Handbook of Porphyrin Science

with Applications to Chemistry, Physics, Materials Science, Engineering, Biology and Medicine

Volume 6

NMR and EPR Techniques

Karl M. Kadish ▪ Kevin M. Smith ▪ Roger Guilard

Editors

World Scientific

How to go to your page

This eBook contains five volumes, beginning with Volume 6. Each volume has its own page numbering scheme, consisting of a volume number and a page number, separated by a hyphen.

For example, to go to page 5 of Volume 6, type v6-5 in the “page #” box at the top of the screen and click “Go.” To go to page 5 of Volume 8, type v8-5 in the "page #" box… and so forth.

Handbook of Porphyrin Science

with Applications to Chemistry, Physics, Materials Science, Engineering, Biology and Medicine

This page intentionally left blank

Handbook of Porphyrin Science

with Applications to Chemistry, Physics, Materials Science, Engineering, Biology and Medicine

Volume 6

NMR and EPR Techniques

Editors

Karl M. Kadish
University of Houston, USA

Kevin M. Smith
Louisiana State University, USA

Roger Guilard
Université de Bourgogne, France

World Scientific

NEW JERSEY • LONDON • SINGAPORE • BEIJING • SHANGHAI • HONG KONG • TAIPEI • CHENNAI

Published by

World Scientific Publishing Co. Pte. Ltd.

5 Toh Tuck Link, Singapore 596224

USA office: 27 Warren Street, Suite 401-402, Hackensack, NJ 07601

UK office: 57 Shelton Street, Covent Garden, London WC2H 9HE

British Library Cataloguing-in-Publication Data
A catalogue record for this book is available from the British Library.

HANDBOOK OF PORPHYRIN SCIENCE
with Applications to Chemistry, Physics, Materials Science, Engineering, Biology and Medicine (Volumes 6–10)

ISBN-13 978-981-4307-18-5 (Set)
ISBN-13 978-981-4307-19-2 (Vol. 6)

Typeset by Stallion Press
Email: enquiries@stallionpress.com

Printed in Singapore.

Contents

Preface

Although the porphyrin and tetrapyrrole research area was regarded as "fully matured" during the 20th century, as evidenced for example by the awarding of numerous Nobel Prizes to its principal researchers, new advances and accomplishments in the field still amaze us as editors. The area continues to blossom and to expand into new areas of science and applications that would probably never have occurred to our 20th century heroes. An earlier *Porphyrin Handbook* assembled the large amount of factual data that had been accumulated during the 20th century. Our new venture, the *Handbook of Porphyrin Science* takes a completely new look at our research area and comprehensively details the contemporary science now appearing in the scientific literature that would indeed have been hard to predict even 10 years ago. In particular, fundamentally new methodologies and potential commercial applications of the beautiful compounds that we all love are exemplified, fully recognizing the subtitle of the series — "with applications to chemistry, physics, materials science, engineering, biology and medicine".

The three of us have complementary expertise in physical chemistry, synthetic and bioorganic chemistry, and in synthetic and mechanistic organometallic chemistry; this has enabled us to cover the whole field of porphyrin science and applications, and to devise comprehensive volume and author content. As of the date of writing, between the three of us, we have published more than 1600 tetrapyrrole research articles, and hold 31 patents related to commercial applications of porphyrin science. So we do know our field, and this has enabled us to assemble a first-rate group of experts who have written comprehensive up-to-date chapters with accuracy and authority; we thank our authors for their cooperation and willingness to go along with our highly ambitious schedule for production of these volumes.

We look forward to comments from our readers, and to suggestions that might enable us to expand our basic interests and scientific coverage even further. Meanwhile, we hope that porphyrin researchers, old, new and of the future, will enjoy reading these volumes just as much as we enjoyed planning and, with the help of World Scientific Publishing Company, producing them from manuscript to published article, in a timely manner.

Karl M. Kadish (Houston, Texas, USA)
Kevin M. Smith (Baton Rouge, Louisiana, USA)
Roger Guilard (Dijon, Bourgogne, France)
January, 2010

This page intentionally left blank

Contributing Authors*

Hasrat Ali
Université de Sherbrooke
Sherbrooke, Québec, Canada
Chapter 16

Cristina Alonso
University of Hull
Kingston-upon-Hull, HU6 7RX, UK
Chapter 17

Edith Antunes
Rhodes University
Grahamstown, 6139, South Africa
Chapter 34

Naoki Aratani
Kyoto University
Kyoto 606-8502, Japan
aratani@kuchem.kyoto-u.ac.jp
Chapter 1

Teodor Silviu Balaban
Karlsruhe Institute of Technology
D-76021 Karlsruhe, Germany
Silviu.Balaban@int.fzk.de
Chapter 3

Alan L. Balch
University of California, Davis
Davis, CA 95616, USA
balch@chem.ucdavis.edu
Chapter 40

David P. Ballou
University of Michigan
Ann Arbor, MI 48109-5606, USA
Chapter 28

Faye Bowles
University of California, Davis
Davis, CA 95616, USA
Chapter 40

Ross W. Boyle
University of Hull
Kingston-upon-Hull, HU6 7RX, UK
r.w.boyle@hull.ac.uk
Chapter 17

Ozguncem Bozkulak
Childrens Hospital Los Angeles
Los Angeles, CA 90027, USA
Chapter 22

Martin Bröring
Technische Universität Carolo-Wilhelmina zu Braunschweig
Hagenring 30, Braunschweig, Germany
m.broering@tu-bs.de
Chapter 41

Kevin Burgess
Texas A&M University
College Station, TX 77842, USA
burgess@tamu.edu
Chapter 37

*Full contact information for authors can be found on the title page of each chapter.

José A.S. Cavaleiro
University of Aveiro
3810-193 Aveiro, Portugal
jcavaleiro@ua.pt
Chapter 9

Sung Cho
Yonsei University
Seoul, 120-747, Korea
Chapter 5

Daniel P. Collins
University of South Carolina
Columbia, SC 29208, USA
Chapter 28

John H. Dawson
University of South Carolina
Columbia, SC 29208, USA
dawson@mail.chem.sc.edu
Chapter 28

Ilia G. Denisov
The University of Illinois
Urbana, IL 61801, USA
Denisov@illinois.edu
Chapter 26

Charles Michael Drain
Hunter College of The City University of New York
New York, NY 10065, USA
cdrain@hunter.cuny.edu
Chapter 15

Francis D'Souza
Wichita State University
Wichita, KS 67260-0051, USA
Francis.DSouza@wichita.edu
Chapter 4

Florence Duclairoir
Institut Nanosciences et Cryogénie
38054 Grenoble cedex 9, France
Chapter 47

Manivannan Ethirajan
Roswell Park Cancer Institute
Buffalo, NY 14263, USA
Chapter 19

Alessandro Feis
University of Florence
I-50019 Sesto Fiorentino, Italy
Chapter 31

Angela Ferrario
Childrens Hospital Los Angeles
Los Angeles, CA 90027, USA
Chapter 22

Kimberly B. Fields
University of South Florida
Tampa, FL 33620, USA
Chapters 13, 43

Takamitsu Fukuda
Osaka University
Toyonaka 560-0043, Japan
tfukuda@chem.sci.osaka-u.ac.jp
Chapter 42

Shunichi Fukuzumi
Osaka University
Suita, Osaka 565-0871, Japan
fukuzumi@chem.eng.osaka-u.ac.jp
Chapter 46

Hiroyuki Furuta
Kyushu University
Fukuoka 819-0395, Japan
hfuruta@cstf.kyushu-u.ac.jp
Chapter 10

Jean-Paul Gisselbrecht
Université de Strasbourg
67000 Strasbourg, France
gissel@unistra.fr
Chapter 14

Charles J. Gomer
University of Southern California
Los Angeles, CA 90027, USA
Chapter 22

Bruno Grimm
Friedrich-Alexander-University Erlangen-Nuremberg
91058 Erlangen, Germany
Chapter 2

Dirk M. Guldi
Friedrich-Alexander-University Erlangen-Nuremberg
91058 Erlangen, Germany
dirk.guldi@chemie.uni-erlangen.de
Chapter 2

Anita Hausmann
Friedrich-Alexander-University Erlangen-Nuremberg
91058 Erlangen, Germany
Chapter 2

Takashi Hayashi
Osaka University
Suita 565-0871, Japan
thayashi@chem.eng.osaka-u.ac.jp
Chapter 23

Petra Hellwig
Université de Strasbourg
67000 Strasbourg, France
hellwig@chimie.u-strasbg.fr
Chapter 36

Yoshio Hisaeda
Kyushu University
Fukuoka 819-0395, Japan
yhisatcm@mail.cstm.kyushu-u.ac.jp
Chapter 48

Barry D. Howes
University of Florence
I-50019 Sesto Fiorentino, Italy
Chapter 31

Akira Ikezaki
Toho University
Ota-ku, Tokyo 143-8540, Japan
Chapter 32

Osamu Ito
Tohoku University
Sendai, 981-3215, Japan
Chapter 4

Anabella Ivancich
Centre Nationale de la Recherche Scientifique (URA 2096)
F-91191 Gif-sur-Yvette, France
Chapter 31

Christophe Jeandon
Université de Strasbourg
67000 Strasbourg, France
cjeandon@unistra.fr
Chapter 14

Norbert Jux
Universität Erlangen-Nürnberg
91054 Erlangen, Germany
norbert.jux@chemie.uni-erlanger.de
Chapter 20

Axel Kahnt
Friedrich-Alexander-University Erlangen-Nuremberg
91058 Erlangen, Germany
Chapter 2

David Kessel
Wayne State University School of Medicine
Detroit, MI 48201, USA
dhkessel@med.wayne.edu
Chapter 21

Dongho Kim
Yonsei University
Seoul, 120-747, Korea
dongho@yonsei.ac.kr
Chapters 5, 6

Kil Suk Kim
Yonsei University
Seoul, 120-747, Korea
Chapter 6

Nagao Kobayashi
Tohoku University
Sendai 980-8578, Japan
nagaok@mail.tains.tohoku.ac.jp
Chapters 33, 42

Lechosław Latos-Grażyński
University of Wrocław
Wrocław 50 383, Poland
llg@wchuwr.pl
Chapter 8

Genxi Li
Nanjing University
Nanjing 210093, PR China
genxili@nju.edu.cn
Chapter 27

Jong Min Lim
Yonsei University
Seoul, 120-747, Korea
Chapter 6

Aurore Loudet
Texas A&M University
College Station, TX 77842, USA
Chapter 37

Evgeny A. Lukyanets
Organic Intermediates and Dyes Institute
Moscow, 123995, Russia
rmeluk@niopik.ru
Chapter 11

Marian Luna
Childrens Hospital Los Angeles
Los Angeles, CA 90027, USA
Chapter 22

Hiromitsu Maeda
Ritsumeikan University
Kusatsu 525-8577, Japan
maedahir@ph.ritsumei.ac.jp
Chapter 38

Jean-Claude Marchon
Institut Nanosciences et Cryogénie
38054 Grenoble cedex 9, France
jean-claude.marchon@cea.fr
Chapter 47

M. Victoria Martínez-Díaz
Universidad Autónoma de Madrid
28049-Madrid, Spain
Chapter 45

Frederic Melin
Université de Strasbourg
67000 Strasbourg, France
Chapter 36

Shingo Nagano
Tottori University
Tottori 680-8552, Japan
Chapter 25

Mikio Nakamura
Toho University
Ota-ku, Tokyo 143-8540, Japan
mnakamu@med.toho-u.ac.jp
Chapter 32

Wonwoo Nam
Ewha Womans University
Seoul 120-750, South Korea
wwnam@ewha.ac.kr
Chapter 44

Victor N. Nemykin
University of Minnesota Duluth
Duluth, MN 55812, USA
vnemykin@d.umn.edu
Chapter 11

Maria G.P.M.S. Neves
University of Aveiro
3810-193 Aveiro, Portugal
Chapter 9

Tebello Nyokong
Rhodes University
Grahamstown, 6139, South Africa
t.nyokong@ru.ac.za
Chapter 34

Yoshiki Ohgo
Toho University
Ota-ku, Tokyo 143-8540, Japan
Chapter 32

Tetsuo Okujima
Ehime University
Matsuyama 790-8577, Japan
Chapter 7

Noboru Ono
Ehime University
Matsuyama 790-8577, Japan
ononbr@dpc.ehime-u.ac.jp
Chapter 7

Atsuhiro Osuka
Kyoto University
Kyoto 606-8502, Japan
osuka@kuchem.kyoto-u.ac.jp
Chapter 1

Ravindra K. Pandey
Roswell Park Cancer Institute
Buffalo, NY 14263, USA
ravindra.pandey@roswellpark.org
Chapter 19

Nayan J. Patel
Roswell Park Cancer Institute
Buffalo, NY 14263, USA
Chapter 19

Miłosz Pawlicki
University of Wrocław
Wrocław 50 383, Poland
Chapter 8

Sébastien Richeter
Université Montpellier 2
34095 Montpellier Cedex 5, France
sebastien.richeter@univ-montp2.fr
Chapter 14

Beate Röder
Humboldt-Universität zu Berlin
12489 Berlin, Germany
roeder@physik.hu-berlin.de
Chapter 20

Natalie Rucker
Childrens Hospital Los Angeles
Los Angeles, CA 90027, USA
Chapter 22

Joshua V. Ruppel
University of South Florida
Tampa, FL 33620, USA
Chapters 13, 43

Romain Ruppert
Université de Strasbourg
67000 Strasbourg, France
rruppert@unistra.fr
Chapter 14

Aoife Ryan
Trinity College Dublin
Dublin 2, Ireland
Chapter 12

Wolfgang Seitz
Friedrich-Alexander-University
Erlangen-Nuremberg
91058 Erlangen, Germany
Chapter 2

Mathias O. Senge
Trinity College Dublin
Dublin 2, Ireland
sengem@tcd.ie
Chapter 12

Natalia N. Sergeeva
Trinity College Dublin
Dublin 2, Ireland
Chapter 12

Hisashi Shimakoshi
Kyushu University
Fukuoka 819-0395, Japan
Chapter 48

Jae-Yoon Shin
Yonsei University
Seoul, 120-747, Korea
Chapter 6

Yoshitsugu Shiro
Harima Institute
Hyogo 679-5148, Japan
yshiro@riken.jp
Chapters 24, 25

Martha Sibrian-Vazquez
Portland State University
Portland, OR 97201, USA
Chapter 18

Sunaina Singh
Hunter College of The City University of
New York
New York, NY 10065, USA
Chapter 15

Stephen G. Sligar
The University of Illinois
Urbana, IL 61801, USA
s-sligar@uiuc.edu
Chapter 26

Giulietta Smulevich
University of Florence
I-50019 Sesto Fiorentino, Italy
giulietta.smulevich@unifi.it
Chapter 31

Nicole L. Snyder
Hamilton College
Clinton, NY 13323, USA
Chapters 13, 43

Fabian Spänig
Friedrich-Alexander-University Erlangen-Nuremberg
91058 Erlangen, Germany
Chapter 2

Tatyana Spolitak
University of Michigan
Ann Arbor, MI 48109-5606, USA
Chapter 28

Hiroshi Sugimoto
Harima Institute
Hyogo 679-5148, Japan
Chapter 24

Osamu Takikawa
National Center for Geriatrics and Gerontology
Obu, Aichi 474-8522, Japan
Chapter 24

Alison Thompson
Dalhousie University
Halifax, Nova Scotia, Canada
alison.thompson@dal.ca
Chapter 39

Motoki Toganoh
Kyushu University
Fukuoka 819-0395, Japan
Chapter 10

Augusto C. Tomé
University of Aveiro
3810-193 Aveiro, Portugal
Chapter 9

Tomas Torres
Universidad Autónoma de Madrid
28049-Madrid, Spain
tomas.torres@uam.es
Chapter 45

Paola Turano
University of Florence
I-50019 Sesto Fiorentino, Italy
turano@cerm.unifi.it
Chapter 30

Md. Imam Uddin
Dalhousie University
Halifax, Nova Scotia, Canada
Chapter 39

Johan E. van Lier
Université de Sherbrooke
Sherbrooke, Québec, Canada
Johannes.Van.Lier@USherbrooke.ca
Chapter 16

Maria da Graça H. Vicente
Louisiana State University
Baton Rouge, LA 70803, USA
vicente@lsu.edu
Chapter 18

Sam P. de Visser
The University of Manchester
Manchester M1 7DN, UK
sam.devisser@manchester.ac.uk
Chapter 44

F. Ann Walker
University of Arizona
Tucson, AZ 85721-0041, USA
awalker@email.arizona.edu
Chapter 29

Jacek Waluk
Polish Academy of Sciences
01-224 Warsaw, Poland
waluk@ichf.edu.pl
Chapter 35

Sam Wong
Childrens Hospital Los Angeles
Los Angeles, CA 90027, USA
Chapter 22

Tabitha E. Wood
Dalhousie University
Halifax, Nova Scotia, Canada
Chapter 39

Frank Xu
Childrens Hospital Los Angeles
Los Angeles, CA 90027, USA
Chapter 22

Hiroko Yamada
Ehime University
Matsuyama 790-8577, Japan
Chapter 7

Jaesung Yang
Yonsei University
Seoul, 120-747, Korea
Chapter 5

Hyejin Yoo
Yonsei University
Seoul, 120-747, Korea
Chapter 5

Min-Chul Yoon
Yonsei University
Seoul, 120-747, Korea
Chapter 6

Zin Seok Yoon
Yonsei University
Seoul, 120-747, Korea
Chapter 5

X. Peter Zhang
University of South Florida
Tampa, FL 33620, USA
pzhang@cas.usf.edu
Chapters 13, 43

Contents of Volumes 1–10

Volume 1 Supramolecular Chemistry

Volume 2 Synthesis and Coordination Chemistry

Volume 3 Synthetic Methodology

Volume 4 Phototherapy, Radioimmunotherapy and Imaging

Volume 5 Heme Proteins

Volume 6 NMR and EPR Techniques

Volume 7 Physicochemical Characterization

Volume 8 Open-Chain Oligopyrrole Systems

Volume 9 Electronic Absorption Spectra — Phthalocyanines

Volume 10 Catalysis and Bio-Inspired Systems — Part I

This page intentionally left blank

29 NMR and EPR Spectroscopy of Paramagnetic Metalloporphyrins and Heme Proteins

F. Ann Walker

Department of Chemistry and Biochemistry, University of Arizona, 1306 E. University B1, Tucson, AZ 85721-0041, USA

I. Introduction and Background

Magnetic resonance techniques, both nuclear magnetic resonance (NMR) and electron paramagnetic resonance (EPR) spectroscopies are excellent techniques for investigating the structure, bonding, dynamics, electron configurations and magnetism of transition metal complexes, and this certainly includes metalloporphyrins. Of course, EPR techniques can only be used when there are odd numbers of unpaired electrons present, either on the metal itself or in some cases, on the ligand(s). The most common number of unpaired electrons present in systems which are studied by EPR spectroscopy is one, although five is another fairly common number, and three is also possible. The development of pulsed EPR techniques, which make possible the study of all magnetic nuclei that are within 3–5 Å of the site of the unpaired electron (usually the metal, although there are an increasing number of cases of macrocycle π-cation or π-anion radicals that have been studied). The types of magnetic resonance techniques, both those belonging to the EPR and to the NMR family, that are commonly used to study metalloporphyrin complexes are summarized and briefly described in Table 1. Although the results of pulsed EPR experiments are mentioned, where appropriate, the experiments and the detailed description of the results is beyond the scope of this chapter. Some of these may be found in a review published in *Inorganic Chemistry*.[1]

While EPR spectroscopy requires the complex to have at least one unpaired electron or multiple unpaired electrons, NMR techniques can be utilized whether the complex is diamagnetic or paramagnetic, and a large number of the metallic elements and/or their compounds have paramagnetic states ($S \geq 1/2$). In fact, a number of the transition metals have several oxidation states that are reasonably stable and can be studied by NMR spectroscopy, and for a given oxidation state there are often several different spin states that are possible. However, not all of these oxidation/spin state possibilities have the "proper" relaxation properties to be easily studied by NMR spectroscopy, as we will discuss later in Section II.B. This author has been involved in the writing of the previous chapters on NMR of paramagnetic metalloporphyrins,[2–4] and within the 30 year time span covered up to the present, some of the systems previously thought to be impossible to study by NMR spectroscopy have been reported, including chromium(III), manganese(IV), copper(II) and silver(II) porphyrins. In most of these cases it has been ^{2}H NMR spectroscopic investigations, where the chemical shifts are extremely similar to those of the corresponding ^{1}H complexes, but the linewidths of the resonances can be as much as a factor of 42 sharper, which have made possible the detection of signals previously thought to be entirely too broad to observe. Discussion of such systems will be found in Sections II.B.2, IV.B.7 and IV.H.1, IV.H.3.

Table 1. Common NMR and EPR experiments used for investigating paramagnetic metalloporphyrins.

NMR experiment	Information Obtained
1D ^{1}H, ^{2}H or ^{13}C	Chemical shift → isotropic or paramagnetic shift → mechanism of spin delocalization; from temperature dependence → information about excited states.
1D NOE difference spectroscopy	Proximity of one type of proton to another, up to a distance of about 5 Å. A spectrum is obtained in which a particular resonance is irradiated. Then a reference, off-resonance irradiation dataset is acquired and the reference is subtracted from the first. The irradiated peak appears as a strong negative peak, and those peaks that are due to protons in close proximity appear as either weak negative or positive peaks, depending on the size of the molecule.
1D saturation transfer difference spectroscopy (also called STD)	Identifies resonances that are involved in chemical exchange. The experiment is the same as that used for 1D NOE difference spectroscopy. Both irradiated peak and that (those) connected to it by chemical exchange are of negative phase if the reference spectrum is subtracted from each peak irradiated.
2D COSY; TOCSY	Correlation SpectroscopY; Total Correlation SpectroscopY. J-coupling information is obtained; helps identify components of a spin system such as an ethyl or propionate group.
2D HETCOR; HMQC	HETeronuclear CORrelation spectroscopy, a ^{13}C-detected 2D heteronuclear experiment; Heteronuclear Multiple Quantum Correlation spectroscopy, a ^{1}H-detected heteronuclear 2D experiment. C-H J-coupling information is obtained in both cases; both identify which proton(s) are bound to which carbon. HMQC has a much higher signal-to-noise (at least a factor of 4) ratio than HETCOR.
2D HMBC	Heteronuclear Multiple Bond Correlation spectroscopy, a modification of the HMQC experiment which allows detection of long-range H-C J-couplings. Very useful for assigning the spectra of unsymmetrical metalloporphyrins.
2D NOESY; EXSY; ROESY	Nuclear Overhauser and Exchange SpectroscopY (sensitive to both through-space (NOE) and chemical exchange processes; NOEs may be zero for intermediate-sized molecules, i.e., many metalloporphyrins); Exchange SpectroscopY (the same experiment), which identifies protons in chemical exchange with each other; Rotating frame Overhauser and Exchange SpectroscopY (also sensitive to both through-space and chemical exchange, but shows NOEs the opposite phase and chemical exchange peaks the same phase as the diagonal, no matter what the size of the molecule).
Continuous wave EPR	g-values → orbital of the unpaired electron; superhyperfine couplings, **a** or **A**, due to nuclei that are strongly coupled to the unpaired electron.

(*Continued*)

Table 1. (*Continued*)

NMR Experiment	Information Obtained
ESEEM	Electron Spin Echo Envelope Modulation → signals due to all nuclei that are so weakly coupled to the unpaired electron that they show no superhyperfine couplings in the continuous wave EPR spectrum. Magnetic field (g-value → dependence of the intensity and frequency of "double quantum" proton peaks near twice the Larmor frequency → orientation of the g-tensor; similar analysis of the ^{14}N and/or ^{2}H peaks also provides very useful bonding and structural information. Intensities of ESEEM peaks are usually readily fit quantitatively to theoretical models.
HYSCORE	2D Hyperfine Sublevel CORrElation spectroscopy: A two dimensional ESEEM experiment, $\pi/2 - \tau - \pi/2 - T_1 - T_2 - \pi/2 - \tau -$ echo, in which correlation is produced between nuclear frequencies in the spin manifolds for an electronic transition. In a HYSCORE experiment, the time between the second $\pi/2$ and π pulse is varied in one dimension and the time between the π and third $\pi/2$ pulse is varied in a second dimension. A two- dimensional FT gives the 2D spectra which can be analyzed in terms of the frequencies of the nuclei involved. As in an ESEEM experiment, the peaks observed are essentially an NMR spectrum of nuclei that are coupled to the electron. However, the 2D technique allows one to separate overlapping peaks. Peaks appearing in the upper right and lower left quadrants typically arise from nuclei in which the hyperfine coupling is less than the Larmor frequency. They appear at the Larmor frequency of the nucleus, separated by the hyperfine coupling. Peaks from nuclei in which the hyperfine interaction is greater than the Larmor frequency of the nucleus appear in the upper left and lower right quadrants. The HYSCORE spectrum can become very complicated for nuclei with a spin I greater than 1/2, with many peaks arising from the additional complication of addition nuclear Zeeman and quadrupole levels. Even with the complexity of the spectra, HYSCORE on complicated systems with multiple nuclei can make ESEEM spectra that would be difficult or impossible to interpret much more manageable.

NMR spectroscopy is particularly valuable for studying paramagnetic metalloporphyrins because the unpaired electrons "illuminate" the heme or other metalloporphyrin center by causing paramagnetic shifts of the protons (or carbons) of the macrocycle, the axial ligand(s) of the metal and, in the case of heme proteins, nearby protein residues, that are exquisitely sensitive to heme substituents, axial ligand effects such as histidine imidazole N–H hydrogen-bonding[5,6] or deprotonation,[5] axial ligand plane orientation,[5,7,8] methionine-SCH_3 chirality,[9] and cyanide

off-axis tilting (in protein complexes such as cyanometmyoglobin),[10,11] as well as the effect of nonbonded protein substituents,[5,12] on the electronic state of the heme. The chemical shifts of the heme macrocycle of heme proteins, also known as paramagnetic or hyperfine shifts if the metal is paramagnetic, are extremely sensitive to all of these factors, as well as to others that will be enumerated in later sections of this chapter, and much can be learned by carrying out a detailed study of a paramagnetic heme protein. Because of this extreme sensitivity, it is sometimes difficult to determine the relative importance of all the factors that might affect the chemical shifts. For this reason, a number of investigators have carried out detailed NMR investigations of appropriately designed model hemes or other metal tetrapyrroles having relatively high molecular symmetry (as compared to naturally-occurring hemes), in order to probe the importance of such factors as substituent effects, electronic asymmetry due to unsymmetrical substitution, axial ligand basicity and steric effects, axial ligand plane orientation, thermodynamics and kinetics of axial ligand binding, exchange and rotation, and hydrogen-bonding effects of these ligands on the NMR spectra of metalloporphyrins. The results of a large number of these investigations have been summarized previously in at least a dozen important chapters or books.[2–5,13–20] However, the focus in all but four of these[2–4,15] has been on heme proteins, where the metal ion was either iron(II) or iron(III). For that reason, this chapter will focus on the proton (and deuteron) NMR spectroscopy of metalloporphyrins of all known oxidation and spin states that have occurred since the literature search for the publication of the previous chapters in *The Porphyrins*[2] and *The Porphyrin Handbook*,[4] with only occasional detailed recapitulation of earlier topics at points where a background must be built up before the recent work can be discussed. The ^{13}C chemical shifts of a number of metalloporphyrins and heme proteins, and occasionally, the ^{19}F chemical shifts will also be discussed. Parts of this chapter will cover some of the same topics as *The Porphyrin Handbook* chapter[4] published about ten years ago, which is necessary for completeness. The NMR spectra of the heme centers of heme proteins will be discussed where the results of NMR studies of paramagnetic metalloporphyrins have direct relevance to interpretations of the heme protein data, or vice versa. In particular, a section on NMR spectroscopy of the nitrophorins and heme oxygenases, and a brief update on other heme proteins, is included (Section IV.A.10).

A. Structures and Electron Configurations of Metalloporphyrins

Structural formulas **1**–**3** show the general structures of porphyrins. The structures of closely related ring systems, including chlorins, isobacteriochlorins, dioxoisobacteriochlorins and corroles are shown in Structures **4**–**7**. Examples of the substituents present on commonly investigated metal macrocycles are summarized in

1

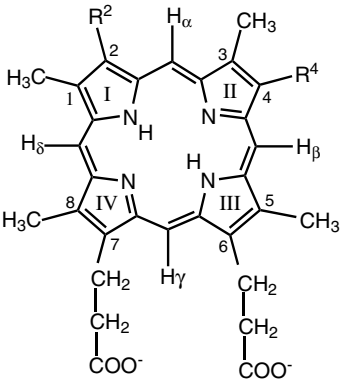
R2
Hα
CH3
H3C
R4
I
II
III
IV
Hδ
Hβ
H3C
CH3
Hγ
CH2
CH2
COO-
CH2
CH2
COO-

2

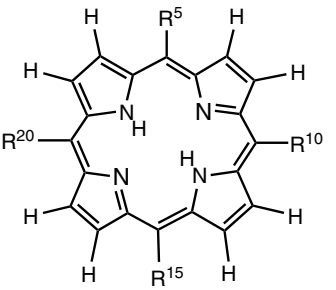
H
R5
R20
R10
R15

3

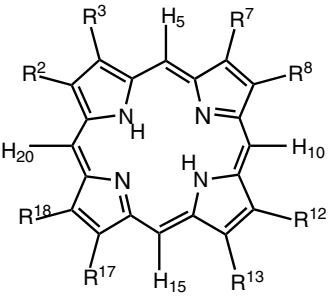
R3
H5
R7
R2
R8
H20
H10
R18
R12
R17
H15
R13

4

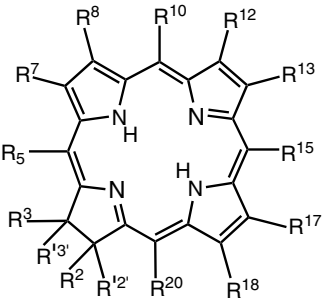
R8
R10
R12
R7
R13
R5
R15
R3
R17
R2
R20
R18

5

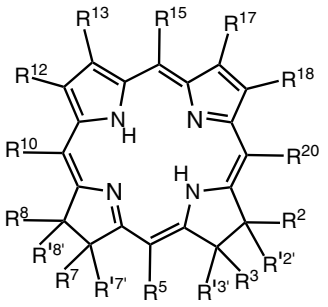
R13
R15
R17
R12
R18
R10
R20
R8
R2

6

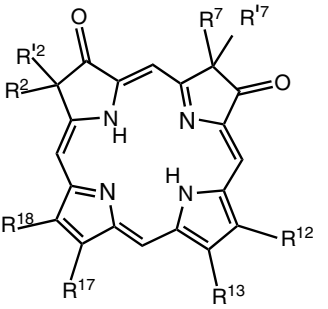
O
R7
R'7
R'2
R2
O
R18
R12
R17
R13

7

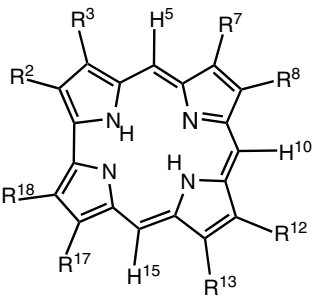
R3
H5
R7
R2
R8
H10
R18
R12
R17
H15
R13

Tables 2–5. Porphyrin macrocycles can be classified as derivatives of natural porphyrins, of which deuteroporphyrin IX is considered the parent. The arrangement of the peripheral substituents of natural porphyrin derivatives is shown in Structure **1**, with the 1–8 and α–δ numbering system used in much of the NMR literature, and the nature of the variable substituents, the common names of the macrocycle and the symbols used in this chapter, are listed in Table 2. For cases in which the propionic acid side chains in Structure **1** are esterified, for example, as dimethyl esters, the symbol will have DME appended to the abbreviation. Two

Table 2. Natural porphyrin dianion derivatives.[a]

2,4-Substituent	Name	Symbol
2,4-H	Deuteroporphyrin IX	DP^{2-}
2,4-Divinyl	Protoporphyrin IX	PP^{2-}
2,4-Diethyl	Mesoporphyrin IX	MP^{2-}
2,4-Dibromo	Dibromodeuteroporphyrin	Br_2DP^{2-}
2,4-Diacetyl	Diacetyldeuteroporphyrin	Ac_2DP^{2-}
2-Acetyl, 4-H	2-Monoacetyldeuteroporphyrin	$2\text{-}AcDP^{2-}$
2-H, 4-Acetyl	4-Monoacetyldeuteroporphyrin	$4\text{-}AcDP^{2-}$

[a]See Structure **1** for structural formula of the parent free-base porphyrin.
If the propionates are esterifed, DME is appended to symbolize dimethyl ester.
[a]See Structure **2** for structural formula of the free base porphyrin.

Table 3. *Meso*-substituted synthetic porphyrin dianion derivatives.[a]

R^5, R^{10}, R^{15}, R^{20}	Name	Symbol
H	Porphine	Po^{2-}
Phenyl	Tetraphenylporphyrin	TPP^{2-}
p-Tolyl	Tetra-*p*-tolylporphyrin	$p\text{-}TTP^{2-}$
m-Tolyl	Tetra-*m*-tolylporphyrin	$m\text{-}TTP^{2-}$
o-Tolyl	Tetra-*o*-tolylporphyrin	$o\text{-}TTP^{2-}$
p-Chlorophenyl	Tetra-*p*-chlorophenylporphyrin	$(p\text{-Cl})4TPP^{2-}$
Mesityl	Tetramesitylporphyrin	TMP^{2-}
N-Methyl-4-Pyridyl	Tetra-*N*-methyl-4-pyridylporphyrin	$(p\text{-MePy})_4P^{2+}$ or $T(p\text{-MePy})P^{2+}$
p-SO_3-Phenyl	Tetra-*p*-sulfonatophenylporphyrin	$TPPS^{6-}$
Mono-m-NO_2-Phenyl, tris-*m*-F-Phenyl	5-(*m*-nitrophenyl)-10,15,20-tris-(*m*-fluorophenyl)-porphyrin	$(m\text{-}NO_2)(m\text{-F})_3TPP^{2-}$
Methyl	Tetra-methylporphyrin	$TMeP^{2-}$
n-Propyl	Tetra-*n*-propylporphyrin	$Tn PrP^{2-}$
iso-Propyl	Tetra-*i*-propylporphyrin	$Ti PrP^{2-}$
Cyclohexyl	Tetra-cyclohexylporphyrin	$TCxP^{2-}$

[a]See Structure **2** for structural formula of the free base porphyrin.

Table 4. Pyrrole-substituted synthetic porphyrin dianion derivatives.[a]

R^2	R^3	R^7	R^8	R^{12}	R^{13}	R^{17}	R^{18}	*meso*[b]	Name	Symbol
H	H	H	H	H	H	H	H	H	Porphine	Po^{2-}
Ethyl	Ethyl	Ethyl	Ethyl	Ethyl	Ethyl	Ethyl	Ethyl	H	Octaethylporphyrin	OEP^{2-}
Ethyl	Methyl	Ethyl	Methyl	Ethyl	Methyl	Ethyl	Methyl	H	Etioporphyrin I	$EP\text{-}I^{2-}$
Ethyl	Methyl	Methyl	Ethyl	Ethyl	Methyl	Methyl	Ethyl	H	Etioporphyrin II	$EP\text{-}II^{2-}$
Ethyl	Ethyl	Ethyl	Ethyl	Ethyl	Ethyl	Ethyl	Ethyl	Phenyl	Octaethyltetraphenylporphyrin	$OETPP^{2-}$
–N=CH–CH=N		H	H	H	H	H	H	Phenyl	Quinoxalinotetraphenylporphyrin	$QTPP^{2-}$

[a]See Structure **3** for structural formula of the free base porphyrin.
[b]*meso* = 5,10,15,20 positions; the OETPP and QTPP dianions are hybrids of Structures **2** and **3**.

Table 5. Structures of well-known chlorin, isobacteriochlorin, dioxoisobacteriochlorin and corrole derivatives.

R^2	R^3	R^7	R^8	R^{12}	R^{13}	R^{17}, R'^{17}	R^{18}, R'^{18}	*meso*[b]	Name	Symbol
Chlorins, [a]Structure **4**										
H	H	H	H	H	H	H,H	H,H	Phenyl	Tetraphenylchlorin	TPC^{2-}
Et	Et	Et	Et	Et,	Et	Et,H	Et,H	H	Octaethylchlorin	OEC^{2-}
PrO^{-c}	Me	Me	V	Me	V	Me,OH	OH, PrO^{-c}	H	Heme *d*	None
Me	V	Me	V	Me	C=O | CH_2–15–*meso*	H,MePropionate	H,Me	5, 10, 20-H, 15–CH_2–C=O connected to 13–C	Pyropheophorbide *a*	None
Me	V	Me	Et		CO_2Me	H,MePropionate		5,10,20-H, 15-CH_2CO_2Me	Chlorin e_6	None

R^2	R^3	R^7	R^8	R^{12}, R'^{12}	R^{13} R'^{13}	R^{17}, R'^{17}	R^{18}, R'^{18}	*meso*[b]	Name	Symbol
Isobacteriochlorins, [a]Structure **5**										
Et	Et	Et	Et	Et, H	Et, H	Et, H	Et, H	H	Octaethylisobacteriochlorin	$OEiBC^{2-}$
AcO^{-c}	PrO^{-c}	PrO^{-c}	AcO^{-c}	H,PrO^{-c}	H,PrO^{-c}	H,PrO^{-c}	H,PrO^{-c}	H	Siroheme	None

(*Continued*)

Table 5. (*Continued*)

$R^2R'^2$	$R^7R'^7$	R^{12}	R^{13}	R^{17}	R^{18}	*meso*[b]	Name	Symbol
Dioxoisobacteriochlorins, [α] Structure **6**								
Me,AcO^{-}[c]	Me,AcO^{-}[c]	Me	PrO^{-}[c]	$AcrO^{-}$[c]	Me	H	Heme d_1	None

R^2	R^3	R^7	R^8	R^{12}	R^{13}	R^{17}	R^{18}	*meso*[b]	Name	Symbol
Corroles, [a] Structure **7**										
	Me	Me	Me	Me	Me	Me	Me	H	Octamethylcorrole	$OMCor^{3-}$ or Me_8Cor^{3-}
Et	Me	Et	Et	Et	Et	Me	Et	H	7,13-Dimethylhexaethlcorrole	7,13-$Me_2Et_6Cor^{3-}$

[a]See Structure **4** for structural formula of the free base chlorin, Structure **5** for that of the free base isobacteriochlorin, Structure **6** for that of the free base dioxoisobacteriochlorin, and Structure **7** for that of the corrole.
[b]meso.5,10,15,20 positions for all but the corrole (5,10,15).
[c]AcO^{-} = acetate; PrO^{-} = propionate; $AcrO^{-}$ = acrylate.

types of synthetic porphyrins, those having either *meso* or β-pyrrole substituents, are shown in Structures **2** and **3**, respectively, and common substituents, IUPAC numbering system, ligand names and abbreviations are given in Tables 3 and 4, respectively.

Chlorins, isobacteriochlorins, 2,7-dioxoisobacteriochlorins and corrole macrocycles are shown in Structures **4**–**7**, respectively, and examples of high symmetry macrocycles of each type, with common substituents, ligand names and abbreviations are summarized in Table 5. Chang and coworkers have been instrumental in proving the structures of several of the so-called "green hemes", including heme d (actually a chlorin, 5,6-dihydroxy protochlorin IX[21]) and heme d_1 (actually a porphinedione or 2,7-dioxoisobacteriochlorin[22]). Other related ring structures that are involved in the stepwise oxidation of the heme to verdoheme and beyond are shown in Structures **8**–**13**, including 5-hydroxyporphyrins (oxophlorins), Structures **8**, oxaporphyrins (verdohemes), Structures **9**, azaporphyrins, **10**, formylbiliverdins, **11**, dioxodipyrromethanes, **12** and dialkyldipyrromethanes, **13**. The structures of other related macrocycles, including etioporphycene, porphyrazines (*meso*-tetraazaporphyrins), phthalocyanines and texaphyrin, are shown in Structures **14**–**17**, respectively. An example of how saturated β-pyrrole bonds can create an optically active macrocycle is shown in Structure **18** for the 5-coordinate high-spin state of chloroiron *trans*,*trans*-octaethylchlorin.

8

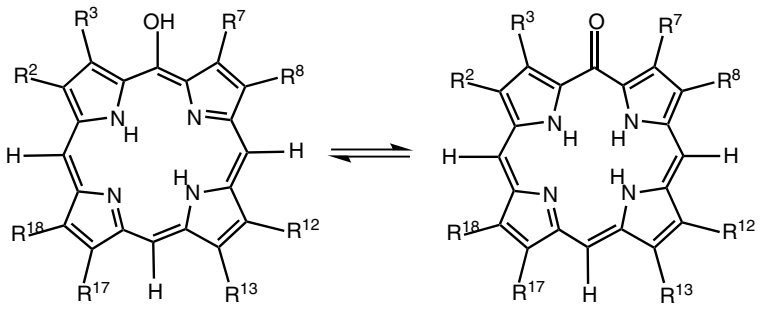

9

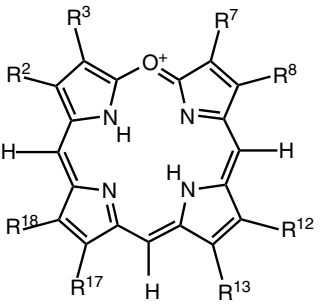

10

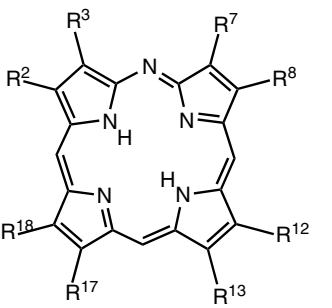

11

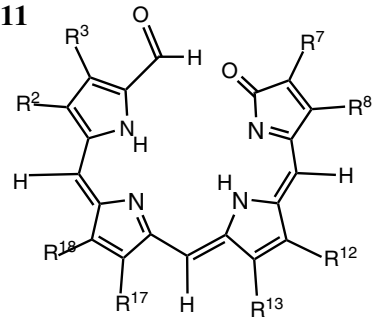

12

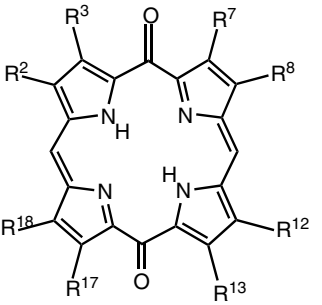

13

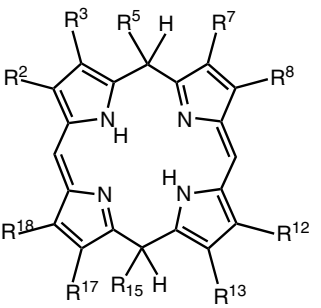

14

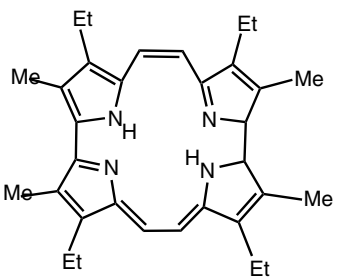

15

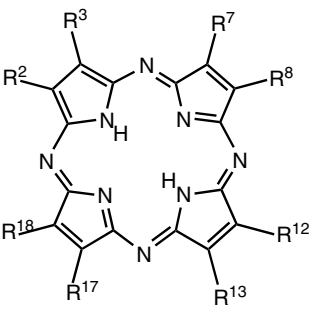

16

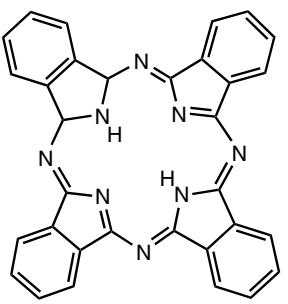

17

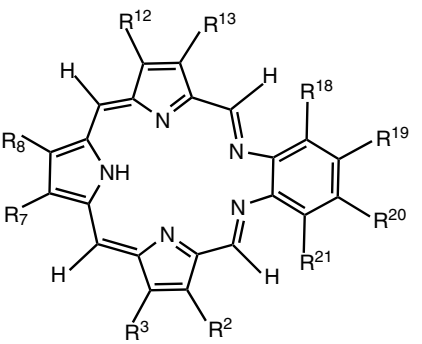

18

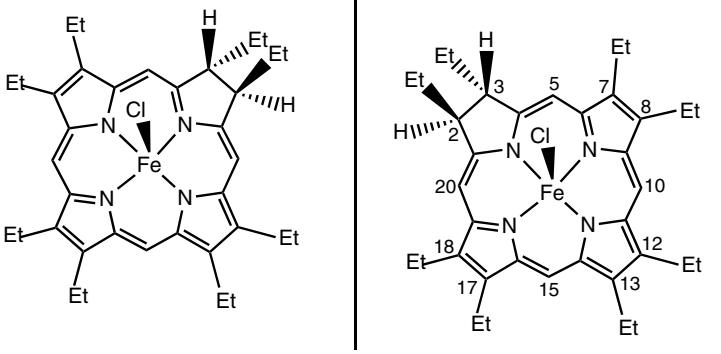

Coordination numbers possible for synthetic and natural metalloporphyrins include 4-coordinate (no axial ligands), 5-coordinate (one axial ligand), 6-coordinate (two axial ligands) and 7- to 9-coordinate (one bidentate ligand and up to three monodentate ligands, as observed for certain lanthanide porphyrins) geometries. The number of axial ligands, and their nature, have dramatic influences on the spin state, optical spectra, EPR g-values and in some cases superhyperfine coupling constants, NMR paramagnetic shifts, Mössbauer isomer shifts, quadrupole splittings and hyperfine coupling constants, as well as reduction potentials and reactivity towards reagents such as molecular oxygen, carbon monoxide, nitric oxide, alkyl halides, alkenes, alkynes and many others.

The molecular and electronic structures of metalloporphyrins may, in certain cases, depend on solvent, anion and degree of aggregation. Deuterated solvents are almost invariably used, except when deuterated porphyrin ^2H signals are being observed. Some solvents, including water (D_2O), dimethylsulfoxide (DMSO-d_6), dimethylformamide (DMF-d_7), methanol (CD_3OD), pyridine-d_5, and tetrahydrofuran (THF-d_8) may coordinate to the metal, or may simply change the dielectric constant of the medium, if strongly-binded ligands are separately provided for the metalloporphyrin. Water and alcohols can also be hydrogen-bond donors to the axial ligands. Chlorinated hydrocarbons, including chloroform ($CDCl_3$), methylene chloride (CD_2Cl_2) and dichloroethane ($C_2D_4Cl_2$), are typically good at dissolving metalloporphyrins, although they may contain traces of acid (DCl) that could react with the metalloporphyrin. Aromatic hydrocarbons, such as toluene-d_8, can interact with the π-system of the porphyrin, both to help dissolve the complex and also to change the π-acidity or -basicity of the macrocycle, as in the case of Co^{II} porphyrins. Carbon disulfide, CS_2, is also good at dissolving uncharged porphyrins. Anions can stabilize either high-spin states (halides, alkoxy, aryloxy, polyoxo anions) or low-spin states (cyanide, aryl, alkyl anions) if they remain coordinated to the metalloporphyrin when dissolved in the chosen solvent.

The known or suspected oxidation states of iron porphyrins, the most commonly studied metalloporphyrins, range from Fe^{I} (d^7) to (possibly) Fe^{V} (d^3). Among these, the possible spin states include high-, intermediate- and low-spin states of Fe^{II} (d^6) and Fe^{III} (d^5), high- and low-spin Fe^{I} (d^7) and Fe^{IV} (d^4), although there have been no reports of high-spin Fe^{I} or high-spin Fe^{IV}. In comparison, for the metals of the first transition series on either side of iron, cobalt porphyrins, both Co^{II} (d^7) and Co^{III} (d^6) complexes have been studied, with reports of both high- and low-spin Co^{II} complexes as a function of porphyrin substituents, but only low-spin (diamagnetic) Co^{III} porphyrins. For manganese porphyrins, Mn^{II} (d^5), Mn^{III} (d^4), Mn^{IV} (d^3), and possibly Mn^{V} (d^2), the latter two as oxomanganese(IV) and oxomanganese(V), have been studied by NMR spectroscopy; Mn^{II} exhibits only the high-spin state while Mn^{III} exhibits both high- and low-spin states, and the two highest oxidation states both appear to be high-spin. Chromium porphyrins have been studied as Cr^{II} (d^4) and Cr^{III} (d^3), the latter of which has extremely broad lines. Although nickel macrocycle complexes are known for Ni^{I} (d^9), Ni^{II} (d^8) and Ni^{III} (d^7), only the Ni^{II} (d^8) systems have been studied by NMR spectroscopy; the 5- and 6-coordinate complexes are paramagnetic, while the 4-coordinate complexes are diamagnetic. Copper porphyrins are known only as Cu^{II} (d^9), which have very broad lines. For most of these metals, the corrole ring is said to stabilize a higher apparent metal oxidation state than do the porphyrin or reduced porphyrin rings, although it often turns out that the electron is missing from the macrocycle rather than the metal. The only diamagnetic members of the extensive series of possible oxidation and spin states are low-spin d^6 6- (and sometimes 5-) coordinate Fe^{II}, Ru^{II}, Os^{II}, 6-coordinate Co^{III}, Rh^{III}, and 4-coordinate Ni^{II}, Pd^{II} and Pt^{II}. The NMR spectra observed for representative examples of each of the possible oxidation and spin states will be discussed in Section IV.

II. Principles

A. Proton Chemical Shifts

The chemical shifts which are observed for protons in paramagnetic molecules are the result of a combination of diamagnetic and paramagnetic contributions. These contributions are additive:

$$\delta_{obs} = \delta_{dia} + \delta_{para}. \quad (1)$$

The diamagnetic contribution, δ_{dia}, is the chemical shift which would have been observed if the molecule had no unpaired electron(s). It is directly evaluated by

recording the NMR spectrum of an appropriate diamagnetic analog of the molecule of interest, usually one containing a diamagnetic metal such as Zn(II), Ni(II), or Cd(II). The metal-free (free base) porphyrin, H_2P is sometimes used if no diamagnetic metal complex is available; the chemical shifts of the protons of a metal-free porphyrin are usually within ~0.2 ppm of those of a diamagnetic metal complex.

The paramagnetic contribution, δ_{para}, is often called the hyperfine shift, δ_{hf}, since it arises from the hyperfine interaction (scalar coupling) of an unpaired electron with the proton nucleus of interest, or the isotropic shift, δ_{iso}, since it is typically observed for molecules or ions in homogeneous solution, where electron spin relaxation and molecular rotation are both generally rapid, and thus yield an isotropic spectrum. The paramagnetic shift consists of two terms, the contact and the pseudocontact (or electron-nuclear dipolar) contributions:

$$\delta_{para} = \delta_{iso} = \delta_{hf} = \delta_{obs} - \delta_{dia} = \delta_{con} + \delta_{pc}. \quad (2)$$

The contact (δ_{con}) and pseudocontact (δ_{pc}) terms arise because spin delocalization from the unpaired electron, usually located on the metal ion, to the protons at the periphery of the molecule, can occur either through chemical bonds or through space (or a combination of the two, as in the case of high- and low-spin Fe^{III} porphyrins, see also Sections IV.A.6 and IV.A.8). The sign convention which will be used throughout this chapter is the one commonly used by all chemists: δ_{obs} is positive if the resonance is at higher frequency (lower shielding) than that of tetramethylsilane (TMS), and negative if the resonance is at lower frequency (higher shielding) than that of TMS. Hence, δ_{para} is positive when the resonance is at lower, and negative when it is at higher shielding than that of the diamagnetic reference compound. This is the reverse of the sign convention that was used in the earlier literature for paramagnetic complexes, including several of the earlier reviews.[2,13] The signs of all contact and pseudocontact (dipolar) shifts reported in earlier publications have been changed herein to conform to the now-accepted sign convention.

1. *Contact Shifts*

Contact shifts of protons, deuteriums, carbons and other nuclei in paramagnetic molecules originate from scalar coupling between electron spins and individual nuclei. In the most general case, the contact shift depends on the principal components of the electronic g-tensor of the paramagnetic center (g_{ii}), the magnetic susceptibility tensor of the molecule (χ_{ii}) and the Fermi hyperfine (contact) coupling

constant (A_h) for coupling the spin of the electron to the spin of the nucleus of interest:[23]

$$\delta_{con} = \left[\frac{A_h}{3\gamma_N \hbar \mu_B}\right]\left[\frac{\chi_{xx}}{g_{xx}} + \frac{\chi_{yy}}{g_{yy}} + \frac{\chi_{zz}}{g_{zz}}\right], \tag{3}$$

where μ_B is the Bohr magneton, χ_{ii} are the molecular magnetic susceptibilities, and g_{ii} are the g-values along each of the principal axes of the molecule. If a single spin state with an isotropic g-tensor is populated, and to the extent that the Curie law is valid, Eq. 3 reduces to a simpler form that is usually applicable to metalloporphyrins:[24,25]

$$\delta_{con} = \frac{A_h \langle g \rangle \mu_B S(S+1)}{3\gamma_N \hbar kT}, \tag{4}$$

where S is the total electron spin quantum number, $\langle g \rangle$ is the average (isotropic) g-value, μ_B is the Bohr magneton, γ_N is the magnetogyric ratio of the nucleus in question, and T is the absolute temperature. Thus, in simple, well-behaved systems, contact shifts are expected to vary linearly with 1/T and to extrapolate to zero at infinite temperature (1/T = 0). However, in cases where a thermally-accessible excited state exists, as is typically the case with low-spin Fe^{III} porphyrins and heme proteins, as well as many other cases, the contact shifts may not extrapolate to zero at infinite temperature, and an expanded form of the Curie law must be employed,[25] as will be discussed later in Section II.A.3.

The interpretation of the contact contributions to the paramagnetiic shifts of protons or deuteriums of paramagnetic molecules in terms of the covalency of metal-ligand bonds relies to a large extent on the McConnell equation:[26]

$$A_H = \frac{Q\rho_C}{2S}, \tag{5}$$

where A_H is the hyperfine coupling constant for each individual proton, Q is a constant for a given type of proton and ρ_C is the unpaired spin density of the electron at the carbon to which the proton is attached; the same holds for deuterium nuclei, which have almost identically the same chemical shifts, contact shifts and pseudocontact shifts as protons. For the case of spin delocalization to a π orbital on the carbon, $Q_H = -63$ MHz, and the contact shifts are negative (to lower frequency or higher shielding). If the proton directly bound to a carbon which has spin density in a π orbital is replaced by a methyl or other aliphatic group, Q_{CH2R} is positive and somewhat variable, because it depends on the rate of rotation

(or preferred orientation, if rotation is slow) of the methyl or other aliphatic group; values of +70 to +75 MHz have been used.[27,28] For alkyl groups larger than CH_3, preferred orientations are the rule, and Q can vary from nearly zero to +100 MHz, but follows the general expression:

$$A_{CH_2R} = \frac{Q_{CH_2R}\rho_C}{2S} = \frac{(B_0 + B_2 \cos^2 \varphi)\rho_C}{2S}, \quad (6)$$

where B_0 and B_2 are positive numbers, and φ is the angle between the C–C–H plane and the p_z orbital axis on the aromatic carbon. B_2 is usually small, and, since $\cos^2\varphi$ is positive for all angles φ, Q_{CH_2R} is always positive. Therefore, if π spin delocalization occurs to a particular carbon atom, a proton directly bound to that carbon will have a contact shift to lower frequency (higher shielding, δ_{con} negative), while replacement of the proton at that carbon position with a methyl or other aliphatic group will produce a contact shift to higher frequency (lower shielding, δ_{con} positive). Such reversal in the sign of paramagnetic shifts for H and CH_3 or CH_2R or CHR_2 at a given position is a clear sign of dominance of the paramagnetic shifts by π spin delocalization, as will be seen in many parts of this chapter. For spin delocalization to a σ-symmetry orbital on the carbon, Q is positive and depends on the number of σ bonds through which the spin is delocalized. For the electron in the 1s orbital of the hydrogen atom, A_H is 1419 MHz, a positive quantity.[29] For protons attached to carbons in metalloporphyrins, where metal electrons are delocalized through either σ or π orbitals of the carbons, the amount of spin density at a given proton on the periphery of the molecule is miniscule in comparison to the hydrogen atom, and is not directly comparable to 1419 MHz because the hydrogens in chemical compounds are involved in chemical bonds.

For σ spin delocalization to protons connected to a carbon framework, Q is also positive, and the spin density, ρ_C, is attenuated sharply as the number of σ bonds between the unpaired electron and the proton increases. In any case, the positive sign of Q means that the contact shifts are positive (to high frequency or low shielding) when σ spin delocalization occurs to the carbon to which the proton is attached. Thus, if the contact contribution to the paramagnetic shifts of protons in molecules such as metalloporphyrins can be separated from the pseudocontact (dipolar) contribution, the pattern of shifts to lower and higher frequencies, as directly-bound protons are replaced by methyl groups at the same symmetry positions on the ring, for example, readily reveals the mechanism(s) of spin delocalization to each symmetry position. This will be discussed further after the pseudocontact (dipolar) shift has been introduced, and after the general strategies for separation of the contact and pseudocontact contributions to the paramagnetic shift have been summarized.

2. *Pseudocontact (Dipolar) Shifts*

a. *Pseudocontact shifts of metalloporphyrin substituents*

The electron-nuclear dipolar contribution to the paramagnetic shift is now usually called the pseudocontact contribution. This is actually a misnomer, since the electron-nuclear dipolar shift contains no contribution from scalar coupling of the electron spin with the spin of the nucleus of interest, that is, no Fermi contact term. Rather, the electron-nuclear dipolar shift results from through-space dipolar coupling of the electronic and nuclear magnetic moments which arise from either the magnetic anisotropy of the metal ion or from zero-field contributions (in cases where the total spin of the ion is greater than one-half). Nevertheless, the use of the term "pseudocontact" to describe the dipolar shift is well entrenched in the literature of heme proteins, as well as throughout the high-resolution NMR community, and we will thus use this term throughout this chapter. However, one must be aware of the fact that it represents the through-space dipolar interaction between the unpaired electron(s) and the nucleus of interest, which should more correctly be called the dipolar shift. In fact, in Section II.A.2.c later, "dipolar couplings" in which a protein (that often includes a metal with one or more unpaired electron) is discussed, these are dipolar couplings between ^{1}H and ^{15}N nuclei. For nuclei other than protons, ligand-centered pseudocontact (dipolar) shifts may also arise from unpaired spin density in π-orbitals,[23,24] but this is not the case for protons. For pseudocontact shifts of protons by S > 1/2 metal atoms or ions it can be shown that

$$\delta_{pc} = \frac{N_A}{24\pi}\left\{\frac{[2\chi_{zz} - (\chi_{xx} + \chi_{yy})](3\cos^2\theta - 1)}{r^3} + \frac{3[\chi_{xx} + \chi_{yy})](\sin^2\theta\cos 2\Omega)}{r^3}\right\}, \quad (7)$$

where N_A is Avogadro's number, χ_{ii} are the principal components of the molecular magnetic susceptibility tensor in SI units (note that $\chi(SI) = (4\pi \times 10^{-7})\chi(cgs\ emu)$), θ is the angle between the proton-metal vector and the z molecular axis, r is the length of this vector, and Ω is the angle between the projection of this vector on the xy plane and the x axis.[24,30,31] The terms $(3\cos^2\theta - 1)/r^3$ and $(\sin^2\theta\cos 2\Omega)/r^3$ are typically known as the axial and rhombic geometric factors, G_{ax} and G_{rh}, respectively, and the terms in Eq. 7 to which they belong are often called the axial and rhombic contributions to the pseudocontact shift, respectively. Axial geometric factors for protons at the β-pyrrole and *meso* positions (Structures **2** and **3**, $R_1 - R_8$ and $R_\alpha - R_\delta$, respectively) of the commonly utilized model hemes, tetraphenylporphinatoiron, (TPP)Fe, octaethylporphinatoiron, (OEP)Fe[2,4] and tetramesitylporphyrinatoiron, (TMP)Fe[32–34] have been calculated from X-ray crystallographic data for the low-spin iron(III) complexes, and are presented in Table 6

Table 6. Axial geometric factors for iron(III) porphyrinates which have planar and ruffled cores.

	Position	$\langle(3\cos^2\theta - 1)r^{-3}\rangle$, in $10^{26}m^{-3}$	Relative geometric factors
Porphyrins with Planar Cores			
TPP	*o*-H	–36.0[a]	1.00
	m-H	–16.7[a] (–17.1)[b]	0.463 (0.475)
	p-H	–14.8[a]	0.410
	o-CH_3	(–15.5)[b]	(0.431)
	m-CH_3	–10.5[a]	0.292
	p-CH_3	–11.0[a] (–11.1)[b]	0.306 (0.308)
	pyrrole-H	–70.3[a] (–75.4)[b]	1.95 (2.09)
OEP	α-CH_2	–42.5[a]	1.18
	meso-H	–110.0[a]	3.06
R-Pyridine	2,6-H	211.6[a]	–5.98
	3,5-H	115[a]	–3.19
	4-H	101[a]	–2.81
	4-CH_3	68[a]	–1.89
R-Imidazole	1-H	135[c]	–3.75
	1-CH_3	80[c] (82.6)[b]	–2.22 (–2.29)
	2-H	216[c] (277)[b]	–6.00 (–7.69)
	2-CH_3	<2[c]	0.00
	4-H	209[c] (269)[b]	–5.80 (–7.47)
	5-H	134[c] (148)[b]	–3.74 (–4.11)
	5-CH_3	75[c]	–2.14
Porphyrins with Ruffled Cores			
TMP	*o*-CH_3	+13.0 to +28.6[d] (50.7)	–0.361 to –0.794 (–1.41)
		–33.6 to –38.3[d] (–44.7)	0.933 to 1.06 (1.24)
	m-H	–6.8 to –14.7[d] (–1.8)	0.189 to 0.408 (0.050)
		–20.4 to –22.2[d] (–20.7)	0.567 to 0.617 (0.575)
	p-CH_3	–9.3 to –10.1[d] (–7.7)	0.258 to 0.280 (0.214)
	Pyrrole-H	–75.1[d] (–75.7)	2.09 (2.10)
R-Pyridine	2,6-H	261.1[d]	–7.25
	3,5-H	121.6[d]	–3.38
R-Imidazole	1-H	(—)	
	1-CH_3	(91.1)[e]	(–2.53)
	2-H	(—)	
	2-CH_3	(96.8)[e]	(–2.69)
	4-H	(138)[e]	(–3.83)
	5-H	(125)[e]	(–3.47)

[a]Bonnett, R.; Czechowski, F.; Latos-Grażyński, L. *J. Chem. Soc. Chem. Commun.* **1990**, 849–851.
[b]For [(TMP)Fe(NMeIm)$_2$]$^+$, Safo, M. K.; Gupta, G. P.;Watson, C. T.; Simonis, U.; Walker, F. A.; Scheidt, W. R. *J. Am. Chem. Soc.* **1992**, *114*, 7066–7075. Geometric factors given in parentheses.
[c]Watson, C. T. Ph.D. Dissertation, University of Arizona, 1996.
[d]Range of values observed for [(TMP)Fe(4-CNPy)$_2$]$^+$, Inniss, D.; Soltis, S. M.; Strouse, C. E. *J. Am. Chem. Soc.* **1988**, *110*, 5644–5650, and [(TMP)Fe(4-NMe$_2$Py)$_2$]$^+$, Safo, M. K.; Gupta, G. P.; Watson, C. T.; Simonis, U.; Walker, F. A.; Scheidt, W. R. *J. Am. Chem. Soc.* **1992**, *114*, 7066–7075.
[e]For [(TMP)Fe(1,2-Me$_2$Im)$_2$]$^+$, Balch, A. L.; Cornman, C. R.; Safari, N.; Latos-Grażyński, L. *Organometallics* **1990**, *9*, 2420–2421. Geometric factors given in parentheses.

for both iron(III) porphyrins with planar cores and those with ruffled cores (represented by (TMP)Fe^{III} with pyridine or hindered imidazole ligands). It is interesting to note that the pyrrole-H and mesityl *p*-CH_3 groups are not much affected by ruffling of the porphyrin ring, while the mesityl *o*-CH_3 and *m*-H groups have two geometric factors each, and the values of these depend somewhat on the degree of ruffling of the porphyrin ring. Pyridine 2,6-H and 3,5-H geometric factors for ruffled porphyrin complexes are somewhat larger than those reported earlier for planar porphyrin complexes, presumably because of the slightly shorter $Fe–N_{ax}$ bond lengths in the former complexes. Although these geometric factors have been obtained for low-spin iron(III) porphyrins, they are usually applicable to other metalloporphyrins unless M–L bond lengths are significantly different.

If the complex of interest has only one thermally-populated spin multiplet with effective spin S,[25,30] then:

$$\chi_{ii} = \left\{ \frac{\mu_0 (\mu_B)^2 S(S+1)}{3kT} \right\} g_{ii}{}^2, \tag{8}$$

where μ_0 is the permeability of free space and μ_B is the Bohr magneton (note that $\chi(SI) = (4\pi \times 10^{-7})\chi(cgs\ emu)$), and Eq. 8 can be simplified to

$$\delta_{pc} = \left\{ \frac{\mu_0 (\mu_B)^2 S(S+1)}{72\pi kTr_3} \right\} \times \left\{ [2g_{zz}{}^2 - (g_{xx}{}^2 + g_{yy}{}^2)](3\cos^2\theta - 1) + 3(g_{xx}{}^2 - g_{yy}{}^2)(\sin^2\theta \cos 2\Omega) \right\}. \tag{9}$$

This equation is the form that is often used for calculation of the pseudocontact contribution to the paramagnetic shift. However, Horrocks and Greenberg[30] showed some 35 years ago that second-order Zeeman (SOZ) contributions to the magnetic susceptibilities of heme systems range from ~3% (cytochrome b_5) to ~10% (cytochrome *c*) to 25% (metmyoglobin cyanide) of those of the first-order Zeeman (FOZ) effect (Curie behavior), and are of opposite sign for cytochrome *c* and metmyoglobin cyanide, but of the same sign for cytochrome b_5. Furthermore, excited electronic states of the metal ion that are thermally populated to varying extents as a function of temperature can lead to non-Curie behavior (nonzero intercepts at 1/T = 0).[25,31] As will be shown in Section II.A.3, this can lead, in the limit, to a reversal in the temperature dependence of the paramagnetic shifts of a complex over a broad temperature range of study. Thus, g-values cannot be used to quantitatively calculate the pseudocontact contributions to the paramagnetic shifts in very many cases, although the fact that they are usually the only magnetic anisotropy data available often makes it very tempting to use them. At the worst,

they at least give important *qualitative* information as to the importance of the pseudocontact contribution to the paramagnetic shift, and for that reason the EPR g-values of representative metalloporphyrins will be summarized in the sections following.

For heme proteins, *magnetic susceptibility anisotropies* can be calculated from Eq. 7 by fitting the protein side chain and backbone chemical shifts that cannot arise from the contact shift, but this is usually not possible for simple metalloporphyrins because of the difficulty of separating the contact and pseudocontact contributions for nuclei that are not many bonds away from the metal. (Examples of the determination of magnetic susceptibility anisotropies are discussed below in the following section.) However, Eq. 9 is sometimes useful for estimating the sizes of the pseudocontact shifts in two complexes for protons at the same molecular positions, when these complexes have different g-values (although note that different g-values lead to different sizes of deviations, as mentioned in the previous paragraph). Thus, if the size of a pseudocontact shift is known for one complex from some independent means, and if the g-values of both complexes are known, the pseudocontact shift of the second complex may be estimated by scaling it by the ratio of the g_{ii}^2 factors for the axial and rhombic terms by using Eq. 9. Examples of the use of such procedures are presented in Sections III.B.2 and III.B.3.

For pseudocontact shifts of metal complexes having S > 1/2, where the g-tensor is sometimes totally symmetric, magnetic anisotropy can still be present if the zero-field splitting, D, is large. In this case, Kurland and McGarvey[23] have shown that the pseudocontact contribution to the paramagnetic shift exhibits a $1/T^2$ dependence. The simplified equation for S = 5/2 is:

$$\delta_{pc} = -\left\{\frac{28\mu_0 \langle g \rangle^2 (\mu_B)^2 D}{36\pi k^2 T^2 r^3}\right\}\{3\cos^2\theta - 1\}, \qquad (10)$$

where μ_0 is the permeability of free space = $4\pi \cdot 10^{-7}[T \cdot m \cdot A^{-1}]$. (Note that a useful SI-unit equivalence for calculation purposes is $J = m^2 \cdot T \cdot A$.) The classic case of high-spin iron(III) porphyrins, where D-values range from 5.6 cm^{-1} (F^-) to 11 cm^{-1} (Cl^-) to 16.4 cm^{-1} (I^-),[35] yields curved Curie plots that result from a contact term that is linear in 1/T (Eq. 4) and a pseudocontact term that results from Eq. 10, with dependence on $1/T^2$.[2,4,36]

b. *Measurement of magnetic susceptibility anisotropies of ferriheme proteins*

Two examples of the determination of magnetic susceptibility anisotropies for proteins, in both cases for metmyoglobin are, first for the S = 1/2 cyanide complex

of sperm whale metmyoglobin, where Emerson and La Mar experimentally determined the paramagnetic pseudocontact shifts for noncoordinated amino acid side-chain protons in the heme pocket of sperm whale cyanometmyoglobin[10] and used them to determine, in solution, the orientation of the principal axes for the paramagnetic susceptibility tensor relative to the heme iron molecular coordinates.[11] The determination was made by a least-squares search for the unique Euler rotation angles which convert the geometric factors in the molecular (crystal) coordinates to ones that correctly predict each of 41 pseudocontact shifts measured[11] by using the magnetic anisotropies computed previously by Horrocks and Greenberg.[30] An excellent fit to experimental shifts was obtained, which also provided predictions that allowed subsequent new assignments to be made. The magnetic axes are oriented so that the z axis is tipped ~15° from the heme normal toward the heme 6-*meso*-H and coincides approximately with the characterized FeCO tilt axis in the isostructural MbCO complex.[37] The FeCO and FeCN units are isostructural, and so the authors proposed that the dominant protein constraint that tips the magnetic z axis from the heme normal was the tilt of the FeCN by steric interactions with the distal residues. The rhombic magnetic axes were found to align closely with the projection of the proximal His imidazole plane on the heme, which confirmed that the His–Fe bonding provided the protein constraint that orients the in-plane anisotropy.[11] (This worked well for cyanometmyoglobin because the histidine imidazole plane is aligned very close to one of the N_P–Fe–N_P axes; a different relationship would hold if the imidazole plane were aligned along the α,γ or β,δ *meso* directions, as in cytochromes *c* and nitrophorins, as discussed later in Section II.C.3.)

In this work[11] the actual axial and rhombic magnetic susceptibility anisotropies, $\Delta\chi_{ax}$ and $\Delta\chi_{rh}$, were not reported. However, La Mar and coworkers returned to cyanometmyoglobin later and determined not only the orientations of the magnetic susceptibility axes, but also the anisotropies;[38] the resulting axial, $\Delta\chi_{ax} = (2.48 \pm 0.30) \times 10^{-8}$ m^3mol^{-1}, and rhombic anisotropy, $\Delta\chi_{rh} = -(0.58 \pm 0.03) \times 10^{-8}$ m^3mol^{-1} were found at 25 °C.[38] These values agree well with the theoretical estimates of Horrocks and Greenberg ($\Delta\chi_{ax} = 2.24 \times 10^{-8}$ m^3mol^{-1}, $\Delta\chi_{rh} = -0.60 \times 10^{-8}$ m^3mol^{-1}).[31] (The values calculated from the First Order Zeeman (FOZ) term only, i.e., the squares of the g-values (Eq. 9), which, for met-MbCN are 3.45, 1.89, and 0.72[39] are as follows: $\Delta\chi_{ax} = 3.90 \times 10^{-8}$ m^3mol^{-1}, $\Delta\chi_{rh} = -1.21 \times 10^{-8}$ m^3mol^{-1} at 25 °C, both of which are considerably larger than the measured values (~30–35% for $\Delta\chi_{ax}$; a factor of two for $\Delta\chi_{rh}$). Thus as reported previously,[30,31] using the g-values may overemphasize both the axial and rhombic anisotropy.)

The axial magnetic anisotropies of ferric cyanide heme complexes are expected to be larger than those of bis-histidine or His-imidazole complexes, because the g-values for the latter are not so widely different from each other, as

in the case of the cyanide complexes, with their large values of g_{max}, as mentioned above. For example, the nitrophorin-imidazole complexes, which have g-values identical to those of cytochromes b_5 (3.02, 2.25, 1.46)[143] have axial and rhombic anisotropies calculated therefrom of $\Delta\chi_{ax} = 2.18 \times 10^{-8}$ m^3mol^{-1}, and $\Delta\chi_{rh} = -1.20 \times 10^{-8}$ m^3mol^{-1} at 25 °C. Although these values may be larger than would be found by actual measurement,[38] the axial and rhombic magnetic anisotropies are not much different whether only the FOZ term or the FOZ + SOZ terms are used, according to Horrocks and Greenberg.[30,31] The $\Delta\chi_{rh}$ obtained from the g-values of $[TPPFe(ImH)_2]^+$, as a function of axial ligand plane angle of the (parallel) imidazole ligand planes, was used for the angle plot shown in Figure 11, and thus the pseudocontact contribution may be somewhat over-estimated, although for bis-imidazole-coordinated hemins, probably not by much.

In the NMR study of La Mar *et al.*,[38] quantitative determination of the magnetic anisotropies as a function of temperature allowed the quantitative separation of contact and pseudocontact shifts for the iron ligands.[38] The heme contact shifts reflect the expected dominant π spin density at the pyrrole positions, but the *meso*-protons were said to exhibit low-field contact shifts indicative of unpaired spin in a σ orbital. It was felt that such delocalized σ spin density could arise from either deformation of the heme from planarity or the loss of σ/π separation for the d_{xz} and d_{yz} orbitals when the major magnetic axis is tilted strongly from the heme normal, as is experimentally observed.[38] The observed anomalous temperature dependences of the heme methyl and axial His ring contact shifts, as well as that of the rhombic anisotropy, are all consistent with thermal population of the excited orbital state[38] (Section II.C.3).

The use of paramagnetism-based constraints for solution structure refinement has also been described for a high spin iron(III)-containing protein (metmyoglobin).[40] Metmyoglobin is known to have an axial water, and thus this was a study of a 6-coordinate high-spin ferriheme protein. It was considered a particularly challenging system due to the unfavorably high ratio between its magnetic susceptibility and its magnetic anisotropy, coupled with relatively long electron spin relaxation times.[40] The cross-correlation between internuclear dipole–dipole interactions and the time average of the electronic magnetic moment (Curie spin) was measured for 61 backbone NH nuclear pairs and used as structural constraint.[40] The magnetic anisotropy tensor parameters calculated after refinement using the energy-minimized average structure were found to be $\Delta\chi_{ax} = -(1.51 \pm 0.18) \times 10^{-8}$ m^3mol^{-1} and $\Delta\chi_{rh} = (1.02 \pm 0.18) \times 10^{-8}$ m^3mol^{-1}.[40] The average structure has a backbone RMSD from the X-ray structure of 0.70 Å.[40] Thus, the 6-coordinate, high-spin aqua complex of metmyoglobin is much less anisotropic than the low-spin cyanide complex discussed above, but with opposite signs of the anisotropies to those of the cyanide complex.

Pseudocontact shifts can also be useful in providing structural restraints in solid-state NMR spectroscopy of microcrystalline proteins that contain paramagnetic metal ions, and have been used to study the matrix metalloproteinase, MMP-12, containing cobalt(II).[41,42]

c. *Residual dipolar couplings of proteins for structure determination*

The dipole–dipole interaction between magnetic nuclei, the leading term of which is described in Eq. 11, is actually the basis of the nuclear Overhauser effect (NOE):

$$H_{\mathrm{Dij}} = -\left[\frac{\gamma_{\mathrm{i}}\gamma_{\mathrm{j}}\mathrm{h}}{2\pi^2\mathrm{r}^3}\right] < \left[\frac{3\cos^2\theta - 1}{2}\right] > \mathrm{I}_{\mathrm{zi}}\mathrm{I}_{\mathrm{zj}}, \tag{11}$$

where the γ values are the magnetogyric ratios for the nuclei i and j, h is Planck's constant, r is the distance between the nuclei, θ is the angle between the internuclear vector and the applied magnetic field, and the I_z are the spin operators for the two nuclei. In principle, the interaction would manifest itself as a splitting of NMR resonances into doublets. When nuclear pairs are directly bonded, as in a ^{1}H–^{15}N amide pair, for example, the interaction would add to the scalar coupling normally seen in nondecoupled high-resolution NMR spectra. Variations in scalar couplings due to dipolar effects are not normally observed in high-resolution spectra because of motional averaging denoted by the brackets in Eq. 11. All motions occurring on time scales short compared to the reciprocal of the dipolar interaction in Hz ($< 10^{-3}$ seconds for ^{1}H–^{15}N and r = 1 Å) contribute to the averaging, including molecular tumbling in solution.

For diamagnetic molecules at moderate field strengths, molecules have little preference in orientation, the tumbling samples a nearly isotropic distribution, and the term inside the bracket goes to zero. If, however, a molecule has a preference in orientation, an average interaction would persist, and the splitting of resonances would vary from their nominal scalar couplings by an amount that depends on the angle θ for each N–H bond vector. Actually, most molecules have preferred orientations in the presence of a magnetic field, because most have anisotropic magnetic susceptibility tensors, χ. Different orientations result in induced magnetic moments of different sizes, and the energies of interactions of these moments with the magnetic field are different. It is clear in Eq. 11 that measurement of residual dipolar couplings can provide powerful structural constraints through their relationship to the angle θ and the internuclear distance r. The effects of averaging simply need to be separated. When many interactions exist within the same molecule, and they are averaged by the same motions, this separation is possible. The

conditions for structural application are therefore well defined: large anisotropy of susceptibility, large magnetic field, and numerous interactions, preferably ones where either r or θ is known.[43]

In 1995, it was shown by Prestegard and coworkers that the dipolar contributions to the splitting of ^{15}N resonances of ^{1}H–^{15}N amide pairs in multidimensional high-field NMR spectra of field-oriented cyanometmyoglobin could be measured.[43] The splittings appeared as small field-dependent perturbations of normal scalar couplings, usually of the order of up to ±2–3 Hz. The paramagnetic protein was found to tend to align to a small extent with the magnetic field vector of a high-field spectrometer, in this first case a 750 MHz NMR spectrometer, so that the dipolar contributions to the ^{1}H,^{15}N amide couplings were not completely averaged. More than 90 resonances were assigned to specific sequential sites in the protein. A specially designed two-dimensional HSQC experiment was used to collect data at 750 MHz, from which splittings of the ^{15}N resonance in the indirect dimension could be measured (coupling-enhanced HSQC). The sequence is based on a gradient-enhanced water-flip-back-HSQC,[44] but incorporates an extra ^{15}N 180° pulse during t_1 evolution. The pulse was simultaneous with the usual 180° ^{1}H pulse, but both were positioned accordion-style to allow pure dipolar splitting evolution for half the period and chemical shift plus dipolar splitting evolution for the other half the period. This sequence scaled chemical shift dispersion so that a smaller spectral width and longer evolution time could be used. For the 750 MHz data set, 200 complex t_1 points were collected with a total t_2 acquisition time of 182 ms. The total experiment time was 14 hours, with a recycling rate of 0.5 s^{-1}.[43] While most variations are small compared to the typical ^{15}N line width, they are measurably different. Splittings range from 96 to 90 Hz. If scalar couplings alone were responsible for the splitting, nearly all pairs would be split by 94 ± 1 Hz. The splittings are also field dependent ($\propto B_0^2$), and thus the dipolar contributions should increase by a factor of 2.25 in going from 500 to 750 MHz,[43] and a additional factor of 1.44 on going from 750 MHz to currently-available high-field systems (900 MHz). This field dependence can be exploited to allow separation of the scalar and dipolar contributions to the observed splitting. The dipolar contributions could be correlated with predictions based on the known susceptibility and known structure of the protein. The implication of these residual dipolar couplings was that they could be used as an additional source of information for protein structure determination in solution. The same methods have been utilized more recently for study of methemoglobin[45] and a number of other systems.[46–50]

Since the first report for cyanometmyoglobin,[43] a number of ways of increasing the alignment of the paramagnetic molecule with the magnetic field of the NMR spectrometer have been developed; most of these rely on crowding the molecules of interest with large substances such as bicelles, phage particles or liquid

crystals, all of which themselves tend to align with a magnetic field. In many of these cases no paramagnetic metal is necessary. Residual dipolar couplings of ±10 Hz can be achieved by adjusting the concentration of bicelles in the mixture, for example, or by changing their axis of alignment by adding a paramagnetic metal that will bind to the bicelles. In addition, means of attaching a paramagnetic metal site, usually housing a lanthanide ion with multiple unpaired electrons[51,52] or several lanthanide ions,[53] to the protein of interest, have been developed, which make it possible to apply the technique of partial alignment of any protein with the strong magnetic field of a high-field NMR spectrometer (750–900 MHz), so that residual dipolar couplings can be measured and used as an additional kind of restraint to allow structure determination of larger and larger proteins.[54] Applications not only to proteins, but also nucleic acids and carbohydrates are envisioned,[54] and a number of these have already been published.[55–78]

3. *Temperature Dependence of Contact and Pseudocontact Shifts*

The temperature dependence of the paramagnetic shifts of paramagnetic complexes in general has often been explained as following the Curie law:[2–4,13]

$$\delta_{iso} \propto \frac{C}{T}, \tag{12}$$

where C is a combination of all the terms present in Eqs. 4 and 9, except in those cases for which the pseudocontact shift obeys Eq. 10. This is approximately true, despite the discussion of the pseudocontact shifts of high-spin metalloporphyrins, which exhibit T^{-2} dependence (Eq. 10). However, as described previously elsewhere,[25] in many cases there are excited states that are within 1–3 kT or so of the ground state, and hence paramagnetic complexes with such a thermally-accessible excited state do not follow the simple Curie law, but rather an expanded Curie law that takes into account the excited state:[25]

$$\delta_n^{con} = \left(\frac{F}{T}\right)\left\{\frac{W_1 C_{n1}{}^2 + W_2 C_{n2}{}^2 e^{-\Delta E/kT}}{W_1 + W_2 e^{-\Delta E/kT}}\right\}, \tag{13}$$

where δ_n^{con} is the contact shift of each proton or carbon of interest, F is the Curie factor that relates the contact shift to the orbital coefficients, T is the absolute temperature, W_1 and W_2 are the weighting factors for the ground and excited state orbitals (equal if the spin multiplicities of ground and excited states are the same), C_{n1} and C_{n2} are the orbital coefficients for position n in the ground and excited states (in the ground state the values of C_{n1} and C_{n2} should be similar to those of the McConnell equation, ρ_C, of Eqs. 5 and 6, unless ΔE is small), respectively, ΔE

is the energy separation between ground and excited states, k is the Boltzmann constant. Several model ferrihemes and ferriheme proteins,[25,79] including a Mo^V-appended $[(TPP)Fe(NMeIm)_2]^+$ complex,[80] for which one axial ligand is prevented from rotating by the bulky 2,3-Mo^V complex, have been analyzed in this manner, as will be discussed below. The values of ΔE range from very small for nonhindered unsymmetrically-substituted $(TPP)Fe^{III}$ derivatives[25] to 160 cm^{-1} for the Mo^V-appended $[(TPP)Fe(NMeIm)_2]^+$ complex,[25,80] 400–700 cm^{-1} for cytochrome b_5,[25,81] and 500 cm^{-1} for *Aplysia* cyanometmyoglobin.[25,82] In these cases ΔE values represent the difference in energy between the two 3e(π) orbitals (see Figure 2) of the heme, and hence also the ΔE between the d_{xz} and d_{yz} orbitals of low-spin iron(III), Figure 1. Another case that has been analyzed in terms of the expanded Curie law of Eq. 13 involves the so-called spin-admixed S = 3/2–5/2 or 5/2–3/2 states of ferric tetraphenylporphyrin perchlorates, where either the 5/2 or 3/2 state is the ground state,[83] as discussed in Section IV.A.**7**, and shown in Figure 27. Therefore, from NMR spectra one not only learns about the electronic ground state, but also, frequently, the first excited electronic state of the complex. The temperature-dependence fitting program TDF for Windows, written by Dr. Nikolai Shokhirev, can be downloaded from the World Wide Web,[84] saved in a directory and

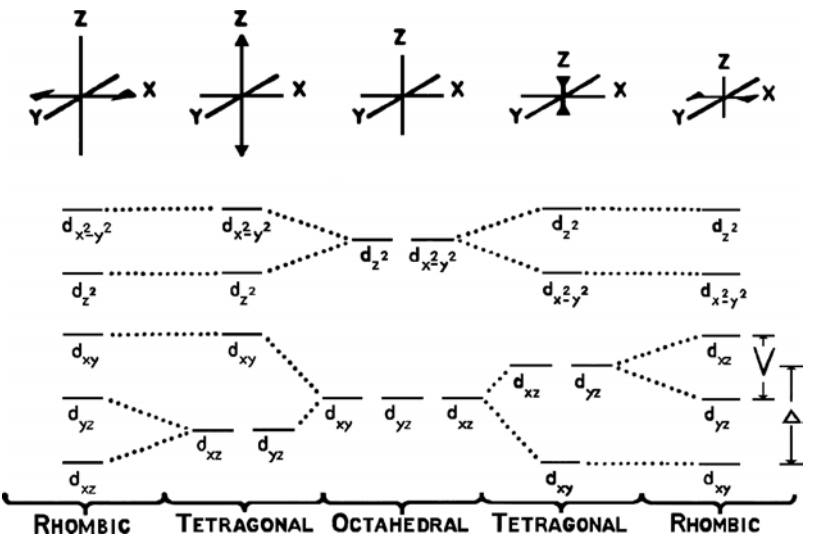

Figure 1. Possible lowering of symmetry of the d-orbitals from octahedral symmetry (center) to either tetragonal or rhombic symmetry. The porphyrin ring itself creates a tetragonal splitting, while planar axial ligands and/or macrocycle asymmetry create a rhombic splitting pattern. One of the two patterns on either side of the central octahedral pattern typically occurs for most metal porphyrinates. Reprinted from Walker, F. A. *Coord. Chem. Rev.* **1999**, *185–186*, 471–534 with permission from Elsevier.

unzipped for use. Assuming that the temperature dependence of the paramagnetic shifts can be fit by either Eq. 4 + 9 (the Curie law), 4 + 10 (Curie law + $1/T^2$ term) or Eq. 13, the system may be considered to be well-behaved, so as to lead to the possibility of separating the contact and pseudocontact contributions to the paramagnetic shift. Detailed approaches to this separation will be presented in Section III.B, after further consideration of the mechanisms of spin delocalization that comprise the contact term.

B. Nuclear Relaxation and Linewidths

In this section the focus will be on relaxation mechanisms[85] that affect only T_2, that is, chemical exchange effects, as well as those that affect both T_1 and T_2.

1. *Chemical Exchange Line Broadening and EXSY Cross Peaks*

Line broadening effects on 1D NMR spectra that result from chemical exchange have been discussed in depth elsewhere.[2,4,86,87] Dynamic processes that can be conveniently monitored are those whose rates are comparable to the chemical shift differences, $\nu_A - \nu_B$, in frequency units, between the exchanging sites A and B.[2,4,86,87] Paramagnetism often permits the resolution of magnetically nonequivalent environments that could not be resolved in a comparable diamagnetic system. In addition, since paramagnetism leads to such a large, nonlinear expansion in the chemical shift range, the chemical shift differences between exchanging environments are likely to be much larger, which permits the characterization of much faster dynamic processes by line broadening techniques. Two-dimensional NMR techniques based on the NOESY(EXSY) or ROESY experiments[88] permit the measurement of much slower rates of chemical exchange, at temperatures where line broadening is not even apparent. An example of such a study of a chemical exchange process is the case where the unsymmetrical axial ligands of $[(TMP)Fe(2\text{-}MeImH)_2]^+$ create four pyrrole-H, four *o*-CH_3, four *m*-H and two *p*-CH_3 environments that are then connected in matrices of cross peaks by chemical exchange as the axial 2-methylimidazole ligands rotate. From the intensity of the cross peaks, the rates of axial ligand rotation could be measured.[89] The rates of axial ligand rotation in the slow exchange regime could also be measured by saturation transfer[90] and by T_2 relaxation times,[91] the latter technique being useable over the same temperature range as the older line broadening techniques. Not only the paramagnetic low-spin iron(III) complexes could be studied by the 2D NMR technique, but also their diamagnetic cobalt(III) and iron(II) analogs.[89,92] This system will be considered in greater detail in Section IV.A.8.

2. *Proton T_1 and T_2 Relaxation Times, as Controlled by Electron Spin Relaxation Times, T_{1e}*

All of these relaxation times have important consequences with respect to whether or not the resonances of interest will be detectable or not.

a. *Electron spin relaxation times, T_{1e} or τ_s*

In the case of an example system which has electron spin S = 1/2, the electron spin relaxation time T_{1e} (sometimes also called τ_s) must be very short compared to the inverse of the electron-nuclear hyperfine coupling constant of the nuclei of our metalloporphyrin complex, $T_{1e} \leq (A/h)^{-1}$, and there are additional factors that make it typically necessary that it be much shorter than that.[93] Organic free radicals, including porphyrin π-cation radicals or their metal complexes, typically have T_{1e}s of 10^{-5} to 10^{-7} seconds, which is too long to achieve this averaging, while metal complexes may have T_{1e}s that range from 10^{-7} to 10^{-13} seconds.[93] Metals that have the longest T_{1e}s include VO^{2+}, Cu^{2+}, Mn^{2+} and Gd^{3+},[93] and to our knowledge, no proton NMR spectra (other than those of phenyl ring substituents of TPP derivatives[2,4]) of these metalloporphyrins have been reported to date, although the ^2H resonances of Cu^{II} porphyrins can be detected by ^2H NMR spectroscopy, as discussed in Section IV.H.1 and shown in Figure 80. Some of these ions have electron configurations that are either d^1 or d^9, for which there are no low-lying excited states to which the ground state is connected by spin-orbit coupling (as is the case of low-spin d^5 and d^7), and thus long T_{1e}s, well-resolved EPR spectra and poorly-resolved NMR spectra, or else, for S > 1/2 systems such as manganese(II), gadolinium(III), and to a lesser extent chromium(III) and manganese(IV), the zero-field splitting constants are small, which leads to long T_{1e}s,[94] well-resolved EPR spectra and poorly-resolved NMR spectra; again, ^2H NMR spectroscopy of appropriately deuterium-labeled complexes makes detection of resonances possible in a number of cases, as discussed below in Sections IV.E and H.3.

On the other hand, high-spin iron(III) and manganese(III) have large zero-field splittings[94] and give well-resolved NMR spectra. It is sometimes possible to extend the range of T_{1e}s over which resonances can be detected, for example for chromium(III) porphyrins, by substituting the protons in the complex of interest with deuterium atoms, which gives a theoretical factor of up to approximately 42 sharpening of the resonances, as discussed in more detail in Section II.D.2.

b. *Nuclear spin-lattice relaxation times, T_1*

The spin-lattice or longitudinal relaxation time of the protons of the metalloporphyrin complex under investigation is typically abbreviated T_1. T_1s are

typically measured by the Inversion-Recovery experiment, as described in various textbooks.[95–99] T_1s must be measured before any 2D NMR experiments are attempted, and typically in a protein having a paramagnetic metal center there is a very wide range of proton T_1s, from those farthest away and thus unaffected by the unpaired electron(s) (500 ms – 1 second if the solution has not been de-gassed with Ar or N_2) to shorter than 3 ms for protons bound to the direct ligands of high-spin iron(III). Although both contact and pseudocontact relaxation effects may be present, the most common situation is that pseudocontact relaxation dominates, especially for nuclei that are not directly connected to the metal through π bonds. Such pseudocontact relaxation results from dipolar coupling between the electron spin of the metal and the nuclear spin of the protons of interest within a given molecule, which is not averaged to zero by rapid rotation of the molecule. Usually, the inverse relaxation times, or relaxation rates, $R_1 = T_1^{-1}$, are proportional to τ_c/r^6, where τ_c is the rotational correlation time of the molecule. A more detailed look at the dependence of R_1 on molecular correlation time, however, shows that the dependence is actually given by:

$$R_1 = T_1^{-1} = \left(\frac{2}{15}\right)\left(\frac{\mu_0}{4\pi}\right)\left[\frac{g_N{}^2(\mu_N)^2\langle g\rangle^2(\mu_B)^2 S(S+1)}{\hbar^2 r^6}\right] \times\left[\frac{7\tau_c}{\left(1+\omega_S{}^2\tau_c{}^2\right)}+\frac{3\tau_c}{\left(1+\omega_I{}^2\tau_c{}^2\right)}\right], \quad (14)$$

where μ_0 is the permeability of free space, g_N is the nuclear g-value, μ_N is the nuclear Bohr magneton (also symbolized as β_N), $\langle g\rangle$ is the average electronic g-value of the metal complex, μ_B is the electron Bohr magneton (also symbolized as β in some of the EPR literature), S is the electron spin of the metal complex, r is the distance between the electron and the nucleus of interest, ω_I is the nuclear Larmor frequency and ω_S is the Larmor frequency of the electron.[93] Of course, there may be an added contact contribution to the R_1s of Eq. 14, especially for protons very near the metal.

For high-spin metals with zero-field splittings, it has been shown that although the exact equation governing T_{1e} differs for the various metal ions being considered,[94] the electron spin relaxation rate for a given metal ion can always be expressed as:

$$T_{1e}{}^{-1} \propto D^2 f(\tau_c), \quad (15)$$

where D is the zero-field splitting constant and τ_c is the rotational correlation time. Thus, linewidths (LW) for high-spin metal complexes should be given by:

$$LW \propto D^{-2}. \tag{16}$$

This relationship holds best for Fe^{III} porphyrinates, where linewidths decrease in the order $N_3^- > Cl^- > Br^- > I^-$.[94] Thus, Fajer and coworkers[100] and the author's coworkers[101] have used this fact to choose I^- as the best anion to produce the sharpest lines for high-spin Fe^{III} chlorins, oxochlorins and dioxoisobacteriochlorins.

Importantly, in connection with the basic $\tau_c r^{-6}$ dependence of R_1 is that the resonances of protons closest to the metal center typically have the shortest T_1s and thus their connectivities are hardest to detect in 2D NMR experiments. Because τ_c depends on solvent viscosity and temperature, changes in any of these factors may make significant changes in the T_1s of the protons, and may thus determine whether 2D cross peaks may be detected or not.

The excellent resolution of the ^1H NMR spectra of dicyanoiron(III) complexes of 2,4-disubstituted deuteroporphyrins was used by La Mar and coworkers to investigate in detail the proton pseudocontact relaxation by delocalized spin density.[102] If only the unpaired electrons on the metal contribute, nuclear relaxation of protons in low-spin iron(III) porphyrins by T_1 and T_2 processes should be given by:

$$R_1 = T_1^{-1} = 6Kr^{-6}T_{1e}, \tag{17}$$

$$R_2 = T_2^{-1} = 7Kr^{-6}T_{1e} + \left(\frac{1}{3}\right)S(S+1)A_h{}^2T_{1e}. \tag{18}$$

where $K = (1/15)\gamma_H{}^2\langle g\rangle^2(\mu_B)^2S(S+1)$.[102] This should mean that the T_1s of all ring CH_3 should be the same, since r^{-6} is identical for all ring CH_3. However, there is a marked difference in the T_1s of the four methyl groups of natural hemin derivatives that increases as the spread of the methyl resonances increases; the methyl with the largest paramagnetic shift has the shortest T_1.[102] These results were explained in terms of a sum of metal-centered pseudocontact relaxation and the pseudocontact relaxation by the delocalized spin density, ρ_C, in the aromatic carbon to which the methyl group is attached, which yields a modification of Eq. 17:

$$R_1 = T_1^{-1} = 6K[R_M{}^{-6} + \rho_C{}^2R_L{}^{-6}]T_{1e}, \tag{19}$$

where R_M is the distance from the metal center to the proton of interest, and R_L is the distance from the aromatic carbon to the proton. The quantity ρ_C is proportional to

the observed contact shift, as described by Eqs. 4 and 5. Thus, in line with the predictions of Eq. 19, a linear relationship was observed between the observed T_1^{-1} and $(\delta_{con})^2$. From the intercept, assuming $R_M = 6.15$ Å, T_{1e} was determined to be 1.8×10^{-12} seconds, and independent of the basicity of the porphyrins in these model compounds.[102] The slope of this line indicates that $R_M^{-6} = \rho_C^2 R_L^{-6}$ for a contact shift of −19 ppm. Assuming R_L ~1.9 Å, this yields $\rho_C = 0.03$. Thus, 0.03 of an unpaired electron in a carbon p orbital causes paramagnetic pseudocontact relaxation of the appended methyl proton of a magnitude comparable to that from the iron center,[102] and pseudocontact relaxation from both ligand-centered and metal-centered spin density must be considered in analyzing heme methyl T_1s, not only in model complexes, but also in heme proteins.

Ligand-centered pseudocontact relaxation is probably a contributor to the short T_1s of the pyrrole-H of TPP complexes of low-spin iron(III) and the *meso*-H of OEP and natural porphyrin complexes of high-spin iron(III), since R_L ~1.08 Å. This could make the ligand-centered pseudocontact relaxation term 33 times larger for a pyrrole-H than a pyrrole-CH_3 with the same magnitude contact shift. The difference in T_1s observed for low-spin iron(III) complexes of β-pyrrole-substituted porphyrins such as OEP and the natural porphyrins[102] as compared to those of TPP and other *meso*-substituted porphyrins are approximately of this magnitude.[3] However, another possible contribution to the short T_1s of the protons of imidazole and pyridine complexes of $(TPP)Fe^{III}$ could be the rapid modulation of the chemical shifts of the pyrrole-H in complexes where planar axial ligands rotate synchronously or asynchronously at a rate comparable to the energy separation of the $3e(\pi)$ orbitals.[103] This energy separation can be approximated as that between the d_{xz} and d_{yz} orbitals, as calculated from the EPR g-values (Section IV.A.8.a). This energy separation is of the order of up to 540–800 cm^{-1}, depending on the value chosen for the spin-orbit coupling constant,[2,4] (see Section IV.A.8.a). This energy separation translates to a ΔE of up to $1.6–2.4 \times 10^{13}$ s^{-1}. In comparison, the energy barrier to rotation of nonhindered imidazoles on $(TPP)Fe^{III}$ has been estimated as 3.3 kJ/mol for synchronous and 5.4 kJ/mol for asynchronous rotation.[90] These barriers lead to calculated rate constants of 1.6×10^{12} s^{-1} for synchronous rotation and 7.2×10^{11} s^{-1} for asynchronous rotation of ligands. The fact that the rate constant for synchronous rotation of axial ligands is within a factor of ten of the energy separation of the $3e(\pi)$ orbitals suggests that this mechanism of shortening of the T_1 and T_2 relaxation times is probably very important for low-spin $(TPP)Fe^{III}$ complexes. In support of this, TPP-related ferriheme complexes that have axial ligands that are "fixed" in orientation (i.e., that are rotating slowly on the NMR timescale) have much longer T_1s (up to 50 ms)[80,103] than do simple, unhindered $[(TPP)Fe^{III}L_2]$ complexes (9 ms or shorter).[104]

c. *Nuclear spin–spin relaxation times, T_2*

When chemical exchange is absent, spin–spin proton or transverse relaxation time in a paramagnetic metal complex is T_2, for which the inverse (R_2) is also often proportional to τ_c/r^6 if pseudocontact relaxation dominates. But the more detailed dependence on correlation time τ_c has a different relationship involving nuclear and electronic Larmor frequencies:

$$R_2 = T_2^{-1} = \left(\frac{1}{15}\right)\left(\frac{\mu_0}{4\pi}\right)\left[\frac{g_N{}^2(\mu_N)^2\langle g\rangle^2(\mu_B)^2 S(S+1)}{\hbar^2 r^6}\right] \times\left[\frac{13\tau_c}{1+\omega_S{}^2\tau_c{}^2}+\frac{3\tau_c}{1+\omega_I{}^2\tau_c{}^2}+4\tau_c\right], \quad (20)$$

where all terms have the same definitions as in Eq. 14. Of course, there may be added to Eq. 20 a contact contribution,[93] especially for protons very close to the metal, and in addition, there may be an additional term, especially for metals which have multiple unpaired electrons, due to Curie relaxation. This term is another type of pseudocontact relaxation which is proportional to $B_o{}^2S^2(S+1)^2\tau_c/T_2r^6$,[35] where B_o is the magnetic field, and is thus most noticeable at very high magnetic fields for large values of S. [It has not been possible to detect it for low-spin iron(III) porphyrins at 500 MHz.[103]] Most metalloporphyrins are not in the extreme narrowing limit at most common NMR frequencies and in most solvents, and so T_2 is usually shorter than T_1. For cases in which there is sizable magnetic anisotropy, linewidths become broader due to this factor, which shortens the electronic T_{1e} (Section II.B.2.a). Sternlicht first derived the expression for the nuclear relaxation rate for complexes possessing magnetic anisotropy:[105]

$$R_2 = T_2^{-1} = \left[\frac{2\gamma_N(\mu_B)^2 S(S+1)}{3r^6}\right]\left[\langle g\rangle^2 + g_{\|}{}^2\cos^2\theta + g_{\perp}{}^2\sin^2\theta\right]\tau_c, \quad (21)$$

where $\langle g\rangle^2$ is the square of the average g-value, r is the proton-metal distance, θ is the angle between the z-axis and the vector r, and all other quantities have their usual definitions. Thus, if $g_{\|}$ is aligned along the z-axis of the complex, as is usually the case, and only the pyrrole-H, for which $\theta = 90°$, are considered, the lines will be broadened in proportion to the size of $\langle g\rangle^2 + g_{\perp}{}^2$. This relationship provides an alternate means of accounting for the linewidths

of the pyrrole-H resonances of $[(TPP)FeL_2]^{+/-}$ complexes for L = CN^- as compared to ImH, discussed in the section above (where the g-values are 0.83 and 1.96, respectively, based on the g-values listed in Table 12), but may not account for the linewidths of low-spin cobalt(II) porphyrins, discussed in Section IV.C.1.

C. Spin Density and Bonding: Mechanisms of Spin Delocalization

Unpaired electrons of 3d metalloporphyrins of various oxidation and spin states are expected to be mainly localized either on the metal or on the porphyrin ring. If the unpaired electron is largely localized on the metal, it is expected to be located in one or more of the metal d-orbitals, while if it is localized on the porphyrin ring, it is expected to be found in either the HOMO (for metalloporphyrin π-cation radicals, $[(P^{-\bullet})M]^+$) or the LUMOs (for π-anion radicals, $[(P^{3-\bullet})M]^-$, or dianions, $[(P^{4-\bullet})M]^{2-}$). For metalloporphyrins in which the unpaired electron is located in one or more of the d-orbitals, spin delocalization can occur through either σ or π orbitals. In the latter case, the spin transfer can arise through either ligand-to-metal (L $\rightarrow$ M) spin transfer (the usual situation), which involves overlap of a filled π orbital with a half-filled d_π orbital, or rarely, by metal-to-ligand (M $\rightarrow$ L) spin transfer or "back-bonding", which involves overlap of an empty π orbital with a half-filled d_π orbital. Thus, an understanding of the symmetry properties and relative energies of the metal and porphyrin orbitals will be of value in understanding the possible mechanisms of spin delocalization to the protons on the periphery of the porphyrin ring.

1. *The Metal Ion*

The relative energies of the five d-orbitals are generally expected to be as shown in one of the sections of Figure 1, although individual variations in these relative energies are observed and are discussed in Section IV. The relative energies of the d-orbitals, beginning in the center of Figure 1, of an ideally octahedral complex (O_h point group) is shown, but it is not expected that the porphyrin will (probably ever) have the same ligand field as the axial ligands. Therefore, we descend to tetragonal symmetry by going to the right or the left of the center of the diagram, to the right if the axial ligands are of stronger field than the porphyrin ring, to the left if they are of weaker field; typically "stronger field" or "weaker field" is controlled by π-donor and π-acceptor properties of the axial ligands. Strong π-donor ligands (highly basic pyridines such as 4-dimethylaminopyridine or almost any imidazole) typically shift the system to the right side tetragonal section of the diagram, whereas strong π-acceptor ligands (cyanide ion, organic isocyanides,

low-basicity pyridines) typically shift the system to the left side tetragonal section of the diagram. Whether the electrons will be paired (low-spin) or unpaired (high-spin) depends on the splitting between the three lower-energy d-orbitals and the two higher-energy d-orbitals, which typically depends on the σ-donor strength of the axial ligands, and/or on whether the coordination number is five rather than six. Whether the orbitals are further split to rhombic symmetry depends on the nature of the axial ligands and their orientations (planar, in parallel, but not perpendicular planes) and on the electron configuration of the metal.

Metalloporphyrins which have been successfully studied by NMR spectroscopy are listed in Table 7. For many of these the metal may be either high-spin, in some cases intermediate-spin, or low-spin. Thus, metalloporphyrins have a rich variety of potential electron configurations. The valence electrons are almost invariably located in the 3d orbitals of the metal, except in the relatively rare cases of true π-cation radicals of $PFe^{II}(NO)$, $PRu^{II}(CO)$ or one-electron oxidized cobalt(III) porphyrins or related macrocycles or of π-cation radicals of bromoiron(III) oxophlorins,[106] but probably not the supposed π-cation radicals of iron(II) complexes of reduced hemes bound to organic isonitrile ligands,[107] which are more likely low-spin iron(III) complexes of the $(d_{xz},d_{yz})^4(d_{xy})^1$ ground state. In 4-, 5- and 6-coordinate metalloporphyrins, the d-orbitals consist of three general symmetry types: (1) The σ-symmetry orbitals that interact with the porphyrin nitrogens and with axial ligands (strictly speaking, in the idealized D_{4h} symmetry of 4- and 6-coordinate metalloporphyrins, these orbitals are of a_1 (d_{z^2}) and b_1 ($d_{x^2-y^2}$) symmetry, but in any case, they are engaged in σ-bonding interactions only); (2) the d_π orbitals, d_{xz} and d_{yz}, which can engage in π-bonding with filled (the common situation) or empty (uncommon) π-symmetry orbitals of the porphyrin ring as well as the axial ligands; and (3) the d_{xy} orbital, which is nonbonding, both in relation to the porphyrin ring and the axial ligands, at least when the porphyrin ring is planar. However, it becomes capable of π-bonding if the porphyrin ring is ruffled, as discussed in Section II.C.2, or if the metal is 5-coordinate and significantly out of the plane of the bonding nitrogens of the porphyrin or other macrocycle, as discussed in Sections II.C.4 and IV.A.6.b,c.

2. *The Porphyrin Ring*

Both 4- and 6-coordinate metalloporphyrins have effective D_{4h} symmetry, if the effects of planar axial ligands and potentially unsymmetrically-placed porphyrin substituents are neglected. Each porphyrin nitrogen supplies a σ-symmetry lone pair that points directly toward the porphyrin nitrogens along the *x*, *-x*, *y* and *-y* axes, and a single π-symmetry p-orbital that is perpendicular to the plane of the porphyrin ring, the p_z orbital of the bonding nitrogen. Not only does the bonding nitrogen have an available π-symmetry p_z orbital, but so do each of the C_α, C_β and

Table 7. Oxidation and spin states of metalloporphyrins for which NMR spectra have been reported.

Metal	Oxidation state	Spin state	Electron configuration
Cr	II	S = 2 High-spin	$(d_{xy})^1(d_{xz},d_{yz})^2(d_{z}2)^1$
	III	S = 3/2 High-spin	$(d_{xy})^1(d_{xz},d_{yz})^2$
	IV	S = 0 Diamagnetic	$(d_{xy})^2$
Mn	II	S = 5/2 High-spin	$(d_{xy})^1(d_{xz},d_{yz})^2(d_{z}2)^1(d_{x}2_{-y}2)^1$
	III	S = 2 High-spin	$(d_{xy})^1(d_{xz},d_{yz})^2(d_{z}2)^1$
		S = 1 Low-spin?	$(d_{xy})^2(d_{xz},d_{yz})^2$
	IV	S = 3/2 High-spin	$(d_{xy})^1(d_{xz},d_{yz})^2$
Fe	I	S = 1/2 Low-spin	$(d_{xy})^2(d_{xz},d_{yz})^4(d_{z}2)^1$
	II	S = 0 Low-spin (diamagnetic)	$(d_{xy})^2(d_{xz}, d_{yz})^4$
		S = 1 Intermediate-spin	$(d_{xy})^2(d_{z}2)^2(d_{xz}, d_{yz})^2$
		S = 2 High-spin	$(d_{xy})^2(d_{xz},d_{yz})^2(d_{z}2)^1(d_{x}2_{-y}2)^1$
	III	S = 1/2 Low-spin	$(d_{xy})^2(d_{xz},d_{yz})^3$ or $(d_{xz},d_{yz})^4(d_{xy})^1$
		S = 3/2 Intermediate spin	$(d_{xy})^2(d_{xz},d_{yz})^2(d_{z}2)^1$
		S = 5/2 High-spin	$(d_{xy})^1(d_{xz},d_{yz})^2(d_{z}2)^1(d_{x}2_{-y}2)^1$
	IV	S = 1 Low-spin	$(d_{xy})^2(d_{xz},d_{yz})^2$
	V?	S = 3/2? High-spin	$(d_{xy})^1(d_{xz},d_{yz})^2$?
Ru	II	S = 0 Diamagnetic	$(d_{xy})^2(d_{xz},d_{yz})^4$
	III	S = 1/2 Low-spin	$(d_{xz},d_{yz})^4(d_{yz})^1$
Co	II	S = 1/2 Low-spin	$(d_{xy})^2(d_{xz},d_{yz})^4(d_{z}2)^1$
		S = 3/2 High-spin	$(d_{xy})^2(d_{xz},d_{yz})^3(d_{z}2)^1(d_{x}2_{-y}2)^1$
	III	S = 0 Diamagnetic	$(d_{xy})^2(d_{xz},d_{yz})^4$
		S = 1 Intermediate-spin	$(d_{xy})^2(d_{xy})^2(d_{xz},d_{yz})^2$?
Rh	II	S 0 = 1 /2 Low-spin	$(d_{xy})^2(d_{xz},d_{yz})^4(d_{z}2)^1$
	III	S = 0 Diamagnetic	$(d_{xy})^2(d_{xz},d_{yz})^4$
Ir	III	S = 0 Diamagnetic	$(d_{xy})^2(d_{xz},d_{yz})^4$
Ni	II	S = 0 Low-spin (diamagnetic)	$(d_{xy})^2(d_{xz},d_{yz})^4(d_{z}2)^2$
		S = 1 High-spin	$(d_{xy})^2(d_{xz},d_{yz})^4(d_{z}2)^1(d_{x}2_{-y}2)^1$
Cu	II	S = 1/2	$(d_{xy})^2(d_{xz},d_{yz})^4(d_{z}2)^2(d_{x}2_{-y}2)^1$
Ag	II	S = 1/2	$(d_{xy})^2(d_{xz},d_{yz})^4(d_{z}2)^2(d_{x}2_{-y}2)^1$
Ce	IV	S = 0 Diamagnetic	f^0
	III	S = 1/2[a]	f^1
La	III	S = 0	f^0
Pr	III	S = 0[a]	f^2
Nd	III	S = 3/2[a]	f^3
Sm	III	S = 5/2[a]	f^5
Eu	III	S = 3[a]	f^6
Gd	III	S = 7/2[a]	f^7
Tb	III	S = 3[a]	f^8
Dy	III	S = 5/2[a]	f^9
Ho	III	S = 2[a]	f^{10}
Er	III	S = 3/2[a]	f^{11}
Tm	III	S = 1[a]	f^{12}
Yb	III	S = 1/2[a]	f^{13}
Lu	III	S = 0	f^{14}

[a]For the lanthanides, S is not a good quantum number.

C_m carbons of the porphyrin skeleton. Earlier[108–112] and recent workers[113–116] have developed more-or-less sophisticated molecular orbital treatments of the porphyrin ring and related macrocycles. In each of these treatments, π molecular orbitals are constructed based on the symmetry properties of the idealized D_{4h}-symmetry porphyrin ring. Hückel MO treatments are qualitatively useful if exact energy separations are not needed.[117] A program has been developed which utilizes the Huckel MO treatment and allows visualization of the molecular orbitals of the porphyrin and related macrocycles, and is available on the Web.[118] The 24 p_z orbitals of the porphine macrocycle are thus combined to produce 24 molecular orbitals (2 a_{1u}, 4 a_{2u}, 3 b_{1u}, 3 b_{2u}, and 6 e_g sets), 13 of which are filled by the 26 p_z electrons of the 24 atoms of the porphyrin nucleus. Although the theories differ in detail, all agree that the frontier and near-frontier orbitals are, in order of increasing energy, $3e(\pi) < 1a_{1u}(\pi) \sim 3a_{2u}(\pi) < 4e(\pi^*)$, using the notation of Longuet-Higgins, *et al*.[108] The $3e(\pi)$, $1a_{1u}(\pi)$ and $3a_{2u}(\pi)$ orbitals are filled, while the $4e(\pi^*)$ orbitals are empty. All theories agree further that the latter are the LUMOs of the porphyrin ring, while the HOMO(s) may be either $1a_{1u}(\pi)$, $3a_{2u}(\pi)$, or the d_{xy} or $d\pi$ orbitals, depending on the oxidation state of the metal, the porphyrin and degree of reduction of the macrocycle (chlorins and isobacteriochlorins), substituents[119] and the axial ligand(s) present. The symmetry properties and electron distributions predicted are shown in Figure 2, left and right, which have been calculated using the program MPorphW.[118] The two pictures show the electron density distributions observed if the nodal planes of the π-symmetry orbitals are placed along the porphyrin nitrogens, as usually shown (Figure 2, left), or along the *meso* positions, an equivalently correct representation (Figure 2, right). As will be shown below, the orbitals of Figure 2 left, are similar to those of the chlorin ring, while those of Figure 2 right, are similar to those of most other macrocycles.

There is at least one case where the metal d_{xy} orbital of a d^1 metalloporphyrin lies lower in energy than the highest-energy filled porphyrin orbital, and thus gives rise to a non-Aufbau filling of the orbitals. This is the case of the V^{IV}=O porphyrin complexes of both OEP and TPP, as well as the phthalocyanine complex (Pc).[120] The EPR spectra of these complexes are indeed those of the $(d_{xy})^1$ metal-based electron configuration,[121,122] yet one-electron oxidation removes an electron from the porphyrin ligand rather than from the $b_2(d_{xy})$ orbital,[123] and one-electron reduction places an electron into an empty porphyrin-based orbital rather than with the single electron in the b_2 (d_{xy}) orbital.[124] Similar behavior has been observed for oxoiron(IV) porphyrinates.[125] These observations have been interpreted in the past to mean that the valence porphyrin orbitals are very close in energy to the metal-based orbitals.

To determine the relative energies and nature of the positive ion states of VO(OEP) in the gas phase, the valence photoelectron spectra of this and related porphyrin and phthalocyanine molecules have been collected.[120] The photoelectron

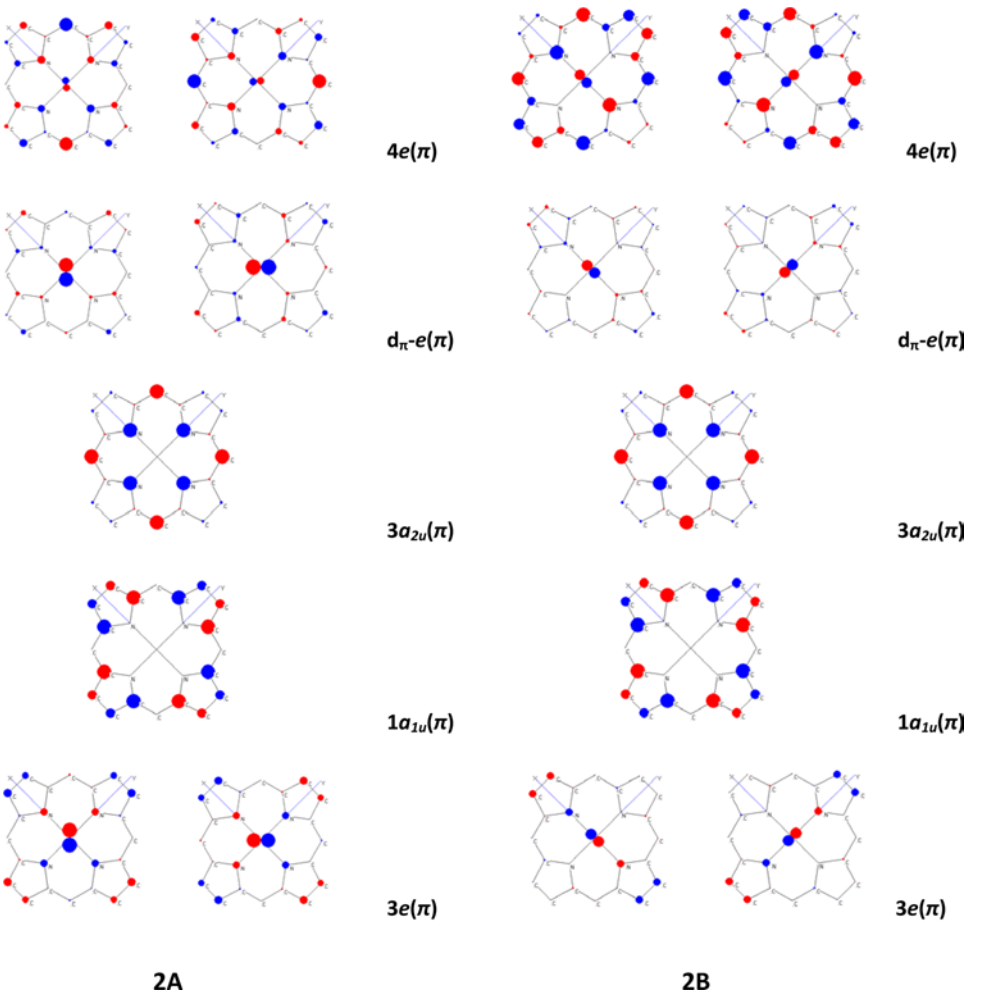

Figure 2. Frontier molecular orbitals of the porphyrin ring, including the mainly metal d_π–e(π) combination orbitals that are usually the HOMOs and/or SOMOs of a metalloporphyrin. Two equivalent representations of the orbitals are shown, with nodes through the nitrogens (left) or the *meso* positions (right). In practice, when axial ligands are also bound to the metal, nodes could be placed at any arbitrary angle in between these two, as long as the nodes of the two orbitals are at right angles to each other. The actual positions of the nodes will depend upon the orientation of planar axial ligand(s).[8] The relative sizes of the circles at each atom represent the relative orbital electron density coefficients, C_i^2, which should be closely related to spin density coefficients, ρ_C. Calculated using the program MPorphW.[118]

spectra show that the lowest energy ionization of VO(OEP) and of vanadyl phthalocyanine, VO(Pc), in the gas phase is from a filled ligand-based orbital, as found for the oxidation of VO(OEP) in condensed phases.[123] The photoelectron spectra also show the unusual result that ionization from the singly occupied metal d

orbital of these molecules requires considerably more energy (at least 1 eV) than ionization from the $3a_{2u}(\pi)$ and $1a_{1u}(\pi)$ doubly occupied porphyrin orbitals, and that the energies associated with high-spin stabilization are extremely small. These observations imply a non-Aufbau occupation of the molecular orbitals. Electronic structure calculations indicate that this non-Aufbau behavior is strongly favored by the electron–electron repulsion energies, regardless of electron relaxation energies with ionization, correlation energies, exchange energies, or other contributions. The large energy associated with this non-Aufbau behavior of vanadyl porphyrins suggests that such behavior may be important in the chemistry of other metalloporphyrins, certainly those of the +4 state for first-row transition metals, and the fundamental basis for this behavior may have important implications for the most stable states of other molecules.[120]

In spite of the non-Aufbau filling of the orbitals of vanadium(IV)[120] and iron(IV)[125] porphyrins, for the vast majority of cases of first-row transition metals in the +2 and +3 oxidation states the d_{xy} and d_π orbitals are believed to lie at similar or perhaps higher energy than the porphyrin or related macrocycle HOMO, and thus the d_π-$e(\pi)$ combined orbital set has been included in Figure 2, just above the $1a_{1u}(\pi)$ and $3a_{2u}(\pi)$ orbitals, in addition to the $3e(\pi)$ porphyrin-only orbitals, which are lower in energy than $1a_{1u}(\pi)$ and $3a_{2u}(\pi)$. The d_π-$e(\pi)$ set of Figure 2 are approximately 75% metal in character, and the orbital coefficients depicted are very similar in ratio to those of the porphyrin-based $3e(\pi)$ orbitals.

For electronic absorption spectra, excitations from $1a_{1u}(\pi)$ and $3a_{2u}(\pi)$ to $4e(\pi^*)$ give rise to the so-called α, β and Soret bands in the visible spectra[109–112] while excitations from $1a_{1u}(\pi)$ and $3a_{2u}(\pi)$ to d_π-$e(\pi)$ give rise to the near infrared charge transfer transitions that have been studied for heme models and proteins by MCD spectroscopy.[126,127] Porphyrin π-cation radicals $[H_2P^{\bullet}]^+$, or their metal(II)-bound counterparts, $[M^{II}P^{-\bullet}]^+$ have either $a_{2u}(\pi)$ or $a_{1u}(\pi)$ unpaired electrons, depending on whether they do or do not have *meso* substituents, respectively,[128] although this can change with the oxidation state and coordination number of the metal and other factors.[128] However, although either the $1a_{1u}(\pi)$ or $3a_{2u}(\pi)$ orbital is typically the HOMO of the porphyrin ring itself (excluding the largely metal-based d_π-$e(\pi)$ orbitals), neither of these orbitals have the proper symmetry to overlap with the d_π orbitals of the metal if the porphyrin ring is planar. In this case, only the $3e(\pi)$, which are lower in energy than either $1a_{1u}(\pi)$ or $3a_{2u}(\pi)$, and can form the depicted d_π–$e(\pi)$ hybrids, and the $4e(\pi^*)$ orbitals, which are higher in energy than either $1a_{1u}(\pi)$ or $3a_{2u}(\pi)$, have the proper symmetry for overlap with the metal d_π orbitals. The $4e(\pi^*)$ orbitals were earlier believed to interact strongly with the d_π orbitals in 5-coordinate Fe^{II}, Fe^{III} and Ni^{II} porphyrin complexes.[2–7] However, as will be shown later in Sections II.C.3 and IV.A.4.a(i), there is no longer any evidence that the $4e(\pi^*)$ orbitals are involved in spin delocalization in any of the metalloporphyrin

complexes to be discussed, even though they have proper symmetry to interact with the d_π orbitals via M $\rightarrow$ P π bonding. Since the 3e(π) orbitals are filled, the type of overlap interaction that can occur between them and the metal d_π orbitals is P $\rightarrow$ M (or, more generally, L $\rightarrow$ M) π bonding. Clearly, the only way in which this type of bonding interaction can lead to spin delocalization from metal to porphyrin π system is if the metal d_π orbitals are partially, but not completely, filled. Thus, spin delocalization via interaction between the filled 3e(π) orbitals and the metal d_π orbitals can occur only if the metal electron configuration is (d_{xz},d_{yz}).[1–3]

In cases where the porphyrin ring is strongly ruffled, the p_z orbitals of the porphyrin nitrogens are twisted away from the normal to the mean porphyrin plane, and thus have components of the p_z orbitals of the nitrogens that lie in the mean (xy) plane of the macrocycle. These components of the "twisted" p_z orbitals have the proper symmetry to interact with the metal d_{xy} orbital, as shown in Figures 3[129] and 4c,[130] and an interaction such as that shown presumes that the energies of the metal and interacting porphyrin orbitals are quite similar, unlike the case for the vanadyl porphyrin discussed above. Consistent with this presumption, while V^{IV}=O porphyrins have no distortion of the porphyrin ring other than a slight doming that places the metal somewhat above the plane of the four nitrogens in the direction of the oxo group, low-spin Fe^{III} porphyrins having two π-acceptor axial ligands such as *t*-BuNC, are strongly ruffled, even though the axial ligands are small. The porphyrin orbital that has proper symmetry to interact with the metal d_{xy} orbital in this case is the $3a_{2u}(\pi)$ orbital,[129] Figure 2. (Such a porphyrin-metal d_{xy}-$a_{2u}(\pi)$ combined orbital has not been depicted in Figure 2, but it would presumably lie above the d_π-e(π) set of the left or right sides of Figure 1, respectively.)

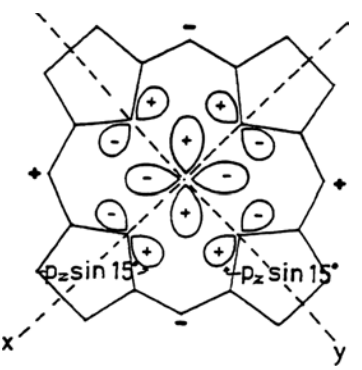

Figure 3. Possible interactions of the d_{xy} orbital with the porphyrin nitrogens in the case of strong S_4 ruffling. The remaining nitrogen p_z projections have proper symmetry to allow delocalization via the $a_{2u}(\pi)$ porphyrin orbital. Modified from Safo, M. K.; Walker, F. A.; Raitsimring, A. M.; Walters, W. P.; Dolata, D. P.; Debrunner, P. G.; Scheidt, W. R. *J. Am. Chem. Soc.* **1994**, *116*, 7760–7770, with permission from the American Chemical Society.

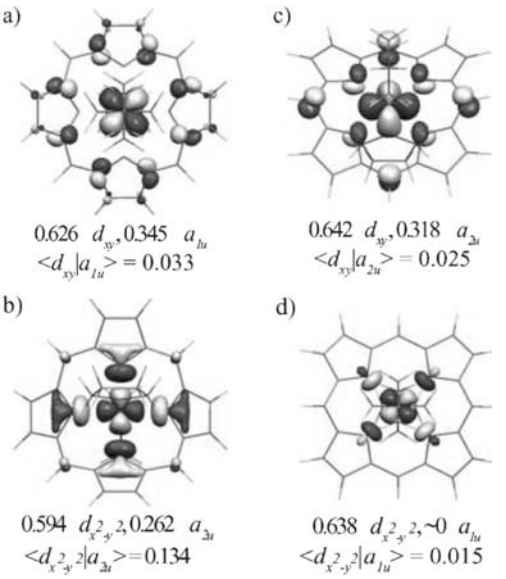

Figure 4. Molecular orbitals based on spin-restricted calculations which depict the bonding interactions between **(a)** d_{xy} and $1a_{1u}(\pi)$ and **(b)** $d_x2_{-y}2$ and $3a_{2u}(\pi)$ for saddled porphyrins, and the bonding interactions between **(c)** d_{xy} and $3a_{2u}(\pi)$ and **(d)** $d_{x^2-y^2}$ and $1a_{1u}(\pi)$ for ruffled porphyrins. The corresponding orbital contributions and the effective orbital overlap in space are also shown under each molecular orbital. Reprinted from Cheng, R.-J.; Wang, Y.-K.; Chen, P.-Y.; Han, Y.-P.; Chang, C.-C. *Chem. Commun.* **2005**, 1312–1314, with permission of the Royal Society of Chemistry.

A ruffled conformation of a metalloporphyrin also allows an additional nontraditional interaction between a metal d-orbital and a porphyrin π orbital: In a ruffled conformation the $d_{x^2-y^2}$ orbital can interact with the porphyrin $1a_{1u}(\pi)$ orbital; these interactions are shown in Figure 4d. As a result of such a ruffled conformation, a metalloporphyrin with an unpaired electron in the d_{xy} orbital would be expected to have spin delocalization to the porphyrin $3a_{2u}(\pi)$ orbital, while one with an unpaired electron in the $d_{x^2-y^2}$ orbital would be expected to have spin delocalization to the porphyrin $1a_{1u}(\pi)$ orbital. Conversely, if a metalloporphyrin is highly saddled, the interactions of these two orbitals with the two aforementioned π orbitals is reversed; in this case, as shown in Figure 4a, when the porphyrin is saddled, the d_{xy} orbital has proper symmetry to interact with the $1a_{1u}(\pi)$ orbital, and delocalization from d_{xy} to $1a_{1u}$ is allowed, while as shown in Figure 4b, the $d_{x^2-y^2}$ orbital has proper symmetry to interact with the $3a_{2u}(\pi)$ orbital and delocalization from $d_{x^2-y^2}$ to $3a_{2u}(\pi)$ is allowed. The d_{xy}-$1a_{1u}(\pi)$ interaction is clearly important in the case of the bis-*t*-BuNC complex of $OETPPFe^{III}$ discussed in Section IV.A.8.c.

If the unpaired electron is mainly localized in a porphyrin π-symmetry orbital, rather than in a metal d-orbital, as would be the case for PFe^{II} π-cation radicals,

then the system is described as a metalloporphyrin π-cation or -anion radical. The electron configuration of π-cation radicals, $[M^{II}(P^{-\bullet})]^+$, is typically either $(1a_{1u})^1$ or $(3a_{2u})^1$, since one or the other of these orbitals is typically the HOMO of the porphyrin π system. In the case of the $(3a_{2u})^1$ π-cation radical, confusion can arise as to whether the electron is mainly porphyrin-based or mainly metal-based with a half-filled d_{xy} orbital. (Simple Hückel MO theory, assuming a flat porphyrin ring, is not able to show this interaction.) Both NMR and EPR spectroscopy are useful for differentiating between these two, for the NMR spectra of porphyrin-based radicals usually have very large spin density at the *meso*-carbons, and EPR spectra of porphyrin-based radicals are extremely sharp (unless the metal has unpaired d-electrons, as for $[Fe^{IV}{=}O\ P^{-\bullet}]$ Compound I centers discussed in Section IV.A.13), with both $g_{\|}$ and $g_{\perp}$ being slightly greater than 2.0 and ranging from 2.001 to 2.003, while for metal-based low-spin d^5 configuration $(d_{xz},d_{yz})^4(d_{xy})^1$ ground state systems $g_{\|}$ is less than 2.0 while $g_{\perp}$ is greater than about 2.2 in most cases,[131] as discussed further in Section IV.A.8.c (see, however, Ref. 132). π-Anion radicals typically have the electron configuration $(4e)^1$, and dianions $(4e)^2$, and again have g-values ranging from 2.001 to 2.003.

In the case of chlorins (dihydroporphyrins), Structure **4**, the chemical reduction of one pyrrole ring reduces the symmetry of the molecule, and thus removes the degeneracy of the $3e(\pi)$ and $4e(\pi^*)$ orbitals. Hückel molecular orbital calculations[118,133] predict the electron density pattern and nodal properties shown in Figure 5 for the corresponding chlorin π orbitals. An important feature of these modified orbitals is the fact that the former $1a_{1u}(\pi)$ orbital, in the chlorin case of Figure 5 denoted A_{-1}, has the proper symmetry at the nitrogens of rings II and IV to allow overlap with a d_π orbital, d_{xz} in the coordinate system shown.[133] This has important consequences for the pattern of spin delocalization observed for both high- and low-spin iron(III) complexes of chlorins, discussed in Sections IV.A.6.c and IV.A.8.i, respectively. Similar modifications of the electron density distribution and symmetry properties of the A,B-tetrahydroporphyrins, better known as isobacteriochlorins, Structure **5**, and dioxoisobacteriochlorins related to heme d_1,[22] Structure **6**, are also expected. The electron density pattern and nodal properties of the corresponding orbitals of isobacteriochlorins calculated with the program MPorphW,[118] are shown in Figure 6. In each case of lower than four-fold symmetry, the orbitals are labeled A (antisymmetric with respect to the two-fold axis) or S (symmetric with respect to the twofold axis), and are numbered 1, −1 and −2, depending on whether they are empty, highest filled or next-highest filled, respectively. The d_π-$e(\pi)$ type orbitals are labeled $d–A_{-2}$ and $d–S_{-2}$ in each MO diagram. However, the electron density pattern for the bacteriochlorins, which have *trans*-saturated pyrrole rings, and their relatives, the *trans*-dioxobacteriochlorins, both of which have a 2-fold rotation axis

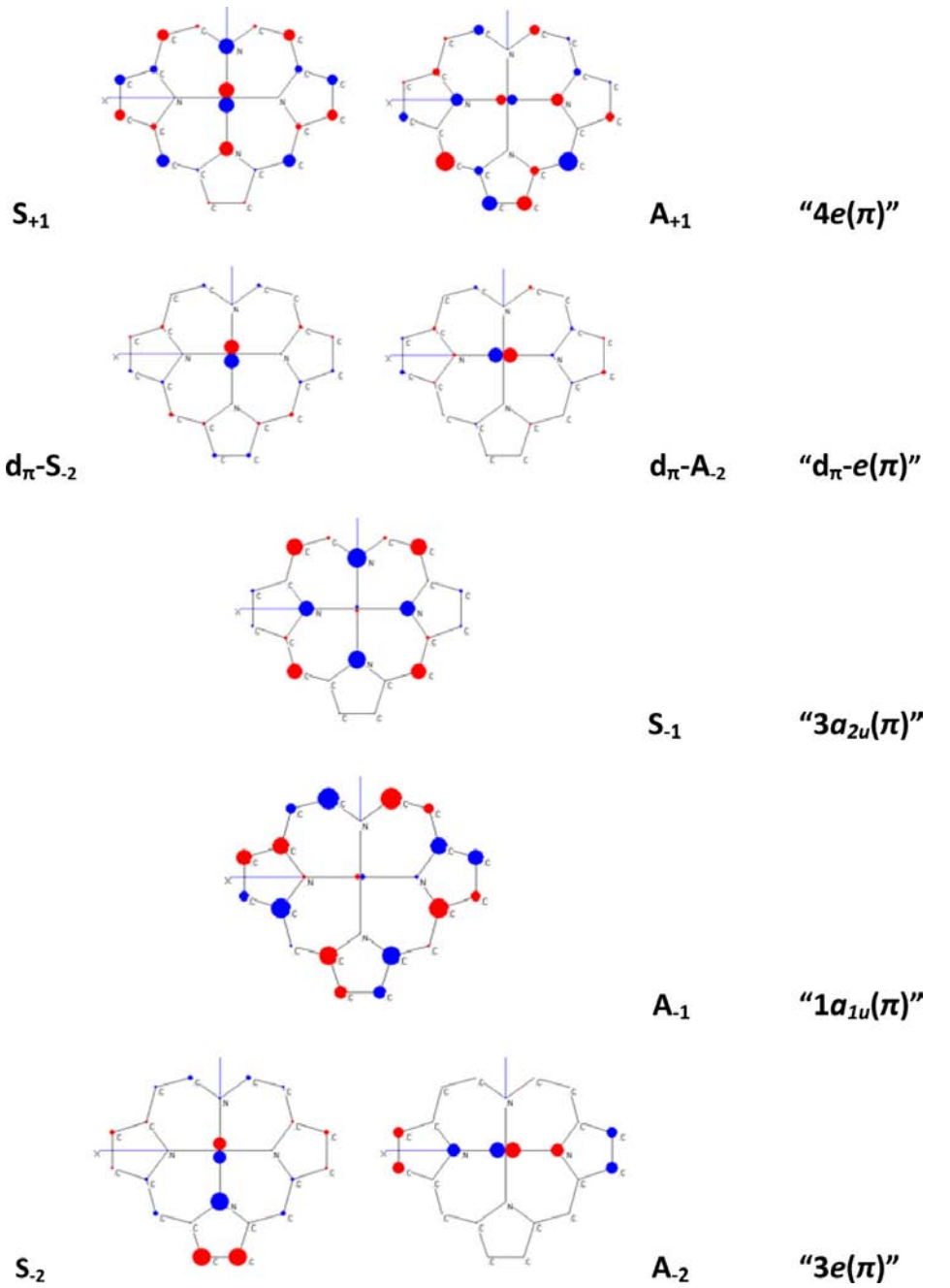

Figure 5. Frontier molecular orbitals of the chlorin ring, including the mainly metal d_π–$e(\pi)$ combination orbitals that are usually the HOMOs and/or SOMOs of a metalloporphyrin. The relative sizes of the circles at each atom represent the relative orbital electron density coefficients, C_i^2, which should be closely related to spin density coefficients, ρ_C. Calculated using the program MPorphW.[118]

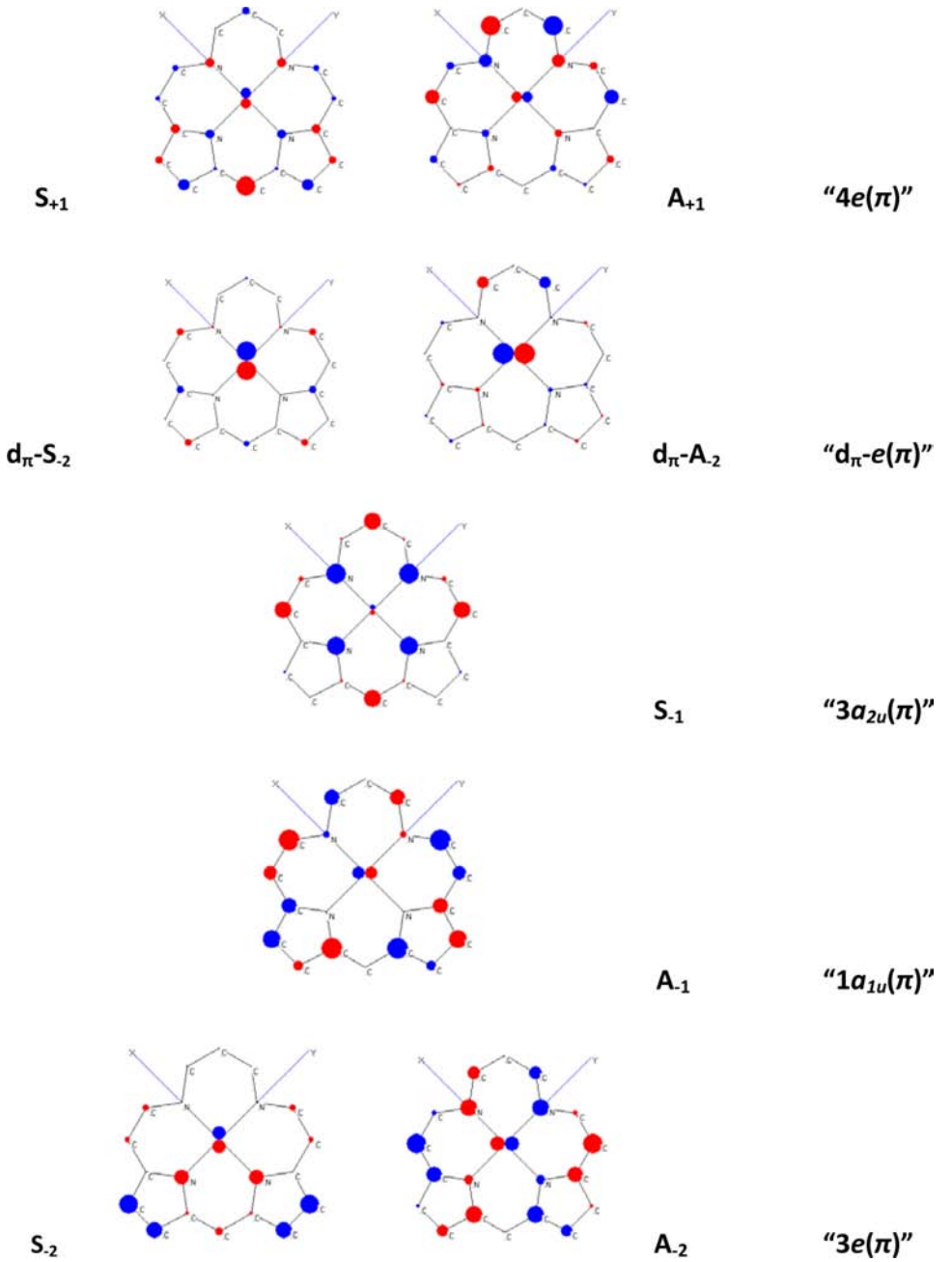

Figure 6. Frontier molecular orbitals of the isobacteriochlorin ring, including the mainly metal d_π–e(π) combination orbitals that are usually the HOMOs and/or SOMOs of a metalloporphyrin. The relative sizes of the circles at each atom represent the relative orbital electron density coefficients, C_i^2, which should be closely related to spin density coefficients, ρ_C. Calculated using the program MPorphW.[118]

perpendicular to the plane of the macrocycle, have higher symmetry, and do not show the mixing of the $1a_{1u}(\pi)$ and d_{xz} orbital.

The corrole ring system (Structure **7**) is closely related to the porphyrins, and they also have frontier orbitals corresponding to those of the above-mentioned ring systems. These orbitals of the corrole ring, calculated with the program MPorphW,[118] are shown in Figure 7, where it is interesting to note that the energies of the S_{-1} and d-S_{-2} and d-A_{-2} orbitals are inverted. Perhaps this helps to explain the ease of removal of one π electron from the corrole ring, which will be discussed in Section IV for the Fe, Co, Ni, Mn and Cu corroles.

3. *The Effect of Axial Ligand Plane Orientation on the Combined Contact and Pseudocontact Shifts of Low-Spin Ferriheme Proteins and Synthetic Hemins with Hindered Axial Ligand Rotation*

Low-spin ferriheme complexes with the electron configuration $(d_{xy})^2(d_{xz},d_{yz})^3$, or any other system which has one or two unpaired electrons in the d_π orbitals, and also has one or two axial ligands with a π-symmetry lone pair of electrons that can act as a π-donor to the metal (in addition to the σ-symmetry lone pair), may be able to control the electron density distribution at the heme β- and *meso*-carbons. This should be evident from the two sets of molecular orbitals for the porphyrin ring shown in Figures 2A and B, where the p-orbitals in the center of Figure 2A are shown with their nodal planes along the N–Fe–N axes of the porphyrin at 90° angles to each other, while the p-orbitals in the center of Figure 2B are shown with their nodal planes along the C_{meso}–C_{meso} positions, also at 90° angles to each other for the two orbitals. These p-orbitals in fact represent the π-symmetry lone pair of electrons provided by a ligand, and the implication is that a π-donor ligand can determine the orientation of the nodal plane of the half-filled metal d_π orbital, and consequently, the particular $3e(\pi)$ orbital of the porphyrin used for porphyrin $\rightarrow$ metal π donation and hence spin delocalization to the porphyrin ring. As also stated in the caption of Figure 2, nodes could be placed at any arbitrary angle in between these two, as long as the nodes of the two orbitals are at right angles to each other. The actual positions of the nodes will depend on the orientation of planar axial ligand(s).[8] The relative sizes of the circles at each atom represent the relative orbital electron density coefficients, C_i^2, which should be closely related to the relative spin density coefficients, ρ_C, and thus the contact shift at each atom, discussed in Section II.A.1, Eqs. 3–6. For a system having the *x*- and *y*-axes of the heme oriented as shown in Figure 8, the dependence of the contact shift on the orientation of the nodal plane of the axial ligand should change as shown in Figure 9.

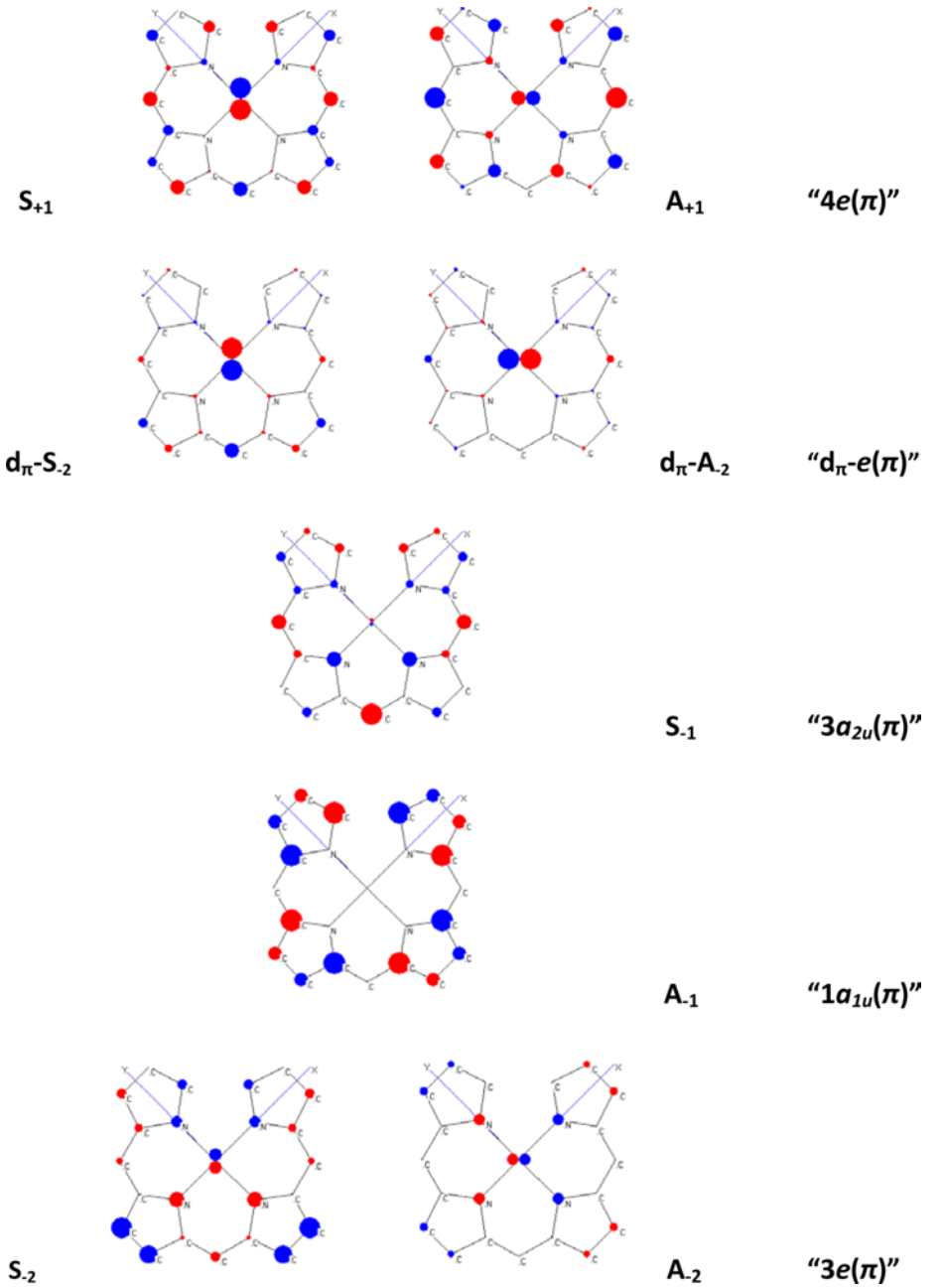

Figure 7. Frontier molecular orbitals of the corrole ring, including the mainly metal d_π–e(π) combination orbitals that are usually the HOMOs and/or SOMOs of a metalloporphyrin. The relative sizes of the circles at each atom represent the relative orbital electron density coefficients, C_i^2, which should be closely related to spin density coefficients, ρ_C. Note that although there is no line connecting the directly-bonded pyrrole rings, the calculations were done assuming a bond. Calculated using the program MPorphW.[118]

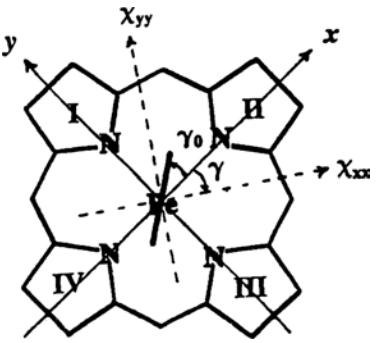

Figure 8. Heme ring with definition of axes (right-hand coordinate system) and axial ligand rotation angle, γ_0, and position of the magnetic axis χ_{xx} if counterrotation by an angle γ takes place. If the axial ligand plane is aligned along the *x* axis of the heme group, as shown, then the expectation is that the minimum magnetic susceptibility tensor component, χ_{xx}, will be aligned coincident with the axial ligand plane, along the molecular *x* axis. As the ligand rotates counterclockwise, χ_{xx} rotates in a clockwise direction in the majority of cases. Reprinted from Shokhirev, N. V.; Walker, F. A. *J. Am. Chem. Soc.* **1998**, *120,* 981–990, with permission from the American Chemical Society.

It has also been shown that as the angle of the nodal plane of the axial ligand rotates, the angle of the χ_{xx} and χ_{yy} tensors (as well as g_{xx} and g_{yy}) should change in the opposite direction, as shown in Figure 8, according to the principle of the counter-rotation of the g(χ)-tensor.[134] In ESEEM (Electron Spin Echo Envelope Modulation) spectroscopic studies of certain model ferriheme complexes it became clear that while the orientation of g_{zz} is the same for all complexes studied (pyrazole,[135] 3-aminopyrazole,[136] 4-dimethylaminopyridine[137] and imidazole[137] complexes of model hemes, and the histamine complex of the heme protein nitrophorin 1,[138] as well as the imidazole complex of iron(III) octaethylchlorin[139]), the orientations of g_{xx} and g_{yy} differ in a manner that suggests that as the axial ligands rotate counterclockwise by an angle γ_0 from being eclipsed with the porphyrinate nitrogens, g_{xx} and g_{yy} rotate clockwise by an angle $\gamma = -\gamma_0$, as diagrammed in Figure 8. It was also possible to demonstrate theoretically that this should be the case for most ferriheme systems.[140] Hence, when the (parallel) axial ligands lie over the porphyrin nitrogens, their nodal planes are aligned along g_{xx}, while when they lie over the porphyrin *meso* positions, their nodal planes are aligned along g_{yy}. This finding has considerable importance for NMR studies of ferriheme proteins, and counter-rotation of the g-tensor with rotation of axial ligands away from the porphyrin nitrogen axes can now be expected to occur in almost all cases.[7,137] Therefore, the dependence of the pseudocontact shift on the orientation of the nodal plane of the axial ligand should change as shown in Figure 10, where the magnetic anisotropy has been calculated from the g-values, Eq. 9. As can be

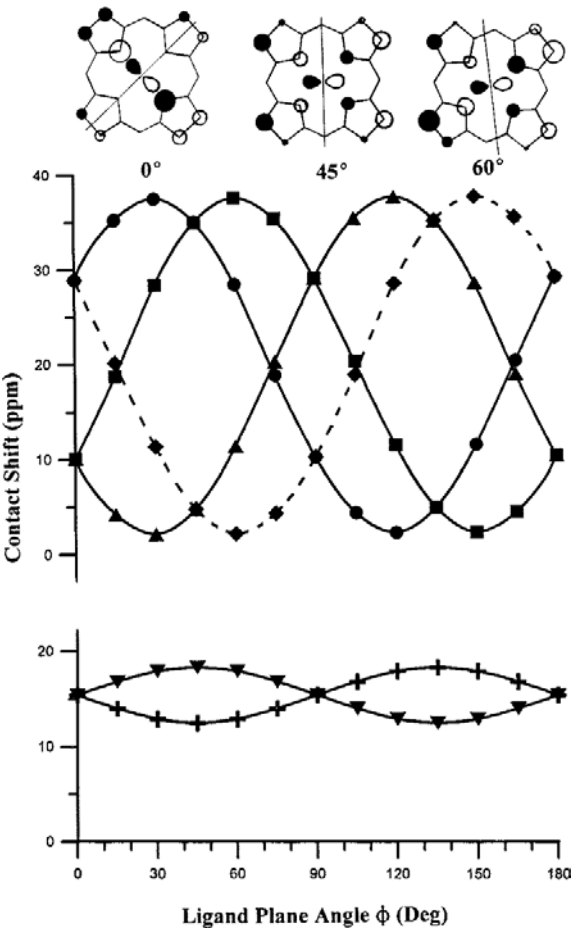

Figure 9. Plot of the dependence of the contact shifts of a symmetrical hemin on the orientation of a planar axial ligand (or two parallel axial ligands). Pictures of the spin density distribution for key angles (0°, 45°, 60°) are shown in the *inserts*. The plot is general, as if for octamethylhemin; in reality, the two α-protons of the 6,7 positions of naturally occurring hemins will have different contact shifts, because of the particular dihedral angle of each of the α-CH_2 protons of the propionates, and the 2,4-positions of protohemin will have different contact shifts, because of the presence of vinyl groups. The 2,6-positions of the symmetrical hemin are represented by a *dashed line*. • β-alkyl positions 1 and 5; ◇ β-alkyl positions 2 and 6; ▲ β-alkyl positions 3 and 7; ■ β-alkyl positions 4 and 8; ▼ α and γ *meso*-H; + β and δ *meso*-H. Reprinted from Shokhirev, N. V.; Walker, F. A. *J. Biol. Inorg. Chem.* **1998**, *3*, 581–594, with permission from Elsevier Publishing Company.

seen, for the imidazole-coordinated hemes whose contact and pseudocontact shift data were used in these calculations,[8] the contact shift is by for the most important at the β-pyrrole positions, while the pseudocontact shift is most important at the *meso* positions.

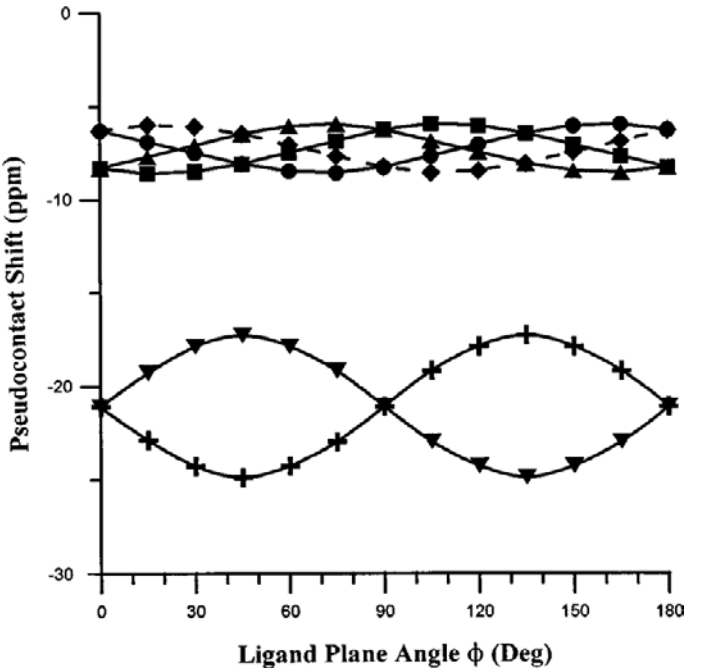

Figure 10. Plot of the dependence of the dipolar (pseudocontact) shift on the orientation of a planar axial ligand (or two parallel axial ligands). Again, the plot is general, as if for octamethylhemin. Counter-rotation of the in-plane **g**-tensor with rotation of the axial ligands was assumed.[88] • β-alkyl positions 1 and 5; ♦ β-alkyl positions 2 and 6; ▲ β-alkyl positions 3 and 7; ▪ β-alkyl positions 4 and 8; ▼ α and γ *meso*-H; + β and γ *meso*-H. The 2,6 positions are represented by a *dashed line*. Reprinted from Shokhirev, N. V.; Walker, F. A. *J. Biol. Inorg. Chem.* **1998**, *3*, 581–594, with permission from Elsevier Publishing Company.

The combination of the contact and pseudocontact contributions to the paramagnetic shift as a function of the angle of the axial ligand, γ, Figure 8 is as shown in Figure 11, when allowance is made for the substituent effect of the vinyl groups (which shifts the 1-Me and 3-Me to somewhat less positive chemical shifts than otherwise expected).[8] This angular dependence has been found to apply to a large number of ferriheme proteins,[8,141–150] as well as to the mono-Mo^{IV}=O-substituted derivative of $[TPPFe(NMeIm)_2]^+$ (Figure 14) and a number of other model heme systems. A program is available on the internet that calculates the relative heme methyl shifts.[151] Other similar methods, which emphasize only the contact interaction, have also been developed,[152–154] but have been used only in equation form. A variation of this angle plot, for high-spin iron(III) porphyrins,[141] shown in Figure 60 below, which is 90° shifted from that shown in Figure 11, and is also available.[151] The reasons for the 90° shift are discussed in Section IV.A.10.a(i).

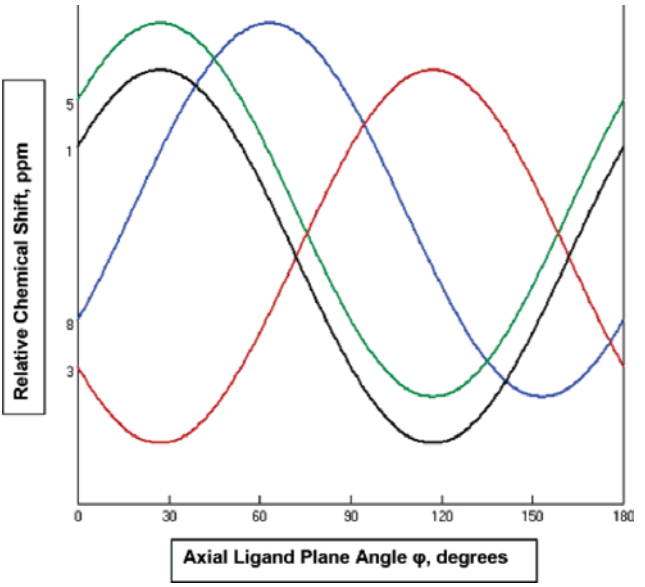

Figure 11. Relative chemical shifts of the heme methyls vs. ligand plane angle or effective ligand plane angle if two planar ligands are present, as calculated for low-spin ferrihemes. Reprinted from Shokhireva, T. Kh.; Smith, K. M.; Berry, R. E.; Shokhirev, N. V.; Balfour, C.; Zhang, H.; Walker, F. A. *Inorg. Chem.* **2007**, *46*, 170–178, with permission from the American Chemical Society.

4. *Mechanisms of Spin Delocalization through Chemical Bonds, and Strategies for Separation of Contact and Pseudocontact Shifts*

In Section II.A.1, it was mentioned that the McConnell Eqs. 5 and 6 and the opposite sign of Q for spin density in π and σ carbon orbitals make it possible for spin delocalization through the σ and π systems to be differentiated. Thus, all paramagnetic shifts of protons that are connected to the unpaired electron only by σ bonds should be in the same direction, whether the proton is directly attached to a conjugated π system or is separated by one or more saturated C–C bonds. On the other hand, if π delocalization mechanisms are involved, the same theory predicts that the sign of the contact shift of the proton bound to the carbon atom that is part of the π system will be opposite to that of a proton that is separated by a saturated C–C bond (Section I.A.1). Thus, π spin delocalization is characterized by a reversal in the sign of the paramagnetic shift when a proton that is directly attached to a carbon which is part of a π system is replaced by an aliphatic group such as $–CH_3$ or $–CH_2–$. Therefore, by judicious choice of model hemes, such as those shown in Structure **2**, with $R_2 – R_{18}$ = H and $R_5 – R_{20}$ = phenyl or alkyl, as contrasted to Structure **3**, with $R_2 – R_{18}$ = alkyl and $R_5 – R_{20}$ = H, it has been possible to assign the mechanism of spin delocalization to the β-pyrrole and *meso* positions

of the porphyrin ring for a number of oxidation and spin states of a number of metalloporphyrins.[2,4]

Some generalizations can be made as to the relative importance of the contact and pseudocontact contributions by analysis of the pattern of paramagnetic shifts for a newly-discovered spin or oxidation state of a metalloporphyrin. For example, if the sign of the paramagnetic shift reverses when protons directly bound to the aromatic carbons of the macrocycle or the axial ligands are replaced by methyl or other alkyl groups, then it may be assumed that the π contact contribution dominates the paramagnetic shift at that position. If so, then the nodal properties of the porphyrin or axial ligand π orbital involved may allow one to evaluate the residual pseudocontact contribution to the paramagnetic shift. For example, in low-spin iron(III) porphyrins having a $(d_{xy})^2(d_{xz},d_{yz})^3$ ground state, the paramagnetic shifts at the β-pyrrole positions (Structure **3**, $R_2 - R_{18}$) reverse in sign when –H is replaced by $-CH_2CH_3$, while those at the *meso* positions (Structure **2**, $R_5 - R_{20}$) are small and shifted to lower shielding for both –H and $-CH_2R$. Thus, it was concluded that the contact contribution results from π-symmetry spin delocalization which involves the $3e(\pi)$ orbitals of the porphyrin, since these orbitals have nodes at the *meso* ($R_5 - R_{20}$) positions, while the $4e(\pi^*)$ orbitals have much larger coefficients for the wave functions of the *meso* carbons than for those of the β-pyrrole carbons,[108] as shown in Figure 2. Thus, any observed paramagnetic shifts of *meso* substituents were assumed to be caused by the pseudocontact contribution. In tetraphenylporphyrin complexes such as $[(TPP)Fe(NMeIm)_2]^+$, the phenyl *ortho*-, *meta*- and *para*-H paramagnetic shifts were found to be directly proportional to the calculated geometric factors for those protons. Thus, scaling the *ortho*- or *meta*-H paramagnetic shifts by the ratio of the axial geometric factors for those protons to the axial geometric factor for the β-pyrrole protons allowed estimation of the axial pseudocontact contribution to the paramagnetic shift of the β-pyrrole protons.[2,4] The same procedure was found to be less successfully applicable to other axial ligand complexes of $(TPP)Fe^{III}$, as will be discussed in Section IV.A.8, because alternation in the sign of the *meso*-phenyl-H paramagnetic shifts (*o*-, *p*-H of opposite sign to *m*-H) indicated the existence of significant π contact contribution to the paramagnetic shifts of those protons, in the order imidazoles < cyanide < pyridines.[2,4] Such alternation in sign (for low-spin iron(III) porphyrins) is now usually taken as an indication of the $(d_{xz},d_{yz})^4(d_{xy})^1$ ground state, with significant delocalization that involve the $3a_{2u}(\pi)$ orbital, as is the case for $[(TPP)Fe(t\text{-}BuNC)_2]^+$.[155]

Whenever the $d_{x^2-y^2}$ orbital is half occupied it has been found that there is a large σ contact contribution to the paramagnetic shifts of the β-pyrrole protons; this provides a major difference in the pattern of spin delocalization of high-spin iron(III) (d^5) and manganese(III) (d^4) porphyrins.[2,4] Such a σ contact contribution

can be readily recognized by its attenuation as aliphatic carbons are inserted between the porphyrin ring and the protons. The presence of large σ spin density at the pyrrole positions does not rule out the possibility of large π spin density at the *meso* positions, if the d_π orbitals of a 6-coordinate high-spin metal center contain at least one unpaired electron, or if the metal is 5-coordinate and located out of the mean plane of the porphyrin, in which case an unpaired electron in the d_{z^2} orbital can directly overlap with the porphyrin $3a_{2u}(\pi)$ orbital to allow large π spin delocalization to the *meso* carbons (see Section IV.A.4.a(i));[156] high-spin iron(II) and -(III) and nickel(II) porphyrins exhibit such a pattern of contact shifts, plus a much smaller pseudocontact shift term in the case of the iron complexes that is readily separable from the contact contribution because it varies according to $1/T^2$,[2,4] Eq. 10. It should be noted that this d_{z^2}–$3a_{2u}(\pi)$ interaction for 5-coordinate high-spin d^6 and d^5 iron porphyrins now replaces the earlier explanation of π spin density at the *meso*-carbons of 5-coordinate metalloporphyrins with a half-filled d_{z^2} orbital, that of mixing of the filled $3e(\pi)$ orbitals with the empty $4e(\pi^*)$ orbitals, so that there is currently no need to invoke the participation of the $4e(\pi^*)$ orbitals in spin delocalization in these systems.[156] Comparison of 5- and 6-coordinate high-spin iron(III) porphyrins and related macrocycles indicates a large σ spin density at the *meso* as well as β-pyrrole positions of the 6-coordinate complexes, but σ spin density only at the β-pyrrole, but π spin density at the *meso* positions for 5-coordinate complexes, as discussed in Section IV.A.6.b,c.

Cases for which the pseudocontact contribution dominates the paramagnetic shifts are readily recognized by the direct proportionality of the paramagnetic shifts to the geometric factors of the protons of interest. Several examples of this situation are the paramagnetic shifts of the phenyl protons of $[(TPP)Fe(R\text{-}Im)_2]^+$ complexes, as discussed in Section IV.A.8.b, the π-cation radicals of iron(III) porphyrins, as discussed in Section IV.A.11, and of cobalt(II) porphyrins, as discussed in Section IV.C.1.

D. Methods of Assignment of the ^{1}H NMR Spectra of Paramagnetic Metalloporphyrins

1. *Substitution of H by CH_3 or Other Substituent*

The original assignment of pyrrole-H, *meso*-H, *o*-, *m*-, and *p*-phenyl-H of symmetrically-substituted model hemes was made by this method,[2,4] and it needs no further elaboration. Balch and Renner[157] used it to assign the phenyl resonances of the ferryl porphyrin complexes, $[(TPP)Fe^{IV}{=}O]$, discussed in Section IV.A.13, and the author's group used it for assigning and interpreting

the nature of the β-pyrrole and *meso* resonance shifts of iron(III) corrolate π-cation radicals.[114,158,159]

2. *Deuteration of Specific Groups*

Methods have been developed by Smith, Goff, Dolphin, Strauss, and others, for specifically deuterating certain positions of both naturally-occurring and synthetic porphyrins or metalloporphyrins, as summarized in detail previously.[3] Although ^{2}H NMR investigation of deuterium-labeled diacetyldeuterohemin incorporated into sperm whale myoglobin was reported early,[160] Goff and coworkers[161–164] and, more recently, Balch and coworkers,[165] have repeatedly demonstrated the utility of ^{2}H NMR spectroscopy for assignment, and indeed, detection of resonances in model hemes. As pointed out, the linewidths of ^{2}H resonances, in Hz, could be narrowed by as much as $(\gamma_D/\gamma_H)^2$; that is, to 1/42 the line widths of the ^{1}H signals,[161] although experimentally, the pyrrole-H and pyrrole-D linewidths of [(TPP)FeCl] differ by only a factor of 10 (280 Hz and 28 Hz, respectively). The *o*-D of [(d_{20}-TPP)FeCl] are much sharper than the *o*-H of [(TPP)FeCl], and the *m*-D occur as a singlet, due to averaging of the two *m*-D environments of this 5-coordinate complex on the shorter time scale (lower frequency) of deuterium NMR.[161] Godziela and Goff utilized the increased sharpness of ^{2}H resonances to detect the pyrrole-D resonance of [(pyrrole-d_8-TPP)Cu^{II}] (1150 Hz wide at half-height) and *meso*-D resonance of [(d^4-OEP)Cu^{II}] which are totally undetectable in the protonated analogs,[164] and Li and Goff utilized this increased sharpness of ^{2}H resonances of the $-CD_3$ and $-C_2D_5$ groups, and wider spectral bandwidth (in terms of ppm available for ^{2}H to detect the α-D of iron(III) alkyl complexes,[163] which were previously undetected.[166] Karlin and coworkers have used pyrrole-deuterated TPP derivatives to good advantage to assign the pyrrole resonances of their cytochrome c oxidase models, as discussed in Section IV.A.4.a(iii). Chromium(III) porphyrins, whose ^{1}H resonances are very poorly resolved,[94] show well-resolved ^{2}H resonances for the pyrrole-D (−16.7 ppm at 24 °C) and phenoxide-D of [(TPP)Cr(OPh)],[165] as shown in Figure 12.

Specifically methyl-deuterated hemins were employed by La Mar, Smith and coworkers[167–169] to assign the methyl resonances of model hemes and heme proteins, and the author's group have used them to assign the heme methyl resonances of nitrophorins 1 and 4.[143,170] Strauss and coworkers[171] and Balch *et al.*[165] have used both ^{1}H and ^{2}H NMR spectroscopy in a complementary fashion to show that the signals that disappear from the ^{1}H spectrum upon deuteration are the only ones that appear in the ^{2}H spectrum. In many cases it is now possible to use 2D ^{1}H NMR techniques to carry out these assignments, if T_1 and T_2 relaxation times are long enough, as discussed in Section II.D.5.

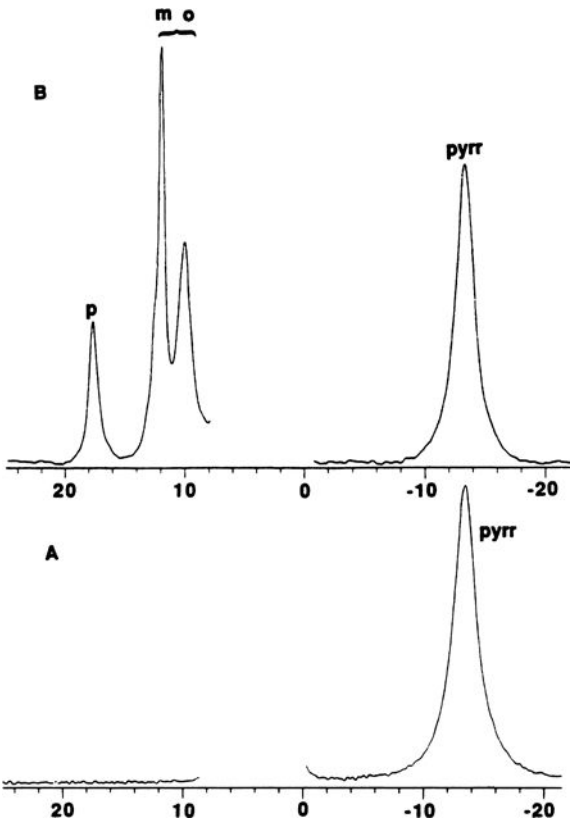

Figure 12. 46.0 MHz ^{2}H NMR spectra of (A) [(d_8-TPP)Cr^{III}(OPh)(THF)] and (B) [(d_8-TPP)Cr^{III}(OPh-d_5)(THF)] in THF solution at 24 °C, with chemical shift scale in ppm. Resonance assignments: pyrr, pyrrole deuterons; *o, m, p = ortho, meta, para* deuterons of the phenoxy ligand. Reprinted from Balch, A. L.; Latos-Grażyński, L.; Noll, B. C.; Olmstead, M. M.; Zovinka, E. P. *Inorg. Chem.* **1992**, *31*, 1148–1151, with permission from the American Chemical Society.

3. *2D ^{13}C Natural Abundance HMQC Spectra and Specific or Complete ^{13}C Labeling of Protohemin for the Assignment of Heme Resonances in Proteins*

A method that can be used by all researchers who have access to an inverse heteronuclear broadband or ^{13}C (^{1}H detect) probe is the $^{1}H\{^{13}C\}$-HMQC experiment. This allows correlation of the ^{13}C and ^{1}H chemical shifts of heme substituents and is especially useful for paramagnetic heme proteins, where some heme resonances are invariably buried under the protein resonance envelope,[141–146,172–179] but the author's group has also used it to investigate the chloroiron(III) corrolate π-radicals, [$Fe^{III}Cl(Corr)^{2-\bullet}$],[159] which are neutrally-charged species, as discussed

further in Section IV.A.11.e. Turner has used this method to aid the assignment of heme proteins since 1995,[173–179] and it is particularly useful for the bis-histidine bound tetra-heme cytochromes c_3.[173,179] We have also found these spectra to be very helpful in identifying and confirming the ^{1}H chemical shifts of heme and nearby protein substituents whose resonances may or may not be resolved outside the protein resonance envelope. By using the information obtained from the HMQC spectra the author's group has been able to assign most, if not all, of the heme substituent resonances of the axial ligand complexes of the nitrophorins,[141–145] and an example spectrum is shown in Figure 64. These heme resonances are fairly easy to assign because of their unique ^{1}H,^{13}C shifts. Model heme complexes have also been assigned with the aid of ^{1}H{^{13}C}-HMQC spectra,[228] as shown below in Figure 15. The unique shifts are a result of a combination of the contact, pseudocontact and diamagnetic contributions to the chemical shifts of both nuclei,[172] which shift these cross peaks well outside the normal ranges observed for the two nuclei in diamagnetic compounds, and thus make them easy to recognize and assign.

To observe these ^{1}H,^{13}C cross peaks in the HMQC spectrum of a low-spin Fe(III) heme protein requires at least a 1 mM concentration (2 mM is preferable) of ferriheme protein at ^{13}C natural abundance, and requires an approximate 24-hour experiment time. Any modern NMR spectrometer equipped with an inverse (^{1}H observe) ^{13}C or broadband probe can be used, and 500 MHz as the ^{1}H Larmor frequency is certainly sufficient for all systems that have been investigated thus far. All of the ^{1}H{^{13}C}-HMQC spectra presented in the author's group papers have been recorded at 500 MHz. Since inverse ^{13}C or inverse broadband probes are common on modern spectrometers, the use of this experiment is strongly recommended to find the heme ^{1}H resonances which are obscured by the protein resonances, and to then look for these resonances in the WEFT-NOESY spectra of the proteins, to permit complete assignment of the heme resonances. Protein side chains that are close to the heme iron, especially the histidine ligand β-CH_2 and α-CH cross peaks, as well as methyl-, methylene- and aromatic-containing side chains of amino acids that are within ~4 Å of Fe also have unusual ^{1}H,^{13}C chemical shifts because of the pseudocontact interaction, and can then be followed in the NOESY spectra to assign the side chains of those amino acids.

Another method for assigning heme resonances that relies on correlations to the ^{13}C chemical shifts of the heme has been used by Rivera and coworkers to prepare specifically ^{13}C-labeled heme precursors, δ-aminolevulinic acid molecules labeled at one of the four carbons of that molecule.[180] The first committed precursor in the biosynthetic pathway to heme and other tetrapyrrole synthesis is δ-aminolevulinic acid (ALA), as shown in Figure 13.[181] Condensation of two molecules of ALA results in porphobilinogen (PBG), the building block of tetrapyrrole synthesis, Figure 13.[182] Subsequently, four molecules of PBG are initially condensed head-to-tail to form the hydroxymethyl bilane (HMB) intermediate.

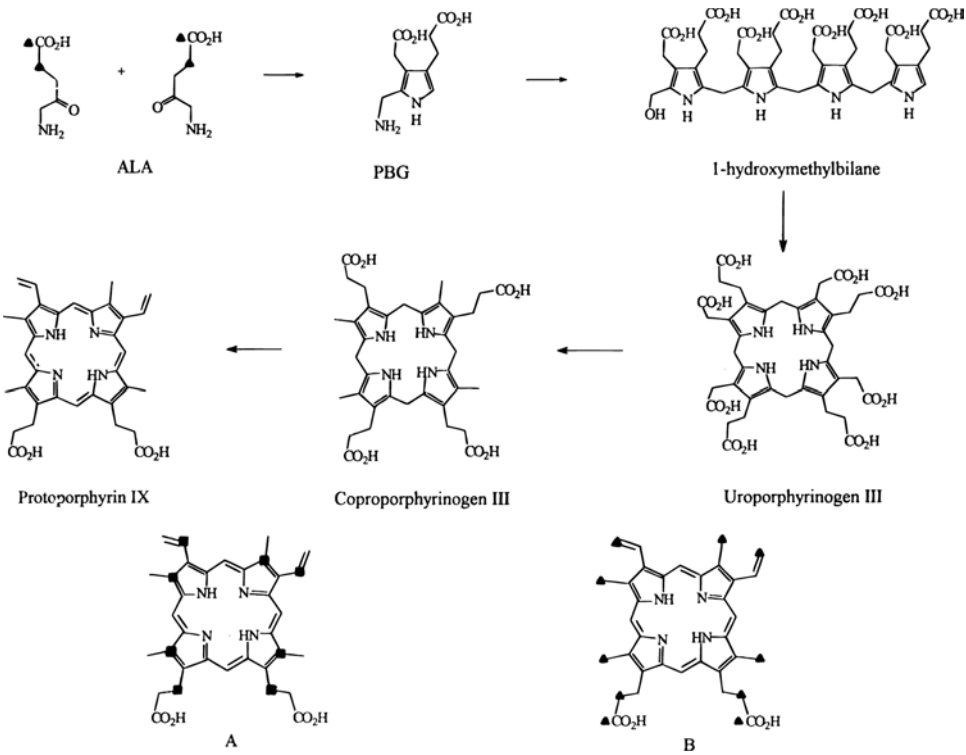

Figure 13. Schematic representation of the heme biosynthetic pathway in which δ-aminolevulinic acid is the first committed precursor. The introduction of iron into protoporphyrin IX, which is catalyzed by ferrochelatase, is not shown in the scheme. When [3-^{13}C]-δ-ALA is used as heme precursor, heme labeled at positions denoted by ■ in structure A is obtained. When [1,2-^{13}C]-δ-ALA is used as heme precursor, heme labeled at positions denoted by ▲ in structure B is obtained. Reprinted from Rodriguez-Marañón, M. J.; Qiu, F.; Stark, R. E.; White, S. P.; Zhang, X.; Foundling, S. I.; Rodriguez, V.; Schilling, III, C. L.; Bunce, R. A.; Rivera, M. *Biochemistry* **1996**, *35*, 16378–16390, with permission from the American Chemical Society.

This intermediate is cyclized to uroporphyrinogen III (uro'gen III) with rearrangement of ring D, as shown in Figure 13. The next step on the route to heme is the decarboxylation of the four acetate groups in uro'gen III by a single enzyme, uroporphyrinogen decarboxylase, to produce coproporphyrinogen III (copro'gen III, Figure 13). This step is followed by oxidative decarboxylation of propionates in pyrrole rings A and B of copro'gen III to give protoporphyrinogen IX. These decarboxylations are again carried out by a single enzyme, copro'gen oxidase, and involve the removal of six hydrogen atoms, one from each of the *meso* positions and two from nitrogen atoms. The last step in the biosynthesis of heme is the insertion of Fe^{2+} into the macrocycle by the enzyme ferrochelatase, which is not included in Figure 13. The many details of porphyrin biosynthesis can be found in

the reviews cited here[181–184] and in references therein, which describe the careful and elegant work carried out in the course of approximately two decades that led to the elucidation of the biosynthesis of heme, chlorophylls and vitamin B_{12}. It has been found that the expression of the genes for several heme proteins in *E. coli* leads to the induction of heme synthesis, and that if the desired ^{13}C-labeled δ-aminolevulinic acid is provided in the bacterial growth medium, the heme will be labeled[180,185] at the positions shown in Figure 13 for 1,2-[186] as compared to 3-^{13}C-labeled ALA.[180] Usually it is necessary to use minimal media to insure that the bacteria will not synthesize their own (unlabeled) ALA.[185] Totally labeled ^{13}C-ALA is commercially available, and has been used to label all carbons of protohemin in proteins.[186] 3-^{13}C-labeled ALA is also commercially available (Cambridge Isotope Laboratories for both). Methods for synthesis of the ^{13}C labeled isomers of δ-aminolevulinic acid that are not available commercially have been developed,[187] and thus specifically ^{13}C-labeled hemes can be synthesized and used for NMR investigations. Specific ^{1}H/^{13}C/^{13}C experiments have been developed,[188,189] and used to completely assign the ^{13}C heme resonances of rat outer mitochondrial membrane (OM) cytochrome b_5.[190] It is also very useful for assigning particular heme resonances, as shown in a very readable article in *Inorganic Chemistry*,[191] where the *meso*-carbon resonances of high-spin wild-type sperm whale-Mb (known to be 6-coordinate with a water bound to the sixth position of iron(III)), and its H64V mutant (known to be a 5-coordinate complex), were used to illustrate how specifically ^{13}C-labeled hemins can be used to assign the *meso*-carbon chemical shifts, and thus the coordination number of the high-spin heme. This methodology was then used to determine that a recently-discovered ferriheme protein from *Shigella dysenteriae* (ShuT) is 5-coordinate.[191]

4. *Saturation Transfer NMR Experiments*

Wüthrich and coworkers used these methods in 1980 to assign the heme resonances of ferricytochrome b_5 which was in chemical exchange with ferrocytochrome b_5, the heme resonances of which had been assigned by NOE techniques.[192] However, for hemes and metalloporphyrins in general outside the proteins, it was earlier thought that electron exchange may be sufficiently rapid so that in many cases separate resonances from the reduced and oxidized metal states of the complexes are not observed.[193–196] We have not found this to be generally true for model hemes at proton frequencies of 300 MHz or higher for either electron exchange or ligand exchange. We have thus used saturation transfer to assign resonances of the high-spin complexes of both model hemes and heme proteins, for which the low-spin resonances have been assigned by mainly 2D NMR techniques.[115,141–146] In the case of other types of chemical exchange, for example,

ligand exchange[197,198] or ligand rotation,[90] saturation transfer provides an effective means of assigning proton resonances of groups that are interchanged by means of the chemical exchange process, and also of estimating the rates of the process (with a cautionary note about possible contributions from spin diffusion).[90]

The most common current presentation of saturation transfer spectra is as difference spectra, called by some STD spectra, where an off-resonance saturation control spectrum is subtracted from each of the on-resonance saturation transfer spectra to give a large negative-pointing peak for each high-spin resonance which is irradiated, and a small negative-pointing peak for the low-spin resonance to which it is linked by saturation transfer, as shown in Figure 36 for assignment of part of the resonances of trans-OECFeCl, and Figure 59 for assignment of the heme resonances of high-spin NP2.

5. *NOE Difference Spectroscopy*

La Mar and coworkers[19,199–203] have used this technique extensively to assign the resonances of the heme group in ferriheme proteins; it is much more easily applied to large molecules, such as proteins, than to small, such as model hemes, since the large size of the proteins insures that the NOE will be negative. On the other hand, for model hemes in liquids of low viscosity, the rotational correlation time, τ_c, is in the intermediate motion limit,[203] such that the predicted steady-state NOE enhancement, though negative at low temperatures (−70 °C or lower in $CDCl_3$ or CD_2Cl_2), is small. This was earlier thought to be the reason that steady-state NOEs were sometimes not observed for model hemes,[203] although Barbush and Dixon[204] showed that the dicyanoiron(III) complex of protohemin gave small NOEs (1% negative) in DMSO-d_6 at 30 °C. Thus, the more serious limitation is that paramagnetic relaxation undermines the NOE.[205] However, if paramagnetic relaxation is independent of motion, as has been found to be the case, then it is possible to recover the NOE by slowing down the rate of molecular reorientation for both low-spin iron(III)[206] and high-spin iron(III) complexes.[133] Few model hemes are soluble in highly viscous solvents other than ethylene glycol or supercooled DMSO, and this may limit the application of NOE difference spectroscopy to model hemes. However, we have found that in general, at room temperature in CD_2Cl_2 or $CDCl_3$, positive steady-state NOEs of metalloporphyrins can be readily detected by NOE difference spectroscopy,[115,207] which is more successful than NOESY experiments, which depend on transient NOEs. At temperatures of −70 °C and below, negative steady-state NOEs of metalloporphyrins of the size of metal TPPs in these same solvents can be readily detected by NOE difference spectroscopy.[115,159,204] The case of a Mo^V-appended (TPP)Fe^{III} bis-N-methylimidazole complex, where two NOEs were detected at −58 °C in CD_2Cl_2,[80] is discussed in

the next Section II.D.6, and shown in Figure 17b; however, this is very close to the temperature where the sign of the NOE changes from positive to negative, which makes the NOEs very weak.

6. *Two-Dimensional NMR Techniques*

In addition to the natural-abundance $^{1}H\{^{13}C\}$-HMQC experiment discussed earlier in Section II.D.3, both ^{1}H-^{1}H scalar couplings and through-space NOEs can be detected for paramagnetic complexes under favorable circumstances. In terms of scalar-coupled systems, COSY (homonuclear correlation spectroscopy),[203,208–214] TOCSY (Total Correlation SpectroscopY, the rotating frame analog of COSY), HETCOR (heteronuclear correlation spectroscopy),[215,216] HMQC (heteronuclear multiple quantum correlation)[141–145,159,172–179] and HMBC[217] (heteronuclear multiple bond correlation) spectra of paramagnetic iron porphyrins have been reported. The success of these experiments is strongly limited by the short T_2 relaxation times of most paramagnetic complexes. For bis-N-methylimidazole complexes of iron(III) tetraphenylporphyrins, typical T_2s of the pyrrole-H are 8–9 ms,[209] or shorter,[104] while for dicyano and monocyano, monoimidazole complexes of β-pyrrole substituted iron(III) porphyrins, T_2s are usually much longer (T_2s for the ring CH_3s of (cyano)(imidazole)protohemin IX are 36–40 ms, and those of the *meso*-H are 21–32 ms),[218] as discussed in Section II.B.2.b. Short T_2 relaxation times can lead to significant cancellation of the antiphase components when J is small, and may prevent detection of cross-peak intensity.[219] However, on the positive side, the fact that T_2s are short for paramagnetic complexes means that the experiments can be run much faster than for diamagnetic compounds, since it makes no sense to acquire data over more than about 1.5–2T_2. In fact, if the acquisition time in t_2 is much longer than 2 × (longest T_2), significant cross peak intensity is lost.[209]

Because of the need to keep the acquisition time, A_t, short, of necessity the digital resolution of 2D NMR experiments for paramagnetic compounds decreases, since $A_t = N/F$, where N is the total number of real data points in the t_2 dimension and F is the spectral bandwidth. Likewise, acquiring many blank data blocks in the t_1 dimension only adds to the total experiment time, so the number of t_1 blocks typically acquired for model hemes with very short T_2s may be 256, 128 or even 64, yielding even poorer digital resolution in the t_1 dimension. However, this is often not a problem because of the large dispersion of the signals of many paramagnetic complexes. The apparent digital resolution can be improved by zero-filling one or more times in either or both dimensions. DQF-COSY experiments often give better resolution than magnitude COSY experiments.[212] An example of a magnitude COSY spectrum, that of $[(OEOP)Fe^{III}(CN)_2]$,[220] is shown in Figure 14.

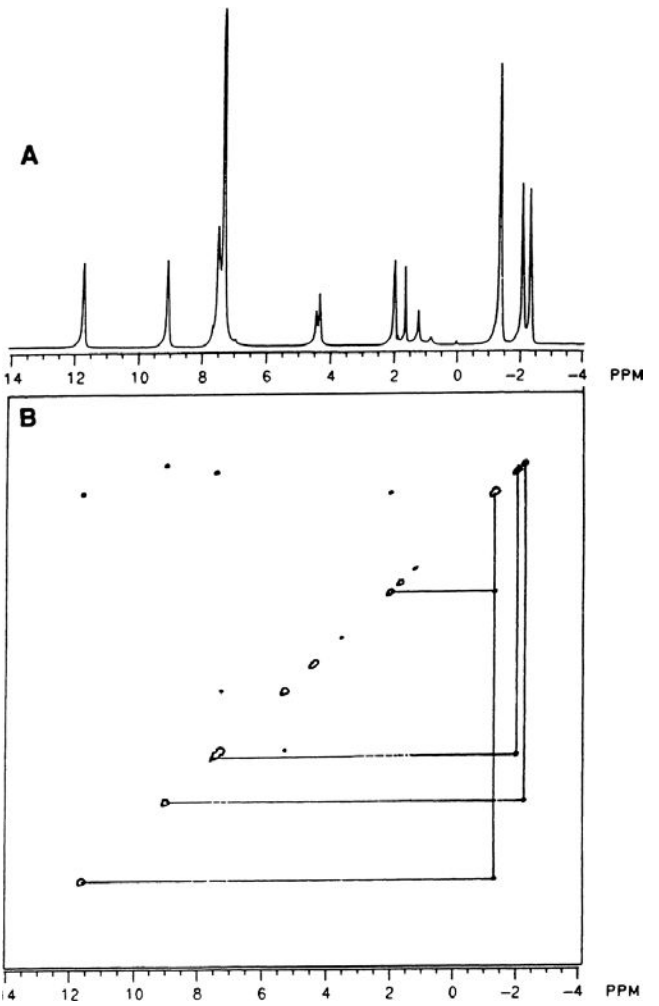

Figure 14. (A) ^{1}H NMR 1D and (B) M-COSY spectrum of $[(OEOP)Fe^{III}(CN)_2]$ in $CDCl_3$ at 20 °C. Reprinted from Gregson, A. K. *Inorg. Chem.* **1981**, *20,* 81–87, with permission from the American Chemical Society.

There have been reported fewer examples of heteronuclear correlation spectra of paramagnetic iron porphyrins, but the ^{13}C–^{1}H heteronuclear correlation (HETCOR) map of dicyanoprotohemin IX has been reported,[221] as has that of *Geleorhinus japonicus* (shark) metcyanomyoglobin.[215] Timkovich has reported the relayed $^{1}H\{^{13}C\}$ scalar correlation spectrum (HMQC) and the long-range ^{1}H–^{13}C scalar correlation (heteronuclear multiple-bond correlation, or HMBC) spectrum of dicyanoprotohemin IX,[216] Banci *et al*. have reported the $^{1}H\{^{13}C\}$ HMQC spectra of the bis-(imidazole) complex of protohemin IX, as well as metmyoglobin

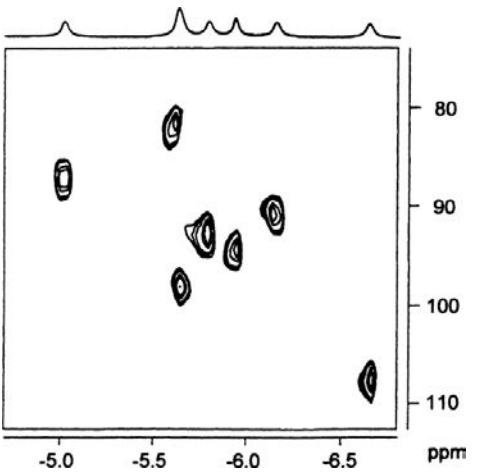

Figure 15. The pyrrole region of the 300MHz ^{1}H-^{13}C HMQC spectrum of $[(2\text{-Cl-TPP})Fe^{III}(CN)_2]^-$ in methanol-d_4 at 294 K. Reprinted from Wojaczynski, J.; Latos-Grażyński, L.; Hrycyk, W.; Pacholska, E.; Rachlewicz, K.; Sżterenberg, L. *Inorg. Chem.* **1996**, *35*, 6861–6872, with permission from the American Chemical Society.

cyanide and ferricytochrome b_5,[222] and Latos-Grażyński and coworkers[223] have reported the $^{1}H\{^{13}C\}$ HMQC spectrum of a monopyrrole substituted TPP derivative, $[(2\text{-Cl-TPP})Fe(CN)_2]^-$. Part of the 2D map of the latter complex is shown in Figure 15. As mentioned above in Section II.D.3, the natural-abundance $^{1}H\{^{13}C\}$-HMQC experiment is very helpful in the assignment of heme resonances within proteins, although only low-spin ferriheme proteins can be studied. Skidmore and Simonis have shown that the HMBC correlations of the α-C and β-H of an unsymmetrically phenyl-substituted derivative of $[(TPP)Fe(NMeIm)_2]^+$ could be observed, despite the short T_1s and T_2s of the protons.[217]

2D Spectra using the NOESY/EXSY (Nuclear Overhauser enhancement and chemical Exchange SpectroscopY) and ROESY (Rotating frame Overhauser and chemical Exchange SpectroscopY) techniques can also be valuable in obtaining dynamic and three-dimensional structural information concerning model hemes. The observation of NOESY cross peaks depends on the mixing time, τ_m, being of the order of the T_1 relaxation times of the protons between which an NOE is expected.[104] Since the T_1s of protons of paramagnetic iron porphyrins can be 8–9 ms or shorter, and decrease as the temperature is lowered[104,224] (in comparison, T_1s of ring CH_3s of dicyanoprotohemin IX are in the range of 150–190 ms[102]), it is important to find experimental conditions that will maximize the lengths of the T_1s. Degassing the sample with argon can lengthen the T_1s by 1–3 ms,[104] which can make the difference between an unsuccessful and a successful experiment in some cases. Latos-Grażyński and coworkers[223] have used a combination of COSY

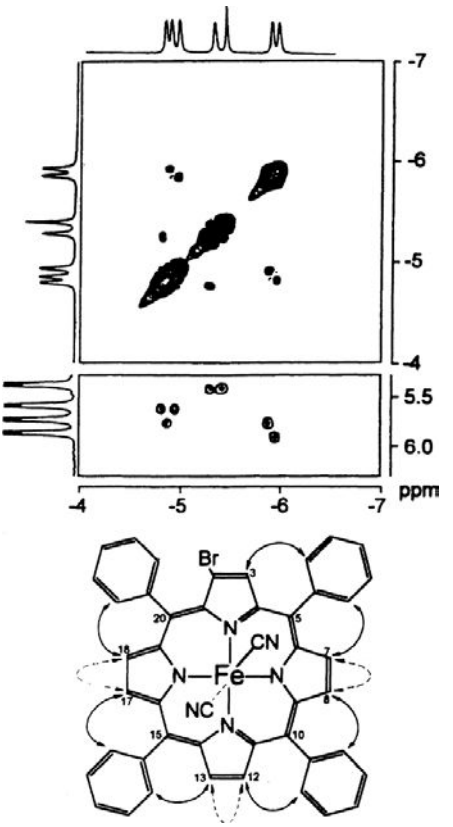

Figure 16. 2D ^{1}H NMR spectra of $[(2\text{-Br-TPP})Fe^{III}(CN)_2]^-$ in methanol-d_4 at 293 K. The upper box presents the COSY map of the pyrrole region, while the lower one shows a fragment of the NOESY spectrum with cross-peaks derived from contacts of *o*-phenyl and pyrrole protons. These contacts are indicated by solid arrows in the molecular scheme. Dashed arrows correspond to COSY cross- peaks. Two *ortho* protons on each phenyl ring are equivalent. Reprinted from Wojaczynski, J.; Latos-Grażyński, L.; Hrycyk, W.; Pacholska, E.; Rachlewicz, K.; Szterenberg, L. *Inorg. Chem.* **1996**, *35*, 6861–6872, with permission from the American Chemical Society.

and NOESY spectra to assign the pyrrole-H resonances of $[(2\text{-Br-TPP})Fe(CN)_2]^-$, as demonstrated in Figure 16. The author's research group has used NOESY spectra acquired at several (low) temperatures to measure the rate constants for chemical exchange due to axial ligand rotation[89] and to investigate the three-dimensional structure (at −74 °C) of $[(TMP)Fe(2MeImH)_2]^+$ in CD_2Cl_2.[104] Chemical exchange is evidenced by cross peaks between all protons of a given type whose magnetic environments are interchanged by the chemical exchange process,[89] as is discussed further in Section IV.A.8.l, whereas at very low temperatures, only the true NOE cross peaks are observed.[104] From the rotating frame NOE cross peaks of the

ROESY spectrum, the low-temperature, three-dimensional structure of the complex was deduced,[225] as discussed in Section IV.A.8.b(iii). In another example, a combination of chemical exchange and NOE cross peaks are observed for mono-*o*-phenyl substituted derivatives of $[(TPP)Fe(NMeIm)_2]^+$ due to hindered rotation of one of the axial ligands.[226]

Mixed success appears to have been experienced with rotating frame experiments using paramagnetic complexes. TOCSY spectra of $[(OETPP)Fe(NMeIm)_2]^+$ have readily been obtained;[214] here the T_1s and T_2s of the α-CH_2 protons of the ethyl groups are much longer than those of the pyrrole-H of the TPP derivatives. ROESY spectra provide an excellent method for distinguishing cross peaks resulting from NOEs (ROEs) and chemical exchange in model hemes.[225,227] However, in one case cross peaks observed in the NOESY experiment were not seen in the ROESY map.[227] A combination of COSY and NOE difference spectra, together with proton T_1s, were utilized to totally assign the pyrrole-H resonances of an unsymmetrically substituted low-spin iron(III) porphyrin having a bulky oxomolybdenum(V) substituent bound to the 2,3-phenyl positions of one phenyl ring, as shown in Figure 17 for $[((2,3\text{-MoOL})TTP)Fe(NMeIm)_2]^+$.[80] Scalar couplings between resonances 2,6 and 4,8 are seen in the COSY spectrum, Figure 18, left panel. NOE difference spectra showed that peaks 2 and 4 were in close proximity, Figure 18, right panel. These assignments for the long-T_1 and -T_2 protons led to two possible assignments of peaks 2, 4, 6 and 8; peaks 1, 3, 5 and 7, however, could be unambiguously assigned to protons h, a, g and b, respectively, on the basis of their short T_1s and T_2s, leading to the two possible assignments of the eight pyrrole-H resonances shown in Figure 18. Since the sharper half of the pyrrole-H resonances observed are correlated either by scalar or by pseudocontact coupling, it is clear that the observed eight pyrrole-H resonances must arise from a single molecular species and not from multiple species with different structures; the broader half of the resonances arise from the four pyrrole-H that are closest to the Mo(V) center.

Earlier COSY and NOESY studies of other unsymmetrically substituted derivatives of $[(TPP)Fe(NMeIm)_2]^+$ which showed the existence of two sets of COSY cross peaks and two different sets of NOESY cross peaks that appeared to allow the complete assignment of the four pyrrole-H resonances observed for these complexes[211] was later shown not to have any NOESY cross peaks, when phase-sensitive NOESY experiments were utilized,[103] and it was also shown in the latter work that the short T_1s of the protons (9 ms) for the distance over which the NOE would have to be transferred from one pyrrole ring to the adjacent one (5.4 Å) precludes detection of NOESY cross peaks for these complexes,[103] as well as for $[(TMP)Fe(2MeImH)_2]^+$, where T_1s are much longer (35 ms). (The steady-state NOE difference spectra used for the Mo-appended $(TPP)Fe^{III}$ complex of

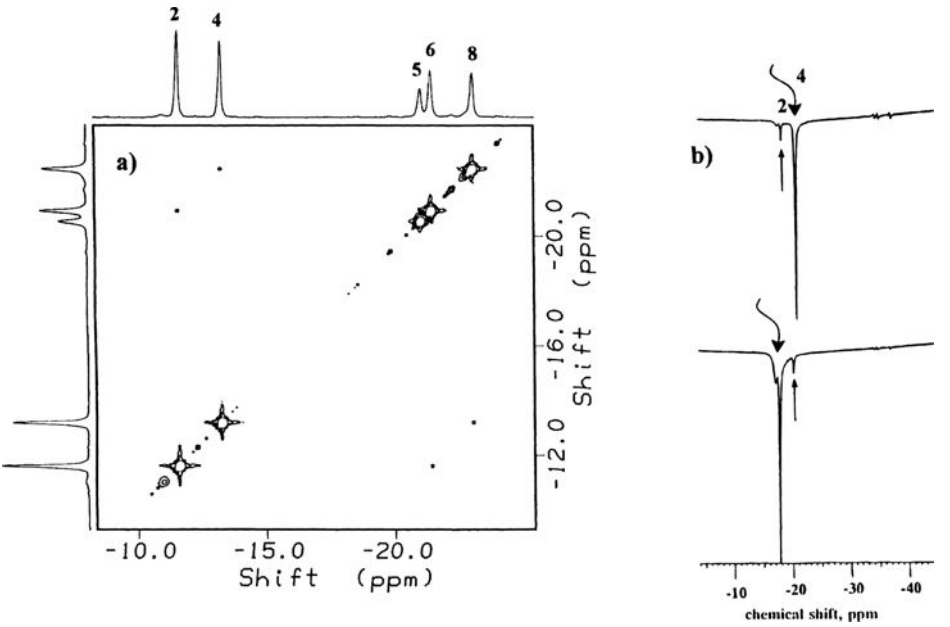

Figure 17. Left: 500MHz COSY map of the pyrrole-H region of [((2,3-MoOL)TTP)$Fe^{III}(NMeIm)_2]^+$ at 300 K. Note the cross peaks between resonances 2 and 6 and resonances 4 and 8, which indicate in each case that the pair of pyrrole protons are scalar coupled and are therefore in the same pyrrole ring. Reprinted from supplementary Figure S3 from Basu, P.; Shokhirev, N. V.; Enemark, J. H.; Walker, F. A. *J. Am. Chem. Soc.* **1995**, *117*, 9042–9055. Right: 500MHz NOE difference spectrum for [(2,3-MoL)TTP)$(NMeIm)_2$]Cl in CD_2Cl_2 at 215 K, showing the peak irradiated and the NOE observed. Reprinted from Basu, P.; Shokhirev, N. V.; Enemark, J. H.; Walker, F. A. *J. Am. Chem. Soc.* **1995**, *117*, 9042–9055, with permission from the American Chemical Society.

Figure 17, right panel[80] can detect much smaller NOEs than can the NOESY experiment, where transient NOEs are measured.) The magnitude NOESY experiments utilized in the earlier work produced cross peaks that were consistent with the expected shape of the π orbital utilized for spin delocalization,[211] but probably resulted from overlap of ridges in the magnitude NOESY spectra.

III. Spectral Analysis

A. Resolution and Assignment

The facility with which well-resolved ^1H (and ^{13}C) NMR spectra of paramagnetic metalloporphyrins can be obtained depends completely on the nature of the metal ion and its oxidation and spin states. Narrow lines are observed under the condition $T_{1e} \leq (A/h)^{-1}$ (see Section II.B.2.a), and in fact, $T_{1e} \leq \tau_c$.[2,4] As mentioned

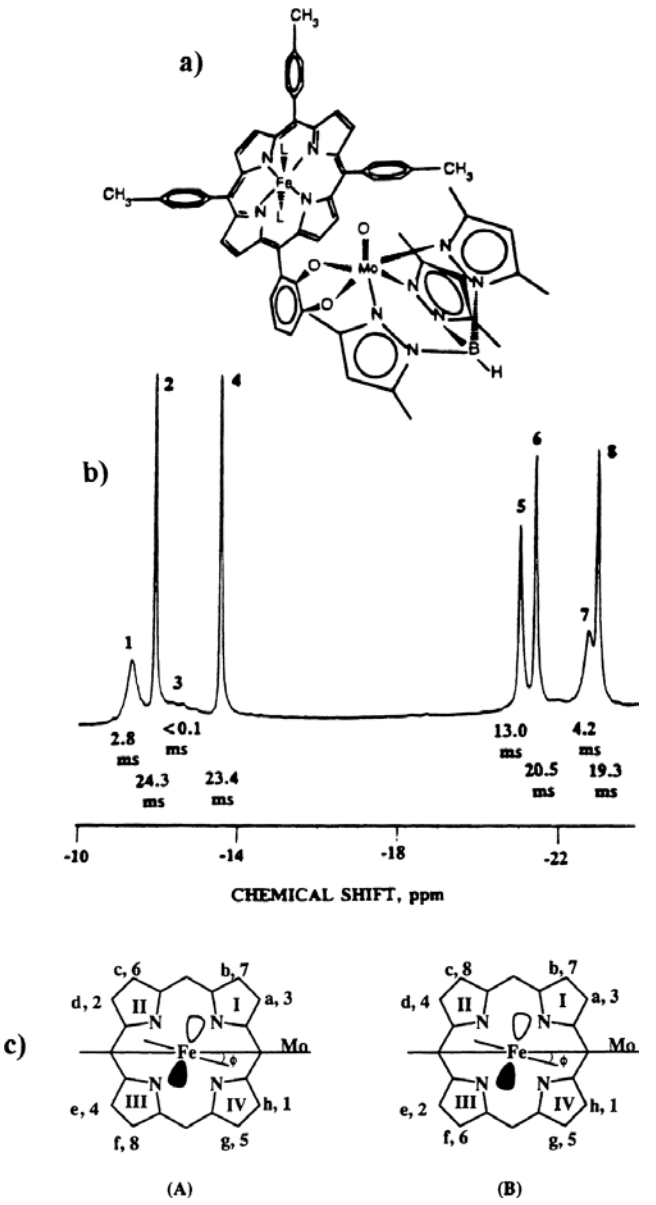

Figure 18. (a) Structure, (b) 500 MHz 1D spectrum of the pyrrole protons of [((2,3-MoOL)TTP)$Fe^{III}(NMeIm)_2]^+$ at 296 K in CD_2Cl_2. Peak numbering increases in order from lower to higher shielding. This is, not coincidentally, the order of increasing contact shifts of the pyrrole protons. (c) Two possible assignments of the pyrrole resonances of [((2,3-MoOL)TTP)$Fe(NMeIm)_2]^+$. Part A shows the assignment most consistent with the isotropic shifts of the protons H_c, H_d, H_e and H_f. Reprinted from Basu, P.; Shokhirev, N. V.; Enemark, J. H.; Walker, F. A. *J. Am. Chem. Soc.* **1995**, *117*, 9042–9055, with permission from the American Chemical Society.

above, VO^{2+}, Cu^{2+}, Mn^{2+} and Gd^{3+} do not satisfy this condition and have few if any resolved resonances for any of their complexes. Cu^{2+}, with T_{1e} values $> 10^{-9}$ seconds, comes the closest to violating this rule, especially in cases where it forms dimeric complexes,[228] but there are no reports of the ^1H NMR spectra of copper(II) porphyrins. However, as mentioned above, Godziela and Goff have observed the pyrrole-D resonance of [(d_8-TPP)Cu], as well as the deuterium resonances of [(d_{20}-OEP)Cu] and the silver(II) analog.[164] The 1150-Hz linewidth of the ^2H signal from the pyrrole-D resonance of [(d_8-TPP)Cu] (see Figure 80) would predict a linewidth of up to 48.3 kHz for the corresponding ^1H resonance of the protonated analog, which explains the fact that no such ^1H resonance has been detected. Chromium(III) porphyrins, with T_{1e} values $> 5 \times 10^{-10}$ seconds, give extremely broad ^1H spectra, but much better resolved ^2H spectra,[165] as shown in Figure 12. The linewidth of the ^2H resonance of the pyrrole-deuterons is about 125 Hz, which represents a major decrease over the greater than 3 kHz (undetectable) linewidth of the ^1H resonance of (TPP)CrCl,[94] and the difference between detectable and nondetectable signals. ^1H linewidths of up to 250–300 Hz are observed for high-spin iron(III) and manganese(III) porphyrins, but the larger range of shifts for the iron(III) porphyrins make it much easier to assign the spectra than for the manganese(III) analogs.

Most probably one of the simplest low-spin iron(III) porphyrin proton NMR spectra is that of $[(TPP)Fe(NMeIm)_2]^+$, shown in Figure 19. All resonances are well-resolved at 300 MHz, much better so than the original 100 MHz spectrum of the same complex shown in Figure 4 of Ref. 2. In comparison, the spectrum of the $[(mono\text{-}m\text{-}nitro, tris\text{-}m\text{-}fluoro\text{-}TPP)Fe(NMeIm)_2]^+$ complex, Figure 20a, shows four inequivalent pyrrole-H resonances and several kinds of phenyl resonances, yet is fairly easy to assign, except for an ambiguity in the assignment of the pyrrole-H resonances in the separate pyrrole rings; COSY spectra allow the pairs of resonances within a given pyrrole ring to be assigned, but the relationship of the two pyrrole rings to each other has not been determined, despite earlier belief to the contrary.[211] Using predictions of the shape of the π orbital used for spin delocalization, the ambiguity can be reduced to twofold, as was done for the $[(2,3\text{-MoOL})(TPP)Fe(NMeIm)_2]^+$ complex[80] shown in Figure 18.

Yet another unsymmetrically-substituted low-spin $(TPP)Fe^{III}$ derivative is that demonstrated by the mono-β-pyrrole-substituted complexes prepared and studied by Latos-Grażyński and coworkers.[223] In these cases there are seven unique β-pyrrole resonances, whose chemical shifts change with the nature of the substituent, as shown for a series of substituents in Figure 41. Even a single deuterium substituent lifts the degeneracy of the pyrrole-H resonances, as demonstrated in the inset of Figure 41. By comparison of Figures 20 and 21 the wide range of spreads of the pyrrole-H resonances are seen, yet their basic relatedness to the simple

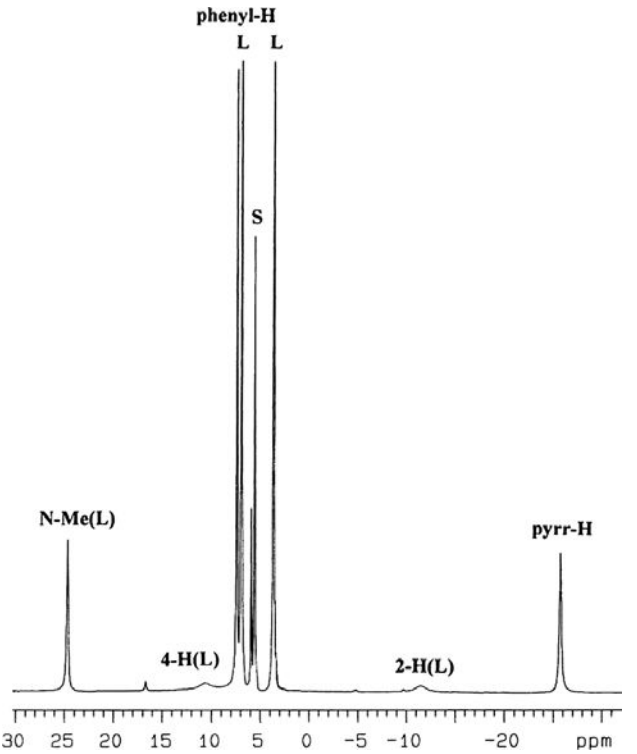

Figure 19. 300 MHz 1D NMR spectrum of $[(TPP)Fe^{III}(NMeIm)_2]^+$ recorded in CD_2Cl_2 at −45 °C. S = solvent, L = free ligand. (T. K. Shokhireva, unpublished work.)

spectrum of $[(TPP)Fe(NMeIm)_2]^+$, Figure 20, is evident. Similar relatedness in the face of increased complexity can be observed between the ^1H NMR spectrum of $[(OEP)Fe(NMeIm)_2]^+$ and an unsymmetrical derivative of this complex, $[(E_6A_2P)Fe(NMeIm)_2]^+$, where E = ethyl and A = diethylcarboxamide,[210] Figure 22. Natural porphyrin complexes of low-spin iron(III) have been studied for many years. A classic example of these spectra is shown in Figure 22, where the methyl regions of a series of 2,4-disubstituted deuteroporphyrinatoiron(III) bis-(cyanide) complexes[168] are shown.

^1H NMR spectra of high-spin iron(III) complexes of [(TPP)FeCl] and [(OEP)FeCl] in $CDCl_3$ and DMSO-d_6 are shown in Figure 23. As is evident, the pyrrole-H and pyrrole-CH_2 chemical shifts of the two porphyrinates have the same signs but the magnitude of the CH_2 shift is much smaller. The change in solvent from $CDCl_3$ to DMSO-d_6 does not greatly affect the chemical shifts of the pyrrole position resonances, but the *meso*-H resonance shifts approximately 100 ppm to higher frequency in the coordinating solvent. This will be considered in greater detail in Sections IV.A.6.a and IV.A.6.b.

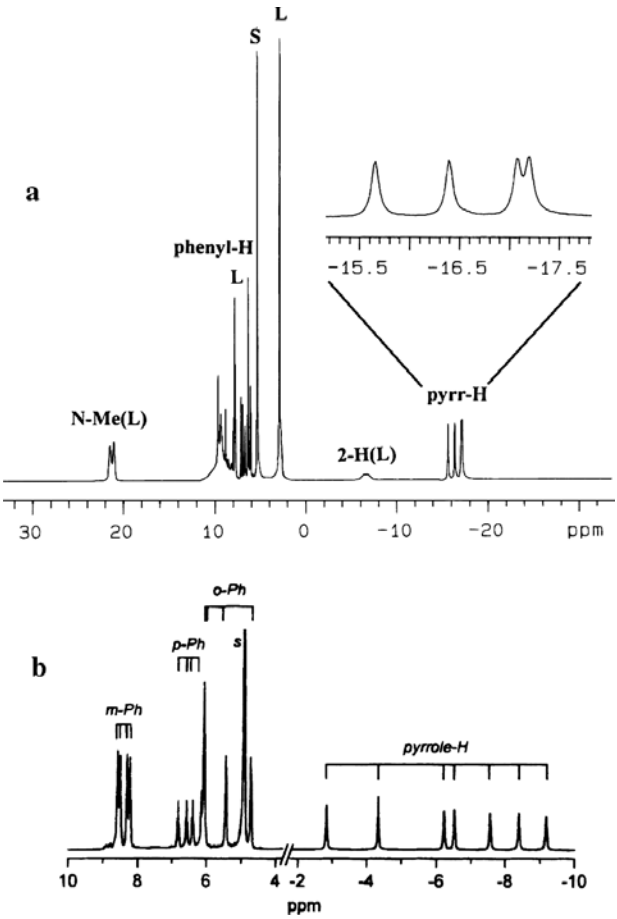

Figure 20. (a) 300MHz 1D NMR spectrum of $[((m\text{-}NO_2)_1(m\text{-}F)_3TPP)Fe^{III}(NMeIm)_2]^+$ recorded in CD_2Cl_2 at 290 K. S = solvent, L = free ligand. Note the two N-Me signals from ligands coordinated on the same and opposite sides to the *m*-NO_2. The coordinated ligand 2-H is also broadened by this inequivalence. (T. K. Shokhireva, unpublished work.) b) 300 MHz 1D ^1H NMR spectrum of $[(2\text{-}CN\text{-}TPPFe^{III}(CN)_2]^-$ in methanol-d_4 at 293 K. Reprinted from Wojaczyński, J.; Latos-Grażyński, L.; Hrycyk, W.; Pacholska, E.; Rachlewicz, K.; Szterenberg, L. *Inorg. Chem.* **1996**, *35*, 6861–6872, with permission from the American Chemical Society.

Similarly to chromium(III) porphyrins, d^3 manganese(IV) porphyrins have quite broad ^1H resonances, which are much better resolved as the deuterium-substituted analogs, when observed by ^2H NMR spectroscopy. As is shown in Figure 24, the pyrrole-D resonance of the TMP complex of oxomanganese(IV) is more than twice as broad as that of the corresponding complex of chloromanganese(III).[229] However, the observed pyrrole-D shifts are relatively similar, as will be discussed further in Sections IV.E.2 and IV.E.7, because of the major

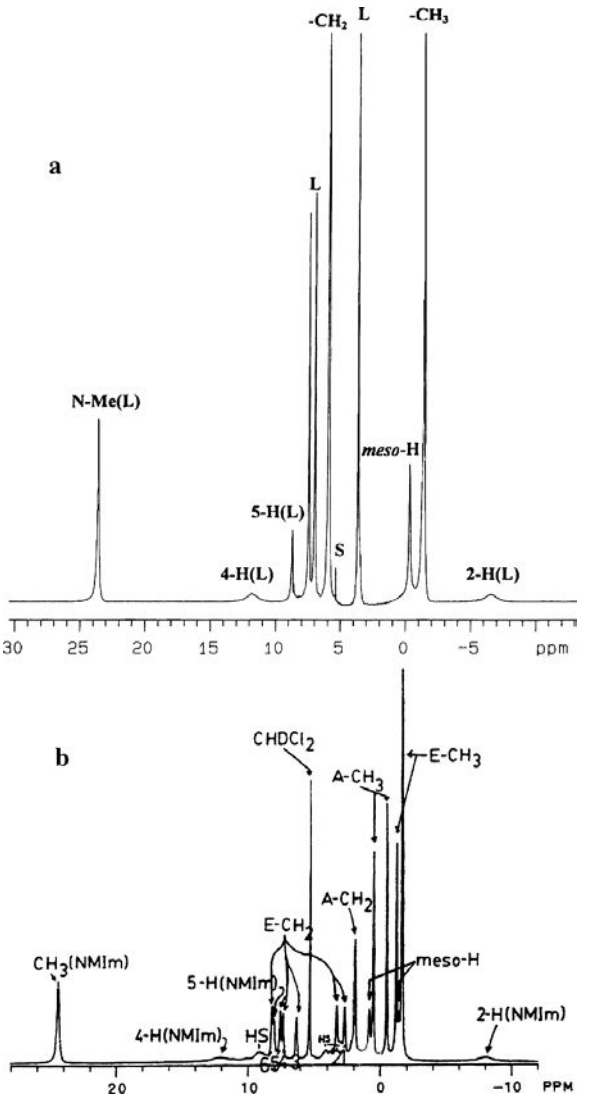

Figure 21. (a) 300 MHz 1D ^{1}H NMR spectrum of $[(OEP)Fe^{III}(NMeIm)_2]^+$ in CD_2Cl_2 at –45 °C. S = solvent, L = free ligand. (T. K. Shokhireva, unpublished work.) (b) 300 MHz 1D ^{1}H NMR spectrum of $[(E_6A_2P)Fe^{III}(NMeIm)_2]^+$ in CD_2Cl_2 at –45 °C. The broad peaks marked HS are due to the presence of a small amount of the high-spin complex, $[(E_6A_2P)FeCl]$. Modified from Isaac, M. F.; Simonis, U.; Lin, Q.; Suffian, D. J.;Wilson, D. L.; Walker, F. A. *Inorg. Chem.* **1993**, *32*, 4030–4041, with permission from the American Chemical Society.

importance of π delocalization involving the two d_π unpaired electrons present in both oxidation states.

Even though most cobalt(II) porphyrins are low-spin and have rather broad ^{1}H resonances with relatively small shifts that are largely pseudocontact in origin

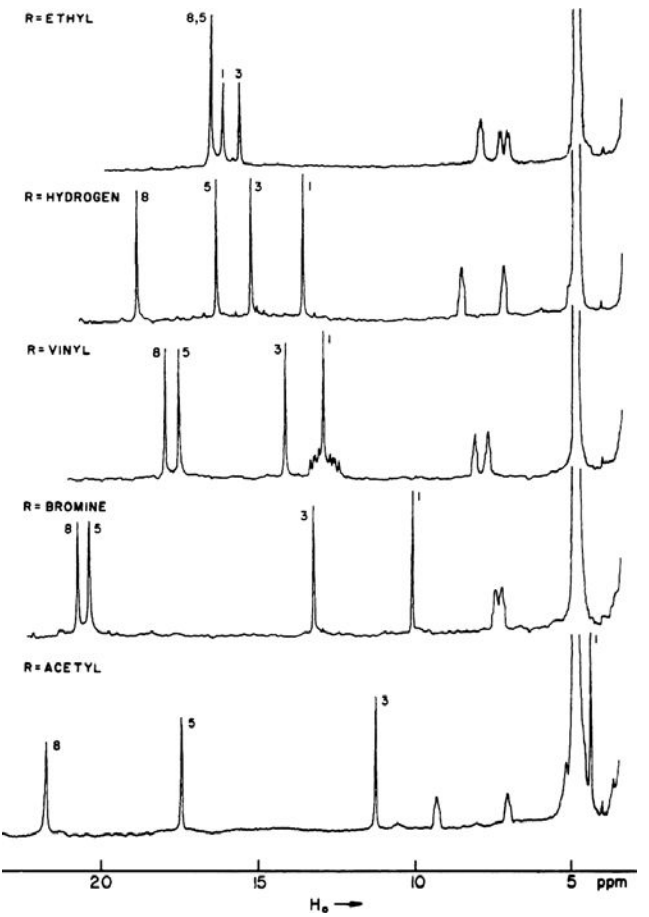

Figure 22. ^{1}H NMR spectra of the methyl regions of $[(2,4\text{-}R_2\text{deuteroporphyrin})Fe^{III}(CN)_2]^-$ in methanol-d_4 at 25 °C for R = ethyl, hydrogen, vinyl, bromine and acetyl. The methyls were assigned by ^{2}H substitution. Reprinted from La Mar, G. N.; Viscio, D. B.; Smith, K. M.; Caughey, W. S.; Smith, M. L. *J. Am. Chem. Soc.* **1978**, *100*, 8085–8092, with permission from the American Chemical Society.

(paramagnetic shifts of up to +19 ppm for the *meso*-H of the OEP complex at 35 °C), the ^{1}H NMR spectra of the chlorocobalt(II) N-methylporphyrin complexes of TPP and OEP,[230] shown in Figure 25, are those of high-spin cobalt(II) centers, and are quite a bit sharper. The lower symmetry of the N-methylporphyrin ligand creates many more resonances for each complex.

B. Analysis of Shifts

Both contact and pseudocontact shifts vary in their relative and absolute contributions to the paramagnetic shifts of the protons on the periphery of the porphyrin

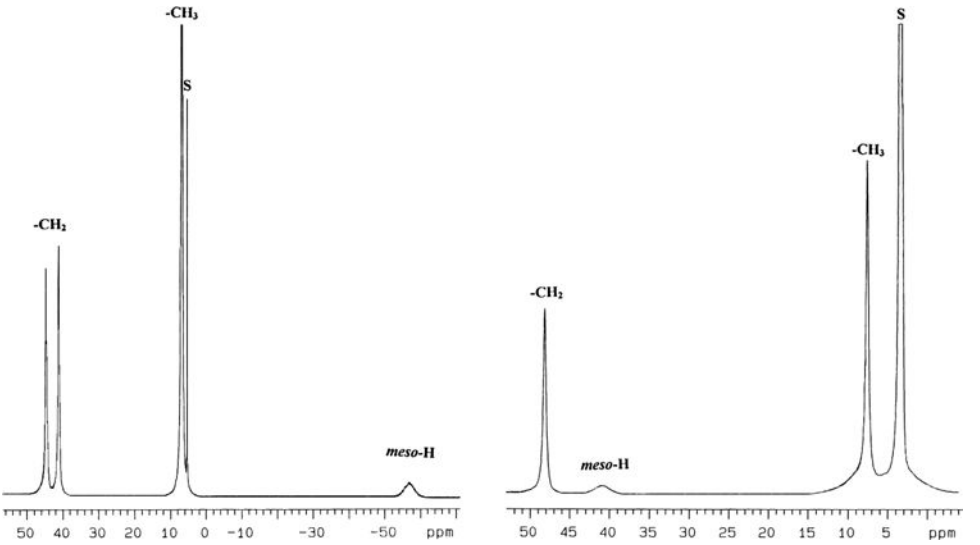

Figure 23. Left: 300 MHz 1D ^{1}H NMR spectrum of HS [(OEP)FeCl] in CD_2Cl_2, and right: DMSO-d_6 at 294 K. (T. K. Shokhireva, unpublished work.)

and axial ligands, depending on the electron configuration and magnetic anisotropy of the metal ion involved. Some knowledge of the magnetic properties and possible electron configurations of the particular system is required in order to begin the process of separating these two terms. Usually it is desired to gain insight into the contact contribution to the paramagnetic shifts, in order to determine what orbital or orbitals is/are used for spin delocalization. In order to do this the pseudocontact contribution to the paramagnetic shifts must be determined and subtracted. The approaches employed depend on the type of magnetic data available. For many electron configurations and spin states, EPR data are available to determine whether or not there is magnetic anisotropy or zero-field splitting that could give rise to a pseudocontact shift. Crystallographic data are available for a number of metalloporphyrins that allow calculation of the axial geometric factors, $(3\cos^2\theta-1)/r^3$, which are part of Eqs. 9 and 10. These axial geometric factors can then be used in one of three ways to separate out the pseudocontact contribution to the paramagnetic shift: (1) *analysis of curvature in the Curie plot*, (2) *empirical methods that rely on a comparison of predicted and computed relative pseudocontact shifts*, and (3) *use of EPR g-values with Eq. 9*. The rhombic geometric factors may be needed in some cases, but in general the rhombic contribution to the pseudocontact shift averages to zero for metalloporphyrins in homogeneous solution, where any nonhindered axial ligands are rotating extremely rapidly. The same is definitely not true of heme proteins, where axial ligands are usually fixed in position, often by hydrogen-bonds and crowding of protein side chains.

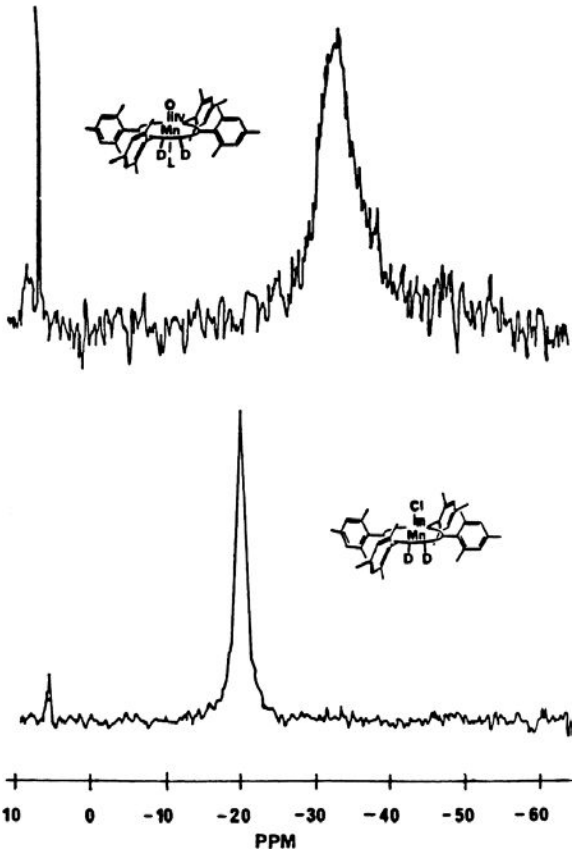

Figure 24. ^{2}H NMR spectra of [(d_8-TMP)Mn^{IV}(O)] (top) and [(d_8-TMP)Mn^{III}Cl] (bottom) in CH_2Cl_2 at –40 °C. The resonance at 5.2 ppm is $CHDCl_2$. Reprinted from Groves, J. T.; Stern, M. K. *J. Am. Chem. Soc.* **1988**, *110*, 8628–8638, with permission from the American Chemical Society.

1. *Curvature in the Curie Plot over the Temperature Range of the Measurement*

When one begins a study of a paramagnetic metalloporphyrin it is important to obtain the temperature dependence of the paramagnetic shifts of the metal complex over as wide a temperature range as possible. For complexes in which axial ligands are bound to the metal, this generally means going to very low temperatures, since axial ligand dissociation may be expected to become significant at or above ambient temperatures for most metalloporphyrins except those of cobalt(III). The mechanism of ligand exchange is generally dissociative,[231] and the intermediate in the ligand exchange processes may be of a different spin state, such as the case of low-spin iron(III), in which the

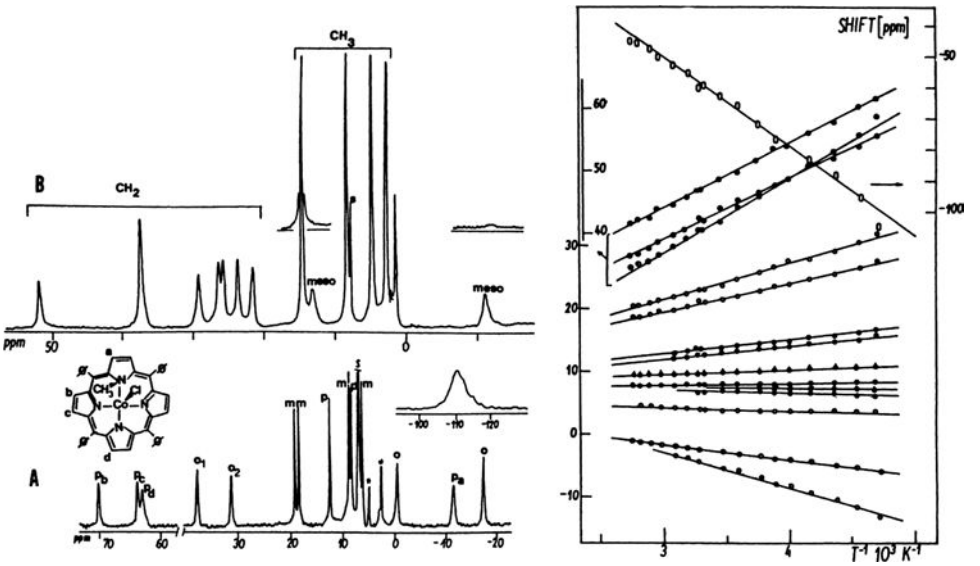

Figure 25. Left: ^{1}H NMR spectra of (A) [(N-CH_3TPP)Co^{II}Cl] in CD_2Cl_2 at –80 °C (N–CH_3 resonance shown in the insert) and (B) [(N–CH_3OEP)Co^{II}Cl] in $CDCl_3$ at –60 °C (inserts present changes due to *meso* deuteration). Abbreviations: P_x, pyrrole; *o, ortho*; *m, meta*; *p, para*. Right: Plot of the temperature dependence of the shifts of [(N–CH_3TPP)CoCl] in CD_2Cl_2: (open circles) *ortho*; (solid circles) *meta*; (solid circles with "tail") *para*; (long ovals) N–CH_3; (half-filled circles) pyrrole. Reprinted from Latos-Grażyński, L. *Inorg. Chem.* **1985**, *24*, 1104–1105, with permission from the American Chemical Society.

5-coordinate intermediate is high-spin. The presence of a small amount of this high-spin mono-ligand intermediate can shift the NMR resonances of the low-spin bis-ligand complex in the direction of those of the high-spin intermediate, and thus cause deviations from the expected temperature dependences based on Curie law (Eq. 11) or expanded Curie law (Eq. 13). Hence, the temperature dependence must be free of such chemical exchange due to ligand dissociation, which generally means working at low (sometimes very low) temperatures. Deuterated solvents typically used for obtaining Curie plots over wide temperature ranges include methylene chloride (mp –97 °C, bp 40 °C), chloroform (mp –64 °C, bp 61 °C), dimethylformamide (mp –61 °C, bp 153 °C), methanol (mp –98 °C, bp 65 °C) or toluene (mp –93 °C, bp 111 °C). Curie plots will typically show whether there is some unusual magnetic behavior of the system. Such unusual magnetic behavior includes: nonzero intercepts due to SOZ and/or excited state contributions to the pseudocontact shifts,[25,30] curvature due to hindered rotation of substituent groups, and curvature due to zero-field splitting contributions to the pseudocontact shift, Eq. 10, as described previously.[2,4]

a. *Zero-field splitting contributions to the pseudocontact shift*

In Section II.A.2 it was shown that zero-field splitting contributions can be separated if the temperature dependence [*over the range of temperatures at which the NMR spectra were measured*] follows a general expression

$$\delta_{iso} = \alpha T^{-1} + \varepsilon T^{-2}, \tag{22}$$

where $\alpha = g\mu_B AS(S+1)/18\gamma_H\hbar k$, $\varepsilon = -(28g^2(\mu_B)^2 D/9\gamma_N{}^2 k^2 r^3)(3\cos^2\theta - 1)$, and D is the zero-field splitting parameter. This has been used previously for separating the contact and pseudocontact contributions to the paramagnetic shifts of high-spin iron(III) porphyrins,[2,4,36] and Latos-Grażyński and coworkers have used it in the study of high-spin nickel(II) porphyrins that have sizeable zero-field splittings,[230] Section IV.F.

b. *Nonzero intercepts of the Curie plot*

Should the Curie plot for all proton resonances of the molecule appear to be linear over the temperature range of the measurements, but the intercepts of the paramagnetic shifts be nonzero, it is likely that there are significant SOZ contributions to the pseudocontact shifts,[30] and/or there is a significant temperature-dependent contribution from an excited state with a different pattern of spin delocalization than that of the ground state,[25] as discussed in Section II.A.3, Eq. 13. Some knowledge as to what types of excited states may be involved is necessary in order to analyze the temperature dependence. For example, if the ground state has a low-spin state (for example, S = 0 or S = 1/2) while the excited state has a higher-spin state (for example, S = 1 or S = 3/2 or 5/2, respectively), the proper weighting factors W_1 and W_2 must be used in Eq. 13. Various scenarios can tried using the program TDFw, available on the World Wide Web.[84] Examples of the use of Eq. 13 for analysis of the temperature dependence of a low-spin $TPPFe^{III}$ complex and of two intermediate spin [$((2,6\text{-}X_2)_4TPP)FeOClO_3$] complexes are shown in Figures 26 and 27, respectively. The only difficulty in using this treatment to separate the pseudocontact and contact shifts is that it assumes that the two have the same temperature dependence, and that the ground and excited state contributions are related in a particular way to the orientation of the nodal plane of the e(π) orbital of low-spin iron(III) for the ground and excited states. It was first thought that this would be a problem, because although the rhombic contribution to the magnetic anisotropy of Eq. 9 is expected to change sign between the ground and excited states, it was believed that the axial contribution to Eq. 9 would not. However, it has since been shown that for low-spin iron(III) the axial pseudocontact shift is opposite in sign for the excited state than it is for the ground state, because the

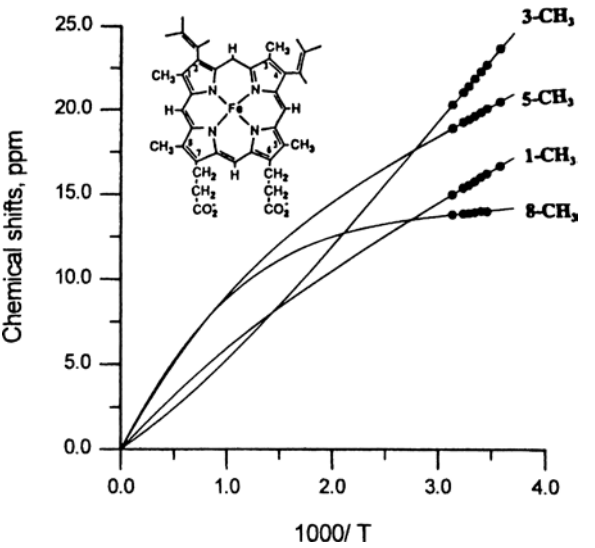

Figure 26. Plot of the fit of Eq. 13 to the calculated contact shifts of the pyrrole-H for [(2,3-MoL)TTPFe^{III}(NMeIm)$_2$]$^+$. The value of ΔE obtained from this fit is 211 ± 25 cm^{-1}, an intermediate value that is smaller than V/λ. Spin density coefficients obtained from this fit are, for the ground state, (c) 0.164, (d) 0.0059, (e) 0.0049, (f) 0.0158, (g) 0.0156 and (h) 0.0046, while for the excited state they are (c) 0.0141, (d) 0.0212, (e) 0.0199, (f) 0.0120, (g) 0.0114 and (h) 0.0195. These values compare reasonably with the magnitudes of those obtained from simple Hückel calculations. Reprinted from Shokhirev, N. V.; Walker, F. A. *J. Phys. Chem.* **1995**, *99*, 17795–17804, with permission from the American Chemical Society.

g-values of the excited state are opposite in magnitude than they are for the ground state.[172] This actually simplifies the fitting of data to Eq. 13, but it provides no means of separating the contact and pseudocontact shifts.

2. *Empirical Methods*

Usefulness of these approaches depends on it being possible to demonstrate relatively unambiguously that the shift(s) for some functional group(s) are either totally pseudocontact or totally contact in origin. In either case, it is then possible to assess the magnitude of the pseudocontact shift at all other positions of interest in the complex. This analysis depends on the fact that the relative pseudocontact shifts for nonequivalent protons in a complex are determined solely by the relative geometric factors.[2,4,23,24] Hence, in an axial case,

$$(\delta_{pc})_i : (\delta_{pc})_j : (\ldots) = \left[\frac{3\cos^2\theta_i - 1}{r_i^3}\right] : \left[\frac{3\cos^2\theta_j - 1}{r_j^3}\right] : [\ldots]. \qquad (23)$$

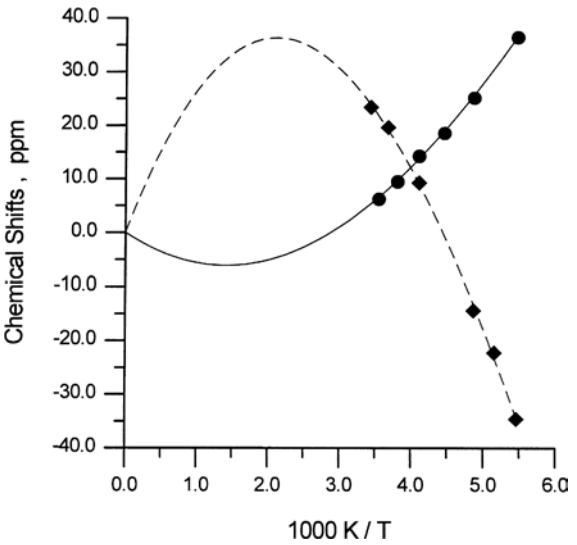

Figure 27. Plot of the fit of Eq. 13 to two spin-admixed $[(2,6\text{-}X_2)_4TPPFe^{III}OClO_3]$ complexes, where the filled circles are for X = F and the filled diamonds for X = Br. In the former case, the S = 5/2 state is the ground state, while for the latter, the S = 3/2 state is the ground state. Reprinted from Nesset, M. J. M.; Cai, S.; Shokhireva, T. K.; Shokhirev, N. V.; Jacobson, S. E.; Jayaraj, K.; Gold, A.; Walker, F. A. *Inorg. Chem.* **2000**, *39*, 532–540, with permission of the American Chemical Society.

If a certain set of protons exhibits relative shifts that are inconsistent with a pattern expected from spin delocalization, but are in quantitative or semiquantitative agreement with relative computed geometric factors, then the paramagnetic shifts may be assumed to be wholly pseudocontact in origin for these positions, for it is extremely unlikely that contact shifts would scale exactly parallel to the pseudocontact shifts. The known pseudocontact shifts for these positions then permit the determination of the pseudocontact contributions to all other shifts for the complex using the ratios of the geometric factors. Examples of a case where this works well and another where it does not, and it is thus possible to use this analysis to show that the shifts are largely or totally contact in origin, are shown in Figure 28. Both involve the phenyl protons of (TPP)Fe complexes. Plotting the observed paramagnetic shifts of the phenyl protons vs. the calculated geometric factors calculated for the *o*-H, *m*-H and *p*-H (Figure 28, left) yields a linear correlation for $[(RTPP)Fe^{II}]$, indicating essentially 100% pseudocontact contribution to the phenyl-H shifts,[232] but for $[TPPFe(t\text{-}BuNC)_2]^+$ (Figure 28, right) the observed shifts deviate significantly in opposite directions for the *o,p*-H and the *m*-H, which indicates that in the latter case the shifts are largely, if not completely, contact in origin.[155] Calculation

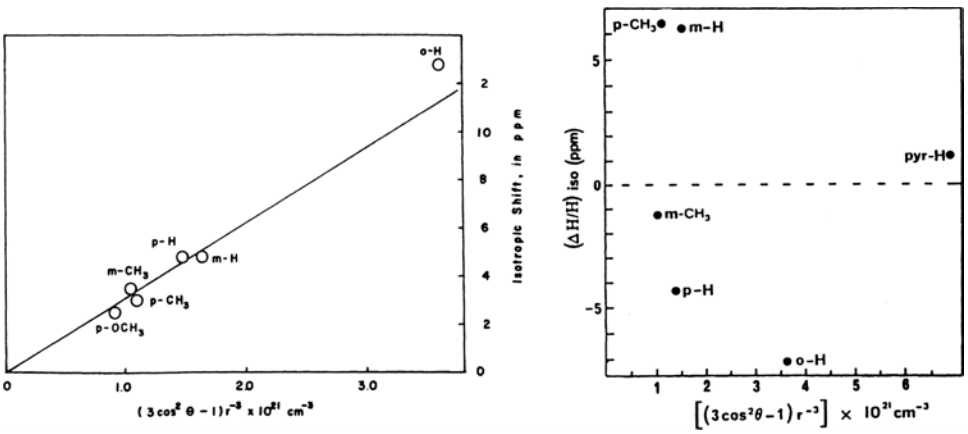

Figure 28. Left: Plot of the isotropic shifts for *meso*-aryl substituents in [(RTPP)Fe^{II}] in benzene-d_6 at 25 °C vs the calculated geometric factor, $\langle(3\cos^2\theta - 1)/r^3\rangle$, showing all aryl resonances close to the theoretical line. Reprinted from Goff, H. M.; La Mar, G. N.; Reed, C. A. *J. Am. Chem. Soc.* **1997**, *99*, 3641–3646, with permission of the American Chemical Society. Right: Plot of the isotropic shifts for *meso*-aryl substituents in [(RTPP)Fe^{III}(*t*-BuNC)$_2$]$^+$ in CD_2Cl_2 at 25 °C vs the calculated geometric factor, $\langle(3\cos^2\theta - 1)/r^3\rangle$ showing all aryl resonances deviating significantly from any theoretical line. The deviations of the experimental points from the straight line through the origin yield the contact shift for each position. Reprinted from Simonneaux, G.; Hindre, F.; Le Plouzennec, M. *Inorg. Chem.* **1989**, *28*, 823–825, with permission from the American Chemical Society.

of the pseudocontact contribution to the pyrrole-H shifts of the bis-(imidazole) or (amino ester) complexes showed that the pseudocontact shift is a minor part of the paramagnetic shift at the pyrrole-H position, thus showing that there is a large contact shift at the β-pyrrole positions for the bis-(imidazole) and -(amino ester) complexes of low-spin iron(III) porphyrins. However, the bis-isocyanide complex of (TPP)Fe^{III} has a totally different pattern of shifts, with vanishingly small pseudocontact shifts at all hydrogen positions, but very large contact shifts at the phenyl-H positions and only a very small (positive) contact shift at the pyrrole-H position. This indicates that these two complexes use different porphyrin (and metal d) orbitals for spin delocalization, as will be discussed in greater detail below. Cobalt(II) porphyrins were earlier shown to have mainly pseudocontact shifts of the phenyl-H, as well as the pyrrole-H positions.[2,4,233] In contrast, manganese(III) porphyrins were shown to have predominantly π contact shifts at both the *meso*-aryl and pyrrole-H positions.[2,4,234] High-spin nickel(II) complexes have very small g-anisotropy, but sizeable zero-field splittings, which produce measurable pseudocontact shifts at the pyrrole positions, which can be separated from the contact shifts by use of Eq. 22, as discussed in Section IV.F.

3. *g-Tensor Anisotropy*

When two complexes have similar geometries but different EPR g-values, the g-values measured at low temperatures (4–77 K) can be used to calculate the axial ($g_{\parallel}^2$–$g_{\perp}^2$), and if necessary, the rhombic g anisotropies (g_{xx}^2–g_{yy}^2). If the sizes of the pseudocontact shifts are known for one of the complexes, those of the other can be estimated by scaling the pseudocontact shifts of the known complex by the ratios of the known g anisotropies of the two, according to Eq. 9. Such procedures have been used previously with good success for low-spin iron(III) porphyrins, $[(RTPP)Fe(ImH)_2]^+$,[2,4] but not for $(RTPP)Co^{II}$ complexes, where axial solvation at both ambient temperatures and 77 K strongly decreases the g-anisotropy measured from polycrystalline samples. Temperature-dependent axial solvation is the case for these cobalt(II) porphyrins.[2,4] For low-spin ferriheme proteins, the g-tensor anisotropy factoring method was used to estimate the pseudocontact shifts of metmyoglobins-cyanide and related molecules, and of cytochromes *c*.[8]

IV. Effect of Metal Ion and Spin State on Bonding

The large majority of NMR studies of paramagnetic metalloporphyrins have involved iron porphyrins of various oxidation and spin states. Thus, this section will begin with a study of iron porphyrins and will then be expanded to the other paramagnetic metalloporphyrins of the transition and lanthanide series.

A. Iron Porphyrins

The types of M-P bonding interactions and the ranges and signs of paramagnetic shifts found for iron porphyrins and the heme proteins are very dependent on oxidation state and spin state of the metal. In fact, the spectra are so characteristically similar within each class of iron(III) porphyrin complexes alone (high-spin, oxo-bridged dimers, intermediate-spin, low-spin with two different electron configurations), and so different between classes, that NMR spectroscopy is a valuable diagnostic tool for determining the nature of the axial ligands and spin state in a newly prepared iron(III) porphyrin complex. The same is also true for iron(II), iron(I) and iron(IV) porphyrin complexes, and thus each of these will be considered individually.

1. *Iron(I) Porphyrins*

Although iron(I) porphyrin complexes are known, only a few of them, such as the low-spin d^7 bis-(pyridine) iron(I) complex of a *meso*-alkoxyporphyrin which bears

an –OR group in one of the *meso* positions,[235] and low-spin d^7 iron(I) complexes of tetraphenylporphyrin, etioporphyrin and octaethylporphyrin[236] have been investigated by either proton or deuterium NMR spectroscopy, and there have been no new reports of their investigation in the past ten years. Proton or deuterium NMR spectra of the iron(I) species are of diagnostic value for determining the ground state of the metal ion, since characteristic positive paramagnetic shifts for certain resonances have been observed. For (tetraphenylporphyrinato)iron(I) the pyrrole-^{2}H signal is observed at about +29 ppm, and the *meso*-D signal of (etioporphyrinato)iron(I) and (octaethylporphyrinato)iron(I) at +14.5 ppm.[236] Pseudocontact shifts are relatively small. Hence, the pyrrole-^{2}H experiences predominantly a contact shift. Based on magnetic measurements and EPR studies of these complexes ($g_\perp = 2.28$ and $g_\parallel = 1.93$ for $[(TPP)Fe]^-$ and $g_\perp = 2.24$ and $g_\parallel = 1.92$ for $[(OEP)Fe]^-$, respectively, with $g_\perp > g_\parallel$,[236,237]) a spin state of S = 1/2 is widely accepted, with the unpaired electron residing in the d_{z^2} orbital, by analogy to cobalt(II) porphyrins.[238]

2. *Diamagnetic Iron(II) Porphyrins*

Ferrous porphyrin complexes are biologically relevant since they are active site analogs of the oxygen transport and storage proteins, hemoglobin and myoglobin. However, synthetic iron(II) porphyrins are easily oxidized, and thus proper care is needed to handle them. The resonance shifts observed in the NMR spectra of the diamagnetic complexes can be used as a convenient reference for determining the magnitude and the direction of the paramagnetic shifts in structurally related paramagnetic complexes.[2-4]

a. *Six-coordinate diamagnetic complexes*

Proton NMR spectra of 6-coordinate ferrous porphyrin complexes show proton resonances in the diamagnetic region. The pyrrole proton signals are shifted to slightly lower shielding by the large ring current effect of the porphyrin macrocycle and are observed at or near 9 ppm. The phenyl proton resonances in this and other complexes are found at 7 to 8 ppm, whereas the resonances of the axial ligands are shifted to high shielding as a consequence of the large ring current of the macrocycle. More extensive discussion of the diamagnetic 6-coordinate iron(II) porphyrin NMR spectra is provided elsewhere.[3,239] Diamagnetic iron(II) complexes derived from chelated protohemes, in which a coordinating imidazole ligand is provided by an alkyl imidazole attached to one or both of the heme propionates (see Figure 42) and in which CO represents the sixth ligand[240] provide examples of 6-coordinate heme models related to natural porphyrins. The porphyrin ring current affects the signals of these complexes in a characteristic

way: *meso*-protons are deshielded (9.7 ppm), vinyl protons are found at 6 to 8 ppm, and side chain protons are strongly shielded.

Several diamagnetic 6-coordinate ruthenium(II) porphyrins have been investigated by ^{1}H NMR spectroscopy, and their chemical shifts are included in Table 8, together with the shifts of other diamagnetic metalloporphyrins that may serve as convenient diamagnetic references for calculating the paramagnetic shifts of paramagnetic metalloporphyrins.

Despite the common belief that only one 2-substituted imidazole will bind to iron(II) porphyrins, and that such complexes are excellent models for T-state hemoglobins, the bis-1,2-dimethylimidazole complex of (TMP)Fe^{II} has been prepared and investigated by X-ray crystallography,[32] magnetic Mössbauer spectroscopy at 4.2 K[241] and by proton NMR spectroscopy in d_8-toluene at −70 to −90 °C.[92] Both of the latter techniques confirm that the complex is diamagnetic, but it has unique spectral parameters because of the strong ruffling of the porphyrinate ring that must occur in order for these sterically hindered ligands to bind to Fe^{II}. The NOESY spectrum of [(TMP)Fe^{II}(1,2-Me$_2$Im)$_2$] at −80 °C is very similar to that of [(TMP)Co^{III}(1,2-Me$_2$Im)$_2$]$^+$ at room temperature,[92] as shown in Figure 29. This similarity in the 2D spectra confirms the similarity in molecular structure of these two complexes, as well as their structural similarity to the highly ruffled paramagnetic iron(III) analog.[32,227] Multinuclear (^{13}C, ^{17}O, ^{57}Fe) NMR studies of diamagnetic carbonmonoxy heme proteins and synthetic model compounds have also been reported.[242]

Compounds with modified ring systems such as the *meso*-oxidized derivative of octaethylporphyrin, OEOP, which as the iron complex is a green pigment known as an iron *meso*-oxaporphyrin or verdoheme, Structure **9**, are low-spin iron(II) diamagnetic centers when bound to two pyridine axial ligands.[220] Their high-spin 5-coordinate halide counterparts are discussed in Section IV.A.4.b(vi).

b. *Five-coordinate diamagnetic complexes*

Chemical shift values of 5-coordinate iron(II) porphyrin complexes are very similar to those observed for the 6-coordinate complexes. Examples of 5-coordinate species are iron(II) alkyl complexes of *meso*-tetraphenylporphyrin, such as [(TPP)Fe($CH_2CH_2CH_3$)]$^-$ and [(TPP)Fe(CH_2CH_3)]$^-$.[243,244] Resonances for the σ-alkyl hydrogens are shielded by the ring current effect of the macrocycle.

3. *Intermediate-Spin Iron(II) Porphyrins: Observed Shifts and the Mechanism of Spin Delocalization*

Four-coordinate ferrous porphyrins have an intermediate spin state (S = 1). Some of these have been studied by various physical methods, and three possible ground

Table 8. [1]H Chemical shifts of four-, five- and six-coordinate diamagnetic metalloporphyrins.[a]

Compound	Temperature (°C)	Chemical shifts, ppm								
		Solvent	Pyrr-H	*Ortho*	*Meta*	*Para*	Alkyl-CH_2	Alkyl-CH_3	Pyrr-CH_n	*Meso*-H
Four-Coordinate Complexes										
[(*p*-TTP)Ni]	25	$CDCl_3$	8.55	7.75	7.39	2.66(Me)				
[(*o*-TTP)Ni]	25	$CDCl_3$	8.41	7.76, 1.92(Me)	7.36	7.47				
[(*p*-TTP)Zn]	25	$CDCl_3$	8.75	7.95	7.40	2.67(Me)				
[(*o*-TTP)ZN]	25	$CDCl_3$	8.59	7.89, 2.59(Me)	7.47	7.47				
Five-coordinate complexes										
$[(TTP)FeCH_2CH_2CH_3]^-$	23	benzene-d_6	8.1		7.0–7.5		$6.0x–1.5\beta$	–0.5		
$[(TTP)FeCH_2CH_3]^-$	23	toluene-d_8	8.1				–2.25	–6.19		
$[(TTP)CoCH_2CH_3]$	21	benzene-d_6	—	—	—	—	–3.07	–4.60		
$[((2,4,6\text{-}(OEt)_3)_4TPPFeCO]$	25	toluene-d_8	8.61	3.87[b],0.56[c]	7.0–7.5	4.28[b],1.58[c]				
[(TMP)RhI]		benzene-d_6	8.83	2.32,1.75(Me)	7.22,7.02	2.43(Me)				
$[(TMP)RhCH_3]$		benzene-d_6	8.75	2.26,1.75(Me)	7.20,7.07	2.43(Me)		–5.25		
[(TMP)RhH]		benzene-d_6	8.77	2.14,1.79(Me)	7.03,6.95	2.43(Me)		–39.99(H)		
$[(TTP)RuH]^-$		THF-d_8	7.60	7.78,7.74	7.35	2.55(Me)		–57.04(H)		
$[(TTP)Ru(CH_3)_2]$		THF-d_8	9.67	7.92	7.51	2.63(Me)		–2.78(CH_3)		
$[(OEP)Ru(CH_3)_2]$		THF-d_8						–3.51(CH_3)	3.88(CH_2)	9.67
$[(TTP)Ru(CHCH_3)]$		benzene-d_6	8.73	8.14,8.05	7.33,7.23	2.39(Me)		13.03(–CH),		
$[(TTP)Ru(CH_2{=}CH_2)]$		THF-d_8	8.37	7.95	7.49	2.39(Me)		–3.54($CH_2{=}CH_2$)		

(*Continued*)

Table 8. (*Continued*)

Compound	Temperature (°C)	Solvent	Chemical shifts, ppm							
			Pyrr-H	*Ortho*	*Meta*	*Para*	Alkyl-CH_2	Alkyl-CH_3	Pyrr-CH_n	*Meso*-H
Six-Coordinate Complexes										
[((2,4,6-$(OEt)_3)_4$TPPFe$(CO)_2$]	25	toluene-d_8	8.77	3.88[b],0.55[c]	6.55	4.29[b],1.58[c]				
[((*p*-*t*-Bu)$_4$TPP)Ru(CO)(Py)]		benzene-d_6	8.64	7.95,8.15	7.66,7.72	1.59(*t*-Bu)				
[((*p*-*t*-Bu)$_4$TPP)Tu$(Py)_2$]		benzene-d_6	8.69	8.28	7.61	1.44(*t*-Bu)				
[((*p*-*t*-Bu)$_4$TPP)Ru$(4\text{-CNPY})_2$]		benzene-d_6	8.80	8.83	7.72	1.47(*t*-Bu)				
[(OEP)Ru$(4\text{-CNPY})_2$]		benzene-d_6							3.85 CH_2 1.80 CH_3	9.40
[(PP)Fe$(Py)_2$]	25	D_2O/CTAB[d]							2.6–3.1	9.4, 9.56
[(TTP)Ru(NO)Cl]		benzene-d_6	9.16	8.11,7.91	~7.5	2.39(Me)				
[(TTP)Co(Py)CH_2CH_3]	21	pyridine-d_5	—	—	—	—	–3.41	–4.18		
[(TPP)Fe$(N\text{-MeIm})_2$]	–21	CD_2Cl_2	8.33	8.02	7.64	7.64				
[(TMP)Fe$(N\text{-MeIm})_2$]	–21	CD_2Cl_2	8.08	1.84(Me)	7.17	4.01(Me)				
[(TMP)Fe$(1,2\text{-Me}_2\text{IM})_2$]	–90	toluene-d_8	8.6	0.4,0.8, 3.0,3.05(Me)	7.02–7.2	2.4,2.45(Me)				
[(TMP)Co$(1,2\text{-Me}_2\text{Im})_2$]	21	CD_2Cl_2	8.9	–0.95,0.15, 2.9(2)(Me)	7.0,7.6	2.6(Me)				

[a]Taken from references 2, 92, 196, 244, 908–912, 918 and 963.
[b]–CH_2 of –OEt.
[c]–CH_3 of –OEt.
[d]CTAB = cetyltrimethylammonium bromide.

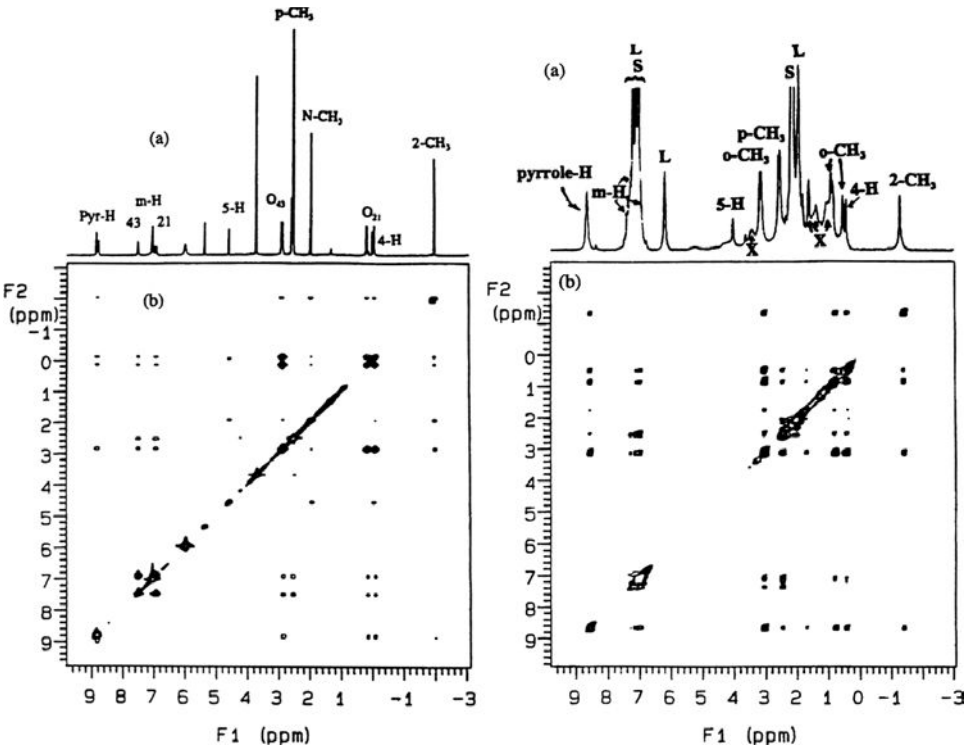

Figure 29. Left: (a) 1D 300 MHz ^{1}H NMR spectrum of $[(TMP)Co^{III}(1,2\text{-}Me_2Im)_2]^+$ in CD_2Cl_2 at +21 °C, showing the four separate *o*-CH_3 resonances observed for this complex, which are in slow exchange on the NMR time scale. (b) 2D phase-sensitive NOESY/EXSY spectrum, recorded at the same temperature with a mixing time of 700 ms, showing chemical exchange (multiple contours) and NOE (single circles) cross peaks. The peaks at 2.5, 3.7, 6.0 and 7.0 ppm are due to excess 1,2-Me_2Im in the solution, and the peak at 5.3 ppm is due to $CDHCl_2$. Right: (a) 1D 300 MHz ^{1}H NMR spectrum of $[(TMP)Fe^{II}(1,2\text{-}Me_2Im)_2]$ in toluene-d_8, recorded at −90 °C. (b) Phase-sensitive ^{1}H NOESY/EXSY spectrum recorded at the same temperature with a mixing time of 500 ms, showing both chemical exchange and NOE cross peaks. Note the similar pattern of *o*-CH_3 resonances for the Co^{III} (left) and Fe^{II} (right) complexes. In addition to the major peaks of the complex, intense resonances due to solvent (S), free ligand (L) and several unknown impurities (X) are marked; none of these show cross peaks in the 2D spectrum. Reprinted from Polam, J. R.; Shokhireva, T. Kh.; Raffii, K.; Simonis, U.; Walker, F. A. *Inorg. Chim. Acta* **1997**, *263*, 109–117, with permission from Elsevier Publishing Company.

states, each consistent with certain physical properties, have been proposed: $^3A_{2g}$ $(d_{xy})^2(d_{z^2})^2(d_{xz},d_{yz})^2$; ^3E_g $(d_{xy})^2(d_{z^2})^1(d_{xz},d_{yz})^3$; and $^3B_{2g}$ $(d_{xy})^1(d_{z^2})^1(d_{xz},d_{yz})^4$.[245] Most proton NMR studies of a variety of planar, 4-coordinate iron(II) complexes of synthetic porphyrin macrocycles favor the $^3A_{2g}$ ground state.[232,245–248] These complexes are generally synthesized in situ in benzene-d_6, toluene-d_8[246–248] or dichloromethane-d_2,[249,250] by reduction of the corresponding iron(III) porphyrins

using either the chromous, aqueous dithionite, the zinc amalgam, or sodium borohydride[251,252] reduction techniques. Representative ^{1}H NMR spectra of [(TPP)Fe] and the iron(II) complexes of deuteroporphyrin IX and protoporphyrin IX are shown in Figures 30 and 31, respectively. Large paramagnetic shifts are observed, as summarized in Table 9.

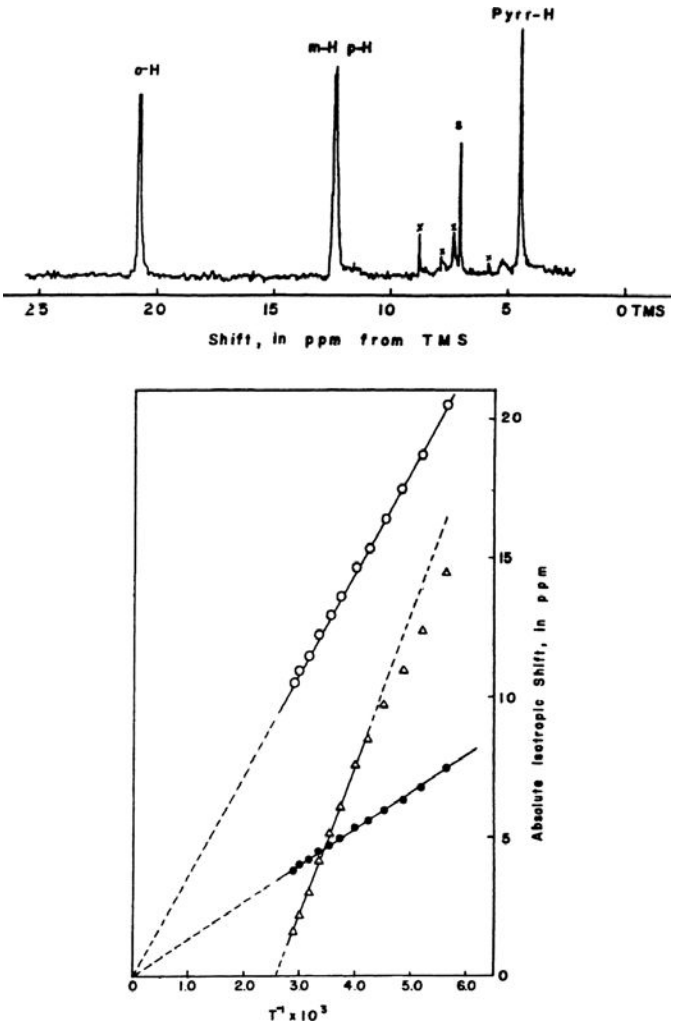

Figure 30. Top: 1D ^{1}H NMR of 0.25 mM [(TPP)Fe^{II}] in benzene-d_6 at 25 °C. The *m*-H/*p*-H clearly split apart at low temperatures to yield the resolved resonances. The *o*-H exhibits a ~8Hz doublet due to the *m*-H. S = solvent, C_6D_5H, and X = impurity. Bottom: Curie plot for the spectrum shown above. Open circles, *o*-H, filled circles; *m*-H; triangles, pyrrole-H. The shift scale is positive for the phenyl-H and negative for the pyrrole-H. Reprinted from Goff, H. M.; La Mar, G. N.; Reed, C. A. *J. Am. Chem. Soc.* **1977**, *99*, 3641–3646, with permission of the American Chemical Society.

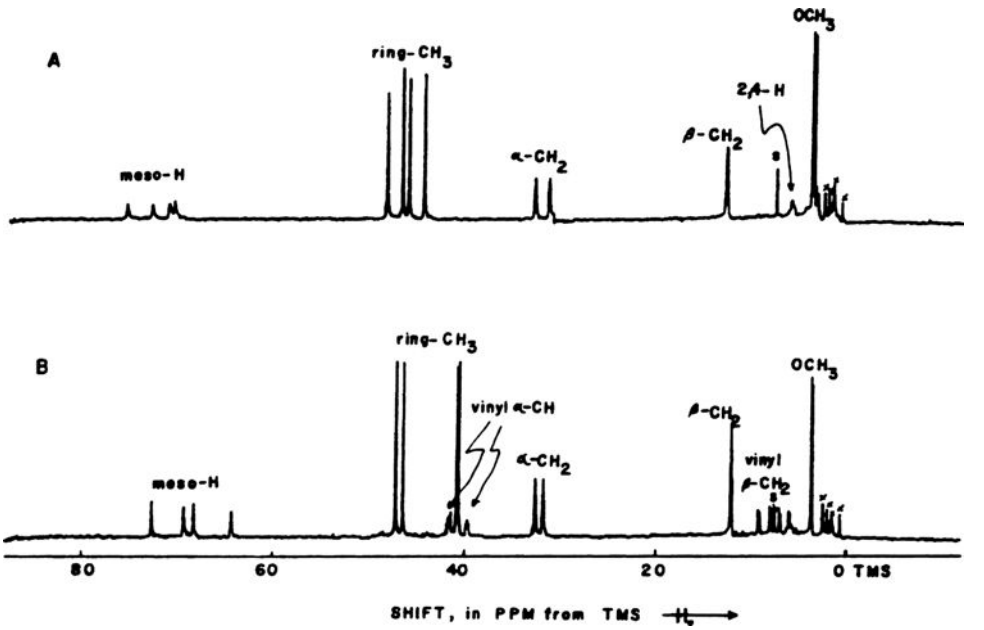

Figure 31. Proton NMR spectra of 1.0 mM benzene-d_6 solutions of (A) [(DP)Fe^{II}] and [(PP)Fe^{II}] at 25 °C. All multiplet structure characteristic of the diamagnetic porphyrin is maintained in each case. S = solvent residual C_6D_5H, and X = impurity. Reprinted from Goff, H. M.; La Mar, G. N.; Reed, C. A. *J. Am. Chem. Soc.* **1977**, *99*, 3641–3646, with permission from the American Chemical Society.

The paramagnetic shifts of the TPP, RTPP and OEP iron(II) complexes have been analyzed and discussed in detail elsewhere,[2–4,246] and can be summarized as follows: Except for the pyrrole protons, all proton resonances are significantly shifted to lower shielding, as seen in Figures 30 and 31. Such a bias of shifts in one direction indicates that at least a major portion of the paramagnetic shifts is a result of the pseudocontact interaction, a result expected, since the 4-coordinate iron(II) molecules are highly magnetically anisotropic.[246] For the synthetic (tetraarylporphinato)iron(II) derivatives the phenyl-H resonances are essentially totally pseudocontact in nature,[232] as demonstrated in Figure 28, left panel. These dominant pseudocontact shifts result from large magnetic anisotropies, $\chi_{\parallel} > \chi_{\perp}$. The paramagnetic shifts for the pyrrole protons of these complexes are found to be small and negative, which suggests that these shifts arise from both contact and pseudocontact contributions which have opposite signs. Negative pyrrole-H paramagnetic shifts are associated with the absence of spin in the $d_{x^2-y^2}$ orbital and at least one unpaired electron in the d_{xz} or d_{yz} orbital.[2,4] The π contact shift requires unpaired spin in d_{xz} and d_{yz} and strongly supports the $^3A_{2g}$ ground state configuration, $(d_{xy})^2(d_{z^2})^2(d_{xz},d_{yz})^2$.[246] The iron(II) complexes of the natural porphyrins also

Table 9. Observed isotropic shifts of four-coordinate, intermediate spin ferrous complexes of synthetic and natural porphyrins.

	Chemical shift, ppm						
Synthetic porphyrin	TPP	*m*-TTP	*p*-TTP	(*p*-Cl)$_4$TPP	OEP	T-*n*-PrP	$T_{piv}PP$
Pyrrole-H	–4.1	–4.4	–3.9	–3.9		–4.4	–4.8
Pyrrole-α-CH_2					29.7		
Pyrrole-β-CH_2					11.0		
meso-H					8.4		
o-H	12.8	13.3	13.2	12.2			11.4
m, m′-H	4.8	5.1	4.9	4.6			4.5, 4.6
p-H	4.8	5.1					5.0
m-CH_3		3.5					
p-CH_3			3.0				

	Chemical shift, ppm				
Natural porphyrin	MP	DP	PP	Br_2DP	Ac_2DP
meso-H (average)	64.1	62.0	59.3	51.1	57.9
1,3,5,8-CH_3 (average)	44.3	42.5	40.2	39.0	33.4
6,7-α-CH_2	30.5, 30.1	29.2, 27.8	29.1, 28.3	27.5, 27.5	26.1, 23.8
β-CH_2	9.8, 9.6	9.1, 9.1	8.7, 8.7	7.2, 6.9	7.2, 6.5
2,4-R	30.2, 28.4	3.0, 3.0	33.1, 31.5		9.2, 11.2
	11.2, 10.4		2.5, 1.3		
			0.5, 0.5		

[a]Data taken from Refs. 232, 246, 249 and 250.

exhibit large paramagnetic shifts at low concentrations; at higher concentrations they tend to aggregate.[246,247]

X-ray crystal structures and NMR studies of (OEP)Fe^{II} and the chlorin complex, (OEC)Fe^{II} were reported, by Strauss and coworkers, as a function of temperature.[248] In the solid state, the chlorin macrocycle is significantly S_4 ruffled, while the parent porphyrin macrocycle is nearly planar. Large paramagnetic shifts with significant pseudocontact contributions were observed for (OEP)Fe^{II}, as shown in Figure 32, which were analyzed as described earlier by Goff and La Mar.[246] However, the paramagnetic shifts of (OEC)Fe^{II} could only be fit to straight lines with large nonzero intercepts.[248] The unusual intercepts of the linear plots of the resonances of the (OEC)Fe^{II} complex were suggested to result from a large temperature-independent paramagnetism.[248] These unusual intercepts are more likely caused by a thermally-accessible excited state which has a different electron configuration and thus a very different pattern of spin delocalization via the contact interaction,[25] as demonstrated by the solid lines of Figure 33. A likely candidate for this excited state is the ^3E_g state, with $d_{xy}^2d_{z^2}^1d_{xz}^2d_{yz}^1$ electron

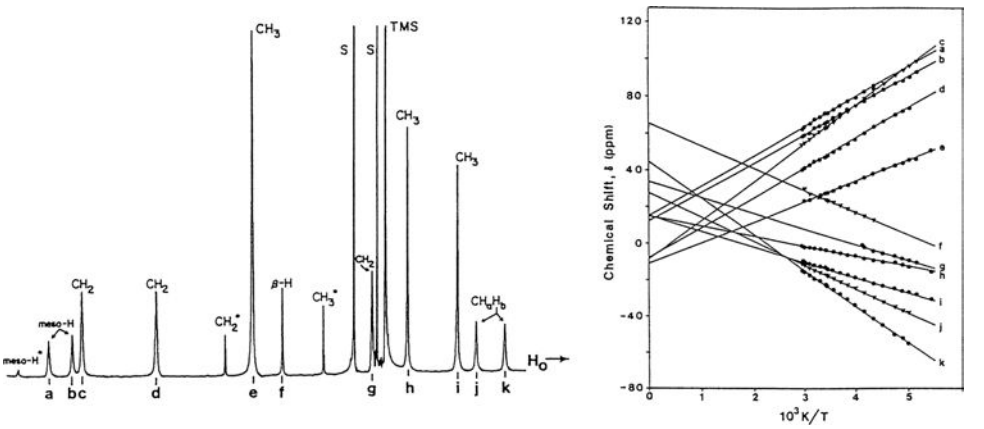

Figure 32. Left: 100 MHz ^{1}H NMR spectrum of [(OEC)Fe^{II}] in toluene-d_8 at 6 °C. Signal assignments are indicated (S = solvent). The resonances marked with asterisks are due to [(OEP)Fe^{II}]. Right: Curie plot of the resonances of [(OEC)Fe]. The solid lines are linear least-squares fits to the data, and are extrapolated to 1/T = 0. Reprinted from Strauss, S. H.; Silver, M. E.; Long, K. M.; Thompson, R. G.; Hudgens, R. A.; Spartalian, K.; Ibers, J. A. *J. Am. Chem. Soc.* **1985**, *107*, 4207–4215, with permission from the American Chemical Society.

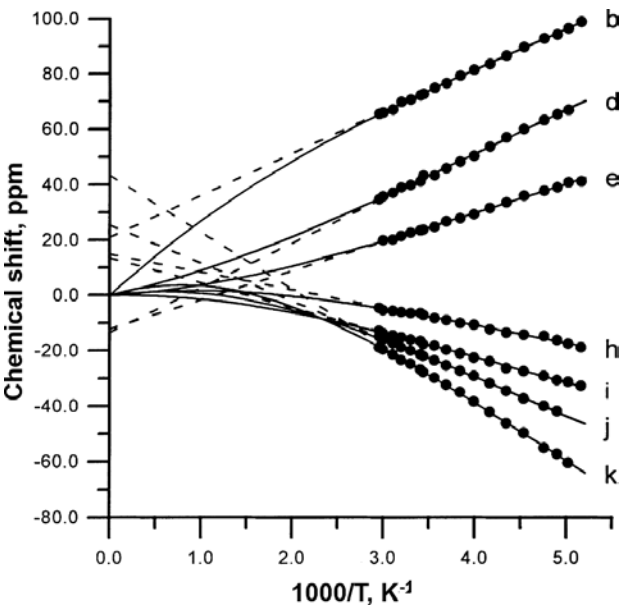

Figure 33. Plot of the fit of Eq. 13 to selected resonances of [(OEC)Fe^{II}].[192] The ΔE determined from this plot is 345 cm^{-1}. (N. V. Shokhirev, unpublished work.)

configuration which would thus remove the possibility of spin delocalization to S_{-2} and cause an apparent increased weighting of the A_{-2} orbital as the temperature is increased.

These results can be explained by using the theory of McGarvey,[245] which explains the pseudocontact and contact shifts for 4-coordinated ferrous complexes for the general case of nonaxial symmetry. $^3A_{2g}$ appears to be the ground state for all intermediate spin iron(II) porphyrins, for which the ground state is spin-orbit coupled to the ^3E_g excited state at a particular energy, 600 cm^{-1} for [(OEC)Fe^{II}] and [(OEP)Fe^{II}], and 1000 cm^{-1} for [(TPP)Fe^{II}]. With addition of the contact shift consequences of an excited state in which d_{xz} is filled (that is, the E_g excited state, Figure 33, solid line), the contact shifts are more clearly understood.

The NMR spectrum of 4-coordinate 2,7,12,17-tetra-*n*-propylporphycene, (TPrPc)Fe^{II}, Structure **14**, in toluene-d_8 at 293 K has been reported to have pyrrole-H resonances at −37.52 ppm, *meso*-H at +71.56 ppm, and α-CH_2 at +27.47 ppm.[253] These chemical shifts are consistent with an S = 1 ground electronic state.

4. *Five-Coordinate High-Spin Iron(II) Porphyrins: Observed Shifts and the Mechanism of Spin Delocalization*

Five-coordinate high-spin ferrous porphyrin complexes with imidazole or pyridine as axial ligand have been of interest because they represent not only direct models of the oxygen transport and storage proteins deoxyhemoglobin and deoxymyoglobin, but they are also fairly good models of the reduced states of cytochrome P450 and chloroperoxidase, in which the single axial ligand is a cysteine thiolate. NMR investigations have been reported for a number of these models, as will be described below. Models of the heme a_3/Cu_B center of cytochromes *c* oxidase, C*c*O, and of the heme/nonheme centers of the C*c*O-like nitrite reductases, NORs, are also discussed in this section, although many of these models start with no or unknown fifth ligand.

a. *Models of deoxyhemoglobin and deoxymyoglobin*

High-spin ferrous complexes can be obtained by addition of a moderate excess of a 2-substituted imidazole or a pyridine to the corresponding 4-coordinated intermediate-spin iron(II) derivatives at ambient temperatures.[246] The paramagnetic shifts of the pyrrole-H in the TPP complexes are positive, and those of the phenyl protons are negative, with typical paramagnetic shifts of +43.5 ppm for the pyrrole-H and −1.0 to −1.5 ppm for the *o*-, *m*-, and *p*-phenyl protons. For 5-coordinate (OEP)Fe^{II} complexes, paramagnetic shifts of −7.0 ppm (chemical shift ~+4 ppm) for the *meso*-H and +8.5 ppm for the pyrrole-α-CH_2 protons have been reported.[246]

The paramagnetic shifts of a number of natural and synthetic high-spin iron(II) porphyrinate complexes are listed in Table 10. The phenyl-H paramagnetic shifts of high-spin (TPP)Fe^{II} are small and negative (Table 10), which suggests that the high-spin complexes exhibit only very small magnetic anistropy.[246] The predominant contribution at the β-pyrrole positions must therefore be contact in origin. The pyrrole-H and α-CH_2 paramagnetic shifts are positive (to higher frequency) (Table 10), which is indicative of primarily σ spin delocalization. The small negative *meso*-H shifts suggest only moderate π delocalization to the *meso* positions. This contact shift pattern, with dominance of σ-spin transfer to the pyrrole positions, is characteristic of an unpaired electron in the $d_{x^2-y^2}$ orbital, which leads to a ground state of $(d_{xy})^2(d_{xz},d_{yz})^2(d_{z^2})^1(d_{x^2-y^2})^1$ for the high-spin ferrous ion.

Moderate π delocalization to the *meso* position was until recently considered indicative of interaction of the partially filled d_π orbitals with e-symmetry porphyrin π orbitals, because while the $3e(\pi)$ orbitals have nodes at the *meso* positions, the d_π orbitals were earlier believed to "encourage" mixing of the $3e(\pi)$ with the $4e(\pi^*)$ orbitals, thereby introducing some π electron density to the *meso* positions, as indicated in Figure 2. However, more recently it has been shown that for 5-coordinate complexes, the out-of- plane position of the iron allows the half-filled d_{z^2} orbital to directly overlap with the $3a_{2u}(\pi)$ orbital to permit π spin density to be delocalized to the *meso* carbons, as shown in Figure 34. This possibility arises solely because the metal is out of the plane of the macrocycle.[156] Thus, at the present time, there is no evidence that the $4e(\pi^*)$ orbitals are involved at all in the spin delocalization of high- or intermediate-spin Fe^{II} or Fe^{III} porphyrinates.[156] This mechanism of spin delocalization is possible for all 5-coordinate iron porphyrinates which have a half-occupied d_{z^2} orbital, and hence 5-coordinate high-spin Fe^{II} and Fe^{III} and intermediate-spin Fe^{II} and Fe^{III} should all show spin density at the *meso*-carbons via this d_{z^2}–$3a_{2u}(\pi)$ spin delocalization mechanism.[156] This mechanism should also apply to high-spin 5-coordinate nickel(II) porphyrins, as is found to be the case (Section IV.F).

Other models of deoxyhemoglobin and deoxymyoglobin involved so-called tailed picket fence porphyrins[254] and pocket porphyrins,[255] in which the axial imidazole ligand that coordinates to the metal ion is covalently linked to the porphyrin. For the tailed picket fence porphinatoiron(II) complexes, four pyrrole-H peaks were observed in the ^1H NMR spectra, centered at a chemical shift of +56 ppm (paramagnetic shift +47.5 ppm).[254,255] This paramagnetic shift is similar to those of other high-spin iron(II) porphyrinates.[246] The pyrrole-H peaks shift with temperature according to the Curie law, and at −5 °C and below new sets of resonances between +10 and −10 ppm appear, which indicated disproportionation of two molecules of the 5-coordinate, high-spin iron(II) complex to yield one 4-coordinate, intermediate-spin iron(II) complex and one diamagnetic, 6-coordinate, low-spin iron(II) complex by intermolecular sharing of axial ligands.[254]

Table 10. Isotropic shifts of five-coordinate (S = 2) synthetic and natural iron(II) porphyrins.[a]

		Phenyl							
Porphyrin	Ligand	pyrr-H	pyrr-α-CH_2	pyrr-β-CH_3	*meso*-H	*o*-H	*m*-H	*p*-H	$-CH_3$
TPP[b]	2-MeImH	43.4				–1.00	–0.70	–1.02	
	Bu-S^-	52.0				2.7, 0.0	1.3, 1.2	0.4	
m-TTP[b]	2-MeImH	43.4				–1.07	–0.62	–1.03	–0.69
	Bu-S^-	51.3				2.4, –0.3	1.2, 0.2	0.3	
p-TTP[b]	2-MeImH	43.7				–1.05	–0.67		–0.37
	Bu-S^-	52.2				2.5, –0.1	1.2, 1.1		0.8
OEP[b]	2-MeImH		8.5	–0.37	–6.7				
	Bu-S^-		10.7, 6.7	1.7	–10.4				

Natural Porphyrin	Ligand	1,3,5,8-CH_3 [d]	6,7-α-CH_2	6,7-β-CH_2	6,7-OCH_3	2,4-R
MPDME[b,c]	2-MeImH	9.8, 9.6, 9.5, 5.6	7.3, 7.1	–1.0	–0.4	7.3, 7.1[e]
						0.0, –0.6 [f]
DPDME[b,c]	2-MeImH	9.3, 9.0, 8.8, 4.3	7.3, 7.0	–1.1	–0.4	44.8, 41.3[g]
PPDME[b,c]	2-MeImH	9.5, 8.8, 8.3, 3.6	7.6, 7.2	–0.9	–0.4	7.4, 3.6[h]
						2.2, 0.9[i]
						–1.4, –2.7[j]
Br_2DPDME[b,c]	2-MeImH	9.7, 9.7, 9.5, 3.5	7.6, 7.4	–0.9	–0.4	
Ac_2DPDME[b,c]	2-MeImH	6.7, 6.7, 5.8, –1.9	6.2, 5.2	–0.6	–0.3	–1.2, –2.1[k]

[a]Data taken from Ref. 2.
[b]In benzene-d_6 at 25 °C. Shifts in ppm, referenced to diamagnetic porphyrins.
[c]*meso*-H resonances located in the region of 3 to 5 ppm and not well resolved.
[d]The methyl resonances are given in order of their position on the porphyrin ring (8,5,3,1), Structure **1**.
[e]α-CH_2.
[f]β-CH_3.
[g]Pyrrole-H.
[h]Vinyl-α-CH.
[i]Vinyl β-CH(cis).
[j] Vinyl β-CH(trans).
[k]Acetyl-CH_3.

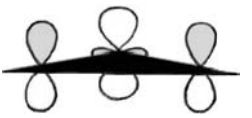

Figure 34. Overlap of the metal d_{z^2} orbital with the porphyrin $3a_{2u}(\pi)$ orbital when the metal is out of the plane of the porphyrin nitrogens.[159] Modified from Nardis, S.; Paolessee, R.; Licoccia, S.; Fronczek, F. R.; Vicente, M. G. H.; Shokhireva, T. K.; Walker, F. A. *Inorg. Chem.* **2005**, *44*, 7030–7046, with permission from the American Chemical Society.

b. *Models for the reduced states of cytochrome P450 and chloroperoxidase*

Five-coordinate mercaptide (thiolate) complexes of iron(II) in which the porphyrin is derived from substituted and unsubstituted tetraphenylporphyrins or from octaethylporphyrin, deuteroporphyrin, protoporphyrin IX dimethyl ester or etioporphyrin I, and the mercaptide moiety from *n*-butyl-, *n*-propyl and ethyl mercaptide (thiolate) (BuS^-, PrS^-, EtS^-), can be obtained by chromous acetylacetonate reduction of the corresponding iron(III) chloride complexes.[256] The α-CH_2 shifts for the alkyl thiolate ligands of the model compounds are very large and appear at around +250 ppm, whereas the signals for the β-CH_2 protons are located at around −2 ppm for the TPP complexes and at −5 to −7 ppm for the natural derivatives.[257] Based on this assignment, the methylene protons for the axial cysteinate of ferrous cytochrome $P450_{CAM}$ and ferrous chloroperoxidase were found to resonate at +279 ppm and +200 ppm, respectively.[256] As summarized in Table 10, the pyrrole protons of the TPP complexes have chemical shifts of +59 to +64 ppm, whereas the phenyl-H have fairly small shifts (*o*-H: 8–10 ppm, *m*-H: 8–9 ppm, *p*-H at 8 ppm). The ring $-CH_2$ protons for the octaethylporphyrin and etioporphyrin complexes resonate at around +11 and +15 ppm, whereas the *meso*-H chemical shift is −0.3 to −0.4 ppm.[256,257] The *meso*-H paramagnetic shifts to negative ppm can only be explained by π spin delocalization, again via $3a_{2u} \rightarrow d_{z^2}$ π donation.[156] Nevertheless, the paramagnetic shifts of at least 250 ppm for the methylene resonances of the coordinated thiolate ligand support a very efficient σ spin delocalization to this ligand.[257]

c. *Models for the heme a_3-Cu_B and heme-nonheme Fe centers of cytochrome oxidase and NO reductase*

Since the two classes of enzymes, cytochrome *c* oxidases (C*c*O) and some of the bacterial nitric oxide reductases (NOR), have very similar architectures for the three metal sites in the subunit that actually does the reduction, they are frequently grouped together into a large enzyme superfamily.[258] A very brief synopsis of the

architectures of the two classes of enzymes is that in both classes there is one heme that is bis-His-coordinated (which could be a heme *a*, *b* or *c*), while the other heme (which could be an *a*, *b*, *o* or *d*) in the C*c*Os is mono-His-coordinated, with the open site very close to the so-called Cu_B center, which is coordinated to three His, one of which is covalently linked to a carbon of the aromatic side chain of Tyr, but in the (bacterial-only) NORs there is (usually) a nonheme Fe center in place of the Cu_B center. CcOs use 4 electrons and 4 protons to reduce O_2 to 2 H_2O, while NORs use 2 electrons and 2 protons to reduce 2 NO to N_2O and H_2O.[259,260] There are also a number of other types of bacterial NORs,[259] including one type that that is a cytochrome P450 enzyme.[261] Each is the/a terminal reductase of their respective respiratory chains.

Two groups have been active in the field of cytochrome oxidase (C*c*O) models during the past ten years, those of Collman and Karlin; not surprisingly, both groups have also branched into modeling NOR. Every paper of Karlin's has the NMR spectra of the (usually) paramagnetic complexes produced and studied therein, while only a few papers of Collman have NMR spectra, and those that do are usually of the diamagnetic precursors that contain no metal. In part this is because of the generally higher molecular symmetry of the models of Karlin; Collman's models tend to have very low molecular symmetry, which means that nearly every proton is unique. Thus, although many papers have been published by Collman and coworkers, those which have an NMR or EPR component are mainly the ones discussed herein.

Several designs have been created by Collman and coworkers, including a number that could be called tailed tri-picket fence porphyrins which knit the three pickets that do not provide a ligand to the iron in the porphyrin ring into a 3-coordinate site that will bind copper, usually to three imidazoles. Designs based on a triazacyclononane, three N- or C-substituted imidazole "pickets",[262] or a single "picket" with three imidazole ligands based on a trisimidazolylmethane or — methanol,[263] with the other two pickets providing protection of the bimetallic center, have been tried. The preparation of all of these models has required monumental synthetic efforts by the members of the group.[262,263] The same three types were shown in pictures in 2001.[264]

In 2002, a paper on binuclear Fe/Cu models for C*c*O was published in which the "picket" that carries the imidazole that binds to Fe on the proximal side carries a *p*-CF_3-phenyl group bound to the 5-carbon of the imidazole ring (the carbon adjacent to the nitrogen that is part of the "picket").[265] This CF_3 group is said to be a useful analytical tool. The ^{19}F NMR spectrum of the Fe/Cu complex shows that the diamagnetic $Fe^{II}CO$ site exists as a mixture of at least three product isomers with very closely spaced ^{19}F chemical shifts of –63.4 ppm vs. $CF_3SO_3^-$ in DMF-d_7.[265] No variable temperature studies are mentioned, nor any explanation

provided for the at least three isomers; the copper center was presumed to be Cu^{I}. A ^{1}H NMR spectrum of the Fe^{II}–CO complex (under N_2) and the presumed bis-CO complex (under CO) shows shifts of the 4-H(Im) of the three distal imidazole-containing pickets (2:1 by symmetry) that are consistent with binding of CO to Cu^{I} as well as Fe^{II} under these conditions.[266] A Zn/Cu complex was also prepared, which gave a Cu^{II} EPR signal having $g_{\|} = 2.28$, $g_{\perp} = 2.07$, $A_{\|} = 175$ G, $A_{\perp} = 13$ G and $A_N(g_{\perp}) = 15$ G.[266]

Another paper, this one on distal metal effects in cobalt porphyrins related to C*c*O, was also published in 2002.[266] This paper used the tri-distal-imidazole-picket-containing porphyrin, with the fourth picket also ending in an imidazole that binds to the cobalt on the proximal side. ^{1}H NMR spectra (9–4 ppm) of the metal-free, Fe^{II}–CO, and Co^{III}–X are shown; these are low-symmetry complexes so most protons show individual resonances, most of which are not assigned. Three EPR figures are shown of the Co–O_2 complex, both in the absence and presence of Cu.[266] The spectra and the idea were based on this author's 1985 paper on the Co–O_2 complex of mono-*ortho*-acetamidophenyl-TPP, which showed hindered rotation of O_2 because of hydrogen-bonding to the N-H of the *ortho*-acetamide.[267] Resonance Raman spectra of the $^{16}O_2$ and $^{18}O_2$ complexes are also shown.[266] Later, a study of water-soluble Co^{II} porphyrins and their O_2 complexes, with similar EPR spectra, were shown.[266] Collman and coworkers have also used electrochemical methods to study the catalytic reaction of models of C*c*O with O_2.[269–272]

In a paper published in 2003 on spectroscopic evidence for a heme-superoxide/Cu(I) intermediate in a functional model of C*c*O it was reported that the NMR resonances between 9 and 10 ppm in this either high-spin or intermediate spin Fe^{II}/Cu^{I} complex are the pyrrole-H resonances, which then move to 8.2–8.4 ppm on binding O_2.[273] However, as mentioned above, the pyrrole-H for a high-spin, 5-coordinate Fe^{II} complex are in the range of +43 to +52 ppm at ambient temperatures (Table 10), and there are no resonances in the +9 to +10 ppm region. This table was taken from the chapter in *The Porphyrins*,[2] and thus these chemical shifts have been known since before 1979. For intermediate-spin Fe^{II} (assuming that the MeCN-d_3/THF-d_8 solvent produced the intermediate-spin state) the pyrrole-H resonances are at −4 to −5 ppm (Table 9), while the *o*-H of the phenyl rings are in the +11 ppm region (for the picket fence porphyrin). Thus, it is not clear what the ligation of this complex was before O_2 was added, or, in fact, afterwards; it would have been wise to have looked for resonances over the range of ± 50 ppm in order to be certain that the complex was properly characterized. Later, the same group showed the results of a single-turnover reaction in a related C*c*O model, this one having a phenoxyl group attached at the 2-carbon of the phenoxyl to the 5-carbon of one imidazole of the three used to bind the copper on the distal

side of the iron porphyrin (this is a methyl-substituted phenoxyl, with the methyl *para* to the OH).[274] An EPR spectrum is shown, which is said to be that of a phenoxyl radical, but the scale over which it was recorded was from 2600 to 4000 G. A phenoxyl radical should have hyperfine splitting from the remaining three CH phenyl ring positions, and the entire spectrum should be quite sharp and extend over not more than 20–40 G at the very most, whereas the top to bottom of the derivative shape shown covers a magnetic field range of at least 80 G. In short, the EPR spectrum looks much more like that of a Cu^{II} complex. A similar EPR spectrum was shown in the *Science* paper on this complex.[272]

A later model of NOR, with Fe both in the porphyrin ring and in the 3-imidazole site, reacts with NO to give first an EPR signal of a S = 3/2 nonheme Fe–NO center (at −80 °C), which, upon warming, changes to a S = 1/2 heme Fe–NO center (at up to 25 °C).[275] A later model of C*c*O, again with the 3-imidazole site, this time containing copper, binds to azide to produce either a $Cu^{I}/Fe^{III}–N_3$ low-spin complex with EPR g-values of 2.75, 2.22 and ~1.87 (calc) or a $Cu^{II}/Fe–N_3$ complex.[276]

Karlin has used what he calls F_8TPPFe^{II}, or $[(2,6\text{-}F_2)_4TPPFe^{II}]$, as his heme model and either "untethered" $TMPACu^{I}(MeCN)$ (TMPA = tris-(2-pyridylmethylamine),[277–279] a tetra-coordinating ligand to Cu^{I} or MePY2 (bis-(2-pyridylethyl)methylamine,[280] a tri-coordinating ligand) or a "tethered" form with two 2-pyridyl groups unchanged and the third making a connection through the 6-position (later also the 5-isomer) of that pyridyl ring to the *ortho* position of one phenyl group on the porphyrin, called ^{6}L, which are tetra-coordinating,[281,282] and other designs which are tri-coordinating[283] ligands to Cu^{I}. These designs give either 4-fold ("untethered" or 2-fold ("tethered") symmetry of the porphyrin system, which is very useful for NMR studies. In 1999 they reacted the $Fe^{II}…Cu^{I}$ complex of ^{6}L with O_2 and observed the $Fe^{III}–OO–Cu^{II}$ intermediate and the $Fe^{III}–O–Cu^{II}$ final product,[281] which were characterized by UV-vis and ^{1}H or ^{2}H (for the d_8-pyrrole complex) NMR spectroscopy at 193 K in acetone. The starting complex gave pyrrole-H resonances at +90 to +80 ppm, the μ-peroxo-bridged intermediate complex gave extremely broad pyrrole-H resonances in the same region, plus very broad pyridyl resonances at −78 ppm, and the final μ-oxo-bridged complex gave 3–4 very broad pyrrole-H resonances in the +90–100 ppm region and very broad pyridyl-H resonances at −64 ppm.[281] These chemical shifts were said to be a result of antiferromagnetic coupling to yield a S = 2 spin state. A full study of the "untethered" $(F_8TPPFe)^{II}$ + $(MePY2)Cu^{I}$ and its reaction with O_2 published the same year[284] confirmed this spin state by the Evans method[376,377] and also showed much sharper ^{1}H NMR resonances because of the higher symmetry; for the μ-oxo-bridged complex at 297 K the pyrrole-H signal was at +67.7 ppm, CH_2–PY at +23.4, +18.9 ppm, pyridyl-H at +1.2, −2.7, −23.5, −37.2 ppm, CH_2-N at −87.7, −155.4 ppm, and CH_3–N at −189.4 ppm.[284] Protonation of the

oxo bridge was also investigated, and the pK_a for that protonation was found to be 16.7–17.6 in CH_3CN or 9.6 ± 2 in water.[284] Later the "untethered" $(F_8TPP)Fe^{II}$ + $(TMPA)Cu^{I}$ + O_2 system was studied and both the μ-peroxo and μ-oxo-bridged complexes were characterized by ^1H NMR spectroscopy at −40 °C in CD_3CN (pyrrole-H +68 and +83 ppm, Py-H −11, −20, and −28 ppm, respectively).[285] Cyanide-bridged complexes were also investigated and shown to have a pyrrole-H resonance at 170 ppm for the 1:1 complex and 160 ppm for the 1Fe:2Cu complex.[286]

In a study in 2001, Karlin and coworkers investigated the reversible dioxygen addition to F_8TPPFe^{II}, where the porphyrin was deuterated on the pyrrole positions.[287] At 193 K the pyrrole-D resonance in THF solvent moved from +93 ppm (+56 ppm at RT, consistent with high-spin Fe^{II}) to +8.9 ppm upon oxygenation to form **2**, the superoxide complex of F_8TPPFe^{III}. On warming this sample to RT and then cooling to 193 K to observe the ^2H NMR yielded complete conversion to $(F_8TPP\text{-}d_8)Fe^{III}$–OH ($\delta_{pyrr}$ = +125 ppm, 193 K).[287] That **2** was not the μ-peroxo dimer, PFe^{III}–OO–$Fe^{III}P$, was clear because La Mar, Balch and coworkers have shown this species to have δ_{pyrr} = +15–17 ppm, as is discussed below in Section IV.A.6.a. ^{19}F NMR chemical shifts for $(F_8TPP)Fe^{II}$, $(THF)(F_8TPP)Fe^{III}$–O_2^- and $(F_8TPP)Fe^{III}$–OH, all at 193 K in THF, are −116, −111, −113 (1:1), and −83 (1:2:1) ppm, respectively.[287] In CH_2Cl_2 the chemical shift of (F_8TPPFe^{II}) at 293 K were quite different, +4.9 ppm, which shifts to −3 ppm at 193 K, because it is intermediate spin (S = 1) Fe^{II}, Table 9; the ^2H chemical shift for $[(F_8TPP)Fe]_2$–O_2^{2-} at 193 K is +17.5 ppm.[287] Treatment of the μ-peroxo dimer with a Lewis base such as NMeIm or *p*-diethylaminopyridine yielded (B)$(F_8TPP)Fe^{IV}$=O, δ_{pyrr} = +3.5 ppm at 193 K.[287] All of these chemical shifts are consistent with those reported by other workers in the field, as discussed in Sections IV.A.3, IV.A.6.a and IV.A.12.b. The ^{19}F chemical shifts in CH_2Cl_2 were also reported. Thermodynamic and kinetic parameters were determined in EtCN and THF solvents.[287]

Similar investigations of the TMPA-tethered $(F_6TPP)Fe^{II}$ complex called $(^6L)Fe^{II}$ the following year, without copper bound,[282] showed very similar UV-vis and ^1H, ^{19}F NMR spectra for the O_2 adduct and its final breakdown product, the Fe^{III}–OH complex, at room temperature, but in the absence of O_2 the pyrrole-H resonances in CD_2Cl_2 were at +45.0, +46.4, +47.9 and +48.4 ppm, and similar chemical shifts in acetone-d_6 and acetonitrile-d_3, and there were also resonances of the pyridyl ligands at both +24.4 (to +20.6) and −12.9 (to −8.2) ppm in CD_2Cl_2 (and the other two solvents), which was again explained by the binding of one of the pyridyl ligands to Fe^{II} (with dynamic equilibrium among two of the three pyridyl ligands).[282] However, in THF-d_8 the pyrrole-H resonances were at +52.8, +54.0, +57.7, +58.4 ppm at room temperature, and the pyrrole-D resonances of the deuterated analog were at +95 and +79 ppm (1:1, both broad) at 193 K in THF,

which suggested that at low temperatures THF was able to successfully compete for one Fe^{II} coordination site. The pyrrole-D resonance of the O_2 complex was at 8.9 ppm and of the –OH complex was at +121 ppm, both at 193 K,[282] as observed for the $(F_8TPP)Fe^{II/III}$ compounds[287] discussed above. In CH_2Cl_2 the ^2H resonances were at +43 to +46 ppm for (^{6}L-d_8)Fe^{II} complex (again indicating 5-, not 4-coordinate as for the parent $(F_8TPP)Fe^{II}$) at 293 K, a single broad resonance at 75 ppm at 193 K for the same species, 9.3 ppm for the O_2 complex, 17.0 ppm for the μ-peroxo dimer, which appeared to rearrange to the Fe^{III}–O_2^- monomer in the presence of high concentrations of O_2, and +122 ppm for the Fe^{III}–OH final decomposition compound.[282]

Addition of CO to the "empty" (^{6}L)Fe^{II} and its (^{5}L)Fe^{II} counterpart (^{6}L has the pyridyl of TMPA linked to the 6-position of the pyridine ring, while ^{5}L has it linked to the 5-position) gave Fe–CO complexes with ν_{CO} at 1976 and 1978 cm^{-1}, respectively, and ^{13}CO chemical shifts of 207.0, 207.1 (~1:1) and 206.8, 207.0 (minor) ppm, respectively, in THF-d_8.[288] For the Cu^I-bound complexes, these values for Fe–CO binding were shifted only slightly (ν_{CO} at 1971 and 1973 cm^{-1}; δ_{13CO} at 207.0 (minor), 208.1 ppm for the 6L isomer and 206.8 (minor), 207.4 ppm for the ^{5}L isomer). (The two values are believed to be for the "outside" and "inside" binding CO isomers.) For Cu^I–CO binding, using TMPA-Cu^I as the standard, ν_{CO} was at 2091 cm^{-1} in THF, δ_{13CO} at 180.3 ppm; for the Fe^{II}…Cu^I complexes, ν_{CO} was at 2093 cm^{-1} for the ^{6}L complex and 2091 cm^{-1} for the ^{5}L complex, δ_{13CO} at 178.2 and 172.4 ppm for ^{6}L and ^{5}L, respectively. ^2H NMR pyrrole shifts for the Cu^I-loaded (^{6}L)Fe^{II} and (^{5}L)Fe^{II} complexes were +54.2, +56.7 (broad) ppm in the absence and +8.8–8.9 ppm in the presence of CO for ^{6}L and +54.0–58.8 (1:1:1:1) and 8.7–8.8 ppm, respectively, for ^{5}L. These are believed to be bis-CO complexes.

A variation on this ligand system was also created in which one pyridyl ligand was replaced by an imidazole ligand, which was further bound to a phenol.[289] Upon oxygenation of this Cu^I ligand complex a superoxo complex formed which rapidly reacted with the starting Cu^I complex to form a Cu^{II}–O_2–Cu^{II} dimer.[289] With $(F_8TPP)Fe^{II}$ a μ-peroxo dimer was formed, as shown by ^1H and ^2H NMR spectroscopy. It was shown that a stable heme-peroxo-copper species can be generated even in the presence of an imidazole-phenol group in close proximity.[289]

Tridentate Cu^I ligands have also been studied in their binding to Cu^I and its diatomic ligand complexes.[290] It was again shown that the O_2 complex generates the peroxo-bridged (S = 2) complex with the Cu ligand being a bis-pyridyl, monotertiary aliphatic amine. Reactivity with CO and PPh_3 was also studied.[290]

$(F_8TPP)Fe^{II}$ + $(TMPA)Cu^I$ + O_2 generated a dimeric μ-peroxo complex which was characterized by X-ray crystallography. The Fe–O–Cu bond angle was nearly linear (171.6°) with the distance between Fe and Cu being 3.58 Å. The

pyrrole-H resonance is at +40.6 ppm (293 K), and protonated –OH bridged complex at 110 ppm.[290]

The ligand architecture of the "tethered" complexes was studied in 2007. It was found that the relatively low ν(O–O) frequencies observed in the 3-coordinate Cu ligand complexes suports a μ–η^2–η^2-peroxo ligation to both iron and Cu.[292] There is no reaction between (F_8TPP)Fe^{III}–O_2^{2-})–Cu^{II}(TMPA) and CO, as observed for (^{6}L)Fe^{III}–O_2^{2-}–Cu^{II}. Rather, the complex behaves more like it has tridentate chelation to Cu, as though the bridging pyridyl ligand is no longer coordinated. This result suggested that the bonding at the metal-peroxide core in the latter complex was weaker than in the TMPA complex. Overall, the (F_8TPP)Fe^{III}–O_2^{2-}–Cu^{II} complex appeared to be the most stable heme-peroxo-copper complex studied.[292] In another paper in 2007, the (F_8TPP)Fe^{III}–O_2–Cu^{II}(TMPA) complex were further characterized by resonance Raman, ^{1}H NMR, Mössbauer and UV-vis spectroscopies.[293] This work was summarized in a review article.[294]

Finally, this group has investigated heme-nonheme diiron complexes as models of the active site of NOR. A crystal structure of the ^{6}Lfe–O–FeCl complex was solved, where Cl^- is a sixth ligand of the nonheme Fe^{III}.[295] The complex is found to have S = 0 by SQUID susceptometry (J = –114.82 cm^{-1}). In spite of that the ^{1}H NMR spectra show pyrrole-H chemical shifts of about +15–16 ppm and pyridyl-H chemical shifts of +10–15 ppm, and larger shifts for the TMPA-CH_2 protons (+24, +27 ppm). Mössbauer data are also reported.[295] The O_2, CO and NO adducts of this complex were reported the following year. RR spectroscopy showed that NO reacted with the complex to produce a dinitrosyl complex, with ν_{NO}(nonheme) = 1798 cm^{-1} and ν_{NO}(heme) = 1689 cm^{-1}.[295] A later study of a Fe^{II}…Cu^{I} model showed that ^{6}LFe(NO) (without Cu-loading) gave a typical Fe^{II}–NO EPR spectrum, the Fe^{III}–Cu^{II} fully oxidized complex gave a high-spin Fe^{III} (g = 6) signal and a typical axial Cu^{II} signal, while the reaction of NO with this complex appears to give Fe^{II}–NO with a fairly similar EPR signal + N_2O, i.e., a reaction of 3 NO molecules with this bimetallic complex.[296] A bis-NO-bound iron porphyrin complex is believed to be an intermediate. Further elaboration of this system has been published recently,[297] in which reductive coupling of NO that fits the stoichiometric reaction:

$$2\ \bullet NO(g) + Fe^{II} + Cu^{I} + 2\ H^+ \rightarrow N_2O(g) + Fe^{III} + Cu^{II} + H_2O. \qquad (24)$$

This reaction is equivalent to one enzyme turnover. As part of this work, the authors showed that the Cu^{II} product has a "reverse" axial EPR signal, i.e., with $g_\perp > g_\parallel$.[297] This occurs when Cu^{II} has a trigonal bipyramidal structure where the axial ligands have higher ligand field than do the equatorial ligands, which thus places the d_{z^2} orbital highest in energy and yields an EPR signal with $g_\perp \sim 2.22$, $g_\parallel \sim 2.02$, $A_\perp \sim 105$ G, $A_\parallel \sim 71$ G.[297,298]

d. *Hydroxide or fluoride complexes*

In addition to thiolate ligands, other anions such as hydroxide or fluoride can also coordinate to ferrous tetraphenylporphyrin or etioporphyrin complexes. Characteristic ^{1}H NMR shifts reveal that the resulting fluoride or hydroxide complexes $[(TPP)Fe(OH)]^-$, $[(TPP)FeF]^-$, $[(Etio)Fe(OH)]^-$, $[(Etio)FeF]^-$ are 5-coordinate and high-spin.[299,300] The positive pyrrole-H shifts in the TPP complexes (+32.8 and +30.3 ppm for the hydroxide and fluoride complexes, respectively) and the positive ring methyl and methylene shifts in the OEP complexes again indicate mainly σ spin delocalization.[299,300] The pyrrole-H resonances of $[(TPP)Fe(OH)]^-$ and $[(TPP)FeF]^-$ are less deshielded than those in other 5-coordinate complexes. This bias to smaller paramagnetic shifts reflects the importance of π spin delocalization in the porphyrin ring. Such π spin density at the pyrrole carbon positions results in a partial cancellation of the proton shifts at those positions due to σ delocalization.[300] The methyl and methylene proton signals in $[(Etio)Fe(OH)]^-$ and $[(Etio)FeF]^-$ appear at low shielding (CH_3, +18.3 ppm, CH_2, +14.9, +12.5 ppm; CH_3, masked, CH_2, +13.0, +14.0 ppm, respectively) and resemble those in other high-spin iron(II) complexes, which is consistent with σ spin delocalization from the singly occupied $d_{x^2-y^2}$ orbital. The *meso*-H resonances are at −12.0 ppm and −10.5 ppm, respectively, which implies that π spin delocalization to the *meso* positions is important.[156]

e. *N-Alkyl (aryl) porphyrin complexes*

N-substituted porphyrins, such as N-alkyl and N-aryl porphyrins are models for cytochrome P450 heme alkylation. These derivatives are known to be formed as inactivation products of hepatic cytochrome P450 by a variety of molecules, including simple alkenes, such as ethylene.[301–303] N-alkylporphyrins have been identified as metabolic products of drugs produced by animal liver cytochromes P450.[302] To model certain aspects of these mechanisms, iron(II) monohalide complexes of N-substituted porphyrin complexes such as N-methyltetraphenylporphyrin, *N*-methyloctaethylporphyrin[304] or [N-(2-phenyl-2-oxoethyl) tetraphenylporphyrin],[303] and iron (II) complexes containing a metallacycle[302] were structurally characterized. A paramagnetic shift pattern characteristic of paramagnetic compounds and consistent with the C_s symmetry of the complexes,[304] is observed in the NMR spectra of these complexes. The N-methyl, N-aryl or N-alkyl resonances are observed in a unique window of +60 to +160 ppm, and reflect a σ spin transfer mechanism.[304] Two of the four pyrrole protons are shifted to the +25 to +60 ppm region (the other two are observed at slightly higher shielding than TMS), the pyrrole CH_2 protons appear in the spectral region of +5 to +35 ppm, and the

meso-H are at −9.5 ppm. The phenyl-H resonances, with one set of phenyl groups which exhibits negative *o*-H and *p*-H paramagnetic shifts and positive *m*-H shifts of essentially the same magnitude, is consistent with π spin delocalization at the *meso* positions,[156] and argues strongly for negligible axial anisotropy for two phenyl rings, and thus for the entire complex. Since the pseudocontact shifts are negligible, the pyrrole-H paramagnetic shifts are thus predominantly contact in origin and reflect the effect of the lowered symmetry. Addition of imidazole ligands to the ferrous halide complexes of N-methyltetraphenyl- and N-methyloctaethylporphyrin results in the formation of the corresponding 5-coordinate imidazole complexes in which imidazole replaces the axial halide ligand. The overall porphyrin resonance pattern and the peak width in these adducts are retained.[304]

f. *Nitrene complexes*

It was proposed that the iron complexes found upon metabolic oxidation of 1,1-dialkylhydrazines by hepatic cytochrome P450 might involve an iron-nitrene bond.[305] Therefore, (porphinato)iron-nitrene complexes were investigated. High-spin, ferrous nitrene complexes, in which the nitrene moiety is inserted into the iron-porphyrin pyrrole nitrogen bond, were synthesized by reaction of (tetraaryl-porphinato)iron(II) complexes with the free nitrene NNC_9H_{18} at −80 °C. ^{1}H NMR data favor the well-defined high-spin ferrous (S = 2) state, with a resonance pattern that parallels that of the thiolate complexes discussed above in Section IV.A.4.a(ii).

g. *Verdoheme analogs: Iron(II) complexes of octaethyloxaporphyrin, OEOP*

In 1930 Warburg and Negelein created a green pigment from heme that they called verdoheme.[306] This pigment was investigated further by Lemberg[307] and Fischer.[308] Much later, Jackson and coworkers[309] showed that a *meso*-oxaporphyrin derivative can be created by oxidation of iron(III) octaethylporphyrin in pyridine by dioxygen in the presence of a reducing agent (hydrazine or ascorbic acid). This macrocycle is called octaethyloxaporphyrin, or verdoheme, OEOP, Structure **9**, a monoanionic ligand in this resonance structure. Balch and coworkers investigated this reaction by NMR spectroscopy.[220] Treatment of diamagnetic $[(OEOP)Fe^{II}(Py)_2]^+$ with HCl yields the 5-coordinate [(OEOP)FeCl]. The ethyl CH_2 resonances extend from +7 to +31 ppm, and adjacent resonances belong to individual CH_2 groups (peaks 1,2; 3,4; 5,6; and 7,8).[220] However, the assignment of the four ethyl groups to the four symmetry-related positions on the OEOP macrocycle has not been reported. The three *meso*-H have chemical shifts of +16 and +29.5 ppm (intensities 2:1,

respectively). Such positive chemical shifts suggest significant σ delocalization to the *meso* positions, since the $d_{x^2-y^2}$ orbital is half-filled. The reaction of iron verdohemes with phenylmagnesium bromide to form paramagnetic iron-phenyl complexes has also been reported.[310]

h. *"N-confused" or "N-inverted" iron(II) porphyrins and related N-modified macrocycle complexes*

If one pyrrole ring is "inverted" so that it binds to porphyrin *meso*-carbons through the 2- and 4-carbons of that individual pyrrole ring, a 2-aza-21-carbaporphyrin is created, where the 21-CH is pointing directly at the iron.[311,312] The $Fe^{II}Br$ complex of this porphyrin, (*H*CTPP*H*)$Fe^{II}Br$, is 5-coordinate and high-spin, with β-pyrrole resonances which reflect the combination of σ and π spin density expected (+45 (1), +44 (2), +38 (2) ppm, and β-NH at −7.5 ppm, 298 K).[313] The uniquely large paramagnetic shift of the inner H(21) (812 ppm, 298 K) indicates a Fe^{II}-{C(21)-H} agostic interaction.[313] Addition of I_2 or Br_2 to a solution of (*H*CTPP*H*)$Fe^{II}Br$ in the absence of O_2 results in 1-electron oxidation to yield [(*H*CTPP*H*)$Fe^{III}Br]^+$, which has pyrrole-H resonances at +115.2, +112.9, +107.9, +91.5, +50.7, +35.9, and −32.8 ppm and the 2-NH at −31.2 ppm.[314] If instead the (*H*CTPP*H*)$Fe^{II}Br$ complex is oxidized by 1-electron with O_2, accompanied by deprotonation of the C(21)H fragment and formation of an Fe–C(21) bond, an intermediate-spin, 5-coordinate iron(III) complex, (*H*CTPP)$Fe^{III}Br$, is formed which has pyrrole-H resonances at +7.2, −10.6, −19.2, −20.6, −23.2, −24.9 and −43.2 ppm, and 2–NH at −76.6 ppm.[314] In the subsequent step of oxidation an O atom is inserted into the preformed Fe^{III}–C(21) bond to produce [(CTPP*O*)$Fe^{III}Br]^-$, which is a high-spin Fe^{III} center (pyrrole-H resonances at +106.3, +82.2, +69.4, +68.5, +53.5, +48.1 and +37.5 ppm).[314] Protonation at the 2–N atom produces (*H*CTPP*O*)FeBr, which has pyrrole-H resonances at +117.3, +80.0, +76.8, +69.1, +59.1, +31.3 and +29.3 ppm, and 2–NH at −25.0 ppm. Structures of the two latter complexes were also obtained.[314] A similar study of the iron complexes of the N-methylated and C-methylated and the C- and N-dimethylated versions of this CTPP ligand has also been reported.[315]

Another N-confused macrocycle was created in the pyriporphyrin family, by linking a 3,5-disubstituted pyridine ring in place of a pyrrole ring, with the pyridine nitrogen facing outward.[316,317] This is formally called 8,11,18,21-tetraaryl-3-aza-*m*-benziporphyrin, (PyP*H*)H, a monoanionic macrocycle with a CH pointing toward the center of the macrocycle ring. The iron(II) complex of this macrocycle[316] has similar reactivity and ^1H chemical shifts to those of the N-confused porphyrin macrocycle discussed in the preceding paragraph, and the benziporphyrins discussed below.

As a variation on the theme of different donor atoms to Fe^{II}, the 5,10,15,20-tetraphenyl-21-*N*-pyriporphyrin ligand (derived from a 2,6-substituted pyridine) was

created and its Fe^{III} complex studied briefly.[318] The numbering system of the pyridine ring in this compound is that the 2,4-H are adjacent to the link to the *meso*-carbons and the 3-H is *para* to the pyridine nitrogen. The Zn^{II} complex has been characterized structurally, and the NMR spectrum of the high-spin dichloroiron(III) and low-spin dicyanoiron(III) complexes have been reported at ambient temperature.[318] For the pyrrole-H and 2,4-H of the high-spin dichloro complex, the ^1H resonances are at +86, +80, +74 and +60 ppm, but not assigned, with the 3-H of the pyridine ring being at +30 ppm. For the same resonances of the low-spin dicyano complex, there are pyrrole-H at +16, +6.5 and +5 ppm, 2,4-H at −3 ppm, and 3-H at +10.5 ppm.[318] This pattern of shifts for the pyrrole-H resonances of the dicyanoiron(III) complex strongly suggests that it has a $(d_{xz},d_{yz})^4(d_{xy})^1$ electronic ground state, and it is likely that the angles expected for the pyridine 6-membered ring atoms as compared to the pyrrole 5-membered ring atoms would encourage ruffling of the macrocycle.

As another variation on the theme of different donor atoms to Fe^{II}, the 5,10,15,20-tetraphenyl-21-oxaporphyrin ligand (derived from furan) was created and its Fe^{II} and Fe^{III} complexes studied.[319,320] The Fe^{III} complexes are more stable,[319] except for the cyanide complex in the presence of excess cyanide, and are discussed in Section IV.A.6.c(V). The Fe^{III} complexes can be reduced to Fe^{II} with moderate reducing agents, and $(OTPP)Fe^{II}Cl$ is 5-coordinate and high-spin, with pyrrole-H resonances at +39.3, +29.5 and −6.4 ppm and the furan β-H at +33.2 ppm at 295 K.[319] The autoreduced cyanide complex, $[(OTPP)Fe^{II}(CN)_2]^-$, is diamagnetic, with furan β-H at 8.56 ppm and pyrrole-H at 8.40, 8.35, and 8.06 ppm.[319] Titration of either $(OTPP)Fe^{III}Cl_2$ or $(OTPP)Fe^{II}Cl$ with *n*-BuLi in toluene-d_8 at 205 K resulted in the formation of $(OTPP)Fe^{II}(CH_2CH_2CH_2CH_3)$.[319] This compound decomposes by hemolytic cleavage of the Fe–C bond to produce $(OTPP)Fe^{I}$, which is a low-spin d^7 complex (d_{z^2} unpaired electron), at least at low temperatures, with g-values of 2.234, 2.032 and 1.990.[319] This complex exhibited pyrrole-H resonances at +156.2, +126.5 and +76.3 ppm and furan resonance at +161.4 ppm at 273 K;[319] these are unprecedentedly large pyrrole-H shifts for iron(I) porphyrins[319] (Section IV.A.1), and this author thinks may suggest that the spin state may be high-spin d^7 at ambient temperatures. Later studies of the reactions of the Fe^{II} oxaporphyrins with phenylmagnesium bromide showed that two σ-aryl groups could bind to form an anionic complex.[320] Oxidation of that complex with Br_2 produced the mono-phenyl, mono-Br six-coordinate complex.[320]

5. *Possible Iron(II) Porphyrin π-Cation Radicals*

The first step of *meso*-oxidation of the porphyrin ring places a hydroxyl group at one *meso* position, Structure **8**, which can then be deprotonated to yield a trianion, which is usually written as a ketonic oxygen, as also shown in Structure **8**, or, if oxidized by

one electron, a single bonded oxygen with a radical at that *meso*-carbon, with two deprotonated nitrogens. Morishima *et al*.[321] reported the NMR spectrum of the one-electron oxidized complex of deprotonated mono-(*meso*-OH-OEP)Fe^{II}, recorded either in pyridine-d_5 or in pyridine/methanol/HC1 solution, which showed two resonances at −154 and −111 ppm which were assigned to the *meso*-protons based on deuterium labeling.[321] An unusual non-Curie temperature-dependence was found for all resonances. The explanation provided was that the iron(II) oxophlorin radical was thermally admixed between nearly degenerate $b_2(\pi)$ and $a_2(\pi)$ (Figure 2) radical states. As the temperature is increased, the $a_2(\pi)$ (Figure 2) contribution of the radical state was believed to become greater, thereby allowing an increase in spin density at the β-pyrrole carbon atoms. However, based in part on their EPR spectra,[321] as discussed in more detail in Section IV.A.8.f and shown in Figure 51, most of which have axial spectra, and all with g-values too different from 2.00 to be carbon/nitrogen-based radicals, these bis-(pyridine) complexes of iron oxophlorins are clearly low-spin iron(III) oxophlorin complexes which have the less-common $(d_{xz},d_{yz})^4(d_{xy})^1$ ground state, with a d_{xy}-based unpaired electron rather than a porphyrin π-based unpaired electron.[131] The anomalous temperature dependence is likely the result of thermal excitation to a low-lying $(d_{xz},d_{yz})^3(d_{xy})^2$ excited state.[131] Further discussion of this and related low-spin iron(III) complexes with the unpaired electron in the d_{xy} orbital will be presented in Sections IV.A.8.a, IV.A.8.c and IV.A.8.e.

The preparation and investigation of iron(II) nitrosyl π-cation radicals of octaethylchlorin and octaethylisobacteriochlorin, as models for reaction intermediates of nitrite reductase were also reported by Morishima and coworkers.[322] The π-cation radicals had well-resolved hyperfine-shifted NMR resonances that were characteristic of an $a_2(\pi)$-type radical state of the iron(II) chlorin (see Figure 5), because of the extremely large positive shifts of the 7,8-H of the chlorin (+190 ppm). Likewise, the 2,3,7,8-deuterium signals of the multiple isomers of the isobacteriochlorin complex were observed between +150 and +260 ppm, while the *meso*-D signals were observed at +35 to +37 ppm (5-D), +18 to +22 ppm (10,20-D) and +87 to +89 ppm (15-D).[322] Non-Curie behavior of the deuterium resonances was interpreted in terms of a valence isomerization involving the $(ON)Fe^{II}$ chlorin π-cation radical and the Fe^{II}–NO^+ chlorin complex. This valence isomerization was also observed in the presence of imidazole.[322]

6. *High-Spin Iron(III) Porphyrins: Observed Shifts and the Mechanism of Spin Delocalization*

a. *Five-coordinate, monomeric iron(III) porphyrin complexes*

^{1}H NMR spectra of simple high-spin, 5-coordinate halide complexes of synthetic and natural porphyrins have been reported and discussed in detail.[2,4] In these

complexes, the metal is significantly out of the plane, and thus gives rise to two *o*-H and *m*-H signals for TPP derivatives and two α-CH_2 resonances for OEP and *meso*-alkyl porphyrin complexes. High-spin iron(III) (S = 5/2) has a ^6A ground state, for which the g-tensor is isotropic. However, relatively large splittings of the zero-field Kramers' doublets, ±1/2, ±3/2, ±5/2, give rise to pseudocontact shifts that are proportional to D/T^2, according to Eq. 10 (Section IV.A.2), and D-values estimated from analysis of the Curie plots are similar to those measured from far-infrared magnetic resonance measurements of (DPDME)FeX.[35] The solution proton NMR spectra of a number of monomeric, 5-coordinate, high-spin iron(III) porphyrins have been reported,[161,323–339] including those having X^- = OH^-, OR^-, OO^{2-}, ROO^-, N_3^-, RC_2^-, NCS^-, $RCOO^-$, NO_3^-, $OTeF_5^-$, SO_4^{2-}, HSO_4^-, RSO_3^-, WS_4^{2-}, (triazolate)$^-$ and (tetrazolate)$^-$. Of these, the NO_3^- complex is known to have the anion binding in a bidentate fashion to iron(III) in the solid state,[336] and both it and the RSO_3^- complexes (as well as the [((TPP)Fe)$_2$SO$_4$] dimer discussed in part d of this section) are believed to have bidentate anions in solution, based on the similarity of their pyrrole-H paramagnetic shifts at 299 K (+72.5, +72.9 ppm, respectively), as compared to monodentate Cl^-, RO^- and $RCOO^-$ (78–80 ppm).[336] (Carboxylates bind to iron(III) porphyrins as monodentate ligands.[335]) Zero-field splitting constants, D, have been estimated for some of these anions, and the order of increase in D appears to be $N_3^- < NCS^- < Cl^- \sim OTeF_5^- \sim N_4C(CH_3)^- < N_4C(C_6H_5)^-$.[329,337] The ions NCS^-, Cl^-, Br^- and I^- in [(TPP)FeX] have D = 5.1, 6.0, 12.5 and 13.5 cm^{-1}, respectively,[333,334] and OH^- in (TMP)FeOH has D = 8.9 cm^{-1}.[323]

The contact shifts of the 5-coordinate high-spin Fe^{III} complexes are large at both pyrrole and *meso* positions, but the mechanism of spin delocalization differs at these two sites. The contact shifts at the β-pyrrole positions are to lower shielding for both pyrrole-H (δ_{con} ~ +61 to +68 ppm at 29 °C) and pyrrole-α-CH_2 (δ_{con} ~ +30, +34 ppm), indicating that spin is delocalized from high-spin iron(III) to these positions through the σ-bond framework of the porphyrin. Such large σ spin delocalization is observed only in metalloporphyrins in which the $d_{x^2-y^2}$ orbital of the metal is half-occupied,[2,4] and is an important signature of half-occupancy of this orbital. In contrast, at the *meso* positions, the contact shifts are to higher shielding for *meso*-H (δ_{con} = −80 ppm at 29 °C) and to lower shielding for *meso*-α-CH_2 (δ_{con} ~+50 ppm).[2,4] This reversal in sign of the contact shift is a clear indication of spin delocalization through π orbitals to the *meso* positions. Since each d-orbital of high-spin iron(III) is half occupied, it is clearly possible that both σ and π spin delocalization can occur. Of the π-symmetry frontier orbitals of the porphyrin that have proper symmetry to overlap with metal orbitals (Figure 2) in these 5-coordinate high-spin Fe^{III} complexes where the metal is out-of-the-plane of the porphyrin nitrogens, it is the $3a_{2u}(\pi)$ orbital that interacts with the metal d_{z^2} orbital via

porphyrin → metal π donation (Figure 34) to permit π spin density to be delocalized to the *meso*-carbons.[156] This mechanism is different than discussed previously,[2,4] in which it was believed that the 4e(π*) orbitals, which have large wave function coefficients at the *meso* positions (Figure 5), allowed π-back-bonding from the d_{xz} and d_{yz} orbitals as the mechanism of spin delocalization.[2,4] The small π spin density at the β-pyrrole carbons of the $3a_{2u}(\pi)$ orbital, which interacts with the d_{z^2} orbital, and the larger π spin density expected at those positions for the 3e(π) orbitals, which can interact with the half-filled d_{xz},d_{yz} orbitals, suggest that the large positive shifts observed for the pyrrole-H are actually the balance of a much larger positive shift due to σ-delocalization and a negative shift due to π-delocalization. This becomes even more clear when the proton NMR spectra of reduced hemes such as iron(III) chlorins, isobacteriochlorins, and dioxoisobacteriochlorins, as well as the numerous macrocycles created by coupled oxidation of hemes are considered, Sections IV.A.6.c(i)–(vii).

Recent additions to the findings from NMR spectroscopic studies of the halide complexes of iron(III) porphyrins includes those arising from the study of the dodecasubstituted porphyrins, especially the octaalkyltetraphenylporphyrins. These complexes have been shown to be at least partially S = 5/2,3/2 spin-admixed complexes, and are thus discussed below in Section IV.A.7.

Notable among these 5-coordinate, monomeric, high-spin iron(III) complexes is the hydroxide complex, because of the difficulty encountered in preventing its well-known hydrolysis to form the μ-oxo dimer:

$$2\ (P)FeOH \leftrightarrows (P)Fe\text{-}O\text{-}Fe(P) + H_2O. \qquad (25)$$

This problem was solved by using tetraphenylporphyrin ligands having *o,o′*-substituents on the phenyl rings, such as $-CH_3$ (TMP), $-OCH_3$ ($(2,4,6\text{-}(OCH_3)_3)_4TPP$),[323] or halogens (–F or –Cl),[326] very bulky *m,m′*-substituents such as *t*-butyl,[324] or by use of superstructured porphyrins such as "basket-handle"[340] or "picket fence"[341] or related water-soluble "picket fence" derivatives.[342] The equilibrium represented by Eq. 25 was utilized to develop a possible pH-sensitive contrast agent for MRI.[343] It, and the additional equilibria between the diaqua and hydroxide complexes, have been studied for the water-soluble tetraphenylporphinesulfonate[344] and tetrakis-(tetrafluorotri-methylaminophenyl) porphyrin[327] complexes of iron(III), and for naturally-derived hemins in aqueous detergent micelles.[345–347] It is also worth noting that while the 5-coordinate hydroxide complex of synthetic iron(III) porphyrinates is high-spin, the 6-coordinate hydroxide complexes of ferriheme proteins are often low-spin, and in some cases mixed low- and intermediate-spin.[19] This subject is discussed in Sections IV.A.10.a(ii) and IV.A.10.b.

The peroxide complex, $[(TPP)FeO_2]^-$, was prepared from $[(TPP)Fe^{II}]$ and superoxide, O_2^-,[161] and is an example of the facile redox that takes place between iron(II) and dioxygen and its redox active reduced derivatives, superoxide and peroxide. The NMR spectrum is clearly diagnostic of a high-spin iron(III) porphyrin.

Formation of $(P)Fe^{III}OO$-*t*-Bu from $(P)Fe^{II}$ and t-BuOOH requires working at very low temperatures (−70 °C), to prevent thermal decomposition to $(P)Fe^{IV}O$ and *t*-BuO•:

$$[(TMP)Fe^{II}] + t\text{-Bu-OOH} \rightarrow [(TMP)Fe^{III}\text{-OO-}t\text{-Bu}] + \text{side products}, \quad (26)$$

$$[(TMP)Fe^{III}\text{-OO-}t\text{-Bu}] \rightarrow [(TMP)Fe^{IV}{=}O] + t\text{-BuO}\bullet, \quad (27)$$

followed by further reactions. Decomposition is catalyzed by bases, such as *N*-methyl-imidazole.[331] The chemical and NMR properties of the $(Fe^{IV}{=}O)^{2+}$ unit will be discussed in Section IV.A.12. The pyrrole-H shifts of the 5-coordinate OH^-, *t*-Bu-O^-, and *t*-Bu-OO^- complexes of $(TMP)Fe^{III}$ at −70 °C (+116.4, +122, +114 ppm, respectively)[331] suggest that OH^- and *t*-Bu-OO^- have similar values of the zero-field splitting constant D, while that for *t*-BuO^- may be larger. The smaller (and similar) value of the zero-field splitting constant for OH^- and *t*-Bu-OO^- are interesting in light of the use of the OH^- complex of hemin-bound heme oxygenase as a model for the HOO^- complex of that enzyme, discussed in Section IV.A.10.b.

Latos-Grażyński and coworkers have investigated the effect of a single β-pyrrole substituent on [(TPP)FeCl] on the pattern of pyrrole-H resonances.[223] The single pyrrole-H resonance of [(TPP)FeCl] at about +80 ppm at 293 K is split into up to seven resonances, in which the 3-H (the proton in the same pyrrole ring, next to the substituent) has the most extreme shift: to lower shielding if the substituent is electron-withdrawing (+104 ppm for 2-NO_2), and to higher shielding if it is electron-donating (+49 ppm for 2-$NHCH_3$), while the remaining six pyrrole-H signals are spread around +80 ppm,[223] as shown in Figure 35.

Introduction of a single *meso* substituent into $ClFe^{III}$(OEP) results in significant changes in the geometric and/or spectroscopic properties of this complex.[348] The mono-*meso*-substituted iron(III) complexes $ClFe^{III}$(*meso*-X-OEP), where X = Ph−, *n*-Bu−, MeO−, Cl−, NC−, HC(O)−, and O_2N−, were isolated and characterized by their UV/vis and paramagnetically-shifted ^1H NMR spectra. The structures of both $ClFe^{III}$(*meso*-Ph-OEP) and $ClFe^{III}$(*meso*-NC-OEP) were determined by X-ray crystallography. Both molecules have five-coordinate structures typical for high-spin (S = 5/2) iron(III) complexes. However, the porphyrins themselves no longer have the domed shape seen in $ClFe^{III}$(OEP), and the N_4 coordination

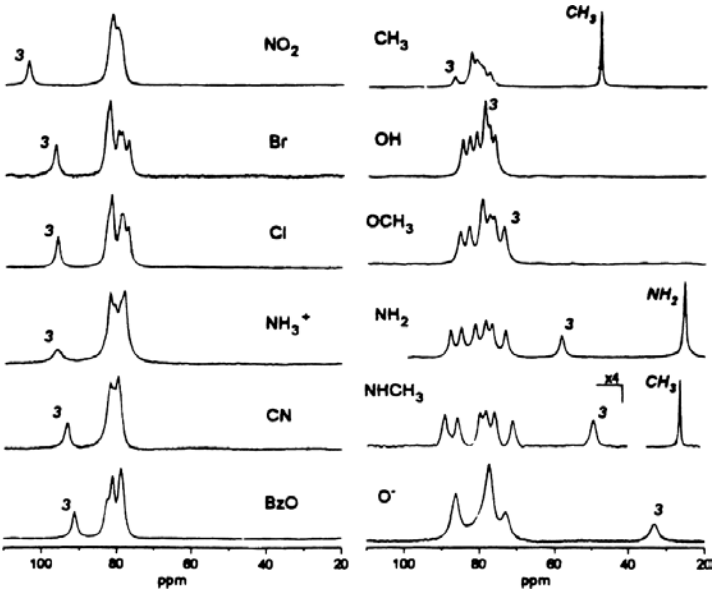

Figure 35. 300 MHz ^{1}H NMR spectra of the pyrrole-H region of a series of high-spin [(2-X-TPP)Fe^{III}Y] complexes in $CDCl_3$ at 293 K. The respective X substituents are shown on each trace. Y = Cl for all complexes except Y = OH for [(2-O-TPPFe^{III}(OH)]$^-$. The 3-pyrrole-H resonance is labeled in each case by 3. Reprinted from Wojaczyński, J.; Latos-Grażyński, L.; Hrycyk, W.; Pacholska, E.; Rachlewicz, K.; Szterenberg, L. *Inorg. Chem.* **1996**, *35*, 6861–6872, with permission from the American Chemical Society.

environment possesses a slight rectangular distortion. These high-spin, mono-*meso*-substituted iron(III) complexes display ^{1}H NMR spectra in chloroform-d solution which indicate that the conformational changes seen in the solid-state structures are altered by normal molecular motion to produce spectra consistent with C_s molecular symmetry. The CH_2 resonances at 298 K (at +43.7 and +41.6 ppm for OEPFeCl) were spread over the region +47.3 to +35.1 ppm for the *n*-butyl-substituted complex and +43.7 to +36.3 ppm for the methoxy-substituted complex, with all other complexes having resonances within these ranges. The *meso*-H resonance(s) (at −55.5 ppm for OEPFeCl) are at −57.9 (*cis*) and −74.3 (*trans*) ppm for the *n*-butyl-substituted complex and −63 (*cis*) and −75 (*trans*) ppm for the methoxy-substituted complex, but different chemical shifts for the phenyl (−65.9 (*cis*) and −58.5 (*trans*) ppm), chloro (−63.7 (*cis*) and −60.7 (*trans*) ppm), cyano (−39.8 (*cis*) and −25.3 (*trans*) ppm) and nitro (−57.3 (*cis*) and −44.4 (*trans*) ppm),[348] which perhaps reflects variable out-of-plane distances for Fe^{III} among these complexes.[156]

Iron(II) N-methylporphyrin complexes are readily oxidized to 5-coordinate high-spin iron(III) N-methylporphyrin halide cations.[349] At −50 °C in $CDCl_3$, [(MeTPP)FeCl]. has pyrrole-H chemical shifts of +128, +92, +70 ppm; the β-pyrrole

chemical shift of the N-methylpyrrole unit was found to be at 2.4 ppm using [(d_8-MeTPP)FeCl]$^+$ and detection by ^{2}H NMR spectroscopy.[349] The three remaining pyrrole rings appear to have similar average amounts of spin delocalization as those of [(TPP)FeCl]; only the modified pyrrole ring suffers sharply decreased spin transfer. The four *m*-H resonances of the N-MeTPP ligand have an almost identical average observed shift to the two of [(TPP)FeCl] at the same temperature.[349] The linewidths, Δ, of the proton resonances of the chloride and bromide complexes differ in proportion to the zero-field splitting parameter, D ($\Delta \propto D^{-2}$), with $\Delta_{Br} > \Delta_{Cl}$, as for the [(TPP)FeX] analogs.[94] The chemical shifts for [(MeOEP)FeCl]$^+$ and [(OEP)FeCl] show similar features, apart from the large asymmetry in spin delocalization caused by N-methylation.[349]

Although it had been known for more than 25 years in 1999 that alkyl groups of 5-coordinate porphyrin complexes such as OEPFeCl are diastereotopic,[350–352] Nakamura and coworkers conducted a detailed study of the coalescence of the CH_2 groups of Et, Pr and the methyl groups of *i*-Pr groups of *meso*-tetraalkyl porphyrinatoiron(III) chloride and determined the activation free energies of each.[353] The coalescence temperatures determined (−72, −60, −62 °C) are specific to the NMR frequency used (300 MHz in their case),[353] and the free energies calculated do not represent a barrier to rotation of the group, but rather a 1-point measurement of the temperature at which rotation of the alkyl group becomes fast enough to average the chemical shifts of the diastereotopic protons on the NMR timescale at 300 MHz — or the temperature at which the rate of chloride exchange averages the environments of the diastereotopic protons.[351,352] In any case, it is not a meaningful result.

The etioporphycene (Structure **14**) complex of chloroiron(III) has the bridging 9,10,19,20-"vinyl"-H at −12 ppm, the 3,6,13,16-CH_3 resonance at +79 ppm and the two α-CH_2 resonances at +37 and +24 ppm at 298 K in $CDCl_3$.[354] The iron(III)X complexes of 2,7,12,17-tetra-*n*-propylporphycene,[355] with X = PhO^-, Cl^-, Br^-, I^-, and ClO_4^-, demonstrate pyrrole-H shifts that depend strongly on anion (+65.3, +28.5, −7.8, −49.4 and −77.1 ppm, respectively, in CD_2Cl_2 at 294 K). The behavior of the chloroiron complex of etioporphycene[354] and the phenolatoiron complex of TPrPc[355] are very similar to that observed for 5-coordinate chloroiron porphyrins discussed above, but the halide and perchlorate complexes of TPrPc exhibit progressively greater spin-admixture, to the point where the perchlorate complex is quite pure S = 3/2.[355] The phenyl compound of etioporphycene appears to be low-spin d^5,[354] and will be discussed in Section IV.A.8.h.

b. *Six-coordinate monomeric high-spin iron(III) porphyrin complexes*

When ligands of medium coordinative ability with counterions that bind weakly are present, iron(III) porphyrins form high-spin, 6-coordinate complexes. This is

the case for [(TPP)FeI] in 1:3 mixed $CDCl_3/CD_2Cl_2$ solutions with added DMSO.[356] The concentration dependence of both [(TPP)FeI] and DMSO on the formation of the complex confirmed that the stoichiometry of the complex was 2 DMSO:1 Fe^{III}. The paramagnetic shift of the pyrrole-H of $[(TPP)Fe(DMSO)_2]^+I^-$ in 3:1 CD_2Cl_2:$CDCl_3$ at −72 °C is ~101 ppm, as compared to ~121 ppm for the 5-coordinate [(TPP)FeI] parent.[356] Dimethylformamide, DMF, also coordinates to [(TPP)FeI] to form 6-coordinate complexes.[195,356,357] Strongly electron-withdrawing 2,4-substituents of natural porphyrins induce a ring methyl paramagnetic shift spread similar to that observed in met-aquamyoglobins, which suggested to the authors of that work that the in-plane asymmetry in high-spin ferriheme proteins may arise from peripheral heme-apoprotein interactions.[357] However, this author suggests that it is more likely that the methyl shift spread observed for the proteins is strongly influenced by the orientation of the nodal plane of the axial (proximal) ligand such as a His-imidazole plane, via π-donation from the filled π orbital of the axial ligand to one of the half-filled d_π orbitals of high-spin iron(III), which, in turn, may decrease the amount of Fe → P π spin delocalization into the porphyrin ring involving that orbital. This hypothesis is supported by the patterns of heme methyl shifts for the resting (HS Fe^{III}) and met-cyano (LS Fe^{III}) states of horseradish peroxidase (HRP), which have heme methyl shifts in the order 5 > 1 > 8 > 3[358] and 8 > 3 > 5 > 1,[359] respectively (Figure 60 as compared to Figure 11). The reversal of the two pairs of almost oppositely-related methyl shifts is consistent with the fact that the histidine ligand lies close to the N_I–Fe–N_{III} vector of the protoporphyrin IX ring for HRP, so that for the high-spin iron(III) state, the d_{xz} unpaired electron, which can be delocalized to the histidine imidazole ring, is not as available to produce π spin delocalization to the 3e(π) orbital that has large electron density at the 1,2 and 5,6 positions of the heme[141] as is the other 3e(π) orbital, that has large electron density at the 3,4 and 7,8 positions of the heme and can interact with the d_{yz} unpaired electron to produce larger contact shifts at those positions. In contrast, for the low-spin state there is only one unpaired electron, so the 3,4 and 7,8 positions of the heme feel the majority of the spin density, even though some spin density is delocalized to the histidine ring. We have used this principle to explain the relative heme methyl shifts in high-spin Fe^{III} heme proteins,[141] as shown in Figure 60.

A major difference in the ^1H NMR spectra of 5- and 6-coordinate high-spin iron(III) porphyrins is the *reversal in sign of the paramagnetic shift for the meso-H*, as shown in Figure 24 and Table 10. This reversal was noted in 1979 for derivatives of natural hemins in DMSO-d_6.[357] The 90–95 ppm shift of the *meso*-H resonance to higher frequency, from about −55 to +40 ppm as the iron goes from 5- to 6-coordination, and presumably from out-of-plane to in-plane,

begged for an explanation at the time of the writing of the first *Porphyrin Handbook* chapter.[4] This question was answered by Cheng *et al.*,[156] who showed that the unpaired electron in the d_{z^2} orbital of 5-coordinate, but not 6-coordinate, high-spin Fe^{III} had the proper symmetry to overlap with the $3a_{2u}(\pi)$ filled porphyrin orbital, thus allowing P → Fe π donation and major spin delocalization to the *meso* positions of the heme. Thus the positive shift of pyrrole-CH_3 and α-CH_2 for 6- as compared to 5-coordinate Fe^{III} indicates that the 6-coordinate complexes have decreased π-delocalization to the β-pyrrole and *meso* positions of the porphyrinate ring because of the loss of the delocalization to the $3a_{2u}(\pi)$. This point is important in comparing the *meso*-H shifts of porphyrins, chlorins and isobacteriochlorins,[171] Table 11, discussed in the next subsection. The comparison of the size of the pyrrole–H and $–CH_2$ paramagnetic shifts of 5- and 6-coordinate high-spin (OEP)Fe^{III} and (TPP)Fe^{III}, as well as the pyrrole-H and $–CH_3$ paramagnetic shifts of the corresponding deuterohemin complex provide additional details: The pyrrole-H shifts are ~20% smaller and the pyrrole–CH_2 and $–CH_3$ shifts ~20% larger in the 6- than the 5-coordinate complexes, which indicates a smaller π contribution to the paramagnetic shifts at the β-pyrrole positions of the 6- than the 5-coordinate complexes.[357] The chemical shifts are totally consistent with lack of involvement of the $3a_{2u}(\pi)$ orbital in the 6-coordinate complexes, and there is thus no need to postulate a change in the energy of the d_π orbitals of high-spin iron(III) between the 5- and 6-coordinate complexes.[357] Comparison of 5- and 6-coordinate high-spin natural hemin derivatives suggests that some redistribution in spin density occurs among the β-pyrrole substituents upon change in coordination. Hence, upon reconstitution of heme proteins with deuterohemin, the relative pyrrole–H and $–CH_3$ shifts may serve as a useful indicator of the state of occupation of the sixth site in high-spin hemoproteins (+66, +46 ppm, respectively, 5-coordinate; +55, +64 ppm, respectively, 6-coordinate; –22, +15 ppm, respectively, low-spin).[356]

A 6-coordinate high-spin iron(III) porphyrin complex is produced if [(TPP)FeF] is reacted with hydrated tetrabutylammonium fluoride ($Bu_4NF•3H_2O$) in dichloromethane[360]: The bis-fluoride anionic complex, $[(TPP)FeF_2]^-$, is stable ($K_f = 4 \times 10^3\ M^{-1}$ at 25 °C), and is characterized by larger pyrrole-H (+85.8 ppm as compared to +72 ppm for the bis-DMSO complex discussed above) and *o,p*-phenyl-H paramagnetic shifts and slightly smaller *m*-phenyl-H paramagnetic shifts. Lack of splitting of the *o*- and *m*-phenyl signals of $[(TPP)FeF_2]^-$ supports the assumption of diaxial fluoride coordination with the metal in the plane of the porphyrin.[360,361] Greater linewidths of the ^1H signals of $[(TPP)FeF_2]^-$ suggest that the bis-fluoride complex has a smaller zero-field splitting constant D than the mono-fluoride complex discussed above.

Table 11. Isotropic shifts of five- and six-coordinate high-spin iron(III) porphyrins, chlorins and isobacteriochlorins.[a–c]

Macrocycle (anion)	Chemical shifts, ppm				
Five-coordinate Complexes					
Porphyrins	Pyrr-α-CH_2	Pyrr-CH_3	Pyrr-H	*meso*-H	
DPDME(Cl^-)[a]	36, 39, 41	45	66	–67	
OEP (Cl^-)[c,d]	39.8	—	—	–55.6	
Chlorins	Pyrr-α-CH_2	Pyrroline-α-CH_2	Pyrroline-H	meso-H	
t-OEC (Cl^-)[c,d]	50.4, 46.3,	26.7, 18.6, 15.4,	21.6, 20.3	–44.3	[15 or 20]
	45.3(3), 43.8,	10.9		–53.2	[15 or 20]
	42.9, 38.6,			–82.0	[5 or 10]
	40.9, 38.6,			–91.2	[5 or 10]
	35.5(2), 34.7				
Isobacteriochlorins					
ttt-OEiBC(Cl^-)[c,d]	70.1,61.8,	29.7, 27.2, 18.2(2),	40.7, 25.9,	–38.4	[15]
	56.8,51.7,	14.1(2), 8.0(2)	20.0, 4.3	–77.7	[10, 20]
	40.9,39.9,			–116.2	[5]
	37.6,34.6				
tct-OEiBC(Cl^-)[c,d]	68.2,62.4,	28.0, 24.0, 15.9(2),	38.7, 33.0,	–31.1, –48.8	[15]
	57.2,50.4,	14.3(2), 10.5(2)	28.0, 16.3	–69.8, –90.2	[10, 20]
	44.6,41.3,			–111.3, –126.8	[5]
	35.0,34.5				
2,7-dioxoOEiBC(I^-)[e]	79.7, 70.3,	21.3, 20.5,		–44	[15]
	65.0(2), 58.2,	18.9, 17.8		–70	[10]
	55.8, 50.3,			–83	[20]
	48.4, 48.2,			–113	[5]
	44.7, 43.4, 43.0				

(*Continued*)

Table 11. (*Continued*)

Macrocycle (anion)	Chemical shifts, ppm				
Six-coordinate Complexes					
Porphyrins	Pyrr-α-CH_2	Pyrr-CH_3	Pyrr-H	*meso*-H	
PP(Cl)[b]	39.0,38.0, 35.7(2)	63.2, 62.2, 57.7, 54.4	—	50, 46, 48 (2)	
DP(Cl)[b]	43.7(2), 41.0(2)	64.3, 61.2	0.55(2)	–29 (4)	
OEP(CF_3SO_3)[c,e]	47.9(16)	—	—	40.1 (4)	
Chlorins	Pyrr-α-CH_2	Pyrroline- α-CH_2	Pyrroline-H	*meso*-H	
t-OEC(CF_3SO_3)[c,e]	60.6(4), 52.8(2), 36.4(2), 35.5(2)	16.5(2), 8.6(2)	81.3(2)	31.7 29.6	[15, 20] [5, 10]
Isobacteriochlorins					
ttt-OEiBC(CF_3SO_3)[c,f]	84.3(2), 83.7(2), 30.6(2), 29.4(2)	19.1(2), 17.1(2)	131.0(2), 72.6(2)	34.2 21.4 0.7	[10, 20] [15] [5]
tct-OEiBC(CF_3SO_3)[c,f]	85.4(2), 82.6(2), 30.6(2), 29.2(2)	16.2(2), 12.8(2)	125.1(2), 69.8(2)	29.8 17.4	[10, 20] [15]

[a]Caughey, W. S.; Koski, W. S. *Biochemistry* **1962**, *1*, 923; solvent = $CDCl_3$, T = 35 °C. [b]Budd, D. L.; La Mar, G. N.; Langry, K. C.; Smith, K. M.; Nayyir-Mazhir, R. *J. Am. Chem. Soc.* **1979**, *101*, 6091–6096; solvent = DMSO-d_6, T = 25 °C. [c]Sullivan, E. P.; Grantham, J. D.; Thomas, C. S.; Strauss, S. H. *J. Am. Chem. Soc.* **1991**, *113*, 5264–5270.
[d]Solvent = toluene-d_8, T = 20 °C. [e]Barkigia, K. M.; Chang, C. K.; Fajer, J.; Renner, M. W. *J. Am. Chem. Soc.* **1992**, *114*, 1701–1707. Solvent = CD_2Cl_2, T = 20 °C. [f]Solvent = 50:50 *v/v* CD_2Cl_2/DMSO-d_6, T = 20 °C.

c. *Monomeric complexes of reduced or oxidized ferrihemes*

i. Iron(III) sulfhemins

Iron(III) complexes of several naturally-occurring chlorins have been investigated by ^{1}H NMR spectroscopy, including the bis-DMSO complex of the stable green sulfhemin prosthetic group extracted from sulfmyoglobin,[133,362] and that of (pyropheophorbide a)iron(III).[208,301] The positive *meso*-H paramagnetic shifts suggest 6-coordinate, bis-(DMSO) complexes in each case. Three of the ring CH_3s of sulfhemin C exhibit essentially unperturbed contact shifts relative to hemin, with only the 3-CH_3 (on the saturated ring) having a sharply attenuated shift, which thus identified the saturated ring as II[133] in the nomenclature of Structure 1; see also Structure **4** and Figure 5. For [(pyropheophorbide a)iron(III)], large paramagnetic shifts for the 1, 3, and 5-CH_3 groups, and relatively small shift for the 8-CH_3 is consistent with the saturated ring being IV[208,301] in the nomenclature of Structure 1; see also Structure 4 and Figure 5. The patterns observed are consistent with those observed for complexes of (OEC)Fe^{III},[301] discussed below.

ii. Iron(III) octaethyl- and tetraphenylchlorin

The symmetry properties of the former d_π–3e(π) (d-S_{-2} and d-A_{-2}, Figure 5) orbitals on going from the porphyrin to the chlorin, Figures 2 and 5, respectively, as well as the change in symmetry of the formerly $a_{1u}(\pi)$ orbital, the A_{-1} orbital of Figure 5, such that it can overlap with the d_{xz} orbital of the metal,[133] have important effects on the NMR spectra of high-spin iron(III) chlorins. With two chiral carbons, *trans*-(OEC)FeCl has two enantiomers that are mirror images of each other (Structure **18**). These two enantiomers have exactly the same NMR spectrum, and thus it is not necessary (and would not be possible) to separate them. The ^{1}H spectrum of high-spin *trans*-(OEC)FeCl (and its $OTeF_5^-$ and NCS^- anion counterparts) and tetraphenylchlorin (TPC) (X = Cl^-, $OTeF_5^-$) were reported and compared to those of the corresponding OEP and TPP complexes.[363] The assignments of the *meso* protons were made by selective deuteration.[363] Unlike its bis(ligand) complexes discussed in Section IV.A.8.i, (OEC)FeCl does not have C_2 symmetry. Thus, there should be a total of 16 different CH_2 resonances (12 from pyrrole-CH_2 groups and 4 from the pyrroline-CH_2 groups) from the eight ethyl groups, two different pyrroline protons, and four different *meso* protons, as reported previously.[363] Thus, the claim of slow or no interconversion between supposed ruffled conformations of *trans*-(OEC)FeCl,[364] as evidenced by the presence of four *meso*-H signals, relied on the misconception that the 5,20 and 10,15 *meso*-H could interconvert via ring inversion of the macrocycle when in a nonplanar conformation. In contrast, the observation of only two *meso*-H signals for

(*cis*-3,4-dihydroxyoctaethylchlorinato) iron(III) chloride at room temperature, which split into four resonances at low temperatures,[364] is indeed indicative of macrocycle inversion of this nonplanar chlorin.

Although the types of protons of (OEC)FeCl were assigned previously,[363] the full resonance assignments for high-spin (OEC)FeCl were obtained in the author's laboratory by using saturation transfer difference (STD) techniques,[115] as shown in Figure 36. To conduct the STD experiments, an NMR sample containing a mixture of (OEC)FeCl and its low-spin complex, [(OEC)Fe(4-Me_2NPy)$_2$]Cl, was made by adding less axial ligand to the solution of (OEC)FeCl than necessary to fully form the bis(ligand) complex (4-Me_2NPy:(OEC)FeCl = 1:1). Only the ^{1}H NMR resonances of (OEC)FeCl and [(OEC)Fe(4-Me_2NPy)$_2$]$^+$ were observed in this sample, and thus no mono(ligand) complex was present, because of its relative instability, which clearly causes it to disproportionate to the HS chloride and LS bis(ligand) complexes. The saturation transfer experiments were carried out on this mixture. Irradiation of the pyrrole-CH_2 peaks of the high-spin (OEC)FeCl form and observation of the saturation transfer to the corresponding peaks of the low-spin species, which had already been assigned (see Section IV.A.8.i), which arise from chemical exchange between the two, when recorded as a difference spectrum, allow the peaks of (OEC)FeCl to be assigned. The control spectrum (Figure 36a) shows the assignments derived for all the CH_2 groups and pyrroline protons from the experiments shown in Figure 36b–o, except for two peaks from the pyrroline-2,3-CH_2 protons, which are under or very close to the envelope of resonances of the low-spin [(OEC)Fe(4-Me_2-NPy)$_2$]Cl.[115] The saturation transfer difference experiments which led to the assignments of the four *meso* protons[115] are consistent with the assignments in the literature obtained by selective deuteration of the chlorin ring, and are thus not shown herein.

An interesting finding in the saturation transfer experiments shown in Figure 36 was that when any resonance from one of the pyrrole-CH_2 groups is irradiated, besides the chemical exchange signal from the corresponding low-spin species, there was another negative-phase signal observed from the high-spin form of (OEC)FeCl. This ST resonance was from the chemical exchange between two CH_2 protons in two different but symmetry-related (such as positions 12,13 or 7,18 or 8,17) ethyl groups. This chemical exchange arises from the binding, loss, and rebinding of chloride ion on the opposite side of the chlorin ring in the process of exchange with the 4-Me_2NPy ligands. For example, for one of the two CH_2 protons at position 8, if the chloride ion leaves when 4-Me_2NPy binds, a different Cl^- can bind to the metal center on the opposite side when 4-Me_2NPy leaves, and this proton will thereby have its chemical environment changed to that of a CH_2 proton at position 17 by virtue of the enantiomeric relationship shown in Structure 18. This process only occurs in the mixture of (OEC)FeCl and [(OEC)Fe(4-Me_2NPy)$_2$]Cl,

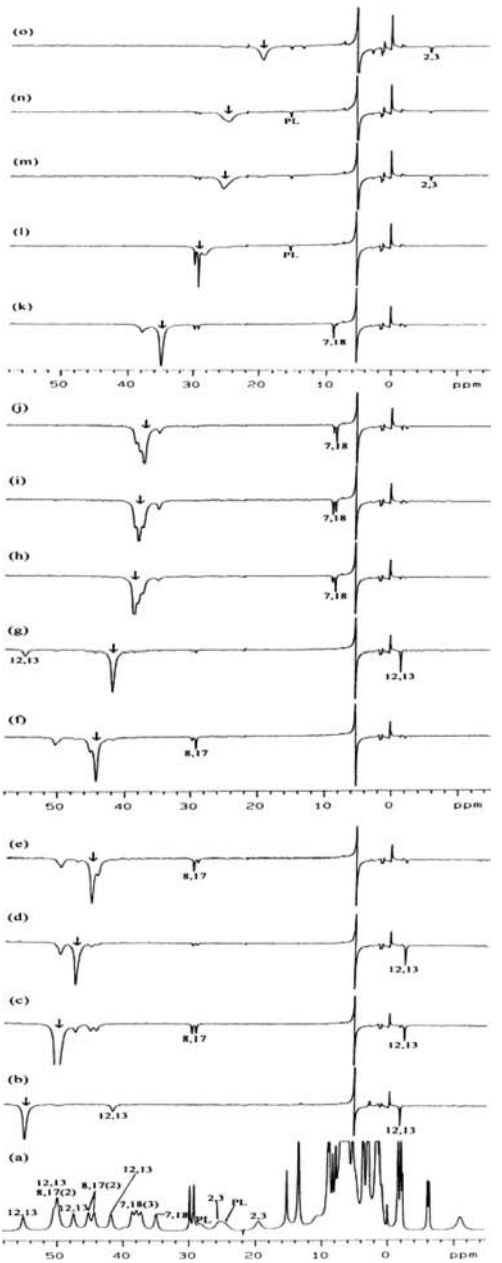

Figure 36. Bottom (a): ^{1}H NMR spectrum of high-spin (OEC)FeCl in CD_2Cl_2 at 30 °C. Above, (b-j): 1D saturation transfer difference spectra of the same complex in solution with enough pyridine-d5 to complex about 10% of the complex. An arrow shows the resonance irradiated in each STD spectrum and the negative-pointing low-spin resonance to which it correlates is numbered. Some NOEs are also observed (positive phase). Five additional STD spectra can be seen in the Supporting Information of the publication. Reprinted from the Supporting Information, Figure S8, of Cai, S.; Lichtenberger, D. L.; Walker, F. A. *Inorg. Chem.* **2005**, *44*, 1890–1903, with permission from the American Chemical Society.

among all ligand complexes studied.[115] (NMeIm and HIm bind too tightly and exchange too slowly to produce saturation transfer signals, while pyridine and 4-CNPy do not bind tightly enough and exchange too rapidly to allow resolved high-spin resonances to be observed.)[115] As a result, chemical exchange signals were observed between two symmetry-related CH_2 groups of the 4-Me_2NPy-containing sample. This chemical exchange was also observed in the NOESY/EXSY spectrum of the mixture of (OEC)FeCl and [(OEC)Fe(4-Me_2NPy)$_2$]Cl.[115] Since there are a total of 10 pyrrole-CH_2 peaks in the paramagnetically-shifted region from 36 to 56 ppm, 5 pairs of cross-peaks should be and are observed (the 2,3-CH_2 resonances are not present in this spectral region).[115]

Interestingly, in the NOESY/EXSY spectrum, only chemical exchange between the CH_2 protons of the high-spin (OEC)FeCl is observed.[115] Chemical exchange between (OEC)FeCl and [(OEC)Fe(4-Me_2NPy)$_2$]Cl was not observed in the NOESY/EXSY spectrum because of the large difference in the relaxation rates of these two species.[115] Thus, it is clear that if one wants to observe the chemical exchange or NOE between a rapidly and a slowly relaxing resonance, the steady-state experiment is a much better choice than the NOESY/EXSY experiment. By irradiating the rapidly-relaxing peak and observing the change of the slowly-relaxing peak, one can avoid the disadvantage of the NOESY experiment, the decrease of the signal during the t_1 increment and mixing time due to the fast relaxation rate of the fast-relaxing species.

The (TPC)FeCl complex pyrrole-H and pyrroline-H resonances, first reported by Strauss and coworkers,[363] were assigned, again by STD spectroscopy from the [(TPC)Fe(4-NMe_2Py)$_2$]$^+$Cl$^-$ complex.[365] In this case there are no chiral carbons. The pyrrole-H resonances are found at +86 (7,18), +77 (12,13), and +66 (8,17) ppm, while the pyrroline-H are found at −2 ppm. As is apparent, the various types of pyrrole protons in the TPC complexes and the various types of pyrrole methylene protons in the OEC complexes exhibit a large range of paramagnetic shifts ($\Delta\delta$ ~30 ppm at 300 K). For both TPC anion complexes, two pyrrole-H resonances are at higher shielding and one is at lower shielding than the pyrrole-H resonance for the TPP homologue, while for the OEC complexes the mirror image of this pattern is observed: Two sets of four pyrrole CH_2 resonances are at lower shielding and one set of four is at higher shielding than the average pyrrole CH_2 resonance for the OEP homologues. However, it should also be noted that the average pyrrole-α-CH_2 shift is larger for the chlorin (+42 ppm) than the porphyrin (+39.8 ppm), although this does not change the higher/lower frequency shift pattern by very much. This reversal in pattern on going from the TPC complexes to the OEC complexes is almost certainly due to the π component of the contact shift at the β-pyrrole position for the two types of complexes. These results suggest that the amount of spin density distributed from the iron atom to the protons in the pyrrole

groups of the macrocycle is nearly the same for 5-coordinate high-spin iron(III) porphyrins and chlorins, but is distributed quite asymmetrically among the various pyrrole positions in the chlorin complexes.[363]

The differential rate of substitution of deuterium at the two chemically different types of *meso*-H positions of OECFeCl under acidic and basic conditions,[171,366,367] as mentioned above, allowed assignment of the two types of *meso*-H; the absolute assignment of the four was achieved by saturation transfer.[115] For the 5-coordinate chloroiron(III) complex, the two *meso*-H adjacent to the reduced ring have a much larger negative paramagnetic shift, and hence a larger π contact shift, than those farther away from it (and much more negative than the *meso*-H paramagnetic shift of (OEP)FeCl as well),[171] which suggests that the S_{-1} orbital, the analog of the $3a_{2u}(\pi)$ orbital of the corresponding porphyrin, (compare Figures 2 and 5), is heavily involved in this π spin delocalization via delocalization of the d_{z^2} unpaired electron in this 5-coordinate chlorin complex.[156] But at the same time, utilizing the "antisymmetric" d_π electron, additional π spin delocalization from the A_{-1} orbital, which is the analog of the $1a_{1u}(\pi)$ orbital of the corresponding porphyrin (compare Figures 2 and 5, can also contribute spin density to the two *meso* positions closest to the pyrroline ring. Thus both the A_{-1} and S_{-1} MOs can contribute, via separate unpaired electrons and separate π molecular orbitals, to the large spin density at those positions. The *meso* positions closest to the saturated pyrrole ring are also those that exchange protons more rapidly with deuterium under acid conditions,[171] and are thus most electron-rich, which is consistent with the relative molecular orbital coefficients of A_{-1}. In contrast, for the 6-coordinate high-spin iron(III) OEC complex, the paramagnetic shift of the two *meso*-H adjacent to the pyrroline ring is only slightly smaller than that of the other two. In addition, both types of *meso*-H of the 6-coordinate complex have less positive paramagnetic shifts than the corresponding OEP complex, which is consistent with the loss of delocalization via the d_{z^2} unpaired electron to the S_{-1} orbital in this 6-coordinate complex.[156]

Peroxoiron(III) chlorin complexes have been prepared from $(OEC)Fe^{III}$ and $(TMC)Fe^{III}$ plus two equivalents of superoxide anion.[368] These complexes exhibit rhombic high-spin EPR spectra, with two resolved g-values of about 9 and 4.2. The NMR spectrum of the $(TMC)Fe^{III}(O_2^{2-})$ complex at −25 °C in acetonitrile showed three pyrrole-H resonances at +79, +72 and +67 ppm and the pyrroline resonance at −62 ppm. The *meta*-H of the mesityl rings is found at 7 ppm.[368]

iii. Two iron(III) octaethylisobacteriochlorin isomers

Iron(III) five- and six-coordinate complexes of both *trans-trans-trans* (*ttt*) and *trans-cis-trans* (*tct*) octaethylisobacteriochlorin, OEiBC, Structure **5**, have also

been investigated.[171] A number of resonances were assigned by means of deuterium substitution, with utilization of both ^{1}H and ^{2}H NMR spectroscopy, as described in Section II.D.2. For the 6-coordinate complexes of both isomers, the spread of the observed shifts of the pyrrole-α-CH_2 is larger for both isomers (*ttt*, $\Delta\delta$ = +54.9; *tct*, +56.2 ppm) than it is for the 5-coordinate complexes (*ttt*, $\Delta\delta$ = +35.5; *tct*, +33.7 ppm). Again, for the 5-coordinate complexes, the out-of-plane position of iron(III) and its anion makes each pyrrole and pyrroline proton magnetically unique in the *ttt* isomer, and those plus the *meso*-H unique in the *tct* isomer. The larger spread of pyrrole-α-CH_2 resonances for 6- vs. 5-coordinate complexes is also mirrored in the pyrroline α-CH_2 and –H resonances (see Table 11).

In the case of the 5-coordinate complexes, the *meso*-H resonances are all at very negative chemical shift, indicating large π spin delocalization to the *meso* positions because of the d_{z^2}-S_{-1} interaction[156] and the d_{xz}-A_{-1} interaction (Figure 5). The large spread (*ttt*, $\Delta\delta$ = 77.8; *tct*, 95.7 ppm) indicates π contact shifts in the order 5 >> 10,20 > 15. This is the opposite order from that observed for the rate of base-catalyzed *meso*-H exchange for deuterium in the metal-free (OEiBC)H_2 isomers,[171] and is thus the same as the order of decreasing electron density at the *meso* positions in each isomer. Thus, the π contact shift pattern at the *meso* positions is indicative of spin delocalization via filled π orbitals, that is, iBC $\rightarrow$ Fe π donation, probably mainly from the formerly $3a_{2u}(\pi)$ orbital of the porphyrin, denoted S_{-1} for the isobacteriochlorin, Figure 6, to the d_{z^2} orbital.[156]

Paramagnetic shifts of the *meso*-H in 6-coordinate DMSO adducts of the two isomers are quite different from those of the 5-coordinate complexes just discussed; as for the chlorin and porphyrin complexes, the sign reverses, indicating a dominance of σ spin delocalization at the *meso*, as well as the pyrrole positions, because of the allowed overlap between the $3a_{2u}(\pi)$-like orbital and the half-filled d_{z^2} metal orbital when the metal is out of the plane of the porphyrin nitrogens.[156] In addition, the spread of the *meso*-H resonances decreases on going from 5- to 6-coordination to 33.5 (*ttt*) and 29.1 (*tct*) ppm. More importantly, the order of the resonances changes, such that the minor π spin delocalization that occurs at the *meso* positions of the 6-coordinate complexes decreases in the order 5 > 15 > 10,20. This pattern is indicative of weak π delocalization via the filled S_{-1} π orbital of a ruffled macrocycle, that is, weak iBC $\rightarrow$ Fe π back-bonding, in addition to a large σ spin delocalization to all macrocycle positions.

iv. An iron(III) monooxochlorin complex

(Monooxooctaethylchlorinato)-iron(III) chloride, (oxo-OEC)FeCl, has been investigated by X-ray crystallography and by1D ^{1}H NMR spectroscopy.[207] The structure shows the iron to be 0.46 Å out of the 24-atom mean plane and 0.25 Å

out of the plane of the four nitrogens.[207] More recently, the CH_2 resonances of (oxo-OEC)FeI, which has much sharper NMR resonances, were assigned by saturation transfer from the $[(\text{oxo-OEC})\text{Fe}(2\text{MeImH})_2]^+\text{I}^-$ complex.[101] (oxo-OEC)FeCl has no C_2 axis, and thus there are 15 unique CH_2 resonances, which range in chemical shift from +69 to +46 ppm at 25 °C.[101] There are also four unique *meso*-H resonances, at −46, −51, −77, and −81 ppm.[101] The temperature dependence is as expected from Eq. 22.[101]

v. Two iron(III) dioxooctaethylisobacteriochlorin complexes

The ^{1}H NMR spectrum of a chloroiron(III) 3,7-dioxooctaethylisobacteriochlorin derived from OEP in CD_2Cl_2[100] shows a very similar pattern of chemical shifts for the *meso*-H, in this case indicating contact shifts in the order 5 > 20 > 10 > 15, with a spread of 69 ppm (Table 11). The spread of the pyrrole-α-CH_2 resonances is 36.7 ppm, with an average chemical shift of +49.4 ppm and that for the pyrroline α-CH_2 resonances is 3.5 ppm, with an average chemical shift of +19.6 ppm. Yang *et al*. attempted to make more detailed assignments of this complex, but were only able to separate the most highly-shifted CH_2 resonances into three groups, *a*, *b* and *c*, with assignments from 68.5 to 47 ppm of *a*, *b*, *a*, *c*, *b* and *c*.[101] Further assignments were not possible because of the lack of NOE interactions that could be detected. Except for the small spread of the pyrroline-α-CH_2 resonances, which is consistent with the structure of this reduced heme, the pattern is very similar to that of the [(OEiBC)FeCl] isomers reported by Sullivan *et al*.,[171] Table 11. Both groups who have studied the NMR spectra of the 3,7-dioxooctaethylisobacteriochlorin complex have used the iodide salt,[100,101] which has the sharpest ^{1}H resonances of all the halides.[94]

The trans-dioxoisobacteriochlorin complex, 2,12-dioxo-octaethylisobacteriochlorin complex, (2,12-dioxo-OEiBCFeI), was very easy to assign from the NOESY spectrum, based on cross peaks from 7,17 to 7,17, 8,18 to 7,17, 3,13 to 3,13 and 3,13 to 3,13-CH_2 protons. Thus, the CH_2 assignments are 7,17 > 8,18 > 8,18, 7,17 > 3,13 > 3,13 ≥ 3,13 > 3,13.[101] The 3,13-CH_2s are in the saturated rings. Thus, the largest spin density is at the 7,8 and 17,18 positions of the macrocycle, the aromatic pyrrole rings.[101]

vi. The iron(III) complex of tetraphenyl-21-oxaporphyrin

The 6-coordinate complex, $(\text{OTPP})\text{Fe}^{\text{III}}\text{Cl}_2$, which has one furan ring in place of a pyrrole ring, is a typical high-spin iron(III) complex, with pyrrole-H resonances at +86.2, +67.9 and +66.3 ppm and the furan β-H at +47.7 ppm.[319] This complex can undergo 1-electron reduction to $(\text{OTPP})\text{Fe}^{\text{II}}\text{Cl}$,[319] as discussed earlier in

Section IV.A.4.a(vii). It can also react with 2 equivalents of cyanide to produce $(OTPP)Fe^{III}(CN)_2$, which has pyrrole-H resonances at −16.2, −24.6 and −40.5 ppm and the furan β-H at −5.4 ppm.[319] In the presence of excess cyanide it is autoreduced to $[(OTPP)Fe^{II}(CN)_2]^-$, as was also discussed in Section IV.A.4.a(vii).

vii. The high-spin iron(III) complexes of mono-*meso*-octaethyloxaporphyrin and mono-*meso*-octaethylazaporphyrin

As was shown in Section IV.A.4.a(vi), oxidation of (OEP)FeCl in pyridine by O_2 in the presence of a reducing agent ("coupled oxidation") produces the *meso*-oxa derivative known as $[(OEOP)Fe^{II}Cl]$,[220] ring Structure **9**. One-electron oxidation of this complex in the presence of excess chloride ion produces $[(OEOP)Fe^{III}Cl_2]$, whose NMR spectrum in $CDCl_3$ at −60 °C shows four CH_2 resonances between +45 and +90 ppm, and two *meso*-H at +60 and +73 ppm (intensity 2:1, respectively). At 297 K these four resonances are found between +35 to +60 ppm.[369] As for the 6-coordinate iron(III) isobacteriochlorin complexes discussed earlier in Section IV.A.6.c(ii), this pattern suggests spin delocalization via the former $3a_{2u}(\pi)$ orbital of the porphyrin, that is, S_{-1} of Figure 6, in addition to a large σ-delocalization to all macrocycle positions.

Treatment of $Cl_2Fe^{III}(OEOP)$ in CD_2Cl_2 with a 1.0 M solution of KOD yields three intermediates with a total range of methylene resonances from +80 to −65 ppm.[369] These have been sorted out to identify the intermediates, first $[Cl_2Fe(OEBOH)]^-$, which has nine methylene resonances between +16.4 and +8.6 ppm and seven more strongly shielded methylene resonances from 0.2 to −11.5 ppm; second, the anion-substituted complex of the same open macrocycle, with one Cl^- replaced by OH^-; and third, the diketo form, which has only one OH^- ligand, [(HO)Fe(OEBO)].[369] The mixed anion intermediate has eight methylene resonances in the +10 to +65 ppm region and another eight in the −20 to −70 ppm region of the spectrum, which show COSY cross peaks between adjacent methylene resonances throughout most of the spectrum (1–2, 3–4, 5–6, and 7–8, but some variation in the remaining eight, with 9–10, 11–12, 13–15, 14–16). It is likely that this wide range of chemical shifts is indicative of radical character in the OEBO complex, but this has not been fully elucidated. The diketo [(HO)Fe(OEBO)] intermediate also exhibits individual methylene resonances, 13 of which are resolved outside the crowded diamagnetic region and ranges in chemical shift from +47 to 0 ppm; the two *meso*-H resonances are at +77 (1) and −7 (2) ppm.[369]

When $[(OEOP)Fe^{II}(Py)_2]Cl$ is treated with ammonia, followed by sulfuric acid and finally HCl, the complex $[(OEAP)Fe^{III}Cl]$ or $[(HOEAP)Fe^{III}Cl_2]$ is obtained if an excess of HCl is used.[370] The 5- and 6-coordinate high-spin iron(III) centers have rather different NMR spectra, with the eight ethyl CH_2 resonances of the 5-coordinate

complex lying between +39 and +50 ppm and the *meso*-H lying at about −18 and −26 ppm (intensities 1:2, respectively) at 23 °C.[370] In contrast, the four ethyl CH_2 resonances of the 6-coordinate dichloro complex lie between about +62 and +90 ppm while the *meso*-H lie at about +23 and +46 ppm (intensities 1:2, respectively) at −78 °C, and the *meso*-N–H proton is at about −46 ppm.[370] When the chloride anions are exchanged for nitrate and the complex is dissolved in DMSO-d_6, the four CH_2 resonances lie between +29 and +32 ppm at 23 °C, while only one *meso*-H resonance is observed, at +36 ppm.[370] These findings for the 6-coordinate complexes are also consistent with a combination of σ and π spin delocalization, as for the 6-coordinate iron(III) isobacteriochlorins and [(OEOP)$Fe^{III}Cl_2$] discussed in Section IV.A.6.c(ii) and the previous paragraph, respectively.

d. *Bridged dimeric complexes of high-spin iron(III) porphyrins and chlorins*

Several of the properties of μ-oxo dimers of iron(III) porphyrins, formed by hydrolysis of the hydroxide complex (Eq. 25) or by reaction of molecular oxygen with iron(II) porphyrins (Eq. 26), have been investigated, including their ^1H and ^{13}C NMR spectra, infrared and Raman spectra, Mössbauer spectra, magnetic susceptibilities and crystal and molecular spectra. These linear (P)Fe–O–Fe(P) units are antiferromagnetically coupled dimers of high-spin iron(III), although attempts to measure the coupling constant, −2J, from the temperature dependence of the magnetic susceptibility or NMR paramagnetic shifts have yielded a range of values.[2,4,371] Magnetic susceptibility results for [((TPP)Fe)$_2$O] in the solid state give −2J = 271 cm^{-1},[372] while values of 258 cm^{-1},[373] and 312 cm^{-1},[374] have been obtained from ^1H and ^{13}C NMR results, respectively. Calculation of −2J from the temperature dependence of the NMR spectra of these complexes is complicated by the possibility of pseudocontact, ZFS and contact contributions to the paramagnetic shifts.[2,4] In any case, the paramagnetic shifts of the protons of these (P)Fe–O–Fe(P) dimers are significantly different from those of the high-spin iron(III) monomers,[2,4] with all resonances occurring between +7 and +14 ppm at 320 K. Similar NMR spectra are observed for the reduced porphyrin analog, [((TPC)Fe)$_2$O], with the addition of two signals from the two types of protons in the pyrroline ring in the 2–4 ppm region.[373] The tetraphenylchlorin complex has a very similar derived value of −2J (265 cm^{-1}). The shift to lower frequency of the pyrroline protons suggests either (1) a sizable π contact shift to higher shielding, which possibly arises from spin delocalization via the $a_{1u}(\pi)$ counterpart of the porphyrin ring, that is, the A^{-1} orbital of Figure 5, or (2) a large rhombic component to the paramagnetic shift, as previously discussed for monomeric, 4-coordinate S = 1 complexes of the reduced hemes (OEC)Fe, (TPC)Fe and (TPiBC)Fe.[248]

The preparation of a series of mixed metal μ-oxo dimers of the type (P)Fe–O–Cr(P′) from (P)Fe^{II} and (P′)Cr=O hve been reported.[375] Their ^{1}H NMR spectra are characterized by resonances of the (P)Fe in the positions found for the symmetrical (P)Fe–O–Fe(P) dimer, and a resonance at +38 ppm due to the pyrrole-H of the chromium porphyrin unit. The peak at ~13 ppm was not present when (OEP)Fe^{II} was used as the iron starting material instead of (TPP)Fe^{II},[375] which confirms that this resonance is due to the pyrrole-H of the iron unit. The temperature dependence of the magnetic susceptibility of the mixed-metal dimer leads to its formulation as antiferromagnetically coupled Fe^{III} (S = 5/2) and Cr^{III} (S = 3/2), which yields S′ = 1, with −2J ~260–300 cm^{-1} and D_{Fe} and g_{Fe} ranging from 3.8 to 4.9 cm^{-1} and 1.98–2.05, respectively, if it is assumed $D_{Cr} \sim -1$ cm^{-1}.[375] Similar binuclear μ-oxo dimers can be made in which the iron complex is the phthalocyanine.[375]

An intermediate in the oxidation of 4-coordinate iron(II) porphyrins to the (P)Fe–O–Fe(P) μ-oxo dimer via Eqs. 28a–c:

$$\underset{A}{(P)Fe^{II}} + O_2 \rightarrow \underset{B}{(P)FeO_2}, \tag{28a}$$

$$\underset{B}{(P)FeO_2} + \underset{A}{(P)Fe^{II}} \rightarrow \underset{C}{(P)Fe^{III}–OO–Fe^{III}(P)} \rightarrow 2\underset{D}{(P)Fe^{IV}=O}, \tag{28b}$$

$$\underset{D}{(P)Fe^{IV}=O} + \underset{A}{(P)Fe^{II}} \rightarrow \underset{E}{(P)Fe^{III}–O–Fe^{III}(P)}, \tag{28c}$$

the μ-peroxo dimer, C, of tetra-(*m*-tolyl)porphinatoiron(III), has been detected by NMR spectroscopy at low temperatures.[378] The μ-peroxo complex, C, has a larger paramagnetic shift for the pyrrole-H at all temperatures, and has an antiferromagnetic coupling constant, −2J, that is about 30% smaller than that for the μ-oxo dimer, E, and the magnetic moment[376,677] decreases from 2.6 μ_B at −50 °C to about 2.2 μ_B at −80 °C, both consistent with weaker antiferromagnetic coupling in the μ-peroxo complex.[378]

Addition of dioxygen to 2,7,12,17-tetra-*n*-propylporphycene, (TPrPc)Fe^{II}, produces its μ-peroxo dimer, which has a pyrrole-H chemical shift of +17.99 ppm in d_8-toluene at 173 K and shows distinct nonCurie temperature dependence because of strong antiferromagnetic coupling.[253] It is stable at 203 K but converts to the μ-oxo dimer at higher temperatures. When the μ-peroxo dimer is reacted with nitrogen bases (pyridine-d_5, NMeIm) it forms the ferryl complex, B(TPrPc)Fe^{IV}=O, which has pyrrole-H at −1.32 ppm, *meso*-H at +11.80 ppm at 223 K; it reacts with triphenylphosphine to produce triphenylphosphine oxide.[253]

Related reactions of 4-coordinate (P)Fe^{II} complexes with *p*-benzoquinone and its derivatives yield hydroquinone dianion bridged iron(III) porphyrin dimers that are characterized by very small antiferromagnetic coupling constants, –2J ~7.2–31 cm^{-1}.[379] Accordingly, the ^1H NMR spectra of these complexes are fairly characteristic of high-spin iron(III) monomeric complexes, with the pyrrole-H resonance at +62–74 ppm at 23 °C.[380] However, the Curie plots show the opposite type of curvature from that of simple monomeric high-spin iron(III) complexes, due to the (small) antiferromagnetic coupling between the iron(III) centers in these dimers.

Several μ-nitrido dimers have been reported, including [(TPP)Fe–N–Fe(TPP)],[381] [(Pc)Fe–N–Fe(Pc)],[382] mixed porphyrin-phthalocyanine complexes such as [(TPP)Fe–N–Fe(Pc)],[383] all of which involve formally Fe^{III}–Fe^{IV} paramagnetic centers, in which each iron is said to behave as though it is +3.5, that is, a delocalized single unpaired electron. This contrasts with the Fe–Ru analog dimers, which behave as Fe^{IV}–Ru^{III} centers.[384] For the di-iron compounds, a single unpaired electron could result from antiferromagnetic coupling of high-spin iron(III) (S = 5/2) and high-spin iron(IV) (S = 2), intermediate-spin iron(III) (S = 3/2) and intermediate-spin iron(IV) (S = 1), or low-spin iron(III) (S = 1/2) and low-spin iron(IV) (S = 0), although the precedent of the μ-oxo dimer of iron(III) porphyrins would suggest that these 5-coordinate centers should be high-spin. In any event, neither the high-spin/high-spin nor intermediate-spin/intermediate-spin antiferromagnetically coupled cases could allow a delocalized electron, for transfer of one electron from iron(III) to iron(IV) would create a different spin state, and the corresponding Fe^{III}–Fe^{IV} μ-nitrido dimer of the iron cyclams has localized valences.[385] The mixed-valence Mn–Fe d^8 systems behave as Mn^{IV}–Fe^{III} and are formally diamagnetic.[386] One-electron oxidation of [(TPP)Mn–N–Fe(Pc)] produces the Mn^{IV}–Fe^{IV} oxidation state, and the oxidized dimers can coordinate pyridine to form mono- and bis-(pyridine) adducts. Up to six additional electrons can be removed from the (IV)–(IV) dimer. The complexes have been characterized by electrochemical techniques, EPR, Mössbauer and resonance Raman spectroscopy,[386] but not by NMR spectroscopy.

Dimeric dinegative oxoanion SO_4^{2-} and CrO_4^{2-}, $[((P)Fe)_2XO_4]$ complexes have been shown to have both ^1H and ^{13}C NMR resonances that are sharp and at very similar paramagnetic shifts to those of monomeric, high-spin iron(III) complexes,[336,387] which suggests that antiferromagnetic coupling is very weak or nonexistant in these dimeric complexes. Very small deviations from Curie behavior were noted, suggesting that zero-field splitting of high-spin iron(III) is very small; this fact and the slightly smaller pyrrole-H paramagnetic shifts of $[((TPP)Fe)_2(SO_4)]$, suggest that the sulfate anion may be acting as a bidentate chelating ligand to each iron(III).

High-spin iron(III) oxophlorins readily dimerize intermolecularly when in the *meso*-hydroxyporphyrin resonance form,[388] Structure **8**. In these 5-coordinate

high-spin iron(III) dimeric centers, antiferromagnetic coupling is very weak and the ^{1}H NMR shift pattern is similar to those of the monomeric chloro- or bromoiron(III) complexes discussed in Section IV.A.6.c(v). The eight ethyl-CH_2 resonances lie between +18 and +39 ppm and show significant differences in T_1s and T_2s depending on their distances from the other iron(III) center, while the *meso*-H resonances are observed at −28 and −98 ppm (intensities 2:1, respectively) in $CDCl_3$ at 28 °C,[388] as observed for other 5-coordinate high-spin iron(III) macrocycles discussed above.

A type of intermolecular dimer formation has also been observed for the unsymmetrically substituted 5-(2-hydroxyphenyl)-10,15,20-tritolylporphyrin complex of iron(III), in which the *o*-OH functions of one molecule are deprotonated and bind as PhO^- ligands to the Fe(III) of a second molecule, which in turn binds its deprotonated *o*-OH function to the iron(III) of the first. Despite this intramolecular dimeric structure, the proton NMR spectra reveal pyrrole-H signals in the +80 ppm region at 25 °C, which is diagnostic of an isolated high-spin iron(III) center, and the magnetic moments in solution[376,377] ($6.0 \pm 0.2\ \mu_B$) and solid-state ($5.91 \pm 0.05\ \mu_B$) match the spin-only value for high-spin iron(III), thus indicating that antiferromagnetic coupling is extremely small.[328]

Several covalently linked di-iron(III) diporphyrins, linked through an alkyl chain to the *ortho*-OH of a single phenyl ring on each porphyrin, have been reported by Wolowiec and Latos-Grażyński, who have also studied the cyanide coordination of them.[389] High-spin complexes in which each iron is coordinated to one cyanide, a bridging low-spin tricyano complex, plus a low-spin tetracyano complex are observed. The NMR spectrum of the tricyano complex that includes a μ-cyano bridge shows evidence of at least 16 pyrrole-H resonances between −12 and −19 ppm at 293 K in $CDCl_3$. This is believed to be due to the unsymmetrical nature of the μ-cyano bridge.[389] Oligomerization of the iron(III), gallium(III) and manganese(III) complexes of (2-hydroxyphenyl)triphenylporphyrin creates head-to-tail trimeric complexes that have been characterized by X-ray crystallography and by NMR spectroscopy.[390–392] The unique 3-H resonances of the iron(III) trimer occur at −90, −95 and −99 ppm for the different stereoisomers, while the other pyrrole-H resonances occur in the +62–81 ppm range.[390,392] The diamagnetic gallium(III) trimer has the 3-H resonances at 1.82, 2.18 and 2.82 ppm.[391] Mixed-metal trimers have also been prepared and characterized by NMR spectroscopy.[392]

7. *Intermediate-Spin Iron(III) Porphyrins: Observed Shifts and the Mechanism of Spin Delocalization*

When weakly-coordinating anionic axial ligands such as ClO_4^-,[15,393–400] $CF_3SO_3^-$,[374] SbF_6^-,[400–402] and $C(CN)_3^-$[374,403] or two weakly-basic pyridine ligands (in the case of β-pyrrole alkyl-substituted porphyrins such as OEP and etioporphyrin, EP), such

as 3-chloropyridine[404] and 3,5-dichloropyridine;[400,405] are present, iron(III) porphyrins exhibit a broad derivative-shaped EPR feature near g = 4[374,397,400,405] and NMR spectra that show anti-Curie behavior.[15,334,396,406] Many of these spectral features are similar to those of the cytochromes *c′*, including the EPR,[400,407,408] near-IR MCD,[400,409,410] Mössbauer[395,402,405,411] and resonance Raman[412,413] spectra, and the NMR spectra of *Chromatium vinosum* cytochrome *c′*, but not those of *Rhodospirillum rubrum*, *Rhodospirillum molischianum* and *Rhodopseudomonas palustris*.[414] Thus, it may be that *C. vinosum* cytochrome *c′* is the anomaly among this type of cytochromes *c*. Interestingly, it is the *C. vinosum* protein that has been studied most frequently by other spectroscopic techniques. The cytochromes *c′* are known to contain 5-coordinate heme *c*, with no distal residues present that are capable of hydrogen-bonding to endogenous ligands.[415,416] Moss and Maltempo have proposed the existence of an intermediate-spin (S = 3/2) state with a quantum-mechanical admixture of the more common high-spin (S = 5/2) state for the protein.[411,417,418] This differs from a simple S = 3/2 → S = 5/2 equilibrium, in that the EPR and Mössbauer features are unique, rather than simply a superposition of the expected spectra of the two spin states, and the ground state is composed of contributions from each state.[406]

The dramatic anti-Curie dependence of the pyrrole-H resonance of [(TPP)FeOClO$_3$] from about −20 ppm at −45 °C to +20 ppm at +54 °C[396] is a now-familiar hallmark of the ^{1}H NMR spectra of spin-admixed S = 3/2,5/2 model heme species. Smaller shifts in the *meso*-H (~ 0 to about −9 ppm) and pyrrole-α-CH$_2$ (−40 to about −33 ppm from −40 to +50 °C) resonances are observed for [(OEP)FeOClO$_3$].[334,374,396] At low temperatures, the S = 3/2 contribution to the spin-admixed state increases,which leads to depopulation of the $d_{x^2-y^2}$ orbital of the S = 5/2 state, and thus decreases the large σ contact shift contribution so characteristic of simple high-spin 5- and 6-coordinate iron(III) porphyrins (Section IV.A.6.a and IV.A.6.b). The NMR spectra have been fit to a model based on a d-orbital splitting pattern modified from the tetragonal pattern on the right side of Figure 1, with the energies of d_{z^2} and $d_{x^2-y^2}$ reversed,[406] where $\Delta = E_{x^2-y^2} - E_{xy} = 34{,}100$ cm^{-1}, $\delta_1 = E_{xz,yz} - E_{xy} = 2{,}500$ cm^{-1}, $\delta_2 = E_{x^2-y^2} - E_{z^2} = 25{,}000$ cm^{-1} and $g_\parallel = 2.0$, and the best values of $\zeta = 200$ cm^{-1}, $g_\perp = 4.77$, with the ground state wave function composed of 61% $^4A_2$ and 39% $^6A_1$ for [TPPFeOClO$_3$], and $\zeta = 120$ cm^{-1}, $g_\perp = 4.39$, with the ground state wave function composed of 80% $^4A_2$ and 20% $^6A_1$ for [(OEP)FeOClO$_3$].

Weak-field anions tend to stabilize the S = 3/2 ground state of the spin-admixed 3/2,5/2 systems, increasing in the order $CF_3CO_2^- \sim CF_3SO_3^- < C(CN)_3^- < ClO_4^-$ for (TPP)Fe^{III} [374] and $CF_3SO_3^- < C(CN)_3^- \sim ClO_4^- < SbF_6^-$ for (OEP)Fe^{III}.[374,400] The low-basicity ligand, 3,5-dichloropyridine, appears to stabilize the S = 3/2 ground state in [(OEP)Fe(3,5-Cl$_2$Py)$_2$]$^+$ about as well as ClO_4^- or SbF_6^-.[400] For *para*-substituted derivatives of [(TPP)FeOClO$_3$], the S = 5/2 contribution increases in

the order *p*-OCH_3 < *p*-H < *p*-Cl < *p*-CF_3,[399] so electron-donating substituents on the phenyl rings favor the S = 3/2 ground state, where the $d_{x^2-y^2}$ orbital is depopulated. Consistent with this, the 2,4,6-trimethoxy derivative, [((2,4,6-$(OCH_3)_3)_4$TPP)$FeOClO_3$] has the most negative reported chemical shift of the pyrrole-H (−30.6 ppm),[398] and thus appears to be the "purest" S = 3/2 complex. However, the temperature dependence of the paramagnetic shifts has not been reported. The shift to higher frequency (δ_{obs} positive) of the *m*-phenyl-H indicates a pseudocontact contribution of positive sign, consistent with the EPR parameters ($g_\perp > g_\parallel$) obtained for [(TPP)$FeOClO_3$].[406]

A series of perchloratoiron(III) complexes of four 2,6- and one 2,4,6-phenyl substituted tetraphenylporphyrin ligands have been investigated as a function of temperature by ^{1}H NMR spectroscopy.[83] The 2,6-phenyl substituents consisted of –H, –F, –Cl, and –Br, and the 2,4,6-phenyl substituents were $-CH_3$. A wide range of temperature dependences, ranging from negative slopes with very large positive 1/T = 0 intercepts (Cl ~ Br > CH_3 > H) to positive slope with very large negative 1/T = 0 intercept (F), were observed, as shown in Figure 37. The NMR results were combined with EPR spectroscopic data, theoretical calculations and curve fitting procedures to arrive at a consistent overview of the variety of temperature

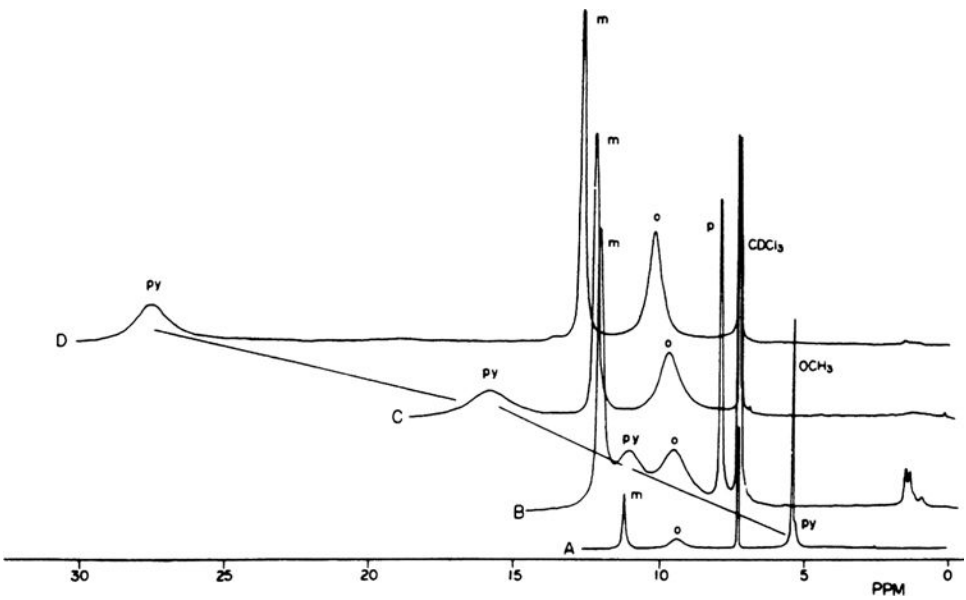

Figure 37. 250 MHz ^{1}H NMR spectrum of 4-substituted phenyl derivatives of [(TPP)$Fe^{III}OClO_3$]: (A) 4-OCH_3; (B) H; (C) 4-Cl; (D) 4-CF_3. Proton designations: *o, ortho*-H; *m, meta*-H; *p, para*-H; py, pyrrole-H. Solutions are ~2mM in $CDCl_3$ at 29 °C. Reprinted from Toney, G. E.; Gold, A.; Savrin, J.; ter Haar, L. W.; Sangaiah, R.; Hatfield, W. E. *Inorg. Chem.* **1984**, *23*, 4350–4352, with permission from the American Chemical Society.

dependent behaviors observed. This overview relies on the premise that in addition to the ground state, one (or more) thermally accessible excited states are populated to varying degrees over the temperature range of the NMR and EPR measurements. If only one excited state is considered, the analysis is consistent with the ground state being S = 3/2 (or largely S = 3/2) and the excited state being the high-spin state (S = 5/2) for all of the complexes except for [{$(2,6\text{-}F_2)_4$TPP}$FeOClO_3$], where the high-spin state (or largely S = 5/2) is the ground state and the intermediate-spin state (S = 3/2) is the excited state.[83] This is another example (see also Ref. 419) of *ortho*-phenyl substituents having opposite electronic effects to those of the *meta*- and *para*-phenyl counterparts.

The dodecasubstituted porphyrin macrocycles octaethyl- and octamethyltetraphenylporphyrin (OETPP and OMTPP, respectively),[420,421] and to a lesser extent tetra-(β,β'-tetramethylene) tetraphenylporphyrin (TC_6TPP),[421] are prevented from being planar macrocycles because of steric interference between the β-substituents and the phenyl rings. OETPPFeCl and OMTPPFeCl have highly saddled conformations with only a small ruffling contribution, with two opposite pyrrole rings having their β-carbons significantly above the plane of the four nitrogens, and the other two pyrrole rings having their β-carbons significantly below that plane, 1.15(11)[420,422] and 1.05(10)[420] Å, respectively. These distortions are less extreme for TC_6TPPFeCl, which also shows significantly more mixing of saddling and ruffling (Normal-coordinate Structure Decomposition (NSD) calculations for (TC_6TPP)FeCl resulted in the following lowest energy modes: B_{2u}(sad) = 1.9985, B_{1u}(ruff) = 1.3508, a small domed component, A_{2u}(dome) = 0.1457, and close to zero values for all the others).[421] The kinetics of nonplanar ring inversion for all three of these complexes, as well as $TC_6TPPFeONO_2$ have been studied by ^{1}H NMR spectroscopy,[420,421] as discussed later in Section IV.A.8.e. In all cases the Fe^{III} is out-of-plane with respect to the porphyrin nitrogens (0.43, 0.51[420] and 0.530(1)[421] Å, respectively). Unlike "flat" (Por)FeCl complexes, the ^{1}H NMR ($\delta(CH_2)_{av}$ ~ 35 ppm at ambient temperatures, curved Curie plots) and EPR ($g_\perp$ ~ 5.2–5.8, $g_\parallel$ = 2) spectra and magnetic susceptibility (μ_{eff} = 4.8–5.2 μ_B) of all three complexes show evidence of being of S = 3/2,5/2 spin-admixed iron complexes.[420,421] The nitrate complex, $TC_6TPPFeONO_2$, was found to have the metal less out-of-plane of the four nitrogens [0.359(1) Å], and to have a correspondingly higher fraction of S = 3/2 character (about 20%, as compared to 2.7% for the chloride complex).[420]

The highly ruffled intermediate-spin [(TEtPrP)Fe$(THF)_2$]$^+$ has been shown to adopt a novel $(d_{xz},d_{yz})^3(d_{xy})^1(d_{z^2})^1$ ground state, while the highly saddled porphyrin [(OETPP)Fe$(THF)_2$]$^+$ has a conventional $(d_{xy})^2(d_{xz},d_{yz})^3(d_{z^2})^1$ ground state, on the basis of the difference in *meso*-^{13}C chemical shifts (+104 vs. −244 ppm, respectively).[423] The same trend holds for the 5-coordinate perchlorate complexes

(+342 vs. –47 ppm, respectively).[423] The halide complexes of the highly ruffled F, Cl^- and Br^- complexes are high-spin, while the I^- complex adopts an admixed S = 5/2,3/2 state.[424] In contrast, the OETPPFeX complex, wher X = I, is a pure intermediate spin complex, on the basis of the *meso*-^{13}C chemical shifts.[424] Another study showed that weak donor ligands such as pyridine-N-oxide, DMSO, DMF, MeOH, THF, 2-MeTHF and dioxane create either high- or intermediate-spin iron centers depending on the structure of the porphyrin ring (TPP (flat), TiPrP (ruffled), and OETPP (saddled)). Again, *meso*-^{13}C chemical shifts were used to reach these conclusions.[425,426] The same 5-coordinate geometries can also be achieved with various 2-substituted imidazoles, and these complexes are also intermediate-spin or spin-admixed.[427]

Five-coordinate halide-ligated complexes of iron(III) porphycene and corphycene have been prepared and studied by X-ray crystallography, Mössbauer, ^1H NMR and EPR spectroscopy and SQUID magnetometry. It was found that the etioporphycene-iodide complex exhibits a mainly S = 3/2 spin state with a small amount of S = 5/2 admixture. In contrast, all of the other halide complexes of both macrocycles show the reverse, a mainly S = 5/2 spin state with a small amount of S = 3/2 admixture.[428]

Bis-ethanol complexes of iron(III) *meso*-tetrachiroporphyrinatoiron(III) (derived from (1R)-cis-caronaldehyde acid methyl ester and pyrrole), and abbreviated $(TMCP)Fe^{III}$, were formed by the reaction of the chloroiron(III) complex with $AgClO_4$ in $EtOH/CHCl_3$.[429] The crystal structures of two distinct products were obtained and found to be $[(TMCP)Fe^{III}(EtOH)_2]\ ClO_4$ and $[(TMCP)Fe^{III}(EtOH)(H_2O)]ClO_4$. Fe-O distances were long (2.173(5) – 2.272(4) Å).[429] The magnetic moment ($\mu_{eff} = 3.8\ \mu_B$), Mössbauer spectrum ($\delta = 0.35(1)$ mm s^{-1}, $\Delta E_Q = 3.79(1)$ mm s^{-1}), and EPR spectrum at 80 K ($g_\perp = 4.0$, $g_\parallel = 2.00$) were all consistent with a nearly pure S = 3/2 ($^4A_2$) ground state with very little rhombic distortion.[429] The NMR spectrum in $CDCl_3$ — EtOH showed the pyrrole-H at about –30 ppm, which is consistent with depopulation of the $d_{x^2-y^2}$ orbital;[429] no temperature of this measurement is given.

Calculations of Mössbauer and NMR data for various S = 3/2 and spin-admixed iron porphyrin complexes, covering four-, five-, and six-coordinate states and three commonly seen porphyrin conformations: planar, ruffled, and saddled have been carried out.[430] Most of the results provided reasonable comparison to experimental data.

8. *Low-Spin Iron(III) Porphyrins*

The low-spin iron(III) porphyrins have always been of major interest, and continue to be so, both because of the richness of information that can be obtained

about the nature of the orbital of the unpaired electron (this richness is aided by the good-to-excellent resolution of the spectra), and because of the relevance of this spin state to a variety of heme proteins (the ferricytochromes *a*, *b*, *c*, *d*, *f* and *o*, the cyanomet forms of the dioxygen-carrying proteins myoglobin and hemoglobin, the cyanide complexes of a number of peroxidases and other related heme oxidases and monooxygenases).

For a number of years it was accepted that low-spin iron(III) hemes have a $(d_{xy})^2(d_{xz},d_{yz})^3$ ground state, with spin delocalization via P → Fe π donation from the filled 3e(π) porphyrin orbitals to the single hole in the d_{xz},d_{yz} set, which leads to π contact shifts being observed at the β-pyrrole positions and no π contact shifts at the *meso* positions.[2,4] In addition, it has been shown that pseudocontact shifts, at least at the β-pyrrole carbons, are much smaller than contact shifts for this electron configuration, and a factoring method was developed, based on the axial geometric factors $((3\cos^2\theta - 1)/r^3)$ of the protons at various locations around the heme and the supposition that there was no contact shift at the *meso* positions (Refs. 2, 4, and references therein), as discussed in Sections II.C and D. This method was found to work well for bis-(imidazole) complexes of iron(III) porphyrins, but somewhat less well for dicyano and bis-(pyridine) complexes, in that order.[2–4] The reason for the increasing failure of the supposition that there was no contact shift at the *meso* positions was variously ascribed to "polarization" of the σ electronic system by the π-symmetry unpaired electron and increased π-bonding interactions of the porphyrin ring with the metal due to weaker σ-bonding from axial ligands to iron(III).[2,4] New results from a number of laboratories, discussed below, clarify this situation to show the importance of delocalization from the filled $3a_{2u}(\pi)$ orbital into the half-empty d_{xy} orbital in ruffled ferriheme complexes which are bound to strong π-acceptor ligands such as alkyl or aryl isocyanides. The $3a_{2u}(\pi)$ orbital has very large electron density at the *meso* carbons (Figure 2), but very small electron density at the β-pyrrole carbons. For other ligand complexes that also have ruffled conformations, there can be partial mixing of a d_{xy} component into a largely $(d_{xz},d_{yz})^3$ electron configuration, but the very large electron density at the *meso* carbons (Figure 2) means that even a small amount of d_{xy} mixing can increase the spin density at the *meso* carbons rather dramatically.

Although the pseudocontact shifts at the β-pyrrole carbons of low-spin ferrihemes are relatively small, it is desirable to calculate them according to Eq. 7, and to do so it is necessary to know the principal values of the magnetic susceptibility tensor, χ_{ii}. Furthermore, the pseudocontact shifts at the *meso*-carbons of low-spin ferrihemes are much larger than the contact shifts, as shown in Figures 9 and 10. However, these principal values of the magnetic susceptibility tensor are usually not available, especially for model hemes. Hence, the principal values of the g-tensor, g_{ii}, which are often readily available from EPR spectroscopy or a combination of

EPR and magnetic Mössbauer spectroscopies,[131,431] are used (Eq. 9), with the cautionary notes concerning the importance of the SOZ contribution presented in Section II.A. Thus, the g-values of a large range of complexes have been measured, and a representative group of these is presented in Table 12, where the axial g-anisotropy factor, $[g_{zz}^2 - (1/2)\,(g_{xx}^2 + g_{yy}^2)]$ or $g_{\|}^2 - g_{\perp}^2$, which is proportional to the axial pseudocontact shift, and the rhombic g-anisotropy factor, $g_{xx}^2 - g_{yy}^2$, which is proportional to the rhombic pseudocontact shift (see Section II.A.2), as well as the Δ/λ and V/Δ d-orbital splitting parameters and percent d_{xy} character of the orbital of the unpaired electron, discussed below, are also included. It can be seen from the data of Table 12 that the axial anisotropy increases in the order ImH < CN^-, and that the axial anisotropy of pyridine complexes depends strongly on the particular pyridine and the particular porphyrin. It is clear from the calculated axial anisotropies based on EPR g-values that the pseudocontact contribution to the paramagnetic shift should increase in the order ImH < CN^- < Py, for all but the least basic pyridines, but this is not usually observed.[2,4] In fact, the pseudocontact contribution usually decreases, while the contact contribution to the paramagnetic shift of *meso* substituents increases. This point is related to a change in the electronic ground state from $(d_{xy})^2(d_{xz},d_{yz})^3$ to $(d_{xz},d_{yz})^4(d_{xy})^1$, and will be discussed further below. For the time being, one should note that not only have bis-(imidazole), dicyano and bis-(pyridine) complexes of iron(III) porphyrins been studied, but also bis-(isonitrile), bis-(ammine), bis-(amino ester), bis-(phosphine), and mixed imidazole-imidazole, imidazole-imidazolate, imidazole-pyridine, pyridine-cyanide, imidazole-cyanide, imidazole-phosphine and a number of other mixed-ligand complexes. Each of these combinations has special features that will be discussed separately. First, the g-values of low-spin iron(III) porphyrins will be discussed, including those which have the historically common $(d_{xy})^2(d_{xz},d_{yz})^3$ electron configuration, those which clearly have the increasingly recognized $(d_{xz},d_{yz})^4(d_{xy})^1$ electron configuration, as well as those for which it is not clear what the electron configuration is.

a. *Griffith's three-orbital theory and experimental EPR data for low-spin iron(III) porphyrins and related macrocycles*

Extensive investigations of the molecular structures, EPR and NMR spectra, and in some cases Mössbauer spectra of well-defined low-spin ferriheme model compounds with imidazoles, high-basicity pyridines, pyrazoles, cyanide ions or organic isocyanides as the axial ligands have provided conclusive evidence of the existence of two different types of $(d_{xy})^2(d_{xz},d_{yz})^3$ ground state complexes, one of which is characterized by single-feature EPR signals[431,432] known as "large g_{max}" or HALS (highly-anisotropic low-spin) signals (Figure 38a) that are only observed

Table 12. The g-values of selected low-spin iron(III) porphyrins and ferriheme proteins.

Porphyrin	L, L′	g_1[a]	g_2[a]	g_3[a]	$(g_{\|\|}^2-g_\perp^2)$[b]	$(g_{xx}^2-g_{yy}^2)$[c]	Δ/λ[d]	V/λ[e]	V/Δ	a[f]	b[f]	c[f]	$\%d_{xy}$[g]	Ref.
						$(d_{xy})^2(d_{xz},d_{yz})^3$ "Large g_{max}" EPR signal								
TPP	2 2-MeImH	3.41	1.87	0.82	9.54	–2.82	2.96	0.88	0.30	0.884	0.434	0.176	3.1	431
TPP	2 Py	3.70	1.12	–0.46	12.96	–1.04	2.16	0.17	0.08	0.742	0.640	0.243	5.9	440
TPP	2 PMe_3	3.59	—	—	11.3	UK[i]								h
TPP	2 CN^-	3.70	1.05	0.52	13.00	–0.83	6.87	0.44	0.06	0.817	0.547	0.091	0.8	440
TPP	1 CN^-, 1Py	3.31	1.76	0.34	9.35	–2.98	2.07	0.66	0.32	0.824	0.483	0.231	5.3	440
TMP	2 2-MeImH	3.17	—	—	~7.1	UK[i]								455
TMP	2 1,2-Me_2Im	3.02	—	—	~5.68	UK[i]								533
TMP	2 4-NMe_2Py	3.44	1.80	0.92	10.07	–2.39	3.64	0.89	0.24	0.891	0.429	0.150	2.2	34
TMP	2 PMe_3	3.55	—	—	~10.9	UK[i]								h
OETPP	2 2-MeImH	3.27	—	—	~8.04	UK[i]								214
OETPP	2 NMeIm	3.18	—	—	~7.17	UK[i]								214
OETPP	2 CN^-	3.47	—	—	~10.06	UK[i]								214
OEP	2 PMe_3	3.54	—	—	~10.8	UK[i]								h
OEP	2 CN^-	3.73	—	—	~12.9	UK[i]								h
TTP	1 Ph^-	3.54	1.7	(0.76)[j]	~10.8	~2.3	3.53	0.76	0.22	0.875	0.464	0.157	2.5	331
TPP	2 CN^-	3.70	1.05	0.52	13.00	–0.83	6.87	0.44	0.06	0.817	0.547	0.091	0.8	489
PP	2 CN^-	3.75	2.42	1.03	10.60	–4.80	2.33	1.06	0.45	0.962	0.424	0.217	4.7	o
PP	2 Py	3.53	1.35	<0.8	11.23	–1.18	3.34	0.49	0.15	0.854	0.478	0.096	0.9	o
PP	1 CN^-, 1 Im^-	3.1	2.2	1.4	6.2	–2.9	3.36	1.56	0.46	0.949	0.304	0.143	2.1	489
Myoglobin cyanide	Imh, CN^-	3.45	1.89	0.93	9.68	–2.71	3.36	0.94	0.28	0.895	0.417	0.158	2.5	39
Leghemoglobin *n*-butylamine	ImH, $BuNH_2$	3.38	2.05	(0.61)[j]	9.14	–3.83	2.03	0.85	0.42	0.874	0.466	0.232	5.4	39
CCP(CN) Mitochondrial	1ImH, 1CN^-	3.17	2.08	0.98	7.41	–3.37	2.49	1.14	0.46	0.898	0.374	0.188	3.5	o
Cyt. b_{562}	2ImH	3.44	—	—	~9.75	UK[i]								433
$C_4{}^+b_{566}$	2 ImH	3.75	—	—	~13.09	UK[i]								433

(*Continued*)

Table 12. (*Continued*)

Porphyrin	L, L′	g_1[a]	g_2[a]	g_3[a]	$(g_{\|\|}^2-g_\perp^2)$[b]	$(g_{xx}^2-g_{yy}^2)$[c]	Δ/λ[d]	V/λ[e]	V/Δ	a[f]	b[f]	c[f]	$\%d_{xy}$[g]	Ref.
						$(d_{xy})^2(d_{xz},d_{yz})^3$ Normal rhombic EPR signal								
TPP	2 NMeIm	2.89	2.29	1.55	4.50	–2.86	3.17	2.03	0.64	0.961	0.248	0.138	1.9	488
TPP	2 4-NMe_2Py	2.79	2.28	1.66	3.78	–2.47	3.60	2.34	0.65	0.970	0.216	0.120	1.4	488
OETPP	2 N-MeIm	2.73	2.37	1.64	3.30	–2.93	2.81	2.50	0.89	0.969	0.207	0.139	1.9	214
TPP	2 PzH	2.62	2.38	1.71	2.57[k,l]	–2.74[k,l]	2.77[k,l]	2.96[k,l]	1.07[k,l]	0.975[k,l]	0.177[k,l]	0.131[k,l]	1.7[k,l]	135
TPP	2 3-MePzH	2.58	2.38	1.74	2.31[k]	–2.65[k]	2.78[k]	3.20[k]	1.15[k]	0.977[k]	0.166[k]	0.127[k]	1.6[k]	488
TPP	2 3-NH_2PzH	2.39	2.28	1.86	1.38[k]	–1.74[k]	3.74[k]	4.70[k]	1.26[k]	0.984[k]	0.111[k]	0.089[k]	0.8[k]	136
TPP	2 Im^-	2.73	2.28	1.76	3.30	–2.10	4.25	2.70	0.64	0.983	0.190	0.102	1.0	455
TMP 2	N-MeIm	2.89	2.33	1.57	4.39	–2.94	3.09	2.07	0.67	0.966	0.244	0.140	2.0	33
TMP	2 3-CH_3PzH	2.58	2.43	1.76	2.16[k]	–2.81[k]	2.54[k]	3.31[k]	1.30[k]	0.983[k]	0.161[k]	0.131[k]	1.7[k]	34
TMP	2 4-CH_3PzH	2.61	2.42	1.74	2.37[k]	–2.83[k]	2.62[k]	3.13[k]	1.19[k]	0.980[k]	0.170[k]	0.133[k]	1.8[k]	[h]
TMP	2 3-NH_2PzH	2.38	2.31	1.93	1.15[k]	–1.60[k]	3.96[k]	5.50[k]	1.39[k]	0.998[k]	0.096[k]	0.080[k]	0.6[k]	[h]
OEP	2 N-MeIm	2.99	2.27	1.51	5.20	–2.73	3.27	1.82	0.56	0.960	0.270	0.144	2.1	[h]
OEP	2 4-NMe_2Py	2.82	2.28	1.64	4.00	–2.49	3.62	2.26	0.62	0.969	0.224	0.121	1.5	33
OEP	2 4-CNPy	HS[m]												[h]
OEP	2 3-MePzH	2.63	2.37	1.72	2.63[k]	–2.66[k]	2.52[k]	2.95[k]	1.17	0.976[k]	0.178[k]	0.127[k]	1.6[k]	[h]
OEP	2 4-MePzH	2.65	2.36	1.72	2.76[k]	–2.61[k]	3.04[k]	2.88[k]	0.95	0.977[k]	0.181[k]	0.125[k]	1.6[k]	[h]
PP	2 ImH	2.92	2.25	1.55	4.79	–2.66	3.50	1.94	0.55	0.961	0.255	0.130	1.7	490
PP	2 Im^-	2.74	2.27	1.76	3.38	–2.06	4.39	2.66	0.61	0.983	0.192	0.100	1.0	490
OMCor	2 ImH	2.58	2.21	1.82	2.56	–1.57	4.57	3.08	0.67	0.983	0.156	0.080	0.6	853
OEC	2 ImH	2.51	2.37	1.73	2.00[k]	–2.62[k]	2.57[k]	3.39[k]	1.32[k]	0.972[k]	0.155[k]	0.127[k]	1.6[k]	483
OE*i*BC	2 ImH	2.49	2.37	1.71	1.93[k]	–2.69[k]	2.47[k]	3.39[k]	1.37[k]	0.968[k]	0.155[k]	0.131[k]	1.7[k]	483
TPC	2 ImH	2.49	2.39	1.75	1.81	–2.65[k]	2.46[k]	3.59[k]	1.46[k]	0.975[k]	0.148[k]	0.128[k]	1.6[k]	445
Sulfmyoglobin cyanide	ImH, CN^-	2.65	2.43	1.65	2.71[k]	–3.18[k]	2.34[k]	2.75[k]	1.18[k]	0.970[k]	0.191[k]	0.149[k]	2.2[k]	[p]
Bovine Cyt b_5 Mitochondrial	2 ImH	3.03	2.23	1.43	5.67	–2.92	3.23	1.68	0.52	0.950	0.289	0.145	2.1	[q]
Cyt. c	1 ImH, 1RSMe	3.06	2.25	1.25	6.05	–3.50	2.56	1.48	0.58	0.897	0.318	0.175	3.1	471
Cyt. a	2 ImH	3.03	2.24	1.24	5.90	–3.48	2.52	1.49	0.59	0.928	0.315	0.176	3.1	442

(*Continued*)

Table 12. (*Continued*)

Porphyrin	L, L′	g_1[a]	g_2[a]	g_3[a]	$(g_{\|\|}^2-g_\perp^2)$[b]	$(g_{xx}^2-g_{yy}^2)$[c]	Δ/λ[d]	V/λ[e]	V/Δ	a[f]	b[f]	c[f]	$\%d_{xy}$[g]	Ref.
						$(d_{xz},d_{yz})^4(d_{xy})^1$ EPR signal								
TPP	2 4-CNPy	2.63	2.63	0.96	–6.00[n]	0.00[n]	–1.75[n]	0.00[n]	0.00[n]	0.285[n]	0.285[n]	0.897[n]	80.4[n]	[h]
TMP	2 4-CNPy	2.53	2.53	1.56	–3.97[n]	0.00[n]	–2.92[n]	0.00[n]	0.00[n]	0.183[n]	0.183[n]	0.956[n]	91.4[n]	33
TMP	2 CN^-	2.56	2.56	1.70	–3.66[n]	0.00[n]	–3.31[n]	0.00[n]	0.00[n]	0.164[n]	0.164[n]	0.979[n]	95.8[n]	[h]
TiPrP	2 CN^-	2.35	2.35	1.82	–2.21[n]	0.00[n]	–4.82[n]	0.00[n]	0.00[n]	0.110[n]	0.110[n]	0.979[n]	95.9[n]	529
QTPP	2 CN^-	2.51	2.25	1.75	–2.62[n]	1.24[n]	–4.36[n]	–2.06[n]	0.47[n]	0.102[n]	0.155[n]	0.970[n]	94.2[n]	532
TPP	2 t-BuNC	2.21	2.21	1.93	–1.16[n]	0.00[n]	–8.32[n]	0.00[n]	0.00[n]	0.060[n]	0.060[n]	0.945[n]	89.5[n]	463
OEP	2 t-BuNC	2.28	2.28	1.83	–1.85[n]	0.00[n]	–5.47[n]	0.00[n]	0.00[n]	0.096[n]	0.096[n]	0.975[n]	95.2[n]	463
$(C_3F_7)_4P$	2 Py	2.07	2.007?	1.99	–0.20[n]	0.26[n]	–26.4[n]	~0.00[n]	~0.00[n]	0.004[n]	0.020[n]	0.998[n]	99.6[n]	132
OEC	2 ImH	2.51	2.37	1.73	–2.97[n]	0.68[n]	–3.83[n]	–0.88[n]	0.23[n]	0.127[n]	0.155[n]	0.972[n]	94.5[n]	483
TPC	2 ImH	2.49	2.39	1.75	–2.89[n]	0.49[n]	–3.92[n]	–0.66[n]	0.17[n]	0.128[n]	0.148[n]	0.975[n]	95.1[n]	445
OEiBC	2 ImH	2.49	2.37	1.71	–2.98[n]	0.58[n]	–3.76[n]	–0.73[n]	0.19[n]	0.131[n]	0.155[n]	0.968[n]	93.7[n]	483
Sirohemin	2 CN^-	2.37	2.37	1.78	–2.45[n]	0.00[n]	–4.39[n]	0.00[n]	0.00[n]	0.121[n]	0.121[n]	0.974[n]	94.9[n]	573
Sulfmyoblobin cyanide	2 CN^-	2.65	2.43	1.65	–3.74[n]	1.12[n]	–3.24[n]	–0.96[n]	0.30[n]	0.149[n]	0.191[n]	0.970[n]	94.1[n]	[p]
Heme d_1 of Cyt. *cd*$_1$														
T. *pantotropha*	ImH, Tyr	2.52	2.19	1.84	–2.19[n]	1.55[n]	–3.57[n]	–0.39[n]	0.11[n]	0.073[n]	0.142[n]	0.983[n]	96.6[n]	[r]
P. *aeruginosa*	ImH, ?	2.43	2.51	1.71	–3.18[n]	–0.40[n]	–3.61[n]	–1.62[n]	0.45[n]	0.157[n]	0.142[n]	0.972[n]	94.4[n]	[r]
T. *denitrificans*	ImH, ?	2.50	2.43	1.70	–3.19[n]	0.35[n]	–3.57[n]	–0.39[n]	0.11[n]	0.144[n]	0.157[n]	0.970[n]	94.1[n]	[s]

(*Continued*)

Table 12. (*Continued*)

[a]Unless otherwise indicated, calculations using g_1, g_2, and g_3 assume $g_1 = g_{zz}$, $g_2 = g_{yy}$, $g_3 = g_{xx}$

[b]$(g_{||}^2 - g_{\perp}^2) = [g_{zz}^2 + (1/2)(g_{xx}^2 + g_{yy}^2)]$, the axial magnetic anisotropy term in Eq. 9.

[c]$(g_{xx}^2 - g_{yy}^2)$ is the rhombic magnetic anisotropy term in Eq. 9.

[d]The tetragonal splitting of the d-orbitals. Calculated from Eq. 32.

[e]The rhombic splitting of the d-orbitals. Calculated from Eq. 31.

[f]Calculated from Eqs. 29, 30.

[g]$\%d_{xy} = 100c^2$.

[h]Watson and Walker, unpublished data.

[i]Unknown; $|g_{xx}^2 + g_{yy}^2|$ expected to be small.

[j]Calculated from $g_{zz}^2 + g_{yy}^2 + g_{xx}^2 = 16$.[453]

[k]Calculated assuming the same assignment of g-values as that given in a). Leads to $V/\Delta > 2/3$, and indicates an "improper" axis system.[448]

[l]Axis system known (by ESEEM investigations) to be that defined in a).

[m]Only a high spin signal observed; either complex did not form, or else it is high spin.

[n]Calculated assuming $g_1 = -g_{xx}$, $g_2 = g_{yy}$, $g_3 = -g_{zz}$. Gives rise to small V/Δ, which suggests a "proper" axis system.[448]

[o]Rhynard, D.; Lang, G.; Spartalian, K.; Yonetani, T. *J. Chem. Phys.* **1979**, *71*, 3715–3721.

[p]Berzofsky, J. A.; Peisach, J.; Blumberg, W. E. *J. Biol. Chem.* **1971**, 246, 3367–3377.

[q]Bois-Poltoratsky, R.; Ehrenberg, A. *Eur J. Biochem.* **1967**, *2*, 361.

[r]Cheesman, M. R.; Ferguson, S. J.; Moir, W. B.; Richardson, D. J.; Zumft, W. G.; Thomson, A. *J. Biochemistry* **1997**, *36*, 16267.

[s]Huynh, B. H.; Lui, M. C.; Moura, J. J. G.; Moura, I.; Ljungdahl, P. O.; Münck, E.; Payne, W. J.; Peck, H. D.; DerVartanian, D. V.; LeGall, J. *J. Biol. Chem.* **1982**, *257*, 9576.

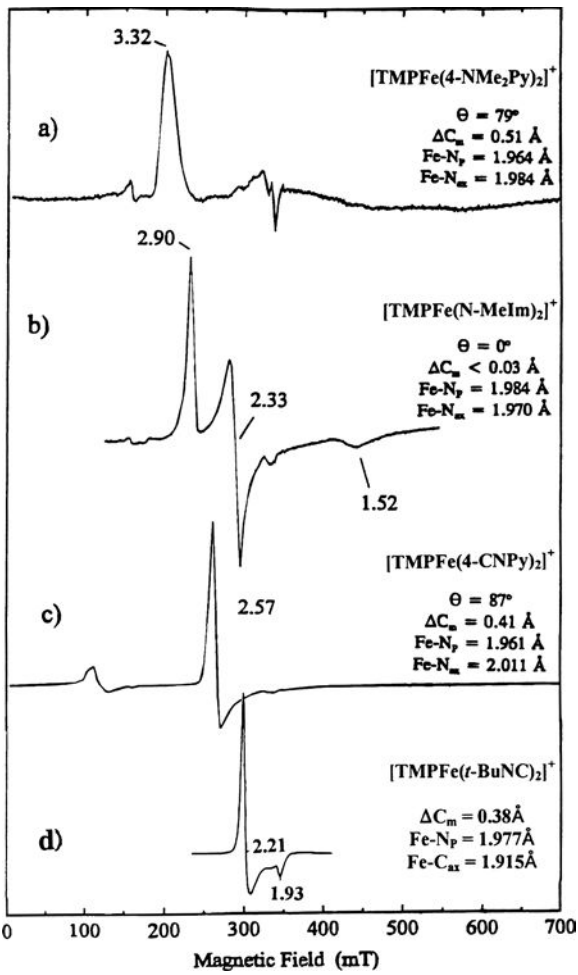

Figure 38. Typical types of EPR spectra exhibited by low-spin ferriheme complexes. (a) "large g_{max}," as in the case of $[(TMP)Fe(4\text{-}NMe_2Py)_2]^+$; b) normal rhombic, as in the case of $[(TMP)Fe(NMeIm)_2]^+$; (c) axial, with large difference between $g_{\|}$ and $g_{\perp}$, as in the case of $[(TMP)Fe(4\text{-}CNPy)_2]^+$; d) axial, with small difference between $g_{\|}$ and $g_{\perp}$, as in the case of $[(TMP)Fe(t\text{-}BuNC)_2]^+$. Relative orientation of the axial ligands is given in each case by θ. Both Fe-N(porphyrin) and Fe-axial ligand bond lengths are given, as well as the deviation of the *meso*-carbons from the mean plane of the porphyrin ring, ΔC_m, a measure of ruffling. In (a)–(c), minor impurity signals are also observed. Reprinted from Walker, F. A. *Coord. Chem. Revs.* **1999**, *185-186*, 471–534, with permission from Elsevier Publishing Company.

at very low temperatures (4–20 K), while the other of which is characterized by well-resolved rhombic EPR signals (Figure 38b) that are usually observed at temperatures up to 77 K. EPR signals of the former type had been observed for a number of poorly-characterized low-spin ferriheme centers in membrane-bound proteins, particularly those of the *b* hemes of mitochondrial Complex III,[433,434]

which are now known to have bis-histidine coordination.[435–439] Correlated structural and EPR studies have provided proof that the "large g_{max}" EPR signal is indicative of near-degeneracy of d_{xz} and d_{yz}.[431,432,434] For complexes with planar axial ligands, near-degeneracy correlates with perpendicular alignment of these ligands.[32–34,131,431,440]

The other type of $(d_{xy})^2(d_{xz},d_{yz})^3$ ground-state complexes, which has well-resolved rhombic EPR signals (Figure 38b), and includes all of the cytochromes b_5,[441] mitochondrial cytochrome *a*,[442] and methemoglobin-imidazole,[443] among many other heme proteins, some of whose EPR parameters are summarized in Table 12, are found to have parallel or near-parallel alignment of the planar axial ligands and marked difference in energy between d_{xz} and d_{yz}. Rhombic EPR spectra and the data derived from them were previously analyzed by Blumberg and Peisach using their "Truth Diagrams" to predict the axial ligands of each ferriheme protein center that gave rise to such a spectrum.[444–447] More recently, Taylor,[448] and later a number of other workers,[449–451] have discovered EPR spectra that are nearly or strictly axial, and have provided evidence that such spectra are indicative of the $(d_{xz},d_{yz})^4(d_{xy})^1$ electron configuration, in which g_{zz} is the smallest, rather than the largest g-value, as shown in Figures 38c, and d.

The theory developed by Griffith for low-spin ferriheme complexes assumed that the $d_{x^2-y^2}$ and d_{z^2} (σ-bonding) orbitals were very high in energy and thus did not mix with the other three d-orbitals, and thus were not involved in determining the g-values of complexes of this spin state.[452,453] Therefore, he developed a 3-orbital model for the g-values of low-spin ferrihemes. This approach was much later developed by Taylor[448] to provide expressions that allowed calculating the relative energies of the d_{yz}, d_{xz} and d_{xy} from the g-values. The wave functions of the lowest-energy Kramers doublet are given by:

$$\begin{aligned} |+\rangle &= a|d_{yz}^{+}\rangle - ib|d_{xz}^{+}\rangle - c|d_{xy}^{-}\rangle, \\ |-\rangle &= -a|d_{yz}^{-}\rangle - ib|d_{xz}^{-}\rangle - c|d_{xy}^{+}\rangle, \end{aligned} \tag{29}$$

and the normalization condition

$$a^2 + b^2 + c^2 = 1.000, \tag{30}$$

should hold. The three former t_{2g} orbitals are thus mixed by spin-orbit coupling; the three g-values are then given in terms of the mixing coefficients *a*, *b* and *c* as:[448]

$$g_{xx} = 2[a^2 - (b + c)^2]; \quad g_{yy} = 2[(a + c)^2 - b^2]; \quad g_{zz} = 2[(a + b)^2 - c^2]. \tag{31}$$

Thus, the experimental g-values of low-spin iron(III) complexes can be used to calculate the orbital mixing coefficients, and thereby provide information as to the individual d-orbital character of the orbital of the unpaired electron. In some cases two of the g-values must be measured by single crystal EPR spectroscopy,[440,454–457] or estimated from Mössbauer spectra at 4.2 K in the presence of an applied magnetic field.[33,431,458] Taylor[448] showed that the g-values could also be utilized to calculate the energy separation of the three formerly t_{2g} orbitals:

$$\frac{V}{\lambda} = \frac{E_{yz} - E_{xz}}{\lambda} = \frac{g_{xx}}{g_{zz} + g_{yy}} + \frac{g_{yy}}{g_{zz} - g_{xx}}, \tag{32}$$

$$\begin{aligned} \frac{\Delta}{\lambda} &= \frac{E_{yz} - E_{xy}}{\lambda} - \frac{V}{2\lambda}, \\ &= \frac{g_{xx}}{g_{zz} + g_{yy}} + \frac{g_{zz}}{g_{yy} - g_{xx}} - \frac{V}{2\lambda}, \end{aligned} \tag{33}$$

where V is the energy difference between the d_{xz} and d_{yz} orbitals, Δ is the energy difference between the d_{xy} and the average of the d_{xz} and d_{yz} orbitals, and λ is the spin-orbit coupling constant, whose value is 460 cm^{-1} for the free ferric ion[459] and somewhat smaller for fairly covalent iron(III) complexes such as the ferriheme centers of interest here.[460] The results of such calculations indicate that the parallel orientation is lower in energy for those cases in which the electron configuration is $(d_{xy})^2(d_{xz},d_{yz})^3$.[431]

One complication in using Eqs. 32 and 33 to determine the energy separations of d_{xy}, d_{xz}, and d_{yz} is that EPR measurements allow calculation of the magnitude, but not the sign, of the g-values of the paramagnetic center. Common use of the expressions derived by Taylor[448] usually assumes that the product of the three g-values, $g_{xx}g_{yy}g_{zz}$, is positive, as has been shown for several heme proteins by Münck, Huynh and coworkers.[461] Furthermore, Taylor showed that $g_{zz} + g_{yy} - g_{xx}$ must be positive.[448] These two conditions, along with Eq. 31, limit the possible choices of signs for the measured g-values. Most workers have also assumed that:

$$g_{xx}^2 + g_{yy}^2 + g_{zz}^2 = 16. \tag{34}$$

This expression allows the third g-value to be estimated in cases in which g-strain precludes its direct measurement,[462] as has been done for many of the "large g_{max}" centers listed in Table 12. However, while this limit appears to hold for systems having fairly pure $(d_{xy})^2(d_{xz},d_{yz})^3$ ground states, it has been shown that for systems having fairly pure $(d_{xz},d_{yz})^4(d_{xy})^1$ ground state, the sum of the squares of the g-values

has been reported to be as small as 13.1–13.5 for bis-(isocyanide) complexes,[449,463] and could be as small as 12, in the limit of no spin-orbit mixing of d_{xy} with the two d_π orbitals.[129,449,463]

The EPR parameters for a number of low-spin ferriheme models and proteins having "large g_{max}", normal rhombic and near-axial types of spectra are included in Table 12. Based on the orbital mixing coefficients, *a*, *b* and *c*, the orbital of the unpaired electron in all of the cases presented in Table 12 is a mixture of contributions from the three formerly t_{2g} orbitals. In particular, for the bis-isonitrile complexes of (TPP)Fe^{III}, the unpaired electron is largely in the d_{xy} orbital (and thus Δ/λ is negative),[449] but small amounts (0.4% each) of the d_{xz} and d_{yz} orbitals are mixed into the orbital of the unpaired electron. As is evident, high-basicity pyridine and imidazole complexes of iron(III) porphyrinates have been shown to be good models,[33,431] of the bis-(histidine)-coordinated cytochromes a, b and c that are involved in electron transfer in a large number of organisms, including cytochromes b_5,[444,464] and c_3,[465,466] as well as the membrane-bound cytochromes b recently shown to have bis-(histidine) coordination, including the two b hemes of mitochondrial "Complex III" (also known as ubiquinone-cytochrome c oxidoreductase)[434–439] and those of chloroplast cytochrome b_6.[467–470] The g-values of all of these complexes clearly indicate that the electron configuration is $(d_{xy})^2(d_{xz},d_{yz})^3$, and all have $g_{zz} > g_{yy} > g_{xx}$.[434]

For some years it was common practice to assign the largest g-value to the direction of the heme normal, on the basis of results of studies of several proteins, including single crystal EPR data for cytochrome *c*,[471] methemoglobin cyanide[443] and several model hemes.[440,455] On the basis of Griffith's theory[452,453] and Taylor's formulation,[448] this assignment was consistent with the d_{yz} orbital being the major contributor to the orbital of the unpaired electron, that is, a~1. However, Taylor showed that this sometimes leads to larger calculated energy separations between d_{xz} and d_{yz} (V/λ) than between their average and the lowest-energy d_{xz} orbital (Δ/λ), a situation that he described as an "Improper Axis System."[448] In such cases, he suggested, by permutation of the assignment of g-values one could arrive at calculated ligand field energy differences that obeyed the expected relationship $V/\lambda < 2/3$. This permutation typically led to a change in the major contributor to the orbital of the unpaired electron from (d_{xz},d_{yz}) to d_{xy}, that is, c~1, and indicated that d_{xy} was higher in energy than d_{xz} and d_{yz}, and thus yielded the "novel" electron configuration $(d_{xz},d_{yz})^4(d_{xy})^1$. Examples of systems, for which this permutation of the assignment of g-values was found to be necessary, included the bis-imidazole complex of octaethyl- and tetraphenylchloriniron(III),[448] the bis-(4-cyanopyridine),[129] -(*t*-butylisocyanide)[463] and –(2,6-xylylisocyanide)[449] complexes of (TPP)Fe^{III} and the bis-pyridine complex of $((C_3F_7)_4P)Fe^{III}$,[132] although the latter has g-values extremely close to those of a free radical, and thus may be a low-spin d^6 Fe^{II} center coordinated to a porphyrin π-cation radical, $P^{-\bullet}$.

Another type of complex that also appears to have this electronic ground state is that derived from *meso*-hydroxyoctaethylporphyrinatoiron(III) either by formation of the benzoyloxy esters[321] or by simple deprotonation of the hydroxy group to form the macrocycle known as an oxophlorin, OEPO, Structure **8**.[321,472–475] The NMR spectra of [OEPOFe(Py)$_2$] in $CDCl_3$ show four methylene resonances with chemical shifts that range from +33 to −2 ppm and *meso*-H resonances at −110 (2) and −153 (1) ppm. The EPR spectrum is axial with $g_\perp = 2.30$, $g_\parallel = 1.76$, and the sum of the squares of the g-values = 13.68,[472] rather than 16 Eq. 33. The authors suggested possible electron configurations of [(Py)$_2$Fe^{II}(OEPO$^{\bullet}$)] or [(Py)$_2$Fe^{III}(OEPO^{-})].[472] They later described it as the latter, although they have also said it can be described by any of three canonical structures, the third being [(Py)$_2$Fe^{I}(OEPO^{+})].[475] This system is discussed further in Section IV.A.8.f.

The preparation and characterization of bis-imidazole and bis-pyridine complexes of octamethyltetraphenylporphyrinatoiron(III), OMTPPFe^{III}, octaethyltetraphenylporphyrinatoiron(III), OETPPFe^{III}, and tetra-β,β'-tetramethylenetetraphenylporphyrinatoiron(III), TC_6TPPFe^{III}, have been reported: *paral*-[FeOMTPP(NMeIm)$_2$]Cl, *perp*-[FeOMTPP(NMeIm)$_2$]Cl, [FeOETPP(NMeIm)$_2$]Cl, [FeTC_6TPP(NMeIm)$_2$]Cl, [FeOMTPP(4-Me$_2$NPy)$_2$]Cl, and [FeOMTPP(2-MeImH)$_2$]Cl.[476] Crystal structure analysis shows that *paral*-[FeOMTPP(NMeIm)$_2$]Cl has its axial ligands in close to parallel orientation (dihedral angle = 19.5°), while *perp*-[FeOMTPP(NMeIm)$_2$]Cl has the axial imidazole ligand planes oriented at 90° to each other and 29° away from the closest N_P–Fe–N_P axis. [FeOETPP(NMeIm)$_2$]Cl has its axial ligands close to perpendicular orientation (dihedral angle = 73.1°). In all three cases the porphyrin core adopts relatively purely saddled geometry.[476] The [FeTC_6TPP(NMeIm)$_2$]Cl complex is the most planar and has the highest contribution of a ruffled component in the overall saddled structure compared to all other complexes in this study. (The estimated numerical contribution of saddled and ruffled components is 0.68:0.32, respectively.) Axial ligand planes are perpendicular to each other and 15.3° away from the closest N_P–Fe–N_P axis. The Fe–N_P bond is the longest in the series because [FeTC_6TPP(NMeIm)$_2$]Cl has the least distorted porphyrin core. In addition to these three complexes, two crystalline forms each of [FeOMTPP(4-Me$_2$NPy)$_2$]Cl and [FeOMTPP(2MeImH)$_2$]Cl were obtained. In all four of these cases the axial planes are in nearly perpendicular planes in spite of quite different geometries of the porphyrin cores (from purely saddled to saddled with 30% ruffling). The EPR spectral type correlates with the geometry of the OMTPP, OETPP and TC_6TPP complexes.[476] For the *paral*-[FeOMTPP(NMeIm)$_2$]Cl, a rhombic signal with g = 2.71, 2.51, 1.54 is consistent with nearly parallel axial ligand orientation. For all other complexes of this study, "large g_{max}" signals are observed ($g_{max} = 3.61 – 3.27$), as are observed for nearly perpendicular ligand plane arrangement. On the basis of this and previous work, the change from "large g_{max}"

to normal rhombic EPR signal occurs between axial ligand plane dihedral angles of 70° and 30°.[476] Additional complexes were prepared, including two imidazole, N-benzylimidazole, and N-methylimidazole complexes, [(OETPP)Fe(ImH)$_2$]Cl, [(OETPP)Fe(NBzIm)$_2$]Cl, and [(OETPP)Fe(NMeIm)$_2$]Cl.[477] Despite large variation in axial ligand size and major saddling of the porphyrin core, the unit cell parameters for all complexes are very similar; each structure has the same basic motif, with large voids formed by the extended porphyrin framework (filled by ordered or disordered axial ligands and disordered solvent), which allows differently sized ligands to fit within the same cell dimensions.[477] Each porphyrin core adopts a saddled conformation with $|\Delta C_\beta|$ = 1.13–1.15 Å. The dihedral angles between axial ligand planes, $\Delta\varphi$, are far from being either ideal parallel or perpendicular: 30.1°, 57.2° for [(OETPP)Fe(ImH)$_2$]Cl (molecules **1** and **2**), 56.8° for [(OETPP)Fe(NBzIm)$_2$]Cl, and 16.0°, 44.6°, 59.6°, and 88.1° for [(OETPP)Fe (NMeIm)$_2$]Cl, which has disordered axial ligands.[477]

Among the complexes of this study,[477] an axial ligand $\Delta\varphi$ of 56.8° is found to be the largest "parallel" angle (as defined by the observation of a normal rhombic or Type II, Figure 38, EPR signal[131] (N-BzIm, g = 3.08, 2.19, 1.31)), while 57.2° is found to be the smallest "perpendicular" $\Delta\varphi$ (as defined by the observation of a "large g_{max}" or Type I EPR signal (ImH, g_{max} = 3.24)). From the results of this and previous studies,[476,478] it appears that the size of the largest g for Types I and II[131] complexes varies continuously, with no break between the two,[477] as shown in Figure 39. While the switch in EPR signal type, from Type II to Type I,[131] appears to be very sharp in this study,[477] this may be somewhat artificial based on limited numbers of examples and the required saddle distortion of the (OETPP)Fe^{III} complexes. However, in comparison to several proteins with dihedral angles near 60° and Type II EPR spectra,[131] it was concluded that the switch in EPR signal type occurs near 57° ± 3–5°.[477]

Bis-pyridine complexes where the pyridine ligand ranges in basicity from 3,4-dimethylpyridine to 4-acetylpyridine have axial EPR spectra with $g_\perp$ in the range of 2.31 to 2.20 and $g_\parallel$ in the range of 1.73 to 1.90, respectively, as shown in Figure 51B, and were originally interpreted as being π-cation radicals of the iron(II) macrocycle.[321] However, these g-values deviate much too much from 2.0 to represent porphyrin-based unpaired electrons. As discussed in Section IV.A.8.c, there is obviously quite a bit of porphyrin $a_{2u}(\pi)$ character to the delocalized unpaired electron density, but based on the g-values (and the NMR spectra discussed below) the electron configuration of the 6-coordinate oxophlorin complexes is low-spin iron(III) with a $(d_{xz},d_{yz})^4(d_{xy})^1$ ground state. For the chlorin and isobacteriochlorin complexes the EPR spectra are rhombic with close spacing of the two largest g-values, while in all of the porphyrin complexes of this ground state the EPR spectra are axial (Table 12). There are however, a number of cases for which V/Δ has

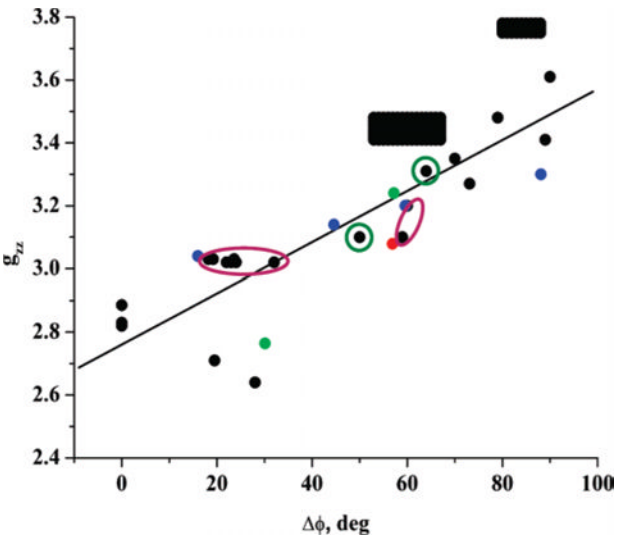

Figure 39. Correlation of the largest *g* value with the dihedral angle between axial ligand planes. Symbols: black, structures and *g* values reported previously are generally from Table 13 except for the points in color: red, N-benzylimidazole complex, 100% $\Delta\varphi = 56.8°$; green, HIm complex, 50% $\Delta\varphi = 30.1°$, 50% $\Delta\varphi = 57.2°$; blue, N-methylimidazole complex, 32% 16.0°, 45% 44.6°, 10% 59.6°, 13% 88.1°. The two points represented as black rectangles, centered at 60° and 84°, represent the range of *g* values and the average current histidine imidazole plane dihedral angles of the b_H and b_L hemes, respectively, of 10 recent structures of Complex III from a wide range of species, with the deviations from the averages for each shown by the width and height of the two rectangles. Proteins other than Complex III cytochromes *b* are enclosed in ovals or circles, purple for water-soluble proteins and green for membrane-bound proteins. Reprinted from Yatsunyk, L. A.; Dawson, A.; Carducci, M. D.; Nichol, G. S.; Walker, F. A. *Inorg. Chem.* **2006**, *45*, 5417–5428, with permission from the American Chemical Society.

been shown to be greater than two-thirds in systems that are unequivocally $(d_{xy})^2(d_{xz},d_{yz})^3$ ground states,[135,136,479,480] especially when the properties of the NMR spectra, discussed later in Section IV.A.8.b are considered. This calls into question the validity of the "Proper Axis System" rule,[448] and clarifies the fact that low-spin iron(III) chlorins, when bound to most nitrogen heterocycles *do not* have $(d_{xz},d_{yz})^4(d_{xy})^1$ ground states, but rather have $(d_{xy})^2(d_{xz},d_{yz})^3$ ground states, even though $V/\Delta > 2/3$.[138]

A part of the inconsistency between EPR and NMR results in such cases is that there are a number of systems which have a different electronic ground state at low temperatures, at which EPR studies are typically done, than they do at ambient temperatures, at which NMR studies are typically done. Such a case was shown to be that of the *t*-butylperoxide adduct of [TPPFe(OCH_3)],[481] which was unequivocally shown by pulsed EPR spectroscopy to have a $(d_{xy})^2(d_{xz},d_{yz})^3$ electronic

ground state at 4.2 K, but a thermal equilibrium between the $(d_{xy})^2(d_{xz},d_{yz})^3$ and $(d_{xz},d_{yz})^4(d_{xy})^1$ electron configurations by NMR spectroscopy at 178 K that became almost pure $(d_{xz},d_{yz})^4(d_{xy})^1$ at higher temperatures. The temperature dependence of the ^{13}C chemical shift of the *meso*-^{13}C of the TPP ligand of $[TPPFe(OCH_3)(OO^tBu)]^-$ was followed between 178 and 231 K in toluene-d_8, and was found to reverse chemical shift directions at about 195 K.[481] Above that temperature the ^{13}C chemical shift of the *meso*-^{13}C of the TPP exhibits anti-Curie temperature dependence. However, *the temperature dependence cannot be fit by assuming a thermally-accessible excited state*.[481] Rather, *it can only be fit by assuming a thermodynamic equilibrium between a planar heme conformation with an electron configuration* $(d_{xy})^2(d_{xz},d_{yz})^3$ *that is stable at very low temperatures* (at which the pulsed EPR spectral investigations were performed), *and a ruffled heme conformation with an electron configuration* $(d_{xz},d_{yz})^4(d_{xy})^1$ *that is stable at ambient temperatures*[481] (at which the NMR spectral investigations were performed). There are undoubtedly a number of other such examples that have not as yet been investigated carefully.

Iron(III) chlorin complexes, such as $[(TPC)Fe(ImH)_2]^+$,[483] have been particularly problematic in defining their electronic ground state. On the basis of his "Proper Axis System" rule Taylor assigned the electronic ground state of $[(TPC)Fe(ImH)_2]^+$ and $[(OEC)Fe(ImH)_2]^+$ to be $(d_{xz},d_{yz})^4(d_{xy})^1$,[448] with g_{zz} thus being the smallest g-value. This has been accepted by all those who have since studied iron(III) chlorins. However, the author's research group found that ESEEM and ENDOR data obtained at 4.2 K are consistent with g_{zz} being the largest g-value,[139] and the NMR data to be discussed below, obtained over the temperature range −90 to +30 °C, are consistent with the $(d_{xy})^2(d_{xz},d_{yz})^3$ ground state, with g_{zz} being the largest g-value.[115,482] Interestingly, the magnitudes of the three g-values of the chlorin complex $[(OEC)Fe(ImH)_2]^+$ (2.51, 2.37, 1.71)[135] are very similar to those of $[(TPP)Fe(PzH)_2]^+$ (2.64, 2.36, 1.71),[135] and the ground state of the former is the same as that of the latter.[139]

There are therefore two quite distinct, limiting ground states for low-spin iron(III) porphyrinates that give rise to three different types of EPR spectra: (1) the generally observed $(d_{xy})^2(d_{xz},d_{yz})^3$ state, for which $g_{zz} > g_{yy} > g_{xx}$, and for which the EPR spectra may be either rhombic or "large g_{max}" in appearance, depending on the relative orientation of planar axial ligands, and (2) the $(d_{xz}, d_{yz})^4(d_{xy})^1$ state, for which $g_{xx} \sim g_{yy} > g_{zz}$, where the d_{xz},d_{yz} pair are degenerate, or nearly so, and below the d_{xy} orbital in energy. For symmetrical porphyrinate rings, this latter electronic state leads to an axial EPR spectrum, with $2.6 \geq g_\perp > 2 > g_\parallel$,[129,132,449,463] and $g_\parallel$ may not be resolved due to g-strain. Equations 28–32 can be utilized to determine the energy differences among the three orbitals, and will be found to have the order shown in Figure 2, left-hand side. For this electron configuration, Eq. 33 does not

hold, but rather, the sum of the squares of the g-values is markedly less than 16, though usually larger than 13. It is becoming increasingly clear that the $(d_{xz},d_{yz})^4(d_{xy})^1$ ground state is not as uncommon or "unusual" as might have been thought, although not all workers have recognized their systems as being low-spin iron(III) complexes of the "unusual" ground state, rather than low-spin d^6 iron(II) π-cation radicals.

b. *NMR studies of low-spin iron(III) porphyrins having the $(d_{xy})^2(d_{xz},d_{yz})^3$ ground state*

Bis-imidazole and -high-basicity pyridine complexes of synthetic and natural ferrihemes are the epitome of the $(d_{xy})^2(d_{xz},d_{yz})^3$ electronic ground state, as has been seen earlier on the basis of their EPR spectra. The ~1.9% d_{xy} character of the orbital of the unpaired electron (Table 12) via spin-orbit coupling is not readily noticed. Thus, spin delocalization is observed almost entirely to the pyrrole-H positions and only to an extremely small extent to the *meso* positions, consistent with P $\rightarrow$ Fe π delocalization via the 3e(π) filled orbitals of the porphyrin,[2,4] Figure 2. In addition, there can be pseudocontact shifts of the *meso*-H of approximately −6 ppm for synthetic and natural ferrihemes, and much more variable pseudocontact shifts for ferriheme proteins (Figure 10).

Paramagnetic shifts of the protons of the porphyrin, and their separation into contact and pseudocontact contributions, of the bis-imidazole complexes of iron(III) with symmetrical synthetic porphyrins such as tetraphenylporphyrin (TPP), 5,10,15,20-tetra-(*n*-propyl)porphyrin (T-*n*-PrP) and octaethylporphyrin (OEP), as well as a number of natural porphyrins, and the nature of spin delocalization to the imidazole ligand, have been reviewed.[2,3,41] The proton NMR spectra of $[(TPP)Fe(NMeIm)_2]^+$ and $[(OEP)Fe(NMeIm)_2]^+$ are presented earlier in this chapter in Figures 19 and 21a, respectively. There have been a number of investigations of (1) the effect of porphyrin substituents on the pattern of spin delocalization, (2) the effect of imidazole deprotonation on the pattern and extent of spin delocalization, and (3) the effect of imidazole plane orientation on the paramagnetic shifts of porphyrin protons, each of which were reviewed in detail in 1993.[3] Therefore, each of those topics will be summarized only briefly.

i. Effect of porphyrin substituents on the pattern of spin delocalization

The effect of porphyrin substituents was first studied by La Mar, Caughey and coworkers on the bis-cyanide complexes of a number of naturally-derived ferrihemes.[2,4,168,169] These NMR studies showed that the spread of the heme methyl resonances is strongly dependent on the nature of the 2,4-substituents of the heme,

Structure **1**, in a manner that may now be interpreted as being a function of both the electron density distribution in each of the 3e(π) orbitals as modified by the electronic effects of the substituents,[211] and the energy separation between the two.[25] Since then, a number of studies of bis-cyanide complexes of naturally-occurring and synthetic ferrihemes have shown that in certain cases the ground state of the low-spin iron(III) is not purely $(d_{xy})^2(d_{xz},d_{yz})^3$, as will be discussed further in Section IV.A.8.d, but this complication was not present in the original study. This early study is a benchmark in our understanding of the effect of substituents on the pattern of spin delocalization in the porphyrin ring of low-spin iron(III) porphyrins. The methyl chemical shifts of a representative series of these complexes were shown above in Figure 22. Recently it has been shown that in addition to using pseudocontact shifts in the solution structure determination of low spin ferriheme proteins, the contact shifts of propionate α-protons can also be used as further structural constraints, with the propionates of rat cytochrome b_5 having been refined in this way.[484]

The pattern of paramagnetic shifts of unsymmetrically phenyl-substituted derivatives of $[(TPP)Fe(NMeIm)_2]^+$ has been reviewed in detail elsewhere.[3] Examples of the spectra of such complexes are shown above in Figures 17 and 20a. Series of mono-*meso*-substituted TPPs have been synthesized and investigated by NMR spectroscopy.[419,485,486] It was found that for unsymmetrically substituted TPPs of the type $[((X)_1(Y)_3TPP)Fe(NMeIm)_2]^+$, where X and Y are located in the *meta*- or *para*-position of its respective phenyl ring, the pyrrole-H resonance, centered at about ~−16 ppm at 33 °C for the parent compound, $[(TPP)Fe(NMeIm)_2]^+$, is split into either three signals of intensity 1:1:2 (or four signals of equal intensity, where the two signals with largest negative chemical shift are very close together) if X is more electron-withdrawing than Y or 2:1:1 (or four signals of equal intensity having the two signals with least negative paramagnetic shift very close to each other) if X is more electron-donating than Y. However, for mono-*ortho*-X or 2,6-X_2 (Y = *p*-OCH_3) derivatives, the pattern is that expected for an electron-donating substituent, even when X is a halogen,[419] as shown in Figure 40. The apparently anomalous behavior of *ortho*-substituents was hypothesized to be due to direct overlap of the electron cloud of the halogen with that of the π system of the porphyrin ring.[419] Vangberg and Ghosh[487] have reported density functional calculations that support this hypothesis.

The EPR g-values of all of the unsymmetrically substituted $(TPP)Fe^{III}$ complexes are essentially identical,[488] so the variation in the spread of the pyrrole-H resonances must be largely due to a change in the contact contribution as the difference in electron-donating/withdrawing properties of the phenyl substituents increases, which suggests redistribution of the spin density in response to the difference in electronic effects of the substituents.

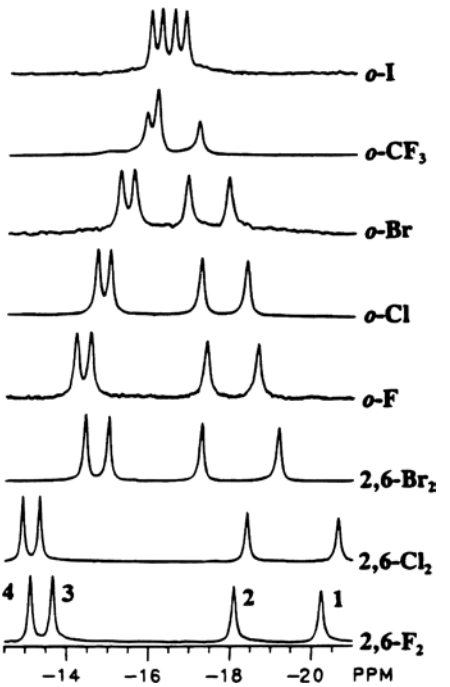

Figure 40. ^{1}H NMR spectra of the pyrrole-H resonances of the low-spin iron(III) complexes [((*o*-X)- or (2,6-X_2))(*p*-OCH_3)$_3$TPP)Fe(NMeIm)$_2$]$^+$ in $CDCl_3$ at 33 °C. Reprinted from Koerner, R.; wright, J. L.; Nesset, M. J. M.; Ding, X. D.; Aubrecht, K.; Watson, R.; Barber, R. A.; Tipton, A. R.; Norvell, C. J.; Mink, L. M.; Simonis, U.; Walker, F. A. *Inorg. Chem.* **1998**, *37*, 733–745, with permission from the American Chemical Society.

Both high- and low-spin ferriheme derivatives of (TPP)Fe^{III} in which there is a single substituent on one of the β-pyrrole positions, the 2-position, have been prepared and investigated by Latos-Grażyński and coworkers.[223] For the low-spin bis-cyanide complexes in methanol-d_4, a wide range of patterns of pyrrole-H resonances for the remaining seven pyrrole protons was observed, as shown in Figure 41. The insert is that of the pyrrole-H resonances of the 2-deuterium complex, which show that even the very small change in substituent, from H to D, breaks the symmetry of the remaining pyrrole-H resonances and creates a measurable substituent effect, particularly for the 3-H. In some cases it was possible to assign all pyrrole-H resonances using NOESY techniques, as shown in Figure 16. Both the patterns and the average chemical shift of the pyrrole-H resonances vary significantly, and in no case are the average shifts of the pyrrole-H indicative of a pure $(d_{xy})^2(d_{xz},d_{yz})^3$ ground state (−7 to −2 ppm at 293 K),[223] in spite of a possible contribution of hydrogen-bond donation from the solvent to the coordinated cyanide.[488] Thus, although a detailed analysis of the pseudocontact (small) and

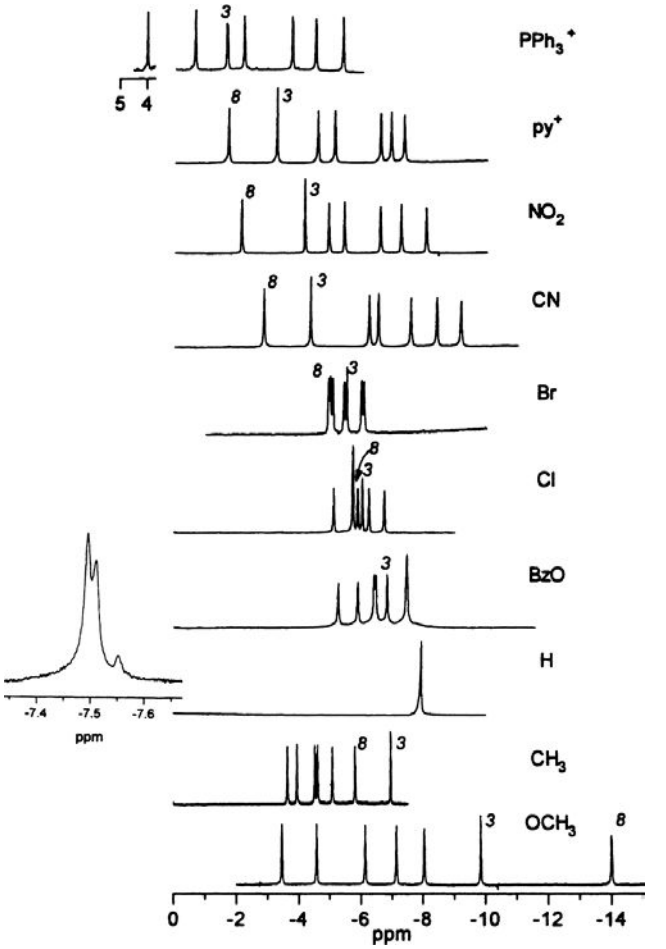

Figure 41. 300 MHz ^{1}H NMR spectra of the pyrrole region of a series of low-spin [(2-X-TPP)$Fe^{III}(CN)_2$]$^-$ complexes in methanol-d_4 at 293 K. X substituents are marked on each trace. The most characteristic 3-H and 8-H pyrrole resonances are labeled by 3 and 8, respectively. The X = D pyrrole-H pattern is shown in the insert to the left of the other spectra. Reprinted from Wojaczyński, J.; Latos-Grażyński, L.; Hrycyk, W.; Pacholska, E.; Rachlewicz, K.; Szterenberg, L. *Inorg. Chem.* **1996**, *35*, 6861–6872, with permission from the American Chemical Society.

contact (large) contributions to the paramagnetic shifts of the pyrrole-H was attempted, the situation is probably even more complicated than thought, because of some contribution of the $(d_{xz},d_{yz})^4(d_{xy})^1$ electron configuration as a thermally-accessible excited state, a situation that will be discussed further in Section IV.A.8.d, where the effect of single *meso*-substitution on the chemical shifts of [OEPFe$(CN)_2$]$^-$ complexes[348] is also discussed. The temperature dependences of these spectra, however, have not been reported.

ii. The shifts of coordinated imidazole ligands and the effect of imidazole deprotonation on the pattern and extent of spin delocalization

(a) *Neutral imidazole ligands*

Paramagnetic shifts of the protons of the imidazole ligands of $[(TPP)Fe(R\text{-}Im)_2]^+$, and their separation into contact and pseudocontact contributions, have been reported.[2,4,489] The pseudocontact shifts of all imidazole protons are positive (to low shielding), while the contact contributions are negative at all ring positions. Since the time of the original study it has been found that the imidazole ligand shifts are consistent with delocalization into the filled π orbital that has large density on the bonding nitrogen.[490] Hence, imidazoles interact with low-spin iron(III) as π donors, and the mechanism of spin delocalization is Im $\rightarrow$ Fe π bonding. This orbital has large π electron density at the 2-position and very small π electron density at the 4- and 5-position. For low-spin iron(III) porphyrins which have a $(d_{xy})^2(d_{xz},d_{yz})^3$ electronic ground state, the pseudocontact contribution to the paramagnetic shift is positive at all axial proton positions. Thus the positive shifts of the imidazole 4-H and 5-H are indicative of mainly pseudocontact shifts at those positions, while the negative shift of the 2-H is the balance of a positive pseudocontact shift and a negative contact shift caused by large π delocalization at that position. The same conclusion (L $\rightarrow$ Fe π bonding) has been reached concerning the interaction of strongly basic pyridines with low-spin iron(III), while weakly basic pyridines are found to act as π acceptors toward low-spin iron(III).[34,491]

It is found that two N–CH_3 and two 2-H signals of the imidazole moiety are well resolved when one phenyl ring has an *ortho*- or *meta*-substituent in the unsymmetrically phenyl-substituted derivatives of $[(TPP)Fe(NMeIm)_2]^+$ discussed in Section IV.A.8.b(ii).[80,226,419,486] Thus, the NMeIm ligands on the two sides of the porphyrin plane have different contact and/or pseudocontact shifts. These differences may be due to different contributions of the two ligands to the orientation of the nodal plane of the complex, which would be expected to affect both the contact and pseudocontact contributions to the paramagnetic shifts of the protons of the two ligands.[8] However, if the ligands are rotating very fast on the NMR timescale, then the two ligands cannot contribute to the orientation of the nodal plane of the 3e(π) orbital used for spin delocalization. In this case the differences in chemical shift of the two N–Me groups must be the result of different Fe–N bond lengths for the two ligands, which result from a nonplanar conformation of the porphyrin ring which results from the unsymmetrically-placed substituents, Usually, if one of those substituents is at an *ortho*-phenyl position, there will be a ruffling distortion to remove steric hindrance between this *ortho*-substituent and the rotating axial ligand. That ruffling distortion will contribute to strengthening the bond between the iron and the axial ligand on the same side of the plane as the

ortho-substituent, and weakening the bond between the iron and the axial ligand on the opposite side of the plane.

(b) *Imidazolate ligands*

Deprotonation of the coordinated imidazole ligands of $[(TPP)Fe(ImH)_2]^+$ results in large shifts in the resonances of the protoporphyrin and imidazole ring protons to lower frequency,[490] and a concommitant decrease in the g-anisotropy of the complex (Table 12). Thus, the pseudocontact contributions to the paramagnetic shifts of imidazolate ligand protons are decreased in magnitude as compared to those of the neutral ligands.[490] The contact contribution is decreased to somewhat over half that observed for the neutral ligand at H-4′ and approximately doubled at the H-5′ position of the ring, which suggests that deprotonation of the imidazole leads to an increase in the strength of L $\rightarrow$ Fe π donation.[490] The increased value of Δ/λ (Table 12) is consistent with this conclusion.

iii. Effect of imidazole plane orientation on the paramagnetic shifts of low-spin iron(III) porphyrins

For some time it has been known that the orientation of planar axial ligands is significant in producing the large spread of the methyl resonances of the protoporphyrin ring of heme proteins,[2–5,8,13,16,141–150] as is discussed earlier in Section II.C.3. A number of investigations of model hemes have been carried out aimed at testing this hypothesis.[80,226,492–495] Since the barrier to rotation of axial ligands in model hemes is very low,[89–92,496] a number of systems that involve covalent attachment of one or both axial ligands have been investigated.[488,492–494] However, such covalent attachment often leads to lower symmetry than desired.[488,492] Nevertheless, the importance of axial ligand plane orientation was clearly demonstrated by the fact that eight ring-CH_3 resonances were observed for the diastereomeric mixture of two coordination isomers of the dichelated protohemin monocyanides of Traylor and Berzinis, with a total spread of 17.1 ppm in DMSO-d_6 at ambient temperature,[492] as shown in Figure 42. Although two isomers are present, this approaches the known spread of the –CH_3 resonances in heme proteins (for example, 11.5 ppm for cyanoferricytochrome *c*,[497] 22.3 ppm for sperm whale cyanometmyoglobin,[10] and 27.1 ppm for HRPCN[498]), where axial ligands are held in particular orientations by the protein. (And as it turns out, the two outer CH_3 signals, 17.1 ppm apart, are in fact from the same isomer, as discussed below.)

2D NMR techniques have been used by this research group to assign a number of the resonances of the two isomers of Traylor and Berzinis' dichelated protohemin cyanide complexes.[499] As shown in Figure 43, NOESY/EXSY spectra at room temperature have shown that the methyl resonances of the two geometrical

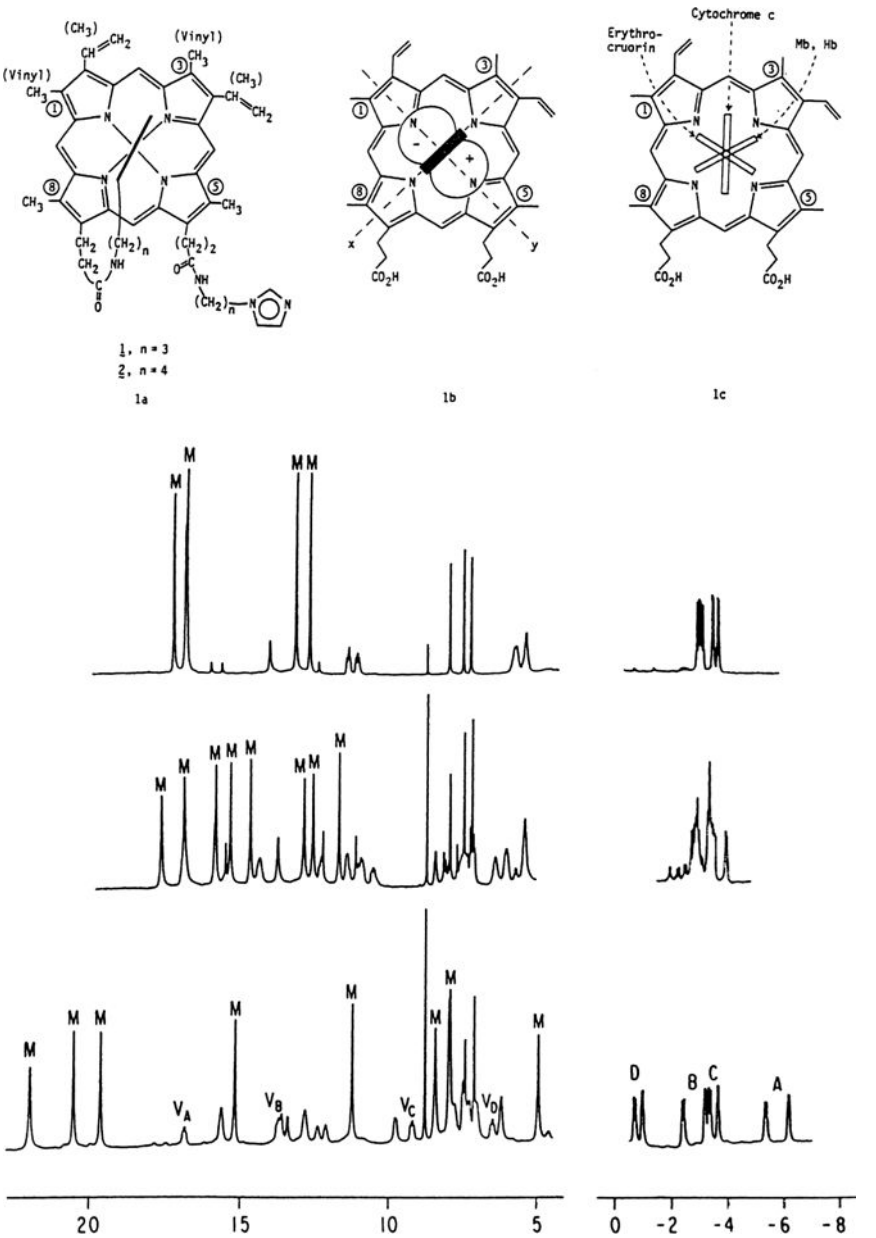

Figure 42. Top: (1a) Structures of one of the four diastereomeric isomers of the dichelated protohemin monocyanide complexes of Traylor and Berzinis; (1b) interaction of the imidazole p orbital with the d_{yz} orbital of the metal; (1c) orientation of axial imidazole planes in three heme proteins. Bottom: NMR spectra of cyanide complexes of the hemins 1 (lower trace), 2 (middle trace), and the complex with two freely rotating N-methylimidazole ligands (upper trace). Methyl group resonances are identified as M, and vinyl group resonances are identified as VA, VB, VC and VD (α-H), and A, B, C, D (β-CH_2). Reprinted from Traylor, T. G.; Berzinis, A. P. *J. Am. Chem. Soc.* **1980**, *102*, 2844–2846, with permission from the American Chemical Society.

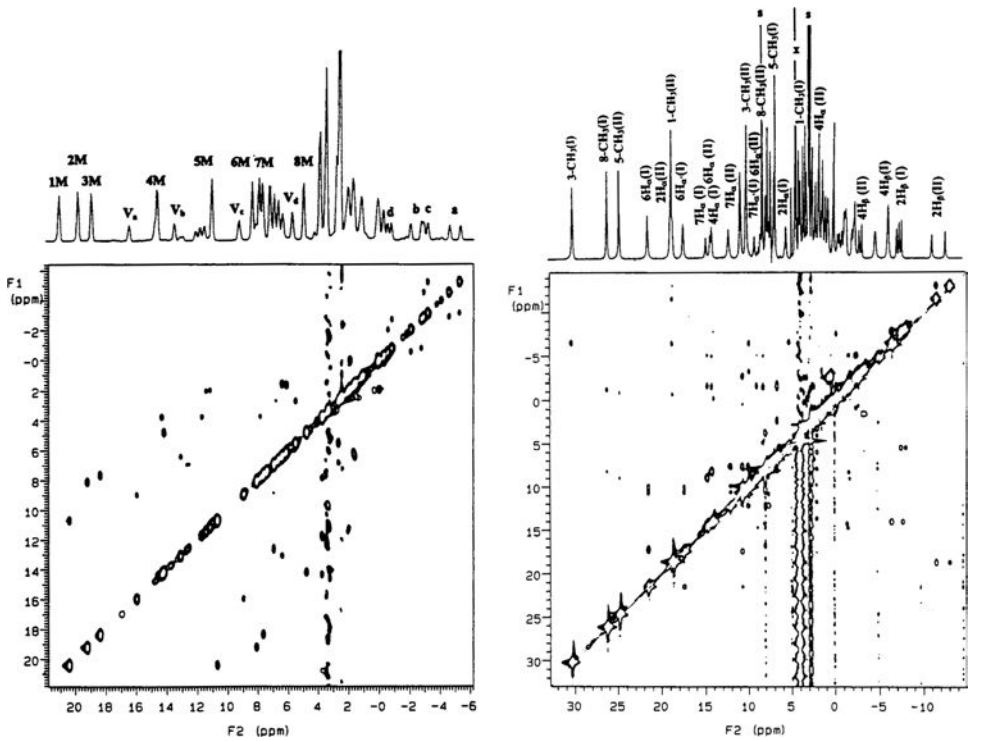

Figure 43. Left: 1D and NOESY/EXSY spectrum of the dichelated protohemin cyanide isomers recorded at 300 MHz in DMSO-d_6 at 35 °C. Note the strong chemical exchange cross peaks that result from exchange of the 6- and 7-imidazole groups and thus link the resonances of one isomer to their partners in the other isomer. As is evident, heme methyl resonances are linked 1M ↔ 5M, 2 ↔ 6, 3 ↔ 7, and 4 ↔ 8 by chemical exchange. Right: 1D and 2D NOESY and COSY spectra of **1** at -57 °C in DMF-d_7. The COSY spectrum (below the diagonal) shows the connectivities between α-H and β-H within each vinyl group. The NOESY spectrum (above the diagonal) shows NOEs between 3-CH_3-(**I**) (30.2 ppm) and 4H-β_t(**I**) (–6.4 ppm); 5-CH_3(**II**) (18.4 ppm) and 6Hα'(**II**) (9.0 ppm); 1-CH_3(**II**) (18.6 ppm) and 2H-β_t(**II**) (–11.5 ppm); 3-CH_3(**II**) (9.9 ppm) and 4H-β_t(**II**) (–3.1 ppm); 8-CH_3(**I**) (26.1 ppm) and 7Hα'(**I**) (8.1 ppm). Reprinted from Minniear, A. B.; Shokhireva, T. Kh.; Walker, F. A. *Inorg. Chem.* **1999**, *38*, 5856–5859, with permission from the American Chemical Society.

isomers are related by chemical exchange in pairs 1 ↔ 5, 2 ↔ 6, 3 ↔ 7 and 4 ↔ 8. DQF-COSY spectra allow assignment of vinyl and propionate resonances, and NOESY spectra recorded at −57 °C allow assignment of the 1- and 3-methyl resonances by NOEs to the 2- and 4-vinyls, respectively. The assignment of methyl resonances, from large to small chemical shift, is 3(**A**), 5(**B**), 8(**A**), 1(**B**), 3(**B**), 5(**A**), 8(**B**), 1(**A**), where **B** represents the isomer shown in Figure 42 top 1a.[492] Thus, isomer **A** has methyl order 3 > 8 ≥ 5 > 1 and is responsible for the 17.1 ppm spread of the heme methyl resonances, while isomer **B** has methyl group order

5 > 1 ≥ 3 > 8 and has a 12.5 ppm spread of its methyl resonances. The ligand of isomer **B** is actually rotated about 10° clockwise (rather than counterclockwise, as shown) from the N_{II}–N_{IV} axis of Figure 42 top 1a, and that of isomer **A** is rotated about 10° counterclockwise from the N_{I}–N_{III} axis of the 6-imidazole bound isomer. Thus, the methyl shifts are approximately those predicted by the angles 100° (**A**) and 170° (**B**) of Figure 11.

The tetramesitylporphyrin complex, $[(TMP)Fe(2MeImH)_2]^+$, proton NMR spectrum exhibits four pyrrole-H, four *ortho*-CH_3, four *meta*-H and two *para*-CH_3 resonances at temperatures below −30 °C, even though the porphyrin is symmetrically substituted[104,496] as shown in Figure 44. The multiplicity of porphyrin resonances was explained in terms of fixed orientations of the 2-methylimidazole ligands at low temperatures.[496] It has been shown by NOESY techniques at very low temperatures that the observed NOEs are consistent with the axial ligands lying over the *meso* positions of the porphyrin ring in perpendicular planes, with only two pyrrole-H giving rise to NOE cross peaks.[104] A complete assignment of the NMR spectrum was achieved from ROESY spectra of the complex,[225] as demonstrated in Figure 45. Such orientations of the hindered 2MeImH ligands are

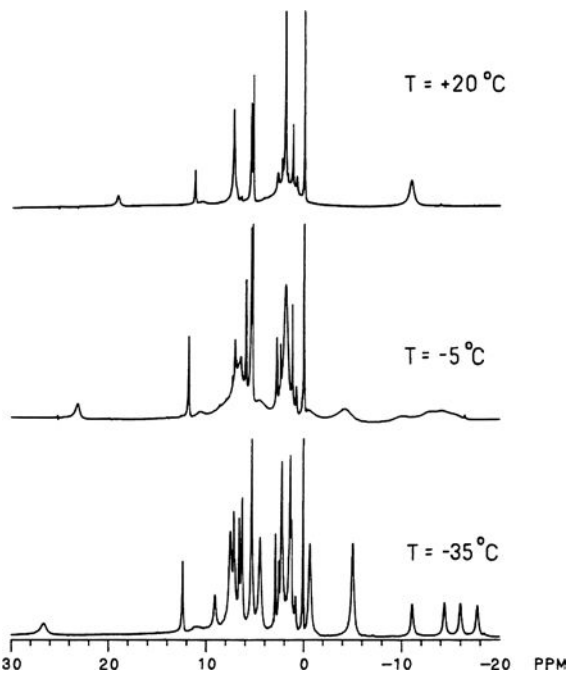

Figure 44. Temperature dependence of the 300 MHz 1D ^{1}H NMR spectrum of $[(TMP)Fe^{III}(2MeImH)_2]^+$. Reprinted with permission from the Ph.D. dissertation of K. I. Momot, University of Arizona, 1998.

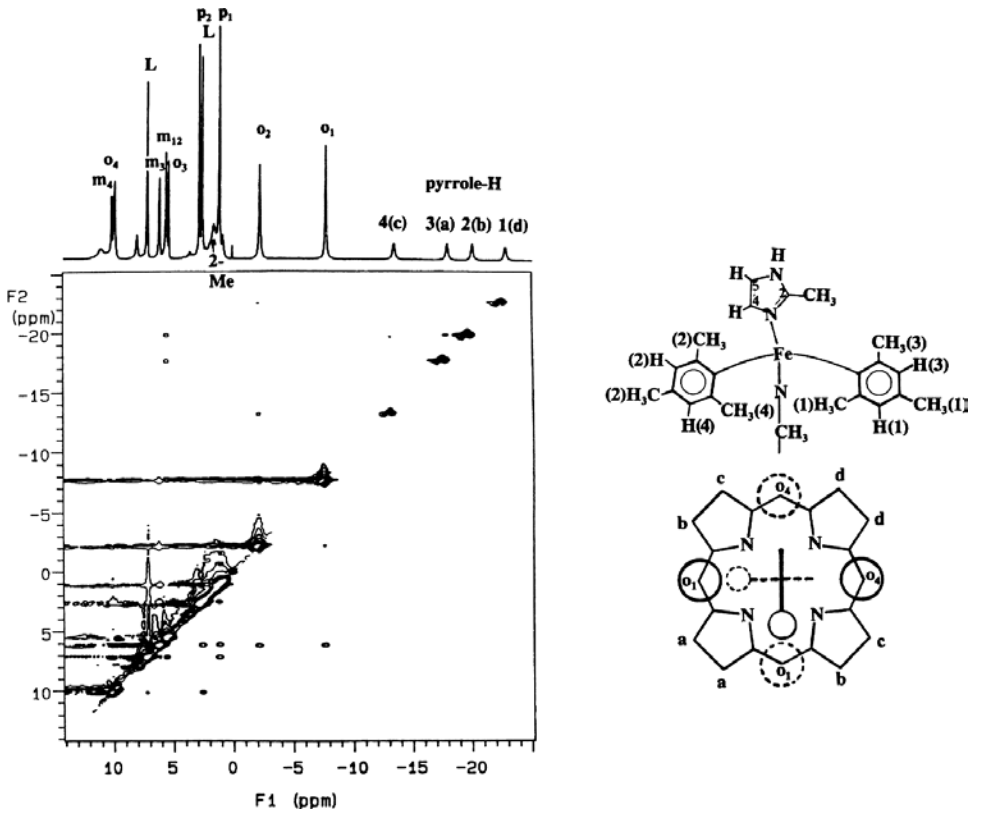

Figure 45. Left: 300 MHz ROESY spectrum of $[(TMP)Fe^{III}(2MeImH)_2]^+$ in CD_2Cl_2 at –75 °C. A much deeper contour, necessary to observe the weak ROEs between pyrrole-H(2) and -(4) and between pyrrole-H and *ortho*-CH_3 resonances, is shown in the half of the ROESY spectrum above the diagonal. Chemical exchange cross peaks are the same phase as the diagonal and are shown in multi-contour dark lines, while ROE cross-peaks are the opposite phase to the diagonal and are shown in single circles. Right: Assignment of the resonances on the basis of the ROESY spectrum. The assignment of mesityl protons is shown in the top structure and of mesityl and ligand 2-CH_3 groups in relation to pyrrole-H in the bottom structure. Reprinted from Shokhireva, T. K.; Nesset, M. J. M.; Walker, F. A. *Inorg. Chim. Acta* **1998**, *272*, 204–210, with permission from Elsevier Publishing Company.

expected in order that the Fe–N_{ax} bond lengths are short enough to allow the complex to be low-spin, and have been confirmed by the X-ray crystal structure for $[(TMP)Fe(1,2\text{-}Me_2Im)_2]^+Cl^-$.[32] Thus, the porphyrin ring is not sensitive to the symmetry of the axial ligands unless their substituents require that they bind to the metal in a tilted manner, off the axis normal to the plane of the porphyrin ring.

Nakamura and Groves first reported the coalescence behavior of the pyrrole-H, *o*-CH_3, *p*-CH_3, and *m*-H resonances of $[(TMP)Fe(2MeImH)_2]^+$ as the temperature is lowered from room temperature to –48 °C[496] (Figure 44). They correctly

ascribed this behavior to a slowing of axial ligand rotation as the temperature is lowered, and calculated activation parameters from complete line shape analysis of the two *p*-CH_3 signals of the TMP ligand. For the rotation of 2MeImH ($\Delta H^{\ddagger} = 54 \pm 2$ kJ/mol; $\Delta S^{\ddagger} = +16 \pm 7$ J/K-mol) and 1,2-Me_2Im ($\Delta H^{\ddagger} = 52 \pm 3$ kJ/mol; $\Delta S^{\ddagger} = +22 \pm 15$ J/K-mol).[496] Although their proposed structure of the low-temperature complex, in which ligand rotation is hindered, was later modified on the basis of NOESY investigations of this system[104] and the X-ray crystal structure of the bis-1,2-dimethylimidazole complex,[32] the activation parameters clearly describe the barriers to rotation of the two 2-substituted imidazoles. These barriers are considerably lower than those for axial ligand exchange,[583] discussed in Section IV.A.8.l, and clearly represent a totally different kinetic process.

The rates of ligand rotation have been measured by EXSY (see definition: Table 1) techniques for $[(TMP)FeL_2]^+$ and $[((2,6\text{-}X_2)_4TPP)FeL_2]^+$, where L = 2MeImH and X = Cl and Br,[89] for $[(TMP)CoL_2]^+$, where L = 2MeImH and 1,2-Me_2Im[89,92] and for $[(TMP)Fe^{II}L_2]$, where L = 1,2-Me_2Im.[92] Saturation transfer[90] and T_2 measurements,[91] and molecular mechanics calculations[90] have also been done for $[(TMP)FeL_2]^+$, where L = 2MeImH. Each of these systems represents a case of a four-site chemical exchange process having a single rate constant. The volume intensities of the cross- and diagonal peaks in the ROESY spectra, such as those shown in Figure 29 for the diamagnetic cobalt(III) and iron(II) complexes, can be used to calculate the rate constant at each temperature, using expressions derived from simple expansion of the expressions of Ernst, Bodenhausen and Wokaun[500] from two- to four-site exchange. For systems having four such sites, there are three possible patterns of weak and strong cross-peaks that can be obtained, depending on the sequential relationship of the chemical shifts and the spatial relationships of the four sites, as shown in Figure 46. The pyrrole-H resonances of $[TMPFe(2MeImH)_2]^+$ exhibit the pattern shown in Figure 46b, while the *o*-CH_3 resonances of the same complex exhibit the pattern shown in Figure 46c and the *o*-CH_3 resonances of the cobalt(III) analog exhibit the pattern shown in Figure 46d.

The rates of ligand rotation measured by saturation transfer difference spectra yielded somewhat higher values of the activation parameters $\Delta H^{\ddagger}$ and $\Delta S^{\ddagger}$ (59 kJ/mol and +41 J/molK, respectively)[90] than did the DNMR, EXSY or T_2 methods (54 and +16;[496] 41 and +3;[83] 48 and −10,[91] respectively, where all entropies of activation are within experimental error of zero). It is likely that spin diffusion occurs during the long irradiation times required for the saturation transfer experiments, which alters the intensities of the apparent saturation transfer peaks,[91] and thus this method is probably not the best for measuring rates of ligand rotation (and possibly other processes as well).

Other axial ligands rotate much more rapidly on all of the metal centers studied than do hindered imidazoles. The $[(TMP)Co(4\text{-}NMe_2Py)_2]^+$ complex shows

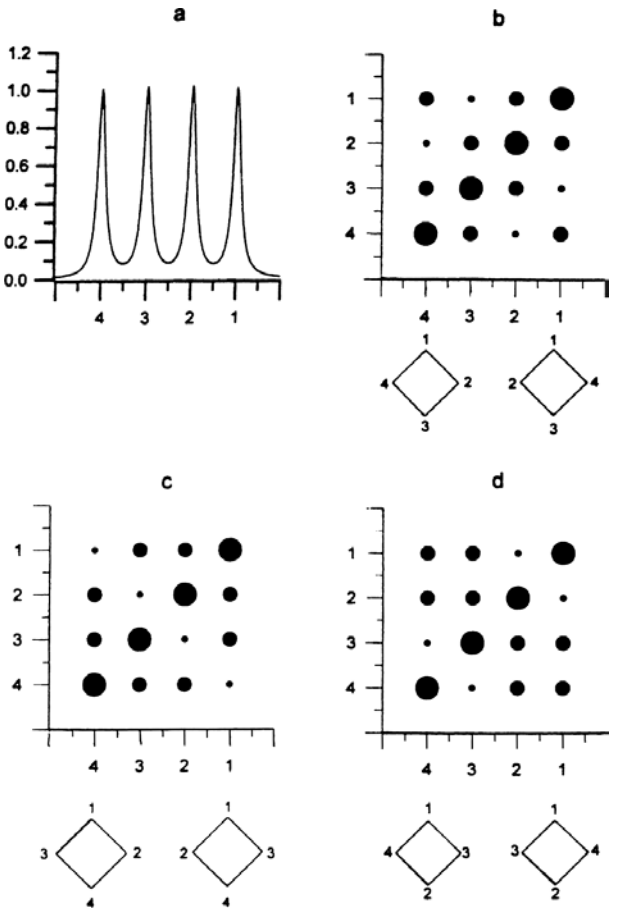

Figure 46. Computer simulation of the four-site chemical exchange process for four equally-separated exchanging peaks 1-4 observed in the 1D NMR spectrum, together with the three different possible 2D EXSY patterns that result from the possible spatial locations of the protons that give rise to the four resonances. Note that in each case there are four relatively weak cross-peaks and eight much stronger cross-peaks. These patterns result from "first-order" and "second-order" cross-peaks that depend on the spatial relationship between the exchanging protons and thus which protons can exchange upon one (or more) step(s) of chemical exchange. Reprinted from Shokhirev, N. V.; Shokhireva, T. Kh.; Polam, J. R.; Watson, C. T.; Raffii, K.; Simonis, U.; Walker, F. A. *J. Phys. Chem. A* **1997**, *101*, 2778–2886, with permission from the American Chemical Society.

broadening of the *o*-CH_3 resonance at 300 MHz at –90 °C that is indicative of a slowing of the rate of 4-NMe_2Py rotation and thus the creation at lower temperatures of two different types of mesityl *o*-CH_3 groups.[92] It is not possible to cool the solution to a low enough temperature to go through coalescence and see the two *o*-CH_3 resonances, at least at 300 MHz. Using line-broadening expressions in the fast-exchange regime,[86,87] and assuming what the final difference in frequency, $\Delta\nu$,

would be for the two *o*-CH_3 resonances, it was possible to estimate the rate constants over the temperature range 188–228 K and to determine the activation parameters $\Delta H^{\ddagger}$ and $\Delta S^{\ddagger}$ for this complex. The latter are 26 kJ/mol and −60 J/K-mol for the bis-(4-NMe_2Py) complex,[92] as compared to 48 kJ/mol and −62 J/K-mol for the bis-(2MeImH) complex and 44 kJ/mol and −84 J/K-mol for the bis-(1,2-Me_2Im) complex.[89] The reason for the very negative values of $\Delta S^{\ddagger}$ for the cobalt(III) complexes, as compared to the near-zero values for the corresponding iron(III) complexes, is not known, but may have to do with solvation differences arising from the difference in anion used (BF_4^- for cobalt(III), ClO_4^- for iron(III)).[89] The extrapolated rate constant for rotation of 4-NMe_2Py ligands at 298 K on (TMP)Co^{III} is at least 1.1×10^6 s^{-1}, as compared to 5.1 s^{-1} for 1,2-Me_2Im on the same metal,[92] a factor of at least 2×10^5 increase for the substituted pyridine. Since ligand rotation is much faster for (TMP)Fe^{III} complexes than for (TMP)Co^{III} (at least a factor of 700 times faster at 298 K),[89] it is not surprising that it has not been possible to obtain evidence of slowed rotation of pyridines or nonhindered imidazoles on low-spin iron(III) porphyrinates over the temperature ranges accessible in common NMR solvents. As for (TMP)Fe^{II}, estimation of a rate constant of ligand rotation for the bis-(1,2-Me_2Im) complex at −80 °C from the intensity of the EXSY cross peaks (Figure 29) of about 1 s^{-1}, and assumption of similar $\Delta H^{\ddagger}$ to those of the corresponding (TMP)Fe^{III} and (TMP)Co^{III} systems, suggests that the rate constant at 298 K could be of the order of 2×10^4 s^{-1}, similar to that of the iron(III) complex.[92]

It was reported by Nakamura that the same multiplicity of pyrrole-H, *o*-CH_3, *m*-H and *p*-CH_3 resonances were observed for the corresponding 2-methylbenzimidazole complex,[501] although the paramagnetic shifts of the TMP protons, their anti-Curie behavior, and the single observed EPR feature at g = 2.6 are all consistent with a $(d_{xz},d_{yz})^4(d_{xy})^1$ ground state having thermal occupancy of the $(d_{xy})^2(d_{xz},d_{yz})^3$ excited state, discussed in Section IV.A.8.c.

iv. Bis-ammine, amino ester and phosphine complexes

Though it has been reported that iron(III) porphyrins undergo autoreduction in the presence of aliphatic amines[502] and phosphines,[503] several workers have succeeded in obtaining the proton NMR spectra of several of these complexes. Kim and Goff found that although aliphatic amines caused autoreduction, the bis-ammonia complex was stable.[504] The NMR spectrum of $[(TPP)Fe(NH_3)_2]^+$ $SO_3CF_3^-$, recorded in CD_2Cl_2 at 25 °C is clearly indicative of a low-spin iron(III) complex with the "normal" $(d_{xy})^2(d_{xz},d_{yz})^3$ ground state, with pyrrole-H resonance at −21 ppm and phenyl resonances close to their diamagnetic positions. An interesting feature of the spectrum is the extremely large positive paramagnetic shift of the ammonia protons (+240.6 ppm). The Curie plots are linear for all protons of the TPP ligand, indicating a simple

electronic ground state. The EPR spectrum, recorded at 5.2 K, has a "large g_{max}" signal at g = 3.75, nearly the limit for low-spin iron(III), which indicates that there is very little, if any, rhombic splitting of d_{xz} and d_{yz}.[504] This is the expected situation for axial ligands that have no planes of symmetry and no π-bonding orbitals.

Simonneaux and coworkers have more recently reported the synthesis and characterization of low-spin bis-amino ester (the amino group of the carboxy-esterified amino acid) iron(III) porphyrin and chlorin complexes.[505,506] By using several esters of valine and leucine, they were able to prevent the autoreduction of the $(TPP)Fe^{III}$ center. The bis-(amino ester) complexes thus formed are partial models of cytochrome *f*, which has the N-terminal amino group coordinated to the heme, as well as a histidine imidazole.[507] The porphyrin complexes are typical $(d_{xy})^2(d_{xz},d_{yz})^3$ ground state complexes with the pyrrole-H resonance at −23.0 ppm at 293 K and "large g_{max}" EPR signals at g_{zz} = 3.56–3.57, as well as a zero-crossing derivative feature at g_{yy} = 1.77–1.76.[505] The nonzero intercepts of the Curie plot suggest that the $(d_{xz},d_{yz})^4(d_{xy})^1$ excited state is thermally accessible.[505] The tetraphenylchloriniron(III) complex has a rhombic EPR spectrum, with g-values of 2.70, 2.33, and 1.61.[506]

The bis-(trimethylphosphine) complex, $[(TPP)Fe(PMe_3)_2]ClO_4$ shows a similar NMR spectrum;[508] the pyrrole-H resonance is observed at −19.6 ppm in CD_2Cl_2 at 20 °C. In this case, however, the PMe_3 methyl-H have an paramagnetic shift of −2.4 ppm, and a derived contact shift of −13.3 ppm. The opposite sign of the contact shift, as compared to that of the bis-(NH_3) complex discussed above, is consistent with the fact that although NH_3 can act only as a σ-donor, PMe_3 can act both as a σ-donor and a π-acceptor, the latter due to the presence of the empty 3d orbitals. Clearly, this π-acceptor character has a very large effect on the observed paramagnetic shift of the axial ligand protons. The EPR g-values reported in this work are g = 2.687, 2.088 and 1.680, from measurements at 140 K.[508] However, at 8 K the only signal found present by the author of this chapter is a "large g_{max}" signal at g = 3.5 (Table 12). Based on this latter spectrum, the effective pseudocontact contribution to the paramagnetic shift at 20 °C is negative at all TPP positions, and the ground state appears to be essentially pure $(d_{xy})^2(d_{xz},d_{yz})^3$. The mixed ligand PMe_3-NMeIm complex was also reported,[509] and has been used as a model for PMe_3-bound heme proteins, as discussed by Simonneaux.[510] The synthesis and characterization of the bis-dimethylphenylphosphine complex of tetraphenylchlorinatoiron(III) and –(II) has also been reported.[511]

v. Mixed-ligand complexes

Numerous ^1H NMR spectra of mixed-ligand complexes have been reported, including (N-RIm)(2MeImH),[493,494] (NMeIm)(R-Py),[512] (R-Py)(R′-Py),[512] (ImH)(Im^-),[490]

(ImH)(CN^-),[490] (2MeImH)(CN^-),[513] (Im^-)(CN^-),[490] (NMeIm)(CN^-),[514,515] (R-Py)(CN^-),[512] (ImH)(OR^-),[331] (Py)($C{\equiv}CR^-$),[330] (NMeIm)(PMe_3),[508,509] (Py)(PMe_3),[508] (ImH)(p-$NO_2C_6H_4O^-$)[331] and (NMeIm)(R^-) and (Py)(R^-) (R^- = aryl, alkyl or carbanion).[516] Most of these are direct models for the cyanide[5,16] or phosphine[517,518] complexes of a number of heme proteins. The mixed-ligand complexes involving R^- will be discussed in Section IV.A.8.d.

Mixed hindered/nonhindered imidazole ligation of (TPP)Fe^{III} produces a pyrrole-H paramagnetic shift (−13.0 ppm for (2MeImH)(NMeIm) at 34 °C) that is intermediate to those of the two symmetrical bis-imidazole complexes (−11.8 ppm for bis-(2MeImH); −16.5 ppm bis-(NMeIm),[494] while covalent attachment of the nonhindered imidazole to the TPP ligand produces a large spread of the pyrrole-H resonances.[493,494]

Complexes of (TPP)Fe^{III} with mixed phosphine-nitrogen donor axial ligands have very similar pyrrole-H shifts to those of the bis-L complexes: At 20 °C for (NMeIm)(PMe_3), δ_{iso} = −27.3 ppm as compared to −27.8 ppm for $(PMe_3)_2$,[508,509] and −26.4 ppm for $(NMeIm)_2$.[486] However, while for (Py)(PMe_3) at 20 °C, δ_{iso} = −28.8 ppm, δ_{iso} is about −21 ppm for the bis-(pyridine) complex.[519] Thus, it would appear that the phosphine ligand stabilizes the "normal" $(d_{xy})^2(d_{xz},d_{yz})^3$ ground state of the mixed-ligand complex containing pyridine, as compared to the mixed $(d_{xz},d_{yz})^4(d_{xy})^1/(d_{xy})^2(d_{xz},d_{yz})^3$ ground state of the bis-(pyridine) complex. (See Section IV.A.8.d.) The PMe_3 complexes of myoglobin and hemoglobin have one and two methyl-H resonances from the coordinated phosphine, respectively, which may suggest some difference in the α and β heme distal environments of hemoglobin. Each of these PMe_3 methyl resonances have different paramagnetic shifts, suggesting some difference in either steric or electronic factors at the heme center of these proteins when bound to the phosphine;[517] permutation of the ring-CH_3 resonance order (Structure 1) for met-Mb(PMe_3) (5 > 8 > 1 > 3) as compared to met-Mb(CN), met-Mb(N_3) and met-Mb(Im) (5 > 1 > 8 > 3) (Structure **1**) suggests a possible steric factor of the phosphine ligand.[518]

c. *Observed shifts and the mechanism of spin delocalization for the $(d_{xz},d_{yz})^4(d_{xy})^1$ ground state*

Of the "pure" $(d_{xz},d_{yz})^4(d_{xy})^1$ systems having EPR g-values near 2.0 that have also been studied by NMR spectroscopy, the first report was for that of [(TPP)Fe(*t*-BuNC)$_2$]$^+$.[155] The ^{1}H NMR resonances, with pyrrole-H resonance at +10 ppm at 298 K was shown to follow the Curie law. The solution magnetic susceptibility of the complex was measured by the Evans method,[376,377] which also clearly showed that this was a S = 1/2 paramagnetic complex.[155] Strong alternation in the direction of the *meso*-phenyl-H shifts (Figure 28) suggested large π spin density at the

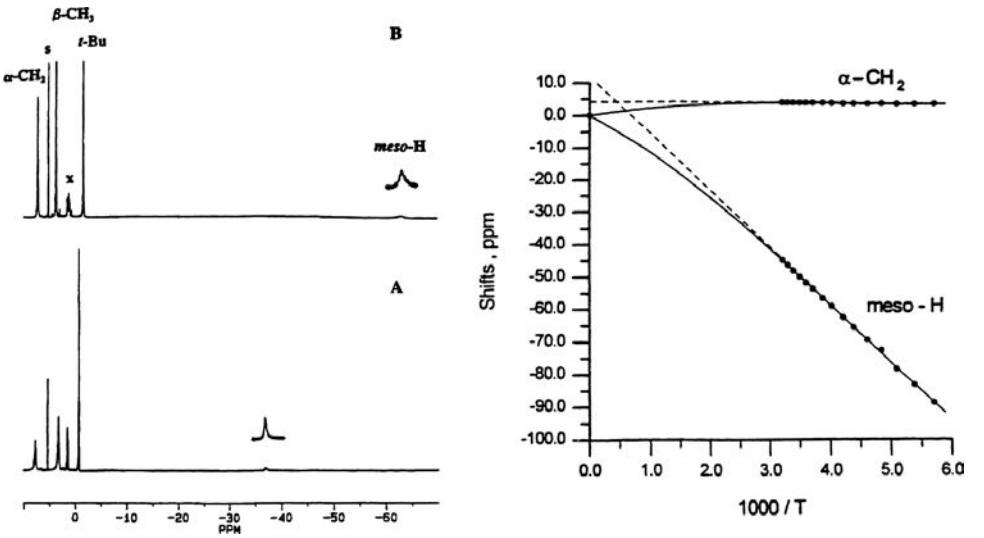

Figure 47. Left: 300 MHz 1D ^{1}H NMR spectrum of $[(OEP)Fe^{III}(t\text{-BuNC})_2]^+$ in CD_2Cl_2 recorded at (A) 303 K and (B) 195 K. Assignments of the resonances are given in (B). Right: Curie plot of the *meso*-H and α-CH_2 resonances of $[(OEP)Fe(t\text{-BuNC})_2]^+$. The dashed lines show the linear dependence, while the solid lines show the temperature dependence expected on the basis of a thermally-accessible excited state with $\Delta E = 296$ cm^{-1}. The derived orbital coefficients for the ground and excited state orbitals are 0.0332 and 0.0084 for the *meso*-H and 0.0004 and 0.0116 for the α-C to which the α-CH_2 are attached, respectively. The *meso*-H orbital coefficients are approximately one-quarter and twice those expected for the $3a_{2u}(\pi)$ and $3e(\pi)$ orbitals, respectively, on the basis of simple Hückel calculations. The β-C orbital coefficients obtained from the temperature dependence of the α-CH_2 resonance are in the right relative size order for those expected for the β-pyrrole carbons for those two orbitals ($\rho_C = 0.004$ and 0.051, respectively). Reprinted from Walker, F. A.; Nasri, H.; Turowska-Tyrk, I.; Mohanrao, K.; Watson, C. T.; Shokhirev, N. V.; Debrunner, P. G.; Scheidt, W. R. *J. Am. Chem. Soc.* **1996**, *118*, 12109–12118, with permission from the American Chemical Society.

meso positions.[155] A later NMR, EPR and magnetic Mössbauer study showed that for $[(OEP)Fe(t\text{-BuNC})_2]^+$, there is very small π delocalization to the β-pyrrole positions, as evidenced by only a 0.5 ppm shift to lower shielding of the α-CH_2 resonances, while there is very large π spin delocalization to the *meso*-H positions of $[(OEP)Fe(t\text{-BuNC})_2]^+$,[463] as shown in Figure 47, where the *meso*-H resonance is at −37 ppm at 30 °C, −63 ppm at −78 °C and −80 ppm at −98 °C. There is some σ spin delocalization to the β-pyrrole positions, for the TPP analog has observed pyrrole-H shifts of about 10 ppm, which amounts to about a 1 ppm shift to lower shielding. The Curie plot for $[(OEP)Fe(t\text{-BuNC})_2]^+$ is also shown in Figure 47, where it can be seen that there is a thermally-accessible excited state.[25] In this case the ΔE is the energy difference between the $(d_{xz},d_{yz})^4(d_{xy})^1$ ground state and the $(d_{xz},d_{yz})^3(d_{xy})^2$ excited state. For $[(OEP)Fe(t\text{-BuNC})_2]^+$, this ΔE is 296 cm^{-1}.[463] For

the related substituted $[(TPP)Fe(2,6\text{-xylylisocyanide})_2]^+$ complexes, it is difficult to estimate ΔE from NMR data.[449] The report of the EPR spectrum of the bis-pyridine complex of $((C_3F_7)_4PFe^{III}$, where $\sum g^2 = 12.53$,[132] unfortunately did not include the NMR spectrum. This spectrum would allow unambiguous assigment of the location of the unpaired electron (metal or porphyrin π).

The bis-(*tert*-butylisocyanide) complexes of three dodecasubstituted iron porphyrinates (OETPP, OMTPP; and TC_6TPP) have been prepared and studied by EPR and ^1H NMR spectroscopy.[520] From the results it has been found that the ground states of the bis-(*t*-BuNC) complexes of OETPP, OMTPP, and TC_6TPP are mainly (99.1–99.4%) $(d_{xz},d_{yz})^4(d_{xy})^1$ electron configurations, with an excited state lying 700 cm^{-1} to higher energy for the OMTPP complex, and probably at lower and higher energies, respectively, for the OETPP and TC_6TPP complexes.[520] In the ^1H NMR spectra the $(d_{xz},d_{yz})^4(d_{xy})^1$ electron configurations of all three complexes are indicated by the large and positive *meso*-phenyl-H shift differences, $\delta_m-\delta_o$ and $\delta_m-\delta_p$, and close to the diamagnetic shifts of groups (CH_3 or CH_2) directly attached to the β-carbons. However, in comparison to *meso*-only substituted porphyrinates such as $[FeTPP(t\text{-BuNC})_2]ClO_4$, the *meso*-phenyl shift differences are much smaller, especially for the OETPP complex.[520] 2D NOESY spectra show that the flexibility of the porphyrin core decreases with increasing nonplanar distortion in the order $TC_6TPP > OMTPP > OETPP$ and in the same order the stability of the binding to *t*-BuNC ligands decreases.[520] The structures of two crystalline forms of $[FeOMTPP(t\text{-BuNC})_2]ClO_4$ were determined by X-ray crystallography. Both structures showed purely saddled porphyrin cores and somewhat off-axis binding of the isocyanide ligands.[520]

Although no structure of the corresponding $[FeOETPP(t\text{-BuNC})_2]ClO_4$ complex was determined, it is clear that it is more purely and more rigidly saddled than the corresponding OMTPP complex. Thus, as mentioned above in Section II.C.2 and shown in Figure 4a, in a saddled porphyrin conformation, the d_{xy} orbital has proper symmetry to interact with the $1a_{1u}(\pi)$ porphyrin orbital,[130] which has nodes at the *meso*-carbons and very small electron density at the β-pyrrole carbons. The fact that the OETPP complex does have at least small π delocalization to the *meso*-carbons suggests that there are ruffling modes that can be activated to some extent in this basically purely saddled iron porphyrinate; however, the lower stability of this complex than that of the OMTPP complex suggests that neither ruffling modes nor delocalization via the $1a_{1u}(\pi)$ orbital are favored by low-spin iron(III) when bound to isocyanide ligands. To our knowledge, this is the first example of a porphyrin complex with a purely saddled conformation that adopts the $(d_{xz},d_{yz})^4(d_{xy})^1$ ground state. All structurally-characterized complexes of this electron configuration reported previously are ruffled. Therefore, it was concluded that a ruffled geometry stabilizes the $(d_{xz},d_{yz})^4(d_{xy})^1$ ground state, but is not necessary for its

existence.[520] It should be added that if a ruffled geometry is not possible, a saddled geometry can also allow delocalization of a d_{xy} unpaired electron via the $1a_{1u}(\pi)$ orbital,[130] although less enthusiastically. Overall we can say that putting bulky groups on the *meso*-carbons of a porphyrin certainly encourages ruffling and the $(d_{xz},d_{yz})^4(d_{xy})^1$ ground state.[451]

By substituting the four phenyl rings of OETPP with 3,5-bis(trifluoromethyl) groups, Nakamura and coworkers were able to turn the bis-*t*-BuNC complex into a $(d_{xy})^2(d_{xz},d_{yz})^3$ ground state system.[521] The bis-*t*-BuNC complex of octaethylmonoazaporphyriniron(III) also appears to have a $(d_{xy})^2(d_{xz},d_{yz})^3$ ground state.[522]

d. *The mixed ground state behavior of bis-cyanide complexes of low-spin ferrihemes: Observed shifts and the mechanism of spin delocalization*

The cyanide ligand has been used for both model hemes and heme proteins for many reasons: (1) CN^- enforces the low-spin state for most iron(III) systems; (2) it is not a planar ligand and hence does not create in-plane magnetic anisotropy (unless it binds in a bent Fe–C–N fashion); (3) CN^- is small and can enter the heme pocket of most heme proteins; (4) it may (or may not) be a good mimic of other ligands (O_2, CO, NO) that bind to heme proteins; (5) since it binds more readily to iron(III) than to iron(II), CN^- produces a coordination geometry, in a paramagnetic state of iron, that is relevant to many active sites of heme proteins (the paramagnetism "illuminates" the heme in the NMR spectrum of the protein); and finally, and most importantly, (6) the NMR spectra of dicyanohemin complexes are well resolved, since the lines are quite narrow, due to very rapid electron spin relaxation times and long proton T_1s and T_2s. (Both T_1s and T_2s are much longer for dicyano and monocyano, monoimidazole than for bis-imidazole complexes of most, if not all, iron(III) porphyrins,[102,218] as discussed in Section II.B.2.) This excellent resolution, combined with the availability of high-field NMR spectrometers, has made it possible to identify a number of iron porphyrins in coals and to assess their degree of carbonification,[523–525] to allow detection of very long-range isotope shifts in β-vinyl deuterated derivatives of dicyanoprotohemin IX,[526] and to allow a variety of heteronuclear 2D NMR experiments to be carried out on dicyanoprotohemin IX.[216,222] Dicyano and (cyano)(pyridine) complexes of natural hemins have also been studied in aqueous detergent micelles.[527,528]

The NMR spectra of the bis-cyanide complexes of a number of naturally-derived ferrihemes were, as mentioned above, reported before 1979,[2,168,169] the spectra of some of which are shown in Figure 22. These NMR studies showed that the spread of the heme methyl resonances is strongly dependent on the nature of the 2,4-substituents of the heme,[168,169] Structure **1**. There was, even in 1979, some

indication that the *meso*-H of these bis-cyanide complexes were exposed to more spin density than were those of the corresponding bis-(imidazole) complexes. Nevertheless, the "large g_{max}" EPR spectrum of $[(PP)Fe(CN)_2]^-$[443] indicated that this was clearly a $(d_{xy})^2(d_{xz},d_{yz})^3$ ground state system. Simple $[(TPP)Fe(CN)_2]^-$ complexes have also been studied by NMR spectroscopy,[514] but with no evidence of "anomalous" contact shifts for the resonances, aside from a small alternation in the direction of the phenyl-H shifts. However, since then it has been shown that the bis-(cyanide) complexes of *meso*-substituted iron(III) porphyrinates having alkyl substituents of increasing size ($H < CH_3 < C_2H_5 <$ *i*-Pr),[450,529] *meso*-tetrachiroporphyrinatoiron(III) derived from (1R)-cis-caronaldehyde acid methyl ester and pyrrole,[530] *meso*-tetracyclohexylporphyrinatoiron(III),[531] quinoxalinotetraphenylporphyrinatoiron(III),[532] tetramesitylporphyrinatoiron(III)[533] and even mono-(*ortho*-substituted) derivatives of (TPP)Fe^{III}[419] show varying degrees of shift of the pyrrole-H resonances toward the limiting +10.82 ppm value indicative of the purest $(d_{xz},d_{yz})^4(d_{xy})^1$ ground state reported thus far.[531] These more recent results have been interpreted as demonstrating the extremely low energy barrier to ruffling of the porphyrinate ring, as well as the interconnection (and perhaps continuum) between the $(d_{xy})^2(d_{xz},d_{yz})^3$ and $(d_{xz},d_{yz})^4(d_{xy})^1$ ferriheme complexes. The bis-2-methylimidazole complex of tetrakis-(*meso*-isopropyl)porphyrinatoiron(III) and the bis-1,2-dimethylimidazole complex of tetrakis-(*meso*-cyclohexyl)porphyrinatoiron(III) are other cases where NMR spectra indicative of the $(d_{xz},d_{yz})^4(d_{xy})^1$ ground state are observed, with four pyrrole-H resonances at 3.2, 4.3, 7.4 and 7.8 ppm at −35 °C for the *meso*-isopropyl derivative,[513,534,535] and 11.1, 10.6, 7.6 and 6.2 ppm at −20 °C for the *meso*-cyclohexyl derivative,[531] respectively. Presumably, the bulky *meso*-isopropyl and –cyclohexyl groups encourage the porphyrin to ruffle even more than does a *meso*-phenyl or –mesityl group, which hence stabilizes the $(d_{xz},d_{yz})^4(d_{xy})^1$ ground state.

However, all of these solution studies are in contradiction to the solid state studies (X-ray crystallography, EPR and Mössbauer spectroscopies reported by Scheidt *et al.*,[536] who find that in the solid state, whether the heme is ruffled or not, the ground electron configuration is always $(d_{xy})^2(d_{xz})^2(d_{yz})^1$, with the energy gap between d_{xz} and d_{yz} being quite small ($\leq$ ~600 cm^{-1}) and variable. For bis-cyanide derivatives, the two limiting ground states can be close in energy, and there is not a single structural feature that assures that bis-cyanoiron(III) porphyrinates will not have the $(d_{xy})^2(d_{xz})^2(d_{yz})^1$ ground configuration. Small perturbations of the bis-cyanoiron(III) porphyrinate systems may be sufficient to tip them into the alternate $(d_{xz},d_{yz})(d_{xy})^1$ state, but these require a solution state.[536]

Introduction of a single *meso* substituent into $K[(NC)_2Fe(OEP)]$ results in significant changes in the spectroscopic (and probably geometric, although no structures are available) properties of these complexes.[348] In methanol solution in the

presence of excess potassium cyanide, the low-spin six-coordinate complexes $K[(NC)_2Fe^{III}$(*meso*-R-OEP)], where R = Ph–, *n*-Bu–, MeO–, Cl–, NC–, HC(O)– and O_2N–. The ^1H NMR spectra of these show that electron-donating substituents produce a relocation of the *meso*-proton chemical shifts to higher shielding, with observed shifts from +3.32 ppm for $[OEPFe(CN)_2]^-$ to +5.50 (*cis*), +3.10 (*trans*) ppm for the formyl-substituted complex and −3.50 (*cis*), −10.31 (*trans*) ppm for the chloro-, −7.49 (*cis*), −10.74 (*trans*) ppm for the methoxy-, and −10.46 (*cis*), −17.15 (*trans*) ppm for the *n*-butyl-substituted complex.[348] This relocation was interpreted in terms of increased contribution from the $(d_{xz},d_{yz})^4(d_{xy})^1$ ground electronic state as the *meso* substituent becomes more electron donating,[348] and suggests that electron-donating substituents may encourage ruffling of the porphyrin ring.

As has been pointed out elsewhere,[131] a correlation between the degree of ruffling of low-spin iron(III) porphyrinates whose structures have been reported and their electronic ground states can be made: If the average deviation of the *meso*-carbons, ΔC_m, is 0.55 Å or greater, the electronic ground state is $(d_{xz},d_{yz})^4(d_{xy})^1$, while if it is smaller than 0.51 Å the electronic ground state is $(d_{xy})^2(d_{xz},d_{yz})^3$. The single anomaly in this correlation is the bis-1,2-Me_2Im complex of $(TMP)Fe^{III}$, which has the largest value of ΔC_m, 0.72 Å,[32] but whose EPR spectral type is intermediate between that of a "large g_{max}" and that of an axial system.[533] The g_{max} value of 3.02 is much smaller than those of most other bis-(hindered imidazole) complexes (3.3 and greater, Table 12) but larger than any of the axial $(d_{xz},d_{yz})^4(d_{xy})^1$ species (2.6 and smaller, Table 12). In fact, the EPR signal for this complex is very broad, as was also observed earlier for the $(TMP)Fe^{III}$ complex with 3-chloropyridine,[34] which was also considered to be very close to the crossover point of the two electronic ground states. Thus, the $[(TMP)Fe(1,2\text{-}Me_2Im)_2]^+$ complex is seen as being "frustrated" by having strong π donor ligands that strongly favor the $(d_{xy})^2(d_{xz},d_{yz})^3$ ground state, but a very ruffled porphyrinate ring that strongly favors the $(d_{xz},d_{yz})^4(d_{xy})^1$ ground state, and hence having some features of each electronic ground state. For the one octaethylporphyrinatoiron(III) complex having the $(d_{xz},d_{yz})^4(d_{xy})^1$ ground state, the value of ΔC_m, is 0.38 Å,[463] which suggests that this β-pyrrole substituted, tetra-*meso*-H porphyrinate, the most similar to the naturally occurring ferriheme centers, switches to the $(d_{xz},d_{yz})^4(d_{xy})^1$ ground state at far lower degrees of ruffling than do the tetraphenylporphyrinates. No structures of *meso*-alkyl porphyrinato-iron(III)-bis-ligand complexes having $(d_{xz},d_{yz})^4(d_{xy})^1$ ground states have yet been reported; it would certainly be interesting to compare the structures of the series of bis-(cyanide) complexes reported by Nakamura *et al.*[529] and those of Latos-Grażyński *et al.*[530,532] The impression, based on NMR results, however, is that *meso*-substituted porphyrinates ruffle very readily, and are probably much more ruffled than the octaethylporphyrinate and the naturally-occurring

porphyrinates. Analysis of the distortions observed for the heme centers of a number of heme proteins[537,538] and structural studies of nickel(II) *meso*-(*t*-butyl)porphyrins[539] appear to bear this out. In contrast, the structures of *meso*-ethynylphenyl- and *meso*-diethynylphenylporphyrins are not ruffled,[540] and their bis-cyanide complexes have pyrrole-H shifts of −14 ppm for the symmetrical tetra-*meso*-(ethynylphenyl) porphyriniron(III) complex, or somewhat less for mixed-*meso*-substituted porphyrins at 298 K.[540]

The bis-cyanide complex of octaethyloxaporphyriniron(III) has an EPR spectrum that could be consistent with either ground state (g-values of 2.4, 2.2 and 1.8), but the NMR spectrum is clearly consistent with the $(d_{xy})^2(d_{xz},d_{yz})^3$ ground state, with α-CH_2 resonances ranging from +12 to +2 ppm and *meso*-H resonances at +4.5 ppm.[541] Consistent with this ground state, the crystal structure shows a planar porphyrin ring. The rhombic EPR signal of this bis-(cyanide) complex must arise from the asymmetry of the macrocycle.

e. *The mixed ground state behavior of bis-(pyridine) complexes of low-spin ferrihemes: Observed shift trends and the mechanism of spin delocalization*

The early work on the bis-pyridine complexes of Fe^{III} β-alkyl porphyrins such as $[(OEP)Fe(R\text{-}Py)_2]^+$, where R-Py = substituted pyridine, has been reviewed elsewhere.[2–4] A model that explains the paramagnetic shifts and solution magnetic susceptibilities of the $[(OEP)Fe(R\text{-}Py)_2]^+$ complexes was developed that includes contributions from the ^2E, $^6A_1(5/2)$, $^6A_1(3/2)$, $^4A_2(3/2)$ and $^2B_2(1/2)$ states.[542] For $[(OEP)Fe(3\text{-}ClPy)_2]^+$ at 320 K the percent contribution of each of these components to the E″ ground state is calculated to be 77%, 1%, 10%, 8% and 3%, respectively. The first and second excited states, both E′, are composed mainly of $^6A_1(1/2)$ and $^2E(1/2)$; hence, magnetic moments of these complexes may not rise above 4.5 μ_B, even though the ground state is not S = 3/2.[542] Interestingly, two different spin states (S = 3/2 and an S = 1/2 ↔ 5/2 equilibrium) have been observed for $[(OEP)Fe(3\text{-}ClPy)_2]^+$ in the crystalline state, depending on the relative and absolute orientations of the 3-chloropyridine ligands: When the φ angles are near 45° (ligands lying over the *meso* positions) and the ligands are in perpendicular planes, the complex was found to have a spin equilibrium,[543] while when the φ angles are small (ligands lying nearly over the porphyrin nitrogens) and the ligands are in nearly parallel planes, the spin state of the complex was found to be S = 3/2.[544,545] $[(OEP)Fe(3\text{-}CNPy)_2]^+$ also crystallizes as a S = 3/2 ground state complex with the axial ligands in parallel planes over the porphyrin nitrogens.[546] Certainly, all orientations are expected to be observed in solution, where axial ligands are expected to rotate rapidly over the temperature ranges investigated; hence

the solution magnetic susceptibility and NMR results[542,547] and the X-ray crystallographic and solid state magnetic susceptibility, EPR and Mössbauer results[543–546] are all consistent with the fact that low-basicity pyridine complexes of the type $[(OEP)Fe(R\text{-}Py)_2]^+$, as well as those of the natural porphyrins,[547] are very close to the magnetic triple point of S = 1/2, 3/2 and 5/2.[542] However, in the case of the basic pyridine complex, $[(OEP)Fe(4\text{-}NMe_2Py)_2]^+$, the S = 1/2 state alone, with a pure $(d_{xy})^2(d_{xz},d_{yz})^3$ ground state, is stabilized at all temperatures,[2,4,33] as it is for all bis-(imidazole) complexes.

Compared with the complex spin state behavior of β-alkylsubstituted porphyrins discussed above, all known bis-(pyridine) complexes of Fe^{III} tetraphenylporphyrins are low-spin.[2,4,34,491,519] Nevertheless, their behavior is not as simple as that of the corresponding bis-(imidazole) complexes. While it has been found in all cases that the pyrrole-H resonance shifts to lower shielding as the basicity of the pyridine decreases,[2,4,34,491,519] all TPP complexes not having *ortho*-phenyl substituents show Curie behavior, albeit with very small temperature dependence for $[(TPP)Fe(4\text{-}CNPy)_2]^+$,[519] while TPP derivatives which have *ortho*-phenyl substituents, such as $[(TMP)Fe(R\text{-}Py)_2]^+$,[34,491] exhibit anti-Curie behavior when R-Py is a low-basicity pyridine (3-CNPy, 4-CNPy). The *meta*-phenyl-H paramagnetic shift also increases dramatically as the basicity of the pyridine decreases, so that for low-basicity pyridines it is no longer possible to assume that the *meso*-phenyl-H paramagnetic shifts are totally due to the pseudocontact contribution.[491] The shift of the pyrrole-H resonance to lower shielding and the increasing contact shift of the *meta*-phenyl-H of the TMP, the anti-Curie behavior of the weakly basic pyridine complexes, and the change in the size (and sign) of the pseudocontact contribution to the paramagnetic shift are indicative of a progressive change in the ground state of these low-spin iron(III) complexes. For $(TMP)Fe^{III}$ complexes with pyridines of decreasing basicity, the pyrrole-H resonance position at −80 °C shifts from −30.9 ppm ($4\text{-}NMe_2Py$) to +2.1 ppm (4-CNPy).[34,491] The latter is clearly not a $(d_{xy})^2(d_{xz},d_{yz})^3$, but rather a $(d_{xz},d_{yz})^4(d_{xy})^1$ ground state complex. Because the shift is a smooth function of the pK_a of the conjugate acid of the pyridine ligand, it is difficult to say where the $(d_{xy})^2(d_{xz},d_{yz})^3$ electron configuration ends and the $(d_{xz},d_{yz})^4(d_{xy})^1$ begins, partly because the energy separation between the two electronic ground states decreases as one moves from the right to the left extreme of the orbital diagram of Figure 1, and so both states are populated thermally as a function of the particular ligand and the temperature. Curie plots of the whole series of pyridine ligand complexes create a family of lines of decreasing negative slope to increasing positive slope as one goes from $[(TMP)Fe(4\text{-}NMe_2Py)_2]^+$ to $[(TMP)Fe(4\text{-}CNPy)_2]^+$.[491]

When axial imidazole or pyridine ligands are bound to low-spin iron(III) porphyrins in perpendicular planes, as discussed above, only one resolved EPR

feature, the "large g_{max}" signal discussed above, is observed.[33,34,431,458] The other two g-values are not resolved, probably due to g-strain, but they can be estimated by single crystal EPR techniques[440] or by magnetic Mössbauer spectroscopy at 4.2 K.[33,431,458] The g-values available are included in Table 12. The g_{max} values of nine bis-R-pyridine complexes of (TMP)Fe^{III} decrease in size from 3.48 to 2.53 as the pK_a of the conjugate acid of the pyridine decreases from 9.7 (4-NMe_2Py) to 1.1 (4-CNPy), with the type of EPR spectrum changing from "large g_{max}", with $g_{max} = g_{zz}$ in the former case, to an axial signal, with $g_{max} = g_{xx} = g_{yy}$ in the latter.[34] Structures of seven of these complexes have been reported.[32–34] In all of these complexes the axial ligands are in perpendicular planes lying over the *meso* positions of the porphyrin ring, with strong ruffling of the porphyrin core in order to reduce steric crowding between the *o*–CH_3 groups and the pyridine ligands, as shown in Figure 48. This strong ruffling produces two oblong "cavities" at right angles to each other, one above and one below the plane of the porphyrin ring, which hold the axial ligands in perpendicular planes over the *meso* positions. The EPR spectrum of $[(TPP)Fe(4\text{-}CNPy)_2]^+$ is also axial in both frozen solution and the solid state, and the X-ray crystal structure shows that the axial ligands are also in perpendicular planes lying over the *meso* positions, with a strongly ruffled porphinato core, even though there are no *ortho*-phenyl substituents.[129] The axial EPR spectra, with $g_\perp > g_\parallel$, Table 12, are indicative of a $(d_{xz},d_{yz})^4(d_{xy})^1$ ground state.[129] MCD studies of

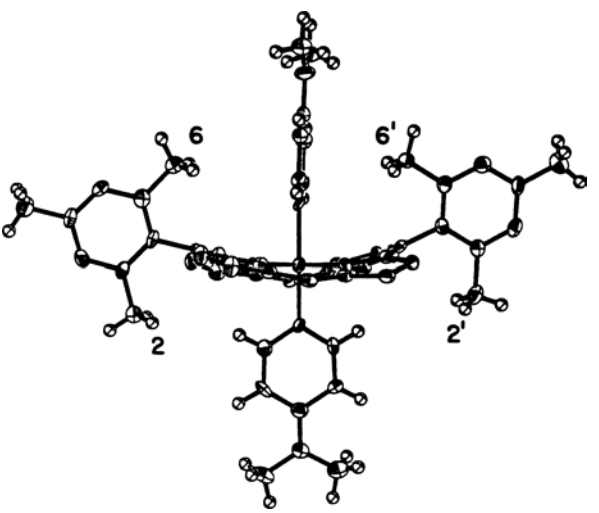

Figure 48. ORTEP diagram showing the arrangement of the effectively coplanar mesityl rings and the axial ligands of $[(TMP)Fe^{III}(4\text{-}NMe_2Py)_2]^+$. Hydrogen atoms have been drawn artificially small, and two of the mesityl rings have been deleted to improve clarity. Reprinted from Safo, M. K.; Gupta, G. P.; Walker, F. A.; Scheidt, W. R. *J. Am. Chem. Soc.* **1991**, *113*, 5497–5510, with permission from the American Chemical Society.

the TMP analog are also consistent with the $(d_{xz},d_{yz})^4(d_{xy})^1$ ground state.[127] Thus, low-basicity pyridines stabilize the less common $(d_{xz}, d_{yz})^4(d_{xy})^1$ electronic ground state for low-spin iron(III), though not as strongly as do isonitrile ligands.[155]

A change in ground state of low-spin iron(III) from the usual $(d_{xy})^2(d_{xz},d_{yz})^3$ to the "unusual" $(d_{xz},d_{yz})^4(d_{xy})^1$ electron configuration occurs smoothly through the series of pyridine complexes of both (TPP)Fe^{III} [514] and (TMP)Fe^{III},[34,491] but the trend is much more pronounced for the TMP complexes, which made it apparent that this change in the ground state was the reason for the $pK_a(BH^+)$ dependence of the paramagnetic shifts in both cases. This $pK_a(BH^+)$ dependence is due to profound effects of the electron configuration of the metal on both the pseudocontact and contact contributions to the paramagnetic shift. For the pseudocontact shift, a change in sign of the axial magnetic anisotropy term (Eqs. 7 and 9) occurs at some $pK_a(BH^+)$ between that of 4-dimethylaminopyridine and 3-cyanopyridine,[491] since the former complex has $g_{zz} > g_{yy} > g_{xx}$[33] while the latter has $g_{xx} = g_{yy} > g_{zz}$.[34] However, the actual anisotropies in homogeneous solution at −80 °C appear to be smaller than those calculated from the g-values (Eq. 9) as a result of thermal population of the "other" electron configuration. If the axial g-anisotropies derived from the g-values of Table 12 are compared to those estimated from the NMR shifts of model low-spin ferrihemes it becomes evident that g-values measured at 77 K and below may not be good indicators of the actual magnetic anisotropy of the complexes at the temperatures of the NMR measurements (183 K and above), and that in many cases the actual magnetic anisotropy may be of opposite sign from that predicted by the g-values measured at very low temperatures (Table 12).

The bis-4-dimethylaminopyridine, bis-1-methylimidazole, bis-cyanide,[548] and bis-4-cyanopyridine[549] complexes of iron(III) octamethyltetraphenylporphyrin, (OMTPP)Fe^{III}, octaethyltetraphenylporphyrin, (OETPP)Fe^{III}, its perfluorinated phenyl analog, (F_{20}OETPP)Fe^{III}, and tetra-(β,β'-tetramethylene)tetraphenylporphyrin, (TC_6TPP)Fe^{III}, have been prepared and characterized by ^{1}H NMR spectroscopy. Complete spectral assignments have been made using 1D and 2D techniques. The temperature dependences of the proton resonances of the complexes show significant deviations from simple Curie behavior and evidence of ligand exchange, ligand rotation, and porphyrin ring inversion at ambient temperatures. At temperatures below the point where dynamics effects contribute, the temperature dependences of the proton chemical shifts of the complexes could be fit to an expanded version of the Curie law (Eq. 12) using the temperature-dependent fitting program developed in this laboratory.[25,84] The results show that, although the ground state differs for various axial ligand complexes and is usually fully consistent with that observed by EPR spectroscopy at 4.2 K, the excited state often has S = 3/2 (or S = 5/2 in the cases where the ground state has S = 3/2). The EPR spectra (4.2 K) of bis-4-dimethylaminopyridine and bis-1-methylimidazole

complexes show "large g_{max}" signals with g_{max} = 3.20 and 3.12, respectively, and the latter also shows a normal rhombic EPR signal, indicating the presence of low-spin (LS) $(d_{xy})^2(d_{xz},d_{yz})^3$ ground states for both. The bis-cyanide complex also yields a large g_{max} EPR spectrum with g = 3.49 and other features that could suggest that some molecules have the $(d_{xz},d_{yz})^4(d_{xy})^1$ ground state. All of these complexes have been characterized by X-ray crystallography.[476,477,549]

For the bis-4-CNPy complexes, the magnetic resonance data depend on the porphyrin macrocycle, as first reported by Nakamura *et al*.[550] An axial EPR signal is observed ($g_\perp$ = 2.49, $g_\parallel$ = 1.6) in frozen solutions of both [FeOMTPP(4-CNPy)$_2$]ClO_4 and [FeTC$_6$TPP(4-CNPy)$_2$]ClO_4 at 4.2 K, which is indicative of the low spin (S = 1/2), $(d_{yz},d_{xz})^4(d_{xy})^1$ electronic ground state for these two complexes.[549] However, in CD_2Cl_2 at 183 K the CH_2 chemical shift of [FeTC$_6$TPP(4-CNPy)$_2$]ClO_4 is +6.8 ppm, which indicates the same spin state as seen in the EPR spectrum, while the CH_3 chemical shift of [FeOMTPP(4-CNPy)$_2$]ClO_4 is +31.4 ppm, which indicates that the latter complex has a higher spin state, identified as S = 3/2.[549] At 273 K the same two chemical shifts are 51.3 and 65.4 ppm, which indicates that both of these complexes have spin states S = 3/2 at ambient temperatures.[549] In contrast, the EPR spectra of [FeOETPP(4-CNPy)$_2$]ClO_4 at 4.2 K are typical of the S = 3/2 state, with g-values of 5.21, 4.25, and 2.07, in agreement with Nakamura *et al*.[550] However, distinct from previous conclusions, large negative phenyl-H shift differences δ_m–δ_o and δ_m–δ_p in the ^{1}H NMR spectra indicate significant negative spin density at the *meso*-carbons, and the larger than expected positive CH_2 shifts (+66.1, +14.8 ppm at 183 K, +45.7, +14.0 ppm at 273 K) are also consistent with a significant population of the S = 2 Fe^{II}, S = 1/2 porphyrin π-radical state, with antiferromagnetic coupling between the metal and porphyrin unpaired electrons.[549] This is the first example of this type of porphyrin-to-metal electron transfer to produce a partial or complete porphyrinate radical state, with antiferromagnetic coupling between metal and macrocycle unpaired electrons in an iron porphyrinate.

The dynamics of porphyrin ring inversion of a number of iron(III) complexes of octamethyltetraphenylporphyrin, (OMTPP)Fe^{III}; octaethyltetraphenylporphyrin, (OETPP)Fe^{III}; octaethyltetra(perfluorophenyl)porphyrin, (F_{20}OETPP)Fe^{III}; and tetra-β,β-tetramethylenetetraphenylporphyrin, (TC$_6$TPP)Fe^{III}, having either one (Cl^-, ClO_4^-) or two [4-(dimethylamino)pyridine, 4-Me$_2$NPy; 4-cyanopyridine, 4-CNPy, N-methylimidazole, NMeIm; tert-butylisocyanide, *t*-BuNC; or cyanide, CN^-] axial ligands were characterized by 1D dynamic NMR (DNMR) and 2D ^{1}H NOESY/EXSY spectroscopies as a function of temperature.[421,549,551] An example of the compounds studied and the types of spectra analyzed is shown in Figure 49, where it can be seen that some compounds could be studied both above and below the coalescence temperature, using fast-exchange techniques in the higher

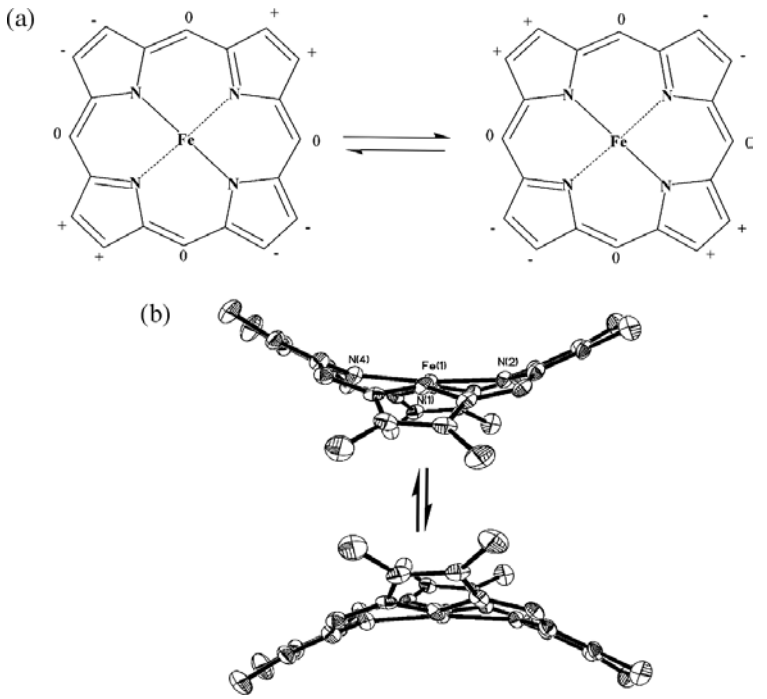

Figure 49. *Top*: Representation of the macrocycle inversion process for the saddle structure of a dodecasubstituted metalloporphyrin: (a) Displacements of the atoms with respect to the porphyrin mean plane are shown as + above the plane, — below the plane, and 0 in the plane; (b) ring inversion approximated using the ORTEP plot generated from the crystal structure of [FeOMTPP(2-MeImH)$_2$]Cl (phenyl ring and axial ligands have been omitted for clarity); ring inversion results in exchange between methyl (for OMTPP) or methylene (for OETPP, F_{20}OETPP, and TC_6TPP) protons.[551] *Middle*: Stacked ^{1}H 300 MHz NMR spectra (low shielding region only) that show broadening of the methyl signal in (OMTPP)FeCl with decreasing temperature.[551] The intensities of all resonances are on a common scale. Reprinted from Yatsunyk, L. A.; Ogura, H.; Walker, F. A. *Inorg. Chem.* **2005**, *44*, 2867–2881, with permission from the American Chemical Society. *Bottom*: 300 MHz ^{1}H NMR spectrum of (OMTPP)FeCl and the lower-shielding part of the NOESY/EXSY spectrum at –80 °C, with 5-ms mixing time; * represents impurities.[548] Reprinted from Yatsunyk, L. A.; Shokhirev, N. V.; Walker, F. A. *Inorg. Chem.* **2005**, *44*, 2848–2866, with permission from the American Chemical Society.

temperature region and 2D NOESY/EXSY (slow-exchange) techniques in the lower temperature region. The activation parameters, $\Delta H^{\ddagger}$, $\Delta S^{\ddagger}$, and $\Delta G^{\ddagger}_{298}$, and the extrapolated rate constants at 298 K for three chloride, one perchlorate, and three bis-(4-Me_2NPy) complexes as well as [FeOETPP(NMeIm)$_2$]Cl, [FeOETPP(*t*-BuNC)$_2$]ClO_4, and Na[FeOETPP(CN)$_2$] have been determined. The results indicate that there is a wide range of flexibility for the porphyrin core (k_{ex}^{298} = 10–10^7 s^{-1}) that decreases in the order TC_6TPP > OMTPP > F_{20}OETPP ≥ OETPP,

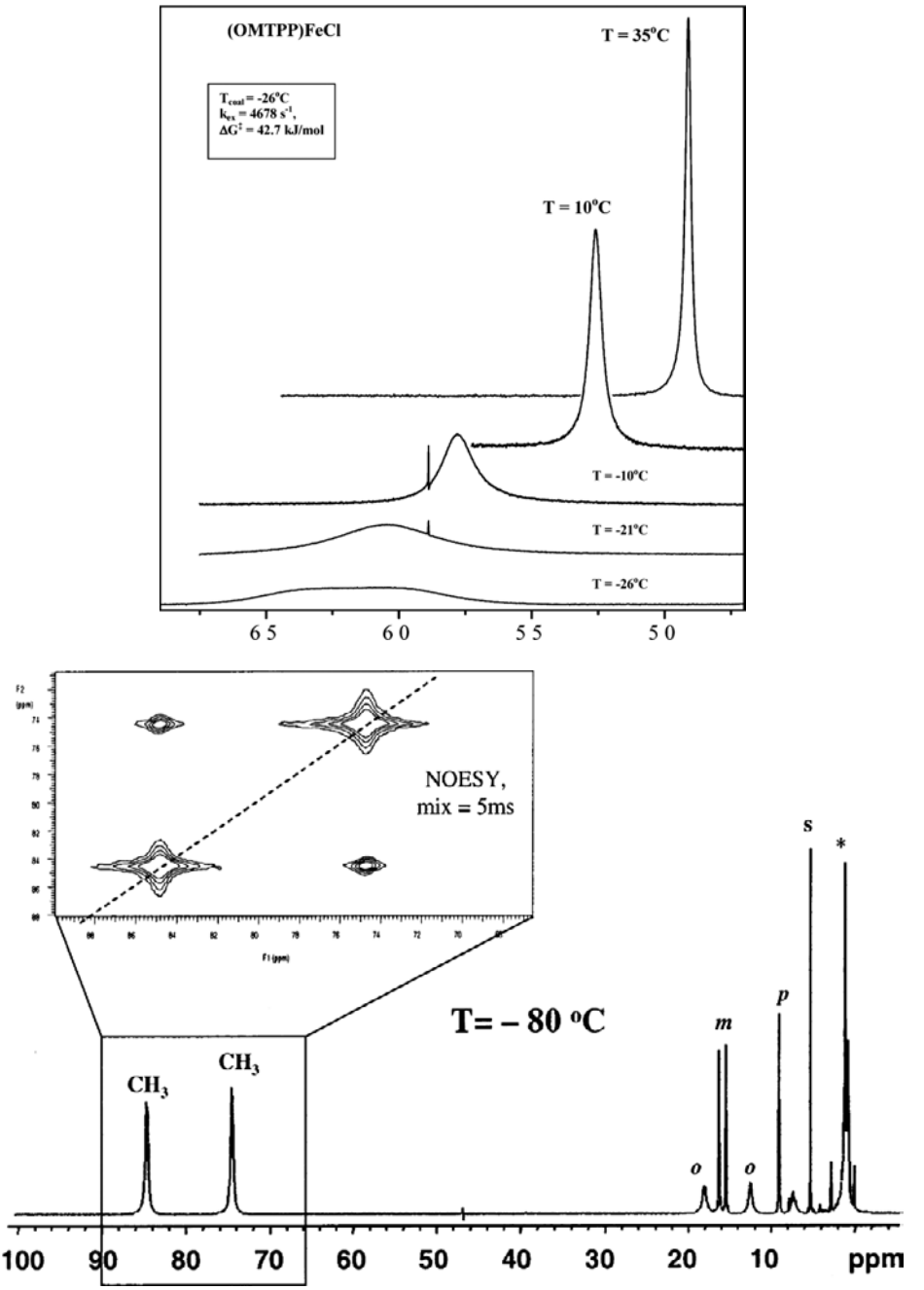

Figure 49. (*Continued*)

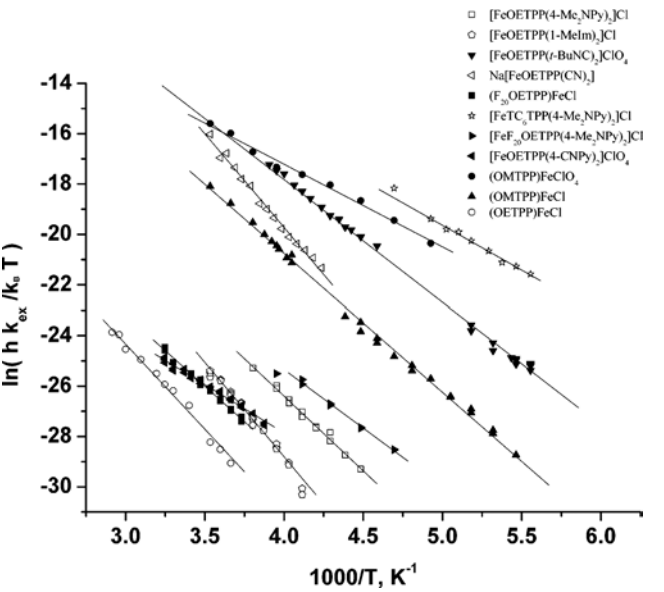

Figure 50. Eyring plots of the kinetics data obtained for porphyrin ring inversion in octaalkyltetraphenyliron(III) five- and six-coordinate porphyrins. Reprinted from Yatsunyk, L. A.; Ogura, H.; Walker, F. A. *Inorg. Chem.* **2005***, 44,* 2867–2881, with permission from the American Chemical Society.

which correlates with increasing porphyrin nonplanarity.[551] To determine the effect of axial ligands, the free energy of activation, Eyring plots were constructed and $\Delta G^{\ddagger}_{298}$ for $OETPPFe^{III}$ and $OMTPPFe^{III}$ bis-ligated complexes were calculated for the complexes with 4-Me_2NPy, NMeIm, or 4-CNPy (~59 kJ mol^{-1}), and for complexes with small cylindrical ligands (*t*-BuNC and CN^-) (~37 kJ mol^{-1}), as well as the S = 3/2, 5/2 spin-admixed chloroiron(III) complexes, as shown in Figure 50. These data suggest that the $\Delta G^{\ddagger}_{298}$ for planar ligand rotation is roughly 20–25 kJ mol^{-1}.[551]

f. *The mixed ground state behavior of bis-(pyridine) complexes of low-spin iron(III) complexes of oxophlorins and meso-amino porphyrins*

The bis-(pyridine) complexes (pyridines of a range of basicities) of the deprotonated *meso*-hydroxyoctaethylporphyrinatoiron(III), also called the oxophlorin complex, where the oxoplorin ligand is OEPO, formally $OEPO^{3-}$, Structure **8**, the bis-(N-methylimidazole) and bis-(imidazole) complexes, as well as the bis-(pyridine) or cyanide, pyridine complexes of the same iron(III) macrocycle all show two *meso*-H resonances (ratios 2:1) at very negative chemical shifts.[321,472,473,552] (The oxophlorin derived from protoheme is an intermediate in the oxidation of

heme to verdoheme by the enzyme heme oxygenase.[220]) The methylene and methyl resonances of both [$(Py)_2$FeOEPO] and [$(Py)_2$FeEtioPO] were assigned by 1D NOE difference spectroscopy; for the former, the methylene resonances were found at +30 (2-CH_2), +15 (3-CH_2), +4.7 (4-CH_2) and −3 (1-CH_2) ppm, and, as mentioned above, the *meso*-H were found at −110 and −153 ppm,[475] assignments that indicate major spin delocalization to an orbital with $a_{2u}(\pi)$-like symmetry.

Three resonance structures of the macrocyclic OEPO complex, which involve Fe^{III}, Fe^{II}, or Fe^{I} have been considered,[475] as mentioned in Section IV.A.8.a. To clarify the electron configuration, the electronic and geometric structures of $(Py)_2Fe^{III}$(OEPO), $(ImH)_2Fe^{III}$(OEPO)•2THF, and $(ImH)_2Fe^{III}$(OEPO)•1.6$CHCl_3$ have been examined by single-crystal X-ray diffraction, measurement of magnetic moments as a function of temperature, and by EPR and NMR spectroscopy.[553] The results clearly show that both complexes exist in the Fe^{III} oxophlorin trianion form rather than the Fe^{II} oxophlorin radical form previously established for (2,6-xylylNC)$_2Fe^{II}$(OEPO$^{\bullet}$).[554] In the solid state from 10 to 300 K, [$(Py)_2Fe^{III}$(OEPO)] exists in the high-spin (S = 5/2) state with the axial ligands in parallel planes, a planar porphyrin, and long axial Fe–N distances.[553] However, in solution it exists predominantly in a low-spin (S = 1/2) form. In contrast, the structures of $(ImH)_2Fe^{III}$(OEPO)•2THF and $(ImH)_2Fe^{III}$(OEPO)•1.6$CHCl_3$ consist of porphyrins with a severe ruffled distortion, axial ligands in nearly perpendicular planes, and relatively short axial Fe–N distances. The crystallographic, magnetic, EPR, and NMR results all indicate that $(ImH)_2Fe^{III}$(OEPO) exists in the low-spin Fe^{III} form in both the solid state and in solution.[553] The *meso*-H resonances of the bis-ImH complex were found at −25 ppm, which suggests a $(d_{xz},d_{yz})^4(d_{xy})^1$ electron configuration, but their temperature dependence is curved; the EPR spectrum at 4 K is rhombic, with g-values 2.72, 2.27 and 1.64.[553] These facts can be rationalized if the electron configuration at 4 K is $(d_{xy})^2(d_{xz},d_{yz})^3$, while that at ambient temperature is $(d_{xz},d_{yz})^4(d_{xy})^1$; whether this change is the result of a temperature-dependent equilibrium between the two, as found for the [TPPFe(OCH_3)(OO-^{t}Bu)]$^-$ case[481] discussed in Section IV.A.8.a, or a thermally-accessible excited state, is not clear. The bis-cyanide complex was also investigated and formulated as $[(CN)_2Fe^{III}(OEPO)]^{2-}$.[473]

[$(Py)_2Fe^{III}$OEPO$^-$] ↔ [$(Py)_2Fe^{II}$(OEPO$^{\bullet}$)] reacts with NO in the strict absence of O_2 to produce a dimer, $[(Py)(NO)Fe^{II}(OEPO)]_2$,[555] which has a 15-*meso*-15-*meso* bond. Its ^{1}H NMR spectrum at −10 °C has eight equally intense methylene resonances with chemical shifts of 18.9, 8.4, 4.3, 2.0, 1.6, 1.2, −1.6, and −4.8 ppm and two *meso*-H resonances at −95.9 and −148.2 ppm; the −148.2 ppm *meso*-H is at the bridging carbon. The reaction can be reversed upon purging with N_2.[555] The crystal structure of the dimer has been obtained and shows that the Fe–N–O unit is bent (138°), as expected for this $\{FeNO\}^7$ center.[555]

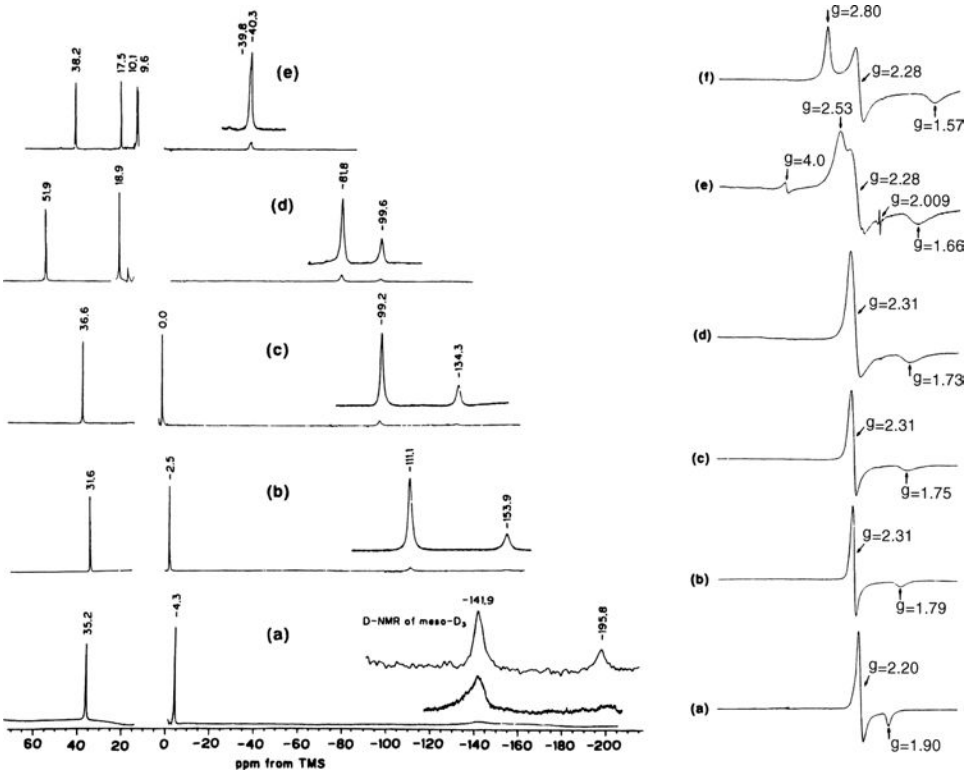

Figure 51. Left: ^{1}H NMR spectra of [(OEPO)Fe^{III}(R-Py)$_2$] measured in the ligand as solvent: (a) 4-acetylpyridine; (b) pyridine-d_5; (c) 4-methylpyridine; (d) 3,4- dimethylpyridine; (e) N-methylimidazole. Sharp signals are due to observable α-CH_2 (additional signals buried in the diamagnetic region), while insets of broad signals represent the *meso*-H. Note the decreasing meso-H shifts as the basicity of the ligands decreases. Right: EPR spectra of the same complexes measured at 77 K. (f) is [OEPOAc)Fe^{III}(ImH)$_2$] in CH_2Cl_2. Note the shift from rhombic to axial spectra and the decrease in g-anisotropy as the basicity of the ligands decreases. Reprinted from Morishima, I.; Fujii, H.; Shiro, Y. *J. Am. Chem. Soc.* **1986**, *108*, 3858–3860, with permission from the American Chemical Society.

Chemical shifts of the *meso*-H resonances of a series of [(R-Py)$_2$FeOEPO] complexes decrease as the basicity of the axial ligand increases and range from –141.9, –195.8 ppm (4-AcPy) to –81.8, –99.6 ppm (3,4-Me$_2$Py) to –40.3, –39.8 ppm (NMeIm),[321] and –118, –152 ppm (bis-pyridine) and –70, –90 ppm (Py, CN^-),[472–475] as shown in Figure 51. The bis-(hydrazine) adduct has *meso*-H shifts of –39 and –44 ppm.[552]) This is another interesting case of the degree of $a_{2u}(\pi)$ character decreasing as the basicity of the axial ligand increases, as observed previously also for the pyridine complexes of (TMP)Fe^{III},[34,491] and as discussed in Section IV.A.8.d above. As discussed earlier in Section IV.A.8.a, the EPR spectra also change in concert with the NMR spectra, such that the 4-AcPy complex has the axial spectrum with

the smallest difference between $g_\perp$ and $g_\parallel$, while 3,4-Me_2Py has the largest difference, and the NMeIm and ImH complexes have rhombic signals, as shown in Figure 51, right hand side. Clearly the oxophlorin ring system has a much greater tendency to have the $(d_{xz},d_{yz})^4(d_{xy})^1$ ground state than does the porphyrin ring, with a given axial ligand, yet the trend is still the same as for the (TMP)Fe^{III} system with pyridines of increasing basicity.[34,491] These oxophlorin-based complexes were originally assigned to be $[(OEPO^{-\bullet})Fe^{II}]^+$ π-cation radical electronic structures.[321] However, neither the EPR g-values, Figure 51, right, (which deviate too much from 2.0 to represent porphyrin-based unpaired electrons), nor the sharpness of the *meso*-H NMR signals, Figure 51, left, (which do, however, become broader with lower-basicity pyridine ligands),[321] are consistent with the unpaired electron being localized in the porphyrin π orbitals, because organic radicals in the absence of any other source of unpaired electrons (such as the $[(P^{-\bullet})Fe^{II}NO]^+$ complexes reported by Morishima and coworkers[322]) have extremely broad to undetectable NMR signals, because of their short electron spin relaxation times. Nevertheless, the large, negative *meso*-H shifts for the 4-acetylpyridine complex of octaethyloxophloriniron(III)[472,473] could represent up to 72% occupation of the $a_{2u}(\pi)$ orbital by the unpaired electron, while the *meso*-H shift of the [(OEP)Fe(*t*-BuNC)$_2$]$^+$ complex represents much less (only about 27%) occupation of that orbital, if simple Hückel calculations[211] are at all meaningful. Thus, this series of varying basicity pyridine complexes of octaethyloxophloriniron(III) may represent the closest approach to a smooth transition from a $(d_{xz},d_{yz})^4(d_{xy})^1$ ground state to a porphyrin-based $3a_{2u}(\pi)$ unpaired electron-low-spin iron(II) electron configuration found thus far. These systems should be compared to the $[(OEP^{-\bullet})Ru(CO)Br)]$ and $[(OEP^{-\bullet})Ru(CO)]^+$ ClO_4^- complexes discussed in Section IV.B later, where there is a clear shift from the ruthenium(III) to ruthenium(II) π-radical states, with relatively small differences in chemical shifts — at least of the pyrrole substituents.

Treatment of the bis-pyridine complexes of a series of mono-*meso*-substituted iron(II) derivatives of octaethylporphyrin, where the *meso*-substituent is NO_2, CN, HC(O), Cl, OMe, phenyl, or *n*-butyl, with hydrogen peroxide in the strict absence of dioxygen in d_5-pyridine at −30 °C yielded stable oxophlorin derivatives, as long as the samples were protected from exposure to dioxygen.[556] These reactions yielded mixtures of three possible oxygenation products, $[(Py)_2Fe$(*cis-meso*-R-OEPO)], $[(Py)_2Fe$(*trans-meso*-R-OEPO)], and $[(Py)_2Fe$(OEPO)]. The yield of $[(Py)_2Fe$(OEPO)], which results from replacement of the unique *meso* substituent, as a function of the identity of the *meso* substituent, decrease in the order NO_2 > HC(O) ~ CN ~ Cl > OMe > Ph, Bu, which suggests that the species responsible for attack on the porphyrin periphery is nucleophilic in nature. The ^{1}H NMR spectra of the products show methylene resonances in the +25 ppm region, but with

quite a wide variation in the separation between the *cis* resonances (largest for formyl (+16, +24 ppm), smallest for methoxy (+25 to +26 ppm)). The *meso*-H resonances were found in the −125 to −225 ppm region, with the *trans* isomer's *meso*-H resonance generally being at lower shielding than the two widely-spaced *cis* isomer *meso*-H resonances.[556] A mechanism involving isoporphyrin formation through attack of hydroxide ion on a cationic iron porphyrin with an oxidized porphyrin ring is suggested.[556] The identity of the unique *meso* functionality also affects the regiospecificity of substitution when the unique *meso* group is retained. Although random attack at the two different *meso* sites is expected to yield a *cis*/*trans* product ratio of 2, the observed ratios vary in the following order: cyano, 5.0; chloro, 3.2; formyl, 2.6; methoxy, 1.9; phenyl, 1.4.[556]

Pyridine solutions of $ClFe^{III}$(*meso*-NH_2-OEP) undergo oxidative ring opening when exposed to dioxygen.[557] The high-spin iron(III) complex, $ClFe^{III}$(*meso*-NH_2-OEP), was isolated and characterized by X-ray crystallography. In the solid state, it has a five-coordinate structure typical for a high-spin (S = 5/2) iron(III) complex. In $CDCl_3$ the ^1H NMR spectrum of $ClFe^{III}$(*meso*-NH_2-OEP) is characteristic of a high-spin, five-coordinate complex which is unreactive toward dioxygen. However, in pyridine-d_5 solution a temperature-dependent equilibrium exists between the high-spin (S = 5/2), six-coordinate complex, {(Py)$ClFe^{III}$(*meso*-NH_2-OEP)}, and the six-coordinate, low spin (S = 1/2 with the less-common $(d_{xz},d_{yz})^4(d_{xy})^1$ ground state) complex, $[(Py)_2Fe^{III}$(*meso*-NH_2-OEP)$]^+$. Such pyridine solutions are air-sensitive, and the remarkable degradation has been monitored by ^1H NMR spectroscopy.[557] These studies reveal a stepwise conversion of $ClFe^{III}$(*meso*-NH_2-OEP) into an open-chain tetrapyrrole complex in which the original amino group and the attached *meso*-carbon atom have been converted into a nitrile group.[557] Additional oxidation at an adjacent *meso* carbon occurs to produce a ligand that binds iron by three pyrrole nitrogen atoms and the oxygen atom introduced at a *meso* carbon. This open-chain tetrapyrrole complex itself is sensitive to attack by dioxygen and is converted into a tripyrrole complex that is stable to further oxidation and has been isolated[557] and investigated by NMR spectroscopy.[558] The process of oxidation of the iron(III) complex, $ClFe^{III}$(*meso*-NH_2-OEP), has been compared with that of the iron(II) complex, $(Py)_2Fe^{II}$(*meso*-NH_2-OEP);[559] both converge to form identical products.

g. *Low-spin Fe^{III} complexes of meso–meso-linked 5,5′-bis(10,15,20-triphenylporphyrin)*

The ^1H NMR spectra of iron(III) complexes of dimeric 5,5′-bis-(10,15,20-triphenylporphyrin) [$(TrPPH_2)_2$], 5,5′-bis(10,15,20-tris(*p*-methoxyphenyl)porphyrin) [$(Tr(p\text{-MeOP})PH_2)_2$], and hybrid $(TrPPH_2)(Tr(p\text{-MeOP})PH_2)$ and the respective

monomeric 5,10,15-triphenylporphyrin ($TrPPH_2$) and 5,10,15-tris(*p*-methoxyphenyl) porphyrin [Tr(*p*-MeOP)PH_2] were investigated in order to investigate the impact of a direct *meso–meso* linkage on the electronic structure of corresponding high- and low-spin iron(III) porphyrins.[560] The following species, covering the representative spin/oxidation states, have been investigated: $(TrPP)_2(Fe^{III}Cl)_2$ (high spin); $[(TrPP)_2(Fe^{III}(CN)_2)_2]^{2-}$ (low spin); $[(TrPP)_2(Fe^{III}Cl)_2]$+ (high-spin iron(III), diporphyrin radical); $[(TrPP^{-\bullet})_2(Fe^{III}Cl)_2]^{2+}$ (high-spin iron(III), diradical of diporphyrin). The iron(III) diporphyrins $(TrPP)_2(Fe^{III}Cl)_2$, $[(TrPP)_2(Fe^{III}(CN)_2)_2]^{2-}$, $\{[(TrPP)Fe^{III}(CN)_2][(Tr(p\text{-}MeOP)P)Fe^{III}(CN)_2]\}^{2-}$, and $[(TrPP)_2(Fe^{III}Cl)_2]^{2+}$ revealed the same ^{1}H NMR features which have been typically encountered in the spectra of the relevant monomeric complexes. Thus magnetic interactions between the two subunits via the skeleton appear to be minor. This is consistent with the structures, in which the two porphyrin planes are perpendicular to each other. The characteristic broadening and/or paramagnetic shifts of 3-H and 7-H resonances were determined and are diagnostic features of the *meso–meso* linkage. One-electron, ligand-based oxidation of $(TrPP)_2(Fe^{III}Cl)_2$ to produce $[(TrPP)_2(Fe^{III}Cl)_2]^+$ was observed with the unpaired electron delocalized over both macrocycles.[560]

h. *Five-coordinate low-spin iron(III) porphyrins and a porphycene*

Publications on the NMR spectra of a number of low-spin iron(III) complexes bound to one alkyl, aryl or silyl axial ligand have appeared;[166,516,561–563] the chemical shifts of typical examples are presented in Table 13. The group IV anions are expected to be extremely strong σ-donors, and indeed, they are able to stabilize both low-spin iron(II)[243] and low-spin iron(III) in a 5-coordinate state, except when four or five electronegative fluorine atoms are present on the aryl ring, in which case the 5-coordinate complexes are high-spin.[564] For the low-spin complexes, porphyrin β-pyrrole-H and $-CH_2$ shifts are indicative of the "normal" $(d_{xy})^2(d_{xz},d_{yz})^3$ ground state, with spin delocalization via P $\rightarrow$ Fe π bonding.[516] The α-H of alkyl groups had not been detected under any condition until Li and Goff[163] reported the ^{2}H NMR spectra of [(d_8-TPP)Fe(CD_3)] and [(d_8-TPP)Fe(C_2D_5)] in toluene at 25 °C, recorded over a very large spectral width at 55 MHz: For the CD_3 group, δ_{obs} = 532 ppm, and for the C_2D_5 group, δ_{obs} for the CD_2 group is 562 ppm, with the CD_3 signal of the ethyl group at −117 ppm. These are the largest chemical shifts reported thus far for iron porphyrins; the low frequency of the ^{2}H nucleus makes possible the use of spectral bandwidths that correspond to such a large number of ppm. Widths of the α-CD_3 and $-CD_2$ resonances are reasonably narrow, 80 and 115 Hz, respectively, in both THF and toluene.[163] In light of the expected narrowing of deuterium resonances of up to a factor of 42 over those of protons at the same molecule positions (Section II.D.2), it is not surprising that $-CH_3$ and

Table 13. Chemical shifts of five-coordinate iron(III) porphyrins with alkyl, aryl and silyl ligands.

Porphyrin	R[a]	T °C	Solvent	δ (Rβ-H), ppm	δ (pyrr-H), ppm	Ref.
TPP	$Si(CH_3)_3$	24	$C_6D_5CD_3$	–1.2	–21.7	565
TTP	$C(CH_3)_3$	0	$C_6D_5CD_3$	–111.5	–21.0	578
TPP	CH_3	21	C_6D_6	—	–19.2	561
	CH_4H_9	21	C_6D_6	–63.7	–18.4	561
	C_6H_5	21	C_6D_6	–81.0	–17.6	561
	$(p\text{-}CH_3)C_6H_4$	21	C_6D_6	–84.7	–16.9	561
TTP	CH_3	–70	$C_6D_5CD_3$	—	–34.0	331
	C_2H_5	–70	$C_6D_5CD_3$	154.0	–34.0	578
	$n\text{-}C_3H_7$	–70	$C_6D_5CD_3$	–27.4	–35.0	578
	$CH(CH_3)_2$	–70	$C_6D_5CD_3$	–145.6	–32.6	578
	$C(CH_3)_2$	–70	$C_6D_5CD_3$	–135.5	–33.7	578
	1-adamantane	–70	$C_6D_5CD_3$	–33.3	–17.9	578
	4-camphor	–70	$C_6D_5CD_3$	–30.8	–42.8, –48.7	578
	$[NMeIm][CH_3]$	–70	$C_6D_5CD_3$	—	–37.0	331
	$[NMeIm][C_2H_5]$	–70	$C_6D_5CD_3$	–94.0	–36.0	331
TMP	$[NMeIm][C_6H_5]$	–60	$CDCl_3$	–69.0	–34.0	516
TPP	$[Py][C_6H_5]$	21	C_5D_5N	–55.0	–21.2	562
$(p\text{-}CF_3)_4$TPP	C_6H_5	21	C_6D_6	–84.27	–17.97	564
	C_6F_4H	21	C_6D_6	—	63.32	564
	C_6F_5	21	C_6D_6	—	66.67	564
	$[Py][C_6H_5]$	21	C_5D_5N	–58.85	–21.18	564
	$[Py][C_6F_4H]$	21	C_5F_5N	—	–16.63	564
	$[Py][C_6F_5]$	21	C_5D_5N	—	–16.43	564

Porphyrin	R[a]	T °C	Solvent	δ (Rβ-H), ppm	δ(*meso*), ppm	$\delta(\alpha\text{-}CH_2)$, ppm	Ref.
OEP	CH_3	21	C_6D_6	—	3.32	2.43, –2.13	561
	$n\text{-}C_4H_9$	21	C_6D_6	–58.6	3.55	2.33, –1.70	561
	C_6H_5	21	C_6D_6	–79.9	5.53	4.46, –1.70	561
	C_6F_4H	21	C_6D_6	—	–48.56	39.91, 42.89	564
	C_6F_5	21	C_6D_6	—	–55.01	41.71, 42.69	562
	$[Py][C_6H_5]$	21	C_5D_5N	–55.7	–3.23	0.07, –2.27	562
	$[Py][C_6F_4H]$	21	C_5D_5N	–	1.94	3.78, 5.60	564
	$[Py][C_6F_5]$	21	C_5D_5N	—	2.28	4.18, 5.81	564

[a]R = alkyl, aryl or silyl ligand.

α-CH_2 signals have not been detected. It has been possible to separate the β-H and more distant proton paramagnetic shifts of the 1-adamantane complex, [(TTP)Fe(1-adamantane)], into contact and pseudocontact contributions.[563] Contact shifts within the 1-adamantane group (as well as other alkyl groups) are negative, since the unpaired electron of low-spin iron(III) is in a π-symmetry orbital, while the spin must be delocalized to the alkyl group via σ-delocalization. It was noted, however, that whereas the β-methyl resonances of the ethyl, isopropyl,

and *tert*-butyl groups have characteristic resonances at about –115 ppm (at 20 °C), the β-methylene groups of *n*-propyl, *n*-butyl, 1-adamantane, and 4-camphor appear at least 50 ppm to lower shielding than these, due to the importance of the $\cos^2\varphi$ term in Eq. 6.[563] The much smaller shift of the silyl methyl protons,[565] Table 13, seems to suggest the possibility of competing σ and π delocalization mechanisms for this heavier coneger of the *tert*-butyl anion. For aryl anions bound to iron(III), the alternating sign pattern of aryl-H contact shifts (Table 13) is indicative of mainly π spin delocalization to the aryl group.[516] Addition of *N*-methylimidazole or pyridine to either 5-coordinate low-spin or high-spin iron(III) porphyrins produces low-spin mixed-ligand complexes, in which the paramagnetic shifts of the phenyl-H or alkyl groups bound to iron are decreased,[516] probably due to decreased $R^- \rightarrow Fe$ σ (and, in the case of R^- = aryl, π as well) delocalization from the R group to the metal. Thus, the effect of adding a sixth ligand, which decreases the contact shifts of the aryl-H, suggests that the aryl anion acts as either a strong σ donor or a π donor, rather than a π acceptor toward low-spin iron(III). However, the planar nature of the aryl ligand is not sufficient to produce a resolved rhombic EPR spectrum for [(TTP)Fe(C_6H_5)]; instead, a "large g_{max}" signal at g = 3.54 is observed, with a broad feature at about g ~ 1.7,[331] indicating near-degeneracy of d_{xz} and d_{yz}, probably due to the strong σ-donor nature of the aryl ligand. Addition of pyridine shifts this signal to g = 3.86 and the broad feature to higher field (lower g-value).[331] Comparison of the ^{1}H chemical shifts of the phenyl and 2,3,5,6-tetrafluorophenyl complexes of both (OEP)Fe^{III} and ((*p*-CF_3)$_4$TPP)Fe^{III} with d_5-pyridine reveals a shift to higher frequency in approximate proportion to the geometric factors for all porphyrin resonances as the electronegative fluorine atoms are substituted onto the phenyl ring; the 4-H of that ring shifts to lower frequency by about the same geometric factor proportion,[564] a clear indication that the major difference in the paramagnetic shifts is due to the pseudocontact contribution. Thus, it appears that the magnetic anisotropy of the low-spin 6-coordinate complexes [(OEP)Fe(C_6F_4H)(Py)] and [((p-CF_3)$_4$TPP)Fe(C_6F_4H)(Py)], as well as the perfluorophenyl analogs, is considerably smaller than that of the phenyl complexes. The EPR spectra of these 6-coordinate, low-spin fluorophenyl complexes have not been reported.

A report of NMR studies on an iron(III) phenyl etioporphycene (Structure **14**) has appeared.[354] The 3,6,13,16-CH_3 resonance is at +11.5 ppm while the α-CH_2 resonances are at 8 and 3.3 ppm and the 9,10,19,20-"vinyl"-H are at +6.7 ppm, and the phenyl-H are at –5.5 (*o*,*p*-H) and +3.7 (*m*-H) ppm. The pattern of shifts is similar to that of the corresponding [(OEP)Fe(C_6H_5)],[561] although the aryl-H shifts are much smaller in magnitude for the porphycene complex, and the alkyl shifts are somewhat smaller.[354] The EPR spectra of the phenyliron(III) porphycene complex and its pyridine adduct have been reported: The g-values are 2.29, 2.27 and

1.94 for the 5-coordinate and considerably more anisotropic for the pyridine adduct. The above-quoted g-values are consistent with the $(d_{xz},d_{yz})^4(d_{xy})^1$ ground state, a very different result than obtained for the TTP analog, which has a "large g_{max}" EPR signal at g = 3.54 and a broad feature at g ~ 1.7.[563] A pure $(d_{xz},d_{yz})^4(d_{xy})^1$ ground state should have very small paramagnetic shifts and Curie plot intercepts of zero, whereas the phenyliron(III) etioporphycene has negative intercepts for all types of protons.[354] This suggests that there is a thermally-accessible $(d_{xy})^2(d_{xz},d_{yz})^3$ excited state, as has been found for many other $(d_{xz},d_{yz})^4(d_{xy})^1$ ground state systems discussed above.

i. *Low-spin iron(III) complexes of reduced hemes*

A number of investigations of the NMR spectra of the dicyano complexes of two reduced hemes have been reported.[133,206,207,566–568] The structure of sulfhemin isomer C, extracted from sulfmyomoglobin cyanide, was determined by NMR techniques,[133,566–568] and shown to be reduced at pyrrole ring II, Structure **1**. Reduction of the porphyrin ring to the chlorin changes the symmetries and molecular orbital coefficients of the frontier orbitals,[133] as shown in Figure 5. The pattern of paramagnetic shifts of this prosthetic group is indicative of delocalization not only from L $\rightarrow$ Fe π donation from the filled A_{-2} orbital of the chlorin (the modification of one of the 3e(π) orbitals of the porphyrin ring), but also from the filled A_{-1} orbital of the chlorin, which, unlike the $1a_{1u}$ orbital of the porphyrin, has proper symmetry to overlap with the d_{xz} orbital of the metal. The NMR spectra of all three of the modified hemin complexes have been observed and assigned as the metmyoglobin cyanide complexes.[362,569] Similar investigation of the dicyanoiron(III) complex of a chlorophyll a derivative, pyropheophorbide a methyl ester, in which it is ring D or IV, Structure **1**, that is reduced, and a fifth ring is present that bridges positions 13 and 15, yielded total assignment of the ^{1}H NMR spectrum of this "green heme" complex, as well as the corresponding bis-(imidazole) complex.[206] Later, the assignments were confirmed by 2D NMR techniques.[208] Again, the pattern of paramagnetic shifts was explained in terms of spin delocalization via L $\rightarrow$ Fe π donation from the A_{-2} and A_{-1} filled π orbitals of the chlorin (Figure 5).[206]

The NMR and EPR spectra of a series of pyridine complexes $[(OEC)Fe(L)_2]^+$ (L = 4-Me_2NPy, Py, and 4-CNPy) have been investigated.[115] The EPR spectra at 4.2 K suggest that with a decrease of the donor strength of the axial ligands, the complexes change their ground state from $(d_{xy})^2(d_{xz},d_{yz})^3$ to $(d_{xz},d_{yz})^4(d_{xy})^1$. The NMR data from 303 to 183 K show that at any temperature within this range the chemical shifts of pyrrole-8,17-CH_2 protons increase with a decrease in the donor strength of the axial ligands. The complete peak assignments of the $[(OEC)Fe(L)_2]^+$ complexes of this study have been made from COSY and NOE

difference experiments.[115] The pyrrole-8,17-CH_2 and pyrroline protons show large chemical shifts (hence indicating large π spin density on the adjacent carbons which are part of the π system), while pyrrole-12,13-CH_2 and -7,18-CH_2 protons show much smaller chemical shifts, as predicted by the spin densities obtained from molecular orbital calculations, both Hückel and DFT; the DFT calculations additionally show close energy spacing of the highest five filled orbitals [of the Fe(II) complex] and strong mixing of metal and chlorin character in these orbitals that is sensitive to the donor strength of the axial substituents.[115] The EPR spectra of the bis-ImH and -4-NMe_2Py complexes are rhombic, with g-values of 2.54, 2.39, 1.72 and 2.85, 2.47, 1.85, respectively, while those of the bis-Py and –4–CNPy complexes have only one resolved feature, at $g_\perp$ = 2.47 and 2.37, respectively; the bis-*t*-BuNC complex, however, has a rhombic EPR signal, with g-values of 2.32, 2.18, 1.93,[115] which are consistent with the $(d_{xz},d_{yz})^4(d_{xy})^1$ electron configuration in a complex where the macrocycle does not have 4-fold symmetry.

The pattern of chemical shifts of the pyrrole-CH_2 protons of [(OEC)Fe(*t*-BuNC)$_2$]$^+$ looks somewhat like that of [(OEC)Fe(4-Me_2NPy)$_2$]$^+$, while the chemical shifts of the *meso*-protons are qualitatively similar to those of [(OEP)Fe(*t*-BuNC)$_2$]$^+$. The temperature dependence of the chemical shifts of [(OEC)Fe(*t*-BuNC)$_2$]$^+$ shows that it has a mixed $(d_{xz},d_{yz})^4(d_{xy})^1$ and $(d_{xy})^2(d_{xz},d_{yz})^3$ electron configuration that cannot be resolved by temperature-dependent fitting of the proton chemical shifts, with a S = 5/2 excited state that lies somewhat more than 2 kT at room temperature above the ground state; the observed pattern of chemical shifts is the approximate average of those expected for the two S = 1/2 electronic configurations, which involve the a-symmetry SOMO of a planar chlorin ring with the unpaired electron predominantly in the d_{yz} orbital and the b-symmetry SOMO of a ruffled chlorin ring with the unpaired electron predominantly in the d_{xy} orbital.[115] A rapid interconversion between the two, with calculated vibrational frequency of 22 cm^{-1}, explains the observed pattern of chemical shifts, while a favoring of the ruffled conformation explains the negative chemical shift (and thus the negative spin density at the α-pyrroline ring carbons), of the pyrroline-H of [TPCFe(*t*-BuNC)$_2$]$^+CF_3SO_3^-$.[570]

Thus, although most of the chlorins studied thus far by ^{1}H NMR spectroscopy clearly have $(d_{xy})^2(d_{xz},d_{yz})^3$ ground states when bound to imidazoles or high-basicity pyridines (despite their g-values, Table 12), when bound to strong π-acceptor ligands, they, like their porphyrin analogs, do have $(d_{xz},d_{yz})^4(d_{xy})^1$ ground states.

The NMR and EPR spectra of two bis-imidazole and three bis-pyridine complexes of tetraphenylchlorinatoiron(III), (TPC)Fe(L)$_2^+$ (L = Im-d_4, 2MeImH, 4-Me_2NPy, Py, and 4-CNPy), have been investigated.[365] The full resonance assignments of the [(TPC)Fe(L)$_2$]$^+$ complexes of this study have been made from correlation spectroscopy (COSY) and nuclear Overhauser enhancement spectroscopy

(NOESY) experiments and Amsterdam density functional (ADF) calculations. Unlike the $[(OEC)Fe(L)_2]^+$ complexes reported previously,[115] the NMR data for the $[(TPC)Fe(L)_2]^+$ complexes of this study indicate that the ground state is S = 1/2 for each bis-ligand complex, whereas a higher spin state was present at NMR temperatures for the Py and 4-CNPy complexes of $(OEC)Fe^{III}$. The pyrrole-8,17 and pyrroline-H of all $[(TPC)Fe(L)_2]^+$ show large magnitude chemical shifts (hence indicating large spin density on the adjacent carbons that are part of the π system), while pyrrole-12,13-CH_2 and −7,18-CH_2 protons show much smaller chemical shifts, as predicted by the spin densities obtained from ADF calculations.[365] The magnitude of the chemical shifts decreases with decreasing donor ability of the substituted pyridine ligands, with the nonhindered imidazole ligand having slightly larger magnitude chemical shifts than the most basic pyridine, even though its basicity is significantly lower (4-Me_2NPyH^+ $pK_a = 9.7$, H_2Im^+, $pK_a = 6.65$ (adjusted for the statistical factor of two protons)). The temperature dependence of the chemical shifts of all but the 4-Me_2NPy bis-ligand complexes studied over the temperature range of the NMR investigations shows that they have mixed $(d_{xy})^2(d_{xz},d_{yz})^3/(d_{xz},d_{yz})^4(d_{xy})^1$ electron configurations that cannot be resolved by temperature-dependent fitting of the proton chemical shifts, with an S = 3/2 excited state in each case that in most cases lies at more than kT at room temperature above the ground state.[365] The observed pattern of chemical shifts of the 4-CNPy complex and analysis of the temperature dependence indicate that it has a pure $(d_{xz},d_{yz})^4(d_{xy})^1$ ground state and that it is ruffled, because ruffling mixes the $a_{2u}(\pi)$-like orbital of the chlorin into the singly occupied molecular orbital (SOMO). This mixing accounts for the negative chemical shift of the pyrroline-H (−6.5 ppm at −40 °C) and thus the negative spin density at the pyrroline-α-carbons, but the mixing is not to the same extent as observed for $[(TPC)Fe(t\text{-}BuNC)_2]^+$, whose pyrroline-H chemical shift is −36 ppm at 25 °C.[570] As mentioned above, peak assignments for high-spin (TPC)FeCl have been made by saturation transfer techniques that depend on chemical exchange between this complex and its bis-4-Me_2NPy adduct.[365]

A series of low-spin six-coordinate (tetraphenylchlorinato)iron(III) complexes $[Fe(TPC)(L)_2]^+$ (L = NMeIm, CN^-, 4-CNPy, and *t*-BuNC) which have their *meso*-carbons labeled with ^{13}C have been prepared, and their ^{13}C NMR spectra have been examined to aid in interpreting the electronic structure. These complexes were all found to exist as the mixture of the two isomers, with $(d_{xy})^2(d_{xz},d_{yz})^3$ and $(d_{xz},d_{yz})^4(d_{xy})^1$ ground states. The contribution of the $(d_{xz},d_{yz})^4(d_{xy})^1$ isomer increased as the axial ligand changes from NMeIm, to CN^- (in CD_2Cl_2 solution), CN^- (in CD_3OD solution), and 4-CNPy, and then to *t*-BuNC as revealed by the *meso*- and pyrroline-carbon chemical shifts; the *meso*-carbon signals at +146 and −19 ppm in $[Fe(TPC)(NMeIm)_2]^+$ shifted to +763 and +700 ppm in $[Fe(TPC)(t\text{-}BuNC)_2]^+$.[571] In the case of the CN^- complex, the population of the $(d_{xz},d_{yz})^4(d_{xy})^1$

isomer increased to a great extent when the solvent was changed from CD_2Cl_2 to CD_3OD. This result is ascribed to the stabilization of the d_{xz} and d_{yz} orbitals of iron(III) caused by hydrogen bonding between methanol and the coordinated cyanide ligand.[571] Comparison of the *meso*-^{13}C NMR data of the TPC complexes with those of the TPP, OEP, and OEC complexes revealed that the populations of the $(d_{xz},d_{yz})^4(d_{xy})^1$ isomer in TPC complexes are much larger than those in the corresponding TPP, OEC, and OEP complexes carrying the same axial ligands.[571]

Sirohemin is an iron(III) isobacteriochlorin that is found in sulfite and assimilatory nitrite reductases.[572] The dicyanoiron(III) complex of the extracted macrocycle has been studied by NMR spectroscopy,[573] where it was shown that the 13- and 17- α-CH_2 protons of the propionates of the two fully aromatic pyrrole rings have resonances in the +13.7 to +10.3 ppm region, while the 12- and 18-CH_2 resonances of the acetate groups of the same two pyrrole rings lie in the +7.0–5.2 ppm region at 15 °C in D_2O, pH 6.0. The 2- and 7- methyls of the saturated pyrrole rings are found in the diamagnetic region at 3.2 and 0.6 ppm, and the four *meso*-H resonances occur at −5.1, −26.3, −30.4 and −58.1 ppm.[573] The basis for assignment of these *meso*-H resonances to the 5, 10, 15 and 20 positions[573] is not clear, for it does not follow the symmetry of the molecule, and thus the expected spin densities at the *meso* positions. Only COSY spectra have been reported, and not NOESY spectra, which would have allowed unambiguous assignment of all (or at least most) of the resonances. The large negative *meso*-H shifts are indicative of $3a_{2u}$-type L → Fe spin delocalization of the unpaired electron for the ground state, consistent with a $(d_{xz},d_{yz})^4(d_{xy})^1$ electronic ground state. Consistent with this, an axial EPR signal is observed at low temperatures (15–20 K) with g-values of 2.37 and 1.78.[573] The shifts of the *meso*-H resonances to high shielding compared to the spin densities calculated from the simple Hückel program, MPorphW,[118,211] suggest an assignment 15 < 5 < 10,20, but this should be confirmed on the basis of NOESY spectra. The 13 and 17 α-CH_2 resonances exhibit anti-Curie behavior, suggesting that the $(d_{xz},d_{yz})^3(d_{xy})^2$ excited state is thermally accessible. Based on the anti-Curie behavior of the 13,17-α-CH_2 resonances but the "Curie" behavior of the *meso*-H, the excited state orbital is probably the former 3e(π) orbital having a node through the 5,15 *meso* carbons. The sirohemin bis-cyanide complex of the sulfite reductase protein has very similar NMR spectra, and the sulfite and nitrite complexes of the sirohemin-containing protein are fairly similar as well.[573] Thus, the electronic ground states of this low-spin iron(III) isobacteriochlorin and the chlorins discussed at the beginning of this section are different, and it thus appears that all reduced hemes cannot be classified as having the same electronic ground state, but rather only the isobacteriochlorins (and possibly also dioxoisobacteriochlorins) have the less-common $(d_{xz},d_{yz})^4(d_{xy})^1$ ground state as the dicyano complexes.

j. *Low-spin iron(III) complexes of N-alkylporphyrins*

Enzymatic turnover of cytochrome P450 enzymes causes formation of N-substituted porphyrins; they are also formed by the reaction of substituted hydrazines with heme proteins. Their formation results in the inactivation of the proteins involved.[574,575] N-substituted porphyrins are also inhibitors of the enzymes ferrochelatase and heme oxygenase.[576] Their iron(II) complexes are surprisingly stable to oxidation in air,[577] but upon oxidation with halogens or the thianthrene π-cation radical they form high-spin iron(III) complexes, which readily bind axial ligands such as cyanide or imidazoles.[578] The NMR spectra of iron(III) complexes of both N-methyl-tetra-(*p*-tolyl) porphyrin (N-MeTTP) and *N*-methyl-tetramesitylporphyrin (N-MeTMP) complexes having one or two cyanide, and two imidazole or 5-methylimidazole ligands show the effects of the lowered symmetry of the porphyrin: Three of the four pyrrole-H resonances of [(N-MeTMP)Fe$(CN)_2$] occur at very high shielding. In the case of the bis-(5-MeImH) or the bis-ImH complex, six of the eight pyrrole-H resonances are resolved, indicating the effect of the N-methyl group on hindering the rotation of at least the 5-MeImH ligand on the same side of the porphyrin plane.[578] Two-dimensional NMR methods would allow assignment of the observed pyrrole-H resonances and identification of the two that occur in the 0–7 ppm region and are obscured by the presence of excess ligand, as well as investigation of possible kinetic processes involving ligand rotation in this system.

k. *Thermodynamics of axial ligation of iron(III) porphyrins*

Previous reports[2,489] have shown that the equilibrium constants for ligand addition to the axial positions of iron(III) porphyrins can be readily measured by observing the relative intensity of peaks due to known proton types within the starting material, [(P)FeX], and product, [(P)Fe(X)(L)] or [(P)FeL_2]$^+X^-$, if the rate of ligand exchange is slow on the NMR time scale. The intermediate complex, [(P)Fe(X)(L)], can be either 6-coordinate, as implied by the parentheses and brackets, or 5-coordinate, as a tight ion pair, [{(P)FeL}$^+X^-$], and is often not detected by UV-visible spectroscopy.[579,580] However, NMR spectroscopic investigations at temperatures above 25 °C indicate conclusively that it is present in measureable concentrations in many cases.[2,231,489] Ligands for which binding constants to either tetraarylporphinatoiron(III) or protohemin have been measured by NMR techniques include imidazoles,[197,198,489,581–583] cyanide,[581] and pyridine/water.[345] In $CDCl_3$ it was found that NMR measurement of the overall binding constants, β_2, for addition of two substituted imidazole (RIm) ligands to a series of tetraphenylporphinatoiron(III) halides yielded values of β_2 similar to those measured by

UV-visible spectroscopy.[579] Only the overall binding constant, β_2, could be measured by NMR spectroscopy at 25 °C and below.[489] A more detailed summary of this work has been presented previously.[3]

l. *Kinetics of axial ligand exchange*

Investigations of the dynamics of axial ligand exchange in the low-spin iron(III) complex $[(TPP)Fe(NMeIm)_2]^+Cl^-$ in $CDCl_3$ by observing line broadening of the coordinated NMeIm N-methyl peak as a function of temperature were first reported by La Mar and Walker.[231] It was established that even in the presence of excess ligand, ligand exchange proceeds by a dissociative mechanism which involves a 5-coordinate $(P)FeL^+X^-$ transition state:

$$[(P)FeL_2]^+ \leftrightarrows [[(P)FeL]^+]^\ddagger + L \quad k_1, \tag{35}$$

$$[[(P)FeL]^+]^\ddagger + L^* \leftrightarrows [(P)FeLL^*]^+ \quad \text{rapid.} \tag{36}$$

These studies were extended by Satterlee et al. to characterize the axial lability of various imidazoles and pyridines in bis-ligated low-spin ferric complexes of synthetic porphyrins, including tetraphenyl- and tetra-*n*-propylporphyrins.[583] Typical activation parameters determined in this study are $\Delta H^\ddagger$ = 17–20 Kcal/mol (71–84 kJ/mol), $\Delta S^\ddagger$ = 15–19 eu (63–79 J/K-mol). More recently it has been shown by a combination of saturation transfer, line width analysis and line shape analysis in the intermediate exchange rate region that, as for the TPP complexes, ligand exchange in sterically more hindered (tetramesitylporphinato)iron(III) complexes is also dissociative.[197,198] Dissociation rates of axially coordinated imidazoles measured for TPP and TMP complexes reveal that the axial lability of coordinated imidazoles increases with increasing steric bulk of the base; that is, 2-methylimidazole complexes have larger dissociation rate constants than the corresponding *N*-methylimidazole species. The increased lability is believed to be due to the steric repulsion between the alkyl substituent in the 2-position of the imidazole ring and the porphyrin macrocycle. Overall it was determined that TPP complexes are more labile than TMP counterparts. However, the stability of the TMP complexes is invariably greater than their TPP counterparts, as discussed in Section IV.A.8.k. In fact, the rate constants are inversely proportional to the equilibrium constants, β_2,[198] which suggests that this reaction indeed proceeds as described by Eqs. 35 and 36, and that $\beta_2/K_2 = k_f/k_r$, where $k_r = k_1$.

Kinetics of ligand exchange on cobalt(III) porphyrins have been studied by saturation transfer techniques at high temperatures and compared to those of the corresponding iron(III) porphyrins, where the ligands were all 1-alkyl, 2-alkyl or

1,2-dialkylimidazoles.[584] It was found that 2-alkylimidazoles (Me, Et, i-Pr) exchange 24–40 times more rapidly than NMeIm, and 1,2-Me_2Im exchanges 1400 times more rapidly than NMeIm for (TPP)Co^{III} and 40–200 (Me, Et, i-Pr) and 200 times more rapidly than NMeIm for (TPP)Fe^{III} at 90 °C. In comparison, the rates of ligand exchange on TMPCo^{III} were found to be slower and much more similar to each other for all ligands studied (0.074 vs. 0.2 s^{-1} for NMeIm, 0.38 vs. 8.2 s^{-1} for 2MeImH and 0.011 vs. 280 s^{-1} for 1,2-Me_2Im). Similarly, the rates of ligand exchange on TMPFe^{III} were found to be slower than those for TPPFe^{III} (0.71×10^4 vs. 6.8×10^4 s^{-1} for NMeIm, 1.7×10^4 vs. 160×10^4 for 2MeImH and 5.2×10^4 vs. 1200×10^4 s^{-1} for 1,2-Me_2Im). The reason for the slower rates of ligand exchange for the TMP complexes was suggested to be the attractive interaction between the *ortho*-methyls and the imidazole π system, or the lowered repulsion between ligand atoms and the porphyrin ring in the ruffled, perpendicularly-oriented axial ligand complexes of 2-alkylimidazoles.[584] The latter is undoubtedly the most important reason.

9. *Electron Exchange Between Low-Spin Iron(III) and Low-Spin Iron(II) Porphyrins*

Heme protein electron self-exchange has been studied by NMR spectroscopy since 1965, when Kowalsky first discovered the line broadening in mixed ferro-/ferri-samples of horse heart cytochrome *c*, which was not present in samples of the pure ferro- or ferri- protein.[585] The electron self-exchange reaction can be written as:

$$\underset{\mathrm{L}}{\overset{\mathrm{L}}{\mathrm{Fe}^{*\mathrm{III}}}} + \underset{\mathrm{L}}{\overset{\mathrm{L}}{\mathrm{Fe}^{\mathrm{II}}}} \leftrightarrows \underset{\mathrm{L}}{\overset{\mathrm{L}}{\mathrm{Fe}^{*\mathrm{II}}}} + \underset{\mathrm{L}}{\overset{\mathrm{L}}{\mathrm{Fe}^{\mathrm{III}}}}, \tag{37}$$

where the hemes were inside the cytochrome *c* protein. Kowalsky estimated the rate of electron exchange as ~5×10^4 $M^{-1}s^{-1}$ at pH 6.6, ~25 °C.[585] Gupta, Koenig and Redfield followed up on this report in 1972 with NMR studies on mixed solutions of the two oxidation states of cytochrome *c*.[586] They found that the rate of exchange of oxidation states by electron transfer was sensitive to the conformation of the protein molecules, and that the electron transfer process *in vitro* arose from binary collisions. At low ionic strengths, the rate was found to be affected by the electrostatic charge on the protein molecules.[586] Wüthrich and coworkers used this method to measure the self-exchange rate for *Pseudomonas aeruginosa* cytochrome c_{551} as 1.2×10^7 $M^{-1}s^{-1}$ at pH 7.0, 42 °C in 1976,[587] and of *Euglena gracilis* cytochrome c_{552} as 5×10^4 at pH 7.0, 29 °C in 1977.[588]

Thereafter the rates of electron exchange between several ferro- and ferricytochromes *c* and *b* were studied in more detail by Dixon and coworkers.[589–591] Electron self-exchange was measured by measurement of NMR linewidths and chemical shifts for cytochromes c_{551} from *Pseudomonas aeruginosa* and *Pseudomonas stutzeri*.[589] The rate for *P. aeruginosa* cytochrome c_{551} was found to be 1.2×10^7 $M^{-1}s^{-1}$ at 40 °C in 50 mM phosphate at pH 7. For *P. stutzeri* under the same conditions the rate was found to be 4×10^7 $M^{-1}s^{-1}$.[589] The electron-transfer self-exchange rate constant of trypsin-solubilized bovine liver microsomal cytochrome b_5 was also investigated as a function of temperature and ionic strength. Calculations based on ^{1}H NMR spectra acquired using the inversion-recovery method determined this rate constant to be 2.6×10^3 $M^{-1}s^{-1}$ at pH 7.0, $\mu = 0.1$ M (sodium phosphate), 25 °C, with $AH^{\ddagger} = 5.5$ kcal mol^{-1} and $AS^{\ddagger} = -23$ eu. The rate constant increases with ionic strength, and reaches a value of 4.5×10^4 $M^{-1}s^{-1}$ at $\mu = 1.5$ M. Analysis of the data in terms of Marcus theory gives a reorganization energy, λ, in the range 0.9–1.3 eV mol^{-1}.[591] Finally, the ionic strength dependence of the electron self-exchange rate constants of cytochromes *c*, c_{551}, and b_5 were measured and analyzed[590] in terms of a monopole-dipole formalism.[592] The self-exchange rate constants, extrapolated to infinite ionic strength, of horse heart cytochrome *c*, *Pseudomonas aeruginosa* cytochrome c_{551}, and bovine cytochrome b_5 were found to be 5.1×10^5, 2×10^7, and 3.7×10^5 $M^{-1}s^{-1}$, respectively, at 27, 40 and 25 °C, respectively; cytochrome *c* showed almost no ionic strength dependence, while the other two proteins showed strong ionic strength dependence below 0.2 M, with the rate of change decreasing from 0.2 M up to 1.6 M, the highest ionic strength investigated.[590] The control of electron transfer by the size and shape of the protein was investigated using a model which accounted for the distance of the heme from each of the surface atoms of the protein. These calculations indicated that the difference between the electrostatically corrected self-exchange rate constants of cytochromes *c* and c_{551} is due only in part to the different sizes (103 vs., 72 amino acids, respectively) and heme exposures of the two proteins.[590]

The role of the protein in controlling the rate of electron transfer between two cytochrome molecules which differ only in the oxidation state of the iron, is generally believed to involve electron transfer through the heme edges exposed to the solvent. The role of the protein in this process could best be assessed by investigating the factors that control electron transfer in hemes themselves; that is, the electron self-exchange rate constants between two hemes free in solution needed to be determined (Eq. 37). Dixon and coworkers employed NMR line broadening methods to determine electron self-exchange rate constants in a variety of heme model compounds with the goal of establishing how changes in porphyrin or axial ligand structure and in macrocycle saturation affect the exchange

rates.[196,593–595] The electron self-exchange rates for various bis-N-methylimidazole complexes of iron porphyrins determined at −21 °C in CD_2Cl_2 are found to range from 8.1×10^7 $M^{-1}s^{-1}$ for the TPP complex to 5.3×10^7 $M^{-1}s^{-1}$ for the 3-MeTPP derivative and do not vary in a regular fashion with increase of steric crowding on the periphery of the porphyrin macrocycle. The total range was less than a factor of 2. Similar rate constants were measured for systems with sterically bulky imidazole ligands, such as N-butylimidazole, which suggests that increasing the steric bulk at either the heme site or on the axial ligand has almost no effect on the rate constants of electron exchange. Changes in the degree of saturation of the macrocycle also affect the rate constants in a minor way. Similar rate constant values were obtained for both the OEP and the octaethylisobacteriochlorin complexes, thus indicating little effect of the macrocycle on the electron transfer rate, perhaps due to counterbalancing effects in either the inner or outer sphere reorganization and orbital occupation.[595]

This conclusion was also drawn from the analysis of the rate constants for the dicyano derivatives, $[(TPP)Fe^{III/II}(CN)_2]^{2-}$, for which rate constants ranging from 1.0×10^7 to 5.8×10^7 $M^{-1}s^{-1}$ at 37 °C in deuterated dimethyl sulfoxide solution were obtained.[196] The value of the rate constant obtained for the heme undecapeptide derived from cytochrome *c* proteolysis (1.3×10^7 $M^{-1}s^{-1}$) is comparable to those of other model compounds[195] and indicates that the rate constants for model hemes are approximately a factor of 10 larger than those found in cytochromes with 80–90 amino acids. This also argues that the heme exposure to the solvent seems not to be a major factor that controls the rate constants for electron self exchange in cytochromes. However, complexes with axial imidazoles bearing NH groups have self-exchange rate constants which are a factor of 2–3 smaller than those with N-alkyl imidazole substituents, which indicates that hydrogen bonding or complete deprotonation of the axial imidazole nitrogen atom may play an important role in controlling electron transfer rates.[595]

10. *^{1}H and ^{13}C NMR Spectroscopy of High- and Low-Spin Ferriheme Proteins: The Nitrophorins and Heme Oxygenases*

a. *NMR spectroscopy of the nitrophorins*

Several species of blood-sucking insects, including the Amazon river-based kissing bug, *Rhodnius prolixus*,[596–599] and the common bedbug, *Cimex lectularius*,[600,601] have developed the strategy of causing vasodilation by injecting the NO-transporting heme proteins known as nitrophorins (NP) into the tissues and capillaries of their victims. On rise in pH from ~5–6 in the salivary glands of the insect to ~7.3–7.5 upon injection of the saliva into the victim's tissues, and the dilution of the protein, NO

dissociates. This NO can pass through cell walls to reach the capillaries, and thereby allow their dilation. At the same time, in the case of the *Rhodnius* NPs, the insect's bite triggers release of histamine by the victim's mast cells and platelets.[602,625] This histamine readily binds to the distal heme site of the nitrophorins. Both of these actions permit the insect to remain on the victim for a longer period of time to obtain a sufficient blood meal before detection. One of the nitrophorins, NP2, has an additional activity which helps the insect obtain its blood meal, that of binding with coagulation factors IX (fIX) and IXa (fIXa).[603] The health concerns raised by the insect bites are discussed in detail elsewhere.[604–610]

It was discovered very early in the study of the nitrophorins that the heme-NO complex found in the salivary glands of the *Rhodnius* NPs is EPR silent,[597] as shown in Figure 52. The homogenate of the salivary gland pairs of 100 insects exhibited a small g = 6 signal, which grew larger when argon gas was equilibrated with the sample for extensive periods of time, and disappeared when NO gas was

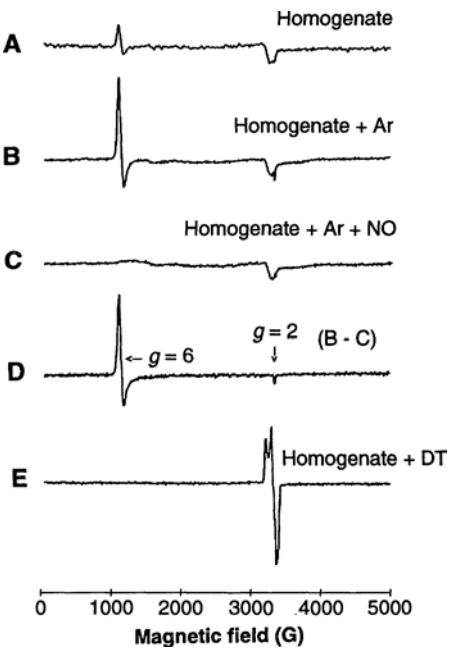

Figure 52. EPR spectra of 100 pairs of *Rhodnius* salivary glands obtained in 125 μL of PBS (A) before argon equilibration; (B) after equilibration in an argon atmosphere for 4 hours; and (C) after equilibration of (B) with NO for 2 min. (E) is the homogenate as in (A) treated with dithionite (DT) to reduce Fe(III) to Fe(II). All spectra are presented on the same scale except (E), which is shown reduced 3x in amplitude. Reprinted with permission from Ribeiro, J. M. C.; Hazzard, J. M. H.; Nussenzveig, R. H.; Champagne, D. E.; Walker, F. A. *Science* **1993**, *260,* 539–541 with permission from the American Association for the Advancement of Science.

subsequently equilibrated with the sample. Subtraction of the EPR spectrum of the NO-added sample from that of the argon-equilibrated sample yielded an axial EPR spectrum with g-values of 6.0 and 2.0, which is characteristic of 5-coordinate, high-spin ferriheme centers having histidine as the sixth ligand (Figure 52D). Thus, the NO-bound NP sample was EPR silent, as expected for a $\{FeNO\}^6$ center in the nomenclature of Feltham and Enemark,[611] in which the number of metal electrons plus the π^* electron of NO are counted. In the absence of NO, the heme center was clearly high-spin Fe(III). In order to obtain the typical EPR spectrum known for heme-NO samples[612] it was necessary to pre-reduce the untreated sample with dithionite and then to equilibrate this dithionite-treated sample with NO, as shown in Figure 52E. The observed EPR spectrum of the resulting sample is that of a 6-coordinate $\{FeNO\}^7$ center, where the sixth ligand is a nitrogen donor,[612] in this case a histidine. The NPs are unique among heme proteins in having stable $\{FeNO\}^6$ centers. This is the result of having a number of negatively-charged protein side chains at physiological pH within 8–16 Å of Fe, all but one of which help to stabilize the formal positive charge on iron(III).[613] As a result of the stabilization of the iron(III)-NO state, the dissociation constants for NO release are in the nM to μM range,[614] a very appropriate size of K_d for biological systems, rather than the pM range of the more typical iron(II)-NO K_ds,[615] which would prevent the NO from being utilized by the insect to help obtain a sufficient blood meal. Interestingly, the iron(II)-NO K_ds of the nitrophorins are even smaller than those (fM range).[614]

In common with the *Rhodnius* nitrophorins, the *Cimex* nitrophorin (*c*NP) was also found to bind one molecule of NO to the stable iron(III) form of the protein to form an EPR-silent $\{FeNO\}^6$ center.[601] However, in contrast to the *Rhodnius* NPs, in the absence of NO the EPR spectrum of the *Cimex* NP is rhombic, with g-values of 7.25, 4.75, and 1.90, which are typical of the high-spin iron(III) form of cytochromes P450.[616] This EPR spectrum thus indicated that in *c*NP the ferriheme is bound to a cysteine ligand. Also in contrast to the *Rhodnius* NPs, when the *c*NP is exposed to high concentrations of NO, two molecules of NO can bind, one to the one-electron-reduced iron(II) form to produce a $\{FeNO\}^7$ center whose EPR spectrum showed that the center was a 5-coordinate heme-NO complex,[612] i.e., that the iron(II) heme had lost its cysteine ligand.[601] The other NO was shown in the crystal structure to be bound to the cysteine, to form a thionitrosyl, SNO.[601] The conclusions which were based the EPR spectra, that the ferriheme center in the absence of NO was bound to a cysteine thiolate, and that the $\{FeNO\}^7$ center was 5-coordinate, with a bent Fe–N–O bond, were also confirmed by the structure of *c*NP in the absence and presence of two molecules of NO.[601] It is probable that the two-NO-bound form is not physiologically relevant, but it is interesting that it can form when the crystals are soaked in mother liquor containing NO. Because

the *c*NP protein has a mass of 30 kD and is thus not that easy to study by multinuclear, multidimensional protein NMR spectroscopy, and because initial characterization of it by 1D ^{1}H NMR spectroscopy revealed that only two heme resonances were exposed outside the spectral envelope of the protein, it will not be discussed further in this chapter.

For further investigation of the *Rhodnius* NPs, a cDNA library was produced from the salivary glands, and the gene for the most abundant nitrophorin, NP1, was cloned[599] and expressed.[617] The genes for NP2, NP3 and NP4 were later also cloned, sequenced, and found to be similar in sequence to NP1.[618] Two additional nitrophorins, designated NP5 and NP6,[619] were later detected in the five nymphal stages of development. The cDNA of another nitrophorin, designated NP7, was found in fifth instar nymphs.[620] The N-terminal sequence of NP5 is very similar to that of NP4 and that of NP6 is very similar to those of NP2 and NP3.[621] The sequences of the four NPs found in the adult insect, plus NP7, are shown in Figure 53, where it can be seen that there are a number of conserved features in the protein sequence, including the four cysteines, the His 59(57)(60), the Leu 123(122)(125) and Leu133(132)(135). NP7 is very different in sequence from NP1–NP4. It shows most similarity to NP2 and NP3 (63 and 64% identity, respectively). NP1 and NP4 are 91% identical in sequence, while NP2 and NP3 have 78% sequence identity. Many residues conserved in NP1–4 are very different in NP7, such that the sequence identity among the five proteins is only 32% (39% among NP1–4). NP7 has different properties than the other *Rhodnius* nitrophorins, in that it binds to anionic phospholipid membranes.[620] Its pI is 9.21,[622] which is much higher than

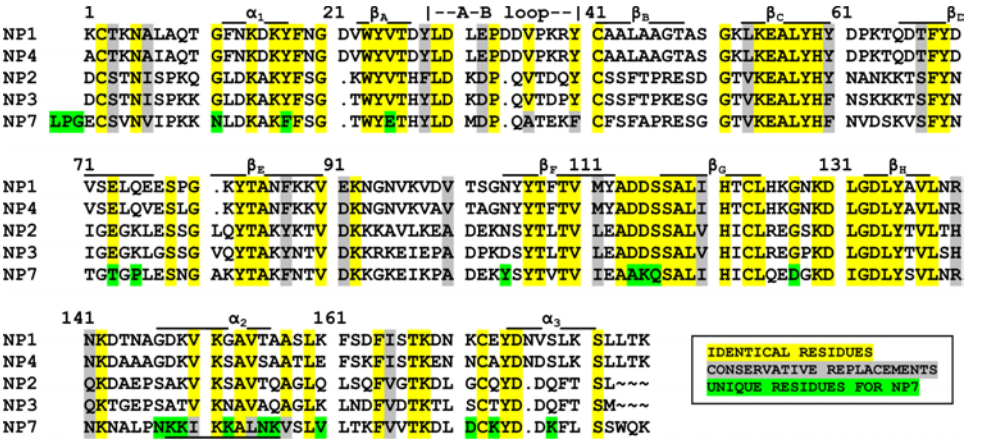

Figure 53. Sequences of five of the nitrophorins from *Rhodnius prolixus,* arranged to show sequence identities within the two groups; NP7 has greatest homology to NP2 and NP3. Helices and β sheet strands are labeled α and β, respectively. Definition of secondary structure is based on the structure of NP4.

those of the others (NP1–4 pI 7.97, 7.53, 6.94, 7.75, respectively[599]), so that if it were present in the saliva of the adult insects, from which NP1–4 were separated on a mono-P chromatofocusing column on an FPLC with triethanolamine HCl buffer at pH 8.4, it would have been missed. NP7 has been partially characterized[622–624] and is under further study in the laboratory of Dr. Markus Knipp at the Max-Planck-Institute for Bioinorganic Chemistry, Mülheim, Germany.

The *Rhodnius* NPs have a molecular mass of about 20 kDa. Crystallographic data show that the tertiary structure of the NPs is that of a β-barrel with a histidine residue that serves as the proximal ligand to the heme.[604] The 3-dimensional structures of various ligand complexes of recombinant NP1,[625,626] NP4[627–632] and NP2[633,634] by X-ray crystallography show that the protein fold of the nitrophorins belongs to a diverse class of proteins called lipocalins,[635,636] a family of relatively small secreted proteins that typically bind small, principally hydrophobic molecules such as pheromones,[637–639] retinol,[640,641] prostaglandins,[640,642] retinoic acid,[643] and biliverdin.[640,644–647] The structures of the cyanide and histamine complexes of NP1 and the NO complex of NP4 are shown in Figure 54. The ferriheme *b* molecule is bound to the protein via the imidazole nitrogen of His59 in NP1 and NP4 (His57 in NP2, NP3, and His60 in NP7). The immediate heme distal ligand-binding pocket is hydrophobic, although there are several glutamate and aspartate amino acid side chains at a somewhat greater distance (Figure 54). To date, these are the only known heme proteins with the heme inside a β-barrel.

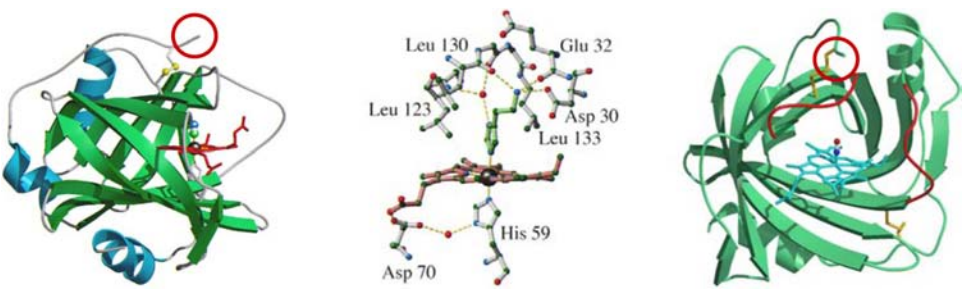

Figure 54. Left: Ribbon structure of NP1-CN,[620] with the A-B loop shown unstructured, sticking out in front of the heme propionate (PDB file 3NP1). Center: Heme binding site of NP1-histamine.[620] Note the proximity of Asp-30 and Glu-32 to the heme center (PDB file (1NP1). Reprinted from Weichsel, A.; Andersen, J. F.; Champagne, D. E.; Walker, F. A.; Montfort, W. R. *Nature Struct. Biol.* **1998**, *5*, 304–309 with permission from *Nature*. Right: Ribbon structure of NP4-NO,[623] showing the closed form of the A-B and G-H loops (red) and the N-terminal amino group above and adjacent to the C2-C122 disulfide bond (red). The two loops are well-resolved in this structure (PDB file 1ERX). Reprinted from Weichsel, A.; Andersen, J. F.; Roberts, S. A.; Montfort, W. R. *Nat. Struc. Biol.* **2000**, *7*, 551–554, with permission from *Nature*.

As is clearly shown in Figure 54 right, the structure of NP4-NO, now at 0.85 Å resolution, shows the heme to be highly nonplanar; this nonplanarity is largely a result of ruffling deformation of the heme. Among the structures of the nitrophorins now available (of NP1, NP2 and NP4), it is found that NP2 structures are most ruffled, with the average deviation of the *meso*-carbons, ΔC_m, being much larger for NP2 than for NP4 ligand complexes with NO, CN^-, ImH, Hm, NH_3, and even for the HS H_2O complex (50.8 vs. 30.3; 40.8 vs. 31.0; 27.0 vs. 15.0; 40.5 vs. 19.5; 39.8 vs. 22.7; 46.3 vs. 25.5, respectively, in 0.01 Å). Thus, the degree of ruffling of the various ligand complexes differs, yet the pattern of ΔC_m significantly larger for NP2 than for NP4 is preserved throughout. Probably the reason for this is the shorter length of both β-strand A and the A-B loop for NP2 (and NP3) than for NP4 (and NP1), Figure 53. The reason for some ruffling of the heme in all NPs is clear from the structure of apo-NP2, discussed below in Section IV.A.10.a(vii), where it is found that when heme is inserted into the apoprotein, the β-barrel must stretch horizontally in order for heme to bind, and the heme itself must also distort in order to fit within the β-barrel. As will be discussed below, the ruffling of the nitrophorin heme leads to several properties of the NPs that are not seen for other heme proteins.

We have made over 80 mutants of the nitrophorins, some of which will be discussed below. Goodin and coworkers have also made at least one mutant of NP1, the H57C mutant.[648] This mutant was characterized by UV-vis, resonance Raman, and room temperature MCD spectroscopies, and by X-ray crystallography. There is some evidence from low temperature measurements (MCD) that the cysteine binds weakly to Fe, although in the structures obtained, imidazole is able to replace the Cys and bind to both the proximal and the distal sites.[648] Histamine also can bind to the distal site, as it does in the native proteins,[648] NP1, NP2 and NP4 (PDB files 1NP1, unsubmitted, and 1IKE, respectively). NMR spectroscopy would be the best way to determine if the Cys ligand actually binds to heme iron at ambient temperatures.

NMR spectroscopy has played an important role in the characterization of the *Rhodnius* nitrophorins.[141–146,170,613,622–624,649] The proteins are stable in the ferriheme state (which is stabilized by the presence of multiple carboxylate side chains, nine for NP2 at distances of 7.99 to 18.45 Å from iron[613]), either as the high-spin (S = 5/2) aqua complex which is present in the absence of added ligand, or the low-spin (S = 1/2) form which is present in the presence of added electron-pair donor ligands such as histamine and various imidazoles or cyanide ion. The diamagnetic Fe^{III}–NO complex is also stable enough for NMR study, and considerable NMR data have been collected, although none are published at present.

The first report, in 1999, of the ^1H NMR spectrum of the imidazole complex of NP1, purified from the insect salivary glands,[626] was acquired from a sample

obtained by purification of approximately 5000 gland pairs of protein (of which NP1 was the major component, 50% of the nitrophorin fraction, 25% of the total protein present). This sample showed two possible protohemin methyl resonances, at +25.3 ppm and +13.0 ppm.[626] Additional experiments, however, showed that the +13.0 ppm resonance was the result of the accidental superposition of three 1-proton resonances at pH* 7.0 (pH* indicates the value measured with a pH meter and glass electrode, without correction for the deuterium isotope effect). When recombinant protein was available, after 1998, it was possible to investigate more highly purified protein samples.[141–146,170] Soon thereafter it was found that as is the case for the protein sequences (Figure 53), the rates of NO release also fall into two groups, with NP1 and NP4 having much larger k_ds than NP2 and NP3.[614]

i. NMR investigations of the high-spin forms of the nitrophorins from *Rhodnius prolixus*

The result of the first studies of the high-spin recombinant proteins, however, was highly disappointing for NP1 and NP4, because there were many overlapping heme resonances in the +70 to +30 ppm region,[170] as shown in Figure 55. High-spin NP2, however, showed paramagnetically-shifted heme substituent resonances that could be interpreted as having relative peak areas of 6:3:4:1:1:1:1:1.[141] As shown in Figure 55, there were also three small resonances, which were only about 1/8th of the intensity of the peaks of area 3, at +69, +68 and +56 ppm (and a fourth expected heme methyl resonance later shown to be at about +51 to +53 ppm which overlapped with the more intense resonances),[141,142] which were later shown to be the result of a minor (**A**) heme orientation.[170] The three small peaks were at first not assigned[141,142] because the crystal structure of NP2–NH_3 had definitively shown only one heme orientation.[633] However, it soon became clear, by following the intensities of the heme resonances as a function of time following addition of hemin, that either the crystals used for determining the structure of NP2–NH_3[633] contained only the major (**B**) heme orientation (presumably because the protein molecules containing the minor (**A**) heme orientation did not crystallize with the major (**B**) form), or else X-ray crystallography was unable to detect the minor (12–13% **A**) heme orientation (Figure 56).

Heme orientation in the nitrophorins has been defined in terms of the view of the heme from the distal pocket side, with the proximal His57 of NP2 being behind the plane of the heme. Viewed in this way, the major heme orientation for NP2 is **B**, with counterclockwise numbering of the heme substituents, as shown in Figure 56B. As has been known for many years, heme *b*-containing proteins may contain either one heme orientation exclusively, or, more frequently, both heme

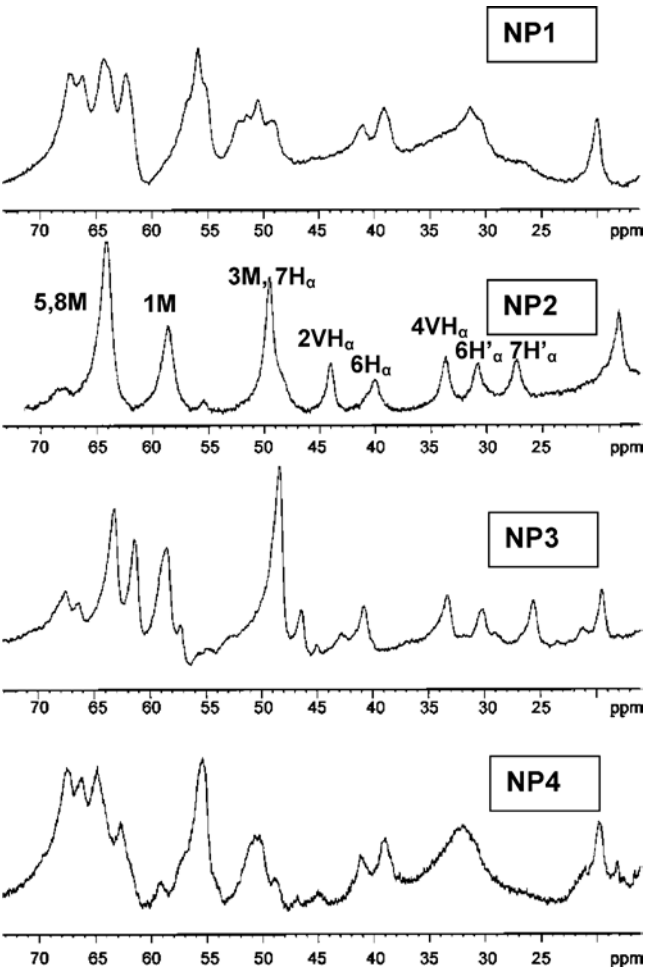

Figure 55. 1D ^{1}H NMR spectra of the high-frequency (16–73 ppm) region of the four NPs in the absence of added ligand at 25 °C, recorded at 500 MHz. The more intense resonances in the 55–68 ppm region for NP1 and NP4 and in the 49–67 ppm region for NP2 and NP3 are those of the eight heme methyls of the two heme rotational isomeric proteins (Figure 51). Resonance assignments given for NP2 were reported previously.[141] Reprinted from Shokhireva, T. Kh.; Smith, K. M.; Berry, R. E.; Shokhirev, N. V.; Balfour, C.; Zhang, H.; Walker, F. A. *Inorg. Chem.* **2007**, *46*, 170–178, with permission from the American Chemical Society.

orientations, with one or the other (**A** or **B**) being predominant, as first reported by La Mar and coworkers for the methemoglobins from the insect *Chironomus thummi thummi*[650] and sperm whale metmyoglobin.[651] The ratio of the two heme orientations, **A** and **B**, is the result of thermodynamic equilibrium between the two that depends on the steric requirements of the 2,4-vinyl substituents of the protohemin molecule in the particular protein's heme binding pocket (Figure 56).

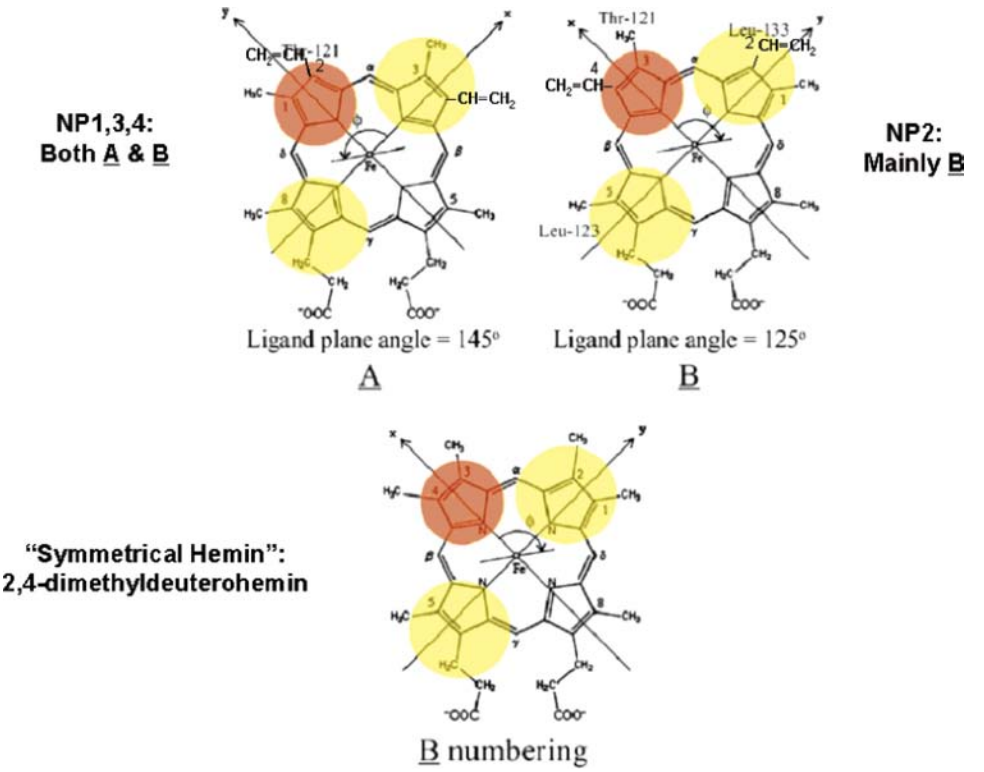

Figure 56. Top: **A** and **B**: the two isomers that result when protohemin IX is inserted into the heme pocket of a protein, with the circles showing the location of specific distal side chains for the nitrophorins. The orange circle represents the side chain of Thr121 for NP1 and NP4, Ile120 for NP2 and NP3, while the yellow circles represent the side chains of Leu123 and Leu133 for NP1 and NP4, Leu122 and Leu132 for NP2 and NP3. The proximal His59 (NP1, NP4) or His57 (NP2, NP3) is behind the plane of the heme. The equilibrium **A**:**B** ratio for each of the wild-type recombinant proteins is 1:1 (NP1, NP4), 1:8 (NP2), and 1:4 (NP3); mutation of Thr121 of NP1 to Ile changes the equilibrium **A**:**B** ratio to 1:8.[170] Bottom: 2,4-dimethyldeuterohemin, herein called the "symmetrical hemin". By convention, methyl numbering according to the **A** isomer is used for the symmetrical hemin. Reprinted from Shokhireva, T. Kh.; Smith, K. M.; Berry, R. E.; Shokhirev, N. V.; Balfour, C.; Zhang, H.; Walker, F. A. *Inorg. Chem.* **2007**, *46*, 170–178, with permission from the American Chemical Society.

[For a dramatic example of how a single residue can affect the heme orientation, see the story of NP7, NP7(E27V,Q) and NP2(V24E).[145,623,624]]

To prove unambiguously that the reason for the poorly-resolved spectra of NP1 and NP4 was nearly equal abundance of heme orientations **A** and **B**, the four NPs were also reconstituted with 2,4-dimethyldeuterohemin, the so-called "symmetrical hemin," also shown in Figure 56, which greatly simplified the spectra of all four nitrophorins;[170] more detailed studies of these high-spin symmetrical hemin complexes and some of their mutants were carried out,[170] as shown in

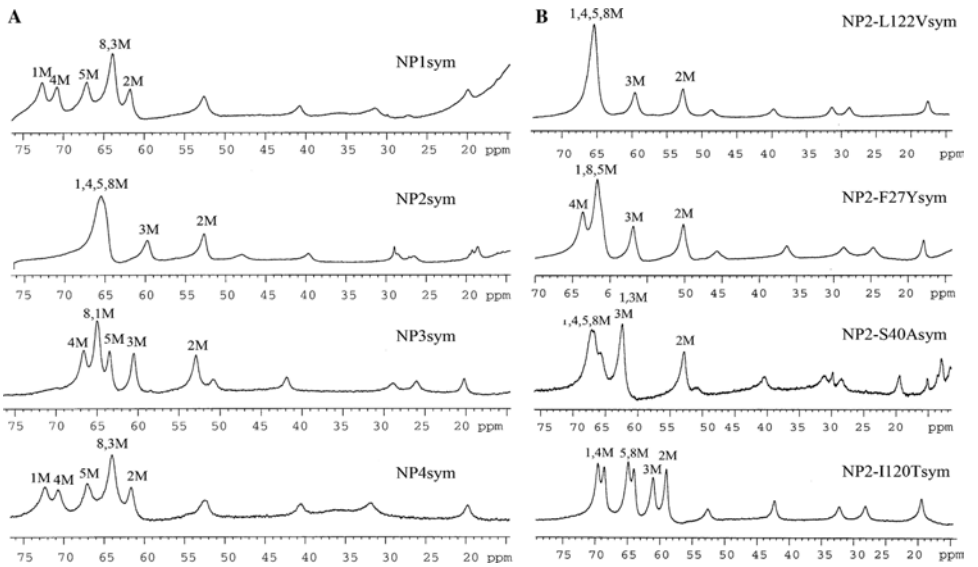

Figure 57. ^{1}H 1D NMR spectra of high-spin complexes of NP1sym–NP4sym (a) and the NP2sym mutants L122V, F27Y, S40A, and I120T (b) with symmetrical heme, all at 25 °C, pH* 7.0, recorded at 500 MHz. The NP2 sample used in spectra (a) and the NP2–S40A sample used in spectra (b) both have small amounts of a low-spin species present (a result of an adventitious ligand introduced during expression or purification), but this does not affect the chemical shifts of the high-spin complexes. Reprinted from Shokhireva, T. Kh.; Shokhirev, N. V.; Berry, R. E.; Zhang, H.; Walker, F. A. *J. Biol. Inorg. Chem.* **2008**, *13*, 941–959, with permission from Elsevier Publishing Company.

Figure 57 for NP1–NP4 and several mutants of NP2. However, it is now clear that there is a further contribution to the poorly-resolved spectra for NP1 and NP4 shown in Figure 55, and that is dynamics of the heme seating. This dynamics was clearly evident in the NOESY/EXSY spectra of the L44F mutant of NP1, as shown in Figure 58, where the EXSY cross peaks between two sets of heme methyl resonances for each heme orientation were evident; the positions of these cross peaks suggest a rotation about the H59 imidazole-Fe bond of approximately 10°.[144] The same type of broadened heme substituent resonances are present in the 1D spectrum of wild-type NP1, although the change in heme seating appears to be smaller and is more difficult to analyze in the wild-type protein case.[652]

The heme methyl resonances of high-spin NP2 were assigned by saturation transfer difference from the already-assigned low-spin complex with N-methylimidazole,[141] as shown in Figure 59, while the heme methyl resonances of high-spin NP1 and NP4 were assigned with the help of specifically deuterium-labeled isomers of protohemin provided by Professor Kevin M. Smith, the 5-CD_3, 5,8-$(CD_3)_2$, and 1,3-$(CD_3)_2$ isomers.[170] This latter method was used for many years by

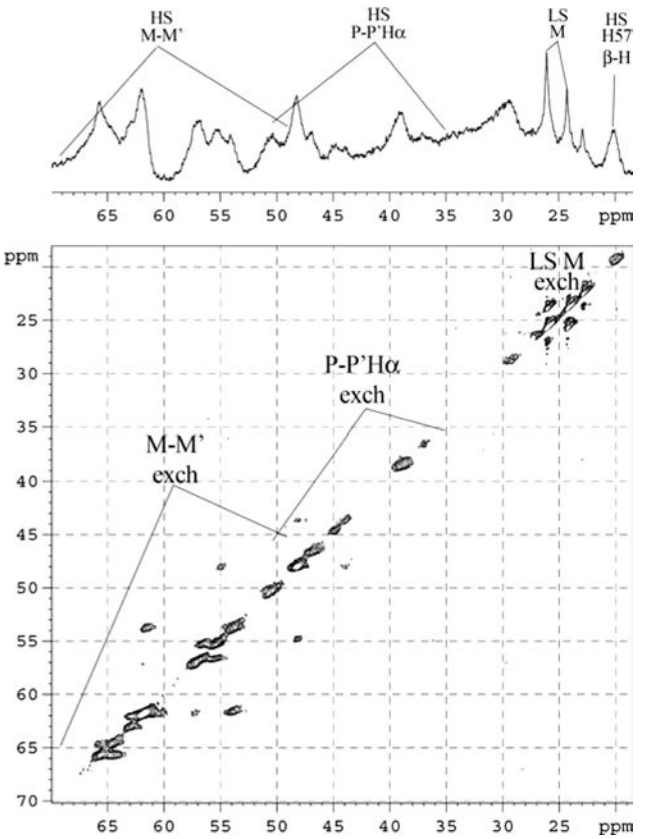

Figure 58. Water-eliminated Fourier transform (WEFT) nuclear Overhauser enhancement spectroscopy (NOESY) spectrum of the NP1(L44F)-ImH complex for the protohemin-containing protein at 35 °C, pH 7.0, recorded at 500 MHz. The sample contains both high-spin and low-spin forms of the mutant protein. The NMR spectrum shows both **A** and **B** orientations of the protohemin and chemical exchange between two high-spin forms for both **A** and **B** isomers, with different nodal plane orientations (**A′**, **B′**). At the same time, the low-spin complex shows chemical exchange (**A**–**A′**) for 3Me. Note that there are no exchange spectroscopy (EXSY) peaks between the high-spin and low-spin complexes. The frequency difference (approximately $1.4–2 \times 10^4$ Hz) between the high- and low-spin species, which are additionally in chemical exchange with each other, is much larger than the inverse mixing time of the NOESY experiment (33–100 Hz), while the off rate for ligand exchange for histamine is of the order of 5.6×10^{-2} s^{-1}, and even if it is a factor of 100 faster for N-methylimidazole (NMeIm), it would be much too slow to allow ligand exchange between low- and high-spin forms of the protein on the time scale of the NOESY experiments. Reprinted from Shokhireva, T. Kh.; Shokhirev, N. V.; Berry, R. E.; Zhang, H.; Walker, F. A. *J. Biol. Inorg. Chem.* **2008**, *13*, 941–959, with permission from Elsevier Publishing Company.

La Mar, Smith, and their coworkers to assign the heme resonances of many ferriheme proteins, as summarized in Ref. 19.

Wüthrich and Keller used the saturation transfer method very early to assign the heme resonances of ferricytochrome b_5 using the assignments already made

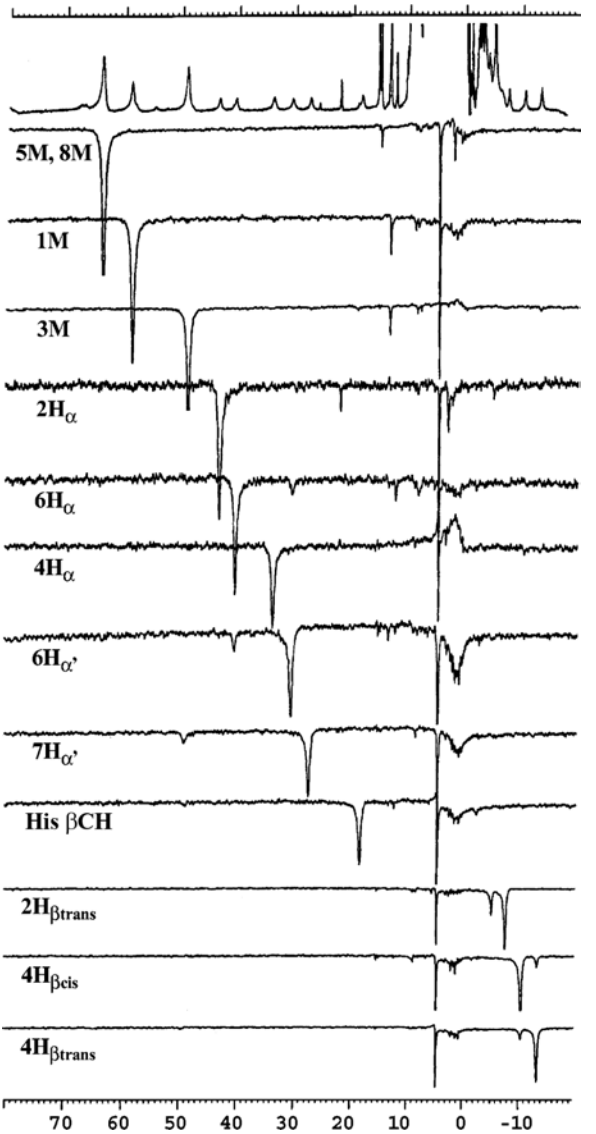

Figure 59. 1D ^{1}H saturation transfer difference spectra (STD) of a mixture of NP2 and the NP2-NMeIm complex at 37 °C and pH* 7.0, recorded at 500 MHz. Reprinted from Shokhireva, T. Kh.; Shokhirev, N. V.; Walker, F. A. *Biochemistry* **2003**, *42*, 679–693, with permission from the American Chemical Society.

for ferrocytochrome b_5,[192] and we have used it to assign the resonances of high-spin NP2 from the already-assigned resonances of the NMeIm complex of NP2.[141] The order of the heme methyl chemical shifts for the high-spin NP2 major **B** heme orientation is 5 = 8 > 1 > 3, while for the **A** heme orientation it is 8 > 5 > 1 > 3,

and the ratio **A**:**B** = 1:8.[170] For NP1,[170] NP3[146] and NP4[170] the order for the **A** isomer is also 8 > 5 > 1 > 3 while the order for the **B** isomer is 5 > 8 > 1 > 3 in all cases; the ratio **A**:**B** = 1:1,[170] 1:4,[141] 1.1:1,[170] respectively, as compared to 1:8 for NP2.[170] The orientation of the His59(57) imidazole plane could be predicted for each of these by using the angle plot specific for high-spin ferrihemes shown in Figure 60,[141] which is rotated by 90° from that of the low-spin ferrihemes,[8] which was discussed earlier in Section IV.A.8.b(iii), Figure 11.

An important property of the nitrophorins is the behavior of the mobile loops that form the opening to the heme distal pocket, the A–B and G–H loops. These are shown in red in the ribbon diagram of NP4-NO at pH 5.6, Figure 54, right. At this low pH, for the NO complex, the loops are well-ordered and there are hydrogen-bonds from several side chains of the A–B loop to side chains or backbone atoms of the G-H loop, so as to "close the door" to the heme pocket entrance.[627] This closed loop conformation is shown best by NP4 when bound to NO, as well as to some other ligands at low pH.[629–631] In contrast, structures solved at high pH (usually 7.5), including that of NP1-CN shown in Figure 54, left, have poorly-ordered loops that give rise to very diffuse electron density, because of the presence of multiple conformations of those loops; in the best-case scenarios, one or two open loop conformations can be modeled.[629–631] The change in loop conformation for NP4 as a function of pH has been used to develop models for the role of loop conformation in determining the rate of NO release from the nitrophorins.[629–631,653–655]

However, while for NP4 the first residue of the recombinant protein is Ala1,[627] as is true for native NP4 as well,[656] recombinant NP1, NP2 and NP3 carry the Met0 which results from the start codon of the recombinant gene. These three native nitrophorins have as their first amino acid one that has a charged side chain, Lys1, Asp1, and Asp1, respectively,[656] and while the native proteins are produced by cleavage of a leader sequence whose role is believed to be to allow export of the proteins to the salivary glands, the recombinant proteins were first produced by simply deleting the leader gene sequence and placing the start codon immediately before the codon for the first amino acid. *E. coli* has a methionine aminopeptidase (MAP) that cleaves methionine from newly-synthesized proteins which have a hydrophobic amino acid as the first amino acid of the mature protein sequence, but this MAP does not have activity to cleave Met0 from a protein whose first amino acid has a charged side chain. Therefore, recombinant NP1 produced from this gene has sequence M0K1C2…,[625] and NP2 and NP3 have sequence M0D1C2....[633] In the structure of NP2-NH_3 (PDB file 1EUO) it was clear that the side chain of M0 prevented the A–B loop from attaining its closed loop conformation. Thus, the NP2(D1A) gene was prepared and that mutant protein was expressed and studied in detail.[649] It was found that there were significant

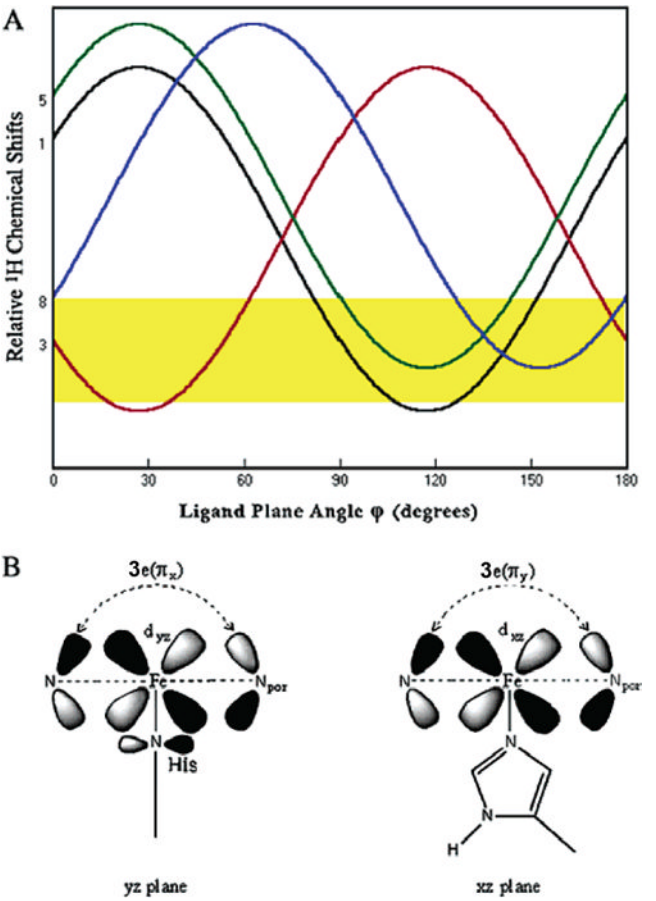

Figure 60. (A) Dependence of heme methyl shifts on the axial ligand nodal plane orientation angle φ for high-spin ferrihemes.[141] The angle φ is defined in Figure 51. No chemical shifts are provided on this modified plot, which is thus generically applicable to any high- or low-spin histidine-ligated heme protein, although the approximate end of the protein diamagnetic resonance envelope appropriate for low-spin ferrihemes is marked; for high-spin iron(III) proteins, the observed methyl shift pattern is that of the angle that is 90° shifted from the axial ligand plane orientation.[151] (B) Iron d_{xz} and d_{yz}, axial ligand π filled orbital on the binding nitrogen, and porphyrin $3e(\pi_x)$ and $3e(\pi_y)$ orbital interactions for high-spin ferrihemes. The transfer of spin density from the d_{yz} orbital of Fe to the histidine π orbital occurs by His $\rightarrow$ d_{yz} π donation, while the transfer of spin density from the d_{xz} orbital of Fe occurs by porphyrin $\rightarrow$ d_{xz} orbital by $3e(\pi_y)$ π donation. Therefore, the $3e(\pi_y)$ orbital obtains greater spin density than does the $3e(\pi_x)$ orbital, and therefore gives rise to the 90° shift in the angle plot shown. This mechanism is modified from that discussed in Ref. 141 because of the finding that the $4e(\pi^*)$ orbitals are not involved in spin delocalization.[156] Although H_2O is bound weakly to the sixth position of the high-spin nitrophorins, it is not expected to interact unequally with the d_{xz} and d_{yz} orbitals of the metal. Modified from Shokhireva, T. Kh.; Shokhirev, N. V.; Walker, F. A. *Biochemistry* **2003**, *42*, 679–693, with permission from the American Chemical Society.

differences between that point mutant protein and the wild-type, M0-containing protein: (1) While the equilibrium ratio of heme orientations **A** and **B** for the M0-containing protein was 1:8 (Figure 57), for NP2(D1A) **A**:**B** = 1:22 at equilibrium.[649] (2) While the $t_{1/2}$ for heme **A**:**B** equilibration of NP2(M0D1) was ~2 hours, that for NP2(D1A) was ~42 hours.[649] (3) Once ligand was added to NP2(D1A) there was no further **A** ⇆ **B** equilibration over periods of weeks. For NP2(M0D1) ligand complexes there was slow equilibration over periods of weeks.[649] (4) At pH 5.5 the midpoint potential of NP2(D1A) was about 30 mV more negative than that of NP2(M0D1) in the absence of added axial ligand (−318 vs. −287 mV), while at pH 7.5 the difference was only about half as great (−325 vs. −310 mV);[649] the axial ligand complexes (NO, Hm, ImH) in general had almost identical E_ms at pH 5.5 (NO: 48 vs. 49 mV; Hm: −408 vs. −410 mV; ImH: −400 vs. −423 mV, respectively), but at pH 7.5 the differences were in general greater (NO: −20 vs. +8 mV; Hm: −440 vs. −474 mV; ImH: −453 vs. −454 mV).[649] (5) In spite of these differences, the K_ds at pH 7.5 were identical for NP2(D1A) and NP2(M0D1) (K_d = 5.0 nM (NO), 10.0 nM (Hm), 40 nM (ImH)).[649] (6) The rate constants for Hm binding and release (k_{on}, k_{off}, respectively) were a factor of 2.5–5 larger for NP2(M0D1) than for NP2(D1A) (5×10^6, 2×10^6 $M^{-1}s^{-1}$; 0.056, 0.011 s^{-1}, respectively).[649] (7) The crystal structure of NP2(D1A)-NH_3 (PDB file 2EU7) showed that the A–B and G–H loops were much more closed, albeit not as closed as those of NP4-NO at low pH (PDB file 1ERX). However, what were very similar between the two proteins were the chemical shifts of the high-spin ferriheme resonances, as well as their NMeIm complexes,[649] which thus indicates that the interaction between the heme substituents and the protein, as well as the His57 orientation, were relatively unchanged by the D1A mutation and A–B loop conformation change. Since the publication of that work, a soluble expression system with export of the protein to the periplasm of *E. coli*, together with cleavage of the export sequence to leave D1 as the first amino acid has been successfully engineered,[657] and future NMR studies will use native NP2. The same soluble expression system has been achieved for NP1, and could in principle be achieved for NP3;[657] however, NP4 still requires its original recombinant gene, which begins with the start codon, immediately before the codon for A1, and the original purification of the apoprotein inclusion bodies obtained during expression[627] to obtain native NP4(A1).

ii. pH titration of the high-spin nitrophorins from *Rhodnius prolixus*

As shown in Figure 23 and discussed in Section IV.A.6.b earlier, the *meso*-H resonance of $OEPFe^{III}$ in DMSO, where the iron(III) porphyrin is 6-coordinate with two DMSO molecules bound axially, is observed at about +41 ppm at ambient

temperature. For symmetrical hemin-reconstituted nitrophorins, occasionally it is possible to see at least some of the broad *meso*-H resonances in the 33–45 ppm region of the ^{1}H NMR spectra of the high-spin proteins, as is evident in the NP1sym and NP4sym spectra[144] of Figure 57A, but usually these resonances are too broad to be observed. Based on the best-case examples and analogy to most other high-spin ferriheme proteins that have one protein-provided axial ligand (except peroxidases),[19] we have assumed that all four of the *Rhodnius* NPs of the adult insect have a water molecule bound on the distal side of the heme. In support of this, we have done pH titrations for NP2 and NP3 and found that they behave quite differently.[146]

What has been known for a long time about ferriheme proteins is that if they have only one protein-provided ligand, in the absence of added exogenous ligands, the aqua complex deprotonates at some basic pH to leave a hydroxide bound to Fe^{III} — or, a 5-coordinate ferriheme center without a bound water molecule reacts with hydroxide to produce a 6-coordinate ferriheme center. The reactions for metmyoglobin have been described as follows:[19]

$$\text{metMbH}_2\text{O} + \text{OH}^- \leftrightarrows \text{metMbOH} + \text{H}_2\text{O}, \tag{38a}$$

$$\text{metMb} + \text{OH}^- \leftrightarrows \text{metMbOH}. \tag{38b}$$

For ferroheme proteins it is not so common to have a water bound to Fe^{II} at low pH, and thus reaction (38b) may be more common for Fe^{II} than for Fe^{III}. As pointed out previously,[19] the hydroxide complex may exist as an equilibrium mixture of S = 5/2 and S = 1/2 spin states, with characteristic temperature dependence for the equilibrium. This point, and inclusion of an S = 3/2 possibility as well, becomes quite important for the heme oxygenases (HOs),[658,659] discussed later in Section IV.A.10.b.

For NP2 this water/hydroxide has a pK_a of about 10.5, and the spin state changes cleanly from S = 5/2 to S = 1/2,[144] as shown in Figures 61c and d, where the growing resonances of the high-pH form (the hydroxide complex) are clearly in the expected chemical shift range for a low-spin complex, with a compressed chemical shift scale which is indicative of the $(d_{xz},d_{yz})^4(d_{xy})^1$ electronic ground state (see next section) (19.0 (3M), 13.0 (5M), 10.7 (8M), 6.5 (1M) at 30 °C).[146] As can be seen, beyond the half-titration point the high-spin resonances become increasingly broadened, so that at pH = 10.99 most features of the high-spin ^{1}H NMR spectrum are too broad to interpret (Figure 61e), yet the low-spin resonances are still quite sharp.[146] This signifies that the rate of deprotonation of the HS form is approaching the difference in frequency between the HS and LS resonances, $(\nu_{HS(5M)}-\nu_{LS(5M)})$, which is about 25.5 kHz at 500 MHz and 30 °C for 5M,

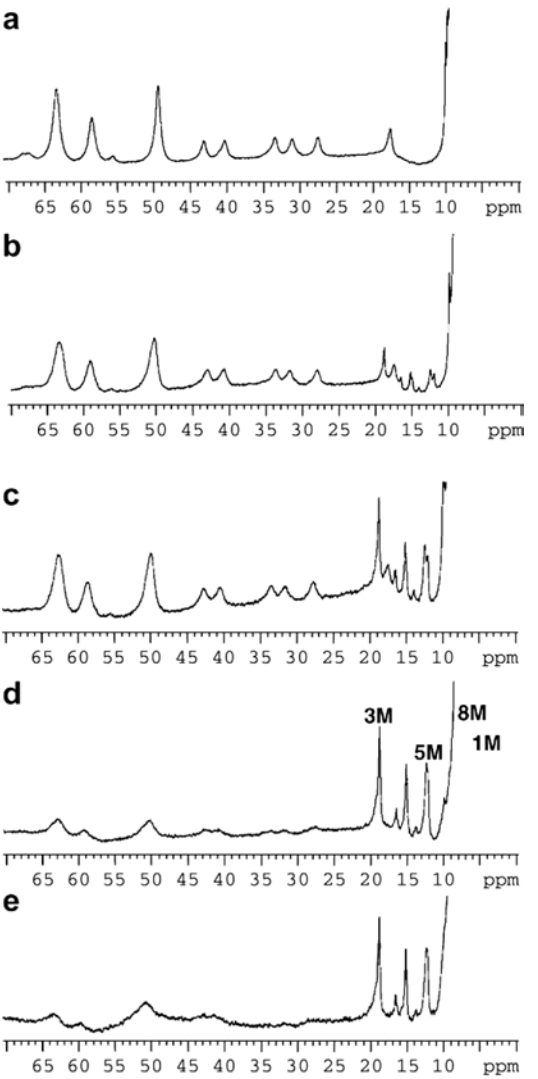

Figure 61. pH titration of NP2 in the absence of added axial ligand, recorded at 500 MHz, 25 °C. pH* values (uncorrected for the deuterium isotope effect) are (a) 7.10, (b) 9.90, (c) 10.30, (d) 10.86, (e) 10.99, (f) plot of pH dependence vs. fraction of hydroxo complex formed (from the relative intensities of the 3Me resonance of the high-spin aquo and the hydroxo complexes). From these data the pK_a of the water molecule bound to NP2 is estimated to be 10.5 (uncorrected for the deuterium isotope effect). Note that spectrum (e) shows the beginning of observable kinetic averaging of the NMR signals of the high-spin aquo and the hydroxo complexes that is quite far advanced at pH* 9.6 for NP3.[146] Methyl resonance assignments for the hydroxo complex[146] are marked on (d). Reprinted from Shokhireva, T. Kh.; Berry, R. E.; Zhang, H.; Shokhirev, N. V.; Walker, F. A. *Inorg. Chim. Acta* **2008**, *361*, 925–940, with permission from Elsevier Publishing Company.

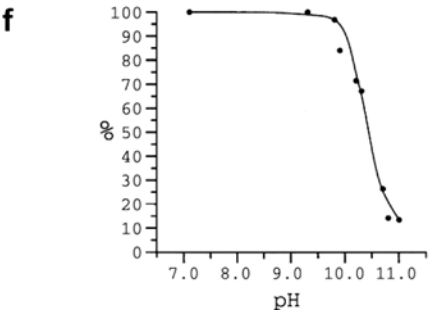

Figure 61. (*Continued*)

26.7 kHz for 8M, or that the rate constant for deprotonation is on the order of $2.6–2.7 \times 10^4$ s^{-1}.

However, for NP3 the same titration does not give well-resolved resonances of the hydroxide complex, but rather the high-spin aqua complex is in chemical exchange with the hydroxide complex on the NMR timescale, and resonances of both are broad and poorly resolved above pH 8.[146] Thus the results are not as clear, beyond the fact that 3M is the methyl resonance having the largest chemical shift for NP3–OH, as for NP2–OH[146] (Figure 61). A rough estimate of the pK_a of NP3–OH is ~9.9–10.[146] It is surprising that the rate of proton exchange is so different for the two proteins, when both the aqua and hydroxide complexes have very similar chemical shifts of the heme resonances. The calculated isoelectric points[660] of NP2 and NP3 are similar (6.1 and 6.5, respectively), and thus probably cannot explain the difference in the rate of proton exchange. Additional examples of deprotonation of the water bound to high-spin ferriheme proteins will be discussed in the section on heme oxygenases (Section IV.A.10.b).

iii. NMR investigations of the low-spin forms of the nitrophorins from *Rhodnius prolixus,* and comparison to other heme proteins

The low-spin (S = 1/2) complexes of the nitrophorins of interest to their biological functions of NO-binding and release and histamine binding include the histamine (Hm) complexes, their simpler models, the imidazole (ImH) complexes, other imidazole complexes (N-methylimidazole, NMeIm, and 2-methylimidazole, 2MeImH), which may be less stable and thus good candidates for saturation transfer studies aimed at assigning the hyperfine-shifted heme resonances of the high-spin complexes, and the cyanide (CN^-) complexes, which have been used as paramagnetic models for the diamagnetic NO complexes.[143–146] All of these have been studied in detail for all four of the major nitrophorins of the adult insect[141–146] and for a number of their mutants, and most have been studied for NP7 and several

of its mutants.[145,623,624] Most of the exogenous ligand complexes of the NPs are extremely stable, with binding constants for ImH and Hm both being 10^8 M^{-1} or larger (K_ds < 100 μM) at pH 7.5,[613] and that for cyanide estimated to be of the order of 10^{12} M^{-1} (K_d ~1 pM) at pH 7.5.[613] The binding constants for NMeIm and 2MeImH are several orders of magnitude smaller than those for ImH and Hm.[661]

In 1998, Shokhirev and Walker showed that the methyl and *meso*-H resonances of low-spin ferriheme proteins are strongly affected by the orientation of the plane of one or possibly both axial ligands, because the orientation of that plane determines the nodal plane orientation of the 3e(π) orbital that is involved in spin delocalization from low-spin iron(III) by Por $\rightarrow$ Fe π donation, and the angular dependence of the pseudocontact contribution to the paramagnetic shifts.[8] Thus, as the planar axial ligand is rotated to a certain angle in a particular ferriheme protein, as defined by Figure 8, so also is the nodal plane of the 3e(π) orbital rotated by simple rehybridization of the two Hückel orbitals, combined with the change in the angle of the pseudocontact contribution,[140,211] as discussed above in Section II.C.3 and shown in Figures 9–11. This concept was shown to apply to a large number of ferriheme proteins[8] and many more[141–150] since that original publication. A program called Shift Patterns[151] was developed for plotting methyl and *meso*-H chemical shifts as a function of ligand plane angle in a general way that is independent of the effect of ligand donor strength (that is, the pattern of relative spacings is used, rather than exact chemical shifts). By use of this program, it is possible to determine the orientation of the nodal plane of the heme 3e(π) orbital utilized for spin delocalization, if the heme methyl order has been assigned, by using the relative spacings of the resonances, with an accuracy in most cases to ±2–3°. Several systems for which this program did not predict the correct relative chemical shifts, for example *N. europae* cytochrome c_{552},[662] were later shown to have an unusual heme methyl chemical shift order (5 > 8 > 3 > 1) and a highly compressed chemical shift range because of dynamic flipping of the methionine ligand's methyl group on the NMR timescale, which has the effect of averaging the chemical shifts of the heme substitutents for the two possible nodal plane orientations of the methionine ligand.[663–666]

The NP2-ImH complex has been studied at pH* 7.0,[141–143,145] 5.5[145,624] and 4.0.[145] As can be seen in the 1D spectrum at these three pH* values shown in Figure 62, besides the major **B** orientation and minor **A** orientation, the 1D ^{1}H NMR spectrum at pH* 5.5 exhibits an extra set of three hyperfine-shifted resonances between 24 and 22 ppm which increased remarkably in intensity on lowering the pH* to 4.0. Peaks were assigned from the pH* 5.5[624] and the pH* 4.0[145] WEFT-NOESY spectra (Figure 63) and from the pH* 5.5[624] and pH* 4.0 ^{1}H{^{13}C}-HMQC spectra.[145] For the major **B** heme orientation of NP2, the order of heme methyl chemical shifts is the same from pH* 7.0 to 4.0, 3 > 5 > 1 > 8.[145] From the angle plot (Figure 11),[8,151] we can see that although the chemical shifts of the heme

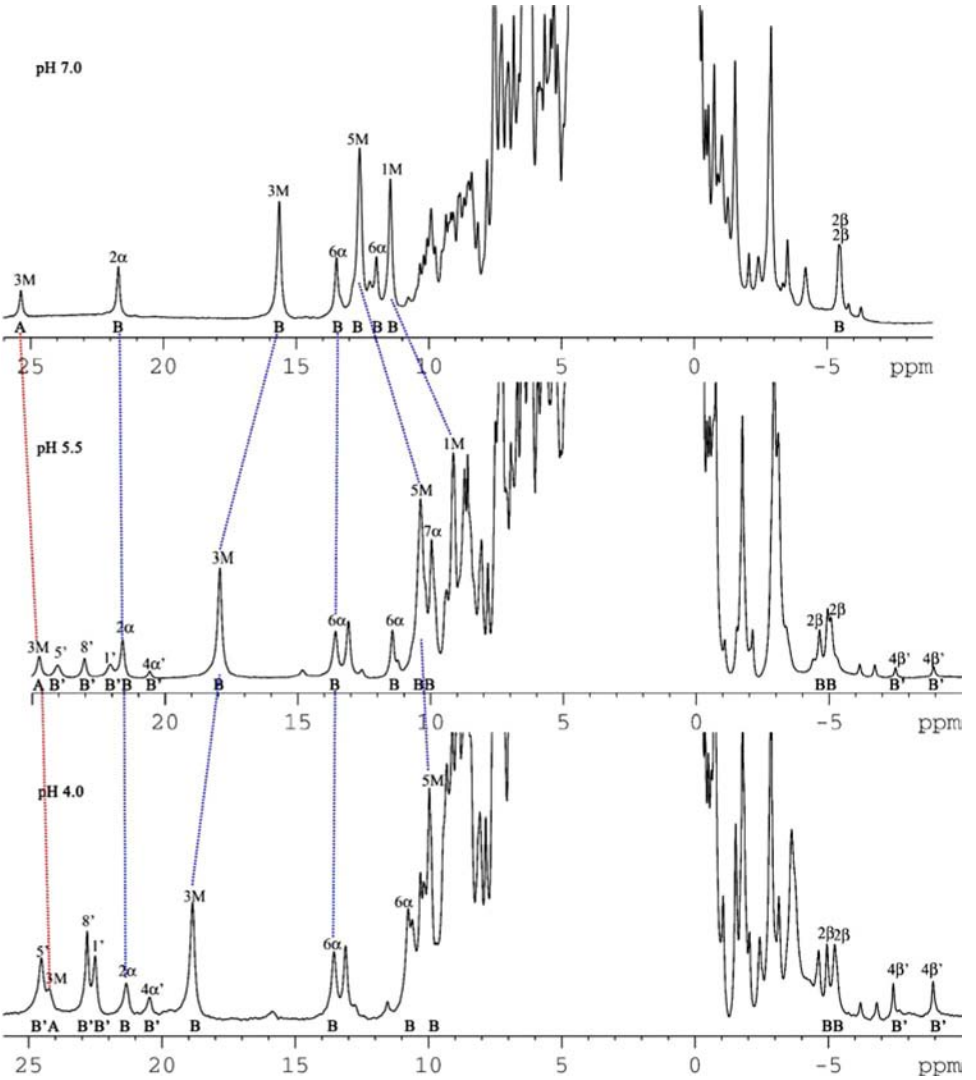

Figure 62. 1D ^{1}H NMR spectra of the hyperfine-shifted resonances of NP2-ImH at pH* 7.0 (top), pH* 5.5 (middle), pH* 4.0 (bottom), recorded at 25 °C at 600 MHz. Lines showing the variation in chemical shift of heme resonances of **A** (red) and **B** (blue) are displayed. Reprinted from Yang, F.; Knipp, M.; Berry, R. E.; Shokhireva, T. K.; Zhang, H.; Walker, F. A. *J. Biol. Inorg. Chem.* **2009**, *14*, 1077–1095, with permission from Elsevier Publishing Company.

methyls change quite a bit, the effective ligand nodal plane angle varies by only a few degrees, in the range of 150–154°; this angle represents the orientation of the exogenous ImH ligand for the **B** heme orientation, while for the **A** orientation the angle is believed to be 116–120°, although because of chemical exchange, not enough resonances of the **A** heme orientation of NP2-ImH have been observed to

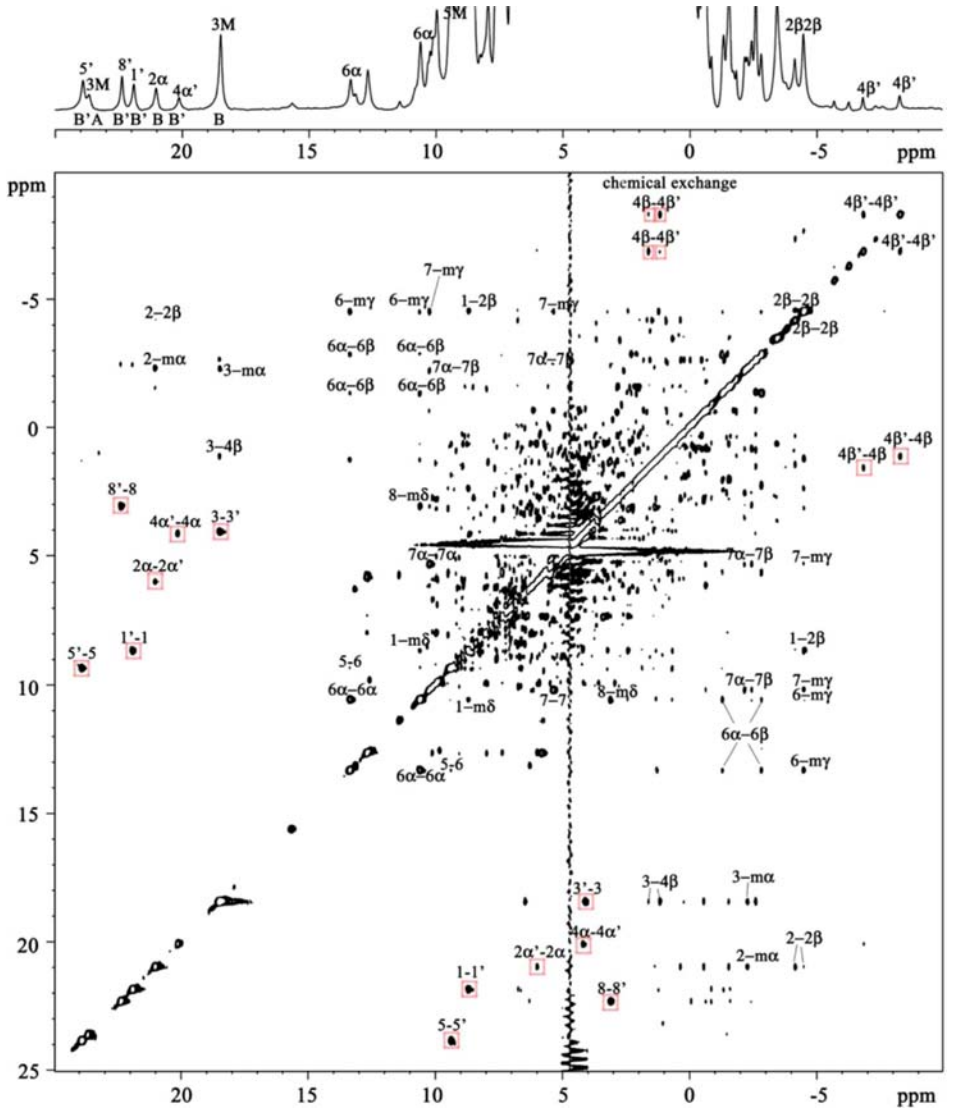

Figure 63. 1D ^{1}H and WEFT-NOESY/EXSY NMR spectra of NP2-ImH in D_2O, buffered with 30 mM Na_2DPO_4/acetic acid-d_4 (pH* 4.0), recorded at 33 °C and 600 MHz. There are both chemical exchange cross peaks between **B′** and **B** (red boxed), and NOESY cross peaks for **B**. Reprinted from Yang, F.; Knipp, M.; Berry, R. E.; Shokhireva, T. K.; Zhang, H.; Walker, F. A. *J. Biol. Inorg. Chem.* **2009**, *14*, 1077–1095, with permission from Elsevier Publishing Company.

define the angle well. Thus, the heme methyl chemical shifts change rapidly with the small changes in axial ligand orientation over this angle range.

Chemical exchange was observed in the NOESY/EXSY spectra of NP2-ImH at pH* 5.5[624] and 4.0[145] between the additional signals and the 5M, 1M, 8M and

3M resonances of the **B** orientation, which shows that these resonances are caused by an additional species with **B** heme orientation, which we have called **B′**. The methyl resonances of **B′** are easily assigned from the chemical exchange cross peaks between **B′** and **B** from the NOESY (EXSY) spectrum (Figure 63). In contrast to the methyl resonance order 3 > 5 > 1 > 8 obtained for **B**, **B′** exhibits the order 5 > 8 > 1 > 3 at both pH* 5.5[624] and pH* 4.0.[145] The effective nodal plane angle of **B′** (~42°) is about 110° different from that of **B** (~152°).[145] Since the proximal His imidazole plane orientation is about 135° from the heme axis defined by the line connecting N_{II} and N_{IV}[633,634] (Figure 8), it is obvious that the effective nodal plane angle obtained from the angle plot is dominated by the exogenous ligand ImH for NP2, as was observed previously at pH* 7.0,[141] and within 5° (156.9°) of the angle observed in the crystal structure (PDB file 1PEE).Thus the ImH plane in isomer **B** is nearly parallel (a difference in angle of ~17°) to the His57 imidazole plane, while in isomer **B′** the ImH plane is nearly perpendicular to the His imidazole plane (a difference of ~93°). Therefore, for simplicity, we can describe the two isomers as having parallel (**B**) and perpendicular (**B′**) ImH plane orientation.

Although a perpendicular orientation of the ImH ligand of NP2-ImH was not observed in our previous study of wt NP2 at pH* 7.0,[141] the **B′** orientation was seen for the symmetrical hemin complex, NP2sym-NMeIm,[146] and for the protohemin NP2 L → V mutants at pH* 7.0: NP2(L122V)-ImH, NP2(L132V)-ImH, and NP2(L122V, L132V)-ImH,[142] as well as for the other three major NPs of the adult insect, both for the protohemin[143,144] and the symmetrical hemin[146] complexes. However, for NP7-ImH, only the **A** heme orientation has been observed, and there is no chemical exchange, probably because of the crowding in the heme-binding pocket due to the presence of E27.[145,623,624]

Both Leu122 and Leu132 point from the β-strands above the heme pocket toward the distal side of the heme (Figure 54, center), and at the time of publication of the first study of the single and double Leu → Val mutants[142] it was believed that the perpendicular ImH orientation was permitted by the shorter Val side chain, which was able to create enough space in the distal pocket to allow ImH ligand rotation. It is now clear that it was only an accident of fate that the perpendicular orientation of ImH, **B′**, with chemical exchange between **B′** and **B** for wt NP2-ImH was not observed at pH 7.0, and that the reason for the existence of the perpendicular ImH orientation is the presence of a minor ruffled conformation of the heme, which cannot accommodate the parallel ImH ligand, but can allow binding of ImH in the perpendicular orientation; dissociation and re-binding of ImH, all within the distal pocket, are thus required in the exchange reaction.[143–145]

By measuring the NOESY/EXSY cross peak and diagonal peak intensities of wt NP2-ImH at low pH, the rate constants and equilibrium constant of interchange between **B′** and **B** can be calculated by use of the program “Two Site Exchange of

NMR Lines" developed in this laboratory.[667] From the results of this calculation, the equilibrium constant K_{eq} for the reaction **B′** ⇆ **B** at pH* 5.5 is larger (8.0) than that at pH* 4.0 (3.4). This is also easily seen from the 1D ^{1}H NMR spectra (Figure 62), that the peaks from **B′** at pH* 4.0 are relatively more intense than are those at pH* 5.5. The NOESY/EXSY spectra at different temperatures and different mixing times show that as the temperature decreases, the **B′** orientation is more favored.[145] Thus, at low temperature the ImH ligand has more tendency to be perpendicular to the His57 imidazole plane than at room temperature. The rate constants for the reaction **B′** ⇆ **B** (k_f, k_r = 8 and 1 s^{-1} at pH 5.5; 6.7 and 1.9 s^{-1} at pH 4.0, respectively, both at 33 °C)[145] also show that different mixing times in the EXSY experiments give the same rate constant, and thus confirm that both the rate and equilibrium constants are independent of mixing time.[145] NOESY/EXSY spectra of wild-type (wt) NP2–ImH and its L122V and L132V distal pocket single mutants and the L122V,L132V double mutant also exhibit chemical exchange cross peaks.[142] The rate of interconversion of the two forms at pH 7.5 could be estimated from the NOESY/EXSY diagonal and cross peak intensities (k_f ~ 54 s^{-1}, k_r ~ 0.5 s^{-1}, $K_{eq} = k_f/k_r$ = 100 or larger),[142] where the major **B** ImH orientation angle is somewhat larger than that found for the wt NP2–ImH complex (168–170°).[141] NMR spectroscopic investigations of the more sterically-demanding 2-methylimidazole ligand (2MeImH) showed that it binds to all three distal pocket mutants to create low-spin six-coordinate Fe^{III} complexes which have the protein-provided H57-imidazole and the distal 2MeImH in nearly perpendicular planes; it also binds to the wt protein in the presence of higher concentrations of 2MeImH, but yields a different ligand plane orientation (about 20° different) than is present in any of the three distal pocket mutants.[142] The crystal structure of the double mutant-ImH complex shows an approximately perpendicular angle which is different than any of those observed in solution (φ = 19.5°, $\Delta\varphi$ = 69.1°, PDB file 1PM1), and is highly ruffled, although not as ruffled as the wild-type (ΔC_m = 38.8 in 0.01Å).[634] In contrast, the orientation angle φ determined for the ImH of the **B′** species in solution is 56°. While both of these give similar dihedral angles to the H57 plane ($\Delta\varphi$ = 69° vs. 74°, since in both cases the dihedral angle less than 90° is measured), the orientation of the ImH ligand for the **B′** species is different by about 36° in solution from its orientation in the solid state.

The relevance of the **B′** ⇆ **B** exchange processes, whose rates can be measured by NOESY/EXSY techniques,[142,145] to the kinetics of NO release from the nitrophorins[668,669] is that **B′** ⇆ **B** exchange clearly involves loss of the ligand, but not loss from the distal pocket, followed by its re-binding in a different orientation. As shown above, the rate constant for ImH orientation change from **B** to **B′** for NP2 (L122V,L132V) at pH 5.5, is k_r ~ 0.5 s^{-1} at pH 7.5,[142] whereas the rate of NO loss from the binding pocket of wild-type NP2 has been measured at pH 8.0

as k_{off} ~ 0.12 s^{-1},[668] and at pH 7.5 as 0.16 s^{-1}.[669] Although NO is a much smaller ligand, and thus might be expected to have a faster rate of dissociation than ImH, the wild-type NP2 pocket is much more crowded than is that for the L → V double mutant.[634] And also, crystal structures of the NO complexes of NP2 and NP4 have shown that the A-B and G-H loops are in the closed conformation, whereas crystal structures of the ImH complexes of both NPs have shown that the A-B and G-H loops are fairly open.[628–634] In addition, in the **B/B′** case, it is likely that the ImH ligand does not completely leave the protein, but simply slides away from the binding site and then slides back in, in a different orientation (it cannot simply rotate through an angle of ~90° because of the bulky Leu122 and Leu132 side chains, Figure 54, center). The k_r values for **B/B′** kinetics of wild-type NP2-ImH at low pH (k_r ~ 1.9 s^{-1} at pH 4.0 and 1 s^{-1} at pH 5.5)[145] are considerably larger than k_r for the **B/B′** kinetics of ImH orientation change of the NP2 L → V double mutant,[142] but k_r (as well as the fraction of **B′**) decreases with increasing pH, which is consistent with the fact that the kinetics are not observed by EXSY techniques at pH 7.0,[141–143,145] and also suggests that at pH 7.5,[669] the rate of NO dissociation and ImH reorientation are rather similar.

The NMR spectra of NP2-histamine (Hm) have been studied by NMR spectroscopy at three different pH* values (6.5, 5.5, 4.5). The assignments at each pH* value were derived from WEFT-NOESY and $^1H\{^{13}C\}$-HMQC spectra.[145] The major **B** orientation at pH* 6.5 is 3 > 5 > 1 > 8, with 3,5,1-methyls very similar in chemical shift, but 8M is far from the other three and falls in the diamagnetic region.[145] From the angle plot (Figure 11), it can be seen that the effective ligand nodal plane orientation is 156–157°, which is similar to that for the ImH complex. Chemical exchange between the major **B** Hm imidazole plane orientation, which is fairly close to parallel to H57 ($\Delta\varphi = 37.6°$ from the unpublished X-ray structure of NP2(D1A)-Hm,[634] $\Delta\varphi$ = 22° from the NMR chemical shifts of the heme methyls[145]), and a very small amount of **B′** Hm orientation at pH* 5.5 and 4.5, which has the Hm imidazole plane nearly perpendicular (84°) to that of H57.[145] The intensities of the NOESY/EXSY cross peaks were too small to allow accurate measurement of the rate and equilibrium constants.[145] It is clear that the larger size of Hm as compared to its simple model, ImH, limits the ability Hm to bind in a perpendicular orientation. It is also very clear that the orientation of the Hm ligand cannot change by such a large amount unless the ligand leaves the distal binding pocket and then re-enters in a different orientation.

In Figure 64 the $^1H\{^{13}C\}$-HMQC spectra of NP2-Hm at pH* 6.5 is shown; the $^1H,^{13}C$ cross peaks of all heme substituents, except for 4Vα and the *meso*-CH, are clearly observed for the **B** heme isomer; they are fairly easy to assign because of their unique $^1H,^{13}C$ shifts.[145] These unique shifts are a result of a combination of the contact, pseudocontact and ring current contributions to the chemical shifts

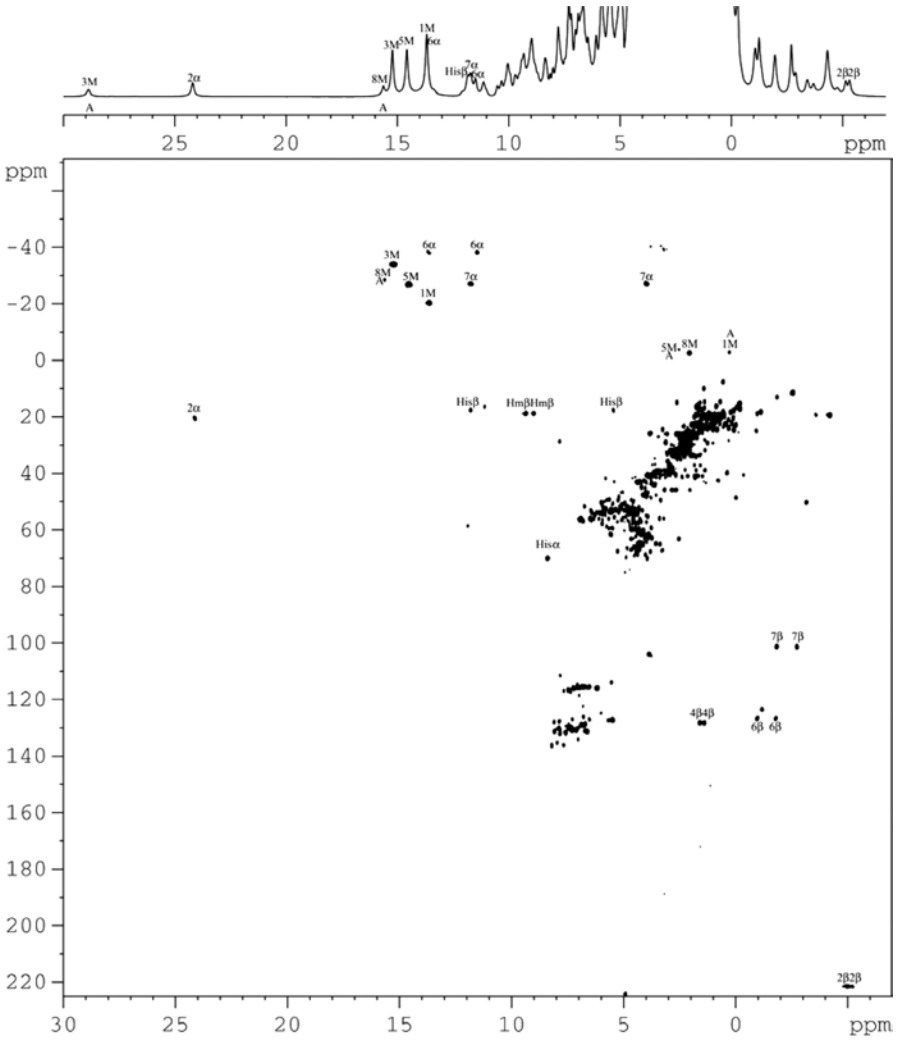

Figure 64. 1D ^{1}H and ^{1}H-^{13}C HMQC spectra of NP2–Hm in D_2O, buffered with 30 mM Na_2DPO_4/acetic acid-d_4 (pH* 6.5), recorded at 35 °C and 500 MHz. Reprinted from Yang, F.; Knipp, M.; Berry, R. E.; Shokhireva, T. K.; Zhang, H.; Walker, F. A. *J. Biol. Inorg. Chem.* **2009**, *14*, 1077–1095, with permission from Elsevier Publishing Company.

of both nuclei,[172] which shift these cross peaks well outside the normal ranges observed for the two nuclei in diamagnetic compounds, and thus make them easy to recognize and assign. The β-vinyl and α- and β-propionate C-H cross peaks can be spotted because pairs of protons have cross peaks to the same carbon. ^{1}H resonances of the 2- and 4α and $-\beta$ vinyl resonances are confirmed by their NOESY cross peaks, as are also the 6- and 7α and β propionate resonances,[145] Figure 64.

Other CH_2 groups that are easily recognized are those of His57 β-CH_2, ^{13}C chemical shift +17.6 ppm, ^1H chemical shifts +11.8 and +5.3 ppm for the **B** heme orientation, and in addition, the cross peaks from the histamine β-CH_2 group (adjacent to the imidazole ring) are also observed, ^{13}C chemical shift +18.7 ppm, ^1H chemical shifts +9.4 and +9.0 ppm. The ^1H His57 β-CH_2 chemical shifts are also confirmed by the NOESY spectra.[145,670] Additional ^1H,^{13}C cross peaks from protein methyls of I120, L122 and L132, which are close to the heme are also seen, with ^{13}C chemical shifts of 10–30 ppm and ^1H chemical shifts of 0 to −5 ppm.[670] There is a rough linear correlation between ^1H and ^{13}C shifts of the heme methyls that helps in the assignment of the heme methyl resonances and the electronic ground state of the ferriheme center.[671] This correlation is based on the contributions to the contact, pseudocontact and ring current shifts of heme substituents.[172]

With regard to the minor **A** isomer, the heme methyl ^1H,^{13}C cross peaks, except for that of 3M, are also observed in Figure 64. The ^1H,^{13}C cross peak for the most hyperfine-shifted methyl resonance is often not observed because it is broader than the other three methyl resonances, as expected from its larger ^1H chemical shift and thus larger expected spin density on its β-pyrrole carbon.[8] In addition, when chemical exchange is involved, as for the wild-type NP2-ImH complex $^1H\{^{13}C\}$-HMQC spectrum at low pH*, not all heme substituent cross peaks are observed, even for the major **B** isomer (6α, 7α, 2α and 4α are not observed).[145]

The wt NP2-CN complex has been investigated at four different pH values, pH* 7.0, 6.5, 5.5 and 4.5. 1D ^1H NMR spectra at pH* 6.5 and 4.5 are shown in Figure 65. Since CN^- is cylindrical, an exogenous ligand plane cannot be discussed in this case. However, as shown previously,[143–145] the nonplanarity of the heme still creates a ruffling nodal plane α for isomer **A** of around 157–159°, and for isomer **B** of around 108–112°. The orientation of this ruffling nodal plane, as determined from the NMR data agrees well with one of the two ruffling nodal planes seen from the crystal structure, that which is near the nitrogen and center of the pyrrole ring I and III for the **B** heme isomer or II and IV for the **A** heme isomer, which are just clockwise to the positions of Leu132 and Leu122 above the mean plane of the heme,[143] Figure 56. In contrast, for isomer **B′** this nodal plane α is around 19°, which is 90° from the just-discussed ruffling nodal plane, and the methyl order is 1 > 5 > 3 > 8. The methyl order for the **B** isomer is 3 > 8 > 1 > 5 at all three pH values, as we have seen for NP–CN complexes at pH 7.0.[143] The fact that 1M has larger chemical shift than 5M has previously been explained by the large degree of ruffling of the heme and somewhat off-axis binding of the cyanide.[143] The methyl order for the **A** isomer is characterized by 3M having similar chemical shift to 5M, and 1M having similar chemical shift to 8M (Figure 11).

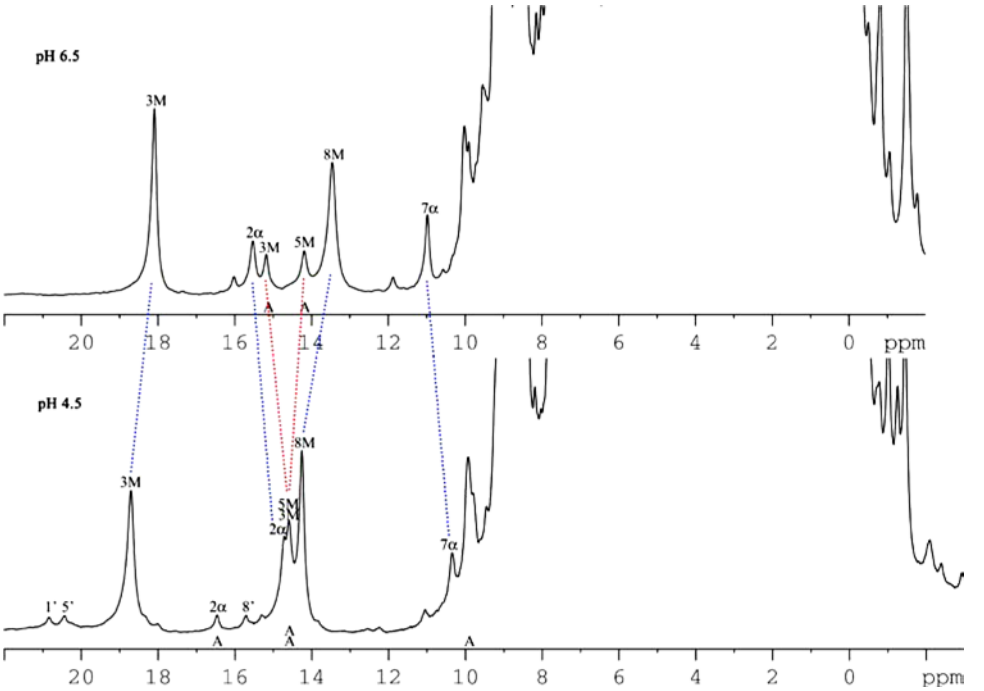

Figure 65. 1D ^{1}H NMR spectra of the hyperfine-shifted resonances of NP2-CN at pH* 6.5 (top) and pH* 4.5 (bottom), recorded at 35 °C at 500 or 600 MHz. Lines showing the variation in chemical shift of heme resonances of **A** (red) and **B** (blue) are displayed. Reprinted from Yang, F.; Knipp, M.; Berry, R. E.; Shokhireva, T. K.; Zhang, H.; Walker, F. A. *J. Biol. Inorg. Chem.* **2009**, *14*, 1077–1095, with permission from Elsevier Publishing Company.

All methyl orders for **A**, **B** and **B′** isomers are different from those of the ImH and Hm complexes.[145] In the ^{1}H{^{13}C}-HMQC spectrum the ^{1}H,^{13}C cross peaks for all heme substituents except the *meso*-CH are observed; His57 β-CH_2 cross peaks are also not seen.[145]

As for the case of the ImH and Hm complexes, resonances from a **B′** species are observed as the pH* is lowered. Although they are very weak in the 1D spectra, the **B′–B** exchange cross peaks for the methyl resonances are relatively strong in the NOESY/EXSY spectra. And by comparing the 1D spectra at pH* 6.5 and pH* 4.5 (Figure 65), the **B′** methyl peaks are relatively stronger at pH* 4.5; thus the trend is the same as seen for the ImH and Hm complexes. Since cyanide is a cylindrical anion and has no ligand plane, the **B′** isomer does not arise from distal ligand rotation, but from dynamic changes in heme symmetry, as concluded previously.[143–145] It is already known that the NP2-CN complex is very ruffled (PDB file 2HYS[143]), and as concluded previously[143–145] the **B′** species is a different ruffled form, with different orientation of the ruffling ridges. Although not observed

in the solid state, protein dynamics in solution at ambient temperatures allow the minor ruffled form to occur transiently on the NMR timescale.

iv. Heme ruffling of the nitrophorins and comparison to other heme proteins

This summary of the NMR spectra of the low-spin ImH, Hm and CN^- complexes of the nitrophorins shows that they are uniquely different from most other ferriheme proteins. Both heme orientations are observed,[142–146,170] except in the case of NP7,[622–624] and there are two orientations of planar axial ligands (ImH, Hm) observed for the major (**B**) heme isomer, which are in chemical exchange on the NMR timescale with each other at lower pH* for NP2,[145] but at all pH values for the other three major NPs.[143,144,146] The cyanide complexes also show chemical exchange, which helps to explain its nature for all ligands studied: A dynamic change in ruffling which is active on the NMR timescale.[143–146] To our knowledge there has been no report of such ruffling dynamics for any other class of ferriheme protein, although the reason is fairly obvious: No other class of heme proteins has such ruffled ferriheme centers as do the *Rhodnius* NPs. This high degree of ruffling is believed to contribute to the very negative midpoint potentials of these proteins, which stabilizes the iron(III) state which can release NO with nM to μM K_ds, whereas the iron(II) state would have pM to fM K_ds.[142,613] One of the effects of this ruffling that has been investigated recently, the average and the spread of the heme methyl resonances,[143,146] will be discussed in the following paragraphs. As these proteins are studied further, additional aspects of the effects of this ruffling will undoubtedly come to light.

In comparison to the nitrophorins, most of the ferriheme proteins for whose cyanide complexes the ^{1}H NMR spectra have been reported are those of myoglobins, hemoglobins, and peroxidases,[8,19,672–674] almost all of which have the histidine imidazole plane aligned along one or the other of the N_P–Fe–N_P axes (Figure 8, φ ~0 or ~90°). Such alignment of the imidazole plane "discourages" ruffling of the heme, whereas the orientation of H57(59) over the β,δ-*meso* carbons, as in the *Rhodnius* nitrophorins, "encourages" ruffling. In addition, the two leucine residues in the distal pocket (L123 and L133 for NP1[625] and NP4,[629] L122 and L132 for NP2[633] and NP3) that are in van der Waals contact with the heme and are believed to further encourage the heme to ruffle, with important consequences in terms of the stability of the Fe^{III}–NO oxidation state.[605,606] Ruffling of a ferriheme tends to stabilize the d_{xz} and d_{yz} orbitals of the iron and, in the limit, leads to a change in the electron configuration of low-spin iron(III) from the more common $(d_{xy})^2(d_{xz},d_{yz})^3$ to the less common $(d_{xz},d_{yz})^4(d_{xy})^1$ configuration[129] discussed in Section IV.A.8.c. This change in electron configuration brings about major

changes in the g-values measured by EPR spectroscopy, as well as major decreases in the proton chemical shifts of the β-pyrrole substituent resonances of the ferriheme. Both of these effects are aided by overlap between the half-filled d_{xy} orbital of iron and the porphyrin $3a_{2u}(\pi)$ molecular orbital.[129] This orbital has large spin density at the nitrogens and *meso*-carbons and very small spin density at the β-pyrrole carbons, Figures 2 and 3. Ruffling of the heme has important functional consequences for the nitric oxide complexes for which the cyanide complex is a model, in that strong ruffling of the heme should help to maintain the $Fe^{III}(d_{xz},d_{yz})^4(d_{xy})^1$–NO• electron configuration rather than the $Fe^{II}(d_{xz},d_{yz})^4(d_{xy})^2$–$NO^+$ electron configuration, which thus helps to facilitate NO release.[605,606]

Thus, as concluded previously,[143] the spread of the heme methyl proton resonances of monocyano ferriheme proteins should be a measure of the degree of d_{xy} character of the metal unpaired electron and thus also of the degree of ruffling of the heme. In Table 14 are summarized the heme methyl proton chemical shifts for a number of ferriheme-cyanide complexes of heme proteins, including the three nitrophorins for which crystal structures are available. As is apparent, there are two classes of ferriheme-cyanide complexes: those which have a spread of the heme methyl resonances of 19.1–29.3 ppm and those which have a spread of 7.2–14.7 ppm. The group with the larger spread of heme methyl resonances includes most of the metmyoglobin cyanides, except for those of *Aplysia* and *Dolabella*, the hemoglobins of *Scapharca* and human, but not lower organism hemoglobins, *Pseudomonas aeruginosa* hemin-containing heme oxygenase-CN in both the normal and alternate seatings, but not human or *Corynebacterium diphtheria* hemin-containing heme oxygenase cyanides. By this criterion of large spread of the heme methyl resonances, we would expect these ferriheme-cyanide proteins to have planar hemes and pure $(d_{xy})^2(d_{xz},d_{yz})^3$ electron configurations in aqueous solution at ambient temperatures. On the other hand, *Aplysia*[675] and *Dolabella*[676] metmyoglobin cyanides, *Scapharca*[677] and human[676] hemoglobin cyanides, human[678] and *Corynebacterium diphtheria* hemin-containing heme oxygenase cyanide,[678] M80A cytochrome *c* cyanide,[679] microperoxidase-8-cyanide,[680] and horse cytochrome *c* cyanide[681] probably all have at least somewhat ruffled hemes, as do the *Rhodnius* nitrophorins.[625–634] In support of this statement, the structure of ferric *Aplysia limacina* Mb,[682] its CN^-, N_3^-, SCN^-, F^-, and imidazole complexes,[683] and several mutants where the mutated group is not near the heme binding pocket,[684] as well as the *Scapharca inaequivalis* tetrameric HbII–CO[685] all show that the histidine imidazole plane is aligned closer to the *meso–meso* axis than to the N–Fe–N axis. And although the heme is modeled as being planar in these crystal structures, it is very likely that in solution a low-energy vibration can take the heme from a planar conformation to a ruffled or possibly a saddled one. Human metHbCN dimer has the His-imidazole plane closer to the N–Fe–N axis

Table 14. Methyl proton shift patterns for histidine/cyanide-coordinated ferriheme proteins.

Protein	His-imidazole plane angle (°)	Methyl shift order	Methyl shifts (ppm)	Spread (ppm)	Average shift (ppm)	Ref.
Sperm whale metMbCN	178	5 > 1 > 8 > 3	27.0, 18.6, 12.9, 4.8	22.2	15.8	672
Elephant metMbCN	178	5 > 1 > 8 > 3	25.3, 16.5, 11.8, 5.9	19.4	14.9	11
G. japonica metMbCN	~178	5 > 1 > 8 > 3	25.1, 16.3, 10.5, 5.7	19.1	14.5	[a]
M. japonicas metMbCN	~178	5 > 1 > 8 > 3	25.9, 16.6, 10.2, 5.7	20.2	14.6	[a]
Human metHb A CN α	159	5 > 1 > 8 > 3	20.9, 15.9, 8.7, 8.0	12.9[b]	13.4	676
Human metHb A CN β	164	5 > 1 > 8 > 3	20.9, 14.7, 8.8, 8.1	12.6[b]	13.1	676
Glycera metHbCN	95	8 > 3 > 5 > 1	19.9, 18.8, 6.5, 0.6	19.2	11.5	[c]
Chironomus thumi thumi						
metHbCN III	~85	8 > 3 > 5 > 1	29.5, 22.2, 7.2, 3.4	26.1	15.6	[d]
IV	~85	8 > 3 > 5 > 1	28.9, 21.4, 7.5, 3.9	25.0	15.4	[d]
Aplysia metMbCN	145–154	3 > 5 > 1 > 8	17.8, 15.7, 11.8, 9.9	7.9[b]	13.8	672
Scapharca metHbCN	~142	3 > 5 > 1 > 8	17.1, 12.7, 12.6, 7.8	9.3[b]	12.6	676
Dolabella metMbCN	~145	3 > 5 > 1 > 8	17.4, 15.1, 11.8, 10.2	7.2[b]	13.6	677
HRPCN	95	8 > 3 > 5 > 1	29.9, 25.1, 6.4, 2.9	27.0	16.1	[a, e]
LiPCN	120	3 > 8 > 5 > 1	30.1, 20.5, 3.3, 0.8	29.3	13.6	[e, f]

(*Continued*)

Table 14. (*Continued*)

Protein	His-imidazole plane angle (ϒ)	Methyl shift order	Methyl shifts (ppm)	Spread (ppm)	Average shift (ppm)	Ref.
Human Heme-HOCN	125	3 > 8 > 5 > 1	19.6, 10.5, 9.0, 5.0	14.7[b]	11.0	678
C. diphtheriae Heme-HOCN	125	3 > 8 > 5 > 1	19.2, 10.6, 8.5, 5.4	13.7[b]	10.9	678
P. aeruginosa Heme-HOCN	35	5 > 1 > 8 > 3	27.7, 22.7, 19.0, 4.4	23.3	18.5	678
P. aeruginosa Heme-HOCN alternate seating	105	3 > 8 > 5 > 1	24.6, 16.3, 5.4, 1.7	22.8	12.0	678
M80A cyt *c* CN	~45	8 > 5 > 1 > 3	22.5, 19.5, 15.4, 11.3	11.2[b]	17.2	679
MP8-CN	~45	8 > 5 > 1 > 3	23.2, 21.7, 16.4, 10.6	12.6[b]	18.0	680
Horse cyt *c* CN	~45	5 > 8 > 1 > 3	23.1, 21.5, 16.6, 11.4	11.7[q]	18.2	681
NP1-CN **A**	139	3 > 5 > 1 > 8	16.7, 13.3, 10.8, 7.3	9.4[q]	12.1	143
B	131	3 > 8 > 1 > 5	20.9, 13.0, 8.2, 7.3	13.6[q]	12.4	143
NP4-CN **A**	138	3 > 5 > 1 > 8	16.9, 12.9, 10.2, 7.7	9.2[q]	11.9	143
B	132	3 > 8 > 1 > 5	19.4, 12.5, 8.6, 7.9	11.5[q]	12.1	143
NP2-CN **A**	138	3 > 5 > 1 > 8	15.8, 14.2, 9.3, 7.9	7.9[q]	11.8	143
B	132	3 > 8 > 1 > 5	18.4, 13.4, 9.7, 7.8	10.6[q]	12.3	143
Protohemin-CN in DMSO	—	8 > 5 > 3 > 1	16.3, 15.9, 12.3, 10.3	6.3	13.6	204

[a]Yamamoto, Y.; Suzuki, T. *Biochim. Biophys. Acta* **1996**, *1293*, 129–139.
[b]Heme methyl spread less than 15 ppm.
[c]Alam, S. L.; Satterlee, J. D. *Biochemistry* **1994**, *33,* 4008–4018.
[d]Zhang, W.; La Mar, G. N.; Gersonde, K. *Eur. J. Biochem.* **1996**, *237*, 841–853.
[e]Pierattelli, R.; Banci, L.; Turner, D. L. *J. Biol. Inorg. Chem.* **1996**, *1*, 320
[f]Banci, L.; Bertini, I.; Pierattelli, R.; Tien, M.; Vila, A. *J. Am. Chem. Soc.* **1995**, *117*, 8659–8667.

than these,[686] but the angles are still far from the N–Fe–N axis as compared to sperm whale, horse, or elephant Mb. The near-*meso–meso* orientation of the His-imidazole plane in each of these cases would "encourage" the ruffled conformation, and thus the NMR observation of very small spread of the heme methyl resonances of the cyanide complexes is consistent with a ruffled heme macrocycle at room temperature.

Ruffling seems to inevitably lead to at least some degree of contribution from the $(d_{xz},d_{yz})^4(d_{xy})^1$ electron configuration.[129] Even for model hemes with sterically bulky imidazole ligands, for which the EPR spectra are of the "large g_{max}" type (Section IV.A.8.a), the average β-pyrrole–H or $-CH_3$ chemical shift magnitude at a given temperature is invariably smaller than for those bound to non-bulky imidazole ligands (−17 vs. −10 ppm for $[TPPFe(NMeIm)_2]^+$ and $[TMPFe(2MeImH)_2]^+$, respectively, both at 300 K, although there may be a small effect of hydrogen-bonding in the latter case). Notably, as just discussed for those ferriheme protein cyanides for which structures are available, and as based on the order of heme methyl resonances for the other members of the latter group of proteins, all have histidine imidazole planes oriented near either the β,δ- or the α,γ-*meso*-carbons, which "encourages" ruffling.[129] The degree of d_{xy} unpaired electron contribution does not have to be major, and in most cases is not major, for all of the members of this second group of ferriheme cyanides have larger spreads of the methyl resonances than does protohemin bis-cyanide in DMSO-d_6 (6.3 ppm spread, Table 14),[204] where there is no ligand plane. But an increase in the degree of d_{xy} character has the effect of yielding a much smaller *spread* of the heme methyl resonances, and a smaller *average heme methyl chemical shift* than the first group, and thus suggests that the hemes of these complexes are quite ruffled.

Interestingly, the EPR spectra of the nitrophorin-cyanide complexes are very similar to that of metMbCN, which indicates that at 4.2 K the electron configuration of both complexes is pure $(d_{xy})^2(d_{xz},d_{yz})^3$. This means that the NP1-CN electron configuration must change with temperature. A similar change in electron configuration with temperature was observed for a model of heme oxygenase, $[TPPFe(OCH_3)(t\text{-BuOO})]^-$, which also exhibited a $(d_{xy})^2(d_{xz},d_{yz})^3$ electron configuration with a planar heme at 4.2 K but a $(d_{xz},d_{yz})^4(d_{xy})^1$ electron configuration with a ruffled heme at ambient temperature,[481] as discussed above in Section IV.A.8.a.

v. Nitrite reductase activity of nitrophorin 7

He and Knipp have recently shown that NP7 reacts with sodium nitrite at pH 7.5 to produce NP7-NO and other products.[687] Resonance Raman spectroscopy was used to prove that the product was indeed NP7-NO.[687] The NP-NO complex is indeed EPR silent, and the ^1H NMR spectrum of the NP2 product is identical to

NP2-NO.[688] By quantitating the products using the Griess reaction,[689] the stoichiometry of the reaction was shown to be:

$$3\ NO_2^- + 2\ H^+ \rightarrow 2\ NO + NO_3^- + H_2O. \quad (39)$$

The nitrophorin, as a Fe^{III} protein, is simply a catalyst of this reaction, and does not itself undergo redox. This is a different reaction with nitrite than that of myoglobin and other Fe^{II} heme proteins, in which the protein is oxidized to Fe^{III},[690,691] and the oxidized (met) forms do not react with nitrite.[692,693]

vi. Dimerization of NP4

Of the four major nitrophorins in the adult *Rhodnius* insect, NP4 is by far the best for X-ray crystallography because it crystallizes in only one space group (C2) and yields structures of very high resolution (0.85 Å for NP4-NH_3 at pH 7.4, PDB file 1X8P, 0.97 Å for NP4-NO at pH 5.6, PDB file 1YWB). All structures of NP4 and its ligand complexes have four molecules per unit cell, and each is a monomer; there are no major interactions between one molecule and another. However, at NMR concentrations (1 mM, 50 mM acetate buffer at pH 5.5), NP4 is a dimer, and it remains mainly so to well above pH 7.5 at 1 mM concentration.[694] In fact, dimer formation at pH 5.0 provides an excellent method for purifying NP4, by size-exclusion chromatography.[694] NP4 containing the symmetrical hemin (Figure 56) is most useful for studies of the monomer-dimer equilibrium by $^1H\{^{15}N\}$-HSQC.

If histamine is added to NP4, the dimer dissociates, with each monomer having histamine bound to the distal side of the Fe^{III} heme; the apoprotein is also monomeric.[694] However, both high-spin NP4 and the NP4-NO complex are dimeric. One particular mutant of holo-NP4, the D30A mutant is, however, monomeric at all pH values in the absence of added ligand. In the wild-type protein, the histamine complex has a hydrogen-bond between the histamine $-NH_3^+$ side chain and D30. Thus, it is believed that D30 and a heme carboxylate are involved in this dimerization, but it is not yet clear what other groups may be involved.[694] NP2 has the analogous aspartate, D29, but does not dimerize, either as the wild-type (M0-containing) or as the native form (D1 as first residue, with no M0). NP1 also contains D30 and is 90% identical in sequence to NP4, but perhaps because it contains M0 (see Section IV.A.10.a(i) earlier), NP1 wild-type does not dimerize. However, newly-prepared native NP1, with K1 as the first residue and no M0, does dimerize, and in all respects behaves very similarly to NP4,[694] except for being a less stable dimer.

Several years ago a paper was published by Ambrus and coworkers,[695] on work done at the University of Arizona during the time when we were actively

studying the NP4 dimer, including by mass spectrometry. This study showed that NP4 dimerized, and that in the gas phase, as detected by mass spectrometry, (studied in the same MS facility as we were using), it formed up to octomers.[695] The DOESY NMR spectra of dimeric NP4 in solution were investigated, but it was remarked by the authors that the solvent HOD resonance was much broader than expected, and the authors did not understand why.[695] Ambrus had admitted to this author several years prior to that publication that he did not understand what the word "paramagnetic" meant; presumably he has never learned.

vii. NMR spectroscopy of apo-nitrophorin 2

NP2 in the absence of heme has been studied by multidimensional NMR spectroscopy at pH 6.5.[696] An NP2 sample with an N-terminus having residues GSHM before the D1 residue that begins the native protein sequence was used for this study. These residues were left following cleavage of an *N*-terminal His_6-tag that aided the purification of the doubly-labeled protein.[696] All but a few $^{1}H,^{15}N$ cross peaks (~8) in the $^{1}H\{^{15}N\}$-HSQC spectrum were assigned and the 3-dimensional structure was solved, first by using only the N–H and Cα-H NOEs, and later using a multitude of side-chain NOEs as well.[696] Refinement of the solution structure[696] shows it to be almost identical to that of the holoprotein obtained by X-ray crystallography,[633] as well as to apo-NP4, which was also solved by X-ray crystallography at pH 5.6.[697] The paper describing this structure provides little detail about the structure, other than "removal of the heme from NP4 has very little effect on (the protein's) structure: The heme binding cavity remains open and loops near the cavity entrance respond to lower pH in the same manner as the intact protein,"[697] meaning that the A-B and G-H loops form the closed loop conformation. Diffuse electron density was also found within the β-barrel, which the authors hypothesized resulted from one or more buffer or cryoprotectant molecules.[697]

The overall similarity of the calculated NMR structure of apoNP2 to the structure of the NP2 holoprotein[633] is remarkable. However, the packing of the β-barrel itself is not entirely identical; the insertion of the heme results in a widening of the the β-barrel opening in the holoprotein parallel to the plane of the macrocycle, by outward displacement of the D and E β-strands by ~1.4 Å. The ability of the extensively H-bonded β-barrel core to undergo such an expansion is somewhat counterintuitive, considering the rigidity that might be expected for this protein fold. However, H/D exchange rates, measured with SOFAST-HMQC[698] for the backbone amides, indicate that the backbone of the β-barrel core opposite to the side that faces the α2 helix is fully accessible to the solvent, and thus must possess significant structural plasticity. The "roof" of the heme cavity undergoes important structural rearrangements on heme binding. Steric clashes between heme and the

L132 side chain result in upward displacement of the H-strand, while downward rearrangement of the G β-strand brings the L122 side-chain into close contact with the heme, presumably by displacing water molecules from the heme cavity of the apoprotein as heme binds. It is noteworthy that both of these residues are conserved among all NPs.

The H/D exchange lifetimes indicate that the residues that show the slowest H/D exchange rates are localized on the α2 helix and F, G, H and A strands of the β-barrel. The slow exchange rates are indicative of the presence of a compact hydrophobic core involving the FGHA part of the β-barrel with the opposing side of the barrel exhibiting a higher degree of plasticity. Higher plasticity may account for the fact that the heme ruffling (and therefore its E_m) is insensitive to the bulkiness of the hydrophobic side chain residues located in that part of the protein. However, the steric requirements of the residues located in the rigid part of the β-barrel do disrupt the planarity of the heme, and undoubtedly modulate its E_m significantly. The rigidity of the β-barrel fold makes it uniquely suited for heme proteins such as the NO-carrying/releasing NP proteins, where a very strong electrochemical stabilization of the oxidized metal center is required. Mainly α-helical proteins cannot exert such pressure on the heme, and thus have flat hemes with much higher E_ms, meaning that Fe^{III} is much more easily reduced to Fe^{II} when the heme is flat. Thus, for release of NO with nM K_ds, the ruffled heme thus helps maintain the Fe^{III} oxidation state.

The $^1H\{^{15}N\}$-HSQC spectrum of the high-spin protohemin-containing holo-NP2 aqua complex showed doubling of a significant number of resonances because of the **A**:**B** disorder of the protohemin (1:8 at equilibrium[170]). Therefore the symmetrical hemin, Figure 56, with the GSHM0D1 N-terminus present, was used for detailed studies. Nearly complete assignment of the backbone spin-systems of the ligand-free high-spin holo-NP2 was obtained.[696] Not including the prolines and N-terminal GSHM sequence, the following were not observed in the 3D triple-resonance experiments and thus were not assigned: Y38, C39, S40, L55, Y56, H57, F66, I120, L122, L129, and L132. Backbone amide groups of all of these are located within 10 Å of the S = 5/2 metal center in the crystal structure (2A3F), and are thus expected to be broadened significantly. The holoprotein shows significantly greater dispersion of $^1H\{^{15}N\}$-HSQC resonances, due to pseudocontact shifts and the macrocycle ring current.[696] As a result, it was possible to obtain all assignments from HNCACB/CBCA(CO)NH and HNCA/HN(CO)CA experiments alone.[696] Further study of the structure and especially the dynamics of NP2 over multiple time scales is ongoing, but, based on the information about the role of extra residues at the N-terminus gained from the study of NP2(D1A) discussed above in Section IV.A.10.a(i), by using a construct which has the native N-terminus, and a C-terminus His_6-tag to allow rapid purification of small isotopically labeled protein samples.[699]

b. *NMR spectroscopy of the hemin-containing heme oxygenases*

Heme oxygenases (HOs) are found in organisms as simple as bacteria and as complex as humans. They are also found in plants, where they are soluble enzymes in which the product biliverdin is a starting point for the construction of linear, light-sensing tetrapyrrole pigments.[700] The heme oxygenase proteins bind hemin, which is then both the active site of the enzyme, as well as its substrate. A histidine is the heme ligand, and there is no distal His. The oxygenase mechanism is believed to involve a ferric hydroperoxide intermediate, as discussed below, rather than the ferryl Compound I species common to cytochromes P450.[701] The heme ring is cleaved at the *meso*-α-carbon in the case of animals, in a reaction that requires three molecules of O_2, seven electrons and nine protons,[702] and produces inorganic iron, carbon monoxide and a tetrapyrrole, biliverdin, which is subsequently reduced to bilirubin; both biliverdin and bilirubin are powerful antioxidants. Pathogenic bacteria such as *Pseudomonas aeruginosa* (*Pa*), *Corynebacterium diphtheriae* (*Cd*) and *Neisseriae meningitidis* (*Nm*) use their heme oxygenase enzymes to "mine" iron from their hosts, and the HOs of these organisms are not necessarily regioselective for the α-*meso*-carbon; for example *Pa*-HO (sometimes called PigA) produces 70% δ-, 30% β-biliverdin,[147] while wild-type *Cd*-HO (sometimes called HmuO) produces 100% α-biliverdin,[148,703] as does *Nm*-HO (sometimes called HemO).[704]

For humans there are two well-characterized isoforms of heme oxygenase, HO-1 and HO-2.[705,706] HO-1 is an inducible isoform, 33 kDa, that is expressed in response to stress (oxidative stress, hypoxia, heavy metals, cytokines, etc.). HO-2 is the constituitive isoform, 36 kDa, which is expressed under homeostatic conditions, and carries an extra ~20 amino acids at the N-terminus. Both human HOs have a C-terminal hydrophobic tail (~25 amino acids), which can be cleaved,[705] that binds them to microsomes, and both HO-1 and HO-2 are ubiquitously expressed and catalytically active. The X-ray crystal structures of human,[707–712] rat[713–717] and four bacterial (*Nm*,[718,718] *Cd*,[720] *Pa*,[721] and *Synechocystis sp.* PCC 6803[722]) HOs have been reported. An example structure, that of *Pa*-HO, is shown in Figure 66. As can be seen, the protein is highly helical, with the heme sandwiched between helices I,II and VII,VIII. The distal helix VII,VIII is very tightly packed against the O_2-binding site of the heme, and a Gly residue is believed to be very important to the activity of the enzyme, as discussed below. In mammals the transfer of electrons from NADPH to the enzyme is mediated by cytochrome P450 reductase,[723] while *Pa*-HO has a NADPH-binding, FAD-containing ferredoxin reductase, *Pa*-FPR, which shuttles the electrons to *Pa*-HO.[724] A small ferredoxin, *Pa*-Bfd, that can incorporate a $[2Fe\text{-}2S]^{2+/1+}$ center, had earlier been thought to shuttle the electrons from *Pa*-FPR to *Pa*-HO, but that was found not to be the case;

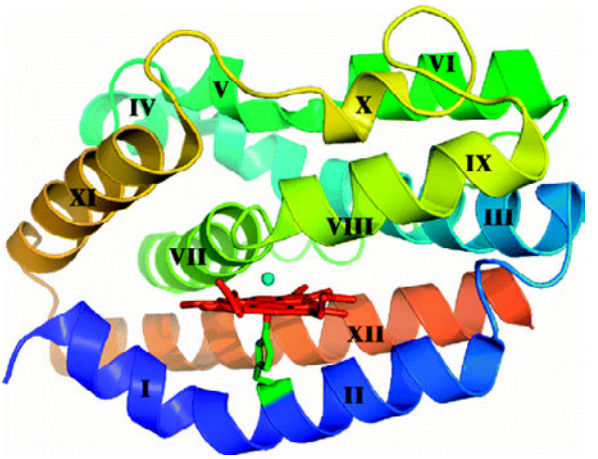

Figure 66. Structure of *Pa*-HO in its ferric resting state (PDB file: 1SK7) illustrating the α-helical fold, the positioning of the heme, and the axial coordination by a His-imidazole and water ligands. The heme is "sandwiched between the proximal helices (I and II) and the distal helices (VII and VIII). The loop between the two distal helices is typically referred to as the helix kink. Reprinted from Rodriguez, J. C.; Zeng, Y.; Wilks, A.; Rivera, M. *J. Am. Chem. Soc.* **2007**, *129*, 11730–11742, with permission from the American Chemical Society.

Pa-FPR does the job alone.[724] It is interesting that both the mammalian and the bacterial (at least in *P. aeruginosa*) HO enzymes get their electrons from flavin-containing reductases. More recently it was discovered that the mobilization of iron from bacterioferritin B requires the binding of apo-Bfd, and to date it appears that Bfd does not function as a normal electron-transfer ferredoxin, despite the fact that one can assemble a 2Fe,2S cluster in its fold.[725]

NMR spectroscopy has been used by the groups of both La Mar and Rivera to study the bacterial HOs, while La Mar initially and even recently has studied mammalian, and most often the human HO-1. The La Mar papers are technically extremely detailed and do not lend themselves to being presented as figures in a review article. In spite of that, the work is extremely well done. La Mar and his group do not begin by assigning the $^{1}H\{^{15}N\}$-HSQC spectrum and work outward to the side chains, but rather begin with the side chains that are affected by the presence of the paramagnetic heme.[678] If the structure of the protein is not available, they use the NOESY and TOCSY spectra of the low-spin cyanoferrihemin state to assign the side chain resonances of all residues which interact with the substituents of the hemin, and use the expected pseudocontact shifts to refine the assignment of these residues, and their exact placement.[678] From this point they will go back to the high-spin and apoprotein states and look at the NOESY and TOCSY spectra of the apoprotein and see which resonances are "bleached" by binding of the paramagnetic heme, based on the protein sequence, side chain type

(usually focusing on the aromatic resonances), and assign these in light of the assignments for the low-spin cyanoferihemin state. If the structure of the protein is available, they proceed in the same general way, but use the protein structure to choose the side chains on which to focus, and again use the expected pseudocontact shifts to refine the placement of these residues.[727] The Rivera papers tend to utilize newer multidimensional NMR methods, which include those for complete assignment of the protein sequence, the side chains, and their dynamics, methods that capitalize on isotopic labeling of the heme or of the polypeptide.

NMR spectroscopy has been used to study HOs for three main purposes: (a) To investigate propionate-polypeptide interactions, which, to a large extent, seat the heme in the pocket and determine regioselectivity (in their absence the heme is free to undergo large-amplitude in-plane motions, which appears to be a property so far unique to HOs); (b) to investigate the heme electronic structure and its possible implications in heme catabolism; and (c) to investigate dynamic-reactivity relationships, including those which involve water molecules in the distal pocket. Each of these topics will be covered in turn in the bacterial HO section.

i. NMR study of high- and low-spin mammalian heme oxygenases

The first paper from the La Mar group, on recombinant rat HO, appeared in 1994,[726] and is referenced in the Porphyrin Handbook chapter.[19] The labeling of the spectra in Figures 2 and 3 of that work does not agree with the captions given, but can be interpreted by studying the spectra in the Porphyrin Handbook chapter.[19] It was reported that rat HO-1 had ~1:1 heme heterogeneity (later refined as 55:45%[678]) and an "unusual hemin electronic structure that is characterized by large differences in delocalized spin density for the two positions within a given pyrrole, rather than the more conventional large differences between adjacent pyrroles."[726] This "unusual" hemin electronic structure was caused by the fact that the axial histidine was aligned close to two of the *meso* carbons (β,δ) rather than along the heme nitrogens (Figure 11), as had been the case for the myoglobins and hemoglobins that had been studied earlier by this group. The pattern was recognized as being similar to one published previously for model hemes having one unique substituent on one phenyl ring of the $[TPPFe(NMeIm)_2]^+$ (where one relatively electron-donating substituent leads to choice of the former $3e(\pi)$ orbital with node passing through the two *meso*-C which do not contain that unique substituent as the orbital preferred for spin delocalization, Figure 2, left, Figures 18 and 40),[211] but was believed by the authors to be due to "a perturbation of the heme by the protein matrix," one that might "activate the heme for attack at the α-*meso* position."[726] The heme heterogeneity did not affect the α-*meso* selectivity of human HO-1.[726]

In 1998 the second publication by La Mar and coworkers appeared, the first on recombinant human HO-1, hereafter called hHO-1, in which 2D NMR studies of substrate-free hHO-1 (apo-hHO-1) were reported.[678] This paper is also referenced in the Porphyrin Handbook chapter.[19] A cluster of nine mobile aromatic residues whose signals were largely "bleached" on binding high-spin hemin reappear at different chemical shifts in the low-spin cyanide-inhibited hHO-hemin complex.[678] There was also heme heterogeneity for hHO-1, but the ratio of the two heme orientations was about 3:1 (later refined to 3.5:1[727]) after adding "excess cyanide" and equilibrating for 2–3 days.[678] (Interestingly, the nitrophorins NP2 and NP3, which have heme **A**:**B** orientations significantly different from 1:1,[143,146] do not equilibrate the two heme orientations over time periods of weeks to months after addition of even a single equivalent of cyanide or other strong-field ligand. This is in agreement with the difference in protein fold of the two classes of proteins, and also suggests that the heme binding constant to hHO-1 is much smaller than that to the NPs, which is consistent with the function of each of these proteins.)

Resonance assignments allowed placement of the aromatic clusters into proximal, distal or peripheral positions over specific pyrrole rings, based on dipolar (NOE) contacts and/or relaxation effects. The three aromatic clusters were located, one on the proximal side adjacent to the axial His, and the other two peripheral and distal to the pyrrole I/II junction, the site of heme oxidation.[678] The heme methyl NOE contacts, when compared to those of globins or peroxidases, were judged to reflect an "open" pocket, where hemin binds in the preformed aromatic cluster of hHO with pyrrole rings I and II and parts of pyrrole ring IV buried in the protein, with pyrrole ring III largely exposed to the solvent, and with the proximal side oriented toward the protein surface and the distal site toward the protein interior.[678] A distal labile proton was located, which was found to serve as the H-bond donor to cyanide, and was felt to likely be the origin of the spectroscopically-detected pK_a of ~7.6 in the hHO-hemin complex, and was felt to probably arise from the same distal residue that serves as the H-bond donor to the activated O_2. The distal base was identified as a Tyr.[678]

Three years later, in 2001, after the crystal structure of hHO-1 had appeared,[707] the Tyr was identified as two Tyr, Y58 and Y137, both on the distal side of the heme binding pocket.[727] It was found, by identifying unique protein resonances by using the crystal structure information, that the major heme isomer was the opposite one to that shown in the crystal structure, and a distal four-ring aromatic cluster had moved 1–2 Å closer to the heme, which allowed for stronger H-bonds from the two Tyr.[727] The Fe-CN orientation showed a ~20° tilt of the distal ligand from the heme normal in the direction of the *α-meso* position, which suggested that the close placement of the distal helix over the heme exerted control of sterospecificity

by both blocking access to the β, γ, and δ-*meso* positions and by tilting the axial ligand, i.e., a proposed peroxide, toward the α-*meso* position.[727] The same group then used the symmetrical hemin (Figure 56), 2,4-dimethyldeuterohemin, to further characterize the heme binding site of hHO-1.[728] A unique distal network was found that involves particularly strong hydrogen-bonds, as well as inter-aromatic contacts. It was proposed that this network stabilized the position of the catalytically critical distal helix Asp-140 carboxylate.[728] Most of the residues of the distal helix (Y134 to L147) and a number of others were assigned. G143 had the largest observed N–H, CαH1 and CαH2 shifts, and the pseudocontact contribution could not be modeled without off-axis binding of the cyanide ligand.[728] Later the same year a study of eight strong hydrogen-bonds from immobilized water molecules within the strong distal H-bonding network of cyanide-inhibited hHO were detected by NMR spectroscopy.[729] It was demonstrated that significant magnetization transfer from the bulk water signal to these eight labile protons did not result from chemical exchange, but rather from direct nuclear Overhauser effect, due to the dipolar interaction of these labile protons with "ordered" water molecules.[729] The enzyme labile-proton-to-water-proton distances were estimated as ~3 Å. It was proposed that the role of the strong H-bonding network was to immobilize numerous water molecules which both stabilize the activated hydroperoxy species and also funnel protons to the active site.[729]

A study of "substrate-free" human heme oxygenase (apo-hHO-1) published in 2004[730] identified five conserved secondary structural elements and detected highly characteristic dipolar or H-bond interactions among these elements to confirm a strongly-conserved folding topology of helices C–H relative to that of substrate complexes in either solution or crystals. Correction of the chemical shifts for paramagnetic and porphyrin ring current influences in the paramagnetic substrate complex revealed that the strength of all but one of the relatively robust H-bonds was conserved in apo-hHO, and that similar ordered water molecules were located near these H-bond donors, as in the substrate-bound complexes.[730] The unique and significant weakening of the Y58-OH H-bond to the catalytically critical D140 carboxylate in apo-hHO was suggested to arise from removal of the axial H-bond acceptor ligand rather than the loss of substrate. The interhelical positions of the conserved strong H-bonds were seen to argue for a structural role in maintaining a conserved structure for helices C–H on loss of substrate.[730] While it was found that the structure and H-bond network were largely conserved upon loss of substrate, the variably increased rate of NH lability dictated a significant loss of dynamic stability in the conserved structure, particularly near the distal helix F.[730]

Although there are three additional papers on the topic of hHO-1 published after 2004, they seem to be aimed at goals related to the bacterial proteins, and will

therefore be discussed below, together with the bacterial HOs studied by the La Mar group.

ii. NMR studies of bacterial heme oxygenases

Meanwhile, Rivera began his NMR investigations of heme proteins on outer mitochondrial membrane cytochrome b_5 (OMb_5) in 1996,[186] following publication of the method used for preparing ^{13}C-labeled heme by expressing this protein in ^{13}C medium the year before,[180] and discussed earlier in Section II.D.3, Figure 13. The 1996 paper was a study of the role played by the propionates of OMb_5 in the electrostatic binding to cytochrome *c*.[186] Although the role of OMb_5 was unknown when the gene for the rat protein was synthesized and the protein investigated in the early 1990s,[731–733] it is now known that cytochromes *c* and OMb_5 are redox partners in the intermembrane space of mitochondria of at least three eukaryotes (rat, mouse, human).[734] In addition, OMb_5 has been shown to be the electron donor to mitochondrial amidoxime reducing component, mARC, a newly-identified molybdoenzyme in the outer mitochondrial membrane;[735,736] OMb_5 in this case is reduced by a mP450 reductase.[735,737,738]

For the study of cytochrome *c*/OMb_5 interactions, titrations of three ^{13}C-hemin-containing OMb_5 isomers, where the three were prepared from 1-^{13}C-ALA, 3-^{13}C-ALA and (1,2-^{13}C)$_2$-ALA (Figure 13), with horse cyt *c* showed clearly that only the heme propionate located on the exposed heme edge of OMb_5 participates in formation of this electrostatic complex. It was also shown that the stoichiometry of the complex is 1:1, and it has a conditional binding constant of 3.8×10^4 M^{-1} at $\mu = 0.02$ M.[186] As part of this work, the X-ray crystal structure of OMb_5 was solved at 2.7 Å and was shown to be almost identical to that of bovine microsomal cytochrome b_5, when compared at medium resolution.[186] Follow-ups to this study included complete isomer-specific ^{1}H and ^{13}C NMR assignments of the heme resonances of rat liver OMb$_5$,[190] which exists as a 1:1 ratio of the two heme orientations. For this study a variety of NMR experiments were used, including HMBC, INADEQUATE, and the more commonly used HMQC, NOESY and COSY experiments,[190] and a new experiment, called INEPT-INADEQUATE.[188,189] This experiment was created because assignments that would normally be performed with the aid of HMBC experiments in diamagnetic molecules proved difficult in the active site of a paramagnetic heme protein where $T_2^{-1} > {}^2J_{CH}$. To circumvent this problem, a new method was presented to selectively detect ^{1}H in ^1H_n–^{13}C–^{13}C fragments biosynthetically introduced into the active sites of heme proteins.[189] The pulse sequence combines well-known building blocks such as INEPT to transfer ^{1}H spin magnetization to bonded ^{13}C nuclei, followed by INADEQUATE to generate ^{13}C–^{13}C double-quantum coherence that is selected with

pulsed field gradients, and finally reverse-INEPT to transfer the magnetization back to ^{1}H nuclei for subsequent observation.[189] This $^{1}H_{n}$–^{13}C–^{13}C edited experiment took advantage of the relatively large values of $^{1}J_{CH}$ and $^{1}J_{CC}$, which avoid the long interpulse delays in HMBC that compromise the detectability of rapidly-relaxing nuclei. The potential applicability of the pulse sequence was first demonstrated by its contribution to the unambiguous assignment of the carbonyl carbons in the heme propionates of ferricytochrome b_5,[189] and then to the complete ^{1}H and ^{13}C assignment of both hemin isomers of ferriheme OMb_5.[190]

Additional directions in the study of OMb_5 involved probing the differences between rat liver OMb$_5$ and bovine microsomal cytoderome b_5[739] and comparing the large difference in plasticity of the two proteins,[740] but the observation that most related to future studies of heme oxygenases was the fact that the H63M mutant of OMb_5, which was prepared for a totally different purpose, when purified by ion exchange chromatography in air, became green in color.[741] Further study showed that the protein contained a product of coupled oxidation of heme, verdoheme.[741] Later study of the H39V mutant of OMb_5,[742] which could catalyze oxidation of heme to biliverdin in the presence of hydrazine and O_2, provided the important insight that catalase (an enzyme that disproportionates 2 H_2O_2 to H_2O and O_2) did not inhibit formation of biliverdin by this OMb_5 mutant, and thus no free H_2O_2 was produced.[742] However, the H63V mutant under the same conditions led to formation of verdoheme, but was completely inhibited by catalase, and only *meso*-hydroxyheme was produced under those conditions.[742] These findings illustrated the subtle but important mechanistic differences between the coupled oxidation reaction, where exogenous H_2O_2 reacts with a ferrous heme site to produce hydroxyheme, and heme oxygenation, where a ferric hydroperoxide moiety hydroxylates the heme to hydroxyheme (Section IV.A.6.c(vii)).

(a) *Heme propionate-polypeptide interactions dictate regioselectivity in HOs*

By this time, Rivera was well into the study of *Pa*-HO, in collaboration with Wilks and coworkers.[147] *Pa*-HO is an interesting bacterial heme oxygenase, in that it is not specific for oxidation at the *α-meso* position, but rather at the *β*- and *δ-meso* positions (30% and 70%, respectively[147]). Since *Pseudomonas aeruginosa* only uses the heme to obtain iron, it does not matter where the heme ring is attacked. In a paper published in 2002,[147] Rivera used specifically ^{13}C-labeled ALAs to produce specifically ^{13}C-labeled hemes in OMb_5, which could then be extracted and inserted into apo-*Pa*-HO (Figure 13, Section II.D.3). Using these labeled-heme-HOs it was possible to study the heme resonances by ^{1}H and ^{13}C NMR and resonance Raman spectroscopy.[147] Whereas the rR spectra indicated that the heme-iron ligation in *Pa*-HO is homologous to that observed in previously studied *α*-hydroxylating

HOs, the NMR studies suggested that the heme in this enzyme is seated in a manner that is distinct from that observed for all α-hydroxylating HOs for which structures were available (hHO-1 and *Nm*-HO at that time). It was found that the heme of *Pa*-HO is rotated in-plane by ~110°, so that the δ-*meso*-C of the major orientational isomer is located within the HO-fold in close to the same place where the α-hydroxylating enzymes typically place the α-*meso*-C.[147] The unusual heme seating displayed by *Pa*-HO, which was elucidated solely on the basis of ^{1}H and ^{13}C NMR spectroscopic studies, was later confirmed by X-ray crystallography.[721] The unusual heme seating places the heme propionates so that they point in the direction of the solvent-exposed heme edge. This orientation appears to originate mainly from the absence of stabilizing interactions between the polypeptide and the heme propionates,[147] which in hHO-1 and *Nm*-HO involve Lys16 and Tyr134, and Lys16 and Tyr112, respectively; the corresponding residues in *Pa*-HO are Asn19 and Phe117.

In agreement with this, preparation of the N19K/F117Y double mutant of *Pa*-HO produced a protein which showed a mixture of two distinct heme seatings, one of which was identical to that of wild-type *Pa*-HO, while the other had the alternative heme seating that was rotated by ~110°, and is very similar to the heme seating in h-HO-1 and *Nm*-HO.[147] Chemical exchange was observed between protein molecules having the two heme seatings for both heme orientational isomers, as shown in the EXSY spectrum of Figure 67, and thus the change in heme seating is active on the NMR timescale.[147] The authors proved that it was the heme that was moving, rather than the axial histidine imidazole plane, by finding an NOE from one of the γ-Me of Val33 to 1M and 3′M of the heme. The products of the *Pa*-HO double mutant were α- (55%), β- (10%) and δ-biliverdin (35%).[147]

In 2004, Rivera, Wilks and coworkers investigated the regioselectivity of the Arg-177 mutants of *Corynebacterium diphtheriae* heme oxygenase as a consequence of in-plane heme disorder.[743] This study was prompted by the report that R183E and R183D mutants of rat HO-1 produce approximately 30% δ-biliverdin.[744] Two plausible mechanisms were proposed to explain the observations. (a) Electrostatic repulsion between E183 (D183) and one of the heme propionates forces the heme to rotate, thereby placing the δ-*meso* carbon in a position that is susceptible to oxidation, or (b) rearrangement of the distal pocket structure is triggered by the formation of an H-bond between E183 (D183) and K179.[744] A change in the pK_a for the Fe^{III}–H_2O to Fe^{III}–OH transition of the mutants was interpreted as being consistent with rearrangement of the H-bond network in the distal pocket. The large similarities between the high-frequency portion of the ^{1}H NMR spectra corresponding to the wild-type and R183E and R183D mutants were interpreted to indicate that the heme in the mutants is not rotated to a significant extent.[744]

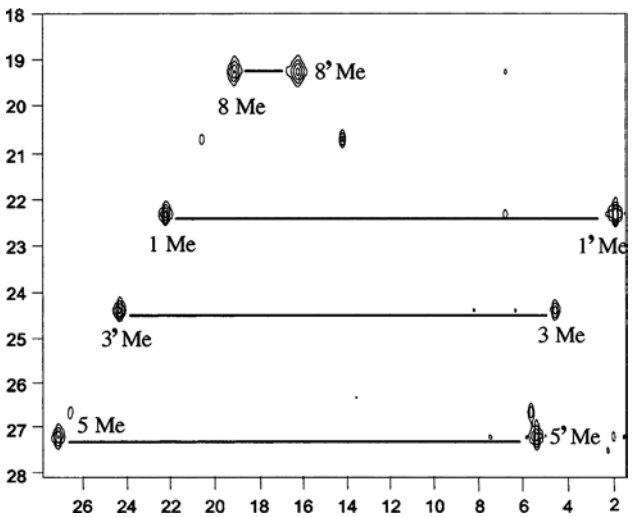

Figure 67. EXSY spectrum of the double mutant of *Pa*-HO-CN. The heme methyl resonance arising from the wild-type and alternative heme seatings are labeled as 1, 3, 5, 8 and 1′, 3′, 5′, 8′, respectively, recorded at 10 °C. Reprinted from Caignan, G. A.; Deshmukh, R.; Wilks, A.; Zeng, Y.; Huang, H.; Moënne-Loccoz, P.; Bunce, R. A.; Eastman, M. A.; Rivera, M. *J. Am. Chem. Soc.* **2002**, *124*, 14879–14892, with permission from the American Chemical Society.

Rivera, Wilks and coworkers re-examined this issue by studying the corresponding R177 mutants in HO from *Corynebacterium diphtheriae*, *Cd*-HO.[743] The replacement of R177 with E or D results in the formation of approximately 55% α- and 45% δ-biliverdin, whereas the R177A mutant retains α-regioselectivity. In addition, the K13N/Y130F/R177A triple mutant catalyzed the formation of 60% δ-, and 40% α-biliverdin, while single mutants K13N and Y130F did not appreciably change the regioselectivity of the reaction.[743] The pK_a of the Fe^{III}–H_2O to Fe^{III}–OH transition in wild-type *Cd*-HO is 9.1, and those of the R177E, R177D, R177A and K13N/Y130F/R177A mutants are 9.4, 9.5. 9.2 and 8.0, respectively. Thus, no obvious correlation exists between the changes in *pK*a and the altered regioselectivity. NMR spectroscopic studies conducted with the R177D and R177E mutants of *Cd*-HO revealed the presence of three heme isomers: A major (*M*) and a minor (*m*) heme orientational isomer related by a 180° rotation about the α–γ *meso* axis and an alternative seating (*m*′) which is related to *m* by an 85° in-plane rotation of the macrocycle.[743] The in-plane rotation of *m* to acquire conformation *m*′ is triggered by electrostatic repulsion between the side chains of D or E at position 177 and heme propionate-6. As a consequence, the δ-*meso* carbon in *m*′ is placed in the position occupied by the α-*meso* carbon in *m*, where it is susceptible to hydroxylation and subsequent formation of δ-biliverdin.[743]

In 2005, Rivera and Wilks and coworkers also investigated a chimera prepared from heme oxygenases from *Pa* and *Nm*, where *Nm*-HO was used, but with a chimeric piece of *Pa*-HO, in which the 107–142 distal helix part of *Nm*-HO was replaced by residues 112–147 of *Pa*-HO to produce *Nm*-HOch.[745] Electronic absorption spectra, resonance Raman and FTIR spectroscopic studies confirm that the orientation and hydrogen-bonding properties of the proximal His ligand are not significantly altered in the chimera relative to those of the wild-type proteins. The catalytic turnover of the *Nm*-HOch-heme complex yields almost exclusively α-biliverdin and a small but reproducible amount of δ-biliverdin.[745] NMR spectroscopic studies revealed that the altered regioselectivity to the chimeric protein likely stems from a dynamic equilibrium between two alternate in-plane conformations of the heme (in-plane heme disorder). Replacement of Lys16 with Ala and Met31 with Lys in the chimeric protein in an effort to tune key polypeptide-heme propionate contacts largely stabilized the in-plane conformer which was conducive to δ-*meso* hydroxylation.[745]

In 2006, La Mar and coworkers produced a triple mutant of hHO-1 that was designed to make it behave like the *Pa*-HO studied by Rivera, Wilks and coworkers in 2002. This triple mutant was K18E/E29K/R183E.[746] Mutation of Glu29 to Lys, which places a positive charge where it can interact with a heme carboxyl if the heme rotates ~90°, causes a slight loss of regiospecificity, but combined with the R183E and K18E mutations results primarily in β/δ-*meso* oxidation of the heme under all conditions.[746] NMR analysis of heme binding to the triple mutant confirmed rotation of the heme in the active site. Kinetic studies demonstrated that mutations of Arg183 greatly impair the rate of the P450 reductase-dependent reaction, in accord with the earlier finding that Arg183 is involved in binding of the reductase to hHO-1, but has little effect on the ascorbate reaction. Mutations of Asp140 and Tyr58 that disrupt the active site hydrogen-bonding network impair catalytic rates, but do not influence the oxidation regiochemistry.[746] The results indicated both that the oxidation regiochemistry is largely controlled by ionic interactions of the heme propionate groups with the protein, and that shifts in regiospecificity involve rotation of the heme about an axis perpendicular to the heme plane,[746] both of which were in agreement with the original report of Rivera and Wilks and coworkers in 2002[147] and their subsequent investigations of the R177E mutant of *Cd*-HO in 2004[743] and the *Nm*-HO-*Cd*-HO chimera in 2005.[745] Later analysis of the symmetrical hemin (Figure 56) complex of this mutant again showed that the protein contacts for the major solution isomers of both substrates dictate ~90° in-plane clockwise rotation relative to that seen in the wt *Nm*-HO.[747] The conventional interpretation of the pattern of substrate methyl hyperfine shifts, however, indicated substrate rotations of only ~50°. This paradox was resolved by demonstrating that the axial His25 imidazole ring also rotated counterclockwise

with respect to the protein matrix in the mutant relative to that in wild-type *Nm*-HO.[747] The axial His25 CβH hyperfine shifts were shown to serve as independent probes of the imidazole plane orientation relative to the protein matrix. It was stated that the pattern of heme methyl hyperfine shifts cannot be used alone to determine the in-plane orientation of the substrate as it relates to the stereospecificity of heme cleavage, without explicit consideration of the orientation of the axial His imidazole plane relative to the protein matrix.[747] This is obvious, as shown by Rivera and coworkers on wild-type *Pa*-HO-CN, where they found an NOE between heme methyls 1 (major) and 3′ (minor) and a methyl of the protein at –0.75 ppm, which was tentatively assigned as a γ-Me of Val33;[147] if this is true, then the His ligand has not changed its orientation, but rather the heme has rotated by ~110°.

In 2006, La Mar and coworkers also characterized the spontaneous "aging" of *Nm*-HO via cleavage of the C-terminus in contact with the substrate.[748] 2D NMR characterization of the cyanide-inhibited substrate complex showed that the C-terminal interactions between Arg208/His209 and the exposed pyrrole of the protohemin substrate in the "native" *Nm*-HO complex is lost in the "aging". Mass spectrometry and N-terminal sequencing of wild-type and "aged" *Nm*-HO reveal that the "aging process involves cleavage of the Arg208;His209 dipeptide."[748] The construction of the double deletion mutant without these two amino acids, and its NMR comparison as both the resting state substrate complex and its cyanide-inhibited complex with the "aged" *Nm*-HO reveal that cleavage of this C-terminal dipeptide is the only modification that takes place during the aging. Comparison with cyanide ligand binding constants reveal a factor of ~1.7 greater CN^- affinity in the native than the "aged" *Nm*-HO.[748] The rate of protohemin degradation and its stereoselectivity are unaffected by the C-terminal truncation. However, the free α-biliverdin yield in the presence of desferrioxamine is significantly increased in the "aged" *Nm*-HO and its deletion mutant relative to wild-type, which argues for a role of the *Nm*-HO C-terminus in modulating product release.[748] The facile cleavage of Arg208/His209 in the resting state complex, with a half-life of ~24 hours at 25 °C, suggested that previous characterization of *Nm*-HO may have been carried out on mixtures of native and "aged" NM-HO, which may account for the "lost" C-terminal residues in the crystal structure.[748] A follow-up on this study was published later the same year, in which the symmetrical hemin was used instead of protohemin.[749] The His207 from the C-terminus was found to interact with the substrate $1CH_3$, as opposed to the $8CH_3$ in the protohemin complex. The different mode of interaction of H207 with the alternate substrates was attributed to the 2-vinyl group of protohemin sterically interfering with the optimal orientation of the proximal helix Asp27 carboxylate that serves as acceptor to the strong H-bond by the peptide of His207.[749] The symmetrical hemin (Figure 56) complex

aged in a manner similar to that of protohemin, with mass spectrometry and N-terminal sequencing indicating that the Arg208/His209 dipeptide is cleaved in that case as well.[749] The symmetrical hemin complex of wild-type *Nm*-HO populates an equilibrium isomer stabilized in low phosphate concentration for which the axial His imidazole ring is rotated by ~20° from that in the wild-type. The His ring reorientation is attributed to Asp24 serving as the H-bond acceptor to the His207 peptide NH, rather than to the His23 ring $N_{\delta}H$, as in the crystals.[749]

(b) *NMR studies of heme electronic structure and its potential implications to the mechanism of heme oxidation*

In 2003, Rivera, Wilks and their coworkers published a second paper on *Pa*-HO, in which they studied the hydroxide complex as a model for the hydroperoxide complex, the activated form of the enzyme which attacks its own *meso*-carbon.[658] A ^{1}H titration similar to that shown in Figure 61 yielded an approximate pK_a of the water bound to the heme of *wt Pa*-HO of ~9.6 by this author's rough estimate; there was no remaining sign of high-spin resonances at pH 10.3.[658] The chemical shifts of the three exposed methyl groups of the major (70%) form of *Pa*-HO observed outside the diamagnetic envelope were about 23, 17 and 14 ppm at 25 °C,[658] which are considerably larger than in the NP2 case (19, 15 and 13 ppm, also at 25 °C).[146] However, the orientation of the imidazole plane of the His ligand is about 90–110° different for the two proteins, which would lead to a larger average heme methyl chemical shift for *Pa*-HO as compared to NP2 at a given temperature, assuming both of them are low-spin.[8] The ^{1}H chemical shifts of this *Pa*-HO-OH complex, however, were smaller than those of the cyanide complex of *Pa*-HO, (pH 7.4–10.0).[658]

To study the system further, ^{13}C labeling of the heme was done, in which 5-^{13}C-ALA was used to produce *meso*- and α-pyrrole ^{13}C-labeled heme, and 4-^{13}C-ALA was used to produce α- and β-pyrrole ^{13}C-labeled heme.[658] Analysis of the heme core carbon resonances revealed that the coordination of hydroxide in the distal site of the enzyme resulted in the formation of at least three populations of Fe^{III}–OH complexes with distinct electron configurations and probable nonplanar ring distortions that are in slow exchange relative to the NMR timescale.[658] The authors showed that the orbital of the unpaired electron makes a dramatic difference in the core carbon atoms of the heme, most of which (except for the *meso*-C) do not have protons attached, and thus had not previously been probed. The ^{13}C resonances of these core atoms have totally different chemical shifts, both absolute and relative, for the three electron configurations found to be important in this study,[658] as shown in Figure 68. The most abundant population (~88% at 37 °C) exhibited a spin crossover between S = 1/2 and S = 3/2 spin states (2/3 and 1/3 contribution, respectively, at 37 °C), and the two less abundant populations exhibited

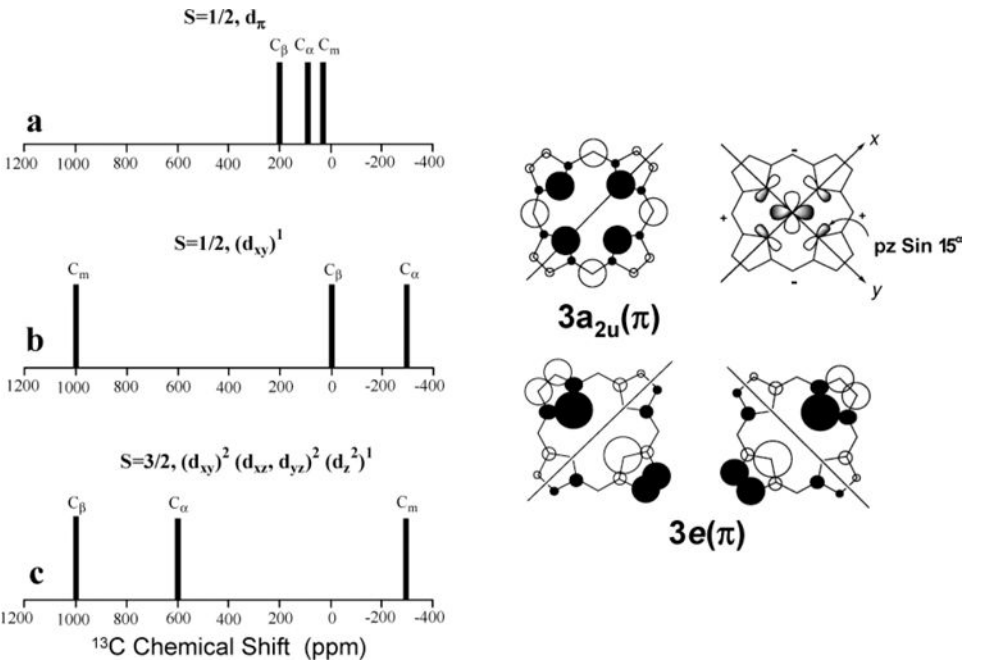

Figure 68. Left: Typical porphyrin core carbon chemical shifts for (a) Fe^{III}-porphyrinates with S = 1/2, d_π electron configuration, (b) Fe^{III}-porphyrinates with the S = 1/2, $(d_{xy})^1$ electron configuration, and (c) Fe^{III}-porphyrinates with the S = 3/2, $(d_{xy})^2(d_{xz},d_{yz})^2(d_z2)^1$ electron configuration. Right: Schematic representation (adapted from Ref. 84) of the $3a_{2u}(\pi)$ and $3e(\pi)$ porphyrin orbitals. The relative sizes of the circles at each atom are proportional to the calculated electron density. The possible interactions between the d_{xy} orbital and the porphyrin nitrogens of a ruffled porphyrin which allow spin delocalization into the $3a_{2u}(\pi)$ orbital are shown schematically next to this orbital. Reprinted from Caignan, G. A.; Deshmukh, R.; Zheng, Y.; Wilks, A.; Bunce, R. A.; Rivera, M. *J. Am. Chem. Soc.* **2003**, *125*, 11842–11852, with permission from the American Chemical Society.

pure S = 3/2 (~10% at 37 °C) and S = 1/2, $(d_{xy})^1$ (~2% at 37 °C) electron configurations, as shown in Figure 69. The major species shows strong temperature dependence of the Cα and Cβ resonances, from ~400 ppm at 37 °C to ~250 ppm at 0 °C, which is opposite the direction expected for Curie behavior, and suggests that the S = 1/2 d_π contribution to the spin-crossover species increases as the temperature is lowered.[658] In line with the work of others on model hemes,[423–429] the interconversion between these species at higher temperatures was believed to be facilitated by the interconversion among various nonplanar conformations of the porphyrin ring.[658] It was proposed that the highly organized network of water molecules in the distal pocket of heme oxygenase, by virtue of donating a hydrogen bond to the coordinated hydroxide ligand, lowers its ligand field strength and thereby increases the field strength of the porphyrin (equatorial) ligand, which

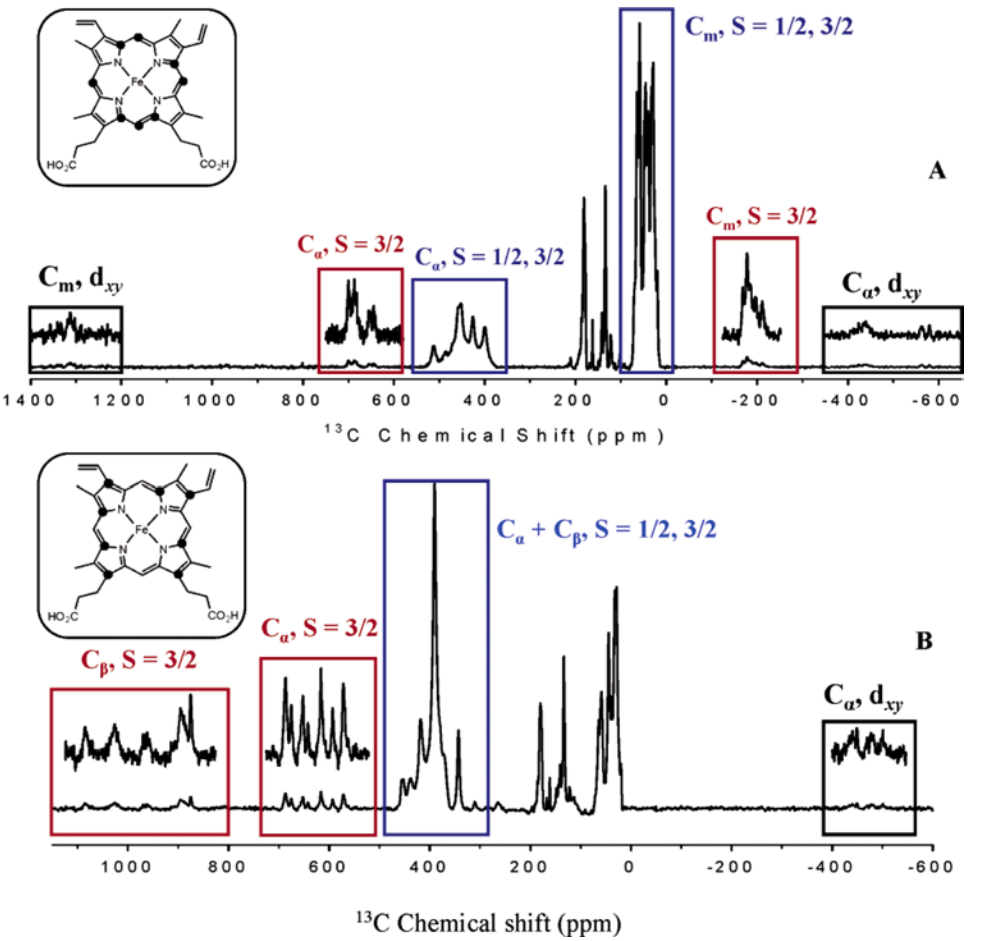

Figure 69. ^{13}C NMR spectra (37 °C) of *Pa*-HO-OH (pH* = 10.3) reconstituted with heme labeled at the C_α and C_m (A) and C_α and C_β carbons (B). Peaks corresponding to the populations exhibiting the S = 1/2,3/2 spin state crossover are highlighted by blue boxes, and peaks corresponding to the population with the S = 3/2 spin state are highlighted by red boxes. Reprinted from Caignan, G. A.; Deshmukh, R.; Zheng, Y.; Wilks, A.; Bunce, R. A.; Rivera, M. *J. Am. Chem. Soc.* **2003**, *125*, 11842–11852, with permission from the American Chemical Society.

results in nonplanar deformations of the macrocycle.[658] This tendency to deform from planarity, which is imparted by the ligand field strength of the coordinated OH^-, is likely reinforced by the flexibility of the distal pocket in HO.[658] The authors suggested that if the ligand field strength of coordinated OOH^- in heme oxygenase is modulated in a similar manner, the resultant large spin density at the *meso* carbons and nonplanar deformation of the porphyrin ring may prime the macrocycle to actively participate in its own hydroxylation.[658] This work will be

discussed further below, after discussion of a paper by La Mar and coworkers[659] that misquoted the results of this study[658] in the abstract of that paper.

In 2006, the La Mar group published a paper in which the 2003 paper of Rivera and coworkers on the hydroxide complex of *Pa*-HO[658] was attacked, first in the abstract of the 2006 paper.[659] Instead of the *Pa*-HO complex, La Mar and coworkers used the *Nm*-HO complex, and their abstract says in part, "The available [pseudocontact] shifts allowed the quantitation of both the orientation and anisotropy of the paramagnetic susceptibility tensor [of *Nm*–HO–OH]. The resulting positive sign, and reduced magnitude of the axial anisotropy relative to the cyanide complex, dictate that the orbital ground state is the conventional "d_π" $(d_{xy})^2(d_{xz},d_{yz})^3$); and not the unusual "$d_{xy}$" ($d_{xz}^2d_{yz}^2d_{xy}$) orbital ground state reported for the hydroxide complex of the homologous heme oxygenase (HO) from *Pseudomonas aeruginosa*[658] and proposed as a signature of the HO distal cavity."[659] There are several factual errors in these two sentences:

(1) Rivera *et al*. did *not* report that the "d_{xy}" electron configuration was the orbital ground state of *Pa*-HO–OH, but rather, as summarized above, they reported that there were at least three species present in the solution, *the major one of which (88% at 37 °C) had a mixed spin state of S = 3/2 (1/3) and S = 1/2 (2/3) d_π, the latter of which became more important as the temperature was lowered*;[658] a pure S = 3/2 ground state species was found to account for 10%; and *the d_{xy} ground state species was reported to comprise 2% at 37 °C.*[658]

(2) Rivera *et al*. did not propose "the d_{xy} ground state as a signature of the HO distal cavity." They did propose that at higher temperatures, such as 37 °C, the heme was able to access a number of nonplanar conformations, and that as the temperature was decreased the heme ring became less flexible and more rigidly planar.[658] They also *mentioned* the model heme paper on the *t*-butylperoxide, methoxide complex of $TPPFe^{III}$,[481] discussed earlier in Section IV.A.8.a. This author was one of the coauthors (with Rivera) of that paper, which clearly showed, by pulsed EPR spectroscopy *at 4.2 K, that the electronic ground state was purely $(d_{xy})^2(d_{xz},d_{yz})^3$, a conventional d_π electronic ground state, yet at room temperature the ^{13}C-meso-carbon shift was very large, which suggested at least some population of a $(d_{xz},d_{yz})^4(d_{xy})^1$ electronic ground state*. By fitting the temperature dependence of the ^{13}C chemical shift over the temperature range of the liquid state of the solvent (CD_2Cl_2) it was also shown that *the two were connected, not as ground and excited state configurations, but as a chemical equilibrium, probably between a planar porphyrin conformation that was stable at low temperatures, and a ruffled porphyrin conformation which became populated at higher temperatures by dynamic changes in porphyrin conformation*.[481] For some reason this paper has raised

the ire of several research groups,[659,750] who certainly did not read it carefully; in addition, some simply ignored it[751] because of what others[659,750] had said (incorrectly) about it. In the comments in the abstract of the 2006 La Mar group paper being discussed,[659] much of the ire expressed toward Rivera actually came from the mistaken convolution of the 2003 paper on *Pa*-HO[658] and the incorrectly-perceived conclusions of the model heme paper.[481]

(3) *Pa*-HO and *Nm*–HO are *not* homologous proteins, unless one believes that protein fold is the only thing important. Even so, they are only 37% identical in sequence;[752] *Nm*-HO is 26% identical in sequence with hHO-1,[753] while *Pa*-HO is only about 14% identical in sequence with hHO-1.[752,753]

(4) *Pa*-HO has a pK_a of the water molecule bound to Fe of about 9.6,[658] whereas *Nm*-HO has a pK_a of at least 10.3[659] (both of these values have been estimated by this author from the titration spectra shown in the two publications[658,659]). This could make it more difficult to obtain 2D NMR spectra of the completely deprotonated form of the *Nm*-HO protein, and the authors mention strong chemical exchange cross peaks in their NOESY(EXSY) spectra of *Nm*-HO-OH.[659] This was not a problem in the *Pa*-HO-OH study, in part because ^{13}C spectra (1D) were recorded, where, because of the much larger chemical shift differences for ^{13}C, the system is not in chemical exchange on the NMR time scale.

(5) La Mar and coworkers mention that the temperature dependence of the heme methyl shifts of Nm-HO-OH do not behave the Curie law, with "weak Curie behavior for 3M (apparent intercept at $T^{-1} = 0$ of 19 ppm) and weak anti-Curie behavior for the 8M peak (apparent intercept at $T^{-1} = 0$ of 30 ppm)."[659] This strongly indicates that spin states in addition to S = 1/2 are involved. The chemical shifts of the heme methyl protons alone, presented in both papers,[659,658] are rather different for the two proteins, but only three of each were assigned. They are in the order 3 > 8 > 5 > 1 for *Nm*-HO–OH, with chemical shifts of about 20, 19, and 13 ppm;[659] based on the angle plot it is likely that 1M is at about 10 ppm, which would mean that the spread of the resonances is about 10 ppm and the average about 15.5 ppm. Those for *Pa*-HO–OH are somewhat larger (methyl shifts from 24 to about 12 ppm, spread of 12–12.5 ppm, average shift of ~16.6 ppm),[658] as expected for the larger average chemical shift of the *Pa*-HO–OH protein due to the difference in histidine imidazole plane orientation.[8] Thus, it is probable that the heme methyl chemical shifts of the two HO–OH complexes are indicative of the same spin state or mixture of spin states, although not necessarily in the same percentages.

The *Pa*-HO–OH shifts are, however, much smaller than those of all of the metMb–OH complexes whose chemical shifts have been reported previously,

which range from nearly 40 to 20 ppm.[754–759] All of these hydroxide complexes have small spreads of the four heme methyl resonances (10.5–12.1 ppm), and large average heme methyl shifts (35.3–33.1 ppm), with T. *akamusi* metHbV–OH having the smallest spread (10 ppm) and the smallest average shift (25.9 ppm). The order of heme methyl resonances for the metMb–OH and one metHb–OH complexes ($5 \geq 8 > 3 > 1$ for most) does not match any prediction of the angle plot that is based on a low-spin $(d_{xy})^2(d_{xz},d_{yz})^3$ electron configuration (Figure 11). The large sizes of the methyl shifts and their order thus suggest strongly that the spin state is not S = 1/2 for metMb–OH complexes, a conclusion that had been implied in the section of Ref. 19 which discussed the hydroxide complexes. In line with the findings of Rivera and coworkers, based on ^{13}C chemical shifts of the heme substituent resonances of *Pa*-HO–OH,[658] we suspect that metMb–OH complexes are mixed S = 3/2,1/2 spin state complexes with considerably more S = 3/2 character than exhibited by *Pa*-HO–OH.

In 2005, Rivera and Wilks and coworkers investigated the azide complexes of *Pa*-HO and *Nm*-HO by ^1H and ^{13}C NMR spectroscopy.[149] These complexes were shown to exist as an equilibrium mixture of two populations, one exhibiting an S = 1/2 $(d_{xy})^2(d_{xz},d_{yz})^3$ electron configuration and planar heme and a second with a novel S = 3/2, $(d_{xz},d_{yz})^3(d_{xy})^1(d_{z^2})^1$ spin state and likely nonplanar heme.[149] At physiologically relevant temperatures, the equilibrium is shifted in the direction of the population exhibiting the novel S = 3/2 electron configuration and nonplanar heme, whereas at temperatures approaching the freezing point of water, the equilibrium is shifted in the direction of the population with the S = 1/2 d_π electronic structure and planar heme. These findings indicate that the microenvironment of the distal pocket in heme oxygenase is unique among heme-containing proteins, in that it lowers the σ-donating (field strength) ability of the distal ligand and, therefore, promotes the attainment of heme electronic structures thus far only observed in heme oxygenase.[149] When the field strength of the distal ligand is slightly lower than that of azide, such as OH^-,[658] the corresponding complex exists as a mixture of populations with likely nonplanar hemes and electronic structures that place significant spin density at the *meso* positions. The ease with which these unusual heme electronic structures are attained by heme oxygenase is likely related to activation of *meso*-carbon reactivity which, in turn, facilitates hydroxylation of a *meso*-carbon by the obligatory ferric hydroperoxide intermediate.[149]

Also in 2005, Rivera, Wilks and coworkers used 5-^{13}C-ALA to synthesize a combination *meso*- and α-labeled heme (Figure 13) and used it to reconstitute apo-*Nm*-HO, to investigate the nature of the verdoheme oxidation product that is formed by α-*meso* oxidation.[760] The ^{13}C NMR data indicated that the ferrous verdoheme complex of *Nm*-HO is six-coordinate and diamagnetic, with a proximal

His and distal hydroxide as axial ligands. The coordination number and spin state of the verdoheme-HO complex are in stark contrast to the 5-coordinate and paramagnetic nature of the heme-HO complex, and heme centers in general.

Several years later, in 2009, La Mar and coworkers used the hHO-1 azide complex[761] to attack Rivera and coworkers a second time. They claimed that the spin state of the azide complex was pure S = 1/2, and that 2D ^{1}H NMR assignments of the substrate and substrate-contact (protein) residue signals revealed a pattern of substrate methyl contact shifts that placed the lone iron π-spin in the d_{xz} orbital, rather than the d_{yz} orbital found in the cyanide complex. They reported that comparison of iron spin relaxivity, magnetic anisotropy, and magnetic susceptibilities argued for a low-spin, $(d_{xy})^2(d_{xz},d_{yz})^3$, ground state in both azide and cyanide complexes.[761] The switch from singly-occupied d_{yz} for the cyanide to d_{xz} for the azide complex of hHO was shown to be consistent with the orbital hole determined for the azide π-plane in the latter complex, which is ~90° in-plane rotated from that of the imidazole π-plane.[761] The induction of the altered orbital ground state in the azide relative to the cyanide hHO complex, as well as the mean low-field bias of methyl hyperfine shifts and their paramagnetic relaxivity relative to those in globins, indicated to the authors that azide exerts a stronger ligand field in hHO than in the globins, or that the distal H-bonding to azide is weaker in hHO than in globins.[761]

The two problems with these conclusions are (1) the assumption that everything that *Pa*-HO and *Nm*-HO do is identical to what hHO-1 does and thus the spin states of the three must of necessity be the same, and (2) the assumption[761] that the azide complex of hHO-1 is low-spin. Both Rivera and coworkers[149] and La Mar and coworkers[761] found orders of heme methyls that are not consistent with the low-spin state for a relatively flat hemin molecule, that is, 5M having a smaller chemical shift than 1M, whereas it should be the reverse.[8] The protohemin complexes of *Pa*-HO and *Nm*-HO could be ruffled enough to give rise to the ruffling-caused reversal of this order that has been observed for the nitrophorins,[143] but it could also be, as Rivera and coworkers concluded for this complex, that the spin state is not pure S = 1/2. For the protohemin complex studied by Rivera *et al.*,[149] this reversal is a very likely sign that the spin state that gives rise to the heme methyl chemical shifts is not actually that of a single low-spin state, but rather of some sort of hybrid or average with a state of different spin multiplicity. For the symmetrical hemin complex (Figure 56) studied by La Mar and coworkers, the 5M and 1M groups within the same complex should have the same chemical shift,[761] no matter what the orientation of the ligand orbitals are, unless there is some sort of serious protein-caused distortion of the heme that affects one and not the other of these heme methyls, which has not been shown in the crystal structures. Yet for the symmetrical hemin hHO-1 complex, 1M > 5M by about 0.7 ppm,

whereas for the cyanide complex, 5M > 1M by about 0.8 ppm.[761] Therefore, it is very likely that Rivera is correct that the ground state of the azide complex is not pure S = 1/2, and that a S = 3/2 component is involved.

(c) *NMR spectroscopic studies of dynamic reactivity relationships*

In 2006, Rivera and coworkers investigated the azide and cyanide-inhibited complexes of *Pa*-HO.[762] The azide complex was chosen for study because this ligand has lower ligand field strengthZ than cyanide, and it appears to have readily-available nonplanar heme macrocycle conformations, and also because of the bent conformation of the Fe–NNN unit, which was expected to be similar in angle to that of the Fe–OOH unit, and because the crystal structure of the azide complex of rat HO-1 appears to have a hydrogen-bond between conserved the Gly143 amide N-H (Gly 125 in *Pa*-HO) and the coordinating nitrogen of the azide ligand.[714] This hydrogen-bond is not possible for the approximately linear cyanide ligand, both because of its geometry and because there is no lone pair of electrons on the coordinating atom, a carbon in that case. The cyanide complex was chosen for study because it clearly has the $(d_{xy})^2(d_{xz},d_{yz})^3$ electron configuration, which is strongly expected to favor a rigid, flat heme macrocycle.[762]

Nearly complete backbone assignments (>93%) for both complexes, of all nonproline residues were assigned, with the majority of the nonassigned residues corresponding to the first 10 amino terminal residues. Resonances strongly affected by heme iron paramagnetism were assigned with the aid of selective amino acid labeling and experiments tailored to detect fast relaxing signals, whereas the rest of the polypeptide was assigned using conventional three-dimensional NMR experiments.[762] Amide chemical shift assignments were used to monitor the rate of exchange of backbone protons in H/D exchange experiments, and the protection factors for each peptide bond were calculated, as shown in the plots in Figure 70. The polypeptide in the *Pa*-HO-N_3 complex was found to be significantly less prone to H/D exchange than the polypeptide in *Pa*-HO-CN, which was interpreted to indicate that *Pa*-HO-N_3 is conformationally less flexible than *Pa*-HO-CN.[762] The differences in protection factors (protection from H/D exchange, as calculated from the rate constants for H/D exchange using the procedures described by Englander[763]) extend to regions of the protein remote from the heme iron and distal ligand. When the differences in protection factors are mapped onto the X-ray crystal structure of *Pa*-HO, the pattern observed suggests that the distinct chemical properties imparted by the coordination of azide as compared to cyanide to the heme iron are transmitted to the polypeptide by a network of structural water molecules that extend from the active site to the surface of the enzyme,[762] as had been studied for hHO-1 by La Mar and coworkers.[678,728–730] While the ^{1}H amide resonance of Gly125 was too broad to detect, the corresponding ^{15}N resonance was

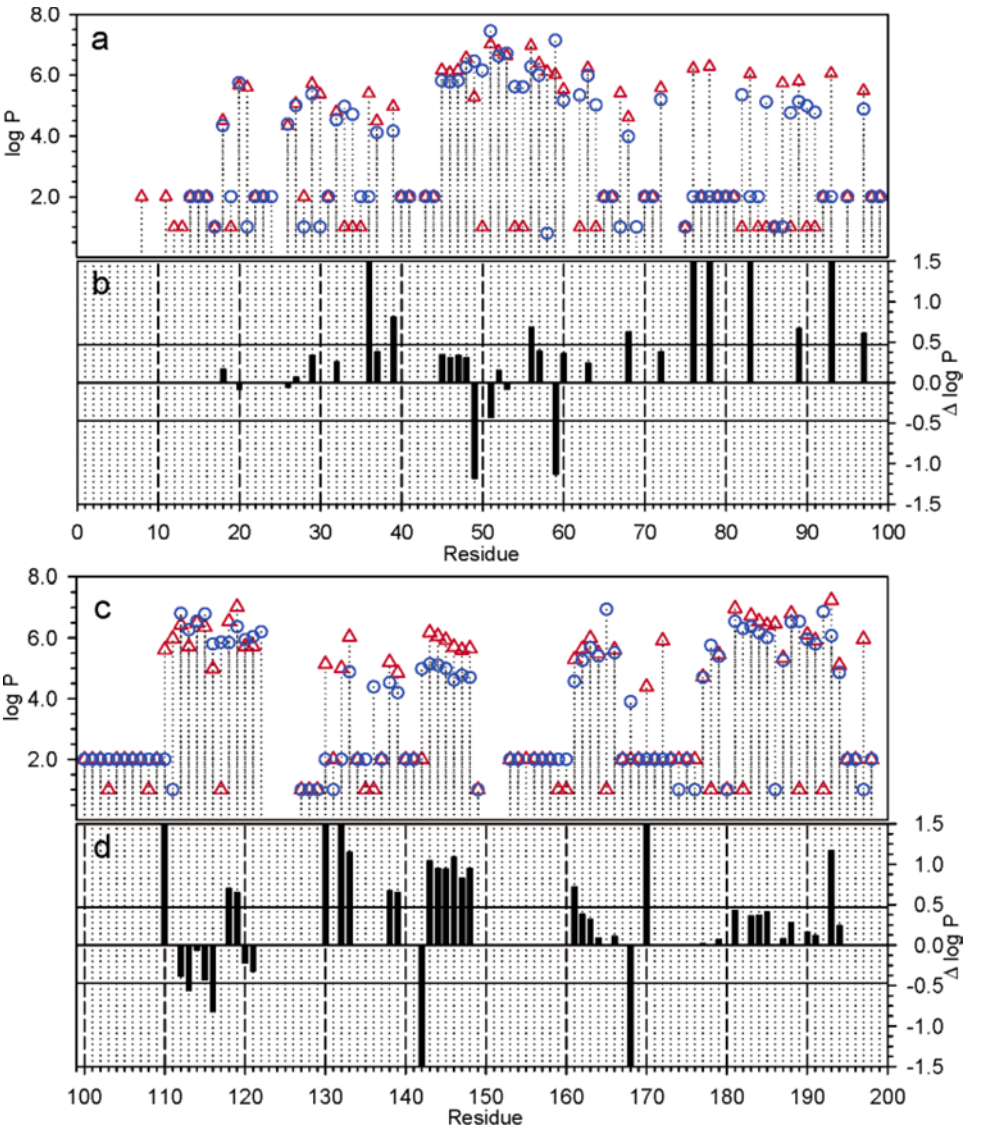

Figure 70. (a and c) Per residue protection factors obtained from amide H/D exchange experiments with *pa*-HO–N_3 (red triangles) and *Pa*-HO–CN (blue circles). A value of log $P = 2$ was arbitrarily given to residues exhibiting exchange rates too fast to be measured, and a value of log $P = 1$ was given to residues not included in the analysis due to either peak overlap or lack of assignments. (b and d) Per residue differences in protection factors ($\Delta\log P = \log P_{azide} - \log P_{cyanide}$) between the *Pa*-HO–$N_3$ and *Pa*-HO–CN. The average difference of all residues is indicated by the horizontal line. Bars reaching the maximum vertical scale ($\Delta\log P = 1.5$) correspond to residues exhibiting exchange rates measurable in *Pa*-HO–N_3 but too fast to measure in the *Pa*-HO–CN (not included in the computation of the average difference). Reprinted from Rodriguez, J. C.; Wilks, A.; Rivera, M. *Biochemistry* **2006**, *45*, 4578–4592, with permission from the American Chemical Society.

found to exhibit a large shift to lower shielding, large linewidth, steep temperature dependence, and a larger than usual shift to higher shielding of the deuterium isotope effect.[762] These properties indicated unpaired spin delocalization from the heme iron to the Gly ^{15}N atom via formation of a hydrogen-bond between the coordinated azide nitrogen and the Gly125 N–H.[762] Thus, this study provided the first clear comparison of the dynamic properties of a heme protein bound to two different axial ligands, and it showed major differences between the two ligand complexes of *Pa*-HO in terms of their H/D exchange rates.

In 2007, Rivera and coworkers presented a detailed look at the hydrogen-bonding network in *Pa*-HO by multidimensional NMR spectroscopy. Relaxation-compensated Carr-Purcell-Meiboom-Gill (rc-CPMG) NMR experiments were used to investigate the μs to ms motions in *Pa*-HO in its ferric state, inhibited by CN^- or N_3^-, and in its ferrous state, inhibited by CO.[764] Comparative analysis of the data from the three forms indicated that the nature of the coordinated distal ligand affects the μs-ms conformational freedom of the polypeptide in regions of the enzyme not only close to, but also far removed from the heme iron and distal ligand sites, as shown in Figure 71. Interpretation of the dynamic information in the context of the crystal structure of resting state *Pa*-HO showed that residues involved in the network of structural hydrogen-bonded waters characteristic of HOs undergo μs-ms motions in *Pa*-HO–CN (Figure 71a), which was studied as a model of the highly paramagnetic S = 5/2 resting form.[764] In comparison, similar motions are suppressed in the *Pa*-HO–CO (Figure 71d) and *Pa*-HO–N_3 (Figure 71b) complexes, which were studied as mimics of the obligatory oxyferrous and ferric-hydroperoxide intermediates, respectively, in the catalytic cycle of heme degradation.[764] These findings suggested that in addition to proton delivery to the nascent Fe^{III}–OO^- intermediate during catalysis, the hydrogen-bonding network serves two additional roles (i) to propagate the electronic state (reactive state) in each of the distinct steps of the catalytic cycle to key, but remote, sections of the polypeptide, via small rearrangements in the network of hydrogen-bonds and (ii) to modulate the conformational freedom of the enzyme, which thus allows it to adapt to the demanding changes in axial coordination state and substrate transformations that take place during the catalytic cycle.[764] This idea was probed by disrupting the H-bonding network in *Pa*-HO by replacing R80 with L. NMR spectroscopic studies conducted with R80L-*Pa*-HO-N_3 (Figure 71c) and R80-L-*Pa*-HO-CO (not shown) revealed that the mutant exhibited nearly global conformational disorder, which is absent in the equivalent complexes of the wild type enzyme.[764] As shown in Figure 72, the crystal structure of Pa-HO highlights the roles of R80, along with E52 and E56, in stabilizing the network of hydrogen-bonding waters in the distal pocket of *Pa*-HO. The "chaotic" disorder in the R80L mutant is likely related to its significantly lower efficiency in hydroxylating heme in the presence of H_2O_2, relative to the wild-type enzyme.[764] This work has given us an entirely

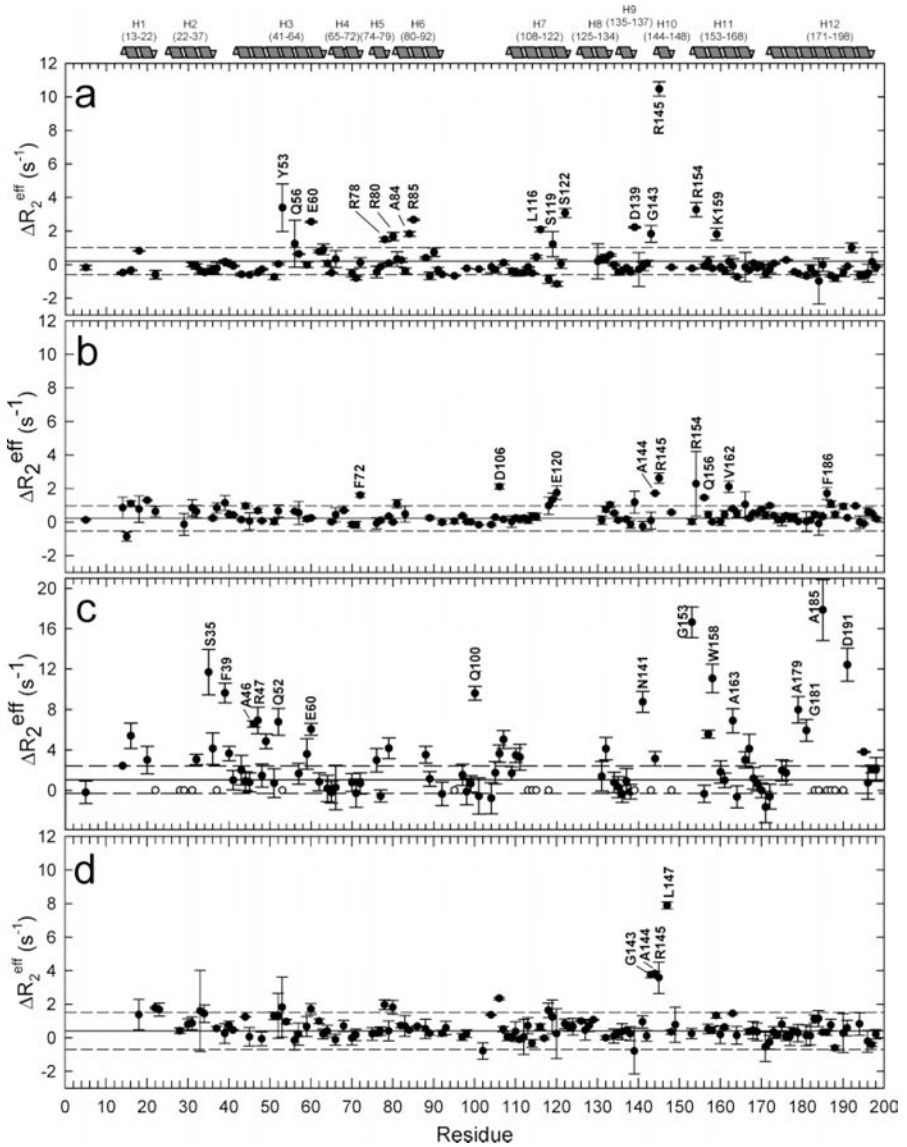

Figure 71. Per residue effect of axial ligand coordination on the backbone ^{15}N relaxation dispersion $\Delta R_2^{eff}(\nu_{CPMG})$ of *Pa*-HO axially coordinated with (a) CN^-, (b) N_3^-, and (d) CO. The per residue plot in (c) shows values of $\Delta R_2^{eff}(\nu_{CPMG})$ obtained for the R80L-*Pa*-HO mutant coordinated with N_3^-, which was prepared with the aim of disrupting the hydrogen-bonding network in *Pa*-HO. The horizontal line represents the average error obtained from two measurements, and the horizontal segmented lines represent 3 standard deviations above and below the average. Residues with $\Delta R_2^{eff}(\nu_{CPMG})$ values more positive than the segmented line representing 3 standard deviations above the mean are considered to be in conformational exchange in the μs–ms time regime sampled by the (constant time) ct-CPMG experiments utilized in these investigations. Reprinted from Rodriguez, J. C.; Zeng, Y.; Wilks, A.; Rivera, M. *J. Am. Chem. Soc.* **2007**, *129*, 11730–11742, with permission from the American Chemical Society.

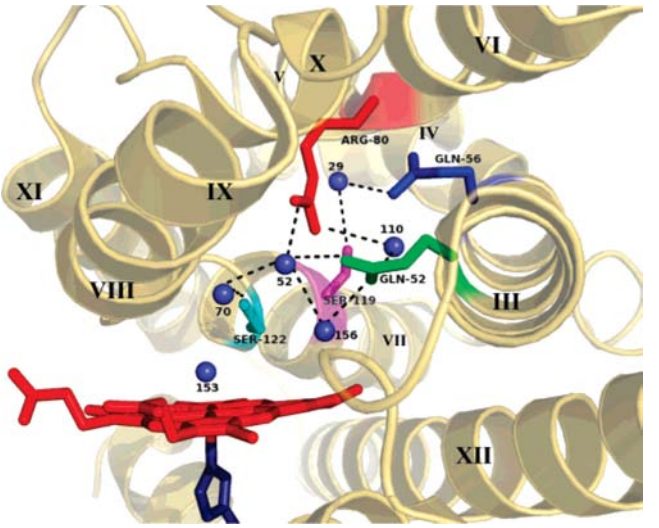

Figure 72. View of *Pa*-HO highlighting structural water molecules networked by hydrogen bonds to themselves and to side chains of key residues, some of which (Gln52, Gln56, and Arg80) are harbored by helices where μs–ms conformational exchange is observed in *Pa*-HO–CN but not in *Pa*-HO–N_3 or *Pa*-HO–CO. Reprinted from Rodriguez, J. C.; Zeng, Y.; Wilks, A.; Rivera, M. *J. Am. Chem. Soc.* **2007**, *129*, 11730–11742, with permission from the American Chemical Society.

new view of heme oxygenases, and one would expect that further studies of the dynamics of various forms of these interesting proteins will be presented in the future.

As indicated by the preceding paragraphs, the dynamics of HO are tightly coupled to the structured waters in the distal pocket of this enzyme. La Mar and coworkers recognized the importance of the structured waters near the heme iron of HOs and have studied the distal water network for a number of years.[678,728–730] In 2003 when La Mar moved into the field of bacterial heme oxygenases with a collaboration with Ikeda-Saito on *Corynebacterium diphtheriae*,[765] before the crystal structure of that enzyme had been reported, he and his coworkers used the human HO (hHO) complex as a homology model. It was demonstrated that not only the spatial contacts among residues and between residues and heme, but also the magnetic axes that can be related to the direction and magnitude of the steric tilt of the Fe–CN unit are strongly conserved in the two HO complexes.[765] The results indicated that very similar contributions of steric blockage of several *meso* positions and steric tilt of the attacking ligand were operative. A distal hydrogen-bonding network that involved numerous very strong H-bonds and immoblized water molecules was identified in *Cd*-HO that is analogous to that previously identified in hHO.[728] The NMR results were completely consistent with the crystal structure of the *Nm*-HO substrate complex. The H-bond network/ordered water

molecules are proposed to orient the distal water molecule near the catalytically key Asp136 (Asp140 in hHO-1) that stabilizes the hydroperoxy intermediate.[765] The dynamic stability of this H-bond network in *Cd*-HO was found to be significantly greater than in hHO, and was suggested to account for the lower catalytic rate in bacterial HO compared with mammalian HO.[765]

The next year, 2004, La Mar and coworkers began a study of *Nm*-HO.[766] This enzyme exhibits less sequence homology to mammalian HO (25%) than does *Cd*-HO (35%). Solution ^{1}H NMR spectroscopy was utilized to define the active site molecular and electronic structure of the cyanide-inhibited, substrate bound complex for comparison with those provided by several crystal structures.[766] Extensive assignments by solely ^{1}H NMR 2D methods revealed a structure that was very strongly conserved with respect to the crystal structure, although H/D exchange indicated dynamically much more stable distal and proximal helices than those for other HOs. Several residues found with alternate orientations in crystal structures of water- and NO-ligated complexes were shown to occupy positions found solely in the NO complex,[719] which confirmed that there may be structural accommodations in response to ligating the substrate complex with a bent, diatomic, H-bond-acceptor ligand.[766] The observed pseudocontact shifts of the cyanide complex allowed the determination of the magnetic axes that showed that the Fe–CN unit is tilted ~10° toward the *α-meso* position, which thereby was thought might facilitate the *α*-stereoselectivity of the enzyme.[766] Numerous labile protons with larger than usual low-shielding bias were identified, and, in common with the other HO complexes, shown to participate in an extended, distal side H-bond network. This H-bond network appeared to order several water molecules, most, but not all, of which have been detected crystallographically.[766] A series of three C-terminal residues, His207-Arg208-His209, are not detected in crystal structures. However, ^{1}H NMR spectroscopy finds two residues, His207 and likely Arg208, in contact with pyrrole ring D,[766] which in crystal structures is exposed to solvent. The nature of the NOEs led the authors to propose a H-bond between the proximally-oriented His207 ring and the carboxylate of Asp27, and a salt-bridge between the terminus of Arg208 and the reoriented 7-propionyl carboxylate.[766] While numerous ordered water molecules are found near both propionates in the crystal structure, they found much larger water NOEs to the 6- than the 7-propionate, which suggested that water molecules near the 7-propionate had been expelled from the cavity by the insertion of Arg208 into the distal pocket.[766] The conversion of the 7-propionate link from the N-terminal region (Lys16) to the C-terminal region (Arg208) in the ligated substrate complex was found to both close the heme cavity more tightly, and was thought to facilitate product exit, the rate-limiting step in the enzyme activity.[766]

In 2005, La Mar and coworkers studied the high-spin iron(III) complex of *Nm*-HO,[767] to assess the prospects for definitive assignment of hyperfine-shifted

and — relaxed residue protons and the interpretation of those shifts in terms of the anisotropy and orientation of the paramagnetic susceptibility tensor, χ. 1D/2D ^{1}H NMR data, together with analyses of paramagnetic relaxation and a preliminary estimate of the magnetic anisotropy, revealed a χ that was anisotropic and oriented along the Fe-His bond vector.[767] Together with T^{-2} dependence of the shifts, $\Delta\chi_{ax}$ yields a zero-field splitting constant, $D = 9.1\ cm^{-1}$, which is expected to serve as a very sensitive probe of H-bond interactions between the iron-ligated water and a series of distal ordered water molecules that are implicated in the mechanism of HO action.[767] The side chains, Gln49 and His53, which are involved in the stabilization of catalytically relevant water molecules, were found to exhibit orientations rotated by 180° about the β-γ bonds in solution relative to those in the crystal.[767] The H-bond donor strengths of Gln49 and His53 were found to respond appropriately to H-bond donor (water) versus H-bond acceptor (cyanide) ion ligands. Very slow NH exchange for the N-terminal portion of the distal helix suggested that an intrinsically "unstable" distal helix may be valid only for the C-terminal portion.[767]

In 2006, La Mar and coworkers[768] described the study of the hydrogen-bonding of ligated water in ferric, high-spin, resting-state *Nm*-HO. Several hemes were utilized that had electron-withdrawing substituents on the hemin periphery. It was found that the pattern of ^{1}H NMR-detected pseudocontact shifts due to the paramagnetic anisotropy of the high-spin Fe^{III} center is strongly conserved among the complexes, with the magnitude of pseudocontact shifts or magnetic anisotropy $\Delta\chi_{ax}$ ($\propto D/T^2$, Eq. 10) increasing in the order 2,4-substituent formyl < vinyl < methyl.[768] The unique changes in the axial field strength implied by the variable zero-field splitting were found to be in accord with expectations for the axial water serving as a stronger H-bond donor in the order of hemin substituents formyl > vinyl > methyl. It was found that Gln49 and His53, ~10 Å from the iron, sensed the change in the ligated water H-bonding to the three nonligated, ordered water molecules that link the two side chains to the iron ligand.[768]

c. *NMR spectroscopy of miscellaneous other heme proteins*

Since publication of the chapter on Nuclear Magnetic Resonance of Hemoproteins in 2000 by La Mar, Satterlee and de Ropp[19] and the chapter on Solution Structures of Hemoproteins in the same volume,[20] there have been some developments on NMR spectroscopy of heme proteins not covered above that should be mentioned, at least briefly. A study of the solution NMR determination of the seating(s) of mono-*meso*-nitro-etioheme-1 in myoglobin has been published and the implications for steric constraints to meso position access in heme degradation by coupled oxidation discussed.[769] This study is distantly related to the HO systems discussed above. A further study of axial interactions of the proximal and distal His in the

cyanomet complexes of the isolated chains and of the 65 kDa intact tetramer of human hemoglobin A was published,[770] as were two papers on the H42A mutant (distal His) of horseradish peroxidase, one on the high-spin ferric form[771] and one on the low-spin ferric cyanide complex[772] and also a study of the electronic structure and magnetic properties of the high-spin ferrous heme in deoxymyoglobin from *Aplysia limacina*.[773] Solution NMR characterization of the equilibrium heme orientational disorder and its functional consequences in the bis-His-coordinated mouse Neuroglobin was reported,[674] although it was later shown that the orientation of the two His ligands is somewhat different in solution[774] than in the crystalline state.[775–777] A study of the bis-His-coordinated human cytoglobin has also been reported.[778] A review of the study by NMR spectroscopy of the mechanisms of electron transfer in heme proteins and models of them has been published, which covers not only iron porphyrin and heme protein self-exchange, but also multiheme intraprotein and interprotein electron transfer.[779] Cytochromes b_5,[780–786] b_{562},[787–790] mitochondrial *c*,[791–795] folding of cytochromes *c*,[796–802] yeast *c*,[803,804] bacterial *c*,[805–813] Mn peroxidase and its models,[814–816] cytochrome *c* complexing with cytochrome b_5,[817,818] Cu_A of cytochrome oxidase,[819] cytochrome *f* complexing with plastocyanin,[820] a heme chaperone[821] and a hemophore[822–824] have been studied by multidimensional NMR spectroscopy, and the ^{1}H NMR spectra of cytochrome *c* in a micellar environment have been investigated.[825,826]

Finally, the hemophore HasAp from *Pseudomonas aeruginosa*, from the heme acquisition system of that organism, which is secreted as a 205-residue-long protein which is subsequently cleaved at the C-terminal to produce mainly a 184-residue-long truncated protein that scavenges heme[827] has been characterized in the crystalline state by X-ray crystallography and in solution by NMR spectroscopy.[828] The X-ray crystal structure of truncated HasAp revealed a polypeptide with $\alpha\beta$ fold and a ferriheme coordinated axially by His32 and Tyr75, with the side chain of His83 poised to accept a hydrogen bond from the Tyr75 phenolic acid group.[828] NMR investigations conducted with full-length HasAp showed that the carboxyl-terminal tail (21 residues) is disordered and conformationally flexible.[828] NMR spectroscopic investigations aimed at studying a complex between apo-HasAp and human methemoglobin were stymied by the rapid heme capture by the hemophore. In an effort to circumvent this problem, NMR spectroscopy was used to monitor the titration of ^{15}N-labeled holo-HasAp with hemoglobin.[828] These studies allowed identification of a specific area on the surface of truncated HasAp, which encompasses the axial ligand His32 loop, that serves as a transient site of interaction with hemoglobin, for which it appeared that a putative encounter complex between apo-HasAp and hemoglobin exists that leads to efficient hemoglobin-heme capture by the hemophore.[828] Similar experiments conducted with full-length ^{15}N-labeled holo-HasAp and hemoglobin revealed a

transient interaction in full-length HasAp similar to that observed in the truncated hemophore.[828] The spectral perturbations observed while these interactions were being investigated, however, are weaker than those observed for the interaction between hemoglobin and truncated HasAp, which suggested that the disordered tail in the full-length HasAp must be proteolyzed in the extracellular milieu to make HasAp a more efficient hemophore.[828]

11. *Iron(III) Macrocycle π-Cation Radicals*

Single-electron oxidation of iron(III) porphyrins may lead to either iron(III) porphyrin π-cation radicals or iron(IV) porphyrins, depending on the axial ligation of the metal and the reaction conditions. In this section, the systems that have been formulated as iron(III) porphyrin π-cation radicals, and in the next section, the iron(IV) porphyrins will be considered. Note that a so-called "metalloporphyrin π-cation radical" is actually a metal ion in some positive oxidation state, M^{n+}, where n is 2 or larger, bound to a porphyrin π-anion radical, $P^{-\bullet}$. Since a porphyrin typically binds to a metal as a −2 anion (because the two protons on the nitrogens of the free-base prophyrins, H_2P, have been removed), removal of one electron from the porphyrin π system to produce the π-radical yields as mononegative, or π-anion radical. If the change on the metal is +2 or higher, then the entire unit, $[MP^{-\bullet}]^{n+}$ is cationic. This the term "porphyrin π-cation radical" is a misnomer. It is only a *cation* because it is bound to a metal of charge +2 or higher!

Considering the three different spin states observed for iron(III) porphyrins, it is not surprising to find that all three have been observed for the one-electron ring-oxidized complexes. Some high-spin, monomeric iron(III) porphyrins give rise to antiferromagnetically coupled S = 2 species;[829–831] others give rise to a noninteracting S = 5/2, S = 1/2 species;[831] spin-admixed S = 3/2,5/2 iron(III) porphyrin complexes give rise to spin-admixed π-cation radical species of either S = 5/2, 3/2[374] or S = 3/2,5/2[832] ground state; and low-spin iron(III) porphyrins give rise to low-spin iron(III) porphyrin π-cation radical species.[833] Although this work was reported previously,[4] it is summarized here for completeness.

a. *High-spin iron(III) porphyrin π-cation radicals*

Anodic oxidation of [(TPP)FeCl] in the presence of perchlorate or hexafluoroantimonate salts, or chemical oxidation with an iron(III) porphyrin π-cation radical of higher oxidation potential, produces a S = 5/2,S = 1/2 antiferromagnetically coupled (effectively $S_{tot} = 2$) 5-coordinate $[(TPP^{-\bullet})Fe^{III}Cl]^+$ π-cation radical[831] which has its pyrrole-H resonance at +66.1 ppm (compared to +79.4 ppm for [(TPP)FeCl]) and its phenyl-H at +37.6, +34.4 (*ortho*), −12.4 (*meta*) and +29.5 ppm (*para*) (compared to −6, 13.3, 12.2, and 6.35 ppm, respectively, for the parent) at 26 °C in CD_2Cl_2.[834] The

large, alternating shifts of the phenyl-H are indicative of large π spin density at the *meso* positions, which suggests that the electron has been removed from the $3a_{2u}(\pi)$ orbital, Figures 2 and 3. However, the sign of the shifts, δ_o positive, δ_m negative, is the opposite of that usually seen for metalloporphyrin π-cation radicals when there is large π spin density seen the *meso*-phenyl positions,[374] as is expected when the porphyrin radical spin is antiferromagnetically coupled to the metal spins. The Curie plots are linear, but the *o*-H has a very large, negative intercept. The X-ray crystal structure of [(TTP)FeCl]SbF_6 consists of isolated 5-coordinate $[(TPP)FeCl]^+$ units, in which the porphyrin macrocycle is strongly S_4 saddled.[831]

In comparison, the NMR spectrum of [(OEP)FeCl]ClO_4 shows relatively small shifts of the pyrrole-α-CH_2 to lower frequency (δ_{obs} = +30.5, +29.6 ppm at 20 °C, as compared to +43.1, +39.5 ppm at 30 °C for the parent) and a large shift of the *meso*-H to lower shielding (δ_{obs} = −18 ppm at 20 °C, compared to −54 ppm at 30 °C for [(OEP)FeCl]), which suggested to the authors that in this case the electron is removed from the $1a_{1u}$ orbital,[834] Figure 2.

π-Cation radicals of (P)Fe–O–Fe(P) species, the μ-oxo dimers of iron(III) porphyrins, are convenient chemical oxidants of the chloroiron porphyrins,[834] and they are interesting species in their own right. Those in which P = TPP or one of its derivatives also have larger phenyl-H paramagnetic shifts than the parent complexes, again with alternating signs, suggesting the same $(a_{2u})^1$ ground state for the metalloporphyrin π-cation radical, in this case delocalized over the two porphyrin rings; the pyrrole-H paramagnetic shift is affected much less (usually δ_{obs} decreases by ~1 ppm). The dication of the μ-oxo dimer can also be prepared, and exhibits attenuated paramagnetic shifts as compared to the monocation.[834]

Several groups have studied the neutrally-charged μ-nitrido dimer of (TPP)Fe, $[((TPP)Fe)_2N]$.[403,835] It is isoelectronic with the iron porphyrin π-cation radical of the μ-oxo dimers discussed above, but has rather different ^{1}H NMR spectra. Whereas $[((TPP)Fe)_2O]^+$ has resonances at 12.3 (pyrr-H), 1.3 (*o*-H), 11.7 (*m*-H) and 3.2 ppm (*p*-H), $[((TPP)Fe)_2N]$ has broad, overlapping resonances at 8.6, 8.3 and 7.6 ppm,[403,835] which suggests that its description as a delocalized system which has two $Fe^{3.5+}$ may be better than considering it to be a delocalized diiron porphyrin π-cation radical. If one-electron oxidation is carried out with I_2/Ag^+, a species with a much sharper NMR spectrum, with resonances at 8.32 (pyrr-H), 7.85 and 7.64 ppm (phenyl-H) is produced. This complex is believed to consist of Fe^{IV}–N^{-III}–Fe^{IV}.[835] Very small temperature dependence over the range +26 to −55 °C suggests that the metals are strongly antiferromagnetically coupled. The complex has a magnetic moment[376,377] of less than 1.8 μ_B at room temperature. Unlike $[((TPP)Fe)_2O]^+$ or $[((TPP)Fe)_2O]^{2+}$, both of which autoreduce in the presence of pyridine, $[((TPP)Fe)_2N]^+$ readily coordinates one or two pyridine ligands; stepwise addition can be observed by monitoring the pyridine *o*-H resonances at −1.26 ppm (1:1) and −1.46 ppm (2:1).[835]

b. *Spin-admixed and intermediate-spin iron(III) porphyrin π-cation radicals*

Electrochemical one-electron oxidation of $[(TPP)Fe(ROH)_2]ClO_4$, where ROH is water or ethanol, in the presence of perchlorate salts, produces the neutrally-charged complex $[(TPP^{-\bullet})Fe(OClO_3)_2]$, a 6-coordinate complex described as a S = 5/2, S = 1/2, non-interacting high-spin species because of its room temperature magnetic moment in the solid state (μ_{eff} = 6.5 ± 0.2 μB).[831] Its NMR spectrum at 25 °C in CD_2Cl_2 revealed paramagnetic shifts of +22.6 (pyrr-H), −27.1 (*o*-H), +27 (*m*-H), −20.6 ppm (*p*-H), suggesting a π-radical of a_{2u} type. However, investigation of this system in CH_2Cl_2 in the presence of electrolyte as a function of temperature, utilizing pyrrole- and phenyl-deuterated TPPs to eliminate the resonances of the large amount of tetra-(*n*-propyl)-ammonium perchlorate electrolyte present, revealed that although the pyrrole-D resonance shifts to higher shielding as the temperature is lowered, the Curie plots are not linear.[374] Rather, they have very steep slopes and very negative intercepts, and are curved at higher temperatures, which indicates that in this spin-admixed state, the ground state is largely S = 5/2.[374] The solution magnetic moment,[376,377] 4.8 ± 0.4 μ_B, is much lower than that observed in the solid state,[831] which suggests antiferromagnetic coupling of the metal and porphyrin spins.

The complexity of the behavior of iron(III) porphyrin π-radicals, and those of tetra-mesitylporphyrin in particular, is demonstrated by the properties of $[(TMP^{-\bullet})Fe(OClO_3)_2]$ in various solvents.[832] This π-radical of iron(III) was prepared by oxidation of $[(TMP)FeOClO_3]$ with ferric perchlorate, isolation and then dissolution in CD_2Cl_2. The temperature dependent behavior is the opposite that observed for $[(TPP)Fe(OClO_3)_2]$ in CH_2Cl_2, with the pyrrole-H resonance at very high shielding at low temperatures (δ_{iso} negative) and at low shielding at higher temperatures (δ_{iso} positive).[832] These results indicate that in the case of the TMP complex, the S = 3/2 ground state is greatly favored over the spin admixed 3/2,5/2 or 5/2,3/2 ground states. Treatment of the latter iron(III) porphyrin π-radical complex with two equivalents of sodium methoxide produced the electron configuration isomer, the d^4 iron(IV) porphyrin complex,[832] discussed in Section IV.A.12.

As an illustration of the chemical reactivity of these iron(III) porphyrin π-radicals, $[(TPP^{-\bullet})Fe(OClO_3)_2]$ reacts with the nucleophiles nitrite ion or triphenylphosphine to produce the mono-β-substituted iron(III) porphyrins.[836] The products were isolated as the 6-coordinate dichloride complexes, $[((2\text{-}NO_2)TPP^{-\bullet})FeCl_2]$ and $[((2\text{-}PPh_3)TPP^{-\bullet})FeCl_2]$, respectively; the latter was characterized by X-ray crystallography and ^{1}H NMR spectroscopy in CD_2Cl_2 for the bis-imidazole complexes.[836] Similar reaction of the π-radical of $(TPP)Fe^{III}$ with pyridine produces the (2-pyridiniumtetraphenylporphyrin)iron(III) bis-(pyridine) complex, as

well as an unstable 5-pyridiniumylisotetraphenylporphyrinato)iron(III) and its 5,10-dipyridiniumyltetraphenylporphodimethene)iron(III) complex.[837]

c. *Low-spin iron(III) porphyrin π-cation radicals*

Though complexes of the type $[(P)Fe(ImH)_2]^+$ could not be electrochemically oxidized to π-cation radicals, titration of the high-spin $[((p\text{-}OCH_3)_4TPP^{-\bullet})FeCl]ClO_4$ in CD_2Cl_2 with imidazole at −38 °C produced a transient complex whose pyrrole-H, *o*-H and *m*-H resonances were at −32.7, −236.3, and +24.8 ppm, respectively.[833] When the sample was warmed to room temperature, immediate autoreduction to the iron(III) porphyrin occurred. The temperature dependence of the pyrrole-H resonance of the transient radical was reasonably linear, and the deviation of the extrapolated shift at 1/T = 0 from the diamagnetic position was no greater than observed for low-spin $[(TPP)Fe(ImH)_2]^+$.[833] The alternating pattern of phenyl-H shifts suggests large π spin delocalization to the *meso* positions, indicative of a $3a_{2u}$ ground state for the radical; however, the sign of the shifts, δ_o negative, δ_m positive, is the reverse of that observed for the parent $[(TPP)FeCl]ClO_4$ complexes discussed above, which suggests a difference in the coupling of metal and porphyrin spins, possibly a switch from antiferromagnetic to ferromagnetic coupling, as in the case of the iron corroles discussed in Section IV.A.11.e. The high-spin radical complex appears to be the exception,[833] as discussed above. For the corresponding low-spin etioporphyrin complex, the ring α-CH_2 and −CH_3 resonances were at +50.4 and +133.1 ppm at −51 °C; the *meso*-H signal could not be detected.[833]

d. *Iron(III) π-cation radicals of oxophlorins*

Balch and coworkers oxidized the iron(III) oxophlorin (*meso*-hydroxyporphyrin) dimer complex of octaethylporphyrin, $[Fe^{III}(OEPO)]_2$ discussed in Section IV.A.6.c(vi) above, with Br_2 to yield two new, highly-oxidized complexes, $BrFe^{III}(OEPO\bullet)$ and $Br_2Fe^{III}(OEPOx)$ (where OEPO• and OEPOx are the octaethyloxophlorin dianion radical and the oxidized octaethyloxophlorin monoanion, respectively), in which the experimental data (especially ^1H NMR spectra) suggest that it is the ligand rather than the iron that undergoes oxidation. $BrFe^{III}(OEPO\bullet)$ has been characterized crystallographically, as well as by magnetic susceptibility (μ_{eff} = 4.9(2) μ_B at 23 °C), and NMR spectroscopy (*meso*-H resonances at extremely low shielding, +344 (1) and +232 (2) ppm, four CH_2 resonances at about +60 ppm, two near 0 ppm, and two at about −10 ppm at 24 °C), as shown in Figure 73, bottom.[106] The authors recognized these data to be indicative of a nominally 3^- anionic macrocycle which was actually a 2^- anion and hence

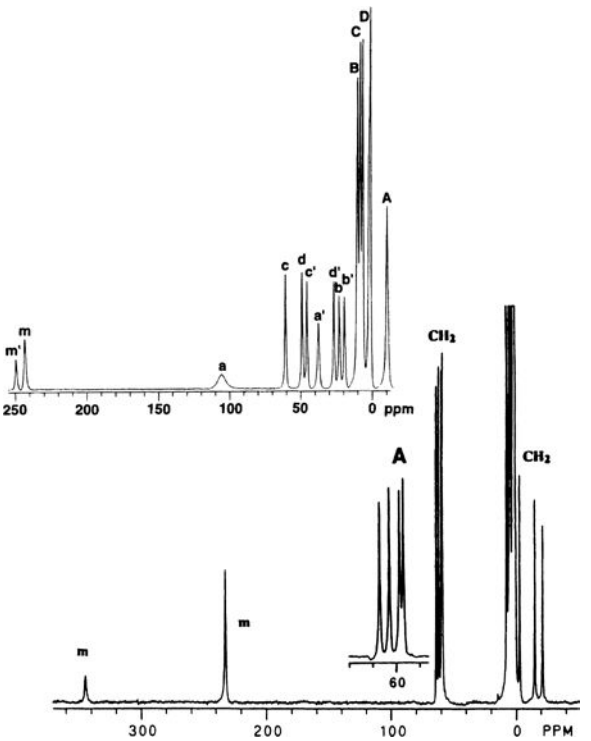

Figure 73. Top: 300 MHz ^{1}H NMR spectrum of $[((OEPO)Fe)_2]^+$ in $CDCl_3$ at 25 °C. Resonance assignments are made on the basis of the dimeric structure. Methylene resonances are identified by lower-case letters a-d′ while methyl resonances have been denoted by capital letters A-D. Cross peaks in the M-COSY spectrum (not shown) connect resonances in ethyl groups as follows: b,b′,B; c,c′,C; d,d′,D. Reprinted from Balch, A. L.; Latos-Grażyński, L.; St. Claire, T. N. *Inorg. Chem.* **1995**, *34*, 1395–1401, with permission from the American Chemical Society. Bottom: 300 MHz ^{1}H NMR spectrum of $[(OEPO^{2-\bullet})Fe^{III}Br]$ in $CDCl_3$ at 24 °C. Inset A shows an expansion of the methylene resonances at about 60 ppm. Reprinted from Balch, A. L.; Latos-Grażyński, L.; Noll, B. C.; Szterenberg, L.; Zovinka, E. P. *J. Am. Chem. Soc.* **1993**, *115*, 11846–11854, with permission from the American Chemical Society.

an iron macrocycle π-radical with the electron mainly located on the oxygen atom, which was antiferromagnetically coupled to high-spin Fe^{III}, and they suggested the $3a_{2u}(\pi)$-type orbital of the macrocycle as the half-filled orbital, Figure 7. Thus, this is an antiferromagnetically-coupled S = 5/2 Fe^{III}, S = 1/2 $OEPO^{2-\bullet}$ complex.[106] These results were very helpful to the author and her coworkers in explaining the ^{1}H NMR spectrum of the chloroiron(III) corroles as antiferromagnetically-coupled S = 3/2 Fe^{III}, S = 1/2 $Corr^{2-\bullet}$ complexes, discussed later in Section IV.A.11.e.

The two-electron oxidized octaethyloxophlorin complex, $[(OEPOx^{1-})FeBr_2]$, has both NMR and EPR spectra indicative of high-spin iron(III), indicating that the macrocycle has no unpaired electrons. The EPR g-values are 5.9 and 2.0, with

superhyperfine coupling on the $g_{\|}$ feature due to the two axial bromide ions. The NMR spectrum has four equally intense $-CH_2$ resonances in the +60 and +30 ppm region, plus two broad *meso*-H resonances at +34 and +21 ppm (intensities 1:2, respectively), a pattern typical of 6-coordinate high-spin iron(III) porphyrins, Section IV.A.6.b. The magnetic moment is 5.8 ± 2 μ_B.[106] The infrared spectrum shows a ketonic function at 1734 cm^{-1}, which indicates that the macrocycle has been oxidized. The self-dimer of iron(III) octaethyloxophlorin, where each iron is coordinated to the oxo group of the other oxophlorin ring, undergoes one-electron oxidation with silver perchlorate to give an iron macrocycle π-radical in which the single unpaired electron is delocalized over the two macrocycles.[838,839] The *meso*-H resonances are found at +250 and +243 ppm (intensities 1:2, respectively), while broad CH_2 resonances due to the ethyl groups closest to the oxo group and thus to the iron(III) of the other macrocycle are found at +106 and +37 ppm and sharper CH_2 resonances are found at +62 to +20 ppm, as shown in Figure 73, top. Like the monomeric $OEPO^{-\bullet}$ radical discussed above, the very large positive shifts of the *meso*-H resonances are indicative of an a_{2u}-type radical which is antiferromagnetically coupled to the high-spin iron(III) centers. Consistent with this, the magnetic moment is 4.8 μ_B per metal.[838]

e. *Iron(III) corrole π-radicals*

As discussed earlier, the corrole macrocycle (Structure **6**) lacks one *meso*-C and one double bond, as compared to the porphyrin. It is thus a −3-charged macrocycle and as such may either stabilize higher oxidation states of first-row transition metals or be more readily oxidized to a metal macrocycle π-radical itself. Although the slightly smaller ring size might suggest stabilization of the higher oxidation state of the metal, the more common situation is that a π-radical of the metal corrole ring is stabilized, as pointed out in Section II.C.2 and Figure 7. For a time it was believed that the chloroiron complex of octaethylcorrole (OECorr or Et_8Corr), as well as the μ-oxo dimer of the same iron macrocycle, were examples of iron(IV) corrolate complexes.[840] However, the ^{1}H NMR spectra of the chloroiron complexes of octamethylcorrole (OMCorr or Me_8Corr) show methyl signals at +40, +31, +18 and +16.6 ppm and *meso*-H at +175 and +166 ppm (intensities 1:2, respectively),[158,841] which are more indicative of the pattern observed for the chloroiron(III) octaethyloxophlorin neutrally charged π-radical[106] discussed earlier in Section IV.A.11.d and shown in Figure 73. The chloroiron 7,13-dimethylhexaethylcorrole gives a methyl signal at +18 ppm and six $-CH_2$ resonances between +40 and −10 ppm and *meso*-H resonances at +187 and +174 ppm (intensities 1:2, respectively) at −60 °C.[158] The magnetic moment (Evans method)[376,377] is 3.0 μ_B, which indicates a formal spin state S = 1. Thus, it was concluded that the iron is

intermediate spin (S = 3/2), and the corrolate radical is antiferromagnetically coupled to the metal, $Fe^{III}Corr^{2-\bullet}$.[158] In contrast, Gross and coworkers have stated repeatedly, without convincing scientific reasoning, that the electron configuration is S = 1 $Fe^{IV}Corr^{3-}$.[842–846] Additional studies of the chloroiron corrolates has shown conclusively that these are all S = 3/2 $Fe^{III}Corr^{2-\bullet}$ systems.[1,114,847–851] The triphenylcorrolatoiron chloride complex was studied by Mössbauer as well as NMR spectroscopy, and more recently by X-ray absorption spectroscopy.[852] While Mössbauer spectroscopy was unable to clearly differentiate the two possible electron configurations,[114,851] NMR spectroscopy clearly shows that phenyl-H resonances of chloroiron triphenylcorrolates (*o*-H +23–25 ppm, *m*-H −2.5 to −3.5 ppm; *p*-H +17 to +19 ppm) mirror those of the *meso*-H in showing large π spin delocalization to the *meso* positions, which is consistent with a π-radical being present in these metal complexes.[114,847,848–850] Calculations have been extremely important in explaining the spin coupling.[114,851,852]

Unlike the chloroiron corrolates, the phenyliron corrolate complex is best formulated as S = 1 $Fe^{IV}Corr^{3-}$, but again with negative spin density at all nitrogens and *meso*-carbons of the macrocycle, yet with the net spin density on the corrolate ring being virtually zero; the phenyl carbanion carbon has relatively large negative spin density of −0.15 and the iron +2.05. On the basis of all of the results, it was concluded that in both the chloroiron and phenyliron complexes the corrolate ring is noninnocent, in the chloroiron complex to a much larger extent than in the phenyliron complex.[114,852]

When treated with imidazole, the chloroiron hexaethyldimethylcorrole complex, [(7,13-Me_2Et_6Corr)FeCl], produces a new set of small peaks due to an imidazole complex, presumably the mono-(imidazole) complex. Increasing the concentration of imidazole increases the intensity of these peaks and creates another new set of peaks, but it is not possible to fully form the bis-(imidazole) complex at ambient temperatures. Cooling the sample to −60 °C in the presence of more than two equivalents of imidazole causes the disappearance of all signals except those of the bis-imidazole complex, whose methyl and $-CH_2$ resonances are found at +44, +14, −5.7 and −10 ppm, and *meso*-H at −93 and −107 ppm (intensities 2:1, respectively).[158] The large negative shifts of the *meso*-H suggest that in this low-spin complex the metal and corrole radical electrons are ferromagnetically coupled. In frozen CD_2Cl_2 at 4.2 K the EPR spectrum of this complex is that of a typical rhombic low-spin iron(III) complex, with g-values of 2.58, 2.21 and 1.82, and no evidence of the corrole radical spin.[158] In agreement with this, the magnetic moment at −60 °C is 1.7 μ_B.[158] This suggests that the complex forms a dimer in which the corrole radicals are spin paired and thus EPR silent. Similar behavior was observed earlier for the one-electron oxidized form of vanadyl octaethylporphyrin.[123]

Cyanide complex formation of (7,13-dimethyl-2,3,8,12,17,18-hexaethylcorrolato)iron chloride, [(7,13-Me_2Et_6Corr)FeCl], in dimethylformamide, DMF-d_7, was studied by ^{1}H NMR spectroscopy.[853] It was found that a bis-cyanide complex forms initially, in which the electron configuration is that of a low-spin Fe^{III} corrolate(2–•) π-radical,[853] a neutrally-charged radical. This complex is not stable, and is readily reduced by an excess of cyanide in the solution. The reduction occurs at the corrole ring instead of on the iron center, to give the monocyanide complex of the low-spin Fe^{III} corrolate(3–), [(7,13-Me_2Et_6Corr)FeCN]$^-$.[853] Thus, this is a case where an axial ligand serves as a reducing agent of the macrocycle, and not of the metal.[854]

The bis-pyridine complex of the $Fe^{III}Corr^{3-}$ state is a typical low-spin Fe^{III} complex, which has also been studied by X-ray absorption spectroscopy.[854] Monopyridine complexes of the 1-electron-reduced Fe(III) corroles have also been studied.[840]

One-electron oxidation of the iron(III) corrole π-radicals is discussed in Section IV.A.13.

12. *Iron(IV) Porphyrins*

Three types of iron(IV) porphyrin complexes have been studied by ^{1}H, and in some cases, ^{2}H NMR spectroscopy. All of of these complexes have spin state S = 1: The low-spin d^4 complex [(TPP)Fe(OCH_3)$_2$] mentioned in Section IV.A.11.a,[832] the deep red, 5-coordinate ferryl, $(Fe^{IV}=O)^{2+}$ complexes[855] and the 6-coordinate adducts of these ferryl complexes, the (B)$(Fe^{IV}=O)^{2+}$ complexes,[855–857] and the iron(IV) phenyl complex.[157] The pattern of spin delocalization observed in each of these systems is unique, as summarized in Table 15, despite the similar magnetic

Table 15. Chemical shifts of representative high-valent iron porphyrin species.

		Chemical shift, ppm				
Compound	T, °C	Pyrr-H	*o*-CH_3	*m*-H	*p*-CH_3	Ref.
[(TMP)Fe(OCH_3)$_2$]	–78	–37.5	2.4	7.72	2.86	832
[(TMP)FeO]	–70	8.4	3.3	6.4, 6.0	2.6	855
[(TMP)FeO(NMeIm)]	–30	4.6	3.2, 1.6	7.4	2.7	855
[(TMP)Fe(Ph)(Br)]	–50	–51	4.2, 3.8	10.6, 10.7	3.2	157
[(TPP)Fe(m-$CH_3C_6H_5$)]ClO_4 [a]	–60	–72	13.4, 12.5	8.1, 7.8	9.5	157
[d_8-(TPP)Fe(O)(F)]•	–78	–1				361
[(TPP)Fe(O)(F)]•	–46	V.B.[b]	–45 (*o*-H)	47.7	–32.0 (p–H)	361
[(TMP)FeO]$^+$•	–70	–21	25, 28	62	10	893
[(TMP)FeO]$^+$•	–77	–27	24, 25	68	11.1	892
[(TMTMP)FeO]$^+$•	–80	145 (CH_3)	56 (*meso*-H)			894

[a]Phenyl resonances: *o*-H, not observed; *m*-H, –56 ppm; *p*-H, –91 ppm.
[b]Very broad.

moments. The ferryl and iron(IV) phenyl cases have direct application to active states in heme proteins.

a. *Six-coordinate, bis-methoxide iron(IV) porphyrins*

As discussed earlier (Section IV.A.11.a), Groves and coworkers[832] have reported the valence isomerization of the iron(III) porphyrin π-radical in the presence of methoxide:

$$\underset{Fe^{III}P^{-\bullet}}{[(TMP)Fe(OClO_3)_2]} + 2\ CH_3O^- \leftrightarrows \underset{Fe^{IV}P^{2-}}{[(TMP)Fe(OCH_3)_2]} + 2\ ClO_4^-. \quad (40)$$

This species is characterized by relatively large π contact shifts to the β-pyrrole positions (−37.5 ppm at −78 °C in CD_2Cl_2/5% methanol-d_4), and relatively small, if any, shifts at the *meso* positions,[832] thus implicating the 3e(π) orbitals in spin delocalization. Wolowiec and Latos-Grażyński have produced this species by reaction of dimethyldioxirane with deuterated dichloromethane/methanol (4:1).[858] The ferryl π-cation radical, $[(TMP^{-\bullet})Fe{=}O(CD_3OD)]^+$ was also produced in this medium by warming the sample from 203 to 233 K for 15 min.[858] This species is unstable in basic solution.

b. *Five- and six-coordinate ferryl, $(Fe{=}O)^{2+}$, porphyrin complexes*

Ferryl complexes have been implicated in the reaction mechanisms of peroxidases and cytochromes P450. For horseradish peroxidase, two intermediates are spectroscopically detectable.[859] Compound I, formed on addition of peroxide to the resting iron(III) form of the enzyme, is a green species that is formally two oxidation levels higher than the resting state, and is widely believed to consist of an $(Fe^{IV}{=}O)^{2+}$ unit complexed to a porphyrin π-anion radical to yield $[Fe^{IV}{=}O\ P^{-\bullet}]^+$. NMR investigations of such complexes are discussed in Section IV.A.13. Compound II, which is red, and is obtained upon one-electron reduction of Compound I, also possesses a $(Fe^{IV}{=}O)^{2+}$ unit, in this case complexed to a normal porphyrin dianion.

Model hemes containing the ferryl unit have been prepared and investigated by ^{1}H NMR spectroscopy at low temperatures by Balch and La Mar and coworkers.[332,855,857,860] The ferryl species have been produced by thermal decomposition (at −30 °C) of the μ-peroxo dimer of $(P)Fe^{III}$, formed from reaction of 2 $(P)Fe^{II}$ with molecular oxygen at −70 °C, Eqs. 41 and 42,[855] by base catalyzed cleavage of the μ-peroxo dimer at similar low temperatures:[855–857]

$$\underset{Fe^{III}\text{-}O_2{}^{2-}Fe^{III}}{(P)Fe\text{-}OO\text{-}Fe(P)} + 2\ B \leftrightarrows 2\ \underset{(B)(Fe^{IV}{=}O),}{(B)(P)Fe{=}O}, \quad (41)$$

where reaction (41) is the same as the second part of reaction (27b), or by base catalyzed cleavage of (P)Fe(OOCHR$_2$) complexes:[332]

$$(P)Fe(OOCHR_2) + B \leftrightarrows (B)(P)Fe^{IV}{=}O + \bullet OCHR_2 \downarrow (P)Fe^{III}OH + O{=}CR_2 + B. \qquad (42)$$

Both the 5- and 6-coordinate ferryl porphyrin complexes have very small observed shifts of all resonances, as summarized in Table 15. Nevertheless, the Curie plots for all resonances are strictly linear, and the observed shifts extrapolate to close to the diamagnetic positions for each type of proton.[855] Investigation of 6-coordinate (imidazole or pyridine) adducts of synthetic ferryl porphyrins and ferryl myoglobin led to detection of broad, weak axial imidazole (histidine) resonances at −11 and −16 ppm in ferryl myoglobin at 35 °C.[860] Analysis of the hyperfine shifts of the axial ligands are consistent with imidazole → Fe π donation similar to that seen in low-spin iron(III) complexes with two imidazolate or one imidazolate and one cyanide ligand,[490] although the contact shifts are much smaller in the iron(IV) complexes.[860] For axial pyridine complexes, the dominant π bonding leads to spin polarization effects by the d_π spin, which leads to contact shift patterns very similar to those reported for low-spin iron(III) porphyrin bis-(pyridine) complexes,[519] but much smaller than those reported for the iron(IV) complexes.[860] These results indicate that the coordinated ligand is located trans to a strongly π-donating oxo ligand, where there is significant spin delocalization from the d_{xz},d_{yz} orbitals to the π_x and π_y orbitals of oxygen by this π donation in both the model compounds and ferryl myoglobin.[860] The small observed shifts are entirely consistent with theoretical calculations,[861,862] which indicate substantial π interaction between iron and oxygen orbitals and effective localization of unpaired spin density within the $(Fe^{IV}{=}O)^{2+}$ unit, a significant amount of which may be localized on the oxygen, which is in line with the reactivity of this group.[863,864]

c. *Five-coordinate iron(IV) phenyl porphyrins*

Single-electron oxidation of phenyliron(III) tetraarylporphyrin complexes with bromine in chloroform at −60 °C produces deep red solutions whose ^{1}H and ^{2}H NMR spectra indicate that they are the corresponding iron(IV) complexes.[157] As summarized in Table 15, the pyrrole-H are found at −60 to −70 ppm, while porphyrin aryl chemical shifts are almost exclusively pseudocontact in nature. The iron phenyl resonances at ~ −300 ppm (*o*-H), −50 to −75 ppm (*m*-H), −43 ppm (*m*-CH_3), ~ −100 ppm (*p*-H) and +112 ppm (*p*-CH_3),[157] indicative of large π spin delocalization to the phenyl ring. However, the nonalternation in sign for the

meta-phenyl-H paramagnetic shift and nonreversal in sign on substitution of CH_3 at the *meta* position suggests some degree of σ spin delocalization to the phenyl ring. In comparison to the phenyl iron(III) porphyrin complexes discussed in Section IV.A.8.f, except for the *meta*-phenyl position, the chemical shift pattern is similar for the two oxidation states, except that the shifts of the Fe(IV) phenyl complexes (Table 15) are larger than those for the iron(III) phenyl complexes (Table 15). This may not be surprising when one considers the electron configurations of the two: For the low-spin aryl iron(III) porphyrins, the electron configuration is $(d_{xy})^2(d_{xz},d_{yz})^3$, with one π-symmetry unpaired electron, while for the low-spin aryl iron(IV) porphyrins, the electron configuration is $(d_{xy})^2(d_{xz},d_{yz})^2$, with two π-symmetry unpaired electrons. However, it should be noted that because of symmetry considerations, only one of the d_π electrons can be delocalized to the aryl group. The aryl iron(IV) porphyrins are thermally unstable, and upon warming convert cleanly to N-phenylporphyrin complexes of iron(II) by reductive elimination.[157] Phenyl migration, which produces a green pigment, is known to occur under aerobic conditions in protein systems such as cytochrome P450, catalase, hemoglobin or myoglobin. The phenyl heme is produced by attack of aryl hydrazines in the presence of oxygen,[575,865] and probably goes through a phenyl iron(IV) intermediate. These N-arylporphyrin complexes of iron are readily demetalated, which leads to destruction of function of the heme protein.

d. *Comparison of iron(IV) porphyrins and iron(III) porphyrin π-radicals*

Balch and Renner[157] concluded that axial ligands play a major role in determining the electronic distribution within highly oxidized iron porphyrins. It has been found that an oxo ligand, a phenyl ligand or two methoxy ligands favor the iron(IV) porphyrin dianion structure, while two halide ions, imidazole or perchlorate ligands produce the iron(III) porphyrin π-radical monoanion electronic structure. The ability of the iron π unpaired electron to interact with the axial ligand(s) appears to make a major contribution to these differences.

13. *Iron(IV) Porphyrin π-Radicals*

In Section IV.A.12.b it was mentioned that the green Compound I species observed in peroxidase enzymes, which contains an iron porphyrin that is two oxidation levels above $(P)Fe^{III}$, consists of a ferryl porphyrin radical, $[(P^{-\bullet})(Fe^{IV}{=}O)^{2+}]^+$. The ferryl unit, complexed to a porphyrin π-anion radical, is a transient and very reactive species (either in the enzymes or in model hemes) and can readily insert the oxygen atom into many C–H bonds.[863,864] Horseradish peroxidase Compound I, in

which the heme iron is bound to a histidine imidazole ligand, was first assigned as an a_{2u} radical, while catalase Compound I, in which the heme iron is also bound to a histidine imidazole ligand, was believed to be an a_{1u} radical.[866,867] It was later shown that all of these heme Compound I states, including those of the cytochromes P450,[864] have a_{1u} radicals which are weakly antiferromagnetically coupled to S = 1 Fe^{IV}=O and give EPR signals near g_{eff} = 2,[868–876] although the breadth of the signal and its symmetrical shape suggests a mixture of weakly antiferromagnetic and weakly ferromagnetic coupling.[872] Compounds I of cytochromes P450 are much less stable than those of peroxidases and catalases, and in many cases cannot even be trapped by freeze-quench EPR experiments, although their decomposition products to Fe^{IV}=O protein radicals have been trapped in a few cases.[877–879] They have also been trapped in stopped-flow experiments. Chloroperoxidase, in which the heme is bound to a cysteine thiolate ligand, has a Compound I with a radical that is fairly strongly antiferromagnetically coupled to S = 1 Fe^{IV}=O, which thus gives S_{eff} = 1/2 and g-values of 1.64, 1.73 and 2.00.[880]

In contrast, different EPR spectra have been reported for the Compound I of *Micrococcus lysodeikticus* catalase[881] and that of ascorbate peroxidase,[882] which suggest *ferromagnetic* coupling of the S = 1/2 radical and the Fe^{IV}=O to yield a S_{eff} = 3/2 state. The Compound I form of these enzymes also show a S_{eff} = 3/2 state with EPR g-values of ~4 and ~2, although there are two subtypes, one which has a rhombic signal (g_{eff} = 4.5, 3.5, 1.98), and the other axial ($g_{\perp eff}$ ~3.4–3.3, $g_{\parallel eff}$ ~2). The catalase-peroxidases (KatGs) of a number of bacteria,[883–885] most importantly *Mycobacterium tuberculosis*,[886–888] show both catalase and peroxidase activity, and this enzyme activates the currently best drug against this disease, the pro-drug isoniazid. In fact, these examples are part of a continuum of spectra observed for Compounds I, which range from a g = 2 signal with extremely broad wings, indicative of antiferromagnetic coupling of radical and Fe^{IV} electrons, to rhombic and axial signals indicative of weak ferromagnetic coupling of these electrons; a good example of the range of signals observed thus far is shown in Figure 26 of the chapter on structure-function relationships in heme peroxidises in this series,[889] which includes the Compounds I of HRP, isoforms I and III of turnip peroxidases,[890] a KatG mutant,[888] ascorbate peroxidase,[882] and a model heme complex discussed below. It should be noted that most peroxidases, and particularly the KatGs, have more than the usual number of tyrosines and tryptophans in the protein sequence, and some of these that are near the heme center provide sites from which the ferryl porphyrin π-cation radical can capture an electron (more often Trp),[885,888,890] which gives a ferryl porphyrin-protein radical state, $[PFe^{III}=O](Trp^{\bullet})^{+}$ for example, and protein radical EPR signals may be observed, or they may show variable coupling to the S = 1, PFe^{IV}=O center, depending on the distance of the

protein radical from the PFe^{IV}=O center. This state may be the actual one that allows substrate oxidation, if there is no substrate binding site near the heme.[885,888–891]

No less that four research groups have investigated the NMR spectra of model complexes of this reactive species,[332,360,892–902] and Nanthakumar and Goff[897] have stabilized an iron(IV) porphyrin radical in the absence of the oxo group by using fluoro substituents on the TPP phenyl rings. Weiss, Gold and coworkers[897–901] have also generated oxoferrylporphyrin radicals by *m*-chloroperbenzoic acid oxidation of the chloro- and trifluoromethanesulfonato complexes of [(TMP)Fe^{III}] and the trifluoromethanesulfonato complex of tetra-(2,6-dichlorophenyl) porphinatoiron(III), [$((2,6\text{-}Cl_2)_4$TPP)Fe^{III}]. The ferryl porphyrin π-cation radical, [$(TMP^{-\bullet})(Fe{=}O)(CD_3OD)]^+$ can also be produced by reaction of dimethyldioxirane with [(TMP)$FeOClO_3$] in deuterated methylene chloride/methanol (4:1) at 203 K followed by warming the sample to 233 K for 15 min.[858] This species was found to be unstable in basic solution. The EPR and Mössbauer spectra of all of these species were found to be those of $[Fe^{IV}{=}O\ Por^{-\bullet}]^+$ in which the porphyrin π-radical was an $a_{2u}(\pi)$ type, not $a_{1u}(\pi)$, and fairly strongly ferromagnetically coupled to the $S = 1$ Fe=O center, rather than antiferromagnetically coupled, as found for the HRP-containing heme enzyme systems.[874–880] Only in the case of a crowded porphyrin with β-tetramethyl,tetraaryl substitution has the $a_{1u}(\pi)$ radical state, with weak ferromagnetic coupling, been stabilized.[895,900] Later, these workers found that the tetra-mesityl- and -2,6-dichlorophenylporpholactones also produced the $a_{1u}(\pi)$ radical state, but again weakly ferromagnetically coupled.[902] In fact, no model complexes have been created which reproduce the HRP- or CPO-type EPR and Mössbauer spectra that are mainly weakly or strongly antiferromagnetically coupled.[874–880]

The $a_{2u}(\pi)$ strongly ferromagnetically-coupled radical complexes have rhombic EPR spectra at 10 K (g-values of 4.47, 3.50, 1.98 for the TMP case, 4.26, 3.68 and 1.990 for the 2,6-dichlorophenylporphyrin case), and Mössbauer spectra indicative of stronger coupling between the Fe^{IV}=O and porphyrin π-radical electrons ($J_0 \sim$ 38–43 cm^{-1}), while the porpholactones, with their $a_{1u}(\pi)$ radical states, have "axial" EPR spectra at 10 K, which were nevertheless analyzed as being rhombic (g-values of 3.48, 3.85, 1.99 for the tetramesitylporpholactone and 3.16, 3.64, 1.99 for the tetra-2,6-dichlorophenylporpholactone), and weaker ferromagnetic coupling between the Fe^{IV}=O and porphyrin π-anion radical electrons $[Fe^{IV}{=}O\ P^{-\bullet}]^+$ ($J_0 \sim 11$–17 cm^{-1}).[902] Fujii and coworkers obtained similar results for these two radical states.[895] Thus, the differences in the coupling of the ferromagnetically-coupled radicals are subtle, although they produce quite different EPR spectra, as shown in Figure 74.

In all but one case,[896,903] "hindered" or "protected" porphyrins, such as tetramesitylporphyrin (TMP),[332,892,893] 2, 7,12,17-tetramethyl -3, 8,13,18- tetramesitylporphyrin (TMTMP),[894,895,900] or tetra-(2,6-difluorophenyl)porphyrin ($(2,6\text{-}F_2)_4$TPP) or (F_8TPP))[903] were used for these model studies. In the case of the TMP

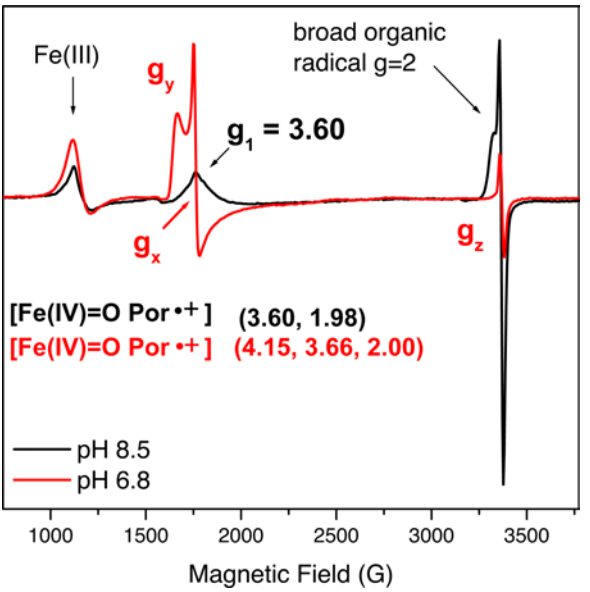

Figure 74. EPR spectrum of the [Fe^{IV}=O $Por^{-\bullet}$] Compound I species formed upon reaction of nitrophorin 2 with 5-fold excess peroxyacetic acid. The rhombic signal with effective g-values of (4.15, 3.66, 2.0) consistent with a strong ferromagnetic coupling is observed at lower pH (6.0 here), while a change to weak ferromagnetic coupling is observed at higher pH values (8.5 here). The Compound I spectrum at pH 6.0 is very similar to that observed for the [Fe^{IV}=O $Por^{-\bullet}$] intermediate formed by ascorbate peroxidase and the ferryl (TMTMP) model complex of Ayougou *et al.*[900] and Fujii *et al.*[895] (see Figure 27 in Ref. 883). The radical signal at g = 2 that contributes to the Compound I spectrum of NP2 obtained at pH 8.5 is consistent with that of a protein-based radical formed as a subsequent intermediate,[905] similar to the cases observed in catalase-peroxidases.[883–888]

complexes, it was found that the porphyrin π-radical is of the a_{2u} type, since large π spin density is detected at the *meso*-phenyl-H and $-CH_3$ positions, as well as a smaller amount of π spin delocalization at the β-pyrrole positions,[128,893] as summarized in Table 15. However, the TMTMP complex has an unpaired electron in the a_{1u} orbital, since the very large pyrrole-CH_3 paramagnetic shift indicates large spin delocalization to the pyrrole positions.[128,895,900] The pyrrole-CH_3 resonance at 132 ppm and the *meso*-H resonance at +54 ppm are shifted to +111 ppm and −1 ppm, respectively, upon binding imidazole.[895] In comparison, pyrrole-CH_3 and *meso*-H shifts for the ferryl complex of protohemin are 4 and 16 ppm, respectively.[857]

Use of *meso*-tetra-2,6-substituted phenyl porphyrins having chloro or nitro substituents produces iron(IV) porphyrin radical states that have more a_{1u} radical character (mixed into the largely a_{2u}-type radical) than is observed for other tetraphenyl-type porphyrins: Using tetrakis-5,10,15,20-(2,6-dichlorophenyl)porphyrin, 5-(2-chloro-6-nitrophenyl), 10,15,20-tris(2,6-dichlorophenyl)porphyrin,

5-(2,6-dinitrophenyl), 10,15,20-tris(2,6-dichlorophenyl)porphyrin as compared to TMP and 2-iodo TMP, pyrrole-H shifts of −61; −54 to −56; −51 to −55; −28; and −24 to −27 ppm, respectively, are observed at −65 °C.[900] In contrast, the fully-a_{1u} radical state of the porpholactones show pyrrole-H shifts of −5 to −20 ppm for the tetramesityl complex and −40 to −60 for the 2,6-dichlorophenyl complex, with the phenyl *meta*-H resonances mirroring this difference in reverse (+20 to +35 ppm for the tetramesityl complex and +10 to +15 ppm for the 2,6-dichlorophenyl complex).[902] Despite the differences in chemical shifts for these two complexes, the low temperature EPR spectra show both of them to be $a_{1u}(\pi)$ radicals.

Goff and coworkers prepared a 6-coordinate, oxo, fluoro complex, [(TPP)Fe=O(F)], by addition of *m*-chloroperbenzoic acid to $[(TPP)FeF_2]^{-\bullet}$ in dichloromethane, or by reaction of the μ-oxo dimer diradical, $[((TPP^{-\bullet})Fe)_2O(ClO_4)_2]$, with excess $Bu_4NF\bullet 3H_2O$ in CD_2Cl_2. This complex has very small pyrrole-D shifts and large, alternating signs for the phenyl-H,[361] which indicate a radical of a_{2u} type. This species has EPR signals at g = 4.2, 3.9 and 3.5 at 5 K, but not higher, which suggests an overall S = 3/2 species composed of S = 1 iron(IV) and the S = 1/2 porphyrin radical.[361] This is presumably the valence isomer of the iron(V) porphyrin species obtained from the fluorinated TPP derivative,[903] discussed in Section IV.A.14.

Nitrophorin 2 also reacts with H_2O_2[904] or peroxyacetic acid to give EPR spectra similar to these, with the rhombic signal seen at pH = 5.5–6.8 and the axial signal at pH 7.7–8.6,[905] as shown in Figure 74, g-values of 4.03, 3.80, and 2.00, and 3.8, ~2.0, respectively. The rhombic spectrum is believed to arise from stabilization of the $a_{2u}(\pi)$ radical state by strong ruffling of the heme, which is relaxed by loss of H-bonds at high pH, and becomes an $a_{1u}(\pi)$ radical state.[905] In fact, it may be that the difference between the EPR spectra of the model heme systems is that the *meso*-substituted models encourage ruffling, which stabilizes the $a_{2u}(\pi)$ radical state, while the β-pyrrole-substituted models prevent ruffling, which stabilizes the $a_{1u}(\pi)$ radical state. As in the KatGs, the ferryl porphyrin π-radical electron can be transferred to protein side chains, in this case only to tyrosines.[905]

Nanthakumar and Goff's nonferryl iron(IV) porphyrin radical or iron(V) complex, probably $[((2,6\text{-}F_2)_4TPP)FeCl](ClO_4)_2$,[896,903] which is produced by two-electron electrochemical oxidation of $[((2,6\text{-}F_2)_4TPP)FeCl]$ in dichloromethane, has reversed phenyl-H shifts (+30.5 and −2.0 ppm for *m*-H and *p*-H, respectively) from those of the one-electron reduced iron(III) porphyrin radical (−3.5, −4.5 (*m*-H) and +16.0 ppm (*p*-H)) discussed in Section IV.A.11, and the pyrrole-H signal has moved from +85.5 ppm to −5 ppm upon oxidation from the iron(III) to the iron(IV) porphyrin radical. Although this pyrrole-H shift is similar to those observed for ferryl porphyrin radicals, Table 15, solution characterization of the two-electron oxidized product of $[((2,6\text{-}F_2)_4TPP)FeCl]$ provides no evidence of an oxo ligand.[896]

The chloroiron (III) corrole π-radicals discussed in Section IV.A.11.e[840] can be oxidized by one electron to create an antiferromagnetically coupled iron(IV) corrole π-cation radical.[906] The magnetic moment of $[(Et_8Corr)Fe(Ph)]^+$ is 1.78 μ_B at 293 K, and the EPR spectra of this phenyl complex, as well as the chloro complex, are indicative of an overall S = 1/2 system (g = 2.17, 2.04, 2.01 and 2.12, 2.07, 2.02, respectivly).[906] These species have not been characterized by NMR spectroscopy.

14. *Iron(V) Porphyrins*

The single report of a possible Fe(V) porphyrin is that of Nanthakumar and Goff,[896,903] in which they used highly electronegative fluorine substituents on the phenyl rings and the strong oxidizing agent, m-chloroperbenzoic acid, to produce a red complex with Soret band at 430 nm and visible band at 550 nm, similar to those of $(P)Fe^{IV}$=O complexes,[897] but with different NMR and EPR spectra. The pyrrole-D signal was observed at +1.3 ppm at 210 K. The EPR spectrum at moderate temperatures (g = 4.38, 3.11 and 2.70, plus a g = 2 radical signal from decomposition products) is believed to be indicative of a S = 3/2 species,[903] rather than a S = 1 iron(IV)/S = 1/2 porphyrin radical species, which is expected to be EPR silent above ~5 K.[903] However, a recent study of related halogenated high-valent iron porphyrins using tetrakis-5,10,15,20-(2,6-dichlorophenyl)porphyrin, 5-(2-chloro-6-nitrophenyl), 10,15,20-tris(2,6-dichlorophenyl)porphyrin, 5-(2,6-dinitrophenyl), 10,15,20-tris(2,6-dichlorophenyl)porphyrin and others, mentioned in the previous section, yield somewhat different rhombic EPR spectra at 10 K (g-values of 4.26, 3.68 and 1.99), pyrrole-H shifts of −61 to −51 ppm at −65 °C, and Mössbauer and resonance Raman spectra indicative of iron(IV) π-cation radicals.[900] The researchers comment that the Mössbauer data are inconsistent with formulation of these complexes as high-spin iron(V).[900] However, the large difference in the chemical shift of the pyrrole-H reported by Nanthakumar and Goff[896,903] and by Jayaraj *et al.*[900] raises the question as to whether the same species was detected in the two studies. Thus, perhaps the possibility of the existence of an Fe(V) porphyrin should be retained — but with a question mark.

B. Ruthenium and Osmium Porphyrins

Unlike the extensive chemistry and NMR spectroscopy of Fe^{I}–Fe^{IV}=O π-cation radicals discussed in Section IV, the reported NMR studies of porphyrin complexes of the heavier elements of the iron group involve mainly diamagnetic compounds. Fairly recent examples include the oligomeric ruthenium(II) porphyrin complexes of mono-(2- or 4-pyridyl)-tri-tolyl- or tri-(4-*t*-butylphenyl)porphyrin,[907] a number of complexes formed by scission of the Ru–Ru bond of

dimeric Ru^{II} complexes[908] or reductive cleavage of that bond,[909] complexes of (TPP)Ru^{III} with NO and anions,[910] osmium(II) porphyrin ylides,[911] oligomeric osmium(II) porphyrin complexes of mono-(3- or 4-pyridyl)-triphenylporphyrin[912] and dioxoruthenium(VI) porphyrins.[913]

Dimeric metal–metal bonded ruthenium(II) complexes of OEP, TPP and TTP, prepared by vacuum pyrolysis of the corresponding [(P)Ru$(Py)_2$] monomeric complexes, have been studied by NMR spectroscopy.[914] These dimeric ruthenium(II) porphyrins are paramagnetic and have a formal Ru=Ru double bond, with an overall d-electron configuration $\sigma^2\pi^4\delta^2\delta^{*2}\pi^{*2}$. The NMR spectra of the TPP and OEP complexes at 30 °C are shown in Figure 75, where it can be seen that the unusually high resolution (for a paramagnetic complex) of the resonances, including all spin–spin splittings, is helpful in assigning them. The negative chemical shift of the pyrrole-H resonance of the TPP complex and the positive chemical shifts of the $-CH_2$ resonances of the OEP complex, as well as the near-diamagnetic shift of the *meso*-H of the latter complex,[914] are all diagnostic of unpaired electrons in the d_π orbitals of the two metals, which is totally consistent with the d-electron configuration. The Os_2 and RuOs analogs also have this electron configuration.[915] However, the d^4–d^6 dimeric mixed metal MoRu,[916,917] WOs,[916] WRu,[918] and

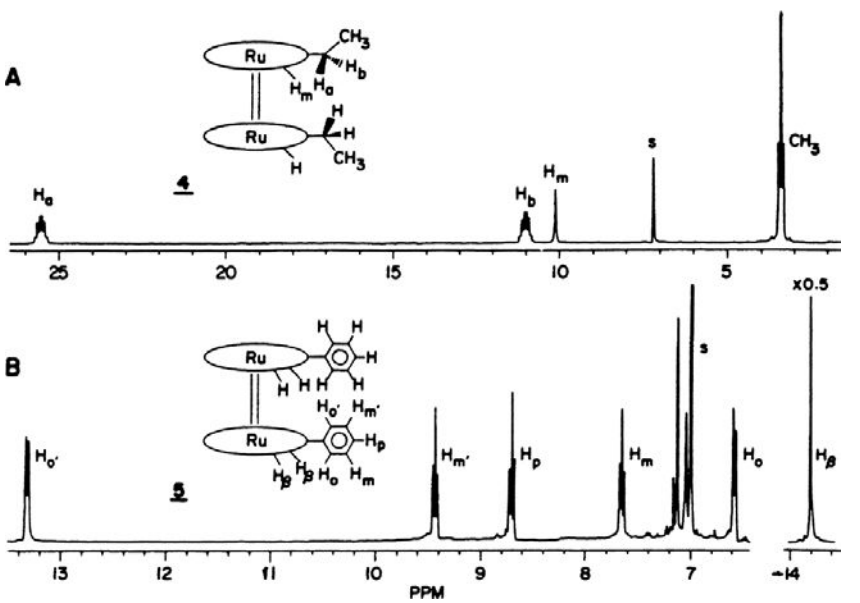

Figure 75. 100 MHz ^1H NMR spectra of $[(P)Ru^{II})]_2$. A: $[(OEP)Ru]_2$ in oxygen-free benzene-d_6. B: $[(TPP)Ru]_2$ in oxygen-free toluene-d_8. Reprinted from Collman, J. P.; Barnes, C. E.; Collins, T. J.; Brothers, P. J. *J. Am. Chem. Soc.* **1981**, *103*, 7030–7032, with permission from the American Chemical Society.

MoOs[918] complexes have the δ^* and π^* orbitals reversed in energy, as is evidenced by the fact that they are paramagnetic.

C. Cobalt Porphyrins

Cobalt porphyrins do not occur naturally, but the related vitamin B_{12} corrins (also called cobalamins) are important in a number of carbon skeleton rearrangements, methyl group transfers and reduction of amino and hydroxyl groups to the hydrocarbon level.[919] In these reactions, cobalt(I), cobalt(II) and cobalt(III) were implicated in the various enzymatic transition states. X-ray crystallographic structure determinations of methionine synthase[920] and methylmalonyl CoA mutase[921] were very informative concerning the binding of the cobalamin to its protein and the possible mechanism of action of the enzyme. In addition, cobalt(II)-reconstituted hemoglobins and myoglobins were extensively investigated in an attempt to elucidate further information concerning quaternary structural interconversions,[922] geometry of the metal–O–O bond,[923–926] and the rate of rotation of bound O_2 by EPR lineshape analysis techniques.[927]

Just one report of NMR investigations of cobalt(II)-reconstituted hemoglobins or myoglobins has appeared, and that one shows an extremely broad peak at +26 or +29 ppm, depending on whether the cobalt(II) is in the α or the β chains of the hemoglobin molecule.[928] These resonances are believed to be due to the *meso*-H of the protoporphyrin IX-cobalt(II). Several broad peaks are also observed in the −5 to −10 ppm region.[928] The breadth of these signals is probably a result of the decreased g-anisotropy of 5-coordinate cobalt(II) porphyrins (as compared to the 4-coordinate complexes), which decreases the paramagnetic shifts of these species. This point will be discussed further in the next section.

1. *Low-Spin Cobalt(II) Porphyrins*

a. *Observed shifts and the pseudocontact interaction*

Table 16 lists the typical paramagnetic shifts for several natural and synthetic cobalt(II) porphyrins. As pointed out previously,[2,4,233] all shifts are to lower shielding. Because the electronic ground state of low-spin cobalt(II) is $^2A_1$ ($d_{z^2}{}^1$), and because the d_{z^2} orbital interacts only very weakly with the σ system of the porphyrin ligand, the majority of the paramagnetic shift at all positions is a result of the pseudocontact interaction. The pseudocontact shifts can be caluclated by use of the factoring method outlined in Section III.B.2 indicates that the majority of the paramagnetic shift is pseudocontact, with small contact shifts at the *meso* (+4 ppm) and pyrrole (−2.4, H; −1.6 ppm, CH_2, at 35 °C) positions.[2,4,233]

Table 16. Chemical shifts of cobalt(II) porphyrins.[a,b]

Porphyrin	Proton position	δ_{iso}, ppm	δ_{dip},[c] ppm	δ_{con}, ppm	Ref.
TTP[d]	Pyrrole-H	7.0[e]	9.4	–2.4	233
	o-H (CH_3)	5.0[e] (2.68,1.29, 1.97, –0.35)[f]	5.0	~0	
	m-H	2.15[e]	2.3	~0	
	p-H (CH_3)	2.03[e] (1.45)[g]	2.05 (1.52)	~0 (~0)	
OEP[d,h]	Pyrrole-CH_2 (CH_3)	4.73 (4.05)	5.2	~ –1.6	233
	meso-H	19.0	15.0	4.0	
EP	Pyrrole-CH_3	4.73			931
	Pyrrole-CH_2 (CH_3)	4.66 (3.92)			
	meso-H	17.57			
MPDME	Pyrrole-CH_3	4.35			931
	Pyrrole-CH_2 (CH_3)	4.4 (3.67)			
	meso-H	16.62			

[a]Adapted from La Mar, G. N.; Walker, F. A. In *The Porphyrins*, Dolphin, D., Ed.; Academic Press: New York, 1979; Vol. IVB, pp. 57–161, with correction of sign for the currently-accepted sign convention.
[b]Referenced against the diamagnetic Ni(II) complex unless otherwise specified.
[c]Calculated by the factoring method of Section III.B.2.
[d]Temperature = 35 °C, solvent = $CDCl_3$.
[e]Shifts taken from [(TPP)Co].
[f]Shifts taken from [(*o*-TTP)Co].
[g]Shifts taken from [(*p*-TTP)Co].
[h]Reference against free ligand.
[i]Temperature = 26 °C, solvent = $CDCl_3$.

Pseudocontact shifts calculated from Eq. 9 by use of g-values, obtained from low-temperature EPR measurements of polycrystalline samples of cobalt(II) porphyrins[238] are in approximate agreement with those calculated by the factoring method (Eq. 23) at room temperature, but deviate at low temperatures because of solvation of the axial positions of the cobalt(II) porphyrin at lower temperatures. Furthermore, the EPR spectra of cobalt(II) porphyrins in solution are very sensitive to solvation of the axial positions,[929] and do not allow calculation of the pseudocontact shifts observed at room temperature.

The g-values of a number of cobalt(II) porphyrins have been reported previously[238,929] and discussed with respect to their effect on the g-anisotropy that gives rise to the pseudocontact interaction ($g_\parallel^2 - g_\perp^2$, Eq. 9).[2,4] Four-coordinate, polycrystalline cobalt(II) porphyrins have very large differences between $g_\perp$ and $g_\parallel$, with values of 3.25–3.29 and 1.83–1.79, respectively, such that $g_\parallel^2 - g_\perp^2$ is of the order of –7.3 to –7.6, while in toluene solution the g-values are 2.85–2.93 and 1.97–1.95 and this anisotropy decreases to –4.1 to –4.8; in $CHCl_3/CH_2Cl_2$ the g-values are 2.38 and 1.97 and it decreases to –1.78. In the presence of a Lewis base, the g-values

more closely approach 2, with $g_\perp = 2.32$ and $g_\parallel = 2.03$ for the NMeIm complex in toluene, and the value of $g_\parallel^2 - g_\perp^2$ shrinks to −1.2 or even smaller.[2,4] Thus, the observed paramagnetic shifts of [(TPP)Co^{II}] of +7 ppm (pyrrole-H) and [(OEP)Co^{II}] of +19 ppm (*meso*-H) at 35 °C in $CDCl_3$ (at which temperature there is very little solvation of the axial positions of the cobalt(II)) are expected to shrink to 1.2 and 2.5 ppm, respectively, if the mono-(NMeIm) complex is formed, or even more, if the g-anisotropy calculated by the factoring method of Section III.B.2 (−8.2) is used. These very small paramagnetic shifts are not very useful for NMR investigations of cobalt(II) porphyrins or cobalt-substituted heme proteins, and only in one case have such resonances have been reported for a protein.[928] Furthermore, since linewidths are dominated by the pseudocontact interaction, which in this case is more complex than Eq. 19 because of the magnetic anisotropy of low-spin cobalt(II), the proton resonances were postulated to become broader as the magnetic anisotropy becomes smaller.[2,4] However, according to Sternlicht's expression for the nuclear relaxation rate for complexes possessing magnetic anisotropy[105] (Section II.B.2.c, Eq. 21), resonances of protons that are in the plane of the porphyrin should be sharpened according to the ratio of $[\langle g \rangle^2 + g_\perp^2]$, or to about 5/9 their value for 5- as compared to 4-coordinate low-spin cobalt(II) porphyrins. No good test of this relationship has been reported.

The complete dominance of the pseudocontact interaction suggested early that cobalt(II) porphyrins might be used as "shift reagents," to determine stereochemistry of molecules with which they associate.[930,931] This has been reported by Uemori and Kuyno for some "jellyfish" type porphyrins having bridging alkyl groups across two opposite *meso* positions of a "picket fence"-type 4-coordinate cobalt(II) porphyrin.[932] The phenyl-H shifts vary linearly with their geometric factors, which suggests that their shifts are mainly pseudocontact in nature. Ironically, although the use of cobalt(II) porphyrins as shift reagents has not occurred for axial ligand complexes (largely because of the reduced magnetic anisotropy that occurs when ligands are bound to the axial positions of cobalt(II)), certain diamagnetic cobalt(III) porphyrins have been proposed as "chiral shift reagents," based on ring-current shifts of coordinated amine ligands.[933]

b. *Oxidation of cobalt(II) porphyrins to produce π-radical dimers*

Cobalt(II) porphyrins can undergo one-electron oxidation from either the cobalt d or porphyrin π orbitals depending on the choice of porphyrin and reaction media. Oxidation of (OEP)Co^{II} in the presence of ligands such as H_2O and CO produces diamagnetic 5- and 6-coordinate complexes of (OEP)Co^{III},[934–939] while in the absence of additional ligands to coordinate the Co^{III}, the oxidation occurs from a porphyrin π molecular orbital to produce a π-radical complex $[(OEP^{-\bullet})Co^{II}]^+$.[934–937]

The paramagnetic monomer (S = 1) interconverts to a diamagnetic dimer, $[(OEP)Co^{II}]_2^{2+}$. The bonding in the dimer is believed to involve both porphyrin π–π bonding, probably similar to that in the vanadyl porphyrin π-cation radical dimer,[123] and in addition, weak Co^{II}–Co^{II} ($3d_{z^2}$–$3d_{z^2}$) bonding, weaker than that observed in $[(OEP)Rh^{II}]_2^{2+}$ discussed in Section IV.D.

c. *Low-spin cobalt(II) oxaporphyrins and porphodimethenes*

As mentioned earlier, in the coupled oxidation of $[(OEP)Fe^{II}(Py)_2]$, the first product is $[(OEPO)Fe^{II}(Py)_2]$, where OEPO is the monoanion of octaethyl-5-hydroxoporphyrin, also called octaethyloxophlorin, Structure **8**. Further oxidation of this complex produces a mixture of the iron(II) complex of octaethyl-5-oxaporphyrin, Structure **9**, $[(OEOP)Fe^{II}(Py)_2]$, also known as octaethylverdoheme, and $[(OEB)Fe^{III}(Py)_2]$, where OEB is the trianion of octaethylbilindione, the hydrolysis product of verdoheme. Since the Co^{II} complexes of both of the final products are more stable than the Fe^{II} complexes, the cobalt(II) oxoporphyrin complex, $[(OEOP)Co^{II}]PF_6$ was investigated by ^1H NMR and shown to have chemical shifts and linewidths consistent with a low-spin cobalt(II) complex.[939] The magnetic moment of the complex is 1.9 μ_B, in solution at 25 °C,[376,377] which confirms the S = 1/2 state. Two *meso*-H resonances are observed at +30 and +21 ppm (intensities 2:1, respectively), three $-CH_2$ resonances at +8, +4 and −2 ppm (intensities 4:4:8, respectively), and two $-CH_3$ resonances at +5 and +2 ppm (intensities 12:12, respectively).[940]

The other product of coupled oxidation of $[(OEP)Fe^{II}(Py)_2]$, mentioned above, is octaethylbilindione, H_3OEB, from which the iron has been lost. (H_3OEB is the diketone formed when the formyl carbon of Structure 11 is removed by oxidation.) Balch and coworkers have studied the effect that complexation of H_3OEB by metal ions has on the redox properties of the resulting complexes. While the iron complex is important in the coupled oxidation process, which occurs upon treatment of this complex with dioxygen in pyridine solution in the presence of a reducing agent,[220,941] it is unstable with respect to loss of iron.[942] However, the cobalt complex, Co(OEB), is stable to both metal ion dissociation and toward dioxygen.[943] The Co(OEB) complex consists of a cobalt ion with approximately planar coordination that is surrounded by four pyrrole nitrogen atoms of the helical ligand. The ^1H NMR spectrum has marked temperature dependent changes.[940] These changes are most prominent in the *meso*-H resonances and indicate that there is thermal population of a low-lying paramagnetic state. This behavior may result from low-spin/high-spin equilibrium for Co^{III}, or from thermal equilibrium between $[(OEB^{3-})Co^{III}]$ (S = 0) and $[(OEB^{2-\bullet})Co^{II})]$, the oxidized ligand radical dianion, or from temperature dependent coupling of ligand and metal spins in $[(OEB^{\bullet})Co^{II})]$.[940] Spectral data indicate that ((OEB)Co] reversibly coordinates pyridine ligands.

The four-membered electron transfer series involving $[Co(OEB)]^n$ with n = +1, 0, −1, −2 has been studied electrochemically and by oxidation with I_2.[942] All complexes are monomeric, and all but Co(OEB) appear to contain Co^{II}. The ^1H NMR spectrum of the 1-electron-oxidized species, $[Co^{II}(OEBOx)]I_3$, shows eight methylene resonances with chemical shifts that range from +16 to −11 ppm, four methyl resonances at 5.55, 3.73, 0.49 and 0.20 ppm, and two *meso*-H resonances, at −20 (2) and +12.62 (1) ppm, which, by the multiplicity of signals observed, suggests that the I_3^- ion is only loosely bound.[942]

Coordination of cobalt(II) with octaethylformylbiliverdin, Structure **11**, formed by coupled oxidation of cobalt(II) octaethylporphyrin, followed by dissociation of the cobalt, produces a complex whose NMR spectrum is consistent with a low-spin cobalt(II) complex of this formylbiliverdin.[944] *Meso*-H and *meso*-formyl resonances are observed at +34, +26, +11 and +3 ppm, and CH_2 resonances range from +19 to −12 ppm. Six CH_3 resonances, two of double intensity, are also observed between +8 and −2 ppm.[944] The pattern of shifts is similar to that of the symmetrical [(OEP)Co] complex, except for the wide spread of the *meso* shifts. The resonances are considerably sharper than those of [(OEP)Co], however, and excellent COSY spectra have been obtained. The EPR spectrum of the OEFB complex in toluene solution in the presence of pyridine yields a spectrum similar to that of [(OEP)Co] bound to one pyridine molecule,[238] with g-values of 2.465, 2.181, 2.001, except that it is rhombic rather than axial. Molecular oxygen readily binds to this complex, to produce the typical Co–O_2 EPR signal.[944]

d. *High-spin cobalt(II) N-alkylporphyrins and alkoxy adducts of oxaporphyrins*

Most cobalt(II) porphyrins are low-spin (S = 1/2) and have rather broad ^1H resonances with relatively small shifts that are largely pseudocontact in origin,[2,4] but the ^1H NMR spectra of the chlorocobalt(II) N-methylporphyrin complexes of TPP and OEP, shown in Figure 25, are those of high-spin cobalt(II) centers (S = 3/2), and are quite a bit sharper.[230] The lower symmetry of the N-methylporphyrin ligand creates many more resonances for each complex. The Curie plots for these resonances are linear but do not extrapolate to the diamagnetic region for the pyrrole-H or N–CH_3. The phenyl-H, however, exhibit paramagnetic shifts as expected if they are mainly pseudocontact in origin,[230] and the pyrrole substituent shifts are indicative of mainly σ delocalization, as expected. The N,N′-vinylene-linked cobalt(II) porphyrins prepared by addition of free-base porphyrins to a C_2H_2 complex of cobalt(III) octaethylporphyrin, followed by oxidative rearrangement and addition of cobalt(II) or other metal to the free-base N-vinylporphyrin have been

reported.[945] The patterns of *meso*-H and β-CH_2 shifts are similar to those of the simple N-alkylporphyrin complexes of $Co^{II}Cl$.[230] When the planar macrocycle octaethyloxaporphyrincobalt(II), discussed in the previous section, is opened by alkoxide addition, helical complexes are formed. These complexes have much sharper resonances, with larger chemical shifts,[946] than the (OEPO)Co^{II} precursor.[940] For the ethoxy product, *meso*-H resonances are observed at about +70 and +55 ppm, and porphyrin β-CH_2 resonances from +40 to about 0 ppm, with the ethoxy $-CH_2$ resonance at −20 ppm, while for the methoxy product all shifts are increased somewhat.[946] These large chemical shifts are not consistent with low-spin cobalt(II), but rather are similar to the chemical shifts of the cobalt(II) N-alkylporphyrins discussed in the previous paragraph. Indeed, the chemical shifts for the two types of cobalt(II) complexes are similar.

2. *High-Spin Cobalt(II) Complexes of a Weak-Field Porphyrin Ligand*

The cobalt(II) complexes of β-pyrrole-fluoro substituted TPP, (F_8TPP)Co^{II}, and perfluorinated TPP, (F_{28}TPP)Co^{II}, are not pure low-spin cobalt(II) complexes, but rather, have varying degrees of low-spin/high-spin character.[947] For the latter complex, the magnetic moment (Evans method, 25 °C, $CDCl_3$)[376,377] is 2.15 μ_B and the β-pyrrole-F shift is −124.8 ppm (as compared to −145.4 ppm for the Zn(II) complex), while the mono-pyridine complex displays a higher magnetic moment of 2.82 μ_B and a β-pyrrole-F shift of −104.6 ppm. Formation of the 6-coordinate complex, in pyridine-d_5 as solvent, created a nearly pure high-spin cobalt(II) center, with a magnetic moment of 3.82 μ_B and a β-pyrrole-F shift of −20.5 ppm, similar to that observed for the bis-(THF) complex (−1.6 ppm). The most positive shift observed for these complexes was the bis-(N-methylimidazole) complex shift, +141.1 ppm.[947] The more positive the β-pyrrole-F shift, the more fully populated the $d_{x^2-y^2}$ orbital is believed to be. Of the two possible S = 3/2 ground states, $^4A_{2g}$, $(d_\pi)^4(d_{xy})^1(d_{z^2})^1(d_{x^2-y^2})^1$, and ^4E_g, $(d_{xy})^2(d_\pi)^3(d_{z^2})^1(d_{x^2-y^2})^1$, the latter is believed to be the ground state of these complexes because of the similarity of the bis-(pyridine) and −(THF) shifts.[947] Neither the EPR spectrum nor the temperature dependence of the ^{19}F NMR shifts have been reported.

3. *Alkylcobalt(III) Porphyrins: Agostic Interactions or Paramagnetic Excited States?*

X-ray crystallography and ^1H and ^{13}C NMR spectroscopy have been used to study apparantly diamagnetic alkylcobalt(III) porphyrins.[948] Porphyrins studied included OEP, TTP, OEC and OEiBC, while alkyl groups included methyl, ethyl, propyl and butyl. Agostic interactions between the β-protons and the metal had previously

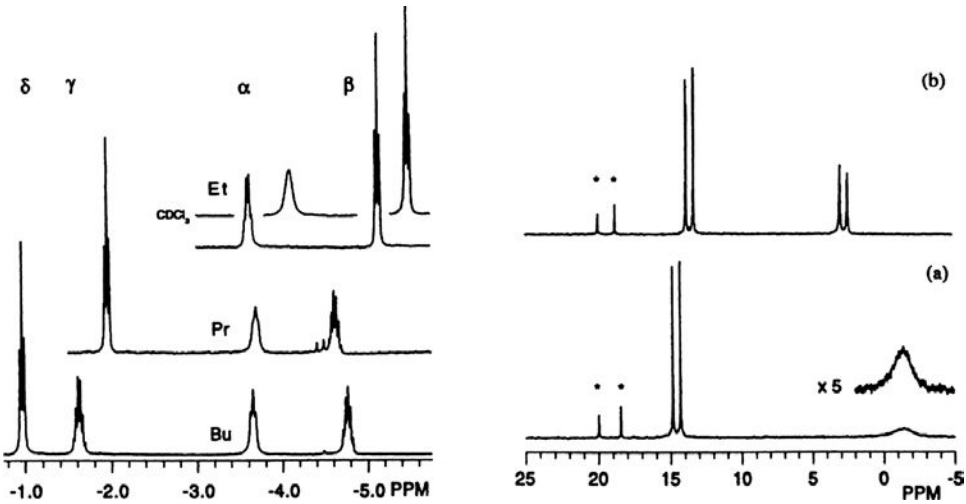

Figure 76. Left: 270 MHz ^{1}H NMR spectra of the axial alkyl groups of [(OEP)Co^{III}(R)] in C_6D_6. Right: 67.9 MHz ^{13}C NMR spectra of the high-shielding region of [(OEP)Co($^{13}C_2H_5$)] in C_6D_6 (a) and in C_5D_5N (b). The inset in spectrum (a) is a fivefold expansion of the α-carbon peak. Peaks indicated with asterisks are the natural abundance CH_3 and CH_2 peaks of OEP. Reprinted from Cao, Y.; Petersen, J. L.; Stolzenberg, A. M. *Inorg. Chim. Acta* **1997**, *263*, 139–148, with permission from Elsevier Publishing Company.

been suggested to explain the broad, ^{1}H resonances of the β-protons of the alkyl group that are shifted to higher shielding,[949] as shown in Figure 76, left. (This shift of the β-protons to higher shielding relative to the α-H is inconsistent with the expectations of ring-current shifts of diamagnetic aromatic compounds.) The three-dimensional structure of the OEP-ethyl complex, [(OEP)Co(Et)], has been determined, and shows no evidence of agostic interactions in the solid state. Furthermore, the ^{13}C resonances of carbons bound to cobalt are very broad and have unusual shifts to higher shielding (Figure 76, right) that are probably better explained by the effects of the quadrupolar ^{59}Co nucleus and to paramagnetic contact shifts that arise from thermal population of an excited state.[948] Organocobalt-mediated radical polymerization of acrylic acid in water has been studied using a water-soluble Co^{II} porphyrin, tetra(3,5-disulfonatomesityl)porphyrin. Low polydispersity, high molecular weight poly(acrylic acid) (PAA) was formed rapidly by the aqueous polymerization of acrylic acid initiated by an azo radical source (V-70) in the presence of this Co^{II} porphyrin. The pyrrole-H resonance of paramagnetic (TMPS)Co^{II} disappears during the induction period of this reaction.[950] Exchange of organic radicals between solution and organo-cobalt complexes was experimentally observed and the reaction pathway was probed through DFT calculations.

Cyanoisopropyl radicals from AIBN (2,2′-azobisisobutyronitrile) enter solutions of cobalt(II) tetramesitylporphyrin ((TMP)$Co^{II\bullet}$) and vinyl acetate (VAc) in benzene and react to produce transient hydride (TMP)Co–H and radicals ($\bullet CH(OAc)CH_2C(CH_3)_2CN$) that proceed on to form organo-cobalt complexes (TMP)Co-$CH(OAc)CH_3$ and (TMP)Co–$CH(OAc)C(CH_3)_2CN$, respectively.[951] Rate constants for near-degenerate exchange of radicals in solution with organo-cobalt complexes are deduced from ^1H NMR studies and kinetic modeling. Associative radical interchange of the latent radical groups in organo-cobalt porphyrin complexes with freely diffusing radicals in solution that is observed in this system provides a pathway for mediation of living radical polymerization of vinyl acetate.[951–953]

4. *A Cobalt(III) Porphyrin π-Cation Radical*

Anodic oxidation of [(OEP)Co^{II}] in the presence of a carbon monoxide atmosphere creates the [(OEP)$Co^{III}(CO)]^+$ π-cation radical complex, whereas in the presence of a dinitrogen atmosphere, a [$(OEP^{-\bullet})Co^{II}]^+$ π-cation radical.[954] The two complexes were characterized by IR spectroscopy; NMR spectra of these species have not been reported. While the NMR spectrum of this species has not been reported, it is probably diamagnetic. The two-electron oxidized complex in the absence of CO yields a species formulated as [$(OEP^{-\bullet})Co^{III}]^{2+}$ $2Br^-$, which exhibited a methylene proton signal at +23 ppm with a halfwidth of 900 Hz, and a broad *meso*-H signal at −81 ppm (linewidth not given, spectrum not shown). At 275 K the latter signal had a paramagnetic shift of −91 ppm, which corresponds to an electron density at the *meso*-C of 0.054 (Eq. 5). This is considerably larger than that at the *meso*-C of the isoelectronic [(OEP)Ru(CO)]$^+$ (0.027), and is probably more indicative of the limiting shift of an $a_{2u}(\pi)$ cation radical-based unpaired electron in a porphyrin macrocycle, although as mentioned in Section IV.B, the EPR spectrum of [$(OEP^{-\bullet})Mg]^+$ yields a splitting constant of 1.48 G, which translates to an electron density at the *meso*-C of 0.066 (Eq. 5), or a contact shift of −107 ppm.

D. Rhodium Porphyrins

The majority of rhodium porphyrins reported to date are diamagnetic dimers.[955] However, if the more sterically bulky tetramesitylporphyrin is used instead, stable monomeric complexes are formed.[956,957] These complexes have NMR spectra and EPR spectra typical of a low-spin d^7 metal with a d_{z^2} unpaired electron. The g-values of the 4-coordinate [(TMP)Rh^{II}] in toluene glass are $g_\perp = 2.65$ and $g_\parallel = 1.915$,[956] similar to those of 4-coordinate cobalt(II) porphyrins.[238] The proton NMR shifts of the porphyrin protons in C_6D_6 at 296 K are +18.3 ppm (pyrrole-H), +3.35 ppm (*o*-CH_3), +8.87 ppm (*m*-H) and +3.51 (*p*-CH_3).[956] The pyrrole-H shift is slightly larger

than that of [(TPP)Co] (+15.5 ppm at 35 °C),[233] which indicates slightly larger pseudocontact shifts, probably, for the rhodium(II) porphyrin. A study of the reactivity of the (TMP)Rh^{II} complex, also described as (TMP)Rh•, with O_2 gave rise to formation of a monomeric O_2 complex, which could also form a peroxo-bridged dimer with another (TMP)Rh•. O_2 could also react with (TMP)Rh-H to yield (TMP)RhOOH.[958] All species were characterized by ^{1}H NMR spectroscopy.

Rh^{III} water-soluble tetra(*p*-sulfonatophenyl)porphyrin has been used to study the reactions of olefins in water to form β-hydroxyalkyl complexes,[959] and the tetrakis(3,5-disulfonatomesityl)porphyrin complex of Rh^{III} has been used to study the reaction with H_2, CO and olefins in water to form formyl and alkyl complexes.[960] Although most detectable species were diamagnetic Rh^{III} complexes, both Rh^{I} and Rh^{II} intermediates were implicated.

Paramagnetic Rh^{II} complexes, Rh(OEP)(PEt_3) and Rh(TPP)(PEt_3), result from addition of PEt_3 to the corresponding metallohydrides, Rh(Por)H, under rigorously anaerobic and anhydrous conditions.[961] According to low-temperature EPR studies ($g_\perp = 2.018$, $g_\parallel = 1.982$ for the mono-PEt_3 complex, $g_\perp = 2.021$, $g_\parallel = 1.973$ for the bis-PEt_3 complex), the HOMO of both complexes is said to be mainly porphyrin based, and not the metal-based $d\sigma^*_{Rh-P}(d_{z^2})$ bond, as reported earlier by Wayland *et al.*[956] However, these g-values are too far from 2.003 and 2.002 to be porphyrin-based radicals, yet they are much closer to these values than that for the Rh(TMP)(PEt_3) (2.116, 2.004, respectively). The ^{1}H NMR resonances for the pyrrole-CH_2 and $-CH_3$ are at 10.2 and −0.7 ppm, respectively. However, the phosphine ligand resonances are said to have a chemical shift of +21 ppm (broad) for all 15 H,[961] which is not what one would expect for CH_2 and CH_3 protons of PEt_3. In the presence of dioxygen the O_2 adduct is formed, which has EPR spectra ($g_\parallel = 2.002$, $g_\perp = 1.982$)[961] similar to those of the Co-O_2 adduct;[238] in both of these complexes the unpaired electron is mainly on O_2 (superoxide ion complex of the M^{III} porphyrinate).

Tris-(mesityl),mono-(*p*-hydroxyphenyl)porphyrin has been used to construct an $-O-(CH_2)_6-O-$bridged porphyrin dimer that, following insertion of rhodium(II), reacts with CO ($P_{CO} = 0.3–0.9$ atm) at room temperature to form the Rh–CO–CO–Rh bridged dimer, which has eight unique pyrrole-H doublets in the 8.18–8.86 ppm region of the ^{1}H NMR spectrum.[962] This presumably indicates that the –C(O)–C(O)– unit binds in such a way as to make the protons of the two rings inequivalent. It would be interesting to investigate the COSY and NOESY spectra of this complex, in order to determine which pyrrole-H are in the same pyrrole ring and which pyrrole-H are in adjacent pyrrole rings, in order to determine the three-dimensional structure of this complex. Warming the sample over the temperature range 300–350 K causes broadening of the resonances, indicating homolytic cleavage of the C–C bond. The activation parameters for this homolytic

cleavage are $\Delta H^{\ddagger} = 88 \pm 4$ kJ/mol and $\Delta S^{\ddagger} = 54 \pm 13$ J/K.mol. The rhodium(II) dimer also reacts with ethylene and 1,3-butadiene to produce the Rh–C_n–Rh bridged complexes, and with CO and H_2O, EtOH, H_2 or CH_4 to produce the H-Rh, Rh-formyl, (EtOC(O))Rh, Rh-formyl, formyl-Rh,Rh-formyl and formyl-Rh,Rh-acetyl organometallic complexes, respectively, all of which have been characterized by ^1H and ^{13}C NMR spectroscopy.[962]

The same diporphyrin ligand system, and one with a more rigid m-xylylene spacer were used to study the dimethyl complex, which has the nondecoupled Rh-$^{13}CH_3$ ^1H signal at −5.29 ppm ($J_{CH} = -141$ Hz) and the ^{13}C signal as a quartet of doublets at −13.58 ppm ($J_{CH} = -141$ Hz, $J_{C103Rh} = -29$ Hz).[963] The dirhodium(II) derivatives were generated by photolysis of the dimethyl complexes, and are stable bimetalloradicals because of the ligand steric demands prohibit Rh^{II}–Rh^{II} bonding.[963] EPR spectra of the dirhodium(II) derivatives ($g_\perp = 2.64$, $g_\parallel = 1.90$), their 5-coordinate triphenylphosphine adducts ($g_\perp = 2.17$, $A_\perp$ (^{31}P) = 756 MHz, $g_\parallel = 2.00$ $A_\parallel$ (^{31}P) = 1016 MHz, $A_\parallel$ (^{103}Rh) = 61 MHz) , and their O_2 adducts ($g_1 = 2.080$, A_1(^{31}P) = 50.9 MHz, $g_2 = 2.005$, A_2(^{31}P) = 50.5 MHz, $g_3 = 1.996$, A_3(^{31}P) = 50.3 MHz) are reported. The ^1H resonance for the pyrrole-H of the 4-coordinate Rh^{II} porphyrin was at +19 ppm at ambient temperature, and the temperature dependence of that resonance extrapolated to 7.53 ppm, which is only about 1.5 ppm from its diamagnetic position;[963] i.e., the complex follows the Curie law quite well. The kinetic advantage of bimetalloradical complexes for substrate reactions that have two metal-centered radicals in the transition state was demonstrated by reactions of dihydrogen with dirhodium(II) bimetalloradical complexes: The ^{103}Rh-H doublet at −40.03 ppm clearly showed that addition of a small amount of H_2 first formed a species in which both Rh centers in the same few dimers were hydrogenated, but over the period of nearly a month it converted to the overall most stable species, in which twice the number of dimers had one RhH and one 4-coordinate Rh^{II} center in each dimer.[963] Methanol reacts with the ligand-free Rh^{II} complex exclusively by C–H bond cleavage to form Rh-CH_2OH and Rh-H centers, and very slowly went on to form H_2 and two Rh–CH_2OH centers in each molecule.[964] This work was further extended to investigate the strength of the C–H bonds in a series of substrates CH_3R (R = H, CH_3, OH, C_6H_5) using the *m*-xylyl diether tethered diporphyrin ligand. Bimolecular substrate reactions involving the intramolecular use of two metalloradical centers and preorganization of the four-centered transition state (M•···X···Y···•M) result in large rate enhancements as compared to termolecular reactions of monoradicals.[965] NMR spectroscopy played an important role in this study.

The Rh–Rh bond dissociation energy of $[(OEP)Rh^{II}]_2$, to give the paramagnetic monomers,

$$[(OEP)Rh]_2 \leftrightarrows 2\ [(OEP)Rh^{\bullet}], \tag{43}$$

has been evaluated using ^{1}H NMR line broadening techniques.[955] At room temperature, all porphyrin resonances are sharp, but as the temperature is raised from 294 to 373 K all resonances broaden. Analysis of the line broadening of the *meso*-H resonance at 9.28 ppm in benzene-d_6 yielded an activation energy E_a +77 ± 3 kJ/mol.[955] Using this value and available data for the bond dissociation energy of H_2 and the reaction of the dimer with H_2:[966]

$$[(OEP)Rh]_2 + H_2 \leftrightarrows 2\ [(OEP)RhH], \tag{44}$$

it was possible to calculate the bond dissociation energy of [(OEP)RhH]

$$[(OEP)RhH] \leftrightarrows [(OEP)Rh^{\bullet}] + H^{\bullet}, \tag{45}$$

as 259 kJ/mol or 61.8 kcal/mol.[955] Using this value, the activation data for the formation of [(OEP)Rh-CHO]:[967]

$$[(OEP)RhH] + CO \leftrightarrows [(OEP)Rh–CHO], \tag{46}$$

and the formyl radical,[968] the bond dissociation energy for the homolytic bond cleavage of [(OEP)Rh–CHO]:

$$[(OEP)Rh–CHO] \leftrightarrows [(OEP)Rh^{\bullet}] + {}^{\bullet}CHO, \tag{47}$$

was calculated to be 243 kJ/mol or 58 kcal/mol.[955] Thus, NMR spectroscopic line-broadening techniques provide a useful method for measuring bond dissociation energies that cannot readily be measured by other methods.

E. Manganese Porphyrins

The manganese(III) porphyrins have been studied for quite some time, probably first for their unusual optical properties, which were interpreted as reflecting extensive manganese-porphyrin π bonding.[969] The complexes are always high-spin d^4, S = 2, and may be 5-coordinate [(P)MnX] or 6-coordinate [(P)MnX(B)], where X is a halide or pseudohalide and B is a Lewis base. Manganese porphyrins have not been shown to exist in or play any role in the functioning of biological systems, but the high-valent states (manganese(V) porphyrins or manganese(IV) porphyrin π-cation radicals) have been shown to be good models of the reactivity of the enzymatically active high-valent states of cytochromes P450, peroxidases, catalases and chloroperoxidase.[970,971]

1. *High-Spin Manganese(II) Porphyrins*

High-spin manganese(II) porphyrin complexes are produced by reduction of manganese(III) porphyrins with zinc amalgam[161] or autoreduction with hydroxide or other OR^- anions.[972] Both 4-coordinate and 5-coordinate (OH^- or OR^- coordinated) complexes can be produced.[161,972] The 4-coordinate complexes have slightly smaller positive pyrrole-H shifts (+34 to +35 ppm at 25 °C)[161,972] than the 5-coordinate complexes (+37 ppm at 25 °C).[161,972] Although these shifts are not nearly as positive as those of high-spin iron(III) porphyrins (Section IV.A.6.a), the spin state of the manganese(II) porphyrins is believed to be high-spin d^5.[972] The binding constants of imidazole, pyridine and DMSO to [(TPP)Mn] have been measured electrochemically in dichloroethane (0.1 M TBAP), and are large, with log K_1 = 4.12, 4.55 and 4.38 log M^{-1}, respectively.[973] The NMR spectra of these 5-coordinate manganese(II) complexes have not been reported. The complex of potassium superoxide with [(TPP)Mn^{II}] shows a pyrrole-D resonance at +32 ppm at 25 °C.[161] The magnetic moment of 5.0 μ_B suggests that the electronic ground state is high-spin manganese(II) coupled antiferromagnetically to the $O_2^{-\bullet}$ axial ligand. This differs from the iron case, where the electron configuration is high-spin iron(III)-O_2^{2-}.[161]

2. *High-Spin Manganese(III) Porphyrins*

The high-spin d^4 electron configuration of [(P)Mn^{III}X] complexes leads to negative shifts for the β-pyrrole-H (−30 ppm in $CDCl_3$ at 35 °C) and positive shifts for the β-pyrrole-CH_2 (+18 ppm),[234] which suggests significant π spin delocalization to the β-pyrrole positions, while *meso*-phenyl resonances are shifted only a small amount in an alternating fashion that suggests a small amount of π spin density at the *meso* positions. [(OEP)Mn^{III}Cl], however, has a *meso*-H shift of +41.4 ppm at 35 °C in $CDCl_3$,[234] which rules out large π spin delocalization from the $3a_{2u}(\pi)$ orbital of the porphyrin ring to the Mn^{III} half-filled d_{z^2} orbital.[156] Thus, the filled $3e(\pi)$ orbitals are utilized for P → Mn π donation. However, this does not account for the large positive shift of the *meso*-H of the OEP complex, which can only be explained in terms of significant σ spin delocalization to the *meso* positions or by a Mn^{II}–$a_{2u}(\pi)$ radical configuration (see below), since the g-anisotropy of high-spin manganese(III) is fairly small.[2,4] EPR spectra of these manganese(III) porphyrins are not detectable at X- or Q-band because the microwave quantum is too small, but have been measured at 226–544 GHz.[974] The zero-field splitting parameters for [(TPP)MnCl], [(DPDME)MnCl] and several tetraazaporphyrin derivatives were found to be in the range D = −2.27 to −2.62 cm^{-1}, with $g_{\|}$ = 1.822 to 2.0.[974] Water-soluble manganese(III) porphyrins have been investigated as possible

water relaxation agents for MRI applications. As expected, porphyrin aggregation decreases the relaxivity of these complexes.[975]

3. *Low-Spin Manganese(III) Porphyrins*

Only three examples of apparant low-spin d^4 (S = 1) manganese(III) porphyrins have been reported: The bis-(cyanide), bis-(imidazolate) and bis-(4-methylimidazolate) complexes. The magnetic moments (Evans method)[376,377] range from 3.0 to 3.7 μ_B,[976] which is higher than the spin-only value of 2.83 μ_B expected for two unpaired electrons, but a T-state system should have considerable spin-orbit coupling with consequent increase in the magnetic moment. The red-brown bis-(cyanide) complexes tend to autoreduce over a period of hours to green high-spin manganese(II) complexes, based on the magnetic moments of the products ($5.8 \pm 0.2\ \mu_B$).[376,377,976] In all of the TPP complexes investigated the β-pyrrole-H resonance is shifted to higher shielding (−14.7, −18.1 and −18.1 ppm, respectively, at 26 °C in DMSO-d_6).[976] These pyrrole-H shifts are indicative of π spin delocalization, probably involving P → Mn π donation from the filled 3e(π) orbitals to the d_{xz},d_{yz} half-filled orbitals of the metal, which thus indicates an electron configuration $(d_{xy})^2(d_{xz},d_{yz})^2$. However, the $[(OEP)Mn(CN)_2]^-$ and $[(Etioporphyrin)Mn(CN)_2]^-$ complexes have very large positive *meso*-H shifts (+34 and +37 ppm, respectively), as shown in Figure 77, which are inconsistent with π delocalization from the metal to the *meso* positions.[976] These large, positive *meso*-H shifts are reminiscent of the iron(III) porphyrin and corrole π-radical spectra discussed in Section IV.A.11.c–v (although with less positive shifts), as well as the Mn corrole spectra discussed in the following Section (IV.E.4) (with very similar shifts). Thus, this author suggests that these "low-spin manganese(III) porphyrins" may actually be intermediate spin (S = 3/2) manganese(II) porphyrin π-radicals, which would be consistent with the observed β-pyrrole shifts of H and CH_2, and would further be consistent with the positive *meso*-H shift if the porphyrin cation electron is antiferromagnetically coupled to the metal electrons. Further study of "low-spin manganese(III) porphyrins," including EPR measurements and the temperature dependence of the NMR spectra, should be carried out in order to obtain a more complete understanding of these complexes.

4. *"Manganese(III) Corrole" at Low Temperatures = Manganese(II) Corrole π-Cation Radical at Ambient Temperatures*

In Section IV.A.10.e it was mentioned that the corrole ring may either stabilize higher oxidation states of metal ions, or may be readily oxidized to the corrole

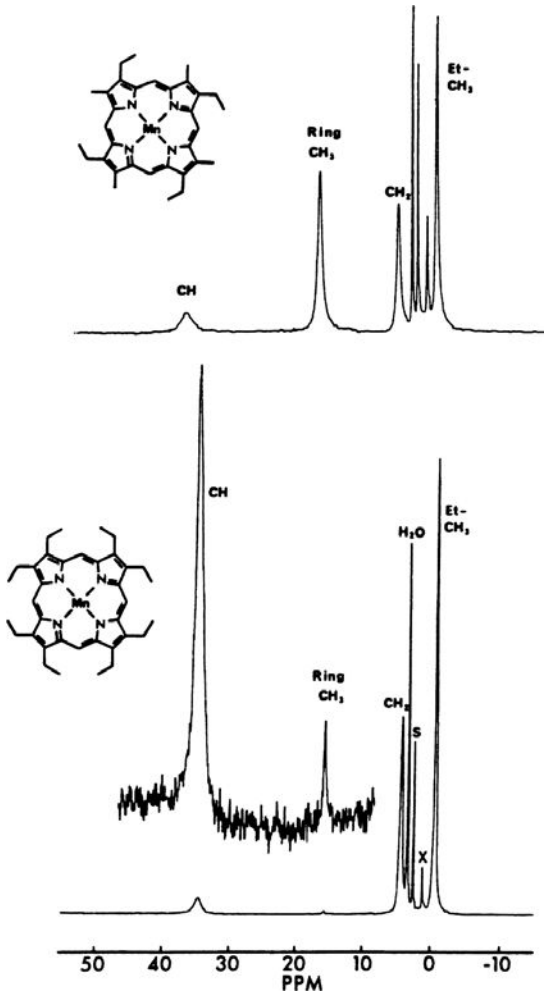

Figure 77. ^{1}H NMR spectra of dicyano complexes of (P)Mn^{III} in DMSO-d_6 at 26 °C (0.005 M manganese porphyrin, solutions saturated with KCN). Bottom: [(OEP)Mn^{III}(CN)$_2$]$^-$; top: [(etioporphyrin)Mn^{III}(CN)$_2$]$^-$. Reprinted from Hansen, A. P.; Goff, H. M. *Inorg. Chem.* **1984**, *23*, 4519–4525, with permission from the American Chemical Society.

π-radical state. Isolation of a putative manganese(III) corrole seemed strange, in that the complex was 4-coordinate.[977] On closer examination, it became clear that in this case the NMR spectra of the 4-coordinate, square planar complex were more consistent with a manganese(II) corrole π-radical electron configuration.[978] The manganese dimethylhexaethylcorrole complex in frozen pyridine solution has an EPR spectrum at 77 K which is characteristic of intermediate-spin manganese(II) (S = 3/2), probably due to the fact that the radical spins on adjacent molecules are paired, as in the low-spin iron(III) π-radical complex of the same

macrocycle, discussed in Section IV.A.10.e. Consistent with this, the X-ray crystal structure shows that the molecular packing of the molecules is such that there is strong overlap of the π systems of the corrole rings to form infinite stacks of molecules.[978] The NMR spectra in pyridine-d_5 of a series of manganese complexes with alkylcorrole isomers (Me_8Corr, 2,18-Me_2Et_6Corr, 3,17-Et_2Me_6Corr, 7,13-Et_2Me_6Corr, 8,12-Et_2Me_6Corr and its 5,15-deuterated analog, 7,13-Me_2Et_6Corr, and 7,8,12,13-Me_4Corr) provide a complete mapping of the spin density in the corrole ring: As in the case of the chloroiron corroles discussed in Section IV.A.11.e, the 5,15- and 10-*meso*-H are at positive chemical shifts (+70.5 and +25 ppm, respectively) because of the antiparallel spin of the corrole π-radical electron, while the 3,17-H and 2,18-H of [(Me_4Corr)Mn] are at very negative chemical shifts (−40 and −123 ppm, respectively)[978] because of large π spin density at those ring positions due to the d_{xz} and d_{yz} unpaired electrons of the S = 3/2 manganese(II) center (while the $3a_{2u}(\pi)$-type orbital, S_{-1}, has small spin density at the β-pyrrole positions, Figure 7). The methyl and methylene proton shifts are positive, confirming the large π spin density at those ring positions due to the d_{xz} and d_{yz} unpaired electrons. Like the 2,18-H, the 2,18-CH_3 and –CH_2 have the largest shifts (+112.4 and +55 ppm, respectively). Next in magnitude are the 8,12-CH_3 and –CH_2 shifts (+64.3 and +35.6 ppm, respectively), followed by the 3,17-CH_3 and –CH_2 shifts (+45.5 and +21.5 ppm, respectively), and finally the 7,13-CH_3 and –CH_2 shifts (+15.8 and ~+8 ppm, respectively).[978] In all cases the CH_3 shifts are very close to twice the size of the –CH_2 shifts, and the pattern of large-small, small-large shifts as one moves away from the directly-bound pyrrole rings is very characteristic of the spin density distribution in the d-A_{-2} orbital, Figure 7. Thus, it appears that the manganese(II) electrons are delocalized by L → Mn π bonding, while the corrole π-radical electron is in the $3a_{2u}(\pi)$-equivalent orbital, S_{-1} (Figure 7). The reason for the much smaller *meso*-H shifts for the Mn complex (+70.5 and +25 ppm (intensities 2:1, respectively)) as compared to the FeCl complex (+175 and +166 ppm (intensities 1:2, respectively)[158]) is at present unclear, but one may guess that it probably has to do either with a difference in the strength of the antiferromagnetic coupling in the two metal complexes or with aggregation to allow partial coupling of the radical spins in these 4-coordinate complexes. Further studies will be required in order to obtain a full explanation of the magnetic interactions in the two metal complexes, both of which are d^5 π-radical centers having metal spin state S = 3/2.

An entirely different situation was found for these complexes at very low temperatures, where high-field and frequency electron paramagnetic resonance (HFEPR) of solid (8,12-diethyl,2,3,7,13,17,18-hexamethylcorrolato)manganese(III) shows that in the solid state they are well described as an S = 2 (high-spin) Mn^{III}

complex of a trianionic ligand, [$Mn^{III}Corr^{3-}$],[979] just as Mn^{III} porphyrins are described as [$Mn^{III}P^{2-}]^{+}$.[980,981] Comparison among the structural data and spin Hamiltonian parameters reported for [$Et_2Me_6CorrMn$], Mn^{III} porphyrins, and a different Mn^{III} corrole, [(tpfc)Mn($OPPh_3$)], previously studied by HFEPR,[982] shows that despite the molecular asymmetry of the corrole macrocycle, the electronic structure of the Mn^{III} ion is roughly axial. However, in corroles, the S = 1 (intermediate-spin) state is much lower in energy than in porphyrins, regardless of axial ligand. HFEPR of [$Et_2Me_6CorrMn$] measured at 4.2 K in pyridine solution shows that the S = 2 [$Mn^{III}Corr^{3-}$] system is maintained, with slight changes in electronic parameters that are likely the consequence of axial pyridine ligand coordination.[979] The present result is the first example of the detection by HFEPR of a Mn^{III} complex *in solution*. Over a period of hours in pyridine solution at ambient temperature, however, the S = 2 Mn^{III} spectrum gradually disappears leaving a signal with g = 2 and ^{55}Mn hyperfine splitting.[979] Analysis of this signal, also observed by conventional EPR, leads to its assignment to a manganese species that could arise from decomposition of the original complex. The low-temperature S = 2 [$Mn^{III}Corr^{3-}$] state is in contrast to that at room temperature, which is described as a S = 1 system deriving from antiferromagnetic coupling between an S = 3/2 Mn^{II} ion and a corrole-centered radical cation: [$Mn^{II}Corr^{2-\bullet}$],[978] as discussed above. The authors state in the abstract that "This temperature-dependent valence state isomerization has been observed for other metallotetrapyrroles."[979] However, to determine whether this is in fact what is happening, it would be worthwhile to study the temperature dependence of the NMR spectrum, in, say toluene-d_8 down to at least –90 °C, to determine whether evidence can be obtained for or against the valence isomerization.

"Manganese(III) octaethylcorrole" in d_8-toluene has rather different chemical shifts, with *meso*-H at +93 and +68 ppm (intensities 2:1, respectively) and $-CH_2$ resonances at +72, +40, +19 and +4.3 ppm.[983] The very positive *meso*-H shifts are still characteristic of a manganese(II) macrocycle π-cation radical formulation, but probably with somewhat stronger antiferromagnetic coupling in this case.

5. *Manganese(III) Porphyrin π-Radicals and Their Transformation to Dichloromanganese(IV) Porphyrins*

[(TMP)$Mn^{III}Cl$] can be chemically oxidized with $Fe(ClO_4)_3$, which leads to the porphyrin-oxidized red product [(pyrrole-d_8-$TMP^{-\bullet}$)$Mn^{III}(ClO_4)_2$], which has its pyrrole-D signal at –48 ppm at room temperature.[984] Magnetic susceptibility measurements and EPR spectroscopy show that the total spin of the complex changes from S = 5/2 at high temperatures (300 K) to S = 3/2 at low temperatures

(100 K).[972] Ligand exchange of the perchlorato ligands to chloride anions is accompanied by a change of the oxidation site from porphyrin to metal, resulting in green [(pyrrole-d_8-TMP)$Mn^{IV}(Cl)_2$], which has its pyrrole-D signal at −38 ppm at room temperature, an EPR spectrum with $g_\perp = 4$ and $g_\parallel = 2$ and a magnetic moment of 3.7 μ_B in solution[376,377] and 3.6 μ_B in the solid state, indicating a spin state S = 3/2. This high-valent metal complex can effect chlorine atom transfer to olefins and natural substrates of chloroperoxidases.[984] The related dimethoxy complex, [(TPP)$Mn^{IV}(OCH_3)_2$], has a somewhat higher magnetic moment (3.9 μ_B) in the solid state and solution.[376,377,985] The EPR spectra of this complex and the related bis-(azide) and bis-(isocyanate) complexes are highly anisotropic, with g-values of 5.43, 2.4, 1.6 (methoxy), similar values for the azide complex, and 5.96, 3.92, 2.01 for the bis-(isocyanate).[986]

6. *Oxomanganese(IV) Porphyrins*

Addition of *m*-chloroperbenzoic acid to [(TMP)MnCl] under basic conditions yields the red complex [(TMP)Mn=O], which has been characterized by optical, infrared, EPR and NMR spectroscopy, as well as mass spectrometry and chemical reaction with β-methylstyrene.[229] Use of pyrrole-deuterated TMP resulted in a pyrrole-D signal at −32 ppm in CD_2Cl_2 at −40 °C of about 2.4 kHz in width, as shown above in Figure 24, which is indicative of π spin delocalization. The EPR spectrum shows g-values of 4 and 2, consistent with an S = 3/2 center. The observed shift of the pyrrole-D of this d^3 [(P)Mn=O] complex[229] is considerably larger than those of the d^3 [(P)CrCl] complexes, discussed in Section IV.H.3.

F. Nickel Porphyrins

Several nickel(II) porphyrins have been used as diamagnetic reference compounds for the investigation of paramagnetic metalloporphyrins, as well as a T-state model in mixed-metal hemoglobins and a model for the nickel macrocyclic complex known as Factor F430 that is the active site of methyl coenzyme M reductase, a methane-forming enzyme. In all of these cases, nickel(II) is diamagnetic. However, there are a number of paramagnetic nickel porphyrins that have been investigated by NMR spectroscopy. The first report of the study of a paramagnetic nickel(II) porphyrin by NMR spectroscopy was that of Abraham and Swinton,[987] who studied the binding of piperidine to (MP)Ni^{II}. They concluded that a 5-coordinate complex was formed, although it was later shown by optical methods that the corresponding TPP complexes are 6-coordinate.[988] A study of the pyrrolidine complexes by UVvisible and resonance Raman spectroscopy and molecular simulations measured the stepwise binding constants (K_1 = 1.1 M^{-1}, K_2 = 3.8 M^{-1} in

CH_2Cl_2),[989] and suggest that there are several nonplanar porphyrin ring conformations (domed, saddled, ruffled) that can occur for the 5-coordinate complex. No mention was made of the likely spin state of each of these possible conformations, although the implication of the discussion was that the 5-coordinate complex is paramagnetic.[989]

The best way of insuring that nickel(II) will have a coordination number greater than four, and thus be paramagnetic, is to create positive charge(s) on the porphyrin ring. Such is the case for both N-alkyl- or N-arylporphyrins as well as the thia-, selena- or carbaporphyrins. In all of these cases, an anion is bound to the nickel(II), which is thereby forced to be 5-coordinate. Latos-Grażyński and coworkers have synthesized and investigated a number of modified macrocycles, where one of the porphyrin nitrogens is replaced by another donor group. These include O, S, Se, NO, N–CH_3 and C. In each case, the modified macrocycle carries an overall charge of −1, so an anion is always bound to one of the axial positions of the metal. Furthermore, since the hybridization of the unique heteroatom is different than that of the "aromatic" nitrogens of the porphyrin, there is always a distortion in the bond angle of the metal-heteroatom bond that distorts the macrocycle from planarity. The first of these studies involved the preparation of the chloronickel(II) complexes of *N*-methyltetraphenyl porphyrin and *N*-methyloctaethylporphyrin.[230] For the N-MeTPP complex, the three types of pyrrole-H from unmodified pyrrole rings are found at +68.2, +72.6 (adjacent pyrrole rings) and +33.7 ppm (opposite pyrrole ring) (in $CDCl_3$ at −60 °C), while the N-methyl pyrrole ring pyrrole-H is found at −9.8 ppm. Pseudocontact shifts of +6.7 to +7.7 ppm, which arise from a zero-field splitting (Eq. 10) were calculated for the pyrrole-H resonances using Eq. 22, which indicates that the majority of the observed shifts are due to the contact interaction. The large positive contact shifts observed at the β-pyrrole positions of the unmodified pyrrole rings are consistent with population of the $d_{x^2-y^2}$ orbital, while the negative contact shifts of the N-methyl pyrrole β-H suggests some π spin density in that pyrrole ring. Multiple phenyl-H resonances are found in the +12.7 to +2.4 ppm range. The N–CH_3 signal is found at +177.8 ppm.[230] Geometric factors for the N-methylporphyrin complexes of $Ni^{II}Cl$ were also reported.[230]

For [(N-MeOEP)NiCl] the pattern of observed shifts is consistent with the conclusions reached above: –CH_2 resonances are observed at +39.0, +34.6, +23.6, +18.8, +16.4, +13.9, +11.7 and +3.0 ppm, while *meso*-H resonances are observed at −15.2 and −20.1 ppm in $CDCl_3$ at −60 °C, and the N–CH_3 resonance is observed at +190.2 ppm. The negative shift of the *meso*-H was explained in terms of spin-orbit mixing of the d_{z^2} and $d_{x^2-y^2}$ unpaired electrons with the d_{xz} and d_{yz} orbitals, which could introduce π spin density at the *meso* positions,[230] as had been suggested earlier.[2] The same explanation could account for the difference in shifts of

the pyrrole-H in the two pyrrole rings adjacent to that carrying the methyl group. However, as pointed out earlier,[4] it seems unlikely that spin-orbit coupling could account for such large differences in contact shift, and therefore another explanation should be found. Thermal population of a $(d_{xy})^2(d_{z^2})^2(d_{x^2-y^2})^2(d_{xz},d_{yz})^2$ excited state, discussed below for the dioxoporphyrin, was suggested not to be an option because of the strict adherence of the shifts to Curie law behavior, Eq. 11.[4] Now, with the explanation of Cheng *et al.*,[156] we can interpret the *meso*-H shifts and the small π spin delocalization to the pyrrole positions as being fully consistent with the 5-coordinate chloronickel(II) center, where overlap of the half-filled d_{z^2} orbital with the $3a_{2u}(\pi)$-like filled orbital of the macrocycle can allow P $\rightarrow$ Fe π donation to the d_{z^2} orbital. The chemical shifts of the porphyrin protons of all modified macrocycle complexes of chloronickel(II) are summarized in Table 17.

Treatment of [(NMeTPP)NiCl] with deuterated aryl Grignard reagents yields the deuterated σ-aryl complexes of nickel(II).[990] At −70 °C in toluene, these complexes have fairly similar (except for the pyrrole-H in the ring opposite the N-methyl) pyrrole-H (+72.6, +52.0, ~ −0.7 ppm) and N-methyl β-H (−21.5 ppm) chemical shifts to those of the starting chloro complex (+75.7, +70.1, +30.3 ppm and −14.2 ppm, respectively), and the phenyl-D resonances are all very large and positive (+568 (*o*), +148 (*m*), +62.8 (*p*) ppm, which indicates mainly σ delocalization to the aryl ring. These patterns are similar to those of the corresponding thiaporphyrin complexes, discussed below.

The nickel(II) thiaporphyrin complex, [(STPP)NiCl], has a similar pattern of pyrrole-H and phenyl-H resonances to that of the N-MeTPP analog. Pyrrole-H resonances were assigned using NOE difference spectral methods, and it was shown that, for the three unmodified pyrrole rings, as one moves away from the thiophene ring the pyrrole-H shifts are +64.6, +32.5 and +30.9 ppm, while the thiophene β-H resonance appears at −29.8 ppm at 298 K in $CDCl_3$,[991] as shown in Figure 78. Replacement of the chloride ion by bromide or iodide decreases the magnitude of the observed shifts of the pyrrole-H and thiophene-H, which is consistent with the expectation that the pseudocontact contribution is dependent on the zero-field splitting created by the particular halide. In DMSO and methanol the chemical shifts of the pyrrole-H are increased (+67.7, +35.9, +56.3 ppm and +68.5, +36.0 and +57.0 ppm, respectively), especially that of the protons in the pyrrole ring opposite the thiophene ring. In the same solvents, the chemical shift of the thiophene β-H become smaller in magnitude (−23.4 and −22.0 ppm, respectively). In $CDCl_3$ with varying amounts of added *n*-butylamine, two species are observed, with pyrrole-H resonances at +63.9, +31.7, +35.6 ppm (1:1 mole ratio) and +64.5, +32.2, +42.0 ppm (1:4 mole ratio), respectively, and thiophene β-H resonances at −26.7 and −25.5 ppm, respectively. Because of the similarity in the shifts of the second *n*-butylamine complex to those observed in DMSO and methanol, it is probable that

Table 17. Chemical shifts of chloronickel(II) modifed porphyrins.

Modifed porphyrin	Solvent	T, °C	Pyrrole-H or $-CH_2$	Modified ring-H or $-CH_2$	Phenyl-H or *meso*-H	Ref.
N-MeOEP	$CDCl_3$	–60	38.95, 30.55,[a,b] 23.57, 18.75,[a,b] 15.43, 13.90 [a,b]	11.73, 2.95[a,b]	–15.18[c] (5,20) –20.06[c] (10,15)	230
N-MeTPP	$CDCl_3$	–60	33.67, 72.64,[d] 68.19 [d]	–9.84[e]	8.44,5.91[f] (o) 11.40,12.74[f] (o) 10.39,9.14[f] (m) 10.84,11.23[f] (m)	230
ODPDTP[g]	$CDCl_3$	–70	84.5, 24.8,[d] 81.6[d]	40.1[e]	numerous	994
SDPDTP	$CDCl_3$	–70	97.6, 46.4,[d] 41.7[d]	–56.4[e]	numerous	994
STPP	$CDCl_3$	25	30.91, 32.51,[d] 64.58 [d]	–29.84 [e]	8.10[f] (o) 9.93, 9.81, 9.74[f] (m) 6.17, 7.53[f] (p)	991
SeDPDTP[g]	$CDCl_3$	20	68.3, 40.2,[d] 17.1[d]	–38.7[e]		993
2-NH-21CH_3CTPP	$CDCl_3$	20	58.06, 58.06,[d] 52.40, 48.25,[d] 26.53, 24,86[d]	2.04[e] (3-H)	numerous	996
2-NCH_3-21CH_3CTPP	$CDCl_3$	20	59.69, 55.95,[d] 50.91, 49.33,[d] 28.15, 27.16[d]	–2.03[e] (3-H)	numerous	996
trans-O_2TPP[h]	$CDCl_3$	–50	64.11	41.8		995

[a]CH_2.
[b]Assignment not reported; modified ring-CH_2 assumed to be those with the smallest shifts.
[c]*Meso*-H.
[d]Pyrrole-H.
[e]Modifed ring-H.
[f]Phenyl-H.
[g]Diphenyldi(p-tolyl)porphyrin.
[h]Dioxotetraphenylporphyrin, i.e., with two trans nitrogens replaced by oxygens.

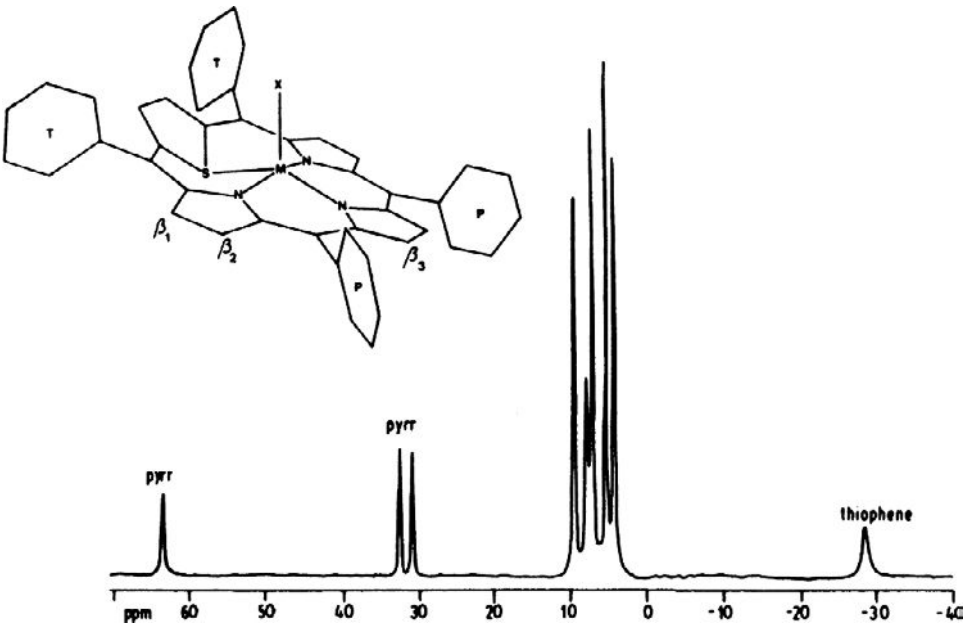

Figure 78. ^{1}H NMR spectrum of [(STPP)NiCl] in $CDCl_3$ at 298 K. Reprinted from Chmielewski, P. J.; Latos-Grażyński, L.; Pacholska, E. *Inorg. Chem.* **1994**, *33*, 1992–1999, with permission from the American Chemical Society.

all three of these are bis-ligand complexes with the halide displaced. Addition of N-methylimidazole also appears to form both mono- and bis-ligand complexes that are in fast exchange with each other and the starting material.[991] Consistent with the importance of a fifth ligand in creating the high-spin state, removal of the halide ion by treatment with $AgClO_4$ yields a diamagnetic thiaporphyrin complex. The chemical shifts of porphyrin protons are summarized in Table 17.

Use of Fenske-Hall calculations to investigate the molecular orbitals of the thiaporphyrin revealed that the extra lone pair on the sulfur creates an extra set of π-symmetry orbitals, where the former $a_{1u}(\pi)$ and this additional π orbital are transformed into two new orbitals, one of which can interact directly with $d_{x^2-y^2}$ when the thiophene ring makes a 30° angle with the plane of the three pyrrole rings.[991] This orbital has extremely large spin density at the sulfur, large π spin density at the β-H of the thiophene ring, and varying spin density at the three unique pyrrole β–H positions, as shown in Figure 79. Thus, this π delocalization, plus the large σ delocalization expected at the pyrrole positions due to population of the $d_{x^2-y^2}$ orbital, account for the pattern of contact shifts observed for the pyrrole-H.[991]

Treatment of [(SDPDTP)NiCl] (SDPDTP = 5,20-diphenyl, 10,15-ditolyl-21-thiaporphyrin) with deuterated aryl Grignard reagents yields the σ-aryl complexes

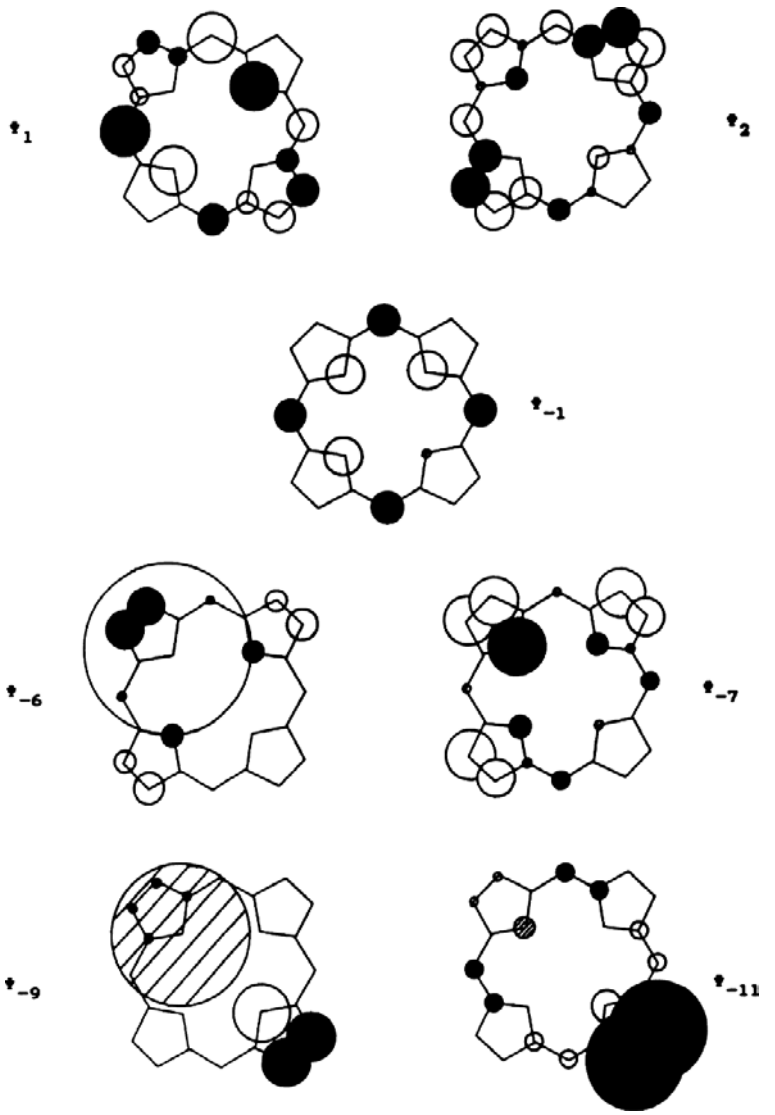

Figure 79. Molecular orbitals of the 21-thiaporphyrin ring, showing the two sulfur π orbitals (cross-hatched circles for φ_{-9} and φ_{-11}, large empty and filled circles for φ_{-6} and φ_{-7}); φ_{-9} can interact in a sigma fashion with the $d_{x}2_{-y}2$ orbital. Reprinted from Lisowski, J.; Latos-Grażyński, L.; Szterenberg, L. *Inorg. Chem.* **1992**, *31*, 1933–1940, with permission from the American Chemical Society.

of nickel(II).[990] At −70 °C in toluene, these complexes have similar (except for the pyrrole-H in the ring opposite the thiophene) pyrrole-H (+87.0, +35.4, ~+2 ppm) and thiophene β-H (−58.0 ppm) chemical shifts to those of the starting chloro complex (+97.6, +46.4, +41.7 ppm and −56.4 ppm, respectively), and the phenyl-D

resonances are all very large and positive (+616 (*o*), +170 (*m*), +76 (*p*) ppm, indicating mainly σ delocalization to the aryl ring.[990] These patterns are similar to those of the corresponding N-MeTPP complexes mentioned above.

Single-electron reduction of [(STPP)NiCl] yielded complexes that could be formulated in terms of the contribution of two canonical forms: nickel(I) thiaporphyrin and nickel(II) thiaporphyrin anion radical.[992] The resonances were assigned by preparation of the deuterated complexes, either [(d_6-STPP)NiCl] or [(d_2-STPP)NiCl]. The three pyrrole-D resonances were found to be at −66.5, +28.8 and +23.7 ppm, while the thiophene-D resonance was at +41 ppm at 298 K in toluene.[992] Addition of a ligand to the axial position of nickel(I) caused a shift of the negative pyrrole-D resonance to higher shielding, to −8.3 ppm for the SO_2 adduct and −43.3 ppm for the $PMePh_2$ complex. The other resonances, if observed, were less affected by the presence of the axial ligand.[992] A combination of σ and π delocalization mechanisms were considered to account for the paramagnetic shift pattern. ^{61}Ni enrichment of [(STPP)Ni] yielded the nickel hyperfine coupling constants for the complex, whose g-values are consistent with a nickel(I) $d_{x^2-y^2}$ unpaired electron ($g_1 = 2.109$, $g_2 = 2.039$, $g_3 = 2.031$).[992]

The corresponding selenaporphyrin complex, [(SeDPDTP)NiCl], where DPDTP = diphenyldi-*p*-tolylporphyrin, has similar pyrrole-H and selenophene β-H chemical shifts (+68.3, +40.2, +17.1 and −38.7 ppm, respectively)[993] which show small shifts on addition of one or two (or more) equivalents of imidazole. In this case the bis-(imidazole) complex is considerably more stable than in the thiaporphyrin case, and thus limiting chemical shifts of the coordinated ligand could be obtained for the N–H, 2-, 4- and 5-H at 298 °C in $CDCl_3$ (+71.0, +55.3, +59.2, +49.6 ppm, respectively). All of these shifts are indicative of a major role of σ delocalization to the axial imidazoles. Addition of an aryl Grignard to this chloride complex produces the corresponding Ni-phenyl complex,[994] which has similar pyrrole-H and selenophene β-H shifts to those of the corresponding 21-thiaporphyrins, except for the pyrrole-H opposite to the selenophene ring. Whereas the thiaporphyrin phenylnickel(II) complex has that pyrrole-H resonance at +2.5 ppm, the corresponding selenophene complex has it at −15 ppm at 203 K in toluene.[994]

The corresponding 21-oxaporphyrin complexes, [(ODPDTP)NiCl] and [(ODPDTP)NiPh] have also been reported.[994] While the chloride complex shows quite similar pyrrole-H chemical shifts (+84.5, +24.8 and +81.6 ppm) to those of the N-MeTPP analog,[230] the furan β-H are observed at +40.1 ppm, rather than at −21.5 ppm as in the N-MeTPP case. For the phenyl complex, the β-H in the pyrrole ring opposite the modified ring have a chemical shift of −13.1 ppm, similar to that observed for the selenophene ring of the corresponding Se-substituted macrocycle, but the furan β-H resonance is again uniquely at a positive chemical shift (+30.0 ppm).[994] The dichloro- and dicyanonickel(II) complexes of

21,23-dioxatetraphenylporphyrin have also been reported and show positive shifts for both pyrrole and furan β-H (+64.1, +41.8 ppm and +36.6, +26.7 ppm, respectively), while the diphenyl complex shows very negative chemical shifts for these two types of macrocyle β-H (−143.1, −31.6 ppm, respectively) at 243 K in toluene-d_8.[995] The authors propose that there is a change in the electron configuration from $(d_{xy})^2(d_{xz},d_{yz})^4(d_{z^2})^1(d_{x^2-y^2})^1$ (as usually observed for high-spin nickel(II)) to $(d_{xy})^2(d_{z^2})^2(d_{x^2-y^2})^2(d_{xz},d_{yz})^2$, where the two unpaired electrons are each in one of the two d_π orbitals. Consistent with this, the phenyl-H resonances appear at +5.5 (*o*) and −4.5 (*m*) ppm.[995] This change in electron configuration seems quite extreme, and it may well be that the normally-expected electron configuration, together with macrocycle to Ni π donation to the half-filled d_{z^2} orbital,[156] even in this 6-coordinate Ni^{II} center, where the metal may be out of the plane of the four nitrogens, represents the actual situation. Warming these diphenylnickel(II) complexes resulted in their decomposition to nickel(I) species that have typical g-values of a d^9 system (2.411, 2.161, 2.049 for the phenyl complex in THF and 2.298, 2.140, 2.093 for the chloride complex). NMR signals could not be observed for these species.[995]

The nickel(II) complex of the "frustrated" porphyrin, 2-aza-5,10,15,20-tetraphenyl-21-carbaporphyrin ($CTPPH_2$) and its C-21-methyl analog have been prepared.[996] The C-21-methyl analog has been characterized structurally and contains a carbon-nickel bond, with the geometry about the carbon being very close to tetrahedral. The complex is diamagnetic. If the 2-N is also methylated, a paramagnetic complex (2-NCH_3-21-CH_3CTPP)NiCl is formed.[996] This complex shows seven separate pyrrole-H resonances when deuterated methyl bromide is used to prepare the di-CD_3 labeled complex.[996] The chemical shifts of pyrrole-protons are summarized in Table 17. Treatment of this dimethyl complex with phenyl Grignard reagents, phenyllithium created the Ni^{II}-σ-phenyl complex, which is high-spin.[997] One-electron reduction with excess PhLi yields [(2-NCH_3-21-CH_3CTPP)Ni^{II}Ph]$^-$, in which the macrocycle has become a π-anion radical. The presence of two paramagnetic centers in this complex produces remarkable variations in spectral patterns, including pyrrole resonances at both low and high shielding (+103.8, +96.7, −25.4, −51.0, −92.2, −114.8 ppm, and sign alternations of the *meso*-phenyl resonances (*ortho* −77.8, −79.3 ppm; *meta* +48.8, +48.0 ppm, *para* −85.7, −86.5 ppm, all at 253 K.[997] Different products are obtained with n-BuLi.

As a variation on the theme of porphyrin macrocycles with different donor atoms to the metal, the *meta*- and *para*-benziporphyrins have been investigated.[998–1000] These are macrocycles where one pyrrole ring has been replaced by either a *meta*- or a *para*-bound benzene ring. The *para*-bound macrocycle does not bind metals, but the *meta*-bound macrocycle, with a CH pointing in the same direction as the N of a typical porphyrin or the CH of the N-confused porphyrin discussed above, does react with Ni^{II} to produce 5-coordinate $Ni^{II}Cl$ complexes that have the 22-H

at about +205 ppm.[998] It appears that the H of the 22-CH can be removed so that the metal can form a diamagnetic 4-coordinate complex with the metal, but that upon HCl addition the complex becomes 5-coordinate and paramagnetic, with an H bound to the 22-carbon.[999]

As another variation on the theme of porphyrin macrocycles with different donor atoms to the metal, the coordinating properties of acetoxy-*meta*-benziporphyrin, (TPBPOAc)H have been investigated for a number of metal ions.[1001] Insertion of Ni, Pd and Fe results in the cleavage of the acetoxy group to yield complexes (TPBPO)M^{II} or $M^{III}X$, but no cleavage if M = Zn or Cd. The TPBPO ligand has one phenolate oxygen which can act as a ligand to the metal. The Pd^{II} and Ni^{II} complexes are 4-coordinate and diamagnetic, while the Fe^{III} complex is high-spin and 5-coordinate. Upon reaction with acetyl chloride the phenolate oxygen is again esterified and the Ni^{II} takes on a distorted 4-coordinate geometry with chloride as the fourth ligand. This complex is paramagnetic, with pyrrole-H resonances at about +65, +55 and +23 ppm.

As a final variation on the theme of porphyrin macrocycles with different donor atoms to the metal, the coordinating properties of the tetraaryl-21-vacataporphyrin (butadieneporphyrin, or annulene-porphyrin hybrid), which contains a vacant site instead of a heteratomic bridge, has been synthesized and its Zn, Cd and Ni complexes investigated.[1002] Two isomers can be made, with the cis-butadiene inside or outside the center of the macrocycle. Both isomers can form complexes with Ni^{II} in which one chloride ion is also bound to the metal. A 6-coordinate bis-imidazole complex can also be made; both are paramagnetic, with resonances extending from the diamagnetic region to about +67 ppm at 298 K.[1002] All of this work has been reviewed recently.[1003]

The EPR spectrum of the one-electron oxidized form of nickel(II) octaethylcorrole has been reported. The spectrum is axial with $g_{\perp} = 2.02$ and $g_{\parallel} = 2.00$,[983] which is suggestive of a π-radical of nickel(II), as proposed previously,[1004] although a g-value of 2.02 is very large for a carbon-centered unpaired electron. Either a d_{xy} unpaired electron for nickel(III) or the dioxygen complex of the d^7 nickel(III) center are also possible.

Electrolysis of 0.5 equivalents of the nickel(II) corrole produced $[(OECorr)Ni]_2^+$, whose EPR spectrum showed similar g-values but was broader than that of the monomeric nickel(III) complex.[983] Neither of these complexes has been characterized by NMR spectroscopy.

G. Lanthanide Porphyrins

The success of lanthanide, Ln^{III}, complexes as "shift reagents" for simplifying second-order NMR spectra of organic compounds with O or N functional groups,[1005,1006]

the extension of "shift reagent" techniques to the determination of the conformation of molecules, including biomolecules, in solution,[1007] and the use of other lanthanide ions as "broadening reagents,"[1008] especially in magnetic resonance imaging (MRI) applications, to increase contrast in images of tissues, has inevitably led to the preparation and investigation of lanthanide and actinide porphyrins. Because the oxidation state of stable lanthanide ions is typically +3, an anionic axial ligand is needed. Because of the higher coordination number preference of lanthanide ions, bidentate anionic ligands such as acylacetonate ($acac^-$) are often bound, or else a diporphyrin-$Ln^{III}H$ or di-Ln^{III}-triporphyrin "triple decker" complex is formed. Yet another means of satisfying the coordination desires of the lanthanide(III) ions is to used the "expanded porphyrin" texaphyrin, Structure **17**, along with two anionic ligands.

Lanthanide(III) porphyrin complexes were reported by Horrocks and coworkers,[1009,1010] for the [(TPP)Ln(acac)] complexes where Ln = Pr (f^2) to Lu (f^{14}). The aryl proton resonance shifts were found to be consistent with a dominant pseudocontact interaction with the metal atom situated significantly out of the porphyrin plane by ~1.6–1.8 Å (fit using the chemical shifts of the aryl protons) for the Yb^{III} and Eu^{III} complexes, respectively. The β-diketonate proton resonances are shifted to higher shielding, while the pyrrole-H resonance is usually shifted to lower shielding.[1010] The resonance shifts of the Yb^{III} complex are linear in 1/T with nonzero intercepts. Several of these complexes serve as "shift reagents" toward heterocyclic amines and alcohols, and it is believed that two of these ligands can bind on the same side as the β-diketonate, due to the large displacement of the metal from the porphyrin plane. The lutetium(III) complex is diamagnetic, and serves as a "ring-current" shift reagent to higher shielding, while ytterbium(III), erbium(III) and thulium(III) yield sizable shifts to lower shielding, terbium(III), dysprosium(III) and holmium(III) yield sizable shifts to higher shielding and praseodymium(III), neodymium(III), samarium(III) and europium(III) yield only small shifts of the "substrate" protons to lower shielding. In all cases, the direction of the shifts of the "substrate" were the same as those of the TPP protons, which suggests that the systems have effective axial symmetry on the NMR time scale, and, on average, the "substrate" occupies the equatorial region, where $(3\cos^2\theta - 1)$ is negative.[1010] Horrocks and Hove reported the preparation and NMR study of water-soluble lanthanide porphyrins based on tetra-*p*-sulfonatophenylporphyrin, $TPPS^{6-}$.[1011] Buchler and coworkers[1012,1013] and Machida and coworkers[1014–1016] reported the synthesis of diporphyrin sandwich compounds of cerium(IV) of the type [$(OEP)_2Ce$], [$(TPP)_2Ce$] (and a number of *p*-substituted derivatives of TPP) and [(TPP)(OEP)Ce]. The diamagnetic "double decker"' metallotetraphenylporphyrin complexes have the pyrrole-H resonance at 8.1–8.3 ppm for the neutrally-charged complexes in $CDCl_3$, and the *o*-H at 9.3–9.4 and 6.2–6.3 ppm for the "outside" and "inside" phenyl protons, and the *m*-H at more variable positions, depending on *p*-phenyl substituent, but again differing by up to

1.2 ppm, with the "inside" *m*-H at higher shielding (smaller chemical shift) than the "outside" *m*-H.[1012] The [$(OEP)_2Ce$] complex has the *meso*-H resonance at 9.11 ppm, the *exo*-CH at 4.20 ppm, the *endo*-CH at 3.86 ppm, and the $-CH_3$ at 1.68 ppm.[1017]

Two cofacial porphyrins, with 1,8-bis[5-(2,8,13,17-tetraethyl-3,7,12,18-tetramethyl)porphyrin]anthracene, DPA^{4-}, and 1,8-bis-[5-(2,8,13,17-tetraethyl-3,7,12,18- tetramethyl) porphyrin]biphenylene, DPB^{4-}, have been synthesized, and their dilutetium(III) complexes prepared.[1018] A crystal structure shows that the lutetium(III) ions are bridged by two hydroxides, and a methanol molecule is also bound to one of the lutetium(III) centers. These complexes are diamagnetic and have all resonances in the −1 to +10 region of the NMR spectrum.

Buchler and coworkers prepared the first di-lanthanide triple-decker molecules,[1017] in which two lanthanide(III) ions are bound to three porphyrins. The diamagnetic La^{III} complex [$(OEP)_3La_2$] has the external OEP resonances at +8.19 ppm (*meso*-H), $-CH_2$ resonances at +3.72 and +3.37 ppm, and $-CH_3$ resonance at +0.95 ppm, and the internal OEP resonances at +8.13 ppm (*meso*-H), $-CH_2$ at +4.09 ppm, and $-CH_3$ at +2.59 ppm, while the paramagnetic Ce^{III} complex has the external OEP resonances at +3.47 ppm (*meso*-H), $-CH_2$ resonances at +0.72 and −0.15 ppm and $-CH_3$ resonance at +2.08 ppm, and the internal OEP resonances at −8.12 ppm (*meso*-H), $-CH_2$ at −5.33 ppm and $-CH_3$ at −5.00 ppm. Thus the paramagnetic shifts of all resonances except the external $-CH_3$ are indicative of the mainly pseudocontact nature of the shifts.

A series of lanthanide complexes of texaphyrin, Structure **17**, have been synthesized and investigated by NMR spectroscopy.[1019] The complexes studied had the formula [$(Tx)Ln(NO_3)_2$], where Ln = Ce, Pr, Nd, Sm, Eu, Tb, Dy, Ho, Er, Tm and Yb. The ^1H resonances were assigned on the basis of 1D NOE, COSY and ROESY experiments, as well as line width and paramagnetic shift analysis. No reports of lanthanide porphyrin NMR studies have appeared since 1999.

H. Miscellaneous Metalloporphyrins which Have Extremely Broad Lines

1. *Copper(II) and Silver(II) Porphyrins*

As discussed in Section II.B.2.a, the electron configuration d^9 is one for which there are no low-lying excited states to which the ground state is connected by spin-orbit coupling (as is the case of low-spin d^5 and d^7), and thus ions with this electron configurations have long T_{1e}s,[93] well-resolved EPR spectra and poorly-resolved NMR spectra. Both of these metals have the single unpaired electron in the $d_{x^2-y^2}$ orbital, with $g_\parallel = 2.169$, $g_\perp = 2.062$ for [$(EP)Cu^{II}$][1020] and $g_\parallel = 2.104$, $g_\perp = 2.029$ for [$(DPDME)Ag^{II}$].[1021] To our knowledge, no proton NMR spectra (other than those of phenyl ring substituents of TPP derivatives,[2,4,164]) of these metalloporphyrins have been reported to date. Deuterium substitution at the pyrrole positions of

(TPP)Cu^{II}, and *meso* and β-CH_2 of (OEP)Cu^{II} and $-Ag^{II}$ has permitted detection of the β-pyrrole substituent resonances, as shown in Figure 80 for the copper(II) complexes. The extremely broad (1.15 kHz) pyrrole-D resonance of [(d_8-TPP)Cu^{II}][164] suggests that the ^1H resonance could be as broad as 48 kHz! The chemical shift at 25 °C is about +41 ppm, consistent with σ delocalization of the $d_{x^2-y^2}$ unpaired electron, and gives us an estimate of the positive contact shift contribution from a single unpaired electron in the $d_{x^2-y^2}$ orbital for a +2 metal. The *meso*-D and β-pyrrole $-CD_2$ resonances of [(d_{20}-OEP)Cu^{II}] are found at −6.2 ppm and +11.5 ppm, respectively, at 25 °C, while those of [(d_{20}-OEP)Ag^{II}] are found at −15.1 and +17.3 ppm, respectively. The $-CD_2$ resonance is about 103 Hz wide, suggesting that the $-CH_2$ resonance could be up to 4.3 kHz wide. However, in retrospect, the $-CH_2$ resonance of [(OEP)Cu^{II}] was found to be barely detectable, Figure 80, now that it is known where to look, and it is not nearly as broad as predicted by the ratio of 42. The pyrrole-D resonance of [(d_8-TPP)Ag^{II}] could not be detected.[164]

The *meso*-D shift to higher shielding, unlike those of 5-coordinate high-spin iron(III) porphyrins (Section IV.A.6.a) and 6-coordinate high-spin nickel(II) porphyrins (Section IV.F),[156] is counter-intuitive, and may represent polarization of the π-symmetry paired spin by the $d_{x^2-y^2}$ unpaired electron;[164] at least it is fairly small. The copper(II) complex of the thiaporphyrin, (STPP), has been prepared and examined by NMR spectroscopy.[992] The pyrrole-D resonances are observed at +49.9, +38.5 and +29.6 ppm, and the thiophene-H resonance at −9 ppm for the 5-coordinate [(d_6-STPP)CuCl] at 298 K in toluene solution. The phenyl resonances are clustered around 7.5 ppm, and they show the shift pattern typical of π delocalization: *meta*-H to lower shielding, *ortho*- and *para*-H to higher shielding with respect to their diamagnetic resonances.[992]

One-electron oxidation of [(d_8-TPP)Cu^{II}] and [(d_{20}-TPP)Cu^{II}] produces complexes in which the pyrrole-D signal appears at +13.4 ppm and the *o*, *m* and *p*-D resonances are at −4.9, +15.8 and −1.01 ppm, respectively.[164] The pyrrole-D resonance is considerably sharper (~ +220 Hz) than for the parent complex. The alternating pattern of phenyl-D shifts suggests that this complex has an $a_{2u}(\pi)$ unpaired electron. In contrast, study of [(d_{20}-OEP)Cu^{III}]$^+$ and [(d_4-OEP)Cu^{III}]$^+$ showed the β-pyrrole-CH_2 resonance to be at +17.1 ppm and the *meso*-D at −4.1 ppm, which suggested to the authors that in this case the electron has been removed from the $a_{1u}(\pi)$ orbital.[164] It is also possible that, if the complex is 5-coordinate, there may be delocalization from the $a_{2u}(\pi)$ orbital to the half-filled d_{z^2} orbital.[156]

Aggregation of copper(II) porphyrins under various conditions has been investigated in detail by EPR spectroscopy.[1022] The close proximity of the two copper centers in the aggregated forms produces not only a $m_S = \pm 1$ allowed transition in the 3100–3300 G region of the X-band EPR spectrum, but also a $m_S = \pm 2$ "double quantum" spin-forbidden transition at half the magnetic field, near 1500–1600 G.[1022]

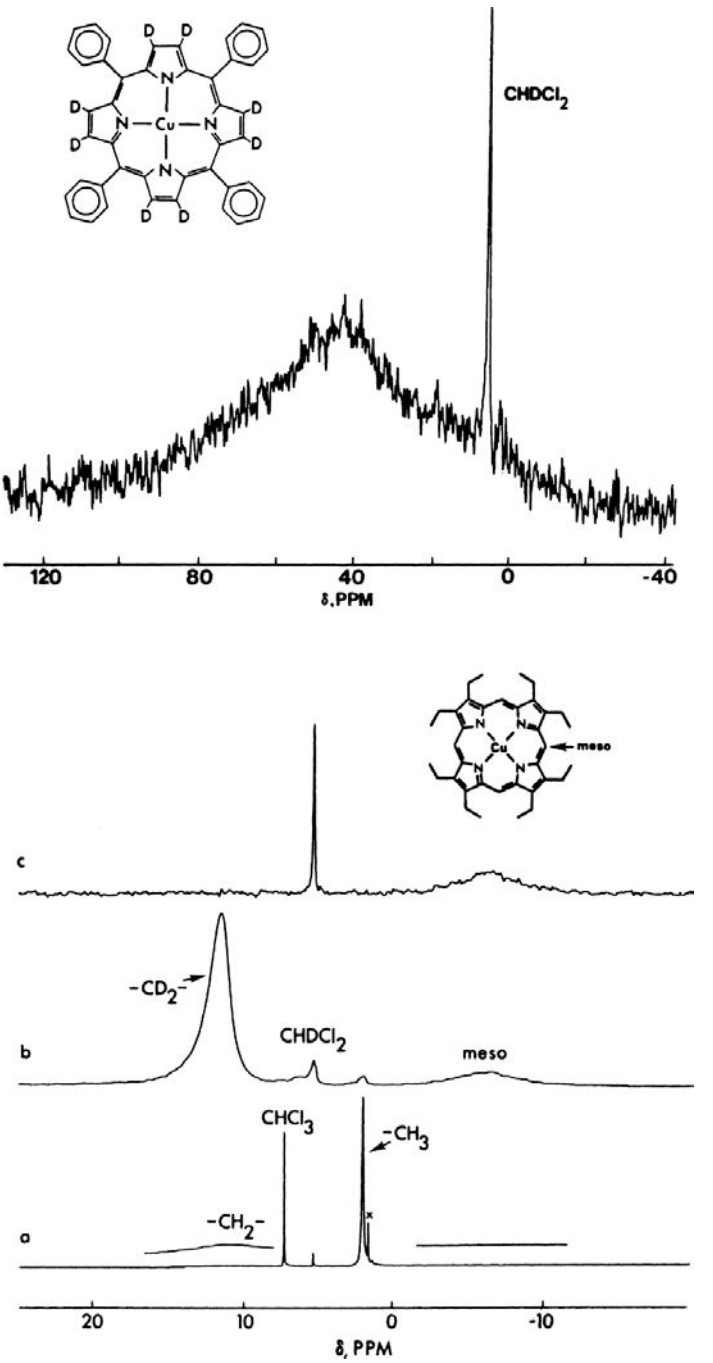

Figure 80. Top: ^{2}H NMR spectrum of [(d_8-TPP)Cu] in CH_2Cl_2 at 25 °C. Bottom: Proton and deuterium NMR spectra of (OEP)Cu: (a) proton NMR spectrum of [(OEP)Cu] in $CDCl_3$; (b) deuterium NMR spectrum of [(d_{20}-OEP)Cu] in CH_2Cl_2; deuterium NMR spectrum of [(d_4-OEP)Cu] in CH_2Cl_2, all recorded at 25 °C. Reprinted from Godziela, G. M.; Goff, H. M. *J. Am. Chem. Soc.* **1986**, *108*, 2237–2243, with permission from the American Chemical Society.

Following that publication, several singly- and doubly-bridged dicopper diporphyrins have been synthesized and studied by EPR spectroscopy to determine the geometry of the dimeric porphyrin.[1023] The distance between the copper atoms in the diporphyrins was determined from the ratio of the intensity of the half-field transitions to the intensity of the allowed transitions and by computer simulation of the spectra. The values obtained by the two methods were in good agreement and ranged from 4.1 to 5.6 Å. The porphyrin planes were parallel within experimental uncertainty. The angle between the interspin vector and the normal to the porphyrin planes (slip angle) was determined by computer simulation of the spectra and values ranged from 20° to 45°. For the majority of the diporphyrins the separation between the porphyrin planes was 3.9 ± 0.1 Å. In an anthracene pillared diporphyrin the interplanar separation was 4.6 Å. The simulations of the spectra indicated that the absolute value of the copper-copper exchange interaction, J, was > 0.3 cm^{-1}.[1023]

2. *Vanadium(IV) Porphyrins*

As is the case for copper(II) and silver(II) porphyrins, vanadyl (VO^{2+}) porphyrins, with a d_{xy}^1 electron configuration also have no low-lying excited states to which the ground state is connected by spin-orbit coupling, and thus ions with this electron configurations have long T_{1e}s,[93] well-resolved EPR spectra and poorly-resolved NMR spectra. Furthermore, unlike copper(II) and silver(II) porphyrins, the g-tensor of vanadyl porphyrins is nearly isotropic.[121,122] Thus extremely small pseudocontact shifts are expected, and in addition, no contact shifts are expected for complexes of this nonruffled metalloporphyrin. The paramagnetic shifts of vanadyl porphyrins are thus expected to be extremely small. Except for several VOTPP entries in Table 32 of Ref. 2, which listed the pyrrole-H and phenyl-H shifts as those expected for diamagnetic porphyrins (Zn(II), Ni(II)), no other reports of proton NMR studies of monomeric vanadyl porphyrins have appeared. However, the preparation and characterization of a π-cation radical derivative of a vanadyl porphyrinate, $[VO(OH_2)(OE\,P^{-\bullet})]SbCl_6$ by chemical oxidation of [VO(OEP)] has been reported, and the formulation has been confirmed by a single-crystal X-ray structure determination.[123] EPR spectra were measured for $[VO(OH_2)(OE\,P^{-\bullet})]SbCl_6$ in the solid (powder) state, in a single crystal, and in fluid and frozen solution. The solution-state EPR spectra of $[VO(OH_2)(OE\,P^{-\bullet})]SbCl_6$ were found to be quite distinct, with vanadium hyperfine lines resolved, and with different spectra in fluid and frozen solution. The solution spectra are identical to those reported earlier by others.[1024–1026] In the solid state, the EPR spectrum of a polycrystalline sample consists of a single broad line with g = 1.99; single-crystal spectra also show vanadium hyperfine-splitting consistent with V–V coupling. The solid-state EPR intensity increases with increasing temperature. $[VO(OH_2)(OE\,P^{-\bullet})]SbCl_6$ was also characterized by a detailed temperature-dependent (6–300 K) magnetic susceptibility study. Satisfactory fits of the temperature-dependent

moments were obtained from a model in which the vanadyl electron is ferromagnetically coupled to the porphyrin π-radical electron ($J_{V\text{-}R} = 63\ cm^{-1}$) and the two radical spins are antiferromagnetically coupled ($J_{R\text{-}R} = -139\ cm^{-1}$). This model also gave a satisfactory prediction of all solid-state EPR properties.[123] The intramolecular ferromagnetic coupling is consistent with the principle of cospatial, orthogonal magnetic orbitals. The intermolecular antiferromagnetic coupling appears to arise from a novel, steplike orientation of pairs of $[VO(OEP^{-\bullet})]^+$ radicals. Unfortunately, no NMR studies of this radical system at ambient temperatures were reported.

3. *Chromium Porphyrins*

Until recently, there was little information about the paramagnetic shifts of chromium(III) porphyrins because of the extreme broadness of the resonances.[2,4,165] However, as discussed in Section II.D.2 and shown in Figure 12, deuterium labeling of several chromium(III) porphyrins has allowed observation of the ^2H resonances of these complexes.[165] The shifts observed for [(d_8-TPP)Cr(OPh-d_5)] at 24 °C are −13.4 ppm (pyrrole-D) and +19, +11.5, +10 ppm (*p*-H, *m*-H, *o*-H, respectively), while the pyrrole-D shift of [(d_8-TPP)CrCl] is −16.7 ppm in THF but −17.5 ppm in $CHCl_3$ and CH_2Cl_2, all at 23–24 °C. Addition of imidazole to a sample in the latter solvent shifts the pyrrole-D to a limiting value of −23 ppm, probably due to formation of a mono-imidazole complex.[165] These shifts are consistent with the expected electron configuration for chromium(III): $(d_{xy})^1(d_{xz})^1(d_{yz})^1$, where the d_{xy} unpaired electron could contribute a maximum of +1–2 ppm shift that will decrease the negative shift expected for the two d_π electrons. (However, the porphyrinate ring of [(TPP)Cr(OPh)(THF)] appears to be planar, with the Cr in the plane of the porphyrin nitrogens,[165] and if the THF remains coordinated in $CHCl_3$ and CH_2Cl_2, then the d_{xy} electron may not provide any delocalization.) Even taking this contribution into account, however, the pyrrole-D shift is not nearly as negative as might have been expected on the basis of the pyrrole-H shifts of low-spin iron(III) porphyrins having the $(d_{xy})^2(d_{xz},d_{yz})^3$ electron configuration (Figure 19); if the two d_π unpaired electrons each contributed the same as the single d_π unpaired electron of low-spin iron(III), then a chemical shift of about −41 ppm at 25 °C should be expected, assuming no contact contribution from the d_{xy} electron, whereas the observed pyrrole-D shifts range from −13 to −17 ppm for the 5-coordinate complexes. Thus, it appears that at least in this case, two d_π electrons do not lead to significantly greater spin delocalization from the 3e(π) orbitals of the porphyrin ring to the d_π orbitals of chromium(III) than does the one of low-spin iron(III). The temperature dependence of the pyrrole-D resonance of [(d_8-TPP)Cr(OPh)(THF)] in THF solution is strictly Curie in nature, while the intercepts of the phenoxide deuterons deviate somewhat from their predicted diamagnetic shifts in an alternating fashion that suggests some

π spin density is delocalized to the phenoxide axial ligand.[165] In fact, it may be this spin delocalization that decreases the pyrrole-H shift somewhat.

The d^4 chromium(II) porphyrin, [(d_8-TPP)Cr], prepared by one-electron reduction of [(d_8-TPP)CrCl], has a larger negative pyrrole-D shift than any of the chromium(III) complexes mentioned above, –34.9 ppm at 24 °C.[165] The presumed electron configuration is $(d_{xy})^1(d_{xz})^1(d_{yz})^1(d_{z^2})^1$, and the d_{z^2} electron is expected to contribute essentially nothing to the contact shifts, because the Cr^{II} is not expected to be out of the plane of the porphyrin nitrogens.[156] Thus, chromium(II) has a pyrrole-D shift closer to that expected for the chromium(III) analog, and the reason for the difference is not clear. The temperature dependence of the pyrrole-D shift is linear, with an extrapolated shift at infinite temperature of 12 ppm, which suggests only a small contribution from a thermally-accessible excited state.

In the presence of an excess of pyridine, the pyrrole-D resonance shifts to about +12.8 ppm, suggesting a change in electron configuration. A similar shift is observed when imidazole is added.[165] The magnetic moment of the bis-(pyridine) complex of [(d_8-TPP)Cr] is 2.9 μ_B at 23 °C,[376,377] indicating two unpaired electrons.[165] The positive value of the pyrrole-D shift is suggestive of no unpaired electrons in the d_{xz} or d_{yz} orbitals, unless there is an unusually large positive pseudocontact shift for this S = 1 chromium(II) porphyrin that cancels the expected negative contact shift, such as those observed for low-spin d^4 iron porphyrins.[157,832] Additional low-spin chromium(II) porphyrin complexes must be investigated before a complete understanding of the contributions to the paramagnetic shifts can be obtained. The linewidth of the ^{1}H signal of the pyrrole-H is sharp enough[165] that such a study could be done with protonated porphyrin ligands.

An oxochromium(IV) complex has also been investigated. When [(d_8-TPP)CrCl] is reacted with *tert*-butylhydroperoxide at –40 °C, followed by warming, a new ^{2}H signal is observed at +9.2 ppm at 23 °C.[165] However, the hydroperoxide also attacks the porphyrin to produce an isoporphyrin,[165] which makes it difficult to study the diamagnetic d^2 chromium(IV) center in detail. Nevertheless, the fact that the complex is diamagnetic suggests that the electron configuration is $(d_{xy})^2$. This is consistent with the electron configuration of oxovanadium(IV) porphyrins, $(d_{xy})^1$.[121,122] No further reports of NMR studies of chromium porphyrins of any oxidation state have appeared since 1999.

I. Summary of Paramagnetic Shifts and Mechanisms of Spin Delocalization for the Metalloporphyrins

In Table 18 are summarized the magnitudes and directions of contact and pseudocontact shifts for first row transition metal porphyrins, the nature (σ or π) of the contact shifts, and the nature of the pseudocontact contribution for each metal in

Table 18. Summary of spin delocalization patterns of metalloporphyrins of various oxidation and spin states.

Metal	Oxidation state	Number of d electrons	Spin state	Orbital of unpaired electron(s)	Pseudocontact shifts	Contact shifts		Dominant type of π charge transfer
						Pyrrole-C	*meso*-C	
Cr	II	4	S = 2	$(d_{xy})^1(d_{xz}, d_{yz})^2(d_{z^2})^1$	N.D.	π	N.D.	P⇒M
			S =1	$(d_{xy})^1(d_{z^2})^1$?	N.D.	σ	N.D.	(?)
	III	3	S = 3/2	$(d_{xy})^1(d_{xz}, d_{yz})^2$	(Small)	π	N.D.	P⇒M
	IV	2	S = 0	—	—	—	—	—
Mn	II	5	S = 5/2	All 5 d	Large (+) exp. $\alpha D/T^2$ exp.	σ	π	P⇒M
	II $Por^{-\bullet}$	5	S = 3/2,1/2	$(3a_{2u})^1(d_{z^2})^1(d_{xz},d_{yz})^2$ $Por^{-\bullet}$ AF coupled	Medium(+) exp. $\alpha(g_{\parallel}^2-g_{\perp}^2)/T$ expected	π	Small	P⇒M
	III	4	S = 2	$(d_{xy})^1(d_{xz},d_{yz})^2(d_{z^2})^1$	(Small)	π	σ?	P⇒M
			S = 1?	$(d_{xz},d_{yz})^2$?	N.D	π	σ?	
(See Mn(II) $Por^{-\bullet}$ (π-cation radical) for more likely electron configuration)								
	IV	3	S = 3/2	$(d_{xy})^1(d_{xz},d_{yz})^2$	(Small)	π	N.D.	P⇒M
Fe	I	7	S = 1/2	$(d_{z^2})^1$	Medium (+) $\alpha(g_{\parallel}^2-g_{\perp}^2)/T$	(–Shifts)	Small (σ?)	—
	II	6	S = 0	—	—	—	—	—
			S = 1	$(d_{xz},d_{yz})^2$	Large (+) $\alpha(g_{\parallel}^2-g_{\perp}^2)/T$	π	0	P⇒M
	II	6	S = 2	$(d_{xz},d_{yz})^2(d_{z^2})^1(d_{z^2-y^2})^1$	(Small)	σ	π	P⇒M
	II $Por^{-\langle}$	6(paired)	S = 1/2	$(3a_{2u})^1$	None	Small π	Large π	—

(*Continued*)

Table 18. (*Continued*)

Metal	Oxidation state	Number of d electrons	Spin state	Orbital of unpaired electron(s)	Pseudocontact shifts	Contact shifts		Dominant type of π charge transfer
						Pyrrole-C	*meso*-C	
	III	5	S = 1/2	$(d_{xz},d_{yz})^3$	Large (–) $\alpha(g_{\|}^2-g_{\perp}^2)/T$	π	Small (σ?)	P⇒M
			S = 1/2	$(d_{xy})^1$	Small (+) $\alpha(g_{\|}^2-g_{\perp}^2)/T$	0?	π	P⇒M
			S = 3/2	$(d_z2)^1(d_{xz},d_{yz})^2$	Medium (+) $\alpha(g_{\|}^2-g_{\perp}^2)/T$	π	π	P⇒M
			S = 3/2,5/2 admixed	$(d_{xz},d_{yz})^2(d_{x^2-y^2})^?$	Small (+) Mixed	π, σ mixed	Mixed	P⇒M
	III	5	S = 5/2	all 5 d	Large (+) $\alpha D/T^2$	σ	π	P⇒M
	III $Por^{-\bullet}$	5	S = 3	$(3a_{2u})^1$, plus all 5 d for TPPs	N.D.[a]		Large + π	—
			S = 2	$(3a_{2u})^1$, plus all 5 d	N.D.	σ	Large – π	—
			S = 1	$(3a_{2u})^1(d_{xz},d_{yz})^2(d_{z^2})^1$	N.D.[a]	π	Large – π	—
			S = 1	$(3a_{2u})^1(d_{xz},d_{yz})^3$	N.D.[a](?)	π	Large + π	P⇒M
	IV	4	S = 1	$(d_{xz},d_{yz})^2$	N.D.[a]	π	Small	P⇒M
			S = 1	ferryl $(d_{xz},d_{yz})^2$, but much spin delocalized to oxo	Small $\alpha(g_{\|}^2-g_{\perp}^2)$	Small π	0	P⇒M
			S = 1	phenyl $(d_{xz},d_{yz})^2$	Small	Large π	Small ?	P⇒M
	IV$Por^{-\bullet}$	4	S = 1/2	$(3a_{2u})^1(d_{xz},d_{yz})^2(TMP^{-\bullet})$	N.D.[a]	Small π	Large –?	P⇒M
			S = 1/2	$(1a_{1u})^1(d_{xz},d_{yz})^2$ (TMTMP)	N.D.[a]	Large π	Small ?	P⇒M
	V?	3	S = 3/2	$(d_{xy})^1(d_{xy},d_{yz})^2$	N.D.[a]	~0	N.D.	N.D.

(*Continued*)

Table 18. (*Continued*)

Metal	Oxidation state	Number of d electrons	Spin state	Orbital of unpaired electron(s)	Pseudocontact shifts	Contact shifts		Dominant type of π charge transfer
						Pyrrole-C	*meso*-C	
Ru	II	6	S = 0	—	—	—	—	—
	III	5	S = 1/2	$(d_{xy})^1$	Small (+) $\alpha(g_\parallel{}^2-g_\perp{}^2)/T$	~0	π	P⇒M
	IV	4	S = 1	$(d_{xy},d_{yz})^2$	N.D.[a]	Large π	~0	P⇒M
	VI	2	S = 0	—	—	—	—	—
Co	II	7	S = 1/2	$(d_{z^2})^1$	Medium (+) $\alpha(g_\parallel{}^2-g_\perp{}^2)/T$	(Shifts)	Small (σ?)	—
			S = 3/2	$(d_{xz},d_{yz})^3(d_{z^2})^1(d_{x^2-y^2})^1$	Medium	σ	Small	—
	II Por$^{-\cdot}$	7	S = 1	$(3a_{2u})^1(d_{z^2})^1$	Medium (+) expected	Small	Small	—
Co	III	6	S = 0	—	—	—	—	—
Ni	II	8	S = 0	—	—	—	—	—
	II	8	S = 1	$(d_{z^2})^1(d_{x^2-y^2})^1$	Medium (–) $\alpha D/T^2$	σ	π	P⇒M
Cu, Ag	II	9	S = 1/2	$(d_{x^2-y^2})^1$	Small (+)	σ	?	—
	II Por$^{-\cdot}$	9	S = 1	$(3a_{2u})^1(d_{x^2-y^2})^1$	N.D.	σ	π	—
Ln	III	0–14	Variable	variable	Large (+ or –)	Very small	Very small	—

N.D. = not determined.

each oxidation state and each spin state. As can be seen, for the contact shift, σ spin delocalization to the porphyrin or related macrocycle is seen when there is an unpaired electron in the $d_{x^2-y^2}$ orbital, while π spin delocalization is seen when there is an unpaired electron in the d_{xz} or d_{yz} orbital (or both), or, if the macrocycle is ruffled or saddled, if there is an unpaired electron in the d_{xy} orbital. In every example seen thus far, delocalization of both σ and π spin density occurs by macrocycle to metal electron donation, which leaves a hole or partial hole on the macrocycle, which is readily sensed by the protons (and carbons) of the macrocycle, and it has been estimated that 3% of an unpaired electron in a π orbital of a particular carbon leads to a contact shift of approximately −20 ppm for the proton bound to that carbon. The π-symmetry orbitals most frequently involved in P → M electron delocalization, which give rise to π spin delocalization to the carbons of the macrocycle, are the $3e(\pi)$ orbitals, which have proper symmetry for interaction with the d_{xz} and d_{yz} orbitals of the metal. However, if the macrocycle is ruffled, the $3a_{2u}(\pi)$ orbital has proper symmetry to interact with the d_{xy} orbital (and the $1a_{1u}(\pi)$ orbital has proper symmetry to interact with the $d_{x^2-y^2}$ orbital), while if the macrocycle is saddled, the $3a_{2u}(\pi)$ orbital has proper symmetry to interact with the $d_{x^2-y^2}$ orbital (and the $1a_{1u}(\pi)$ orbital has proper symmetry to interact with the d_{xy} orbital). If the metal is out of the plane of the porphyrin nitrogens (as in a 5-coordinate metalloporphyrin complex), there can be a different means of involving the $3a_{2u}(\pi)$ orbital in spin delocalization, in this case by P → M π donation from the $3a_{2u}(\pi)$ orbital to the half-filled d_{z^2} orbital of the metal (for high-spin d^5, d^6 and d^8); this spin delocalization is prohibited if the complex binds a second axial ligand. A major finding of the past ten years is that there is at this time no evidence for the involvement of the $4e(\pi^*)$ orbitals in spin delocalization for any metalloporphyrin.

V. Acknowledgments

This chapter is dedicated to the memory of Professor Richard Koerner of Pennsylvania State University, whose life ended much too soon, on December 17, 2002, as a result of pneumonia. As an undergraduate in the author's laboratory, Richard did the majority of the work reported in Ref. 419. Richard obtained his Ph.D. at U. C. Davis where he worked with Professor Alan L. Balch on projects referenced in this chapter that involved "deconstructing" the heme ring. He then became a postdoctoral fellow with Professor Richard H. Holm, and went from there to Penn State University in the fall of 2001, where he began his independent career.

The author wishes to thank Dr. Nikolai V. Shokhirev for continually updating and modifying the programs on his website, especially ShiftPatterns, MPorphW and TDFW, so that they are more and more useful to those who wish to analyze the chemical shifts or spin density distributions of metalloporphyrins and related

macrocycles. She also wishes to thank all of her present and former talented coworkers for their positive contributions to the work from this laboratory which is discussed in this chapter, and Mary Sparks, who prepared the structures and tables.

VI. References

1. Walker, F. A. *Inorg. Chem*. **2003**, *42*, 4526–4544.
2. La Mar, G. N.; Walker, F. A. In *The Porphyrins*; Dolphin, D., Ed.; Academic Press: New York, **1979**; Vol. IVB, pp. 57–161.
3. Walker, F. A.; Simonis, U. In *Biological Magnetic Resonance*; Berliner, L. J.; Reuben, J., Eds.; Plenum: New York, **1993**; Vol. 12, pp. 133–274.
4. Walker, F. A. In *The Porphyrin Handbook*; Kadish, K. M.; Smith, K. M.; Guilard, R., Eds.; Academic Press: Boston, **2000**, Chapter 36, Vol. 5, pp. 81–183.
5. Satterlee, J. D. In *Metal Ions in Biological Systems*; Sigel, H., Ed; Marcel Dekker: New York, **1987**; Vol. 21, pp. 121–185.
6. Thanabal, V.; de Ropp, J. S.; La Mar, G. N. *J. Am. Chem. Soc*. **1988**, *110*, 3027–3035.
7. McLachlan, S. J.; La Mar, G. N.; Lee, K. B. *Biochim. Biophys. Acta* **1988**, *957*, 430–445.
8. Shokhirev, N. V.; Walker, F. A. *J. Biol. Inorg. Chem.* **1998**, *3*, 581–594.
9. Keller, R. M.; Schejter, A.; Wüthrich, K. *Biochim. Biophys. Acta* **1980**, *626*, 15–22.
10. Emerson, S. D.; La Mar, G. N. *Biochemistry* **1990**, *29*, 1545–1556.
11. Emerson, S. D.; La Mar, G. N. *Biochemistry* **1990**, *29*, 1556–1566.
12. Lee, K.-B.; La Mar, G. N.; Kehres, L. A.; Fujinari, E. M.; Smith, K. M.; Pochapsky, T. C.; Sligar, S. D. *Biochemistry* **1990**, *29*, 9623–9631.
13. La Mar, G. N. In *Biological Applications of Magnetic Resonance*; Shulman, R. G., Ed.; Academic Press: New York, **1979**; pp. 305–343.
14. Keller, R. M.; Wüthrich, K. In *Biological Magnetic Resonance*; Berliner, L. J.; Reuben, J., Eds.; Plenum Press: New York, **1981**, Vol. 3, pp. 1–52.
15. Goff, H. M. In *Iron Porphyrins*; Lever, A. B. P.; Gray, H. B., Eds.; Addison-Wesley: Reading, MA, **1983**; Part 1, pp. 239–281.
16. Satterlee, J. D. *Ann. Reports. NMR Spectrosc.* **1986**, *17*, 79–179.
17. Bertini, I.; Turano, P.; Vila, A. *Chem. Rev.* **1993**, *93*, 2833–2932.
18. Yamamoto, Y. *Ann. Rep. NMR Spectrosc.* **1998**, *36*, 1–77.
19. La Mar, G. N.; Satterlee, J. D.; de Ropp, J. S. In *The Porphyrin Handbook*; Kadish, K. M.; Smith, K. M.; Guilard, R., Eds.; Academic Press: New York, **2000**; Chapter 37, pp. 185–298.
20. Banci, L.; Bertini, I.; Luchinat, C.; Turano, P. In *The Porphyrin Handbook*, Kadish, K. M.; Smith, K. M.; Guilard, R., Eds.; Academic Press: New York, **2000**; Vol. 5, Chapter 39, pp. 323–350.
21. Sotiriou, C.; Chang, C. K. *J. Am. Chem. Soc.* **1988**, *110*, 2264–2270.
22. Chang, C. K.; Wu, W. *J. Biol. Chem.* **1986**, *261*, 8593–8596.
23. Kurland, R. J.; McGarvey, B. R. *J. Magn. Reson.* **1970**, *2*, 286–300.
24. Jesson, J. P. In *NMR of Paramagnetic Molecules*; La Mar, G. N.; Horrocks, W. D.; Holm, R. H., Eds.; Academic Press: New York, **1973**; pp. 1–53.
25. Shokhirev, N. V.; Walker, F. A. *J. Phys. Chem.* **1995**, *99*, 17795–17804.
26. McConnell, H. M. *J. Chem. Phys.* **1956**, *24*, 764–766.
27. McLachlan, A. D. *Mol. Phys.* **1958**, *1*, 233–240.

28. Chestnut, D. B. *J. Chem. Phys.* **1958**, *29*, 43–47.
29. Carrington, A.; McLachlan, A. D. *Introduction to Magnetic Resonance*; Harper & Row: New York, **1967**; p. 80.
30. Horrocks, W. D.; Greenberg, E. S. *Biochim. Biophys. Acta* **1973**, *322*, 38–44.
31. Horrocks, W. D.; Greenberg, E. S. *Mol. Phys.* **1974**, *27*, 993–999.
32. Munro, O. Q.; Marques, H. M.; Debrunner, P. G.; Mohanrao, K.; Scheidt, W. R. *J. Am. Chem. Soc.* **1995**, *117*, 935–954.
33. Safo, M. K.; Gupta, G. P.; Walker, F. A.; Scheidt, W. R. *J. Am. Chem. Soc.* **1991**, *113*, 5497–5510.
34. Safo, M. K.; Gupta, G. P.; Watson, C. T.; Simonis, U.; Walker, F. A.; Scheidt, W. R. *J. Am. Chem. Soc.* **1992**, *114*, 7066–7075.
35. Brackett, G. D.; Richards, P. L.; Caughey,W. S. *J. Chem. Phys.* **1971**, *54*, 4383–4401.
36. La Mar, G. N.; Eaton, G. R.; Holm, R. H.; Walker, F. A. *J. Am. Chem. Soc.* **1973**, *95*, 63–75.
37. Kuriyan, J.; Wilz, S.; Karplus, M.; Petsko, G. A. *J. Mol. Biol.* **1986**, *192,* 133–1541.
38. Nguyen, B. D.; Xia, Z.; Yeh, D. C.; Deaguero, H.; La Mar, G. N. *J. Am. Chem. Soc.* **1999**, *121*, 208–217.
39. Thomson, A. J.; Gadsby, P. M. A. *J. Chem. Soc., Dalton Trans.* **1990**, 1921–1928.
40. Turano, P.; Battaini, G.; Casella, L. *Chem. Phys. Lett.* **2003**, *373*, 460–463.
41. Balayssac, S.; Bertini, I.; Lelli, M.; Luchinat, C.; Maletta, M. *J. Am. Chem. Soc.* **2007**, *129*, 2218–2219.
42. Balayssac, S.; Bertini, I.; Bhaumik, A.; Lelli, M. ; Luchinat, C. *Proc. Natl. Acad. Sci. USA* **2008**, *105*, 17284–17289.
43. Tolman, J. R.; Flanagan, J. M.; Kennedy, M. A.; Prestegard, J. H. *Proc. Natl. Acad. Sci. USA* **1995**, *92*, 9279–9283.
44. Kay, L. E.; Xu, G. Y.; Yamazaki, T. *J. Magn. Reson. A* **1994**, *109*, 129–133.
45. Sahu, S. C.; Simplaceanu, V.; Gong, Q.; Ho, N. T.; Glushka, J. G.; Prestegard, J. H.; Ho, C. *J. Am. Chem. Soc.* **2006**, *128*, 6290–6291.
46. Salvatore, B. A.; Ghose, R.; Prestegard, J. H. *J. Am. Chem. Soc.* **1996**, *118,* 4001–4008.
47. Tian, F.; Al-Hashimi, H. M.; Craighead, J. L.; Prestegard, J. H. *J. Am. Chem. Soc.* **2001**, *123,* 485–492.
48. Tolman, J. R.; Al-Hashimi, H. M.; Kay, L. E.; Prestegard J. H. *J. Am. Chem. Soc.* **2001**, *123,* 1416–1424.
49. Tian, F.; Valafar, H.; Prestegard, J. H. *J. Am. Chem. Soc.* **2001**, *123,* 11791–11796.
50. Seidel III, R. D.; Zhuang, T.; Prestegard, J. H. *J. Am. Chem. Soc.* **2007**, *129,* 4834–4839.
51. Su, X.-C.; McAndrew, K.; Huber, T.; Otting, G. *J. Am. Chem. Soc.* **2008**, *130*, 1681–1687.
52. Kamen, D. E.; Cahill, S. M.; Girvin, M. E. *J. Am. Chem. Soc.* **2007**, *129*, 1846–1847.
53. Martin, L. J.; Hähnke, M. J.; Nitz, M.; Wöhnert, J.; Silvaggi, N. R.; Allen, K. N.; Schwalbe, H.; Imperiali, B. *J. Am. Chem. Soc.* **2007**, *129*, 7106–7113.
54. Prestegard, J. H. *Nat. Struct. Biol.* **1998**, *5*, 517–522.
55. Dames, S. A.; Aregger, R.; Vajpai, N.; Bernado, P.; Blackledge, M.; Grzesiek, S. *J. Am. Chem. Soc.* **2006**, *128*, 13508–13514.
56. Atreya, H. S.; Garcia, E.; Shen, Y.; Szyperski, T. *J. Am. Chem. Soc.* **2007**, *129*, 680–692.
57. Meier, S.; Strohmeier, M.; Blackledge, M.; Grzesiek, S. *J. Am. Chem. Soc.* **2007**, *129*, 754–755.
58. Burton, R. A.; Tjandra, N. *J. Am. Chem. Soc.* **2007**, *129(5)*, 1321–1326
59. Cho, M.-K.; Kim, H.-Y.; Bernado, P.; Fernandez, C. O.; Blackledge, M.; Zweckstetter, M. *J. Am. Chem. Soc.* **2007**, *129*, 3032–3033.

60. Showalter, S. A.; Brüschweiler, R. *J. Am. Chem. Soc.* **2007**, *129*, 4158–4159.
61. Markwick, P. R. L.; Bouvignies, G.; Blackledge, M. *J. Am. Chem. Soc.* **2007**, *129*, 4724–4730.
62. Mukrasch, M. D.; Markwick, P.; Biernat, J.; von Bergen, M.; Bernadó, P.; Griesinger, C.; Mandelkow, E.; Zweckstetter, M.; Blackledge, M. *J. Am. Chem. Soc.* **2007**, *129*, 5235–5243.
63. Hu, K.; Vögeli, B.; Clore, G. M. *J. Am. Chem. Soc.* **2007**, *129*, 5484–5491.
64. Kummerlöwe, G.; Auernheimer, J.; Lendlein, A.; Luy, B. *J. Am. Chem. Soc.* **2007**, *129*, 6080–6081.
65. Vögeli, B.; Ying, J.; Grishaev, A.; Bax, A. *J. Am. Chem. Soc.* **2007**, *129*, 9377–9385.
66. Meier, S.; Grzesiek, S.; Blackledge, M. *J. Am. Chem. Soc.* **2007**, *129*, 9799–9807.
67. Pileio, G.; Guo, Y.; Pham, T. N.; Griffin, J. M.; Levitt, M. H.; Brown, S. P. *J. Am. Chem. Soc.* **2007**, *129*, 10972–10973.
68. Sprangers, R.; Kay, L. E. *J. Am. Chem. Soc.* **2007**, *129*, 12668–12669.
69. Bertini, I.; Gupta, Y. K.; Luchinat, C.; Parigi, G.; Peana, M.; Sgheri, L.; Yuan, J. *J. Am. Chem. Soc.* **2007**, *129*, 12786–12794.
70. Schuetz, A.; Junker, J.; Leonov, A.; Lange, O. F.; Molinski, T. F.; Griesinger, C. *J. Am. Chem. Soc.* **2007**, *129*, 15114–15115.
71. Lorieau, J.; Yao, L.; Bax, A. *J. Am. Chem. Soc.* **2008**, *130*, 7536–7537.
72. Marsh, J. A.; Baker, J. M. R.; Tollinger, M.; Forman-Kay, J. D. *J. Am. Chem. Soc.* **2008**, *130*, 7804–7805.
73. Hansen, D. F.; Vallurupalli, P.; Kay, L. E. *J. Am. Chem. Soc.* **2008**, *130*, 8397–8405.
74. Hus, J.-C.; Salmon, L.; Bouvignies, G.; Lotze, J.; Blackledge, M.; Brüschweiler, R. *J. Am. Chem. Soc.* **2008**, *130*, 15927–15937.
75. Yao, L.; Vögeli, B.; Ying, J.; Bax, A. *J. Am. Chem. Soc.* **2008**, *130*, 16518–16520.
76. De Simone, A.; Richter, B.; Salvatella, X.; Vendruscolo, M. *J. Am. Chem. Soc.* **2009**, *131*, 3810–3811.
77. Baldwin, A. J.; Hansen, D. F.; Vallurupalli, P.; Kay, L. E. *J. Am. Chem. Soc.* **2009**, *131*, 11939–11948.
78. Thiele, C. M.; Maliniak, A.; Stevensson, B. *J. Am. Chem. Soc.* **2009**, *131*, Articles ASAP?
79. Bertini, I.; Luchinat, C.; Parigi, G. *Eur. J. Inorg. Chem.* **2000**, 2473–2480.
80. Basu, P.; Shokhirev, N. V.; Enemark, J. H.; Walker, F. A. *J. Am. Chem. Soc.* **1995**, *117*, 9042–9055.
81. Keller, R. M.; Wüthrich, K. *Biochim. Biophys. Acta* **1972**, *285*, 326–336.
82. Peyton, D. H.; La Mar, G. N.; Pande, U.; Ascoli, F.; Smith, K. M.; Pandey, R. K.; Parish, D. W.; Bolognesi, M.; Brunori, M. *Biochemistry* **1989**, *28*, 4880±4887.
83. Nesset, M. J. M.; Cai, S.; Shokhireva, T. Kh.; Shokhirev, N. V.; Jacobson, S. E.; Jayaraj, K.; Gold, A.; Walker, F. A. *Inorg. Chem.* **2000**, *39*, 532–540.
84. Program TDFw; http://www.shokhirev.com/nikolai/programs/prgsciedu.html, manual of use also available.
85. Swift, T. J. In *NMR of Paramagnetic Molecules*; La Mar, G. N.; Horrocks, W. D.; Holm, R. H., Eds; Academic Press: New York, **1973**; Chapter 2.
86. Sandstrom, J. *Dynamic NMR Spectroscopy*; Academic Press: New York, **1982**.
87. Oki, M. *Application of Dynamic NMR Spectroscopy to Organic Chemistry*; VCH: Deerfield Beach, Florida, **1985**.
88. Neuhaus, D.; Williamson, M. The *Nuclear Overhauser Effect in Structural and Conformational Analysis*; VCH: New York, **1989**.

89. Shokhirev, N. V.; Shokhireva, T. Kh.; Polam, J. R.; Watson, C. T.; Raffii, K.; Simonis, U.; Walker, F. A. *J. Phys. Chem. A* **1997**, *101*, 2778–2786.
90. Momot, K. I.; Walker, F. A. *J. Phys. Chem. A* **1997**, *101*, 2787–2795.
91. Momot, K. I.; Walker, F. A. *J. Phys. Chem. A* **1998**, *102*, 10682–10688.
92. Polam, J. R.; Shokhireva, T. Kh.; Raffii, K.; Simonis, U.; Walker, F. A. *Inorg. Chim. Acta* **1997**, *263/1–2*, 109–117.
93. Bertini, I.; Luchinat, C. In Physical Methods for Chemists, 2nd ed. 2; Drago, R. S., Ed.; Saunders: Mexico, **1992**; Chapter 12.
94. La Mar, G. N.; Walker, F. A. *J. Am. Chem. Soc.* **1975**, *97*, 6950–6956.
95. Derome, A. E. *Modern NMR Techniques for Chemistry Research*; Pergamon: New York, **1987**.
96. Sanders, J. K. M.; Hunter, B. K. *Modern NMR Spectroscopy, A Guide for Chemists*, 2nd ed.; Oxford University Press: Oxford, **1993**.
97. Evans, J. N. S. *Biomolecular NMR Spectroscopy*; Oxford University Press: New York, **1995**.
98. Cavanagh, J.; Fairbrother, W. J.; Palmer III, A. G.; Skelton, N. J. *Protein NMR Spectroscopy: Principles and Practice;* Academic Press: San Diego, CA, **1996**.
99. Jacobsen, N. E. *NMR Spectroscopy Explained: Simplified Theory, Applications and Examples for Organic Chemistry and Structural Biology*, Wiley Interscience: New York, **2007**.
100. Barkigia, K. M.; Chang, C. K.; Fajer, J.; Renner, M. W. *J. Am. Chem. Soc.* **1992**, *114*, 1701–1707.
101. Yang, F.; Kumar, M. R.; Walker, F. A. Manuscript in preparation.
102. Unger, S. W.; Jue, T.; La Mar, G. N. *J. Magn. Reson.* **1985**, *61*, 448–456.
103. Momot, K. I.; Walker, F. A. *J. Phys. Chem. A* **1997**, *101*, 9207–9216.
104. Walker, F. A.; Simonis, U. *J. Am. Chem. Soc.* **1991**, *113*, 8652–8657.
105. Sternlicht, H. *J. Chem. Phys.* **1965**, *42*, 2250.
106. Balch, A. L.; Latos-Grażyński, L.; Noll, B. C.; Szterenberg, L.; Zovinka, E. P. *J. Am. Chem. Soc.* **1993**, *115*, 11846–11854.
107. Sullivan, E. P.; Strauss, S. H. *Inorg. Chem.* **1985**, *28*, 3093–3095.
108. Longuet-Higgins, H. C.; Rector, C. W.; Platt, J. R. *J. Chem. Phys.* **1950**, *18*, 1174–1181.
109. Zerner, M.; Gouterman, M.; Kobayashi, H. *Theor. Chim. Acta* **1966**, *6*, 363.
110. Gouterman, M. In *The Porphyrins*; Dolphin, D., Ed.; Academic Press: New York, **1978**; Vol. III, pp. 1–165.
111. Antipas, A.; Buchler, J. W.; Gouterman, M.; Smith, P. D. *J. Am. Chem. Soc.* **1978**, *100*, 3015–3024.
112. Binstead, R. A.; Crossley, M. J.; Hush, N. S. *Inorg. Chem.* **1991**, *30*, 1259–1264.
113. Ghosh, A. *Acc. Chem. Res.* **1998**, 31, 189–198.
114. Zakharieva, O.; Schünemann, V.; Gerdan, M.; Licoccia, S.; Cai, S.; Walker, F. A.; Trautwein, A. X. *J. Am. Chem. Soc.* **2002**, *124*, 6636–6648.
115. Cai, S.; Lichtenberger, D. L.; Walker, F. A. *Inorg. Chem*. **2005**, *44*, 1890–1903.
116. Neese, F. ORCA — *An ab initio, Density Functional and Semiemperical Program Package*, Version 2.5–20, **2007** ed., Universität Bonn, Germany, **2007**.
117. Gouterman, M. Personal communication **2005**.
118. MPorphW, an interactive simple Hückel program for Windows, with visualization of the orbitals, their nodal properties and energies is available: http://www.shokhirev.com/nikolai/programs/prgsciedu.html, program MPorphW. The input of this program can be modified to include planar axial ligands, to remove double bonds, atoms, or to change the energy of a

meso-C, to simulate the effect of -OH substitution at a *meso*-C, for example. This program was last updated September 8, **2009**.

119. Gruhn, N. E.; Lichtenberger, D. L.; Ogura, H.; Walker, F. A. *Inorg. Chem.* **1999**, *38*, 4023–4027.
120. Westcott, B. L.; Gruhn, N. E.; Michelsen, L. J.; Lichtenberger, D. L. *J. Am. Chem. Soc.* **2000**, 122, 8083–8084.
121. Bernal, I.; Rieger, P. H. *Inorg. Chem.* **1963**, *2*, 256–262.
122. Kivelson, D.; Lee, S.-K. *J. Chem. Phys.* **1964**, *41*, 1896–1903.
123. Schulz, C. E.; Song, H. S.; Lee, Y. J.; Mondal, J. U.; Mohanrao, K.; Reed, C. A.; Walker, F. A.; Scheidt, W. R. *J. Am. Chem. Soc.* **1994**, *116*, 7196–7203.
124. Lin, C.-Y.; Spiro, T. G. *Inorg. Chem.* **1996**, *35*, 5237–5243.
125. Czarnecki, K.; Proniewicz, L. M.; Fujii, H.; Kincaid, J. R. *J. Am. Chem. Soc.* **1996**, *118*, 4680–4685 and references therein.
126. Cheesman, M. R.; Greenwood, C.; Thomson, A. J. *Adv. Inorg. Chem.* **1991**, *36*, 201–255.
127. Cheesman, M. R.; Walker, F. A. *J. Am. Chem. Soc.* **1996**, *118*, 7373–7380.
128. Fajer, J.; Davis, M. S. In *The Porphyrins*; Dolphin, D., Ed.; Academic Press: New York, **1979**; Vol. IV, pp. 197–256.
129. Safo, M. K.; Walker, F. A.; Raitsimring, A. M.; Walters, W. P.; Dolata, D. P.; Debrunner, P. G.; Scheidt, W. R. *J. Am. Chem. Soc.* **1994**, *116*, 7760–7770.
130. Cheng, R.-J.; Wang, Y.-K.; Chen, P.-Y.; Han, Y.-P.; Chang, C.-C. *Chem. Commun*. **2005**, 1312–1314.
131. Walker, F. A. *Coord. Chem. Revs.* **1999**, *185–186*, 471–534.
132. Moore, K. T.; Fletcher, J. T.; Therien, M. J. *J. Am. Chem. Soc.* **1999**, *121*, 5196–5209.
133. Chatfield, M. J.; La Mar, G. N.; Parker, W. O.; Smith, K. M.; Leung, H.-K.; Morris, I. K. *J. Am. Chem. Soc.* **1988**, *110*, 6352–6358.
134. Shokhirev, N. V.; Walker, F. A. *J. Am. Chem. Soc.* **1998**, *120*, 981–990.
135. Raitsimring, A. M.; Borbat, P.; Shokhireva, T. Kh.; Walker, F. A. *J. Phys. Chem.* **1996**, *100*, 5235–5244.
136. Schünemann, V.; Raitsimring, A. M.; Benda, R.; Trautwein, A. X.; Shokhireva, T. Kh.; Walker, F. A. *J. Biol. Inorg. Chem.* **1999**, *4*, 708–716.
137. Raitsimring, A. M.; Walker, F. A. *J. Am. Chem. Soc.* **1998**, *120*, 991–1002.
138. Astashkin, A. V.; Raitsimring, A. M.; Walker, F. A. *Chem. Phys. Lett.* **1999**, *306*, 9–17.
139. Astashkin, A. V.; Raitsimring, A. M.; Walker, F. A. *J. Am. Chem. Soc*. **2001**, *123*, 1905–1913.
140. Shokhirev, N. V.; Walker, F. A. *J. Am. Chem. Soc.* **1998**, *120*, 981–990.
141. Shokhireva, T. Kh.; Shokhirev, N. V.; Walker, F. A. *Biochemistry* **2003**, *42*, 679–693.
142. Shokhireva, T. Kh.; Berry, R. E.; Uno, E.; Balfour, C. A.; Zhang, H.; Walker, F. A. *Proc. Natl. Acad. Sci. USA* **2003**, *100*, 3778–3783.
143. Shokhireva, T. Kh.; Weichsel, A.; Smith, K. M.; Berry, R. E.; Shokhirev, N. V.; Balfour, C.; Zhang, H.; Montfort, W. R.; Walker, F. A. *Inorg. Chem.* **2007**, *46*, 2041–2056.
144. Shokhireva, T. Kh.; Shokhirev, N. V.; Berry, R. E.; Zhang, H.; Walker, F. A. *J. Biol. Inorg. Chem.* **2008**, *13*, 941–959.
145. Yang, F.; Knipp, M.; Berry, R. E.; Shokhireva, T. K.; Zhang, H.; Walker, F. A. *J. Biol. Inorg. Chem*. **2009**, *14*, 1077–1095.
146. Shokhireva, T. Kh.; Berry, R. E.; Zhang, H.; Shokhirev, N. V.; Walker, F. A. *Inorg. Chim. Acta* **2008**, *361*, 925–940.

147. Caignan, G. A.; Deshmukh, R.; Wilks, A.; Zeng, Y.; Huang, H.; Moënne-Loccoz, P.; Bunce, R. A.; Eastman, M. A.; Rivera, M. *J. Am. Chem. Soc.* **2002**, *124*, 14879–14892.
148. Zeng, Y.; Deshmukh, R.; Caignan, G. A.; Bunce, R. A.; Rivera, M.; Wilks, A. *Biochemistry* **2004**, *43*, 5222–5238.
149. Zeng, Y.; Caignan, G. A.; Bunce, R. A.; Rodriguez, J. C.; Wilks, A.; Rivera, M. *J. Am. Chem. Soc.* **2005**, *127*, 9794–9807.
150. Deshmukh, R.; Zeng, Y.; Furci, L. M.; Huang, H.; Morgan, B. N.; Sander, S.; Alontaga, A. Y.; Bunce, R. A.; Moënne-Loccoz, P.; Rivera, M.; Wilks, A. *Biochemistry* **2005**, *44*, 13713–13723.
151. Program Shift Patterns, http://www.shokhirev.com/nikolai/programs/prgsciedu.html
152. Bertini, I.; Luchinat, C.; Parigi, G.; Walker, F. A. *J. Biol. Inorg. Chem.* **1999**, *4*, 515–519; 846.
153. Turner, D. L.; Brennan, L.; Messias, A. C.; Teodoro, M. L.; Xavier, A. V. *Eur. Biophys. J.* **2000**, *29*, 104–112.
154. Turner, D. L. *J. Biol. Inorg. Chem.* **2000**, *5*, 328–332.
155. Simonneaux, G.; Hindre, F.; Le Plouzennec, M. *Inorg. Chem.* **1989**, *28*, 823–825.
156. Cheng, R.-J.; Chen, P.-Y.; Lovell, T.; Liu, T.; Noodleman, L.; Case, D. A. *J. Am. Chem. Soc.* **2003**, *125*, 6774–6783.
157. Balch, A. L.; Renner, M. W. *J. Am. Chem. Soc.* **1986**, *108*, 2603–2608.
158. Cai, S.; Walker, F. A.; Licoccia, S. *Inorg. Chem.* **2000**, *39*, 3466–3478.
159. Nardis, S.; Paolessee, R.; Licoccia, S.; Fronczek, F. R.; Vicente, M. G. H.; Shokhireva, T. Kh.; Walker, F. A. *Inorg. Chem*. **2005**, *44*, 7030–7046.
160. Oster, O.; Neireiter, G. W.; Clouse, A. O.; Gurd, F. R. N. *J. Biol. Chem.* **1975**, *250*, 7990–7996.
161. Shirazi, A.; Goff, H. M. *J. Am. Chem. Soc.* **1982**, *104*, 6318–6322.
162. Hickman, D. L.; Goff, H. M. *J. Am. Chem. Soc.* **1984**, *106*, 5013–5014.
163. Li, Z.; Goff, H. M. *Inorg. Chem. Soc.* **1992**, *31*, 1547–1548.
164. Godziela, G. M.; Goff, H. M. *J. Am. Chem. Soc.* **1986**, *108*, 2237–2243.
165. Balch, A. L.; Latos-Grażyński, L.; Noll, B. C.; Olmstead, M. M.; Zovinka, E. P. *Inorg. Chem.* **1992**, *31*, 1148–1151.
166. Arasasingham, R. D.; Balch, A. L.; Cornman, C. R.; Latos-Grażyński, L. *J. Am. Chem. Soc.* **1989**, *111*, 4357–4363.
167. Evans, B.; Smith, K. M.; La Mar, G. N.; Viscio, D. B. *J. Am. Chem. Soc.* **1977**, *99*, 7070–7073.
168. La Mar, G. N.; Viscio, D. B.; Smith, K. M.; Caughey,W. S.; Smith, M. L. *J. Am. Chem. Soc.* **1978**, *100*, 8085–8092.
169. La Mar, G. N.; Budd, D. L.; Viscio, D. B.; Smith, K. M.; Langry, K. C. *Proc. Natl. Acad. Sci. USA* **1978**, *75*, 5755–5759.
170. Shokhireva, T. Kh.; Smith, K. M.; Berry, R. E.; Shokhirev, N. V.; Balfour, C.; Zhang, H.; Walker, F. A. *Inorg. Chem.* **2007**, *46*, 170–178.
171. Sullivan, E. P.; Grantham, J. D.; Thomas, C. S.; Strauss, S. H. *J. Am. Chem. Soc.* **1991**, *113*, 5264–5270.
172. Banci, L.; Bertini, I.; Luchinat, C.; Pierattelli, R.; Shokhirev, N. V.; Walker, F. A. *J. Am. Chem. Soc.* **1998**, *120*, 8472–8479.
173. Turner, D. L.; Salgueiro, C. A.; Schenkels, P.; LeGall, J.; Xavier, A. V. *Biochim. Biophys. Acta* **1995**, *1246*, 24–28.
174. Turner, D. L. *Eur. J. Biochem.* **1995**, *227*, 829–837.

175. Costa, H. S.; Santos, H.; Turner, D. L. *Eur. Biophys. J.* **1996**, *25*, 19–24.
176. Brennan, L.; Turner, D. L. *Biochim. Biophys. Acta* **1997**, *1342*, 1–12
177. Louro, R. O.; Medina, M.; Aguiar, A. P.; Hervás, M.; De la Rosa, M.; Gómez-Moreno, C.; Turner, D. L.; Xavier, A. *J. Biol. Inorg. Chem.* **1998**, *3*, 68–73.
178. Louro, R. O.; Correia, I. J.; Brennan, L.; Coutinho, I. B.; Xavier, A. V.; Turner, D. L. *J. Am. Chem. Soc.* **1998**, *120*, 13240–13247.
179. Louro, R. O.; Pessanha, M.; Reid, G. A.; Chapman, S. K.; Turner, D. L.; Salgueiro, C. A. *FEBS Lett.* **2002**, *531*, 520–524.
180. Rivera, M.; Walker, F. A. *Anal. Biochem.* **1995**, *230*, 295–302.
181. Warren, M. J.; Scott A. I. *Trends Biochem. Sci.* **1990**, *15*, 486–489.
182. Leeper, F. J. *Nat. Prod. Rep.* **1985**, *2*, 19–47.
183. Scott, A. I. *Acc. Chem. Res.* **1990**, *23*, 308–317.
184. Scott, A. I. *Angew. Chem. Int. Ed. Engl.* **1993**, *32*, 1223–1376.
185. Filippov, I.; Knipp, M.; Berry, R. E.; Yang, F.; Zhang, H.; Walker, F. A. to be submitted.
186. Rodríguez-Marañón, M. J.; Qiu, F.; Stark, R. E.; White, S. P.; Zhang, X.; Stephen, I. Foundling, S. I.; Rodríguez, V.; Schilling, C. L., III; Bunce, R. A.; Rivera, M. *Biochemistry* **1996**, *35*, 16378–16390.
187. Bunce, R. A.; Schilling III, C. L.; Rivera, M. *J. Labelled Compd. and Radiopharm*. **1997**, 39, 669–675.
188. Qiu, F.; Stark, R. E.; Rivera M. *NMR Newsletter* **1996**, 5–6.
189. Qiu, F.; Rivera, M.; Stark, R. E. *J. Magn. Reson.* **1998**, 130, 76–81.
190. Rivera, M.; Qiu, F.; Bunce, R. A.; Stark, R. E. *J. Biol. Inorg. Chem.* **1999**, *4*, 87–98.
191. Alontaga, A. Y.; Bunce, R. A.; Wilks, A.; Rivera, M. *Inorg. Chem.* **2006**, *45*, 8876–8881.
192. Keller, R.; Wüthrich, K. *Biochim. Biophys. Acta* **1980**, *621*, 204–217.
193. Weightman, J. A.; Hoyle, N. J.; Williams, R. J. P. *Biochim. Biophys. Acta* **1971**, *244*, 567–572.
194. Kimura, K.; Peerson, J.; Wilson, M.; Cookson, D. J.; Williams, R. J. P. *J. Inorg. Biochem* **1981**, *15*, 11–25.
195. Dixon, D.W.; Barbush, M.; Shirazi, A. *Inorg. Chem.* **1985**, *24*, 1081–1087.
196. Shirazi, A.; Barbush, M.; Ghosh, S.; Dixon, D. W. *Inorg. Chem.* **1985**, *24*, 2495–2502.
197. Nakamura, M. *Chem. Lett. (Japan)* **1988**, 453–456.
198. Nakamura, M. *Inorg. Chim. Acta* **1989**, *161*, 73–80.
199. Johnson, R. D.; Ramaprasad, S.; La Mar, G. N. *J. Am. Chem. Soc.* **1983**, *105*, 7205–7206.
200. Ramaprasad, S.; Johnson, R. D.; La Mar, G. N. *J. Am. Chem. Soc.* **1984**, *106*, 5330–5335.
201. Ramaprasad, S.; Johnson, R. D.; La Mar, G. N. *J. Am. Chem. Soc.* **1984**, *106*, 3632–3635.
202. Unger, S.W.; LeComte, J. T. J.; La Mar, G. N. *J. Magn. Reson.* **1985**, *64*, 521–526.
203. Yu, C.; Unger, S. W.; La Mar, G. N. *J. Magn. Reson.* **1986**, *67*, 346–350.
204. Barbush, M.; Dixon, D. W. *Biochem. Biophys. Res. Commun.* **1985**, *129*, 70–75.
205. Dugad, L. B.; La Mar, G. N.; Unger, S. W. *J. Am. Chem. Soc.* **1990**, *112*, 1386–1392.
206. Licoccia, S.; Chatfield, M. J.; La Mar, G. N.; Smith, K. M.; Mansfield, K. E.; Anderson, R. R. *J. Am. Chem. Soc.* **1989**, *111*, 6087–6093.
207. Cai, S.; Belikova, E.; Yatsunyk, L.; Stolzenberg, A. M.; Walker, F. A. *Inorg. Chem.* **2005**, *44*, 1882–1889.
208. Keating, K. A.; de Ropp, J. S.; La Mar, G. N.; Balch, A. L.; Shaiu, F.-Y.; Smith, K. M. *Inorg. Chem.* **1991**, *30*, 3258–3263.
209. Lin, Q.; Simonis, U.; Tipton, A. R.; Norvell, C. J.; Walker, F. A. *Inorg. Chem.* **1992**, *31*, 4216–4217.

210. Isaac, M. F.; Simonis, U.; Lin, Q.; Suffian, D. J.; Wilson, D. L.; Walker, F. A. *Inorg. Chem.* **1993**, *32*, 4030–4041.
211. Tan, H.; Simonis, U.; Shokhirev, N. V.; Walker, F. A. *J. Am. Chem. Soc.* **1994**, *116*, 5784–5790.
212. Walker, F. A. In Spectroscopic Methods in Bioinorganic Chemistry; Solomon, E. I.; Hodgson, K., Eds.; ACS Symposium. Series; No. 692 American Chemical Society: Washington, DC, **1998**; pp. 30–61.
213. Luo, Y.; Peyton, D. H.; Yee, S. *Biochim. Biophys. Acta* **1998**, *1388*, 66–76.
214. Ogura, H.; Yatsunyk, L.; Medforth, C. J.; Smith, K. M.; Barkigia, K. M.: Renner, M. W.; Melamed, D.; Walker, F. A. *J. Am. Chem. Soc.* **2001**, *123*, 6564–6578.
215. Yamamoto, Y.; Nanai, N.; Chujo, R.; Suzuki, T. *FEBS Lett.* **1990**, *264*, 113–116.
216. Timkovich, R. *Inorg. Chem.* **1991**, *30*, 37–42.
217. Skidmore, K.; Simonis, U. *Inorg. Chem.* **1996**, *35*, 7470–7472.
218. Bertini, I.; Capozzi, F.; Luchinat, C.; Turano, P. *J. Magn. Reson.* **1991**, *95*, 244–252.
219. Ernst, R. R.; Bodenhausen, G.; Wokaun, A. *Principles of Nuclear Magnetic Resonance in One and Two Dimensions*; Clarendon Press: Oxford, England, **1987**; Chapter 8.
220. Balch, A. L.; Latos-Grażyński, L.; Noll, B. C.; Olmstead, M. M.; Szterenberg, L.; Safari, N. *J. Am. Chem. Soc.* **1993**, *115*, 1422–1429.
221. Yamamoto, Y.; Fujii, N. *Chem. Lett. (Japan)* **1987**, 1703–1706.
222. Banci, L.; Bertini, I.; Pierattelli, R.; Vila, A. J. *Inorg. Chem.* **1994**, *33*, 4338–4343.
223. Wojaczynski, J.; Latos-Grażyński, L.; Hrycyk, W.; Pacholska, E.; Rachlewicz, K.; Szterenberg, L. *Inorg. Chem.* **1996**, *35*, 6861–6872.
224. de Ropp, J. S.; La Mar, G. N. *J. Am. Chem. Soc.* **1991**, *113*, 4348–4350.
225. Shokhireva, T. Kh.; Nesset, M. J. M.;Walker, F. A. *Inorg. Chim. Acta* **1998**, *272/1–2*, 204–210.
226. Walker, F. A.; Simonis, U.; Zhang, H.; Walker, J. M.; Ruscitti, T. M.; Kipp, C.; Amputch, M. A.; Castillo, B. V.; Cody, S. H.; Wilson, D. L.; Graul, R. E.; Yong, G. J.; Tobin, K.; West, J. T.; Barichievich, B. A. *New J. Chem.* **1992**, *16*, 609–620.
227. Simonis, U.; Dallas, J. L.; Walker, F. A. *Inorg. Chem.* **1992**, *31*, 5349–5350.
228. Abriata, L. A.; Ledesma, G. N.; Pierattelli, R.; Vila, A. J. *J. Am. Chem. Soc.* **2009**, *131*, 1939–1946.
229. Groves, J. T.; Stern, M. K. *J. Am. Chem. Soc.* **1988**, *110*, 8628–8638.
230. Latos-Grażyński, L. *Inorg. Chem.* **1985**, *24*, 1104–1105.
231. La Mar, G. N.; Walker, F. A. *J. Am. Chem. Soc.* **1972**, *94*, 8607–8608.
232. Goff, H. M.; La Mar, G. N.; Reed, C. A. *J. Am. Chem. Soc.* **1977**, *99*, 3641–3646.
233. La Mar, G. N.; Walker, F. A. *J. Am. Chem. Soc.* **1973**, *95*, 1790–1796.
234. La Mar, G. N.; Walker, F. A. *J. Am. Chem. Soc.* **1975**, *97*, 5103–5107.
235. Sano, S.; Suguira, Y.; Maeda, Y.; Ogawa, S.; Morishima, I. *J. Am. Chem. Soc.* **1981**, *103*, 2888–2890.
236. Hickman, D. L.; Shirazi, A.; Goff, H. M. *Inorg. Chem.* **1985**, *24*, 563–566.
237. Donohoe, R. J.; Atamian, M.; Bocian, D. F. *J. Am. Chem. Soc.* **1987**, *109*, 5593–5599.
238. Walker, F. A. *J. Am. Chem. Soc.* **1970**, *92*, 4235–4244.
239. Medforth, C. In *The Porphyrin Handbook*; Kadish, K. M.; Smith, K. M.; Guilard, R., Eds.; Academic Press: New York, **2000**; Chapter 35, pp. 1–80.
240. Traylor, T. G.; Chang, C. K.; Geibel, J.; Berzinis, A.; Mincey, T.; Cannon, J. *J. Am. Chem. Soc.* **1979**, *101*, 6716–6731.

241. Grodzicki, M.; Flint, H.; Winkler, H.; Walker, F. A.; Trautwein, A. X. *J. Phys. Chem. A* **1997**, *101*, 4202–4207.
242. Kalodimos, C. G.; Gerothanassis, I. P.; Pierattelli, R.; Troganis, A. *J. Inorg. Biochem.* **2000**, *79*, 371–380.
243. Balch, A. L.; Cornman, C. R.; Safari, N.; Latos-Grażyński, L. *Organometallics* **1990**, *9*, 2420–2421.
244. Latos-Grażyński, L.; Cheng, R. J.; La Mar, G. N.; Balch, A. L. *J. Am. Chem. Soc.* **1982**, *104*, 5992–6000.
245. McGarvey, B. R. *Inorg. Chem.* **1988**, *27*, 4691–4698.
246. Goff, H. M., La Mar, G. N. *J. Am. Chem. Soc.* **1977**, *99*, 6599–6606.
247. Migita, K.; La Mar, G. N. *J. Phys. Chem.* **1980**, *84*, 2953–2957.
248. Strauss, S. H.; Silver, M. E.; Long, K. M.; Thompson, R. G.; Hudgens, R. A.; Spartalian, K.; Ibers, J. A. *J. Am. Chem. Soc.* **1985**, *107*, 4207–4215.
249. Mispelter, J.; Momenteau, M.; Lhoste, J. M. *Mol. Phys.* **1977**, *33*, 1715–1728.
250. Mispelter, J.; Momenteau, M.; Lhoste, J. M. *J. Chem. Phys.* **1980**, *72*, 1003–1012.
251. Mink, L. M.; Polam, J. R.; Christensen, K. A.; Bruck, M. A.; Walker, F. A. *J. Am. Chem. Soc*. **1995**, *117*, 9329–9339.
252. Polam, J. R.; Wright, J. L.; Christensen, K. A.; Walker, F. A.; Flint, H.; Winkler, H.; Grodzicki, M.; Trautwein, A. X. *J. Am. Chem. Soc.* **1996**, *118*, 5272–5276.
253. Rachlewicz, K.; Latos-Grażyński, L.; Vogel, E. *Inorg. Chem.* **2000**, *39*, 3247–3251.
254. Collman, J. P.; Brauman, J. I.; Doxsee, K. M.; Halbert, T. R.; Bunnenberg, E.; Linder, R. E.; La Mar, G. N.; Del Gaudio, J.; Lang, G.; Spartalian, K. *J. Am. Chem. Soc.* **1980**, *102*, 4182–4192.
255. Collman, J. P.; Brauman, J. I.; Collins, T. J.; Iverson, B. L.; Lang, G.; Pettman, R. B.; Sessler, J. L.; Walters, M. A. *J. Am. Chem. Soc.* **1983**, *105*, 3038–3052.
256. Lukat, G.; Goff, H. M. *Biochim. Biophys. Acta* **1990**, *1037*, 351–359.
257. Parmely, R. C.; Goff, H. M. *J. Inorg. Biochem.* **1980**, *12*, 269–280.
258. Saraste, M.; Castresana, J. *FEBS Lett.* **1994**, *341*, 1–4.
259. Zumft, W. G. *J. Inorg. Biochem.* **2005**, *99*, 194–215.
260. Wasser, I. M.; de Vries, S.; Moënne-Loccoz, P.; Schröder, I.; Karlin, K. D. *Chem. Rev.* **2002**, *102,* 1201–1234.
261. Daiber, A.; Shoun, H.; Ullrich, V. *J. Inorg. Biochem.* **2005**, *99*, 185–193.
262. Collman, J. P.; Rapta, M.; Bröring, M.; Raptova, L.; Schwenninger, R.; Boitrel, B.; Fu, L.; L'Her, M. *J. Am. Chem. Soc.* **1999**, *121*, 1387–1388.
263. Collman, J. P.; Zhong, M.; Wang, Z.; Rapta, M.; Rose, E. *Org. Lett.* **1999**, *1*, 2121–2124.
264. Collman, J. P.; Zhong, M.; Costanzo, S.; Zhang, C. *J. Org. Chem.* **2001**, *66*, 8252–8256.
265. Collman, J. P.; Sunderland, C. J.; Boulatov, R. *Inorg. Chem.* **2002**, *41*, 2282–2291.
266. Collman, J. P.; Berg, K. E.; Sunderland, C. J.; Aukauloo, A.; Vance, M. A.; Solomon, E. I. *Inorg. Chem.* **2002**, *41*, 6583–6596.
267. Walker, F. A.; Bowen, J. H. *J. Am. Chem. Soc.* **1985**, *107*, 7632–7635.
268. Collman, J. P.; Yan, Y.-L.; Eberspacher, T.; Xie, X.; Solomon, S. I. *Inorg. Chem*. **2005**, *44*, 9628–9630.
269. Boulatov, R.; Collman, J. P.; Shiryaeva, I. M.; Sunderland, C. J. *J. Am. Chem. Soc.* **2002**, *124*, 11923–11935.
270. Shiryaeva, I. M.; Collman, J. P.; Boulatov, R.; Sunderland, C. J. *Anal. Chem.* **2003**, *75*, 494–502.

271. Devaraj, N. K.; Decreau, R. A.; Ebina, W.; Collman, J. P.; Chidsey, C. E. D. *J. Phys. Chem. B* **2006**, *110*, 15955–15962.
272. Collman, J. P.; Devaraj, N. K.; Decreau, R. A.; Yang, Y.; Yan, Y. L.; Ebina, W.; Eberspacher, T. A.; Chidsey, C. E. D. *Science* **2007**, *315*, 1565–1568.
273. Collman, J. P.; Sunderland, C. J.; Berg, K. E.; Vance, M. A.; Solomon, E. I. *J. Am. Chem. Soc.* **2003**, *125*, 6648–6649.
274. Collman, J. P.; Decréau, R. A.; Yan, Y.; Yoon, J.; Solomon, E. I. *J. Am. Chem. Soc.* **2007**, *129*, 5794–5795.
275. Collman, J. P.; Dey, A.; Yang, Y.; Decréau, R. A.; Ohta, T.; Solomon, E. I. *J. Am. Chem. Soc.* **2008**, *130*, 16498–16499.
276. Collman, J. P.; Dey, A.; Decréau, R. A.; Yang, Y. *Inorg. Chem.* **2008**, *47*, 2916–2918.
277. Nanthakumar, A.; Fox, S.; Murthy, N. N.; Karlin, K. D.; Ravi, N.; Huynh, B. H.; Orosz, R. D.; Day, E. P.; Hagen, K. S.; Blackburn, N. J. *J. Am. Chem. Soc.* **1993**, *115*, 8513–8514.
278. Karlin, K. D.; Nanthakumar, A.; Fox, S.; Murthy, N. N.; Ravi, N.; Huynh, B. H.; Orosz, R. D.; Day, E. P. *J. Am. Chem. Soc.* **1994**, *116*, 4753–4763.
279. Nanthakumar, A.; Fox, S.; Murthy, N. N.; Karlin, K. D. *J. Am. Chem. Soc.* **1997**, *119*, 3898–3906.
280. Kopf, M.-A.; Neuhold, Y.-M.; Zuberbühler, A. D.; Karlin, K. D. *Inorg. Chem.* **1999**, *38*, 3093–3102.
281. Ghiladi, R. A.; Ju, T. D.; Lee, D.-H.; Moënne-Loccoz, P.; Kaderli, S.; Neuhold, Y.-M.; Zuberbühler, A. D.; Woods, A. S.; Cotter, R. J.; Karlin, K. D. *J. Am. Chem. Soc.* **1999**, *121*, 9885–9886.
282. Ghiladi, R. A.; Karlin, K. D. *Inorg. Chem.* **2002**, *41*, 2400–2407.
283. Kopf, M.-A.; Karlin, K. D. *Inorg. Chem.* **1999**, *38*, 4922–4923.
284. Kopf, M.-A.; Neuhold, Y.-M.; Zuberbühler, A. D.; Karlin, K. D. *Inorg. Chem.* **1999**, *38*, 3093–3102.
285. Ghiladi, R. A.; Hatwell, K. R.; Karlin, K. D.; Huang, H.; Moënne-Loccoz, P.; Krebs, C.; Huynh, B. H.; Marzilli, L. A.; Cotter, R. J.; Kaderli, S.; Zuberbühler, A. D. *J. Am. Chem. Soc.* **2001**, *123*, 6183–6184.
286. Corsi, D. M.; Murthy, N. N.; Young, Jr., V. G.; Karlin, K. D. *Inorg. Chem.* **1999**, *38*, 848–858.
287. Ghiladi, R. A.; Kretzer, R. M.; Guzei, I.; Rheingold, A. L.; Neuhold, Y.-M.; Hatwell, K. R.; Zuberbühler, A. D.; Karlin, K. D. *Inorg. Chem.* **2001**, *40*, 5754.
288. Kretzer, R. M.; Ghiladi, R. A.; Lebeau, E. L.; Liang, H.-C.; Karlin, K. D. *Inorg. Chem.* **2003**, *42*, 3016–3025.
289. Kim, E.; Kamaraj, K.; Galliker, B.; Rubie, N. D.; Moënne-Loccoz, P.; Kaderli, S.; Zuberbühler, A. D.; Karlin, K. D. *Inorg. Chem.* **2005**, *44*, 1238–1247.
290. Kim, E.; Helton, M. E.; Lu, S.; Moënne-Loccoz, P.; Incarvito, C. D.; Rheingold, A. L.; Kaderli, S.; Zuberbühler, A. D.; Karlin, K. D. *Inorg. Chem.* **2005**, *44*, 7014–7029.
291. Chufán, E. E.; Verani, C. N.; Puiu, S. C.; Rentschler, E.; Schatzchneider, U.; Incaravito, C.; Rheingold, A. L.; Karlin, K. D. *Inorg. Chem.* **2007**, *46*, 3017–3026.
292. Chufán, E. E.; Mondal, B.; Gandhi, T.; Kim, I.; Rubie, N. D.; Moënne-Loccoz, P.; Karlin, K. D. *Inorg. Chem.* **2007**, *46*, 6382–6394.
293. Ghiladi, R. A.; Chufán, E. E.; del Rio, D.; Solomon, E. I.; Krebs, C.; Huynh, B. H.; Huang, H.; Moënne-Loccoz, P.; Kaderli, S.; Honecker, M.; Zuberbühler, A. D.; Marzilli, L.; Cotter, R. J.; Karlin, K. D. *Inorg. Chem.* **2007**, *46*, 3889–3902.
294. Chufán, E. E.; Puiu, S. C.; Karlin, K. D. *Acc. Chem. Res.* **2007**, *40*, 563–572.

295. Wasser, I. M.; Martens, C. F.; Verani, C. N.; Rentschler, E.; Huang, H.; Moënne-Loccoz, P.; Zakharov, L. N.; Rheingold, A. L.; Karlin, K. D. *Inorg. Chem.* **2004**, *43*, 651–662.
296. Wang, J.; Schopfer, M. P.; Sarjeant, A. A. N.; Karlin, K. D. *J. Am. Chem. Soc.* **2009**, *131*, 450–451.
297. Wang, J.; Schopfer, M. P.; Puiu, S. C.; Sarjeant, A. A. N.; Karlin, K. D. *Inorg. Chem.* **2009**, *48*, 0000–0000.
298. Maiti, D.; Lee, D.-H.; Sarjeant, A. A. N.; Mau, M. Y. M.; Solomon, E. I.; Gaoutchenova, K.; Sundermeyer, J.; Karlin, K. D. *J. Am. Chem. Soc.* **2008**, *130*, 6700–6701.
299. Yu, B.-S.; Goff, H. M. *J. Am. Chem. Soc.* **1989**, *111*, 6558–6562.
300. Shin, K.; Kramer, K.; Goff, H. M. *Inorg. Chem.* **1987**, *26*, 4103–4106.
301. Balch, A. L.; Cheng, R. J.; La Mar, G. N.; Latos-Grażyński, L. *Inorg. Chem.* **1985**, *24*, 2651–2656.
302. Battioni, J.-P.; Artaud, I.; Dupre, D.; Leduc, P.; Mansuy, D. *Inorg. Chem.* **1987**, *26*, 1788–1796.
303. Komives, E. A.; Tew, D.; Olmstead, M. M.; Ortiz de Montellano, P. R. *Inorg. Chem.* **1988**, *26*, 1788–1796.
304. Balch, A. L.; Chan, Y.-W.; La Mar, G. N.; Latos-Grażyński, L.; Renner, M. W. *Inorg. Chem.* **1985**, *24*, 1437–1443.
305. Mahy, J. P.; Battioni, P.; Mansuy, D.; Fisher, J.; Weiss, R.; Mispelter, J.; Morgenstern-Badarau, I.; Gans, P. *J. Am. Chem. Soc.* **1984**, *106*, 1699–1706.
306. Warburg, O.; Negelein, E. *Chem. Ber.* **1930**, *63*, 1816–1818.
307. Lemberg, R. *Biochem. J.* **1935**, *29*, 1322–1336.
308. Fischer, H.; Libowitsky, H. *Z. Physiol. Chem.* **1938**, *255*, 209.
309. Jackson, A. H.; Kenner, G.W.; Smith, K. M. *J. Am. Chem. Soc.* **1966**, *88*, 4539–4541.
310. Lord, P. A.; Latos-Grażyński, L.; Balch, A. L. *Inorg. Chem.* **2002**, *41*, 1011–1014.
311. Chmielewski, P. J.; Latos-Grażyński, L.; Rachlewicz, K.; Glowiak, T.; *Angew. Chem., Int. Ed. Engl.* **1994**, *33*, 779-781.
312. Furuta, H.; Asano, T.; Ogawa, T. *J. Am. Chem. Soc.* **1994**, *116*, 767–768.
313. Rachlewicz, K.; Wang. S.-W.; Peng, C.-H.; Hung, C.-H.; Latos-Grażyński, L. *Inorg. Chem.* **2003**, *42*, 7348–7350.
314. Rachlewicz, K.; Wang. S.-W.; Ko, J.-L.; Hung, C.-H.; Latos-Grażyński, L. *J. Am. Chem. Soc.* **2004**, *126*, 4420–4431.
315. Rachlewicz, K.; Gorzelańczyk, D.; Latos-Grażyński, L. *Inorg. Chem.* **2006**, *45*, 9742–9747.
316. Myśliborski, R.; Latos-Grażyński, L. *Eur. J. Org. Chem.* **2005**, 5039–5048.
317. Myśliborski, R.; Rachlewicz, K.; Latos-Grażyński, L. *Inorg. Chem.* **2006**, *45*, 7828–7834.
318. Myśliborski, R.; Latos-Grażyński, L.; Szterenberg, L. *Eur. J. Org. Chem*. **2006**, 3064–3068.
319. Pawlicki, M.; Latos-Grażyński, L. *Inorg. Chem.* **2002**, *41*, 5866–5873.
320. Pawlicki, M.; Latos-Grażyński, L. *Inorg. Chem.* **2004**, *43*, 5564–5571.
321. Morishima, L.; Fujii, H.; Shiro, Y. *J. Am. Chem. Soc.* **1986**, *108*, 3858–3860.
322. Ozawa, S.; Fujii, H.; Morishima, I. *J. Am. Chem. Soc.* **1992**, *114*, 1548–1554.
323. Cheng, R.-J.; Latos-Grażyński, L.; Balch, A. L. *Inorg. Chem.* **1982**, *21*, 2412–2418.
324. Balch, A. L.; Latos-Grażyński, L.; Noll, B. C.; Phillips, S. L. *Inorg. Chem.* **1993**, *32*, 1124–1129.
325. Miyamoto, T. K.; Tsuzuki, S.; Hasegawa, T.; Sasaki, Y. *Chem. Lett. (Japan)* **1983**, 1587–1588.
326. Woon, T. C.; Shirazi, A.; Bruice, T. C. *Inorg. Chem.* **1986**, *25*, 3845–3846.
327. La, T.; Miskelly, G. M.; Bau, R. *Inorg. Chem.* **1997**, *36*, 5321–5328.

328. Goff, H. M.; Shimomura, E. T.; Lee, Y. J.; Scheidt, W. R. *Inorg. Chem.* **1984**, *23*, 315–321.
329. Guilard, R.; Perrot, I.; Tabard, A.; Richard, P.; Lecomte, C.; Liu, Y. H.; Kadish, K. M. *Inorg. Chem.* **1991**, *30*, 27–37.
330. Behere, D. V.; Goff, H. M. *J. Am. Chem. Soc.* **1984**, *106*, 4945–4950.
331. Arasasingham, R. D.; Cornman, C. R.; Balch, A. L. *J. Am. Chem. Soc.* **1989**, *111*, 7800–7805.
332. Arasasingham, R. D.; Balch, A. L.; Cornman, C. R.; de Ropp, J. S.; Eguchi, K.; La Mar, G. N. *Inorg. Chem.* **1990**, *29*, 1847–1850.
333. Behere, D. V.; Birdy, R.; Mitra, S. *Inorg. Chem.* **1982**, *21*, 386–390.
334. Dugad, L. B.; Mitra, S. *Proc. Indian Acad. Sci.* **1984**, *93*, 295–311.
335. Oumous, H.; Lecomte, C.; Protas, J.; Cocolios, P.; Guilard, R. *Polyhedron* **1984**, *3*, 651–659.
336. Phillippi, M. A.; Baenziger, N.; Goff, H. M. *Inorg. Chem.* **1981**, *20*, 3904–3911.
337. Kellett, P. J.; Pawlik, M. J.; Taylor, L. F.; Thompson, R. G.; Levstik, M. A.; Anderson, O. P.; Strauss, S. H. *Inorg. Chem.* **1989**, *28*, 440–447.
338. Crawford, P. W.; Ryan, M. D. *Inorg. Chim. Acta* **1991**, *179*, 25–33.
339. Kim, Y. O.; Song, B.; Goff, H. M. *Inorg. Chem.* **1993**, *32*, 1304–1305.
340. Lexa, D.; Momenteau, M.; Saveant, J.-M.; Xu, F. *Inorg. Chem.* **1985**, *24*, 122–127.
341. Gunter, M. J.; McLaughlin, G. M.; Berry, K. J.; Murray, K. S.; Irving, M.; Clark, P. E. *Inorg. Chem.* **1984**, *23*, 283–300.
342. Hambright, P.; Turner, A.; Cohen, J. S.; Lyon, R. C.; Katz, A.; Neta, P.; Adeyemo, A. *Inorg. Chim. Acta* **1987**, *128*, L11–L14.
343. Helpern, J. A.; Curtis, J. C.; Hearshen, D.; Smith, M. B.; Welch, K. M. A. *Magn. Reson. Med.* **1987**, *5*, 302–305.
344. Ivanca, M. A.; Lappin, A. G.; Scheidt, W. R. *Inorg. Chem.* **1991**, *30*, 711–718.
345. Mazumdar, S.; Medhi, O. K.; Mitra, S. *Inorg. Chem.* **1988**, *27*, 2541–2543.
346. Mazumdar, S. J. *Chem. Soc., Dalton Trans.* **1991**, 2091–2096.
347. Mazumdar, S.; Medhi, O. K.; Mitra, S. *Inorg. Chem.* **1991**, *30*, 700–705.
348. Kalish, H.; Camp, J. E.; Stepien, M.; Latos-Grażyński, L.; Olmstead, M. M.; Balch, A. L. *Inorg. Chem.* **2002**, *41*, 989–997.
349. Balch, A. L.; La Mar, G. N.; Latos-Grażyński, L.; Renner, M. W. *Inorg. Chem.* **1985**, *24*, 2432–2436.
350. Walker, F. A.; La Mar, G. N. *Ann. NY Acad. Sci.* **1973**, *206*, 328–348.
351. La Mar, G. N. *J. Am. Chem. Soc.* **1973**, *95*, 1662–1663.
352. Reference 2, Fig. 24.
353. Ikeue, T.; Ohgo, Y.; Uchida, A.; Nakamura, M.; Fujii, H.; Yokoyama, M. *Inorg. Chem.* **1999**, *38*, 1276–1281.
354. Kadish, K. M.; Tabard, A.; Van Caemelbecke, E.; Aukauloo, A. M.; Richard, P.; Guilard, R. *Inorg. Chem.* **1998**, *37*, 6168–6175.
355. Rachlewicz, K.; Latos-Grażyński, L.; Vogel, E.; Ciunik, Z.; Jerzykiewicz, L. B. *Inorg. Chem.* **2002**, *41*, 1979–1988.
356. Zobrist, M.; La Mar, G. N. *J. Am. Chem. Soc.* **1978**, *100*, 1944–1946.
357. Budd, D. L.; La Mar, G. N.; Langry, K. C.; Smith, K. M.; Nayyir-Mazhir, R. *J. Am. Chem. Soc.* **1979**, *101*, 6091–6096.
358. de Ropp, J. S.; La Mar, G. N. *J. Am. Chem. Soc.* **1991**, *113*, 4348–4350.
359. Thanabal, V.; de Ropp, J. S.; La Mar, G. N. *J. Am. Chem. Soc.* **1987**, *109*, 265–272.
360. Hickman, D. L.; Goff, H. M. *Inorg. Chem.* **1983**, *22*, 2787–2789.
361. Hickman, D. L.; Nanthakumar, A.; Goff, H. M. *J. Am. Chem. Soc.* **1988**, *110*, 6384–6390.

362. Chatfield, M. J.; La Mar, G. N.; Smith, K. M.; Leung, H.-K.; Pandey, R. K. *Biochemistry* **1988**, *27*, 1500–1507.
363. Pawlik, M. J.; Miller, P. K.; Sullivan, E. P.; Levstik, M. A.; Almond, D. A.; Strauss, S. H. *J. Am. Chem. Soc.* **1988**, *110*, 3007–3012.
364. Ozawa, S.; Watanabe, Y.; Morishima, I. *Tetrahedron Lett.* **1994**, *35*, 4141–4144.
365. Cai, S.; Shokhireva, T. Kh.; Lichtenberger, D. L.; Walker, F. A. *Inorg. Chem.* **2006**, *45*, 3519–3531.
366. Bonnett, R.; Gale, I. A. D.; Stephenson, G. F. *J. Chem. Soc. C* **1967**, 1168–1172.
367. Whitlock, H. W.; Hanauer, R.; Oester, M. Y.; Bower, B. K. *J. Am. Chem. Soc.* **1969**, *91*, 7485–7489.
368. Ozawa, S.; Watanabe, Y.; Morishima, I. *Inorg. Chem.* **1994**, *33*, 306–313.
369. Latos-Grażyński, L.; Wojaczyński, J.; Koerner, R.; Johnson, J. J.; Balch, A. L. *Inorg. Chem.* **2001**, *40*, 4971–4977.
370. Balch, A. L.; Olmstead, M. M.; Safari, N. *Inorg. Chem.* **1993**, *32*, 291–296.
371. Scheidt, W. R.; Reed, C. A. *Chem. Rev.* **1981**, *81*, 543–555.
372. Helms, J. H.; ter Haar, L. W.; Hatfield, W. E.; Harris, D. L.; Jayaraj, K.; Toney, G. E.; Gold, A.; Newborn, T. D.; Pemberton, J. R. *Inorg. Chem.* **1986**, *25*, 2334–2337.
373. Strauss, S. H.; Pawlik, M. J.; Skowyra, J.; Kennedy, J. R.; Anderson, O. P.; Spartalian, K.; Dye, J. L. *Inorg. Chem.* **1987**, *26*, 724–730.
374. Boersma, A. D.; Goff, H. M. *Inorg. Chem.* **1984**, *23*, 1671–1676.
375. Liston, D. J.; Kennedy, B. J.; Murray, K. S.; West, B. O. *Inorg. Chem.* **1985**, *24*, 1561–1567.
376. Evans, D. F. *J. Chem. Soc.* **1959**, *2003*.
377. For superconducting magnets, the revised equation must be used: Sur, S. K. *J. Magn. Reson.* **1989**, *82*, 169–173.
378. Chin, D.-H.; Del Gaudio, J.; La Mar, G. N.; Balch, A. L. *J. Am. Chem. Soc.* **1977**, *99*, 5486–5488.
379. Kessel, S. L.; Hendrickson, D. N. *Inorg. Chem.* **1980**, *19*, 1883–1889.
380. Balch, A. L.; Hart, R. L.; Latos-Grażyński, L. *Inorg. Chem.* **1990**, *29*, 3253–3256.
381. Bottomley, L. A.; Gorce, J.-N.; Goedken, V. L.; Ercolani, C. *Inorg. Chem.* **1985**, *24*, 3733–3737.
382. Ercolani, C.; Hewage, S.; Heucher, R.; Rossi, G. *Inorg. Chem.* **1992**, *32*, 2975–2977.
383. Ercolani, C.; Jubb, J.; Pennesi, G.; Russo, U.; Trigiante, G. *Inorg. Chem.* **1995**, *34*, 2535–2541.
384. Ercolani, C.; Floris, B. In *Phthalocyanines–Properties and Applications*; Leznoff, C. C.; Lever, A. B. P., Eds.; VCH Publishers: New York, **1993**; Vol. 2, pp. 1–42.
385. Grapperhaus, C. A.; Mienert, B.; Bill, E.; Weyhermüller, T.; Wieghardt, K. *Inorg. Chem.* **2000**, *39,* 5306–5317.
386. Donzello, M. P.; Ercolani, C.; Kadish, K. M.; Ou, Z.; Russo, U. *Inorg. Chem.* **1998**, *37*, 3682–3688.
387. Godziela, G. M.; Ridnour, L. A.; Goff, H. M. *Inorg. Chem.* **1985**, *24*, 1610–1611.
388. Balch, A. L.; Latos-Grażyński, L.; Noll, B. C.; Olmstead, M. M.; Zovinka, E. P. *Inorg. Chem.* **1992**, *31*, 2248–2255.
389. Wolowiec, S.; Latos-Grażyński, L. *Inorg. Chem.* **1994**, *33*, 3576–3586.
390. Wojaczyński, J.; Latos-Grażyński, L. *Inorg. Chem.* **1995**, *34*, 1044–1054.
391. Wojaczyński, J.; Latos-Grażyński, L. *Inorg. Chem.* **1995**, *34*, 1054–1062.
392. Wojaczyński, J.; Latos-Grażyński, L.; Olmstead, M. M.; Balch, A. L. *Inorg. Chem.* **1997**, *36*, 4548–4554.

393. Dolphin, D. H.; Sams, J. R.; Tsin, T. B. *Inorg. Chem.* **1977**, *16*, 711–713.
394. Kastner, M. E.; Scheidt, W. R.; Mashiko, T.; Reed, C. A. *J. Am. Chem. Soc.* **1978**, *100*, 666–667.
395. Reed, C. A.; Mashiko, T.; Bentley, S. D.; Kastner, M. E.; Scheidt, W. R.; Spartalian, K.; Lang, G. *J. Am. Chem. Soc.* **1979**, *101*, 2948–2958.
396. Goff, H. M.; Shimomura, E. *J. Am. Chem. Soc.* **1980**, *102*, 31–37.
397. Masuda, H.; Taga, T.; Osaki, K.; Sugimoto, H.; Yoshida, Z.-I.; Ogoshi, H. *Inorg. Chem.* **1980**, *19*, 950–955.
398. Toney, G. E.; ter Haar, L. W.; Savrin, J. E.; Gold, A.; Hatfield, W. E.; Sangaiah, R. *Inorg. Chem.* **1984**, *23*, 2561–2563.
399. Toney, G. E.; Gold, A.; Savrin, J.; ter Haar, L. W.; Sangaiah, R.; Hafield, W. E. *Inorg. Chem.* **1984**, *23*, 4350–4352.
400. Kintner, E. T.; Dawson, J. H. *Inorg. Chem.* **1991**, *30*, 4892–4897.
401. Shelly, K.; Bartczak, T.; Scheidt, W. R.; Reed, C. A. *Inorg. Chem.* **1985**, *24*, 4325–4330.
402. Gupta, G. P.; Lang, G.; Reed, C. A.; Shelly, K.; Scheidt, W. R. *J. Chem. Phys.* **1987**, *86*, 5288–5293.
403. Summerville, D. A.; Cohen, I. A.; Hatano, K.; Scheidt, W. R. *Inorg. Chem.* **1978**, *17*, 2906–2910.
404. Scheidt, W. R.; Geiger, D. K.; Hayes, R. G.; Lang, G. *J. Am. Chem. Soc.* **1983**, *105*, 2625–2632.
405. Scheidt, W. R.; Osvath, S. R.; Lee, Y. J.; Reed, C. A.; Shavez, B.; Gupta, G. P. *Inorg. Chem.* **1989**, *28*, 1591–1595.
406. Dugad, L. B.; Marathe, V. R.; Mitra, S. *Proc. Indian Acad. Sci.* **1985**, *95*, 189–205.
407. Maltempo, M. M.; Moss, T. H.; Cusanovich, M. A. *Biochim. Biophys. Acta* **1974**, *342*, 290–305.
408. Maltempo, M. M. *Biochim. Biophys. Acta* **1975**, *379*, 95–102.
409. Rawlings, J.; Stephens, P. J.; Nafie, L. A.; Kamen, M. D. *Biochemistry* **1977**, *16*, 1725–1729.
410. Yoshimura, T.; Suzuki, S.; Nakahara, A.; Iwasaki, H.; Masuko, M.; Marsubara, T. *Biochim. Biophys. Acta* **1985**, *831*, 267–274.
411. Moss, T. H.; Bearden, A. J.; Bartsch, R. G.; Cusanovich, M. A. *Biochemistry* **1968**, *7*, 1583–1591.
412. Teraoka, J.; Kitagawa, T. *J. Phys. Chem.* **1980**, *84*, 1928–1935.
413. Hobbs, J. D.; Larsen, R. W.; Meyer, T. E.; Hazzard, J. H.; Cusanovich, M. A.; Ondrias, M. R. *Biochemistry* **1990**, *29*, 4166–4174.
414. La Mar, G. N.; Jackson, J. T.; Dugad, L. B.; Cusanovich, M. A.; Bartsch, R. G. *J. Biol. Chem.* **1990**, *265*, 16173–16180.
415. Weber, P. C.; Howard, A.; Xuong, N. H.; Salemme, F. R. *J. Mol. Biol.* **1981**, *153*, 399–424.
416. Finzel, B. C.; Weber, P. C.; Hardman, K. D.; Salemme, F. R. *J. Mol. Biol.* **1985**, *186*, 627–743.
417. Maltempo, M. M. *J. Chem. Phys.* **1974**, *61*, 2540–2547.
418. Maltempo, M. M.; Moss, T. H. *Quart. Rev. Biophys.* **1976**, *9*, 181–215.
419. Koerner, R.; Wright, J. L.; Nesset, M. J. M.; Ding, X. D.; Aubrecht, K.; Watson, R.; Barber, R. A.; Tipton, A. R.; Norvell, C. J.; Mink, L. M.; Simonis, U.; Walker, F. A. *Inorg. Chem.* **1998**, *37*, 733–745.
420. Cheng, R.-J.; Chen, P.-Y.; Gau, P.-P.; Chen, C.-C.; Peng, S.-M. *J. Am. Chem. Soc.* **1997**, *119*, 2563–2569.

421. Yatsunyk, L. A.; Walker, F. A. *J. Porphyrins Phthalocyanines* **2005**, *9*, 214–228.
422. Schünemann, V.; Gerdan, M.; Trautwein, A. X.; Haoudi, N.; Mandon, D.; Fischer, J.; Weiss, R.; Tabard, A.; Guilard, R. *Angew. Chem. Int. Ed.* **1999**, *38,* 3181–3183.
423. Sakai, T.; Ohgo, Y.; Ikeue, T.; Takahashi, M.; Takeda, M.; Nakamura, M. *J. Am. Chem. Soc.* **2003**, *125*, 13028–13029.
424. Sakai, T.; Ohgo, Y.; Ikeue, T.; Takahashi, M.; Takeda, M.; Nakamura, M. *J. Am. Chem. Soc.* **2003**, *125*, 13028–13029.
425. Ohgo, Y.; Ikeue, T.; Nakamura, *Inorg. Chem.* **2002**, *41*, 1698–1700.
426. Hoshino, A.; Ohgo, Y.; Nakamura, M. *Inorg. Chem.* **2005**, *44*, 7333–7344.
427. Ikezaki, A.; Nakamura, M. *Inorg. Chem.* **2002**, *41*, 6225–6236.
428. Ohgo, Y.; Neya, S.; Ikeue, T.; Takahashi, M.; Takeda, M.; Funasaki, N.; Nakamura, M. *Inorg. Chem.* **2002**, *41*, 4627–4629.
429. Simonato, J.-P.; Pécaut, J.; Le Pape, L.; Oddou, J.-L. ; Jeandey, C.; Shang, M. ; Scheidt, W. R.; Wojaczyński, J.; Wolowiec, S.; Latos-Grażyński, L.; Marchon, J.-C. *Inorg. Chem.* **2000**, *39*, 3978–3987.
430. Ling, Y.; Zhang, Y. *J. Am. Chem. Soc.* **2009**, *131*, 5386–6388.
431. Walker, F. A.; Huynh, B. H.; Scheidt, W. R.; Osvath, S. R. *J. Am. Chem. Soc.* **1986**, *108*, 5288–5297.
432. Salerno, J. C.; Leigh, J. S. *J. Am. Chem. Soc.* **1984**, *106*, 2156–2159.
433. Salerno, J. C. *J. Biol. Chem.* **1984**, *259*, 2331–2336.
434. Berry, E. A.; Walker, F. A. *J. Biol. Inorg. Chem.* **2008**, *13*, 481–498.
435. Xia, D.; Yu, C.-A.; Kim, H.; Xia, J.-Z.; Kachurin, A. M.; Zhang, L.; Yu, L.; Deisenhofer, J. *Science* **1997**, *277*, 60–66.
436. Iwata, S.; Lee, J. W.; Okada, K.; Lee, J. K.; Iwata, M.; Rasmussen, B.; Link, T. A.; Ramaswamy, S.; Jap, S. K. *Science* **1998**, *281*, 64–71.
437. Zhang, Z.; Huang, L.; Shulmeister, V. M.; Chi, Y.-I.; Kim, K. K.; Hung, L. W.; Crofts, A. R.; Berry, E. A.; Kim S.-H. *Nature* **1998**, *392*, 677–684.
438. Berry, E. A.; Huang, L.-S.; Zhang, Z.; Kim, S.-H. *J. Bioenerg. Biomembr.* **1999**, *31*, 177–190.
439. Hunte, C.; Koepke, J.; Lange, C.; Rossmanith, T.; Michel, H. *Structure* **2000**, *8*, 669–684.
440. Inniss, D.; Soltis, S. M.; Strouse, C. E. *J. Am. Chem. Soc.* **1988**, *110*, 5644–5650.
441. Guzov, V. I.; Houston, H. L.; Murataliev, M. B.; Walker, F. A.; Feyereisen, R. *J. Biol. Chem.* **1996**, *271*, 26637–26645 and references therein.
442. Aasa, R.; Albracht, S. P. J.; Falk, K. E.; Fanne, B.; Vanngard, T. *Biochim. Biophys. Acta* **1976**, *422*, 260–272.
443. Hori, H. *Biochim. Biophys. Acta* **1971**, *251*, 227–235.
444. Blumberg, W. E.; Peisach, J. In *Probes of Structure and Function of Macromolecules and Membranes*; Chance, B.; Yonetani, T.; Mildvan, A. S., Eds.; Academic Press: New York, **1971**; Vol. 2, p. 215.
445. Peisach, J.; Blumberg, W. E.; Adler, A. D. *Ann. NY Acad. Sci.* **1973**, *206*, 310–327.
446. Brautigan, D. L.; Feinberg, B. A.; Hoffman, B. M.; Margoliash, E.; Peisach, J.; Blumberg, W. E. *J. Biol. Chem.* **1977**, *252*, 574–582.
447. Palmer, G. In *The Porphyrins*; Dolphin, D., Ed.; Academic Press: New York, 1979; pp. 313–353.
448. Taylor, C. P. S. *Biochim. Biophys. Acta* **1977**, *491*, 137–149.
449. Simonneaux, G.; Schünemann, V.; Morice, C.; Carel, L.; Toupet, L.; Winkler, H.; Trautwein, A. X.; Walker, F. A. *J. Am. Chem. Soc.* **2000**, *122*, 4366–4377.

450. Nakamura, M.; Ikeue, T.; Ikezuki, A.; Ohgo, Y.; Fujii, H. *Inorg. Chem.* **1999**, *38*, 3857–3862.
451. Ikeue, T.; Ohgo, Y.; Saitoh, T.; Yamaguchi, T.; Nakamura, M. *Inorg. Chem.* **2001**, *40*, 3423–3434.
452. Griffith, J. S. *Nature* **1957**, *180*, 30–31.
453. Griffith, J. S. *Mol. Phys.* **1971**, *21*, 135–139.
454. Quinn, R.; Valentine, J. S.; Byrn, M. P.; Strouse, C. E. *J. Am. Chem. Soc.* **1987**, *109*, 3301–3309.
455. Quinn, R.; Nappa, M.; Valentine, J. S. *J. Am. Chem. Soc.* **1982**, *104*, 2588–2595.
456. Soltis, S. M.; Strouse, C. E. *J. Am. Chem. Soc.* **1988**, *110*, 2824–2829.
457. Byrn, M. P.; Katz, B. A.; Keder, N. L.; Levan, K. R.; Magurany, C. J.; Miller, K. M.; Pritt, J. W.; Strouse, C. E. *J. Am. Chem. Soc.* **1983**, *105*, 4916–4922.
458. Flint, H.; Trautwein, A. X.; Winkler, H.; Grodzicki, M.; Wright, J. L.; Polam, J. R.; Walker, F. A. *J. Inorg. Biochem.* **1995**, *59*, 493, and *ICAME-95 Conference Proceedings* **1995**, *50*, 839–842.
459. Figgis, B. N.; Lewis, J. In *Techniques of Inorganic Chemistry*; Jonassen, H. B.; Weissberger, A., Eds.; Wiley Interscience: New York, **1965**; Vol. IV, p. 159.
460. Baker and Lewis obtained values of 260–270 cm^{-1} for nonheme low-spin Fe(III) complexes (*J. Chem. Soc., Dalton Trans.* **1975**, 598–602). Maltempo has used the value of 300 cm^{-1} for low-spin ferrihemes, while Levin and Brill obtained a value of 350 cm^{-1} for metmyoglobin complexes (*J. Phys. Chem.* **1988**, *92*, 5103–5110). We have used 400 cm^{-1} as the maximum possible value of λ.
461. Huynh, B. H.; Emptage, M. H.; Münck, E. *Biochim. Biophys. Acta* **1978**, *534*, 295–306.
462. De Vries, S.; Albracht, S. P. J. *Biochim. Biophys. Acta* **1978**, *546*, 334–340.
463. Walker, F. A.; Nasri, H.; Turowska-Tyrk, I.; Mohanrao, K.; Watson, C. T.; Shokhirev, N. V.; Debrunner, P. G.; Scheidt,W. R. *J. Am. Chem. Soc.* **1996**, *118*, 12109–12118.
464. Mathews, F. S.; Czerwinski, E. W.; Argos, P. In *The Porphyrins*; Dolphin, D., Ed.; Academic Press: New York, **1979**; Vol. VII, pp. 108–147.
465. Pierrot, M.; Haser, R.; Frey, M.; Payan, F.; Astier, J.-P. *J. Biol. Chem.* **1982**, *257*, 14341–14348.
466. Higuchi, Y.; Kusunoki, M.; Matsuura, Y.; Yasuoka, N.; Kakudo, M. *J. Mol. Biol.* **1984**, *172*, 109.
467. Stroebel, D.; Choquet, Y.; Popot, J.-L.; Picot, D. *Nature* **2003**, *426*, 413–418.
468. Kurisu, G.; Zhang, H.; Smith, J. L.; Cramer, W. A. *Science* **2003**, *302*, 1009–1014.
469. Cramer, W. A.; Zhang, H.; Yan, J.; Curisu, G. ; Smith, J. L. *Annu. Rev. Biochem.* **2006**, *75*, 769–790.
470. Yamashita, E.; Zhang, H.; Cramer, W. A. *J. Mol. Biol.* **2007**, *370*, 39–52.
471. Mailer, C.; Taylor, C. P. S. *Can. J. Biochem.* **1972**, *50*, 1048–1055.
472. Balch, A. L.; Noll, B. C.; Reid, S. M.; Zovinka, E. P. *Inorg. Chem.* **1993**, *32*, 2610–2611.
473. Balch, A. L.; Koerner, R.; Latos-Grażyński, L.; Noll, B. C. *J. Am. Chem. Soc.* **1996**, *118*, 2760–2761.
474. Balch, A. L.; Koerner, R.; Latos-Grażyński, L.; Lewis, J. E.; St. Claire, T. N.; Zovinka, E. P. *Inorg. Chem.* **1997**, *36*, 3892–3897.
475. Kalish, H. R.; Latos-Grażyński, L.; Balch, A. L. *J. Am. Chem. Soc.* **2000**, *122*, 12478–12486.
476. Yatsunyk, L. A.; Carducci, M. D.; Walker, F. A. *J. Am. Chem. Soc.* **2003**, *125*, 15986–16005.
477. Yatsunyk, L. A.; Dawson, A.; Carducci, M. D.; Nichol, G. S.; Walker, F. A. *Inorg. Chem.* **2006**, *45*, 5417–5426.

478. Ogura, H.; Yatsunyk, L.; Medforth, C. J.; Smith, K. M.; Barkigia, K. M.; Renner, M. W.; Melamed, D.; Walker, F. A. *J. Am. Chem. Soc.* **2001**, *123*, 6564–6578.
479. Devaney, P. W. Ph.D. Dissertation, University of Illinois, **1980**.
480. Balch, A. L.; Koerner, R.; Latos-Grażyński, L.; Lewis, J. E.; St. Claire, T. N.; Zovinka, E. P. *Inorg. Chem.* **1997**, *36*, 3892–3897.
481. Rivera, M.; Caignan, G. A.; Astashkin, A. V.; Raitsimring, A. M.; Shokhireva, T. Kh.; Walker, F. A. *J. Am. Chem. Soc*. **2002**, *124*, 6077–6089.
482. Cai, S.; Shokhireva, T. Kh.; Lichtenberger, D. L.; Walker, F. A. *Inorg. Chem*. **2006**, *45*, 3519–3531.
483. Stolzenberg, A. M.; Strauss, S. H.; Holm, R. H. *J. Am. Chem. Soc.* **1981**, *103*, 4763–4778.
484. Bertini, I.; Luchinat, C.; Rosato, A. *Inorg. Chim. Acta* **2000**, *297*, 199–205.
485. Walker, F. A.; Balke, V. L.; McDermott, G. A. *J. Am. Chem. Soc.* **1982**, *104*, 1569–1574.
486. Walker, F. A.; Benson, M. *J. Phys. Chem.* **1982**, *86*, 3495–3499.
487. Vangberg, T.; Ghosh, A. *J. Am. Chem. Soc.* **1998**, *120*, 6227–6230.
488. Walker, F. A.; Reis, D.; Balke, V. L. *J. Am. Chem. Soc.* **1984**, *106*, 6888–6898.
489. Satterlee, J. D.; La Mar, G. N. *J. Am. Chem. Soc.* **1976**, *98*, 2804–2808.
490. Chacko, V. P.; La Mar, G. N. *J. Am. Chem. Soc.* **1982**, *104*, 7002–7007.
491. Watson, C. T.; Cai, S.; Shokhirev, N. V.; Walker, F. A. *Inorg. Chem*. **2005**, *44*, 7468–7484.
492. Traylor, T. G.; Berzinis, A. P. *J. Am. Chem. Soc.* **1980**, *102*, 2844–2846.
493. Goff, H. M. *J. Am. Chem. Soc.* **1980**, *102*, 3252–3254.
494. Walker, F. A. *J. Am. Chem. Soc.* **1980**, *102*, 3254–3256.
495. Walker, F. A.; Buehler, J.; West, J. T.; Hinds, J. L. *J. Am. Chem. Soc.* **1983**, *105*, 6923–6929.
496. Nakamura, M.; Groves, J. T. *Tetrahedron* **1988**, *44*, 3225–3230.
497. Wüthrich, K. *Proc. Natl. Acad. Sci. USA* **1969**, *63*, 1071–1078.
498. Thanabal, V.; de Ropp, J. S.; La Mar, G. N. *J. Am. Chem. Soc.* **1987**, *109*, 265–272.
499. Minniear, A. B.; Shokhireva, T. Kh.; Walker, F. A. *Inorg. Chem*. **1999**, *38*, 5856–5859.
500. Reference 219, Chapters 6 and 9.
501. Nakamura, M.; Nakamura, N. *Chem. Lett. (Japan)* **1991**, 1885–1888.
502. Hwang, Y. C.; Dixon, D. W. *Inorg. Chem.* **1986**, *25*, 3716–3718 and references therein.
503. La Mar, G. N.; Del Gaudio, J. *Adv. Chem. Ser*. 162: Bioinorganic Chemistry II, **1977**, pp. 207–226.
504. Kim, Y. O.; Goff, H. M. *Inorg. Chem.* **1990**, *29*, 3907–3908.
505. Morice, C.; Le Maux, P.; Simonneaux, G. *Inorg. Chem.* **1998**, *37*, 6100–6103.
506. Simonneaux, G.; Kobeissi, M.; Toupet, L. *Inorg. Chem.* **2003**, *42*, 1644–1651.
507. Martinez, S. E.; Huang, D.; Szczepaniak, A.; Cramer, W. A.; Smith, J. L. *Structure* **1994**, *2*, 95–105.
508. Simonneaux, G.; Sodano, P. *Inorg. Chem.* **1988**, *27*, 3956–3959.
509. Simonneaux, G.; Sodano, P. J. *Organomet. Chem.* **1988**, *349*, C12-C14.
510. Simonneaux, G. In *The Porphyrin Handbook*; Kadish, K. M.; Smith, K. M.; Guilard, R., Eds.; Academic Press: New York, **2000**; Chapter 38, pp. 299–322.
511. Kobeissi, M.; Toupet, L.; Simonneaux, G. *Inorg. Chem*. **2001**, *40,* 4494–4499.
512. Bold, T. J. Ph.D. Dissertation, University of California, Davis, **1978**.
513. Nakamura, M.; Ikeue, T.; Fujii, H.; Yoshimura, T.; Tajima, K. *Inorg. Chem.* **1998**, *37*, 2405–2414.
514. La Mar, G. N.; Del Gaudio, J.; Frye, J. S. *Biochim. Biophys. Acta* **1977**, *498*, 422–435.
515. La Mar, G. N.; Frye, J. S.; Satterlee, J. D. *Biochim. Biophys. Acta* **1976**, *428*, 78–90.

516. Balch, A. L.; Renner, M. W. *Inorg. Chem.* **1986**, *25*, 303–307.
517. Simonneaux, G.; Bondon, A.; Sodano, P. *Inorg. Chem.* **1987**, *26*, 3636–3638
518. Simonneaux, G.; Bondon, A.; Sodano, P. *Biochim. Biophys. Acta* **1990**, *1038*, 199–203.
519. La Mar, G. N.; Bold, T. J.; Satterlee, J. D. *Biochim. Biophys. Acta* **1977**, *498*, 189–207.
520. Yatsunyk, L. A.; Walker, F. A. *Inorg. Chem.* **2004**, *43*, 4341–4352.
521. Ohgo Y.; Hoshino, A.; Okamura, T.; Uekusa, H.; Hashizume, D.; Ikezaki, A.; Nakamura, M. *Inorg. Chem.* **2007**, *46*, 6193–6207.
522. Nakamura, K.; Ikezaki, A.; Ohgo, Y.; Ikeue, T.; Neya, S.; Nakamura, M. *Inorg. Chem.* **2008**, *47*, 10299–10307.
523. Bonnett, R.; Czechowski, F.; Latos-Grażyński, L. *J. Chem. Soc. Chem. Commun.* **1990**, 849–851.
524. Czechowski, F.; Latos-Grażyński, L. *Naturwiss.* **1990**, *77*, 578–581.
525. Czechowski, F.; Latos-Grażyński, L.; Wolowiec, S. *Organ. Geochem.* **1994**, *21*, 1059–1068.
526. Medforth, C. J.; Shiau, F.-Y.; La Mar, G. N.; Smith, K. M. *J. Chem. Soc., Chem. Commun.* **1991**, 590–592.
527. Mazumdar, S. *J. Phys. Chem.* **1990**, *94*, 5947–5953.
528. Mazumdar, S.; Medhi, O. K.; Mitra, S. *J. Chem. Soc., Dalton Trans.* **1990**, 1057–1061.
529. Nakamura, M.; Ikeue, T.; Fujii, H.; Yoshimura, T. *J. Am. Chem. Soc.* **1997**, *119*, 6284–6291.
530. Wolowiec, S.; Latos-Grażyński, L.; Mazzanti, M.; Marchon, J.-C. *Inorg. Chem.* **1991**, *36*, 5761–5771.
531. Wolowiec, S.; Latos-Grażyński, L.; Toronto, D.; Marchon, J.-C. *Inorg. Chem.* **1998**, *37*, 724–732.
532. Wojaczyński, J.; Latos-Grażyński, L.; Głowiak, T. *Inorg. Chem.* **1997**, *36*, 6299–6306.
533. Shokhireva, T. Kh.; Raitsimring, A. M.; Walker, F. A. Unpublished results.
534. Nakamura, M.; Tajima, K.; Tada, K.; Ishizu, K.; Nakamura, N. *Inorg. Chim. Acta* **1996**, *224*, 113–124.
535. Nakamura, M.; Ikeue, T.; Neya, S.; Funasaki, N.; Nakamura, N. *Inorg. Chem.* **1996**, *35*, 3731–3732.
536. Li, J.; Noll, B. C.; Schulz, C. E.; Scheidt, W. R. *Inorg. Chem.* **2007**, *46*, 2286–2298.
537. Jentzen, W.; Song, X.-Z.; Shelnutt, J. A. *J. Phys. Chem. B* **1997**, *101*, 1684–1699;
538. Shelnutt, J. A.; Song, X.-Z.; Ma, J.-G.; Jia, S.-L.; Jentzen, W.; Medforth, C. J. *Chem. Soc. Rev.* **1998**, *31*, 31–41.
539. Song, X.-Z.; Jentzen, W.; Jaquinod, L.; Khoury, R. G.; Medforth, C. J.; Jia, S.-L.; Ma, J.-G.; Smith, K. M.; Shelnutt, J. A. *Inorg. Chem.* **1998**, *37*, 2117–2128.
540. Berlicka, A.; Latos-Grazynski, L.; Lis, T. *Inorg. Chem.* **2005**, *44*, 4522–4533.
541. Balch, A. L.; Noll, B. C.; Safari, N. *Inorg. Chem.* **1993**, *32*, 2901–2905.
542. Gregson, A. K. *Inorg. Chem.* **1981**, *20*, 81–87.
543. Scheidt, W. R.; Geiger, D. K.; Haller, K. J. *J. Am. Chem. Soc.* **1982**, *104*, 495–499.
544. Scheidt, W. R.; Gouterman, M. In *Iron Porphyrins*, Lever, A. B. P.; Gray, H. B., Eds.; Addison-Wesley: Reading, MA; Part I, **1983**; pp. 89–140.
545. Scheidt,W. R.; Geiger, D. K.; Lee, Y. J.; Reed, C. A.; Lang, G. *Inorg. Chem.* **1987**, *26*, 1039–1045.
546. Safo, M. K.; Gupta, G. P.; Orosz, R. D.; Reed, C. A.; Scheidt, W. R. *Inorg. Chim. Acta* **1991**, *184*, 251–258.
547. Hill, H. A. O.; Morallee, K. G. *J. Am. Chem. Soc.* **1972**, *94*, 731–738.
548. Yatsunyk, L.; Shokhirev, N. V.; Walker, F. A. *Inorg. Chem.* **2005**, *44*, 2848–2866.

549. Yatsunyk, L.; Walker, F. A. *Inorg. Chem.* **2004**, *43*, 757–777.
550. Ikue, T.; Ohgo, Y.; Ongayi, O.; Vicente, M. G. H.; Nakamura, M. *Inorg. Chem.* **2003**, *42*, 5560–5571.
551. Yatsunyk, L. A.; Ogura, H.; Walker, F. A. *Inorg. Chem.* **2005**, *44*, 2005 2867–2881.
552. St. Claire, T. N.; Balch, A. L. *Inorg. Chem.* **1999**, *38*, 684–691.
553. Rath, S. P.; Olmstead, M. M.; Balch, A. L. *Inorg. Chem.* **2006**, *45*, 6083–6093.
554. Rath, S. P.; Olmstead, M. M.; Balch, A. L. *J. Am. Chem. Soc.* **2004**, *126*, 6379–6386.
555. Rath, S. P.; Koerner, R.; Olmstead, M. M.; Balch, A. L. *J. Am. Chem. Soc.* **2003**, *125*, 11798–11799.
556. Kalish, H.; Camp, J. E.; Stepien, M.; Latos-Grażyński, L.; Balch, A. L. *J. Am. Chem. Soc.* **2001**, *123*, 11719–11727.
557. Rath, S. P.; Kalish, H.; Latos-Grażyński, L.; Olmstead, M. M.; Balch, A. L. *J. Am. Chem. Soc.* **2004**, *126*, 646–654.
558. Rath, S. P.; Olmstead, M. M.; Latos-Grażyński, L.; Balch, A. L. *J. Am. Chem. Soc.* **2003**, *125*, 12578–12579.
559. Kalish, H.; Lee, H. M.; Olmstead, M. M.; Latos-Grażyński, L.; Rath, S. P.; Balch, A. L. *J. Am. Chem. Soc.* **2003**, *125*, 4674–4675.
560. Wojaczynski, J.; Latos-Grażyński, L.; Chmielewski, P.; Van Calcar, P.; Balch, A. L. *Inorg. Chem.* **1999**, *38*, 3040–3050.
561. Cocolios, P.; Lagrange, G.; Guilard, R. *J. Organomet. Chem.* **1983**, *253*, 65–79.
562. Lançon, D.; Cocolios, P.; Guilard, R.; Kadish, K. M. *Organometallics* **1984**, *3*, 1164–1170.
563. Balch, A. L.; Hart, R. L.; Latos-Grażyński, L.; Traylor, T. G. J. *Am. Chem. Soc.* **1990**, *112*, 7382–7388.
564. Kadish, K. M.; Tabard, A.; Lee, W.; Liu, Y. H.; Ratti, C.; Guilard, R. *Inorg. Chem.* **1991**, *30*, 1542–1549.
565. Kim, Y. O.; Goff, H. M. *J. Am. Chem. Soc.* **1988**, *110*, 8706–8707.
566. Chatfield, M. J.; La Mar, G. N.; Balch, A. L.; Lecomte, J. T. J. *Biochem. Biophys. Res. Commun.* **1986**, *135*, 309–315.
567. Chatfield, M. J.; La Mar, G. N.; Lecomte, J. T. J.; Balch, A. L.; Smith, K. M.; Langry, K. C. *J. Am. Chem. Soc.* **1986**, *108*, 7108–7110.
568. Bondoc, L. L; Chau, M.-H.; Price, M. A.; Timkovich, R. *Biochemistry* **1986**, *25*, 8458–8466.
569. Chatfield, M. J.; La Mar, G. N.; Kauten, R. J. *Biochemistry* **1987**, *26*, 6939–6950.
570. Simonneaux, G.; Kobeissi, M. *J. Chem. Soc., Dalton Trans*. **2001**, 1587–1592.
571. Ikezaki, A.; Nakamura, M.; Juillard, S.; Simonneaux, G. *Inorg. Chem.* **2006**, *45*, 6728–6739.
572. Crane, B. R.; Siegel, L. M.; Getzoff, E. D. *Science* **1995**, *270*, 59–67.
573. Kaufman, J.; Sigel, L. M.; Spicer, L. D. *Biochemistry* **1993**, *32*, 8782–8791.
574. Ortiz de Montellano, P. R.; Correia, M. A. *Annu. Rev. Pharmacol. Toxicol.* **1983**, *23*, 481.
575. Ortiz de Montellano, P. R.; Reich, N. O. In *Cytochrome P450, Structure, Mechanism and Biochemistry*; Ortiz de Montellano, P. R., Ed.; Plenum Press: New York, **1986**; pp. 273–314.
576. Lavallee, D. K. *The Chemistry and Biochemistry of N-Substituted Porphyrins*; VCH Publishers: New York, **1987**.
577. Anderson, O. P.; Kopelov, A. B.; Lavallee, D. K. *Inorg. Chem.* **1980**, *19*, 2101–2107.
578. Balch, A. L.; Cornman, C. R.; Latos-Grażyński, L.; Olmstead, M. M. *J. Am. Chem. Soc.* **1990**, *112*, 7552–7558.
579. Walker, F. A.; Lo, M. W.; Ree, M. T. *J. Am. Chem. Soc.* **1976**, *98*, 5552–5560.

580. Walker, F. A.; Balke, V. L.; West, J. T. *J. Am. Chem. Soc.* **1985**, *107*, 1226–1233.
581. Wang, J.-T.; Yeh, H. J. C.; Johnson, O. F. *J. Am. Chem. Soc.* **1978**, *100*, 2400–2405.
582. Nakamura, M.; Nakamura, N. *Chem. Lett. (Japan)* **1990**, 181–184.
583. Satterlee, J. D.; La Mar, G. N.; Bold, T. J. *J. Am. Chem. Soc.* **1977**, *99*, 1088–1093.
584. Nakamura, M. *Bull. Chem. Soc. Jpn.* **1995**, *68*, 197–203.
585. Kowalsky, A. *Biochemistry* **1965**, *4*, 2382–2388.
586. Gupta, R. K.; Koenig, S. H.; Redfield, A. G. *J. Magn. Reson.* **1972**, *7*, 66–73.
587. Keller, R. M.; Wüthrich, K.; Pecht, I. *FEBS Lett.* **1976**, *70*, 180–184.
588. Keller, R. M.; Wüthrich, K.; Schejter, A. *Biochim. Biophys. Acta* **1977**, *491*, 409–415.
589. Timkovich, R.; Cai, M. L.; Dixon, D. W. *Biochem. Biophys. Res. Commun.* **1988**, *150*, 1044–1050.
590. Dixon, D. W.; Hong, X.; Woehler, S. E. *Biophys. J.* **1989**, *56*, 339–351.
591. Dixon, D. W.; Hong, X.; Woehler, S. E.; Mauk, A. G.; Sishta, B. P. *J. Am. Chem. Soc.* **1990**, *112*, 1082–1088.
592. van Leeuwen, J. W. *Biochim. Biophys. Acta* **1983**, *743*, 408–421.
593. Dixon, D. W.; Barbush, M.; Shirazi, A. *J. Am. Chem. Soc.* **1984**, *106*, 4638–4639.
594. Dixon, D.W.; Barbush, M.; Shirazi, A. *Inorg. Chem.* **1985**, *24*, 1081–1087.
595. Dixon, D. W.; Woejler, S.; Hong, X.; Stolzenberg, A. *Inorg. Chem.* **1988**, *27*, 3682–3685.
596. Ribeiro, J. M. C.; Gonzales, R.; Marinotti, O. *Br. J. Pharmacol.* **1990**, *101*, 932–936.
597. Ribeiro, J. M. C.; Hazzard, J. M. H.; Nussenzveig, R. H.; Champagne, D. E.; Walker, F. A. *Science* **1993**, *260*, 539–541.
598. Moncada, S.; Martin, J. F. *Lancet* **1993**, *341*, 1511.
599. Champagne, D. E.; Nussenzveig, R.; Ribeiro, J. M. C. *J. Biol. Chem.* **1995**, *270*, 8691–8695.
600. Valenzuela, J. G.; Walker, F. A.; Ribeiro, J. M. C. *J. Exper. Med.* **1995**, *198*, 1519–1526.
601. Weichsel, A.; Maes, E. M.; Andersen, J. F.; Valenzuela, J. G.; Shokhireva, T. Kh.; Walker, F. A.; Montfort, W. R. *Proc. Natl. Acad. Sci. USA* **2005**, *102*, 594–599.
602. Ribeiro, J. M. C.; Walker, F. A. *J. Exp. Med.* **1994**, *180*, 2251–2257.
603. Gudderra, N. P.; Ribeiro, J. M. C.; Andersen, J. F. *J. Biol. Chem.* **2005**, *280*, 25022–25028.
604. Walker, F. A.; Montfort, W. R. In *Adv. Inorg. Chem.*; Mauk A. G.; Sykes, A. G. Eds.; Academic Press: San Diego, **2001**; Vol. 51, Chapter 5, pp. 295–358
605. Walker, F. A. *J. Inorg. Biochem*. **2005**, *99*, 216–236.
606. Walker, F. A. In: *The Smallest Biomolecules: Diatomics and their Interactions with Heme Proteins*, Ghosh, A., Ed.; Elsevier B. V.; **2008**; pp. 378–428.
607. Neva, F. A. In: *Cecil Textbook of Medicine*; Wyngaarden, J. B.; Smith, L. H. Eds.; Saunders, Hartcourt Brace Jovanovich, Inc.: Philadelphia, Ed. 18, **1988**; Section 383, pp. 1865–1869.
608. Kirchhoff, L. V. In: *Harrison's Principles of Internal Medicine*; Wilson, J. D.; Braunwald, E.; Isselbacher, K. J.; Petersdorf, R. G.; Martin, J. B.; Fauci, A. S.; Root, R. K. Eds.; McGraw-Hill: New York; Ed. 12, **1991**; pp. 791–793.
609. Kirchhoff, L. V. *N. Engl. J. Med.* **1993**, *329*, 639.
610. http://www.cdc.gov/ncidod/dpd/parasites/chagasdisease/default.htm
611. Feltham, R. D.; Enemark, J. H. *Coord. Chem. Rev.* **1974**, *13*, 339–406.
612. Wayland, B. B.; Olson, L. W. *J. Am. Chem. Soc.* **1974**, *96*, 6037–6041.
613. Berry, R. E.; Shokhirev, M. N.; Ho, A. Y. W.; Yang, F.; Shokhireva, T. K.; Zhang, H.; Weichsel, A.; Montfort, W. R.; Walker, F. A. *J. Am. Chem. Soc.* **2009**, *131*, 2313–2327.
614. Andersen, J. F.; Ding, X. D.; Balfour, C.; Champagne, D. E.; Walker, F. A.; Montfort, W. R. *Biochemistry* **2000**, *39*, 10118–10131.

615. Traylor, T. G.; Sharma, V. S. *Biochemistry* **1992**, *31*, 2847–2849.
616. Peisach, J., Blumberg, W. E., Ogawa, S., Rachmilewitz, E. A.; Oltzik, R. *J. Biol. Chem.* **1971**, *246*, 3342–3355.
617. Andersen, J. F.; Weichsel, A.; Balfour, C.; Champagne, D. E.; Montfort, W. R. *Structure* **1998**, *6*, 1315–1327.
618. Champagne, D. E.; Ribeiro, J. M. C. Unpublished work.
619. Moreira, M. F.; Coelho, H. S. L.; Zingali, R. B.; Oliveira, P. L.; Masuda, H. *Insect Biochem. Mol. Biol.* **2003**, *33*, 23–28.
620. Andersen, J. F.; Gudderra, N. P.; Francischetti, I. M. B.; Valenzuela, J. G.; Ribeiro, J. M. C. *Biochemistry* **2004**, *43*, 6987–6994.
621. Ribeiro, J. M. C. Personal communication.
622. Knipp, M.; Zhang, H.; Berry, R. E.; Walker, F. A. *Prot. Expr. Purif.* **2007**, *54*, 183–191.
623. Knipp, M.; Yang, F.; Berry, R. E.; Zhang, H.; Shokhirev, M. N.; Walker, F. A. *Biochemistry* **2007**, *46*, 13254–13268.
624. Yang, F.; Zhang, H.; Knipp, M. *Biochemistry* **2009**, *48(2)*, 235–241.
625. Weichsel, A.; Andersen, J. F.; Champagne, D. E.; Walker, F. A.; Montfort, W. R. *Nature Struct. Biol.* **1998**, *5*, 304–309.
626. Ding, X. D.; Weichsel, A.; Balfour, C.; Shokhireva, T. Kh.; Pierik, A.; Averill, B. A.; Montfort, W. R.; Walker, F. A. *J. Am. Chem. Soc.* **1999**, *121*, 128–138.
627. Andersen, J. F.; Weichsel, A.; Balfour, C. A.; Champagne, D. E.; Montfort, W. R. *Structure* **1998**, *6*, 1315–1327.
628. Weichsel, A.; Andersen, J. F.; Roberts, S. A.; Montfort, W. R. *Nat. Struc. Biol.* **2000**, *7*, 551–554.
629. Roberts, S. A.; Weichsel, A.; Qiu, Y.; Shelnutt, J. A.; Walker, F. A.; Montfort, W. R. *Biochemistry* **2001**, *40,* 11327–11337.
630. Maes, E. M.; Weichsel, A.; Andersen, J. F.; Shepley, D.; Montfort, W. R. *Biochemistry* **2004**, *43,* 6679–6690.
631. Kondrashov, D. A.; Roberts, S. A.; Weichsel, A.; Montfort, W. R. *Biochemistry* **2004**, *43*, 13637–13647.
632. Maes, E. M.; Roberts, S. A.; Weichsel, A.; Montfort, W. R. *Biochemistry* **2005**, *44*, 12690–12699.
633. Andersen, J. F.; Montfort, W. R. *J. Biol. Chem.* **2000**, *275*, 30496–30503.
634. Weichsel, A.; Berry, R. E.; Zhang, H.; Walker, F. A.; Montfort, W. R. (1999–2002) PDB files available (http://www.rcsb.org/): 1PEE, 1PM1, 1T68, 2A3F, 2ACP, 2AH7, 2AL0, 2ALL, 2AMM, 2ASN, 2EU7, 2HYS, 2GTF.
635. Flower, D. R. *Biochem. J.* **1996**, *318*, 1–14.
636. Flower, D. R. *Biochim. Biophys. Acta* **2000**, *1482*, 44–56.
637. Marie, A. D.; Veggerby, C.; Robertson, D. H. L.; Gaskell, S. J.; Hubbard, S. J.; Martinsen, L.; Hurst, J. L.; Beynon, R. *J. Protein Science* **2001**, *10*, 411–417.
638. Spinelli, S.; Vincent, F.; Pelosi, P.; Tegoni, M.; Cambillau, C. *Eur. J. Biochem.* **2002**, *269*, 2449–2456.
639. Lazar, J.; Greenwood, D. R.; Rasmussen, L. E. L.; Prestwich, G. D. *Biochemistry* **2002**, *41*, 11786–11794.
640. Newcomer, M. E.; Jones, T. A.; Aqvist, J.; Sundelin, J.; Eriksson, U.; Rask, L.; Peterson, P. A. *EMBO J.* **1984**, *3*, 1451–1454.
641. Newcomer, M. E.; Ong, D. E. *Biochim. Biophys. Acta* **2000**, *1482*, 57–64.

642. Nagata, A.; Suzuki, Y.; Igarashi, M.; Eguchi, N.; Ton, H.; Urade, Y.; Hayashi, O. *Proc. Natl. Acad. Sci. USA* **1991**, *88*, 4020–4024.
643. Newcomer, M. E. *Structure* **1993**, *1*, 7–18.
644. Riley, C. T.; Barbeau, B. K.; Keim. P. S.; Kezdy, F. J.; Heinrikson, R. L.; Law, J. H. *J. Biol. Chem.* **1984**, *259*, 13159–13165.
645. Holden, H. M.; Rypniewski, W. R.; Law, J. H.; Rayment, I. *EMBO J.* **1987**, *6*, 1565–1570.
646. Huber, R.; Schneider, M.; Epp, O.; Mayr, I.; Messerschmidt, A.; Pflugrath, J.; Kayser, H. *J. Mol. Biol.* **1987**, *195*, 423–434.
647. Huber, R.; Schneider, M.; Mayr, I.; Muller, R.; Deutzmann, R.; Suter, F.; Zuber, H.; Falk, H.; Kayser, H. *J. Mol. Biol.* **1987**, *198*, 499–513.
648. Vetter, S. W.; Terentis, A. C.; Osborne, R. L.; Dawson, J. H.; Gooden, D. B. *J. Biol. Inorg. Chem.* **2009**, *14*, 179–191.
649. Berry, R. E.; Shokhireva, T. Kh.; Filippov, I.; Shokhirev, M. N.; Zhang, H.; Walker, F. A. *Biochemistry* **2007**, *46*, 6830–6843.
650. La Mar, G. N.; Overkamp, M.; Sick, H.; Gersonde, K. *Biochemistry* **1978**, *17*, 352–361.
651. La Mar, G. N.; Budd, D. L.; Smith, K. M.; Langry, K. C. *Proc. Natl. Acad. Sci. USA* **1978**, *75*, 5755–5759.
652. Shokhireva, T. K. Unpublished work.
653. Kondrashov, D.A.; Montfort, W. R. *J. Phys. Chem. B* **2007**, *111*, 9244–9252.
654. Marti, M. A.; Lebrero, M. C. G.; Roitberg, A. E.; Estrin, D. A. *J. Am. Chem. Soc.* **2008**, *130*, 1611–1618.
655. Swails, J. M.; Meng, Y.; Walker, F. A.; Marti, M. A.; Estrin, D. A.; Roitberg, A. E. *J. Phys. Chem. B* **2009**, *113*, 1192–1201.
656. http://www.ncbi.nlm.nih.gov/Genbank/database
657. Berry, R. E.; Zhang, H.; Walker, F. A. To be published.
658. Caignan, G. A.; Deshmukh, R.; Zheng, Y.; Wilks, A.; Bunce, R. A.; Rivera, M. *J. Am. Chem. Soc.* **2003**, *125*, 11842–11852.
659. Ma, L.-H.; Liu, Y.; Zheng, X.; Yoshida, T.; La Mar, G. N. *J. Am. Chem. Soc.* **2006**, *128*, 6657–6668.
660. EMBL WWW Gateway to Isoelectric Point Service, http://www.embl-heidelberg.de/cgi/pi-wrapper.pl.
661. Berry, R. E.; Walker, F. A. Unpublished work.
662. Timkovich, R.; Cai, M.; Zhang, B.; Arciero, D. M.; Hooper, A. B. *Eur. J. Biochem.* **1994**, *226*, 159–168.
663. Zhong, L.; Wen, X.; Rabinowitz, T. M.; Russell, B. S.; Karan, E. F.; Bren, K. L. *Proc. Natl. Acad. Sci. USA* **2004**, *101*, 8637–8642.
664. Wen, X.; Bren, K. L. *Biochemistry* **2005**, *44*, 5225–5233.
665. Wen, X.; Bren, K. L. *Inorg. Chem.* **2005**, *44*, 8587–8593.
666. Wen, X.; Patel, K. M.; Russell, B. S.; Bren, K. L. *Biochemistry* **2007**, *46*, 2537–2544.
667. Shokhirev, N. V.; Walker, F. A. (2000) Two Site Exchange of NMR Lines http://www.shokhirev.com/nikolai/programs/prgsciedu.html
668. Andersen, J. F.; Ding, X. D.; Balfour, C.; Champagne, D. E.; Walker, F. A.; Montfort, W. R. *Biochemistry* **2000**, *39*, 10118–10131.
669. Berry, R. E.; Walker, F. A. Unpublished results.
670. Shokhireva, T. K.; Yang, F.; Walker, F. A. Manuscript in preparation.
671. Yang, F.; Walker, F. A. Manuscript in preparation.

672. La Mar, G. N.; Smith, K. M.; Gersonde, K.; Sick, H.; Overkamp, M. *J. Biol. Chem.* **1980**, *255*, 66–70.
673. La Mar, G. N.; de Ropp, J. S.; Smith, K. M.; Langry, K. C. *J. Biol. Chem.* **1981**, *256*, 237–243.
674. Du, W.; Syvitski, R.; Dewilde, S.; Moene, L.; La Mar, G. N. *J. Am. Chem. Soc.* **2003**, *125*, 8080–8081.
675. Wu, Y.; Basti, M.; Gambacurta, A.; Chiancone, E.; Ascoli, F.; La Mar, G. N. *Biochim. Biophys. Acta* **1996**, *1298*, 261–275.
676. Kolczak, U.; Han C.; Sylvia, L. A.; La Mar, G. N. *J. Am. Chem. Soc.* **1997**, *119*, 12643–12654.
677. Yamamoto, Y.; Suzuki, T. *Biochim. Biophys. Acta* **1993**, *1163*, 287–296.
678. Gorst, C. M.; Wilks, A.; Yeh, D. C.; Ortiz de Montellano, P. R.; La Mar, G. N. *J. Am. Chem. Soc.* **1998**, *120*, 8875–8884.
679. Banci, L.; Bertini, I.; Bren, K. L.; Cremonini, M. A.; Gray, H. B.; Luchinat, C.; Turano, P. *J. Biol. Inorg. Chem.* **1996**, *1*, 117–126.
680. Low, D. W.; Gray, H. B.; Duus, J. Ø. *J. Am. Chem. Soc.* **1997**, *119*, 1–5.
681. Brennan, L.; Turner, D. L. *Biochim. Biophys. Acta* **1997**, *1342*, 1–12.
682. Bolognesi, M.; Onesti, S.; Gatti, G.; Coda, A.; Ascenzi, P.; Brunori, M. *J. Mol. Biol.* **1989**, *205*, 529–544.
683. Conti, E.; Moser, C.; Rizzi, M.; Mattevi, A.; Lionetti, C.; Coda, A.; Ascenzi, P.; Brunori, M.; Bolognesi, M. *J. Mol. Biol.* **1993**, *233*, 498–508.
684. Federici, L.; Savino, C.; Musto, R.; Travaglini-Allocatelli, C.; Cutruzzola, F.; Brunori, M. *Biochem. Biophys. Res. Commun.* **2000**, *269*, 58–63.
685. Royer, Jr., W. E.; Heard, K. S.; Harrington, D. J.; Chiancone, E. *J. Mol. Biol.* **1995**, *253*, 168–186.
686. Brucker, E. A. PDB file 1O1I, deposited 11/19/2002.
687. He, C.; Knipp, M. J. *Am. Chem. Soc.* **2009**, *131*, 12042–12043.
688. Yang, F.; Knipp, M.; Walker, F. A., unpublished work.
689. Beda, N.; Nedospasov, A. *Nitric Oxide* **2005**, *13*, 93–97.
690. Shiva, S.; Huang, Z.; Grubina, R.; Sun, J.; Ringwood, L. A.; MacArthur, P. H.; Xu, X.; Murphy, E.; Darley-Usmar, V. M.; Gladwin, M. T. *Circ. Res.* **2007**, *100*, 654–661.
691. Gladwin, M. T.; Grubina, R.; Doyle, M. P. *Acc. Chem. Res.* **2009**, *42*, 157–167.
692. Wanat, A.; Gdula-Argasinska, J.; Rutkowska-Zhik, D.; Witko, M.; Stochel, G.; van Eldik, R. *J. Biol. Inorg. Chem.* **2002**, *7*, 165–176.
693. Fernandez, B. O.; Ford, P. C. *J. Am. Chem. Soc.* **2003**, *125*, 10510–10511.
694. Berry, R. E.; Yang, F.; Shokhireva, T. K.; Zhang, H.; Montfort, W. R.; Walker, F. A. To be submitted to *Biochemistry*.
695. Ambrus, A.; Friedrich, K.; Somogyi, A. *Anal. Biochem.* **2006**, *352*, 286–295.
696. Filippov, I.; Walker, F. A. Manuscript in preparation.
697. Amoia, A. A.; Montfort, W. R. *Protein Sci.* **2007**, *16*, 2076–2081.
698. Schanda, P.; Kupce, E.; Brutscher, B. *J. Biomol. NMR* **2005**, *33*, 199–211.
699. Yang, F.; Berry, R. E.; Zhang, H.; Walker, F. A. Research in progress.
700. Beale, S. I. *Chem. Rev.* **1993**, *93*, 785–802.
701. Ortiz de Montellano, P. R. In *Cytochrome P450, Structure, Mechanism and Biochemistry*; Ortiz de Montellano, P. R., Ed.; Plenum Press: New York, **1995**; pp. 245–304.
702. Tenhunen, R.; Marver, H. S.; Schmid, R. *J. Biol. Chem.* **1969**, *244*, 6388–6394.
703. Wilks, A.; Moënne-Loccoz, P. *J. Biol. Chem.* **2000**, *275*, 11686–11692.

704. Zhu, W.; Wilks, A.; Stojiljkvic, I. *J. Bacteriol.* **2000**, *182*, 6783–6790.
705. Maines, M. D. *FASEB J.* **1988**, *2*, 2557–2568.
706. Yoshida, T.; Migita, C. T. *J. Inorg. Biochem.* **2000**, *82*, 33–41.
707. Schuller, D. J.; Wilks, A.; Ortiz de Montellano, P. R.; Poulos, T. L. *Nat. Struct. Biol.* **1999**, *6*, 860–867.
708. Lad, L.; Wang, J.; Li, H.; Friedman, J.; Bhaskar, B.; Ortiz de Montellano, P. R.; Poulos, T. L. *J. Mol. Biol.* **2003**, *336*, 527–538.
709. Wang, J.; Niemevz, F.; Lad, L.; Huang, L.; Alvarez, D. E.; Buldain, G.; Poulos, T. L.; Ortiz de Montellano, P. R. *J. Biol. Chem.* **2004**, *279,* 42593–42604.
710. Wang, J.; Lad, L.; Poulos, T. L.; Ortiz de Montellano, P. R. *J. Biol. Chem.* **2005**, *280,* 2797–2806.
711. Lad, L.; Koshkin, A.; Ortiz de Montellano, P. R.; Poulos, T. L. *J. Biol. Inorg. Chem.* **2005**, *10,* 138–146.
712. Bianchetti, C. M.; Yi, L.; Ragsdale, S. W.; Phillips Jr., G. N. *J. Biol. Chem.* **2007**, *282,* 37624–37631.
713. Sugishima, M.; Omata, Y.; Kakuta, Y.; Sakamoto, H.; Noguchi, M.; Fukuyama, K. *FEBS Lett.* **2000**, *471*, 61–66.
714. Sugishima, M.; Sakamoto, H.; Higashimoto, Y.; Omata, Y.; Hayashi, S.; Noguchi, M.; Fukuyama, K. *J. Biol. Chem.* **2002**, *277*, 45086–45090.
715. Sugishima, M.; Sakamoto, H.; Noguchi, M.; Fukuyama, K. *Biochemistry* **2003**, *42*, 9898–9905.
716. Sugishima, M.; Sakamoto, H.; Noguchi, M.; Fukuyama, K. *J. Mol. Biol.* **2004**, *341*, 7–13
717. Sato, H.; Sugishima, M.; Sakamoto, H.; Higashimoto, Y.; Shimokawa, C.; Fukuyama, K.; Palmer, G.; Noguchi, M. *Biochem. J.* **2009**, *419,* 339–345.
718. Schuller, D. J.; Zhu, W.; Stojiljkovic, I.; Wilks, A.; Poulos, T. L. *Biochemistry* **2001**, *40*, 11552–11558.
719. Friedman, J.; Lad, L.; Deshmukh, R.; Li, H.; Wilks, A.; Poulos, T. L. *J. Biol. Chem.* **2003**, *278*, 34654–34659.
720. Unno, M.; Matsui, T.; Chu, G. C.; Couture, M.; Yoshida, T.; Rousseau, D. L.; Olson, J. S.; Ikeda-Saito, M. *J. Biol. Chem.* **2004**, *279*, 21055–21061.
721. Friedman, J.; Lad, L.; Li, H.; Wilks, A.; Poulos, T. L. *Biochemistry* **2004**, *43*, 5239–5245.
722. Sugishima, M.; Hagiwara, Y.; Zhang, X.; Yoshida, T.; Migita, C. T.; Fukuyama, K. *Biochemistry* **2005**, *44,* 4257–4266.
723. Liu, Y.; Ortiz de Montellano, P. R. *J. Biol. Chem.* **2000**, *275*, 5297–5307.
724. Wang, A.; Zeng, Y.; Han, H.; Weeratunga, S.; Morgan, B. N.; Moënne-Loccoz, P.; Schönbrunn, E.; Rivera, M. *Biochemistry* **2007**, *46*, 12198–12211.
725. Weeratunga, S. K.; Sovell, S.; Battaile, K. P.; Fisher, C. J.; Gee, C. E.; Rivera, M. *Biochemistry* **2009**, *48*, 7420–7431.
726. Hernandez, G.; Wilks, A.; Paolesse, R.; Smith, K. M.; Ortiz de Montellano, P. R.; La Mar, G. N. *Biochemistry* **1994**, *33*, 6631–6641.
727. La Mar, G. N.; Asokan, A.; Espiritu, B.; Yeh, D. C.; Auclair, K.; Ortiz de Montellano, P. R. *J. Biol. Chem.* **2001**, *276*, 15678–15687.
728. Li, Y.; Syvitski, R. T.; Auclair, K.; Wilks, A.; Ortiz de Montellano, P. R.; La Mar, G. N. *J. Biol. Chem.* **2002**, *277*, 33018–33031.
729. Syvitski, R. T.; Li, Y.; Auclair, K.; Ortiz de Montellano, P. R.; La Mar, G. N. *J. Am. Chem. Soc.* **2002**, *124*, 14296–14297.

730. Li, Y.; Syvitski, R. T.; Auclair, K.; Ortiz de Montellano, P. R.; La Mar, G. N. *J. Biol. Chem.* **2004**, *279*, 10195–10205.
731. Rivera, M.; Barillas-Mury, C.; Christensen, K. A.; Little, J. W.; Wells, M. A.; Walker, F. A. *Biochemistry* **1992**, *31*, 12233–12240.
732. Meyer, T. E.; Rivera, M.; Walker, F. A.; Mauk, M. R.; Mauk, A. G.; Cusanovich, M. A.; Tollin, G. *Biochemistry* **1993**, *32*, 622–627.
733. Rivera, M.; Wells, M. A.; Walker, F. A. *Biochemistry* **1994**, *33*, 2161–2170.
734. Altuve, A.; Wang, L.; Benson, D. R.; Rivera, M. *Biochem. Biophys. Res. Commun.* **2004**, *314*, 602–609.
735. Havemeyer, A.; Bittner, F.; Wollers, S.; Mendel, R.; Kunze, T.; Clement, B. *J. Biol. Chem.* **2006**, *281*, 34796–34802.
736. Gruenewald, S.; Wahl, B.; Bittner, F.; Hungeling, H.; Kanzow, S.; Kotthaus, J.; Schwering, U.; Mendel, R. R.; Clement, B. *J. Med. Chem.* **2008**, *51*, 8173–8177.
737. Bernheim, M. *Enzymologia* **1972**, *43*, 167–176.
738. Clement, B.; Lomb R.; Möller, W. *J. Biol. Chem.* **1997**, *272*, 19615–19620.
739. Altuve, A.; Silchenko, S.; Lee, K.-H.; Kuczera, K.; Terzyan, S.; Zhang, Y.; Benson, D. R.; Rivera, M. *Biochemistry* **2001**, *40*, 9469–9483.
740. Simeonov, M.; Altuve, A.; Massiah, M. A.; Wang, A.; Eastman, M. A.; Benson, D. R.; Rivera, M. *Biochemistry* **2005**, *44*, 9308–9319.
741. Rodriguez, J. C.; Rivera, M. *Biochemistry* **1998**, *37*, 13082–13098.
742. Avila, L.; Huang, H.; Damaso, C. O.; Lu, S.; Moënne-Loccoz, P.; Rivera, M. *J. Am. Chem. Soc.* **2003**, *125*, 4103–4110.
743. Zeng, Y.; Deshmukh, R.; Caignan, G. A.; Bunce, R. A.; Rivera, M.; Wilks, A. *Biochemistry* **2004**, *43*, 5222–5238.
744. Zhou, H.; Migita, C. T.; Sato, M.; Sun, D.; Zhang, X.; Ikeda-Saito, M.; Fujii, H.; Yoshida, T. *J. Am. Chem. Soc.* **2000**, *122*, 8311–8312.
745. Deshmukh, R.; Zeng, Y.; Furci, L. M.; Huang, H.; Morgan, B. N.; Sander, S.; Alontaga, A. Y.; Bunce, R. A.; Moënne-Loccoz, P.; Rivera, M.; Wilks, A. *Biochemistry* **2005**, *44*, 13713–13723.
746. Wang, J.; Evans, J. P.; Ogura, H.; La Mar, G. N.; Ortiz de Montellano, P. R. *Biochemistry* **2006**, *45*, 61–73.
747. Ogura, H.; Evans, J. P.; Ortiz de Montellano, P. R.; La Mar, G. N. *Biochemistry* **2008**, *47*, 421–430.
748. Liu, Y.; Ma, L.-H.; Zhang, X.; Yoshida, T.; Satterlee, J. D.; La Mar, G. N. *Biochemistry* **2006**, *45*, 3875–3886.
749. Liu, Y.; Ma, L.-H.; Zhang, X.; Yoshida, T.; Satterlee, J. D.; La Mar, G. N. *Biochemistry* **2006**, *45*, 13875–13888.
750. Garcia-Serres, R.; Davydov, R. M.; Matsui, T; Ikeda-Saito, M.; Hoffman, B. M.; Huynh, B. H. *J. Am. Chem. Soc.* **2007**, *129*, 1402–1412.
751. Chen, H.; Moreau, Y.; Derat, E.; Shaik, S. *J. Am. Chem. Soc.* **2008**, *130*, 1953–1965.
752. Ratliff, M.; Zho, W.; Seshmukh, R.; Wilks, A.; Stojiljkovic, I. *J. Bacteriol.* **2001**, *183*, 6394–6403.
753. Zhu, W.; Wilks, A.; Stojiljkovic, I. *J. Bacteriol.* **2000**, *182*, 6783–6790.
754. Krishnamoorthi, R.; La Mar, G. N.; Mizukami, H.; Romero, A. *J. Biol. Chem.* **1984**, *259*, 265–270.
755. Yamamoto, Y.; Chûjô, R.; Inoue, Y.; Suzuki, T. *FEBS Lett.* **1992**, *310*, 71–74.
756. Qin, J.; Pande, U.; La Mar, G. N.; Ascoli, F.; Ascenzi, P.; Cutruzzolá, F.; Travaglini-Allocatelli, C.; Brunori, M. *J. Biol. Chem.* **1993**, *268*, 24012–24021.

757. Yamamoto, Y.; Suzuki, T.; Hori, H. *Biochim. Biophys. Acta* **1993**, *1203*, 267–275.
758. Koshikawa, K.; Yamamoto, Y.; Kamimura, S.; Matsuoka, A.; Shikama, K. *Biochim. Biophys. Acta* **1998**, ***1385***, 89–100.
759. Luo, Y.; Peyton, D. H.; Yee, S. *Biochim. Biophys. Acta* **1998**, *1388*, 66–76.
760. Damaso, C. O.; Bunce, R. A.; Barybin, M. V.; Wilks, A.; Rivera, M. *J. Am. Chem. Soc.* **2005**, *127*, 17582–17583.
761. Ogura, H.; Evans, J. P.; Peng, D.; Satterlee, J. D.; Ortiz de Montellano, P. R.; La Mar, G. N. *Biochemistry* **2009**, *48*, 3127–3137.
762. Rodriguez, J. C.; Wilks, A.; Rivera, M. *Biochemistry* **2006**, *45*, 4578–4592.
763. S. W. Englander: http://hx2.med.upenn.edu/download.html contains a spread sheet that can be used to calculate these protection factors from the rate constants for H/D exchange.
764. Rodriguez, J. C.; Zeng, Y.; Wilks, A.; Rivera, M. *J. Am. Chem. Soc.* **2007**, *129*, 11730–11742.
765. Li, Y.; Syvitski, R. T.; Chu, G. C.; Ikeda-Saito, M.; La Mar, G. N. *J. Biol. Chem.* **2003**, *278*, 6651–6663.
766. Liu, Y.; Zhang, X.; Yoshida, T.; La Mar, G. N. *Biochemistry* **2004**, *43*, 10112–10126.
767. Liu, Y.; Zhang, X.; Yoshida, T.; La Mar, G. N. *J. Am. Chem. Soc.* **2005**, *127*, 6409–6422.
768. Ma, L.-H.; Liu, Y.; Zhang, X.; Yoshida, T.; Langry, K. C.; Smith, K. M.; La Mar, G. N. *J. Am. Chem. Soc.* **2006**, *128*, 6391–6399.
769. Wang, J.; Li, Y.; Ma, D.; Kalish, H.; Balch, A. L.; La Mar, G. N. *J. Am. Chem. Soc.* **2001**, *123*, 8080–8088.
770. La Mar, G. N.; Kolczak, U.; Tran, A.-T. T.; Chien, E. Y. T. *J. Am. Chem. Soc.* **2001**, *123*, 4266–4274.
771. Asokan, A.; de Ropp, J. S.; Newmyer, S. L.; Ortiz de Montellano, P. R.; La Mar, G. N. *J. Am. Chem. Soc.* **2001**, *123*, 4243–4254.
772. de Ropp, J. S.; Sham, S.; Asokan, A.; Newmyer, S.; Ortiz de Montellano, P. R.; La Mar, G. N. *J. Am. Chem. Soc.* **2002**, *124*, 11029–11037.
773. Ma, D.; Musto, R.; Smith, K. M.; La Mar, G. N. *J. Am. Chem. Soc.* **2003**, *125*, 8494–8504.
774. Walker, F. A. *J. Biol. Inorg. Chem.* **2006**, *11*, 391–397.
775. Pesce, A.; Dewilde, S.; Nardini, M.; Moens, L.; Ascenzi, P.; Hankeln, T.; Burmester, T.; Bolognesi, M. *Structure* **2003**, *11*, 1087–1095.
776. Vallone, B.; Nienhaus, K.; Brunori, M.; Nienhaus, G. U. *Proteins Struct. Funct. Bioinf.* **2004**, *56*, 85–94.
777. Vallone, B.; Nienhaus, K.; Matthes, A.; Brunori, M.; Nienhaus, G. U. *Proc. Natl. Acad. Sci. USA* **2004**, *101*, 17351–17356.
778. Bondarenko, V.; Dewilde, S.; Moens, L.; La Mar, G. N. *J. Am. Chem. Soc.* **2006**, *128*, 12988–12999.
779. Simonneaux, G.; Bondon, A. *Chem. Rev.* **2005**, *105*, 2627–2646.
780. Arnesano, F.; Banci, L.; Bertini, I.; Koulougliotis, D.; Monti, A. *Biochemistry* **2000**, *39*, 7117–7130.
781. Banci, L.; Bertini, I.; Rosato, A.; Scacchieri, S. *Eur. J. Biochem.* **2000**, *267*, 755–766.
782. Bertini, I.; Luchinat, C.; Turano, P. *J. Biol. Inorg. Chem.* **2000**, *5*, 761–764.
783. Banci, L.; Bertini, I.; Branchini, B.; Hajieva, P.; Spyroulias, G. A.; Turano, P. *J. Biol. Inorg. Chem.* **2001**, *6*, 490–503.
784. Banci, L.; Bertini, I.; Felli, I. C.; Hajieva, P.; Viezzoli, M. S. *J. Biomol. NMR* **2001**, *20*, 1–10.
785. Banci, L.; Bertini, I.; Cavallaro, G.; Luchinat, C. *J. Biol. Inorg. Chem.* **2002**, *7*, 416–426.
786. Giachetti, A.; La Penna, G.; Perico, A.; Banci, L. *Biophys. J.* **2004**, *87*, 498–512.

787. Arnesano, F.; Banci, L.; Bertini, I.; Ciofi-Baffoni, S.; de Lumley Woodyear, T.; Johnson, C. M.; Barker, P. D. *Biochemistry* **2000**, *39*, 1499–1514.
788. Arnesano, F.; Banci, L.; Bertini, I.; van der Wetering, K.; Czisch, M.; Kaptein, R. *J. Biomol. NMR* **2000**, *17*, 295–304.
789. Assfalg, M.; Banci, L.; Bertini, I.; Ciofi-Baffoni, S.; Barker, P. D. *Biochemistry* **2001**, *40*, 12761–12771.
790. Banci, L.; Bertini, I.; Felli, I. C.; Sarrou, J. *J. Magn. Reson.* **2005**, *172*, 191–200.
791. Bertini, I.; Castellani, F.; Luchinat, C.; Martini, G.; Parigi, G.; Ristori, S. *J. Phys. Chem.* **2000**, *104*, 10653–10658.
792. Bertini, I.; Huber, J. G.; Luchinat, C.; Piccioli, M. *J. Magn. Reson.* **2000**, *147*, 1–8.
793. Banci, L.; Bertini, I.; Liu, G.; Reddig, T.; Tang, W.; Wu, Y.; Zhu, D. *J. Biol. Inorg. Chem.* **2001**, *6*, 628–637.
794. Barker, P. B.; Bertini, I.; Del Conte, R.; Ferguson, S. J.; Hajieva, P.; Tomlinson, P.; Turano, P.; Viezzoli, M. S. *Eur. J. Biochem.* **2001**, *268*, 4468–4476.
795. Assfalg, M.; Bertini, I.; Dolfi, A.; Turano, P.; Mauk, A. G.; Rosell, F. I.; Gray, H. B. *J. Am. Chem. Soc.* **2003**, *125*, 2913–2922.
796. Berners-Price, S.; Bertini, I.; Gray, H. B.; Spyroulias, G. A.; Turano, P. *J. Inorg. Biochem.* **2004**, *98*, 814–823.
797. Bertini, I.; Rosato, A.; Turano, P. *J. Porph. Phtal.* **2004**, *8*, 238–245.
798. Pascal, G.; Briux, M.; Rico, M.; Ciofi-Baffoni, S.; Banci, L.; Ramachandran Shastry, M. C.; Roder, H.; de Lumley Woodyear, T.; Johnson, C. M.; Fersht, A. R.; Barker, P. D. *J. Mol. Biol.* **2005**, *346*, 331–344.
799. Worrall, J. A., Diederix, R. E., Prudencio, M., Lowe, C. E., Ciofi-Baffoni, S., Ubbink, M., and Canters, G. W. *Chem. Bio. Chem.* **2005**, 6, 747–758.
800. Furlan, S.; La Penna, G.; Banci, L.; Mealli, C. *J. Phys. Chem. B* **2007**, *8*, 1157–1164.
801. Assfalg, M.; Bertini, I.; Del Conte, R.; Giachetti, A.; Turano, P. *Biochemistry* **2007**, *46*, 6232–6238.
802. La Penna, G.; Furlan, S.; Banci, L. *J. Biol. Inorg. Chem.* **2007**, *2*, 180–193.
803. Borsari, M.; Dikaya, E.; Dikiy, A.; Gonchar, M. V.; Maidan, M. M.; Pierattelli, R.; Sibirny, A. A. *Biochim. Biophys. Acta* **2000**, *1543*, 174–188.
804. Assfalg, M.; Bertini, I.; Turano, P.; Mauk, A. G.; Winkler, J. R.; Gray, H. B. *Biophys. J.* **2003**, *84*, 3917–3923.
805. Assfalg, M.; Bertini I.; Turano, P.; Bruschi, M.; Durand, M. C.; Giudici-Orticoni, M. T.; Dolla A. *J. Biomol. NMR* **2002**, *22*, 107–122.
806. Banci, L.; Bertini, I.; Ciurli, S.; Dikiy, A.; Dittmer, J.; Rosato, A.; Sciara, G.; Thompsett, A. *ChemBioChem* **2002**, *3*, 299–310.
807. Bartalesi, I.; Bertini I.; Hajieva P.; Rosato A.; Vasos, P. *Biochemistry* **2002**, *41*, 5120–5130.
808. Assfalg, M.; Bertini, I.; Bruschi, C.; Michel, C.; Turano, P. *Proc. Natl. Acad. Sci. USA* **2002**, *99*, 9750–9754.
809. Bartalesi, I.; Bertini, I.; Ghosh, K.; Rosato, A.; Turano, P. *J. Mol. Biol.* **2002**, *321*, 693–701.
810. Bartalesi, I.; Bertini, I.; Rosato, A. *Biochemistry* **2003**, *42*, 739–745.
811. Bertini, I.; Ghosh, K.; Rosato, A.; Vasos, P. R. *Biochemistry* **2003**, *42*, 3457–3463.
812. Bertini, I.; Faraone-Mennella, J.; Gray, H. B.; Luchinat, C.; Parigi, G.; Winkler, J. R. *J. Biol. Inorg. Chem.* **2004**, *9*, 224–230.
813. Bartalesi, I.; Bertini, I.; Di Rocco, G.; Ranieri, A.; Rosato, A.; Vanarotti, M.; Viezzoli, M. S.; Vasos, P. *J. Biol. Inorg. Chem.* **2004**, *5*, 600–608.

814. Santucci, R.; Bongiovanni, C.; Marini, S.; Del Conte, R.; Tien, M.; Banci, L.; Coletta, M. *Biochem. J.* **2000**, *349*, 85–90.
815. Banci, L.; Bartalesi, I.; Ciofi-Baffoni. S.; Tien, M. *Biopolymers* **2002**, *72*, 38–57.
816. Redaelli, C.; Monzani, E.; Santagostini, L.; Casella, L.; Sanangelantoni, A. M.; Pierattelli, R.; Banci, L. *Chem. Bio. Chem.* **2002**, *3*, 226–233.
817. Bertini, I.; Hajieva, P.; Luchinat, C.; Nerinovski, K. *J. Am. Chem. Soc.* **2001**, *123*, 12925–12926.
818. Banci, L.; Bertini, I.; Felli, I. C.; Krippahl, L.; Kubicek, K.; Moura, J. J. G.; Rosato, A. *J. Biol. Inorg. Chem.* **2003**, *8*, 777–786.
819. Bertini, I.; Cavallaro, G.; Rosato, A. *J. Biol. Inorg. Chem.* **2005**, *10*, 613–624.
820. Musiani, F.; Dikiy, A.; Semenov, A. Y.; Ciurli, S. *J. Biol. Chem.* **2005**, *280*, 18833–18841.
821. Arnesano, F.; Banci, L.; Barker, P. D.; Bertini, I.; Rosato, A.; Su, X. C.; Viezzoli, M. S. *Biochemistry* **2002**, *41*, 13587–13594.
822. Caillet-Saguy, C.; Delepierre, M.; Lecroisey, A.; Bertini, I.; Piccioli, M.; Turano, P. *J. Am. Chem. Soc.* **2006**, *128*, 150–158.
823. Caillet-Saguy, C.; Turano, P.; Piccioli, M.; Lukat-Rodgers, G.; Czjzek, M.; Guigliarelli, B.; Izadi-Pruneyre, N.; Delepierre, M.; Rodgers, K.; Lecroisey, A. *J. Biol. Chem.* **2008**, *283*, 5960–5970.
824. Caillet-Saguy, C.; Piccioli, M.; Turano, P.; Izadi-Pruneyre, N.; Delepierre, M.; Bertini, I.; Lecroisey, A. *J. Am. Chem. Soc.* **2009**, *131*, 1736–1744.
825. Chevance, S.; Le Rumeur, E.; de Certaines, J. D.; Simonneaux, G.; Bondon, A. *Biochemistry* **2003**, *42*, 15342–15351.
826. Bertini, I.; Turano, P.; Vasos, P. R.; Chevance, S.; Bondon, A.; Simonneaux, G. *J. Mol. Biol.* **2004**, *336*, 489–496.
827. Letoffé, S.; Redeker, V.; Wandersman, C. *Mol. Microbiol.* **1998**, *28*, 1223–1234.
828. Alontaga, A. Y.; Rodriguez, J. C.; Schönbrunn, E.; Becker, A.; Funke, T.; Yuki, E. T.; Hayashi, T.; Stobaugh, J.; Moënne-Loccoz, P.; Rivera, M. *Biochemistry* **2009**, *48*, 96–109.
829. Phillippi, M. A.; Shimomura, E. T.; Goff, H. M. *Inorg. Chem.* **1981**, *20*, 1322–1325.
830. Scholz, W. F.; Reed, C. A.; Lee, Y. J.; Scheidt, W. R.; Lang, G. *J. Am. Chem. Soc.* **1982**, *104*, 6791–6793.
831. Buisson, G.; Deronzier, A.; Duee, E.; Gans, P.; Marchon, J.-C.; Regnard, J.-R. *J. Am. Chem. Soc.* **1982**, *104*, 6793–6795.
832. Groves, J. T.; Quinn, R.; McMurry, T. J.; Nakamura, M.; Lang, G.; Boso, B. *J. Am. Chem. Soc.* **1985**, *107*, 354–360.
833. Goff, H. M.; Phillippi, M. A. *J. Am. Chem. Soc.* **1983**, *105*, 7567–7571.
834. Phillippi, M. A.; Goff, H. M. *J. Am. Chem. Soc.* **1982**, *104*, 6026–6034.
835. Kadish, K. M.; Rhodes, R. K.; Bottomley, L. A.; Goff, H. M. *Inorg. Chem.* **1981**, *20*, 3195–3200.
836. Malek, A.; Latos-Grażyński, L.; Bartczak, T. J.; Zadlo, A. *Inorg. Chem.* **1991**, *30*, 3222–3230.
837. Rachlewicz, K.; Latos-Grażyński, L. *Inorg. Chem.* **1995**, *34*, 718–727.
838. Balch, A. L.; Latos-Grażyński, L.; St. Claire, T. N. *Inorg. Chem.* **1995**, *34*, 1395–1401.
839. Balch, A. L.; Koerner, R.; Latos-Grazynski, L.; Noll, B. C. *J. Am. Chem. Soc.* **1996**, *118*, 2760–2761.
840. Vogel, E.; Will, S.; Tilling, A. S.; Neumann, L.; Lex, J.; Bill, E.; Trautwein, A. X.; Wieghardt, K. *Angew. Chem., Int. Ed. Engl.* **1994**, *33*, 731–735.

841. Licoccia, S.; Paci, M.; Paolesse, R.; Boschi, T. *J. Chem. Soc. Dalton Trans.* **1991**, 461–466.
842. Gross, Z. *J. Biol. Inorg. Chem.* **2001**, *6*, 733–738.
843. Gross, Z.; Galili, N.; Saltsman, I. *Angew. Chem.*, *Int. Ed.* **1999**, *38*, 1427–1429.
844. Simkovich, L.; Galili, N.; Saltsman, I.; Goldberg, I.; Gross, Z. *Inorg. Chem.* **2000**, *39*, 2704–2705.
845. Simkhovich, L.; Goldberg, I.; Gross, Z. *Inorg. Chem.* **2002**, *41*, 5433–5439.
846. Simkhovich, L.; Gross, Z. *Inorg. Chem.* **2004**, *43*, 6136–6138.
847. Cai, S.; Licoccia, S.; D'Ottavi, C.; Paolesse, R.; Nardis, S.; Bulach, V.; Zimmer, B.; Shokhireva, T. Kh.; Walker, F. A. *Inorg. Chim. Acta* **2002**, *339*, 171–178.
848. Yatsunyk, L.; Walker, F. A. *Inorg. Chim. Acta* **2002**, *337*, 266–274.
849. Nardis, S.; Paolessee, R.; Licoccia, S.; Fronczek, F. R.; Vicente, M. G. H.; Shokhireva, T. K.; Walker, F. A. *Inorg. Chem*. **2005**, *44*, 7030–7046.
850. Walker, F. A.; Licoccia, S.; Paolesse, R. *J. Inorg. Biochem.* **2006**, *100*, 810–837.
851. Roos, B. O.; Veryazov, V.; Conradie, J.; Taylor, P. R.; Ghosh, A. *J. Phys. Chem. B* **2008**, *112*, 14099–14102.
852. DeBeer George, S.; Hocking, R. K.; Walker, F. A.; Licoccia, S.; Gross, Z.; Solomon, E. I. To be submitted.
853. Cai, S.; Licoccia, S.; Walker, F. A. *Inorg. Chem*. **2001**, *40*, 5795–5798.
854. Hocking, R. K.; Wasinger, E. C.; Yan, Y.; deGroot, F. M. F.; Walker, F. A.; Hodgson, K. O.; Hedman, B.; Solomon, E. I. *J. Am. Chem. Soc.* **2007**, *129*, 113–125.
855. Balch, A. L.; Chan, Y.-W.; Cheng, R.-J.; La Mar, G. N.; Latos-Grażyński, L.; Renner, M. W. *J. Am. Chem. Soc.* **1984**, *106*, 7779–7785.
856. Chin, D. H.; Balch, A. L.; La Mar, G. N. *J. Am. Chem. Soc.* **1980**, *102*, 1446–1448.
857. La Mar, G. N.; de Ropp, J. S.; Latos-Grażyński, L.; Balch, A. L.; Johnson, R. B.; Smith, K. M.; Parish, D. W.; Cheng, R. J. *J. Am. Chem. Soc.* **1983**, *105*, 782–787.
858. Wolowiec, S.; Latos-Grażyński, L. *Inorg. Chem.* **1998**, *37*, 2984–2988.
859. Marnett, L. J.; Weller, P.; Battista, J. R. In *Cytochrome P450, Structure, Mechanism and Biochemistry*; Ortiz de Montellano, P. R., Ed.; Plenum Press: New York; **1986**; pp. 29–76.
860. Balch, A. L.; La Mar, G. N.; Latos-Grażyński, L.; Renner, M. W.; Thanabal, V. *J. Am. Chem. Soc.* **1985**, *107*, 3003–3007.
861. Loew, G. H.; Herman, Z. S. *J. Am. Chem. Soc.* **1980**, *102*, 6114–6115.
862. Hanson, L. K.; Chang, C. K.; Davis, M. S.; Fajer, J. *J. Am. Chem. Soc.* **1981**, *103*, 663–670.
863. McMurry, T. J.; Groves, J. T. In *Cytochrome P450, Structure, Mechanism and Biochemistry*; Ortiz de Montellano, P. R., Ed.; Plenum Press: New York, **1986**; pp. 1–28.
864. Ortiz de Montellano, P. R. In *Cytochrome P450, Structure, Mechanism and Biochemistry*; Ortiz de Montellano, P. R., Ed.; Plenum Press: New York, **1986**; pp. 217–272.
865. Kunze, K. L.; Ortiz de Montellano, P. R. *J. Am. Chem. Soc.* **1983**, *105*, 1380–1381.
866. Dolphin, D.; Forman, A.; Borg, D. C.; Fajer, J.; Felton, R. H. *Proc. Natl. Acad. Sci. USA* **1971**, *68*, 614–618.
867. Dolphin, D.; Felton, R. H. *Acc. Chem. Res.* **1974**, *7*, 26–32.
868. Schulz, C. E.; Devaney, P. W.; Winkler, H.; Debrunner, P. G.; Doan, N.; Chiang, R.; Rutter, R.; Hager, L. P. *FEBS Lett.* **1979**, *103*, 102–105.
869. Roberts, J. E.; Hoffman, B. M.; Rutter, R.; Hager, L. P. *J. Biol. Chem.* **1981**, *256*, 2118–2121.
870. Roberts, J. E.; Hoffman, B. M.; Rutter, R.; Hager, L. P. J. *Am. Chem. Soc*. **1981**, *103,* 7654–7656.
871. Rutter, R.; Valentine, M.; Hendrich, M. P.; Hager, L. P.; Debrunner, P. G. *Biochemistry* **1983**, *22*, 4759–4774.

872. Schulz, C. E.; Rutter, R.; Sage, J. T.; Debrunner, P. G.; Hager, L. P. *Biochemistry* **1984**, *23*, 4743–4754.
873. Dawson, J. H.; Kaw, L.-S.; Penner-Hahn, J. E.; Sono, M.; Eble, K. S.; Bruce, G. S.; Hager, L. P.; Hodgson, K. O. J. *Am. Chem. Soc.* **1986**, *108*, 8114–8116.
874. Dunford, H. B. *Heme Peroxidases*; John Wiley & Sons: New York, **1999**.
875. Bill, E. *Hyperfine Int.* **1994**, *90*, 143–158.
876. Ivancich, A.; Jouve, H. M.; Sartor, B.; Gaillard, J. *Biochemistry* **1997**, *36,* 9356–9364.
877. Schünemann, V.; Jung, C.; Trautwein, A. X.; Mandon, D.; Weiss, R. *FEBS Lett*. **2000**, *179*, 149–154.
878. Schünemann, V.; Lendzian, F.; Jung, C.; Contzen, J.; Barra, A.-L.; Sligar, S. G.; Trautwein, A. X. *J. Biol. Chem*. **2004**, *279*, 10919–10930.
879. Jung, C.; Lendzian, F.; Schünemann, V.; Richter, M.; Böttger, L. H.; Trautwein, A. X.; Contzen, J.; Galander, M.; Ghosh, D. K.; Barra, A.-L. *Magn. Reson. Chem.* **2005**, *43*, S84–S95.
880. Rutter, R.; Hager, L. P.; Dhonau. H.; Hendrich, M.; Valentine M.; Debrunner, P. G. *Biochemistry* **1984**, *23*, 6809–6816.
881. Benecky, M.; Frew, J. E.; Scowen, N.; Jones, P.; Hoffman, B. M. *Biochemistry* **1993**, *32*, 11929–11933.
882. Patterson, W.; Poulos, T. L.; Goodin, D. B. *Biochemistry* **1995**, *34*, 4342–4345.
883. Ivancich, A.; Jakopitsch, C.; Auer, M.; Un, S.; Obinger, C. J. *Am. Chem. Soc*. **2003**, *125*, 14093–14102.
884. Carpena, X.; Wiseman, B.; Deemagarn, T.; Herguedas, B.; Ivancich, A.; Singh, R.; Loewen, P. C.; Fita, I. *Biochemistry* **2006**, *45,* 5171–5179.
885. Colin, J.; Wiseman, B.; Switala, J.; Loewen, P. C.; Ivancich, A. *J. Am. Chem. Soc.* **2009**, *131*, 8557–8563.
886. Zhang, Y.; Heym, B.; Allen, B.; Young, D.; Cole, S. *Nature* **1992**, *13*, 591–593.
887. Johnsson, K.; Froland, W. A.; Schultz, P. G. *J. Biol. Chem.* **1997**, *272*, 2834–2840.
888. Singh, R.; Switala, J.; Loewen, P. C.; Ivancich, A. *J. Am. Chem. Soc.* **2007**, *129*, 15954–15963.
889. Smulevich, G.; Feis, A.; Howes, B. D.; Ivancich, A. Structure-function relationships in heme peroxidases: New insights from electronic absorption, resonance Raman and multi-frequency Electron Paramagnetic Resonance spectroscopies, In the *Handbook of Porphyrin Science*; Kadish, K. M.; Smith, K. M.; Guilard, R., Eds.; World Scientific: Singapore, **2010**, Volume 6, Chapter 31.
890. Ivancich, A.; Mazza, G.; Desbois, A. *Biochemistry* **2001**, *40,* 6860–6866.
891. Deemagarn, T.; Wiseman, B.; Carpena, X.; Ivancich, A.; Fita, I.; Loewen, P. C. *Prot. Struct. Funct. Bioinf.* **2007**, *66*, 219–228.
892. Groves, J. T.; Haushalter, R. C.; Nakamura, M.; Nemo, T. E.; Evans, B. J. *J. Am. Chem. Soc.* **1981**, *103*, 2884–2886.
893. Balch, A. L.; Latos-Grażyński, L.; Renner, M. W. *J. Am. Chem. Soc.* **1985**, *107*, 2983–2985.
894. Fujii, H.; Ichikawa, K. *Inorg. Chem.* **1992**, *31*, 1110–1112.
895. Fujii, H.; Yoshimura, T.; Kamada, H. *Inorg. Chem.* **1996**, *35,* 2373–2377.
896. Nanthakumar, A.; Goff, H. M. *Inorg. Chem.* **1991**, *30*, 4460–4464.
897. Gold, A.; Jayaraj, K.; Doppelt, P.; Weiss, R.; Chottard, G.; Bill, E.; Ding, X.; Trautwein, A. X. *J. Am. Chem. Soc.* **1988**, *110*, 5756–5761.
898. Bill, E.; Ding, X.-Q.; Bominaar, E. L.; Trautwein, A.; Winkler, H.; Handon, D.; Weiss, R.; Gold, A.; Jayaraj, K.; Hatfield, W. E.; Kirk, M. L. *Eur. J. Biochem.* **1990**, *188*, 665–672.

899. Mandon, D.; Weiss, R.; Jayaraj, K.; Gold, A.; Terner, J.; Bill, E.; Trautwein, A. X. Inorg. Chem. **1992**, *31*, 4404–4409
900. Ayougou, K.; Mandon, D.; Fischer, J.; Weiss, R.; Müther, M.; Schünemann, V.; Trautwein, A. X.; Bill, E.; Terner, J.; Jayaraj, K.; Gold, A.; Austin, R. N. *Chem. Eur. J.* **1996**, *2,* 1159–1163.
901. Jayaraj, K.; Terner, J.; Gold, A.; Roberts, D. A.; Austin, R. N.; Mandon, D.; Weiss, R.; Bill, E.; Müther, M.; Trautwein, A. X. *Inorg. Chem.* **1996**, *35*, 1632–1640.
902. Jayaraj, K.; Gold, A.; Austin, R. N.; Ball, L. M.; Terner, J.; Mandon, D.; Weiss, R.; Fischer, J.; DeCian, A.; Bill, E.; Müther, M.; Schünemann, V.; Trautwein, A. X. *Inorg. Chem.* **1997**, *36,* 4555–4566.
903. Nanthakumar, A.; Goff, H. M. *J. Am. Chem. Soc.* **1990**, *112*, 4047–4049.
904. Ribeiro, J. M. C *Insect Biochem. Mol. Biol.* **1998**, *28*, 1051–1057.
905. Singh, R.; Berry, R. E.; Yang, F.; Zhang, H.; Walker, F. A.; Ivancich, A. *Biochemistry*, in press **2010**.
906. Van Caemelbecke, E.; Will, S.; Autret, M.; Adamian, V. A.; Lex, J.; Gisselbrecht, J.-P.; Gross, M.; Vogel, E.; Kadish, K. M. *Inorg. Chem.* **1996**, *35*, 184–192.
907. Funatsu, K.; Imamura, T.; Ichimura, A.; Sasaki, Y. *Inorg. Chem.* **1998**, *37*, 4986–4995.
908. Collman, J. P.; Brothers, P. J.; McElwee-White, L.; Rose, E.; Wright, L. J. *J. Am. Chem. Soc.* **1985**, *107*, 4570–4571.
909. Collman, J. P.; Brothers, P. J.; McElwee-White, L.; Rose, E. *J. Am. Chem. Soc.* **1985**, *107*, 6110–6111.
910. Bohle, D. S.; Hung, C.-H.; Smith, B. D. *Inorg. Chem.* **1998**, *37*, 5790–5806.
911. Djukic, J.-P.; Young, V. G.; Woo, L. K. *Organometallics* **1994**, *13*, 3995–4003.
912. Kariya, N.; Imamura, T.; Sasaki, Y. *Inorg. Chem.* **1998**, *37*, 1658–1660.
913. Groves, J. T.; Quinn, R. *J. Am. Chem. Soc.* **1985**, *107*, 5790–5792.
914. Collman, J. P.; Barnes, C. E.; Collins, T. J.; Brothers, P. J. *J. Am. Chem. Soc.* **1981**, *103*, 7030–7032.
915. Collman, J. P.; Arnold, H. A. *Acc. Chem. Res.* **1993**, *26*, 586–592.
916. Collman, J. P.; Harford, S. T.; Maldivi, P.; Marchon, J.-C. *J. Am. Chem. Soc.* **1998**, *120*, 7999–8000.
917. Collman, J. P.; Harford, S. T.; Franzen, S.; Marchon, J.-C.; Shreve, A. P.; Woodruff, W. H. *Inorg. Chem.* **1999**, *38*, 2085–2092.
918. Collman, J. P.; Harford, S. T.; Franzen, S.; Shreve, A. P.; Woodruff, W. H. *Inorg. Chem.* **1999**, *38*, 2093–2097.
919. Dolphin, D., Ed. *Vitamin B_{12}*; Wiley Interscience: New York, **1982**; Vols. 1 and 2.
920. Drennan, C. L.; Huang, S.; Drummond, J. T.; Matthews, R. G.; Ludwig, M. L. *Science* **1994**, *266*, 1669–1674.
921. Mancia, F.; Keep, N. H.; Nakagawa, A.; Leadlay, P. F.; McSweeney, S.; Rasmussen, B.; Bösecke, P.; Diat, O.; Evans, P. R. *Structure* **1996**, *4*, 339–350.
922. Hoffman, B. M. In *The Porphyrins*; Dolphin, D., Ed.; Academic Press: New York, **1979**; Vol. 7, pp. 403–472.
923. Chien, J. C. W.; Dickenson, L. C. *Proc. Natl. Acad. Sci. USA* **1972**, *69*, 2783–2787.
924. Dickenson, L.C.; Chien, J. C. W. *Proc. Natl. Acad. Sci. USA* **1980**, *77*, 1235–1239.
925. Hori, H.; Ikeda-Saito, M.; Yonetani, T. *Nature* **1980**, *288*, 501–502.
926. Hori, H.; Ikeda-Saito, M.; Froncisz, W.; Yonetani, T. *J. Biol. Chem.* **1982**, *257*, 3636–3642.
927. Bowen, J. H.; Shokhirev, N. V.; Raitsimring, A. M.; Buttlaire, D. H.; Walker, F. A. *J. Phys. Chem. B* **1997**, *101*, 8683–8691.

928. Ikeda-Saito, M.; Inabushi, T.; McDonald, G. G.; Yonetani, T. *J. Biol. Chem.* **1978**, *253*, 7134–7137.
929. Walker, F. A. *J. Magn. Reson.* **1974**, *15*, 301–318.
930. Hill, H. A. O.; Sadler, P. J.; Williams, R. J. P.; Berry, C. D. *Ann. N.Y. Acad. Sci.* **1973**, *206*, 247–267
931. Hill, H. A. O.; Sadler, P. J.; Williams, R. J. P. *J. Chem. Soc., Dalton Trans.* **1973**, 1663–1667.
932. Uemori, Y.; Kyuno, E. *Inorg. Chim. Acta* **1990**, *174*, 109–117.
933. Toronto, D.; Sarrazin, F.; Pecaut, J.; Marchon, J.-C.; Shang, M.; Scheidt, W. R. *Inorg. Chem.* **1998**, *37*, 526–532.
934. Salehi, A.; Oertling, W. A.; Babcock, G. T.; Chang, C. K. *J. Am. Chem. Soc.* **1986**, *108*, 5630–5631.
935. Oertling, W. A.; Salchi, A.; Chung, Y. C.; Leroi, G. E.; Chang, C. K.; Babcock, G. T. *J. Phys. Chem.* **1987**, *91*, 5887–5898.
936. Erler, B. S.; Scholy, W. F.; Lee, Y. J.; Scheidt, W. R.; Reed, C. A. *J. Am. Chem. Soc.* **1987**, *109*, 2644–2652.
937. Schmidt, E.; Zhang, H.; Chang, C. K.; Babcock, G. T.; Oertling, W. A. *J. Am. Chem. Soc.* **1996**, *118*, 2954–2961.
938. Gasyna, Z.; Stillman, M. J. *Inorg. Chem.* **1990**, *29*, 5101–5109.
939. Mu, X. H.; Kadish, K. M. *Inorg. Chem.* **1989**, *28*, 3743–3747.
940. Balch, A. L.; Mazzanti, M.; St. Claire, T. N.; Olmstead, M. M. *Inorg. Chem.* **1995**, *34*, 2194–2300.
941. Balch, A. L.; Latos-Grażyński, L.; Noll, B. C.; Olmstead, M. M.; Safari, N. *J. Am. Chem. Soc.* **1993**, *115*, 9056–9061.
942. Attar, S.; Balch, A. L.; Van Calcar, P. M.; Winkler, K. *J. Am. Chem. Soc.* **1997**, *119*, 3317–3323.
943. Balch, A. L.; Mazzanti, M.; Noll, B. C.; Olmstead, M. M. *J. Am. Chem. Soc.* **1994**, *116*, 9114–9122.
944. Koerner, R.; Olmstead, M. M.; Ozarowski, A.; Phillips, S. L.; Van Calcar, P. M.;Winkler, K.; Balch, A. L. *J. Am. Chem. Soc.* **1998**, *120*, 1274–1284.
945. Setsune, J.; Takeda, H.; Ito, S.; Saito, Y.; Ishimaru, Y.; Fukuhara, K.; Saito, Y.; Kitao, T.; Adachi, T. *Inorg. Chem.* **1998**, *37*, 2235–2246.
946. Latos-Grażyński, L.; Johnson, J.; Attar, S.; Olmstead, M. M.; Balch, A. L. *Inorg. Chem.* **1998**, *37*, 4493–4499.
947. Smirnov, V. V.; Woller, E. K.; DiMagno, S. G. *Inorg. Chem.* **1998**, *37*, 4971–4978.
948. Cao, Y.; Petersen, J. L.; Stolzenberg, A. M. *Inorg. Chim. Acta* **1997**, *263*, 139–148.
949. Al-Akhdar, W. A.; Belmore, K. A.; Kendrick, M. J. *Inorg. Chim. Acta* **1989**, *165*, 15–17.
950. Peng, C.-H.; Fryd, M.; Wayland, B. B. *Macromolecules* **2007**, *40*, 6814–6819.
951. Li, S.; de Bruin, B.; Peng, C.-H.; Fryd, M.; Wayland, B. B. *J. Am. Chem. Soc.* **2008**, *130*, 13373–13381.
952. Peng, C.-H.; Scricco, J.; Li, S.; Fryd, M.; Wayland, B. B. *Macromolecules* **2008**, *41*, 2368–2373.
953. Peng, C.-H.; Li, S.; Wayland, B. B. *Inorg. Chem.* **2009**, *48*, 5039–5046.
954. Hu, Y.; Han, B. C.; Bao, L. Y.; Mu, X. H.; Kadish, K. M. *Inorg. Chem.* **1991**, *30*, 2444–2446.
955. Wayland, B. B.; Coffin, V. L.; Farnos, M. D. *Inorg. Chem.* **1988**, *27*, 2745–2747.
956. Wayland, B. B.; Sherry, A. E.; Poszmik, G.; Bunn, A. G. *J. Am. Chem. Soc.* **1992**, *114*, 1673–1681.

957. Wayland, B. B.; Sherry, A. E.; Bunn, A. G. *J. Am. Chem. Soc.* **1993**, *115*, 7675–7684.
958. Cui, W.; Wayland, B. B. *J. Am. Chem. Soc.* **2006**, *128*, 10350–10351.
959. Fu, X.; Li, S.; Wayland, B. B. *J. Am. Chem. Soc.* **2006**, *128*, 8947–8954.
960. Fu, X.; Li, S.; Wayland, B. B. *Inorg. Chem.* **2006**, *45*, 9884–9889.
961. Collman, J. P.; Boulatov, R. *J. Am. Chem. Soc.* **2000**, *122*, 11812–11821.
962. Zhang, X.-X.; Parks, G. F.; Wayland, B. B. *J. Am. Chem. Soc.* **1997**, *119*, 7938–7944.
963. Zhang, X.-X.; Wayland, B. B. *Inorg. Chem.* **2000**, *39*, 5318–5325.
964. Cui, W.; Zhang, P.; Wayland, B. B. *J. Am. Chem. Soc.* **2003**, *125*, 4994–4995.
965. Cui, W.; Wayland, B. B. *J. Am. Chem. Soc.* **2004**, *126*, 8266–8274.
966. Farnos, M. D. Ph.D. Thesis, University of Pennsylvania, **1987**.
967. Farnos, M. D.; Woods, B. A.; Wayland, B. B. *J. Am. Chem. Soc.* **1986**, *108*, 3659–3663.
968. McMillen, D. F.; Golden, D. M. *Ann. Rev. Phys. Chem.* **1982**, *33*, 493–532.
969. Boucher, L. J. *Coord. Chem. Revs.* **1972**, *7*, 289–329.
970. Stern, M. K.; Groves, J. T. In *Manganese Redox Enzymes*; Pecoraro, V. L., Ed.; VCH: New York, **1992**; pp. 233–259.
971. Mansuy, D. *Coord. Chem. Revs.* **1993**, *125*, 129–142.
972. Arasasingham, R. D.; Bruice, T. C. *Inorg. Chem.* **1990**, *29*, 1422–1427.
973. Kelly, S. L.; Kadish, K. M. *Inorg. Chem.* **1982**, *21*, 3631–3639.
974. Goldberg, D. P.; Telser, J.; Krzystek, J.; Montalban, A. G.; Brunel, L.-C.; Barrett, A. G. M.; Hoffman, B. M. *J. Am. Chem. Soc.* **1997**, *119*, 8722–8723.
975. Kellar, K. E.; Foster, N. *Inorg. Chem.* **1992**, *31*, 1353–1359.
976. Hansen, A. P.; Goff, H. M. *Inorg. Chem.* **1984**, *23*, 4519–4525.
977. Boschi, T.; Licoccia, S.; Paolesse, R.; Tehran, M. A.; Pelizzi, G.; Vitali, F. *J. Chem. Soc., Dalton Trans.* **1990**, 463–468.
978. Licoccia, S.; Morgante, E.; Paolesse, R.; Polizio, F.; Senge, M. O.; Tondello, E.; Boschi, T. *Inorg. Chem.* **1997**, *36*, 1564–1570.
979. Krzystek, J.; Telser, J.; Hoffman, B. M.; Brunel, L.-C.; Licoccia, S. *J. Am. Chem. Soc.* **2001**, *123*, 7890–7897.
980. Goldberg, D. P.; Telser, J.; Krzystek, J.; Montalban, A. G.; Brunel, L. C.; Barrett, A. G. M.; Hoffman, B. M. *J. Am. Chem. Soc.* **1977**, *119*, 8722–8723.
981. Krzystek, J.; Telser, J.; Pardi, L. A.; Goldberg, D. P.; Hoffman, B. M.; Brunel, L. C. *Inorg. Chem.* **1999**, *38*, 6121–6129.
982. Bendix, J.; Gray, H. B.; Golubkov, G.; Gross, Z. *J. Chem. Soc., Chem. Commun*. **2000**, 1957–1958.
983. Kadish, K. M.; Adamian, V. A.; Van Caemelbecke, E.; Gueletii, E.; Will, S.; Erben, C.; Vogel, E. *J. Am. Chem. Soc.* **1998**, *120*, 11986–11993.
984. Kaustov, L.; Tal, M. E.; Shames, A. I.; Gross, Z. *Inorg. Chem.* **1997**, *36*, 3503–3511.
985. Camenzind, M. J.; Hollander, F. J.; Hill, C. L. *Inorg. Chem.* **1982**, *21*, 4301–4308.
986. Camenzind, M. J.; Hollander, F. J.; Hill, C. L. *Inorg. Chem.* **1983**, *22*, 3776–3784.
987. Abraham, R. J.; Swinton, P. F. *J. Chem. Soc. B* **1969**, 903–908.
988. Walker, F. A.; Hui, E.; Walker, J. M. *J. Am. Chem. Soc.* **1975**, *92*, 2390–2397.
989. Jia, S.-L.; Jentzen, W.; Shang, M.; Song, X.-Z.; Ma, J.-G.; Scheidt, W. R.; Shelnutt, J. A. *Inorg. Chem.* **1998**, *37*, 4402–4412.
990. Chmielewski, P. J.; Latos-Grażyński, L. *Inorg. Chem.* **1992**, *31*, 5231–5235.
991. Lisowski, J.; Latos-Grażyński, L.; Szterenberg, L. *Inorg. Chem.* **1992**, *31*, 1933–1940.
992. Latos-Grażyński, L.; Chmielewski, P. J.; Olmstead, M. M.; Balch, A. L. *Inorg. Chem.* **1996**, *35*, 566–573.

993. Latos-Grażyński, L.; Pacholska, E.; Chmielewski, P. J.; Olmstead, M. M.; Balch, A. L. *Inorg. Chem.* **1996**, *35*, 566–573.
994. Pacholska, E.; Chmielewski, P. J.; Latos-Grażyński, L. *Inorg. Chim. Acta* **1998**, *273*, 184–190.
995. Chmielewski, P. J.; Latos-Grażyński, L. *Inorg. Chem.* **1998**, *37*, 4179–4183.
996. Chmielewski, P. J.; Latos-Grażyński, L.; Glowiak, T. *J. Am. Chem. Soc.* **1996**, *118*, 5690–5701.
997. Chmielewski, P. J.; Latos-Grażyński, L. *Inorg. Chem.* **2000**, *39*, 5639–5647.
998. Stępień, M.; Latos-Grażyński, L.; Szterenberg, L. *Inorg. Chem.* **2004**, *43*, 6654–6662.
999. Stępień, M.; Latos-Grażyński, L.; Szterenberg, L.; Panek, J.; Latajka, Z. *Inorg. Chem.* **2004**, *43*, 4566–4580.
1000. Stępień, M.; Latos-Grażyński, L. *Acc. Chem. Res.* **2005**, *38*, 88–98.
1001. Stępień, M.; Latos-Grażyński, L. *Inorg. Chem.* **2003**, *42*, 6183–6193.
1002. Pacholska-Dudziak, E.; Skonieczny, J.; Pawlicki, M.; Szterenberg, L.; Latos-Grażyński, L. *Inorg. Chem.* **2005**, *44*, 8794–8803.
1003. Pacholska-Dudziak, E.; Latos-Grażyński, L. *Eur. J. Inorg. Chem.* **2007**, 2594–2608.
1004. Will, S.; Lex, J.; Vogel, E.; Schmickler, H.; Gisselbrecht, J.-P.; Haubtmann, C.; Bernard, M.; Gross, M. *Angew. Chem.* **1997**, *109*, 367–371.
1005. Sanders, J. K.; Williams, D. H. *Nature* **1972**, *240*, 365–390.
1006. Cockerill, A. F.; Davies, G. L. O.; Harden, R. C.; Rackham, D. M. *Chem. Revs.* **1973**, *73*, 553–588.
1007. Kemple, M. D.; Ray, B. D.; Lipkowitz, K. B.; Prendergast, F. G.; Nageswara Rao, B. D. *J. Am. Chem. Soc.* **1988**, *110*, 8275–8287.
1008. Zhang, X.; Chang, C. A.; Brittain, H. G.; Garrison, J. M.; Telser, J.; Tweedle, M. F. *Inorg. Chem.* **1992**, *31*, 5597–5600.
1009. Wong, C.-P.; Venteicher, R. F.; Horrocks, W. DeW., Jr. *J. Am. Chem. Soc.* **1974**, *96*, 7150–7151.
1010. Horrocks, W. DeW., Jr.; Wong, C.-P. *J. Am. Chem. Soc.* **1976**, *98*, 7157–7162.
1011. Horrocks, W. DeW., Jr.; Hove, E. G. *J. Am. Chem. Soc.* **1998**, *100*, 4386–4392.
1012. Buchler, J. W.; De Cian, A.; Fischer, J.; Kihn-Botulinski, M.; Paulus, H.; Weiss, R. *J. Am. Chem. Soc.* **1986**, *108*, 3652–3659.
1013. Buchler, J. W.; Nawra, M. *Inorg. Chem.* **1994**, *33*, 2830–2837.
1014. Jiang, J.; Machida, K.; Yamamoto, E.; Adachi, G. *Chem. Lett.* **1991**, 2035–2038.
1015. Jiang, J.; Machida, K.; Yamamoto, E.; Adachi, G. *Bull. Chem. Soc. Jpn.* **1992**, 1990–1992.
1016. Jiang, J.; Machida, K.; Adachi, G. J. *Alloys Comp.* **1993**, *192*, 296–299.
1017. Lay, K. L.; Buchler, J. W.; Kenny, J. E.; Scheidt, W. R. *Inorg. Chim. Acta* **1986**, *123*, 91–97.
1018. Lachkar, M.; Tabard, A.; Brandes, S.; Guilard, R.; Atmani, A.; De Cian, A.; Fischer, J.; Weiss, R. *Inorg. Chem.* **1997**, *36*, 4141–4146.
1019. Lisowski, J.; Sessler, J. S.; Lynch, V.; Mody, T. D. *J. Am. Chem. Soc.* **1995**, *117*, 2273–2285.
1020. Roberts, E. M.; Koski, W. S. *J. Am. Chem. Soc.* **1960**, *82*, 3006–3010.
1021. Kneubühl, F. K.; Koski, W. S.; Caughey, W. S. *J. Am. Chem. Soc.* **1961**, *83*, 1607–1609.
1022. Smith, T. D.; Pilbrow, J. R. *Coord. Chem. Rev.* **1974**, *13*, 173–278 and references therein.
1023. Eaton, S. S.; Eaton, G. R.; Chang, C. K. *J. Am. Chem. Soc.* **1985**, *107*, 3177–3184.
1024. Lemtur, A.; Chakravortay, K.; Dhar, T. K.; Subramanian, J. *J. Phys. Chem.* **1984**, *88*, 5603–5608.
1025. Luckhurst, G. R.; Setaka, M.; Subramanian, J. *Mol. Phys.* **1976**, *32*, 1299–1309.
1026. Subramanian, J. In *Porphyrins and Metalloporphyrins*; Smith, K. M., Ed.; Elsevier: Amsterdam, **1975**; pp. 555–589.

This page intentionally left blank

30 Heme Acquisition by Hemophores: A Lesson from NMR

Paola Turano

Magnetic Resonance Center (CERM) and Department of Chemistry,
University of Florence, Via Luigi Sacconi 6,
I-50019 Sesto Fiorentino, Italy

List of Abbreviations

Ccm	cytochrome c maturation
CRINEPT	cross-correlated relaxation-enhanced polarization transfer
DPC	dodecyl phosphocholine
HAS	heme acquisition system
HO	heme oxygenase
HSQC	heteronuclear single quantum correlation
LbpA	lactoferrin binding protein A
LbpB	lactoferrin binding protein B
NOESY	nuclear Overhauser effect spectroscopy
PBP	periplasmic binding protein
TbpA	transferrin binding protein A
TbpB	transferrin binding protein B
TROSY	transverse relaxation-optimized spectroscopy

I. Biological Background

Iron is an essential element for virtually all living organisms. It has been reported that the iron content in bacteria is of the order of 10^5–10^6 iron ions per cell.[1] Virtually all living microorganisms require a minimum effective concentration of 10^{-8} M for growth.[2]

Iron ranks fourth in abundance of all elements on the Earth's crust,[3] but its bioavailability is limited. Under aerobic conditions iron(III) is the dominant oxidation state and is characterized by an extremely low solubility (of the order of 10^{-18} M, at pH of 7.4).[4] Iron(II) is more soluble, but available to organisms only in anaerobic environments. In the presence of air, it becomes toxic due to its redox chemistry which leads to the formation of ferric iron and reactive oxygen species.

As a consequence of these considerations, iron in biological systems is found tightly sequestered by high-affinity iron-binding proteins.[5] Bacteria have developed a number of mechanisms to acquire iron, allowing their survival in free iron-poor environments.[1,2,6–8] In Gram-negative bacteria, a number of pathways have been identified which rely (i) on iron ion uptake through siderophores; (ii) on iron ion uptake from transferrin/lactoferrin; (iii) on the use of heme as an iron source through its direct uptake in free form or from heme-binding proteins; and (iv) on the uptake of heme mediated by hemophore proteins. All these processes share common key elements (Figure 1) i.e., an outer membrane receptor, a periplasmic binding protein (PBP), and an inner membrane ATP-binding cassette (ABC) transporter. The transport through the outer membrane receptor requires the action of the TonB system (TonB, ExbB, and ExbD).[8]

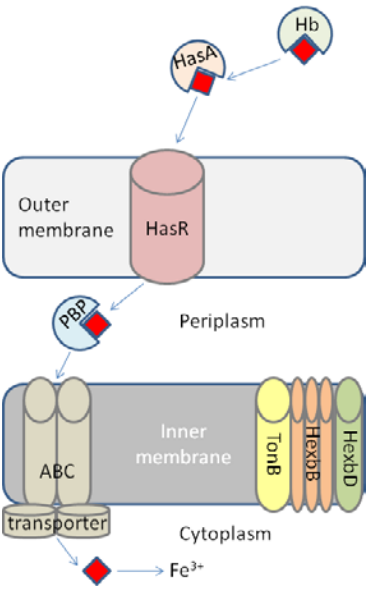

Figure 1. Schematic representation of the key elements of the heme acquisition system in Gram-negative bacteria. The hemophore protein HasA uptakes heme (red diamond) from a host protein (here hemoglobin, Hb) and delivers it to the outer membrane receptor (HasR). The other key components for heme delivery to the cytoplasm and iron abstraction are a periplasmic binding protein (PBP), an inner-membrane ABC transporter, and the TonB system (TonB, ExbB, ExbD). In the cytosol, heme oxygenase or functionally analogous enzymes extract iron(III) from heme.

Siderophores are low molecular weight (MW < 1000 Da) and high affinity ($K_{aff} > 10^{30}$) iron chelators.[9,10] Their biosynthesis is induced by intracellular iron deficiency and they are secreted into the extracellular milieu to scavenge iron. They are able to dissolve insoluble iron(III) species and facilitate its transport into the cell. Siderophores are structurally well characterized and numerous studies are available on the mechanism of the siderophore-mediated iron acquisition system.[11,12]

In vertebrate hosts, only a small amount of iron is extracellular and bound to the glycoproteins transferrin or lactoferrin. In many pathogenic bacteria, such as *Neisseria meningitidis* and *Haemophilus influenza,* extraction of the iron atoms from the host's iron carriers occurs via outer membrane receptors, the TbpB/TbpA and LbpB/LbpA proteins.[13–15] These two-component receptors are constituted by a membrane-anchored binding protein (the B-protein) and an integral membrane protein (the A-protein), specific for transferrin (Tb) and lactoferrin (Lb), respectively.

Nevertheless, in vertebrates, most irons are intracellular, either stored in ferritin or inserted in the protoporphyrin ring of heme-containing proteins, mainly

hemoglobin. Microorganisms can up take the heme either as a free heme (whose concentration in living systems is however very low due to its cytotoxicity) or as heme associated with host hemoproteins (hemoglobin, hemoglobin–haptoglobin, heme-albumin, heme-hemopexin, and myoglobin).[16–18] The uptake relies either on the two-component receptor HpuA/HpuB, an analog of the transferrin/lactoferrin system, which binds hemoglobin, hemoglobin–haptoglobin, and apohaptoglobin, or on the single-component HmbR receptor, specific only for hemoglobin.

The second mechanism that bacteria use to extract iron from heme uses specialized bacterial proteins, termed hemophores.[1,7,19,20] They are extracellularly secreted and acquire heme from the environment, usually extracting it from heme proteins. The hemophore then delivers heme to a specific outer membrane receptor, where the process of heme transport to the cytoplasm initiates and proceeds through the steps common to the other iron-uptake mechanisms described above (Figure 1). The ensemble of proteins involved in the hemophore-dependent process constitutes the heme acquisition systems (HAS). The use of heme as an iron source requires iron abstraction from the heme. This process occurs in the bacterial cytoplasm, where the heme is degraded, through oxidative cleavage, to biliverdin, carbon monoxide, and free iron by the enzyme heme monooxygenase (HO). [21] Non-HO homolog heme degrading enzymes have also been described for some bacteria.[22–25] Very recently two enzymes that promote iron extraction from heme preserving the tetrapyrrole ring intact have been reported.[26]

The focus of this chapter is on the use of NMR to investigate structure and chemistry of some components and key steps of the mechanism of the heme acquisition system in Gram-negative bacteria.

II. Hemophore Protein HasA

A. Heme-Loaded HasA

Under conditions of iron limitation, the Gram-negative bacterium *Serratia marcescens* secretes HasA, a monodomain 19 kDa protein, which acts as a hemophore. This protein was the first hemophore to be discovered and the only one structurally characterized until now. The X-ray crystal structure of the heme loaded form of HasA shows an original $\alpha+\beta$ fold, with a seven-stranded antiparallel β-sheet on one side of the protein and four α-helices on the other side (Figure 2a). Two loops, L1 and L2, connect the α and β faces of the molecule and provide the heme-iron(III) axial ligands, H32 through its Nε2 and Y75 through its Oη. His/Tyr coordination is quite atypical for heme proteins in native states; it has been reported only for the cytochrome c maturation protein (CcmE),[27] and for the oxidized form of the cytochrome cd_1 nitrite reductase.[28] A H-bond between H83 Nε2 and the Y74 Oη was observed in two out of the three crystal structures available

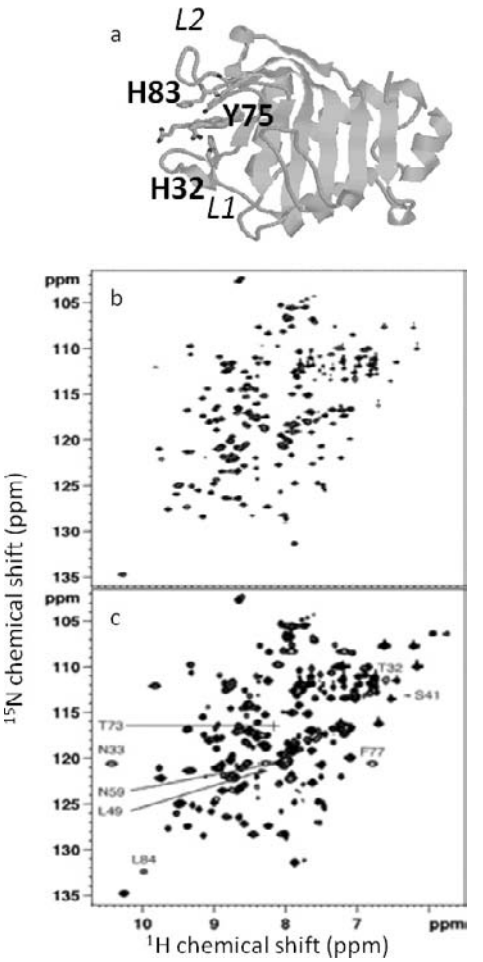

Figure 2. The X-ray crystal structure of holoHasA (PDB ID 1B2V). (a) Loop L1 provides the H32 ligand. Loop L2 bears the Y75 ligand and H83. In this structure an H-bond between Y75 Oη and H83 Nε2 is present. ^{1}H–^{15}N HSQC (b) and paramagnetic tailored ^{1}H–^{15}N HSQC (c) of the holoprotein. A set of peaks (here labeled) due to residues in the proximity of the paramagnetic center is detectable only in the latter experiment. (Panels b and c are adapted from Ref. 33.)

(PDB ID 1B2V at pH 4.6 and PDB ID 1DKO at pH 8.0).[29,30] In the third structure (PDB ID 1DKH at pH 6.5)[30] H83 does not interact with Y75 while it is involved in a hydrogen bond with a water molecule.

In order to learn about the heme-coordination environment in solution and the possible relevance of second coordination sphere interactions on the heme binding properties of HasA, a number of studies have been conducted by NMR.

It is worth mentioning that both X-ray crystallography[29,30] and NMR[31–34] reveal the presence of two orientations, with a relative ratio of the order of 70:30, for the

heme inserted in the hemophore that differ for a rotation of 180° around the α, γ-*meso* axis. This phenomenon, commonly observed in b-type heme proteins,[35–37] results in a doubling of the peaks of the heme resonances, the axial ligands and most of the heme-binding pocket residues. For the sake of clarity, no mention to the presence of the minor species will be made in the remaining of this chapter; all the considerations presented for the major species are assumed to hold equally for the major one as well.

1. *NMR of the Gallium(III) Derivative*

The presence of iron(III) complicates NMR spectral analysis due to the important paramagnetic effects induced by the metal ion on surrounding residues. An initial characterization of HasA in solution was therefore carried out using the gallium(III)-heme derivative as a diamagnetic analog of the holoprotein; gallium(III) and iron(III) have the same charge, similar atomic radius (0.62 Å vs. 0.65 Å) and similar coordination preferences. The backbone assignment of gallium(III)–HasA provided evidence of intact secondary structures with respect to iron(III)–HasA.[32]

$^{1}H–^{15}N$ multiple bond connectivity spectra[38] for the detection of $^{15}N–^{1}H$ correlations via $^{3}J_{NH}$ coupling constants were used to characterize the protonation state of the imidazole ring of His residues in the protein.[39] Patterns of ^{3}J connectivities between non-exchangeable imidazole protons Hδ2 and Hε1 and Nδ1 and Nε2 allowed the identification of all these nuclei for the His residues present in HasA, i.e. H17, H32, H83, H128, H133, and H179. The ^{15}N chemical shifts of the imidazole nitrogens are diagnostic for their protonation state[40–42]: in a fully protonated, positively charged, imidazole ring, both nitrogens resonate on average at 175 ppm; in a neutral imidazole ring, the deprotonated nitrogen typically resonates at about 250 ppm, whereas the protonated nitrogen resonates at about 165 ppm; intermediate chemical shift values are indicative of fast exchange between the two tautomers. Involvement in H bonding affects the above shift values up to 10 ppm: the shift of a nitrogen behaving as an acceptor in a hydrogen bond decreases, whereas that of a nitrogen behaving as a donor increases.

In gallium(III)–HasA, a relatively low chemical shift value was measured for the Nδ1 of H83 (227.3 ppm) and attributed to the involvement of this nitrogen in a hydrogen bond, presumably as an acceptor of the hydroxyl proton Hη of Y75,[39] by analogy with the X-ray data.[29]

2. *NMR of the Iron(III) Derivative*

a. *^{1}H NMR*

Heme methyl chemical shifts in iron(III) provide a signature of the spin state of heme iron.[35] In high-spin iron(III) heme proteins, they resonate in the 60–100 ppm

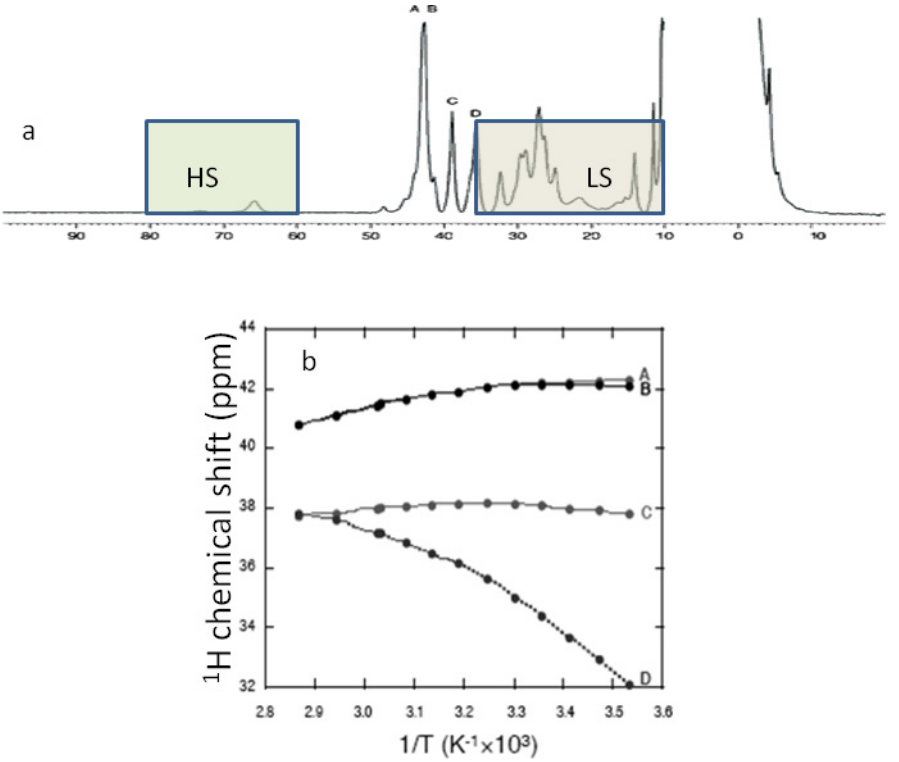

Figure 3. The ^{1}H NMR spectrum of iron(III) heme-loaded HasA recorded at 700 MHz and 303 K (a). The resonances attributed to the heme methyl resonances are labeled A–D. Typical ranges for the chemical shift of heme methyls in high-spin and low-spin iron(III) heme proteins are indicated by the semitransparent boxes. The temperature dependence of the chemical shift for heme methyl resonances does not follow the Curie behavior (b). (Adapted from Ref. 33.)

range. In low-spin iron(III) heme proteins their chemical shifts range between 5 and 35 ppm. In HasA, the heme methyl resonances have chemical shift values intermediate between those expected for a purely S = 5/2 heme iron(III) and those for a purely S = 1/2 heme iron(III),[33] being observed at 42.7 (two overlapping signals at 303 K), 38.9, and 35.7 ppm (Figure 3a). At a field of 16.4 T, heme methyl T_1 values are 8–9 ms, and line widths of the order of 400 Hz. Similar chemical shift and T_1 values have been reported for heme proteins undergoing high-spin/low-spin equilibria, which are fast on the chemical shift NMR time scale.[43,44] The non-linear temperature dependence of the heme methyl chemical shift values (Figure 3b) further supports the nonpure spin nature of heme–iron(III) in HasA.

The relatively low chemical shift (about 70 ppm) for the exchangeable resonance of Hδ1 H32, its large line width (about 1000 Hz) and the short T_1 value (< 2 ms)

are consistent with literature data on intermediate spin state systems.[45] As typical for nonpurely low-spin heme proteins,[35] the Hδ1 of the bound His is the only signal of an axial ligand detectable in the ^{1}H NMR spectra.

b. *Heteronuclear detection*

The sensitivity of NMR experiments depends critically on the type of nucleus that is detected during acquisition, with a $\gamma^{3/2}$ dependence, where γ is the gyromagnetic ratio of the detected nucleus. This translates into a factor of eight in sensitivity at advantage of ^{1}H-detected experiments over ^{13}C-detected experiments, and into a factor of 31 over ^{15}N-detected experiments. Consequently, virtually all modern biomolecular NMR experiments detect protons during acquisition.[46] The sensitivity of the NMR experiment is also dependent on the nature of the excited nucleus, being directly proportional to its γ value. During the last decade, hardware developments, in particular the advent of cryoprobes, have sensibly increased the sensitivity of the NMR experiments. Therefore, while the relative sensitivity of proton detection and heteronuclear detection remains that predicted by theory, heteronuclear-detected NMR experiments can now be brought into a sensitivity range that makes them feasible even for biomolecular applications.

Development of special probes optimized for ^{13}C sensitivity has given a particular impulse to ^{13}C-NMR with respect to ^{15}N-NMR. While 1D ^{15}N-detected experiments on proteins are nowadays possible, they still suffer from very low sensitivity. By contrast, a number of ^{13}C NMR experiments aimed at sequential and side chain assignments in proteins have been developed that exploit the heteronuclear backbone ^{13}C′–^{15}N and ^{15}N–Cα scalar couplings, as well as the large homonuclear carbon–carbon scalar couplings (30–70 Hz) for coherence transfer.[47–57]

This protonless NMR approach has been proposed as particularly useful in systems characterized by short relaxation times.[58–63] The large proton gyromagnetic ratio that is responsible for the high sensitivity of ^{1}H-NMR experiments also causes large dipole–dipole interactions that lead to short relaxation times and may broaden lines beyond detection with increasing molecular mass or in the presence of paramagnetic centers. In this context, heteronuclei, which are characterized by smaller gyromagnetic ratios, may represent probes with better performances.

By taking advantage of the new NMR tools available for the investigation of fast relaxing biomolecules, a better understanding of the coordination environment and electronic structure of the iron(III)–heme loaded HasA was obtained.

i. ^{13}C NMR

^{13}C-NMR permits researchers to learn about the axial coordination of heme iron in holoHasA.[33] Standard ^{1}H–^{15}N HSQC (Figure 2b) experiments provided peaks for

the NH backbone of all residues but the N-terminal one and 15 amino acids located close to the paramagnetic center (they are amino acids 32–34, 41, 42, 50, 60, 74–78, 83–85). With paramagnetic tailored ^{1}H–^{15}N HSQC experiments, which used fast repetition rates and short INEPT delays, the eight peaks corresponding to residues T33, N34, S42, L50, T60, T74, F78, and L85 could be retrieved (Figure 2c); but resonances for H32, N41, Y75, T76, L77, H83, and T84 remained undetectable. ^{13}C-direct detection experiments, in particular ^{13}C–^{13}C COSY and the CACO spectra, provided the assignment of all protein residues beside the two axial ligands H32 and Y75, and L76. Signals of H83 could be detected only in paramagnetic tailored ^{13}C-spectra (Figure 4).

Although ^{13}C experiments are much more robust for paramagnetic systems than the standard assignment strategy based on ^{1}H-detected experiments, the heme axial ligands could only be detected in 1D ^{13}C experiments. The monodimensional ^{13}C spectrum of holoHasA shows well-resolved peaks that are heavily hyperfine shifted. Most of them are observed downfield in the 220–770 ppm region and have T_1 values of the order of 1–13 ms, (Figure 5a). The upfield signals at −22 and −32 ppm have

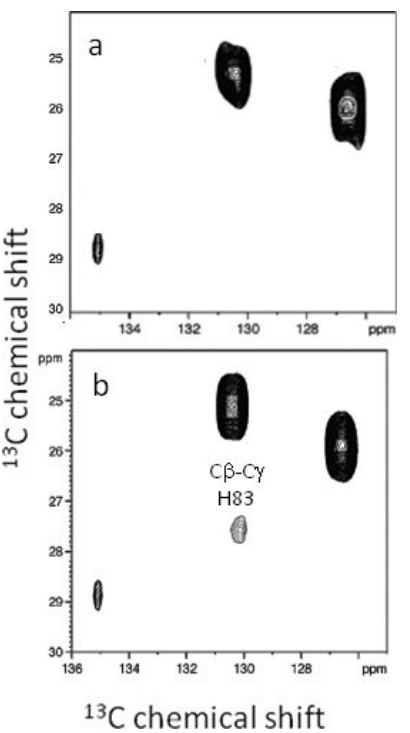

Figure 4. Portion of the ^{13}C–^{13}C COSY spectrum of the holoprotein containing the Cβ–Cγ cross peaks for His residues (a) and its paramagnetic tailored version (b). The Cβ–Cγ correlation for H83 is only detectable in the latter spectrum. (Adapted from Ref. 33.)

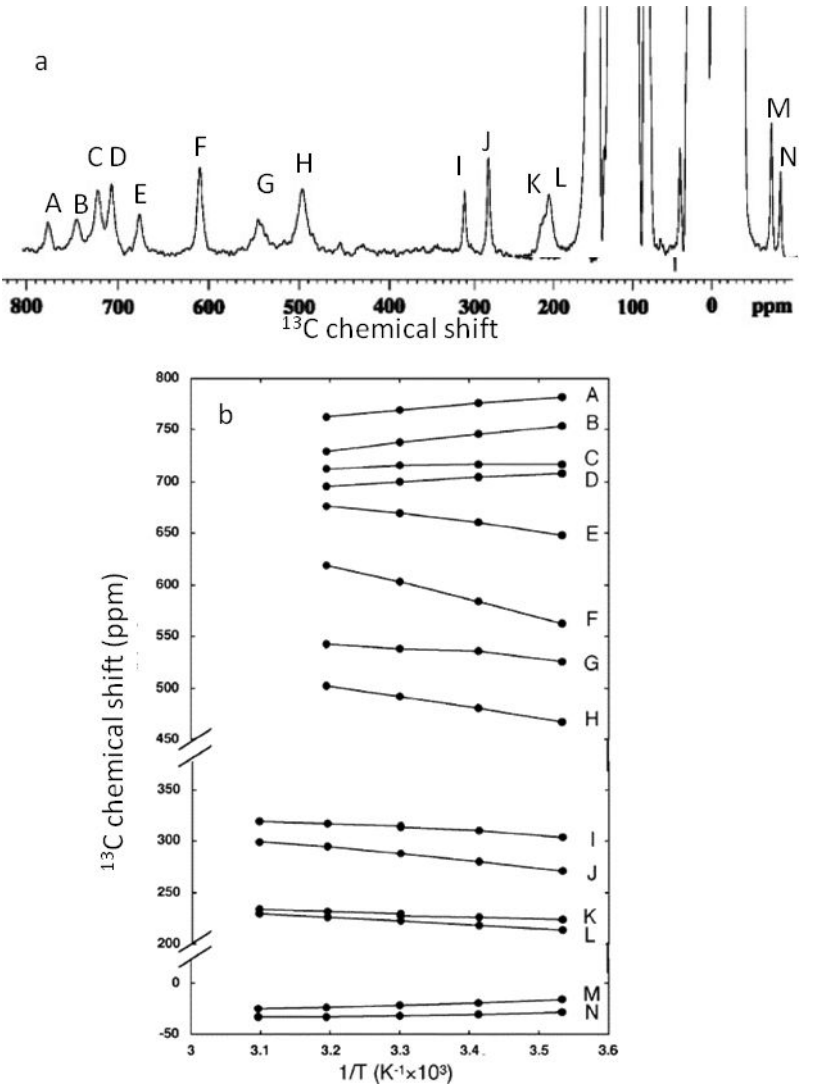

Figure 5. The ^{13}C NMR spectrum of iron(III) heme-loaded HasA recorded at 700 MHz and 303 K (a). The hyperfine-shifted resonances are labeled A–N. Resonances attributed to Y75 have shifts that decrease with temperature, while resonances attributed to H32 have shifts that increase with temperature (b). (Adapted from Ref. 33.)

longer T_1 values (in the 70–90 ms range). The chemical shift, T_1, and line width values of the hyperfine shifted resonances can only be consistent with the hypothesis that they originate from the coordinating residues (the heme was not ^{13}C-enriched and therefore its resonances could not be detected in these spectra). From the comparison of the ^{13}C spectra of the wild type protein and of its Y75A variant,

it was possible to discriminate between Y75 and H32 resonances. The two sets of signals could also be clustered based on their behavior as a function of temperature (Figure 5b). Those attributed to Y75 have shifts that decrease upon increasing temperature, whereas those attributed to H32 have shifts that increase upon increasing temperature. This behavior could be rationalized assuming a temperature-dependent chemical equilibrium between two limit spin states: a low-spin species, S = 1/2, and a high-spin species, S = 5/2, the latter being characterized by substantially larger hyperfine shifts and becoming more populated at higher temperature. In the fully low spin limit species, both H32 and Y75 are strong iron axial ligands; in the purely high spin limit species, Y75 is no longer bound to the heme iron, which becomes five-coordinate. Upon increasing temperature, the shift of H32, which remains invariably coordinated to iron, increases because of the increase in total spin and therefore of the unpaired electron delocalization on its ring. On the contrary, the shifts of Y75 decrease because in the high spin form the Tyr *t* is no more a ligand and therefore its signals do not experience any contact shifts anymore.

In the range of experimentally accessible temperatures, both H32 and Y75 coordinate iron, the latter most probably thanks to the H-bond with H83, which imposes a partial tyrosinate character to Y75 and makes it a better ligand for iron(III).

ii. ^{15}N NMR

Monodimensional ^{15}N-direct detected experiments were used for the identification of the imidazole nitrogen atoms of His residues, with the aim to assign the ^{15}N nuclei of the axial ligand H32 and the key residue H83. A broad signal (70 Hz), with a chemical shift strongly dependent upon temperature (181.2 ppm at 303 K to 193.4 ppm at 317 K) (Figures 6a and 6b) is detectable. This resonance therefore experiences important paramagnetic effects; it is also present in the 1D ^{15}N spectra of the holoH83A mutant (Figure 6c). On this basis, it was assigned to the Nδ1 of H32. The H83 Nε2 was assigned to a relatively sharp resonance present at about 179 ppm at 303 K (Figure 6a); its identification relied on the observation that no corresponding resonance could be detected in the analogous spectrum of the H83A mutant (see Figure 6c and Section II.B). The shift value for the H83 Nε2 resonance in the iron(III) wild-type protein differs by +12.9 ppm with respect to that of the gallium(III) protein. A similar effect is observed for the Cβ of H83, which shows a +7.05 ppm chemical shift variation with respect to the gallium(III) form. Such relatively large observed differences in chemical shift are not explainable in terms of structural differences with respect to the gallium protein, because ^{13}C chemical shifts are very little dependent on the local environment of the nucleus. Furthermore, the observed chemical shift differences cannot be accounted for simply on the basis of pseudocontact shifts that, for the location of these nuclei with respect to the paramagnetic

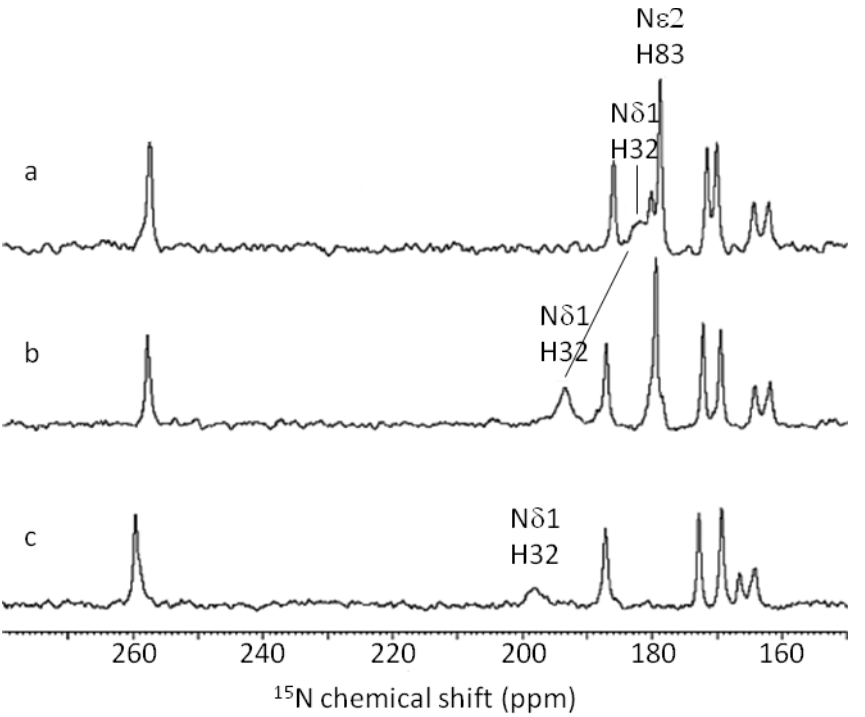

Figure 6. Monodimensional ^{15}N NMR spectra of wild-type holoHasA at 303 K (a); wild-type holoHasA at 317 K (b), and H83A at 317 K (c). All the spectra have been recorded at pH 5.5. (Adapted from Ref. 33.)

center and magnetic axes, were estimated to be < 1 ppm in absolute value. Therefore, contact shift contributions had to be invoked; unpaired spin-density transfer from the ligand to the second coordination sphere nuclei has already been reported, for example, in the case of a tyrosine H-bonded to the cyanide iron ligand in the low-spin iron(III) cyanide adduct of M80A cytochrome *c*.[64,65] The hyperfine shift values observed for the abovementioned H83 nuclei further support the presence of a H-bond between H83 Nδ1 and the iron-ligated Y75 Oη, allowing the delocalization of the iron(III) unpaired spin density onto the imidazole ring of H83. Consistently, the resonance of the Nδ1 of H83 could not be detected, most probably because it is broadened beyond detection by contact shift contributions to its T_2. Of course, the same consideration holds for the Nε2 of H32, which is directly bound to iron(III).

B. The H83A Variant

The hypothesis that H83 in wild-type HasA modulates the strength of the Tyr–iron bond was further confirmed by the characterization of the H83A variant.[34]

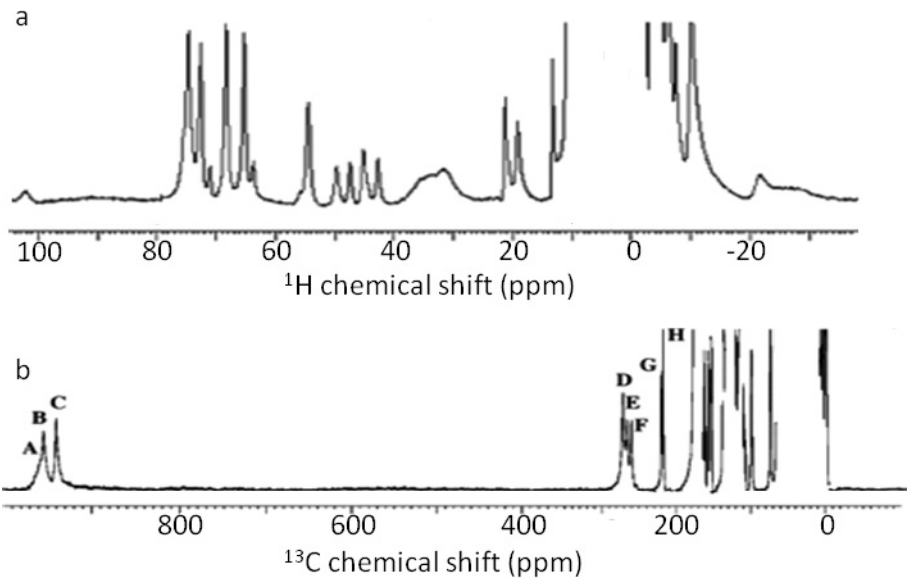

Figure 7. Monodimensional ^{1}H (a) and ^{13}C (b) NMR spectra of H83A recorded at pH values of 5.2 and 5.6, respectively. (Adapted from Ref. 34.)

Replacement of H83 with an alanine causes detachment of the tyrosine ligand, thus giving rise to pentacoordinate, a purely high-spin species that is dominant at neutral pH. The ^{1}H NMR spectrum obtained at 303 K and acidic-neutral pH values for H83A displays heme-methyl resonances between 60 and 80 ppm, and a broad exchangeable resonance at 102.3 ppm, attributed to the Hδ1 of the axial His ligand; resonances with such shifts are typical of high-spin species (Figure 7a).[35] Longitudinal relaxation times are shorter than 1 ms for the four heme methyls and for the H32 Hδ1 and of the order of 4–5 ms for all the other downfield-shifted signals. The hyperfine-shifted resonances exhibit a Curie behavior, consistent with a pure high spin state. The ^{1}H NMR spectrum of holoH83A shows a broad feature at –25 ppm, attributable to *meso* H-peaks. Upfield resonance for *meso* protons are indicative of pentacoordination,[35] a conclusion further supported by resonance Raman, and UV-visible spectroscopy. Monodimensional ^{13}C and ^{15}N NMR spectra also point to the same conclusion (Figures 7b and 76, respectively). In the ^{15}N NMR spectrum the resonance of the Nδ1 of H32 remains as broad as expected for a coordinating residue. In the ^{13}C NMR spectrum the number of hyperfine shifted resonances decreases with respect to the wild type, consistent with the presence of a single axial ligand. The cross peak of Y75 in the ^{13}C–^{13}C COSY spectrum of H83A is detected in the typical Cβ–Cγ region (Figure 8), as expected for a noncoordinating residue. As already observed for the signals of the heme methyls and H32 Hδ1 in the ^{1}H NMR spectrum, the average shift

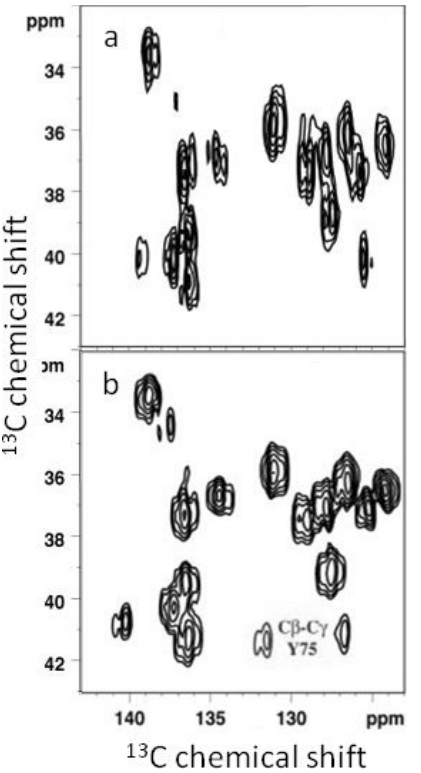

Figure 8. Portion of the ^{13}C–^{13}C COSY spectrum of the holoprotein containing the Cβ–Cγ cross peaks for Tyr residues for wild-type holoHasA (a) and H83A (b). The Cβ–Cγ correlation for Y75 is only detectable in the latter spectrum. (Adapted from Ref. 34.)

of the hyperfine-shifted ^{13}C resonances increases up to 900 ppm, consistently with an increased hyperfine shift contribution due to the change from an intermediate to a high spin state. The chemical shifts of the ^{13}C hyperfine-shifted resonances have a regular Curie dependence, which is normal for a pure spin state.

The ^{1}H NMR spectrum of holoH83A at acidic and neutral pH exhibits unresolved overlapping signals between 20 and 40 ppm (Figure 7a), whose intensity increases with respect to that of the high spin species upon increasing pH. NMR together with a panel of other spectroscopic techniques has established the existence of series of pH-depended equilibria, summarized in Figure 9. It shows that when Y75 is detached from heme binding, the "distal" site of the heme becomes accessible to exogenous ligands. This opening of an access to the heme iron, which does not imply any important conformational change of protein backbone (as deducible from ^{1}H–^{15}N HSQC) has suggested that the protein state found in H83A may represent a possible mechanistic intermediate in the heme transfer reactions involving HasA: the uptake reaction from host hemoproteins and/or the delivery reaction to the membrane receptor HasR.

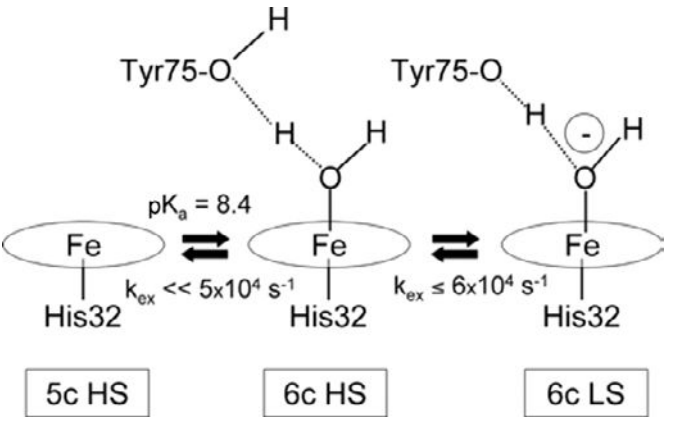

Figure 9. The heme iron spin state and the coordination sphere of holoH83A have been defined over a wide range of pH values. At variance with the wild-type case, variations in iron coordination number and spin state as a function of pH are observed and summarized in this figure. In solution at acidic pH the major form of holoH83A is a high-spin five-coordinate species, having as fifth ligand H32. At increasing pH values, the five-coordinate high-spin species decreases in intensity at the advantage of a high-spin and a low-spin six-coordinate species. The latter is dominant at alkaline pH values. (Adapted from Ref. 34.)

C. Apo HasA

The structure of the apoprotein has been determined by NMR with standard methodology.[66] It shows an intact structure for the α and β portions of the protein. The conformation of loop L2 does not differ much from that of the holoprotein. Notably, the Y75–H83 hydrogen bond is maintained in the apoprotein. In contrast, loop L1 undergoes a major conformational change that gives rise to an "opening" of the structure with respect to the heme-loaded form (Figure 10a). Loop L1 is far more mobile in the apo than in the gallium(III) form of the protein. The ^{1}H–^{15}N HSQC spectrum of the apoprotein (Figure 10b) differs from that of the heme-loaded HasA due to the conformational differences of the unstructured parts of the protein backbone. The conformational rearrangements accompanying heme binding to HasA (Figures 2a and 10a) have led to the description of the hemophore structure as resembling a "fish biting the heme".[29]

III. HasA–HasR Interaction

A. ^{1}H–^{15}N NMR Spectra

The shift patterns of ^{1}H–^{15}N correlations for backbone amides represent a clear signature of the open conformation of apoHasA and of the closed conformation of the heme-loaded HasA, common to both the gallium(III) and the iron(III) derivatives.

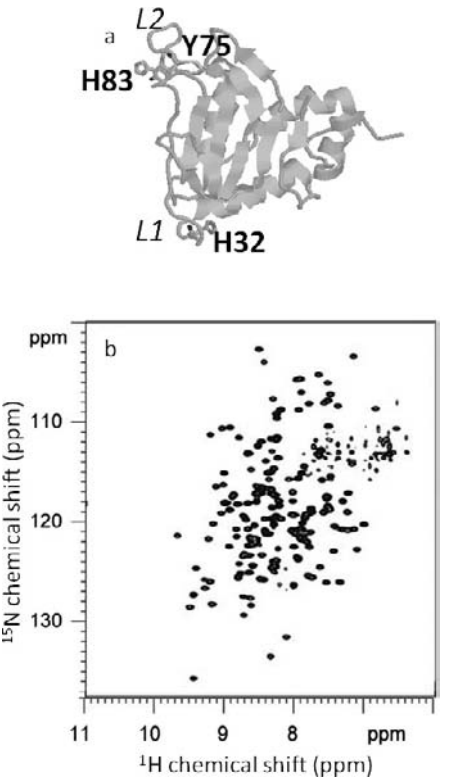

Figure 10. The average NMR solution structure of apoHasA (PDB ID 1YBJ) (a). The two loops, and in particular loop L1, have a different conformation with respect to the holoprotein, where they provide the heme iron axial ligands. $^{1}H–^{15}N$ HSQC of the apoprotein (b). (Panel b is adapted from Ref. 33.)

In addition, the presence of iron(III) in the holoprotein gives rise to hypefine shift contributions for the backbone nuclei in its surroundings and line broadening (even beyond detection) on some of them (Section II.A.2 and Figure 2c). Changes in this NMR signature have been used to monitor the variations occurring upon interaction between HasA and its membrane receptor HasR, in the presence and in the absence of heme.[67]

HasR is a large protein (98 kDa)[68] which could be solubilized in DPC micelles up to a concentration of the order of 300 μM. Both holo and apoHasA form a stable complex with HasR under these experimental conditions. Nevertheless, the low solubility of the system combined with the large total molecular weight of the protein–protein complex embedded in micelles required the use of an *ad hoc* strategy. NMR heavily suffers from molecular size limitations; with increasing molecular mass, the slow molecular tumbling of the complex in solution causes fast

transverse relaxation that broadens signals beyond detection in standard $^{1}H–^{15}N$ HSQC experiments. It is a common practice to alleviate line broadening effects using isotope enrichment with ^{2}H for nonexchangeable hydrogens; this isotope enrichment decreases the magnitude of dipolar interactions provided by the protein frame, thus significantly reducing nuclear spin relaxation rates.[69] For this purpose, ^{2}H (99.7 ± 0.1%),^{15}N-labeled HasA was used in the complex with unlabeled HasR. Even with this optimal isotope-labeling, instead of the conventional NMR HSQC spectra, detection of $^{1}H–^{15}N$ correlations of the low molecular weight component HasA in the supramolecular structure of the complex required the use of CRINEPT-TROSY experiments.[70] Constructive use of cross-correlated relaxation phenomena in transverse relaxation-optimized spectroscopy (TROSY)[71] combined with cross-correlated relaxation-enhanced polarization transfer (CRINEPT)[70,72] provided spectra as those reported in Figure 11a, where most of the resonances of

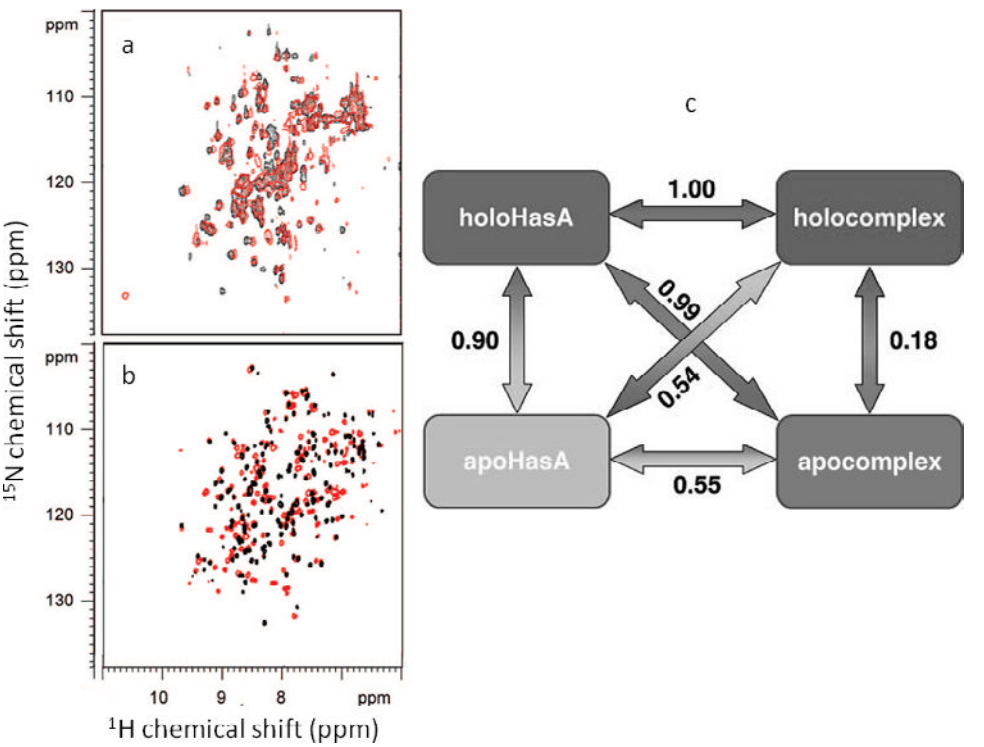

Figure 11. Superimposition of the CRINEPT-TROSY spectra obtained in DPC micelles for apoHasA–HasR (black trace) with holoHasA–HasR (red trace) (a), and apoHasA (black trace) with holoHasA (red trace) (b). Representation of the results obtained from the statistical analysis of the spectral profiles for apoHasA, holoHasA, apoHasA–HasR, and holoHasA–HasR (c). Numbers reported on each arrow are the values of the normalized distance matrix obtained for each pair of spectra. (Adapted from Ref. 67.)

the hemophore protein were still detectable in its complexed forms, although with sensibly increased line widths and consequent reduction in resolution.

1. *Chemical Shift Perturbation Mapping*

Chemical shift perturbation is the most widely used NMR method to map protein interfaces.[73] The interaction with a partner molecule causes environmental changes on the protein interface and, hence, affects the chemical shifts of the nuclei in this area. In addition, if upon interaction there are conformational changes involving the observed protein, they will also be revealed by chemical shift changes. Complex formation between apoHasA and HasR induces a number of chemical shift variations (Figures 11a and 11b, black traces). Two types of signals were useful for analysis of the chemical shift mapping: (1) signals experiencing minimal chemical shift changes (<0.25 ppm), if any, and therefore belonging to regions of apoHasA that are not affected by the presence of the receptor; (2) signals that undoubtedly disappear from their original well-resolved position in the free apoHasA spectrum upon complex formation and are therefore severely affected when binding to the receptor. Residues whose behavior could not be safely defined, mainly because they fall in crowded spectral regions, were unsound for the analysis and were not used to map the interaction. Residues of class 2 are all clustered around the heme binding pocket (Figure 12a) indicating an heavy involvement of L1, L2 and amino acids on strands 2–6 in the interaction surface area. With a similar approach, it was

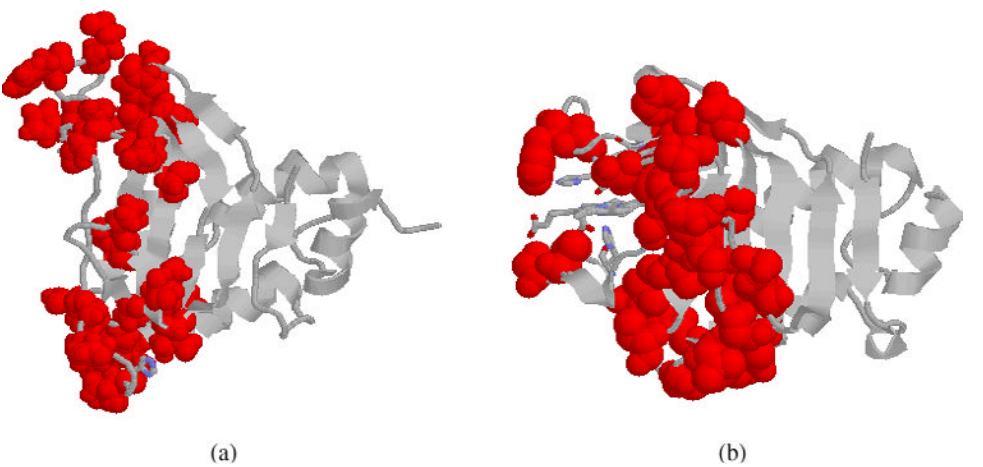

Figure 12. Chemical shift perturbation mapping for apoHasA–HasR (a) and holoHasA–HasR (b). Perturbed residues (red spheres) define the surface contact area on the hemophore upon binding to the receptor. In the holoHasA structure the heme, its axial ligands and H83 are shown as sticks.

possible to map the residues affected upon *complex* formation between holoHasA and HasR; most of the resonances of class 2 in the holoHasA–HasR complex (Figure 12b) coincide with those experiencing chemical shift changes in apoHasA upon binding to HasR. When not coincident, they are located in protein regions found to belong to the interaction area in the apoHasA–HasR complex. Therefore, two important conclusions could be drawn from the chemical shift perturbation mapping: (i) the interaction area was unequivocally identified; (ii) it resulted that the contact surface area between the hemophore and its receptor is independent of the presence of the heme in the complex.

2. *Spectral Profiling*

Identification of the residues at the interface constitutes an important achievement for the structural and mechanistic characterization of the complex; however, the information content embedded in the spectra of Figure 11 is richer. From the simple visual inspection of the spectra of Figures 11a and 11b, it is apparent that differences in the chemical shift signature that characterize free apoHasA and free holoHasA are essentially quenched in their complexes with HasR, This concept could be better rationalized taking advantage of an approach that is used in NMR-based metabolomics, where differences in the metabolic signature of different individuals are quantified in terms of distance matrix without the need of any peak assignment.[74] The obtained results are summarized in Figure 11c, from which it emerges that spectral patterns for the four available protein forms (free apoHasA, free holoHasA, apoHasA in the complex with HasR, and holoHasA in the complex with HasR) carry unique features that are conformation specific. A normalized distance matrix value of 1 is attributed to the most distant pair of spectra, that is the pair holoHasA/holocomplex. The second most distant pair is constituted by the spectra of holoHasA and apoHasA. On the contrary, apoHasA–HasR and holoHasA–HasR spectra are very close (0.18; a value equal to 0 would correspond to spectral identity). Normalized distance matrix values of 0.55 and 0.54 are obtained for apoHasA compared with apocomplex and holocomplex, respectively. In summary, signal patterns are substantially identical for the two complexes, relatively similar for the two pairs apoHasA/apoHasA–HasR and apoHasA/holoHasA–HasR, whereas holoHasA is different from all the others. A clear outcome from this statistical analysis is that three conformations are accessible to HasA in solution: the isolated holoprotein, the isolated apoprotein, and the conformation in the complex. The spectral features for the complex are much closer to those of the isolated apoHasA than those of the isolated holoHasA. Therefore the closed conformation of holoHasA and the paramagnetic effects on its spectra, that is the two factors determining its spectral signature, are not shared with the complex.

While the standard chemical shift mapping perturbation allowed the identification of the interaction area for both apo- and holo-hemophores, the statistical analysis of the spectral fingerprint in terms of distance matrix permitted inference about the differences and similarities in the structure of apoHasA and holoHasA in their isolated forms and in their complex with HasR. In addition, a number of individual conformations accessible to the protein in solution is also defined through the statistical analysis.

B. The Fate of the Heme

Signals of residues on loops L1 and L2 that were undetectable in the holoHasA ^{1}H–^{15}N spectra due to severe paramagnetic line broadening are observed in the holocomplex at shifts typical for apoHasA, strongly suggesting that upon complex formation, the heme group is not located on the hemophore protein anymore, but is transferred to HasR. This important mechanistic hypothesis could have been better supported by the detection of the signals of H32 and Y75 for the holocomplex in diamagnetic ^{13}C–^{13}C spectra (by analogy with the finding for Y75 in the H83A; see Section II.B and Figure 8). Unfortunately, the combination of large molecular weight and relatively low concentration of the complex prevented the detection of aromatic Cβ–Cγ signals with enough resolution and signal-to-noise in complexes.

Given the intrinsic low sensitivity of ^{13}C-direct detected NMR experiments, lack of any detectable hyperfine-shifted resonance in monodimensional spectra for the diluted samples typical of these large and poorly soluble complexes does not constitute a reliable negative proof of the breaking of the heme iron axial bonds.

The definitive proof for the working hypothesis of heme transfer from the hemophore to the receptor upon complex formation came from the X-ray crystal structure of the complex published at the same time as the NMR characterization (Figure 13).[75] In the structure of the ternary complex HasA–HasR–heme, the heme is found to be no longer bound to HasA but axially coordinated to two His residues of HasR (H603 and H189, located on the extracellular face of the receptor) (Figure 13). This implies a transfer of the heme over a distance of about 9 Å. In the same complex, a rotation of the His83 side chain is observed that would reduce the Y75 binding ability and therefore could impair sliding back of the heme to the HasA heme-binding site.

While X-ray crystallography provided a clear evidence of the heme transfer and of the reorientation of H83,[75] the loop containing His32 could not be modeled due to missing electron density (residues 29 to 38) possibly due to multiple conformations or disorder. The NMR spectra,[67] instead, allowed detection of

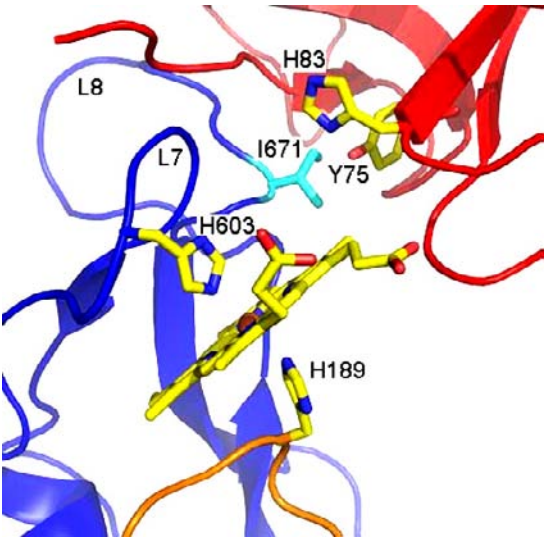

Figure 13. The heme binding site in the X-ray crystal structure of the ternary complex: HasA–HasR–heme. HasA is shown as red ribbon, HasR in blue. Key residues on both proteins are labeled. (Adapted from Ref. 75.)

resonances of this loop, indicating that it has the same arrangement in both complexes and that its conformational features are close to those of the apoprotein. These considerations show the complementarity of the two approaches for the study of complex biomolecular assemblies.

IV. Interaction with Hemoglobin

In *Pseudomonas aeruginosa,* a hemophore named HasAp, which shares 50% identity with *S. marcescens* HasA has been identified.[76] From X-ray crystallography[77] HasAp was found to share with HasA the fold and the axial heme–iron coordination by H32 and Y75. The orientation of the side chain of H83 places its Nδ1 within hydrogen-bond distance from Y75 Oη.

An extensive assignment of the protein backbone NMR resonances was performed with triple resonance experiments on uniformly labeled ^{13}C-, ^{15}N-samples as well as with a number of amino acid selective ^{15}N-enriched samples.[77] The amide backbone identification constituted the starting point for a chemical shift perturbation mapping of the interaction between HasAp and hemoglobin.

In vivo heme internalization through HasR and release of the apo-hemophore requires energy provided by the TonB system.[78,79] *In vitro*, the HasA–HasR interaction gives rise to a stable complex that remains associated even after the heme

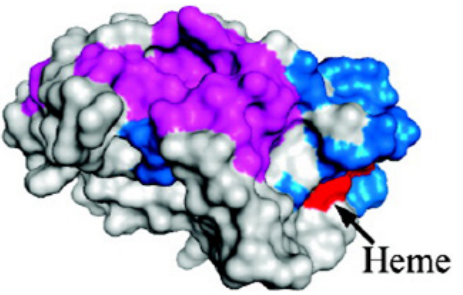

Figure 14. Surface representation of the structure of holo-HasAp where residues whose peaks exhibit chemical shift perturbations upon titration with met-Hb are highlighted in magenta and residues whose resonances disappear upon addition of met-Hb are highlighted in blue. (Adapted from Ref. 77.)

has been transferred from the hemophore to the receptor.[67] This allowed the characterization of the complexes reported in the previous section.

On the contrary, the interaction of apoHasAp and met-Hb gives rise to a rapid transfer of the heme to the hemophore followed by complex dissociation.[77] Therefore, the identification of the possible interaction area between the two partner proteins was studied in a binary system constituted by holoHasAp and met-Hb. Two segregated surface areas on the hemophore have been identified (Figure 14), one where $^{1}H–^{15}N$ connectivities display chemical shift perturbations upon interaction with met-Hb and the other where signals become broadened beyond detection. The former are due to residues mainly located on helix $\alpha 2$ and on the hairpins connecting $\beta 3$ to $\beta 4$ and $\beta 6$ to $\beta 7$. The latter mainly belong to loop L1 and to some portions of loop L2; their behavior has been interpreted in terms of increased conformational dynamics between the open and closed conformations of this loop that gives rise to line broadening beyond detection. A second interpretation of the data is that the loop bearing H32 may represent a second binding area with different affinity for the heme carrier. No attempts to quantify paramagnetic effects of the heme iron(III) in met-Hb on the chemical shifts of the residues of HasAp has been reported. However, it cannot be ruled out as a possible contribution to the observed signal line broadening.

V. Concluding Remarks

In 2000, Bertini and coworkers reviewed the available solution NMR structures of small low-spin heme proteins[80] and showed that the goal of obtaining solution structures for S = 1/2 iron(III) heme proteins as good as those for the diamagnetic iron(II) forms had been reached, mainly thanks to the use of paramagnetism-based

constraints such as pseudocontact shifts[81–84] and residual dipolar couplings.[85,86] During the last decade, structure determination of low-spin ferriheme proteins in solution has become routine.

In the meantime, NMR has gained importance as a structural biology study technique, substantially raising the bar for the size of macromolecules that can be studied. The exploitation of cross-correlated techniques in ^{1}H-detected NMR and the use of ^{13}C-direct detection, in combination with specific sample labeling techniques, represents a very important breakthrough for the detailed analysis of large systems and in particular for large protein–protein assemblies.[62,63,70,87–94] ^{13}C direct detection has also demonstrated its potentiality in reducing the blind zone around paramagnetic centers characterized by $S > 1/2$.[33,34,58,61,95–97]

The present chapter reviews the first application of these strategies to the characterization of the heme uptake: heteronuclear detection experiments proved to be extremely valuable to unravel the first and second coordination sphere effect on the iron electronic structure in HasA[33,34] while cross-correlated ^{1}H–^{15}N NMR provided important structural and mechanistic insights on the protein–protein interactions assisting the heme transfer process.[67]

VI. Acknowledgments

I'm deeply indebted to all the people who have worked with me on HasA characterization: Ivano Bertini and Mario Piccioli at CERM, and Célia Caillet-Saguy, Muriel Delepierre and Anne Lecroisey at Institut Pasteur, who introduced us to the problem and with whom we have established a fruitful and pleasant long-term collaboration.

VII. References

1. Wandersman, C.; Stojiljkovic, I. *Curr. Opin. Microbiol.* **2000**, *3*, 215–220.
2. Braun, V.; Hantke, K. In *Transition Metals in Microbial Metabolism*; Winkelmann G.; Carano C. J., Eds.; Harwood Academic Publishers: Amsterdam, **1997**, pp. 81–116.
3. Stiefel, E. I. In *Biological Inorganic Chemistry*; Bertini, I.; Gray, H. B.; Stiefel, E. I.: Valentine, J. S., Eds.; University Science Books: Sausalito (CA), **2007**, pp. 7–30.
4. Neilands, J. B.; Nakamura, K. In *Handbook of Microbial Iron Chelates*; Winkelmann, G., Ed.; CRC Press: Boca Raton (FL), **1991**, pp. 1–14.
5. Bertini, I.; Sigel, A.; Sigel, H., Eds. *Handbook on Metalloproteins*; Marcel Dekker: New York, **2001**, p. 1.
6. Andrews, S. C.; Robinson, A. K.; Rodriguez-Quiñones, F. *FEMS Microbiol. Rev*. **2003**, *27*, 215–237.
7. Wandersman, C.; Delepelaire, P. *Annu. Rev. Microbiol.* **2004**, *58*, 611–647.
8. Krewulak, K. D.; Vogel, H. J. *Biochim. Biophys. Acta* **2008**, *1778*, 1781–1804.
9. Boukhalfa, H.; Crumbliss, A. L. *Biometals* **2002**, *15*, 325–339.

10. Raymond, K. N.; Denz, E. In *Iron Transport in Bacteria*; Crosa, J. H.; Mey, A. R.; Payne, S. M., Eds.; ASM Press: Washington, **2004**, pp. 3–17.
11. Ferguson, A. D.; Deisenhofer, J. *Cell* **2004**, *116*, 15–24.
12. Zawadzaka, A. M.; Abergel, R. J.; Nichiporuk, R.; Andersen, U. N.; Raymond, K. N. *Biochemistry* **2009**, *48*, 3645–3657.
13. Gray-Owen, S. D.; Schryvers, A. B. *Trends Microbiol.* **1996**, *4*, 185–191.
14. Schryvers, A. B.; Stojiljkovic, I. *Mol. Microbiol.* **1999**, *32*, 1117–1123.
15. Boulton, I. C. G. A. R.; Shergill, J. K.; Joannou, C. L.; Evans, R. W. *J. Theor. Biol.* **1999**, *198*, 497–505.
16. Lewis, L. A.; Dyer, D. W. *J. Bacteriol.* **1995**, *177*, 1299–1306.
17. Lewis, L. A.; Gray, E.; Wang, Y. P.; Roe, B. A.; Dyer, D. W. *Mol. Microbiol.* **1997**, *23*, 737–749.
18. Lewis, L. A.; Gipson, M.; Hartman, K.; Ownbey, T.; Vaughn, J.; Dyer, D. W. *Mol. Microbiol.* **1999**, *32*, 977–989.
19. Cescau, S.; Cwerman, H.; Letoffe, S.; Delepelaire, P.; Wandersman, C.; Biville, F. *Biometals* **2007**, *20*, 603–613.
20. Tong, Y.; Guo, M. *Arch. Biochem. Biophys.* **2009**, *481*, 1–15.
21. Kikuchi, G.; Yoshida, T.; Noguchi, M. *Biochem. Biophys. Res. Commun.* **2005**, *338*, 558–567.
22. Wu, R.; Skaar, E. P.; Zhang, R.; Joachimiak, G.; Gornicki, P.; Schneewind, O.; Joachimiak, A. *J. Biol. Chem.* **2005**, *280*, 2840–2846.
23 Friedman, D. B.; Stauff, D. L.; Pishchany, G.; Whitwell, C. W.; Torres, V. J.; Skaar, E. P. *PLoS. Pathog.* **2006**, *2*, e87.
24. Puri, S.; O'Brian, M. R. *J. Bacteriol.* **2006**, *188*, 6476–6482.
25. Lee, W. C.; Reniere, M. L.; Skaar, E. P.; Murphy, M. E. *J. Biol. Chem.* **2008**, *283*, 30957–30963.
26. Letoffe, S.; Heuck, G.; Delepelaire, P.; Lange, N.; Wandersman, C. *Proc. Natl. Acad. Sci. USA* **2009**, *106*, 11719–11724.
27. Uchida, T.; Stevens, J. M.; Daltrop, O.; Harvat, E. M.; Hong, L.; Ferguson, S. J.; Kitagawa, T. *J. Biol. Chem.* **2004**, *279*, 51981–51988.
28. Nurizzo, D.; Silvestrini, M. C.; Mathieu, M.; Cutruzzola, F.; Bourgeois, D.; Fulop, V.; Hajdu, J.; Brunori, M.; Tegoni, M.; Cambillau, C. *Structure* **1997**, *5*, 1157–1171.
29. Arnoux, P.; Haser, R.; Izadi, N.; Lecroisey, A.; Delepierre, M.; Wandersman, C.; Czjzek, M. *Nat. Struct. Biol.* **1999**, *6*, 516–520.
30. Arnoux, P.; Haser, R.; Izadi-Pruneyre, N.; Lecroisey, A.; Czjzek, M. *Proteins* **2000**, *41*, 202–210.
31. Izadi-Pruneyre, N.; Wolff, N.; Castagne, C.; Czisch, M.; Wandersman, C.; Delepierre, M.; Lecroisey, A. *J. Biomol. NMR* **1999**, *14*, 193–194.
32. Deniau, C.; Couprie, J.; Simenel, C.; Kumar, V.; Stojiljkovic, I.; Wandersman, C.; Delepierre, M.; Lecroisey, A. *J. Biomol. NMR* **2001**, *21*, 189–190.
33. Caillet-Saguy, C.; Delepierre, M.; Lecroisey, A.; Bertini, I.; Piccioli, M.; Turano, P. *J. Am. Chem. Soc.* **2006**, *128*, 150–158.
34. Caillet-Saguy, C.; Turano, P.; Piccioli, M.; Lukat-Rodgers, G.; Czjzek, M.; Guigliarelli, B.; Izadi-Pruneyre, N.; Rodgers, K.; Delepierre, M.; Lecroisey, A. *J. Biol. Chem.* **2008**, *283*, 5960–5970.
35. Bertini, I.; Turano, P.; Vila, A. J. *Chem. Rev.* **1993**, *93*, 2833–2932.
36. Arnesano, F.; Banci, L.; Bertini, I.; Felli, I. C. *Biochemistry* **1998**, *37*, 173–184.
37. Arnesano, F.; Banci, L.; Bertini, I.; Felli, I. C.; Koulougliotis, D. *Eur. J. Biochem.* **1999**, *260*, 347–354.
38. Bax, A.; Summers, M. F. *J. Am. Chem. Soc.* **1986**, *108*, 2093–2094.

39. Wolff, N.; Deniau, C.; Letoffe, S.; Simenel, C.; Kumar, V.; Stojiljkovic, I.; Wandersman, C.; Delfini, M.; Lecroisey, A. *Protein Sci.* **2002**, *11*, 757–765.
40. Van Dijk, A. A.; Scheek, R. M.; Dijkstra, K.; Wolters, G. K.; Robillard, G. T. *Biochemistry* **1992**, *31*, 9063–9072.
41. Pelton, J. G.; Torchia, D. A.; Meadow, N. D.; Roseman, S. *Protein Sci.* **1993**, *2*, 543–558.
42. Bhattacharya, S.; Sukits, S. F.; MacLaughlin, K. L.; Lecomte, J. T. *Biophys. J.* **1997**, *73*, 3230–3240.
43. Wu, J. Z.; La Mar, G. N.; Yu, L. P.; Lee, K. B.; Walker, F. A.; Chiu, M. L.; Sligar, S. G. *Biochemistry* **1991**, *30*, 2156–2165.
44. Qin, J.; La Mar, G. N.; Dou, Y.; Admiraal, S. J.; Ikeda-Saito, M. *J. Biol. Chem.* **1994**, *269*, 1083–1090.
45. La Mar, G. N.; Budd, D. L.; Smith, K. M.; Langry, K. C. *J. Am. Chem. Soc.* **1980**, *102*, 1822–1827.
46. Serber, Z.; Richter, C.; Moskau, D.; Boehlen, J.-M.; Gerfin, T.; Marek, D.; Haeberli, M.; Baselgia, L.; Laukien, F.; Stern, A. S.; Hoch, J. C.; Dötsch, V. *J. Am. Chem. Soc.* **2000**, *122*, 3554–3555.
47. Bertini, I.; Duma, L.; Felli, I. C.; Fey, M.; Luchinat, C.; Pierattelli, R.; Vasos, P. R. *Angew. Chem. Int. Ed.* **2004**, *43*, 2257–2259.
48. Babini, E.; Felli, I. C.; Lelli, M.; Luchinat, C.; Pierattelli, R. *J. Biomol. NMR* **2005**, *33*, 137.
49. Bermel, W.; Bertini, I.; Duma, L.; Emsley, L.; Felli, I. C.; Pierattelli, R.; Vasos, P. R. *Angew. Chem. Int. Ed.* **2005**, *44*, 3089–3092.
50. Bermel, W.; Bertini, I.; Felli, I. C.; Pierattelli, R.; Vasos, P. R. *J. Magn. Reson.* **2005**, *172*, 324–328.
51. Bermel, W.; Bertini, I.; Felli, I. C.; Piccioli, M.; Pierattelli, R. *Progr. NMR Spectrosc.* **2006**, *48*, 25–45.
52. Bermel, W.; Bertini, I.; Felli, I. C.; Kümmerle, R.; Pierattelli, R. *J. Magn. Reson.* **2006**, *178*, 56–64.
53. Bermel, W.; Bertini, I.; Felli, I. C.; Lee, Y.-M.; Luchinat, C.; Pierattelli, R. *J. Am. Chem. Soc.* **2006**, *128*, 3918–3919.
54. Bermel, W.; Felli, I. C.; Kümmerle, R.; Pierattelli, R. *Concepts Magn. Reson.* **2008**, *32A*, 183–200.
55. Felli, I. C.; Brutscher, B. *ChemPhysChem*. **2009**, 10, 1356–1368.
56. Bermel, W.; Bertini, I.; Felli, I. C.; Pierattelli, R. *J. Am. Chem. Soc.* **2009**, *131*, 15339–15345.
57. Felli, I. C.; Glaser, S. J.; Pierattelli, R.; Luy, B. *J. Biomol. NMR* **2009**, *43*, 187–196.
58. Bermel, W.; Bertini, I.; Felli, I. C.; Kümmerle, R.; Pierattelli, R. *J. Am. Chem. Soc.* **2003**, *125*, 16423–16429.
59. Bertini, I.; Felli, I. C.; Kümmerle, R.; Moskau, D.; Pierattelli, R. *J. Am. Chem. Soc.* **2004**, *126*, 464–465.
60. Bertini, I.; Felli, I. C.; Kümmerle, R.; Luchinat, C.; Pierattelli, R. *J. Biomol. NMR* **2004**, *30*, 245–251.
61. Bertini, I.; Felli, I. C.; Luchinat, C.; Parigi, G.; Pierattelli, R. *ChemBioChem.* **2007**, *8*, 1422–1429.
62. Bermel, W.; Felli, I. C.; Matzapetakis, M.; Pierattelli, R.; Theil, E. C.; Turano, P. *J. Magn. Reson.* **2007**, *188*, 301–310.
63. Matzapetakis, M.; Turano, P.; Theil, E. C.; Bertini, I. *J. Biomol. NMR* **2007**, *38*, 237–242.
64. Banci, L.; Bertini, I.; Bren, K. L.; Gray, H. B.; Sompornpisut, P.; Turano, P. *Biochemistry* **1995**, *34*, 11385–11398.

65. Bren, K. L.; Gray, H. B.; Banci, L.; Bertini, I.; Turano, P. *J. Am. Chem. Soc.* **1995**, *117*, 8067–8073.
66. Wolff, N.; Izadi-Pruneyre, N.; Couprie, J.; Habeck, M.; Linge, J.; Rieping, W.; Wandersman, C.; Nilges, M.; Delepierre, M.; Lecroisey, A. *J. Mol. Biol.* **2008**, *376*, 517–525.
67. Caillet-Saguy, C.; Piccioli, M.; Turano, P.; Izadi-Pruneyre, N.; Delepierre, M.; Bertini, I.; Lecroisey, A. *J. Am. Chem. Soc.* **2009**, *131*, 1736–1744.
68. Ghigo, J. M.; Letoffe, S.; Wandersman, C. *J. Bacteriol.* **1997**, *179*, 3572–3579.
69. Fiaux, J.; Bertelsen, E. B.; Horwich, A. L.; Wüthrich, K. *J. Biomol. NMR* **2004**, *29*, 289–297.
70. Riek, R.; Wider, G.; Pervushin, K.; Wüthrich, K. *Proc. Natl. Acad. Sci. USA* **1999**, *96*, 4918–4923.
71. Pervushin, K.; Riek, R.; Wider, G.; Wüthrich, K. *Proc. Natl. Acad. Sci. USA* **1997**, *94*, 12366–12371.
72. Brüschweiler, R.; Ernst, R. R. *J. Chem. Phys.* **1992**, *96*, 1758–1766.
73. Zuiderweg, E. R. *Biochemistry* **2002**, *41*, 1–7.
74. Assfalg, M.; Bertini, I.; Colangiuli, D.; Luchinat, C.; Schaefer, H.; Schuetz, B.; Spraul, M. *Proc. Natl. Acad. Sci. USA* **2008**, *105*, 1420–1424.
75. Krieg, S.; Huché, F.; Diederichs, K.; Izadi-Pruneyre, N.; Lecroisey, A.; Wandersman, C.; Delepelaire, P.; Welte, W. *Proc. Natl. Acad. Sci. USA* **2009**, *106*, 1045–1050.
76. Letoffe, S.; Redeker, V.; Wandersman, C. *Mol. Microbiol.* **1998**, *28*, 1223–1224.
77. Alontaga, A. Y.; Rodriguez, J. C.; Schönbrunn, E.; Becker, A.; Funke, T.; Yukl, E. T.; Hayashi, T.; Stobaugh, J.; Moënne-Loccoz, P.; Rivera, M. *Biochemistry* **2009**, *48*, 96–109.
78. Paquelin, A.; Ghigo, J. M.; Bertin, S.; Wandersman, C. *Mol. Microbiol.* **2001**, *42*, 995–1005.
79. Letoffe, S.; Delepelaire, P.; Wandersman, C. *J. Bacteriol.* **2004**, *186*, 4067–4074.
80. Banci, L.; Bertini, I.; Luchinat, C.; Turano, P. In *The Porphyrin Handbook*; Kadish K. M.; Smith K. M.; Guilard R., Eds.; Academic Press: San Diego, CA, **2000**, pp. 323–350.
81. Capozzi, F.; Cremonini, M. A.; Luchinat, C.; Sola, M. *Magn. Reson. Chem.* **1993**, *31*, S118–S127.
82. Banci, L.; Bertini, I.; Bren, K. L.; Cremonini, M. A.; Gray, H. B.; Luchinat, C.; Turano, P. *J. Biol. Inorg. Chem.* **1996**, *1*, 117–126.
83. Banci, L.; Bertini, I.; Gori Savellini, G.; Romagnoli, A.; Turano, P.; Cremonini, M. A.; Luchinat, C.; Gray, H. B. *Proteins Struct. Funct. Genet.* **1997**, *29*, 68–76.
84. Banci, L.; Bertini, I.; Cremonini, M. A.; Gori Savellini, G.; Luchinat, C.; Wüthrich, K.; Güntert, P. *J. Biomol. NMR* **1998**, *12*, 553–557.
85. Tolman, J. R.; Flanagan, J. M.; Kennedy, M. A.; Prestegard, J. H. *Proc. Natl. Acad. Sci. USA* **1995**, *92*, 9279–9283.
86. Banci, L.; Bertini, I.; Huber, J. G.; Luchinat, C.; Rosato, A. *J. Am. Chem. Soc.* **1998**, *120*, 12903–12909.
87. Riek, R.; Fiaux, J.; Bertelsen, E. B.; Horwich, A. L.; Wuthrich, K. *J. Am. Chem. Soc.* **2002**, *124*, 12144–12153.
88. Salzmann, M.; Wider, G.; Pervushin, K.; Senn, H.; Wüthrich, K. *J. Am. Chem. Soc.* **1999**, *121*, 844–848.
89. Pervushin, K. *Q. Rev. Biophys.* **2000**, *33*, 161–197.
90. Riek, R.; Pervushin, K.; Wüthrich, K. *TIBS* **2000**, *25*, 462–468.
91. Salzmann, M.; Pervushin, K.; Wider, G.; Senn, H.; Wüthrich, K. *J. Am. Chem. Soc.* **2000**, *122*, 7543–7548.
92. Braun, D.; Wüthrich, K.; Wider, G. *J. Magn. Reson.* **2003**, *165*, 89–94.

93. Eletsky, A.; Kienhofer, A.; Pervushin, K. *J. Biomol. NMR* **2001**, *20*, 177–180.
94. Turano, P.; Lalli, D.; Felli, I. C.; Theil, E. C.; Bertini, I. The iron pathway to the central cavity of ferritin. *Proc. Natl. Acad. Sci. USA* **2010**, *107*, 545–550.
95. Babini, E.; Bertini, I.; Capozzi, F.; Felli, I. C.; Lelli, M.; Luchinat, C. *J. Am. Chem. Soc.* **2004**, *126*, 10496–10497.
96. Bertini, I.; Luchinat, C.; Parigi, G.; Pierattelli, R. *ChemBioChem.* **2005**, *6*, 1536–1549.
97. Bertini, I.; Luchinat, C.; Parigi, G.; Pierattelli, R. *Dalton Trans.* **2008**, 3782–3790.

This page intentionally left blank

31 Structure–Function Relationships Among Heme Peroxidases: New Insights from Electronic Absorption, Resonance Raman and Multifrequency Electron Paramagnetic Resonance Spectroscopies

Giulietta Smulevich,* Alessandro Feis,* Barry D. Howes* and Anabella Ivancich†

*Dipartimento di Chimica, Università di Firenze, Via della Lastruccia 3, I-50019 Sesto Fiorentino (FI), Italy

†Centre Nationale de la Recherche Scientifique (URA 2096) and CEA-Saclay, iBiTec-S, Laboratoire de Hyperfréquences, Métalloprotéines et Systèmes de Spin, F-91191 Gif-sur-Yvette, France

I. General Introduction

The principal objective of this chapter is to provide an overview of our current understanding of the structure and function of heme-containing peroxidases which belong to the plant and animal peroxidase superfamilies, with an emphasis on recent insights obtained from UV-vis electronic absorption and resonance Raman (RR) studies. In order to highlight the enzymatic mechanism of peroxidases, recent findings from multifrequency electron paramagnetic resonance (EPR) spectroscopy are also discussed. The relatively recently discovered family of bifunctional peroxidases, which are encoded by the *katG* gene in different bacteria, archebacteria and fungi, and which are phylogenetically related to heme peroxidases but are structurally and functionally more complex than the latter, are included.

In general, peroxidases include a very large group of enzymes (with or without heme) that reduce peroxide and oxidize a wide variety of substrates. In particular, heme-containing peroxidases, which almost invariably have the Fe-protoporphyrin IX chromophore (see below), use hydrogen peroxide as the

electron acceptor to catalyze a number of oxidative reactions using various substrates as donors, which are converted into radicals. Peroxidases typically catalyze a reaction of the form

$$\text{ROOR}' + \text{electron donor } (2e^-) + 2H^+ \rightarrow \text{ROH} + \text{R}'\text{OH}$$

Heme peroxidases are found in bacteria, fungi, plants and animals. On the basis of sequence similarity, they can be divided into two superfamilies: one found in bacteria, fungi and plants, and the other in animals.

Plant, fungal and bacterial peroxidases constitute a superfamily which has been divided into three classes, based on sequence alignment and biological origin.[1,2] Animal peroxidases make up a group of homologous proteins which constitute a separate peroxidase superfamily[3] characterized by a markedly different amino acid sequence, overall structure and prosthetic group properties compared to plant, fungal or bacterial peroxidases. Animal peroxidases evolved independently from the plant, fungal and bacterial superfamily and most likely belong to a different gene family. Recently, evolutionary relationships among animal heme peroxidases have been proposed after advanced phylogenetic analysis.[4]

In addition to these two families, a new category of peroxidases has recently been identified, known as the dye-decolorizing peroxidase-type (DyP-type) peroxidase family.[5] Eighty putative members of this family have been included in databases such as PeroxiBase (http://peroxibase.isb-sib.ch) and Pfam.[6] They are not considered members of the plant or animal peroxidase superfamily because of their specific primary and tertiary structures and unique reaction characteristics. Although the characterization of the function and structure of these proteins is still in the early stages, they appear to be bifunctional enzymes with hydrolase or oxygenase activities, in addition to the typical peroxidase activity. A review focusing on the DyP-type peroxidase family has just been published.[7] Furthermore, chloroperoxidase (CPO) and *Pseudomonas aeruginosa* cytochrome c peroxidase do not belong to the two peroxidase superfamilies mentioned above. They are dimeric proteins and each monomer is divided into two domains, both containing a covalently bound *c*-type cytochrome and a Ca^{2+} ion bound between the two domains.[8,9] CPO from *Caldariomyces fumago*[10] differs from plant peroxidases mainly in that the proximal ligand is not a histidine residue but a cysteine thiolate, in common with the cytochrome P450 enzyme. It is also characterized by an unusual distal heme pocket.[11,12] Although its biological role is the chlorination of organic substrates, it also shows peroxidase-, catalase- and p450-type reactions.[13] *P. aeruginosa* cytochrome c peroxidase[8] belongs to the bacterial peroxidases responsible for catalyzing the two-electron reduction of hydrogen peroxide to water, a key function within the cellular detoxification pathway of reactive oxygen

species in microbes.[14] The abovementioned structural differences, particularly with regard to the heme pocket of CPO and *P. aeruginosa* cytochrome *c* peroxidase, have led to their classification as a different family. Hence, they will not be discussed in this chapter.

The availability of three-dimensional structural data for members of the peroxidase superfamilies has increased dramatically in recent years. The new crystal structure data combined with site-directed mutagenesis has allowed the roles of many of the catalytic residues conserved across the three classes of the plant peroxidase superfamily, as well as in the animal superfamily, to be well understood.

A. Resonance Raman Spectroscopy

Spectroscopic techniques have been fundamental to the comprehension of peroxidase function under physiological conditions.[15] In particular, resonance Raman (RR) spectroscopy, which has been widely applied to the study of heme proteins,[16] has made a significant contribution to the understanding of the molecular interactions at the peroxidase active sites. The extreme sensitivity of RR spectroscopy to alterations in the surroundings of the heme, in combination with site-directed mutagenesis and X-ray structural data, has given insight into the influence exerted on protein architecture in the vicinity of the active site by key amino acids and furnished critical information on protein flexibility, functionality and stability.[17,18] Moreover, in recent years, the extensive developments of Raman microscopy have opened up interesting new perspectives. This technique, consisting of an optical microscope coupled to a Raman spectrometer, allows one to collect Raman signals from small regions of a crystal. A schematic view of the experimental setup for Raman microscopy is shown in Figure 1.[19] The comparison of detailed Raman spectra for peroxidases in crystal and solution forms has offered a means of bridging crystallographic and solution studies, providing a powerful synergy with X-ray-crystallographic analysis.

B. Multifrequency Electron Paramagnetic Resonance Spectroscopy

Electron paramagnetic resonance (EPR) is a spectroscopical technique based on the response of paramagnetic molecules (those having unpaired electrons) to an applied external magnetic field. Transition metal ions and organic radicals are naturally occurring paramagnetic molecules, which have crucial roles in catalytic reactions and related electron transfer processes in metalloproteins.[20] Accordingly, EPR spectroscopy has been extensively used to obtain structural and functional information of active sites in metalloproteins.[20] In the case of heme peroxidases, important information on the spin state and coordination number can be obtained from the EPR spectrum of the heme active sites of the resting enzymes.[21]

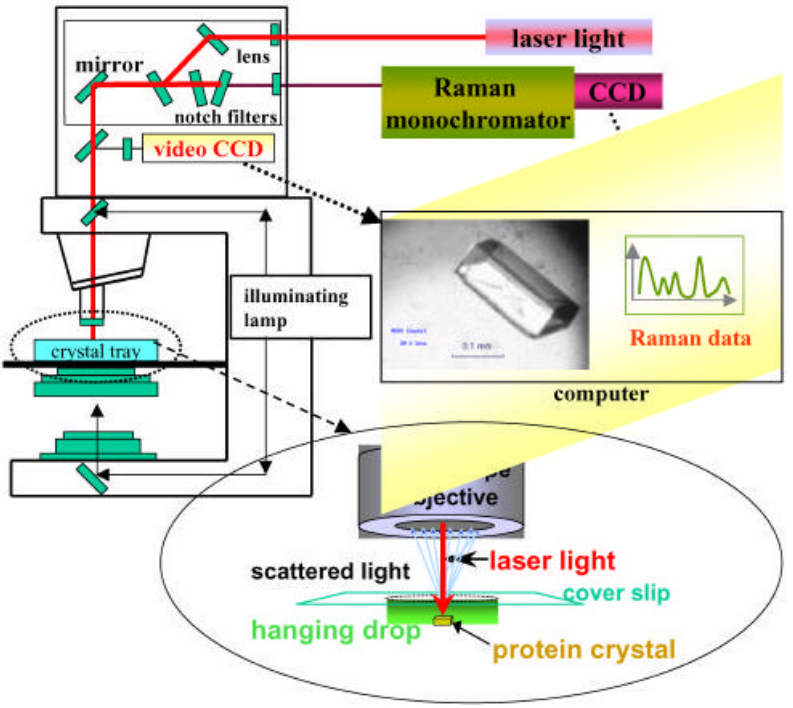

Figure 1. Raman microscope coupled to a laser and spectrometer**.** Crystals are placed with a small amount of mother liquor in a hanging drop under a cover glass, or mounted with a small amount of mother liquor in a capillary tube which is then sealed. The crystal can be viewed via a long focal length objective and a video of a charge-coupled device (CCD) camera for optical imaging. The same objective is used for both the sample excitation and the collection of the back-scattered radiation. The beam focused on the crystal can be viewed on the computer monitor. A magnified view of a protein crystal as observed under the microscope objective is also shown. (Reprinted with permission from Carey, P. R.; Dong, J. *Biochemistry* **2004**, *43*, 8885–8893. © 2004, American Chemical Society.)

Moreover, the intermediates formed during the catalytic cycle of peroxidases, and resulting from changes in the oxidation state of the heme iron and formation of radical species, can be monitored by EPR spectroscopy.[22–24] EPR spectrometers employing continuous wave irradiation at standard frequencies (9 GHz, the so-called X-band) have been widely used for the characterization of the environment of the heme site in peroxidases (reviewed in Ref. 15), since the EPR spectrum obtained from samples in frozen solutions is very sensitive to geometry changes induced by varying the pH (see for example Ref. 25) and/or by the effect of site-directed mutations affecting directly or indirectly the proximal and distal heme sides (see for example Ref. 26). The information obtained from the 9 GHz EPR spectrum is limited, in particular for unequivocal determination of the chemical

nature and magnetic interactions of organic radical intermediates with the heme iron (a good example is given in Ref. 27). The development of EPR spectrometers that use higher microwave frequencies (ranging from 95 to 360 GHz) and the related higher magnetic fields (up to 14 T), as well as the development of the theoretical and experimental aspects related to their application to characterize cofactors in metalloproteins,[28,29] constitute a crucial advancement in the understanding of the putative role of protein-based radicals formed as alternative catalytic intermediates in peroxidases.[30,31] Accordingly, it is only recently that substantial evidence from multifrequency EPR spectroscopy has challenged the view of the heme moiety as the unique site for reaction with substrates via higher valence intermediates, in particular the [Fe(IV)=O $Por^{\bullet+}$] species. As will be discussed in this chapter (see Sections II.F.3 and III.D.2), both peroxidases and catalase–peroxidases can stabilize [Fe(IV)=O $Trp^{\bullet}$] or [Fe(IV)=O $Tyr^{\bullet}$] species with well-defined radical sites that are formed subsequently to the [Fe(IV)=O $Por^{\bullet+}$] intermediate by intramolecular electron transfer. Such radical species can play the role of alternative reactive intermediates in the oxidation of specific substrates.

II. Superfamily of Plant, Fungal and Bacterial Peroxidases

The superfamily of plant, fungal and bacterial peroxidases is divided into three classes of structurally related peroxidases[1] and comprises proteins which are present in a wide variety of living organisms. Comprehensive analyses of the origins of the nonanimal peroxidase superfamily have recently been reported.[32,33] Plants contain two groups of heme peroxidases: intracellular peroxidases of prokaryotic origin (class I) and classical or secretory plant peroxidases (class III). Class I includes cytochrome c peroxidase (CCP), ascorbate peroxidase (APX) and catalase–peroxidases (KatGs), which have recently raised considerable interest. In fact, despite their striking sequence homologies to the members of class I of the plant peroxidase superfamily, they exhibit peroxidase and substantial catalase activities similar to those of monofunctional catalases.

Horseradish peroxidase isoenzyme C (HRPC) is the most extensively studied prototype of class III, but in the last decade many other members of this class have been studied, including horseradish isoenzyme A (HRPA2), barley (BP1), soybean (SBP), peanut (PNP) and *Arabidopsis thaliana* (ATP). In particular, the entire peroxidase gene family of the plant *Arabidopsis thaliana* has recently been fully described.[34,35] The 73 class III peroxidase genes in *Arabidopsis thaliana*, encoding what are predicted to be 71 stable enzymes folded similarly to HRP C, were used for surveying the evolutionary relationships among peroxidases in the plant kingdom.[35]

The remaining group of peroxidases in the plant peroxidase superfamily are of fungal origin (class II) and include well-characterized examples such as *Coprinus cinereus* peroxidase (CIP), *Coprinus macrorhizus* peroxidase (CMP), *Arthromyces ramosus* peroxidase (ARP) and the lignin (LIP) and manganese peroxidases from white-rot fungi (MNP). Since CIP and ARP peroxidases are identical in both their covalent structure and enzymatic properties,[36] we will refer to these peroxidases by the name ARP/CIP, unless differently stated.

Plant peroxidases are involved in a wide range of biological functions, such as defence against stress (class I), metabolism of lignin (classes II and III), developmental processes and defence against environmental changes (class III).[37]

A. Heme Pocket

After the first three-dimensional structure of yeast cytochrome *c* peroxidase (CCP), solved more than two decades ago,[38] in the last 20 years many other three-dimensional structures of native peroxidases with and without substrates have been determined by X-ray crystallography. Seven of these structures have been extensively discussed by Poulos in a chapter devoted to peroxidases in the previous handbook of porphyrins,[13] namely CCP,[38] lignin peroxidase (LIP),[39–41] ARP/CIP,[42,43] manganese peroxidase (MNP),[44] APX,[45] peanut peroxidase (PNP),[46] HRPC[47] and barley peroxidase (BP1).[48] Recently, other structures of native proteins have been obtained, namely those of *Arabidopsis thaliana* A2 (ATPA2)[49,50] and N (ATPN),[51] soybean peroxidase (SBP),[52] and catalase–peroxidase from different origins.[53–57] At present, more than 300 structures can be found in the Protein Data Bank (http://www.rcsb.org/pdb/home/home.do), including native, recombinant, mutated proteins and their complexes with substrates and small ligands.

The X-ray structures clearly show that the overall helix-rich protein fold is conserved. Moreover, although the three classes show less than 20% amino acid sequence identity, all peroxidases contain invariant amino acids in the heme cavity important for catalytic activity, as predicted on the basis of the amino acid alignment.[1] As shown in Figure 2, these conserved residues (distal His, Arg, Asn and proximal His, Asp) are connected by an extended hydrogen-bond network through various water molecules. In particular, on the proximal side of the heme the axial His ligand of the heme iron is hydrogen-bonded to a buried carboxylate group of an Asp residue. Moreover, the catalytic His residue on the distal side is hydrogen-bonded to an Asn residue.

The role played by the key amino acids has been studied by kinetic methods and spectroscopic techniques in a number of peroxidases. Moreover, the application of site-directed mutagenesis to these proteins provided important insight into heme pocket interactions.

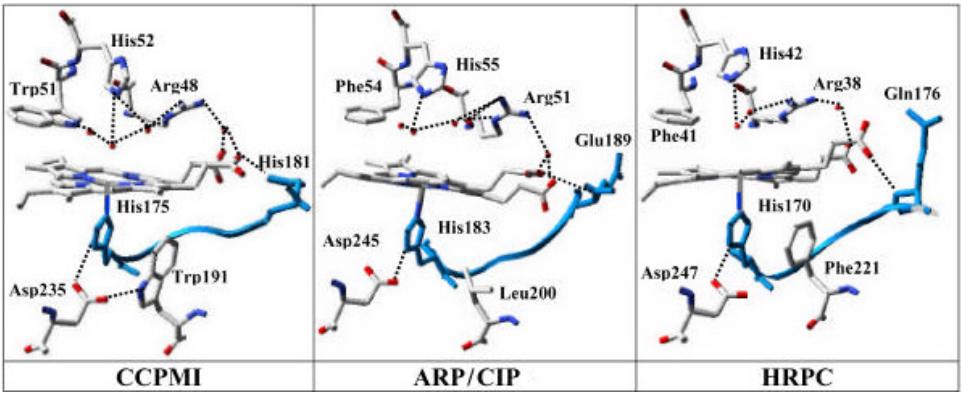

Figure 2. Structural diagram of the heme pocket of recombinant CCP (CCPMI) (PDB 1CCP), ARP/CIP (1GZB) and HRPC (1ATJ). Dotted lines indicate H-bonds. Water molecules are also shown. The loop connecting the proximal Fe-ligand with the residue H-bonded to the heme propionyl is shown in blue. (Reprinted with permission from Smulevich, G.; Feis, A.; Howes, B. D. *Acc. Chem. Res.* **2005**, *38*, 433. © 2005, American Chemical Society.)

The combination of X-ray crystallography and the extensive resonance Raman studies on wild-type (WT) proteins and various site-directed mutants representative of the three classes of the plant superfamily, namely cytochrome *c* peroxidase (class I),[17,58–62] ARP/CIP (class II)[63–66] and HRPC (class III),[18,63.67–69] has allowed the identification of many common characteristics of these enzymes.

1. *Fe(III) Resting State*

In the Fe(III) resting state, the heme iron sixth coordination site is vacant (pentacoordinate, 5c) or bound weakly to water (hexacoordinate, 6c), emphasizing that one coordination site must be free to enable peroxides or other ligands to bind and react with the protein.[17] However, while the resting state of the proteins belonging to either class I or II is mainly 5c high-spin (5cHS), a distinctive characteristic of the class III peroxidases is a pentacoordinate quantum-mechanically mixed-spin (5cQS) state. The QS state reflects a quantum-mechanical admixture of intermediate ($S = 3/2$) and high ($S = 5/2$) spin states, and is very unusual in biological systems. Among the various class III peroxidases so far studied, the proportion of the $S = 3/2$ state increases in the order HRPC < HRPA2 < SBP < BP1.[70–73] Figure 3 compares the high-frequency region resonance Raman spectra of the Fe(III) forms of different representatives of peroxidases belonging to class III. The progressive increase in frequency of the core size marker bands on passing from wt HRP to the F221M HRP mutant reflects an increasing proportion of the intermediate spin species in the QS state.

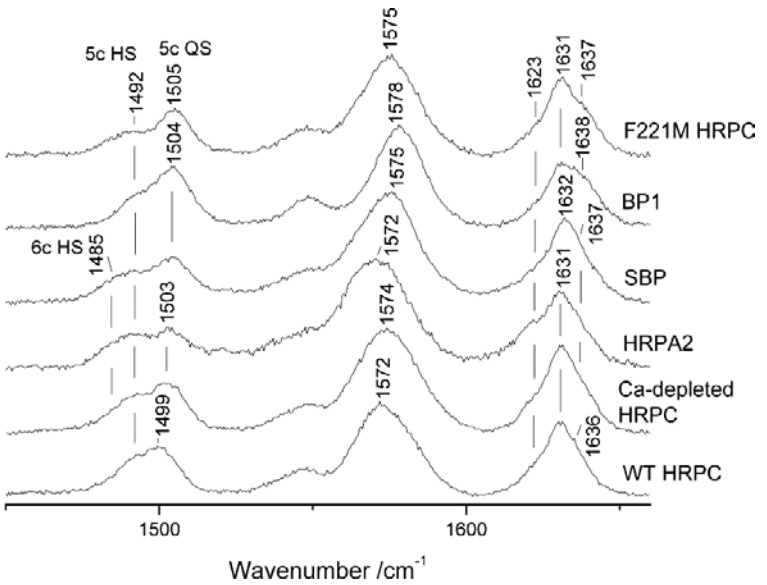

Figure 3. High-frequency region resonance Raman spectra of the Fe(III) forms of different representatives of peroxidases belonging to class III: WT HRPC, soybean peroxidase (SBP), the F221M mutant of HRPC (pH 7.0), HRPA2 (pH 7.3), Ca-depleted HRPC (pH 7.8), barley peroxidase (BP1) (pH 6.5). Excitation wavelength 406.7 nm (WT HRPC, Ca-depleted HRPC, HRPA2, SBP, F221M HRPC) and 413.1 nm (BP1). 5cHS and 6cHS indicate the bands ν_3 due to five- and six-coordinate high spin, respectively, and 5cQS indicates the band from the quantum-mechanically mixed-spin state.

The spectroscopic characteristics of the QS spin state (for both penta- and hexacoordination) have been reviewed previously.[18,74] The 5cQS state is characterized (Figure 4, *left*) by a blue-shifted UV-vis absorption spectrum compared to those of a 5cHS heme, higher frequency of the RR core-size marker bands, which cannot be assigned to either 5cHS or hexacoordinate high-spin (6cHS) hemes but closely resemble those characteristic of hexacoordinate low-spin (6cLS) hemes, and EPR spectra with g_{12} values in the range $4 < g_{12} < 6$, typical only of a QS heme.

The binding of benzohydroxamic acid (BHA) to class II and III peroxidases induces the formation of a 6c state (see below), which in class III peroxidases has been assigned to a quantum-mechanically mixed-spin (6cQS) heme (Figure 4, *right*). The latter is characterized by absorption spectra in which the Soret band sharpens with about a 35% increase of the extinction coefficient and red-shifts about 4 nm with respect to those of a 5cQS state, similar to those of a 6cHS heme, RR core-size marker band frequencies which resemble those of a 5cHS system, and EPR spectra with g_{12} values in the range $4 < g_{12} < 6$.

The structural origin and functional significance of the QS states remain elusive. The most widely suggested origins, a weak axial ligand field[75] or a saddle-shaped

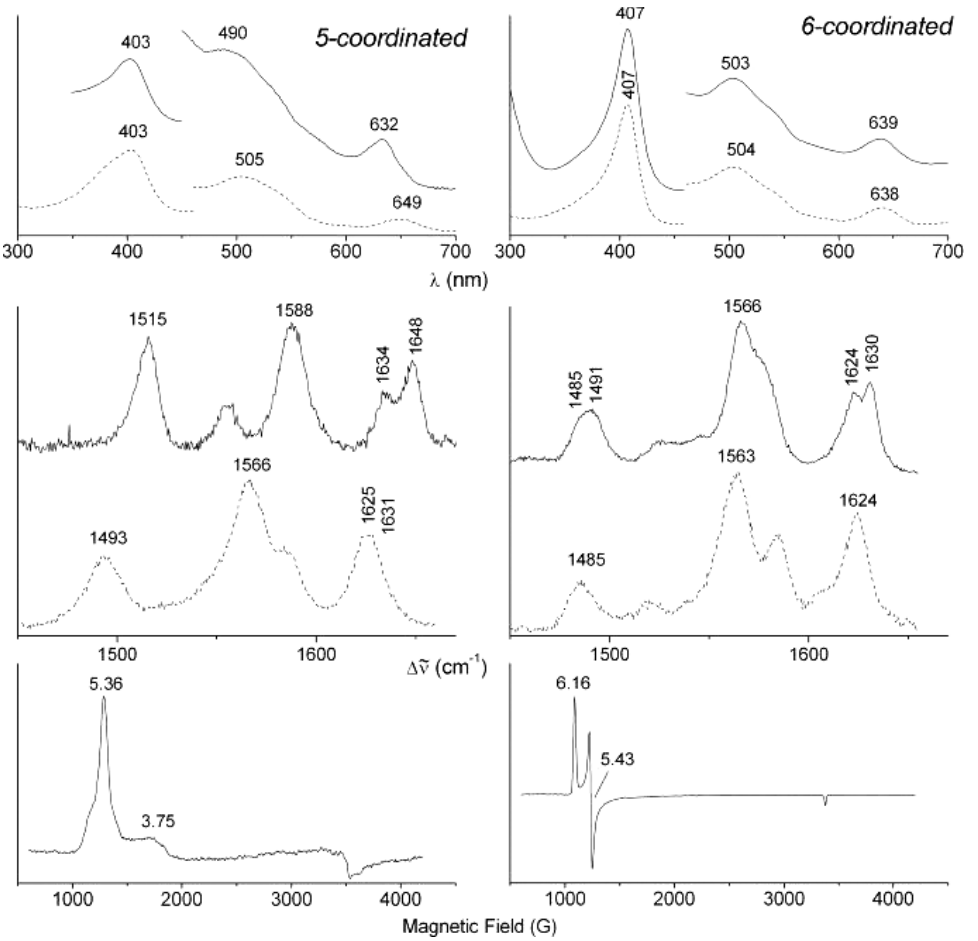

Figure 4. From top to bottom. Absorption, RR and EPR spectra at 10 K (solid line) and room temperature (RT) (dashed line). (Left) barley peroxidase (BP1) at 10 K (5cQS) and ARP/CIP at RT (5cHS); (right) HRPC–BHA at 10 K (6cQS) and CIP/ARP–BHA at RT (6cHS). (Reprinted with permission from Smulevich, G.; Feis, A.; Howes, B. D. *Acc. Chem. Res.* **2005**, *38*, 433. © 2005 American Chemical Society.)

heme deformation,[76] are not sufficient to cause the QS states. However, an analysis of the heme conformation by the normal-coordinate structural decomposition (NSD) method of all the X-ray crystal structures of peroxidases contained in the Protein Data Bank[77] revealed that the peroxidases exhibit a conserved out-of-plane distortion equal to, or larger than, that of the cytochromes. The heme of cytochrome is highly distorted by covalent attachments at the heme periphery. Moreover, the mainly saddled deformation of the peroxidase heme is observed for all of the peroxidase X-ray structures. In addition, contributions from other deformation types

were found, namely ruffling (varying from 0.6 to 0.2 Å) and other small deformation components (doming, waving[53]) usually with a negative sign.[73]

Recently, the out-of-plane modes of horseradish peroxidase (HRP) in different spin, oxidation and ligation states have been measured by RR spectra with (near) Soret excitation.[78] The nonplanar modes of the heme are Raman-inactive for planar macrocycles, but become RR-active in the presence of out-of-plane deformations. A variety of out-of-plane modes such as γ_5, γ_6, γ_7 (A_{2u}), γ_{21} and γ_{22} (E_g), γ_{15} (B_{2u}) and γ_{11} (B_{1u}) have been observed in the Fe(III) 5cHS, QS and 6cLS states as well as in the 5cHS Fe(II) form. The appearance of these bands is clearly indicative of nonplanar deformations. In addition, in the Fe(III) hydroxo-6cLS state observed at alkaline pH,[79] a substantial reduction of the ruffling distortion was found, whereas the doming deformation remained largely unaffected by the change of the iron spin and ligation state.

The spectroscopic characterization of peroxidases has mainly been performed on the proteins in solution. The importance of applying Raman spectroscopy to biomolecular crystals was recognized in the 1970s.[80,81] In the 1980s and 1990s, new technologies permitted the development of Raman microscopy, where an optical microscope is coupled to a Raman spectrometer to collect Raman signals from sample regions as small as a few micrometers. A review of the application of Raman microscopy to proteins has recently been published.[82,83] Pioneering applications of Raman microscopy in cell biology have also been reported.[84,85] More recently a number of nonresonant, resonant or polarized Raman studies have been reported on heme proteins.[60,86–88] In the last 20 years, single-crystal microresonance Raman spectra on heme-containing peroxidases have been obtained on CCP[89] and some of its site-directed mutants,[90] HRP-C,[91] SBP,[52] ATPA2[50] and ARP/CIP.[74,91] Comparison between the spectroscopic data of the protein in solution and crystal forms not only showed that the coordination could be different from that determined by X-ray crystallography, but also revealed the presence of artefacts induced either by the temperature used to acquire the data (see below) or by the chemicals used for crystallization. In fact, the difficulties which are sometimes encountered in crystallizing proteins are often overcome by the addition of salts or hydrophilic compounds to the crystallizing medium that help the crystallization process. However, the chemicals can modify the active site of the protein, since the structural balance that determines the coordination state in a heme protein can be very delicate. In the first application of micro-Raman to peroxidases it was found that, unlike WT CCP, the Trp51Phe CCP mutant showed a dominant 5-c heme population in the single crystal[90,92] whereas in solution the 6-c form was dominant.[58] The different coordination state was mimicked by adding 2-methyl-2,4-pentanediol (MPD) to the solution and was attributed to the dehydrating effect of MPD, which is present during crystallization.[90]

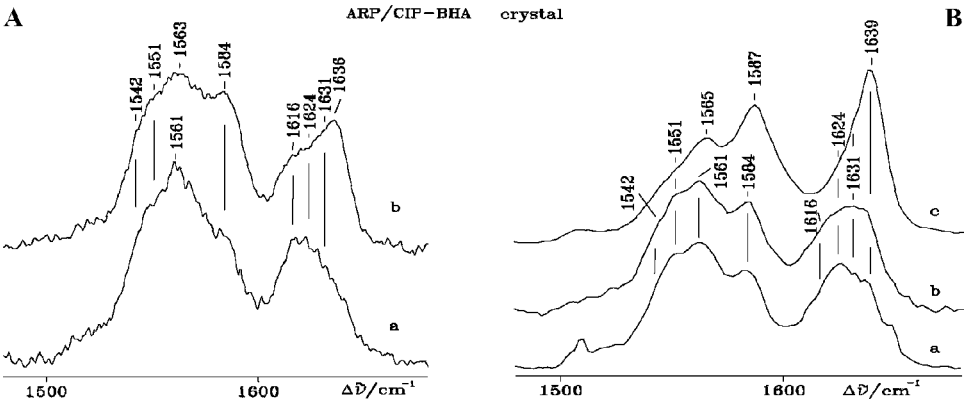

Figure 5. (A) RR spectra of ARP/CIP–BHA as a single crystal soaked in (a) Na_2SO_4 and in (b) $(NH_4)_2SO_4$. (B) RR spectra of ARP/CIP–BHA soaked in $(NH_4)_2SO_4$ taken at different laser power on the crystal surface: (a) 100 μW; (b) 180 μW; (c) 550 μW. (Reprinted with permission from Indiani, C.; Santoni, E.; Becucci, M.; Boffi, A.; Fukuyama, K.; Smulevich, G. *Biochemistry* **2003**, *42*, 14066–14074. ©2003, American Chemical Society.)

Figure 5 shows the RR spectra[93] of ARP/CIP-BHA for 514.5 nm excitation as a single crystal (a) obtained from a soaking solution containing Na_2SO_4 and (b) obtained from a soaking solution containing $(NH_4)_2SO_4$. Although the same experimental conditions were applied, it is evident that the presence of $(NH_4)_2SO_4$ induces the formation of a 6cLS heme, as judged by the intensity increase of the bands at 1584 cm^{-1} (ν_{19}) and at 1636 cm^{-1} (ν_{10}). These findings clearly indicate that the characteristics of the protein crystal depend critically on its preparation and suggest that the micro-Raman technique may offer a sensitive tool for the screening of sample preparation.

The laser power at the sample might also be a factor inducing artefacts. In this particular case, the amount of the 6cLS heme depends on the laser power at the sample surface during the RR experiment. For single crystals of ARP/CIP-BHA soaked in $(NH_4)_2SO_4$, the higher the laser power, the greater the intensity of the bands characteristic of the 6cLS (Figure 5B). A laser power of 550 μW on the crystal gave rise to an almost pure 6cLS heme with core size marker bands at 1551 cm^{-1} (ν_{38}), 1565 cm^{-1} (ν_{11}), 1587 cm^{-1} (ν_{19}), and 1639 cm^{-1} (ν_{10}) (Figure 5B, spectrum c).

Finally, the combined analysis of solution and single-crystal data allows one to obtain also critical information on protein flexibility and the existence of possible alternative conformations, as in the case of recombinant *Arabidopsis* peroxidase, ATPA2.[50] Figure 6 compares the RR spectra of ATP A2 crystals obtained at room temperature with those of the protein solution at different pH values. Different ATPA2 crystals from the same batch of crystals exhibited two slightly different RR spectra. Crystal I (Figure 6c) was identical to the ATP A2 in solution at pH 7.5

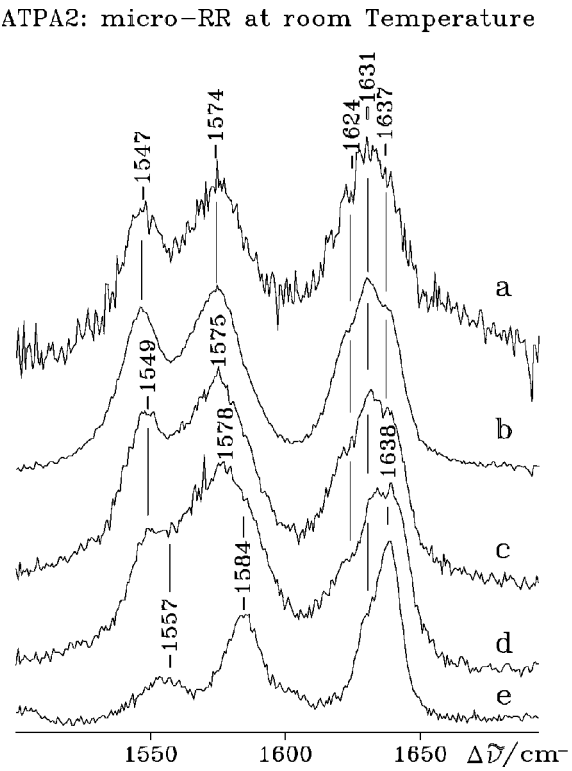

Figure 6. Micro-RR spectra of ATPA2 crystals. (a) ATPA2 dissolved in the crystallization medium at pH 6.6; (b) ATP A2 in bicine buffer at pH 7.5; (c) ATPA2 crystal form I; (d) ATPA2 crystal form II, (e) ATP A2 in glycine buffer at pH 10.6. Experimental conditions: 514.5 nm excitation, 5 cm^{-1} resolution, and 50 μW and 2.1 mW laser power in crystal and solution samples, respectively. The laser beam was moved to a new surface spot of the crystal every 60 s, and the spectra were added to give the total accumulation time. (Reprinted with permission from Nielsen, K. L.; Indiani, C.; Henriksen, A.; Feis, A.; Becucci, M.; Gajhede, M.; Smulevich, G.; Welinder, K. G. *Biochemistry* **2001**, *40*, 11013–11021. © 2001, American Chemical Society.)

(Figure 6b). Crystal II (Figure 6d) exhibited additional weak bands compared to crystal I at 1557 (ν_{11}), 1584 (ν_{19}) and 1638 (ν_{10}) cm^{-1}. They were due to the presence of a small amount of 6cLS heme, as judged by comparison with the spectrum of ATPA2 at pH 10.5 (Figure 6e), which is a pure 6cLS form. The differences observed between crystals I and II were not induced by the crystallization medium, since the spectrum of ATPA2 dissolved in the medium (Figure 6a) gave rise to a spectrum almost identical to that in bicine at pH 7.5. Moreover, the presence of an artefact due to the laser-induced heating of the crystal could be ruled out since no damage was detected on the surface of the crystals after irradiation with the very low power applied, and no spectral changes were observed during the exposure time. The experimental conditions giving rise to the slightly

different crystal spectra are not clear, but crystal II demonstrates that it is possible to induce the formation of a 6cLS heme in ATPA2 even at room temperature, confirming the presence of a flexible distal side.

2. *Extended Network of H-Bonds*

Peroxidases are characterized by the presence of an extended network of H-bonds coupling the distal and proximal sides of the heme, constituted on the distal side by water molecules H-bonded to His and Arg, the heme propionate and the proximal His ligated to the heme iron (Figure 2). As a consequence of the high polarity of the distal cavity and the extended H-bond network involving water molecules and conserved distal and proximal amino acids, the coordination state of peroxidases can be dramatically affected by chemical conditions. The distal arginine and histidine residues have been extensively mutated in the various peroxidases. Resonance Raman spectroscopy clearly indicated that the mutation modifies the heme coordination and perturbs the proximal Fe–imidazole (Fe–Im) bond strength, as a consequence of charge distribution, size, and H-bonding acceptor/donor properties of the substituting amino acid.[18] Therefore, the H-bond network preserves the protein function and keeps intact the coupling between the proximal and distal residues.

Interestingly, the coordination and spin states of the heme in peroxidases are also markedly sensitive to changes of temperature. The importance of low-temperature experiments on proteins is often underestimated, since very low temperatures and the frozen state are nonphysiological and, therefore, are considered to give little useful insight into structure–function relationships. However, from a spectroscopic point of view, low-temperature experiments give rise to narrower spectral bands, allowing one to separate bands which would overlap at room temperature. Moreover, some techniques, such as EPR spectroscopy, must be applied at liquid nitrogen or helium temperatures due to the magnetic relaxation properties of the heme iron. One of the main disadvantages of low-temperature measurements on hemoproteins and, in particular, peroxidases, is their sensitivity to temperature-dependent conformational changes, which may alter the spin and coordination states of the heme iron. The temperature effect on the heme iron has become an important issue over the last decade, with the increased use of synchrotron radiation as an X-ray source, many protein structures have also been solved at liquid nitrogen temperature. In fact, macromolecular crystals commonly suffer rapid radiation damage during room temperature X-ray data collection, and most macromolecular crystal diffraction data are now collected at or near 100 K. The benefits of cryocrystallography include reduced secondary radiation damage and, usually, higher-resolution and better-quality data.[94] Therefore, if the maximum

advantage is to be gained from the comparison of results obtained by various techniques in different temperature ranges, it is important to establish whether any reversible or irreversible changes have been caused by the variation in temperature. Many RR and electronic absorption data have proven that a significant number of peroxidases undergo a temperature-induced transition from a 5c- to a 6cLS heme. Moreover, conformational changes in the heme cavity, including a contraction of the heme core, reorientation of the vinyl group in position 2 of the porphyrin macrocycle, and binding of the distal His to the Fe atom, often occur.[73,95–98] The recent study of plant anionic horseradish peroxidase HRPA2 and the orthologous *Arabidopsis* peroxidase ATPA2, produced recombinantly in *E. coli*, provides an example of how spectroscopy, crystallography and enzyme kinetics can complement each other.[50] It was shown that the location of a water molecule, which might be important for reactivity, could be different at low temperatures and, therefore, not representative of the active state of the protein under physiological conditions. While the crystal structure of ATPA2 at 1.45 Å resolution at 100 K showed a water molecule at 2.1 Å from the heme iron,[49] a distance which could impede activity since the water molecule is expected to be ligated to the heme iron, the X-ray-crystallographic and single-crystal/solution resonance Raman studies at room temperature confirmed that the sixth coordination position of the ATPA2 heme iron is essentially vacant,[50,71] showing a 5c heme iron. In fact, the UV-vis (Figure 7A) and RR (Figure 7B) spectra at room temperature of ATPA2 and HRPA2 are identical and characteristic of a mixture of three species: 5cHS, 6cHS and 5cQS. This last species is predominant at room temperature, as in many other class III peroxidases. Hence, ATPA2 and HRPA2 have the same coordination previously described for other class III plant peroxidases.

When the temperature is lowered at neutral pH, the UV-vis spectra of ATPA2 (Figure 7C)[50] and HRPA2[98] undergo major changes and exhibit isosbestic points at 590, 514 and 465 nm. The spectra are consistent with the presence of two types of 6cLS hemes — a bis-histidyl type and a hydroxyl type — coexisting with the 5cQS species. All the forms are characterized by high RR frequencies, indicating a contraction of the heme core at low temperatures. The changes were reversible and much more pronounced than those seen for SBP,[97] HRPC[95] and BP1,[73] indicating that the A2 type peroxidases have an unusually flexible heme cavity, possibly of importance for the catalytic process.

3. *Vinyl–Protein Interaction*

The heme prosthetic group of peroxidases has two vinyl substituents in positions 2 and 4 (Figure 8) which are conjugated to the porphyrin macrocycle to a different extent, depending on the protein in question. As a consequence, the absorption

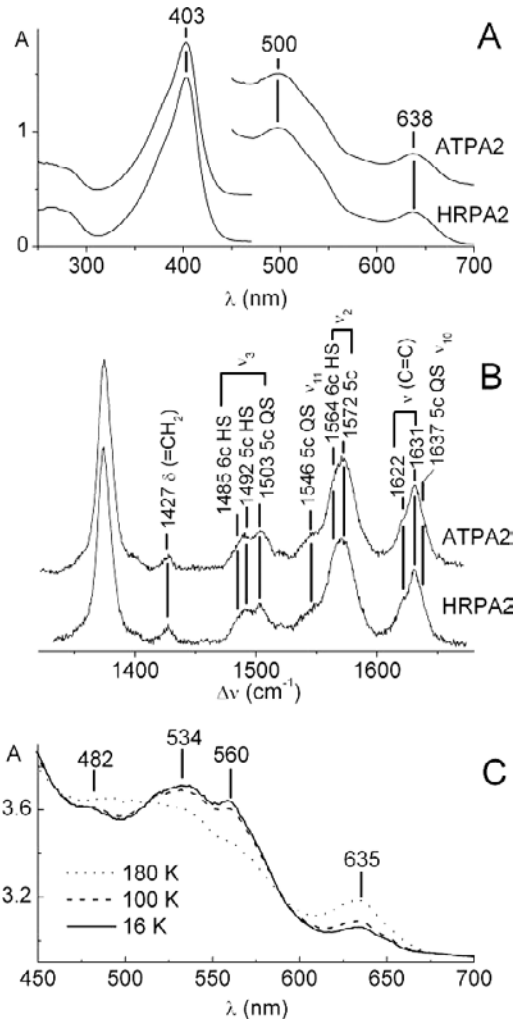

Figure 7. (A) Electronic absorption spectra of Fe(III) ATPA2 and HRPA2, at pH 7.5, in bicine buffer at room temperature. The region between 450 and 700 nm has been expanded eight fold. (B) Corresponding RR spectra obtained with Soret excitation (406.7 nm excitation). (C) Electronic absorption spectra of Fe(III) ATPA2, at pH 7.5, in bicine buffer at 180, 100 and 16 K. (Reprinted with permission from Nielsen, K. L.; Indiani, C.; Henriksen, A.; Feis, A.; Becucci, M.; Gajhede, M.; Smulevich, G.; Welinder, K. G. *Biochemistry* **2001**, *40,* 11013–11021. © 2001 American Chemical Society.)

maxima of the Fe-protoporphyrin IX prosthetic group are related not only to the coordination/spin state of the heme but also to the degree of conjugation between the heme group and its two vinyl substituents.[18,99] Therefore, the electronic coupling between the vinyl groups and the porphyrin modulates the energy of the π–π^* transitions and furnishes an enhancement mechanism for the vibrational

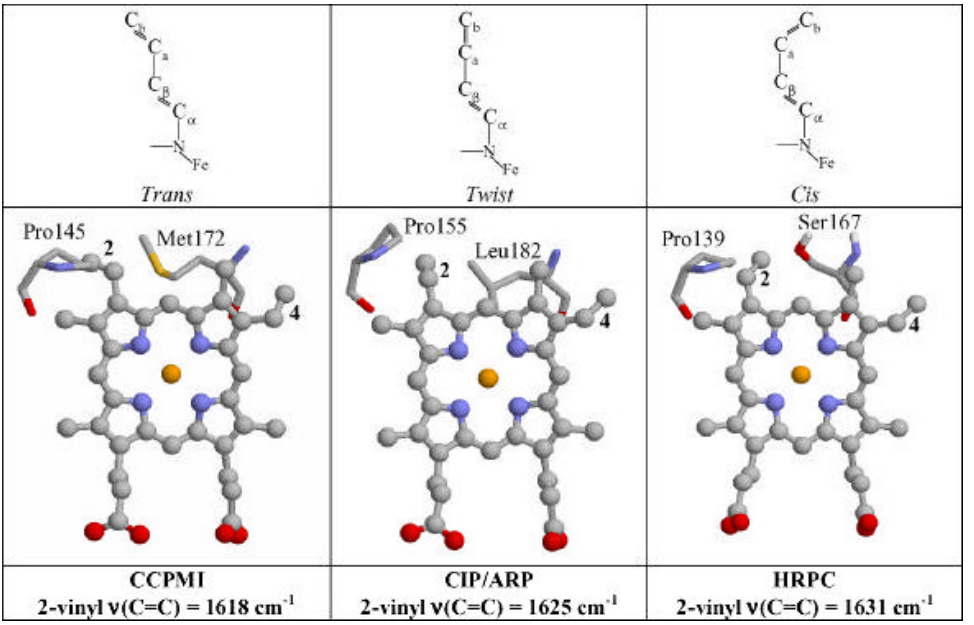

Figure 8. Schematic representations (top) of the different 2-vinyl conformations and structures (bottom) viewed along the *z* axis, perpendicular to the heme plane, of CCPMI, ARP/CIP and HRPC. (Reprinted with permission from Smulevich, G.; Feis, A.; Howes, B. D. *Acc. Chem. Res.* **2005**, *38*, 433. © 2005 American Chemical Society.)

modes of the vinyls in the RR spectra.[100] The conjugation can induce an upshift of the UV-vis maxima of up to 10 nm, as clearly observed in the electronic absorption spectra of plant peroxidases. In fact, despite their largely invariant coordination and spin state and the close similarity of their RR spectra, the Soret band wavelength varies from 398 nm in BP1[73] to 408 nm in CCP[101] as a consequence of the degree of conjugation between the porphyrin macrocycle and the vinyl substituents.[102]

To rationalize this effect, the absorption and RR spectra of selected mutants and fluoride complexes of various peroxidases have been analyzed in detail in relation to their X-ray structures.[99] The X-ray structures revealed that the vinyl orientation among the various plant peroxidases differs mainly at position 2, as a consequence of different steric hindrances imposed by the protein matrix. The ν(C=C) vinyl stretching frequency was found to be a sensitive probe of the degree of electronic conjugation between vinyl and porphyrin and, hence, the RR vinyl stretching frequencies can vary markedly. As the constraint on the 2-vinyl diminishes, the conjugation between the vinyl and the porphyrin decreases, the 2-vinyl ν(C=C) stretching frequency increases, and a large frequency separation is observed between the two ν(C=C) stretching modes in the RR spectra. When the protein matrix exerts weak or

no constraints on the 2-vinyl group, two distinct ν(C=C) stretching modes are found in the RR spectra. A relationship between the ν(C=C) stretching frequency and the torsion angle, τ, of the 2-vinyl group, involving the relative orientations of vinyl (C_b–C_a) and pyrrole (C_β–C_α) C=C double bond π planes, has been established.[99] The maximum and minimum conjugation between the vinyl group and the porphyrin macrocycle is observed when the vinyl and pyrrole double bond π planes are mutually parallel ($\tau = 140°$) and perpendicular ($\tau = 50°$), respectively. Three limiting vinyl conformations (trans, twist and cis) are sketched in Figure 8.[18] The amino acid that interacts with vinyl 2 is possibly that at position 172 (CCP numbering), which is methionine in CCP, leucine in class II peroxidases and serine in ascorbate peroxidase (APX) and class III peroxidases. The repulsive interaction between the vinyl group and the amino acid is strongest in CCP (class I) and weakens on passing from class II to class III peroxidases and APX (class I). On the basis of the spectroscopic data, amino acid sequence alignment, and the distances between the vinyl Ca and Cb atoms and the surrounding amino acids as determined by the X-ray structures, the role of a variety of interactions, including van der Waals contacts, π–π electron interactions, and C–H–––O H-bonds, has been inferred.[99] The vinyl group orientations appear to depend on the concerted orientations of the distal helix B and proximal helix F axes, controlled by the H-bonds between the distal arginine, a heme propionyl group, and an amino acid on the extended strand adjacent to proximal helix F.

4. *Imidazolate Character of the Proximal Iron Ligand*

The conserved H-bond between the N_δ atom of the imidazole ligand and the carboxylate group of the aspartic side chain, which acts as H-bond acceptor, imparts an imidazolate character to the proximal heme ligand (Figure 9). This effect can be detected by RR spectroscopy, since the imidazolate character induces an increase in the frequency of the ν(Fe–Im) stretching mode (between 230 and 250 cm^{-1}) of the 5c Fe(II) state. Moreover, the polarity of the H-bond results in a downshift of the frequency of the ν(Fe–Im) stretching mode at alkaline pH and upon buffer deuteration due to a weakening of the H-bond interaction, as shown in early work by Kitagawa and coworkers.[103–105]

This pH effect on the ν(Fe–Im) frequency has been observed for all heme peroxidases so far studied (see Table 1). However, within the plant peroxidase superfamily, the RR spectral features of classes I and II noticeably differ from those of class III. In fact, at neutral pH, the peroxidases belonging to the first two classes (Table 1) show a broad band due to the coexistence of two bands at very different frequencies. They have been assigned to two tautomers: in one tautomer the proton resides on the imidazole, while in the other the proton is transferred to the carboxylate (Figure 9). On the contrary, peroxidases of class III at neutral pH

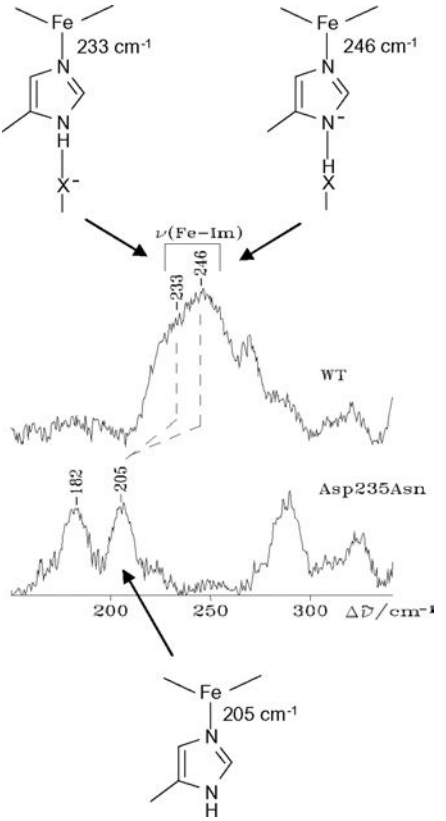

Figure 9. Low-frequency RR spectra of Fe(II) recombinant CCP(MKT) and the Asp235Asn mutant. The broad Fe-His stretching band observed in Fe(II) CCP is composed of two ν(Fe-His) modes, assigned to tautomers of the H-bond between the His175 N_δ proton and the Asp235 carboxylate chain. In one tautomer, the proton resides on the imidazole [ν(Fe-His) = 233 cm^{-1}], while in the other, the proton is transferred to the carboxylate [ν(Fe-His) = 246 cm^{-1}]. Disruption of the H-bond in the mutant lowers the frequency of [ν(Fe-His) to 205 cm^{-1}.[58,62] (Reprinted with permission from Smulevich, G.; Feis, A.; Howes, B. D. *Acc. Chem. Res.* **2005**, *38*, 433. © 2005, American Chemical Society.)

show only one tautomer, their RR spectra being characterized by a sharp band at a relatively high frequency (Table 1). A possible explanation of this behavior might derive from a different geometry of the H-bond between the proximal His and Asp (contained in helix H) residues compared to the members of classes I and II, which inhibits the formation of a double-well potential for the imidazole proton.

The replacement of the Asp carboxylate group with the amide group of an asparagine in ARP/CIP[64] and in CCP[58,62] causes a dramatic frequency lowering (about 40 cm^{-1}) of the ν(Fe–Im) stretch (Figure 9 and Table 1). In addition, the rupture of the His–Asp H-bond interaction upon mutation causes a change in the

Table 1. RR frequencies (cm^{-1}) of the ν(Fe–Im) stretching mode for various heme-containing peroxidases and selected site-directed mutants of the key residues of the heme pocket.

Protein	Acid pH	Alk. PH	Ref.
Class I			
CCP	247–233 (sh)	233	58, 62, 202
D235N–CCP	205	205	58, 62
H52L–CCP	242–227 (sh)	205–229–248	59
R48L	242–227	206	58
H181G–CCP	241–229 (sh)	203	59
APX	234–207 (w)	232–204 (w)	96
Syn. KatG	253–205 (w)	251–203 (w)	110
Syn. D152S	250 (s) 237 (m)	250 (m) 237 (s)	108
Syn. I248F	250 (s) 237 (w)	250 (s) 237 (m)	108
Syn. D402E	251–202 237–213		112
M. tub. KatG	244	241.228 (sh)	113
M. tub. KatG	244		114
Class II			
ARP/CIP	230–211(w)	211	63
D245N–CIP	204		64
H51L–CIP	230–211	211	65
LIP	244–230		291
MNP	248–236		292
Class III			
HRP–C	244	241	103
R38K	240		293
HRPA2	252	246	103
SBP	246	246	72
BP1	237		73
JRP isoenzymes	Ranging from 246 to 252	Ranging from 241 to 248	105
TP-1	252	248	105
TP-3	251	246	105
TP-7	248	244	105

JRP: Japanese radish peroxidase; TP: turnip peroxidase.

heme coordination and spin states from a 5cHS heme to a 6cLS bis–His heme. Therefore, the His–Asp H-bond interaction not only modulates the Fe–His bond strength but also restrains the Fe from moving into the heme plane and binding a distal water or the distal His.

B. Heme Pocket in Catalase–Peroxidases

In this section we will treat separately catalase–peroxidases (KatGs), since in the last few years they have aroused considerable interest. In fact, despite their striking

sequence homologies to CCP, they are the only members of the plant peroxidase superfamily exhibiting both peroxidase and substantial catalase activities. Many spectroscopic and functional studies have been published. Moreover, four crystal structures of different KatGs have recently become available, namely those from *Haloarcula marismortui*,[53] *Burkholderia pseudomallei*,[54] *Mycobacterium tuberculosis*[56] and *Synechococcus* PCC 7942.[106] They all revealed that the proximal and distal heme pockets contain conserved amino acids at almost identical positions as in other class I peroxidases, such as CCP and APX. In particular, both the proximal triads His/Trp/Asp (His290, Trp341 and Asp402) in *Synechocystis* numbering (which is used here) and the distal His/Arg/Trp (His123, Arg119 and Trp122) together with the H-bond interactions are conserved (Figure 10).

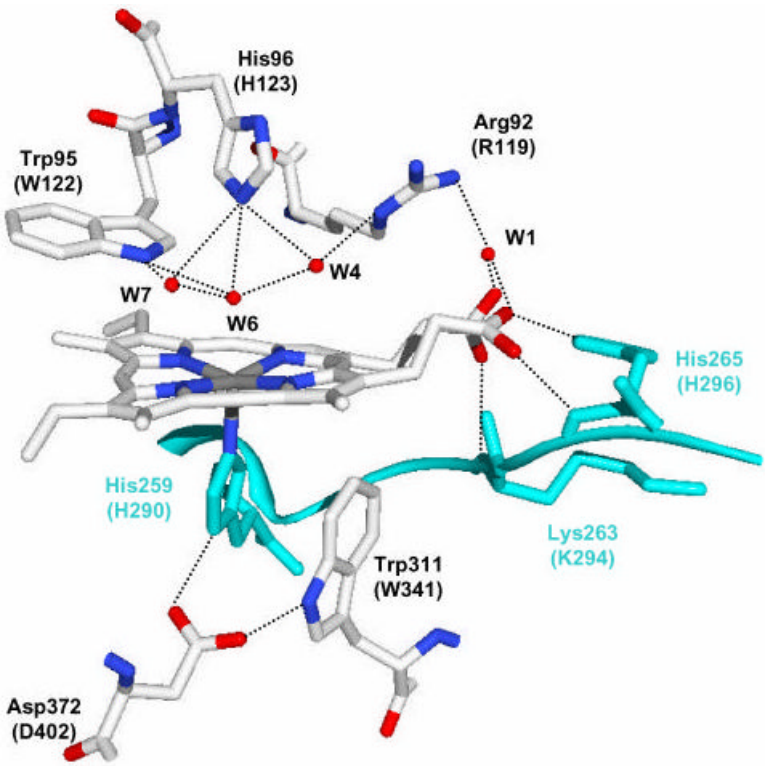

Figure 10. Structural diagram of the extended hydrogen-bond network connecting the distal and proximal sides of the heme pocket of *H. marismortui* KatG. The loop containing the proximal Fe-ligand (His290) and the residues hydrogen-bonded to the heme propionyls is shown in cyan. Residue numbers are for *H. marismortui* KatG (*Synechocystis* numbering in parentheses). (Reprinted from *J. Inorg. Biochem.* **2006**, *100*, 568–585. Smulevich, G.; Jakopitsch, C.; Droghetti, E.; Obinger, C., Probing the structure and bifunctionality of catalase–peroxidase (KatG). © 2006, with permission from Elsevier.)

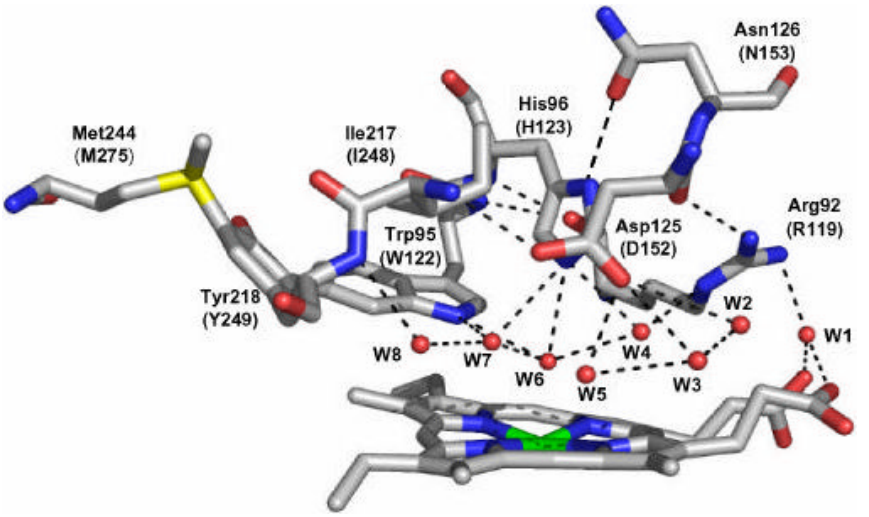

Figure 11. Zoom views of the distal side heme pocket of *H. marismortui* KatG. The amino acid numbering is for *H. marismortui* KatG (*Synechocystis* numbering in parentheses). (Reprinted from *J. Inorg. Biochem.* **2006**, *100*, 568–585. Smulevich, G.; Jakopitsch, C.; Droghetti, E.; Obinger, C., Probing the structure and bifunctionality of catalase–peroxidase (KatG). © 2006, with permission from Elsevier.)

However, the X-ray structures also revealed features unique to KatG. In the vicinity of the active site, novel covalent bonds between chains of the three considered distal residues, (Trp122, Tyr249 and Met275) (Figure 11) were found. Other specific KatG features are three large loops, two of them (indicated as LL1 and LL2) showing highly conserved sequence patterns.[107] Both LL1 and LL2 constrict the access channel of H_2O_2 to the heme group on the distal side. The LL1 insertion, in particular, is positioned at one edge of the heme between helices D and E, thereby connecting the distal and proximal catalytic domains and controlling the flexibility and character of the bond between the proximal histidine and the Fe(III) iron (Figure 12). In addition to the covalently linked distal Tyr249, LL1 contains other residues highly conserved in all KatGs, namely Ile248, Asn251, Pro252 and Glu253.[108]

Furthermore, Glu253 creates an acidic entrance to the channel characterized by a pronounced funnel shape and a continuum of water molecules (Figure 13). At the narrowest part of the funnel, the highly conserved residues Asp152 and Ser335 control the access to the distal side residues Arg119, His123 and Trp122. Ser335 is situated along the access channel, and probably H-bonded to the carbonyl oxygen atom of the heme propionate group. The side chain carboxyl group of Asp152 points toward the heme pocket at 7.8 Å from the heme iron and is H-bonded to two distal water molecules forming part of an extended H-bond network. The

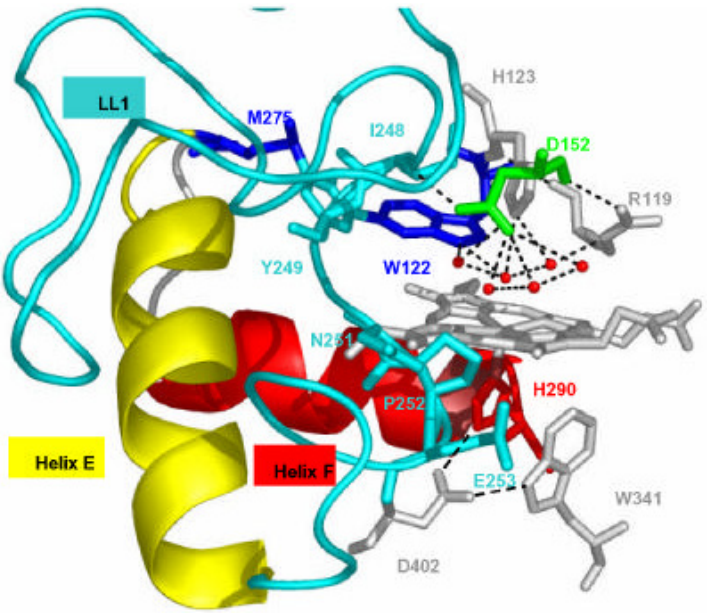

Figure 12. LL1 connecting the distal heme side with helices E (yellow) and F (red). Coordinates are from *H. marismortui* KatG but residue numbering is for *Synechocystis*. Typical peroxidase residues are depicted in gray and the proximal histidine in red. The distal aspartate is shown in green, residues forming the covalent adduct in blue, and residues belonging to LL1 in cyan. Only selected waters (in red) are shown. Dashed lines indicate hydrogen bonds, inferred on the basis of distance criteria. (Reprinted from *J. Inorg. Biochem.* **2006**, *100*, 568–585. Smulevich, G.; Jakopitsch, C.; Droghetti, E.; Obinger, C., Probing the structure and bifunctionality of catalase–peroxidase (KatG). © 2006, with permission from Elsevier.)

presence of this novel Asp residue in the distal heme cavity provides some structural constraints in KatG. In fact, Asp152 is H-bonded to the LL1 residue Ile248 and is adjacent to Asn153, which is conserved in all plant-type peroxidases[1] and H-bonded to the distal His (Figure 11).

Extensive spectroscopic and kinetic studies (see Ref. 109 and references therein) have been performed on WT and selected variants of KatGs from different sources in order to understand how the structural features typical of KatG correlate with its bifunctional activity. Mutagenesis of both proximal and distal side residues of KatG affects selectively the function inhibiting mainly the catalase but not the peroxidase activity. Moreover, marked differences in the structural role of conserved amino acids and H-bond networks in KatG with respect to the other plant peroxidases were found.

RR has been mainly applied to the study of the cyanobacterium *Synechocystis* PCC 6803 (overexpressed in *E. coli*) KatG and selected mutants[108,110–112] and *M. tuberculosis* KatG and selected mutants.[113–118]

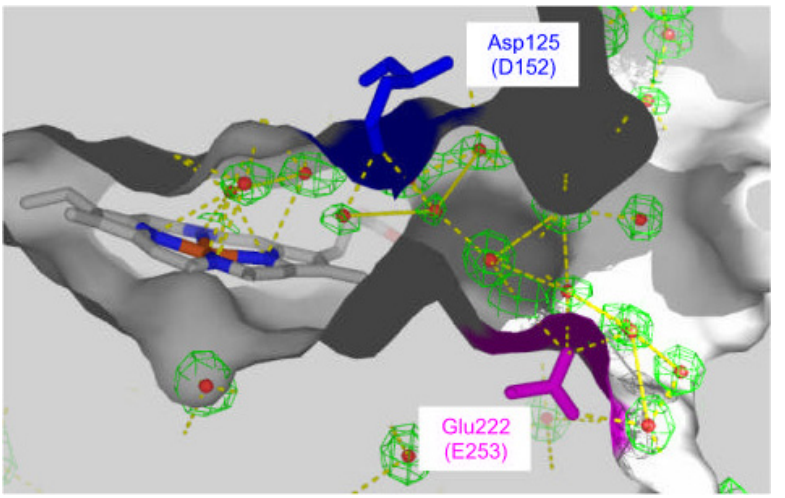

Figure 13. Slab view of the main access channel for H_2O_2 of *H. marismortui* KatG. The 2Fo_Fc electron density map of the water molecules in the channel modeled at 1σ is shown in green and inferred hydrogen bonds are indicated in yellow. Asp125 (D152) and Glu222 (E253) are drawn as sticks and colored blue and magenta, respectively. (Reprinted from *J. Inorg. Biochem.* **2006**, *100*, 568–585. Smulevich, G.; Jakopitsch, C.; Droghetti, E.; Obinger, C., Probing the structure and bifunctionality of catalase–peroxidase (KatG). © 2006, with permission from Elsevier.)

1. *KatG from Synechocystis*

The electronic absorption and RR spectra of Fe(III) KatG from *Synechocystis* are characterized by a predominant 5cHS heme with a small amount of both 6cHS and 6cLS hemes (Figure 14).[108]

Upon reduction the protein becomes predominantly 5cHS.[110] At pH 5.7, two ν(Fe–Im) stretching modes have been assigned at 205 and 253 cm^{-1}, the frequency being correlated with the strength of the H-bond between the proximal His and the Asp carboxylate side chain. As for CCP and APX (see Table 1), the band at 205 cm^{-1} corresponds to a species whose proton resides on the imidazole, while the band at 253 cm^{-1} corresponds to a form where the proton is transferred to the carboxylate (Figures 15 and 16). The absence of a decrease in the intensity ratio between the two bands upon changing the pH suggested that the two species are independent as in APX[96] and not in equilibrium as in CCP[58,62] or ARP/CIP.[63]

Based on the results obtained from the characterization of various site-directed mutants, marked differences in the structural role of the conserved amino acids and H-bond networks in KatG with respect to the other plant peroxidases were found. Mutations affecting the proximal His–Asp or Asp–Trp H-bond interactions dramatically alter not only the enzymatic activity[119] but also the coordination and spin states, as observed for other heme peroxidases.[18] In fact, as for the other heme

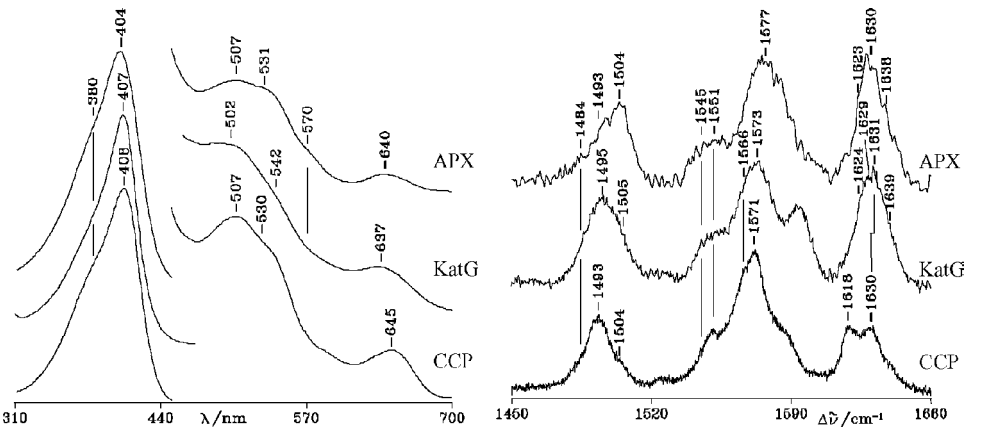

Figure 14. (Left) Electronic absorption spectra of Fe(III) CCP, KatG and APX at neutral pH in phosphate buffer. The region between 450 and 700 nm has been expanded eight fold. (Right) Corresponding RR spectra obtained with 413.1 nm (CCP and APX) and 406.7 nm (KatG) excitation wavelengths. (Reprinted with permission from Heering, H. A.; Indiani, C.; Regelsberger, G.; Jakopitsch, C.; Obinger, C.; Smulevich, G. *Biochemistry* **2002**, *41*, 9237–9247. © 2002 American Chemical Society.)

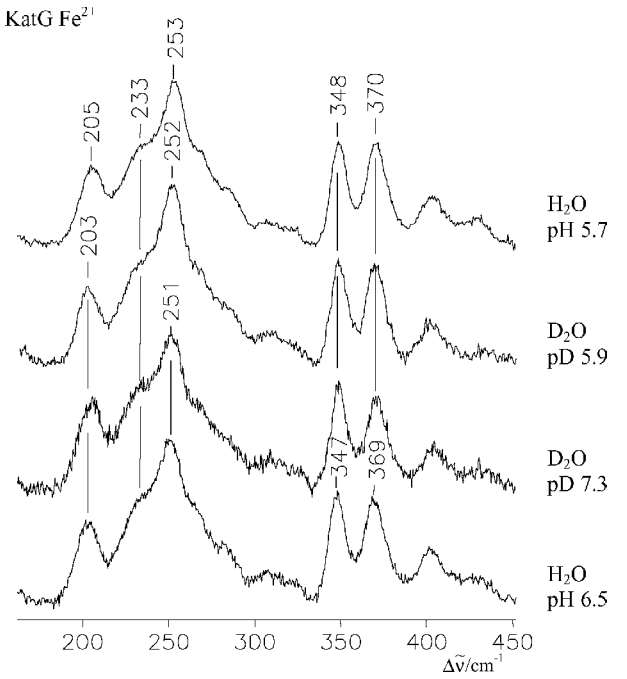

Figure 15. RR spectra of Fe(II) KatG in the low-frequency region in H_2O (pH 5.7 and 6.5) and D_2O (pD 5.9 and 7.3). (Reprinted with permission from Heering, H. A.; Indiani, C.; Regelsberger, G.; Jakopitsch, C.; Obinger, C.; Smulevich, G. *Biochemistry* **2002**, *41*, 9237–9247. © 2002 American Chemical Society.)

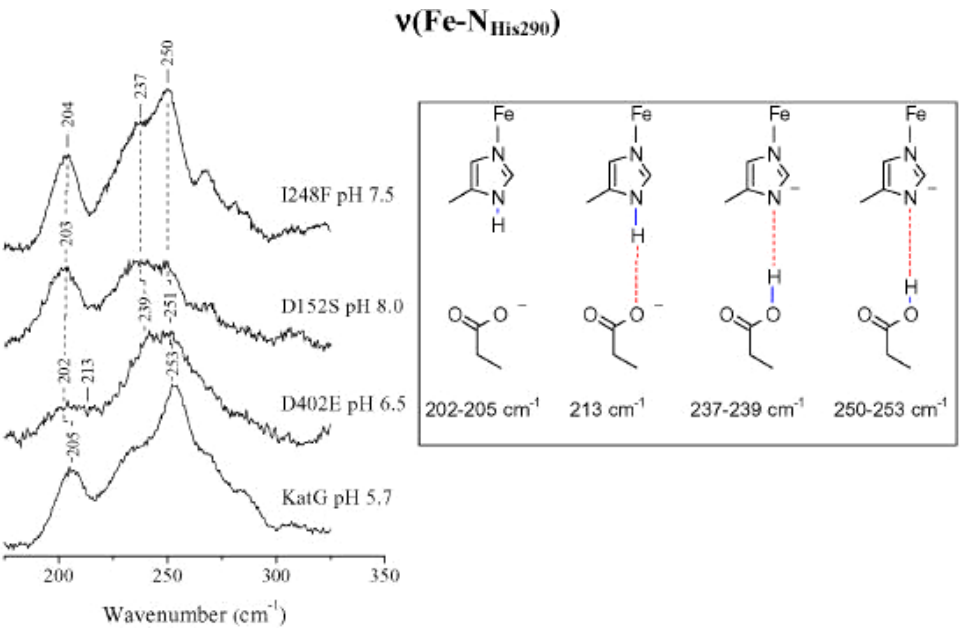

Figure 16. (Left) Low-frequency RR spectrum of Fe(II) WT KatG from *Synechocystis* and its Asp402Glu (D402E), Asp152Ser (D152S) and Ile248Phe (I248F) mutants obtained by excitation at 441.6 nm. (Right) Schematic representation of the different proximal H-bonds corresponding to the various frequencies of the *v*(Fe–Im) stretching modes. The Fe–Im frequency increases as the proton becomes progressively more distant from the imidazole. (Reprinted from *J. Inorg. Biochem.* **2006**, *100*, 568–585. Smulevich, G.; Jakopitsch, C.; Droghetti, E.; Obinger, C., Probing the structure and bifunctionality of catalase–peroxidase (KatG). © 2006, with permission from Elsevier.)

peroxidases, KatG contains a H-bond network connecting the proximal and the distal sides of the heme pocket (Figure 10). However, unlike the other plant peroxidases, mutation of the proximal key residues alters to differing degrees the heme architecture, weakening the heme binding. Partial loss of the heme, accompanied by the concomitant presence of a 6cLS heme due to the binding of an internal ligand to the heme, was revealed by both RR and electronic absorption.[112] The major role played by the proximal His–Asp H-bond in the stability of the KatG architecture was also directly confirmed by the Fe–Im bond strength, as measured via the RR frequency of the Fe–Im stretching mode. The experiment highlighted that the *v*(Fe–Im) stretching mode frequency is the result of a delicate equilibrium of the H-bonds between the conserved proximal His (His290) and Asp residues (Asp402) and between the Asp residue (Asp402) and the nitrogen atom of the indole group of Trp341. The disruption of the N_{Trp}–O_{Asp} H-bond in the W341F mutant strengthens the Fe–Im bond, resulting in a protein which maintains the spectral and kinetic properties of the WT protein. On the contrary, the combined

effect of the disruption of the Trp–Asp H-bond and absence of the π–π interaction between the His and the aromatic ring, as in the W341A mutant, completely destabilized the protein architecture. Moreover, the RR spectrum of the Fe(II) D402E mutant showed the presence of two different conformers, each characterized by two Fe–Im stretching modes at 202 and 251 cm^{-1}, as the WT enzyme, and at 213 and 237 cm^{-1}. The new conformer is likely a consequence of the novel Glu–His H-bond formed in the mutant (Figure 16), which, therefore, maintains its native HS character and peroxidase activity.[119]

Contrary to expectations, mutation of three distal amino acid side chains, Trp122, Tyr249 and Met275, involved in the two covalent bonds located on the distal side of the heme (Figures 11 and 12) does not significantly affect the Fe–Im bond strength [as judged by the RR ν(Fe–Im) band frequency] or the coordination state (as judged by the core size marker band frequencies), compared to the WT protein. However, unlike the WT protein, the variants show a tendency to lose the heme group. Interestingly, the Trp122Ala and Trp122Phe mutants showed a decreased alkaline transition pKa and, as a consequence, the Fe(III) RR spectra showed the presence of an aquo-6cHS heme and hydroxo-6cLS hemes coexisting with the 5cHS state at neutral pH. Therefore, when the complete crosslink is absent (Tyr249Phe and Trp122Phe or Trp122Ala) or only partially formed (Met275Ile), the heme binding is weakened and the protein is destabilized.[112]

Mutation of the conserved Trp, Arg and His distal residues perturbs the distal Fe coordination state and weakens the proximal Fe–Im bond. This is a consequence of the H-bond network which, via the distal water molecules, Trp, His and Arg residues, connects the distal and proximal sides of the heme pocket, as found for other plant peroxidase members (Figure 10).[18,110] As with the Arg51Asn CIP[65] or Trp51Phe CCP mutants,[58] substitution of the distal Arg with an Asn, or the distal Trp with either Ala or Phe residues,[110] facilitated binding of the distal water molecule to the iron. Similarly, a water molecule also binds the heme iron upon alteration or disruption of the Asn–His H-bond, by replacing the hydrogen-acceptor carboxamide group of the Asn153 residue with an aspartate carboxylate group (N153D) or an aliphatic residue (N153A). In fact, alteration or disruption of the Asn–His H-bond alters the distal His basicity, preventing the distal His from binding the distal water molecule. However, unlike plant peroxidases, distal mutation alters also the stability of the heme architecture. The Arg119Ala mutant was found to be particularly unstable, easily losing the prosthetic group even at neutral pH. The His123Glu variant also loses the heme at neutral pH, probably as a consequence of the nearby negatively charged Asp152 residue, a unique characteristic of KatGs. The study of variants that disrupt the H-bonding between Asp152, which resides in the distal cavity, and Ile248, located on the LL1 chain (Figures 11 and 12), gave important insight into the structural architecture characteristic of

only KatGs. RR data and structural analysis demonstrate the existence of a very rigid and ordered structure resulting from interactions of LL1 residues with both distal and proximal residues and the heme itself. This distal H-bond represents a novel link between the proximal and distal sides of the heme cavity and is important for the stability of the heme pocket and for maintaining the proximal H-bond strength. Substitution of Ile248 by Phe, or Asp152 with Ser, present in CCP, makes KatG spectroscopically and structurally similar to CCP. Mutation increases the 5cHS form at the expense of the aquo-6c species and drastically alters the proximal His–Asp H-bond interaction. Two pH-sensitive bands were found in the RR spectra of the Fe(II) forms at about 237 and 250 cm^{-1} (Figure 16 and Table 1), reminiscent of the 233 and 247 cm^{-1} doublet found in CCP,[62,120] corresponding to tautomeric forms of the H-bond between the His290 and Asp402 carboxylate side chain. These results confirm that perturbation of the Asp152–Ile248 H-bond leads to changes at the proximal heme site which are mediated by LL1 and its connection with helices E and F, with helix F carrying the proximal histidine (Figure 12). Moreover, since these mutations increase the peroxidase activity with a concomitant dramatic reduction of the overall catalase activity, it was suggested that small structural perturbations and disruption of the H-bond networks have only a small impact for compound I formation (see Section II.F), which is common to catalatic and peroxidatic activity, but a defined extended H-bond network is crucial for selectively guiding and binding the (second) peroxide molecule necessary for the catalatic activity.[108]

2. *KatG from Mycobacterium tuberculosis*

KatG from *M. tuberculosis* is important for the virulence of this pathogen because of its role in the removal of peroxide in infected host macrophages.[121–123] Moreover, *M. tuberculosis* KatG is of great interest in the field of tuberculosis research, since it plays a direct role in activation of the prodrug isoniazid, a potent antituberculosis drug which has been in use for more than half a century since its discovery in 1952.[124] The growing worldwide problem of resistance to this drug due to mutations in the katG gene has been addressed in clinical and biochemical studies often focused on the 315 position. The S315T variant has been produced in the laboratory and studied in detail, since this mutation is that most commonly found in isoniazid resistant bacteria.[56,125] As mentioned above, the Ser residue is situated along the substrate access channel, and is probably H-bonded to the carbonyl oxygen atom of the heme propionate group. Recently, an explanation for isoniazid resistance in the S315T mutant was found in the loss of the high-affinity drug-binding site, since the methyl group of the threonine residue restricts the narrow opening at the bottom of a substrate access channel.[125] Nevertheless, the

S315T mutant preserves the enzyme functions, thereby preserving bacterial physiology and virulence.[126]

Recombinant KatG and selected variants from *M. tuberculosis* have been extensively studied by optical and RR spectroscopy, giving apparently discordant results, characterized by variability of the heme spin and coordination states. However, recently the RR examination of Fe(III) KatG from *M. tuberculosis* under a variety of conditions, including the presence of fluoride, chloride or isoniazid, and isolated at different stages during purification in different buffers, allowed the Fe(III) heme structural heterogeneity to be explained, and underlined that it contains a heterogeneous population of heme species that present distinct spectroscopic properties.[115,118] The RR results reveal that a 5c heme form of KatG could be isolated, but that coordination and spin state changes are unavoidable during handling of the enzyme under a variety of conditions, as reported earlier for CCP.[127] Therefore, while the 5c form (HS and QS) predominates in the freshly isolated enzymes, a 6c heme species accumulates in the resting enzyme after purification. This form has been shown to have a unique structure containing weakly associated water on the heme distal side and it is the favored reactant for ligand binding. In particular, the use of resting enzyme samples with different proportions of the 5c and 6c forms, as well as the use of the KatG mutants with replacements at residue 315, which have different tendencies to create the 6c form, allowed the authors to demonstrate that the 6cHS species binds cyanide more rapidly and is the preferred heme state for peroxide binding. In particular, RR provided direct evidence for favored binding of cyanide to the 6c S315T mutant.

Fe(II) KatG from *M. tuberculosis* also shows contrasting results. While two pH-dependent ν(Fe–Im) stretches at 244 and 228 cm^{-1} have been reported,[113] in a more recent report[114] only the 244 cm^{-1} ν(Fe–Im) stretching mode has been observed. The Fe–Im stretching vibration is detected also at 244 cm^{-1} in the Fe(II) forms of the S315T variant.[116] Minimal, if any, perturbation of the distal heme pocket in the S315T mutant has been observed. Instead, the S315T mutation seems to induce small changes in the KatG conformation/dynamics of the ligand access channel, as indicated by CO rebinding kinetics in flash photolysis experiments. Therefore, as noted above, it is suggested that substitution of Ser315 with Thr confers resistance to isoniazid by reducing accessibility to the KatG heme pocket by steric hindrance in the access channel. However, since the actual binding site of isoniazid in KatG and its S315T mutant remains elusive, this model may be relevant only when isoniazid binds inside the heme pocket, and modification of an isoniazid binding site outside the heme pocket by the mutation cannot be ruled out.[116]

The characterization of the *M. tuberculosis* Tyr229Phe and Met255Ile mutants,[115] in agreement with the slight differences noted between the WT protein

from *M. tuberculosis* and that from *Synechocystis* PCC 6803, showed spectroscopic features slightly different from those of the corresponding mutants of *Synechocystis*. The Met255Ile variant has a significantly greater relative population of the 6cHS heme than either WT KatG or the Tyr229Phe mutant. Similar to the corresponding mutants of *Synechocystis* KatG, this latter mutant of *M. tuberculosis* has decreased steady-state catalase activity and enhanced peroxidase activity. In addition, since it shows a significantly reduced affinity for isoniazid,[128] it has been proposed that the Trp–Tyr–Met linkage, absent in the Y229F variant, may be required for establishing the proper geometry of the residues that contribute to the formation of a small-molecule binding site.[54] Moreover, although disruption of the cross-linked adduct in the Y229F mutant does not seem to affect H-bonding in the proximal heme pocket, since the Fe–Im stretching frequency is the same for the Fe(II) Tyr229Phe variant and WT protein,[117] the absence of the covalent linkage perturbs the active site. RR spectra of the Fe(III) Y229F variant are consistent with a significant amount of the 6cLS heme and a more planar heme compared to WT KatG. Moreover, changes in the properties of the CO (see below) and NO vibrations indicate that their binding geometry and their steric and electrostatic interactions with distal residues are modified in the Y229F variant.[117] These observations support the idea that loss of the cross-linked triad by the Y229F mutation causes rearrangement of distal heme pocket residues and perturbs their H-bonding interactions with ligands bound to the heme.[114,116] The authors proposed that the Met–Tyr–Trp cross-linked adduct stabilizes a distal H-bonding network that is disrupted in the Y229F variant due to rearrangement of distal residues. This network includes Ile228, which forms a H-bond with Asp137. In *Synechocystis* KatG, the analogous Asp (Asp152) plays an important role in stabilization of the LL1 loop which is anchored by Tyr229.[53,54,56,107,111,129] Asp137 forms a H-bond with Arg104 which interacts with a water molecule that is H-bonded to the heme propionates.[56] Perturbation of H-bonding to the heme propionates can explain the difference in heme planarity and pH sensitivity between the Y229F variant and WT KatG.[114] Differences in the steric and electrostatic environment of their distal heme pockets are most likely due to rearrangement of distal pocket residues and, to a lesser extent, perturbation of the H-bonding network. Figure 17 shows the proposed H-bonding network. The integrity of the covalent adduct seems crucial for the stability of the LL1 loop, the maintenance of the proposed H-bonding network and, in general, of the heme pocket architecture.

C. Calcium Binding Sites

In addition to the conserved residues, the peroxidases of classes II and III have two calcium binding sites, one distal and one proximal to the heme plane (as shown

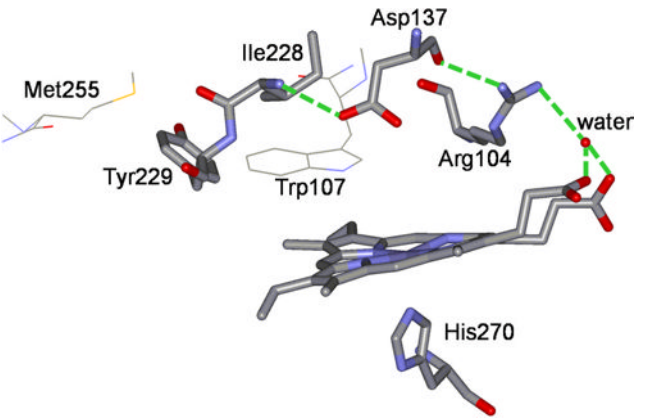

Figure 17. H-bonding network between Tyr229 and heme propionate groups that may be perturbed in the Y229F mutant of KatG from *M. tuberculosis*. The dotted lines indicate the H-bonds with lengths shorter than 3 Å. (Reprinted from *J. Inorg. Biochem.* **2006**, *101*, 422–433. Kapetanaki, S. M.; Zhao, X. B.; Yu, S. W.; Magliozzo, R. S.; Schelvis, J. P. M., Modification of the active site of *Mycobacterium tuberculosis* KatG after disruption of the Met–Tyr–Trp cross-linked adduct. © 2006, with permission from Elsevier.)

for HRPC in Figure 18), which are important for maintaining protein stability and activity.[1,39,44] These features are absent from class I peroxidases. However, APX has a K^+ binding site on the proximal site.[45] As with the effect of Ca^{2+} ion removal from peroxidases of classes II and III (see below), the electronic absorption and MCD spectra of the engineered K-site APX mutant, which has had its potassium cation binding site removed, gave rise to a bis-imidazole ligated heme system. Therefore, it appears that upon removal of the proximal K^+ ion the protein undergoes a conformational change to yield a bis-histidine coordination structure in both the Fe(III) and Fe(II) oxidation states at neutral pH.[130]

Figure 18 shows the local structure in the proximity of the distal and proximal Ca^{2+} ion binding sites of native HRPC.[47] Both Ca^{2+} ion sites are seven-coordinate, with ligands composed of side chain oxygen atoms and carbonyl groups and one water molecule in the case of the distal site. The distal and proximal Ca^{2+} ions are structurally coupled to the active site (His42 and His170, respectively) through an intermediate residue adjacent in sequence (Asp43 and Thr171, respectively). Each of these intermediate residues provides two bonds to the corresponding Ca^{2+} ion; therefore, the loss of either Ca^{2+} ion has considerable potential to perturb the active site structural and catalytic properties.

Although peroxidases of the plant superfamily display primary structure homology, the role of calcium in maintaining the function of the enzyme is different between classes II and III. The class II peroxidases MNP and LIP showed complete loss of activity after calcium release, in contrast to the class III peroxidases

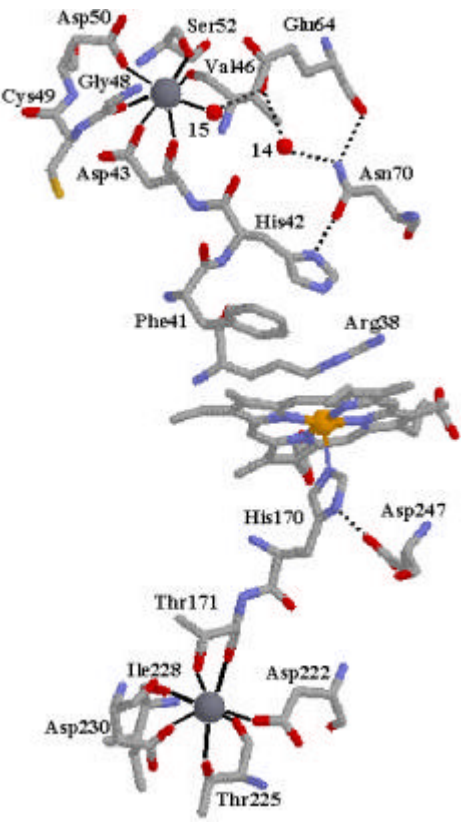

Figure 18. The structural features of the heme pocket of HRPC, showing the distal and proximal Ca^{2+} ion-binding sites, heme group and principal residues. Bonds with the Ca^{2+} ions are shown as continuous lines and hydrogen bonds as dashed lines.

HRPC, HRPA1 and PNP, which retained 40–60% of their activity after calcium release.[131,132] This difference between the two classes of peroxidases was attributed to different locations of intramolecular disulfide bridges.[133] Moreover, spectroscopic and functional studies of many class III peroxidases indicate that one of the two Ca^{2+} ions may play a more important role in maintaining the heme pocket structural characteristics necessary for high catalytic activities.[131,134] Loss of activity, observed under thermal and alkaline inactivation for many classes II and III peroxidases, has been correlated with the loss of one or both calcium ions. Thermal[135] and alkaline[136] inactivation of LIP has been correlated with loss of calcium ions and formation of an inactive bis-histidyl hexacoordinate low-spin (6cLS) heme state. In apparent contrast with alkaline inactivation, which results in the loss of both calcium ions, thermal inactivation causes the loss of only the more weakly bound distal calcium ion. Likewise, thermal inactivation of MNP has been correlated

with loss of a distal calcium ion and formation of an inactive 6cLS state.[133,137] Perturbation of the distal calcium binding site by construction of the site-directed mutant, Asp47Ala, resulted in an enzyme that had properties identical to those of thermally inactivated MNP.[133] ^{1}H-NMR studies on class III peanut peroxidase could not distinguish the structural contributions of each calcium ion. However, it was evident that binding of the two Ca^{2+} ions was required in order not to compromise the structural properties and activity of the enzyme.[138]

Removal of the bound calcium ions from native HRPC results in a considerable decrease in activity and thermal stability.[131,134,139–142] Calcium is required to maintain the structural integrity of the heme in its optimal geometry for catalysis, which is lost upon calcium depletion.[143] Moreover, based on the spectroscopic results obtained upon mutation of the amino acids involved in the H-bonding network around the heme,[144–147] it was concluded that the Ca^{2+} ion on the distal side of the heme plays a determining role. Unlike the abovementioned studies, RR and UV-vis spectra firmly favor the proximal Ca^{2+} ion as the first to be lost.[148] In fact, in the Fe(II) form, the ν(Fe–Im) stretching mode downshifts 27 cm^{-1}, revealing a significant structural perturbation of the proximal cavity near the His ligand. Since the Thr171 residue, adjacent to the proximal His, provides two coordination bonds to the proximal Ca^{2+} ion (Figure 18), it is reasonable to expect that loss of only this Ca^{2+} ion would cause a change in the disposition of the histidine leading to a weakening of the His–Asp hydrogen bond and, therefore, of the heme iron–His170 interaction. The binding properties of the distal cavity are maintained since, as for native HRPC, the Ca^{2+}-depleted enzyme binds benzohydroxamic acid in its Fe(III) state, and CO in its Fe(II) state, suggesting that modification of the distal cavity by Ca^{2+} depletion is not particularly extensive and/or can be easily reversed. However, unlike the native protein, observation of a bis-histidyl LS heme in reduced Ca^{2+}-depleted HRPC indicates that loss of calcium induces some conformational change in the heme pocket. Alteration of the distal side heme structure enables the imidazole group of the distal histidine to bind to the sixth coordination position of the reduced heme iron. In agreement with the loss of the proximal calcium ion is the finding that a similar LS heme is formed in Fe(II) HRPC[69] upon mutation of the proximal Phe221 residue, which is stacked approximately parallel to the proximal histidine ligand. Clearly, alteration of the proximal heme side can be transmitted to the distal cavity, inducing some flexibility in the position of the distal histidine.

Interestingly, the mutation of F190 in MNP (equivalent to F221 of HRPC) by either Ile or Ala has also a marked destabilizing effect on the enzyme,[149] giving rise to a 6cLS bis-histidyl complex.[150] The formation of this complex requires displacement of helix B to enable the distal His46 to coordinate with the heme iron atom. Moreover, it has been suggested that this mutation also results in the loss of

the distal calcium ion.[151] However, the calcium ions of class II fungal peroxidases such as LIP and MNP are more labile than those of class III plant peroxidases.[136] The difference between the lability of the distal calcium in classes II and III peroxidases is due mainly to the disulphide bridge between Cys44 and Cys49, which is unique to the latter.[1] This restricts the flexibility of distal helix B and limits movement of His42 in the distal heme cavity of HRPC.

The role of Ca^{2+} ions has also been addressed by computer simulations. A 500 ps[143,152] and 2 ns[153] molecular dynamics calculation on the native HRP structure and those produced by computer simulation techniques after partial and total Ca^{2+} depletion have been performed. The NSD analysis of the heme group revealed that the deformation of the heme group from D_{4h} symmetry, significant in the native form,[154] upon total Ca^{2+} depletion changed both the in-plane and out-of-plane distortions with a decrease of nonplanarity.[152,154] NSD analysis showed also a lack of coupled dynamics of the heme and protein motion[153] after Ca^{2+} removal. In addition, polarized RR spectroscopy on partially Ca^{2+}-depleted samples[155] suggested more significant structural effects than those previously reported[148] and somewhat different changes in the spin state of the heme. These different results have been attributed to differences in the sample preparation techniques, even if they appear to be similar.

Recently, the native and totally Ca^{2+}-depleted forms of HRPC have been compared by using pH-, pressure-, viscosity- and temperature-dependent UV absorption, CD, H/D exchange-FTIR spectroscopy and by binding of the substrate benzohydroxamic acid. It has been reported that Ca^{2+} depletion does not change the alpha helical content of the protein, but strongly modifies the tertiary structure and dynamics to yield a homogeneously loosened molten globule-like structure. The observed tertiary changes in the heme pocket have been related to changes in the dipole orientation and coordination of a distal water molecule. Deprotonation of distal His42, linked to Asp43 which is coordinated with the distal Ca^{2+}, perturbs an H-bonding network connecting this Ca^{2+} to the heme crevice that involves the distal water.[156] Moreover, unlike the previously observed effects noted after one Ca^{2+} ion depletion,[148] the authors did not observe effects that required involvement of a role for the proximal Ca^{2+}. The significant structural effects on the overall protein structure and also in the heme pocket reported in this study indicate that the binding of the distal Ca^{2+} is of critical importance.

D. Binding Sites for Substrates: Benzohydroxamic and Salicylhydroxamic Acids

The mechanism of substrate binding and catalysis in heme peroxidases has been reviewed previously.[2,157] The application of site-directed mutagenesis enabled

significant progress to be made in understanding the roles of the amino acid residues involved in substrate binding. The combination of X-ray crystallography and Raman spectroscopy has been particularly informative, highlighting the effects of hydroxamic acid binding to peroxidases. In particular, comparison of detailed Raman spectra for complexes in crystal and solution forms provides a means of bridging crystallographic and solution studies.[17]

The binding of nonphysiological substrates, such as aromatic hydroxamic acids, to peroxidases has been extensively investigated with the aim of probing the aromatic donor binding site. In particular, X-ray structures have been solved for the complexes formed between HRPC and benzohydroxamic acid (BHA),[158] and ARP/CIP with both BHA[159] and salicylhydroxamic acid (SHA).[160] The comparison between these structures reveals that the location of the aromatic rings in the active site is similar (Figure 19).

The aromatic ring is located in the distal cavity, nearly parallel to the heme plane. The hydroxamic acid moiety forms H-bonds with the conserved distal His, Arg and Pro55 residues. The additional hydroxyl group of SHA (compared to BHA) does not form H-bonds with any amino acid residue in the heme cavity. In addition, a hydrophobic pocket surrounding the aromatic ring of the substrate was found in HRPC, which is not present in ARP/CIP.[158] The aromatic molecule does not bind directly to the heme iron, but the addition of SHA or BHA to HRPC and ARP/CIP displaces water molecules from the distal cavity, leaving only one molecule of water close to the heme iron. The iron–water distances in the HRPC–BHA, ARP/CIP–BHA and ARP/CIP–SHA complexes were found to be 2.6,[158] 2.7[159] and 2.8 Å,[160] respectively. Considering the rather long Fe–H_2O distance, there have been conflicting interpretations concerning the extent to which BHA affects the binding of the water molecule to the Fe atom. While NMR proton hyperfine shifts indicated that the HRPC–BHA complex was a five-coordinate high-spin (5cHS) species,[70] based on electronic absorption,[161] resonance

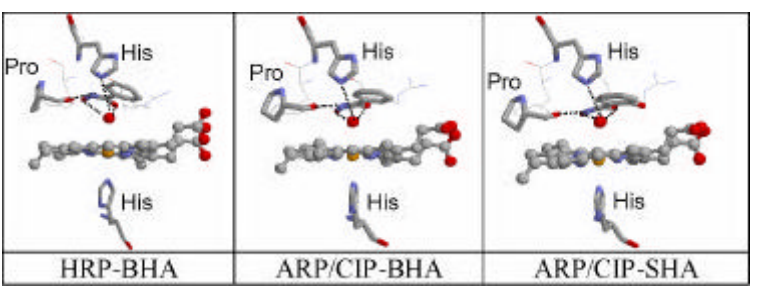

Figure 19. Comparison of the heme pocket of HRPC with BHA,[158] and ARP/CIP with both BHA[159] and SHA.[160]

Raman[67,95,162,163] and EPR,[164] it was concluded that binding of BHA to both HRPC and ARP/CIP[74,91] induces the formation of a six-coordinate high-spin (6cHS) heme. Comparison of the RR spectra of single-crystal and solution samples of the complex demonstrated that this form derives from a water molecule bound to the heme iron.[91,93] However, the solution spectra for HRPC and ARP/CIP complexed with BHA differ in terms of the amount of the 6c form present. This difference was correlated with the small variation observed by X-ray crystallography in the iron–water distance between HRPC–BHA (2.6 Å), ARP/CIP–BHA (2.7 Å) and ARP/CIP–SHA (2.8 Å), which is longer than the usual iron–ligand distance (2.1 Å). The combined analysis of the spectroscopic data and X-ray crystal structures of the ARP/CIP–SHA complex indicates that the Fe–H_2O distance measured by X-ray diffraction is an average resulting from the 5c and 6c species in equilibrium which, however, are directly revealed by RR spectroscopy.[93] Figure 20 compares the RR spectra of solution and single-crystal samples of the ligand-free ARP/CIP and its complexes with SHA and BHA at pH 5.5. It can be seen that there are no substantial differences in the band frequencies between the solution and the crystalline states. The Fe(III) protein at pH 5.5 is a pure 5cHS.[63,93] Upon addition of either BHA or SHA, changes in the frequency and relative intensities of the core size marker bands are observed, clearly indicating the formation of a 6cHS (ν_{11} at 1542, ν_{19} at 1561 and ν_{10} at 1616 cm^{-1}) at the expense of the 5cHS species (ν_{11} at 1551, ν_{19} at 1568, and ν_{10} at 1631 cm^{-1}), which remains in a small amount, as judged by the bands at 1631 cm^{-1} (ν_{10}) and the shoulder at 1551 cm^{-1} (ν_{11}). The ARP/CIP–SHA complex gives rise to spectra characterized by features that are in

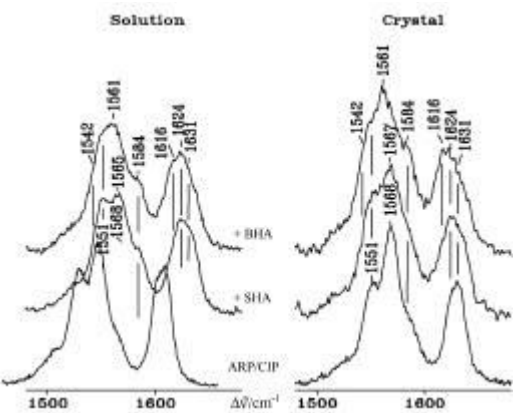

Figure 20. Comparison between solution (left) and single-crystal (right) RR spectra of ARP/CIP–BHA and ARP/CIP–SHA, obtained with the 514.5 nm line of an Ar^+ laser. (Reprinted with permission from Indiani, C.; Santoni, E.; Becucci, M.; Boffi, A.; Fukuyama, K.; Smulevich, G. *Biochemistry* **2003**, *42*, 14066–14074. © 2003 American Chemical Society.)

between those typical of the free and BHA ligated protein, since it contains a higher amount of the 5cHS heme. The RR spectra of the crystals are characterized by a striking enhancement of the inverse-polarized ν_{19} mode at 1568 cm^{-1} (ARP/CIP) 1567 cm^{-1} (ARP/CIP–SHA), and 1561 cm^{-1} (ARP/CIP–BHA), which does not depend on the orientation of the crystal in the laser beam, but is likely the result of a larger ruffled distortion of the heme for the crystalline form of ARP[73] with respect to the protein in solution.

E. Ligand Binding

It is well known that heme pocket proximal and distal amino acid residues control ligand binding in heme proteins. For example, the conserved distal histidine of vertebrate globins has been shown to be important in fine-tuning the ligand affinities via H-bond stabilization involving its N_ε proton.[165,166] In peroxidases, the H-bond stabilization of the incoming ligand by the distal residues is of particular importance, since they have a more polar distal cavity compared to globins. The postulated mechanism of peroxide decomposition relies on the concerted roles played by the proximal histidine together with the distal histidine and arginine residues, through H-bonds and charge stabilization, as originally proposed by Poulos and Kraut.[167] Furthermore, the H-bond between the N_δ proton of the distal His and a conserved Asn residue, and/or the presence of the positively charged guanidinium group of the distal Arg in the proximity of the distal His, depresses its p*K*a to values between 4 and 5,[59] forcing the N_ε of the imidazole ring to act as an H-bond acceptor. Therefore, many studies on peroxidases have been devoted to understanding whether the different cavity characteristics of the globins and peroxidases are also reflected in the binding of other exogenous ligands. Crystal structures of the complexes formed between CCP and CN^-, NO, CO and F^- revealed that significant changes are induced in the distal cavity upon adduct formation. The disposition of the distal Arg and His residues is significantly perturbed, and there is a rearrangement of the water molecules present in the active site.[168] In the case of the CCP–CN complex, all three distal residues, Arg48, Trp51 and His52, can potentially form H-bonds with the N atom of cyanide; the ligand in the CCP–F complex is directly H-bonded to the Trp51 and Arg48 residues, whereas the distal His appears H-bonded to a water molecule, which in turn interacts strongly with the fluoride. The interaction between Arg48 and F^- is possible because the distal Arg undergoes a conformational change that places it within H-bonding distance of F^-. Clearly, the fact that the X-ray structures of both the CCP fluoride complex and the CCP compound I (see Section II.F) show that the distal Arg48 adopts an "in" position, which enables Arg48 to H-bond with the ferryl O and the fluoride ligand,[169] highlights the effectiveness of the fluoride ligand in

probing the distal heme cavity of CCP, CIP and HRPC. The electronic absorption and RR data on a carefully chosen selection of site-directed mutants for these peroxidases allowed diagnostic correlations to be established between spectroscopic parameters, and the number and nature of H-bonding partners in the corresponding fluoride complexes.[65]

Upon fluoride binding, despite the fact that all the peroxidases under investigation showed almost identical RR spectra characteristic of six-coordinate high-spin species, the position of the charge transfer band (CT1) in the electronic absorption spectra varied between 610 and 620 nm. In general, the wavelength of this band depends on the p and π donor capability of the axial ligands[61,64,170] and, therefore, it is a sensitive probe of axial ligand polarity and of its interaction with the distal protein residues. The stronger the H-bond from the ligand to a distal residue, the lower the CT1 wavelength. The opposite effect is observed when the ligand acts as an H-bond acceptor. This trend is illustrated by the effect on the CT1 band of mutation of the distal Trp/Phe residue in CCP and CIP, respectively (Table 2 from Ref. 18). The CT1 wavelength of the fluoride complex of both CCP–F and the Phe54Trp CIP variant is greater than that observed for CIP–F or the Trp51Phe CCP variant. In fact, while in the first case the bound F^- receives H-bonds from the distal Arg, Trp, and a water molecule, in the CCP Trp51Phe mutant and in CIP, the number of H-bonds is reduced from three to two. The loss of Trp, which acts as an H-bond donor, blueshifts the CT1 band.

The combined analysis of the UV-vis and RR data on peroxidases has highlighted that the complex mechanism of stabilization of anionic ligands exerted by the distal amino acids resembles that of compound I formation during peroxidase catalysis, where ligand stabilization by the distal Arg is coupled to protonation of the distal His. Clearly, the mechanism of stabilization of the fluoride ligand exerted by the distal residues is different between myoglobin and peroxidases. In peroxidases, the Arg is the determinant in controlling the ligand binding via a

Table 2. Soret and CT1 bands (nm) of peroxidase–fluoride complexes.[18]

Proteins	Soret	CT1	H-bonds with fluoride		
CCP	406	617	H_2O	Trp51	Arg48
His52Leu CCP	406	617	?	Trp51	Arg48
Trp51Phe CCP	406	613	H_2O		Arg48
ARP/CIP	406	615	H_2O		Arg51
Phe54Trp ARP/CIP	407	618	H_2O	Trp54	Arg51
Arg51Gln ARP/CIP	405	613	H_2O	Trp54	Gln51
HRPC	404	611	H_2O		Arg38
His42Leu HRPC	403	610	?		Arg38
Myoglobin	406	610	H_2O	His64	

strong H-bond between the positively charged guanidinium group and the anion. Mutation of Arg to Leu decreases the stability of the complex 900-fold, suggesting that this interaction stabilizes the complex by 4 kcal/mol. The distal His also contributes to the stability of the fluoride complex, presumably by accepting a proton from HF and H-bonding, through a water molecule, to the anion. Mutation of His to Leu decreases the stability of the fluoride complex 30-fold, suggesting that this interaction is much weaker than the interaction with the distal Arg. For Mb, the distal His is solely responsible for stabilization of the exogenous ligand.

On the basis of RR studies, the involvement of the distal residues in the stabilization of the CN^-,[171,172] and OH^- ligands[67,79] has also been proposed. In particular, for the HRP–OH[67] and CIP–OH complexes[65] both the distal Arg and His interact, in a concerted manner, via H-bonds with the ligand. The positive guanidinium group of the distal Arg is strongly H-bonded to the ligand, since upon mutation of the Arg the hydroxyl is not able to bind to the iron atom in both proteins. The distal His plays a secondary role, but is also H-bonded to the bound ligand, giving rise to a 6cLS heme.[65,67] Interestingly, WT CCP does not bind OH^- at alkaline pH. In fact, the alkaline transition induces a conformational change that permits the distal His52 to bind the Fe atom, forming a bis-His 6cLS heme. When this residue is replaced by Leu, the hydroxide ligand instead binds to the Fe atom.[59]

CO binds to the heme iron of peroxidases in the Fe(II) oxidation state. The interactions between the oxygen of the CO and the distal residues are weaker than in the case of fluoride complexes. Therefore, conformational transitions, such as that induced by fluoride in CCP, have not been observed. X-ray structures are available for the CCP–CO and HRPC–CO complexes.[173,174] In the case of HRPC, the angles and distances between the oxygen atom of CO and the side chains of His and Arg indicate a strong H-bond with His42 and a weaker one with Arg38 (Figure 21).[174] For CCP, the distance between the oxygen atom of CO and Arg48 is greater than 3.2 Å and it appears that the ligand interacts with the guanidinium group via an H-bond with a water molecule. Whether or not His52 is H-bonded with CO is less certain. However, His52 is close enough for H-bonding (within 2.8 Å) to CO.

The heme protein adducts with CO are the most frequently studied Fe(II)–ligand complexes, since CO is a sensitive vibrational probe of heme binding sites in proteins. In particular, polar interactions and the formation of H-bonds between the bound CO and the distal residues increase the extent of back-donation from the Fe d_π to the CO π^* orbitals. As a consequence, the Fe–C bond strengthens while the CO bond weakens, thereby increasing the ν(FeC) vibrational frequencies and decreasing the ν(CO) frequencies.[175,176] There is an inverse linear correlation between the ν(FeC) and ν(CO) frequencies which depends on the extent of π back-bonding (Figure 22).

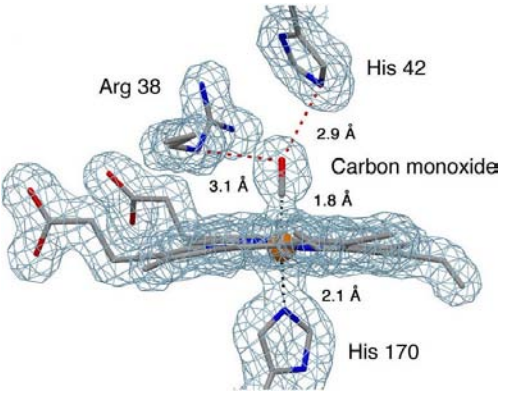

Figure 21. Refined crystal structures, showing the active site of the HRPC–CO complex. (Reprinted with permission from Carlsson, G. H.; Nicholls, P.; Svistunenko, D.; Berglund, G. I.; Hajdu, *J. Biochem.* **2005**, *44*, 635–642. © 2005, American Chemical Society.)

The CO adducts of many members of the plant peroxidase families have been obtained. It is clear from Table 3 that the study of CO–peroxidase complexes has benefited greatly from the availability of site-directed mutants. In fact, comparison between wild-type and mutated proteins has enabled clarification as to which CO–amino-acid interactions are most important.

The main results obtained by vibrational spectroscopy for heme peroxidases can be summarized as follows:

(i) The CO complexes of heme peroxidases differ markedly from those of sterically hindered model CO–porphyrin complexes, being sensitively dependent on interactions between the CO molecule and adjacent amino acids.

(ii) Multiple pH-dependent conformers may be present in the CO complexes of peroxidases. On the basis of distal mutations, it has been demonstrated that the conformers differ in terms of their H-bond interactions between the oxygen of the bound CO and the distal His or Arg.[127,170,177–179] In particular, at neutral pH, while only one form has been found for the CCP–CO complex, HRPC–CO has two different conformers deriving from different protein–CO interactions. The RR and IR results on the CCP–CO complex in solution revealed that the oxygen atom of the bound CO is H-bonded with a distal residue,[120] subsequently identified as the distal Arg.[59] However, this H-bond interaction is weaker than that observed for the HRP–CO form I, characterized by ν(FeC) and ν(CO) at 539 and 1906 cm^{-1}, respectively (Figure 22 and Table 3). This result agrees with the conclusions obtained from the comparative

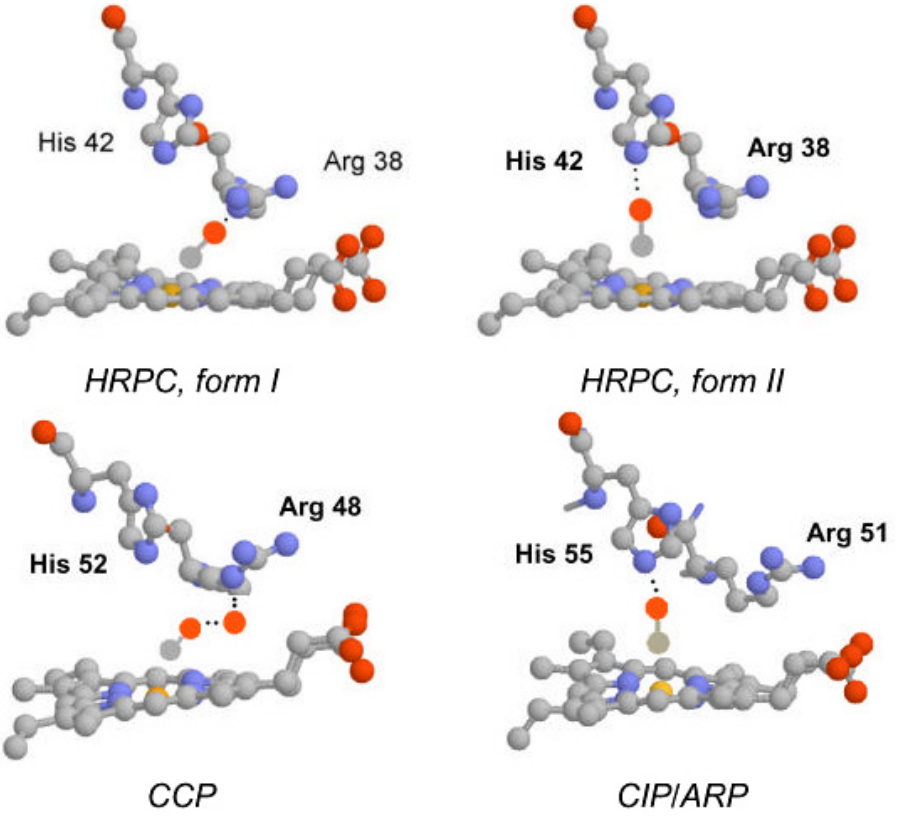

CO complex	ν_{FeC}	ν_{CO}	*symbol*
Tea peroxidase	545	1892	△
HRPC, form I	539	1906	○
CCP	530	1922	□
CIP	519	1930.5	◊
HRPC, form II	516	1934	○
HRPC, acid pH	492	1967	○

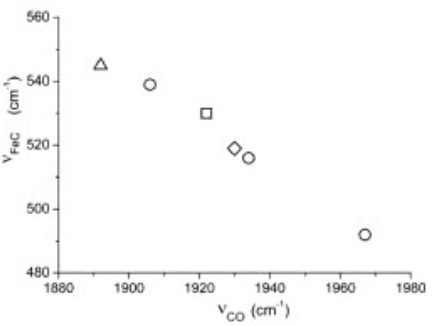

Figure 22. H-bonding interactions of bound CO in HRPC, CCP and ARP/CIP. The structure of CCP–CO is adapted from Ref. 174. The other structures are pictorial representations based on the RR results. The table and plot show the inverse linear ν_{FeC}/ν_{CO} frequency correlation for the above proteins and for the extreme back-bonding cases of HRPC–CO at acid pH[170] and the CO complex of tea ascorbate peroxidase.[290] (Reprinted with permission from Smulevich, G.; Feis, A.; Howes, B. D. *Acc. Chem. Res.* **2005**, *38*, 433. © 2005, American Chemical Society.)

Table 3. Vibrational frequencies (cm^{-1}) of the FeCO unit in the Fe(II)–CO complexes of ARP/CIP, HRPC, CCP, KatG and selected mutants at different pH values. In parentheses is indicated the ^{13}CO isotopic shift.

	ν_{CO}	(cm^{-1})	ΔD_2O	ν_{FeC}	(cm^{-1})	δ_{FeCO}	Ref.
Acid forms							
Class I							
CCP	1922		–2	530	(–5)		120
CCPMI	1922			503			″
Arg48Leu CCPMI	1941			500	(–8)		″
Arg48Lys CCPMI	1936			510	(–6)		″
Trp51Phe CCPMI	1932			528	(–5)		″
Asp235Asn CCPMI	1933			531	(–5)		″
M. tub. KatG	1926			522		584	294
S315T *M. tub.* KatG	1926			520		585	″
M. tub. KatG	1925			525	(–6)	586	116
Y229F *M. tub.* KatG	1930			523		586	117
Class II							
ARP/CIP	1930.5		–1	519	(–5)		181
Asp245Asn	1939.5			517	(–6)		″
Arg51Lys	1934.5			514			″
Arg51Gln	1933			518			″
Arg51Asn	1932			519	(–3)		″
	1942			506	(–3)		″
Arg51Leu	1925	(–43)		533	(–5)		″
	1943			519	(–5)		″
	1938.5	(–44)		521	(–6)		″
Phe54Trp	1919			528			″
	1930			518			″
	1942			508			″
Phe54Val	1944			508			″
Class III							
HRPC (form I)	1906		–2	539	(–4)		127, 170, 177–179
HRPC (form II)	1933		–1	516	(–5)		″
HRPC (pH 3)	1967			492			170
Arg38Leu	1941.5		–1	515	(–5)		295
Phe41Val (form a)	1912		–1	526	(–5)		68
Phe41Val (form b)	1919		–1	519	(–5)		″
TcAPXII[a]	1892	(–44)		545	(–5)		290
	1908	(–42)		537	(–6)		
Alkaline forms							
Class I							
CCP	1948			503			127
CCPMI	1948			507	(–7)		120
Arg48Leu	1951			500	(–4)		″
Arg48Lys	1945			507	(–5)		″

(*Continued*)

Table 3. (*Continued*)

	ν_{CO}	(cm^{-1})	ΔD_2O	ν_{FeC}	(cm^{-1})	δ_{FeCO}	Ref.
Asp235Asn	1951			505	(–5)		″
M. tub. KatG	1965			499			294
S315T *M. tub.* KatG	1956			500			″
Class II							
ARP/CIP	1951			503	(–3)		181
Asp245Asn	1959			503	(–4)		″
Arg51Lys	1948			507			″
Arg51Gln	1947			502			″
Arg51Asn	1952			495	(–4)		″
Arg51Asn	1942			506	(–3)		″
Arg51Leu	1956			503			″
Arg51Leu	1925	(–43)		533	(–5)		″
Phe54Trp	1956			503			″
Class III							
HRPC	1933			530			295, 296
TcAPXII[a]	1930	(–47)		516	(–6)		290
	1946	(–46)		503	(–5)		″

[a]Cationic ascorbate peroxidase isoenzyme II from tea.

study of compound I formation upon mutation of the distal Arg and His in CCP and HRPC. The removal of the positively charged guanidinium group of Arg from the active site is more critical in HRPC than in CCP.[180] In the other conformer of HRPC–CO, form II (characterized by ν(FeC) and ν(CO) at 516 and 1934 cm^{-1}), His42 is the interacting residue. The vibrational frequencies of this latter conformer are very similar to those observed for the ARP/CIP–CO complex[181] (see point iv).

(iii) The H-bonding capability of the distal Arg residue influences the water molecule occupancy of the distal cavity, which orchestrates the H-bond network of the distal cavity and the ability to form stable complexes between anionic ligands and the heme Fe atom. However, it is not essential to stabilize the CO ligand, as in the case of ARP/CIP–CO, demonstrating that Arg51 of ARP/CIP does not interact with the CO molecule directly, but modulates the back-bonding and the CO dissociation rate.[181]

(iv) The capability of CO to form H-bonds with the distal residues clearly depends on their geometrical disposition and the size of the distal cavity. The Fe(II) ARP/CIP–CO complex is characterized by a much more open cavity than the other peroxidases. On the basis of the X-ray structure of the Fe(III) protein[42] (Figure 23), it appears that only the His residue is able to interact with the CO ligand, since the location of the Arg residue precludes its interaction with the CO.

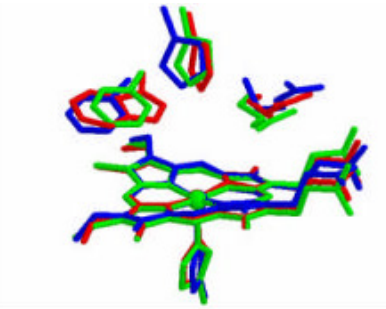

Distances (Å) between the Fe atom and the N atoms of the distal Arg				Residues involved in H-bonds with CO
	N_ε	NH_1	NH_2	
HRPC	4.6	5.8	6.7	His Arg
CCPMI	5.5	7.0	7.7	H_2O Arg
ARP/CIP	6.3	8.0	8.3	His

Figure 23. Comparison between the heme pocket of HRPC,[46] CCPMI[92] and ARP/CIP.[42] The table reports the relative distances between the Fe atom and the N atom of the distal Arg, together with residues involved in the H-bonds with the bound CO, as inferred on the basis of the RR spectra.

By comparing the structures of Fe(III) CCP(MI)[92] and HRPC,[46,47] it can be seen that the terminal nitrogen atom of the distal Arg is located at a shorter distance (about 1 Å) from the heme iron in HRPC than in CCP. This characteristic accounts for the stronger H-bond interaction with CO in HRPC compared to CCP. Moreover, both the distal His and Arg residues in HRPC are involved in H-bond interactions with the coordinated CO. The different geometric dispositions and p*K*a's of the distal residues in the two proteins are considered to be responsible for the different stabilization mechanisms.

F. Catalytic Intermediates

Peroxidases catalyze the oxidation of a wide variety of organic and inorganic substrates at the expense of hydrogen peroxide via the formation of two higher-valence intermediates, commonly named compounds I and II.[157,182] The initial step in the catalytic mechanism is heterolysis of the O–O bond of hydrogen peroxide, resulting in compound I and water. Compound I is two oxidation equivalents higher than the resting form, containing an iron oxoferryl center [Fe(IV)=O] and a porphyrin cation radical ($Por^{\bullet+}$). As will be discussed later, in some peroxidases the

radical can be formed on an amino acid residue (as in the case of CCP, in which the long-lived intermediate known as compound ES consists of a ferryl porphyrin with a radical localized on the Trp191 residue).[30]

Compound I is then reduced back to the resting state by two sequential one-electron oxidations of two substrates, SH, via the intermediate compound II [Fe(IV)=O].

The reaction can be summarized as follows:

$$\text{Resting state Fe(III)} + H_2O_2 \rightarrow \text{Compound I [Fe(IV)=O Por}^{\bullet+}\text{]} + H_2O$$

$$\text{Compound I [Fe(IV)=O Por}^{\bullet+}\text{]} + SH \rightarrow \text{Compound II [Fe(IV)=O]} + S^{\bullet}$$

$$\text{Compound II [Fe(IV)=O)]} + SH \rightarrow \text{Resting state Fe(III)} + S^{\bullet} + H_2O$$

It is of note that, historically, the terms "compound I" and "compound II" have been used to refer to the two reactive intermediates formed in the catalytic cycle of HRP and for which the electronic structures are [Fe(IV)=O Por$^{\bullet+}$] and [Fe(IV)=O], respectively, as shown in the above reaction scheme. They also reflect the idea that only the heme is the catalytically active species. In order to underline the differences observed in the case of CCP, in which the more stable and detectable intermediate has a different electronic structure, [Fe(IV)=O Trp$^{\bullet+}$], the term "compound ES" was given to it. As will be described in the following section, a higher degree of complexity in the reactive intermediates has been elucidated in the past few years, in particular for the bifunctional peroxidases. Hence, the use of the nomenclature — compound I, compound II and compound ES — for these more complex cases can be misleading, and it is preferable to use the actual electronic structure to accurately define the reactive intermediates. In this section, the terms "compound I" and "compound II" are used in the description of the HRP case and ES in the case of CCP, since there is no ambiguity. Furthermore, they reflect the commonly used terminology in the literature. For the more complex and recently characterized cases, the electronic structure will be used.

The conserved distal His and Arg residues, which render the heme cavity of peroxidases much more polar than in the globins, are involved in acid-base catalysis and cleavage of the peroxide O–O bond during the catalytic cycle. The postulated mechanism of peroxide decomposition relies on the concerted roles played by the proximal histidine, the distal histidine and arginine, through H-bonds and charge stabilization, as originally proposed by Poulos and Kraut.[167] In particular, the distal His functions as an acid/base catalyst that assists in the deprotonation of hydrogen peroxide and facilitates its binding to the heme iron, and the distal Arg assists in charge stabilization during the formation of compound I. The proximal His ligand of the heme iron is H-bonded to a conserved Asp residue which imparts an imidazolate

character. The imidazolate character of the proximal heme ligand has been proposed to stabilize the ferryl intermediate due to its electron-donating properties.

On the distal side, the concerted interactions of His and Arg with hydroperoxide bound to the heme have been called "the pull effect", and the increased electron donation of the proximal imidazole ligand is called "the push effect" since it stabilizes the high oxidation state of the iron in compound I, leading to the rapid reaction of peroxidases with hydrogen peroxide.[38]

1. *X-Ray Structures of Intermediates*

In a recent review, the novel high-resolution X-ray structures of resting state CCP[169] and HRP[47] together with those of their reactive intermediates,[183] are compared and extensively discussed.[184] Figure 24 shows the distal (His and Arg) and proximal (His and Asp) key residues in the heme cavities of HRPC and CCP, and the H-bond interactions between these residues and water molecules. In addition, H-bonds between the ferryl-ligated oxygen, the key residues and the closest water molecules are shown for the high-valence intermediates. The proximal heme cavity of CCP contains a Trp residue (Trp191, the site for the radical formation) and a Met residue (Met172), which in HRP are substituted by Phe221 and Ser167, respectively (not shown in the figure).

The higher resolution of the recent crystal structures of Fe(III) CCP and compound ES[169] enables very accurate determination of the changes in heme parameters which occur upon reaction with hydrogen peroxide. In particular:

(iii) In the resting state of CCP a distal water molecule is at 2.33 Å from the iron and is H-bonded to the distal His52. This form corresponds to a predominant 5cHS heme state with a minor 6c aquo form, as observed in the single-crystal RR spectra.[89] Upon passing from the resting Fe(III) state to compound ES, the His–Fe bond distance increases and the iron moves into the porphyrin plane, leading to shorter pyrrole N–Fe bonds. The Fe(IV)–O bond distance is 1.87 Å, more similar to HRP compound II (1.84 Å) than HRP compound I (1.71 Å).

(iv) The distal Arg48 residue, a key residue for the formation of compound ES, in resting state CCP occupies two positions: an "out" position close to the heme propionate and an "in" position close to the heme iron. In compound ES, only the "in" position exists, which enables Arg48 to H-bond with the ferryl O ligand.[169] The "in" position has also been observed in the CCP fluoride complex.[173]

(v) In the resting state, the proximal Met172 residue is also best modeled in terms of two conformations. In compound ES, Met172 occupies the position closer to the proximal His175 ligand. The distance between the Met172 SG atom and His175 varies from 6.4 Å in the resting state position to 4.4 Å in compound ES.

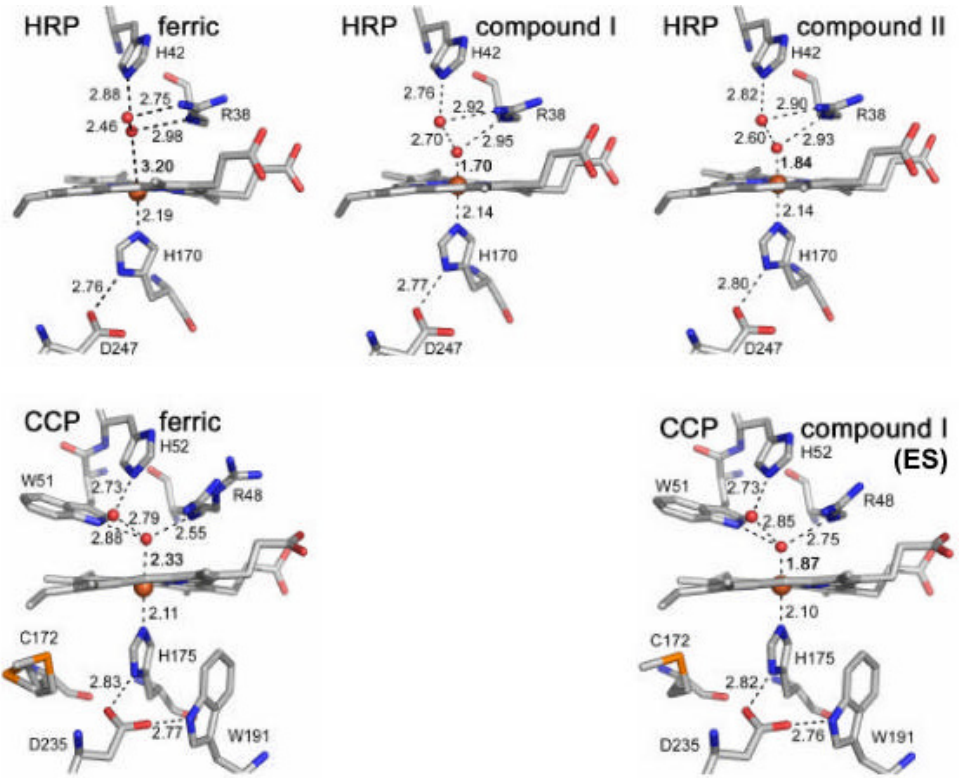

Figure 24. Crystal structure of the heme cavity with key residues of resting state HRP, and CCP, together with their intermediate compounds. Hydrogen bonds based on distance criteria are indicated by dashed lines. Distances are in Å. The following color coding is used: carbon is light gray, oxygen red, nitrogen blue, sulfur dark yellow and iron orange. (A) Fe(III), compounds I and II HRP (1ATJ, 1HCH, 1H55); (B) Fe(III) and compound I (ES) CCP (1ZBY, 1ZBZ).[47,169,183] Since the Fe^{4+}–O distance observed for HRP-II at neutral pH is quite close to 1.87 Å, as found for CCP compound I (ES), this latter has been positioned below HRP compound II, to underline their similarities. (Adapted from *J. Inorg. Biochem.* **2006**, *100*, 460–476. Hersleth, H. P.; Ryde, U.; Rydberg, P.; Gorbitz, C. H.; Andersson, K. K., Crystallographic and spectroscopic studies of peroxide-derived myoglobin compound II and occurrence of protonated Fe-IV-O. © 2006, with permission from Elsevier.)

Finally, a region between residues 193–195 also shows an ordering process upon passing from the Fe(III) state to the compound ES intermediate. The ordering of Met172 and the 193–195 residues region have been suggested to provide electrostatic stabilization of the cationic Trp191 radical.[185]

The crystal structures of the HRP Fe(III) resting state and its compounds I and II are shown in Figure 24A.[47,183] The Fe(III) state has a water molecule in the active site within H-bonding distance to His42, at 3.20 Å from the iron. This leads to a

Table 4. Resonance Raman frequencies (cm^{-1}) and assignments for resonance Raman bands of resting state and intermediate compounds of HRP.[74,148,197,198,293]

Mode[a]	Pol.	Resting state 6cQS	Resting state 5cQS	[Fe(IV)=O Por$^{\bullet+}$] 6cLS	[Fe(IV)=O] 6cLS	Δ^b	Predominant mode composition
ν_{10} (B_{1g})	dp	1620	1636	1636	1639	–3	$\nu(C_\alpha–C_m)$
Vinyl $\nu_{C=C}$		1630			1630		Vinyl $\nu_{C=C}$ (2)
Vinyl $\nu_{C=C}$		1624			1620		Vinyl $\nu_{C=C}$ (4)
ν_{37} (E_u)	p	1579	1584	1614	1602	+12	*c*
ν_2 (A_{1g})	p	1566	1572	1606	1587	+19	$\nu(C_\beta–C_\beta)$
ν_{11} (B_{1g})	dp	1547	1553	1570	1560	+10	$\nu(C_\beta–C_\beta)$
ν_{38} (E_u)	dp				1552		*c*
ν_3 (A_{1g})	p	1491	1499	1504	1509	–5	$\nu(C_\alpha–C_m)_{sym}$
ν_{28} (B_{2g})				1458	1472	–14	$\nu(C_\alpha–C_m)_{sym}$
Vinyl	dp	1427		1428	1427	+1	Vinyl $\delta(=CH_2)_s$
ν_{29} (B_{2g})		1404		1402	1398	+4	ν(pyr quarter ring)
ν_4 (A_{1g})	p	1373		1359	1379	–20	ν(pyr half ring)$_{sym}$
ν_{21} (A_{2g})		1305		1322			δ (=C_mH)
	ap			1164			
ν_{14} (B_{1g})	dp	1131		1135			$\nu(C_\beta$–vinyl)
				974			
ν_{46} (B_u)				946			
				927			
γ_4 (A_{1u})	dp			828	831		
				809	808		
$\nu_{Fe(IV)=O}$	p				789		$\nu_{Fe(IV)=O}$ alk. pH
$\nu_{Fe(IV)=O}$	p			794	774	+20	$\nu_{Fe(IV)=O}$ pH 7, isoenzymes B, C
$\nu_{Fe(IV)=O}$	p			786			$\nu_{Fe(IV)=O}$ pH 4.4, isoenzymes B, C
ν_{15} (B_{1g})	dp			758	756		
					746		
				715	718		
$2\nu_8$ (A_{1g})	p			692			
ν_7 (A_{1g})	p				679		
				648			

[a] Mode numbering and predominant mode compositions follow Refs. 297 and 298.
[b] Frequency differences in cm^{-1} between the [Fe(IV)=O Por$^{\bullet+}$] and [Fe(IV)=O] species.
[c] The predominant mode compositions, $C_\beta–C_\beta$ vs. $C_\alpha–C_m$ for ν_{37} and ν_{38}, are not yet certain.[297,298]

predominant pentacoordinate state, as confirmed by the RR spectra of the single crystal[91] (Table 4), with the iron being slightly shifted toward the proximal side of the heme plane, giving rise to a saddle-shaped distortion. The same type of distortion is seen in compounds I and II, even if the iron becomes six-coordinated and is positioned in the heme plane. In compounds I and II, the oxygen ligated to the iron is H-bonded to the N_ε of Arg38 and to a (putative leaving) water molecule, which in turn is H-bonded to the $N_{\varepsilon 2}$ of His42 and to NH_1 of the distal Arg38. One-electron reduction from

compound I to compound II does not change the Fe–His170 bond, giving rise only to small changes in the two Arg38 and His42 H-bonding distances. However, compound II differs from compound I as a consequence of the elongation of the Fe–O bond, which is 1.70 Å in compound I and 1.84 Å in compound II. This can be interpreted as a protonation of the oxygen, which would change the Fe–O interaction from a double bond in compound I to a single bond in compound II.

The intermediates of the heme-containing enzymes have been extensively studied for many years by different spectroscopic methods, such as UV/visible, near-IR, CD, EPR, resonance Raman, Mossbauer, ENDOR and MCD (magnetic circular dichroism). In this section the results obtained by multifrequency EPR and RR spectroscopies will be discussed. To illustrate the electronic absorption spectra of peroxidase intermediates, we show in Figure 25 the well-characterized case of HRPC.[186] Compound I (green trace) exhibits the characteristic electronic absorption spectrum of an [Fe(IV)=O Por$^{\bullet+}$] species.[187,188] Restoration of an electron to the porphyrin ring generates the [Fe(IV)=O] species (red trace).[24,189]

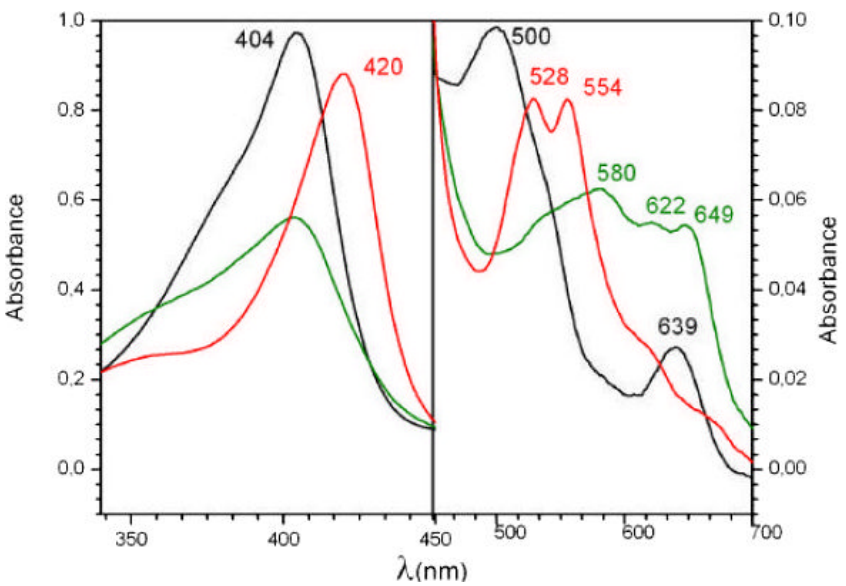

Figure 25. The UV-vis electronic absorption spectra of horseradish peroxidase C in the resting [Fe(III)] state and the catalytic intermediates. The first committed intermediate formed in the catalytic cycle and upon the two-electron reaction of the Fe(III) enzyme (black trace) with hydrogen peroxide is the [Fe(IV)=O Por$^{\bullet+}$] species (green trace), The corresponding 9 GHz EPR spectrum is shown in Figure 27. The 60% hypochromicity of the Soret band (404 nm) and the charge-transfer band at 649 nm are characteristics of the [Fe(IV)=O Por$^{\bullet+}$] species. A clear shift, and narrowing of the Soret band together with the appearance of the α and β bands at 528 and 554 nm, are characteristic of the [Fe(IV)=O] species (red trace) and result from the one-electron reaction of the [Fe(IV)=O Por$^{\bullet+}$] with the substrate.

2. *Resonance Raman Characterization of Intermediates*

In a previous edition of *The Porphyrin Handbook*, Kincaid extensively reported the RR data obtained on the intermediate compounds of peroxidases.[172] Moreover, recently, in a special issue of the *Journal of Inorganic Biochemistry* devoted to high-valent iron intermediates in biology, a number of articles reviewed the RR results obtained on the intermediate compounds of peroxidases.[184,186,190]

In principle, RR spectroscopy is well suited for investigating the intermediates of the peroxidase cycle since the vibrational frequencies of the [Fe(IV)=O] and [Fe(IV)=O Por$^{\bullet+}$] intermediates are different (Figure 26, from Ref. 186). In fact, following the four-orbital model proposed by Gouterman,[191] the formation of a porphyrin π cation radical results from the removal of an electron from either of the two highest-occupied molecular orbitals, a_{1u} and a_{2u}, which are nearly degenerate. Hence, the compound I species which is formed that is of either $^2A_{1u}$ or $^2A_{2u}$ symmetry, is expected to give rise to vibrational frequencies different from those of the nonradical intermediate.[187,188,192–194] Therefore, (i) the identification of the frequencies of the in-plane heme skeletal modes enables the nature of the electronic ground states to be characterized and (ii) the frequency of the ν(Fe(IV)=O) stretching mode, which can be identified via the solvent oxygen exchange since its frequency is ^{18}O-sensitive, should provide information on the characteristics of the intermediate compounds. However, RR spectra for intermediates of the [Fe(IV)=O Por$^{\bullet+}$] type have sometimes been contradictory, due to the weakness of the RR signals from porphyrin π cation radical species, the presence of strong signals due to impurities, and further complications arising from the photolability, which causes the [Fe(IV)=O Por$^{\bullet+}$] signals to appear similar to those of the [Fe(IV)=O] species or other forms.

Table 5 compares the absorption maxima of resting state and oxidized intermediates of several heme-containing peroxidases. Table 6 compares the corresponding RR frequencies for the ν(Fe(IV)=O) stretching modes of the intermediate compounds.

A comparison of these results, together with the structure of the resting states and the intermediate compounds when available, allows a number of conclusions to be drawn:

(i) The [Fe(IV)=O Por$^{\bullet+}$] species exhibits unique and characteristic vibrational spectra, in agreement with the studies of synthetic systems which indicate that its vibrational signatures are different from the nonradical forms. The frequencies and band assignments are given in Table 6.

(ii) The vibrational spectra of the various ferryl intermediates so far detected in peroxidases, namely LIP,[195] ARP/CIP,[196] HRPA and HRPC,[197,198] CCP (compound ES),[199] KatG,[200] are very similar.

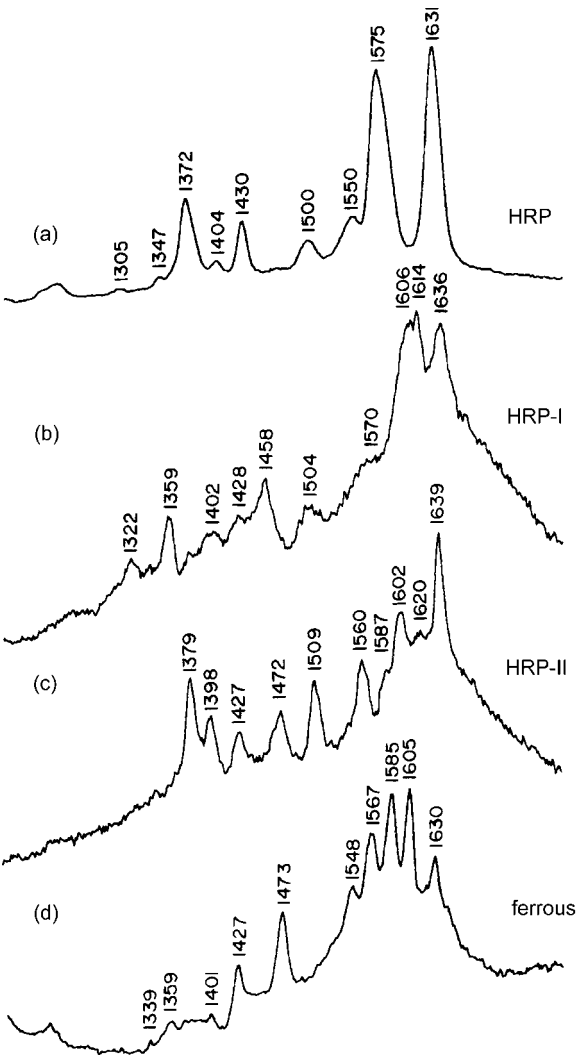

Figure 26. Resonance Raman spectra of: (a) resting horseradish peroxidase; (b) compound I; (c) compound II; (d) Fe(II) horseradish peroxidase; 356.4 nm excitation, pH 6.8. (Reprinted from *J. Inorg. Biochem.* **2006**, *100*, 480–501. Terner, J.; Palaniappan, V.; Gold, A.; Weiss, R.; Fitzgerald, M. M.; Sullivan, A. M.; Hosten, C. M. Resonance Raman spectroscopy of oxo-iron(IV) porphyrin pi-cation radical and oxoiron(IV) hemes in peroxidase intermediates.)

(iii) The ν(Fe=O) mode gives rise to a polarized band (ρ = 1/8) characterized by ^{18}O-sensitivity (see Table 4). The intensity of the metal–oxo vibration is greatly enhanced using Soret excitation between 400 and 450 nm.[186] However, recently a new Raman excitation profile maximum of an oxygen-to-iron charge-transfer transition for the ν(Fe=O) mode at 580 nm was found.[201]

Table 5. Electronic absorption maxima (nm) of the Fe(III) resting state and the intermediate compounds of HRPC, CCP and ARP/CIP.

Protein	Resting state	[Fe(IV)=O Por$^{\bullet+}$]	[Fe(IV)=O] and [Fe(IV)=O Trp$^{\bullet+}$] CCP[a]	Ref.
HRPC	403, 498, 643	400, 525(sh), 577, 622(sh), 651	420, 527, 555	299
CCP	408, 507, 647		418, 530, 560	300, 301
ARP/CIP	405, 504, 645	402, 658	419, 530, 554	302

[a] The Fe(IV)–O distance observed for [Fe(IV)=O] HRP at neutral pH is quite close to 1.87 Å, as found for [Fe(IV)=O Trp$^{\bullet+}$] CCP. Moreover, the electronic absorption of this latter compound is very similar to the [Fe(IV)=O] species of both HRP and ARP/CIP. Therefore, as for Table 6, these compounds are placed in the same column to underline their similarities.

Table 6. Resonance Raman frequencies (cm^{-1}) of the $\nu_{Fe(IV)=O}$ stretching mode observed for the intermediate compounds of HRPA, HRPC, CCP and ARP/CIP. The isotopic shift (in cm^{-1}) observed in $H_2{}^{18}O_2$ is reported in parentheses.

Protein	[Fe(IV)=O Por$^{\bullet+}$]	[Fe(IV)=O] and [Fe(IV)=O Trp$^{\bullet+}$] CCP[a]	Ref.
HRPA		789 (34), pH 11 778 (34), pH 5	211
HRPC	792 (38), pH 7.0 786 (29), pH 4.4	787 (30), pH 11 788 (31), pH 10.6 775 (30), pH 7	186, 189, 201, 208, 211, 303–305
ARP/CIP	781 (37, 50), pH 7.3	787 (38), pH 9.6 788 (39)	196, 201
CCP		753 (28) 767	199, 202

The authors obtained RR spectra of the ferryl intermediates for both HRPC and ARP/CIP excited at 580 and 590 nm, respectively, characterized by spectra of remarkably high quality, similar to those typical of Soret excitation (Tables 4 and 6).

(iv) Unlike the frequency reported for the [Fe(IV)=O Por$^{\bullet+}$] intermediate, the RR frequencies of the ν(Fe(IV)=O) stretching mode observed for the [Fe(IV)=O] intermediate in HRPA, HRPC and ARP/CIP at similar pH values are very similar. We will discuss hereafter the RR frequency in the context of the high-resolution structures of the intermediate compounds of HRPC and CCP. The RR frequencies of the ν(Fe(IV)=O) stretching mode of HRPC and CCP intermediates agree well with their expected structures. Comparing the two intermediates for HRPC at neutral pH, the ν(Fe=O) vibration occurs at 792 cm^{-1}

for the [Fe(IV)=O Por$^{\bullet+}$] intermediate, and 17 cm^{-1} lower (775 cm^{-1}) for the [Fe(IV)=O] state. The crystal structures[183] indicate that a water molecule in the heme distal pocket moves 0.1 Å closer to the ferryl oxygen upon the formation of the [Fe(IV)=O] intermediate. Moreover, the [Fe(IV)=O] intermediate differs from [Fe(IV)=O Por$^{\bullet+}$] due to the elongation of the Fe–O bond, i.e. 1.70 Å vs. 1.84 Å. This can be interpreted as a protonation of the oxygen, which would change the Fe–O interaction from a double bond in the [Fe(IV)=O Por$^{\bullet+}$] intermediate to a single bond in [Fe(IV)=O], in agreement with the RR downshift observed for the ν(Fe=O) band. Therefore, the RR 18 cm^{-1} downshift observed for the ν(Fe(IV)=O) stretching mode of HRP upon conversion to the ferryl species can be attributed to the formation of ferryl oxygen by means of charge transfer and proton transfer, accompanied by an increase in H-bonding strength with a nearby water molecule. The Fe(IV)–O distance observed in the crystallographic structure of HRP in the [Fe(IV)=O] intermediate state at neutral pH is quite close to 1.87 Å, as found for the [Fe(IV)=O Trp$^{\bullet+}$] intermediate from CCP. In the latter case, Poulos and coworkers suggested that this Fe^{4+}–O distance corresponds to a single Fe(IV)–O bond.[169] It is noteworthy that the RR frequency of the ν(Fe=O) band in the CCP ferryl intermediate is even lower than that of the HRP ferryl intermediate (775 cm^{-1}), being observed at 753 cm^{-1} or 767 cm^{-1} in two different reports.[199,202] This is consistent with an increased H-bonding to the ferryl oxygen in CCP, as the oxygen is H-bonded to Arg48 and Trp51, whereas the homologous Phe41 of HRP is unable to form an H-bond. Moreover, the X-ray structure of CCP shows that the guanidinium side chain of Arg48 swings in to make close contact with the ferryl oxygen.

Prior to the determination of the X-ray structure, the Fe(IV)–O distance of HRP compound II was determined by EXAFS. The EXAFS studies on HRP in the 1980s showed two different bond lengths for compound II, 1.64 Å and 1.93 Å, while only a short bond was observed for CCP (1.67 Å) and (Mb 1.69 Å).[203–205] Clearly, the inconsistency between the reported HRP-II Fe–O bond lengths has resulted in considerable confusion. However, a recent study by Gray and coworkers gave only a short Fe–O distance for HRP.[206] Moreover, the Fe–O bond length in HRP-II was found to be pH-sensitive, being 1.90 Å at pH 7 and 1.72 Å at pH 10,[207] suggesting a transition from single bond to double bond. The Raman frequencies of the ν(Fe(IV)=O) group are also pH-sensitive, increasing from 775 cm^{-1} at neutral pH to 789 cm^{-1} at alkaline pH. The pH effects on the ν(Fe(IV)=O) frequency of HRP-II[208–211] and the ν(Fe^{2+}–Im) stretching frequency[103] have been attributed to ionization of the same distal histidine, His42, with a perturbation of the distal H-bonding network by the protonation status of $N_{\epsilon 2}$ and orientation of a bridging distal

water molecule, as suggested by Terner.[186] This interpretation appears to be confirmed by the effect of the mutation of His42 to glutamic acid or glutamine. The ν(Fe(IV)=O) stretch of compound II observed at 775 cm^{-1} in the wild type at neutral pH shifts to 789 cm^{-1} in the mutant, a frequency that compares well with that observed in the wild-type compound II at alkaline pH. This was attributed to lack of an H-bond to the ferryl oxygen due to the absence of the distal His.[146] Therefore, the presence of H-bonding between the oxoferryl iron and distal residues in peroxidases lowers this frequency relative to those of synthetic model compounds.

(v) The ν(Fe(IV)=O) stretch of compound II is also sensitive to deuteration. An upshift of 3 cm^{-1} upon deuteration was observed for the neutral/lower pH ν(Fe=O) frequencies, accompanied by dramatic increases in intensity.[209,211,212] This change has been attributed to a deuterium-induced decrease in the strength of the H-bond between the ferryl oxygen and the protonated Arg38.[186]

Several theoretical and experimental investigations have raised the question of whether the protonated ferryl Fe(IV)–OH species might be a better description than Fe(IV)=O for compounds I and II.[184,190] The protonation status of the ferryl group, as well as the presence of a distal-pocket proton delivery network linked to the oxo ligand, can play an important role in proton-coupled electron transfer during catalysis. In this regard, the presently available experimental data are not in complete agreement. As noted in the foregoing discussion, high-resolution crystal structures of the compound II intermediate of HRPC and the [Fe(IV)=O $Trp^{\bullet+}$] intermediate of CCP indicate that the ferryl oxygen is protonated.[169,183] In both cases precautions were taken to ensure that reduction of the active centers induced by the X-ray radiation did not occur. In the case of CCP compound ES, UV-vis of dissolved crystals and single-crystal EPR at low temperature before and after X-ray exposure were used to characterize the heme state. No reduction was observed.

Particularly elaborate procedures were utilized for the intermediate of HRP, which is more suseptible to photoreduction than CCP, including the use of a multicrystal data collection strategy and monitoring of the electronic absorption spectum of the crystals at 100 K before and after X-ray exposure with a microspectrophotometer. This procedure enabled nearly pure compounds I and II to be studied. An analysis of the available RR data by Terner and coworkers is in accord with a protonated status for the ferryl oxygen. On the basis of a comparison of the ν(Fe(IV)=O) stretching frequencies and oxygen atom solvent exchangeability of many heme proteins at various pHs, they noted that oxygen atom solvent exchangeability is more pronounced at lower pH and the corresponding ν(Fe(IV)=O) stretching frequencies are lower. The authors concluded that this implies that compound II has at least a partial Fe(IV)–OH character, conferred by

strong H-bonding from within the distal pocket, which contributes to the substantial lowering of the *v*(Fe(IV)=O) stretching frequencies of compounds II relative to those of model compounds.[186] As pointed out by Babcock and coworkers, though,[213] it is important to recall in such a discussion that the pH-dependent shift of *v*(Fe(IV)=O) to lower frequency upon protonation of the distal histidine cannot be unambiguously assigned to the H-bond formed with the Fe=O group. Protonation of the distal histidine also strengthens the proximal Fe–N(His) bond through the H-bonding network linking the distal and proximal sides of the heme, which would lead to a lower *v*(Fe(IV)=O) frequency. RR studies of distal-site-directed mutants of HRP have clearly demonstrated that disruption of the H-bonds between distal residues leads to a downshift of the proximal Fe–N(His) stretching frequency.[67] However, it is noteworthy that, at least in the case of HRP, no variation in the proximal Fe-His170 bond is detected upon conversion from compound I to compound II.[183] Behan and Green suggest that the available RR and Mossbauer data are not consistent with a protonated ferryl oxygen.[190] In particular, application of Badger's rule shows good agreement between RR data of Fe–O stretching frequencies and Fe-oxo distances determined by EXAFS measurements. The contrast of these conclusions with respect to that resulting from the crystal structures is proposed to depend on the possibility that, since some reduction of high-valent hemes might occur in the X-ray beam during data collection,[214] the observed Fe–O distance determined by the X-ray structure might be affected by such a reduction. This suggestion appears to be contradicted by a recent work where high-resolution crystal structures of myoglobin in the pH range 5.2–8.7 have been used as models for the peroxide-derived compound II intermediates in heme peroxidases.[215] In this work a combination of X-ray crystallography, microspectrophotometry, RR on both solution and single crystals, and Mössbauer spectroscopy were used to elucidate the structure of Mb compound II. The compound II state of myoglobin in crystals was controlled by single-crystal microspectrophotometry before and after synchrotron data collection. Radiation-induced changes were observed resulting in an unknown unstable intermediate H, which by heating regenerates compound II. Based on the crystallographic and spectroscopic data, the authors suggest that for Mb compound II the observed Fe–O bond length (1.86–1.90 Å) is consistent with that of a single bond, the presence of an Fe(IV) center being indicated by Mössbauer spectroscopy. Since this long Fe–O bond for compound II is also consistent with those measured for compound II of HRP, catalases, and the isoelectric compound ES in CCP, the authors concluded that this finding is probably a general feature of the compound II states and the isoelectric compound ES states in heme proteins. However, recent EPR and ENDOR studies of cryoreduced compound II of various peroxidases and myoglobin[216] suggest that the high-valent iron center of globin and HRP compounds II, as

well as that of CCP compound I (CCP-ES), is $[Fe(IV)=O]^{2+}$ and that its cryoreduction produces $[Fe(IV)–OH]^{+}$. This product is formed presumably because the heme is linked to a distal-pocket hydrogen bonding/proton delivery network through an H-bond to the "oxide" ligand. The data also indicate that Mb and HRP compounds II exist as two major conformational substates.

3. *Multifrequency EPR Spectroscopy: Identification and Reactivity of Intermediates*

EPR spectroscopy has been widely used for elucidating the electronic structure of active sites in heme-containing proteins.[21,217] As mentioned before, specific information on the iron oxidation, spin state and coordination number can be obtained from the low-temperature (4 K) EPR spectrum of the heme iron. Moreover, the intermediates resulting from changes in the oxidation state of the heme iron and formation of radical species can be monitored by EPR spectroscopy. RR and EPR spectroscopies are fairly complementary techniques for the characterization of hemes (see for example Ref. 218). The information inferred from the low-temperature 9 GHz EPR spectrum of peroxidases in their resting (Fe(III)) state is less detailed than that obtained from the RR spectrum (see previous section), although EPR spectroscopy has proven to be important in elucidating long-range interactions of amino acid residues with the heme iron.[26] In the case of reactive intermediates, the distinct EPR spectra (g-tensors) and magnetic properties of the heme iron and radicals involved, as well as the possibility of characterizing the radicals formed as substrate products of the reaction, render the EPR technique particularly advantageous.[219] Heme peroxidases, in particular HRP and CCP, have been extensively and thoroughly characterized by EPR spectroscopy. Comprehensive reviews on the topic are available, and hence only selected aspects will be discussed in this section with the aim of highlighting putative new research directions. A very complete description of the full body of work on HRP and CCP can be found in the book *Heme Peroxidases*, by Dunford.[15]

The 9 GHz EPR spectrum, recorded at 4 K, of the first committed intermediate in the catalytic cycle of HRP that is formed upon reaction of the Fe(III) enzyme with hydrogen peroxide, shows a very broad EPR signal extending over about 2500 G (Figure 27). Such a broad spectrum is hardly detected at temperatures higher than 30 K, due to relaxation broadening.[220] It was necessary to combine 9 GHz EPR and Mössbauer spectroscopies to assign such an abnormal EPR spectrum to that of a porphyrin cation radical magnetically coupled to the ferryl iron, the $[Fe(IV)=O\ Por^{\bullet+}]$ species.[221] The model proposed by Schulz and coworkers to explain the unusually broad EPR spectrum considers that the effective g values of the EPR spectrum depend on the interaction parameter (J), the zero-field splitting

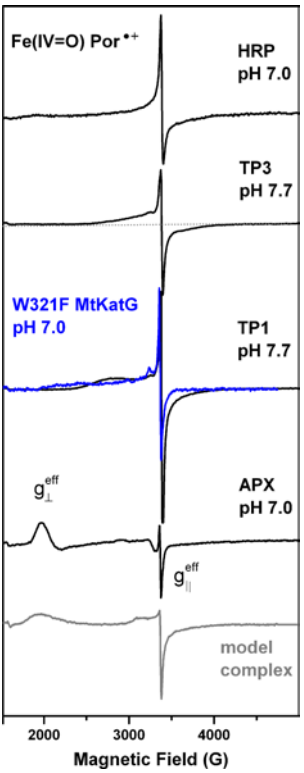

Figure 27. The 9 GHz EPR spectra, recorded at 4 K, of the [Fe(IV)=O Por$^{\bullet+}$] species formed during the reaction of hydrogen peroxide with horseradish peroxidase (HRP), isoforms 1 and 3 of turnip peroxidase (TP1 and TP3), and ascorbate peroxidase (APX). In the case of the W321F variant of *M. tuberculosis* catalase–peroxidase (W321F KatG), it was possible to trap the otherwise short-lived [Fe(IV)=O Por$^{\bullet+}$] intermediate, when incubating the enzyme with five-fold excess of isoniazid prior to the 2s mixing with 15-fold excess of peroxyacetic acid.[31] The [Fe(IV)=O (tmtmp)$^{\bullet+}$] species was obtained upon addition of 10-fold excess of m-cholorobenzoic acid in deuterated methanol to solutions of Fe(III) triflate [Fe(III)Tf(tmtmp)] in methylene chloride or butyronitrile at –78° C.[225] The experimental conditions used for the spectra of HRP, TP1, TP3 and APX are the same as in Ref. 25.

(D) of the oxoferryl iron, and the g values of the interacting species. To a first approximation, when the Zeeman energy is small compared to the zero-field splitting, the effective g-values are given by

$$g_{\|}^{\text{eff}} = g_{\text{rad}},$$

$$g_{\perp}^{\text{eff}} = g_{\text{rad}} + 2\, g_{\perp}^{\text{Fe}}\, (J/D),$$

where g_{rad} is the g value of the isolated porphyrinyl radical (taken as isotropic and approximately equal to 2.0, if considering the resolution of the 9 GHz EPR

spectrum), $g_{\perp}^{Fe}$ represents the g component of the oxoferryl iron ($g_{\perp}^{Fe} = 2.28$ and $g_{\parallel}^{Fe} = 1.94$),[222] and D is the zero-field splitting parameter of the oxoferryl iron. The EPR spectrum of the exchange-coupled species arises from the lowest of the three Kramers doublets, which is well separated in energy from the other two, and can be represented as an effective spin $S^{eff} = 1/2$. A thorough description of the model and its implications was provided by Hoffman and coworkers.[223,224] It is of note that differences in the strength of the exchange-coupling interaction (J) are reflected in the different shapes of the EPR spectra of the [Fe(IV)=O Por$^{\bullet+}$] intermediates in peroxidases, as illustrated in Figure 27. However, in all cases the overall width and temperature dependence of the signals are very similar. Moreover, the estimated values of $J/D = 0.4$, obtained by using the above-mentioned model and the observed effective g values (Figure 27) of the different peroxidases, agree well with a weak ferromagnetic interaction similar to that of the oxoferryl triflate π cation radical obtained from the [Fe(III)Tf(tmtmp)] model complex.[225] The EPR signal observed for the [Fe(IV)=O Por$^{\bullet+}$] intermediate formed upon addition of hydrogen peroxide to the isoforms of turnip peroxidase at basic pH shows a sharp central resonance at $g = 2.0$ with broad asymmetric wings, as in the case of HRP (Figure 27, top). In the cases of ascorbate peroxidase[226] and the turnip isoforms at acidic pHs,[25] the [Fe(IV)=O Por$^{\bullet+}$] intermediate shows an axial signal with the observed $g_{\perp}^{eff}$ between 2.56 and 3.4, and $g_{\parallel}^{eff} = 2.0$ (Figure 27, bottom). The possible correlation of the sign (negative for antiferromagnetic and positive for ferromagnetic) and strength of the exchange interaction with the reactivity of the [Fe(IV)=O Por$^{\bullet+}$] intermediate remains to be explored. In particular, this open question becomes relevant in the light of the remarkable differences observed for the lifetimes of the [Fe(IV)=O Por$^{\bullet+}$] intermediates among different peroxidases, and the possibly correlated propensity to form subsequent protein-based radical intermediates by intramolecular electron transfer, as in the case of isoform 7 of turnip peroxidase at basic pH.[25]

CCP is an interesting example of such a case. The [Fe(IV)=O Por$^{\bullet+}$] intermediate is extremely short-lived, and readily converts to the [Fe(IV)=O Trp$_{191}^{\bullet+}$] species (for a review, see Ref. 15). The electronic absorption spectrum characteristic of the [Fe(IV)=O Por$^{\bullet+}$] species can be detected only when the site for the formation of the Trp radical is removed, i.e. the W191F variant.[227] Even in this case, the transition from the [Fe(IV)=O Por$^{\bullet+}$] to the ferryl species is observed within 8 ms.[227] The mechanism for the selective stabilization of the porphyrin or tryptophanyl radicals is not well understood. As shown in Figure 27, APX forms a relatively stable [Fe(IV)=O Por$^{\bullet+}$] intermediate even though the proximal side Trp, equivalent to Trp191 in CCP (see Figure 2), is conserved. From a comparative study of the active site structure of APX and CCP, including mutations[169] and theoretical calculations,[169,228] it was proposed that the electrostatic environment and redox potentials of the porphyrin or the protein redox cofactors are responsible

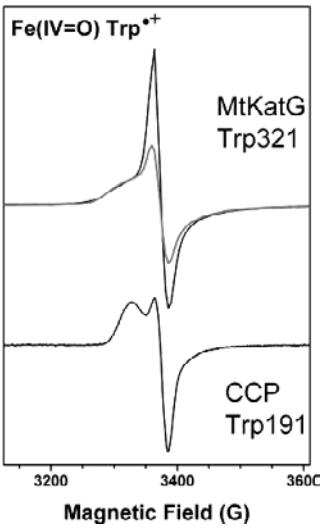

Figure 28. The 9 GHz EPR spectra, recorded at 4 K, of the [Fe(IV)=O Trp$^{\bullet+}$] intermediates formed in *M. tuberculosis* catalase–peroxidase (MtKatG, radical site Trp321) upon reaction with peroxyacetic acid[31] and in cytochrome *c* peroxidase (CCP, radical site Trp191) upon reaction with hydrogen peroxide.[27] The 400 G-broad spectra of the Trp radicals reflect the exchanged-coupling interaction with the ferryl iron. The two narrower (isolated) protein-based radicals (shown in Figure 29) centered at $g \approx 2$, which contributed to the central part of the [Fe(IV)=O $Trp_{321}^{\bullet+}$] spectrum (top, black trace), were not formed when the enzyme was preincubated with the isoniazid substrate prior to the reaction with peroxyacetic acid (top, gray trace).

for the differences in the stabilities of the radicals. The 9 GHz EPR spectrum of CCP upon reaction with hydrogen peroxide (Figure 28) is different from that of HRP, APX and turnip peroxidase isoforms. The axial EPR signal (about 400 G wide) observed at 9 and 35 GHz could be modeled by a weak exchange coupling interaction between a tryptophanyl radical and the oxoferryl moiety,[30] including a distribution in *J* values, with ferro- and antiferromagnetic coupling.[224,229] EPR and ENDOR spectroscopies combined with site-directed mutagenesis studies unequivocally identified the site of the radical formation as Trp 191 (located on the proximal side of the heme cavity of CCP; see Figure 2). In a more recent study, multifrequency (9–285 GHz) EPR spectroscopy and spectral simulations were used to further characterize the [(Fe(IV)=O) Trp$^{\bullet+}$] intermediate in CCP.[27] The tryptophanyl radical, having an exchange coupling interaction with the oxoferryl moiety, could be modeled by a powder pattern spectrum with effective *g* values that depend on the interaction parameters, the zero-field splitting (*D*) of the oxoferryl iron, and the *g* values of the interacting species. The use of multiple frequencies (9, 95, 190 and 285 GHz) to record the EPR spectrum provided more strict constraints on the

spectral simulations. Moreover, by modeling the spin coupling as an anisotropic interaction, instead of as a sum of isotropic exchange terms,[224] it was possible to obtain a representation which was consistent both with the frozen solution and the single-crystal data. In addition, the inherently superior resolution of high-field EPR spectroscopy permitted unequivocal identification of a transient tyrosyl radical formed 60 s after the addition of one equivalent of hydrogen peroxide to the wild-type CCP at 0 °C. The Tyr radical disappeared after 1 h incubation at 0 °C, unlike the long-lived [Fe(IV)=O Trp191$^{\bullet+}$] intermediate. Accordingly, the ambiguities about the "narrow" signal reported previously for CCP[224,230,231] could be clarified by the higher resolution of the *g* values at higher frequencies/higher fields.[27]

Other cases of peroxidases that form a short-lived [Fe(IV)=O Por$^{\bullet+}$] intermediate are LIP[232] and versatile peroxidases.[233] These peroxidases together with MNP are the fungal enzymes playing a key role in the ligninolytic cycle (for a review, see Ref. 15). As in the case of CCP, multifrequency EPR and ENDOR studies have unequivocally identified a Trp radical intermediate in versatile peroxidases,[234] although the site for the radical formation differs from that of CCP. In lignin peroxidase, structural data[235,236] and site-directed mutagenesis studies[232] led to the proposal of a surface Trp residue (Trp171) surrounded by negatively charged residues, as the oxidation site for the substrate veratryl alcohol (VA). No direct evidence from EPR spectroscopy on the formation of Trp171$^{\bullet}$ species, or its reactivity with VA, has been reported to date, a fact tentatively explained by the short-lived nature of the radical.[237] No major differences are observed in the crystal structures of lignin[235] and versatile[238] peroxidases that could explain the remarkably different stability of the Trp$^{\bullet}$ in these two enzymes. Hence, as in the case of CCP and APX, understanding the physicochemical properties that determine the stability and reactivity of the Trp radical intermediate remained an open issue. Recently, an EPR characterization of LIP variants that were designed to modify the microenvironment of the putative Trp$^{\bullet}$ radical site, inequivocally showed that the radical is formed on Trp171 and it is the reactive species with VA.[239]

Catalase–peroxidases constitute yet another case of enzymes in which porphyrin- and protein-based radical intermediates with different stability have been detected. These bifunctional enzymes are homodimeric, each monomer containing two sequence-related domains but only the N-terminal domain binds the heme cofactor.[53,54,56,106] The overall structure of the N-terminal domain has similar topology to that of CCP,[53] yet these enzymes have a catalase-like activity comparable to that of monofunctional catalases, in contrast to monofunctional peroxidases. These unique features of KatGs, together with the fact that KatGs are considered as ancestors of monofunctional peroxidases, render this family of heme enzymes an appealing system in which to investigate the role of alternative electron transfer pathways involving Trp and Tyr as alternative cofactors in the catalytic cycle of peroxidases and catalases. A powerful combination of multifrequency EPR

spectroscopy, isotopic labeling of tryptophan and tyrosine residues, and site-directed mutagenesis has been applied to characterize the chemical nature of the intermediates formed in the peroxidase-like reaction of KatGs from *Synechocystis* PCC6803[26,240] and *Mycobacterium tuberculosis*.[31,241–243] The formation of the [Fe(IV)=O Por$^{\bullet+}$] species and two subsequent protein-based radical intermediates, Trp$^{\bullet}$ and Tyr$^{\bullet}$, was discerned by their distinct EPR spectra.[240] Moreover, Trp106 was shown to be the unique site for the formation of the Trp$^{\bullet}$ despite the high number of Trp residues in *Synechocystis* KatG.[26] Trp106 belongs to a KatG-specific short stretch of residues on the enzyme surface that results in the heme propionates of KatGs being less surface-exposed compared to those of monofunctional peroxidases. Kinetic studies on *Synechocystis* KatG using stopped-flow absorption spectrophotometry showed that an [Fe(IV)=O Por$^{\bullet+}$] intermediate is formed upon reaction with peroxyacetic acid (for a review, see Ref. 109). In the case of *M. tuberculosis* KatG, comparative kinetic studies using stopped-flow electronic absorption spectrophotometry showed that the [Fe(IV)=O Por$^{\bullet+}$] intermediate is shorter-lived than that of *Synechocystis* KatG.[244] Accordingly, the broad EPR spectrum of the [Fe(IV)=O Por$^{\bullet+}$] species in *M. tuberculosis* KatG could not be detected,[31] even when the rapid-mix freeze-quench technique was applied to prepare the EPR samples.[241] Interestingly, the short-lived [Fe(IV)=O Por$^{\bullet+}$] intermediate could be detected when *M. tuberculosis* KatG was incubated with isoniazid prior to the reaction with peroxyacetic acid (see Figure 27, blue trace).[31] The assignment of the chemical nature of the radical intermediates formed in *M. tuberculosis* KatG based on EPR studies is controversial. Magliozzo and coworkers assigned their 9 GHz EPR spectra of MtKatG to a tyrosyl radical species formed on Tyr353, a residue which is not conserved in other KatG enzymes.[242] Later, a revised interpretation of the same 9 GHz EPR data together with the 130 GHz EPR spectrum of the radicals led the same authors to propose the formation of a Trp$^{\bullet}$, as a minority species to Tyr$^{\bullet}$.[243] More recent studies by Ivancich and coworkers, in which multifrequency (9–285 GHz) EPR spectroscopy combined with selective deuterium labeling of Trp and Tyr residues was applied to investigate the intermediates of the wild-type MtKatG and selected Trp variants, concluded that two Trp$^{\bullet}$ radicals are formed.[31] Trp321, the same site as in cytochrome *c* peroxidase, was identified as one of the radical sites in MtKatG.[31] Accordingly, a broad EPR signal was clearly detected in the 9 GHz EPR spectrum of *M. tuberculosis* KatG (Figure 28). Comparison of the exchange-coupled Trp$^{\bullet}$ spectra of *M. tuberculosis* KatG and CCP shows that they have a different line shape (see Figure 28), an effect that is most probably explained by a different distribution of the ferro- and antiferromagnetic components of the exchange coupling of the Trp radical (see above). The narrow signal contributing to the central part of such a spectrum (see Figure 28) was shown to arise from the other, not exchange-coupled Trp$^{\bullet}$

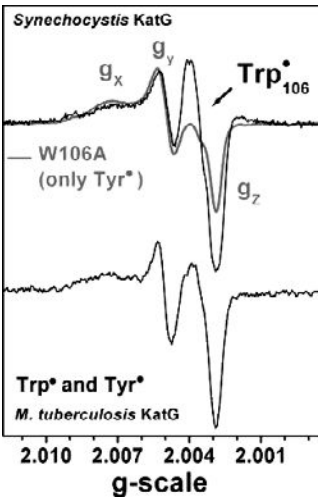

Figure 29. The high-field/high-frequency (10 T, 285 GHz) EPR spectra of the $Trp^{\bullet}$ and $Tyr^{\bullet}$ formed in the wild-type (top, black trace) and W106A variant (top, gray trace) of *Synechocystis* PCC6803 catalase–peroxidase, and wild-type *M. tuberculosis* catalase–peroxidase (bottom, black trace) upon reaction with peroxyacetic acid. The spectra were recorded at 10 K, using a frequency modulation of 30 kHz and a field modulation of 10 G. The (initial) sample concentration was 1 mM and 40 μL volume; a 15-fold excess of peroxyacetic acid was used for the 10 s reaction performed in ice. The site for the radical in *Synechocystis* KatG is Trp106,[26] so only the signal of the $Tyr^{\bullet}$ with g values of $g_x = 2.0064(4)$, $g_y = 2.0040(5)$ and $g_z = 2.0020(8)$ was detected in the W106A variant (top, gray trace).

species by using selective deuteration of Trp and Tyr residues and the higher resolution of g tensors at higher fields/higher frequencies (Figure 29). However, the site for the formation of this (isolated) $Trp^{\bullet}$ is not the same as in *Synechocystis* KatG (see above). The differences observed between the two KatGs with regard to the radical sites reveal that catalase–peroxidases are similar to the monofunctional peroxidases in the stabilization of different radical intermediates.

For a long time, it has been considered that CCP was the exception among heme peroxidases because the stable [Fe(IV)=O $Trp^{\bullet+}$] species is the oxidizing intermediate in the reaction with the substrate cytochrome *c*. Such a reaction was shown to require a well-defined electron transfer pathway[245] between the unique radical site, Trp191, and the binding site for cytochrome *c* on the surface.[185] Nonetheless, CCP uses the short-lived [Fe(IV)=O $Por^{\bullet+}$] intermediate for the oxidation of small molecules such as guaiacol, pyrogallol, aniline and mesidine that can access the δ-meso heme edge through the solvent channel,[246] like in all other peroxidases. A recent crystal structure of CCP that was crystallized with bound isoniazid showed that this aromatic molecule also binds close to the δ-meso heme edge.[247] Recent findings on the specific role of Trp radicals as oxidizing species in

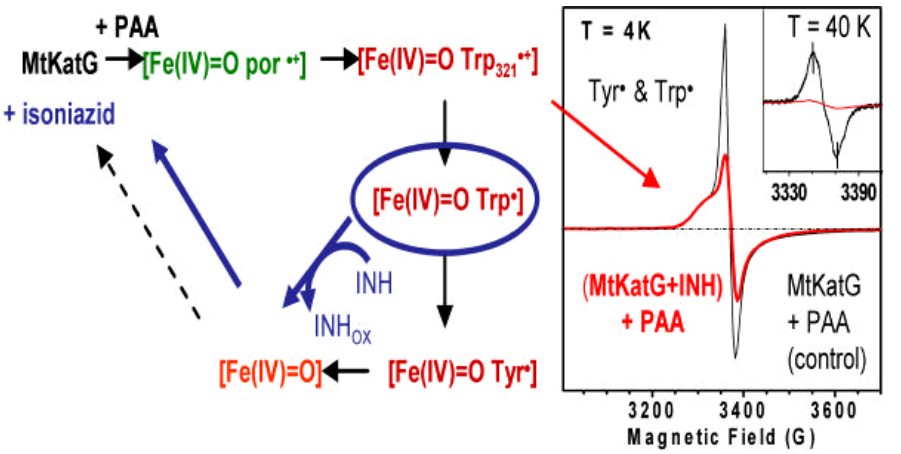

Figure 30. Scheme of the intermediates, detected by multifrequency EPR spectroscopy, in *M. tuberculosis* KatG upon reaction with peroxyacetic acid (PAA). The electronic structure of the intermediates included in the scheme is based on the direct detection and characterization of the corresponding EPR spectra, with the exception of the [Fe(IV)=O] species, which is EPR-silent (integer spin). Yet, it is possible to infer the formation of the missing signal when comparing the Fe(III) conversion and the yield of the detected intermediates. The Trp• not exchange-coupled (circled in blue) was concluded to be the reactive species for the peroxidase-like reaction of MtKatG with isoniazid as a substrate.[31]

the reaction with substrates in other peroxidases and catalase–peroxidases[31,232,236,248] support the hypothesis that, in heme enzymes, specific Trp (or Tyr) residues can either play a role in facilitating electron transfer between redox cofactors[249,250] or act as true intermediates in the peroxidase cycle.[31] The reactivity of *M. tuberculosis* and *Synechocystis* KatGs with isoniazid was also carefully monitored by using EPR spectroscopy in order to identify the intermediate responsible for the oxidation of isoniazid.[31,251] The results show that in *Synechocystis* KatG, the isoniazid substrate can react readily with the [Fe(IV)=O Por•+] species.[251] In contrast, in *M. tuberculosis* KatG the reactive species was shown to be the [Fe(IV)=O Trp•] (Figure 30) formed subsequently to the [Fe(IV)=O Trp_{321}•+] intermediate.[31] These findings indicate that, in both KatGs and monofunctional peroxidases, the observed variability of Trp sites where the subsequent intermediates to the [Fe(IV)=O Por•+] can be stabilized, appears to be correlated with differences in substrate binding sites.

III. Superfamily of Animal Peroxidases

Animal peroxidases are classified in a separate superfamily, which is often indicated as the superfamily of mammalian peroxidases for historical reasons.

The superfamily includes myeloperoxidase (MPO), eosinophil peroxidase (EPO), lactoperoxidase (LPO) and thyroid peroxidase (TPO). Both MPO and EPO are involved in the immune system response. MPO is produced by neutrophil cells and released during phagocytosis, whereas EPO is secreted by eosinophil cells. LPO can be found in milk and other fluids. All of these proteins react with H_2O_2 and form intermediate compounds, which are related to those already discussed in the section describing plant peroxidases. The specific electron donors are small inorganic anions, and particularly chloride, bromide and thiocyanate. The resulting acids, HOCl, HOBr and HOSCN, have a strong antimicrobial activity. The production of these reactive species is considered to be the biological function of MPO, EPO and LPO. Thyroid peroxidase has a different function, being involved in the synthesis of thyroid hormones. Both the chemical properties and the biomedical aspects of animal peroxidases have been reviewed in recent articles.[252–254]

A. Covalent Links and Heme Structure

From the chemical point of view, the most noteworthy structural property of animal peroxidases is the presence of covalently linked heme cofactors. The Fe-protoporhyrin IX tetrapyrrole ring is bound to the protein matrix by chemical bonds at rings A and C. The protein–heme link is the result of posttranslational modifications, the mechanisms of which are currently being clarified.[255]

MPO is a unique case, bearing three covalent bonds (Figure 31): an ester bond at ring C, resulting from oxidation of methyl 5 and esterification to an aspartate side chain (Asp94); a similar ester bond at ring A between methyl 1 and a glutamate residue (Glu242); an unusual sulfonium bond (also at ring A) between the

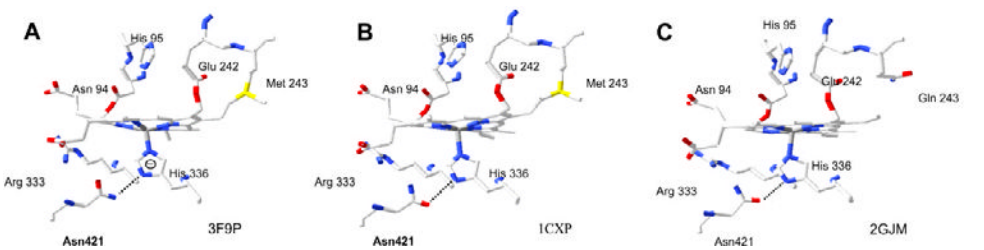

Figure 31. (A) Heme structure and porphyrin–protein linkages in human glycosilated myeloperoxidase according to the coordinate file 3F9P.[261] H-bonding between the NH2 group of Asn 421 and *anionic* His336 has been proposed. Covalent bonding between heme and Glu242 is limited to 20% of the molecules. (B) Heme structure and porphyrin–protein linkages in human myeloperoxidase according to the coordinate file 1CXP.[259] In this structure, Asn421 is H-bonded to *neutral* His336 through its amide carbonyl.[259,269] (C) Structure of the active site[259] of bovine LPO (2GJM).[263] The numbering of the residues follows that of MPO.

b-carbon atom of vinyl 2 and a methionine residue (Met243). Both LPO[256] and EPO[257] have two covalent bonds, namely, ester bonds between methyl 1 and Glu242 (MPO alignment number) and between methyl 5 and Asp 94 (Figure 31).

There are several effects of the covalent links on the heme structure that can be clearly seen by spectroscopy and X-ray crystallography: distortion from planarity, symmetry lowering, and changes in the electronic structure.

B. X-Ray Structures: An Overall View

X-ray structures of MPO have been published for one glycoform of canine[258] and human origin.[259,260] In the X-ray structure of human MPO obtained at −180 °C with 1.8 Å resolution (Figure 31B),[259] the heme tetrapyrrole ring appears to be considerably distorted from planarity, since rings A and C are tilted toward the protein distal side. The iron atom is slightly displaced toward the proximal side (0.2 Å below the line connecting the N atoms of rings B and D), and is coordinated with the proximal His residue (His336) with a bond length Fe–N = 2.19 Å. The imidazole ring of His336 is H-bonded with Asn421, at variance with plant peroxidases where the proximal His is H-bonded with the carboxylate group of an Asp residue (see Figure 2). In all the MPO structures, the distal heme cavity contains not only the His/Arg couple (His95, Arg239), which is common to plant peroxidases, but also a glutamine residue (Gln91). Moreover, a network of water molecules has been localized in the distal cavity. The water molecules are H-bonded with the distal residues, a heme propionate on ring C, and between themselves. One of them lies at 2.9 Å from both His95 nitrogen and the heme iron, which suggests H-bonding to the histidine and weak coordination to the iron.

The very recent crystal structure of a mixture of MPO glycoforms (hMPOm), obtained directly by purification from human leukocytes, exhibits several significant differences compared to previous MPO structures reported in the literature.[261] The variations include heme-to-protein linkages, sites and extent of glycosylation. First of all, X-ray modeling, cross-checked by molecular dynamics simulations, gave new insights into the interaction between proximal His336 and Asn421, strongly suggesting that the imidazole of His336 could be present as imidazolate. Moreover, it was underlined that the His–Asn–Arg interaction is important in the maintenance of both the proximal and the distal heme cavity architecture as well as the catalytic properties of MPO. Upon replacing Asn421 by Asp, a 10 nm blue shift of the Soret band was observed in the UV-vis spectrum, as well as complete loss of the chlorination activity. Another difference with published MPO structures concerns the heme-to-protein bonds in hMPOm. On the basis of the electron density maps, two alternative conformations of the side chain of Glu242 are suggested. In hMPOm the majority of the ester bond with Glu242 is broken, whereas

both the sulfonium ion linkage and the second ester bond are fully present. Therefore, the heme is still considerably distorted, but flatter compared to the other published structures (Figure 31A).

Structures of bovine LPO, both in the resting state and as a complex with SCNO,[262] goat LPO,[256] buffalo LPO (2GJM)[263] and its complex with SCN^-,[264] have recently become available. The heme cofactor in LPO is less distorted than in MPO (Figure 31C), mainly because of the absence of the covalent link with Met at ring A. The Fe–His bond length and the Fe–distal water distance are 2.14 Å and 2.65 Å, respectively.[256] The proximal His is H-bonded with the Asn437 residue, which corresponds to the Asn421 of MPO. A comparison between the structure of the SCN^- complex of (bovine and buffalo) LPO and that of the SCN^- complex of (human) MPO[260] has led to the suggestion that the structural determinant for the substrate specificity of LPO, i.e. preference for the oxidation of SCN^- rather than halides, is the conformation of the loop which extends from Arg418 to Phe431.

C. Resonance Raman and Electronic Absorption Spectroscopies

In a previous edition of *The Porphyrin Handbook*, Kincaid extensively reported the RR data obtained on the various mammalian peroxidases, including the Fe(III) and Fe(II) states, their exogenous ligand adducts and catalytic intermediates.[172] Therefore, in this chapter we focus on the new results obtained in the last decade.

The electronic absorption spectrum of MPO has been known to be anomalous since the first protein preparations became available.[265] The Soret band maximum lies at 428 nm, the α and β bands at 570 and 622 nm, respectively, and the CT1 band at 690 nm. All these maxima are markedly redshifted compared with the wavelengths of both high- and low-spin Fe(III) heme-containing proteins. Clarification of the origin of the red shift could be obtained with the aid of site-directed mutagenesis combined with electronic and RR spectroscopies. This is best illustrated (Figure 32) by the spectral properties of the MPO mutant, where Met243 is substituted with Thr. Mutation of the Met243 residue prevents the formation of the sulfonium heme–protein link.[266–268] In particular, the absorption and magnetic circular dichroism spectra of the M243T mutant and of its CN complexes become similar to those of other heme proteins. Recently, the comparison between the RR spectra of wt MPO and M243T[269] showed that the iron coordination is the same in the two proteins, since the ν_3 core-size marker band frequency indicates a 6cHS heme (the ν_2 marker band frequency is not coincident with that expected for such a spin state, since it is coupled to the stretching mode of the vinyl groups, which are quite different in the two proteins). In spite of the common coordination, the RR intensities are quite different, and in particular: (i) the RR spectrum of MPO shows intense bands due to nontotally symmetric modes,

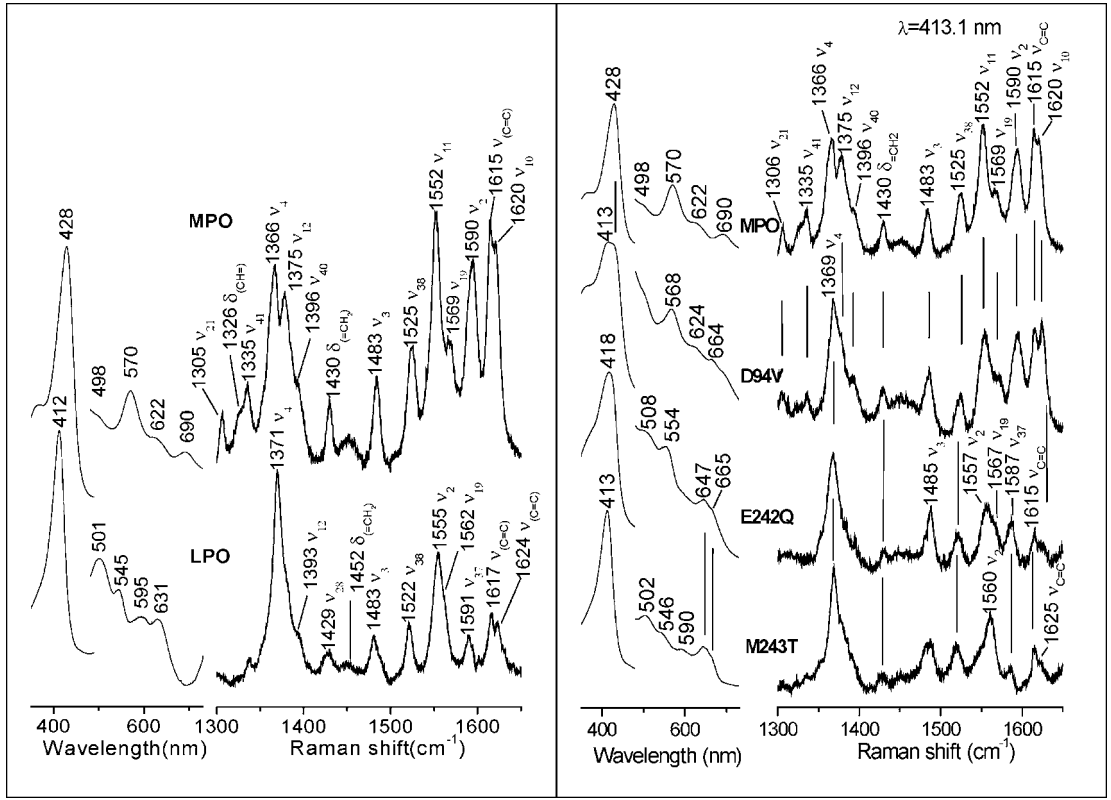

Figure 32. (Left) Electronic absorption and RR spectra of Fe(III) LPO and MPO. The intensity in the visible region is expanded four-fold. The spectra in the Soret region have been shifted along the coordinate axis to allow better visualization. (Right) Electronic absorption and RR spectra in the high-frequency region of Fe(III) MPO and its Asp94Val, Glu242Gln and Met243Thr mutants. (Adapted from: Zederbauer, M.; Furtmueller, P. G.; Brogioni, S.; Jakopitsch, C.; Smulevich, G.; Obinger, C. *Nat. Prod. Rep.* **2007**, *24*, 571–584. Reproduced by permission of The Royal Society of Chemistry.)

e.g. ν_{12}, ν_{11}, ν_{19} and ν_{10}, which suggest that the heme macrocycle symmetry is lowered to C_2, with the C_2 axis perpendicular to the heme plane; (ii) the spectrum of M243T is dominated by totally symmetric modes, indicating a heme with D_{4h} pseudosymmetry. However, the combined analysis of the RR spectra of M243T, Glu242Gln and Asp94Val mutants demonstrates that the heme is distorted to some extent even in the absence of the sulfonium linkage, possibly owing to the residual covalent linkages with Asp and Glu which contribute to the distortion from the planar conformation and the lowered symmetry. In fact, despite the absence of the sulfonium linkage in the Met243 variant, its RR spectra retain some unusual features compared to other heme proteins, such as a remarkable enhancement of several out-of-plane low-frequency modes. Fe(II) MPO maintains the spectroscopic complexity observed for the Fe(III) form. In fact, the electronic absorption spectrum is rather unique, being red-shifted with respect to other heme proteins, with a Soret maximum at 472 nm. Concomitantly, its vibrational spectrum is very complex. Moreover, as for the Fe(III) form, mutation of the D94, E242 and M243 alters the spectroscopic features of the corresponding Fe(II) species, causing a blue-shift of the Soret band with a concomitant reduction in the complexity of the Raman spectra.[266–268,270,271]

Both the absorption spectra[253] and the RR spectra[272] of the resting state of LPO are similar to those of "regular" hexacoordinated heme proteins, e.g. Fe(III) myoglobin (Figure 32).

In contrast with Fe(II)MPO, the Fe(II) state of LPO displays a time-dependent equilibrium between multiple species. The presence of multiple Fe(II)LPO species has been demonstrated by magnetic circular dichroism,[273] and by electronic absorption spectroscopy and ligand-binding kinetics.[274,275] A recent RR spectroscopy study[276] has allowed the characterization of three different forms of Fe(II)LPO on the basis of their ν(Fe–His) stretching frequencies. In particular, the species with absorption maxima at 444, 432 and 425 nm display a ν(Fe–His) band at 254, 221 and 227 cm^{-1}, respectively (Table 7 and Figure 33). The species with the weakest Fe–Im bond [ν(Fe–His) at 221 cm^{-1}] does not appear immediately, but develops with time. An interesting finding is that the M243T and M243V MPO mutants exhibit a similar behaviour, whereas mutations at D94 and E243 yield a single, stable Fe(II) form with a ν(Fe–His) at 243 cm^{-1},[276] similar to the band observed in wt MPO at 246 cm^{-1} (Figure 34).[277] Therefore, only the presence of the sulfonium linkage in MPO prevents the slow conformational change observed for Fe(II)LPO; when it is absent Fe(II) MPO is less stable.

In the low-frequency region both MPO and LPO are characterized by ν(Fe–His) stretching frequencies at markedly high frequencies (248–255 cm^{-1}), with the ν(Fe–His) of LPO being slightly higher than the ν(Fe–His) of MPO.[163,271] This fairly high RR frequency suggests a substantial imidazolate character of the proximal histidine which could not be justified by the X-ray structures since the H-bond acceptor

Table 7. Electronic absorption maxima (nm) and resonance Raman frequencies (cm^{-1}) of the different Fe(II) forms observed for LPO, MPO, and its Met243Thr, Met243Val, Asp94Val and Glu242Gln mutants. From Ref. 276.

	Species I		Species II		Species III	
	UV-vis Soret	RR ν(Fe–Im)	UV-vis Soret	RR ν(Fe–Im)	UV-vis Soret	RR ν(Fe–Im)
LPO	444 nm pH = 8.5 t = 0	254 cm^{-1}	432 nm pH = 8.5 t = 60 min. pH = 5.0	221 cm^{-1}	425 nm pH = 8.5 t = 0 pH = 6.0	227 cm^{-1}
M243T MPO	445 nm t = 0	248 cm^{-1}	433 nm t = 10 min.	232 cm^{-1}		
M243V MPO	450 nm pH = 9.0 t = 0	248 cm^{-1}	434 nm pH = 9.0 t = 15 min. pH = 7.0	232 cm^{-1}		
D94V MPO	474 nm	243 cm^{-1}				
E242Q MPO	458 nm	243 cm^{-1}				
MPO	474 nm	246 cm^{-1}				

in animal peroxidases was found to be the amide oxygen of a conserved Asn.[253] At present, the crystal structure of hMPOm together with molecular dynamics simulations support the RR findings which suggest that a neutral proximal histidyl imidazole would have unfavorable H-bonding interactions, whereas a deprotonated His336 would strengthen the Fe–imidazole bond.[261] The authors suggest that in animal peroxidases the NH2 group of the Asn421 (MPO numbering) is oriented toward the unprotonated N_δ of the proximal His, while its carbonyl group interacts with the (positively charged) guanidinium group of Arg333 (Figure 31A).

RR spectroscopy of the CO complex of MPO has not been performed, since MPO is one of the very few examples of heme proteins which cannot bind CO,* contrasting with EPO[274] and LPO.[278]

RR spectroscopy of EPO has been performed both on the isolated enzyme and on eosinophil granulocytes.[279] The analysis of the spectra, which were obtained using a micro-Raman spectrophotometer with excitation wavelengths at 413.1, 514.5 and 660 nm, has demonstrated that the coordination of Fe(III)EPO is the same as that of Fe(III)LPO.

*Very weak CO binding to MPO has been recently demonstrated by differential Fourier transform infrared spectroscopy. (Murphy, E. J.; Marechal, A.; Segal, A. W.; Rich, P. R. *Biochemistry* **2010**, *49*, 2150–2158.)

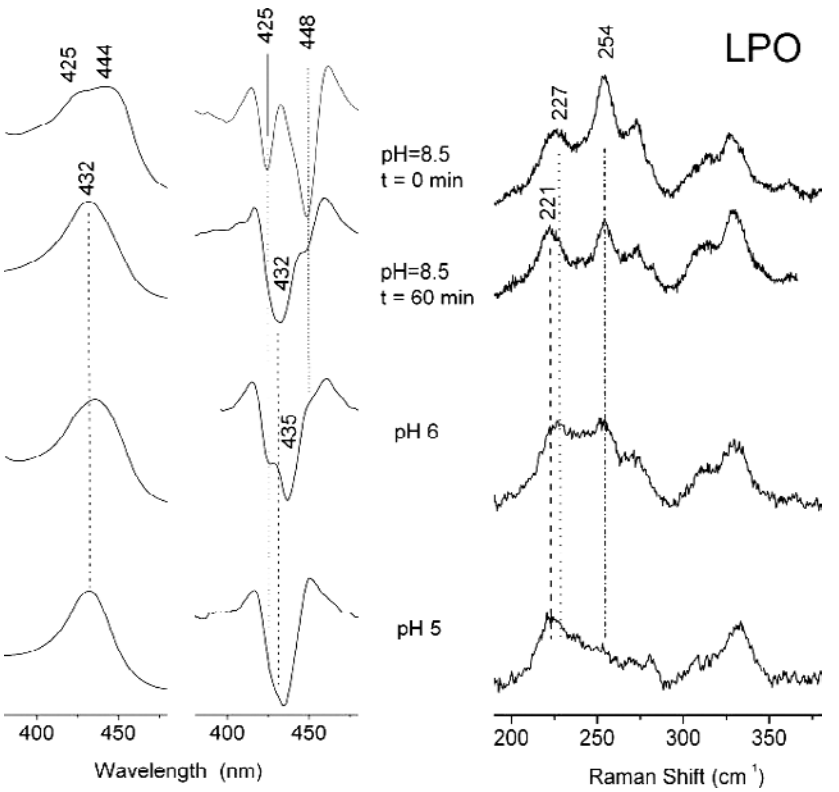

Figure 33. *From left to right*: Absorption, second derivative absorption, and resonance Raman spectra of Fe(II) lactoperoxidase at pH 8.5, 6 and 5. The set of spectra at pH 8.5 demonstrates the slow conformational change occurring in the first hour after sample reduction. The absorption maxima/shoulders for the different species, and the corresponding frequency of the *v*(Fe–Im) stretching bands, are marked.

D. Catalytic Intermediates

1. *Resonance Raman and Electronic Absorption Studies*

The reactive intermediates of animal peroxidases have only been partially characterized by means of RR spectroscopy, due to their instability. No new experiments have been performed recently and the complete set of available data has been already reported in the previous *Handbook* series.[172] The rapid-scan electronic absorption spectra of the reaction of MPO with hydrogen peroxide are shown in Figure 35.[252] The Fe(III) spectrum (bands at 430, 570 and 690 nm) displays significant spectral changes upon addition of a 10-fold excess hydrogen peroxide (hypochromicity of the Soret band and appearance of a charge-transfer band at 625 nm). These variations, observed within 100 ms, were assigned to the

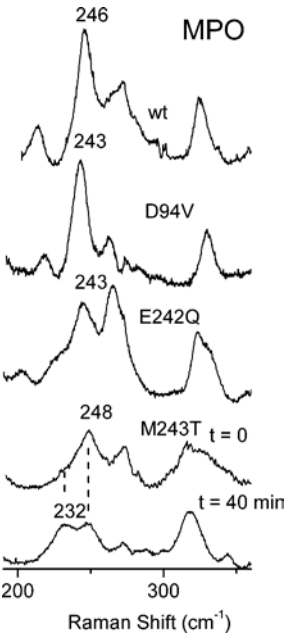

Figure 34. Resonance Raman spectra of Fe(II) myeloperoxidase and of its mutants D94V, E242Q and M243T. In this last mutant, a slow conformational change — similar to the lactoperoxidase case — occurs in the first hour after sample reduction. The frequency of the *ν*(Fe–Im) stretching band is marked.

[Fe(IV)=O Por$^{\bullet+}$] intermediate (compound I). Further spectral changes (shift of the Soret band to 456 nm and increase in intensity of the band at 625 nm) were assigned to the ferryl intermediate (compound II). The spectrum characterized by a Soret band at 453 nm and a CT band at 625 nm was assigned to the oxygen complex, often termed "compound III."

Optical spectroscopy has been performed for MPO in the ferryl oxidation state (compound II)[280] at pH 7.0 and 10.7, giving evidence of two distinct ferryl species at neutral and alkaline pH with a pKa of about 9. The two species are characterized by different electronic absorption spectra. However, the corresponding features in the RR spectra could not be detected. In fact, an isotopic $^{16}O/^{18}O$ shift was present only in the spectra at pH 10.7, which allowed assignment of a band at 782 cm^{-1} to the Fe=O stretching mode.

The RR spectra of the ferryl intermediate (compound II) was reported for LPO at pH 6.8; the intermediate was stable for 2–3 min under laser irradiation. A noteworthy feature is the very low frequency (745 cm^{-1}) of the Fe=O stretching band.[199] Furthermore, the frequency of the Fe–O_2 stretching band (531 cm^{-1}) in compound III is particularly low in LPO.[281]

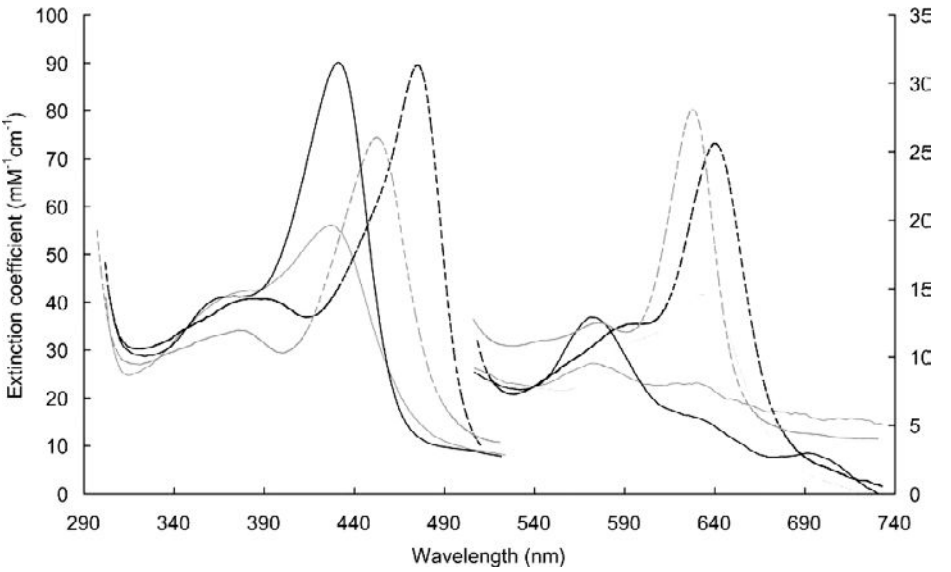

Figure 35. Absorption spectra of redox intermediates of myeloperoxidase at pH 7.0: Fe(III) protein (black and bold), compound I (gray), compound II (black and thin) and compound III (gray dashed line). In addition, Fe(II) MPO is shown (black dashed line). (Reprinted from *Arch. Biochem. Biophys.* **2005**, *445*, 199–213. Furtmüller, M.; Zederbauer, M.; Jantschko, W.; Helm, J.; Bogner, M.; Jakopitsch, C.; Obinger, C. Active site structure and catalytic mechanisms of human peroxidases. © 2005, with permission from Elsevier.)

2. *Multifrequency EPR Spectroscopy Combined with Stopped-Flow Electronic Absorption Spectrophotometry*

The recently available X-ray crystal structures of bovine (PDB entry 2GJ1) and caprine[256] LPO obtained at 2.34 Å and 2.4 Å resolution, respectively, confirmed the previous proposal of a deeply buried heme site.[282] The channel allowing the access of substrates from the enzyme surface to the distal side of the heme in caprine LPO is cylindrical in shape, with a diameter of approximately 6 Å.[256] The structures of the enzyme complexed with thiocyanate (PDB entry 2IPS), 2-hydroxybenzohydroxamic acid (also known as salicylhydroxamic acid) (PDB entry 2QPK) and acetylsalicylic acid (PDB entry 2QQT) have also been deposited and reveal a substrate binding site on the heme distal side, in close contact with the iron and the distal histidine. Such a binding site is favorable for a heme-edge type of reaction with aromatic (or small) substrates, typical of peroxidases.[158,159] Kinetic studies on the reaction of LPO with hydrogen peroxide[283] and hypochlorous acid[119] led to the conclusion that the [Fe(IV)=O Por$^{\bullet+}$] species was the reactive intermediate. Indirect evidence for the formation of protein-based radical species as isomers of the [Fe(IV)=O Por$^{\bullet+}$] intermediate was reported. In one case, spin-trapping

experiments indicated the formation of one protein radical, and Mass Spectrometry analysis showed that a surface residue, Tyr289, was the cause of the enzyme dimerization, via a dityrosine crosslink.[284] Kinetic studies of the LPO reaction with *p*-substituted phenols showed that the enzyme reactivity was correlated with the redox potential of these substrates.[285] These authors invoked a tyrosyl radical intermediate to explain the very low enzyme reactivity, measured at pH 5 for p-substituted phenols containing an amino group.[285] More recently, multifrequency (9–285 GHz) EPR spectroscopy combined with stopped-flow electronic absorption spectrophotometry was applied in order to directly detect the radical(s) and unequivocally determine their electronic nature and microenvironment, as well as their putative catalytic competence in the reaction of milk LPO with hydrogen peroxide as a function of pH.[219] The use of high frequency/high field (285 GHz/10 T) to record the EPR spectrum provides enhanced resolution of the *g* tensor components (*g* values) of organic radicals, which are unresolved in the EPR spectrum recorded at conventional (9 GHz) frequencies. In particular, Tyr$^\bullet$ and Trp$^\bullet$ can be clearly discerned from their 285 GHz EPR spectrum, based on the higher *g* anisotropy (defined as $\Delta g = g_Z - g_X$) of Tyr radicals (as illustrated in Figure 29). Further information about the microenvironment of the protein-based radical can also be obtained from the 285 GHz EPR spectrum, since the g_x value of tyrosyl radicals is sensitive to the presence of H-bonds or positively charged residues.[218] The high-field EPR spectrum of LPO upon reaction with five-fold excess hydrogen peroxide showed the predominant signal of a Tyr$^\bullet$, with *g* values of g_x = 2.0077(0), g_y = 2.0039(5) and g_z = 2.0020(8) at pH = 8.0, and of g_x = 2.0066(2), g_y = 2.0039(5) and g_z = 2.0020(8) at pH ≤ 7.5 (Figure 36, left panel). The corresponding EPR spectra recorded at 9 GHz showed differences in the (unresolved) proton hyperfine couplings of Tyr$^\bullet$ (Figure 36, central panel) that were consistent with the changes observed at the higher frequency. Taken together, the differences in g_x values (detected in the 285 GHz EPR spectra) and the proton hyperfine couplings (detected in the 9 GHz EPR spectra) were indicative of two chemically different Tyr radicals as a function of pH. Accordingly, a single Tyr with a pH-dependent microenvironment or, alternatively, two Tyr with different microenvironments are consistent with the EPR spectra. Interestingly, the different microenvironment of Tyr$^\bullet$ could be related to the reactivity of the radical (see below), as has been shown in the case of the Tyr_D and Tyr_Z radicals in photosystem II.[286] Another feature revealed by the 285 GHz EPR spectrum of LPO upon reaction with hydrogen peroxide was the additional intensity contributing to the g_y–g_z spectral region of the Tyr$^\bullet$ signal. The narrower signal agreed well with that expected for Trp$^\bullet$, as observed in the cases of *Synechocystis* and *M. tuberculosis* KatGs (see Figure 29). Such a less anisotropic signal was better observed in the HF EPR spectrum of a commercial LPO sample at pH 6.8 (Figure 36, left panel,

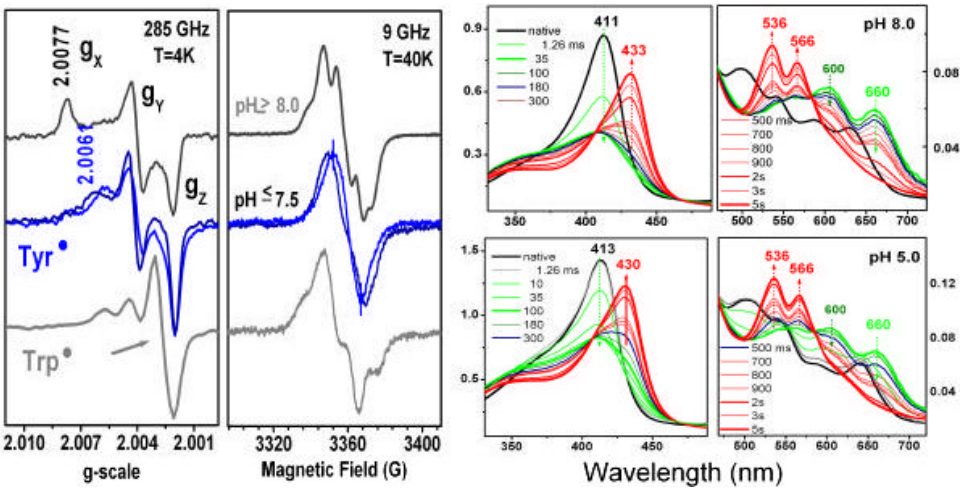

Figure 36. The 285 GHz (left panel) and 9 GHz (central panel) EPR spectra of the Trp• and Tyr• intermediates formed by the reaction of lactoperoxidase with five-fold excess hydrogen peroxide at 0 °C and as a function of pH (4 = pH = 10). For both frequencies, the spectra obtained at pH 8 (left and central panels, top; gray trace) are representative of all spectra obtained for samples at basic pH values (pH = 8), and the spectra at pH 5 (left and central panels, middle; black trace) are representative of those obtained at neutral and acidic pH values (4 = pH = 7.5). The signal with smaller g anisotropy ($\Delta g = g_z - g_x = 0.0014$) and contributing to the g_y–g_z region of the Tyr• spectrum ($\Delta g = g_z - g_x = 0.0044$) recorded at 285 GHz (left panel, top; black trace) was totally consistent with the expected g values of a Trp•, as shown in the case of *Synechocystis* KatG (Figure 29). Such a signal was clearly observed in the commercial lactoperoxidase sample (left panel, bottom; black thin trace) due to the different relative yield of Trp• and Tyr• species. The right panel shows rapid-scan electronic absorption spectra of the reaction of lactoperoxidase with five-fold excess hydrogen peroxide at 5 °C and monitored up to 5 s. The experiments were carried out at pH 8 (top) and pH 5 (bottom). Selected representative spectra are shown. The resting (Fe(III)) enzyme is shown in black, the [Fe(IV)=O Por•+] in green, the transition to the ferryl species in blue and the ferryl intermediate in red. Experimental conditions are described in Ref. 219.

bottom spectrum), for which the 9 GHz EPR spectrum (Figure 36 central panel, bottom spectrum) showed an overall broader signal and different shape, both spectra indicating a higher yield of the Trp• signal (relative to the Tyr• signal) in this sample. The difference in relative yields of the Tyr and Trp radicals may be related to variations in purification steps reflecting different contents of the enzyme isoforms. The absence of the broad signal (2500 G overall width) consistent with the [Fe(IV)=O Por•+] intermediate (see Section II.F.3) in the 9 GHz EPR spectrum of lactoperoxidase was clearly explained by the complementary kinetic information obtained from the rapid-scan electronic absorption spectra of the reaction of LPO with hydrogen peroxide, in conditions (pH and mixing temperature) comparable to those of the EPR experiments (Figure 36, right panel). Accordingly, the

[Fe(IV)=O Por$^{\bullet+}$] intermediate (hypochromicity of the Soret band and shift of the CT band to 660 nm) was shown to be formed within 35 ms at pH 8 and 100 ms at pH 6 (Figure 36, right panel, thick green trace) and the transition to the ferryl-like spectrum (shift of the Soret band to 433 nm and two distinct new CT bands at 536 nm and 566 nm) was achieved within 2 s, which is the mixing time used in the EPR experiments. It is important to note that the electronic absorption spectrum of an [Fe(IV)=O] intermediate as observed in the case of HRP (see Figure 25) is indistinguishable from that of an [Fe(IV)=O Tyr$^{\bullet}$] or [Fe(IV)=O Trp$^{\bullet}$] species, because the bands corresponding to Tyr$^{\bullet}$ (405–410 nm) and Trp$^{\bullet}$ (510–560 nm) are completely masked by the heme bands.[287,288] Information obtained from the EPR spectra and the rapid-scan electronic absorption spectra of the reaction of LPO with hydrogen peroxide unequivocally allowed one to clearly identify the short-lived [Fe(IV)=O Por$^{\bullet+}$], [Fe(IV)=O Trp$^{\bullet}$] and [Fe(IV)=O Tyr$^{\bullet}$] intermediates, and a final [Fe(IV)=O] species (Figure 37).

The combination of EPR and stopped-flow measurements was also used to characterize the reaction of LPO with two types of substrates (small aromatic vs. bulkier organic molecules). Two different mechanisms for substrate oxidation were distinguished in LPO.[219] The [Fe(IV)=O Por$^{\bullet+}$] intermediate was shown to be responsible for the oxidation of *o*-dianisidine, *o*-anisidine, and benzohydroxamic acid via a

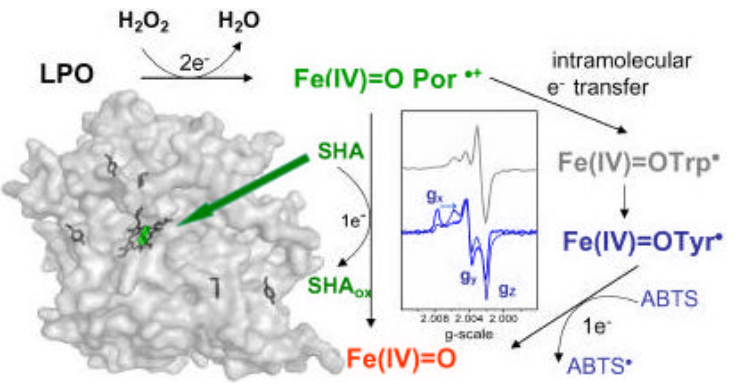

Figure 37. Scheme of the catalytic intermediates, detected by combining multifrequency EPR spectroscopy and stopped-flow electronic absorption spectrophotometry in lactoperoxidase. The global view of the crystal structure of lactoperoxidase, highlighting the five tyrosine residues identified as candidates for the radical site based on the high-field EPR spectroscopy studies, is also shown. Tyr433 and Tyr468 are close to the surface, and Tyr7 and Tyr71 are directly exposed on it; Tyr177 is located deeper in the protein, adjacent to a putative secondary access channel. The deeply buried heme site is partially visible at the end of the narrow access channel. The figure was prepared using the coordinates deposited in the Protein Data Bank (accession code 2GJ1). The [Fe(IV)=O Por$^{\bullet+}$] intermediate was shown to be the reactive species with bezohydroxamic acid (BHA) and small substrates, while the oxidation of ABTS by the [Fe(IV)=O Tyr$^{\bullet}$] intermediate was favored at pH 5.

heme-edge reaction, and of mitoxantrone (1,4-dihydroxy-5,8-bis[2-(2-hydroxyethylamino)ethylamino]-anthracene-9,10-dione) via long-range electron transfer (favored at pH 8), but not involving the [Fe(IV)=O Tyr$^{\bullet}$] intermediate. It is important to note that a very recent paper discussing the crystal structures of milk lactoperoxidase complexes with benzohydroxamic acid concluded that the proximity of the oxygen atom of the hydroxyl group of this substrate to the heme iron (a distance of 3.3 Å) and apparent displacement of water molecules of the heme distal side would block the peroxide binding site and prevent enzymatic action.[289] Such a conclusion is at odds with the stopped-flow measurements, since these experiments clearly demonstrated that the [Fe(IV)=O Por$^{\bullet+}$] intermediate readily reacted with benzohydroxamic acid.[219] Accordingly, care must be taken when concluding about enzymatic reactions based on a static view of the enzyme and the substrates. Interestingly, it was shown that at pH 5 the formation of the [Fe(IV)=O Tyr$^{\bullet}$] intermediate was in competition with the oxidation of mitoxantrone, and that this intermediate was responsible for the efficient reaction with ABTS (2,2′-azino-bis(3-ethylbenzthiazoline-6-sulphonic acid).[219] In conclusion, lactoperoxidase showed similarities to cytochrome *c* peroxidase, lignin peroxidase and catalase–peroxidases with regard to the formation of protein-based radical intermediates as alternative oxidation species for substrates that cannot access the heme site (Figure 37).

IV. Acknowledgments

We thank members of our research groups and coworkers who are responsible for some of the work reviewed in this chapter; their names are listed in the appropriate references.

V. References

1. Welinder, K. G. *Curr. Opin. Struct. Biol.* **1992**, *2*, 388–393.
2. Veitch, N. C.; Smith, A. T. *Adv. Inorg. Chem.* **2001**, *51*, 107–162.
3. Kimura, S.; Ikeda-Saito, M. *Proteins Struct. Funct. Genet.* **1988**, *3*, 113–120.
4. Loughran, N. B.; O'Connor, B.; O'Fagain, C.; O'Connell, M. J. *BMC Evol. Biol.* **2008**, *8*.
5. Sugano, Y.; Muramatsu, R.; Ichiyanagi, A.; Sato, T.; Shoda, M. *J. Biol. Chem.* **2007**, *282*, 36652–36658.
6. Bateman, A.; Coin, L.; Durbin, R.; Finn, R. D.; Hollich, V.; Griffiths-Jones, S.; Khanna, A.; Marshall, M.; Moxon, S.; Sonnhammer, E. L. L.; Studholme, D. J.; Yeats, C.; Eddy, S. R. *Nucleic Acids Res.* **2004**, *32*, D138–D141.
7. Sugano, Y. *Cell. Mol. Life Sci.* **2009**, *66*, 1387–1403.
8. Dunford, H. B. Chloroperoxidase and *Pseudomonas* Cytochrome *c* Peroxidase. In *Heme Peroxidases*; Dunford, H. B., Ed.; Wiley-VCH: New York, **1999**; pp. 323–348.
9. De Smet, L.; Savvides, S. N.; Van Horen, E.; Pettigrew, G.; Van Beeumen, J. J. *J. Biol. Chem.* **2006**, *281*, 4371–4379.

10. Griffin, B. W. Chloroperoxidase: a review. In *Peroxidases in Chemistry and Biology*; Everse, J., Everse, K. E., Grisham, M. B., Eds. CRC: Boca Raton, Florida; **1991**; pp. 85–138.
11. Sundaramoorthy, M.; Terner, J.; Poulos, T. L. *Structure* **1995**, *3*, 1367–1377.
12. Sundaramoorthy, M.; Terner, J.; Poulos, T. L. *Chem. Biol.* **1998**, *5*, 461–473.
13. Poulos, T. L. Peroxidase and cytochrome P450 structures. In *The Porphyrin Handbook*; Kadish, K., Smith, K. M., Guilard, R., Eds. **2000**; pp. 189–218.
14. Dunford, H. B.; Stillman, J. S. *Coord. Chem. Rev.* **1976**, *19*, 187–251.
15. Dunford, H. B. *Heme Peroxidases*; Wiley-VCH: New York, **1999**.
16. Spiro, T. G. *Biological Applications of Raman Spectroscopy, Vol. III*; Wiley-Interscience: New York, **1988**.
17. Smulevich, G. *Biospectroscopy* **1998**, *4*, S3–S17.
18. Smulevich, G.; Feis, A.; Howes, B. D. *Acc. Chem. Res.* **2005**, *38*, 433–440.
19. Carey, P. R.; Dong, J. *Biochemistry* **2005**, *43*, 8885–8893.
20. Stubbe, J.; van der Donk, W. A. *Chem. Rev.* **1998**, *98*, 705–762.
21. Palmer, G. *Electron Paramagnetic Resonance of Hemoproteins*; Addison-Wesley: Reading, Massachusetts, **1983**; pp. 43–88.
22. Blumberg, W. E.; Peisach, J.; Wittenberg, B. A.; Wittenberg, J. B. *J. Biol. Chem.* **1968**, *243*, 1854–1862.
23. Wittenberg, B. A.; Kampa, L.; Wittenberg, J. B.; Blumberg, W. E.; Peisach, J. *J. Biol. Chem.* **1968**, *243*, 1863–1870.
24. Peisach, J.; Blumberg, W. E.; Wittenberg, B. A.; Wittenberg, J. B. *J. Biol. Chem.* **1968**, *243*, 1871–1880.
25. Ivancich, A.; Mazza, G.; Desbois, A. *Biochemistry* **2001**, *40*, 6860–6866.
26. Jakopitsch, C.; Obinger, C.; Un, S.; Ivancich, A. *J. Inorg. Biochem.* **2006**, *100*, 1091–1099.
27. Ivancich, A.; Dorlet, P.; Goodin, D. B.; Un, S. *J. Am. Chem. Soc.* **2001**, *123*, 5050–5058.
28. Bennatii, M.; Prisner, T. F. *Rep. Prog. Phys.* **2005**, *68*, 411–448.
29. Moebius, K.; Savitsky, A. *High-Field EPR Spectroscopy on Proteins and Their Model Systems: Characterization of Transient Paramagnetic States*, Royal Society of Chemistry: Cambridge, **2009**.
30. Sivaraja, M.; Goodin, D. B.; Smith, M.; Hoffman, B. M. *Science* **1989**, *245*, 740.
31. Singh, R.; Switala, J.; Loewen, P. C.; Ivancich, A. *J. Am. Chem. Soc.* **2007**, *129*, 15954–15963.
32. Duroux, L.; Welinder, K. G. *J. Mol. Evol.* **2003**, *57*, 397–407.
33. Passardi, F.; Bakalovic, N.; Teixeira, F. K.; Margis-Pinheiro, M.; Penel, C.; Dunand, C. *Genomics* **2007**, *89*, 567–579.
34. Tognolli, M.; Penel, C.; Greppin, H.; Simon, P. *Gene* **2002**, *288*, 129–138.
35. Welinder, K. G.; Justesen, A. F.; Kjaersgard, I. V. H.; Jensen, R. B.; Rasmussen, S. K.; Jespersen, H. M.; Duroux, L. *Eur. J. Biochem.* **2002**, *269*, 6063–6081.
36. Kjalke, M.; Andersen, M. B.; Schneider, P.; Christensen, B.; Schulein, M.; Welinder, K. G. *Biochim. Biophys. Acta* **1992**, *1120*, 248–256.
37. Everse, J. *Peroxidases in Chemistry and Biology*; CRC Press: Boca Raton, Florida, **1991**.
38. Finzel, B. C.; Poulos, T. L.; Kraut, J. *J. Biol. Chem.* **1984**, *259*, 13027–13036.
39. Edwards, S. L.; Raag, R.; Wariishi, H.; Gold, M. H.; Poulos, T. L. *Proc. Natl. Acad. Sci. USA* **1993**, *90*, 750–754.
40. Poulos, T. L.; Edwards, S. L.; Wariishi, H.; Gold, M. H. *J. Biol. Chem.* **1993**, *268*, 4429–4440.
41. Piontek, K.; Glumoff, T.; Winterhalter, K. *FEBS Lett.* **1993**, *315*, 119–124.
42. Kunishima, N.; Fukuyama, K.; Matsubara, H.; Hatanaka, H.; Shibano, Y.; Amachi, T. *J. Mol. Biol.* **1994**, *235*, 331–344.

43. Petersen, J. F. W.; Kadziola, A.; Larsen, S. *FEBS Lett.* **1994**, *339*, 291–296.
44. Sundaramoorthy, M.; Kishi, K.; Gold, M. H.; Poulos, T. L. *J. Biol. Chem.* **1994**, *269*, 32759–32767.
45. Patterson, W. R.; Poulos, T. L. *Biochemistry* **1995**, *34*, 4331–4341.
46. Schuller, D. J.; Ban, N.; van Huystee, R. B.; McPherson, A.; Poulos, T. L. *Structure* **1996**, *4*, 311–321.
47. Gajhede, M.; Schuller, D. J.; Henriksen, A.; Smith, A. T.; Poulos, T. L. *Nat. Struct. Biol.* **1997**, *4*, 1032–1038.
48. Henriksen, A.; Welinder, K. G.; Gajhede, M. *J. Biol. Chem.* **1998**, *273*, 2241–2248.
49. Østergaard, L.; Teilum, K.; Mirza, O.; Mattsson, O.; Petersen, M.; Welinder, K. G.; Mundy, J.; Gajhede, M.; Henriksen, A. *Plant. Mol. Biol.* **2000**, *44*, 231–243.
50. Nielsen, K. L.; Indiani, C.; Henriksen, A.; Feis, A.; Becucci, M.; Gajhede, M.; Smulevich, G.; Welinder, K. G. *Biochemistry* **2001**, *40*, 11013–11021.
51. Mirza, O.; Henriksen, A.; Ostergaard, L.; Welinder, K. G.; Gajhede, M. *Acta Crystallogr. D Biol. Crystallogr.* **2000**, *56*, 372–375.
52. Henriksen, A.; Mirza, O.; Indiani, C.; Teilum, K.; Smulevich, G.; Welinder, K. G.; Gajhede, M. *Protein Sci.* **2001**, *10*, 108–115.
53. Yamada, Y.; Fujiwara, T.; Sato, T.; Igarashi, N.; Tanaka, N. *Nat. Struct. Biol.* **2002**, *9*, 691–695. Accession pdb code: 1ITK.
54. Carpena, X.; Loprasert, S.; Mongkolsuk, S.; Switala, J.; Loewen, P. C.; Fita, I. *J. Mol. Biol.* **2003**, *327*, 475–489.
55. Carpena, X.; Melik-Adamyan, W.; Loewen, P. C.; Fita, I. *Acta Crystallogr. D Biol. Crystallogr.* **2004**, *60*, 1824–1832.
56. Bertrand, T.; Eady, N. A. J.; Jones, J. N.; Nagy, J. M.; Jamart-Gregoire, B.; Raven, E. L.; Brown, K. A. *J. Biol. Chem.* **2004**, *279*, 38991–38999.
57. Carpena, X.; Wiseman, B.; Deemagarn, T.; Singh, R.; Switala, J.; Ivancich, A.; Fita, I.; Loewen, P. C. *EMBO Rep.* **2005**, *6*, 1156–1162.
58. Smulevich, G.; Mauro, J. M.; Fishel, L. A.; English, A. M.; Kraut, J.; Spiro, T. G. *Biochemistry* **1988**, *27*, 5477–5485.
59. Smulevich, G.; Miller, M. A.; Kraut, J.; Spiro, T. G. *Biochemistry* **1991**, *30*, 9546–9558.
60. Smulevich, G.; Spiro, T. G. *Methods Enzymol.* **1993**, *Metallobiochem. Part C* **1993**, *226*, 397–408.
61. Smulevich, G.; Neri, F.; Willemsen, O.; Choudhury, K.; Marzocchi, M. P.; Poulos, T. L. *Biochemistry* **1995**, *34*, 13485–13490.
62. Smulevich, G.; Hu, S. Z.; Rodgers, K. R.; Goodin, D. B.; Smith, K. M.; Spiro, T. G. *Biospectroscopy* **1996**, *2*, 365–376.
63. Smulevich, G.; Feis, A.; Focardi, C.; Tams, J.; Welinder, K. G. *Biochemistry* **1994**, *33*, 15425–15432.
64. Smulevich, G.; Neri, F.; Marzocchi, M. P.; Welinder, K. G. *Biochemistry* **1996**, *35*, 10576–10585.
65. Neri, F.; Indiani, C.; Welinder, K. G.; Smulevich, G. *Eur. J. Biochem.* **1998**, *251*, 830–838.
66. Neri, F.; Indiani, C.; Baldi, B.; Vind, J.; Welinder, K. G.; Smulevich, G. *Biochemistry* **1999**, *38*, 7819–7827.
67. Howes, B. D.; Rodriguez-Lopez, J. N.; Smith, A. T.; Smulevich, G. *Biochemistry* **1997**, *36*, 1532–1543.
68. Heering, H. A.; Smith, A. T.; Smulevich, G. *J. Inorg. Biochem.* **1999**, *74*, 157.
69. Howes, B. D.; Veitch, N. C.; Smith, A. T.; White, C. G.; Smulevich, G. *Biochem. J.* **2001**, *353*, 181–191.

70. de Ropp, J. S.; Mandal, P.; Brauer, S. L.; Lamar, G. N. *J. Am. Chem. Soc.* **1997**, *119*, 4732–4739.
71. Feis, A.; Howes, B. D.; Indiani, C.; Smulevich, G. *J. Raman Spectrosc.* **1998**, *29*, 933–938.
72. Nissum, M.; Feis, A.; Smulevich, G. *Biospectroscopy* **1998**, *4*, 355–364.
73. Howes, B. D.; Schiodt, C. B.; Welinder, K. G.; Marzocchi, M. P.; Ma, J. G.; Zhang, J.; Shelnutt, J. A.; Smulevich, G. *Biophys. J.* **1999**, *77*, 478–492.
74. Indiani, C.; Feis, A.; Howes, B. D.; Marzocchi, M. P.; Smulevich, G. *J. Am. Chem. Soc.* **2000**, *122*, 7368–7376.
75. Scheidt, W. R.; Reed, C. A. *Chem. Rev.* **1981**, *81*, 543–555.
76. Cheng, R. J.; Chen, P. Y.; Gau, P. R.; Chen, C. C.; Peng, S. M. *J. Am. Chem. Soc.* **1997**, *119*, 2563–2569.
77. Jentzen, W.; Song, X. Z.; Shelnutt, J. A. *J. Phys. Chem. B* **1997**, *101*, 1684–1699.
78. Huang, Q.; Schweitzer-Stenner, R. *J. Raman Spectrosc.* **2005**, *36*, 363–375.
79. Feis, A.; Marzocchi, M. P.; Paoli, M.; Smulevich, G. *Biochemistry* **1994**, *33*, 4577–4583.
80. Yu, N.-T.; Liu, C. S. *J. Am. Chem. Soc.* **1972**, *94*, 5127–5128.
81. Yu, N.-T. *J. Am. Chem. Soc.* **1974**, *96*, 4664–4668.
82. Carey, P. R. *Ann. Rev. Phys. Chem.* **2006**, *57*, 527–554.
83. Carpentier; P.; Royant, A.; Ohana, J.; Bourgeois, D. *J. Appl. Cryst.* **2007**, *40*, 1113–1122.
84. Loppnow, G. R.; Barry, B. A.; Mathies, R. A. *Proc. Natl. Acad. Sci. USA* **1989**, *86*, 1515–1518.
85. Puppels, G. J.; Demul, F. F. M.; Otto, C.; Greve, J.; Robertnicoud, M.; Arndtjovin, D. J.; Jovin, T. M. *Nature* **1990**, *347*, 301–303.
86. Zhu, L. Y.; Sage, J. T.; Champion, P. M. *Biochemistry* **1993**, *32*, 11181–11185.
87. Sage, J. T.; Morikis, D.; Champion, P. M. *J. Biol. Chem.* **1989**, *90*, 3015–3032.
88. Sawyer, S.; Hester, R. E. *FEBS Lett.* **1984**, *174*, 219–222.
89. Smulevich, G.; Wang, Y.; Edwards, S. L.; Poulos, T. L.; English, A. M.; Spiro, T. G. *Biochemistry* **1990**, *29*, 2586–2592.
90. Smulevich, G.; Wang, Y.; Mauro, J. M.; Wang, J. M.; Fishel, L. A.; Kraut, J.; Spiro, T. G. *Biochemistry* **1990**, *29*, 7174–7180.
91. Smulevich, G.; Feis, A.; Indiani, C.; Becucci, M.; Marzocchi, M. P. *J. Biol. Inorg. Chem.* **1999**, *4*, 39–47.
92. Wang, J. M.; Mauro, J. M.; Edwards, S. L.; Oatley, S. J.; Fishel, L. A.; Ashford, V. A.; Xuong, N. H.; Kraut, J. *Biochem.* **1990**, *29*, 7160–7173.
93. Indiani, C.; Santoni, E.; Becucci, M.; Boffi, A.; Fukuyama, K.; Smulevich, G. *Biochemistry* **2003**, *42*, 14066–14074.
94. Garman, E. *Curr. Opin. Struct. Biol.* **2003**, *13*, 545–551.
95. Smulevich, G.; English, A. M.; Mantini, A. R.; Marzocchi, M. P. *Biochemistry* **1991**, *30*, 772–779.
96. Nissum, M.; Neri, F.; Mandelman, D.; Poulos, T. L.; Smulevich, G. *Biochemistry* **1998**, *37*, 8080–8087.
97. Indiani, C.; Feis, A.; Howes, B. D.; Marzocchi, M. P.; Smulevich, G. *J. Inorg. Biochem.* **2000**, *79*, 269–274.
98. Howes, B. D.; Feis, A.; Indiani, C.; Marzocchi, M. P.; Smulevich, G. *J. Biol. Inorg. Chem.* **2000**, *5*, 227–235.
99. Marzocchi, M. P.; Smulevich, G. *J. Raman Spectrosc.* **2003**, *34*, 725–736.
100. Spiro, T. G.; Li, H. Y. Resonance Raman Spectroscopy of metalloporphyrins. In *Biological Applications of Raman Spectroscopy, Vol. III*; Spiro, T. G., Ed.; John Wiley & Sons: New York, **1988**; pp. 1–37.

101. Yonetani, T.; Wilson, D. F.; Seamonds, B. *J. Biol. Chem.* **1966**, *22*, 5347–5352.
102. Neri, F.; Kok, D.; Miller, M. A.; Smulevich, G. *Biochemistry* **1997**, *36*, 8947–8953.
103. Teraoka, J.; Kitagawa, T. *J. Biol. Chem.* **1981**, *256*, 3969–3977.
104. Teraoka, J.; Kitagawa, T. *Biochem. Biophys. Res. Commun.* **1980**, *93*, 694–700.
105. Kitagawa, T. The heme protein structure and the iron histidine stretching mode. In *Biological Applications of Raman Spectroscopy, Vol. III*; Spiro, T. G., Ed.; Wiley & Sons: New York, **1988**; pp. 97–131.
106. Wada, K.; Tada, T.; Nakamura, Y.; Kinoshita, T.; Tamoi, M.; Shigeoka, S.; Nishimura, K. *Acta Crystallogr. D Biol. Crystallogr.* **2002**, *58*, 157–159.
107. Za mocky, M.; Regelsberger, G.; Jakopitsch, C.; Obinger, C. *FEBS Lett.* **2001**, *492*, 177–182.
108. Jakopitsch, C.; Droghetti, E.; Schmuckenschlager, F.; Furtmuller, P. G.; Smulevich, G.; Obinger, C. *J. Biol. Chem.* **2005**, *280*, 42411–42422.
109. Smulevich, G.; Jakopitsch, C.; Droghetti, E.; Obinger, C. *J. Inorg. Biochem.* **2006**, *100*, 568–585.
110. Heering, H. A.; Indiani, C.; Regelsberger, G.; Jakopitsch, C.; Obinger, C.; Smulevich, G. *Biochemistry* **2002**, *41*, 9237–9247.
111. Santoni, E.; Jakopitsch, C.; Obinger, C.; Smulevich, G. *Biochemistry* **2004**, *43*, 5792–5802.
112. Santoni, E.; Jakopitsch, C.; Obinger, C.; Smulevich, G. *Biopolymers* **2004**, *74*, 46–50.
113. Lukat-Rodgers, G. S.; Wengenack, N. L.; Rusnak, F.; Rodgers, K. R. *Biochemistry* **2000**, *39*, 9984–9993.
114. Kapetanaki, S.; Chouchane, S.; Girotto, S.; Yu, S. W.; Magliozzo, R. S.; Schelvis, J. P. M. *Biochemistry* **2003**, *42*, 3835–3845.
115. Chouchane, S.; Girotto, S.; Kapetanaki, S.; Schelvis, J. P. M.; Yu, S. W.; Magliozzo, R. S. *J. Biol. Chem.* **2003**, *278*, 8154–8162.
116. Kapetanaki, S. M.; Chouchane, S.; Yu, S. W.; Zhao, X. B.; Magliozzo, R. S.; Schelvis, J. P. M. *Biochemistry* **2005**, *44*, 243–252.
117. Kapetanaki, S. M.; Zhao, X. B.; Yu, S. W.; Magliozzo, R. S.; Schelvis, J. P. M. *J. Inorg. Biochem.* **2007**, *101*, 422–433.
118. Ranguelova, K.; Suarez, J.; Metlitsky, L.; Yu, S. W.; Brejt, S. Z.; Brejt, S. Z.; Zhao, L.; Schelvis, J. P. M.; Magliozzo, R. S. *Biochemistry* **2008**, *47*, 12583–12592.
119. Jakopitsch, C.; Regelsberger, G.; Furtmuller, P. G.; Ruker, F.; Peschek, G. A.; Obinger, C. *J. Inorg. Biochem.* **2002**, *91*, 78–86.
120. Smulevich, G.; Mauro, J. M.; Fishel, L. A.; English, A. M.; Kraut, J.; Spiro, T. G. *Biochemistry* **1988**, *27*, 5486–5492.
121. Rouse, D. A.; Devito, J. A.; Li, Z. M.; Byer, H.; Morris, S. L. *Mol. Microbiol.* **1996**, *22*, 583–592.
122. Musser, J. M. *Emerg. Infect. Dis.* **1996**, *1996*, 1–17.
123. Marttila, H. J.; Soini, H.; Huovinen, P.; Viljanen, M. K. *Antimicrob. Agents Chemother.* **1996**, *40*, 2187–2189.
124. Robitzek, E. H.; Selikoff, I. J. *Am. Rev. Tuberc.* **1952**, *65*, 402–410.
125. Zhao, X. B.; Yu, H.; Yu, S. W.; Wang, F.; Sacchettini, J. C.; Magliozzo, R. S. *Biochemistry* **2006**, *45*, 4131–4140.
126. Pym, A. S.; Saint-Joanis, B.; Cole, S. T. *Infect. Immun.* **2002**, *70*, 4955–4960.
127. Smulevich, G.; Evangelista-Kirkup, R.; English, A. M.; Spiro, T. G. *Biochemistry* **1986**, *25*, 4426–4430.
128. Yu, S.; Girotto, S.; Zhao, X. B.; Magliozzo, R. S. *J. Biol. Chem.* **2003**, *278*, 44121–44127.

129. Jakopitsch, C.; Auer, M.; Regelsberger, G.; Jantschko, W.; Furtmuller, P. G.; Ruker, F.; Obinger, C. *Biochemistry* **2003**, *42*, 5292–5300.
130. Cheek, J.; Mandelman, D.; Poulos, T. L.; Dawson, J. H. *J. Biol. Inorg. Chem.* **1999**, *4*, 64–72.
131. Shiro, Y.; Kurono, M.; Morishima, I. *J. Biol. Chem.* **1986**, *261*, 9382–9390.
132. Rodríguez Marañón, M. J.; Stillman, M. J.; van Huystee, R. B. *Biochem. Biophys. Res. Commun.* **1993**, *194*, 332.
133. Sutherland, G. R. J.; Zapanta, L. S.; Tien, M.; Aust, S. D. *Biochemistry* **1997**, *36*, 3654–3662.
134. Ogawa, S.; Shiro, Y.; Morishima, I. *Biochem. Biophys. Res. Commun.* **1979**, *90*, 674–678.
135. Nie, G. J.; Aust, S. D. *Biochemistry* **1997**, *36*, 5113–5119.
136. George, S. J.; Kvaratskhelia, M.; Dilworth, M. J.; Thorneley, R. N. F. *Biochem. J.* **1999**, *344*, 237–244.
137. Sutherland, G. R. J.; Aust, S. D. *Biochemistry* **1997**, *36*, 8567–8573.
138. Barber, K. R.; Maranon, M. J. R.; Shaw, G. S.; vanHuystee, R. B. *Eur. J. Biochem.* **1995**, *232*, 825–833.
139. Haschke, R. H.; Friedhoff, J. M. *Biochem. Biophys. Res. Commun.* **1978**, 1039–1042.
140. Morishima, I.; Kurono, M.; Shiro, Y. *J. Biol. Chem.* **1986**, *261*, 9399.
141. Pappa, H. S.; Cass, A. E. G. *Eur. J. Biochem.* **1993**, *212*, 227–235.
142. Chattopadhyay, K.; Mazumdar, S. *Biochemistry* **2000**, *39*, 263–270.
143. Laberge, M.; Huang, Q.; Schweitzer-Stenner, R.; Fidy, J. *Biophys. J.* **2003**, *84*, 2542–2552.
144. Tanaka, M.; Nagano, S.; Ishimori, K.; Morishima, I. *Biochemistry* **1997**, *36*, 9791–9798.
145. Tanaka, M.; Morimoto, A.; Ishimori, K.; Morishima, I. *Pure Appl. Chem.* **1998**, *70*, 911–916.
146. Tanaka, M.; Ishimori, K.; Mukai, M.; Kitagawa, T.; Morishima, I. *Biochemistry* **1997**, *36*, 9889–9898.
147. Tanaka, M.; Ishimori, K.; Morishima, I. *Biochemistry* **1998**, *37*, 2629–2638.
148. Howes, B. D.; Feis, A.; Raimondi, L.; Indiani, C.; Smulevich, G. *J. Biol. Chem.* **2001**, *276*, 40704–40711.
149. Kishi, K.; Hildebrand, D. P.; van Someren, M. K.; Gettemy, J.; Mauk, A. G.; Gold, M. H. *Biochemistry* **1997**, *36*, 4268–4277.
150. Youngs, H. L.; Moënne-Loccoz, P.; Loehr, T. L.; Gold, M. H. *Biochemistry* **2000**, *39*, 9994–10000.
151. Banci, L.; Bertini, I.; Capannoli, C.; Del Conte, R.; Tien, M. *Biochemistry* **1999**, *38*, 9617–9625.
152. Laberge, M.; Szigeti, K.; Fidy, J. *Biopolymers* **2004**, *74*, 41–45.
153. Laberge, M.; Kovesi, I.; Yonetani, T.; Fidy, J. *Biopolymers* **2006**, *82*, 425–429.
154. Huang, Q.; Szigeti, K.; Fidy, J.; Schweitzer-Stenner, R. *J. Phys. Chem.B* **2003**, *107*, 2822–2830.
155. Huang, Q.; Laberge, M.; Szigeti, K.; Fidy, J.; Schweitzer-Stenner, R. *Biopolymers* **2003**, *72*, 241–248.
156. Szigeti, K.; Smeller, L.; Osvath, S.; Majer, Z.; Fidy, J. *Biochim. Biophys. Acta Proteins Proteomics* **2008**, *1784*, 1965–1974.
157. Smith, A. T.; Veitch, N. C. *Curr. Opin. Chem. Biol.* **1998**, *2*, 269–278.
158. Henriksen, A.; Schuller, D. J.; Meno, K.; Welinder, K. G.; Smith, A. T.; Gajhede, M. *Biochemistry* **1998**, *37*, 8054–8060.
159. Itakura, H.; Oda, Y.; Fukuyama, K. *FEBS Lett.* **1997**, *412*, 107–110.
160. Tsukamoto, K.; Itakura, H.; Sato, K.; Fukuyama, K.; Miura, S.; Takahashi, S.; Ikezawa, H.; Hosoya, T. *Biochemistry* **1999**, *38*, 12558–12568.

161. Schonbaum, G. R. *J. Biol. Chem.* **1973**, *248*, 502–511.
162. Teraoka, J.; Kitagawa, T. *J. Phys. Chem.* **1980**, *84*, 1928–1935.
163. Kitagawa, T.; Hashimoto, S.; Teraoka, J.; Nakamura, S.; Yajima, H.; Hosoya, T. *Biochemistry* **1983**, *22*, 2792.
164. Gupta, R. K.; Mildvan, A. S.; Schonbaum, G. R. *Biochem. Biophys. Res. Commun.* **1979**, *89*, 1334–1340.
165. Aime, S.; Fasano, M.; Paoletti, S.; Cutruzzola, F.; Desideri, A.; Bolognesi, M.; Rizzi, M.; Ascenzi, P. *Biophys. J.* **1996**, *70*, 482–488.
166. Vojtechovský, J.; Chu, K.; Berendzen, J.; Sweet, R. M.; Schlichting, I. *Biophys. J.* **1999**, *77*, 2153–2174.
167. Poulos, T. L.; Kraut, J. *J. Biol. Chem.* **1980**, *255*, 8205.
168. Edwards, S. L.; Poulos, T. L. *J. Biol. Chem.* **1990**, *265*, 2588–2595.
169. Bonagura, C. A.; Bhaskar, B.; Shimizu, H.; Li, H. Y.; Sundaramoorthy, M.; McRee, D. E.; Goodin, D. B.; Poulos, T. L. *Biochemistry* **2003**, *42*, 5600–5608.
170. Smulevich, G.; Paoli, M.; De Sanctis, G.; Mantini, A. R.; Ascoli, F.; Coletta, M. *Biochemistry* **1997**, *36*, 640–649.
171. Al-Mustafa, J.; Kincaid, J. R. *Biochemistry* **1994**, *33*, 2191–2197.
172. Kincaid, J. R. Resonance Raman spectra of heme proteins and model compounds. In *The Porphyrin Handbook*; Kadish, K., Smith, K. M., Guilard, R., Eds.; Academic: New York, **2000**; pp. 225–292.
173. Edwards, S. L.; Poulos, T. L.; Kraut, J. *J. Biol. Chem.* **1984**, *259*, 12988.
174. Carlsson, G. H.; Nicholls, P.; Svistunenko, D.; Berglund, G. I.; Hajdu, *J. Biochemistry* **2005**, *44*, 635–642.
175. Phillips, G. N.; Teodoro, M. L.; Li, T. S.; Smith, B.; Olson, J. S. *J. Phys. Chem. B* **1999**, *103*, 8817–8829.
176. Ray, G. B.; Li, X. Y.; Ibers, J. A.; Sessler, J. L.; Spiro, T. G. *J. Am. Chem. Soc.* **1994**, *116*, 162–176.
177. Barlow, C.; Ohlsson, P.-I.; Paul, K. G. *Biochemistry* **1976**, *1976*, 2225.
178. Evangelista-Kirkup, R.; Smulevich, G.; Spiro, T. G. *Biochemistry* **1986**, *25*, 4420–4425.
179. Uno, T.; Nishimura, Y.; Tsuboi, M.; Makino, R.; Iizuka, T.; Ishimura, Y. *J. Biol. Chem.* **1987**, *262*, 4549–4556.
180. Rodriguez-Lopez, J. N.; Smith, A. T.; Thorneley, R. N. F. *J. Biol. Chem.* **1996**, *271*, 4023–4030.
181. Feis, A.; Santoni, E.; Neri, F.; Ciaccio, C.; De Sanctis, G.; Coletta, M.; Welinder, K. G.; Smulevich, G. *Biochemistry* **2002**, *41*, 13264–13273.
182. English, A. M.; Tsaprailis, G. *Adv. Inorg. Chem.* **1995**, *34*, 79–125.
183. Berglund, G. I.; Carlsson, G. H.; Smith, A. T.; Szoke, H.; Henriksen, A.; Hajdu, *J. Nature* **2002**, *417*, 463–468.
184. Hersleth, H. P.; Ryde, U.; Rydberg, P.; Gorbitz, C. H.; Andersson, K. K. *J. Inorg. Biochem.* **2006**, *100*, 460–476.
185. Pelletier, H.; Kraut, J. *Science* **1992**, *258*, 1748–1755.
186. Terner, J.; Palaniappan, V.; Gold, A.; Weiss, R.; Fitzgerald, M. M.; Sullivan, A. M.; Hosten, C. M. *J. Inorg. Biochem.* **2006**, *100*, 480–501.
187. Dolphin, D.; Forman, A.; Borg, D. C.; Fajer, J.; Felton, R. H. *Proc. Natl. Acad. Sci. USA* **1971**, *68*, 614–618.
188. Dolphin, D.; Felton, R. H. *Acc. Chem. Res.* **1974**, *7*, 26–32.

189. Terner, J.; Sitter, A.; Reczek, C. M. *Biochim. Biophys. Acta* **1985**, *828*, 73–80.
190. Behan, R. K.; Green, M. T. *J. Inorg. Biochem.* **2006**, *100*, 448–459.
191. Gouterman, M. In *The Porphyrins*; Dolphin, D., Ed.; Academic: New York, **1978**; pp. 1–169.
192. Terner, J.; Gold, A.; Weiss, R.; Mandon, D.; Trautwein, A. X. *J. Porph. Phthal.* **2001**, *5*, 364.
193. Dolphin, D. *Israel J. Chem.* **1981**, *21*, 67–71.
194. Skillman, A. G.; Collins, J. R.; Loew, G. H. *J. Am. Chem. Soc.* **1992**, *114*, 9538–9544.
195. Andersson, L. A.; Renganathan, V.; Loehr, T. M.; Gold, M. H. *Biochemistry* **1987**, *26*, 2258–2263.
196. Proshlyakov, D. A.; Paeng, I. R.; Paeng, K. J.; Kitagawa, T. *Biospectroscopy* **1996**, *2*, 317–329.
197. Palaniappan, V.; Terner, J. *J. Biol. Chem.* **1989**, *264*, 16046–16053.
198. Hosten, C. M.; Sullivan, A. M.; Palaniappan, V.; Fitzgerald, M. M.; Terner, J. *J. Biol. Chem.* **1994**, *269*, 13966–13978.
199. Reczek, C. M.; Sitter, A.; Terner, J. *J. Mol. Struct.* **1989**, *214*, 27–41.
200. Kapetanaki, S. M.; Chouchane, S.; Yu, S. W.; Magliozzo, R. S.; Schelvis, J. P. M. *J. Inorg. Biochem.* **2005**, *99*, 1401–1406.
201. Ikemura, K.; Mukai, M.; Shimada, H.; Tsukihara, T.; Yamaguchi, S.; Shinzawa-Itoh, K.; Yoshikawa, S.; Ogura, T. *J. Am. Chem. Soc.* **2008**, *130*, 14384–14385.
202. Hashimoto, S.; Teraoka, J.; Inubushi, T.; Yonetani, T.; Kitagawa, T. *J. Biol. Chem.* **1986**, *261*, 11110–11118.
203. Penner-Hahn, J. E.; Eble, K. S.; McMurry, T. J.; Renner, M.; Balch, A. L.; Groves, J. T.; Dawson, J. H.; Hodgson, K. O. *J. Am. Chem. Soc.* **1986**, *108*, 7819–7825.
204. Chance, B.; Powers, L.; Ching, Y.; Poulos, T. L.; Schonbaum, G. R.; Yamazaki, I.; Paul, K. G. *Arch. Biochem. Biophys.* **1984**, *235*, 596–611.
205. Chance, M.; Powers, L.; Kumar, C.; Chance, B. *Biochemistry* **1986**, *25*, 1259–1265.
206. Green, M. T.; Dawson, J. H.; Gray, H. B. *Science* **2004**, *304*, 1653–1656.
207. Chang, C. S.; Yamazaki, I.; Sinclair, R.; Khalid, S.; Powers, L. *Biochemistry* **1993**, *32*, 923–928.
208. Oertling, W. A.; Babcock, G. T. *Biochemistry* **1988**, *27*, 3331–3338.
209. Makino, R.; Uno, T.; Nishimura, Y.; Iizuka, T.; Tsuboi, M. *J. Biol. Chem.* **1986**, *261*, 8376–8382.
210. Hashimoto, S.; Nakajima, Y.; Yamazaki, I.; Tatsuno, Y.; Kitagawa, T. *FEBS Lett.* **1986**, *208*, 305–307.
211. Sitter, A.; Reczek, C. M.; Terner, J. *J. Biol. Chem.* **1985**, *260*, 7515–7522.
212. Hashimoto, S.; Tatsuno, Y.; Kitagawa, T. *Proc. Natl. Acad. Sci. USA* **1986**, *83*, 2417–2421.
213. Oertling, W. A.; Kean, R. T.; Wever, R.; Babcock, G. T. *Inorg. Chem.* **1990**, *29*, 2633–2645.
214. Corbett, M. C.; Latimer, M. J.; Poulos, T. L.; Sevrioukova, I. F.; Hodgson, K. O.; Hedman, B. *Acta Crystallogr. D Biol. Crystallogr.* **2007**, *63*, 951–960.
215. Hersleth, H. P.; Uchida, T.; Rohr, A. K.; Teschner, T.; Schuenemann, V.; Kitagawa, T.; Trautwein, A. X.; Gorbitz, C. H.; Andersson, K. K. *J. Biol. Chem.* **2007**, *282*, 23372–23386.
216. Davydov, R.; Osborne, R. L.; Kim, S. H.; Dawson, J. H.; Hoffman, B. M. *Biochemistry* **2008**, *47*, 5147–5155.
217. Walker, F. A. "NMR and EPR of metalloporphyrins and heme proteins," Vol. VIII. In *Handbook of Porphyrin Science*; Kadish, K.; Smith, K. M.; Guilard, R., Eds.; Academic: New York, **2010**.
218. Ivancich, A.; Mattioli, T. A.; Un, S. *J. Am. Chem. Soc.* **1999**, *121*, 5743–5753.
219. Fielding, A. J.; Singh, R.; Boscolo, B.; Loewen, P. C.; Ghibaudi, E. M.; Ivancich, A. *Biochemistry* **2008**, *47*, 9781–9792.

220. Colvin, J. T.; Rutter, R.; Stapleton, H. J.; Hager, L. P. *Biophys. J.* **1983**, *41*, 105–108.
221. Schulz, C. E.; Devaney, P. W.; Winkler, H.; Debrunner, P. G.; Doan, N.; Chiang, R.; Rutter, R.; Hager, L. P. *FEBS Lett.* **1979**, *103*, 102–105.
222. Rutter, R.; Hager, L. P.; Dhonau, H.; Hendrich, M.; Valentine, M.; Debrunner, P. *Biochemistry* **1984**, *23*, 6809–6816.
223. Benecky, M. J.; Frew, J. E.; Scowen, N.; Jones, P.; Hoffman, B. *Biochemistry* **1993**, *32*, 11929–11933.
224. Houseman, A. L. P.; Doan, P. E.; Goodin, D. B.; Hoffman, B. M. *Biochemistry* **1993**, *32*, 4430–4443.
225. Ayougou, K.; Mandon, D.; Fischer, J.; Weiss, R.; Müther, M.; Schünemann, V.; Trautwein, A.; Bill, E.; Terner, J.; Jayaraj, K.; Gold, A.; Austin, R. *Chem. Eur. J.* **1996**, *2*, 1159–1163.
226. Patterson, W. R.; Poulos, T. L.; Goodin, D. B. *Biochemistry* **1995**, *34*, 4342–4345.
227. Erman, J. E.; Vitello, L. B.; Mauro, J. M.; Kraut, J. *Biochemistry* **1989**, *28*, 7992–7995.
228. Jensen, G. M.; Bunte, S. W.; Warshel, A.; Goodin, D. B. *J. Phys. Chem. B* **1998**, *102*, 8221–8228.
229. Huyett, J. E.; Doan, P. E.; Gurbiel, R.; Houseman, A. L. P.; Sivaraja, M.; Goodin, D. B.; Hoffman, B. M. *J. Am. Chem. Soc.* **1995**, *117*, 9033–9041.
230. Hori, H.; Yonetani, T. *J. Biol. Chem.* **1985**, *260*, 349–355.
231. Fishel, L. A.; Farnum, M. F.; Mauro, J. M.; Miller, M. A.; Kraut, J. *Biochemistry* **1991**, *30*, 1986–1996.
232. Doyle, W. A.; Blodig, W.; Veitch, N. C.; Piontek, K.; Smith, A. T. *Biochemistry* **1998**, *37*, 15097–15105.
233. Martinez, M. J.; Ruiz-Dueñas, F. J.; Guillen, F.; Martinez, A. T. *Eur. J. Biochem.* **1998**, *237*, 424–432.
234. Pogni, R.; Teutloff, C.; Lendzian, F.; Basosi, R. *Appl. Magn. Res.* **2007**, *31*, 509–526.
235. Choinowski, T.; Blodig, W.; Winterhalter, K. H.; Piontek, K. *J. Mol. Biol.* **1999**, *286*, 809–827.
236. Blodig, W.; Smith, A. T.; Doyle, W. A.; Piontek, K. *J. Mol. Biol.* **2001**, *305*, 851–861.
237. Blodig, W.; Smith, A. T.; Winterhalter, K.; Piontek, K. *Arch. Biochem. Biophys.* **1999**, *370*, 88–92.
238. Perez-Boada, M.; Ruiz-Dueñas, F. J.; Martinez, A. T.; Pogni, R.; Basosi, R.; Choinowski, T.; Piontek, K.; Martinez, M. J. *J. Mol. Biol.* **2006**, *354*, 385–402.
239. Smith, A. T.; Doyle, W. A.; Dorlet, P.; Ivancich, A. *Proc. Natl. Acad. Sci. USA* **2009**, *106*, 16084–16089.
240. Ivancich, A.; Jakopitsch, C.; Auer, M.; Un, S.; Obinger, C. *J. Am. Chem. Soc.* **2003**, *125*, 14093–14102.
241. Chouchane, S.; Girotto, S.; Yu, S.; Magliozzo, R. S. *J. Biol. Chem.* **2002**, *277*, 42633–42638.
242. Zhao, X.; Girotto, S.; Yu, S.; Magliozzo, R. S. *J. Biol. Chem.* **2004**, *279*, 7606–7612.
243. Ranguelova, K.; Girotto, S.; Gerfen, G. J.; Yu, S.; Suarez, J.; Metlitsky, L.; Magliozzo, R. S. *J. Biol. Chem.* **2007**, *282*, 6255–6264.
244. Jakopitsch, C.; Vlasits, J.; Wiseman, B.; Loewen, P. C.; Obinger, C. *Biochemistry* **2007**, *56*, 1183–1193.
245. Hays Putnam, A.-M.; Lee, Y.-T.; Goodin, D. B. *Biochemistry* **2009**, *48*, 1–3.
246. Wilcox, K. S.; Jensen, G. M.; Fitzgerald, M. M.; McRee, D. E.; Goodin, D. B. *Biochemistry* **1996**, *35*, 4858–4866.
247. Metcalfe, C.; MacDonald, I. K.; Murphy, E. J.; Brown, K. A.; Raven, E. L.; Moody, P. C. E. *J. Biol. Chem.* **2008**, *10*, 6193–6200.

248. Pogni, R.; Vazquez-Duhalt, R.; Giansanti, S.; Teutloff, C.; Verdin, J.; Valderrama, B.; Lendzian, F.; Lubitz, W.; Basosi, R. *Biochemistry* **2005**, *44*, 4267–4274.
249. Shih, C.; Museth, A. K.; Abrahamsson, M.; Blanco-Rodriguez, A. M.; Di Biblio, A.; Sudhamsu, J.; Crane, B. R.; Ronayne, B. R.; Towrie, M.; Vlcek Jr, A.; Richards, J. H.; Winkler, J. R.; Gray, H. B. *Science* **2008**, *320*, 1762.
250. Colin, J.; Wiseman, B.; Switala, J.; Loewen, P. C.; Ivancich, A. *J. Am. Chem. Soc.* **2009**, *131*, 8557–8563.
251. Colin, J.; Jakopitsch, C.; Obinger, C.; Ivancich, A. *Appl. Magn. Res.* **2009**, in press.
252. Furtmüller, M.; Zederbauer, M.; Jantschko, W.; Helm, J.; Bogner, M.; Jakopitsch, C.; Obinger, C. *Arch. Biochem. Biophys.* **2006**, *445*, 199–213.
253. Zederbauer, M.; Furtmueller, P. G.; Brogioni, S.; Jakopitsch, C.; Smulevich, G.; Obinger, C. *Nat. Prod. Rep.* **2007**, *24*, 571–584.
254. Davies, M. J.; Hawkins, C. L.; Pattison, D. I.; Rees, M. D. *Antioxid. Redox Signal.* **2008**, *10*, 1199–1234.
255. Ortiz de Montellano, P. R. *Drug Metab. Rev.* **2008**, *40*, 405–426.
256. Singh, A. K.; Singh, N.; Sharma, S.; Singh, S. B.; Kaur, P.; Bhushan, A.; Srinivasan, A.; Singh, T. P. *J. Mol. Biol.* **2008**, *376*, 1060–1075.
257. Oxvig, C.; Thomsen, A. R.; Overgaard, M. T.; Sorensen, E. S.; Hojrup, P.; Bjerrum, M. J.; Gleich, G. J.; Sottrup-Jensen, L. *J. Biol. Chem.* **1999**, *274*, 16953–16958.
258. Zeng, J.; Fenna, R. E. *J. Mol. Biol.* **1992**, ***226***, 185–207.
259. Fiedler, T. J.; Davey, C. A.; Fenna, R. E. *J. Biol. Chem.* **2000**, *275*, 11964–11971.
260. Blair-Johnson, M.; Fiedler, T. J.; Fenna, R. E. *Biochemistry* **2001**, *40*, 13990–13997.
261. Carpena, X.; Vidossich, P.; Schroettner; K.; Callisto, B. M.; Banerjee, S.; Stampler, J.; Soudi, M.; Furtmueller, P. G.; Rovira, C.; Fita, I.; Obinger, C. *J. Biol. Chem.* **2009**, *284*, 25929–25937.
262. Singh, A. K.; Singh, N.; Sharma, S.; Shin, K.; Takase, M.; Kaur, P.; Srinivasan, A.; Singh, T. P. *Biophys. J.* **2009**, *96*, 646–654.
263. Sheikh, I. A.; Ethayathulla, A. S.; Singh, A. K.; Singh, N.; Sharma, S.; Singh, T. P. *PDB Data Bank* **2006**.
264. Sheikh, I. A.; Singh, A. K.; Singh, N.; Sinha, M.; Singh, S. B.; Bhushan, A.; Kaur, P.; Srinivasan, A.; Sharma, S.; Singh, T. P. *J. Biol. Chem.* **2009**, *284*, 14849–14856.
265. Andrews, P. C.; Krinsky, N. I. *J. Biol. Chem.* **1981**, 4218.
266. Kooter, I. M.; Moguilevsky, N.; Bollen, A.; Sijtsema, N. M.; Otto, C.; Dekker, H. L.; Wever, R. *Eur. J. Biochem.* **1999**, *264*, 211–217.
267. Kooter, I. M.; Koehler, B. P.; Moguilevsky, N.; Bollen, A.; Wever, R.; Johnson, M. K. *J. Biol. Inorg. Chem.* **1999**, *4*, 684–691.
268. Kooter, I. M.; Moguilevsky, N.; Bollen, A.; van der Veen, L. A.; Otto, C.; Dekker, H. L.; Wever, R. *J. Biol. Chem.* **1999**, *274*, 26794–26802.
269. Brogioni, S.; Feis, A.; Marzocchi, M. P.; Zederbauer, M.; Furtmuller, P. G.; Obinger, C.; Smulevich, G. *J. Raman Spectrosc.* **2006**, *37*, 263–276.
270. Floris, R.; Moguilevsky, N.; Puppels, G. J.; Jacquet, A.; Renire, R.; Bollen, A.; Wever, R. *J. Am. Chem. Soc.* **1995**, *117*, 3907–3911.
271. Manthey, J. A.; Boldt, N. J.; Bocian, D. F.; Chan, S. I. *J. Biol. Chem.* **1986**, *261*, 6734–6741.
272. Zbylut, S. D.; Kincaid, J. R. *J. Am. Chem. Soc.* **2002**, *124*, 6751–6758.
273. Sharonov, Y. A. *FEBS Lett.* **1995**, *377*, 512–514.
274. Abu-Soud, H. M.; Hazen, S. L. *Biochemistry* **2001**, *40*, 10747–10755.

275. Galijasevic, S.; Saed, G. M.; Diamond, M. P.; Abu-Soud, H. M. *J. Biol. Chem.* **2004**, *279*, 39465–39470.
276. Brogioni, S.; Stampler, J.; Furtmuller, P. G.; Feis, A.; Obinger, C.; Smulevich, G. *Biochim. Biophys. Acta Proteins Proteomics* **2008**, *1784*, 843–849.
277. Babcock, G. T.; Ingle, R. T.; Oertling, W. A.; Davis, J. C.; Averill, B. A.; Hulse, C. L.; Bolscher, B. G. J.; Wever, R. *Biochim. Biophys. Acta* **1985**, *828*, 58–66.
278. Hu, S. Z.; Treat, R. W.; Kincaid, J. R. *Biochemistry* **1993**, *32*, 10125–10130.
279. Salmaso, B. L. N.; Puppels, G. J.; Caspers, P. J.; Floris, R.; Wever, R.; Greve, J. *Biophys. J.* **1994**, *67*, 436–446.
280. Oertling, W. A.; Hoogland, H.; Babcock, G. T.; Wever, R. *Biochemistry* **1988**, *27*, 5395–5400.
281. Hu, S. H.; Kincaid, J. R. *J. Am. Chem. Soc.* **1991**, *113*, 7189–7194.
282. De Gioia, L.; Ghibaudi, E. M.; Laurenti, E.; Salmona, M.; Ferrari, R. P. *J. Biol. Inorg. Chem.* **1996**, *1*, 476–485.
283. Kimura, S.; Yamazaki, I. *Arch. Biochem. Biophys.* **1979**, *198*, 580–588.
284. Lardinois, O. M.; Medzihradszky, K. F.; Ortiz de Montellano, P. R. *J. Biol. Chem.* **1999**, *274*, 35441–35448.
285. Monzani, E.; Gatti, A. L.; Profumo, A.; Casella, L.; Gullotti, M. *Biochemistry* **1997**, *36*, 1918–1926.
286. Un, S.; Dorlet, P.; Rutherford, A. W. *Appl. Magn. Reson.* **2001**, *21*, 341–361.
287. Ivancich, A.; Jouve, H. M.; Sartot, B.; Gaillard, *J. Biochemistry* **1997**, *36*, 9356–9364.
288. Wiseman, B.; Colin, J.; Smith, A. T.; Ivancich, A.; Loewen, P. C. *J. Biol. Inorg. Chem.* **2009**, *14*, 801–811.
289. Singh, A. K; Singh, N.; Sinha, M.; Bhushan, A.; Kaur, P.; Srinivasan, A.; Sharma, S.; Singh, T. P. *J. Biol. Chem.* **2009**, *284*, 20311–20318.
290. Heering, H. A.; Jansen, M. A. K.; Schneider-Belhaddad, F.; Smith, A. T.; Thorneley, R. N. F.; Smulevich, G. *J. Inorg. Biochem.* **2001**, *86*, 256.
291. Kuila, D.; Tien, M.; Fee, J. A.; Ondrias, M. A. *Biochemistry* **1985**, *24*, 3394–3397.
292. Mino, Y.; Wariishi, H.; Blackburn, N. J.; Loehr, T. L.; Gold, M. H. *J. Biol. Chem.* **1988**, *263*, 7036.
293. Smulevich, G.; Paoli, M.; Burke, J. F.; Sanders, S. A.; Thorneley, R. N. F.; Smith, A. T. *Biochemistry* **1994**, *33*, 7398–7407.
294. Lukat-Rodgers, G. S.; Wengenack, N. L.; Rusnak, F.; Rodgers, K. R. *Biochemistry* **2001**, *40*, 7149–7157.
295. Feis, A.; Rodriguez-Lopez, J. N.; Thorneley, R. N. F.; Smulevich, G. *Biochemistry* **1998**, *37*, 13575–13581.
296. Rodriguez-Lopez, J. N.; George, S. J.; Thorneley, R. N. F. *J. Biol. Inorg. Chem.* **1998**, *3*, 44–52.
297. Hu, S. Z.; Smith, K. M.; Spiro, T. G. *J. Am. Chem. Soc.* **1996**, *118*, 12638–12646.
298. Li, X. Y.; Czernuszewicz, R. S.; Kincaid, J. R.; Stein, P.; Spiro, T. G. *J. Phys. Chem.* **1990**, *94*, 47–61.
299. Dunford, H. B. Spectroscopy of horseradish peroxidase. I: Optical, resonance Raman, magnetic circular dichroism, X-ray absorption and diffraction. In *Heme Peroxidases*; Dunford, H. B., Ed.; Wiley-VCH: New York, **1999**; pp. 135–174.
300. Yonetani, T.; Ray, G. S. *J. Biol. Chem.* **1965**, *240*, 4508.
301. Pond, A. E.; Bruce, G. S.; English, A. M.; Sono, M.; Dawson, J. H. *Inorg. Chim. Acta* **1998**, *276*, 250–255.

302. Andersen, M. B.; Hsuanyu, Y.; Welinder, K. G.; Schneider, P.; Dunford, H. B. *Acta Chem. Scand.* **1991**, *45*, 1080–1086.
303. Palaniappan, V.; Fitzgerald, M. M.; Sullivan, A. M.; Shifflett, J.; Terner, J. In *Time-Resolved Vibrational Spectroscopy*; Takahashi, H., Ed.; Springer-Verlag: Berlin, **1992**; pp. 32–35.
304. Kincaid, J. R.; Zheng, Y. H.; AlMustafa, J.; Czarnecki, K. *J. Biol. Chem.* **1996**, *271*, 28805–28811.
305. Hashimoto, S.; Tatsuno, Y.; Kitagawa, T. *Proc. Jpn. Acad. B–Phys.* **1984**, *60*, 345–348.

This page intentionally left blank

Index to Volume 6

C

D

E

F

G

H

I

K

L

M

N

R

S

T

V

X

Z

Handbook of Porphyrin Science

with Applications to Chemistry, Physics, Materials Science, Engineering, Biology and Medicine

Volume 7

Physicochemical Characterization

Karl M. Kadish ▪ Kevin M. Smith ▪ Roger Guilard

Editors

World Scientific

Handbook of Porphyrin Science

with Applications to Chemistry, Physics, Materials Science, Engineering, Biology and Medicine

This page intentionally left blank

Handbook of Porphyrin Science

with Applications to Chemistry, Physics, Materials Science, Engineering, Biology and Medicine

Volume 7

Physiochemical Characterization

Editors

Karl M. Kadish
University of Houston, USA

Kevin M. Smith
Louisiana State University, USA

Roger Guilard
Université de Bourgogne, France

World Scientific

NEW JERSEY • LONDON • SINGAPORE • BEIJING • SHANGHAI • HONG KONG • TAIPEI • CHENNAI

Published by

World Scientific Publishing Co. Pte. Ltd.

5 Toh Tuck Link, Singapore 596224

USA office: 27 Warren Street, Suite 401-402, Hackensack, NJ 07601

UK office: 57 Shelton Street, Covent Garden, London WC2H 9HE

British Library Cataloguing-in-Publication Data
A catalogue record for this book is available from the British Library.

HANDBOOK OF PORPHYRIN SCIENCE
with Applications to Chemistry, Physics, Materials Science, Engineering, Biology and Medicine
(Volumes 6–10)

ISBN-13 978-981-4307-18-5 (Set)
ISBN-13 978-981-4307-20-8 (Vol. 7)

Typeset by Stallion Press
Email: enquiries@stallionpress.com

Printed in Singapore.

Contents

Preface

Although the porphyrin and tetrapyrrole research area was regarded as "fully matured" during the 20th century, as evidenced for example by the awarding of numerous Nobel Prizes to its principal researchers, new advances and accomplishments in the field still amaze us as editors. The area continues to blossom and to expand into new areas of science and applications that would probably never have occurred to our 20th century heroes. An earlier *Porphyrin Handbook* assembled the large amount of factual data that had been accumulated during the 20th century. Our new venture, the *Handbook of Porphyrin Science* takes a completely new look at our research area and comprehensively details the contemporary science now appearing in the scientific literature that would indeed have been hard to predict even 10 years ago. In particular, fundamentally new methodologies and potential commercial applications of the beautiful compounds that we all love are exemplified, fully recognizing the subtitle of the series — "with applications to chemistry, physics, materials science, engineering, biology and medicine".

The three of us have complementary expertise in physical chemistry, synthetic and bioorganic chemistry, and in synthetic and mechanistic organometallic chemistry; this has enabled us to cover the whole field of porphyrin science and applications, and to devise comprehensive volume and author content. As of the date of writing, between the three of us, we have published more than 1600 tetrapyrrole research articles, and hold 31 patents related to commercial applications of porphyrin science. So we do know our field, and this has enabled us to assemble a first-rate group of experts who have written comprehensive up-to-date chapters with accuracy and authority; we thank our authors for their cooperation and willingness to go along with our highly ambitious schedule for production of these volumes.

We look forward to comments from our readers, and to suggestions that might enable us to expand our basic interests and scientific coverage even further. Meanwhile, we hope that porphyrin researchers, old, new and of the future, will enjoy reading these volumes just as much as we enjoyed planning and, with the help of World Scientific Publishing Company, producing them from manuscript to published article, in a timely manner.

Karl M. Kadish (Houston, Texas, USA)
Kevin M. Smith (Baton Rouge, Louisiana, USA)
Roger Guilard (Dijon, Bourgogne, France)
January, 2010

This page intentionally left blank

Contributing Authors*

Hasrat Ali
Université de Sherbrooke
Sherbrooke, Québec, Canada
Chapter 16

Cristina Alonso
University of Hull
Kingston-upon-Hull, HU6 7RX, UK
Chapter 17

Edith Antunes
Rhodes University
Grahamstown, 6139, South Africa
Chapter 34

Naoki Aratani
Kyoto University
Kyoto 606-8502, Japan
aratani@kuchem.kyoto-u.ac.jp
Chapter 1

Teodor Silviu Balaban
Karlsruhe Institute of Technology
D-76021 Karlsruhe, Germany
Silviu.Balaban@int.fzk.de
Chapter 3

Alan L. Balch
University of California, Davis
Davis, CA 95616, USA
balch@chem.ucdavis.edu
Chapter 40

David P. Ballou
University of Michigan
Ann Arbor, MI 48109-5606, USA
Chapter 28

Faye Bowles
University of California, Davis
Davis, CA 95616, USA
Chapter 40

Ross W. Boyle
University of Hull
Kingston-upon-Hull, HU6 7RX, UK
r.w.boyle@hull.ac.uk
Chapter 17

Ozguncem Bozkulak
Childrens Hospital Los Angeles
Los Angeles, CA 90027, USA
Chapter 22

Martin Bröring
Technische Universität Carolo-Wilhelmina zu Braunschweig
Hagenring 30, Braunschweig, Germany
m.broering@tu-bs.de
Chapter 41

Kevin Burgess
Texas A&M University
College Station, TX 77842, USA
burgess@tamu.edu
Chapter 37

*Full contact information for authors can be found on the title page of each chapter.

José A.S. Cavaleiro
University of Aveiro
3810-193 Aveiro, Portugal
jcavaleiro@ua.pt
Chapter 9

Sung Cho
Yonsei University
Seoul, 120-747, Korea
Chapter 5

Daniel P. Collins
University of South Carolina
Columbia, SC 29208, USA
Chapter 28

John H. Dawson
University of South Carolina
Columbia, SC 29208, USA
dawson@mail.chem.sc.edu
Chapter 28

Ilia G. Denisov
The University of Illinois
Urbana, IL 61801, USA
Denisov@illinois.edu
Chapter 26

Charles Michael Drain
Hunter College of The City University of New York
New York, NY 10065, USA
cdrain@hunter.cuny.edu
Chapter 15

Francis D'Souza
Wichita State University
Wichita, KS 67260-0051, USA
Francis.DSouza@wichita.edu
Chapter 4

Florence Duclairoir
Institut Nanosciences et Cryogénie
38054 Grenoble cedex 9, France
Chapter 47

Manivannan Ethirajan
Roswell Park Cancer Institute
Buffalo, NY 14263, USA
Chapter 19

Alessandro Feis
University of Florence
I-50019 Sesto Fiorentino, Italy
Chapter 31

Angela Ferrario
Childrens Hospital Los Angeles
Los Angeles, CA 90027, USA
Chapter 22

Kimberly B. Fields
University of South Florida
Tampa, FL 33620, USA
Chapters 13, 43

Takamitsu Fukuda
Osaka University
Toyonaka 560-0043, Japan
tfukuda@chem.sci.osaka-u.ac.jp
Chapter 42

Shunichi Fukuzumi
Osaka University
Suita, Osaka 565-0871, Japan
fukuzumi@chem.eng.osaka-u.ac.jp
Chapter 46

Hiroyuki Furuta
Kyushu University
Fukuoka 819-0395, Japan
hfuruta@cstf.kyushu-u.ac.jp
Chapter 10

Jean-Paul Gisselbrecht
Université de Strasbourg
67000 Strasbourg, France
gissel@unistra.fr
Chapter 14

Charles J. Gomer
University of Southern California
Los Angeles, CA 90027, USA
Chapter 22

Bruno Grimm
Friedrich-Alexander-University Erlangen-Nuremberg
91058 Erlangen, Germany
Chapter 2

Dirk M. Guldi
Friedrich-Alexander-University Erlangen-Nuremberg
91058 Erlangen, Germany
dirk.guldi@chemie.uni-erlangen.de
Chapter 2

Anita Hausmann
Friedrich-Alexander-University Erlangen-Nuremberg
91058 Erlangen, Germany
Chapter 2

Takashi Hayashi
Osaka University
Suita 565-0871, Japan
thayashi@chem.eng.osaka-u.ac.jp
Chapter 23

Petra Hellwig
Université de Strasbourg
67000 Strasbourg, France
hellwig@chimie.u-strasbg.fr
Chapter 36

Yoshio Hisaeda
Kyushu University
Fukuoka 819-0395, Japan
yhisatcm@mail.cstm.kyushu-u.ac.jp
Chapter 48

Barry D. Howes
University of Florence
I-50019 Sesto Fiorentino, Italy
Chapter 31

Akira Ikezaki
Toho University
Ota-ku, Tokyo 143-8540, Japan
Chapter 32

Osamu Ito
Tohoku University
Sendai, 981-3215, Japan
Chapter 4

Anabella Ivancich
Centre Nationale de la Recherche Scientifique (URA 2096)
F-91191 Gif-sur-Yvette, France
Chapter 31

Christophe Jeandon
Université de Strasbourg
67000 Strasbourg, France
cjeandon@unistra.fr
Chapter 14

Norbert Jux
Universität Erlangen-Nürnberg
91054 Erlangen, Germany
norbert.jux@chemie.uni-erlanger.de
Chapter 20

Axel Kahnt
Friedrich-Alexander-University Erlangen-Nuremberg
91058 Erlangen, Germany
Chapter 2

David Kessel
Wayne State University School of Medicine
Detroit, MI 48201, USA
dhkessel@med.wayne.edu
Chapter 21

Dongho Kim
Yonsei University
Seoul, 120-747, Korea
dongho@yonsei.ac.kr
Chapters 5, 6

Kil Suk Kim
Yonsei University
Seoul, 120-747, Korea
Chapter 6

Nagao Kobayashi
Tohoku University
Sendai 980-8578, Japan
nagaok@mail.tains.tohoku.ac.jp
Chapters 33, 42

Lechosław Latos-Grażyński
University of Wrocław
Wrocław 50 383, Poland
llg@wchuwr.pl
Chapter 8

Genxi Li
Nanjing University
Nanjing 210093, PR China
genxili@nju.edu.cn
Chapter 27

Jong Min Lim
Yonsei University
Seoul, 120-747, Korea
Chapter 6

Aurore Loudet
Texas A&M University
College Station, TX 77842, USA
Chapter 37

Evgeny A. Lukyanets
Organic Intermediates and Dyes Institute
Moscow, 123995, Russia
rmeluk@niopik.ru
Chapter 11

Marian Luna
Childrens Hospital Los Angeles
Los Angeles, CA 90027, USA
Chapter 22

Hiromitsu Maeda
Ritsumeikan University
Kusatsu 525-8577, Japan
maedahir@ph.ritsumei.ac.jp
Chapter 38

Jean-Claude Marchon
Institut Nanosciences et Cryogénie
38054 Grenoble cedex 9, France
jean-claude.marchon@cea.fr
Chapter 47

M. Victoria Martínez-Díaz
Universidad Autónoma de Madrid
28049-Madrid, Spain
Chapter 45

Frederic Melin
Université de Strasbourg
67000 Strasbourg, France
Chapter 36

Shingo Nagano
Tottori University
Tottori 680-8552, Japan
Chapter 25

Mikio Nakamura
Toho University
Ota-ku, Tokyo 143-8540, Japan
mnakamu@med.toho-u.ac.jp
Chapter 32

Wonwoo Nam
Ewha Womans University
Seoul 120-750, South Korea
wwnam@ewha.ac.kr
Chapter 44

Victor N. Nemykin
University of Minnesota Duluth
Duluth, MN 55812, USA
vnemykin@d.umn.edu
Chapter 11

Maria G.P.M.S. Neves
University of Aveiro
3810-193 Aveiro, Portugal
Chapter 9

Tebello Nyokong
Rhodes University
Grahamstown, 6139, South Africa
t.nyokong@ru.ac.za
Chapter 34

Yoshiki Ohgo
Toho University
Ota-ku, Tokyo 143-8540, Japan
Chapter 32

Tetsuo Okujima
Ehime University
Matsuyama 790-8577, Japan
Chapter 7

Noboru Ono
Ehime University
Matsuyama 790-8577, Japan
ononbr@dpc.ehime-u.ac.jp
Chapter 7

Atsuhiro Osuka
Kyoto University
Kyoto 606-8502, Japan
osuka@kuchem.kyoto-u.ac.jp
Chapter 1

Ravindra K. Pandey
Roswell Park Cancer Institute
Buffalo, NY 14263, USA
ravindra.pandey@roswellpark.org
Chapter 19

Nayan J. Patel
Roswell Park Cancer Institute
Buffalo, NY 14263, USA
Chapter 19

Miłosz Pawlicki
University of Wrocław
Wrocław 50 383, Poland
Chapter 8

Sébastien Richeter
Université Montpellier 2
34095 Montpellier Cedex 5, France
sebastien.richeter@univ-montp2.fr
Chapter 14

Beate Röder
Humboldt-Universität zu Berlin
12489 Berlin, Germany
roeder@physik.hu-berlin.de
Chapter 20

Natalie Rucker
Childrens Hospital Los Angeles
Los Angeles, CA 90027, USA
Chapter 22

Joshua V. Ruppel
University of South Florida
Tampa, FL 33620, USA
Chapters 13, 43

Romain Ruppert
Université de Strasbourg
67000 Strasbourg, France
rruppert@unistra.fr
Chapter 14

Aoife Ryan
Trinity College Dublin
Dublin 2, Ireland
Chapter 12

Wolfgang Seitz
Friedrich-Alexander-University
Erlangen-Nuremberg
91058 Erlangen, Germany
Chapter 2

Mathias O. Senge
Trinity College Dublin
Dublin 2, Ireland
sengem@tcd.ie
Chapter 12

Natalia N. Sergeeva
Trinity College Dublin
Dublin 2, Ireland
Chapter 12

Hisashi Shimakoshi
Kyushu University
Fukuoka 819-0395, Japan
Chapter 48

Jae-Yoon Shin
Yonsei University
Seoul, 120-747, Korea
Chapter 6

Yoshitsugu Shiro
Harima Institute
Hyogo 679-5148, Japan
yshiro@riken.jp
Chapters 24, 25

Martha Sibrian-Vazquez
Portland State University
Portland, OR 97201, USA
Chapter 18

Sunaina Singh
Hunter College of The City University of
New York
New York, NY 10065, USA
Chapter 15

Stephen G. Sligar
The University of Illinois
Urbana, IL 61801, USA
s-sligar@uiuc.edu
Chapter 26

Giulietta Smulevich
University of Florence
I-50019 Sesto Fiorentino, Italy
giulietta.smulevich@unifi.it
Chapter 31

Nicole L. Snyder
Hamilton College
Clinton, NY 13323, USA
Chapters 13, 43

Fabian Spänig
Friedrich-Alexander-University Erlangen-Nuremberg
91058 Erlangen, Germany
Chapter 2

Tatyana Spolitak
University of Michigan
Ann Arbor, MI 48109-5606, USA
Chapter 28

Hiroshi Sugimoto
Harima Institute
Hyogo 679-5148, Japan
Chapter 24

Osamu Takikawa
National Center for Geriatrics and Gerontology
Obu, Aichi 474-8522, Japan
Chapter 24

Alison Thompson
Dalhousie University
Halifax, Nova Scotia, Canada
alison.thompson@dal.ca
Chapter 39

Motoki Toganoh
Kyushu University
Fukuoka 819-0395, Japan
Chapter 10

Augusto C. Tomé
University of Aveiro
3810-193 Aveiro, Portugal
Chapter 9

Tomas Torres
Universidad Autónoma de Madrid
28049-Madrid, Spain
tomas.torres@uam.es
Chapter 45

Paola Turano
University of Florence
I-50019 Sesto Fiorentino, Italy
turano@cerm.unifi.it
Chapter 30

Md. Imam Uddin
Dalhousie University
Halifax, Nova Scotia, Canada
Chapter 39

Johan E. van Lier
Université de Sherbrooke
Sherbrooke, Québec, Canada
Johannes.Van.Lier@USherbrooke.ca
Chapter 16

Maria da Graça H. Vicente
Louisiana State University
Baton Rouge, LA 70803, USA
vicente@lsu.edu
Chapter 18

Sam P. de Visser
The University of Manchester
Manchester M1 7DN, UK
sam.devisser@manchester.ac.uk
Chapter 44

F. Ann Walker
University of Arizona
Tucson, AZ 85721-0041, USA
awalker@email.arizona.edu
Chapter 29

Jacek Waluk
Polish Academy of Sciences
01-224 Warsaw, Poland
waluk@ichf.edu.pl
Chapter 35

Sam Wong
Childrens Hospital Los Angeles
Los Angeles, CA 90027, USA
Chapter 22

Tabitha E. Wood
Dalhousie University
Halifax, Nova Scotia, Canada
Chapter 39

Frank Xu
Childrens Hospital Los Angeles
Los Angeles, CA 90027, USA
Chapter 22

Hiroko Yamada
Ehime University
Matsuyama 790-8577, Japan
Chapter 7

Jaesung Yang
Yonsei University
Seoul, 120-747, Korea
Chapter 5

Hyejin Yoo
Yonsei University
Seoul, 120-747, Korea
Chapter 5

Min-Chul Yoon
Yonsei University
Seoul, 120-747, Korea
Chapter 6

Zin Seok Yoon
Yonsei University
Seoul, 120-747, Korea
Chapter 5

X. Peter Zhang
University of South Florida
Tampa, FL 33620, USA
pzhang@cas.usf.edu
Chapters 13, 43

Contents of Volumes 1–10

Volume 1 Supramolecular Chemistry

Volume 2 Synthesis and Coordination Chemistry

Volume 3 Synthetic Methodology

Volume 4 Phototherapy, Radioimmunotherapy and Imaging

Volume 5 Heme Proteins

Volume 6 NMR and EPR Techniques

Volume 7 Physicochemical Characterization

Volume 8 Open-Chain Oligopyrrole Systems

Volume 9 Electronic Absorption Spectra — Phthalocyanines

Volume 10 Catalysis and Bio-Inspired Systems — Part I

This page intentionally left blank

32 Electronic and Magnetic Structures of Iron Porphyrin Complexes

Mikio Nakamura,*,† Yoshiki Ohgo* and Akira Ikezaki*

*Department of Chemistry, Faculty of Medicine, Toho University, Ota-ku, Tokyo 143-8540, Japan

†Division of Chemistry, Graduate School of Science, Toho University, Funabashi 274-8510, Japan

I. Introduction

Heme proteins play important roles in various aspects of biological processes, which include oxygen transport in hemoglobin, oxygen storage in myoglobin, electron transfers in various cytochromes, disproportionation of hydrogen peroxide in catalase, and oxidation of organic substrates in cytochrome P450.[1–3] Figure 1 shows an example of enzymatic reactions, i.e. oxidation of organic substrates catalyzed by cytochrome P450.[4–9] The active site of cytochrome P450 contains a heme, the iron of which is connected to the protein via a thiolate linkage of a cysteinate residue. In the resting state of cytochrome P450, the iron adopts a six-coordinate ferric low-spin state (A), Fe^{III}(S = 1/2), with water as a sixth axial ligand. However, once organic substrate is incorporated into the substrate binding pocket, all the water molecules in the pocket are excluded and consequently the iron adopts the five-coordinate ferric high-spin state (B), Fe^{III}(S = 5/2), with cysteinate as the sole axial ligand. The redox potential increases on going from the six-coordinate low-spin state to the five-coordinate high-spin state, which makes the reduction of iron(III) much easier. As a result, the five-coordinate ferric high-spin state is converted to the five-coordinate ferrous high-spin state (C), Fe^{II}(S = 2), having cysteinate as an axial ligand. Next follows the oxygen-binding step. Thus, the addition of dioxygen to the high-spin ferrous heme leads to the formation of an oxygen-bound diamagnetic species, which is considered to adopt either a six-coordinate ferrous low-spin state with dioxygen (O_2) as the sixth axial ligand (D), Fe^{II}(S = 0), or a six-coordinate ferric low-spin state with superoxide anion radical ($O_2^{\bullet-}$) as the sixth ligand (D′), Fe^{III}(S = 1/2); $O_2^{\bullet-}$ (S = 1/2). In the latter case, the observed diamagnetism could be explained in terms of the strong antiferromagnetic coupling between Fe^{III}(S = 1/2) and S = 1/2 superoxide anion radical. After the second one-electron reduction, the heme adopts a very labile six-coordinate ferric low-spin state, Fe^{III}(S = 1/2), with peroxide (O_2^{2-})(E) or hydroperoxide(F) as the sixth ligand. The latter complex receives a proton and releases a water molecule

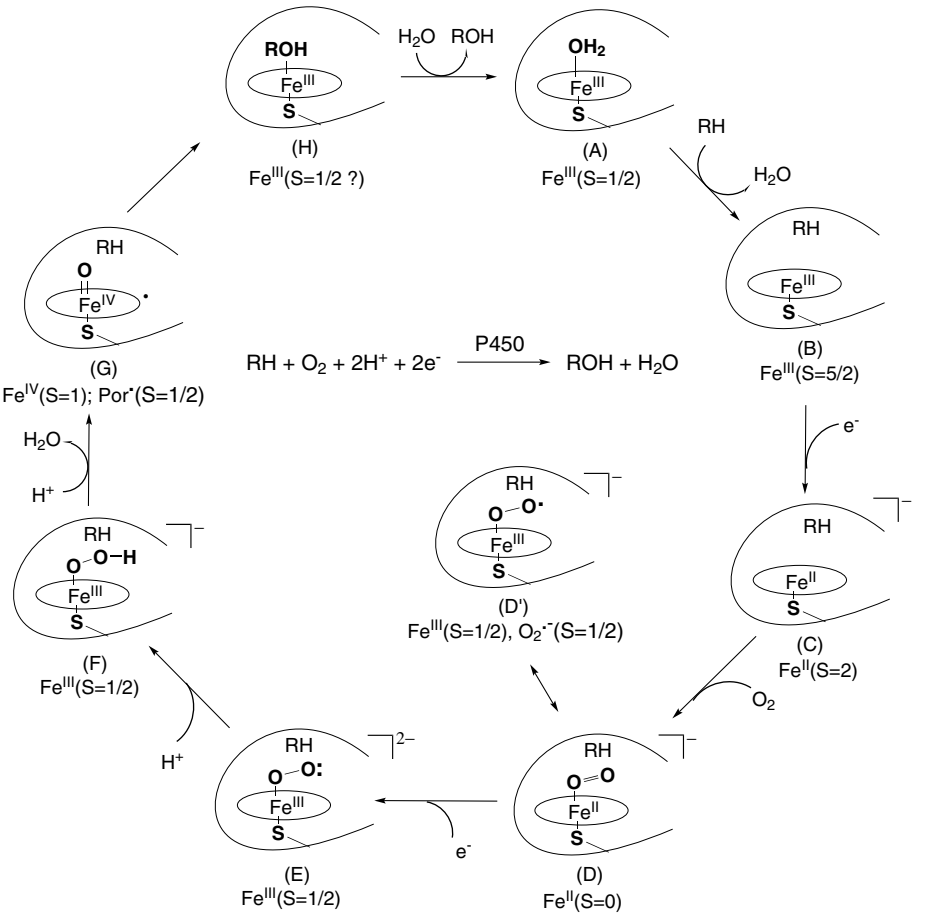

Figure 1. Catalytic mechanism proposed for cytochrome P450. (Adapted from Refs. 4–9.)

to form what is called compound I, a reactive intermediate which is believed to be a six-coordinate low-spin $Fe^{IV} = O$ species with porphyrin cation radical(G), $[(Fe^{IV} = O)(Por^{\cdot})]^{+}$.[10–17] The oxygen is then transferred from the reactive intermediate to the organic substrate to form an alcohol.

As this example shows, the iron porphyrin complexes change their electronic and coordination structures during the enzymatic reaction. Each of the iron porphyrin complexes plays a crucial role in each step of the catalytic cycle by utilizing the physicochemical properties specific to the heme. Thus, it is very important to reveal the detailed physicochemical properties of various iron porphyrin complexes with different electronic and coordination structures. For these purposes, the use of model complexes is quite important because one can characterize them by means of a number of techniques such as UV–vis, IR, CV, NMR, EPR,

resonance Raman, CD, MCD, Mössbauer, SQUID, EXAFS, and X-ray crystallography.[18,19] In addition, these measurements, which are sometimes difficult to perform in proteins, can be done even under extreme conditions Among the techniques mentioned above, ^{1}H and ^{13}C NMR spectroscopy are particularly useful, since they provide detailed information on the electronic structures of the complexes in solution at various temperatures.[20–31] This is because the half-occupied iron 3d orbital interacts with the specific σ and π molecular orbitals of the porphyrin and increases the spin density at the specific carbon and nitrogen atoms of the complex. Consequently, the ^{13}C NMR signals of the carbon atoms with large spin density appear at extremely upfield or downfield positions. Similarly, the ^{1}H NMR signals of the hydrogen atoms directly attached to the carbon atoms with large spin density are observed outside of the so-called diamagnetic region, i.e. 0–10 ppm. Thus, one can determine which 3d orbitals of the iron have unpaired electrons by an analysis of the observed ^{1}H and ^{13}C NMR chemical shifts. In other words, the chemical shift can be an excellent probe for revealing the electronic structure of paramagnetic iron porphyrin complexes.

Through extensive studies using various spectroscopic, magnetic, and structural analyses, it is now clear that the spin states of iron porphyrins are controlled by the nature and number of axial ligands, electronic effects of peripheral substituents, deformation of the porphyrin ring, etc.[25,26,28–35] In the case of low-spin iron(III) porphyrins, while the six-coordinate complexes carrying axial ligands with strong field strength (such as imidazole and cyanide) exhibit a low-spin (S = 1/2) state, the five-coordinate complexes carrying an anionic ligand such as halide and acetate show a high-spin (S = 5/2) state. If the field strengths of anionic ligands are extremely weak, the complexes adopt a rare intermediate-spin (S = 3/2) state.[36] Figure 2 shows three kinds of spin states in iron(III) porphyrins.[30]

Furthermore, each spin state could have a different electron configuration. This is most explicitly exemplified in the low-spin complexes which exhibit either the $(d_{xy})^2(d_{xz}, d_{yz})^3$ or the $(d_{xz}, d_{yz})^4(d_{xy})^1$ electronic ground state, as shown in

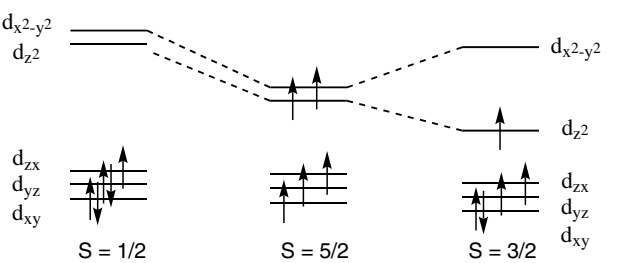

Figure 2. Spin states of iron(III) porphyrins. (Adapted with permission from Ref. 30. Copyright 2006, Elsevier Science.)

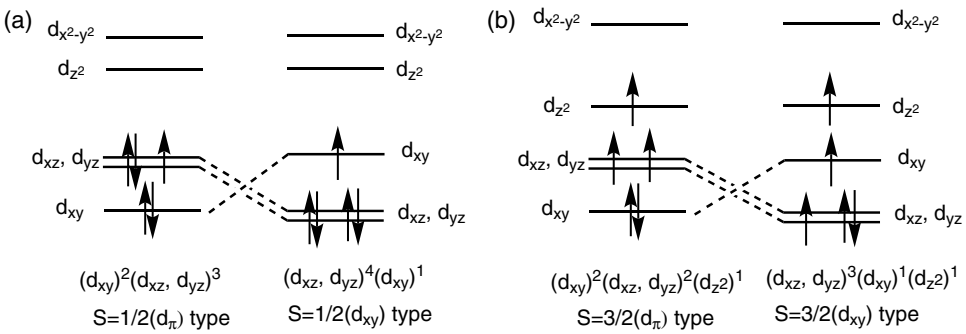

Figure 3. Two types of electronic ground states in (a) low-spin and (b) intermediate-spin iron(III) porphyrins. (Adapted with permission from Ref. 373. Copyright 2003, American Chemical Society.)

Figure 3[25,26,28–31]; they are abbreviated as S = 1/2(d_π) type and S = 1/2(d_{xy}) type, respectively. Similarly, at least two electronic ground states, $(d_{xy})^2(d_{xz}, d_{yz})^2(d_{z^2})^1$ and $(d_{xz}, d_{yz})^3(d_{xy})^1(d_{z^2})^1$, exist even in the intermediate-spin complexes[37]; they are abbreviated as S = 1/2(d_π) type and S = 1/2(d_{xy}) type, respectively. The assignment of the electronic ground states of the specific intermediate-spin complexes such as $[Fe(T^iPrP)(THF)_2]^+$ and $[Fe(OETPP)(THF)_2]^+$ is still a controversial issue.[37–39]

The one-electron oxidation of iron(III) porphyrins should form either an iron(III) porphyrin cation radical or an iron(IV) porphyrin.[26,40] Actually, however, most of the papers reported previously have shown the formation of iron(III) porphyrin cation radicals. These radical species give characteristic ^{1}H NMR spectra, where some of the signals appear at extraordinary upfield or downfield positions due to the presence of an unpaired electron in the porphyrin orbitals.[26,40] The unpaired electron cannot be independent of the paramagnetic iron center. It could interact with the paired and/or unpaired electrons in the iron 3d orbitals. Consequently, the ^{1}H NMR spectra should be affected by the spin states and electron configurations of the iron(III) ions. In other words, the electronic and magnetic structures of iron(III) porphyrin cation radicals could be completely different, depending on the electron configuration of the iron(III) ions. In the case of iron(IV) porphyrins, the iron could adopt the S = 0 and S = 2 spin states, though all the complexes reported to date show the S = 1 spin state.

The two-electron oxidation of iron(III) porphyrins should give either one of the four possible electronic structures, i.e. iron(V) porphyrin, iron(IV) porphyrin cation radical, iron(III) porphyrin dication, or iron(III) porphyrin N-oxide.[11,12] The iron porphyrins with this oxidation state are quite important, since the reactive intermediates that appear transiently in the catalytic cycle of heme proteins such

as catalase, peroxidase, and cytochrome P450 are supposed to adopt these oxidation states.[4–9]

In this review, we will describe the formation and spectroscopic properties of synthetic iron porphyrins with various oxidation states, spin states, electron configurations, and coordination structures. Special emphasis will be placed on the iron porphyrin complexes with unusual electronic and magnetic properties. The synthetic iron porphyrin complexes described in this review are summarized in Scheme 1 together with their abbreviations.

II. NMR and EPR Methods to Determine the Electronic Structures

A. Orbital Interactions

It is very important to understand the iron–porphyrin orbital interactions to reveal the electronic structures of the complexes. Thus, before discussing the electronic structures of various iron porphyrin complexes, the iron–porphyrin orbital interactions will be surveyed. Figure 4 shows the frontier orbitals of a zinc porphyrin with D_{4h} symmetry, calculated by the DFT method.[41] The symmetry presentation of metal and porphyrin orbitals in six-coordinate planar D_{4h} complexes is given in Table 1.[42,43] Among these orbitals, the occupied $3e_g$ and vacant $4e_g$* orbitals can interact with the iron d_π(d_{xz} and d_{yz}) orbitals. If the complex in question has half-occupied d_π orbitals as in the case of low-spin iron(III) complexes with the $(d_{xy})^2(d_{xz}, d_{yz})^3$ ground state, the unpaired electron can delocalize to the porphyrin ring by the d_π–$3e_g$ interactions especially to the pyrrole C_β atoms because the $3e_g$ orbitals have a relatively large coefficient at these carbon atoms, as shown in Figure 4.[20,23,26,28–31] In principle, all the frontier orbitals of the porphyrin except for the e_g orbitals are orthogonal to any of the iron 3d orbitals and thus there should be no interaction other than the d_π–$3e_g$ and d_π–$4e_g$* interactions. However, porphyrin rings are flexible and are easily deformed by steric and electronic effects of the peripheral substituents and the axial ligands.[44–51] Typical deformation modes frequently encountered both in synthetic iron porphyrins and in naturally occurring heme proteins are ruffling, saddling, and doming, as given in Figure 5.[50] The ruffling indicates that the *meso* carbon atoms deviate from the mean plane up and down alternately, while the saddling indicates that the β carbon atoms deviate similarly. Doming is typical of five-coordinate iron porphyrin complexes where iron is placed out of the plane defined by the four nitrogen atoms of the pyrrole rings. If the porphyrin ring deforms in a ruffled or saddled fashion in six-coordinate iron porphyrins, some iron–porphyrin orbital interactions can be symmetry allowed, which are originally forbidden in a planar D_{4h} complex. For example, although the

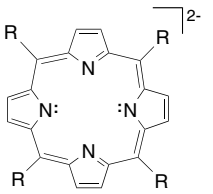

TRP

R	TRP
H	THP
Metyl(Me)	TMeP
Ethyl(Et)	TEtP
Propyl(^{n}Pr)	T^{n}PrP
Cyclopropyl(^{c}Pr)	T^{c}PrP
Cyclohexyl(^{c}Hx)	T^{c}HxP
Isopropyl(^{i}Pr)	T^{i}PrP
1-Ethylpropyl(EtPr)	TEtPrP
tert-Butyl(^{t}Bu)	T^{t}BuP

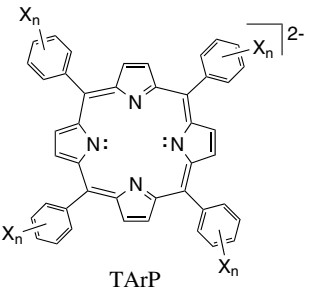

TArP

X_n	TArP
H	TPP
3-Me	3-Me-TPP
4-Me	4-Me-TPP
4-OMe	4-OMe-TPP
2,6-F_2	2,6-F_2-TPP
2,6-Cl_2	2,6-Cl_2-TPP
2,4,6-Me_3	Me_3-TPP or TMP
2,4,6-Et_3	Et_3-TPP
2,4,6-$^{i}Pr_3$	$^{i}Pr_3$-TPP
2,4,6-$(OMe)_3$	2,4,6-$(OMe)_3$-TPP
2,3,4,5,6-F_5	F_5-TPP
2,6-OSi(^{i}Pr)$_3$	2,6-$(OSi^{i}Pr_3)_2$-TPP

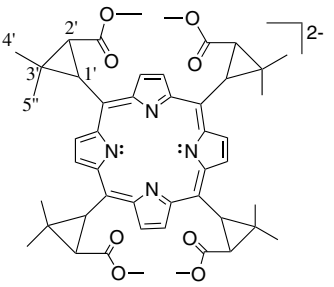

TMCP

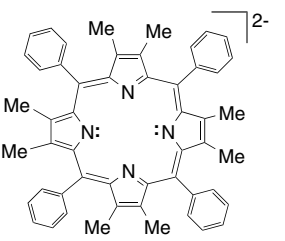

OMTPP

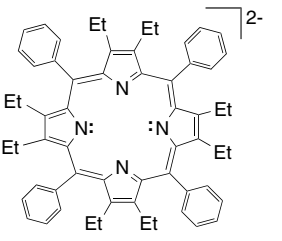

OETPP

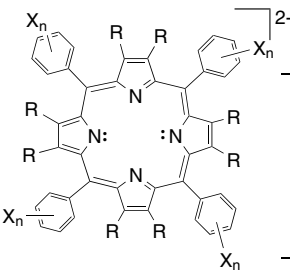

X_n
4-OCH_3
4-CF_3
2,6-Cl_2
3,5-Me_2
3,5-$^{t}Bu_2$
3,5-$(CF_3)_2$

OMTArP(R=Me)
OETArP(R=Et)

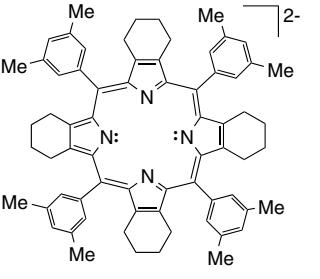

TBTXP

Scheme 1. Dianions of porphyrins and porphyrin analogs discussed in this chapter.

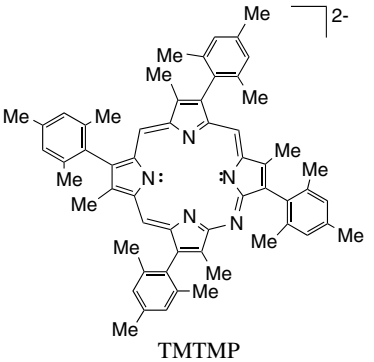

TMTMP

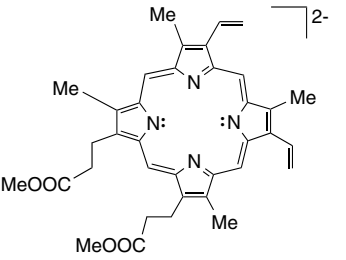

ProtoIXMe$_2$

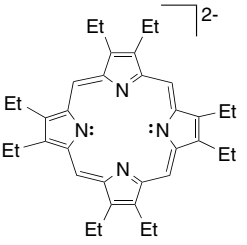

OEP

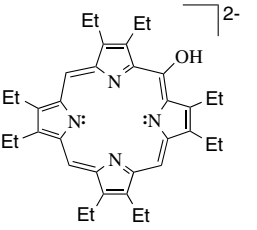

OEPO

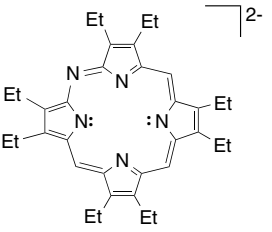

MAzP

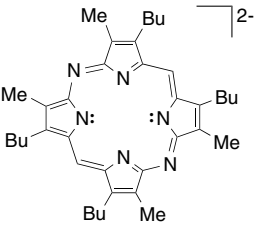

DAzP

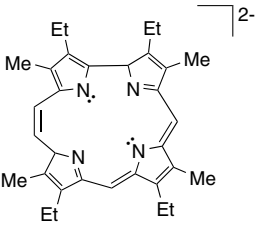

EtioHPc

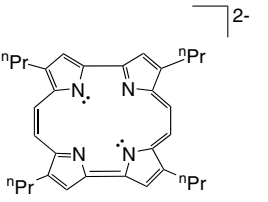

TPrPc

Scheme 1. (*Continued*)

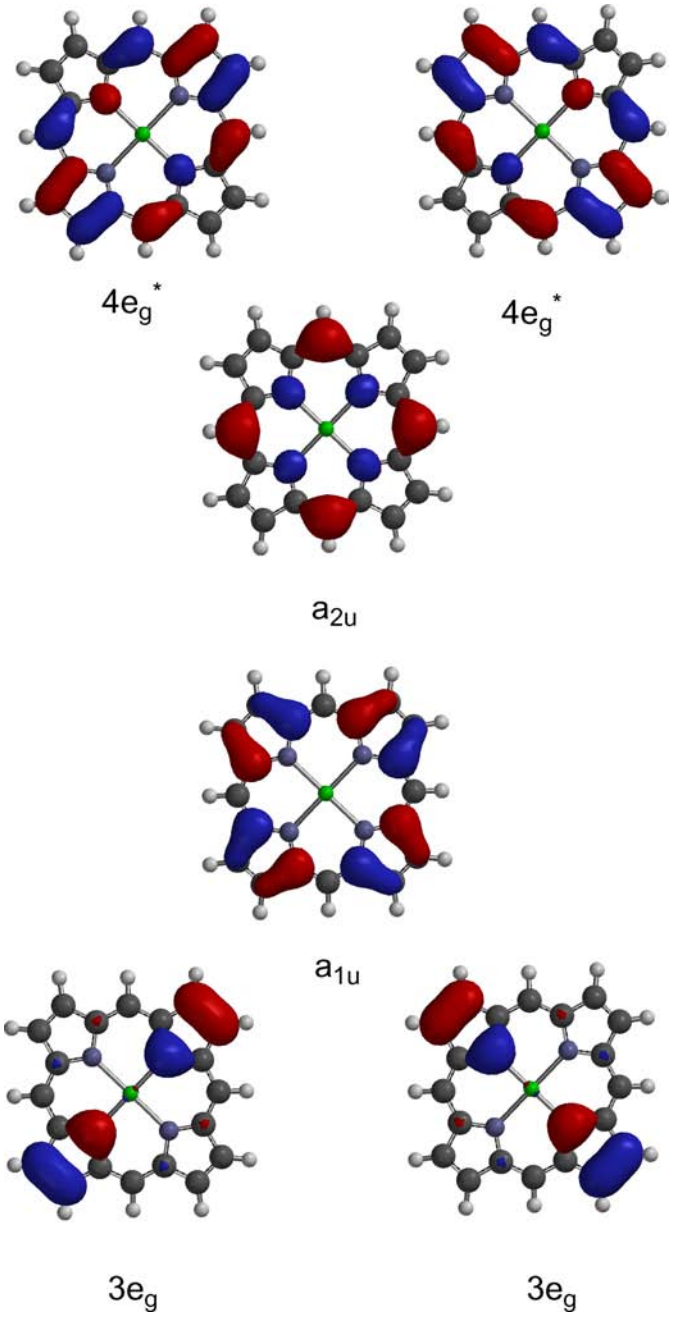

Figure 4. Frontier orbitals of a D_{4h} zinc porphyrin calculated by the DFT method. (Ikezaki, A. Unpublished results.[41])

Table 1. Correlation table for the molecular orbitals of metal porphyrin complexes.[a]

	D_{4h} Planar	D_{2d} Ruffled	D_{2d} Saddled	C_{4v} Domed
Metal				
$d_{x^2-y^2}$	b_{1g}	b_1	b_2	b_1
d_{z^2}	a_{1g}	a_1	a_1	a_1
$d_{xz,yz}$	e_g	e	e	e
d_{xy}	b_{2g}	b_2	b_1	b_2
Porphyrin				
$4e_g$*	$4e_g$*	e	e	e
a_{1u}	a_{1u}	b_1	b_1	a_2
a_{2u}	a_{2u}	b_2	b_2	a_1
$3e_g$	$3e_g$	e	e	e

[a]Source: Refs. 42 and 43.

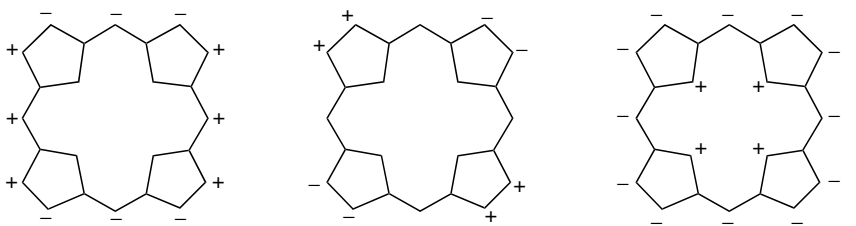

Figure 5. Major deformation modes of porphyrin: (a) ruffled, (b) saddled, and (c) domed deformation. Only the most significant displacements are shown. + indicates displacements above the mean plane and — indicates displacements below the mean plane. (Modified with permission from Senge, M. O. *The Porphyrin Handbook*; Kadish, K. M.; Smith, K. M.; Guilard, R.; Eds.; Academic Press: San Diego, CA, **2000**; Vol. 1, Chapter 6, p. 241.[50])

porphyrin a_{2u} orbital is orthogonal to any of the metal 3d orbitals in a planar D_{4h} complex, it can interact with the iron d_{xy} and $d_{x^2-y^2}$ orbitals if the porphyrin ring deforms in a ruffled or saddled fashion, respectively, as shown in Table 1.[42,43] Similarly, although the a_{1u} orbital is orthogonal to any of the iron 3d orbitals in the planar D_{4h} complex, it can interact with the $d_{x^2-y^2}$ orbital in the ruffled complex and with the d_{xy} orbital in the saddled complex. The symmetry presentation given in Table 1 also indicates that the d_π–$3e_g$ and d_π–$4e_g$* interactions in planar D_{4h} complexes can be maintained even in the deformed complexes since the d_π and e_g orbitals in D_{4h} complexes are signified as e symmetry in ruffled and saddled D_{2d} complexes as well as in domed C_{4v} complexes. Thus, the energy levels of iron 3d orbitals are finely modulated by the degree and mode of porphyrin deformation.

B. NMR Spectroscopy

As mentioned above, a number of techniques have been used to elucidate the electronic structures of iron porphyrin complexes. Among them, ^{1}H and ^{13}C NMR are particularly useful because they provide detailed information on the electronic structures of the complexes in solution at various temperatures.[20,31] In this section, discussion will be confined to the low-spin iron(III) porphyrins and to a description of how NMR spectra are useful for characterization of the two types of electronic ground state, $(d_{xy})^2(d_{xz}, d_{yz})^3$ and $(d_{xz}, d_{yz})^4(d_{xy})^1$, that the low-spin complexes adopt.[25,26,28–31] The NMR characteristics of the complexes with other spin states and oxidation states will be mentioned later.

1. *^{1}H NMR Spectroscopy*

Figure 6 shows the ^{1}H NMR spectra of low-spin $[Fe(T^{n}PrP)(DMAP)_2]^+$(a) and $[Fe(T^{i}PrP)(4\text{-}CNPy)_2]^+$(b) taken in CD_2Cl_2 solution at 213 K.[52] Extensive studies

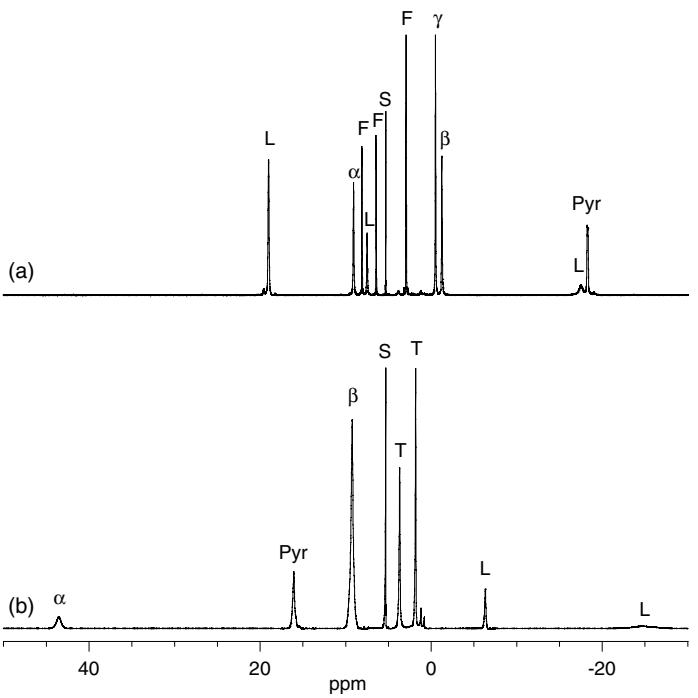

Figure 6. ^{1}H NMR spectra of (a) $[Fe(T^{n}PrP)(DMAP)_2]^+$ and (b) $[Fe(T^{i}PrP)(4\text{-}CNPy)_2]^+$ taken in CD_2Cl_2 solution at 213 K. Signal assignments: pyr shows the pyrrole-H signal; *α*, *β*, and γ indicate the meso alkyl-H signals; F and L are the free and coordinated ligand-H signals; S and T are the solvent and THF signals. (Adapted with permission from Ref. 52. Copyright 2000, American Chemical Society.)

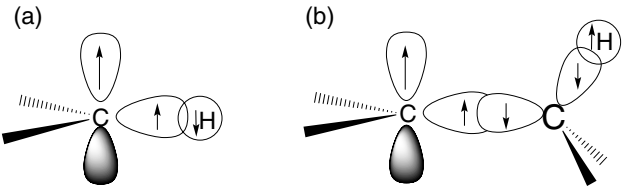

Figure 7. Spin polarization from the π spin on the pyrrole C_β atoms. The effect of π spin density on the carbon atom toward (a) the directly bonded hydrogen atom and (b) the hydrogen atom through two σ-bonds. (Modified from Refs. 28 and 53.)

have revealed that the former adopts the $(d_{xy})^2(d_{xz}, d_{yz})^3$ ground state while the latter adopts the $(d_{xz}, d_{yz})^4(d_{xy})^1$ ground state.[52] Thus, the large upfield shift of the pyrrole-H signal, $\delta = -18.5$ ppm, in $[Fe(T^nPrP)(DMAP)_2]^+$ can be explained in terms of the interaction between the half-occupied d_π orbital and the filled $3e_g$ orbital. As mentioned in the previous section, the unpaired electron in the d_π orbital is delocalized to the porphyrin ring especially on the pyrrole C_β atoms since the $3e_g$ orbital has a relatively large coefficient on these carbon atoms (see Figure 4 for the $3e_g$ orbitals). Consequently, the pyrrole-H signal shows a large upfield shift due to the spin polarization mechanism. Figure 7a shows the spin polarization of the pyrrole C–H σ bond caused by the π spin density on the C_β atoms.[28,53] In contrast, the *meso*-CH(α) signal appears at $\delta = 8.0$ ppm, which is rather close to the corresponding signal in the diamagnetic complex. The result is understandable, because the $3e_g$ orbital has zero coefficient on the *meso*-C atoms. Thus, *the large upfield shift of the pyrrole-H signal together with the small isotropic shift of the* meso-*CH(α) signal are the characteristic features of the ^{1}H NMR spectra of low-spin [Fe(TRP)L$_2$]$^+$ with the $(d_{xy})^2(d_{xz}, d_{yz})^3$ ground state, where R is the alkyl groups attached to the* meso-*C atoms.*

In the case of $[Fe(T^iPrP)(4\text{-}CNPy)_2]^+$, the unpaired electron is in the iron d_{xy} orbital, which is delocalized to the porphyrin ring by the d_{xy}–a_{2u} interaction in the ruffled porphyrin framework. It is understandable that the pyrrole-H signal of this complex appears at $\delta = 16$ ppm, rather close to the pyrrole-H signal, $\delta = 9.4$ ppm, of diamagnetic $[Co(TEtP)(2\text{-}MeIm)_2]^+$,[54] since the a_{2u} orbital has a fairly small coefficient at the C_β atoms. A small downfield shift should be ascribed to the dipolar contribution of the low-spin iron(III) with the $(d_{xz}, d_{yz})^4(d_{xy})^1$ ground state. In contrast, the *meso*-CH(α) signal appears at an extremely downfield position, $\delta = 43$ ppm. The large downfield shift is also understandable since the a_{2u} orbital has a large coefficient at the *meso*-C atoms, which induces the large downfield shift to the *meso*-CH(α) signal by the spin polarization mechanism, as shown in Figure 7b. Thus, *the large downfield shift of the meso-CH(α) signal together with the small isotropic shift of the pyrrole-H signal are the characteristic features of*

the ^{1}H NMR spectra of low-spin[Fe(TRP)L$_2$]$^{\pm}$-with the (d_{xz}, d_{yz})^4(d_{xy})^1 ground state.

In low-spin iron(III) porphyrins having aryl groups at the *meso* positions, [Fe(TArP)L$_2$]$^+$, the *meta*-H chemical shift can be a good probe of the electronic ground state. The theoretical background is as follows[55–59]: the observed chemical shift (δ_{obs}) of the *meta*-H signal can be given by Eq. 1, where δ_{iso} is the isotropic shift and δ_{dia} is the chemical shift of the *meta*-H signal in a suitable diamagnetic complex such as [Co(TArP)L$_2$]$^+$.[60,61] The δ_{iso} value, which is the sum of the contact and dipolar shift, δ_{con} and δ_{dip}, respectively, can be expressed by Eq. 2 in the case of the complexes with axial symmetry, where K_{con} and K_{dip} are positive constants, ρ_C^{meta} is the spin density at

$$\delta_{obs} = \delta_{iso} + \delta_{dia}, \tag{1}$$

$$\delta_{iso} = \delta_{con} + \delta_{dip} = \frac{-K_{con}\rho_C^{meta} + K_{dip}(\chi_{\parallel} - \chi_{\perp})(3\cos^2\theta - 1)/r^3}{T}, \tag{2}$$

the *meta*-C atom, θ is the angle between the nucleus(m-H)–metal(Fe) vector and the z axis, and r is the length of this vector. The term $(3\cos^2\theta - 1)/r^3$ is referred to as the axial geometric factor. As mentioned previously, the spin density at the *meso*-C atoms in low-spin (d_{xy})^2 (d_{xz}, d_{yz})^3 type complexes is supposed to be zero. Therefore, both the isotropic shift and the slope of the Curie plots for the *meta*-H should be negative. This is because the ρ_C^{meta} value is nearly zero and the ($g_{\parallel}^2 - g_{\infty}^2$) $(3\cos^2\theta - 1)/r^3$ is negative; the latter term is negative because $g_{\parallel}^2 - g_{\infty}^2$ is positive in the (d_{xy})^2 (d_{xz}, d_{yz})^3 type complexes,[25] while $(3\cos^2\theta - 1)/r^3$ is negative for the *meta*-H. In contrast, the low-spin (d_{xz}, d_{yz})^4(d_{xy})^1 type complexes have a sizable amount of spin density on the *meso*-C atoms due to the interaction between the half-occupied d_{xy} and filled a_{2u} orbitals. The positive spin at the *meso*-C atoms is delocalized to the attached phenyl rings and induces a positive π spin density at the *ortho*- and *para*-C and a negative π spin density at the *meta*-C atoms.[28] Thus, the slope for the contact shift, $-K_{con}\rho_C^{meta}$, should be positive. In addition, the slope for the dipolar shift, ($g_{\parallel}^2 - g_{\infty}^2$) $(3\cos^2\theta - 1)/r^3$, should also be positive because the $g_{\parallel}^2 - g_{\infty}^2$ value is negative in the (d_{xz}, d_{yz})^4(d_{xy})^1 type complexes.[25,53] Consequently, it is expected that the *meta*-H signal appears more downfield than the corresponding signal of the diamagnetic complex and that the slope of its Curie plots is positive. This tendency is clearly seen in the Curie plots of the *meta*-H signals of [Fe(OMTPP)L$_2$]$^{\pm}$. As shown in Figure 8,[62] the Curie slope is negative if L is HIm, CN^-, and DMAP, and positive if L is ^{t}BuNC. Thus, we can conclude that the HIm, CN^-, and DMAP complexes adopt the (d_{xy})^2(d_{xz}, d_{yz})^3 ground state while the ^{t}BuNC complex adopts the (d_{xz}, d_{yz})^4(d_{xy})^1

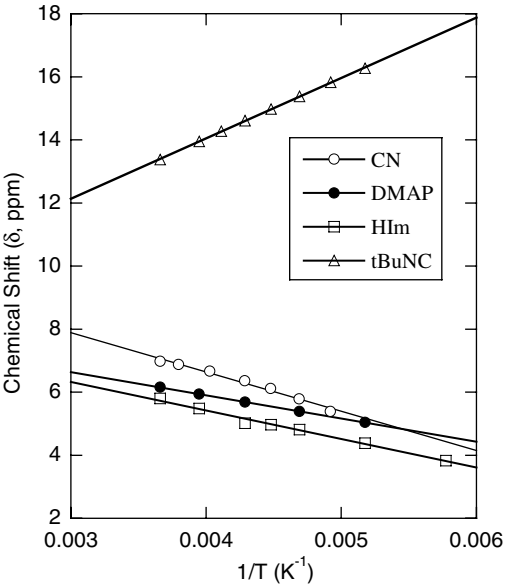

Figure 8. Curie plots of the *meta*-H signals of $[Fe(OMTPP)L_2]^+$, where L is HIm, CN^-, DMAP, and ^{t}BuNC. (Adapted with permission from Ref. 62. Copyright 2003, American Chemical Society.)

ground state. Therefore, *Curie plots of the meta-H signal can predict the electronic ground state of low-spin* $[Fe(TArP)L_2]^{\pm}$.

Walker and coworkers[28] have proposed that the electronic ground state of low-spin iron(III) porphyrins having *meso*-aryl groups such as $[Fe(TPP)L_2]^+$, $[Fe(OETPP)L_2]^+$, and $[Fe(TPC)L_2]^+$ can be determined by the $\delta_m - \delta_p$ and $\delta_m - \delta_o$ values; δ_o, δ_m, and δ_p are the chemical shifts of the *ortho*-, *meta*-, and *para*-phenyl signals, respectively. If $\delta_m - \delta_p$ and $\delta_m - \delta_o$ are both large and positive, then the complex has large amounts of positive spin at the *meso*-C atoms, which in turn indicates that the complex adopts the $(d_{xz}, d_{yz})^4(d_{xy})^1$ ground state. In contrast, if $\delta_m - \delta_p$ and $\delta_m - \delta_o$ are small with $\delta_m - \delta_p$ positive and $\delta_m - \delta_o$ usually negative, then the complex adopts the $(d_{xy})^2(d_{xz}, d_{yz})^3$ ground state since the *meso*-C atoms have little or no spin density.

2. *^{13}C NMR Spectroscopy*

Figure 9 shows the ^{13}C NMR spectra of (a) $[Fe(T^nPrP)(DMAP)_2]^+$, (b) $[Fe(T^cPrP)(2\text{-MeIm})_2]^+$, and (c) $[Fe(T^iPrP)(4\text{-CNPy})_2]^+$ taken in CD_2Cl_2 solution at 298 K.[52] The chemical shifts of the three kinds of carbon atoms constituting the porphyrin core, i.e. C_{meso}, C_α, and C_β, are quite different among these complexes. In the case

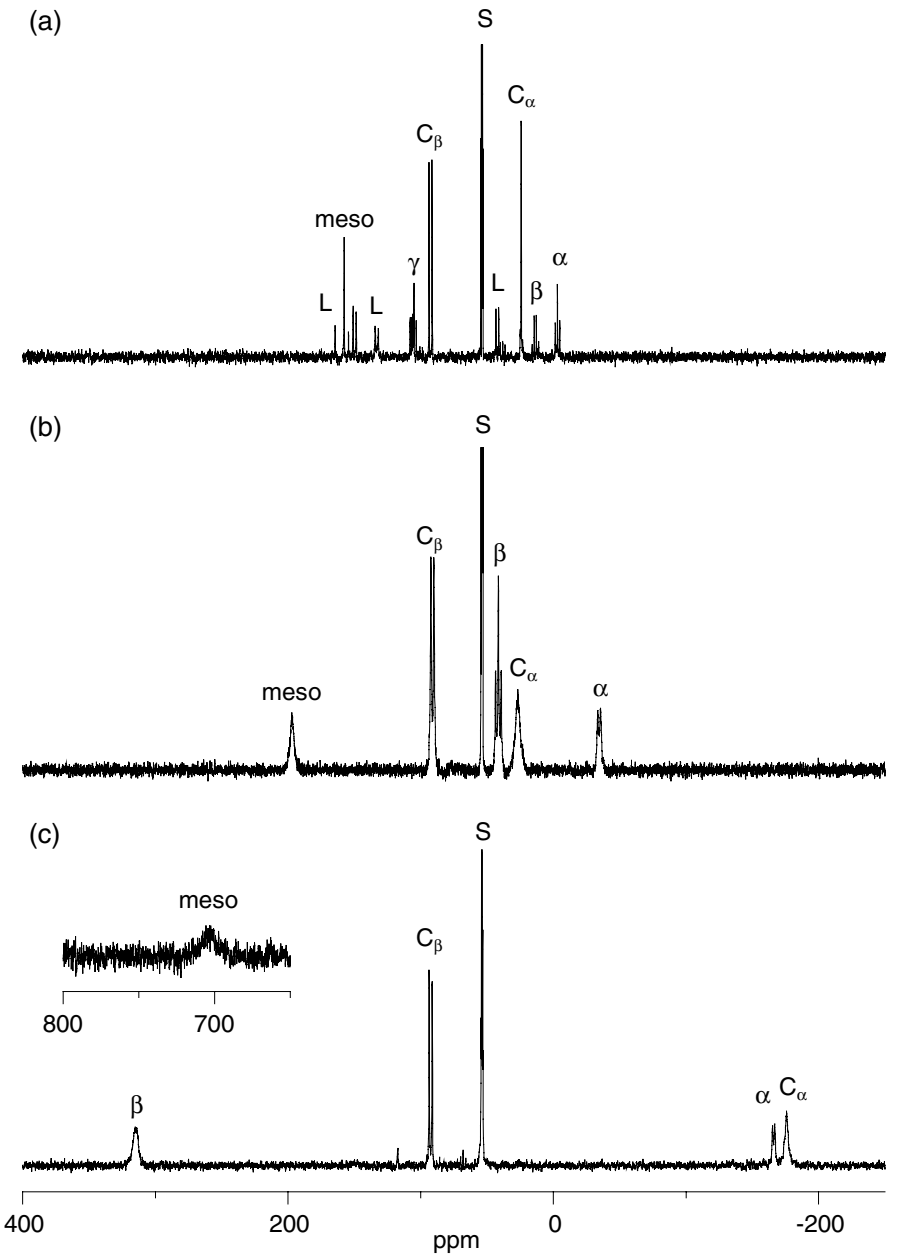

Figure 9. ^{13}C NMR spectra of (a) $[Fe(T^nPrP)(DMAP)_2]^+$, (b) $[Fe(T^cPrP)(2\text{-MeIm})_2]^+$, and (c) $[Fe(T^iPrP)(4\text{-CNPy})_2]^+$ taken in CD_2Cl_2 solution at 298 K. Signal assignment: C_α, C_β, and *meso* are the *α*-, *β*-, and *meso*-carbon atoms, respectively; *α*, *β*, and *γ* are the *α*-, *β*-, and *γ*-carbons of the *meso*-alkyl groups, respectively; and S and L are the signals for the solvent and coordinating ligand, respectively. Both coordinating and free ligand signals are not observable in (b) and (c) at this temperature. (Adapted with permission from Ref. 52. Copyright 2000, American Chemical Society.)

of $[Fe(T^nPrP)(DMAP)_2]^+$, the chemical shifts of these carbon signals are 157.7, 24.3, and 92.6 ppm, respectively, while they are 707, −176, and 92.5 ppm, respectively, in the case of $[Fe(T^iPrP)(4\text{-}CNPy)_2]^+$. The large downfield shift of the C_{meso} signal together with the large upfield shift of the *meso*-C_α signal in $[Fe(T^iPrP)(4\text{-}CNPy)_2]^+$ is understandable since the *meso*-C atoms have large spin density due to the d_{xy}–a_{2u} interaction in a highly ruffled porphyrin framework. However, a slightly upfield-shifted C_β signal, δ = 73.6 ppm, in the $(d_{xy})^2(d_{xz}, d_{yz})^3$ type $[Fe(T^nPrP)(HIm)_2]^+$ needs to be explained, as the C_β atoms also have relatively large spin density due to the interaction between the half-occupied d_π and fully occupied $3e_g$ orbital. In fact, the large upfield shift of the pyrrole-H signal, δ = −21.5 ppm at 223 K, is a direct indication that the C_β atoms certainly have a considerable amount of spin density.

In the case of ^{13}C NMR spectroscopy, the chemical shift of the specific carbon atom is determined not only by the spin density of the carbon in question but also by the spin density on the neighboring carbon atoms. Thus, the isotropic shift of the carbon signal (δ_{iso}), which is obtained by the subtraction of the corresponding chemical shift of a diamagnetic complex (δ_{dia}) from the observed chemical shift (d_{obs}), is given by Eq. 3,

$$\delta_{iso} = \delta_{obs} - \delta_{dia} = \delta_{con} + \delta_{dip}{}^{MC} + \delta_{dip}{}^{LC}, \tag{3}$$

where δ_{con}, $\delta_{dip}{}^{MC}$, and $\delta_{dip}{}^{LC}$ represent the metal-centered dipolar shift, ligand-centered dipolar shift, and contact shift, respectively.[21,31,55–59] The metal-centered dipolar shift in the complexes with axial symmetry is defined by Eq. 4,

$$\delta_{dip}{}^{MC} = \frac{(1/2\pi)(\chi_{\parallel} - \chi_{\perp})(3\cos^2\theta - 1)}{r^3},^{58} \tag{4}$$

where χ's are molecular susceptibilities, θ is the angle between the nucleus–metal vector and the z axis, r is the length of this vector, and the term $(3\cos^2\theta - 1)/r^3$ is the axial geometric factor. $\delta_{dip}{}^{LC}$ is assumed to be proportional to the π-spin density ρ^π-at the observed carbon atom and is given by Eq. 5,[55–59,63]

$$\delta_{dip}{}^{LC} = -(\chi_{\parallel} - \chi_{\perp})K\rho^\pi, \tag{5}$$

where K is a positive constant. Thus, $\delta_{dip}{}^{LC}$ is negative in the $(d_{xy})^2(d_{xz}, d_{yz})^3$ type complexes while it is positive in the $(d_{xz}, d_{yz})^4(d_{xy})^1$ type complexes, provided that ρ^π is positive.

Carbon contact shifts originate from unpairing of carbon 1s electrons and unpairing of the three carbon sp^2 bonding pairs. Thus, the isotropic shift of

C_{meso}, C_α, C_β, and *meso*-C_α signals can be given by Eqs. 6–9, respectively,[63–66] where the S^C term indicates polarization of the 1s orbital, the $Q^C_{CC'}$ term reflects polarization of the three sp^2 bonds by the π-spin density at the observed carbon atom, and the $Q^C_{C'C}$ term represents polarization of the C–C bond by the π spin densities centered on the neighboring carbon atoms; the S^C, $Q^C_{CC'}$, Q^C_{CH}, and $Q^C_{C'C}$ values are estimated to be −35.5, +40.3, +54.6, and −39.0 MHz, respectively.[63,64] The F^C value is defined as $F^C = 2\pi g\mu_B S(S + 1)/3\gamma_C kT$,[65] where γ_C is the magnetogyric ratio of carbon, k is the Boltzmann constant, and μ_B is the Bohr magneton.

For the C_{meso} signal,

$$\begin{aligned}\delta_{iso}(C_{meso}) &= \delta_{obs} - \delta_{dia} = \delta_{con} + \delta_{dip}{}^{LC} + \delta_{dip}{}^{MC}(C_{meso}) \\ &= [(S^C + 3Q^C_{CC'})\rho^\pi_{meso} + (2Q^C_{C'C})\rho^\pi_\alpha]F^C + (\chi_\perp - \chi_\parallel)K\rho^\pi_{meso} \\ &\quad + \delta_{dip}{}^{MC}(C_{meso}). \end{aligned} \tag{6}$$

For the C_α signal,

$$\begin{aligned}\delta_{iso}(C_\alpha) &= [(S^C + 2Q^C_{CC'} + Q^C_{CN})\rho^\pi_\alpha + (Q^C_{C'C}\rho^\pi_\beta + Q^C_{C'C}\rho^\pi_{meso} + Q^C_{N'C}\rho^\pi_N)]F^C \\ &\quad + (\chi_\perp - \chi_\parallel)K\rho^\pi_\alpha + \delta_{dip}{}^{MC}(C_\alpha). \end{aligned} \tag{7}$$

For the C_β signal,

$$\begin{aligned}\delta_{iso}(C_\beta) &= [(S^C + 2Q^C_{CC'} + Q^C_{CH})\rho^\pi_\beta + (Q^C_{C'C}\rho^\pi_\beta + Q^C_{C'C}\rho^\pi_\alpha)]F^C \\ &\quad + (\chi_\perp - \chi_\parallel)K\rho^\pi_\beta + \delta_{dip}{}^{MC}(C_\beta). \end{aligned} \tag{8}$$

For the *meso*-C_α((alkyl) signal,

$$\delta_{iso}(meso\text{-}C_\alpha) = Q^C_{C'C}\rho^\pi_{meso}F^C + \delta_{dip}{}^{MC}(meso\text{-}C_\alpha). \tag{9}$$

Let us consider the isotropic shifts of the C_{meso} signal in $[Fe(T^nPrP)(HIm)_2]^+$ adopting the $(d_{xy})^2(d_{xz}, d_{yz})^3$ ground state. The major interactions should occur between the d_π and $3e_g$ orbitals. Since the $3e_g$ orbital has zero coefficient at the C_{meso} atoms, we can simplify the isotropic shift of the C_{meso} signal given in Eq. 6 by assuming that $\rho_{meso} = 0$. Thus, Eq. 6 is converted into Eq. 6′:

$$\delta_{iso}(C_{meso}) = (2Q^C_{C'C})\rho^\pi_\alpha F^C + \delta_{dip}{}^{MC}(C_{meso}). \tag{6′}$$

The $\delta_{iso}(C_{meso})$ value must be negative in the $(d_{xy})^2(d_{xz}, d_{yz})^3$ type complexes because both $Q^C_{C'C}$ and $\delta_{dip}{}^{MC}(C_{meso})$ are negative; $\delta_{dip}{}^{MC}(C_{meso})$ given in Eq. 4 is negative because $\chi_\parallel - \chi_\perp$ is positive in the $(d_{xy})^2(d_{xz}, d_{yz})^3$ type complexes while the axial geometric factor $(3\cos^2\theta - 1)/r^3$ is negative for the C_{meso} atoms. In fact, the

C_{meso} signal of this complex is observed at 84.9 ppm at 298 K, which is more upfield by 36.1 ppm than the corresponding signal of diamagnetic Zn(TPP).[67]

As for the isotropic shift of the C_β signal given in Eq. 8, this can be rewritten into Eq. 8′ by using the Q^C and S^C values:

$$\delta_{iso}(C_\beta) = [(60.7\rho^\pi{}_\beta - 39.0\rho^\pi{}_\alpha)]F^C + (\chi_\perp - \chi_\parallel)K\rho^\pi{}_\beta + \delta_{dip}{}^{MC}(C_\beta). \quad (8')$$

Since the $(\chi_\perp - \chi_\parallel)K\rho^\pi{}_\beta$ and $\delta_{dip}{}^{MC}(C_\beta)$ values are negative for the $(d_{xy})^2(d_{xz}, d_{yz})^3$ type complexes, the $\delta_{iso}(C_\beta)$ is not always positive although the $(d_{xy})^2(d_{xz}, d_{yz})^3$ type complexes have relatively large $\rho^\pi{}_\beta$ values. This is the reason why the C_β signal in $[Fe(T^nPrP)(HIm)_2]^+$ is observed at δ = 87.0 ppm at 298 K, which is 45.0 ppm further upfield than the corresponding signal of diamagnetic Zn(TPP).[67]

For the low-spin complexes with the $(d_{xz}, d_{yz})^4(d_{xy})^1$ ground state, such as $[Fe(T^iPrP)(4\text{-}CNPy)_2]^+$, the unpaired electron in the d_{xy} orbital is delocalized to the porphyrin ring by the d_{xy}–a_{2u} interaction in a ruffled porphyrin framework. Since the a_{2u} orbital has a negligibly small coefficient at the C_α and C_β atoms, the isotropic shift of the C_{meso} signal can be approximated as Eq. 6″ by assuming that $\rho_\alpha = 0$ and $\rho_\beta = 0$:

$$\delta_{iso}(C_{meso}) = (S^C + 3Q^C{}_{CC'})F^C\rho^\pi{}_{meso} + (\chi_\perp - \chi_\parallel)K\,\rho^\pi{}_{meso} + \delta_{dip}{}^{MC}(C_{meso}). \quad (6'')$$

Since the $(S^C + 3Q^C{}_{CC'})$, $(\chi_\perp - \chi_\parallel)K$, and $\delta_{dip}{}^{MC}$ values are all positive for the $(d_{xz}, d_{yz})^4(d_{xy})^1$ type complexes, the C_{meso} signal should appear at a fairly downfield position. If the complex adopts a quite pure $(d_{xz}, d_{yz})^4(d_{xy})^1$ ground state, the d_{xy} orbital is located far above the d_π orbital. In such a case, the $\rho^\pi{}_{meso}$ value should be quite large, due to the strong d_{xy}–a_{2u} interaction. Consequently, the C_{meso} signal appears at a more downfield position. In fact, the C_{meso} signal is observed at δ = 707 ppm at 298 K in the case of $[Fe(T^nPrP)(4\text{-}CNPy)_2]^+$, which is more downfield by 586 ppm than the corresponding signal of the diamagnetic complex.[52] Therefore, *the chemical shift of the* C_{meso} *signal is an excellent probe not only for determineing the electronic ground state of low-spin iron(III) porphyrins but also for evaluating the purity of the* $(d_{xz}, d_{yz})^4(d_{xy})^1$ *ground state.* Figure 10 shows the correlation of chemical shifts between pyrrole-H and *meso*-C signals in a number of low-spin iron(III) porphyrins taken at 223 K.[68] As revealed in the figure the downfield shift of the *meso*-C signal is proportional to that of the pyrrole-H signal if the chemical shift of the pyrrole-H signal is less than 10 ppm; the correlation coefficient reaches as much as 0.9863. However, once the chemical shift of the pyrrole-H exceeds δ = 10 ppm, the chemical shift of the *meso*-C signal exhibits a steep increase. As a result, there seems to be no correlation in the chemical shifts of these two signals in the complexes where the pyrrole-H signals exceed 10 ppm. In fact, while

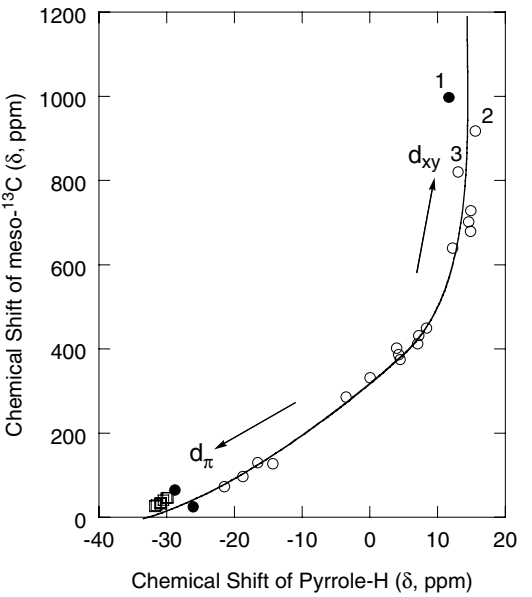

Figure 10. Relation of chemical shifts between pyrrole-H and *meso*-^{13}C nuclei at 223 K obtained from 18 $[Fe(TRP)L_2]^{\pm}$ (*), 3 $[Fe(TPP)L_2]^{\pm}$ (•), and 8 $[Fe(TArP)L_2]^{\pm}$(□). d_{xy} and d_{π} indicate the $(d_{xz}, d_{yz})^4(d_{xy})^1$ and the $(d_{xy})^2(d_{xz}, d_{yz})^3$ ground state, respectively. Numbers in the graph, **1**, **2**, and **3**, indicate the *meso*-C chemical shifts of $[Fe(TPP)(^tBuNC)_2]^+$, $[Fe(T^nPrP)(4\text{-}CNPy)_2]^+$, and $[Fe(T^iPrP)(4\text{-}CNPy)_2]^+$, respectively. (Adapted with permission from Ref. 68. Copyright 2003, Royal Society of Chemistry.)

the pyrrole-H chemical shifts of $[Fe(TPP)(^tBuNC)_2]^+$(**1**), $[Fe(T^nPrP)(4\text{-}CNPy)_2]^+$(**2**), and $[Fe(T^iPrP)(4\text{-}CNPy)_2]^+$(**3**) are 11.7, 13.0, and 15.6 ppm, the *meso*-C chemical shifts for these complexes are 997, 820, and 918 ppm, respectively. It should be interesting to determine the *meso*-C chemical shifts of $[Fe(T^nPrP)(^tBuNC)_2]^+$ and $[Fe(T^iPrP)(^tBuNC)_2]^+$. However, no reports have been published concerning the observation of the *meso*-C signals in $[Fe(TRP)(^tBuNC)_2]^+$, where R is an alkyl group attached to the *meso*-C atoms. Probably, these signals should appear extremely downfield with very broad bandwidths due to the large spin density on the *meso*-C atoms.

C. EPR Spectroscopy

EPR spectroscopy is also a powerful tool for determining the electronic structure of iron porphyrins.[25,26,28–30,69–71] High-spin complexes exhibit their $g_{\perp}$ and $g_{\parallel}$ signals at *ca*. 6.0 and 2.0, while the intermediate-spin complexes show them at *ca*. 4.0 and 2.0. In the case of low-spin complexes, there are three types of EPR spectra. Complexes that adopt the $(d_{xy})^2(d_{xz}, d_{yz})^3$ ground state exhibit either rhombic or

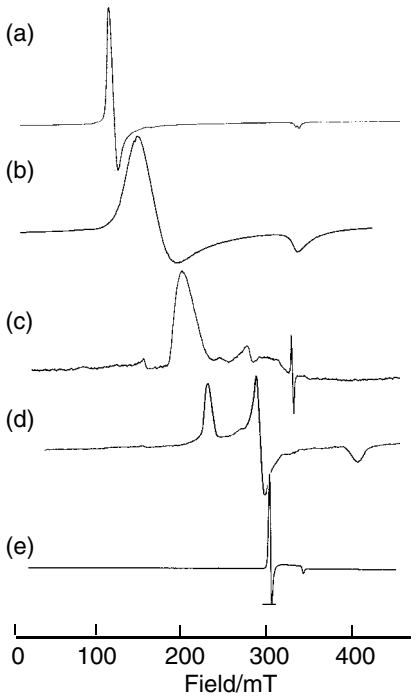

Figure 11. EPR spectra of iron(III) porphyrins with various electronic structure: (a) Fe(T^{i}PrP)F, (b) [Fe(T^{c}PrP)(THF)$_2$]$^+$, (c) [Fe(OETPP)(2-MeIm)$_2$]$^+$, (d) [Fe(OEP)(DMAP)$_2$]$^+$, and (e) [Fe(T^{n}PrP)(^{t}BuNC)$_2$]$^+$ taken in frozen CH_2Cl_2 solution at 4 K. (Adapted from Refs. 81, 82, 83, 84 and 52, respectively.)

large g_{max} type spectra, depending on the orientation of planar axial ligands such as imidazole and pyridine. The complexes with parallel-aligned axial ligands show rhombic type spectra, while those with perpendicularly aligned axial ligands show large g_{max} type spectra.[72–74] Complexes with linear ligands such as cyanide also exhibit large g_{max} type spectra.[75] According to the work of Yatsunyk and coworkers,[76] the spectral type changes from rhombic to large g_{max} type if the dihedral angle between the axial ligand planes exceeds *ca*. 57°. In contrast, the complexes that adopt the $(d_{xz}, d_{yz})^4(d_{xy})^1$ ground state always exhibit axial type spectra where $g_\perp$ values are smaller than 2.6.[26,28–30,77–79] In Figure 11 are shown the EPR spectra of (a) Fe(TEtPrP)F,[80] (b) [Fe(T^{c}PrP)(THF)$_2$]$^+$,[81] (c) [Fe(OETPP)(2-MeIm)$_2$]$^+$,[82] (d) [Fe(OEP)(DMAP)$_2$]$^+$,[83] and (e) [Fe(T^{c}PrP)(4-CNPy)$_2$]$^+$ taken in frozen CH_2Cl_2 solution at 4 K.[52] These complexes are examples that adopt the (a) high-spin state, (b) intermediate-spin state, (c) low-spin $(d_{xy})^2(d_{xz}, d_{yz})^3$ ground state with perpendicularly aligned axial ligands, (d) low-spin $(d_{xy})^2(d_{xz}, d_{yz})^3$ ground state with parallel aligned axial ligands, and (e) low-spin $(d_{xz}, d_{yz})^4(d_{xy})^1$ ground state.

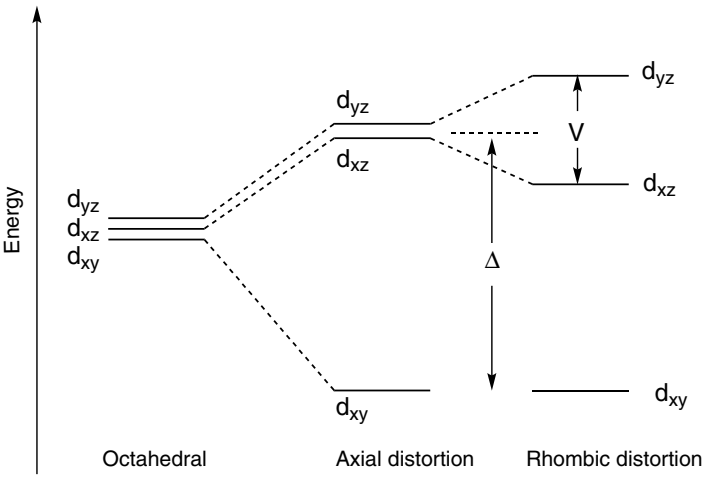

Figure 12. Energy levels of the three t_{2g} orbitals as the symmetry is reduced from being octahedral with axial distortion and rhombic distortion. (Adapted from Ref. 69.)

Once the three *g* values are obtained from the EPR spectra in low-spin iron(III) porphyrins, it is possible to calculate the relative energy levels of the 3d orbitals using Eqs. 10 and 11 developed by Taylor,[71] where V is the energy difference between the d_{xz} and d_{yz} orbitals, Δ is the energy difference between the d_{xy} and the average of the d_{xz} and d_{yz} orbitals, as shown in Figure 12, and λ is the spin–orbit coupling constant. This constant has the value of 460 cm^{-1} for the free ferric ion and a much smaller value in iron(III) porphyrins.

$$\frac{V}{\lambda} = \frac{E_{yz}}{\lambda} - \frac{E_{xz}}{\lambda} = \frac{g_x}{g_z + g_y} + \frac{g_y}{g_z - g_x}, \tag{10}$$

$$\frac{\Delta}{\lambda} = \frac{E_{yz}}{\lambda} - \frac{E_{xy}}{\lambda} - \frac{V}{2\lambda} = \frac{g_x}{g_z + g_y} + \frac{g_z}{g_y - g_x} - \frac{V}{2\lambda}. \tag{11}$$

III. Low-Spin Iron(III) Porphyrins

A. General Considerations

As shown in Figure 3, there are two types of electronic ground state in low-spin iron(III) porphyrin complexes. One is a commonly observed $(d_{xy})^2(d_{xz}, d_{yz})^3$ ground state and the other is a less common $(d_{xz}, d_{yz})^4(d_{xy})^1$ ground state.[26,28–30] Studies have revealed that complexes carrying axial ligands with strong σ-donating and weak π-accepting ability, such as imidazole and dimethylaminopyridine (DMAP), adopt

the common $(d_{xy})^2(d_{xz}, d_{yz})^3$ state. In contrast, complexes carrying axial ligands with strong π-accepting ability, such as *tert*-BuNC and 4-CNPy, prefer the less common $(d_{xz}, d_{yz})^4(d_{xy})^1$ state. Walker, Scheidt and others have explained that the d_π orbitals in the latter complexes are stabilized by interaction with the low-lying $\pi*$ orbital of the ligand to the points which are lower than the d_{xy} orbital.[78,79] As a result, the unpaired electron occupies the d_{xy} orbital to form the $(d_{xz}, d_{yz})^4(d_{xy})^1$ ground state. Generally speaking, low-spin complexes should exist as an equilibrium mixture of two spin isomers, i.e. electron configurational isomers, as given by Eq. 12.

$$(d_{xy})^2(d_{xz},d_{yz})^3 \underset{\longleftarrow}{\overset{K}{\longrightarrow}} (d_{xz},d_{yz})^4(d_{xy})^1. \tag{12}$$

If the energy difference between two isomers is rather small, two isomers should exist in a comparable ratio. In contrast, if the d_{xy} orbital is located far above the d_π orbitals in the energy diagram, then the isomer with the $(d_{xy})^2(d_{xz}, d_{yz})^3$ ground state should exist exclusively. The spectroscopic properties of the complex, therefore, change depending on the energy difference between the d_{xy} and d_π orbitals.

The rate for interconversion between two electron configurational isomers is generally very fast on the NMR time scale. Therefore, the observed chemical shift for the ^1H and ^{13}C signal is the average of the chemical shifts of two isomers, which is expressed by Eq. 13,

$$\delta_{\text{obs}} = \frac{1}{1+K}\,\delta_{d_\pi} + \frac{K}{1+K}\,\delta d_{xy}. \tag{13}$$

Figure 13 shows the Curie plots of the pyrrole-H signals of a series of low-spin iron(III) porphyrins, $[Fe(T^cPrP)L_2]^{\pm}$, where axial ligands are 4-CNPy, Py, 3-MePy, CN^-, DMAP, and HIm.[52] As shown in the figure, all the complexes except $[Fe(T^cPrP)(CN)_2]^-$ exhibit good linearity although the slopes of the lines are different depending on the axial ligands. The low-spin complexes with the positive slope have the spin isomer with the $(d_{xz}, d_{yz})^4(d_{xy})^1$ ground state as the major component, while those with the negative slope have the spin isomer with the $(d_{xy})^2(d_{xz}, d_{yz})^3$ground state as the major component. The curvature in Curie plots of the pyrrole-H signal in $[Fe(T^cPrP)(CN)_2]^-$ can be explained in terms of the temperature dependence of the equilibrium constant *K* shown in Eq. 12.

In contrast to the case of the NMR spectra, both of the spin isomers could be directly observed by EPR spectroscopy since the rate for interconversion between two isomers shown in Eq. 12 should be slow enough on the EPR time scale at 4.2 K. Figure 14 displays the EPR spectrum of $[Fe(Et\text{-}TPP)(CN)_2]^-$ taken in frozen

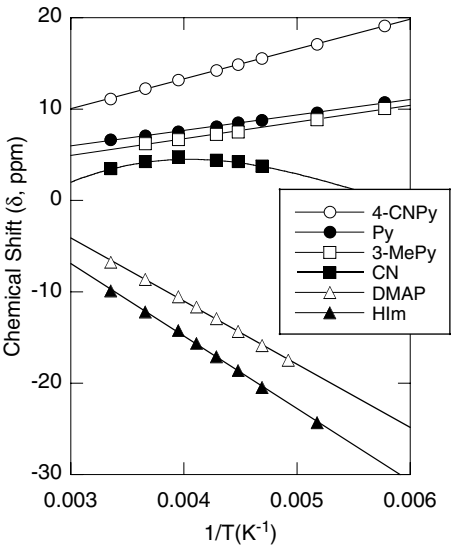

Figure 13. Curie plots of the pyrrole-H signals of a series of $[Fe(T^cPrP)L_2]^+$. (Adapted with permission from Ref. 52. Copyright 2000, American Chemical Society.)

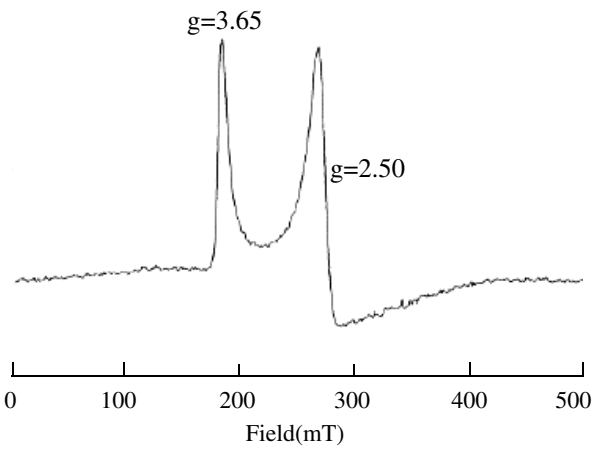

Figure 14. EPR spectrum of $[Fe(Et\text{-}TPP)(CN)_2]^-$ taken in frozen CH_3CN solution at 4.2 K. (Adapted with permission from Ref. 84. Copyright 2002, American Chemical Society.)

acetonitrile solution at 4.2 K, which clearly shows two types of EPR signals: one is a large g_{max} type signal with $g = 3.65$ and the other is an axial signal with $g = 2.50$.[84] Thus, the complex exists as a mixture of two electron configurational isomers at 4.2 K; one adopts the $(d_{xy})^2(d_{xz}, d_{yz})^3$ ground state while the other adopts the $(d_{xz}, d_{yz})^4(d_{xy})^1$ ground state. If we assume that the equilibrium constant between

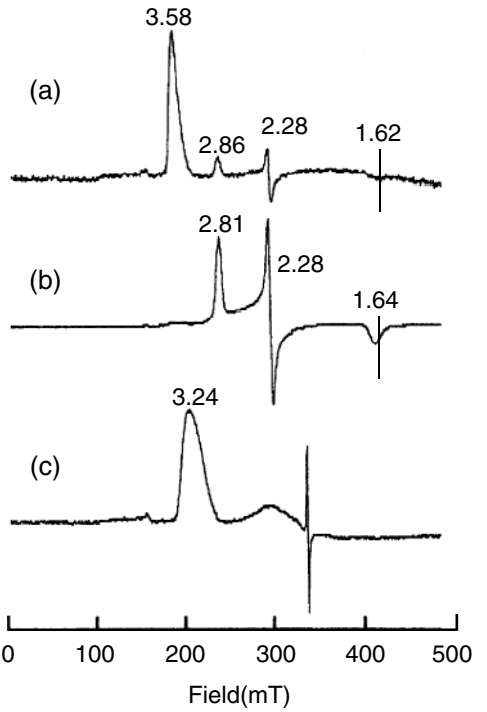

Figure 15. EPR spectra of (a) $[Fe(TMTMP)(DMAP)_2]ClO_4$, (b) $[Fe(OEP)(DMAP)_2]^+$, and (c) $[Fe(OETPP)(DMAP)_2]ClO_4$ taken in frozen CH_2Cl_2 solution at 4.2 K. (Reprinted with permission from Ref. 83. Copyright 2000, Chemical Society of Japan.)

two isomers is *ca*. 10 in favor of the $(d_{xz}, d_{yz})^4(d_{xy})^1$ isomer, the $\Delta G°$ is calculated to be 80 J/mol at 4.2 K. Thus, this phenomenon is observable when the difference in thermodynamic stability of the isomers is fairly small.

The EPR spectrum can differentiate the conformational isomers as well. Figure 15 shows the EPR spectra of (a) $[Fe(TMTMP)(DMAP)_2]ClO_4$, (b) $[Fe(OEP)(DMAP)_2]^+$, and (c) $[Fe(OETPP)(DMAP)_2]ClO_4$ taken in frozen CH_2Cl_2 solution at 4.2 K.[83] As shown in Figure 15(a), $[Fe(TMTMP)(DMAP)_2]^+$ gives two sets of signals, i.e. rhombic type signals at $g = 2.86$, 2.28, and 1.62 and a large g_{max} type signal at $g = 3.58$. The EPR spectrum of the former isomer resembles that of $[Fe(OEP)(DMAP)_2]^+$ shown in Figure 15b, indicating that the axial ligands are aligned parallel above and below the porphyrin ring. In contrast, the EPR spectrum of the other isomer resembles that of $[Fe(OETPP)(DMAP)_2]^+$ shown in Figure 15c, suggesting that the axial ligands are aligned perpendicularly. It is clear from Figure 15a that the perpendicular isomer predominates over the parallel isomer. EPR measurement at various temperatures could yield the thermodynamic

parameters, $\Delta H°$ and $\Delta S°$, which would help us understand the properties of these biologically relevant complexes.

B. Factors Affecting the Electronic Ground States

There are several factors that affect the electronic ground states of low-spin iron(III) porphyrins.[26,30,31] Four major factors that should be considered are (i) number and nature of axial ligands, (ii) electronic effects of peripheral substituents, (iii) deformation of porphyrin rings, and (iv) solvent effects. Among them, the number and nature of axial ligands are the most important factor that affects the electronic ground state of low-spin iron(III) porphyrins. In this section will be described in detail how these factors affect the electronic structure by using various model complexes given in Scheme 1.

1. *Axial Ligands*

Axial ligands can directly affect the energy level of the iron d_{z^2} orbital by σ donation. If the coordination atom of the axial ligand is a part of an aromatic ring such as imidazole or pyridine, then the ligand can also affect the energy levels of the iron d_π orbitals by donating or accepting π electrons. Axial ligands with strong σ-donating and weak π-accepting ability, such as HIm and CN^-, lead to the formation of low-spin complexes with the common $(d_{xy})^2(d_{xz}, d_{yz})^3$ ground state, while those with low-lying π^* orbitals, such as 4-CNPy and ^{t}BuNC, stabilize complexes with the less common $(d_{xz}, d_{yz})^4(d_{xy})^1$ ground state.[26,30,31] Safo and coworkers[78] have measured the ^{1}H NMR chemical shifts of $[Fe(TMP)L_2]^+$ and correlated them with the pKa(BH^+) values of a wide variety of nitrogen bases (Ls) ranging from pKa 9.7 (DMAP) to 1.1 (4-CNPy). Table 2 lists the chemical shifts (δ_{obs}) and isotropic shifts (δ_{iso}) of *meso*-H and pyrrole-H signals together with the pKa values of the conjugate acids; the isotropic shift is defined by Eq. 1. The data in the table indicate that the magnitude of the *meso*-H isotropic shift increases while that of the pyrrole-H decreases as the axial ligand becomes less basic.[78] The result is interpreted in terms of a smooth change in the electronic ground state from largely $(d_{xy})^2(d_{xz}, d_{yz})^3$ to at least 50% $(d_{xz}, d_{yz})^4(d_{xy})^1$ as the energy level of the ligand π^* orbital decreases. It should be noted that low-spin complexes with the $(d_{xy})^2(d_{xz}, d_{yz})^3$ ground state such as $[Fe(TMP)(DMAP)_2]^+$, have relatively large π spin density on the pyrrole C_β atoms, which induces a large upfield shift of the pyrrole-H signal. In contrast, the low-spin complexes with the $(d_{xz}, d_{yz})^4(d_{xy})^1$ ground state, such as $[Fe(TMP)(4\text{-}CNPy)_2]^+$, have fairly small π spin density on the pyrrole C_β atoms, inducing a fairly small upfield shift of the pyrrole-H signal.

Table 2. ^{1}H NMR Chemical Shifts of a Series of $[Fe(TMP)L_2]^+$ at 193 K in CD_2Cl_2.

		δ_{obs}		δ_{iso}	
Ligand	pKa(BH^+)	m-H	Pyrrole-H	m-H	Pyrrole-H
DMAP	9.70	4.85	–30.9	–2.42	–39.5
2-MeIm	7.56	7.77	–20.4	0.5	–29.0
1-MeIm	7.33	5.01	–31.3	–2.26	–39.9
3,4-Me_2Py	6.46	7.48	–21.2	0.21	–29.7
3,5-Me_2Py	6.15	7.12	–23.0	–0.15	–31.6
4-MePy	6.02	8.22	–18.2	0.95	–26.8
3-MePy	5.68	8.36	–17.8	1.09	–26.4
Py	5.22	9.47	–13.3	2.20	–21.9
3-ClPy	2.84	10.85	–10.3	3.58	–18.9
3-CNPy	1.45	13.07	–4.4	5.80	–13.0
4-CNPy	1.1	14.59	2.1	7.32	–6.5

Source: Ref. 78.

Simonneaux and coworkers[85] have reported that iron(III) porphyrins with phosphonite derivatives, such as $P(OMe)_2Ph$ and $P(OEt)_2Ph$, also exhibit the $(d_{xz}, d_{yz})^4(d_{xy})^1$ ground state, as revealed from the ^{1}H NMR and EPR data. The pyrrole-H signal appears at +2.6 ppm at 293 K for $[Fe(TPP)(P(OEt)_2Ph)]^+$. The EPR spectrum is axial with $g_\perp = 2.36$ and $g_\parallel = 1.91$ for $[Fe(4\text{-Me-TPP})(P(OEt)_2Ph)]^+$.[86] In contrast, the corresponding bis-phosphine complex $[Fe(TPP)(PMe_3)_2]^+$ adopts the $(d_{xy})^2(d_{xz}, d_{yz})^3$ ground state, as indicated by the upfield shift of the pyrrole-H signal, i.e. –19.6 ppm at 303 K.[87] Since the pKa values of the conjugate acids of phosphorus ligands decrease in the order $PMe_3 > PMe_2Ph > P(OMe)_2Ph > P(OMe)_3$,[88] the result can be ascribed to the presence of a low-lying π^* orbital in phosphonite ligands. The $\delta_m - \delta_p$ and $\delta_m - \delta_o$ values for $[Fe(TPP)(PPh(OEt)_2)]^+$ are 6.34 and 4.64 ppm, respectively, while those for $[Fe(TPP)(PMe_3)_2]^+$ are 0.42 and 1.78 ppm, respectively, supporting the above-mentioned assignment of the ground state.

Latos-Grazynski, Marchon, and coworkers[89] have reported the ^{1}H NMR spectra of a series of low-spin iron(III) chiroporphyrins $[Fe(TMCP)L_2]^{\pm}$. Because of the presence of bulky chiral cyclopropyl groups at the *meso* positions, the complexes are projected to be highly ruffled. Thus, the bis-CN complex gives two pyrrole-H signals even at ambient temperature; one is due to the 2-, 3-, 12-, and 13-H and the other is due to the 7-, 8-, 17-, and 18-H. In the case of complexes carrying hindered axial ligands, such as 2-MeIm or 1,2-Me_2Im, two atropisomers, I and II, exist due to hindered rotation about the imidazole-*N* and iron(III) bond.[90–93] Each isomer gives four pyrrole-H signals and two cyclopropyl CH(1′) signals. In Table 3, the axial ligands are arranged in the descending order of the pyrrole-H chemical shifts, which exactly corresponds to the descending order of

Table 3. ^{1}H NMR chemical shifts (CD_2Cl_2, 293 K) of a series of $[Fe(TMCP)L_2]^{\pm}$.

Ligand (L)	Solvent		Pyrrole-H	Pyrrole-H(ave)	*Meso*-CH	*Meso*-CH(ave)
CN^-	CD_3OD		11.12, 10.56	10.84	101.87	101.87
CN^-	$CDCl_3$		3.57, 3.23	3.40	69.12	69.12
1,2-Me_2Im[a]	CD_2Cl_2	I	–4.93, –4.08, –0.99, –0.66	–2.67	55.73, 41.12	48.44
		II	–4.95, –2.44, –1.79, –0.20	–2.35	57.49, 43.37	50.43
2-MeIm[a]	CD_2Cl_2	I	–7.83, –7.22, –4.11, –4.11	–5.81	41.12, 28.1	34.61
		II	–7.83, –5.94, –5.08, –3.72	–5.64	41.77, 29.95	35.86
1-MeIm	CD_2Cl_2		–8.31, –8.18	–8.25	23.96	23.96
Him	CD_2Cl_2		–10.16, –9.97	–10.07	15.83	15.83

[a]The complex has two atropisomers, I and II, due to the slow rotation of axial ligands around the N–Fe bond. (Source: Ref. 89.)

the isopropyl-CH(1′) chemical shifts. Thus, it is clear that the electronic ground state changes from $(d_{xz}, d_{yz})^4(d_{xy})^1$ to $(d_{xy})^2(d_{xz}, d_{yz})^3$ as the axial ligand varies from CN^- (in CD_3OD) to HIm. The data in Table 3 indicate that the population of the $(d_{xz}, d_{yz})^4(d_{xy})^1$ isomer increases (i) if the CD_2Cl_2 solvent is replaced by CD_3OD in the bis-CN complex and (ii) if a methyl group is introduced into the 2-position of the imidazole. These two aspects will be discussed in Section III.B.3.

The effect of axial ligands on the electronic ground states of low-spin iron(III) porphyrins is most explicitly seen in the *meso*-alkyl-substituted complexes, i.e. $[Fe(TRP)L_2]^{\pm}$.[52] Table 4 lists the ^{1}H and ^{13}C NMR chemical shifts (CD_2Cl_2, 223 K) of a series of $[Fe(T^nPrP)L_2]^{\pm}$, $[Fe(T^cPrP)L_2]^{\pm}$, and $[Fe(T^iPrP)L_2]^{\pm}$. The EPR g values taken in frozen CH_2Cl_2 solution at 4.2 K are also listed. The ligands are arranged in ascending order of the pyrrole-H chemical shifts except for 4-CNPy and ^{t}BuNC; the pyrrole-H signal of the 4-CNPy complex in each series appears slightly more downfield than that of the ^{t}BuNC complex. The ligand arrangement in Table 4 corresponds to the ascending order of the CH(α)-H and *meso*-C and the descending order of the CH(α)-C and C_α chemical shifts. The large downfield shift of the pyrrole-H and *meso*-C signals, which is observed when the axial ligand changes from HIm to ^{t}BuNC, indicates that the electronic ground state changes from nearly pure $(d_{xy})^2(d_{xz}, d_{yz})^3$ in the HIm complex to nearly pure $(d_{xz}, d_{yz})^4(d_{xy})^1$ in the ^{t}BuNC complex in $[Fe(T^nPrP)L_2]^{\pm}$ and $[Fe(T^cPrP)L_2]^{\pm}$.

The situation is a little different, however, in the case of $[Fe(T^iPrP)L_2]^{\pm}$. Even the pyrrole-H signal of the HIm complex is observed considerably downfield, at 0.11 ppm, as compared with the corresponding signals in $[Fe(T^nPrP)(HIm)_2]^+$ and $[Fe(T^cPrP)(HIm)_2]^+$; these are observed at –21.45, and –18.70 ppm, respectively. Similarly, the *meso*-C signal appears considerably downfield, at 331.6 ppm, in $[Fe(T^iPrP)(HIm)_2]^+$ as compared with 73.1 and 97.1 ppm in $[Fe(T^nPrP)(HIm)_2]^+$

Table 4. ^{1}H and ^{13}C NMR chemical shifts (CD_2Cl_2, 223 K) and EPR g values (CH_2Cl_2, 4.2 K) of a series of (a) $[Fe(T^nPrP)L_2]^{\pm}$, (b) $[Fe(T^cPrP)L_2]^{\pm}$, and (c) $[Fe(T^iPrP)L_2]^{\pm}$.

	^{1}H NMR				^{13}C NMR						EPR			
Ligand (L)	Pyrrole-H	CH(a)	CH(β)		*meso*-C	CH(α)	CH(β)	CH(γ)	C_α	C_β	g_1	g_2	g_3	Ground State[c]
(a) $[Fe(T^nPrP)L_2]^{\pm}$														
HIm	–21.45	1.72	–1.47		73.1	14.5	64.5	12.4	0.0	73.6	2.90	2.35	(1.45)[b]	d_π
DMAP	–16.68	9.73	–0.92		130.5	–7.3	108.6	12.6	–2.2	84.3	3.10	2.10		d_π
2-MeIm	–8.20	21.3	0.79		a	a	a	a	a	a	2.85	2.10		d_π
CN^-	–3.48	30.9	0.09		336.1	–56.6	249.7	17.9	–72.7	61.2	2.51	2.51		d_{xy}
3-MePy	4.49	51.4	1.77		470.0	–120.6	348.8	16.9	–88.5	77.0				(d_{xy})
Py	7.07	57.9	1.65		526.5	–140.6	385.7	17.6	–108.2	74.3	2.55	2.55		d_{xy}
4-CNPy	13.03	88.5	0.68		814.7	–245.1	574.2	23.0	–262.7	66.0	2.46	2.46	1.68	d_{xy}
^{t}BuNC	12.65	118.5	–4.16		d	d	d	d	d	84.7[e]	2.16	2.16	1.95	d_{xy}
(b) $[Fe(T^cPrP)L_2]^{\pm}$														
HIm	–18.70	10.88	–1.52	–2.26	97.1	–6.2	17.5		11.8	79.6	2.87	2.42		d_π
DMAP	–14.31	26.37	–1.21	–2.81	127.4	–25.4	29.7		8.5	88.0	3.10	2.00		d_π
2-MeIm	–12.27	35.48	–9.29	d	149.1	d	d		–62.0	d	2.90	2.10		d_π
	–9.98	51.32	–6.50		231.6				–36.1					
	–7.25		–3.28						37.7					
	–4.46		–2.06						39.8					
CN^-	4.28	91.87	–0.15	–1.82	386.7	–98.9	91.4		–84.2	61.2	2.49	2.49		d_{xy}
3-MeIm	7.25	115.25	–0.27	–3.35	431.6	–133.0	102.8		–71.1	79.6				(d_{xy})
Py	8.39	121.35	–0.35	–3.93	448.9	–141.5	106.8		–81.3	78.7	2.56	2.56		d_{xy}
4-CNPy	14.89	189.49	–1.56	–4.16	680.1	–240.8	155.9		–211.9	71.7	2.49	2.49	1.58	d_{xy}
^{t}BuNC	14.70	d	–4.23		d	d	d		d	91.0	2.16	2.16	1.95	d_{xy}

(*Continued*)

Table 4. (*Continued*)

Ligand (L)	^{1}H NMR			^{13}C NMR						EPR			Ground State[c]
	Pyrrole-H	CH(a)	CH(β)	*meso*-C	CH(α)	CH(β)	CH(γ)	C_α	C_β	g_1	g_2	g_3	
(c) $[Fe(T^iPrP)L_2]^{\pm}$													
HIm	0.11	16.14	3.91	331.6	–55.3	172.5		–28.3	76.5	2.55	2.55		d_{xy}
DMAP	4.00	19.79	4.78	402.2	–76.6	207.3		–47.2	81.1	2.54	2.54		d_{xy}
2-MeIm	2.76	19.26	4.10	379.2	–65.4	d		–28.1	65.6	2.58	2.58		d_{xy}
	4.12	23.09	3.47	488.7	–104.2			–34.3	67.6				
	7.50		6.51					–93.4	80.4				
	8.15		7.51					–123.7	85.4				
CN^-	12.26	28.68	6.67	639.6	–134.5	309.4		–186.0	54.7	2.42	2.42	1.74	d_{xy}
3-MePy	14.66	33.20	7.76	702.5	–170.6	339.2		–165.2	71.6				(d_{xy})
Py	14.94	33.95	7.83	728.6	–179.3	349.3		–179.3	71.4	2.52	2.52	1.60	d_{xy}
4-CNPy	15.62	41.63	8.87	917.5	–242.9	425.1		–293.5	74.8	2.41	2.41	1.79	d_{xy}
^{t}BuNC	12.93	50.82	10.03	d	d	d		d	98.8[e]	2.16	2.16	1.96	d_{xy}

[a]Measurement was difficult due to the low solubility. [b]Calculated from $g_x^2 + g_y^2 + g_z^2 = 16$. [c]The electronic ground state was determined at 4.2 K from the EPR spectra. The d_π and d_{xy} represent the $(d_{xy})^2(d_{xz}, d_{yz})^3$ and $(d_{xz}, d_{yz})^4(d_{xy})^1$ ground state, respectively. [d]Signals were too broad to detect. [e]Data at 298 K. (Source: Refs. 52 and 82.)

and $[Fe(T^cPrP)(HIm)_2]^+$, respectively. The EPR spectrum of $[Fe(T^iPrP)(HIm)_2]^+$ taken at 4.2 K shows a broad signal at $g = 2.55$, which should be classified as axial-type.

These results strongly indicate that $[Fe(T^iPrP)(HIm)_2]^+$ is a unique example that adopts the $(d_{xz}, d_{yz})^4(d_{xy})^1$ ground state in spite of the coordination of HIm; all of the bis-HIm complexes reported previously adopt the $(d_{xy})^2(d_{xz}, d_{yz})^3$ ground state. The anomaly observed in $[Fe(T^iPrP)(HIm)_2]^+$ can be ascribed to the deformation of the porphyrin ring, which will be discussed in the next section. On the basis of the data listed in Tables 2–4, it is concluded that the population of the $(d_{xz}\ d_{yz})^4(d_{xy})^1$ type isomer increases as the axial ligand changes from HIm to ^{t}BuNC in the order given by Eq. 14:

$$\begin{aligned} &HIm < DMAP,\ 1\text{-}MeIm < 2\text{-}MeIm < 1,2\text{-}Me_2Im < CN^- \\ &< 3\text{-}MePy < Py < 3\text{-}CNPy,\ 4\text{-}CNPy < {}^t\text{BuNC}. \end{aligned} \tag{14}$$

2. *Electronic Effects of Peripheral Substituents*

In addition to the field strengths of axial ligands, the electronic ground state of low-spin iron(III) porphyrins can be influenced by the electronic effect of peripheral substituents. Table 5 lists the ^{1}H and ^{13}C NMR chemical shifts of a series of $[Fe(p\text{-}X\text{-}TPP)(CN)_2]^-$.[94] Figure 16a shows the Hammett plots for the *meso*-C isotropic shifts, where the isotropic shifts are determined in CD_2Cl_2 and CD_3OD solutions separately.[94] In both solvents, the Hammett plot yields a good straight line. While the isotropic shifts are positive, +18.7 to +85.2 ppm, in all the complexes examined in CD_3OD solution they are negative, −24.3 to −43.5 ppm, in CD_2Cl_2 solution. Furthermore, the slope of the line is −69.5 ppm in CD_3OD solution which is more than three times as much as that in CD_2Cl_2 solution. The positive isotropic shifts in CD_3OD solution indicate that the *meso*-C atoms have positive spin density, which in turn indicates that all the complexes given by $[Fe(T(p\text{-}X)PP)(CN)_2]^-$ adopt the $(d_{xz}, d_{yz})^4(d_{xy})^1$ ground state in CD_3OD solution regardless of the kind of *p*-substituents. The large negative slope observed in CD_3OD solution then indicates that the $(d_{xz}, d_{yz})^4(d_{xy})^1$ ground state is stabilized as the electron-donating ability of the *p*-substituent increases. In contrast, the negative isotropic shifts together with the insensitive substituent effect suggest that all the complexes adopt the $(d_{xy})^2(d_{xz}, d_{yz})^3$ ground state in CD_2Cl_2 solution. The isotropic shifts of the C_α signals obtained in CD_2Cl_2 and CD_3OD at 298 K are also plotted against the Hammett σ_p values, and they are shown in Figure 16b. Although the Hammett plots show good linearity in both CD_2Cl_2 and CD_3OD, the slopes are rather small, 7.5 (CD_2Cl_2) and 22.6 (CD_3OD) ppm, as compared with those of the *meso*-C Curie plots. Thus, the isotropic shifts of the C_α signals are less

Table 5. NMR chemical shifts of $[Fe(4\text{-}X\text{-}TPP)(CN)_2]^-$ determined in CD_2Cl_2 and CD_3OD solutions at 298 K: (a) ^1H NMR, (b)^{13}C NMR chemical shifts.

	CD_2Cl_2			CD_3OD		
X	Pyrrole-H	*o*	*m*	Pyrrole-H	*o*	*m*
$-OCH_3$	−16.09	4.48	5.97	−6.31	5.47	7.80
$-CH_3$	−16.12	4.47	6.26	−6.78	5.46	8.06
–H	−16.55	4.55	6.36	−7.69	5.61	8.04
–F	−16.82	4.50	6.00	−8.32	5.65	7.62
–Cl	−16.97	4.44	6.27	−8.98	5.57	7.82
$-CF_3$	−17.62	4.56	6.45	−10.46	5.73	7.86
–CN	−17.62	4.51	6.46	−11.11	5.66	7.80

	CD_2Cl_2				CD_3OD			
X	*Meso*	C_α	C_β	*Ipso*	*Meso*	C_α	C_β	*Ipso*
$-OCH_3$	94.4	40.2	89.8	118.0	203.9	21	88.3	89.5
$-CH_3$	93.5	40.3	89.9	123.1	195.8	22.4	88.6	96.6
–H	89.0	41.3	90.3	127.2	183.8	26.6	89.4	103.8
–F	84.2	42.4	90.6	124.1	173.2	30.7	90.2	102.7
–Cl	81.1	42.9	90.9	127.3	163.7	33.3	90.8	107.9
$-CF_3$	74.8	43.9	91.6	134.1	145.8	38.5	92.4	119.0
–CN	74.3	47.3	92.9	135.8	136.5	41.3	93.3	122.5

Source: Ref. 94.

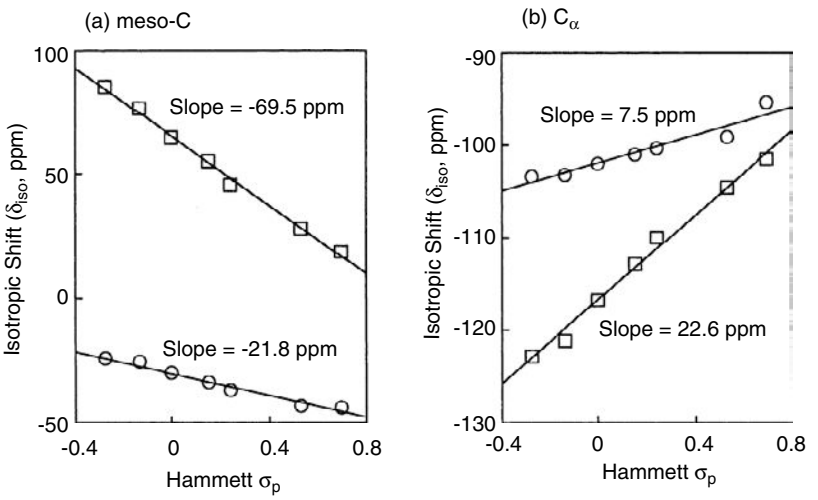

Figure 16. Plots of the carbon isotropic shifts of $[Fe(p\text{-}X\text{-}TPP)(CN)_2]^-$ against Hammett σ_p values in CD_2Cl_2 and CD_3OD at 298 K: (a) *meso*-C and (b) C_α. The symbols ○ and □ are isotropic shifts obtained in CD_2Cl_2 and CD_3OD solutions, respectively. (Adapted with permission from Ref. 94. Copyright 2002, Elsevier Science.)

sensitive to the *p*-substituents than those of the *meso*-C signals. As the population of the $(d_{xy})^2(d_{xz}, d_{yz})^3$ type isomer increases, the spin density at the *meso*-C decreases and that at the C_α increases. Thus, the positive and negative slopes in Hammett plots observed for the *meso*-C and pyrrole C_α signals, respectively, indicate that the electron-withdrawing substituents stabilize the $(d_{xy})^2(d_{xz}, d_{yz})^3$ state. The electronic ground state determined by the NMR spectra is supported by the EPR spectra taken in frozen CH_2Cl_2 solution at 4.2 K. These complexes commonly exhibit a strong signal at $g = 3.6$ in CH_2Cl_2 solution, while they commonly exhibit a strong signal at $g = 2.5$ in CH_3OH solution regardless of the kind of *p*-substituents. The results clearly indicate that these complexes adopt the $(d_{xy})^2(d_{xz}, d_{yz})^3$ and $(d_{xz}, d_{yz})^4(d_{xy})^1$ ground states in frozen CH_2Cl_2 and CH_3OH solutions, respectively, at 4.2 K. It should be noted here that the EPR spectra are less sensitive to subtle changes in the electronic ground state as compared with the NMR spectra.

There is another good example showing that the electron-withdrawing *meso* substituents stabilize the $(d_{xy})^2(d_{xz}, d_{yz})^3$ ground state. Compare the spectroscopic data of $[Fe(TPP)(^tBuNC)_2]^+$ with those of $[Fe(F_{20}–TPP)(^tBuNC)_2]^+$.[82] The porphyrin ring in the latter complex should be electron-deficient because of the presence of a strong electron-withdrawing pentafluorophenyl (C_6F_5) group at each *meso* position. In accordance with the general tendency of bis-^{t}BuNC complexes, both $[Fe(TPP)(^tBuNC)_2]^+$ and $[Fe(F_{20}\text{-}TPP)(^tBuNC)_2]^+$ adopt the less common $(d_{xz}, d_{yz})^4(d_{xy})^1$ ground state, as revealed by the axial type EPR spectra. However, the $g_\perp$ and $g_\parallel$ values are quite different; they are 2.18 and 1.93 in the former complex, and 2.31 and 1.86 in the latter. Similarly, the pyrrole-H signals of $[Fe(TPP)(^tBuNC)_2]^+$ and $[Fe(F_{20}\text{-}TPP)(^tBuNC)_2]^+$ appear at 11.7 and 5.48 ppm at 223 K, respectively. The results clearly indicate that the d_{xy} orbitals of both complexes are located above the d_π orbitals. However, the energy gaps between the d_{xy} and d_π orbitals are very different; they are calculated to be 9.16 and 5.55λ for $[Fe(TPP)(^tBuNC)_2]^+$ and $[Fe(F_{20}\text{-}TPP)(^tBuNC)_2]^+$, respectively, according to Eqs. 10 and 11.

The examples given above indicate that electron-donating groups at the *meso* positions stabilize the $(d_{xz}, d_{yz})^4(d_{xy})^1$ ground state while electron-withdrawing groups stabilize the $(d_{xy})^2(d_{xz}, d_{yz})^3$ ground state. The electronic effects of the peripheral substituents are most explicitly observed in saddle-shaped $[Fe(OETArP)L_2]^\pm$ where Ar represents various substituted phenyl groups, such as 4-CH_3O, H, 4-CF_3, and 3,5-$(CF_3)_2$, and the axial ligand (L) is either HIm or ^{t}BuNC.[95] Tables 6 and 7 list the ^{1}H and ^{13}C NMR chemical shifts of these complexes taken in CD_2Cl_2 solution at 298 K together with those of the corresponding diamagnetic zinc complexes, Zn(OETArP).[95] In the ^{1}H NMR spectra of $[Fe(OETArP)(HIm)_2]^+$, most of the signals exhibit no drastic change depending on the *meso* phenyl substituents. In contrast, the ^{1}H and ^{13}C signals in $[Fe(OETArP)(^tBuNC)_2]^+$ exhibit considerable

Table 6. ^{1}H NMR chemical shifts of [Fe(OETArP)(HIm)$_2$]$^+$, [Fe(OETArP)(^{t}BuNC)$_2$]$^+$, and [Zn(OETArP)] taken in CD_2Cl_2 solutions at 298 K.

Complexes Aryl Substituent	$\Sigma\sigma$	CH_2	CH_2(ave)	CH_3	*o*	*m*	*P*	^{t}Bu
[Fe(OETArP)(Him)$_2$]$^+$								
4-MeO	–0.27	4.74, 10.98[a]	7.86 [a]	0.74	5.64	5.49	3.35[b]	
H	0.00	4.37, 10.34[a]	7.34	0.86	4.97	5.80	6.73	
4-CF_3	0.54	4.32, 10.69	7.51	0.92	4.90	6.00	—	
2,6-Cl_2	—	5.54, 9.71[a]	7.63	1.18	—	5.42	6.32	
3,5-$(CF_3)_2$	0.86	3.56, 10.91[a]	7.24	1.05	5.23		1.17	
[Fe(OETArP)(^{t}BuNC)$_2$]$^+$								
4-MeO	–0.27	7.10	7.10	1.14	5.10	10.55	—	–1.55[a]
H	0.00	7.46	7.46	1.32	5.54	11.05	6.31	–1.53[a]
4-CF_3	0.54	9.93	9.93	1.27	7.00	10.14	—	–1.03[a]
2,6-Cl_2	—	12.39	12.39	1.73	—	9.35	7.53	–1.03[a]
3,5-$(CF_3)_2$	0.86	10.83	10.83	1.36	7.96		7.96	–0.95[a]
Zn(OETArP)								
4-MeO	–0.27	2.10, 2.65	2.38	0.45	8.19	7.24	4.07 [b]	—
H	0.00	2.01, 2.61	2.31	0.46	8.31	7.67	7.79	—
4-CF_3	0.54	1.97, 2.63	2.30	0.49	8.52	8.03	—	—
2,6-Cl_2	—	2.45	2.45	0.71	—	7.76	7.65	—
3,5-$(CF_3)_2$	0.86	1.52	1.52	1.26	8.87	—	8.36	—

[a]Extrapolated values; signals are too broad at ambient temperature. [b]Methoxy signal. (Source: Ref. 95.)

Table 7. ^{13}C NMR chemical shifts of $[Fe(OETArP)(HIm)_2]^+$, $[Fe(OETArP)(^tBuNC)_2]^+$, and Zn(OETArP) taken in CD_2Cl_2 solutions at 298 K.

Complex Aryl Substituent	$\Sigma\sigma$	*Meso*	C_α	C_β	*o*	*m*	*p*	*Ipso*	$CH_2(\alpha)$	$CH_3(\beta)$
$[Fe(OETArP)(HIm)_2]^+$										
4-MeO	–0.27	–2	182[a]	179[a]	102	111	156	163	–23	91
H	0.00	7	162[a]	167[a]	107	124	125	162	–24	87
4-CF_3	0.54	5	157[a]	166[a]	108	122	—	166	–24	86
2,6-Cl_2	—	–7	149[a]	161[a]	113	128	128	154	–27	92
3,5-$(CF_3)_2$	0.86	6	144[a]	164[a]	109	128	119	161	–25	85
$[Fe(OETArP)(^tBuNC)_2]^+$										
4-MeO	–0.27	430	–11	143	317	126	171	n.d.	0	58
H	0.00	417	–5	143	310	144	138	37	–2	59
4-CF_3	0.54	280	79	152	244	135	n.d.	98	–10	75
2,6-Cl_2	—	166	136	157	205	133	133	125	–21	93
3,5-$(CF_3)_2$	0.86	194	117	161	207	139	126	128	–18	87
[Zn(OETArP)]										
4-MeO	–0.27	119	148[a]	144[a]	135	113	160	135	19.9	17.5
H	0.00	119	147[a]	144[a]	136	127	128	142	19.8	17.5
4-CF_3	0.54	118	147[a]	144[a]	136	124	131	145	20.0	17.4
2,6-Cl_2	—	113	147[a]	144[a]	141	129	131	139	20.0	16.1
3,5-$(CF_3)_2$	0.86	too broad to detect								

[a]The assignments of the α and β signals could be reversed. (Source: Ref. 95.)

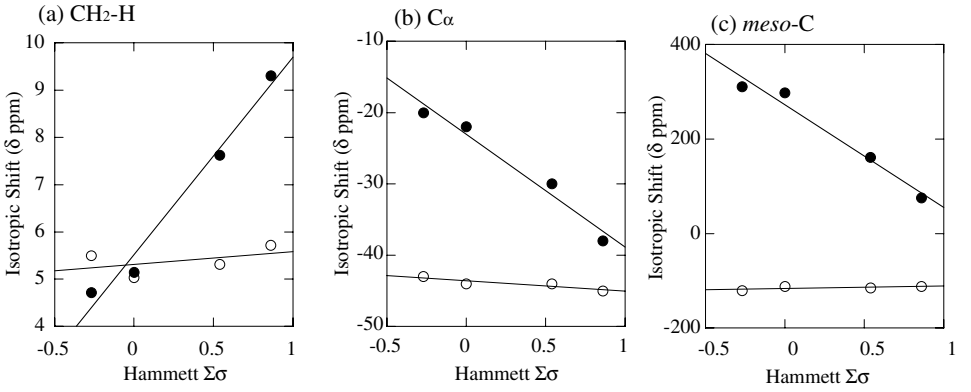

Figure 17. Hammett plots of the ^{1}H and ^{13}C NMR isotropic shifts of $[Fe(OETArP)(HIm)_2]^+$ (○) and $[Fe(OETArP)(^tBuNC)_2]^+$ (●). (a) CH_2-H, (b) C_α, and (c) *meso*-C. (Adapted with permission from Ref. 95. Copyright 2007, American Chemical Society.)

substituent dependence. Figure 17 shows the Hammett plots of some ^{1}H and ^{13}C signals of $[Fe(OETArP)(HIm)_2]^+$ and $[Fe(OETArP)(^tBuNC)_2]^+$.[95] For each signal, the substituent effect on the chemical shifts is considerably larger in $[Fe(OETArP)(^tBuNC)_2]^+$ than in $[Fe(OETArP)(HIm)_2]^+$ The isotropic shift of the CH_2–H signal of $[Fe(OETArP)(^tBuNC)_2]^+$ increases from +4.72 to +9.31 ppm with increase in the Hammett σ value, as shown in Figure 17a.

Correspondingly, the isotropic shift of the C_α signal decreases from −20 to −38 ppm, as shown in Figure 17b. The isotropic shift of the *meso*-C signal exhibits the largest change; it decreases from 311 to 76 ppm, as shown in Figure 17c. Thus, the Hammett plot for the *meso*-C signal shows a large negative slope, −220 ppm, in $[Fe(OETArP)(^tBuNC)_2]^+$ as compared with +5.4 ppm in $[Fe(OETArP)(HIm)_2]^+$. The results suggest that the spin density of the C_β gradually increases while that of the *meso*-C drastically decreases with increase in the Hammett σ value, which in turn indicates that the electronic ground state in $[Fe(OETArP)(^tBuNC)_2]^+$ gradually changes from $(d_{xz}, d_{yz})^4(d_{xy})^1$ to $(d_{xy})^2(d_{xz}, d_{yz})^3$. The change in the electronic ground state is further confirmed by the EPR spectra shown in Figure 18. As expected, $[Fe(OETArP)(HIm)_2]^+$ exhibits either rhombic or large g_{max} type spectra typical of the low-spin $(d_{xy})^2(d_{xz}, d_{yz})^3$ type complexes. In the case of $[Fe(OETArP)(^tBuNC)_2]^+$, all the complexes except the 3,5-$(CF_3)_2$ complex show axial type spectra characteristic of low-spin complexes with the $(d_{xz}, d_{yz})^4(d_{xy})^1$ ground state. Only the 3,5-$(CF_3)_2$ complex exhibits a rhombic type spectrum, which unambiguously indicates that this complex adopts the $(d_{xy})^2(d_{xz}, d_{yz})^3$ ground state in spite of the coordination of ^{t}BuNC. Thus, it is clear on the basis of the NMR and EPR data that the electronic ground state of $[Fe(OETArP)(^tBuNC)_2]^+$ gradually changes

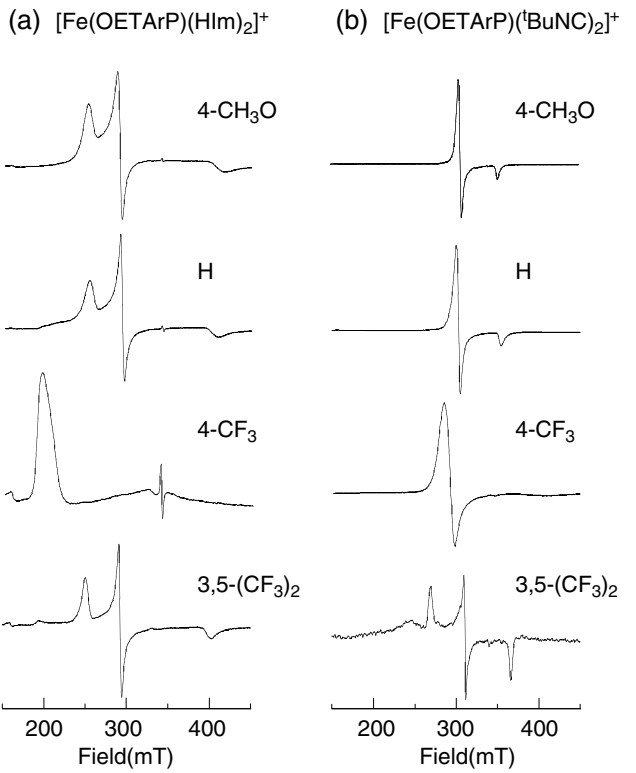

Figure 18. EPR spectra of a series of $[Fe(OETArP)(HIm)_2]^+$ and $[Fe(OETArP)(^tBuNC)_2]^+$ taken in CH_2Cl_2 solutions at 4.2 K. (Adapted with permission from Ref. 95. Copyright 2007, American Chemical Society.)

from nearly pure $(d_{xz}, d_{yz})^4(d_{xy})^1$ to nearly pure $(d_{xy})^2(d_{xz}, d_{yz})^3$ as the *meso*-aryl substituent changes from 4-CH_3O to 3,5-$(CF_3)_2$. Figure 19 shows the relative energy levels of the d_{xy}, d_{yz}, and d_{xz} orbitals of a series of $[Fe(OETArP)(^tBuNC)_2]^+$ obtained on the basis of the EPR *g* values in frozen CH_2Cl_2 solution at 4.2–20 K according to Eqs. 10 and 11. In the figure, the average value of the energy levels of the three d orbitals is fixed at a constant value. The 3,5-$(CF_3)_2$ complex is the first example of a low-spin iron(III) porphyrin that shows the $(d_{xy})^2(d_{xz}, d_{yz})^3$ ground state in spite of the coordination of ^{t}BuNC.

Electronic effects of peripheral substituents on the electronic ground state can be explained as follows: electron-donating *meso* substituents should destabilize the porphyrin π orbitals, especially the a_{2u} orbital, because this orbital has large coefficients at the *meso* positions. As a result, the interaction between the d_{xy} and a_{2u} orbitals is strengthened since the energy gap separating these two orbitals decreases as shown in Figure 20a, which in turn lifts the d_{xy} orbital above the d_π

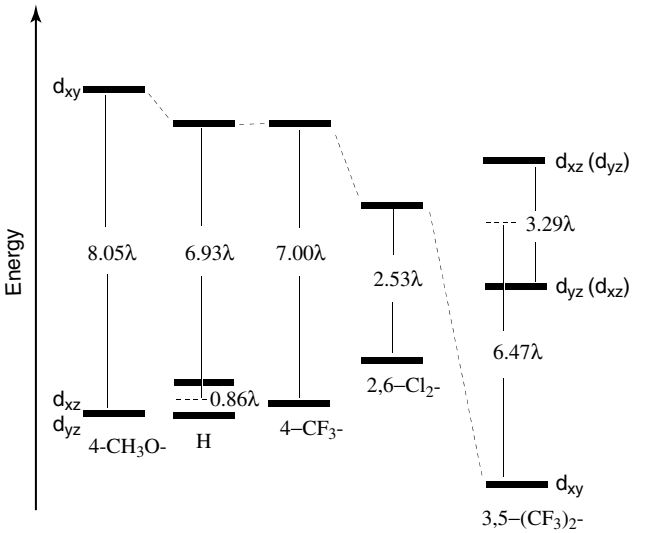

Figure 19. Relative energy levels of the d_{xy}, d_{yz}, and d_{xz} orbitals of a series of [Fe(OETArP)(^{t}BuNC)$_2$]$^+$. (Adapted with permission from Ref. 95. Copyright 2007, American Chemical Society.)

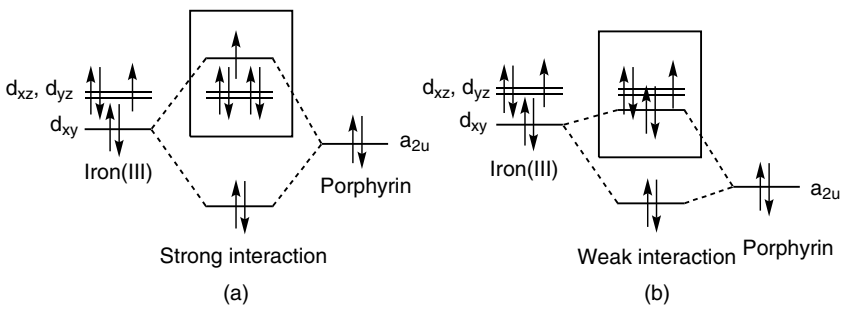

Figure 20. Schematic presentation of the change in energy levels in iron 3d orbitals by the introduction of substituents on the *meso* phenyl ring: (a) electron-donating substituents, (b) electron-withdrawing substituents. (Adapted with permission from Ref. 94. Copyright 2002, Elsevier Science.)

orbitals.[94] In contrast, electron-withdrawing *meso* substituents stabilize the a_{2u} orbital, and weaken the a_{2u}–d_{xy} interaction, as shown in Figure 20b. Consequently, the energy level of the d_{xy} orbital is lowered and thus the $(d_{xy})^2(d_{xz}, d_{yz})^3$ ground state is stabilized.

It should be noted here that the low-spin complex with the purest ever reported $(d_{xz}, d_{yz})^4(d_{xy})^1$ ground state is not the bis-^{t}BuNC complex, but the bis-Py complex with strongly electron-withdrawing heptafluoropropyl (C_3F_7) groups at the *meso* positions, $[Fe(T(C_3F_7)P)(Py)_2]^+$.[96] This complex shows $g_\perp$ and $g_\parallel$ signals at 2.07

and 1.99, respectively. The energy gap (Δ) between the d_{xy} and d_π orbitals reaches as much as -26.4λ, which is much larger than that of $[Fe(T^iPrP)(^tBuNC)_2]^+$ ($g_\perp$ = 2.16, $g_\parallel$ = 1.96; $\Delta/\lambda = -11.3$). At present, it is difficult to explain why this complex adopts the purest $(d_{xz}, d_{yz})^4(d_{xy})^1$ ground state despite the presence of strongly electron-withdrawing C_3F_7 groups at the *meso* positions. The highly ruffled structure expected for this complex could strengthen the d_{xy}–a_{2u} interaction and lift the d_{xy} orbital. In addition, the low-lying $4e_g$* orbitals of $T(C_3F_7)P$ could lower the iron d_π orbitals by the d_π–$4e_g$* interactions to stabilize the $(d_{xz}, d_{yz})^4(d_{xy})^1$ ground state. Anyway, because of the presence of a highly ruffled structure together with strongly electron-withdrawing *meso* substituents, $[Fe(T(C_3F_7)P)(Py)_2]^+$ should be an interesting complex for further electronic structure investigations. Unfortunately, however, this complex seems to be so unstable that the only spectroscopic data reported are from the EPR spectrum at 4.2 K.

3. *Deformation of the Porphyrin Ring*

Porphyrins are intrinsically planar 18π aromatic macrocycles. However, because the porphyrin ring is not a rigid macrocycle, it can be easily deformed in order to relieve the steric repulsion that occurs between a peripheral substituents and/or between a peripheral substituent and an axial ligand.[44–51] Deformation of the porphyrin ring affects the energy levels of the 3d orbitals of the iron, and in some cases changes the electronic ground state.[52,89,97–101] This is because the ring deformation always shortens the Fe–N bond to destabilize the $d_{x^2-y^2}$ orbital. Even the energy level of the t_{2g} orbitals should be affected by deformation of the porphyrin ring. Although the porphyrin a_{1u} and a_{2u} orbitals are orthogonal to any of the iron 3d orbitals in a planar D_{4h} complex, they can interact with the iron d_{xy} and $d_{x^2-y^2}$ orbitals if the porphyrin ring deforms, as shown in Table 1.[42,43] It has already been described in detail that the porphyrin a_{2u} orbital can interact with the iron d_{xy} orbital if the normally planar complex deforms in a D_{2d} ruffled fashion. It is also well known that the a_{2u} orbital can interact with the $d_{x^2-y^2}$ orbital if the complex deforms in a D_{2d} saddled fashion.[102,103] Similarly, the interaction between a_{1u} and $d_{x^2-y^2}$ orbitals is symmetry-allowed in a ruffled D_{2d} complex, and the interaction between a_{1u} and d_{xy} is symmetry-allowed in a saddled D_{2d} complex, as listed in Table 1.[38,42,43,104]

a. *Ruffled deformation*

Extensive structural and theoretical studies have revealed that the introduction of bulky substituents at the *meso* positions induces the highly ruffled deformation of the porphyrin ring.[105–108] In contrast, the introduction of aryl groups at the *meso*

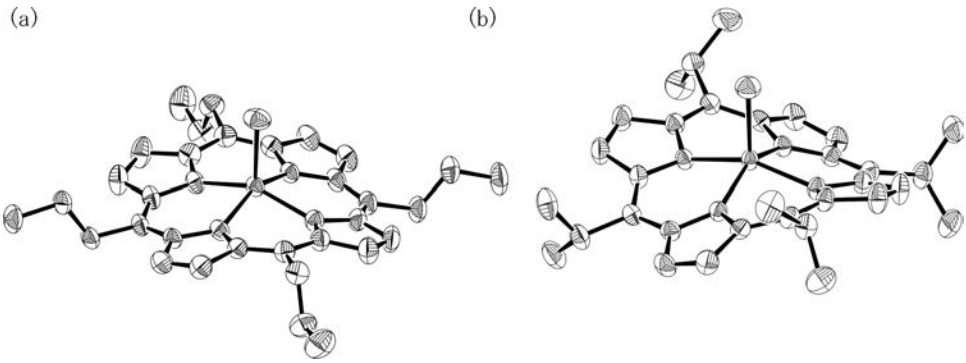

Figure 21. Molecular structure of (a) Fe(T^{n}PrP)Cl and (b) Fe(T^{i}PrP)Cl. (Adapted with permission from (a) Ref. 110, copyright 1999 American Chemical Society, and (b) Ref. 111, copyright 1999 International Union of Crystallography.)

positions does not usually affect porphyrin planarity because of the less bulky nature of the pseudoperpendicular phenyl group as compared with the alkyl group; note that the half-thickness of the benzene ring is 1.85 Å while that of a methyl group is 2.0 Å.[109] As the bulkiness of the *meso*-alkyl group increases, the ruffling of the porphyrin ring increases correspondingly.[105] Figure 21 shows the molecular structures of Fe(T^{n}PrP)Cl and Fe(T^{i}PrP)Cl.[110,111] Obviously, the porphyrin ring of the latter complex is ruffled to a greater extent. Thus, examination of the electronic structure of $[Fe(TRP)(CN)_2]^-$, where R is H, Me, Et, and ^{i}Pr, should reveal the relationship between porphyrin deformation and the electronic structure. Figure 22 shows the ^{1}H NMR spectra of a series of $[Fe(TRP)(CN)_2]^-$ taken in CD_2Cl_2 solution at 298 K.[97] As the *meso*-R changes from H to Me, Et, and then to the ^{i}Pr group, the pyrrole-H signal moves from −17.2 to −1.5, −2.0, and then to +10.0 ppm, suggesting clearly that the electronic ground state changes from $(d_{xy})^2(d_{xz}, d_{yz})^3$ to $(d_{xz}, d_{yz})^4(d_{xy})^1$. The results can best be explained in terms of destabilization of the d_{xy} orbital due to the d_{xy}–a_{2u} interaction, which is strengthened as the ruffling of the porphyrin ring increases on going from the R=H to the R=^{i}Pr complex.

In Table 8 are collected all the spectroscopic data of these complexes, including the ^{1}H NMR chemical shifts, the ^{13}C NMR chemical shifts of the coordinating CN^- ligand, and the EPR *g* values. The crystal field parameters obtained from the EPR *g* values are also listed.[97] Among these data, the chemical shifts of the coordinating CN^- ligand need to be explained. The chemical shift of the cyanide ligand moves downfield on going from the H to Me, Et, and then to the ^{i}Pr complex. Thus, the chemical shifts should reflect the electronic ground state of the complex. Various ferric porphyrin complexes with bis-CN coordination have been examined by ^{13}C NMR.[112–116] Their chemical shifts are in the range of −2000 to −2400 ppm.

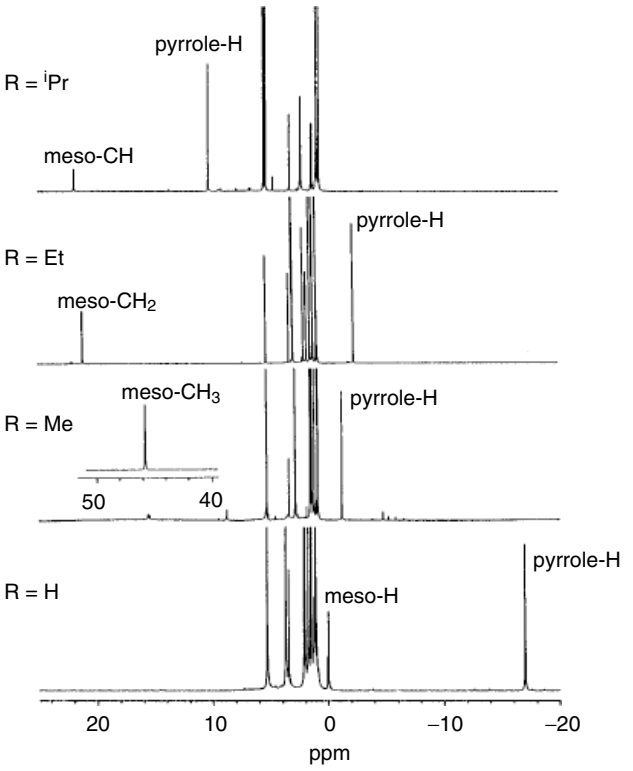

Figure 22. ^{1}H NMR spectra of a series of $[Fe(TRP)(CN)_2]^-$ taken in CD_2Cl_2 solution at 298 K. (Adapted with permission from Ref. 97. Copyright 1997, American Chemical Society.)

Table 8. NMR and EPR data of $[Fe(TRP)(CN)_2]^-$ determined in (a) CD_2Cl_2 solution and (b) CD_2Cl_2/CD_3OD solution together with the crystal field parameters.

	^{1}H NMR (248 K)			^{13}C NMR (248 K)	EPR (4.2 K)				
R	Pyrrole-H	CH(α)	CH(β)	CN^-	g_x	g_y	g_z	Δ/λ^C	V/λ^C
(a) CD_2Cl_2 Solution									
H	–23.19	(–2.99)[a]	—	–2973	—	—	3.65	—	—
Me	0.34	64.21	—	–1840	2.46	2.46	—	—	—
Et	–2.26	27.54	2.51	–2054	2.48	2.48	—	—	—
^{i}Pr	11.94	26.93	6.45	–1530	2.43	2.43	1.73	–3.83	–3.83
(b) CD_2Cl_2/CD_3OD Solution									
H	–21.73	(0.03)[a]	—	–2963	—	—	3.5	—	—
Me	8.65	99.05	—	–1401	2.43	2.43	1.69	–3.63	–3.63
Et	8.27	48.43	4.71	–1557	2.47	2.47	1.61	–3.20	–3.20
^{i}Pr	12.76	29.69	6.84	–1389	2.35	2.35	1.82	–4.82	–4.82

[a]Chemical shits of the *meso*-H signal. (Source: Ref. 97.)

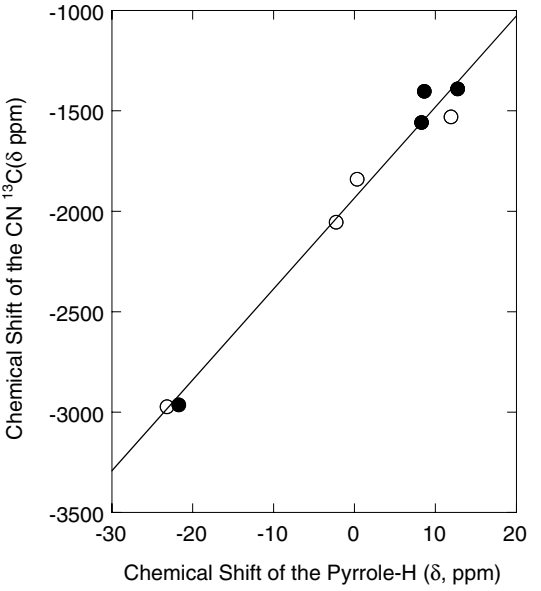

Figure 23. Correlation of the chemical shifts between the pyrrole-H and CN^- carbon signals in a series of [Fe(TRP)$(CN)_2$]. White circles are the chemical shifts in CD_2Cl_2 and black circles are those in CD_2Cl_2–CD_3OD. (Adapted with permission from Ref. 97. Copyright 1997, American Chemical Society.)

In the case of the complexes carrying both cyanide and imidazole ligands, the iron-bound cyanide signal is observed far more upfield: −3500 to −4300 ppm.

Figure 23 shows the correlation of the chemical shifts between the pyrrole-H and CN carbon signals in $[Fe(TRP)(CN)_2]^-$.[97] A fairly good correlation suggests that the change in chemical shifts of the CN carbon signal has the same origin as that of the pyrrole-H signal. In other words, the chemical shifts of the coordinating cyanide are controlled by the electronic ground state of the low-spin iron(III) ion. Cheng and coworkers have carried out DFT calculations for planar $[Fe(TPP)(CN)_2]^-$ and ruffled $[Fe(T^iPrP)(CN)_2]^-$.[117] Figure 24 shows the molecular orbitals involving d_{xy} and d_π obtained by the spin-restricted ADF calculations. In the case of the $(d_{xy})^2(d_{xz}, d_{yz})^3$ type low-spin complexes, the unpaired electron in the d_π orbital should interact with the CN π orbitals to induce positive spin density at the CN carbon atom, as shown in Figure 24b. Consequently, the CN carbon signal is expected to appear at a downfield position. Actually, however, the CN signals in the six-coordinate bis-CN and mixed cyanide–imidazole complexes are observed at extremely upfield positions, i.e. −2000 to −4300 ppm. The upfield shift is ascribed to indirect spin polarization via σ bonding interaction between d_{z^2} and the CN^- lone pair. Thus, the axial CN^- donates more positive spin density to

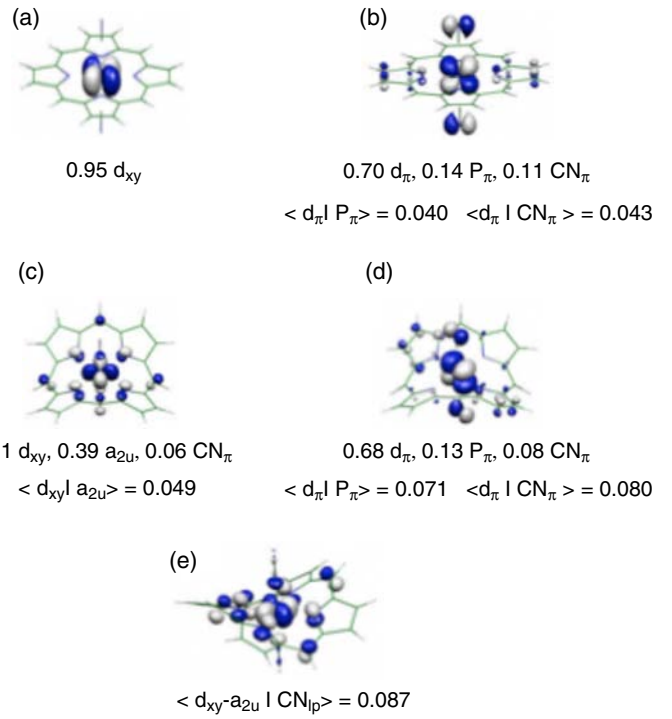

Figure 24. Molecular orbitals based on spin-restricted calculations depict the bonding characteristics of d_{xy} and d_{xz}, d_{yz} for $[FeP(CN)_2]^-$ complexes with planar [(a), (b)] and ruffled [(c), (d)] macrocycle conformation. Bonding interaction between d_{xy} and cyanide lone pairs is depicted in (e), a perspective view of (c). The corresponding major orbital contributions and the effective orbital overlap in space are also shown under each molecular orbital. (Reprinted with permission from Ref. 104. Copyright 2009, Royal Society of Chemistry.)

the vacant d_{z^2} orbital, which results in negative spin density at the CN^- carbon atom. The large upfield shift of the CN^- carbon signals indicates that the spin polarization mechanism predominates over the spin delocalization mechanism.

In the case of the low-spin $(d_{xz}, d_{yz})^4(d_{xy})^1$ type complexes, the CN^- π orbital is orthogonal to the half-occupied iron d_{xy} orbital. Consequently, the negative spin on the CN^- carbon should be much larger in the $(d_{xz}, d_{yz})^4(d_{xy})$ type complexes and induces a much larger upfield shift of the CN^- carbon signal in these complexes. This expectation is, however, against the experimental facts. Thus, there should be some direct spin delocalization mechanism between the half-occupied iron d_{xy} orbital and the axial cyanide. Cheng and coworkers have found that there is an unexpected bonding interaction between iron d_{xy} and cyanide lone pair in ruffled $[Fe(Por)(CN^-)_2]^-$, as shown in Figure 24e.[117] Because of this bonding interaction specific to the ruffled complexes, the spin density of the CN^- carbon in

Table 9. Slopes of the Curie plots (ppm K) of the pyrrole-H signals in $[Fe(R_3\text{-TPP})L_2]^+$ together with the chemical shifts.[a]

	Slope (ppmiK)				Chemical Shifts (δ ppm)[b]			
Ligand (L)	H	Me	Et	^{i}Pr	H	Me	Et	^{i}Pr
HIm	–8.58	–8.31	–8.37	–7.25	–27.4	–27.0	–27.4	–25.5
1-MeIm	–8.68	–8.62	–8.65	–8.05	–27.9	–27.7	–28.1	–27.0
2-MeIm	–8.56	–6.01	–5.97	–5.47	–23.3	–18.2	–18.7	–17.6
2-EtIm	–8.74	–5.68	–6.40	–5.74	–22.3	–16.8	–19.0	–18.2
2-^{i}PrIm	–8.00	–5.53	–6.12	–5.12	–21.8	–17.6	–19.1	–14.0
1,2-Me_2Im	–8.67	–4.53	–5.37	–4.55	–21.4	–13.6	–16.3	–15.2
1-Me-2-^{i}PrIm	—	–3.88	–4.19	–4.15	—	–12.8	–14.0	–13.9
BzIm	–8.55	–5.25	–5.93	–5.22	–22.3	–16.7	–18.2	–16.9

[a] Chemical shifts were determined in CD_2Cl_2 solution. [b]Chemical shifts of the pyrrole-H signals at 217 K. (Source: Ref. 119.)

$[Fe(T^iPrP)(CN^-)_2]^-$ becomes much less negative than for all the other low-spin complexes.

There are several more examples suggesting that the ruffled deformation stabilizes the $(d_{xz}, d_{yz})^4(d_{xy})^1$ ground state. Table 9 lists the slopes of the Curie plots of pyrrole-H signals in a series of $[Fe(R_3\text{-TPP})L_2]^+$, where R are H, Me, Et, and ^{i}Pr groups and L are various imidazole ligands.[119] From the data in the table, it is possible to extract the general tendency that the slope increases when both of the following two conditions are satisfied: (i) the *meso*-phenyl group has substituents at the *ortho* positions and (ii) the imidazole ligand has an alky substituent at position 2 of the ring.

Low-spin complexes that satisfy these two conditions should have a ruffled porphyrin ring because of the steric repulsion between the bulky axial ligand and the *ortho* alkyl substituents of the porphyrin. In fact, the X-ray molecular structure of $[Fe(TMP)(1,2\text{-}Me_2Im)_2]^+$ is highly ruffled, in contrast to that of $[Fe(TMP)(1\text{-}MeIm)_2]^+$, as shown in Figure 25.[118,120] The highly ruffled conformation creates mutually perpendicular clefts along the C_{meso}–Fe–C_{meso} axes above and below the porphyrin ring. The planar axial ligands coordinate to the iron(III) along these clefts to minimize their steric repulsion with the porphyrin core. Consequently, the $(d_{xz}, d_{yz})^4(d_{xy})^1$ ground state is stabilized due to the d_{xy}–a_{2u} interaction which is specific to the ruffled deformation. Similar examples can be seen in *meso*-alkyl-substituted complexes such as $[Fe(TCHP)L_2]^+$ and $[Fe(TMCP)L_2]^+$.[89,121] The pyrrole-H signals of these complexes move downfield by 3.6 (298 K) and 5.7 (223 K) ppm, respectively, as the axial 1-MeIm ligand is replaced by 1,2-Me_2Im. Similarly, the pyrrole-H signal of $[Fe(T^nPrP)(2\text{-}MeIm)_2]^+$ appears more downfield by 13.3 ppm than the corresponding signal of $[Fe(T^nPrP)(HIm)_2]^+$. $[Fe(TMP)(2\text{-}MeBzIm)_2]^+$ is a special case.[122] This complex exhibits the pyrrole-H signal *ca.* 2 ppm

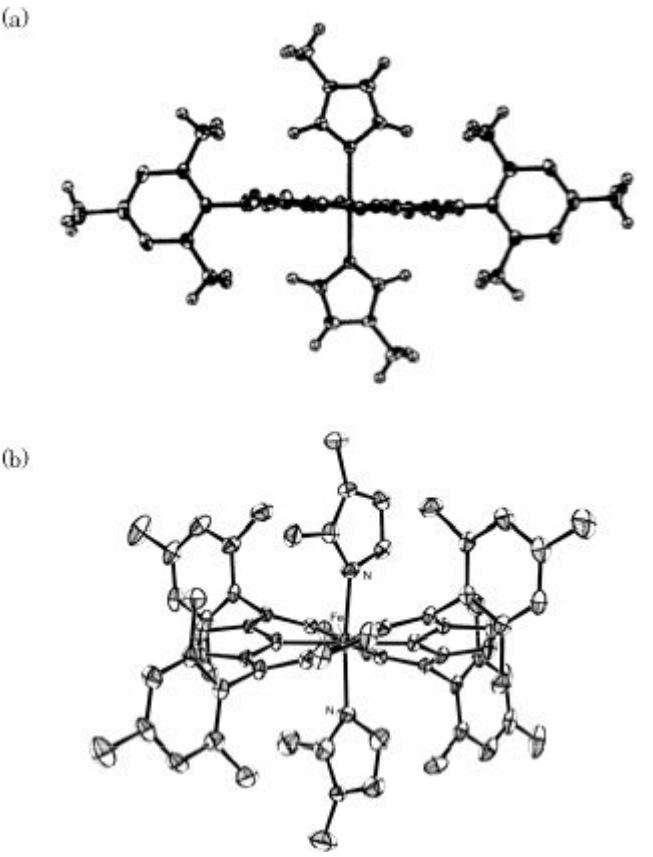

Figure 25. ORTEP diagrams of (a) $[Fe(TMP)(1\text{-}MeIm)_2]^+$ and (b) $[Fe(TMP)(1,2\text{-}Me_2Im)_2]^+$. The thermal ellipsoids enclose 30% probability. Hydrogen atoms are omitted for clarity. (Adapted with permission from: (a) Ref. 118, copyright 1991 American Chemical Society; and (b) Ref. 120, copyright 1995 American Chemical Society.)

at 206 K and the *meso*-C signal at 321 ppm at 221 K. The EPR spectrum exhibits a single band at $g = 2.6$. All these data strongly indicate that the complex adopts the $(d_{xz}, d_{yz})^4(d_{xy})^1$ ground state because of the highly ruffled structure expected for this complex.[122] On the basis of the data in Tables 3, 4 and 9, it is reasonable to conclude that *the ruffling of the porphyrin ring stabilizes the* $(d_{xz}, d_{yz})^4(d_{xy})^1$ *ground state* if other conditions such as basicity and number of the axial ligands and the electronic effect of peripheral substituents are similar.

b. *Saddled deformation*

Next, the effect of another typical mode of porphyrin deformation, the saddled deformation, on the electronic ground state of the low-spin iron(III) porphyrins is

Table 10. EPR *g* values and crystal field parameters of a series of $[Fe(Por)(^tBuNC)_2]^+$.

Porphyrin substituent	g_1	g_2	g_3	Δ	*V*
T^iPrP	2.16	2.16	1.96	–11.3	0
T^cPrP	2.16	2.16	1.95	–10.7	0
T^nPrP	2.16	2.16	1.95	–10.7	0
TPP	2.18	2.18	1.93	–9.16	0
F_5-TPP	2.31	2.31	1.86	–5.53	0
OMTPP	2.20	2.17	1.95	–9.79	1.32
TBTXP	2.21	2.21	1.94	–8.60	0
OETArP					
4-OCH_3	2.216	2.216	1.925	–8.05	0
H	2.29	2.25	1.92	–6.93	0.86
4-CF_3	2.250	2.250	1.908	–7.00	0
2,6-Cl_2	2.370	2.370	1.680	–2.53	0
3,5-$(CF_3)_2$	2.524	2.186	1.859	6.47	3.29
ProtoIXMe$_2$	2.30	2.30	1.86	–5.63	0
OEP	2.29	2.29	1.86	–5.73	0

Source: Refs. 82 and 95.

considered. As mentioned above, low-spin iron(III) complexes with the axial ligands having low-lying π^* orbitals, such as ^{t}BuNC, almost always adopt the $(d_{xz}, d_{yz})^4(d_{xy})^1$ ground state. However, the energy gap between the d_{xy} and d_π orbitals shown as Δ in Figure 12 should be different among bis-^{t}BuNC complexes. Therefore, the effect of the saddled deformation can be evaluated by comparison of the Δ values in a wide variety of $[Fe(Por)(^tBuNC)_2]^+$ complexes. Table 10 lists the EPR *g* values of these complexes taken in frozen CH_2Cl_2 solution at 4.2 K together with the crystal field parameters, Δ and *V*.[82,95] As the data in Table 10 show, the $|\Delta|$ value increases in the order given by Eq. 15:

$$\text{ProtoIXMe}_2, \text{OEP} < \text{OETPP} < \text{TPP}, \text{OMTPP} < T^nPrP, T^cPrP, T^iPrP. \quad (15)$$

It is clear that the OETPP core prefers the $(d_{xy})^2(d_{xz}, d_{yz})^3$ ground state as compared with the TPP core. However, it is difficult to generalize whether or not this order indicates that the saddled deformation of the porphyrin ring actually stabilizes the $(d_{xy})^2(d_{xz}, d_{yz})^3$ ground state. This is because OETPP has eight electron-donating ethyl groups at the C_β positions as compared with TPP, which should affect the electronic ground state of the low-spin iron(III) complexes. In fact, the substitution of alkyl groups at the pyrrole C_β atoms seems to stabilize the $(d_{xy})^2(d_{xz}, d_{yz})^3$ ground state since the energy gaps between the d_{xy} and d_π orbitals in OEP and ProtoIXMe$_2$ complexes are much smaller than in OETPP. What is more puzzling is that the energy gap in the OMTPP complex is similar to that of TPP although

OMTPP is known to have a highly saddled structure as in the case of OETPP.[50] In fact, X-ray crystallographic analysis has revealed that $[Fe(OMTPP)(^tBuNC)_2]^+$ has a pure saddled structure.[123] It should be noted, however, that the only bis-^{t}BuNC complex that adopts the $(d_{xy})^2(d_{xz}, d_{yz})^3$ ground state is $[Fe(OETArP)(^tBuNC)_2]^+$, where aryl (Ar) is the electron-withdrawing 3,5-$(CF_3)_2$Ph group. In contrast, the TPP complex with the strongly electron-withdrawing pentafluorophenyl groups at the *meso* positions, $[Fe(F_{20}\text{-TPP})(^tBuNC)_2]^+$, still maintains the $(d_{xz}, d_{yz})^4(d_{xy})^1$ ground state. Thus, it can be said with reservation that *the* $(d_{xy})^2(d_{xz},d_{yz})^3$ *ground state is stabilized to some extent if the porphyrin ring is saddled.*

All the $(d_{xz}, d_{yz})^4(d_{xy})^1$ type complexes in which the molecular structures have been determined by X-ray crystallography exhibit the ruffled structure. However, $[Fe(OMTPP)(^tBuNC)_2]^+$ has a purely saddled porphyrin core in the solid state though it adopts the $(d_{xz}, d_{yz})^4(d_{xy})^1$ ground state.[123] Therefore, the ruffled geometry is not necessary for the existence of the $(d_{xz}, d_{yz})^4(d_{xy})^1$ ground state. However, $[Fe(OMTPP)(^tBuNC)_2]^+$ shows the *meso*-C signal at an extremely downfield position in CD_2Cl_2 solution, i.e. 979 ppm at 223 K, which is quite close to that of $[Fe(TPP)(^tBuNC)_2]^+$, at 997 ppm.[82] The result clearly indicates that the *meso*-C atoms of $[Fe(OMTPP)(^tBuNC)_2]^+$ certainly have large amounts of spin density though the complex shows a purely saddled structure in the solid state. The large downfield shift of the *meso*-C signal could be an indication that the ring conformation in solution is different from that in the solid. There could be an effective spin delocalization mechanism from the $(d_{xz}, d_{yz})^4(d_{xy})^1$ iron(III) to the porphyrin ring even in purely saddled $[Fe(OMTPP)(^tBuNC)_2]^+$. Interestingly, both axial ligands in this complex are tilted in opposite directions.[123] Tilted axial ligand binding seems to be a common characteristic of the bis-^{t}BuNC complexes since the axial ligands in $[Fe(OEP)(^tBuNC)_2]^+$ and $[Fe(TPP)(^tBuNC)_2]^+$ are also tilted; they are tilted in the same direction in these complexes.[74] Obviously, both experimental and theoretical studies are necessary in order to reveal the spin delocalization mechanism in purely saddled $[Fe(OMTPP)(^tBuNC)_2]^+$.

4. *Solvent Effects*

In general, solvent can affect the electronic ground state because it can vary the field strengths of the axial ligands. An example is the *methanol effect* on the electronic ground state of bis-CN complexes. As shown in Tables 3, 5 and 8, addition of methanol greatly stabilizes the $(d_{xz}, d_{yz})^4(d_{xy})^1$ ground state. La Mar and coworkers pointed out many years ago that hydrogen bonding between the coordinated cyanide and solvent molecules decreases σ-donation and increases the π-accepting ability of the cyanide ligand, which lowers the d_{xz} and d_{yz} relative to the d_{xy} orbital, and hence the energy gap Δ shown in Figure 12.[124] Figure 26 shows the

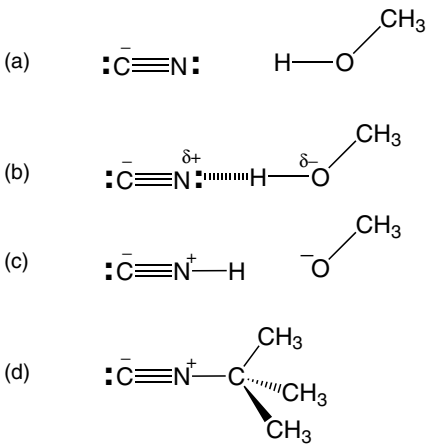

Figure 26. Relationship between cyanide and methanol: (a) no interaction, (b) hydrogen bonding, (c) limiting case of the hydrogen bonding where H^+ is completely transferred to the nitrogen atom, and (d) structural formula of *tert*-butylisocyanide. (Modified with permission from Ref. 84. Copyright 2002, American Chemical Society.)

interaction between cyanide and methanol.[84] The limiting structure of hydrogen bonding, where the proton is completely transferred to the nitrogen atom as given in Figure 26c, has a structural formula similar to ^{t}BuNC given in Figure 26d. Thus, hydrogen bonding should lower the π^* orbital of cyanide, which in turn stabilizes the iron d_π orbitals by d_π–p_{π^*} interactions to the points that are lower than the d_{xy} orbital. Consequently, the d_{xy} orbital has an unpaired electron to adopt the $(d_{xz}, d_{yz})^4(d_{xy})^1$ ground state. Bis-CN complexes are suitable for revealing the effect of solvent on the electronic ground state because the energy difference between the d_π and d_{xy} orbital is small. This means that the small perturbation to the coordinated cyanide could change the energy levels of the 3d orbitals of low-spin iron(III) complexes and alter their physicochemical properties. Table 11 lists the ^{13}C NMR chemical shifts of $[Fe(Et_3\text{-TPP})(CN^-)_2]^-$ obtained in various solvents at 253 K, which clearly indicate that the downfield shift of the *meso*-C signal increases in the order given in Eq. 16.[84]

$$\begin{aligned} CCl_4 < C_6D_6,\ C_6D_5CD_3,\ CD_3CN < (CD_3)_2CO,\ &\text{DMSO-}d_6,\ \text{DMF-}d_7 \\ < CD_2Cl_2 < CDCl_3 < CD_3OD. \end{aligned} \tag{16}$$

Examination of the data in Table 11 reveals the following relationships between the *meso*-C chemical shifts at 253 K and solvents: (i) the *meso*-C signal appears fairly downfield, δ = 275 ppm, in a protic solvent such as methanol; (ii) large differences in chemical shifts are observed even among nonpolar

Table 11. ^{13}C NMR chemical shifts of $[Fe(Et_3\text{-}TPP)(CN)_2]^-Bu_4N^+$ determined in various solvents at 253 K.

Solvent	Meso	C_α	C_β	Ipso	o	m	p
CD_3OD	275.4	–17.0	76.6	68.8	236.5	130.0	146.5
$CDCl_3$	191.4	9.3	76.2	91.8	202.0	125.6	142.5
CD_2Cl_2	172.3	10.4	78.5	97.0	193.2	125.3	143.1
DMF-d_7	134.9	18.6	78.0	106.9	178.4	125.0	143.1
DMSO-d_6[a]	130.8	16.2	78.5	107.0	176.4	124.5	142.4
$(CD_3)_2CO$	123.3	20.7	77.2	109.9	174.2	124.4	142.6
CD_3CN	100.3	20.4	81.1	113.4	165.1	123.4	142.6
$C_6D_5CD_3$	96.1	25.2	80.3	116.7	164.9	123.9	142.2
C_6D_6[a]	95.5	23.8	79.6	116.1	164.5	123.7	142.1
CCl_4	79.6	25.6	82.2	119.1	158.2	122.6	140.8

[a]The values are extrapolated from high temperature. (Source: Ref. 84.)

solvents; for example, the chemical shifts in $CDCl_3$ and CD_2Cl_2 are $\delta = 191$ and 172 ppm, respectively, as compared with δ = 80–100 ppm in toluene-d_8 ($C_6D_5CD_3$), benzene-d_6 (C_6D_6), and CCl_4; (iii) the *meso*-C signals appear in a quite narrow range, $\delta = 129 \pm 6$ ppm, in dipolar aprotic solvents, such as DMF-d_7, DMSO-d_6, and acetone-d_6, which are located between those for the two types of nonpolar solvents mentioned above; (iv) the *meso* signal in acetonitrile-d_3 (CD_3CN) appears rather close to that in $C_6D_5CD_3$ or C_6D_6, *ca.* 100 ppm, though CD_3CN is classified as a dipolar aprotic solvent.

As mentioned in Eqs. 6′ and 6″, the isotropic shifts of the *meso*-C signals are positive (downfield shift) in the complexes with the $(d_{xz}, d_{yz})^4(d_{xy})^1$ ground state, while they are negative (upfield shift) in those with the $(d_{xy})^2(d_{xz}, d_{yz})^3$ ground state. Figure 27 shows the Curie plots of the *meso*-C signal of $[Fe(Et_3\text{-}TPP)(CN)_2]^-$ taken in various solvents. The chemical shifts of diamagnetic $[Co(Et\text{-}TPP)(CN)_2]^-$ are almost constant, 115.5 ± 0.6 ppm, at 298 K in various solvents. Curie plots of the *meso*-C signal of $[Co(Et\text{-}TPP)(CN)_2]^-$ determined in CD_2Cl_2 solution are also given in Figure 27. This line separates the Curie plots of the $(d_{xy})^2(d_{xz}, d_{yz})^3$ type complexes from those of the $(d_{xz}, d_{yz})^4(d_{xy})^1$ type complexes. From the viewpoint of the *meso*-C Curie plots, the solvents can be classified into four types — type A — protic solvents such as CD_3OD; type B — nonpolar solvents such as $CDCl_3$ and CD_2Cl_2; type C — dipolar aprotic solvents such as DMF-d_7, DMSO-d_6, and acetone-d_6; Type D — nonpolar solvents such as toluene-d_8, benzene-d_6, and CCl_4. While the complex adopts the $(d_{xz}, d_{yz})^4(d_{xy})^1$ ground state in the solvents classified as types A–C, it shows the $(d_{xy})^2(d_{xz}, d_{yz})^3$ ground state in the solvents classified as type D. Figure 27 also indicates that the $(d_{xz}, d_{yz})^4(d_{xy})^1$ character is the largest in type A solvents, followed by types B and C. It should be noted that

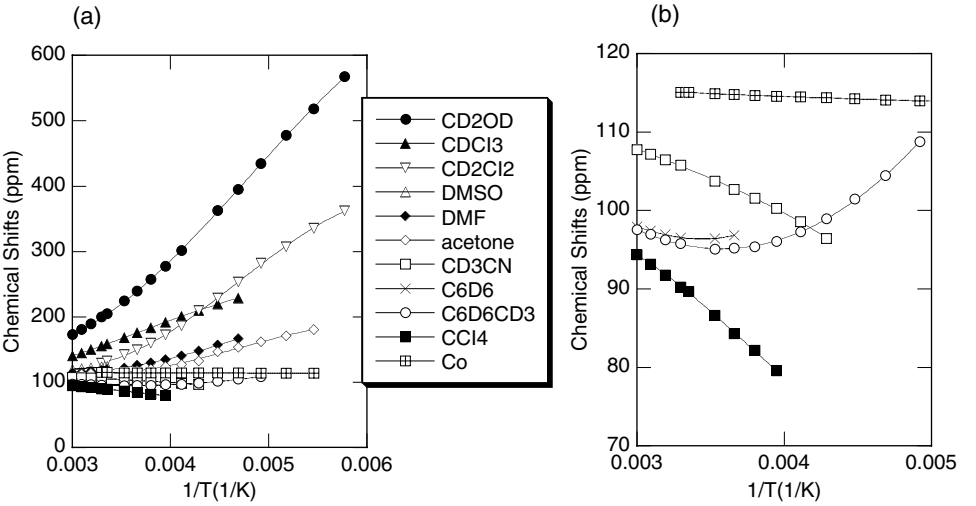

Figure 27. Curie plots of the *meso*-C signals in $[Fe(Et_3\text{-TPP})(CN)_2]^-Bu_4N^+$. (a) In all the solvents examined and (b) in nonpolar solvents such as CCl_4, C_6D_6, and $C_6D_5CD_3$ as well as in a dipolar aprotic solvent such as CD_3CN. Curie plots of the *meso*-C signal of diamagnetic $[Co(Et_3\text{-TPP})(CN)_2]^-Bu_4N^+$ taken in CD_2Cl_2 solution are also given. (Adapted with permission from Ref. 84. Copyright 2002, American Chemical Society.)

Table 12. ^{1}H NMR chemical shifts of $[Fe(Et_3\text{-TPP})(CN)_2]^-$ determined at various solvents 298 K and 253 K.

	298 K		253 K	
Solvent	Pyrrole-H	*m*	Pyrrole-H	*m*
CD_3OD	–6.89	8.44	–4.75	9.69
$CDCl_3$	–9.59	7.54	–9.97	8.13
CD_2Cl_2	–12.10	7.09	–12.28	7.74
DMF-d_7	–13.10	6.81	–15.28	7.05
DMSO-d_6	–12.50	7.24	–15.69[a]	7.39[a]
$(CD_3)_2CO$	–13.57	6.67	–16.11	6.91
CD_3CN	–15.07	6.52	–19.76	6.20
$C_6D_5CD_3$	–15.23	6.49	–18.66	6.63
C_6D_6	–15.06	6.50	–18.98[a]	6.41[a]
CCl_4	–15.53	6.77	–20.43	6.58

[a]The value is extrapolated from high temperature. (Source: Ref. 84.)

acetonitrile-d_3(CD_3CN) is an exceptional case; the complex exhibits the $(d_{xy})^2(d_{xz}, d_{yz})^3$ ground state in this solvent, though the solvent is classified as a type C solvent. Table 12 shows the ^{1}H NMR chemical shifts taken in various solvents at 298 K and 253 K. As mentioned, the chemical shifts of the pyrrole-H and *meta*-H

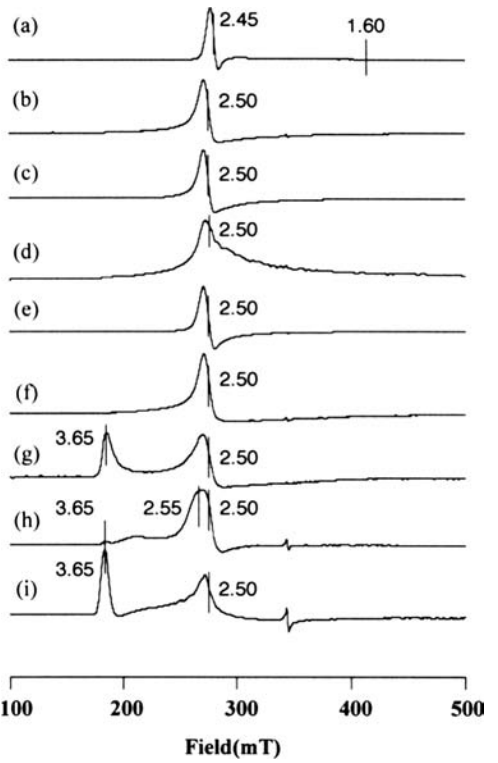

Figure 28. EPR spectra of $[Fe(Et_3\text{-}TPP)(CN)_2]^-Bu_4N^+$ taken in frozen solutions at 4.2 K: (a) CD_3OD, (b) $CDCl_3$, (c) CD_2Cl_2, (d) DMF-d_7, (e) DMSO-d_6, (f) $(CD_3)_2CO$, (g) CD_3CN, (h) $C_6D_5CD_3$, and (i) C_6D_6. (Reprinted with permission from Ref. 84. Copyright 2002, American Chemical Society.)

signals are good probes of the electronic ground state. The order of the chemical shifts of these signals is the same as is given in Eq. 15. Thus, the data listed in Table 12 are totally consistent with those obtained using ^{13}C-NMR spectroscopy.

Figure 28 shows the EPR spectra of complexes taken in various frozen solvents at 4.2 K.[84] While the complex shows only the axial type signals centered at $g = 2.5$ in types A–C solvents, it exhibits both the axial type ($g = 2.5$) and large g_{max} type ($g = 3.7$) signals in type D solvents, indicating that two kinds of electron configurational isomers are present in the frozen solutions. Thus, the EPR results are totally consistent with the NMR results. Again, acetonitrile behaves like type D solvent, though it is classified as type C.

Type A solvents such as methanol are good proton donors in hydrogen bonding with coordinating cyanide, which lowers the π^* orbital of cyanide and stabilizes the $(d_{xz}, d_{yz})^4(d_{xy})^1$ ground state. The effect of hydrogen bonding is more explicitly observed when much stronger proton donors are added, as shown in

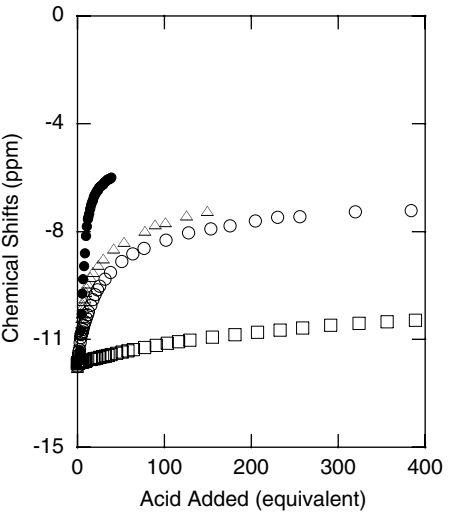

Figure 29. Change in the ^{1}H NMR pyrrole-H shift against the acid added. Each acid was added to a solution containing $[Fe(Et_3\text{-TPP})(CN)_2]^-Bu_4N^+$ and CN^- in 1:2 molar ratios at 298 K: CH_3COOH (●), C_6H_5OH (Δ), CD_3OD (○), and $CDCl_3$ (□). (Adapted with permission from Ref. 84. Copyright 2002, American Chemical Society.)

Figure 29.[84] The downfield shift of the pyrrole-H signal increases as the acidity of the solvents increases, as shown in the following order: $CD_3OD < C_6H_5OH < CH_3COOH$.

As for the type B solvents such as chloroform, they are known to be much stronger proton donors than other compounds having C–H bonds on the basis of C–H···X distances in the crystal.[125–127] Formation of C–H···X hydrogen bonding is also reported for dichloromethane in the crystal.[128] The presence of C–H···X hydrogen bonding has been reported even in solution between chloroform and pyridine or between chloroform and DMSO.[129] Thus, it must be a reasonable assumption to ascribe the stabilization of the $(d_{xz}, d_{yz})^4(d_{xy})^1$ ground state in $CDCl_3$ and CD_2Cl_2 to the weak C–D···N hydrogen bonding between the coordinated cyanide and solvent molecules.[130]

In type C solvents such as DMF and DMSO, the chemical shifts of the *meso*-C and pyrrole-H signals are located between those obtained in the two types of nonpolar solvents, types B and D. On the basis of the NMR results, it is concluded that the energy gap between the d_{xy} and d_π orbitals in type C solvents is less than that in type B solvents, which should be ascribed to the difference in proton donor ability among these solvents. The proton donor ability is estimated by the C–H···X bond distances in the crystal, where X = N, O, or Cl. In fact, X-ray crystallographic studies have revealed that the C–H···X bond distances of acetonitrile,

DMSO, and acetone are longer than those of $CHCl_3$ and CH_2Cl_2, supporting the hypothesis mentioned above.[128] Among the type C solvents examined in this study, CD_3CN differs from the others and resembles the type D solvents. In fact, the chemical shifts of the *meso*-C signals are 96.5 and 99.0 ppm in CD_3CN and $C_6D_5CD_3$, respectively, at 233 K. Similarly, the EPR spectrum in frozen CH_3CN shows both axial and large g_{max} type signals, as in the case of C_6D_6 solutions. Thus, CD_3CN behaves like type D solvents, which could be ascribed to the weak proton donor ability.

C. Low-Spin Complexes with a Rare Electronic Ground State

In the previous sections, the factors that affect the electronic ground state of low-spin iron(III) porphyrins have been described in detail. In general, low-spin complexes carrying imidazole (HIm) as axial ligand adopt the $(d_{xy})^2(d_{xz}, d_{yz})^3$ ground state while those carrying *tert*-butylisocyanide (^{t}BuNC) adopt the $(d_{xz}, d_{yz})^4(d_{xy})^1$ ground state. In this section, we will describe the reverse cases: bis-HIm and bis-^{t}BuNC complexes that adopt the $(d_{xz}, d_{yz})^4(d_{xy})^1$ and the $(d_{xy})^2(d_{xz}, d_{yz})^3$ ground state, respectively.[131] Preparation and characterization of such complexes should deepen our understanding of the electronic structures of iron(III) porphyrins as well as heme proteins.

1. *Bis-Imidazole Complexes that Adopt the $(d_{xz}, d_{yz})^4(d_{xy})^1$ Ground State*

As mentioned in the previous section, low-spin complexes with the $(d_{xz}, d_{yz})^4(d_{xy})^1$ ground state exhibit axial type EPR spectra. However, EPR spectra reflect the electronic structure at the extremely low temperature where the measurement is carried out. For determination of the electronic structure at ambient temperature, ^1H and ^{13}C NMR spectroscopy serve a useful role. Chemical shift data listed in Tables 2–8 suggest that low-spin complexes adopting the $(d_{xz}, d_{yz})^4(d_{xy})^1$ ground state at ambient temperature satisfy the following three conditions: (i) $\delta > 0$ ppm for the pyrrole-H signal, (ii) $\delta > 200$ ppm for the *meso*-C signal, and (iii) positive Curie slopes for these signals. As for the pyrrole-H chemical shifts, some complexes adopt the $(d_{xz}, d_{yz})^4(d_{xy})^1$ ground state even if the pyrrole-H signals appear more upfield, i.e. *ca.* −10 ppm, at ambient temperature. There are several bis-HIm complexes reported previously that satisfy the NMR criteria mentioned above. They are highly ruffled $[Fe(T^iPrP)(HIm)_2]^+$ and $[Fe(T^iPrP)(2\text{-}MeIm)_2]^+$.[52,132] At 298 K, the pyrrole-H and *meso*-C chemical shifts are 1.1 and 287 ppm, respectively, for $[Fe(T^iPrP)(HIm)_2]^+$ and 4.9 and 356 ppm, respectively, for $[Fe(T^iPrP)(2\text{-}MeIm)_2]^+$. Curie slopes are all positive for these signals. Thus, it is clear that both of these complexes adopt the $(d_{xz}, d_{yz})^4(d_{xy})^1$ ground state at ambient temperature

in spite of the coordination of imidazole ligands. The $(d_{xz}, d_{yz})^4(d_{xy})^1$ ground states of these complexes are directly confirmed at 4.2 K by the EPR spectra, since they exhibit g_∞ signals at 2.55 and 2.58.[52,132] Other complexes such as $[Fe(T^cHxP)(HIm)_2]^+$ and $[Fe(T^cHxP)(1,2\text{-}Me_2Im)_2]^+$ also adopt the $(d_{xz}, d_{yz})^4(d_{xy})^1$ ground state at ambient temperature, since the pyrrole-H chemical shifts are 2.81 and 7.83 ppm, respectively, at 293 K.[121] Stabilization of the $(d_{xz}, d_{yz})^4(d_{xy})^1$ ground state of these complexes is ascribed to the highly ruffled structure of the porphyrin ring, which raises the energy level of the d_{xy} orbital by the a_{2u}–d_{xy} interaction to the point that is higher than the d_π orbitals. As shown in Eq. 12, low-spin complexes exist as an equilibrium mixture of two spin isomers. Thus, the chemical shifts of the pyrrole-H and *meso*-C signals are determined by Eq. 13. The pyrrole-H chemical shifts of 1.1 and 4.9 ppm observed in $[Fe(T^iPrP)(HIm)_2]^+$ and $[Fe(T^iPrP)(2\text{-}MeIm)_2]^+$, respectively, suggest that the population of the $(d_{xz}, d_{yz})^4(d_{xy})^1$ isomer is not exclusively large. There is no doubt that $[Fe(T^tBuP)(HIm)_2]^+$ should give a much purer $(d_{xz}, d_{yz})^4(d_{xy})^1$ type low-spin complex, since the presence of bulky *tert*-butyl groups at the *meso* positions should ruffle the porphyrin ring to the greatest extent. Unfortunately, insertion of iron into $H_2(T^tBuP)$ to form for example $Fe(T^tBuP)Cl$ seems to be difficult, as up to now there has been no report describing the formation of this very interesting complex. Probably, the narrow N_4 cavity expected for this highly ruffled porphyrin ring hampers the iron insertion reaction. However, there are a couple of examples of T^tBuP complexes having paramagnetic metal ions, such as $[Cu(T^tBuP)]$ and $[Mn(T^tBuP)(OAc)]$, which exhibit quite interesting properties caused by the deformed structure.[108,133]

2. *A Bis*-Tert-*Butylisocyanide Complex Adopting the* $(d_{xy})^2(d_{xz}, d_{yz})^3$ *Ground State*

The first example of a bis-^{t}BuNC complex adopting the $(d_{xy})^2(d_{xz}, d_{yz})^3$ ground state is the iron(III) diazaporphyrin, $[Fe(DAzP)(^tBuNC)_2]^+$.[134] This complex exhibits various unusual spectroscopic characteristics that have never been observed in other bis-^{t}BuNC complexes, such as $[Fe(OEP)(^tBuNC)_2]^+$. Table 13 lists the spectroscopic data of various bis-^{t}BuNC complexes, including $[Fe(DAzP)(^tBuNC)_2]^+$.[134] Figure 30 shows the Curie plots of the α-CH_2 and *meso*-H signals of $[Fe(DAzP)(^tBuNC)_2]^+$ and $[Fe(OEP)(^tBuNC)_2]^+$, which strongly indicate the difference in electronic structure of these complexes.[134] The major spectroscopic differences are as follows: (i) the α-CH_2 signals of $[Fe(DAzP)(^tBuNC)_2]^+$ and $[Fe(OEP)(^tBuNC)_2]^+$ are observed at δ = 17.8 and 7.6 ppm at 298 K, respectively, suggesting that $[Fe(DAzP)(^tBuNC)_2]^+$ has a sizable amount of spin density at the pyrrole C_β atoms; (ii) the *meso*-H signals of $[Fe(DAzP)(^tBuNC)_2]^+$ and $[Fe(OEP)(^tBuNC)_2]^+$ appear at δ = 19.2 and −37.7 ppm, respectively, indicating that the *meso*-C atom

Table 13. Spectroscopic data of some $[Fe(Por)(^tBuNC)_2]^+$.

Porphyrin (Por)	^{1}H NMR[a] $\delta_{tert\text{-}Bu}$ (ppm)	^{13}C NMR[a] δ_{meso} (ppm)	EPR g Values[b]	IR ν_{CN} (cm^{-1})[c]	Ground State[d]
DAzP	6.60[e]	21[e]	3.01 2.05 1.5[e]	2213[e]	d_π
OETPP	–2.84[f]	416[f]	2.29 2.25 1.92[f]	2195[e]	d_{xy}
OEP	–1.32[f]	491[f]	2.29 2.29 1.86[f]	2193[g]	d_{xy}
OMTPP	–2.70[f]	979[f]	2.20 2.17 1.95[f]	2193[e]	d_{xy}
TPP	–2.86[f]	997[f]	2.18 2.18 1.93[f]	2200[g]	d_{xy}
T^{n}PrP	–2.12[f]	Too broad[f]	2.16 2.16 1.95[f]	2190[e]	d_{xy}
T^{i}PrP	–2.36[f]	Too broad[f]	2.16 2.16 1.96[f]	2193[e]	d_{xy}

[a] δ ppm, CD_2Cl_2, 223 K. [b] CH_2Cl_2, 4–12 K. [c] CH_2Cl_2, 298. [d] d_π and d_{xy} indicate the $(d_{xy})^2(d_{xz}, d_{yz})^3$ and $(d_{xz}, d_{yz})^4(d_{xy})^1$ ground states, respectively. [e] Ref. 134. [f] Ref. 82. [g] Ref. 74.

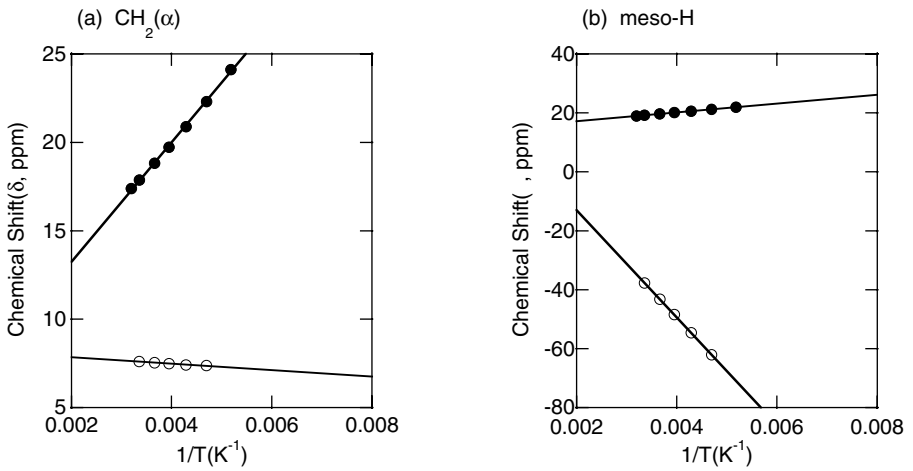

Figure 30. Curie plots of (a) $CH_2(\alpha)$ and (b) *meso*-H signals of $[Fe(DAzP)(^tBuNC)_2]^+$ (●) and $[Fe(OEP)(^tBuNC)_2]^+$ (○). (Adapted with permission from Ref. 134. Copyright 2006, Royal Society of Chemistry.)

of $[Fe(DAzP)(^tBuNC)_2]^+$ has a negative spin while that of $[Fe(OEP)(^tBuNC)_2]^+$ has a large positive spin; (iii) while the *meso*-C signal of $[Fe(DAzP)(^tBuNC)_2]^+$ appears upfield, at $\delta = 21$ ppm at 223 K, that of $[Fe(OEP)(^tBuNC)_2]^+$ appears significantly downfield, at $\delta = 491$ ppm; analysis of the isotropic shifts reveals that the spin densities at the *meso*-C atoms are –0.012 and +0.028 for $[Fe(DAzP)(^tBuNC)_2]^+$ and $[Fe(OEP)(^tBuNC)_2]^+$, respectively; (iv) the EPR spectrum of $[Fe(DAzP)(^tBuNC)_2]^+$ is rhombic while that of $[Fe(DAzP)(DMAP)_2]^+$ is axial. All these results strongly indicate that $[Fe(DAzP)(^tBuNC)_2]^+$ adopts the $(d_{xy})^2(d_{xz}, d_{yz})^3$ ground state despite the coordination of ^{t}BuNC.

The CN stretching frequency of the coordinating ^{t}BuNC in [Fe(DAzP)(^{t}BuNC)$_2$]$^+$ is 2213 cm^{-1}, which is higher by 13–20 cm^{-1} than the corresponding values for all the other bis-^{t}BuNC complexes as listed in Table 13. The higher frequency indicates stronger σ-bonding and/or weaker π-back-bonding in [Fe(DAzP)(^{t}BuNC)$_2$]$^+$ as compared with other bis-^{t}BuNC complexes.[135] A reasonable explanation is that because of the presence of two electronegative nitrogen atoms at the *meso* positions, the a_{2u}-like orbital in DAzP is stabilized as shown in Figure 20. As a result, the a_{2u}–d_{xy} interaction is weakened, which makes the iron(III) ion electron poor. Consequently, the σ-donation from ^{t}BuNC is strengthened and/or π-back-donation from iron(III) to the axial ligand is weakened, both of which contribute to the higher CN stretching frequency in [Fe(DAzP)(^{t}BuNC)$_2$]$^+$ compared with other bis-^{t}BuNC complexes.

Another interesting finding in Table 13 is the chemical shift of the *tert*-butyl signal. While [Fe(DAzP)(^{t}BuNC)$_2$]$^+$ exhibits its *tert*-butyl signal at 6.6 ppm at 223 K, all the other complexes exhibit the signal further upfield, −1 to −3 ppm. The large difference in chemical shifts can be explained in terms of the difference in dipolar shifts. In the case of coordinating *tert*-butyisocyanide, the major part of the methyl isotropic shift should come from the dipolar shift; the contribution of the contact shift should be negligibly small, since three σ-bonds separate the proton and nitrogen atoms. As shown in Eq. 2, the dipolar shift is given by $K_{dip}[(g_{\parallel}^2 - g_{\infty}^2)(3\cos^2\theta - 1)/r^3]/T$. Since the sign of $g_{\parallel}^2 - g_{\infty}^2$ is positive in the $(d_{xy})^2(d_{xz}, d_{yz})^3$ and negative in the $(d_{xz}, d_{yz})^4(d_{xy})^1$ type low-spin complex, the *tert*-butyl signal should appear downfield and the Curie slope should be positive if the complex adopts the $(d_{xy})^2(d_{xz}, d_{yz})^3$ ground state; note that the geometric factor $(3\cos^2\theta - 1)/r^3$ is positive for the *tert*-butyl protons. In contrast, the *tert*-butyl signal of the $(d_{xz}, d_{yz})^4(d_{xy})^1$ type complex appears somewhat upfield and the Curie slope should be negative since $(g_{\parallel}^2 - g_{\infty}^2)(3\cos^2\theta - 1)/r^3$ is negative. Thus, the chemical shift and the Curie slope of the *tert*-butyl signal can be good probes for the electronic structure of bis-^{t}BuNC complexes.[134] Figure 31 shows the Curie plots of the methyl signals in 11 kinds of bis-^{t}BuNC complexes.[82,134] It is evident that the methyl signal appears somewhat downfield and the Curie slope is positive only in [Fe(DAzP)(^{t}BuNC)$_2$]$^+$, which clearly indicate that the complex adopts the $(d_{xy})^2(d_{xz}, d_{yz})^3$ ground state despite the coordination of ^{t}BuNC.

It is interesting to elucidate the electronic structure of the corresponding monoazaporphyrin complex, [Fe(MAzP)(^{t}BuNC)$_2$]$^+$. This complex shows an NMR spectrum similar to that of [Fe(DAzP)(^{t}BuNC)$_2$]$^+$; notably, downfield-shifted $CH_2(\alpha)$, *meso*-H, and *tert*-butyl methyl signals.[136] Furthermore, the EPR spectrum taken in frozen CH_2Cl_2 solution shows three signals at g = 2.84, 2.26, 1.58. These data clearly indicate that the complex adopts the $(d_{xy})^2(d_{xz}, d_{yz})^3$ ground state. Thus, introduction of only one nitrogen atom into a *meso* position of

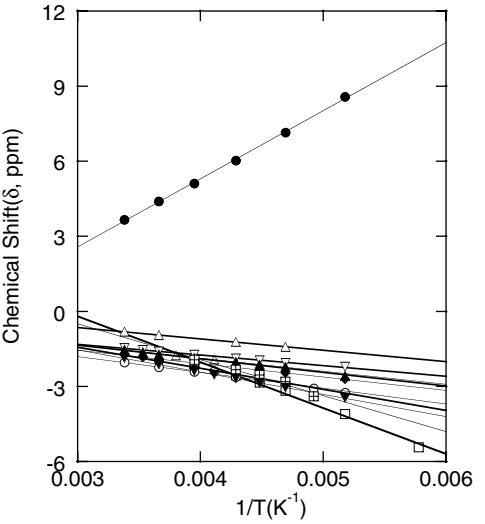

Figure 31. Curie plots of the methyl signals of coordinating ^{t}BuNC in various [Fe(Por)(^{t}BuNC)$_2$]$^+$ complexes. The methyl signal of [Fe(DAzP)(^{t}BuNC)$_2$]$^+$ is given by the symbol ●, the Curie plots of which clearly indicate the positive slope. Other porphyrins are OETPP, OMTPP, OEP, TMeP, TEtP, T^{n}PrP, T^{c}PrP, T^{i}PrP, ProtoIXMe$_2$, and TPP. The Curie plots of these complexes exhibit the negative slopes. (Adapted with permission from Ref. 134. Copyright 2006, Royal Society of Chemistry.)

[Fe(OEP)(^{t}BuNC)$_2$]$^+$ is sufficient to convert the electronic ground state from $(d_{xz}, d_{yz})^4(d_{xy})^1$ to $(d_{xy})^2(d_{xz}, d_{yz})^3$.

IV. Mixed High-Spin and Intermediate-Spin Complexes

A. General Considerations

Five-coordinate iron(III) porphyrin complexes, Fe(Por)X, with anionic axial ligands (X^-) such as chloride and methoxide, usually exhibit the high-spin (S = 5/2) state.[32–35,137–139] This is because the iron(III) ion deviates from the porphyrin plane in these complexes to stabilize the $d_{x^2-y^2}$ orbital. If axial chloride or acetate is replaced by a much weaker anionic ligand such as ClO_4,[140–147] $C(CN)_3$,[148,149] or SbF_6,[149] then the d_{z^2} orbital is stabilized and the $d_{x^2-y^2}$ orbital is destabilized.[32] The destabilization of the $d_{x^2-y^2}$ orbital is ascribed to contraction of the out-of-plane distance of iron.[32] As a result, these complexes are expected to adopt the intermediate-spin (S = 3/2) state. Actually, however, they exhibit not a pure S = 3/2 but a mixed S = 3/2, 5/2 spin state. The mixed S = 3/2, 5/2 spin state has been considered to be a quantum-mechanical admixture caused by spin–orbit coupling between the high-spin and intermediate-spin states, and not a thermal equilibrium

between two spin states.[147,150–153] However, some complexes have also been found that exhibit thermal equilibrium between the S = 3/2 and S = 5/2.[101,154–156] In this section, the spectroscopic properties of mixed S = 3/2 and S = 5/2 complexes will be described, together with the conditions for obtaining an essentially pure intermediate-spin complex.

B. Formation of Pure Intermediate-Spin Complexes

In general, formation of pure intermediate-spin complexes is quite difficult. In order to obtain this state, one has to expand the energy gap between the $d_{x^2-y^2}$ and d_{z^2} orbitals. Stabilization of the d_{z^2} orbital should be attained by coordination of the axial ligand with extremely weak field strength. Destabilization of the $d_{x^2-y^2}$ orbital is possible if an iron porphyrin with short Fe–N bonds is used.

1. *Axial Ligands with Extremely Weak Field Strength*

a. *Magnetochemical series*

^{1}H NMR spectroscopy is a good method for determining the contribution of the S = 3/2 in the mixed S = 3/2, 5/2 spin state.[20–31] This is because the pure high-spin complex exhibits its pyrrole-H signal fairly downfield due to the presence of an unpaired electron in the $d_{x^2-y^2}$ orbital; the unpaired electron in this orbital delocalizes to the pyrrole-H position through σ-bonds and induces a large downfield shift of the pyrrole-H signal. In contrast, the $d_{x^2-y^2}$ orbital is depopulated in the pure S = 3/2 complexes. As mentioned in Section II.B, the S = 1/2 complexes with the $(d_{xy})^2(d_{xz}, d_{yz})^3$ ground state exhibit pyrrole-H signals somewhat upfield due to the interaction between half-occupied d_π and fully occupied $3e_g$ orbitals. The pyrrole-H signals in the S = 3/2 complexes should appear even further upfield because they could have two unpaired electrons in both of the d_π orbitals. In fact, the chemical shift of the pyrrole-H signal in Fe(TPP)$[Ag(Br_6CB_{11}H_6)_2]$, which is considered to adopt an essentially pure intermediate-spin state, reaches –60 ppm.[36,156,157] If the chemical shifts of the pyrrole-H signals of the pure S = 5/2 and pure S = 3/2 complexes are determined to be δ_{high} and δ_{int}, respectively, then the contribution of the S = 3/2 spin state, signified as Int(%), in the analogous complex with the mixed S = 3/2, 5/2 spin state should be given by Eq. 17, where δ_x is the chemical shift of the pyrrole-H signal of the complex in question[80]:

$$\mathrm{Int}(\%) = \left[\frac{\delta_{\mathrm{high}} - \delta_x}{\delta_{\mathrm{high}} - \delta_{\mathrm{int}}} \right] \times 100. \tag{17}$$

It should be noted that Eq. 17 is valid if the chemical shift of the pyrrole-H signal is proportional to the contribution of the S = 3/2 state.

EPR spectroscopy is also a good method for determination of the spin state.[26,28–30,69] High-spin complexes exhibit a $g_\perp$ signal at 6.0, while the intermediate-spin complexes show the signal at 4.0. Depending on the contribution of the S = 3/2 in the mixed S = 5/2 and S = 3/2 complex, the $g_\perp$ value varies in the range between 4.0 and 6.0. Thus, the contribution of the intermediate-spin state, Int(%), is given by Eq. 18[69]:

$$\mathrm{Int}(\%) = \left[\frac{6.0 - g_\perp}{2}\right] \times 100. \tag{18}$$

On the basis of the pyrrole-H chemical shifts and EPR $g_\perp$ values, Reed and Guiset succeeded in ranking the weakness of anionic ligands (X) in five-coordinate Fe(TPP)X complexes, and denoted the hierarchy given in Eq. 19 as the *magnetochemical series*[36,157,158]:

$$\begin{aligned}[\mathrm{Ag(Br_6CB_{11}H_6)_2}]^- &< \mathrm{CB_{11}H_{12}^-} < \mathrm{SbF_6^-} < \mathrm{Co(C_2B_9H_{11})_2^-} < \mathrm{AsF_6^-} < \mathrm{ClO_4^-} \\ &< \mathrm{C(CN)_3^-} < \mathrm{CF_3SO_3^-} < \mathrm{BF_4^-} < \mathrm{ONC(CN)_2^-} < \mathrm{ReO_4^-} \\ &< \mathrm{OTeF_3^-} < \mathrm{I^-} < \mathrm{Br^-} < \mathrm{Cl^-}. \end{aligned} \tag{19}$$

The weakest anionic ligand is determined to be $[\mathrm{Ag(Br_6CB_{11}H_6)_2}]^-$, since the pyrrole-H signal is observed at the most upfield position, i.e. $\delta = -60$ ppm at 298 K. Moreover, Reed and coworkers have reported that $\mathrm{H(CHB_{11}Cl_{11})}$ is the strongest isolable acid presently known, which in turn indicates that $\mathrm{CHB_{11}Cl_{11}^-}$ is the weakest anionic ligand.[159] The magnetochemical series is also applicable to porphyrin isomers such as porphycene. The pyrrole signal of (TPrPc)FeX moves upfield as the axial ligand (X) changes from $\mathrm{PhO^-}$ to $\mathrm{Cl^-}$, $\mathrm{Br^-}$, $\mathrm{I^-}$, and then to $\mathrm{ClO_4^{-\bullet}}$, which corresponds to spin state change from S = 5/2 to S = 3/2.[160]

Six-coordinate iron(III) porphyrin complexes usually show the low-spin state. However, the complex can adopt a rare high-spin state if a neutral ligand has oxygen as the coordinating atom as exemplified by DMSO and DMF.[161–164] Fluoride is unique, because it can bind Fe(TPP)F to form $\mathrm{Fe(TPP)F_2^-}$.[165,166] These complexes commonly exhibit the pyrrole-H signals at extremely downfield positions, i.e. 70–90 ppm at 298 K. As in the case of five-coordinate complexes, the high-spin state is converted into the intermediate-spin state if the field strength of the oxygen ligand is weakened. Table 14 lists the ^{1}H and ^{13}C NMR chemical shifts as well as EPR g values for a series of $[\mathrm{Fe(TPP)L_2}]^+$, where L is an oxygen ligand.[167–169] The pyrrole-H signal moves upfield from 71 to 3 ppm as the axial ligand changes from 4-MePyNO to THF, demonstrating the increase in the S = 3/2 contribution.

Table 14. ^{1}H NMR, ^{13}C NMR, and EPR data of $[Fe(TPP)L_2]^+$.

	^{1}H NMR[a]				^{13}C NMR[a]			EPR[b]		
Ligand (L)	Pyrrole-H	*o*	*m*	*p*	C_α	C_β	*Meso*	*g* Values		
4-MePyNO	70.7	12.7	9.4	9.7	1625	1248	26	6.11	5.81	2.00
3,5-Me_2PyNO	71.0	12.8	9.4	9.7	1636	1249	29	5.85		2.00
PyNO	68.9	13.3	9.5	9.8	1617	1240	27	6.00		2.00
4-ClPyNO	67.2	13.2	9.7	9.9	1594	1218	25	5.85		2.00
DMSO	67.2	13.0	9.6	9.7	1538	1226	10	5.85		2.01
DMF	60.2	13.5	9.9	9.9	1474	1179	13	5.85		2.00
CH_3OH	48.1	13.8	10.1	10.0	1261	1024	37	5.69		2.00
THF	3.1	14.1	10.1	10.3	547	518	60	4.59		2.00
								6.03	5.48	2.00

[a]CD_2Cl_2, 298 K; [b] CH_2Cl_2, 4.2 K. (Source: Ref. 168.)

In Table 14, the axial ligands are arranged in descending order of the pyrrole-H chemical shifts, which therefore corresponds to the magnetochemical series for oxygen ligands given in Eq. 20:

$$\begin{aligned} &\text{THF} < \text{Et}_2\text{NNO} < \text{MeOH} < \text{DMF} < \text{DMSO} < \text{4-ClPyNO} \\ &\quad < \text{PyNO} < \text{3,5-Me}_2\text{PyNO, 4-MePyNO.} \end{aligned} \tag{20}$$

It should be noted that the C_α and C_β signals move upfield as the axial ligand changes from 4-MePyNO to THF. Similarly, the EPR $g_\perp$ value decreases in the same order. The order of the field strengths of some ligands, such as PyNO, substituted PyNOs, and DMSO, are difficult to determine from the data in Table 14 because of the similarity of the chemical shifts; the pyrrole-H and C_α signals are observed in a narrow range, 71.0–67.2 ppm and 1638–1538 ppm, respectively. The magnetochemical series of oxygen ligands given in Eq. 20 is determined on the basis of the pyrrole-H chemical shifts of both planar $[Fe(TPP)L_2]^+$ and ruffled $[Fe(T^iPrP)L_2]^+$, as will be described in detail in Section IV.B.2.a(ii). If the porphyrin is fixed in a series of $[Fe(Por)L_2]^+$, THF should be the best ligand for obtaining a six-coordinate complex where the contribution of the intermediate-spin state is the largest.[167–169]

b. *Four-coordinate iron(III) porphyrin cation*

As the field strength of the anionic axial ligand (X) is weakened in the magnetochemical series given in Eq. 18, the iron(III) ion in five-coordinate Fe(Por)X is brought to the center of the porphyrin ring. Consequently, the $d_{x^2-y^2}$ orbital is

greatly destabilized. In contrast, the Fe-X bond is elongated to stabilize the d_{z^2} orbital. The limiting case is the complex that has no axial ligand [i.e. four-coordinate iron(III) porphyrin cation]. Such a complex has been prepared recently by Suslick and coworkers.[170]

Treatment of Fe[2,6-(OSi^{i}Pr$_3$)$_2$-TPP]Cl with various silver salts AgY (Y = $CB_{11}H_6Br_6^-$, SbF_6^-, ClO_4^-, $CF_3SO_3^-$) yields a series of anion-exchanged complexes Fe[2,6-(OSi^{i}Pr$_3$)$_2$-TPP]Y, where the porphyrin has very bulky 2,6-bis(triisopropylsiloxy)phenyl groups at the *meso* positions. Surprisingly, CD_2Cl_2 solutions of these complexes exhibit pyrrole-H signals at exactly the same position, i.e. −81 ppm at 290 K. The anions examined in this study are very different within the magnetochemical series. In fact, the pyrrole-H chemical shifts of Fe(TPP)Y are −60, −31.5, −13, and 39.3 ppm for $CB_{11}H_6Br_6$, SbF_6, ClO_4, and CF_3SO_3, respectively. Thus, the anomalous result indicates that the complexes are four-coordinate iron(III), where iron(III) adopts the pure intermediate-spin state. In fact, the crystal structure of Fe[2,6-(OSi^{i}Pr$_3$)$_2$-TPP]($CB_{11}H_6Br_6$) confirms the absence of an axial ligand. The average Fe–N bond length is 1.94 ± 0.01 Å, with the iron situated in the porphyrin plane. Because of the bulky 2,6-bis(triisopropylsiloxy)phenyl groups at the *meso* positions, there are cavities above and below the porphyrin ring. The carborane anion ($CB_{11}H_6Br_6^-$) is located outside of the cavity. The solution magnetic moment determined by the Evans method is 4.1 μ_B in CH_2Cl_2 solution between 298 and 190 K, and the SQUID data show no change between 300 and 10 K. EPR spectra show a signal at $g_\perp = 4.2$ in both frozen solution and the crystalline state. The Mössbauer spectra obtained at 6 K show an IS value of 0.33 mm/s, which is typical of intermediate-spin complexes. But the complex shows a very large QS value which reaches 5.16 mm s^{-1}.[171–173] All these data clearly indicate that Fe[2,6-(OSi^{i}Pr$_3$)$_2$-TPP]($CB_{11}H_6Br_6$) is the first example of a four-coordinate iron(III) porphyrin that adopts an essentially pure intermediate-spin state.

As mentioned earlier, the pyrrole-H signal of this complex appears at −81 ppm, which is more upfield by 13–20 cm^{-1} than another essentially pure intermediate-spin Fe(TPP)($CB_{11}H_6Br_6$).[36,157,158] The results suggest that the pyrrole-H chemical shifts are different even among pure intermediate-spin complexes, probably because of the difference of the out-of-plane distance of the iron(III) ion from the N_4 plane. Thus, Eq. 16 should be carefully applied to five-coordinate complexes because the pyrrole-H chemical shifts are determined not only by the contribution of the intermediate-spin state but also by the out-of-plane distance of the iron(III) ion.

2. *Deformation of the Porphyrin Ring*

As mentioned earlier, the destabilization of the $d_{x^2-y^2}$ and stabilization of the d_{z^2} orbital are the necessary conditions for obtaining intermediate-spin complexes.

Since the deformation of the porphyrin ring usually contracts the Fe–N bond length,[32–35] it should raise the energy level of the $d_{x^2-y^2}$ orbital. Consequently, the electronic structure is perturbed by the ring deformation. Since the typical modes for deformation are ruffled and saddled, in this section it will be discussed how such deformation affects the spin state in the mixed S = 5/2 and S = 3/2 spin system.

a. *Ruffled deformation*

i. Five-coordinate complexes

Ruffling of the porphyrin ring affects the energy levels of the iron d orbitals. As mentioned in Sections II.A and II.B, the d_{xy} orbital can interact with the porphyrin a_{2u} orbital in the ruffled porphyrin framework. Consequently, the d_{xy} orbital is lifted in the energy diagram. The $d_{x^2-y^2}$ orbital is also lifted, due to the contraction of the equatorial Fe–N bonds, which is commonly observed in highly ruffled iron(III) porphyrin complexes.[35] Because of the destabilization of the $d_{x^2-y^2}$ orbital, the ruffled complexes tend to adopt the intermediate-spin state. Figure 32 shows the ^{1}H NMR spectra of a series of five-coordinate Fe(TEtPrP)X.[80] The upfield shift of the pyrrole-H signal is clearly seen as the axial ligand changes from Cl^- to I^-, and then to ClO_4^-. Table 15 lists the ^{1}H NMR chemical shifts of Fe(TEtPrP)X and the structurally analogous Fe(T^{i}PrP)X.[80] Figure 33 shows the Curie plots of the

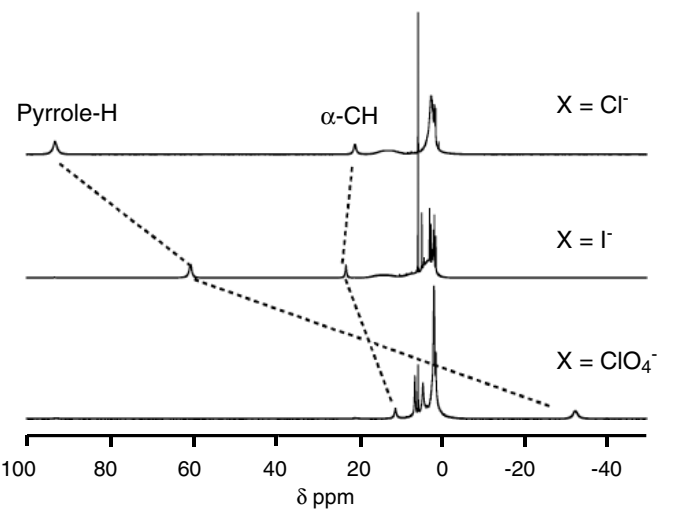

Figure 32. ^{1}H NMR spectra of a series of [Fe(TEtPrP)X] taken in CD_2Cl_2 solution at 298 K. (Adapted with permission from Ref. 80. Copyright 2004, American Chemical Society.)

Table 15. ^{1}H NMR and EPR data of [Fe(TEtPrP)X] and [Fe(T^{i}PrP)X].

	^{1}H NMR[a]			EPR[c]			
Complex X	Pyrrole-H	CH_α	Int(%)[b]	g_1	g_2	g_3	Int(%)[d]
[Fe(TEtPrP)X]							
F	97.0	15.8	0	5.92	5.92	1.99	4
Cl	93.1	20.5	3	6.11	5.90	2.00	0
Br	85.2	22.2	9	5.95	5.93	1.99	3
I	60.4	22.7	28	5.50	3.02	1.80	87
I[e]	85.1	23.5	9	5.94	5.94	2.01	3
ClO_4	−32.8	10.8	100	4.09	4.09	1.98	96
[Fe(T^{i}PrP)X]							
F	97.1	22.3	0	5.95	5.95	2.00	3
Cl	90.4	28.3	5	6.16	5.71	2.00	3
Br	73.9	28.8	18	5.92	5.92	1.99	4
I	20.7	22.8	60	5.34	3.02	1.85	91
ClO_4	−31.2	13.8	100	4.90	3.50	1.90	90

[a]CD_2Cl_2, 298 K. [b]Determined on the basis of the pyrrole-H chemical shifts at 298 K. [c]CH_2Cl_2, 4.2 K. [d]Determined on the basis of the EPR g values at 4.2 K. [e]In toluene-d_8 solution. (Source: Ref. 80.)

pyrrole-H signals of Fe(TEtPrP)X and Fe(T^{i}PrP)X.[80] The Curie lines are drawn so that they intercept the ordinate axis at the chemical shifts of the corresponding diamagnetic complexes, *ca*. 9.5 ppm. In both Fe(TEtPrP)X and Fe(T^{i}PrP)X, the pyrrole-H signals of the F^- complexes appear in the most downfield position, δ = *ca*. 97 ppm at 298 K, and move further downfield linearly versus 1/*T*. The pyrrole-H signals of the Cl^- complexes show similar temperature dependence. These results suggest that the F^- and Cl^- complexes in both systems are in a pure high-spin state. By contrast, the pyrrole-H signals of the ClO_4^- complexes appear at the most upfield positions, −34 and −31 ppm, and move further upfield almost linearly versus 1/*T*. Thus, the ClO_4^- complexes are considered to be in an essentially pure intermediate-spin state. The pyrrole signals of the Br^- and I^- complexes appear between those of the F^- and ClO_4^- complexes, and their Curie lines exhibit considerable curvature. The results suggest that they are in the mixed S = 3/2 and S = 5/2 spin state and that the contribution of the S = 3/2 increases as the temperature is lowered. Thus, in the ruffled complexes, even the Br^- complexes exhibit considerable contribution of the S = 3/2 state. If we assume that the F^- and ClO_4^- complexes are in the pure S = 5/2 and S = 3/2 spin state, respectively, then the contribution of the S = 3/2, Int(%), can be estimated on the basis of the pyrrole-H chemical shifts by Eq. 17. As mentioned, the Int(%) value determined by Eq. 17 is an approximate value especially in the five-coordinate complexes because the

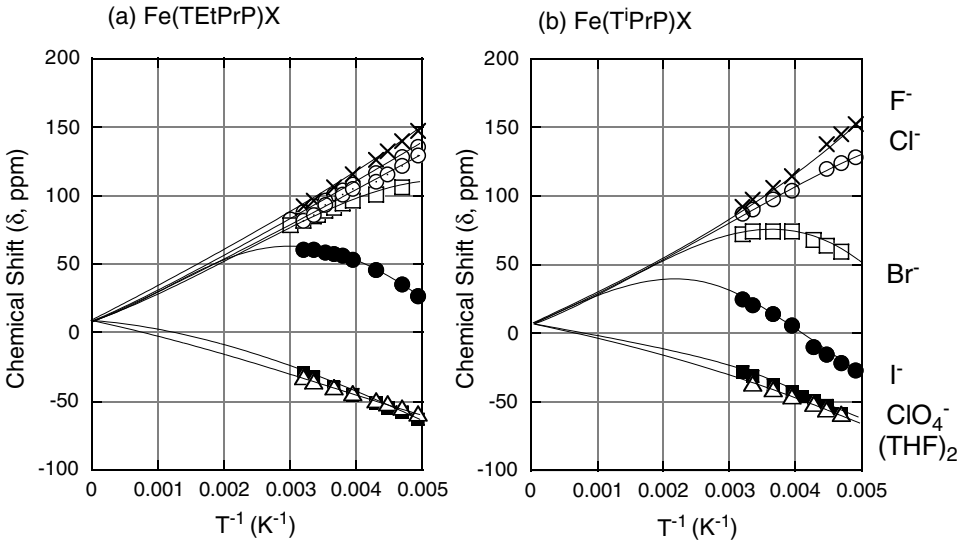

Figure 33. Curie plots of the pyrrole-H signals taken in CD_2Cl_2 solution: X = F (×), Cl (○), Br (□), I (•), ClO_4 (■), and $(THF)_2$ (Δ). Curie plots of [Fe (TEtPrP)I] determined in toluene-d_8 solution is given by ⊙. (Adapted with permission from Ref. 80. Copyright 2004, American Chemical Society.)

chemical shifts of the pyrrole-H signal in the pure high-spin or pure intermediate-spin complexes could change, depending on the out-of-plane distance of the iron(III) ion. The Int(%) values of [Fe(TEtPrP)X] and [Fe(TⁱPrP)X] listed in Table 15 indicate that they are very much dependent on the solvent used. While the Int(%) of [Fe(TEtPrP)I] is 28% at 298 K in CD_2Cl_2 solution, it is only 9% in toluene-d_8 solution at the same temperature.[80]

Figure 34 shows the EPR spectra of [Fe(TEtPrP)X] taken in frozen CH_2Cl_2 solution.[80] The EPR *g* values are listed in Table 15. Once these values are determined, it is possible to estimate the Int(%) values by using Eq. 18. The data in the table suggest that, while the F^-, Cl^-, and Br^- complexes are essentially in the high-spin state, I^- complexes such as [Fe(TEtPrP)I] and [Fe(TⁱPrP)I] are mainly in the intermediate-spin state with Int(%) values of 87% and 91%, respectively. Since the Int(%) values of [Fe(TEtPrP)I] and [Fe(TⁱPrP)I] are estimated by the ^{1}H NMR method to be 28% and 60% at 298 K, respectively, they increase as the temperature is lowered from 298 to 4.2 K. In contrast, the Int(%) values of the Br^- complexes seem to decrease with decreasing temperature.

The data in Table 15 also indicate that the Int(%) of [Fe(TEtPrP)I] varies depending on the conditions.[80] Although the complex exhibits a mixed S = 5/2 and S = 3/2 spin state in CH_2Cl_2 solution, it shows a pure S = 5/2 value both in toluene

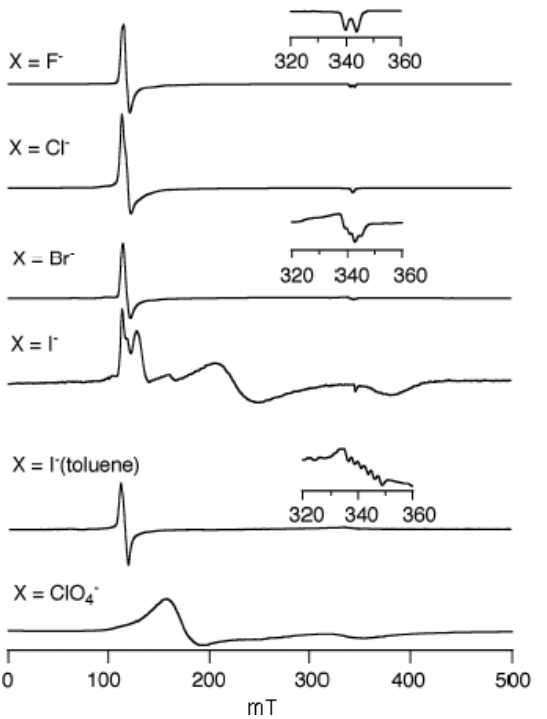

Figure 34. EPR spectra of a series of [Fe(TEtPrP)X] taken in frozen CH_2Cl_2 solution at 4.2 K. (Adapted with permission from Ref. 80. Copyright 2004, American Chemical Society.)

solution and in the solid state; the $g_\perp$ and $g_\parallel$ values are 5.94 and 2.01 in toluene solution and 5.98 and 2.05 (not shown in the table) in the solid state, respectively. The difference in spin states of [Fe(TEtPrP)I] in solution and in the solid state is not a very unusual phenomenon. For example, iodo(etiohemiporphycenato)iron(III) exhibits an S = 3/2 state with a minor contribution of S = 5/2 in solution.[174] The same complex shows, however, a quite pure S = 5/2 spin state in the solid. The difference is ascribed to the extraordinarily labile nature of the iodide ion in iodo(etiohemiporphycenato)iron(III). Thus, the iron is pulled toward the N_4 cavity in solution and, consequently, the complex adopts the intermediate-spin state. In the crystal lattice, however, packing forces could contract the labile Fe–I bond. Thus, the iron is lifted from the N_4 cavity toward the iodide, resulting in the formation of a typical high-spin five-coordinate structure. The difference in spin states of [Fe(TEtPrP)I] in solution and in the solid state could be explained similarly. The labile nature of the spin state mentioned above is one of the characteristics of the five-coordinate iron(III) porphyrin complexes, because similar lability in the spin state has been observed in five-coordinate iron(III) porphyrin complexes in biological systems such as cytochromes c′.[175]

ii. Six-coordinate complexes

Table 16 lists the ^{1}H and ^{13}C NMR chemical shifts, as well as EPR *g* values, of a series of six-coordinate $[Fe(T^{i}PrP)L_2]^+$.[168] The axial ligands are arranged according to the magnetochemical series for oxygen ligands shown in Eq. 18. Comparison of the ^{1}H NMR chemical shifts between $[Fe(TPP)L_2]^+$ and $[Fe(T^{i}PrP)L_2]^+$ listed in Tables 14 and 16, respectively, reveals that each pyrrole-H signal shifts upfield to a different extent on going from planar $[Fe(TPP)L_2]^+$ to ruffled $[Fe(T^{i}PrP)L_2]^+$. These results suggest that *the* S = 3/2 *character increases as the planar TPP is replaced by ruffled* $T^{i}PrP$, as in the case of the five-coordinated complexes. Consequently, the difference in pyrrole-H chemical shifts increases among the 4-MePyNO, PyNO, 4-ClPyNO, and DMSO complexes, which enables a ranking of the field strength for oxygen ligands, as shown in Eq. 20.

The ^{13}C NMR chemical shifts of the C_α and C_β signals correlate well with those of the pyrrole-H chemical shifts, suggesting that these signals can also be good probes of the contribution of the S = 3/2 spin state. In contrast, the chemical shifts of the *meso*-C signals exhibit a poor correlation.

The data in Tables 14 and 16 indicate that the complex with a highly ruffled porphyrin ring and a fairly weak oxygen ligand such as $[Fe(T^{i}PrP)(THF)_2]^+$ shows an essentially pure intermediate-spin state.[98,99,168] Figure 35 displays the molecular structure of (a) $[Fe(T^{i}PrP)(THF)_2]^+$ and (b) $[Fe(TEtP)(THF)_2]^+$.[176,177] The porphyrin ring of the former complex is highly ruffled. The average deviations of the *meso*-C atoms in $[Fe(T^{i}PrP)(THF)_2]^+$ and $[Fe(TEtP)(THF)_2]^+$ are 0.629 and 0.244 Å, respectively, and the average equatorial Fe–N bond lengths are 1.967 and

Table 16. ^{1}H NMR, ^{13}C NMR, and EPR data of $[Fe(T^{i}PrP)L_2]^+$.

	^{1}H NMR[a]			^{13}C NMR[a]			EPR[b]	
Ligand (L)	Pyrrole-H	CH	CH_3	C_α	C_β	*Meso*	*g* Values	
4-MePyNO	58.5	10.8	6.2	1262	1038	97	5.85	2.00
3,5-Me_2PyNO	57.6	10.9	6.3	1239	1015	97	5.70	2.00
PyNO	41.7	9.9	6.1	1031	865	110	5.70	2.00
4-ClPyNO	35.2	10.7	5.8	889	756	114	5.75	1.99
DMSO	–7.7	8.0	4.6	226	290	126	4.2	2.00
DMF	–21.5	7.3	4.2	24	138	145	4.2	2.00
MeOH	–28.3	7.3	n.d.	–47	86	142	4.1	2.00
THF	–35.5	5.7	4.9	–122	22	115	4.0	1.97
2-MeTHF	–37.3	6.4	5.7	–154	n.d.	127	4.1	2.00
Dioxane	–39.8	5.9	n.d.	–156	9	118	4.1	2.00

[a]CD_2Cl_2, 298 K; [b]CH_2Cl_2, 4.2 K. (Source: Ref. 168.)

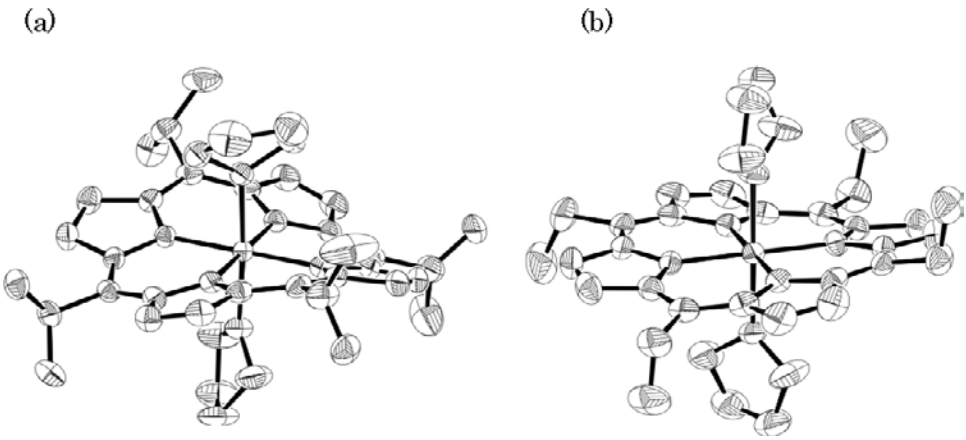

Figure 35. ORTEP diagrams of $[Fe(T^iPrP)(THF)_2]^+$ and $[Fe(TEtP)(THF)_2]^+$. (Adapted with permission from: (a) Ref. 176 and (b) Ref. 177. Copyright 2001, 1999, International Union of Crystallography.)

2.006 Å, respectively. As a result, the former adopts an essentially pure S = 3/2 spin state while the latter shows a mixed S = 5/2 and S = 3/2 spin state.[168,177] The average equatorial Fe–N bond lengths in planar complexes such as $[Fe(OEP)(THF)_2]^+$ and $[Fe(TPP)(THF)_2]^+$ are 1.999 and 2.040 Å, respectively.[178,179] Consequently, these complexes exhibit the mixed S = 5/2 and S = 3/2 spin state.

b. *Saddled deformation*

The saddled deformation of the porphyrin core also affects the energy levels of the 3d orbitals. Although the saddled deformation decreases the overlap between the iron $d_{x^2-y^2}$ orbital and the nitrogen lone pair for geometrical reasons, it should raise the energy level of the $d_{x^2-y^2}$ orbital since the interaction between and a_{2u} orbitals becomes symmetry-allowed in D_{2d} saddled complexes, as shown in Table 1.[42,43] In addition, the interaction should be enhanced because the Fe–N bonds in OETPP complexes are in general much shorter than those of the corresponding TPP complexes. The most explicit example showing the $d_{x^2-y^2}$–a_{2u} interaction is the cation radical, $[Cu(II)(OETPP^{\cdot})]^+$, reported by Fajer *et al.*[102] The complex exhibits sharp ^1H NMR lines, indicative of a diamagnetic species, which is ascribed to strong antiferromagnetic coupling between the half-occupied $d_{x^2-y^2}$ orbital and the half-occupied a_{2u} orbital.[103] Thus, the $d_{x^2-y^2}$ orbital can be destabilized in highly saddled complexes, which increases the contribution of the intermediate-spin state.

i. Five-coordinate complexes

Table 17 shows the ^{1}H NMR and EPR data of a series of five-coordinate Fe(OETPP)X, where X = F^-, Cl^-, Br^-, I^-, and ClO_4^-.[180,181] The Int(%) values estimated at 4.2 K by Eq. 17 clearly indicate that, while the F^- and Cl^- complexes are in the S = 5/2 state with a minor contribution of S = 3/2, the Br^- and I^- complexes adopt the S = 3/2 state with a minor contribution of S = 5/2. The ClO_4^- complex exhibits an essentially pure S = 3/2 spin state. It should be noted that the Int(%) values of ruffled Fe(TEtPrP)Br and Fe(T^{i}PrP)Br are 3% and 4%, respectively, while the Int(%) value is 89% in saddled Fe(OETPP)Br. Thus, *the saddled OETPP core stabilizes the S = 3/2 spin state more effectively than the corresponding ruffled T^{i}PrP core* if the axial ligands are the same. The possibility of the saddled porphyrin ring stabilizing the intermediate-spin state was first proposed by Cheng *et al.* in the discussion of the spin state of Fe(OETPP)Cl.[182] Although the Int(%) of Fe(OETPP)Cl is not as high as proposed,[183] saddled complexes such as Fe(OETPP)I are certainly in a pure intermediate-spin state in spite of the coordination of the halide, ion as Cheng *et al.* pointed out from the theoretical point of view.[183] Figure 36a shows the Mössbauer spectrum of Fe(OETPP)I taken for a microcrystalline sample at 77 K. The IS and QS values are 0.42 and 3.05 mm s^{-1}, respectively. The large QS value indicates that the complex is in the $S = 3/2$ spin state. Figure 36b shows the temperature dependence of the effective magnetic moments measured by SQUID magnetometry. The μ_{eff} values are 3.8–3.9 μ_B over a wide range of temperature, which are quite close to the spin-only value, 3.87 μ_B, expected for the S = 3/2 state. Thus, Fe(OETPP)I adopts a quite pure intermediate-spin state both in solution and in the solid state.[180]

Table 17. ^{1}H NMR and EPR data of Fe(OETPP)X together with Int(%) values.

	^{1}H NMR[a]						EPR[b]				
Complex	CH_2		CH_3	*o*	*m*	*p*	*g* Values			Int (%)	Ref.
Fe(OETPP)F	24.1	35.4	1.6	8.1	12.9	7.0	6.50	5.30	2.00	5	180
	38.4	45.0	3.7	10.6	13.1						
Fe(OETPP)Cl	20.1	32.1	1.8	9.1	12.2	7.5	6.56	5.27	1.97	4	180
	34.8	49.0	3.2	11.5	12.4						
Fe(OETPP)Br	18.1	32.6	1.0	10.4	11.7	8.4	4.95	3.50	1.95	89	180
	34.3	45.8	2.3	13.5	12.2						
Fe(OETPP)I	11.9	29.3	0.4	12.6	10.3	9.6	4.14	4.14	2.00	93	180
	32.1	47.3	0.9	15.8	10.8						
Fe(OETPP)ClO_4	13.0	42.7	0.7	13.4	7.1	9.8	4.05	4.05	2.1	98	181

[a]In CD_2Cl_2 at 298 K. [b]Frozen CH_2Cl_2 solutions at 4.2 K.

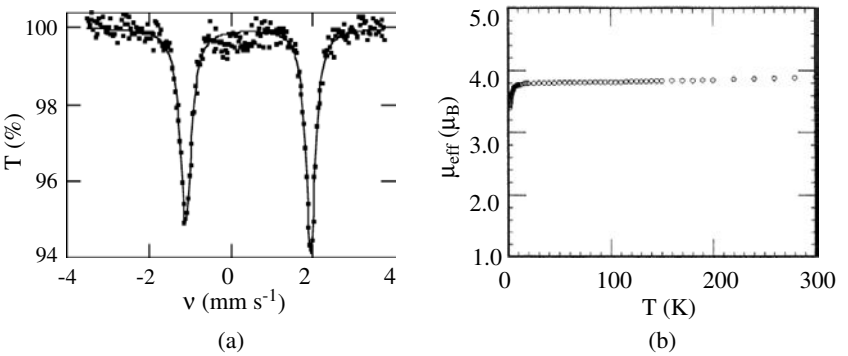

Figure 36. (a) Mössbauer spectrum of Fe(OETPP)I taken for a microcrystalline sample at 77 K. (b) Temperature dependence of the effective magnetic moments (μ_{eff}) measured by SQUID magnetometry. (Adapted with permission from Ref. 180. Copyright 2002, Royal Society of Chemistry.)

Table 18. ^{1}H NMR, ^{13}C NMR, and EPR data of $[Fe(OETPP)L_2]^+$.

	^{1}H NMR[a]						^{13}C NMR[a]			EPR[b]		
Ligand (L)	CH_2		CH_3	*o*	*m*	*p*	C_α	C_β	*Meso*	*g* Values		
4-MePyNO	21.0	44.2	2.4	14.7	8.7	10.3	598	601	–19	5.54		2.00
3,5-Me_2PyNO	18.6	43.8	2.4	14.7	8.4	10.4	504	498	–40	5.69		2.00
PyNO	20.0	43.8	2.2	15.3	7.4	10.6	555	512	–63	5.73	4.35	2.00
DMSO	15.4	39.2	0.9	17.2	7.4	10.6	485	398	–139	4.2		2.01
DMF	11.6	37.7	-0.1	15.8	6.1	11.4	419	250	–221	4.2		2.00
MeOH	11.7	37.0	0.3	15.8	5.9	11.5	409	239	–211	4.1		1.97
THF	11.0	38.7	0.3	15.8	5.6	11.5	394	215	–269	4.0		2.0

[a]CD_2Cl_2, 298 K; [b]CH_2Cl_2, 4.2 K. (Source: Ref. 168.)

ii. Six-coordinate complexes

The ^{1}H NMR, ^{13}C NMR, and EPR data of a series of six-coordinate $[Fe(OETPP)L_2]^+$ are listed in Table 18.[168] The complexes with weak axial ligands such as THF, MeOH, DMF, and DMSO exhibit $g_\perp$ signals from 4.0 to 4.2, suggesting that the complexes are in an essentially pure intermediate-spin state. These complexes commonly exhibit fairly upfield *meso*-C signals, which should be ascribed to the interaction between the filled a_{2u} and empty $d_{x^2-y^2}$ orbital in saddle-shaped complexes.[42,43] This interaction induces positive spin in the $d_{x^2-y^2}$ orbital, leaving the negative spin in the a_{2u} orbital by the spin polarization mechanism, and shifts the *meso*-carbon signal to an upfield position. In addition, the d_π–$3e_g$ interaction should also contribute to the upfield shift of the *meso*-carbon signals, especially when the complexes adopt the S = 3/2 state with the $(d_{xy})^2(d_{xz}, d_{yz})^2(d_{z^2})^1$ electronic

ground state because of the presence of two unpaired electrons in the d_π orbitals, as shown in Figure 3b.

C. Electronic Ground State in Intermediate-Spin Complexes

In the case of low-spin iron(III) porphyrins, it is now well established that there are two types of electronic ground states, i.e. $(d_{xy})^2(d_{xz}, d_{yz})^3$ and $(d_{xz}, d_{yz})^4(d_{xy})^1$. The complexes adopting the less common $(d_{xz}, d_{yz})^4(d_{xy})^1$ ground state almost always have highly ruffled structures. In contrast, the saddled structure tends to stabilize the $(d_{xy})^2(d_{xz}, d_{yz})^3$ ground state. Therefore, it is expected that even in the intermediate-spin complexes, there should be two different electronic ground states, $(d_{xz}, d_{yz})^3(d_{xy})^1(d_{z^2})^1$ and $(d_{xy})^2(d_{xz}, d_{yz})^2(d_{z^2})^1$ abbreviated as $S = 3/2(d_{xy})$ and $S = 3/2(d_\pi)$, respectively, as shown in Figure 3b. It seems to be quite natural, by analogy with the low-spin complexes, to assume that ruffled intermediate-spin $[Fe(T^iPrP)(THF)_2]^+$ should adopt the $S = 3/2(d_{xy})$ ground state while the saddled intermediate-spin $[Fe(OETPP)(THF)_2]^+$ should adopt the $S = 3/2(d_{xy})$ ground state.[37]

Table 19 lists the ^1H and ^{13}C NMR chemical shifts of ruffled and saddled low-spin and intermediate-spin complexes. The isotropic shifts of these complexes are also listed in bold. As the data in the table indicate, both the ^1H NMR and ^{13}C NMR data are totally different between ruffled and saddled complexes even if the spin state is the same, which in turn indicates that the electronic ground state could be different between ruffled and saddled complexes.[37,98,168] Reed and Guiset reported that $Fe(TPP)(Br_6CB_{11}H_6)$ is a pure intermediate-spin state, as is revealed from the presence of an extremely upfield-shifted pyrrole-H signal, i.e. −62 ppm.[157] In contrast, the pyrrole-H chemical shift is −31 ppm in $Fe(T^iPrP)ClO_4$ although the complex is also proven to be in an essentially pure intermediate-spin state.[37] On the basis of the large difference in pyrrole-H chemical shifts, *ca.* 31 ppm, between these two S = 3/2 complexes, Nakamura and coworkers proposed that highly ruffled intermediate-spin complexes such as $Fe(TEtPrP)ClO_4$ and $[Fe(T^iPrP)(THF)_2]^+$ should adopt the novel $S = 3/2$ (d_{xy}) ground state.[37] This is because the $S = 3/2(d_{xy})$ complexes have only one unpaired electron in the d_π orbitals; the presence of the unpaired electron in the d_π orbital is the major factor contributing to the upfield shift of the pyrrole-H signals. The electronic ground state mentioned above is further supported by the fact that the difference in pyrrole-H chemical shifts between low-spin $[Fe(T^iPrP)(4\text{-}CNPy)_2]^+$ and $[Fe(TPP)(HIm)_2]^+$ adopting $S = 1/2(d_{xy})$ and $S = 1/2(d_\pi)$, respectively, is also quite large, *ca.* 30 ppm.[52,82] The large difference can be explained in terms of the number of unpaired electrons in the d_π orbitals; $[Fe(T^iPrP)(4\text{-}CNPy)_2]^+$ has no unpaired electron in the d_π orbitals, while $[Fe(TPP)(HIm)_2]^+$ has one. Thus, $[Fe(T^iPrP)(THF)_2]^+$ is expected to be the first example of the intermediate-spin complex adopting the $S = 3/2(d_{xy})$ ground state.

Table 19. ^{1}H NMR and ^{13}C NMR chemical shifts and isotropic shifts[a] of some low-spin and intermediate-spin complexes.

	^{1}H NMR[b]							^{13}C NMR[b]									
Complexes	Pyrrole-H	Py-CH_2	Py-CH_2(ave)	Py-CH_3	*meso*-CH_a(*o*)	*meso*-CH_b(*m*)	*meso*-(*p*)	C_α	C_β	CH_2	CH_3	*meso*	*meso*-CH_α(*o*)	*meso*-CH_β(*m*)	*meso*-(*p*)	Spin State (S)	Ref.
[Fe(T^{n}PrP)	–12.2				5.1	–0.03		33	87			85	14	67		1/2(d_π)	52
$(HIm)_2]^+$	**–21.6**				**0.5**			**–108**	**–43**			**–32**	**–22**	**37**			
[Fe(T^{i}PrP)	13.6				31.4	7.0		–176	93			707	–166	315		1/2(d_{xy})	52
$(4\text{-CNPy})_2]^+$	**4.3**				**26.8**	**4.9**		**–317**	**–37**			**591**	**–202**	**293**			
[Fe(OETPP)		4.4 10.3	7.4	0.9	(5.0)	(5.8)	(6.7)	162	167	–24	87	7	(107)	(124)	(125)	1/2(d_π)	82
$(HIm)_2]^+$			**5.1**	**0.4**	**(–3.3)**	**(–1.9)**	**(–1.1)**	**15**	**23**	**–44**	**70**	**–112**	**(–29)**	**(–3)**	**(–3)**		
[Fe(OETPP)		7.5	7.5	1.3	(5.5)	(11.1)	(6.3)	–4	144	–0.5	59	418	(310)	(145)	(139)	1/2(d_{xy})	82
$(^t\text{BuNC})_2]^+$			**5.2**	**0.8**	**(–3.3)**	**(3.4)**	**(–1.5)**	**–152**	**–1**	**–22**	**42**	**298**	**(174)**	**(17)**	**(10)**		
[Fe(T^{i}PrP)	–35.5				5.7	4.9		–122	22			115	51	14		3/2	98
$(THF)_2]^+$	**–44.6**				**0.9**	**–2.8**		**–262**	**–111**			**–8**	**17**	**–15**			
[Fe(T^{i}PrP)	–38.7				9.0	4.4		–213	28			210	14	63		3/2	184
$(PhCHO)_2]^+$	**–47.8**				**4.2**	2.3		**–353**	**–103**			**88**	**–21**	**34**			
[Fe(OETPP)		11.1 38.7	24.9	0.3	(15.8)	(5.6)	(11.5)	394	215	–55	215	–269	(–74)	(118)	(116)	3/2	98
$(THF)_2]^+$			**22.6**	**–0.2**	**(7.49)**	**(–2.1)**	**(3.71)**	**247**	**71**	**–75**	**198**	**–388**	**(–210)**	**(–9)**	**(–12)**		
[Fe(OETPP)		13.7 42.0	27.9	–0.8	(16.5)	(5.3)	(12.1)	470	266	–56	203	–295	(–73)	(129)	(114)	3/2	100
$(4\text{-CNPy})_2]^+$			**24.9**	**–1.3**	**(8.19)**	**(–2.4)**	**(4.31)**	**323**	**122**	**–76**	**186**	**–414**	**(–209)**	**(2)**	**(–14)**		

[a]Isotropic shifts are determined on the basis of the chemical shifts of diamagnetic Ni(T^{n}PrP) and Zn(OETPP) and they are given in boldface. [b]Chemical shifts are determined in CD_2Cl_2 at 298 K.

The data in Table 19 indicate, however, that the isotropic shift of the *meso*-C signal of $[Fe(T^iPrP)(THF)_2]^+$ is negative, −8 ppm. Although it is more downfield than the corresponding value, −32 ppm, in $[Fe(T^nPrP)(HIm)_2]^+$ adopting the S = 1/2(d_π) state, it is much more upfield than the corresponding value, 591 ppm, in the $(d_{xz}, d_{yz})^4(d_{xy})^1$ type $[Fe(T^iPrP)(4\text{-}CNPy)_2]^+$. The outcome might be the suggestion that $[Fe(T^iPrP)(THF)_2]^+$ exists not as a pure S = 3/2(d_{xy}) complex but as a mixture of S = 3/2(d_{xy}) and S = 3/2(d_π) where S = 3/2(d_π) predominates over S = 3/2(d_{xy}). How can a much purer S = 3/2(d_{xy}) complex be obtained? In the case of low-spin complexes, the pure S = 1/2(d_{xy}) complex is obtained by the combination of a highly ruffled porphyrin and axial ligands with low-lying π^* orbitals. This is because ruffling of the porphyrin core raises the energy level of the d_{xy} orbital by way of the a_{2u}–d_{xy} interaction. Furthermore, axial ligands with low-lying π^* orbitals lower the d_π orbitals via the d_π–p_π^* interaction. Therefore, $[Fe(T^iPrP)(4\text{-}CNPy)_2]^+$ and $[Fe(T^iPrP)(^tBuNC)_2]^+$ are considered to be the purest examples of an S = 1/2(d_{xy}) complex.[52,82]

To obtain a much purer S = 3/2(d_{xy}) complex, it is necessary to use a weak oxygen ligand that has low-lying π^* orbitals. In Table 19 are added the NMR data of one such complex, $[Fe(T^iPrP)(PhCHO)_2]^+$.[184] This complex should adopt a much purer S = 3/2(d_{xy}) state, because benzaldehyde has a low-lying π^* orbital. The intermediate-spin state of this complex has been confirmed on the basis of EPR data; the g_∞ value is 4.1 in frozen CH_2Cl_2 solution at 4.2 K. In fact, the isotropic shift of the *meso*-C signal of $[Fe(T^iPrP)(PhCHO)_2]^+$ appears as high as +88 ppm. The positive and negative isotropic shifts of the *meso*-C and the *meso*-CH_α carbon signals, respectively, strongly indicate that the *meso*-C atoms have sizable amounts of positive spin, which in turn indicates that the d_{xy} orbital is half-occupied.

The S = 3/2(d_π) ground state in $[Fe(OETPP)(THF)_2]^+$ is supported by the isotropic shift of the pyrrole-CH_2 carbon signals. While the isotropic shift of this signal in $[Fe(OETPP)(THF)_2]^+$ is −75 ppm as listed in Table 19, it is only −44 ppm in $[Fe(OETPP)(HIm)_2]^+$. Since the isotropic shift of the pyrrole-CH_2 carbon signal is proportional to the spin density on the C_β atoms, this result indicates that the spin density on the C_β atoms in $[Fe(OETPP)(THF)_2]^+$ is nearly 1.8 times as high as that in $[Fe(OETPP)(HIm)_2]^+$, which in turn indicates that $[Fe(OETPP)(THF)_2]^+$ has two unpaired electrons in the d_π orbitals.[37]

Assignment of the electronic ground state of intermediate-spin complexes such as $[Fe(T^iPrP)(THF)_2]^+$ and $[Fe(OETPP)(THF)_2]^+$ is a good target for theoretical calculations. Cheng and coworkers reported, on the basis of DFT calculations, that $[Fe(T^iPrP)(THF)_2]^+$ and $[Fe(OETPP)(THF)_2]^+$ should adopt the S = 3/2(d_π) and S = 3/2(d_{xy}) states, respectively, which is an opposite assignment of the previously mentioned electronic ground states.[38] In the saddled complex, the calculation

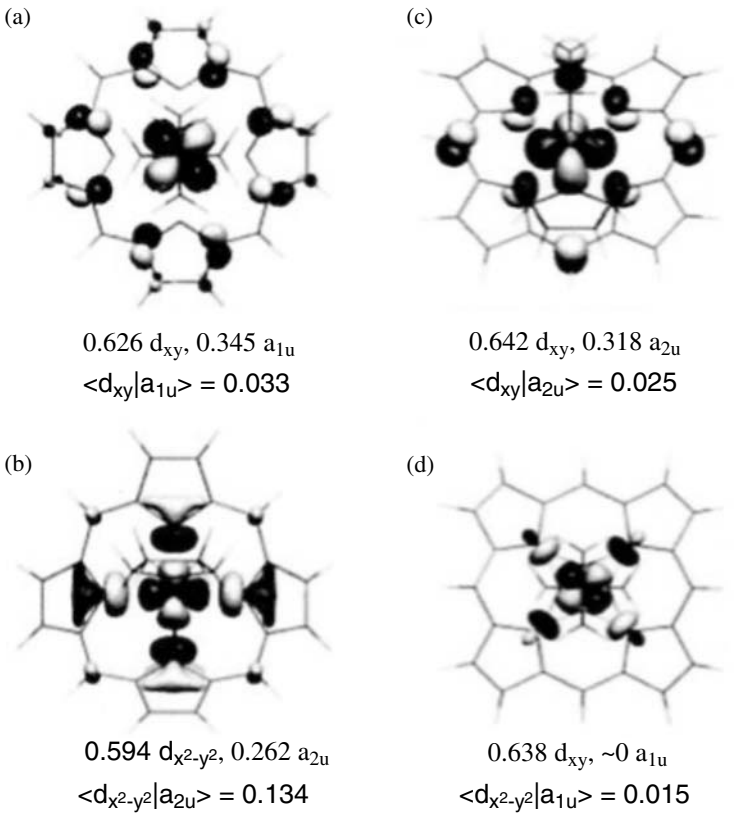

Figure 37. Bonding interactions between (a) d_{xy}–a_{1u}, (b) $d_{x^2-y^2}$–a_{2u} for saddled $[FeP(THF)_2]^+$, and the bonding interactions between (c) d_{xy}–a_{2u} and (d) $d_{x^2-y^2}$–a_{1u} for ruffled $[FeP(THF)_2]^+$. (Adapted with permission from Ref. 38. Copyright 2005, Royal Society of Chemistry.)

reveals the presence of two symmetry-allowed bonding interactions. One is a well-established interaction between a_{2u} and $d_{x^2-y^2}$ orbitals, and the other is the interaction between a_{1u} and d_{xy} orbitals. As shown in Figure 37, the bonding interaction between a_{1u} and d_{xy} orbitals in the saddled complex is unexpectedly strong; it is much stronger than the bonding interaction between a_{2u} and d_{xy} orbitals in a ruffled complex. As a result, the d_{xy} orbital in the saddled complex is lifted above the d_π orbital to form the $S = 3/2(d_{xy})$ electronic ground state. Table 20 shows the net spin population and the nuclear spin populations for each symmetry-distinct atom type for $[Fe(OETPP)(THF)_2]^+$ and $[Fe(T^iPrP)(THF)_2]^+$ with high-spin and two different intermediate-spin states, $S = 3/2(d_{xy})$ and $S = 3/2(d_\pi)$, obtained by spin-unrestricted ADF calculations.[38] As for saddled $[Fe(OETPP)(THF)_2]^+$, the data listed in Table 20 suggest that both $^4A_1$ and ^4E explain correctly the existence of extraordinarily upfield-shifted *meso*-C signals since both have large negative

Table 20. Net spin populations and the [nuclear spin populations] in the order of 10^{-4} on each symmetry-distinct atom type for bis-THF complexes from unrestricted DFT calculations.

$[Fe(OETPP)(THF)_2]^+$	$^6A_2$, S = 5/2		$^4A_1$, S = 3/2(d_π)		^4E, S = 3/2(d_{xy})	
meso-C	76	[3.8]	–232	[–26.6]	–384	[–52.2]
C_α	195	[46.5]	129	[3.3]	207	[42.6]
C_β	325	[75.2]	295	[31.7]	171	[17.8]
ipso-C	0	[9.6]	22	[7.7]	49	[25.4]
Pyrrole-CH_3	11	[5.5]	11	[4.7]	0	[–0.1]
	8	[2.5]	5	[1.1]	7	[3.1]
$[Fe(T^iPrP)(THF)_2]^+$	$^6A_2$, S = 5/2		$^4A_1$, S = 3/2(d_π)		^4E, S = 3/2(d_{xy})	
meso-C	387	[52.3]	–109	[–11.7]	583	[90.0]
C_α	28	[52.5]	125	[–13.7]	–120	[–38.6]
C_β	207	[73.7]	216	[8.7]	40	[–5.7]
meso-CH_α	–28	[–11.7]	5	[1.0]	–36	[–14.9]
Pyrrole-H	–2	[1.8]	–20	[–4.2]	–3	[–0.7]

Source: Ref. 38.

net spin populations on the *meso*-C atoms. However, the fact that C_α is more downfield-shifted than the C_β signal in saddled $[Fe(OETPP)(THF)_2]^+$ suggests that ^4E should be the leading contribution to this unusual intermediate-spin state complex.[38] DFT calculations also suggest that the intermediate-spin $[Fe(OETPP)(4\text{-}CNPy)_2]^+$ adopts the S = 3/2 (d_{xy}) rather than the S = 3/2(d_π) ground state.[117] As for ruffled $[Fe(T^iPrP)(THF)_2]^+$, the DFT calculations predict an extraordinarily large downfield shift for the *meso*-C signal if the complex adopts the ^4E, S = 3/2(d_{xy}) ground state. Thus, $[Fe(T^iPrP)(THF)_2]^+$ is concluded to adopt the $^4A_1$, S = 3/2(d_π) electronic ground state.[38]

Ling and Zhang have applied quantum-chemical calculations to predict the Mössbauer and NMR properties of various S = 3/2 iron(III) porphyrins with planar, ruffled, and saddled conformations.[39] The calculations correctly reproduced the Mössbauer QS and IS values as well as the ^1H and ^{13}C NMR chemical shifts. An interesting new observation is the dependence of d_{z^2} ordering on the Fe–N distance; the d_{z^2} orbital is relatively stabilized as the Fe–N_P bond distance decreases. Consequently, the d_{z^2} orbital is usually of the lowest energy due to a weaker interaction along the z-axis as compared to the stronger interactions in the *x*–*y* plane from the shorter Fe–N contact. Thus, the frontier iron MO orderings in S = 3/2 complexes are different from those reported previously if the Fe–N bond distance is less than 1.975 Å. The orbital ordering in ruffled $[Fe(T^iPrP)(THF)_2]^+$ is $d_{x^2-y^2} > d_\pi > d_{xy} > d_{z^2}$, while that in saddled $Fe(OETPP)ClO_4$ is $d_{x^2-y^2} > d_{xy} > d_\pi > d_{z^2}$. In the case of $[Fe(OETPP)(4\text{-}CNPy)_2]^+$ where the Fe–N distance is 1.975 Å, the orbital orderings become $d_{x^2-y^2} > d_{xy} > d_{z^2} > d_\pi$. Presence

or absence of the unpaired electron in the d_{z^2} orbital should affect the chemical shifts of the coordinating ligand. Thus, further systematic NMR experiments focusing on the chemical shifts of axial ligands together with theoretical studies are necessary in order to fully understand the electronic structure of the intermediate-spin complexes.

V. Spin Crossover in Iron(III) Porphyrins

A. General Considerations

The spin crossover phenomenon was first discovered in 1931 for iron(III) tris-dithiocarbamate complexes.[171–173,185–187] Since then many transition metal complexes showing thermal spin crossover phenomena have been found both in the solid state and in solution. Most of the complexes that exhibit the spin crossover phenomenon contain Fe(II), Fe(III), and to a lesser extent Co(II), Co(III), Mn(II), Mn(III), Ni(II), and Mo(II).[185–187] Among them, Fe(II) complexes have been most extensively studied because of their potential uses as electronic and optical switching and memory devices.[188] In the case of iron(III) porphyrins, there are three possible spin states: high-spin (S = 5/2), intermediate-spin (S = 3/2), and low-spin (S = 1/2) states. Thus, there should be three kinds of spin crossover processes; the ones between S = 5/2 and S = 1/2, between S = 3/2 and S = 1/2, and between S = 5/2 and S = 3/2, as shown in Figure 38.[30] The spin crossover process between S = 5/2 and S = 1/2 has been actively studied in six-coordinated complexes since its first observation in metmyoglobin by Beetlestone and George in 1964.[189] Since then ample examples have been reported in hemoproteins such as hemoglobin,[190] cytochrome P450,[191] cytochrome c peroxidase, etc.[192–194] As in the case of hemoproteins, spin crossover phenomena between S = 5/2 and S = 1/2 have been found

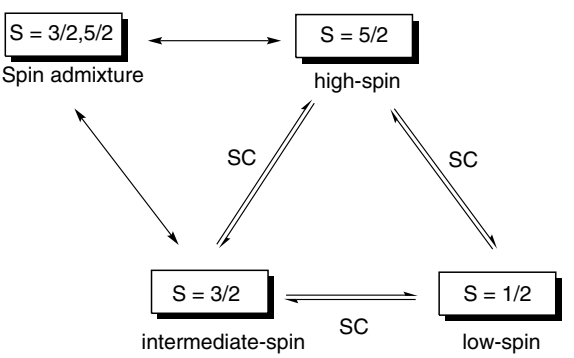

Figure 38. Possible spin crossover(SC) processes between two spin states. (Adapted with permission from Ref. 30. Copyright 2006, Elsevier Science.)

also in synthetic iron(III) porphyrins. Typical examples are azide complexes such as $[Fe(OEP)(3\text{-}ClPy)_2]^+$ and $[Fe(TPP)(N_3)_2]^-$ reported by Scheidt *et al.*,[195,196] and $[Fe(Por)(N_3)(1\text{-}MeIm)]$ reported by Neya *et al.*,[197,198] (Note: Por indicates various porphyrin isomers, such as corrphycene, porphycene, and hemiporphycene.)[199] Each porphyrin isomer has a unique size and shape of the cavity surrounded by the four pyrrole nitrogen atoms. Thus, the electronic and magnetic properties of these complexes are specific.[200–203] In mixed azide and imidazole complexes, $[Fe(Por)(N_3)(1\text{-}MeIm)]$, corrphycene stablizes the high-spin state while porphycene and hemiporphycene stabilize the low-spin state.[198]

On the other hand, the spin crossover between S = 3/2 and S = 1/2 had not been observed in iron porphyrins until recently, although two examples have been reported in iron(III) complexes without a porphyrin ligand. They are $[Fe^{III}(TMC)(NO)](BF_4)_2$ and $[Fe^{III}(L\text{-}N_4Me_2)(S_2C_6H_4)](ClO_4)\oplus 0.5H_2O$,[204,205] where TMC, L-$N_4Me_2$, and $S_2C_6H_4$ are 1,4,8,11-tetramethyl-1,4,8,11-tetraazacyclotetradecane, *N*,*N*′-dimethyl-2,11-diaza[3.3](2,6) pyridinophane, and 1,2-benzendithiolate, respectively. The first example of an iron(III) porphyrin complex to show spin crossover between S = 3/2 and S = 1/2 was observed by Ikeue and coworkers in highly saddled $[Fe(OETPP)L_2]^+$ having a nitrogen base such as Py or 4-CNPy as an axial ligand (L).[100,200]

It has long been considered that the mixed S = 3/2 and S = 5/2 is not a thermal equilibrium between S = 3/2 and S = 5/2 but a quantum mechanical spin admixture caused by spin–orbit coupling between the two spin states.[150,151] In other words, the thermal spin crossover between S = 3/2 and S = 5/2 does not exist in principle. In fact, all the mixed S = 3/2 and S = 5/2 complexes exhibited averaged NMR and EPR signals. However, several examples have been reported that have to be explained in terms of a spin crossover between S = 3/2 and S = 5/2.[101,154–156] Understanding the mechanism for the spin crossover processes is quite important, since they take place in various biological processes.[190–194,206–208] In this section, we will first describe complexes that exhibit the rare spin crossover processes between S = 3/2 and S = 1/2. We will then introduce a couple of new complexes that exhibit the spin crossover between S = 5/2 and S = 3/2.

B. Spin Crossover Between S = 3/2 and S = 1/2

1. *$[Fe(OETPP)L_2]^+$*

Six-coordinate complexes with a nitrogen base such as imidazole or pyridine usually show a low-spin state. As mentioned in the previous section, saddle-shaped complexes tend to stabilize the intermediate-spin state. Examples are [Fe(OETPP)I],[180] $[Fe(OETPP)ClO_4]$,[181] and $[Fe(OETPP)(THF)_2]^+$.[98] As listed in Tables 17 and 18,

Table 21. ^{1}H NMR chemical shifts of $[Fe(OETPP)L_2]^+$ and $[Fe(OMTPP)L_2]^+$ taken in CD_2Cl_2 solution at 298 K and 193 K.

	^{1}H NMR				^{13}C NMR		
Complex Ligand (L)	Pyrrole-CH(α)	*o*-H	*m*-H	*p*-H	*Meso*	C_α	C_β
$[Fe(OETPP)L_2]^+$	298 K						
DMAP	4.8 11.8	5.4	5.9	6.9	3	168	176
Py	11.1 32.3	13.0	5.8	10.4	–186	384	244
4-CNPy	13.7[a] 41.8	16.5[a]	5.3	12.1	–295	470	266
THF	11.1 38.7	15.8	5.6	11.5	–236[a]	394	215
^{t}BuNC	7.5	5.5	11.1	6.3	419	–4	144
	193 K						
DMAP	2.6 13.1	1.2	4.2	5.5	–53	122	159
Py	6.5 23.7	4.8	4.8	6.8	–88	224	211
4-CNPy	14.6[a] 64.3	21.1[a]	3.6	14.6	–500	664	328
THF	25.7 59.8	11.1	4.4	13.6	–291	n.d.	n.d.
^{t}BuNC	5.6 18.1	6.7	11.4	6.8	341	74	137
$[Fe(OMTPP)L_2]^+$	298 K						
DMAP	19.7	5.3	6.4	6.7	48	110	164
Py	48.6	10.8	7.2	9.1	–9	205	214
4-CNPy	63.9	13.2	6.8	3.6	–68	243	242
THF	62.0	11.6	6.6	4.4	–1	n.d.	n.d.
^{t}BuNC	1.4	3.1	12.8	11.4	701	–207	113
	193 K						
DMAP	21.8	2.1	5.0	5.5	3.4	50	147
Py	22.6	4.1	8.0	6.3	163	42	158
4-CNPy	36.9	7.5	9.6	7.9	224	109	188
THF	91.3	17.6	5.9	12.1	–105	n.d.	n.d.
^{t}BuNC	–3.9	–0.2	16.3	3.6	1153[b]	–484	77

[a]Values are revised from the original ones. [b]Data obtained by the extrapolation from high temperature. (Source: Refs. 62 and 82.)

these complexes adopt an essentially pure intermediate-spin state. It is then expected that even the complexes carrying nitrogen bases with a weak-field ligand should exhibit a quite pure intermediate-spin state if the porphyrin is highly saddled. Table 21 lists the ^{1}H and ^{13}C NMR chemical shifts of $[Fe(OETPP)L_2]^+$ and $[Fe(OMTPP)L_2]^+$, where Ls are nitrogen bases such as DMAP, Py, and 4-CNPy.[62,100] The chemical shifts of $[Fe(OETPP)(THF)_2]^+$ and $[Fe(OETPP)(^tBuNC)_2]^+$,[82,98] which are well characterized as the intermediate-spin and low-spin complexes, respectively, are also listed for comparison. As the axial ligand changes from DMAP to Py, and then to 4-CNPy in Table 21, the CH_2, *o*-H, and *p*-H signals of $[Fe(OETPP)L_2]^+$ exhibit a downfield shift and approach the corresponding signals of $[Fe(OETPP)(THF)_2]^+$. In addition, the large upfield shift of the *meso*-C and the

downfield shift of the C_α signals of $[Fe(OETPP)(4\text{-}CNPy)_2]^+$ resemble those of $[Fe(OETPP)(THF)_2]^+$. These NMR results suggest that the spin state actually changes from S = 1/2 in the DMAP complex to S = 3/2 in the 4-CNPy complex. In fact, the solution magnetic moments of $[Fe(OETPP)(4\text{-}CNPy)_2]^+$ determined by the Evans method in CD_2Cl_2 solution are 4.2 ± 0.1 μ_B at 193–298 K, which is close to the spin-only value expected for the S = 3/2 complexes.[100]

It is interesting to compare the electronic structures of saddled $[Fe(OETPP)L_2]^+$ carrying nitrogen bases with those of the corresponding ruffled $[Fe(T^nPrP)L_2]^+$.[52,62,100] In the case of ruffled $[Fe(T^nPrP)L_2]^+$, all the complexes maintain the low-spin state although the electronic ground state changes from $(d_{xy})^2(d_{xz}, d_{yz})^3$ to $(d_{xz}, d_{yz})^4(d_{xy})^1$ on going from DMAP to Py, and then to 4-CNPy, as shown in Table 4.[52] In the case of saddled $Fe(OETPP)L_2^+$, however, while strong σ-donating and weak π-accepting ligands such as HIm and DMAP give a low-spin complex with the $(d_{xy})^2(d_{xz}, d_{yz})^3$ ground state, weak σ-donating and strong π-accepting ligands such as 4-CNPy form intermediate-spin complexes.[62,100] Thus, in the saddled complexes, *it is the spin state that changes depending on the field strength of the axially coordinating nitrogen ligands.*

The data in Table 21 indicate that the ^1H and ^{13}C signals of $[Fe(OETPP)Py_2]^+$ are located between those of low-spin $[Fe(OETPP)(DMAP)_2]^+$ and intermediate-spin $[Fe(OETPP)(4\text{-}CNPy)_2]^+$. These results suggest that low-spin and intermediate-spin $[Fe(OETPP)Py_2]^+$ coexist as an equilibrium mixture in CD_2Cl_2 solution at 298 K. Figure 39a shows the Curie plots of the CH_2–H signals of $[Fe(OETPP)L_2]^+$,

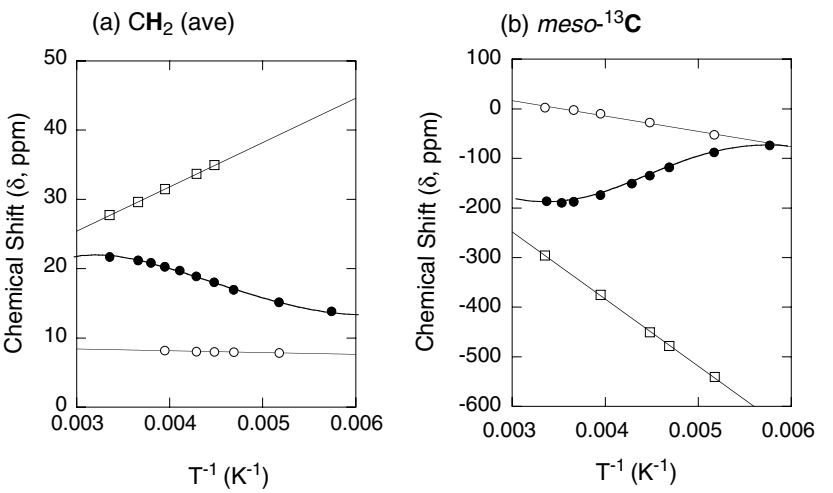

Figure 39. Curie plots of the (a) CH_2 and (b) *meso*-C signals of $[Fe(OETPP)(DMAP)_2]^+$ (★), $[Fe(OETPP)(Py)_2]^+$ (•), and $[Fe(OETPP)(4\text{-}CNPy)_2]^+$ (□). (Adapted with permission from Ref. 100. Copyright 2001, WILEY-VCH Verlag GmbH.)

where Ls are DMAP, Py, and 4-CNPy.[100] While the Curie plots of the DMAP and 4-CNPy complexes give good linearity, the Curie plots of the Py complex exhibit considerable curvature. A similar tendency is observed in the Curie plots of the *meso*-C signals shown in Figure 39b.[100] Although both the CH_2 and *meso*-C signals of the Py complex appear close to the corresponding signals of the 4-CNPy complex at ambient temperature, they approach those of the DMAP complex at lower temperature. The curvature of the Curie lines of $[Fe(OETPP)Py_2]^+$ clearly indicates that spin crossover takes place between S = 3/2 and S = 1/2. In contrast, $[Fe(OETPP)(DMAP)_2]^+$ and $[Fe(OETPP)(4\text{-}CNPy)_2]^+$ maintain the S = 1/2 state and the S = 3/2 spin state, respectively, in the temperature range examined. The equilibrium constant for the spin crossover process (K_{SC}) in CD_2Cl_2 solution is determined at several temperatures on the basis of the *meso*-C chemical shifts according to Eq. 20, where δ_{DMAP}, δ_{Py}, and $\delta_{4\text{-}CNPy}$ are the *meso*-C chemical shifts of the DMAP, Py, and 4-CNPy complexes, respectively:

$$S = \frac{1}{2} \underset{\longleftarrow}{\overset{K_{SC}}{\longrightarrow}} S = \frac{3}{2},$$
$$K_{SC} = \frac{S = \frac{3}{2}}{S = \frac{3}{2}} = \frac{\delta_{DMAP} - \delta_{Py}}{\delta_{Py} - \delta_{4-CNPy}}. \quad (20)$$

The plots of $\log(K_{SC})$ vs. $1/T$ show a good linearity from which the thermodynamic parameters are determined as follows: $\Delta H° = 17$ kJ mol^{-1} and $\Delta S° = 67$ J mol^{-1} K^{-1}. Although the spin crossover process between the S = 1/2 and S = 3/2 states is not unprecedented in iron(III) complexes,[204,205] $[Fe(OETPP)Py_2]^+$ is actually the first example in iron(III) porphyrin complexes.[100] It should be noted here that $[Fe(OETPP)Py_2]^+$ adopts the $(d_{xy})^2(d_{xz}, d_{yz})^3$ ground state at lower temperatures on the basis of the upfield-shifted *m*-H and *meso*-C signals listed in Table 21.

What are the magnetic properties of these complexes in the solid state? Table 22 lists the Mössbauer parameters of a series of $[Fe(OETPP)L_2]^+$ measured at ambient and liquid nitrogen temperatures.[98] At ambient temperature, the QS value of $Fe(OETPP)(DMAP)_2^+$ is 2.21 mm s^{-1}, which is within the range of the low-spin state. In contrast, the QS value of $[Fe(OETPP)(4\text{-}CNPy)_2]^+$ is quite large, 3.26 mm s^{-1}, and is close to that of $[Fe(OETPP)(THF)_2]^+$, suggesting that this complex adopts the intermediate-spin state. The QS value of $[Fe(OETPP)Py_2]^+$ is 2.76 mm s^{-1}, which is between the QS values of the DMAP and 4-CNPy complexes. Thus, the Py complex exists as a mixture of the S = 3/2 and the S = 1/2 spin states at ambient temperature in the solid. As the temperature is lowered to 80 K, the QS value of the DMAP complex is maintained while that of the Py complex decreases to 2.26 mm s^{-1}. These results indicate that the Py complex adopts predominantly

Table 22. Mössbauer parameters and spin states of $[Fe(OETPP)L_2]^+$ and $[Fe(OMTPP)L_2]^+$.

Complex Ligand(L)		T / K	IS / mm s^{-1}	QS / mm s^{-1}	Γ_1 / mm s^{-1}	Γ_2 / mm s^{-1}	Spin State
$[Fe(OETPP)L_2]^+$							
DMAP		290	0.19	2.21	0.27	0.32	1/2
		80	0.26	2.31	0.55	0.89	1/2
Py		290	0.32	2.76	0.27	0.29	1/2,3/2
		80	0.25	2.29	0.47	0.64	1/2
4-CNPy	Site A	295	0.37	3.26	0.32	0.33	3/2
	Site A	80	0.57	3.03	0.47	0.47	3/2
	Site B	80	0.20	2.70	0.64	0.64	1/2
THF		290	0.41	3.65	0.32	0.26	3/2
		80	0.50	3.50	0.77	0.49	3/2
$[Fe(OMTPP)L_2]^+$							
DMAP		290	0.16	1.86	0.30	0.33	1/2
		70	0.23	1.89	0.38	0.54	1/2
Py		299	0.19	2.18	0.23	0.26	1/2
		78	0.25	2.18	0.33	0.42	1/2

Source: Refs. 100 and 209.

the low-spin state at 80 K. In the case of the 4-CNPy complex, two doublets (sites A and B) appear below 230 K. Since the IS and QS values for sites A and B are in the range of intermediate-spin and low-spin states, respectively, the complexes with different spin states coexist at low temperature. Thus, a rare spin crossover occurs even in $[Fe(OETPP)(4\text{-}CNPy)_2]^+$ in the solid state. Figure 40 shows the effective magnetic moments (μ_{eff}) measured on microcrystalline samples with a SQUID magnetometer over 2–300 K. The results confirm that the DMAP complex is in the low-spin state while the THF complex is in the pure intermediate-spin state over a wide range of temperatures.[100] Figure 40 also indicates that a major part of the Py complex is in the S = 1/2 state below 150 K, though the population of the S = 3/2 ground state considerably increases above this temperature. Similarly, the 4-CNPy complex is a mixture of the S = 1/2 and S = 3/2 states below 200 K though it exists almost exclusively as the S = 3/2 above 200 K. On the basis of the Mössbauer and SQUID results, it is clear that *not only* $[Fe(OETPP)Py_2]^{\pm}$ *but also* $[Fe(OETPP)(4\text{-}CNPy)_2]^{\pm}$ *exhibits the spin crossover process in the solid state.*

2. $[Fe(OMTPP)L_2]^+$ and $[Fe(TBTXP)L_2]^+$

Figure 41 shows the Curie plots of (a) the CH_3–H and (b) the *meso*-C signals of $[Fe(OMTPP)L_2]^+$, where L is DMAP, Py, 4-CNPy, THF, and ^{t}BuNC.[62] Among

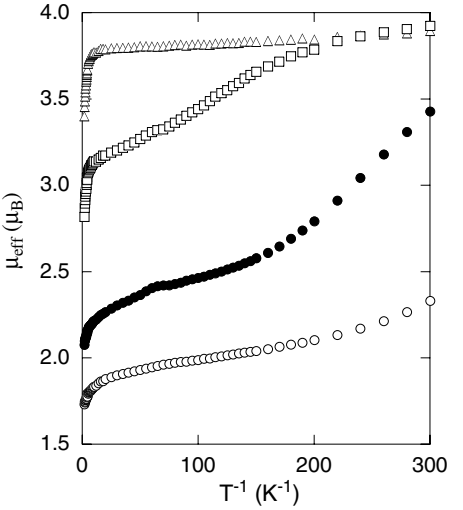

Figure 40. Temperature dependence of the effective magnetic moments of $[Fe(OETPP)L_2]^+$. L = DMAP (○); Py (●); 4-CNPy (□); and THF(Δ). (Adapted with permission from Ref. 100. Copyright 2001, WILEY-VCH Verlag GmbH.)

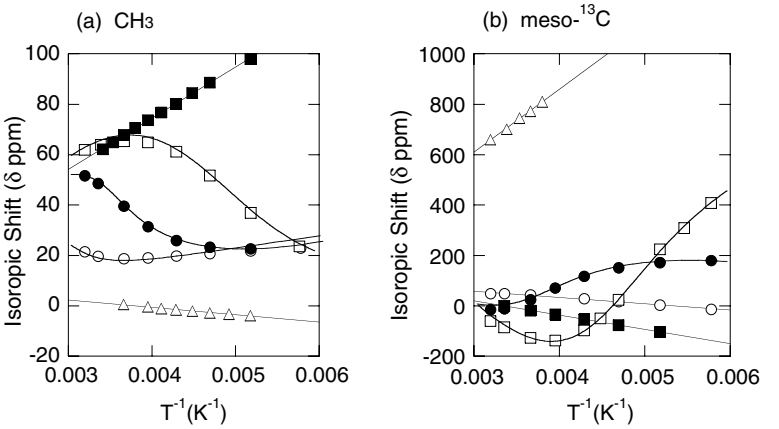

Figure 41. Curie plots of the (a) CH_3–H and (b) *meso*-^{13}C signals of $[Fe(OMTPP)(DMAP)_2]^+$ (○), $[Fe(OMTPP)(Py)_2]^+$ (●), $[Fe(OMTPP)(4\text{-}CNPy)_2]^+$ (□), $[Fe(OMTPP)(THF)_2]^+$ (■), and $[Fe(OMTPP)(^tBuNC)_2]^+$ (Δ). (Adapted with permission from Ref. 62. Copyright 2003, American Chemical Society.)

these complexes, $[Fe(OMTPP)(THF)_2]^+$ shows a good linearity, suggesting that the complex is in a quite pure S = 3/2 spin state. Similarly, the Curie plots of the *meso*-C signals of both $[Fe(OMTPP)(DMAP)_2]^+$ and $[Fe(OMTPP)(^tBuNC)_2]^+$ exhibit good linearity with negative and positive slopes, respectively, suggesting

that the former adopts S = 1/2 with the $(d_{xy})^2(d_{xz}, d_{yz})^3$ ground state while the latter adopts S = 1/2 with the $(d_{xz}, d_{yz})^4(d_{xy})^1$ ground state.[62] In contrast, the Curie plots of $[Fe(OMTPP)Py_2]^+$ and $[Fe(OMTPP)(4\text{-}CNPy)_2]^+$ shown in Figure 41a exhibit a curvature, suggesting that the spin crossover takes place between S = 3/2 and S = 1/2 in both of these complexes. Inspection of the Curie lines for the *meso*-C signals shown in Figure 41b reveals, however, that the magnetic behaviors of $[Fe(OMTPP)L_2]^+$ (L = Py and 4-CNPy) are quite different from those of $[Fe(OETPP)L_2]^+$ (L = Py). As the temperature is lowered, the Curie line of $[Fe(OMTPP)(4\text{-}CNPy)_2]^+$ (□) moves away from that of $[Fe(OMTPP)(DMAP)_2]^+$ (○) and approaches that of $[Fe(OMTPP)(^tBuNC)_2]^+$ (Δ). Similar temperature dependence is observed for $[Fe(OMTPP)Py_2]^+$ (•), though the deviation from the Curie line of $[Fe(OMTPP)(DMAP)_2]^+$ (○) is much smaller. $[Fe(TBTXP)L_2]^+$ exhibits a similar curvature in Curie plots if L is Py or 4-CNPy though the spin crossover phenomenon from S = 3/2 to S = 1/2 starts at higher temperature. These results suggest that the spin crossover pathways of OMTPP and TBTXP complexes are different from those of OETPP complexes. *While the spin state of* $[Fe(OETPP)Py_2]^{\pm}$ *changes from* S = *3/2 to* S = *1/2 with the* $(d_{xy})^2(d_{xz}, d_{yz})^3$ *ground state as the temperature is lowered, that of* $[Fe(OMTPP)(4\text{-}CNPy)_2]^{\pm}$ *and* $[Fe(OMTPP)Py_2]^{\pm}$ *changes from* S = *3/2 to* S = *1/2 with the* $(d_{xz}, d_{yz})^4(d_{xy})^1$ *ground state.*[62]

What are the magnetic properties of $[Fe(OMTPP)L_2]^+$ in the solid state? Table 22 also shows the Mössbauer parameters of the DMAP and Py complexes.[209] The IS values increase from 0.16 to 0.23 mm s^{-1} in $[Fe(OMTPP)(DMAP)_2]^+$ and from 0.19 to 0.25 mm s^{-1} in $[Fe(OMTPP)(Py)_2]^+$ as the temperature is lowered from 290 to 77 K. In contrast, the QS values are almost constant in this temperature range; they are 1.86–1.90 mm s^{-1} for $[Fe(OMTPP)(DMAP)_2]^+$ and 2.13–2.18 mm s^{-1} for $[Fe(OMTPP)Py_2]^+$. Thus, these complexes maintain the low-spin state over a wide range of temperature. The low-spin state assignment of $[Fe(OMTPP)(DMAP)_2]^+$ and $[Fe(OMTPP)Py_2]^+$ is further supported by the effective magnetic moments determined by SQUID magnetometry; they are 2.1–2.8 μ_B in the temperature range of 50–300 K.[209] Thus, the magnetic behavior of $[Fe(OETPP)Py_2]^+$ and of $[Fe(OMTPP)Py_2]^+$ are quite different in the solid. *While* $[Fe(OETPP)Py_2]^{\pm}$ *shows a spin crossover between the S = 3/2 and S = 1/2 spin states,* $[Fe(OMTPP)Py_2]^{\pm}$ *maintains the* S = *1/2 spin state in the solid state.*[209]

3. $[Fe(MAzP)L_2]^{\pm}$ and $[Fe(OEP)L_2]^{\pm}$

Table 23 shows the ^1H NMR chemical shifts of (a) $[Fe(MAzP)L_2]^{\pm}$ and (b) $[Fe(OEP)L_2]^{\pm}$ taken in CD_2Cl_2 solution at 298 K (upper) and 223 K (lower).[136] Figures 42 and 43 show the Curie plots of the *meso*-H and CH_3 signals of some selected complexes, respectively.[136]

Table 23. ^{1}H NMR chemical shifts of $[Fe(MAzP)L_2]^{\pm}$ and $[Fe(OEP)L_2]^{\pm}$ taken in CD_2Cl_2 solution at 298 K (upper) and 223 K (lower).

Complex Ligand (L)	CH_2				CH_2 (Ave)	CH_3 (Ave)	*m*(1H)[a]	*m*(2H)[a]	*m* (Ave)
$[Fe(MAzP)L_2]^{\pm}$									
DMAP	6.38	6.38	6.89	7.10	(6.69)	(–0.63)	1.50[b]	2.41[b]	(2.11)
	4.86	5.03	6.21	6.45	(5.64)	(–2.59)	–5.43	6.45	(–3.93)
1-MeIm	6.57	6.68	7.38	7.70	(7.08)	(–0.42)	—	—	—
	5.53	5.53	7.99	8.35	(6.85)	(–1.65)	—	—	—
CN^-	5.78	6.03	6.47	6.73	(6.25)	(–1.59)	–0.20	1.90	(1.20)
	4.64	5.36	5.36	6.27	(5.41)	(–2.81)	–7.72	–3.78	(–5.09)
^{t}BuNC	14.17	14.44	14.61	15.32	(14.64)	(2.73)	9.79	11.47	(10.91)
	16.48	16.75	16.80	18.14	(17.04)	(4.28)	10.74	13.68	(12.70)
Py	10.27	10.60	10.93	11.26	(10.77)	(0.01)	2.82	4.17	(3.72)
	8.11	8.78	9.62	9.67	(9.05)	(–2.15)	–5.73	–3.05	(–3.94)
4-CNPy	23.52	24.15	25.10	25.96	(24.68)	(3.83)	18.48	17.50	(17.83)
	15.16	13.54	14.84	15.46	(14.72)	(–0.71)	–0.32	2.04	(1.25)
3,5-Cl_2Py	30.01	31.89	32.64	33.95	(32.12)	(4.27)	26.75	24.45	(25.22)
	33.54	34.96	36.70	37.74	(35.74)	(4.17)	30.05	28.36	(28.94)
THF	27.75	29.74	30.50	32.10	(30.02)	(4.73)	27.6	24.3	(26.54)
	33.30	34.91	36.77	38.14	(35.78)	(5.65)	—	—	—

(*Continued*)

Table 23. (*Continued*)

Complex Ligand(L)	CH_2	CH_2 (Ave)	CH_3 (Ave)	*m*(1H)[a]	*m*(2H)[a]	*m* (Ave)
$[Fe(OEP)L_2]^{\pm}$						
DMAP	6.73	6.73	–0.41	—	1.82	—
	4.64	4.64	–1.49	—	–4.60	—
1-MeIm	7.06	7.06	–0.24	—	2.90	—
	5.82	5.82	–1.56	—	–0.82	—
CN^-	4.63	4.63	–0.66	—	0.72	—
	4.58	4.58	–2.59	—	—5.04	—
^{t}BuNC	7.61	7.61	3.19	—	–37.71	—
	7.40	7.40	3.18	—	–58.17	—
Py	14.71	14.71	1.26	—	7.00	—
	8.50	8.50	–0.25	—	–3.83	—
4-CNPy	28.06	28.06	4.11	—	20.45	
	15.10	15.10	0.62	—	0.84	
3,5-Cl_2Py	38.8	38.8	6.27		32.0	
	46.3	46.3	7.7		46.3	
THF	38.13	38.13	6.20		39.50	
	50.51	50.51	8.13		60.04	

[a]m(1H), m(2H): *meso*-H signals corresponding to 1H and 2H, respectively. [b] Extrapolated values from low temperature. (Source: Ref. 136.)

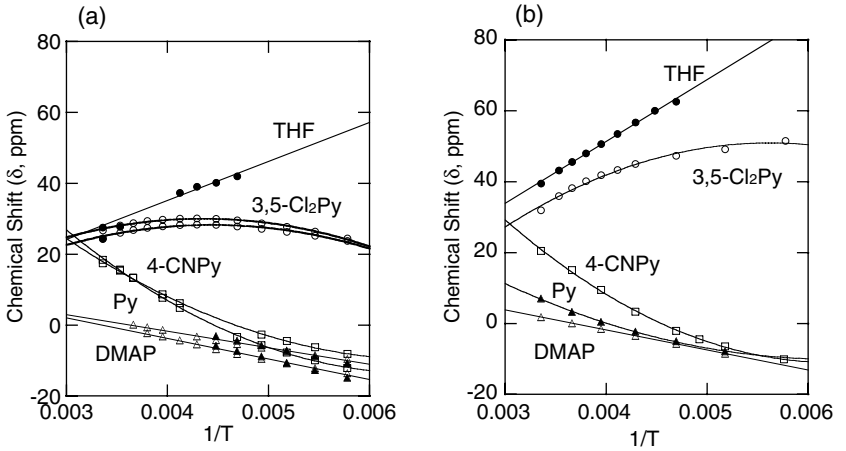

Figure 42. Curie plots of the *meso*-H signals in (a) $[Fe(MAzP)L_2]^+$ and (b) $[Fe(OEP)L_2]^+$. (Adapted with permission from Ref. 136. Copyright 2008, American Chemical Society.)

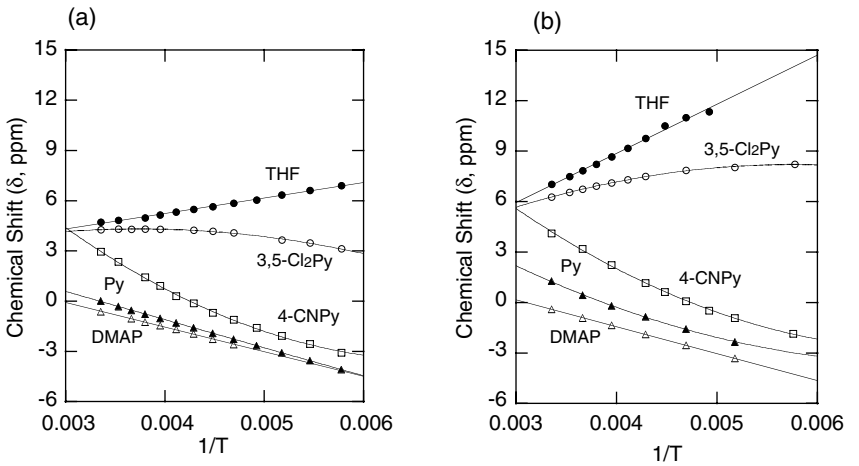

Figure 43. Curie plots of the CH_3 signals in (a) $[Fe(MAzP)L_2]^+$ and (b) $[Fe(OEP)L_2]^+$. (Adapted with permission from Ref. 136. Copyright 2008, American Chemical Society.)

As listed in Table 23a, $[Fe(MAzP)L_2]^{\pm}$ complexes carrying axial ligands with strong field strength such as DMAP, 1-MeIm, and CN^- exhibit their CH_2 signals at downfield positions, 6–8 ppm, and the *meso*-H signals at upfield positions, 1–3 ppm. In addition, all the signals of these complexes show fairly good linearity in the Curie plots. The ^1H NMR characteristics mentioned above suggest that these complexes adopt the low-spin state with the $(d_{xy})^2(d_{xz}, d_{yz})^3$ ground state. The small downfield shifts of the CH_2 signals can be explained in terms of the interaction

between the half-filled iron d_π and the filled $3e_g$-like orbitals of MAzP. The upfield shift of the *meso*-H signals should mainly be caused by the dipolar contribution in the $(d_{xy})^2(d_{xz}, d_{yz})^3$ type complexes.

The CH_2 and *meso*-H signals of $[Fe(MAzP)(4\text{-}CNPy)_2]^+$ and $[Fe(MAzP)(3,5\text{-}Cl_2Py)_2]^+$ appear much further downfield than those of low-spin complexes with the $(d_{xy})^2(d_{xz}, d_{yz})^3$ ground state; the chemical shifts of the CH_2 and *meso*-H signals of the 3,5-Cl_2Py complex reach as far as 32.12 (ave) and 25.22 (ave) ppm, respectively, at 298 K. The large downfield shift of the CH_2 signals at 298 K suggests that these complexes are either in the S = 3/2 spin state with two unpaired electrons in the d_π orbitals or in the S = 5/2 spin state with an unpaired electron in the $d_{x^2-y^2}$ orbital. It is difficult to differentiate the S = 5/2 from the S = 3/2 spin state on the basis of the CH_2 chemical shifts, because they appear downfield in both the S = 3/2 and S = 5/2 complexes. In such a case, the chemical shifts of the β-CH_3 signals and their temperature dependence should be a good probe for determining the spin states since the S = 5/2 complexes exhibit β-CH_3 signals further downfield than the S = 3/2 complexes; the unpaired electron can be delocalized to the CH_3 protons through σ-bonds in the S = 5/2 complexes. The data in Table 23a indicate that the CH_3 signals of the 4-CNPy and 3,5-Cl_2Py complexes appear at 3.83 and 4.27 ppm, respectively. Since the CH_3 signals of high-spin Fe(MAzP)Cl appear at 6.9–7.5 ppm, it is reasonable to conclude that they are mainly in the S = 3/2 state.

As shown in Figures 42a and 43a, the *meso*-H and CH_3 signals of $[Fe(MAzP)(4\text{-}CNPy)_2]^+$ show large upfield shifts as the temperature is lowered and approach those of the low-spin DMAP complex. These result can be explained in terms of spin crossover from the mainly S = 3/2 to the mainly S = 1/2 state. Similar temperature dependence is observed in $[Fe(MAzP)(3,5\text{-}Cl_2Py)_2]^+$, though the degree of the spin crossover is much smaller; the *meso*-H signals still appear far downfield even at 223 K. Thus, the magnetic behaviors of the 4-CNPy and 3,5-Cl_2Py complexes resemble those of $[Fe(OETPP)Py_2]^+$ and $[Fe(OMTPP)Py_2]^+$, since all of these complexes exhibit the spin transition from S = 3/2 to S = 1/2. However, the magnetic behavior of $[Fe(MAzP)Py_2]^+$ is different from that of $[Fe(OETPP)Py_2]^+$ and $[Fe(OMTPP)Py_2]^+$, because it maintains the S = 1/2 spin state even at ambient temperature; the average chemical shift of the CH_2 signals at 298 K is 10.77 ppm, which is not much different from 6.69 ppm for the low-spin DMAP as listed in Table 23a.

Comparison of the electronic structures between $[Fe(MAzP)L_2]^\pm$ and $[Fe(OEP)L_2]^\pm$ should be useful for elucidating the effect of a nitrogen atom at one of the *meso* positions. Figures 42 and 43 suggest that the electronic structure of $[Fe(MAzP)L_2]^\pm$ is surprisingly similar to that of $[Fe(OEP)L_2]^\pm$ if the axial ligand is the same. Close inspection of the data in Table 23 reveals, however, that the

chemical shifts and the temperature dependence of the CH_3 signals are different in the two 3,5-Cl_2Py complexes. While the CH_3 signals in [Fe(MAzP)(3,5-Cl_2Py)$_2$]$^+$ appear at 4.27 ppm on average at 298 K, the corresponding signal in [Fe(OEP)(3,5-Cl_2Py)$_2$]$^+$ is observed much more downfield, at 6.27 ppm. These results indicate that the $d_{x^2-y^2}$ orbital in the OEP complex has a much larger spin population than in the MAzP complex. In other words, the population of the S = 5/2 state increases on going from [Fe(MAzP)(3,5-Cl_2Py)$_2$]$^+$ to [Fe(OEP)(3,5-Cl_2Py)$_2$]$^+$. Furthermore, the Curie plots of the CH_3 signals of these complexes presented in Figure 43 indicate that the averaged CH_3 signal in the MAzP complex shows a small negative slope, while that of the OEP complex exhibits a positive slope. The negative slope of the CH_3 signal in [Fe(MAzP)(3,5-Cl_2Py)$_2$]$^+$ is consistent with spin crossover from mainly S = 3/2 at 298 K to the mixed S = 3/2 and S = 1/2 state at 173 K. In contrast, the positive slope in [Fe(OEP)(3,5-Cl_2Py)$_2$]$^+$ suggests that the contribution of the S = 5/2 spin state is dominant even at 173 K. EPR spectra support this conclusion, because [Fe(MAzP)(3,5-Cl_2Py)$_2$]$^+$ exhibits S = 1/2 while [Fe(OEP)(3,5-Cl_2Py)$_2$]$^+$ shows the mixed S = 3/2 (major) and S = 5/2 (minor) states at 4.2 K; the $g_\perp$ values of these complexes are 3.46 and 4.23, respectively, in frozen CH_2Cl_2 solution.[136] The low-spin state in [Fe(MAzP)(3,5-Cl_2Py)$_2$]$^+$ at 4.2 K can be explained in terms of a destabilization of the $d_{x^2-y^2}$ orbital caused by the smaller N_4 cavity of the MAzP core as compared with the OEP core. An X-ray crystallographic analysis reported by Balch and coworkers has also revealed that the average Fe–N_p bond in Fe(MAzP)Cl is 2.044 Å, which is *ca*. 0.02 Å shorter than that in Fe(OEP)Cl.[210,211]

4. *Structural Consequences of Spin Crossover*

It is interesting to know how the coordination structure and the surrounding lattice of [Fe(OETPP)Py_2]$^+$ change during the spin crossover process in the solid state. Temperature dependence of the crystal and molecular structures of [Fe(OETPP)Py_2]$^+$ and [Fe(OMTPP)Py_2]$^+$ is instructive.[209,212] Figure 44 shows the molecular structures of [Fe(OETPP)Py_2]$^+$ and [Fe(OMTPP)Py_2]$^+$ determined at 298 K, together with the perpendicular displacements of the peripheral atoms from the least-squares plane.[209,212] The maximum deviation among the $C_{20}N_4Fe$ core is observed for one of the pyrrole β carbon atoms, which is 1.31 Å for [Fe(OETPP)Py_2]$^+$ and 1.10 Å for [Fe(OMTPP)Py_2]$^+$. Deviation of the *meso*-carbon from the least-squares plane is at most 0.05 Å in [Fe(OETPP)Py_2]$^+$, while it is as much as 0.19 Å in [Fe(OMTPP)Py_2]$^+$. Thus, the OETPP complex adopts a pure saddled structure while the OMTPP core includes some ruffling. This does not mean that the saddled OMTPP core is generally much easier to ruffle than the corresponding OETPP core. In fact, the structural analysis of [Fe(OMTPP)(^{t}BuNC)$_2$]$^+$ reveals

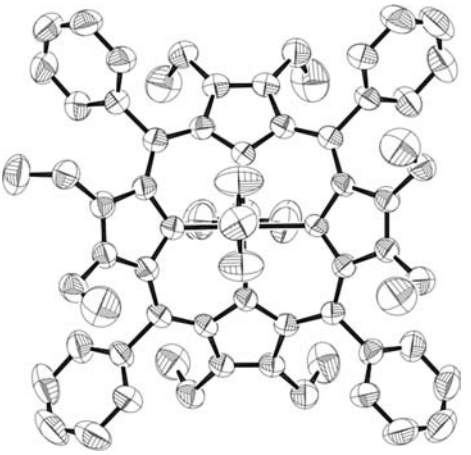

(a) $[Fe(OETPP)Py_2]ClO_4$

(b) $[Fe(OMTPP)Py_2]ClO_4$

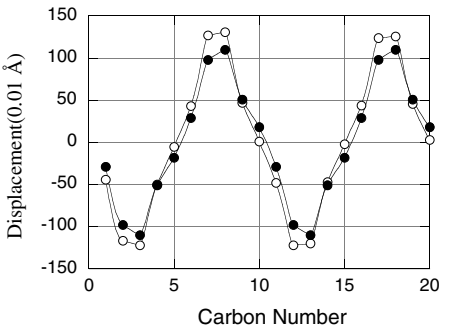

(c) Perpendicular displacement

Figure 44. ORTEP diagrams of (a) $[Fe(OETPP)Py_2]^+$ and (b) $[Fe(OMTPP)Py_2]^+$. (c) Perpendicular displacement of the core atoms from the mean plane for $[Fe(OETPP)Py_2]^+$ (○) and $[Fe(OMTPP)Py_2]^+$ (●). (Adapted with permission from: (a) Ref. 212, copyright 2002 American Chemical Society; and (b), (c) Ref. 209. Copyright 2004, WILEY-VCH Verlag GmbH.)

Table 24. (a) Crystallographic details and (b) bond lengths for $[Fe(OETPP)Py_2]ClO_4$ at three different temperatures.

	298 K	180 K	80 K
(a) Crystallographic Details			
Formula		$C_{70}H_{70}N_6FeClO_4.2CH_2Cl_2$	
Mol wt		1320.47	
Crystal system		monoclinic	
Space group		$P2_1/n$	
Z		4	
b(Å)	13.972(1)	13.800(2)	13.857(1)
c(Å)	19.481(1)	17.870(2)	17.764(1)
β(Å)	26.750(3)	26.237(3)	26.184(2)
B(deg)	101.493(3)	101.375(3)	101.411(1)
V(Å^3)	6969.0(10)	6343.3(12)	6318.0(6)
R1	0.0759	0.0943	0.0923
wR2	0.2435	0.1958	0.2016
GOF	1.073	0.978	1.010
Bonds	298 K	180 K	80 K
(b) Bond Lengths (Å^3) and Rotation Angles ($\phi\bar{u}$)			
Fe1–N1	1.967(2)	1.950(3)	1.960(3)
Fe1–N2	1.997(3)	1.958(3)	1.955(3)
Fe1–N3	1.975(2)	1.953(3)	1.965(3)
Fe1–N4	2.000(3)	1.954(3)	1.947(3)
Fe1–N5	2.197(3)	2.039(4)	2.001(3)
Fe1–N6	2.204(3)	2.042(4)	1.984(3)
Fe1–N_p[a]	1.985(3)	1.954(3)	1.957(3)
Fe–N_{ax}[b]	2.201(3)	2.041(4)	1.993(3)
ϕ[c]	1.1(4)		6.3(3)
	3.6(3)		11.6(3)

[a]Average bond length of the equatorial bonds. [b]Average bond length of the axial bonds. [c]Dihedral angle between the coordinated pyridine and N_p–Fe–N_{ax} plane. (Source: Ref. 212.)

that the OMTPP core shows a quite pure saddled structure in spite of the coordination of ^{t}BuNC, which usually induces the ruffled deformation of the porphyrin core.[123] Table 24 lists the crystallographic and structural data for $[Fe(OETPP)Py_2]^+$.[212] The axial and equatorial bond lengths given at three different temperatures clearly indicate that most of the bonds contract at lower temperature. The shortening of the axial bonds is much larger than that of the equatorial ones. The average axial and equatorial bonds, Fe–N_{ax} and Fe–N_p, have shown 9.5% and 1.4% contraction, respectively, as the temperature is lowered from 298 to 80 K. The data in Table 24 also demonstrate that the bond contraction between 298 and 180 K is much larger than that between 180 and 80 K; the bond contraction for Fe–N_{ax} is 0.160 and

0.048 Å for each temperature range, respectively, while that for Fe–N_p is 0.031 and < 0.01 Å.[212]

Another notable change in structure is the rotation angle ϕ of the pyridine ligand; ϕ is defined as the dihedral angle between the coordinated pyridine and N_p–Fe–N_{ax} plane. The pyridine ligands are placed almost along the diagonal Np–Fe–Np axes perpendicularly above and below the porphyrin; ϕ values for two ligands are fairly small, 1.1° and 3.6°, at 298 K. The rotation angle increases, however, from 1.1° and 3.6° to 6.3° and 9.7° as the temperature is lowered to 80 K. The increase in the rotation angle can be ascribed to a shortening of the Fe–N_{ax} bond at lower temperatures.

Because of the bond contraction, the steric repulsion between the ligand and pyrrole nitrogen atoms should increase. Thus, the conformation at $\theta = 3.6°$, which is most stable at 298 K, where Fe–N_{ax} is 2.201 Å, is no longer stable at 80 K, where Fe–N_{ax} is 1.993 Å. These results suggest that the rotation of the axial ligand is quite important for minimizing steric repulsion that is caused by bond contraction at lower temperatures. Figure 45 illustrates how the molecule adjusts its structure to maintain the most stable conformation as the temperature is raised or lowered.[212]

The data in Table 24a indicate that the unit cell decreases by 9.3% in volume on going from 298 to 80 K because of packing forces. In this crystal, the *a*, *c*, and *b* axes almost coincide with the N1–N3, N2–N4, and N5–N6 axes, respectively; N1, N2, N3, and N4 are porphyrin nitrogen atoms, while N5 and N6 are pyridine nitrogen atoms. Examination of the crystal data in Table 24 reveals that the lattice contractions along the *a*, *c*, and *b* axes are 1.2%, 1.9%, and 3.3%, respectively, in the temperature range of 298–180 K. Correspondingly, the bond contraction takes

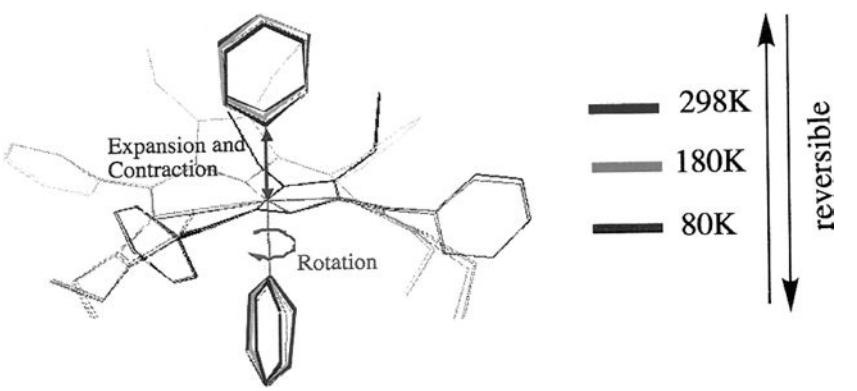

Figure 45. Temperature-dependent structural change in $[Fe(OETPP)Py_2]^+$ at three different temperatures. (Adapted with permission from Ref. 200. Copyright 2002, American Chemical Society.)

place by 1.0%, 2.2%, and 7.3% for Fe1–N1(N3), Fe1–N2(N4), and Fe1–N5(N6), respectively. It should be noted that, as the temperature is lowered from 298 to 180 K, the largest contraction of the unit cell occurs along the *b* axis, which results in the largest contraction of the Fe–N_{ax} bonds. *It is this shortening of the axial bonds that destabilizes the* d_{z^2} *orbital and induces the spin transition from S* = 3/2 *to S* = 1/2.[209]

The phenomenon observed in the crystal seems to be closely connected with the functional tuning process of some heme proteins such as leghemolobin in the dioxygen binding process.[213] Orientation changes of the proximal and distal histidine ligands together with Fe–N bond contraction induce a change in the spin state. In this sense, the crystal of $[Fe(OETPP)Py_2]^+$ may be regarded as a superstructure parallel to a protein matrix in its constraining function.[212]

C. Spin Crossover Between S = 3/2 and S = 5/2

1. *Monoaqua Complexes of Saddled Porphyrins*

In the previous section, it was reported that highly saddled complexes with fairly weak axial ligands such as $[Fe(OETPP)(THF)_2]ClO_4$ and $Fe(OETPP)ClO_4$ adopt a quite pure intermediate-spin state.[98,181] Furthermore, the analogous complexes such as $[Fe(OETPP)(Py)_2]^+$ and $[Fe(OMTPP)(Py)_2]^+$ with much stronger nitrogen bases exhibit a novel spin crossover between S = 3/2 and S = 1/2.[100,209,212] Similar spin crossover has been reported by Rivera and coworkers in the heme metabolism process mediated by human heme oxygenase.[206,207] While the spin crossover between S = 5/2 and S = 1/2 and between S = 3/2 and S = 1/2 have been observed both in heme proteins and in model heme complexes, the spin crossover between S = 5/2 and S = 3/2 has never before been observed.

As previously mentioned, the mixed S = 5/2 and S = 3/2 spin state is considered to be a quantum-mechanical spin admixture caused by spin–orbit coupling between the S = 3/2 and S = 5/2 spin states.[150,151] However, Ohgo and coworkers have found that highly saddled complexes $[Fe(OMTArP)(H_2O)]ClO_4$, where Ar is 3,5-dimethylphenyl (3,5-Me_2Ph) and 3,5-bis(*tert*-butlyl)phenyl (3,5-$^t Bu_2$Ph), exhibit an unprecedented example of spin crossover between the S = 3/2 and S = 5/2 spin states.[101] Figure 46 shows the X-ray molecular structures of these complexes, both of which have highly saddled five-coordinated monoaqua complexes.[101] Table 25 shows geometric parameters of these complexes together with those of some analogous complexes.[101] Short Fe–Np bond lengths together with the small out-of-plane displacement of the iron(III) ion indicate that these complexes are in the intermediate-spin state. Extremely downfield-shifted methyl signals together with downfield-shifted *o*- and *p*-H signals in the ^{1}H NMR spectra

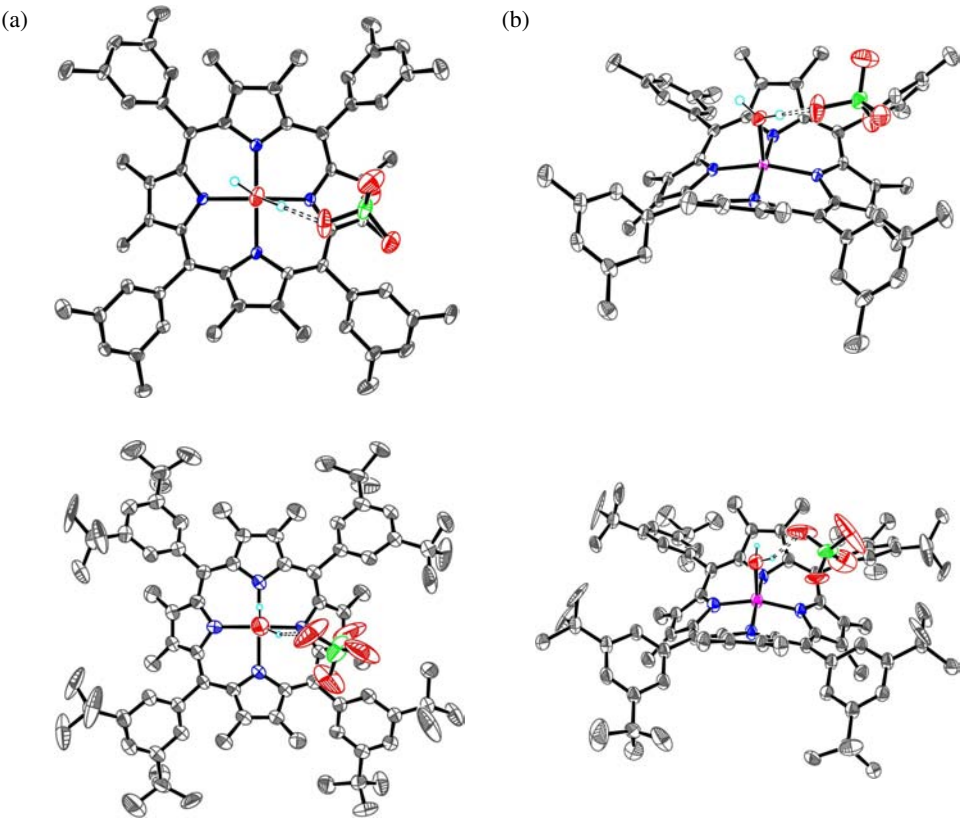

Figure 46. Molecular structures of $[Fe(OETArP)(H_2O)]^+$, where (a) Ar = 3,5-Me_2Ph and (b) Ar = 3,5-^{t}Bu_2Ph. Hydrogen bonds are shown as dotted lines. (Adapted with permission from Ref. 101. Copyright 2006, Royal Chemical Society.)

also support the intermediate-spin state proposal for these complexes; the chemical shifts of the py-CH_3, *o*-H, and *m*-H signals are 60.1, 11.7, and 9.12 ppm, respectively, for the 3,5-Me_2Ph complex, and 60.4, 11.7, and 9.12 ppm, respectively, for the 3,5-^{t}Bu_2Ph complex.

Temperature-dependent EPR spectra taken in frozen CH_2Cl_2 solution are given in Figure 47.[101] As shown in this figure, both complexes exhibit a strong signal at *ca*. 4.0 at 70 K, indicating that they adopt the intermediate-spin state. As the temperature is lowered, the intensity of the signal at 4.0 decreases while that at 6.0 increases. The EPR spectra at 4 K exhibit two types of signal characteristic of the high-spin and intermediate-spin species. The *g* values, determined by computer simulations of the observed spectra, are as follows: (a) 6.10, 5.90, 2.00 (S = 5/2) and 4.20, 3.80, 2.10 (S = 3/2); (b) 6.10, 5.90, 2.00 (S = 5/2); 4.37, 3.77, 1.99 (S = 3/2). When the temperature is further lowered, the intensity of the high-spin

Table. 25. Comparison of geometric parameters in five-coordinated saddle-shaped iron(III) porphyrin complexes.

Complex	Fe–N_p[a]	Fe–X_{ax}[b]	ΔFe[c]	Δ_{max}[d]	N_4 area[e]	Ref.
[Fe(OMTArP)(H_2O)]$^+$						
Ar = 3,5-Me_2Ph	1.946(4)	2.084(4)	0.285(2)	1.35	7.45	101
[Fe(OMTArP)(H_2O)]$^+$						
Ar = 3,5-$^t Bu_2$Ph	1.960(2)	2.056(2)	0.232(1)	1.32	7.59	101
[Fe(OMTPP)Cl]	2.034	2.247	0.464	1.22	7.87	182
[Fe(OETPP)Cl]	2.030	2.242	0.467	1.32	7.83	182
[Fe(OETPP)ClO_4]	1.963	2.059	0.262	1.32	7.59	181

[a]Bond length (Å) between iron and pyrrole nitrogen. [b]Bond length (Å) between iron and axial ligand. [c]Out-of-plane deviation (Å) of iron (III) ion from the N_4 plane. [d]Peripheral atoms that exhibit the largest deviation (Å) from the N_4 plane. [e]The area (Å^2) of the plane consisting of the four nitrogen atoms of the pyrrole rings.

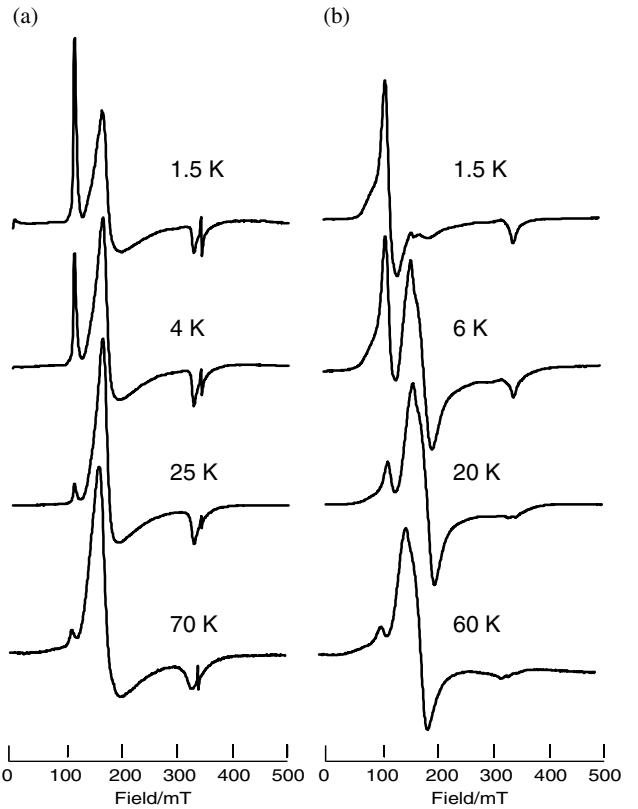

Figure 47. EPR spectra of [Fe(OMTArP)(H_2O)]$^+$ taken in frozen CH_2Cl_2 solution, where (a) Ar = 3,5-Me_2Ph and (b) Ar = 3,5-$^t Bu_2$Ph. (Adapted with permission from Ref. 101. Copyright 2006, Royal Society of Chemistry.)

signal increases, especially in the 3,5-^{t}Bu$_2$Ph complex; this complex exists exclusively as a high-spin complex at 4.2 K. The process is reversible, because the original spectra are completely reproduced when the temperature is raised back to 70 K. The temperature dependence of the EPR spectra could best be explained in terms of the unprecedented spin crossover between S = 5/2 and S = 3/2. The populations of each species are determined by computer simulations of the observed spectra. The van't Hoff plots yield $\Delta H°$ and $\Delta S°$ values corresponding to the equilibrium given in Eq. 21.

$$S = \frac{5}{2} \underset{\longleftarrow}{\overset{K}{\longrightarrow}} S = \frac{3}{2}. \tag{21}$$

The values are 60 J·mol^{-1} and 48·J·mol^{-1}·K^{-1} for the 3,5-Me$_2$Ph, and 100 J·mol^{-1} and 19 J·mol^{-1}·K^{-1} for 3,5-^{t}Bu$_2$Ph complexes, respectively.

2. *Monoazide Complexes*

Neya and coworkers have found that the azide complex of iron(III) porphycene, [Fe(TPrPc)N$_3$], exhibits interesting spectroscopic and magnetic behavior.[154] In the ^{1}H NMR spectra, the pyrrole-H signal appears at 19 ppm at 298 K and shifts to −30 ppm when the temperature is lowered to 200 K. The EPR spectrum is nearly axial with $g_\infty = 5.41$(ave) and $g_\parallel = 2.00$, suggesting that Int(%) = 30% at 5 K. The QS value in the Mössbauer spectrum increases from 2.20 mm s^{-1} at 290 K to 2.68 mm s^{-1} at 77 K, which also supports the S = 3/2 contribution increasing at lower temperature. The effective magnetic moment is 4.80 μ_B at 290 K and decreases to 4.06 μ_B at 50 K. All of these data suggest that the complex is in a mixed S = 5/2 and S = 3/2 spin state. It is very difficult to determine if the complex is in a thermal equilibrium between S = 5/2 and S = 3/2, or in a spin admixture of the two spin states; all the complexes except [Fe(OETArP)(H$_2$O)]$^+$ exhibit averaged NMR, EPR, and Mössbauer signals.[101] Neya and coworkers considered IR spectroscopy to be a good method for observing directly the two spin state isomers expected for [Fe(TPrPc)N$_3$]. This is because the approximate time scale of IR is 10^{-13} s, which is shorter than the time scales of EPR, NMR, and Mössbauer spectroscopy; they are are 10^{-4}–10^{-8}, 10^{-1}–10^{-9}, and 10^{-7} s^{-1}, respectively.[212] Consequently, IR spectroscopy should discriminate the thermal spin-state equilibrium from the quantum-mechanical spin admixture. In fact, the IR spectra given in Figure 48 show two separate absorptions centered at 2049 and 2066 cm^{-1}. They are assigned to the azide stretching band for the S = 3/2 and S = 5/2 spin-state isomers, respectively. Increase of the 2049 cm^{-1} band and concomitant decrease of the 2066 cm^{-1} band with decreasing temperature, accompanied by the 2054 cm^{-1} isosbestic point,

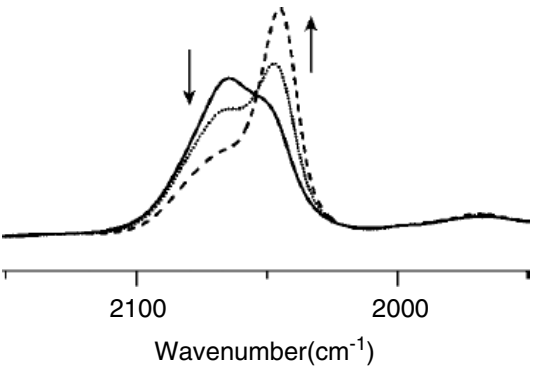

Figure 48. The IR absorption spectra of Fe(T^nPrPc)N_3 in chloroform. Temperature decreases (295, 254, 216 K) as indicated by the arrow. (Adapted with permission from Ref. 154. Copyright 2007, Wiley-VCH Verlag GmbH & Co. KGaA.)

demonstrate that the S = 5/2 and S = 3/2 isomers are in a thermal equilibrium. The IR analysis further reveals that [Fe(T^iPrP)N_3] also exhibits a similar spin crossover between S = 5/2 and S = 3/2.[155] Thus, it seems that spin crossover phenomena are possible between any two of the three spin states in iron(III) porphyrin complexes.[101,154,155]

D. Spin Crossover in Monoimidazole Complexes

Cytochromes c′ are a unique class of heme proteins found in photosynthetic, denitrifying, and nitrogen-fixing bacteria.[215] These proteins are usually found as dimers. In spite of low homology in the amino acid sequences, the overall folding of the monomers is similar. They possess a heme prosthetic group covalently bound to the protein via two thioether linkages that are provided by a conserved Cys–X–Y–Cys–His motif near the C-terminal region.[215–222] The heme iron is five-coordinate with a solvent-exposed histidine residue. Although X-ray crystallographic analyses have revealed the structural similarity among these proteins, the microenvironment around the heme center is slightly different among the proteins. Thus, the solvent-exposed histidine residue can participate in hydrogen bonding with water molecules and/or basic protein residues in a slightly different way among the proteins. These proteins are considered to adopt a unique spin state, a quantum-mechanical admixture of a high-spin (S = 5/2) and an intermediate-spin (S = 3/2) state,[150,151] although some examples have been found showing the thermodynamic equilibrium between S = 5/2 and S = 3/2 spin state isomers, as described in the previous section.[101,154–156] The contribution of the S = 5/2 or 3/2 state changes depending on the bacterial source and the spectroscopic methods

applied for the measurements.[223] In most cases, the oxidized form of iron is predominantly in the S = 5/2 spin state though the contribution of the S = 3/2 state increases in cytochromes c′ isolated from some bacteria, such as C. *vinosum* and *Rb. capsulatus*.[223] To reveal the ambiguous spin state of these proteins, both structural and spectroscopic studies with synthetic monoimidazole complexes are necessary. In fact, the isolation of monoimidazole complexes is quite difficult because of the formation of the corresponding stable bis-adducts.[224–227] The only structurally characterized complex is [Fe(OEP)(2-MeIm)]ClO_4, reported by Scheidt *et al.* in 1985.[228] This complex maintains the S = 5/2 state at least above 60 K. In this section, the spectroscopic, magnetic, and crystallographic properties of monoimidazole complexes such as $[Fe(TMP)L]^+$,[229,230] $[Fe(TMTMP)L]^+$,[231] and $[Fe(OETPP)L]^+$ will be described.[232]

1. *[Fe(TMP)L]⁺ and [Fe(TMTMP)L]⁺*

In principle, it is possible to obtain monoimidazole complexes by the reaction of iron(III) porphyrins with a 1.0 equivalent of the imidazole ligand. In the case of the reaction between Fe(TPP)ClO_4 and 1-MeIm, however, not only [Fe(TPP)(1-MeIm)]$^+$ but also [Fe(TPP)(1-MeIm$_2$)]$^+$ is formed. Furthermore, contamination with water leads to the formation of μ-oxo dimer $[Fe(TPP)]_2O$ according to the reaction mechanism shown in Scheme 2.[229] If a 1.0 equivalent of sterically hindered imidazole such as 1,2-Me_2Im or 2-MeBzIm is added in place of 1-MeIm, then the μ-oxo dimer is formed predominantly, together with a small amount of monoimidazole complex.[229] It is then expected that the addition of a 1.0 equivalent of hindered imidazoles to [Fe(TMP)]ClO_4 could form the corresponding monoimidazole complexes [Fe(TMP)L]ClO_4 as the sole product, since formation of the μ-oxo dimer is prohibited due to the presence of the *o*-methyl groups. In fact, a quite pure monoimidazole complex can be obtained by the addition of a 1.0 equivalent of the hindered ligand.[230] Figure 49 shows the ^{1}H NMR spectrum of (a) [Fe(TMP)]ClO_4 and (b) $[Fe(TMP)(2\text{-MeIm})]^+$ taken in CD_2Cl_2 solution at 298 K.[230] The pyrrole-H signal of $[Fe(TMP)(2\text{-MeIm})]^+$ is observed at 35.1 ppm, suggesting that the complex adopts the mixed high-spin and intermediate-spin state. Because of the five-coordinate structure, two *m*-H signals are observed at 14.3 and 13.2 ppm.

$$Fe(TPP)ClO_4 + H_2O \rightleftharpoons [Fe(TPP)(H_2O)]ClO_4$$

$$[Fe(TPP)(H_2O)]ClO_4 + L \rightleftharpoons Fe(TPP)(OH) + HL^+ClO_4^-$$

$$Fe(TPP)(OH) + Fe(TPP)ClO_4 + L \rightleftharpoons [Fe(TPP)]_2O + HL^+ClO_4^-$$

Scheme 2. Mechanism for the formation of μ-oxo dimmer.

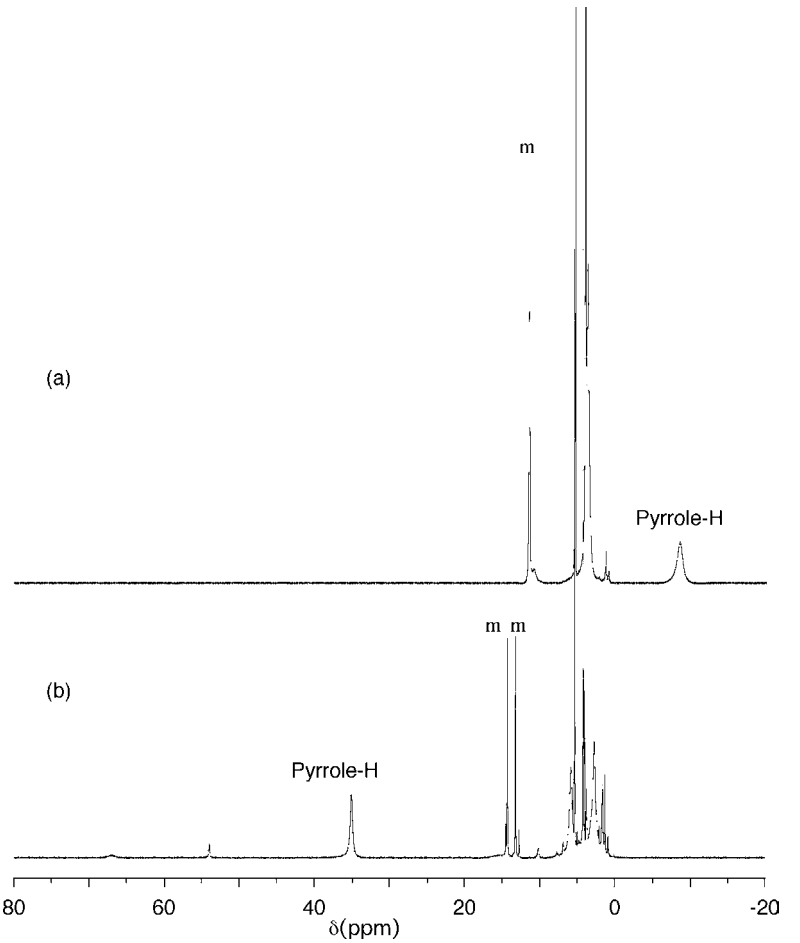

Figure 49. ^{1}H NMR spectra of (a) Fe(TMP)ClO_4 and (b) [Fe(TMP)(2-MeIm)]$^+$ taken in CD_2Cl_2 at 298 K. (Adapted with permission from Ref. 230. Copyright 2002, American Chemical Society.)

Table 26a lists the ^{1}H NMR chemical shifts of a series of [Fe(TMP)L]ClO_4 together with the Int(%) values obtained from Eq. 16, where the chemical shifts of the high-spin and intermediate-spin complexes, δ_{high} and δ_{int}, are considered to be +80 and −60 ppm, respectively.[230] Table 26b shows the ^{1}H NMR chemical shifts of a series of [Fe(TMTMP)L]ClO_4, where the mesityl and methyl groups are attached to the C_β atoms and no substituent is attached to the *meso*-C atoms.[231]

Among the axial ligands listed in Table 26a, there is no doubt that 4,5-Cl_2Im stabilizes the intermediate-spin state most effectively, which should be ascribed to the weaker σ-donating and stronger π-accepting ability as compared with other ligands. In contrast, 2-^{t}BuIm greatly stabilizes the high-spin state; the pyrrole-H signal is observed at 78.4 ppm, which indicates that Int(%) is only 1%. In the case

Table 26. 1H NMR chemical shifts (d, ppm) of (a) $[Fe(TMP)L]ClO_4$[a] and (b) $[Fe(TMTMP)L]ClO_4$[b] determined at 298 K in CD_2Cl_2 solution together with Int(%).

Axial ligands (L)	Pyrrole-H		*m*-H			Int(%)
(a) $[Fe(TMP)L]ClO_4$[c]						
HIm	20.7	(15.1)	13.2	12.5	(16.9, 15.5)	42
5-MeIm	31.0	(40.4)	13.7	12.8	(18.1, 16.4)	35
2-MeIm	35.1	(29.3)	14.3	13.2	(17.5, 15.6)	32
2-EtIm	32.4	(16.9)	14.1	13.1	(16.7, 15.0)	34
2-^{i}PrIm	30.5	(4.4)	14.0	13.1	(15.9, 14.5)	35
2-(1-EtPr)Im	54.1	(84.4)	15.4	14.1	(20.2, 17.5)	19
2-^{t}BuIm	78.4	(122.6)	13.0	12.0	(17.2, 15.1)	1
1,2-Me_2Im	25.4	(29.6)	13.9	12.9	(17.8, 15.9)	39
1-Me-2-EtIm	19.0	(–12.0)	13.4	12.6	(14.9, 13.6)	44
1-Me-2-^{i}PrIm	13.9	(–23.5)	13.2	12.4	(14.1, 13.0)	47
BzIm	27.7	(28.4)	14.0	13.0	(18.2, 16.1)	37
5,6-Me_2BzIm	43.3	(70.1)	14.9	13.6	(19.2, 16.8)	26
2-MeBzIm	27.0	(–13.4)	14.1	13.0	(14.8, 13.2)	38
1, 2-Me_2BzIm	13.7[d]	(–26.61)	13.5	12.5[d]	(14.1, 12.7)	47
4,5-Cl_2Im	–15.3[d]	(–56.2)	10.5	10.5[d]	(12.4, 11.6)	68
Cl^-[e]	79.8	(125.2)	15.9[d]	14.3[d]	(22.2, 19.2)	0
ClO_4^-[f]	–9.3	(–61.6)	11.4	—	(11.6)	64

Axial Ligand(L)	Pyrrole-Me	*o*-Me		*m*-H		*p*-Me	*Meso*
(b) $[Fe(TMTMP)L]ClO_4$							
HIm	69.2	8.0	4.8	14.4	13.5	5.5	–16.6
5-MeIm	70.3	8.2	5.0	14.5	13.7	5.8	–20.1
2-MeIm	70.0	8.8	5.1	14.5	13.8	6.2	–31.9

[a]Ref. 230. [b]Ref. 231. [c]Data in parentheses are the chemical shifts at 193 K. [d]Data are obtained by extrapolation from low temperature. [e][Fe(TMP)Cl]. [f]$[Fe(TMP)]ClO_4$.

of $[Fe(TMP)(2\text{-}^t BuIm)]ClO_4$, the distance between the ligand and the porphyrin ring should be the largest among the complexes listed in Table 26a because of the severe steric repulsion between the *tert*-butyl group and the porphyrin core. As a result, the iron(III) ion is pulled toward the imidazole nitrogen, which increases the out-of-plane distance of the iron(III) ion and stabilizes the high-spin state. The out-of-plane distance should decrease as the axial ligand changes from 2-^{t}BuIm to 2-(1-EtPr)Im, and then to 2-RIm (R = Me, Et, ^{i}Pr), resulting in stabilization of the intermediate-spin state of the corresponding complexes. In fact, the Int(%) values of the 2-(1-EtPr)Im and 2-RIm (R = Me, Et, ^{i}Pr) complexes are 19% and 32–35%, respectively.

The data in Table 26a also indicate that the introduction of the 1-Me group to the 2-Rim (R = Et, ^{i}Pr) ligand stabilizes the intermediate-spin state. Thus, the

pyrrole-H chemical shift moves upfield from 4.4 to −23.5 ppm at 193 K as the axial ligand changes from 2-^{i}PrIm to 1-Me-2-^{i}PrIm. A similar upfield shift, from 16.9 to −12.0 ppm, is observed as the axial ligand changes from 2-EtIm to 1-Me-2-EtIm. However, the pyrrole-H signal shows no appreciable change as the axial ligand changes from 1-MeIm to 1,2-Me_2Im. Introduction of the 1-Me group should regulate the conformation of the 2-^{i}Pr and 2-Et substituents in such a way that the Me groups of these substituents face the porphyrin ring. As a result, the tilting angle of the Fe–N_{axial} bond from the heme normal should increase by the introduction of the 1-Me group, which weakens the field strengths of these ligands and stabilizes the intermediate-spin state.

Table 27 lists the ^{13}C NMR chemical shifts where axial ligands are arranged in the same order given in Table 26. The chemical shifts of the C_α and C_β signals correlate well with those of the pyrrole-H chemical shifts. On the basis of the data in Tables 26 and 27, the order of the Int(%) values in the imidazole complexes is given by Eq. 22:[230]

$$\begin{aligned} 2\text{-}^{t}\text{BuIm} << 2\text{-(1-EtPr)Im} < \text{HIm, 5-MeIm, 2-RIm (R = Me, Et, }^{i}\text{Pr)}, \\ 1,2\text{-Me}_2\text{Im} < \text{1-Me-2-RIm (R = Et, }^{i}\text{Pr)} < 4,5\text{-Cl}_2\text{Im}. \end{aligned} \quad (22)$$

It is interesting to discuss how the spin state of a monoimidazole complex is affected by the solvents. While the pyrrole-H signal is observed at 35.0 ppm in

Table 27. ^{13}C NMR chemical shifts (δ, ppm) of some carbon signals in [Fe(TMP)L]ClO_4 determined at 298 K in CD_2Cl_2 solution.

Axial ligands (L)	C_α	C_β	*Meso*	*Ortho*	
HIm	637	748	305	274	259
5-MeIm	774	855	322	290	273
2-MeIm	755	888	393	314	302
2-EtIm	717	862	391	311	299
2-^{i}PrIm	679	836	390	308	297
2-(1-EtPr)Im	1051	1148	448	351	342
2-^{t}BuIm	1294	1343	368	322	302
1,2-Me_2Im	643	800	375	300	290
1-Me-2-EtIm	545	727	368	291	282
1-Me-2-^{i}PrIm	446	654	368	285	277
BzIm	690	809	349	293	281
5,6-Me_2BzIm	914	1002	381	320	306
2-MeBzIm	549	775	437	316	309
1, 2-Me_2BzIm	383	645	413	241	216
Cl^{-}[a]	1204	1327	525	408	372
ClO_4^{-}[b]	176	−377	252	217	

[a][Fe(TMP)Cl]. [b][Fe(TMP)]ClO_4. (Source: Ref. 230.)

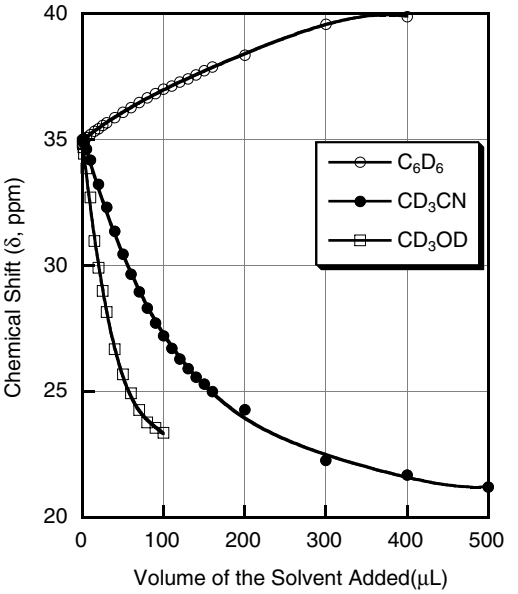

Figure 50. Change in chemical shifts of the pyrrole protons observed by the addition of various amounts of C_6D_6, CD_3CN, or CD_3OD into a CD_2Cl_2 solution of [Fe(TMP)(2-MeIm)]ClO_4 at 25 °C. (Adapted with permission from Ref. 230. Copyright 2002, American Chemical Society.)

CD_2Cl_2 solution, it moves upfield as a polar solvent such as CD_3CN or CD_3OD is added to the CD_2Cl_2 solution of [Fe(TMP)(2-MeIm)]ClO_4; the pyrrole signals reachs 27.2 and 23.4 ppm in CD_2Cl_2 solutions containing 15% CD_3CN and 15% CD_3OD, respectively. In contrast, the pyrrole signal moves downfield, and appears at 37.0 ppm in CD_2Cl_2 solutions containing 15% of nonpolar C_6D_6. Figure 50 shows the change in chemical shifts of the pyrrole signals observed by addition of (a) C_6D_6, (b) CD_3CN, and (c) CD_3OD.[230] The upfield shift of the pyrrole-H signals in polar solvents corresponds to the increase in the intermediate-spin character. This result indicates that the Fe(III)–N_{axial} bond is weakened as the polarity of the solvent increases. In other words, the 2-MeIm ligand behaves as a weaker ligand in a polar solvent than in a less polar solvent. Thus, the Fe(III) ion is pulled toward the center of the N_4 cavity, resulting in an increase in Int(%). In nonpolar solvents such as benzene, the Fe(III)–N_{axial} bond is strengthened, resulting in a decrease in Int(%). In the present study, it has been shown experimentally that the population of the S = 3/2 isomer increases as polar solvents such as methanol and acetonitrile are added. It is expected that the NH of the coordinated imidazole ligand participates in hydrogen bonding with polar solvents such as methanol. If this is the case, the hydrogen bonding would increase the S = 3/2 contribution. In fact, the X-ray crystallographic analysis of *Rb. capsulatus* has shown hydrogen bonding between

the coordinated imidazole(His122) and a water molecule.[219] Correspondingly, the S = 3/2 contribution of cytochrome c′ reached as high as 40%.[223] In contrast, the structural analysis of *R. molischianum* has shown that the coordinated imidazole (His122) is not involved in hydrogen bonding.[233] Therefore, the S = 3/2 contribution decreased to 13% as determined by EPR spectgroscopy;[223] the S = 3/2 contribution was estimated to be 0% by ^{1}H NMR spectroscopy.[234] On the basis of these results, it is proposed that *the hydrogen bonding of solvent molecules to the coordinated histidyl imidazole ligand somewhat weakens the ligand field strength and increases the S* = 3/2 *contribution in the mixed S* = 5/2, 3/2 *spin system.*[230]

2. *[Fe(OETPP)L]$^+$*

In the previous section, spectroscopic studies of the spin state of a wide variety of monoimidazole model complexes, $[Fe(TMP)L]^+$, were described. However, structural studies of these monoimidazole complexes have been hampered because of the difficulty of obtaining good crystals.[225] Ikezaki and coworkers have prepared the saddle-shaped monoimidazole complexes, $[Fe(OETPP)L]ClO_4$, and determined their crystal and molecular structures.[232] In this section, the spectroscopic and magnetic properties of structurally characterized $[Fe(OETPP)L]ClO_4$, where L is Him and 2-MeIm, will be described together with spectroscopic data of the L = 2-MeBzIm complex.

These complexes are prepared by the addition of a 1.0 equivalent of HIm, 2-MeIm, or 2-MeBzIm, respectively, to CH_2Cl_2 solutions of $[Fe(OETPP)(THF)_2]ClO_4$. Figure 51 shows the molecular structure of $[Fe(OETPP)(2\text{-MeIm})]ClO_4$

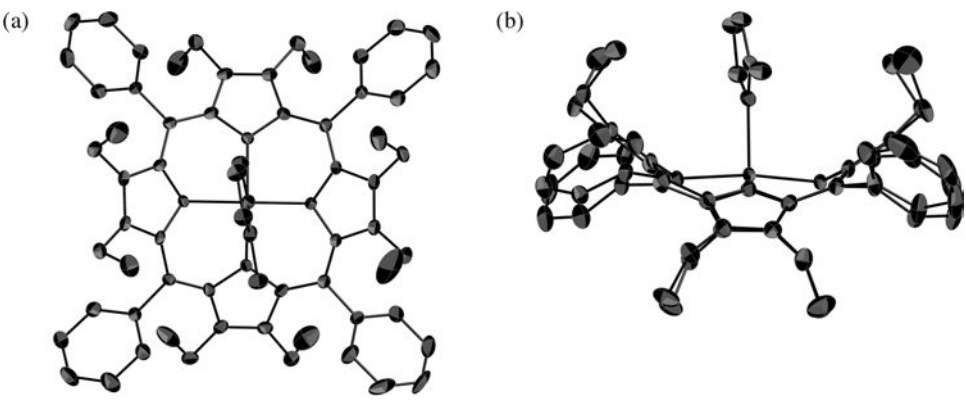

Figure 51. Molecular structure of $[Fe(OETPP)(2\text{-MeIm})]ClO_4$ presented by ORTEP diagrams: (a) viewed from the top and (b) viewed from the side. Thermal ellipsoids are drawn to enclose 50% probability. (Adapted with permission from Ref. 232. Copyright 2009, Wiley-VCH Verlag GmbH & Co. KGaA.)

Table 28. Structural comparison of five-coordinate iron(III) porphyrinates.

Complexes	S[a]	Fe–N_p(Å)	Fe–L_{ax}(Å)	Δ(Å)	Ref.
[Fe(OEP)(2-MeIm)]ClO_4	5/2	2.038(6)	2.068(4)	0.36	228
[Fe(OETPP)Cl]	5/2	2.031(5)	2.2418(23)	0.47	182
[Fe(OETPP)ClO_4]	3/2	1.963(7)	2.059(6)	0.25	181
[Fe(OETPP)(HIm)]ClO_4	3/2	1.969(3)	2.066(3)	0.24	232
[Fe(OETPP)(2-MeIm)]ClO_4	3/2	1.966(2)	2.079(2)	0.26	232

[a]Spin state.

determined by X-ray crystallography at 120 K. Table 28 lists the structural parameters of these complexes together with those of the analogous five-coordinate complexes. As shown in Figure 51, $[Fe(OETPP)(2\text{-}MeIm)]^+$ exhibits a highly saddled porphyrin core. The average Fe–N_p lengths are 1.969(3) Å, which is quite close to the average Fe–N_p length of S = 3/2 Fe(OETPP)ClO_4, i.e. 1.963(7) Å,[181] and is much shorter than that of S = 5/2 $[Fe(OEP)(2\text{-}MeIm)]^+$, i.e. 2.038(6) Å.[228] In contrast, the Fe–N_{axial} bond length of $[Fe(OETPP)(2\text{-}MeIm)]^+$ is slightly larger than that of $[Fe(OEP)(2\text{-}MeIm)]^+$. The axial 2-MeIm ligand is aligned along the N–Fe–N axis. Deviation of the Fe(III) ion from the 4N mean plane is small, 0.26 Å, which is again quite close to that of Fe(OETPP)ClO_4, 0.25 Å.[181a] The similarity between the structural parameters of $[Fe(OETPP)L]^+$ (L = HIm, 2-MeIm) and those of Fe(OETPP)ClO_4 suggests that the monoimidazole complexes adopt the S = 3/2 form in the solid state at 120 K.

The intermediate-spin state of these complexes can also be verified by Mössbauer spectroscopy. Figure 52 shows the Mössbauer spectra taken for microcrystalline samples in the temperature range of 300–80 K. In both $[Fe(OETPP)(HIm)]^+$ and $[Fe(OETPP)(2\text{-}MeIm)]^+$, the QS values are almost constant, 3.06 ± 0.01 and 3.03 ± 0.01 mm s^{-1}, respectively. Even at 4 K the QS values are nearly the same. On the basis of the X-ray crystallographic and Mössbauer spectroscopic studies, it is concluded that the two kinds of monoimidazole complexes retain the $S = 3/2$ state over a wide range of temperature, i.e. from 4 K to 300 K in the solid state.[232]

Although these complexes adopt the intermediate-spin state in the solid, they could adopt a different spin state in solution, as exemplified for Fe(TEtPrP)I.[80] The spin state in solution can be determined by ^1H NMR, ^{13}C NMR, and EPR spectroscopy.

Table 29 lists the ^1H NMR and ^{13}C NMR chemical shifts determined in CD_2Cl_2 solutions at 298 K. Curie plots of the signals in these complexes exhibit good linearity, suggesting that they maintain a single spin state over the NMR temperature range, i.e. 298–173 K. Negative $\delta(meta)$–$\delta(para)$ values together with the negative

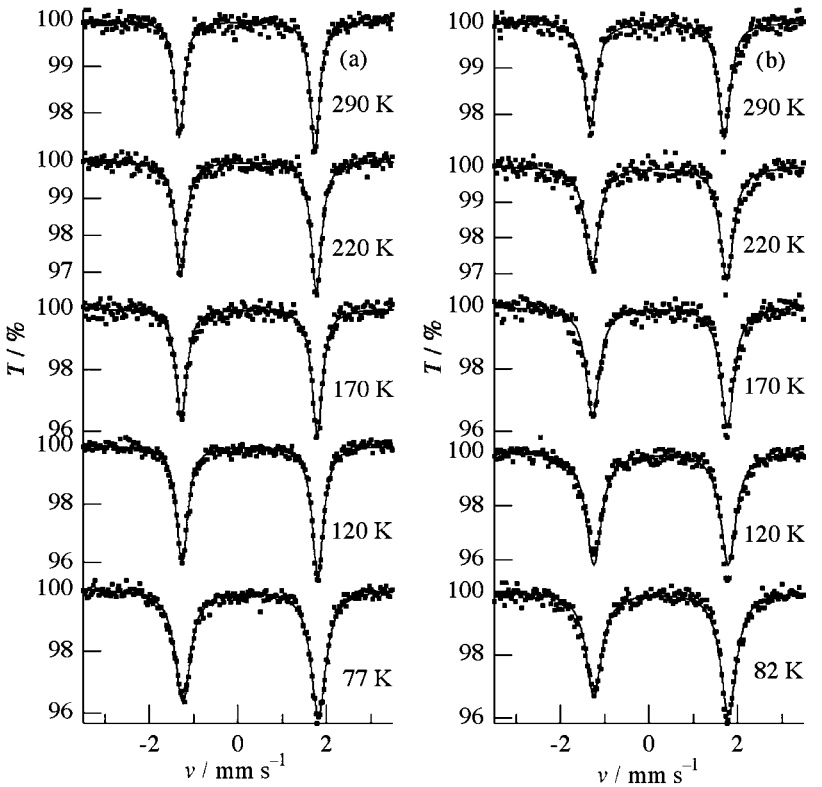

Figure 52. Mössbauer spectra of (a) [Fe(OETPP)(HIm)]$^+$ and (b) [Fe(OETPP)(2-MeIm)]$^+$ taken for the microcrystalline samples. (Adapted with permission from Ref. 232. Copyright 2009, from Wiley-VCH Verlag GmbH & Co.)

Curie slopes of the *m*-H signals indicate that the *meso*-carbon atoms have negative spin, which in turn indicates that these complexes adopt the S = 3/2 state; five-coordinate high-spin Fe(III) porphyrins should have positive spin at the *meso*-carbon atoms and thus give positive $\delta(meta)$–$\delta(para)$ values, as in the case of Fe(OETPP)Cl. The solution magnetic moment of [Fe(OETPP)(2-MeIm)]$^+$ determined by the Evans method is 4.2 μ_B at 298 K and is invariant down to 173 K. This value is close to the spin-only value expected for the S = 3/2 spin state.

^{13}C NMR chemical shifts of these complexes are also listed in Table 29. The C_α and C_β signals appear considerably further upfield than those in high-spin Fe(OETPP)Cl, which can be ascribed to the presence of the vacant $d_{x^2-y^2}$ orbital. Considerable upfield shifts of the *meso* signal, −79, −54, and 11 ppm for the HIm, 2-MeIm, and 2-MeBzIm complexes, respectively**,** satisfy the condition required for the saddle-shaped intermediate-spin complexes. Large upfield shifts are also observed for the CH_2 signals. The average chemical shifts of these signals are

Table 29. ^{1}H and ^{13}C NMR chemical shifts of Fe(OETPP)Cl, Fe(OETPP)ClO_4, and [Fe(OETTPP)L]$^{+}$, where L = HIm, 2-MeIm, and 2-MeBzIm taken in CD_2Cl_2 at 298 K.

Axial Ligand	Spin State	^{1}H NMR										^{13}C NMR										Ref.
		CH_2		CH_3		*o*		*m*		*p*	Ligand	CH_2		CH_3		C_α		C_β		*meso*		
Cl^-	5/2	20.1	32.1	1.8	3.2	9.1	11.5	12.2	12.4	7.5	—	53	61	116	163	525	642	973		456		182[d]
		34.8	49.0								—											232
ClO^-_4	3/2	13.0	42.7	0.7		13.4		7.1		9.8	—	−66		220		195		248		−47		232
HIm	3/2	9.4	18.3	−1.0	1.7	11.8	14.8	6.9	7.4	10.0	42.9 78.3	−49	−47	173	227	275	378	270	308	−79		232
		24.3	52.4								93.7											
2-MeIm	3/2	9.0	18.4	−1.1	1.6	11.3	14.6	7.0	7.6	9.8	65.0 104.1	−50	−40	169	229	240	349	279	314	−54		232
		20.6	54.4																			
2-MeBzIm	3/2	7.9	8.3	−1.0	−0.3	10.7	13.9	7.4	7.9	9.4		−55	−54	164	174	289, 298,		311, 316,		7.7		232
		18.6	19.5	1.0[b]								−41	−31	233	236	331[c]				13.6		
		20.1	57.0[a]																			

[a]Signals at 19.5 and 57.0 ppm correspond to 4H. Other signals correspond to 2H. [b]Signals at −1.0, −0.3, and 1.0 ppm correspond to 6H, 6H, and 12H, respectively. [c]Either C_α or C_β signals. [d]^{1}H NMR: Ref. 182. ^{13}C NMR: Ref. 232.

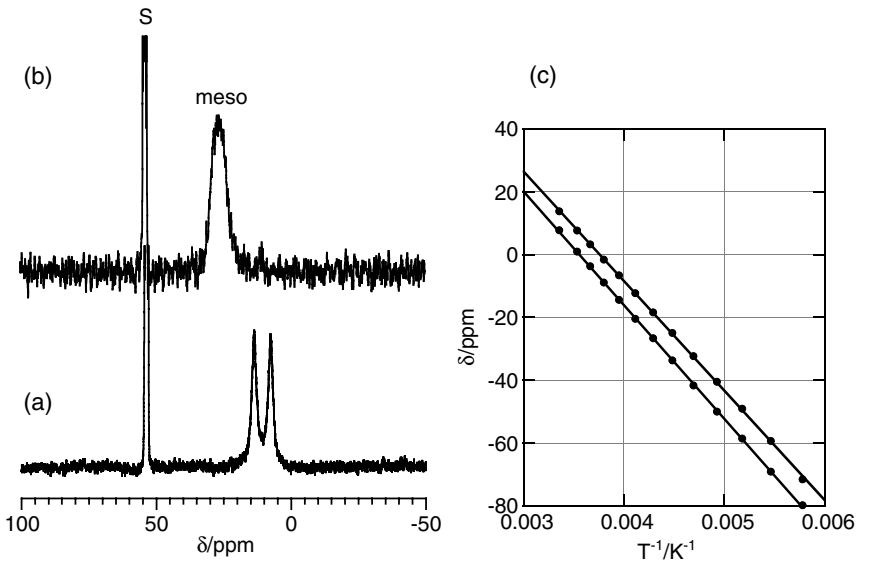

Figure 53. Temperature dependence of the *meso*-C signals in [Fe(OETPP)(2-MeBzIm)]$^+$ at (a) 298 K and (b) 338 K. (c) Curie plots of the *meso*-C signals. (Adapted with permission from Ref. 232. Copyright 2009, Wiley-VCH Verlag GmbH & Co.)

almost constant, –48, –49, and –45 ppm, which are close to the corresponding chemical shift in intermediate-spin Fe(OETPP)ClO_4. Thus, the ^{13}C NMR results also suggest that these complexes are in the S = 3/2 spin state in CD_2Cl_2 solution.

As shown in Figure 53a, the *meso*-C shows two signals at 7.7 and 13.6 ppm at 298 K, suggesting that the ligand rotation about the Fe–N_{axial} bond is slow on the NMR time scale, even at ambient temperature.[90–93,235–239] These signals have broadened and coalesced at 338 K as shown in Figure 53b, from which the activation free energy ($\Delta G^{\neq}$) for rotation is estimated to be 64 kJ mol^{-1}. A similar phenomenon is observed in the 2-MeIm complex at lower temperature; $\Delta G^{\neq}$ is 35 kJ mol^{-1} at 197 K. In contrast, the HIm complex maintains a single *meso*-C signal even at 183 K. The extremely high barrier to rotation in the 2-MeBzIm complex can be ascribed to the fact that the bulky 2-MeBzIm ligand is situated in the cavity created by the saddled porphyrin ring, as is speculated from the molecular structure of the analogous 2-MeIm complex shown in Figure 51b.

Figure 54 shows the EPR spectra of the HIm and 2-MeIm complexes taken in frozen CH_2Cl_2 solution. As shown in Figure 54a, the 2-MeIm complex exhibits a major signal at $g = 5.9$ together with a minor signal at $g = 4.0$, which clearly indicates that the major component adopts the S = 5/2 state at 60 K. As the temperature is further lowered, the signal at $g = 4.0$ decreases in intensity and completely disappears at 4 K. Thus, the [Fe(OETPP)(2-MeIm)]$^+$ complex is in a quite pure

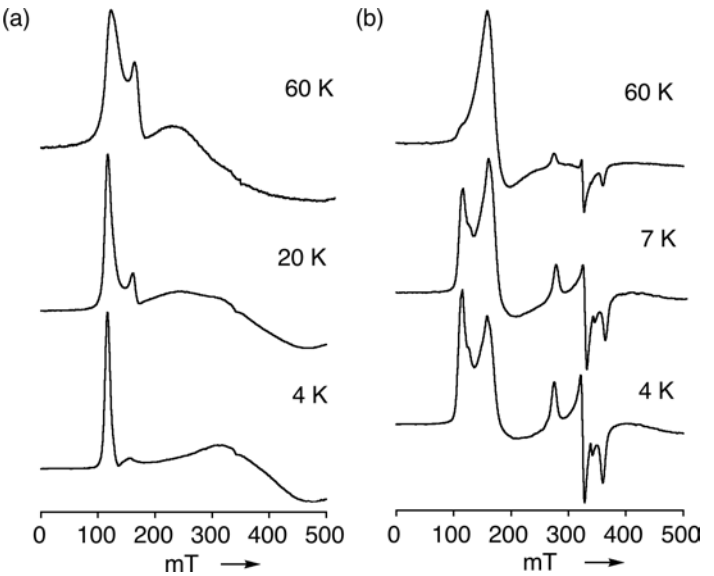

Figure 54. Temperature-dependent EPR spectra of (a) $[Fe(OETPP)(2\text{-MeIm})]^+$ and (b) $[Fe(OETPP)(HIm)]^+$ recorded in CH_2Cl_2 solution. (Adapted with permission from Ref. 232. Copyright 2009, Wiley-VCH Verlag GmbH & Co.)

S = 5/2 state at 4 K. The process is reversible, since the original spectrum is completely reproduced when the temperature is raised back to 60 K. The NMR and EPR spectra can best be explained in terms of spin crossover from the S = 3/2 to the S = 5/2 spin state as the temperature is lowered.

The EPR spectra of the HIm complex shown in Figure 54b are even more unusual. This complex exhibits a major signal at $g = 4.0$ at 60 K though some weak signals are observed at a higher field. As the temperature is lowered, the signal at $g = 4.0$ decreases in intensity while the signals at $g = 6.0$, 2.5, 2.1 increase. At 4 K, the HIm complex exists as a mixture of three species with different spin states: an S = 5/2 species with $g_\perp = 6.0$, an S = 3/2 species with $g_\perp = 4.0$, and an S = 1/2 species with $g = 2.47$, 2.10, 1.55. Formation of the S = 1/2 and S= 5/2 complexes can be ascribed to the disproportionation given by Eq. 23:

$$2[Fe(OETPP)(HIm)]^+ \leftrightarrows [Fe(OETPP)(HIm)_2]^+ + Fe(OETPP)ClO_4. \qquad (23)$$

This possibility is, however, completely ruled out, since $Fe(OETPP)ClO_4$ is well characterized as an essentially pure S = 3/2 complex.[37,180,181] Furthermore, the g values of $[Fe(OETPP)(HIm)_2]ClO_4$ determined under the same conditions are 2.72, 2.37, and 1.64, which are different from those of the S = 1/2 complex observed at 4 K.[82] Thus, it is reasonable to deduce that the S = 5/2 and S = 1/2

complexes are spin isomers and that they exist as an equilibrium mixture with the S = 3/2 complex.

Existence of the three kinds of spin isomers indicates that there are three different structures in [Fe(OETPP)(HIm)]ClO_4 at extremely low temperatures. The spin crossover from the S = 3/2 to the S = 1/2 spin state at lower temperature induces a contraction of the Fe–N(axial) and Fe–N(equatorial) bonds, as in the case of [Fe(OETPP)Py_2]$^+$ listed in Table 24(b).[212] Similar spin crossover is known in the five-coordinate iron(II) porphyrin [Fe(TPP)(CN)]$^-$ reported by Scheidt and coworkers.[234] This complex exhibits a decrease in both the Fe–CN bond length and the out-of-plane distance of the iron(II) ion by 0.23 and 0.28 Å, respectively, as structural consequences of the spin crossover from the S = 2 spin state at 400 K to the S = 0 spin state at 100 K.

In contrast to the spin crossover from the S = 3/2 to the S = 1/2 spin state, spin crossover from the S = 3/2 to the S = 2/5 spin state should increase the out-of-plane displacement of the iron(III) ion toward the axial imidazole ligand as the temperature is lowered. As mentioned in the previous section, the five-coordinate saddle shaped monoaqua complex [Fe(OMTArP)(H_2O)]$^+$ also exhibits spin crossover from S = 3/2 to S = 5/2 at extremely low temperature.[101]

The question arises as to why two kinds of spin crossover processes take place simultaneously only in [Fe(OETPP)(HIm)]$^+$. In the case of [Fe(OETPP)(2-MeIm)]$^+$ and [Fe(OETPP)(2-MeBzIm)]$^+$ carrying hindered imidazole ligands, the approach of the axial ligand toward the porphyrin ring should be hampered due to steric repulsion between the axial ligand and the porphyrin core. A space-filling model of the crystal structure of [Fe(OETPP)(2-MeIm)]$^+$ suggests that a further approach of the ligand toward the porphyrin ring is impossible because of steric repulsion between the ligand methyl and the *meso*-phenyl groups. For this reason, [Fe(OETPP)(2-MeIm)]$^+$ and [Fe(OETPP)(2-MeBzIm)]$^+$ exhibit only one type of spin crossover process, S = 3/2 to S = 5/2, in contrast to the case of [Fe(OETPP)(HIm)]$^+$. Thus, the electronic structure of monoimidazole complexes is quite different from those of other five-coordinate complexes, Fe(Por)X, where X is an anionic ligand such as ClO_4^- or Cl^-.

As is well known, imidazole and alkyl-substituted imidazoles are intrinsically strong-field ligands. In monoimidazole complexes, however, the field strength of imidazole varies drastically due to steric interactions with the porphyrin core and/or peripheral substituents. These steric interactions should influence not only the Fe–N_{axial} bond lengths but also the Fe–N_{axial} tilt angle from the heme normal plane. All of these structural changes affect the field strength of imidazole ligands and result in the formation of a unique complex showing the S = 5/2, S = 3/2, and S = 1/2 spin states as an equilibrium mixture. Figure 55 summarizes the magnetic behavior of [Fe(OETPP)(HIm)]$^+$. These findings cast light on the long-standing mystery of the ambiguous spin state of cytochromes c′.[215]

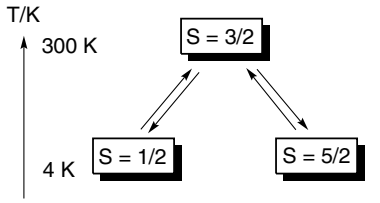

Figure 55. The spin crossover in the saddle-shaped monoimidazole complex [Fe^{III}(OETPP)(HIm)]$^+$. (Adapted with permission from Ref. 332. Copyright 2009, Wiley-VCH Verlag GmbH & Co.)

VI. Oxidized Products of Iron(III) Porphyrin Complexes

A. One-Electron-Oxidized Products

High-valent iron porphyrin complexes have been extensively studied both experimentally and theoretically because they play important roles in the catalytic cycles of a number of heme enzymes.[4–17] One-electron oxidation of iron(III) porphyrins should form either an iron(IV) porphyrin or an iron(III) porphyrin cation radical. However, most publications have reported the formation of iron(III) porphyrin cation radicals. These radical species give characteristic ^{1}H NMR spectra, where some of the signals appear at extraordinary upfield or downfield positions due to the presence of half-occupied porphyrin orbitals.[11,26,40]As mentioned in the previous sections, iron(III) porphyrin complexes can adopt various electronic structures, including the S = 5/2, S = 3/2, and S = 1/2 spin states.[25–35] Some complexes exhibit spin crossover phenomena between two of the three spin states. Furthermore, each spin state can have different electron configurations, as is well exemplified in the low-spin complexes which adopt either the $(d_{xy})^2(d_{xz}, d_{yz})^3$ or the $(d_{xz}, d_{yz})^4(d_{xy})^1$ electronic ground state.[25–31] Similarly, at least two types of electronic ground states exist even in the intermediate-spin complexes, i.e. $(d_{xy})^2(d_{xz}, d_{yz})^2(d_{z^2})^1$ and $(d_{xz}, d_{yz})^3(d_{xy})^1(d_{z^2})^1$.[37–39,104,168,184] The unpaired electron in the porphyrin orbital cannot be independent of the paramagnetic iron center. It can interact with the paired and/or unpaired electrons in the iron 3d orbitals. Consequently, the ^{1}H NMR spectra should be affected by the spin states and electron configurations of the iron(III) ions.[40] In the case of iron(IV) porphyrins, the iron can adopt the S = 0, S = 1, or S = 2 spin state, though no examples have ever been reported for S = 0 and S = 2. The unpaired electrons in the S = 1 complexes can be delocalized to the porphyrin ring by the interactions with the porphyrin π orbitals to give characteristic ^{1}H NMR spectra. For these reasons, ^{1}H NMR spectroscopy has been used as a powerful tool for determining the fine electronic structures of one-electron oxidized products of iron(III) porphyrins. In this section, we will describe the characteristic features of the NMR spectra of one-electron-oxidized products

of iron(III) porphyrins such as iron(III) porphyrin cation radicals and iron(IV) porphyrins. These oxidized products are signified as follows for the anionic ligand X^-; $[Fe^{III}(Por^{\cdot})]^{2+}$, $[Fe^{III}(Por^{\cdot})X]^+$, $[Fe^{III}(Por^{\cdot})X_2]$, $[Fe^{IV}(Por)]^{2+}$, $[Fe^{IV}(Por)X]^+$, and $[Fe^{IV}(Por)X_2]$. The oxidation number is added to avoid confusion.

1. *Iron(III) Porphyrin Cation Radicals*

a. *High-spin iron(III) porphyrin cation radicals*

One-electron oxidation of iron(III) porphyrins was reported by Goff *et al.*[240] These authors electrochemically oxidized a series of [Fe(TPP)X], where X is an anionic ligand such as F^-, Cl^-, Br^-, I^-, or ClO_4^-, and found that the one-electron oxidation potentials are quite insensitive to the axial ligands; the first oxidation potentials are *ca.* 1.1 V for all the complexes examined.[240] Consequently, these oxidized species are characterized as iron(III) porphyrin cation radicals, $[Fe^{III}(TPP^{\bullet})X]^+$, rather than iron(IV) porphyrins, $[Fe^{IV}(TPP)X]^+$. Marchon, Reed, and coworkers chemically oxidized $[Fe^{III}$(4-Me-TPP)Cl] by using the hexachloroantimonate salt of phenoxathiin cation radical $(Phenox^{\bullet})SbCl_6$ and obtained $[Fe^{III}$(4-Me-TPP$^{\cdot}$)Cl$](SbCl_6)$.[241] The X-ray crystal structure of $[Fe^{III}$(4-Me-TPP$^{\bullet}$)Cl$](SbCl_6)$ revealed that the crystal lattice consists of discrete $[Fe^{III}$(4-Me-TPP$^{\bullet}$)Cl$]^+$ and $SbCl_6^-$ ions where the porphyrin core is strongly S_4-saddled.[241] In the chemical oxidation of $[Fe^{III}$(TPP)Cl], the porphyrin cation radical $[Fe^{III}$(TPP$^{\cdot}$)Cl$](ClO_4)$ thus formed exhibits a pyrrole-H signal at 66.1 ppm at 299 K, which indicates that the iron(III) ion maintains the high-spin (S = 5/2) state.[242] The cation radical nature of the porphyrin ring can clearly be seen in the ^{1}H NMR spectra of these complexes. The characteristics in ^{1}H NMR spectra are the chemical shifts of the *meso*-phenyl signals. They are at 37.6, 34.4 ppm for the *o*-H, −12.4 ppm for the *m*-H, and 29.5 ppm for the *p*-H.[242] Observation of two kinds of *o*-H signals is a direct indication that the iron is five-coordinate. The presence of extremely downfield- or upfield-shifted *meso*-phenyl-H signals indicates that the *meso*-carbon atoms have a large amount of spin density, which in turn indicates that the a_{2u} orbital of the porphyrin is half-occupied. As mentioned in the previous section, the unpaired electron at the *meso*-carbon atoms should induce an upfield shift of the *o*- and *p*-H signals and a downfield shift of the *m*-H signals. Thus, the chemical shift pattern of the *meso*-phenyl signals in $[Fe^{III}(TPP^{\bullet})Cl]^+$ suggests that the *meso*-carbon atoms have a sizeable amount of negative spin, which can only be explained in terms of antiferromagnetic coupling between the radical and metal spins.[240,242] In fact, the Mössbauer spectroscopy and magnetic susceptibility studies of the solid sample indicate that the complex shows a strong antiferromagnetic coupling between the S = 5/2 iron(III) ion and the S = 1/2 porphyrin radical to lead to an

overall S = 2 spin state.[241,243,244] [Fe^{III}(TDP)Cl] is similarly oxidized to form [Fe^{III}(TDP$^{\bullet}$)Cl]$^{+}$.[245] The pyrrole-H signal appears at 72 ppm at 217 K. Upfield shifts of the *o*-CH_3 signals at −8.0 and −10.3 ppm in [Fe^{III}(TDP$^{\cdot}$)Cl]$^{+}$ correspond to the downfield shifts of the *o*-H signals in [Fe^{III}(TPP$^{\bullet}$)Cl]$^{+}$, suggesting that [Fe(TPP$^{\cdot}$)Cl]$^{+}$ and [Fe^{III}(TDP$^{\cdot}$)Cl]$^{+}$ adopt the same electronic structure.[245]

While the *meso*-phenyl signals of [Fe^{III}(TPP)Cl] exhibit large isotropic shifts upon one-electron oxidation, the isotropic shift of the *meso*-H signal is reduced in the case of [Fe^{III}(OEP)Cl]; the *meso*-H signal appears at −54 ppm in [Fe^{III}(OEP)Cl], while it appears at −18 ppm in oxidized [Fe^{III}(OEP$^{\bullet}$)Cl]$^{+}$.[242] Similarly, the isotropic shifts of the CH_2 signals are reduced upon one-electron oxidation; the CH_2 signals appear at 43.1 and 39.5 ppm in [Fe^{III}(OEP)Cl], while they are observed at 30.5 and 29.6 ppm in [Fe^{III}(OEP$^{\bullet}$)Cl]$^{+}$. Reduced isotropic shifts in [Fe^{III}(OEP$^{\bullet}$)Cl]$^{+}$ can be explained in terms of electron removal from the a_{1u} orbital; the a_{1u} orbital has a large coefficient at the C_{α} atoms, as shown in Figure 4. Thus, the unpaired electron in the a_{1u} orbital in [Fe^{III}(OEP$^{\bullet}$)Cl]$^{+}$ is delocalized to the C_{α} atoms and should shift the *meso*-H signal to downfield positions. However, the NMR chemical shifts can also be explained in terms of the weak antiferromagnetic coupling of the a_{2u} radical with the metal spins;[26] the a_{2u} orbital can interact with the iron d_{z^2} orbital in five-coordinate C_{4v} complexes, as shown in Table 1. The antiferromagnetic coupling between the iron(III) and a_{2u} radical spins is most explicitly observed in the analogous iron(III) octaethyloxophlorin radical, [Fe^{III}(OEPO$^{\bullet}$)Br].[246] Because of the large negative spin at the *meso*-C atoms, the *meso*-H signals resonate at extremely downfield positions, i.e. 344 and 232 ppm. Table 30 lists the chemical shifts of some iron(III) porphyrin cation radicals together with those of the precursors. These data indicate that complexes carrying aryl groups at the *meso* positions exhibit similar chemical shifts. Thus, these complexes are classified as high-spin iron(III) cation radicals where the a_{2u} radical spin antiferromagnetically couples with metal spins.[149,247,248]

^{13}C NMR spectroscopy is quite useful for determination of the electronic structures of iron(III) porphyrin complexes.[30,31,208] Little is known, however, of the ^{13}C NMR spectra of iron(III) porphyrin radicals although their importance and usefulness as probes of the electronic structure of radical species was pointed out many years ago.[249] This is because some ^{13}C NMR signals in radical species are quite difficult to observe due to their extreme broadness. In fact, the ^{13}C NMR spectrum of [Fe^{III}(TPP$^{\bullet}$)Cl]$^{+}$ exhibits only four signals at 1050, 958, 137, and 8.7 ppm for C_{β}, C_{ipso}, *m*-C, and *p*-C, respectively. No *meso*-C signal is observed even by the use of *meso*-^{13}C (99% ^{13}C)–enriched [Fe^{III}(TPP$^{\bullet}$)Cl]$^{+}$. Hoshino and Nakamura have determined the ^{13}C NMR chemical shifts of [Fe^{III}(TPP$^{\bullet}$)Cl]$^{+}$ by the titration method.[250] As shown in Figure 56, addition of only 0.075 equivalents of [Fe^{III}(TPP$^{\bullet}$)Cl]$^{+}$ to the CD_2Cl_2 solution of [Fe^{III}(TPP)Cl] shifts the *meso*-C signal

Table 30. ^{1}H NMR chemical shifts of (a) high-spin iron(III) porphyrin cation radicals $[Fe^{III}(Por^{\cdot})Cl]^+$ and (b) their parent complexes $[Fe^{III}(Por)Cl]$ taken at ambient temperatures.

	Pyrrole			*Meso*					
Complexes	H	$CH_2(\alpha)$	$CH_3(\alpha)$	*o*-H(CH_α)		*m*-H(CH_β)		*p*-H	Ref.
(a) $[FeIII(Por^{\cdot})X]^+$									
$[Fe^{III}(OEP)Cl]^+$	—	30.5, 29.6	—	–18[c]		—		—	242
$[Fe^{III}(TPP^{\cdot})Cl]^+$	66.1	—	—	37.6	34.4	–12.4		29.5	242
$[Fe^{III}(TDP^{\cdot})Cl]^+$	68.0	—	—	–8.0[b]	–10.3[b]	2.0[b]		13.7	245
$[Fe^{III}(4\text{-OMe-TPP}^{\cdot})Cl]^+$	59.9	—	—	48.1		–9.8		–5.7[b]	242
$[Fe^{III}(3\text{-Me-TPP}^{\cdot})Cl]^+$	68.7	—	—	44.5	42.6	–13.0	5.9[b]	37	241
$[Fe^{III}(4\text{-Me-TPP}^{\cdot})Cl]^+$	64.8	—	—	48.0		–14.7		–30.5[b]	241
$[Fe^{III}(2,6\text{-}F_2TPP^{\cdot})Cl]^+$	85.5	—	—	–140[d]		–3.5	–4.3	16.0	247
$[Fe^{III}(OMTPP^{\cdot})Cl]^+$	—	—	69.9, 63.0	39.7	36.9	–11.0	–12.5	31.7	248
$[Fe^{III}(OETPP^{\cdot})Cl]^+$	—	71.2, 56.1 24.7, 16.6	—	37.6	34.9	–10.1	–11.5	28.8	248
$[Fe^{III}(T^iPrP^{\cdot})Cl]^+$	64.6	—	—	(–38.1)	—	(–9.6)		—	[e]
(b) $[Fe^{III}(Por^{\cdot})X]^+$									
$[Fe^{III}(OEP)Cl]$	—	43.1, 39.5	—	–54[c]	—	—	—	—	242
$[Fe^{III}(TPP)Cl]$	80.1	—	—	6.2	3.8	12.6	12.0	5.8	248
$[Fe^{III}(TDP)Cl]$	79.7	—	—	6.2[b]	3.7[b]	(3.8)	(3.3)	8.0	[e]
$[Fe^{III}(4\text{-OMe-TPP})Cl]$	79.6	—	—	ca. 6	—	12.8	11.9	5.2[b]	242
$[Fe^{III}(2,6\text{-}F_2TPP)Cl]$	80.0	—	—	–78.5[d]	–81.0[d]	13.5	11.8	7.0	247
$[Fe^{III}(OMTPP)Cl]$	—	—	51.1	11.3	8.6	12.5	12.2	7.4	248
$[Fe^{III}(OETPP)Cl]$	—	49.0, 34.8 32.1, 20.1		11.5	9.1	12.4	12.2	7.5	248
$[Fe^{III}(T^iPrP)Cl]$	90.5	—	—	(28.9)	—	(9.5)	—	—	97

[a]Data in parentheses are the chemical shifts of the *meso*-alkyl signals. [b]CH_3. [c]*Meso*-H. [d]*o*-F. [e]Nakamura M., *et al.*; unpublished results.

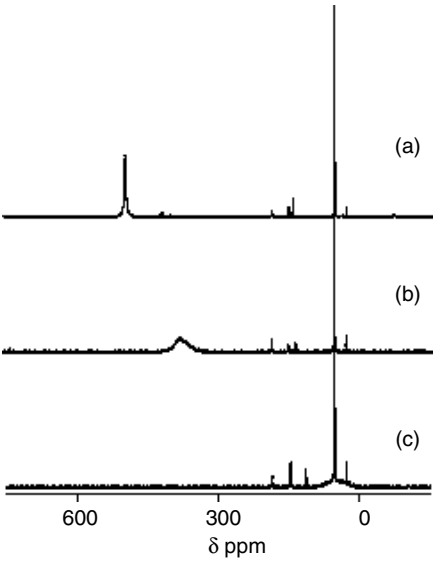

Figure 56. Change in the ^{13}C NMR spectrum of *meso*-^{13}C–enriched [Fe^{III}(TPP)Cl] observed when (a) 0.00, (b) 0.075, and (c) 0.23 equivalents of *meso*-^{13}C–enriched cation radical [Fe(TPP$^{\bullet}$)Cl]$^{+}$ were added in CD_2Cl_2 solution at 298 K. (Adapted with permission from Ref. 250. Copyright 2005, Royal Society of Chemistry.)

from 495 to 376 ppm.[251,252] Furthermore, the half-heigth width ($W_{1/2}$) increases from 306 to 2530 Hz. When 0.23 equivalents of the radical are added, the *meso* signal with $W_{1/2}$ = 3890 Hz appears at 48.0 ppm. The signal is no longer observed after the addition of 0.3 equivalents of the radical. Since the electron exchange between [Fe^{III}(TPP)Cl] and [Fe^{III}(TPP$^{\cdot}$)Cl]$^{+}$ is fast on the ^{13}C NMR time scale, the observed chemical shift δ_{obs} is expressed by Eq. 24 in the presence of x equivalents of the radical, where δ_N and δ_R are the chemical shifts of the carbon atoms in [Fe^{III}(TPP)Cl] and [Fe^{III}(TPP$^{\cdot}$)Cl]$^{+}$, respectively. Plots of δ(obs) against 1/(1 + x) yield a straight line, from which the chemical shifts of *meso*-C, C_α, and *o*-C are determined to be −1910, 2230 and −721 ppm, respectively. Four other signals at 1050, 958, 137, and 8.7 ppm are assigned to C_β, *ipso*-C, *m*-C, and *p*-C, respectively. The ^{13}C NMR chemical shifts of [Fe^{III}(TPP$^{\cdot}$)Cl]$^{+}$ are summarized in Table 31 together with those of some high-spin [Fe^{III}(Por)X]. The large upfield shift of the *meso*-C signal is a direct indication of antiferromagnetic coupling in this species. Because of the large negative spin at the *meso*-C and pyrrole-N atoms, the neighboring C_α signal appears at an extraordinary downfield position, i.e. 2230 ppm.

$$\delta(\text{obs}) = \delta_R + \frac{\delta_N \bar{G} \delta_R}{1 + x}. \tag{24}$$

Table 31. ^{13}C NMR chemical shifts of $[Fe^{III}(TPP^{\cdot})Cl]^{+}$ and those of some high-spin $[Fe^{III}(Por)X]$ determined in CD_2Cl_2 solution at 298 K.[a]

	Pyrrole				*Meso*					
Complexes	C_α	C_β	CH_2	CH_3	*Meso*	*Ipso*	*o*(CH_α)	*m*(CH_β)	*p*(CH_c)	Ref.
$[Fe^{III}(TPP^{\bullet})Cl]^{+}$	*2230*	1050	—	—	*–1910*	958	*–721*	137	8.7	250
$[Fe^{III}(TPP)Cl]$	1204	1321	—	—	495	–71.7	417, 400	152, 148	143	250–252
$[Fe^{III}(OETPP)Cl]$	642, 525	972	162, 116	61, 55	456	25	353, 349	144	148	68
$[Fe^{III}(T^{i}PrP)Cl]$	1056	1360	—	—	670	—	(–199)	(358)	—	b
$[Fe^{III}(T^{n}PrP)Cl]$	1166	1369	—	—	592	—	(–194)	(504)	(28)	b

[a]Chemical shifts written in *italic* are obtained by the titration method. [b]Nakamura, M. *et al.*, unpublished results.

b. *Mixed high-spin and intermediate-spin iron(III) porphyrin cation radicals*

As mentioned in Section IV, iron(III) complexes carrying weak-field axial ligands adopt the mixed high-spin and intermediate-spin state. What is the electronic structure of the corresponding iron(III) porphyrin cation radicals? Marchon, Reed, and others oxidized $[Fe(TPP)]ClO_4$ by using thianthrene cation radical perchlorate, $(Thian)^{\bullet+}ClO_4^-$, or $Fe(ClO_4)_3$ and obtained the iron(III) porphyrin cation radical $[Fe^{III}(TPP^{\bullet})(ClO_4)_2]$.[241] The X-ray crystal structure of $[Fe^{III}(TPP^{\bullet})(ClO_4)_2]$ reveals that, unlike the highly saddled $[Fe^{III}(TPP^{\bullet})Cl](SbCl_6)$ core, the $[Fe^{III}(TPP^{\bullet})(ClO_4)_2]$ core is nearly planar.[241] The ^1H NMR spectrum shows that the pyrrole-H signal appears at 31.4 ppm, and the *o*-, *m*-, and *p*-H signals appear at −19.3, 34.7, and −12.9 ppm, respectively, at 298 K.[241,246] Thus, the chemical shifts of $[Fe^{III}(TPP^{\bullet})(ClO_4)_2]$ are quite different from those of $[Fe^{III}(TPP^{\bullet})Cl](SbCl_6)$. It should be noted that the signs of chemical shifts of the phenyl protons are reversed; they are 36.0 (ave), −12.3, and 29.5 ppm for the *o*-, *m*,- and *p*-H signals, respectively, in the case of $[Fe^{III}(TPP^{\bullet})Cl](SbCl_6)$.[242] The NMR data suggest that the *meso*-C atoms of $[Fe^{III}(TPP^{\bullet})(ClO_4)_2]$ have a large amount of positive spin, which indicates that there is no appreciable antiferromagnetic coupling in this complex. The result is understandable, because the half-occupied a_{2u} orbital is orthogonal to any of the iron 3d orbitals in the planar D_{4h} complex. The solution magnetic moment of this complex ranges from 4.4 to 5.2 μ_B, depending on samples preparation.[246] The NMR spectrum of analogous $[Fe^{III}(TPP^{\bullet})(SO_3CF_3)_2]$ shows the pyrrole-H signal at 43.9 ppm at 305 K and the *o*-, *m*-, and *p*-H signals at −17.1, 31.3, and −11.3 ppm, respectively, at 309 K. Table 32 lists the chemical shifts of one-electron-oxidized $[Fe^{III}(TPP^{\bullet})X_2]$ together with those of the parent $[Fe^{III}(TPP)X]$ where X is a weak-field anionic ligand such as ClO_4^- or $CF_3SO_3^-$. The data in the table indicate that the pyrrole-H signals in both $[Fe^{III}(TPP^{\bullet})X_2]$ and $[Fe^{III}(TPP)X]$ move upfield as the axial ligand X changes from $CF_3SO_3^-$ to ClO_4^-; note that ClO_4^- is a much weaker ligand than $CF_3SO_3^-$ in the magnetochemical series shown in Eq. 18.[36,157,158] Thus, the pyrrole-H chemical shifts of these complexes are mainly determined by the contribution of the S = 3/2 spin state. It should be noted that the electronic structure of $[Fe^{III}(TPP^{\bullet})(ClO_4)_2]$ in solution seems to be different from that in the solid, because the solid sample of $[Fe^{III}(TPP^{\cdot})(ClO_4)_2]$ exhibits a magnetic moment of 6.5 μ_B, which suggests the presence of ferromagnetic coupling between the radical spin and the high-spin iron(III) spins.[241] As listed in Table 32, the chemical shifts of $[Fe^{III}(TMP^{\cdot})(ClO_4)_2]$ are very sensitive to solvent and temperature.[253] In CD_2Cl_2 solution at 294 K, the ^1H NMR spectrum shows the pyrrole-H signal at 18.7 ppm and the *o*-CH_3, *m*-H, and *p*-CH_3 signals at 20, 55, and 12.5 ppm, respectively. Thus, the complex has large positive spin at the *meso*-C atoms due to the formation of the a_{2u} radical. As the temperature is lowered, the pyrrole-H signal moves

Table 32. ^{1}H NMR chemical shifts of mixed high-spin and intermediate-spin iron(III) porphyrin cation radicals [Fe^{III}(Por·)XY] and their precursors [Fe^{III}(Por)X], where X and Y are weak anionic ligands.[a]

				Meso-phenyl			
Complex	T (K)	Solvent	Pyrrole-H	*o*-H	*m*-H	*p*-H	Ref.
[Fe^{III}(TPP·)$(SO_3CF_3)_2$]	309	CD_2Cl_2	43.9[b]	–17.1	31.3	–11.3	149
[Fe^{III}(TPP·)$(ClO_4)_2$]	298	CD_2Cl_2	31.4	–19.3	34.7	–12.9	149
[Fe^{III}(4-Me -TPP·)$(ClO_4)_2$]	293	CD_2Cl_2	31.6	–16.6	31.6	(31.6)	254
[Fe^{III}(TMP·)$(ClO_4)_2$]	294	CD_2Cl_2	18.7	(20)	55	(12.5)	253
	195	CD_2Cl_2	–22.5	(32.2)	90.9	(19.7)	253
	195	CD_2Cl_2/ CD_3OD[c]	ca. 100[d]	(41)	122, 119	(27)	253
	294	toluene-d_8	39.6	(21.1)	58.2	(12.3)	253
	195	toluene-d_8	61	(39)	115	(23)	253
[Fe^{III}(TPP)](SO_3CF_3)	302	$CDCl_3$	39.3	9	12.5	7.5	149
[Fe^{III}(TPP)]ClO_4	302	$CDCl_3$	13.0	9.2	11.9	7.7	149
[Fe^{III}(TMP)]ClO_4	295	CD_2Cl_2	–12.5	(3.35)	10.52	(3.86)	253
	195	CD_2Cl_2/ CD_3OD[c]	47.9	(4.82)	11.9	(5.96)	253

[a]Data in parentheses are the chemical shifts of the methyl signals. [b]Data at 305 K. [c][Fe^{III}(TMP·)$(ClO_4)_2$] is converted to high-spin [Fe^{III}(TMP•)$(CD_3OD)_2$]$(ClO_4)_2$ in CD_2Cl_2/5% CD_3OD solution. [d]Three signals are observed at 93.1, 102, 108 ppm.

upfield while the *meso*-phenyl signals shift further downfield. At 195 K, the pyrrole-H signal is observed at –22.5 ppm while the *o*-CH_3, *m*-H, and *p*-CH_3 signals appear at 32.2, 90.9, and 19.7 ppm, respectively. The NMR spectral behavior suggests that the interaction between the a_{2u} radical and iron(III) spins is fairly weak and that the spin state of iron(III) changes from the mixed S = 5/2, S = 3/2 at state 294 K to the mainly S = 3/2 state at 195 K. In toluene-d_8 solution, however, the pyrrole-H signal moves downfield from 39.6 ppm at 294 K to 61 ppm at 195 K. This result can be explained in terms of an increase in population of the high-spin state in nonpolar toluene-d_8 solution.[249] Upon addition of methanol-d_4 to the CD_2Cl_2 solution of [Fe(TMP•)$(ClO_4)_2$] at 195 K, the pyrrole-H signal shows a large downfield shift from –22.5 to *ca.* 100 ppm. Thus, [Fe(TMP•)$(ClO_4)_2$] is converted into [Fe(TMP•)$(CD_3OD)_2$]$(ClO_4)_2$, which is in a high-spin state with the a_{2u} porphyrin cation radical. Although both [Fe(TMP•)$(CD_3OD)_2]^{2+}$ and [Fe(TMP•)Cl^+] have high-spin iron(III) ions, the radical spin in the former complex is almost independent of the high-spin iron(III).

c. *Low-spin iron(III) porphyrin cation radicals*

It is possible to obtain six-coordinate low-spin iron(III) porphyrin cation radicals [Fe^{III}(Por•)$L_2]^{2+}$ by addition of neutral axial ligands L to the S = 5/2 or mixed

S = 3/2, S = 5/2 iron(III) porphyrin cation radicals such as $[Fe^{III}(TPP^{\bullet})Cl]^{+}$ and $[Fe^{III}(TMP^{\bullet})(ClO_4)_2]$. Depending on the nature of the axial ligands and the deformation mode of the porphyrin ring, the low-spin iron(III) ions adopt either the $(d_{xy})^2(d_{xz}, d_{yz})^3$ or the $(d_{xz}, d_{yz})^4(d_{xy})^1$ ground state. Thus, the interaction of the porphyrin radical with these two types of iron(III) ions should be different.

i. Iron(III) with the $(d_{xy})^2(d_{xz}, d_{yz})^3$ electron configuration

Addition of imidazole to a CD_2Cl_2 solution of $[Fe^{III}(TPP^{\bullet})Cl^{+}]$ at 235 K yields the corresponding bis-HIm complex $[Fe^{III}(TPP^{\bullet})(HIm)_2]^{2+}$.[255] This complex shows the pyrrole-H, *o*-, *m*-, and *p*-H signals at −40.1, −31.7, 30.4, and −22.1 ppm, respectively, at 235 K. The NMR data suggest that the oxidized bis-HIm complexes are best described as low-spin iron (III) porphyrin cation radicals, where the radical spin is in the a_{2u} orbital. The solution magnetic moment for the analogous $[Fe^{III}(4\text{-}OMe\text{-}TPP^{\cdot})(HIm)_2]^{2+}$ is 2.8 ± 0.2 μ_B, suggesting that this spin does not strongly couple with the metal spin. The result is indicative of a planar porphyrin structure where the a_{2u} orbital is orthogonal to any of the iron 3d orbitals. As mentioned in Section III, the pyrrole-H chemical shifts are affected by the electronic ground state of low-spin iron(III). While low-spin complexes with the $(d_{xy})^2(d_{xz}, d_{yz})^3$ ground state exhibit pyrrole-H signals rather upfield due to d_{π}–$3e_g$ interactions, those with the $(d_{xz}, d_{yz})^4(d_{xy})^1$ ground state exhibit them close to their diamagnetic positions, as shown in Tables 2–5. Thus, it is clear that $[Fe^{III}(TPP^{\bullet})(HIm)_2]^{2+}$ adopts the S = 1 $(d_{xy})^2(d_{xz}, d_{yz})^3(a_{2u})^1$ ground state.

Addition of imidazole ligands such as 2-MeIm and HIm to a CD_2Cl_2 solution of $[Fe^{III}(TDP^{\bullet})Cl^{+}]$ at 195 K forms $[Fe^{III}(TDP^{\bullet})(2\text{-}MeIm)_2]^{2+}$ and $[Fe^{III}(TDP^{\bullet})(HIm)_2]^{2+}$, respectively.[245] Figure 57 shows the ^1H NMR spectra of (a) $[Fe^{III}(TDP^{\bullet})Cl^{+}]$, (b) $[Fe^{III}(TDP^{\bullet})(2\text{-}MeIm)_2]^{2+}$, and (c) $[Fe^{III}(TDP^{\bullet})(2\text{-}MeIm\text{-}d_6)_2]^{2+}$ taken in CD_2Cl_2 solution at 217 K. As shown in Figure 57b, $[Fe^{III}(TDP^{\bullet})(2\text{-}MeIm)_2]^{2+}$ exhibits four pyrrole-H signals at −45.6, −45.9, −51.7, and −54.7 ppm at 217 K. Similarly, the complex shows four *o*-CH_3 signals at 42.4, 34.0, 8.0, and 6.7 ppm, four *m*-CH_3 signals at 4.7, 3.7, −0.6, and −0.7 ppm, and two *p*-H signals at −1.0 and −2.1 ppm. The number of signals indicates that rotation of the coordinating 2-MeIm is hindered on the ^1H NMR time scale to form a C_2 structure wherein the axial ligands are aligned perpendicularly along the C_{meso}–Fe–C_{meso} axes above and below the porphyrin ring, as in the case of the parent $[Fe^{III}(TDP)(2\text{-}MeIm)_2]^{+}$ complex.[90–93,235–238] Since the large downfield shifts of the *o*-CH_3 signals correspond to the large upfield shift of the *o*-H signal in the analogous $[Fe^{III}(TPP^{\bullet})(HIm)_2]^{2+}$ compound, it is clear that $[Fe^{III}(TDP^{\bullet})(2\text{-}MeIm)_2]^{2+}$ adopts the same electronic structure as $[Fe(TPP^{\bullet})(HIm)_2]^{2+}$, i.e. the S = 1, $(d_{xy})^2(d_{xz}, d_{yz})^3(a_{2u})^1$ ground state. Table 33 lists the chemical shifts of various low-spin

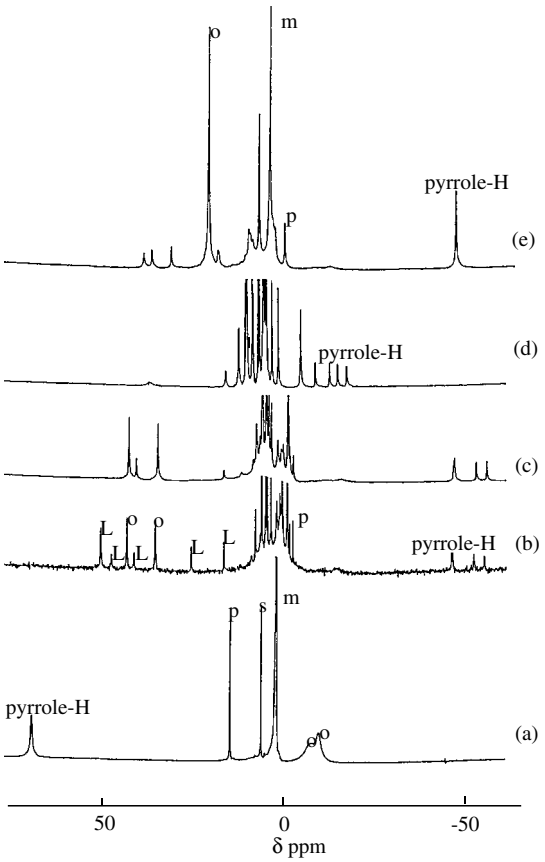

Figure 57. ^{1}H NMR spectra taken in CD_2Cl_2 solution at 217 K: (a) [Fe^{III}(TDP•)Cl], (b) [Fe^{III}(TDP•)(2-MeIm)$_2$]$^{2+}$ obtained by the addition of 4.0 equivalents of 2-MeIm to [Fe^{III}(TDP•)Cl], (c) [Fe^{III}(TDP•)(2-MeIm-d_5)$_2$]^2, (d) [Fe^{III}(TDP)(2-MeIm)$_2$]$^+$ obtained after standing the sample at 298 K for 10 min, and (e) [Fe^{III}(TDP•)(HIm)$_2$]$^{2+}$ obtained by the addition of 4.5 equivalents of HIm to [Fe^{III}(TDP•)Cl]. The Symbols o, m, and p indicate the *o*-CH_3, *m*-CH_3, and *p*-H signals, respectively. The symbols L and s indicate the ligand and solvent signals, respectively. (Adapted with permission from Ref. 245. Copyright 1996, Chemical Society of Japan.)

iron(III) porphyrin cation radicals [Fe^{III}(Por•)L_2]$^{2+}$ together with the parent [Fe(Por)L_2]$^+$, respectively.

ii. Iron(III) with the $(d_{xz}, d_{yz})^4(d_{xy})^1$ electron configuration

As mentioned in Section III, highly ruffled low-spin [Fe(T^iPrP)L_2]$^+$ adopts the less common $(d_{xz}, d_{yz})^4(d_{xy})^1$ ground state regardless of the kind of axial ligands.[30,31,52,82] In fact, the pyrrole-H and *meso*-C signals of [Fe(T^iPrP)(HIm)$_2$]$^+$ appear at downfield positions, namely 0.1 and 332 ppm, respectively, at 223 K, which unambiguously

Table 33. ^{1}H NMR chemical shifts of low-spin iron(III) porphyrin cation radicals $[Fe^{III}(Por^{\cdot})L_2]^{2+}$ [(a), (b), and (c)] and those of thier precursors $[Fe^{III}(Por)L_2]^{+}$ [(a′), (b′), and (c′)] where L is neutral ligand.[a]

			Meso					
Complexes	T (K)	Pyrrole-H	*o*-H	*m*-H	*p*-H	CH(a)	CH(b)	Ref.
(a) $[Fe(TArP^{\bullet})L_2]^{2+}$								
$[Fe(TPP^{\bullet})(HIm)_2]^{2+}$	235	–40.1	–31.7	30.4	–22.1			255
$[Fe(4\text{-}OMe\text{-}TPP^{\bullet})(HIm)_2]^{2+}$	235	–32.7	–36.3	24.8	(12.9)			255
$[Fe(2,4,6\text{-}(OMe)_3\text{-}TPP^{\bullet})(HIm)_2]^{2+}$	243	–40.4	(12.8)	26.7	(9.5)			255
$[Fe(TDP^{\bullet})(HIm)_2]^{2+}$	217	–49.1	(19.0)	(2.2)	–1.8			245
$[Fe(TDP^{\bullet})(2\text{-}MeIm)_2]^{2+}$	217	–49.5[b]	(22.8)[b]	(1.8)[b]	–1.6[b]			245
(b) $[Fe(TRP^{\bullet})L_2]^{2+}$								
$[Fe(TEtP^{\bullet})(HIm)_2]^{2+}$	223	–36.0				230.9	15.5	256
$[Fe(T^nPrP^{\bullet})(HIm)_2]^{2+}$	223	–34.1				232.6	–8.8	256
$[Fe(T^iPrP^{\bullet})(HIm)_2]^{2+}$	223	–20.4				42.4	9.0	256
$[Fe(TEtP^{\bullet})(2\text{-}MeIm)_2]^{2+}$	223	–33.7[b]				206.6[b]	14.4[b]	256
$[Fe(T^nPrP^{\bullet})(2\text{-}MeIm)_2]^{2+}$	223	–30.9[b]				208.2[b]	ca. –7	256
$[Fe(T^iPrP^{\bullet})(2\text{-}MeIm)_2]^{2+}$	223	–21.7[b]				47.9[b]	9.4[b]	256
(c) $[Fe(TMP^{\bullet})L_2]^{2+}$								
$[Fe(TMP^{\bullet})(HIm)_2]^{2+}$	213	–53.2	(20.1)	52.1	(7.0)			257
$[Fe(TMP^{\bullet})(4,5\text{-}Cl_2Im)_2]^{2+}$	213	–25.6	n.d.	24.8	(4.0)			257
$[Fe(TMP^{\bullet})(^t BuNC)_2]^{2+}$	213	4.64	(2.66)	6.78	(2.24)			257

(*Continued*)

Table 33. (*Continued*)

Complex	T (K)	Pyrrole-H	*Meso*					Ref.
			o-H	*m*-H	*p*-H	CH(a)	CH(b)	
(a′) [Fe(TArP)L_2]$^+$								
[Fe(TPP)(HIm)$_2$]$^+$	298	–16.8	5.1	6.2	6.3			c
[Fe(4-OMeTPP)(HIm)$_2$]$^+$	298	–16.6	5.0	5.8	(3.2)			c
[Fe(2,4,6-(OMe)$_3$-TPP)(HIm)$_2$]$^+$	298	–16.8	(1.7)	5.1	(3.8)			c
[Fe(TDP)(HIm)$_2$]$^+$	298	–16.4	(0.8)	(1.6)	6.1			c
(b′) [Fe(TRP)L_2]$^+$								
[Fe(TEtP)(HIm)$_2$]$^+$	223	–21.2				1.3	–1.2	256
[Fe(T^{n}PrP)(HIm)$_2$]$^+$	223	–20.9				2.4	–1.0	256
[Fe(T^{i}PrP)(HIm)$_2$]$^+$	223	0.6				16.5	3.9	256
[Fe(TEtP)(2-MeIm)$_2$]$^+$	223	–9.4				16.7	1.1	256
[Fe(T^{n}PrP)(2-MeIm)$_2$]$^+$	223	–8.8				19.8	0.8	256
[Fe(T^{i}PrP)(2-MeIm)$_2$]$^+$	223	5.6[b]				21.2[b]	5.4[b]	256
(c′) [Fe(TMP)L_2]$^+$								
[Fe(TMP)(HIm)$_2$]$^+$	298	–16.8	(0.9)	6.0	(1.6)			c
[Fe(TMP)(4,5-Cl$_2$Im)$_2$]$^+$	298	–9.4	(2.2)	10.0	(3.1)			c
[Fe(TMP)(^{t}BuNC)$_2$]$^+$	298	7.1	(5.5)	18.2	(4.2)			c

[a]Data in parentheses are the chemical shifts of the methyl signals. [b]Averaged value. [c]Ikezaki, A. *et al.*, unpublished results.

indicates that the complex is in the $(d_{xz}, d_{yz})^4(d_{xy})^1$ ground state; these are actually the only examples of bis-HIm complexes that adopt the $(d_{xz}, d_{yz})^4(d_{xy})^1$ ground state. Therefore, it is expected that the one-electron-oxidized product, $[Fe(T^iPrP^{\bullet})(HIm)_2]^{2+}$, should have a $(d_{xz}, d_{yz})^4(d_{xy})^1(a_{2u})^1$ ground state. However, the data in Tables 33b indicate that the pyrrole-H signal appears somewhat upfield, at $\delta =$ −20.4 ppm, as compared with $\delta = 0.1$ ppm in the parent $[Fe(T^iPrP)(HIm)_2]^+$. Thus, the electronic structure of low-spin iron(III) ion switches from $(d_{xz}, d_{yz})^4(d_{xy})^1$ to $(d_{xy})^2(d_{xz}, d_{yz})^3$ as the electron is removed from the porphyrin ring. Since the *meso*-CH(α) signal is observed at a downfield position, 42.4 ppm, the electronic structure of $[Fe(T^iPrP^{\bullet})(HIm)_2]^{2+}$ can be expressed as S = 1, $(d_{xy})^2(d_{xz}, d_{yz})^3(a_{2u})^1$. These results suggest that the $(d_{xy})^2(d_{xz}, d_{yz})^3(a_{2u})^1$ ground state is more stable than the $(d_{xz}, d_{yz})^4(d_{xy})^1(a_{2u})^1$ ground state. This is understandable, because the a_{2u} orbital is stabilized to a great extent by the one-electron oxidation. As a result, the interaction between the d_{xy} and a_{2u} orbitals in $[Fe(T^iPrP^{\cdot})L_2]^{2+}$ is weakened, which stabilizes the d_{xy} orbital to form the complex with the S = 1, $(d_{xy})^2(d_{xz}, d_{yz})^3(a_{2u})^1$ ground state. Figure 58 shows the ^{1}H NMR spectra of (a) $[Fe(TEtP^{\bullet})(HIm)_2]^{2+}$ and (b) $[Fe(T^iPrP^{\bullet})(2\text{-MeIm})_2]^{2+}$.[256] It is clear that the electronic structure of these complexes is also described as S = 1 $(d_{xy})^2(d_{xz}, d_{yz})^3(a_{2u})^1$ because of the presence of the upfield-shifted pyrrole-H signal together with the downfield-shifted *meso*-CH_α signals. Close inspection of the data in Table 33 reveals that the pyrrole-H signal in $[Fe(TRP^{\cdot})(HIm)_2]^{2+}$ moves downfield from −36.0 to −20.4 ppm as the *meso* substituent changes from Et to the much bulkier ^{i}Pr group. This result suggests that the population of the $(d_{xz}, d_{yz})^4(d_{xy})^1(a_{2u})^1$ spin isomer increases relative to that of the $(d_{xy})^2(d_{xz}, d_{yz})^3(a_{2u})^1$ isomer as the ruffling of the porphyrin ring increases. It should be noted that the $(d_{xz}, d_{yz})^4(d_{xy})^1(a_{2u})^1$ spin isomer should really be expressed as S = 0, $(d_{xz}, d_{yz})^4(d_{xy}, a_{2u})^2$ since the half-occupied d_{xy} orbital is expected to interact antiferromagnetically with the half-occupied a_{2u} orbital in the ruffled porphyrin structure.[43] These results suggest that, in order to obtain $[Fe(Por^{\cdot})L_2]^{2+}$ with the S = 0, $(d_{xz}, d_{yz})^4(d_{xy}, a_{2u})^1$ ground state, the axial ligand should have low-lying π^* orbitals. Needless to say, ^{t}BuNC is the best candidate for obtaining such a complex since almost all the low-spin complexes of porphyrins and porphyrin analogs carrying a ^{t}BuNC ligand exhibit the $(d_{xz}, d_{yz})^4(d_{xy})^1$ ground state; the only examples showing the $(d_{xy})^2(d_{xz},d_{yz})^3$ ground state are the monoazaporphyrin $[Fe(MAzP)(^tBuNC)_2]^+$,[136] the diazaporphyrin $[Fe(DAzP)(^tBuNC)_2]^+$,[134] and the highly saddled $[Fe(OETArP)(^tBuNC)_2]^+$ with electron-withdrawing aryl groups at the *meso* positions.[95]

Ikezaki and coworkers prepared a series of $[Fe(TMP^{\bullet})L_2]^{2+}$ (L = HIm, 4,5-Cl_2Im, and ^{t}BuNC) complexes by addition of axial ligands L to a CD_2Cl_2 solution of $Fe(TMP^{\bullet})(ClO_4)_2$ at 195 K.[257] Figure 59 displays the ^{1}H NMR spectra of these complexes taken at 173 K. As shown in Figure 59a, the pyrrole-H and *m*-H signals

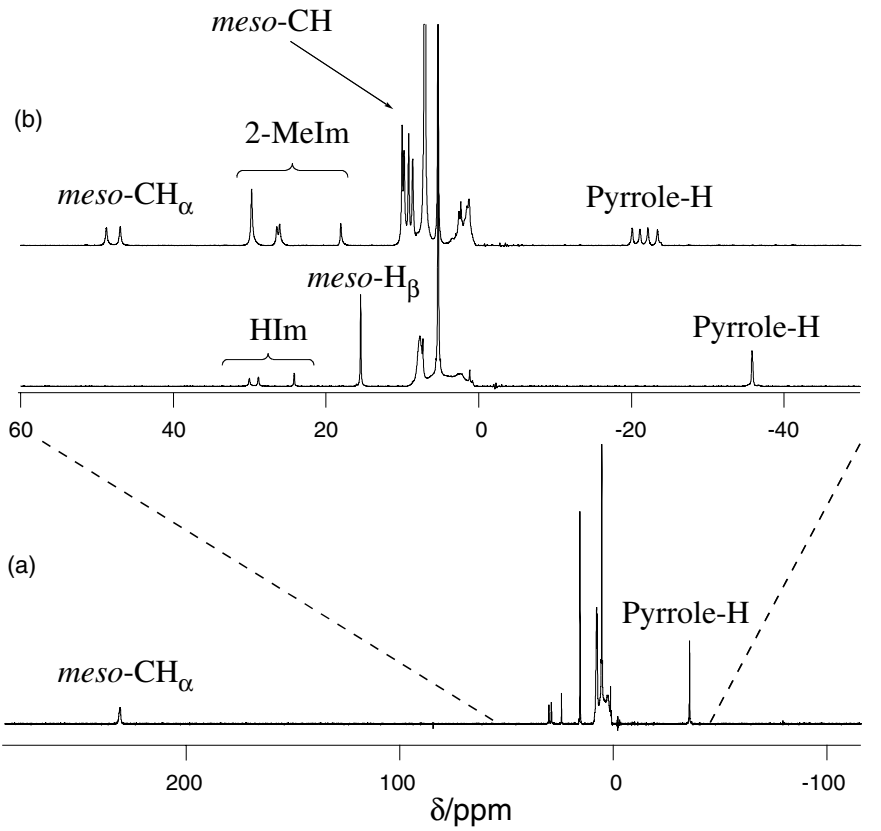

Figure 58. ^{1}H NMR spectra of low-spin iron(III) porphyrin cation radicals taken in CD_2Cl_2 solution at 223 K: (a) $[Fe(TEtP^{\bullet})(HIm)_2]^{2+}$ together with the expanded spectrum, (b) $[Fe(T^iPrP^{\bullet})(2\text{-MeIm})_2]^{2+}$. (Adapted with permission from Ref. 256. Copyright 2003, Royal Society of Chemistry.)

of $[Fe(TMP^{\bullet})(HIm)_2]^{2+}$ are observed at −70.8 and 65.7 ppm, respectively, at 173 K, which clearly indicates that the complex adopts the S = 1, $(d_{xy})^2(d_{xz}, d_{yz})^3(a_{2u})^1$ ground state. If axial HIm is replaced by 4,5–Cl_2Im, the pyrrole-H and *m*-H signals shift to *ca.* −26 and 24 ppm, respectively, as shown in Figure 59b; these signals split into several lines at this temperature due to slow rotation of the 4,5-Cl_2Im ligand.[90–93] Thus, the isotropic shifts are greatly reduced on going from $[Fe(TMP^{\bullet})(HIm)_2]^{2+}$ to $[Fe(TMP^{\bullet})(4,5\text{-}Cl_2Im)_2]^{2+}$. In the case of $[Fe(TMP^{\bullet})(^tBuNC)_2]^{2+}$, all the signals are observed in the so-called diamagnetic region, from 1.7 to 6.8 ppm in this case, as shown in Figure 59c. The effective magnetic moment of this complex is 0.45 μ_B at 173 K and 0.57 μ_B at 223 K. The ^{1}H NMR chemical shifts of both the cation radical $[Fe(TMP^{\bullet})L_2]^{2+}$ and the parent $[Fe(TMP)L_2]^+$ are listed in Tables 33c and 33c′, respectively. In neutral $[Fe(TMP)L_2]^+$, the pyrrole-H signal moves downfield from −16.8 to −9.4, and then to 7.1 ppm at 298 K as the axial

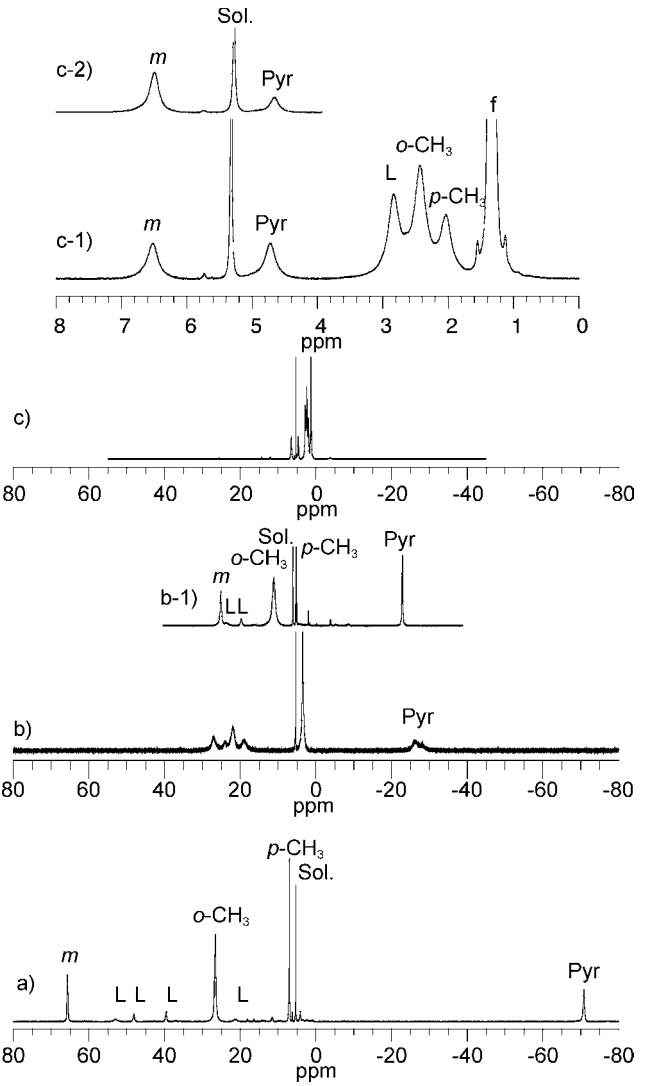

Figure 59. (a) ^{1}H NMR spectrum of $[Fe(TMP^{\bullet})(HIm)_2]^{2+}$ taken in CD_2Cl_2 solution at 173 K. (b) ^{1}H NMR spectrum of $[Fe(TMP^{\bullet})(4,5\text{-}Cl_2Im)_2]^{2+}$ taken in CD_2Cl_2 solution at 173 K. The same sample taken at 253 K is given in inset (b-1). (c) ^{1}H NMR spectrum of $[Fe(TMP^{\bullet})(^tBuNC)_2]^{2+}$ taken in CD_2Cl_2 solution at 173 K. Inset (c-1) shows the 0–8 ppm region and inset (c-2) shows the spectrum obtained from the pyrrole-d_8 complex. (Adapted with permission from Ref. 257. Copyright 2008, Royal Society of Chemistry.)

ligand changes from HIm to 4,5-Cl_2Im, and then to ^{t}BuNC. These results indicate a change in the electronic ground state from $(d_{xy})^2(d_{xz}, d_{yz})^3$ to $(d_{xz}, d_{yz})^4(d_{xy})^1$. A similar tendency is observed in the cation radical $[Fe(TMP^{\bullet})L_2]^{2+}$. The pyrrole-H signal moves downfield from –53.2 to –25.6, and then to 4.6 ppm, which can also be

ascribed to the change in electron configuration of the low-spin iron(III) from $(d_{xy})^2(d_{xz}, d_{yz})^3$ to $(d_{xz}, d_{yz})^4(d_{xy})^1$. The diamagnetic nature of $[Fe(TMP^{\bullet})(^tBuNC)_2]^{2+}$ can then be explained in terms of strong antiferromagnetic coupling between the half-occupied d_{xy} and half-occupied a_{2u} orbitals in a highly ruffled porphyrin framework. Thus, the electronic ground state of $[Fe(TMP^{\bullet})(HIm)_2]^{2+}$ and $[Fe(TMP^{\bullet})(^tBuNC)_2]^{2+}$ should be expressed as S = 1, $(d_{xy})^2(d_{xz}, d_{yz})^3(a_{2u})^1$ and S = 0, $(d_{xz}, d_{yz})^4(d_{xy}, a_{2u})^2$, respectively. The pyrrole-H signal of $[Fe(TMP^{\bullet})(4,5\text{-}Cl_2Im)_2]^{2+}$ is observed just between the pyrrole-H signals of $[Fe(TMP^{\bullet})(HIm)_2]^{2+}$ and $[Fe(TMP^{\bullet})(^tBuNC)_2]^{2+}$, which indicates that $[Fe(TMP^{\bullet})(4,5\text{-}Cl_2Im)_2]^{2+}$ exists as an equilibrium mixture of two kinds of spin isomers as expressed by Eq. 25:

$$S = 1,\ (d_{xy})^2(d_{xz}, d_{yz})^3(a_{2u})^1 \leftrightarrows S = 0,\ (d_{xz}, d_{yz})^4(d_{xy}, a_{2u})^2. \quad (25)$$

The pyrrole-H and *m*-H signals of $[Fe(TMP^{\bullet})(^tBuNC)_2]^{2+}$ are observed to be more upfield by 4.2 and 0.8 ppm than the corresponding signals of diamagnetic $[Co(TMP)(^tBuNC)_2]^+$. Similarly, the *meso*-C signal of $[Fe(TMP^{\bullet})(^tBuNC)_2]^{2+}$ appears at 160 ppm at 173 K, which is more downfield by 42 ppm than is the corresponding signal of diamagnetic $[Co(TMP)(^tBuNC)_2]^+$. Figure 60 shows the Curie plots of the *m*-H and pyrrole-H signals of the three complexes. Clearly, the isotropic shift of each signal decreases as the axial ligand changes from HIm to

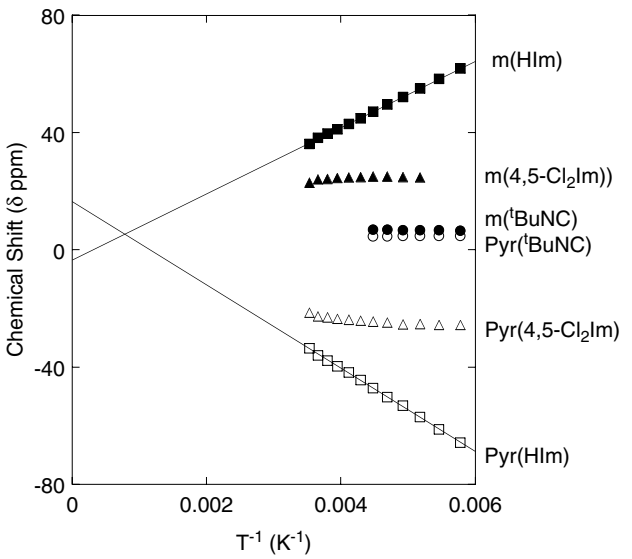

Figure 60. Curie plots of the *m*-H(m) and pyrrole-H(Pyr) chemical shifts of $[Fe(TMP^{\bullet})L_2]^{2+}$. (Adapted with permission from Ref. 257. Copyright 2008, Royal Society of Chemistry.)

4,5-Cl_2Im, and then to ^{t}BuNC. The Curie plot of the *meso*-C signal of $[Fe(TMP^{\bullet})(^t BuNC)_2]^{2+}$ exhibits a small downfield shift at higher temperatures. These results indicate that $[Fe(TMP^{\bullet})(^t BuNC)_2]^{2+}$ exists mainly as the S = 0, $(d_{xz}, d_{yz})^4(d_{xy}, a_{2u})^2$ spin isomer with a small population of the S = 1, $(d_{xy})^2$ $(d_{xz}, d_{yz})^3(a_{2u})^1$spin isomer. The population of the latter isomer increases only slightly at higher temperatures, as is revealed from the temperature dependence of the effective magnetic moments. However, a slight increase in population of the paramagnetic isomer greatly affects the signal width. That should be the reason why the *meso*-C signal disappears as the temperature is raised. As shown in Figure 56, the *meso*-C signal of [Fe(TPP)Cl] broadens to a great extent when 0.075 equivalents of $[Fe(TPP^{\bullet})Cl]^+$ are added.

On the basis of the data described above, low-spin iron(III) porphyrin cation radicals denoted by $[Fe(Por^{\bullet})L_2]^{2+}$ exist in either one of the three possible electronic ground states. They exist (i) predominantly as S = 1, $(d_{xy})^2(d_{xz}, d_{yz})^3(a_{2u})^1$ as in the case of $[Fe(TMP^{\cdot})(HIm)_2]^{2+}$, (ii) predominantly as S = 0, $(d_{xz}, d_{yz})^4(d_{xy}, a_{2u})^2$ as in the case of $[Fe(TMP^{\cdot})(^t BuNC)_2]^{2+}$, and (iii) as an equilibrium mixture of S = 1, $(d_{xy})^2(d_{xz}, d_{yz})^3(a_{2u})^1$ and S = 0, $(d_{xz}, d_{yz})^4(d_{xy}, a_{2u})^2$, as in the case of $[Fe(TMP^{\bullet})(4,5\text{-}Cl_2Im)_2]^{2+}$.[257]

2. *Iron(IV) Porphyrin Complexes*

a. *Iron(IV) porphyrins with an Fe^{IV}=O bond*

Iron(IV) porphyrins are in general quite unstable and difficult to obtain. Most of the iron(IV) complexes reported to date have an Fe^{IV}=O group, since they are more stable than the corresponding iron(IV) complexes without the Fe^{IV}=O bond. Balch, La Mar, and coworkers reported the first example of an Fe^{IV}=O complex [(Fe^{IV}=O)(3-Me-TPP)(1-MeIm)] obtained by addition of 1-MeIm to the peroxo-bridged dimer [(3-Me-TPP)Fe^{III}O–OFe^{III}(3-MeTPP)].[258,259] The iron(IV) oxidation state has been confirmed by the solution magnetic moment, which is $2.9 \pm 0.1\ \mu_B$ at 221 K and is invariant down to 183 K. Furthermore, the Mössbauer spectrum has revealed that the isomer shift of the iron atom is 0.11 mm s^{-1} at 4.2 K, which is characteristic of an iron(IV) complex.[260] In the ^{1}H NMR spectra, all the signals are observed between 5 and 10 ppm. The temperature dependence of the paramagnetic shift of each signal strictly follows the Curie law over a wide temperature range. The complex reacts instantaneously with Fe^{II}(3-Me-TPP) to form quantitatively the μ-oxo dimer [(3-Me-TPP)Fe^{III}]$_2$O. Thus, the electronic structure of [(Fe^{IV}=O)(3-Me-TPP)(1-MeIm)] should be given as S = 1, $(d_{xy})^2(d_{xz}, d_{yz})^2$. Thermal decomposition of the peroxobridged dimer of sterically hindered TMP, [(TMP)Fe^{III}O–OFe^{III}(TMP)], yields the five-coordinate [(Fe^{IV}=O)(TMP)].[261,262]

Similarly, thermal decomposition of the alkylperoxo complex [Fe^{III}(TMP)(OO^{t}Bu)] produces [(Fe^{IV}=O)(TMP)].[263] Although electrochemical and chemical one-electron oxidation of [Fe(Por)Cl] have produced [Fe(Por$^{\bullet}$)Cl]$^+$, as mentioned in the previous section, the same oxidation of [Fe(Por)(OH)] produces [(Fe^{IV}=O)(Por)] if Por has *o*-phenyl substituents that prevent the formation of a μ-oxo dimer.[264–267] Later, Groves *et al.* reported a convenient preparative method for [(Fe^{IV}=O)(TMP)]; namely, ligand metathesis of the iron(III) cation radical, [Fe^{III}(TMP$^{\cdot}$)(ClO_4)$_2$], over moist basic alumina.[268] Although [(Fe^{IV}=O)(TMP)] is unstable in CH_2Cl_2 solution and forms [Fe^{III}(TMP)Cl] within a minute at ambient temperature, it is much more stable in benzene solution.[268] Figure 61 shows the ^{1}H NMR spectrum of [(Fe^{IV}=O)(TMP)] taken in CD_2Cl_2 solution at 195 K together with the UV spectrum taken in benzene solution at room temperature. The ^{1}H NMR chemical shifts of various Fe^{IV}=O complexes are listed in Table 34.[231,253,258,261,268–272] As is revealed from the data in the table, the isotropic shift of each signal in both five- and six-coordinate Fe=O complexes is quite small. Since these complexes adopt the S = 1, $(d_{xy})^2(d_{xz}, d_{yz})^2$ ground state, one can expect that the pyrrole-H signals should appear extremely upfield due to an interaction between half-filled iron d_π and filled porphyrin $3e_g$ orbitals, as in the case of the S = 3/2 iron(III) complexes such as [Fe^{III}(T^{i}PrP)($THF)_2$]$^+$ and [Fe^{III}(TPP)]Ag($Br_6CB_{11}H_6$)$_2$;[98,157] the chemical shift of the pyrrole-H signal reaches as much as −62 ppm in the latter complex at 298 K.

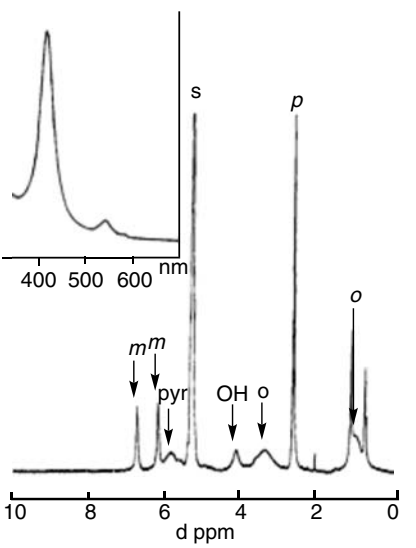

Figure 61. ^{1}H NMR spectrum of (Fe^{IV} = O)(TMP) in CD_2Cl_2 solution at 195 K. The peaks marked *p*, *m*, and *o* are *p*-Me, *m*-H, and *o*-Me. The peak marked OH is due to the *p*-Me of Fe^{III}(TMP)(OH). Inset: UV spectrum in benzene at room temperature. (Adapted with permission from Ref. 268. Copyright 1994, American Chemical Society.)

Table 34. ^{1}H NMR chemical shifts of iron(IV) porphyrin complexes.[a]

Complex	T (K)	Pyrrole-H	*Meso*-H	*o*-H	*m*-H	*p*-H	Ref.
[(Fe^{IV} = O)(TMP)]	195	5.85	—	(3.40, 1.05)	6.75, 6.20	(2.70)	268
	193	6.5	—	(3.5, 1.0)	6.6, 6.0	(2.7)	231
	203	8.4	—	(3.3, n.d.)	6.4, 6.0	(2.6)	261
	273	7.30	—	(2.80, 1.25)	6.35, 6.70	(2.60)	269
[(Fe^{IV} = O)(3-MeTPP)(1-MeIm)]	200	5.1	—	8.7	7.8	7.8	258
[(Fe^{IV} = O)(TMP)(1-MeIm)]	213	—	—	(3.6, n.d.)	7.5	(2.74)	261
	243	4.6	—	(3.2, 1.6)	7.4	(2.67)	261
	193	3.8	—	(3.8, 1.2)	7.2, 2.1	(2.8)	231
[(Fe^{IV} = O)(TMP)(OMe-d_3)]$^{-2}$	243	–4.1	—	(1.5)	—	(2.7)	270
[(Fe^{IV} = O)(TPP)(L)][b]	197	1.2	—	9.1	7.9	8.3	271
[(Fe^{IV} = O)(TPP)(1-MeIm)]	193	5.05	—	9.2	7.9	7.9	261
[(Fe^{IV} = O)(TpivPP)(THF)]	223	7.2	—	12.9	9.3, 8.7	7.7	272
[(Fe^{IV} = O)(2,6-Cl_2-TPP)(DMF)]	223	14.1	—	—	4.01	4.01	272
[(Fe^{IV} = O)(OEP)(1-MeIm)]	222	–1[c]	15	—	—	—	273
[(Fe^{IV} = O)(EtioP)(1-MeIm)]	222	–1[c]	16	—	—	—	273
[(Fe^{IV} = O)(TMTMP)]	193	(8.6)	33.3	(3.8, 1.5)	8.8, 7.3	(2.6)	231
[(Fe^{IV} = O)(TMTMP)(1-MeIm)]	193	(4.7)	17.2	(2.8, 1.6)	8.1, 7.3	(2.5)	231
[(Fe^{IV} = O)(TMTMP)(1,2-Me_2Im)]	193	(4.8)	18.0	(3.5, 1.7)	8.1, 7.3	(2.4)	231
[Fe^{IV}(TMP)($OMe)_2$]	195	–37.5		(2.4)	7.72	(2.86)	253

[a]Data in parentheses are the chemical shifts of the methyl signals. [b]Chemical shifts are obtained from Figure 1 of Ref. 271. The axial ligand (L) is not specified. [c]Pyrrole-CH_2.

Table 35. Gross atomic spin populations of high-valent iron porphyrins.[a]

	Fe	L_{axial}	N_{por}	C_α	C_β	C_{meso}
$Fe^{V}(P)(N)^{b}$	1.579	1.550	–0.018	–0.004	–0.003	–0.002
$Fe^{IV}(P)(NH)^{c}$	0.775	1.289	–0.003	0.000	0.000	–0.006
$Fe^{IV}(P)(O)^{c}$	1.199	0.826	–0.009	0.003	0.001	–0.006
$Fe^{V}(P)(O)(F)^{b}$	2.134	0.961	–0.036	0.000	–0.003	0.000
$Fe^{IV}(\text{“}a_{2u}\text{”-}P^{\bullet})(O)(F)^{b}$	1.110	0.904	0.114	–0.045	–0.006	0.221
$Fe^{IV}(\text{“}a_{1u}\text{”-}P^{\bullet})(O)(F)^{b}$	1.111	0.888	–0.048	0.141	0.029	–0.051

[a]P and P· indicate porphyrin and porphyrin cation radical, respectively. [b]S = 3/2. [c]S = 1. (Source: Refs. 274, 275.)

Table 35 lists the gross atomic spin populations determined by DFT calculations for various high-valent iron complexes.[274,275] As shown in the table, most of the unpaired electrons in the Fe^{IV}=O complexes are localized on the axial part, i.e. iron and oxygen atoms, and the amount of the total spin density on the porphyrin ring is negligibly small. Thus, the theoretical study explains why the isotropic shifts of the peripheral proton signals in Fe^{IV}=O complexes are negligibly small in spite of the presence of two unpaired electrons in the d_π orbitals.

b. *Iron(IV) porphyrins without an Fe=O bond*

While there are ample examples of iron(IV) complexes with an Fe=O bond, iron(IV) complexes without the Fe=O bond are quite rare. The only example is the bis-methoxo complex, $[Fe(TMP)(OMe)_2]$, which is prepared by the addition of methoxide to the iron(III) porphyrin cation radical, $[Fe^{III}(TMP^{\bullet})(ClO_4)_2]$, as shown in Eq. 26.[253]

$$Fe^{III}(TMP^{\bullet})(ClO_4)_2 + 2MeO^- \leftrightarrows [Fe^{IV}(TMP)(OMe)_2] + 2ClO_4^- \qquad (26)$$

The electronic structure of $[Fe^{IV}(TMP)(OMe)_2]$ has been examined by various spectroscopic methods. Figure 62 shows the ^1H NMR spectrum of this complex taken in $CDCl_3$ at 223 K. The ^1H NMR chemical shifts of this complex are listed in Table 34. The characteristic is that the pyrrole-H signal appears at an extremely upfield position, $\delta = -37.5$ ppm at 195 K, while the other signals such as *o*-CH_3, *m*-H, and *p*-CH_3 are quite close to their diamagnetic positions. The effective magnetic moment, μ_{eff}, is 2.9 ± 0.2 μ_B between 229 and 193 K in CH_2Cl_2 solution. Thus, the complex is best described as an iron(IV) porphyrin with the S = 1, $(d_{xy})^2(d_{xz}, d_{yz})^2$ ground state, which is further verified by the Mössbauer and EXAFS data.[276] Because of the absence of the Fe=O bond, the unpaired electrons

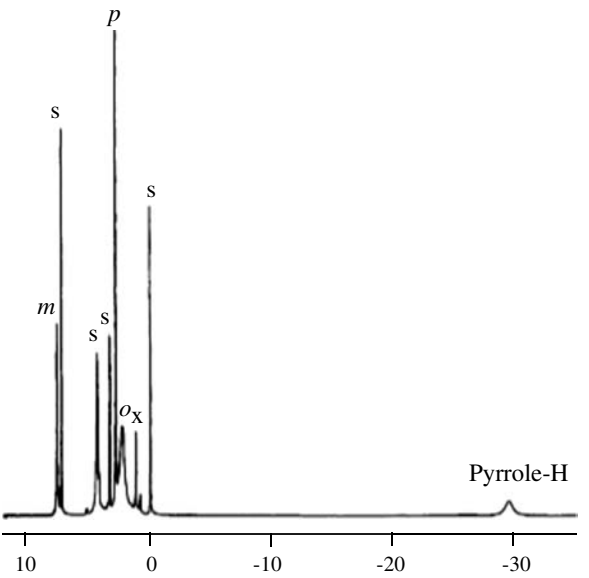

Figure 62. ^{1}H NMR spectra of [Fe^{IV}(TMP)$(OCH_3)_2$] taken in $CDCl_3$ solution at 223 K. (Adapted with permission from Ref. 253. Copyright 1985, American Chemical Society.)

in the d_{xz} and d_{yz} orbitals delocalize to the porphyrin ring by interaction with the filled $3e_g$ orbitals to induce a large upfield shift of the pyrrole-H signal. That is the reason why the ^{1}H NMR spectrum of [(Fe^{IV}=O)(TMP)] shown in Figure 61 is quite different from that of [Fe^{IV}(TMP)$(OCH_3)_2$] shown in Figure 62, although both complexes adopt the S = 1, $(d_{xy})^2(d_{xz}, d_{yz})^2$ ground state. A ^{13}C NMR study further reveals that [Fe^{IV}(TMP)$(OCH_3)_2$] has negligibly small spin density at the *meso*-C atoms because the *meso*-C signal appears at 64.3 ppm, at 213 K; the *meso*-C signal of low-spin [Fe^{III}(T^nPrP)$(HIm)_2$]$^+$ with the $(d_{xy})^2(d_{xz}, d_{yz})^3$ ground state appears at 73.1 ppm as listed in Table 4.[52] [Fe^{IV}(TMP)$(OCH_3)_2$] can be produced together with the two-electron-oxidized product, [(Fe^{IV}=O)($TMP^{\bullet}$)]$^+$, by oxidation of Fe^{III}(TMP)(ClO_4) with iodosylbenzene or dimethyldioxirane in mixed CD_2Cl_2 and CD_3OD solution.[277,278]

It was expected that the addition of strong anionic ligands to a solution of iron(III) porphyrin cation radical would produce an iron(IV) porphyrin as in the case of [Fe^{IV}(TMP)$(OMe)_2$]. Among various anionic ligands, F^- should be a suitable ligand since it is highly ranked in the magnetochemical series proposed by Reed *et al.*[157,158] In fact, the electrochemical oxidation of $Fe^{III}(TPP)F_2^-$ is unique, in the sense that the first oxidation wave is at +0.68 V.[165,166] Since the first oxidation wave for most five-coordinate iron(III) porphyrins is *ca.* +1.1 V, the corresponding wave for [$Fe^{III}(TPP)F_2]^-$ has been suggested to be due to an iron-centered

oxidation to form the iron(IV) species, $[Fe^{IV}(TPP)F_2]$. However, the complex is too unstable to obtain an NMR spectrum. A density functional study has also predicted that one-electron oxidation of $[Fe^{III}(TPP)F_2]^-$ should form the iron(IV) porphyrin, $[Fe^{IV}(Por)F_2]$, rather than the iron(III) porphyrin cation radical.[279] However, *ab initio* CASPT2 calculations by Ghosh and Taylor favor a high-spin porphyrin cation radical as the ground state by a significant energetic margin over an iron(IV) porphyrin.[280,281] Thus, the electronic structure of the one-electron oxidized product of high-spin $[Fe^{III}(TPP)F_2]^-$ is still ambiguous and further experimental studies are necessary.

B. Two-Electron-Oxidized Products of Iron(III) Porphyrins

As shown in Figure 1, a reactive intermediate in the catalytic reaction of cytochrome P450 is considered to be two oxidizing equivalents above the ferric state. There are several kinds of two-electron-oxidized species.[12,285] They are an oxoiron(V) porphyrin $[(Fe^{V}{=}O)(Por)]^+$[11,12,26,282–284]; a six-coordinate iron(V) porphyrin without an $Fe^{V}{=}O$ bond $[Fe^{V}(Por)(X)(Y)]^+$ where X and Y are anionic ligands; an oxoiron(IV) porphyrin cation radical $[(Fe^{IV}{=}O)(Por^{\bullet})]^+$[11,12,26,277,285]; a six-coordinate iron(IV) porphyrin cation radical without an $Fe^{IV}{=}O$ bond $[Fe^{IV}(Por^{\bullet})(X)(Y)]^+$; an iron(III) porphyrin N-oxide[12,285,286,287]; and an iron(III) porphyrin dication.[12,285,288,289] Figure 63 shows some of the two-electron-oxidized-complexes mentioned above.[285]

In the case of naturally occurring heme proteins that are involved in oxidation reactions, the reaction intermediate where the second oxidation equivalent is placed on the iron ligand has been denoted as compound I. The nature of compound I in heme proteins such as peroxidase, catalase, and cytochrome P450 has been considered to be an oxoiron(IV) porphyrin cation radical $[(Fe^{IV}{=}O)(Por^{\bullet})]^+$.[4–17] In this section we will describe the electronic structures of $[(Fe^{IV}{=}O)(Por^{\bullet})]^+$ together with other two-electron-oxidized complexes such as the oxoiron(V) porphyrin $[(Fe^{V}{=}O)(Por)]^+$, the iron(III) porphyrin N-oxide, and the iron(III) porphyrin dication.

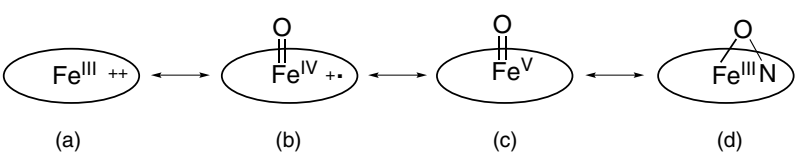

Figure 63. Two-electron-oxidized species of iron(III) porphyrin complexes: (a) Iron(III) porphyrin dication; (b) iron(IV) porphyrin radical cation; (c) iron(V) porphyrin; (d) iron(III) porphyrin N-oxide. (Adapted with permission from Ref. 285. Copyright 2002, Elsevier Science.)

1. *Oxoiron(IV) Porphyrin Cation Radicals*

The first example of an oxoiron(IV) porphyrin cation radical was reported by Groves *et al.* in 1981.[277] These authors examined the oxidation of [Fe(TMP)Cl] with 1.5 equivalents of *m*-CPBA in CD_2Cl_2–CD_3OD-methanol (4:1) solution at 195 K and obtained a green intermediate. The pyrrole-H signal of [Fe(TMP)Cl] at δ 120 ppm disappears and a new signal appears at δ –27 ppm. Figure 64 shows the ^{1}H NMR spectrum of the green intermediate taken at 195 K in CD_2Cl_2-CD_3OD. The *o*-Me signals appear at 26 and 24 ppm, the *m*-H signal at 68 ppm, and the *p*-Me signal is at 11.1 ppm. Thus, the green intermediate has an unpaired electron in the a_{2u} orbital. These chemical shifts are highly temperature dependent and obey the Curie law between 237 and 184 K. The magnetic susceptibility was determined by the Evans method to be 4.2 μ_B, which is slightly larger than the expected value, μ_{eff} = 3.87 μ_B, for an S = 3/2 system. The visible spectrum shows a broad Soret band at 406 nm and another broad band centered at 645 nm. The Mössbauer spectrum derived from ^{57}Fe-enriched [Fe(TMP)Cl] shows a quadrupole doublet centered at 0.05 mm/s (QS = 1.49 mm/s). Treatment of a CH_2Cl_2-CH_3OH solution of the green intermediate with norbornene in the presence of $H_2{}^{18}O$ yields ^{18}O-incorporated norbornene oxide, which clearly indicates the presence of an Fe^{IV}=O unit in the intermediate. Thus, the complex is best expressed as

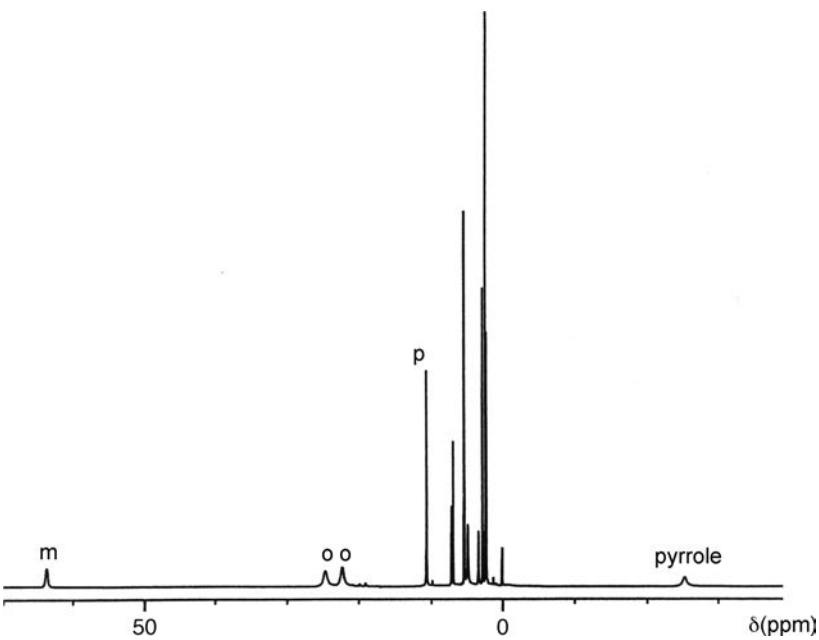

Figure 64. ^{1}H NMR spectrum of [(Fe^{IV}=O)($TMP^{\bullet}$)]$^+$ taken in CD_2Cl_2–CD_3OD at 195 K. (Adapted with permission from Ref. 277. Copyright 1981, American Chemical Society.)

$[(Fe^{IV}{=}O)(TMP^{\bullet})]^+$, a compound I analog of HRP and cytochrome P450. The large downfield shift of the *m*-H signals together with the large upfield shift of the pyrrole-H signals indicate the presence of an a_{2u} radical together with the half-occupied d_π orbital(s). Thus, the electronic structure of $[(Fe^{IV}{=}O)(TMP^{\bullet})]^+$ can be expressed as $(d_{xy})^2(d_{xz},d_{yz})^2(a_{2u})^1$. The EPR spectrum of $[(Fe^{IV}{=}O)(TMP^{\bullet})]^+$ shows signals at 4.47, 3.50, and 1.98, which suggest the presence of ferromagnetic coupling between the iron(IV) ion and the porphyrin cation radical to form the S = 3/2 state.[290,291] Resonance Raman spectroscopy shows a band at 828 cm^{-1} for Fe=O.[292] The EXAFS reveals the Fe=O length to be 1.6 Å, which is close to the Fe=O lengths of compound I and compound II of HRP.[293] In order to investigate the relationship between structure and reactivity of $[(Fe^{IV}{=}O)(Por^{\bullet})]^+$, various oxoiron(IV) porphyrin cation radicals have been prepared using *m*-CPBA or ozone as oxidizing reagents.[227,294–297] In Table 36 are listed the ^{1}H NMR chemical shifts of such complexes.

Fujii found that the pyrrole-H signal in $[(Fe^{IV}{=}O)(TArP^{\bullet})]^+$ shifts upfield from −27.6 to −44.1, −65.5, and then to −72.7 ppm as the *meso*-aryl substituent changes from (2,4,6-Me_3)phenyl to (2-Cl-6-Me)phenyl, (2,6-Cl_2)phenyl, and then to (2,4,6-Cl_3)phenyl.[295] In contrast, the paramagnetic shift of the *m*-H signal decreases with the same change in the *meso*-aryl substituent, as listed in Table 36. These results are interpreted in terms of a mixing of the a_{1u} radical state with the original a_{2u} radical state; note that the a_{2u} orbital is stabilized relative to the a_{1u} orbital by introduction of electronegative substituents at the *meso* position. Thus, in the complex having strongly electron-withdrawing pentafluorophenyl (C_6F_5) groups at the *meso* positions, i.e. $[(Fe^{IV}{=}O)(F_5\text{-}TPP^{\bullet})]^+$, the pyrrole-H signal appears at an extremely upfield position, −96 ppm at 193 K, which indicates that the a_{1u} radical character predominates over the a_{2u} radical character.[295]

Oxo-iron(IV) porphyrin cation radicals with the a_{1u} radical character can also be expected for $[(Fe^{IV}{=}O)(TMTMP^{\bullet})]^+$. TMTMP has four methyl and four mesityl groups at the pyrrole β carbon atoms, as shown in Scheme 1. Thus, it is expected that the electronic structure and reactivity of $[(Fe^{IV}{=}O)(TMTMP^{\cdot})]^+$ should resemble compound I of naturally occurring heme proteins such as HRP and peroxidase. A wide variety of pyrrole-substituted complexes such as $[(Fe^{IV}{=}O)(TMTMP^{\bullet})]^+$ and $[(Fe^{IV}{=}O)(TArP^{\bullet})]^+$ have been prepared.[295] The ^{1}H NMR chemical shifts of these complexes are also listed in Table 36. Extremely large downfield shifts of the pyrrole β-methyl signals suggest that the pyrrole β-carbon atoms have large spin density, which is consistent with formation of the a_{1u} radical. The *meso*-H signals of some complexes appear rather downfield, i.e. 7–55 ppm. These results indicate that the *meso*-carbon atoms have a sizable amount of negative spin density, which is induced by the large positive spin density on the pyrrole α-carbon atoms characteristic of the a_{1u} radical. The EPR spectrum of $[(Fe^{IV}{=}O)(TMTMP^{\bullet})]^+$ shows signals at g = 3.6 and 2.0, which are close to those of compound I of

Table 36. ^{1}H NMR chemical shifts of iron(IV) porphyrin cation radicals [(Fe^{IV} = O)(Por$^{\bullet}$)X].[a]

Complex	*T* (K)	Pyrrole-H	*Meso*	*o*-Me	*m*-H	*p*-Me	Ref.
[(Fe^{IV} = O)(TMP$^{\bullet}$)X]							
X = F	193	–13.0		26.9, 24.1	71.4	10.7	296
X = Cl	196	–27		26, 24	68	11.1	277
	193	–6.7		23.3, 20.2	60.6	10.7	296
X = OAc	193	–8.3		28.5, 25.7	76.2	11.3	296
X = $OSO_2CF_3^-$	193	–26.2		26.8, 24.3	68.6	11.3	296
X = $OClO_3$	193	–26.9		26.0, 23.5	65.3	11.1	296
	193	–27.4		26.4, 23.9	66.4	11.3	231
X = NO_3^-	193	–19.4		27.8, 25.3	72.5	10.2	231
X = 3-F-4-NO_2-PhO^-	193	–13.7		26.9, 25.4	71.7	11.3	231
[(Fe^{IV} = O)(TMP$^{\bullet}$)L]$^{+}$							
L = CD_3OD	231	–25.7		22.5, 21.3	65.4	10.8	278
L = HIm[b]	193	–11.3		27.5, 26.4	74.8, 73.1	11.7	231
L = 2-MeIm[b]	193	–9.8		broad	broad	11.3	231
L = 5-MeIm[b]	193	–11.1		25.8, 24.2	74.9, 73.2	11.2	231
[(Fe^{IV} = O)(2,6-Cl_2-TPP$^{\bullet}$)]$^{+c}$	213	–60.8			31	n.d.	291
[(Fe^{IV} = O)[2,4,6-$(OMe)_3$-TPP$^{\bullet}$]$^{+c}$	203	–33.2			36.0, 31.6	n.d.	291
[(Fe^{IV} = O)(TArP$^{\bullet}$)]$^{+b}$							
Ar = 2-Cl-6-MePh	193	–44.1		24.4,21.7	55.5, 7.8, 47.7		295
Ar = 2,6,-Cl_2Ph	193	–65.5			34.8		295
Ar = 2,4,6-Cl_3Ph	193	–72.7			30.0		295

(*Continued*)

Table 36. (*Continued*)

Complex	*T* (K)	Pyrrole-H	*Meso*	*o*-Me	*m*-H	*p*-Me	Ref.
[(Fe^{IV} = O)(TMTMP$^{•}$)X]							
X = $OClO_3$	193	(135.5)	55.6	9.6, 7.6	15.0, 14.2	3.6	231
X = NO_3	193	(127.7)	34.7	8.3, 7.4	14.6, 13.8	3.3	231
X = 3-F-4-NO_2-PhO	193	(101.9)	–1.0	7.7, 6.6	13.7, 13.3	3.2	231
[(Fe^{IV} = O)(TMTMP$^{•}$)L]$^{+}$ [b]							
L = Him	193	(113.2)	0.0	8.7, 7.5	13.4, 12.6	3.2	231
L = 2-MeIm	193	(123.7)	–14.8	9.3, 8.0	15.0, 14.2	2.9	231
L = 5-MeIm	193	(111.8)	–4.0	8.6, 7.4	13.4, 12.6	3.1	231
[(Fe^{IV} = O)(TMTArP$^{•}$)]ClO_4							
Ar = 2,4,6-Me_3Ph	203	(139.0)	53.4		14.9, 14.0		295
Ar = 2-Cl-6-MePh	203	(151.8)	32.4, 30.8, 30.5, 29.1, 28.1, 27.3		12.8, 12.7, 12.6, 12.1, 12.0, 11.9, 11.8, 11.1		295
Ar = 2,6-Cl_2Ph	203	(164.7)	–3.0		10.9, 9.8		295
Ar = 2,4,6-Cl_3Ph	203	(166.9)	–7.5		10.5, 9.4		295

[a]Data in parentheses are the chemical shifts of the pyrrole methyl signals. [b]Counter anion is ClO_4^-. [c] Counter anion is $CF_3SO_3^-$.

Micrococcus lysodeikticus catalase and ascorbate peroxidase.[297,298] Thus, compound I of these enzymes should adopt the a_{1u} radical state.[299]

2. *Iron(III) Porphyrin N-Oxides*

A bridged iron porphyrin N-oxide has been suggested as a reactive intermediate in the catalytic cycle of cytochrome P-450 on the basis of the crystal structure of N-bridged iron porphyrin carbenes,[300–306] several metalloporphyrn N-oxides,[307–309] and an N-bridged nitrene.[310] The first iron(III) porphyrin N-oxide, which is isoelectronic with the iron(IV) porphyrin cation radical, was prepared and characterized by Groves and Watanabe.[286] Addition of two equivalents of mCPBA to a toluene solution of [Fe^{III}(TMP)(mCB)] at 273 K yielded a new complex together with bis(3-chlorobenzoyl)peroxide. The UV–vis spectrum of this complex showed a dramatically red-shifted Soret band at 441 nm. The ^{1}H NMR spectrum taken at 223 K showed *m*-H signals at 17.2, 15.0, and 13.8 ppm (relative intensity 1:2:1) and *p*-CH_3 signals at 4.2 and 3.9 ppm. The EPR spectrum showed strong signals at $g = 4.3$. The solution magnetic moment determined by the Evans method is $5.4 \pm 0.1\ \mu_B$ at 248 K in toluene-d_8 solution. The electronic structure of this complex has been assigned as rhombically distorted high-spin iron(III) on the basis of the presence of the downfield-shifted *m*-H signal. Mechanistic studies have revealed that the iron(III) porphyrin N-oxide is formed via homolytic O–O bond cleavage of the coordinated *m*-chlorobenzoylperoxo ligand. At higher concentration or under acidic conditions, the oxo-iron(IV) porphyrin cation radical [(Fe^{IV}=O)($TMP^{\bullet}$)]$^+$ is formed by heterolytic O–O bond cleavage.[287,311]

3. *Iron(III) Porphyrin Dications*

The first well-characterized iron(III) porphyrin dication was reported by Watanabe and coworkers.[288,289] The complex was prepared by the reaction of an iron(III) porphyrin N-oxide, Fe^{III}(TMP N-oxide), with trifluoroacetic acid in toluene at low temperature. The EPR spectrum taken at 77 K shows two signals at 9.5 and 4.25. The intensity of these signals decreases upon warming the solution to afford the EPR silent iron(III) cation radical. The pyrrole-D signal in pyrrole deuterated [Fe^{III}(TMP N-oxide)] appears at 118 ppm at 193 K, which indicates that the complex adopts the ferric high-spin state.

4. *Iron(V) Porphyrins*

Two groups have reported the formation of iron(V) porphyrins. Nanthakumar and Goff oxidized pyrrole deuterated [Fe^{III}(F_2-TPP)F_2]$^-$ with *m*-CPBA in CH_2Cl_2

solution in the presence of excess fluoride ions and obtained a red complex.[282a] The product shows the pyrrole-D signal at 1.3 ppm at 210 K. This signal is observable even at 290 K although it is converted rapidly to the starting $[Fe^{III}(F_2\text{-}TPP)F_2]^-$ complex along with partial decomposition of the porphyrin. The chemical shift of the pyrrole-D signal obeys the Curie law from 220 to 270 K with a *y* intercept at 7.3 ppm. The phenyl proton signals are observed at 9.0 and 15.0 ppm, unlike the case for iron porphyrin cation radical species. The red complex shows a Soret band at 430 nm and a Q band at 550 nm. The EPR spectrum taken at 80 K exhibits three distinct signals at $g = 4.38, 3.11, 2.70$. Its solution magnetic moment at 210 K is $4.1 \pm 0.2\ \mu_B$, which is close to the spin-only value expected for $S = 3/2$. Since an iron(IV) compound with $S = 1$ is expected to be EPR-silent, the red complex appears to be the first example of an iron(V) porphyrin. It should be noted that this complex is observed only in the presence of a large excess of fluoride ligands. Thus, the red complex can be expressed as either $[Fe^V(F_2\text{-}TPP)F_2]^+$ or $[(Fe^V{=}O)(F_2\text{-}TPP)F]$.

Formation of an iron(V) porphyrin was also reported by Morishima *et al.*[283,284] They oxidized $[Fe^{III}(2,6\text{-}Cl_2\text{-}TPP)(OCOAr)]$ with 1.8 equivalents of *p*-nitroperbenzoic acid (*p*-NPBA) in CH_2Cl_2 solution in the presence of nine equivalents of *m*-chlorobenzoic acid at 183 K and obtained the green oxo-iron(IV) porphyrin cation radical $[(Fe^{IV}{=}O)(2,6\text{-}Cl_2\text{-}TPP^{\bullet})]^+$. This green solution turns red upon addition of four equivalents of methanol. The red complex exhibits characteristic UV–vis bands at 418 and 546 nm, which are similar to those of the $Fe^{IV}{=}O$ species, but very different from those of iron(III) porphyrin dications and iron(III) porphyrin N-oxides.[286–289] The pyrrole-D and *meta*-D signals of the deuterated red complex appear at −35.1 and 8.0 ppm, respectively. While the green complex is EPR silent, the red one exhibits EPR signals at 4.33, 3.69, and 1.99 at 4.2 K in frozen CH_2Cl_2 solution. Both green and red complexes are reduced by two equivalents of tetra-n-butylammonium iodide. The red complex reacts with norbornene even at 183 K to form norbornene oxide, though this reactivity is about 10 times less than for the green complex. The solution magnetic susceptibility of the red complex is $4.0 \pm 0.2\ \mu_B$, indicating that the complex has three unpaired electrons. The red complex ισ also obtained by addition of 1.8 equivalents of pentafluoroiodosylbenzene in the presence of 200 equivalents of methanol. Taken all together, the red complex is isoelectronic with the green one $[(Fe^{IV}{=}O)(2,6\text{-}Cl_2\text{-}TPP^{\bullet})]^+$ and is best expressed as an oxo-iron(V) porphyrin $[(Fe^V{=}O)(2,6\text{-}Cl_2\text{-}TPP)]^+$.

The iron(V) porphyrins reported by the two groups are similar in UV–vis and magnetic properties. However, the former complex is relatively stable even at ambient temperature while the latter decomposes at 208 K to the starting high-spin iron(III) complex after several hours. In addition, the ^2H NMR chemical shifts of the deuterated complexes are totally different. While the former complex shows

the pyrrole-D signal at +1.3 ppm at 210 K, the latter complex shows it at −35.1 ppm at 178 K. The difference in chemical shifts of pyrrole-D signals could be explained in terms of the difference in axial ligands. In the case of the former complex, the iron(V) species is obtained only in the presence of a large excess of fluoride ions. Thus, the complex could be expressed as $[Fe^{V}(F_2\text{-TPP})F_2]^+$ rather than $[(Fe^{V}{=}O)(F_2\text{-TPP})F]$. Even in such a case, it is still difficult to explain why two kinds of iron(V) species exhibit such a large difference in pyrrole-D chemical shifts. As mentioned in the previous section, the ^{1}H NMR spectrum of $[(Fe^{IV}{=}O)(TMP)]$ is very different from that of $[Fe^{IV}(TMP)(OMe)_2]$ though both of the complexes adopt the iron(IV) with the $(d_{xy})^2(d_{xz}, d_{yz})^2$ electronic ground state. In this case, the former complex with the Fe^{IV}=O bond shows the pyrrole-H signal close to the diamagnetic position, at 5.85 ppm at 195 K, while the latter complex exhibits it at −37.5 ppm at the same temperature, as shown in Table 34.

Jayaraj *et al.* oxidized similar complexes [Fe(Por)Cl], where Por has strongly electron-withdrawing aryl groups at the *meso* positions, including [Fe(2,6-Cl_2-TPP)Cl]. The ^{1}H NMR, UV–vis, Mössbauer, EPR, and resonance Raman spectra indicated the formation of an oxo-iron(IV) porphyrin radical cation $[(Fe^{IV}{=}O)(Por^{\bullet})]^+$ with an a_{1u} cation radical even in the presence of methanol.[312] On the basis of the spectroscopic data, Jayaraj *et al.* ruled out the possible structural assignment of high-spin iron(V) coordinated to the neutral porphyrin ligand. Dey and Ghosh reported that DFT calculations suggest that the oxo-iron(IV) porphyrin cation radical is more stable than the corresponding oxo-iron(V) complex.[239] However, since the ^{1}H NMR spectra of Nanthakumar and Goff, Morishima *et al.*, and Jayaraj *et al.* are all different, it is impossible to rule out the existence of the iron(V) porphyrins reported by Nanthakumar and Goff as well as by Morishima *et al.* Further experimental and theoretical studies are necessary in order to fully characterize these iron(V) porphyrins.

VII. Acknowledgments

The authors would like to thank all their current and former coworkers and students whose names are given in the references of this chapter. We are especially indebted to Dr. Takahisa Ikeue of Shimane University, Professor Masashi Takahashi of Toho University, and Professor Saburo Neya of Chiba University. Without their cooperation, our contributions to this field would have been much smaller. Work in the authors' laboratories was financially supported by the Research Center for Materials with Integrated Properties in Toho University, a Research Promotion Grant from Toho University Graduate School of Medicine, Sumitomo Foundation, and a Grant-in-Aid for Scientific Research from MEXT, Japan.

VIII. References

1. Lippard, S. J.; Berg, J. M. *Principles of Bioinorganic Chemistry*; University Science Books: Mill Valley, CA, **1994**.
2. Kaim, W.; Schwederski, B. *Bioinorganic Chemistry: Inorganic Elements in the Chemistry of Life*; John Wiley & Sons: New York, **1994**.
3. Groves, J. T. Models and mechanisms of cytochrome P450 action. In *Cytochrome P450: Structure, Mechanism, and Biochemistry*, 3rd ed.; Ortiz de Montellano, P. R., Ed.; Kluwer/Plenum: New York, **2004**; pp. 1–44.
4. Groves, J. T. *Proc. Natl. Acad. Sci.* USA **2003**, 100, 3569.
5. Zhou, H.; Groves, J. T. J. *Porphyrins Phthalocyanines* **2004**, 8, 125.
6. Dawson, J. H.; Sono, M. *Chem. Rev.* **1987**, 87, 1255.
7. Denisov, I. G.; Makris, T. M.; Sligar, S. G.; Schlichting, I. *Chem. Rev.* **2005**, 105, 2253.
8. Shaik, S.; Kumar, D.; de Visser, S. P.; Altun, A.; Thiel, W. *Chem. Rev.* **2005**, 105, 2279.
9. Meunier, B.; de Visser, S. P.; Shaik, S. *Chem. Rev.* **2005**, 104, 3947.
10. Groves, J. T.; Shalyaev, K.; Lee, J. Oxometalloporphyrins in oxidative catalysis. In *The Porphyrin Handbook*; Kadish, K. M.; Smith, K. M.; Guilard, R., Eds.; Academic Press: San Diego, CA, 2000; Vol. 4, pp. 17–40.
11. Weiss, R.; Gold, A.; Trautowein, A. X.; Terner, J. High-valent iron and manganese complexes of porphyrins and related macrocycles. In *The Porphyrin Handbook*; Kadish, K. M.; Smith, K. M.; Guilard, R., Eds. Academic Press: San Diego, CA, 2000; Vol. 4, pp. 65–96.
12. Watanabe, Y. High-valent intermediates. In *The Porphyrin Handbook*; Kadish, K. M.; Smith, K. M.; Guilard, R., Eds.; Academic Press: San Diego, CA, 2000; Vol. 4, pp. 97–117.
13. Holm, R. H.; Kennepohl, P.; Solomon, E. I. *Chem. Rev.* **1996**, 96, 2239.
14. Costas, M.; Mehn, M. P.; Jensen, M. P.; Que, L., Jr. *Chem. Rev.* **2004**, 104, 939.
15. Behan, R. K.; Green, M. T. J. *Inorg. Biochem.* **2006**, 100, 502.
16. Conradie, J.; Wasbotten, I.; Ghosh, A. J. *Inorg. Biochem.* **2006**, 100, 502.
17. Pan, Z.; Zhang, R.; Newcomb, M. J. *Inorg. Biochem.* **2006**, 100, 502.
18. Solomon, E. I.; Lever, A. B. P., Eds.; *Inorganic Electronic Structure Spectroscopy*; John Wiley & Sons: New York, **1999**, Vol. 1.
19. Que, L. Jr., Ed.; *Physical Method in Bioinorganic Chemistry: Spectroscopy and Magnetism*; University Science Books: Sausalito, CA, **2000**.
20. La Mar, G. N.; Walker, F. A. NMP studies of paramagnetic metalloporphyrins. In *The Porphyrins*; Dolphin, D., Ed.; Academic Press: New York, **1979**; Vol. IV, pp. 61–157.
21. Goff, H. M. Nuclear magnetic resonance of iron porphyrins. In *Iron Porphyrins*, *Part 1*; Lever, A. B. P.; Gray, H. B., Eds.; *Physical Bioinorganic Chemistry Series 1*; Addison-Wesley: Reading, Massachusetts, 1983; pp. 237–281.
22. Bertini, I.; Luchinat, C. In *NMR of Paramagnetic Molecules in Biological Systems*; Lever, A. B. P., Ed.; *Physical Bioinorganic Chemistry Series 3*; Benjamin/Bummings: Menlo Park, CA, 1986; pp. 165–229.
23. Walker, F. A.; Simonis, U. Proton NMR spectroscopy of model hemes. In *Biological Magnetic Resonance*; Berliner, L. J.; Reuben, L., Eds.; NMR of Paramagnetic Molecules, Vol. 12; Plenum Press: New York, **1993**; pp. 133–274.
24. Bertini, I.; Luchinat, C. In *NMR of Paramagnetic Substances*; Lever, A. B. P., Ed. *Coord. Chem. Rev.*, Vol. 150, Elsevier: Amsterdam, **1996**; p. 296.
25. Walker, F. A. *Coord. Chem. Rev.* **1999**, 185–186, 471.

26. Walker, F. A. Proton NMR and EPR spectroscopy of paramagnetic metalloporphyrins. In *The Porphyrin Handbook*; Kadish, K. M.; Smith, K. M.; Guilard, R., Eds.; Academic Press: San Diego, CA, **2000**; Vol. 5, pp. 81–183.
27. La Mar, G. N.; Satterlee, J. D.; De Ropp, J. S. Nuclear magnetic resonance of hemoproteins. In *The Porphyrin Handbook*; Kadish, K. M.; Smith, K. M.; Guilard, R., Eds.; Academic Press: San Diego, CA, **2000**; Vol. 5, pp. 185–298.
28. Walker, F. A. *Inorg. Chem.* **2003**, 42. 4526.
29. Walker, F. A. *Chem. Rev.* **2004**, 104, 589.
30. Nakamura, M. *Coord. Chem. Rev.* **2006**, 250, 2271.
31. Nakamura, M.; Ohgo, Y.; Ikezaki, A. J. *Inorg. Biochem.* **2008**, 102, 433.
32. Scheidt, W. R.; Reed, C. A. *Chem. Rev.* **1981**, 81, 543.
33. Scheidt, W. R.; Lee, Y. J. *Struct. Bond.* **1987**, 64, 1.
34. Scheidt, W. R.; Gouterman, M. Ligands, spin state, and geometry in hemes and related metalloporphyrins. In *Iron Porphyrin*, Part 1; Lever, A. B. P.; Gray, H. B., Eds.; Addison-Wesley: Reading, MA, 1983; pp. 89–139.
35. Scheidt, W. R. Systematics of the stereochemistry of porphyrins and metalloporphyrins. In *The Porphyrin Handbook*; Kadish, K. M.; Smith, K. M.; Guilard, R., Eds.; Academic Press: San Diego, CA, **2000**; Vol. 3, pp. 49–112.
36. Evans, D. R.; Reed, C. A. *J. Am. Chem. Soc*. 2000, *122*, 4660.
37. Sakai, T.; Ohgo, Y.; Ikeue, T.; Takahashi, M.; Takeda, M.; Nakamura, M. J. *Am. Chem. Soc*. **2003**, *125*, 13028.
38. Cheng, R.-J.; Wang, Y.-K.; Chen, P.-Y.; Han Y.-P.; Chang, C.-C. *Chem. Commun.* **2005**, 1312.
39. Ling, Y.; Zhang, Y. *J. Am. Chem. Soc*. **2009**, *131*, 6386.
40. Ikezaki, A.; Ohgo, Y.; Nakamura, M. *Coord. Chem. Rev*. **2009**, *253*, 2056.
41. Ikezaki, A. Unpublished result. Calculated by *Spartan* '04 software; Wavefunction, Inc.: Irvine, CA, **2004**.
42. Cheng, R.-J.; Chen, P.-Y.; Lovell, T.; Liu, T.; Noodleman, L.; Case, D. A. *J. Am. Chem. Soc.* **2003**, *125*, 6774.
43. Conradie, J.; Ghosh, A. J. *Phys. Chem. B*. **2003**, *107,* 6486.
44. Barkigia, K. M.; Berber, M. D.; Fajer, J.; Medforth, C. J.; Renner, M. W.; Smith, K. M. *J. Am. Chem. Soc*. **1990**, *112*, 8851.
45. Bushnell, G. W.; Louie, G. V.; Brayer, G. D. *J. Mol. Biol*. **1990**, *214,* 585.
46. Kunishima, N.; Fukuyama, K.; Matsubara, H.; Hatanaka, H.; Shibano, Y.; Amachi, T. *J. Mol. Biol*. **1994**, *235*, 331.
47. Hobbs, J. D.; Shelnutt, J. A. *J. Protein Chem*. **1995**, *14*, 19.
48. Shelnutt, J. A.; Song, X.-Z.; Ma, J.-G.; Jia, S.-L.; Jentzen, W.; Medforth, C. J. *Chem. Soc. Rev.* **1998**, *27*, 31.
49. Ma, J.-G.; Zhang, J.; Franco, R.; Jia, S.-L.; Moura, I.; Moura, J. J. G.; Kroneck, P. M. H.; Shelnutt, J. A. *Biochemistry* **1998**, *37*, 12431.
50. Senge, M. O. Highly substituted porphyrins. In *The Porphyrin Handbook*; Kadish, K. M.; Smith, K. M.; Guilard, R., Eds.; Academic Press: San Diego, CA, **2000**; Vol. 1, pp. 239–347.
51. Shelnutt, J. A. Molecular simulations and normal-coordinate structural analysis of porphyrins and heme proteins. In *The Porphyrin Handbook*; Kadish, K. M.; Smith, K. M.; Guilard, R., Eds.; Academic Press: San Diego, CA, **2000**; Vol. 7, pp. 167–223.
52. Ikeue, T.; Ohgo, Y.; Saitoh, T.; Nakamura, M.; Fujii, H.; Yokoyama, M. *J. Am. Chem. Soc*. **2000**, *122*, 4068.

53. Ming, L.-J. Nuclear magnetic resonance of paramagnetic metal centers in proteins and synthetic complexes. In *Physical Method in Bioinorganic Chemistry: Spectroscopy and Magnetism*; Que, L., Jr., Ed.; University Science Books: Sausalito, CA. 2000; pp. 375–464.
54. Saitoh, T.; Ikeue, T.; Ohgo, Y.; Nakamura, M. *Tetrahedron* **1997***, 53,* 12487.
55. Turner, P.; Gunter, M. J. *Inorg. Chem*. **1994**, *33*, 1406.
56. Mispelter, J.; Momenteau, M.; Lhoste, J.-M. Heteronuclear magnetic resonance. In *NMR of Paramagnetic Molecules*; Berliner, L. J.; Reuben, J., Eds.; Biological Magnetic Resonance, Vol. 12; Plenum Press: New York, **1993**; pp. 299–355.
57. Phillipi, M. A.; Goff, H. M. *J. Chem. Soc. Chem. Commun*. **1980**, 455.
58. Heller, C.; McConnell, H. M. *J. Chem. Phys*. **1960**, *32*, 1535.
59. McLachlan, A. D. *Mol. Phys*. **1958**, *1*, 233.
60. Nakamura, M. *Bull. Chem. Soc. Jpn*. **1995**, *68*, 197.
61. Nakamura, M.; Ikezaki, A. *Chem. Lett*. **1995**, 733.
62. Ikeue, T.; Ohgo, Y.; Ongayi, O.; Vicente, M. G. H.; Nakamura, M. *Inorg. Chem.* **2003**, *42*, 5560.
63. Kurland, R. J.; McGarvey, B. R. *J. Magn. Reson*. **1969**, *2*, 286.
64. Karplus, M.; Fraenkel, G. K. *J. Chem. Phys*. **1961**, *35*, 1312.
65. Wütrich, K.; Baumann, R. *Helvetica Chim. Acta* **1973**, 56, 585.
66. Strom, E. T.; Underwood, G. R.; Jurkowitz, D. *Mol. Phys*. **1972**, *24*, 901.
67. Strohmeier, M.; Orendt, A. M.; Facelli, J. C.; Solum, M. S.; Pugmire, R. J.; Parry, R. W.; Grant, D. M. *J. Am. Chem. Soc*. **1997**, *119*, 7114.
68. Nakamura, M.; Hoshino, A.; Ikezaki, A.; Ikeue, T. *Chem. Commun.* **2003**, 1862.
69. Palmer, G. Electron paramagnetic resonance of hemoproteins. In *Iron Porphyrins, Part II*; Lever, A. B. P.; Gray, H. B. Eds.; Physical Bioinorganic Chemistry Series 2; Addison-Wesley: Reading, MA. 1983; pp. 43–88.
70. Bohan, T. L. *J. Magn. Reson.* **1977**, *26*, 109.
71. Taylor, C. P. S. *Biochim. Biophys. Acta* **1977**, *491*, 137.
72. Walker, F. A.; Reis, D.; Balke, V. J. *J. Am. Chem. Soc*. **1984**, *106*, 6888.
73. Walker, F. A.; Huynh, B. H.; Scheidt, W. R.; Osvath, S. R. *J. Am. Chem. Soc*. **1986**, *108*, 5288.
74. Walker, F. A.; Nasri, H.; Turowska-Tyrk, I.; Mohanrao, K.; Watson, C. T.; Shokhirev, N. V.; Debrunner, P. G.; Scheidt, W. R. *J. Am. Chem. Soc*. **1996**, *118*, 12109.
75. Inniss, D.; Soltis, S. M.; Strouse, C. E. *J. Am. Chem. Soc*. **1988**, *110*, 5644.
76. Yatsunyk, L.A.; Dawson, A.; Carducci, M. D.; Nichol, G. S.; Walker, F. A. *Inorg. Chem*. **2006**, *45*, 5417.
77. Simonneaux, G.; Schünemann, V.; Morice, C.; Carel, L.; Toupet, L.; Winkler, H.; Trautwein, A. X.; Walker, F. A. *J. Am. Chem. Soc*. **2000**, *122*, 4366.
78. Safo, M. K.; Gupta, G. P.; Watson, C. T.; Simonis, U.; Walker, F. A.; Scheidt, W. R. *J. Am. Chem. Soc*. **1992**, *114*, 7066.
79. Safo, M. K.; Walker F. A.; Raitsimring, A. M.; Walters, W. P.; Dolata, D. P.; Debrunner, P. G.; Scheidt, W. R. *J. Am. Chem. Soc*. **1994**, *116*, 7760.
80. Sakai, T.; Ohgo, Y.; Hoshino, A.; Ikeue, T.; Saitoh, T.; Takahashi, M.; Nakamura, M. *Inorg. Chem*. 2004, *43*, 5034.
81. Ikeue, T. *et al.* Unpublished result.
82. Ikeue, T.; Ohgo, Y.; Saitoh, T.; Yamaguchi, T.; Nakamura, M. *Inorg. Chem*. **2001**, *40*, 3423.
83. Ikeue, T.; Yamaguchi, T.; Ohgo, Y.; Nakamura, M. *Chem. Lett*. **2000**, *29*, 3423.
84. Ikezaki, A.; Nakamura, M. *Inorg Chem.* **2002**, *41*, 2761.

85. Guillemot, M.; Simonneaux, G. *J. Chem. Soc. Chem. Commun*. **1995**, 2093.
86. Pilard, M.-A.; Guillemot, M.; Toupet, L.; Jordanov, J.; Simonneaux, G.; *Inorg. Chem*. **1997**, *36*, 6307.
87. Simonneaux, G.; Sodano, P. *Inorg. Chem*. **1988**, *27*, 3956.
88. Rahman, M. M.; Liu, H. Y.; Ericks, K.; Prock, A.; Giering, W. P. *Organometallics* **1989**, *8*, 1.
89. Wołowiec, S.; Latos-Grażyński, L.; Mazzanti, M.; Marchon, J.-C. *Inorg. Chem*. **1997**, *36*, 5761.
90. Nakamura, M.; Groves, J. T. *Tetrahedron* **1988**, *44*, 3225.
91. Walker, F. A.; Simonis, U. *J. Am. Chem. Soc*. **1991**, *113*, 8652.
92. Nakamura, M. *Chem. Lett*. **1992**, 2423.
93. Nakamura, M.; Ikeue, T.; Neya, S.; Funasaki, N.; Nakamura, N. *Inorg. Chem*. **1996**, *35*, 3731.
94. Ikezaki, A.; Ikeue, T.; Nakamura, M. *Inorg. Chim. Acta* **2002**, *335*, 91.
95. Ohgo, Y.; Hoshino, A.; Okamura, T.; Uekusa, H.; Hashizume, D.; Ikezaki, A. Nakamura, M. *Inorg. Chem.* **2007**, *46*, 8193.
96. Moore, K. T.; Fletcher, J. T.; Therien, M. J. *J. Am. Chem. Soc.* **1999**, *121*, 5196.
97. Nakamura, M.; Ikeue, T.; Fujii, H.; Yoshimura, T. *J. Am. Chem. Soc*. **1997**, *119*, 6284.
98. Ikeue, T.; Saitoh, T.; Yamaguchi, T.; Ohgo, Y.; Nakamura, M.; Takahashi, M.; Takeda, M. *Chem. Commun*. **2000**, 1989.
99. Simonato, J.-P.; Pécaut, J.; Le Pape, L.; Oddou, J.-L.; Jeandey, C.; Shang, M.; Scheidt, W. R.; Wojaczyński, J.; Wołowiec, S.; Latos-Grażyński, L.; Marchon, J.-C. *Inorg. Chem*. **2000**, *39*, 3978.
100. Ikeue, T.; Ohgo, Y.; Yamaguchi, T.; Takahashi, M.; Takeda, M.; Nakamura, M. *Angew. Chem. Int. Ed*. 2001, *40*, 2617.
101. Ohgo, Y.; Chiba, Y.; Hashizume, D.; Uekusa, H.; Ozeki, T.; Nakamura, M. *Chem. Commun.* **2006**, 1935.
102. Renner, M. W.; Barkigia, K. M.; Zhang, Y.; Medforth, C. J.; Smith, K. M.; Fajer, J. *J. Am. Chem. Soc.* **1994**, *116*, 8582.
103. Shao, J.: Steene, E.; Hoffman, B. M.; Ghosh, A. *Eur. J. Inorg. Chem*. **2005**, 1609.
104. Cheng, R.-J.; Chao, C.-W.; Han, Y.-P.; Chen, Y.-C.; Ting, C.-H. *Chem. Commun*. **2009**, 2180.
105. Jentzen, W.; Simpson, M. C.; Hobbs, J. D.; Song, X.; Ema, T.; Nelson, N. Y.; Medforth, C. J.; Smith, K. M.; Veyrat, M.; Mazzanti, M.; Ramasseul, R.; Marchon, J.-C.; Takeuchi, T.; Goddard, III, W. A.; Shelnutt, J. A. *J. Am. Chem. Soc.* **1995**, *117*, 11085
106. Senge, M. O.; Ema, T.; Smith, K. M. *J. Chem. Soc. Chem. Commun.* **1995**, 733.
107. Medforth, C. J.; Muzzi, C. M.; Shea, K. M.; Smith, K. M.; Abraham, R. J.; Jia, S.; Shelnutt, J. A. *J. Chem. Soc. Perkin Trans. 2*. **1997**, 839.
108. Ikezaki, A.; Nakamura, M. *Chem. Lett*. **2005**, *34*, 1046.
109. Li, W.-K.; Zhou, G.-D.; Mak, T. C. W. Advanced structural inorganic chemistry. In *IUCr Texts on Crystallography 10*; Oxford University Press; **2008**; Chapter 4.
110. Ikeue, T.; Ohgo, Y.; Uchida, A.; Nakamura, M.; Fujii, H.; Yokoyama M. *Inorg. Chem*. **1999**, *38*, 1276.
111. Ohgo, Y.; Ikeue, T.; Nakamura, M. *Acta Crystallogr. Sect. C 55* **1999**, 1817.
112. Goff, H. *J. Am. Chem. Soc.* **1977**, *99*, 7723.
113. Fujii, H. *J. Am. Chem. Soc*. **2002**, *124*, 5936.
114. Mao, J.; Zhang Y.; Oldfield, E. *J. Am. Chem. Soc*. **2002**, *124*, 13911.
115. Hada M. *J. Am. Chem. Soc*. **2004**, *126*, 486.
116. Nonaka, D.; Wariishi, H.; Fujii, H. *Biochemistry* **2009**, *48*, 898.

117. Cheng, R.-J.; Lee, C.-H.; Chao, C.-W. *Chem. Commun*. **2009**, 2526.
118. Safo, M. K.; Gupta, G. P.; Walker, F. A.; Scheidt, W. R. *J. Am. Chem. Soc*. **1991**, *113*, 5497.
119. Nakamura, M.; Tajima, K.; Tada, M.; Ishizu, K.; Nakamura, N. *Inorg. Chim. Acta* **1994**, *224*, 113.
120. Munro, O. Q.; Marques, H. M.; Debrunner, P. G.; Mohanrao, K.; Scheidt, W. R. *J. Am. Chem. Soc*. **1995**, *117*, 935.
121. Wołowiec, S.; Latos-Grażyński, L.; Toronto, D.; Marchon, J.-C. *Inorg. Chem*. **1998**, *37*, 724.
122. Nakamura, M.; Nakamura, N. *Chem. Lett*. **1991**, 1885.
123. Yatsunyk, L. A.; Walker, F. A. *Inorg. Chem*. **2004**, *43*, 4341.
124. La Mar, G. N.; Gaudio, J. D.; Frye, J. S.; *Biochim. Biophys. Acta* **1977**, *498*, 422.
125. Desiraju, G. R. *J. Chem. Soc. Chem. Commun.* **1989**, 179.
126. Pedireddi, V. R.; Desiraju, G. R. *J. Chem. Soc. Chem. Commun.* **1992**, 988.
127. Steiner, T. *J. Chem. Soc. Chem. Commun.* **1994**, 2341.
128. Steiner, T. *New J. Chem.* **1998**, 1099.
129. Allerhand, A.; Schleyer, P. v. R. *J. Am. Chem. Soc.* **1963**, *85*, 1715.
130. Nishio, M.; Umezawa, Y.; Honda, K.; Tsuboyama, S.; Suezawa, H. *Cryst. Eng. Comm.* **2009**, *11*, 1757.
131. Nakamura, M.; Ohgo, Y.; Ikezaki, A. *J. Inorg. Biochem.* **2008**, *102*, 433.
132. Nakamura, M.; Ikeue, T.; Fujii, H.; Yoshimura, T.; Tajima, K. *Inorg. Chem*. **1998**, *37*, 2405.
133. Senge, M. O.; Bischoff, I.; Nelson, N. Y.; Smith, K. M. *J. Porphyrins Phthalocyanines* **1999**, *3*, 99.
134. Ohgo, Y.; Neya, S.; Uekusa, H.; Nakamura, M. *Chem. Commun*. **2006**, 4590.
135. Stuzhin, P. A.; Vagin, S. I.; Hanack, M. *Inorg. Chem.* **1998**, *37*, 2655.
136. Nakamura, K.; Ikezaki, A.; Ohgo, Y.; Ikeue, T.; Neya, S.; Nakamura, M. *Inorg. Chem*. **2008**, *47*, 10299.
137. Scheidt, W. R.; Finnegan, M. G. *Acta Crystallogr.* **1989**, *C45*, 1214.
138. Lecomte, C.; Chadwick, D. L.; Coppens, P.; Stevens, E. D. *Inorg. Chem*. **1983**, *22*, 2982.
139. Hatano, K.; Uno, T. *Bull. Chem. Soc. Jpn*. **1990**, *63*, 1825.
140. Dolphin, D. H.; Sams, J. R.; Tsin, T. B. *Inorg. Chem*. **1977**, *16*, 711.
141. Kastner, M. E.; Scheidt, W. R.; c, T.; Reed, C. A. *J. Am. Chem. Soc.* **1978**, *100*, 666.
142. Reed, C. A.; Mashiko, T.; Bentley, S. P.; Kastner, M. E.; Scheidt, W. R.; Spartalian, K.; Lang, G.; *J. Am. Chem. Soc*. 1979, *101*, 2948.
143. Goff, H. M.; Shimomura, E. *J. Am. Chem. Soc*. 1980, *102*. 31.
144. Masuda, H.; Taga, T.; Osaki, K.; Sugimoto, H.; Yoshida, Z. I.; Ogoshi, H. *Inorg. Chem.* **1980**, *19*, 950.
145. Toney, G. E.; terHaar, L. W.; Savrin, J. E.; Gold, A.; Hatlfield, W. E.; Sangaiah, R. *Inorg. Chem*. **1984**, *23*, 2561.
146. Toney, G. E.; Gold, A.; Savrin, J. E.; terHaar, L. W.; Sangaiah, R. *Inorg. Chem*. **1984**, *23*, 4350.
147. Kintner, E. T.; Dawson, J. H. *Inorg. Chem*. **1991**, *30*, 4892.
148. Summerville, D. A.; Cohen, I. A.; Hatano, K.; Scheidt, W. R. *Inorg. Chem.* **1978**, *17*, 2906.
149. Boersma, A. D.; Goff, H. M. *Inorg. Chem.* **1984**, *23*, 1671.
150. Maltempo, M. M.; Moss, T. H.; Cusanovich, M. A. *Biochim. Biophys. Acta* **1974**, *342*, 290.
151. Maltempo, M. M. *J. Chem. Phys*. **1974**, *61*, 2540.
152. Gupta, G. P.; Lang, G.; Reed, C. A.; Shelly, K.; Scheidt, W. R. *J. Chem. Phys*. **1987**, *86*, 5288.
153. Gupta, G. P.; Lang, G.; Lee, Y. J.; Scheidt, W. R.; Shelly, K.; Reed, C. A. *Inorg. Chem*. **1987**, 26, 3022.

154. Neya, S.; Takahashi, A.; Ode, H.; Hoshino, T.; Hata, M.; Ikezaki, A.; Ohgo, Y.; Takahashi, M.; Hiramatsu, H.; Kitagawa, T.; Furutani, Y.; Kandori, H.; Funasaki, N.; Nakamura, M. *Eur. J. Inorg. Chem*. **2007**, 3188.
155. Neya, S.; Takahashi, A.; Ode, H.; Hoshino, T.; Ikezaki, A.; Ohgo, Y.; Takahashi, M.; Furutani, Y.; Lórentz-Fonfría, V. A.; Kandori, H.; Hiramatsu, H.; Kitagawa T.; Teraoka, J.; Funasaki, N.; Nakamura, M. *Bull. Chem. Soc. Jpn*. **2008**, *81*, 136.
156. Djukic, B.; Dube, P. A.; Razavi, F.; Seda, T.; Jenkins, H. A.; Britten, J. F.; Lemaire, M. T. *Inorg. Chem.* **2009**, *48*, 699.
157. Reed, C.A.; Guiset, F. *J. Am. Chem. Soc*. **1996**, *118*, 3281.
158. Reed, C. A. *Inorg. Chim. Acta* **1997**, *263*, 95.
159. Juhasz, M.; Hoffmann, S.; Stoyanov, E.; Kim, K.-C.; Reed, C. A. *Angew. Chem. Int. Ed*. **2004**, *43*, 5352.
160. Rachlewicz, K.; Latos-Grazynski, L.; Vogel, E.; Ciunik, Z.; Jerzykiewicz, L. B. *Inorg. Chem.* **2002**, *41*, 1979.
161. Zobrist, M.; La Mar, G. N. *J. Am. Chem. Soc*. **1978**, *100*, 1945.
162. Budd, D. L.; La Mar, G. N. Langry, K. C.; Smith, K. M.; Nayyir-Mazhir, R. *J. Am. Chem. Soc*. **1979**, *101*, 6091.
163. Dixon, D. W.; Barbush, M.; Shirazi, A. *Inorg. Chem.* 1985, *24*, 1081.
164. de Ropp, J. S.; La Mar, G. N. *J. Am. Chem. Soc*. **1991**, *113*, 4348.
165. Hickman, D. L.; Goff, H. M. *Inorg. Chem*. **1983**, *22*, 2787.
166. Hickman, D. L.; Nanthakumar, A.; Goff, H. M. *J. Am. Chem. Soc*. **1988**, *110*, 6384.
167. Hoshino, A.; Nakamura, M. *Chem. Lett.* **2004**, *33.* 1234.
168. Hoshino, A.; Ohgo, Y.; Nakamura, M. *Inorg. Chem.* **2005**, *44,* 7333.
169. Nakamura, M. *Angew. Chem. Int. Ed.* **2009**, *48*, 2638.
170. Fang, M.; Wilson, S. R.; Suslick, K. S. *J. Am. Chem. Soc*. **2008**, *130*, 1134.
171. Sams, J. R.; Tsin, T. B. Mössbauer spectroscopy of iron porphyrins. In *The Porphyrins*; Dolphin, D., Ed.; Academic: New York, **1978**; Vol. 4, pp. 425–478.
172. Debrunner, P. G. Mössbauer spectroscopy of iron porphyrins. In *Iron Porphyrin*, *Part III*; Lever, A. B. P.; Gray, H. B., Eds.; Physical Bioinorganic Chemistry, Vol 4; VCH: New York, **1989**; pp. 139–234.
173. Gütlich, P.; Ensling, J. Mössbauer spectroscopy. In *Inorganic Electronic Structure and Spectroscopy*, *Vol. 1*; Solomon, E. I., Lever A. B. P., Eds.; John Wiley & Sons: New York, **1999**; pp. 161–211.
174. Ohgo, Y.; Neya, S.: Takahashi, M.; Takeda, M.; Funasaki, N.; Nakamura, M. *Chem. Lett*. **2003**, *32*, 526.
175. Weiss, R.; Gold, A.; Terner, J. *Chem. Rev*. **2006**, *106*, 2550.
176. Ohgo, Y.; Saitoh, T.; Nakamura, M. *Acta Crystallogr.* **2001**, *C57*, 233.
177. Ohgo, Y.; Saitoh, T.; Nakamura, M. *Acta Crystallogr.* **1999**, *C55*, 1284.
178. Masuda, H.; Taga, T.; Osaki, K.; Sugimoto, H.; Yoshida, Z.-I.; Ogoshi, H. *Bull. Chem. Soc. Jpn.* **1982**, *55*, 3891.
179. Chen, L.; Yi, G.-B.; Wang, L.-S.; Dharmawardana, U. R.; Dart, A. C.; Khan, M. A.; Richter-Addo, G. B. *Inorg. Chem*. **1998**, *37*, 4677.
180. Nakamura, M.; Ikeue, T.; Ohgo, Y.; Takahashi, M.; Takeda, M. *Chem. Commun.* **2002**, 1198.
181. Barkigia, K. M.; Renner, M. W.; Fajer, J. *J. Porphyrins Phthalocyanines.* **2001**, *5*, 415.
182. Cheng, R.-J.; Chen, P.-Y.; Gau, P.-R.; Chen, C.-C.; Peng, S.-M. *J. Am. Chem. Soc*. **1997**, *119*, 2563.

183. Schünemann, V.; Gerdan, M.; Trautwein, A. X.; Haoudi, N.; Mandon, D.; Fischer, J.; Weiss, R.; Tabard, A.; Guilard, R. *Angew. Chem. Int. Ed*. **1999**, *38*, 3181.
184. Ikezaki, A.; Ohgo, Y.; Watanabe, T.; Nakamura, M. *Inorg. Chem. Commun*. **2008**, *11*, 1198.
185. Gütlich, P.; Ensling, J. Spin transition in iron(II) compounds. In *Inorganic Electronic Structure and Spectroscopy*; Solomon, E. I.; Lever A. B. P., Eds.; John Wiley & Sons: New York, **1999**; Vol. 2, pp. 575–622.
186. Gütlich, P.; Hauser, A. *Coord. Chem. Rev.* **1990**, *97*, 1.
187. Gütlich, P.; Hauser, A. Spiering, H. *Angew. Chem. Int. Ed. Engl.* **1994**, *33*, 2024.
188. Kahn, O.; Kröber, J.; Jay, C. *Adv. Mater.* **1992**, *4*, 718.
189. Beetlestone, J.; George, P. *Biochemistry* **1964**, *3*, 707.
190. Iizuka, T.; Kotani, M. *Biochim. Biophys. Acta* **1968**, *154*, 417.
191. Sligar, S. G. *Biochemistry* **1976**, *15*, 5399.
192. Yonetani, T.; Iizuka, T.; Asakura, T. *J. Biol. Chem*. **1972**, *247*, 863.
193. Iizuka, T.; Kotani, M. Yonetani, T. *Biochim. Biophys. Acta Enzymol.* **1968**, *167*, 257.
194. Iizuka, T.; Yonetani, T. *Adv. Biophys*. **1970**, *1*, 157.
195. Scheidt, W. R.; Geiger, D. K.; Haller, K. J. *J. Am. Chem. Soc.* **1982**, *104*, 495.
196. Ellison, M. K.; Nasri, H.; Xia, Y.-M.; Marchon, J.-C.; Schulz, C. E.; Debrunner, P. G.; Scheidt, W. R. *Inorg. Chem*. **1997**, *36*, 4804.
197. Neya, S.; Tsubaki, M.; Hori, H.; Yonetani, T.; Funasaki, N. *Inorg. Chem*. **2001**, *40*, 1220.
198. Neya, S.; Chang, C. K.; Okuno, D.; Hoshino, T.; Hata, M.; Funasaki, N. *Inorg. Chem*. **2005**, *44*, 1193.
199. Sessler, J. L.; Gebauer, E.; Vogel, E. Porphyrin isomers. In *The Porphyrin Handbook*; Kadish, K. M.; Smith, K. M.; Guilard, R., Eds.; Academic Press: San Diego, CA, **2000**; Vol. 4, pp. 1–54.
200. Ohgo, Y.; Neya, S.; Ikeue, T.; Funasaki, F.; Takahashi, M.; Takeda, M.; Nakamura, M. *Inorg. Chem.* **2002**, *41*, 4627.
201. Ohgo, Y.; Neya, S.; Ikeue, T.; Funasaki, F.; Nakamura, M. *Acta Crystallogr.* **2001**, *C57*, 1046.
202. Ohgo, Y.; Neya, S.; Ikeue, T.; Funasaki, F.; Takahashi, M.; Takeda, M.; Nakamura, M. *Inorg Chem.* **2002**, *41*, 4627.
203. Ohgo, Y.; Neya, S.; Takahashi, M.; Takeda, M.; Nakamura, M. *Chem. Lett.* **2003**, *32*, 526.
204. Hodges, K. D.; Wollmann, R. G.; Kessel, S. L.; Hendrickson, D. N.; Van Derveer, D. G.; Barefield, E. K. *J. Am. Chem. Soc*. **1979**, *101*, 906.
205. Koch, W. O.; Schünemann, V.; Gerdan, M.; Trautwein, A. X.; Krüger, H.-J. *Chem. Eur. J.* **1998**, *4*, 686.
206. Zeng, Y.; Caignan, G. A.; Bunce, R. A.; Rodriguez, J. C.; Wilks, A.; Rivera, M. *J. Am. Chem. Soc*. **2005**, *127*, 9794.
207. Caignan, G. A.; Deshmukh, R.; Zeng, Y.; Wilks, A.; Bunce, R. A.; Rivera, M. *J. Am. Chem. Soc*. **2003**, *125*, 11842.
208. Rivera, M.; Caignan, G. A. *Anal. Bioanal. Chem*. **2004**, *378*, 1464.
209. Ohgo, Y.; Ikeue, T.; Takahashi, M.; Takeda, M.; Nakamura, M. *Eur. J. Inorg. Chem.* **2004**, 798.
210. Balch, A. L.; Olmstead, M. M.; Safari, N. *Inorg. Chem.* **1993**, *32*, 291.
211. Ernst, J.; Subramanian, J.; Fuhrhop, J.-H. *Z. Naturforsh. A* **1977**, 32, 1129.
212. Ohgo, Y.; Ikeue, T.; Nakamura, M. *Inorg. Chem.* **2002**, *41*, 1698.
213. Harutyunyan, E. H.; Safonova, T. N.; Kuranova, I. P.; Popov, A. N.; Teplyakov, A. V.; Obmolova, G. V.; Rusakov, A. A.; Vainshtein, B. K.; Dodson, G. G.; Wilson, J. C.; Perutz, M. F. *J. Mol. Biol.* **1995**, *251*, 104.

214. Shriver, D. F.; Atkins, P. W.; Langford, C. H. *Inorganic Chemistry*, 2nd ed.; Oxford University Press; **1994**; pp. 111–113.
215. Weiss, R.; Gold, A.; Terner, J. *Chem. Rev*. **2006**, *106*, 2550.
216. Yasui, M.; Harada, S.; Kai, Y.; Kasai, N.; Kusunoki, M.; Matsuura, Y. *J. Biochem (Tokyo)* **1992**, *111*, 317.
217. Ren, Z.; Meyer, T.; McRee, D. E. *J. Mol. Biol*. **1993**, *234*, 433.
218. Tahirov, T. H.; Misaki, S.; Meyer, T. E.; Cusanovich, M. A.; Higuchi, Y.; Yasuoka, N. *Nat. Struct. Biol.* **1996**, *3*, 459.
219. Tahirov, T. H.; Misaki, S.; Meyer, T. E.; Cusanovich, M. A.; Higuchi, Y.; Yasuoka, N. *J. Mol. Biol.* **1996**, *259*, 467.
220. Dobbs, A. J.; Anderson, B. F.; Faber, H. R.; Baker, E. N. *Acta Crystallogr.* **1996**, *D52*, 356.
221. Archer, M.; Banci, L.; Dikaya, E.; Romão, M. J. *J. Biol. Inorg. Chem*. **1997**, *2*, 611.
222. Shibata, N.; Iba, S.; Misaki, S.; Meyer, T. E.; Bartsch, R. G.; Cusanovich, M. A.; Morimoto, Y.; Higuchi, Y.; Yasuoka, N. *J. Mol. Biol*. **1998**, *284*, 751.
223. Fujii, S.; Yoshimura, T.; Kamada, H.; Yamaguchi, K.; Suzuki, S.; Shidara, S.; Takakuwa, S. *Biochim. Biophys. Acta* **1995**, *1251*, 161.
224. Quinn, R.; Nappa, M.; Valentine, J. S. *J. Am. Chem. Soc.* **1982**, *104*, 2588.
225. Gupta, G. P.; Lang, G.; Scheidt, W. R.; Geiger, D. K.; Reed, C. A. *J. Chem. Phys*. **1985**, *83*, 5945.
226. Gupta, G. P.; Lang, G.; Scheidt, W. R.; Geiger, D. K.; Reed, C. A. *J. Chem. Phys*. **1986**, *85*, 5212.
227. Fujii, H.; Yoshimura, T.; Kamada, H. *Inorg. Chem*. **1997**, *36*, 6142.
228. Scheidt, W. R.; Geiger, D. K.; Lee, Y. J.; Reed, C. A.; Lang, G. *J. Am. Chem. Soc.* **1985**, *107*, 5693.
229. Ikezaki, A.; Nakamura, M. *J. Inorg. Biochem*. **2001**, *84*, 137.
230. Ikezaki, A.; Nakamura, M. *Inorg. Chem*. **2002**, *41*, 6225.
231. Takahashi, A.; Kurahashi, T.; Fujii, H. *Inorg. Chem*. **2009**, *48*, 2614.
232. Ikezaki, A.; Takahashi, M.; Nakamura, M. *Angew. Chem. Int. Ed.* **2009**, *48*, 6300.
233. Finzel, B. C.; Weber, P. C.; Hardman, K. D.; Salemme, F. R. *J. Mol. Biol*. **1985**, *186*, 627.
234. La Mar, G. N.; Jackson, J. T.; Dugad, L. B.; Cusanovich, M. A.; Bartsch, R. G. *J. Biol. Chem.* **1990**, *265*, 16173.
235. Nakamura, M.; Nakamura, N. *Chem. Lett.* **1991**, 627.
236. Nakamura, M.; Tajima, K.; Tada, K.; Ishizu, K.; Nakamura, N. *Inorg. Chim. Acta* **1994**, *224*, 113.
237. Zhang, H.; Simonis, U.; Walker, F. A. *J. Am. Chem. Soc.* **1990**, *112*, 6124.
238. Basu, P.; Raitsimring, A. M.; Enemark, J. H.; Walker, F. A. *Inorg. Chem*. **1997**, *36*, 1088.
239. Neya, S.; Funasaki, N.; Nakamura, M. *Biochim. Biophys. Acta* **1992**, *117*, 243.
240. Phillippi, M. A.; Shimomura, E. T.; Goff, H. M. *Inorg. Chem.* **1981**, *20*, 1322.
241. Gans, P.; Buisson, G.; Duée, E.; Marchon, J.-C.; Erler, B. S.; Scholz, W. F.; Reed, C. A. *J. Am. Chem. Soc.* **1986**, *108*, 1223.
242. Phillippi, M. A.; Goff, H. M. *J. Am. Chem. Soc.* **1982**, *104*, 6026.
243. Buisson, G.; Deronzier, A.; Duée, E.; Gans, P.; Marchon, J.-C.; Regnard, J.-R. *J. Am. Chem. Soc.* **1982**, *104*, 6793.
244. Scholz, W. F.; Reed, C. A.; Lee, Y. J.; Scheidt, W. R.; Lang, G. *J. Am. Chem. Soc.* **1982**, *104*, 6791.
245. Nakamura, M.; Kawasaki, Y. *Chem. Lett.* **1996**, *25*, 805.

246. Balch, A. L.; Latos-Grażyński, L.; Noll, B. C.; Szterenberg, L.; Zovinka, E. P. *J. Am. Chem. Soc.* **1993**, *115*, 11846.
247. Nanthakumar, A.; Goff, H. M. *Inorg. Chem.* **1991**, *30*, 4460.
248. Nakamura, M.; Yamaguchi, T.; Ohgo, Y. *Inorg. Chem.* **1999**, *38*, 3126.
249. Hanson, L. K.; Chang, C. K.; Davis, M. S.; Fajer, J. *J. Am. Chem. Soc.* **1981**, *103*, 663.
250. Hoshino, A.; Nakamura, M. *Chem. Commun.* **2005**, 915.
251. Mispelter, J.; Momenteau, M.; Lhoste, J.-M. *J. Chem. Soc. Dalton Trans.* **1981**, 1729.
252. Goff, H. M.; Shimomura, E. T.; Phillippi, M. A. *Inorg. Chem.* **1983**, *22*, 66.
253. Groves, J. T.; Quinn, R.; McMurry, T. J.; Nakamura, M.; Lang, G.; Boso, B. *J. Am. Chem. Soc.* **1985**, *107*, 354.
254. Rachlewicz, K.; Latos-Grazynski, L. *Inorg. Chem*. **1996**, *35*, 1136.
255. Goff, H. M.; Phillippi, M. A. *J. Am. Chem. Soc.* **1983**, *105*, 7567.
256. Ikeue, T.; Ohgo, Y.; Nakamura, M. *Chem. Commun.* **2003**, 220.
257. Ikezaki, A.; Tukada, H.; Nakamura, M. *Chem. Commun.* **2008**, 2257.
258. Chin, D.-H.; Balch, A. L.; La Mar, G. N. *J. Am. Chem. Soc.* **1980**, *102*, 1446.
259. Chin, D.-H.; La Mar, G. N.; Balch, A. L. *J. Am. Chem. Soc.* **1980**, *102*, 5945.
260. Simmoneaux, G.; Scholtz, W. F.; Reed, C. A. *Biochim. Biophys. Acta* **1982**, *716*, 1.
261. Balch, A. L.; Chan, Y.-W.; Cheng, R.-J.; La Mar, G. N.; Latos-Grazynski, L.; Renner, M. W. *J. Am. Chem. Soc.* **1984**, *106*, 7779.
262. Balch, A. L.; La Mar, G. N.; Latos-Grazynski, L.; Renner, M. W.; Thanabal, V. *J. Am. Chem. Soc.* **1985**, *107*, 3003.
263. Arasasingham, R. D.; Cornman, C. R.; Balch, A. L. *J. Am. Chem. Soc.* **1989**, *111*, 7800.
264. Lee, W. A.; Calderwood, T. S.; Bruice, T. C. *Proc. Natl. Acad. Sci. U.S.A*. **1985**, *82*, 4301.
265. Calderwood, T. S.; Lee, W. A.; Bruice, T. C. *J. Am. Chem. Soc.* **1985**, *107*, 8272.
266. Groves, J. T.; Gilbert, J. A. *Inorg. Chem.* **1986**, *25*, 123.
267. Swistak, C.; Mu, X. H.; Kadish, K. M. *Inorg. Chem*. **1987**, *26*, 4360.
268. Groves, J. T.; Gross, Z.; Stern, M. K. *Inorg. Chem.* **1994**, *33*, 5065.
269. Balch, A. L.; Cornman, C. R.; Latos-Grażyński, L.; Renner, M. W. *J. Am. Chem. Soc.* **1992**, *114*, 2230.
270. Shin, K.; Goff, H. M. *J. Am. Chem. Soc.* **1987**, *109*, 3140.
271. Schappacher, M.; Weiss, R. *J. Am. Chem. Soc.* **1985**, *107*, 3736.
272. Gold, A.; Jayaraj, K.; Doppelt, P.; Weiss, R.; Chottard, G.; Bill, E.; Ding, X.; Trautwein, A. X. *J. Am. Chem. Soc.* **1988**, *110*, 5756.
273. La Mar, G. M.; de Ropp, J. S.; Latos-Grazynski, L.; Balch, A. L.; Johnson, R. B.; Smith, K. M.; Parish, D. W.; Cheng, R.-J. *J. Am. Chem. Soc.* **1983**, *105*, 782.
274. Ghosh, A. Almöf, J.; Que, L., Jr. *J. Phys. Chem*. **1994**, *98*, 5576.
275. Dey, A.; Ghosh, A. *J. Am. Chem. Soc.* **2002**, *124*, 3206.
276. Penner-Hahn, J. E.; McMurry, T. J.; Renner, M.; Latos-Grazynsky, L.; Eble, K. S.; Davis, I. M.; Balch, A. L.; Groves, J. T.; Dawson, J. H.; Hodgson, K. O. *J. Biol. Chem.* **1983**, *258*, 12761.
277. Groves, J. T.; Haushalter, R. C.; Nakamura, M.; Nemo, T. E.; Evans, B. J. *J. Am. Chem. Soc.* **1981**, *103*, 2884.
278. Wołowiec, S.; Latos-Grażyński, L. *Inorg. Chem.* **1998**, *37*, 2984.
279. Jones, D. H.; Hinman, A. S.; Ziegler, T. *Inorg. Chem.* **1993**, *32*, 2092.
280. Ghosh, A.; Persson, B. J.; Taylor, P. R. *J. Biol. Inorg. Chem.* **2003**, *8*, 507.
281. Ghosh, A.; Taylor, P. R. *J. Chem. Theory Comput.* **2005**, *1*, 597.

282. Nanthakumar, A.; Goff, H. M. *J. Am. Chem. Soc*. **1990**, *112*, 4047.
283. Yamaguchi, K.; Watanabe, Y.; Morishima, I. *J. Chem. Soc. Chem. Commun.* **1992**, 1721.
284. Murakami, T.; Yamaguchi, K.; Watanabe, Y.; Morishima, I. *Bull. Chem. Soc. Jpn.* **1998**, *71*, 1343.
285. Fujii, H. *Coord. Chem. Rev.* **2002**, *226*, 51.
286. Groves, J. T.; Watanabe, Y. *J. Am. Chem. Soc*. **1986**, *108*, 7836.
287. Groves, J. T.; Watanabe, Y. *J. Am. Chem. Soc*. **1988**, *110*, 8443.
288. Watanabe, Y.; Tekehira, K.; Shimazu, M.; Hayakawa, T.; Orita, H.; Kaise, M. *J. Chem. Soc. Chem. Commun.* **1990**, 1262.
289. Tsurumaki, H.; Watanabe, Y.; Morishima, I. *J. Am. Chem. Soc*. **1993**, *115*, 11784.
290. Bill, K.; Ding, X.-Q.; Bominaar, E. L.; Trautwein, A. X.; Winkler, H.; Mandon, D.; Weiss, R.; Gold, A.; Jayaraj, K.; Hatfield, W. E.; Kirk, M. L. *Eur. J. Biochem.* **1990**, *188*, 665.
291. Mandon, D.; Weiss, R.; Jayaraj, K.; Gold, A.; Terner, J.; Bill, E.; Trautwein, A. X. *Inorg. Chem.* **1992**, *31*, 4404.
292. Hashimoto, S.; Tatsuno, Y.; Kitagawa, T. *J. Am. Chem. Soc.* **1987**, *109*, 8096.
293. Penner-Hahn, J. E.; Eble, K. S.; McMurry, T. J.; Renner, M.; Balch, A. L.; Groves, J. T.; Dawson, J. H.; Hodgson, K. O. *J. Am. Chem. Soc*. **1986**, *108*, 7819.
294. Sugimoto, H.; Tung, H.-C.; Sawyer, D. T. *J. Am. Chem. Soc*. **1988**, *110*, 2465.
295. Fujii, H. *J. Am. Chem. Soc*. **1993**, *115*, 4641.
296. Gross, Z.; Nimri, S. *Inorg. Chem.* **1994**, *33*, 1731.
297. Benecky, M.; Frew, J. E.; Scowen, N.; Jones, P.; Hoffman, B. M. *Biochemistry* **1993**, *32*, 11929.
298. Patterson, W.; Poulos, T. L.; Goodin, D. B. *Biochemistry* **1995**, *34*, 4342.
299. Fujii, H.; Yoshimura, T.; Kamada, H. *Inorg. Chem*. **1996**, *35*, 2373.
300. Mansuy, D.; Lange, M.; Chottard, J. C. *J. Am. Chem. Soc*. **1978**, *100*, 3213.
301. Mansuy, D.; Lange, M.; Chottard, J. C. *J. Am. Chem. Soc*. **1979**, *101*, 6437.
302. Chevrier, B.; Weiss, R.; Lange, M.; Chottard, J. C.; Mansuy, D. *J. Am. Chem. Soc*. **1981**, 103, 2899.
303. Mansuy, D.; Morgenstern-Bararau, I.; Lange, M.; Gans, P. Z. *Inorg. Chem*. **1982**, 21, 1427.
304. Latas-Grazynski, L.; Cheng, R.-J.; La Mar, G. N.; Balch, A. L. *Inorg. Chem.* **1981**, *103*, 4270.
305. Olmstead, M. M.; Cheng, R.-J.; Balch, A. L. *Inorg. Chem*. **1981**, *21*,4143.
306. Castro, C. E.; Wade, R. S. *J. Org. Chem*. **1985**, *50*, 5342.
307. Andrews, L. E.; Bonnett, R.; Ridge, R. J.; Appelman, E. H. *J. Chem. Soc. Perkin Trans.* **1983**, *1*, 103.
308. Balch, A. L.; Chan, Y. W.; Olmstead, M. M.; Renner, M. W. *J. Am. Chem. Soc*. **1985**, *107*, 2393.
309. Balch, A. L.; Chan, Y. W.; Olmstead, M. M. *J. Am. Chem. Soc*. **1985**, *107*, 6510.
310. Mahy, J.-P.; Battioni, P.; Mansuy, D. *J. Am. Chem. Soc*. **1986**, *107*, 1079.
311. Yamaguchi, K.; Watanabe, Y.; Morishima, I. *Inorg. Chem.* **1992**, *31*, 156.
312. Jayaraj, K.; Terner, J.; Gold, A.; Roberts, D. A.; Austin, R. N.; Mandon, D.; Weiss, R.; Bill, E.; Müther, M.; Trautwein, A. X. *Inorg. Chem*. **1996**, *35*, 1632.

33 Optically Active Porphyrin Systems Analyzed by Circular Dichroism

Nagao Kobayashi

Department of Chemistry, Graduate School of Science, Tohoku University, Sendai 980-8578, Japan

I. Introduction

Circular dichroism (CD) is detected as the difference between the absorption of left and right circularly polarized light when equal amounts of left and right polarized light interact with chiral molecules, i.e. $\Delta A = A_l - A_r$, where A_l and A_r are the absorptions of left and right circularly polarized light respectively.[1–6] Depending on the relative sizes of A_l and A_r, the observed CD can be either positive or negative. Since normal porphyrins (Por) are planar achiral molecules, they do not show CD *per se*. However, when chiral substituents are linked (they are called extrinsically active) or molecules are intrinsically optically active, or when a plurality of Pors have the proper (chiral) mutual orientation, CD is often observed. In this chapter, the fundamental aspects of CD theory which may be required to understand the chapter are first described, and then Por systems analyzed using this spectroscopy are introduced in roughly chronological order. Here, discussion is confined to electronic CD, since Pors are chromophores having absorptions in the near-UV to near-IR regions. Syntheses of some representative optically-active Pors are also introduced, even where the CD spectra are not necessarily well-analyzed. In particular, some systems are interesting from the view point of CD analysis even if their CD spectra are not analyzed or even reported.

II. Fundamentals of Circular Dichroism

A. Phenomenological and Theoretical Basis

Since CD is defined as the difference of absorbance between left and right circularly polarized light, we should first know about electronic absorption spectra. When chromophores are excited by electromagnetic radiation in the form of light, the transition of the electron from the initial to the final orbital is associated with a charge migration or electron cloud redistribution, which leads to an electronic dipole (μ). For each electronic transition, an electronic and a magnetic transition dipole can be defined. If the initial and final states are labeled i and j respectively, a linear charge displacement brings about an electronic transition dipole, μ_{ij}, while an electron rotation produces a magnetic transition moment $\mathbf{m}_{ij}$. The experimental

absorption intensity is obtained by integration of spectra whose abscissa is expressed by a unit proportional to energy, and this is directly related to the oscillator strength $\mathbf{f}_{ij}$ that is proportional to $|\mu_{ij}|^2 + |\mathbf{m}_{ij}|^2$. For symmetry reasons, the electronic dipole term is often much larger (*ca*. five orders of magnitude) than the magnetic dipole, so that if the absorption is strong, it is generally called an electric-dipole allowed transition, and this is the case for almost all aromatic molecules without chirality. In the case of optically active molecules, a magnetic transition moment is also produced, i.e. both μ_{ij} and $\mathbf{m}_{ij}$ have some value. The direction of $\mathbf{m}_{ij}$ is determined using the right hand grip rule. If the second through fifth fingers follow the movement of charge, then the thumb points in the direction of $\mathbf{m}_{ij}$. The CD intensity $\mathbf{R}_{ij}$, called the *rotational strength,* is experimentally obtained from the integral of the CD curves. $\mathbf{R}_{ij}$ is proportional to the scalar product of μ_{ij} and $\mathbf{m}_{ij}$, i. e. $\mathbf{R}_{ij} = \mu_{ij} * \mathbf{m}_{ij}$, and can have both signs. As mentioned above, the intensity of the electronic absorption spectra is roughly proportional to $|\mu_{ij}|^2$ and that of the CD spectra $\mu_{ij} * \mathbf{m}_{ij}$. CD is therefore generally obtained only in the same wavelength region as the electronic absorption spectra. An intense CD is observed only when either μ_{ij} or $\mathbf{m}_{ij}$ is large, so that if the electronic absorption is weak, the CD is also often weak. There is a rule that the integral of the CD over the whole electromagnetic spectrum is zero. Although CD spectra of only one sign are sometimes observed, in such cases the spectra of the counter sign is hidden at shorter wavelengths than the instrumental limit.

B. Porphyrin Chromophores

Porphyrins (Figure 1) have an almost square planar shape, so that metallocomplexes are approximated as chromophores of D_{4h} or D_4 symmetry, while metal-free

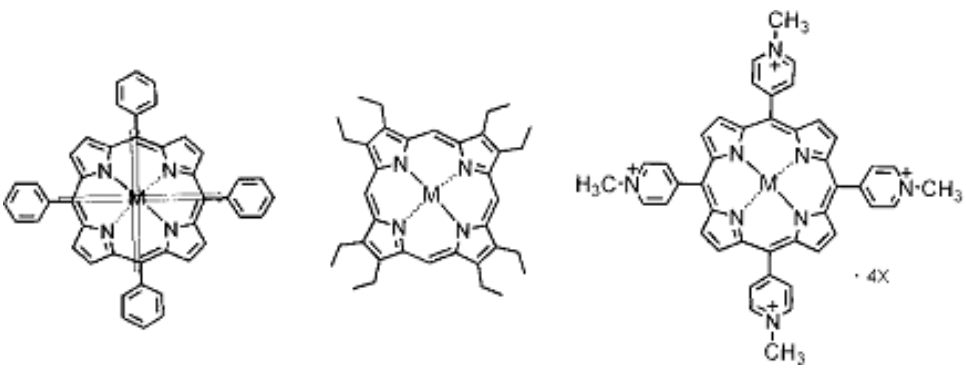

Figure 1. Metalloporphyrin chromophores and degenerate transition dipoles. In the case of *meso*-aryl porphyrins, one dipole is along 5 and 15-positions while another is along 10 and 20-positions.

derivatives have D_{2h} or D_2 symmetry. Depending on the type or position of substituent groups, the symmetry can be lowered further. The porphyrins usually used for chiroptical systems are often 5,10,15,20-tetraphenylporphyrin and its derivatives. When there is no other substituent on the periphery, the lowest two excited states are doubly degenerate and the x- and y-directions are set on the lines connecting the *trans meso–meso* positions, while this can be changed by peripheral substituent groups on the pyrrole ring. For example, in the case of tetraphenylporphyrin, when a carboxyl group is introduced at the para position of one of the four phenyl groups in order to link to the OH groups of natural products, the two orthogonal transition dipoles in the π-plane are still lying along the *trans meso–meso* directions. In the case of chlorins, where one of the four pyrrole rings is reduced, the two axes are aligned along the *trans pyrrole–pyrrole* directions. Chlorophylls have an extra carbocyclic ring between one pyrrole ring and the meso positions, so that in this case, the precise direction of the two dipoles has to be determined by MO calculations. On the other hand, D_{4h} or D_4 symmetric metallophthalocyanines have two degenerate transition dipole moments along the *trans pyrrole–pyrrole* directions.

C. Exciton Coupling

Typical exciton coupling is seen when a plurality of chromophores with electric dipole-allowed transitions interact through space, maintaining independence as a chromophore. Depending on the arrangement or orientation in space, the resultant spectra become different (Figure 2).[7,8] When two (or more) chromophores are in a cofacial arrangement, the absorption spectrum shifts to shorter wavelengths, which is often called an H-aggregate if the constituent chromophores are numerous. Another typical orientation is the almost parallel head-to-tail type which produces a spectrum at longer wavelengths compared to that of the constituent chromophore. If many chromophores are arranged in this fashion, this is called a

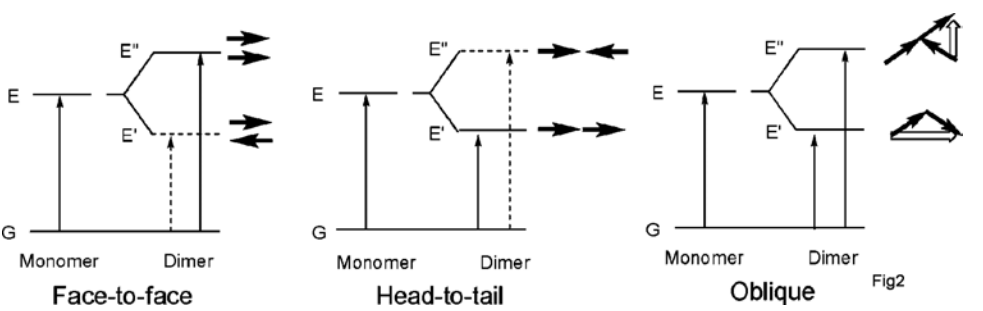

Figure 2. Band splitting of face-to-face, head-to-tail, and oblique dimers.

J-aggregate. A more general type is the case where the chromophores are arranged obliquely in space. Under these conditions, theoretically, two absorption peaks would appear at both a longer and shorter wavelength compared to the absorption peak of the monomer, although depending on the spatial arrangement and distance of the chromophores, two peaks are not always clearly seen. For a theoretical analysis, the use of two identical chromophores and a C_2 or lower symmetry arrangement is particularly important for CD spectroscopy. This exciton coupling method has been widely applied in order to determine the configuration and conformation of natural products and organic compounds. Although not necessarily stated explicitly, there are several important points to consider when using this method. These are: (1) The chromophores must retain independence. If the chromophores are mutually conjugated, this often leads to an incorrect analysis; (2) It is desirable to use chromophores which have intense absorption in the wavelength region where the substrates do not absorb, and (3) It is desirable to use chromophores whose direction of transition moment is established. From these standpoints, *para*-dimethylaminobenzoic acid and 5-*p*-carboxyphenyl-10,15,20-triphenylporphyrin have been widely used as chromophores. The former case has strong absorption ($\varepsilon = ca.$ 28,000–30,000) at *ca.* 310–320 nm, where natural products have almost no absorption. *Para*-dimethylaminobenzoic acid has a permanent dipole along the axis connecting the dimethylamino and carboxyl groups, and the transition moment at the longest wavelength band lies in this direction.[9] In the case of porphyrins, the Soret band lies at a longer wavelength at *ca.* 410–420 nm, and its absorption coefficient reaches[8,9] the order of *ca.* 5 or 6×10^5 so that this chromophore can be used for further analysis of large substrates where dimethylaminobenzoic acid is of limited use.

Figure 3 illustrates an example of the exciton coupling of a 1,2-diol bis(4-substituted benzoate). Here, one would like to know the configuration of the two carbon atoms to which OH groups are linked. The important point to note is that the direction of the transition moment at the longest wavelength (the line connecting the carboxyl C and the para position of the benzene ring) is almost parallel to that of the C–O of C–OH. As shown in Figure 3(b), upon exciton coupling between two benzoate chromophores, the excited state splits into two energy levels, while the ground state remains as a single state. The energy gap of 2V in the excited state is called the *Davydov splitting*. As a result, there are two electronic transitions leading to two absorption bands. If the two transition moments are not coplanar, the magnetic moment generated by the oscillating dipole **1** will be non-orthogonal to dipole **2**. Thus, excitations to the two split energy levels give rise to the CD Cotton effect of mutually opposite signs (Figure 4) which are separated by the energy gap $\Delta\lambda$ (= 2V, Davydov splitting). Summation of the component Cotton effects results in a solid curve having two extrema. The maximum at longer

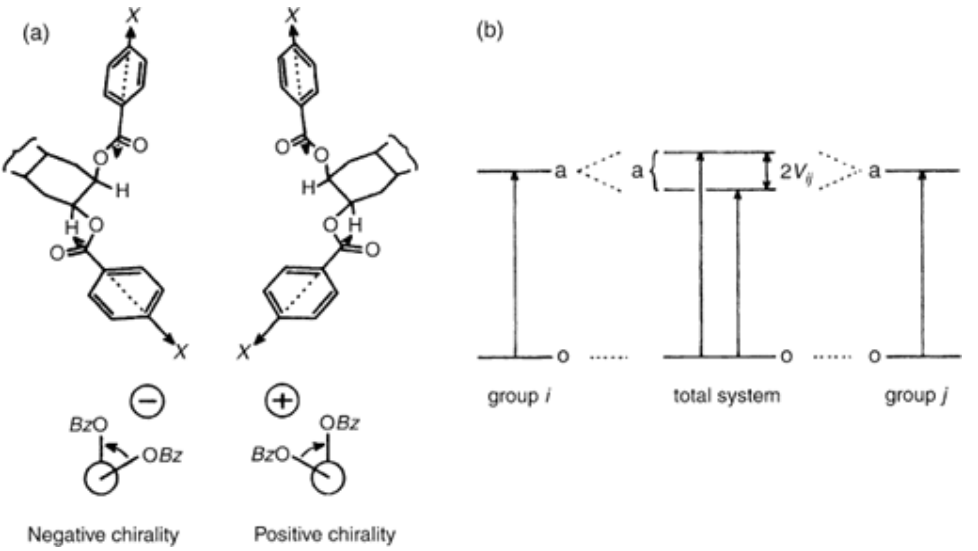

Figure 3. (a) Exciton coupling between two identical chromophores (degenerate system), as exemplified by the system of 1,2-diol bis(4-substituted benzoate); (b) by exciton coupling, the excited states split into two energy levels; the energy gap $2V_{ij}$ is called Davydov splitting (redrawn from Ref. 7).

wavelength is called the first Cotton effect, while that at shorter wavelength is called the second Cotton effect. The amplitude of split Cotton effects is defined as $\Delta\varepsilon_1$–$\Delta\varepsilon_2$, where $\Delta\varepsilon_1$ and $\Delta\varepsilon_2$ are the intensities of the first and second Cotton effects. In the case of UV spectra, summation of two component spectra often leads to a single broadened maximum because in many cases, the energy gap $\Delta\lambda$ is relatively small compared to the bandwidth. Provided the electronic transition dipole moments of the two chromophores constitute a clockwise screw sense (positive exiton chirality), as exemplified by the dibenzoate on the right hand side of Figure 3a, the sign of the first CD Cotton effect (lower energy side) is positive and that of the second Cotton effect (higher energy side) is negative (Figure 4, right). When the two dipole moments make a counter-clockwise screw sense (negative exciton chirality as shown on the left hand side of Figures 3a and 4), the signs of the first and second Cotton effects are negative and positive, respectively. Since the $\Delta\lambda$ is small, the resulting CD spectrum has a bisignate shape with respect to the absorption maximum. The amplitude of a CD spectrum, which is defined as the distance between the peak and trough of a split CD curve is (i) inversely proportional to the square of the interchromophoric distance, (ii) proportional to the absorption coefficient of their chromophores and (iii) dependent on the interchromophoric projection angle with a maximum at approximately 70 degrees and minima at 0 and 180 degrees.[10]

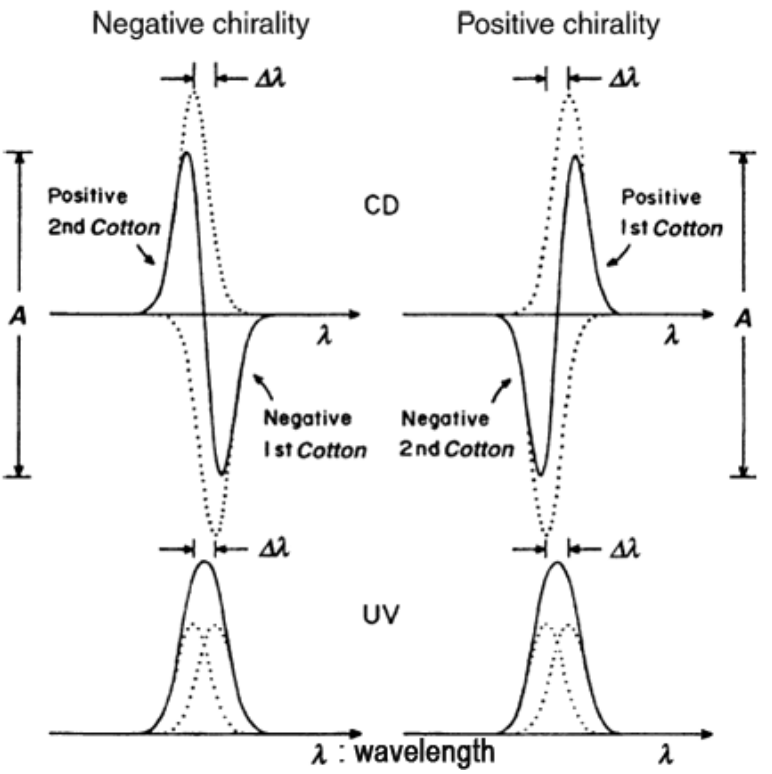

Figure 4. Typical pattern of CD and electronic absorption spectra of exciton coupling system. Summation of two component Cotton effects (dotted line) of opposite signs separated by Davydov splitting ($\Delta\lambda$) yields CD and absorption curves of solid line; positive chirality gives positive first and negative second CD Cotton effects, whereas negative chirality gives negative first and positive second Cotton effects; the amplitude (A) is defined as: $A = \Delta\varepsilon_1 - \Delta\varepsilon_2$ where $\Delta\varepsilon_1$ and $\Delta\varepsilon_2$ are intensities of the first and second Cotton effects. (left) Counter-clockwise and (right) clockwise of two identical exciton coupling chromophores leads to negative (left) and positive (right) chirality (redrawn from Ref. 7).

III. Natural Heme and Synthetic Heme Systems

A. Natural Heme Systems

CD spectra of hemoproteins began to appear at the end of the 1960s, but interpretation of the spectra has rarely been attempted. As an example, Figure 5 shows the spectra of human hemoglobin.[11] Although four hemes are included (in a strict sense, heme means an iron porphyrins found in nature), there is almost no heme–heme interaction, so that these can be regarded as representative monomeric heme spectra. One observes large negative CD troughs at 222 and 208 nm in the 200–250 nm region, which have been assigned to n–π^* and π–π^* transitions in an α-helix, and the helix content can be estimated therefrom. Although several

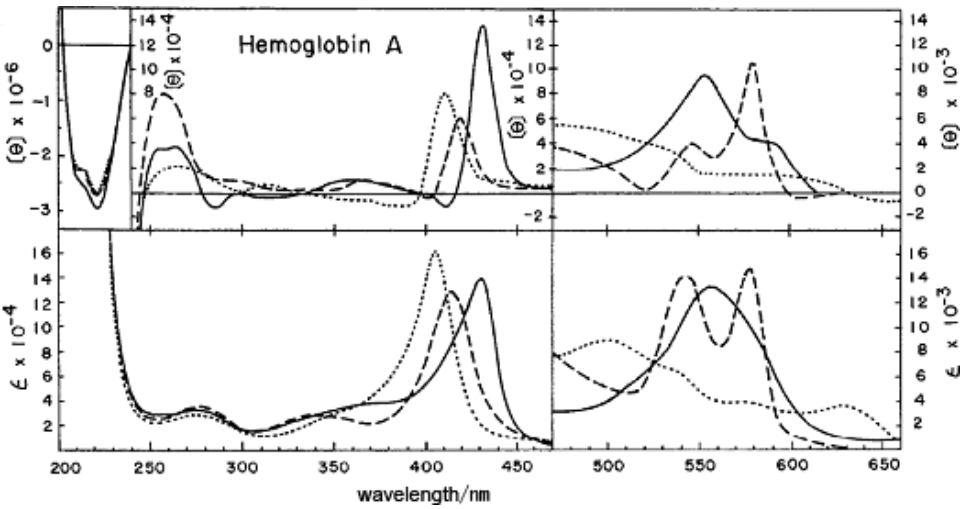

Figure 5. CD and electronic absorption spectra of native human hemoglobin. Oxygenated hemoglobin (broken lines), deoxygenated hemoglobin (solid lines), and methemoglobin (dotted lines) (redrawn from Ref. 11).

methods are reported to estimate the helix content from the negative CD intensity, the estimated helix contents are in good agreement with the data from X-ray analysis for myoglobin, lisozyme, ribonuclease, and chimotripcin.[12] Greenfield and Fasman[12] and others[13,14] further suggested a method from which the content of α-helix, β-sheet structure and random coil structure in unknown samples can be estimated.[12–15] However, the contribution of porphyrin chromophores to the CD in this region is small, so not many porphyrin chemists are interested in CD in this region.[16] The CD of heme in the 250–300 nm region is generally produced by aromatic amino acids.[17] However, only a CD peak at *ca.* 260 nm commonly appears for hemoglobin,[11] myoglobin,[18] and cytochrome *c*,[19] and its intensity varies depending on the spin and oxidation of the central iron. Furthermore, this peak is observed in hemeoctapeptides[20] not containing aromatic amino acids, S–S bonding, or SH groups so that it is believed to be a heme-related CD peak.

The *ca.* 320–650 nm region has been assigned to the porphyrin chromophore. As clearly shown in Figure 5, the shapes of the CD spectra resemble those of the electronic absorption, and the sign is positive except in a small region at shorter wavelengths than the Soret band. Although many hemoproteins show this kind of CD pattern, only larvae cytochrome *b*-563[21] and *b*-555[22] from the housefly, *Musca domestica L.* (Figure 6), cytochrome b2 from bakers' yeast L-lactate dehydrogenase,[23,24] indoleamine-2,3-dioxygenase,[25,26] and lamprey hemoglobin[27] give negative CD troughs corresponding to almost all the absorption peaks. In addition, a

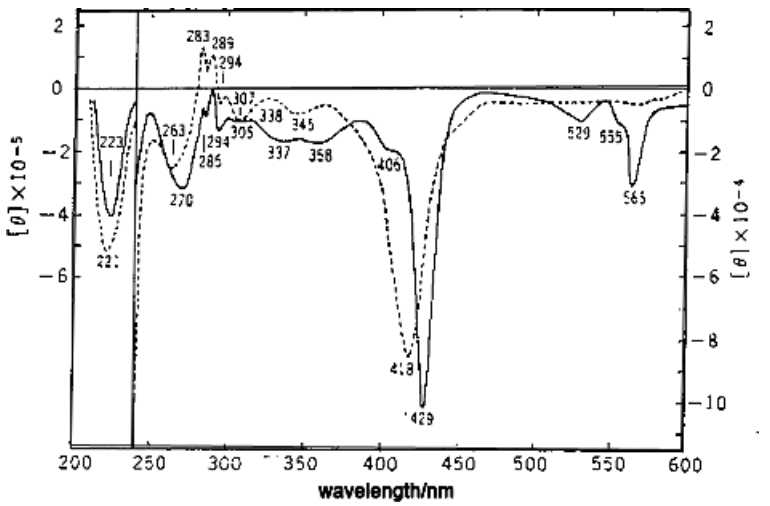

Figure 6. CD spectra of larval ferri- (broken line) and ferrocytochrome *b*-563 (solid line) from *Musca domestica L.* (redrawn from Ref. 21)

dispersion type CD is observed for the Soret band of a cytochrome *c*[28] and human hemoglobin.[27] These differences of CD Cotton effects were once conjectured to reflect the difference of the functions of hemoproteins,[21] but were insufficient to allow generalization. Furthermore, some information or facts had been accumulated on the Soret and visible region CD up to the mid-70s. For example, changing the oxidation state of the heme iron induces CD changes in both the aromatic amino acid (200–250 nm) and porphyrin chromophore (*ca.* 320–650 nm) regions.[29] For this phenomenon, the change of the sixth ligand and the out-of-plane shift of iron from the porphyrin plane were suggested as the origin.[19] No satisfactory explanation was given for the changes in intensity and shape in the visible region CD peaks accompanying a change of the axial ligand. On the other hand, the Soret CD of tetrameric hemoglobin could not be expressed as a summation CD of the constituting four subunits.[30]

Under such circumstances, Hsu and Woody were the first to attempt a theoretical analysis of the CD spectra of hemoproteins whose several structures were analyzed by X-ray spectroscopy.[31] Before calculation, they extracted rotational data from experimental data. The Soret rotational strengths in metmyoglobin and hemoglobin were estimated to be 0.5 and 0.2 Debye–Bohr magnetons (DBM, 1 DBM = 0.9273×10^{-38} cgs unit), respectively. They considered, with respect to the shape, intensity, and sign of the Soret and visible CD spectra of X-ray-analyzed myoglobin and hemoglobin, that the interaction between transitions in heme and the excited states in the globin skeleton and side chains is responsible. On the basis of Kirkwood's theory[32] as extended by Tinoco[33], they then calculated the interaction

between the Soret or Q transition and π–π^* transitions of aromatic amino acids, π–π^* and n–π^* transitions of polypeptides, and σ–σ^* transitions of alkyl groups located in the proximity of the heme, and obtained results which could be rationalized with the experimental data. According to these authors, the sign and intensity of the Soret and Q band CD are determined by interaction between the transitions in heme and the allowed π–π^* transitions of aromatic amino acids. The calculated myoglobin rotational strengths arising from interaction with allowed π–π^* transitions in aromatic side chains are 0.306 (Rx = 1.295, Ry = –0.989), 0.0146, –0.0050, and 0.1619 DBM for the Soret, Q, N, and L band respectively. These are qualitatively in agreement with the experimental results. Here, the Q band rotational strength was positive and about one order of magnitude smaller than that of the Soret band. Among the aromatic residues, His(64,7E), His(97,2FG), Phe(33,14B), Tyr(103,4G) and Tyr(146, 23H) give major contributions. His(64,7E) is the distal histidine that is close to the sixth ligand of the iron. The fifth ligand, His(93,8F), gives only a small effect because its imidazole group sits in a rather symmetrical position with respect to the heme, and the imidazole plane is nearly perpendicular to the heme plane. Because of the closeness of the proximal imidazole and heme, one might expect that the resultant Soret rotational strength would be sensitive to the relative position of these two groups. Accordingly, calculations were carried out with the imidazole plane rotated by 0–90 degrees and tilted by 1–10 degrees with respect to the heme plane. In all cases, the calculated Rx and Ry are almost equal in magnitude and opposite in sign. Hence, the proximal histidine was concluded not to play a major role in induced Cotton effects of the heme proteins.

In a similar manner, calculations for horse hemoglobin show that the α and β chains have contributions to the average rotational strength which are nearly equal in magnitude and opposite in sign (α chain, 0.631 DBM; β chain, –0.634 DBM).[31] Among the aromatic residues in the α chain, His-58, Phe-33, Phe-43, Phe-98, Try-42, Try-140, and Trp-14 make the major contributions to the rotational strength. For the β chain, the major contributions come from His-63, His-69, Phe-42, Phe-41, Phe-71, Phe3-85, Phe-103, Tyr-130, and Trp-15. Again the proximal histidines, His-87 of the α chain and His-92 of the β chain, give only small net contributions to the Soret rotational strength. It was found that,[31] because of the strongly allowed transitions in the far-UV region, tyrosine and tryptophan at a distance of 10–15 Å from the heme group give significant rotational strength to the heme transitions. The calculated Soret rotational strength due to intersubunit interactions was 0.1 DBM, as compared to the experimental 0.23 DBM for human oxyhemoglobin.

In order to estimate the extent of coupling of the heme transitions with transitions in the polypeptide backbone, the 220 nm (n–π^*) and then the 190 nm (π–π^*)

bands of amides (about 120 in all) were considered.[31] The net contribution to the Soret rotational strength from these two types of coupling was negligibly small (0.003 DBM). In calculating the coupling of heme transitions with transitions in the alkyl side chains, 65 side chains in myoglobin were included. The intensity of the σ–σ^* transition in the C–C bond was fairly large, but the induced Soret rotational strength through coupling with these transitions was at most only a few hundredths of a DBM, partly because of the large energy separation between the Soret and σ–σ^* transitions (~280 nm). The total contribution to the myoglobin Soret rotational strength from the σ–σ^* transitions of the 65 alkyl side chains was only 0.04 DBM.

Later, similar results were obtained for the CD band of hemoglobin III from *Chironomus*[34] and cytochome *c* peroxidase from baker's yeast (*Saccharomyces cerevisiae*).[35] A small negative Cotton effect seen at shorter wavelengths in the Soret band of Figure 5 was reproduced by taking the direction of the transition of the Soret band into account (experimental data were reproduced when the two Soret components are polarized towards the bridging methine carbons[31]). When calculations were performed assuming that the vinyl groups at the 2 and 4 positions of protoporphyrin IX were rotated by 45°,[36] the contribution of negative CD was revealed in the Soret band region. In particular, the effect of the two vinyl groups was so marked that the CD sign and intensity produced by interaction between the heme transition and π–π^* transitions of the aromatic amino acids may be canceled when two vinyl groups are rotated in a similar direction.

Figure 7a shows the CD spectrum of a undecapeptide–CO complex purified from horse heart cyctochome *c*.[37] This compound contains only a heme and an eleven amino acid peptide (Val-Glu-Lys-Cys-Ala-Gln-Cys-His-Thr-Val-Glu), and has been considered to be the simplest heme model compound (a heme is linked to two Cys units). With increasing concentration, it aggregates in a head-to-tail fashion, and the intermolecular distances are estimated to be 10 and 13 Å, respectively, when the iron is in trivalent and divalent states (in the case of heme octapeptides where a Val-Glu-Lys unit was removed from heme undecapeptide,[38] they form a card-type aggregate and the interplanar distance is considered to be less than 7 Å[39]). In the spectra, the solid line shows the aggregated state, and can be explained by an exciton coupling interaction. The minus-to-plus pattern of almost similar intensity from longer wavelengths associated with the Soret peak indicates that the molecules are aggregated in a left-handed manner.[1,7] Figure 7b shows the CD spectra of monomeric ferric (solid line) and ferrous hemes (broken line) coordinated by an imidazole molecule as a fifth ligand. Although the spectra are similar in shape to those of Figure 5, theoretical calculations were carried out incorporating various factors,[37] since the intensity was much larger than that seen in Figure 5. The Soret CD intensity was estimated taking into account the

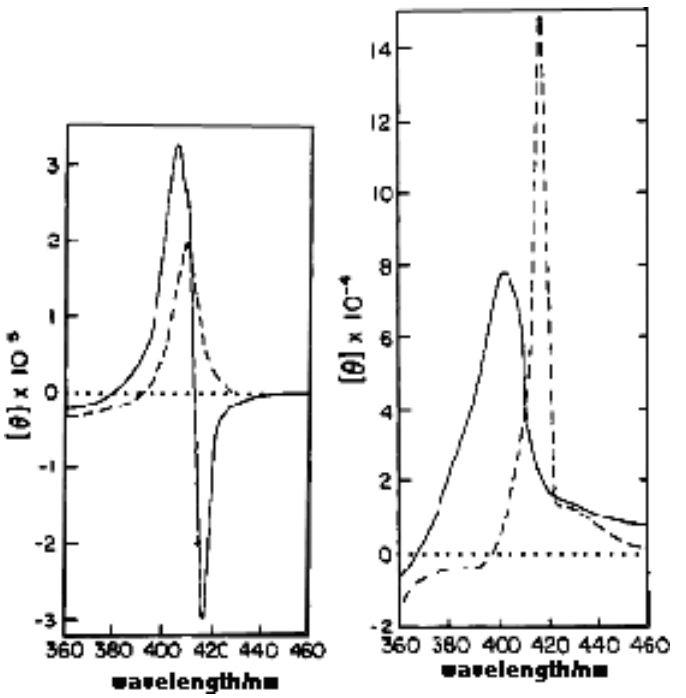

Figure 7. (a) CD spectrum of the CO complex of reduced heme undecapeptide at two different concentrations, 6.2×10^{-3} M (solid line) and 1.5×10^{-6} M (broken line), at pH 7.4. (b) CD spectrum of the heme undecapeptide (concentration = 7.3×10^{-5} M) from equine heart cytochrome *c* in the presence of 0.1 M imidazole in aqueous solution, ferric (solid line, pH 9) and ferrous (broken line, pH 8.4) state (redrawn from Ref. 37).

deformation of the heme plane from the X-ray data,[40] in addition to the π–π^* transition of imidazole, π–π^* and n–π^* of peptides, and polarization of the bonding. As a consequence, it was found that the n–π^* of peptides can be neglected and that the contribution of the π–π^* of imidazole was also small. That is, when imidazole was coordinated as an axial ligand, the intensity did not change whether one or two imidazole molecules were coordinated. The π–π^* transition of peptides and the polarization effect of the sulfur of thioether were found to produce large positive and negative CDs respectively. The polarization effect of the group depended on the models used, and the experimental data could only be reproduced when the symmetry axis was situated approximately along the C=O bond. In addition, it was concluded that the asymmetry of the ligand fields give little contribution.

In recent years, the CD of reconstituted hemoproteins has attracted attention.[41–46] When heme is inserted into apoprotein, the most stable orientation equilibrium is not always attained immediately, sometimes taking a few minutes to several weeks to complete. If the porphyrin is deformed and if the front and back

sides can be discriminated, the process can be followed as a change in the CD spectra. Since the same process can also be monitored by NMR, the ratio of front and back sides can be estimated by comparing the CD and NMR spectra. When naturally occurring hemes are used, the CD spectrum approaches that of natural hemoproteins with elapsing time, but occurs almost instantaneously (milliseconds) in the case where synthetic porphyrins having a plane of symmetry are used.[45,46] The latter case is considered to be produced as a result of the front and back sides being identical.

As an example, Figure 8 (top) shows the Soret CD spectra of native and reconstituted sperm whale myoglobin in the carbonmonoxy form at pH 7.4,[42] and the

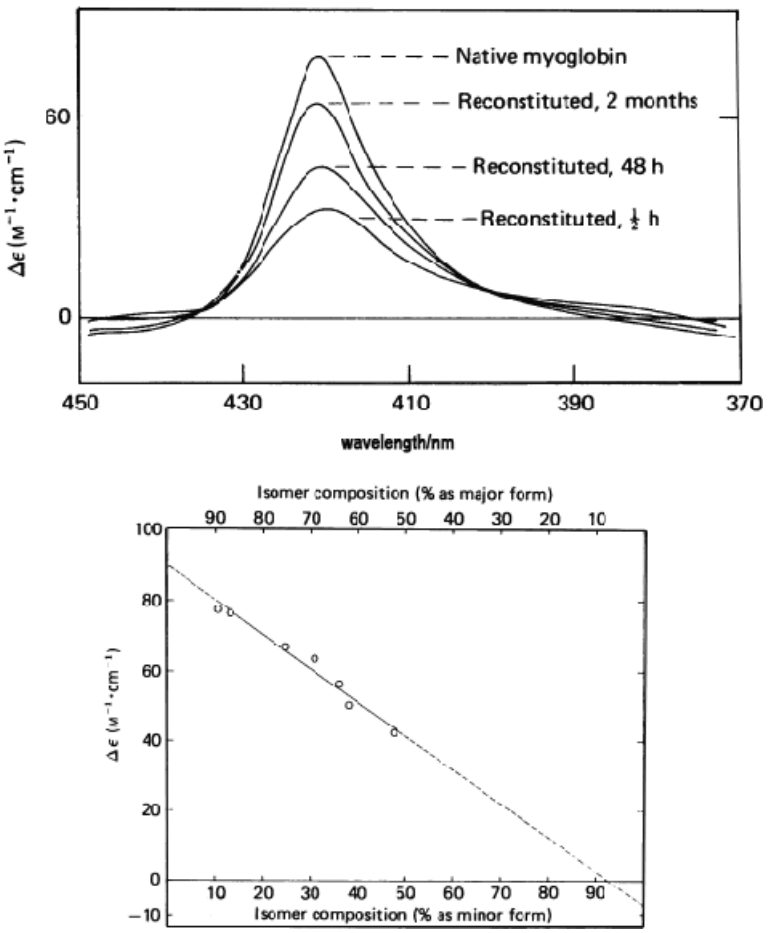

Figure 8. CD spectra of carbomonoxymyoglobin in 0.1 M sodium phosphate buffer (top), and correlation of CD signal with percentage isomer composition (bottom) (redrawn from Refs. 42 and 44).

correlation of CD intensity with isomer composition determined from the ^{1}H NMR spectra (Figure 8b), major and minor refers to native and disordered forms, respectively).[46] By extrapolation of the results in Figure 8 (bottom), the CD intensities of the pure native and pure disordered orientations were predicted, so that using these values, the native orientation in sperm whale myoglobin at equilibrium was found to be predominant (90%) with 10% of the disordered form still persisting.

Reports on the CD spectra of hemoproteins in the near-IR region are very rare. Iron(II) cytochome *c* shows very broad, weak absorptions between 600 and 1000 nm, and the corresponding CD spectra have been reported (Figure 9).[47] In this hemoprotein, the fifth and sixth coordination sites are occupied by methionyl sulfur and histidyl nitrogen. The anisotropy factor (four times the CD intensity divided by the absorption intensity,[48] i.e. 4R/D) is about 0.002, which is larger than those of typical magnetic dipole-forbidden π–π transitions by about one order of magnitude. This relatively much larger anisotropy factor for the near-IR band, compared to the porphyrin π–π transitions, permitted the authors to identify some of the near-IR bands as due to magnetic dipole allowed *d*–*d* transitions. The low absorption intensity compared with the porphyrin π–π transition was also consistent with this conclusion. Both the absorption and CD spectra were simultaneously

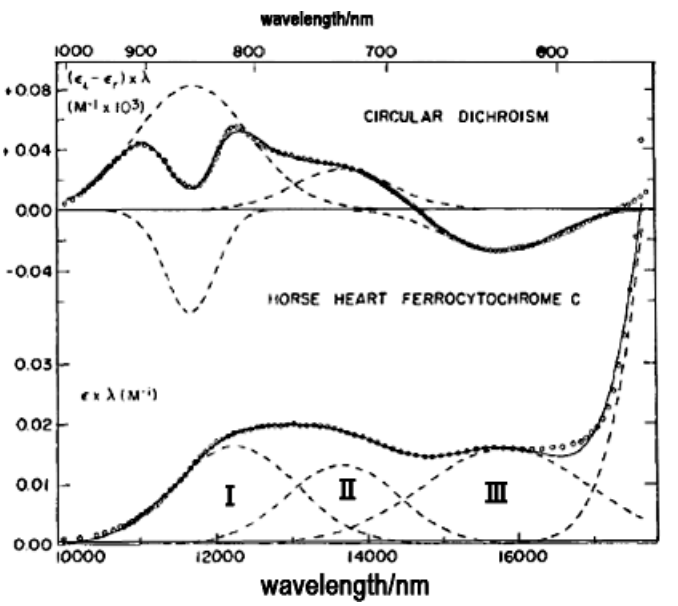

Figure 9. Absorption and CD spectra of horse heart ferrocytochrome *c* with resolution into Gaussian bands using a least-square method. Circles are the experimental points, dashed lines are the Gaussian components, and the solid lines are the Gaussians (the fit) (redrawn from Ref. 47).

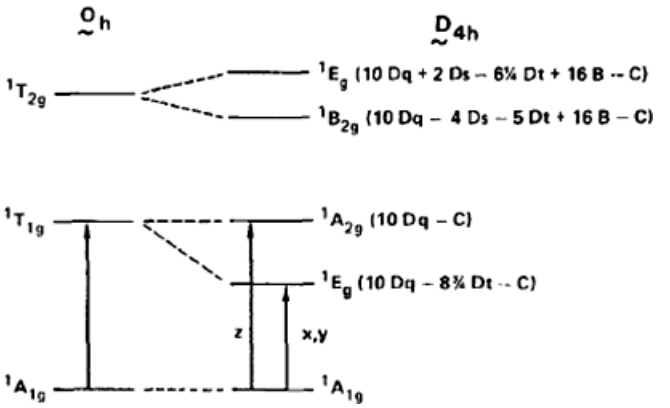

Figure 10. Singlet states of a low-spin d^8 iron in a tetragonal crystal field with first-order energies relative to the ground state. Also indicated are the magnetic dipole allowed transitions from the ground state which are allowed in octahedral symmetry (redrawn from Ref. 47).

fitted on the assumption that the corresponding band has a similar energy and bandwidth. Three components were required in the absorption spectra (bands I to III in order of ascending energy), while two CD components were included associated with band I. These fits were analyzed using the lowest excited singlet states in Figure 10.[49,50] In this *magnetic* dipole radiation field (600–1000 nm), only in-plane polarized *electric* dipole intensity can contribute to the rotational strength of *d–d* transitions, since for a transition to be optically active, *electric and magnetic* transition dipole vectors must be parallel or antiparallel.[1] As shown in Figure 10, the lowest and second lowest ligand–field transitions are polarized along the x, y (in-plane) and z-axes, respectively. The lowest transition can therefore borrow intensity from the nearby intense in-plane polarized, electric dipole-allowed π–π transitions. As a result, the CD intensity in the lowest transition region was expected to be larger than the other region. Indeed, between 900 and 1000 nm, the anisotropy factor was estimated to be 0.013, which is more than 6 times larger than in the other region, so that band I was assigned to $^1A_{1g} \rightarrow {}^1E_g$.[47] The two CD components in this region were then presumed to be the components of the doubly degenerate ^1E_g states.

In Ref. 50, an $^1A_{2u}$ charge-transfer state was predicted by the authors to lie close to ^1E_g. This charge-transfer state arises by promotion of an electron from the top-filled porphyrin π-orbital to an empty iron d_{z2} orbital. Therefore, this transition is polarized normal to the porphyrin plane (z-axis). Taking into account that this CT transition is predicted at 17,000 cm^{-1},[49] either band II (14,400 cm^{-1}, *ca.* 795 nm) or III (15,800 cm^{-1}, *ca.* 633 nm) can be assigned to this CT band. Thus, the use of CD spectroscopy coupled with electronic absorption spectroscopy enabled

the analysis of *d–d* transitions. Although for low-spin iron(II) carboxymyoglobin, the lowest energy *d–d* transitions and z-polarized CT transitions of similar energy were found at 16,000 and 19,000 cm^{-1}, which are higher than the observed 14,400 and 15,800 cm^{-1} for ferrous cytochrome *c*, this was attributed to a weaker ligand-field for the latter. These differences are further attributed to differences in the fifth and sixth ligands, which in carboxymyoglobin are hystidyl nitrogen and carbon monoxide.

The near-IR CD of bovine liver catalase (Figure 11) has also been measured.[51] Native Fe(III) catalase shows a very intense near-IR CD peak at 880 nm with $[\theta] = 30{,}000$ and a shoulder at 970 nm. When an extraneous ligand was added, the magnitude of the CD bands decreased in the order of native > azide > cyanide.[50] Fe(III) catalase is known to have a high-spin character compared with other hemeproteins, since one of the axial ligands is phenolate, different from the imidazole of most hemoproteins.[52] Indeed, the effective Bohr magneton numbers for native catalase and its azide and cyanide analogs are 5.96, 5.86, and 2.63, respectively,[53] indicating that both the native and azide forms are ferric high-spin and

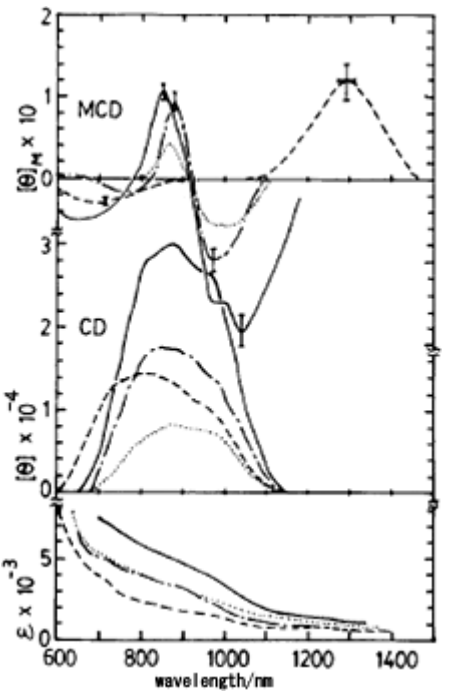

Figure 11. Near-IR MCD, CD and absorption spectra for native Fe(III) bovine liver catalase (solid lines), and its azide (dotted broken lines), cyanide (broken lines), and imidazole (dotted lines) derivatives (redrawn from Ref. 51).

that cyanide is a ferric low-spin compound. MCD spectra in this region showed dispersion type Faraday *A* terms except for cyanide, and at a shorter wavelength than for other ferric hemoproteins. From these spectroscopic results,[54–57] the near-IR band has been assigned to a charge-transfer transition from porphyrin a_{1u}, a_{2u} (π) to iron e_g (dπ) orbitals. However, the reason for the extraordinarily strong CD has not yet been elucidated.

Although high-spin ferrous myoglobin shows positive CD bands at *ca*. 1330, 970, and 760 nm with low anisotropy factors of 0.01, 0.001, and 0.0001, respectively, favoring the assignments as charge-transfer transitions or magnetically forbidden *d–d* transitions, no definitive assignment has yet been performed.[58] However, from the energy of transitions in the CD spectra, the bands at 1330 and 760 nm have been tentatively assigned to a *d–d* and some charge-transfer transition, respectively.

A few reports of the vibrational CD (VCD) spectra for hemoproteins or reconstituted hemoproteins have been reported in the literature.[59–61] VCD spectra of the asymmetric stretch of azide ligated to the heme of a series of evolutionally diverse and site-directed mutant hemoglobin and myoglobin (Mb) were anomalously intense in most cases examined. These papers also demonstrated its intriguing sensitivity to subtle protein-ligand interactions between the azide ligand and distal globin amino acid residues based on the observation of a drastic decrease in the VCD intensity of the azide stretching in a variety of metMb whose distal histidine was replaced by other amino acids. Figure 12 shows the IR and VCD spectra of several myoglobin and hemoglobin species. In the absorption spectra, some species show bands at *ca*. 2044 and 2022 cm^{-1}, the former of which was assigned as derived from the ionically bound high-spin azide form and second as derived from the covalently bound low-spin azide form. Interestingly, the only species which have large anisotropy ratios (-8.0 to -9.5×10^{-4}) showed a negative VCD sign corresponding to the low-spin band.[59] The authors considered several factors in trying to find the origin of the heme-azide VCD spectra. For negative anisotropy values, the electric and magnetic dipole transition moments must orient in roughly opposite directions such that their scalar vector projection on one another is negative, while the magnetic dipole transition moment must be unusually large in relation to the accompanying electric dipole transition moment. As the most likely source of the large circulating electron current for the magnetic dipole transition, the authors further considered the heme-ring with a large number of π-electrons (*ca*. 20). The observed anisotropy values of *ca*. 10^{-3} in the VCD spectrum demonstrate that the lone azide oscillator generates a large magnetic dipole transition moment. Long-range electron flow, the coupling of electric current to the nuclear moment of the azide ligand, a polarizability mechanism and vibronic coupling have all been suggested as possible mechanisms for this.

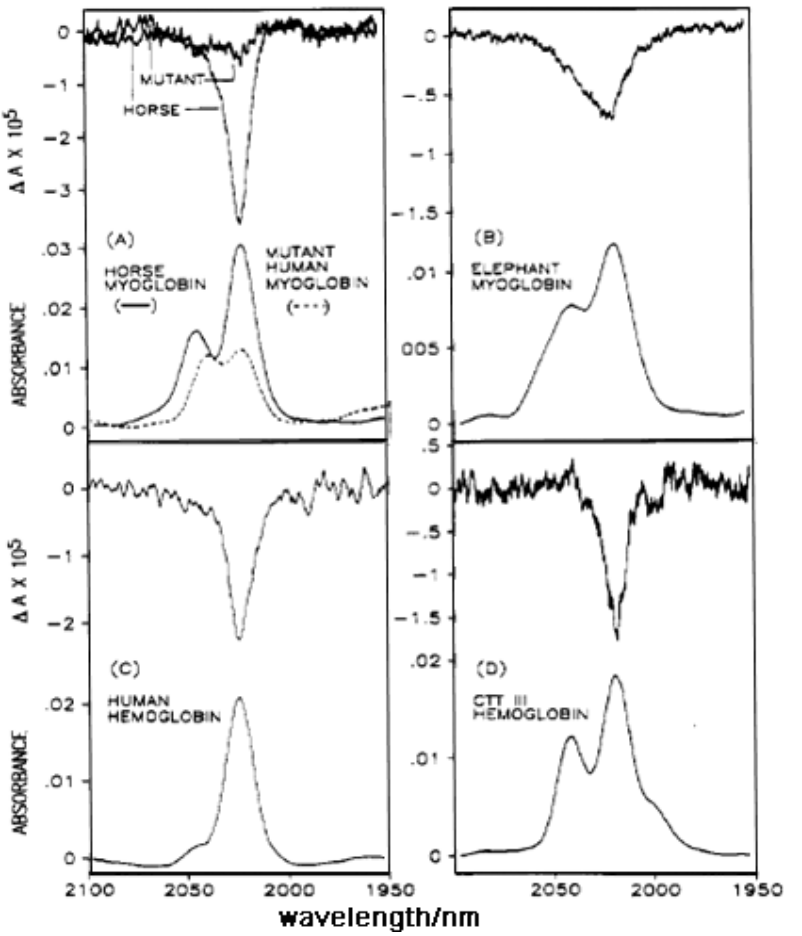

Figure 12. IR absorption and VCD spectra of the following: (A) 11.5 mM horse metMbN_3, and 7.1 mM mutant (Asn E11) human metMbN_3 with 2.7 mM unbound N_3–; (B) 6.0 mM elephant MbN_3; (C) 8.0 mM human HbN_3; (D) 6.0 mM CTT III HbN_3, pH 7 with 0.01M phosphate buffer (redrawn from Ref. 59).

In order to clarify the VCD mechanism of the azide ligand, Teraoka *et al.* then investigated the VCD spectra of metMb with a variety of extraneous ligands (SCN^-, OCN^-, CN^-, and CO), in addition to a reconstituted azidometMb with ironoctaethylporphyrin (FeOEP) (Figure 13a).[60] No VCD band was observed for the reconstituted azidometMb, although the dipole strength was as great as that of native metMb with an iron-protoporphyrin IX and both 2024 (low-spin) and 2042 cm^{-1} (high-spin) absorption bands appeared (Figure 13b). From this observation, it was proposed that the asymmetry of the porphyrin ring may be an important factor for the strong VCD signal. The metMb cyanide complex exhibited an

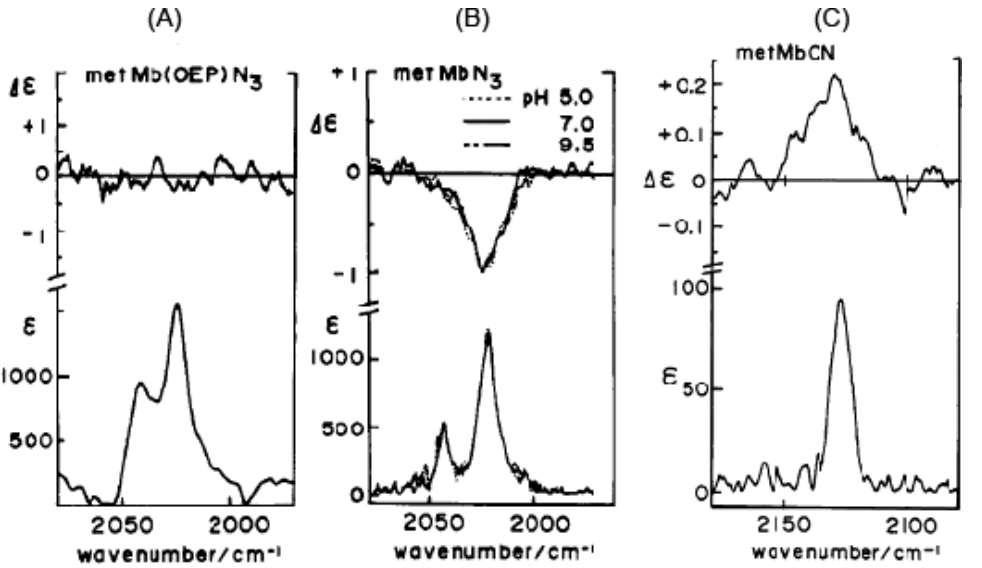

Figure 13. Absorption and VCD spectra of (A) 2.3 mM of metMb(OEP)N_3 reconstituted with iron-octaethylporphyrin at pH 7.0 (B) 2.3 mM metMbN_3 and (C) 13.5 mM (KCN) metMbCN at ph 7.0 (redrawn from Ref. 60).

extraordinarily strong positive VCD band (Figure 13c), i.e. in the opposite sense to the case of the azide complex, corresponding to the CN stretching vibration, while no VCD band was observed for metMb with SCN^-, OCN^-, or CO axial ligands. The anisotropy value of the VCD band of metMb cyanide was 2.8×10^{-3}, which is almost four times stronger than that of metMb azide and opposite in sign. They concluded that the relative orientation of the electric and magnetic dipole moments induced by the stretching of a ligand is approximately parallel for the cyanide but antiparallel for the azide in the ferric low-spin state.

B. Synthetic Heme Systems

In this section, only systems designed to mimic heme systems or systems containing both porphyrin and polypeptides are described. Ikeda and Nezu reported the absorption and CD spectra for aqueous solutions of a water-soluble porphyrin,[62,63] *meso*-tetra(4N-methylpyridinium)porphyrin tosylate (TMpyP tosylate), in the presence of poly(L-glutamic acid) or poly(S-carboxymethyl-L-cystein) at different pH values. At neutral and alkaline pH, where poly(L-glutamic acid) is randomly coiled, essentially no CD was induced in the Soret region over a wide range of [polypeptide]/[TMpyP] ratios. At acidic pH, where poly(L-glutamic acid) is helical, a positive CD band and a negative CD band were induced at 415 and

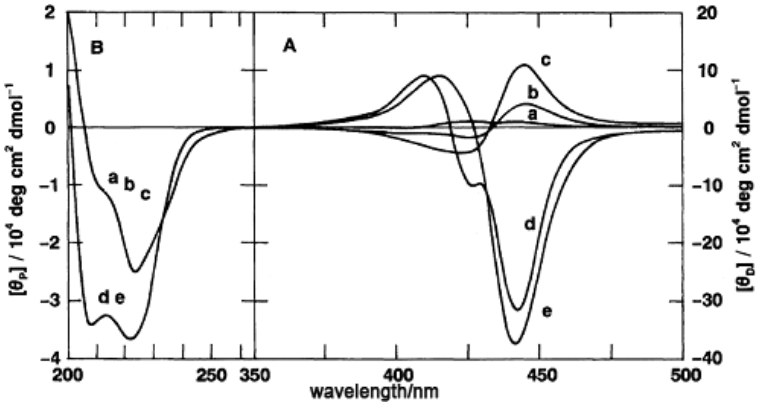

Figure 14. CD spectra of TMpyP mixed with poly(L-glutamic acid) at pH 4.4 (poly(L-glutamic acid) makes α-helix at pH smaller than *ca.* 6). [TMpyP] = 1.00×10^{-5} M, [poly(L-glutamic acid)]/[TMpyP]: a, 1.0; b, 5.0; c, 10.0; d, 50.0 (redrawn from Ref. 63).

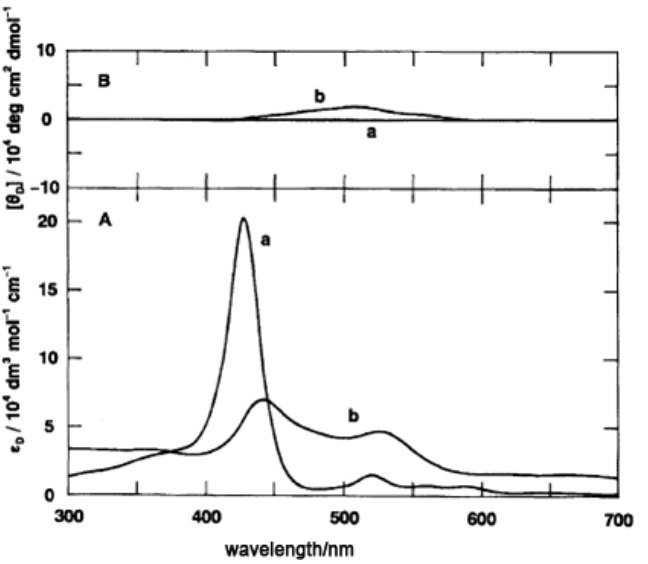

Figure 15. Absorption and CD spectra of TMpyP aqueous solutions in the presence of poly(S-carboxymethyl-L-cyctein) at [poly(S-carboxymehtyl-L-cystein)]/[TMpyP] = 100. [TMpyP] = 1.00×10^{-5} M. a, pH7.41; b, pH 4.49 (redrawn from Ref. 63). Poly(S-carboxymehtyl-L-cystein) exists as random coil and β-sheet structures at pH 7.41 and 4.49, respectively.

442 nm, respectively if the [polypeptide]/[TMpyP] ratio was high, but this induced CD became considerably weaker as the [polypeptide]/[TMpyP] ratio was lowered (Figure 14). In the presence of poly(S-carboxymethyl-L-cyctein), the absorption spectra differ considerably depending on the pH (Figure 15).[63] At neutral and

alkaline pH, where the polypeptide exists as a random coil structure, the absorption spectrum was typically that of normal porhyrins. At pH 5.5, where the polymer exists as a β-sheet structure, the Soret band shifted to longer wavelength and the Q band concomitantly increased. Although no CD was induced when the peptide had a coil structure, a weak and broad CD was induced when the peptide adopted the β-sheet structure, but strangely only in the Q band region. Although the absorption and CD spectral behavior of TMpyP in the presence of polypeptide was thus described phenomonologically, no explanation has been given by way of interpretation.

Fukushima studied the effect of NaCl on the absorption and CD spectra of a system comprising poly(Glu-Val-Lys-Val) (molecular weight, *ca.* 14,000) and diprotonated tetrakis(4-sulphonatophenyl)porphyrin (TPPS) in aqueous solution.[64] Experiments were carried out mainly at pH 4, where poly(Glu-Val-Lys-Val) exists in a β-sheet structure and the central two pyrrole imine nitrogens of TPPS are diprotonated. In the absence of poly(Glu-Val-Lys-Val), diprotonated TPPS shows a Soret band at 434 nm ascribed to monomeric species. As a result of the addition of poly(Glu-Val-Lys-Val) or NaCl, a new peak due to aggregates appears at around 489 nm. Interesting CD behavior was observed when [poly(Glu-Val-Lys-Val)]/[TPPS]= 1:5 (Figure 16), depending on the NaCl concentration. As seen in curves a–c in Figure 16, when the NaCl concentration was typically less than 250 mM, the sign of the CD curve changed from minus to plus in ascending energy corresponding to both the 434 and 489 nm absorption bands, thus suggesting that the

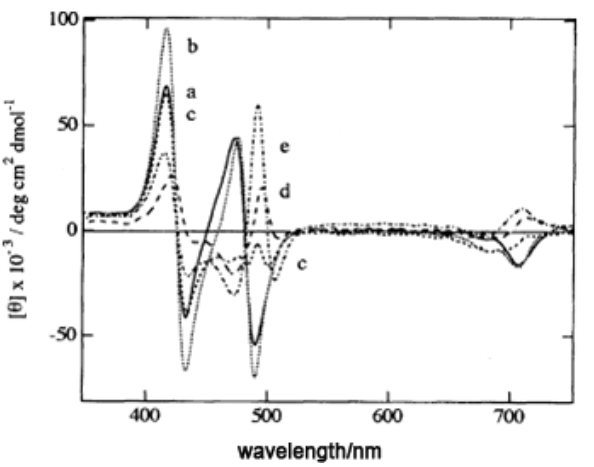

Figure 16. CD spectra of 6.67×10^{-5} M TPPS (5,10,15,20-tetrakis(4-sulfonatophenyl)porphyrin) in aqueous solution at pH 4.0 and [poly(Glu-Val-Lys-Val)]/[TPPS]=2 in the presence of poly(Glu-Val-Lys-Val) at different NaCl concentrations. [NaCl]: a, 0 mM; b, 100 mM; c, 250 mM; d, 500; e, 1000 mM (redrawn from Ref. 64).

aggregates adopt an S-chiral conformation. Although a dispersion type CD curve was observed in the 434 nm region where the author assigned a monomeric TPPS Soret band, this was ascribed to two different monomeric species bound consecutively to different sites located on the polypeptide. When the NaCl concentration was increased to 500 and 1000 mM (curves *d* and *e*), the CD sign corresponding to the 489 nm absorption band changed from plus to minus in ascending energy. The author, therefore, concluded that the helicity of the aggregates changed from S to R with increasing NaCl concentration. Since the ellipticity at 217 nm for the polypeptide was unchanged with increase of the NaCl concentration, the above CD change upon increase of NaCl concentration was thought to be unrelated to any polypeptide conformational change. Thus, it was presumed that an increase in the ionic strength induced a chiral conformational transition due to the prevention of electrostatic interaction between TPPS and the polypeptide. By conducting experiments under various conditions, the author claimed that four types of aggregate were obtained. However, it was difficult to carry out quantitative analysis, since the conformation between the porphyrin and polypeptide is unknown.

The CD and absorption spectra of synthetic peptide-sandwiched mesoheme have been reported by several groups. Benson and coworkers prepared compound **1** (Figure 17, top) using iron(III) mesoporphyrin IX,[65] and **2** (Figure 17, middle) using iron(III) mesoporphyrin II.[66] A theoretical analysis of the CD data has not been attempted. However, interestingly, compound **1** showing a negative CD ($[\theta] = -80{,}000$) corresponding to the Soret absorption band in water exhibited reduced intensity with increasing helix content as a result of the addition of the helix-stabilizing cosolvent (1,1,1,3,3,3-hexafluoro-2-propanol) to *ca.* $[\theta] = -15{,}000$.[65] For this phenomenon, they inferred that a greater alignment of the peptide backbone amides alters the average orientation of the transition dipoles of the amides relative to the Bx and By transitions of the heme. In contrast, compound **2** showed a positive CD in helix-stabilizing co-solvent.[66]

Pavone and coworkers[67,68] prepared hemoprotein model compounds containing iron or cobalt 3,7,12,17-tetramethylporphyrin (deuteroporphyrin IX) (Figure 17, bottom). In the case of the cobalt(III) complex, they succeeded in separating two equally abundant Δ and Λ complexes using HPLC.[68] These isomers showed either a negative (Δ isomer) or positive (Λ isomer) CD envelope corresponding to the Soret absorption peaks (Figure 18). Interestingly, the absolute CD intensity was different, i.e. a negative trough of the Δ isomer was about twice as large as the positive peak of the Λ isomer. By using the CD intensity at 222 nm assigned to an α-helix, it was revealed that helix content in the Δ isomer is always larger than that in the Λ isomer under similar conditions.

Sakamoto and coworkers designed and synthesized a series of amphiphilic two α-helix peptides, which bound iron(III) mesoporphyrin IX through a ligation

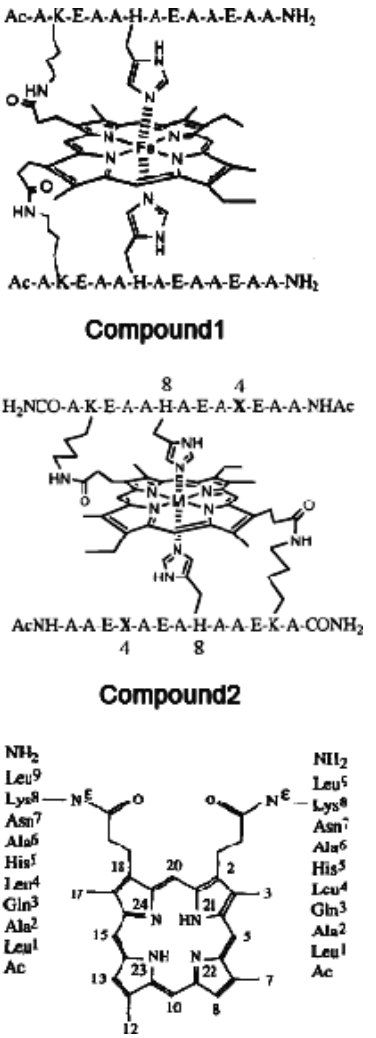

Figure 17. Peptide-sandwiched mesohemes reported by Benson *et al.* (left and middle) and monochrome reported by Pavone *et al.* (right) (redrawn from Refs. 65, 66 and 67). The meaning of A, K, E, H are not explicitly described even in original papers, although they are amino acid residues.

of two histidine (His) residues.[69] These peptides contain 17 amino acid residues. Hydrophobic Phe, Ile, Leu, Val, and Ala residues (Figure 19) were systematically substituted into the peptide structure around the axial ligands in order to explore how hydrophobic and/or steric effects alter the interaction between the peptides and the heme. In Figure 19, eight positions designated by X and Y were substituted. Figure 20 shows the CD spectra in the 190–250 nm region in the absence (broken lines) and presence (solid lines) of the heme. CD curves with an intense

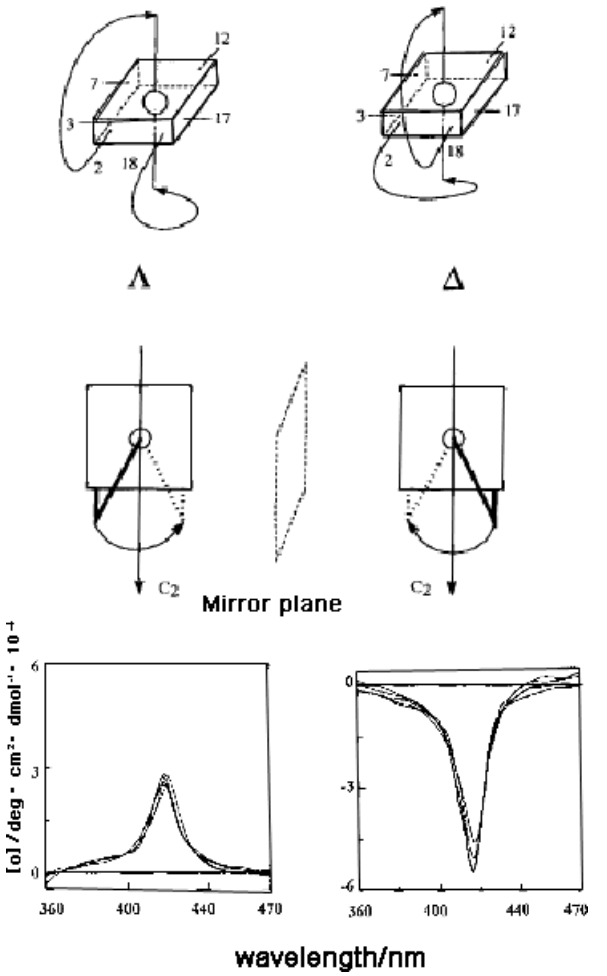

Figure 18. Schematic representation of the Δ and Δ isomer configuration of the cobalt(III) complex of Pavones' mesoheme (Fig. 17, bottom), and their CD spectra in the Soret region at various trifluoroethanol concentration (0–30%) (redrawn from Ref. 68). The fifth and sixth positions are coordinated by histidinyl imidazole.

positive peak at 190 nm and weaker negative troughs at 209 and 222 nm, such as (j) in this figure, indicate that the peptides are forming an α-helix. In many cases (a, b, c, e, f, j, k, and f), the peptide exists as an α-helix, but in the presence of the heme the CD intensity often increased, indicating an increase in the α-helicity. This was attributed to a ligation of the peptides to iron through the His residue. Namely, in acidic pH where the His residue was protonated and therefore the ligation was disabled, this kind of increase was not observed. In cases d, g, h and l of Figure 20, the helix content in some peptides, particularly those containing

(a)

Ac-A A E A X Y K A H A E Y X A K A A-GGG C-NH_2

Ac-A A E A X Y K A H A E Y X A K A A-GGG C-NH_2

Peptide	X	Y	Peptide	X	Y
H2α17-FF	Phe	Phe	H2α17-VV	Val	Val
H2α17-FL	Phe	Leu	H2α17-VL	Val	Leu
H2α17-LF	Leu	Phe	H2α17-LV	Leu	Val
H2α17-II	Ile	Ile	H2α17-AA	Ala	Ala
H2α17-IL	Ile	Leu	H2α17-AL	Ala	Leu
H2α17-LI	Leu	Ile	H2α17-LA	Leu	Ala
H2α17-LL	Leu	Leu			

(b)

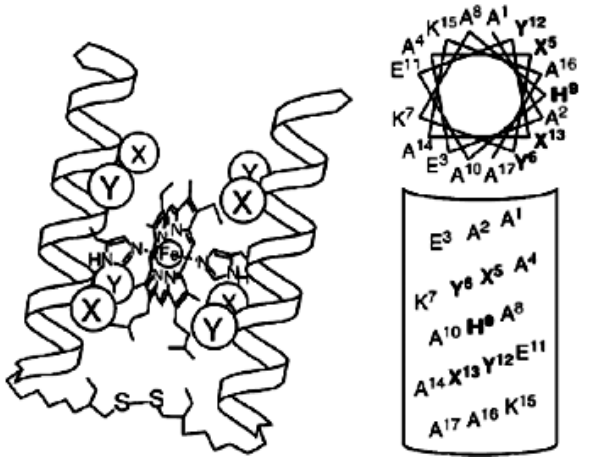

Figure 19. Structure of the designed peptide, H2α17-XY (a) Amino acid sequence of H2α17-XY; (b) Schematic illustration of two-α-helix peptide structure bound to the heme and helix wheel and net drawings of the 17-peptide (redrawn from Ref. 69).

valine, appeared very low in the absence of the heme. However, even in these cases, α-helix was generated by the addition of the heme except for case g (β-sheet structure in both absence and presence of the heme).

Figure 21 shows the CD spectra in the Soret region, which were collected under similar conditions as in Figure 20. The heme bound to the Ile- and Val-containing peptides, except for H2a17-VV, showed a strong induced CD peak in the Soret region, which was split into a negative peak at longer wavelengths and a positive peak at shorter wavelengths (d–f, h, l). The crossover wavelengths were coincident with those of the maximum position of the Soret peak, and the intensities of both positive and negative peaks were almost equal, indicating that the induced Soret CD was derived from exciton coupling with heme-heme interactions.

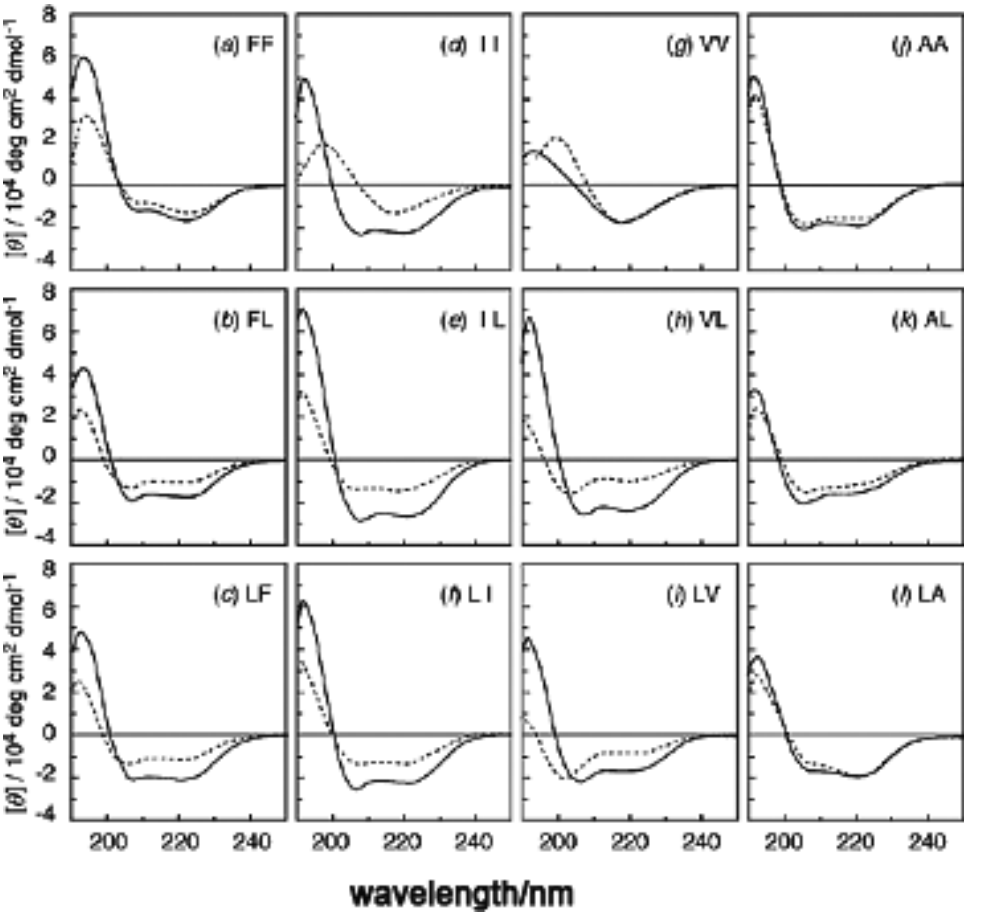

Figure 20. CD spectra of H2α17-FF (a), -FL (b), -LF (c), -II (d), -IL (e), -LI (f), -VV (g), -VL (h), -LV (i), -AA (j), -AL (k), and -LA (l) in the absence (broken lines) and presence (solid lines) of heme (redrawn from Ref. 69).

The split Cotton effect indicated that the heme groups were highly oriented in close positions in the self-assembled peptides. Among the Ile- Val-containing peptides, the most hydrophobic H2a17-IL showed the largest Soret CD peaks. On the other hand, the most hydrophilic H2a17-LV showed the smallest Soret CD peaks. These results were taken to imply that the mutual orientation and distance of heme molecules in the assembled peptides varied depending on the hydrophobicity and/or arrangement of hydrophobic residues around the heme.

The CD spectrum of heme bound to H2a17-FL was characterized by a negative peak at longer wavelengths and a weak positive peak at shorter wavelengths (b). These data suggest that two hemes are left-handed in (d–f, h, l). The CD spectra of the heme in the presence of H2a17-VV, -AA, -AL, and -LA (g, j–l) showed a

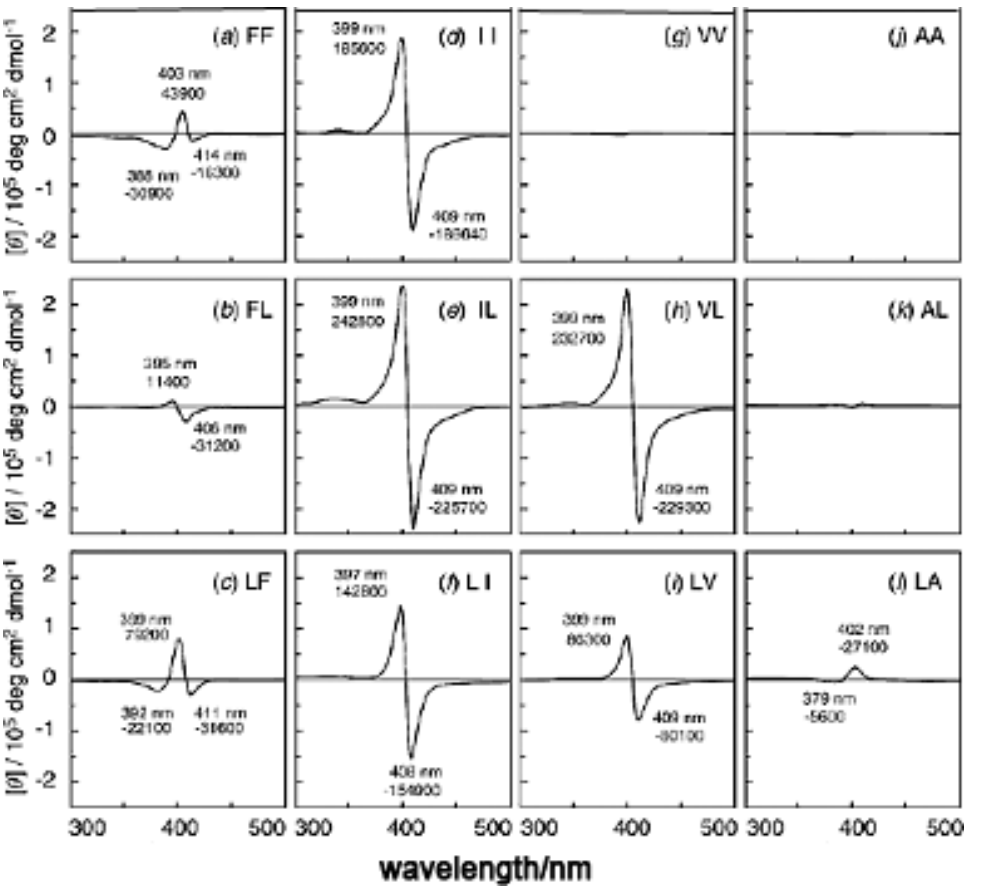

Figure 21. The Soret CD spectra of heme in the presence of H2α17-FF (a), -FL (b), -LF (c), -II (d), -IL (e), -LI (f), -VV (g), -VL (h), -LV (i), -AA (j), -AL (k), and -LA (l) in the absence (broken lines) and presence (solid lines) of heme (redrawn from Ref. 69).

small or no induced CD in the Soret region, suggesting that the peptide could not bind the heme effectively.

IV. Chlorophyll, Bacteriochlorophyll, Chlorin, and Bacteriochlorin Systems

A. Natural Chlorophyll and Bacteriochlorophyll Monomer and Dimer Systems

1. *Chlorophyll* a *and Bacteriochlorophyll* a *and Their Derivatives*

Of the few existing reports on the CD of chlorophylls,[70–73] that by Housser and Sauer is the most detailed.[73] The CD, MCD, and absorption spectra of chlorophyll

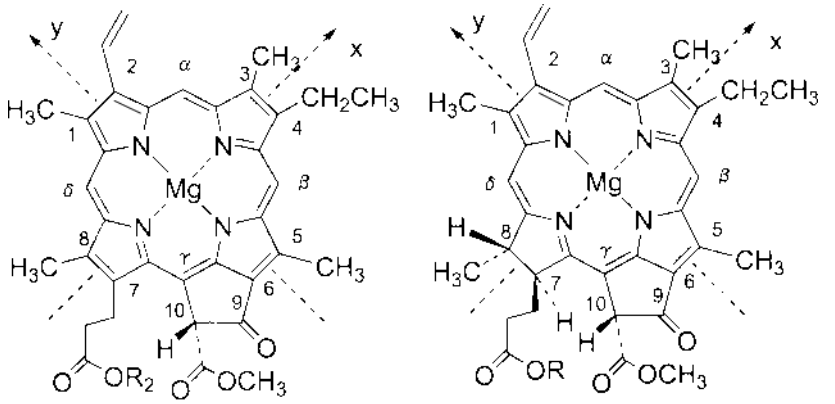

Figure 22. Molecular structures of protochlorophyll *a* and chlorophyll *a,* showing the absolute configuration of the asymmetrically placed ring substituents reported for chlorophyll *a*.

a (Chl *a*), pheophytin *a* (Pheo *a*, the metal-free complex of Chl *a*), pyrochlorophyll *a* (pyroChl *a*, the compound obtained by removal of the C-10 carbomethoxy group from Chl *a*), pyropheophytin *a*, (pyroPheo *a*, the metal-free compound of pyroChl *a*), and as protochlorophyll pigments, photochlorophyll *a* (PChl *a*), and 4-vinylprotochlorophyll *a* (VPChl *a*) were reported together with those of some of their dimers in Ref. 73. (Figure 22 contains the structures of protochlorophyll *a* and Chl *a*[73]). Before their analysis, it was known, as an empirical interpretation, that the effects of alternation in the asymmetry of the substitution at carbon atoms C-10 (in the cyclopentanone ring V) and C-7 and C-8 (of ring IV) are found to be directly related to the signs and amplitudes of the CD bands.[71,72] For example, from their optical activity data, Wolf *et al.*[71] succeeded in confirming that the 10-carbomethoxy group present in methyl pheophorbide *a* is in the *trans* configuration relative to the propionic acid side chain on C-7.

Figure 23 shows the CD, MCD and absorption spectra of Chl *a* and pyroChl *a*, while Figure 24 shows the spectra of Pheo *a* and pyroPheo *a* (note these are metal-free compounds of Chl *a* and pyroChl *a* in Figure 23). Note that in each figure, in the pyro compounds, the 10-carbomethoxy group is eliminated from Chl *a* or Pheo *a*. The optical spectra of PChl *a* (Figure 25) and its demetalated species, protopheophytin *a* (PPheo *a*, Figure 26) are quite different from those of Figures 23 and 24, since the pyrrole ring IV in the proto compounds is unsaturated, which is different from the compounds in Figures 23 and 24 (see Figure 22). Several general observations can be made from an examination of these spectra. In some cases, a strong MCD band is observed to correspond to a weak or non-existent CD band, e.g. the Qx(00) bands of Chl *a* and pyroChl *a* in Figure 23 and of Pheo *a* in

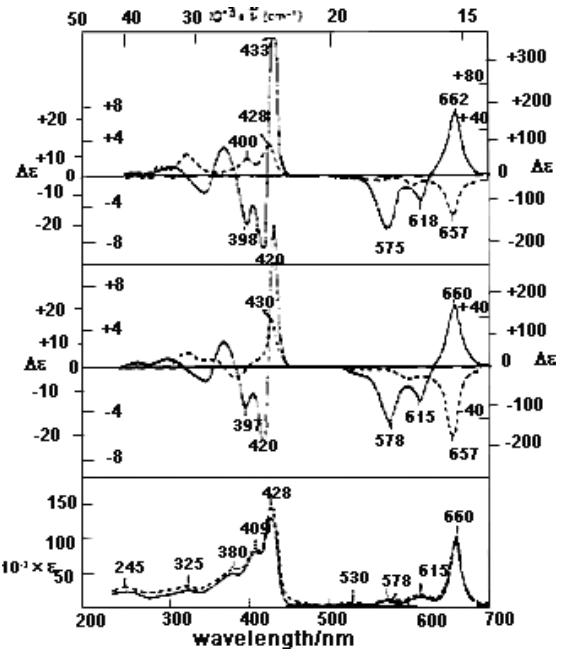

Figure 23. CD (broken lines) and MCD (solid lines) (upper and middle curves) and absorption (lower curve) spectra of Chl *a* and pyroChl *a* in ether. In absorption spectra, solid and broken line are for Chl *a* and pyroChl *a*, respectively (redrawn from Ref. 73).

Figure 24. As seen in Figures 23 and 24, the almost degenerate B bands (Soret bands) are more clearly resolved in the MCD compared to the CD spectra. On the other hand, the longest wavelength component in the Soret region appears in the CD but not in the MCD spectra of PChl *a* (Figure 25) and PPheo *a* (Figure 26). Optical activity data of the chlorophyll *a* and protochlorophyll *a* pigments in ether are summarized in Table 1.[73]

The CD spectra of the group of compounds show some distinct correlations with molecular structure, particularly for the Q band. The relevant data are summarized in Table 2.[73] Since CD is sensitive to slight conformational changes,[1–7,9,10] one has to be aware of the structural differences in the species studied. Chl *a* contains substituents asymmetrically placed at ring carbons C-7, C-8, and C-10. PChl *a* has only the C-10 substituent asymmetry, and pyroChl *a* has only the C-7 and C-8 asymmetries, by virtue of the loss of the C-10 carboxymethyl substituent and its replacement by a proton upon pyrolysis. As seen in Figures 23 and 24, Chl *a* and pyroChl *a* show negative and positive CD corresponding to the Q and Soret bands, respectively, while their metal-free derivatives, Pheo *a* and pyroPheo *a* exhibit positive, negative, and positive CD corresponding to the Qy(00), Qx(00), and Soret bands, respectively. In addition, as is discernible from a comparison

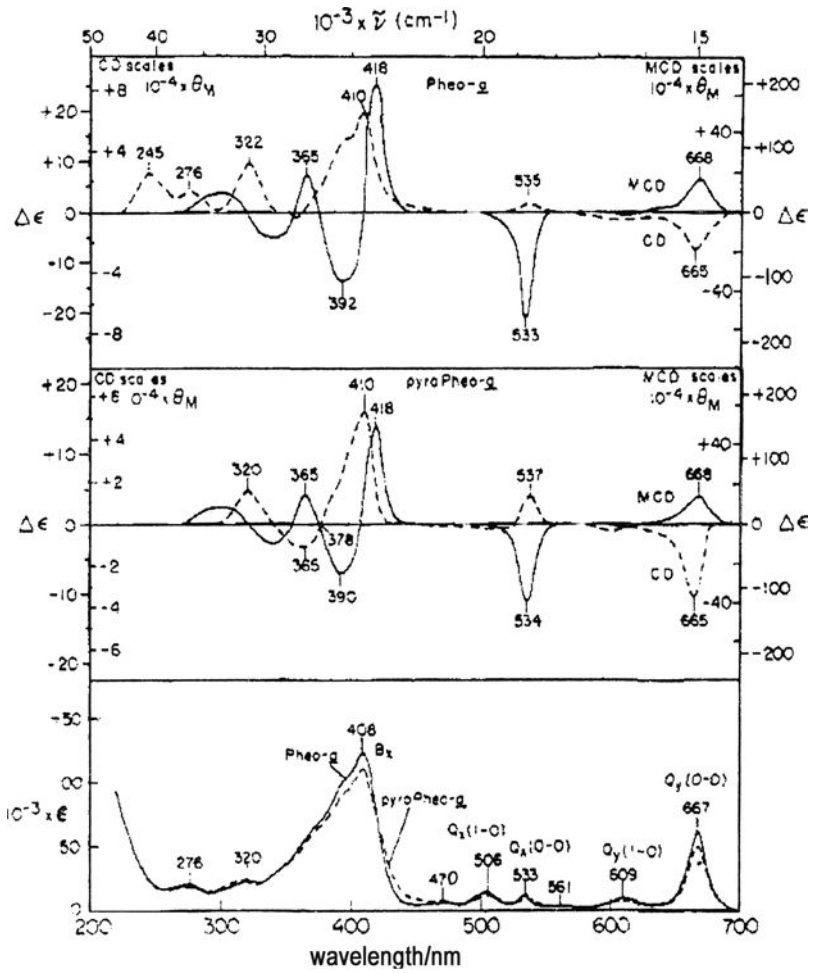

Figure 24. CD (broken lines) and MCD (solid lines) (upper and middle curves) and absorption (lower curve) spectra of Pheo *a* and pyroPheo *a* in ether. In absorption spectra, solid and broken line are for Chl *a* and pyroChl *a*, respectively. These are the metal-free compounds of the compounds in Figure 23 (redrawn from Ref. 73).

between Chl *a* and pyroChl *a* (Figure 23) and between Pheo *a* and pyroPheo *a* (Figure 24), the loss of asymmetry at the C-10 carbon atom commonly produces an increase in the CD intensities of the chlorophyll pigments. From the MCD spectra in Figures 25 and 26, the splitting of the Qy and Qx components is smaller for PChl *a* and PPheo *a* than for the species in Figures 23 and 24, due to the unsaturation of ring IV. Corresponding to the split Q components, the CD sign of PChl *a* (Figure 25) changes from positive to negative in ascending energy, while negative CD was observed for the Q band of Chl *a* and PChl *a* at the longest

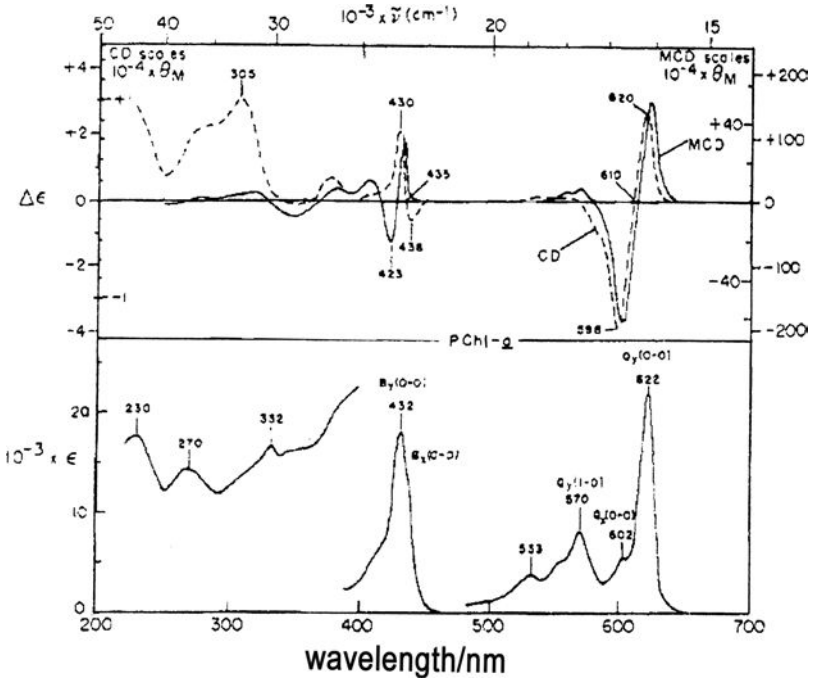

Figure 25. CD (broken line) and MCD (solid line) (upper) and absorption (lower) spectra of PChl *a* in ether. (redrawn from Ref. 73). As seen in Figure 22, in PChl *a,* the pyrrole ring IV is unsaturated different from Chl. a whose ring IV is saturated.

wavelength. An analysis of the behavior for PPheo *a* was more difficult since its CD was much smaller in magnitude (Figure 26). From the MCD sign, which is positive and negative at 640 and 593 nm, respectively, the longest wavelength band was assigned as a Qx component, which is different from other derivatives. A negative CD trough was observed corresponding to the Qx band.

The authors calculated the anisotropy factors using a point dipole to represent the electric transition moments, and compared these with experimentally obtained values (Table 3).[73] Although the calculated values were smaller than the experimental quantities by at least an order of magnitude, the sign was reproduced. It was found that the contribution to the CD of the carboxymethyl substituent at carbon atom C-10 of the cyclopentenone ring V is of an opposite sign compared to the C-7 and C-8 substituents of ring V. For the C-10 substituent, the CD contributions were positive in the y-polarization direction and negative in the x-polarization direction, while the reverse was true for the C-7 and C-8 substituents (x polarization through rings II–IV). It was also suggested that the substituents at C-10 and at C-7 and C-8 are probably the only ones responsible for the visible CD.

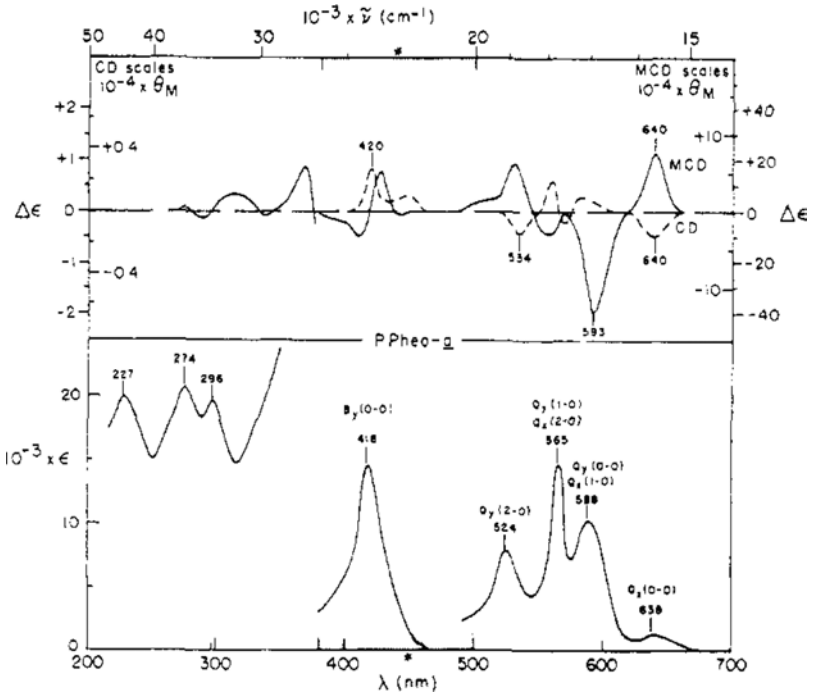

Figure 26. CD (broken line) and MCD (solid line) (upper) and absorption (lower) spectra of PPheo *a* in ether (redrawn from ref. 73). PPheo *a* is the metal-free compound of PChl *a* in Fig. 22.

The formation of aggregates gives rise to important modifications in the absorption and optical activity compared to the corresponding monomers. Figures 27–29 show the spectra of the dimer species in CCl_4. The Chl *a* (Figure 27), pyroChl *a* (Figure 28), and PChl *a* (Figure 29) spectra are characterized by the appearance of split components in the Q and B monomer absorption bands upon formation of the dimers, concomitant with hypochromicity of the dimer absorption compared with the monomer. The Qy bands of Chl *a* and pyroChl *a* clearly show absorption shoulders on the long-wavelength side, and the maxima are shifted slightly to the red. In the Soret region, the bandwidths become larger and the maxima are also shifted slightly to longer wavelength. On the other hand, the Q and B transitions of the aggregated PChl *a* are shifted to shorter wavelength compared to the monomer. The Q transitions for PChl *a* (Figure 29) do not show any clear splitting in the absorption, but the bandwidth is slightly increased. The B transition, however, showed a very distinct separation of components for the aggregate (436 and 455 nm, respectively).

The CD spectra of the dimers provide clear evidence of additional splitting. In the case of Chl *a* and pyroChl *a* (Figures 27 and 28), the Qy bands exhibit positive

Table 1. Optical activity of the chlorophyll and protochlorophyll pigments in ether (from Ref. 73).

Absorption spectra ($\varepsilon_{max} \times 10^{-3}$)			Optical activity ($\Delta\varepsilon(\lambda_{max})$)	
λ_{max}, nm	(mole/l)$^{-1}$ cm^{-1}	Assignments	CD	MCD
Chi *a*				
661	86.3	Qy(0–0)	−13.8(657 nm)	+160(662 nm)
615	12.6	Qy(1–0)		−60.5(618 nm)
575	6.8	Qx(0–0)		−130(575 nm)
530	3.4	Qx(1–0)		
428	113	Bx(0–0) By(0–0)	+11.0(428 nm)	+355(434.5 nm) −177(420 nm)
PyroChl *a*				
661	80	Qy(0–0)	−21(657 nm)	+156(660 nm)
615	13.9	Qy(1–0)		−78(615 nm)
578	8	Qx(0–0)		−135(578 nm)
530	4.5	Qx(1–0)		
428	123	Bx(0–0) By(0–0)	+14.7(428 nm)	+333(433 nm) −194(420 nm)
Pheo *a*				
667	61	Qy(0–0)	−79(665 nm)	+48(668 nm)
609	9.15	Qy(1–0)		−4.9(610 nm)
561	3.75	Qy(2–0)		
533	12	Qx(0–0)	+0.86(535 nm)	−165(532 nm)
506	13.8	Qx(1–0)		
470	5.85	Qx(2–0)		
408	123	Bx(0–0) By(0–0)	+20.3(410 nm)	+190(418 nm) −105(390 nm)
PyroPheo *a*				
667	49	Qy(0–0)	−10.5(665 nm)	+37(668 nm)
609	7.8	Qy(1–0)		−6.5(610 nm)
561	3.95	Qy(2–0)		
535	9.9	Qz(0–0)	−3.7(537 nm)	−119(534 nm)
507	12.1	Qx(1–0)		
470	7.45	Qx(2–0)		
408	109	Bx(0–0) By(0–0)	+17.25(410 nm)	+149(418 nm) −80(388 nm)
PChl *a*				
622	22	Qy(0–0)	+3.0(624 nm)	+130(622 nm)
602	5.35	Qx(0–0)	−3.75(600 nm)	−188(601 nm)
570	8.05	Qy(1–0)		+22.5(568 nm)
556(sh)	5.05	Qx(1–0)?		+19.4(557 nm)
533	3.75	Qy(2–0)?		+8.15(535 nm)
438	137	Bx(0–0)	−7.55(438 nm)	
432	182	By(0–0)	+25(432 nm)	+91(432 nm) −65(423 nm)

(*Continued*)

Table 1. (*Continued*)

Absorption spectra ($\varepsilon_{max} \times 10^{-3}$)			Optical activity ($\Delta\varepsilon(\lambda_{max})$)	
λ_{max}, nm	(mole/l)$^{-1}$ cm^{-1}	Assignments	CD	MCD
PPheo *a*				
638	1.32	Qx(0–0)	–0.50(638 nm)	+22(638 nm)
588	10.2	Qy(0–0), Qx(1–0)?	?	–40(593 nm)
565	14.5	Qy(1–0), Qx(2–0)?	?	–9(560 nm)
524	7.7	Qy(2–0)?	?	+19(530 nm)
432(sh)	82.5	Bx(0–0)	?	
418	145	By(0–0)	+8.7(418 nm)	+153(427 nm) –98(410 nm)

CD corresponding to the shoulders in the absorption bands (677 and 680 nm, respectively), cross zero near the absorption peaks (664 and 670 nm), and show negative CD bands on their short wavelength sides (659 and 661 nm). For the B transition, the behavior is reversed, with the negative CD band being on the long wavelength side. In the case of PChl *a*, the longest wavelength component (628 nm) is negative, while it is positive for Chl *a* and for pyroChl *a*. In the region of overlap between the x and y components, the effects add together, which may be the reason for the very intense negative CD band centered at 443.5 nm.

In order to interprete the CD spectra in Figures 23–29, the bands must first be properly assigned. For this, the knowledge of MCD and theoretical treatment of Kirkwood[32] was utilized. Thus, the long wavelength transition was assigned as y-polarized for all compounds except PPheo *a* in Figure 26 (x-polarized). Implicit in the Kirkwood model is the assumption that each of the asymmetric centers acts independently on the transition moments. Accordingly, it was expected that the observed rotational strengths can be accounted for by a summation of the interactions associated with each significant asymmetric site on the porphyrin ring. This was observed quantitatively for the different compounds studied for the Qy transitions of PChl *a*, pyrroChl *a*, and Chl *a*. However, it cannot be tested further for the Qx bands, because the corresponding CD component could not be distinguished. The correspondence of calculation and experiment was insufficient, since the calculated CD intensity was weaker than the experimentally observed intensity by one order.

In the case of strongly interacting dimers, the oscillators associated with corresponding transitions in different molecules couple with each other, leading to a splitting of each of the excited states, and producing CD components associated with each of the new transitions. From previous studies, the spectrum in CCl_4 was

Table 2. Experimental values of absorption and rotational strengths of chlorophylls and protochlorophylls in ether (from Ref. 73).

		PChl*a*	PyroChl *a*	Chi *a*	PPheo *a*	PyroPheo *a*	Pheo *a*
λ_{max}, nm	Qy	622	661	661	588, 565 (?)	667	667
	Qx	602	578	575	638	535	533
ω_{max}, cm^{-1}	Qy	16,080	15,130	15,130	17,010 17,700	14,990	14,990
	Qz	16,610	17,300	17,390	15,670	18,690	18,760
$10^{-3}\varepsilon_{max}$, $(mole/1)^{-1}$ cm^{-1}	Qy	22	80	86.3	10.2 14.5	49	61
	Qx	5.35	8	6.8	1.32	9.9	12
Band width $\Delta\omega$, cm^{-1}	Qy	325	420	390	570,[a] 530	405	405
	Qx	450[a]	780[a]	760[a]	440[a]	490[a]	490[a]
Oscillator strength $f = 4.33 \times 10^{-9} \int \varepsilon(\omega) d\omega$	Qy	0.0	0.155	0.155	0.027 0.0355	0.091	0.114
	Qx	0.0110	0.029	0.024	0.0027	0.0225	0.027
Dipole strength 10^{36} μ^2, $(esu\ cm)^2$	Qy	4.35	21.7	21.7	3.34, 4.24	12.9	16.1
	Qx	1.42	3.53	2.91	0.36	2.54	3.06
Molecular ellipticity	Qy	+10	−69	−46	?	−35	−26
$10^{-3}(\theta_M)_{max}$, 10^{-2} $deg(mole/1)^{-1}$ cm^{-1}	Qx	−12.4			−1.65	+12.2	+2.85
Rotational strength	Qy	+1.48	−14.3	−8.7	?	−6.9	−5.2
$10^{40}R_A$(cgs)	Qx	−1.82			−0.34	+2.4	+0.55
$10^4 4R_A/\mu^2 = 10^4\Delta\varepsilon_{max}/\varepsilon_{max}$	Qy	+1.36	-2.6	−1.60	?	-2.15	-1.30
	Qx	−7.0			−3.8	+3.7	+0.72
$10^8 4R_A/\mu^2\ \omega_{max} = 10^8\Delta\varepsilon_{max}/\varepsilon_{max}$ cm	Qy	+0.85	−1.73	−1.06	?	−1.43	−0.86
	Qx	−4.22			−2.42	+2.00	+0.38

Table 3. Comparison of experimental and calculated anisotropy factors for chlorophyll and protochlorophyll pigments (from Ref. 73).

Asymmetry Centers	Transition	Experimental $10^8\Delta\varepsilon/\varepsilon\omega$, cm		Calculated $10^8 4\pi\Sigma f_{ij}$, cm
		PChl *a*	PPheo *a*	
C-10	Qy	+0.85		+0.107
	Qx	–4.22	–2.42	–0.180
		PyroChl *a*	pyroPheo *a*	
C-7, C-8	Qy	–1.73	–1.43	–0.45
	Qx		+2.00	+0.198
		Ch *a*	Pheo *a*	
C-7, C-8, C-10	Qy	–1.06	–0.86	+0.062
	Qx		+0.38	+0.018

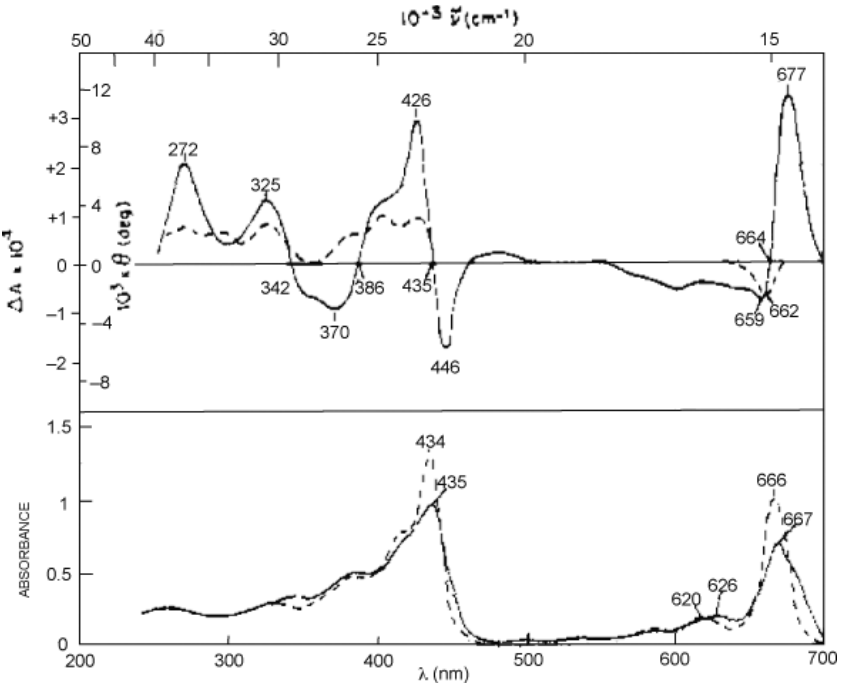

Figure 27. CD and absorption spectra of Chl *a* dimer in CCl_4 (redrawn from Ref. 73).

thought to be that of dimers, and in detailed studies by Katz and coworkers, the molecules were proposed to be oriented so that the C-9 carbonyl group of one molecule interacts with the central magnesium of the other.[74] (Note that the so-called Fischer nomenclature was used by Katz and coworkers because the work

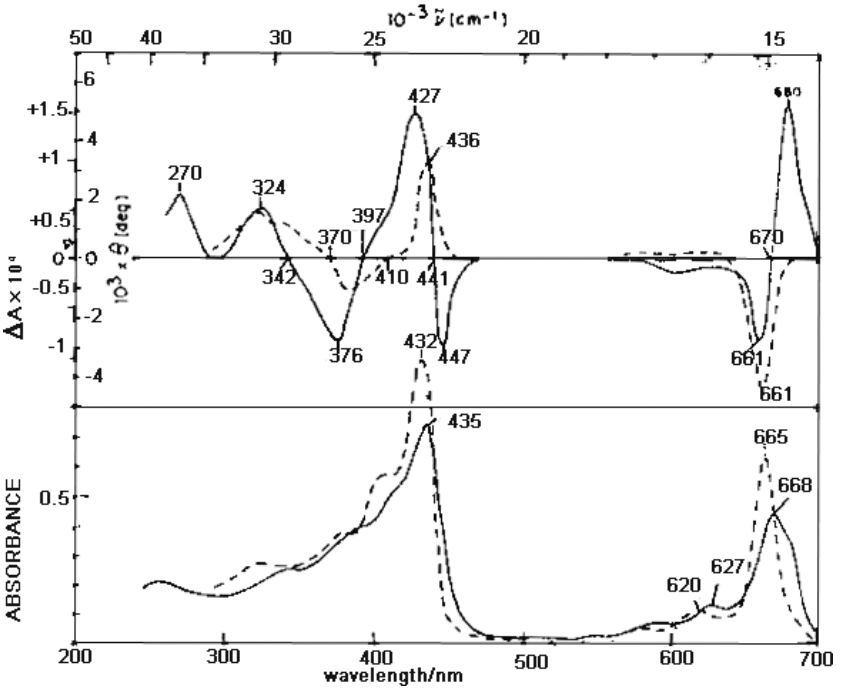

Figure 28. CD and absorption spectra of pyroChl *a* dimer in CCl_4 (redrawn from Ref. 73).

pre-dates adoption of the IUPAC system). Furthermore, the CD data of Katz and coworkers showed that the porphyrin rings do not lie in parallel planes, but that one molecule is inclined with respect to the other. Examination of the short wavelength regions of the dimer spectra for Chl *a* and pyroChl *a* in Figures 27 and 28 shows a very close correspondence between the two, even though the corresponding monomer spectra are quite dissimilar (Figure 23). This was taken as evidence to indicate marked similarities in the dimer structures of Chl *a*, pyroChl *a*, Chl *b* and BChl. The inclusion of pyroChl *a* in this group was significant, in that it does not posses a carboxymethyl substituent on the C-10 carbon, indicating further that the carboxymethyl substituent on C-10 has no significant influence on the formation of the dimer. In the case of PChl *a*, where ring IV is not reduced, the CD spectrum of the aggregated dimer species is quite different (Figure 29). Here, the longest wavelength component of the CD is negative for the aggregated PChl *a* (solid curve) whereas it is positive for each of the other molecules. Thus, it was concluded that PChl *a* has a significantly different dimer structure from that of Chl *a* and the other molecules. The major difference in molecular structure between PChl *a* and the other molecules is that the first C-C bond of the propionic ester substituent at C-7 lies in the porphyrin plane for PChl *a*, but is at an almost

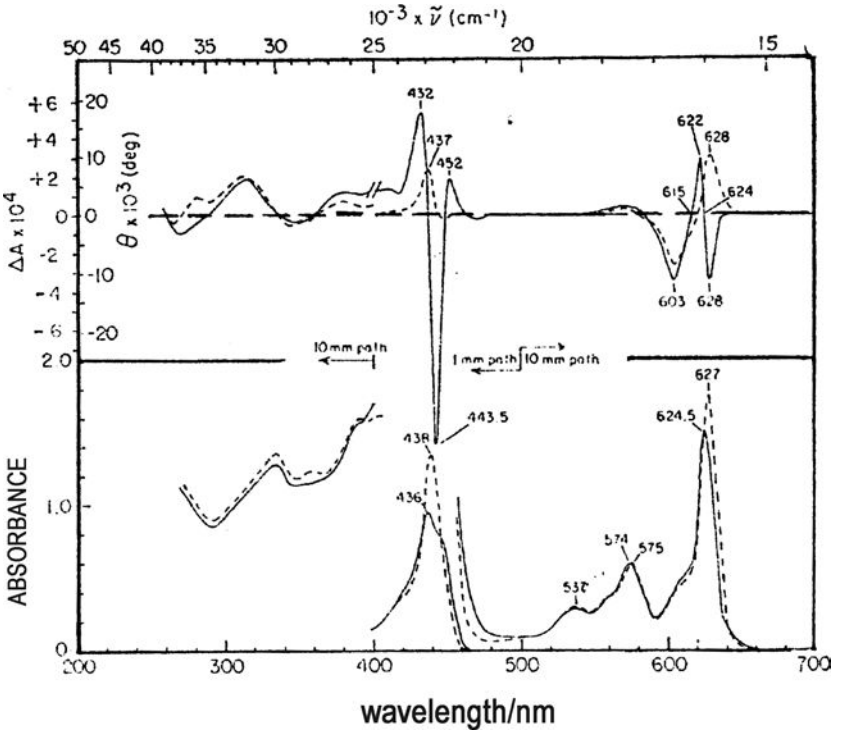

Figure 29. CD and absorption spectra of PChl *a* dimer in CCl_4 (redrawn from Ref. 73).

tetrahedral angle for the others. Since this group is farther from the proposed point of interaction at C-9 than the C-10 carboxymethyl group, the authors could not connect the dimer structure to the CD spectra.

2. *Bacteriochlorophylls* c, d, e *and* g

Although the structures of bacteriochlorophyll (BChl) *c, d, e* and *g* (Figure 30) were established before the end of the 20th century, little is known about their CD spectra.[75–88] BChl *c in vivo* is a mixture of at least five homologs, all of which form aggregates in organic solvents such as CH_2Cl_2, $CHCl_3$, and CCl_4. Various groups have reported absorption and CD spectra under various conditions. However, the spectra are sensitive to changes in both position and intensity from group to group, depending on the pre-treatment, concentration, temperature, and solvent used for the measurements. The spectra of two species which appear reliable from the experimental data are shown here. The first is the spectra of epimerically pure BChl *c*, isolated from *Chlorobium tepidum* (Figure 31),[85] and the other is the spectra of BChl *g* and *g′* from *Heliobacterium chlorum* (Figure 32).[81] The structure of

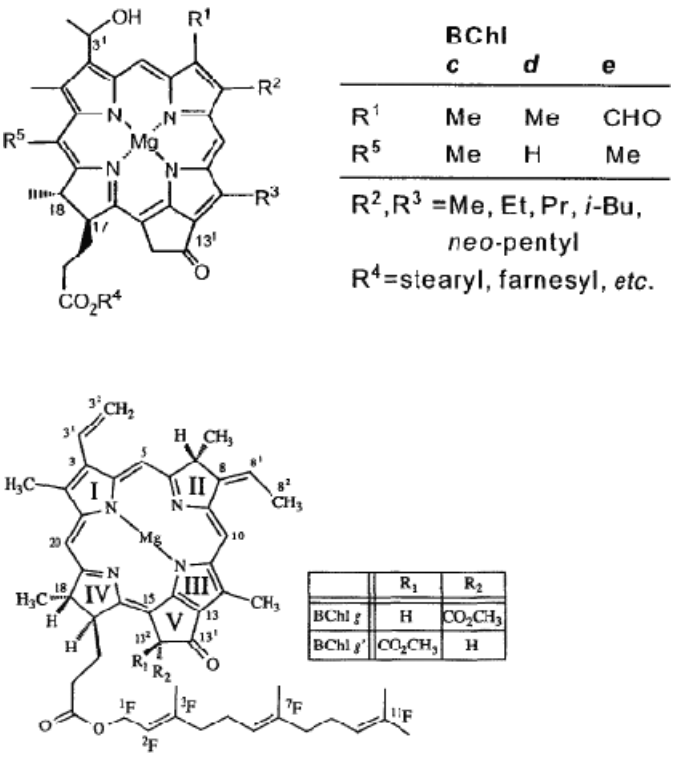

Figure 30. Structures of bacteriochlorophyll *c, d, e* and *g* (redrawn from Refs. 81 and 84).

quite unstable BChl *g* resembles that of BChl *b*, both pigments containing the unusual ethylidene group at ring II (Figure 30). Photoisomerization of BChl *g* at ring II yields Chl *a*, the main chlorophyll of oxygenic photosynthesis. BChl *g′* is the 13^2-epimer of BChl *g*. In the case of BChl *c*, a strong CD peak and trough were observed corresponding to the Q and Soret bands, respectively, while in the case of BChl *g* and *g′*, the CD sign at both the Q and Soret absorption peaks was the same, positive for BChl *g′* and negative for BChl *g*. Although the absorption spectra of BChl *g* and *g′* are very similar, the CD spectra are distinctly different, not only in sign but also in the intensity in the Q region. Attempts to interpret the CD spectra of BChl *c, d, e*, and *g* have not been successful.

3. *Light Harvesting Complex 2 (LH2)*

The photosynthetic antenna of purple bacteria consists of two types of light-harvesting antenna complex, termed complex 1 (LH1, the core antenna complex) surrounding the reaction center, and complex 2 (LH2, a peripheral antenna

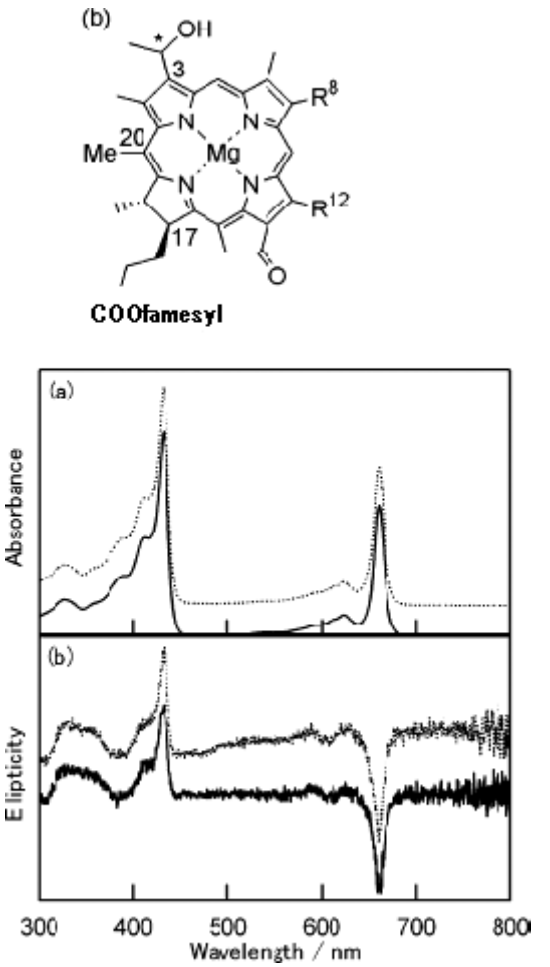

Figure 31. (a) Absorption and (b) CD spectra of synthetic epimerically pure BChl *c* (solid line) and BChl *c* from *Chlorobium tepidum* (doted line) in Et_2O (redrawn from Ref. 85).

complex) positioned away from the reaction center. The crystal structures of bacterial LH2 complexes from two species, *Rhodospirillum (Rs.) molischianum* and *Rhodopseudomonas (Rps.) acidophila* determined in 1995[89] and 1996[90] opened the door to an increasingly detailed understanding of the unusual spectroscopic and dynamic properties of the bacterial antenna complexes. The LH2 from *Rps. acidophila* consists of nine copies of each of two proteins (*a* and *b*), 27 BChl and 18 carotenoid molecules arranged in a ring structure with C9 symmetry. A striking feature is their separation into two parallel rings. The ring of 9 BChl is larger in diameter than the ring of 18 BChl, while the spacing between successive BChl in the ring of 18 is closer, by a factor of two, than the spacing in the ring of 9 BChl

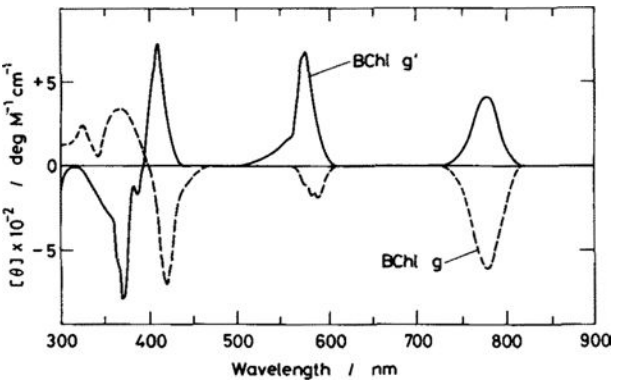

Figure 32. CD spectra of BChl *g* (broken line) and *g′* (solid line) in benzene at room temperature (redrawn from Ref. 81). Although not shown, absorption spectra are very similar except Qx band at around 550–600 nm; the peak of *g′* is sharper.

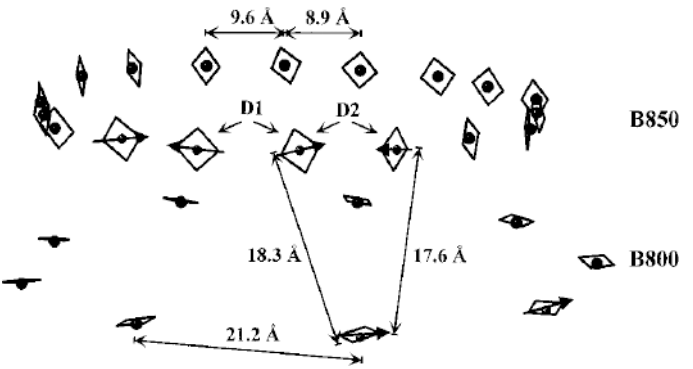

Figure 33. Schematic structure of LH2 from *Rps. acidophila*. The BChl *a* molecules with the central Mg atom are shown. D1 refers to a protomer and D2 refers the dimer between adjacent protomers. The directions of the Qy transition dipole vectors are indicated by vectors. Upper part consists of 18 B850 pigments; below are shown the 9 B800 pigments (redrawn from Ref. 102).

(Figure 33). Thus, the ring of 18 closely-spaced BChl is thought to be responsible for B850 and the ring of 9 widely-spaced BChl for B800.

The absorption spectra of LH2 complexes from different species of purple bacteria features an intense band at 850–860 nm and another band of about half that intensity at *ca*. 800 nm. At shorter wavelengths, there is a single band at *ca*. 590 nm attributable to the Qx band of BChl, while bands in the 400–500 nm region are attributed to carotenoids. The Soret band generally appears around 350–400 nm. The CD spectrum of LH2 exhibits a –/+ pattern in ascending energy, corresponding to the Qy bands at *ca*. 850–860 nm, and a much weaker CD of

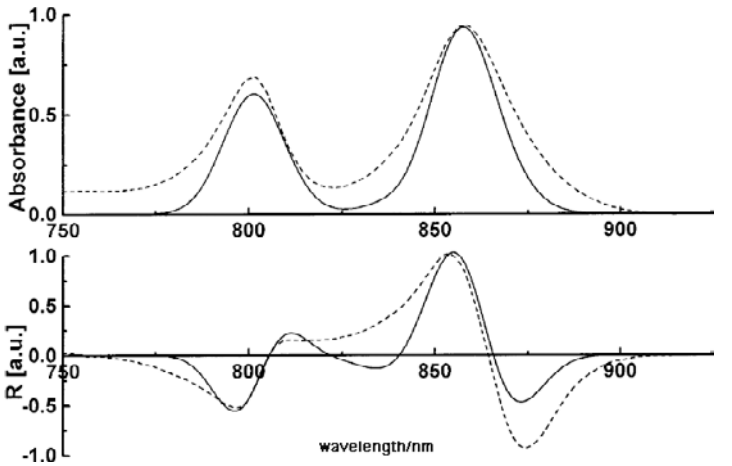

Figure 34. Experimental (dashed lines) and simulated (solid lines) of LH2 antenna of *Rps. acidophila* at room temperature (redrawn from Ref. 102).

negative envelope associated with the *ca*. 800 nm Qy band (Figure 34).[102,104] Linear dichroism studies show that the transition moments of both B800 and B850 lie in the plane of the chromophore membrane (the closely associated BChl in the ring of 18 are arranged in a head-to-head and tail-to-tail fashion around the ring).[106]

Sauer and coworkers[101] were the first to calculate the spectrum of LH2 of *Rps. acidophila* using the X-ray crystal structure.[89] They adopted a point monopole approximation in order to calculate the chromophore-chromophore interactions. The BChl *a* transition energy was first set at 12,500 cm^{-1} corresponding to the absorption wavelength of the B800 ring, where the excitonic interactions are small. By increasing the units of calculation from the protomer (two B850 and one B800), the trimer (one third of the full nonameric complex, with six B850 and three B800), the nonamer (18 B850 and nine B800), they showed that the absorption spectra are essentially additive, to give the spectrum of the complete nonamer. In the case of the protomer, the Q band appeared seemingly as a single peak at *ca*. 12,300 cm^{-1}, while in the trimer, split Q bands appeared at *ca*. 11,900 and 12,000 cm^{-1}, and in the nonamer, finally largely split Q bands were estimated at *ca*. 11,800 and 12,500 cm^{-1}, substantiating that the 850 nm band is essentially produced by excitonic coupling. Finally, to match the experimental spectrum, the transition energies of the B850 molecules were scaled to 12,260 cm^{-1}. In addition, by calculating the set of 18 B850 and the set of nine B800 separately, the authors confirmed that the B800 molecules are sufficiently isolated in LH2, and that the excitonic interaction among molecules in B800 is small. In addition, as seen in Figure 34, although the zero-crossing of the CD spectrum appears at lower energy than the

absorption peak by *ca*. 7 nm. This was explained by the negative rotational strength of the lowest energy state and the positive rotation just above this. Furthermore, because the lowest state has very weak absorption while the state just above it is very strong, the CD zero-crossing is at a lower energy than that of the absorption maximum.

The next higher level of calculation, i.e. an INDO/S calculation, was carried out for B800 (eight pigments) and B850 antenna (16 pigments) of *Rs. molischianum*,[97] which was the largest semi-empirical calculation on bacterial antenna. For calculation of the B850 antenna, the BChl *a* molecule was approximated by a reduced structure containing 44 atoms. The chromophore–chromophore interactions were estimated semi-empirically using the known crystal structure. However, the computed energy levels did not predict the experimental transition energies well.

Linnanto and coworkers then calculated the excitonic spectra of the LH2 antenna complex of *Rps. acidophila* adopting four different approaches.[102] For comparison, the energy levels were first calculated by applying the frequently used dipole-dipole approximation between all the 27 BChl a pigments of a single LH2 complex (case A). In the second level of calculation, the interaction energy between the neighboring B850 BChl *a* molecules was calculated semi-empirically (case B). Here, the values of nearest neighbor interaction matrix elements of the B850 ring were estimated by considering both possible ab–BChl *a* dimers as a supermolecule. By using this method, the special extension of the transition densities and the overlap between the wave functions with nearest neighbor molecules were taken into account. The calculation was further improved (case C) by calculating semiempirically (ZINDO/S) the transition energy of each monomer (B800, B850*a* and B850*b*) with a selected part of the protein. The difference from case B is that the monomer energies were calculated separately instead of using the experimental value of 12,937 cm^{-1} (773 nm).

The transition energies of the B850 BChl *a* monomers were calculated with the histidine residues. The B800 monomer was calculated with the nine nearest amino acids, the part of the phytyl tail of B850 which is in close vicinity of B800, and part of the carotenoid. In this way, the effects of surrounding protein environments were included. The result was then used to recalculate the interaction energy. In the last phase (case D), diagonal and off-diagonal disorder was included in the calculation, in order to account for the inhomogeneous line width of the experimental spectrum. Here, the computation included uncorrected random variation of the values of matrix elements which leads to inhomogeneous broadening of the spectral lines. The transition dipoles were kept fixed, while homogeneous widths of 210 cm^{-1} (B800) and 188 cm^{-1} (B850) were fixed for each transition. The diagonal disorder was 200 cm^{-1} (B800) and 220 cm^{-1} (B850), and the off-diagonal

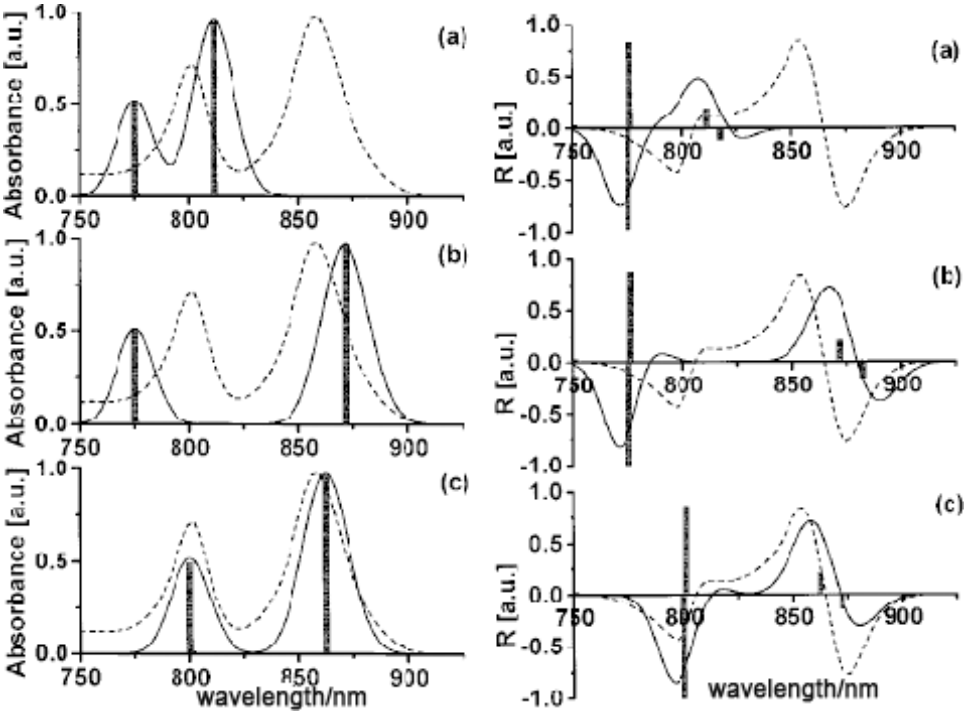

Figure 35. Exciton stick electronic absorption (left) and CD (right) spectra of LH2 complex and simulated spectra with a 350 cm^{-1} Gaussian line width. The experimental spectra at room temperature are shown as dashed lines for comparison. (a), (b) and (c) correspond to cases A, B and C, respectively, in the text (redrawn from Ref. 102).

disorder was 10% of the value of the matrix element. These linewidths were similar to the experimental values.[107–109] The results are clearly shown in Figure 35, together with the experimental spectra (dashed line).

In Case A, the exciton interaction energy between the nearest neighbor BChl *a* of B850 were 346 cm^{-1} (within the protomer) and 249 cm^{-1} (between the protomers). The exciton interaction energies between non-neighboring pigments were of the order of 30–40 cm^{-1}. The absorption intensity was concentrated mainly on four excited states, two of which were red shifted only to 775 nm. The other two states were red shifted to 811 nm, corresponding to a displacement from the Qy transition energy of the monomeric BChl *a* at 773 nm. The energy separation of the two absorption bands was much smaller. Thus, although the calculated values were not accurate, the general shapes of the absorption and CD spectra were in agreement with the experimental results. In case B, the exciton interaction energy between the nearest neighbor BChl *a* of B850 were 771 cm^{-1} (within the protomer) and 712 cm^{-1} (between the protomers), which were twice as large as those in case A.

The calculated absorption intensity was again concentrated mainly on four exciton states, and these four components formed two absorption bands, as in case A. The positions of these absorption bands were at 775 nm corresponding to the B800 transition, and 871 nm associated with B850 transition. The energy separation between the two transitions is about twice as large as is experimentally observed. The CD spectrum consisted of two pairs of lines: one pair centered at around 775 nm with an energy separation of only 17 cm^{-1} and one pair at around 876 nm with an energy separation of 140 cm^{-1}. The sequence of signs of the CD lines was identical with that obtained in case A. In case C, the Qy transition energies of the three monomers were calculated, on the wavelength scale, at 797 (B800), 784 (B850b), and 779 nm (B850a), respectively.

Compared with the Qy transition energy of monomeric BChl *a*, shifts induced by the surroundings of the BChl *a* monomers were −385 (B800), −189 (B850*b*) and −107 (B850*a*) cm^{-1}. The exciton interaction energies between the nearest neighbor BChl *a* of the B850 ring are *ca*. 650 cm^{-1} (within the *a,b*-protomer) and 560 cm^{-1} (between the protomers). The calculated absorption intensity of the whole LH2 complex is again concentrated on four components, and gives rise to two absorption bands at *ca*. 800 and 862 nm (Figure 35 bottom), which are very close to the experimental peaks. The energy separation of these two bands was 910 cm^{-1}, while the energy difference between the low-energy exciton state ^1A and $^{1,2}E_1$ state was 125 cm^{-1}. The CD spectrum consists of two pairs of lines (Figure 35, bottom). One pair is centered at 800 nm with an energy separation of 18 cm^{-1}, and one pair at 867 nm with an energy separation of 125 cm^{-1}. From these results, the authors concluded that the red-shift of the B800 band is to a large extent due to pigment–protein interactions, which is consistent with hole burning data indicating that exciton effects are unimportant for the B800 molecules and therefore, the B800 band.[110] Finally, by introducing diagonal and nondiagonal disorder to the exciton Hamiltonian, the experimental CD and absorption curves were simulated, with the results shown in Figure 34 as solid lines. Good agreement with the experimental spectra was obtained.

B. Synthetic Chlorins, Bacteriochlorins and Their Dimeric and Aggregated Systems

Although the CD spectra of several synthetic chlorin and bacteriochlorin systems have been reported,[111–118] papers which include analysis are very rare. Here, we restrict ourselves to introducing representative spectra of relatively well-defined systems.

Pandy, Kadish, Fukuzumi and coworkers compared the electronic absorption and CD spectra of ring-B reduced chlorins obtained by oxidation of bacteriochlorins

with those of ring-D reduced chlorins (Figures 36 and 37).[117] In these cases, there is a tendency for both the Qy and Soret bands to appear at longer wavelength when the B-ring is reduced (see in particular Figure 37). CD spectra were also reported, and CD peaks and troughs were observed associated with each absorption peak. Interestingly, the CD sign of the ring-B reduced species was opposite to the ring-D reduced species; with respect to the Qy and Soret bands, the B-ring reduced chlorins always gave positive and negative CD signs respectively. Although the authors

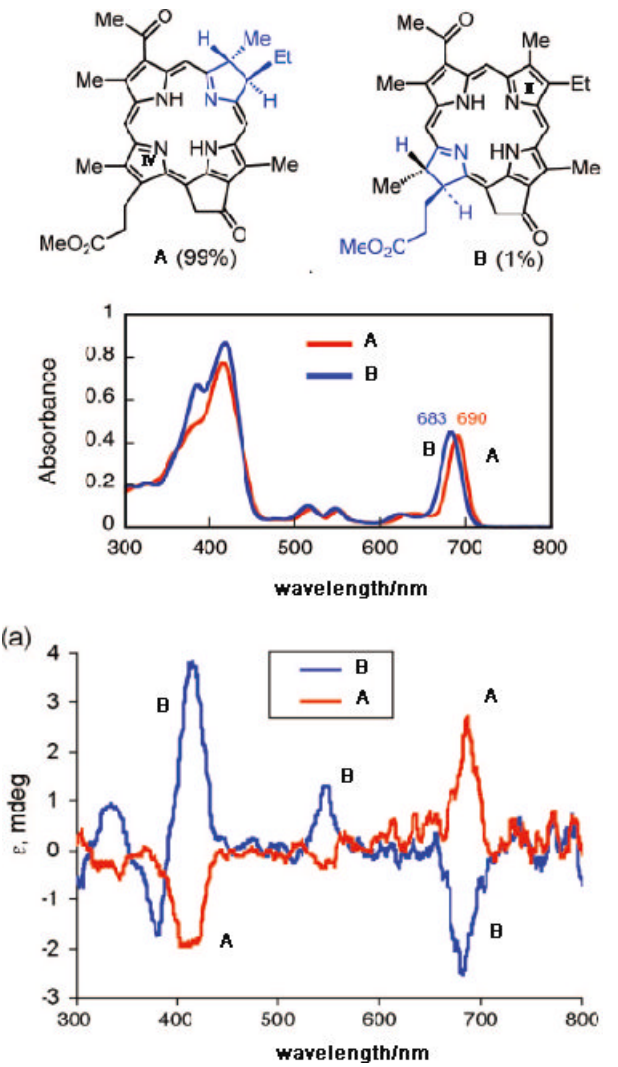

Figure 36. Electronic absorption and CD spectra of ring B or D reduced chlorins containing five-membered rings in CH_2Cl_2 (redrawn from Ref. 117).

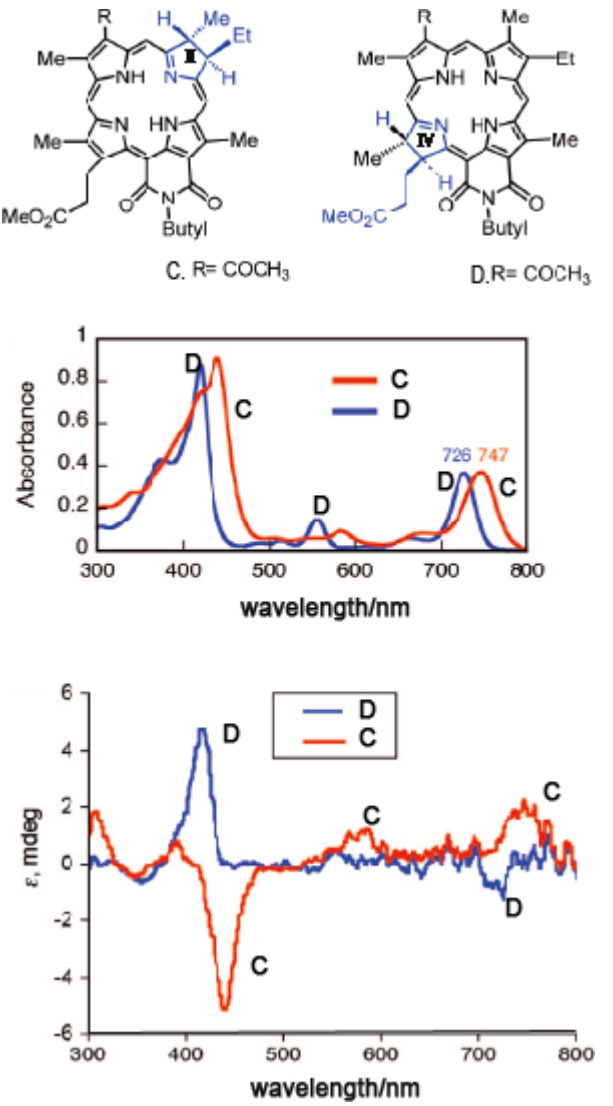

Figure 37. Electronic absorption and CD spectra of ring B or D reduced *N*-butyl-purpurinimide in CH_2Cl_2 (redrawn from Ref. 117).

suggested exciton coupling produced by self-association of the molecules, this interpretation is incorrect, since there are no dispersion type curves associated with absorption peaks, and the intensity is weak so that the spectra are noisy. The spectra shown in Figures 36 and 37 are characteristic of intrinsically active molecules.

Bucks and Boxer reported data of several cofacial chlorophyll-based dimers (Figures 38 and 39).[111] The main structural difference between the compounds in

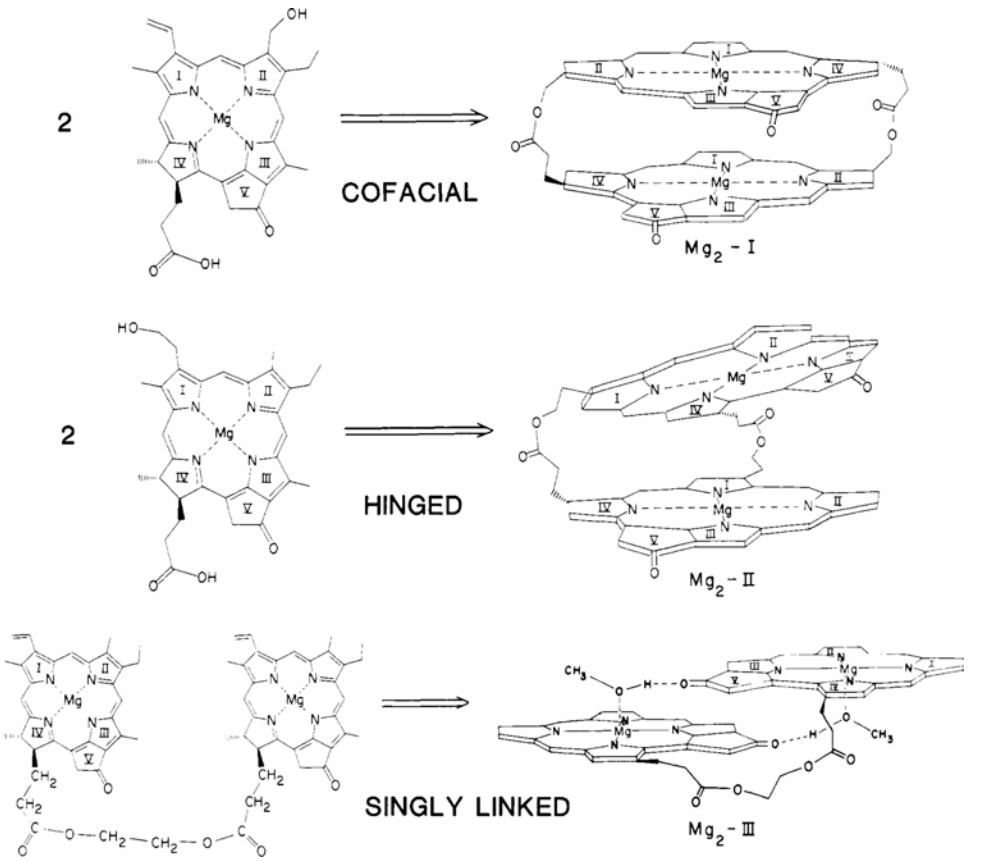

Figure 38. Chemical structures and schematic molecular conformations for the dimers by Bucks and Boxer (redrawn from Ref. 111).

Figures 39 and 40 are that in the former case, five-membered rings are fused while in the latter, six-membered rings are fused. In order to discuss the CD and absorption spectra, an understanding of the conformation is prerequisite. Inspection of a molecular model of the cofacial dimer showed that the macrocycles are parallel, and the angle between the y-axes is about $40 \pm 5°$. The centers might be offset by as much as 3.5 Å, as the rings move closer to maximize their π–π interactions. The structure of the hinged dimer was less well defined because of the considerable flexibility in the connection. For small opening angles of the hinge, the y-axes of the monomers were at approximately 90 degrees to each other. Based on this information, the two components of the cofacial dimer were predicted to be separated by about 700 cm^{-1} (*ca.* 30 nm) with most of the oscillator strength in the higher energy component (8:1, leading to a blue-shift). The rotational strengths of these components should be large, equal and opposite in

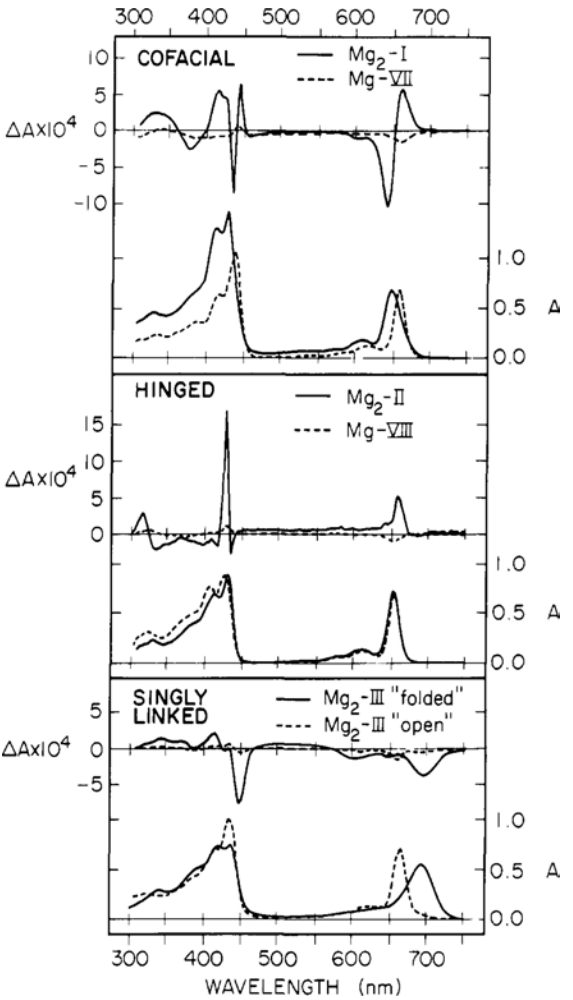

Figure 39. Comparisons of the absorption and CD spectra for the monomers (top and middle, broken lines) and the dimers (top and middle, solid lines) shown in Figure 38. In the bottom, "folded" (solid lines) and "open" (broken lines) forms were obtained by changing the solvent; "folded" was in toluene, and "open" was in toluene:pyridine = 9:1 v/v (redrawn from Ref. 111).

sign, with the band at lower energy positive. In the case of the hinged dimer, the Qy transition should not be split, since the transition moments are perpendicular, and any excitonic components in the CD should cancel out, as is indeed observed (Figure 39, middle). In the singly-linked "folded" dimer, the transition dipole moments are nearly antiparallel, so that nearly all of the oscillator strength is expected to lie in the lower energy component of the split Qy band (leading to a red shift). Although the rotational strength appears to be nearly zero theoretically,

the CD intensity in Figure 39, bottom is not particularly weak, indicating that the dipole coupling effect is still significant.

Kosaka and Tamiaki reported a well-defined cyclic hetero-dyad as a model compound for stacked chlorophylls, together with a linear non-cyclic hetero-dyad (Figure 40).[115] The largest difference of the constituent chlorin units is that one chlorin has a 13-keto carbonyl group while another has no substituent at the 13 position. After NMR analysis and consideration of the total energies obtained by molecular modeling, the cyclic dyad was concluded to take a conformation as shown at the bottom of Figure 40. The Qy absorption maximum of the cyclic dyad and linear dyad appeared at the same wavelength. The Qy and Soret bands of the former were slightly broader in the red and blue regions, respectively, relative to the latter. Intense S-shaped and reversed S-shaped CD signals in the Qy and Soret regions, respectively, of the cyclic dyad demonstrated that the two constituting chlorin units were close enough to give rise to an intramolecular transition dipole-dipole moment interaction. By applying the CD exciton chirality method, the S-shaped signal in the Qy region of the cyclic dyad revealed a "clockwise" rotational orientation of the two Qy transition dipole moments on the N21-N23 axis, which is in accordance with the two electronic transition moments drawn at the bottom of Figure 40 (top view).

Tamiaki and coworkers reported the aggregation of a Zn chlorin.[83] Including previous data,[78] it was known that the central zinc atom, the hydroxyl group at C-3^1 and the keto group at C-13^1 are prerequisites for aggregation. Furthermore, for the aggregation of the Zn chlorin in nonpolar solvents (Figure 41), it was found that the 3^1-hydroxyl oxygen of one chlorin coordinates to the zinc of another as a fifth axial ligand, and that the hydrogen of the ligated hydroxyl binds to the 13^1-carbonyl oxygen of a third molecule. In Figure 41, the spectra drawn as dotted lines are for monomeric species in THF. In this state, the CD is very weak. By adding 1 vol% of hexane, the Qy band shifted to the red, as seen for natural Mg chlorins,[78,118] and an intense dispersion type CD appeared corresponding to the Qy band, indicating the presence of strong exciton coupling due to supramolecular structure formation. As compatible structures, an antiparallel orientation, with head-to-head dimeric building blocks joined by hydrogen bonding and chlorine ring overlapping, has been proposed (Figure 42).

V. Synthetic Porphyrin Monomer Systems

Although several CD spectra of synthetic monomeric porphyrins have been reported, their analysis has been limited. In most cases, only the spectra were reported without explanation. In this section, therefore, only the structures of compounds and their spectra will be presented.

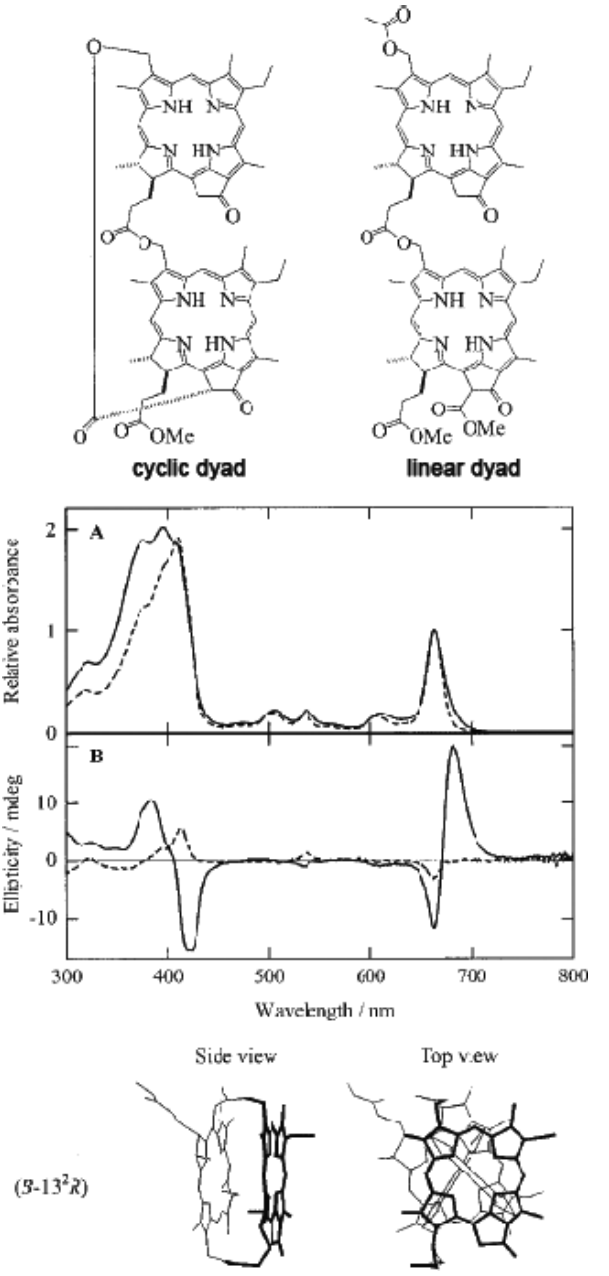

Figure 40. Structures of cyclic (top left) and linear (top right) chlorophyll hetero-dyads and their electronic absorption and CD spectra in CH_2Cl_2. Solid lines are for cyclic dyad. The bottom shows the optimized structure of cyclic dyad, which is consistent with NMR data (redrawn from Ref. 115).

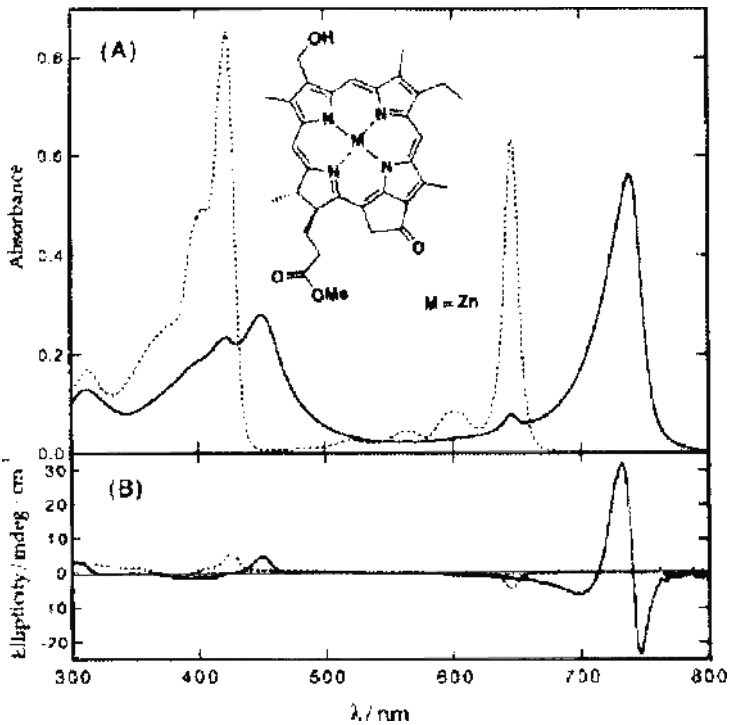

Figure 41. Electronic absorption and CD spectra of a Zn chlorin in THF (solid lines) and THF:hexane (99:1 v/v) (dotted lines) (redrawn from Ref. 83).

Daniell and Bruckner reported the enantiomeric resolution of a ruffled porphyrinoid (Figure 43).[119] As indicated by + and − signs in the structure of this figure, the relative position of the carbon atoms are displaced from the mean plane of the macrocycle. Two enantiomers displayed the Soret and Q bands at 442 and *ca*. 660 nm, and exhibited mirror image CD spectra. The sign at the Soret and Q was opposite for the two enantiomers.

Naruta and coworkers reported four binaphthyl-linked porphyrins and their CD spectra (Figure 44).[120,121] In these cases, S-binaphthyl-linked porphyrins show positive CD in all regions with the R-binaphthyl-linked examples being conversely negative. No explanation was given for these data.

Inoue, Aida and coworkers reported several CD-active porpohyrins[122–127] with one of the simplest examples being shown in Figure 45.[122] In the structure, the ethyl and methyl peripheral substituent groups on the pyrrole rings are oriented in a single-handed manner, so that two structures constitute antipodes depending on whether the RNH group is on this side or the other side of the porphyrin plane. The antipodes showed CD of perfect mirror images in the Soret band region. Pyrrole N-alkylated porphyrins (Figure 46) are conceptually an extension of the

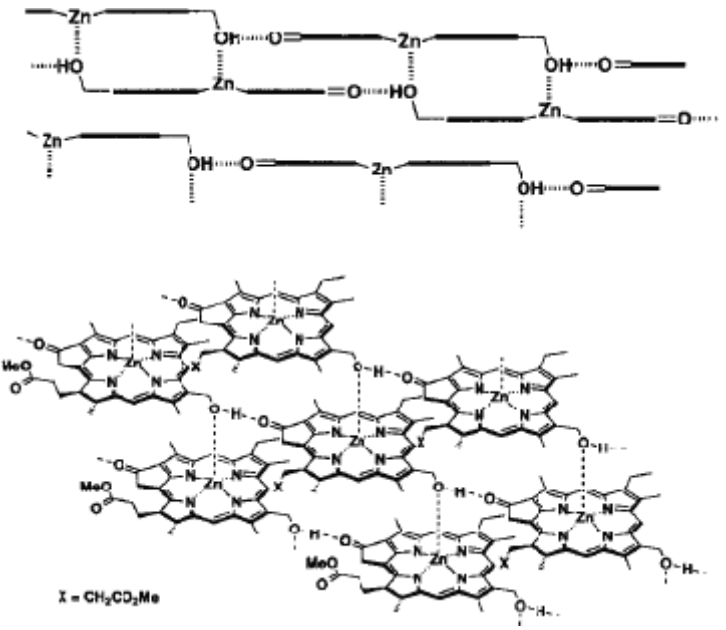

Figure 42. Schematic anti-parallel structures of Zn chlorine aggregates which show spectra drawn in solid lines in Figure 41 (top) and proposed supramolecular (bottom) (redrawn from Ref. 83).

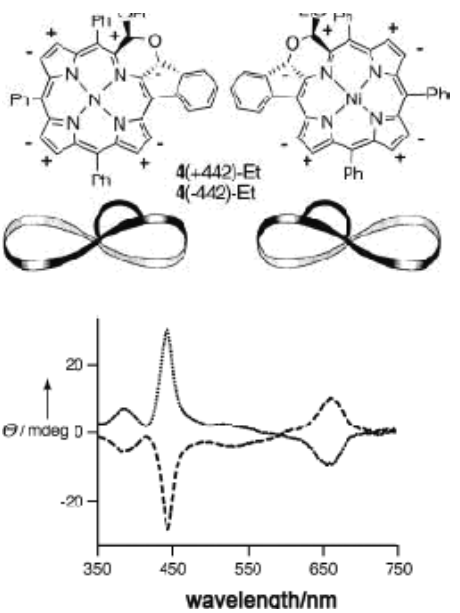

Figure 43. Ruffled porphyrins reported by Daniell and Bruckner, and their CD spectra (redrawn from Ref. 119). The "+" and "–" in the structures indicate the ruffled conformation, that is, the relative position of the carbon atoms with respect to the mean plane of the macrocycle.

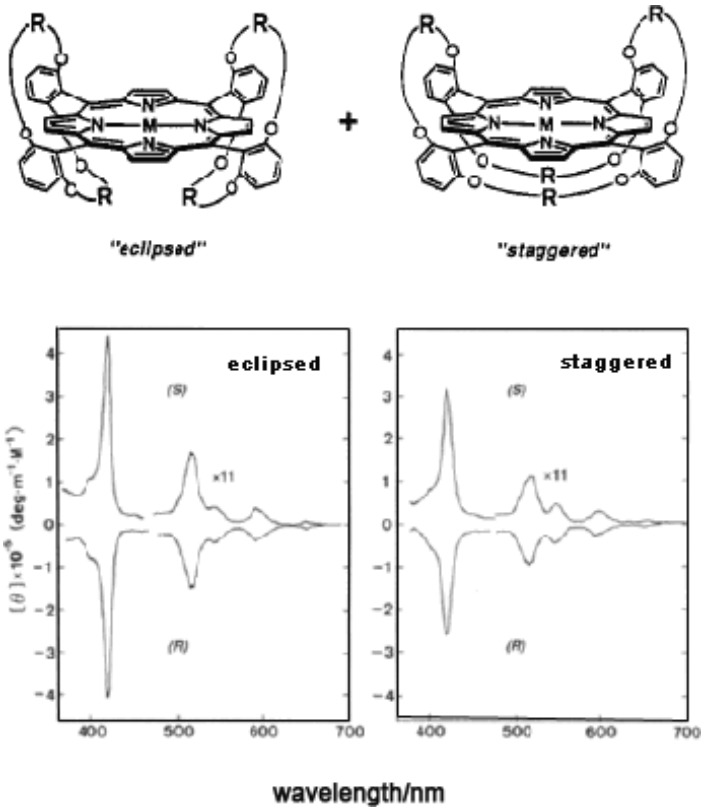

Figure 44. Eclipsed and staggered forms of the four optically active binaphthyl-linked porphyrins reported by Naruta *et al.* (redrawn from Ref. 120). In the structure, the –R– portion represents binaphthyl units.

compounds in Figure 45.[123] Again, methyl and ethyl groups on the pyrrole β-positions are arranged in a single-handed manner, so that these molecules can be enantiomers depending on whether the alkyl group is protruding upwards or downwards from the porphyrin plane. In their case, however, four chiral porphyrins were obtained, since the authors used optically active R and/or S-alkyl groups. No interpretation of the CD spectra was attempted. Strapped porphyrins, shown in Figure 47 are chiral following resolution using optically active HPLC.[124] Although the correspondence between the CD spectra (sign) and enantiomeric structures were not elucidated, the data give insight into the CD generation mechanism. The spectra exhibited in A and B in Figure 47 contain a benzene ring in the strap. However, as C shows, compounds without a benzene ring in the stap also show an intense CD signal at the Soret band, indicating that a benzene ring in the strap portion is not important for strong CD generation. Since the enantiomers in this figure are intrinsically active compounds which do not contain any chiral

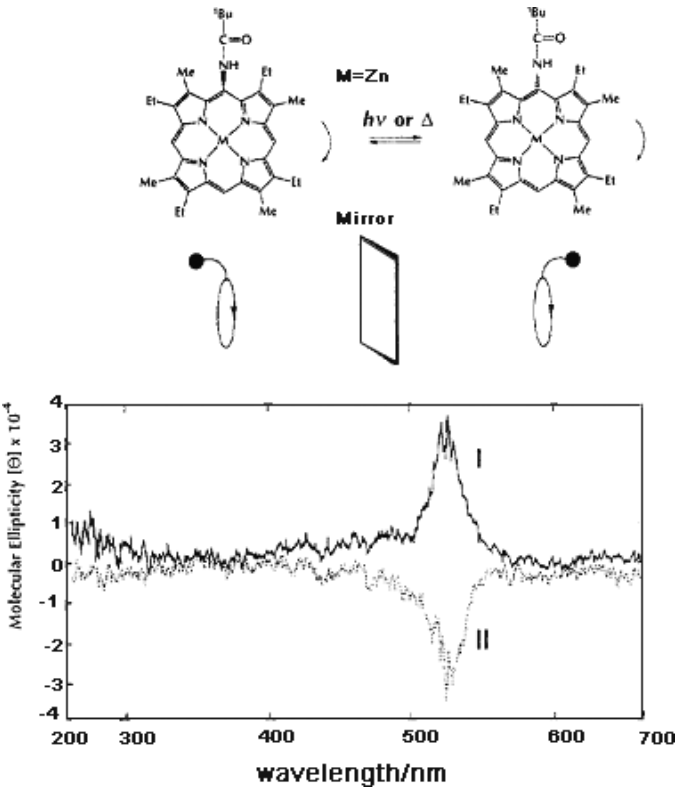

Figure 45. Structures and CD spectra of zinc α-(pivaloylamino)etioporphyrin reported in Ref. 122 (redrawn from Ref. 122). The relationship between the antipodes and CD spectra has not been elucidated.

moiety, the CD can most probably be considered to be generated by interaction of the electronic dipole moment in the amido moiety with that in the porphyrin plane. If optimized structures are obtained, it is now possible to calculate the CD spectra of the compounds in this figure, although this was not possible at the time the paper was published.

The oxophosphorus porphyrins in Figure 48 were also prepared.[125] It was proven beforehand from X-ray data that upon treatment with acid, oxoporphyrins produce the protonated form (cationic hydroxo complex) in which the porphyrin is ruffled and distorted from planarity.[128] The CD spectra of the enantiomers of the ethyl complex in a basic medium (planar oxo form) exhibited mirror-image monosign CD bands in the Soret region with a $[\theta]$ value of approximately 5000 (Figure 48A(a)), while in an acidic medium (ruffled hydroxyl form) the CD intensity was significantly enhanced, to give a $[\theta]$ value of *ca*. 25,000 (Figure 48A (b)). In the case of the phenyl complex, a much clearer pH dependence was observed.

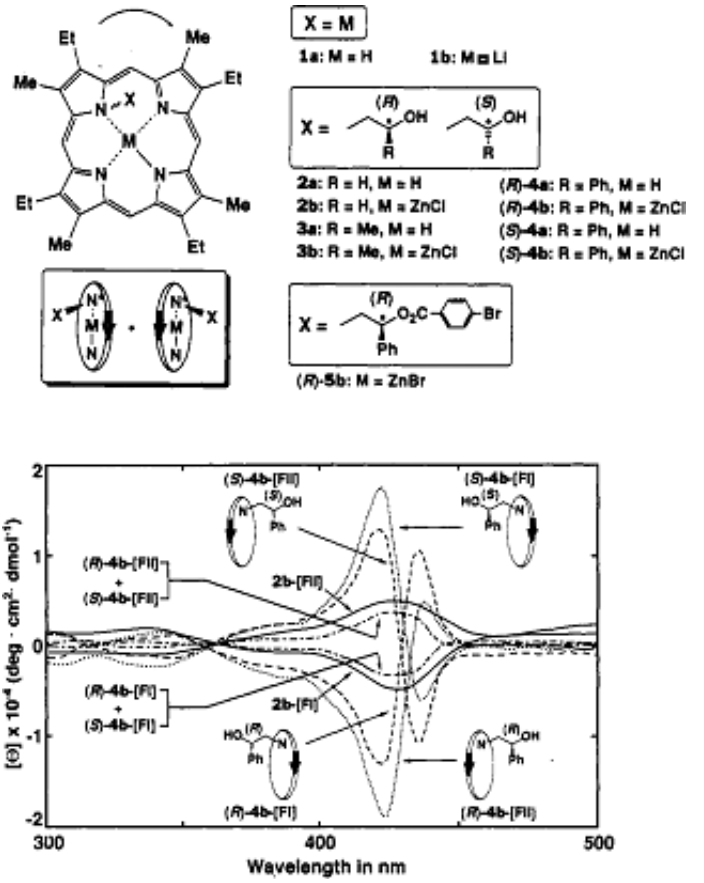

Figure 46. Structures and CD spectra of pyrrole *N*-alkylated porphyrins reported in Ref. 123 (redrawn from Ref. 123).

In basic media (planar oxo form), negative or positive monosignated CD bands were observed, similar to the case of the ethyl complex Figure 48B (a). While in acidic media (ruffled hydroxyl form), the CD showed split Cotton effects (Figure 48B (b)). The authors attributed this difference in the CD profile of the latter compound to an electronic interaction between the porphyrin chromophore and the axial phenyl groups. A D_2-symmetric porphyrin[126] and cobalt porphyrins which have similar structures to those in Figure 46 are also known.[127]

Ogoshi and coworkers reported two types of C_2 symmetric type porphyrin having two chromophores at the opposite positions of a porphyrin moiety (Figure 49).[129,130] In the case of porphyrins containing two naphthyl units, CD spectra were measured in the presence of L or D-amino acids or their esters.[130] In particular, when hydroxyl groups are present in the naphthyl moiety, extraneous amino

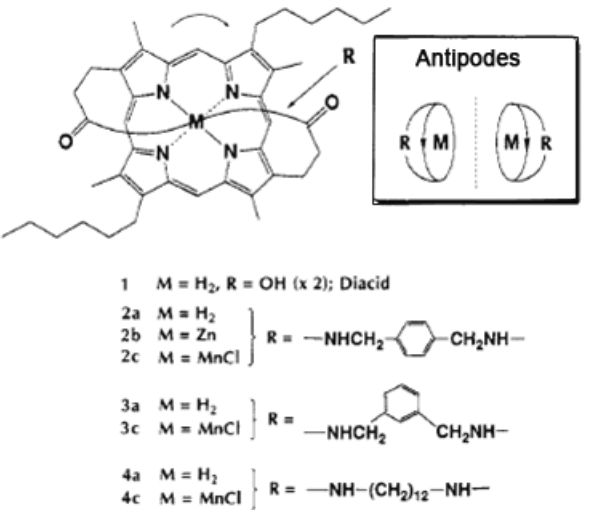

Figure 47. Structures and CD spectra of the antipodes reported in Ref. 124 (redrawn from Ref. 124). The relationship between the antipodes and CD spectra has not been elucidated.

acids fix the mutual special orientation of the naphthyl groups and porphyrin by hydrogen bonding to the OH group and coordinating to the central zinc atom. All of the hydrogen-bonded host-guest complexes exhibited a split Cotton effect; i.e. all complexes with L-aminoacid esters, where the longer wavelength peak of the Soret band was negative and the shorter wavelength peak was positive (Figure 49). However, a single-peak CD was observed if the OH group was changed to OCH_3. For aliphatic amino acid ester-complexes, positive and negative CD envelopes had the same intensity, while for aromatic amino acid esters, the induced CD was not symmetric, and the envelope at longer wavelength was always stronger than that at shorter wavelength. Accordingly, it was concluded that not only hydrogen bonding interactions but also aryl–aryl interactions between the aromatic group of aromatic amino acids and the porphyrin make a contribution to the observed Cotton effects. Since the Soret band consists of two nearly degenerate transitions (Bx and By) in the porphyrin plane, the two being perpendicular to each other, the positive and negative peaks were assigned to the two nearly-degenerate transitions. As possible mechanisms, hydrogen bonding which would fix the orientation of the carbonyl group of the guest amino acid (ester), and consequently the coupling between the magnetic transition dipole moment of the carbonyl group and the electronic transition dipole moment of the porphyrin Soret transitions were considered. A mechanism of coupling between the naphthyl electric transition dipole moment and the two Soret electric transition moments was ruled out, since this mechanism was theoretically found to induce Cotton effects with the same sign in both the Bx and By bands.

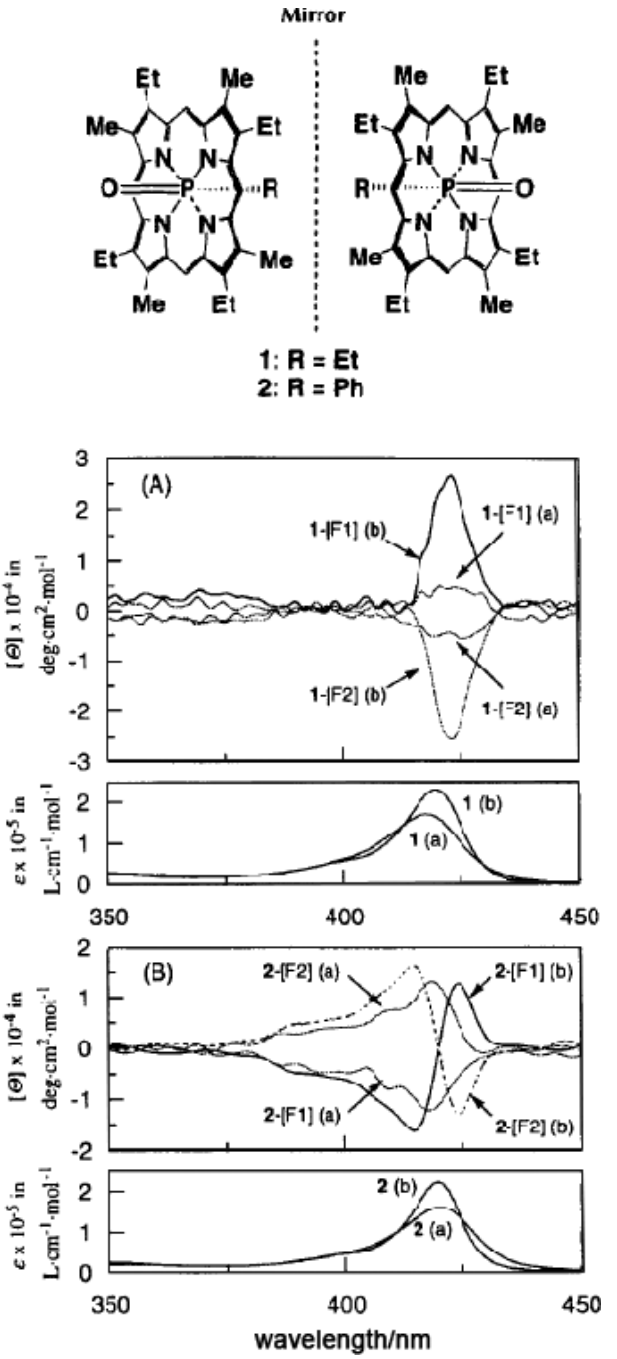

Figure 48. Oxophosphorus porphyrin and their absorption and CD spectra. F1 and F2 means first and second eluted fractions in HPLC experiments, (a) is the planar oxo form obtained under basic conditions and (b) indicates ruffled hydroxy form obtained under acidic conditions (redrawn from Ref. 125).

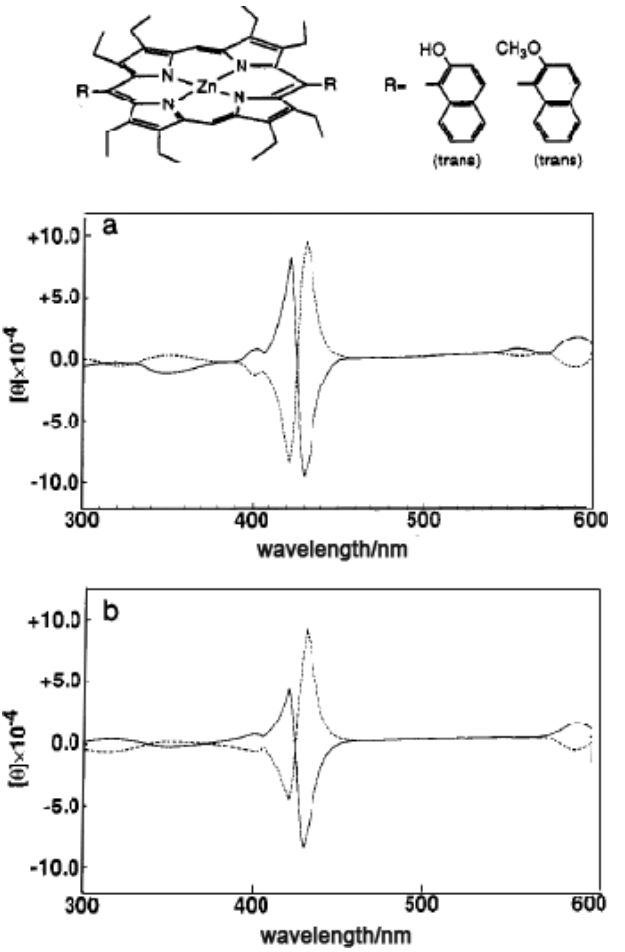

Figure 49. Hydroxy- or methoxy-substituted naphthyl-linked zinc porphyrins and the CD spectra of hydroxynaphthyl-linked porphyrin in the presence of (a) L- (solid line) and D- (broken line) leucine methyl ester, and (b) L-(solid line) and D- (broken line) phenylalanine methyl ester (redrawn from Ref. 130).

VI. Synthetic Porphyrin Dimer and Oligomer Systems

A. Bis-porphyrin Systems Linked to Optically Active Naphthalene Units

Hayashi and coworkers linked two zinc porphyrins to optically active (S)-binaphthyl, and used this as a ditopic coreceptor for a series of diamines. CD spectra were recorded for varying lengths of alkyl group between the two terminal amino groups, (Figure 50).[131] In the absence of diamines, the diporphyrin showed a plus-to-minus CD pattern as viewed from longer wavelength, corresponding to the Soret band, since (S) binaphthyl is a right-handed conformer. When diamines were

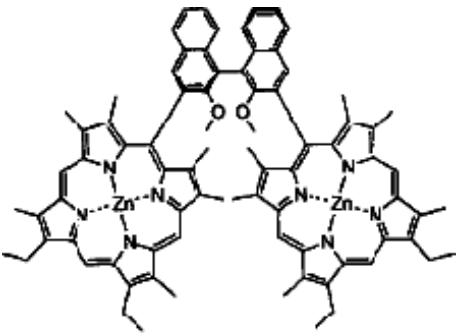

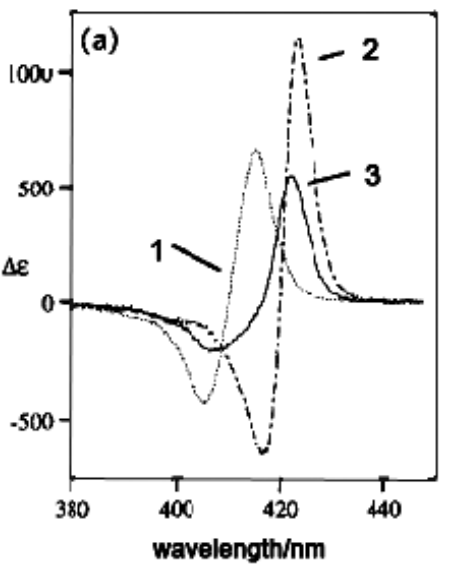

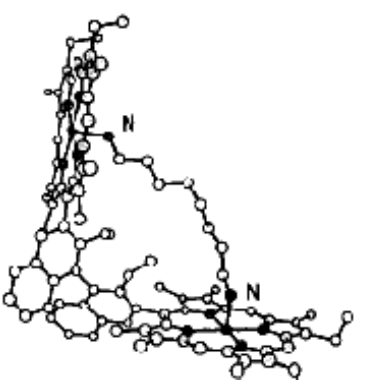

Figure 50. Binaphthayl-linked bis-porphyrin reported by Hayashi *et al*. and its CD spectra in the absence (1) and presence of 1,8-diaminooctane (2) or N-octylamine (3) (modified from Ref. 131).

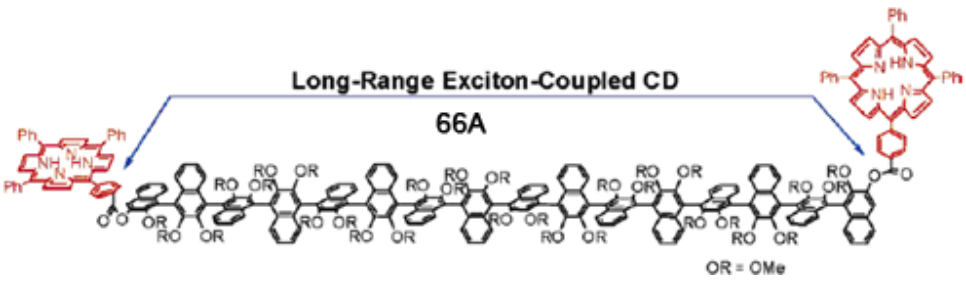

Figure 51. Hexadecanaphthalene that posseses two H_2TPPs (redrawn from Ref. 132).

added to the system, two amino groups coordinate to the zinc ion so that the angle between the two porphyrins changed. When 1,8-diaminooctane was used, the complexation constant was the largest, and the most intense bisignate CD was observed, although it was plus-to-minus in ascending energy. As shown in the proposed structure in Figure 50, the two porphyrins maintain a right-handed helicity in this state.

Tsubaki and coworkers synthesized oligomers of naphthalenes in a right-handed or left-handed manner, and linked tetraphenylporphyrins (H_2TPPs) at the two terminals (Figure 51).[132] By changing the number of naphthalene units, and accordingly the distance between the two porphyrins, they measured long-range exciton-coupled CD. They succeeded in detecting a coupled CD associated with the Soret band of the H_2TPPs separated by *ca.* 66 Å (this is the record to date). However, a rather more intriguing point is the finding of a very clear correlation between chirality and intensity. The authors concluded from the X-ray data of several oligomers and molecular mechanics calculations that the average dihedral angle between the adjacent naphthalene units is *ca.* 89–90 degrees. If this is the case, as shown in Figure 52, when four naphthalene units are linked with only an S-configuration, the two H_2TPPs are orientated in an anticlockwise direction, which leads to a negative exciton-coupled CD spectrum. However, when they are linked through two S- and one R-configuration, the two H_2TPPs are positioned in a clockwise direction, so that a positive split CD is expected. The results are excellent (Figure 53). In this figure, (S)-binaphthalene and (S,R,S)-quaternaphthalane have positively split CD curves, while in the case of (S,S,S)-quaternaphthalene, a negatively coupled CD is exhibited, but the absolute intensity is approximately the same as that of (S,R,S)-quaternaphthalane. With increasing naphthalene units from 4 to 8 and further to 16, the intensity of the observed coupled CD decreased at a ratio of 75:22:6 for the estimated ratio of 4:1:0.25. This is a useful system, since naphthalene units are linked linearly in a straight line and the interdistance of the two porphyrin units can be easily estimated.

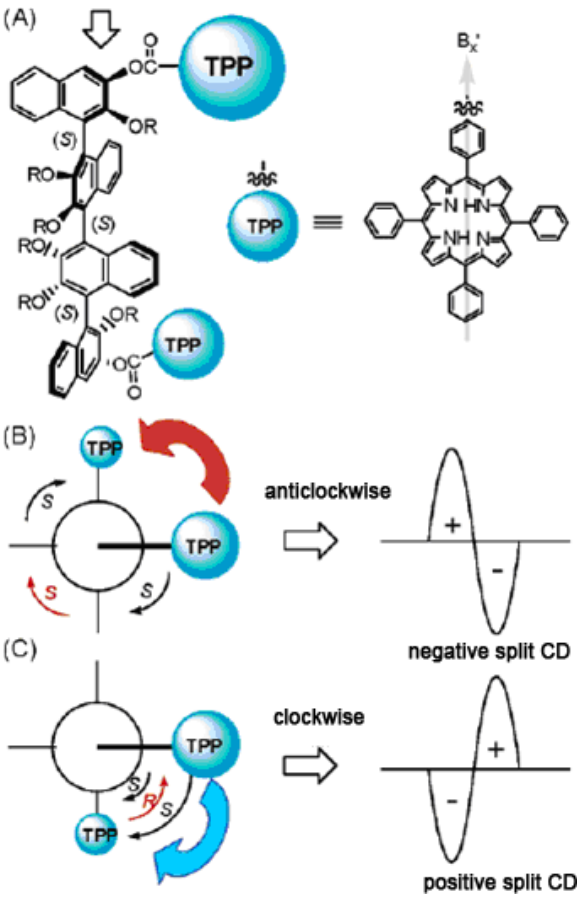

Figure 52. (A) (*S,S,S*)-quaternaphthalene with two H_2TPP units, and presentation of (B) anti-clockwise (*S,S,S*)- and (C) clockwise (*S,R,S*)-quaternaphthalene structures (redrawn from Ref. 132).

B. Dimeric Porphyrin Systems Without Optically Active Substituents

The first optically meso–meso linked porphyrin dimer was reported by Yoshida and Osuka in the year 2000.[133] Soon thereafter, a series of *meso–meso* linked Zn diporphyrins strapped with a dioxymethylene group of various lengths were reported (Figure 54).[134] Shortening the strap length resulted in a gradual decrease of the dihedral angle between the porphyrins and an increasing distortion of the porphyrin ring. The absorption spectrum of relatively unconstrained diporphyrins $\mathbf{S_{10}}$ strapped with a 10-carbon chain exhibits a split Soret band at 414 and 447 nm and a weak Q_{00} and prominent Q_{01} bands, both of which are similar to those of nonstrapped diporphyrin. Shortening the strap length causes systematic changes in the absorption spectra, in which the intensities of the split Soret band decrease, the

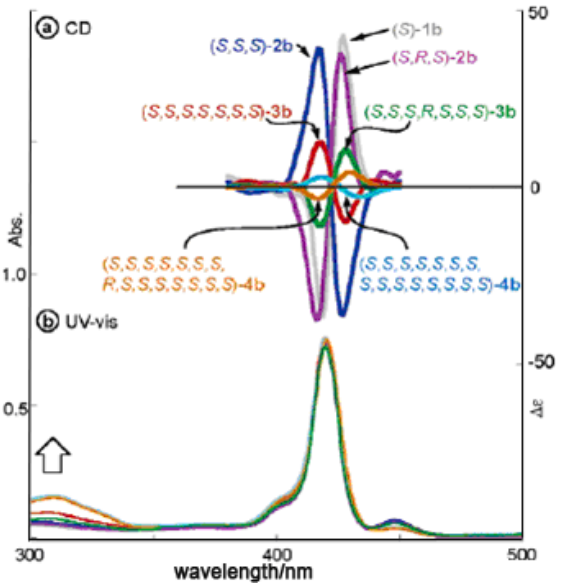

Figure 53. CD and electronic absorption spectra of naphthalene oligomers; (*S*)-2mer, (*S,S,S*)- and (*S,R,S*)-4mers, (*S,S,S,S,S,S,S,S*)- and (*S,S,S,R,S,S,S*)-8mers, and (*S,S,S,S,S,S,S,S,R,S,S,S,S,S,S,S*)- and (*S,S,S,S,S,S,S,S,S,S,S,S,S,S,S,S*)-16mers (redrawn from Ref. 132).

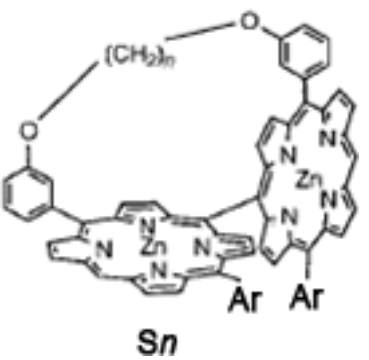

Sn

Figure 54. Strapped porphyrins ***Sn*** (redrawn from Ref. 134).

absorption bands at about 400 nm and longer than *ca*. 460 nm increase in intensity, and a prominent one-band feature of a Q-band becomes a distinct two-band feature with concurrent progressive red-shifts of the lowest Q_{00} band. These strapped porphyrins were separated into the optically active enantiomers through a chiral HPLC column. The two isolated enantiomers displayed opposite Cotton effects, as shown in Figure 55. There was no significant Cotton effect in the Q-band region. The CD spectrum of the fast eluting isomer, S10(A) exhibited Cotton effects,

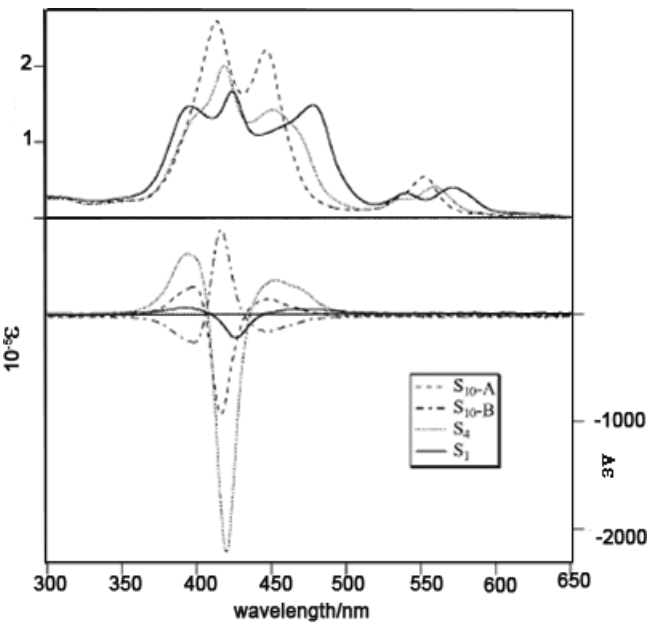

Figure 55. Absorption and CD spectra of several strapped diporphyrins; S_{10}(A), S_{10}(B), S_4(A), and S_2(A) in CH_2Cl_2. A and B means fast and second eluting isomer, respectively (redrawn from Ref. 134).

positive at 446 nm, negative at 416 nm, and positive at 398 nm. These CD spectra were interpreted as a superimposition of two bisignate split Cotton effects with opposite signs. In the case of $\mathbf{S_{10}}$(A), the first Cotton effect at around 430 nm was positive and the second one at around 405 nm was negative, and thus the negative band at 416 nm had the largest intensity. As the strap length was shortened, the first bisignate Cotton effect was red-shifted, while the second one remained at almost the same position. The intensities also changed with the strap length, and the largest intensity was observed for $\mathbf{S_4}$. For oblique diporphyrins, exciton coupling between $\mu_{\perp 1}$ and $\mu_{\perp 2}$ and between $\mu_{//1}$ and $\mu_{//2}$ can explain the three absorption peaks in the absorption spectra, but the CD spectra cannot be explained conceptually. Although not published[135] this kind of CD spectra can be conceptually reproduced if $\mu_{//1}$ and $\mu_{//2}$ are slightly bent.

Bringmann and coworkers reported *meso*-arylated β–β linked diporphyrins and their atropo-enantiomers,[136,137] using Zn, Cu, Ni, and Pd as central metals, or metal-free. Although enantiomers were obtained by repeated resolution using HPLC on a chiral phase, the enantiomeric purity decreased with time, the extent of which varied according to the central metal; after 24 hours, copper and nickel were almost racemic, while zinc was enantiopure. X-ray data revealed that the two nickel porphyrin moieties are largely distorted and have a ruffled conformation,

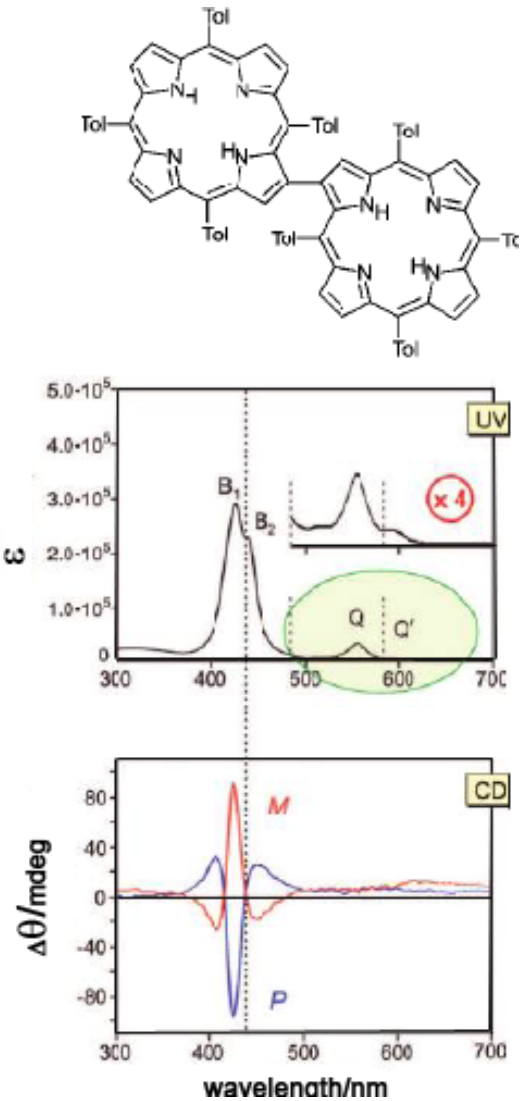

Figure 56. A β–β linked Zn porphyrin dimer and the electronic and CD spectra of their enantiomers (redrawsn from Ref. 137).

while the two zinc porphyrin moieties have a near-planar structure. The CD data were, accordingly, collected for the dizinc porphyrins (Figure 56). Corresponding to the split Soret band, the *P*-enantiomer showed a plus-minus-plus pattern in ascending energy, which is very close or almost identical to the CD pattern observed for the meso–meso linked diporphyrins (Figure 55).[134] The authors did not attempt to explain the spectra either by concept or exciton coupling theory. DFT calculations using a B3LYp/3-21G basis set, however, reproduced a plus-minus-plus CD

pattern for the Soret region of *P*-configurated Zn diporphyrin consistent with experiment.[136]

Matano and coworkers reported the synthesis of *meso*-phenylsulfinyl zinc porphyrins and their self-organization to S-oxo-tethered cofacial dimers.[138] When a hexane:2-propanol (100:1) solution of the above zinc porphyrins were applied to a chiral HPLC, two fractions were obtained in high optical purity. Under conditions where the homodimers and monomer were considered to be present in a 4:1 ratio, the authors measured the CD spectra of these isolated species. The first fraction showed a plus-to-minus pattern in the Soret band region in ascending energy, so that the absolute configuration of this fraction was assigned as *S*. From NMR data, the dimer was considered to be produced through the coordination of an oxygen of S=O to the Zn atoms (Figure 57).

From several *meso–meso*, *meso–β,* and *β–β* linked porphyrin dimers, Osuka and coworkers succeeded in isolating optically active meso–meso and *β–β* doubly linked dimers (Figure 58) whose enantiomers show a mirror-image relationship in their CD spectra.[139] According to the X-ray structure, the two porphyrin rings adopt an almost coplanar, helically twisted conformation, perhaps due to steric repulsion of the hydrogen atoms at the nearest pyrrole *β* protons. Interpretation of the CD spectra was attempted using the exciton chirality method. However, this was an essentially unsuitable system since the constituting porphyrin chromophores were not independent. Indeed, theoretical studies using MCD and TD-DFT calculations later proved that the assignment in Ref. 139 was incorrect; the right-handed dimer showed a mainly positive CD envelope in the Q band region (Figure 59).[140]

Werner, Vogel and coworkers reported the enantiometric separation and determination of the absolute configuration of "figure eight" cyclooctapyrroles (Figure 60).[141] Although this species is not a porphyrin, it is considered to be a porphyrinoid system since two metals can be incorporated utilizing four pyrrole rings each, i.e. the loop-shaped conformation of the macrocycles exhibits two structurally identical, helical N4 cavities. The "figure eight" structure in the solid state was confirmed by X-ray crystallography, and that in the solution by NMR analysis.

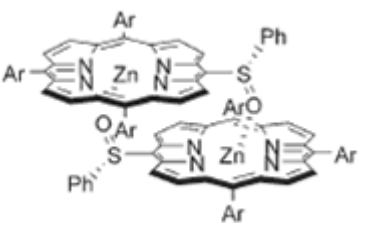

Figure 57. A cofacial dimer of *meso*-phenylsulfinyl zinc porphyrin (redrawn from Ref. 138).

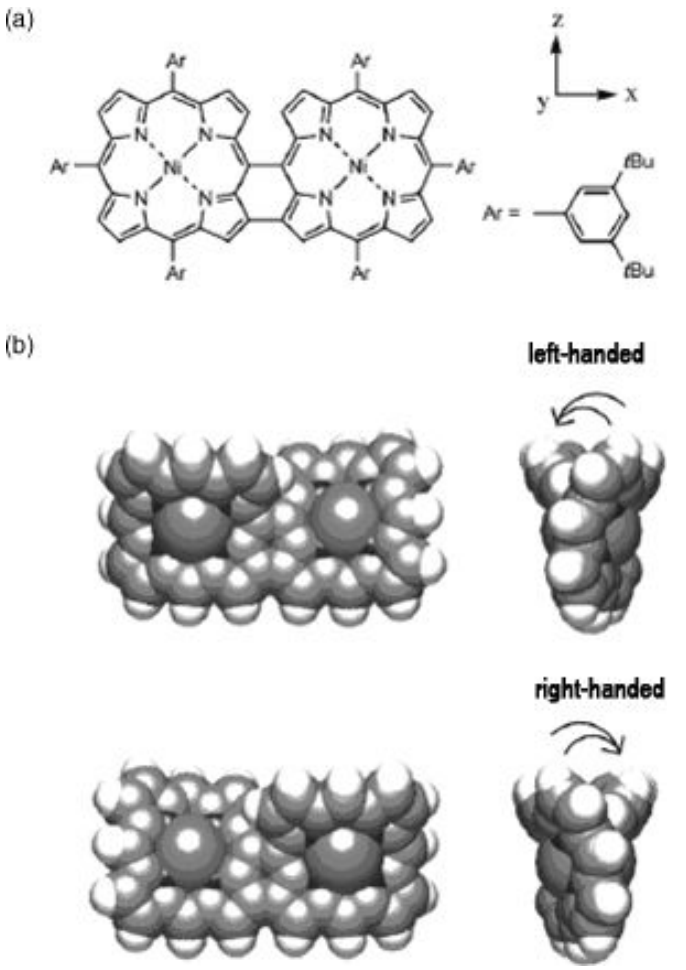

Figure 58. A *meso–meso β–β* doubly linked porphyrin dimer and its left- and right-handed structure (redrawn from Ref. 140).

The four dipyrrin units are almost planar, so that the helical conformation of the two tetrapyrrole substructures is mainly attributable to the torsions of the bipyrrole C–C single bonds (N–C–C′–N′ torsion angle: $\Phi = 30°$). The enantiometric separation was carried out on an HPLC column, and the enantiomers in this figure were optically stable in hexane even at 60 °C. As shown in Figure 60, the (*M,M*) enantiomer (solid line) and (*P,P*) enantiomer (broken line) exhibit exciton-coupled type CD spectra.

Ethane-bridged bis(zinc octaethylporphyrin) complexed with (*R,R*)-1,2-diaminocyclohexane results in a stable 1:1 tweezer complex exclusively as a consequence of its remarkably large association constant ($> 10^7 M^{-1}$).[142] The structure

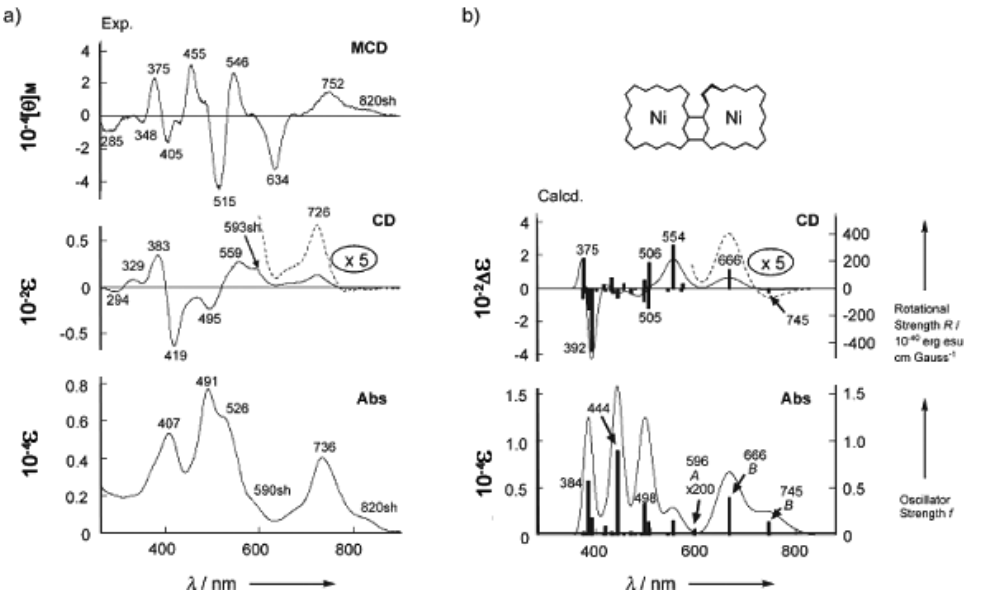

Figure 59. (a) MCD, CD and absorption spectra of the porphyrin dimer in Fig. 58, and (b) calculated CD and absorption spectra obtained as a sum of a Gaussian-type function with a half-band width of 1300 cm^{-1} (redrawn from Ref. 140).

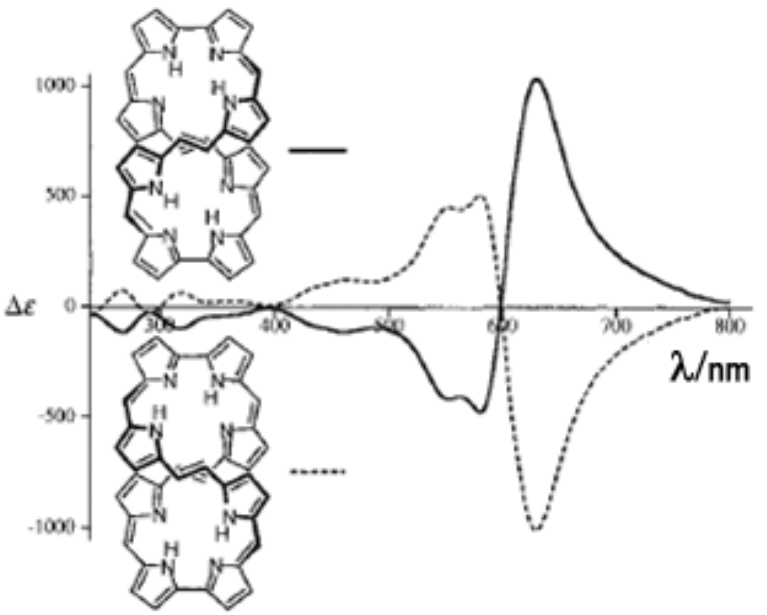

Figure 60. Structures of "figure eight" octapyrrole (*M,M*)- (top) and (*P,P*)- (bottom) enantiomers and their CD spectra (solid and broken lines, respectively) (redrawn from Ref. 141).

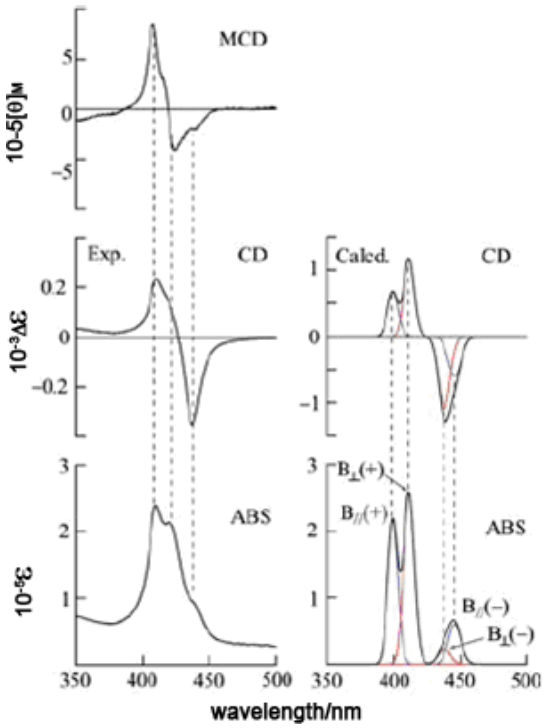

Figure 61. Experimental MCD, CD, and absorption spectra as well as the calculated CD and absorption spectra of the tweezer consisting of ethane-bridged bis(zinc octaethylporphyrin) and (R,R)-1,2-diaminocyclohexane. Each calculated exciton band was described by a single Gaussian curve. The notations plus and minus represent the in-phase and out-of-phase transitions, respectively (redrawn from Ref. 142).

of this chiral tweezer complex was analyzed by X-ray crystallography to have a noncrystallographic pseudo-two fold axis through the centers of the ethano-bridge, and furthermore its electronic and conformational structures in solution were examined by analyzing the CD, MCD, and electronic absorption spectra (Figure 61). In this figure, three well-resolved absorption bands are seen at 410, 419, and 436 nm. The positions of the MCD peaks coincide very closely with these transitions, indicating their nondegenerate character. Importantly, electronic transitions of different polarization exhibit MCD signals of opposite sign, so that it was found accordingly that the two transitions (at 408 and 419 nm) with the same positive CD sign are indeed of different polarization: the higher energy MCD signal (at 408 nm) is positive, while the lower energy MCD signal (at 424 nm) is negative.

To rationalize the experimentally observed spectral data, and taking into account the assignment of the transition polarization, theoretical absorption and

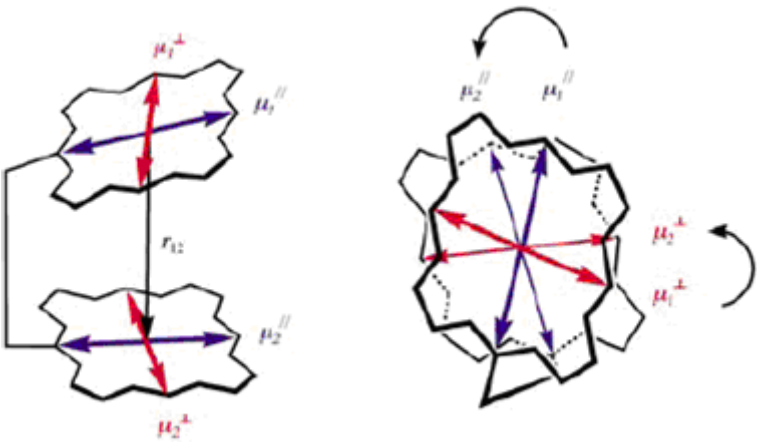

Figure 62. Definition of the direction of the transition dipole moments used in the theoretical analysis. r_{12} is the distance between the centers of gravity of the porphyrin units. The subscripts 1 and 2 are used to distinguish the two chromophores (redrawn from Ref. 142).

CD spectra were calculated using the geometrical parameters obtained from the corresponding crystal structure and the spectral parameters of the corresponding porphyrin monomer on the basis of the Kuhn–Kirkwood coupled-oscillator mechanism.[32,33,143] This tweezer system consists of two identical porphyrin moieties, each having two different transition moments $B_{//}$ and $B_{\perp}$, which have parallel and perpendicular orientations to the ethane bridge, respectively (Figure 62). This arrangement results in two major types of degenerate exciton interaction ($B_{//} - B_{//}$ and $B_{\perp} - B_{\perp}$ couplings), and thus leads to four exciton states. The relative orientation between these two pairs of electronic transition is anticlockwise, which according to the exciton chirarity method[7] predicts the negative chirality that was observed experimentally. The resulting calculated absorption spectrum has three well-resolved bands that are also similar to the experimental results (Figure 61). The face-to-face conformation and short distance between the centers of the interacting electric dipoles ($r_{12} = 6.23$ Å) results in the higher energy $B_{//}(+)$ and $B_{\perp}(+)$ and lower energy $B_{//}(-)$ and $B_{\perp}(-)$ exciton states being well separated. These pairs of states become optically allowed and partially forbidden transitions, respectively, as a consequence of strong exciton interactions that result in the observed absorption profile. Furthermore, the MCD $B_{//}(+)$ and $B_{\perp}(+)$ bands should theoretically be of opposite sign because of their orthogonal polarization, which is in full agreement with the experimental results. A minus-to-plus CD pattern was calculated for the both $B_{//} - B_{//}$ and $B_{\perp} - B_{\perp}$ couplings, and results in one intense negative CD signal at lower energy and two partly resolved, positive CD signals at higher energy. This CD pattern was in good agreement with that observed experimentally.

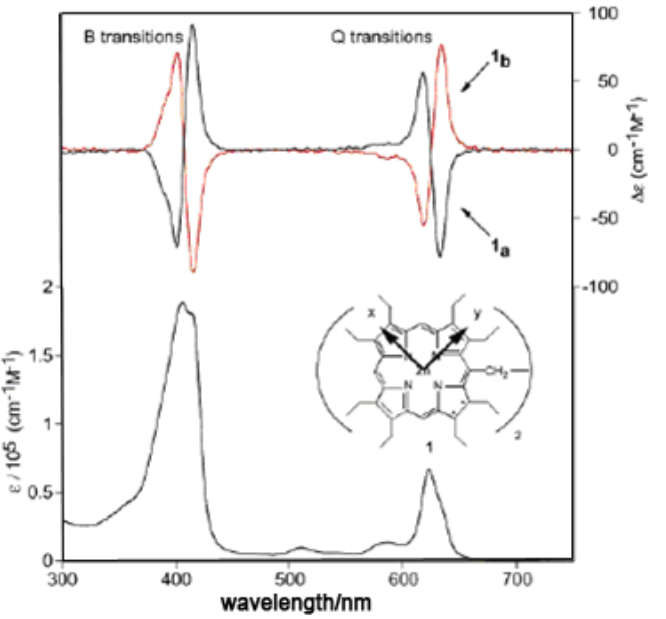

Figure 63. Absorption and CD spectra of two enantiomers ($\mathbf{1}_a$ and $\mathbf{1}_b$) of ethane-bridged bis(zinc octaethylchlorin). $\mathbf{1}_a$ and $\mathbf{1}_b$ are the first and second eluting enantiomers in the HPLC column (redrawn from Ref. 144).

Furthermore, the electronic absorption and CD spectra were nicely reproduced by TD-DFT calculations at the B3LYP/6-31G(d) level.

Ethane-bridged bis(zinc octaethylchlorin) was resolved to yield two enantiomers which exhibit dispersion CD signals in the regions of chlorin B and Q transitions (Figure 63).[146] UV-visible absorption profiles of 1a (first eluting fraction in HPLC column) and 1b (second fraction) are not distinguishable from each other, showing considerable broadening and splitting of the corresponding B and Q bands due to strong excitonic interaction. In the case of the CD spectra, very clear dispersion curves were observed, not only in the B band region but also in the Q band. The positions of the CD peaks and troughs in the B region coincide closely with the maxima of the split B band in the absorption spectrum. The anisotropy factor in the Q band region is more than three times that in the B band region. Furthermore, and importantly, the B and Q signals have opposite CD signs, which is a clear indication of distinct special orientation of the relevant coupling transitions, apparently due to the different polarization along the chlorin x- and y-axes (see Figure 63).

For assignment of the absolute configurations of the two fractions 1a and 1b, the coupling direction of the chlorin's lowest energy Qy electronic transitions is of the utmost importance because of their well-distinguished absorption characteristics.

In particular, the negative sign of the Qy couplet of 1a indicates an anticlockwise orientation of the corresponding transitions, while in the case of 1b, the situation is exactly the opposite. According to X-ray data possessing C_2 symmetry, these bis-chlorins are V-shaped, with the reduced pyrrole rings of two chlorin moieties located at the closest special position to each other. In this geometry, two Qy transitions of the (S,S/S,S)-enantiomer form a clockwise turn that, in accordance with the exciton chirality method, corresponds to positive chirality as determined for 1b. For the (R,R/R,R)-enantiomer the direction of coupling and thus the corresponding chirality sign are opposite, as seen for 1a.

To theoretically confirm this assignment, the CD spectrum of the (R,R/R,R)-enantiomer was calculated using the following approach. Firstly, the spacial geometry of this enantiomer was obtained at the semi-empirical PM3 level using the corresponding crystallographic data as a starting point (interchromophoric distance is 8.16 Å). Under such conditions, a Coulombic rather than electron exchange interaction model is more appropriate to apply for the two chlorin chromophores. In the second step, spectral parameters (exciton energies and transition moments) of the chlorin monomer were obtained from CI calculations at the ZIBDO/S level of zinc 5-methyloctaethylchlorin. The derived absorption spectrum of the monomer consists mainly of four well-distinguished (Qy, Qx, Bx, and By) transitions (Figure 64b), and is typical of chlorin-type chromophores.[73–88] Finally, on the basis of the geometrical and spectral parameters obtained by the point-dipole approximation and the Kuhn-Kirkwood coupled oscillator analysis,[32,33,143] the theoretical electronic absorption and CD spectra of the (R,R/R,R)-enantiomer were calculated (Figure 64a). The calculated spectral features are in good agreement with the experimental spectra of 1a. It is clearly seen that the intensity of the out-of-phase Qy(−) transition is smaller than that of the in-phase Qy(+) transition due to the partially forbidden nature as a result of the V-shaped orientation of these dipoles. A negligibly small CD signal arising from the Qx–Qx coupling is also predicted correctly, since its intensity is proportional to the square of the magnitude of the Qx transition moment. Furthermore, the lower energies of the Qy and Bx transitions, in comparison to the corresponding Qx and By transitions, allow one to attribute the origin of their opposite chirality signs to the different direction of the coupled transitions: i.e., clockwise and anticlockwise for the x and y polarizations, respectively. Thus, this theoretical model nicely reproduces the relative energy levels and intensities of the coupling transitions, particularly the three degenerate Qy–Qy, Qx–Qx, and Bx–Bx couplings. Although there was some overestimation of the CD intensities arising from the By–By coupling, the actual CD signals of the CD By band are expected to be less pronounced due to the smaller excitonic splitting than those of the Bx bands. More importantly, this analysis predicted the negative chirality of the most red-shifted and energetically

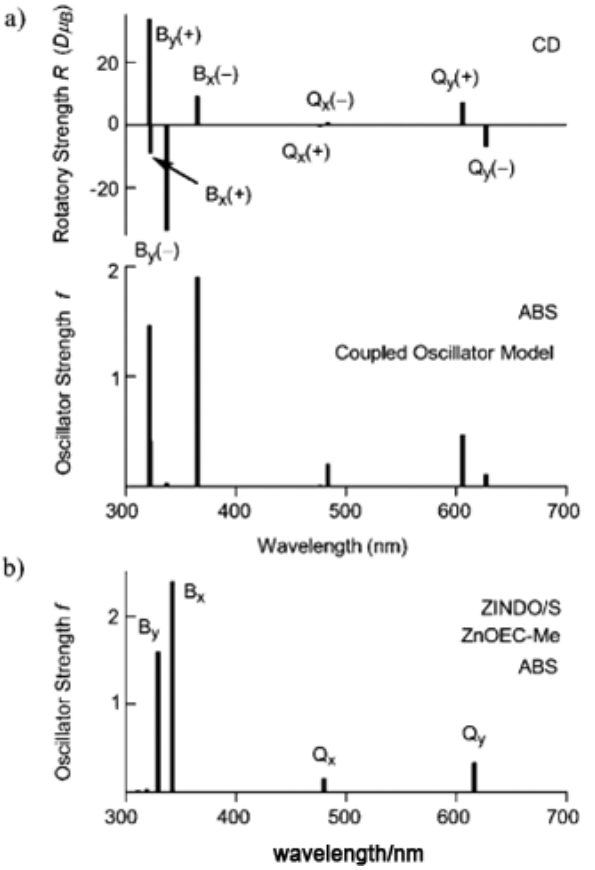

Figure 64. (a) Calculated absorption and CD stick spectra of (*R,R/R,R*)-bis-chlorin drawn in Figure 63 based on the optimized structure. The notations (+) and (–) represent the in-phase and out-of-phase transitions, respectively. (b) Computed linear absorption spectrum of zinc 5-methyloctaethylchlorin (redrawn from Ref. 144).

isolated Qy transitions of 1a, thus unambiguously supporting the assigned absolute configuration.

C. Oligomeric Porphyrin Systems

CD spectra of several oligomeric porphyrin systems have been reported. However, since the systems become complex, virtually no anaysis has been carried out. For example, Osuka and coworkers synthesized *meso*-cinchomeronimide-appended *meso–meso*–linked metal (H_2 and Zn) porphyrin dimers (Figure 65) which can exist as mixtures of six atropisomers.[145] These atoropisomers can be separated since the free rotation of the cinchomeronimide group is considerably restricted

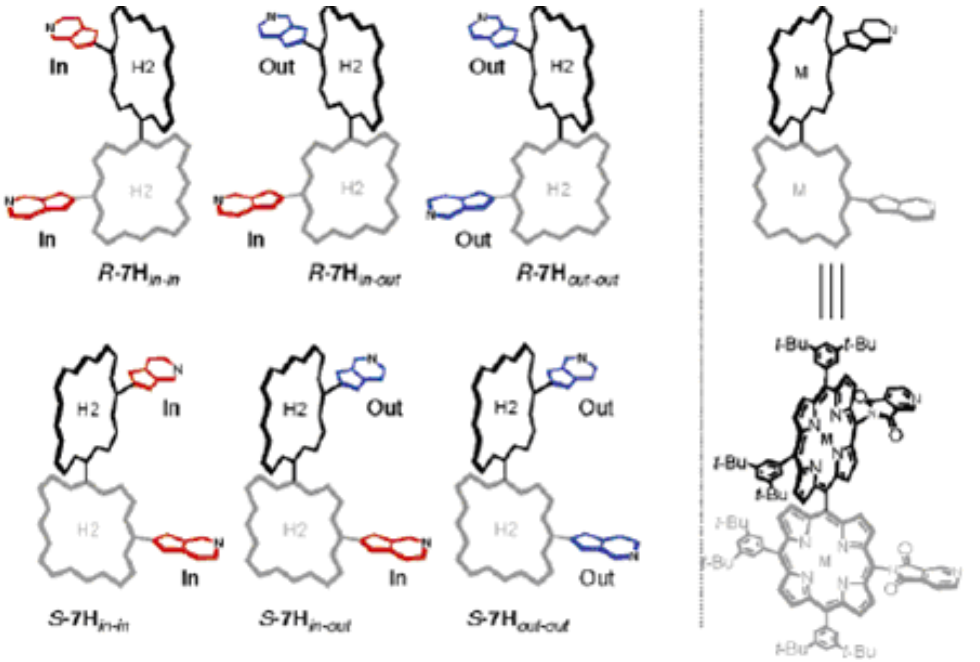

Figure 65. *meso*-Cinchomeronimide appended *meso–meso* linked metal (H_2, Zn) diporphyrin and its six kinds of atropisomers. In the abbreviations, *S* and *R* indicate chirarity, "in" and "out" means whether the nitrogen atoms of cinchomeron moiety is oriented inward and outward, respectively, of the porphyrin plane (redrawn from Ref. 145).

due to the steric hindrance of the two imide-carbonyl groups. Depending on whether the nitrogen atoms of the cinchomeronimide are facing outwards or inwards from the porphyrin plane, these atropisomers are expressed by adding the subscript in–in, in–out, out–out, in addition to handedness (S and R). When the zinc complexes of the separated isomers were dissolved in solution, they exhibited high-fidelity self-sorting assembly, to form discrete cyclic trimers, tetramers, and pentamers with large association constants from $7_{in–in}$, $7_{in–out}$, and $7_{out–out}$, respectively (compound **7** in the paper) (Figure 66). Although the absorption spectra of $R7_{in–in}$, $R7_{in–out}$, and $R7_{out–out}$ (*meso–meso* linked diporphyrin) are practically identical, with two strong Soret peaks at 427 and 465 nm and a Q_{01} band at 574 nm, their self-assembled oligomers showed the CD spectra shown in Figure 67. Although these CD spectra appear to be rationalized by exciton coupling theory, no analysis has been attempted.

Osuka and coworkers reported fairly similar box-type porphyrin enantiomers and their absorption and CD spectra.[146] Although the CD spectra were perfect mirror images of each other (Figure 68), again no explanation was given. Aida and

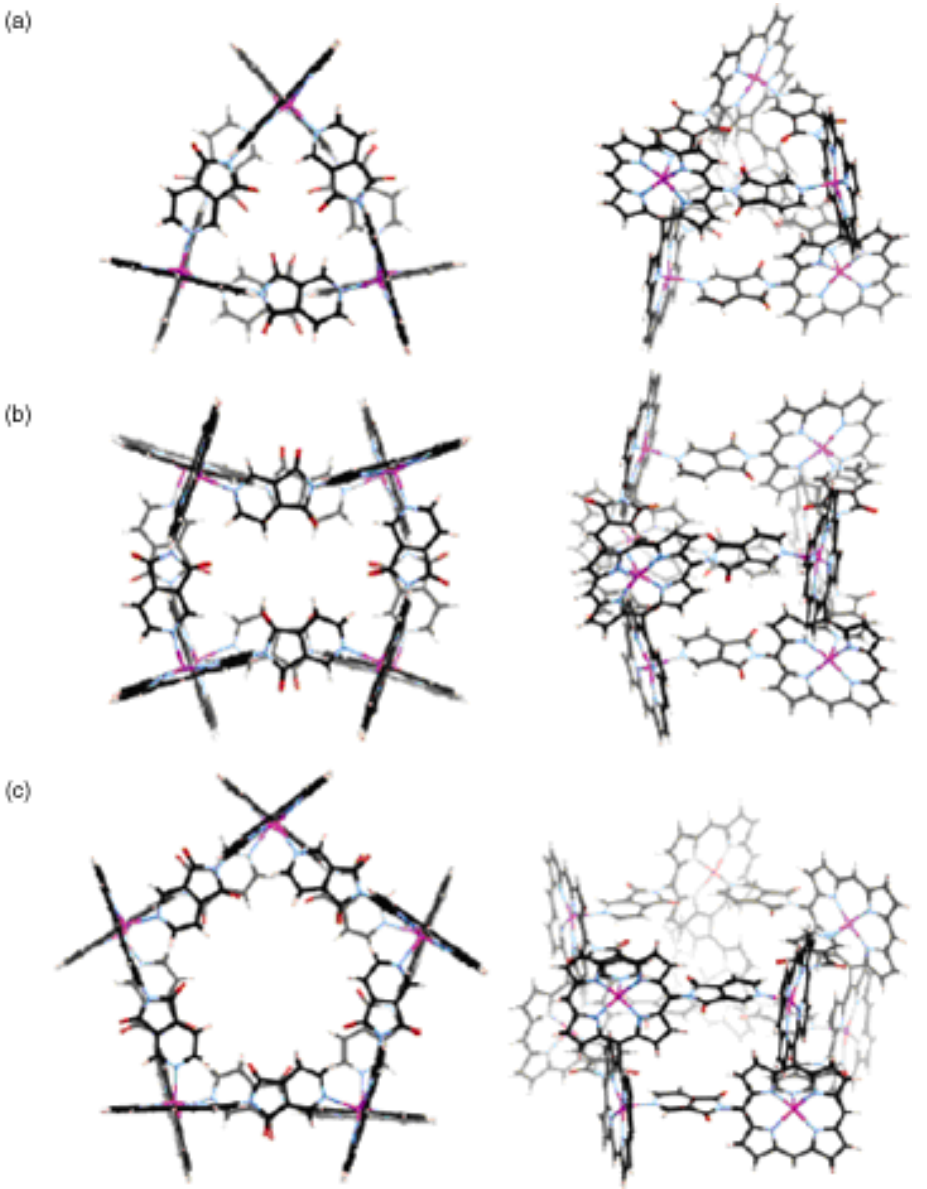

Figure 66. Structures of DFT-calculated (a) (R-$7_{in–in}$)$_3$, (b) (R-$7_{in–out}$)$_4$, and (c) (R-$7_{out–out}$)$_5$. The structure of (c) is very close to that confirmed by X-ray (redrawn from Ref. 145).

coworkers reported box-type porphyrin assemblies having CD spectra very close to those in Figure 68.[147]

Stang and coworkers reported a cyclic tetramer of a 5,15-diphenyl-10,20-dipyridyl metal-free porphyrin connected by four optically active R or S-binaphthyl

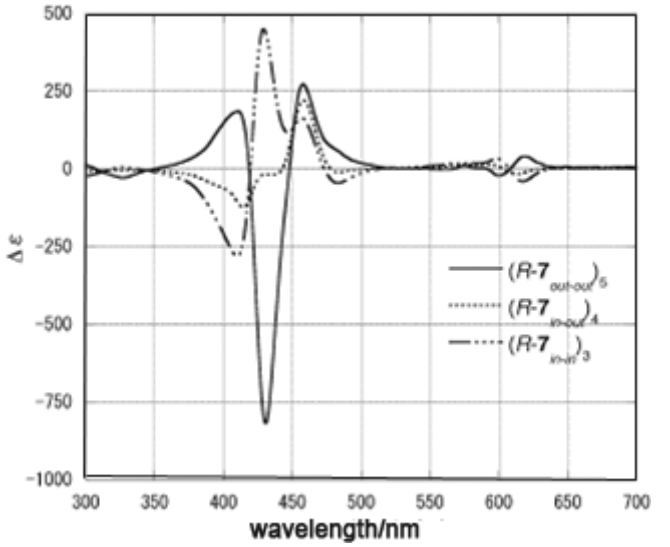

Figure 67. CD spectra of R-7 in $CHCl_3$. Broken dotted, dotted, and solid lines represent the spectra of cyclic trimer, tetramer, and pentamer, respectively in Figure 66 (redrawn from Ref. 145).

(BINAP) units (Figure 69 top) and their electronic absorption and CD spectra (Figure 69 bottom).[148] Although the absorption spectrum is typical of monomeric porphyrin without aggregation, very sharp bisignate CD curves were observed in the Soret band region. The apparent Davydov splitting is 10 nm. The authors suggested three types of coupling interaction: (a) four "adjacent" porphyrin couplings (pairs of porphyrins attached to the same transition metal corner), (b) two "opposing" porphyrin couplings (porphyrins on opposite sides of the macrocycle), and (c) a combination of (a) and (b). Careful examination of the structure revealed that both the "adjacent" and "opposing" pairs of porphyrin chromophores are in the same chiral environment of the BINAP ligands. This was in accord with the signs of the first and the second Cotton effects observed in the CD spectrum for the Soret band of the macrocycle, as well as with the large magnitude of the splitting due to mutual cooperativity. Interestingly, when zinc was inserted into the macrocycle, a bisignate CD was not recorded, but a single peak (when R(+)-BINAP was used) was observed corresponding to the Soret peak. The authors suggested that this is due to the high symmetry (D_{4h}) of the zinc complex. In the case of the metal-free complex, the Bx and By (Soret) transition is separated by about 200–250 cm^{-1} and the direction of transition moment is mutually normal.[149] Thus, when R(+)-BINAP was used as a linkage, the coupling interaction among Bxs may give a negative CD and that among Bys a positive CD. Then, as a result, a

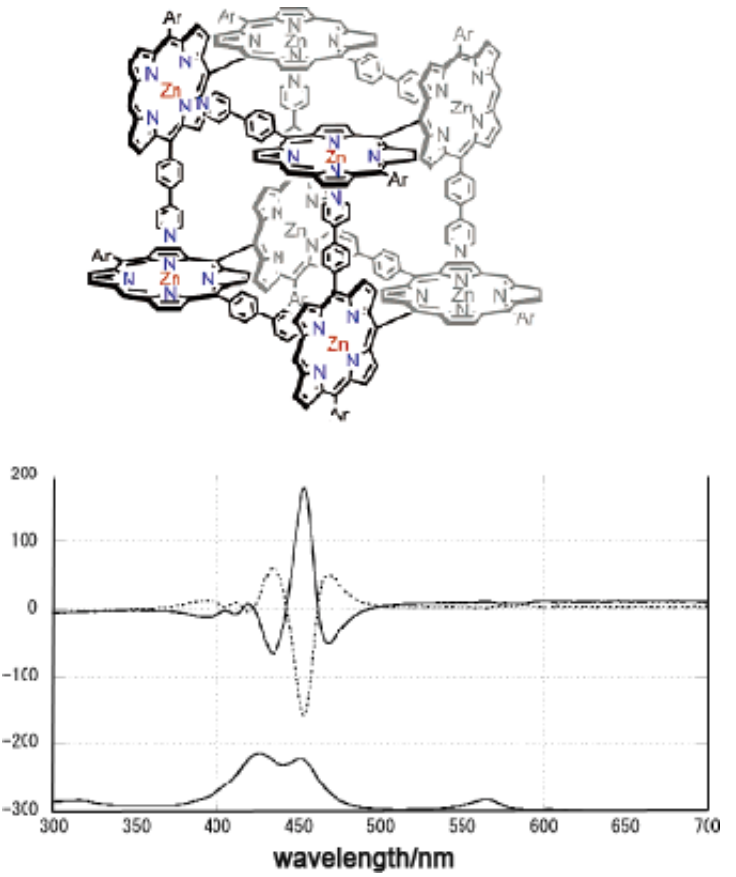

Figure 68. (top) (R)-Isomer structure of tetrameric box type assembly of *meso*-pyridine appended *meso–meso*-linked Zn porphyrin dimer. (bottom) The absorption and CD spectra of the above box type assembly of the Zn porphyrins. CD spectra-isomer relationship is not elucidated, although mirror-like curvatures are recorded (redrawn from Ref. 146).

bisignate CD curve is observed since the energies of Bx and By are very close. Whether this is correct or not has to be judged carefully by considering the optimized structures.

Kimura and coworkers reported (R)- or (S)-BINAP-linked diporphyrins and their CD spectra (Figure 70).[150] Similarly to the abovementioned Stang and coworker's case, metal-free derivatives display bisgnated CD signals in the Soret region. The R-enantiomer exhibited a positive CD sign at 427 nm corresponding to the Soret absorption peak and a negative CD sign at shorter wavelength. When iron was inserted, the bisignate CD signal almost disappeared, and the R-enantiomer showed positive CD in the Soret region, strongly suggesting that the Soret CD is actually induced CD produced by a coupling interaction between the BINAP

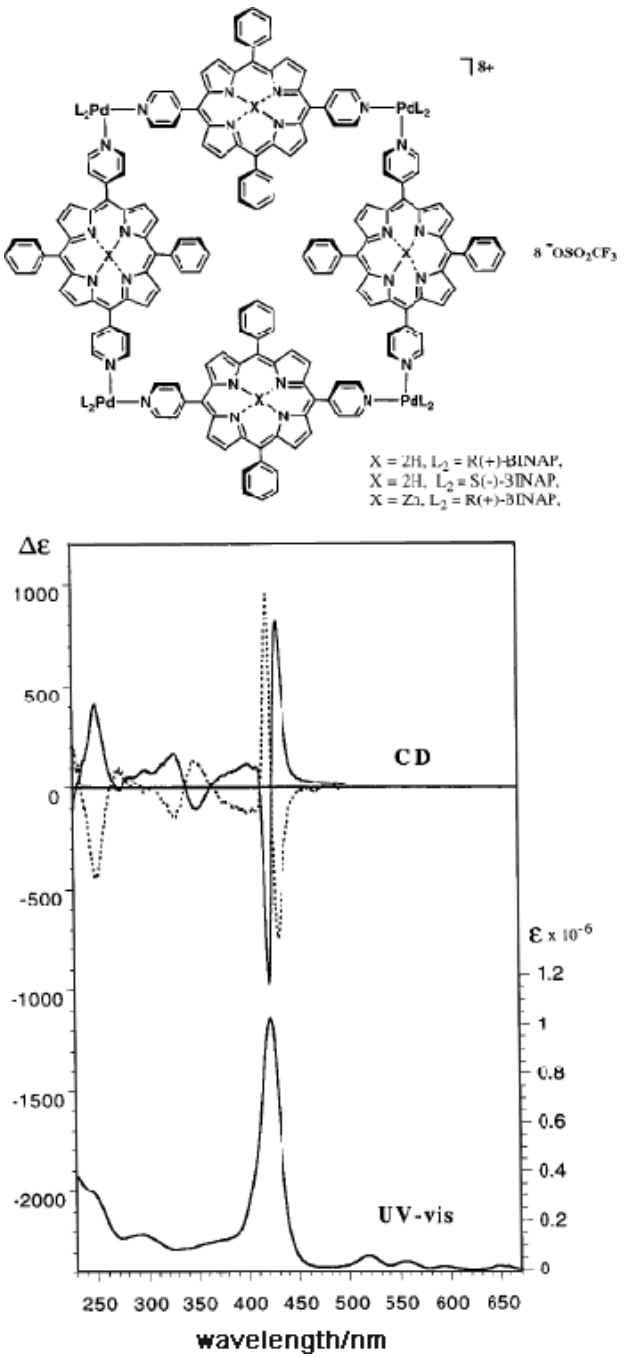

Figure 69. (top) A cyclic tetramer of 5,10-diphenyl-10,20-dipyridyl porphyrin connected by four Pd^{2+} ions. L2 means R(+)- or S(-)-BINAP. X = H_2 or Zn. (bottom) CD and UV-vis spectra of the above tetramer, X = H_2: (solid line) L2 = R(+)-BINAP, (dotted line) L2 = S(–)-BINAP (redrawn from Ref. 148).

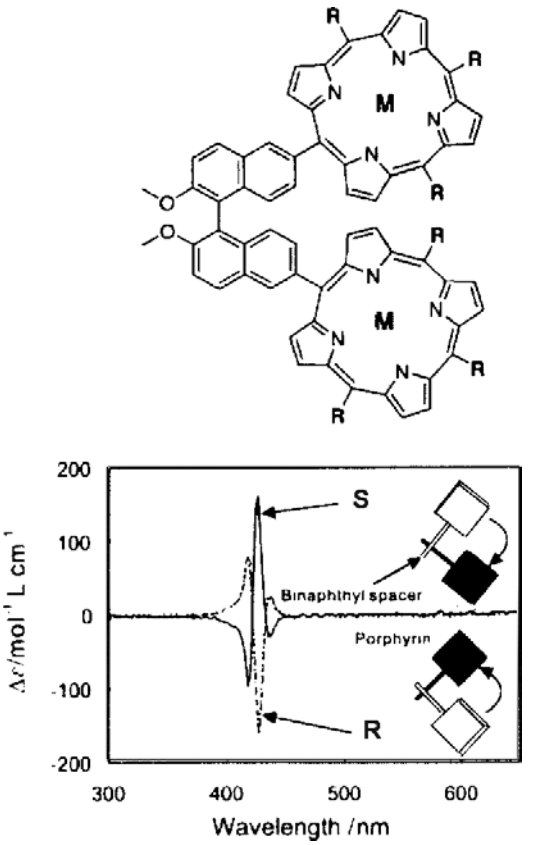

Figure 70. The structure of BINAP-linlked porphyrin dimer by Kimura *et al.* (M = H_2), and their CD spectra. The rotation direction in the inset in the original paper was wrong (here it was fixed) (redrawn from Ref. 150).

chromophore and the porphyrin chromophore.[151] Fe(III) porphyrins generally produce μ-oxo dimers when treated with basic solutions. Kimura and coworkers also treated their iron complexes with aqueous solutions at various pHs, particularly at alkaline pH.[150] Since Fe porphyrins form oligomeric or polymeric μ-oxo complexes intermolecularly, the resulting species began to show bisignate CD curves in the Soret region due to excitonic interaction (Fe–Fe distance is *ca.* 0.38 Å).

Liu, Ji and coworkers reported chiral linear zinc porphyrin arrays constructed from an amino acid-bridged zinc porphyrin dimer and ethylene diamine via self-assembly (Figure 71).[152] Unfortunately, there are several misconceptions in this paper with respect to the interpretation of the electronic absorption and CD spectra. When the positions of the Soret band of zinc porphyrin and amino acid-bridged zinc porphyrins were compared, the band of the

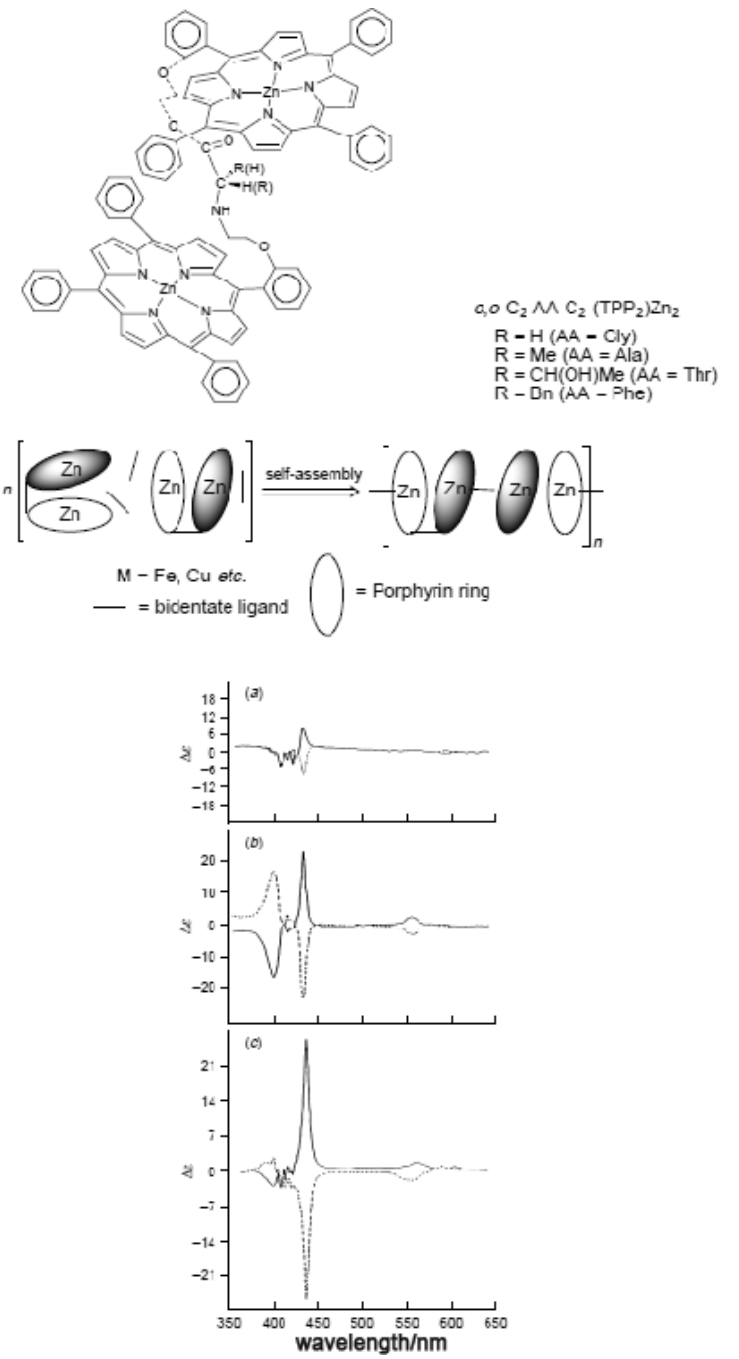

Figure 71. (top) Zn porphyrin dimers bridged by amino acid, (middle) formation of one-dimentional assembly of the zinc porphyrin by the addition of bidentate ligands, and (bottom) CD spectra of some of the Zn dimers in the absence of extraneous ligands (redrawn from Ref. 152).

dimer was at longer wavelength but the difference was always 0–3 nm. The authors concluded that this was due to the formation of a head-to-tail dimer produced by a π–π interaction. Unless there is further clear evidence, such as from NMR, these small values might be considered to be substituent effects or experimental error. The authors insisted that the CD spectra were correlated to chiral π–π stacking of the zinc porphyrins in the dimers even where no bisignate CD curves are seen in Figure 71. Furthermore, it is strange that glycine-bridged dimers show mirror-image CD curves (Figure 71(a)) since there is no L or D-isomer for glycine. Zn porphyrin dimers linked by alanine or threonine showed CD envelopes of either plus or minus in both the Soret and Q band regions. This kind of CD curve can never be explained as being produced by chiral π–π stacking of the zinc porphyrins in the dimers. In the paper, the authors show that the CD curves in Figure 71 are diminished by adding extraneous bidentate ligands. Since zinc porphyrins are generally five-coordinate in the presence of extraneous strong ligands, these data suggest that, in the absence of extraneous bidentate ligands, the amino group and carbonyl oxygen in the bridging moiety coordinate to two zinc ions in the dimer, so that the two porphyrin planes are very close. Accordingly, the CD curves in this figure appear to be produced by interaction of the porphyrin and the amino acid in the bridging moiety. Since the CD envelope changes sign by the use of L- or D-amino acid, this fact also strongly suggests that the CD was induced by the bridging amino acid.

Tamiaki and coworkers reported a similar porphyrin dimer, but with cyclic dipeptides (2,5-piperazinediones) as the linking units, and provided valuable data (Figure 72).[153] A porphyrin monomer with an appended optically active 2,5-piperazinedione gave no CD signal, but a dimer linked by cyclo(L-Tyr-L-Tyr) showed a minus-to-plus CD pattern in ascending energy in the Soret region (left-handed helicity), while a dimer linked by cyclo(D-Tyr-L-Tyr) was CD silent in the same region. These data indicate that the CD was generated by exciton coupling of the two porphyrin chromophores and that the two porphyrins most probably take a C_2 or C_{2v} arrangement in the cyclo(L-Tyr-L-Tyr)-linked dimer.

The CD spectra of water-soluble porphyrins (mostly anionic tetrasulfonate or cationic N-methylpiridinium-4-yl porphyrins) in the presence of D- or L-polyglutamate[154] or poly-L-lysine[155] have been reported. Although the CD spectra show a mirror-image relationship upon changing the coexisting L- or D-amino acid polymer, no detailed analysis was given in these reports, where the porphyrins exist as aggregates.

Sebek and Bour evaluated, with the aid of quantum chemical computations, the magnitudes of the perturbational, dipolar, and direct covalent contributions

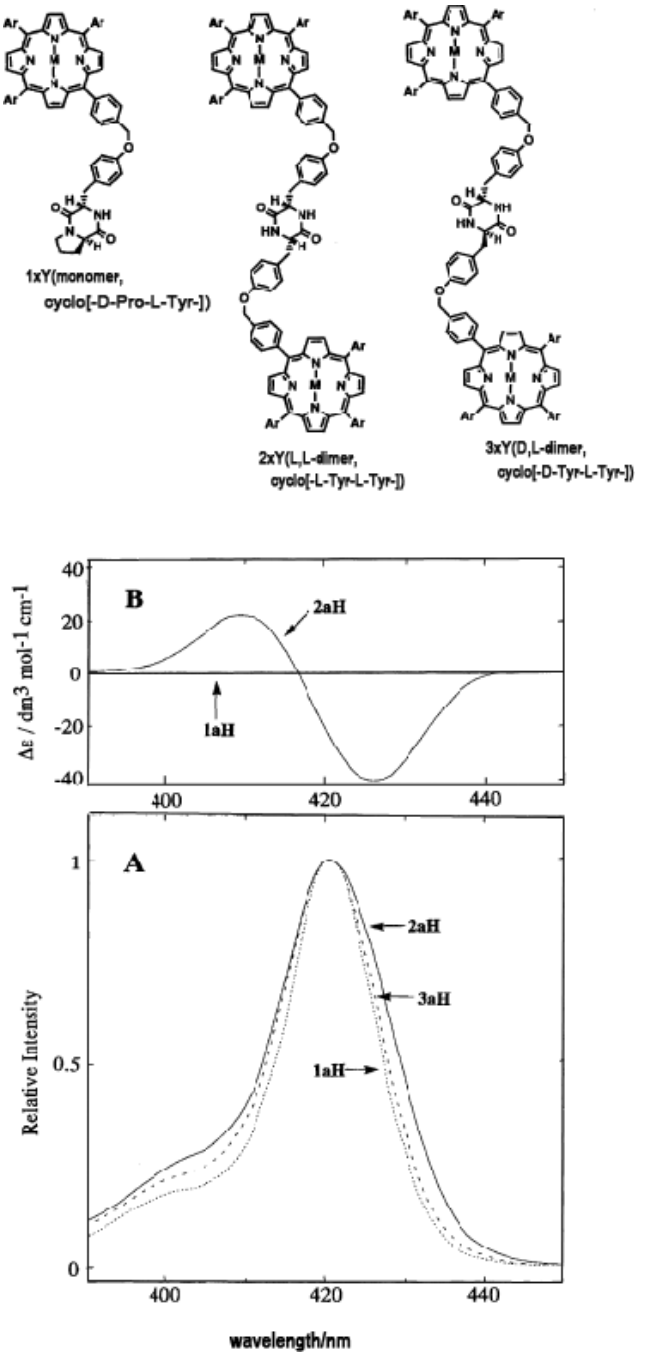

Figure 72. Structures of cyclic dipeptides (2,5-piperazinedione)-appended monopophyrin **1aH**, and cyclic dipeptides (2,5-piperazinedione)-bridged diporphyrin **2aH** and **3aH**. The difference between **2aH** and **3aH** are in the cyclic dipeptide moiety; **2aH** is composed of cyclo(L-Tyr-L-Tyr) while **3aH** consists of cyclo(D-Tyr-L-Tyr) (redrawn from Ref. 153).

to the electronic CD of porphyrin systems.[156] They claimed that TD-DFT, particularly with the hybrid B3LYP functional, are suitable for estimating the electronic excitation energies and spectral intensities. Transition dipole coupling between chirally stacked porphyrins was determined as the most important mechanism contributing to the optical activity. Perturbation models realized by a chirally arranged porphyrin and a point charge provided very small CD signals.

Kim and coworkers discussed the stacking of tetrakis(3-N-methylpyridinium-4-yl)porphyrin on poly[d(A-T)2] (DNA) in terms of electronic absorption, CD, and linear dichroism spectroscopy under different conditions (particularly at various NaCl concentrations).[157] In the investigation of the porphyrin-DNA interactions, a negative CD band in the Soret region has generally been accepted as an intercalated porphyrin, while porphyrin bound at the groove exhibits a positive CD band. A bisignate CD band is pronounced for the stacked porphyrins. In the presence of poly[d(A-$T)_2$], the cationic porphyrins showed bisignate signal changing of plus-to-minus in ascending energy, but this signal changes with time when the NaCl concentration is low. Together with the data of linear dichroism, the authors concluded that the molecular plane of the porphyrin is almost parallel to the DNA base plane under the above conditions. No concrete conclusions were drawn from the CD data in this study.

Aida and coworkers found an interesting phenomenon using their 5,15-bis(4-carboxyphenyl)-10,20-dendronyl zinc porphyrins (Figure 73).[158] As the dendritic moieties, they prepared from first to third generations. When porphyrins containing second generation dendrons at the 10 and 20 positions were dissolved at 5 mM (very concentrated solution) in $CHCl_3$, absorption peaks at 453 and 413 nm were displayed, which were assigned to a J-aggregated species. Similar absorption spectra were obtained when porphyrins contraining third generation dendron were dissolved at 5 mM in benzene. On the other hand, this type of absorption spectrum was not observed for species whose carboxyl groups at 5 and 15 positions were methyl esterified (these showed a single Soret band at *ca*. 423 nm). When the J-aggregated solutions were cast onto glass plates, the authors noticed that the spin-coated films displayed a chirality dominance in the statistical distributions which was dependent on the spinning direction. As seen typically in Figure 73, films spin-coated in a clockwise direction showed a plus-to-minus CD pattern in ascending energy, corresponding to the 453 nm peak, while those films spin-coated in an anticlockwise direction displayed exactly the opposite CD behavior. For this kind of phenomenon to occur, the distance between the porphyrin and dendron units was important: if the distance was too short, the bisignate CD curves were not observed (for details, see Ref. 158).

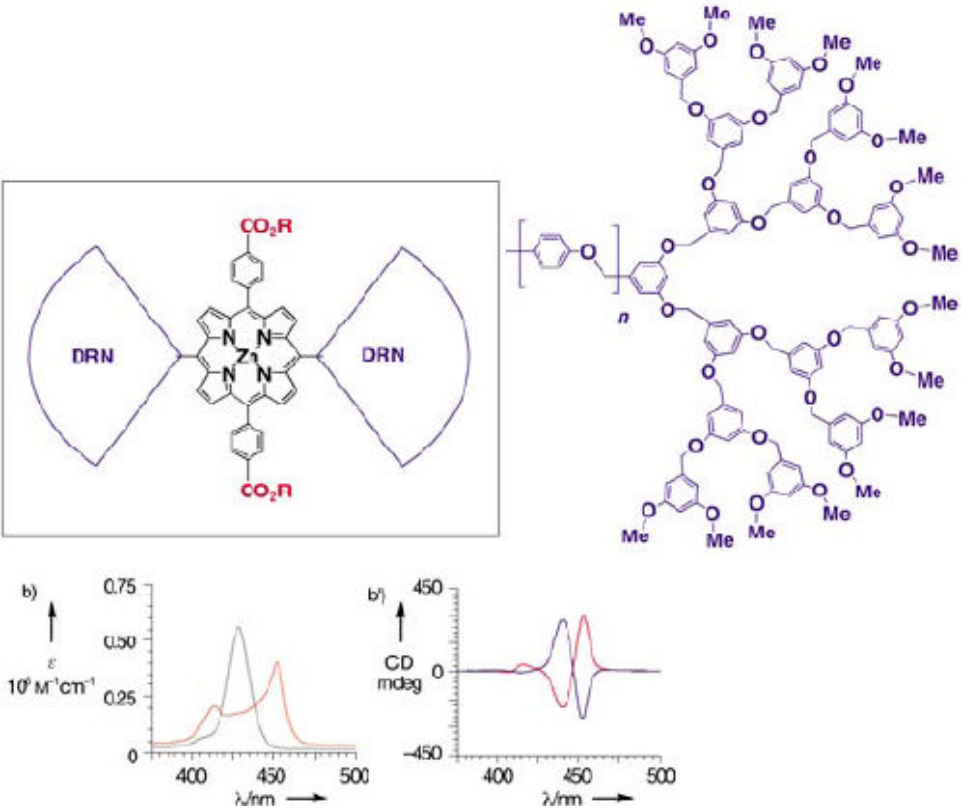

Figure 73. (top left) 5,15-bis(4-carboxyphenyl)-10,20-didendronyl zinc porphyrin prepared by Aida *et al.* (top right) Third generation dendron linked to the 5,15 positions of the zinc porphyrin, (bottm left) the electronic absorption of the porphyrin in this figure (red) and its methyl ester derivative (green) at 5 mM in benzene, and (bottom right) CD spectra of thin films (n = 0,1) prepared by spin-coating in the clockwise (red curves) and counterclockwise (blue curves) directions (redrawn from Ref. 158).

VII. Application of Porphyrins to Conformational Analysis

A. Determination of the Helicity of Polyisocyanides

Takei and coworkers determined the helicity of helical polyisocyanide using exciton coupling of porphyrins.[159] Chiral polyisocyanide was synthesized 35 years ago, in 1974.[160] Since then, nobody has succeeded in finding a relationship between the helicity and CD sign. Takei prepared poly(aryl isocyanide)s with a polymerization degree of 100, where aryl = alkyloxycarbonylphenyl, and furthermore alkyl = (L)- or (D)-menthyl, (D)-isomenthyl, (D)-neopenthyl, (S)-butyl, and (S)-octyl (Figure 74, compounds **1a**–**1f**). Simultaneously, corresponding

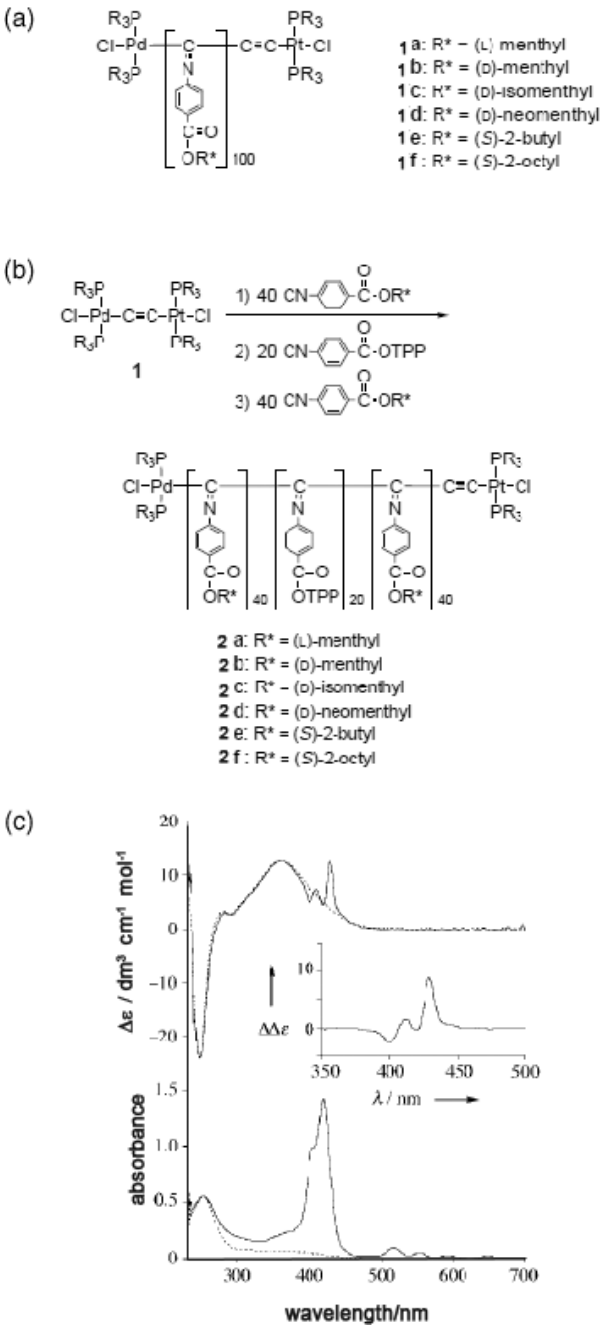

Figure 74. (a) Structures of optically active isocyanide homopolymers, **1a**–**1f** (degree of polymerization (DP) = 100), (b) structures of optically active isocyanide triblock copolymers containing a block with tetraphenylporphyrinyl substituents, **2a**–**2f** (DP = 100), and (c) electronic absorption and CD spectra of **1a** (dotted lines) and **2a** (solid lines). The inset in (c) shows the subtracted CD spectrum: i.e. **2a**–**1a** (redrawn from Ref. 159).

triblock copolymers containing a tetraphenylporphyrin unit as one of two aryl groups were prepared (Figure 74, compounds **2a**–**2f**). As the dotted lines in this figure show, the homopolymer with an (L)-menthyloxycarbonylphenyl group exhibits a very weak broad absorption band between 300 and 500 nm, and a broad positive CD envelope in the same wavelength region. The triblock copolymer showed absorption bands due to the tetraphenylporphyrin moiety; a Soret band in the *ca.* 380–450 nm region and four weak Q peaks in the 500–700 nm region. The CD spectrum is similar in shape to that of the corresponding homopolymer, except in the Soret region, which indicates that the helicity of the homopolymer and the triblock copolymer is the same. Subtraction of the CD spectrum of the homopolymer from that of the triblock copolymer showed a positive-to-negative pattern (positive CD couplet) on going from longer to shorter wavelength (see the inset of (c)) in the Soret region, indicating that the CD spectrum in this region of the copolymer is produced by superimposition of this positive couplet and the broad CD envelope originating from the homopolymer main chain. Then, from the positive-to-negative CD pattern in the Soret region, this copolymer was found to have right-handed helicity. Therefore, the homopolymer poly(aryl isocyanide)s showing a positive CD envelope in the 300–500 nm region was found to be a right-handed polymer. Thus, the CD sign-helicity relationship of the chiral polyisocyanide was elucidated 35 years after its advent. This assignment was opposite to that predicted theoretically, and underlines the importance of experimental evidence.[161] Interestingly, the helicity depended on the configuration (L or D) of the alkyl moiety, being right-handed (P helicity) for (L) and left-handed (M helicity) for (D).

B. Determination of the Absolute Configurations of Natural Products

Nakanishi, Berova, Woody and coworkers applied exciton-coupled CD spectroscopy to determine the absolute configurations of natural products.[162,163] In 1995 and 1996, these authors began using zinc(II) or metal-free 5-(4-carboxyphenyl)-10,15,20-triphenylporphyrins to determine the configuration of steroids and brevetoxin.[162,163] First, with respect to the transition moment directions for the porphyrin Soret band, Woody described in Ref. 163 that we can not expect the porphyrin chromophore to behave like a linear oscillator as previously assumed, instead that it must be treated as a nearly circular oscillator, with nearly degenerate, orthogonal transition moments of approximately the same magnitude. However, in all the cases they examined in which the bis-porphyrin derivative can be compared with bis(*p*-dimethylaminobenzoyl) derivatives, the signs of the Cotton effects were identical that they suggested

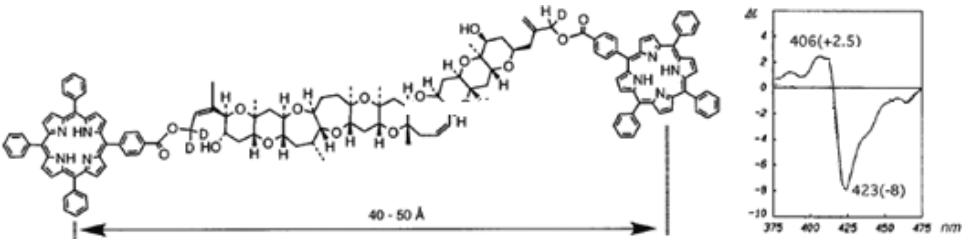

Figure 75. Structure and CD spectra of brevetoxin-bridged porphyrin dimer and its CD spectra in MeOH/water = 4:1 (redrawn from Ref. 163).

that the normal exciton rule for linear oscillators can be used. After all, it was concluded that the effective transition moment can be regarded as being in the 5,15-direction of the porphyrin skeleton. Two porphyrin molecules were linked to steroids and brevetoxin molecules by ester linkages, and utilizing the CD exciton coupling, they determined the absolute configuration. Within the samples examined, all results were consistent with those obtained using bis[*p*-(dimethylamino)benzoates]. There are several merits to using pophyrin chromophores; 1) the absorption coefficient of the Soret band is very large, 2) the position of the Soret band is much longer compared to chromophores found in many natural products, and 3) the polarization direction is known to run along the C-5/C-15 direction.[162] Porphyrins at the termini of dimeric steroids and brevetoxin B exhibited exciton coupling over interchromophoric distances of up to 50 Å (Figure 75).

Several years later, the same authors applied the CD exciton method to gymnocin-B, separated from the red tide species, dinoflagellate *Karenia mikimotoi* at Kushimo, Japan.[164] Gymnocins are a series of cytotoxic marine polycyclic ethers, and in gymnocin-B, two hydroxyl groups are present at C-10 and C-37, separated by *ca*. 20 Å (Figure 76). This exhibited a positive-to-negative sign in ascending energy, showing that two OH groups are in a right-handed configuration.

Since chiral bis-porphyrins are the subject of intense interest as chiral receptors and as probes in the determination of the structure and stereochemistry of natural and synthetic products, Woody and coworkers reconsidered the CD spectra of bis-porphyrins from three classes to provide an improved framework for their interpretation: I, where the porphyrins can adopt a relatively wide range of orientations relative to each other, II, porphyrins having a fixed orientation and III, porphyrins undergoing π-stacking (Figure 77).[165] The calculations primarily utilized the classical polarizability theory of DeVoe (point dipole approximation),[166,167] but were supplemented by a quantum chemical matrix method

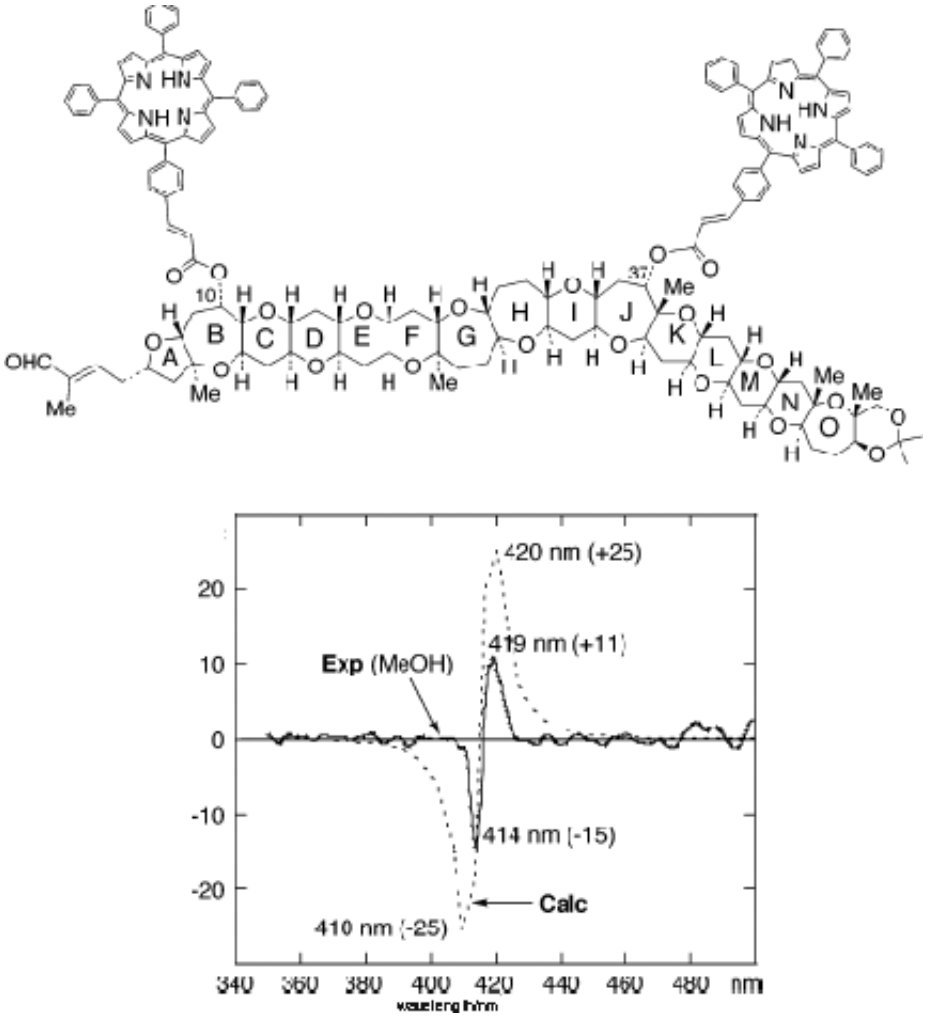

Figure 76. Structure of gymnocin B linked with two tetraphenyl porphyrins at C-10 and C-37 OHs, and its experimental (solid line) and calculated (broken line) CD spectra (redrawn from Ref. 164).

(monopole approximation with the program MATMAC).[168] Class I was represented by three isomers of the diester of 5a-cholestane-3,17-diol with 5-(4′-carboxyphenylporphyrin) (*αβ*, *βα*, *ββ*) (Figure 78). Careful analysis of the torsional degrees of freedom led to two to four minimum-energy conformers for each isomer. The CD spectra in the Soret region were calculated as Boltzmann-weighted averages over the low-energy conformers for each isomer. Three models were used: the effective transition moment model, in which only one of the degenerate Soret components is considered, along the 5–15 direction ($D = 88.3$ D^2);

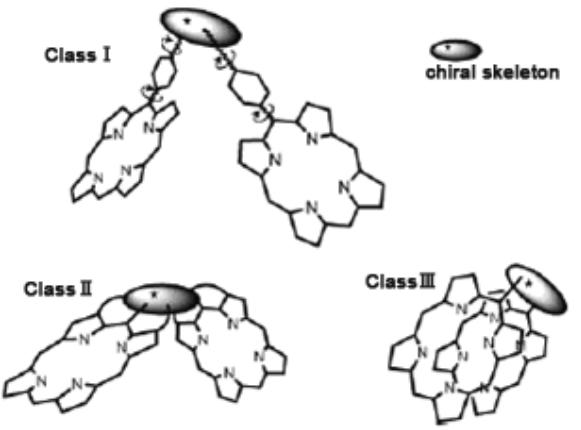

Figure 77. Schematic representations of the three classes of bis-porphyrins. Class I: compounds with unrestricted rotation (about one or more axes). Class II: compounds with two porphyrin rings with fixed special orientation. Class III: compounds with π–π stacked porphyrins (redrawn from Ref. 165).

the circular oscillator model, in which both Soret components are given equal weight ($D = 88.3$ D^2 each); and the hybrid model, in which the 10–20 oscillator is given half the weight ($D = 44.1$ D^2, a value heuristically justified) of the 5–15 oscillator, to mimic the effect of extensive vibrational averaging about the 5–15 direction. All three models predicted Soret exciton couplets with signs in agreement with experiment. Quantitatively, the best results were given by the hybrid and circular oscillator models, validating the widely-used effective transition moment model for qualitative assignments of bis-porphyrin chirality, and thus permitting application of the exciton chirality model. However, simultaneously, it was indicated that for quantitative studies, the circular oscillator or hybrid models should be used. The simplified effective transition moment and hybrid models were justified by the vibrational averaging in class I bis-porphyrins, and it was stressed that they are to be used only with these kinds of system. Two class II bis-porphyrins were also studied by DeVoe method calculations in the circular oscillator model, which yielded good agreement with experiment (Figure 79).[169] For class III bis-porphyrin systems, the calculations gave only qualitative agreement (Figure 80), and limitations in the conformational analysis with the close contacts and dynamic effects in these π-stacked systems precluded quantitative results.

Methods for determination of the absolute configurations of amino acid, amino alcohols, α-hydroxy acids, monoalcohols, primary and secondary monoamines, and α-chiral carboxylic acids by zinc and magnesium porphyrin tweezers were developed mainly by the Nakanishi and Berova and their

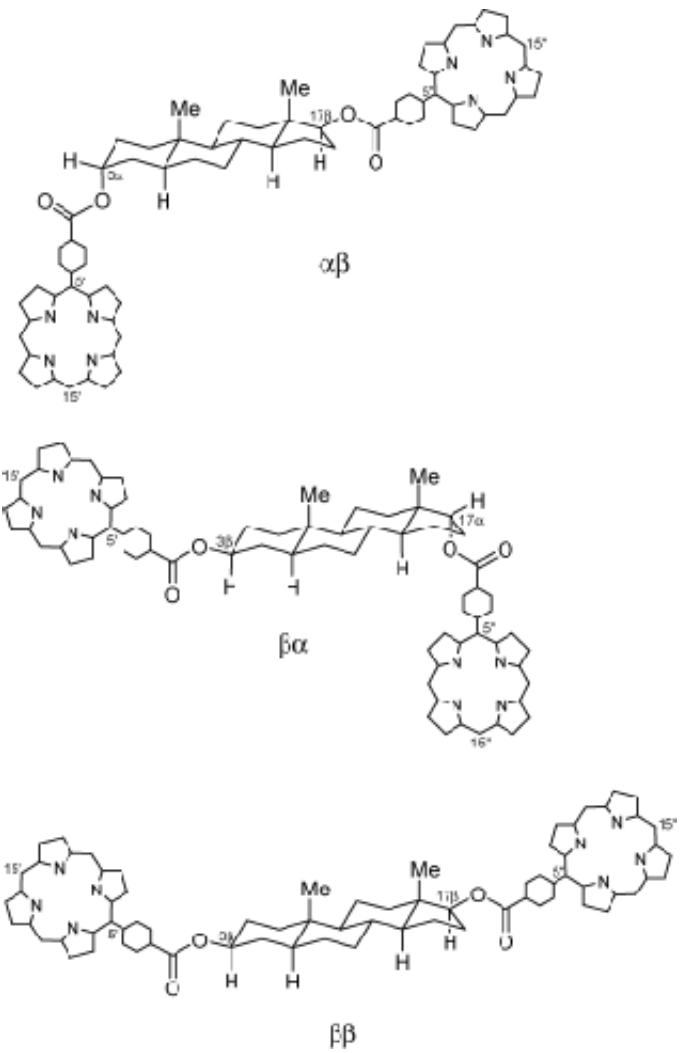

Figure 78. Three isomers ($\alpha\beta$, $\beta\alpha$, $\beta\beta$) of diester of 5α-cholestane-3,17-diol with 5-(4′-carboxyphenyl-10,15,20-triphenylporphyrin (redrawn from Ref. 165).

coworkers over a period of about 10 years from the late 1990s onward.[170–178] The concept is simple (Figure 81). As exemplified in Figure 81, the chiral substrates are linked to the achiral trifunctional bidentate carrier molecule (3-aminopropylamino)acetic acid, and the resultant conjugates are then complexed with dimeric zinc porphyrin hosts, giving rise to 1:1 host/guest sandwiched complexes (primary and secondary amines coordinate to two zinc ions). These complexes exhibit exciton-coupled bisignate CD spectra due to stereo-differentiation, leading to preferred porphyrin helicity. Since the chiral

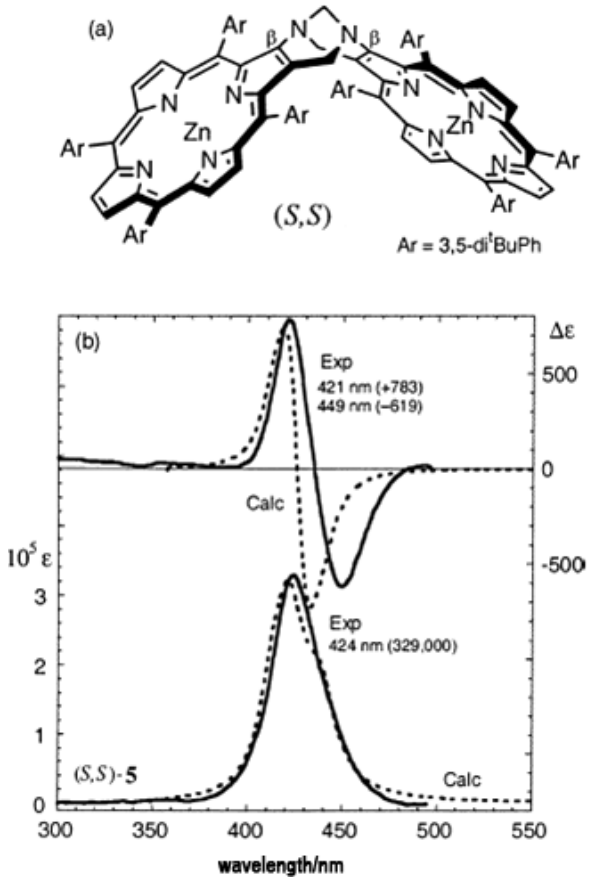

Figure 79. Structure of spactially obliquely fixed diporphyrin and its experimental (solid lines) and calculated (broken lines) electronic absorption and CD spectra (redrawn from Refs. 165 and 169).

sense of twist between the two porphyrins in the complex is dictated by the stereogenic center of the substrate, the sign of the complex determines the absolute configuration at this center. The twist of the porphyrin tweezer in the complex can be predicted from the relative steric sizes of the group flanking the sterogenic center, such that the bulkier group (L) protrudes from the complex sandwich. As an example, the case of (S)-2-(1-hydroxy)ethylnaphthalene (Figure 82) which is shown as a conjugate in Figure 81 can be considered. The schematic representation (Newman projection) depicts the substituent attached to the stereogenic center which leads to the prediction of the CD couplet sign. If the hydroxyl group is placed at the rear, as shown, the clockwise arrangement of L (larger group), M (medium group) and hydrogen results in a positive CD couplet, and *vice versa*. The absolute sense of twist between the porphyrin

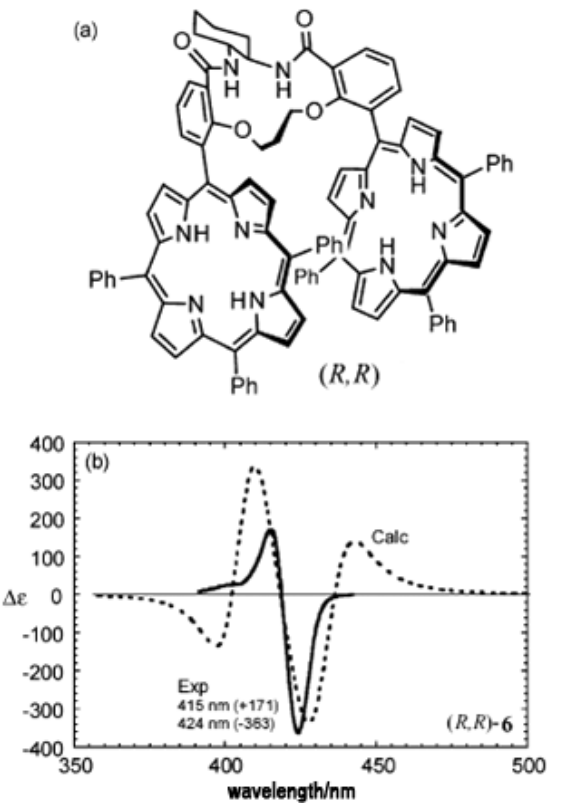

Figure 80. (R,R) ($\alpha\alpha$)-form of diester of 5α-cholestane-3,17-diol with 5-(4′-carboxyphenyl-10,15,20-triphenylporphyrin (redrawn from Ref. 165).

electric transition moments, and hence the sign of the exciton-coupled CD is dependent on whether the P-2 porphyrin of the tweezer coordinates to the secondary amine nitrogen from the direction of the M or L group (Figure 81). The preferred conformer determines the sign of the CD couplet, and hence the observed CD exciton chirality reveals the absolute configuration of the substrate. The assignment of M and L to substituents at the stereogenic center is thus crucial for predicting the sign of the CD couplet. However, at the same time, the authors emphasized that factors other than steric bulk, such as electronic interactions, hydrogen bonding, and rotational degrees of freedom cannot be ignored. The authors discussed L/M based on relative steric factors and electronic factors separately. In Ref. 178, *meso*-tetra(pentafluoro)phenyl zinc porphyrins are used. It is stressed that an electron-withdrawing effect increases the Lewis acidity of the central zinc, thereby facilitating coordination of guest (Lewis base) molecules.

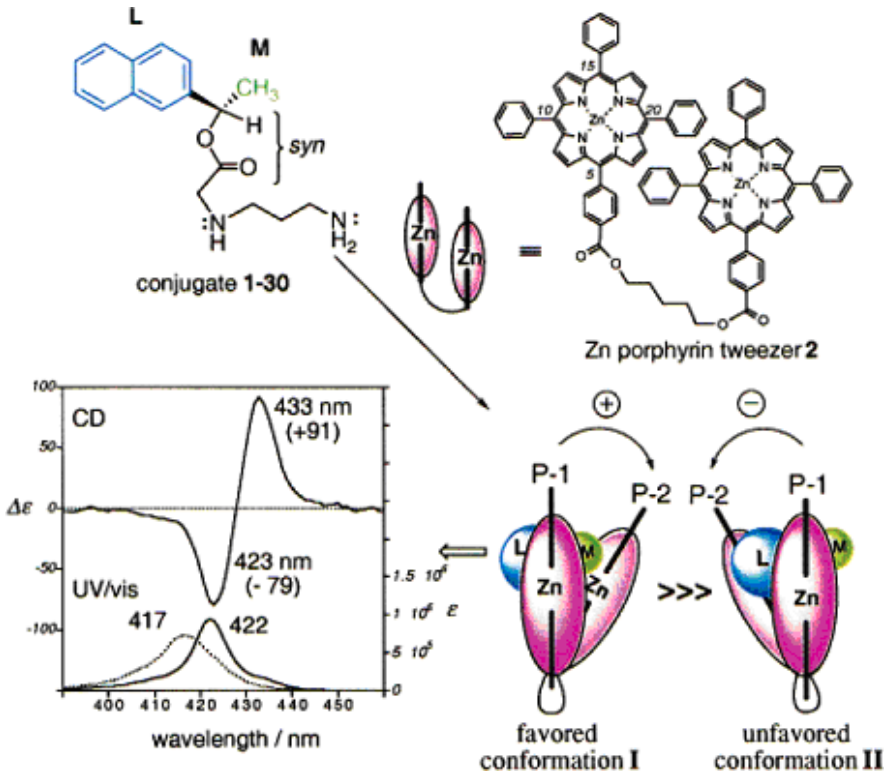

Figure 81. Complex formation between a conjugate and a tweezer leads to two conceivable conformations with opposite sense of twists. The predominant conformation I, the one in which the **L** (larger) group is protruding away from the porphyrin-1/porphyrin-2 sandwich, giving rise to a typical CD couplet representing the sense of twist between the two porphyrins and hence the absolute configuration at the stereogenic center; the broken curve in the absorption spectrum represents the tweezer prior to complexation (redrawn from Ref. 172).

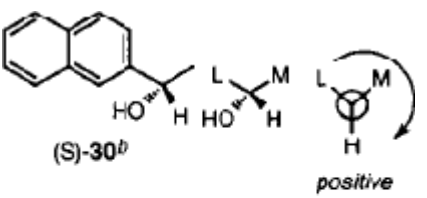

Figure 82. Prediction of CD couplet in the case of (*S*)-2(1-hydroxy)ethylnaphthalene and CD amplitude observed in the experiment. MCH is methylcyclohexane (redrawn from Ref. 172).

VIII. Concluding Remarks

CD spectroscopy is highly sensitive to small conformational changes so great care must be taken in analyzing CD spectra. If X-ray data exist, those coordinates should be used to calculate CD solution spectra, since all conformational analyses reported to date have shown close agreement with the X-ray structures. Some researchers who are unfamiliar with the technique calculate CD spectra based on optimized enantiomeric structures of low symmetry porphyrinic compounds. This should be avoided since near planar porphyrin ligands are often predicted to have deformed low symmetry structures resulting in unrealistic calculated spectra. CD spectral analysis of compounds for which no X-ray data exist must be performed carefully. The most important factors are the distance and angles between the chromophores. If the orientations of the electronic and magnetic transition moments are estimated correctly, the CD sign pattern can often be successfully predicted. Knowledge derived from the assignment of electronic absorption spectra should be used whenever possible. For instance, the use of strong electronic absorption bands can be particularly helpful during CD studies, as described in the context of conformational analyses of natural products. Since many research institutes and universities are now able to provide porphyrinoid researchers with easy access to CD spectrometers, it is important for researchers in the field to fully understand this elegant spectroscopic technique. This can be achieved relatively easily based on a brief study of the theory of circular dichroism and chirality.

IX. References

1. Charney, E. (Ed.) *The Molecular Basis of Optical Activity. Optical Rotatory Dispersion and Circular Dichroism*; John Wiley and Sons: New York, **1979**.
2. *Circular Dichroism: Parinciples and Applications*; Nakanishi, K.; Berova, N.; Woody, R. W. Eds.; Wiley-VCH: New York, **2000**.
3. Lightner, D. A.; Gurst, J. E. *Organic Conformational Analysis and Stereochemistry from Circular Dichroism Spectroscopy*; Wiley-VCH: New York, **2000**.
4. Mason, S. F. *Molecular Optical Activity and the Chiral Discrimination*, Cambridge University Press; Cambridge, **1982**.
5. Roger, A.; Norden, B. *Circular Dichroism and Linear Dichroism*, Oxford University Press: Oxford, **1997**.
6. *Circular Dichroism and the Conformational Analysis of Biomolecules*; Fasman, G. D. Ed.; Plenum Press: New York, **1996**.
7. Harada, N.; Nakanishi, K. *Circular Dichroism Spectroscopy-Exciton Coupling in Organic Stereochemistry;* Oxford University Press: Oxford, **1983.**
8. Satake, A.; Kobuke, Y. *Org. Biomol. Chem.* **2007***, 5,* 1679.
9. Berova, N.; Bari, L. D.; Pescitelli, G. *Chem. Soc. Rev.* **2007***, 36,* 914.
10. Bari, L. D.; Pescitelli, G.; Salvadori, P. *J. Am. Chem. Soc.* **1999***, 121,* 7998.
11. Sugita, Y.; Nagai, M.; Yoneyama, Y. *J. Biol. Chem.* **1971**, *246*, 383.

12. Greenfield, N.; Fasman, G. D. *Biochemistry* **1969**, *8*, 4108.
13. Manavalan, P.: Johnson Jr., W. C. *Nature* **1983**, *305*, 831.
14. Stokkum, I. H. M. ; Spoelder, H. J. W.; Bloemendal, M.; Grondelle, R.; Groen, F. C. A. *Anal. Biochem*. **1990**, *191*, 110.
15. It is known that the error from experiments becomes larger in the hemoproteins containing a large portion of β-sheets and random coil structures.[13,14]
16. Tetrameric hemoglobin may change intensity by 8% due to the exchange of the 6th ligand (Hanisch, G.; Engel, J.; Brunori, M.; Fasold, H. *Eur. J. Biochem.* **1969**, *9*, 335).
17. Hamaguchi, K.; Takesada, K. *Rotatory Dispersion of Proteins*; Tokyo Univ. Press; Tokyo, **1971**.
18. Urry, D. W. *J. Biol. Chem*. **1967**, *242*, 4441.
19. Myer, Y. P. *J. Biol. Chem*. **1968**, *243*, 2115.
20. Zand, R.; Vinogradov, S. *Biochem. Biophys. Res. Commun*. **1976**, *26*, 121.
21. Okada, Y.; Okunuki, K. *J. Biochem. (Tokyo)* **1970**, *67*, 603.
22. Okada, Y.; Okunuki, K. *J. Biochem. (Tokyo)* **1970**, *67*, 487.
23. Tsong, T. Y.; Sturtevant, J. M. *J. Am. Chem. Soc.* **1969**, *91*, 2382.
24. Iwatsubo, M.; Risler, J. L. *Eur. J. Biochem.* **1969**, *9*, 280.
25. Uchida, K.; Shimizu, T.; Makino, R.; Sakaguchi, K.; Iizuka, T.; Ishimura, Y.; Nozawa, T.; Hatano, M. *J. Biol. Chem*. **1983**, *25*, 2519, 2526.
26. Sono, M.; Dawson, J. H. *Biochim. Biophys. Acta* **1984**, *789*, 170.
27. Sugita, Y.; Dohi, Y.; Yoneyama, Y. *Biochim. Biophys. Res. Commun.* **1968**, *31*, 447.
28. Sond, R.; Vinogradov, S. *Arch. Biochem. Biophys.* **1968**, *125*, 94.
29. Bolard, J.; Garnier, A. *Biochim. Biophys. Acta* **1972**, *263*, 535.
30. Geraci, G.; Li, T. K. *Biochemistry* **1969**, *8*, 1848.
31. Hsu, M. C.; Woody, R. W. *J. Am. Chem. Soc.* **1971**, *93*, 3515.
32. Kirkwood, J. G. *J. Chem. Phys.* **1937**, *5*, 479.
33. Tinoco Jr., I. *Adv. Chem. Phys*. **1962**, *4*, 113.
34. Fleischhauer, J.; Wollmer, A. *Z. Naturforsch*. **1972**, *27b*, 530.
35. Sievers, G. *Biochim. Biophys. Acta* **1978**, *536*, 212.
36. Woody, R. In: *Biochemical and Clinical Aspects of Hemoglobin Abnormalities*; Cauhey, W. S. Ed.: Academic Press: New York, **1978**, pp. 279–298.
37. Blauer, G.; Sreerama, N.; Woody, R. W. *Biochemistry* **1993**, *32*, 6674.
38. Urry, D. W. *J. Am. Chem. Soc*. **1967**, *89*, 4190.
39. Urry, D. W.; Pettegrew, J. W. *J. Am. Chem. Soc*. **1967**, *93*, 5276.
40. Takano, T.; Dickerson, R. E. *Proc. Natl. Acad. Sci. USA* **1980**, *77*, 6371.
41. Konishi, Y. K.; Suzuki, H. *J. Biochem.* **1985**, *98*, 1181.
42. Aojula, H. S.; Wilson, M. T.; Drake, A. *Biochem. J*. **1986**, *237*, 613.
43. Light, W. R.; Rohlfs, R. L.; Palmer, G.; Olson, J. S. *J. Biol. Chem*. **1987**, *262*, 46.
44. Aojula, H. S.; Wilson, M. T.; Moore, G. T.; Williamsoin, D. J. *Biochem. J*. **1988**, *250*, 853.
45. Santussi, R.; Ascoli, F.; La Mar, G. N.; Parish, D. W.; Smith, K. M. *Biophys. Chem*. **1990**, *37*, 251.
46. Kobayashi, N.; Osa, T.; Kitashima, M.; Matsuoka, A.; Shikama, K. *Proceedings of the 5th Int. Natl. Conf. on Circular Dichroism*, Colorado, August 18–22, **1993**, p. 201.
47. Eaton, W. A.; Charney, E. *J. Chem. Phys*. **1969**, *51*, 4502
48. The factor "four" is a historical accident. See Moffit, W.; Moscowitz, A. *J. Chem. Phys*. **1959**, *30*, 648.

49. Ballhausen, C. J. *Introduction to Ligand Field Theory*; McGraw-Hill; New York, **1962**.
50. Zerner, M.; Gouterman, M.; Kobayashi, H. *Theor. Chim. Acta* **1966**, *6*, 363.
51. Kobayashi, N.; Osa, T. *Chem. Pharm. Bull*. **1989**, *37*, 3105.
52. Reid, T. J.; Murthy, M. R. N, Sicignano, A.; Tanaka, N.; Musick, W. D. J.; Rossman, M. G. *Proc. Natl. Acad. Sci. USA* **1981**, *78*, 4767.
53. Torri, K.; Iizuka, T.; Ogura, Y. *J. Biochem (Tokyo)* **1970**, *68*, 837.
54. Kobayashi, N.; Nozawa, T.; Hatano, M. *Biochim. Biophys. Acta* **1977**, *493*, 340.
55. Kobayashi, N.; Nozawa, T.; Hatano, M. *Bull. Chem. Soc. Jpn.* **1981**, *54*, 919.
56. Yamamoto, T.; Nozawa, T.; Kobayashi, N.; Hatano, M. *Bull. Chem. Soc. Jpn*. **1982**, *55*, 3059.
57. Kobayashi, N.; Nakai, K. *Chem. Commun.* **2007**, 4077.
58. Nozawa, T.; Yamamoto, T.; Hatano, M. *Biochim. Biophys. Acta* **1976**, *427*, 28.
59. Bormett, R. W.; Asher, S. A.; Larkin, P. J.; Gustafson, W. G.; Rangnathan, N.; Freedman, T. B.; Nafie, L. A.; Barasubramanian, S.; Boxer, S. G.; Yu, N.-T.; Gersonde, K.; Noble, R. W.; Springer, B. A.; Sligar, S. G. *J. Am. Chem. Soc*. **1992**, *114*, 6864.
60. Teraoka, J.; Nakamura, K.; Nakahara, Y.; Kyogoku, Y.; Sugeta, H. *J. Am. Chem. Soc*. **1992**, *114*, 9211.
61. Teraoka, J.; Yamamoto, N.; Matsumoto, Y.; Kyogoku. Y.; Sugeta, H. *J. Am. Chem. Soc*. **1996**, *118*, 8875.
62. Ikeda, S.; Nezu, T.; Ebert, G. *Biopolymers* **1991**, *31*, 1257.
63. Ikeda, S.; Nezu, T. *Bull. Chem. Soc. Jpn.* **1993**, *66*, 18.
64. Fukushima, Y. *Bull. Chem. Soc. Jpn*. **1996**, *69*, 1719.
65. Benson, D. R.; Bradley, R. H.; Zhu, X.; Doughty M. B. *J. Am. Chem. Soc*. **1995**, *117*, 8502.
66. Liu, D.; Williamson, D. A.; Kennedy, M. L.; Williams, T. D.; Morton, M. M.; Benson, D. R. *J. Am. Chem. Soc.* **1999**, *121*, 11798.
67. Nastri, F.; Lombardi, A.; Morelli, G.; Maglio, O.; D'Auria, G.; Pedone, C.; Pavone, V. *Chem. Eur. J.* **1997**, *3*, 340.
68. Nastri, F.; Lombardi, A.; Morelli, G.; Maglio, O.; D'Auria, G.; Pedone, C.; Pavone, V. *Chem. Eur. J*. **1997**, *3*, 350.
69. Sakamoto, S.; Obataya, I.; Ueno, A.; Mihara, H. *J. Chem. Soc., Perkin Trans.* **1999**, *2*, 2059.
70. Wolf, H. *Ann. Chem*. **1966**, *695*, 98.
71. Wolf, H.; Brockman, H.; Biere, H.; Inhoffen, H. H. *Ann. Chem*. **1967**, *704*, 208.
72. Briat, D.; Schooley, D. A.; Records, R.; Bunnenberg, E.; Djerassi, C. *J. Am. Chem. Soc.* **1967**, *89*, 6170.
73. Housser C.; Sauer, K. *J. Am. Chem. Soc*. **1970**, *92*, 779.
74. Katz, J. J.; Strain, H. H.; Leussxing, D. L. ; Dougherty, R. C. *J. Am. Chem. Soc*. **1968**, *90*, 784.
75. Smith, K. M.; Bobe, F. W.; Goff, D. A.; Abraham, R. J. *J. Am. Chem. Soc*. **1986**, *108*, 1111.
76. Smith, K. M.; Craig, G. W.; Kehres, L. A.; Phennig, N. *J. Chromatog*. **1983**, *281*, 209.
77. Smith, K. M.; Goff, D. A.; Fajer, J.; Barkigia, K. M. *J. Am. Chem. Soc*. **1982**, *104*, 3747.
78. Smith, K. M.; Kehles, L. A.; Fajer, J. *J. Am. Chem. Soc*. **1983**, *105*, 1387.
79. Olson, J. M.; Pedersen, J. P. *Photosynth. Res*. **1990**, *25*, 25.
80. Brune, D. C.; Gerola, P. D.; Olson, J. M. *Photosynth. Res*. **1990**, *24*, 253.
81. Kobayashi, M.; Meent, E. J.; Erkelens, C.; Amesz, J.; Ikegami, I.; Wataabe, T. *Biochim. Biophys. Acta* **1991**, *1057*, 89.
82. Tamiaki, H.; Miyata, S.; Kureishi, Y.; Tanikaga, R. *Tetrahedron* **1996**, *52*, 12421.
83. Tamiaki, H.; Amakawa, M.; Shimono, Y.; Tanikaga, R.; Holzwarth, A. R.; Schafner, K. *Photchem. Photobiol.* **1996**, *63*, 92.

84. Miyatake, T.; Tamiaki, H.; Holzwarth, A. R.; Schafner, K. *Helv. Chim. Acta* **1999**, *82*, 797.
85. Sasaki, S.; Mozoguchi, T.; Tamiaki, H. *J. Org. Chem*. **2007**, *72*, 4566.
86. Lehmann, R. P.; Brunisholz, R. A.; Zuber, H. *Photosyn. Res*. **1994**, *41*, 165.
87. Ma, Y. Z.; Cox, R. P. ; Gilltro, T.; Miller, M. *Photosyn. Res.* **1996**, *47*, 157.
88. Zhu, Y.; Lin, S.; Ramakrishna, B. L.; Noort, P. I. *Photosyn. Res.* **1996**, *47*, 207.
89. McDermott, G.; Prince, S.; Freer, A.; Hawthornthwaite-Lawless, A.; Papiz, M.; Cogdell, R.; Isaacs, N. *Nature* **1995**, *374*, 517.
90. Koepke, J.; Hu, X.; Muenke, C.; Schulten, K.; Michel, H. *Structure* **1996**, *4*, 581.
91. Alden, R.; Johnson, E.; Nagarajan, V.; Parson, W.; Law, C.; Cogdell, R. *J. Phys. Chem. B*. **1997**, *101*, 4667.
92. Meier, T.; Zhao, Y.; Chernyak, V.; Mukamel, S. *J. Chem. Phys*. **1997**, *107*, 3876.
93. Wu, H.-M.; Reddy, N. R. S.; Small, G. J. *J. Phys. Chem. B* **1997**, *101*, 651.
94. Sturgis, J. N.; Olsen, D. J.; Robert, B.; Hunter, C. N. *Biochemistry* **1997**, *36*, 2772.
95. Monshouer, R.; Grondelle, R. *Biochim. Biophys. Acta* **1996**, *1275*, 70.
96. Hu, X.; Ritz, T.; Damjanovic, A.; Schulten, K. *J. Phys. Chem. B* **1997**, *101*, 3584.
97. Corey, M. G.; Zerner, M. C.; Hu, X.; Schulten, K. *J. Phys. Chem. B* **1998**, *102*, 7640.
98. Samsen, O. J. G.; Grondelle, R.; Amerongen, H. *Biophys. J*. **1996**, *71*, 1934.
99. Sumi, H. *J. Phys. Chem. B* **1999**, *103*, 252.
100. Scholes, G. D.; Fleming, G. R. *J. Phys. Chem. B* **2000**, *104*, 1854.
101. Sauer, K.; Cogdell, R. J.; Prince, S. M.; Freer, A.; Isaaks, N. W.; Scheer, H. *Photochem. Photobiol*. **1996**, *64*, 564.
102. Linnanto, J.; Korppi-Tommola, J. E. I.; Helenius, V. M. *J. Phys. Chem. B* **1999**, *103*, 8739.
103. Cogdell, R. J.; Scheer, H. *Photochem. Photobiol*. **1985**, *42*, 669.
104. Sauer, K.; Austin, L. A. *Biochemistry* **1978**, *17*, 2011.
105. Philipson, K. D.; Tsai, S. W. C.; Sauer, K. *J. Phys. Chem*. **1971**, *75*, 1440.
106. Bolt, D. J.; Sauer, K.; Shiozawa, J. A.; Drews, G. *Biochim. Biophys. Acta* **1981**, *637*, 342.
107. Jimenez, R. Dikshit, S. N.; Bradforth, S. E.; Flemeing, G. R. *J. Phys. Chem*. **1996**, *100*, 6825.
108. Wu, H.-M.; Small, G. J. *J. Phys. Chem*. **1998**, *102*, 888.
109. Ridley, J. E.; Zerner, M. C. *Theor. Chim. Acta* **1973**, *32*, 111.
110. Reddy, N. R. S.; Wu, H.-M.; Jankowiak, R.; Cogdell, R. J.; Small, G. *Photosynth. Res.* **1996**, *48*, 277.
111. Bucks, R. D.; Boxer, S. G. *J. Am. Chem. Soc.* **1982**, *104*, 340.
112. Tamiaki, H.; Kubota, T.; Tanikawa, R. *Chem. Lett.* 1996, 639.
113. Tamiaki, H.; Holtzwarth, A. R.; Schaffner, K. J. *Photochem. Photobiol. B: Biol*. **1992**, *15*, 355.
114. Cheng, P.; Liddell, P. A.; Ma, X. S. C.; Blankenship, R. E. *Photochem. Photobiol*. **1993**, *58*, 290.
115. Kosaka, N.; Tamiaki, H. *Eur. J. Org. Chem.* **2004**, 2325.
116. Taima, H.; Ojubo, A.; Yoshioka, N.; Inoue, H. *Tetrahedron Lett*. **2005**, *46*, 4161.
117. Liu, C.; Dobhal, M. P.; Cethirajan, M.; Missert, J. R.; Pandy, R. K.; Balasubramanian, S.; Sukumaran, D. K.; Zhang, M.; Kadish, K. M.; Ohkubo, K.; Fukuzumi, S. *J. Am. Chem. Soc*. **2008**, *130*, 14311.
118. Balaban, T. S.; Holzwarth, A. R.; Schaffner, K. *J. Mol. Struc*. **1995**, *349*, 183.
119. Daniell, H. W.; Bruckner, C. *Angew. Chem. Int. Ed*. **2004**, *43*, 1688.
120. Naruta, Y.; Tani, T.; Ishihara, N.; Maruyama, K. *J. Am. Chem. Soc*. **1991**, *113*, 6865.
121. Naruta, Y.; Ishihara, N.; Tani, F.; Maruyama, K. *Bull. Chem. Soc. Jpn.* **1993**, *66*, 158.
122. Konishi, K.; Miyazaki, K.; Aida, T.; Inoue, S. *J. Am. Chem. Soc*. **1990**, *112*, 5639.

123. Konishi, K.; Takahata, Y.; Aida, T.; Inoue, S. *J. Am. Chem. Soc*. **1993**, *115*, 1169.
124. Konishi, K.; Oda, K.; Nishida, K.; Aida, T.; Inoue, S. *J. Am. Chem. Soc.* **1992**, *114*, 1313.
125. Konishi, K.; Suezaki, M.; Aida, T. *Tet. Lett*. **1999**, *40*, 6951.
126. Furusho, Y.; Kimura, T.; Mizuno, Y.; Aida, T. *J. Am. Chem. Soc*. **1997**, *119*, 15267.
127. Konishi, K.; Sugino, T.; Aida, T.; Inoue, S. *J. Am. Chem. Soc.* **1991**, *113*, 6487.
128. Yamamoto, Y.; Nadano, R.; Itagaki, M.; Akiba, K. *J. Am. Chem. Soc*. **1995**, *117*, 8287.
129. Kuroda, Y.; Kato, Y.; Higashioji, T.; Ogoshi, H. *Angew. Chem. Int. Ed*. **1993**, *32*, 723.
130. Mizutani, T.; Ema, T.; Yoshida, T.; Kuroda, Y.; Ogoshi, H. *Inorg. Chem*. **1993**, *32*, 2072.
131. Hayashi, T.; Nonoguchi, M.; Aya, T.; Ogoshi, H. *Tetrahedron Lett*. **1997**, *38*, 1603.
132. Tsubaki, K.; Takaishi, K.; Tanaka, H.; Miura, M.; Kawabata, T. *Org. Lett*. **2006**, *8*, 2587.
133. Yoshida, N.; Osuka A. *Tet. Lett*. **2000**, *41*, 9287.
134. Yoshida, N.; Ishizuka, T.; Osuka, A.; Jeong, D. H.; Cho, H. S.; Kim, D.; Matsuzaki, Y.; Nogami, A.; Tanaka, K. *Chem. Eur. J*. **2003**, *9*, 58.
135. Fukazawa, A. Master thesis, 2008, Tohoku University.
136. Bringmann, G.; Gots, D. C. G.; Gulder, T. A. M.; Reichert, M. *Org. Lett*. **2006**, *8*, 4743.
137. Bringmann, G.; Rudenauer S.; Gots, D. C. G.; Gulder, T. A. M.; Gehrke, T. H.; Bruhn, T.; Kupfer, T.; Radacki, K.; Braunschweg, H.; Heckmann, A.; Lambert, C. *J. Am. Chem. Soc.* **2008**, *130*, 17812.
138. Matano, Y.; Shinozuka, T.; Matsumoto, K.; Imahori, H.; Nakano, H. *Chem. Asian J.* **2007**, *2*, 1417.
139. Tsuda, A.; Furuta, H.; Osuka, A. *J. Am. Chem. Soc*. **2001**, *123*, 10304.
140. Muranaka, A.; Asano, Y.; Tsuda, A.; Osuka, A.; Kobayashi, N. *Chem. Phys. Chem*. **2006**, *7*, 1235.
141. Werner, A.; Michaels, M.; Zander, L.; Lex, J.; Vogel, E. *Angew. Chem. Int. Ed*. **1999**, *38*, 3650.
142. Borovkov, V. V.; Fujii, I.; Muranaka, A.; Hembry, G. A.; Tanaka, T.; Ceuleman, A.; Kobayashi, N.; Inoue, Y. *Angew. Chem. Int. Ed*. **2004**, *43*, 5481.
143. Kuhn, W. *Trans. Faraday Soc*. **1930**, *26*, 293.
144. Borovkov, V. V.; Muranaka, A.; Hembury, G. A.; Origame, Y.; Ponomarev, G. V.; Kobayashi, N.; Inoue, Y. *Org. Lett*. **2005**, *7*, 1015.
145. Kamada, T.; Aratani, T.; Ikeda, T.; Shibata, N.; Higuchi, Y.; Wakamiya, A.; Yamaguchi, S.; Kim, K. S.; Yoon, Z. S.; Kim, D.; Osuka, A. *J. Am. Chem. Soc*. **2006**, *128*, 7670.
146. Kwang, I. W.; Kamada, T.; Ahn, T. K.; Ko, D. M.; Nakamura, T.; Tsuda, A.; Osuka, A.; Kim, D. *J. Am. Chem. Soc*. **2004**, *126*, 16187.
147. Aimi, J.; Oya, K.; Tsuda, A.; Aida, T. *Angew. Chem. Int. Ed*. **2007**, *46*, 2031.
148. Fan, J.; Whithold, J. A.; Olenyuk, B.; Levin, M. D.; Stang, P. J.; Fleisher, E. B. *J. Am. Chem. Soc.* **1999**, *121*, 2741.
149. Seybold, P. G.; Gouterman, M. *J. Mol. Spectrosc*. **1969**, *31*, 1.
150. Kimura, M.; Kitamura, T.; Sano, M.; Muto, T.; Hanabusa, K.; Shirai, H.; Kobayashi, N. *New J. Chem*. **2000**, *24*, 113.
151. Kobayashi, N.; Higashi, R.; Titeca, B. C.; Lamote, F.; Ceulemans, A. *J. Am. Chem. Soc*. **1999**, *121*, 12018.
152. Liu, H.; Huang, J.; Tian, X.; Jiao, X.; Luo, G.; Ji, L. *Chem. Commun*. **1997**, 1575.
153. Tamiaki, H.; Suzuki, S.; Maruyama, K. *Bull. Chem. Soc. Jpn*. **1993**, *66*, 2633.
154. Purrello, R.; Raudino, A.; Scolaro, L. M.; Loisi, A.; Bellacchio, E.; Lauceri, R. *J. Phys. Chem. B* **2000**, *104*, 10900.
155. Nezu, T.; Ikeda, S. *Bull. Chem. Soc. Jpn*. **1993**, *66*, 25.
156. Sebek, J.; Bour, P. *J. Phys. Chem. A* **2008**, *112*, 2920.

157. Park, T.; Shin, J. S.; Han, S. W.; Son, J. K.; Kim, S. K. *J. Phys. Chem. B* **2004**, *108*, 17106.
158. Yamaguchi, T.; Kimura, T.; Matsuda, H.; Aida, T. *Angew. Chem. Int. Ed*. **2004**, *43*, 6350.
159. Takei, F.; Hayashi, H.; Onitsuka, K.; Kobayashi, N.; Takahashi, S. *Angew. Chem. Int. Ed.* **2001**, *40*, 4092.
160. Nolte, R. J. M.; Beijnen, A. J. M.; Drenth, W. *J. Am. Chem. Soc*. **1974**, *96*, 5932.
161. Amabilino, D. B.; Ramos, E.; Serrano, J.-L.; Sierra, T.; Veciana, J. *J. Am. Chem. Soc.* **1998**, *120*, 9126.
162. Matile, S.; Berova, N.; Nakanishi, K.; Novkova, S.; Philipova, I.; Blagoev, B. *J. Am. Chem. Soc.* **1995**, *117*, 7021.
163. Matile, S.; Berova, N.; Nakanishi, K.; Fleischhauer, J.; Woody, R. W. *J. Am. Chem. Soc.* **1996**, *118,* 5198.
164. Tanaka, K.; Itagaki, Y.; Satake, M.; Naoki, H.; Yasumoto, T.; Nakanishi, K.; Berova, N. *J. Am. Chem. Soc.* **2005**, *127*, 9561.
165. Pescitelli, G.; Gavriel, S.; Wang, Y.; Fleischhauser, J.; Woody, R. W.; Berova, N. *J. Am. Chem. Soc.* **2003**, *125*, 7613.
166. DeVoe, H. *J. Chem. Phys*. **1964**, *41*, 393.
167. DeVoe, H. *J. Chem. Phys*. **1965**, *43*, 3199.
168. Zobel, E. Diplomarbeit, RTWH, Aachen, **1989**.
169. Crossly, M. J.; Mackay, L. G.; Try, A. C. *J. Chem. Soc., Chem. Commun.* **1995**, 1925.
170. Huang, X.; Rickman, B. H.; Borhan, B.; Berova, N.; Nakanishi, K. *J. Am. Chem. Soc.* **1998**, *120*, 6185.
171. Rickman, B. H.; Matile, S.; Nakanishi, K.; Berova, N. *Tetrahedron* **1998**, *54*, 5041.
172. Kurtan, T.; Nesnas, N.; Li, Y.-Q.; Huang, X.; Nakanishi, K.; Berova, N. *J. Am. Chem. Soc.* **2001**, *123*, 5962.
173. Huang, X.; Fujioka, N.; Pescitelli, G.; Koehn, F. E.; Williamson, R. T.; Nakanishi, K.; Berova, N. *J. Am. Chem. Soc.* **2002**, *124*, 10320.
174. Lintuluoto, J. M.; Borovkov, V. V.; Inoue, Y. *J. Am. Chem. Soc.* **2002**, *124*, 13676.
175. Proni, G.; Pescitelli, G.; Huang, X.; Nakanishi, K.; Berova, N. *J. Am. Chem. Soc.* **2003**, *125*, 12914.
176. Proni, G.; Pescitelli, G.; Huang, X.; Quraishi, N. Q.; Naanishi, K.; Berova, N. *Chem. Commun.* **2002**, 1590.
177. Yang, Q.; Olmsted, C.; Borhan, B. *Org. Lett.* **2002**, *20*, 3423.
178. Li, X.; Tanasova, M.; Vasileiou, C.; Borhan, B. *J. Am. Chem. Soc.* **2008**, *130*, 1885.

This page intentionally left blank

34 Photochemical and Photophysical Properties of Metallophthalocyanines

Tebello Nyokong and Edith Antunes

Department of Chemistry, Rhodes University, Grahamstown, 6139, South Africa

List of Abbreviations

AcO	acetate
ADMA	anthracene-9,10-bis-methylmalonate
BSA	bovine serum albumin
BHDC	benzyl-*n*-hexadecyldimethyl ammonium chloride
BTH	2,6,-di-tri-tert-butyl-4-methyl phenol
CEL	cremophore EL
CTAC	cetyltrimethylammonium chloride
CTAB	cetyltrimethylammonium bromide
1-ClNP	1-chloronaphthalene
DABCO	1,4,diazobicyclooctane
DCM	dichloromethane
DMF	dimethylformamide
DMSO	dimethylsulfoxide
DPBF	1,3-diphenylisobenzofuran
EC	ethyl cellulose
HPLC	high performance liquid chromatography
HSA	human serum albumin
ISC	intersystem crossing
LB	langmuir-blodgett
LDH	layered double oxide
MPc	metallophthalocyanine
NPc	naphthalocyanine
PBS	phosphate buffer saline (or solution)
Pc	phthalocyanine
PDT	photodynamic therapy
Py	pyridine
d-py	deuterated pyridine
PVC	polyvinyl chloride
SDS	sodium dodecylsulfate

SOLM	singlet oxygen luminescence method
THF	tetrahydrofuran
TX	triton X-100
Φ_F	fluorescence quantum yield
Φ_Δ	singlet oxygen quantum yield
Φ_P	photodegradation quantum yield
τ_T	triplet lifetime

I. Introduction

Phthalocyanines (Pcs) and metallophthalocyanines (MPcs) have a wide variety of applications due to their diverse chemical, structural, electronic and optical properties.[1–7] As a result of their bright blue, green to violet colors and excellent lightfastness, Pcs are used worldwide as dyes and pigments.[7] MPc complexes, in particular CuPcs, are produced in industry on a large scale (~50,000 tons per year). Phthalocyanines show exceptional thermal and chemical stability, with strong acids only protonating conventional MPc complexes.[8–11]

Pcs have found application in rewritable optical media (CD-RW),[1] as photoconducting materials in laser printers and photocopiers,[1] in nonlinear optics,[12] Langmuir-Blodgett (LB) films,[13] semiconductor devices[2,13] and as electrochemical and chemical sensors.[14,15] They have also attracted much attention in oncology as photosensitizers for malignant tumor treatment in photodynamic therapy (PDT). PDT uses a combination of a photosensitizing drug (e.g. MPcs) and light in the presence of molecular oxygen to obtain a therapeutic effect based on selective cell destruction.[4] For use in photocatalysis (photosensitization), MPc complexes containing non-transition metal ions are employed. High triplet state quantum yields and long triplet lifetimes are required for efficient photosensitization, and these criteria may be fulfilled by the incorporation of diamagnetic metals such as zinc, aluminum or silicon into the phthalocyanine macrocycle. A recent review by Ishii and Kobayashi provided the photophysical (singlet and triplet state parameters) data of a range of substituted and unsubstituted MPc complexes,[16] and fast methods for the direct detection of triplet states such as time-resolved electron paramagnetic resonance were discussed. The present chapter focuses chiefly on main group phthalocyanine complexes with emphasis on their photochemical behavior (singlet oxygen and photostability), in addition to some photophysical studies carried out on these complexes. The effects of phthalocyanine ring substituents on these parameters will also be discussed. The common abbreviations employed in this chapter are listed in front. Table 1 lists the phthalocyanine substituents discussed in this chapter. Figure 1 lists MPc (not included in Table 1) and related complexes which will be used in this chapter.

Table 1. General ring (R_1 to R_4) substituents of phthalocyanines.

R can be any of the ring substituents listed in Table 1a. Each ring substituent is represented by **S** followed by an identification number. A **q** following **S1**, **S2**, **S3** and **S4** refers to the quaternized form of the complex. X_1 and X_2 are general axial ligands; X can be any of the axial ligands in Table 1b. The axial ligands are represented by **L** followed by an identification number.

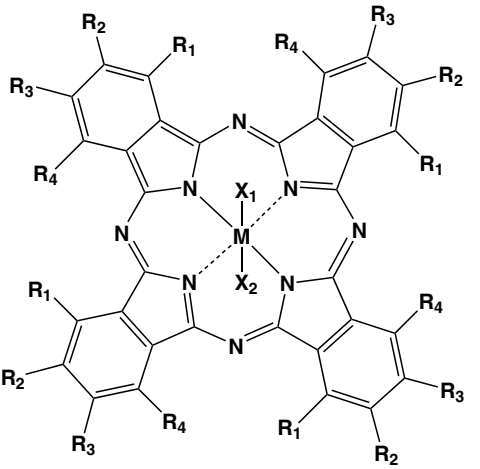

Table 1a. Ring substituents.

Ring substituent (R_1, R_2, R_3, R_4)	Identification number	Ref.
Water solubilizing ligands		
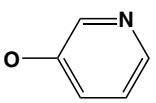	**S1**	67, 69, 98, 115
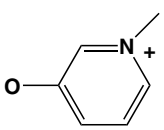	**S1q**	67, 98,115
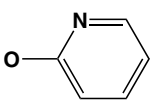	**S2**	70,118,119
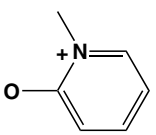	**S2q**	70

(*Continued*)

Table 1a. (*Continued*)

Ring substituent (R_1, R_2, R_3, R_4)	Identification number	Ref.
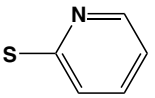	**S3**	68, 70
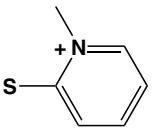	**S3q**	68, 70
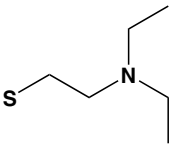	**S4**	72
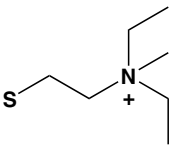	**S4q**	72
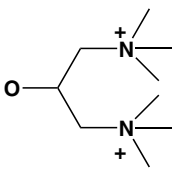	**S5**	73
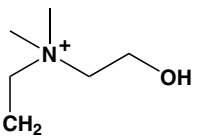	**S6**	74
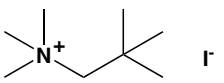	**S7**	75
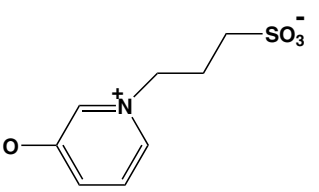	**S8**	76

(*Continued*)

Table 1a. (*Continued*)

Ring substituent (R_1, R_2, R_3, R_4)	Identification number	Ref.
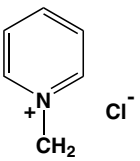	**S9**	74
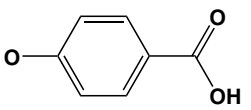	**S10**	36, 54, 78, 97, 156
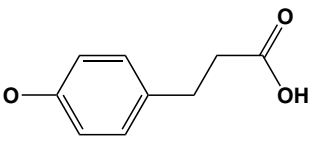	**S11**	78
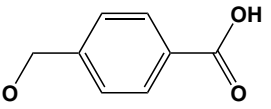	**S12**	79
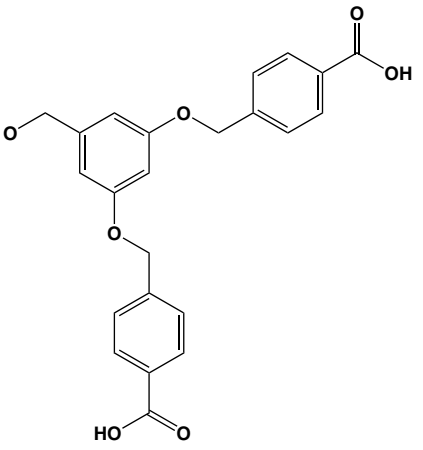	**S13**	79
Other ligands		
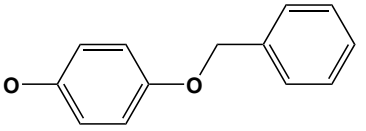	**S14**	89, 139, 118, 179, 186, 188, 198

(*Continued*)

Table 1a. (*Continued*)

Ring substituent (R_1, R_2, R_3, R_4)	Identification number	Ref.
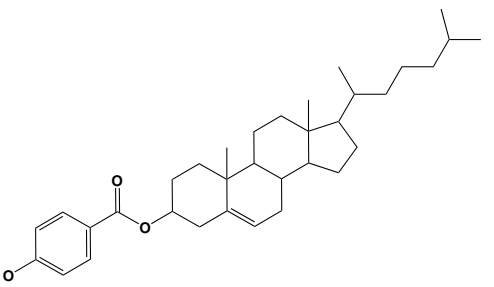	**S15**	36
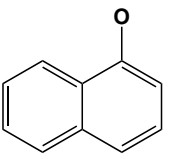	**S16**	36
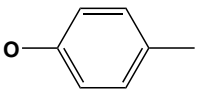	**S17**	36, 41
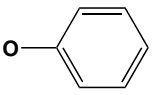	**S18**	8, 36, 44, 45, 54, 127, 136, 139, 148, 156, 177, 179, 184, 191, 200, 186, 211
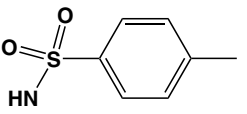	**S19**	132
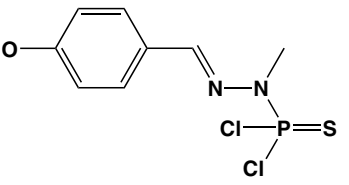	**S20**	134
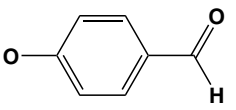	**S21**	36
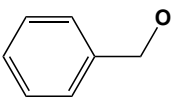	**S22**	136

(*Continued*)

Table 1a. (*Continued*)

Ring substituent (R_1, R_2, R_3, R_4)	Identification number	Ref.
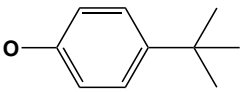	**S23**	8, 33, 36, 37, 41, 54, 88, 139, 148, 156, 157, 177, 179, 184, 186, 191, 200, 211
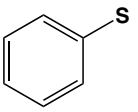	**S24**	36, 137, 139
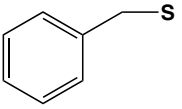	**S25**	136, 137
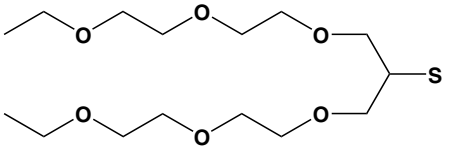	**S26**	138
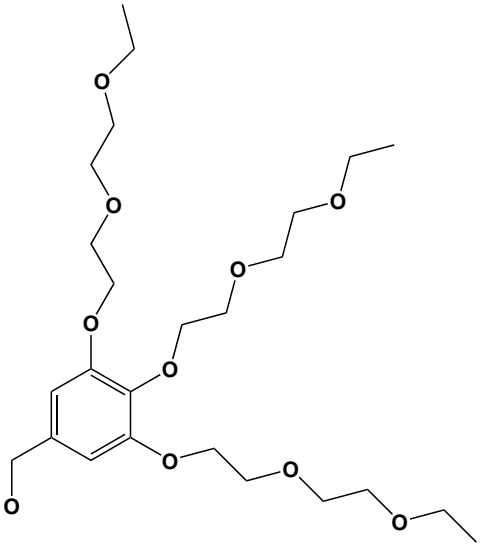	**S27**	149
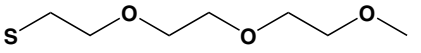	**S28**	100, 150
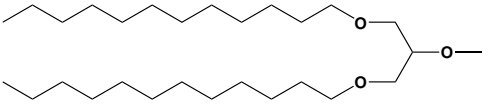	**S29**	143

(*Continued*)

Table 1a. (*Continued*)

Ring substituent (R_1, R_2, R_3, R_4)	Identification number	Ref.
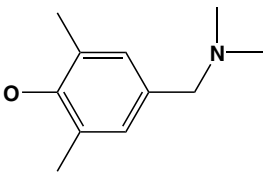	**S30**	88
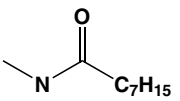	**S31**	87
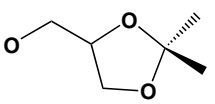	**S32**	147
	**S33**	147
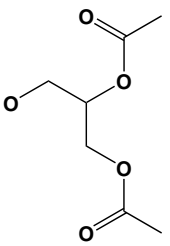	**S34**	147
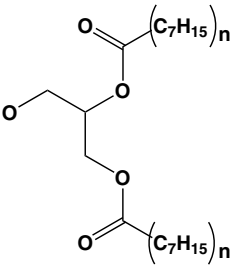	**S35**	147
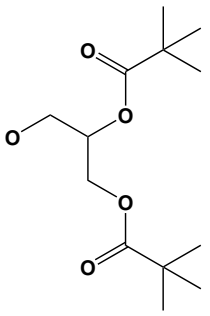	**S36**	147

(*Continued*)

Table 1a. (*Continued*)

Ring substituent (R_1, R_2, R_3, R_4)	Identification number	Ref.
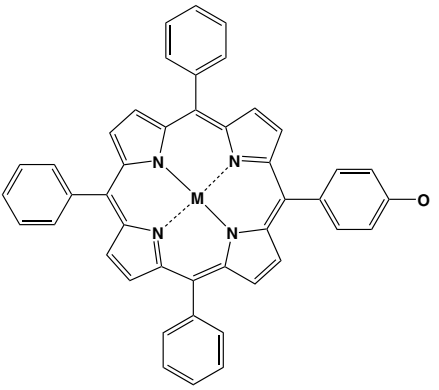	**S37**	151, 168
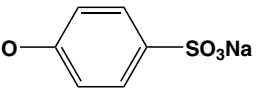	**S38**	148
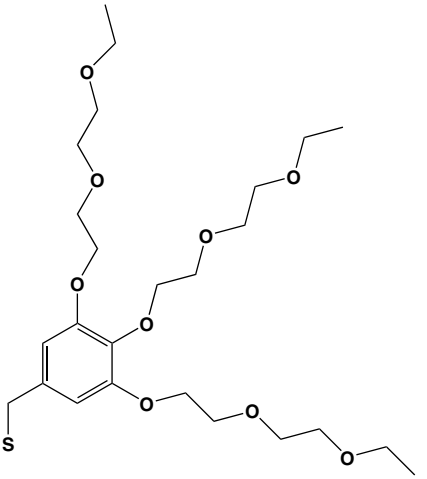	**S39**	149
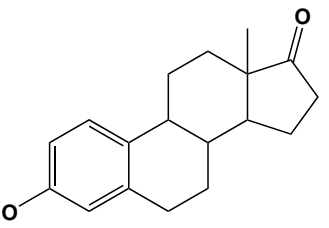	**S40**	36, 37, 45

(*Continued*)

Table 1a. (*Continued*)

Ring substituent (R_1, R_2, R_3, R_4)	Identification number	Ref.
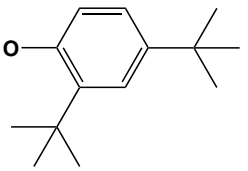	**S41**	36
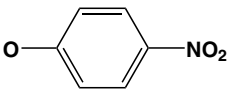	**S42**	36, 45, 156
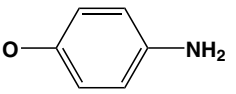	**S43**	36
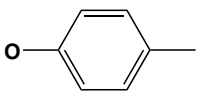	**S44**	36
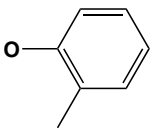	**S45**	45
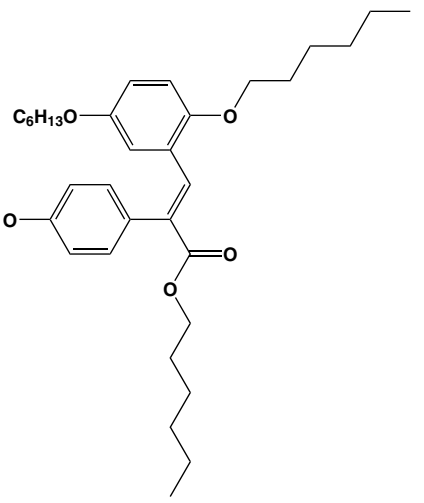	**S46**	161
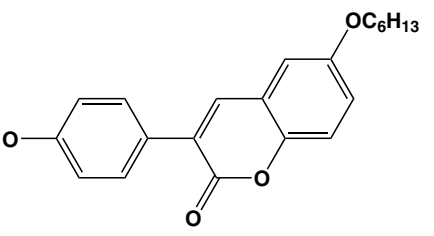	**S47**	161

(*Continued*)

Table 1a. (*Continued*)

Ring substituent (R_1, R_2, R_3, R_4)	Identification number	Ref.
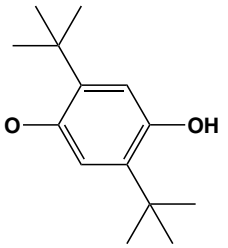	**S48**	160
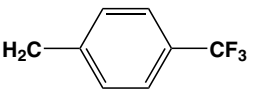	**S49**	159
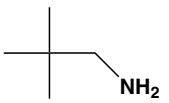	**S50**	75
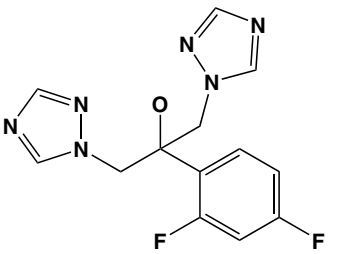	**S51**	158
	**S52**	166
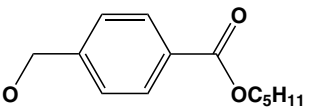	**S53**	79
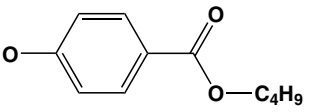	**S54**	78
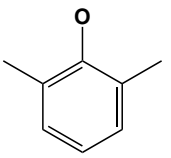	**S55**	164

(*Continued*)

Table 1a. (*Continued*)

Ring substituent (R_1, R_2, R_3, R_4)	Identification number	Ref.
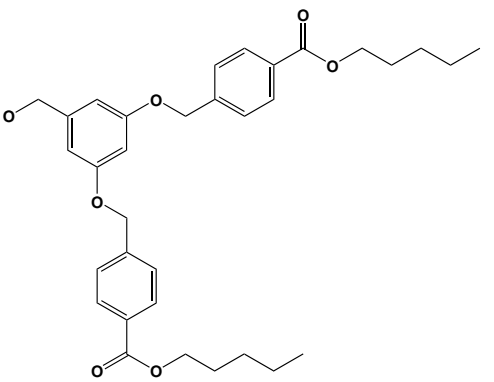	**S56**	79

Table 1b. General axial ligands.

Axial ligand (X_1, X_2)	Identification number	Ref.
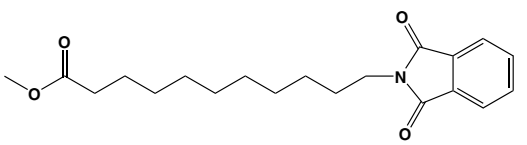	**L1**	141
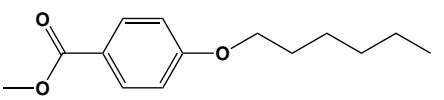	**L2**	141
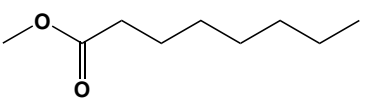	**L3**	141
O_3SCH_3	**L4**	127
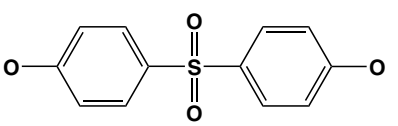	**L5**	183, 185
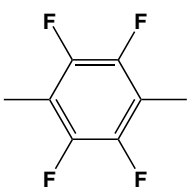	**L6**	183

(*Continued*)

Table 1b. General axial ligands.

Axial ligand (X_1, X_2)	Identification number	Ref.
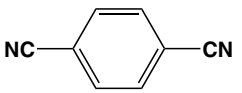	**L7**	183
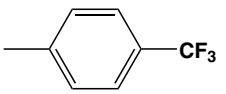	**L8**	182
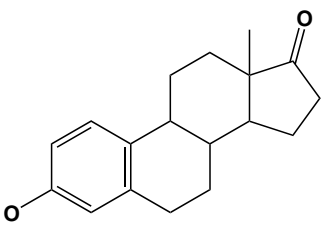	**L9**	45
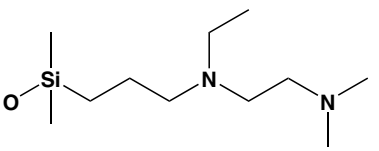	**L10**	145
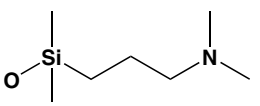	**L11**	145
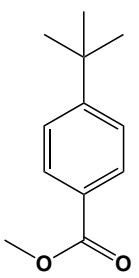	**L12**	195
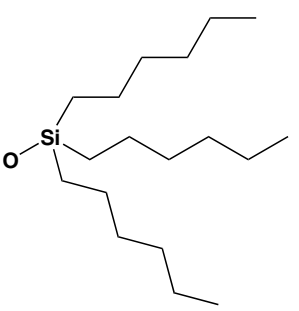	**L13**	44, 127, 193

(*Continued*)

Table 1b. (*Continued*)

Axial ligand (X_1, X_2)	Identification number	Ref.
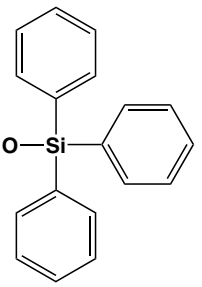	**L14**	44, 127, 193
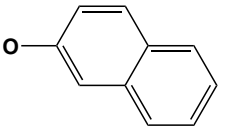	**L15**	44, 127
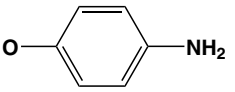	**L16**	44
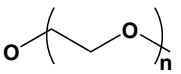	**L17**	192, 194
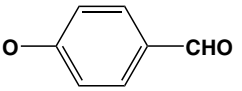	**L18**	127
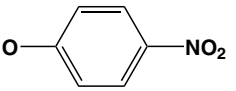	**L19**	127
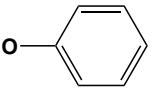	**L20**	127
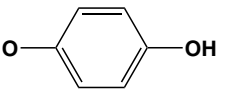	**L21**	127
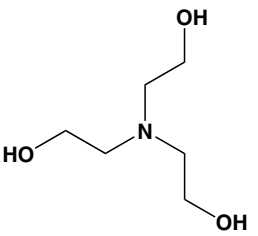	**L22**	127

(*Continued*)

Table 1b. (*Continued*)

Axial ligand (X_1, X_2)	Identification number	Ref.
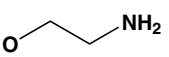	**L23**	127
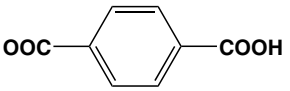	**L24**	127
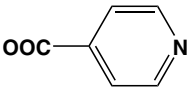	**L25**	127
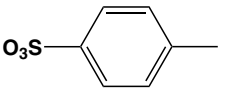	**L26**	127
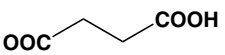	**L27**	127
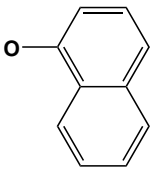	**L28**	44, 127
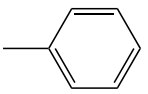	**L29**	202

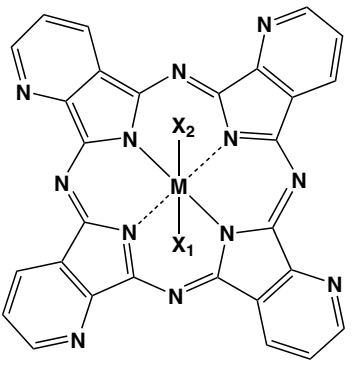

1

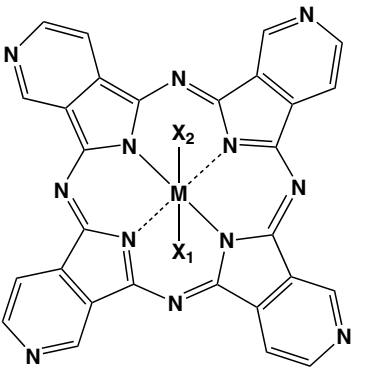

2

Figure 1. Molecular structure of complexes re-drawn from the references provided: **1** (and **1q**),[63] **2** (and **2q**),[87,102] **3** (M = Zn or 2H),[54,97,148] **4** (M = Zn or 2H),[156] **5**,[164] **6**,[164] **7**,[164] **8**,[54,148] **9**,[155] **10**,[181,182] **11**,[181] **12** (M = Ga(III) or In(III)),[183] **13** (M = Zn, Al(III) or Co),[207] **14**.[17]

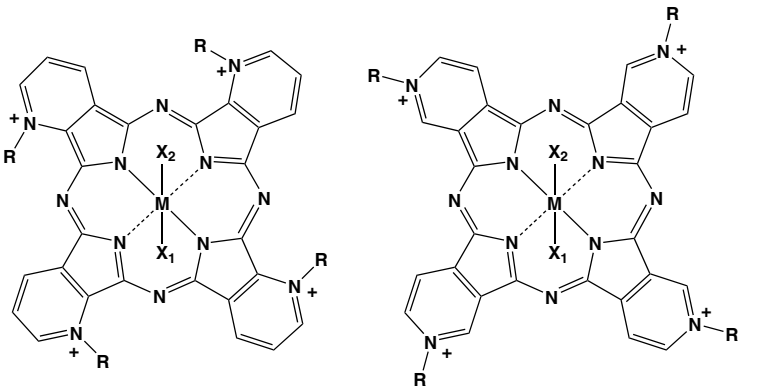

1q (quaternized 1)

2q (quaternized 2)

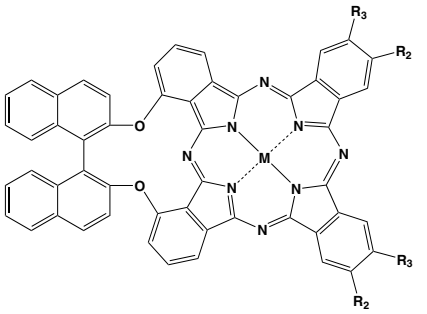

3

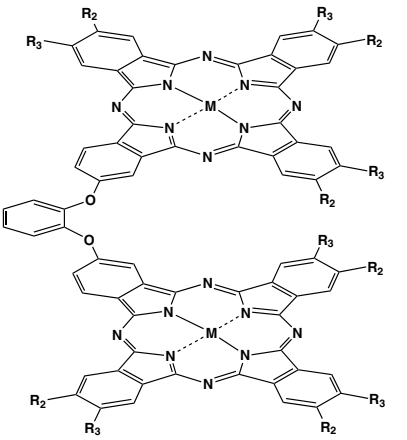

4

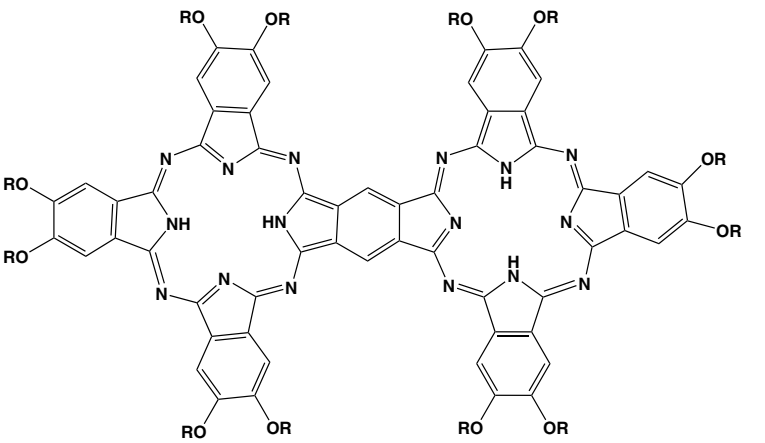

5

Figure 1. (*Continued*)

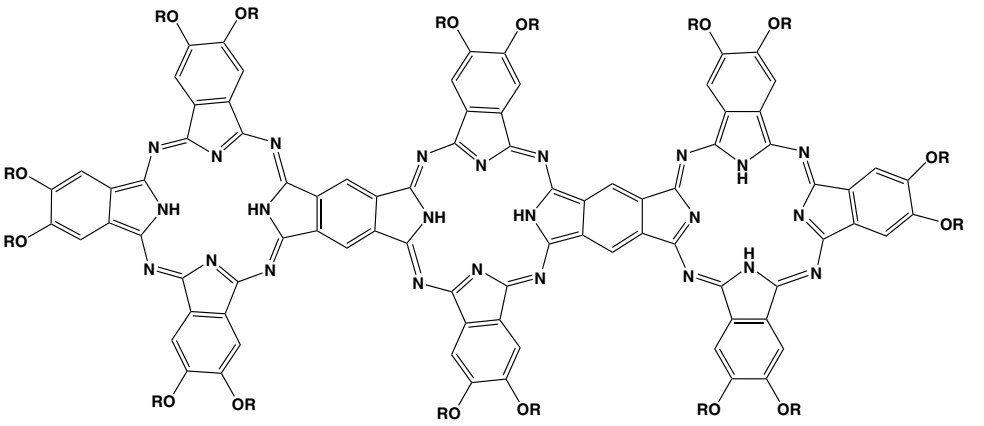

6

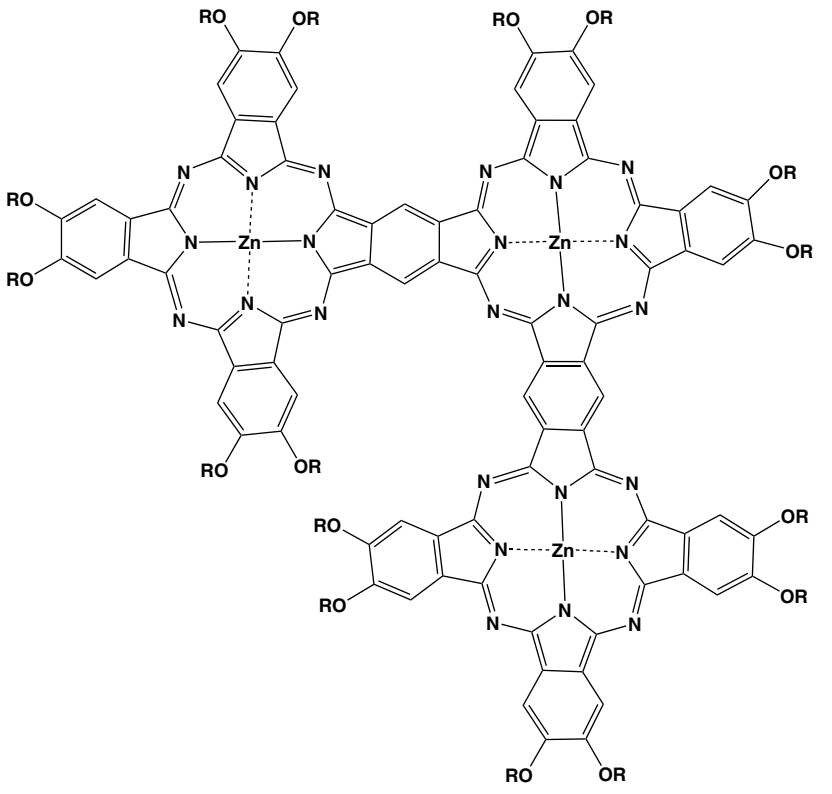

7

Figure 1. (*Continued*)

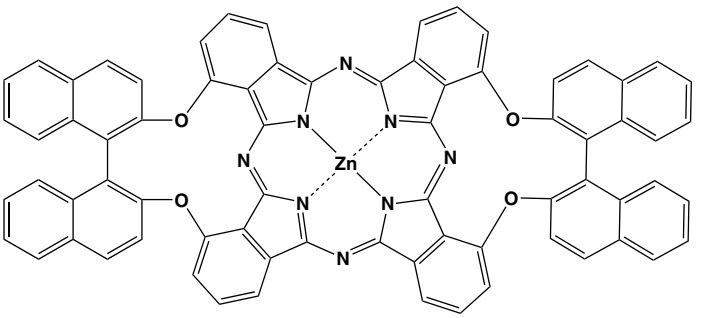

8

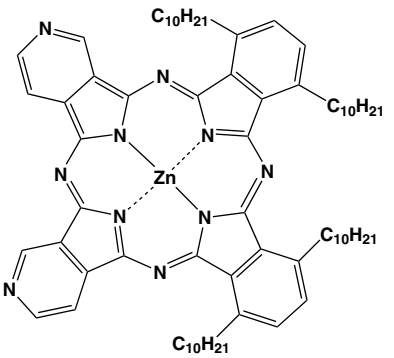

9

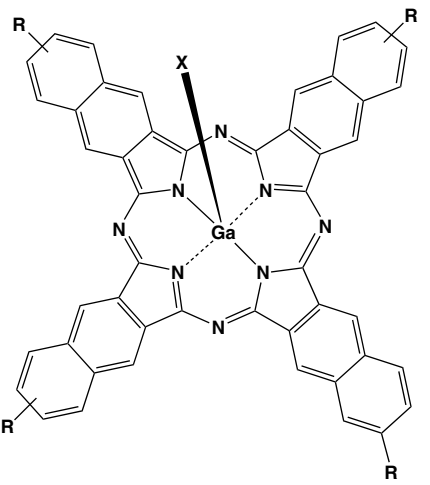

10

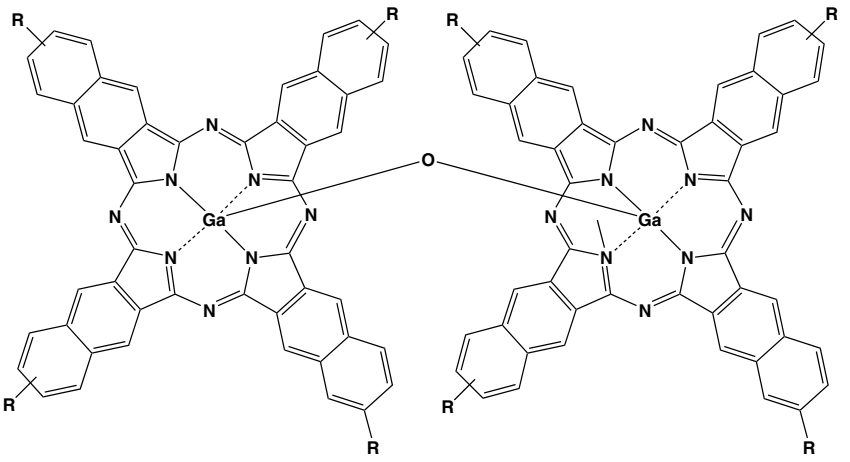

11

Figure 1. (*Continued*)

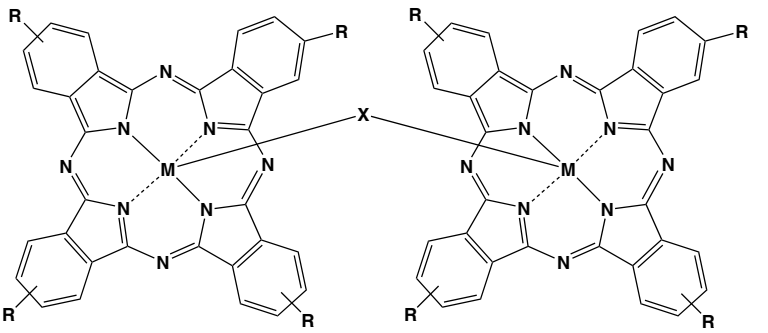

12

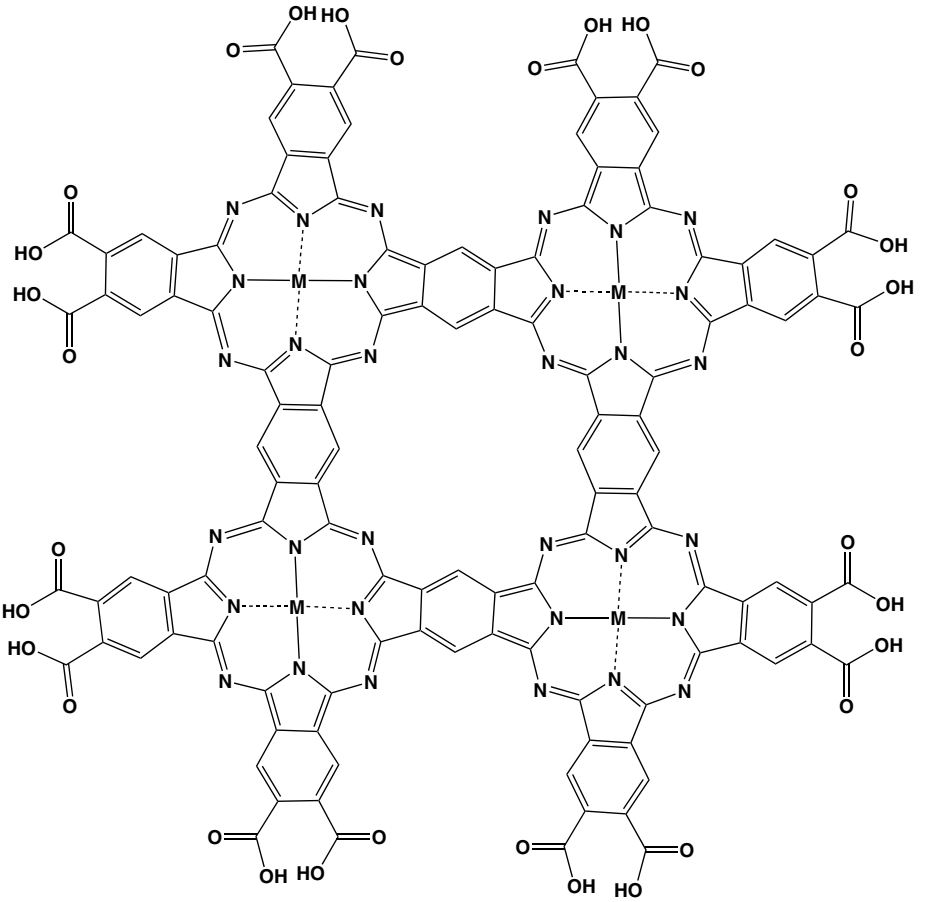

13

Figure 1. (*Continued*)

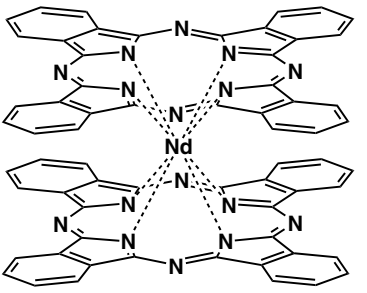

14

Figure 1. (*Continued*)

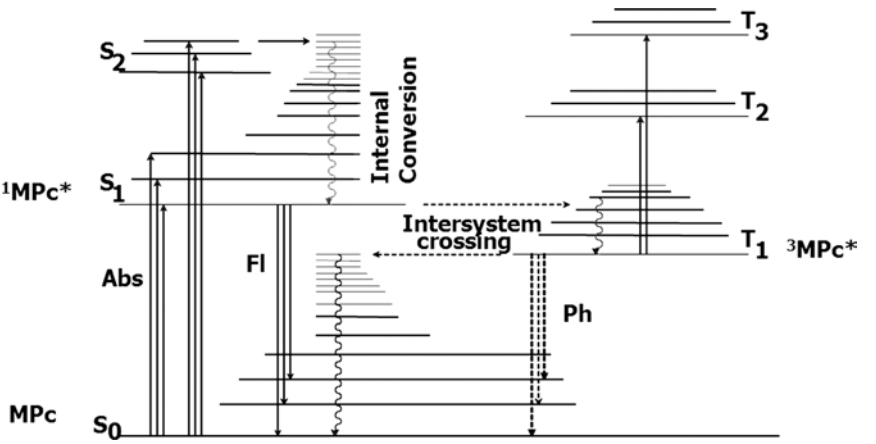

Figure 2. Jablonski diagram. Abs = absorption, Fl = fluorescence, Ph = phosphorescence.

II. Photochemical and Photophysical Parameters

Photochemical studies include singlet oxygen and photodegradation quantum yields, as well as photocatalysis, while photophysical studies include fluorescence and triplet state quantum yields and lifetimes. Since the fluorescence lifetimes have been extensively reviewed,[16] they will not be included in this chapter. Figure 2 shows a Jablonski diagram representing the photophysical processes following light absorption.

A. Singlet Oxygen Quantum Yields (Φ_Δ)

MPc complexes act as photosensitizers for many reactions, including the degradation of pollutants[17–19] and transformation of alkenes and alkanes.[20] Most notable among the uses of Pcs is their use as photosensitizers in oncology, particularly in

$$\mathrm{MPc} \rightarrow {}^{1}\mathrm{MPc}^{*} \xrightarrow{\mathrm{ISC}} {}^{3}\mathrm{MPc}^{*} \quad (1)$$

$${}^{3}\mathrm{MPc}^{*} + {}^{3}\mathrm{O}_2 \rightarrow {}^{1}\mathrm{O}_2 \quad (2)$$

$${}^{1}\mathrm{O}_2 + \mathrm{Subs} \rightarrow \mathrm{Oxidation\ products} \quad (3)$$

Scheme 1. Type II mechanism.[27,38–45] Here, MPc = metallophthalocyanine, ISC = intersystem crossing, Subs = substrate, ${}^{3}\mathrm{O}_2 = \mathrm{O}_2({}^{3}\Sigma_g)$ and ${}^{1}\mathrm{O}_2 = \mathrm{O}_2({}^{1}\Delta_g)$.

$${}^{3}\mathrm{MPc}^{*} + \mathrm{O}_2 \rightarrow \mathrm{MPc}^{+\bullet} + \mathrm{O}_2{}^{-\bullet} \quad (4)$$

$${}^{3}\mathrm{MPc}^{*} + \mathrm{Subs} \rightarrow \mathrm{MPc}^{-\bullet} + \mathrm{Subs}^{+\bullet} \quad (5)$$

$$\mathrm{MPc}^{-\bullet} + \mathrm{O}_2 \rightarrow \mathrm{MPc} + \mathrm{O}_2{}^{-\bullet} \quad (6)$$

$$\mathrm{O}_2{}^{-\bullet} \xrightarrow{\mathrm{H}^{+}} \mathrm{HO}_2{}^{\bullet} \quad (7)$$

$$\mathrm{HO}_2{}^{\bullet} + \mathrm{Subs{-}H} \rightarrow \mathrm{H}_2\mathrm{O}_2 + \mathrm{Subs}^{\bullet} \quad (8)$$

$$\mathrm{Subs}^{+\bullet}, \mathrm{Subs}^{\bullet}, \mathrm{H}_2\mathrm{O}_2 \rightarrow \mathrm{Oxidation\ Products} \quad (9)$$

Scheme 2. Type I mechanism.[27,40] MPc = metallophthalocyanine, Subs = substrate.

photodynamic therapy (PDT).[4,21–28] ZnPc complexes in particular are well known for their photosensitizing abilities,[29–37] while unmetalated phthalocyanine complexes show very little PDT effect.[28] It is believed that during photosensitization (photocatalysis), the MPc molecule is first excited to the triplet state, and then transfers the energy to ground state oxygen, $\mathrm{O}_2({}^{3}\Sigma_g)$, generating excited state oxygen, $\mathrm{O}_2({}^{1}\Delta_g)$, the chief cytotoxic species, which subsequently oxidizes the substrate. This is the Type II mechanism as shown in Scheme 1.[27,38–45]

Singlet oxygen is generated when oxygen in its triplet state (${}^{3}\mathrm{O}_2$) interacts with a sensitizer (in its triplet state, ${}^{3}\mathrm{MPc}^{*}$).Thus singlet oxygen quantum yields are expected to be comparable to the MPc triplet state quantum yields if quenching of the latter by ground state oxygen is efficient.[39] The excited triplet state of the MPc (${}^{3}\mathrm{MPc}^{*}$) can also interact with ground state molecular oxygen or substrate molecules (Eqs. 4 and 5) generating superoxide (Eqs. 4 and 6) and hydroperoxyl radicals (Eq. 7), which subsequently afford oxidation of the substrate (Eqs. 8 and 9) by a Type I mechanism (Scheme 2).[27,40]

It has been reported that the Type II mechanism is more prevalent[39] in photoinitiated oxidation reactions; thus the magnitude of singlet oxygen quantum yield (Φ_Δ), which expresses the amount of singlet oxygen generated per quanta of light, is often employed as a main criterion in choosing the photosensitizers to be used in photocatalytic reactions. Many factors associated with the sensitizers are responsible for the magnitude of the determined quantum yield of singlet oxygen, including: triplet excited state energy, ability of substituents and solvents to

quench the singlet oxygen, the triplet excited state lifetime and the efficiency of the energy transfer between the triplet excited state of the sensitizer and the ground state of oxygen.

The singlet oxygen quantum yields for the MPc complexes may be conveniently determined using a singlet oxygen quencher such as 1,3-diphenylisobenzofuran (DPBF), or by using the singlet oxygen luminescence method (SOLM). The results using the two methods are comparable.[33] Side reactions are excluded when SOLM is employed. When DPBF is employed in micellar solutions, chain reactions occur as a result of the endoperoxide initially formed, but this problem can be overcome by adding sodium thiosulfate which destroys endoperoxide.[33] DPBF is an efficient $^1O_2$ quencher in organic solvents and its disappearance can be readily monitored by following the decrease in its absorption peak at 416 nm [in dimethylsulfoxide (DMSO), for example], as in Figure 3.[33]

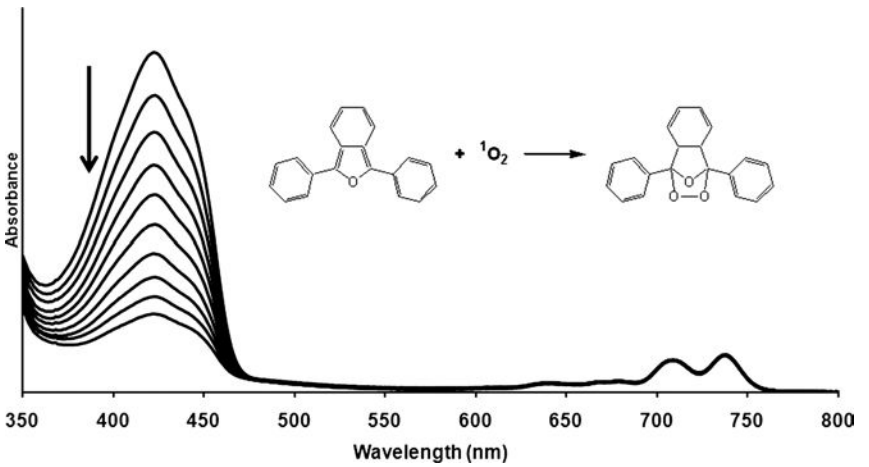

Figure 3. Change in absorption spectra of diphenyl isobenzofuran (DPBF) as singlet oxygen is produced by the phthalocyanine. Inset: Representation of the reaction of singlet oxygen with DPBF.

$$^3O_2 + {}^3MPc^* \xrightarrow{h\nu} {}^1O_2 \quad (10)$$

$$^1O_2 \xrightarrow{k_d} {}^3O_2 \quad \text{Natural decay} \quad (11)$$

$$^1O_2 + DPBF \xrightarrow{k_q} \text{Oxidation products (chemical quenching)} \quad (12)$$

$$^1O_2 + DPBF \xrightarrow{k_{p(DPBF)}} {}^3O_2 + DPBF^* \text{ (physical quenching)} \quad (13)$$

$$^1O_2 + MPc \xrightarrow{k_{p(MPc)}} {}^3O_2 + MPc^* \text{ (physical quenching)} \quad (14)$$

$$^1O_2 + MPc \xrightarrow{k_{q(MPc)}} \text{Chemical reaction (chemical quenching)} \quad (15)$$

Scheme 3. Physical and chemical reactions of DPBF in the presence of $^1O_2$.

Anthracene-9, 10-bis-methylmalonate (ADMA) may be employed as a singlet oxygen quencher in aqueous media by monitoring its disappearance at 380 nm in the presence of singlet oxygen. Scheme 3 shows the fate of $^1O_2$ in the presence of DPBF.

DPBF acts exclusively as a chemical quencher in DMSO and other organic solvents, and thus Eq. 13 may be disregarded. Physical quenching through Eq. 14 may also be ignored since Φ_Δ does not depend on the concentration of the sensitizer (MPc). Furthermore, the reaction rate of the sensitizer with $^1O_2$ according to Eq. 15 is negligible compared to the rate of $^1O_2$ of reaction with DPBF. Thus, only Eqs. 11 and 12 are relevant to the decay of singlet oxygen, and these equations may be used in deriving Eq. 16 for the determination of Φ_Δ employing a standard such as unsubstituted ZnPc[19,35,37]:

$$\Phi_\Delta = \Phi_\Delta^{Std} \frac{W \cdot I_{abs}^{Std}}{W^{Std} \cdot I_{abs}} \tag{16}$$

where Φ_D^{Std} is the singlet oxygen quantum yield for the standard, W and W^{Std} are the DPBF photobleaching rates in the presence of MPc derivatives under investigation and the standard, respectively. I_{abs} and I_{abs}^{Std} are the rates of light absorption by the MPc derivative and standard, respectively. A similar equation may be derived for the use of ADMA as a quencher.

I_{abs} is determined by Eq. 17:

$$I_{abs} \frac{\alpha SI}{N_A} \tag{17}$$

where α is the fraction of light absorbed, S is the cell area irradiated, N_A is Avogadro's constant and I the light intensity.

In the absence of appropriate standards, DPBF (or ADMA) quantum yields (Φ_{DPBF}) are calculated using Eq. 18[33]:

$$\Phi_{DPBF} = \frac{(C_0 - C_t)V}{tI_{abs}} \tag{18}$$

where C_0 and C_t are the respective concentrations of DPBF before and after irradiation, t the irradiation time and V is the volume of the sample. Singlet oxygen quantum yields are then calculated using Eq. 19[33]:

$$\frac{1}{\Phi_{DPBF}} = \frac{1}{\Phi_\Delta} + \frac{1}{\Phi_\Delta} \frac{k_d}{k_a} \frac{1}{[DPBF]} \tag{19}$$

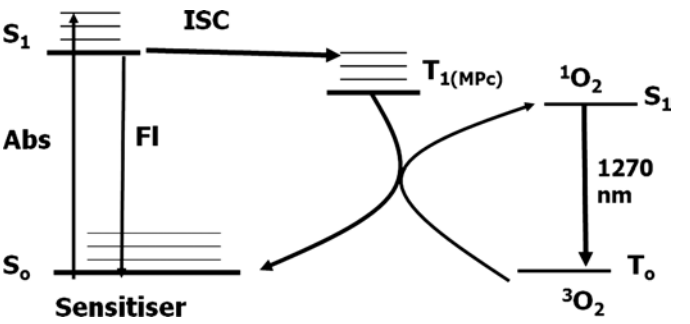

Figure 4. Simplified Jablonski diagram showing the 1270 nm luminescence of singlet oxygen. ISC = intersystem crossing, Fl = fluorescence.

where k_d is the singlet oxygen decay rate constant and k_q the reaction rate constant of DPBF in the presence of singlet oxygen. $1/\Phi_\Delta$ is obtained from the intercept of a plot of $1/\Phi_{DPBF}$ versus 1/[DPBF].

The use of the singlet oxygen luminescence method (SOLM) relies on the luminescence of singlet oxygen at 1270 nm, which is a spin forbidden process (S_1–T_1) (Figure 4), but occurs in an area that is generally free from interference. However, the signal is weak. The dynamic course of $^1O_2$ concentration [$^1O_2$] can be clearly recorded, following Eq. 20 as described theoretically in the literature[38]:

$$[^1O_2] = A\frac{\tau_D}{\tau_T - \tau_D}\left[\exp\left(\frac{-t}{\tau_T}\right) - \exp\left(\frac{-t}{\tau_D}\right)\right] \quad (20)$$

where the τ_D is the lifetime of $^1O_2$, τ_T is the lifetime of MPc at the triplet state, *t* is time in seconds and *A* is a coefficient involved in sensitizer concentration and singlet oxygen quantum yield. The singlet oxygen quantum yield may then be determined by the relative method using a standard such as ZnPc, Eq. 21:

$$\Phi_\Delta = \Phi_\Delta^{Std}\frac{A}{A^{Std}} \quad (21)$$

where Φ_Δ^{Std} is the singlet oxygen quantum yield for the standard, A and A^{std} are the coefficients of the sample and standard, respectively. Standards which are often employed for Φ_Δ are listed in Table 2 in different solvents.[12,27,33,41,42,48]

The equipment employed for the SOLM method is shown in Figure 4, and consists of an ultrasensitive detector such as a Ge detector, combined with a series of filters to minimize background signals. The equipment uses a laser excitation source as shown in Figure 5. A typical signal obtained from the SOLM for singlet oxygen obtained from an MPc complex is shown in Figure 6.

Table 2. Photochemical and photophysical data for complexes commonly used as references for triplet quantum yields (Φ_T), fluorescence quantum yields (Φ_F) and singlet oxygen quantum yields (Φ_Δ).[a]

Complex	Solvent	$\lambda_{Q\ band}$/nm (log ε)	λ_T/nm (log ε)	Φ_T	Φ_F	Φ_Δ	τ_T (μs)	Ref.
ZnPc	Toluene/ 1% py	671.5 (5.25)	490 (4.56)	0.58	0.34	0.54	330	48
ZnPc	DMSO	672 (5.38)		0.50	0.20	0.67	350	41
ZnPc	DMF	670				0.56		33
ZnPc	1-ClNP				0.3			47
ZnPc	Ethanol	670			0.53			33
ZnT*t*BPc	Ethanol	674 (5.20)	490 (4.55)	0.58		0.54	200	12
Li_2Pc	Acetonitrile	665 (5.18)	469 (3.58)	0.60	0.5	0.50	60	50
Chlorophyll *a*	Pyridine					0.59		27
Chlorophyll *a*	Benzene					0.60		27
Chlorophyll *a*	Toluene					0.60		27
Chlorophyll *a*	Ether				0.32			48
Cresyl violet	Methanol					0.54		48
Rhodamine 6G	Ethanol				0.94			46, 49

[a]The following symbols apply to all tables: Φ_F = fluorescence quantum yield (in general the standard used for determination of Φ_F is chlorophyll *a* in ether (Φ_F = 0.32) [49]); Φ_T = triplet quantum yield; Φ_Δ = singlet oxygen quantum yield; τ_T = triplet life time.

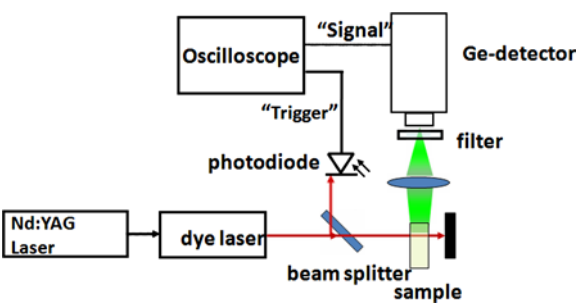

Figure 5. A diagrammatic representation of the singlet oxygen detector system using the singlet oxygen luminescence at 1270 nm.

B. Photodegradation Quantum Yields (Φ_P)

Photostability of MPc complexes is important for their application as photocatalysts (photosensitizers). Photodegradation is the oxidative degradation of a photosensitizer molecule with time into lower molecular weight fragments.[33] Photodegradation generally depends on the structure of the molecule, concentration, solvent and light intensity. It is believed that photodegradation is a $^1O_2$ mediated process, since $^1O_2$ is highly reactive and it can react with macrocyclic metal

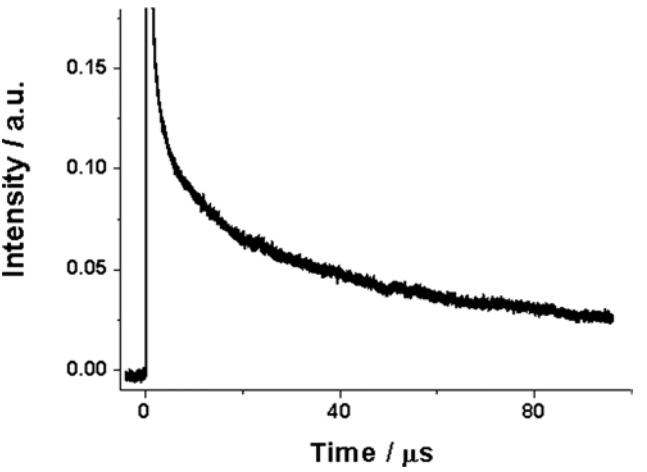

Figure 6. A typical decay curve observed during singlet oxygen determination using its luminescence at 1270 nm.

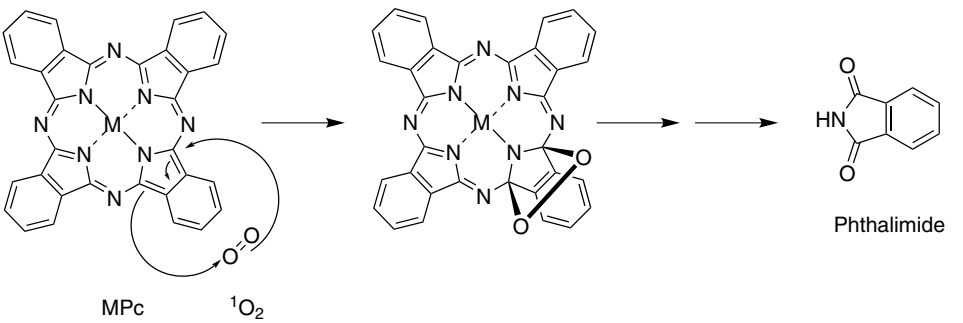

Scheme 4. Photodegradation of phthalocyanine by singlet oxygen. Modified from Ref. 34.

complexes, such as phthalocyanines as shown in Scheme 4.[34] Phthalimide was found to be the photooxidation product following degradation of MPcs.[34] Photodegradation (photobleaching) is characterized by a decrease in the intensity of both the Q- and B-bands, without a shift in maxima or formation of new bands in the visible region. Photobleaching quantum yields (Φ_p) may thus be determined using Eq. 22.[19,33,35,37]

$$\Phi_P = \frac{(C_0 - C_t)VN_A}{I_{abs}St} \tag{22}$$

where C_t and C_0 in mol.l^{-1} are the MPc molar concentrations after and prior to irradiation, respectively, V is the reaction volume, S the irradiated area of the

cell, t the irradiation time, N_A is the Avogadro's number and I_{abs} is defined by Eq. 17.

C. Fluorescence Quantum Yields (Φ_F)

Fluorescence properties of MPcs such as spectral shifts, fluorescence quantum yields and lifetimes are influenced by the presence and nature of the central metal, aggregation, nature of solvent, pH, halogenation, photoinduced electron transfer or electronic energy transfer, amongst other factors. Fluorescence quantum yield (Φ_F) is a measure of the efficiency of the emission process. Fluorescence quantum yields may be determined by the comparative method, using a well-known standard. Equation 23 may be employed,[44–47] using a reference such as chlorophyll *a*:

$$\Phi_F = \Phi_F^{Std} \frac{FA^{Std} n^2}{F^{Std} A (n^{Std})^2} \tag{23}$$

where F and F^{Std} are the areas under the emission curves of the sample and standard, respectively, A and A^{Std} are the absorbances of the sample and standard, respectively, and n and n^{Std} are the refractive indices of the solvents used for sample and standard, respectively. The references often employed for the determination of fluorescence quantum yields (Φ_F) are listed in Table 2.[41,46–50]

D. Triplet State Quantum Yields (Φ_T) and Lifetimes (τ_T)

Population of the triplet state with excited MPc molecules is of importance in visible light driven processes such as photocatalysis (photosensitization), since these excited molecules transfer their energy to ground state oxygen to produce singlet oxygen which is essential in these processes.

Laser flash photolysis gives information about the triplet–triplet absorption and the lifetime of the excited species. The equipment employed is shown diagramatically in Figure 7. The triplet quantum yield (Φ_T) is based on the maximum absorption of the triplet state generated during laser flash photolysis experiments. The triplet state absorption of MPcs is at ~500 nm, a region which is far away from their ground state absorption maximum (Q- band ~700 nm). This provides for easy measurement of the triplet absorption since there is no overlap. Φ_T can be determined using a standard with a known Φ_T, some of the standards are listed in Table 2.[12,41,48,50] The transient absorption due to the triplet state between 450 and 550 nm is accompanied by loss in the absorption in the Soret and Q-band regions due to depletion of the parent compounds (Figure 8). For triplet quantum yield

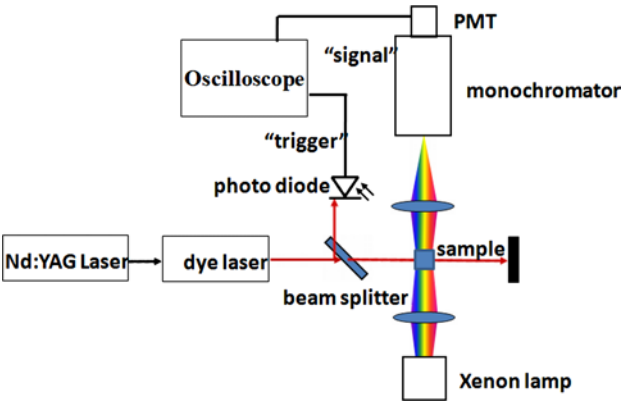

Figure 7. A diagrammatic representation of the laser flash photolysis system used for triplet yields and lifetimes.

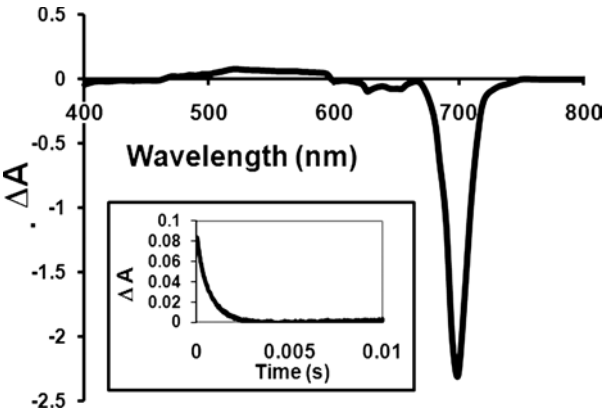

Figure 8. Typical differential absorption spectrum of a metallophthalocyanine (MPc). Inset: Typical triplet decay curve of MPc.

determinations, either the singlet depletion method, Eq. 24,[41,51–54] or triplet absorption method, Eq. 25,[54,55] may be employed:

$$\Phi_T = \Phi_T^{Std} \frac{\Delta A_S \varepsilon_S^{Std}}{\Delta A_S^{Std} \varepsilon_S} \tag{24}$$

$$\Phi_T = \Phi_T^{Std} \frac{\Delta A_T \varepsilon_T^{Std}}{\Delta A_T^{Std} \varepsilon_T} \tag{25}$$

where ΔA_S and ΔA_S^{Std} are the changes in the singlet state absorbance of the MPc derivative and standard (such as ZnPc), respectively. ΔA_T and ΔA_T^{Std} are the

changes in the triplet state absorption of the MPc derivative and the standard, respectively. Φ_T^{Std} is the triplet state quantum yield for the standard. ε_S and ε_S^{Std} are the singlet state extinction coefficients for the MPc derivatives and the standard, respectively. ε_T and ε_T^{Std} are the triplet state extinction coefficients for the MPc derivatives and the standard respectively, and are determined from the molar extinction coefficients of their respective singlet states (ε_S and ε_S^{Std}), the changes in absorbances of the ground singlet states (ΔA_S and ΔA_S^{Std}) and changes in the triplet state absorptions (ΔA_T and ΔA_T^{Std}), according to Eqs. 26 and 27:

$$\varepsilon_T = \varepsilon_S \frac{\Delta A_T}{\Delta A_S} \tag{26}$$

$$\varepsilon_T^{Std} = \varepsilon_S^{Std} \frac{\Delta A_T^{Std}}{\Delta A_S^{Std}} \tag{27}$$

The lifetime of an excited state is the time taken to diminish the population of the molecules in that state to 1/e of its initial concentration. A decay curve (Figure 8 inset) gives the triplet lifetime. The lifetimes of the transients are determined from a software program such as OriginPro 7.5, used in fitting the triplet decay curve. The triplet curve may obey second order kinetics, at high concentrations ($> 1 \times 10^{-4}$ M), due to the triplet–triplet recombination.[56]

III. Water Soluble Phthalocyanine Complexes

For PDT action, it is necessary that the drug be easy to administer via systemic injection into the blood stream. As the blood itself is a water-based system, water solubility then becomes an essential requirement for a PDT drug. Additionally, the drug will have to traverse lipid membranes, meaning that it should also be lipophilic. Water solubility is also essential for use of MPc complexes in the photodegradation of pollutants such as chlorinated phenols under homogeneous conditions. Hence, water soluble Pc complexes will be discussed separately. The most common water-soluble complexes are the sulfonated MPcs.[57,58] Sulfonation[59] by the reaction of MPc complexes with fuming sulfuric acid (containing SO_3) gives a variable mixture of differently sulfonated metallophthalocyanine complexes ($MPc(SO_3^-)_n$, where M = metal ion, n = mixture of 1, 2, 3, or 4 sulfonate groups, which will be represented as $MPc(SO_3)_{mix}$ in this chapter, each containing a variety of positional isomers. Mixed-sulfonated aluminium phthalocyanine [ClAl(III)$Pc(SO_3)_{mix}$], commercially known as Photosens® has been developed as a PDT drug with a fair measure of success.[27] Tetrasulfonated derivatives are generally synthesized by Weber and Busch's method.[60]

Pentasulfonation has been reported in cases where tetrasulfonation was expected.[61]

Tetrapyridinoporphyrazine (Figure 1, complexes **1** and **2**) are phthalocyanines in which the outer benzene rings are replaced with electron-withdrawing pyridine rings.[62] The *N*,*N*′,*N*″,*N*‴-tetramethylated quaternized forms of tetrapyridinoporphyrazines (Figure 1, complexes **1q** and **2q**) are tetrapositively charged and hence water soluble.[62–66] Other positively charged water soluble complexes include quaternized phthalocyanines containing substituents **S1q**, **S2q**, **S3q** or **S4q** which are quaternized forms of **S1**, **S2**, **S3** or **S4**.[67–72] A wide variety of quaternized MPc complexes exist in addition to the ones mentioned above. These include MPc complexes substituted with **S5**,[73] **S6**,[74] **S7**,[75] **S8**,[76] and **S9**.[74] MPcs containing carboxylic acid groups,[77] hence negatively charged, have also been studied. These include MPc complexes substituted with **S10**,[78] **S11**,[78] **S12**,[79] and **S13**.[79] Some cationic phthalocyanines have been found to target vulnerable sites in cells,[80] showing their importance in tumor necrosis and photoinactivation of bacteria.

A. Aggregation Behavior

Aggregation is usually depicted as a coplanar association of rings progressing from monomer to dimer and higher order complexes. Aggregation in MPcs is dependent on the concentration, nature of the solvent, nature of the substituents, complexed metal ions and temperature. In the aggregated state, the electronic structure of the complexed phthalocyanine rings are perturbed, resulting in the alternation of the ground and excited state electronic structures. Water soluble Pc complexes readily form aggregates. Sulfonated MPc complexes often form dimers or higher aggregates in solution.

The relative geometry of the macrocycles determines the spectroscopic behavior of aggregates. According to Kasha's molecular exciton theory,[81] the absorption band of aggregates will be blue-shifted (Figure 9) with respect to the monomer band when the angle between the polarization axes of monomer and the line of molecular center of the aggregate is larger than 54.7°. If the angle is equal to 90°, the molecules are in a face-to-face fashion (the so-called H-type aggregate). On the other hand, when the angle is smaller than the critical angle of 54.7°, the aggregate peak is red-shifted (the so-called J-type aggregate). The cofacial arrangement (common in most Pc aggregates) generally yields the blue-shifted H-aggregates,[82,83] whereas an edge-to-edge arrangement of the J-aggregates is less common. The H aggregates show an absorption band around 630 nm.[82] MPc photosensitizers that form dimers and higher aggregates show a lower photosensitization efficiency.[57,84] Aggregation reduces the lifetimes of the MPc excited state, most probably due to enhanced radiationless excited state dissipation.[83] Therefore, the quantum yields

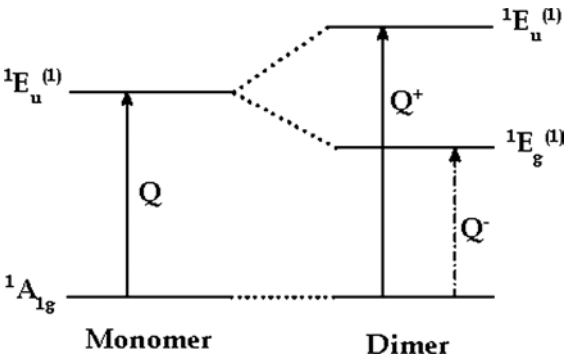

Figure 9. Energy levels showing the transitions involved in aggregated MPc complexes. Modified from Gasyna, Z.; Kobayashi, N.; Stillman, M. J. J. *Chem. Soc. Dalton Trans.* **1989**, 2397–2405, Copyright 1989 Royal Society of Chemistry.

of the excited states and consequently, singlet oxygen generation, are lowered. The degree of sulfonation, isomeric composition and the nature of the central metal ion affect the extent of aggregation. Biological environments support monomerization of phthalocyanines.

1. *Sulfonated Derivatives*

$ClAl(III)Pc(SO_3)_{mix}$, $(OH)_2Si(IV)Pc(SO_3)_{mix}$ and $(OH)_2Ge(IV)Pc(SO_3)_{mix}$ complexes in pH 7.4 buffer show broadening and splitting of the Q-band.[51,53] This behavior is characteristic of the formation of aggregates in sulfophthalocyanines. For these three complexes, addition of a surfactant (Triton X-100) did not bring about any noticeable change in shape and intensity of the spectra, suggesting that these complexes are in a monomeric state. Addition of Triton-X-100 to solutions of $ZnPc(SO_3)_{mix}$ and $(OH)_2Sn(IV)Pc(SO_3)_{mix}$ induced considerable increases in intensity of the low energy band in the visible region, suggesting that the molecules are aggregated and that addition of Triton X-100 breaks up the aggregates.

The degree of aggregation in water increases with lipophilicity,[58] hence the prevalence of the less sulfonated fractions in solution is expected to increase aggregation. High performance liquid chromatography (HPLC) confirmed[53] that $ClAl(III)Pc(SO_3)_{mix}$, $(OH)_2Si(IV)Pc(SO_3)_{mix}$ and $(OH)_2Ge(IV)Pc(SO_3)_{mix}$ had a prevalence of fractions with a higher degree of sulfonation, hence were not aggregated compared with $ZnPc(SO_3)_{mix}$ and $(OH)_2Sn(IV)Pc(SO_3)_{mix}$ complexes which contained less sulfonated fractions and were therefore more aggregated. $ClAl(III)Pc(SO_3)_{mix}$, $(OH)_2Si(IV)Pc(SO_3)_{mix}$ and $(OH)_2Ge(IV)Pc(SO_3)_{mix}$ consisted

mainly (~90%) of tetrasulfonated derivatives, while $ZnPc(SO_3)_{mix}$, and $(OH)_2Sn(IV)Pc(SO_3)_{mix}$ contained approximately the same amounts of the tetra-, tri- and di-sulfonated derivatives.[52] Tetrasubstituted MPc complexes ($MPc(SO_3)_4$) contain positional isomers in a statistical ratio of 1:1:2:4 (for the 2,9,16,23-, 2,10,16,24-, 2,9,17,24- and 2,9,16,24-isomers). The isomers are difficult to separate chromatographically. For a series of $ClAl(III)Pc(SO_3)_n$ complexes, only the di-[85] and tri-sulfonated complexes were essentially monomeric.[42,85]

2. *Carboxylated Derivatives*

The ground state electronic absorption spectra of $(OH)Al(III)Pc(COOH)_8$, $ZnPc(COOH)_8$, $(OH)_2Si(COOH)_8$ and $(OH)_2Ge(IV)Pc(COOH)_8$ in PBS pH 7.4 shows no aggregation, typical of octacarboxysubstituted complexes, whereas tetracarboxylated derivatives ($MPc(COOH)_4$) are aggregated.[19,77,86] The plurality of COOH substituents prevents aggregation. For MPc complexes containing **S12** and **S13** substituents, the former resulted in aggregated MPc complexes, while those containing **S13** were not aggregated due to the bulkiness of the substituent.[79] MPc complexes substituted with **S10** or **S11** were also found to be aggregated.[78]

3. *Quaternized Derivatives*

MPc complexes containing quaternizable groups are constantly reported in the literature.[68–72,74–76,87,88] According to the literature,[64,65] water soluble porphyrazine complexes (complexes **1q** or **2q**; Figure 1) do not form aggregates in aqueous solutions. Positively charged water soluble phthalocyanine complexes containing substituents **S1q**, **S2q**, **S3q** or **S4q** are aggregated in solution.[67–72] For example, ZnPc complexes tetra- or octasubstituted with substituent **S4q** are highly soluble in aqueous media but were aggregated with the monomer band appearing near 700 nm and the band due to aggregates near 640 nm.[72] The presence of the bulky quaternized 2-diethylaminoethanethiol substituent **S4q** at the periphery of the ZnPc does not prevent aggregation of the Pc macrocycles. The addition of a surfactant, Cremophore EL (CEL), to the aqueous solution of these complexes resulted in a decrease in the intensity of the band due to the aggregates, with a concomitant increase in the intensity of the band due to the monomeric species. The disappearance of the peak due to the aggregates was, however, not complete.[72] Addition of Cremophore EL reduced aggregation resulting in increased photoactivity and improved photosensitizing ability for MPcs substituted with **S1q** to **S4q**. Aggregated MPcs are expected to disaggregate and exhibit monomeric behavior in organic solvents, and this was observed

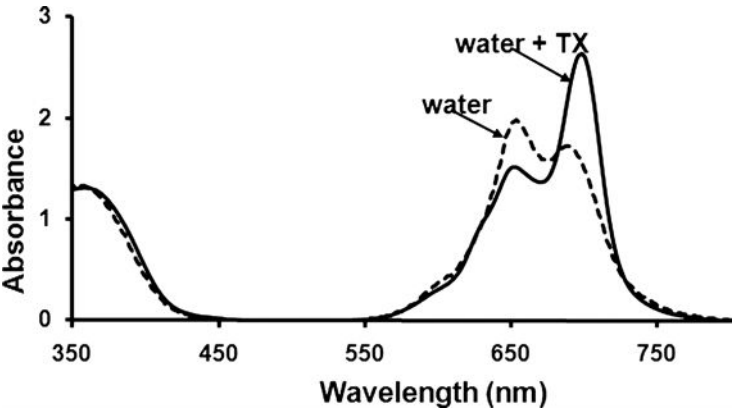

Figure 10. Absorption spectra of In(III)Pc (**S1q** substituent) in water in the presence and absence of Triton X-100 at a concentration of 6.6×10^{-5} mol dm^{-3}. TX = Triton X 100. Reproduced with permission from Ref. 69.

for ZnPc complexes tetra- or octasubstituted with substituent **S4q** in dimethylsulfoxide (DMSO).[72] The presence of trialkylated compounds, due to incomplete quaternization of the outer nitrogen atoms, induces severe aggregation.[87] Water soluble quaternized ZnPc complexes containing **S6**, **S7**, **S8** and **S9** were also found to be aggregated in water.[74–76]

Water soluble ClGa(III)Pc complexes containing **S1q** substituents were not aggregated in water; however their Clln(III)Pc counterparts were aggregated in water.[67,69] It is not clear why the two derivatives show different aggregation behavior. The addition of Triton X-100 to the water solution of the ClIn(III)Pc derivatives resulted in disaggregation, as evidenced by the sharp increase in the intensity of the monomer peak and a decrease in the intensity of the dimer peak (Figure 10).[69] However, the disappearance of the peak due to the aggregate is not complete as judged by the persistence of the peak at 649 nm even after addition of Triton X-100. Water soluble ZnPc complexes containing **S2q** substituents were highly aggregated in water, and the spectra were recorded in a water–pyridine solvent mixture.[70]

B. Fluorescence Spectra and Quantum Yields (Φ_F)

Fluorescence spectral behavior of Pcs has been extensively studied.[16,89–98] Generally in phthalocyanines, the excitation spectra are similar to the absorption spectra and both are mirror images of the fluorescence emission spectra (Figure 11a).[68] However for aggregated MPc complexes, the absorption profile is

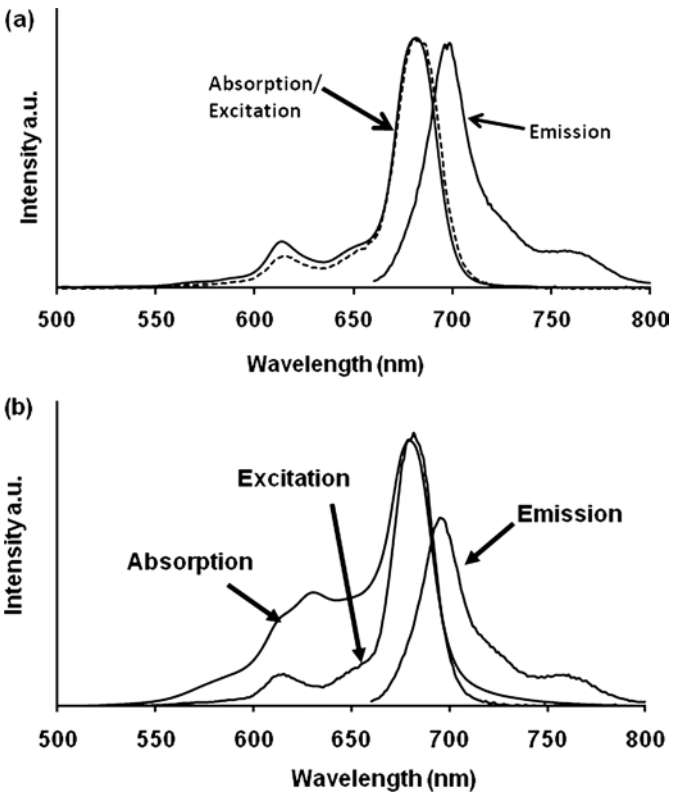

Figure 11. Absorption, excitation and emission spectra of (a) typical MPc (Cl_2Si(IV)Pc tetra substituted on the peripheral position with **S2** substituent) in DMSO. Excitation wavelength = 620 nm. Modified from Ref. 68. (b) A typical aggregated MPc in DMSO. Excitation wavelength = 620 nm. Modified from Ref. 89.

different to that of the fluorescence spectrum, Figure 11b,[89] since aggregates do not fluoresce.

The Φ_F values often increase with increase in the viscosity of the solvent. The relationship between Φ_F and the viscosity (η) of the solvent is given by the Forster-Hoffmann equation (Eq. 28):[99,100]

$$\log \Phi_F = C + x \log \eta. \tag{28}$$

As is the case with other photophysical and photochemical properties of MPc complexes,[101–115] fluorescence behavior is affected by solvent, aggregation and the presence of surfactants or proteins. The fluorescence quantum yield values for water soluble MPc complexes are shown in Table 3. The values are typical of MPc complexes in general, with the exceptions discussed below.

Table 3. Photochemical and photophysical behavior of water soluble phthalocyanines.[a] Refer to Figure 1 and Table 1 for numbering of the complexes.

Complex	Φ_F	Φ_T	Φ_Δ	$\Phi_P \times 10^5$	τ_T (μs)	Solvent	Ref.
			Unmetalated				
$H_2Pc(SO_3)_4$	0.62	0.22	0.09		170	Aqueous	83, 33
	0.60	0.24	0.16			DMF	33
						DMF	92
$H_2Pc(SO_3)_{2(mix)}$			0.02			Triton X-100	114
Complex **3** ($R_2 = R_3 =$ **S10**)	—	0.13	0.13			H_2O	97
	0.12	0.56	0.56			H_2O + CTAC	
	0.04	0.34	0.34			DMSO	
	0.02	0.25	0.25			Methanol	
			Group 2				
$MgPc(SO_3)_{2(mix)}$			0.19			DMSO	114
			Group 4				
$OTi(IV)Pc(SO_3)_{mix}$	0.18					Methanol	113
	0.42					DMSO	
	0.03					PBS	
			Group 5				
$(Cl)_3Ta(V)Pc(SO_3)_{mix}$	0.22					Methanol	113
	0.18					DMSO	
	0.15					PBS	

(*Continued*)

Table 3. (*Continued*)

Complex	Φ_F	Φ_T	Φ_Δ	$\Phi_P \times 10^5$	τ_T (μs)	Solvent	Ref.
			Group 12				
ZnPc							
Carboxylated derivatives							
$ZnPc(COOH)_8$	0.23	0.50	0.32	2.65	160	Aqueous media	77
$ZnPc(COOH)_8$			0.48			DMF/py	33
$ZnPc(COOH)_8$			0.52			pH10	35
$ZnPc(COOH)_4$			0.51			DMF	206
$R_1 = R_4 = H$, $R_2 = R_3 =$ **S10**			0.23	0.24		DMSO	36
$R_1 = R_2 = R_3 = H$, $R_4 =$ **S10**	0.14					DMF	78
$R_1 = R_2 = R_4 = H$, $R_3 =$ **S10**	0.25					DMF	78
$R_1 = R_2 = R_3 = H$, $R_4 =$ **S11**	0.16					DMF	78
$R_1 = R_2 = R_4 = H$, $R_3 =$ **S11**	0.23					DMF	78
$R_1 = R_2 = R_3 = H$, $R_4 =$ **S12**	0.0015					H_2O/0.1 M KOH	79
$R_1 = R_2 = R_3 = H$, $R_4 =$ **S13**	0.006					H_2O/0.1 M KOH	79
(Complex **3**) $R_2 = R_3 =$ **S10**	0.17	0.27	0.31	1.65	90	DMSO	54
(Complex **3**) $R_2 = H$; $R_3 =$ **S10**	0.16	0.25	0.23	0.30	130	DMSO	54
(Complex **4**) $R_2 = H$; $R_3 =$ **S10**	0.06		0.06			DMSO	156
Sulfonated Derivatives							
$ZnPc(SO_3)_{mix}$	0.16	0.53	0.45	3.65	2.95	PBS	52
	0.21	0.61	0.54	7.02	2.37	PBS + TX	52
	0.14	0.86	0.72	13.65	530	DMSO	41, 52
$ZnPc\ (SO_3)_2$		0.46	0.52		270	Methanol	108, 109
	0.16					DMSO	90
$ZnPc(SO_3)_3$	0.12					DMSO	90

(*Continued*)

Table 3. (*Continued*)

Complex	Φ_F	Φ_T	Φ_Δ	$\Phi_P \times 10^5$	τ_T (μs)	Solvent	Ref.
$ZnPc(SO_3)_{2.1(mix)}$			≤0.01			pH 7.4	114
			0.65			TX	
			0.74			DMSO	
$ZnPc(SO_3)_{2.9(mix)}$			0.10			pH 7.4	
			0.70			TX	114
			0.70			DMSO	
$ZnPc(SO_3)_{3.4(mix)}$			0.10			PH 7.4	
			0.69			TX	114
$ZnPc(SO_3)_{3.7(mix)}$			0.49			pH 7.4	
			0.67			TX	114
			0.70			DMSO	
$ZnPc(SO_3)_4$	0.32	0.56			245	Aqueous	83
					165	pH 7.1	94
			≤ 0.01			pH 7.4	114
			0.30			TX	114
			0.68			DMSO	114
	0.28	0.56				DMF	92
			0.52			DMF	33
					50	H_2O	103
			0.70		490	Detergent	107
	0.07	0.88	0.46	4.03	470	DMSO	41
	0.14	0.56			180	H_2O:methanol	93
			0.5			DMF	76
			0.5			H_2O	
	0.12					DMSO	90
$ZnNPc(SO_3)_4$			0.25		110	Detergent	107

(*Continued*)

Table 3. (*Continued*)

Complex	Φ_F	Φ_T	Φ_Δ	$\Phi_P \times 10^5$	τ_T (μs)	Solvent	Ref.
Quaternized Derivatives							
$R_1 = R_4 = H$, $R_3 = R_2 =$ **S1q**	0.0614					DMSO	115
	0.0394					Methanol	
	0.0038					pH 7	
$R_1 = R_2 = R_4 = H$, $R_3 =$ **S2q**	0.17	0.78	0.66		30	Py: H_2O (1:1)	70
$R_1 = R_2 = R_4 = H$, $R_3 =$ **S3q**	0.11	0.43	0.29		10	Py: H_2O (1:1)	70
$R_1 = R_2 = R_3 = H$, $R_4 =$ **S4q**	<0.01	0.15	0.10	9.3	20	PBS	72
	0.03	0.17	0.12	12.2	90	PBS + CEL	
	0.09	0.63	0.51	18.1	200	DMSO	
$R_1 = R_2 = R_4 = H$, $R_3 =$ **S4q**	<0.01	0.28	0.15	10.9	70	PBS	72
	0.02	0.34	0.26	19.0	110	PBS + CEL	
	0.18	0.57	0.62	16.6	210	DMSO	
$R_1 = R_4 = H$, $R_3 = R_2 =$ **S4q**	<0.01	0.17	0.10	5.1	40	PBS	72
	0.01	0.32	0.24	7.7	60	PBS + CEL	
	0.08	0.60	0.49	17.1	220	DMSO	
$R_1 = R_2 = R_4 = H$, $R_3 =$ **S5**			0.6			H_2O	73
			0.32			PBS	
$R_1 = R_4 = H$, $R_3 = R_2 =$ **S6**			0.65			H_2O	74
			0.60			Methanol	
			0.62			Ethanol	
$R_1 = R_2 = R_4 = H$, $R_3 =$**S7**	0.28					pH 7	75
	0.04	<0.001			220	HSA /pH 7	
	0.09	0.16			150	CTAC/pH 7	
	0.09	0.59			140	SDS/pH 7	

(*Continued*)

Table 3. (*Continued*)

Complex	Φ_F	Φ_T	Φ_Δ	$\Phi_P \times 10^5$	τ_T (μs)	Solvent	Ref.
$R_1 = R_4 = H$, $R_3 = R_2 =$ **S9**			0.45			H_2O	74
			0.17			Methanol	
			<0.05			Ethanol	
$R_1 = R_4 = H$, $R_3 = R_2 = OCH_2CH_2N^+(CH_3)_3$	0.30					DMF	165
$R_1 = R_4 = H$, $R_3 = R_2 = SCH_2CH_2N^+(CH_3)_3$	0.26					DMF	165
(Complex **1q**); R = CH_3			0.06			DMSO	63
(Complex **2q**); R = CH_3	0.30		0.50			DMF	102
	0.25		0.71		139	H_2O (SDS)	87
(Complex **2q**); R = $(CH_2)_4COOCH_2CH_3$	0.09		0.55		133	H_2O (SDS)	87
			Group 13				
Al(III)							
(OH)Al(III)Pc$(COOH)_8$	0.27	0.32	0.12	0.26	450	Aqueous media	77
(OH)Al(III)Pc$(COOH)_8$			0.12			DMSO	35
(OH)Al(III)Pc$(COOH)_4$	0.66		0.10			Adsorbed	111
ClAl(III)Pc$(SO_3)_{mix}$	0.44	0.44	0.42	0.40	2.93	PBS	53
	0.34			0.59		BSA/PBS	53
	0.39	0.52	0.48	5.79	800	DMSO	52
ClAl(III)Pc$(SO_3)_2$					520	PBS	95
					505	H_2O	84
	0.54	0.23			1130	D_2O	95, 96
	0.40	0.17			550	pH 7.4	104, 109, 110
		0.24	0.27		775	Methanol	108, 109
					1440	CD_3OD	95
			0.15			pH 7.4/TX	114
			0.39			DMSO	
	0.27					Micelles	85
			0.30			CH_3OD	110

(*Continued*)

Table 3. (*Continued*)

Complex	Φ_F	Φ_T	Φ_Δ	$\Phi_P \times 10^5$	τ_T (μs)	Solvent	Ref.
ClAl(III)Pc$(SO_3)_3$					490	PBS	95
					1150	D_2O	95
			0.42			pH 7.4	95
	0.24					Micelles	85
ClAl(III)Pc$(SO_3)_4$					530	PBS	95
					1140	D_2O	
			0.18			pH10	18, 35
					500	Aqueous	83
					440	pH7.1	94
	0.56	0.28				DMF	92
			0.20			DMF	33
					1160	H_2O/BSA	94
					440	H_2O	
	0.18	0.36			560	H_2O:Methanol	93
$R_1 = R_4 = H$, $R_3 = R_2 =$ **S6**			0.38			H_2O	74
			0.35			Methanol	
			0.35			Ethanol	
$R_1 = R_4 = H$, $R_3 = R_2 =$ **S9**			0.37			H_2O	74
			0.10			Methanol	
			<0.05			Ethanol	
Ga(III)							
ClGa(III)Pc$(SO_3)_2$		0.36	0.38		390	Methanol	108
							109
ClGa(III)Pc$(SO_3)_4$			0.41			DMF	33
		0.36	0.38		420	Methanol	108

(*Continued*)

Table 3. (*Continued*)

Complex	Φ_F	Φ_T	Φ_Δ	$\Phi_P \times 10^5$	τ_T (μs)	Solvent	Ref.
$(AcO)Gd(III)Pc(SO_3)_{2(mix)}$ [d]			0.37			DMSO	114
$ClGa(III)Pc(SO_3)_1(C(CH_3)_3)_3$		0.36	0.38		440	Methanol	108
$ClGa(III)Pc(SO_3)_2(C(CH_3)_3)_2$		0.36	0.38		360	Methanol	108
$ClGa(III)Pc(SO_3)_3(C(CH_3)_3)_1$		0.36	0.38		300	Methanol	108
$R_1 = R_2 = R_3 = H$,	0.19		0.53			DMSO	67
R_4 = **S1q** (X_1 = Cl)	0.07		0.41			H_2O	
$R_1 = R_2 = R_4 = H$,	0.24		0.51			DMSO	67
R_3 = **S1q** (X_1 = Cl)	0.12		0.44			H_2O	
In(III)							
$R_1 = R_4 = H$,	0.03	0.68	0.66	40.0	150	DMSO	98
$R_2 = R_3$ = **S1q** (X_1 = Cl)	0.02	0.59	0.56	1.20	10	H_2O + TX	
$R_1 = R_2 = R_3 = H$,	0.020	0.81	0.44	5.0	70	DMSO	69
R_4 = **S1q** (X_1 = Cl)	0.002	0.66	0.56	71.2	8.2	H_2O	
	0.008	0.67	0.56	87.9	20	H_2O + TX	
$R_1 = R_2 = R_4 = H$,	0.082	0.94	0.68	4.9	50	DMSO	69
R_3 = **S1q** (X_1 = Cl)	0.017	0.73	0.57	68.0	7.2	H_2O	
	0.048	0.82	0.70	103	20	H_2O + TX	
Group 14							
Si(IV)							
$(OH)_2Si(IV)Pc(SO_3)_{mix}$	0.34	0.45	0.49	0.71	2.90	PBS	52
	0.29	0.58	0.52	7.35	439	DMSO	
$(OH)_2Si(IV)Pc(SO_3)_4$	0.10	0.56			280	H_2O: Methanol	93
$(OH)_2Si(IV)Pc(COOH)_8$	0.24	0.34	0.22	86.3	90	Aqueous media	77

(*Continued*)

Table 3. (*Continued*)

Complex	Φ_F	Φ_T	Φ_Δ	$\Phi_P \times 10^5$	τ_T (μs)	Solvent	Ref.
$R_1 = R_4 = H$, $R_3 = R_2 =$ **S1q**, **L1** = **L2** = $OSi(CH_2CH_2CH_3)_3$	0.0518					DMSO	115
$R_1 = R_4 = H$, $R_3 = R_2 =$ **S1q**, **L1** = **L2** = $OSi(CH_2CH_2CH_3)_3$	0.0958					Methanol	115
$R_1 = R_4 = H$, $R_3 = R_2 =$ **S1q**, **L1** = **L2** = $OSi(CH_2CH_2CH_3)_3$	0.0732					pH 7	115
$R_1 = R_4 = H$, $R_3 = R_2 =$ **S1q**, **L1** = **L2** = $OSi(CH_2(CH_3)_2)_3$	0.0763					DMSO	115
$R_1 = R_4 = H$, $R_3 = R_2 =$ **S1q**, **L1** = **L2** = $OSi(CH_2(CH_3)_2)_3$	0.1146					Methanol	115
$R_1 = R_4 = H$, $R_3 = R_2 =$ **S1q**, **L1** = **L2** = $OSi(CH_2(CH_3)_2)_3$	0.0455					pH 7	115
$R_1 = R_4 = H$, $R_3 = R_2 =$ **S1q**, **L1** = **L2** = $OSi(C_6H_5)_2\,C(CH_3)_3$	0.0361					DMSO	115
$R_1 = R_4 = H$, $R_3 = R_2 =$ **S1q**, **L1** = **L2** = $OSi(C_6H_5)_2C(CH_3)_3$	0.0758					Methanol	115
$R_1 = R_4 = H$, $R_3 = R_2 =$ **S1q**, **L1** = **L2** = $OS(C_6H_5)_2C(CH_3)_3$	0.0566					pH 7	115
(Complex **1q**); R = **CH_3**			0.01			DMSO	63

(*Continued*)

Table 3. (*Continued*)

Complex	Φ_F	Φ_T	Φ_Δ	$\Phi_P \times 10^5$	τ_T (μs)	Solvent	Ref.
Ge(IV)							
$(OH)_2$Ge(IV)Pc$(SO_3)_{mix}$	0.30	0.67	0.68	0.45	2.76	PBS	52
	0.24			0.44		BSA/PBS	
	0.21	0.79	0.78	9.74	760	DMSO	
$(OH)_2$Ge(IV)Pc$(SO_3)_4$	0.12	0.81			250	H_2O:methanol	93
$(OH)_2$Ge(IV)Pc$(COOH)_8$	0.13	0.62	0.31	2.12	240	Aqueous media	77
(Complex **1q**); R = **CH_3**			< 0.01			DMSO	63
Sn(IV)							
$(OH)_2$Sn(IV)Pc$(SO_3)_{mix}$	0.05	0.59	0.42	1.59	2.52	PBS	52
	0.19	0.68	0.52	1.77	2.32	PBS/TX	
	0.13	0.87	0.65	14.01	120	DMSO	
(Complex **1q**); R = **CH_3**			0.02			DMSO	63

[a]The following symbols apply to all tables: Φ_F = fluorescence quantum yield (in general the standard used for determination of Φ_F is chlorophyll *a* in ether ($\Phi_F = 0.32$)[48]; Φ_T = triplet quantum yield; Φ_Δ = singlet oxygen quantum yield; Φ_P = photodegradation quantum yield; τ_T = triplet life time. Subscripts = average number of sulfo groups per molecule.

1. *Sulfonated Derivatives*

a. *$MPc(SO_3)_{mix}$ complexes*

For $MPc(SO_3)_{mix}$ complexes, which are a mixture of sulfonated MPc complexes, the determined photophysical and photochemical parameters are an average for each mixture. It is important to report these parameters for the mixtures since such mixtures are already in use in PDT for example. For the aggregated $ZnPc(SO_3)_{mix}$ and $(OH)_2Sn(IV)Pc(SO_3)_{mix}$ complexes,[52] it was only the monomer that fluoresced. For the nonaggregated $(OH)_2Ge(IV)Pc(SO_3)_{mix}$ and $(OH)_2Si(IV)Pc(SO_3)_{mix}$, the excitation spectra are different from the absorption spectra, suggesting that not all the components fluoresced. The fluorescence quantum yields were influenced by the heavy atom effect. Comparing the monomeric $MPc(SO_3)_{mix}$ [M = ClAl(III) (Φ_F = 0.44), $(OH)_2Ge$ (Φ_F = 0.30), $(OH)_2Si$ (Φ_F = 0.34)] complexes in phosphate buffer saline (PBS) in Table 3, Φ_F values were lower for complexes with the heavier atoms (e.g. Ge) due to the heavy atom effect.[52] The aggregated $(OH)_2Sn(IV)Pc(SO_3)_{mix}$ (Φ_F = 0.05) and $ZnPc(SO_3)_{mix}$ (Φ_F = 0.16) complexes showed significantly lower Φ_F values in PBS than the nonaggregated complexes in water[52] and the Φ_F values increased when a surfactant such as Triton X-100 was added (see Table 4). The Φ_F values are generally lower (Table 3) for the $MPc(SO_3)_{mix}$ (M = Zn and $(OH)_2Sn(IV)$) complexes in DMSO than in water (with or without Triton X-100) and this was attributed[52] to the presence of the relatively heavier atoms in DMSO, which may tend to favor intersystem crossing rather than fluorescence. However, in general DMSO gives larger Φ_F values compared to water in Table 3, since there is less aggregation in DMSO.

Bovine serum albumin (BSA) decreased the fluorescence quantum yields of the nonaggregated MPc complexes ($ClAl(III)Pc(SO_3)_{mix}$, $(OH)_2Ge(IV)Pc(SO_3)_{mix}$ and $(OH)_2Si(IV)Pc(SO_3)_{mix}$).[52,53] $ClAl(III)Pc(SO_3)_2$ gave higher Φ_F in D_2O compared to water.[95,96]

For $(Cl)_3Ta(V)Pc(SO_3)_{mix}$, the Φ_F values ranging from 0.15 in PBS to 0.22 in DMSO are not as low as would be expected for the complex containing the heavy Ta central metal. However compared to the corresponding $OTi(IV)Pc(SO_3)_{mix}$ (Φ_F = 0.42) in DMSO, the Φ_F value of 0.18 for $(Cl)_3Ta(V)Pc(SO_3)_{mix}$ is low.[113]

b. *Other $MPc(SO_3)_n$ complexes*

Φ_F values either decreased or remained unchanged as the number of sulfonate groups increase for $ZnPc(SO_3)_2$ (Φ_F = 0.16), $ZnPc(SO_3)_3$ (Φ_F = 0.12), $ZnPc(SO_3)_4$ (Φ_F = 0.07) in DMSO.[41,90,91] When comparing $ZnPc(SO_3)_4$ (Φ_F = 0.28) with $ClAl(III)Pc(SO_3)_4$ (Φ_F = 0.56) and $H_2Pc(SO_3)_4$ (Φ_F = 0.60) in DMF, the Zn complex showed a low Φ_F value (Table 3), but was found to be the best

Table 4. Photochemical and photophysical properties of non-water soluble metal phthalocyanines.[a] Refer to Figure 1 and Table 1 for the numbering of the complexes.

Complex	Ring substituent	Axial ligand	Φ_F	Φ_T	Φ_Δ	$\Phi_P \times 10^5$	τ_T (μs)	Solvent	Ref.
			Unmetalated						
H_2	**Unsubstituted**								
	$R_1 = R_4 = R_2 = R_3 = H$		0.55					$CHCl_3$	130
	Tetrasubstituted								
	$R_1 = R_2 = R_4 = H$, $R_3 = OCH_2C(CH_3)_3$		0.24					$CHCl_3$	130
	$R_1 = R_2 = R_4 = H$, $R_3 = (CH_2)_2O(CH_2)_2OCH_3$				0.19		504	Toluene	88
	$R_1 = R_2 = R_4 = H$, R_3 = **S46**		0.12					DMSO	161
	$R_1 = R_2 = R_4 = H$, R_3 = **S47**		0.21					DMSO	161
	Octasubstituted								
	$R_1 = R_4 = H$, $R_2 = R_3 = O(CH_2)_3CH_3$		0.96					Toluene	130
	$R_2 = R_3 = H$, $R_1 = R4 = O(CH_2)_3CH_3$		0.19					Ethanol	130
	$R_2 = R_3 = H$, $R_1 = R_4 = C_8H_{17}$		0.10					DCM	131
	$R_2 = R_3 = H$, $R_1 = R_4 = C_{10}H_{21}$		0.07					DCM	131
	$R_2 = R_3 = H$, $R_1 = R_4 = C_{12}H_{25}$		0.06					DCM	131
	$R_2 = R_3 = H$, $R_1 = R_4 = C_{14}H_{29}$		0.05					DCM	131
	$R_1 = R_4 = H$, $R_2 = R_3$ = **S19**		0.33					THF	132
			0.03					DMSO	
			0.23					EC	
			0.03					PVC	

(*Continued*)

Table 4. (*Continued*)

Complex	Ring substituent	Axial ligand	Φ_F	Φ_T	Φ_Δ	$\Phi_P \times 10^5$	τ_T (μs)	Solvent	Ref.
	$R_1 = R_4 = H$, $R_2 = R_3 =$ **S55**		0.33		0.10			Toluene	164
	Other								
	Complex **5**, (R = **S55**)		0.04		<0.02			Toluene	164
	Complex **6**, (R = **S55**)		< 0.02		<0.02			Toluene	164
		Group 1							
Li_2	**Unsubstituted**								
	$R_1 = R_4 = R_2 = R_3 = H$		0.50	0.60				CH_3CN	50
	NPc		0.50	0.60				Acetone	50
Mg	**Unsubstituted**								
	$R_1 = R_4 = R_2 = R_3 = H$		0.6					1-ClNP	43
			0.76					—	135
		Group 4							
OTi(IV)	**Tetrasubstituted — nonperipheral (α)**								
	$R_1 = R_2 = R_3 = H$, $R_4 =$ **S18**				0.63	27		DCM	136
	$R_1 = R_2 = R_3 = H$, $R_4 =$ **S22**				0.61	22		DCM	136
	$R_1 = R_2 = R_3 = H$, $R_4 =$ **S24**				0.69	48		DCM	136
	$R_1 = R_2 = R_3 = H$, $R_4 =$ **S24**		0.05	0.31			150	DMSO	137
	$R_1 = R_2 = R_3 = H$, $R_4 =$ **S25**				0.64	45		DCM	136
	$R_1 = R_2 = R_3 = H$, $R_4 =$ **S25**		0.07	0.50			150	DMSO	137

(*Continued*)

Table 4. (*Continued*)

Complex	Ring substituent	Axial ligand	Φ_F	Φ_T	Φ_Δ	$\Phi_P \times 10^5$	τ_T (μs)	Solvent	Ref.
	Tetrasubstituted — peripheral (β)								
	$R_1 = R_2 = R_4 = H$, R_3 = **S18**				0.84	38		DCM	136
	$R_1 = R_2 = R_4 = H$, R_3 = **S22**				0.73	35		DCM	136
	$R_1 = R_2 = R_4 = H$, R_3 = **S24**		0.11		0.82		210	DMSO	137
					0.86	53		DCM	136
	$R_1 = R_2 = R_4 = H$, R_3 = **S25**		0.14		0.70		200	DMSO	137
					0.77	50		DCM	136
	$R_1 = R_2 = R_4 = H$, R_3 = **S26**		0.16	0.78	0.72	1.31	150	DMSO	138
	Octasubstituted — peripheral (β)								
	$R_1 = R_4 = H$, $R_2 = R_3$ = **S14**	$X_1 = O$	0.19	0.45			60	1-ClNP	139
	$R_1 = R_4 = H$, $R_2 = R_3$ = **S18**	$X_1 = O$	0.16	0.23			40	1-ClNP	139
	$R_1 = R_4 = H$, $R_2 = R_3$ = **S23**	$X_1 = O$	0.17	0.56			100	1-ClNP	139
	$R_1 = R_4 = H$, $R_2 = R_3$ = **S24**	$X_1 = O$	0.14	0.13			70	1-ClNP	139
	$R_1 = R_4 = H$, R_3 = **S26**, R_2 = Cl	$X_1 = O$	0.10	0.85	0.78	3.35	220	DMSO	138
Zr(IV)	$R_1 = R_2 = H$, $R_3 = R_4 = H$	$X_1 = X_2$ = Cl	0.006					DMSO	141
	$R_1 = R_2 = H$, $R_3 = R_4 = H$	$X_1 = X_2$ = L1	0.016					DMSO	141
			0.009					Toluene	
	$R_1 = R_2 = H$, $R_3 = R_4 = H$	$X_1 = X_2$ = L2	0.016					DMSO	141
			0.009					Toluene	
	$R_1 = R_2 = H$, $R_3 = R_4 = H$	$X_1 = X_2$ = L3	0.013					DMSO	141
			0.009					Toluene	
			Group 10						
Ni	$R_1 = R_4 = H$, $R_2 = R_3 = C_5H_{11}$		< 0.01					1-ClNP	142
	$R_1 = R_4 = H$, $R_2 = R_3 = C_8H_{17}$		< 0.01					1-ClNP	142
	$R_1 = R_4 = H$, $R_2 = R_3 = C_{12}H_{25}$		< 0.01					1-ClNP	142

(*Continued*)

Table 4. (*Continued*)

Complex	Ring substituent	Axial ligand	Φ_F	Φ_T	Φ_Δ	$\Phi_P \times 10^5$	τ_T (μs)	Solvent	Ref.
Pd	$R_1 = R_4 = H$, $R_2 = R_3 = C_5H_{11}$		< 0.01					1-ClNP	142
	$R_1 = R_4 = H$, $R_2 = R_3 = C_8H_{17}$		< 0.01					1-ClNP	142
	$R_1 = R_4 = H$, $R_2 = R_3 = C_{12}H_{25}$		< 0.01					1-ClNP	142
Zn	**Unsubstituted**								
	$R_1 = R_4 = R_2 = R_3 = H$		0.3					1-ClNP	83
	$R_1 = R_4 = R_2 = R_3 = H$		0.34	0.58	0.54		330	Toluene/%py	48
	$R_1 = R_4 = R_2 = R_3 = D$[d]		0.34	0.58	0.54		330	Toluene/d-py	48
	$R_1 = R_4 = R_2 = R_3 = H$		0.20	0.50	0.67	2.61	350	DMSO	41,157
	$R_1 = R_4 = R_2 = R_3 = H$				0.56			DMF	33
	$R_1 = R_4 = R_2 = R_3 = H$		0.17		0.17		77	Acetone	146
	$R_1 = R_4 = R_2 = R_3 = H$	X_1 = py	0.22		0.48	1.32		DMF	8
		X_1 = pip	0.16		0.31	0.14		DMF	
		X_1 = CN	0.14		0.51	0.12		DMF	
	$R_1 = R_2 = R_3 = R_4 = H$				0.56			DMF/ H_2O	158
					0.62			BHDC Micelles	
	$R_1 = R_2 = R_3 = R_4 = H$				0.55			DMF	76
	$R_1 = R_2 = R_3 = R_4 = H$				0.58			DMF	115
	$R_1 = R_2 = R_3 = R_4 = H$		0.17	0.58	0.58	2.35	330	DMF	100
			0.07	0.65	0.65	0.93	340	Toluene	
	Tetrasubstituted — non-peripheral (α)								
	$R_1 = R_2 = R_3 = H$, R_4 = **S4**		0.07	0.66	0.64	66.2	190	DMSO	72
	$R_1 = R_2 = R_3 = H$, R_4 = **S14**		0.18	0.81	0.76	0.50		DMSO	89
			0.18	0.81	0.77	6.70		Toluene	

(*Continued*)

Table 4. (*Continued*)

Complex	Ring substituent	Axial ligand	Φ_F	Φ_T	Φ_Δ	$\Phi_P \times 10^5$	τ_T (μs)	Solvent	Ref.
	$R_1 = R_2 = R_3 = H$, R_4 = **S29**		0.17	0.65	0.62	139	76	DMF	143
			0.15	0.75	0.71	153	20	Toluene	
	$R_1 = R_2 = R_3 = H$, R_4 = **S48**		0.003		0.693			DMSO	160
	$R_1 = R_2 = R_3 = H$, R_4 = **S54**		0.24					DMF	78
	$R_1 = R_2 = R_3 = H$, $R_4 = OC(CH_3)_3$				0.58			DMF	206
	Tetrasubstituted — peripheral (β)								
	$R_1 = R_2 = R_4 = H$,		0.17	0.68	0.40		7	DMF	119
	R_3 = **S2**		0.077	0.80	0.46		350	DMSO	
	$R_1 = R_2 = R_4 = H$, R_3 = **S4**		0.13	0.71	0.68	66.1	180	DMSO	72
	$R_1 = R_2 = R_4 = H$,		0.23	0.60	0.52	0.33		DMSO	89
	R_3 = **S14**		0.19	0.80	0.58	5.39		Toluene	
	$R_1 = R_2 = R_4 = H$, R_3 = **S23**		0.14	0.85	0.60	3.33	160	DMSO	41,157
	$R_1 = R_2 = R_4 = H$, R_3 = **S23**		0.13		0.42	9.41		DMF	8
	$R_1 = R_2 = R_4 = H$, R_3 = **S23**				0.55			DMF	33
	$R_1 = R_2 = R_4 = H$,				0.58		287	Toluene	88
	R_3 = **S23**				0.47		306	EtOH	
	$R_1 = R_2 = R_4 = H$, R_3 = **S27**		0.10	0.87	0.73	0.22	280	DMSO	149
	$R_1 = R_2 = R_4 = H$, R_3 = **S28**		0.20	0.77	0.64	16.2	230	DMSO	150
	$R_1 = R_2 = R_4 = H$,		0.15	0.64	0.58	3.28	210		
	R_3 = **S28**		0.04	0.67	0.52		180	DMF	100
								Toluene	
	$R_1 = R_2 = R_4$ =H, R_3 = **S29**		0.18	0.60	0.51	2.28	100	DMF	143
			0.16	0.81	0.77	7.90	40	Toluene	

(*Continued*)

Table 4. (*Continued*)

Complex	Ring substituent	Axial ligand	Φ_F	Φ_T	Φ_Δ	$\Phi_P \times 10^5$	τ_T (μs)	Solvent	Ref.
	$R_1 = R_2 = R_4 = H$, R_3 = **S30**				0.59			Ethanol	88
	$R_1 = R_2 = R_4 = H$, R_3 = **S31**		0.18	0.66	0.51		57	Toluene	88
	$R_1 = R_2 = R_4 = H$, R_3 = **S32**		0.28						147
	$R_1 = R_2 = R_4 = H$, R_3 = **S33**		0.3						147
	$R_1 = R_2 = R_4 = H$, R_3 = **S34**		0.32						147
	$R_1 = R_2 = R_4 = H$, R_3 = **S35**		0.32						147
	$R_1 = R_2 = R_4 = H$, R_3 = **S36**		0.26						147
	$R_1 = R_2 = R_4 = H$, R_3 = **S37**		0.03	0.12			230	DMSO	168
			0.02	0.23			240	Toluene	
	$R_1 = R_2 = R_4 = H$, R_3 = **S39**		0.08	0.67	0.65	1.63	370	DMSO	149
	$R_1 = R_2 = R_4 = H$, R_3 = **S46**		0.11					DMSO	161
	$R_1 = R_2 = R_4 = H$, R_3 = **S47**		0.21					DMSO	161
	$R_1 = R_2 = R_4 = H$, R_3 = **S49**		0.25		0.56			THF	159
	$R_1 = R_2 = R_4 = H$, R_3 = **S51**				0.23			DMF/H_2O	158
	$R_1 = R_2 = R_4 = H$, R_3 = **S51**				0.30			BHDC Micelles	158
	$R_1 = R_2 = R_4 = H$, R_3 = **S53**		0.3					THF	79
	$R_1 = R_2 = R_4 = H$, R_3 = **S54**		0.31					DMF	78
	$R_1 = R_2 = R_4 = H$, R_3 = **S56**		0.26					THF	79
	$R_1 = R_2 = R_4 = H$, $R_3 = NH_2$		< 0.022		0.11			DMSO	157
	$R_1 = R_2 = R_4 = H$, $R_3 = NO_2$		< 0.022		0.11			DMSO	157
	$R_1 = R_2 = R_4 = H$, $R_3 = C(CH_3)_3$		0.26	0.58	0.54		200	Ethanol	11
	$R_1 = R_2 = R_4 = H$, $R_3 = OCH_2C(CH_3)_3$		0.25					$CHCl_3$	130

(*Continued*)

Table 4. (*Continued*)

Complex	Ring substituent	Axial ligand	Φ_F	Φ_T	Φ_Δ	$\Phi_P \times 10^5$	τ_T (μs)	Solvent	Ref.
	$R_1 = R_2 = R_4 = H$,				0.44			Toluene	88
	$R_3 = (CH_2)_2O(CH_2)_2OCH_3$				0.42			EtOH	88
	$R_1 = R_2 = R_4 = H$, $R_3 = CH_3$		0.26		0.56			THF	159
	$R_1 = R_2 = R_4 = H$, $R_3 = C(CH_3)_3$				0.61			DMF	206
	Octasubstituted — peripheral (β)								
	$R_1 = R_4 = H$, $R_3 = R_2 =$ **S4**		0.05	0.75	0.62	94.0	200	DMSO	72
	$R_1 = R_4 = H$, $R_3 = R_2 =$ **S14**		0.08	0.47	0.46	0.13		DMSO	89
			0.18	0.78	0.58	2.87		Toluene	
	$R_1 = R_4 = H$, $R_2 = R_3 =$ **S15**				0.44	111		$CHCl_3$	36
	$R_1 = R_4 = H$, $R_2 = R_3 =$ **S16**				0.01			$CHCl_3$	36
	$R_1 = R_4 = H$, $R_2 = R_3 =$ **S17**		0.24	0.63	0.51	2.12	370	DMSO	36,41
	$R_1 = R_4 = H$, $R_2 = R_3 =$ **S18**				0.60	2.53		DMSO	8,36
	$R_1 = R_4 = H$, $R_2 = R_3 =$ **S19**		0.17		0.53	12.1		DMF	
			0.25					THF	132
			0.15					DMSO	
			0.15					EC	
	$R_1 = R_4 = H$, $R_2 = R_3 =$ **S21**				0.34	5.04		DMSO	36
	$R_1 = R_4 = H$, $R_2 = R_3 =$ **S23**				0.73	464		$CHCl_3$	36
					0.52			DMSO	176
	$R_1 = R_4 = H$, $R_3 =$ **S26**, $R_2 = Cl$		0.10	0.85	0.78	3.35	220	DMSO	138
	$R_1 = R_4 = H$, $R_3 = R_2 =$ **S28**		0.13	0.73	0.66	4.56	240	DMF	100
			0.03	0.70	0.41		210	Toluene	
	$R_1 = R_4 = H$, $R_3 = R_2 =$ **S28**		0.13	0.85	0.72	22.0	280	DMSO	150
	$R_1 = R_4 = H$, $R_3 =$ **S28**, $R_2 = Cl$		0.09	0.72	0.67	4.01	230	DMF	100
			0.03	0.71	0.44		190	Toluene	
	$R_1 = R_4 = H$, $R_2 = R_3 =$ **S37**		0.005	0.04			170	DMSO	151

(*Continued*)

Table 4. (*Continued*)

Complex	Ring substituent	Axial ligand	Φ_F	Φ_T	Φ_Δ	$\Phi_P \times 10^5$	τ_T (μs)	Solvent	Ref.
	$R_1 = R_4 = H$, R_3 = **S39**, R_2 = Cl		0.10	0.89	0.80	0.26	240	DMSO	149
	$R_1 = R_4 = H$,				0.64	275		$CHCl_3$	36
	$R_2 = R_3$ = **S40**		0.15		0.43	1.74		DMSO	37
	$R_1 = R_4 = H$, $R_2 = R_3$ = **S41**				0.44	766		$CHCl_3$	36
	$R_1 = R_4 = H$, $R_2 = R_3$ = **S42**				0.36	1.41		DMSO	36
	$R_1 = R_4 = H$, $R_2 = R_3$ = **S43**				0.07	0.86		DMSO	36
	$R_1 = R_4 = H$, $R_2 = R_3$ = **S48**		0.004		0.692			DMSO	160
	$R_1 = R_4 = H$, $R_2 = R_3$ = **Cl**		0.02		0.34		370	DMSO	41
	$R_1 = R_4 = H$, $R_2 = R_3 = SC_4H_9$				0.61	6.4		DMF	152
	$R_1 = R_4 = H$, $R_2 = 3R_3 = (C_6C_{13})_7$, $1R_3 = (CH_2)_{11}SH$)				0.45			Toluene	153
	$R_1 = R_4 = H$, $R_2 = 3R_3 = (C_6C_{13})_7$, $1R_3 = (CH_2)_{11}SH$) – nanoparticles				0.65			Ethanol	153
	$R_1 = R_4 = H$, $R_2 = R_3 = C_{10}H_{21}$			0.26	0.47			THF	162
	$R_1 = R_4 = H$, $R_2 = R_3 = OC_6H_{13}$				0.52			DMF	33
	$R_1 = R_4 = H$, $R_3 = R_2 = OCH_2CH_2N(CH_3)_2$		0.30					DMF	165
	$R_1 = R_4 = H$, $R_3 = R_2 = SCH_2CH_2N(CH_3)_2$		0.26					DMF	165
	$R_1 = R_4 = H$, $R_2 = R_3 = OC(CH_3)_3$				0.58			DMF	206
	$R_1 = R_4 = H$, $R_2 = R_3 = CN$				0.47			DMF	206
	$R_2 = R_3 = H$, $R_1 = R_4 = 4 \times$ **S52**, $4 \times C_{10}H_{21}$				0.92			DMF	166

(*Continued*)

Table 4. (*Continued*)

Complex	Ring substituent	Axial ligand	Φ_F	Φ_T	Φ_Δ	$\Phi_P \times 10^5$	τ_T (μs)	Solvent	Ref.
	$R_2 = R_3 = H$, $R_1 = R_4 = 2 \times$ **S52**, $6 \times C_{10}H_{21}$				0.85			DMF	166
	$R_2 = R_3 = H$,		0.26		0.22		100	THF	154
	$R_1 = R_4 = C_{10}H_{21}$		0.28					Toluene	
	$R_2 = R_3 = H$, $R_1 = R_4 = C_8H_{17}$		0.13					DCM	131
	$R_2 = R_3 = H$, $R_1 = R_4 = C_{10}H_{21}$		0.17					DCM	131
	$R_2 = R_3 = H$, $R_1 = R_4 = C_{12}H_2$		0.16					DCM	131
	$R_2 = R_3 = H$, $R_1 = R_4 = C_{14}H_{29}$		0.13					DCM	131
	Other								
	Complex **1**				0.16			DMSO	63
	Complex **2**		0.35		0.56			DMF	102
	$R_2 = R_3 =$				0.58			DMF	206
	$R_1 = R_4 = F$,		0.04		0.13		<1	Acetone	146
	$R_1 = R_4 = F$, $R_2 = R_3 = C(CF_3)_2F$		0.39		0.21		131	Acetone	146
	$R_1 = R_2 = R_3 = R_4 = OC(CH_3)_3$				0.63			DMF	206
	(Complex **3**)$R_2 = R_3 =$ **S18**		0.17	0.52	0.54	3.28	150	DMSO	54
	(Complex **3**)$R_2 = H$, $R_3 =$ **S18**		0.20	0.45	0.47	0.93	120	DMSO	54,148
	(Complex **3**) $R_2 = R_3 =$ **S23**		0.16	0.70	0.72	3.77	180	DMSO	54
	(Complex **3**) $R_2 = H$, $R_3 =$ **S23**		0.22	0.62	0.58	2.3	90	DMSO	54,148
	(Complex **3**) $R_2 = H$, $R_3 =$ **S38**		0.26		0.37	0.88		DMSO	148
	(Complex **4**) $R_2 = H$, $R_3 =$ **S18**		0.07		0.22			DMSO	156
	(Complex **4**) $R_2 = H$, $R_3 =$ **S23**		0.08		0.14			DMSO	156
	(Complex **4**) $R_2 = H$, $R_3 =$ **S42**		0.06		0.24			DMSO	156
	(Complex **5**) $R_2 = H$, $R_3 =$ **S55**		0.08					THF	164
	(Complex **6**) $R_2 = H$, $R_3 =$ **S55**		< 0.03					THF	164
	(Complex **7**) $R_2 = H$, $R_3 =$ **S55**		< 0.03					THF	164

(*Continued*)

Table 4. (*Continued*)

Complex	Ring substituent	Axial ligand	Φ_F	Φ_T	Φ_Δ	$\Phi_P \times 10^5$	τ_T (μs)	Solvent	Ref.
	(Complex **9**)						26	Film	155
	(Complex **8**)		0.19	0.58	0.68	0.38	150	DMSO	54,148
	$R_1 = R_2 = R_4 = H$, R_3 = **S48**		0.20		0.201			DMSO	160
	(disubstituted)								
	NPc		0.07	0.37	0.19	16.4	126	DMSO	8, 41,157
Cd	**Unsubstituted**								
	$R_1 = R_4 = R_2 = R_3 = H$		0.021	0.77	0.58		5	DMF	119
			0.015	0.70	0.78		30	DMSO	
	Tetrasubstituted — nonperipheral (α)								
	$R_1 = R_2 = R_3 = H$, R_4 = **S2**		0.16	0.70	0.60		10	DMF	118,119
			0.16	0.61	0.44	61.1	40	DMSO	
			0.17		0.50			$CHCl_3$	
			0.18		0.52	55.7		THF	
			0.17					DCM	
	$R_1 = R_2 = R_3 = H$, R_4 = **S14**		0.14	0.51	0.33	56.3		Toluene	118,119
			0.18		0.42	10.9		THF	
			0.15		0.26	61.5		$CHCl_3$	
			0.19	0.53	0.41	16.3		DMF	
			0.045	0.38	0.31	9.2		DMSO	
			0.15			118		DCM	
	$R_1 = R_2 = R_3 = H$, R_4 = **S18**		0.054	0.73	0.58	2.53		Toluene	177
			0.47		0.43	4.01		THF	
			0.39		0.31	2.20		$CHCl_3$	
			0.31	0.49	0.42	3.89		DMF	
			0.063	0.66	0.80	2.86		DMSO	

(*Continued*)

Table 4. (*Continued*)

Complex	Ring substituent	Axial ligand	Φ_F	Φ_T	Φ_Δ	$\Phi_P \times 10^5$	τ_T (μs)	Solvent	Ref.
	$R_1 = R_2 = R_3 = H$, R_4 = **S23**		0.27	0.49	0.40	1.8		Toluene	177
			0.50		0.44	1.67		THF	
			0.49		0.49	3.30		$CHCl_3$	
			0.53	0.56	0.56	2.13		DMF	
			0.055	0.61	0.59	0.19		DMSO	
	Tetrasubstituted — peripheral (β)								
	$R_1 = R_2 = R_4 = H$, R_3 = **S2**		0.017	0.85	0.64		5	DMF	118,119
			0.013	0.83	0.74		30	DMSO	
	$R_1 = R_2 = R_3 = H$, R_3 = **S14**		0.14	0.82	0.042		30	Toluene	118,119
			0.21		0.025			THF	
			0.25		0.015			$CHCl_3$	
			0.13	0.77	0.39	35.8	5	DMF	
			0.10	0.36	0.23		30	DMSO	
			0.27					DCM	
	$R_1 = R_2 = R_4 = H$, R_3 = **S18**		0.13	0.87	0.32	0.98		DMF	177
			0.29		0.31	2.72		THF	
			0.27		0.19	4.40		$CHCl_3$	
			0.29	0.40	0.39	3.55		DMF	
			0.20	0.61	0.41	0.42		DMSO	
	$R_1 = R_2 = R_4 = H$, R_3 = **S23**		0.14	0.76	0.33	0.92		Toluene	177
			0.27		0.27	0.06		THF	
			0.27		0.19	9		$CHCl_3$	
			0.32	0.41	0.26	3.84		DMF	
			0.21	0.54	0.35	2.47		DMSO	
						0.41			

(*Continued*)

Table 4. (*Continued*)

Complex	Ring substituent	Axial ligand	Φ_F	Φ_T	Φ_Δ	$\Phi_P \times 10^5$	τ_T (μs)	Solvent	Ref.
Hg	$R_1 = R_2 = R_3 = R_4 = H$		0.017	0.86	0.57		4	DMF	119
			0.010	0.87	0.82		40	DMSO	
	$R_1 = R_2 = R_4 = H$, R_3 = **S2**		0.009	0.90	0.56		4	DMF	119
			0.005	0.89	0.78		20	DMSO	
		Group 13							
Ga(III)	**Unsubstituted**								
	$R_1 = R_4 = R_2 = R_3 = H$	X_1 = Cl	0.31	0.7				1-ClNP	189
	Ga(III)Pc	X_1 = Cl	0.30	0.69	0.41	0.93	200	DMSO	188
	Tetrasubstituted — nonperipheral (α)								
	$R_1 = R_2 = R_3 = H$, R_4 = **S1**	X_1 = Cl	0.12		0.48			DMSO	67
	$R_1 = R_2 = R_3 = H$, R_4 = **S18**	X_1 = Cl	0.14	0.62	0.64	11.9	230	DMSO	179
	$R_1 = R_2 = R_3 = H$, R_4 = **S23**	X_1 = Cl	0.15	0.54	0.62	20.3	350	DMSO	179
	Tetrasubstituted — peripheral (β)								
	$R_1 = R_2 = R_4 = H$, $R_3 = C(CH_3)_3$	X_1 = Cl					257	Toluene	183
	$R_1 = R_2 = R_4 = H$, R_3 = **S1**	X_1 = Cl	0.19		0.59			DMSO	67
	$R_1 = R_4 = R_2 = H$, R_3 = **S3**	X_1 = Cl	0.30	0.65	0.34		110	DMSO	68
		0.26	0.54	0.33		20		DMF	68
	$R_1 = R_2 = R_4 = H$, R_3 = **S14**	X_1 = Cl	0.23	0.75	0.62	1.92	210	DMSO	188
	$R_1 = R_2 = R_4 = H$, R_3 = **S18**	X_1 = Cl	0.19	0.61	0.64	28.2	270	DMSO	179

(*Continued*)

Table 4. (*Continued*)

Complex	Ring substituent	Axial ligand	Φ_F	Φ_T	Φ_Δ	$\Phi_P \times 10^5$	τ_T (μs)	Solvent	Ref.
	$R_1 = R_2 = R_4 = H$, R_3 = **S23**	X_1 = Cl	0.20	0.45	0.58	23.2	340	DMSO	179
	Octasubstituted (β)								
	$R_1 = R_4 = H$, $R_2 = R_3$ = **S14**	X_1 = Cl	0.13	0.74	0.51	0.5	200	DMSO	188
	$R_1 = R_4 = H$, $R_2 = R_3$ = **S18**								
		X_1 = Cl	0.19	0.66	0.53	1.23	370	DMSO	184
			0.19	0.79	0.66	0.42	20	DMF	
			0.14	0.65	0.68	2.91	79	Toluene	
	$R_1 = R_4 = H$, $R_2 = R_3$ = **S23**	X_1 = Cl	0.22	0.67	0.56	1.77	290	DMSO	184
			0.15	0.74	0.74	1.52	76	DMF	
			0.17	0.75	0.65	2.84	10	Toluene	
	Other								
	Complex **10**, R = $C(CH_3)_3$	X = Cl					21	$CHCl_3$	181,182
	Complex **10**, R = $C(CH_3)_3$	X = **L8**					18	$CHCl_3$	182
	Complex **11**, R = $C(CH_3)_3$						14	$CHCl_3$	181
	Complex **12**, R = $C(CH_3)_3$	X = O					357	Toluene	183
	Complex **12**, R = $C(CH_3)_3$	X_1 = **L5**					667	Toluene	183
	Complex **12**, R = $C(CH_3)_3$	X_1 = **L7**					200	Toluene	183
In(III)									
	Unsubstituted								
	$R_1 = R_4 = R_2 = R_3 = H$	X_1 = Cl	0.031	0.9				1-ClNP	189
	$R_1 = R_4 = R_2 = R_3 = H$	X_1 = Cl	0.018	0.91	0.61	3.43	50	DMSO	188

(*Continued*)

Table 4. (*Continued*)

Complex	Ring substituent	Axial ligand	Φ_F	Φ_T	Φ_Δ	$\Phi_P \times 10^5$	τ_T (μs)	Solvent	Ref.
	Tetrasubstituted — nonperipheral (α)								
	$R_1 = R_2 = R_3$, R_4 = **S1**	X_1 = Cl	0.018	0.93	0.86	3	40	DMSO	69
	$R_1 = R_2 = R_3$ = H, R_4 = **S18**	X_1 = Cl	0.048	0.78	0.88	9.2	40	DMSO	179
	$R_1 = R_2 = R_3$ = H, R_4 = **S14**	X_1 = Cl	0.013	0.97	0.94	0.30	40	DMSO	188
	$R_1 = R_2 = R_3$ = H, R_4 = **S23**	X_1 = Cl	0.015	0.59	0.88	13.9	40	DMSO	179
	Tetrasubstituted — peripheral (β)								
	$R_1 = R_2 = R_4$ = H, $R_3 = C(CH_3)_3$	X_1 = Cl					46	Toluene	183
	$R_1 = R_2 = R_4$ = H, $R_3 = C(CH_3)_3$	X_1 = **L7**					22	Toluene	183
	$R_1 = R_2 = R_4$, R_3 = **S1**	X_1 = Cl	0.017	0.73	0.65	2.4	50	DMSO	69
	$R_1 = R_4 = R_2$ = H,	X1 = Cl	0.03	0.93	0.33		60	DMSO	68
	R_3 = **S3**		0.03	0.89	0.53		50	DMF	68
	$R_1 = R_2 = R_4$ = H, R_3 = **S14**	X_1 = Cl	0.017	0.91	0.87	0.97	50	DMSO	188
	$R_1 = R_2 = R_4$ = H, R_3 = **S18**	X_1 = Cl	0.032	0.69	0.87	24.4	50	DMSO	179
	$R_1 = R_2 = R_4$ = H, R_3 = **S23**	X_1 = Cl	0.019	0.60	0.88	21.4	50	DMSO	179
	Octasubstituted — peripheral (β)								
	$R_1 = R_4$ = H,								
	$R_2 = R_3$ = **S14**	X_1 = Cl	0.017	0.89	0.78	0.27	70	DMSO	188
	$R_1 = R_4$ = H,	X_1 = Cl	0.025	0.84	0.79	1.39	60	DMSO	191
	$R_2 = R_3$ = **S18**		0.018	0.76	0.60	5.64	20	DMF	
			0.023	0.55	0.31	2.75	20	Toluene	
	$R_1 = R_4$ = H,	X_1 = Cl	0.020	0.70	0.72	2.35	50	DMSO	191
	$R_2 = R_3$ = **S23**		0.022	0.61	0.50	4.83	9.5	DMF	
			0.021	0.41	0.30	3.19	10	Toluene	

(*Continued*)

Table 4. (*Continued*)

Complex	Ring substituent	Axial ligand	Φ_F	Φ_T	Φ_Δ	$\Phi_P \times 10^5$	τ_T (μs)	Solvent	Ref.
	Other								
	Complex **12**, R = $C(CH_3)_3$	X = O					42	Toluene	183
	Complex **12**, R = $C(CH_3)_3$	X_1 = **L6**					35	Toluene	183
	Complex **12**, R = $C(CH_3)_3$	X_1 = **L7,** X_2 = Cl					22	Toluene	183
		Group 14							
Si(IV)									
	Unsubstituted								
	$R_2 = R_3 = R_1 = R_4 = H$	X_1 = **L10** X_2 = OH			0.50		139	CH_3CN	145
	$R_2 = R_3 = R_1 = R_4 = H$	$X_1 = X_2$ = **L10**			0.20		188	CH_3CN	145
	$R_2 = R_3 = R_1 = R_4 = H$	X_1 = **L11** X_2 = OH			0.43		113	CH_3CN	145
	$R_2 = R_3 = R_1 = R_4 = H$	$X_1 = X_2$ = **L11**			0.32		160	CH_3CN	145
	$R_2 = R_3 = R_1 = R_4 = H$	$X_1 = X_2$ = **L12**			0.62			DCM	195
	$R_2 = R_3 = R_1 = R_4 = H$	$X_1 = X_2$ = **L13**			0.32	243		THF $CHCl_3$	193
	$R_2 = R_3 = R_1 = R_4 = H$	$X_1 = X_2$ = **L14**			0.29–0.37	213		THF $CHCl_3$	193
		$X_1 = X_2$ = **L17**		0.82	0.16			DMF	192
	$R_2 = R_3 = R_1 = R_4 = H$	$X_1 = X_2$ = OH			0.28			DMSO	63
	$R_2 = R_3 = R_1 = R_4 = H$	$X_1 = X_2$ = **L17**			0.27			Toluene	194
	Octasubstituted — peripheral (β)								
	$R_2 = R_3$ = **S18**, $R_1 = R_4 = H$	$X_1 = X_2$ = Cl	0.21	0.31	0.14	1.0	194	DMSO	44,127
	$R_2 = R_3$ = **S18**, $R_1 = R_4 = H$	$X_1 = X_2$ = OH	0.18	0.30	0.07	–	179	DMSO	44,127
	$R_2 = R_3$ = **S18**, $R_1 = R_4 = H$	$X_1 = X_2$ = **L4**			0.16			DMSO	127

(*Continued*)

Table 4. (*Continued*)

Complex	Ring substituent	Axial ligand	Φ_F	Φ_T	Φ_Δ	$\Phi_P \times 10^5$	τ_T (μs)	Solvent	Ref.
	$R_2 = R_3 =$ **S18**, $R_1 = R_4 = H$	$X_1 = X_2 =$ **L13**	0.29	0.40	0.41	4.1	311	DMSO	44,127
	$R_2 = R_3 =$ **S18**, $R_1 = R_4 = H$	$X_1 = X_2 =$ **L14**	0.34	0.41	0.20	3.0	356	DMSO	44,127
	$R_2 = R_3 =$ **S18**, $R_1 = R_4 = H$	$X_1 = X_2 =$ **L15**	0.02	0.29	0.20	170	260	DMSO	44,127
	$R_2 = R_3 =$ **S18**, $R_1 = R_4 = H$	$X_1 = X_2 =$ **L16**	0.03	0.43	0.03	3.3	271	DMSO	44,193
	$R_2 = R_3 = Cl$, $R_1 = R_4 = H$	$X_1 = X_2 =$ **L17**	0.73		0.38			DMF	192
	$R_2 = R_3 = Br$, $R_1 = R_4 = H$	$X_1 = X_2 =$ **L17**	0.34		0.52			DMF	192
	$R_2 = R_3 = R_1 = R_4 = Cl$	$X_1 = X_2 =$ **L17**			0.42			DMF	194
	$R_2 = R_3 = R_1 = R_4 = Br$	$X_1 = X_2 =$ **L17**			0.55			DMF	194
	$R_2 = R_3 =$ **S18**, $R_1 = R_4 = H$	$X_1 = X_2 =$ **L18**			0.21	200		DMSO	127
	$R_2 = R_3 =$ **S18**, $R_1 = R_4 = H$	$X_1 = X_2 =$ **L19**			0.19	100		DMSO	127
	$R_2 = R_3 =$ **S18**, $R_1 = R_4 = H$	$X_1 = X_2 =$ **L20**			0.21	160		DMSO	127
	$R_2 = R_3 =$ **S18**, $R_1 = R_4 = H$	$X_1 = X_2 =$ **L21**			0.18	400		DMSO	127
	$R_2 = R_3 =$ **S18**, $R_1 = R_4 = H$	$X_1 = X_2 =$ **L22**			0.11	1.9		DMSO	127
	$R_2 = R_3 =$ **S18**, $R_1 = R_4 = H$	$X_1 = X_2 =$ **L23**			0.14	1.7		DMSO	127
	$R_2 = R_3 =$ **S18**, $R_1 = R_4 = H$	$X_1 = X_2 =$ **L24**			0.21	1.8		DMSO	127
	$R_2 = R_3 =$ **S18**, $R_1 = R_4H$	$X_1 = X_2 =$ **L25**			0.14	7.0		DMSO	127
	$R_2 = R_3 =$ **S18**, $R_1 = R_4 = H$	$X_1 = X_2 =$ **L26**			0.15	800		DMSO	127
	$R_2 = R_3 =$ **S18**, $R_1 = R_4 = H$	$X_1 = X_2 =$ **L27**			0.17	1.4		DMSO	127
	$R_2 = R_3 =$ **S18**, $R_1 = R_4 = H$	$X_1 = X_2 =$ **L28**			0.21	170		DMSO	44, 127
	Other								
	Complex **1**	$X_1 = X_2 = OH$			0.21			DMSO	63
	$R_1 = R_4 = R_2 = H$, $R_3 =$ **S3**	X1 = X2 = Cl	0.20	0.80	0.62		130	DMSO	68
			0.2	0.62	0.47		80	DMF	
Si(IV)(Pc)-O-Si(IV)(Pc)	$R_2 = R_3 = R_1 = R_4 = H$		0.22				116	Toluene	196

(*Continued*)

Table 4. (*Continued*)

Complex	Ring substituent	Axial ligand	Φ_F	Φ_T	Φ_Δ	$\Phi_P \times 10^5$	τ_T (μs)	Solvent	Ref.
Si(IV)(Pc)-O-Si(IV)(Pc)-O-Si(IV)(Pc)	$R_2 = R_3 = R_1 = R_4 = H$		0.114				51	Toluene	196
Si(IV)(Pc)-O-Si(IV)(Pc)-O-Si(IV)(Pc)O-Si(IV)(Pc)	$R_2 = R_3 = R_1 = R_4 = H$		0.094				37	Toluene	196
Ge(IV)									
	Unsubstituted								
	$R_2 = R_3 = R_1 = R_4 = H$	$X_1 = X_2$ =OH			0.25			DMSO	63
	Octasubstituted — peripheral (β)								
	$R_2 = R_3$ = **S18**, $R_1 = R_4 = H$	$X_1 = X_2 = Cl$	0.12	0.30	0.18		340	DMSO	45
	$R_2 = R_3$ = **S40**, $R_1 = R_4 = H$	$X_1 = X_2 = Cl$	0.21	0.20	0.18		205	DMSO	45
	$R_2 = R_3$ = **S45**, $R_1 = R_4 = H$	$X_1 = X_2 = Cl$	0.31	0.50	0.24		168	DMSO	45
	Others								
	Complex **1**	$X_1 = X_2 = OH$			0.17			DMSO	63
Sn(IV)									
	Unsubstituted								
	$R_2 = R_3 = R_1 = R_4 = H$	$X_1 = X_2 = OH$			0.26			DMSO	63
	$R_2 = R_3 = R_1 = R_4 = H$	$X_1 = X_2$ = **L9**	0.02	0.08	0.22		18	DMSO	45
	Tetrasubstituted — nonperipheral (α)								
	$R_1 = R_2 = R_3 = H$, R_4 = **S14**	$X_1 = X_2 = Cl$	0.008	0.69	0.75	61.7	30	DMSO	186
	$R_1 = R_2 = R_3 = H$, R_4 = **S18**	$X_1 = X_2 = Cl$	0.008	0.79	0.58	41.0	50	DMSO	186
	$R_1 = R_2 = R_3 = H$, R_4 = **S23**	$X_1 = X_2 = Cl$	0.007	0.76	0.74	43.1	40	DMSO	186

(*Continued*)

Table 4. (*Continued*)

Complex	Ring substituent	Axial ligand	Φ_F	Φ_T	Φ_Δ	$\Phi_P \times 10^5$	τ_T (μs)	Solvent	Ref.
	Tetrasubstituted — peripheral (β)								
	$R_1 = R_4 = R_2 = H$, R_3 = **S3** (Sn(II))		0.012	0.88	0.59		40	DMSO	68
			0.04	0.75	0.57		30	DMF	68
	$R_1 = R_2 = R_4 = H$, R_3 = **S14**	$X_1 = X_2 = Cl$	0.011	0.71	0.73	42.9	30	DMSO	186
	$R_1 = R_2 = R_4 = H$, R_3 = **S18**	$X_1 = X_2 = Cl$	0.014	0.89	0.73	27.9	40	DMSO	186
	$R_1 = R_2 = R_4 = H$, R_3 = **S23**	$X_1 = X_2 = Cl$	0.010	0.75	0.65	17.9	40	DMSO	186
	Octasubstituted — peripheral (β)								
	$R_2 = R_3$ = **S18**, $R_1 = R_4 = H$	$X_1 = X_2 = Cl$	0.04	0.19	0.22		30	DMSO	45
	$R_2 = R_3$ = **S18**, $R_1 = R_4 = H$	$X_1 = X_2 = Cl$	0.04	0.19	0.29		32	DMSO	45
	$R_2 = R_3$ = **S40**, $R_1 = R_4 = H$	$X_1 = X_2 = Cl$	0.01	0.15	0.23		10	DMSO	45
	$R_2 = R_3$ = **S45**, $R_1 = R_4 = H$	$X_1 = X_2 = Cl$	0.06	0.45	0.34		32	DMSO	45
	Octasubstituted — nonperipheral (α)								
	$R_2 = R_3 = H$, $R_1 = R_4$ = **$C_{10}H_{21}$**	$X_1 = X_2 = Cl$	0.23				200	THF	154
			0.15	0.35			10	Toluene	
	$R_2 = R_3 = H$, $R_1 = R_4$ = **C_6H_{13}**	$X_1 = X_2 = Cl$	0.20				90	THF	154
			0.16	0.30			20	Toluene	
	Other								
	Complex **1**	$X_1 = X_2 = OH$			0.15			DMSO	63
Pb									
	Tetrasubstituted — nonperipheral (α)								
	$R_1 = R_2 = R_3 = H$; R_4 = **S18**		0.03	0.72			10	DMF	201
			< 0.01	0.78			40	DMSO	
			0.01	0.82			8	Toluene	

(*Continued*)

Table 4. (*Continued*)

Complex	Ring substituent	Axial ligand	Φ_F	Φ_T	Φ_Δ	$\Phi_P \times 10^5$	τ_T (μs)	Solvent	Ref.
	$R_1 = R_2 = R_3 = H$; R_4 = **S23**		0.02	0.82			9	DMF	201
			> 0.01	0.80			30	DMSO	
			0.05	0.70			7	Toluene	
	Tetrasubstituted — peripheral (β)								
	$R_1 = R_2 = R_3 = H$, R_4 = **S14**		< 0.01	0.80			5	DMF	200
			< 0.01	0.82			40	DMSO	
			0.03	0.83			6	Toluene	
	$R_1 = R_2 = R_4 = H$, R_3 = **S18**		< 0.01	0.75			9	DMF	201
			< 0.01	0.76			20	DMSO	
			0.02	0.77			8	Toluene	
	$R_1 = R_2 = R_4 = H$, R_3 = **S23**		< 0.01	0.78			9	DMF	201
			< 0.01	0.72			30	DMSO	
			0.04	0.78			9	Toluene	
	Octasubstituted — peripheral (β)								
	$R_1 = R_4 = H$, $R_2 = R_3$ = **S14**		< 0.01	0.83			6	DMF	200
			< 0.01	0.84			30	DMSO	
			0.01	0.86			7	Toluene	
	$R_1 = R_4 = H$, $R_2 = R_3$ = **S18**		< 0.01	0.78			5	DMF	201
			0.01	0.76			20	DMSO	
			0.01	0.85			7	Toluene	
	$R_1 = R_4 = H$, $R_2 = R_3$ = **S23**		< 0.01	0.74			5	DMF	201
			< 0.01	0.88			50	DMSO	
			< 0.01	0.74			6	Toluene	

(*Continued*)

Table 4. (*Continued*)

Complex	Ring substituent	Axial ligand	Φ_F	Φ_T	Φ_Δ	$\Phi_P \times 10^5$	τ_T (μs)	Solvent	Ref.
				Group 15					
[Sb(III)]$^+$									
	Unsubstituted								
	$R_2 = R_3 = R_1 = R_4 = H$			0.75		0.31	30	DMSO	199
				0.76		0.52	7	DMF	
	$R_1 = R_4 = H$, $R_2 = R_3 =$ **S18**			0.79		0.42	20	DMSO	199
				0.78		0.61	5	DMF	
				0.77		0.57	7	Toluene	
	$R_1 = R_4 = H$, $R_2 = R_3 =$ **S23**			0.80		0.48	30	DMSO	199
				0.82		0.53	5	DMF	
				0.78		0.81	6	Toluene	
Sb(V)	$R_2 = R_3 = R_1 = R_4 = H$	$X_1 = X_2 = Cl$	0.01					CH_2Cl_2	198
	$R_1 = R_4 = H$, $R_2 = R_3 = C(CH_3)_3$	$X_1 = X_2 = Cl$	0.01					CH_2Cl_2	198
	$R_1 = R_4 = H$, $R_2 = R_3 = C(CH_3)_3$	$X_1 = X_2 = Br$	0.001					CH_2Cl_2	198
P	$R_1 = R_4 = R_2 = R_3 = H$	$X_1 = X_2 = OH$	0.13	0.52			113	DMSO	202
	$R_1 = R_4 = R_2 = R_3 = H$	$X_1 = X_2 =$ **L29**	0.08	0.27			456	DMSO	202

[a]The following symbols apply to all tables: Φ_F = fluorescence quantum yield (in general the standard used for determination of Φ_F is chlorophyll a in ether ($\Phi_F = 0.32$) [49]); Φ_T = triplet quantum yield; Φ_Δ = singlet oxygen quantum yield; Φ_P = photodegradation quantum yield; τ_T = triplet life time.

photosensitizer in terms of cell-killing ability.[92] The low Φ_F value for $ZnPc(SO_3)_4$ could be the result of some aggregation even in organic solvents such as DMF in addition to the heavy atom effect of Zn central metal. The value is also low for this complex in a methanol–water mixture ($\Phi_F = 0.14$).[93] Bovine serum albumin quenches the fluorescence of $ClAl(III)Pc(SO_3)_4$ complexes.[94]

2. *Carboxylated Derivatives*

The absorption spectra of $MPc(COOH)_8$ complexes are mirror images of the fluorescence emission spectra as is usually observed for MPc derivatives, due to a lack of aggregation.[77] Φ_F values for the $MPc(COOH)_8$ [M = Al ($\Phi_F = 0.27$), Zn ($\Phi_F = 0.23$), Ge ($\Phi_F = 0.13$), Si ($\Phi_F = 0.24$)] decrease with an increase in the size of the central metal which is consistent with the strength of the spin-orbit coupling induced by the respective central metals based on their relative masses.[77] The fluorescence quantum yields of $(OH)Al(III)Pc(COOH)_4$ complex adsorbed onto silica particles were found to be higher than in solution[111] (Table 3). The unmetalated form of complex **3** (Figure 1) containing **S10** substituents is water soluble but it is highly aggregated in water and methanol, but mainly monomeric in DMSO (with a low $\Phi_F = 0.04$) and chloroform.[97] The fluorescence quantum yield of this complex in water containing a surfactant cetyl trimethylammonium chloride (CTAC) was $\Phi_F = 0.12$, a value typical of MPc complexes.[97] ZnPc complexes containing **S10** or **S11** substituents gave typical values of Φ_F.[54,78] ZnPc substituted with **S13** ($\Phi_F = 0.006$) gave a higher Φ_F value than **S12** ($\Phi_F = 0.0015$) due to presence of bulkier substituents resulting in less aggregation, however these values are low compared to ZnPc complexes in general in Table 3.[79]

3. *Quaternized Derivatives*

a. *Porphyrazine complexes*

As stated above, the presence of triakylated compounds due to incomplete quaternization of the outer nitrogen atoms induces severe aggregation of porphyrazine complexes,[87] resulting in low Φ_F values which were lower in water (containing sodium dodecylsulfate, SDS) compared to toluene for these complexes. The Φ_F value for quaternized Zn porphyrazine derivatives (complex **2q**, R = CH_3) of 0.30 (Table 3) was similar to that of the corresponding unquaternized complex (complex **2**, $\Phi_F = 0.35$) in DMF.[102]

b. *MPc complexes*

Zwitterionic conjugates of ZnPc complexes exhibited Φ_F values in the region of 0.2 to 0.3 in organic solvents.[101] For ZnPc derivatives octasubstituted with **S1q**

groups, the Φ_F values ranged from 0.0038 to 0.0614 in DMSO, pH 7 and methanol,[115] values which are very low for MPc complexes (Table 3). For the corresponding Si(IV) complexes (containing **S1q**), the values ranged from 0.0361 to 0.1146 for the same solvents, hence showing an improvement.[115] When Zn was employed as a central metal for **S2q** ligands[70] there was considerable aggregation, resulting in a disagreement between absorption and emission spectra. However, in a mixture of water and pyridine (50:50) the complex was less aggregated. Addition of organic solvents normally breaks the aggregates, resulting in monomerization and a mirror image relationship between the fluorescence emission and absorption spectra (Figure 11a).[68] For MPc complexes containing the **S4q** substituent and Zn central metal, there was a lack of agreement between absorption and emission spectra due to aggregation.[72] For these complexes, the band centered around 640 nm associated with the dimer, is not seen in the fluorescence excitation spectra since only the monomer fluoresces. In DMSO, the absorption and fluorescence excitation spectra of the complexes were similar and are mirror images of the emission spectrum. Monomerization of the ZnPc (substituted with **S4q**) leads to enhanced fluorescence and this is noticed in the Φ_F value of this complex in the presence of Cremophore EL and in DMSO compared to the value in aqueous media alone. The Φ_F values followed the trend PBS 7.4 < PBS 7.4 + CEL < DMSO for ZnPc complexes containing the **S4q** substituent.[72] Also in DMSO, Φ_F values for ionic complexes (i.e. those containing an **S4q** substituent) were slightly lower than for the nonionic complexes (i.e. those containing an **S4** substituent).[72] Fluorescence quantum yield values of the ZnPc derivative substituted with **S2q** or **S3q** were found to be 0.17 and 0.11 respectively in a pyridine–water (50:50) mixture,[70] values which are within the range of phthalocyanine complexes (Table 3).

The water soluble ClGa(III)Pc complexes containing **S1q** substituents are not aggregated[67] and, as such, the excitation spectra were similar to absorption spectra and both were mirror images of the fluorescence spectra. The proximity of the wavelength of the Q-band absorption and excitation spectral maxima, suggest that the nuclear configurations of the ground and excited states are similar and are not affected by excitation.

The fluorescence quantum yields of ClGa(III)Pc derivatives peripherally or nonperipherally substituted with **S1q** are typical of MPc complexes (Table 3).[67,98] The peripherally substituted complexes showed marginally higher Φ_F values in comparison to the nonperipherally substituted ClGa(III)Pc and ClIn(III)Pc derivatives (Table 3), suggesting less quenching of the excited singlet state by non-peripheral substitution compared to the peripheral substitution.[67,69]

C. Triplet Quantum Yields (Φ_T) and Lifetimes (τ_T)

1. *Sulfonated Derivatives*

a. *$MPc(SO_3)_{mix}$ complexes*

Triplet quantum yields (Φ_T) are influenced both by the heavy atom effect and aggregation for a series of $MPc(SO_3)_{mix}$ complexes.[52] Φ_T values for the aggregated $(OH)_2Sn(IV)Pc(SO_3)_{mix}$ and $ZnPc(SO_3)_{mix}$, complexes improved upon addition of Triton X-100 (Table 3). For the monomeric $ClAl(III)Pc(SO_3)_{mix}$, $(OH)_2Ge(IV)Pc(SO_3)_{mix}$ and $(OH)_2Si(IV)Pc(SO_3)_{mix}$ complexes, the Φ_T values were lower (considering the same solvent) for the smaller atom, due to the heavy atom effect. Comparing $ZnPc(SO_3)_{mix}$ and $ClAl(III)Pc(SO_3)_{mix}$ complexes, a larger Φ_T value was obtained for the former due to the heavy atom effect, considering the same solvent.

It is important to note that the triplet states of MPc complexes are quenched by oxygen,[88] hence deoxygenation is important for the accurate determination of triplet lifetimes. Values of τ_T for $ZnPc(SO_3)_{mix}$ and MPc complexes in general are very low in water compared to when nonaqueous solvents or D_2O are employed.[93,103,104] This was explained in terms of the near IR spectra of the solvents. Figure 12 shows the near IR absorption spectra of three solvents: DMSO, DMF and H_2O, and how these affect the triplet and singlet oxygen lifetimes in solution.[41] The triplet state energy of ZnPc and many of its derivatives in solution is ~1.12 eV,[27] which corresponds to an absorption wavelength of ~1108 nm. The intensity and broadness of the solvent absorption in this wavelength region should

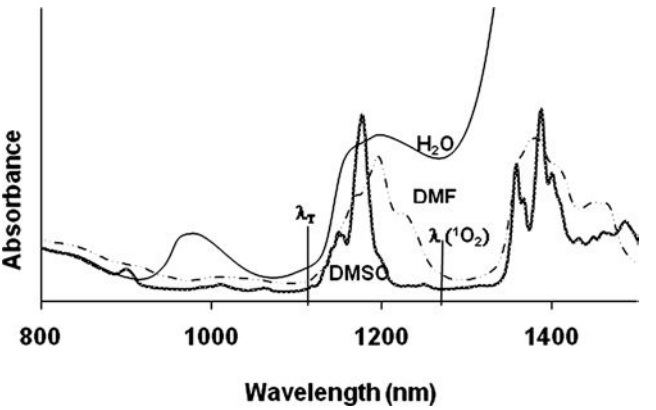

Figure 12. Near IR absorption spectra of some common solvents: DMSO, DMF and water. Reproduced with permission from Ref. 41.

have a considerable effect on the triplet lifetime. H_2O shows a very broad absorption band near 1108 nm, which implies that nonradiative decay and quenching of the sensitizer's triplet state would be more rapid in H_2O than in DMSO or DMF where absorption at 1108 nm is minimal. Thus τ_T values are generally lower in water when compared to DMSO, D_2O or DMF (Table 3). The τ_T values for the $MPc(SO_3)_{mix}$ complexes in DMSO ranged between 120 and 800 μs,[52] the highest value being observed for $ClAl(III)Pc(SO_3)_{mix}$ (800 μs), followed by $(OH)_2Ge(IV)Pc(SO_3)_{mix}$ (760 μs), $(OH)_2Si(IV)Pc(SO_3)_{mix}$ (439 μs), and $ZnPc(SO_3)_{mix}$ (530 μs).

b. *Other $MPc(SO_3)_n$ complexes*

For $ZnPc(SO_3)_4$, the Φ_T value was high in DMSO ($\Phi_T = 0.88$;[41] Table 3). Generally, Φ_T values are higher for $ZnPc(SO_3)_4$ compared to the disubstituted derivatives (Table 3).[108,109] Compared to other substituted ZnPc complexes (such as *tert*-butylphenoxy, methylphenoxy and nitro-substituted ZnPc derivatives), sulfonation of the Pc ring brings about longer triplet lifetimes.[41] The triplet lifetime values for $ZnPc(SO_3)_4$ and $ZnNPc(SO_3)_4$ in the presence of detergents[107] (Table 3), were increased when compared to water alone.[103] There was little effect of the degree of sulfonation on triplet lifetimes,[94,95] when considering the same solvent: compare $ClAl(III)Pc(SO_3)_2$ (τ_T = 520 μs), $ClAl(III)Pc(SO_3)_3$ (τ_T = 490 μs) and $ClAl(III)Pc(SO_3)_4$ (τ_T = 530 μs) in PBS or (τ_T = 1130 μs, 1150 μs and 1140 μs respectively in D_2O in Table 3. Bovine serum albumin (BSA) increases the lifetime of the triplet state of $ClAl(III)Pc(SO_3)_4$ as shown in Table 3.[94] However, association of BSA with ZnPc complexes decreased the triplet quantum yields, suggesting singlet state and/or static triplet quenching of the bound dye by the host protein.[106]

A large τ_T value was obtained for $ClAl(III)Pc(SO_3)_2$ in CD_3OD ($\tau_T = 1440$ μs)[95] compared to $\tau_T = 550$ μs in pH 4 buffer or 775 μs in methanol.[104,108–110] Sulfonated ClGa(III)Pc derivatives show low Φ_T values in methanol,[108] but the triplet state is long lived (τ_T ranging from 300 to 440 μs)[108,109] (See Table 3).

2. *Carboxylated Derivatives*

The variation of Φ_T among the $MPc(COOH)_8$ complexes in aqueous media [Φ_T = 0.0 (Zn), 0.32 (Al), 0.34 (Si) and 0.62 (Ge)] depends on the heavy atom effect which encourages intersystem crossing to the triplet state.[77] The triplet state lifetime values of the $MPc(COOH)_8$ range from 90 μs (M = Si) to 450 μs (M = Al), which is a typical range for many MPc complexes.[77]

For the unmetalated water soluble complex **3** (Figure 1) containing **S10** substituents, Φ_T values were highly solvent dependent, with the highest value being

observed in water containing CTAC ($\Phi_T = 0.56$), followed by DMSO ($\Phi_T = 0.34$), again showing that monomerization increases the photophysical parameters. This complex however, showed very low τ_T values (< 5 μs) in all solvents.[97] For complex **3** (M = Zn and containing **S10** substituent), $\Phi_T = 0.25$ in DMSO for the disubstituted complex, which did not change on tetrasubstitution ($\Phi_T = 0.27$). The lifetime decreased upon moving from the disubstituted to tetrasubstituted complex.[54]

3. *Quaternized Derivatives*

As expected, the presence of CEL gave increased Φ_T values for ZnPc complexes containing the substituent **S4q** compared to the phosphate buffer solution (PBS) alone.[72] An increase in triplet lifetimes (τ_T) in the order, PBS 7.4 < PBS 7.4 + CEL < DMSO were observed with these ZnPc complexes. The lowest τ_T values exhibited in PBS 7.4 are likely due to the fact that the triplet state of MPcs can be quenched by water (Figure 12), in addition to aggregation. The slight increase τ_T values in the presence of CEL may be due to less exposure of the Pc to the aqueous medium as well as a decrease in aggregation. The triplet quantum yields were very low in the presence of HSA for ZnPc tetrasubstituted with **S7** ($\Phi_T < 0.001$) with a reasonable lifetime of $\tau_T = 220$ μs.[75] The Φ_T value increased in the presence of CTAC ($\Phi_T = 0.16$, while the τ_T (= 150 μs) decreased.[75] These values changed in the presence of SDS, i.e. Φ_T increased to 0.59, while τ_T decreased to 140 μs).[75] ZnPc complexes containing other quaternizable substituents such as **S2q** and **S3q** showed typical Φ_T values in the presence of organic solvents (Table 3).

Unsubstituted ClIn(III)Pc and ClIn(III)Pc tetrasubstituted either peripherally or nonperipherally with **S1q** substituents gave shorter lifetimes and correspondingly larger triplet quantum yields (Φ_T) when compared to ZnPc derivatives in general (Table 3), due to the enhanced intersystem crossing induced by the larger In central metal.[69] In DMSO, Φ_T value for the quaternized octasubstituted ClIn(III)Pc containing the substituent **S1q**, ($\Phi_T = 0.68$) is larger than that in water with Triton X-100 ($\Phi_T = 0.59$), which is attributed to increased intermolecular interaction in water compared to that in DMSO.[98] Even in the presence of Triton X-100, some level of aggregation still exists for ClIn(III)Pc complexes containing the substituent **S1q** in water. The Φ_T value for the quaternized ClIn(III)Pc complexes tetrasubstituted with **S1q** substituents at peripheral positions ($\Phi_T = 0.94$, Table 3) was very high in DMSO.

The triplet lifetime values for the ClIn(III)Pc complexes substituted with **S1q** were lower in water when compared to DMSO due to the aggregation in water, and this was also due to absorption by water at the same wavelength as the triplet state of MPc complexes (Figure 12). τ_T values for the quaternized ClIn(III)Pc

complexes (**S1q** substituents, peripheral or nonperipheral, Table 3) were similar to those of the corresponding unquaternized derivatives (**S1** substituents) in DMSO. Addition of Triton X-100 increased the τ_T values in water for these ClIn(III)Pc complexes.

D. Singlet Oxygen Quantum Yields (Φ_Δ)

Energy transfer between the triplet state of photosensitizers and ground state (triplet) molecular oxygen leads to the production of singlet oxygen. Therefore singlet oxygen quantum yield, which is the efficiency of singlet oxygen generation, should depend on the triplet state quantum yield and lifetime, the efficiency of energy transfer, the energy of the triplet state and the ability of the substituents to quench the triplet state among other factors. Thus, the trend in variation of Φ_Δ within an array of photosensitizers should be parallel to the variations in their Φ_T values. Due to the aggregation behavior of MPc complexes, the values of Φ_Δ are expected to increase in the presence of detergents (e.g. Triton X-100), in the same manner as for the Φ_T values.[112]

1. *Sulfonated Derivatives*

a. *$MPc(SO_3)_{mix}$ complexes*

For a range of $MPc(SO_3)_{mix}$ [M = ClAl(III), Zn, $(OH)_2Si(IV)$, $(OH)_2Ge(IV)$] photosensitizers,[52] lower singlet oxygen quantum yields (Φ_Δ) were observed in aqueous solutions (in the absence of detergents) compared to organic solvents or in aqueous media in the presence of detergents (Table 3). The degree of sulfonation has an influence on the production of singlet oxygen. For a series of $ZnPc(SO_3)_{n(mix)}$ (n = an average number of SO_3 groups) complexes (Table 3), Φ_Δ values were almost the same in DMSO, but an increase in Φ_Δ with the value of n is observed in PBS (pH 7.4) in the absence of Triton X-100.[114] The Φ_Δ value is low for the more aggregated $ZnPc(SO_3)_{2.1(mix)}$ ($\Phi_\Delta \leq 0.01$), but high for the mainly monomeric $ZnPc(SO_3)_{3.7(mix)}$ ($\Phi_\Delta = 0.49$) in pH 7.4 buffer (Table 3).[114]

For the unmetalated $H_2Pc(SO_3)_{n(mix)}$, complex, intermolecular hydrogen bonding results in extensive aggregation, with the addition of Triton X-100 leading only to partial monomerization and a low Φ_Δ value (0.02).[114]

b. *Other $MPc(SO_3)_n$ complexes*

In reversed micelles, singlet oxygen quantum yields for the di- and trisubstituted $(OH)Al(III)Pc(SO_3)_n$ complexes were found to be the same as in water, even

though enhanced intersystem crossing was observed in micelles.[42] (OH)Al(III)Pc$(SO_3)_n$ derivatives generally give low Φ_Δ values compared to the corresponding ZnPc derivatives due to the small size of the central Al metal ion compared to Zn.

As observed with ZnPc$(SO_3)_4$, the Φ_Δ value for ZnNPc$(SO_3)_4$ increased in the presence of detergents.[107] However, for ClAl(III)Pc$(SO_3)_4$ (Φ_Δ = 0.20 in DMF and 0.18 in aqueous media) and H_2Pc$(SO_3)_4$ (Φ_Δ = 0.16 in DMF and 0.09 in aqueous media), low singlet oxygen quantum yields (< 0.3) were observed (Table 3).[18,33,35,83,92] The Φ_Δ values for tetrasulfonated MPc complexes were found to increase as follows in DMF: ZnPc$(SO_3)_4$ (Φ_Δ = 0.52) > XGa(III)Pc$(SO_3)_4$ (Φ_Δ = 0.41) > XAl(III)Pc$(SO_3)_4$ (Φ_Δ = 0.2) ~ H_2Pc$(SO_3)_4$ (Φ_Δ = 0.16), (where X represents an anionic axial ligand). In general, Φ_Δ values were higher in DMF than in water or water containing CTAC.[33] MgPc$(SO_3)_2$ gave a low Φ_Δ value in DMSO, most likely due to the large fluorescence expected for small central metals.[114]

2. *Carboxylated Derivatives*

MPc$(COOH)_8$ (M = Al, Zn, Si and Ge) gave low Φ_Δ values even though these complexes are not aggregated. The values increase with the size of the central metal as follows: Al (Φ_Δ = 0.12) < Si (Φ_Δ = 0.22) < Zn (Φ_Δ = 0.32) ≈ Ge (Φ_Δ = 0.31) in aqueous media.[77] When considering the number of carboxyl groups, the Φ_Δ values obtained for ZnPc$(COOH)_8$ (Φ_Δ = 0.48 in DMF) and ZnPc$(COOH)_4$ (Φ_Δ = 0.51 in DMF) were similar (Table 3). For (OH)Al(III)Pc$(COOH)_8$, association via hydrogen bonding occurs, affecting the production of singlet oxygen and hence the photosensitizing ability.[42] Thus, (OH)Al(III)Pc$(COOH)_8$ gave a low Φ_Δ value of 0.12 in DMSO or aqueous media (Table 3).[35,77] For complex **3**, containing Zn as the central metal ion and substituted with **S10**, low Φ_Δ values were obtained for both the tetrasubstituted (Φ_Δ = 0.31) and disubstituted (Φ_Δ = 0.23) complexes.[54] Table 3 shows an even lower Φ_Δ value for complex **4** substituted with **S10**.

3. *Quaternized Derivatives*

a. *Porphyrazine complexes*

For the zinc porphyrazine **2q** complexes substituted with CH_3 or $CH_3COOCH_2CH_3$, singlet oxygen quantum yields were higher in aqueous (SDS) solutions (Table 3) compared to organic solvents.[87] The Φ_Δ value for the quaternized Zn porphyrazine complex (**2q**) of 0.50 (Table 3) was similar to that of the corresponding unquaternized complex (Φ_Δ = 0.56) in DMF (Table 4).[102] For the **1q** complexes containing Ge, Sn and Zn central metals, the Φ_Δ values are very low (< 0.1).

b. *MPc complexes*

Efficient production of singlet oxygen in DMSO was observed with values of S_Δ (= Φ_Δ/Φ_T, which represents the efficiency of quenching of the triplet excited state by singlet oxygen), being near unity for quaternized tetra- or octasubstituted ZnPcs containing the **S4q** substituent.[72] The low Φ_Δ values obtained for these complexes in PBS (Table 3) are consequently due to low Φ_T values, as discussed above. However, a slight improvement is observed in Φ_Δ values in CEL. ZnPc complexes octasubstituted with **S6** or **S9** gave Φ_Δ values which were larger for the former substituent (0.60, 0.62 and 0.65 in methanol, ethanol and water, respectively for **S6**),[74] compared to **S9** which ranged from < 0.05 to 0.45 in the same solvents.[74] For ZnPc tetrasubstituted with **S5** substituents, a Φ_Δ value of 0.6 was obtained in neat water. This was reduced to about 0.32 in phosphate-buffered saline.[73]

As with the ZnPc counterparts, ClAl(III)Pc complexes octasubstituted with **S6** or **S9**, gave Φ_Δ values which were generally larger for **S6** (0.35, 0.35 and 0.38 in methanol, ethanol and water, respectively).[74] The values for **S9** ranged from Φ_Δ < 0.05 to 0.37 in the same solvents.[74] As expected, the Φ_Δ values were larger for ZnPc compared to ClAl(III)Pc due to the heavy atom effect.

Quaternized ClIn(III)Pc complexes (tetrasubstitued with **S1q** substituent at peripheral and nonperipheral positions) showed lower Φ_Δ values (ranging from 0.44 to 0.70; Table 3) when compared to their unquaternarized counterparts (containing **S1**), with Φ_Δ values ranging from 0.65 to 0.86 in various solvents.[69]

In some cases, the Φ_Δ values are low relative to Φ_T for ClIn(III)Pc complexes substituted with **S1q** in Table 3, suggesting inefficient transfer of energy from the triplet state of MPc to triplet state oxygen (and thus the subsequent formation of singlet oxygen). ClIn(III)Pc octasubstituted with **S1q** gave $\Phi_\Delta = 0.66$ in DMSO and $\Phi_\Delta = 0.56$ in water.[98] The lower value in water is ascribed to the quenching of singlet oxygen by water, as demonstrated by the shorter lifetime of singlet oxygen in water (4.2 μs)[116] compared to that in DMSO (30 μs).[117] The Φ_Δ values for ClGa(III)Pc complexes (containing **S1q** substituent) showed that the point of substitution (peripheral or nonperipheral positions) does not affect the Φ_Δ values[67] (Table 3).

E. Photobleaching Quantum Yields (Φ_p)

Observation of the degradation of the molecules under irradiation can be used to study their stability and this is especially important for those molecules intended for use as photocatalysts. The collapse of the absorption spectra without any distortion of the shape (or shifts in wavelength) is generally taken to imply clean photodegradation and is not associated with phototransformation. The

photodegradation (photobleaching) quantum yield (Φ_p) is a measure of the stability of a molecule under photo-irradiation. It is believed that photobleaching is a singlet oxygen-mediated process; hence, its efficiency should depend on the value of Φ_Δ. Thus, oxidative attack of the excited triplet state of MPcs by singlet oxygen brings about photodegradation, since the triplet state is sufficiently long lived to participate in photochemical reactions.

In general, for sulfonated ZnPc derivatives, Φ_p values are of the order of 10^{-5} (Table 3). For a series of $MPc(SO_3)_{mix}$ complexes, photodegradation quantum yield values tend to follow singlet oxygen trends (Table 3).[52,53] Photodegradation quantum yields were found to be high in DMSO for unquaternized peripherally tetra- or octasubstituted ZnPcs containing the **S4** substituent ($\Phi_p = 66 \times 10^{-5}$ in DMSO Table 4) compared to their quaternized counterparts containing the **S4q** substituents ($\Phi_p = 17 \times 10^{-5}$ in DMSO).[72] The lowest values of photodegradation were exhibited in PBS pH 7, for the **S4q** substituent on ZnPc (Table 3),[72] where Φ_Δ values are also low. This confirms that photodegradation is dependent on singlet oxygen.

For quaternized ClIn(III)Pc complexes containing the **S1q** tetrasubstituent at peripheral and nonperipheral positions, the photodegradation quantum yields were almost similar, showing that the point of substitution does not affect stability. For ClIn(III)Pc or ClGa(III)Pc derivatives containing **S1q** as the substituent, the variation of Φ_p follows the same trend as that of Φ_Δ, with Φ_p values being higher in aqueous media compared to DMSO. Hence, the complexes are less stable in the former solvent.[69]

IV. Non-Water Soluble Phthalocyanine Complexes

A. Aggregation Behavior in General

The aggregation tendencies of non-water soluble MPc complexes are attributed to the formation of π–π interactions between adjacent MPc rings. Coordinating solvents may be axially ligated to the central metals in the MPc complexes, thereby preventing columnar aggregation. However the presence of axial or ring substituents is often not sufficient to prevent aggregation. Thus the non-water soluble complexes discussed in this work often show aggregation. CdPc derivatives showed unique aggregation behavior and are therefore discussed in greater detail.[118] The spectrum of CdPc nonperipherally substituted with **S14** is typical of a monomeric species (Figure 13a), whereas that of its peripherally substituted counterpart (with **S14**) tends to be slightly broad in both DMF and DMSO.[118] The spectrum of the latter was quite unusual in DCM or chloroform (Figure 13b), suggesting extensive aggregation. No changes in spectra occurred on addition of the

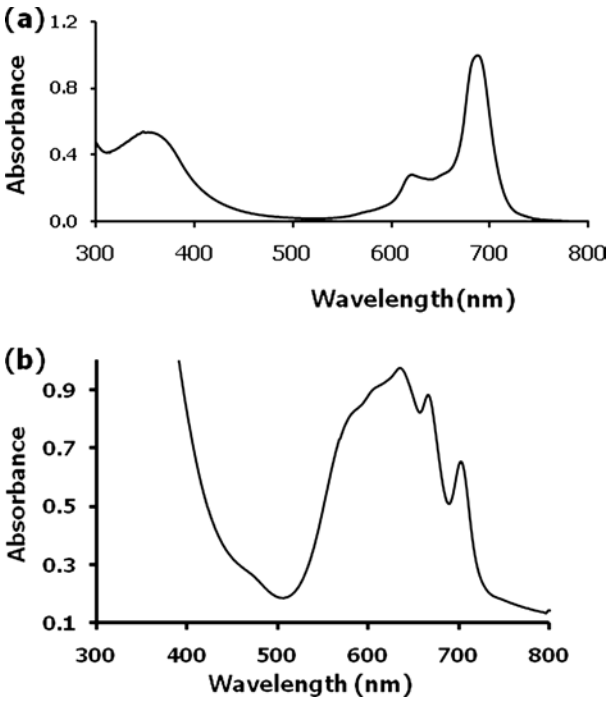

Figure 13. Electronic absorption spectra of CdPc peripherally tetrasubstituted with **S14** ligand in (a) DMSO and (b) DCM. Modified from Ref 118.

surfactant to solutions of CdPc peripherally substituted with **S14**, which is an indication that this complex is in a monomeric state or that the aggregates are too strong to be broken by surfactants. For CdPcs, triple-decker and higher oligomeric complexes have been reported in addition to demetalation.[119–122] The oxidizing and noncoordinating nature of the solvents may also play a role,[123,124] where chlorinated solvents are known to oxidize some MPc complexes.[119,120]

The presence of two sharp bands near 700 nm (Figure 13b) may suggest demetalation. Addition of a metal salt such as zinc acetate to these solutions resulted in the collapse of the two sharp bands confirming that the peaks were due to demetalation. Partial oxidation was also confirmed by addition of reducing agents.[119] Thus in DCM, $CHCl_3$, THF and toluene, CdPc peripherally substituted with **S14** showed partial oxidation and partial demetalation in addition to aggregation.

ZnPc complexes peripherally octasubstituted with **S10**, **S15**, **S16** and **S17** and the octachlorinated ZnPc [$ZnPc(Cl)_8$] complex showed aggregation behavior in organic solvents even at low concentrations ($< 1 \times 10^{-5}$ M).[36] The UV-visible spectrum of ZnPc complexes peripherally octasubstituted with **S18** showed an extra band[8] (the so-called X-band[125]) in nonpolar or less polar solvents such as benzene

and chloroform, but not in solvents of higher polarity such as DMF, acetone and DMSO. The origin of the X band has been explained in terms of the distortion of the Pc ring due to the presence of eight phenyl groups on the peripheral positions of the phthalocyanine ring.[126]

The axially ligated $X_2Si(IV)Pc$ complexes (where X is the negatively charged axial ligand) containing phenoxy groups (**S18**) on the ring showed spectra typical of a monomeric species.[127] For $X_2Si(IV)Pc$ complexes containing axial hydroxyl ligands, aggregation occurs due to hydrogen bonding between the axial hydroxyl groups.[127]

B. Unmetalated, Group 1 and Group 2 Phthalocyanine Complexes

Phthalocyanine complexes are notorious for their lack of solubility in common organic solvents. Unmetalated Pc complexes are generally less soluble compared to their metalated counterparts. Introduction of substituents onto the Pc ring as well as metalation enhances the solubility of these complexes. Thus, as Table 4 shows, there are fewer studies available on unmetalated phthalocyanines.

Unmetalated phthalocyanine complexes substituted with fluorine and terphenyl ligands gave very high fluorescence quantum yields of $\Phi_F = 0.88$.[128] Unsubstituted H_2Pc exhibits a higher Φ_F value ($\Phi_F = 0.55$) in $CHCl_3$ when compared to the complex tetrasubstituted with $OCH_2C(CH_3)_3$ ($\Phi_F = 0.24$) in Table 4.[129,130] Unmetalated phthalocyanines nonperipherally octasubstituted with long chains gave Φ_F values ranging from 0.05 to 0.10 in DCM.[131] On insertion of the Zn central metal, the Φ_F values increased, ranging from 0.13 to 0.17 (Table 4).[131] Unmetalated phthalocyanines octasubstituted with **S19** gave low Φ_F values in DMSO and polyvinyl chloride (PVC), but the values were found to be higher in THF.[132] For this complex, the Φ_F values were generally higher (in THF and ethyl cellulose, EC) than for the corresponding ZnPc derivative (Table 4).[132]

H_2Pc tetrasubstituted with $(CH_2)_2O(CH_2)_2OCH_3$ gave a low singlet oxygen quantum yield (Φ_Δ) of 0.19, but had a long lifetime in toluene (504 μs).[88] A mixture of solutions of anionic 5,10,15,20-sulfonato-phenyl-porphyrin (TSPP) and a positively charged $H_2Pc(SCH_2CH_2N^+(CH_3)_3CH_3SO)_2(NH_2)_2$ complex gave high Φ_Δ values compared to individual components.[129,133] For the phosphorus dendrimers (**S20**) built from an octasubstituted metal free phthalocyanine core, the fluorescence quantum yield increased with an increase in the number of dendrimers.[134] Both Li_2Pc and Li_2NPc complexes gave the same Φ_T and Φ_F values of 0.6 and 0.5 respectively[50] (Table 4), giving $\Phi_T + \Phi_F$ of ~ 1. This suggested that the dominant radiationless decay path was intersystem crossing for these complexes.

There are only a few studies on the photochemical properties of MgPc derivatives. Unsubstituted MgPc was found to give a Φ_F value of 0.76 (Table 4).[135]

Table 5. Selected photocatalytic reactions of MPcs.

MPc complex[a]	Molecule photocatalyzed	Medium[b]	Oxidant	Main product	Product yield (%)[b]	Ref.
Alkenes						
ClGa(III)Pc	1-Hexene	DCM homogeneous	Oxygen	1,2-Epoxyhexane	1.19	211, 235
$R_1 = R_4 = H$, $R_2 = R_3 =$ **S14**, **(c)** (M = ClGa(III))	1-Hexene	DCM homogeneous	Oxygen	1,2-Epoxyhexane	1.08	211, 235
$R_1 = R_4 = H$, $R_2 = R_3 =$ **S23** (M = ClGa(III))	1-Hexene	DCM homogeneous	Oxygen	1,2-Epoxyhexane	1.21	211, 235
ClIn(III)Pc	1-Hexene	DCM homogeneous	Oxygen	1,2-Epoxyhexane	1.22	211, 235
$R_1 = R_4 = H$, $R_2 = R_3 =$ **S14** (M = ClIn(III))	1-Hexene	DCM homogeneous	Oxygen	1,2-Epoxyhexane	1.38	211, 235
$R_1 = R_4 = H$, $R_2 = R_3 =$ **S23** (M = ClIn(III))	1-Hexene	DCM homogeneous	Oxygen	1,2-Epoxyhexane	1.25	211, 235
$R_1 = R_4 = H$, $R_2 = R_3 =$ **S18** (M = OTi(IV))	1-Hexene	DCM homogeneous	Oxygen	1,2-Epoxyhexane		136
$R_1 = R_4 = H$, $R_2 = R_3 =$ **S22** (M = OTi (IV))	1-Hexene	DCM homogeneous	Oxygen	1,2-Epoxyhexane		136
$R_1 = R_4 = H$, $R_2 = R_3 =$ **S24** (M = OTi(IV))	1-Hexene	DCM homogeneous	Oxygen	1,2-Epoxyhexane		136
$R_1 = R_4 = H$, $R_2 = R_3 =$ **S25** (M = OTi(IV))	1-Hexene	DCM homogeneous	Oxygen	1,2-Epoxyhexane		136

(*Continued*)

Table 5. (*Continued*)

MPc complex[a]	Molecule photocatalyzed	Medium[b]	Oxidant	Main product	Product yield (%)[b]	Ref.
$R_2 = R_3 = H$, $R_1 = R_4 =$ **S18** (M = OTi(IV))	1-Hexene	DCM homogeneous	Oxygen	1,2-Epoxyhexane		136
$R_2 = R_3 = H$, $R_1 = R_4 =$ **S22** (M = OTi(IV))	1-Hexene	DCM (homo)	Oxygen	1,2-Epoxyhexane		136
$R_2 = R_3 = H$, $R_1 = R_4 =$ **S24** (M = OTi(IV))	1-Hexene	DCM homogeneous	Oxygen	1,2-Epoxyhexane		136
$R_2 = R_3 = H$, $R_1 = R_4 =$ **S25** (M = OTi(IV))	1-Hexene	DCM homogeneous	Oxygen	1,2-Epoxyhexane		136
ZnPc	Cyclohexene	Dioxan homogeneous	Oxygen	Cyclohexenone	4.4	20
		THF homogeneous	Oxygen	Cyclohexenone	4.3	20
		Benzene homogeneous	Oxygen	Cyclohexenone	1.8	20
		DMF/CH_2Cl_2 homogeneous	Oxygen	Cyclohexenone	6.6	20
Sulfur-containing compounds						
$ZnPc(SO_3)_4$ or $ClAl(III)Pc(SO_3)_4$	2-ME	Aqueous homogeneous	Oxygen	2-Hydroxyethanesulfonic acid		205
	HS^-	Aqueous homogeneous	Oxygen	SO_4^{2-}		205
$ZnPc(SO_3)_4$ $ZnPc(COOH)_4$	2-ME	Aqueous homogeneous	Oxygen	2-Hydroxyethanesulfonic acid		216
$ZnPc(SO_3)_4$ $ZnPc(COOH)_4$	$S_2O_3^-$	Aqueous homogeneous	Oxygen	SO_4^{2-}		216

(*Continued*)

Table 5. (*Continued*)

MPc complex[a]	Molecule photocatalyzed	Medium[b]	Oxidant	Main product	Product yield (%)[b]	Ref.
Phenols						
H_2Pc/Al_2O_3 or H_2Pc/TiO_2	Phenol	H_2O–ethanol (2:1) heterogeneous	Oxygen	CO_2		223
$(NdPc)_2$, Complex **14**	4-Chlorophenol	pH 6–7 heterogeneous	Oxygen	4-Chlorocatechol		17
$CoPc(COOH)_4/TiO_2/Pt$	Phenol	Aqueous media	Oxygen	CO_2	0.10	225
$FePc/SiO_2$	Phenol	Heterogeneous	H_2O_2	p-Hydroquinone p-Benzoquinone		215
FePc@NaY	Phenol	Heterogeneous	H_2O_2	p-Hydroquinone p-Benzoquinone		215
$FeO_2Pc(SO_3)_4$/(LDH)[d]	Phenol	Heterogeneous	Oxygen			220
$ZnPc(SO_3)_4$	Phenol	pH 13	Oxygen	CO_2		224
$ZnPc(SO_3)_4$ or $ClAl(III)Pc(SO_3)_4$	Phenol	Aqueous or ethanol homogeneous	Oxygen	CO_3^{2-}		205
	4-Chlorophenol	Aqueous or ethanol homogeneous	Oxygen			205
	Cyclopentadiene	Ethanol homogeneous		4,5-Epoxypent-2-enaldehyde		205
$ZnPc(SO_3)_{mix}$	4-chlorophenol	pH 10 homogeneous	Oxygen	Benzoquinone	0.0140[c]	35
	Trichlorophenol	pH 7		2,5-Dichloro-1, 4-benzoquinone	0.0105[c]	19
	Pentachlorophenol	pH 7		2,3,5,6-Tetrachloro-1, 4-benzoquinone	0.00392[c]	19
$ZnPc(SO_3)_4$	4-Chlorophenol	pH 10	Oxygen	Benzoquinone	<0.002[c]	35

(*Continued*)

Table 5. (*Continued*)

MPc complex[a]	Molecule photocatalyzed	Medium[b]	Oxidant	Main product	Product yield (%)[b]	Ref.
$ZnPc(SO_3)_n$	Phenol	pH 10	Oxygen	Quinone	0.15[c]	218
	2-Chlorophenol			Quinone	0.24[c]	
	3-Chlorophenol			Quinone	0.20[c]	
	4-Chlorophenol			Quinone	0.20[c]	
	2,6-Dichlorophenol			Quinone	0.21[c]	
	2,4,6-Trichlorophenol			Quinone	0.20[c]	
$ZnPc(COOH)_8$	4-Chlorophenol	pH 10 homogeneous	Oxygen	Benzoquinone	0.0059[c]	35
$ZnPc(COOH)_4/TiO_2/Pt$	Phenol	Aqueous heterogeneous	Oxygen	CO_2	0.10	225
ClAl(III)Pc/CTMAB	4-Chlorophenol	Aqueous heterogeneous	Oxygen			226
	4-Nitrophenol					
	2,4-Dichlorophenol					
	2,4,6-Trichlorophenol					
$ClAl(III)Pc(SO_3)_{mix}$	4-Chlorophenol	pH 10 homogeneous	Oxygen	Benzoquinone	0.0097[c]	35
	Trichlorophenol	pH 7		2,5-Dichloro-1, 4-benzoquinone	0.0118[c]	19
	Pentachloro-phenol	pH 7		2,3,5,6-Tetrachloro-1, 4-benzoquinone	0.00680[c]	19
$ClAl(III)Pc(SO_3)_4$	4-Chlorophenol	pH 10 homogeneous	Oxygen	Benzoquinone	0.0040[c]	35
	Trichlorophenol	pH 7		2,5-Dichloro-1, 4-benzoquinone	0.00540[c]	19
	Pentachloro-phenol	pH 7		2,3,5,6-Tetrachloro-1, 4-Benzoquinone	0.00450[c]	19

(*Continued*)

Table 5. (*Continued*)

MPc complex[a]	Molecule photocatalyzed	Medium[b]	Oxidant	Main product	Product yield (%)[b]	Ref.
$OHAl(III)Pc(SO_3)_4$	Phenol	pH 13 homogeneous	Oxygen	CO_2		224
$(OH)Al(III)Pc(COOH)_3NH_2$	Phenol	pH 3	Oxygen	Benzoquinone		228
	4-Chlorophenol	homogeneous		Benzoquinone		
$ZnPc(COOH)_4/TiO_2$	4-Chlorophenol	Aqueous heterogeneous		CO_2, Cl^-		227
$ClAl(III)Pc(COOH)_8$	4-Chlorophenol	pH 10 heterogeneous	Oxygen	Benzoquinone	<0.002[c]	35
$OHAl(III)Pc(SO_3)_x$	Phenol	pH 10	Oxygen	Quinone	0.39[c]	218
	2-Chlorophenol	homogeneous		Quinone	0.43[c]	
	3-Chlorophenol			Quinone	0.48[c]	
	4-Chlorophenol			Quinone	0.61[c]	
	2,6-Dichlorophenol			Quinone	0.47[c]	
	2,4,6-Trichlorophenol			Quinone	0.40[c]	
$LAl(III)Pc/SiO_2$ (L = Cl or OH)	Phenol	CH_3CN heterogeneous	Oxygen	Quinone		221
$(OH)Ga(III)Pc(SO_3)_4$	Phenol	pH 13 homogeneous	Oxygen	CO_2		224
$(OH)_2Si(IV)Pc(SO_3)_{mix}$	Trichlorophenol	pH 7 homogeneous	Oxygen	2,5-Dichloro-1, 4-benzoquinone	0.00343[c]	19
	Pentachloro-phenol	pH 7		2,3,5,6-Tetrachloro-1, 4-benzoquinone	0.00411[c]	19

(*Continued*)

Table 5. (*Continued*)

MPc complex[a]	Molecule photocatalyzed	Medium[b]	Oxidant	Main product	Product yield (%)[b]	Ref.
$(OH)_2Si(IV)Pc(SO_3)_x$	Phenol	pH 10 homogeneous	Oxygen	Quinone	0.24[c]	218
	2-Chlorophenol			Quinone	0.31[c]	
	3-Chlorophenol			Quinone	0.27[c]	
	4-Chlorophenol			Quinone	0.44[c]	
	2,6-Dichlorophenol			Quinone	0.31[c]	
	2,4,6-Trichlorophenol			Quinone	0.25[c]	
$(OH)_2Sn(IV)Pc(SO_3)_{mix}$	Trichlorophenol	pH 7 homogeneous	Oxygen	2,5-Dichloro-1, 4-benzoquinone	<0.002[c]	19
	Pentachloro-phenol	pH 7		2,3,5,6-Tetrachloro-1, 4-benzoquinone	<0.002[c]	19

[a] PcS_{mix} = mixture of sulfonated Pcs. X refers to an axial ligand, where one was not provided in the reference.
[b] % yield = (Product obtained$_{1,2\text{-epoxyhexane}}$)/(Initial susbstrate)] × 100.
[c] As quantum yield.
[d] LDH = layered double oxide.

C. Group 4 To 11 Phthalocyanine Complexes

For these groups only the OTi(IV)Pc complexes have been relatively intensely studied. OTi(IV)Pc complexes containing the **S14**, **S22-S25**[136–139] substituents at the peripheral and nonperipheral positions have been studied in a variety of solvents. Φ_F values for nonperipherally tetrasubstituted OTi(IV)Pcs are generally lower than that for the corresponding peripherally substituted derivatives (Table 4). The Φ_F values generally increase (or remain the same) for peripherally substituted derivatives, from tetrasubstituted to octasubstituted derivatives. OTi(IV)Pc complexes substituted with polyethylene glycol units gave Φ_F values which ranged from 0.05 to 0.32 (not in Table 4).[140]

Studies on the triplet state properties of OTi(IV)Pc derivatives are few. However, the Φ_T values range from moderate to high, where the highest value of $\Phi_T = 0.85$ was obtained for a OTi(IV)Pc derivative octasubstituted with **S26** in DMSO.[138] The triplet lifetimes are highly dependent on the solvent and substituents present, and the lowest values were obtained for OTi(IV)Pc octasubstituted with **S14** ($\tau_T = 60$ μs) and **S18** ($\tau_T = 40$ μs) in chloronaphthalene.[139] The Φ_Δ values obtained for the OTi(IV)Pc derivatives octasubstituted with substituent **S26** were high, corresponding to high Φ_T values.[138] The Φ_p values for OTi(IV)Pc complexes were within the range typically obtained for MPc complexes, showing stability.

X_2Zr(IV)Pc complexes (where X = Cl, **L1**, **L2** and **L3**), gave very low Φ_F values ranging from 0.006 to 0.016 (Table 4).[141]For PdPc and NiPc complexes containing long chain substituents, low Φ_F values were obtained (<0.01) due to the open-shell nature of the complexes (Table 4).[142]

D. Group 12 Phthalocyanine Complexes

1. *ZnPc Complexes*

a. *Fluorescence quantum yields (Φ_F)*

ZnPc derivatives are the most intensively studied of all MPc complexes photochemically and photophysically, with substituents ranging from **S14** to **S56**.[9,29,41,143–166] Fluorescence quantum yields (Φ_F) for unsubstituted ZnPc is ~ 0.2[41,157] in DMSO and this value is often employed as the reference for Φ_F determinations of other MPc complexes. Φ_F values for unsubstituted ZnPc range from 0.07 to 0.34 in various solvents (Table 4). The values are influenced by the viscosity of the solvent, where lower values are obtained in less viscous solvents.[37] Of the substituted complexes, there are fewer studies on nonperipherally substituted ZnPc derivatives compared to those that are peripherally substituted (Table 4). For ZnPc complexes octasubstituted with **S18** on the peripheral

positions, the fluorescence excitation and emission spectra exhibited two bands. This is associated with the loss of symmetry due to the twisting of the phenyl ring which distorts the molecule.[41]

Fluorescence of aggregated ZnPc complexes such as $ZnPc(NO_2)_4$ and $ZnPc(NH_2)_4$ complexes occurs from the monomeric component,[157] thus the Φ_F values were found to be very low ($\Phi_F < 0.02$; Table 4) for these complexes as expected. Fluorescence quantum yields were not affected by the addition of cyclodextrin,[157] which is known to prevent aggregation in porphyrins.[167] Halogenation of ZnPc derivatives resulted in a decrease in fluorescence quantum yields as expected, due to the heavy atom effect.[30] A decrease in the Φ_F value was observed from ZnPc ($\Phi_F = 0.17$ in acetone) to $ZnPcF_{16}$, ($\Phi_F = 0.04$), followed by an increase for the $ZnPc(C(CF_3)_2F)_8F_8$ complex ($\Phi_F = 0.39$) in acetone[146] (Table 4). This observation is consistent with the notion that aromatic fluorine groups in $ZnPcF_{16}$ are part of the phthalocyanine π system and thus enhance the intersystem crossing. Aliphatic fluorine groups in $ZnPc(C(CF_3)_2F)_8F_8$ are not conjugated with the phthalocyanine π system, resulting in increased fluorescence lifetimes.[146]

The fluorescence quantum yields obtained for ZnPc tetrasubstituted (at peripheral positions) with bulky substituents such as **S46**, **S47**, **S49** or **S54**, are typical of MPc complexes.[78,159,161] ZnPc complexes tetra(α)- or octa(β)-substituted with the **S48** substituent, also a bulky substituent, gave very low fluorescence quantum yields (0.003 and 0.004, respectively) in DMSO, with complete quenching of its fluorescence in aqueous solutions.[160] Low Φ_F values were also obtained for Zn naphthalocyanine (ZnNPc) complexes and this was explained in terms of the fast degradation of these complexes upon photolysis.[41,157] The Φ_F value of ZnPc in the pentamer (β-tetrasubstituted with four **S37** molecules, $\Phi_F = 0.03$ in DMSO; (Table 4), was much smaller than that for ZnPc alone ($\Phi_F = 0.2$), implying that ZnPc fluorescence is quenched in the presence of the porphyrin substituents.[168] The fluorescence spectra of a phthalocyanine–porphyrin complex containing eight units of zinc tetraphenylporphyrin (**S37**) showed extensive energy transfer between the porphyrin and phthalocyanine moieties.[151] The excitation spectra were slightly different from the absorption spectra in terms of Q-band absorption wavelength, suggesting that changes in the nature of the molecules occur upon excitation. Φ_F values upon excitation at the porphyrin Q-band were found to be very small due to energy transfer taking place from the porphyrin units to the phthalocyanine moieity.[151] For the porphyrin–phthalocyanine heterodimer ($ZnTPP\text{-}O\text{-}ZnPc(C(CH_3)_3)_4$), selective excitation of the porphyrin chromophore resulted in a very efficient energy transfer to the phthalocyanine moiety,[169] resulting in very low Φ_F values compared to the individual components. This was also observed for a porphyrin–phthalocyanine hetero dimer linked by a triple bond[170,171] and ZnPc substituted with four tetraphenylporphyrins (**S37**).[168]

Binuclear ZnPc complexes (complex **4**, Figure 1) containing catechol bridges and substituted with **S18**, **S23** and **S42** gave low Φ_F values (Table 4), and this was attributed to a self-quenching process in the binuclear phthalocyanine complexes.[156] Annulated dinuclear (**5**) and trinuclear (**6** and **7**, Figure 1) ZnPc phthalocyanines containing substituent **S55** gave much lower Φ_F values (< 0.03 for **6** and **7** and 0.08 for **5**) compared to the monomeric complex (Φ_F = 0.28), which is in agreement with the reduction in fluorescence lifetime.[164]

b. *Triplet quantum yields (Φ_T) and lifetimes (τ_T)*

The triplet lifetimes of unsubstituted ZnPc in DMSO is relatively long at 350 μs (Table 4). There were no differences in Φ_T (or τ_T) values for ZnPc when compared to the fully deuterated derivative (ZnPc-d_{16})[48] in toluene containing 1% pyridine.

A relatively low τ_T value was reported for ZnPc β-tetrasubstituted with bulky **S23**,[41] τ_T = 160 μs in DMSO, compared to when ZnPc is β-octasubstituted with **S17** or Cl (τ_T = 370 μs) in Table 4. This was explained in terms of the "loose bolt" effect,[41] which accelerates internal conversion. The τ_T values increased with solvent viscosity for β-octasubstituted ZnPc complexes containing **S28** and Cl as substituents (Figure 14).[100]

The triplet lifetimes increased with a decrease in temperature for the ZnPc complexes containing **S32–S36** as substituents.[147] The degree of aggregation decreased for complexes containing bulky substituents, and increased for long alkyl chain substituents.[147] An efficient intersystem crossing was observed for the heterodimer complex consisting of a positively charged porphyrin and a negatively charged phthalocyanine.[172–174]

For ZnPc β-substituted with **S37**, the triplet lifetime decreased compared to the respective monomers. This decrease was dependent on the number of por-

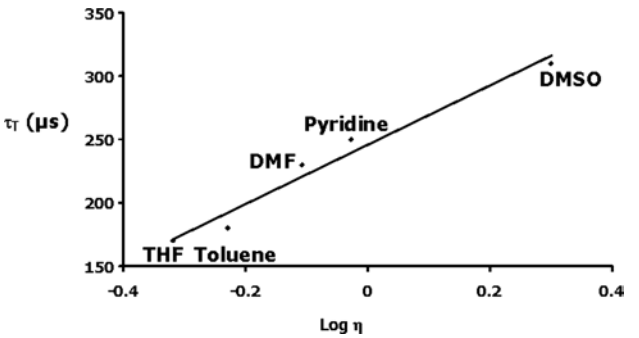

Figure 14. Dependence of ZnPc (**S28** substituent) triplet lifetime on logarithm of solvent viscosities. Reproduced with permission from Ref. 100.

phyrin rings present on the molecules.[168] ZnPc β-tetrasubstituted with **S37** had a triplet lifetime of 230 μs, while the β-octasubstituted derivative gave a τ_T value of 170 μs, in DMSO.[151,168] The triplet quantum yields also decreased with an increase in the number of porphyrin rings: $\Phi_T = 0.12$ for ZnPc (β-tetrasubstituted with **S37**) and 0.04 for ZnPc (β-octasubstituted with **S37**) in DMSO.[151,168] There was a decrease in τ_T values in going from ZnPc ($\tau_T = 77$ μs) to $ZnPcF_{16}$ ($\tau_T < 1$ μs), followed by an increase for the $ZnPc(C(CF_3)_2F)_8F_8$ complex ($\tau_T = 131$ μs) in acetone[146] (Table 4). As discussed above, the differences are explained in terms of changes in the conjugation of the phthalocyanine π system.

Compared with ZnPc ($\tau_T = 350$ μs), the excited states of the complexes **3** and **8** (Figure 1 with τ_T ranging from 90 to 180 μs; See Table 4), were found to be much more short-lived,[54] due to the quenching abilities of naphthalene.[54,148] The binaphthalo complex **8** had a relatively high τ_T (= 150 μs) value (Table 4), which was attributed to its rigid structure. Quantum yields of the triplet state also favor the less aggregated complex **3**, which contains the bulky **S23** substituents.[54] A film of porphyrazine complex **9** was found to have a low τ_T of 26 μs.[155]

c. *Singlet oxygen quantum yields (Φ_Δ)*

In general unsubstituted ZnPc shows higher singlet oxygen quantum yields compared to its substituted derivatives, with a few exceptions such as $ZnPc(SO_3)_{mix}$. For the $ZnPc(NH_2)_4$ complex containing amine functional groups at the β positions, a low Φ_Δ (= 0.11 in DMSO) value was obtained[157] due to the well-known quenching abilities of singlet oxygen by the amino groups, as well as the aggregated nature of this complex. High Φ_Δ values were observed for the monomeric ZnPc peripherally tetrasubstituted with **S23** in DMSO ($\Phi_\Delta = 0.60$)[41,157] and $\Phi_\Delta = 0.58$ in toluene[88] (Table 4). Very high Φ_Δ values were obtained for the monofunctionalized Zn azaphthalocyanines ($\Phi_\Delta = 0.80$) in organic solvents.[175]

For ZnPc complexes β-tetrasubstituted with **S51**, the Φ_Δ values were lower ($\Phi_\Delta = 0.23$ in DMF/water) than for the unsubstituted ZnPc in the same solvent system ($\Phi_\Delta = 56$).[158] The Φ_Δ values increased to $\Phi_\Delta = 0.62$ (for unsubstituted ZnPc) and $\Phi_\Delta = 0.30$ (for **S51** β-tetrasubstituted ZnPc) in benzyl-*n*-hexadecyldimethyl ammonium chloride (BHDC) micelles.[158] For ZnPc complexes β-octasubstituted with **S15–S17**, **S23**, **S41–S43**, aggregation played a significant role in the magnitude of the Φ_Δ values (Table 4).[36] Thus the relatively low Φ_Δ value for **S16** was explained in terms of the aggregated nature of these complexes. ZnPc complexes β-octasubstituted with **S23** gave a larger Φ_Δ value (0.73) in chloroform[36] than in DMSO ($\Phi_\Delta = 0.52$).[176] The $ZnPc(Cl)_8$ complex gave relatively low Φ_Δ values and this is attributed to aggregation.[51] $ZnPc((CH_2)_2O(CH_2)_2OCH_3)_4$ ($\Phi_\Delta = 44$ in toluene) gave a larger Φ_Δ value than the unmetalated $H_2Pc((CH_2)_2O(CH_2)_2OCH_3)_4$

complex with Φ_Δ = 0.19 in toluene (Table 4).[88] Nanoparticles of $ZnPc(C_6C_{13})_7(CH_2)_{11}SH$ complex on gold were found to generate singlet oxygen with higher quantum yields (Φ_Δ = 0.65) compared to their non-nanoparticle form (Φ_Δ = 0.45 Table 4).[153]

A decrease in Φ_Δ values was observed on going from ZnPc (Φ_Δ = 0.17) to $ZnPcF_{16}$ (Φ_Δ = 13) followed by an increase for the $ZnPc(C(CF_3)_2F)_8F_8$ complex (Φ_Δ = 21) in acetone.[146] Axial ligation of ZnPc using cyanide, pyridine and piperidine resulted in a decrease in Φ_Δ. The decrease in Φ_Δ was attributed to the lowering of the triplet energy to a value where energy transfer to ground state oxygen was no longer feasible. ZnPc complexes octasubstituted at the nonperipheral position with two or four **S52** ligands gave very large Φ_Δ values (0.85 and 0.92, respectively).[166] Comparing data obtained for the tetrasubstituted complexes **3** ($R_2 = R_3$) with that for the disubstituted complex **3** (R_3 = H), the latter was observed to have lower Φ_Δ values.[54] The Φ_Δ values for complexes **4** were low compared to the values obtained for monomeric ZnPc and this was attributed to intramolecular coupling of the rings as explained above.[156]

d. *Photodegradation quantum yields (Φ_P)*

ZnPc is stable towards degradation in DMSO[41] compared to some ring substituted derivatives. This was explained in terms of intramolecular vibrations of some ring substituents which quench singlet oxygen as soon as it is formed.[41] The aggregated complexes $ZnPc(NH_2)_4$ and $ZnPc(NO_2)_4$ did not undergo photobleaching, but instead were found to undergo transformation from the aggregated to the monomeric state upon photolysis.[157]

The disubstituted complex **3** (R_3 = H, Figure 1) was found to be generally more stable to photodegradation than the corresponding tetrasubstituted derivative (Complex **3**, $R_3 = R_2$, Table 4). The increase in stability of the former was attributed to the plurality of the bulky substituents which may destabilize the Pc ring in the latter complexes.[54,148]

In general, zinc phthalocyanine complexes β-octasubstituted with the more electron-withdrawing substituted phenoxyl groups (e.g. **S42**) tended to stabilize the phthalocyanine molecule in DMSO in the presence of light.[36] The more electron-donating phenoxyl groups (e.g. **S23** and **S41**) tend to be easily degraded in chloroform,[36] confirming that the photobleaching mechanism involves oxidative degradation of the ring. However in DMSO, ZnPc complexes octasubstituted with **S23** or **S41** were found to be relatively stable[176] (Table 4), through less stable than **S42**. ZnPc complexes octasubstituted with **S15** or **S40** which contain biologically important substituents, i.e. cholesterol and estrone, respectively, were easily degraded in chloroform[36] (Table 4). In THF, ZnPc complexes β-octasubstituted

with **S18** underwent phototransformation rather than photobleaching, resulting in an increase in the low energy band (the X-band), due to the distortion of the ring.[37] $ZnPc(SC_6H_4CH_3)_8$ and $ZnPc(SC_4H_9)_8$ complexes containing thioether substituents were relatively stable ($\Phi_P \sim 6 \times 10^{-5}$; Table 4, with the former showing less stability than the latter, due to the ability of benzene ring to enhance photobleaching.[35,152]

2. *CdPc Complexes*

a. *Fluorescence quantum yields*

The most studied CdPc complexes are those tetrasubstituted with substituents **S2**, **S14**, **S18** and **S23**[118,119,177] at the peripheral and nonperipheral positions. Where there is no aggregation, the absorption spectra are similar to the excitation spectra, and both are mirror images of the emission spectra. The fluorescence excitation and emission spectra of the CdPc containing **S2** were typical of phthalocyanine complexes, with the fluorescence excitation spectrum being a mirror image of the emission spectrum and the latter being similar to the absorption spectra. Hence, no demetalation for this complex upon excitation occurred. However, for CdPc tetrasubstituted with **S14** at the peripheral positions, the excitation spectra show a split in the Q-band in toluene, $CHCl_3$, DCM and THF due to the demetalation discussed above. For this complex, the excitation spectrum was similar to the absorption spectrum of an umetalated derivative, suggesting that the loss of symmetry is due to demetalation upon excitation.[118,119,177]

The fluorescence quantum yields of CdPc derivatives tetrasubstituted with substituents **S18** and **S23** at the nonperipheral positions are generally high in THF and chloroform, compared to MPc complexes in general (Table 4). As discussed above, even though the CdPc derivatives containing **S14** are demetalated in some solvents, it is expected that the heavy atom effect of Cd will still influence the Φ_F values. The Φ_F values for these complexes are typical of MPcs. For CdPc containing **S2** substituents,[118,119] low Φ_F values were obtained for peripheral substitution as expected on the basis of the heavy atom effect of Cd. However, this was not the case for nonperipherally substituted derivatives. Unsubstituted CdPc shows low Φ_F and high Φ_T, as expected for complexes with heavy atoms (Table 4).

b. *Triplet quantum yields and lifetimes*

The Φ_T values for the CdPc derivatives in Table 4 correspond to Φ_F to the extent that, where the values of the latter are low, the former values are high. For CdPc peripherally tetra substituted with **S18**, the sum of Φ_T (0.87) and Φ_F (0.13) was

unity in DMF. This suggests that the dominant radiationless decay path was intersystem crossing for these complexes, as was observed for Li_2Pc and Li_2NPc complexes.[50] The triplet lifetimes for the CdPc derivatives are generally low in Table 4 due to the heavy atom effect.

c. *Photochemistry*

When considering the Φ_Δ values, there is a trend towards lower yields for those phthalocyanines substituted with (benzyloxy)phenoxyl groups (**S14**), particularly at the peripheral positions. This suggests that these groups reduce the ability of the molecules to produce singlet oxygen efficiently, since large Φ_T values were obtained. However, the Φ_Δ values for CdPc containing **S14** at nonperipheral positions were not as low as that for the peripheral substitution (Table 4). The differences could be a result of the change in symmetry upon excitation, as discussed above for the CdPc complexes peripherally substituted with **S14**. Some CdPc complexes containing pyridyloxy substituents (**S2**) underwent phototransformation rather than photodegradation, as indicated by a shift in the Q-band maxima. The phototransformation was ascribed to some distortion of the pyridyloxy-substituted phthalocyanine macrocycle upon exposure to intense light.[118] For CdPc, peripherally substituted with **S14**, no phototransformation or photodegradation was observed in some solvents (toluene, $CHCl_3$, THF and DCM), since no decrease in absorption intensity was observed. The stability of this complex was ascribed to partial oxidation in these solvents.[118] Coordinating solvents such as DMSO are capable of protecting the molecule against oxidative attack, while non-coordinating solvents leave the molecule prone to oxidative attack, giving rise to a high Φ_P yields.

3. *HgPc Complexes*

For HgPc complexes containing an **S2** substituent at the peripheral position, the fluorescence emission spectrum was different from the absorption spectrum in that the former was broad. This suggests the loss of symmetry for the fluorescing molecule, which is most likely due to demetalation as observed for the CdPc complexes above.[119] HgPc complexes containing the **S2** substituent at the peripheral position gave the lowest Φ_F value when compared to the corresponding CdPc and ZnPc derivatives.[119] The order of fluorescence quantum yield values is ZnPc ($\Phi_F = 0.077$) > CdPc ($\Phi_F = 0.013$) > HgPc ($\Phi_F = 0.005$) for these complexes in DMSO. This trend is also observed for the unsubstituted complexes, and is expected due to the spin-orbit coupling induced by the respective central metal ions. In general, the effect of introducing pyridyloxy substituents (**S2**) to peripheral positions on

the HgPc ring is a reduction in Φ_F values (Table 4) when considering the same solvent.[119] The substituents perhaps encourage the deactivation of the excited singlet state via nonradiative means (intersystem crossing and internal conversion) rather than via fluorescence.

As expected, the HgPc complex containing **S2** substituents at peripheral positions has the lowest triplet lifetime when compared to the corresponding ZnPc and CdPc complexes. The order of triplet lifetimes with respect to the central metal ions is Zn(II) (τ_T = 350 μs) > Cd(II) (τ_T = 30 μs) > Hg(II) (τ_T = 20 μs). It is clear from Table 4 that HgPc derivatives give higher Φ_Δ (0.78) and Φ_T (0.89) values than the corresponding ZnPc derivatives (Φ_Δ = 0.46 and Φ_T = 0.80) containing **S2** substituents in DMSO.

E. Group 13 Phthalocyanine Complexes

1. *XAl(III)Pc Complexes*

The studies on non-water soluble XAl(III)Pc complexes (X = negatively charged axial ligand) are limited, since research has focused on water soluble derivatives as indicated above. Given that Al(III) is a small ion, unsubstituted XAl(III)Pc predictably has large Φ_F values ~0.65.[111] Polymer-bound chloroaluminum tricarboxymonoamidephthalocyanine gave a lower Φ_Δ value compared to the unbound (in solution) complex.[178] Singlet oxygen production is restricted on polymers due to decreased lifetimes of the triplet state.[178]

2. *XGa(III)Pc and XIn(III)Pc Complexes*

a. *Fluorescence quantum yields*

The most studied complexes are those that are unsubstituted or those containing **S1**, **S14**, **S18** and **S23** as substituents.[179–189] XGa(III)Pc and XIn(III)Pc complexes are often studied together, so in this work they will also be treated likewise. With a few exceptions, the shapes of the excitation spectra are similar to absorption spectra, both are mirror images of the fluorescent spectra for ClGa(III)Pc complexes. For the tetra(peripheral or nonperipheral)- and octa(peripheral)-substituted ClIn(III)Pc containing **S14** substituents, the shape of the excitation spectra was different to the absorption spectra in that the Q-band of the former showed splitting, unlike the narrow Q-band observed for the latter. This suggests that there are changes in the molecule following excitation, most likely due to loss of symmetry. However, this was not observed for the corresponding ClGa(III)Pc complexes. The difference in the behavior of ClGa(III)Pc and ClIn(III)Pc upon excitation was explained in terms of the larger indium metal that is more displaced from the core

of the phthalocyanine ring. The displacement becomes more pronounced upon excitation, causing a loss of symmetry.

Table 4 shows that the Φ_F values of ClGa(III)Pc complexes are in general typical of MPc complexes. These values are slightly higher for peripherally substituted derivatives compared to the nonperipherally substituted complexes, suggesting less quenching of the excited singlet state by peripheral tetrasubstitution compared to nonperipheral tetrasubstitution. For the ClIn(III)Pc complexes in general, the Φ_F values are very low due to an enhancement in intersystem crossing caused by the presence of the heavier indium atom.

b. *Triplet quantum yields and lifetimes*

For both ClGa(III)Pc and ClIn(III)Pc derivatives, there was a change in spectra following laser irradiation. The spectral changes involved a decrease in the Q-band and an increase in absorption near 590 nm (Figure 15).[188] However, upon exposure of the solution to air, the Q-band increased in intensity and the band around 590 nm decreased, suggesting that this band was due to reduction products of the complexes.[190] The first ring reduction in MPc complexes was characterized by a decrease in the Q-band and the formation of weak bands between 500 and 600 nm.[190] Thus during laser irradiation, the ClGa(III)Pc and ClIn(III)Pc derivatives were partly transformed into an anion (Pc^{-3}) species. The suggested mechanism for the formation of Pc^{-3} in the presence of H donors is shown by Eqs. 29 to 31 (where S–H is an acidic solvent):

$$MPc + h\nu \rightarrow {}^3MPc^* \quad (29)$$

$${}^3MPc^* + S\text{–}H \rightarrow MPc^{\bullet -} + S\text{–}H^{\bullet +} \quad (30)$$

$$MPc^{\bullet -} + O_2 \rightarrow MPc + O_2^{\bullet -} \quad (31)$$

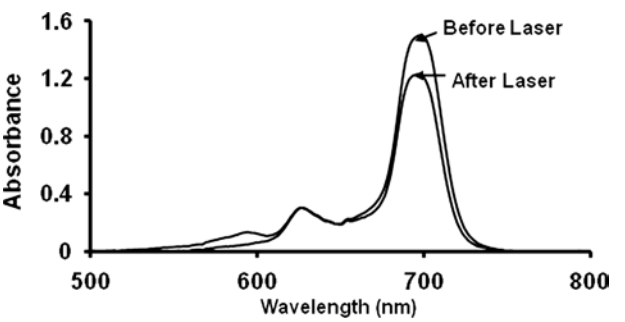

Figure 15. Absorption spectral changes of In(III)Pc tetrasubstituted with **S14** before and after laser irradiation. Reproduced with permission from Ref. 188.

For a series of indium and gallium phthalocyanine monomers as well as bridged dimers, the ClGa(III)Pc complexes were found to have much longer triplet lifetimes compared to the corresponding ClIn(III)Pc complexes, due to the heavy atom effect of In.[173,174]

For complexes **10** and **11** (Figure 1, both naphthalocyanine-based and containing Ga(III) as the central ion), the τ_T values were low in chloroform (ranging from 14 to 21 μs).[181,182] However, for complex **12** (Figure 1, Ga(III) central ion) containing oxygen and **L5** bridges, high τ_T values (357 and 667 μs respectively) in toluene were obtained (Table 4).[183] ClIn(III)Pc complex **12** (Figure 1) containing oxygen ($\tau_T = 42$), **L6** ($\tau_T = 35$) and **L7** ($\tau_T = 22$) bridges gave relatively low τ_T values (Table 4).[183,185,187] The Φ_T values of unsubstituted ClAl(III)Pc, ClGa(III)Pc and ClIn(III)Pc complexes increased with the size of the central metal as follows: ClAl(III) ($\Phi_T = 0.4$) < ClGa(III) ($\Phi_T = 0.7$) < ClIn(III) ($\Phi_T = 0.9$), while the Φ_F values correspondingly decreased (ClAl(III) ($\Phi_F = 0.58$) > ClGa(III) ($\Phi_F = 0.31$) > ClIn(III) ($\Phi_F = 0.031$), in 1-chloronaphthalene due to the heavy atom effect.[189]

In the case of ClGa(III)Pc containing the **S14** substituents, the trend of singlet oxygen quantum yields (in DMSO) was as follows: nonperipherally tetrasubstituted ($\Phi_\Delta = 0.69$) > peripherally tetrasubstituted ($\Phi_\Delta = 0.62$) > peripherally octasubstituted ($\Phi_\Delta = 0.51$). The same trend applied for ClIn(III)Pc derivatives substituted with **S14**, with $\Phi_\Delta = 0.94$, 0.87 and 0.78 respectively. As expected, due to the heavy atom effect ClIn(III)Pc complexes show larger singlet oxygen quantum yields in general (Table 4). The ClGa(III)Pc and ClIn(III)Pc complexes show about the same stability, with Φ_P of the order of 10^{-5} to 10^{-4}.[191] These complexes are however, generally less stable than the corresponding ZnPc derivatives (Table 4).

F. Group 14 and 15 Phthalocyanine Complexes

1. *Photophysics*

a. *X_2Si(IV)Pc complexes*

The axial ligands studied for these complexes range from **L9** to **L28** (Table 4). The most studied complexes are the X_2Si(IV)Pc derivatives.[127,192–196] X_2Si(IV)Pc complexes containing **L12** as the axial ligand (4-*tert*-butylbenzoic acid), giving a rigid conformation, gave a high Φ_F value of 0.62.[195] μ-Oxo Si(IV)Pc complexes containing two, three or four Si(Pc) units showed triplet lifetimes and yields which decreased with an increase in the number of units (Table 4).[196] The change in the nature of axial ligand for Si(IV)Pc complexes has some effect on the fluorescence quantum yields[44,127] (Table 4) ranging from $\Phi_F = 0.02$ to 0.34 for axial ligands OH, Cl, **L13**–**L16** β-octasubstituted with the same ring substituent (**S18**) (Table 4).

β-Octa-chlorinated (Φ_F = 0.73) or brominated (Φ_F = 0.34) Si(IV)Pc complexes containing two poly(ethylene glycol) axial ligands (**L17**) show a larger Φ_F value (in DMF) for the chlorinated complex since bromine encourages intersystem crossing more than chlorine[192] (Table 4), being larger in size.

For unsubstituted X_2Si(IV)Pc complexes containing a series of axial ligands (including phenyl, terphenyl, thienyl and pyrenyl systems), the Φ_F ranged from 0.31 to 0.84 in DCM (values not in Table 4) with the thiophene ligands giving significantly lower Φ_F.[197] It was suggested that the electron-rich thiophene group may quench the excited state by an electron transfer mechanism resulting in a lower value for Φ_F.[197] For unsubstituted Si(IV)Pc complexes containing axial ligands **L10** and **L11**, τ_T values decreased on substitution of one of the axial ligands with a hydroxyl ligand (Table 4).[145]

In the case of the axially ligated X_2Si(IV)Pc complexes containing OH, Cl, **L13–L16** axial ligands and β-octasubstituted with **S18**,[44] triplet state lifetimes vary according to the degree of aggregation, with the aggregated complex (containing OH ligands) showing a shorter lifetime compared to the rest of the complexes in the series (ranging from 194 to 356 μs)[44] in Table 4. For Si(IV)Pc complexes β-octasubstituted with **S18** and containing axial ligands OH, Cl, **L13–L16**, the Φ_T values were low, ranging from 0.29 to 0.43[44] (Table 4).

b. *Other group 14 and 15 phthalocyanine complexes*

The Φ_F values for octasubsubstituted X_2Ge(IV)Pc derivatives are typical of MPc complexes in Table 4. For Cl_2Sn(IV)Pc complexes, Φ_F values are less than 0.01 for tetrasubstituted derivatives due to the size of the Sn central metal ion, but these values increase on octasubstitution (Table 4). The Φ_T values were lower for the $(Cl)_2$Sn(IV)Pc (β-octasubstituted with **S18**, **S40** and **S45**) derivatives compared to the corresponding $(Cl)_2$Ge(IV)Pc derivatives.[45,186] Triplet quantum yields were not affected greatly by changes in axial ligands for X_2Sn(IV)Pc derivatives. The X_2Sn(IV)Pc complex containing estrone (**L9**) as an axial ligand showed very short triplet lifetimes (τ_T = 18 μs), and uncharacteristically low triplet quantum yields (Φ_T = 0.08).[45] The τ_T values were found to be very low for $(Cl)_2$Sn(IV)Pc derivatives in general, ranging from 10 to 32 μs (β-octasubstituted with **S18**, **S40** and **S45**) compared 168 to 340 μs for the corresponding ClGe(IV)Pc complexes (Table 4.)[45]

$[(OH)_2Sb(V)Pc]^+$ complexes showed very low Φ_F values ($\leq$ 0.01) regardless of the axial ligand or peripheral substituent.[198,199] PbPc complexes substituted with **S18** or **S23** gave low Φ_F values due to the presence of the heavy Pb ion. These complexes were demetalated upon excitation, but the effects of the Pb ion (in solution) will still affect the fluorescence behavior.[200,201] This also results in high Φ_T values ranging from 0.70 to 0.88 in Table 4. Phosphorus phthalocyanine

complexes exhibit Φ_F values which are typical of MPc complexes in general, but also show low Φ_T values ($\Phi_T < 0.6$),[202] while high τ_T values were observed for some PPc complexes (Table 4).[202]

2. *Photochemistry*

The Φ_Δ values did not vary much for unsubstituted $(OH)_2$Ge(IV)Pc ($\Phi_\Delta = 0.25$), $(OH)_2$Sn(IV)Pc ($\Phi_\Delta = 0.26$), and $(OH)_2$Si(IV)Pc ($\Phi_\Delta = 0.28$) complexes in DMSO (Table 4).[63] Φ_Δ values for complexes **1** containing Ge(IV), Sn(IV) or Si(IV) as central metals were low, ranging from 0.15 (Sn(IV)), to 0.17 (Ge(IV)) and 0.21 (Si(IV)).[63] When comparing Cl_2Sn(IV)Pc, Cl_2Ge(IV)Pc and Cl_2Si(IV)Pc β-octasubstituted with the same peripheral (**S18**), an increase in Φ_Δ with an increase in the size of the central metal was observed as follows: Si(IV) ($\Phi_\Delta = 0.14$) < Ge(IV) ($\Phi_\Delta = 0.18$) < Sn(IV) ($\Phi_\Delta = 0.22$) in DMSO, due to the heavy atom effect.[45] This effect was also used to explain the higher Φ_Δ value obtained for the Cl_2Ge(IV)Pc complex when the axial chloride ligands are replaced by the iodide ligands.[45,63] For complex Cl_2Sn(IV)Pc containing estrone ligands (**S40**) on the periphery, the Φ_Δ value was similar to when estrone was located axially.[45] For a series of axially substituted Si(IV)Pc derivatives peripherally β-octasubstituted with **S18** and containing axial ligands (OH, Cl, **L13–16**, **L18–28**), the Φ_Δ values varied to some extent with the axial ligand[127] and were generally low, ranging between 0.03 and 0.41 (Table 4).

Photolysis of the less aggregated tetrapyridinoporphyrazine complexes (**1**) containing Sn(IV) or Si(IV) as the central metals in DMSO resulted in degradation accompanied by reduction of the ring. Thus the complexes exhibited a strong tendency towards reductive quenching of the excited states.[63] Attempts to photobleach Ge(IV)Pc complexes containing **S18**, **S40** and **S45** substituents resulted in the reduction of the central Ge(IV) ion to the Ge(II)Pc species,[45] with the Ge(II)Pc compound being stable to photodegradation. However, the corresponding Sn(IV)Pc complexes did not show phototransformation to the Sn(II)Pc species. For the latter complexes, there was evidence of photoreduction of the Pc ring during the photobleaching process with a mechanism similar to Eqs. 29–31.[45]

For Si(IV)Pc complexes containing Cl and **L13–L16** as the axial ligands, attempts to photobleach the Pcs resulted in the well-known axial ligand transformation into a hydroxyl group for all complexes.[44]

V. Photocatalytic Reactions

The use of Pc complexes in oncology as photosensitizers for malignant tumor treatment by photodynamic therapy (PDT) is well-documented and is part of the

current series (see Volume 4). PDT will therefore not be discussed in this chapter, which concentrates on selected photocatalytic reactions of industrial (such as oxidation of alkenes) and environmental importance (such as photodegradation of pollutants). Photodegradation of toxic sulfur compounds, phenols and chlorinated phenols are known to be catalyzed by MPc complexes.[203–231]

Sulfur-containing compounds, such as mercaptans, alkali sulfides, alkali sulfites, and alkali thiosulfates are byproducts of industrial processes and are pollutants in waste and natural waters.[209] The presence of sulfide ions in industrial wastewater (from the oil-processing industry, paper manufacturing, and synthetic fiber production) is of great environmental concern. The complete oxidation of sulfur-containing compounds is an essential solution to environmental problems.

Phenols are widespread in nature and are also produced by normal human metabolism from tyrosines. The bactericidal properties of phenols make them useful in natural defense mechanisms in biological systems. Phenolic compounds may be released into the environment in a number of ways, including during the manufacture of industrial products such as plastics, pharmaceuticals, dyes and pesticides (e.g. pentachlorophenol). Insecticides containing toxic nitrophenols are used in agriculture and tend to persist in the environment.

The oxidation of olefins into useful products is of immense industrial interest. For example, epoxides are useful intermediates obtained on catalytic oxidation of alkenes that are widely used for petrochemicals, fine chemicals and polymers such as oxygen-containing natural products or production of epoxy resins. Use of molecular oxygen as an oxidant for the transformation of alkenes is preferred as it is cheap, environmentally friendly and readily available.[232–234]

Phthalocyanines are employed as sensitizers in the oxidation of chemicals via singlet oxygen since they are able to generate singlet oxygen. Both Type I and II mechanisms may be involved during the photocatalytic degradation or transformation of molecules using MPc complexes. Table 5 summarizes the phenols, sulfur containing compounds and alkenes which are photodegraded by MPc complexes.

A. Sulfur-Containing Compounds

Wöhrle and coworkers developed phthalocyanine complexes for the photocatalysis of sulfur compounds under homogeneous or heterogeneous (impregnated on SiO_2, Al_2O_3, charcoal and TiO_2) conditions.[203] The catalytic and photocatalytic oxidations of sulfide, thiol and phenol derivatives were studied. Heterogeneous photocatalysis resulted in higher activities than homogeneous catalysis. The phthalocyanine and naphthalocyanine complexes studied for photocatalysis included those containing Mg, Al(III), Si(IV) and Zn. Photocatalytic activity of

the oligomers were found to be higher than that of the analogous low molecular weight complexes.[203] 2-Mercaptoethanol, used as an example of a thiol, was photooxidized to the corresponding sulfonic acid.[203]

ZnPc and ClAl(III)Pc are efficient photocatalysts for the oxidation of thiolates or sulfides to sulfonic acids or sulfate. Co-sensitizers involving phthalocyanines $ZnPc(SO_3)_4$ or Ge(IV)Pc (containing substituent **S8**) and CTAC were employed for the photooxidation of 2-mercaptoethanol in aqueous alkaline solutions.[76] Compared to single-component sensitizers, an improvement in the photocatalytic activity is observed in the case of co-sensitization. CTAC reduces aggregation which would otherwise lower photocatalytic activity due to low singlet oxygen quantum yields. $ZnPc(SO_3)_4$ and $ZnPc(COOH)_4$ were studied for the photooxidation of 2-mercapto-ethanol and sodium thiosulfate.[216] In the presence of CTAC, quinoline and ethanol additives, $ZnPc(SO_3)_4$ and $ZnPc(COOH)_4$ were monomerized, resulting in an increase in photocatalytic activity as stated above for CTAC. Monomerization in the presence of quinoline is enhanced due to axial coordination of the base to the central metal atom in the complexes, which impedes the π–π interactions between the phthalocyanine complexes. Increasing solvent viscosity enhances the self-association of the phthalocyanine complexes, lowering photocatalytic activity.[216]

B. Phenols

1. *Phthalocyanine Complexes on Supports*

The homogeneous and heterogeneous photocatalytic oxidation of chlorinated phenols in the presence of oxygen or hydrogen peroxide and MPc complexes has been researched extensively.[215–228] The oxidation products for unsubstituted phenols have been determined to be mainly carbonate and maleic/fumaric acids when using phthalocyanine complexes.[203]

The association of TiO_2 and ZnPc resulted in a small increase (< 6%) in the photodegradation efficiency of phenol over TiO_2 alone. This behavior was expected since the light employed had a maximum absorption at 360 nm, where there is insignificant absorption by ZnPc,[222] showing the need for visible light excitation of the MPc complexes. The photooxidation of phenol was catalyzed by metal-free phthalocyanine (H_2Pc) supported on Al_2O_3 or TiO_2 in the presence of visible light.[223] The rate of phenol photooxidation catalyzed by H_2Pc/TiO_2 was much higher than that obtained for H_2Pc/Al_2O_3. The high photocatalytic activity of the sample is explained by an electron transfer from the conduction band of the excited H_2Pc semiconductor particles to the conduction band of TiO_2 support.[223]

OHAl(III)Pc or ClAl(III)Pc were supported on aminopropyl silica and/or exchange resins and employed for the photocatalytic oxidation of phenol.[221] Resins included IRA 67, IRA 96, Amberlite 200, Amberlite XAD 8, and Dowex. On the whole, the electronic absorption spectra of the grafted photosensitizer were close to its absorption spectra in the homogeneous state. However, the bonding to the support inhibited the photosensitizer, resulting in a loss of the photosensitizing efficiency in some cases. In order to prevent self-quenching or nonaccessibility of the substrate, the amount of the photosensitizer on the support was kept at a low level.[221]

Bentonite was modified with cetyltrimethylammonium bromide (CTMA), then ClAl(III)Pc was inserted successfully into the interlamellar space of CTMA-modified bentonite and employed as a photosensitizer.[226] Under visible light irradiation, the composite catalyst exhibited good photocatalytic activity for degradation of pollutants such as phenol, 4-chlorophenol, 4-nitrophenol, 2,4-dichlorophenol, and 2,4,6-trichlorophenol in an aerated aqueous medium. It was noted, however, that during repeated experiments, the degradation rate of 2,4,6-trichlorophenol was gradually decreased, due to some intermediates formed and sorbed onto the catalyst surface.[226]

(OH)Al(III)Pc$(COOH)_4$ easily adsorbs onto SiO_2, Al_2O_3, and TiO_2 from DMF/aqueous solutions with no desorption. Adsorption of an (OH)Al(III)Pc$(COOH)_4$ onto the TiO_2 surface resulted in a reusable material to perform selective photocatalytic oxidations under visible light irradiation. 4-Chlorophenol was mostly decomposed into CO_2 and chloride ions when an Al(III)Pc$(COOH)_4$/TiO_2 catalyst was employed.[227] Injection of electrons into the semiconductor conduction band from the excited dye leaves a radical cation, initiating the oxidation reactions in these systems. TiO_2 was found to be superior to SiO_2 and Al_2O_3 in terms of the photocatalytic degradation of 4-chlorophenol in the presence of (OH)Al(III)Pc$(COOH)_4$.[227] The products of photodegradation of 4-chlorophenol are CO_2 and Cl^- (Table 5). (OH)Al(III)Pc$(COOH)_4$/TiO_2 was also found to catalyze the photodegradation of 2-chlorophenol, 2,4-dichlorophenol, 2,4,6-trichlorophenol, catechol and others.[227] ZnPc$(COOH)_4$, CuPc$(COOH)_4$ and CoPc$(COOH)_4$ were also found to show photocatalytic activity for the degradation of 4-chlorophenol under visible light.[227] However CuPc$(COOH)_4$ and CoPc$(COOH)_4$ showed low photoactivity, due to their short lifetime in the triplet state.

In another study, TiO_2 sensitized with ZnPc$(COOH)_4$ and CoPc$(COOH)_4$ showed improved photocatalytic activity for the degradation of phenol using visible light.[225] Photodeposition of platinum on MPc$(COOH)_4$/TiO_2 enhanced reaction photoefficiency from ~ < 0.05 (without Pt) to 0.1 (with Pt) in Table 5. The enhanced degradation in the presence of Pt was explained in terms of platinum electron trapping, which is fast enough to compete with electron back transfer,

thereby increasing the probability of interaction with molecular oxygen to form highly reactive oxygen species. The main product of the photooxidation was CO_2.[225]

Hydroxoaluminium tricarboxymonoamide phthalocyanine [(OH)Al(III)Pc-$(COOH)_3(NH_2)$] was adsorbed onto TiO_2 and employed for the photocatalytic degradation (using visible light) of different substrates which included phenol, thiophenol and 4-chlorophenol. The radical cation of the phthalocyanine, produced by electron injection of the dye into the TiO_2 conduction band, was found to be the species responsible for the oxidation of the substrates.[228]

It is known that the most active photocatalysts for the photodegradation of pollutants are phthalocyanines bearing Al, Zn and Si central atoms.[217] FePc is not expected to be effectively activated by the photon flux. However, the photocatalytic activity of FePc (in the presence of hydrogen peroxide) has been reported.[215] FePc adsorbed on silica (FePc/SiO_2) has higher intrinsic activity towards the degradation of phenol in water, than when encapsulated within NaY zeolite (FePc@NaY).[215] While adsorption on silica was reported to be more simple with the solid exhibiting higher photocatalytic activity, FePc/SiO_2 was not found to be suitable in organic media in which iron phthalocyanine may become soluble and/or self-degraded. The preparation of FePc@NaY was more complicated, but permanent immobilization was achieved, rendering a more durable photocatalyst for reuse.[215]

Dioxoiron phthalocyanine tetrasulfonate ($FeO_2Pc(SO_3)_4$) was incorporated inside the space of a layered double oxide hydoxides (LDH).[220] The resulting material exhibited an optical spectrum characteristic of isolated metalated phthalocyanine. Laser flash photolysis of the solid showed the $FeO_2Pc(SO_3)_4$ complex to have a long-lived transient (> 2 ms). The solid is able to act as an effective photocatalyst for the degradation of phenol in aqueous media.

2. *Phthalocyanine Complexes in Solution*

$CuPc(SO_3)_4$ was found to be an effective photocatalyst for the degradation of 4-chlorophenol, 2,4-dichlorophenol and 2,4,6-trichlorophenol in aerated aqueous solutions under visible light ($\lambda > 450$ nm) irradiation.[229] The $CuPc(SO_3)_4$ photosensitizer was found to be stable and could be used repeatedly.[229]

The oxidation of phenol and its chlorinated derivatives (2-chlorophenol, 3-chlorophenol, 4-chlorophenol, 2,6-dichlorophenol and 2,4,6-trichlorophenol) was photocatalyzed by $MPc(SO_3)_n$ (M = OHAl, Zn or $(OH)_2Si$).[218] The chlorinated phenols were transformed at higher rates than phenol with 4-chlorophenol identified as the most reactive molecule with the highest achieved quantum yield of 0.61% at pH 10 (Table 5).[218] The photooxidation of phenol and 2-, 3- and

4-monochlorophenols by irradiation with visible light in aqueous alkaline solutions in the presence of (OH)Al(III)Pc$(SO_3)_4$, (OH)Ga(III)Pc$(SO_3)_4$ and Zn Pc$(SO_3)_4$ as well as oxygen have been reported.[224] The stabilities of the photosensitizers were found to be strongly dependent on the pH and aggregation tendency. The photooxidation products included carbon dioxide and maleic or fumaric acid (Table 5).[224]

Carboxylated polymeric Al and Zn phthalocyanines were also found to be more photocatalytic towards the oxidation of 2-mercaptoethanol than their mononuclear counterparts.[205,206] The photocatalytic activity of the polymer (complex **13**, Figure 1) was also found to be much higher than that for the monomers in the oxidation of phenols.[208] The high photoactivity of the polymers was explained by the presence of intra-molecular triplet–triplet energy transfer between the phthalocyanine macrocycles. The products of the oxidation of phenols in an alkaline medium were the same for both the mono- and polynuclear phthalocyanine complexes that were employed as photocatalysts.[208] Maleic and fumaric acids as well as carbon dioxide were obtained as the final products of the photooxidation.[208] The formation of quinones (Scheme 5) is an intermediate step during the photocatalytic oxidation of phenols at pH 13, before the final destruction of the substrate.[208]

The use of lanthanide diphthalocyanines (complex **14**, Figure 1) as photocatalysts for the degradation (phototransformation) of chlorophenols has been reported.[17] Lutetium diphthalocyanine is an intrinsic semiconductor. Irradiation of catalysts with semiconductor properties such as $NdPc^{2-}$ generates electrons (e^-) and holes (h^+). Once the electrons and holes are produced, the electron scavenging action of molecular oxygen prevents the recombination of the electron–hole pairs. The formation of reactive hydroxyl radicals produced by the reaction between the photogenerated hole, h^+, and OH^- or H_2O is known to be the primary oxidizing agent for the photomineralization of organic pollutants over semiconductor catalysts.

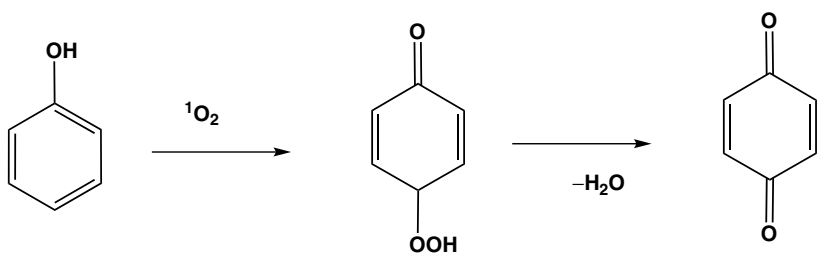

Scheme 5. Formation of quinones as intermediates during photodegradation of phenols. Adapted with permission from Ref. 208.

C. Alkanes and Alkenes

Literature on the use of MPcs as alkene and alkane photocatalysts is scanty; therefore, only a few reports are listed in Table 5. The photocatalytic activities of the various OTi(IV)Pc, ClGa(III)Pc and ClIn(III)Pc complexes towards the oxidation of 1-hexene in the presence of oxygen resulted in 2-epoxyhexane as the main product and 1-hexen-3-ol as the minor product.[136,210] In addition, a correlation was observed between the photocatalytic trends and singlet oxygen quantum yields.

The mechanisms involved (Type I, Scheme 2 or Type II, Scheme 1) in the production of the oxidation products were determined by the use of 1,4-diazabicyclo[2.2.2]octane (DABCO, singlet oxygen quencher) and a radical quencher, 2,6-di-*tert*-butyl-4-methylphenol (BHT). Singlet oxygen was found to be the sole active species in the production of the epoxide, and the radicals were responsible for the formation of the allylic alcohol. Thus, both Type I and Type II mechanisms were involved (Scheme 6). The yields for the products were higher for ClGa(III)Pc and ClIn(III)Pc complexes when compared to OTi(IV)Pc complexes, probably due to larger singlet oxygen quantum yields.[136,211]

ZnPc was employed as a photocatalyst for cyclohexene oxidation, with the following trend in product yield being observed: cyclohexenone > cyclohexene hydroperoxide > cyclohexenol > *trans*-cyclohexane diol > cyclohexene oxide. The suggested mechanism for the formation of the products is shown in Scheme 7.[20]

Excitation of phthalocyanines populates the triplet state, effecting the generation of singlet oxygen which subsequently attacks the Pc complexes, causing

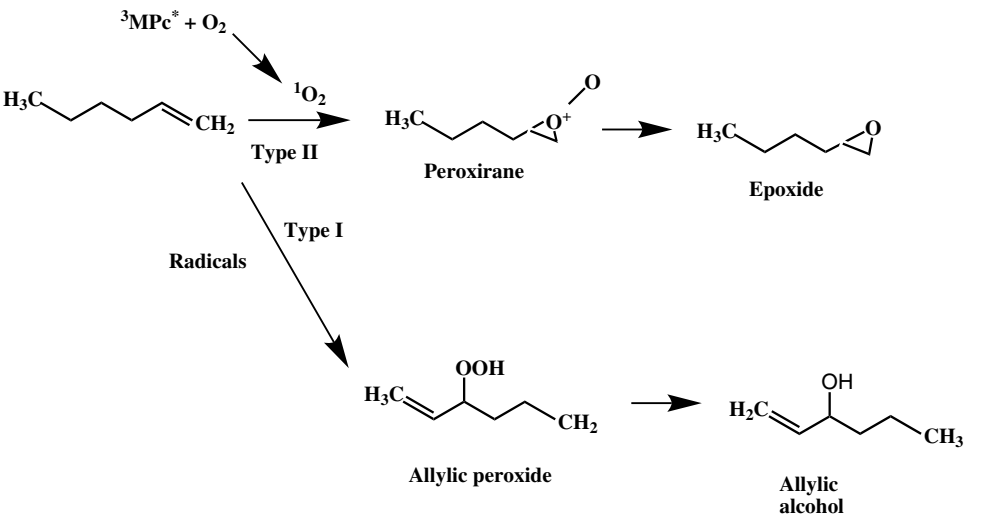

Scheme 6. Proposed mechanism for the formation of the photooxidation products of 1-hexene. Reproduced with permission from Ref. 136.

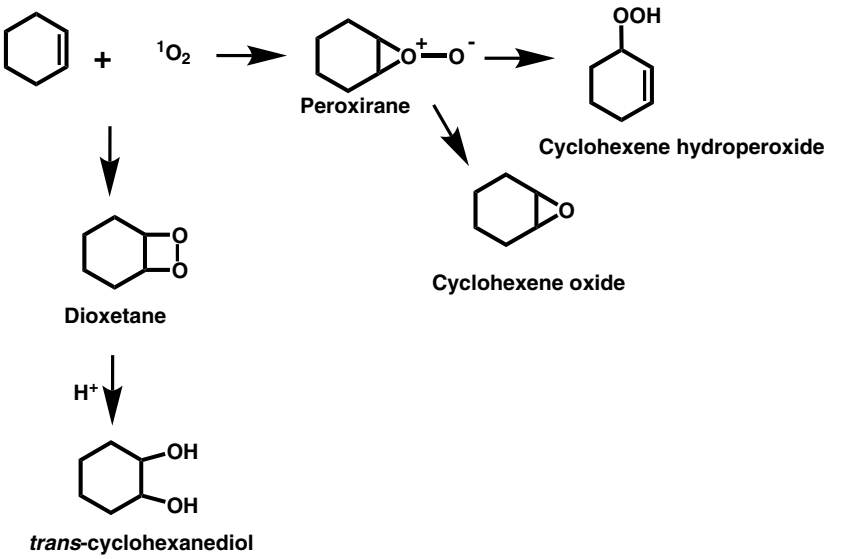

Scheme 7. Suggested mechanism for the formation of photolysis products of cyclohexene. Modified from Ref. 20.

decomposition of the Pc. Electron-withdrawing substituents have been shown to increase catalyst stability and therefore improve product yields.[20] However, unsubstituted or sulfonated MPc complexes tend to decompose upon photolysis, as judged by the decrease in the intensities of both the Q- and Soret bands, for both red and white light.[20,205] For ZnPc, degradation was found to be more pronounced with white light than with red light.[20] The rate of degradation is also affected by light intensity, with low intensity light giving less degradation as expected.

VI. Conclusions

The triplet state, singlet oxygen, photobleaching and fluorescence quantum yields, as well as triplet lifetimes of MPc complexes are hugely affected by the nature of substituents and by the aggregation behavior of the complexes. Water solubility is essential for PDT action as well as other applications of Pc complexes; thus, many studies have been conducted in water and have concentrated on XAl(III)Pc and ZnPc derivatives. A recurring problem, however, is the aggregation behavior of the conventional water soluble MPcs, such as those tetrasubstituted with carboxylic or sulfonated groups. This review shows that there are some known MPc complexes that are water soluble but not aggregated.

The most important parameter for the application of MPc complexes is the singlet oxygen quantum yield. Many factors are responsible for the magnitude of

the determined quantum yield of singlet oxygen. These include: triplet excited state energy, ability of substituents and solvents to quench the singlet oxygen, the triplet excited state lifetime and the efficiency of the energy transfer between the triplet excited state and ground state oxygen. The triplet quantum yields increase for complexes with heavier central metals due to the heavy atom effect, which inevitably shortens the triplet lifetimes. There is considerable literature on singlet oxygen generation ability of the Zn phthalocyanine complexes, with less attention being paid to the other non-transition metals or metalloids (e.g. Ge(IV), Si (IV), Sn(IV), Ga(III) and In(III)) Pcs. Photodegradation generally depends on the structure of the molecule, concentration, solvent and light intensity.

The photocatalytic degradation of a selection of environmental pollutants and industrially important molecules using MPc complexes is also presented in this chapter. There are still very few reports on the use of MPc complexes as photocatalysts compared to their use as catalysts in the presence of oxidants. This is an area where MPc complexes may be applied with a great deal of success, although MPc complexes that are stable to light, such as halogenated derivatives are necessary.

VII. Acknowledgments

This work was supported by the Department of Science and Technology (DST) and National Research Foundation (NRF), South Africa through DST/NRF South African Research Chairs Initiative for Professor of Medicinal Chemistry and Nanotechnology and Rhodes University. Edith Antunes thanks CSIR/Swiss JRF of South Africa for Post-doctoral funding.

VII. References

1. Gregory, P. In *High-Technology Applications of Organic Colourants*; Plenum Press: New York, **1991**; pp. 7–273.
2. McKeown, N. B. In *Phthalocyanine Materials: Synthesis*, *Structure and Function. Chemistry of Solid State Materials*; Cambridge University Press: New York, **1998**; pp. 32–149.
3. Leznoff, C. C.; Lever, A. B. P., Eds.; *Phthalocyanines: Properties and Applications*; VCH Publishers: New York, **1989**, **1993**, **1996**, Vols. 1–4.
4. Okura, I. In *Photosensitization of Porphyrins and Phthalocyanines*; Gordon and Breach Science Publishers: Amsteldijk, The Netherlands, **2001**; pp. 151–213.
5. Dini, D.; Hanack, M. In *Phthalocyanines: Properties and Materials. The Porphyrin Handbook*. Kadish, K. M.; Smith, K. M.; Guilard, R., Eds.; Academic Press: New York, **2003**; Vol. 17, pp. 1–31.
6. Ben-Hur, E.; Chan, W. S. *Spectroscopic and Electrochemical Characterization. The Porphyrin Handbook,* Kadish, K. M.; Smith, K. M.; Guilard, R., Eds.; Academic Press: New York, **2003**; Vol. 19, pp. 1–30.

7. Gregory, P. *J. Porphyrins Phthalocyanines* **1999**, *3*, 468–476.
8. Ogunsipe, A. O.; Nyokong, T. *J. Mol. Struct.* **2004**, *689*, 89–97.
9. Stuzhin, P. A. *J. Porphyrins Phthalocyanines* **1999**, *3*, 500–513.
10. Stuzhin, P. A.; Khelevina, O. G.; Angeoni, S.; Berezin, B. D. In *Phthalocyanines: Properties and Applications*; Leznoff, C. C.; Lever, A. B. P., Eds.; VCH: New York, **1996**; Vol. 4; pp. 19–77.
11. Beeby A.; FitzGerald, S.; Stanley, C. F.; *J. Chem. Soc., Perkin Trans. 2*, **2001**, 1978–1982.
12. Maya, E. M.; Snow, A. W.; Shirk, J. S.; Pong, R. G.; Flom, S. R.; Roberts, G. L. *J. Mater. Chem.* **2003**, *13*, 1603–1613.
13. Iwamoto, M. *J. Mater.Chem.* **2000**, *10*, 99–106.
14. Zagal, J.; Bedioui, F.; Dodelet, J. P., Eds.; *N4-Macrocyclic Metal Complexes,* Springer: New York, **2006**.
15. Snow, A. W.; Barger, W. R. In *Phthalocyanines: Properties and Applications.* Leznoff, C. C.; Lever, A. B. P., Eds.; VCH Publishers: New York, **1989**, Vol. 1 pp. 341–392.
16. Ishii, K.; Kobayashi, N. In *Phthalocyanines: Spectroscopic and Electrochemical Characterization. The Porphyrin Handbook*. Kadish, K. M.; Smith, K. M.; Guilard, R., Eds.; Academic Press: New York, Vol. 16, pp. 1–40.
17. Nensala, N.; Nyokong, T. *J. Mol. Cat.: A Chem.* **2000**, *164*, 69–76.
18. Ichinohe, T.; Miyasaka, H.; Isoda, A.; Kimura, M.; Hanabusa, K.; Shirai, H. *React. Funct. Polym*. **2000**, *43*, 63–70.
19. Ozoemena, K.; Kutznetsova, N.; Nyokong, T. *J. Mol. Catalysis, A: Chem.* **2001**, *176*, 29–40.
20. Sehlotho, N.; Nyokong, T. *J. Mol. Cat. A: Chem.* **2004**, *219*, 201–207.
21. Allen, C. M.; Sharman, W. M.; Van Lier, J. E. *J. Porphyrins Phthalocyanines* **2001**, *5*, 161–169.
22. Rosenthal, I. *Photochem. Photobiol.* **1991**, *53*, 859–870.
23. Spikes, J. D. *Photochem. Photobiol. B: Biol.* **1990**, *6*, 259–274.
24. Spikes, J. D. *Photochem. Photobiol.* **1986**, *43*, 691–699.
25. Bown, S. G.; Tralau, C. J.; Coleridge Smith, P. D.; Akdemir, D. T.; Wieman, T. J. *Br. J. Cancer* **1986**, *54*, 43–52.
26. Brown, S. B.; Truscott, T. G. *Chem. Br.* **1993**, *29*, 955–958.
27. Bonnett, R. In *Chemical Aspects of Photodynamic Therapy*; Gordon and Breach Science: Amsteldijk, The Netherlands, **2000**; pp. 199–222.
28. Zimcik, P.; Miletin, M.; Ponec, J.; Kostka, M.; Fiedler, Z. *J. Photochem. Photobiol. A: Chem.* **2003**, *155*, 127–131.
29. Lukyanets, E. A. *J. Porphyrins Phthalocyanines* **1999**, *3*, 424–432.
30. Zhang, X-F.; Xu, H.-J. *J. Chem. Soc. Faraday Trans.* **1993**, *89*, 3347–3351.
31. Tabata, K.; Fukushima, K.; Oda, K.; Okura, I. *J. Porphyrins Phthalocyanines* **2000**, *4*, 278–284.
32. Martin, P. C.; Gouterman, M.; Pepich, B. V.; Renzoni, G. E.; Schindele, D. C. *Inorg. Chem.* **1991**, *30,* 3305–3309.
33. Spiller, W.; Kliesch, H.; Wohrle, D.; Hackbarth, S.; Roder, B.; Schnurpfeil, G. *J. Porphyrins Phthalocyanines* **1998**, *2*, 145–158.
34. Schnurpfeil, G.; Sobbi, A. K.; Spiller, W.; Kliesch, H.; Wohrle, D. *J. Porphyrins Phthalocyanines* **1997**, *1*, 159–167.
35. Ozoemena, K.; Kutznetsova, N.; Nyokong, T. *J. Photochem. Photobiol. A: Chem.* **2001**, *139*, 217–224.

36. Maree, S.; Nyokong, T. *J. Porphyrins Phthalocyanines* **2001**, *5*, 782–792.
37. Ogunsipe, A.; Maree, D.; Nyokong, T. *J. Mol. Struc.* **2003**, *650*, 131–140.
38. Patterson, M. S.; Madsen, S. J.; Wilson, R. *J. Photochem. Photobiol. B: Biol.* **1990**, *5*, 69–84.
39. Foley, S. Jones, G.; Liuzzi, R.; McGarvey, D. J.; Perry, H. M.; Truscott, T. G. *J. Chem. Soc. Perkin Trans.* **1997**, *2*, 1725–1730.
40. Rosenthal, I.; Ben-Hur, E. *Int. J. Radiat. Biol.* **1995**, *67*, 85–91.
41. Ogunsipe, A.; Chen, J.-Y.; Nyokong, T. *New J. Chem.* **2004**, *28*, 822–827.
42. Kuznetsova, N. A.; Gretsova, N. S.; Derkacheva, V. M.; Mikhalenko, S. A.; Solov'eva, L. I.; Yuzhakova, O. A.; Kaliya, O. L.; Luk'yanets, E. A. *Russ. J. Gen. Chem.* **2002**, *72*, 300–306.
43. Shen, T.; Yuan, Z. L.; Xu, H. Y. *Dyes Pigm.* **1989**, *11*, 77–80.
44. Maree, D.; Nyokong, T.; Suhling, K.; Phillips, D. *J. Porphyrins Phthalocyanines* **2002**, *6*, 373–376.
45. Maree, S.; Phillips, D.; Nyokong, T. *J. Porphyrins Phthalocyanines* **2002**, *6*, 17–25.
46. Ferry-Forgues, S.; Lavabre, D. *J. Chem. Ed.* **1999**, *76*, 1260–1264.
47. Fu, J.; Li, X. Y.; Ng, D. K. P.; Wu, C. *Langmuir* **2002**, *18*, 3843–3847.
48. Bishop, S. M.; Beeby, A.; Parker, A. W.; Foley, M. S. C.; Philips, D. *J. Photochem. Photobiol. A: Chem.* **1995**, *90*, 39–44.
49. Lakowicz, J. R. In *Principles of Fluorescence Spectroscopy*, 2nd Edn.; Kluwer Academic/Plenum Publishers: New York, **1999**; pp. 17–19.
50. Gilat, S. L.; Ebbeseb, T. W. *J. Phys. Chem.* **1993**, *97*, 3551–3554.
51. Ogunsipe, A.; Nyokong, T. *J. Porphrins Phthalocyanines* **2005**, *9*, 121–129.
52. Ogunsipe, A.; Nyokong, T. *J. Photochem. Photobiol. A: Chem.* **2005**, *173*, 211–220.
53. Ogunsipe, A.; Nyokong, T. *Photochem. Photobiol. Sci.* **2005**, *4*, 510–516.
54. Seotsanyana-Mokhosi, I.; Chen, J.-Y.; Nyokong, T. *J. Porphyrins Phthalocyanines* **2005**, *9*, 316–325.
55. Kubát, P.; Mosinger, J. *J. Photochem. Photobiol. A: Chem.* **1996**, *96*, 93–97.
56. Debacker, M. G.; Deleplanque, O.; Van Vlieberge, B.; Sauvage, F. X. *Laser Chem.* **1988**, *8*, 1–11.
57. Dhami, D.; Phillips, D. *J. Photochem. Photobiol. A: Chem.* **1996**, *100*, 77–84.
58. Edrei, R.; Goofried, V.; van Lier, J. E.; Kimel, S. *J. Porphyrins Phthalocyanines* **1998**, *2*, 191–199.
59. Ambroz, M.; Beeby, A.; MacRobert, A. J.; Simpson, M. S. C.; Svensen, R. K.; Phillips, D. *J. Photochem. Photobiol. B: Biol.* **1991**, *9*, 87–95.
60. Weber, J.; Busch, D. *Inorg. Chem.* **1965**, *4*, 469–471.
61. Dixon, D. W.; Gill, F. A.; Sook, B. R. *J. Porphyrins Phthalocyanines* **2004**, *8*, 1300–1310.
62. Moeno, M.; Idowu, M.; Nyokong, T. *Inorg. Chim. Acta* **2008**, *361*, 2950–2956.
63. Seotsanyana-Mokhosi, I.; Kuznetsova, N.; Nyokong, T. *J. Photochem. Photobiol. A: Chem.* **2001**, *140*, 215–222.
64. Wohrle, D.; Gitzel, J.; Okura, I.; Aono, S. *J. Chem. Soc. Perkin Trans. 2* **1985**, 1171–1178.
65. Thamae, M.; Nyokong, T. *J. Electroanal. Chem.* **1999**, *470*, 126–135.
66. Szulinski, W. S.; Kincaid, J. R. *Inorg. Chem.* **1998**, *37*, 5014–5020.
67. Durmuş, M.; Nyokong, T. *Inorg. Chem. Commun.* **2007**, *10*, 333–338.
68. Moeno, S.; Nyokong, T. *J. Photochem. Photobiol. A: Chem.* **2009**, *203*, 204–210.
69. Durmuş, M.; Nyokong, T. *Photochem. Photobiol. Sci.*, **2007**, *6*, 659–668.
70. Moeno, S.; Nyokong, T. *J. Photochem. Photobiol. A: Chem.* **2009**, *201*, 228–236.
71. Sehlotho, N.; Durmuş, M.; Ahsen, V.; Nyokong, T. *Inorg. Chem. Commun.* **2008**, *11*, 479–483.
72. Idowu, M.; Nyokong, T. *Polyhedron* **2009**, *28*, 416–424.

73. Segalla, A.; Borsarelli, C. D.; Braslavsky, S. E.; Spikes, J. D.; Roncucci, G.; Dei, D.; Chiti, G.; Jori, G.; Reddi, E. *Photochem. Photobiol. Sci.* **2002**, *1*, 641–648.
74. Makarov, D. A.; Yuzhakova, O. A.; Silvika, L. K.; Kuznetsova, N.; Negrimovsky, V. M.; Ka;iya, O.; Lukyanets, E. A. *J. Porphyrins Phthalocyanines* **2007**, *11*, 586–595.
75. Rodriquez, M. E.; Fernandez, D. A.; Awruch, J.; Braslavsky, S. E.; Dicello, E. L. *J. Porphyrins Phthalocyanines* **2006**, *10*, 33–42.
76. Łapok, L.; Schnurpfeil, G.; Gerdes, R.; Gorun, S. M.; Suvorova, O.; Kudryavtseva, G. S.; Wohrle, D. *J. Porphyrins Phthalocyanines* **2009**, *13*, 346–357.
77. Idowu, M.; Nyokong, T. *J. Lumin.* **2009**, *129*, 356–362.
78. Ke, M.-R.; Huang, J.-D.; Weng, S.-M. *J. Photochem. Photobiol. A: Chem.* **2009**, *201*, 23–31.
79. Nishida, M.; Momotake, A.; Shinohara, Y.; Nishimura, Y.; Arai, T. *J. Porphyrins Phthalocyanines* **2007**, *11*, 448–454.
80. Ball, D. J.; Mayhew, S.; Wood, S. R.; Griffiths, J.; Vernon, D. I.; Brown, S. B. *Photochem. Photobiol.* **1999**, *69*, 390–396.
81. Kasha M., *Radiat. Res.* **1963**, *20*, 55–70.
82. Kobayashi, T., Ed.; *J-Aggregates*; World Scientific: Singapore, **1996**.
83. Darwent, J. R.; Douglas, P.; Harriman, A.; Poter, G.; Richoux, M. C. *Coord. Chem. Rev.* **1982**, *44*, 83–126.
84. Oldham, T. C.; Eigenbrot, I. V.; Crystal, B.; Phillips, D. *Proc. SPIE* **1996**, *2625*, 266–277.
85. Dhami, S.; Cosa, J. J.; Bishop, S. M.; Phillips, D. *Langmuir* **1996**, *12*, 293–300.
86. Idowu, M.; Nyokong, T; *J. Photochem. Photobiol. A: Chem.* **2009**, *204*, 63–68.
87. Marti, C.; Nonell, S.; Nicolau, M.; Torres, T. *Photochem. Photobiol.* **2000**, *71*, 53–59.
88. Grofcsilk, A.; Baranyai, P.; Bitter, I.; Csokai, V.; Kubinyi, M.; Szegletes, K.; Tatai, J.; Vidóczy, T. *J. Mol. Struct.* **2004**, *704*, 11–15.
89. Durmuş, M.; Nyokong, T. *Spectrochim. Acta: A* **2008**, *69*, 1170–1177.
90. Siejak, A.; Wrobel, D.; Siejak, P.; Olejarz, B.; Ion, R. M. *Dyes Pigm.* **2009**, *83*, 281–290.
91. Zhang, X; Ma, J; Xu, H. *Proc. SPIE* **1993**, *1616*, 372–377.
92. Owens, J. W.; Robins, M. *J. Porphyrins Phthalocyanines* **2001**, *5*, 460–464.
93. Idowu, M.; Nyokong, T. *Polyhedron* **2009**, *28*, 891–896.
94. Lang, K; Wagnerová, D. M.; Engst, P; Kubát, P. *Zietschrift Phys. Chem.* **1994**, *187*, 213–221.
95. Simpson, M. S. C.; Beeby, A.; Bishop, S. M.; MacRobert, A. J.; Parker, A. W.; Phillips, D. *SPIE* **1992**, *1640*, 520–529.
96. Foley, M. S. C.; Beeby, A.; Parker, A. W.; Bishop, S. M.; Phillips, D. *J. Photochem. Photobiol. B: Biol.* **1997**, *38*, 10–17.
97. Seotsanyana-Mokhosi, I.; Nyokong, T. *J. Porphyrins Phthalocyanines* **2005**, *9*, 476–483
98. Durmuş, M.; Erdoğmuş, A.; Ogunsipe, A.; Nyokong, T. *Dyes Pigm.* **2009**, *82*, 244–250.
99. Förster, T.; Hoffmann, G. Z. *Phys. Chem*. **1971**, *75*, 63–76.
100. Ogunsipe, A.; Durmuş, M.; Atilla, D.; Gurek, A. G.; Ahsen, V.; Nyokong, T. *Synth. Met.* **2008**, *158*, 839–847.
101. Li, H.; Fronczek, F. R.; Vicente, M.G.H. *J. Organomet. Chem*. **2009**, *694*, 1607–1611.
102. Dupouy, E. A.; Lazzeri, D.; Durantini, E. N. *Photochem. Photobiol. Sci.* **2004**, *3*, 992–998.
103. Engst, P.; Kubát, P.; Jirsa, M. *J. Photochem. Photobiol. A: Chem.* **1994**, *78*, 215–219.
104. Beeby, A.; Parker, A. W.; Simpson, M. S. C.; Phillips, D. *J. Photochem. Photobiol. B: Biol.* **1992**, *16*, 73–81.
105. Idowu, M.; Nyokong, T. *J. Photochem. Photobiol. A: Chem.* **2008**, *200*, 396–401.

106. Alarcon, X. E.; Edwards, A. M.; Garcia, A. M.; Munoz, M.; Aspee, A.; Borsarelli, C. D.; Lissi, A. E. *Photochem. Photobiol. Sci.* **2009**, *8*, 255–263.
107. Spikes, J. D.; van Lier, J. E.; Bommer, J. C. *J. Photochem. Photobiol.* **1995**, *91*, 193–198.
108. Phillips, D. *Pure Appl. Chem.* **1995**, *67*, 117–126.
109. Bishop, M.; Beeby, A.; Meunier, H.; Parker, A. W.; Foley, M. S. C.; Pjillips, D. *J. Chem. Soc. Faraday Trans.* **1996**, *92*, 2689–2695.
110. Lacey, J. A.; Phillips, D.; Milgrom, L. R.; Yahioglu, G.; Rees, R. D. *Photochem. Photobiol.* **1998**, *67*, 97–100.
111. Iriel, A.; Lagorio, G.; Dicelio, L. E.; San Román, E.; *Phys. Chem. Chem. Phys.* **2002**, *4,* 224–239.
112. Gerhardt, S. A.; Lewis, J. W.; Zhang, J. Z.; Bonnett, R.; McManus, K. A. *Photochem. Photobiol. Sci.* **2003**, *2,* 934–938.
113. Tau, P.; Nyokong, T. *Inorg. Chim. Acta* **2007**, *360*, 2615–2622.
114. Kuznetsova, N. A.; Gretsova, N. S.; Derkacheva, V. M.; Kaliya, O. L.; Lukyanets, E. A. *J. Porphyrins Phthalocyanines* **2003**, *7*, 147–154.
115. Li, H; Jensen, T. J.; Fronczek, F. R.; Vicente, M. G. H.; *J. Med. Chem.* **2008**, *51*, 502–511.
116. Schmidt, R. *J. Am. Chem. Soc.* **1989**, *111*, 6983–6987.
117. Nilsson, R.; Kearns, D. R. *J. Phys. Chem.* **1974**, *78*, 1681–1683.
118. Chidawanyika, W.; Nyokong, T. *J. Photochem. Photobiol. A: Chem.* **2009**, *202*, 99–106.
119. Chidawanyika, W.; Ogunsipe, A.; Nyokong, T. *New J. Chem.* **2007**, *31*, 377–384.
120. Grodkowski, J.; Chambers J. H., Jr.; Neta, P. *J. Phys. Chem.* **1984**, *88*, 5332–5335.
121. Chambrier, I.; Hughes, D. L.; Swarts, J. C.; Isare, B.; Cook, M. J. *Chem. Commun.* **2006**, 3504–3506
122. Chambrier, I.; White, G. F.; Cook, M. J.; *Chem. Eur. J.* **2007**, *13*, 7608–7618.
123. Kuznetsova, N. A.; Okunchikov, V. V.; Dokachera, V. M.; Kahiy, O. L.; Luk'yanets, E. A. *J. Porphyrins Phthalocyanines* **2005**, *9*, 393–397.
124. Winter, G.; Heckmann, H.; Haisch, P.; Eberhardt, W.; Hanack, M.; Lüer, L.; Egelhaaf, H-J.; Oelkrug, D. *J. Am. Chem. Soc.* **1998**, *120*, 11663–11673.
125. Kasuga, K.; Matsuura, N.; Inoue, K.; Handa, M.; Sugimori, T.; Isa, K.; Nakata, M. *Chem. Lett.* **2002**, 352–353.
126. Kobayashi, N.; Fukuda, T.; Ueno, K.; Ogino, H. *J. Am. Chem. Soc.* **2001**, *123*, 10740–10741.
127. Maree, D. M.; Kuznetsova, N. ; Nyokong, T. *J. Photochem. Photobiol. A: Chem.* **2001**, *140*, 117–125.
128. Barker, C. A.; Zeng, X.; Bettington, S.; Batsanov, A. S.; Bryce, M. R.; Beeby, A. *Chem. Eur. J.* **2007**, *13*, 6710–6717.
129. Nyokong, T. *Coord. Chem. Rev.* **2007**, *251*, 1707–1722.
130. Kaneko Y.; Nishimura, Y.; Takane, N.; Arai T.; Sakuragi H.; Kobayashi, N.; Matsuhaga, D.; Pac, C.; Tokumaru, K.; *J. Photochem. Photobiol. A: Chem.* **1997**, *106*, 177–183.
131. Swarts, J. C.; Maree, D. M. *J. Porphyrins Phthalocyanines* **2006**, *11*, 613–617.
132. Topal, S. Z.; Yuksel, F.; Ayse, G.; Ertkin, K.; Yeniguel, B.; Ahsen, V. *J. Photochem. Photobiol. A: Chem.* **2009**, *202*, 205–213.
133. Agirtas, S.; Ion, R.-M.; Bekaroglu, O. *Mat. Sci. Eng.* **2000**, C*7*, 105–110.
134. Leclaire, J.; Dagiral, R.; Fery-Forgues, S.; Coppel, Y.; Donnadieu, B.; Caminade, A.-M.; Majoral, J.-P. *J. Am. Chem. Soc.* **2005**, *127*, 15762–15770.
135. Knyukshto, V. N.; Kuzmitsky, V. A.; Borisevich, E. A.; Volkovoch, D. I.; Bubnova, A. S.; Stuzhin, P. A.; Solovyov, K. N. *J. Appl. Spect.* **2009**, *76*, 341–351.

136. Tau, P.; Nyokong, T. *J. Mol. Cat. A: Chem.* **2007**, *273*, 149–155.
137. Tau, P.; Nyokong, T. *J. Chem. Soc. Dalton Trans.* **2006**, 4482–4490.
138. Atilla, D.; Durmuş, M.; Yılmaz, Ö.; Gürek, A. G.; Ahsen, V.; Nyokong, T. *Eur. J. Inorg. Chem.* **2007**, 3573–3581.
139. Tau, P.; Nyokong, T. *J. Porphyrins Phthalocyanines* **2006**, *10*, 1040–1048.
140. Kang, H.-J.; Kang, E.-H.; Park, S.-W.; Lee, J.-W.; Lee, J.-K. *Macromol. Symposia* **2006**, *235*, 195–200.
141. Tretyakova, I. N.; Chemii, V. Y.; Tomachynski, L. A.; Volkov, S. V. *Dyes Pigm.* **2007**, *75*, 67–72.
142. Ogunbayo, T. B.; Ogunsipe, A.; Nyokong, T. *Dyes Pigm.* **2009**, *82*, 422–426.
143. Durmuş, M.; Ahsen, V.; Nyokong, T. *J. Photochem. Photobio. A: Chem.* **2007**, *186*, 323–329.
144. Kuznetsova, N.; Gretsova, N.; Kalmykova, E.; Makarova, E.; Dashkevich, S.; Negrimovskii, V.; Kaliya, O.; Luk'yanets E. *Russ. J. Gen. Chem.* **2000**, *70*, 133–140.
145. Li, Y. S.; Zaidi, S. I. A.; Rodgers, M. A. J.; Mukhtar, H.; Kenney, M. E.; Oleinick, N. L.; He, J.; Hedy E.; Larkin, H. E.; Rihter, B. D. *Photochem. Photobiol.* **1997** *65*, 581–586.
146. Beveridge, A. C.; Bench, B. A.; Gorun, S. M.; Diebold, G. J. *J. Phys. Chem. A* **2003**, *107,* 5138–5143.
147. FitzGerald, S.; Farren, C.; Stanley, C. F.; Beeby, A.; Bryce, M. R. *Photochem. Photobiol. Sci.* **2002**, *1*, 581–587.
148. Seotsanyana-Mokhosi, I.; Nyokong, T. *J. Porphyrins Phthalocyanines* **2004**, *4*, 1214–1221.
149. Gürol, I.; Durmuş, M.; Ahsen, V.; Nyokong, T. *J. Chem. Soc., Dalton Trans.* **2007**, 3782–3791.
150. Atilla, D.; Saydan, N.; Durmuş, M.; Gürek, A. G.; Khan, T.; Rück, A.; Walt, H.; Nyokong, T.; Ahsen, V. *J. Photochem. Photobio. A: Chem.* **2007**, *186*, 298–307.
151. Zhao, Z.; Nyokong, T.; Maree, M. D. *J. Chem. Soc. Dalton Trans.* **2005**, 3732–3737.
152. Ozoemena, K. I.; Nyokong, T. *Inorg. Chem. Comm.* **2003**, *6*, 1192–1195.
153. Hone, D. C.; Walker, P. I.; Evans-Gowing, R.; FitzGerald, S.; Beeby, A.; Chambrier, I.; Cook, M. J.; Russell, D. A. *Langmuir* **2002**, *18*, 2985–2987.
154. Khene, S.; Cammidge, A. N.; Cook, M. J.; Nyokong, T. *J. Porphyrins Phthalocyanines* **2007**, *11*, 761–770.
155. Sakamoto, K.; Ohno-Okumura, E.; Kato, T.; Kawaguchi, T.; Cook, M. J.; *J. Porphyrins Phthalocyanines* **2003**, *7*, 83–88.
156. Seotsanyana-Mokhosi, I.; Nyokong, T. *J. Porphyrins Phthalocyanines* **2003**, *7*, 167–175
157. Tau, P.; Ogunsipe, A. O.; Maree, S.; Maree, M. D.; Nyokong, T. *J. Porphyrins Phthalocyanines* **2003**, *7*, 439–446.
158. Cormick, M. P.; Rovera, M.; Durantini, E. N. *J. Photochem. Photobiol. A: Chem.* **2008**, *194*, 220–229.
159. Yslas, E. I.; Rivarola, V.; Durantini, E. N. *Bioorg. Med. Chem.* **2004**, *13*, 39–46.
160. Li, H.; Nguyen, N.; Fronczek, F. R.; Vicente, M. G. H. *Tetrahedron* **2009**, *65*, 3357–3363.
161. Camur, M.; Bulut, M.; Kandaz, M.; Gueney, O. *Polyhedron* **2009**, *28*, 233–238.
162. Kaestner, L.; Cesson, M.; Kassab, K.; Christensen, T.; Edminson, P. D.; Cook, M. J.; Chambrier, I.; Jori, G. *Photochem. Photobiol. Sci.* **2003**, *2*, 660–667.
163. Sugimori, T.; Nojima, J.; Ozawa, T.; Handa, M.; Kasuga, K. *Chem. Lett.* **2004**, *33*, 1014–1015.
164. Makarov, S.G; Suvorova, O., Litwinski, C.; Ermilov, E.A.; Roeder, B.; Tsaryova, O.; Dülcks, T.; Wöehrle, D., *Eur. J. Inorg. Chem.* **2007**, *546–552.*
165. Strassert, C. A.; Bilmes, G. M.; Awruch, J.; Dicello, L. E. *Photochem. Photobiol. Sci.* **2008**, *7*, 738–747.

166. Al–Raqa, S. Y. *J. Porphyrins Phthalocyanines* **2006**, *10*, 55–62.
167. Mosinger, J.; Deumié, M.; Lang, K.; Kubát, P.; Wagnerová, D. M. *J. Photochem. Photobiol. A: Chem.* **2000**, *130*, 13–20.
168. Zhao, Z.; Ogunsipe, A. O.; Maree, M.D.; Nyokong, T. *J. Porphyrins Phthalocyanines* **2005**, *9*, 186–197.
169. Tran-Thi, T. H.; Desforge, C.; Thiec, C. *J. Phys. Chem.* **1989**, *93*, 1226–1233.
170. Sutton, J. M.; Boyle, R. W. *Chem. Comm.* **2001**, 2014–2015.
171. Yang, S. I.; Li, J.; Cho, H. S.; Kim, D.; Bocian, D. F.; Holten, D.; Lindsey, J. S. *J. Mater. Chem.* **2000**, *10*, 283–296.
172. Tran-Thi, T. H.; Lipskier, J. E. *J. Chem. Soc., Faraday Trans.* **1992**, *88*, 2129–2137.
173. Chen, Y.; Dini, D.; Hanack, M.; Fujitsuka, M.; Ito, S. *Chem. Comm*. **2004**, 340–341.
174. Chen, Y.; Hanack, M.; Blau, W. J.; Dini, D.; Liu, Y.; Lin, Y.; Bai, J. J. *Mat. Sci.* **2006**, *41*, 2169–2185.
175. Zimcik, P.; Miletin, M.; Novakova, V.; Kopecky, K.; Marcela, M.; Stata, V.; Sedlackova, K. *Aust. J. Chem.* **2009**, *62*, 425–433.
176. Matlaba, P.; Nyokong, T. *Polyhedron* **2002**, *21*, 2463–2472.
177. Chidawanyika, W.; Antunes, E.; Nyokong, T. *J. Photochem. Photobiol. A: Chem.* **2008**, *195*, 183–190.
178. Ramán, E. S. *J. Photochem. Photobiol. A: Chem.* **1996**, *102*, 109–112.
179. Durmuş, M.; Nyokong, T. *Tetrahedron* **2007**, *63*, 1385–1394.
180. Durmuş, M.; Nyokong, T. *Polyhedron* **2007**, *26*, 2767–2776.
181. Chen, Y.; Hanack, M.; Araki, Y.; Ito, O. *Chem. Soc. Rev*. **2005**, *34*, 517–529.
182. Chen, Y.; O'Flaherty, S.; Fujitsuka, M.; Hanack, M.; Subramanian, L. R.; Ito, O.; Blau, W. J. *Chem. Mater.* **2002**, *14*, 5163–5168.
183. Chen, Y.; Araki, Y.; Fujitsuka, M.; Hanack, M.; Ito, O.; O'Flaherty, S. M.; Blau, W. J. *Solid State Comm.* **2004**, *131*, 773–778.
184. Chauke, V.; Ogunsipe, A.; Durmuş, M.; Nyokong, T. *Polyhedron* **2007**, *26*, 2663–2671.
185. Chen, Y.; O'Flaherty, S. M.; Hanack, M.; Blau, W. J.; *J. Mater. Chem*. **2003**, *13*, 2405–2408.
186. Idowu, M.; Nyokong, T. *J. Photochem. Photobiol. A: Chem.* **2008**, *199*, 282–290.
187. Chen, Y.; Araki, Y.; Dini, D.; Liu, Y.; Ito, O.; Fujitsuka, M. *Mat. Chem. Phys*. **2006**, *98*, 212–216.
188. Durmuş, M.; Nyokong, T. *Polyhedron* **2007**, *26*, 3323–3335.
189. Brannon, J. H.; Magde, D. *J. Am. Chem. Soc.* **1980**, *102*, 62–65.
190. Mack, J.; Stillman, M. J. *In Phthalocyanines: Spectroscopic and Electrochemical Characterization. The Porphyrin Handbook,* Kadish, K. M.; Smith, K. M.; Guilard, R., Eds.; Academic Press: New York, **2003**; Vol. 16; pp. 43–113.
191. Chauke, V.; Durmuş, M.; Nyokong, T. *J. Photochem. Photobiol. A: Chem.* **2007**, *192*, 179–187.
192. Huang, J.-D.; Wang, S.; Lo, P.-C.; Fong, W.-P.; Ko, W.-H.; Ng, D. K. P. *New J. Chem.* **2004**, *28*, 348–334.
193. Daziano, J.-P.; Steenken, S.; Chabannon, C.; Mannoni, P.; Chanon, M.; Julliard, M.; *Photochem. Photobiol.* **1996**, *64*, 712–719.
194. Lo, P.-C.; Wang, S.; Zeug, A.; Meyer, M.; Roder, B.; Ng, D. K. P. *Tetrahedron Lett.* **2003**, *44*, 1967–1970.
195. Farren, C.; FitzGerald, S.; Bryce, M. R.; Beeby, A.; Batsanov, A. S.; *J. Chem. Soc. Perkin Trans.* **2002**, *2*, 59–66.

196. Gunaratne, T.; Kennedy, V. O.; Kenney, M. E.; Rodgers, M. A. J. *J. Phys. Chem. A* **2004**, *108*, 2576–2582.
197. Barker, C. A.; Findlay, K. S.; Bettington, S.; Batsanov, A. S.; Perepichka, I. F.; Bryce, M. R.; Beeby, A. *Tetrahedron* **2006**, *62*, 9433–9439.
198. Isago, H.; Miura, K.; Oyama, Y. *J. Inorg. Biochem.* **2008**, *102*, 380–387.
199. Modibane, D.; Nyokong, T. *Polyhedron* **2009**, *28*, 479–484.
200. Modibane, K. D.; Nyokong, T. *Polyhedron* **2009**, *28*, 147–1480.
201. Modibane, D.; Nyokong, T. *Polyhedron* **2008**, *27*, 1102–1110.
202. Antunes, E.; Nyokong, T. *J. Porphyrins Phthalocyanines* **2009**, *13*, 153–160.
203. Wöhrle, D.; Suvorova, O.; Gerdes, R.; Bartels, O.; Łapok, Ł.; Baziakina, N.; Makarov, S.; Słodek, A. *J. Porphyrins Phthalocyanines* **2004**, *8*, 1020–1041.
204. Schneider, G.; Wöhrle, D.; Spiller, W.; Stark, J.; Schulz-Ekloff, G. *Photochem. Photobiol.* **1994**, *60*, 333–342.
205. Gerdes, R.; Bartels, O.; Schneider, G.; Wöhrle, D.; Schulz-Ekloff, G. *Intern. J. Photoenergy* **1999**, *1*, 41–47.
206. Shinohara, H.; Tsaryova, O.; Schnurpfeil, G.; Wohrle, D. *J. Photochem. Photobiol. A: Chem.* **2006**, *184*, 50–57.
207. Iliev, V.; Ileva, A.; *J. Env. Prot. Ecol.* **2001**, *2*, 603–613.
208. Iliev, V.; Mihaylova, A.; Bilyarska, L. *J. Mol. Cat. A: Chem.* **2002**, *184*, 121–130.
209. Moore, J. W.; Moore E. A. In *Environmental Chemistry*; Academic Press: New York, **1976**; pp. 196–255.
210. Iliev, V.; Mihaylova, A. *J. Photochem. Photobiol. A Chem.* **2002**, *149*, 23–30.
211. Chauke, V.; Nyokong, T. *J. Mol. Cat. A: Chem.* **2008**, *289*, 9–13.
212. Lang, K.; Wagnerová, D. W.; Brodilová, J. J. *Photochem. Photobiol. A Chem*. **1993**, *72*, 9–14.
213. Safari, N.; Bahadoran, F. *J. Mol. Cat. A: Chem.* **2001**, *171*, 115–121.
214. Huang, J.-W.; Huang, W.-Z.; Mei, W.-J.; Liu, J.; Hu, S.-G.; Ji, L.-N. *J. Mol. Catal. A: Chem.* **2000**, *156*, 275–278.
215. Alvaro, M.; Carbonell, E.; Espla´; Garcia, M. H. *Appl. Catal. B: Environ*. **2005**, *57*, 37–42.
216. Iliev, V.; Alexiev, V.; Bilyarska, L. *J. Mol. Cat. A Chem.* **1999**, *137*, 15–26.
217. Kluson, P.; Drobek, M.; Zsigmond, A.; Baranyi, J.; Bata, P.; Zarubova, S.; Kalaji, A. *Appl. Catal.B: Environ.* **2009**, *91*, 605–609.
218. Kluson, P.; Drobek, M.; Krejcikova, S.; Krysa, J.; Kalaji, A.; Cajthaml, T.; Rakusan, J. *Appl. Catal. B: Environ.* **2008**, *80*, 321–326.
219. Roman, E. A. S.; Navio, J. A.; Litter, M. I. *J. Advan. Oxid. Technol*. **1998**, *3*, 261–269.
220. Maretti, L.; Carbonell, E.; Alvaro, M.; Scaianoa, J. C.; Garcia, H. *J. Photochem. Photobiol. A: Chem.* **2009**, *205*, 19–22.
221. Pepe, E.; Abbas, O.; Rebufa, C.; Simon, M.; Lacombe, S.; Julliard M. *J. Photochem. Photobiol. A: Chem.* **2005**, *170*, 143–149.
222. Machado, A. E. H.; de Miranda, J. A.; de Freitas, R. F.; Duarte, E. T. F. M.; Ferreira, L. F.; Albuquerque, Y. D. T.; Ruggiero, R.; Sattler, C.; de Oliveira, L. *J. Photochem. Photobiol. A: Chem.* **2003**, *155*, 231–241.
223. Iliev, V. *J. Photochem. Photobiol. A: Chem.* **2002**, *151*, 195–199.
224. Gerdes, R.; Wöhrle, D.; Spiller, W.; Schneider, G.; Schnurpfeil, G.; Schulz-Ekloff, G. *J. Photochem. Photobiol. A Chem.* **1997**, *111*, 65–74.
225. Gilma G. O.; Carlos A. P. M.; Fernando M. O.; Edgar A. P.-M. *Catalysis Today* **2005**, *107–108*, 589–594.

226. Xiong, Z.; Xu, Y.; Zhu, L.; Zhao J. *Environ. Sci. Technol.* **2005**, *39*, 651–657.
227. Sun Q.; Xu, Y. *J. Phys. Chem. C* **2009,** *113*, 12387–12394.
228. Hodak, J.; Quinteros, Litter, C. M. I.; Roman E. S. *J. Chem.* SOC., *Faraday Trans.* **1996**, *92*, 5081–5088.
229. Xu, Y.; Chen, Z. *Chem. Lett*. **2003**, *32*, 592–593.
230. Ranjit, K. T.; Willner, I.; Bossmann, S.; Braun, A. *Research Chem. Interm*.**1999**, *25*, 733–756.
231. Wöehrle, D.; Schlettwein, D.; Schnurpfeil, G.; Schneider, G.; Karmann, E.; Toshida, T.; Kaneko, M. *Polym. Advaced Technol*. **1995**, *6*, 118–30.
232. Cicco, S. R.; Latronica, M.; Mastrorilli, P., Suranna, G. P.; Nobile C. F.; *J. Mol. Catal. A: Chem.* **2001**, *165*, 135–140.
233. Shiragami, T.; Matsumoto, J.; Inoue, H.; Yasuda, M. *J. Photochem. Photobiol. C Photochem. Rev.* **2005**, *6*, 227–248.
234. Brink, M.; Wennerström, O. *J. Photochem. Photobiol. A Chem.* **2001**, *143*, 201–208.
235. V. Chauke, MSc thesis, Rhodes University, **2008**.

This page intentionally left blank

35 Structure, Spectroscopy, Photophysics, and Tautomerism of Free-Base Porphycenes and Other Porphyrin Isomers

Jacek Waluk

Institute of Physical Chemistry, Polish Academy of Sciences,
Kasprzaka 44, 01-224 Warsaw, Poland

List of Abbreviations

CPMAS	cross-polarization magic angle spinning
DFT	density functional theory
EPR	electron paramagnetic resonance
ENDOR	electron-nuclear double resonance
HB	hydrogen bond
HOMO	highest occupied molecular orbital
LCAO	linear combination of atomic orbitals
LUMO	lowest unoccupied molecular orbital
MCD	magnetic circular dichroism
NMR	nuclear magnetic resonance
OECp	2,3,6,7,11,12,17,18-octaethylcorrphycene
OEIPc	2,3,6,7,13,14,17,18-octaethylisoporphycene
OEHPc	2,3,6,7,12,13,17,18-octaethylhemiporphycene
OEPc	2,3,6,7,12,13,16,17-octaethylporphycene
OEPr	2,3,7,8,12,13,17,18-octaethylporphyrin
PDT	photodynamic therapy
PPP	Pariser–Parr–Pople method
TPP	5,10,15,20-tetraphenylporphyrin
TPPo	2,7,12,17-tetraphenylporphycene

I. Introduction

Nature relies upon porphyrins in many fundamental processes involving living matter and light. In photosynthesis, for instance, chlorophylls and bacteriochlorophylls play several roles, acting as light-harvesting pigments and participating in charge separation and transport. Myoglobin and hemoglobin, the proteins responsible for

oxygen binding, transport, and storage, owe their function to the heme prosthetic group, made up of an iron porphyrin. The same compound can also bind nitric oxide or carbon monoxide. Another heme protein, cytochrome *c*, does not bind oxygen, but owing to its redox properties is an essential component of the electron transport chain. In turn, vitamin B_{12} contains a corrin moiety — a reduced porphyrin-like structure with a Co^{2+} ion. Cobalt–porphyrin-containing enzymes are involved in the biosynthesis of hydrocarbons. In a patent, it was proposed to use cobalt-porphyrin complexes as antiobesity agents.[1] All these facts demonstrate that it is quite appropriate to refer to porphyrins as "pigments of life".[2] One should recall in this context that the green color of leaves, the red color of blood, and various hues of red in meat are due to the porphyrin chromophore. Actually, *πορφυριων* (*porphyrion*) is the Greek word for purple.

An enormous number of applications involving porphyrins have been proposed. The Patent Storm US database returns above 15,000 entries with "porphyrin" as a keyword. The corresponding number from a Scopus patent search is 19,500. Among various possible applications, artificial photosynthetic units or dye-sensitized solar cells are extremely promising for photovoltaics. Porphyrins are widely used in photodynamic therapy (PDT) for cancer treatment, in photodiagnostics, and as catalysts and biomimetic models. The prospects of exploiting porphyrin-based nanostructures for sensing applications have been reviewed.[3]

Designing a porphyrin-based system for a particular purpose requires a desired modification of structural, electronic, or spectral parameters. These can be controlled, albeit to a limited degree, by appropriate substitution. Much larger room for improvement is available if the four pyrrole moieties are connected in a different fashion than is found in porphyrin, while maintaining the general $C_{20}N_4H_{14}$ formula and the π-electron conjugated pathway. The synthesis of porphycene, first reported by Vogel and coworkers in 1986,[4] initiated a new area of research, devoted to constitutional isomers of porphyrin. If the N_4 coordination site is to be preserved, the four pyrrole and four methine units can be reshuffled in eight different ways, as demonstrated in a theoretical paper.[5] Thus, seven "nitrogen-in" constitutional isomers of porphyrin can be envisaged. Of those, four have been synthesized as of now: porphycene (**2**), hemiporphycene[6,7] (**3**), corrphycene[8,9] (**4**), and isoporphycene[10,11] (**5**) (Figure 1). In a more systematic nomenclature, each of these compounds may be called [18]porphyrin-(n_1.n_2.n_3.n_4), where the number in square brackets indicates the number of π electrons in the conjugation path and n_i ($0 \le n_i \le 4$) denotes the number of the methine groups in each bridging unit, starting with the highest value and going toward the next highest one. The parent compound can thus be called [18]porphyrin-(1.1.1.1), and porphycene is [18]porphyrin-(2.0.2.0), whereas the names [18]porphyrin-(2.1.1.0), [18]porphyrin-(2.1.0.1), and [18]porphyrin-(3.0.1.0) correspond to hemiporphycene,

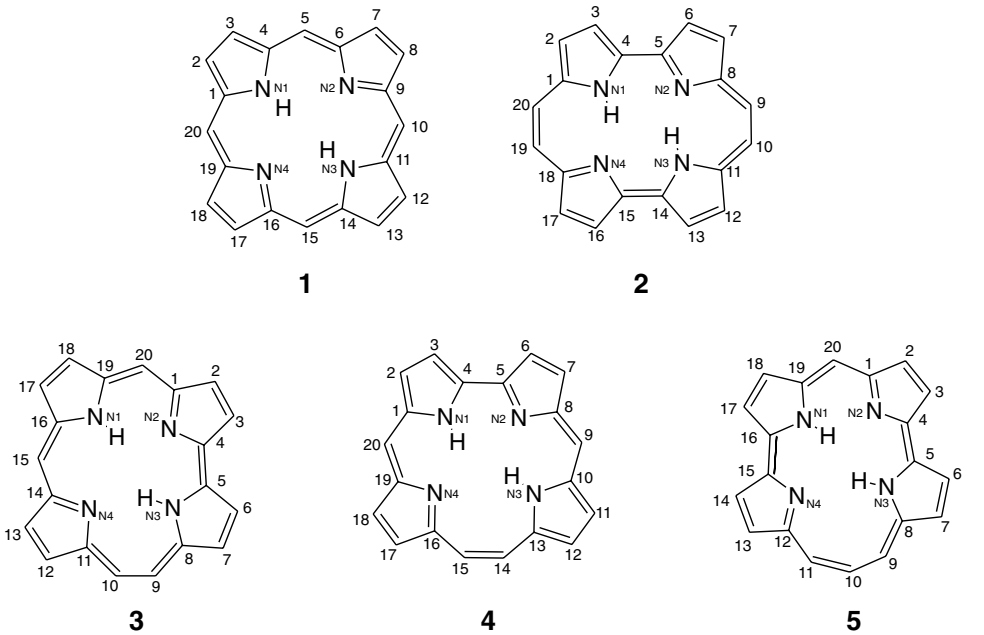

Figure 1. Porphyrin (**1**), porphycene (**2**), hemiporphycene (**3**), corrphycene (**4**), and isoporphycene (**5**). The formulas correspond to the most stable tautomeric form of each isomer (See Table 1).

corrphycene, and isoporphycene, respectively. Interestingly, the chronological order of syntheses of porphyrin isomers correlates with their calculated relative energies (Table 1). One can also see that for porphycene a lower energy is predicted than for porphyrin. This is due to exceptionally strong intramolecular hydrogen bonds in the former. For metal complexes, the energy ordering is reversed, making metalloporphyrins more stable. The highest energies are expected for the three molecules which have not yet been obtained: [18]porphyrin-(2.2.0.0) (**6**), [18]porphyrin-(3.1.0.0) (**7**), and [18]porphyrin-(4.0.0.0) (**8**).

Another type of porphyrin isomer was obtained, initially in the form of *meso* tetraaryl-substituted derivatives, at about the same time as corrphycene and hemiporphycene. In this molecule one of the pyrrole units has its nitrogen atom pointing outward. Accordingly, it has been dubbed inverted[12] or N-confused[13] porphyrin (**9**). These studies were followed by successful syntheses of various core-modified porphyrins, in which the CH unit was replaced by a heteroatom such as O, S, Se, Te.[14,15]

After the initial studies of porphycene, it became obvious that even though the basic properties of the porphyrin chromophore are preserved in the isomer, the quantitative characteristics can be very different. For example, the electronic absorption spectra in the low-energy range are red-shifted and much more intense

Table 1. Calculated relative energies (kcal/mol) of porphyrin isomers. The values correspond to the lowest-energy tautomeric form of each isomer (see formulas **1**–**8**).

	BLYP/6-31G** //3-21G[a]	B3LYP/6-311+G** //6-31G[b]	B3LYP/6-31G**[c]
2 [18]porphyrin-(2.0.2.0) (porphycene)	0.0	0.0	0.0 (0.0)[d]
1 [18]porphyrin-(1.1.1.1)	1.5	0.4	1.0 (1.2)
4 [18]porphyrin-(2.1.1.0) (hemiporphycene)	6.6	6.1	6.0 (6.4)
3 [18]porphyrin-(2.1.0.1) (corrphycene)	13.5	13.4	13.3 (13.8)
5 [18]porphyrin-(3.0.1.0) (isoporphycene)	20.5	21.5	21.0 (21.2)
6 [18]porphyrin-(2.2.0.0)	30.4	33.4	31.4 (32.0)
7 [18]porphyrin-(3.1.0.0)	40.2	42.0	41.9 (42.2)
8 [18]porphyrin-(4.0.0.0)	72.1	69.8	71.5 (71.7)

[a]Ref. 41; [b]Ref. 207; [c]This work. [d]In parentheses are the values including zero-point energy correction.

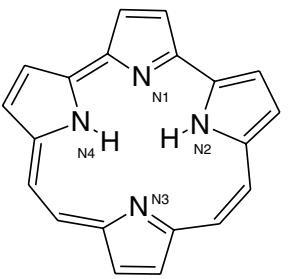

6

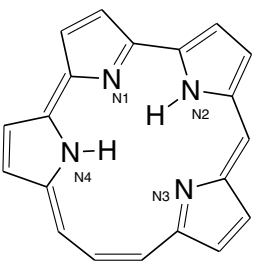

7

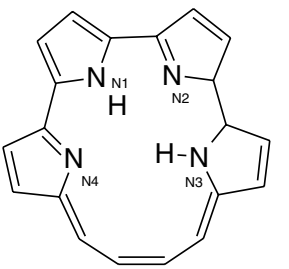

8

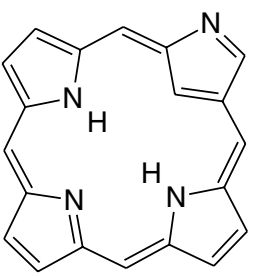

9

than those of the parent compound, which suggested that porphycenes may be better phototherapeutic agents than porphyrin. This hypothesis was soon corroborated[16]; the studies of photodynamic properties of porphycenes are now quite intense.[17] A still unexploited area is the use of porphycenes in artificial light-harvesting systems.

While the investigations of corrphycene, hemiporphycene, and, in particular, isoporphycene have been rather limited, this is not the case for porphycene. About 300 derivatives have been described so far. Most of a few hundred porphycene-related patents propose this chromophore as a photosensitizer in PDT. Other patent applications involve, besides synthetic procedures, information storage, and use of porphycenes as optical recording media, in catalysis, fluorescence immunoassays, molecular imaging, tissue marking, and drug delivery tracking.

With regard to fundamental research, porphycenes have become model molecules for studying the mechanisms of intramolecular double hydrogen transfer, both experimentally[18–40] and theoretically.[41–50] Several factors make porphycenes ideal for that purpose. First, the geometry of the two intramolecular hydrogen bonds is well defined and insensitive to the environment. On the other hand, the hydrogen bond (HB) geometry can be significantly modified by peripheral substitution. Depending on the position of a substituent, both strengthening and weakening of the HBs are possible. Moreover, the substitution pattern can be selected in such a way that the symmetric double minimum character is either preserved or destroyed. A low potential energy barrier facilitates tunneling; the consequences can be monitored both in condensed phases and in the regime of isolated molecules. The spectral and photophysical properties of porphycenes, such as absorption and strong emission in the red spectral region, make them readily amenable to various experimental techniques, including those of high spectral and temporal resolution. Finally, the presence of two intramolecular HBs provides an opportunity to study cooperative effects, both in hydrogen bonding and in proton/hydrogen transfer.

Previous reviews of isomeric porphyrins included both free-base and metal derivatives,[51–57] providing detailed information on synthetic aspects and redox properties. The latter have been studied quite intensely,[58–67] whereas the spectroscopic and photophysical properties have been reviewed less frequently.[19,68,69] The applications of porphycenes in phototherapy have been summarized recently.[17] The present work focuses on structural, spectroscopic, photophysical, and tautomeric properties of free-base porphyrin isomers. After discussing the geometries, in particular the inner cavity parameters crucial for the intramolecular HB characteristics, we analyze the electronic structure. A simple molecular orbital approach is described, which enables one to explain and to predict differences in the electronic absorption patterns of different isomers. Next, photophysical

properties are presented. Understanding both spectral and photophysical behavior is a prerequisite for successful applications based on chromophore–light interactions. Finally, the mechanisms of tautomerism are discussed for ground and electronically excited states. Because porphycenes have been studied much more intensely than other isomers, they are the main object of this work. The relevant data for other porphyrin isomers will be reviewed as well, whenever available.

II. Structure

A. Symmetry and Planarity

The mode of reshuffling of pyrrole units determines the symmetry of the ensuing isomer. Parent free-base porphyrin belongs to the D_{2h} group; in metalloporphyrins the symmetry is even higher — D_{4h}. The corresponding symmetries are C_{2h} and D_{2h} for porphycene, and C_s and C_{2v} for corrphycene. Parent porphycene is planar[4]; an essentially planar ring structure has been found also for 2,7,12,17-tetra-*n*-propylporphycene **10**,[70] 9,10,19,20-tetra-*n*-propylporphycene **11**,[71] 9,10,19,20-tetraphenylporphycene **12**,[72] 2,3-dihydroporphycene **13**,[73] and 2,7,12,17-tetraethyl-3,6,13,16-tetramethylporphycene (etioporphycene, **14**).[74] For the last, replacement of the methyl by ethyl groups, leading to 2,3,6,712,13,16,17-octaethylporphycene (OEPc, **15**), introduces a slight twist[74] (Figure 2).

An interesting pattern is obtained through gradual substitution of 2,7,12,17-tetra-*n*-propylporphycene by bromine in the β' positions (3,6,13,16). In the mono-, dibromosubstituted (at positions 3 and 13) and tribromosubstituted (3,6,13) derivatives, **16**–**18** respectively, the macrocycle is reported to be planar, but it becomes

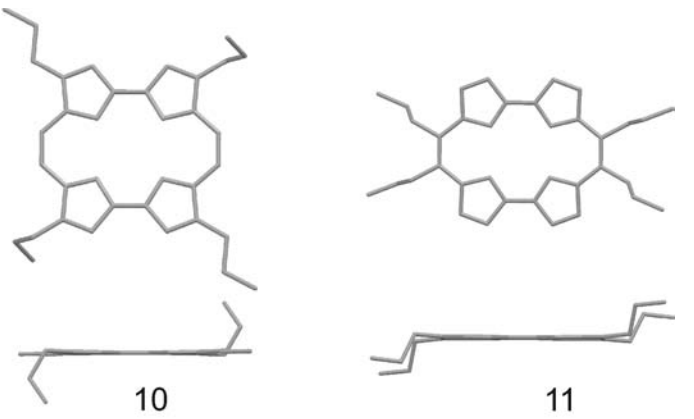

Figure 2. Front and side views of X-ray-determined structures of several free-base porphycene derivatives: **10**,[70] **11**,[71] **12**,[72] **13**,[73] **14**,[74] and **15**.[74] Hydrogen atoms have been omitted for clarity.

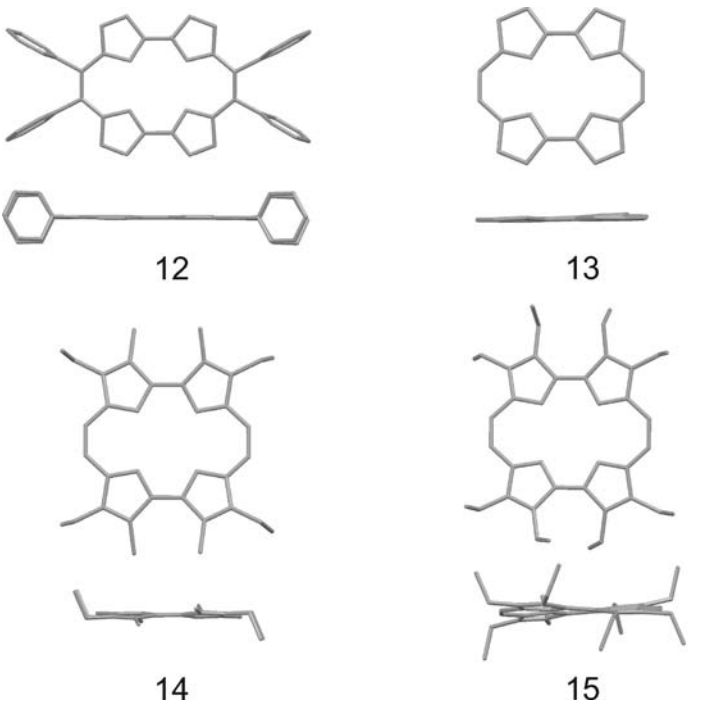

Figure 2. (*Continued*)

distorted in 3,6,13,16-tetrabromo-2,7,12,17-tetra-*n*-propylporphycene **19**.[75] For the last compound, three papers report quite different degrees of distortion.[75–77]

The unsubstituted corrphycene has not yet been obtained. 2,3,6,7,11,12,17,18-Octaethylcorrphycene (OECp, **20**) has a planar macrocyclic ring.[9] An intriguing observation is that in the crystalline phase both protons are located at the adjacent nitrogens belonging to the bipyrrole unit. Such a *cis* tautomeric form (**20a**) is

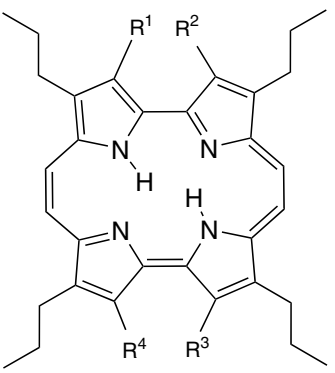

	R^1	R^2	R^3	R^4
16	Br	H	H	H
17	Br	H	Br	H
18	Br	Br	Br	H
19	Br	Br	Br	Br

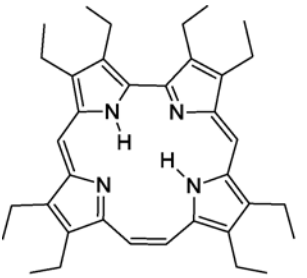

20 *trans*

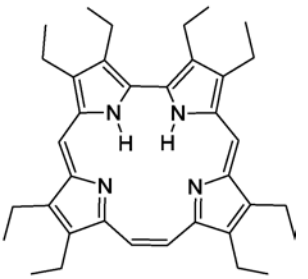

20a cis

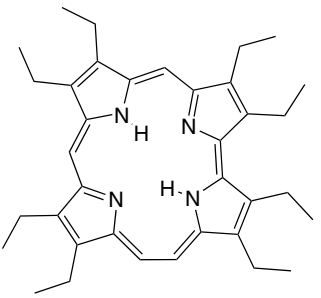

21

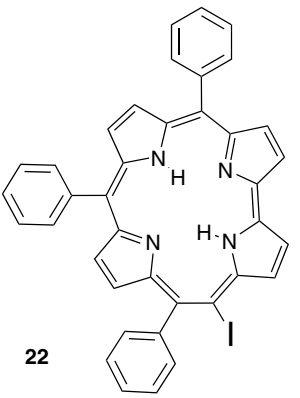

22

predicted by calculations performed for the parent corrphycene to be less stable than the *trans* structure **20** (see Table 3). The NMR data indicate that the latter predominates in solution. Protonation of two cavity nitrogens leads to a strongly nonplanar structure.[78]

Both free-base and metallohemiporphycenes can have at most C_s symmetry, provided that they are planar. Synthesis of the unsubstituted hemiporphycene has not been reported so far. The crystallographic analysis of free-base 2,3,6,7,12,13,17, 18-octaethylhemiporphycene (OEHPc, **21**)[7] reveals a nearly planar conformation, whereas in nickel,[6,56] zinc,[56] magnesium,[56] and iron[79] complexes the macrocycle is slightly saddle-shaped. An even larger distortion from planarity is observed for 5-iodo-6,11,16-triphenylhemiporphycene **22**.[80]

In isoporphycene, the trimethine moiety can assume *cis* or *trans* conformations. Both isomers were isolated in the form of palladium complexes of octaethylisoporphycene (**23a** and **23b**) and found to be almost planar.[7] However, in the *trans* (*E*) isomer **23b**, the central atom of the C_3 bridge lies 0.44 Å above the molecular plane. As in the cases of hemiporphycene and corrphycene, isoporphycene has not yet been obtained in the parent, unsubstituted form.

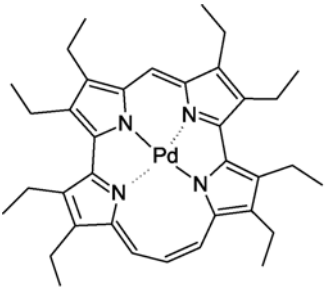

23a

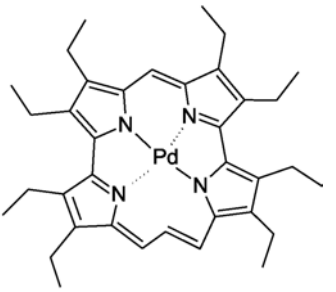

23b

The general tendency predicted by calculations for the high-energy isomers **6**–**8** is that they should be essentially planar in the (*Z*) configuration, whereas the (*E*) structures can be somehow distorted from planarity.[41]

The symmetry can be different for different tautomeric forms of a given isomer. The symmetry predictions given above were based on calculations, which revealed that the most stable structure corresponds to a *trans* form, with the protons on the opposite pyrrole rings. The planar (if possible) *cis* tautomers of porphycene, as well as two out of three *cis* forms of corrphycene, isoporphycene, and **8**, should reveal C_{2v} symmetry. On the contrary, the *cis* forms of **6** should exhibit lower symmetry (C_s) than the *trans* ones.

Geometry optimizations performed at the B3LYP/6-31G** level yield planar structures for all the tautomeric forms of porphyrin and corrphycene. In the other isomers some tautomeric forms become nonplanar, most probably due to the repulsion of the inner hydrogens. The nonplanar structure is predicted for one of the *cis* tautomers of porphycene (**2b**, Figure 8), one of the four possible *cis* forms of hemiporphycene (**3e**, Figure 13), and two tautomeric species of isoporphycene (**5b** and **5c**, Figure 10). In **6**, of the two pairs of *trans* and *cis* forms one is planar (**6** and **6b**, Figure 12), while the other is not (**6a** and **6c**). For **7** (in the *Z* configuration), the planar structure is predicted for only two out of six possible tautomers: the *trans* structure **7** and the *cis* form **7c** (Figure 14). Finally, geometry optimization of **8** yields nonplanar geometry for all possible tautomers (Figure 11).

The shape and size of the internal N_4 cavity are crucial for both metal coordination and intramolecular hydrogen bonding properties. The calculated and experimentally determined N–N distances are shown in Table 2. For parents **1** and **2**, the agreement between experimental and computational results is good. It becomes much worse if the predictions based on calculations for the unsubstituted isomers **3**–**5** are confronted with the experimental data for octaethyl derivatives. The reason is the sensitivity of the geometry of the inner cavity to the substituent, as discussed in the following section.

Table 2. N–N distances (pm) of the inner cavity of porphyrin isomers. Calculated using B3LYP/6-31G** for the lowest-energy tautomer of each form. In parentheses are experimental values.

	N1–N4	N1–N2	N2–N3	N3–N4
1	293.2 (288)[a] (290)[b]	293.2 (289)[a] (291)[b]	293.2 (289)[a] (291)[b]	293.2 (290)[a] (291)[b]
2	265.5 (262.5)[c]	283.8 (282.8)[c]	265.5 (262.5)[c]	283.8 (282.8)[c]
3	320.6 (312.9)[d]	259.5 (270.8)[d]	273.6 (262.7)[d]	292.5 (304.5)[d]
4	274.2 (280.0)[e]	262.5 (253.9)[e]	274.2 (280.4)[e]	353.9 (344.8)[e]
5 (*Z*) isomer	274.0	246.9	274.0	312.8[f]
5 (*E*) isomer	265.7 (254.1)[f]	269.0 (282.6)[f]	264.0 (254.1)[f]	374.2 (390.9)[f]
6	253.8	253.8	324.9	324.9
7	253.0	245.1	281.3	366.0
8	266.0	244.4	266.0	371.3

[a]Ref. 82. [b]Ref. 83. [c]Ref. 4. [d]Ref. 7; data for OEHPc **21**. [e]Ref. 9; data for the *cis* form of OECP (**20a**). [f]Ref. 10; structure of the *E* isomer of 2,3,6,7,13,14,17,18-octaethylisoporphycene.

B. Influence of Substituents on the Geometry of the Internal Cavity

The size of the internal N_4 cavity in porphyrin is remarkably stable with regard to four-fold or eight-fold symmetrical substitution by alkyl or aryl groups. This is illustrated in Figure 3, where the N–N distances are compared for parent porphyrin **1**[81–83] and its derivatives: 2,3,7,8,12,13,17,18-octaethyl- (OEPr, **24**),[84] 5,10,15,20-tetra-*n*-propyl- (**25**),[85] and 5,10,15,20-tetraphenyl- (TPP, **26**).[86,87] An analysis of the Cambridge Crystallographic Database, containing above 500 variously substituted free-base porphyrins, revealed that in about 80% of the compounds the N–N distances oscillate around 292 ± 10 pm. On the other hand, it is possible to strongly distort the cavity, making it rectangular, by substitution, by either aryl or alkyl groups at the opposite *meso* positions, as shown in Figure 3 for 5,15-diphenylporphyrin (**27**)[88] and 5,15-di-*n*-butyl-2,3,7,8,12,13,17,18-octaethylporphyrin (**28**).[89]

Structural studies of the alkyl derivatives of porphycene demonstrate that the dimensions of the N_4 core are significantly affected by the substitution pattern. Interestingly, the same substituent, when placed at different positions, can either decrease or increase the N–N distances (Figure 4). Four-fold alkyl substitution at the *meso* positions (9,10,19,20) leads to a more rectangular cavity, as shown in Figure 3 for the tetramethyl-, (**29**) tetra-*n*-propyl- (**11**),[71] and tetraphenyl- (**12**)[72] derivatives. The opposite effect is obtained in β,β'-octaalkylporphycenes, illustrated by the examples of octaethyl- (**15**)[74] and etioporphycene **14**.[74] Finally, in 2,7,12,17-tetraalkyl derivatives, such as tetra-*n*-propyl- (**10**)[70] and tetra-*tert*-butyl- (**30**), the size of the cavity remains similar to that of the parent, unsubstituted

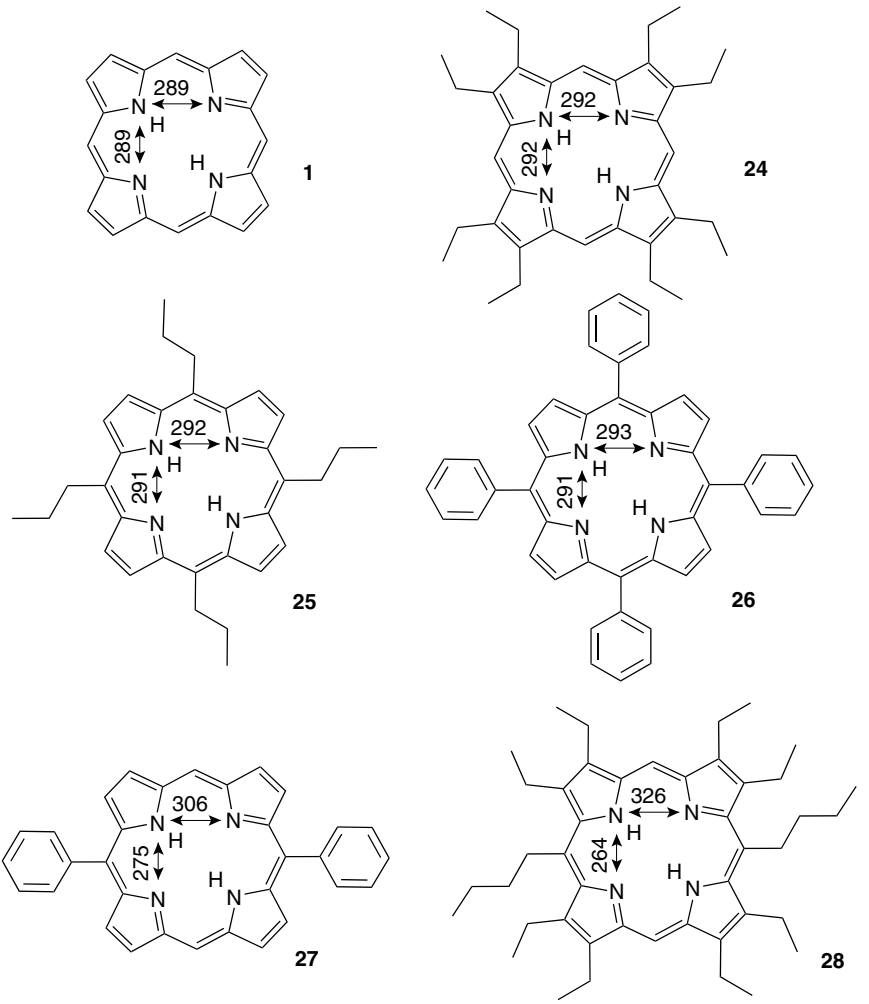

Figure 3. Crystallographically determined internal cavity dimensions (in pm) in differently substituted porphyrins: **1**,[81–83] **24**,[84] **25**,[85] **26**,[86,87] **27**,[88] and **28**.[89]

compound, strongly suggesting that the changes observed for octaalkyl derivatives are mainly due to substituents at the β' positions (3,6,13,16). This conclusion was confirmed by calculations, but has not yet been established experimentally. A strongly distorted structure has been reported for 2,7,12,17-tetraethyl-3,6,13,16-tetrakis(trifluoromethyl)porphycene **31**[90] (Figure 5).

A gradual evolution of the cavity dimensions was observed upon consecutive brominations in β' positions[75] (Figure 6). The first bromine substitution does not noticeably change the geometry of the inner core (see structure **10** in Figure 4). Subsequent introductions of bromine atoms result in the reversal of the short and

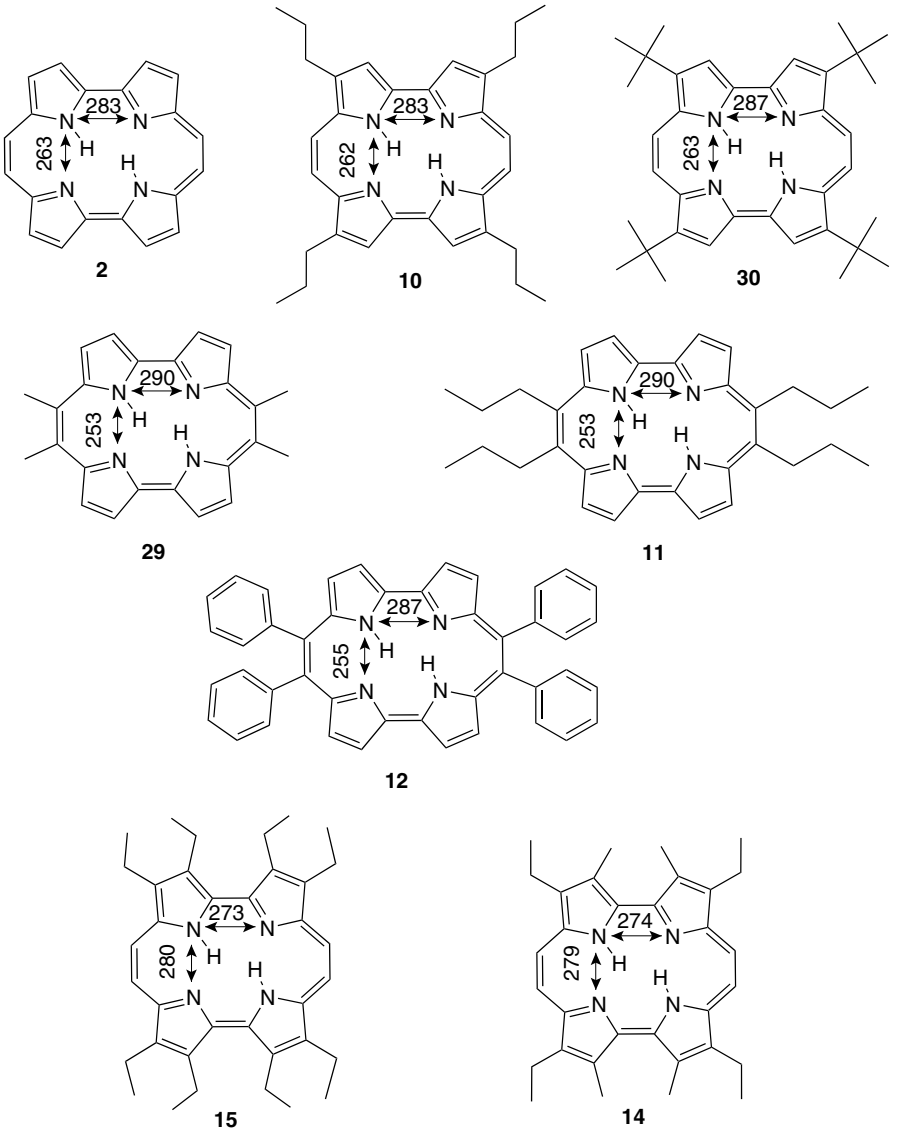

Figure 4. Crystallographically determined internal cavity dimensions (in pm) in differently substituted porphycenes: **2**,[4] **10**,[70] **30**, **29**,[71] **11**,[71] **12**,[72] **15**,[74] and **14**.[74]

long sides of the cavity. In the tetrabromosubstituted derivative **19**, the cavity dimensions are the same as in OEPc **15**.

The position-dependent sensitivity of the porphycene inner core to substitution has a large impact on the strength of two intramolecular hydrogen bonds and on the rate of double hydrogen transfer. As discussed in more detail in Section V,

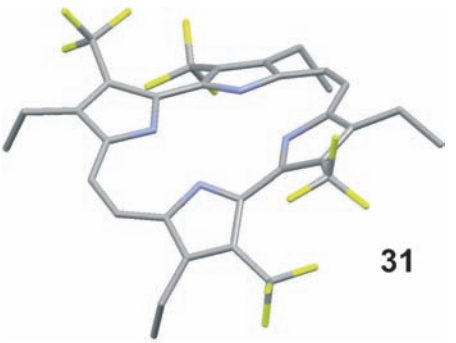

Figure 5. X-ray structure of 2,7,12,17-tetraethyl-3,6,13,16-tetrakis(trifluoro-methyl)porphycene.[90] Hydrogen atoms have been omitted for clarity.

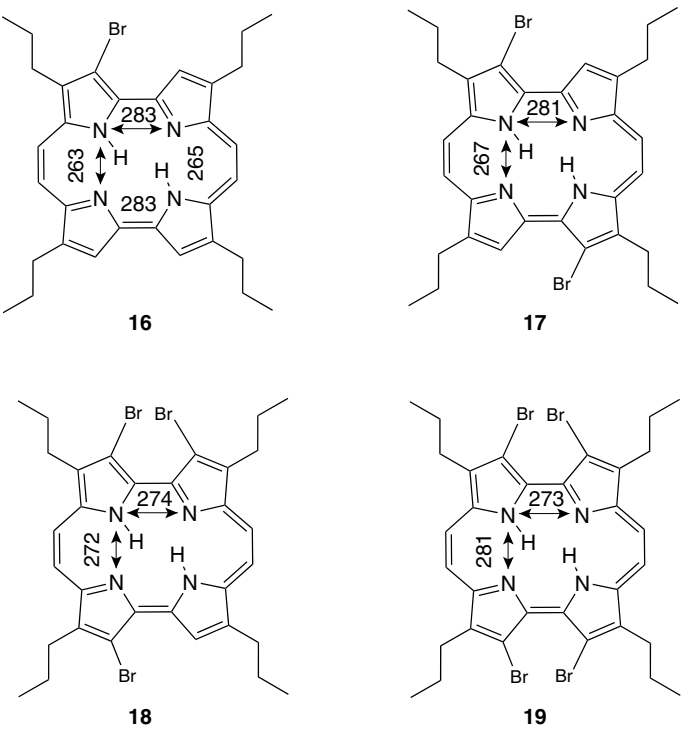

Figure 6. Evolution of the inner core geometry with subsequent bromine substitutions. The X-ray data are taken from Ref. 75.

changing the NH···N distance from 2.80 Å in 2,3,6,7,12,13,16,17-octaethylporphycene **15** to 2.53 Å in 9,10,19,20 tetramethylporphycene **29** or tetra-*n*-propylporphycene **19** results in nearly four orders of magnitude larger tautomerization rates in the *meso*-substituted derivatives, in which the smaller NH···N separation

makes the hydrogen bonds much stronger. It is also instructive to note that fourfold *meso* substitution by methyl and *n*-propyl groups leads in both cases to the same changes in the cavity dimensions, which suggests that the electronic rather than steric factors are of primary importance for the geometry modifications.

C. *Cis–Trans* Tautomerism

The two inner protons may be distributed between the four nitrogens in several ways. In the *trans* form, the protons are positioned at the opposite pyrrole rings, whereas the *cis* structures correspond to their location on the adjacent pyrroles. The *trans* tautomers are predicted to be thermodynamically more stable (Table 3); the relative energies presented in Table 1 for the lowest energy structures of each isomer all correspond to such forms. The number of possible nonequivalent *cis*

Table 3. Relative energies (kcal/mol; in parentheses, the values including zero-point energy correction) and dipole moments calculated (B3LYP/6-31G**) for different tautomeric forms of porphyrin isomers. The energies are given with respect to the lowest-energy tautomer of each isomer.

	Relative Energy (kcal/mol)	Dipole Moment (D)
1	0.0 (0.0)	0.0
1a	8.2 (7.8)	2.10
2	0.0 (0.0)	0.0
2a	2.2 (1.6)	1.17
2b	30.2 (30.3)	1.79
3	0.0 (0.0)	0.58
3a	1.0 (0.9)	0.46
3b	4.2 (3.7)	1.57
3c	5.1 (4.4)	1.94
3d	19.9 (19.4)	1.81
3e	20.5 (20.2)	2.62
4	0.0 (0.0)	0.51
4a	5.2 (4.9)	1.85
4b	5.8 (5.2)	1.40
4c	16.6 (16.0)	2.77
5	0.0 (0.0)	0.53
5a	3.9 (2.9)	1.48
5b	22.3 (22.3)	2.91
5c	23.7 (23.4)	2.29
6	0.0 (0.0)	0.57
6a	1.9 (1.9)	0.84
6b	9.0 (8.6)	1.62
6c	10.2 (9.7)	1.51
7	0.0 (0.0)	0.37
7a	0.5 (0.6)	1.31

(*Continued*)

Table 3. (*Continued*)

	Relative Energy (kcal/mol)	Dipole Moment (D)
7b	7.5 (7.4)	1.69
7c	10.0 (9.3)	1.65
7d	11.0 (10.7)	2.15
7e	12.4 (12.0)	2.96
8	0.0 (0.0)	1.95
8a	8.5 (8.2)	2.86
8b	9.6 (9.7)	1.00
8c	11.5 (10.8)	2.47

and *trans* forms increases with lowering of molecular symmetry. Thus, one *trans* and one *cis* tautomer are expected for porphyrin. More correctly, two chemically equivalent *trans* (**1′** and **1″**) and four equivalent *cis* tautomers (**1a′**–**1a″″**) exist, described by symmetric double or quadruple minimum potentials (Figure 7). One

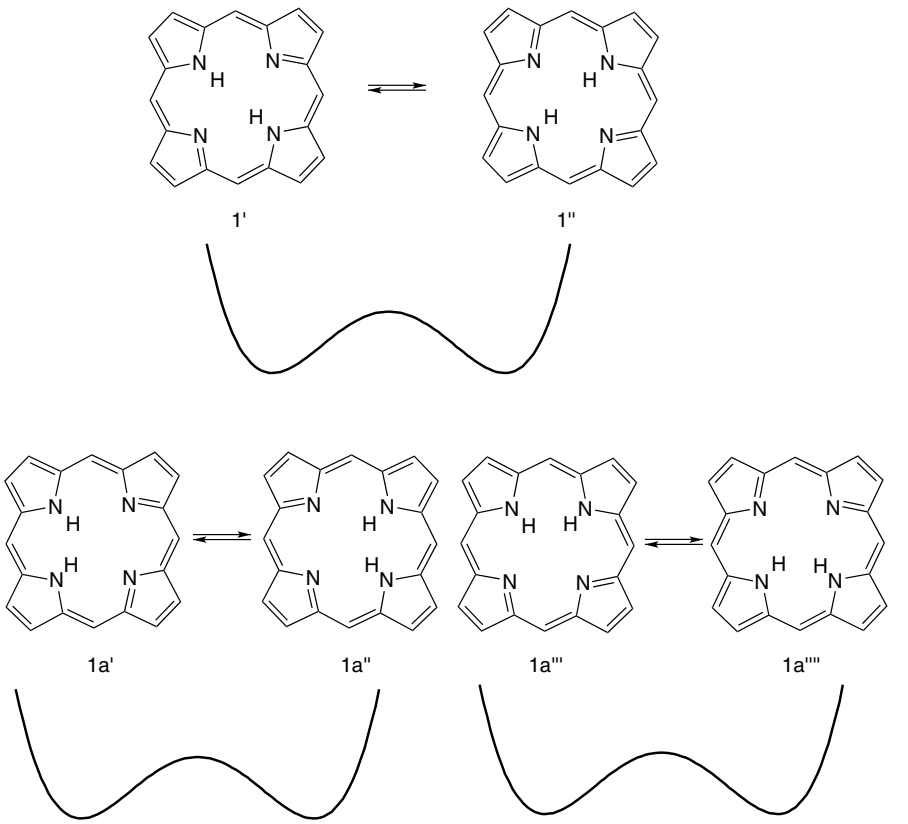

Figure 7. *Trans* (top) and *cis* (bottom) tautomers of porphyrin. Symmetric potential for hydrogen exchange has been schematically indicated.

should note that the four-fold degeneration of the *cis* tautomers does not necessarily imply equal energy barriers for their interconversion. Thus, while the same barrier may be expected for the 1a′–1a″ and 1a‴–1a⁗ transformations, this is not the case for e.g. 1a′–1a‴, if the former process occurs in a concerted fashion. For a conversion such as 1a′–1a‴, a stepwise mechanism is preferable, involving a *trans* form as an intermediate. The interconversion between the equivalent forms, often called a self-exchange process, may be monitored by such techniques as NMR,[18,24,33,37,91–93] or electronic and IR spectroscopy using polarized light.[20,31,32,34–36,94–96] In the regime of an isolated molecule, the two inner protons are delocalized between the four nitrogens, which gives rise to tunneling splittings. These have been observed for porphycene isolated in supersonic jets[22] or helium nanodroplets,[40] and for *meso*-alkylated derivatives in supersonic beams[30] (see Section V).

For porphycene, one pair of equivalent *trans* tautomers and two pairs of equivalent *cis* forms are possible (Figure 8). Corrphycene can exist as a pair of equivalent *trans* structures, but for the *cis* form a symmetric double minimum is

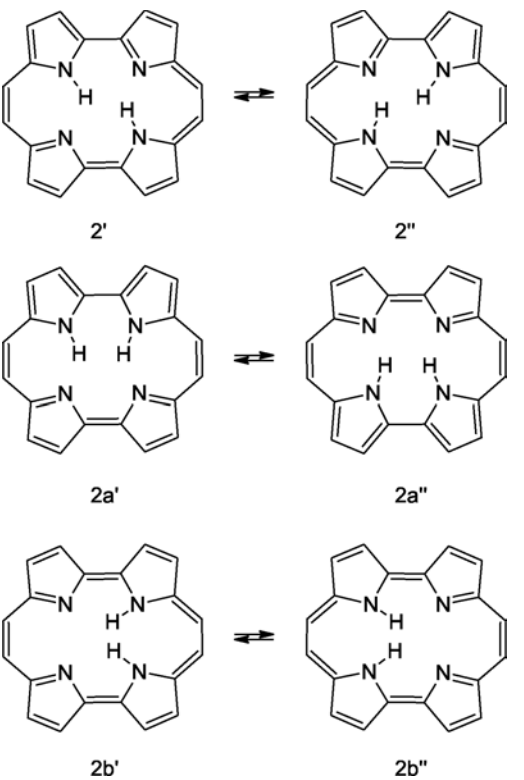

Figure 8. *Trans* and *cis,* pairwise–degenerate tautomers of porphycene.

possible only for one out of three different species (**4c** in Figure 9). The same situation arises for isoporphycene (Figure 10) and [18]porphyrin-(4.0.0.0) **8** (Figure 11). For [18]porphyrin-(2.2.0.0) **6**, two nonequivalent *trans* tautomers and two pairs of degenerate *cis* forms are possible (Figure 12). No degeneracies are expected for hemiporphycene (Figure 13) and [18]porphyrin-(2.2.0.0) **7** (Figure 14). These molecules can assume two *trans* and four *cis* forms, each corresponding to a different energy. Considerations of *E/Z* isomerism and nonplanarity show a

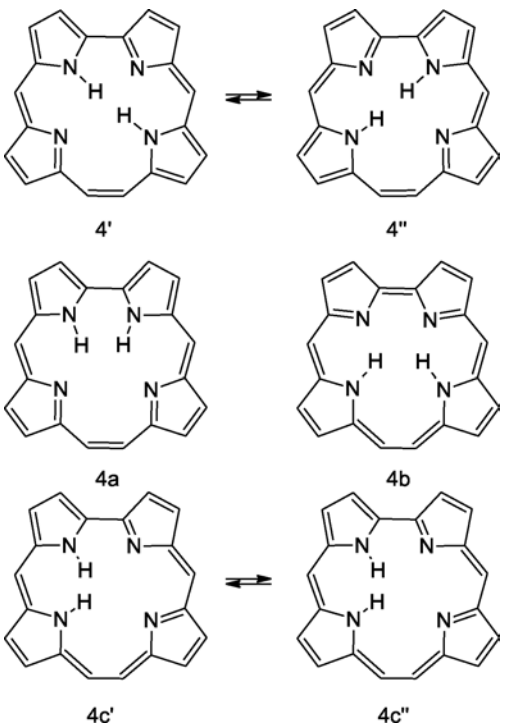

Figure 9. *Trans* and *cis* tautomeric forms of corrphycene.

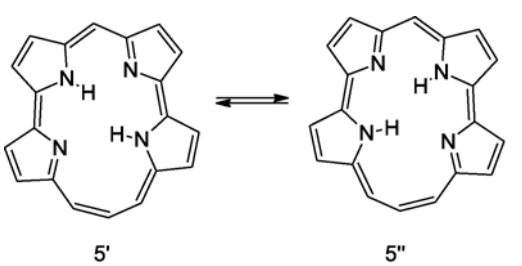

Figure 10. *Trans* and *cis* tautomeric forms of isoporphycene in the (*Z*)-configuration.

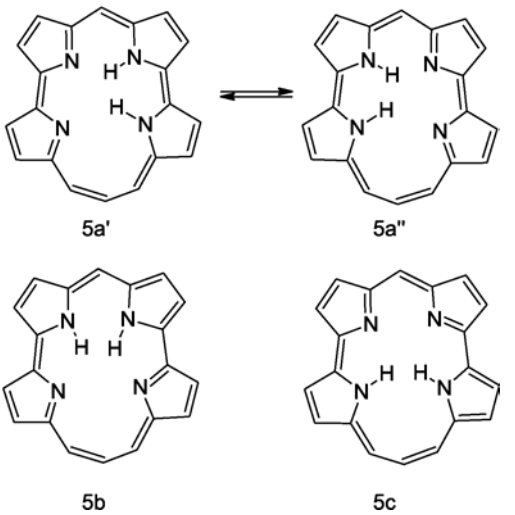

Figure 10. (*Continued*)

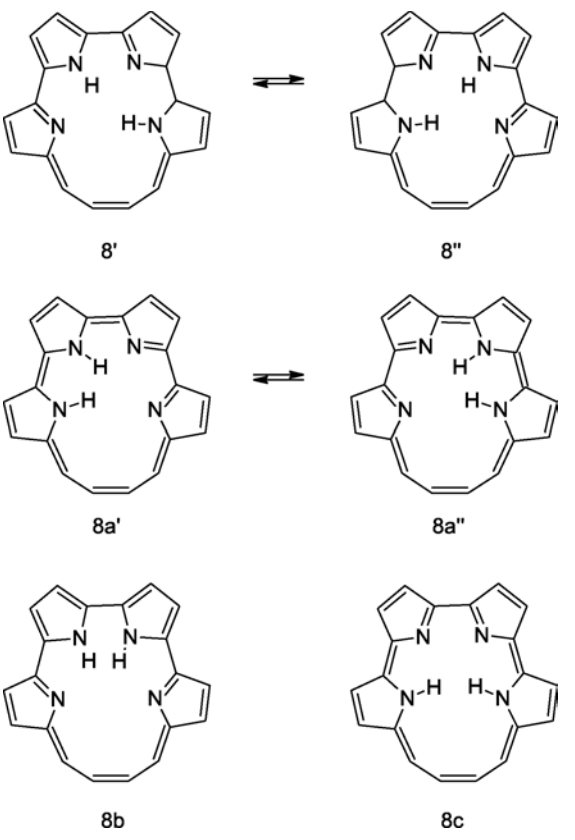

Figure 11. *Trans* and *cis* tautomeric forms of [18]porphyrin-(4.0.0.0).

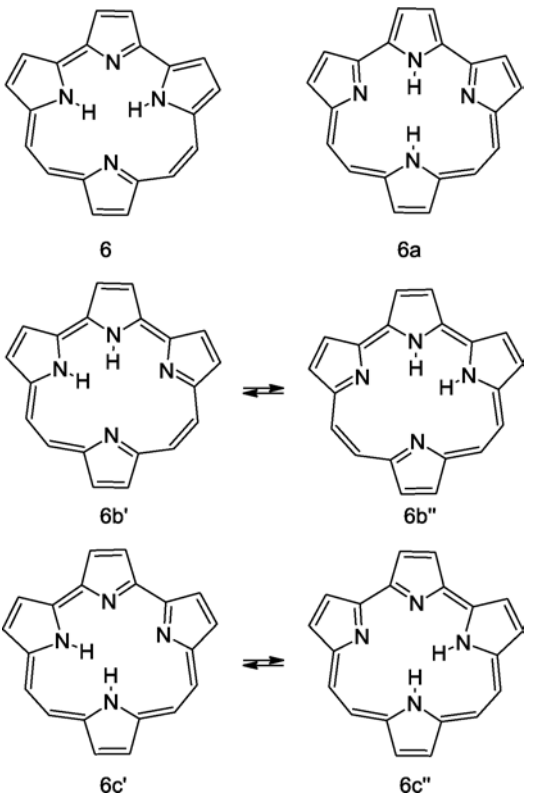

Figure 12. *Trans* and *cis* tautomeric forms of [18]porphyrin-(2.2.0.0).

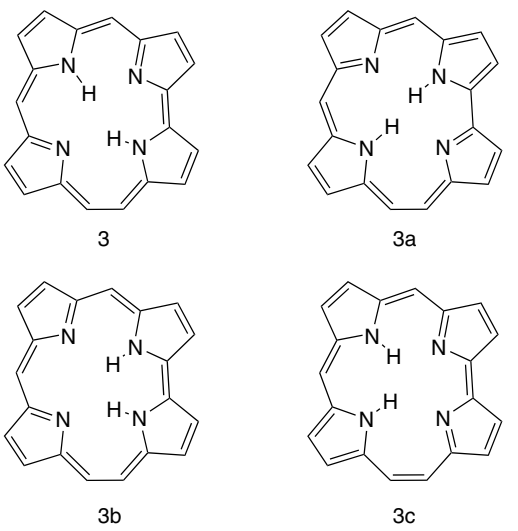

Figure 13. *Trans* and *cis* tautomeric forms of hemiporphycene.

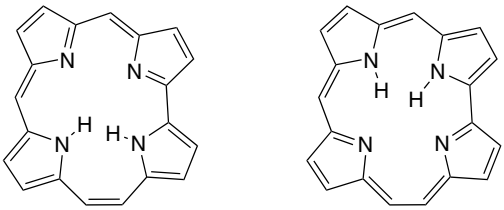

Figure 13. (*Continued*)

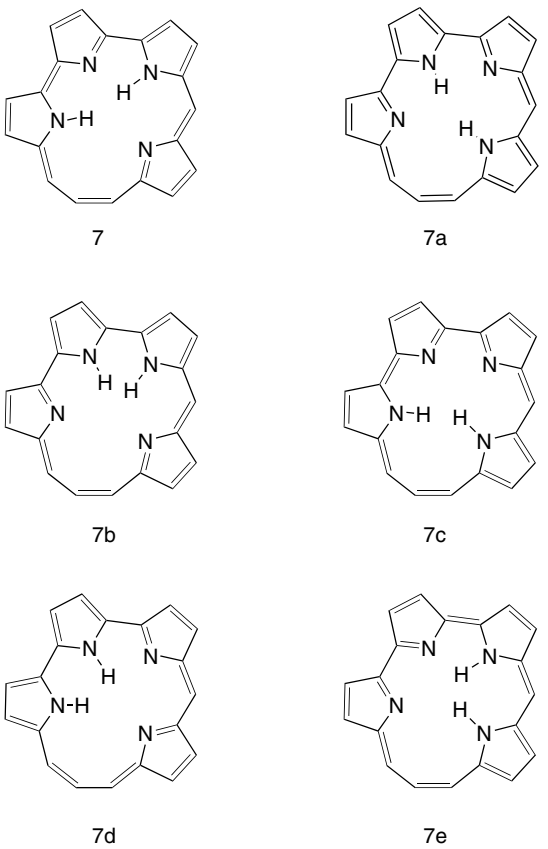

Figure 14. *Trans* and *cis* tautomeric forms of [18]porphyrin-(3.1.0.0).

possibility of lifting the degeneracy and/or increasing the number of tautomeric forms.[41,97,98] Moreover, the relative energies of the *E* and *Z* forms may be changed by substitution. This was demonstrated for free-base isoporphycene.[98] DFT calculations show that the *Z* isomer has lower energy than the *E* form in the parent

compound, but in the octaethylderivatives (analogous to **23a** and **23b**) the ordering is reversed.

III. Spectroscopy

A. Electronic Absorption Spectra

Free-base porphyrins reveal a characteristic electronic absorption pattern.[99] In solutions at room temperature, at least four bands of moderate intensity are observed in the region between 660 and 500 nm. The relative intensities of the bands vary for different derivatives. This observation led to empirical classification into three types: etio, rhodo, phyllo.[100] These so-called Q bands are followed by a very strong transition around 400 nm, referred to as a Soret band. Both Q and Soret bands correspond to two π–π^* electronic transitions. In the parent free-base porphyrin, D_{2h} symmetry dictates that the transition moments in both Q and Soret pairs be orthogonal and lie in the molecular plane. The notation Q_x and Q_y was introduced, reflecting the polarization along the NH–HN direction (Q_x) or perpendicular to it (Q_y). In most cases, the Q_x transitions are observed at lower energies than Q_y. A characteristic is a strong vibronic component lying between the origins of Q_x and Q_y bands. Quite often, its intensity is higher than that of the 0–0 transition of Q_x.

In lower symmetry porphyrins, the Q_x/Q_y notation is no longer strictly correct. It can be replaced by using Q_1 and Q_2, where the indices indicate the energetic order. A more general notation, based on the perimeter model,[99,101–107] refers to the Q transitions as L_1 and L_2, whereas the transitions responsible for the Soret band are denoted as B_1 and B_2.

Qualitatively, the same absorption pattern is preserved in porphyrin isomers, although quantitative differences are substantial and vary for different species. The largest changes are observed between porphyrin and porphycene, particularly in the Q region. Comparison between the electronic absorption spectra of porphyrin **1** and porphycene **2** (Figure 15) shows that the Q (L) bands in porphycene are shifted to the red and the Soret (B) transitions to the blue with respect to their locations in porphyrin. Most spectacular is the increase in Q band intensity, by approximately an order of magnitude, and the reversal of the intensity pattern of vibronic structure: the origins of L transitions, weak in **1**, become dominant (L_1) or quite strong (L_2) in **2**. The intensities of the B bands are similar in the two isomers, the higher maximum value of the absorption coefficient in **1** being compensated for by a greater bandwidth in **2**.

The positions of the L and B transitions and their intensities are presented for selected derivatives of **1**–**5** in Tables 4–6. These values demonstrate that porphyrin

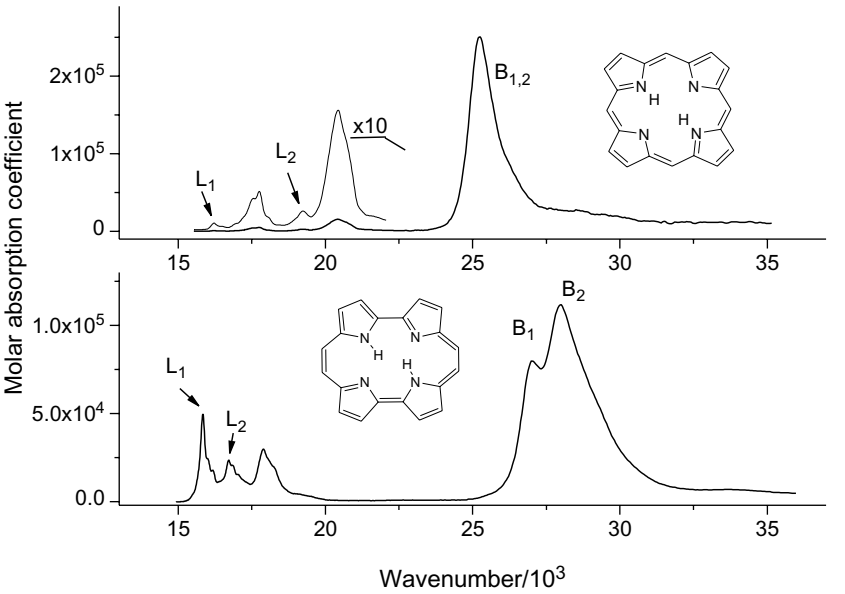

Figure 15. Room temperature electronic absorption spectra of porphyrin **1** in toluene (top) and porphycene **2** in *n*-hexane (bottom), with indicated positions of the Q (L) and Soret (B) transitions.

Table 4. Electronic absorption data for free-base porphyrin and selected derivatives. Band positions are in nm; in parentheses are decadic molar absorption coefficients (ε/1000).

	L_1	L_2	Soret Bands	Solvent	Reference
1	627.5	511.5	372.5	vapor	208
	613.5	518	393.5	CH_2Cl_2	208
	613.4	519.0	390.6	ethanol	208
	617.3	520.8	396.5	benzene	208
			396.5 (264)	benzene	209
	617 (0.84)	520 (2.4)	396.5 (250)	toluene	this work
	612.75	502.91		supersonic jet	191
	612.3			*n*-octane matrix	210
	625.05	531.25		anthracene	211
	612.6[a]	504.9[a]		Ne matrix	95
	613.2[a]	510.2[a]		Ar matrix	95
	613.1[a]	512.2[a]		Kr matrix	95
	614.6/611.1[b]	514.6/516.0[b]		Xe matrix	95
OEPr **24**	622 (5.8)	532 (10.8)	400 (159)	benzene	212
25	657 (5.0)	553 (6.3)	416 (316)	CH_2Cl_2	213
TPP **26**	648 (5.3)	548 (7.8)	418 (415.7)	benzene	214
27	628 (2.0)	535 (3.8)	405 (331)	DMF	215
28	584 (12.6)	516 (26.9)	414 (263)	CH_2Cl_2 +1%NEt_3	89

[a]Average over several sites. [b]Two major sites.

Table 5. Electronic absorption data for porphycene and selected free-base derivatives. Band positions are in nm; in parentheses are decadic molar absorption coefficients (ε/1000).

	L_1	L_2	Soret Bands	Solvent	Reference
2	630 (51.9)	596 (30.4)	370 (139) 358 (107)	benzene	4
	618.4/618.2[a]			supersonic jet	22
	619.35			helium droplets	40
	624.5	591.9		N_2 matrix	156
	625.6	593.0		Ar matrix	156
	627.7	595.9		Kr matrix	156
	632.1	600.3		Xe matrix	156
10	633 (48.2)	600 (34.1)	381 (100.2) 370 (142)	CH_2Cl_2	70
	633 (46.4)	601 (33.3)	371(142)	CH_2Cl_2	75, 216
	631.5 (53.45)			ethanol	156
	628.7	595.8		nitrogen matrix	
45	633/644[b]	603	384, 369.5		23
30	632 (48.5)	601 (35.3)	384/370 (96.3/147)	CH_2Cl_2	217
16	641 (43.8)	607 (28.4)	371 (125)	CH_2Cl_2	75
17	649 (47.3)	613 (29)	372 (132)	CH_2Cl_2	75
18	665 (34.6)	625 (23.8)	375 (113)	CH_2Cl_2	75
19	684 (29.0)	640 (20.6)	387 (104) 379 (107)	CH_2Cl_2	76 75
42	659 (49.9)	628 (45.8)	378 (117.8)	toluene	111
43	656 (54)	627 (56)	387 (121) 376 (151)	toluene	112
44	657 (56)	631 (69)	400 (133)	toluene	112
46	763 (21)	709 (49)	412 (84) 375 (93)	toluene	112
37	656 (39)	619 (25)	376 (107)	CH_2Cl_2	109
38	654 (34.8)	619 (23.6)	375 (103)	CH_2Cl_2	109
33	643	608	380, 369	methanol	108
34–35[c]	653	616	381, 375	methanol	108
36	688	650	385sh, 372	methanol	108
	686	643	387, 371	water	108
29	657 (42.5)		386 (63.8) 369 (141)	CH_2Cl_2	71
39	658 (50.1)		386 (63.1) 372 (170)	CH_2Cl_2	71
11	659 (46)		373 (161.1)	CH_2Cl_2	71, 110
	667	641	394, 377	polyethylene	
40	646	616	384 367	acetonitrile	this work
12	653 (42.5)	625 (31.4)[d]	382 (152.8)	CH_2Cl_2	72
41	655 (38.3)	627 (27.9)[d]	383 (123)	CH_2Cl_2	72
15	665 (30.7)	625 (19.7)	385 (144)	CH_2Cl_2	74

(*Continued*)

Table 5. (*Continued*)

	L_1	L_2	Soret Bands	Solvent	Reference
14	657 (30)	617 (18.4)	382 (144.2)	CH_2Cl_2	74
31	720 (43)	670 (22)	376 (89)	CH_2Cl_2	90
13	595 (29.9)	575[e] (23.8)	402 (74.4) 382 (51.7) 360 (71.4)	benzene	73
47	686 (77)	645 (59)	373 (131)	CH_2Cl_2	113
48	760 (23.7)	698 (38.6)	425 (33.1) 388 (34.4)	toluene	114
49	758 (17)	697 (28)	419 (33) 388 (37)	toluene	115

[a]Tunneling doublet splitting. [b]Two tautomeric forms. [c]The data reported for the mixture of two isomers. [d]Possibly a vibronic component, not the 0–0 origin of L_2. [e]Tentative assignment.

Table 6. Electronic absorption data for selected free-base derivatives of hemiporphycene, corrphycene, and isoporphycene. Band positions are in nm; in parentheses are decadic molar absorption coefficients (ε/1000).

	L_1	L_2	Soret Bands	Solvent	Reference
			Hemiporphycene Derivatives		
OEHPc **21**	632 (10.8)	583 (9)	405 (153.7)	CH_2Cl_2	7
	629 (9.7)	581 (7.6)	418[a] 403[a] (144.7)	acetonitrile	117
22	637 (10.7)	591 (10.4)	419 (190.5)	CH_2Cl_2	80
89	636 (4.8)	588 (4.15)	414 (76)	CH_2Cl_2	6
			Corrphycene Derivatives		
OECp **20**	630 (2.6)	541 (4.0)	414 (151.9)	CH_2Cl_2	9
	629 (2.7)	541 (4.5)	429[a] 412[a] (111.6)	acetonitrile	118
90	632 (1.9)	540 (3.8)	415 (139.4)	benzene	9
91	632 (2)	545sh (2.5)	408 (82.8)	CH_2Cl_2	119
	632 (1)	546sh (1.7)	408 (56)	DMSO	
92	628 (1.05)	550sh (2.7)	411 (93)	CH_2Cl_2	119
	629 (0.9)	550sh (3.6)	411 (88.2)	DMSO	
93	628 (2.5)	551 (5.75)	416 (102)	CH_2Cl_2	120
			Isoporphycene Derivatives		
OEIPc **94**	672 (6.55)	615[b] (4.7) 558[b] (5.7)	434 (117.2)	CH_2Cl_2	10

[a]Peaks separated in MCD spectra, not in absorption. [b]The origin of L_2 has not yet been assigned.

and porphycene represent the extreme cases with regard to the L band intensity. This is further exemplified in Figure 16, where the spectra of four octaethyl derivatives of **1**–**4** are compared. As in the case of the unsubstituted isomers, the largest intensity increase in the Q region is observed for OEPc **15**. The octaethylcorrphycene

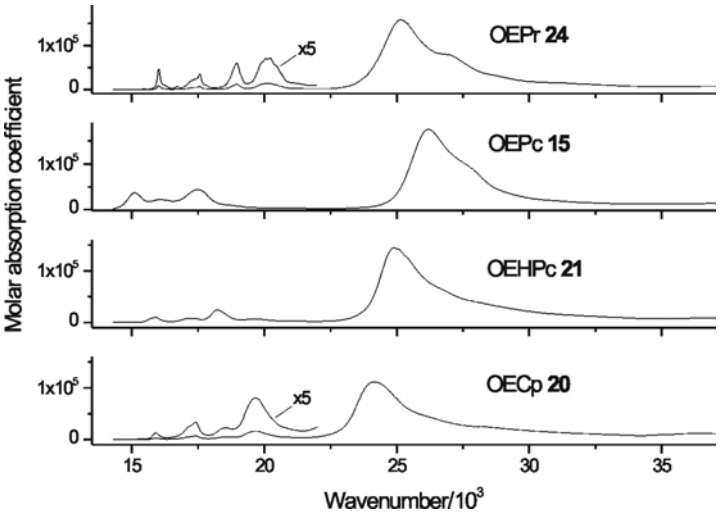

Figure 16. Room temperature absorption spectra for octaethyl derivatives of **1**–**4**, recorded in *n*-hexane solutions.

spectrum resembles that of OEPr **24**, whereas the absorption of OEHPc **21** in the Q region is significantly more intense, but still much less so than in OEPc. This behavior can be readily explained using a perimeter model approach, as presented in Section III.B.

1. *Absorption Spectra of Porphycenes*

The influence of alkyl substitution of porphycene on the electronic absorption spectra is strongly position-dependent, as shown in Figure 17. Very small changes are observed for β-substitution (2,7,12,17). Such an effect could be expected, given that this type of substitution does not lead to considerable geometric alteration. In contrast, adding four alkyl groups in the β' positions (3,6,13,16) induces a significant red shift of both L transitions. The effect is significantly larger for octaethylporphycene **15** than for etioporphycene **14** and 2,7,12,17-tetra-*n*-propyl-3,6,13,16-tetramethylporphycene **32**. This finding suggests that the shift may be related to deviation from planarity, smaller for the two derivatives with methyl substituents. In a series of β'-brominated 2,7,12,17-tetra-*n*-propylporphycenes,[75] planar mono- and dibromoderivatives **16**–**17** reveal small red shifts. In the triply brominated compound **18** both L_1 and L_2 exhibit the same shifts as OEPc **15**, whereas in the tetrabromo derivative **19** the shifts become much larger (see Table 5). The latter is definitely nonplanar, but **18** is not,[75] showing that both nonplanarity and electronic effects may contribute to the shift. This could explain exceptionally large shifts

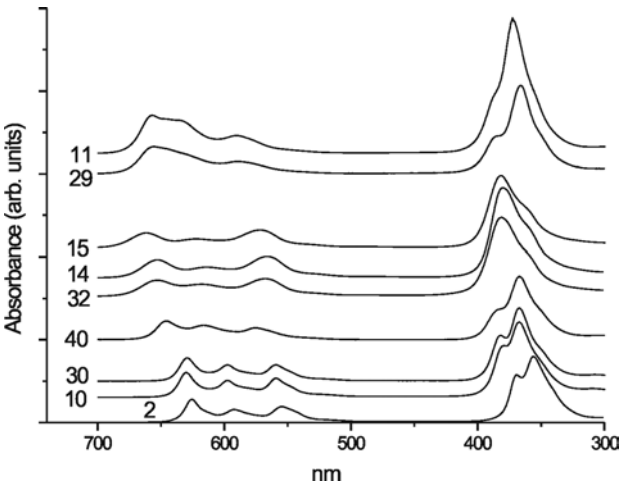

Figure 17. Room temperature absorption spectra in acetonitrile. From bottom to top: porphycene **2**, 2,7,12,17-tetra-*n*-propylporphycene **10**, 2,7,12,17-tetra-*tert*-butylporphycene **30**, 2,7-di-*tert*-butyl-10,19-dimethylporphycene **40**, 2,7,12,17-tetra-*n*-propyl-3,6,13,16-tetramethylporphycene **32**, 2,7,12,17-tetraethyl-3,6,13,16-tetramethylporphycene **14** (etioporphycene), 2,3,6,7,12,13,16,17-octaethylporphycene **15** (OEPc), 9,10,19,20-tetramethylporphycene **29**, 9,10,19,20-tetra-*n*-propylporphycene **11**.

observed for highly nonplanar 2,7,12,17-tetraethyl-3,6,13,16-tetrakis(trifluoromethyl)porphycene **31**.[90] A similar behavior is observed for β'-sulfonated derivatives **33**–**36**.[108] The shifts in the triply sulfonated product **36** are much larger than those observed for singly (**33**) and doubly sulfonated species **34**–**35**. Two sulfonamide derivatives **37**–**38**[109] reveal shifts similar to those of **34** and **35**.

Octaalkyl β,β'-substitution introduces an interesting change in the intensity pattern in the Soret region. As in the parent porphycene and β-substituted derivatives, two features are observed, but with reverse intensities: The lower-energy band, less intense in the parent compound, now becomes dominant.

The red shift of Q bands is also observed for *meso*-substitution (9,10,19,20). In this case, the L_2 transition is stabilized to a larger degree than L_1, which leads to their

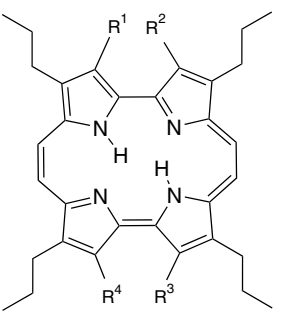

	R^1	R^2	R^3	R^4
33	SO_3Na	H	H	H
34	SO_3Na	H	H	SO_3Na
35	SO_3Na	H	SO_3Na	H
36	SO_3Na	SO_3Na	SO_3Na	H

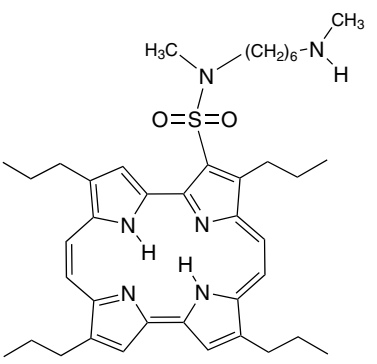

37

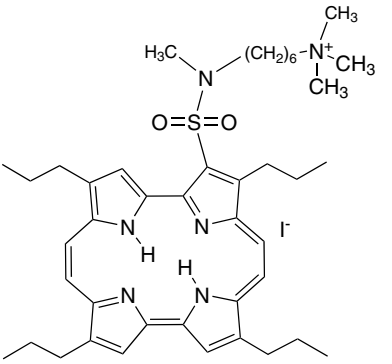

38

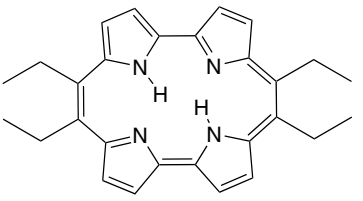

39

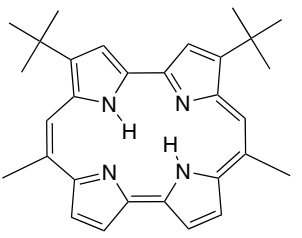

40

near-degeneracy in 9,10,19,20-tetraalkylporphycenes. The two transitions could be resolved by linear dichroism[110] and MCD[19] measurements. Practically the same spectra are observed for porphycene substituted by four methyl (**29**), ethyl (**39**), and *n*-propyl groups (**11**).[71] In contrast to the behavior of octaalkylporphycenes, the intensity pattern in the Soret region resembles that of parent or β-alkylporphycenes.

An interesting case is provided by unsymmetrically substituted porphycene: 2,7-di-*tert*-butyl-10,19-dimethylporphycene (**40**). For this molecule, the shifts of L_1 and L_2 are similar, and the shape of the spectrum in the low-energy region resembles the parent porphycene much more than those of the *meso*-tetraalkyl-substituted compounds (Figure 17).

The absorption spectra of *meso*-aryl-substituted derivatives resemble those of the alkyl-substituted compounds, as demonstrated by the tetraphenyl (**12**) and tetratolyl (**41**) derivatives.[72] This is in line with similar geometries, in particular practically the

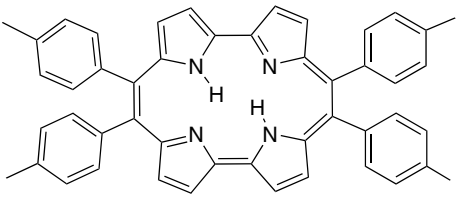

41

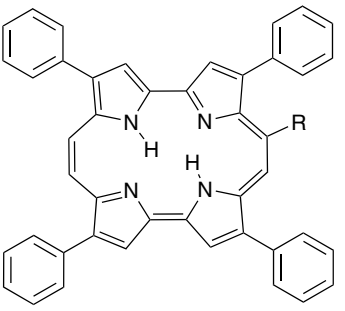

R= H **42**; OAc **43**; NO_2 **44**; NH_2 **46**

same inner cavity dimensions. On the other hand, substitution by phenyl at the β positions leads to significant changes in the absorption. 2,7,12,17-Tetraphenylporphycene (TPPo, **42**)[111] shows significant red shifts of both L_1 and L_2 with respect to the parent porphycene (26 and 29 nm, corresponding to 699 and 855 cm^{-1}, respectively). Substitution of **42** by an acetoxy or nitro group in position 9, leading to **43**–**44**,[112] does not alter the spectrum significantly. Similar behavior was observed for 2,7,12,17-tetra-*n*-propylporphycene and its 9-acetoxy derivative **45**.[23] On the other hand, huge shifts of both Q bands are observed for 9-amino-2,7,12,17-tetraphenylporphycene **46**.[112]

Another way to induce strong shifts of both low-energy transitions is the replacement of β' CH groups by nitrogen atoms, leading to imidacene **47**.[113] Further red shifts are observed when this is combined with aryl substitutions in the β positions, as observed for derivatives **48**[114] and **49**.[115] Interestingly, for the last two cases the red shift is accompanied by a significant decrease in the intensity of both transitions. An even larger decrease in intensity is observed for the Soret bands, so that the absorption spectra of **48** look rather atypical, displaying similar intensities in the Q and Soret regions.[114]

In a review of photophysical properties of porphycenes,[68] Braslavsky and coworkers have reported transition energies for the lowest excited singlet state along with the values of the corresponding absorption coefficients for 38 derivatives (**10**, **45**, **50**–**85**). Some of these compounds (**60**, **78**–**79**, **81**, **85**) and three others (**86**–**88**) have been studied earlier by Richert and coworkers as photodynamic antitumor agents.[16] These datasets and the values presented in Tables 4–6 demonstrate remarkable

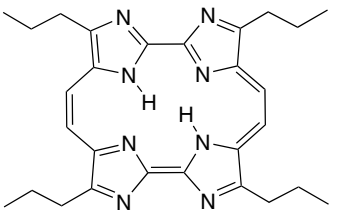

47

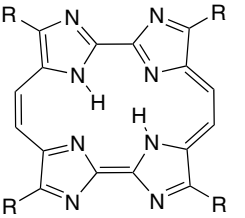

48 R = *p*-BuPh

49 R = *p*-$(CH_2O)(CH_2CH_2O)_3CH_2Ph$

49a R = o-CH_3OPh

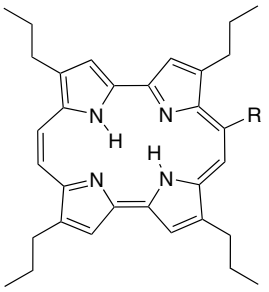

	R
50	OH
51	OCH_3
52	$OCH_2(C_6H_4)CO_2H$
45	$OCOCH_3$
53	$OCO(CH_2)_3CO_2C(CH_3)_3$
54	$OCOCH_2NHCO_2C(CH_3)_3$
55	$OCO(CH_2)_3NHCO_2C(CH_3)_3$

	R
56	NH_2
57	$NHCOCH_3$
58	$NHCO(CH_2)_3CO_2H$
59	$NHCO(CH_2)_3CO_2CH_3$

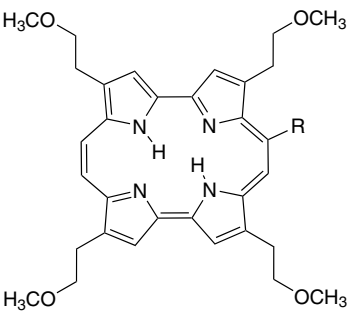

	R
60	H
61	OH
62	OCH_3
63	$O(CH_2)_5CH_3$
64	$OCOCH_3$
65	$OCO(CH_2)_4CH_3$
66	$OCO(CH_2)_7CH_3$
67	$OCO(CH_2)_{16}CH_3$

	R
68	$OCOCH_2NHCO_2C(CH_3)_3$
69	$OCO(C_6H_4)$carotenyl
70	NH_2
71	$NHCOCH_3$
72	$NHCO(CH_2)_3CO_2H$
73	$NHCO(CH_2)_3CO_2CH_3$
74	$N[CO(CH_2)_3CO]$

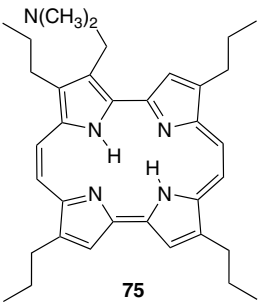

75

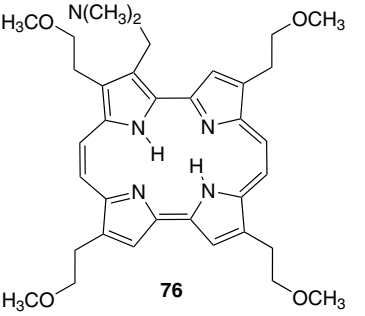

76

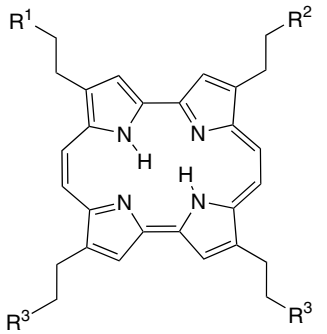

	R^1	R^2	R^3
77	OH	CH_3	CH_3
78	OH	OCH_3	OCH_3
79	OH	OH	CH_3
80	OCH_3	CH_3	CH_3
81	OCH_3	OCH_3	CH_3
82	OC_2H_5	OC_2H_5	OC_2H_5

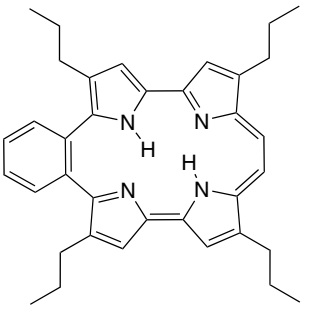

83

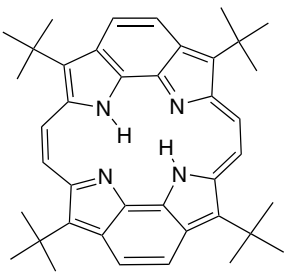

84

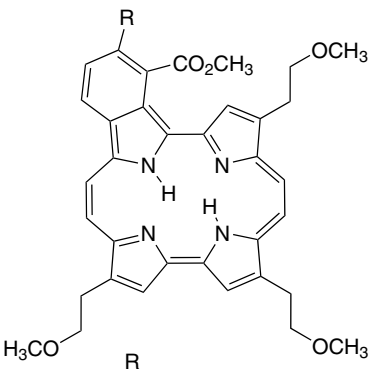

R

85 CO_2H

86 CO_2CH_3

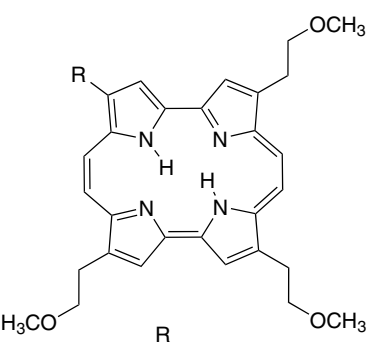

R

87 CH_2CH_2Br

88 $CHCH_2$

stability of the intensity of the S_0–S_1 transition and its high oscillator strength compared with porphyrin and other constitutional isomers. The reason for the insensitivity to the type and position of substituents is the "negative-hard" character of the porphycene chromophore, described in Section III.B. On the other hand, the S_0–S_1

transition energy may be tuned over a large range. These properties make porphycenes very attractive for applications, particularly in photodynamic therapy.

2. *Absorption Spectra of Hemiporphycene, Corrphycene, and Isoporphycene Derivatives*

Absorption spectra of free-base hemiporphycene derivatives have been reported in only a few papers.[6,7,116,117] The data available for OEHPc **21**, 5-iodo-6,11,16-triphenylhemiporphycene **22**[80] and 9-carbethoxy-10,15,20-triphenylhemiporphycene **89**[6] (Figure 16 and Table 6) reveal similar spectral patterns for the three compounds. The Q bands are red-shifted with respect to those of octaethylporphyrin, the shift of Q_2 being larger than that of Q_1. Both shifts are significantly smaller than in octaethylporphycene. The spectra in the Soret region are similar to those of octaethylporphyrin. The values of absorption coefficients are similar for OEPr and OEHPc in the Soret region. In the Q region, hemiporphycenes definitely absorb more strongly. Interestingly, the absorption of **89** is about twice as weak as that of **21** for both the Q and Soret band regions.

Temperature dependence studies have shown that the absorption of **21** in 3-methylpentane is due to both possible *trans* tautomers, analogs of **3** and **3a** in Figure 13.[116] The enthalpy of tautomerization was determined to be 0.65 kcal/mol, in agreement with computational predictions (see Table 3).

The absorption spectra of octaethylhemicorrphycene **20**,[9,118] etiocorrphycene **90**,[9] 2,3,6,7,11,12,17,18-octamethylcorrphycene **91**,[119] 2,3,6,7,11,18-hexamethyl-12,17-bis-(2-methoxycarbonylethyl)corrphycene **92**,[119] and 2,3,6,7,11,18-hexamethyl-12,17-bis-(2-ethoxycarbonyl)corrphycene **93**[120] are all similar and, of all isomers, the closest to the spectra of porphyrins (Figure 16, Table 6), with regard to both

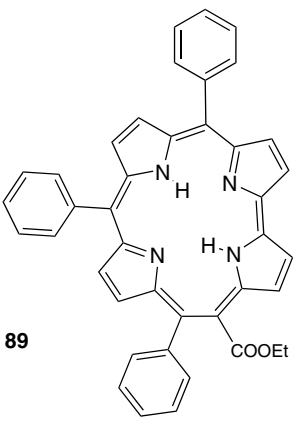

89

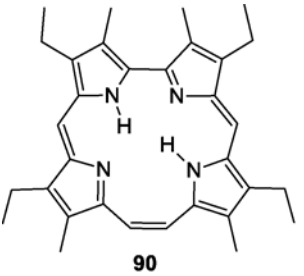

90

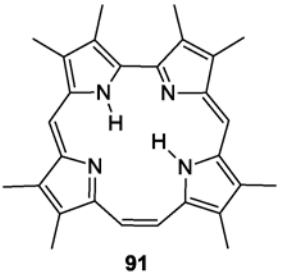

91

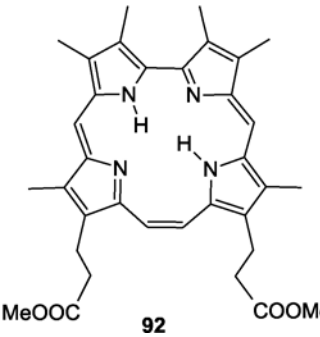

92

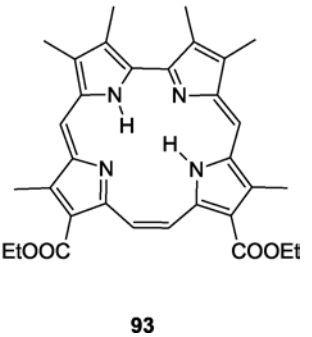

93

spectral positions and intensities. Corrphycene derivatives reveal small and similar red shifts of Q_1, Q_2 and Soret bands with respect to OEPr. The intensities in the Soret region are similar or slightly smaller than in OEPr, whereas those of Q bands are definitely lower. In **90**, the 0–0 transition is very weak, and similar in intensity to that in parent porphyrin. Another similarity is the domination of vibronic peaks over purely electronic 0–0 transition, for both Q_1 and Q_2.

Derivatives of isoporphycene are the least investigated of all the isomers. The data for octaethylisoporphycene (OEIPc, **94**)[10] reveal a spectrum which is strongly red-shifted with respect to that of OEPr. The shifts of both Q bands are similar to those observed for OEPc, but the intensities are definitely smaller, resembling

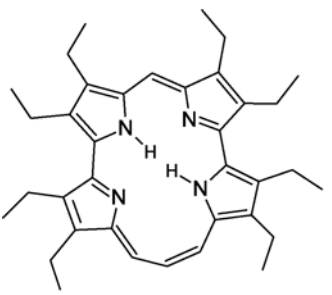

94a

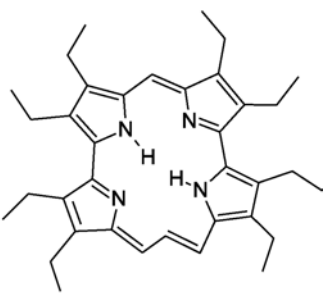

94b

those in hemiporphycene derivatives. The wavelength maximum of the Soret band exhibits the largest shift among all isomers.

It was demonstrated that the *E* (**94b**) and *Z* (**94a**) forms of OEIPc are both present in 3-methylpentane solutions, the *E* isomers being dominant.[116] Using low-temperature fluorescence spectroscopy, it was possible to obtain excitation spectra of both forms; somewhat surprisingly, they turned out to be very similar.

B. Perimeter Model Applied for the Elucidation of Absorption and Magnetic Circular Dichroism Spectra

The electronic absorption spectra of porphyrins exhibit a great sensitivity to structural perturbations, such as substitution, metal complexation, reduction in one or more rings, or fusion of aromatic rings onto the basic skeleton. Still, it is possible to interpret the spectra of diverse porphyrins on the basis of a simple model, developed by Gouterman and coworkers.[99,121,122] In this approach the Q (L) and Soret (B) transitions are described by taking into account the interactions between the four singly excited electron configurations, obtained by promoting an electron from one of the two highest occupied π molecular orbitals (HOMOs) into one of the lowest unoccupied orbitals (LUMOs).

A closely related methodology, based on a perimeter model, was proposed by Michl[104–107] in order to understand absorption and, in particular, magnetic circular dichroism (MCD) spectra of $4N + 2$ π electron aromatic compounds. The perimeter model has been now successfully applied to several hundred compounds, including many porphyrin derivatives.[107,123–144]

Figure 18 presents the absorption and MCD spectra of the octaethyl derivatives of three porphyrin isomers: OEPc **15**, OEHPc **21**, and OECp **20**. The differences in the MCD pattern are dramatic. For OEPc, the MCD intensity for the Q transitions is higher than in the Soret range. In the hemiporphycene derivative, the intensities are almost equal in the two regions. For OECp, larger intensity is observed for the Soret (B) bands; thus, only in this case does the MCD spectrum follow the pattern of the absorption intensity. The MCD signals of both L bands of OECp are extremely weak for the 0–0 transitions. Finally, their signs are opposite to those observed for porphycene and hemiporphycene derivatives. It should be recalled that the sign of the Faraday *B* term is negative for a positive MCD signal, and positive for a negative MCD signal.

These huge differences can readily be explained by simple considerations based on a perimeter model. Using this approach, the compounds are formally derived from an ideal $C_{20}H_{20}^{++}$ perimeter, by distorting its shape and bridging with two NH and two N^- units (Figure 19). This perturbation shifts the orbital energies of the ideal perimeter by an amount which is dictated by the position of the

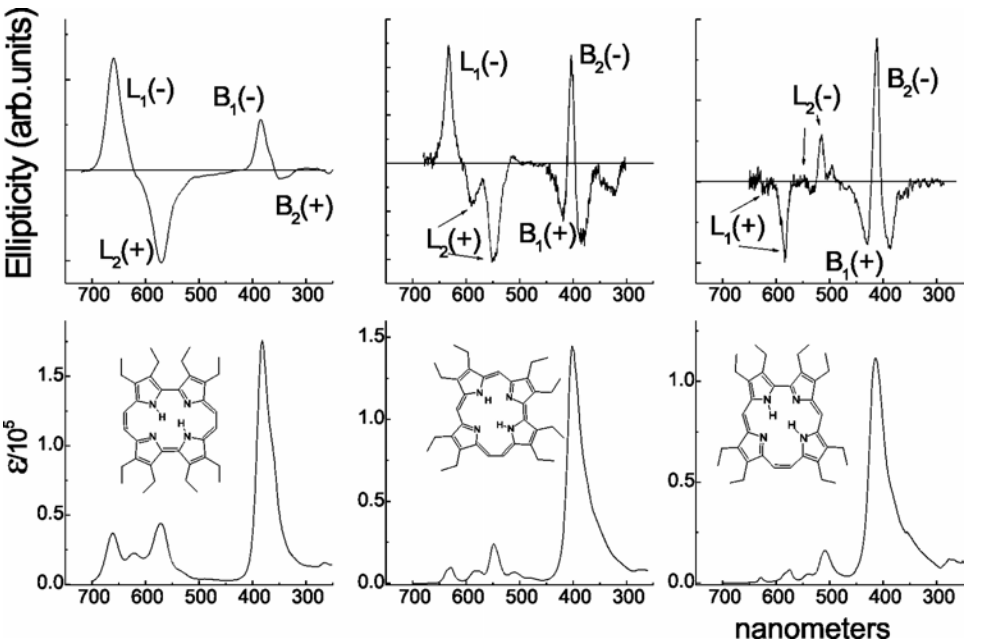

Figure 18. Absorption (bottom) and MCD (top) spectra of OEPc **15** (left), OEHPc **21** (middle), and OECp **20** (right), recorded in aconitrile at 293 K. The location of L and B transitions is indicated, with the sign of a corresponding *B* term.

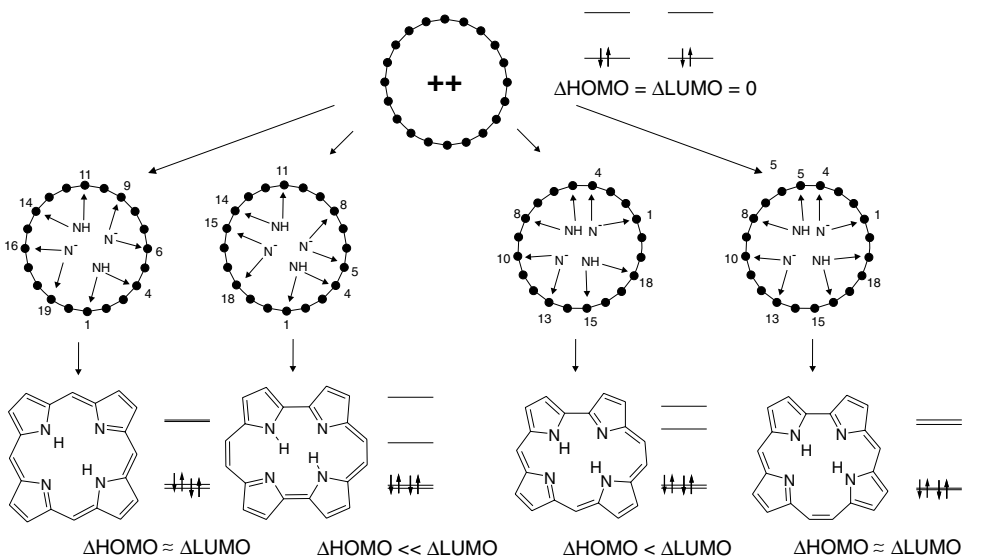

Figure 19. Derivation of porphyrin, porphycene, hemiporphycene, and corrphycene from the $C_{20}H_{20}^{++}$ perimeter, with the resulting HOMO and LUMO splittings.

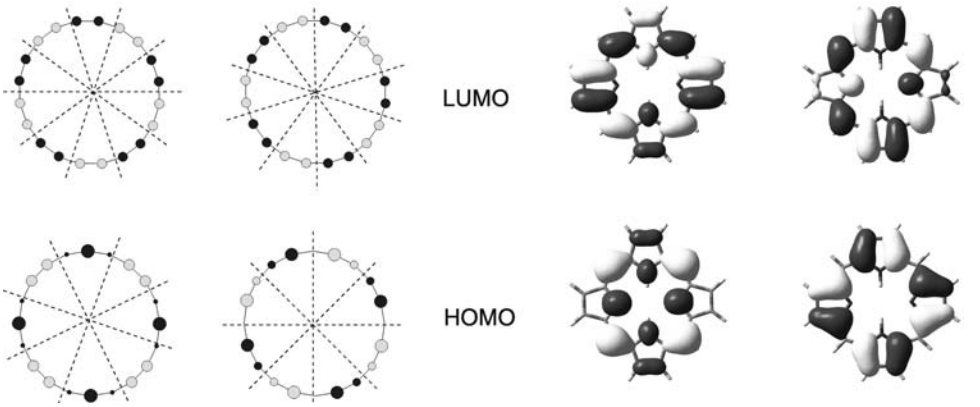

Figure 20. Two highest occupied and two lowest unoccupied orbitals of the unperturbed $C_{20}H_{20}^{++}$ perimeter. Right: The HOMO and LUMO pair calculated for porphyrin.

substituent and the orbital shape. No change in energy is expected if a bridging atom lies in the orbital nodal plane, or if the attachment points lie on nodes. Otherwise, the orbital energy shift should be proportional to the algebraic sum of LCAO coefficients in the bridging positions. It is therefore easy to predict relative orbital energy changes just on the basis of nodal properties. Figure 20 shows the HOMOs and LUMOs of an ideal perimeter compared with the orbitals calculated for porphyrin. The same pattern of nodal planes is evident. The HOMO and LUMO pairs are degenerate in the parent perimeter, but they need not be degenerate after the perimeter has experienced a perturbation leading to a particular molecule. The analysis of the shape of ideal perimeter orbitals, given by symmetry, permits predicting the orbital splittings in porphyrin isomers. In general, HOMOs are less affected than the LUMO pair and no large splitting in the occupied pair is expected (ΔHOMO $\approx$ 0). With regard to LUMOs, they are shifted differently in different isomers. In porphyrin and corrphycene, two bridges raise the energy of one LUMO; the other two bridges, the energy of the other LUMO. Thus no splitting is expected (ΔLUMO $\approx$ 0). On the contrary, in porphycene all four bridges destabilize the energy of one LUMO component, not affecting the other. Hence, a large LUMO splitting is predicted. Hemiporphycene represents an intermediate case, with three bridges interacting with one LUMO component, and only one with the other LUMO. As a result, a moderate LUMO splitting is expected, definitely smaller than for porphycene. The orbital splittings expected for the four isomers are presented in Figure 19.

The values of ΔHOMO and ΔLUMO are the crucial parameters in the perimeter model, since they are contained in the formulas for transition dipole strengths of all four states resulting from the interaction between singly excited

HOMO–LUMO configurations. ΔHOMO and ΔLUMO also enter into the equations for the Faraday terms *A*, *B*, and *C*, which determine the MCD intensity. For free-base porphyrin and isomers, only *B* terms are nonzero. They are expressed by formulas containing two contributions, μ^- and μ^+. The former are practically structure-independent and smaller than the latter, which are very sensitive to molecular structure. Various MCD sign patterns are expected, depending on the value of ΔHOMO and ΔLUMO: a +,–,+,– sequence of *B* term signs of L_1, L_2, B_1, and B_2 transitions is predicted for ΔHOMO > ΔLUMO, whereas the opposite sequence, –,+,–,+, should hold when ΔHOMO < ΔLUMO. Finally, when ΔHOMO = ΔLUMO, a +,+,+,– sequence is expected. However, the equality of ΔHOMO and ΔLUMO may easily be destroyed, even by a weak perturbation. Therefore, the molecules for which ΔHOMO ≈ ΔLUMO have been called "soft" chromophores, indicating that their MCD behavior can be easily changed. In contrast, in molecules for which ΔHOMO > ΔLUMO or ΔHOMO < ΔLUMO the MCD pattern is not easily influenced by perturbation. They have therefore been called "positive-hard" or "negative-hard" chromophores, depending on the sign of ΔHOMO–ΔLUMO.

According to the simple orbital analysis, porphycene, with ΔHOMO << ΔLUMO, should be a strongly negative-hard chromophore, with the negative/positive *B* term MCD pattern for L_1/L_2, not expected to change in different derivatives. Indeed, such a pattern has been observed for all porphycene derivatives studied so far (see Figure 18 as an example), as well as for doubly protonated and doubly deprotonated **2**.[19] The same pattern is expected and observed (Figure 18) for hemiporphycene and its derivatives. On the other hand, corrphycene, similarly to porphyrin, is predicted to be a soft chromophore (ΔHOMO ≈ ΔLUMO). For such a molecule, the MCD signal in the L_1/L_2 region can be extremely weak and dominated by effects not taken into account in the perimeter model, e.g. vibronic interaction. This indeed seems to be the case for OECp. On the other hand, the model predicts strong MCD intensity in the region of B transition, dominated by μ^- terms, with the +,– *B* term sequence for B_1, B_2, exactly as observed (Figure 18). The perimeter model also explains why the MCD intensity falls so drastically in the Soret region upon passing from corrphycene to hemiporphycene and porphycene. The reason is the interplay of μ^- and μ^+ contributions, which are of the opposite signs; the contribution of μ^+ increases with |ΔHOMO–ΔLUMO|, and thus from hemiporphycene to porphycene.

The perimeter model also allows understanding changes in the absorption intensity of the L with respect to the B transitions. The ratio of dipole strengths, D(L)/D(B), should grow, approximately, as $\Delta LUMO^2 - \Delta HOMO^2$. This relation immediately explains the increasing absorption intensity of the Q region in the order porphyrin ≈ corrphycene < hemiporphycene < porphycene. Similar behavior

has been observed for neutral, diprotonated, and doubly deprotonated forms of OEHPc: the prediction, based on theoretical arguments, that D(L)/D(B) should increase in the order dication, neutral molecule, dianion has been confirmed by experiment.[117]

The perimeter model has worked perfectly for hundreds of molecules, including numerous porphyrins. In fact, the predictions regarding the absorption and MCD patterns for all porphyrin isomers were made at the time when only porphycene was available.[5] The MCD experiments for corrphycene[118] and hemiporphycene[117] derivatives, which confirmed the theoretical predictions, were performed a decade later. Table 7 presents a comparison of predictions based on a perimeter model with the results of (i) simple PPP calculations performed in 1990 and (ii) more advanced calculations carried out for the purpose of this work. It is obvious that all the earlier predictions remain valid. The novel calculations improve somewhat the numerical agreement with perimeter model predictions, in particular when reproducing more accurately the soft character of the porphyrin chromophore. The theoretical predictions await experimental verification for four isomers, of which only one (isoporphycene) is available at present.

MCD is a very useful spectroscopic tool for detecting spectral transitions which overlap in the absorption. From the point of view of other applications, such as studies of tautomeric equilibria, solvent effects, etc., the interesting chromophores are those of a soft character, since they are able to respond strongly even to weak perturbations. Of the existing isomers, corrphycene and isoporphycene are obvious choices for such studies. The three isomers which remain to be synthesized should be strongly (**6**, **8**) or moderately (**7**) negative-hard chromophores. They

Table 7. Comparison of frontier orbital splittings predicted by the perimeter model with the results of calculations.

		Calculated			
		PPP[a]		B3LYP/6-31G**	
	Predicted	ΔHOMO[b]	ΔLUMO[b]	ΔHOMO	ΔLUMO
1	ΔHOMO ≈ ΔLUMO	0.82	0.07	0.14	0.02
2	ΔHOMO << ΔLUMO	0.37	1.89	0.06	1.33
3	ΔHOMO < ΔLUMO	0.29	0.69	0.04	0.56
4	ΔHOMO ≈ ΔLUMO	0.11	0.05	0.03	0.07
5	ΔHOMO ≈ ΔLUMO	0.04	0.30	0.03	0.11
6	ΔHOMO << ΔLUMO	0.37	1.88	0.02	1.29
7	ΔHOMO < ΔLUMO	0.20	0.56	0.07	0.66
8	ΔHOMO << ΔLUMO	0.32	1.74	0.14	1.10

[a]Ref. 5. [b]In eV.

should thus exhibit strong absorption in the Q region. In the case of **6** and **8**, similarity to porphycene is expected, whereas the spectral properties of isomer **7** should rather resemble those of hemiporphycene.

The validity of the four orbital and perimeter models has been confirmed for other members of the porphyrinoid family: smaragdyrin isomers,[145] tetraphenylsapphyrins,[146] and doubly protonated cyclohexa-, cyclohepta-, and cyclooctapyrroles.[147] It is reassuring that the predictions based on a simple model are confirmed by high-level *ab initio* computational studies. Nakatsuji and coworkers studied the excited state of porphycene, corrphycene, and porphycene using the symmetry-adapted cluster-configuration interaction method (SAC-CI),[148] concluding that "the differences in the Q-band absorptions among the isomers were clearly explained by the four-orbital model." A rare example of a molecule which requires treatment beyond the four-orbital model is rosarin, a nonaromatic hexapyrrolic expanded porphyrin. For a proper description of its molecular structure, six orbitals have to be taken into account: three occupied and three unoccupied.[149]

The perimeter model has been successfully extended to 4N electron[150–154] (and 4N ± 1 electron)[155] systems, opening up new possibilities for understanding spectral characteristics of large and diverse groups of compounds on the basis of a conceptually unifying treatment.

C. Low-Temperature Spectroscopy of Porphycene

In addition to measurements in solutions and glasses, porphycene and some of its derivatives have been investigated in the regime of molecular isolation, in supersonic jets,[22,28,30] nanohelium droplets,[40] or rare gas and nitrogen cryogenic matrices.[23,42,156–160] The jet and droplet studies are discussed in detail in Section V, since they greatly contribute to the understanding of mechanisms of intramolecular double hydrogen tunneling. The matrix isolation experiments allowed information to be obtained on molecular vibrations in the ground and lowest excited electronic states. Malsch and Hohlneicher compared IR, Raman, UV, and site-selective fluorescence and fluorescence excitation spectra recorded for the parent porphycene.[42] They observed that the rule of mutual exclusion was obeyed in the IR and Raman spectra. This suggests that the spectra are due to the *trans* tautomeric forms, because the *cis* tautomers do not have the inversion center. However, in the opinion of the authors this result does not provide a decisive proof, because the spectra calculated for the *cis* form reproduce the experiment equally well, indicating that the geometry and electronic structure of porphycene are not sensitive to tautomerization. Another surprising result was the absence of the NH stretching vibration in the IR spectrum, even though the calculations predicted that the corresponding band should be the most intense of all.

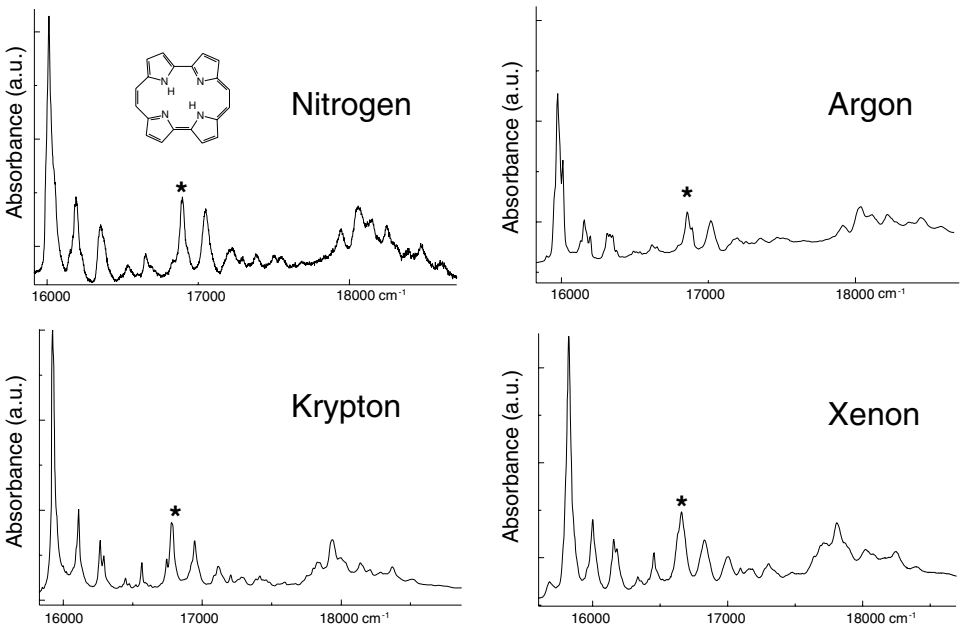

Figure 21. Absorption spectra of porphycene in different matrices at 15 K. The asterisks indicate the origin of the S_1–S_2 transition. (Modified with permission from Ref. 156.)

Comparison of shifts of vibronic bands in different rare gas and nitrogen matrices allowed determination of the electronic origins of the S_0–S_2 transition, normally mixed with the S_0–S_1 vibronic components.[156] The spectra of **2** in four different cryogenic matrices are shown in Figure 21. Comparison with the matrix spectra of parent porphyrin[95] reveals several important differences in the absorption patterns of the two isomers, which could not be so clearly observed in solution: (i) the origins of L_1 and L_2 are much closer to each other in **2** than in **1**; (ii) in contrast to the situation in **1**, where the L_2 transition is much stronger than L_1, the two transitions in **2** are of comparable intensity; actually the transition to the lowest excited singlet state seems to be slightly stronger; (iii) the 0–0 transitions are dominant for both L_1 and L_2 in porphycene, whereas for **1** they are weaker than the vibronic components.

These studies were followed by a series of papers which used molecular dynamics simulation of matrix deposition to analyze the site structure observed in the electronic and IR spectra of porphyrin, porphycene, and tetra-*tert*-butylporphycene embedded in argon and xenon matrices.[161–164] The structure of the main trapping sites has been identified. Interestingly, porphycene occupies the same main site in argon and xenon, whereas for porphyrin the situation is different: the same main site as for porphycene dominates for xenon matrices (Figure 22), but

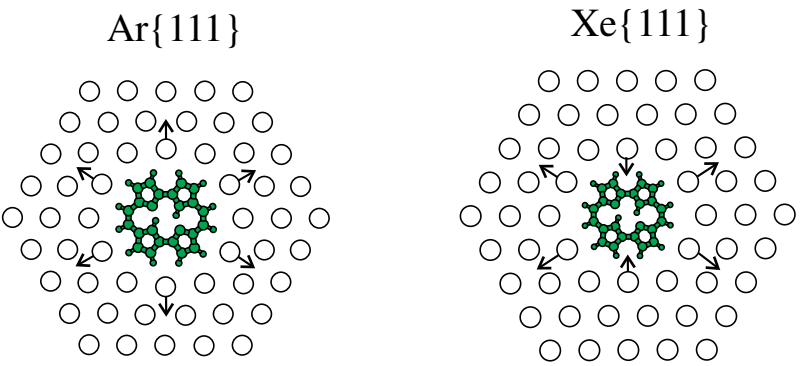

Figure 22. The structure of the main trapping site of porphycene in argon (left) and xenon (right) matrices. (Modified with permission from Ref. 161.)

in argon porphyrin occupies several different substitutional sites. These studies demonstrated that a seemingly minor structural difference in two similar molecules can lead to drastic changes in the absorption pattern of chromophores embedded in cryogenic matrices.

Another conspicuous difference between the electronic spectra of **1** and **2** was the doublet splitting of lines observed for the S_0–S_1 transition in the former, and the absence of splitting in the latter. This was explained by differences in the absolute directions of the transition moments of the two *trans* tautomeric forms with respect to the sides of the hexagonal cavity embedding the molecule. Due to the symmetries of the cavity and the chromophores, for porphycene the interaction of each of the two transition moments with the rare gas atoms forming the cavity should be approximately the same, but this is not the case for porphyrin (Figure 23).

IV. Photophysics

The values of basic photophysical parameters for the parent porphyrin and some derivatives are presented in Table 8. In planar free-base porphyrins the main channel of the S_1 decay is the intersystem crossing to the triplet manifold. Room temperature fluorescence quantum yields are usually of the order of 10% and the fluorescence decays in about 10 ns. The photophysical characteristics drastically change when the macrocycle skeleton becomes nonplanar. This leads to a large decrease in the fluorescence yield and lifetime, as shown in Table 8 by the examples of 5,10,15,20-tetraphenyl-2,3,7,8,12,13,17,18-octamethylporphyrin **95**, 5,10,15,20-tetraphenyl-2,3,7,8,12,13,17,18-octaethylporphyrin **96**, and 2,3,5,7,8,10,12,13,15,-17,18,20-dodecaphenylporphyrin **97**. Interestingly, for these derivatives both internal conversion and intersystem crossing become

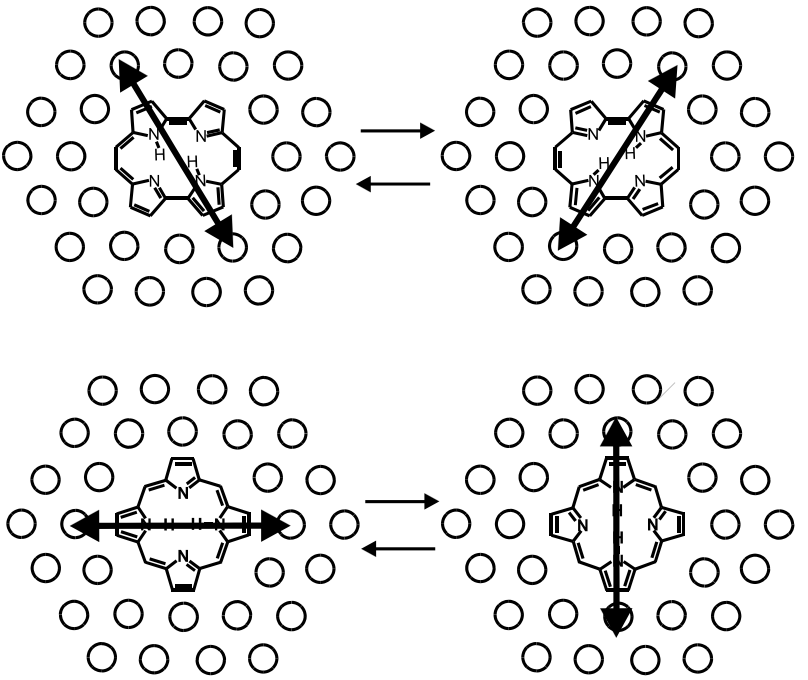

Figure 23. The directions of the S_0–S_1 electronic transition moments in two *trans* tautomeric forms with respect to the rare gas cavity. Top — porphycene; bottom — porphyrin. (Modified with permission from Ref. 161.)

Table 8. Photophysical data for free-base porphyrin and selected derivatives. Φ_F and Φ_T are the quantum yields of fluorescence and triplet formation, respectively. τ_F is the fluorescence decay time (in ns).

	Φ_F	τ_F	Φ_T	Solvent	Reference
1	0.043	9.6		toluene	218
	0.054	15.3		benzene	219
OEPr **24**	0.13	18.9		benzene	219
	0.16	21.7	0.7	toluene	165
			0.75	cyclohexane	220
TPP **26**	0.075	9.0		propanol	218
	0.11	12.4		benzene	219, 221
	0.117	10.8		CH_2Cl_2	222
		12.2	0.74	cyclohexane	220
			0.82	methylcyclohexane	223
			0.84	propanol	224
95	0.003	0.64	>0.5	toluene	165
96	0.005	0.66	>0.5	toluene	165
97	0.006	0.83	>0.5	toluene	165
98	2×10^{-4}	0.046	<0.2	3-methylpentane: isopentane 1:1	166

faster in the distorted macrocycle.[165] On the contrary, the excited state deactivation is dominated by S_1–S_0 internal conversion in ruffled, nonplanar 5,10,15,20-tetra-*tert*-butylporphyrin **98**.[166]

The values of fluorescence quantum yields and lifetimes, as well as those of triplet yields and the efficiencies of singlet oxygen generation, reported for various porphycenes are presented in Table 9. Based on these values are the radiative and radiationless S_1 depopulation rates, shown in Table 10. Additional extensive data containing the values of quantum yields of fluorescence, triplet formation, and singlet oxygen generation for 38 porphycene derivatives are available in the review by Braslavsky and coworkers.[68] In general, fluorescence quantum yields of free-base porphycenes are higher than in porphyrins. This could be expected on the basis of larger absorption coefficients. The radiative constants determined for different porphycenes from the values of fluorescence quantum yields and decay times are very similar for various derivatives, in analogy with the observation of similar absorption coefficients. This comparison suggests that the geometry of most porphycenes is not significantly changed upon excitation.

As long as the porphycene chromophore remains planar (and for nonaryl substituents), both fluorescence and intersystem crossing contribute to the excited state decay with comparable efficiencies, the yield of triplet formation usually being somewhat higher. One should note that internal conversion to the ground state cannot be neglected either. For instance, in the parent porphycene, the yields of fluorescence, intersystem crossing, and internal conversion are 0.36, 0.42, and 0.22, respectively. Very similar values are obtained for 2,7,12,17-tetrapropyl-derivative **10**. When phenyl groups are substituted at the same position, the respective yields become 0.15, 0.33, and 0.52, demonstrating that now the internal conversion becomes the main decay channel. This process definitely takes over when the chromophore becomes nonplanar, as demonstrated for two dibenzoporphycenes: 2,7,12,17-tetra-*t*-butyl-3,6,13,16-dibenzo[*cde*, *mno*]porphycene **84** and its tetramethyl analog **99**,[157,159] as well as by the huge increase in k_{IC} observed upon passing from mono- and dibrominated porphycenes **16–17** to tri- and tetrabrominated derivatives **18** and **19**.[75] However, the increase in k_{IC} is also observed for tetraazaporphycenes which are probably planar, such as **48** and **49a**. This has been interpreted in terms of the energy gap law, since the S_0–S_1 transition in azaporphycenes is strongly shifted to the red with respect to that of the parent compound **2** (see Table 5).[115]

As expected, substitution by heavy atoms leads to an increase in the triplet formation yields. This is clearly observed for brominated porphycenes **16–19**.[75] A finding which awaits explanation is the large decrease in the radiative rates of the nitro (**44)** and amino (**46)** derivatives of TPPo **42**.[112]

Table 9. Photophysical data for porphycene and selected derivatives. Φ_F, Φ_T , and Φ_Δ are the quantum yields of fluorescence, triplet formation, and singlet oxygen generation, respectively. τ_F is the fluorescence decay time (in ns).

	Φ_F	τ_F	Φ_T	Φ_Δ	Solvent	Reference
2	0.36	10.2	0.42	0.30	toluene	225
		8.75			CH_2Cl_2	225
		11.76			methanol	225
				0.34	benzene	226
		11.6		0.32	DPPC vesicles	226
	0.44		0.3		benzene	173
				0.34	benzene, toluene	173
10	0.32	9.76		0.35	toluene	225
				0.36	benzene	226
				0.37	DPPC vesicles	226
	0.38		0.4		benzene	173
				0.36	benzene, toluene	173
	0.37	8.92	0.36	0.36	toluene	75
100	0.14				CH_2Cl_2	179
	0.11				sol–gel silica plate	
OEPc **15**	0.02	5.0	0.04		ethanol	168
	0.017		< 0.1	0.06	toluene	7
42	0.15	4.8	0.33	0.23	toluene	69
43	0.22	4.3		0.19	toluene	112
44	0.033	3.9		0.16	toluene	112
46	0.004	0.81[a]		0.09	toluene	112
84, **99**		0.01–0.02			Ar matrix	157
48	0.03	0.52	0.045	0.013	toluene	111, 115
				0.023	benzene	
49a	0.02	0.34			toluene	115
				0.034	benzene	
33	0.33	8.38			CH_3OD	227
				0.29	D_2O	
34–35[b]	0.17	3.94		0.25	CH_3OD	227
	0.10	1.61			H_2O	
				0.10	D_2O	
36	≈ 0			0.01	CH_3OD	227
	≈ 0				H_2O	
				≈ 0	D_2O	
16	0.08	1.4	0.90	0.90	toluene	75
17	0.03	0.754	0.95	0.95	toluene	75
18	0.006	0.103	0.72	0.71	toluene	75
19	0.002	0.053	0.53	0.49	toluene	75

[a]Average of two lifetimes. [b]The data reported for the mixture of two compounds.

Table 10. The radiative (k_r) and nonradiative rates of S_1 depopulation for porphycene and selected derivatives in room temperature solutions. IC — internal conversion; ISC — intersystem crossing.

	k_r (10^7 s^{-1})	k_{IC} (10^7 s^{-1})	k_{ISC} (10^7 s^{-1})	Solvent	Reference
2	3.5	2.2	4.1	toluene	225
10	3.9	2.3	4.1	toluene	69
	4.1	3.0	4.0	toluene	75
42	3.1	10.8	6.9	toluene	69
43	5.1			toluene	112
44	0.8			toluene	112
46	0.5			toluene	112
48	5.8	110	7.2	toluene	115
49a	5.9	180	8.7	toluene	115
16	5.7	1.4	64	toluene	75
17	4.0	2.7	130	toluene	75
18	5.8	260	700	toluene	75
19	3.8	870	1000	toluene	75
33	3.9			CH_3OD	227
34–35[a]	4.3			CH_3OD	227
	6.2			H_2O	

[a]Mixture of two compounds.

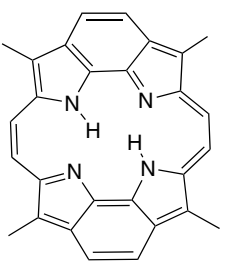

99

Very little is known so far about the photophysics of other porphyrin isomers. Room temperature measurements have been reported for toluene solutions of OEHPc **21** and OECp **20**. The fluorescence is stronger in the hemiporphycene derivative. The ratio of the quantum yields (0.09 in **21** vs. 0.03 in **20**) is very similar to the ratio of absorption coefficients for the transition to L_1 (see Table 6). Both compounds reveal high efficiency of triplet formation (0.9 and 0.6 for **20** and **21**, respectively). They also generate single oxygen, with a quantum yield of 0.48 for **20** and 0.58 for **21**.

A. Mechanism of Excited State Deactivation in Alkylated Porphycenes

Tetraalkyl substitution of porphycene at the β positions has very little influence on the photophysical properties. In contrast, *meso*-substitution has a dramatic effect. This was first observed by Levanon and coworkers, who studied the triplet formation in the parent porphycene and two *n*-propyl derivatives **10** and **11**.[167] At room temperature, comparable triplet yields were observed for all three compounds when triplet–triplet sensitization was used to produce the porphycene in the T_1 state. On the contrary, the triplet formation yield was negligible for the *meso*-derivative when the route to the triplet involved laser excitation followed by intersystem crossing. The triplet state was detectable at temperatures below 240 K. In order to interpret these results, the authors postulated the existence of a thermally activated singlet state lying about 1000 cm^{-1} above S_1. This state would be directly coupled to the ground state, thus providing an efficient channel for S_1 depopulation.

Further studies demonstrated that fluorescence of methyl and *n*-propyl *meso*-substituted porphycenes **29** and **11** can be enhanced not only by lowering the temperature but also by increasing the viscosity of the environment.[39] Actually, embedding the chromophore in a polymer sheet at 293 K is nearly as effective as lowering the temperature to 77 K. Comparison of the effect of temperature on the fluorescence intensity in the parent porphycene **2** and in 9,10,19,20-tetra-*n*-propylporphycene **11** is shown in Figure 24. The fluorescence of **2** is intense already at 293 K and increases only weakly at low temperatures. In contrast, the emission intensity of **11** increases dramatically, by more than two orders of magnitude in the temperature range between 293 and 77 K; this is accompanied by a corresponding increase in the fluorescence decay time. In fact, the emission decay for **11** and the tetramethyl analog **29** is biexponential, since both *trans* and *cis* tautomeric forms are present.

Similar behavior, namely large viscosity dependence of the fluorescence quantum yield and lifetime, was observed for β,β'-substituted octaalkyl derivatives. Again, the emission enhancement can be induced in two different ways: either by viscosity increase or by temperature decrease. An interesting observation is that, for the same solvent, both fluorescence quantum yields and lifetimes are about an order of magnitude higher for octaalkyl-substituted than for *meso*-substituted porphycenes.

Replacement of the two internal protons by deuterons leads to an increase in fluorescence intensity. At the same time, the activation barrier for the depopulation process remains the same for deuterated and nondeuterated derivatives. This can be seen from the same temperature dependence of the emission intensity presented in Figure 24 for both nondeuterated **11** and its deuterated derivative.

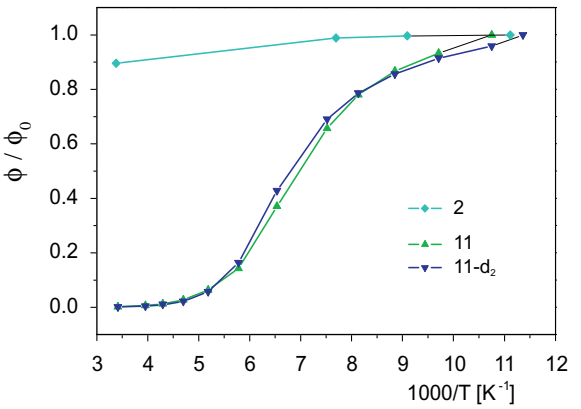

Figure 24. Relative changes of fluorescence quantum yield with temperature, measured for parent porphycene **2** and 9,10,19,20-tetra-*n*-propylporphycene **11**. The results are also presented for the doubly deuterated **11**.

Another observation relevant to the explanation of the depopulation mechanism was provided by comparison of photophysical properties of free-base and zinc octaethylporphycenes.[168] In the zinc derivative, the sum of fluorescence and intersystem crossing quantum yields was found to be close to unity. This was not the case for the free base, for which the value of this sum was very small and solvent-independent. Thus, the internal protons must play a role in the radiationless deactivation. Still, another factor must also be taken into account, responsible for the viscosity dependence. The latter suggests that a large amplitude motion is involved.

The model which was recently proposed to explain the photophysics of alkylated porphycenes[39] is based on the above experimental factors and on the results of calculations performed for three different tautomeric forms of porphycene. The calculations yielded an unusual result for the *cis*-2 form of porphycene (the forms **2b′** and **2b″** in Figure 8): in this tautomer, the state of lowest energy corresponds to an open shell configuration with strongly nonplanar geometry, whereas the planar, closed shell structure has a slightly higher energy. Since the *cis*-2 form is the least stable tautomer of porphycene, both energy levels are located in the vicinity of the first excited state of the *trans* (and *cis*-1) forms. In the correlation of the electronic states of the *trans* and *cis*-2 tautomers (Figure 25), the open shell states of the former must be correlated with the open shell states of the latter. The same is true of the closed shell states. Therefore, the correlation curves must cross along the curve describing the excited state *trans–cis*-2 tautomerization. Since the *cis*-2 structure was found to be strongly nonplanar, the hydrogen transfer coordinate involves not only the proton translocation but also twisting. The observed sensitivity to viscosity can thus be explained.

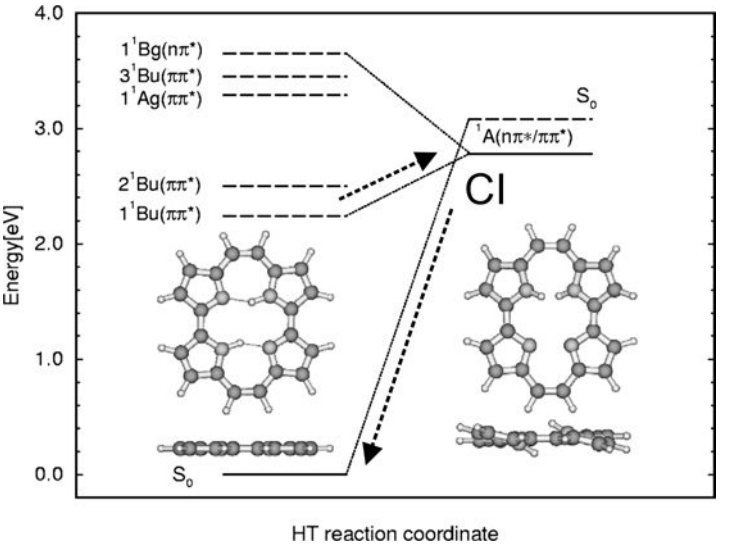

Figure 25. Correlation of the electronic states in the *trans* (left) and *cis*-2 tautomeric forms of parent porphycene. The arrows indicate the path of deactivation involving a conical intersection (CI). (Modified with permission from Ref. 39.)

Preliminary calculations indicate the existence of a conical intersection along the tautomerization coordinate, corresponding to a nonplanar structure, in which the two pyrrolic rings on which the protons reside in the *cis*-2 tautomer are twisted from the molecular plane. For testing the model, four porphycenes — **2**, **40**, **15**, and **29** — were selected as a representative series. In **2** and **40** the emission is strong, whereas for **15** and **29** the fluorescence quantum yield in nonviscous solutions is very low. A perfect correlation was obtained between the experimentally measured S_1 deactivation rate and the calculated difference between the lowest electronic state of *cis*-2 and the energy of the excited S_1 state of the *trans* tautomer. According to the model, this value is a measure of the activation barrier, i.e. the energy required to assume the geometry of the conical intersection. The calculated values increase in the order **29**, **15**, **40**, **2**. This is exactly the order of the experimentally determined S_1 deactivation rates. The model allows one to understand this ordering. If the deactivation were controlled only by nonplanarity, then the largest rate should be expected for the nonplanar octaalkyl derivatives. If, on the other hand, the process is governed by the tautomerization barrier, one should expect the most efficient depopulation in the *meso*-derivatives, which have the shortest, and therefore the strongest, intramolecular hydrogen bonds. The barrier to deactivation via tautomerization should be the largest in octaalkyl derivatives, which have the weakest hydrogen bonds. The fact that the two extreme cases, octaalkyl and *meso*-substituted derivatives, are depopulated most efficiently,

demonstrates that both hydrogen transfer and deviation from planarity contribute to the deactivation. A somewhat similar explanation had been proposed before to account for the lack of emission in strongly nonplanar dibenzoporphycenes.[159]

It remains to be seen whether the above model can be successfully extended to other porphycene derivatives, in particular those containing aryl substituents.

B. Relaxation from Higher Excited States

Picosecond time-resolved absorption and emission studies have been performed for several porphycenes isolated in cryogenic argon and nitrogen matrices.[157,158,160] The transient signals originating in the S_1 state were monitored as a function of time delay from the moment of excitation. An unusually long relaxation time was observed for parent porphycene excited into the Soret region. The relaxed S_1 state was observed only after a delay exceeding 100 ps. On the other hand, no spectral evolution was observed for direct excitation into S_1 (Figure 26). Similar behavior was observed for tetra-*tert*-butylporphycene **30**. On the other hand, the relaxation from higher excited states was found to be very fast for dibenzoporphycenes **84** and **99**. These differences were explained by the rigidity and planarity of the parent porphycene, as opposed to a flexible structure of the dibenzo derivatives. For the latter, the times of relaxation from higher excited states were compared for the chromophore embedded into an argon matrix at 27 K and the same chromophore in a glassy and liquid 2-methyltetrahydrofuran at 93 and 293 K, respectively. The same relaxation times, 9–13 ps, were observed for the glassy and liquid matrices, whereas for Ar the relaxation was significantly longer (16–20 ps).[157]

The dynamics of relaxation from the Soret states has also been studied at room temperature for *meso*-substituted porphycenes **11** and **29**, using a femtosecond fluorescence upconversion technique.[169] An extremely short time, about 50 fs, was determined for the relaxation of the B into the L states. This value is similar to, or even shorter than, the one observed for porphyrin, even though the separation between the Soret and Q bands is nearly twice as large in the case of porphycenes.

The electronic and vibrational relaxation processes occurring after excitation to S_2 were monitored for porphycene **2** in solution at 293 K.[170] The sequence of processes following the excitation includes intramolecular vibrational redistribution, S_2–S_1 internal conversion, and thermal equilibration via energy transfer to the solvent. The last process is the longest and takes about 16 ps in acetonitrile.

C. Triplet State Studies

In view of potential applications in photodynamic therapy, the properties of the triplet states of porphycenes have been intensively studied.[25,68,69,75,112,115,167,168,171–179]

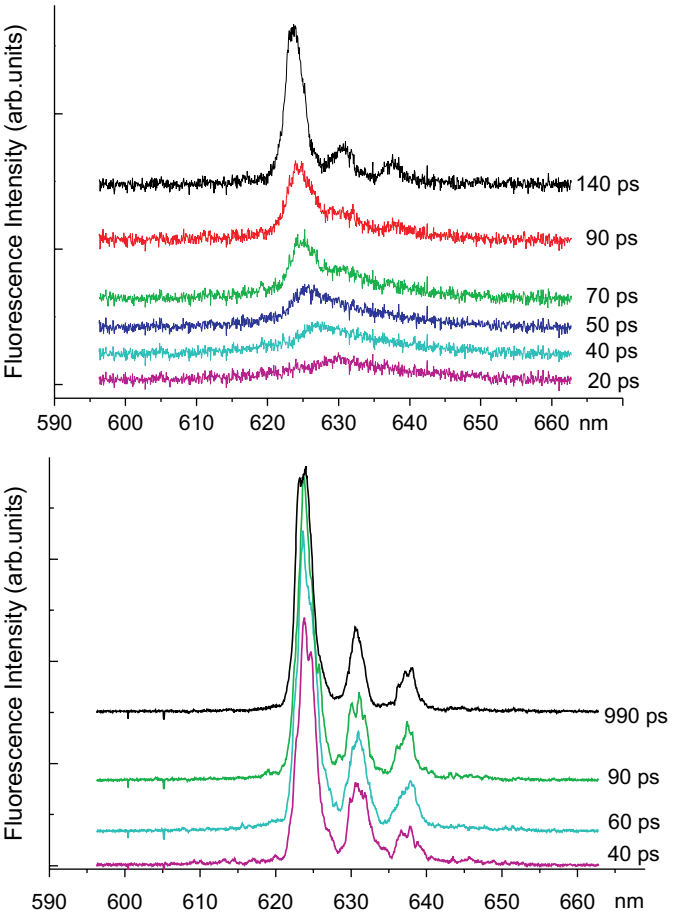

Figure 26. Time evolution of fluorescence spectra of 2 in a nitrogen matrix at 15 K. Bottom: excitation to S_1 (593 nm); top: excitation into the Soret band (355 nm). Time delay from the moment of excitation is indicated for each spectrum. (Modified with permission from Ref. 160.)

As can be inferred by comparing the data in Tables 8 and 9, the triplet state is populated less efficiently than in porphyrins. As a consequence, the efficiency of singlet oxygen generation by porphycenes should be lower. Fortunately, this is compensated for by the fact that porphycenes absorb much more strongly. Moreover, the triplet state usually generates singlet oxygen with a nearly 100% yield (Table 9). Thus, the average value for $^1O_2$ photosensitization, 0.3 ± 0.1, is very close to the usual triplet formation efficiency, which allows porphycenes to be called "excellent photosensitizers".[17] When one is considering practical applications, however, it is to be remembered that the predictions obtained on the basis of *in vitro* experiments may not always be transferable to living systems. This was

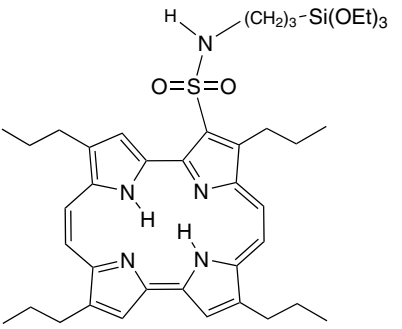

100

demonstrated in a paper by Baumer and coworkers, devoted to singlet oxygen generation by 9-acetoxy-2,7,12,17-tetrakis-(β-methoxyethyl)porphycene **64** in solution.[177] The results showed that, due to very different oxygen concentrations *in vitro* and *in vivo* (lower in the latter), the obtained quantum yield values may be very different in the two cases.

Photosensitizing properties of porphycenes can also be exploited in the solid state. In work by Hisaeda and coworkers,[179] a porphycene derivative **100** was covalently immobilized in a sol–gel silica film. Under irradiation with visible light, singlet oxygen was produced, which was then used for oxidation of 1,5-dihydroxynaphthalene. This procedure could be recycled.

Photoexcited triplet states of several porphycene derivatives have been studied by EPR, ENDOR, and electron spin echo techniques.[25,168,174–176] These measurements resulted in the determination of the zero-field splitting parameters D and E, as well as the hyperfine coupling tensor components. Comparison of the latter with the values calculated for *trans* and *cis* forms of parent porphycene indicated that the molecule exists in the *trans* form in the triplet state.[25]

Very little is known about the triplet state properties of the other porphyrin isomers. Magnetic, kinetic, and structural parameters were determined using time-resolved EPR for OECp **20** and OEHPc **21** in toluene and liquid crystal matrices.[180] For doubly protonated OECp, studied in benzene solutions, the values of the quantum yield of triplet formation and singlet oxygen generation have been determined (0.82 and 0.38, respectively).[181]

V. Tautomerism

A. Tautomerism in Porphyrins

The process of migration of two internal protons between the four nitrogen atoms which form the inner cavity of porphyrin has been studied since the early

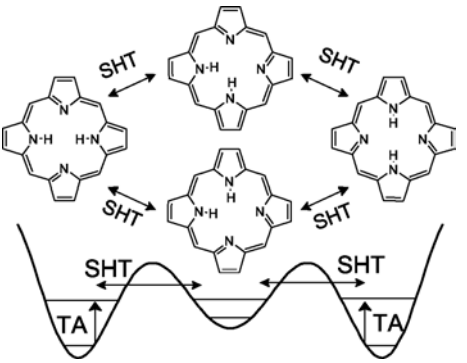

Figure 27. Scheme of stepwise tautomerization in porphyrin: TA — thermal activation; SHT — single hydrogen tunneling.

1970s.[182,183] The main issues considered are related to the stepwise vs. concerted mechanism of the reaction and the role of tunneling. After two decades of investigations, the tautomerization mechanism was established, based mainly on the NMR studies by Limbach and coworkers.[91–93] The reaction proceeds according to a stepwise mechanism, with thermal activation of a level isoenergetic with a transient *cis* tautomer intermediate. The second step involves single hydrogen tunneling through the potential barrier (Figure 27). The model is based on several experimental findings. The HH/DD isotope effect is very large, 17 at 273 K for parent porphyrin[92] and 29 for TPP,[91] whereas the HD/DD effect is much smaller (1.9 and 2.0, respectively). Such behavior is characteristic of a stepwise process which involves two consecutive hydrogen transfer steps via an intermediate. Large isotope effects (11 for **1** at 293 K) indicate tunneling, which is additionally corroborated by nonlinear Arrhenius plots. A remarkable observation is that for the parent porphyrin the tautomerization rate constants and isotope effects are the same for the liquid phase and polycrystalline environment. It was concluded that the liquid state degeneracy of two *trans* tautomers is maintained in the solid phase.[92] Finally, one should mention that the *cis* tautomeric intermediate, crucial for the mechanism, has never been experimentally observed in porphyrins.

The tautomerization occurs in porphyrin not only in the ground electronic state but also after photoexcitation.[184–186] This reaction proceeds even at liquid helium temperatures, in contrast to the dark process, which can be frozen at low temperatures. Such behavior enables photoorientation, i.e. achieving partial alignment of initially isotropic samples by irradiation with linearly polarized light. This methodology has been used for porphyrins isolated in rare-gas matrices.[94,95,187,188] Combining photoorientation with linear dichroism studies enabled polarization assignments for transitions observed in the electronic and IR absorption spectra, as well as detailed characterization of matrix site characteristics.[162,163] The mechanism of photoinduced tautomerization in porphyrin most probably involves a triplet state.[96,189]

B. Tautomerism in Porphycenes

1. *Coherent Double Hydrogen Tunneling in Isolated Molecules*

Quantum mechanics dictates the delocalization of wave functions in a system containing several energy minima separated by barriers, as long as the barriers are finite. Porphyrin and porphycene provide examples of such compounds: two chemically equivalent tautomers are separated by a potential barrier. For such a special, symmetric double minimum case, the two tautomers are equally probable, and the energy levels are split into doublets (Figure 28). Because of selection rules, only certain transitions between tunneling levels are allowed. For the S_0–S_1 electronic absorption or emission, these are the transitions labeled O_+^+ and O_-^- in Figure 28, involving either lower or upper tunneling levels in S_0 and S_1.

The value of the tunneling splitting depends on the mass of the tunneling particle, the distance it has to travel, and the effective tautomerization barrier. Naturally, these parameters should be strongly correlated with the molecular structure, in particular with the strength of the NH···N intramolecular hydrogen bonds. Shorter, more linear hydrogen bonds should yield lower barriers to tautomerization. One could therefore expect a smaller barrier for porphycene than for porphyrin, a prediction which was fully confirmed by calculations.[44,190] As a consequence, tunneling splittings in porphycene should be be larger than in porphyrin. Indeed, the fluorescence excitation spectrum of porphycene isolated

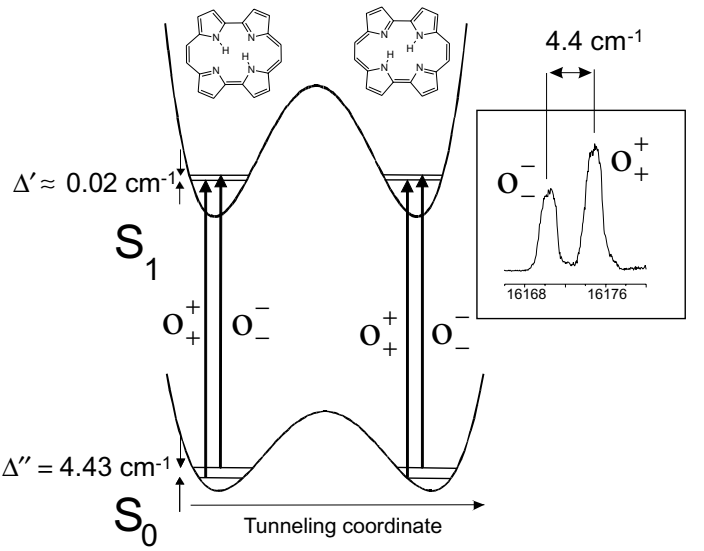

Figure 28. Tunneling splitting due to delocalization of internal protons in porphycene, and the allowed optical transitions between the ground and the lowest excited singlet state. Inset: The 0–0 region of the fluorescence excitation spectrum of porphycene isolated in a supersonic jet, revealing the tunneling splitting.[22]

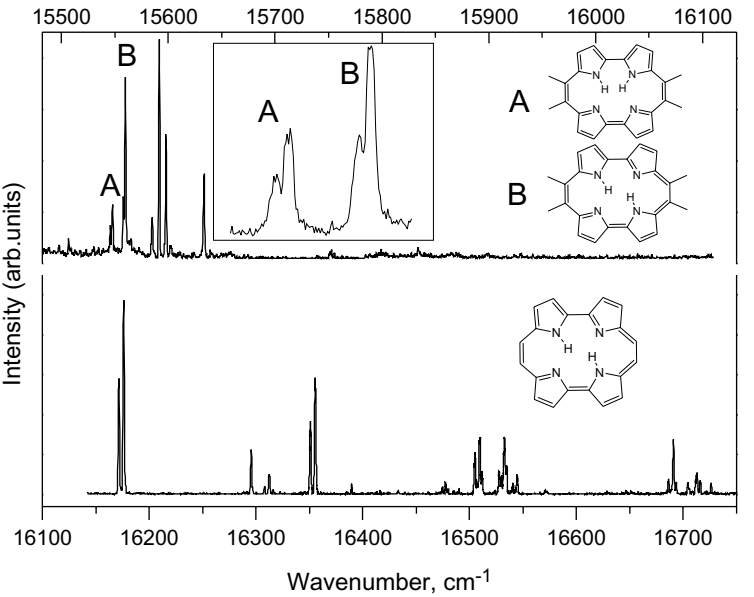

Figure 29. Fluorescence excitation spectra of parent porphycene (bottom) and of 9,10,19,20-tetramethylporphycene **29** (top) isolated in supersonic jets. The inset shows the expanded region of the 0–0 transitions for *cis* (A) and *trans* (B) tautomers of **29**. (Modified with permission from Ref. 30.)

in supersonic jets consists of doublets, separated by 4.4 cm^{-1} (Figures 28 and 29).[22] In contrast, the spectrum of supersonic-jet-isolated porphyrin reveals no splittings.[191]

The proof that the splittings are due to coherent double hydrogen tunneling was provided by experiments on porphycene with one ($Pc–d_1$) or two ($Pc–d_2$) internal protons substituted by deuterons. No splittings were observed under these conditions.

In general, the splittings observed in the spectra express the difference between ground and excited state tunneling splitting values. For a special case where the splitting is negligibly small in one of the states, the separation of the spectral lines becomes equal to the tunneling splitting in the other state involved in the monitored spectral transition. This is the case for porphycene, as revealed by the same values of doublet separation observed for the 0–0 transition and numerous vibronic peaks. Based on the red shifts observed in the spectra of $Pc–d_1$ and $Pc–d_2$, it was concluded that the observed 4.4 cm^{-1} separation of doublet components is practically due entirely to the splitting in the ground electronic state.[22] The finding of a much larger tunneling splitting in the ground electronic state than in the first excited singlet state was explained assuming that the molecule expands upon excitation. In particular, the

two NH···N distances become larger, which weakens the intramolecular hydrogen bonds and thus leads to an increase of the tautomerization barrier. This hypothesis has been confirmed by geometry optimization of electronically excited porphycene.

About a decade later, the conclusions reached on the basis of supersonic jet studies were confirmed and extended by an investigation of porphycene embedded in helium nanodroplets.[40] These studies, carried out at a lower (and, in contrast to the jet, well-defined) temperature of 0.37 K and with better spectral resolution yielded 4.43 cm^{-1} as the tunneling splitting value of the ground state vibrationless level. It was also possible to obtain the respective splitting for Pc–d_1; a value of 0.58 cm^{-1} has been measured. In addition, the value of the splitting in S_1 was estimated at 0.02 cm^{-1}.

Most spectacular were the results of fluorescence measurements, which yielded the tunneling splitting values for different vibrational levels of the electronic ground state. These values were found to depend crucially on the particular vibrational mode. Thus, for some vibrational levels, the splitting values were very close to the value observed for the 0–0 transition. For a 182 cm^{-1} a_g mode, the splitting was much higher — 12 cm^{-1}. On the contrary, for another a_g mode, 145 cm^{-1}, the splitting was found to be so small that it could not be experimentally resolved. It was thus demonstrated that the tunneling is mode-specific. In other words, tautomerization characteristics may be different for different vibrational levels. Some modes can promote the process by lowering the barrier, which is manifested by a larger tunneling splitting. Other vibrations may increase the barrier and thus decrease the splitting. Finally, there exist also "neutral" vibrations, which, when excited, do not change the effective barrier penetrated by the tunneling protons.

The forms of several low-frequency modes, including the "promoting" ($2a_g$), "hindering" ($1a_g$), and two "neutral" ones ($3a_g$ and $4a_g$), are presented in Figure 30. In accordance with chemical intuition, the neutral modes do not greatly affect the hydrogen bond parameters, whereas the others do that to a great extent. Especially instructive is the form of the promoting $2a_g$ mode. For this vibration, the nuclear motions simultaneously make both hydrogen bonds shorter and more linear. The smaller barrier for double hydrogen tunneling (and, in consequence, a larger tunneling splitting) is therefore easy to understand. The behavior of the hindering $1a_g$ mode is the opposite: this vibration results in weakening of the hydrogen bonds.

A detailed supersonic jet study was also performed for two *meso*-substituted porphycenes, **11** and **29**.[30] Since the X-ray and NMR data[71] indicate stronger hydrogen bonds, one could expect larger tunneling splitting values. Indeed, the values for the ground and the lowest excited singlet state were estimated at 15 cm^{-1} and 2 cm^{-1}, respectively. Most interestingly, the potential for tautomerization in **29** was found not to be symmetric, the reason being the coupling between the motion of the internal protons and the methyl substituents. The asymmetry is reversed upon excitation (Figure 31).

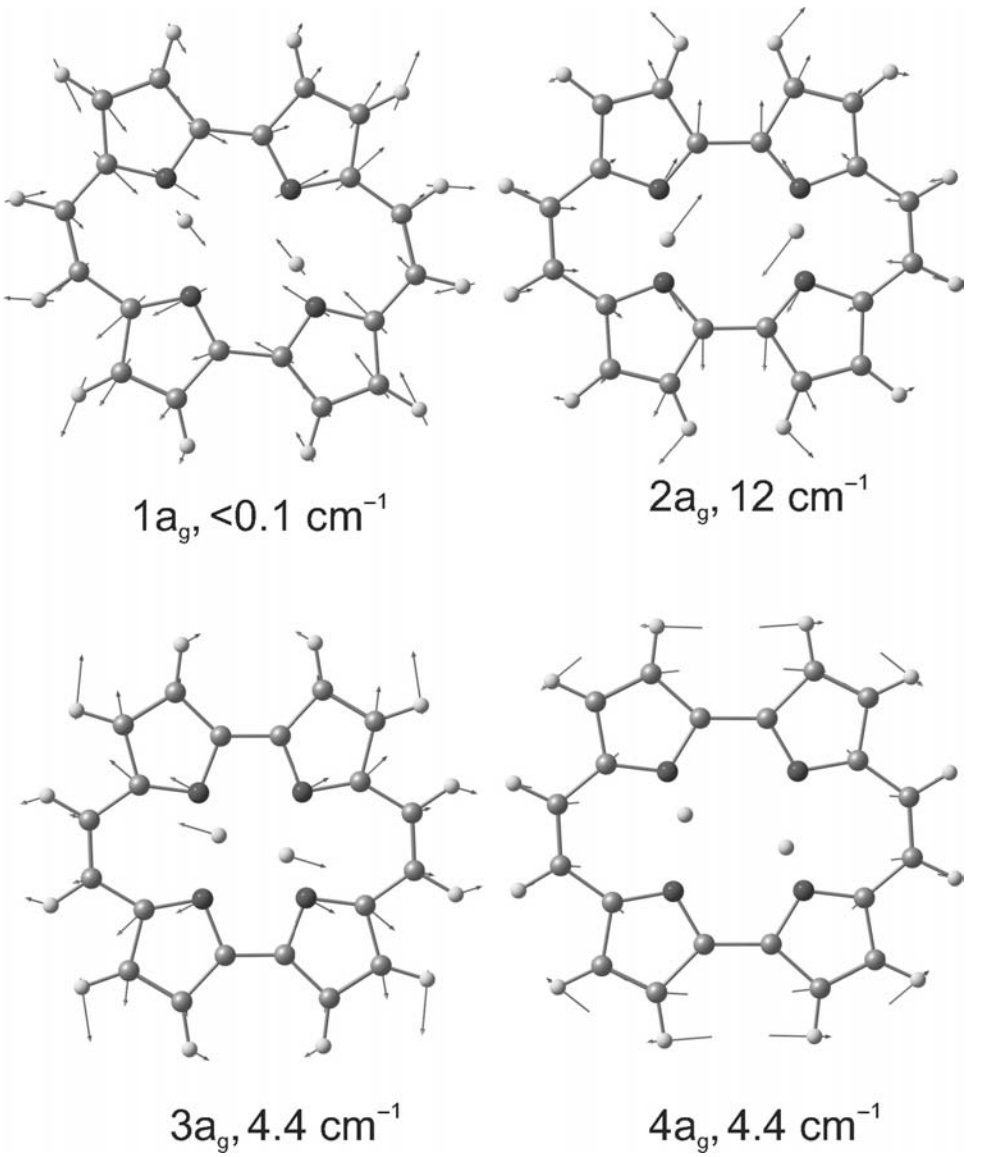

Figure 30. The forms of four lowest-frequency a_g modes of porphycene with the corresponding values of ground state tunneling splittings determined from fluorescence in helium nanodroplets at 0.37 K.[40]

These supersonic jet studies resulted in another valuable finding. The fluorescence excitation spectra of **11** and **29** exhibit a structure consisting of a doublet of doublets (features A and B in Figure 29). One of the doublets disappears upon cooling. In a singly or doubly deuterated derivative, features A and B consist of

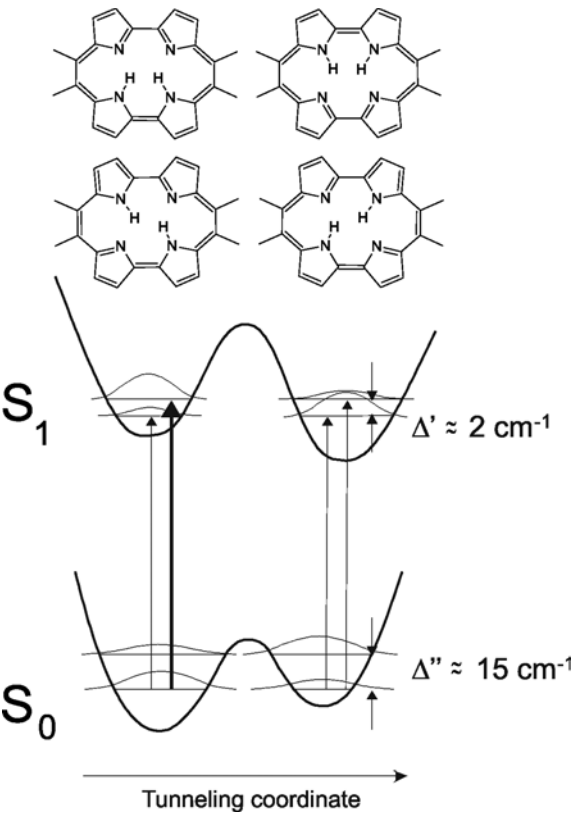

Figure 31. The shapes of potential energy curves governing tautomerization in 9,10,19,20-tetramethylporphycene **29**, with the estimated values of tunneling splitting in the S_0 and S_1 electronic states. (Modified with permission from Ref. 30.)

single lines. These findings were interpreted as an indication of the presence of both *cis* (feature A) and *trans* (feature B) tautomeric forms, each revealing similar tunneling splitting values in S_0 and S_1. The existence of both tautomeric forms was also confirmed for solutions, by observing doubly exponential fluorescence decays.[39] The calculations predict that the two tautomeric forms in **29** should have similar energies, differing by less than 1 kcal/mol. To the author's knowledge, this molecule is so far the only porphycene for which the presence of both *cis* and *trans* tautomeric forms has been reported.

Finally, the results of supersonic jet studies confirmed the existence of a rapid deactivation channel in electronically excited *meso*-alkylated porphycenes. As seen in Figure 29, the fluorescence excitation spectra are limited to a narrow range above the 0–0 transition — less than 200 cm^{-1}. Excitation with higher energy excess leads to the disappearance of fluorescence, indicating the

onset of an efficient radiationless process. According to the model discussed in Section IV.A, the deactivation efficiency should be related to the medium viscosity, extremely low for a supersonic jet. Therefore, the activation energy for this channel in the jet should be lower than that determined from solution studies. This is indeed the case, which provides yet another argument for the model which postulates that the radiationless deactivation of excited porphycenes proceeds along the pathway involving both hydrogen transfer and distortion from planarity.[39]

2. *Molecules in Condensed Phases*

a. *Ground state tautomerism in polycrystalline porphycene*

Early ^{15}N-CPMAS-NMR comparative studies of crystalline porphyrin and porphycene by Limbach and coworkers[18] showed a much larger tautomerization rate in the latter. The line shape analysis allowed one to determine tautomerization rates in porphyrin; they decrease from >30000 s^{-1} at 356 K to 500 s^{-1} at 244 K. For porphycene the rates were too fast to be determined, as no line broadening was detected, even at the lowest available temperature of 107 K. Four sharp lines were observed, indicating the presence of two nonequivalent asymmetric proton transfer systems. Two alternative explanations were proposed: (i) existence of two nonequivalent molecules in the crystal, each having access to two tautomeric states; (ii) equivalence of all the molecules in the crystal, each with four accessible tautomeric states. The nonequivalence of tautomers is due to crystal effects.

Further studies of porphycene enabled determination[24] of the rate constants from the analysis of longitudinal ^{15}N T_1 relaxation times in the temperature range 228–355 K. The tautomerization was found to occur on a nanosecond time scale. The temperature dependence of the rate pointed to the dominant role of tunneling across a barrier of about 8 kcal/mol. A concerted mechanism of tautomerization was suggested, based on strong coupling between the two hydrogen bonds.

Work from Limbach's group,[37] based on high-resolution ^{15}N and ^{2}H NMR spectroscopy and longitudinal relaxometry, yielded several unusual results. The tautomerization rates have been found to decrease sharply at higher temperatures. Above 225 K, the rate was reported to drop by four orders of magnitude. A phase transition was postulated to occur at this temperature. Another unexpected finding was the observation of the same rates of the HH and HD/DD tautomerism. The authors proposed that the reaction occurs in a concerted fashion at high temperatures and as a stepwise process at low temperatures. In the low-temperature region, non-Arrhenius behavior was observed for the DD transfer, indicative of tunneling. Finally, two nonequivalent molecules were detected in

the unit cell, corroborating the hypothesis proposed in the first NMR study on porphycene.[18]

b. *Studies using polarized spectroscopy techniques*

The measurements of fluorescence anisotropy of porphycene showed that the emission is partially depolarized.[19,20] An example is presented in Figure 32. When the molecule is excited into S_1, the anisotropy value is below 0.20 instead of 0.4, expected for parallel orientation of absorbing and emitting transition dipole moments. In turn, for excitation into S_2, the anisotropy is around 0, whereas, judging from the results of calculations, it should be close to –0.2, because the S_0–S_1 and S_0–S_2 transition moments are predicted to be nearly perpendicular.

These results can be understood by assuming a rapid *trans–trans* tautomerization in the excited state. The reaction changes the direction of each transition moment. Tautomerization is equivalent to the reflection of the transition moment in the vertical or horizontal plane perpendicular to the plane of the porphycene macrocycle (Figure 33). In a high-temperature regime, when the reaction occurs many times back and forth before the excited molecule emits a photon, the probabilities of emitting with a transition moment corresponding to that of the initially excited and that of the other tautomer are equal. The observed value of the anisotropy is related to the position of the transition moment in the molecular

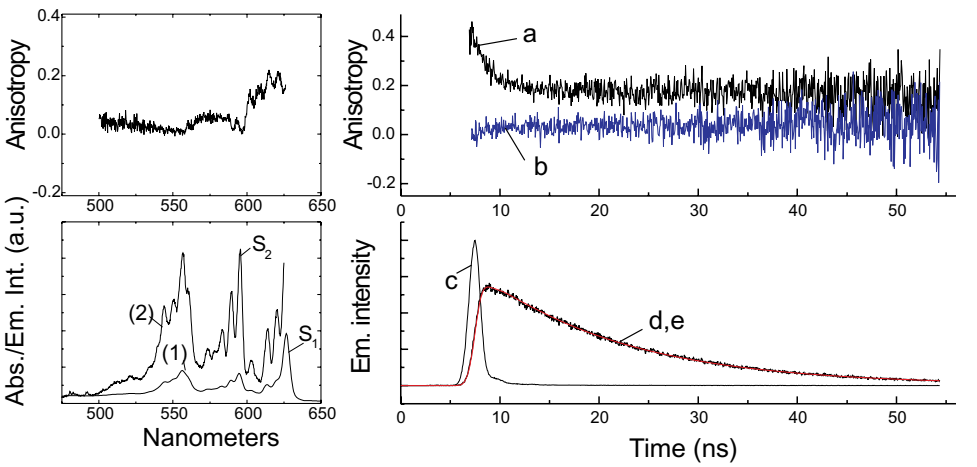

Figure 32. Porphycene in 1:1 methanol:ethanol glass at 97 K. Left — absorption (1) and fluorescence excitation (2); top — anisotropy of fluorescence excitation. Right — decay of anisotropy for excitation into S_1 (625 nm, a) and S_2 (590 nm, b); bottom — experimental (d) and fitted (e) fluorescence decay curve and the excitation profile (c). (Modified with permission from Ref. 32.)

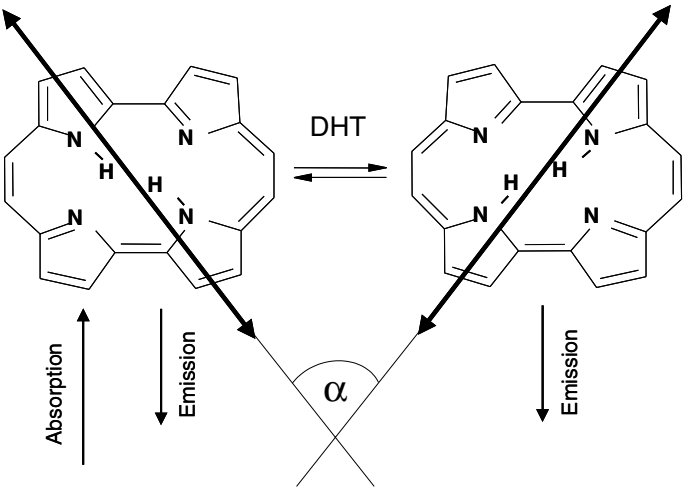

Figure 33. Change in the transition moment direction caused by double hydrogen transfer in porphycene. The structure on the left corresponds to the initially excited form.

plane. Therefore, it is possible to determine the transition moment directions, using fast excited state tautomerization as a tool. This has been performed for the parent porphycene.[20] Even though the symmetry of porphycene is C_{2h}, which allows any direction in the molecular plane, the directions of S_0–S_1 and S_0–S_2 transition moments resemble the situation in free-base porphyrin: the transition to S_1 is polarized approximately along the NH direction, and the transition to S_2 is nearly perpendicular to it. Initial anisotropy studies of OECp indicate similar behavior of the transition moments corresponding to two lowest excited singlet states.

The observation of depolarized fluorescence immediately shows that the dominant tautomeric structure corresponds to the *trans* tautomer, as the direction of the transition moments does not change during the *cis–cis* conversion. *Trans–cis* or *cis–trans* processes would lead to different values of the anisotropy than observed experimentally.

Comparative studies of four different porphycenes, **2**, **10**, **11**, and **15**, performed in *n*-propanol glass at 113 K revealed depolarized fluorescence for all but the last of these compounds. Thus, at this temperature, the reaction is too slow in **15** to occur within the excited state lifetime, about 10 ns. Octaethylporphycene **15** has the largest NH···N distance of all the studied porphycenes, and thus the weakest hydrogen bonding. This explains the lowest tautomerization rate for this molecule. As discussed later in this section, the difference in rates is dramatic, which is most probably due to the tunneling mechanism of hydrogen transfer in porphycenes.

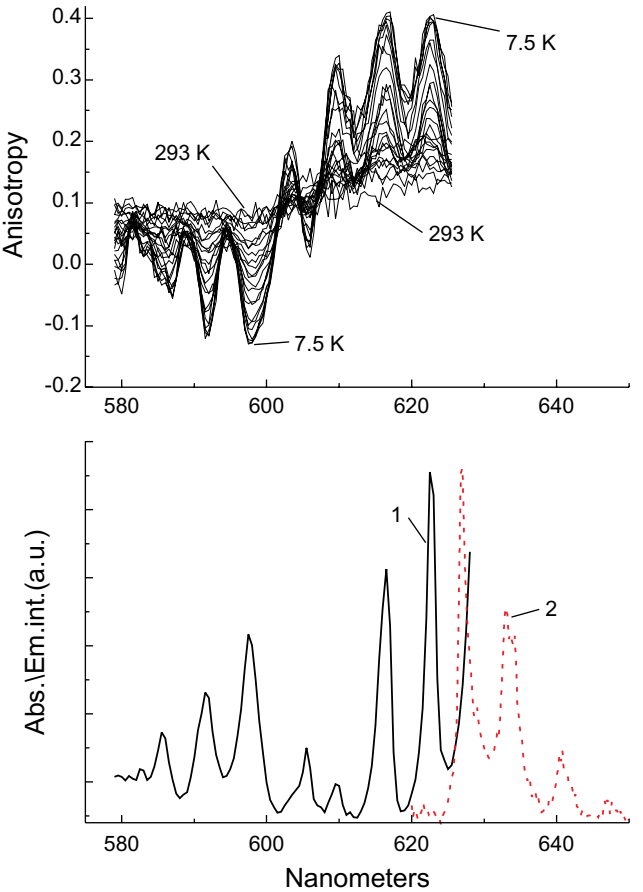

Figure 34. Top: Temperature dependence of the anisotropy of fluorescence excitation recorded between 293 and 7.5 K for porphycene embedded in a poly(vinyl butyral) matrix. Bottom: Fluorescence excitation (1) and fluorescence at 15 K. (Modified with permission from Ref. 32.)

A methodology has been developed[31,32] which enables determination of the excited state tautomerization rates from the analysis of absorption anisotropy, measured in both the stationary and time-resolved modes (see Figures 32 and 34). Studies of the temperature dependence of the anisotropy of porphycene fluorescence (Figure 34) resulted in an Arrhenius plot from which a surprisingly low activation energy, 0.55 kcal/mol, was extracted. This was interpreted as evidence of thermally activated double hydrogen tunneling. The value of the apparent tautomerization barrier is, within the experimental error, equal to the frequency of the $2a_g$, "promoting" mode, which was found to reveal the largest tunneling splitting for the chromophore isolated in helium nanodroplets (See Section V.B.1 and Figure 30).

The methodology was subsequently extended to transient absorption studies, or, more generally, to pump–probe experiments.[35,36] This approach allows determination of the rates not only for the electronically excited but also for the ground state. The rates in both states can be determined in one experiment by changing the pump/probe wavelengths.

Using this technique, the rates of double hydrogen transfer, in both S_0 and S_1, have been measured for porphycene **2** and four derivatives: **11**, **15**, **29**, and **30**.[36] The results are presented in Figure 35 and Table 11. The difference in the rates is striking: the values vary by over three orders of magnitude. The fastest reaction is observed in the two porphycenes in which the hydrogen bonding is the strongest, i.e. **11** and **29**. The slowest rate is obtained for **15**, a molecule with the largest NH···N distance. The values of the rates correlate nicely with ^{1}H chemical shifts, which thus can be treated as good indicators of intramolecular hydrogen bond strength. Other indices, i.e. the X-ray-determined or calculated NH···N, also work nicely

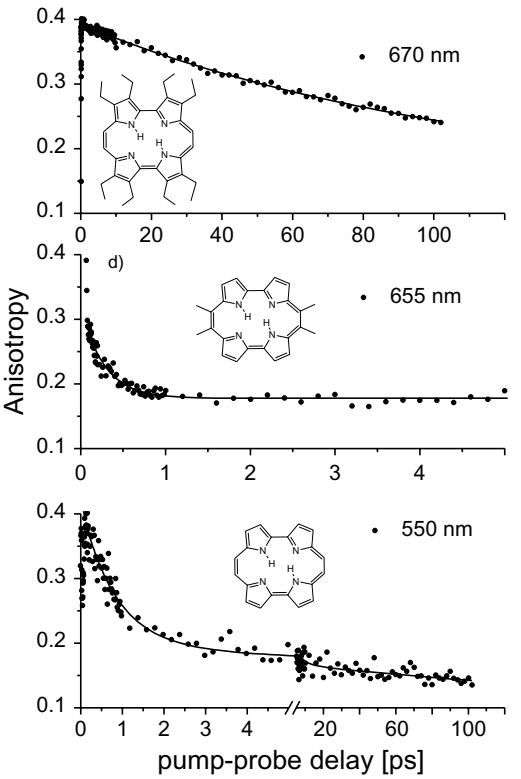

Figure 35. Time-resolved anisotropy of transient absorption measured at 293 K for **2**, **15**, and **29** in ethylene glycol. The wavelength of pump and probe pulses is indicated for each compound.

Table 11. The rates of tautomerization in five different porphycenes in the ground (k_0) and the lowest electronically excited singlet state (k_1), measured at 293 K in ethylene glycol solutions.[36]

	k_0 (s^{-1})	k_1 (s^{-1})
2	$5.8 \cdot 10^{11}$	$7.4 \cdot 10^{10}$
2-d_2[a]	$1.3 \cdot 10^{11}$	$1.5 \cdot 10^{10}$
30	$13.7 \cdot 10^{11}$	$2.0 \cdot 10^{11}$
30-d_2[a]	$1.7 \cdot 10^{11}$	$2.6 \cdot 10^{10}$
11	$\sim 10^{13}$	$1.9 \cdot 10^{12}$
29	$\sim 10^{13}$	$1.9 \cdot 10^{12}$
15	$\sim 10^{10}$	$\leq 10^{9}$

[a]Obtained from the isotope effects measured in O-deuterated ethanol or butanol.

when the corresponding values strongly differ, but fail for geometrically similar structures, like **2** and **30**, for which the tautomerization rates vary by a factor of 2–3. The fact that the change in NH···N separation from 2.53 Å in **11** to 2.80 Å in **15** results in rate constants differing by orders of magnitude provides another argument for the dominant contribution of the tunneling mechanism, even at room temperature.

In all the investigated porphycenes the reaction is slower in S_1, by approximately an order of magnitude, in agreement with the smaller tunneling splittings observed for the excited state.

The same pump and probe methodology was used to determine the rate of an intermolecular process — exchange of internal hydrogen atoms by deuterons provided by the solvent, deuterated alcohol.[35] The reaction, studied for **2** and **30**, turned out to be unusually slow; at 293 K, about 20 hours were required to complete the double deuteration. The kinetic evolution of Pc-d_0, Pc-d_1, and Pc-d_2 populations could be monitored separately for each tautomer (Figure 36). The same value was obtained for the rates of the first and the second deuteration.

The results obtained so far suggest a mechanism for tautomerization in porphycene which is presented in Figure 37, together with the corresponding scheme for porphyrin. As opposed to a stepwise mechanism for the latter, the double hydrogen transfer in porphycene occurs most probably in a concerted fashion. The barrier for the concerted transfer in **2** is significantly lower than in **1**. Moreover, it can be dynamically modulated by vibrational excitation. It is possible that exciting the 182 cm^{-1} promoting mode is sufficient for inducing a rapid tunneling. Remarkably, such energy excess is small with respect to the *cis–trans* energy difference, calculated as about 2 kcal/mol.

Tunneling of two internal hydrogen atoms in condensed phases has been demonstrated to occur at low temperatures by the studies of unsymmetrically

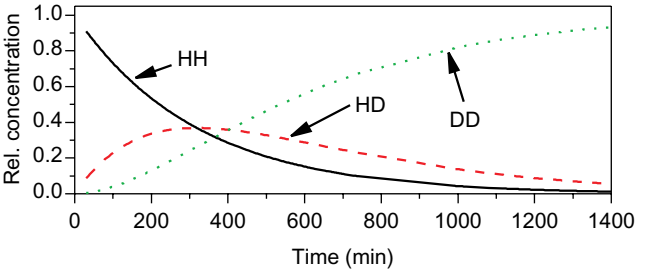

Figure 36. Changes in the relative concentration of three isotopomers of porphycene **2**, measured as a function of time from the moment of dissolving the compound in BuOD at 293 K. (Modified with permission from Ref. 35.)

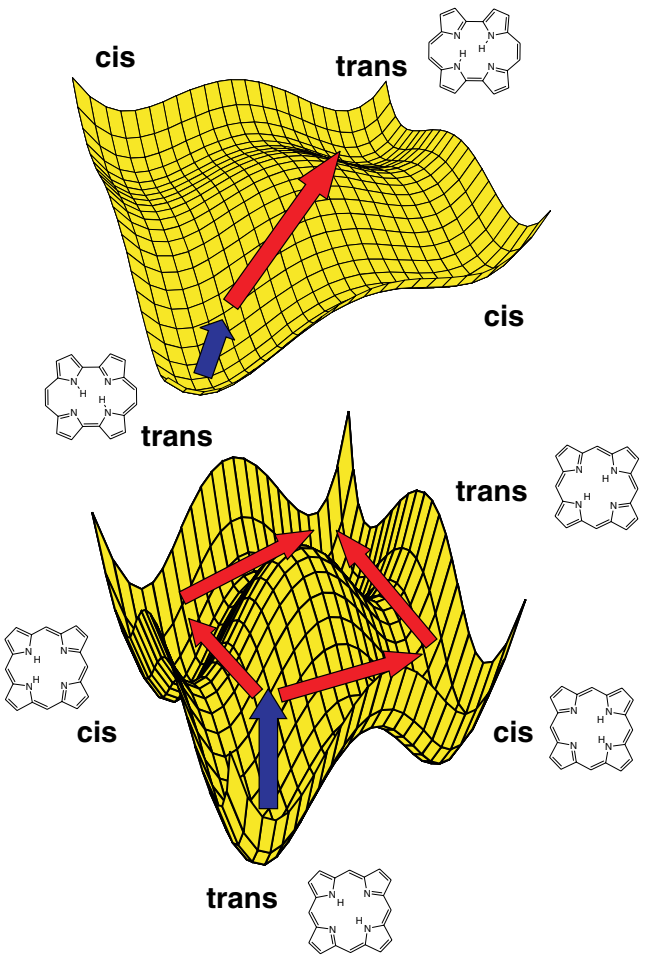

Figure 37. Comparison of the tautomerization pathways in porphyrin and porphycene. (Modified with permission from Ref. 32.)

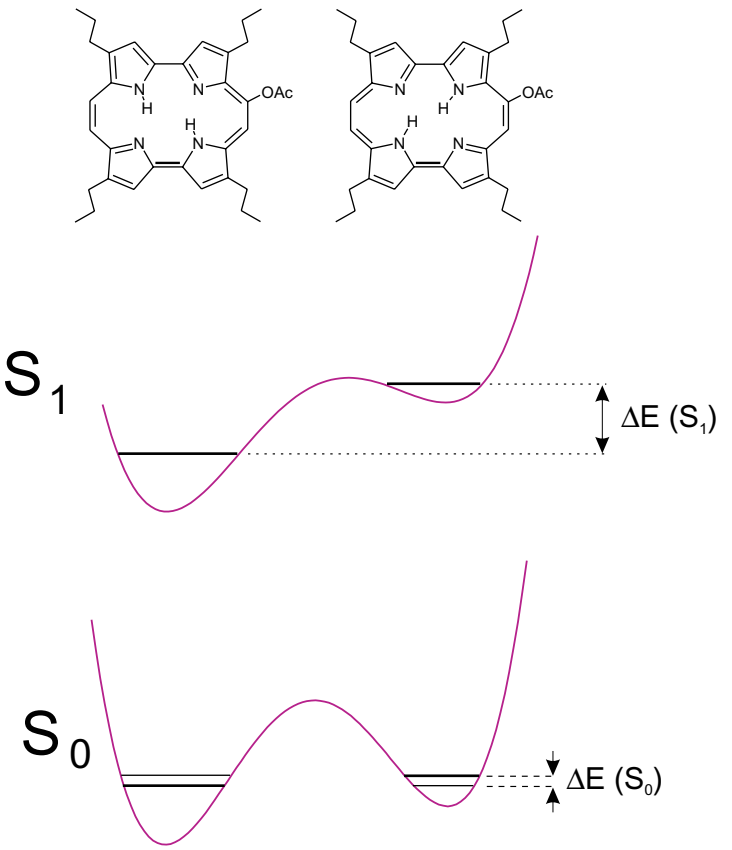

Figure 38. Scheme of potential energy surfaces for the *trans–trans* tautomerization in 9-acetoxy-2,7,12,17-tetra-*n*-propylporphycene. (Modified with permission from Ref. 23.)

substituted acetoxyporphycene **45**.[23] In this molecule, two *trans* tautomers are no longer degenerate. Both forms can be observed in the absorption spectra, their $S_1(0–0)$ transitions differing by about 10 nm. Fluorescence, on the other hand, occurs preferentially from one form, indicating a nonsymmetrical excited state potential. Combined absorption/emission studies, carried out in a large temperature range, showed that the two forms interconvert in the ground electronic state even at temperatures below 20 K. The asymmetry of the potential in S_0 was estimated to be very small, but in S_1 the internal hydrogen atoms become localized (Figure 38).

c. *Tautomerization in the triplet state*

Studies of porphycene by time-resolved EPR, ENDOR, and electron spin echo techniques have been carried out in a large temperature range.[25,174–176] These investigations,

combined with calculations of triplet and singlet geometries, allowed establishing that porphycene exists in the *trans* form in the triplet state.[25] The calculations also indicated that the energy difference between *cis* and *trans* tautomers is larger in T_1 than in S_0 (21.6 vs. 11.25 kJ/mol, B3LYP/6-31G*). The inner cavity is expanded in T_1, the increase in the rectangle sides being about 0.6% with respect to S_0.

Investigations of parent porphycene in a toluene glassy matrix in the temperature range 4–100 K indicated the presence of two triplet state species;[176] only one form is observed at 4 K, whereas the population of the other increases with temperature. This was interpreted as evidence of triplet state tautomerism, with the maximum rate at 100 K estimated at $7 \cdot 10^8$ s^{-1}.

3. *Single Molecule Studies*

Fluorescence detection is one of the favorite techniques in single molecule spectroscopy. It is often coupled with use of polarized light. The fact that the transition moment direction in porphycene changes after tautomerization suggested a possibility of monitoring the double hydrogen transfer reaction in a single chromophore. This was achieved by analyzing spatial profiles of the emission excited with an appropriately polarized laser beam.[29] Figure 39 shows the spatial patterns

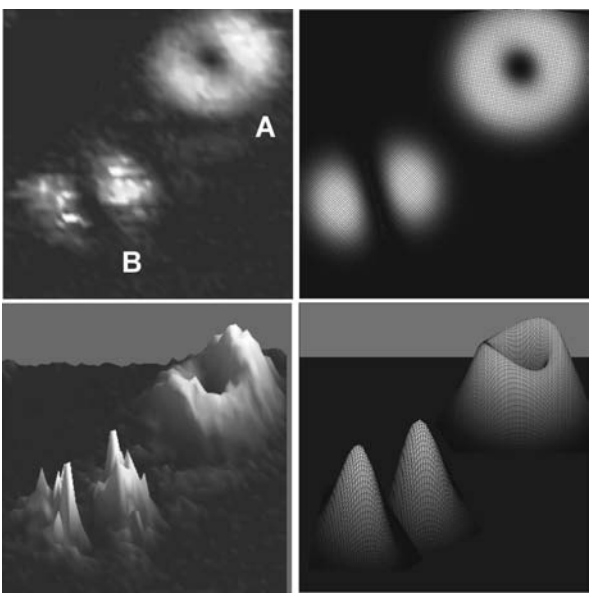

Figure 39. Left: Confocal image of two fluorescing porphycene molecules in PMMA matrix. Right: Simulated patterns. The lower pictures represent 3D plots of the same area as the upper ones. (Adapted with permission from Ref. 29.)

of the emission from two porphycene molecules embedded in poly(methyl methacrylate) film. Simulations demonstrate that a ring pattern cannot be obtained from a single emitting dipole. On the other hand, such a pattern is readily reconstructed assuming two transition dipoles forming an angle of 72°, in excellent agreement with the results obtained for bulk samples in stationary fluorescence[20] and, independently, transient absorption experiments.[36]

While the interpretation of the ring shape as being due to a "dual-dipole emitter" was straightforward, this was not the case with the double lobe pattern. It may be due to a dual emitter molecule which is oriented perpendicular to the surface plane or, alternatively, it may originate from molecules in which, for some reason, the tautomerization is hindered and which therefore emit "normally" as a single dipole. Although the latter case seems less probable, such a possibility had to be checked. The issue was resolved by comparing special patterns of the same single chromophore using two polarization modes, azimuthal and radial (Figure 40).[38] This analysis left no doubt that the emitting single chromophores contain two transition dipoles. Moreover, using two polarization modes of the exciting laser beam, it was possible to determine the 3D orientation of the chromophore in the polymer matrix. For molecules oriented perpendicular to the matrix support plane, such analysis allows one to differentiate the chromophores in which the two transition moments form similar angles with the sample surface from those in which one transition moment is approximately parallel and the other approximately perpendicular to the surface (molecules 2 and 3, respectively, in Figure 40).

So far, tautomerization at a single molecule level has been observed for four different porphycenes, namely **2**, **30**, the "mixed" derivative **40**, and the recently synthesized 2,7,12,17-tetratriphenylmethylporphycene **101**. Given the importance

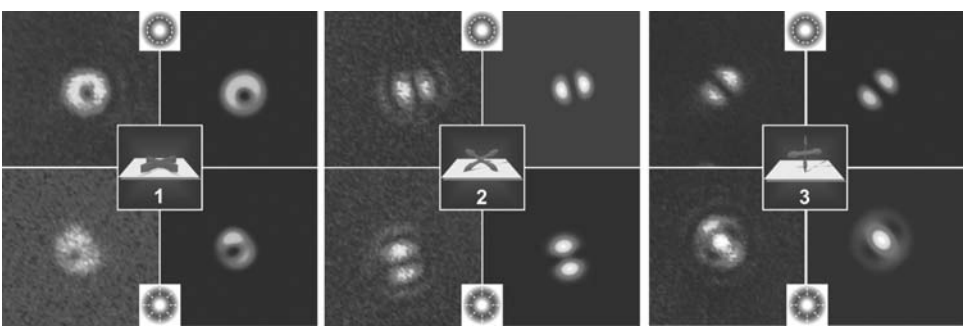

Figure 40. Confocal fluorescence images from single molecules of 2,7,12,17-tetra-*tert*-butylporphycene **30** excited by azimuthally (top) or radially (bottom) polarized laser beam. Left — experiment; right — simulation. The insets show the orientation of the transition moments with respect to the sample surface. (Adapted with permission from Ref. 38.)

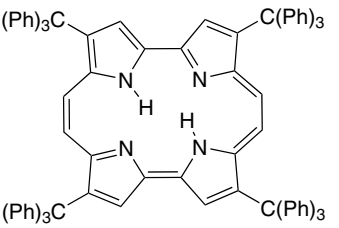

101

of porphycenes in photodynamic therapy and photodiagnostics, this methodology carries great potential for studying biological systems.

VI. Summary and Outlook

Structural, spectral, and photophysical studies of free-base porphycenes reveal important differences with regard to the corresponding characteristics of porphyrins. The rectangular shape of the inner core results in a shorter distance between the nitrogen atoms and, as a consequence, in stronger, more linear hydrogen bonds. This leads to dramatic consequences for the mechanism of tautomerization. All the results obtained so far indicate that, in contrast to the situation in porphyrins, the double hydrogen transfer in porphycenes occurs in a concerted fashion. The low energy barrier for tautomerization leads to tunneling splittings which can be readily detected and characterized quantitatively. Such investigations, carried out for cold, isolated molecules, have shown the mode specificity of the reaction. In turn, experiments in condensed phases based on techniques which use polarized light allow determination of reaction rates in both ground and excited electronic states. Porphycenes thus provide a rare opportunity of probing, for the same system, the characteristics of double hydrogen transfer occurring either in a coherent fashion or as a rate process. In addition, the potential energy barrier for the process can be readily modified by chemically "mild" substituents, such as alkyl groups. Using such procedures, it is possible to increase or decrease the energy barriers and to perturb the symmetry of the double minimum potential. All these factors make porphycenes role models for studying intramolecular hydrogen bonding and tautomerization, and, in particular, such aspects of these phenomena as cooperativity of hydrogen bonding and proton translocation, tunneling, and mode specificity. Those porphycenes which reveal ultrafast hydrogen transfer seem to be promising candidates for quantum control experiments.

Several experimental observations for porphycenes still await interpretation. The large difference in the values of tautomerization rates at room temperature obtained by NMR spectroscopy for polycrystalline porphycene and by optical

techniques for the same molecule in solutions and polymer films has not yet been explained. Interestingly, the two methods yielded similar values at low temperatures. Another finding to be elucidated is the lack of the NH stretching band in the IR spectrum, even though the calculations predict that this transition should be the strongest of all. Evidently, harmonic approximation is not a good model, and the appropriate description has to take into account coupling with other modes, as suggested by the results obtained for porphycene isolated in supersonic jets and helium nanodroplets.

The absorption characteristics of porphycenes, qualitatively similar to those of porphyrins, are quantitatively very different. Larger transition moments for both Q transitions result in stronger absorption and more intense emission. Still, triplet states are populated with reasonable intensities, and the quantum efficiency of singlet oxygen generation is very high. All these properties make porphycenes extremely attractive candidates for use in photodynamic therapy. Actually, comparison of photodynamic activity of several porphycenes, bearing two or four methoxyethyl side chains, with the properties of Photofrin (an FDA-approved, clinically used sensitizer), showed that porphycenes were 17–220 times more active.[16] Since the difference in the extinction coefficient is only about 10-fold, and the triplet formation efficiency may be lower in porphycenes, other factors, such as membrane solubility, must be critical and favorable for porphycenes.

Strong fluorescence makes porphycenes good candidates for cellular imaging. Even more important, perhaps, is the huge sensitivity of the emission intensity in several alkyl-substituted porphycenes to the viscosity of the environment. This property may allow better characterization of localization in the cell and monitoring of cellular metabolism. A procedure for monitoring viscosity in a cell based on chromophores which exhibit viscosity-dependent fluorescence has been proposed recently.[192,193]

Another promising application of porphyrin isomers to biological systems which is being intensively developed[194–205] is to replace the porphyrin moiety in hemoproteins by porphycene, hemiporphycene, and corrphycene derivatives (see Chapter 20, by Hayashi).

The investigations of isomers other than porphycenes are still in the early stage. However, some general comparisons are already possible. Porphycenes, being negative-hard chromophores, have definitely the strongest absorption and, in consequence, the largest radiative constants. Moreover, these characteristics should not vary strongly among different derivatives, though modification of transition energies by substitution is possible. These properties, along with good triplet yield, make porphycenes the best choice for photodynamic therapy sensitizers among all the porphyrin isomers synthesized so far. Of the remaining three isomers, **6** and **8** should be similar to porphycene, as they are also predicted to be strongly negative-hard chromophores.

The small sensitivity of spectral properties of porphycenes to internal perturbations — and even smaller to external perturbations — suggests little use in analytical/sensoring applications. Here, corrphycene, isoporphycene, and their derivatives have greater potential. As soft chromophores, they should be very sensitive even to minor structural perturbations, such as changes in tautomeric equilibria or in the properties of the environment. MCD seems to be a method of choice for monitoring such changes.

Regarding photophysical characteristics, alkyl-substituted porphycenes are quite promising, with their fluorescence greatly affected by the environment. The potential of other isomers is still unknown. Hopefully, these compounds will be the subject of more intensive studies in the years to come. Naturally, availability of cheap and expedient synthetic procedures is a limiting factor. Recent progress in the synthesis of porphycenes[57,72,206] allows an optimistic forecast.

VII. Acknowledgments

The author is indebted to the many colleagues who contributed to the results presented in this work: Michał Gil, Hubert Piwoński, Natalia Urbańska, Alexander Vdovin, Piotr Fita, Czesław Radzewicz, Oksana Pietraszkiewicz, Marek Pietraszkiewicz, Jerzy Sepioł, Yuriy Stepanenko, Alfred Meixner, Alkwin Slenczka, Bernhard Dick, Achim Hartschuh, Clemens Stupperich, Alexander Kyrychenko, Jacek Dobkowski, Paweł Borowicz, Grażyna Orzanowska, Sylwester Gawinkowski, Gabriela Wiosna-Sałyga, Andrzej Mordziński, and Alexander Starukhin. The author is especially grateful to Emanuel Vogel and Josef Michl, who stimulated his interest in porphycenes. The help of Oleksandr Shkurenko in searching the Cambridge Structural Database is greatly appreciated. This work was partially supported by the grant N204 3329 33 from the Polish Ministry of Science and Higher Education.

VIII. References

1. Cobalt–porphyrin complexes and use thereof as an anti-obesity agent. US Patent 6900197, **2005**.
2. Battersby, A. R.; Fookes, C. J. R.; Matcham, G. W. J.; McDonald, E. *Nature (London)* **1980**, *285*, 17.
3. Monti, D.; Nardis, S.; Stefanelli, M.; Paolesse, R.; Di Natale, C.; D'Amico, A. *J. Sensors*, *2009* [doi:10.1155/2009/856053].
4. Vogel, E.; Köcher, M.; Schmickler, H.; Lex, J. *Angew. Chem. Int. Ed. Engl.* **1986**, *25*, 257.
5. Waluk, J.; Michl, J. *J. Org. Chem.* **1991**, *56*, 2729.
6. Callot, H. J.; Metz, B.; Tschamber, T. *New J. Chem.* **1995**, *19*, 155.

7. Vogel, E.; Bröring, M.; Weghorn, S. J.; Scholz, P.; Deponte, R.; Lex, J.; Schmickler, H.; Schaffner, K.; Braslavsky, S. E.; Müller, M.; Pörting, S.; Fowler, C. J.; Sessler, J. L. *Angew. Chem. Int. Ed. Engl.* **1997**, *36*, 1651.
8. Aukauloo, M. A.; Guilard, R. *New J. Chem.* **1994**, *18*, 1205.
9. Sessler, J. L.; Brucker, E. A.; Weghorn, S. J.; Kisters, M.; Schafer, M.; Lex, J.; Vogel, E. *Angew. Chem. Int. Ed. Engl.* **1994**, *33*, 2308.
10. Vogel, E.; Scholz, P.; Demuth, R.; Erben, C.; Broring, M.; Schmickler, H.; Lex, J.; Hohlneicher, G.; Bremm, D.; Wu, Y. D. *Angew. Chem. Int. Ed.* **1999**, *38*, 2919.
11. Vogel, E.; Bröring, M.; Erben, C.; Demuth, R.; Lex, J.; Nendel, M.; Houk, K. N. *Angew. Chem. Int. Ed. Engl.* **1997**, *36*, 353.
12. Chmielewski, P. J.; Latos-Grażyński, L.; Rachlewicz, K.; Glowiak, T. *Angew. Chem. Int. Ed. Engl.* **1994**, *33*, 779.
13. Furuta, H.; Asano, T.; Ogawa, T. *J. Am. Chem. Soc.* **1994**, *116*, 767.
14. Chmielewski, P. J.; Latos-Grażyński, L. *Coord. Chem. Rev.* **2005**, *249*, 2510.
15. Furuta, H.; Maeda, H.; Osuka, A. *Chem. Commun.* **2002**, 1795.
16. Richert, C.; Wessels, J. M.; Müller, M.; Kisters, M.; Benninghaus, T.; Goetz, A. E. *J. Med. Chem.* **1994**, *37*, 2797.
17. Stockert, J. C.; Cañete, M.; Juarranz, A.; Villanueva, A.; Horobin, R. W.; Borrell, J.; Teixidó, J.; Nonell, S. *Curr. Med. Chem.* **2007**, *14*, 997.
18. Wehrle, B.; Limbach, H. H.; Kocher, M.; Ermer, O.; Vogel, E. *Angew. Chem. Int. Ed. Engl.* **1987**, *26*, 934.
19. Waluk, J.; Müller, M.; Swiderek, P.; Köcher, M.; Vogel, E.; Hohlneicher, G.; Michl, J. *J. Am. Chem. Soc.* **1991**, *113*, 5511.
20. Waluk, J.; Vogel, E. *J. Phys. Chem.* **1994**, *98*, 4530.
21. Frydman, B.; Fernandez, C. O.; Vogel, E. *J. Org. Chem.* **1998**, *63*, 9385.
22. Sepioł, J.; Stepanenko, Y.; Vdovin, A.; Mordziński, A.; Vogel, E.; Waluk, J. *Chem. Phys. Lett.* **1998**, *296*, 549.
23. Gil, M.; Jasny, J.; Vogel, E.; Waluk, J. *Chem. Phys. Lett.* **2000**, *323*, 534.
24. Langer, U.; Hoelger, C.; Wehrle, B.; Latanowicz, L.; Vogel, E.; Limbach, H. H. *J. Phys. Org. Chem.* **2000**, *13*, 23.
25. Kay, C. W. M.; Gromadecki, U.; Törring, J. T.; Weber, S. *Mol. Phys.* **2001**, *99*, 1413.
26. Ghosh, A.; Moulder, J.; Bröring, M.; Vogel, E. *Angew. Chem. Int. Ed. Engl.* **2001**, *40*, 431.
27. Lament, B.; Karpiuk, J.; Waluk, J. *Photochem. Photobiol. Sci.* **2003**, *2*, 267.
28. Nosenko, Y.; Jasny, J.; Pietraszkiewicz, M.; Mordziński, A. *Chem. Phys. Lett.* **2004**, *399*, 331.
29. Piwoński, H.; Stupperich, C.; Hartschuh, A.; Sepioł, J.; Meixner, A.; Waluk, J. *J. Am. Chem. Soc.* **2005**, *127*, 5302.
30. Vdovin, A.; Sepioł, J.; Urbańska, N.; Pietraszkiewicz, M.; Mordziński, A.; Waluk, J. *J. Am. Chem. Soc.* **2006**, *128*, 2577.
31. Waluk, J. *Acc. Chem. Res.* **2006**, *39*, 945.
32. Gil, M.; Waluk, J. *J. Am. Chem. Soc.* **2007**, *129*, 1335.
33. Pietrzak, M.; Shibl, M. F.; Bröring, M.; Kühn, O.; Limbach, H. H. *J. Am. Chem. Soc.* **2007**, *129*, 296.
34. Waluk, J. In *Hydrogen-Transfer Reactions*, Hynes, J. T.; Klinman, J. P.; Limbach, H. H.; Schowen, R. L., Eds.; Wiley-VCH: Weinheim, **2007**; Vol. 1, p. 245.
35. Fita, P.; Urbańska, N.; Radzewicz, C.; Waluk, J. *Z. Phys. Chem.* **2008**, *222*, 1165.
36. Fita, P.; Urbańska, N.; Radzewicz, C.; Waluk, J. *Chem. Eur. J.* **2009**, *15*, 4851.

37. Lopez del Amo, J.; Langer, U.; Torres, V.; Pietrzak, M.; Buntkowsky, G.; Vieth, H. M.; Shibl, M. F.; Kühn, O.; Bröring, M.; Limbach, H. H. *J. Phys. Chem. A* **2009**, *113*, 2193.
38. Piwoński, H.; Hartschuh, A.; Urbańska, N.; Pietraszkiewicz, M.; Sepioł, J.; Meixner, A.; Waluk, J. *J. Phys. Chem. C* **2009**, *113*, 11514.
39. Sobolewski, A.; Gil, M.; Dobkowski, J.; Waluk, J. *J. Phys. Chem. A* **2009**, *113*, 7714.
40. Vdovin, A.; Waluk, J.; Dick, B.; Slenczka, A. *ChemPhysChem* **2009**, *10*, 761.
41. Wu, Y. D.; Chan, K. W. K.; Yip, C. P.; Vogel, E.; Plattner, D. A.; Houk, K. N. *J. Org. Chem.* **1997**, *62*, 9240.
42. Malsch, K.; Hohlneicher, G. *J. Phys. Chem. A* **1997**, *101*, 8409.
43. Malsch, K.; Roeb, M.; Karuth, V.; Hohlneicher, G. *Chem. Phys.* **1998**, *227*, 331.
44. Kozlowski, P. M.; Zgierski, M. Z.; Baker, J. *J. Chem. Phys.* **1998**, *109*, 5905.
45. Walewski, Ł.; Krachtus, D.; Fischer, S.; Smith, J. C.; Bala, P.; Lesyng, B. *Int. J. Quantum Chem.* **2006**, *106*, 636.
46. Shibl, M. F.; Pietrzak, M.; Limbach, H. H.; Kühn, O. *ChemPhysChem* **2007**, *8*, 315.
47. Smedarchina, Z.; Shibl, M. F.; Kühn, O.; Fernández-Ramoz, A. *Chem. Phys. Lett.* **2007**, *426*, 314.
48. Smedarchina, Z.; Siebrand, W.; Fernandez-Ramos, A.; Meana-Paneda, R. *Z. Phys. Chem.* **2008**, *222*, 1291.
49. Walewski, Ł.; Bała, P.; Lesyng, B. In *From Computational Biophysics to Systems Biology (CBSB07)*, Hansmann, U. H. E. M. J.; Mohanty, S.; Zimmermann, O., Eds.; John von Neumann Institute for Computing: Jülich, **2007**, (http://www.fz-juelich.de/nic-series/volume36); Vol. 36, p. 291.
50. Walewski, Ł.; Waluk, J.; Lesyng, B. *J. Phys. Chem. A* **2010**, *114*, 2313.
51. Sessler, J. L.; Gebauer, A.; Vogel, E. In *The Porphyrin Handbook*, Kadish, K. M.; Smith, K. M.; Guilard, R., Eds.; Academic: New York, **2000**; Vol. 2, p. 1.
52. Sessler, J. L.; Weghorn, S. J. *Expanded, Contracted & Isomeric Porphyrins*; Elsevier: Oxford, **1997**.
53. Vogel, E. *Pure Appl. Chem.* **1990**, *62*, 557.
54. Sessler, J. L. *Angew. Chem.* **1994**, *33*, 1348.
55. Vogel, E. *Pure Appl. Chem.* **1996**, *68*, 1355.
56. Fowler, C. J.; Sessler, J. L.; Lynch, V. M.; Waluk, J.; Gebauer, A.; Lex, J.; Heger, A.; Zuniga-y-Rivero, F.; Vogel, E. *Chem. Eur. J.* **2002**, *8*, 3485.
57. Sánchez-Garcia, D.; Sessler, J. L. *Chem. Soc. Rev.* **2008**, *37*, 215.
58. Renner, M. W.; Forman, A.; Wu, W.; Chang, C. K.; Fajer, J. *J. Am. Chem. Soc.* **1989**, *111*, 8618.
59. Bernard, C.; Gisselbrecht, J. P.; Gross, M.; Vogel, E.; Lausmann, M. *Inorg. Chem.* **1994**, *33*, 2393.
60. Kadish, K. M.; D'Souza, F.; Van Caemelbecke, E.; Boulas, P.; Vogel, E.; Aukauloo, A. M.; Guilard, R. *Inorg. Chem.* **1994**, *33*, 4474.
61. D'Souza, F.; Boulas, P.; Aukauloo, A. M.; Guilard, R.; Kisters, M.; Vogel, E.; Kadish, K. M. *J. Phys. Chem.* **1994**, *98*, 11885.
62. Guldi, D. M.; Neta, P.; Vogel, E. *J. Phys. Chem.* **1996**, *100*, 4097.
63. Guldi, D. M.; Field, J.; Grodkowski, J.; Neta, P.; Vogel, E. *J. Phys. Chem.* **1996**, *100*, 13609.
64. Rachlewicz, K.; Latos-Grazyński, L.; Vogel, E.; Ciunik, Z.; Jerzykiewicz, L. B. *Inorg. Chem.* **2002**, *41*, 1979.
65. Rachlewicz, K.; Latos-Grażyński, L.; Vogel, E. *Inorg. Chem.* **2000**, *39*, 3247.
66. Gisselbrecht, J. P.; Gross, M.; Vogel, E.; Sessler, J. L. *Inorg. Chem.* **2000**, *39*, 2850.

67. Gisselbrecht, J. P.; Gross, M.; Vogel, E.; Scholz, P.; Bröring, M.; Sessler, J. L. *J. Electroanal. Chem.* **2001**, *507*, 244.
68. Braslavsky, S. E.; Müller, M.; Mártire, D. O.; Pörting, S.; Bertolotti, S. G.; Chakravorti, S.; Koç-Weier, G.; Knipp, B.; Schaffner, K. *J. Photochem. Photobiol. B* **1997**, *40*, 191.
69. Rubio, N.; Prat, F.; Bou, N.; Borrell, J. I.; Teixidó, J.; Villanueva, A.; Juarranz, A.; Cañete, M.; Stockert, J. C.; Nonell, S. *New J. Chem.* **2005**, *29*, 378.
70. Vogel, E.; Balci, M.; Pramod, K.; Koch, P.; Lex, J.; Ermer, O. *Angew. Chem. Int. Ed. Engl.* **1987**, *26*, 928.
71. Vogel, E.; Köcher, M.; Lex, J.; Ermer, O. *Isr. J. Chem.* **1989**, *29*, 257.
72. Anju, K. S.; Ramakrishnan, S.; Thomas, A. P.; Suresh, E.; Srinivasan, A. *Org. Lett.* **2008**, *10*, 5545.
73. Vogel, E.; Köcher, M.; Balci, M.; Teichler, I.; Lex, J.; Schmickler, H.; Ermer, O. *Angew. Chem. Int. Ed. Engl.* **1987**, *26*, 931.
74. Vogel, E.; Koch, P.; Hou, X. L.; Lex, J.; Lausmann, M.; Kisters, M.; Aukauloo, M. A.; Richard, P.; Guilard, R. *Angew. Chem.* **1993**, *32*, 1600.
75. Shimakoshi, H.; Baba, T.; Iseki, Y.; Aritome, I.; Endo, A.; Adachi, C.; Hisaeda, Y. *Chem. Commun.* **2008**, 2882.
76. Will, S.; Rahbar, A.; Schmickler, H.; Lex, J.; Vogel, E. *Angew. Chem. Int. Ed. Engl.* **1990**, *29*, 1390.
77. Aritome, I.; Shimakoshi, H.; Hisaeda, Y. *Acta Crystallogr. Sect. C–Cryst. Struct. Commun.* **2002**, *C58*, o563.
78. Sessler, J. L.; Brucker, E. A.; Lynch, V.; Choe, M.; Sorey, S.; Vogel, E. *Chem. Eur. J.* **1996**, *2*, 1527.
79. Ohgo, Y.; Neya, S.; Takahashi, M.; Takeda, M.; Funasaki, N.; Nakamura, M. *Chem. Lett.* **2003**, *32*, 526.
80. Paolesse, R.; Nardis, S.; Stefanelli, M.; Fronczek, F. R.; Vicente, M. G. H. *Angew. Chem. Int. Ed.* **2005**, *44*, 3047.
81. Webb, L. E.; Fleischer, E. B. *J. Chem. Phys.* **1965**, *43*, 3100.
82. Chen, B.; Tulinsky, A. *J. Am. Chem. Soc.* **1972**, *94*, 4144.
83. Saltsman, I.; Goldberg, I.; Balazs, Y.; Gross, Z. *Tetrahedron Lett.* **2007**, *48*, 239.
84. Lauher, J. W.; Ibers, J. A. *J. Am. Chem. Soc.* **1973**, *95*, 5148.
85. Codding, P. W.; Tulinsky, A. *J. Am. Chem. Soc.* **1972**, *94*, 4151.
86. Kano, K.; Fukuda, K.; Wakami, H.; Nishiyabu, R.; Pasternack, R. F. *J. Am. Chem. Soc.* **2000**, *122*.
87. Silvers, S. J.; Tulinsky, A. *J. Am. Chem. Soc.* **1967**, *89*, 3331.
88. Bond, A. D.; Feeder, N.; Redman, J. E.; Teat, S. J.; Sanders, J. K. M. *Cryst. Growth Des.* **2002**, *2*, 27.
89. Senge, M. O.; Kalisch, W. W.; Bischoff, I. *Chem. Eur. J.* **2000**, *6*, 2721.
90. Hayashi, T.; Nakashima, Y.; Ito, K.; Ikegami, T.; Aritome, I.; Suzuki, A.; Hisaeda, Y. *Org. Lett.* **2003**, *5*, 2845.
91. Schlabach, M.; Wehrle, B.; Rumpel, H.; Braun, J.; Scherer, G.; Limbach, H. H. *Ber. Bunsenges. Phys. Chem.* **1992**, *96*, 821.
92. Braun, J.; Schlabach, M.; Wehrle, B.; Köcher, M.; Vogel, E.; Limbach, H. H. *J. Am. Chem. Soc.* **1994**, *116*, 6593.
93. Braun, J.; Limbach, H. H.; Williams, P. G.; Morimoto, H.; Wemmer, D. E. *J. Am. Chem. Soc.* **1996**, *118*, 7231.
94. Radziszewski, J. G.; Waluk, J.; Michl, J. *Chem. Phys.* **1989**, *136*, 165.

95. Radziszewski, J.; Waluk, J.; Michl, J. *J. Mol. Spectrosc.* **1990**, *140*, 373.
96. Radziszewski, J. G.; Waluk, J.; Nepraš, M.; Michl, J. *J. Phys. Chem.* **1991**, *95*, 1963.
97. Ghosh, A.; Jynge, K. *J. Phys. Chem. B* **1997**, *101*, 5459.
98. Bremm, D.; Lex, J.; Hohlneicher, G. *J. Mol. Struct.* (*Theochem*) **2007**, *802*, 45.
99. Gouterman, M. *J. Mol. Spectrosc.* **1961**, *6*, 138.
100. Stern, A.; Wenderlein, H. *Z. Physik. Chem.* **1936**, *176A*, 81.
101. Platt, J. R. *J. Chem. Phys.* **1949**, *17*, 484.
102. Moffit, W. *J. Chem. Phys.* **1954**, *22*, 320.
103. Moffit, W. *J. Chem. Phys.* **1954**, *22*, 1820.
104. Michl, J. *J. Am. Chem. Soc.* **1978**, *100*, 6801.
105. Michl, J. *J. Am. Chem. Soc.* **1978**, *100*, 6812.
106. Michl, J. *J. Am. Chem. Soc.* **1978**, *100*, 6819.
107. Michl, J. *Tetrahedron* **1984**, *40*, 3845.
108. Baba, T.; Shimakoshi, H.; Hisaeda, Y. *Tetrahedron Lett.* **2004**, *45*, 5973.
109. Mak, N. K.; Kok, T. W.; Wong, R. N. S.; Lam, S. W.; Lau, Y. K.; Leung, W. N.; Cheung, N. H.; Huang, D. P.; Yeung, L. L.; Chang, C. K. *J. Biomed. Sci.* **2003**, *10*, 418.
110. Birklund-Andersen, K.; Vogel, E.; Waluk, J. *Chem. Phys. Lett.* **1997**, *271*, 341.
111. Nonell, S.; Bou, N.; Borrell, J. I.; Teixidó, J.; Villanueva, A.; Juarranz, A.; Cañete, M. *Tetrahedron Lett.* **1995**, *36*, 3405.
112. Arad, O.; Rubio, N.; Sánchez-Garcia, D.; Borrell, J. I.; Nonell, S. *J. Porphyrins Phthalocyanines* **2009**, *13*, 376.
113. Sargent, A. L.; Hawkins, I. C.; Allen, W. E.; Liu, H.; Sessler, J. L.; Fowler, C. J. *Chem. Eur. J.* **2003**, *9*, 3065.
114. Nonell, S.; Borrell, J. I.; Borrós, S.; Colominas, C.; Rey, O.; Rubio, N.; Sánchez-García, D.; Teixidó, J. *Eur. J. Org. Chem.* **2003**, 1635.
115. Rubio, N.; Sánchez-García, D.; Jiménez-Banzo, A.; Rey, Ó.; Borrell, J. I.; Teixidó, J.; Nonell, S. *J. Phys. Chem. A* **2006**, *110*, 3480.
116. Bremm, D.; Hohlneicher, G. *J. Mol. Struct.* **1999**, *480–481*, 591.
117. Gorski, A.; Vogel, E.; Sessler, J. L.; Waluk, J. *Chem. Phys.* **2002**, *282*, 37.
118. Gorski, A.; Vogel, E.; Sessler, J. L.; Waluk, J. *J. Phys. Chem. A* **2002**, *106*, 8139.
119. Falk, H.; Chen, Q. Q. *Monatsh. Chem.* **1996**, *127*, 69.
120. Neya, S.; Nishinaga, K.; Ohyama, K.; Funasaki, N. *Tetrahedron Lett.* **1998**, *39*, 5217.
121. Gouterman, M. *J. Chem. Phys.* **1959**, *30*.
122. Gouterman, M.; Wagnière, G. H.; Snyder, L. C. *J. Mol. Spectrosc.* **1963**, *11*, 108.
123. Keegan, J. D.; Stolzenberg, A. M.; Lu, Y. C.; Linder, R. E.; Barth, G.; Moscowitz, A.; Bunnenberg, E.; Djerassi, C. *J. Am. Chem. Soc.* **1982**, *104*, 4305.
124. Keegan, J. D.; Stolzenberg, A. M.; Lu, Y. C.; Linder, R. E.; Barth, G.; Moscowitz, A.; Bunnenberg, E.; Djerassi, C. *J. Am. Chem. Soc.* **1982**, *104*, 4317.
125. Lu, Y.; Shu, A. Y. L.; Knierzinger, A.; Clezy, P. S.; Bunnenberg, E.; Djerassi, C. *Tetrahedron Lett.* **1983**, *24*, 2433.
126. Keegan, J. D.; Bunnenberg, E.; Djerassi, C. *Spectrochim. Acta Part A* **1984**, *40A*, 287.
127. Lu, Y.; Waleh, A.; Shu, A. Y. L.; Goldbeck, R. A.; Kehres, L. A.; Crandell, C. W.; Wee, A. G. H.; Knierzinger, A.; Gaete-Holmes, R.; *et al*. *J. Am. Chem. Soc.* **1984**, *106*, 4241.
128. Wee, A. G. H.; Shu, A. Y. L.; Bunnenberg, E.; Djerassi, C. *J. Org. Chem.* **1984**, *49*, 3327.

129. Ceulemans, A.; Oldenhof, W.; Gorller-Walrand, C.; Vanquickenborne, L. G. *J. Am. Chem. Soc.* **1986**, *108*, 1155.
130. Goldbeck, R. A.; Tolf, B. R.; Wee, A. G. H.; Shu, A. Y. L.; Records, R.; Bunnenberg, E.; Djerassi, C. *J. Am. Chem. Soc.* **1986**, *108*, 6449.
131. Goldbeck, R. A.; Tolf, B. R.; Bunnenberg, E.; Djerassi, C. *J. Am. Chem. Soc.* **1987**, *109*, 28.
132. Goldbeck, R. A. *Acc. Chem. Res.* **1988**, *21*, 95.
133. Zen'kevich, E. A.; Shul'ga, A. M.; Chernook, A. V.; Filatov, I. V.; Gurinovich, G. P. *Teor. Eksp. Khim.* **1989**, *25*, 295.
134. Yoshimura, T.; Toi, H.; Inaba, S.; Ogoshi, H. *Bull. Chem. Soc. Jpn.* **1992**, *65*, 1915.
135. Franzen, S. *J. Phys. Chem. B* **2002**, *106*, 10482.
136. Stillman, M.; Mack, J.; Kobayashi, N. *J. Porphyrins Phthalocyanines* **2002**, *6*, 296.
137. Mack, J.; Stillman, M. J. In *The Porphyrin Handbook*, Kadish, K. M., Smith, K.M., Guilard, R.; Eds.; Academic: New York, **2003**; Vol. 16, p. 43.
138. Mack, J.; Asano, Y.; Kobayashi, N.; Stillman, M. J. *J. Am. Chem. Soc.* **2005**, *127*, 17697.
139. Muranaka, A.; Yokoyama, M.; Matsumoto, Y.; Uchiyama, M.; Tsuda, A.; Osuka, A.; Kobayashi, N. *ChemPhysChem* **2005**, *6*, 171.
140. Kobayashi, N.; Nakai, K. *Chem. Commun.* **2007**, 4077.
141. Mack, J.; Stillman, M. J.; Kobayashi, N. *Coord. Chem. Rev.* **2007**, *251*, 429.
142. Mack, J.; Bunya, M.; Shimizu, Y.; Uoyama, H.; Komobuchi, N.; Okujima, T.; Uno, H.; Ito, S.; Stillman, M. J.; Ono, N.; Kobayashi, N. *Chem. Eur. J.* **2008**, *14*, 5001.
143. Muranaka, A.; Homma, S.; Maeda, H.; Furuta, H.; Kobayashi, N. *Chem. Phys. Lett.* **2008**, *460*, 495.
144. Kobayashi, N.; Fukuda, T. *Bull. Chem. Soc. Jpn.* **2009**, *82*, 631.
145. Gorski, A.; Lament, B.; Davis, J. M.; Sessler, J.; Waluk, J. *J. Phys. Chem. A* **2001**, *105*, 4992.
146. Lament, B.; Rachlewicz, K.; Latos-Grażyński, L.; Waluk, J. *Chem. Phys. Chem* **2002**, *3*, 849.
147. Gorski, A.; Köhler, T.; Seidel, D.; Lee, J. T.; Orzanowska, G.; Sessler, J. L.; Waluk, J. *Chem. Eur. J.* **2005**, *11*, 4179.
148. Hasegawa, J.; Takata, K.; Miyahara, T.; Neya, S.; Frisch, M. J.; Nakatsuji, H. *J. Phys. Chem. A* **2005**, *109*, 3187.
149. Lament, B.; Dobkowski, J.; Sessler, J. L.; Weghorn, S. J.; Waluk, J. *Chem. Eur. J.* **1999**, *5*, 3039.
150. Höweler, U.; Downing, J. W.; Fleischhauer, J.; Michl, J. *J. Chem. Soc. Perkin Trans. 2* **1998**, 1101.
151. Fleischhauer, J.; Höweler, U.; Michl, J. *Spectrochim. Acta Part. A* **1999**, *55*, 585.
152. Fleischhauer, J.; Höweler, U.; Michl, J. *J. Phys. Chem. A* **2000**, *104*, 7762; erratum, 10866.
153. Fleischhauer, J.; Michl, J. *J. Phys. Chem. A* **2000**, *104*, 7776.
154. Fleischhauer, J.; Raabe, G.; Klingensmith, K. A.; Höweler, U.; Chatterjee, P. K.; Hafner, K.; Vogel, E.; Michl, J. *Int. J. Quantum Chem.* **2005**, *102*, 925.
155. Kramer, B.; Fleischhauer, J.; Michl, J. *Z. Naturforsch.* **1993**, *48a*, 1243.
156. Starukhin, A.; Vogel, E.; Waluk, J. *J. Phys. Chem. A* **1998**, *102*, 9999.
157. Dobkowski, J.; Lobko, Y.; Gawinkowski, S.; Waluk, J. *Chem. Phys. Lett.* **2005**, 128.
158. Dobkowski, J.; Galievsky, V.; Waluk, J. *Chem. Phys. Lett.* **2000**, *318*, 79.
159. Dobkowski, J.; Galievsky, V.; Starukhin, A.; Vogel, E.; Waluk, J. *J. Phys. Chem. A* **1998**, *102*, 4966.
160. Dobkowski, J.; Galievsky, V.; Gil, M.; Waluk, J. *Chem. Phys. Lett.* **2004**, *394*, 410.
161. Kyrychenko, A.; Waluk, J. *J. Chem. Phys.* **2005**, *123*, 064706.

162. Kyrychenko, A.; Waluk, J. *J. Chem. Phys.* **2003**, *119*, 7318.
163. Kyrychenko, A.; Gorski, A.; Waluk, J. *J. Chem. Phys.* **2004**, *121*, 12017.
164. Kyrychenko, A.; Gawinkowski, S.; Urbańska, N.; Pietraszkiewicz, M.; Waluk, J. *J. Chem. Phys.* **2007**, *127*, 134501.
165. Gentemann, S.; Medforth, C. J.; Forsyth, T. P.; Nuro, D. J.; Smith, K. M.; Fajer, J.; Holten, D. *J. Am. Chem. Soc.* **1994**, *116*, 7363.
166. Gentemann, S.; Medforth, C. J.; Ema, T.; Nelson, N. Y.; Smith, K. M.; Fajer, J.; Holten, D. *Chem. Phys. Lett.* **1995**, *245*, 441.
167. Levanon, H.; Toporowicz, M.; Ofir, H.; Fessenden, R. W.; Das, P. K.; Vogel, E.; Kocher, M.; Pramod, K. *J. Phys. Chem.* **1988**, *92*, 2429.
168. Berman, A.; Michaeli, A.; Feitelson, J.; Bowman, M. K.; Norris, J. R.; Levanon, H.; Vogel, E.; Koch, P. *J. Phys. Chem.* **1992**, *96*, 3041.
169. Gil, M.; Organero, J. A.; Waluk, J.; Douhal, A. *Chem. Phys. Lett.* **2006**, *422*, 142.
170. Fita, P.; Radzewicz, C.; Waluk, J. *J. Phys. Chem. A* **2008**, *112*, 10753.
171. Ofir, H.; Regev, A.; Levanon, H.; Vogel, E.; Kocher, M.; Balci, M. *J. Phys. Chem.* **1987**, *91*, 2686.
172. Toporowicz, M.; Ofir, H.; Levanon, H.; Vogel, E.; Köcher, M.; Pramod, K.; Fessenden, R. W. *Photochem. Photobiol.* **1989**, *50*, 37.
173. Nonell, S.; Aramendía, P. F.; Heihoff, K.; Negri, R. M.; Braslavsky, S. E. *J. Phys. Chem.* **1990**, *94*, 5879.
174. Hamacher, V.; Plato, M.; Möbius, K.; Vogel, E. *Appl. Magn. Reson.* **1993**, *4*, 321.
175. Kay, C. W. M.; Möbius, K. *Mol. Phys.* **1998**, *95*, 1013.
176. Kay, C. W. M.; Elger, G.; Möbius, K. *Phys. Chem. Chem. Phys.* **1999**, *1*, 3999.
177. Baumer, D.; Maier, M.; Engl, R.; Szeimies, R. M.; Bäumler, W. *Chem. Phys.* **2002**, *285*, 309.
178. Baier, A.; Maier, M.; Engl, R.; Landthaler, M.; Bäumler, W. *J. Phys. Chem. B* **2005**, *109*, 3041.
179. Shimakoshi, H.; Baba, T.; Iseki, Y.; Endo, A.; Adachi, C.; Watanabe, M.; Hisaeda, Y. *Tetrahedron Lett.* **2008**, *49*, 6198.
180. Shuali, Z.; Berg, A.; Levanon, H.; Vogel, E.; Broring, M.; Sessler, J. L.; Fowler, C.; Weghorn, S. J. *Chem. Phys. Lett.* **1999**, *300*, 687.
181. Mártire, D. O.; Vaveliuk, P.; Bilmes, G. M. *Spectrochim. Acta Part A* **2000**, *56*, 2043.
182. Storm, C. B.; Teklu, Y. *J. Am. Chem. Soc.* **1972**, *94*, 1745.
183. Storm, C. B.; Teklu, Y. *Ann. NY. Acad. Sci.* **1973**, *206*, 631.
184. Solov'ev, K. N.; Zalesski, I. E.; Kotlo, V. N.; Shkirman, S. F. *JETP Lett. (Eng. transl.)* **1973**, *17*, 332.
185. Zalesski, I. E.; Kotlo, V. N.; Sevchenko, A. N.; Solov'ev, K. N.; Shkirman, S. F. *Sov. Phys. Dokl. (Eng. transl.)* **1973**, *17*, 1183.
186. Voelker, S.; van der Waals, J. H. *Mol. Phys.* **1976**, *32*, 1703.
187. Radziszewski, J.; Burkhalter, F. A.; Michl, J. *J. Am. Chem. Soc.* **1987**, *109*, 61.
188. Radziszewski, J.; Michl, J.; Waluk, J. *Proc. SPIE — Int. Soc. Opt. Eng.* **1991**, *1575*, 606.
189. Dvornikov, S. S.; Kuz'mitskii, V. A.; Knyukshto, V. N.; Solov'ev, K. N. *Dokl. Akad. Nauk SSSR* **1985**, *282*, 362.
190. Baker, J.; Kozlowski, P. M.; Jarzecki, A. A.; Pulay, P. *Theor. Chem. Acc.* **1997**, *97*, 59.
191. Even, U.; Jortner, J. *J. Chem. Phys.* **1982**, *77*, 4391.
192. Kuimova, M. K.; Yahioglu, G.; Levitt, J. A.; Suhling, K. *J. Am. Chem. Soc.* **2008**, *130*, 6672.
193. Kuimova, M. K.; Botchway, S. W.; Parker, A. W.; Balaz, M.; Collins, H. A.; Anderson, H. L.; Klaus Suhling, K.; Ogilby, P. R. *Nat. Chem.* **2009**, *1*, 69.
194. Hayashi, T.; Dejima, H.; Matsuo, T.; Sato, H.; Murata, D.; Hisaeda, Y. *J. Am. Chem. Soc.* **2002**, *124*, 11226.

195. Matsuo, T.; Dejima, H.; Hirota, S.; Murata, D.; Sato, H.; Ikegami, T.; Hori, H.; Hisaeda, Y.; Hayashi, T. *J. Am. Chem. Soc.* **2004**, *126*, 16007.
196. Matsuo, T.; Tsuruta, T.; Maehara, K.; Sato, H.; Hisaeda, Y.; Hayashi, T. *Inorg. Chem.* **2005**, *44*, 9391.
197. Hayashi, T.; Murata, D.; Makino, M.; Sugimoto, H.; Matsuo, T.; Sato, H.; Shiro, Y.; Hisaeda, Y. *Inorg. Chem.* **2006**, *45*, 10530.
198. Matsuo, T.; Ikegami, T.; Sato, H.; Hisaeda, Y.; Hayashi, T. *J. Inorg. Biochem.* **2006**, *100*, 1265.
199. Matsuo, T.; Murata, D.; Hisaeda, Y.; Hori, H.; Hayashi, T. *J. Am. Chem. Soc.* **2007**, *129*, 12906.
200. Matsuo, T.; Ito, K.; Nakashima, Y.; Hisaeda, Y.; Hayashi, T. *J. Inorg. Biochem.* **2008**, *102*, 166.
201. Neya, S.; Nakamura, M.; Imai, K.; Funasaki, N. *Chem. Pharm. Bull.* **2001**, *49*, 345.
202. Neya, S.; Tsubaki, M.; Hori, H.; Yonetani, T.; Funasaki, N. *Inorg. Chem.* **2001**, *40*, 1220.
203. Neya, S.; Imai, K.; Hiramatsu, Y.; Kitagawa, T.; Hoshino, T.; Hata, M.; Funasaki, N. *Inorg. Chem.* **2006**, *45*, 4238.
204. Neya, S.; Hoshino, T. *Jinko Ketsueki* **2008**, *16*, 3.
205. Neya, S.; Suzuki, M.; Hoshino, T. *Artif. Organs* **2009**, *33*, 189.
206. Urbańska, N.; Pietraszkiewicz, M.; Waluk, J. *J. Porphyrins Phthalocyanines* **2007**, *11*, 596.
207. Punnagai, M.; Sateesh, B.; Sastry, G. N. *Arkivoc* **2005**, 258.
208. Edwards, L.; Dolphin, D. H.; Gouterman, M.; Adler, A. D. *J. Mol. Spectrosc.* **1971**, *38*, 16.
209. Rimington, C. *Biochem. J.* **1960**, *75*.
210. Voelker, S.; Macfarlane, R. M.; Genack, A. Z.; Trommsdorff, H. P. *J. Chem. Phys.* **1977**, *67*, 1759.
211. Kim, B. F.; Bohandy, J. *J. Mol. Spectrosc.* **1978**, *73*, 332.
212. Eisner, U.; Lichtarowicz, A.; Linstead, R. P. *J. Chem. Soc.* **1957**, 733.
213. Johnstone, R. A. W.; Nunes, M. L. P. G.; Pereira, M. M.; d'A. Rocha Gonsalves, A. M.; Serra, A. C. *Heterocycles* **1996**, *43*, 1423.
214. Fonda, H. N.; Gilbert, J. V.; Cormier, R. A.; Sprague, J. R.; Kamioka, K.; Conolly, J. S. *J. Phys. Chem.* **1993**, *97*, 7024.
215. Lin, C. Y.; Chen, Y. C.; Yao, C. W.; Huang, S. C.; Cheng, Y. H. *Dalton Trans.* **2008**, 793.
216. Milanesi, C.; Biolo, R.; Jori, G.; Schaffner, K. *Laser Med. Sci.* **1991**, *6*, 437.
217. Lausmann, M.; Zimmer, I.; Lex, J.; Lueken, H.; Wieghardt, K.; Vogel, E. *Angew. Chem. Int. Ed. Engl.* **1994**, *33*, 736.
218. Gradyushko, A. T.; Tsvirko, M. P. *Opt. Spectrosc. (Russ.)* **1971**, *31*, 548.
219. Ohno, O.; Kaizu, Y.; Kobayashi, H. *J. Chem. Phys.* **1985**, *82*, 1779.
220. Kikuchi, K.; Kurabayashi, Y.; Kokubun, H.; Kaizu, Y.; Kobayashi, H. *J. Photochem. Photobiol., A* **1988**, *45*, 261.
221. Seybold, P. G.; Gouterman, M. *J. Mol. Spectrosc.* **1969**, *31*, 1.
222. Goll, J. G.; Moore, K. T.; Ghosh, A.; Therien, M. J. *J. Am. Chem. Soc.* **1996**, *118*, 8344.
223. Gurinovich, G. P.; Jagarov, B. M. In *Luminescence of Crystals, Molecules and Solutions*, Williams, F., Ed.; Plenum: New York, **1973**; p. 196.
224. Gradyushko, A. T.; Sevchenko, A. N.; Solovyov, K. N.; Tsvirko, M. P. *Photochem. Photobiol.* **1970**, *11*, 387.
225. Aramendia, P. F.; Redmond, R. W.; Nonell, S.; Schuster, W.; Braslavsky, S. E.; Schaffner, K.; Vogel, E. *Photochem. Photobiol.* **1986**, *44*, 555.
226. Redmond, R. W.; Valduga, G.; Nonell, S.; Braslavsky, S. E.; Schaffner, K.; Vogel, E.; Pramod, K.; Kocher, M. *J. Photochem. Photobiol. B* **1989**, *3*, 193.
227. Baba, T.; Shimakoshi, H.; Endo, A.; Adachi, C.; Hisaeda, Y. *Chem. Lett.* **2008**, *37*, 264.

This page intentionally left blank

36 Recent Applications of Infrared Spectroscopy and Microscopy in Chemistry, Biology and Medicine

Petra Hellwig and Frédéric Melin

Institut de Chimie, UMR 7177, Laboratoire de Spectroscopie Vibrationnelle et Électrochimie des Biomolécules, Université de Strasbourg, 1, rue Blaise Pascal, 67000 Strasbourg, France

List of Abbreviations

4-AcPy	4-acetylpyridine
Arg	arginine
Asn	asparagine
Asp	aspartic acid
ATP	adenosine triphosphate

ATR	attenuated total reflexion
C*a*	α-pyrrolic carbon atoms
C*b*	β-pyrrolic carbon atoms
Cyt	cytochrome
C_n-cap (n = 2, 3)	phenyl-capped tetraphenylporphyrin with $-O(CH_2)_nOCO-$linkers between the cap and the porphyrin
C*m*	*meso* carbon atoms
CASSCF	complete active space self-consistent field
DFT	density functional theory
DFT-SQM	density functional theory with scaled quantum-mechanical force field
2D-IR	two-dimensional infrared
DMAP	4-dimethylaminopyridine
DNA	deoxyribonucleic acid
IR	infrared
FEL	free electron laser
FIR	far-infrared
fs	femtosecond
FTIR	Fourier-transformed infrared
Gln	glutamine
Glu	glutamic acid
Hb	hemoglobin
Im	imidazole
ISP	iron–sulfur protein
Mb	myoglobin
MIR	mid-infrared
MeIm	methylimidazole
Me_2Im	dimethylimidazole
Mepip	methylpiperidine
$NapC_2$-cap	phenyl-capped tetranaphtalenylporphyrin with $-O(CH_2)_2OCO-$linkers between the cap and the porphyrin
NIR	near-infrared
NRVS	nuclear resonance vibrational spectroscopy
OC_3OPor	phenyl-capped tetraphenylporphyrin with $-O(CH_2)_3O-$ linkers between the cap and the porphyrin
OD	optical density
OEP	octaethylporphyrin

Pc	phthalocyanine
MedPiv	medium tail pocket porphyrin
OBTPP	octabromotetraphenylporphyrin
PDT	photodynamic therapy
Pip	piperidine
Piv_2C_n (n = 8, 9, 10, 12)	hybrid basket handle porphyrin with n carbons in the strap
PocPiv	small tail pocket porphyrin
PPIX	protoporphyrin IX
PPIXMe	protoporphyrin IX dimethylester
Py	pyridine
SDS	sodium dodecyl sulfate
SEIRAS	surface-enhanced infrared absorption spectroscopy
SERS	surface-enhanced Raman scattering
SIR	synchrotron infrared emission
SOMO	singly occupied molecular orbital
TalPiv	large tail pocket porphyrin
TAP	*meso* tetra(*p*-anisyl)porphyrin
TCP	twin coronet porphyrin
TCP-py	twin coronet porphyrin with a covalently bound pyridine
TDCPP	*meso* tetra(2,6-dichlorophenyl)porphyrin
TD-DFT	time-dependent density functional theory
TDFPP	*meso* tetra(2,6-difluorophenyl)porphyrin
TD-THz	time-dependent terahertz
THz	terahertz
TMP	*meso* tetramesitylporphyrin
T(*p*-CF_3)PP	*meso* tetra(*p*-trifluoromethylphenyl)porphyrin
T(*p*-CN)PP	*meso* tetra (*p*-cyanophenyl)porphyrin
TPFPP	*meso* tetra(pentafluorophenyl)porphyrin
TPivPP	*meso* tetra($\alpha,\alpha,\alpha,\alpha$-*o*-pivalamidophenyl)porphyrin
T(*p*-OCF_3)PP	*meso* tetra(*p*-trifluoromethoxyphenyl)porphyrin
TPP	*meso* tetraphenylporphyrin
TTP	*meso* tetra(*p*-tolyl)porphyrin
δ	label of in-plane deformation vibrational modes
γ	label of out-of-plane deformation vibrational modes
ν	label of stretching vibrational modes

I. Introduction

Infrared spectroscopy is a versatile technique that can be used for all types of materials, including polymers, biological samples, individual molecules and tissues. Although the theory of infrared spectroscopy has been thoroughly worked out, its scientific basis is currently undergoing a boost, with the application of this analytical technique in biology and biomedicine and the development of new time- and space-resolved techniques in chemistry and biochemistry.

For many years infrared spectroscopy has been a popular technique for analyzing porphyrins and their derivatives.[1–13] The vibrational modes typically found are specific to the porphyrin ring,[4,14,15] its oxidation and spin states,[14,16,17] the central ion and, more importantly, its axial ligands[18–22] and hydrogen bonding environment or interaction.[23,24] Normal coordinate analysis and other theoretical approaches can be applied for detailed analysis. Together with Raman spectroscopy, the technique has developed to a point where it is a standard analytical method that accompanies synthesis and characterization of porphyrin compounds.[25–29] This is especially the case for the mid- and near-infrared spectral ranges, where low cost instruments are available.

Infrared spectroscopy is used to study reaction mechanisms and has been crucially employed in clarifying reaction intermediates within the catalytic cycle of enzymes and their models.[11,30–33] Combination with other techniques, including photo- or redox chemistry, has been realized. Infrared microscopy and infrared imaging have recently emerged, adding the possibility of studying spatial resolution of molecular ensembles, tissues or crystals. The development of the step scan technique and the evolution of laser spectroscopies allowed studies with a time resolution up to the femtosecond (fs) range. The unique combination of molecular level structural information and ultrafast time resolution was achieved by two-dimensional (2D) IR spectroscopies, giving previously inaccessible insight into rapid structural fluctuations, vibrational dynamics and solvent–solute interactions.[34–36] Synchrotron radiation for high resolution gas phase infrared spectroscopy was used in pioneering applications at MAXLab in Sweden[37] and LURE in France,[38] and new facilities have been developed at a number of synchrotrons, including SOLEIL (France), the Australian Synchrotron, IRIS and ANKA (Germany), and the Swiss Light Source. Synchrotron radiation provides an infrared source that is much brighter than conventional thermal sources. This type of light source is ideal for applications requiring high spatial resolution (i.e. spectromicroscopy) or high spectral resolution (<0.001 cm^{-1}).

In this chapter, an overview of recent developments in the area of infrared-light-based spectroscopies is given along with selected examples from the field of porphyrins and their derivatives. Some emphasis will be given to studies of

hemoproteins derived from the respiratory chain. After a summary of the well-established mid-infrared spectral properties of porphyrins and derivatives, we will focus on the emerging NIR and FIR studies as well as IR differential spectroscopy induced by variation of external parameters like the redox state or temperature.

II. Infrared Absorbance Spectra of Porphyrins and Related Compounds

Infrared spectroscopists distinguish three main spectral ranges: the near-infrared (NIR) extends close to the visible from 12,500 to 4000 cm^{-1} (800–2500 nm), the mid-infrared (MIR) from 4000 to 450 cm^{-1} and the far-infrared (FIR) from approximately 450 to 2 cm^{-1} (13.5–0.06 THz). Normal coordinate analysis has been carried out for porphyrins starting from an idealized D_{4h} symmetry, and then the symmetry constraints were relaxed to take into account the deviation from planarity of the macrocycle as well as the rotation of peripheral substituents.[39–42] In D_{4h} symmetry the planar porphyrin core has 71 in-plane vibrational modes, out of which 18 of E_u symmetry are IR-active, and 34 out-of-plane modes, out of which 6 of A_{2u} symmetry are IR-active. *Meso*- or β-substitution of the porphyrin core further increases the number of vibrational modes: the metallotetraphenylporphyrins (MTPPs), for instance, have 169 normal modes, out of which 27% can be characterized by IR spectroscopy. The planar core of phthalocyanines has 165 normal vibration modes, out of which 8 of A_{2u} and 28 of E_u symmetry are IR-active.[43]

A. The Mid-Infrared or Rock Salt Region

The MIR absorption of porphyrins has been described for the simplest porphyrin or substituted ones (such as tetraphenylporphyrin (TPP) and derivatives, octaethylporphyrin (OEP), protoporphyrin IX (PPIX) and hematoporphyrin IX, *N*-methyl porphyrins), a variety of their metal complexes (Mg(II), Mn(II) and Mn(III), Fe(II) and Fe(III), Co(II) and Co(III), Ni(II), Pd(II), Pt(II), Cu(II), Ag(II), Zn(II), Cd(II)) and with or without biologically relevant additional ligands (O_2, CO, NO, imidazoles).[1–13,18] In some cases, a complete quantum-chemistry-based analysis is also available.[40,41] Usually up to four regions can be distinguished in the spectra.[18,39,41,44] Between 500 and 810 cm^{-1} there mostly appear out-of-plane vibrations of the porphyrin (in particular pyrrole folding modes, deformations $\gamma(H_\beta)$) as well as the phenyl deformation bands in the *meso*-phenyl-substituted porphyrins. The second region extends approximately from 900 to 1350 cm^{-1} and encompasses mainly in-plane vibrations (coupled pyrrole breathing and deformation bands, pyrrole half-ring modes, C–H in-plane bending modes). Between 1400 and 1700 cm^{-1} there appear the coupled stretching modes of the =C–N, C=N and

C=C bonds of the porphyrin core and the phenyl substituents. At higher energy (above 3000 cm^{-1}) the weak stretching N–H and C–H bands of the pyrrole and methine bridges can be seen. In addition, the spectra of protoporphyrin IX and hematoporphyrin IX derivatives show the strong pH-dependent absorption peaks of the propionate carbonyl stretches between 1700 and 1750 cm^{-1} and the weaker antisymmetric and symmetric C–H alkyl stretching mode just below 3000 cm^{-1}. The C=C stretching bands of the vinyl substituents of protoporphyrin IX can be found at approximately 1640 cm^{-1}.

A similar analysis of the spectrum can be done for phthalocyanines (Pc): below 900 cm^{-1} are encountered mainly the γ(C–H) and ring out-of-plane ϕ_{C-C} deformations, whereas between 1000 and 1500 cm^{-1} can be found the in-plane C–H bending vibrations. The C=C pyrrole, isoindole and benzene as well as C=N stretching vibrations can usually be distinguished in the spectra, in the region between 1300 and 1600 cm^{-1}. Just above 3000 cm^{-1} can be seen the stretching C–H vibrations.[43,45,46]

Partially reduced metalloporphyrins, such as chlorins, display more complex spectra, due to their lower molecular symmetry. All the modes which were forbidden for porphyrins of D_{4h} symmetry become IR-active in the corresponding chlorins. A strong band in the region 1620–1640 cm^{-1}, attributed to a C_{α}–C_{meso} stretching vibration, seems to be characteristic of chlorins.[47,48]

Several rare-earth double- and triple-decker porphyrins, phthalocyanines or mixed porphyrins–phthalocyanines have also been characterized by IR spectroscopy.[49–51]

1. *Square Planar M(II) Porphyrins and Analogs: Metal-Sensitive Bands*

When studying different monomeric metalloporphyrins with several divalent metals by IR spectroscopy, Thomas and Martell,[18] Boucher and Katz,[7] Ogoshi and coworkers,[44] and Lavallee[1] identified several metal-sensitive bands. Some sharp absorption bands near 960, 980 and 1000 cm^{-1} in the MTPP derivatives and between 920 and 970 cm^{-1} in the protoporphyrin and hematoporphyrin IX dimethyl ester derivatives, and attributed to either an in-plane deformation mode or a C–H rocking mode, shifted to higher frequencies approximately in the order Pt > Pd > Co, Ni > Cu > Ag > Zn > Cd > Mg. This dependency was suggested to be correlated with the strength of the metal–nitrogen bond in these complexes and is consistent with the order of stability of the metalloporphyrins. The weak bands attributed to the C=C and C=N stretches between 1500 and 1700 cm^{-1} also showed some metal dependency in both their frequencies and intensities, especially in the case of nonsubstituted porphyrins, octaethylporphyrin and *N*-methyl tetraphenylporphyrin derivatives.

Metallophthalocyanines show three strong absorptions in the 1000–1200 cm^{-1} region, which are sensitive to the nature of the central metal.[45]

2. *Five- and Six-Coordinate M(II) Porphyrins: Axial Ligand Bands*

Most porphyrin derivatives have been designed and studied to model the active site of hemoproteins which contain iron porphyrins coordinated to one or two axial ligands. Biologically relevant ligands include imidazoles, thiols, O_2, CO, CN^- and NO. The infrared frequencies of the axial ligand after binding can be compared to their respective values for the free ligand, which usually gives valuable insight into the strength and mode of coordination of these ligands to the metalloporphyrin.

a. *Imidazoles*

Mono-imidazole and bis-imidazole ligated iron porphyrins, as models of naturally occurring histidine ligated hemoproteins, have been mainly examined by Raman resonance spectroscopy, and only a few IR studies are available. These ligands show several characteristic bands in the MIR domain, which were assigned for 4-MeIm, 1-MeIm and Im using H/D and $^{14}N/^{15}N$ exchange.[52] The δ(CH) and ring stretching modes have been localized between 1400 and 1500 cm^{-1}, and δ(NH) modes between 1200 and 1350 cm^{-1}. Two specific vibrational modes have also been observed for all these ligands between 1060 and 1100 cm^{-1} and attributed to coupled ν(C–C) and δ(CH) modes and coupled δ(CH) and δ(NH) vibrations. These latter bands are clearly identified in the spectra of bis-imidazole iron porphyrins (Fe(P)$(Im)_2$) as well as in cyt b_{559} of the photosystem II complex, which contains a heme coordinated to two histidines of two distinct transmembrane α-helices.

b. *Dioxygen*

In its free form dioxygen (O_2) is IR-inactive; however, it is possible to observe a $\nu(O_2)$ band in metalloporphyrins and metallophthalocyanines, due to a nonsymmetric binding, but the band is expected to be weak, and therefore quite difficult to identify in the spectra.[53] In addition, O_2 adducts are sometimes formed only at very low temperature, or are quite unstable, requiring special technology for isolation and spectroscopic characterization. For instance, most O_2 adducts of metallotetraphenylporphyrins and octaethylporphyrins without additional axial ligands were obtained by the "matrix isolation" method.[54–59]

The $\nu(O_2)$ frequency shows some dependency on the nature of the metal and the sixth axial ligand. Depending on the family of porphyrins, these effects are small (see in Table 1 the picket fence porphyrins TpivPP and the capped porphyrins) or more pronounced (see the TPP family), and therefore difficult to

Table 1. $\nu(^{16}O_2)$, $\nu(^{16}O^{18}O)$, $\nu(^{18}O_2)$ frequencies measured in cm^{-1} in some O_2 adducts of synthetic porphyrins and hemoproteins.

Complex	$\nu(^{16}O_2)$	$\nu(^{16}O^{18}O)$	$\nu(^{18}O_2)$	Ref.
Cr(TPP)(O_2)(Py)	1142		masked	60
Co(TPP)(O_2)	1278[a]	1252, 1242[a]	1209[a]	55
Co(TPP)(O_2)(1-MeIm)	1142[b]		1071[b]	61
Fe(TPP)(O_2)	1106, 1195[a]	1162[a]	1043, 1127 [a]	54
Mn(TPP)(O_2)	983[a]		933[a]	56
Co(OEP)(O_2)	1275[a]		1202[a]	57
Fe(OEP)(O_2)	1104, 1190[a]	masked	1042, 1124[a]	62
Mn(OEP)(O_2)	991[a]		934[a]	59
Ti(OEP)(O_2)	898			63
Fe(TpivPP)(O_2)(1-MeIm)	1159[c]		1075[c]	64
Co(TpivPP)(O_2)(1-MeIm)	1150[c]		1077[c]	64
Fe(C_2-cap)(O_2)(Py)	1175[d]		1096[d]	61
Fe(C_2-cap)(O_2)(1-MeIm)	1172[b]		1097[b]	61
Co(C_2-cap)(O_2)(1-MeIm)	1176[b]		1084[b]	61
Fe(C_3-cap)(O_2)(1-MeIm)	1160[e]		1080, 1085[e]	61
HbO_2	1107[f]		1065[f]	65
MbO_2	1103[f]		1065[f]	66

[a]Matrix isolation; [b]Solution 3% 1-MeIm/toluene; [c]Nujol mull; [d]Pyridine solution; [e]Solution 3% 1-MeIm/toluene, 195 K; [f]Aqueous solution.

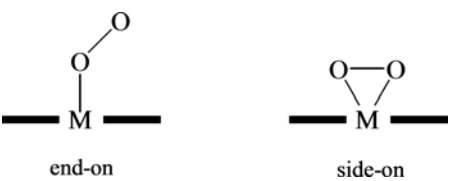

Figure 1. Different modes of coordination of O_2 to metalloporphyrins.

predict and explain.[67] However, the intensity of the $\nu(O_2)$ band, its frequency, and its behavior upon isotopic exchange are considered as good indicators of the mode of binding of the O_2 ligand in these complexes.[61,62] Co(TPP)(O_2) showed a high $\nu(O_2)$ frequency and two $\nu(^{16}O^{18}O)$ frequencies, which is consistent with a superoxide-like end-on mode of coordination (see Figure 1). For Mn(TPP)(O_2) a peroxide-like side-on coordination of O_2 was proposed from EPR studies.[68] This seems to be consistent with the significantly lower value of $\nu(O_2)$ frequency obtained for this complex. It was also suggested that the higher value of $\nu(O_2)$ frequency obtained for Fe(TPP)(O_2) and Fe(OEP)(O_2) could belong to an end-on complex, whereas the lower value could belong to a side-on complex.[58]

c. *Carbon monoxide*

Carbon monoxide (CO) is also a biologically important molecule, since it is produced by heme catabolism. CO binds stronger than O_2 to unprotected hemes, making even the natural level of CO in cells potentially lethal. Therefore nature has developed its own mechanisms for preventing poisoning of hemoproteins by CO.[69] In this connection, a wide diversity of carbonmonoxy iron porphyrin models Fe(P)(CO)(L) (with L an additional nitrogen ligand) have been studied both in solution and in the solid phase to find out the environmental factors controlling the discrimination between CO and O_2 in natural hemoproteins. CO in its free form has a strong absorption band at 2143 cm^{-1}, in a region of the MIR where porphyrins do not show any major absorption, thus making carbonmonoxy metalloporphyrins rather easy to characterize by IR. When it is ligated to a metalloporphyrin, the frequency of this band decreases dramatically, by as much as 220 cm^{-1} (see Table 2). The *d*-electron back-donation mechanism,[70,71] which is well verified in the case of unprotected hemes, allows correlation of the decrease in the ν(CO) frequency with the strength of the Fe–CO bond: the lower the ν(CO) frequency, the stronger the Fe–CO bond.

Table 2 shows that the carbonmonoxy iron metalloporphyrins studied so far exhibited a quite large range of ν(CO) frequencies. Within the same system, it is even possible sometimes to observe several ν(CO) frequencies corresponding to different binding conformations (see for instance the TPP complexes in the solid phase[72] or the carbonmonoxy myoglobin[84] and cytochrome *c* oxidase in Table 2). Such important differences are now thought to arise from secondary interactions between the CO molecule and its environment in the binding pocket of the porphyrin as well as electrostatic effects,[53,72] rather than just deviations from the linearity of the Fe–CO bond, as initially suggested. First, when one is comparing carbonmonoxy metalloporphyrins with different sixth axial ligands L in solution, it appears that this ligand exerts a *trans* effect on the CO ligand, decreasing the ν(CO) frequency in the order 4-acetylpyridine > pyridine > 1-methylimidazole > dimethylaminopyridine > alkyl thiol.[81] Therefore, the more electron-donating this ligand is, the larger the effect will be. However, a very interesting study by Scheidt *et al*. on TPP complexes with different imidazoles (see Table 2)[72] showed that in the solid phase, additional interactions such as hydrogen bondings between bound CO and neighboring imidazoles lead to large differences in the observed ν(CO) frequencies and one of the lowest ν(CO) frequencies observed to date. In contrast, the "twin coronet" porphyrins (TCPs) showed some of the highest ν(CO) frequencies observed so far in metalloporphyrins.[82] These high frequencies were correlated with the presence of polar residues (such as oxygen atoms) close to the oxygen atom of the CO molecule. Therefore proton donors in the binding pocket

Table 2. ν(CO) frequencies measured for some representative iron(II) synthetic porphyrins and hemoproteins.

Complex	$\nu(^{12}C^{16}O)$ (cm^{-1})	Ref.
Fe(TPP)(CO)(1-MeIm)	1969[a]; 1967–1968[b]	72
Fe(TPP)(CO)(2-MeIm)	1972[a]; 1926[b]	72
Fe(TPP)(CO)(1,2-Me_2Im)	1972[a]; 1948, 1953 (solvate 1)[b]; 1963 (solvate 2)[b]	72,73
Fe(TPP)(CO)(Py)	1980	74
Fe(TPP)(CO)(SEt)	1920[c]	75
Fe(OEP)(CO)(1-MeIm)	1965[a]	76
Fe(OEP)(CO)(Py)	1967	70
Fe(PPIX)(CO)(Py)	1970[a]	77
Fe(TpivPP)(CO)(1-MeIm)	1967[a]	64
Fe(PocPiv)(CO)(1-MeIm)	1964[a]	78
Fe(MedPiv)(CO)(1-MeIm)	1954[a]	78
Fe(TalPiv)(CO)(1-MeIm)	1963[a]	78
Fe(C_2-cap)(CO)(1-MeIm)	2002[a]	73
Fe(C_2-cap)(CO)(1,2-Me_2Im)	1999[a]	73
Fe(NapC_2-cap)(CO)(1,2-Me_2Im)	1998[a]	73
Fe(C_3-cap)(CO)(1,2-Me_2Im)	1984[a]	73
Fe(OC_3OPor)(CO)(1-MeIm)	1978[b]	79
Fe(OC_3OPor)(CO)(1,2-Me_2Im)	1974[d]	79
Fe(Piv_2C_8)(CO)(1-MeIm)	1948[a]	80
Fe(Piv_2C_9)(CO)(DMAP)	1947[a]	81
Fe(Piv_2C_9)(CO)(1-MeIm)	1948[a]	80
Fe(Piv_2C_9)(CO)(Py)	1953[a]	81
Fe(Piv_2C_9)(CO)(4-AcPy)	1955[a]	81
Fe(Piv_2C_{10})(CO)(1-MeIm)	1952[a]	80
Fe(Piv_2C_{12})(CO)(DMAP)	1950[a]	81
Fe(Piv_2C_{12})(CO)(1-MeIm)	1958[a]	80
Fe(Piv_2C_{12})(CO)(Py)	1963[a]	81
Fe(Piv_2C_{12})(CO)(4-AcPy)	1966[a]	81
Fe(TCP)(CO)	1990[e]	82
Fe(TCP-py)(CO)	2008[e]	82
HbCO	1951[f]	83
MbCO	1927, 1945, 1969[f]	84
Cytochrome *c* oxidase CO	1966 (form α)[f]; 1956 (form β)[f]	85

[a]Toluene or benzene solution containing an excess of nitrogen base; [b]Crystal nujol mull; [c]Chlorobenzene solution; [d]Krytox oil; [e]Pure sample; [f]In aqueous solution.

seem to favor the $Fe^{\delta+}$=C=$O^{\delta-}$ resonance structure, whereas electron-rich residues favor the $Fe^{\delta-}$–C≡$O^{\delta+}$structure.

In strapped porphyrins such as the "basket handle porphyrins" and in "capped porphyrins," a higher ν(CO) frequency was observed for tighter structures (see the comparison between the "hybrid basket handle porphyrins" with respectively 8, 9, 10, 12 carbon atoms in the strap,[80] and the comparison between C_3-cap and C_2-cap

compounds[73]). In "pocket porphyrins,"[78] the situation is less clear since the ν(CO) frequency of Fe(MedPiv)(CO)(1-MeIm) is lower than that of both the more encumbered Fe(PocPiv)(CO)(1-MeIm) and less encumbered Fe(TalPiv)(CO)(1-MeIm) systems. A combination of steric and electronic interactions between the bound CO and the strap or the cap was invoked to explain all these observations. The high dependency of the ν(CO) frequency on the metal environment in these systems justifies why CO has long been used as a sensor of the binding pocket in both synthetic metalloproteins and hemoproteins.

d. *Cyanide*

The ligand cyanide (CN^-) has been used for a long time as a common inhibitor and ligand of the active site of hemoproteins, mainly with iron in its +III oxidation state. Reduction of the low spin (cyano) Fe(III) hemoproteins usually leads to the (cyano) Fe(II) hemoproteins. However, it is only recently that a (cyano) Fe(II) complex of a synthetic porphyrin has been prepared and characterized, i.e. $[Fe(TPP)(CN)]^-$, by Scheidt and coworkers in 2008.[86] Interestingly, this complex exhibited two strong CN stretching vibrations at 296 K: a major one at 2070 cm^{-1} and a minor one at 2105 cm^{-1}. For comparison, the CN stretching vibration appears at 2098 cm^{-1} in gaseous HCN.[87] With the help of temperature effects, the major band was attributed to a low spin Fe(II) compound whereas the minor band was attributed to a high spin Fe(II) compound.

e. *Nitric oxide*

Many iron nitrosyl metalloporphyrins have been studied, particularly as models of the nitrite reductase enzymes, such as the cytochrome *c* nitrite reductase, which converts nitrite NO_2^- into ammonia NH_3. These compounds belong to the $\{M–NO\}^7$ family of metal nitrosyl complexes[88] (as established by Enemark and Feltham[89]), where the superscript 7 is the sum of *d*-electrons on the metal and electrons in the π^* orbital of NO. Other metalloporphyrins, with cobalt(II) and manganese(II), are also able to bind and activate NO. The corresponding nitrosyl complexes are members of the $\{M–NO\}^8$ and $\{M–NO\}^6$ families, respectively. Bis-nitrosyl metalloporphyrins have been reported, by subsequent reaction at low temperature between a parent mono-nitrosyl porphyrin and excess NO.[90,91]

In its gaseous form, NO absorbs at 1876 cm^{-1}, and this wavenumber decreases upon coordination to a metalloporphyrin (Table 3).

Like the ν(CO) in carbonmonoxy metalloporphyrins, the ν(NO) frequency is highly dependent on the electronic environment of the porphyrin. The macrocycle basicity has a direct influence on its value, as observed when one is comparing the

Table 3. $\nu(^{14}NO)$ frequencies obtained for some synthetic porphyrins.

Complex	$\nu(^{14}N^{16}O)$ (cm^{-1})	Ref.
Fe(OEP)(NO)	1667[a]	92
Fe(TPP)(NO)	1678[a]	92
Fe(PPIXDMe)(NO)	1676[c]	93
Fe(PPIXDMe)(NO)(Py)	1633[d]	93
Fe(PPIXDMe)(NO)(1-MeIm)	1618[e]	93
Fe(TPP)(NO)(1-MeIm)	1625[b]	94
Fe(TPP)(NO)(4-MePip)	1640 (form 1)[b]; 1653–1656 (form 2)[b]	95
Fe(TTP)(NO)	1675[b]	96
Fe(TMP)(NO)	1672[a]	92
Fe(OBTPP)(NO)	1685[b]	96
Fe(TDFPP)(NO)	1687[b]	96
Fe(TDCPP)(NO)	1688[b]	96
Fe(TPFPP)(NO)	1705[b]	96
$Fe(TPP)(NO)_2$	1695 (strong)[f] ; 1777 (weak)[f]	91
Co(OEP)(NO)	1677[b]	97
Co(TPP)(NO)	1680[a]	98
Co(TAP)(NO)	1679[a]	98
Co(T(*p*-OCF_3)PP)(NO)	1687[a]	98
Co(T(*p*-CF_3)PP)(NO)	1690[a]	98
Co(T(*p*-CN)PP)(NO)	1693 [a]	98
Mn(TPP)(NO)	1735[b]	99
Mn(TPP)(NO)(4-MePip)	1740[b]	99
Mn(TTP)(NO)(CH_3OH)	1743[b]	100
Mn(TTP)(NO)(Pip)	1746[b]	100
Mn(TTP)(NO)(1-MeIm)	1738, 1732[b]	100
Mn(TAP)(NO)(Pip)	1748[b]	100
Mn(TAP)(NO)(1-MeIm)	1736[b]	100

[a]Thin layer CH_2Cl_2/electrolyte film; [b]KBr pellet; [c]$CHCl_3$ solution; [d]Pyridine solution; [e]1-MeIm solution; [f]$CHCl_3$ solution, 213 K.

various substituted porphyrins studied. Adding electron-donating substituents on the porphyrin (such as alkyl groups)[92,96] increases the electronic density on the metal, which in turns decreases the NO bond strength through *d*-electron back-donation. In contrast, adding electron-withdrawing substituents (such as $–CF_3$, $–OCF_3$ and halides)[96,98] decreases the electronic density on the metal, which is then less prone to back-donation; therefore the ν(NO) appears at higher frequency. Linear relationships between the ν(NO) frequency and the first oxidation potential of the porphyrin (which is linked to the porphyrin ring basicity) were derived from some of these data.[92] The axial base exerts a *trans* effect on the NO ligand,[93,96] decreasing the ν(NO) frequency in the order alkyl alcohol > piperidine > imidazoles. The ν(NO) frequencies below 1700 cm^{-1}, obtained for the iron(II) and cobalt(II) complexes, are consistent with bent M–N–O geometries, whereas those

of the Mn(II) porphyrins are consistent with a quasi-linear M–N–O geometry.[88] The bis-nitrosyl Fe(TPP)$(NO)_2$ complex, isolated at 213 K, showed a main NO band nearly twice as intense as the corresponding band of the parent mono-nitrosyl Fe(TPP)(NO) compound, suggesting that the two NO ligands have nearly the same electronic structure.[91]

3. *M(II) and M(III) Porphyrins: Redox- and Spin-State-Sensitive Bands*

From the study of 20 hexacoordinated Fe(TPP)(L)(L′) complexes (L and L′ are two additional axial ligands),[14] two structure-sensitive bands were identified; one strongly spin-dependent at 1330–1350 cm^{-1}, called band I; and the other strongly oxidation-state-sensitive at 806–790 cm^{-1}, called band II. Band I was usually observed at 1349–1343 cm^{-1} for low spin iron TPP derivatives and 1341–1333 cm^{-1} for high spin complexes, and was only slightly sensitive to deuteration of the β-pyrrolic protons. Calculations showed that this band corresponds to a highly mixed mode labeled ν_{41} with both some stretching ($\nu(C_\alpha–C_{meso})$ + $\nu(C_{meso}$–phenyl) + ν(pyrrole half ring)) and in-plane deformation ($\delta(C_\beta–H)$) characters.[41] Band II appeared at higher wavenumbers for Fe(III) species than for Fe(II) species and showed a strong shift upon deuteration of the β-pyrrolic protons. It was assigned from calculations to out-of-plane deformation vibrations ($\gamma(C_\beta–H)$ and pyrrole folding, labeled γ_5).[41]

Other studies on biologically relevant porphyrins such as protoporphyrin IX[10] revealed two main redox-sensitive bands; one in the C=C and C=N stretching region at 1575–1525 cm^{-1} involving β carbon atoms and labeled ν_{38}, and the other in the in-plane-deformation region at 1280–1262 cm^{-1} involving *meso* carbon and hydrogen atoms and labeled δ_{42}. A redox-sensitive band similar to band II, in the out-of-plane deformation region but at slightly higher wavenumbers (830–848 cm^{-1}), was also observed for these porphyrins.[101] All these bands are clearly seen in the spectra of hemoproteins[10,102] and are therefore used as specific redox heme markers.

Some axial ligand bands described previously are also highly metal-redox-state-sensitive. Carbonmonoxy iron(III) porphyrins are unknown; however, mono- and bis-cyano iron(III) porphyrins abound,[103] and nitrosyl iron(III) porphyrins have been prepared.[88] Nitrosyl ferric porphyrins belong to the $\{M–NO\}^6$ series and their ν(NO), at significantly higher frequencies than that of the ferrous analogs (see Table 4), is consistent with quasi-linear M–N–O groups and a Fe(II)–NO^+ electronic structure, sometimes suggested for these complexes. Interestingly, a ν(NO) frequency at 1913 cm^{-1} was detected in the reaction of *Paracoccus pantotrophus* cytochrome cd_1 nitrite reductase with nitrite,[104] showing that a nitrosyl ferric heme intermediate is probably formed. The measured ν(CN)

Table 4. Comparison of the $\nu(^{14}NO)$ frequencies in some Fe(II) and Fe(III) metalloporphyrins and hemoproteins.

Complex	$\nu(^{14}NO)$ (cm^{-1})	$\nu(CN)$ (cm^{-1})	Ref.
Fe(II)(OEP)(NO)	1667[a]		92
[Fe(III)(OEP)(NO)]ClO_4	1854[a]		92
Fe(II)(TPP)(NO)	1678[a]		92
[Fe(III)(TPP)(NO)]ClO_4	1848[a]		92
[Fe(II)(TPP)(CN)]K(222)		2070 (LS), 2105 (HS)[b]	86
Fe(III)(TPP)(CN)(Py)		2130 (LS)[b]	103
Fe(II)(Mb)(CN)		2057 (pH 7.8); 2078 (pH 5.3)[c]	105
Fe(III)(Mb)(CN)		2126 (pH 6–8)[c]	105

LS: Low-spin; HS: High-spin; [a]Thin layer CH_2Cl_2/electrolyte film; [b]KBr pellet; [c]Aqueous solution.

frequencies are also higher for the low spin iron(III) than for the low spin iron(II) metalloporphyrins (see Table 4).

4. *Porphyrin π-Cation Radicals*

Oxidation of both synthetic metalloporphyrins and natural hemoproteins can occur either on the metal or on the macrocycle itself, and FTIR allows a clear and simple identification of the oxidation site. The π-cation radicals of TPP metalloporphyrins (Cu, Fe) exhibit a strong band in the region 1270–1295 cm^{-1},[106] assigned by Hu and Spiro to the ν_{41} mode (ν(pyrrole half ring)) using selective deuteration.[107] This mode had been discussed before as being a spin state marker of Fe(II) and Fe(III) TPP derivatives. The increase in intensity of the corresponding IR band, when removing one electron from the porphyrin, was explained by a good matching between the topology of the a_{2u} SOMO of $TPP^{\bullet+}$ and the vibrational phases of ν_{41}. In contrast, π-cation radicals of OEP metalloporphyrins (Cu, Ni) showed increased intensity of two bands between 1550 and 1600 cm^{-1},[106] attributed to C_α–C_{meso} asymmetric stretchings (ν_{37}) and C_β–C_β stretchings (ν_{38}).[107] In this case, the SOMO of the porphyrin radical cation is of a_{1u} symmetry and is topologically adapted to the eigenvectors of ν_{38}. The π-cation radical of the sterically crowded and therefore highly unplanar Cu(II) octaethyltetraphenylporphyrin was also studied by IR spectroscopy.[108] It showed an intensity enhancement of the ν_{41} mode as well, but shifted at higher energy (1355 cm^{-1}), which is a probable consequence of the conformational distorsions in this porphyrin.

From the studies of double-decker actinide and lanthanide phthalocyanines or mixed phthalocyanines–porphyrins, a similar marker band for oxidized phthalocyanines was identified at about 1310 cm^{-1}, and assigned to pyrrole stretching.[49,109,110]

These π-cation radical characteristic bands led to a better understanding of the electronic structure of neutral, oxidized and reduced rare-earth double-decker phthalocyanines, bis-porphyrins or mixed phthalocyanines–porphyrins. Since Pc, TPP and OEP show different marker bands, it was possible to determine where the electronic hole preferentially resides in these complexes. Homoleptic complexes usually showed a delocalization of the hole over the two equivalent macrocycles. However, in (TPP)Eu^{III}(OEP) for instance, the electronic hole was rather localized on the OEP ring, whereas in [(TPP)Ce^{IV}(Pc)]$^+$ the hole could be found on the phthalocyanine.[50,51,110,111]

B. Recent Developments in the Near-Infrared

The NIR is widely used in analytical chemistry, industry and biomedical research.[112,113] In the biomedical field, this technique has gained importance because NIR light penetrates superficial layers (skin, subcutaneous fat, skull, etc.) and is either absorbed by chromophores (oxy- and deoxyhemoglobin and myoglobin) or scattered within the tissue. So-called NIR spectroscopy is a noninvasive and relatively low-cost optical technique that is becoming widely used instrumentation for determining tissue O_2 saturation, changes in hemoglobin volume and, indirectly, brain/muscle blood flow and muscle O_2 consumption.[114–116] Tissue O_2 saturation represents a dynamic balance between O_2 supply and O_2 consumption in the small vessels, such as the capillary, arteriolar and venular bed. Quantitative measurements of blood flow *in vivo* are possible using NIRS and a light-absorbing tracer, which can be applied to evaluate, for example, circulatory responses to exercise and to assess tissue O_2 saturation. The venular O_2 saturation can be estimated with NIRS by applying venous occlusion and measuring changes in oxygenated hemoglobin versus total hemoglobin. These various measurements provide the opportunity to evaluate several important metabolic and circulatory patterns in localized regions of tissue and may be fruitful in the study of occupational syndromes and a variety of diseases. This technique was further developed for NIR-spectroscopic imaging[117,118] and for cancer research.[119–121] Furthermore, absorption bands in the NIR are important in different fields of biomedicine. Extended porphyrins and conjugated porphyrin dimers have been developed, based on their favorable photophysical properties and intracellular behavior. These molecules are suitable for photodynamic therapy (PDT) and similar modalities.[122–126]

In chemistry, several NIR spectroscopic features have been found to be useful for the characterization of porphyrins and hemoproteins.[127,128] For example, "band III" in porphyrins is a fine probe of the heme pocket conformation. This signal, positioned in the NIR at ~760 nm (~13,200 cm^{-1}), is observed only in the deoxygenated derivative of Hb and is attributed to a porphyrin-to-iron charge transfer

electronic transition. This signal is sensitive to heme pocket structural relaxations, and is thus called the "conformation band". Recent studies include the analysis of hemoglobin conformational variations.[129]

C. The Far-Infrared or THz Spectral Region

1. *Modes of a Collective Nature*

The FIR is of great importance due to the rich chemical and physical processes observable in this spectral range and therefore has seen a flurry of research activity.[130–134] The interest in this spectral range is based on the observation that the FIR contribution of a wide range of molecules is dominated by vibrations involving a substantial fraction of the atoms forming the molecule and motion associated with intermolecular hydrogen bond vibrations. Due to their collective nature, such modes are highly sensitive to the intra- and intermolecular structure and thus provide a unique fingerprint of the conformational state of the molecule and effects of its environment.

The interest in this spectral domain originated from the prediction of the collective structural vibrational modes for DNA and other large biological molecules first presented more than 30 years ago.[135] As a consequence, the inter- and intramolecular hydrogen bonding interaction can be characterized and interesting broad features are found for proteins,[136,137] or any system containing hydrogen bonding components such as water.[138] This signal strongly depends on the polarizability of the hydrogen bond.[139] Theoretical predictions indicate a noticeable role of the vibrational anharmonicity in the FIR spectral features.[140]

Any molecule with internal hydrogen bonding structures displays a large broad feature in the FIR/THz range that seems to include dense, overlapping normal modes (see Figure 2).[141–143] Whereas chemists attribute this continuum to the low frequency hydrogen bonding modes,[144] in physics this large signal is named the "boson peak."[145] In crystals, lattice modes are also involved in this spectral region. Since the study of this spectral range for larger molecules and especially for the THz range is very recent, only a few publications are available.

The development of new sources, as well as progress in the interpretation of the results, is very promising.[133,146–151] In addition to the use of synchrotron light sources, so-called free electron lasers (FELs) have been developed for the FIR. FELs allow the generation of electromagnetic radiation in a wide field of frequencies through the proper adjustment of the energy of an electron beam and the field configuration of a magnetic undulator passed by this beam. The energy obtained is significantly higher than from conventional sources.[137,152] FIR or THz spectroscopy is currently being promoted to become a routine technique for

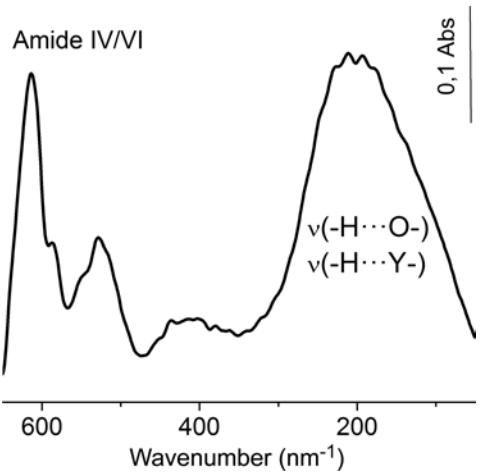

Figure 2. FIR spectrum of cytochrome *c* oxidase from *P. denitrificans,* including the amide region and the low frequency hydrogen bonding feature. Y represents any hydrogen bonding partner. In the spectra of large membrane proteins, the heme modes are less dominant. (Modified from Ref. 6.)

all-day use in science and industry. Quantitative studies show the potential of THz spectroscopy for the detection and identification of intermolecular hydrogen bonds in unknown mixture samples.[153,154]

An interesting example of an application, found in the field of porphyrin research, is the so-called heme "doming" mode. This motion seems to be significantly delocalized, so that distant sites respond to ligand interactions including oxygen binding on vibrational time scales. The delocalization has ramifications for understanding long range interactions in biomolecules, such as those that mediate cooperativity in allosteric proteins. In the spectral region below 300 cm^{-1}, the doming modes, the hydrogen bonding signatures and clearly defined signals of the metal–ligand vibrations are observed. Some examples are given below.

2. *Metal–Ligand Vibrations*

A classic application of the FIR involves the characterization of metal–ligand vibrations. In contrast to resonance Raman data, only a few infrared-spectroscopic reports are available for the FIR region; however, the analysis is often completed by a full theoretical study.[6,52,155,156] In the field of porphyrins, FIR spectra were published for Ni(TPP) using DFT-SQM calculations.[40] Paulat and coworkers presented infrared and resonance Raman spectra of different metalloporphyrin complexes (Fe, Mn and Co) with a Cl^- ligand, together with DFT calculations in the spectral range of 2000–300 cm^{-1}.[41] For Fe(TPP)Cl, a complete vibrational data set

was discussed. The use of FIR is again very important in the field, due to the development of THz spectroscopy and synchrotron-based infrared approaches.[6,8,155–157]

In a recent synchrotron-light-based study, FTIR absorbance data of different heme model compounds in the mid- and low-frequency regions were obtained from thin films of protoporphyrin IX, hemin, hematin, microperoxidase 11 and horse heart cytochrome *c*.[6] The porphyrin model compound data are dominated by ring motions; however, metal–ligand vibrations of noteworthy intensities are typically distinguishable, such as the Fe–Cl vibration at 345 cm^{-1} and the Fe–N vibrational mode at 378–390 cm^{-1}. The Fe–N vibration is especially important for the study of heme proteins, such as hemoglobin, myoglobin, or cytochrome *c* oxidase, where the iron–histidine bond is the only covalent bond between protein and the active site where oxygen binds. This vibration is a marker for changes in protein structure and dynamics.

Whereas the assignment of the Fe–N stretching motions between 250 and 200 cm^{-1} is well accepted for Raman spectra,[9,158] the position in the infrared data is under debate. This question was clarified by studying a model compound. The active site of oxygen-binding proteins was mimicked using the ferric protoporphyrin IX derivative hemin, coordinated to two imidazole molecules and embedded in sodium dodecyl sulfate (SDS) micelles.[155] The detergent simulated the hydrophobic cavity of heme proteins. Both infrared and Raman data are available for this compound.[155,159] The Fe–N motions were tentatively attributed to being involved in the asymmetric ν(Fe–N) vibration (378 cm^{-1}) and the ν(Fe–N) + δ(pyr *trans*) vibration (401 cm^{-1}). Paulat *et al.*[41] reported that the asymmetric Fe–N (N: imidazol-ligand) stretching vibration can be expected at 390 cm^{-1} and the ν(Fe–N) + δ(pyr *trans*) vibration at 402 cm^{-1}. Based on theoretical calculations, Mitchell and colleagues assigned the asymmetric ν(Fe–N) in spectra of Fe(III)(OEP)$(Im)_2$ to a signal at 386 cm^{-1}; the mode is coupled with the out-of-plane pyrrole tilting mode (pyr-tilt).[21] The signal would be expected around 350 cm^{-1} without the coupling of the modes. This assignment was recently confirmed.[156]

Within this context, the dynamics of a five-coordinate deoxymyoglobin model, Fe(TPP)(2-MeIm), is discussed in relation to the active site of the six-coordinate heme protein, carbonmonoxymyoglobin. The iron-imidazole stretching mode was identified at 226 cm^{-1} for the first time in a six-coordinate heme system.[8] The heme in-plane modes with large contributions from the ν_{42}, ν_{49}, ν_{50} and ν_{53} modes of the core porphyrin were identified. In general, the iron modes can be attributed to a coupling with the porphyrin core, the CO ligand, the imidazole ring and/or the phenyl rings. Other significant findings were the observation that vibrations of the porphyrin ring peripheral substituents are strongly coupled to the iron doming mode and that the Fe–C–O tilting and bending modes are related by a negative interaction force constant.[157]

In infrared spectra of proteins, the predominant features can be assigned in general to motions of the amide linkage. It was thus investigated whether or not metal–ligand vibrations could be depicted in the low frequency range. For cytochrome *c* and microperoxidase 11, the Fe–N vibration was seen at 380 cm^{-1}.[6] Microperoxidase is a cytochrome *c* site model with 11 attached amino acids, which is obtained on the basis of a trypsin digestion.[102] The most prominent signal in large proteins, however, is the large internal hydrogen bonding feature (see Figure 2). Ligands coordinated to heme sites in proteins have been extensively characterized in the MIR. Most of the ligands compete with oxygen or NO for their binding site. Based on the strong infrared absorption of these ligands, they have been established as probes for the active site of oxidases, sensors and transporters.[22,160,161] These experiments will be discussed together with reaction-induced FTIR spectroscopy.

D. Using the Effect of Temperature: T-Derivative Spectroscopy

Studies of the temperature dependence of IR spectra make it possible to compare the spectra in various phase states and to clarify the role of intermolecular forces.[19] Data are studied in all accessible temperature ranges. With the help of closed circle cryostats, temperatures down to 4 K can be obtained; however, nitrogen-cooled systems are often sufficient.[162–165] Measurements at low temperatures were also performed to trap reaction intermediates, including dioxygen adducts of heme model compounds in cryogenic matrixes[54,166,167] or unstable complexes.[168] For example, in oxygen carrier models (see Section II.A.2.b), the $\nu(O_2)$ frequency was found between 1100 and 1280 cm^{-1} for end-on ligation, and between 900 and 1000 cm^{-1} for side-on ligation.[58] Isotope labeling of the ligand is typically performed to confirm the assignments.

Temperature-derivative spectroscopy has proven to be a particularly powerful technique for studying protein–ligand interactions. Several ligand binding studies of porphyrins in proteins are known. Myoglobin, a ubiquitous mammalian oxygen storage heme protein, was the first protein with a structure determined by X-ray crystallography[169] and serves as a model system for heme–ligand interactions.[162,170] The most extensively studied form is the complex bound with CO, which is more stable than the protein complexed with the physiological O_2 ligand. A large photodissociation quantum yield and the high intensity of the ν(CO) vibration in the MIR spectral range made the mode accessible for extensive studies, the ligand being utilized as a local probe of structure function and dynamics[160,164,171,172] due to the high sensitivity of the ν(CO) to the heme environment, as discussed in Section II.A.2.c.

Among a large number of excellent studies, the temperature dependence of the slow geminate recombination of CO in oxygen transporters by Frauenfelder and

coworkers, and others, was crucial in initiating an understanding of the dynamics of conformational substates in proteins.[173,174] Barrier crossings associated with conformational changes of the protein-dissociated CO system were determined based on the temperature dependence of the vibrational motions. Geminate ligand rebinding of CO with myoglobin was found to be highly nonexponential at T < 200 K, giving evidence for the trapping of a large number of protein statistical substates at low temperature.[175,176] Measurements are started with a completely photodissociated sample at a temperature around 10 K, where rebinding is extremely slow on the experimental time scale. While linearly increasing the sample temperature with time, FTIR spectra are measured continuously. The absorbance difference spectra, involving information on the different substates, are then calculated from spectra at successive temperatures.

Temperature-dependent investigation of an infrared spectrum can be analyzed by the vibration involved in a signal. Although many of the absorption bands are combination modes, they can be roughly considered as stretching or bending modes. When H-bonding is present, it is more difficult to bend a bond and consequently the frequencies of the bending modes increase with H-bonding. H-bonding will weaken the intramolecular force constant and as a result it shifts the IR absorption of a stretching motion to lower frequency. At higher temperatures, H-bonding is weaker and the respective shifts can be induced. For coupled vibrations this does not always apply.

Temperature-dependent studies also aim to answer questions on the crucial role of H-bonds, since temperature has a large effect on H-bonding, which is both directional and cooperative. For many molecules, H-bonds are what often determine structure, and when extreme temperature disrupts the structure, the IR spectra change. This may be explained with the help of water, which is a liquid at room temperature. As the temperature increases, the motion of water increases, decreasing its H-bonding contribution and thereby changing the IR spectra. Because water H-bonding is temperature-dependent, any vibrational modes that are coupled directly or indirectly to water H-bonding will also be temperature-dependent. Temperature-dependent infrared spectroscopy can monitor such temperature-dependent H-bonding to study conformational changes, binding events or the nature of solvation.

The temperature dependence of a vibrational mode is a strong indication of the presence of H-bonds within a molecular structure, and the shifting of absorption peaks with decreasing temperature may be ascribed to the collective vibrational modes of the molecule. These effects are of special interest in the FIR, where the shift of vibrational peak frequencies with temperature may be used to probe the expansion of the H-bonding network of molecular ensembles or proteins.[23]

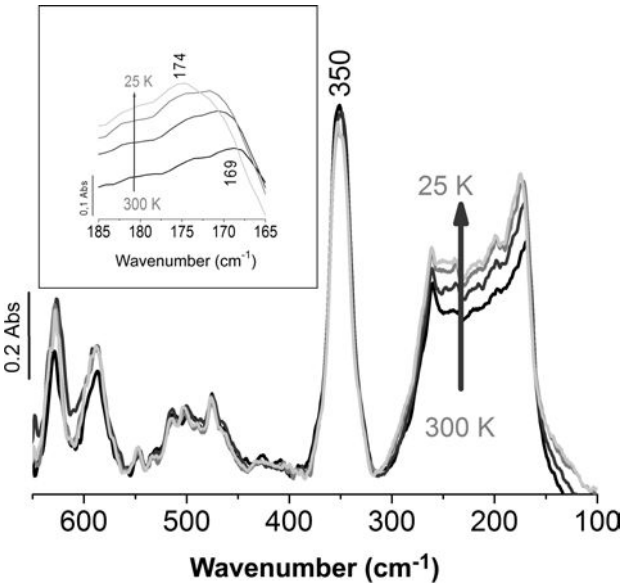

Figure 3. Absorbance spectra between 650 and 100 cm^{-1} of hemin Fe(III)(PPIX)Cl for the temperatures 300, 200, 100 and 25 K. The inset shows an enlarged view of the hydrogen bonding features. (Adapted from Ref. 155.)

Figure 3 shows the temperature dependence of the IR spectrum of hemin, an iron(III) porphyrin derived from red blood cells. Whereas the Fe–Cl vibration at 350 cm^{-1} does not show any noticeable shift,[155] the broad spectral feature between 300 and 100 cm^{-1} increases and up-shifts with temperature, indicating the internal strengthening of the H-bonding interaction, most likely taking place between the hemin propionate groups.

E. Using Pressure in Infrared Spectroscopy

1. *Pressure Dependence of Infrared Spectral Features*

The pressure dependence of vibrational modes is another parameter that can be used to probe signals in the MIR and FIR. Evidently, the samples need to be very stable and the effect should be reversible. Infrared spectroscopy under high pressure is technically challenging, due to the limited space in a pressure cell, such as a diamond anvil cell. Typically, pressures of up to GPa are applied. The signal that will be perturbed by the pressure needs to be sensitive to the local environment and to the orientation of the motion.

The pressure dependence of an infrared mode was used to assign the out-of-plane movement of Fe porphyrins, as described below.[177] Further pressure

dependence studies involve the manipulation of ligands bound to iron in porphyrin complexes and the decrease in the N–O stretching frequency with increasing pressure, which was studied for a nitrosyl complex of iron(II) tetraphenylporphyrin [FeTPP(NO)], for example.[178,179] The decrease in the N–O stretching frequency is based on the increase in the Fe–N–O angle. This kind of effect can be applied to study ligand binding.

2. *Assignment of Heme Doming Modes*

The dynamics of the heme prosthetic group and that of the surrounding group are directly coupled to the properties of the protein and thus its function. The dynamics was especially interesting for the formulation of the allosteric mechanism of hemoglobin, first suggested by Monod *et al.*[180] and put on a sterochemical basis by Perutz.[181] The two-state model was interpreted in terms of an equilibrium between two alternative structures: a tense one (T) with low oxygen affinity, constrained by salt bridges between the C-termini of the four subunits; and a relaxed one (R), lacking these bridges. The equilibrium was thought to be governed primarily by the positions of the iron atoms relative to the porphyrin: the iron is out-of-plane in five-coordinated, high-spin deoxyhemoglobin, and in-plane in six-coordinated, low-spin oxyhemoglobin. The spectral signature of these motions should be included in doming modes.

The optical excitation of six-coordinate hemes induces, via the transitions lying in the plane of the heme, the population of intrinsically short-lived excited states (hundreds of fs to a few ps).[182] These excited states have an antibonding character and can lead to dissociation of the Fe–ligand bond within tens of fs. Dissociation subsequently leads to a heme "doming" within 1 ps.[11] Interestingly, this translation motion of the heme core can be resilient, as observed spectroscopically.[143]

In an interesting synchrotron-light-based experimental and density functional approach, the "doming motion" that is found for the crucial out-of-plane movement of Fe porphyrins was probed. The pressure dependence of vibrational modes was used to identify the doming motion and other related normal modes.[177] A 20 cm^{-1} shift of the respective signal at 53 cm^{-1} could be induced by applying 0.24 GPa to a carbonmonoxy pyridine iron octaethylporphyrin complex. The respective data and the heme motion are shown in Figure 4.

Further theoretical and spectroscopic studies on these doming modes and the analysis of low-lying spin states of iron(II) porphyrin predicted the doming mode of porphyrin to be at 71 cm^{-1}, close to the 75 cm^{-1} frequency determined from coherent reaction dynamics in myoglobin.[17] In most approaches, however, it was not possible to make a definitive assignment, due to either lack of theoretical

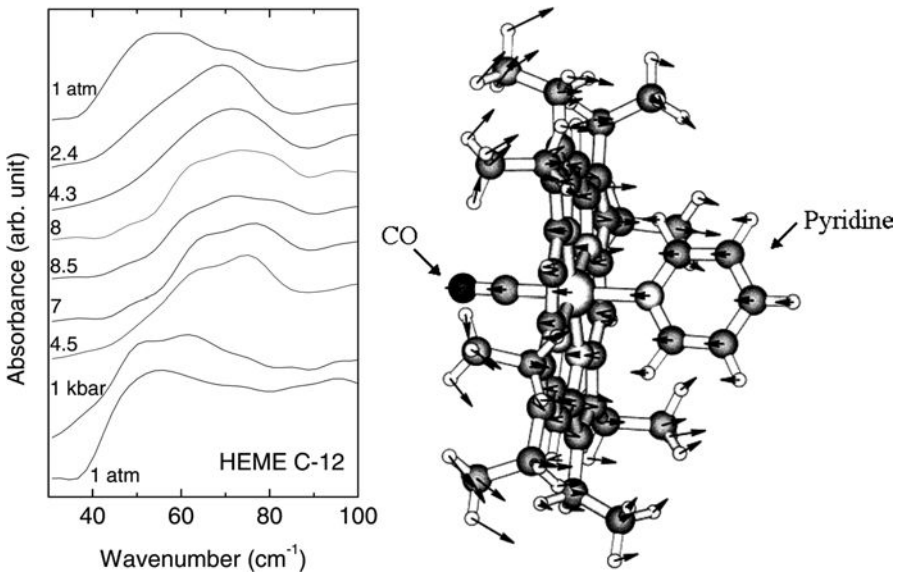

Figure 4. FIR absorption spectra of Fe(OEP)(CO)(Py) determined with the help of synchrotron light. The gasket and sample were ~500 μm thick, with a 500 μm diameter (*left*). The Fe(OEP)(CO)(Py) molecule shows atom displacements for the doming mode (*right*). The Fe atom is located between the CO and pyridine molecules. Nitrogen atoms are bonded to the Fe atom. (Reproduced with permission from Ref. 177; Copyright 2002, National Academy of Sciences, USA.)

calculations or incomplete experimental information such as intensity data or the use of pressure dependence.

F. Space-Resolved Techniques

1. *Infrared Microscopy and Imaging*

The combination of microscopic techniques and infrared spectroscopy has added the possibility of studying surfaces and tissues at molecular resolution and has led to infrared imaging.[183] Chemical, biochemical and biomedical information can be combined with spatial information. This has been one of the most important applications of vibrational spectroscopy to biomedically oriented research during the last decade.[184,185] Studies on living cells and tissue have emerged prominently in recent years. Infrared microscopy was realized for the MIR and the FIR, the latter being called THz imaging.

In chemistry and life sciences, FTIR imaging can be directly applied to the sample, for example to obtain the distribution of a certain compound in a sample. The identification of any compound with a clear vibrational marker is

possible within a large matrix.[186–188] Hemazoin-type porphyrin derivatives have been detected in biological cells, and candidates for photodynamic therapy were identified. NIR molecular imaging probes are being developed based on amphiphilic bisporphyrins and their Yb(III) complexes.[189] Furthermore, the contributions of the classic NIR vibrational markers in tissue, hemoglobin and myoglobin can be monitored.[190] Finally, infrared-fluorescent probes are increasingly important. Their wavelengths penetrate tissue well; therefore these probes are suitable for whole-body imaging.[191] In addition, combination with electrochemical techniques was reported, including the FTIR-microscopic study on self-assembled or immobilized heme layers on different types of electrodes.[192,193] Data of this type are typically obtained with a setup which includes a reflection element and, more recently, which is often coupled to synchrotron light sources.

2. *Working with Synchrotron Light*

The use of synchrotron light for infrared spectroscopy (SIR) and microscopy has dramatically increased during the past couple of years. Worldwide there are an increasing number of synchrotron infrared facilities.[194,195]

Flux for conventional and synchrotron infrared emission are almost equivalent but the opening angle of the edge radiation is narrower from the constant field of the bending magnet; the SIR is emitted into a narrow range of angles. The intensity profiles of the two types of emission at various wavelengths are different. The brightness advantage is thus not based on a higher power produced by the synchrotron, but on the fact that the effective source size is small; a synchrotron infrared source typically fills a 10–20 μm area. For studies below 200 cm^{-1}, synchrotron light is the "best" light source available. For low aperture settings also, the MIR shows a higher brightness.

Imaging has become one of the main applications of synchrotron-light-based infrared spectroscopies.[131,183,196–199] The high brilliance of the infrared light, however, is also of special interest to biochemists and chemists working with transmission techniques in the FIR.[155,177] New approaches include time-resolved measurements in combination with spatial resolution, such as TD–THz.

A recent development is the so-called nuclear resonance vibrational spectroscopy (NRVS), an emerging synchrotron-based approach.[13,200] NRVS achieves the ultimate limit of selectivity for a single atom in a complex molecule, because only the vibrational dynamics of the probe nucleus contribute to the measured signal. The NRVS signal is proportional to the mean square amplitude of the metal along the direction of the X-ray beam, and all modes involved will contribute to the measured spectrum.

III. Reaction-Induced FTIR Difference Spectroscopy

A. Motivation

By using reaction-induced FTIR difference spectroscopy, the reorganization of proteins upon the induced reaction can be monitored without contributions from the background. This technique can also be applied to smaller molecules or any other material. It became an especially important tool for the analysis of reaction mechanisms in enzymes and was essentially improved by spectroscopists working in the field of biochemistry and biophysics. Measurements in aqueous solutions have been made possible, in spite of the high absorptivity of water.[30,201] The first studies were presented by researchers working on bacteriorhodopsin,[202] and on photosynthesis.[10,203,204] Other applications followed.

The success of this approach is based on the possibility of monitoring the vibrational absorption bands of a single –COOH group, or any other residue, in a protein, which contains residues on the order of 10^3. The difficulties are obviously substantial. In practice, this amounts to being able to monitor absorption of about 10^{-5} OD in a background of about 1 OD, which requires very low random noise and drift (1 part in 10^{-6}). Data reported are thus typically obtained by cycling the reaction of interest and averaging a large number of scans and cycles. Several approaches have been used to obtain difference FTIR spectra. The goal in all cases is to maintain the sample at a constant concentration and path length, while perturbing the state of the sample in a way that is informative.

The analysis is based on the presence of specific vibrational marker modes of reactant, intermediate or product states. The outcome or kinetics of the induced reaction can then be interpreted by inspection of the transitions of these marker modes. Site-specific information is obtained for vibrational marker modes that involve nuclear motions of specific molecular side groups. When vibrational normal modes are involved in nuclear motions of extended parts of the molecules, a direct structural insight is usually not obtained. Isotopic substitution reveals the involvement of certain nuclei in the vibrational motions. When, in comparing the experimentally observed vibrational mode pattern with predictions from quantum-chemical calculations, a full correspondence is possible, the three-dimensional structure is derivable. Current quantum-chemical calculation routines, such as density functional theory (DFT), allow for the estimation of the electronic ground state structure of medium-sized molecules. For electronic excited states, including intermediate and product states, reliable results can be obtained with the *ab initio* complete active space self-consistent field (CASSCF) routine, albeit for mid-sized molecules not much larger than 20 atoms. New developments in numerical procedures, such as time-dependent density functional theory (TD-DFT), may prove beneficial in the estimation of larger molecular structures in electronic excited states.

A significant difficulty of the reaction-induced technique is thus the discrimination of individual contributions in the spectrum and their unequivocal assignment. A number of strategies were developed over the years, including the variation of external parameters like pH, pressure, temperature, specific and nonspecific isotope labeling, or, in the case of proteins, site-directed mutagenesis on crucial amino acids. In the following section some reaction-induced approaches are presented.

B. Electrochemically Induced FTIR Difference Spectroscopy

1. *Thin Layer Electrochemistry*

Porphyrin vibrational modes depend on the redox state of the central metal center. It was thus of interest to couple the spectroscopic experiments with electrochemical techniques. For *in situ* infrared-spectroscopic investigations of electrochemical reactions, a number of different techniques were developed. The first thin layer cells were reported in the 1970s[205,206] and that became a well-established tool for investigating porphyrins, phthalocyanines and their derivatives in different redox states.[109,207]

The development of electrochemical cells for infrared-spectroscopic measurements in aqueous solution was achieved in the 1990s. The basic design realized has not been significantly changed since then. It should be noted that implementation for infrared spectroscopy is considerably more complicated when it comes to measurements in aqueous solutions. Moss and colleagues have developed a cell that became successful for redox-induced FTIR-difference-spectroscopic studies on biological molecules in aqueous solution in transmission mode.[208] Fourier transform infrared spectra are obtained on the basis of thin layer electrochemistry of the protein at a modified gold grid electrode. The modification or functionalization of the surface is often done with the help of thiols that covalently bind to the electrode and thus protect the protein from irreversible adsorption onto the gold surface. This spectroelectrochemical thin layer cell allows fast, accurate and reproducible control of the redox situation of the protein. The resulting reduced minus-oxidized infrared difference spectra show the changes in the frequencies and intensities of molecular vibrations that arise from the redox-linked conformational change and coupled protonation changes. The concept of the transmission cell has not been significantly changed since then.

The thin layer electrochemical cell presented in Figure 5 (the path below 10 μm) was used to obtain full redox titration of large proteins. Detailed analysis of heme–heme interactions with cooperative systems, such as the hemes in the

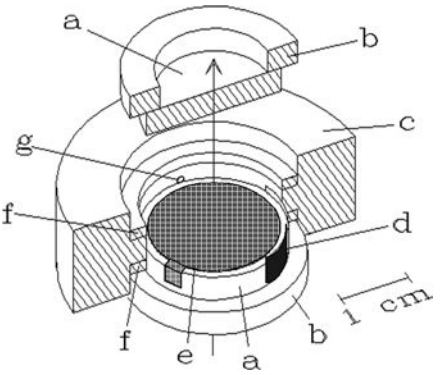

Figure 5. Scheme of a thin layer spectroelectrochemical cell adapted from Ref. 208. In detail: (a) IR window, CaF_2 for MIR, ZnSe for the lower frequency range[101] and diamond or Si for the FIR[52]; (b) plastic ring; (c) cell body; (d) Pt counterelectrode; (e) gold mesh, working electrode, not to scale; (f) rubber O-ring; (g) capillary connection to reference electrode.

bacterial reaction center in photosynthesis[209] or in the cytochrome *c* oxidase from the respiratory chain, was carried out.[210]

2. *Surface-Enhanced Infrared Absorption Spectroscopy*

Another possibility of working with samples that require aqueous solutions is a setup based on the reflection of the infrared light. Attenuated total reflection (ATR) FTIR spectroscopy devices have been successfully combined with electrochemistry.[211] The measurements are performed in reflection mode; therefore the working electrodes may be of any metal or of glassy carbon. Unfortunately, a large sample volume of 20 μL is needed.

A technical solution using a significantly lower sample volume was developed based on surface-enhanced approaches, where the sample is directly adsorbed onto the electrode surface (see Figure 6). This development is based on the seminal discovery of surface-enhanced Raman scattering (SERS) in the early 1970s, which opened up the field of surface-enhanced spectroscopies.[212] The phenomenon was subsequently observed at longer wavelengths and ultimately led to the realization of surface-enhanced infrared absorption spectroscopy (SEIRAS).[213] The practical and theoretical aspects of the phenomenon have more recently been described.[214,215] Characteristic of vibrational techniques, SERS and SEIRAS provide a wealth of molecular information on the level of a single chemical bond.

SERS and SEIRAS are complementary techniques, and each has its own advantages and disadvantages. SERS takes advantage of its enormous enhancement factor (on the order of 10^6–10^{12}). The strongest enhancement results from the

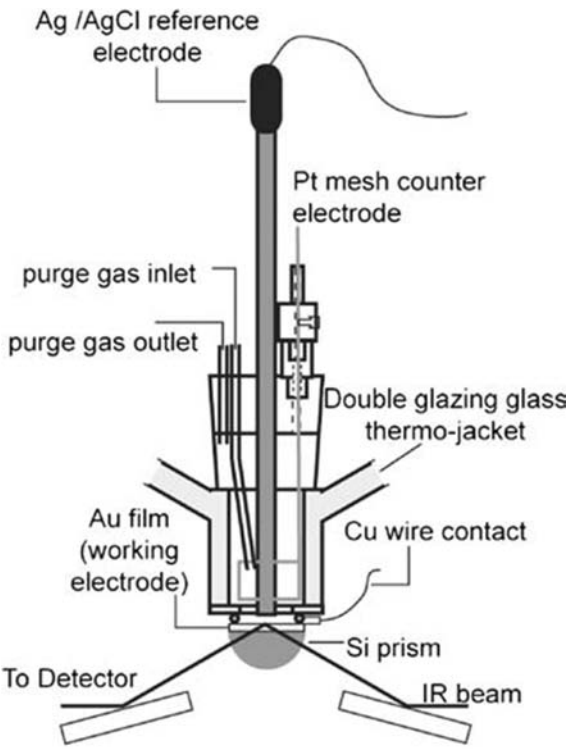

Figure 6. Cell developed for the study of immobilized proteins and other adsorbed species for the SEIRAS technique. (Reproduced with permission from Ref. 216; Copyright 2007, Springer-Verlag.)

resonance condition, if the biomolecule carries a chromophoric cofactor. The Raman signal is very weak and the fluorescence which often accompanies the phenomenon may render detection of the Raman spectrum difficult. Although this is not a problem with SEIRAS, the surface enhancement is modest (about 10–10^3). SEIRAS probes almost all bands of the adsorbed species as long as the vibrational mode includes a dipole component perpendicular to the surface (surface selection rule).[217] Although the enhancement factor of SEIRAS is smaller than that of SERS, the cross-section for infrared absorption is several orders of magnitude higher than the corresponding Raman cross-section. Thus, the weaker enhancement of SEIRAS may be sufficient for many applications.

A number of successful experiments using this technique have been reported.[218,219] Since the signal relay comprises only small amounts of monolayer molecules at the interfaces, measurement with a very small amount of the sample is possible.[216] Surface-enhanced vibrational spectroelectrochemistry constitutes a powerful approach to elucidating the reaction mechanisms and dynamics not only

of smaller molecules but also of immobilized redox proteins. In contrast to traditional electrochemical methods, the combination of SERS and SEIRA provides a direct and detailed molecular picture of all potential-dependent processes of the adsorbed species.

A profound knowledge of the molecular structure and dynamics of immobilized proteins and enzymes that can be obtained by these methods is a prerequisite for the rational design of bioelectronic devices of technological importance. In addition, surface-enhanced vibrational spectroscopies create new possibilities of studying complex biomimetic systems, thereby providing novel insight into fundamental biological processes.

Generally, the influence of electric fields on the various parameters that control electron- and proton-transfer reactions of soluble and membrane-bound proteins, like cytochrome *c*[220] and cytochrome *c* oxidase,[221] can now be studied. Electric fields of a magnitude comparable to those at the interfaces of biomembranes, i.e. the natural reaction environment, may have a substantial influence on redox potentials, protein structure, redox-linked conformational changes and orientation/reorientation of electrostatic complexes; therefore these studies demonstrate a functional role of the electric field effects *in vivo*.

C. Examples of Redox-Induced FTIR Difference Spectra

1. *Studies on Porphyrins and Small Hemoproteins*

Redox-induced FTIR difference spectroscopy was successfully applied for the characterization of the redox-sensitive vibrational modes of porphyrins and hemoproteins. Together with the redox-dependent transitions, signals from the reorganization of the direct environment upon electron transfer become available. These reorganizations may include protonation state changes or conformational movements. Cytochrome *c* and its derivatives are well characterized by the electrochemically induced FTIR-difference-spectroscopic approach.[16,208,222] Data analysis was possible due to several studies on model compounds. An often-used heme *c*-site model is the so-called microperoxidase, which is obtained by trypsic digestion of cytochrome *c*.[10,102] The number of amino acids still attached to the *c*-type heme is indicated by a number.

Figure 7 shows the reduced-minus-oxidized FTIR difference spectra for cytochrome *c* and for imidazole-microperoxidase-8.[10,102,222] In it the positive and negative signals correspond respectively to changes that occur upon reduction or oxidation. Generally, the data include all changes that happen upon the induced reaction. The structural changes are involved in the so-called amide I band, which is observed between 1700 and 1600 cm^{-1} and includes the ν(C=O) vibration of the polypeptide backbone in a hydrogen-bonding-dependent manner.

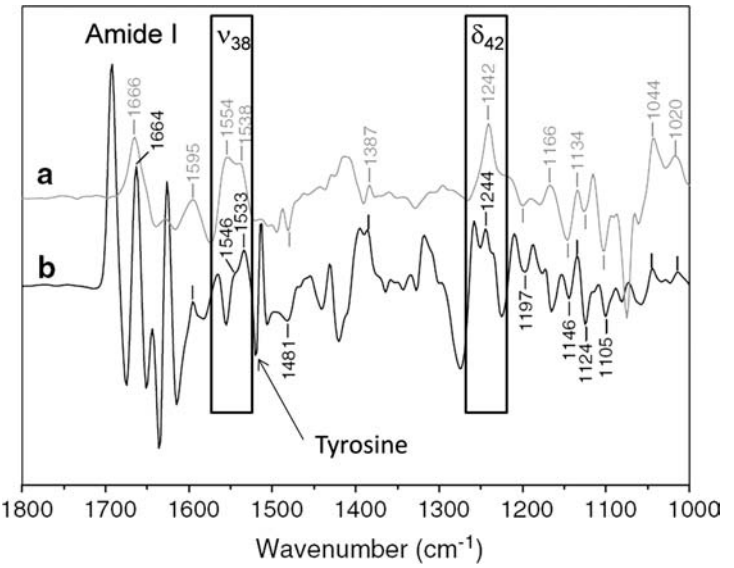

Figure 7. Reduced-minus-oxidized FTIR difference spectra of (a) an imidazole-microperoxidase-8 complex and (b) horse heart cytochrome *c*. (Modified from Ref. 102.)

Furthermore, the amide II signal seen from 1580 to 1520 cm^{-1} may provide information on structural rearrangements. Comparing the difference spectra of cytochrome *c* and the microperoxidase, strong differences can be noticed. This is based on the additional contributions from beta turns and beta sheet segments in the cytochrome *c* data. In addition, signals from amino acids contribute to the spectrum, such as signals characteristic of the protonation of a tyrosine residue at 1518 and 1500 cm^{-1}, a signal that arises in all known cytochrome *c* FTIR difference spectra.[208,222]

The redox-sensitive contribution of the hemes typically observed in the redox-induced difference spectra is the ν_{38} and δ_{42} vibrational modes at 1556–1533 cm^{-1} and 1244 cm^{-1}, respectively, the exact position depending on the type of heme in the protein.[10,102,210,223] The common redox-sensitive markers are summarized in Table 5. An additional heme marker can be found at around 840–830 cm^{-1}, a signal that includes the γ(CH) mode of the porphyrin ring.[101] Several other less intense vibrational modes are found at lower frequencies.

Similar thin layer cells were developed for studies on the nonhydrosoluble synthetic porphyrins in organic media.[224] Redox-induced FTIR difference spectroscopy was used in particular to determine where the removal or addition of an electron takes place, on either the metal or the porphyrin. Using the diagnostic band of π-cation radicals (Section II.A.4), it was for instance proven that the second oxidation of Fe(OEP)(NO) leads to the porphyrin π-cation radical $Fe(OEP^{\bullet})^{2+}$.[92,225–227]

Table 5. Typical redox-sensitive heme vibrations.[210]

Vibration and coupled vibration	Nomenclature	Typical spectral range (cm^{-1})
ν(C*a*C*m*) δ(C*a*C*m*H), δ(C*m*X)	ν_{37}	1560–1625
ν(C*b*C*b*) ν(C*a*C*m*), ν(NC*a*), ν(C*b*X), δ(C*b*X)	ν_{38}	1535–1570
ν(C*a*C*m*)^{sym} ν(NC*a*), ν(C*b*C*b*), ν(C*a*C*m*)	ν_{39}	1450–1490
ν(C*a*C*b*) δ(C*b*X), ν(NC*a*), δ(C*a*C*b*C*b*)	ν_{40}	1435–1450
ν(C*a*N) ν(C*a*C*b*), δ(C*b*X), δ(C*a*C*b*C*b*)	ν_{41}	1360–1395
δ(C*m*H) δ(C*b*X), ν(C*a*N), ν(C*a*C*b*)	δ_{42}	1220–1270

Since the 1980s, most studies describing the combination of electrochemistry with infrared spectroscopy have been carried out in the MIR range.[208,222] More recently, the use of the so-called fingerprint region in the lower frequency range and of the FIR region, which includes signals from metal–ligand vibrations, has started to evolve.[52,101]

2. *Studies on Enzymes from the Respiratory Chain*

Despite the difficulty of obtaining crystal structures from membrane proteins, several high resolution structures of enzymes from the respiratory chain are available. Crucial information like ligand and substrate dynamics, proton acceptor sites and cofactor coupling, however, is essentially obtained by spectroscopic techniques, often in combination with biochemical approaches, including site-directed mutagenesis or monoclonal antibody studies. X-ray crystallography is not sensitive to proton location, due to the weak electron density of the proton and the very high resolution that would be required. Most crystal structures of membrane proteins lack structural information on hydrogen atoms. In contrast, infrared spectroscopy is highly sensitive to the location of protons. In the following paragraphs, an overview of some interesting studies in this field will be presented.

a. *Identification of protonation sites in cytochrome* c *oxidase*

In the cellular respiration process, oxygen reduction is coupled to the formation of an electrochemical membrane proton gradient that drives ATP synthesis. The terminal heme/copper oxidases in the respiratory electron transfer chains reduce oxygen to water and efficiently couple electron and proton transfer.[228] Besides the four protons required for water formation, up to four protons are pumped across the membrane (termed "vectorial protons") by most terminal heme/copper oxidases to contribute to the electrochemical proton gradient. Four redox-active cofactors participate in the electron transfer within the cytochrome *c* oxidase. Cu_A represents

the first acceptor for electrons from cytochrome *c* that are subsequently transferred to heme *a*. Further electron transfer leads to the binuclear heme copper center (heme a_3 and Cu_B), where oxygen is bound and reduced. The crystal structures of several bacterial and mammalian oxidases give a clear view of the architecture of the enzyme active sites and confirm likely sites for the proton transport.[229,230]

Figure 8 shows the oxidized-minus-reduced FTIR difference spectrum of cytochrome *c* oxidase from *Paracoccus denitrificans*.[231] The positive and negative signals correspond respectively to changes that occur upon oxidation or reduction. The vibrational modes observed include redox-dependent changes of the hemes themselves, of the environment of the electron acceptors/donors, and of any coupled protonation or conformational change. In the amide I range (1680–1620 cm^{-1}), the differential signals indicate absorption changes arising from alterations of C=O groups from the polypeptide backbone. These difference signals can be related to subtle perturbations in the structure after the redox process.

In addition, contributions from the formyl group of hemes *a* and a_3, the heme propionates, and from individual amino acid side chains (Asn, Gln and Arg) are expected in this spectral region. In the spectral region from 1560 to 1520 cm^{-1} (the amide II range), essentially contributions from aromatic amino acid side chains and heme C=C groups are observed, as well as antisymmetric COO^- modes caused by protonation/deprotonation or perturbation of COO^- groups (Asp, Glu and heme

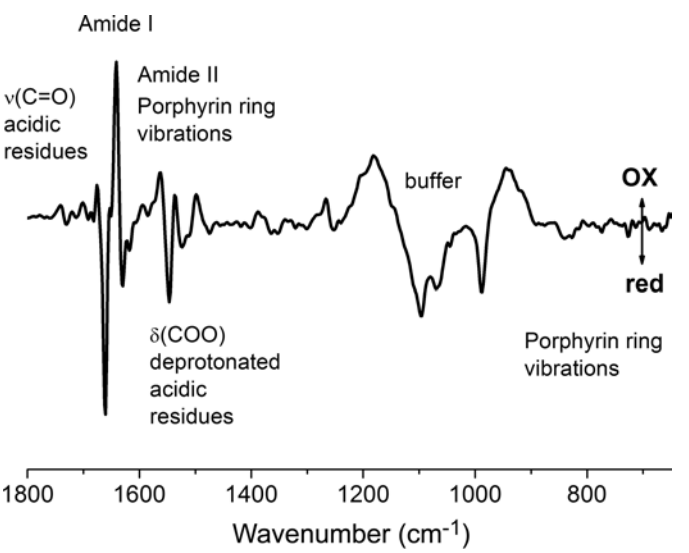

Figure 8. Oxidized-minus-reduced FTIR difference spectrum of the cytochrome *c* oxidase from *P. denitrificans* for the full potential step from –0.5 to 0.5 V versus a Ag/AgCl reference electrode. (Adapted from Ref. 210.)

propionate modes). At 1748 cm^{-1}, a positive signal, correlating with the oxidation of the enzyme, can be seen. In the spectral region above 1710 cm^{-1}, contributions from the ν(C=O) vibrational mode of protonated Asp and Glu side chains are expected exclusively.[232–234]

Some noteworthy differences have been described when comparing the spectra of the same enzyme found in different organisms, such as from the bacterium *Paracoccus denitrificans* and from bovine heart mitochondria.[235,236] This is interesting, since the two oxidases host the same heme centers, hemes *a* and a_3, with far-reaching similarities regarding their environment.[229,230] The same redox-dependent changes of the porphyrin ring, the formyl and vinyl substituent and the heme propionates are expected to manifest themselves in the spectra. The redox-dependent reorganization of an additional amino acid was suggested based on the crystal structure and can be depicted in the spectra together with the protonation reaction induced by the electron transfer.[235,237] The identification of the contribution of one individual amino acid clearly demonstrates the sensitivity of the reaction-induced FTIR-difference-spectroscopic technique. However, the explanation for this additional feature is under debate, since the existence of a third proton pathway was excluded for bacterial enzymes.[238]

Several studies have identified the contributions from individual amino acids within the enzyme. The possible function of individual amino acid side chains as proton acceptor/donor and thus their participation in the proton pathway have often been investigated by site-directed mutagenesis, which involves biochemical perturbation of the individual amino acids. The molecular processes concomitant with the redox reactions of a wild-type and mutant enzyme can be analyzed by combining protein electrochemistry and FTIR difference spectroscopy. Using these techniques the protonation state of glutamic acid 278 in the cytochrome *c* oxidase from *P. denitrificans* was assigned. This residue is the key proton transporter within the proton pump.[239,240] Analysis of the infrared signal was confirmed by groups working on the same enzyme from different organisms.[231,241]

Another way of obtaining information at the molecular level is isotope labeling. ^{13}C-isotope labeling was used to assign the protonation states of the heme propionates within the cytochrome *c* oxidase (see Figure 9). The structure of the heme environment is shown in Figure 10. This labeling was important for identification of the role of the heme propionates during the catalytic cycle. Based on crystallographic data it has been suggested that these propionate groups participate in proton translocation.[229]

Specific isotopic labeling provides an excellent tool for redox-FTIR investigations and avoids structural changes that can arise upon site-directed mutagenesis. A method for providing isotopically labeled cytochrome *c* oxidase was developed that guaranteed a very efficient and specific ^{13}C-enrichment at the carboxyl groups of the heme propionates. The protein obtained from these preparations had

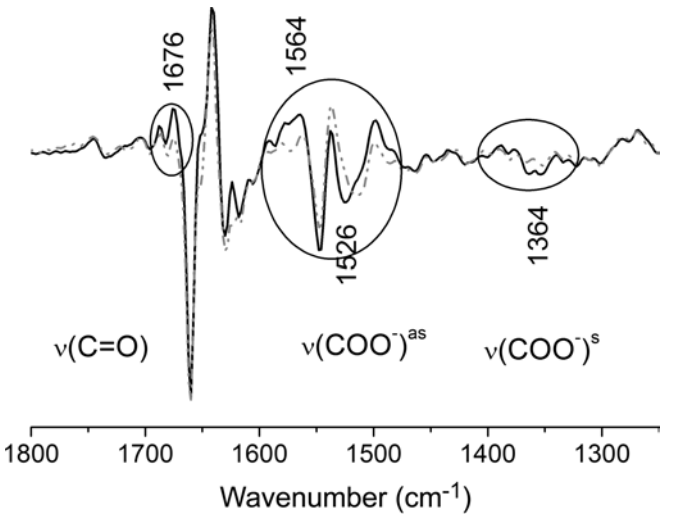

Figure 9. Oxidized-minus-reduced FTIR difference spectra of the cytochrome *c* oxidase from *P. denitrificans* as isolated (full line) and after ^{13}C labeling at the –COOH propionate functions of all hemes in the protein (dotted line). (Modified from Ref. 31.)

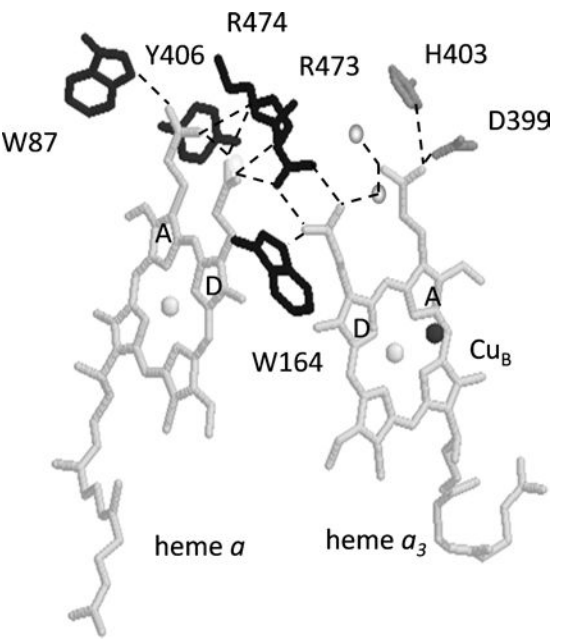

Figure 10. Structure of the heme environment in the cytochrome *c* oxidase from *P. denitrificans*. All amino acids within hydrogen bonding distance of the four heme propionates are shown. (Modified from Ref. 244.)

spectral characteristics and enzymatic activity identical to those of the wild type. The ^{13}C-labeled enzyme was used to identify the signals observed in electrochemically induced FTIR difference spectra of the cytochrome *c* oxidase and to assign their protonation states.[31,242]

Based on direct comparison between the "as-isolated form" of the protein and the oxidase, in which all COOH propionate functions were ^{13}C-labeled, the vibrational modes of heme propionates within a heme protein were distinguished for the first time. As seen in Figure 9, signals at 1570 cm^{-1} and in the 1546–1528 cm^{-1} range were assigned to antisymmetric COO^- modes. A signal at 1390 cm^{-1} was attributed to a symmetric COO^- mode of deprotonated heme propionates. The vibrational mode at 1676 cm^{-1} was attributed to a COOH mode of a protonated heme propionate.[31] The assignments were confirmed for a related oxidase by analogous experiments,[242] and the technique developed was used to clarify the analogous questions in other hemoproteins.[243]

To assign the individual vibrational modes within the spectrum of the full redox step to each of the specific heme propionates, additional experiments were necessary. First, an assignment of the individual heme was made with the help of infrared redox titrations on the basis of the respective redox potential.[210] In addition, site-directed mutagenesis was performed. The crystal structure[229] revealed that all four heme propionates had strong hydrogen bonding interactions with several amino acids (see Figure 10), and with parts of the protein backbone in close proximity.[244] The spectra of mutant proteins of the interacting amino acids have been accompanied by changes of the vibrational modes of the corresponding heme propionate. These changes are based on the variation of the hydrogen bonding toward the respective heme propionate. The respective experiments led to the conclusion that the ring D propionate of heme *a* acts as a proton acceptor upon reduction of cytochrome *c* oxidase, and none of the other three heme propionates seemed to be protonated upon reduction of the enzyme.[244] It was suggested that the ring D propionate of heme a_3 underwent significant conformational changes in its charged state, which might result in a change of the proton arrangement within the cluster of interacting residues and thus cause an increase in net protonation.[244]

b. *The bc_1 complex from the respiratory chain*

The cytochrome bc_1 complex (ubiquinol–cytochrome *c* oxidoreductase; complex III) is one of the fundamental components of the respiratory electron transfer chains located in the inner mitochondrial or bacterial cytoplasmic membranes.[245] The enzyme catalyzes the electron transfer from ubiquinol to cytochrome *c*; this electron transfer is coupled to translocation of protons across the membrane. All bc_1 complexes contain three catalytic subunits: cytochrome *b* with two *b*-type

hemes (hemes b_L and b_H), cytochrome c_1 with a covalently bound *c*-type heme and the Rieske iron–sulfur protein with a [2Fe–2S] cluster (ISP).

Figure 11 shows the different heme contributions that were obtained by addressing the redox step typical of each heme. Control experiments were performed in the visible spectral range, where the contribution typical of each

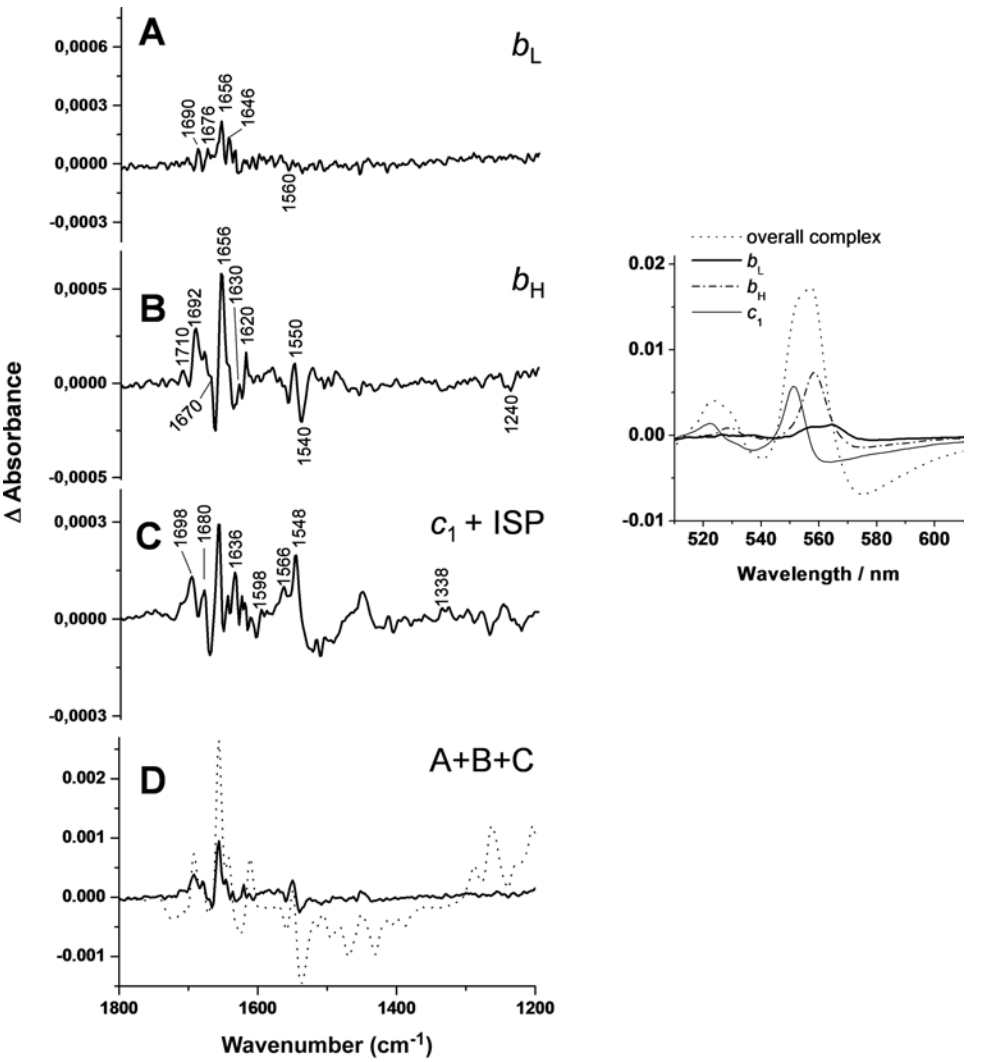

Figure 11. Oxidized-minus-reduced FTIR difference spectra of the individual hemes in the bc_1 complex from *P. denitrificans* (A: heme b_L; B: heme b_H, C: heme c_1 and Rieske Protein; D: comparison of the sum of the A–C spectra (bold line) with the spectrum of the overall complex (dotted line)). The potential steps were selected from the UV/visible titration of the individual hemes (see insert). (Modified from Ref. 248.)

heme type can be distinguished. Redox-induced FTIR difference spectra of the bc_1 complex have been studied by several groups.[211,246–248] The analysis of the contribution of each heme and the coupling of protonation changes to each transition was important for clarifying the interplay between different sites in the protein.

Redox-induced FTIR difference spectra include information on the protonation state of for example the amino acids or the heme propionates in an equilibrium situation. Time-resolved techniques have been developed that allow following the electron transfer and the coupled conformational changes or protonation reactions in "real" time.

D. Time-Resolved Techniques and Photoinduced Reactions

1. *Accessible Time Domains*

Chemistry occurs over a large range of time scales, most of which are accessible to infrared spectroscopy. Elementary steps in chemistry, such as the dynamical event of a chemical bond breaking or bond formation, appear to take place on femtosecond-to-picosecond time scales.[249] Examples of ultrafast chemistry are hydrogen and proton transfer, electron transfer, bond fissions and *cis–trans* isomerizations. Biomolecular reaction dynamics in liquid solutions are dominated by relatively slow mutual diffusion; typical time scales are on the order of nanoseconds. The dynamics of ultrafast condensed phase chemistry are determined not only by the potential energy surfaces of the reactant–product species, but the surrounding solvent also plays a major role in modulating the energy levels of reactants, intermediates and products, as well as the energy barriers separating these species. The outcome of chemical reactions is thus partially different from those for isolated reacting species. Photoinduced chemistry offers the opportunity to trigger the reaction dynamics at a well-defined point in time, and is thus often used for time-resolved approaches.

Rapid scan FTIR is used to study time-resolved motions, from a few milliseconds to seconds. The use of standard rapid scan FTIR spectroscopy is an experimentally accessible approach that allows a time resolution of 60 ms, if a 4.5 cm^{-1} resolution is chosen. Time-resolved FTIR difference spectroscopy experiments often use light-triggered reactions in proteins such as photoreceptors or photosynthetic pigments. The time scale of rapid scan FTIR, however, is also suitable for molecules that are not light-triggered using rapid mixing applications.

Step scan FTIR was developed for the characterization of the functionally important motions that take place in the time window from a few nanoseconds to a few milliseconds. The time-limiting step of the interferometer technique (FT) is the movement of the mirror; the highest velocity possible is the one used in the rapid scan approach. To obtain a higher time resolution, only a fraction of the

interferogram is measured in the step scan approach; this corresponds to a partial movement of the mirror. Then, as a function of the fractions of the interferogram measured, the reaction needs to be cycled to obtain the complete interferogram and consequently, after Fourier transformation, the full spectrum. Obviously, time-resolved step scan FTIR spectroscopy is technically challenging because it is sensitive to vibration and requires long measurement times for data averaging. Consequently, only a limited number of studies have been carried out using step scan FTIR spectroscopy. Step scan FTIR was first established to study the photoinduced reaction of bacteriorhodopsin,[250] and later to characterize the rebinding of CO to hemoglobin and cytochrome *c* oxidase in the nanosecond time range.[12,251]

Ultrafast infrared spectroscopy elucidates molecular structure evolution during ultrafast chemical reactions and represents an exquisite tool for following chemical reactions in real time after applying an optical trigger pulse. It is often used as a single wavelength technique or with short-pulsed laser systems, because the velocity of the mirror in an FT spectrometer limits time resolution (see step scan technique).

This technique is interesting to chemists and biochemists. Following vibrational marker modes in real time provides direct insight into the structural dynamics, as shown in studies on intramolecular hydrogen transfer, bimolecular proton transfer, electron transfer, hydrogen bonding during solvation dynamics, bond fission in organometallic compounds and heme proteins, *cis–trans* isomerization, and transformations in photochromic switch pairs. Femtosecond infrared spectroscopy monitors the site-specific interactions in hydrogen bonds. Furthermore, the conversion between excited electronic states can be followed for intramolecular electron transfer by inspection of the fingerprint IR-active vibrations, in conjunction with quantum-chemical calculations. Excess internal vibrational energy, generated either by optical excitation or by internal conversion from the electronic excited state to the ground state, is observable through transient frequency shifts of IR-active vibrations. An early example of picosecond infrared spectroscopy on excited state intramolecular hydrogen transfer was presented in 1986.[252] The method has mainly been employed on metallocarbonyl compounds[253] and heme proteins.[254–256] With the availability of sensitive MIR detector arrays, it is now possible to fully explore the potential of time-resolved vibrational spectroscopy to gain insight into transient molecular structures involved in chemical reaction pathways.

2. *Light-Induced FTIR Difference Spectroscopy*

a. *Ligand rebinding*

One of the most elementary photoinduced chemical processes is bond fission, where after absorption of a UV-vis photon one or several chemical bonds break

and the molecular fragments separate from each other. In most of the studies, the binding of the ligand or the rebinding of the photodissociated form is followed spectroscopically. Photodissociation is induced by lasers or white flash lamps. The measurements are performed for all temperature ranges and both rapid scan and step scan studies are known.

Groundbreaking work on photodissociation of small molecules using ultrafast UV-vis pump–probe techniques has been reported since the early days of ultrafast spectroscopy.[20,257] As mentioned in Section II.C.2, ligands like CO and CN^- that compete with oxygen for its binding site have been systematically used to analyze all types of oxidases and transporters.[22,160,161] The signal for the CO rebinding is typically found between 1980 and 1910 cm^{-1}.[171] The less-often-studied Fe–CO bending and stretching contributions are found in the FIR at about 574 cm^{-1} and 495 cm^{-1} for hemoproteins and porphyrin models.[258] Polarization-sensitive spectroscopy revealed the orientation of the CO or NO ligands in myoglobin or hemoglobin, either bound to the heme iron or released into the heme pockets. NO rebinding typically takes place in the ps range, in a phase that was suggested to reflect a barrier-less rebinding to the protein.

A number of proteins have been studied by time-resolved spectroscopies. They include NO binding proteins (signaling proteins), like NO synthase, Fix L, CooA or heme-based biological sensors.[172,259–263] Heme-based sensors presently constitute the majority of the proteins known to sense NO, O_2 and CO and to initiate the chemistry required to adapt to changes in their availability. They are found in a great variety of organisms throughout all the kingdoms of life. These signal transducers achieve their responses by coupling a regulatory heme-binding domain to a neighboring transmitter. The past several years have been witness to a staggering rate of advancement in the understanding of how organisms respond to changes in the availability of diatomic molecules that are toxic and/or crucial for survival. Infrared spectroscopy is thus used to characterize the ligand binding properties and, together with mutagenesis studies, defines crucial parameters of their sensoring ability.

b. *Ligand rebinding in cytochrome* c *oxidase*

The active site of the final acceptor of the respiratory chain, the cytochrome *c* oxidase, was structurally characterized in great detail using light-induced rebinding studies. In this enzyme, CO, CN^- and other ligands compete with oxygen for its binding site to the heme a_3–Cu_B binuclear center. As noted before, in contrast to oxygen these ligands give strong infrared bands, and thus represent excellent probes for spectroscopic investigations of cytochrome *c* oxidase.[264]

The negatively charged CN^- ligand was used to examine redox-linked conformational changes at the binuclear site.[265] Of the various possible ligands competing

with oxygen, CO was most extensively used to probe the environment of the binuclear center. It tightly binds to the reduced heme a_3/Cu_B center and can be photolyzed with a quantum yield close to 100%. Ultrafast kinetic studies on the photolysis of CO in the visible and MIR spectral range have provided insight into the primary molecular steps of photodissociation and rebinding.[266,267] In addition, the CO adduct of the cytochrome *c* oxidase has been studied with infrared spectroscopy at cryogenic temperatures.[85,164,268–270]

The thermodynamically favored binding site for CO is the iron of heme a_3. However, it was demonstrated that the binding of CO to heme a_3 proceeds via a CO adduct to Cu_B.[271] After photoexcitation of heme a_3, the Fe–CO bond is broken and CO is transferred to Cu_B, which is only 4.5 Å away from the heme a_3 center.[229] The stability of this intermediate depends on temperature and on CO concentration in the surrounding medium. At ambient and moderately low temperature, this Cu_B–CO adduct is in equilibrium with free CO in the bulk phase, whereas for the enzyme at temperatures below 140 K the Cu_B-bound CO can be trapped. Only transfer of CO within the binuclear center from heme a_3 to Cu_B after photoexcitation is observed.[272,273] The Cu_B binding site is relevant not only to CO but also to the physiological O_2 ligand.[274]

Figure 12 shows such a rebinding experiment for the fully reduced form of the cytochrome *c* oxidase. The positive signal seen corresponds to the Cu–CO vibrational modes and the negative signal to the Fe–CO vibrational modes. In each signal a number of conformers can be distinguished. Based on the analysis of the light-induced FTIR difference spectra on mutants of cytochrome *c* oxidases, the ligands of the Cu_B site and the surrounding loops were predicted, several years before the structure was determined by X-ray crystallography.[275,276]

CO bound to fully reduced cytochrome *c* oxidase exhibits two molecular conformations, termed the α- and the β-form, previously reported for the aa_3 oxidase from *R. sphaeroides*.[277] In wild-type cytochrome *c* oxidase from *P. denitrificans*, the α-form was attributed to signals at 1966/2063 cm^{-1} and the β-form to signals at 1952/2042 cm^{-1}.[85] The relative contribution of the conformers was found to be pH-dependent and suggested to originate from a residue with a pK value of 7.3 in the vicinity of the heme copper center.[277] This pH dependency is lost in mutants in the vicinity of the heme propionates for heme a_3, indicating that an interaction takes place between the active site and the propionates.[278]

Investigation of CO photolysis and rebinding to the fully reduced cytochrome *c* oxidase revealed that CO moves within the binding site and is released from the enzyme at higher temperature. Both CO rebinding at 268 K and at cryogenic temperature result in FTIR difference spectra that are similar with respect to the amide I, amide II and heme modes, but essentially differ due to the motional constraints of the CO molecule at low temperature. In the case of the mixed valence

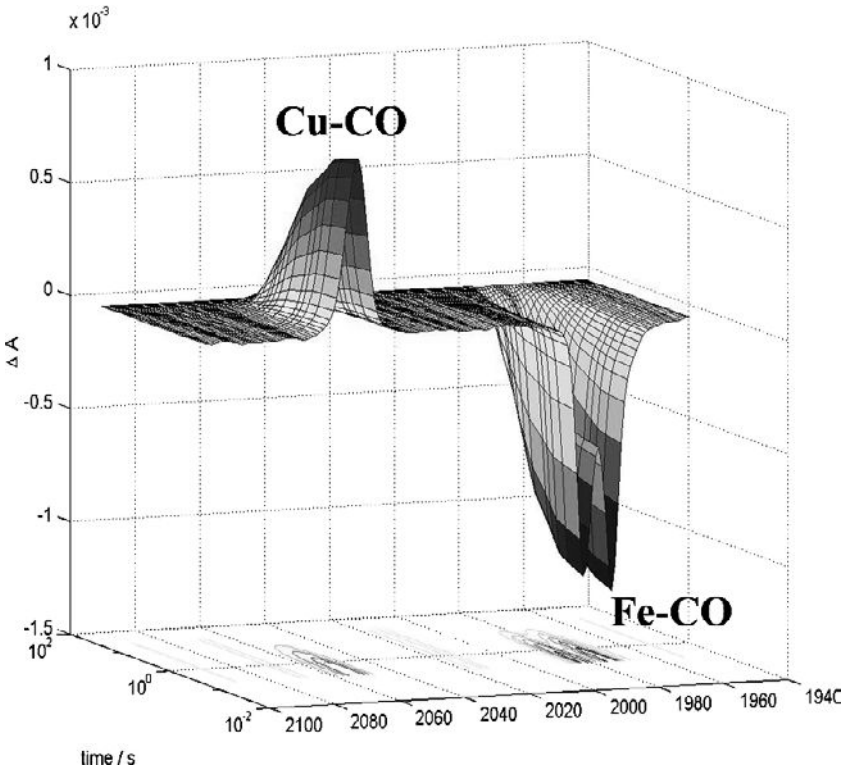

Figure 12. 3D plot of the CO rebinding to the fully reduced cytochrome *c* oxidase from *P. denitrificans* at 140 K. A. (Böhm and P. Hellwig, unpublished data; working conditions as described in Ref. 85.)

cytochrome *c* oxidase, photodissociation of CO initiates "reverse" electron transfer; proton release to the medium is coupled to this reaction.[279,280] Data obtained for the *P. denitrificans* cytochrome *c* oxidase clearly indicated that this reverse electron transfer causes changes at an acidic residue.[85,278] This is illustrated by a difference signal at 1746 cm^{-1}, which is shifted to 1740 cm^{-1} in ^2H_2O. The data obtained from a mutation, where glutamic acid 278 was replaced by a residue that does not contain the COOH function, show the absence of this signal and thus allow identification of this residue as being responsible for the signal. Taking into account the data of the electrostatic calculations,[281] the balance of evidence suggests the possible repositioning of the carboxylate proton in response to changes of the local electric fields rather than proton release, because proton release is still observed in a related mutant enzyme. At low temperature (below 270 K), rotations leading to a proton repositioning are most likely frozen, resulting in the absence of the signal assigned to the prominent glutamic acid 278.

FTIR-spectroscopic study of the CO rebinding is an established observable for the analysis of heme-Cu sites. In addition, the analysis of other heme-containing oxidases was successful, leading for example to the finding of a heme–heme binuclear center in the *bd* oxidase.[282] This type of oxidase is found in prokaryotes and is implicated in the survival of some bacteria, including pathogens, under conditions of low aeration. With a very high affinity for dioxygen (in the nM range), cytochrome *bd* not only couples respiration to the generation of a proton motive force, but also scavenges O_2.[283]

3. *Time-Resolved THz Spectroscopy*

Time domain THz (TD-THz) spectroscopy is a technique that is very promising for its unique time-resolved feature and its applications to dynamic and time-resolved processes. As mentioned above, contributions of metal–ligand vibrations and hydrogen bonding collective motions can be probed in the FIR region (<800 cm^{-1}) and these low frequency modes also involve contributions from water chains in the protein or any hydrogen bonding within the structure.[134,136,284] The spectroscopic characterization of low frequency signals may lead to an understanding of the protein dynamics that give rise to protein function, including ligand accommodation and electron and proton transfer.

TD-THz approaches probe the time-resolved reorganization of water within an induced reaction, such as in protein refolding.[132] The TD-THz technique is a pump–probe approach. The major components are a fs laser, a THz emitter source and a THz detector (FIR). A sample is excited in a desired spectral range and then monitored with a second laser system. Data on intermolecular forces, reaction dynamics or bond formation are accessible due to a fs time resolution. This technique has not yet been used to characterize hemoproteins or porphyrin derivative reactions and its citation here is meant to inspire the use of this promising technique.

4. *Two-Dimensional Infrared Spectroscopy*

a. *The approach*

Similarly, exciting developments have been seen in the field of two-dimensional infrared (2D-IR) spectroscopy; however, this technique has not yet been used for the characterization of the reactions of porphyrins and related compounds. This spectroscopic tool combines structural and ultrafast time resolution.[285] The idea is based on the transferability of the concepts of multidimensional nuclear magnetic resonance (NMR) spectroscopy to IR spectroscopy, which was postulated already

in the earliest publications on 2D-NMR. The first 2D-IR spectrum, however, was measured relatively recently.[286,287] Despite the fact that multidimensional optical techniques are analogs of their NMR counterparts, the time resolution is significantly improved: from ms in NMR to fs in IR.[288,289]

In 2D-IR spectroscopy, the response of complex molecules to sequences of fs infrared pulses is measured. A unique view of the structure, dynamics and fluctuating environments of molecules is provided, such as signatures of conformational and hydrogen-bonding fluctuations, protein folding and chemical exchange processes. Since vibrational spectra of large molecules are complex and congested, the use of a vibrational marker for 2D-IR is essential. A vibrational marker is a signal that should have a spectrally resolved transition in a part of the spectrum that is free of other transitions of the molecule and the solvent and at the same time should have a reasonably large extinction coefficient. Stretching modes with a large transition dipole, such as C=O, amide-I, amide-II, O–H and N–H, are often used in 2D-IR measurements. In addition, isotope labeling can be used to support the analysis. The interpretation is made on the basis of theoretical tools and simulation protocols, based on different approaches, including for example vibrational exciton Hamiltonians or united residue models.[289–291]

The study of metal carbonyls[292,293] demonstrated the unique ability of 2D-IR spectroscopy to resolve vibrational structure and dynamics in multimode systems. It was possible to resolve the transitions between vibrational energy levels, to determine the orientations and relative magnitude of the corresponding transition dipole moments, to measure the coupling between modes due to the anharmonicity of the potential, and finally to probe energy redistribution among the modes as well as energy relaxation to other degrees of freedom. In addition, valuable new information has been obtained on metal-to-ligand charge transfer processes, solvent–solute interactions and fluxionality. The technique is currently being advanced to allow the attribution of distances or bond connectivity patterns in molecules and reach the level of an analytical method.[294] Two examples are given below.

b. *OH stretching and H-bonding in water*

Water dynamics have been studied in detail, most recently using multidimensional nonlinear infrared spectroscopy to acquire structural and dynamical information on fs time scales.[295,296] Many of the unusual properties of liquid water are attributed to its unique structure, which is a random and fluctuating three-dimensional network of hydrogen bonds that link the highly polar water molecules. One of the most direct probes of the dynamics of this network is the infrared spectrum of the OH stretching vibration, which reflects the distribution of hydrogen-bonded

structures and the intermolecular forces controlling the structural dynamics of the liquid. Two-dimensional infrared photon echo and pump–probe studies of the OH stretching vibration provide a sensitive probe of the correlations and couplings in the hydrogen-bonded network of liquid water. Spectral diffusion and resonant energy transfer occur on a time scale much shorter than the average hydrogen bond lifetime of approximately 1 ps. The efficiency of energy redistribution within the hydrogen-bonded network means that liquid water essentially loses the memory of persistent correlations in its structure within 50 fs.[295,296]

c. *Estimating angles and distances between molecules*

One of the great strengths of NMR spectroscopy has been its ability to measure the coupling strength between nuclear spins and subsequently to deduce the distance between them. This capability stems from the relatively simple physics that determines the spin–spin coupling, in which distances interfere. It was shown that for systems in which electrical anharmonicity dominates, the coupling can be well described by the physics of multipole coupling, which corresponds approximately to the dipole–dipole coupling.[297] There are two types of anharmonicities intrinsic to a molecular system. The first of these comprises the lowest order anharmonic terms in a molecular potential energy surface, known as the mechanical anharmonicity. The second is the electrical anharmonicity, defined as the nonlinearity in a molecular electrical dipole moment.

Guo and coworkers analyzed the complex-forming molecular system, phenylacetylene and benzonitrile.[297] Here, the cross-peaks formed by dipolar couplings appear with the predicted strength and at the predicted locations in a 2D-IR spectrum. The polarization dependence of the cross-peaks can be used to deduce the angle between the molecules in question and thereby to estimate the distances between the two interacting modes via the intensities of the intermolecular cross-peaks. 2D-IR spectroscopy can be used to detect weakly interacting complexes and also to analyze their interaction geometry.

E. Perfusion-Induced Approaches; Stopped-Flow and Rapid Mixing

The combination of infrared spectroscopy with conventional mixing or stopped-flow technologies was recently achieved even for aqueous solutions. The main problem during development was the realization of the mixing procedure of the relatively concentrated sample solution with its reactant in an infrared cell with a path of about 50 μm or less. High pressure is needed to achieve instant mixing. The first prototype of a stopped-flow cell for aqueous solution was available in 1995.[298] The cell path was optimized down to 10 μm, allowing studies in the

MIR.[299] The applications of this technique include the characterization of active sites within proteins and their reactions[300,301] and the measurements on chemical and biochemical reactions in a time-resolved manner.[302–304] Typically, a 100 ms mixing time is needed; the reaction is then followed with the time limits of the respective FTIR apparatus. A stopped-flow mixing unit was recently presented combined with an infrared microscope; the setup added spatial information to the data.[305]

An alternative approach that was specifically developed for protein–substrate interaction is perfusion-induced FTIR difference spectroscopy. For example, studies on cytochrome *c* oxidase led to conclusions about oxygen reaction intermediates.[306,307] In order to monitor perfusion-induced difference spectra, it is necessary to create a stable protein layer on the ATR crystal. This can be achieved via direct immobilization or using the hydrophobic properties of some crystals. In the first studies presented, films from the cytochrome *c* oxidase from *Rhodobacter sphaeroides* and beef heart mitochondria were reconstituted with lipids and then adhered to the internal reflection element of the ATR device.[306] This procedure leads to samples with a quite low concentration, since the protein is "diluted" by the lipids. Interestingly, membrane proteins, when separated from the detergent molecules used for solubilization, can be directly applied on the crystal surface. The crystal surface then replaces the hydrophobic membrane. The success of this approach was unexpected, since membrane proteins tend to be extremely unstable; however, a fully functional protein was obtained.[307–309] The principle is evidently suited not only for membrane proteins. The immobilization of any molecule via hydrophobic interaction on the surface of the ATR crystal and subsequent study of the interaction with a partner is possible.

IV. Conclusion

Infrared spectroscopy is a technique that may provide data on the structure, function and dynamics of a molecule. The basic approach uses reaction- or structure-sensitive vibrational markers, such as redox, metal or π-cationic sensitive modes when one is working with porphyrins or hemes. Experimentally, several new approaches have emerged during the last few years, including reaction-induced approaches, ultrafast time-resolved techniques, 2D-IR, imaging and the use of synchrotron light as an infrared source, allowing in particular a better understanding of reaction mechanisms in hemoproteins or identification of protonation sites in proton-pumping enzymes. These recent techniques, mainly developed in the biomedical and biochemical fields, now offer promising applications, such as the real time study of chemical reactions by means of 2D-IR or TD-THz spectroscopy. Infrared spectroscopy is evidently a very

versatile technique, and the development of infrared-light-based techniques is surely far from being finished.

V. References

1. Lavallee, D. K. *Inorg. Chem.* **1978**, *17*, 231–232.
2. Craven, C. W.; Reissmann, K. R.; Chinn, H. I. *Anal. Chem.* **1952**, *24*, 1214–1215.
3. Wetherell, H. R.; Hendrickson, M. J.; McIntyre, A. R. *J. Am. Chem. Soc.* **1959**, *81*, 4517–4520.
4. Vestling, C. S.; Downing, J. R. *J. Am. Chem. Soc.* **1939**, *61*, 3511–3513.
5. Boucher, L. J.; Strain, H. H.; Katz, J. J. *J. Am. Chem. Soc.* **1966**, *88*, 1341–1346.
6. Dörr, S.; Schade, U.; Hellwig, P. *Vib. Spectrosc.* **2008**, *47*, 59–65.
7. Boucher, L. J.; Katz, J. J. *J. Am. Chem. Soc.* **1967**, *89*, 1340–1345.
8. Rai, B. K.; Durbin, S. M.; Prohofsky, E. W.; Sage, J. T.; Ellison, M. K.; Scheldt, W. R.; Sturhahn, W.; Alp, E. E. *Phys. Rev. E* **2002**, *66*, 051904/1–051904/12.
9. Argade, P. V.; Sassardi, M.; Rousseau, D. L.; Inubushi, T.; Ikeda-Saito, M.; Lapidot, A. *J. Am. Chem. Soc.* **1984**, *106*, 6593–6596.
10. Berthomieu, C.; Boussac, A.; Mäntele, W.; Breton, J.; Nabedryk, E. *Biochemistry* **1992**, *31*, 11460–11471.
11. Franzen, S.; Lambry, J. C.; Bohn, B.; Poyart, C.; Martin, J. L. *Nat. Struct. Biol.* **1994**, *1*, 230–233.
12. Hu, X.; Frei, H.; Spiro, T. G. *Biochemistry* **1996**, *35*, 13001–13005.
13. Leu, B. M.; Silvernail, N. J.; Zgierski, M. Z.; Wyllie, G. R.; Ellison, M. K.; Scheidt, W. R.; Zhao, J.; Sturhahn, W.; Alp, E. E.; Sage, J. T. *Biophys. J.* **2007**, *92*, 3764–3783.
14. Oshio, H.; Ama, T.; Watanabe, T.; Kincaid, J.; Nakamoto, K. *Spectrochim. Acta A* **1984**, *40*, 863–870.
15. Procyk, A. D.; Bocian, D. F. *Annu. Rev.* **1992**, *43*, 465–496.
16. Calvert, J. F.; Hill, J. L.; Dong, A. *Arch. Biochem. Biophys.* **1997**, *346*, 287–293.
17. Kozlowski, P. M.; Spiro, T. G.; Bérces, A.; Zgierski, M. Z. *J. Phys. Chem. B* **1998**, *102*, 2603–2608.
18. Thomas, D. W.; Martell, A. E. *J. Am. Chem. Soc.* **1959**, *81*, 5111–5119.
19. Krim, L.; Sorgues, S.; Soep, B.; Shafizadeh, N. *J. Phys. Chem. A* **2005**, *109*, 8268–8274.
20. Lim, M.; Jackson, T. A.; Anfinrud, P. A. *Science* **1995**, *269*, 962–966.
21. Mitchell, M. L.; Li, X. Y.; Kincaid, J. R.; Spiro, T. G. *J. Phys. Chem.* **1987**, *91*, 4690–4696.
22. Suharti, S. L.; de Vries, S.; Moënne-Loccoz, P. *J. Am. Chem. Soc.* **2004**, *126*, 15332–15333.
23. Demmel, F.; Doster, W.; Petry, W.; Schulte, A. *Eur. Biophys. J.* **1997**, *26*, 327–335.
24. Enakieva, Y. Y.; Bessmertnykh, A. G.; Gorbunova, Y. G.; Stern, C.; Rousselin, Y.; Tsivadze, A. Y.; Guilard, R. *Org. Lett.* **2009**, *11*, 3842–3845.
25. Ogoshi, H.; Watanbe, E.; Yoshida, Z.; Kincaid, J.; Nakamoto, K. *J. Am. Chem. Soc.* **1973**, *95*, 2845–2849.
26. Decréau, R. A.; Collman, J. P.; Yang, Y.; Yan, Y.; Devaraj, N. K. *J. Org. Chem.* **2007**, *72*, 2794–2802.
27. Rochford, J.; Chu, D.; Hagfeldt, A.; Galoppini, E. *J. Am. Chem. Soc.* **2007**, *129*, 4655–4665.
28. Fantauzzi, S.; Gallo, E.; Rose, E.; Raoul, N.; Caselli, A.; Issa, S.; Ragaini, F.; Cenini, S. *Organometallics* **2008**, *27*, 6143–6151.
29. Jaquinod, L.; Prévot, L.; Fischer, J.; Weiss, R. *Inorg. Chem.* **1998**, *37*, 1142–1149.
30. Gerwert, K. *Biol. Chem.* **1999**, *380*, 931–935.

31. Behr, J.; Hellwig, P.; Mäntele, W.; Michel, H. *Biochemistry* **1998**, *37*, 7400–7406.
32. Hayashi, T.; Lin, I. L.; Chen, Y.; Fee, J. A.; Moënne-Loccoz, P. *J. Am. Chem. Soc.* **2007**, *129*, 14952–14958.
33. Nienhaus, K.; Knapp, J. E.; Palladino, P.; Royer, W. E.; Nienhaus, G. U. *Biochemistry* **2007**, *46*, 14018–14031.
34. Hochstrasser, R. M. *Proc. Natl. Acad. Sci. USA* **2007**, *104*, 14190–14196.
35. Finkelstein, I. J.; Zheng, J.; Ishikawa, H.; Kim, S.; Kwak, K.; Fayer, M. D. *Phys. Chem. Chem. Phys.* **2007**, *9*, 1533–1549.
36. Bredenbeck, J.; Helbing, J.; Kolano, C.; Hamm, P. *Chemphyschem* **2007**, *8*, 1747–1756.
37. Nelander, B. *Vib. Spectrosc.* **1995**, *9*, 29–41.
38. Roy, P.; Brubach, J. B.; Calvani, P.; deMarzi, G.; Filabozzi, A.; Gerschel, A.; Giura, P.; Lupi, S.; Marcouillé, O.; Mermet, A.; Nucara, A.; Orphal, J.; Paolone, A.; Vervloet, M. *Nucl. Instrum. Methods. A* **2001**, *467–468*, 426–436.
39. Li, X. Y.; Czernuszewicz, R. S.; Kincaid, J. R.; Su, Y. O.; Spiro, T. G. *J. Phys. Chem.* **1990**, *94*, 31–47.
40. Rush III, T. S.; Kozlowski, P. M.; Piffat, C. A.; Kumble, R.; Zgierski, M. Z.; Spiro, T. G. *J. Phys. Chem. B* **2000**, *104*, 5020–5034.
41. Paulat, F.; Praneeth, V. K. K.; Näther, C.; Lehnert, N. *Inorg. Chem.* **2006**, *45*, 2835–2856.
42. Starovoitova, V.; Budarz, T. E.; Wyllie, G. R. A.; Scheidt, W. R.; Sturhahn, W.; Alp, E. E.; Prohofsky, E. W.; Durbin, S. M. *J. Phys. Chem. B* **2006**, *110*, 13277–13282.
43. Zhang, X.; Zhang, Y.; Jiang, J. *Spectrochim. Acta A* **2004**, *60*, 2195–2200.
44. Ogoshi, H.; Saito, Y.; Nakamoto, K. *J. Chem. Phys.* **1972**, *57*, 4194–4202.
45. Seoudi, R.; El-Bahy, G. S.; El Sayed, Z. A. *J. Mol. Struct.* **2005**, *753*, 119–126.
46. Ziminov, A.; Ramsh, S.; Terukov, E.; Trapeznikova, I.; Shamanin, V.; Yurre, T. *Semiconductors* **2006**, *40*, 1131–1136.
47. Scheer, H.; Inhoffen, H. H., Eds. *The Porphyrins*; Academic Press: New York, **1978**; Vol. 2.
48. Andersson, L. A.; Loehr, T. M.; Sotiriou, C.; Wu, W.; Chang, C. K. *J. Am. Chem. Soc.* **1986**, *108*, 2908–2916.
49. Lu, F.; Zhang, L.; Liu, H.; Yan, X. *Vib. Spectrosc.* **2005**, *39*, 139–143.
50. Dennis, K. P. N.; Jiangzhuang, J. *Chem. Soc. Rev.* **1997**, *26*, 433–442.
51. Buchler, J. W.; Ng, D. K. P.; Kadish, K. M.; Smith, K. M.; Guilard, R., Eds.; Academic Press: San Diego, **2000**; Vol. 3, pp. 245–294.
52. Berthomieu, C.; Marboutin, L.; Dupeyrat, F.; Bouyer, P. *Biopolymers* **2006**, *82*, 363–367.
53. Jung, C. *J. Mol. Recognit.* **2000**, *13*, 325–351.
54. Nakamoto, K.; Watanabe, T.; Ama, T.; Urban, M. W. *J. Am. Chem. Soc.* **1982**, *104*, 3744–3745.
55. Kozuka, M.; Nakamoto, K. *J. Am. Chem. Soc.* **1981**, *103*, 2162–2168.
56. Urban, M. W.; Nakamoto, K.; Basolo, F. *Inorg. Chem.* **1982**, *21*, 3406–3408.
57. Urban, M. W.; Nakamoto, K.; Kincaid, J. *Inorg. Chim. Acta* **1982**, *61*, 77–81.
58. Watanabe, T.; Ama, T.; Nakamoto, K. *J. Phys. Chem.* **1984**, *88*, 440–445.
59. Watanabe, T.; Ama, T.; Nakamoto, K. *Inorg. Chem.* **1983**, *22*, 2470–2472.
60. Cheung, S. K.; Grimes, C. J.; Wong, J.; Reed, C. A. *J. Am. Chem. Soc.* **1976**, *98*, 5028–5030.
61. Jones, R. D.; Budge, J. R.; Ellis, P. E.; Linard, J. E.; Summerville, D. A.; Basolo, F. *J. Organomet. Chem.* **1979**, *181*, 151–158.
62. Watanabe, T.; Ama, T.; Nakamoto, K. *J. Phys. Chem.* **1984**, *88*, 440–445.
63. Guilard, R.; Fontesse, M.; Fournari, P.; Lecomte, C.; Protas, J. *J. Chem. Soc. Chem. Commun.* **1976**, 161–162.

64. Collman, J. P.; Brauman, J. I.; Halbert, T. R.; Suslick, K. S. *Proc. Natl. Acad. Sci. USA* **1976**, *73*, 3333–3337.
65. Barlow, C. H.; Maxwell, J. C.; Wallace, W. J.; Caughey, W. S. *Biochem. Biophys. Res. Commun.* **1973**, *55*, 91–95.
66. Maxwell, J. C.; Volpe, J. A.; Barlow, C. H.; Caughey, W. S. *Biochem. Biophy. Res. Commun.* **1974**, *58*, 166–171.
67. Momenteau, M.; Reed, C. A. *Chem. Rev.* **1994**, *94*, 659–698.
68. Hoffman, B. M.; Szymanski, T.; Brown, T. G.; Basolo, F. *J. Am. Chem. Soc.* **1978**, *100*, 7253–7259.
69. Springer, B. A.; Sligar, S. G.; Olson, J. S.; Phillips, G. N., Jr. *Chem. Rev.* **1994**, *94*, 699–714.
70. Buchler, J.; Kokisch, W.; Smith, P. In *Cis, Trans, and Metal Effects in Transition Metal Porphyrins* **1978**; pp. 79–134.
71. Stavrov, S. S.; Decusar, I. P.; Bersuker, I. B. *New J. Chem.* **1993**, *17*, 71–76.
72. Silvernail, N. J.; Roth, A.; Schulz, C. E.; Noll, B. C.; Scheidt, W. R. *J. Am. Chem. Soc.* **2005**, *127*, 14422–14433.
73. Hashimoto, T.; Baldwin, J. E.; Basolo, F.; Dyer, R. L.; Crossley, M. J. *J. Am. Chem. Soc.* **1982**, *104*, 2101–2109.
74. Peng, S.-M.; Ibers, J. A. *J. Am. Chem. Soc.* **1976**, *98*, 8032–8036.
75. Caron, C.; Mitschler, A.; Riviere, G.; Ricard, L.; Schappacher, M.; Weiss, R. *J. Am. Chem. Soc.* **1979**, *101*, 7401–7402.
76. Salzmann, R.; McMahon, M. T.; Godbout, N.; Sanders, L. K.; Wojdelski, M.; Oldfield, E. *J. Am. Chem. Soc.* **1999**, *121*, 3818–3828.
77. Wang, J. H.; Nakahara, A.; Fleischer, E. B. *J. Am. Chem. Soc.* **1958**, *80*, 1109–1113.
78. Collman, J. P.; Brauman, J. I.; Collins, T. J.; Iverson, B. L.; Lang, G.; Pettman, R. B.; Sessler, J. L.; Walters, M. A. *J. Am. Chem. Soc.* **1983**, *105*, 3038–3052.
79. Slebodnick, C.; Duval, M. L.; Ibers, J. A. *Inorg. Chem.* **1996**, *35*, 3607–3613.
80. Desbois, A.; Momenteau, M.; Lutz, M. *Inorg. Chem.* **1989**, *28*, 825–834.
81. Landergren, M.; Baltzer, L. *J. Chem. Soc. Perkin Trans. 2* **1992**, 355–360.
82. Matsu-ura, M.; Tani, F.; Naruta, Y. *J. Am. Chem. Soc.* **2002**, *124*, 1941–1950.
83. Alben, J. O.; Caughey, W. S. *Biochemistry* **1968**, *7*, 175–183.
84. Frauenfelder, H.; Sligar, S.; Wolynes, P. *Science* **1991**, *254*, 1598–1603.
85. Rost, B.; Behr, J.; Hellwig, P.; Richter, O. M.; Ludwig, B.; Michel, H.; Mäntele, W. *Biochemistry* **1999**, *38*, 7565–7571.
86. Li, J.; Lord, R. L.; Noll, B. C.; Baik, M.-H.; Schulz, C. E.; Scheidt, W. R. *Angew. Chem. Int. Ed.* **2008**, *47*, 10144–10146.
87. Satoshi, K.; Takayanagi, M.; Nakata, M. *J. Mol. Struct.* **1997**, *413–414*, 365–369.
88. Scheidt, W. R.; Ellison, M. K. *Acc. Chem. Res.* **1999**, *32*, 350–359.
89. Enemark, J. H.; Feltham, R. D. *Coord. Chem. Rev.* **1974**, *13*, 339–406.
90. Wayland, B. B.; Olson, L. W. *J. Am. Chem. Soc.* **1974**, *96*, 6037–6041.
91. Lorkovic, I.; Ford, P. C. *J. Am. Chem. Soc.* **2000**, *122*, 6516–6517.
92. Mu, X. H.; Kadish, K. M. *Inorg. Chem.* **1988**, *27*, 4720–4725.
93. Maxwell, J. C.; Caughey, W. S. *Biochemistry* **1976**, *15*, 388–396.
94. Piciulo, P. L.; Rupprecht, G.; Scheidt, W. R. *J. Am. Chem. Soc.* **1974**, *96*, 5293–5295.
95. Scheidt, W. R.; Brinegar, A. C.; Ferro, E. B.; Kirner, J. F. *J. Am. Chem. Soc.* **1977**, *99*, 7315–7322.
96. Bohle, D. S.; Hung, C.-H. *J. Am. Chem. Soc.* **1995**, *117*, 9584–9585.
97. Ellison, M. K.; Scheidt, W. R. *Inorg. Chem.* **1998**, *37*, 382–383.

98. Richter-Addo, G. B.; Hodge, S. J.; Yi, G.-B.; Khan, M. A.; Ma, T.; Van Caemelbecke, E.; Guo, N.; Kadish, K. M. *Inorg. Chem.* **1996**, *35*, 6530–6538.
99. Scheidt, W. R.; Hatano, K.; Rupprecht, G. A.; Piciulo, P. L. *Inorg. Chem.* **1979**, *18*, 292–299.
100. Zahran, Z. N.; Lee, J.; Alguindigue, S. S.; Khan, M. A.; Richter-Addo, G. B. *Dalton Trans.* **2004**, 44–50.
101. Dörr, S.; Wolpert, M.; Hellwig, P. *Biopolymers* **2006**, *82*, 349–352.
102. Marboutin, L.; Boussac, A.; Berthomieu, C. *J. Biol. Inorg. Chem.* **2006**, *11*, 811–823.
103. Li, J.; Noll, B. C.; Schulz, C. E.; Scheidt, W. R. *Inorg. Chem.* **2007**, *46*, 2286–2298.
104. George, S. J.; Allen, J. W. A.; Ferguson, S. J.; Thorneley, R. N. F. *J. Biol. Chem.* **2000**, *275*, 33231–33237.
105. Reddy, K. S.; Yonetani, T.; Tsuneshige, A.; Chance, B.; Kushkuley, B.; Stavrov, S. S.; Vanderkooi, J. M. *Biochemistry* **1996**, *35*, 5562–5570.
106. Shimomura, E. T.; Phillippi, M. A.; Goff, H. M.; Scholz, W. F.; Reed, C. A. *J. Am. Chem. Soc.* **1981**, *103*, 6778–6780.
107. Hu, S.; Spiro, T. G. *J. Am. Chem. Soc.* **1993**, *115*, 12029–12034.
108. Barkigia, K. M.; Renner, M. W.; Fajer, J. *J. Phys. Chem. B* **1997**, *101*, 8398–8401.
109. Kadish, K. M.; Moninot, G.; Hu, Y.; Dubois, D.; Ibnlfassi, A.; Barbe, J. M.; Guilard, R. *J. Am. Chem. Soc.* **1993**, *115*, 8153–8166.
110. Chabach, D.; Tahiri, M.; De Cian, A.; Fischer, J.; Weiss, R.; Bibout, M. E. M. *J. Am. Chem. Soc.* **1995**, *117*, 8548–8556.
111. Bian, Y.; Jiang, J.; Tao, Y.; Choi, M. T. M.; Li, R.; Ng, A. C. H.; Zhu, P.; Pan, N.; Sun, X.; Arnold, D. P.; Zhou, Z.-Y.; Li, H.-W.; Mak, T. C. W.; Ng, D. K. P. *J. Am. Chem. Soc.* **2003**, *125*, 12257–12267.
112. Ferrari, M.; Mottola, L.; Quaresima, V. *Can. J. Appl. Physiol.* **2004**, *29*, 463–487.
113. Hoshi, Y. *J. Biomed. Opt.* **2007**, *12*, 062106.
114. Yoshitani, K.; Ohnishi, Y. *J. Anesth.* **2008**, *22*, 502–504.
115. Ndubuizu, O.; LaManna, J. C. *Antioxid. Redox Signal.* **2007**, *9*, 1207–1219.
116. Serebrennikova, Y. M.; Smith, J. M.; Huffman, D. E.; Leparc, G. F.; García-Rubio, L. H. *Opt. Express* **2008**, *16*, 18215–18229.
117. Perrey, S. *Methods* **2008**, *45*, 289–299.
118. Pogue, B. W.; Paulsen, K. D. *Opt. Lett.* **1998**, *23*, 1716–1718.
119. Wang, J.; Davis, S. C.; Srinivasan, S.; Jiang, S.; Pogue, B. W.; Paulsen, K. D. *J. Biomed. Opt.* **2008**, *13*, 041305.
120. Prince, S.; Malarvizhi, S. *Biofactors* **2007**, *30*, 255–263.
121. Kondepati, V. R.; Heise, H. M.; Backhaus, J. *Anal. Bioanal. Chem.* **2008**, *390*, 125–139.
122. Finikova, O. S.; Cheprakov, A. V.; Beletskaya, I. P.; Carroll, P. J.; Vinogradov, S. A. *J. Org. Chem.* **2004**, *69*, 522–535.
123. Detty, M. R.; Gibson, S. L.; Wagner, S. J. *J. Med. Chem.* **2004**, *47*, 3897–3915.
124. Balaz, M.; Collins, H. A.; Dahlstedt, E.; Anderson, H. L. *Org. Biomol. Chem.* **2009**, *7*, 874–888.
125. Kuimova, M. K.; Collins, H. A.; Balaz, M.; Dahlstedt, E.; Levitt, J. A.; Sergent, N.; Suhling, K.; Drobizhev, M.; Makarov, N. S.; Rebane, A.; Anderson, H. L.; Phillips, D. *Org. Biomol. Chem.* **2009**, *7*, 889–896.
126. Hilmey, D. G.; Abe, M.; Nelen, M. I.; Stilts, C. E.; Baker, G. A.; Baker, S. E.; Bright, F. V.; Davies, S. R.; Gollnick, S. O.; Oseroff, A. R.; Gibson, S. L.; Hilf, R.; Detty, M. R. *J. Med. Chem.* **2002**, *45*, 449–461.

127. Dong, A.; Caughey, W. S. *Methods Enzymol.* **1994**, *232*, 139–175.
128. Clay, G. O.; Schaffer, C. B.; Kleinfeld, D. *J. Chem. Phys.* **2007**, *126*, 025102.
129. Schiro, G.; Cupane, A. *Biochemistry* **2007**, *46*, 11568–11576.
130. Schmuttenmaer, C. A. *Chem. Rev.* **2004**, *104*, 1759–1779.
131. Miller, L. M.; Dumas, P. *Biochim. Biophys. Acta* **2006**, *1758*, 846–857.
132. Kim, S. J.; Born, B.; Havenith, M.; Gruebele, M. *Angew. Chem. Int. Ed.* **2008**, *47*, 6486–6489.
133. Kaun, N.; Baena, J. R.; Newnham, D.; Lendl, B. *Appl. Spectrosc.* **2005**, *59*, 505–510.
134. Heugen, U.; Schwaab, G.; Bründermann, E.; Heyden, M.; Yu, X.; Leitner, D. M.; Havenith, M. *Proc. Natl. Acad. Sci. USA* **2006**, *103*, 12301–12306.
135. Eyster, J. M.; Prohofsky, E. W. *Phys. Rev. Lett.* **1977**, *38*, 371–373.
136. Markelz, A. G. *IEEE J. Sel. Top. Quant. Electron*. **2008**, *14*, 180–190.
137. Xie, A.; van der Meer, A. F.; Austin, R. H. *Phys. Rev. Lett.* **2002**, *88*, 018102.
138. Brubach, J. B.; Mermet, A.; Filabozzi, A.; Gerschel, A.; Roy, P. *J. Chem. Phys.* **2005**, *122*, 184509.
139. Zundel, G.; Brzezinski, B. *Pol. J. Chem.* **1998**, *72*, 172–192.
140. Go, N.; Noguti, T.; Nishikawa, T. *Proc. Natl. Acad. Sci. USA*. **1983**, *80*, 3696–3700.
141. Zhang, C.; Durbin, S. M. *J. Phys. Chem. B* **2006**, *110*, 23607–23613.
142. Xu, J.; Plaxco, K. W.; Allen, S. J. *J. Phys. Chem. B* **2006**, *110*, 24255–24259.
143. Leu, B. M.; Zhang, Y.; Bu, L.; Straub, J. E.; Zhao, J.; Sturhahn, W.; Alp, E. E.; Sage, J. T. *Biophys. J.* **2008**, *95*, 5874–5889.
144. Hurley, W. J.; Kuntz Jr., I. D.; Leroi, G. E. *J. Am. Chem. Soc.* **1966**, *88*, 3199–3202.
145. Ryzhov, V. A. *Phys. Solid State* **2002**, *44*, 2229–2233.
146. Martens, S.; Gompf, B.; Dressel, M. *Appl. Opt.* **2009**, *48*, 5490–5496.
147. Ji, Y. B.; Lee, E. S.; Kim, S. H.; Son, J. H.; Jeon, T. *Opt. Express* **2009**, *17*, 17082–17087.
148. Williams, K. K.; Taylor, Z. D.; Suen, J. Y.; Lu, H.; Singh, R. S.; Gossard, A. C.; Brown, E. R. *Opt. Lett.* **2009**, *34*, 3068–3070.
149. Willer, U.; Pohlkötter, A.; Schade, W.; Xu, J.; Losco, T.; Green, R. P.; Tredicucci, A.; Beere, H. E.; Ritchie, D. A. *Opt. Express* **2009**, *17*, 14069–14074.
150. Musheinesh, M. A.; Divin, C. J.; Fessler, J. A.; Norris, T. B. *Opt. Express* **2009**, *17*, 13663–13670.
151. Suen, J. Y.; Tewari, P.; Taylor, Z. D.; Grundfest, W. S.; Lee, H.; Brown, E. R.; Culjat, M. O.; Singh, R. S. *Stud. Health Technol. Inform.* **2009**, *142*, 364–368.
152. Grosse, E. *Phys. Med. Biol.* **2002**, *47*, 3755–3760.
153. Ueno, Y.; Ajito, K. *Anal. Sci.* **2008**, *24*, 185–192.
154. Liu, H. B.; Chen, Y.; Zhang, X. C. *J. Pharm. Sci.* **2007**, *96*, 927–934.
155. Dörr, S.; Schade, U.; Hellwig, P.; Ortolani, M. *J. Phys. Chem. B* **2007**, *111*, 14418–14422.
156. Marboutin, L.; Desbois, A.; Berthomieu, C. *J. Phys. Chem. B* **2009**, *113*, 4492–4499.
157. Rai, B. K.; Durbin, S. M.; Prohofsky, E. W.; Sage, J. T.; Ellison, M. K.; Roth, A.; Scheidt, W. R.; Sturhahn, W.; Alp, E. E. *J. Am. Chem. Soc.* **2003**, *125*, 6927–6936.
158. Kitagawa, T. In *Biological Applications of Raman Spectroscopy*; Spiro, T. G., Ed.; Wiley and Sons: New York, **1988**; Vol. III, pp. 97–131.
159. Boffi, A.; Das, T. K.; della Longa, S.; Spagnuolo, C.; Rousseau, D. L. *Biophys. J.* **1999**, *77*, 1143–1149.
160. Jung, C.; Schulze, H.; Deprez, E. *Biochemistry* **1996**, *35*, 15088–15094.
161. Alben, J. O.; Beece, D.; Bowne, S. F.; Doster, W.; Eisenstein, L.; Frauenfelder, H.; Good, D.; McDonald, J. D.; Marden, M. C.; Moh, P. P.; Reinisch, L.; Reynolds, A. H.; Shyamsunder, E.; Yue, K. T. *Proc. Natl. Acad. Sci. USA* **1982**, *79*, 3744–3748.

162. Nienhaus, K.; Nienhaus, G. U. *Methods Enzymol.* **2008**, *437*, 347–378.
163. Berendzen, J.; Braunstein, D. *Proc. Natl. Acad. Sci. USA.* **1990**, *87*, 1–5.
164. Alben, J. O.; Moh, P. P.; Fiamingo, F. G.; Altschuld, R. A. *Proc. Natl. Acad. Sci. USA* **1981**, *78*, 234–237.
165. Nienhaus, G. U.; Chu, K.; Jesse, K. *Biochemistry* **1998**, *37*, 6819–6823.
166. Collman, J. P.; Gagne, R. R.; Gray, H. B.; Hare, J. W. *J. Am. Chem. Soc.* **1974**, *96*, 6522–6524.
167. Watanabe, T.; Ama, T.; Nakamoto K. *J. Phys. Chem. A* **1984**, *88*, 440–445.
168. Kurtikyan, T. S.; Martirosyan, G. G.; Hakobyan, M. E.; Ford, P. C. *Chem. Commun.* **2003**, *9*, 1706–1707.
169. Kendrew, J. C.; Bodo, G.; Dintzis, H. M.; Parrish, R. G.; Wyckoff, H.; Phillips, D. C. *Nature* **1958**, *181*, 662–666.
170. Brunori, M.; Bourgeois, D.; Vallone, B. *J. Struct. Biol.* **2004**, *147*, 223–234.
171. Spiro, T. G.; Wasbotten, I. H. *J. Inorg. Biochem.* **2005**, *99*, 34–44.
172. Vos, M. H. *Biochim. Biophys. Acta* **2008**, *1777*, 15–31.
173. Ansari, A.; Berendzen, J.; Bowne, S. F.; Frauenfelder, H.; Iben, I. E. T.; Sauke, T. B.; Shyamsunder, E.; Young, R. D. *Proc. Natl. Acad. Sci. USA* **1985**, *82*, 5000–5004.
174. Austin, R. H.; Beeson, K. W.; Eisenstein, L.; Frauenfelder, H.; Gunsalus, I. C. *Biochemistry* **1975**, *14*, 5355–5373.
175. Johnson, J. B.; Lamb, D. C.; Frauenfelder, H.; Müller, J. D.; McMahon, B.; Nienhaus, G. U.; Young, R. D. *Biophys. J.* **1996**, *71*, 1563–1573.
176. Nienhaus, G. U.; Mourant, J. R.; Frauenfelder, H. *Proc. Natl. Acad. Sci. USA* **1992**, *89*, 2902–2906.
177. Klug, D. D.; Zgierski, M. Z.; Tse, J. S.; Liu, Z.; Kincaid, J. R.; Czarnecki, K.; Hemley, R. J. *Proc. Natl. Acad. Sci. USA* **2002**, *99*, 12526–12530.
178. Prémont-Schwarz, M.; Bohle, D. S.; Gilson, D. F. R. *Inorg. Chim. Acta* **2006**, *359*, 3089–3091.
179. Kurtikyan, T. S.; Hovhannisyan, A. A.; Hakobyan, M. E.; Patterson, J. C.; Iretskii, A.; Ford, P. C. *J. Am. Chem. Soc.* **2007**, *129*, 3576–3585.
180. Monod, J.; Wyman, J.; Changeux, J.-P. *J. Mol. Biol.* **1965**, *12*, 88–118.
181. Perutz, M. F. *Nature* **1970**, *228*, 726–739.
182. Petrich, J. W.; Poyart, C.; Martin, J. L. *Biochemistry* **1988**, *27*, 4049–4060.
183. Lasch, P.; Naumann, D. *Biochim. Biophys. Acta.* **2006**, *1758*, 814–829.
184. Zhang, X. C. *Phys. Med. Biol.* **2002**, *47*, 3667–3677.
185. Bhargava, R.; Levin, I. W. *Anal. Chem.* **2001**, *73*, 5157–5167.
186. Malik, Z.; Dishi, M.; Garini, Y. *Photochem. Photobiol.* **1996**, *63*, 608–614.
187. Gravier, J.; Korchowiec, B.; Schneider, R.; Rogalska, E. *Chem. Phys. Lipids* **2009**, *158*, 102–109.
188. Kee, H. L.; Diers, J. R.; Ptaszek, M.; Muthiah, C.; Fan, D.; Lindsey, J. S.; Bocian, D. F.; Holten, D. *Photochem. Photobiol.* **2009**, *85*, 909–920.
189. Jiang, F. L.; Poon, C. T.; Wong, W. K.; Koon, H. K.; Mak, N. K.; Choi, C. Y.; Kwong, D. W.; Liu, Y. *Chembiochem* **2008**, *9*, 1034–1039.
190. Nighswander-Rempel, S. P.; Kupriyanov, V. V.; Shaw, R. A. *Appl. Spectrosc.* **2005**, *59*, 190–193.
191. Shu, X.; Royant, A.; Lin, M. Z.; Aguilera, T. A.; Lev-Ram, V.; Steinbach, P. A.; Tsien, R. Y. *Science* **2009**, *324*, 804–807.
192. He, P.; Hu, N.; Rusling, J. F. *Langmuir* **2004**, *20*, 722–729.
193. Liu, H. H.; Tian, Z. Q.; Lu, Z. X.; Zhang, Z. L.; Zhang, M.; Pang, D. W. *Biosens. Bioelectron.* **2004**, *20*, 294–304.

194. Abo-Bakr, M.; Feikes, J.; Holldack, K.; Wüstefeld, G.; Hübers, H. W. *Phys. Rev. Lett.* **2002**, *88*, 254801.
195. Marinkovic, N. S.; Huang, R.; Bromberg, P.; Sullivan, M.; Toomey, J.; Miller, L. M.; Sperber, E.; Moshe, S.; Jones, K. W.; Chouparova, E.; Lappi, S.; Franzen, S.; Chance, M. R. *J. Synchrotron Radiat.* **2002**, *9*, 189–197.
196. Miller, L. M.; Wang, Q.; Telivala, T. P.; Smith, R. J.; Lanzirotti, A.; Miklossy, J. *J. Struct. Biol.* **2006**, *155*, 30–37.
197. Miller, L. M.; Carlson, C. S.; Carr, G. L.; Chance, M. R. *Cell. Mol. Biol.* **1998**, *44*, 117–127.
198. Schmidt, M.; Lee, J. S.; Grunze, M.; Kim, K. H.; Schade, U. *Appl. Spectrosc.* **2008**, *62*, 171–175.
199. Carr, G. L.; Williams, G. P. *SPIE Conf. Proc.* **1997**, *3153*, 51–59.
200. Scheidt, W. R.; Durbin, S. M.; Sage, J. T. *J. Inorg. Biochem.* **2005**, *99*, 60–71.
201. Zscherp, C.; Barth, A. *Biochemistry* **2001**, *40*, 1875–1883.
202. Braiman, M. S.; Mogi, T.; Marti, T.; Stern, L. J.; Khorana, H. G.; Rothschild, K. J. *Biochemistry* **1988**, *27*, 8516–8520.
203. Nabedryk, E.; Berthomieu, C.; Verméglio, A.; Breton, J. *FEBS Lett.* **1991**, *293*, 53–58.
204. Buchanan, S.; Michel, H.; Gerwert, K. *Biochemistry* **1992**, *31*, 1314–1322.
205. Heineman, W. R.; Kuwana, T.; Hartzell, C. R. *Biochem. Biophys. Res. Commun.* **1972**, *49*, 1–8.
206. Norris, B. J.; Meckstroth, M. L.; Heineman, W. R. *Anal. Chem.* **1976**, *48*, 630–632.
207. Lin, X. Q.; Kadish, K. M. *Anal. Chem.* **1985**, *57*, 1498–1501.
208. Moss, D.; Nabedryk, E.; Breton, J.; Mäntele, W. *Eur. J. Biochem.* **1990**, *187*, 565–572.
209. Fritz, F.; Moss, D. A.; Mäntele, W. *FEBS Lett.* **1992**, *297*, 167–170.
210. Hellwig, P.; Grzybek, S.; Behr, J.; Ludwig, B.; Michel, H.; Mäntele, W. *Biochemistry* **1999**, *38*, 1685–1694.
211. Iwaki, M.; Yakovlev, G.; Hirst, J.; Osyczka, A.; Dutton, P. L.; Marshall, D.; Rich, P. R. *Biochemistry* **2005**, *44*, 4230–4237.
212. Fleischmann, M.; Hendra, P. J.; McQuilla, A. J. *Chem. Phys. Lett.* **1974**, *26*, 163–166.
213. Hartstein, A.; Kirtley, J. R.; Tsang, J. C. *Phys. Rev. Lett.* **1980**, *45*, 201–204.
214. Aroca, R. F.; Ross, D. J.; Domingo, C. *Appl. Spectrosc.* **2004**, *58*, 324–338.
215. Osawa, M. *Near-Field Optics and Surface Plasmon Polaritons* **2001**, *81*, 163–187.
216. Ataka, K.; Heberle, J. *Anal. Bioanal. Chem.* **2007**, *388*, 47–54.
217. Osawa, M. *Bull. Chem. Soc. Jpn.* **1997**, *70*, 2861–2880.
218. Zhang, Z.; Sato, T. I. H.; Watanabe, A.; Ozaki, Y. *Langmuir* **2001**, *17*, 4564–4568.
219. Zhang, Z.; Yoshida, N.; Imae, T.; Xue, Q.; Bai, M.; Jiang, J.; Liu, Z. *J. Colloid Interf. Sci.* **2001**, *243*, 382–387.
220. Ataka, K.; Heberle, J. *J. Am. Chem. Soc.* **2004**, *126*, 9445–9457.
221. Ataka, K.; Giess, F.; Knoll, W.; Naumann, R.; Haber-Pohlmeier, S.; Richter, B.; Heberle, J. *J. Am. Chem. Soc.* **2004**, *126*, 16199–16206.
222. Schlereth, D. D.; Mäntele, W. *Biochemistry* **1993**, *32*, 1118–1126.
223. Lin, C. Y.; Spiro, T. G. *J. Phys. Chem. B* **1997**, *101*, 472–482.
224. Kadish, K. M.; Mu, X. H.; Lin, X. Q. *Electroanalysis* **1989**, *1*, 35–41.
225. Jones, D. H.; Hinman, A. S. *J. Chem. Soc. Dalton Trans.* **1992**, 1503–1508.
226. Kadish, K. M.; Mu, X. H. *P. Appl. Chem.* **1990**, *62*, 1051–1054.
227. Hinman, A. S.; Olorunyolemi, T. *Can. J. Chem.* **1993**, *71*, 1975–1982.
228. Hosler, J. P.; Ferguson-Miller, S.; Mills, D. A. *Annu. Rev. Biochem.* **2006**, *75*, 165–187.
229. Iwata, S.; Ostermeier, C.; Ludwig, B.; Michel, H. *Nature* **1995**, *376*, 660–669.

230. Tsukihara, T.; Aoyama, H.; Yamashita, E.; Tomizaki, T.; Yamaguchi, H.; Shinzawa-Itoh, K.; Nakashima, R.; Yaono R.; Yoshikawa, S. *Science* **1995**, *269*, 1069–1074.
231. Hellwig, P.; Behr, J.; Ostermeier, C.; Richter, O. M.; Pfitzner, U.; Odenwald, A.; Ludwig, B.; Michel, H.; Mäntele, W. *Biochemistry* **1998**, *37*, 7390–7399.
232. Barth, A. *Biochim. Biophys. Acta* **2007**, *1767*, 1073–1101.
233. Vogel, R.; Siebert, F. *Curr. Opin. Chem. Biol.* **2000**, *4*, 518–523.
234. Kötting, C.; Gerwert, K. *Chemphyschem* **2005**, *6*, 881–888.
235. Hellwig, P.; Soulimane, T.; Buse, G.; Mäntele, W. *FEBS Lett.* **1999**, *458*, 83–86.
236. Yoshikawa, S.; Muramoto, K.; Shinzawa-Itoh, K.; Aoyama, H.; Tsukihara, T.; Shimokata, K.; Katayama, Y.; Shimada, H. *Biochim. Biophys. Acta* **2006**, *1757*, 1110–1116.
237. Okuno, D.; Iwase, T.; Shinzawa-Itoh, K.; Yoshikawa, S.; Kitagawa, T. *J. Am. Chem. Soc.* **2003**, *125*, 7209–7218.
238. Salje, J.; Ludwig, B.; Richter, O. M. *Biochem. Soc. Trans.* **2005**, *33*, 829–831.
239. Richter, O. M.; Ludwig, B. *Biochim. Biophys. Acta* **2009**, *1787*, 626–634.
240. Brzezinski, P.; Reimann, J.; Adelroth, P. *Biochem. Soc. Trans.* **2008**, *36*, 1169–1174.
241. Lübben, M.; Prutsch, A.; Mamat, B.; Gerwert, K. *Biochemistry* **1999**, *38*, 2048–2056.
242. Schmidt, B.; Hillier, W.; McCracken, J.; F.-M., S. *Biochim. Biophys. Acta* **2004**, *1655*, 248–255.
243. Mileni, M.; Haas, A. H.; Mäntele, W.; Simon, J.; Lancaster, C. R. *Biochemistry* **2005**, *44*, 16718–16728.
244. Behr, J.; Michel, H.; Mäntele, W.; Hellwig, P. *Biochemistry* **2000**, *39*, 1356–1363.
245. Berry, A. B.; Guergova-Kuras, M.; Huang, L.; Crofts, A. R. *Annu. Rev. Biochem.* **2000**, *69*, 1005–1075.
246. Ritter, M.; Palsdottir, H.; Abe, M.; Mäntele, W.; Hunte, C.; Miyoshi, H.; Hellwig, P. *Biochemistry* **2004**, *43*, 8439–8446.
247. Baymann, F.; Robertson, D. E.; Dutton, P. L.; Mäntele, W. *Biochemistry* **1999**, *38*, 13188–13199.
248. Ritter, M.; Anderka, O.; Ludwig, B.; Mäntele, W.; Hellwig, P. *Biochemistry* **2003**, *42*, 12391–12399.
249. Zewail, A. H. *Science* **1988**, *242*, 1645–1653.
250. Rödig, C.; Siebert, F. *FEBS Lett.* **1999**, *445*, 14–18.
251. Heitbrink, D.; Sigurdson, H.; Bolwien, C.; Brzezinski, P.; Heberle, J. *Biophys. J.* **2002**, *82*, 1–10.
252. Elsaesser, T.; Kaiser, W. *Chem. Phys. Lett.* **1986**, *128*, 231–237.
253. Moore, J. N.; Hansen, P. A.; Hochstrasser, R. M. *J. Am. Chem. Soc.* **1989**, *111*, 4563–4566.
254. Moore, J. N.; Hansen, P. A.; Hochstrasser, R. M. *Proc. Natl. Acad. Sci. USA* **1988**, *85*, 5062–5066.
255. Stoutland, P. O.; Dyer, R. B.; Woodruff, W. H. *Science* **1992**, *257*, 1913–1917.
256. Achterhold, K.; Parak, F. G. *J. Phys. Cond. Matter* **2003**, *15*, 1683–1692.
257. Schotte, F.; Lim, M.; Jackson, T. A.; Smirnov, A. V.; Soman, J.; Olson, J. S.; Phillips, G. N. J.; Wulff, M.; Anfinrud, P. A. *Science* **2003**, *300*, 1944–1947.
258. Hu, S.; Vogel, K. M.; Spiro, T. G. *J. Am. Chem. Soc.* **1994**, *116*, 11187–11188.
259. Jasaitis, A.; Hola, K.; Bouzhir-Sima, L.; Lambry, J. C.; Balland, V.; Vos, M. H.; Liebl, U. *Biochemistry* **2006**, *45*, 6018–6026.
260. Marvin, K. A.; Kerby, R. L.; Youn, H.; Roberts, G. P.; Burstyn, J. N. *Biochemistry* **2008**, *47*, 9016–9028.
261. Lu, S.; Suharti; Vries, S.; Moënne-Loccoz, P. *J. Am. Chem. Soc.* **2004**, *126*, 15332–15333.

262. Bidwai, A. K.; Ok, E. Y.; Erman, J. E. *Biochemistry* **2008**, *47*, 10458–10470.
263. Das, T. D.; Wilson, E. K.; Cutruzzolà, F.; Brunori, M.; Rousseau, D. L. *Biochemistry* **2001**, *40*, 10774–10781.
264. Gilles-Gonzalez, M.-A.; Gonzalez, G. *J. Inorg. Biochem.* **2005**, *99*, 1–22.
265. Tsubaki, M.; Yoshikawa, S. *Biochemistry* **1993**, *32*, 164–173.
266. Einarsdottir, Ó.; Dyer, R. B.; Lemon, D. D.; Killough, P. M.; Hubig, S. M.; Atherton, S. J.; López-Garriga, J. J.; Palmer, G.; Woodruff, W. H. *Biochemistry* **1993**, *32*, 12013–12024.
267. Dyer, R. B.; Peterson, K. A.; Stoutland, P. O.; Woodruff, W. H. *Biochemistry* **1994**, *33*, 500–507.
268. Mitchell, D. M.; Müller, J. D.; Gennis, R. B.; Nienhaus, U. G. *Biochemistry* **1996**, 16782–16788.
269. Park, S.; Pan, L. P.; Chan, S. I.; Alben, J. O. *Biophys. J.* **1996**, *71*, 1036–1047.
270. Puustinen, A.; Bailey, J. A.; Dyer, R. B.; Mecklenburg, S. L.; Wikström, M.; Woodruff, W. H. *Biochemistry* **1997**, *36*, 13195–13200.
271. Georgiadis, K. E.; Jhon, N.-I.; Einarsdottir, Ó. *Biochemistry* **1994**, *33*, 9245–9256.
272. Fiamingo, F. G.; Altschuld, R. A.; Alben, J. O. *J. Biol. Chem.* **1986**, *261*, 12976–12987.
273. Fiamingo, F. G.; Altschuld, R. A.; Moh, P. P.; Alben, J. O. *J. Biol. Chem.* **1982**, *257*, 1639–1650.
274. Oliveberg, M.; Malmström, B. G. *Biochemistry* **1992**, 3560–3563.
275. Calhoun, M. W.; Hill, J. J.; Lemieux, L. J.; Ingledew, W. J.; Alben, J. O.; Gennis, R. B. *Biochemistry* **1993**, *32*, 11524–11529.
276. Hosler, J. P.; Shapleigh, J. P.; Tecklenburg, M. J.; Thomas, J. W.; Kim, Y.; Espe, M.; Fetter, J.; Babcock, G. T.; Alben, J. O.; Gennis, R. B. *Biochemistry* **1994**, *33*, 1194–1201.
277. Mitchell, D. M.; Shapleigh, J. P.; Archer, A. M.; Alben, J. O.; Gennis, R. B. *Biochemistry* **1996**, *35*, 9446–9450.
278. Hellwig, P.; Bohm, A.; Pfitzner, U.; Mantele, W.; Ludwig, B. *Biochim. Biophys. Acta* **2008**, *1777*, 220–226.
279. Mitchell, R.; Rich, P. R. *Biochim. Biophys. Acta* **1994**, *1186*, 19–26.
280. Ädelroth, P.; Sigurdson, H.; Hallen, S.; Brzezinski, P. *Proc. Natl. Acad. Sci. USA* **1996**, *93*, 12292–12297.
281. Kannt, A.; Lancaster, C. R. D.; Michel, H. *Biophys. J.* **1998**, *74*, 708–721.
282. Hill, J. J.; Alben, J. O.; Gennis, R. B. *Proc. Natl. Acad. Sci. U.S.A.* **1993**, *90*, 5863–5867.
283. Jünemann, S. *Biochim. Biophys. Acta* **1997**, *1321*, 107–127.
284. Zhang, C.; Durbin, S. M. *J. Phys. Chem. B* **2006**, *110*, 23607–23613.
285. Hamm, P.; Helbing, J.; Bredenbeck, J. *Annu. Rev. Phys. Chem.* **2008**, *59*, 291–317.
286. Hamm, P.; Lim, M.; Hochstrasser, R. M. *J. Phys. Chem. B* **1998**, *102*, 6123–6138.
287. Ernst, R. R.; Bodenhausen, G.; Wokaun, A. *Principles of Nuclear Magnetic Resonance in One and Two Dimensions*; Oxford: Clarendon, **1987**.
288. Bredenbeck, J.; Helbing, J.; Kolano, C.; Hamm, P. *Chemphyschem* **2007**, *8*, 1747–1756.
289. Zhuang, W.; Hayashi, T.; Mukamel, S. *Angew. Chem. Int. Ed.* **2009**, *48*, 3750–3781.
290. Zhuang, W.; Abramavicius, D.; Hayashi, T.; Mukamel, S. *J. Phys. Chem. B* **2006**, *110*, 3362–3374.
291. Khalili, M.; Liwo, A.; Jagielska, A.; Scheraga, H. A. *J. Phys. Chem. B* **2005**, *109*, 13798–13810.
292. Baiz, C. R.; McRobbie, P. L.; Preketes, N. K.; Kubarych, K. J.; Geva, E. *J. Phys. Chem. A* **2009**, *113*, 9617–9623.

293. Baiz, C. R.; McRobbie, P. L.; Anna, J. M.; Geva, E.; Kubarych, K. J. *Acc. Chem. Res.* **2009**, *42*, 1395–1404.
294. Rubtsov, I. V. *Acc. Chem. Res.* **2009**, *42*, 1385–1394.
295. Kraemer, D.; Cowan, M. L.; Paarmann, A.; Huse, N.; Nibbering, E. T.; Elsaesser, T.; Miller, R. J. *Proc. Natl. Acad. Sci. USA* **2008**, *105*, 437–442.
296. Cowan, M. L.; Bruner, B. D.; Huse, N.; Dwyer, J. R.; Chugh, B.; Nibbering, E. T.; Elsaesser, T.; Miller, R. J. *Nature* **2005**, *434*, 199–202.
297. Guo, R.; Fournier, F.; Donaldson, P. M.; Gardner, E. M.; Gould, I. R.; Klug, D. R. *Phys. Chem. Chem. Phys.* **2009**, 8417–8421.
298. White, A. J.; Drabble, K.; Wharton, C. *Biochem. J.* **1995**, *306*, 843–849.
299. Masuch, R.; Moss, D. A. *Appl. Spectrosc.* **2003**, *57*, 1407–1418.
300. George, S. J.; Kurkin, S.; Thorneley, R. N.; Albracht, S. P. *Biochemistry* **2004**, *43*, 6808–6819.
301. George, S. J.; Andrew, C. R.; Lawson, D. M.; Thorneley, R. N. F.; Eady, R. *J. Am. Chem. Soc.* **2001**, *123*, 9683–9684.
302. Hinsmann, P.; Frank, J.; Svasek, P.; Harasek, M.; Lendl, B. *Lab. Chip.* **2001**, *1*, 16–21.
303. Tolland J. D.; Thorneley, R. N. F. *Biochemistry* **2005**, *44*, 9520–9527.
304. Muthusamy, M.; Ambundo, E. A.; George S. J.; Lippard, S. J.; Thorneley, R. N. F. *J. Am. Chem. Soc.* **2003**, *125*, 11150–11151.
305. Kauffmann, E.; Darton, N. C.; Austin, R. H.; Batt, C.; Gerwert, K. *Proc. Natl. Acad. Sci. USA.* **2001**, *98*, 6646–6649.
306. Nyquist, R. M.; Heitbrink, D.; Bolwien, C.; Wells, T. A.; Gennis, R. B.; Heberle, J. *FEBS Lett.* **2001**, *505*, 63–67.
307. Iwaki, M.; Puustinen, A.; Wikstrom, M.; Rich, P. R. *Biochemistry* **2004**, *43*, 14370–14378.
308. Rich, P. R.; Iwaki, M. *Mol. Biosyst.* **2007**, *3*, 398–407.
309. Iwaki, M.; Rich, P. R. *J. Am. Chem. Soc.* **2004**, *126*, 2386–2389.

Index to Volume 7

B

C

F

G

H

N

O

P

Q

R

S

T

V

W

X

Z

Handbook of Porphyrin Science

with Applications to Chemistry, Physics, Materials Science, Engineering, Biology and Medicine

Volume 8

Open-Chain Oligopyrrole Systems

Karl M. Kadish ▪ Kevin M. Smith ▪ Roger Guilard

Editors

World Scientific

Handbook of Porphyrin Science

with Applications to Chemistry, Physics, Materials Science, Engineering, Biology and Medicine

This page intentionally left blank

Handbook of Porphyrin Science

with Applications to Chemistry, Physics, Materials Science, Engineering, Biology and Medicine

Volume 8

Open-Chain Oligopyrrole Systems

Editors

Karl M. Kadish
University of Houston, USA

Kevin M. Smith
Louisiana State University, USA

Roger Guilard
Université de Bourgogne, France

World Scientific

NEW JERSEY • LONDON • SINGAPORE • BEIJING • SHANGHAI • HONG KONG • TAIPEI • CHENNAI

Published by

World Scientific Publishing Co. Pte. Ltd.

5 Toh Tuck Link, Singapore 596224

USA office: 27 Warren Street, Suite 401-402, Hackensack, NJ 07601

UK office: 57 Shelton Street, Covent Garden, London WC2H 9HE

British Library Cataloguing-in-Publication Data
A catalogue record for this book is available from the British Library.

HANDBOOK OF PORPHYRIN SCIENCE
with Applications to Chemistry, Physics, Materials Science, Engineering, Biology and Medicine
(Volumes 6–10)

ISBN-13 978-981-4307-18-5 (Set)
ISBN-13 978-981-4307-21-5 (Vol. 8)

Typeset by Stallion Press
Email: enquiries@stallionpress.com

Printed in Singapore.

Contents

Preface

Although the porphyrin and tetrapyrrole research area was regarded as "fully matured" during the 20th century, as evidenced for example by the awarding of numerous Nobel Prizes to its principal researchers, new advances and accomplishments in the field still amaze us as editors. The area continues to blossom and to expand into new areas of science and applications that would probably never have occurred to our 20th century heroes. An earlier *Porphyrin Handbook* assembled the large amount of factual data that had been accumulated during the 20th century. Our new venture, the *Handbook of Porphyrin Science* takes a completely new look at our research area and comprehensively details the contemporary science now appearing in the scientific literature that would indeed have been hard to predict even 10 years ago. In particular, fundamentally new methodologies and potential commercial applications of the beautiful compounds that we all love are exemplified, fully recognizing the subtitle of the series — "with applications to chemistry, physics, materials science, engineering, biology and medicine".

The three of us have complementary expertise in physical chemistry, synthetic and bioorganic chemistry, and in synthetic and mechanistic organometallic chemistry; this has enabled us to cover the whole field of porphyrin science and applications, and to devise comprehensive volume and author content. As of the date of writing, between the three of us, we have published more than 1600 tetrapyrrole research articles, and hold 31 patents related to commercial applications of porphyrin science. So we do know our field, and this has enabled us to assemble a first-rate group of experts who have written comprehensive up-to-date chapters with accuracy and authority; we thank our authors for their cooperation and willingness to go along with our highly ambitious schedule for production of these volumes.

We look forward to comments from our readers, and to suggestions that might enable us to expand our basic interests and scientific coverage even further. Meanwhile, we hope that porphyrin researchers, old, new and of the future, will enjoy reading these volumes just as much as we enjoyed planning and, with the help of World Scientific Publishing Company, producing them from manuscript to published article, in a timely manner.

Karl M. Kadish (Houston, Texas, USA)
Kevin M. Smith (Baton Rouge, Louisiana, USA)
Roger Guilard (Dijon, Bourgogne, France)
January, 2010

This page intentionally left blank

Contributing Authors*

Hasrat Ali
Université de Sherbrooke
Sherbrooke, Québec, Canada
Chapter 16

Cristina Alonso
University of Hull
Kingston-upon-Hull, HU6 7RX, UK
Chapter 17

Edith Antunes
Rhodes University
Grahamstown, 6139, South Africa
Chapter 34

Naoki Aratani
Kyoto University
Kyoto 606-8502, Japan
aratani@kuchem.kyoto-u.ac.jp
Chapter 1

Teodor Silviu Balaban
Karlsruhe Institute of Technology
D-76021 Karlsruhe, Germany
Silviu.Balaban@int.fzk.de
Chapter 3

Alan L. Balch
University of California, Davis
Davis, CA 95616, USA
balch@chem.ucdavis.edu
Chapter 40

David P. Ballou
University of Michigan
Ann Arbor, MI 48109-5606, USA
Chapter 28

Faye Bowles
University of California, Davis
Davis, CA 95616, USA
Chapter 40

Ross W. Boyle
University of Hull
Kingston-upon-Hull, HU6 7RX, UK
r.w.boyle@hull.ac.uk
Chapter 17

Ozguncem Bozkulak
Childrens Hospital Los Angeles
Los Angeles, CA 90027, USA
Chapter 22

Martin Bröring
Technische Universität Carolo-Wilhelmina zu Braunschweig
Hagenring 30, Braunschweig, Germany
m.broering@tu-bs.de
Chapter 41

Kevin Burgess
Texas A&M University
College Station, TX 77842, USA
burgess@tamu.edu
Chapter 37

*Full contact information for authors can be found on the title page of each chapter.

José A.S. Cavaleiro
University of Aveiro
3810-193 Aveiro, Portugal
jcavaleiro@ua.pt
Chapter 9

Sung Cho
Yonsei University
Seoul, 120-747, Korea
Chapter 5

Daniel P. Collins
University of South Carolina
Columbia, SC 29208, USA
Chapter 28

John H. Dawson
University of South Carolina
Columbia, SC 29208, USA
dawson@mail.chem.sc.edu
Chapter 28

Ilia G. Denisov
The University of Illinois
Urbana, IL 61801, USA
Denisov@illinois.edu
Chapter 26

Charles Michael Drain
Hunter College of The City University of New York
New York, NY 10065, USA
cdrain@hunter.cuny.edu
Chapter 15

Francis D'Souza
Wichita State University
Wichita, KS 67260-0051, USA
Francis.DSouza@wichita.edu
Chapter 4

Florence Duclairoir
Institut Nanosciences et Cryogénie
38054 Grenoble cedex 9, France
Chapter 47

Manivannan Ethirajan
Roswell Park Cancer Institute
Buffalo, NY 14263, USA
Chapter 19

Alessandro Feis
University of Florence
I-50019 Sesto Fiorentino, Italy
Chapter 31

Angela Ferrario
Childrens Hospital Los Angeles
Los Angeles, CA 90027, USA
Chapter 22

Kimberly B. Fields
University of South Florida
Tampa, FL 33620, USA
Chapters 13, 43

Takamitsu Fukuda
Osaka University
Toyonaka 560-0043, Japan
tfukuda@chem.sci.osaka-u.ac.jp
Chapter 42

Shunichi Fukuzumi
Osaka University
Suita, Osaka 565-0871, Japan
fukuzumi@chem.eng.osaka-u.ac.jp
Chapter 46

Hiroyuki Furuta
Kyushu University
Fukuoka 819-0395, Japan
hfuruta@cstf.kyushu-u.ac.jp
Chapter 10

Jean-Paul Gisselbrecht
Université de Strasbourg
67000 Strasbourg, France
gissel@unistra.fr
Chapter 14

Charles J. Gomer
University of Southern California
Los Angeles, CA 90027, USA
Chapter 22

Bruno Grimm
Friedrich-Alexander-University Erlangen-Nuremberg
91058 Erlangen, Germany
Chapter 2

Dirk M. Guldi
Friedrich-Alexander-University Erlangen-Nuremberg
91058 Erlangen, Germany
dirk.guldi@chemie.uni-erlangen.de
Chapter 2

Anita Hausmann
Friedrich-Alexander-University Erlangen-Nuremberg
91058 Erlangen, Germany
Chapter 2

Takashi Hayashi
Osaka University
Suita 565-0871, Japan
thayashi@chem.eng.osaka-u.ac.jp
Chapter 23

Petra Hellwig
Université de Strasbourg
67000 Strasbourg, France
hellwig@chimie.u-strasbg.fr
Chapter 36

Yoshio Hisaeda
Kyushu University
Fukuoka 819-0395, Japan
yhisatcm@mail.cstm.kyushu-u.ac.jp
Chapter 48

Barry D. Howes
University of Florence
I-50019 Sesto Fiorentino, Italy
Chapter 31

Akira Ikezaki
Toho University
Ota-ku, Tokyo 143-8540, Japan
Chapter 32

Osamu Ito
Tohoku University
Sendai, 981-3215, Japan
Chapter 4

Anabella Ivancich
Centre Nationale de la Recherche Scientifique (URA 2096)
F-91191 Gif-sur-Yvette, France
Chapter 31

Christophe Jeandon
Université de Strasbourg
67000 Strasbourg, France
cjeandon@unistra.fr
Chapter 14

Norbert Jux
Universität Erlangen-Nürnberg
91054 Erlangen, Germany
norbert.jux@chemie.uni-erlanger.de
Chapter 20

Axel Kahnt
Friedrich-Alexander-University Erlangen-Nuremberg
91058 Erlangen, Germany
Chapter 2

David Kessel
Wayne State University School of Medicine
Detroit, MI 48201, USA
dhkessel@med.wayne.edu
Chapter 21

Dongho Kim
Yonsei University
Seoul, 120-747, Korea
dongho@yonsei.ac.kr
Chapters 5, 6

Kil Suk Kim
Yonsei University
Seoul, 120-747, Korea
Chapter 6

Nagao Kobayashi
Tohoku University
Sendai 980-8578, Japan
nagaok@mail.tains.tohoku.ac.jp
Chapters 33, 42

Lechosław Latos-Grażyński
University of Wrocław
Wrocław 50 383, Poland
llg@wchuwr.pl
Chapter 8

Genxi Li
Nanjing University
Nanjing 210093, PR China
genxili@nju.edu.cn
Chapter 27

Jong Min Lim
Yonsei University
Seoul, 120-747, Korea
Chapter 6

Aurore Loudet
Texas A&M University
College Station, TX 77842, USA
Chapter 37

Evgeny A. Lukyanets
Organic Intermediates and Dyes Institute
Moscow, 123995, Russia
rmeluk@niopik.ru
Chapter 11

Marian Luna
Childrens Hospital Los Angeles
Los Angeles, CA 90027, USA
Chapter 22

Hiromitsu Maeda
Ritsumeikan University
Kusatsu 525-8577, Japan
maedahir@ph.ritsumei.ac.jp
Chapter 38

Jean-Claude Marchon
Institut Nanosciences et Cryogénie
38054 Grenoble cedex 9, France
jean-claude.marchon@cea.fr
Chapter 47

M. Victoria Martínez-Díaz
Universidad Autónoma de Madrid
28049-Madrid, Spain
Chapter 45

Frederic Melin
Université de Strasbourg
67000 Strasbourg, France
Chapter 36

Shingo Nagano
Tottori University
Tottori 680-8552, Japan
Chapter 25

Mikio Nakamura
Toho University
Ota-ku, Tokyo 143-8540, Japan
mnakamu@med.toho-u.ac.jp
Chapter 32

Wonwoo Nam
Ewha Womans University
Seoul 120-750, South Korea
wwnam@ewha.ac.kr
Chapter 44

Victor N. Nemykin
University of Minnesota Duluth
Duluth, MN 55812, USA
vnemykin@d.umn.edu
Chapter 11

Maria G.P.M.S. Neves
University of Aveiro
3810-193 Aveiro, Portugal
Chapter 9

Tebello Nyokong
Rhodes University
Grahamstown, 6139, South Africa
t.nyokong@ru.ac.za
Chapter 34

Yoshiki Ohgo
Toho University
Ota-ku, Tokyo 143-8540, Japan
Chapter 32

Tetsuo Okujima
Ehime University
Matsuyama 790-8577, Japan
Chapter 7

Noboru Ono
Ehime University
Matsuyama 790-8577, Japan
ononbr@dpc.ehime-u.ac.jp
Chapter 7

Atsuhiro Osuka
Kyoto University
Kyoto 606-8502, Japan
osuka@kuchem.kyoto-u.ac.jp
Chapter 1

Ravindra K. Pandey
Roswell Park Cancer Institute
Buffalo, NY 14263, USA
ravindra.pandey@roswellpark.org
Chapter 19

Nayan J. Patel
Roswell Park Cancer Institute
Buffalo, NY 14263, USA
Chapter 19

Miłosz Pawlicki
University of Wrocław
Wrocław 50 383, Poland
Chapter 8

Sébastien Richeter
Université Montpellier 2
34095 Montpellier Cedex 5, France
sebastien.richeter@univ-montp2.fr
Chapter 14

Beate Röder
Humboldt-Universität zu Berlin
12489 Berlin, Germany
roeder@physik.hu-berlin.de
Chapter 20

Natalie Rucker
Childrens Hospital Los Angeles
Los Angeles, CA 90027, USA
Chapter 22

Joshua V. Ruppel
University of South Florida
Tampa, FL 33620, USA
Chapters 13, 43

Romain Ruppert
Université de Strasbourg
67000 Strasbourg, France
rruppert@unistra.fr
Chapter 14

Aoife Ryan
Trinity College Dublin
Dublin 2, Ireland
Chapter 12

Wolfgang Seitz
Friedrich-Alexander-University
Erlangen-Nuremberg
91058 Erlangen, Germany
Chapter 2

Mathias O. Senge
Trinity College Dublin
Dublin 2, Ireland
sengem@tcd.ie
Chapter 12

Natalia N. Sergeeva
Trinity College Dublin
Dublin 2, Ireland
Chapter 12

Hisashi Shimakoshi
Kyushu University
Fukuoka 819-0395, Japan
Chapter 48

Jae-Yoon Shin
Yonsei University
Seoul, 120-747, Korea
Chapter 6

Yoshitsugu Shiro
Harima Institute
Hyogo 679-5148, Japan
yshiro@riken.jp
Chapters 24, 25

Martha Sibrian-Vazquez
Portland State University
Portland, OR 97201, USA
Chapter 18

Sunaina Singh
Hunter College of The City University of
New York
New York, NY 10065, USA
Chapter 15

Stephen G. Sligar
The University of Illinois
Urbana, IL 61801, USA
s-sligar@uiuc.edu
Chapter 26

Giulietta Smulevich
University of Florence
I-50019 Sesto Fiorentino, Italy
giulietta.smulevich@unifi.it
Chapter 31

Nicole L. Snyder
Hamilton College
Clinton, NY 13323, USA
Chapters 13, 43

Fabian Spänig
Friedrich-Alexander-University Erlangen-Nuremberg
91058 Erlangen, Germany
Chapter 2

Tatyana Spolitak
University of Michigan
Ann Arbor, MI 48109-5606, USA
Chapter 28

Hiroshi Sugimoto
Harima Institute
Hyogo 679-5148, Japan
Chapter 24

Osamu Takikawa
National Center for Geriatrics and Gerontology
Obu, Aichi 474-8522, Japan
Chapter 24

Alison Thompson
Dalhousie University
Halifax, Nova Scotia, Canada
alison.thompson@dal.ca
Chapter 39

Motoki Toganoh
Kyushu University
Fukuoka 819-0395, Japan
Chapter 10

Augusto C. Tomé
University of Aveiro
3810-193 Aveiro, Portugal
Chapter 9

Tomas Torres
Universidad Autónoma de Madrid
28049-Madrid, Spain
tomas.torres@uam.es
Chapter 45

Paola Turano
University of Florence
I-50019 Sesto Fiorentino, Italy
turano@cerm.unifi.it
Chapter 30

Md. Imam Uddin
Dalhousie University
Halifax, Nova Scotia, Canada
Chapter 39

Johan E. van Lier
Université de Sherbrooke
Sherbrooke, Québec, Canada
Johannes.Van.Lier@USherbrooke.ca
Chapter 16

Maria da Graça H. Vicente
Louisiana State University
Baton Rouge, LA 70803, USA
vicente@lsu.edu
Chapter 18

Sam P. de Visser
The University of Manchester
Manchester M1 7DN, UK
sam.devisser@manchester.ac.uk
Chapter 44

F. Ann Walker
University of Arizona
Tucson, AZ 85721-0041, USA
awalker@email.arizona.edu
Chapter 29

Jacek Waluk
Polish Academy of Sciences
01-224 Warsaw, Poland
waluk@ichf.edu.pl
Chapter 35

Sam Wong
Childrens Hospital Los Angeles
Los Angeles, CA 90027, USA
Chapter 22

Tabitha E. Wood
Dalhousie University
Halifax, Nova Scotia, Canada
Chapter 39

Frank Xu
Childrens Hospital Los Angeles
Los Angeles, CA 90027, USA
Chapter 22

Hiroko Yamada
Ehime University
Matsuyama 790-8577, Japan
Chapter 7

Jaesung Yang
Yonsei University
Seoul, 120-747, Korea
Chapter 5

Hyejin Yoo
Yonsei University
Seoul, 120-747, Korea
Chapter 5

Min-Chul Yoon
Yonsei University
Seoul, 120-747, Korea
Chapter 6

Zin Seok Yoon
Yonsei University
Seoul, 120-747, Korea
Chapter 5

X. Peter Zhang
University of South Florida
Tampa, FL 33620, USA
pzhang@cas.usf.edu
Chapters 13, 43

Contents of Volumes 1–10

Volume 1 Supramolecular Chemistry

Volume 2 Synthesis and Coordination Chemistry

Volume 3 Synthetic Methodology

Volume 4 Phototherapy, Radioimmunotherapy and Imaging

Volume 5 Heme Proteins

Volume 6 NMR and EPR Techniques

Volume 7 Physicochemical Characterization

Volume 8 Open-Chain Oligopyrrole Systems

Volume 9 Electronic Absorption Spectra — Phthalocyanines

Volume 10 Catalysis and Bio-Inspired Systems — Part I

This page intentionally left blank

37 BODIPY® Dyes and Their Derivatives: Syntheses and Spectroscopic Properties

Aurore Loudet and Kevin Burgess

Department of Chemistry, Texas A&M University, P.O. Box 30012, College Station, Texas 77842, USA

I. Introduction

4,4-Difluoro-4-bora-3a,4a-diaza-*s*-indacene, or BODIPY® (hereafter abbreviated to BODIPY) dyes tend to be strongly UV-absorbing molecules that emit sharp fluorescence peaks with high quantum yields. They are relatively insensitive to the polarity and pH of their environment, and are reasonably stable to physiological conditions. Small modifications to their structures enable tuning of their fluorescence characteristics, hence these dyes are widely used to label proteins[1–5] and DNA.[6] However, potential applications of these dyes are so diverse that modifications to the BODIPY framework are desirable for many reasons.

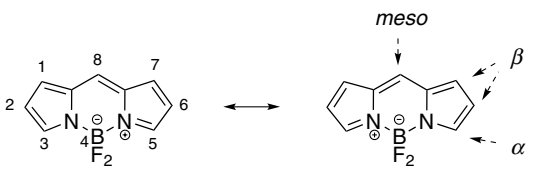

BODIPY dyes
small, intensely fluorescent systems

This chapter summarizes the basic chemistry and spectroscopic properties of common BODIPY-derivatives, and draws attention to ways in which interesting

probes could be prepared. Applications of BODIPYs as labelling reagents,[2,4,7–34] fluorescent switches,[35,36] chemosensors[37–74] and as laser dyes[75] may be interested in this review as a guide to synthesis and spectroscopic properties, but details on use of the dyes in those ways are not included here. Those seeking small amounts of commercially available dyes for labeling should also consult the Invitrogen (formerly Molecular Probes) catalog.[2,76] This chapter is based on a review that was published by us in 2007,[77] but has been updated to include pivotal recent developments in the area.

II. The BODIPY Core

The IUPAC numbering system for BODIPY dyes is different to that used for dipyrromethenes,[78] and this can lead to confusion. However, the terms α-, β-positions, and *meso*- are used in just the same way for both systems.

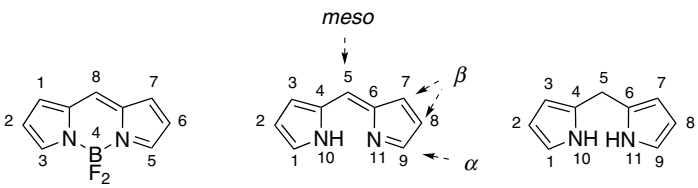

the "BODIPY core" | the "dipyrrin core" of dipyrromethenes | dipyrromethane core

A. Fundamental Properties

BODIPY dyes were first discovered in 1968 by Treibs and Kreuzer.[79] While the syntheses of many substituted BODIPYs have been reported since then, the preparation of the fully unsubstituted BODIPY **1** remained a challenge and has only recently been reported in the literature.[80,81] This is because of synthetic difficulties obtaining this compound related to the fact that the unsubstituted dipyrromethene core is sensitive to nucleophilic addition. Synthesis of the corresponding dipyrromethene precursor has been reported, but this compound is unstable and decomposes above −30 °C to −40 °C.[82] The symmetrical, dimethyl-substituted compound **2** has been prepared[83] and could be considered as a reference to which other simple alkylated BODIPYs can be compared. The symmetrically substituted systems **3** and **4** have apparently not been reported, reflecting synthetic limitations for even some simple BODIPY systems. However, the unsymmetrically substituted BODIPYs **5** and **6** have been prepared.[84] There are relatively minor differences in the reported UV-absorption maxima, fluorescence emission maxima, and quantum yields of these compounds, and these should not be

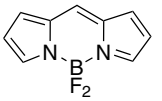

1
MeOH, Φ 0.97
$\lambda_{max\ abs}$ 497 nm
$\lambda_{max\ emiss}$ 504 nm

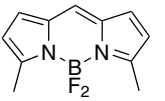

2
EtOH, Φ 0.81
$\lambda_{max\ abs}$ 507 nm
$\lambda_{max\ emiss}$ 520 nm

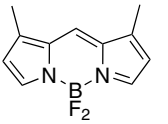

3
unknown

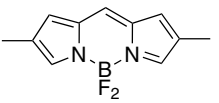

4
unknown

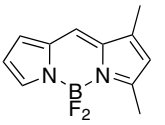

5
EtOH, Φ 0.70
$\lambda_{max\ abs}$ 499 nm
$\lambda_{max\ emiss}$ 509 nm

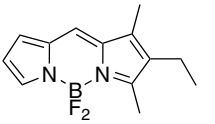

6
EtOH, Φ 0.40
$\lambda_{max\ abs}$ 510 nm
$\lambda_{max\ emiss}$ 520 nm

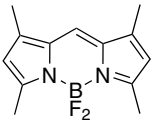

7
EtOH, Φ 0.80
$\lambda_{max\ abs}$ 505 nm
$\lambda_{max\ emiss}$ 516 nm

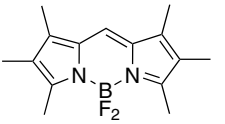

8
EtOH, Φ 0.56
$\lambda_{max\ abs}$ 528 nm
$\lambda_{max\ emiss}$ 535 nm

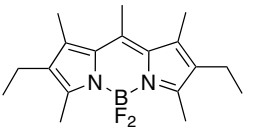

9
EtOH, Φ 0.70
$\lambda_{max\ abs}$ 517 nm
$\lambda_{max\ emiss}$ 546 nm

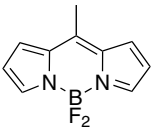

10
unknown

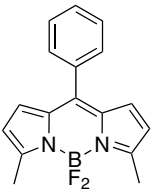

11
MeOH, Φ 0.19
$\lambda_{max\ abs}$ 508 nm
$\lambda_{max\ emiss}$ 521 nm

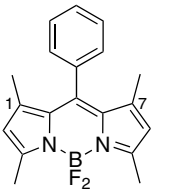

12
MeOH, Φ 0.65
$\lambda_{max\ abs}$ 498 nm
$\lambda_{max\ emiss}$ 508 nm

over-interpreted because small calibration errors are common in these types of experiments. However, when the symmetrically-, tetra-, hexa-, and hepta-alkylated systems **7**,[84,85] **8**, and **9** are included in the comparison then an unambiguous trend towards red-shifted absorption and emission maxima with increased substitution becomes apparent.

Alkylation or arylation at the *meso* position has no special effect on the absorption and emission wavelengths (compare **2** with **11**, and **7** with **12**) even

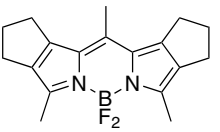

13
EtOH, Φ 0.81
$\lambda_{max\ abs}$ 512 nm
$\lambda_{max\ emiss}$ 535 nm

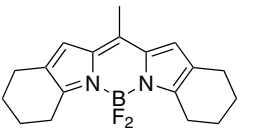

14
EtOH, Φ 0.84
$\lambda_{max\ abs}$ 535 nm
$\lambda_{max\ emiss}$ 560 nm

though this substitution position is structurally unique. However, the quantum yield of the *meso*-phenyl compound **11** is appreciably less than the more substituted analog **12**. Such differences are widely attributed to 1,7-substituents preventing free rotation of the phenyl group reducing loss of energy from the excited states via non-irradiative molecular motions. Consistent with this, introduction of *ortho*-substituents on the phenyl ring has been observed to increase quantum yields, and similar explanations have been invoked.

BODIPY derivatives in which aliphatic rings have been fused to the pyrrole fragments are perhaps more constrained than ones bearing acyclic aliphatic substituents. Nevertheless, the effects on their emission maxima are not always easily rationalized. Compound **13** has a shorter emission wavelength maximum than **9** even though both have three substituents on the pyrrole rings. On the other hand, **14** has only two such attachments, yet it has the longest wavelength fluorescence emission.

B. Syntheses of the Unsubstituted BODIPY 1

There are three recent reports on preparations of **1**.[80,81,86] In the first, BODIPY **1** was prepared by oxidation of the corresponding dipyrromethane.[87] As mentioned above, the dipyrromethene core is very unstable and must be stabilized rapidly after oxidation. Thus, the oxidation was carried out at −78 °C, under nitrogen for 1 hour. Upon completion of the oxidation, the dipyrromethene was reacted *in situ* with DBU and boron trifluoride diethyl etherate to form **1** in 5–10% (Chart 1).[80]

To avoid the oxidation step from the dipyrromethane to dipyrromethene, BODIPY **1** was prepared via the classical asymmetric synthesis route. Thus, condensation of 2-formylpyrrole and 1H-pyrrole, followed by complexation with boron afforded **1**. Although the synthesis is straightforward, the purification is quite extensive and laborious, yielding the target compound in low yield (8%). The author also reported that **1** exhibits a high photochemical (τ_{Fl} 7.2 ns) but low thermal stability, decomposing at temperature above 50 °C.[86]

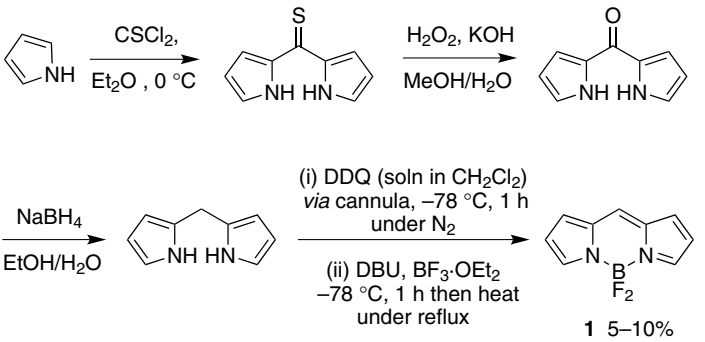

Chart 1.

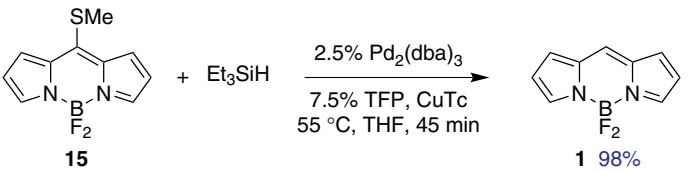

Chart 2.

Chart 2 describes a much more efficient route to **1** affording the target compound in 98% yield.[81] Compound **1** was obtained by reaction of 8-thiomethylBODIPY **15** (synthesis discussed later) with triethylsilane in the presence of a catalytic amount of Pd and a stoichiometric amount of copper(I) thienyl-2-carboxylate (CuTc) in THF at 55 °C for 45 min (Chart 2). BODIPY **1** emits brightly in both nonpolar and polar solvents (Φ ranges from 68 to 93% from nonpolar to polar solvents), and surprisingly was sparingly soluble in water. It is an air-stable, crystalline red solid with excellent bench-life. It is highly recommended to handle it in a well-ventilated fume hood since as a powder, since the authors noticed it causes rather strong nose, skin and throat irritation.

C. Syntheses of Substituted BODIPYs from Pyrroles and Acid Chlorides or Anhydrides

8-Substituted BODIPY® dyes **A** (i.e., ones with substituents in the *meso* position) tend to be relatively easy to prepare via condensation of acyl chlorides with pyrroles (Chart 3).[88,89] These transformations involve unstable dipyrromethene hydrochloride salt intermediates. The intermediate dipyrromethene hydrochlorides are easier to handle and purify as the number of substituents on the pyrrole

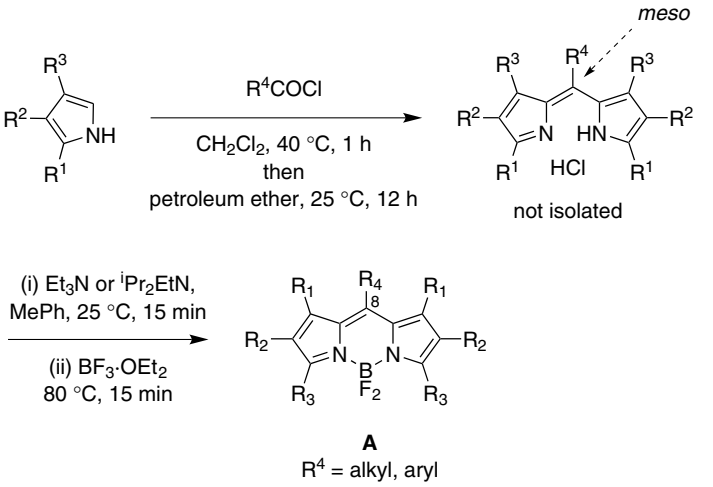

Chart 3.

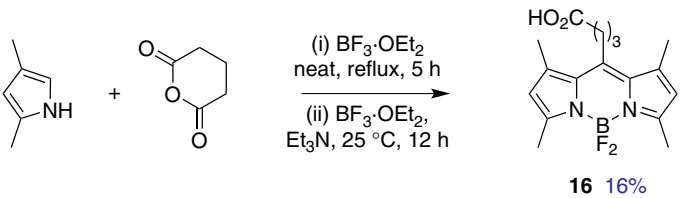

Chart 4.

increases but, even so, these are not generally isolated in syntheses of BODIPY dyes.

Other activated carboxylic acid derivatives could be used in place of acid chlorides in Chart 3. In the particular case of acid anhydrides, this concept has been reduced to practice. Chart 4 shows how the BODIPY derivative **16** was prepared from glutaric anhydride.[28] An attractive feature of this chemistry is that a free carboxylic acid is produced, and this may later be used to attach the probe to target molecules.

D. From Pyrroles and Aldehydes

Syntheses similar to those depicted in Charts 3 and 4 but which use aromatic aldehydes[5] (to the best of our knowledge, *aliphatic* aldehydes have not been reported in this reaction) require oxidation steps. The reagents for these oxidations can introduce experimental complications. Thus, in Chart 5 the oxidant used was

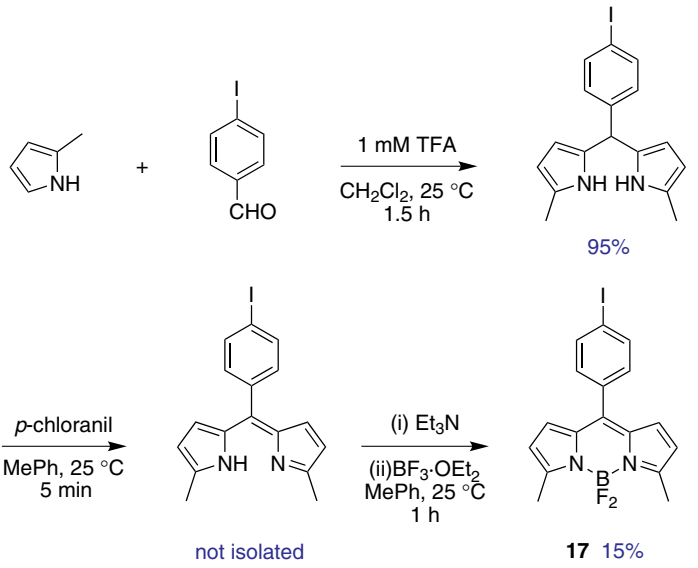

Chart 5.

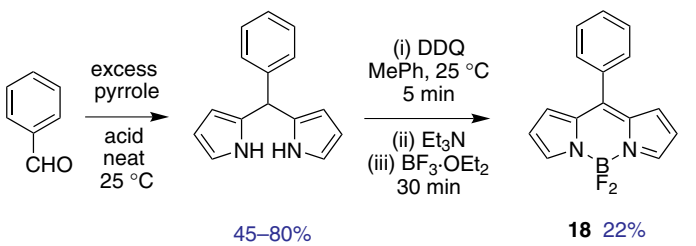

Chart 6.

p-chloranil and eventually the byproducts from this had to be removed (in fact, this was done after complexation with the boron).

α,β-Unsubstituted BODIPYs e.g. **18** can also be prepared from aldehydes using neat conditions.[5] The aldehyde is dissolved in excess pyrrole at room temperature, and the dipyrromethane intermediate (the reduced form of the dipyrromethene) was formed and isolated. The BODIPY dye was obtained after oxidation with DDQ and complexation with boron (Chart 6). Acid chlorides probably would be too reactive to use with pyrrole (since it is unsubstituted and more reactive) so this aldehyde-based approach is the method of choice.

Use of, for instance, halogenated benzaldehydes (or halogenated acid chlorides as above) provides compounds like **17** that can be further elaborated. In another example, systems **19** and **20** were prepared from benzaldehyde derivatives

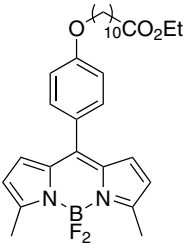

19
CH_2Cl_2, Φ 0.36
$\lambda_{max\ abs}$ 508 nm
$\lambda_{max\ emiss}$ 524 nm

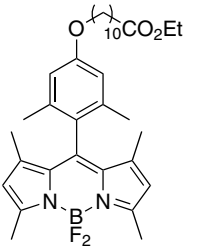

20
CH_2Cl_2, Φ 0.94
$\lambda_{max\ abs}$ 501 nm
$\lambda_{max\ emiss}$ 512 nm

that have long chain acid substituents. These probes were used to investigate dynamic effects in membranes.[16] Presumably *ortho*-substituents were included on the *meso*-aromatic group to restrict rotation of that ring and increase quantum yields.

The fact that a diverse set of aldehydes could be used to prepare *meso*-substituted BODIPYs provides a means to introduce more sophisticated functionalities for specialized purposes. For instance, 8-hydroxyquinoline-2-carboxaldehyde was used to prepare the Hg^{2+}-selective chromo- and fluoroionophore **21**.[51] This probe is highly fluorescent in the presence of transition-metal ions (Co^{2+}, Ni^{2+}, Cu^{2+}, and Zn^{2+}) and heavy-metal ions (Pb^{2+}, Cd^{2+}), but 5 equiv. of mercuric ions reduced its emission by more than 98% (the color of the solution also changed from light amber to red enabling the progress of the complexation event to be visualized). A 1:1 complex with Hg^{2+} is formed in which the dipyrromethene core of **21** adopts a nearly orthogonal conformation with the 8-hydroxyquinoline moiety because of the methyl groups in positions 1- and 7- on the BODIPY core. This particular arrangement displays the binding site of 8-hydroxyquinoline for complexation of metal ions. The shape of these BODIPY-based ligand is such that 2:1 L:M complexes are sterically disfavored.

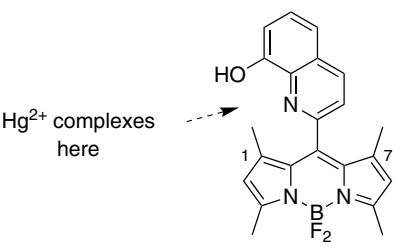

21

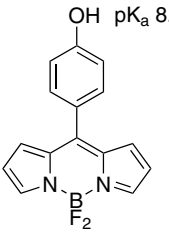

22
MeOH, Φ 0.28
$\lambda_{max\ abs}$ 505 nm
$\lambda_{max\ emiss}$ 517 nm

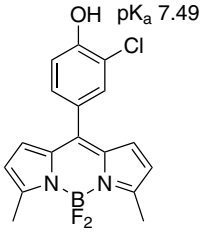

23
MeOH, Φ 0.16
$\lambda_{max\ abs}$ 507 nm
$\lambda_{max\ emiss}$ 520 nm

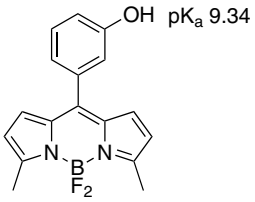

24
MeOH, Φ 0.19
$\lambda_{max\ abs}$ 508 nm
$\lambda_{max\ emiss}$ 521 nm

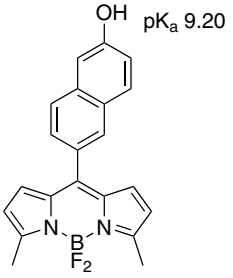

25
MeOH, Φ 0.025
$\lambda_{max\ abs}$ 508 nm
$\lambda_{max\ emiss}$ 522 nm

Fluorescent pH probes **22**–**25** have been prepared from phenolic benzaldehydes (a case where the acid chloride approach would have raised chemoselectivity issues).[59] These compounds are weakly fluorescent in the phenolate form presumably due to charge transfer from the phenolate donor to the excited-state indacene moiety. The pKa of the different derivatives was tuned by varying the aromatic substituent.

It is unusual to use nonaromatic aldehydes to prepare BODIPY derivatives. In this sense the vinylic thioether probe **26** is exceptional. A catalytic amount of ytterbium (III) trifluoromethane sulfonamide was used to mediate the condensation process, the intermediate dipyrromethane was oxidized with DDQ, and complexation with boron trifluoride gave the product, though in very poor yield (Chart 7).[90] The fluorescence emission of compound **26** was red-shifted relative to dyes with a phenyl group at the *meso* position (e.g. **11**). Compound **27** has a sulfide in conjugation with the BODIPY core, just as **26** does. The fluorescence emission maximum of **26** is 26 nm red-shifted compared to **27**, indicating that electron donating groups in this position tend to have that effect.

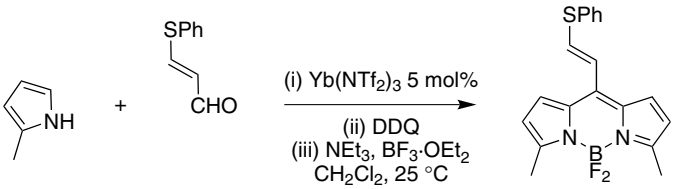

26 2%
MeOH, Φ na
$\lambda_{max\ abs}$ 528 nm
$\lambda_{max\ abs}$ 580 nm

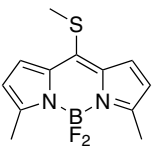

27
MeOH, Φ 0.37
$\lambda_{max\ abs}$ 530 nm
$\lambda_{max\ abs}$ 554 nm

Chart 7.

E. From Ketopyrroles Including Syntheses of Unsymmetrical BODIPYs

Condensations of pyrroles with acid chlorides or with benzaldehyde derivatives, as outlined above, are direct and convenient methods to access symmetrically substituted BODIPY dyes. However, another approach is required to form unsymmetrically substituted ones. Generally, this is achieved via preparations of ketopyrrole intermediates, followed by a Lewis acid mediated condensation of these with another pyrrole fragment.

Schemes 1a and b show reactions of magnesium anions of pyrroles with activated carboxylic acid derivatives to give the corresponding 2-ketopyrroles.[91,92] In part c, one such ketopyrrole is condensed with another pyrrole unit to give a BODIPY framework. That example gives a symmetrical product, but the method is particularly valuable for unsymmetrical ones, as in Scheme 1d.

F. Synthesis of Symmetrical BODIPY from Pyrrole-2-Carbaldehyde

BODIPYs unsubstituted at the *meso* position are usually prepared by condensation of a pyrrole-2-carbaldehyde with a pyrrole. However, Burgess and coworkers have recently reported that similar BODIPY derivatives, without any substituents at the *meso* position, could easily be prepared from the aldehyde alone (Scheme 2).[93]

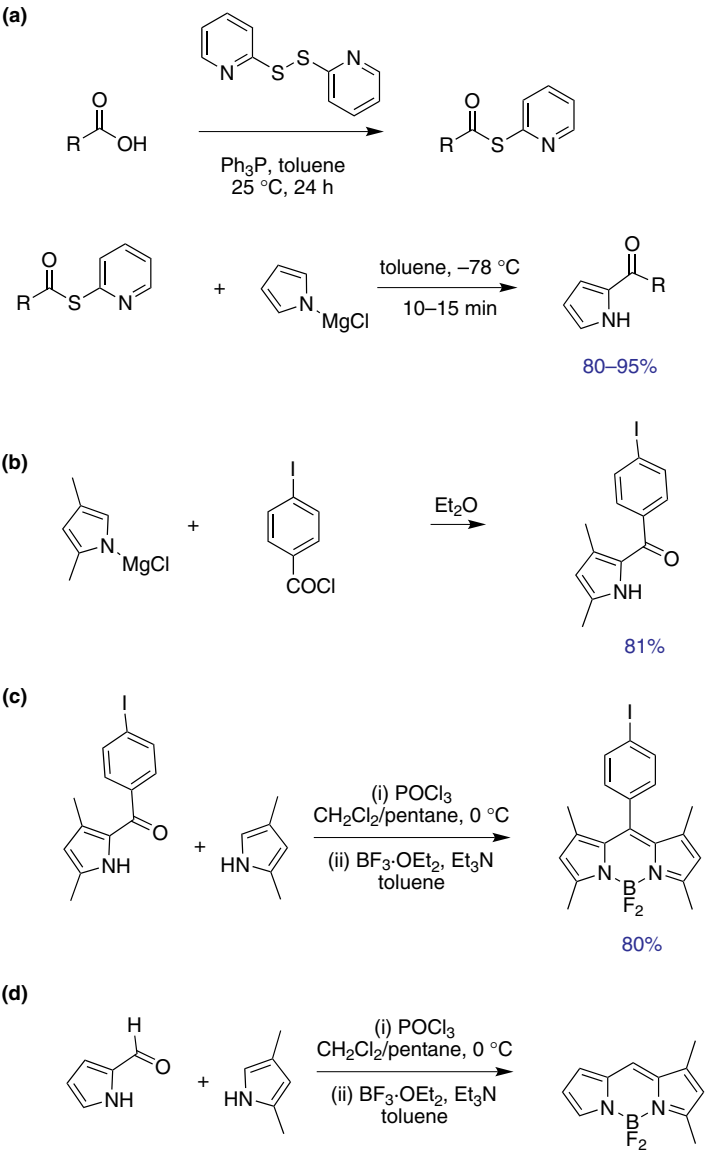

Scheme 1. (**a**) and (**b**) two different methods for production of ketopyrroles from magnesium derivatives of pyrrole, and application of these starting materials in the production of (**c**) symmetrical, and (**d**) unsymmetrical dyes.

Thus, a series of alkyl and aryl substituted BODIPYs i.e. probes **28–30** was prepared from the corresponding pyrrole-2-carbaldehyde and phosphorus oxychloride. The latter seems to be intimately involved in this reaction as the dipyrromethenium cation was not formed when other Lewis acid were used (TFA or $BF_3{\cdot}OEt_2$).

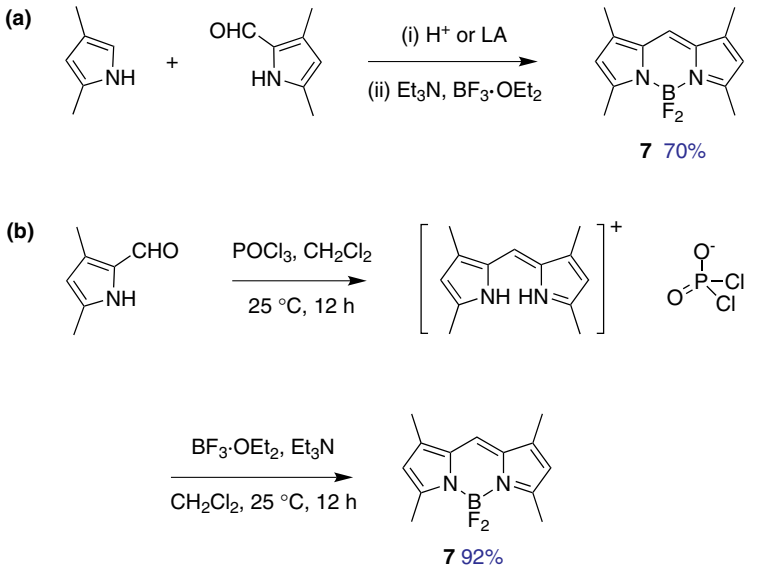

Scheme 2. (**a**) Conventional synthesis of tetramethyl-BODIPY **7**; (**b**) Preparation of tetramethyl-BODIPY **7** from the corresponding pyrrole-2-carbaldehyde and phosphorus oxychloride.

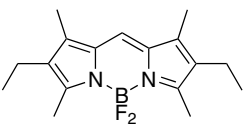

28 75%
(45% conv. method)
CH_2Cl_2, Φ 0.86
$\lambda_{max\ abs}$ 531 nm
ε 87 000 $M^{-1}cm^{-1}$
$\lambda_{max\ emiss}$ 538 nm

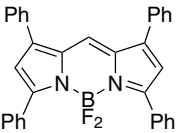

29 21%
CH_2Cl_2, Φ 1.00
$\lambda_{max\ abs}$ 564 nm
ε 78 000 $M^{-1}cm^{-1}$
$\lambda_{max\ emiss}$ 593 nm

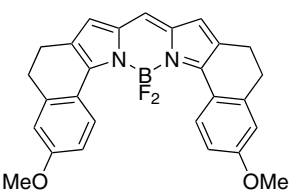

30 85%
CH_2Cl_2, Φ 0.71
$\lambda_{max\ abs}$ 651 nm
ε 149 100 $M^{-1}cm^{-1}$
$\lambda_{max\ emiss}$ 662 nm

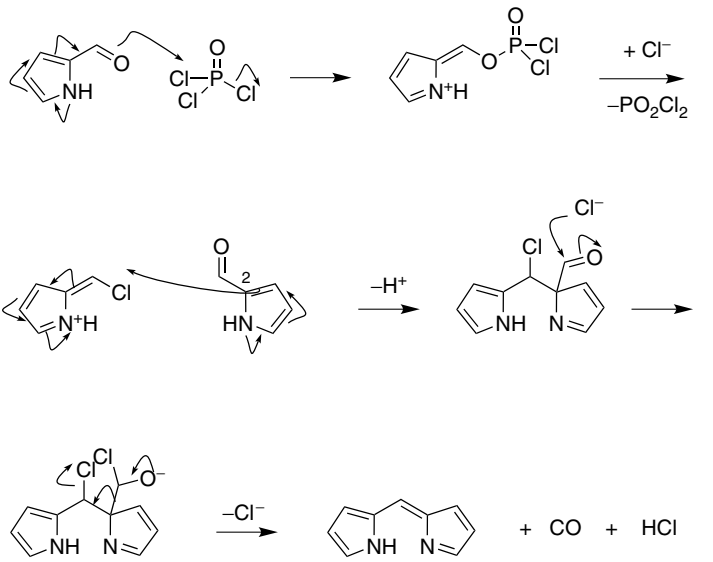

Figure 1. A possible mechanism for the formation of dipyrromethene from pyrrole-2-carbaldehyde and phosphorus oxychloride.

A possible mechanism is that $POCl_3$ reacts with pyrrole-2-carbaldehyde to give a vinylogous Vilsmeier-Haack reagent. Electrophilic attack from the C^2-atom of another pyrrole-2-carbaldehyde on to the vinylogous Vilsmeyer-Hack reagent then leads to the formation of the dipyrromethene (Figure 1). All the new BODIPY dyes prepared emit bright, sharp fluorescent signals. As various substituents were tolerated in the synthesis, probes that emit in the range 516–662 nm could be prepared.

III. Modifications to *meso*-Aromatic Substituents on the BODIPY Core

A. Introduction

The BODIPY core is robust enough to withstand a range of chemical transformations, and a variety of aromatic groups can be introduced at the *meso*-position for appropriately functionalized BODIPY dyes. Alternatively, dyes with special *meso*-groups can be produced via *in vivo* synthesis. These strategies have been used to produce several dyes for many different applications; just a few illustrative ones are shown in Figure 2. For instance, derivatives of this type have been formed as selective sensors of particular redox active molecules (**31**,[53] **32**,[56] **33**,[39] **34**,[94] **35**,[95] **36**[96] and **37**,[97] Figure 2a), pH probes (**38**[46] and **39**,[42] Figure 2b), metal-chelators

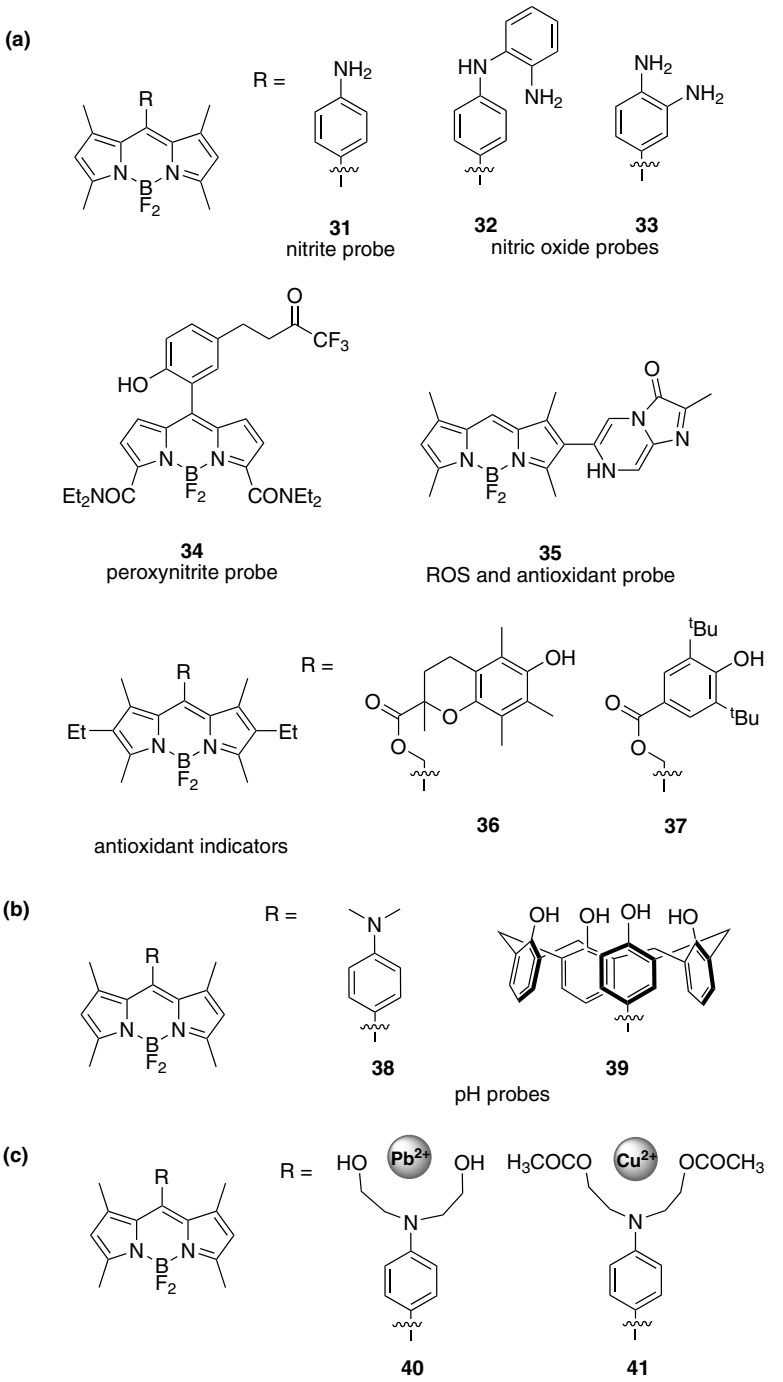

Figure 2. Selected BODIPYs with *meso*-modifications to give: (**a**) selective sensors of particular redox active molecules; (**b**) pH probes; (**c**) metal-chelators; (**d**) biomolecule conjugating groups; and (**e**) cyanide ions.

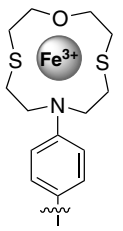

42

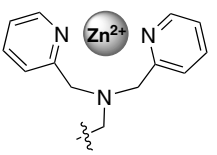

43

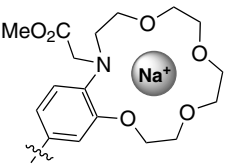

44

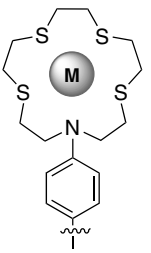

M = Hg^{2+}, Ag^{+}, Cu^{2+}

45

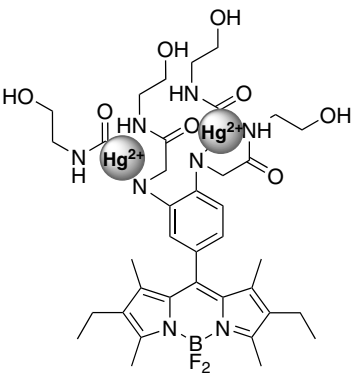

46

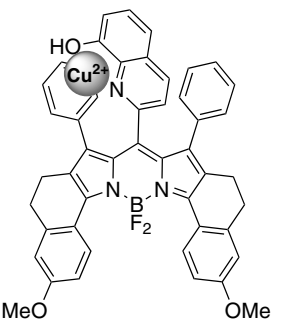

47

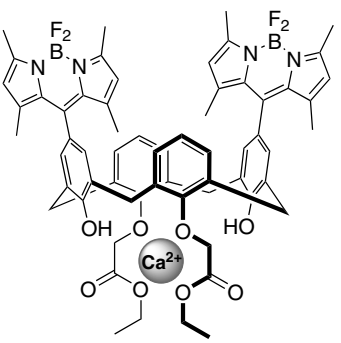

48

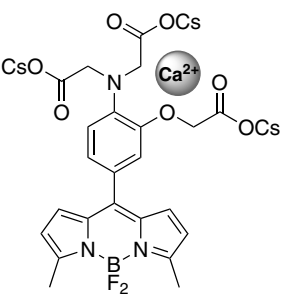

49

Figure 2. (*Continued*)

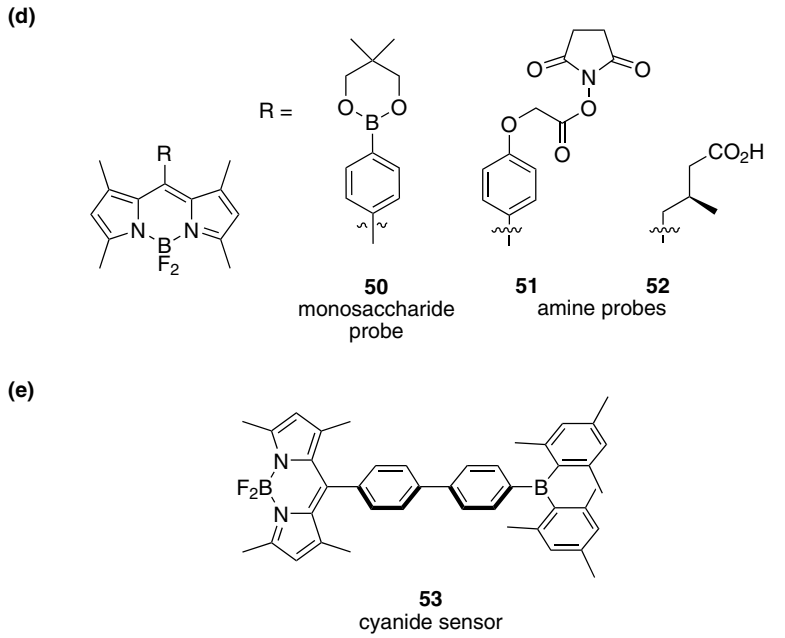

Figure 2. (*Continued*)

(**40**,[70] **41**,[70] **42**,[65] **43**,[58] **44**,[57] **45**,[44] **46**,[71] **47**,[69] **48**,[73] and **49**,[62] Figure 2c), as biomolecule conjugating groups (**50**,[40] **51**,[72] and **52**,[98] Figure 2d) and as sensor for cyanide ions (**53**,[99] Figure 2e).

Here we intend to restrict the discussion to the general concepts that influence the fluorescence properties of *meso*-modified BODIPY dyes; this review does not attempt to give a comprehensive list of all the compounds made. Without exception, the chemosensors operate by perturbing the reduction potential of the *meso*-substituent as illustrated in Figure 3a and b for the case of **36** and **37**, respectively. The next section discusses in more details the electronic effects of these perturbations on fluorescence.

B. Fluorescence Control via Photoinduced Electron Transfer

Transfer of electrons between nonplanar parts of fluorescent molecules modifies their fluorescence intensities.[100] This has been known for some time but Nagano, Ueno and coworkers have skillfully applied calculated orbital energy levels and experimentally determined electrochemical data to rationalize quantum yields. Their initial work with fluorescein derivatives,[101,102] was later expanded to encompass BODIPY systems as described here.[103]

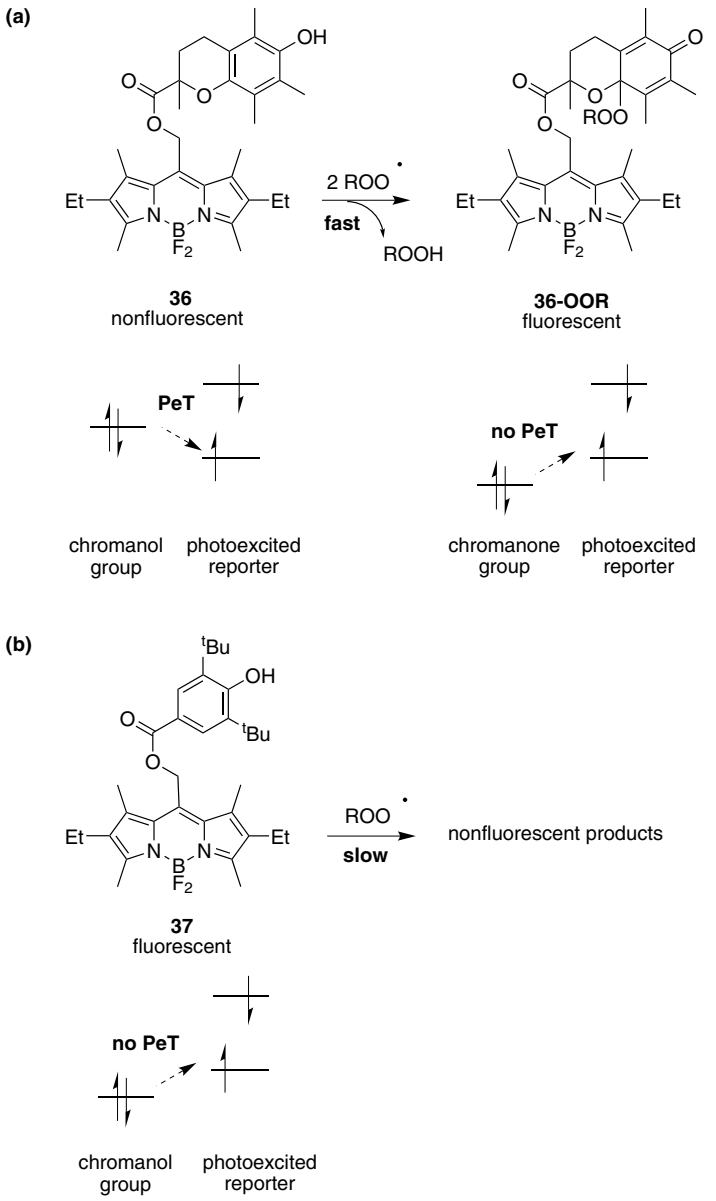

Figure 3. Off/on sensing mechanism for (**a**) **36**; and (**b**) **37** is controlled by PeT from the chromanol group.

Some nonplanar fluorescent molecules can be regarded as a highly fluorescent group with non- (or significantly less) fluorescent substituents (Figure 4a). Some such substituents, depending on their oxidation potentials relative to the excited state of the BODIPY core, can act as electron donors or acceptors. If electron

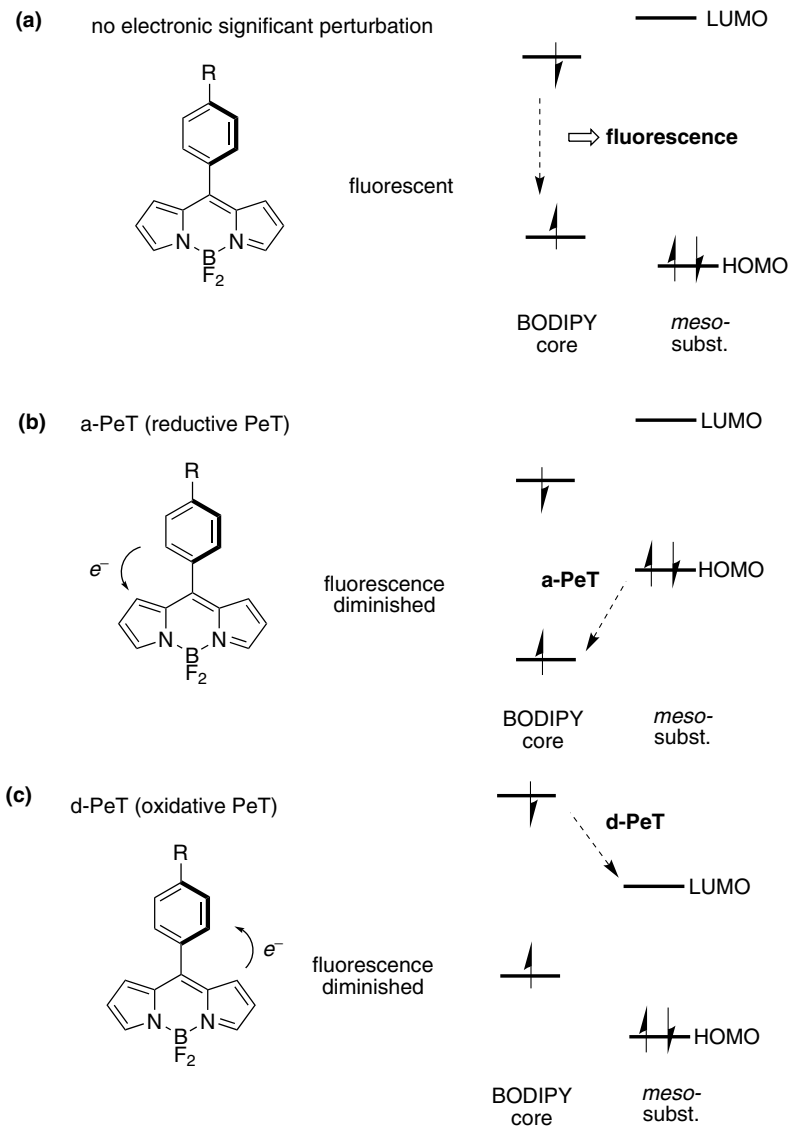

Figure 4. The *meso*-substituent provides: (**a**) no significant electronic perturbation; (**b**) electrons to the excited state; and, (**c**) a low lying LUMO to accept electrons from the excited state.

transfer occurs then the fluorescence is diminished when the fluorescent group in its excited state is reduced. In this situation, the fluorescent group is acting as an acceptor, consequently this may be called reductive-PeT or a-PeT ("a" for acceptor; Figure 4b). However, if the energy states are such that the excited state of the fluorescent group can donate electrons to the substituent LUMO then oxidative-PeT,

d-PeT, occurs ("d" for donor; Figure 4c). Indirectly, solvent polarity has an effect on this process. This is because photoexcitation and oxidation processes involve modification of ground state dipoles, and solvents may stabilize or destabilize these changes according to polarity.

The feasibility of electron transfer can be judged from the change in free energy (ΔG_{PeT}), as described by the Rehm-Weller equation[104]:

$$\Delta G_{PeT} = E_{1/2}\,(D^+/D) - E_{1/2}\,(A/A^-) - \Delta E_{00} - C$$

where

$E_{1/2}\,(D^+/D)$ = ground-state oxidation potential of the donor
$E_{1/2}\,(A/A^-)$ = ground-state reduction potential of the acceptor
ΔE_{00} = excitation energy
C = an electrostatic interaction term.

Nagano and coworkers applied these principles to the triazole-BODIPY derivative **55** (Figure 5) to develop a nitric oxide probe.[52] The low fluorescence of the diamine **54** was explained in terms of reductive PeT. When nitric oxide converts the diamine into the benzotriazole **55** then reductive PeT does *not* occur and fluorescence is observed. Scheme 3 outlines the synthesis of the probe and the oxidized product.

A refinement of these ideas was used to explain why the fluorescence for the compounds **55** decreased in the order **b** > **a** > **c** (Figure 6). This is because the nature of the substituent impacts the reduction potential of the BODIPY core in that order (**b** is the most negative).

Fluorescence of the $Zn^{2=}$ and NO_2^+ chemosensors **56**[54] and **57**[105] has been explained using reductive PeT concepts outlined above. Chelation or nitration makes the reduction potential of the *meso*-substituent more negative, PeT is switched-off, and the probes become fluorescent.

Strongly electron-withdrawing substituents on aromatic *meso*-substituents lower the LUMO of the aromatic system to the level where it might accept electrons from the orbital containing the promoted electron in the BODIPY core (Figure 4c). In such cases *oxidative* PeT comes into play. An illustration of this is the quantum yields of **58**–**60**.[105] For dye **60** oxidative PeT is diminished because the ketones lower the energy of the BODIPY orbital containing the promoted electron.

At least two weaknesses are associated with combining theoretical calculations and electrochemical data to rationalize quantum yields. First, the reduction potentials for the two components are calculated on isolated systems: the fact that they are attached to each other must perturb the actual orbital levels. Second,

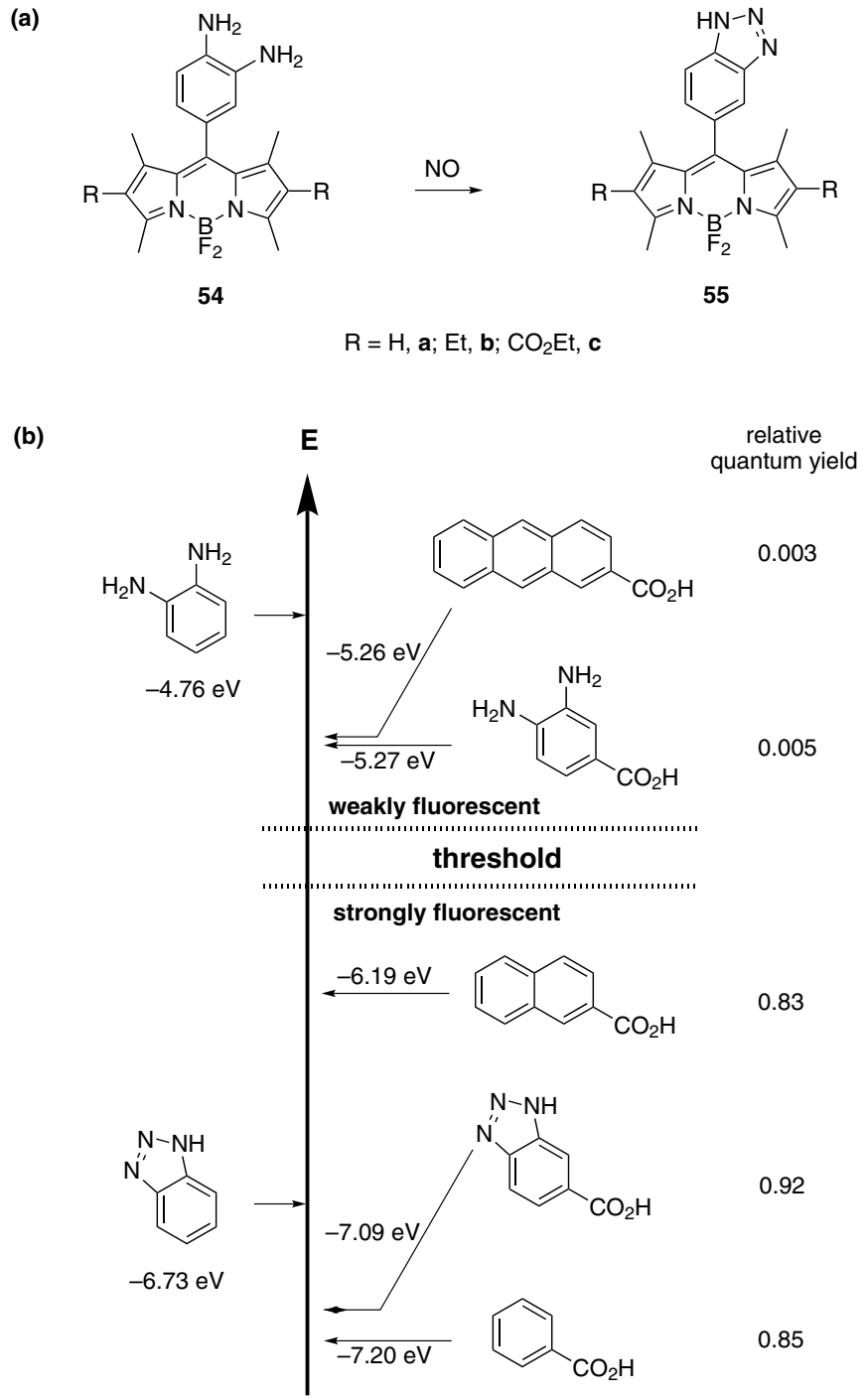

Figure 5. (**a**) Calculated HOMO energy levels of *meso*-substituents for BODIPY **54** and **55**; (**b**) Reductive PeT occurs above the threshold indicated.

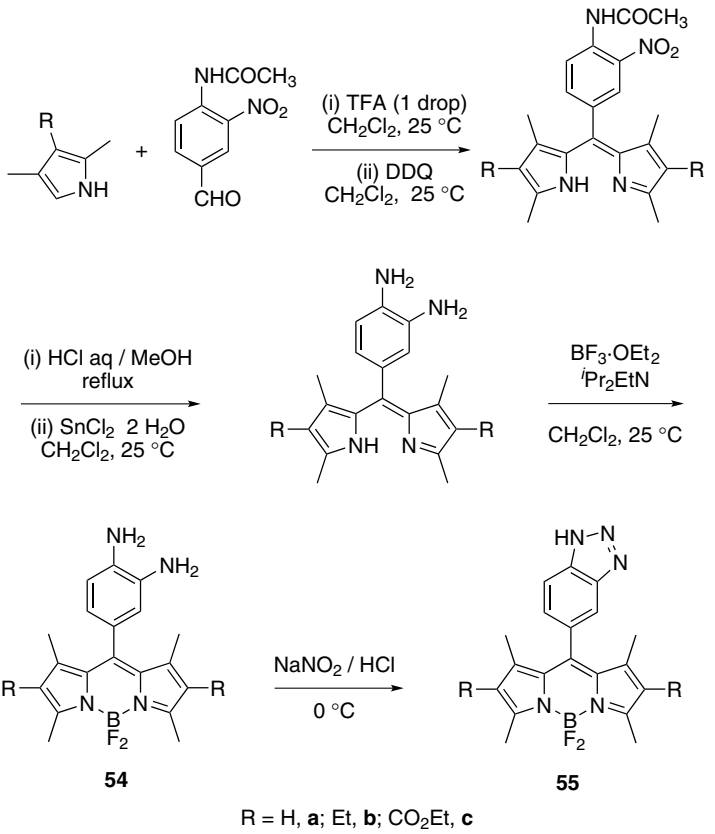

Scheme 3. Synthesis of diaminobenzene- and triazole- BODIPY derivatives **54** and **55.**

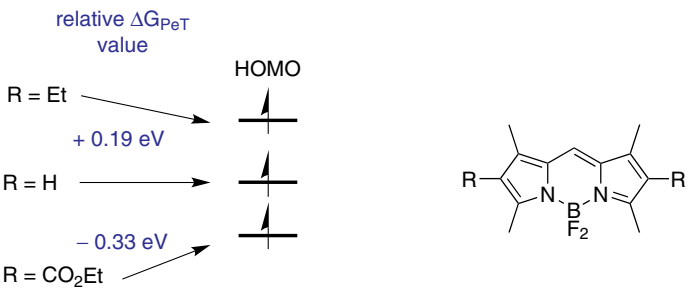

Figure 6. Reductive PeT increases in the order Et < H < CO_2Et.

energies of excited states are notoriously difficult to calculate. Nevertheless, the approach emphasized by Nagano and coworkers helps dispel dogmas that surround fluorescent probes. For instance the assertion that nitro groups or heavy atom substituents always quench fluorescence is simply not true. The reality is that

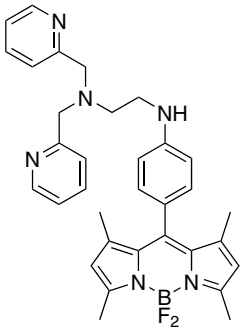

56

$\lambda_{max\ abs}$ 499 nm
$\lambda_{max\ emiss}$ 509 nm
Φ 0.003 (without Zn^{2+})
Φ 0.058 (with Zn^{2+})

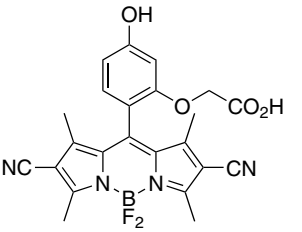

57

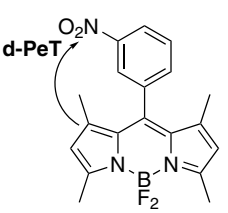

58

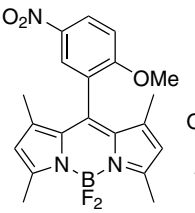

59

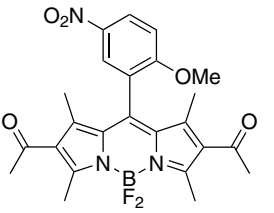

60

	58	**59**	**60**
Φ	0.004	0.023	0.529
ΔG_{PeT} (eV)	0	+ 0.15	+ 0.42

they tend to do so but only if their orbital energy levels interact with the fluorescent chromophore in a way that facilitates PeT.

IV. BODIPYs with Heteroatom Substituents

A. From Electrophilic Substitution Reactions

Simple considerations of mesomeric structures reveal that 2- and 6-positions of the BODIPY core bear the least positive charge, so they should be most susceptible to electrophilic attack (Figure 7). However, there is no definitive study of regioselectivities in these reactions for BODIPYs without pyrrole substituents; almost invariably some of the other positions are blocked by substituents.

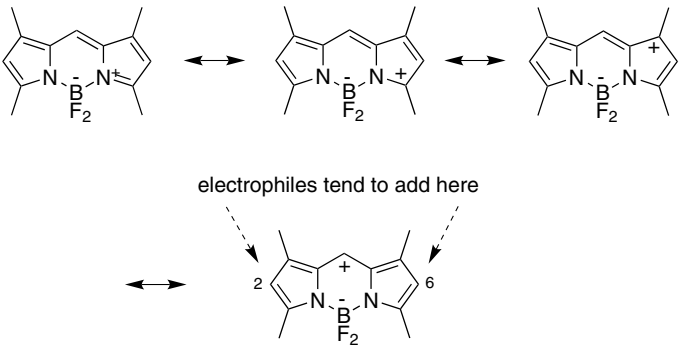

Figure 7. Electrophilic attack on tetramethyl-BODIPY.

1. *Nitration*

The 2,6-dinitro BODIPY dye **61** can be obtained via nitration with nitric acid at 0 °C (Chart 8). In this reaction, the fluorescence quantum yield of the product is much less than that of the starting material.[88,106–108] To the best of our knowledge, this is the only nitration of a BODIPY dye that has been reported in the literature.

2,6-Dinitro-BODIPY **62**[109] and **63**[110–114] have also been reported in the Japanese patent literature for applications as sensitizers and inks. We were unable

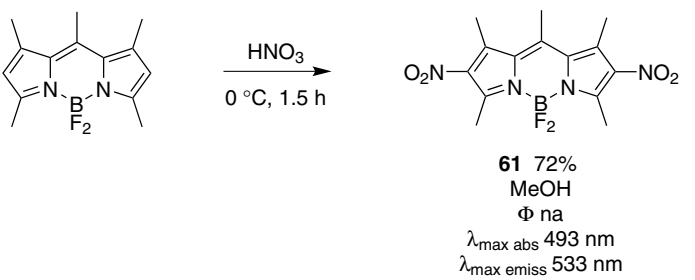

Chart 8.

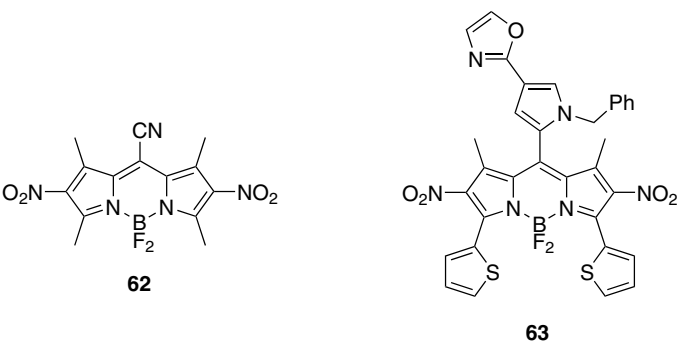

to find procedures for their syntheses and the corresponding spectroscopic data in these documents.

2. *Halogenation*

Bromination of the 1,3,5,7,8-pentamethyl-substituted BODIPY shown in Chart 9 gave the dibromination product **64**.[88,115] Predictably, introduction of bromo substituent onto the dipyrromethene core causes a significant red shift of both the UV-absorption and emission maxima, and it quenches the fluorescence quantum yield via the heavy atom effect.

2,6-Diiodo-tetramethyl BODIPY **65** was prepared as described in Chart 10.[116] Just as for the dibromo-BODIPY **64**, iodo-substituents cause significant red shift of the UV-absorption and fluorescence emission maxima, and decrease the fluorescence quantum yield via the heavy atom effect. Compound **65** is much more resistant to photobleaching than Rose Bengal; this is because the BODIPY core has a more positive oxidation potential than the xanthone unit of Rose Bengal. Compound **65** is an efficient photosensitizer.

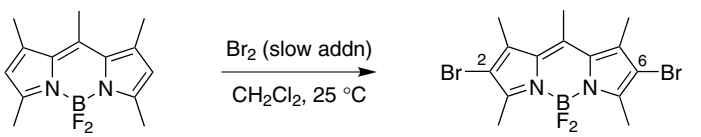

MeOH, Φ 0.95
$\lambda_{max\ abs}$ 492 nm
$\lambda_{max\ emiss}$ 504 nm

64 50%
9:1 MeOH:CH_2Cl_2
Φ 0.45 (CH_2Cl_2)
$\lambda_{max\ abs}$ 516 nm
$\lambda_{max\ emiss}$ 546 nm

Chart 9.

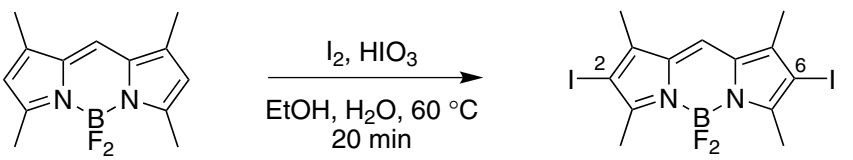

65 83%
MeOH
Φ 0.02 (0.1% (v/v) DMF as cosolvent)
$\lambda_{max\ abs}$ 534 nm
$\lambda_{max\ emiss}$ 548 nm

Chart 10.

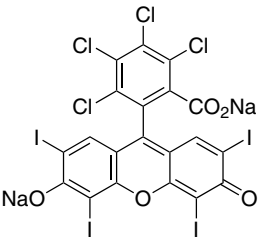

Rose Bengal

2,6-Difluoro- and 2,6-dichloro- BODIPY derivatives **66**[109] and **67**,[110–114] have been applied in electroluminescent devices and sensitizers. Their synthesis has not been reported.

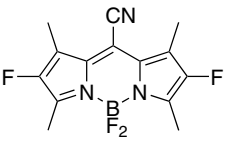

66

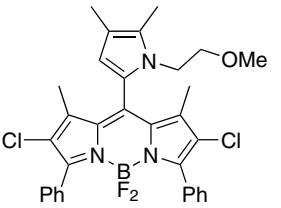

67

Chlorination of the unsubstituted dipyrromethane shown in Scheme 4 occurs preferentially at the α-positions. Thus the 3,5-dichloro BODIPY derivative **68**

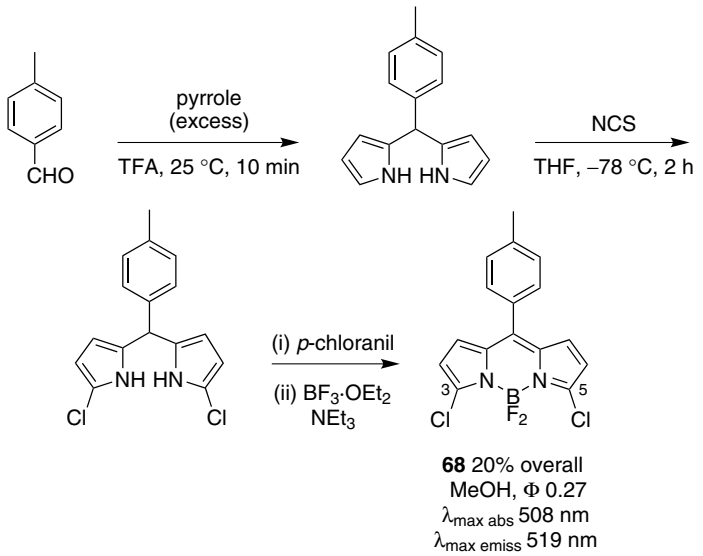

Scheme 4. Preparation of 3,5-dichloro-BODIPY via chlorination of a dipyrromethane intermediate.

could be obtained after oxidation with *p*-chloranil and complexation with boron trifluoride etherate. Applications of such chlorinated materials as S_NAr electrophiles are described later in this chapter.

3. *Potential for Other Electrophilic Substitution Reactions*

BODIPY dyes are intrinsically electron rich, and the reactions shown above illustrate that they will react with electrophiles. It is therefore surprising that the reactions shown above represent the state-of-the-art in this area. There are very few sulfonation reactions (see Section V) despite the importance of water-soluble dyes; most of the sulfonated BODIPY compounds in the Invitrogen catalog (aka Molecular Probes) feature carboxylic acids with sulfonated leaving groups. There are no reports in the literature of some common electrophilic addition processes like Vilsmeier-Haack reactions on BODIPY substrates, but Burgess and coworkers have investigated this type of reaction, and the mono-formylated BODIPY dye could successfully be synthesized in excellent yield (unpublished results).

B. From Nucleophilic Attack on Halogenated BODIPYs

The most common approach to introduce substituents on the 3- and 5-positions of the BODIPY core involve *de novo* syntheses with appropriately substituted pyrroles, but an exciting recent development reaches the same goal via nucleophilic substitution on 3,5-dichloro-BODIPY such as **68**.[117–121] The nucleophiles used so far include alkoxides, amines, thioalkoxides, diethyl malonate anion, and cyanide. These reactions can be stopped at the mono-substitution stage or forced to the disubstitution product (Scheme 5) hence they are useful for access to asymmetric **69** and symmetric **70**, hetero-substituted BODIPY dyes, which would be difficult to obtain by other routes. When cyanide was used as nucleophile, displacement was achieved using Lewis acid activation of trimethylsilyl cyanide. Addition of tin tetrachloride gave selective substitution at the carbon atom, i.e., compound **71**, while boron trifluoride promoted displacement at both the carbon and boron atoms giving the corresponding tetracyanide derivative **72**. S_NAr reactions were successfully used to simultaneously change the BODIPY core structure, its fluorescent properties, and enhance its water solubility (compounds **73–75**). In addition, Burgess and coworkers showed that this process could be used to conjugate dyes to proteins, e.g., to give **76** and **77**.[119]

The spectroscopic effects of electron-donating groups attached to the BODIPY core for the compounds in Scheme 5 were studied. The 3- and 5-substituents had significant effects, shifting both the absorption and/or emission spectra, and

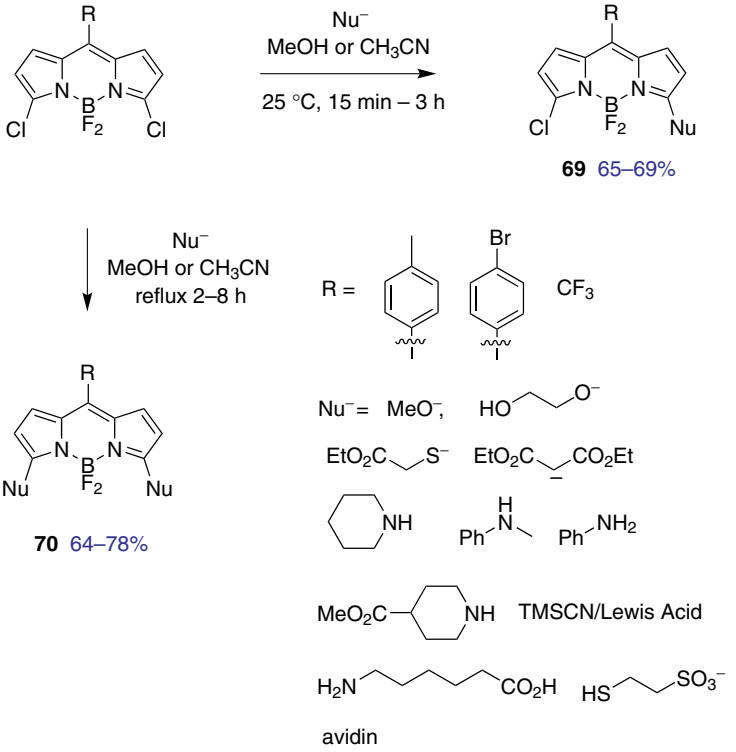

Scheme 5. BODIPY dyes via S_NAr reactions.

changing the fluorescence quantum yields. For example, introduction of an amino- or sulfur-centered nucleophiles results in a significant bathochromic shift (red shift) of both the absorption and emission.[117] Data were collected in methanol (Figure 8); the absorption and emission maxima were red-shifted in cyclohexane but otherwise it was quite similar to that for methanol (data not shown). The quantum yields varied widely with the nature of the nucleophiles and the degree of substitution. In general, mono-substituted dyes tend to have lower quantum yields than the bis-substituted ones. Interestingly, the water-soluble BODIPYs **73–75** have good to excellent quantum yields.

8-(ω-Haloalkyl)-BODIPY dyes **78** and **79** are useful starting materials. These are easily synthesized by condensation of a ω-haloacyl chloride with 3-ethyl-2,4-dimethyl pyrrole (Chart 11).[122]

Compounds **78** and **79** can be used as fluorescent electrophiles and can easily be functionalized by nucleophilic substitution reactions, giving compounds **B**.[49,122] Thus, cysteine-selective fluorescent label, fluorescent amino acids, chemosensors for metal ions[49] and fluorescent pH probes could be prepared.[123]

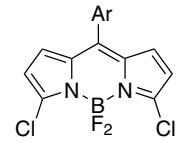

3,5-dichloroBODIPY
MeOH, Φ 0.27
$\lambda_{max\ abs}$ 508 nm
$\lambda_{max\ emiss}$ 519 nm

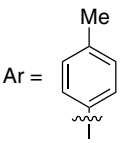

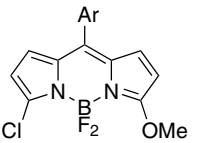

69a
MeOH, Φ 0.062
$\lambda_{max\ abs}$ 499 nm
$\lambda_{max\ emiss}$ 515 nm

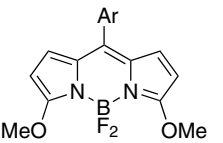

70a
MeOH, Φ 0.20
$\lambda_{max\ abs}$ 510 nm
$\lambda_{max\ emiss}$ 523 nm

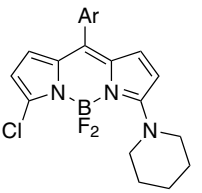

69b
MeOH, Φ 0.002
$\lambda_{max\ abs}$ 479 nm
$\lambda_{max\ emiss}$ 562 nm

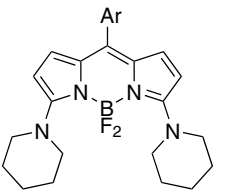

70b
MeOH, Φ 0.011
$\lambda_{max\ abs}$ 572 nm
$\lambda_{max\ emiss}$ 612 nm

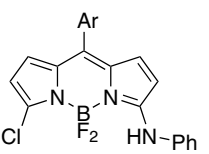

69c
MeOH, Φ 0.003
$\lambda_{max\ abs}$ 498 nm
$\lambda_{max\ emiss}$ 566 nm

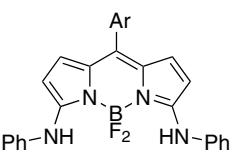

70c
MeOH, Φ 0.45
$\lambda_{max\ abs}$ 588 nm
$\lambda_{max\ emiss}$ 613 nm

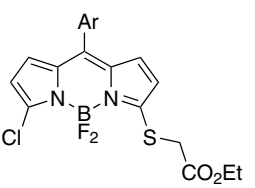

69d
MeOH, Φ 0.26
$\lambda_{max\ abs}$ 536 nm
$\lambda_{max\ emiss}$ 550 nm

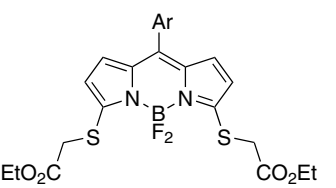

70d
MeOH, Φ 0.50
$\lambda_{max\ abs}$ 564 nm
$\lambda_{max\ emiss}$ 579 nm

Figure 8. Spectroscopic data for some BODIPYs formed by S_NAr reactions.

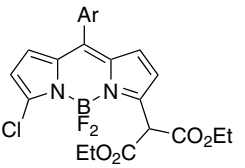

69e
MeOH, Φ 0.28
$\lambda_{max\ abs}$ 508 nm
$\lambda_{max\ emiss}$ 522 nm

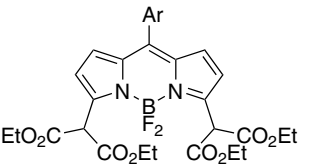

70e
MeOH, Φ 0.35
$\lambda_{max\ abs}$ 509 nm
$\lambda_{max\ emiss}$ 522 nm

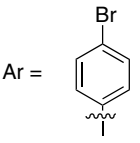

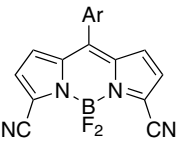

71
MeOH, Φ 0.66
$\lambda_{max\ abs}$ 514 nm
$\lambda_{max\ emiss}$ 526 nm

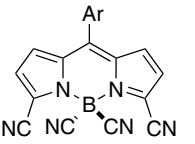

72
MeOH, Φ 0.80
$\lambda_{max\ abs}$ 510 nm
$\lambda_{max\ emiss}$ 523 nm

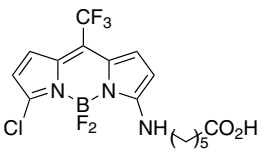

73
pH 7.4, Φ 0.74
$\lambda_{max\ abs}$ 469 nm
ε 17 100 $M^{-1}cm^{-1}$
$\lambda_{max\ emiss}$ 542 nm

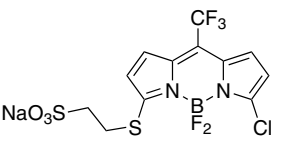

74
pH 7.4, Φ 0.95
$\lambda_{max\ abs}$ 569 nm
ε 57 000 $M^{-1}cm^{-1}$
$\lambda_{max\ emiss}$ 584 nm

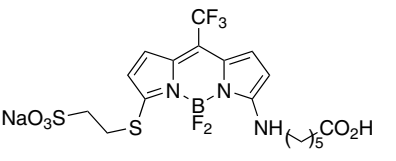

75
pH 7.4, Φ 0.70
$\lambda_{max\ abs}$ 477 nm
ε 41 800 $M^{-1}cm^{-1}$
$\lambda_{max\ emiss}$ 584 nm

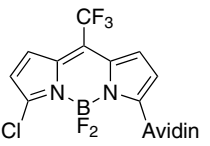

76
pH 7.4
$\lambda_{max\ abs}$ 481 nm
$\lambda_{max\ emiss}$ 546 nm

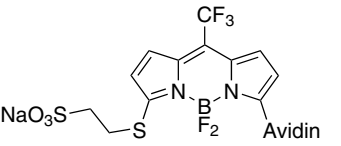

77
pH 7.4
$\lambda_{max\ abs}$ 492 nm
$\lambda_{max\ emiss}$ 592 nm

Figure 8. (*Continued*)

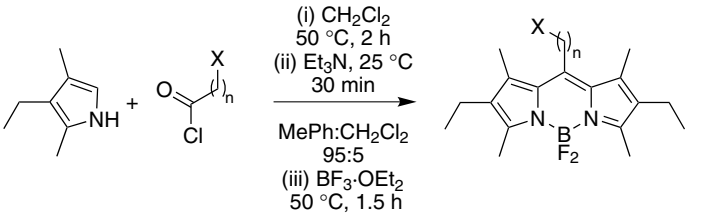

Chart 11.

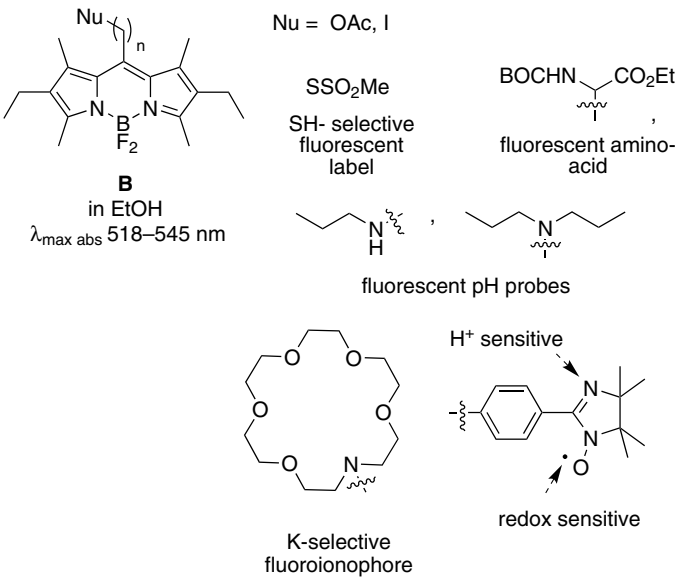

C. From Metal Mediated C-H Functionalization

Pyrroles can be functionalized via palladium-catalyzed activation reactions.[124–126] Burgess and coworkers applied the same strategy to synthesize novel BODIPY dyes via palladium-mediated C-H functionalization (Chart 12).[127] This route provides a direct way to extend the conjugation of the BODIPY core, without a halogenated or metalated intermediate prior to the coupling reaction. Highly fluorescent, mono- (**80**) or disubstituted (**81**) dyes can be obtained. A water-soluble, sulfonated BODIPY dye **80d** was also prepared via this route, but in low yield (2%).

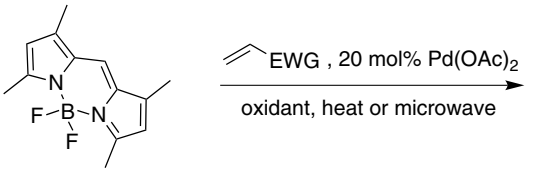

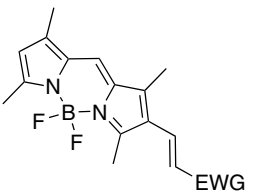

+

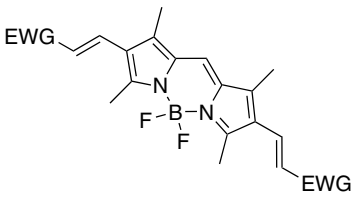

80a–d **81a–d**

EWG =

80a–d	**81a–d**
a CO_2Me EtOH, Φ 0.73 $\lambda_{max\ abs}$ 527 nm $\lambda_{max\ emiss}$ 549 nm	**a** CO_2Me CH_3CO_2Et, Φ 0.51 $\lambda_{max\ abs}$ 559 nm $\lambda_{max\ emiss}$ 580 nm
b $CO_2{}^nBu$ EtOH, Φ 0.73 $\lambda_{max\ abs}$ 528 nm $\lambda_{max\ emiss}$ 551 nm	**b** $CO_2{}^nBu$ EtOH, Φ 0.52 $\lambda_{max\ abs}$ 560 nm $\lambda_{max\ emiss}$ 580 nm
c CO_2H EtOH, Φ 0.42 $\lambda_{max\ abs}$ 531 nm $\lambda_{max\ emiss}$ 570 nm	**c** *not formed*
d SO_3H EtOH, Φ 0.25 $\lambda_{max\ abs}$ 529 nm $\lambda_{max\ emiss}$ 560 nm	**d** *not formed*

Chart 12.

The C-H functionalization process was also applied to α,β-unsaturated esters to form compounds **82** and **83**. Mono- and disubstituted products were obtained, but these do not correspond exactly because the alkene double bond was shifted out of conjugation with the BODIPY core.

Iridium-catalyzed direct borylation of aromatic compounds via C-H bond activation and the use of organoboranes with rhodium catalysis have been extensively explored for new types of C-C bond formation. Recently, Osuka and coworkers

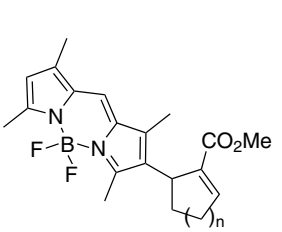

82a–b

a n = 1
EtOH, Φ 0.72
$\lambda_{max\ abs}$ 518 nm
$\lambda_{max\ emiss}$ 525 nm

b n = 2
EtOH, Φ 0.78
$\lambda_{max\ abs}$ 517 nm
$\lambda_{max\ emiss}$ 527 nm

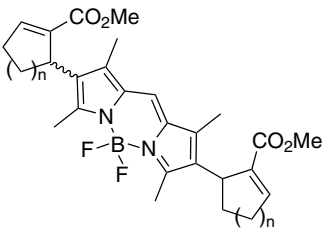

83a–b

a n = 1
EtOH, Φ 0.92
$\lambda_{max\ abs}$ 530 nm
$\lambda_{max\ emiss}$ 539 nm

b n = 2
EtOH, Φ 0.89
$\lambda_{max\ abs}$ 529 nm
$\lambda_{max\ emiss}$ 540 nm

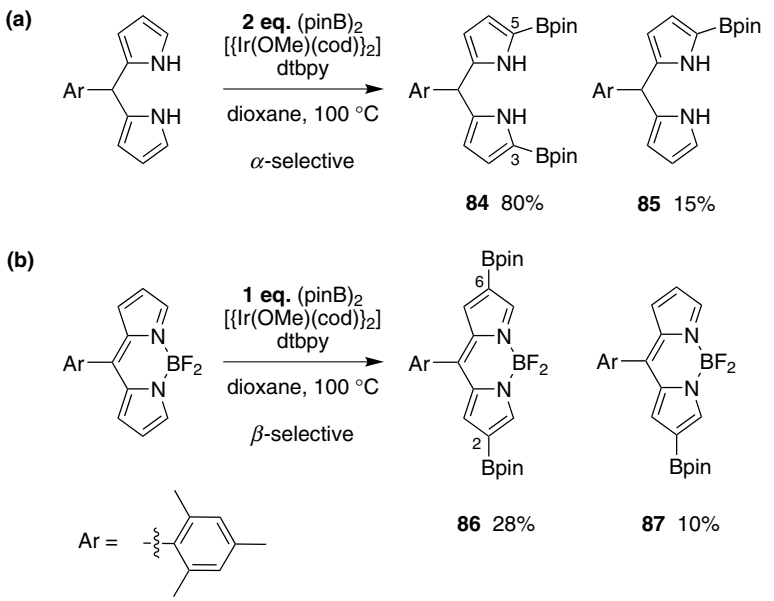

Scheme 6. Borylation of (**a**) *meso*-mesityldipyrromethane, and (**b**), *meso*-mesitylBODIPY.

applied those novel metal-catalyzed methodologies to dipyrromethane and BODIPY dyes.[128] The BODIPY precursor was borylated regioselectively at the 3- and 5-positions (aka α positions), while the corresponding BODIPY reacted at the 2- and 6-positions (aka β positions) (Scheme 6). Borylation of the BODIPY occurred

in low yield probably because of the instability of the dye under the reaction conditions.

Rhodium-catalyzed Heck-type additions were used to prepare α- and β-functionalized BODIPY dyes from **84** and **87** (Scheme 7). Treatment of **84** with hexyl acrylate gave the desired 3,5-double addition products as a mixture of the *E*,*E*- and *E*,*Z*- isomers, **88** and **89**. Oxidation of **88** with DDQ, followed by complexation with boron afforded the corresponding BODIPY **90** (Scheme 7a). Under the same conditions, the BODIPY **86** gave the desired disubstituted product **91** along with some partially saturated compound **92** (Scheme 7b). α, β, γ, δ-Dienote functions were also introduced, but the corresponding products **93** and **94** were obtained in low yields. Photophysical properties of the new dyes were studied in CH_2Cl_2. A substantial red shift for both the absorption and emission was observed upon extending the conjugation of the system. The 3,5-substituted BODIPY dyes exhibit sharp fluorescence peaks, higher extinction coefficients and fluorescence quantum yields, relative to the 2,6- substituted BODIPY dyes **91**.

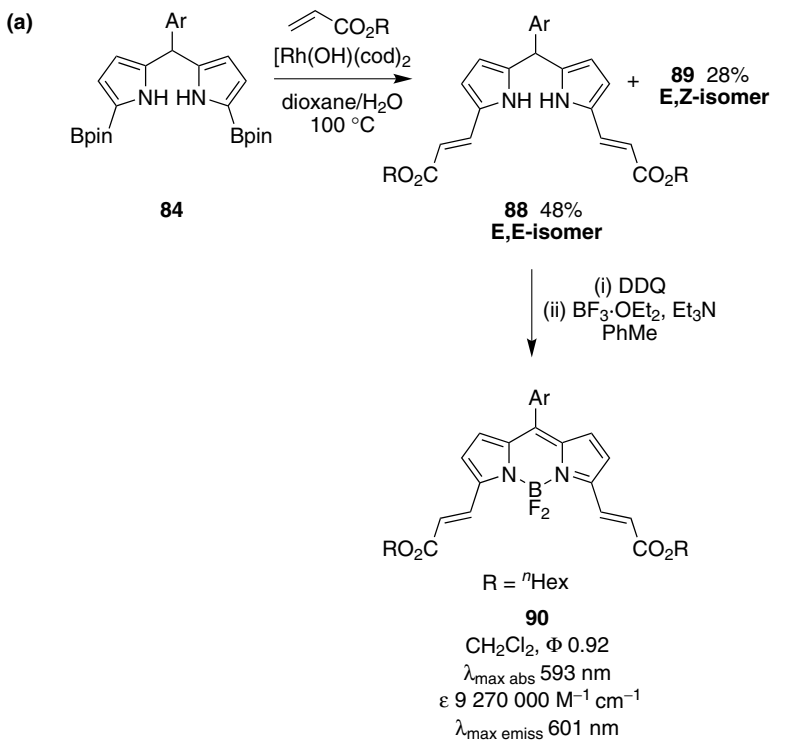

Scheme 7. Functionalization of: (**a)** the 3,5-borylated *meso*-mesityldipyrromethane **84**; and, (**b)** the 2,6-borylated *meso*-mesitylBODIPY **86**; and (**c**), the extended conjugated systems **93** and **94** formed via this approach.

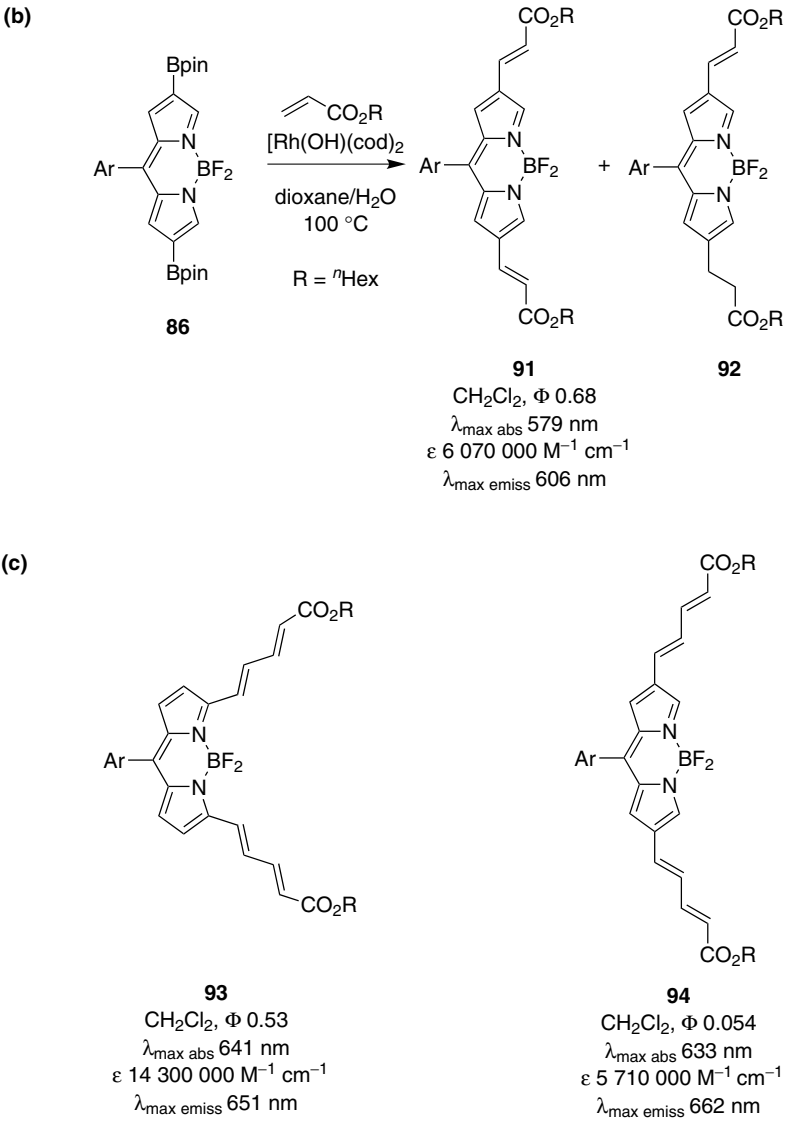

Scheme 7. (*Continued*)

D. From Nucleophilic Attack at the *meso*-Position

BODIPY systems with a *meso*-cyanide substituent are special insofar as they fluoresce at significantly longer wavelengths than the unsubstituted systems.[129] Further, they can be accessed by direct addition of cyanide anion to the dipyrromethene core, followed by oxidation. The first synthetic route developed gave poor overall yields, mainly due to loss of material in forming the

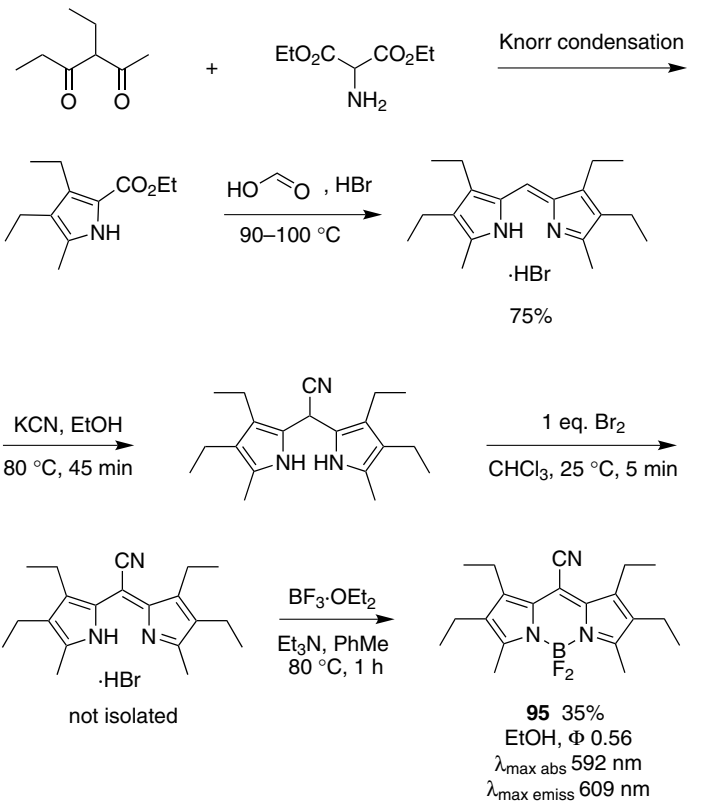

Scheme 8. Cyanopyrromethene-BF_2 complexes via addition of cyanide.

dipyrromethene,[89] but an improved one was published by Boyer and coworkers (Scheme 8).[130] In that work, Knorr condensation of 3-ethylhexan-2,4-dione with diethyl aminomalonate give ethyl 3,4-diethyl-5-methylpyrrole-2-carboxylate. This pyrrole is then converted to the dipyrromethene hydrobromide via the presumed intermediacy of 2-methyl-3,4-diethylpyrrole and its condensation with the α-formyl derivative that is formed *in situ*.

Comparison of compound **95** with other *meso*-cyano BODIPYs (e.g. **96–99**) shows their fluorescence and absorption are about 60 nm red-shifted relative to simple alkyl-substituted BODIPYs. This large bathochromic shift seems attributable to a net stabilization of the BODIPY LUMO via interaction with the cyano group. The presence of the cyano group also significantly reduces the molecular extinction coefficient. Only in the case of **99** where the core bears two ester groups is this red-shift attenuated. Presumably in this case the esters reduce the electron density on the BODIPY core available for delocalization into the nitrile, and this affects the fluorescence emission wavelength.

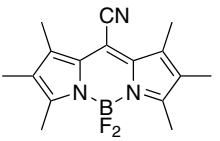

96
MeOH, Φ 0.54
$\lambda_{max\ abs}$ 588 nm
$\lambda_{max\ emiss}$ 612 nm

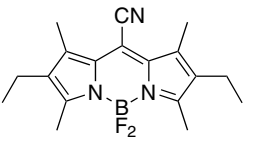

97
dioxane, Φ 0.55
$\lambda_{max\ abs}$ 580 nm
$\lambda_{max\ emiss}$ 620 nm

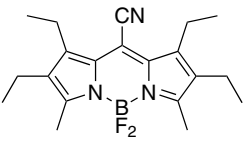

98
MeOH, Φ 0.56
$\lambda_{max\ abs}$ 592 nm
$\lambda_{max\ emiss}$ 609 nm

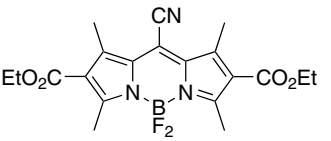

99
dioxane, Φ 0.82
$\lambda_{max\ abs}$ 556 nm
$\lambda_{max\ emiss}$ 589 nm

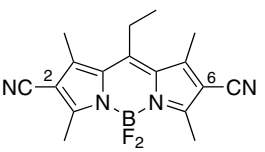

100
dioxane, Φ 0.79
$\lambda_{max\ abs}$ 496 nm
$\lambda_{max\ emiss}$ 511 nm

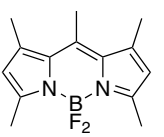

101
dioxane, Φ 0.99
$\lambda_{max\ abs}$ 493 nm
$\lambda_{max\ emiss}$ 519 nm

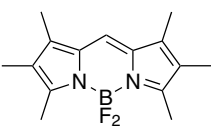

8
MeOH, Φ 0.56
$\lambda_{max\ abs}$ 528 nm
$\lambda_{max\ emiss}$ 552 nm

Red-shifted fluorescence associated with a cyano group is particular to the *meso*-position. 2,6-Dicyano BODIPY **100** has two cyano groups, neither occupies the *meso*-position, and fluorescence from this compound peaks at about the same wavelength as similar BODIPYs without nitrile substituents, e.g. **101** and **8**.[130] Similarly, substitution at the 2- and 6-positions with carboethoxy, acetamido, sulfonate anion, bromo or nitro groups do not produce any red shift.[89,130,131]

A synthesis of sulfur containing BODIPYs under mild conditions was recently achieved via reaction of thiophosgene with substituted pyrroles to give the corresponding thioketone **102**.[90] The latter can then react with various electrophiles to form the dipyrromethene intermediates that were combined with boron trifluoride in presence of base to afford the thio-BODIPY derivatives **27**. These *meso*-thioalkyl groups can be displaced by nucleophiles to give anilino-substituted BODIPY derivative **103** (Scheme 9, see also Chart 2). Amine adduct **103** was not

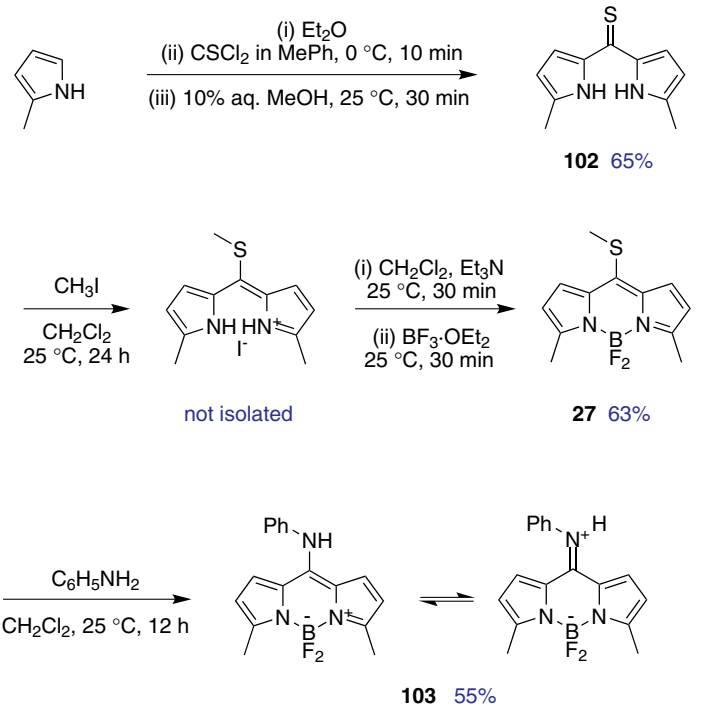

Scheme 9. Synthesis of sulfur- and anilino- BODIPY derivatives.

fluorescent, presumably because of electron transfer from the amine group to the BODIPY core in the excited state.

V. Water-Soluble BODIPY Dyes

A. From Electrophilic Substitution Reactions

Despite the practical value of *water-soluble* BODIPY dyes, very few have been reported. Up to 2008, only a few sulfonated BODIPY dyes had been reported. They were obtained from tetra-, or penta-substituted BODIPYs via treatment with chlorosulfonic acid, then subsequent neutralization with a base (e.g. Chart 13). Monosulfonated systems could be obtained when only one equivalent of chlorosulfonic acid was used. Introduction of the sulfonate groups did not change the absorption and emission spectra significantly relative to the unsulfonated dye. The sulfonated BODIPY dyes **104**–**107** are strongly fluorescent in water and/or methanol, and are claimed to have even better stability than the parent dyes.[88,132–137]

Burgess and coworkers recently developed sulfonation conditions to prepare various functionalized, mono- and bis-sulfonated BODIPY systems, e.g. **108**–**110**.[138]

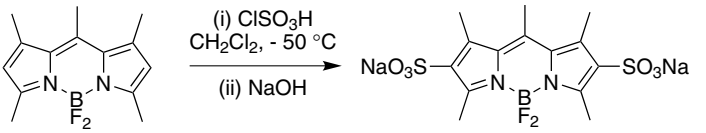

104 40%
MeOH, Φ 0.73 (H_2O)
$\lambda_{max\ abs}$ 492 nm
$\lambda_{max\ emiss}$ 533 nm

Chart 13.

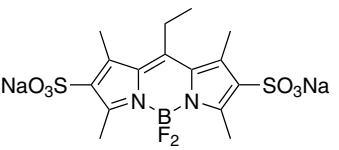

105
MeOH, Φ 0.44
$\lambda_{max\ abs}$ 498 nm
$\lambda_{max\ emiss}$ 530 nm

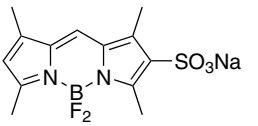

106 80%
MeOH, Φ 0.80
Φ 0.85 (H_2O)
$\lambda_{max\ abs}$ 495 nm
$\lambda_{max\ emiss}$ 515 nm

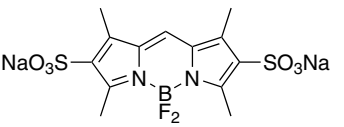

107 60%
H_2O, Φ 0.85
$\lambda_{max\ abs}$ 491 nm
$\lambda_{max\ emiss}$ 510 nm

BODIPY **108** is functionalized with an aryl iodide for elaboration via Pd-mediated couplings. Compound **109** has two chlorine atoms that could be replaced by S_NAr reactions. Probe **110** was designed with an acid functional group to facilitate activation and coupling to amines.

B. From Coupling or Substitution Reactions

So far, three different strategies have been explored to introduce water-soluble groups onto the hydrophobic BODIPY core: (i) S_NAr reaction at the 3-position of 3,5-dichloroBODIPY with 2-mercaptosulfonic acid (Section IV.B),[119] (ii) Heck-coupling in the 2- and 6-positions (Section IV.C)[127] and, (iii) electrophilic sulfonation with chlorosulfonic acid.[138] Only the last approach gives water-soluble BODIPYs in good yields without requiring prior functionalization of the BODIPY

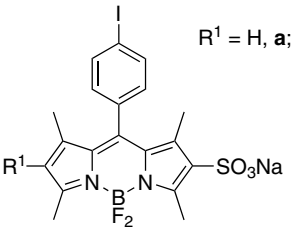

R^1 = H, **a**; R^1 = SO_3Na, **b**

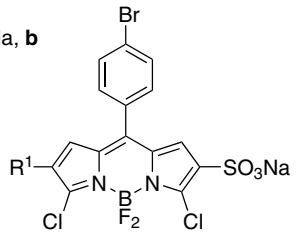

108a 60%
H_2O, Φ 0.47
$\lambda_{max\ abs}$ 494 nm
log ε 5.18 M^{-1} cm^{-1}
$\lambda_{max\ emiss}$ 507 nm

109a 92%
H_2O, Φ 0.27
$\lambda_{max\ abs}$ 509 nm
log ε 4.86 M^{-1} cm^{-1}
$\lambda_{max\ emiss}$ 523 nm

108b 88%
H_2O, Φ 0.34
$\lambda_{max\ abs}$ 498 nm
log ε 5.00 M^{-1} cm^{-1}
$\lambda_{max\ emiss}$ 509 nm

109b 85%
H_2O, Φ 0.41
$\lambda_{max\ abs}$ 512 nm
log ε 4.89 M^{-1} cm^{-1}
$\lambda_{max\ emiss}$ 524 nm

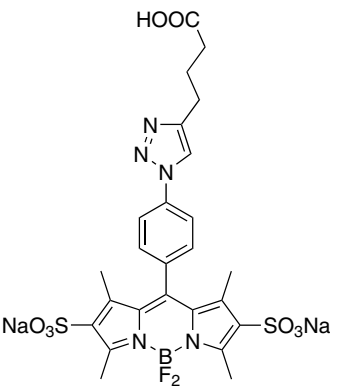

110 42%
H_2O, Φ 0.49
$\lambda_{max\ abs}$ 498 nm
log ε 4.90 M^{-1} cm^{-1}
$\lambda_{max\ emiss}$ 511 nm

core. Recently, Ziessel and coworkers reported two alternative strategies to introduce (poly)sulfonated groups onto the BODIPY core.[139] The first relies on a peptide coupling between α-sulfo-β-alanine and BODIPY **111** (obtained in two steps from the corresponding phenyliodo derivative via Pd-mediated carboalkoxylation, followed by saponification; Chart 14). The mild conditions (NMP-water, pH 8.5, 25 °C) involve in this amine/acid coupling allow the presence of

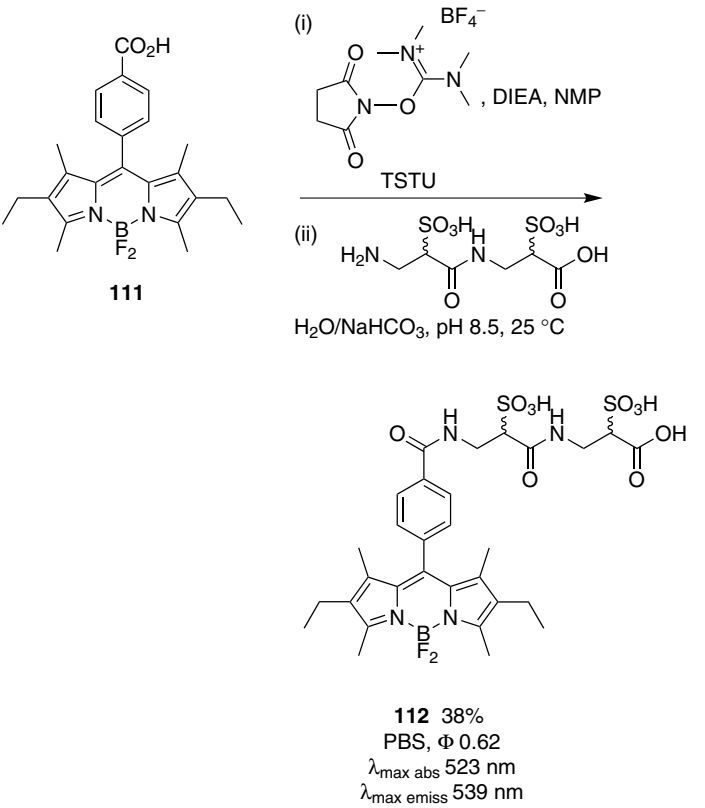

Chart 14.

additional sophisticated functional groups and provide hydrophilic fluorophores with a handle for conjugation to biomolecules.

Ziessel's second strategy to *water-soluble* BODIPYs is based on alkynylation at the 2,6-positions (Chart 15) and/or at the boron center (Chart 16) with 1-dimethylamino-2-propyne, followed by alkylation with propane sultone. Introduction of the hydrophilic linker at the 2- and 6-positions (dye **95**) resulted in a bathochromic shift in the emission spectra relative to dye **116**. BODIPY **116** shows two absorption maxima at 522 and 567 nm in PBS; the latter disappears in EtOH indicating aggregation of the dye in aqueous medium.

VI. Aryl-, Alkenyl-, Alkynyl-Substituted BODIPYs

A. *Meso* Aryl-, Alkenyl- and Alkynyl-Substituted BODIPYs

Meso-substituted BODIPY are usually prepared via condensation of an aryl aldehyde with a large excess of pyrrole under acid catalysis, oxidation with DDQ,

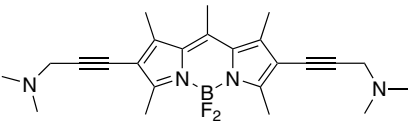

113
CH_2Cl_2, Φ 0.54
$\lambda_{max\ abs}$ 543 nm
$\lambda_{max\ emiss}$ 565 nm

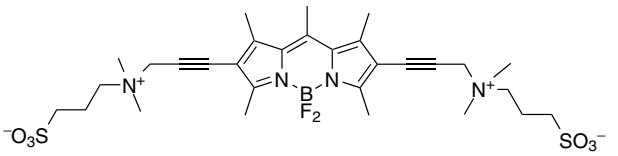

114 58%
PBS, Φ 0.78
$\lambda_{max\ abs}$ 521 nm
$\lambda_{max\ emiss}$ 540 nm

Chart 15.

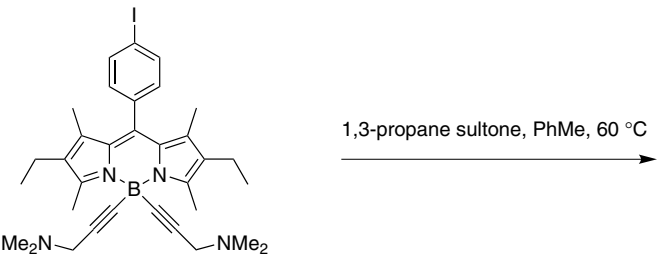

115
CH_2Cl_2, Φ 0.52
$\lambda_{max\ abs}$ 521 nm
$\lambda_{max\ emiss}$ 532 nm

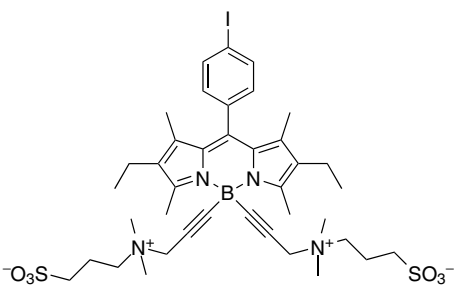

116 62%
PBS, Φ 0.61
$\lambda_{max\ abs}$ 522, 567 nm
$\lambda_{max\ emiss}$ 530 nm

Chart 16.

followed by complexation with BF_3 etherate. Although commonly used, this methodology has several disadvantages; for instance, it includes tedious purifications, synthesis of the aldehyde (if not commercially available), and some functional groups on the aryl aldehyde might be incompatible with acid, and DDQ oxidation.

Inspired by the work of Liebeskind[140] and Biellmann,[90] Peña-Cabrera and coworkers reported a novel, simple and efficient synthesis of *meso*-substituted BODIPY via Pd-catalyzed, Cu(I)-mediated cross-coupling of the 8-thiomethylBODIPY **117** with boronic acids under neutral conditions (Chart 17).[141] Both electron-rich and -poor aryl and alkenyl boronic acids reacted smoothly under the Liebeskind-Srogl coupling conditions. Bromo-aryl derivatives, e.g. compound **118**, could be prepared in good yield without further polymerization (via Suzuki-type reactions) as the Liebeskind-Srogl works in the absence of base. Bulky boronic acids did not compromise either the efficiency of the process as

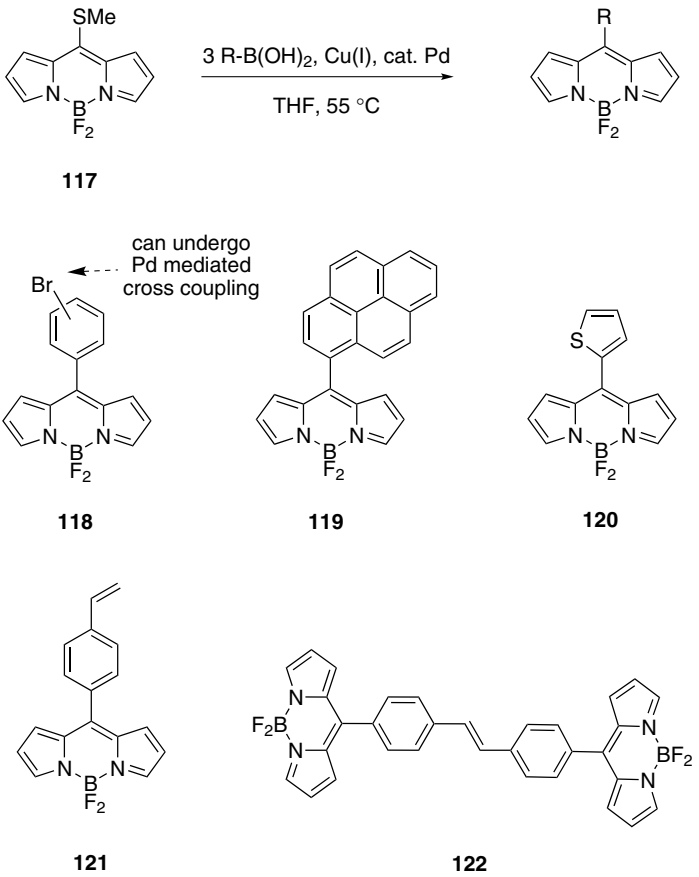

Chart 17.

BODIPY **119** could be prepared in 67% yield in 15 minutes. Heteroaryl boronic acids also showed excellent reactivity. This new route tolerates many functional groups allowing preparation of products that can be further elaborated. Compound **118** containing an aryl bromide can undergo Pd mediated cross coupling. BODIPY **122** was obtained from homometathesis of **121**. No spectroscopic data have been reported yet.

Until recently, there was only one *meso*-vinyl substituted BODIPY dye (compound **26**, Section II.D). Introduction of a vinyl unit at the *meso* position of BODIPY led to a bathochromic shift of the emission maxima, while the absorption did not change. Dyes **124**–**129**, synthesized from BODIPY **123**, illustrate a new series of dyes combining polymethine and dipyrromethene chromophoric fragments.[142] The methyl group of **123** is not highly reactive, but can undergo some condensation reactions. Thus, Vilsmeier-type formylation of **123** gave the disubstituted BODIPY **124**. The hemicyanine dye **126** was obtained by treating the monoformylated product **125** with aniline (Chart 18). BODIPY **124** shows good fluorescent properties. However, the derivatives **125** and **126** are nonfluorescent, presumably due to PeT quenching. Acidification of the solutions of **125** and **126** restores the fluorescence, but that of **125** disappears quickly, and irreversibly.[142]

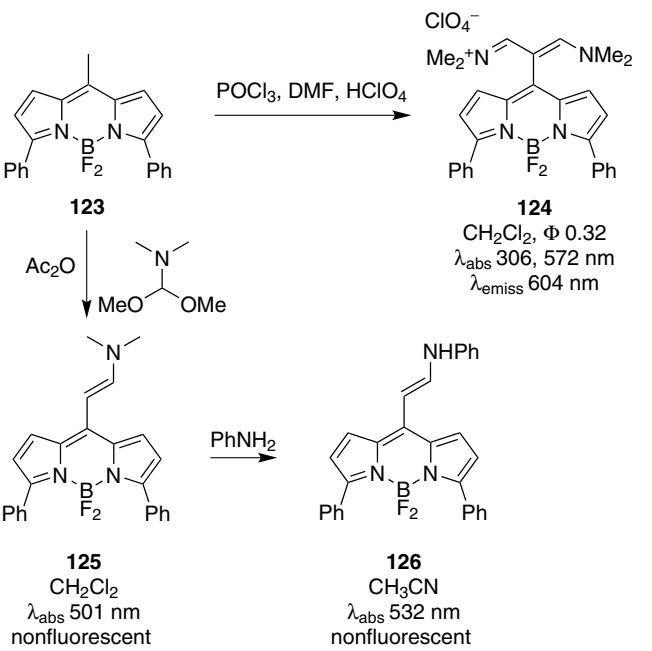

Chart 18.

BODIPY **123** reacts with more active phenyliminovinyl derivatives of heterocycles of low and medium basicity (e.g. 4-pyran, indoline, benz[*c,d*]indole, and benzothiazole) to form dyes such as **127–129** in good yields (Chart 19). Combination of **123** with 2-(phenyliminovinyl)quinoline led to the formation of **131** (Chart 20). The author postulates this may be due to the low electron-withdrawing ability of the BODIPY nucleus, which makes the betaine mesomeric form unfavorable. The contribution of the betaine mesomeric form increases with increasing electron-donating effect of the second terminal nucleus, whereas the stability of the boron complex decreases. Thus, the synthesis of symmetrical dyes such as **132** is difficult due to the formation of the unfavorable anionic form of the BODIPY nucleus.

The physical properties of new polymethine-substituted BODIPY dyes were studied in CH_2Cl_2 and DMF. The merocyanine nature of these dyes manifests itself in the existence of two absorption bands: a short-wavelength band characteristic of the BODIPY core and a more intense, long-wavelength band typical of the

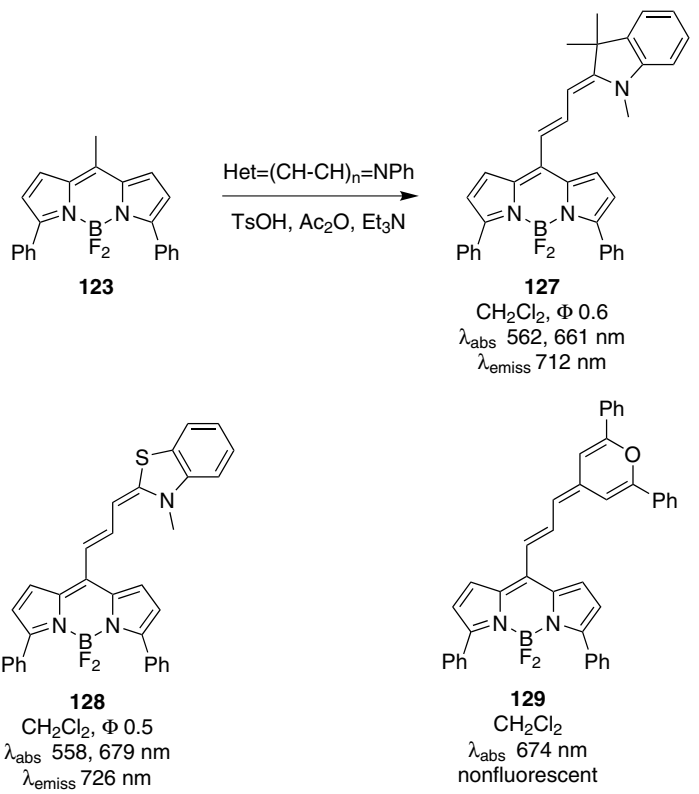

Chart 19.

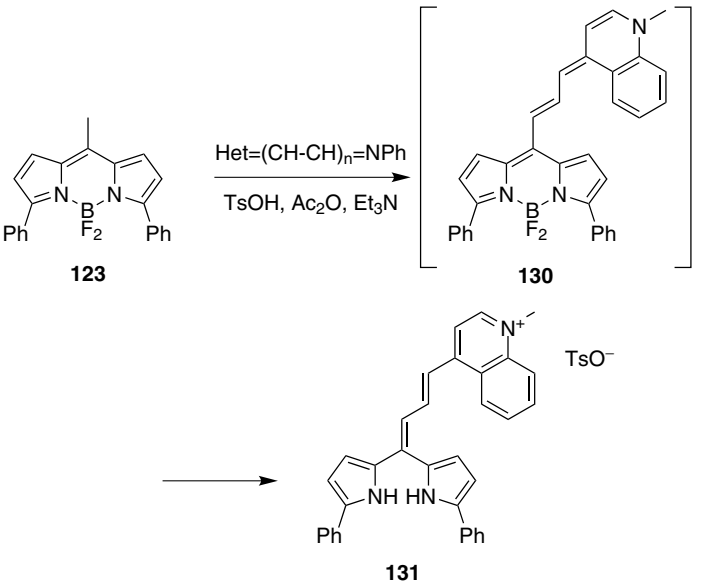

123 **130** **131**

Chart 20.

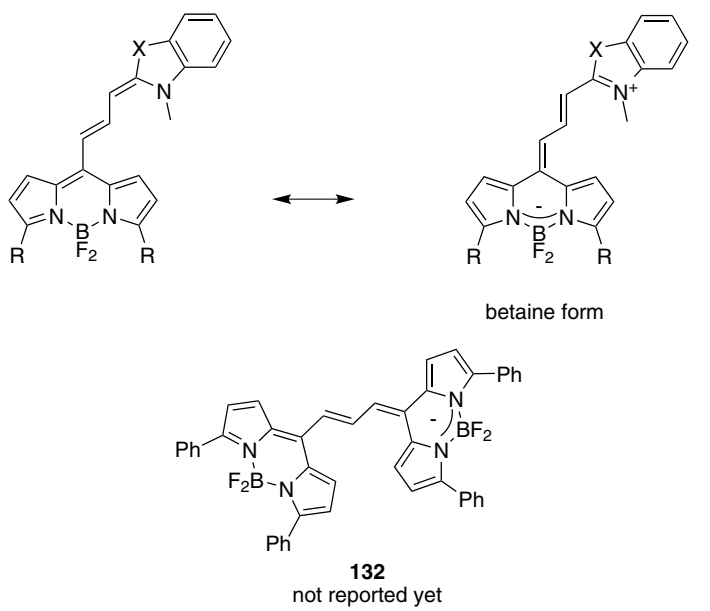

132
not reported yet

polymethine fragment. Upon protonation, the long-wavelength absorption band completely disappears while the one corresponding to the BODIPY nucleus increases. Boradipyrromethenecyanines **127** and **128** are moderately fluorescent in CH_2Cl_2 ($\Phi \sim 0.5$–0.6), and are weakly fluorescent, particularly in polar solvents

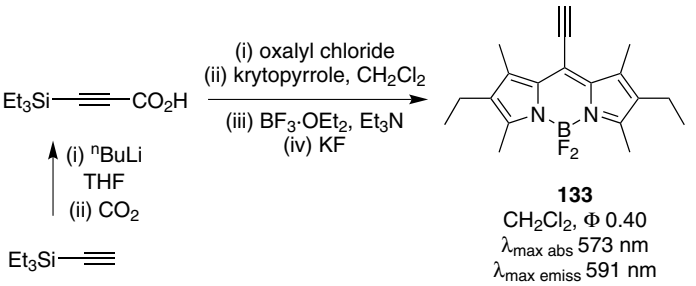

Chart 21.

($\Phi < 0.1$ in DMF). There is no fluorescence increase for these materials upon protonation.

Very few *meso*-alkynyl BODIPYs are known. As far as we are aware, the 8-ethynyl BODIPY **133** is the first one.[143] It was prepared by a classical route, involving condensation of 2,4-dimethyl-3-ethylpyrrole with triethylsilylacetylene acid (generated *in situ*), followed by complexation with BF_3 etherate, and deprotection of the silyl group with potassium fluoride (Chart 21). Compound **133** shows an intense absorption at 573 nm, red-shifted by 30 nm relative to the 8-methyl derivative due to extended conjugation.

B. 3,5-Aryl-Substituted BODIPYs from Aryl-Pyrroles

Aryl-substituted BODIPY dyes can be formed via condensation of the corresponding pyrroles with acyl chlorides.[144,145] The 2-aryl pyrroles used were prepared via Suzuki couplings[146] of *N*-*tert*-butoxycarbonyl-2-bromopyrrole (Chart 22); this was more convenient than starting with less accessible materials like 4-aryl-1-azidobutadienes[147] or a *N*-tosylarylimine.[148,149] Removal of the *N*-BOC protecting group under basic conditions gave the desired aryl pyrroles. These products were found to decompose on standing, rapidly under acidic conditions, and were therefore best formed immediately before use.

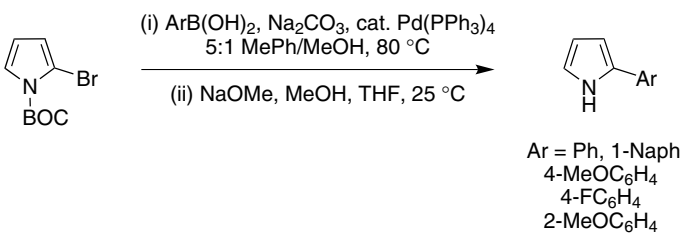

Chart 22.

3,5-Diaryl BODIPY dyes were obtained from the pyrroles shown above, via a one pot, two-step process featuring 4-iodobenzoyl chloride. The 3,5-aryl groups extend the conjugation of the BODIPY systems. Compared to the alkyl-substituted derivatives, e.g. **134** and **135** which have green, fluorescein-like emissions ($\lambda_{max\ emis}$ = 510 nm), both the absorption and emission maxima of 3,5-diaryl substituted BODIPYs **136–140** are shifted to longer wavelengths ($\lambda_{max\ emis}$ = 588–626 nm).[144,145] The *para*-electron-donating group of **138** gives a larger bathochromic shift and increased quantum yield, compared to the compound with that same substituents in the *ortho*-position **140**. Similarly, the extended aromatic substituent naphthalene of **137** red-shifted the emission maximum for this compound. However, the extinction coefficients for **136–140** were not markedly

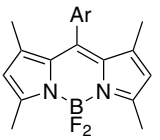

134
$CHCl_3$, Φ 0.64
$\lambda_{max\ abs}$ 500 nm
$\lambda_{max\ emiss}$ 510 nm

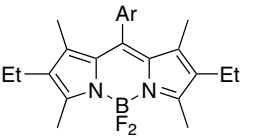

135
$CHCl_3$, Φ 0.78
$\lambda_{max\ abs}$ 524 nm
$\lambda_{max\ emiss}$ 537 nm

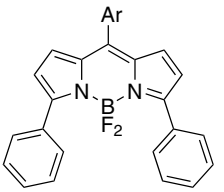

136
$CHCl_3$, Φ 0.20
$\lambda_{max\ abs}$ 555 nm
$\lambda_{max\ emiss}$ 588 nm

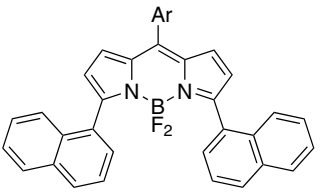

137
$CHCl_3$, Φ 0.38
$\lambda_{max\ abs}$ 542 nm
$\lambda_{max\ emiss}$ 607 nm

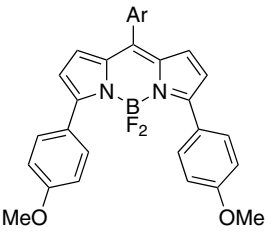

138
$CHCl_3$, Φ 0.42
$\lambda_{max\ abs}$ 582 nm
$\lambda_{max\ emiss}$ 626 nm

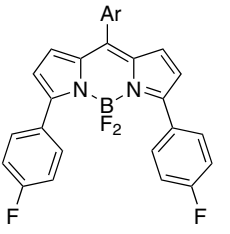

139
$CHCl_3$, Φ 0.22
$\lambda_{max\ abs}$ 555 nm
$\lambda_{max\ emiss}$ 590 nm

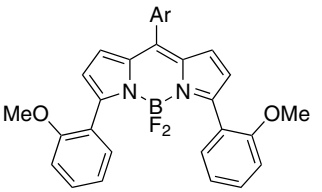

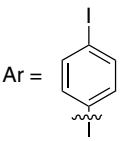

140
$CHCl_3$, Φ 0.08
$\lambda_{max\ abs}$ 545 nm
$\lambda_{max\ emiss}$ 598 nm

increased relative to the alkyl systems **134** and **135** and their fluorescence quantum yields were significantly lower due to non-radiative loss of energy via rotation around the C-Ar bonds.[150]

Similarly to above, the polyphenylated BODIPYs **141–143** were prepared from the corresponding 2,4-diphenylpyrrole or 2,3,4-triphenylpyrrole prepared by Suzuki-Miyaura coupling of 2,3,4-tribromopyrrole with $PhB(OH)_2$ to study the effect of the peripheral phenyl groups on photophysical properties.[151] The peripheral phenyl groups of **141** and **143** are arranged in a propeller-like fashion in the solid state, as shown by X-rays analyses. In THF, the new BODIPY derivatives show strong absorption bands centered around 561–576 nm and fluorescence emission between 597–613 nm. Although, the emissions maxima for the new BODIPYs are close, significant differences were observed in their quantum yields. BODIPYs **29** and **141** have extremely high quantum yields, while dyes **142** and **143** are only moderate (20 and 30%). This marked difference is due to the phenyl ring at the *meso* position; the steric congestion around this group accelerates non-radiative internal conversion. Intense emissions for **142** and **143** were observed when the dyes (1%) were included in PMMA films. This is probably because rotation of the *meso*-phenyl ring is restricted in the solid state.

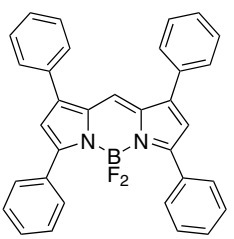

29 21%
CH_2Cl_2, Φ 1.00
$\lambda_{max\ abs}$ 564 nm
ε 78 000 M^{-1} cm^{-1}
$\lambda_{max\ emiss}$ 593 nm

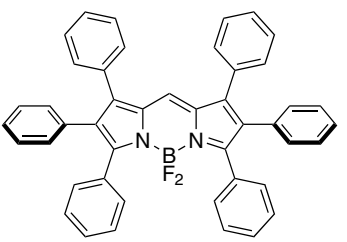

141
THF, Φ 0.96
$\lambda_{max\ abs}$ 576 nm
$\lambda_{max\ emiss}$ 608 nm

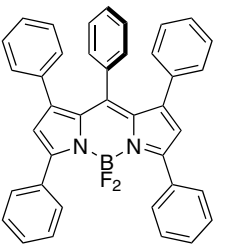

142
THF, Φ 0.31
$\lambda_{max\ abs}$ 561 nm
$\lambda_{max\ emiss}$ 597 nm

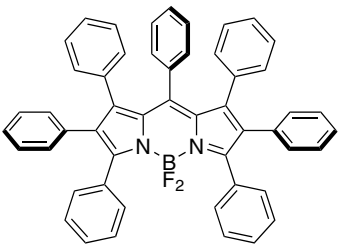

143
THF, Φ 0.20
$\lambda_{max\ abs}$ 573 nm
$\lambda_{max\ emiss}$ 613 nm

Fluorescence of some BODIPYs in solution can be reduced at elevated concentrations due to intermolecular π-stacking. BODIPY dyes can stack in two geometrically distinct forms: H- and J-dimers (Figure 9). The former is most likely a result of intramolecular dimerization, with the stacking of two BODIPY planes with almost parallel $S_0 \rightarrow S_1$ transition dipoles, and anti-parallel electric dipole moments. This dimer is practically non-fluorescent, and exhibits blue-shifted absorption relative to that of the monomer. The J-dimer, in which the $S_0 \rightarrow S_1$ transition dipoles are oriented in planes at 55°, is fluorescent and shows a red-shifted absorption relative to that of the monomer.[152–154]

Compound **144** was designed to sterically prevent dimers formation in solution.[155] Further, the hindered internal rotation of the mesityl rings reduces nonradiative relaxation of excited states, enhancing fluorescence quantum yields. Dyes such as **144** were prepared from mesityl aldehyde and the corresponding pyrrole **145**[156] (made via a Trofimov reaction).[149]

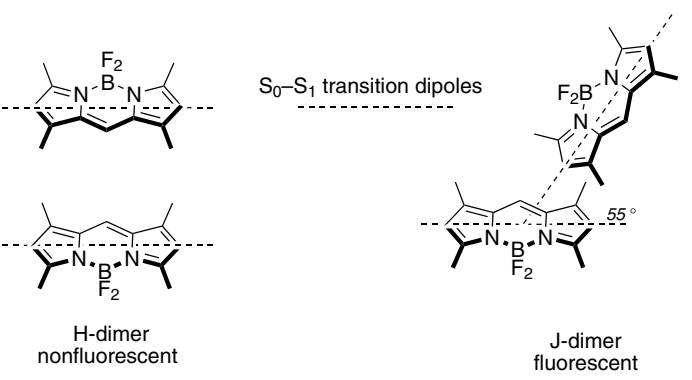

Figure 9. Structures of H-dimer and J-dimer.

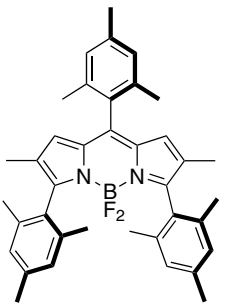

144
CH_2Cl_2, Φ 0.95
$\lambda_{max\ abs}$ 543 nm
$\lambda_{max\ emiss}$ 559 nm

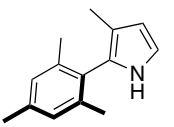

145

C. Knoevenagel Reactions with Benzaldehyde Derivatives to Give Alkenyl Systems

1. *3,5-Styryl-BODIPY Dyes*

3- and 5-Methyl BODIPY substituents are acidic enough to participate in Knoevenagel reactions. Thus, styryl-BODIPY derivatives can be obtained by condensation of 3,5-dimethyl-BODIPYs with aromatic aldehydes (Chart 23).[157,158] With *p*-dialkylaminobenzaldehyde the reaction can be restricted to one condensation (di(dimethylamino)styryl-substituted BODIPY dyes can be obtained with longer reaction time (7d)),[159] but 4-alkoxybenzaldehydes tend to give mixtures corresponding to one and two condensations.[160]

The condensation processes shown in Chart 23 provide BODIPY derivatives that have red-shifted fluorescence, and functional groups that can be used in sensors and molecular logic gates. UV-absorption spectra of compounds from one condensation (e.g. **148** and **149**) tend to reach maxima around 594 nm in MeOH, and their fluorescence emissions are similarly red-shifted. Both the absorption and, particularly, the fluorescence spectra are dependent upon solvent polarity.[161,162] The red shift is more pronounced in polar solvents indicating excitation of the dyes leads to more polarized excited states.

Structures **147**–**149** illustrate some effects of amino substituents in these styryl systems. When the amine is directly conjugated with the styryl group then a maximum red-shift is obtained, but when it is part of the *meso*-substituent then the bathochromic shift is less because this *meso* substituent is nonplanar. Quantum yields for these materials are only high when the amine is protonated disfavoring Intramolecular Charge Transfer (ICT) in the excited state.[157,162] Compound **149** is a metal sensor because complexation to ions alleviates ICT and increases its

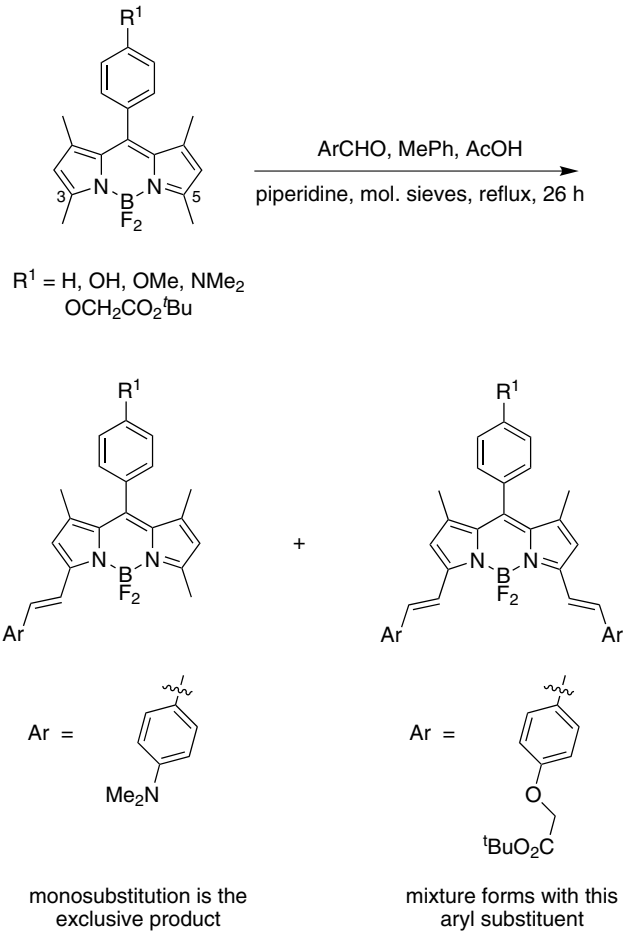

Chart 23.

quantum yield. Introduction of a second styryl group at the 5-position (compound not shown) red-shifts the UV and fluorescence maxima by almost 100 nm and 50 nm, respectively.[159]

BODIPYs **150** and **151** are ICT dyes; they display opposite spectral shifts upon protonation.[163] As expected, upon addition of acid (TFA), emission of **150** is significantly blue-shifted (from 753 to 630 nm) as the ICT donor group dimethylamino functionality is a considerably less effective electron donor when protonated. Conversely, **151** with acid gives a red-shifted absorption spectrum (from 620 to 660 nm).

Compound **152** can be called a molecular and logic gate for generation of singlet oxygen for photodynamic therapy.[164] The chemical inputs of the logic system are Na^+ and H^+ as the pH of tumor tissues is quite acidic, and the intracellular

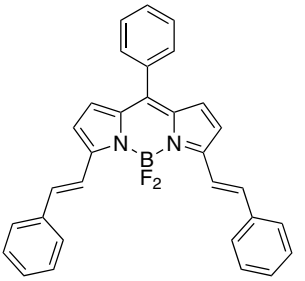

146
CH_3CN, Φ 0.84
$\lambda_{max\ abs}$ 628 nm
$\lambda_{max\ emiss}$ 642 nm

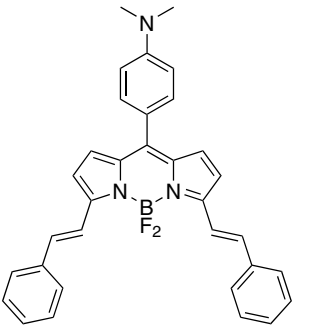

147
CH_3CN, Φ 4×10^{-4}
$\lambda_{max\ abs}$ 620 nm
$\lambda_{max\ emiss}$ 636 nm

$CH_3CN + H^+$, Φ 0.75
$\lambda_{max\ abs}$ 634 nm
$\lambda_{max\ emiss}$ 652 nm

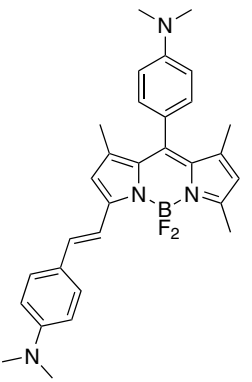

148
H_2O, Φ 9×10^{-4}
$\lambda_{max\ abs}$ 578 nm
$\lambda_{max\ emiss}$ 758 nm

MeOH, Φ 0.10
$\lambda_{max\ abs}$ 594 nm
$\lambda_{max\ emiss}$ 699 nm

$H_2O + 2H^+$, Φ 0.55
$\lambda_{max\ abs}$ 557 nm
$\lambda_{max\ emiss}$ 565 nm

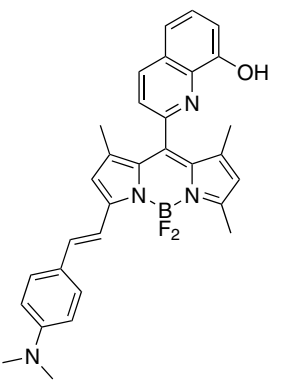

149
MeOH, Φ 0.04
$\lambda_{max\ abs}$ 608 nm
$\lambda_{max\ emiss}$ 738 nm

sodium ion concentration is also significantly higher than normal tissues. The molecular system is an automaton which is to seek the higher concentration of both hydrogen and sodium ions, and release the cytotoxic agent (singlet oxygen).

There is no marked pH dependence for the electronic spectra of the alkoxy-substituted systems **153** and **154**.[160] However, the fluorescence of the

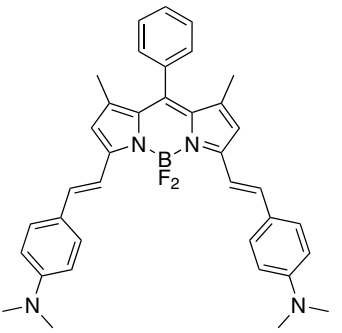

150

$CHCl_3$, Φ n.d.
$\lambda_{max\ abs}$ 700 nm
$\lambda_{max\ emiss}$ 753 nm

$CHCl_3$ + 2 H^+, Φ n.d.
$\lambda_{max\ emiss}$ 630 nm

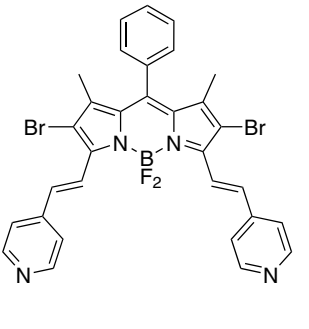

151

$CHCl_3$, Φ n.d.
$\lambda_{max\ abs}$ 620 nm
$\lambda_{max\ emiss}$ 640 nm

$CHCl_3$ + 2 H^+, Φ n.d.
$\lambda_{max\ abs}$ 660 nm
$\lambda_{max\ emiss}$ 677 nm

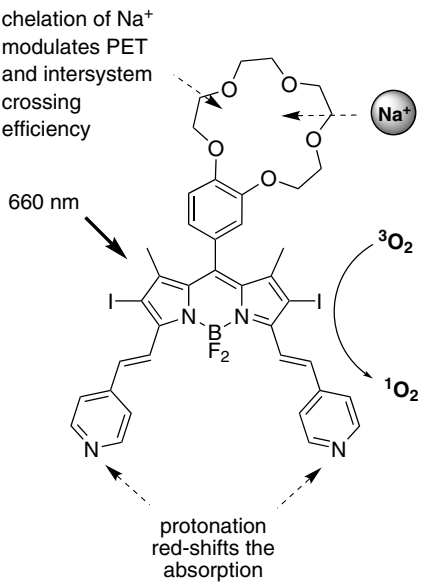

Na^+	H^+	$^1O_2$
0	0	low (1.0)
1	0	low (2.9)
0	1	low (1.0)
1	1	high (6.1)

152

amino-phenol **155** is quenched when the hydroxyl group is deprotonated, but the UV absorbance and fluorescence maxima remain the same; fluorescence is enhanced and there is a blue shift when the amine group is protonated. This molecule has also been compared to a logic gate.[66]

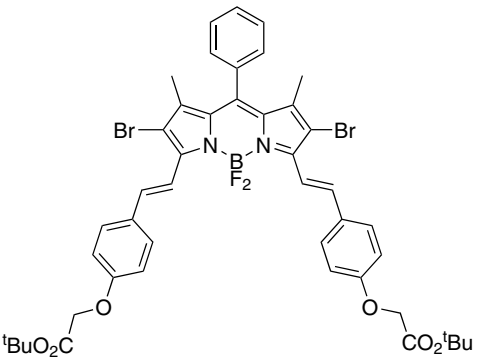

153
^{i}PrOH, Φ 0.42
$\lambda_{max\ abs}$ 657 nm
$\lambda_{max\ emiss}$ 679 nm
fwhm 41 nm

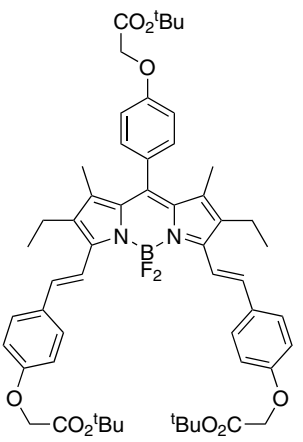

154
^{i}PrOH, Φ 0.40
$\lambda_{max\ abs}$ 657 nm
$\lambda_{max\ emiss}$ 679 nm
fwhm 43 nm

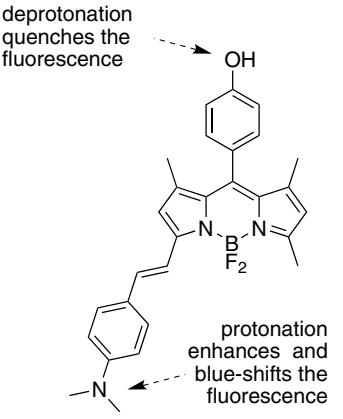

155
THF, Φ 0.25
$\lambda_{max\ abs}$ 565 nm
$\lambda_{max\ emiss}$ 660 nm

THF + H^{+}, Φ 0.85
$\lambda_{max\ abs}$ 525 nm
$\lambda_{max\ emiss}$ 560 nm

THF + OH^{-}, Φ 0.032
$\lambda_{max\ abs}$ 565 nm
$\lambda_{max\ emiss}$ 660 nm

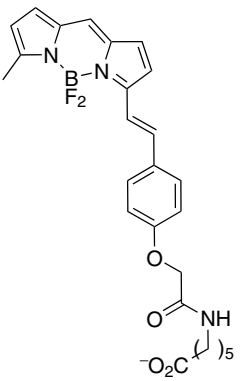

BODIPY 630/650

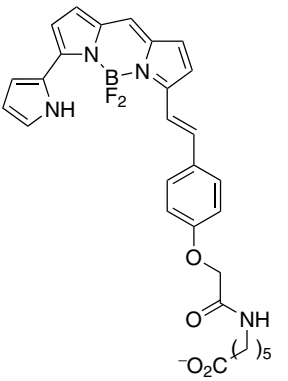

BODIPY 650/665

Although many new styryl BODIPYs have been synthesized, Invitrogen's BODIPY 630/650 and BODIPY 650/665 probes are the only two longest-wavelength amine-reactive BODIPY fluorophores commercially available to date.

Biomolecules labeled at relatively large BODIPY:protein ratios can have diminished fluorescence intensities due to interactions between the probes; the fluorescence can also be red-shifted for the same reason.[165] Small molecules containing two BODIPYs have been produced to test these types of effects. The first prepared were somewhat flexible being based on cyclohexane.[152,153] More recently, rigid ones with cofacial BODIPY dyes have been made and studied. Only one transition dipole moment is possible for these structures. The xanthane unit was chosen as a scaffold since it can be easily functionalized on its 4- and 5-positions. Aldehyde or bis-aldehyde functionalities on the xanthane (**156** or **160**, respectively) were used to construct the BODIPY units by condensation with 2,4-dimethylpyrrole. A 3-methyl substituent on the BODIPY was then reacted with *p*-dimethylaminobenzaldehyde to extend the conjugation (Scheme 10).[166]

Compound **161** has two cofacial BODIPY groups, and the UV absorption maximum of the BODIPY part is blue-shifted (to 478 nm, with a shoulder at 504 nm) relative to 1,3,5,7-tetramethyl-BODIPY **7** and the other control compound **157**. Compound **162**, which has one styryl-extended BODIPY and one tetramethyl-BODIPY substituent, has UV absorption peaks corresponding to both these substituents (455 nm and 575 nm). Upon excitation at 480 nm, the monochromophoric system **157** exhibits a very strong emission at 500 nm, while the fluorescence emission of the di-BODIPY system **161** is significantly quenched; it shows two peaks, one at 505 nm and a broader excimer-type emission at 590 nm. Efficient energy transfer from the donor (tetra-methyl BODIPY) to the acceptor (extended BODIPY) was observed for the system **162**. The cofacial chromophores are separated by approximately 4.5 Å, allowing both energy transfer and formation of an

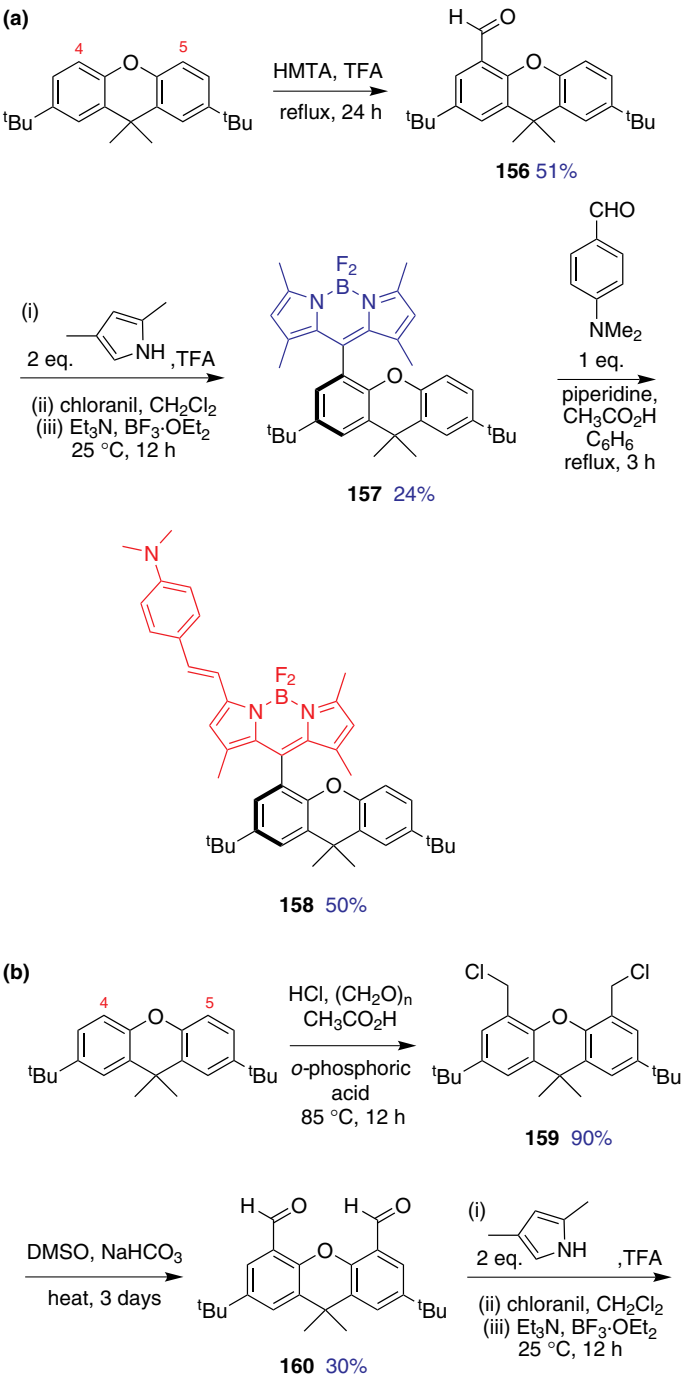

Scheme 10. Syntheses of BODIPY dyes anchored on xanthene units to test self-quenching: (**a**) a system with one BODIPY dye; (**b**) a similar compound with two, where only one has extended conjugation; and, (**c**) another where both have extended conjugation.

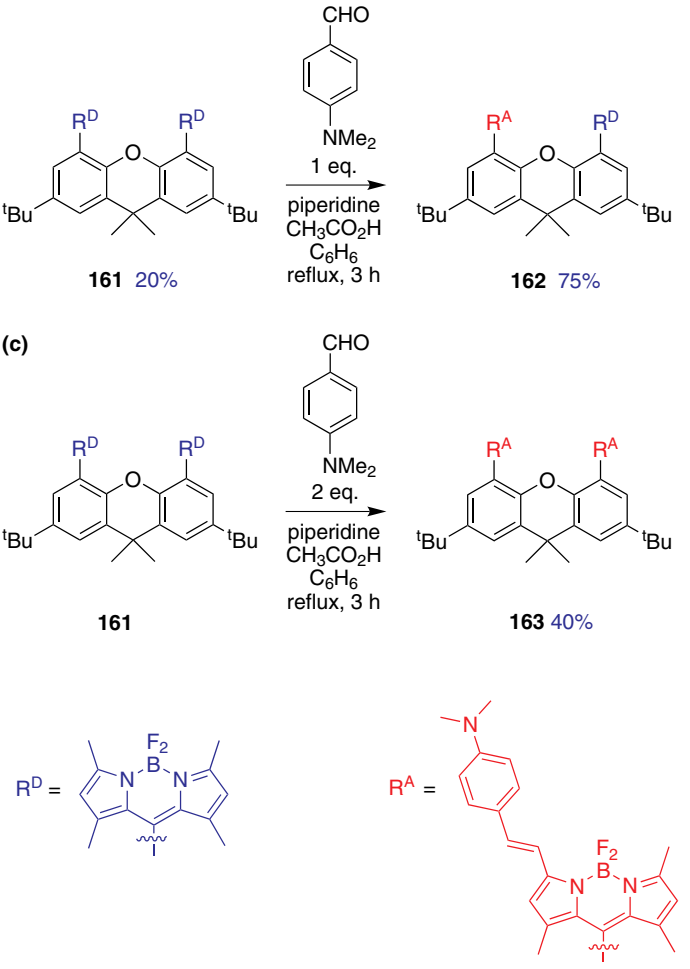

Scheme 10. (*Continued*)

excimer-like state. Incidentally, system **162** acts as an energy transfer cassette; fluorescence emission could be observed at 650 nm from the extended BODIPY (acceptor) upon excitation of the other BODIPY (donor) at 480 nm. More discussion of energy transfer cassettes follows in Section 7.

2. *1,3,5,6-Tetrastyryl-BODIPY Dyes*

Mulliken-charge analysis on the core carbon atoms of tetramethyl-BODIPY **7** revealed that the methyl groups in positions 1 and 7 could be almost as acidic as the 3,5-methyls. Therefore BODIPY dye **164 c**arrying pyridinylethynyl substituents on the 2,6-positions could be condensed with *p*-anisaldehyde to form the

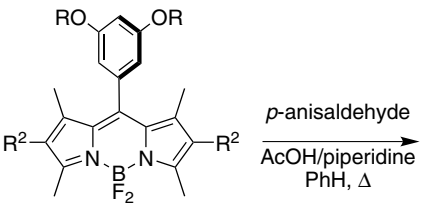

164

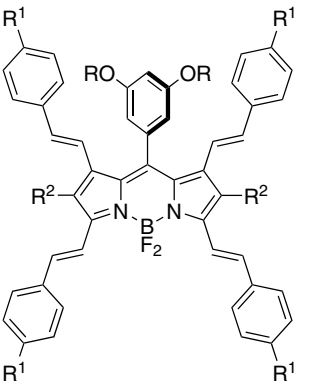

a R^1 = OMe, R^2 = H

b R^1 = OMe, R^2 = Br

c R^1 = OMe, R^2 =

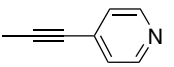

d R^1 = $N(Me)_2$, R^2 =

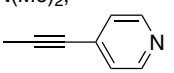

165a–d

	$\lambda_{max\ abs}$ ($CHCl_3$)	ε	$\lambda_{max\ emiss}$	Φ
a	689	127 900	710	0.34
b	700	48 800	727	0.12
c	721	88 200	747	0.42
d	802	141 500	837	0.13

Chart 24.

corresponding tetrastyryl BODIPY derivative **165c** (Chart 24). The styryl groups introduced by the Knoevenagel reaction were exclusively in the *trans (E)* configuration. The 2,6-dibromo derivative **164b** reacted as efficiently as the ethynyl-substituted derivatives. As expected, the 2,6-H BODIPY **164a** reacted slowly and, by stopping the reaction at different times, the mono-, di-, tri- and tetra-styryl derivatives could be obtained. The first methyls to react were exclusively the 3,5-methyls, and tri- and tetra-substituted products were obtained when the concentration of reactants was increased by removal of most of the solvent.[167]

With the exception of **165d**, the new tetrastyryl dyes absorb between 690 and 720 nm, and emit between 710–750 nm. They have large extinction coefficients, and their quantum yields are found to be moderate to high. Compound **165d** is a true near-IR dye, absorbing around 800 nm, and emiting near 837 nm; its quantum

yield tends to be decreased by the strong charge transfer and highly polar excited state.

D. From Palladium-Catalyzed Coupling Reactions at the 3- and 5-Positions

3,5-Dichloro BODIPY derivatives such as **68** have similar reactivities to heterocyclic imidoyl chlorides; this opens a new window for derivatization using transition-metal-catalyzed reactions. Thus, new 3-, 5-aryl, ethenylaryl and ethynylaryl compounds **166** and **167** were obtained via Stille, Suzuki, Heck and Sonogashira couplings (Chart 25).[168,169] The extended conjugation, and mono-/disubstitution patterns, of these dyes give dispersed fluorescence emission maxima within the series. Absorption maxima for the monosubstituted compounds **166** are blue-shifted by 20 nm to 50 nm relative to the disubstituted ones **167**. The largest red shift for both absorption and emission was observed for the styryl substituted derivatives. The dyes with ethenyl- or ethynyl-aryl substituents gave the highest quantum yields (**167c**, 0.92; **166d**, 0.98; and, **167d**, 1.00).[168] The mono-substituted BODIPY dyes can further be derivatized by nucleophilic substitution (see section above) or by another transition-metal-catalyzed coupling reaction to give unsymmetrically substituted probes.

Selectivity for mono-substitution via Pd mediated cross coupling, i.e., Sonogashira and Suzuki on compounds such as **68** is low, and the resulting products are hard to isolate in a pure form. Those problems could be overcome if mono-halogenated BODIPY dyes such as **168** were used. Such systems can be prepared from the corresponding 2-acyl-4-halo- and/or 2-acyl-5-halopyrroles via condensation with another pyrrole in presence of phosphorus oxychloride, followed by complexation with boron (Chart 26).[170] The *meso*-substituent of the BODIPY is introduced during the acylation (via Vilsmeier-Haack reaction) reaction of 2-halogenated pyrroles, allowing for a large number of substituents to be introduced. Furthermore, the spectroscopic properties of the resulting BODIPY can be easily tuned by careful selection of the pyrrole; the red-shifted BODIPY **169** was synthesized from the conformationally restricted 4,5-dihydro-1*H*-benzo[*g*]indole.

The mono-halogenated system **168** can then be further functionalized via Sonogashira or Suzuki cross coupling reactions to give BODIPY **170–172** (Chart 27). The new dyes are strongly fluorescent. Interestingly, the fluorescence quantum yield of the 2-alkynylated dye **170** decreases significantly with increasing solvent polarity (data not shown), while small variations are observed for the corresponding 3-alkynylated dye **171**. Moreover, the absorption maxima of the 3-alkynylated derivative is red-shifted relative to the 2-alkynyl isomer.

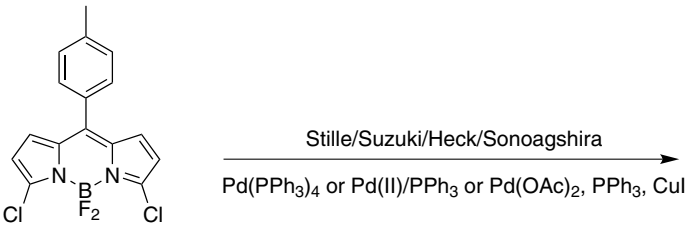

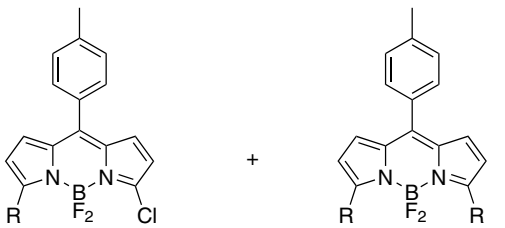

R =

a		MeOH; Φ 0.04 $\lambda_{max\ abs}$ 525 nm $\lambda_{max\ emiss}$ 549 nm	MeOH; Φ 0.21 $\lambda_{max\ abs}$ 547 nm $\lambda_{max\ emiss}$ 582 nm
b	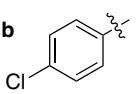	MeOH; Φ 0.03 $\lambda_{max\ abs}$ 525 nm $\lambda_{max\ emiss}$ 549 nm	MeOH; Φ 0.39 $\lambda_{max\ abs}$ 554 nm $\lambda_{max\ emiss}$ 590 nm
c	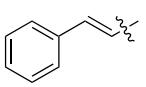	MeOH; Φ 0.55 $\lambda_{max\ abs}$ 564 nm $\lambda_{max\ emiss}$ 579 nm	MeOH; Φ 0.92 $\lambda_{max\ abs}$ 626 nm $\lambda_{max\ emiss}$ 639 nm
d	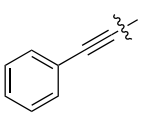	MeOH; Φ 0.98 $\lambda_{max\ abs}$ 556 nm $\lambda_{max\ emiss}$ 569 nm	MeOH; Φ 1.00 $\lambda_{max\ abs}$ 605 nm $\lambda_{max\ emiss}$ 622 nm

Chart 25.

As illustrated above, organometallic cross coupling reactions can extend the conjugation of the BODIPY core. However, such transformations are usually done in basic conditions and/or at high temperature that may cause partial decomposition of the BODIPY dyes. Furthermore, chemoselectivities are hard to control when several halides are present on the same molecule. On the other hand, Liebeskind-Srogl cross coupling is carried out under neutral conditions,[140] and is

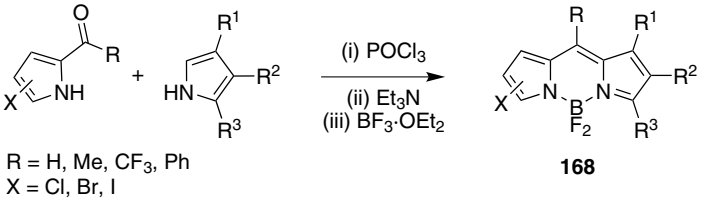

R = H, Me, CF_3, Ph
X = Cl, Br, I

168

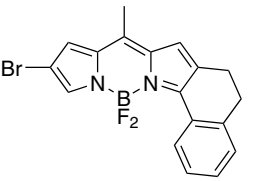

169
PhMe, Φ 0.87
$\lambda_{max\ abs}$ 567 nm
$\lambda_{max\ emiss}$ 583 nm

Chart 26.

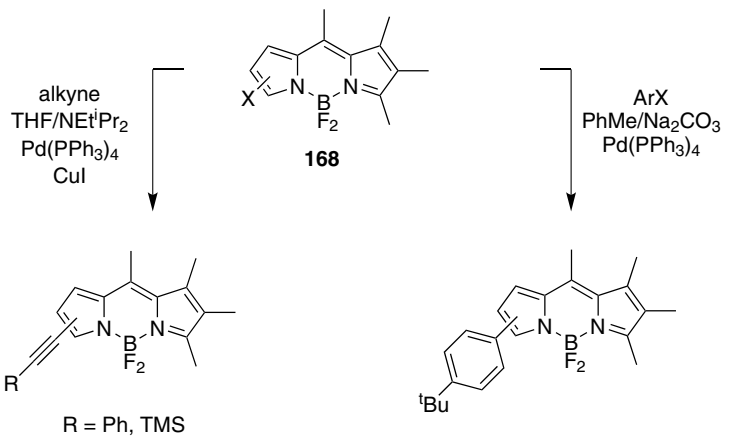

168

R = Ph, TMS

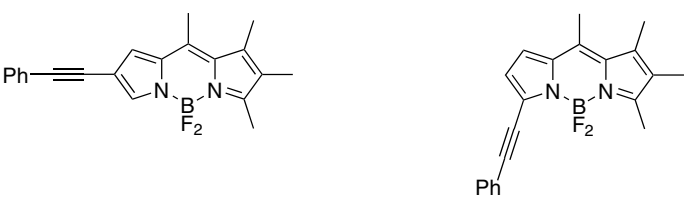

170
PhMe, Φ 0.61
$\lambda_{max\ abs}$ 521 nm
$\lambda_{max\ emiss}$ 561 nm

171
PhMe, Φ 0.93
$\lambda_{max\ abs}$ 542 nm
$\lambda_{max\ emiss}$ 556 nm

Chart 27.

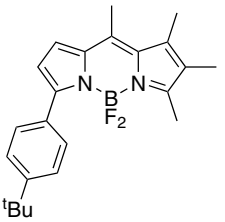

172
PhMe, Φ 0.83
$\lambda_{max\ abs}$ 527 nm
$\lambda_{max\ emiss}$ 553 nm

Chart 27. (*Continued*)

chemoselective for thioalkyl groups over aryl bromides.[171] Thus, Burgess and coworkers recently reported the synthesis of 3,5-aryl BODIPYs **176a–c** via Liebeskind-Srogl cross coupling from the 3,5-thiobutylBODIPY derivative **174** (Chart 28).[172] Electron-rich aryl-tin reagents cleanly gave the disubstituted products. Some monosubstituted product, i.e., **175** was isolated with electron-poor aryl group, but in no case was the aryl-bromide affected.

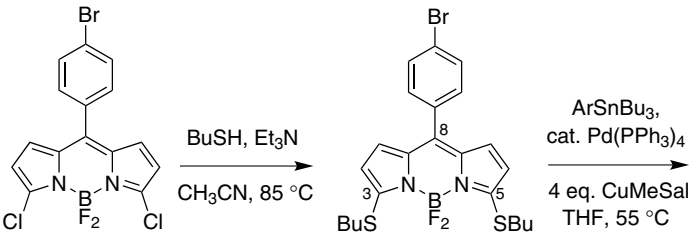

173

174 99%
EtOAc; Φ 0.40
$\lambda_{max\ abs}$ 577 nm
$\lambda_{max\ emiss}$ 595 nm

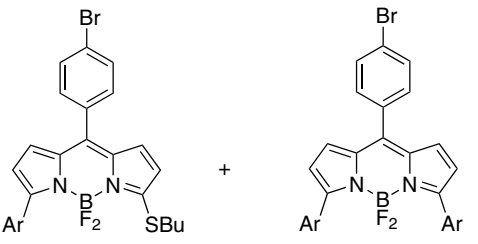

175 a–c **176 a–c**

Chart 28.

Ar =

a		not formed	85% EtOAc; Φ 0.58 $\lambda_{max\ abs}$ 571 nm $\lambda_{max\ emiss}$ 597 nm
b	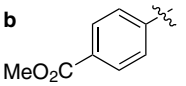	26% EtOAc; Φ 0.14 $\lambda_{max\ abs}$ 555 nm $\lambda_{max\ emiss}$ 588 nm	62% EtOAc; Φ 0.36 $\lambda_{max\ abs}$ 559 nm $\lambda_{max\ emiss}$ 596 nm
c	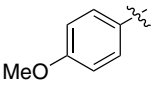	not formed	75% EtOAc; F 0.38 $I\mu_{ax\ abs}$ 581 nm $I\mu_{ax\ emiss}$ 621 nm

Chart 28. (*Continued*)

VII. Energy Transfer Cassettes

A. Through-Space Energy Transfer Cassettes

Two fluorescent entities may be joined in the same molecule to give a "cassette." One of these, the *donor*, may collect radiation efficiently at the excitation wavelength and pass this energy to the second fluorescent moiety that emits it at a longer wavelength. If the mechanism of energy transfer is through space then this system might be called a through-space energy transfer cassette. Energy transfer cassettes are typically used to artificially enhance the Stokes' shift of a probe. Ones featuring BODIPY dyes have been somewhat useful for DNA sequencing on a genomic scale[173] where four distinct fluorescent outputs are required, and usually only one excitation wavelength is used.

Through-space energy transfer efficiencies depend on several factors, including: (i) spectral overlap of the donor emission with the acceptor absorbance; (ii) distance between the donor and the acceptor; (iii) the orientation factors; and, (iv) the effectiveness of alternative de-excitation modes. Cassettes described in this section have no obvious way to transfer energy from donors to acceptors via bonds.

The dendritic light harvesting system **177** with four BODIPY donors and a perylenediimide (PDI) acceptor was constructed via click chemistry.[174] Its UV spectrum is equal to the sum of the donor and acceptor components indicating they are not electronically perturbing each other.[175] The extinction coefficients of **177** at 526 nm (BODIPY λ_{max}) and 582 nm (PDI λ_{max}) are 240 000 and 45 000 $M^{-1}cm^{-1}$, respectively, hence the donor absorption is huge simply because four BODIPY units are involved. No green fluorescence emission from BODIPY was observed

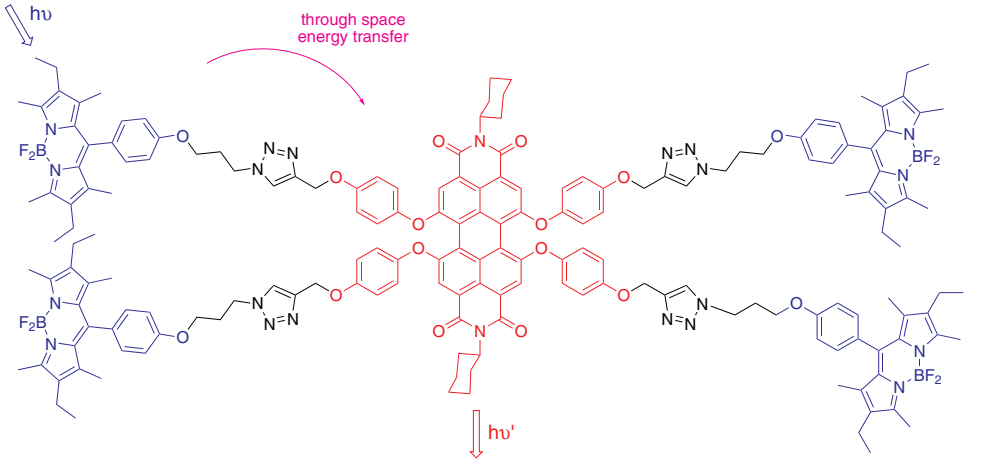

177

upon excitation at 526 nm, indicating efficient energy transfer (99%). Based on the energy transfer efficiency, the authors of this work calculated a Förster critical radius of 47 Å. An "antenna effect" (emission intensity at 618 nm when excited at 526 nm (BODIPY core) divided by that from excitation at 588 nm (at the PDI core)) gave approximately a 3.5-fold enhancement.

Most studies on energy transfer between porphyrins and other chromophores have focused on electron and energy transfer in the plane of the porphyrin. "Vertical" electron and energy transfer from axial ligands, on the other hand, have not been studied extensively but systems **178**–**181** were synthesized to study this phenomenon. An antimony porphyrin was chosen as the acceptor because this central metal can coordinate to ligands with oxygen, nitrogen, or sulfur atoms. Energy transfer from the excited singlet state of the BODIPY to the Sb(TPP) chromophore occurs for **178**, **179** and **181**. This happens with efficiencies in the 13–40% range, decreasing as the length of the methylene bridge increases. Little or no evidence was seen for quenching of the porphyrin excited singlet state by the BODIPY. This was true even when polar solvents were used and the donor and acceptor fragments would be expected to pack against each other. However, for system **180**, which differs from **178** only at the second axial ligand (phenoxy vs. methoxy), the excited singlet state of the Sb(TPP)-acceptor was quenched by the BODIPY and phenoxy ligands. The quenching by the phenoxy group occurs, at least in part, via a nonradiative electron-transfer process.[176]

Systems **182** and **183** are two novel BODIPY-silicon(IV) phthalocyanines (Pc) conjugates.[177] These only differ in their axial substituents; system **182** bears two BODIPY, while **183** has two mono-styryl BODIPY moieties. Upon excitation

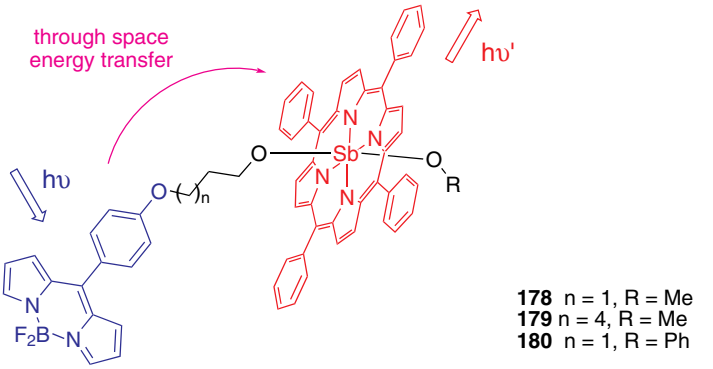
through space
energy transfer
hυ'
hυ
Sb
O
R
n
N
F2B
178 n = 1, R = Me
179 n = 4, R = Me
180 n = 1, R = Ph

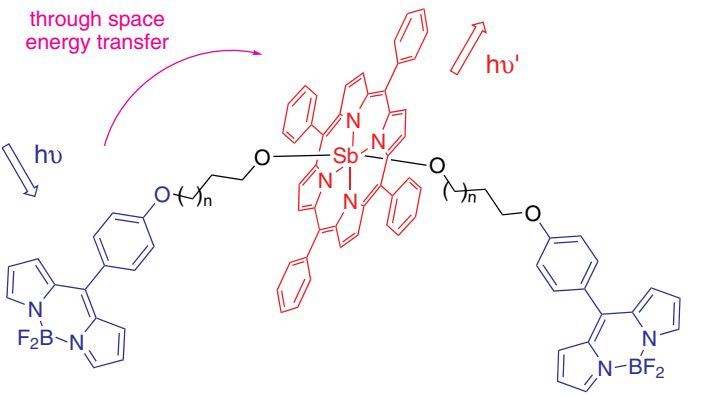
through space
energy transfer
hυ'
hυ
Sb
O
n
N
F2B
N–BF2

181

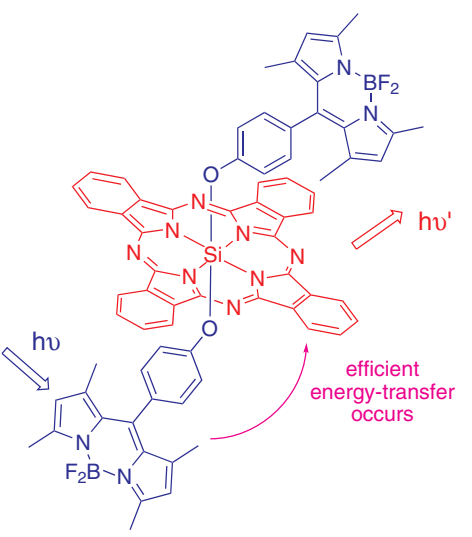
BF2
Si
O
hυ'
hυ
efficient
energy-transfer
occurs
F2B

182

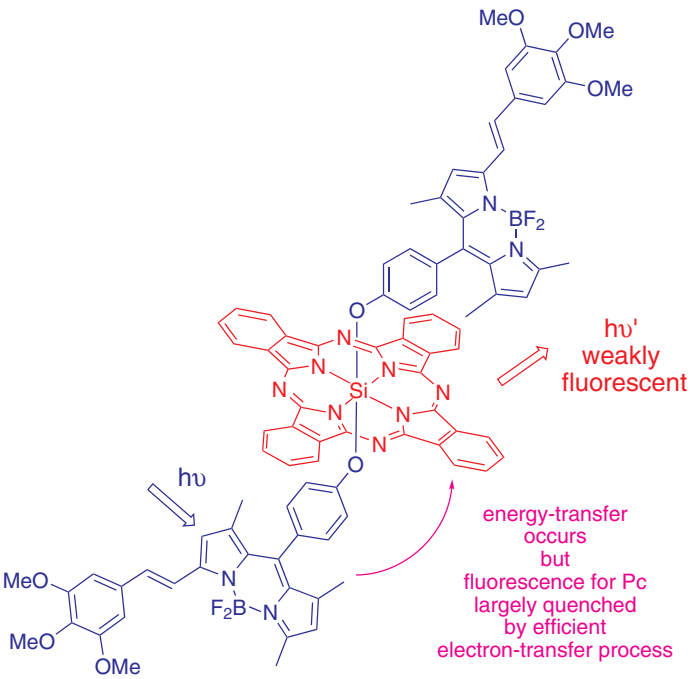

183

at 480 nm, efficient photoinduced energy-transfer (Φ_{ENT} 57%) from the excited BODIPY units to the phthalocyanine (Pc) core was observed for **182**. When the triad **182** was excited directly at the Pc core (615 nm), a strong emission band at 686 nm was observed suggesting that electron-transfer was not taking place to quench the excited Pc. The fluorescence quantum yield of the Pc emission was however significantly lower upon excitation at 480 nm relative to direct excitation of the Pc (Φ = 0.35 vs. 0.60). Surprisingly, upon excitation of the mono-styryl BODIPY units (530 nm) in **183**, a very weak emission band at 686 nm characteristic of the Pc core was observed, and the emission at 580 nm from the BODIPY moieties was also greatly reduced (Φ 0.003 vs. 0.78). This suggests that excitation energy transfer occurred from the initially excited mono-styryl BODIPY units to the Pc core, but, the fluorescence emission of the Pc is largely quenched, probably by an efficient electron-transfer process.

System **184** is another artificial light harvesting system with BODIPY dye donors, but here the energy is transferred to a zinc porphyrin (ZnP), then electron transfer occurs to a fullerene (C_{60}-Im) unit; thus the molecule was called a "supramolecular triad". The Zn-porphyrin connects to the fullerene component via metal to axial-ligand coordination. Both steps in the process were efficient.

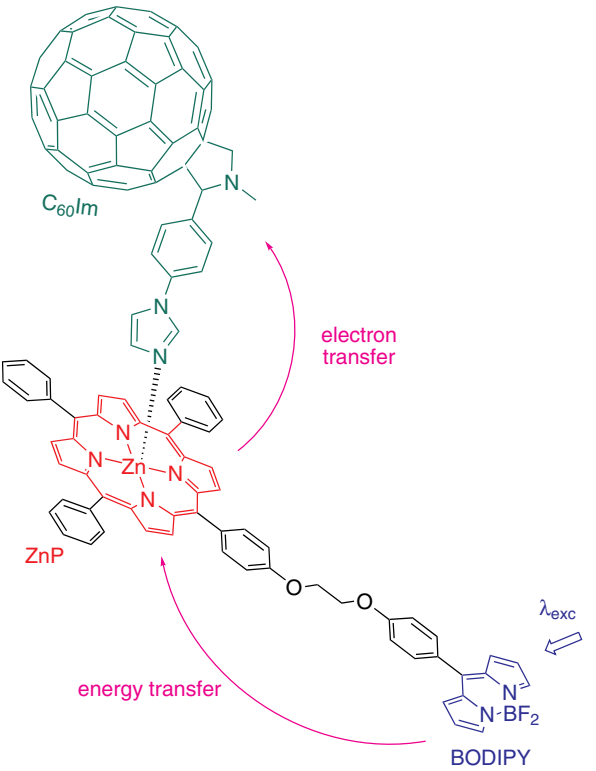

184

Overall, the system was said to mimic the "combined antenna-reaction center" in natural photosynthesis.[178]

Like **178**–**184**, complex **185** also features a donor and an acceptor system linked via axial coordination to a zinc porphyrin.[179] This self-assembling system is based on the exceptional affinity of phenanthroline-strapped zinc porphyrins for *N*-unsubstituted imidazoles.[180,181] Efficient net energy transfer (80%) was observed for excitation of the BODIPY at 495 nm and emission at the free porphyrin. Energy transfer from the excited ZnP-Im complex to the free porphyrin was calculated to be 85%.

Compound **186** was designed to be a molecular switch. It has two stable conformations governed by the bridged resorcin(4)arene scaffold.[182] In the absence of protons (or perhaps other guest cations) the molecule exists in a contracted geometry maximizing FRET (fluorescence resonance energy transfer) between the two BODIPY based probes. Decreased pH values switch the molecule to the expanded conformation and this is evident by the reduced energy transfer. An advantage of using BODIPY dyes in this study is their low sensitivity to pH changes.

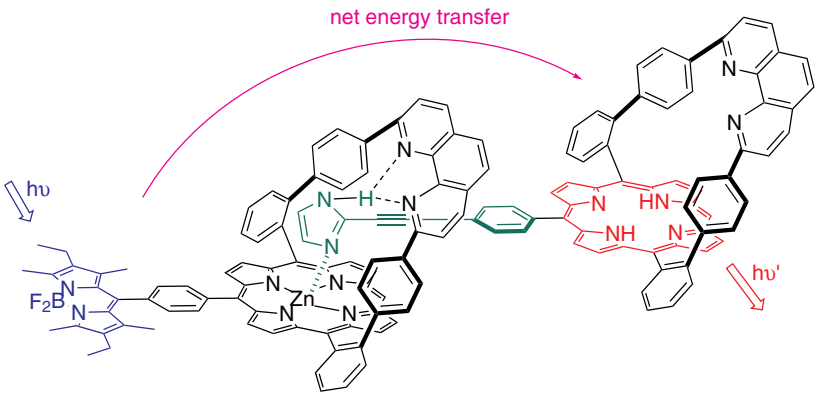

185

The UV spectrum of **186** displays three strong absorption bands assigned to the spacer (λ_{max} 332 nm), the donor (λ_{max} 529 nm) and the acceptor dye (λ_{max} 619 nm), respectively. Upon excitation at 490 nm, two emission bands at 542 nm (donor dye) and 630 nm (acceptor dye) are observed, in a ratio of the donor/acceptor fluorescence intensity of 45:55, indicating low FRET efficiency (possibly due to unfavorable orientations of the transition dipole moments, and/or to the dynamic behavior of the cavitand part). Upon addition of TFA, the emission from the acceptor is nearly completely quenched, whereas the donor fluorescence intensity doubles.

B. Through-Bond Energy Transfer Cassettes

1. *Porphyrin-Based Systems as Models of Photosynthesis*

The prevalent mechanism of through-space energy transfer in most cassettes is likely to be via dipolar couplings, i.e. Förster energy transfer. The rate and efficiency of this is governed by, among other things, the overlap integral between the donor fluorescence and the acceptor absorbance.

If the donor and acceptor dyes are coupled to each other via a conjugated but twisted π-system then the prevalent mechanism of energy transfer is likely to be through bonds. Constraints on through-bond energy transfer are not well understood, but it appears there is no requirement for a good overlap integral. This is important in the design of fluorescent cassettes because, if this is true, there is no obvious limitation on the energy gap between the donor fluorescence and the acceptor absorbance, hence cassettes with huge "apparent Stokes' shifts" could be produced.

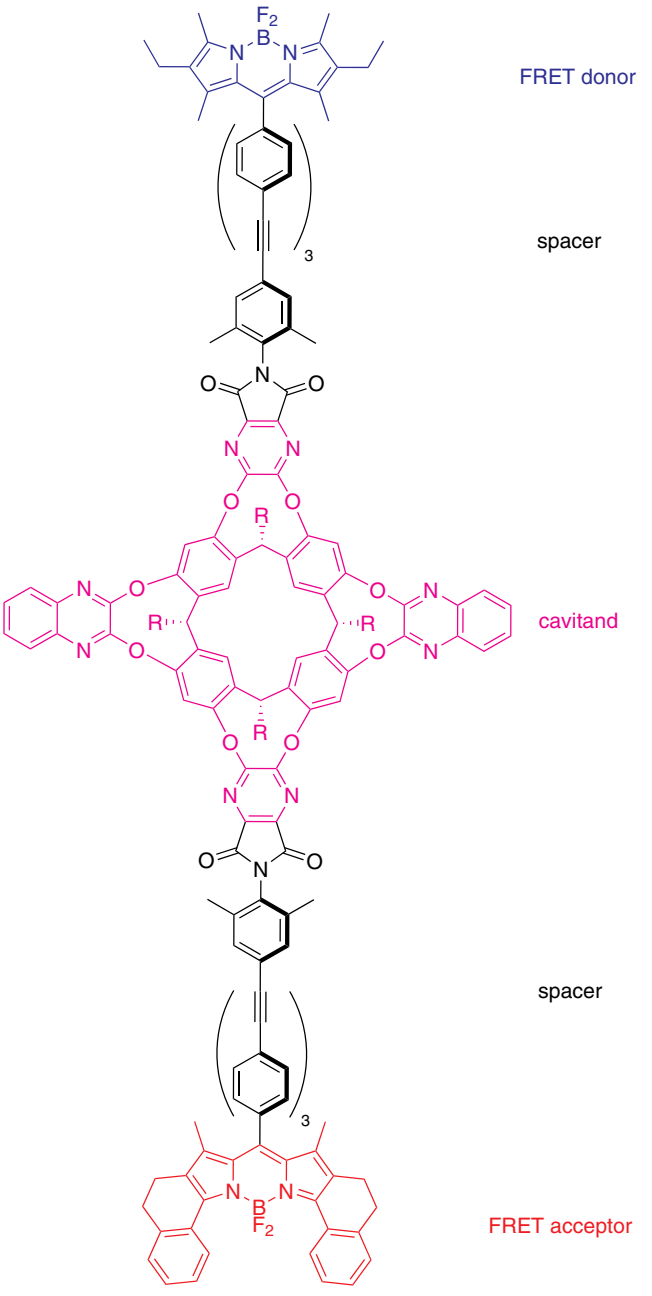

186
R = *n*-C_6H_{13}

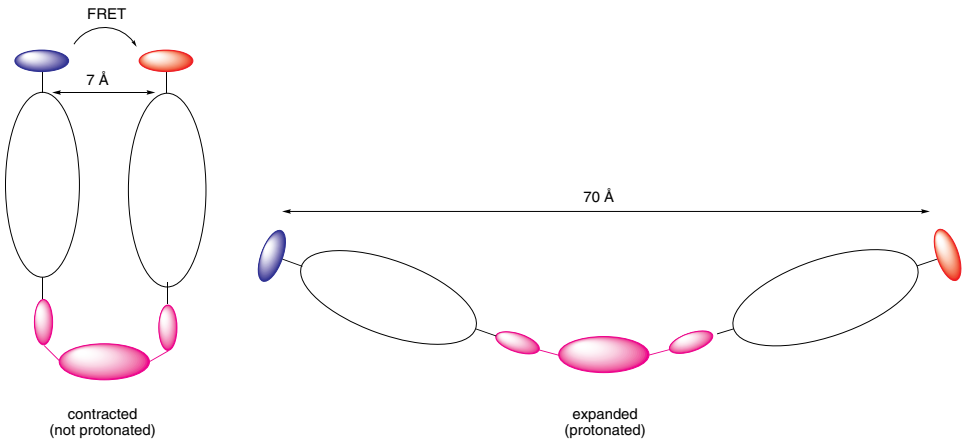

A pioneer of energy transfer systems featuring BODIPY donors was Lindsey who studied them in the context model porphyrin-based systems for photosynthesis.[183] He proposed that the rates and efficiencies of through-bond energy transfer are influenced by:

- steric interactions between the donor/acceptor wherein increased torsional constraints decrease rates and efficiencies of energy transfer;
- frontier orbital characteristics for the HOMO and LUMO; and, related to that,
- the site of attachment of the donor/acceptor to the linker and the nature of the linker.

Lindsey has described the through-bond energy transfer cassette **187** as a "linear molecular photonic wire". It features a BODIPY donor and a free base porphyrin acceptor. This donor-acceptor pair is separated by 90 Å. Efficient energy transfer (76%) from the donor to the acceptor was observed upon excitation at 485 nm (i.e., the donor $\lambda_{max\ abs}$).[184]

Systems **188** and **189** were described as "molecular optoelectronic linear- and T-gates", respectively. In these cassettes, the emission of the acceptor can be turned

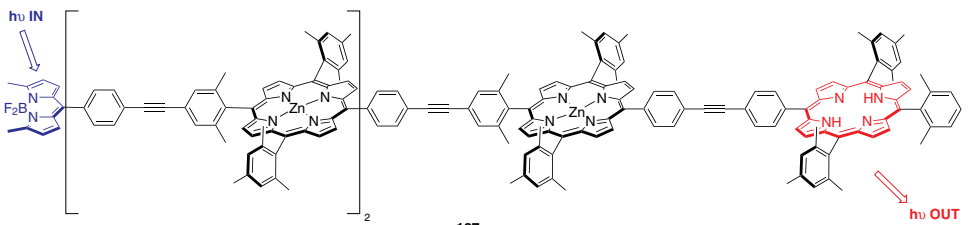

187

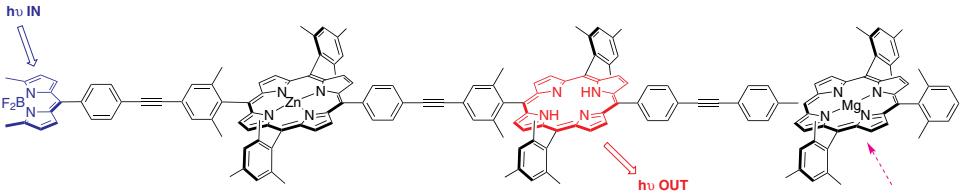

188

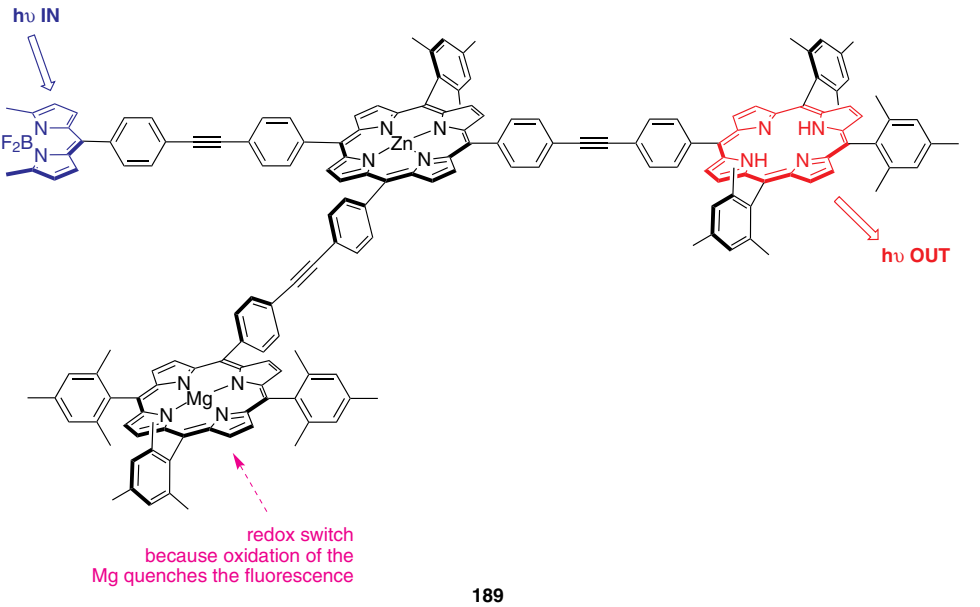

189

on or off via reduction or oxidation of the attached magnesioporphyrin; the latter in its oxidized state quenches fluorescence via ICT. For each cassette more than 80% of energy transfer was observed upon excitation of the BODIPY donor part.[185]

Compounds **190–193** are light-harvesting arrays featuring one, two, or eight BODIPY donors and one porphyrin acceptor. Increasing the number of BODIPY

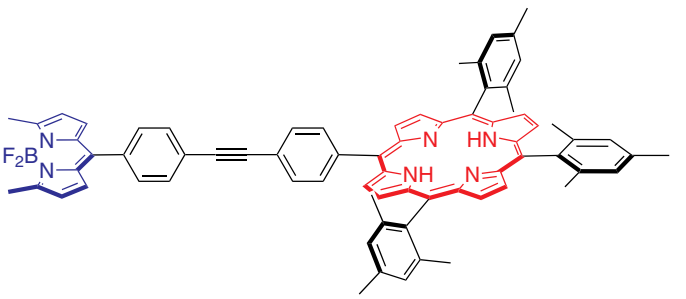

190

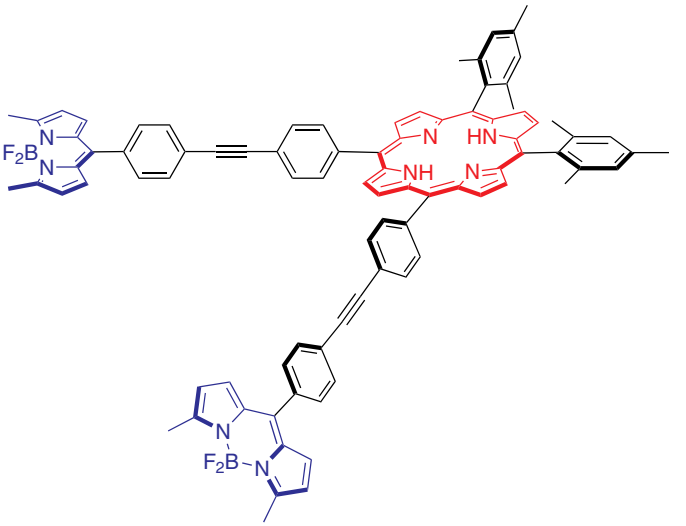

191

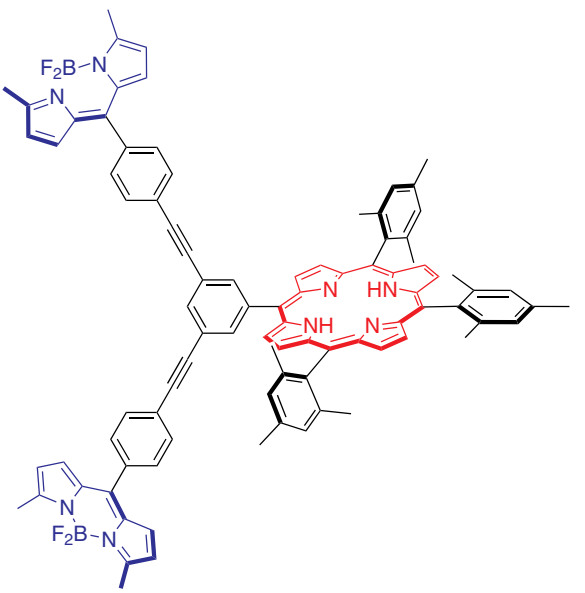

192

donors from one to eight only increases the relative absorption at 516 nm from 68 to 94% (of a BODIPY standard) for the free base porphyrins **190–193**, and from 91 to 99% for the Zn-porphyrin (not shown). Near quantitative energy transfer was observed for the systems containing one or two BODIPY units, but 80–90% energy transfer was observed for the system bearing eight BODIPY units.[186]

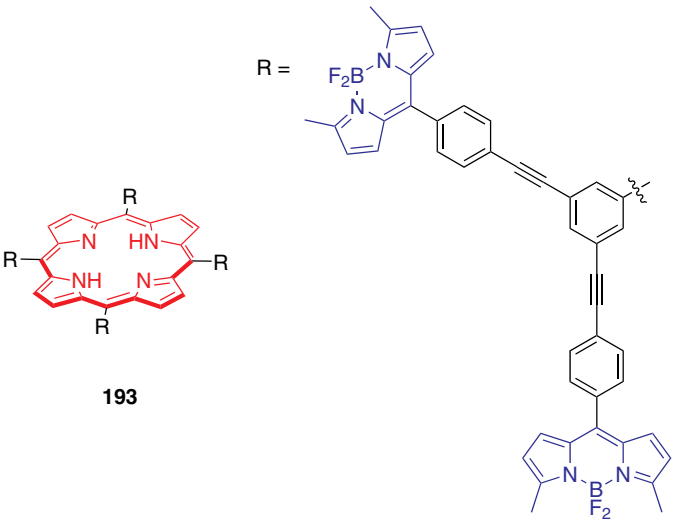

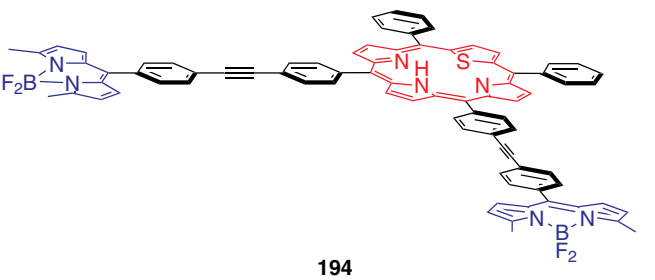

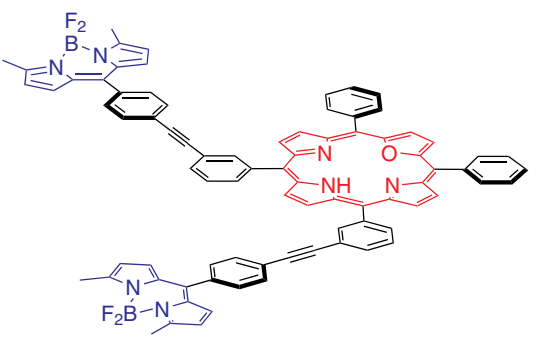

Cassettes **194** and **195** were synthesized from the corresponding thia- and oxo-porphyrins by Sonogashira couplings with 8-(4-iodophenyl)-BODIPY. Excitation of the BODIPY part at 485 nm gave weak emission from the BODIPY core and strong emissions from the porphyrin units, suggesting efficient energy

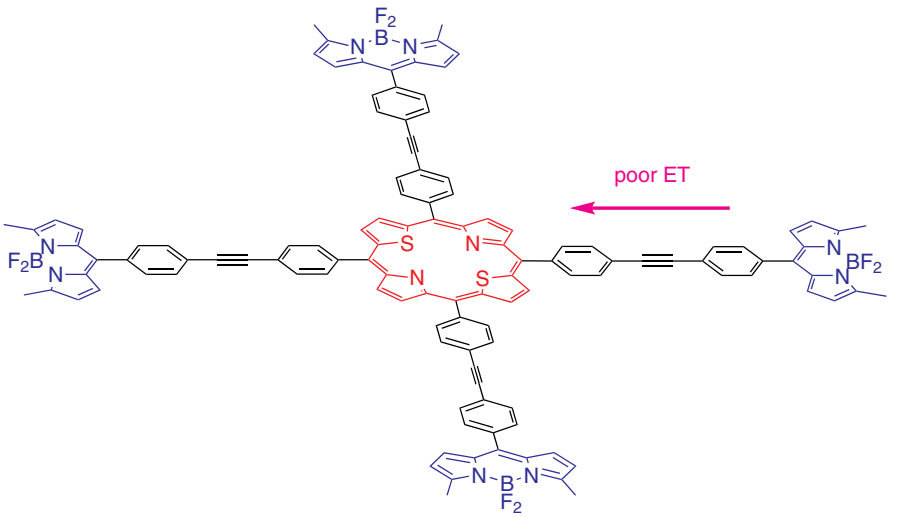

196

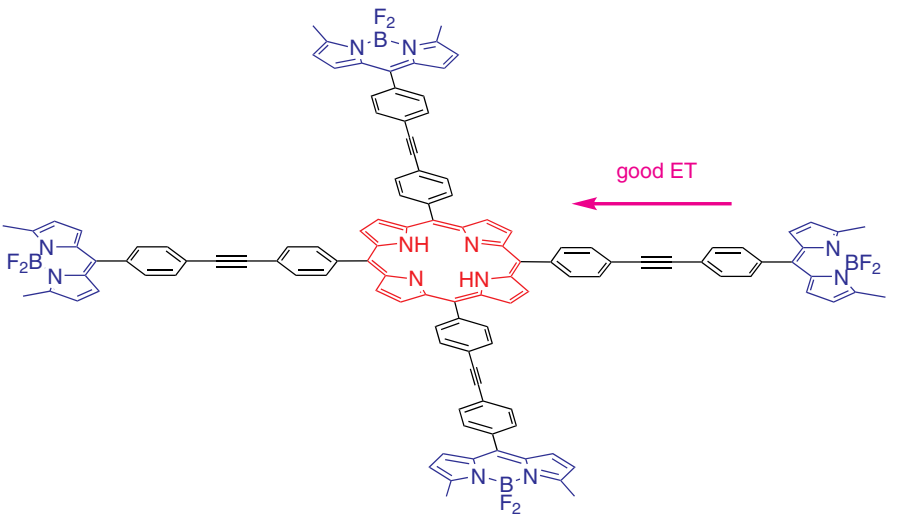

197

transfer. Direct comparison of the efficiencies of energy transfer is difficult because the separations and orientations of the donor and acceptor fragments are different.[187,188] Interestingly, the analogous system with two sulfurs, **196**, gave poor energy transfer (~ 11%) upon excitation at 485 nm,[189] whereas **197** which has a normal porphyrin core gave 97% energy transfer.[190]

2. *Polypyridine Complexes Containing Accessory BODIPY Chromophores*

The dual-dye systems **198**–**205** featuring one or more BODIPY chromophores and a Ru(II) polypyridine complex have been synthesized as models for solar energy conversion and storage. The BODIPY chromophore was chosen for its strong fluorescence, whereas the Ru(II) polypyridine complex was chosen for its relatively intense and long-lived triplet metal-to-ligand charge transfer (MLCT) emission.

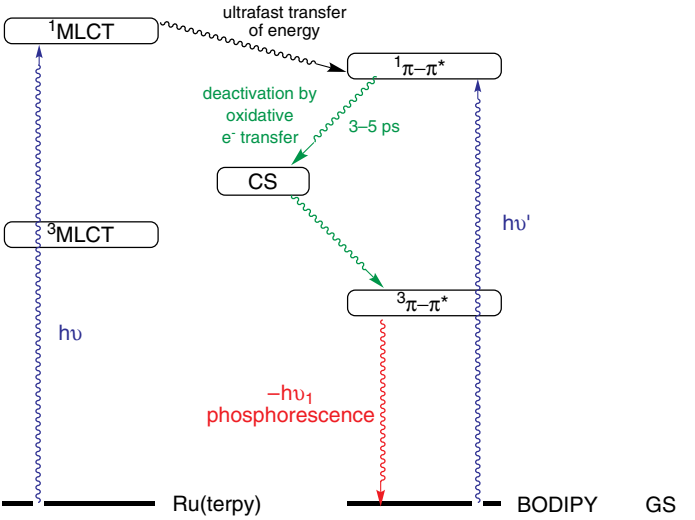

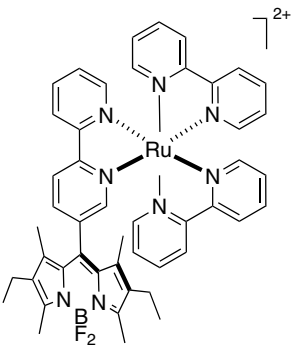

198

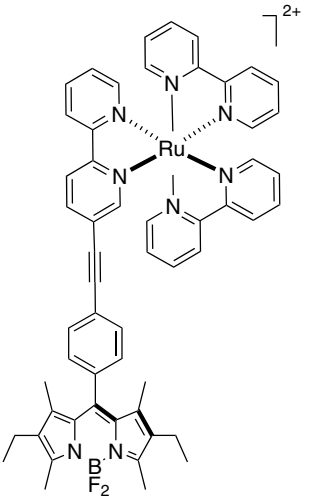

199

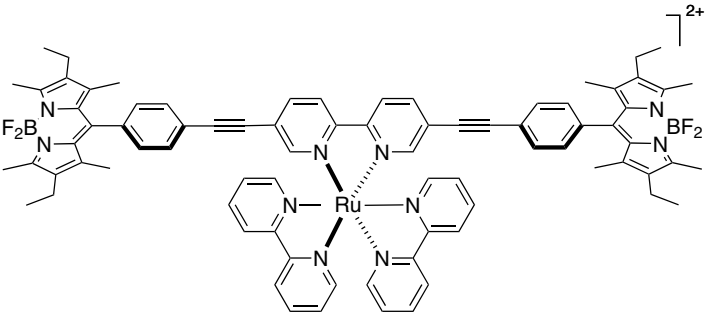

200

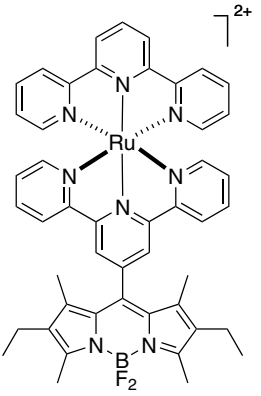

201

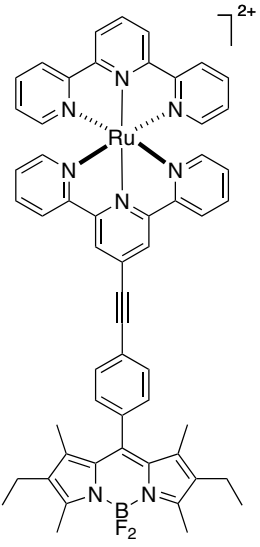

202

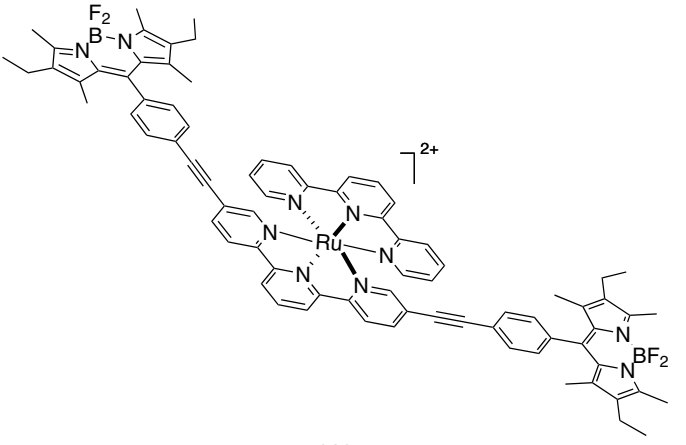

203

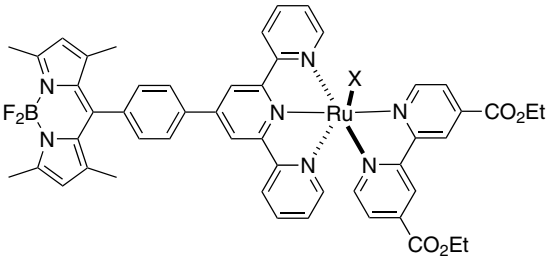

204 X = Cl
205 X = NCS

The pyridine based BODIPY dyes were synthesized by condensation of formylpyridine with 3-ethyl-2,4-dimethylpyrrole.[191–194] The new compounds exhibit intense absorption in the visible region, with a major sharp band at 523 nm (acetonitrile solution) assigned to the π–π^* transition for the dipyrromethene dye and a broader band of lower intensity between 450 and 500 nm. The free ligands are strongly fluorescent both in solution at room temperature and at 77 K in a rigid matrix, but no luminescence could be observed in solution for the Ru complexes, independently of the excitation wavelength. Nanosecond transient absorption spectra, however, revealed a relatively long-lived (ms time scale) excited state for all metal complexes. The latter was identified as the BODIPY-based triplet state, and is believed to be formed through a charge-separated level from the BODIPY-based $^1\pi$–π^* state. At 77 K, all the complexes studied except for **198**, exhibit the BODIPY-based fluorescence, although with a slightly shortened lifetime compared to the free ligands. However, the surprising finding was that **201**–**203** also exhibit a phosphorescence signal assigned to the BODIPY subunits (emission at 774 nm of 50 ms lifetime). This is the first report of phosphorescence for BODIPY based dyes. The authors propose that the phosphorescence is due to the presence of the heavy ruthenium metal, which facilitated intensity to be diverted into the BODIPY $^3\pi$–π^* state from the closely lying metal-based ^{3}MLCT level (for which luminescence decay is highly efficient at 77 K).[192,195,196] Phosphorescence from BODIPY units is certainly unusual. It only was observed here at 77 K for a system coupled with a ruthenium complex, and the efficiency of the process was not determined.

Compounds **204** and **205** combine ruthenium polypyridine units with BODIPY fragments. The BODIPY part ensures a high molar absorption coefficient of the system in the metal-to-ligand charge-transfer region (around 500 nm). The singlet excited states of **204** and **205** are strongly quenched by the presence of ruthenium: energy transfers to the Ru center with high efficiency (93% and 73% for **204** and **205**, respectively), where it is then dissipated via electron transfer and/or singlet to triplet intersystem crossing. The net effect of this arrangement is that these complexes are not fluorescent.[197]

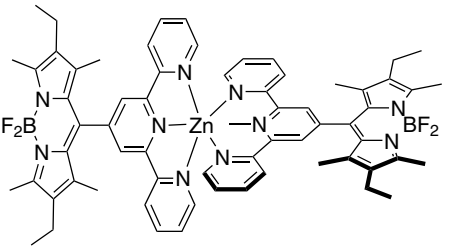

206

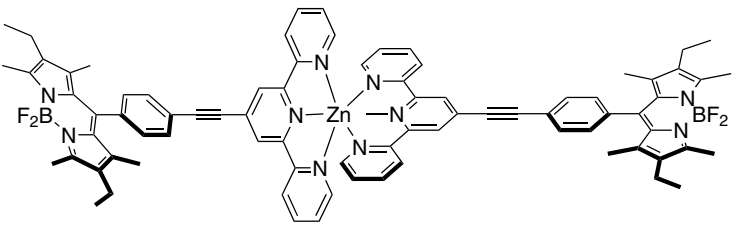

207

Loss of fluorescence when BODIPY dyes are conjugated with metal complexes is common. For instance complexes **206** and **207** have greatly reduced fluorescence relative to the free ligands,[193,194] presumably due to intramolecular electron transfer.[193,198]

Other complexes, e.g. of platinum,[199] containing BODIPY-based ligands have been prepared, but without comment on their fluorescent properties. It is unlikely that such materials will be useful as probes.

3. *Relatively Compact Systems as Potential Probes in Biotechnology*

Porphyrin-based cassettes tend to be larger than is ideal for applications relating to labeling of biomolecules, but the through-bond energy transfer aspect could be useful for applications wherein one source is used and several different outputs must be observed simultaneously. Thus, there has been interest in making smaller through-bond energy transfer cassettes.

BODIPY-based cassettes featuring simple aromatic donors can be prepared from halogenated BODIPYs, e.g. **208** via palladium-mediated cross-coupling reactions.[200] Monoiodinated products can be quite useful for such syntheses. For instance, Chart 29 shows a typical stepwise BODIPY synthesis that was used for this.[200]

Fluorescence quantum yields of compounds **209–212** excited at the donor λ_{max} range from 0.02 to 0.75 (in chloroform). $S_1 \leftrightarrow S_0$ Transition moments of the two chromophores components for compound **213** are mutually perpendicular in all

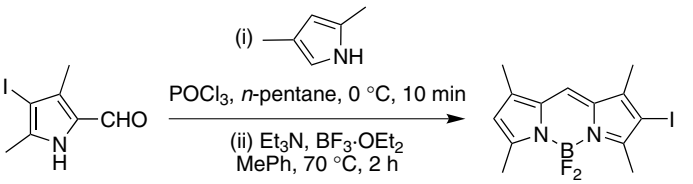

208 36%

Chart 29.

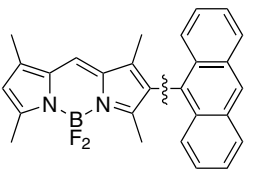

209

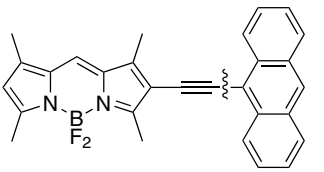

210

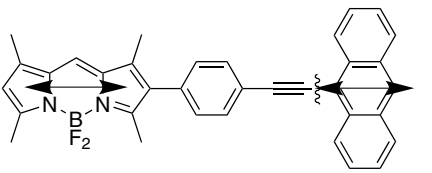

211

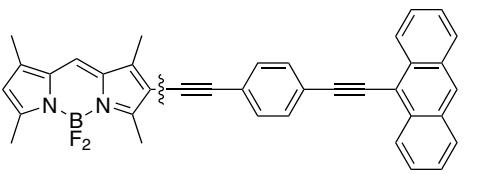

212

conformations. Fast energy transfer, of the order of 0.45 ± 0.08 ps, was observed for this compound. For **209**–**212**, the donor and acceptor $S_1 \leftrightarrow S_0$ transition moments are mutually coaxial with the linker in all conformations. The transfer rate for this set of compounds was *even faster* than for **213**, ~ 200 fs; in fact, this was too fast to be measured accurately.[201] Thus, it appears from this data that parallel and aligned transition moments are ideal for extremely fast energy transfer. The length of the linker in this series of compounds was also varied but not enough derivatives were made to arrive at conclusions relating this parameter with energy-transfer rates.

More recently, energy transfer cassettes like **213** have been prepared; these are similar except that the *meso*-donor group is one or two pyrene units linked with

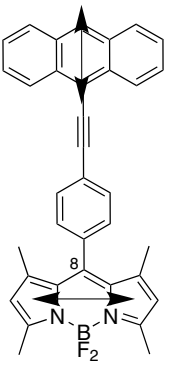

213

alkynes. It was shown that the energy transfer efficiency is reduced when alkyne units are added. Of course, use of conjugated pyrenes as the donor increases the UV absorption at shorter wavelengths and the λ_{max} for that donor-based band; the latter effect decreases the apparent Stokes' shift observed.[202]

Energy transfer cassettes like **214**–**216**, in which two BODIPY chromophores are linked via an acetylenic linker, have been prepared.[182] As the length of the linker increases, energy transfer efficiency decreases from about 98% to ~ 35%. These were described as FRET cassettes, but there is a strong possibility that some of the energy transfer takes place through bonds.

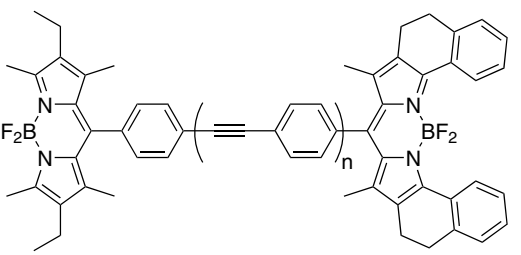

214–216
n = 1, 3, and 6 respectively

Compound **217** represents a novel star-shaped supramolecular multichromophoric system containing three different BODIPY dyes triangularly arranged around a truxene core.[203] The three BODIPY subunits used absorb at different wavelengths, allowing **217** to absorb a large fraction of UV and visible radiation. System **217** was prepared via Sonogashira couplings between the tri-iodo truxene and the corresponding ethynyl BODIPYs. At any excitation wavelength, the emission spectrum of **217** is dominated by a band at 767 nm, indicating that highly efficient and fast energy transfer processes occur within **217**. It is thought that both Dexter-type (from the truxene core to the peripheral BODIPYs) and Förster-type (between the peripheral BODIPYs subunits) mechanisms likely contribute to the overall energy transfer process.

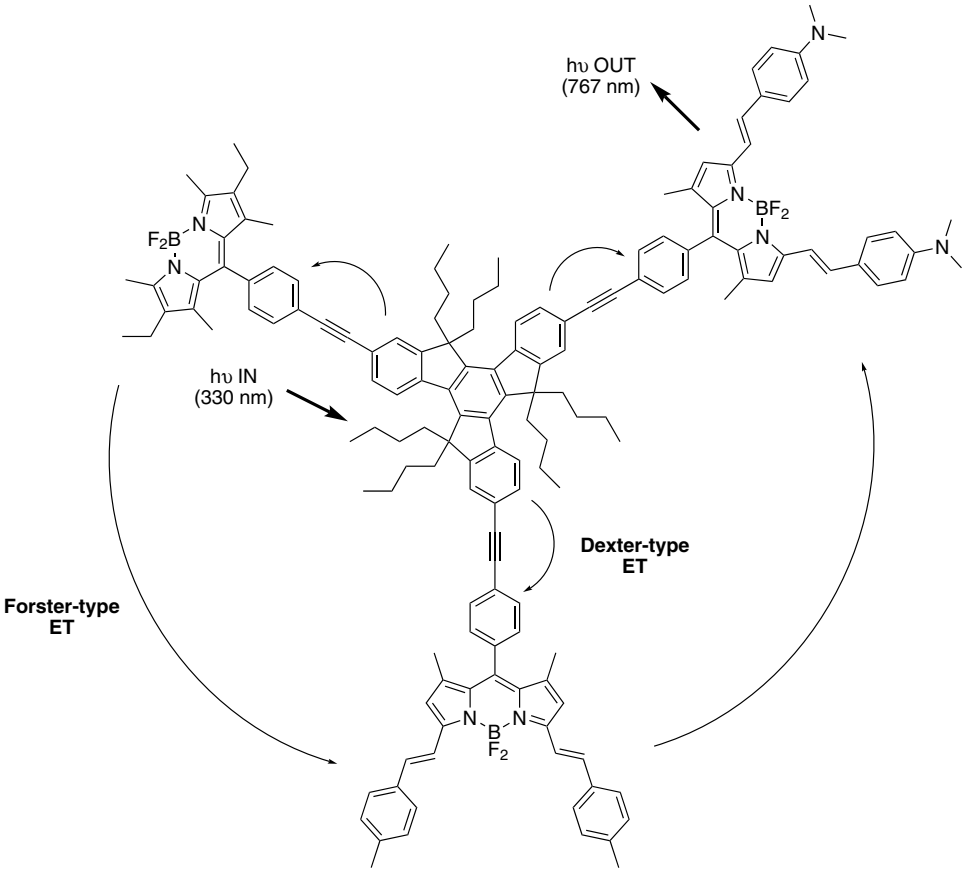

217

The oligothiophene-BODIPY-based donor–acceptor system **218** represents the first example of light-harvesting systems combining BODIPY and thiophenes. Efficient energy transfer was observed from the quaterthiophene to the BODIPY.[204]

A restriction of FRET in observation of protein-protein interactions is that the emission from the donor must overlap with the absorbance of the acceptor. Compounds **209–218** are examples of "through-bond" energy transfer (TBET) cassettes in which the donor relays energy to an acceptor (or more) via twisted π-electron systems. However, these systems are very hydrophobic and have no handle to allow conjugation to biomolecules. *Water-soluble* probes **219–222** were recently reported by Burgess and coworkers.[172,205,206] These TBET cassettes were assembled via Pd-mediated cross coupling (**220**) or via copper-mediated alkyne/azide cycloadditions (**219** and **221–222**). Energy transfer in **220** is highly pH dependent. At pH < 6.0, energy transfer from the donor to the acceptor occurs efficiently and emission at around 600 nm i.e. from the acceptor is observed. In the phenolate form i.e. pH > 8.5, minimal energy transfer occurs and emission at

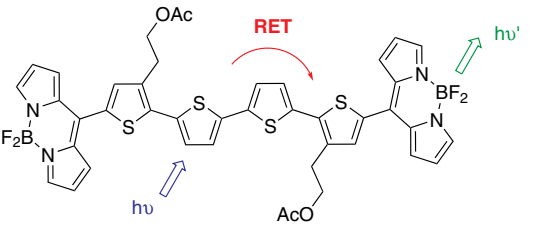

218

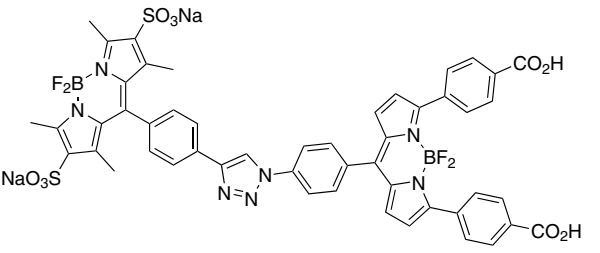

219

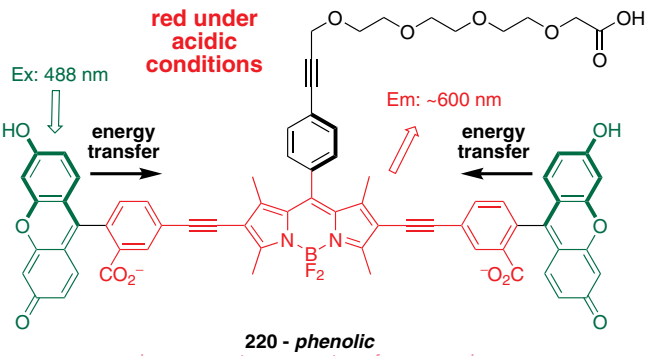

220 - *phenolic*
donor acceptor energy transfer occurs in
phenolic form pH < 6.0

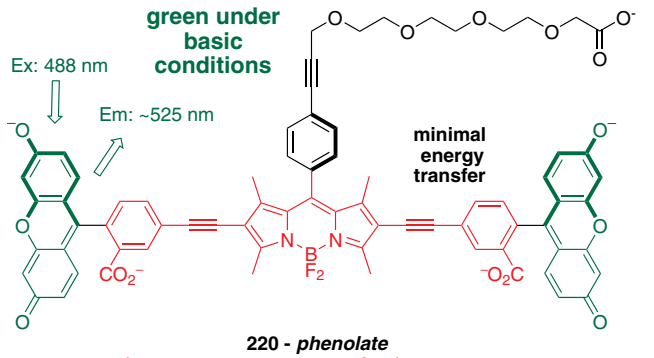

220 - *phenolate*
donor acceptor energy transfer does not occur
for the phenolate pH > 6.5

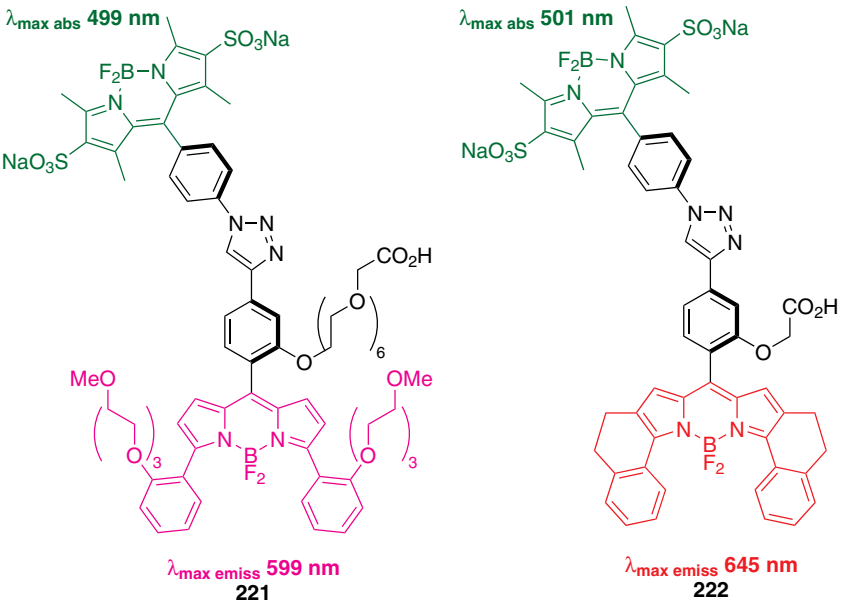

around 525 nm (from the donor) is observed. Thus, this probe is a potentially useful ratiometric pH reporter. Indeed, **220**-BSA conjugate was synthesized and imported inside COS7 cells at 37 or 4 °C via Pep-1[207,208] to measure the pH of the endosomes and cytosol. The pH values of endosomes and cytosol, obtained from

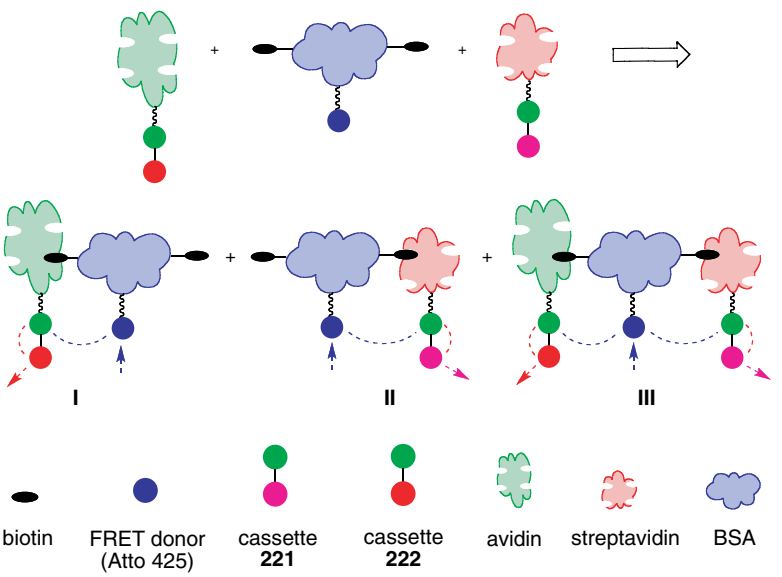

Figure 10. Protein–protein interactions can be monitored with through-bond energy transfer cassettes.

the red/green ratio, were 5.4 and 7.2, respectively; these data are consistent with those expected for such intracellular regions.

Cassettes **221** and **222** possess the same donor and differ only from their acceptor parts (**221** emits at ~ 600 nm, while **222** fluoresce at ~ 645 nm). These probes were used to monitor three-component interactions (via FRET and TBET) as illustrated in Figure 10. A FRET donor (Atto425 attached to BSA-biotin) was mixed with **221**-streptavidin and **222**-avidin conjugates, and the interactions between (strept)avidin and biotin were monitored by observing emissions from **221** and **222** upon excitation at 458 nm.[206] These cassettes allow increased dispersion of fluorescence emissions from a single excitation source.

VIII. BODIPY-Based Polymers

A. Poly(aryleneethynylene)s (PAEs) Co-Containing BODIPY (2,6-Positions)

Organic materials with large and fast nonlinear optical responses are promising for nonlinear devices. One parameter, two-photon absorption (TPA) is a very important third-order nonlinear optic (NLO) effect. Materials with large TPA cross-section are in great demand. In the last decade, many strategies have been developed to design molecules with large TPA cross-section, and it has been shown that conjugation length, molecular symmetry, strength of donor/acceptor groups, and molecular planarity affect TPA cross-section.[209,210]

Polymers **223**–**226** were synthesized under standard Sonogashira cross coupling conditions between the 2,6-diiodoBODIPY and the corresponding arylethynes, and their third-order nonlinear optical properties were studied.[211] The third-order nonlinear properties of these polymers increased with increasing amounts of BODIPY component, i.e. **223** exhibited the largest nonlinear absorption coefficient (β) and effective nonlinear refractive index (η). This indicates that the enhancement of third-order nonlinear optical response in the copolymers is not influenced by the conjugated phenylene motif, but is controlled mainly by the BODIPY component.

Akkaya and coworkers have reported the synthesis of the BODIPY oligomer **227** (via iterative Sonogashira coupling).[212] Decyloxy chains were incorporated on the *meso*-phenyl group of the parent BODIPY dye to keep the oligomer soluble as the chain was extended. As the number, n, of repeating units increases, both the absorption and emission maxima are red-shifted. These bright oligomers can be further elaborated by electrophilic aromatic substitution of the pyrrole moieties of the terminal BODIPYs.

The fluorescent conjugated copolymers **228a**–**c** were prepared by Pd catalyzed Suzuki polymerization of 9,9-dihexylfluorene-2,7-diboronic acid with each of three different 2,6-diiodo-substituted BODIPY monomers.[213] The copolymers absorb between 547–557 nm, and emit brightly (with quantum yield up to 0.85) between

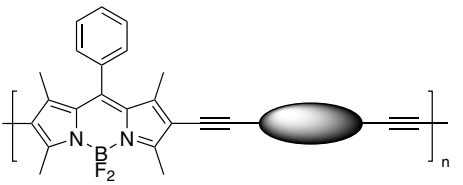

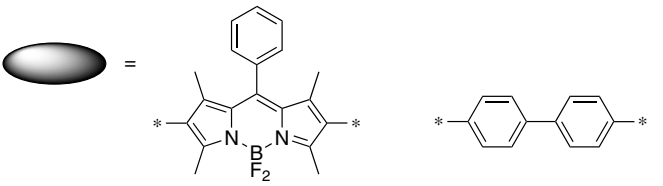

223 **224**

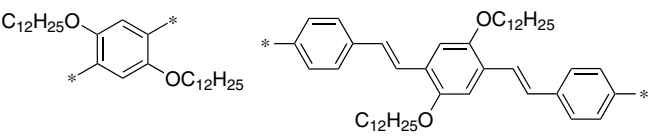

225 **226**

	M_w	PDI	$\lambda_{max\ abs}$	$\lambda_{max\ emiss}$	Φ	$\eta_2 \times 10^{-11}$	$\beta \times 10^{-12}$	BODIPY (%)
223	2134	1.27	640	661	0.24	5.91	200	100
224	7232	1.65	633	664	0.08	2.16	164	61.1
225	9612	1.61	571	615	0.24	4.37	84	40.6
226	5561	1.62	575	637	0.25	-	-	32.6

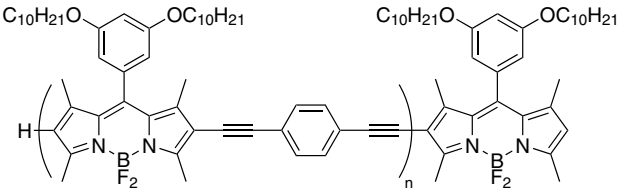

227 n = 0-4

n	$\lambda_{max\ abs}$ ($CHCl_3$)	ε	$\lambda_{max\ emiss}$	Φ
1	551	95 000	586	0.39
2	579	69 000	621	0.45
3	597	118 000	624	0.60
4	592	251 000	620	0.58

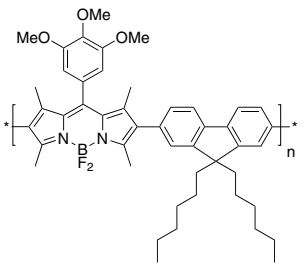

228a 69%
M_n: 22 500 g/mol
CH_2Cl_2, Φ 0.64
$\lambda_{max\ abs}$ 557 nm
$\lambda_{max\ emiss}$ 587 nm

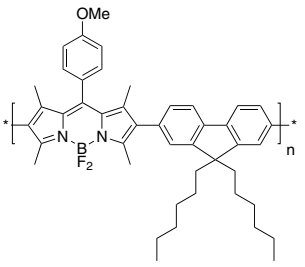

228b 54%
M_n: 19 100 g/mol
CH_2Cl_2, Φ 0.56
$\lambda_{max\ abs}$ 547 nm
$\lambda_{max\ emiss}$ 585 nm

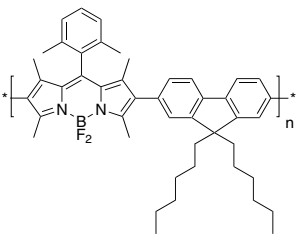

228c 52%
M_n: 18 400 g/mol
CH_2Cl_2, Φ 0.85
$\lambda_{max\ abs}$ 549 nm
$\lambda_{max\ emiss}$ 588 nm

585–588 nm. Furthermore, no fluorescence from the fluorene moiety was observed in the copolymers, indicating efficient photoinduced energy transfer from the fluorene to the BODIPY. In addition, the copolymers display sensitive (and selective) fluorescent responses to fluoride and cyanide anions. Titration with chloride, bromide and iodide anions did not result in significant quenching of the fluorescence.

Polymer **231** was synthesized by electropolymerization of the 2.6-bis(thienyl) BODIPY **229** and compound **230** (3,4-ethyl-enedioxythiophene; EDOT) (Chart 30).[214] Polymer **231** represents a highly stable, environmentally robust electroactive material with well-defined quasi-reversible redox couple, and fast response time

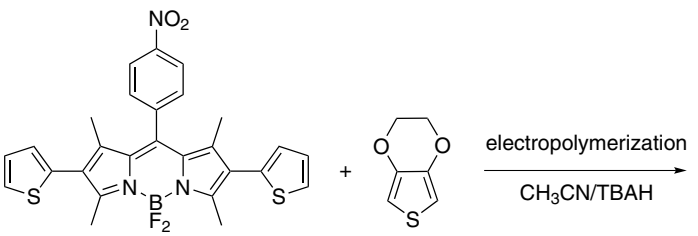

229 **230**

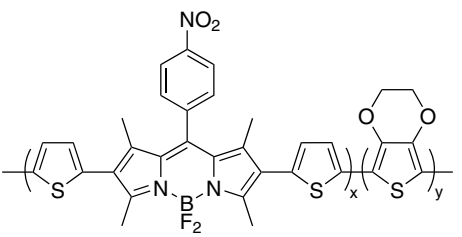

231

Chart 30.

between redox states as well as high coloration efficiency. In addition, the copolymer film exhibited different electrochromic behavior, which can be adjusted by changing the polymerization potential.

B. BODIPY-Based Organoboron Polymer

Based on the work by Ziessel and coworkers, [215–217] Nagai and coworkers prepared the polymers **233 a–c** from monomer **232** via Sonogashira-Hagihara coupling.[218] The latter was prepared from the corresponding BODIPY and Grignard derivative. The Sonogashira-Hagihara coupling reaction of **232** with diynes proceeds via *p*-phenylene-ethynylene formation under mild conditions (Chart 31).

These new BODIPY-based poly(*p*-phenylene-ethynylene)s are highly luminescent and they can form particular or fibrillar nanostructures due to their rod-coil type structure; i.e. the rod and coil segments are a rigid π-conjugated polymer main chain and decyl group, respectively. Scanning electron microscopy (SEM) of

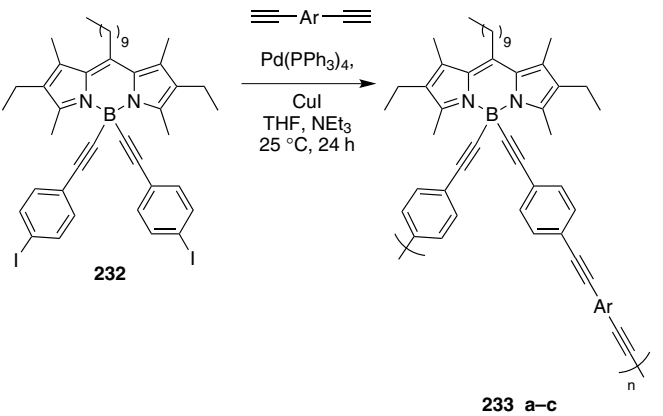

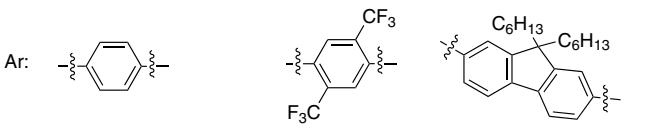

a	**b**	**c**
M_n 30700	M_n 22600	M_n 11300
nm-sized particles and	predominant particles	particles only,
µm-sized fiber-like structures	few fiber-like structures	no fibers
$CHCl_3$, Φ 0.80	$CHCl_3$, Φ 0.71	$CHCl_3$, Φ 0.85
$\lambda_{max\ abs}$ 519 nm	$\lambda_{max\ abs}$ 519 nm	$\lambda_{max\ abs}$ 519 nm
ε 189 000 M^{-1} cm^{-1}	ε 125 000 M^{-1} cm^{-1}	ε 148 000 M^{-1} cm^{-1}
$\lambda_{max\ emiss}$ 532 nm	$\lambda_{max\ emiss}$ 532 nm	$\lambda_{max\ emiss}$ 532 nm

Chart 31.

polymer **233a** revealed nm-sized particles and μm-sized fiber like structures, formed from aggregation of each particle. These fiber-like structures were less in **233b** and not observed in **233c**, suggesting that these architectures result from the steric factor of the substituents in the comonomer units. All polymers showed absorption maxima around 519 nm and emission brightly at around 532 nm.

IX. Substitution of Fluoride Atoms in the BF_2-Group

A. With Alkyl Groups

Some dialkyl-*B* BODIPY compounds have been prepared via reactions of the corresponding dipyrromethenes with bromodimethylborane, dibutylboron triflate, or 9-BBN triflate. Increased steric bulk at the boron atom along this series correlated with *decreased* fluorescence quantum yields. While the substituent at the *meso* position has no effect on the UV absorption and emission spectra, the fluorescence quantum yields strongly depend on the nature of the aryl group. Introduction of steric constraints on the aryl ring increases the quantum yield (compare **234** and **237**, **235** and **238**).[219]

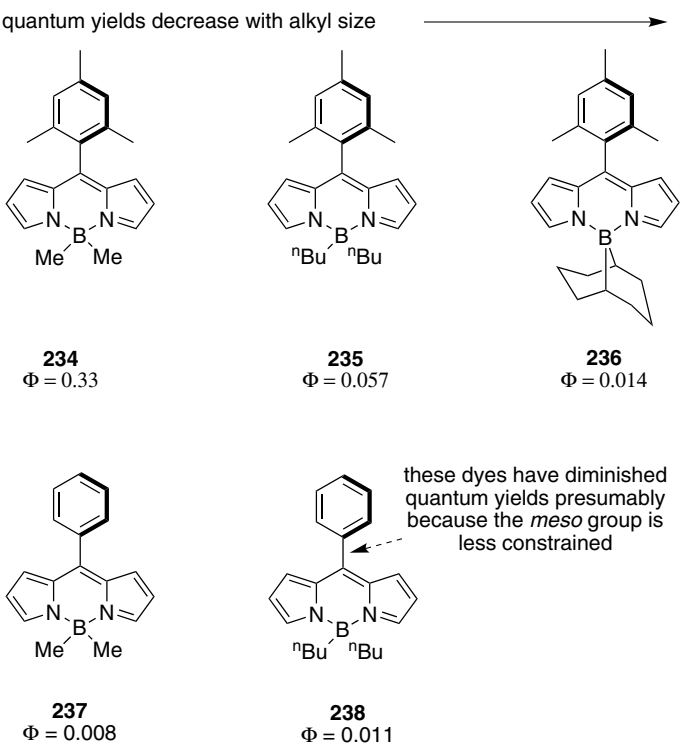

234 $\Phi = 0.33$

235 $\Phi = 0.057$

236 $\Phi = 0.014$

237 $\Phi = 0.008$

238 $\Phi = 0.011$

B. With Aryl Groups

Aryl Grignards can displace fluoride from the boron difluoride entity of BODIPY dyes. In Scheme 11a, at 0 °C, even with excess Grignard reagent, only the monosubstituted products **239** and **240** were obtained, but the disubstituted product **241** was formed by adding the Grignard reagent at room temperature. Reaction of aryl lithium reagents was much faster; these gave only the disubstituted products **242**–**244**, even when just one equivalent of anion was added (Scheme 11b).

The new dyes **239**–**244** are highly fluorescent in solution. While the absorption maximum of the BF_2 parent dye is relatively insensitive to the solvent polarity, the *B*-Ar BODIPYs tend to undergo small red-shifts in more polar solvents. The fluorescence emission maxima of **239**–**244** are also red-shifted relative to the parent BF_2 structures. Compared to the BF_2 parent dye, the Stokes' shift for the *B*-Ar derivatives **239**–**244** is also larger, and sensitive to the size of the aryl substituent. While the fluorescence quantum yield of the BF_2 parent dye is insensitive to the solvent polarity, a modest decrease is observed for **239**–**244** in more polar solvents like ethanol or acetonitrile. In these latter solvents, an increase in the rate of nonradiative decay for the *B*-Ar derivatives is observed. The origin of this

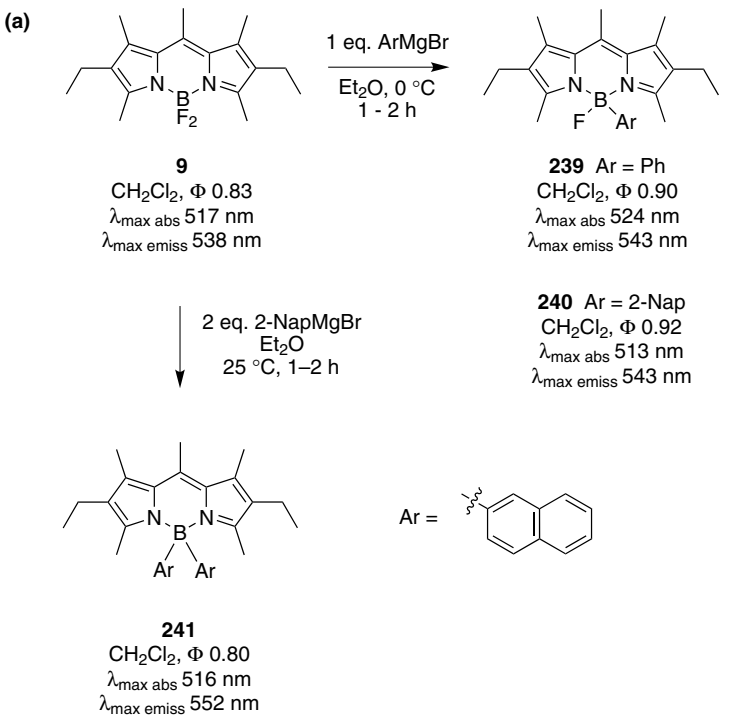

Scheme 11. Synthesis of *C*-BODIPYs using (**a**) aryl Grignard reagents; and, (**b**) aryl lithium reagents.

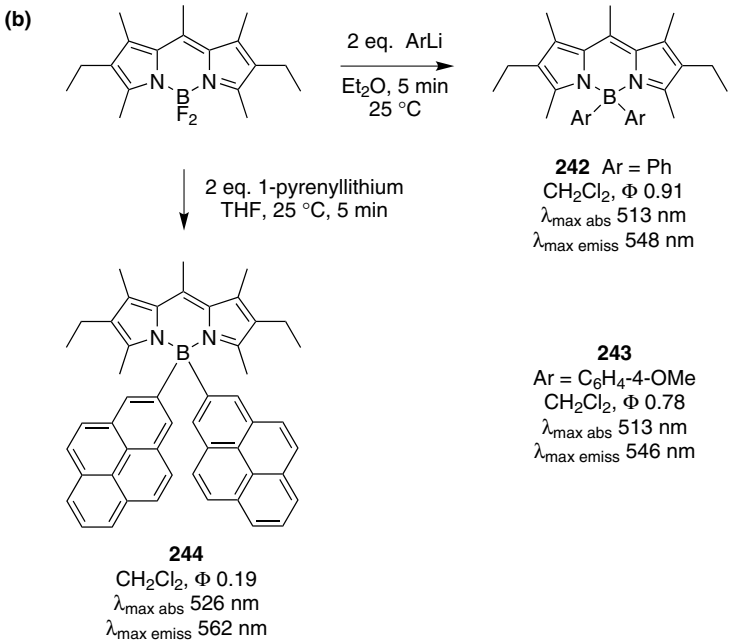

Scheme 11. (*Continued*)

solvent dependence is thought to be a solvophobic effect in which the aryl substituents seek to minimize surface contact with more polar media.

UV absorbance by the aromatic substituents means that these compounds can be regarded as energy transfer cassettes, and when the *B*-Ar groups have good extinction coefficients then there may be some value in this aspect of their properties. The dipyrene system **244** absorbs in the range 230–317 nm corresponding to the $\pi \leftrightarrow \pi^*$ transition of the pyrene units, and emits exclusively (100% energy transfer) from the BODIPY part.[220] However, there is no immediate application of this effect.

C. With Alkyne Groups

Acetylide anions are also good nucleophiles for the displacement of fluoride from the borondifluoride entity of BODIPY dyes. The pyrromethene dialkynyl borane complexes **245** and **246**, for instance, were synthesized from 4-lithioethynyltoluene and 1-lithioethynylpyrene, respectively.[215–217]

Adding groups to the boron atoms does not bring them into conjugation with the BODIPY core. Consistent with this, the absorption spectra of **245** and 2**46** have distinct BODIPY and ethynylaryl components. Upon excitation at 516 nm,

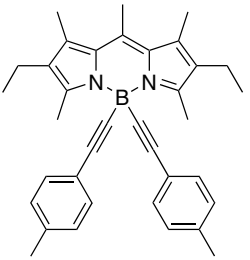

245
CH_2Cl_2, Φ 0.95
$\lambda_{max\ abs}$ 516 nm
$\lambda_{max\ emiss}$ 537 nm

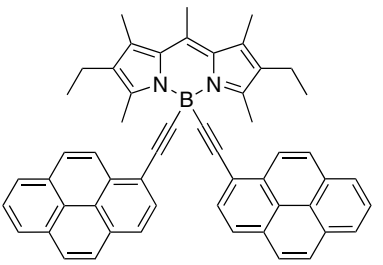

246
CH_2Cl_2, Φ 0.94
$\lambda_{max\ abs}$ 371, 516 nm
$\lambda_{max\ emiss}$ 535 nm

both **245** and **246** emit strongly, with high fluorescence quantum yield, in the region 535–540 nm. For **246**, excitation at 371 nm (pyrene absorption band) did not lead to emission from the pyrene but instead to emission characteristic of the indacene core, indicating an efficient energy transfer from the pyrene to the indacene moiety.[215,216,221]

It is possible to add trimethylsilylacetylide to displace fluoride from BODIPYs, then desilylate under basic conditions and Sonogashira couple to the terminal alkyne, e.g. **248** (Scheme 12). Whereas use of excess sodium hydroxide in the desilylation reaction affords the bis(ethynyl)BODIPY **248**, the monoprotected derivative **249** can be obtained using limited amounts of NaOH and shorter reaction times.[222,223] Access to the monoprotected derivative facilitates introduction of different *B*-alkynes substituents.[216]

Compounds **250–251** can act as energy transfer cassettes, just like the *B*-aryl systems mentioned above. Irradiation of the donor (pyrene or anthracene) was observed to give only BODIPY emission, indicative of a near quantitative energy transfer. BODIPY **253** in which four different chromophores have been covalently linked together represents a more sophiscated cascade-type system.[224] Upon excitation in the pyrene and/or perylene region, efficient energy transfer occurs and emission from the BODIPY is observed.

Terminal alkynes like **249** and **256** can be oxidatively dimerized (Pd^{II} and CuI under aerobic conditions) to give butadiynes **254** and **257** (Scheme 13).[222] Deprotection of the product butadiyne **254** was very slow; for instance, only a mixture of monodeprotected **255a** and bisdeprotected **255b** was isolated after 6 days.[222]

Substitution of the fluoride ligands on boron by polyaryl-alkynide ligands was also performed on the near-IR dye **258**.[225,226] This allows the production of dyes with large virtual Stokes' shift by virtue of intramolecular energy transfer.[227]

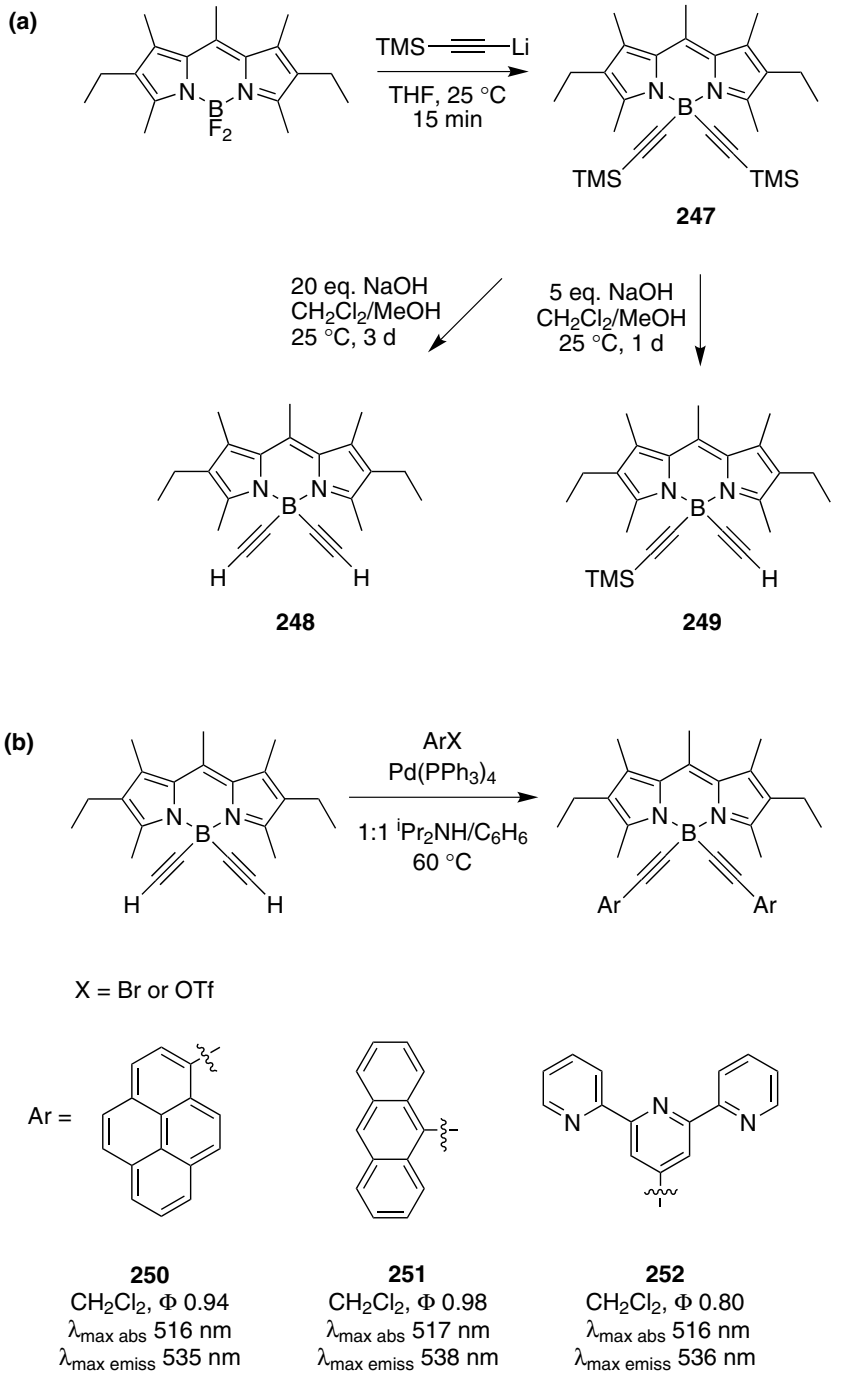

Scheme 12. (**a**) Two-step synthesis of bis(ethynyl)BODIPY **248**, and the monoprotected analog **249**; and, (**b**) some examples of compounds that have been prepared via Sonogashira coupling of **213**.

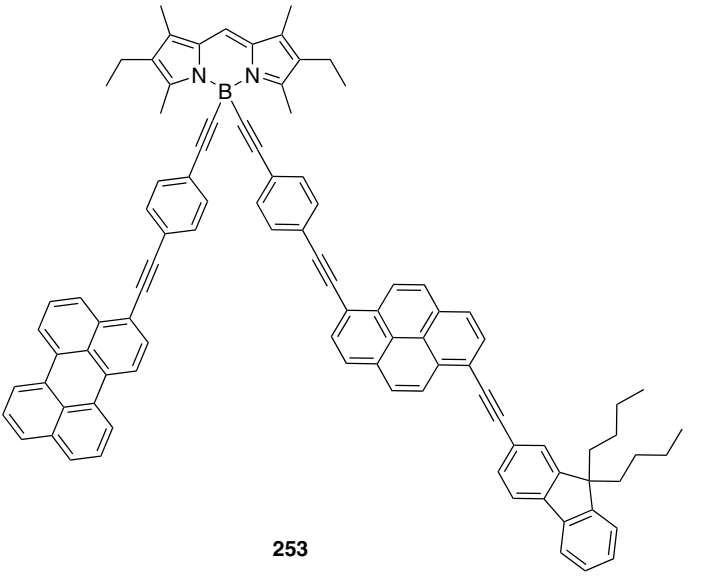

253

Thus, the dialkyne intermediate **259** was obtained by reaction of **258** with the appropriate alkynyl-Grignard reagent. Subsequently, Sonogashira coupling with various ethynylarene derivatives afforded the systems **260**–**264**. All the new dyes exhibit UV absorption maxima at ca. 708 nm with a molar absorptivity of

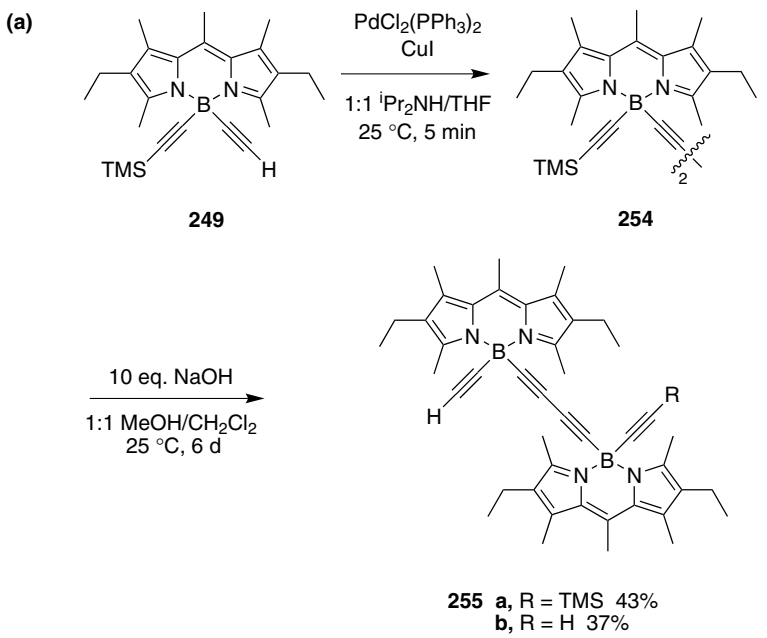

Scheme 13. Synthesis of homocoupled products.

(b)

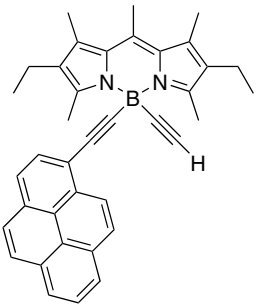

256

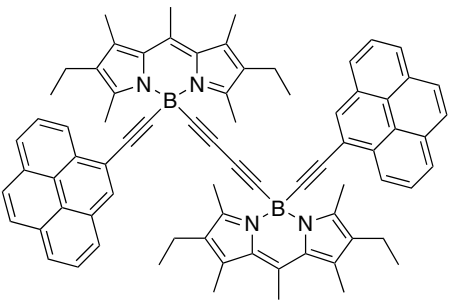

257

Scheme 13. (*Continued*)

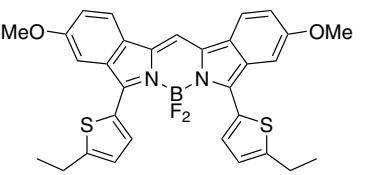

258
CH_2Cl_2, Φ 0.20
$\lambda_{max\ abs}$ 727 nm
$\lambda_{max\ emiss}$ 780 nm

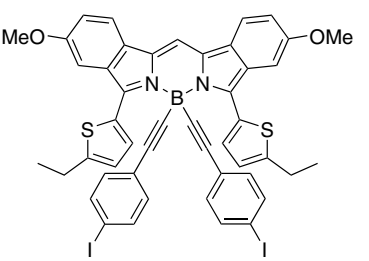

259
CH_2Cl_2, Φ 0.45
$\lambda_{max\ abs}$ 709 nm
$\lambda_{max\ emiss}$ 750 nm

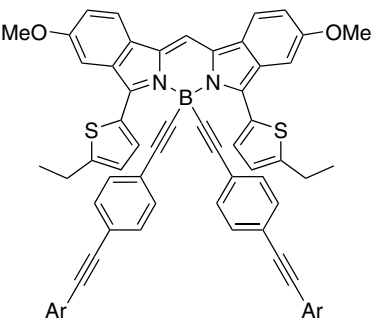

Ar =

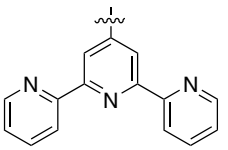

260
CH_2Cl_2, Φ 0.22
$\lambda_{max\ abs}$ 709 nm
$\lambda_{max\ emiss}$ 750 nm

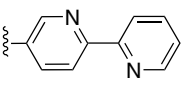

261
CH_2Cl_2, Φ 0.21
$\lambda_{max\ abs}$ 708 nm
$\lambda_{max\ emiss}$ 750 nm

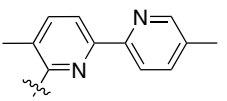

262
CH_2Cl_2, Φ 0.19
$\lambda_{max\ abs}$ 708 nm
$\lambda_{max\ emiss}$ 750 nm

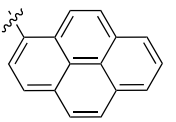

263
CH_2Cl_2, Φ 0.40
$\lambda_{max\ abs}$ 708 nm
$\lambda_{max\ emiss}$ 750 nm

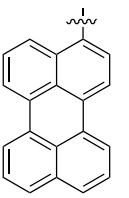

264
CH_2Cl_2, Φ 0.40
$\lambda_{max\ abs}$ 708 nm
$\lambda_{max\ emiss}$ 750 nm

~80 000 M^{-1} cm^{-1}. Higher energy absorption bands assigned to the pyrene, perylene, bis- and tri-pyridine were also observed near 350 and 450 nm. Upon excitation at 708 nm, a broad emission band at 750 nm, with quantum yields between 0.19 and 0.45 was observed in all cases. Fast energy transfer to the central dipyrromethene core was observed upon irradiation of the pyrene and perylene units in **263** and **264**, giving large virtual Stokes'shifts. The efficiency of the energy transfer for compounds **263** and **264** was estimated to 58% and 38%, respectively. Formation of aggregates was observed when the dyes were dissolved at concentrations higher than 10^{-7} M.

The same strategy, i.e. substitution of the fluoride with aryl-alkynides was applied to establish a tetrachromophoric cascade in dye **265**.[226] System **265**

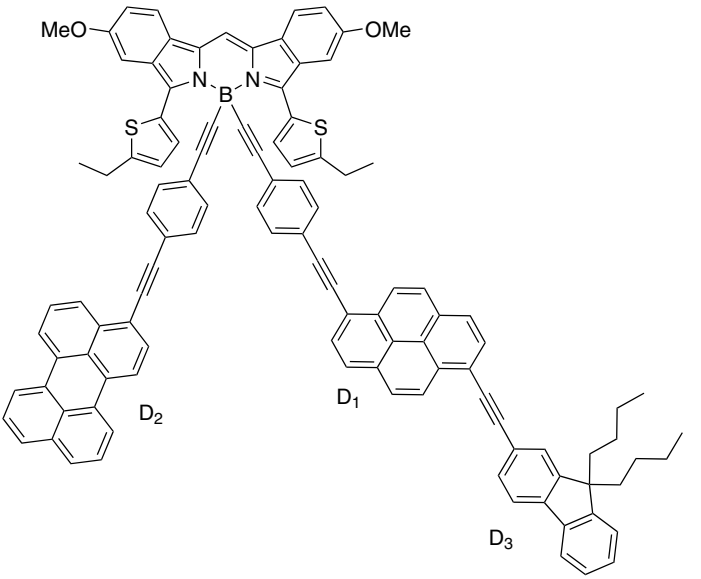

265
CH_2Cl_2
$\lambda_{max\ abs}$ 280, 308, 419,708 nm
$\lambda_{max\ emiss}$ 750 nm

contains three alkynylaryl energy donors, such as pyrene (D_1), perylene (D_2) and fluorene (D_3). As for **253**, selective irradiation in each absorbing subunit (D_1, D_2 or D_3) resulted in a single emission at ca. 750 nm, indicating efficient energy transfer over 25 Å to the BODIPY acceptor emitting.

D. With Alkoxide Groups

The first two *B*-methoxy BODIPYs prepared were **266**–**267**. These were made by reacting the corresponding BF_2 compound with sodium methoxide in methanol (Chart 32). The shape of the absorption and emission spectra were the same for the starting material **12** and the two products, suggesting the change in *B*-substituents had little effect on the electronic states of the boroindacene core. Interestingly, the monomethoxy- and dimethoxy-products were more water-soluble than the corresponding BF_2 compounds.[74]

The only other report of *B*-OR BODIPYs describes syntheses of systems **C** via treatment of the corresponding BODIPY with various alcohols in the presence of aluminum trichloride (Chart 33).[92] This study was more expansive than the first insofar as a more diverse set of alcohols were studied. Thus the alcohols used included simple alkoxy **268**–**270**, aryloxy **271**–**274**, and several diol-derived systems **275**–**278**. Across this series there were only minor changes in the absorbance

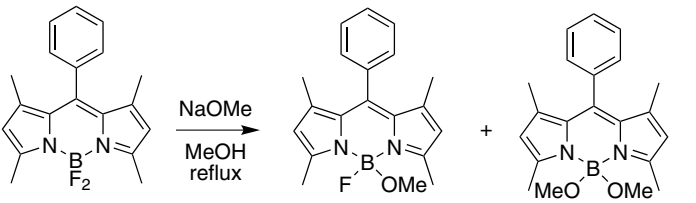

12
MeOH, Φ 0.46
$\lambda_{max\ abs}$ 497 nm
$\lambda_{max\ emiss}$ 507 nm

266
MeOH, Φ 0.45
$\lambda_{max\ abs}$ 498 nm
$\lambda_{max\ emiss}$ 509 nm

267
MeOH, Φ 0.49
$\lambda_{max\ abs}$ 498 nm
$\lambda_{max\ emiss}$ 509 nm

Chart 32.

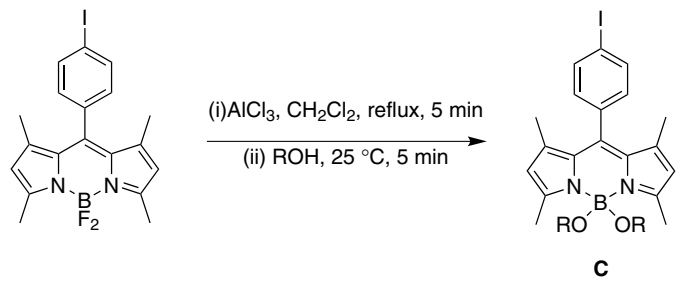

C

R =

268
$CHCl_3$, Φ 0.55
$\lambda_{max\ abs}$ 505 nm
$\lambda_{max\ emiss}$ 519 nm

269
$CHCl_3$, Φ 0.76
$\lambda_{max\ abs}$ 504 nm
$\lambda_{max\ emiss}$ 518 nm

270
$CHCl_3$, Φ 0.65
$\lambda_{max\ abs}$ 506 nm
$\lambda_{max\ emiss}$ 522 nm

271
$CHCl_3$, Φ 0.06
$\lambda_{max\ abs}$ 506 nm
$\lambda_{max\ emiss}$ 517 nm

272
$CHCl_3$, Φ 0.004
$\lambda_{max\ abs}$ 507 nm
$\lambda_{max\ emiss}$ 518 nm

273
$CHCl_3$, Φ 0.065
$\lambda_{max\ abs}$ 506 nm
$\lambda_{max\ emiss}$ 520 nm

274
$CHCl_3$, Φ 0.54
$\lambda_{max\ abs}$ 504 nm
$\lambda_{max\ emiss}$ 516 nm

Chart 33.

$(RO)_2$ =

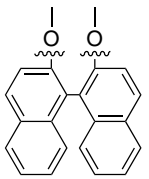

275
$CHCl_3$, Φ 0.002
$\lambda_{max\ abs}$ 506 nm
$\lambda_{max\ emiss}$ 516 nm

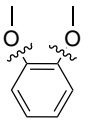

276
$CHCl_3$, Φ 0
$\lambda_{max\ abs}$ 510 nm
$\lambda_{max\ emiss}$ na

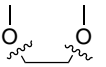

277
$CHCl_3$, Φ 0.14
$\lambda_{max\ abs}$ 507 nm
$\lambda_{max\ emiss}$ 521 nm

278
$CHCl_3$, Φ 0.54
$\lambda_{max\ abs}$ 504 nm
$\lambda_{max\ emiss}$ 522 nm

Chart 33. (*Continued*)

and emission spectra. The *dialkoxy*-BODIPYs **268–270** appear to have higher fluorescence quantum yields than the *diaryloxy*-ones **271–274**, and the systems binaphthol- and catechol-derived systems **275** and **276** have extremely poor quantum yields.

E. Boronium and Borenium BODIPY Cations

Due to their inherent fluorophilicity, organoboron compounds have often been used as fluoride sensors. However, in most cases, binding of fluoride anions with a neutral and/or cationic triarylborane to form the corresponding fluoroborate species results in a turn-off response both in the absorption and emission spectra of the borane; this limits the potential applications of the sensors. Therefore, boron-based fluoride sensors that give a turn-on response are becoming attracting. The BODIPY boronium cation [**280**-DMAP]$^+$, recently reported by Gabbai,[228] can be selectively and rapidly converted to the neutral BODIPY **280**-F in the presence of fluoride anions (Chart 34). Upon binding of the fluoride anion, the fluorescence intensity of the BODIPY increases by a factor of five, giving a response that can be easily detected with the naked eye. A 48% and 6% increase was observed upon addition of chloride and bromide anions to [**280**-DMAP]$^+$, respectively.

In similar work, Piers and coworkers reported the synthesis of the tricoordinate borenium cation **281**-F (Chart 35).[229] This compound is stable in a crystalline form, but decomposes readily (within 20–30 min) in a CD_2Cl_2 solution. Treatment of **281**-F with DIBAL-H gave the unprecedented borenium hydride cation, **282**-H, that was then easily converted to the corresponding boronium **283**-H by treatment with DMAP. Interestingly, compound **282**-H does not appear to promote hydroboration, as no reaction was observed upon treatment with phenylacetylene.

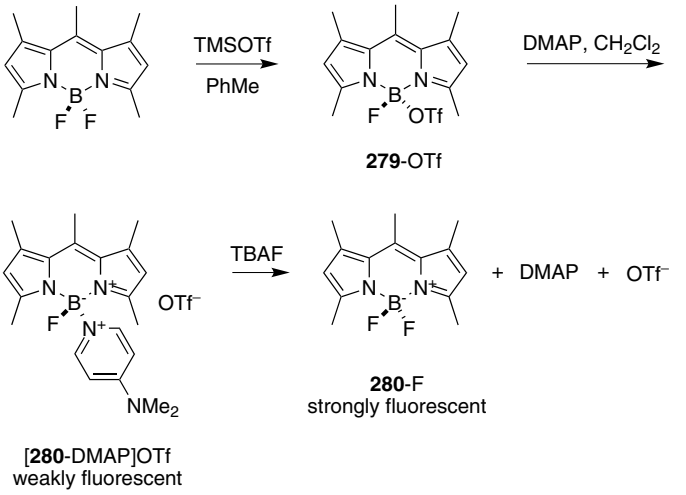

Chart 34.

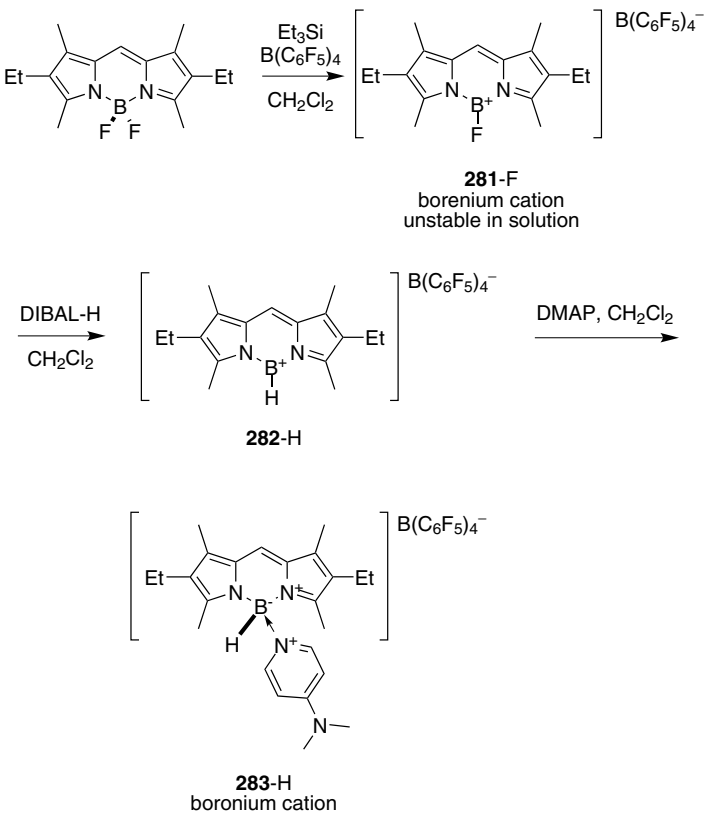

Chart 35.

X. Use of Metals Other Than Boron

The BODIPY core features a boroindacene unit, so compounds where the boron has been substituted with other metals are, strictly speaking, beyond the scope of this review. However, there are a few dipyrromethene anion complexes of other metals that have highly fluorescent spectroscopic characteristics. These are covered here because they are clearly relevant as probes.

Free base dipyrrins react readily with a variety of metals salts to form the corresponding bis(dipyrrinato)-metal(II) or tris(dipyrrinato)-metal(III) complexes, but their fluorescence properties have rarely been studied and they have generally been regarded as non-fluorescent.[230–253] The first discussion of fluorescent properties for zinc complexes of the boraindacene fragment was in 2003.[254,255] The complexes were prepared either from treatment of a purified dipyrrin with zinc acetate, or, a two-step, one-flask approach involving oxidation of a dipyrromethane and complexation of the resulting crude dipyrrin with a $Zn(OAc)_2$ in presence of triethylamine. Complexes **284** and **285** are weakly fluorescent but **286** is a stronger emitter (it has a multinanosecond excited-state lifetime); thus free rotation of the *meso*-phenyl is again implicated as a major pathway for nonradiative relaxation to the ground state for **284** and **285**.

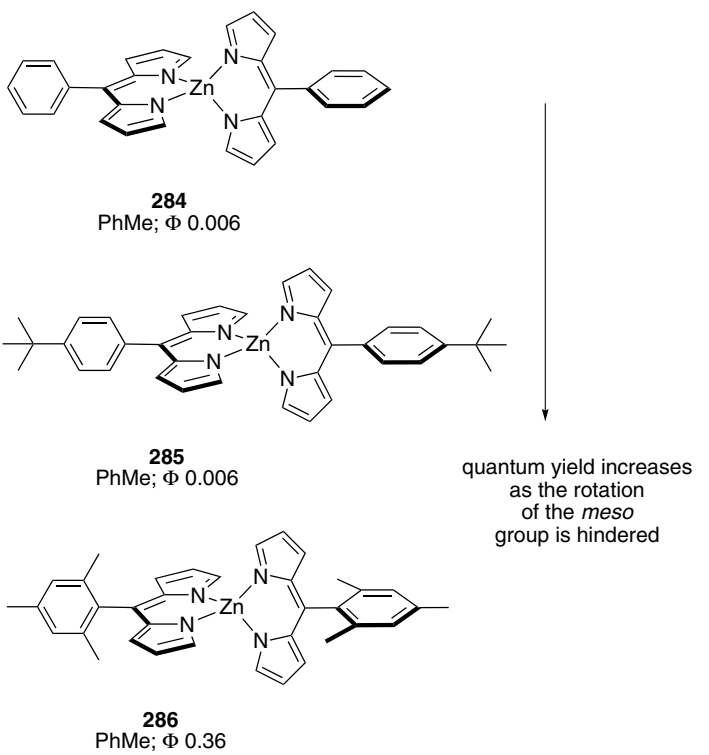

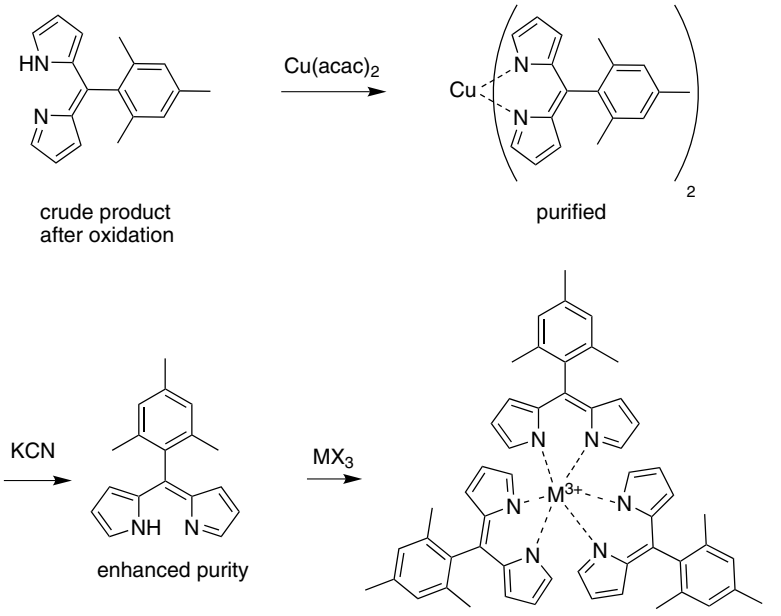

Chart 36.

Porphyrin or phthalocyanine complexes of group 13 metals can be fluorescent; this inspired syntheses of two new dipyrromethenes **287** and **288** from gallium(III) and indium(III), respectively (Chart 36). In hexanes, the new compounds fluoresce green light, with quantum yields of 0.024 and 0.074 for the gallium(III) and indium(III) complexes, respectively.[256]

"Nanoarchitectures" **289a–d** have been fabricated from Zn, Co, Ni, and Cu with dipyrromethene-based ligands, but are only strongly fluorescent with zinc.[257] The

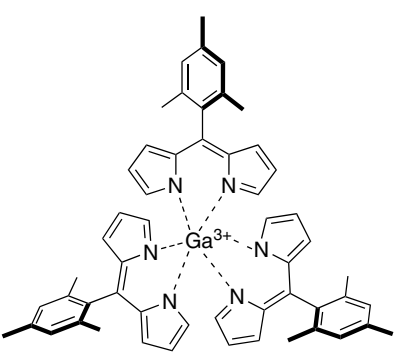

287
hexanes, Φ 0.024
$\lambda_{max\ abs}$ 448 nm
$\lambda_{max\ emiss}$ 528 nm

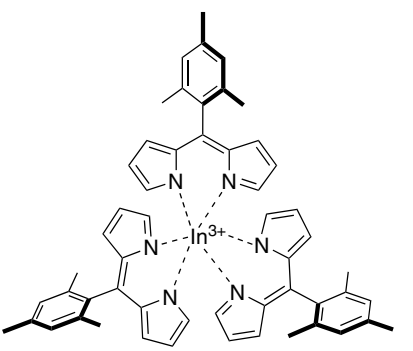

288
hexanes, Φ 0.074
$\lambda_{max\ abs}$ 444 nm
$\lambda_{max\ emiss}$ 522 nm

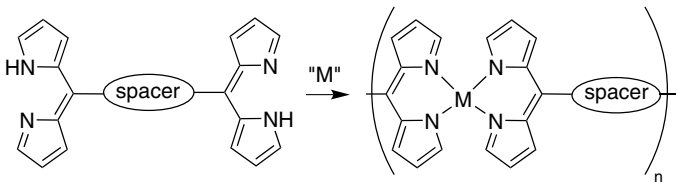

289a–d

spacer =

a

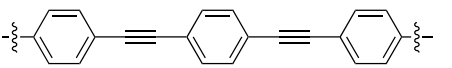

b

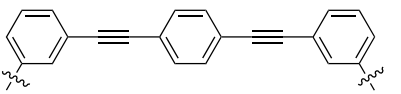

c

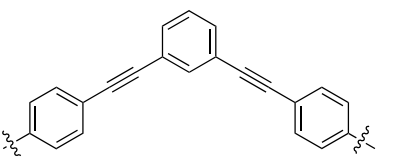

d

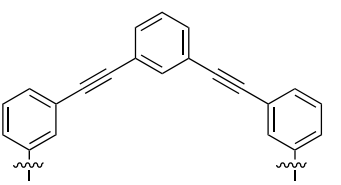

fluorescence emission maxima of the zinc complexes in THF and in the solid state are around 510–515 nm and 532–543 nm, respectively. In acetonitrile, no emission was observed possibly because of aggregation of the particles. Fluorescence emission could be observed on a submicron scale for particles derived from Zn-bridged dipyrromethene oligomers; this is significant because quantum dots formed from clusters of inorganic compounds are considerably larger.

XI. BODIPY-Analogs with Extended Aromatic Conjugation

A. Restricted Systems

As mentioned previously, aryl-substituents on a BODIPY chromophore, e.g. in **136** and **137**, red-shift its absorption and emission spectra, but decrease its fluorescence intensity, presumably because of the free rotation of the aryl groups.[144,145] Consequently, more rigid systems like **290** and **291** where the aryl groups at position 3- and 5- are not freely rotating, were prepared and studied.[258]

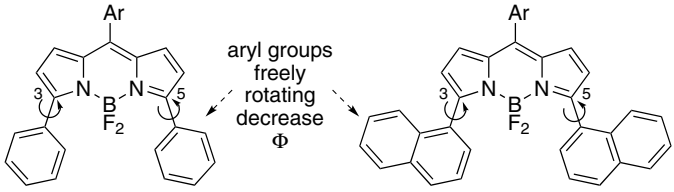

136
$CHCl_3$, Φ 0.20
$\lambda_{max\ abs}$ 555 nm
$\lambda_{max\ emiss}$ 588 nm

137
$CHCl_3$, Φ 0.38
$\lambda_{max\ abs}$ 542 nm
$\lambda_{max\ emiss}$ 607 nm

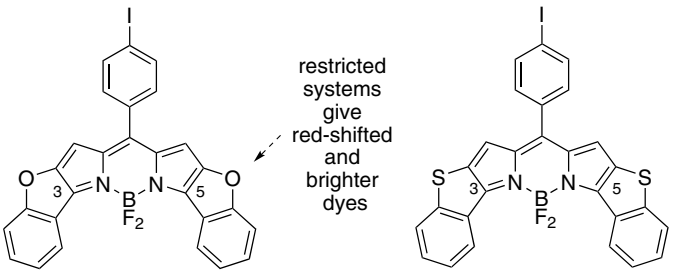

290a
MeOH, Φ 0.34
$\lambda_{max\ abs}$ 637 nm
$\lambda_{max\ emiss}$ 647 nm

290b
MeOH, Φ 0.05
$\lambda_{max\ abs}$ 658 nm
$\lambda_{max\ emiss}$ 673 nm

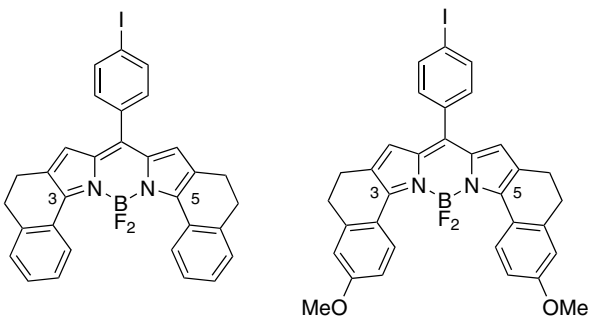

291a
MeOH, Φ 0.38
$\lambda_{max\ abs}$ 634 nm
$\lambda_{max\ emiss}$ 647 nm

291b
MeOH, Φ 0.13
$\lambda_{max\ abs}$ 658 nm
$\lambda_{max\ emiss}$ 673 nm

These absorb and fluoresce more intensely at longer wavelengths, and their quantum yields are generally higher, with the exception of **291b**.

Derivatives **291** and **292** were obtained by condensation of 4-iodobenzoyl chloride with the corresponding pyrrole-based starting materials, which were prepared in several steps as described in Scheme 14. Most of the effort here is in the preparation of the pyrrole based starting materials. Part **a** of Scheme 14 shows

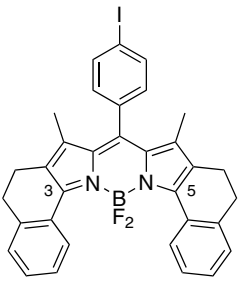

291c
MeOH, Φ 0.72
$\lambda_{max\ abs}$ 619 nm
$\lambda_{max\ emiss}$ 629 nm

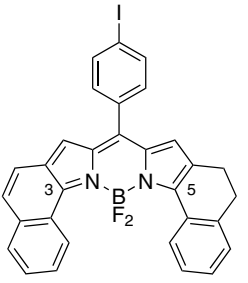

292
MeOH, Φ 0.17
$\lambda_{max\ abs}$ 634 nm
$\lambda_{max\ emiss}$ 668 nm

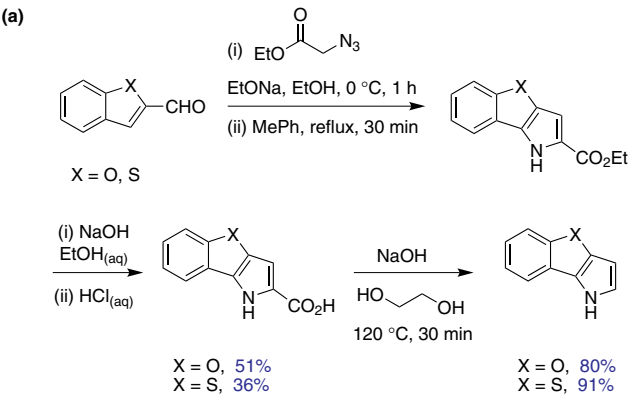

Scheme 14. Syntheses of the pyrrole-based starting materials.

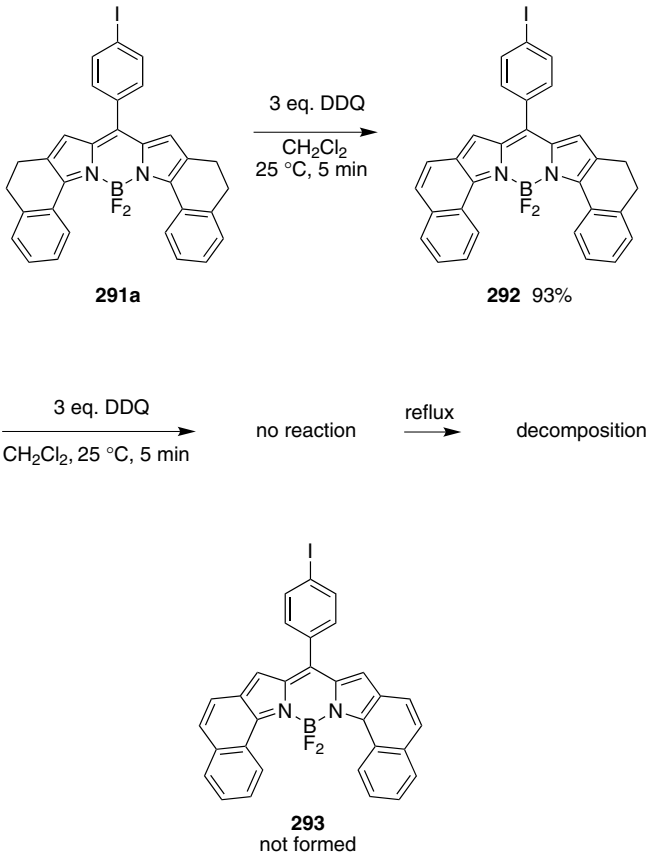

Scheme 15. Synthesis of more conjugated BODIPY derivatives.

a route that featured intramolecular C-H activation by a nitrene, **b** involves a Trofimov reaction,[149] and **c** shows a classical condensation route.[259]

Oxidation of **291a** was attempted, but only the half-oxidized product **292** could be obtained; further treatment with excess DDQ at room temperature overnight gave no reaction (Scheme 15). Semi-empirical calculations showed that the activation energy required to form **293** was excessive compared with the half oxidized form **292** due to steric reasons. The physical properties of the mono-oxidized product were somewhat surprising. First, the maximum absorbance was not shifted to the red relative to **291a**, only the fluorescence emission was shifted to the red by 21 nm. Second, although the conjugation of the system was extended, the extinction coefficient was three times smaller than the reduced form of the dye **291a** (41000 vs. 126250 respectively); the quantum yield was also less than half that of **291a**.

2′-Methoxy substituents on α-aryl groups provide a special opportunity for syntheses of constrained BODIPY dyes. Thus **294**, wherein rotation around a

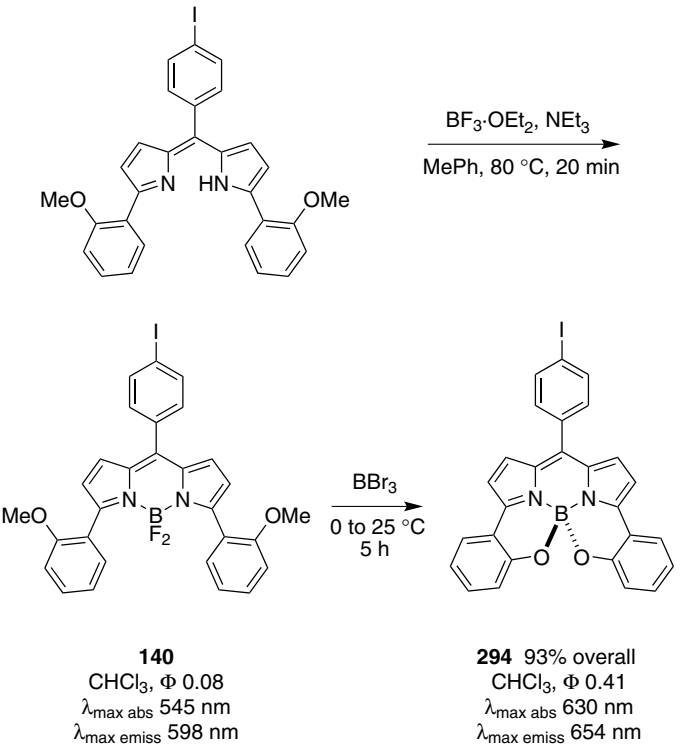

Scheme 16. Synthesis of a new NIR BODIPY dye.

C-Ar bond was prevented by B-O bond formation, was conveniently obtained by demethylation and intramolecular cyclization of **140** (Scheme 16).[260] Dye **294** has a red-shifted, sharper fluorescence emission than the BF_2 parent dye and its quantum yield is 5.5–6.0 times larger. This same approach has also been applied to aza-BODIPYs, e.g., Section XII.C.

Compound **296** could also be obtained directly from the dipyrrin ligand **295** by reaction with $B(OMe)_3$. Thus, a series of chiral Ar-BODIPY derivatives **297** was synthesized from reactions of **295** with arylboronic acids (Scheme 17).[261] The chiral boron center in these Ar-BODIPYs could be used for chiral recognition or for circularly polarized luminescence. The new BODIPYs derivatives **297a–c** show a strong absorption band at around 590 nm and an intense fluorescence centered around 615 nm with quantum yield of 0.63–0.68. As for compound **294**, the B-O linkage caused a red shift of both the absorption and emission.

Bright and long-wavelength emitting fluorophores, named Keio Fluors (KFL), **301** and **302**, based on BODIPY have recently been synthesized by Suzuki and coworkers.[262,263] These new probes were obtained from α-carboxylated furopyrrole **298** and α-formylated furopyrrole **299** in the presence of trifluoroactetic acid

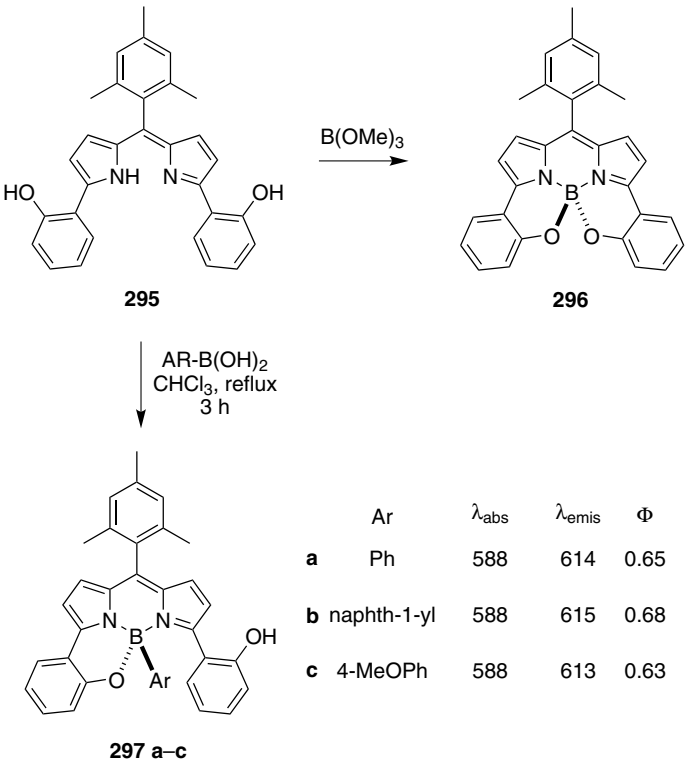

	Ar	λ_{abs}	λ_{emis}	Φ
a	Ph	588	614	0.65
b	naphth-1-yl	588	615	0.68
c	4-MeOPh	588	613	0.63

Scheme 17. Synthesis of chiral Ar-BODIPY dyes.

and trichlorophosphate (Scheme 19a). Preparation of the furopyrroles is described in Scheme 18. Briefly, furopyrrole 5-carboxylic acid **298** was synthesized by a Hemetsberger-Knittel reaction[264,265] on furan-2-carbaldehyde, and the furopyrrole **299** was obtained by α-formylation of the corresponding furopyrrole 5-carboxylic acid **298** (Scheme 18). Symmetrical and asymmetric KFLs can easily be synthesized (Scheme 19).

These new probes cover a wide spectral range from 542 nm to 738 nm. They exhibit high extinction coefficients (118 000–316 000 $M^{-1}cm^{-1}$), sharp emission spectra ($\Delta\lambda_{1/2}$ 16–30 nm) and high quantum yields, even in polar solvents (Φ 0.90–0.97 in EtOH). In addition, their absorption and emission profiles can be finely tuned through synthetic modifications. For example, both absorption and emission can be red-shifted by ca. + 40 nm via fusion of one furan ring gives (**5** vs. **301a**), fusion of two furan rings leads to ca. + 80 nm (**5** vs. **300a**), introduction of a phenyl ring gives ca. + 40 nm (**300a** vs. **304**), introduction of two phenyl rings gives ca. + 70 nm (**300a** vs. **300c**), attachment of one methoxy group in *ortho* or *para*-position of a phenyl ring leads to ca. + 20 nm (**300c** vs. **300b**, **300d**),

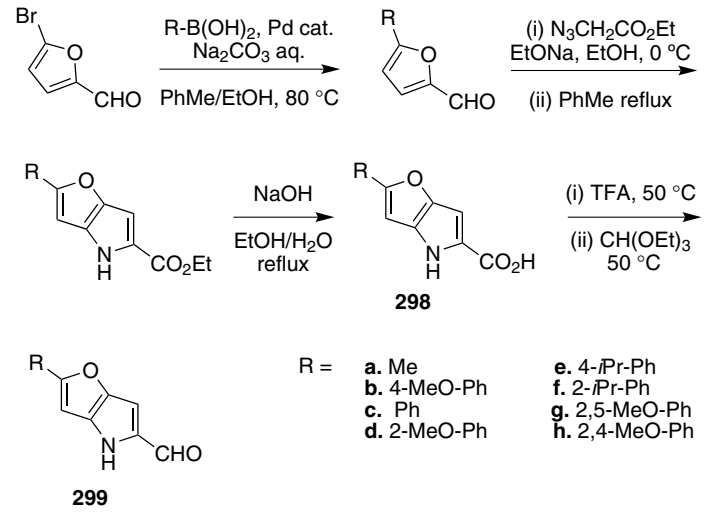

Scheme 18. Synthesis of furopyrroles.

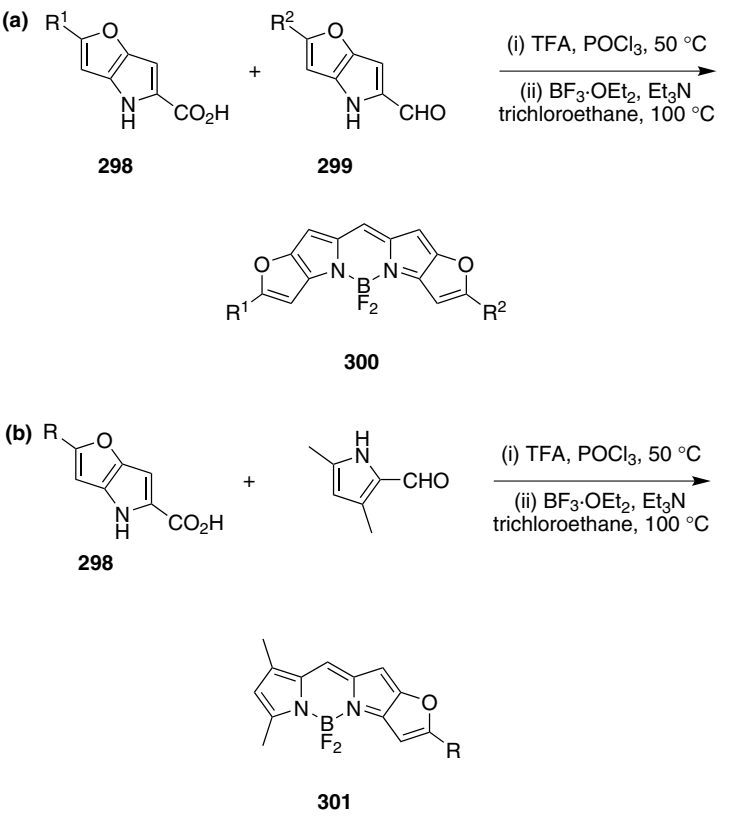

Scheme 19. Synthesis of (**a**) symmetrical and (**b**) unsymmetrical new NIR BODIPY dyes.

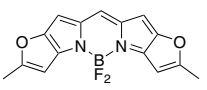

300a 69.4%
$CHCl_3$, Φ 0.96
$\lambda_{max\ abs}$ 579 nm
ε 202 000 M^{-1} cm^{-1}
$\lambda_{max\ emiss}$ 583 nm

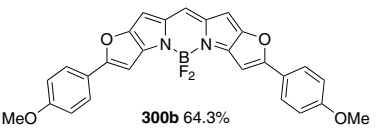

300b 64.3%
$CHCl_3$, Φ 0.86
$\lambda_{max\ abs}$ 673 nm
ε 288 000 M^{-1} cm^{-1}
$\lambda_{max\ emiss}$ 683 nm

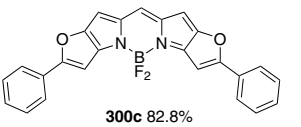

300c 82.8%
$CHCl_3$, Φ 0.90
$\lambda_{max\ abs}$ 652 nm
ε 314 000 M^{-1} cm^{-1}
$\lambda_{max\ emiss}$ 661 nm

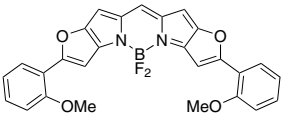

300d 67.4%
$CHCl_3$, Φ 0.91
$\lambda_{max\ abs}$ 671 nm
ε 313 000 M^{-1} cm^{-1}
$\lambda_{max\ emiss}$ 680 nm

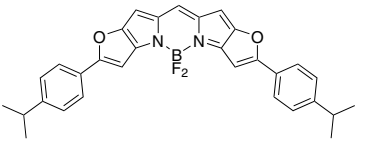

300e 44.5%
$CHCl_3$, Φ 0.97
$\lambda_{max\ abs}$ 662 nm
ε 316 000 M^{-1} cm^{-1}
$\lambda_{max\ emiss}$ 671 nm

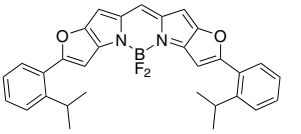

300f 47.6%
$CHCl_3$, Φ 0.87
$\lambda_{max\ abs}$ 629 nm
ε 142 000 M^{-1} cm^{-1}
$\lambda_{max\ emiss}$ 655 nm

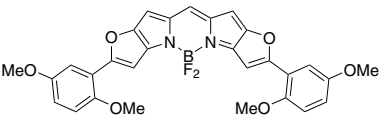

300g 39.3%
$CHCl_3$, Φ 0.82
$\lambda_{max\ abs}$ 679 nm
ε 280 000 M^{-1} cm^{-1}
$\lambda_{max\ emiss}$ 689 nm

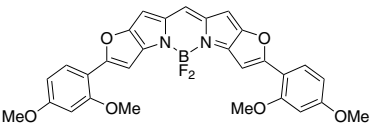

300h 71.6%
$CHCl_3$, Φ 0.81
$\lambda_{max\ abs}$ 690 nm
ε 282 000 M^{-1} cm^{-1}
$\lambda_{max\ emiss}$ 701 nm

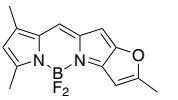

301a 66.8%
$CHCl_3$, Φ 0.96
$\lambda_{max\ abs}$ 542 nm
ε 140 000 M^{-1} cm^{-1}
$\lambda_{max\ emiss}$ 549 nm

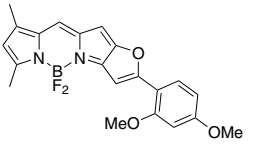

301h 40.3%
$CHCl_3$, Φ 0.95
$\lambda_{max\ abs}$ 596 nm
ε 184 000 M^{-1} cm^{-1}
$\lambda_{max\ emiss}$ 605 nm

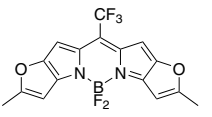

302 39.9%
$CHCl_3$, Φ 0.98
$\lambda_{max\ abs}$ 613 nm
ε 185 000 M^{-1} cm^{-1}
$\lambda_{max\ emiss}$ 620 nm

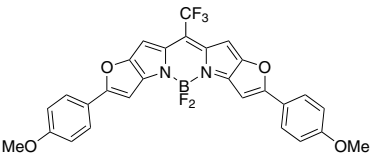

303 58.4%
$CHCl_3$, Φ 0.56
$\lambda_{max\ abs}$ 723 nm
ε 253 000 M^{-1} cm^{-1}
$\lambda_{max\ emiss}$ 738 nm

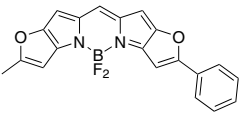

304 44.4%
$CHCl_3$, Φ 0.95
$\lambda_{max\ abs}$ 614 nm
ε 248 000 M^{-1} cm^{-1}
$\lambda_{max\ emiss}$ 620 nm

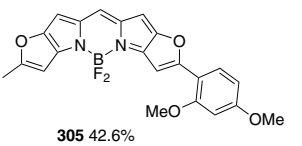

305 42.6%
$CHCl_3$, Φ 0.87
$\lambda_{max\ abs}$ 634 nm
ε 192 000 M^{-1} cm^{-1}
$\lambda_{max\ emiss}$ 644 nm

and introduction of an electron accepting group at the *meso* position gives ca. + 50 nm (**303** vs. **300b**).

B. Extended Aromatic Systems

1. *Di(iso)indomethene Dyes*

Aromatic ring-fused BODIPY derivatives, boron-di(iso)indomethene dyes **307** have been prepared via retro Diels-Alder reactions[266,267] featuring a norbornane-derived pyrrole (Scheme 20).[268] The spectroscopic data for the di(iso)indomethene derivatives **307** are shown below. The nature of the substituents at the *meso* position has no influence on the absorption and emission properties of the new dyes. The new di(iso)indomethene dyes display a red-shifted absorption compared to the bicyclic-BODIPY precursors **306**. The more expanded, conjugated, and rigid di(iso)indomethene BODIPY dyes **307** are also characterized by a significantly higher extinction coefficient relative to the bicyclic-BODIPY dyes **306**. Due to their rigid-fused system, which prevents a nonradiative deactivation of the excited state, bicyclic-BODIPY **306** and di(iso)indomethene BODIPY dyes **307** have small Stokes' shifts. The Stokes' shifts are, however, generally larger for bicyclic-BODIPY dyes **306** than for the di(iso)indomethene derivatives **307**. The absorption and emission spectra of bicyclic-BODIPY **306** and di(iso)indomethene BODIPY dyes **307** are independent of the solvent polarity. The fluorescence quantum yields of the bicyclic-BODIPY dyes **306** are much higher than the corresponding di(iso)indomethene BODIPY dyes **307**.

Other indomethene dyes including **258**[225] and **309–312**[225,269] have been prepared via a different route illustrated in Scheme 21. Substituted 2-acylacetophenones **308**, obtained by oxidation with lead(IV) acetate of the corresponding N-aroylhydrazones[270] formed by condensation of 2-hydroxyacetophenones and hydrazines, were condensed with ammonia to give the dibenzopyrromethene. These were treated with boron trifluoride to give the 3,4:3′,4′-dibenzopyrrometheneboron difluoride core (Scheme 21).

The new dyes **258** and **309–312**[225,269] exhibit very long wavelength absorption and emission bands, and are relatively stable to photobleaching.

2. *Dyes Based on Benz[c,d]indole*

Benz[*c,d*]indole and its derivatives have been used to form deeply colored dyes. Compound **313**, for instance, was obtained by condensation of

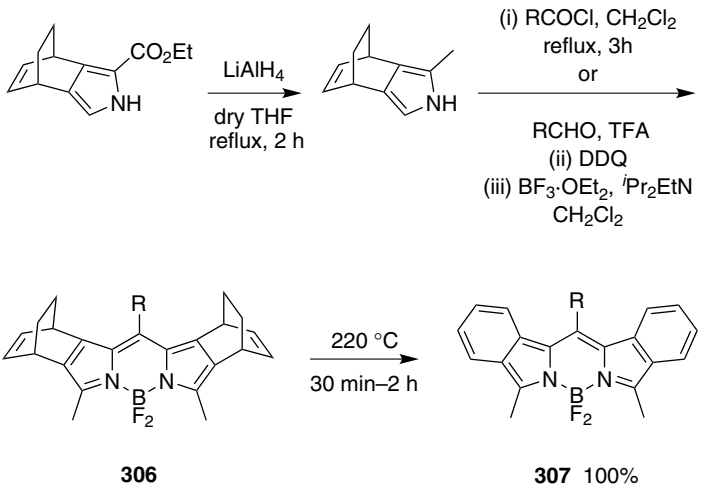

306 **307** 100%

for **307** .....

R =

a
EtOH, Φ 0.28
$\lambda_{max\ abs}$ 603 nm
$\lambda_{max\ emiss}$ 609 nm

b
EtOH, Φ 0.33
$\lambda_{max\ abs}$ 601 nm
$\lambda_{max\ emiss}$ 608 nm

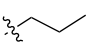

c
EtOH, Φ 0.36
$\lambda_{max\ abs}$ 602 nm
$\lambda_{max\ emiss}$ 608 nm

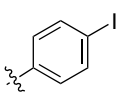

d
EtOH, Φ 0.26
$\lambda_{max\ abs}$ 606 nm
$\lambda_{max\ emiss}$ 614 nm

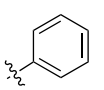

e
CH_3CN, Φ 0.87
$\lambda_{max\ abs}$ 597 nm
$\lambda_{max\ emiss}$ 606 nm

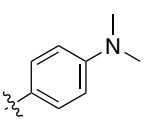

f
CH_3CN, Φ 0.022
$\lambda_{max\ abs}$ 597 nm
$\lambda_{max\ emiss}$ 605 nm

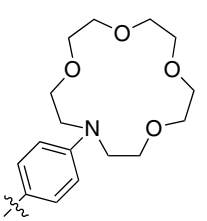

g
CH_3CN, Φ 0.093
$\lambda_{max\ abs}$ 598 nm
$\lambda_{max\ emiss}$ 606 nm

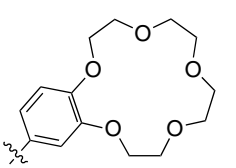

h
CH_3CN, Φ 0.86
$\lambda_{max\ abs}$ 598 nm
$\lambda_{max\ emiss}$ 607 nm

Scheme 20. Extended aromatic dyes from retro-Diels Alder reactions.

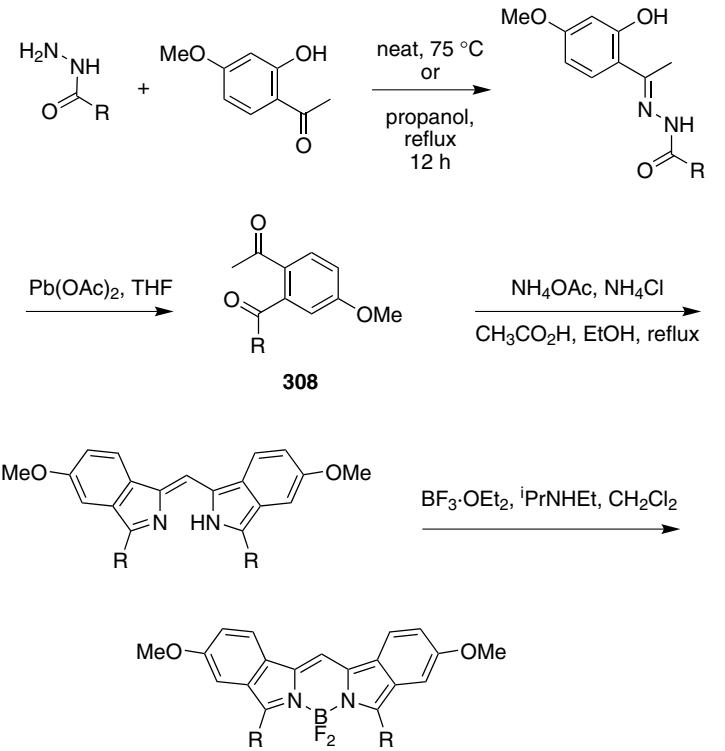

Scheme 21. Synthesis of di(iso)indomethene dyes from 2-acylacetophenone derivatives **308**.

2-methylthiobenz[*c,d*]indolium iodide and 2-methylbenz[*c,d*]indolium iodide, followed by complexation with boron trifluoride etherate (Chart 37). Its fixed planar structure exhibits a sharp absorption band at 618 nm, and fluoresces at 625 nm.[271,272]

3. *Phenanthrene-Fused BODIPY Systems*

2H-Dibenzo[e,g]isoindole (or β-phenanthropyrrole) have also been used to prepare bright, near-IR dyes.[273] Compounds **316** for instance were prepared from ethylphenantro[9,10-*c*]-pyrrole-1-carboxylate **314** via 1-methylphenanthro [9,10-*c*]-pyrrole **315**, then condensation with aromatic aldehydes, oxidation with DDQ and complexation with boron (Chart 38). These new dyes display distorted, "propeller-like" conformations due to the steric hindrance between the *meso* substituent and the large phenanthrene groups. They absorb maximally

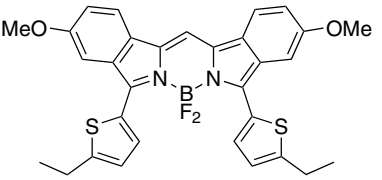

258
CH_2Cl_2, Φ 0.20
$\lambda_{max\ abs}$ 727 nm
$\lambda_{max\ emiss}$ 780 nm

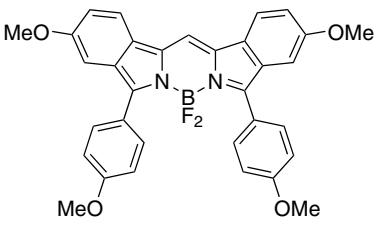

309

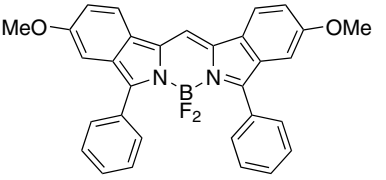

310

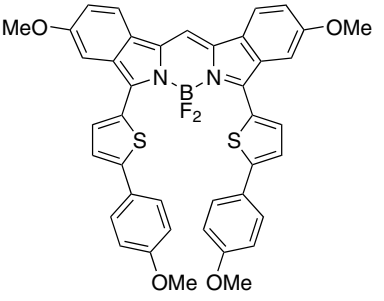

311
CH_2Cl_2
$\lambda_{max\ abs}$ 765 nm
$\lambda_{max\ emiss}$ 827 nm

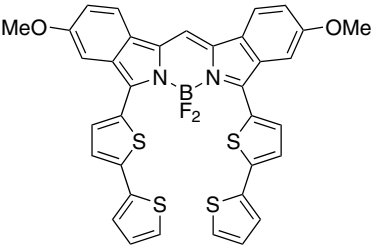

312
CH_2Cl_2
$\lambda_{max\ abs}$ 766 nm
$\lambda_{max\ emiss}$ 831 nm

around 620 nm, and like for pyrrole or isoindole-BODIPY systems, they are insensitive to the solvent polarity, with the exception of **316d,** where the fluorescence is quenched due to fast charge transfer process from the *meso*-dialkylanilino substituent. Unlike BODIPYs, and because of their crowded structure, the nature of the substituent at the *meso* position can influence the electronic properties of dyes **316**: **316c** with the strongest acceptor (CN) shows the longest wavelength absorption and emission, while **316d** with the strongest donor (NMe_2) displays the shortest ones. Furthermore, despite their distorted, "propeller-like" conformations, these new dyes emit brightly (Φ > 0.9). Finally,

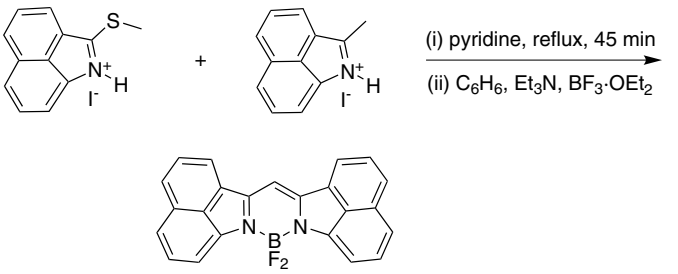

313
DMSO; Φ 0.52
$\lambda_{max\ abs}$ 618 nm
ε 94 000 M^{-1} cm^{-1}
$\lambda_{max\ emiss}$ 625 nm

Chart 37.

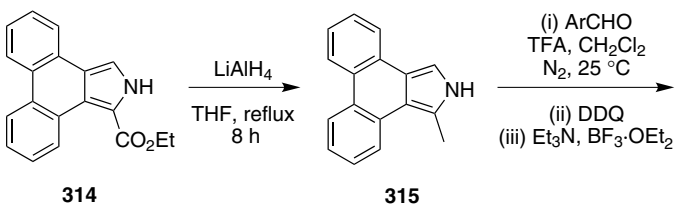

314 **315**

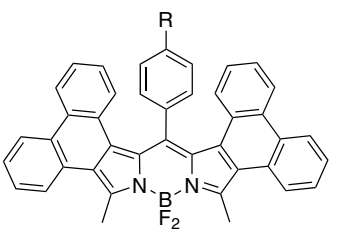

316a R = H, 15%
Bu_2O, Φ 1.00
$\lambda_{max\ abs}$ 630 nm
$\lambda_{max\ emiss}$ 648 nm

316b R = I, 13%
Bu_2O, Φ 0.92
$\lambda_{max\ abs}$ 633 nm
$\lambda_{max\ emiss}$ 654 nm

316c R = CN, 7%
Bu_2O, Φ 0.95
$\lambda_{max\ abs}$ 642nm
$\lambda_{max\ emiss}$ 668 nm

316d R = $N(Me)_2$, 10%
Bu_2O, Φ 0.96
$\lambda_{max\ abs}$ 621 nm
$\lambda_{max\ emiss}$ 636 nm

Chart 38.

these new phenanthro-BODIPYs dyes are a promising platform to design more elaborated near-IR probes as their electronic properties can be finely tuned by changing the nature of the substituent at the *meso* position. Probe **316d** was used as a pH indicator for the acidic range.

4. *Porphyrin-Fused Systems*

Systems **318**–**320** have edge-shared porphyrin and BODIPY parts. They were synthesized from the formylated pyrroloporphyrin **317** via acid-catalyzed condensation with 2,4-dimethylpyrrole. Their UV spectra contain four quite intense bands in the 300–750 nm region, and do not resemble the sum of the spectra of tetraphenylporphyrin (TPP) and of BODIPY. Systems **318** and **320** emit respectively at 693 and 714 nm upon excitation over all the 240–700 nm region with low quantum yields, and **319** did not show any significant fluorescence.[3]

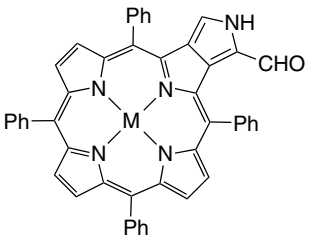

317

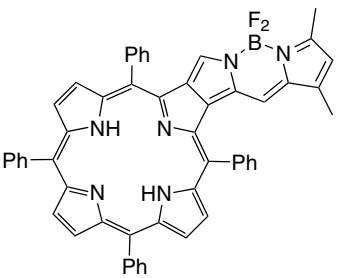

318
CH_2Cl_2, Φ 0.04
$\lambda_{max\ abs}$ 388, 413, 531, 640 nm
$\lambda_{max\ emiss}$ 693 nm

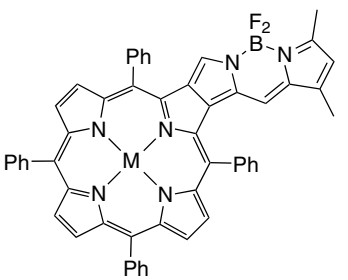

M = Cu
319
CH_2Cl_2, Φ nonfluorescent
$\lambda_{max\ abs}$ 390, 412, 531, 675 nm

M = Zn
320
CH_2Cl_2, Φ 0.053
$\lambda_{max\ abs}$ 392, 415, 539, 676 nm
$\lambda_{max\ emiss}$ 714 nm

5. *Bis-BODIPYs Systems*

Meso-unsubstituted and *meso*-aryl-substituted bis-BODIPYs systems **323** and **325**, respectively, were prepared from their corresponding free-base ligands, i.e. **322** (Scheme 22).[274–276] Water-saturated diethyl ether was a preferred solvent

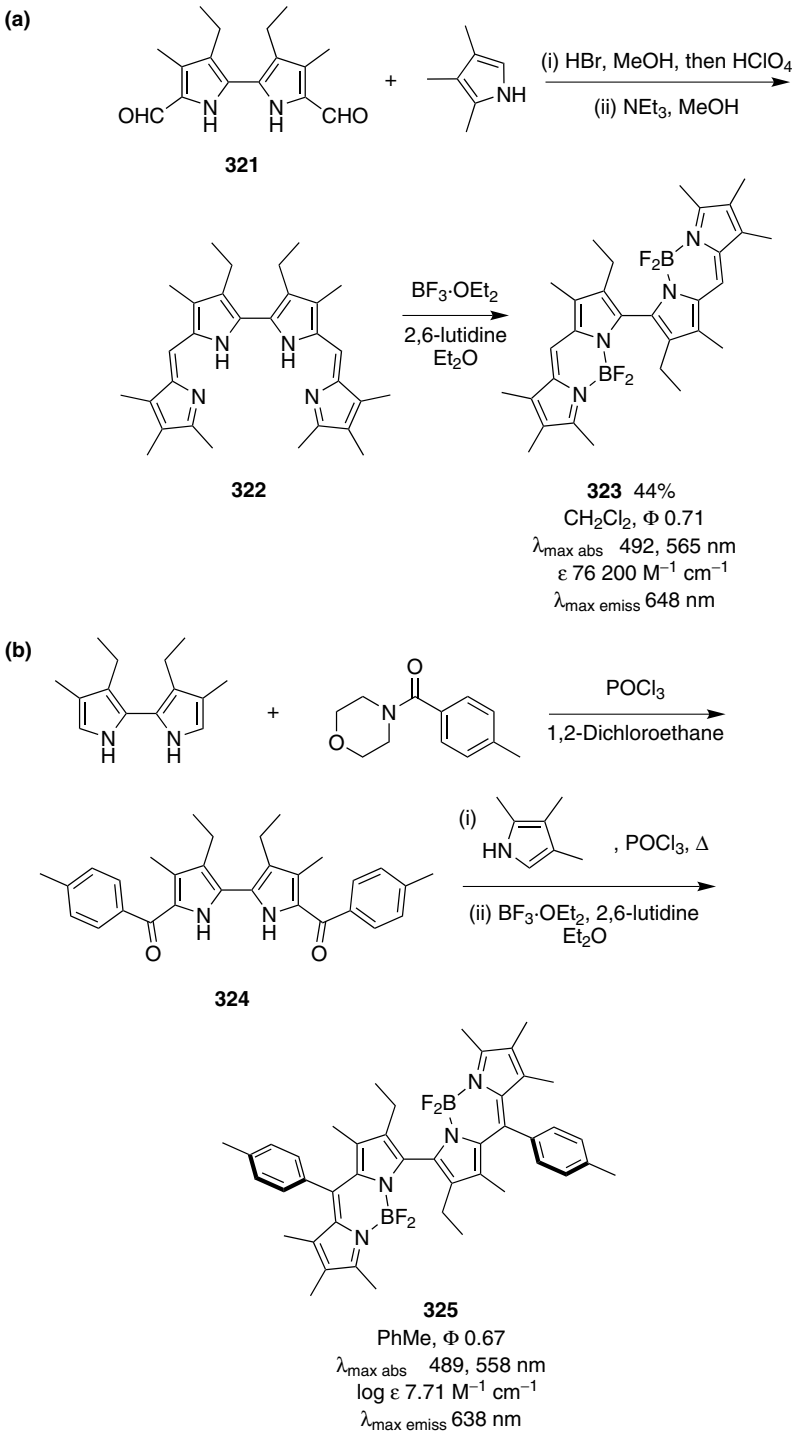

Scheme 22. Synthesis of (**a**) *meso*-unsubstituted and (**b**) *meso*-aryl-substituted bis-BODIPYs.

system for BF_2-coordination on dipyrrin ligands as it reduced the basicity of the fluoride anions and therefore limits side-reaction/decomposition processes, e.g., attack at the *meso*-position of both free ligands and bis-BODIPYs by basic fluoride anions formed *insitu* when the reaction was performed in CH_2Cl_2.

Unlike most classical BODIPYs, which are characterized by a single, strong absorption band at ca. 530 nm, an intense, narrow emission around 540 nm and a small Stokes' shift (200–400 cm^{-1}), these new dimeric chromophores display two major absorption bands with maxima at around 490 and 560 nm, an unstructured, broad emission and a remarkable large Stokes' shift (2200 cm^{-1}). Splitting of the absorption bands was assigned to exciton coupling; this was confirmed by the ratio between the integrated absorption spectra of the dimers and monomers being equal to 2. This exciton splitting had an intramolecular origin as no concentration effect (no aggregation) could be detected on the absorption parameters in the range 10^{-6}–10^{-4} M. No concentration effects could be observed on the luminescence either. Solvent polarity, however, had a significant effect on the luminescence quantum yield and the Stokes' shift. Increasing solvent polarity strongly reduced the luminescent quantum yield, especially on dimers without substituent at the *meso* position. Thus, bis-BODIPYs such as **323** could be used as polarity probes.

When compared to other dimeric BODIPY species, H-type nonluminescent dimers or J-type luminescent dimers, the data obtained for the bis-BODIPYs **323** or **325** were very similar to the one for J dimer, with the exception of the exciton splitting.

Furthermore, unlike BODIPYs, these new dyes exhibit a significant amount of singlet and triplet excited state with a fair ability to sensitize singlet oxygen.[274–276]

XII. Aza-BODIPY Dyes

A. Tetra-Aryl Systems

Synthesis of the azadipyrromethene chromophore **326** (without boron, but with aryl substituents) was first described in the 1940s.[277–279] This, as described below, is the framework for a very interesting set of dyes called the aza-BODIPYs. Two general methods to prepare these compounds were developed. In one, 2,4-diarylpyrroles were converted into their 5-nitroso derivatives, then condensed with a second molecule of pyrrole (Scheme 23a). Scheme 23b shows the second method, in which Michael addition products **D** from chalcones and nitromethane,[277] or cyanide **E**,[278,279] were reacted with formamide (or other ammonia-sources) to give the core **326**. In the first instance, these reactions were performed neat, i.e. without solvent. Soon after, it was realized that use of alcohol

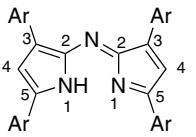

326

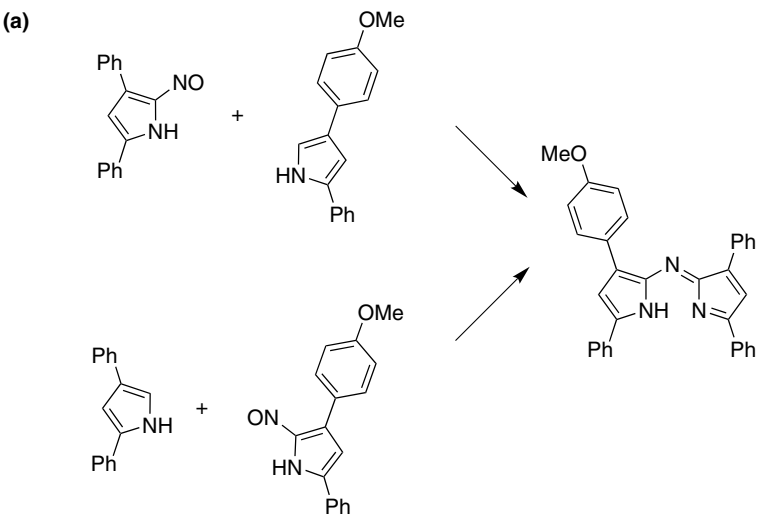

D **E**

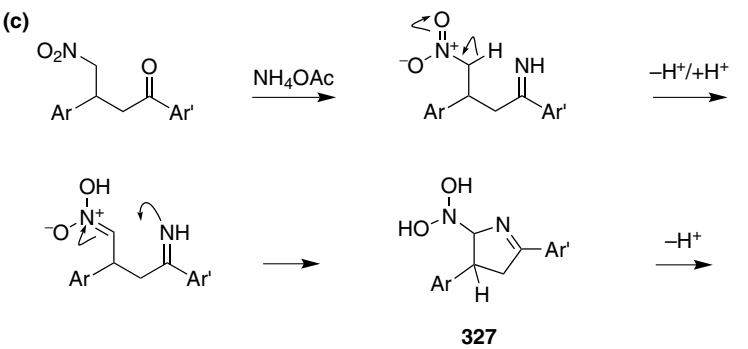

327

Scheme 23. Formation of azapyrromethene from (**a**) nitroso pyrrole; and (**b**) nitrobutyrophenones **D** and keto-nitrile **E**; (**c**) postulated mechanism for the formation of azapyrromethene from nitrobutyrophenones **D** and, (**d**) from keto-nitrile **E**.

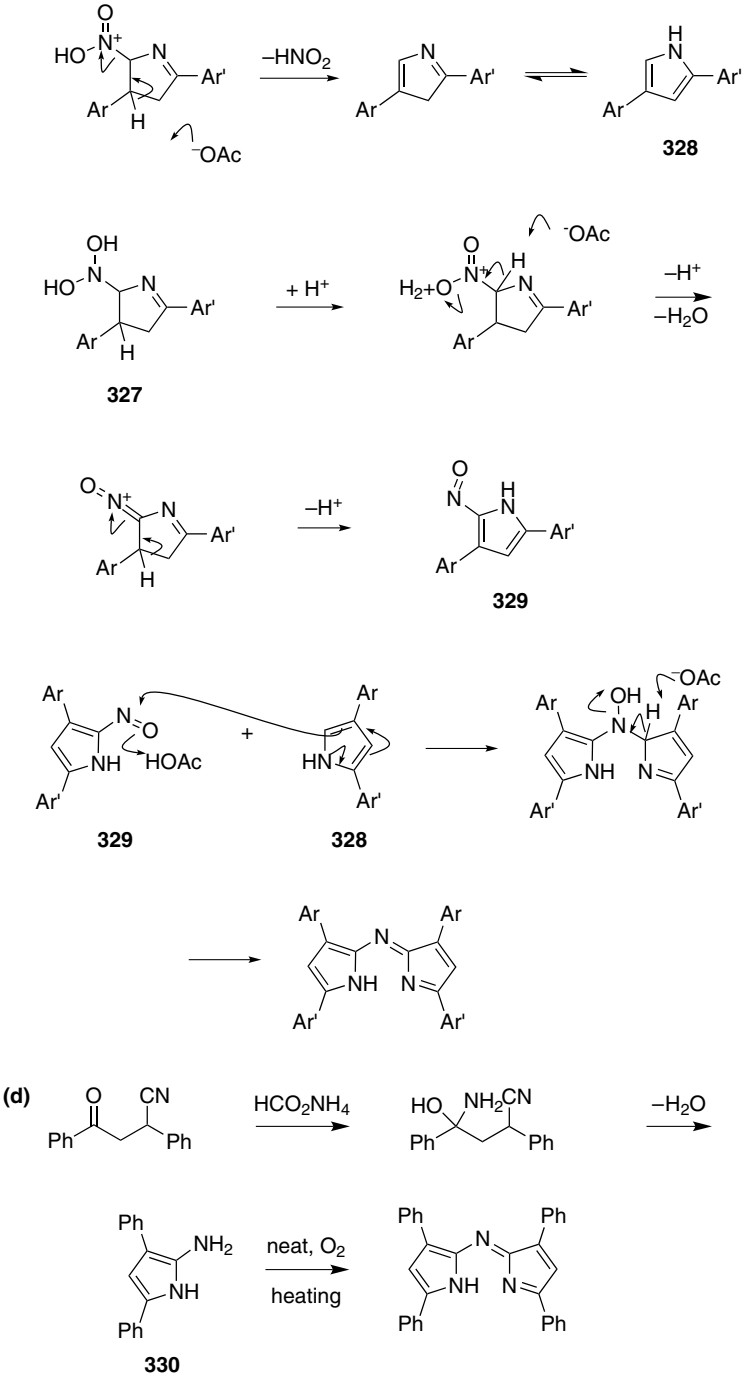

Scheme 23. (*Continued*)

solvents usually causes the azadipyrromethenes to precipitate from the reaction mixture, thus enhancing the ease of isolation and yields. The postulated mechanism for formation of the azadipyrromethene core from the nitromethane adducts is shown in Scheme 23c. It proceeds via pyrrole **328**, which is nitrosylated *in situ* to give **329** that then condenses with another molecule of the pyrrole.

It is also possible to prepare the azadipyrromethene chromophore from cyanide Michael addition products **E** as described in Scheme 23d. Ammonium formate serves as a source of ammonia in the pyrrole-forming condensation step. The 2-amino pyrrole intermediates **330** readily convert to the azadipyrromethene core on heating in the air. Switching from acetate to formate in the dry melt process for the synthesis of **326** nearly doubled the yield to give approximately 50%.[279] Formation of this chromophore seems to be most facile when there are four phenyl substituents, but it is possible to obtain the diphenyl products **333** (below) by slight modification of the reaction conditions.[279]

The first reactions of azadipyrromethenes with boron electrophiles were reported in the early 90s (Scheme 24).[131,280] The aza-BODIPY **332** was made from the 3,5-tetraphenyl azapyrromethene **331** in that way. The less substituted aza-BODIPY **334** could not be obtained after treatment of the corresponding azadipyrromethene **333** with boron trifluoride[280]; however, this might have been an artifact of the particular conditions screened.

Beginning with research largely from O'Shea's group from 2002 onwards, there has been a resurgence of interest in aza-BODIPY dyes, resulting in syntheses of

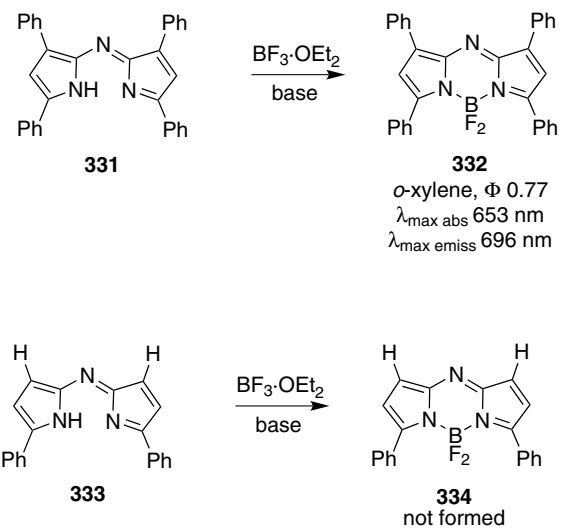

Scheme 24. First syntheses of aza-BODIPY dyes.

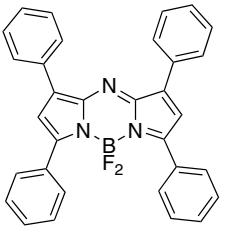

332
$CHCl_3$, Φ 0.34
$\lambda_{max\ abs}$ 650 nm
$\lambda_{max\ emiss}$ 672 nm

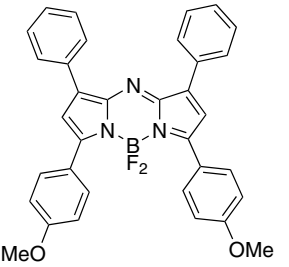

335
$CHCl_3$, Φ 0.36
$\lambda_{max\ abs}$ 688 nm
$\lambda_{max\ emiss}$ 715 nm

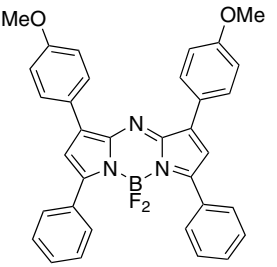

336
$CHCl_3$, Φ 0.23
$\lambda_{max\ abs}$ 664 nm
$\lambda_{max\ emiss}$ 695 nm

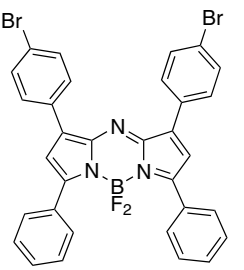

337
$CHCl_3$, Φ 0.34
$\lambda_{max\ abs}$ 658 nm
$\lambda_{max\ emiss}$ 680 nm

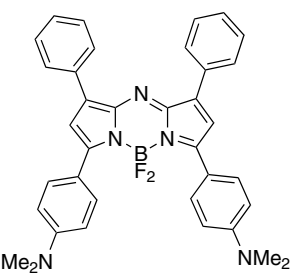

338
$CHCl_3$, Φ na
$\lambda_{max\ abs}$ 799 nm
$\lambda_{max\ emiss}$ 823 nm

dyes like **335**–**338**.[281–284] In this latest era of the field, the azadipyrromethene skeletons are still prepared from nitromethane adducts to the corresponding chalcone according to the route described in Scheme 23c but butanol, rather than methanol or solvent-free conditions, was the preferred medium.[282] The syntheses

were completed by adding $BF_3 \cdot OEt_2$ at room temperature; the intermediate azadipyrromethanes precipitated out in high purities and were not purified beyond washing with ethanol.[281,282]

UV absorption maxima of the tetraarylazadipyrromethene-BF_2 chelates strongly depend on the Ar-substituents. *para*-Electron donating groups on the 5-Ar substituents gives increased extinction coefficients and significant red-shifts in the $\lambda_{max\ abs}$ (149 nm for dimethylamino vs. H, *cf* **338** vs. **332**).[283] *para*-Substitution with an electron donating group on the 3-aryl ring has less impact, but still gives a bathochromic shift (*cf* **335** vs. **336**).[282]

The UV absorption maxima of the aza-BODIPY dyes are relatively insensitive to solvent polarity; only small blue-shifts tend to be observed (6–9 nm) when switching from toluene to ethanol. Their absorptions are sharp, with a full width at half-maximum height (fwhm) varying from 51 to 67 nm in aqueous solution with an emulsifier called Cremophor EL, and 47 to 57 nm in chloroform indicating that the dyes do not aggregate under those conditions. The extinction coefficients range from 75,000 to 85,000 M^{-1} cm^{-1}, which is much greater than substituted porphyrins (3000–5000 M^{-1} cm^{-1}) for instance. This strong absorbance is one of the factors that facilitate efficient singlet-oxygen generation, hence these molecules are potentially useful photosensitizers for photodynamic therapy.[285–288]

Fluorescence emission spectra of the aza-BODIPY dyes reported to date are also relatively insensitive to the solvent polarity. Compounds **332** and **335** to **337** have high fluorescence quantum yields. In the case of **337**, there is a bromine atom attached to the phenyl substituent, but no significant decrease in the quantum yield was observed.[282] On the other hand, introduction of bromine directly into the core of the dye, e.g. compounds **339** to **341** results in a significant decrease of the fluorescence quantum yields, indicating a larger heavy-atom effect and an increased singlet oxygen production.[282] A quantum yield was not reported for **338**, but the

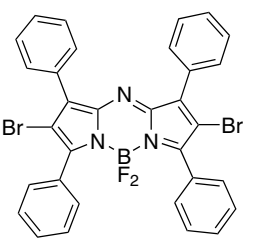

339
$CHCl_3$, Φ 0.01
$\lambda_{max\ abs}$ 650 nm
$\lambda_{max\ emiss}$ 673 nm

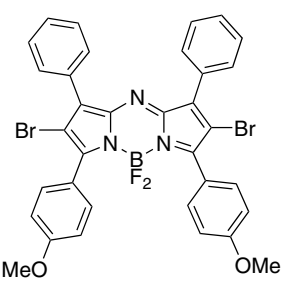

340
$CHCl_3$, Φ 0.10
$\lambda_{max\ abs}$ 679 nm
$\lambda_{max\ emiss}$ 714 nm

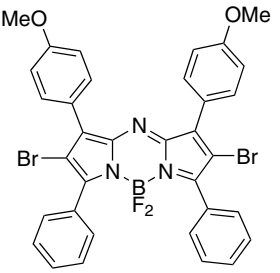

341
$CHCl_3$, $\Phi < 0.01$
$\lambda_{max\ abs}$ 653 nm
$\lambda_{max\ emiss}$ 679 nm

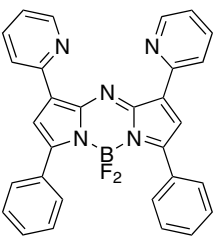

342
CH_3CN; Φ 0.19
$\lambda_{max\ abs}$ 655 nm
$\lambda_{max\ emiss}$ 682 nm

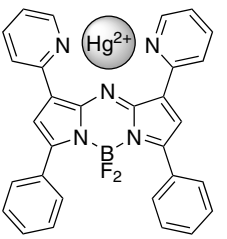

CH_3CN; Φ 0.17
$\lambda_{max\ abs}$ 696 nm
$\lambda_{max\ emiss}$ 719 nm

compound became much more fluorescent under acidic conditions due to variation in the internal charge transfer.[283] Upon addition of acid, the absorption band at 799 nm disappears and a new band at 738 nm appears indicating the monoprotonated form. The later disappears with addition of more acid, and a new band characteristic of the bis-protonated species appears at 643 nm.

Aza-BODIPY dyes mostly have been studied in the context of photodynamic therapy agents, but chemosensors have also been made from these compounds. Compound **342** is highly selective for mercuric ions that become chelated between the 2′-pyridyl groups.[289] Mercuric ion complexation red-shifts both the UV-absorption and fluorescence emission maxima. The dissociation constant was determined to be 5.4×10^{-6} M, with a 1:1 binding stoichiometry.

Compound **343** and **344** are photoinduced electron transfer crown ether chemosensors featuring aza-BODIPY chromophore[290]; they are used as visible sensors for the paralytic shellfish toxin Saxitoxin. Saxitoxin contains guanidine groups, and it is these functional groups that interact with the crown ether part of

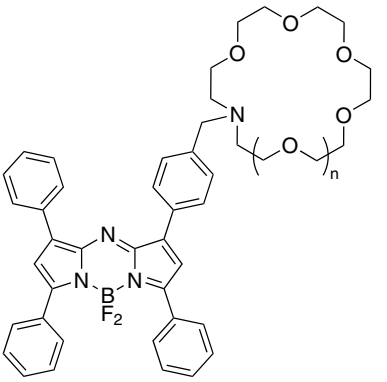

343 n = 1
344 n = 4

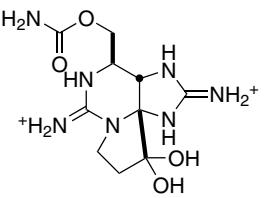

Saxitoxin

these molecules. In the absence of Saxitoxin, PET from the crown ether to the fluorophore quenches the fluorescence. Upon complexation of the toxin, PET can no longer happen and fluorescence is turned on. At 1:1 toxin/crown stoichiometry, the fluorescence enhancement was over 100% for compound **343**. The average binding constant for **343** to Saxitoxin, 6.2×10^5 M^{-1}, was among the highest observed for any chemosensor of that toxin. Compound **344**, which has a larger crown ether bound the toxin less strongly (1.4×10^4 M^{-1}) and gave insignificant fluorescence enhancement. The putative PET mechanism in these systems involves π-stacking of one of the Saxitoxin's guanidiniums to the fluorophore.

B. Extended Aza-BODIPY Systems

1. *Restricted Systems*

Strongly electron-donating groups, rigidifying structural modifications, and embellishments to extend the conjugation of the BODIPY dyes tend to red-shift their fluorescence emissions. Predictably then, similar modifications can be used to push the emission spectra of aza-BODIPY systems into the near-IR.

The "extended" aza-BODIPY systems **345**–**357** were synthesized from 2,4-diarylpyrroles. These starting materials were obtained in good overall yield over four steps from an alkene via (i) addition of iodo azide, (ii) dehydro-halogenation, (iii) pyrrolysis (azirine formation) and (iv) carbanion induced pyrrole formation as shown in Scheme 25.[291,292]

The conformationally restricted aza-BODIPY dyes were then prepared as shown in Scheme 26 via condensation of the pyrrole generated in Scheme 25 with a nitrosopyrrole generated *in situ*, followed by complexation with boron trifluoride. Attempts to condense 2,4-dimethylpyrrole with a nitrosated restricted

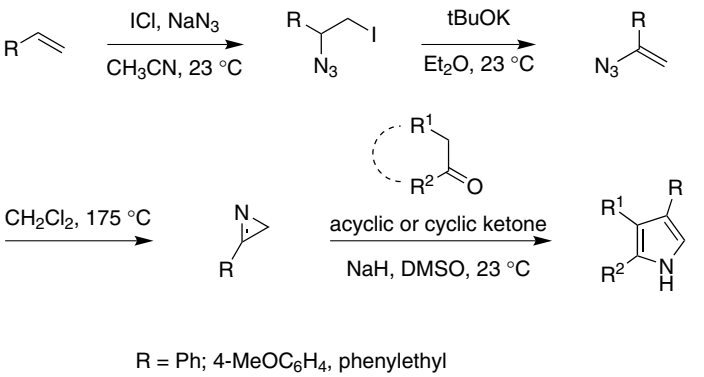

Scheme 25. Synthesis of cyclized/restricted 2,4-diarylpyrroles.

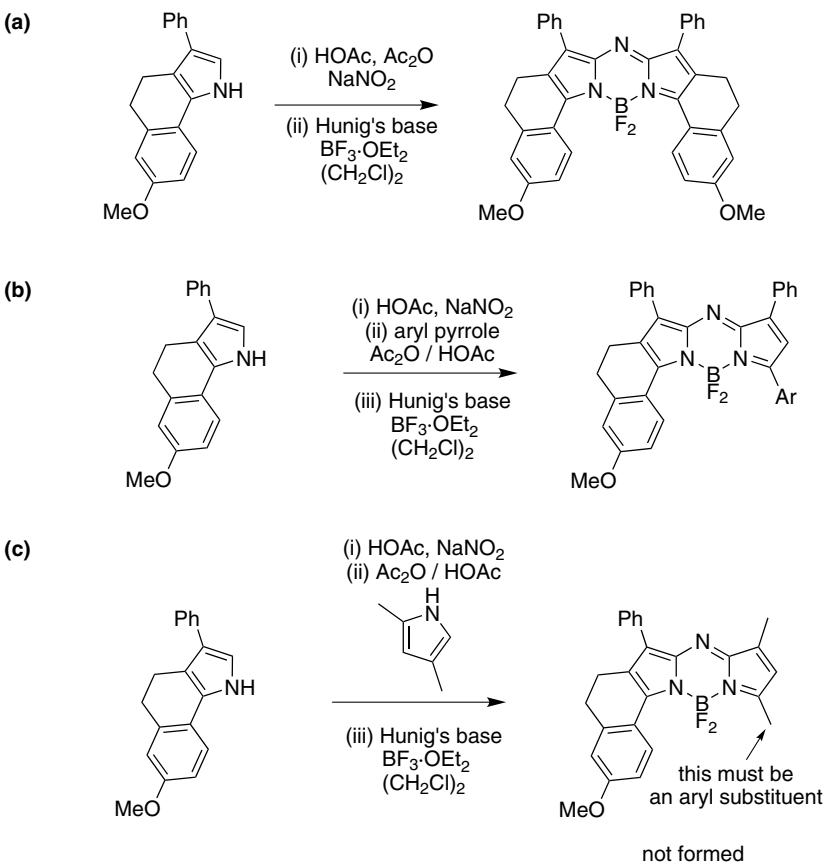

Scheme 26. Synthesis of (**a**), Symmetrical and (**b**), Asymmetrical Conformationally Restricted AzaBODIPY Dyes. (**c**) Reaction with 2-alkyl pyrrole does not yield to the desired product.

2,4-diarylpyrrole failed to give any product, suggesting that the 2-aryl substituent in the pyrrole is essential for the formation of these restricted aza-BODIPY dyes.

All the conformationally restricted systems **345–357** absorb over 650 nm. Dyes **345–347** with both sides incorporated in carbocyclic rings have narrow,

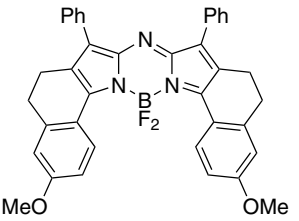

345
$CHCl_3$, Φ 0.28
$\lambda_{max\ abs}$ 740 nm
ε 159000 M^{-1} cm^{-1}
$\lambda_{max\ emiss}$ 752 nm

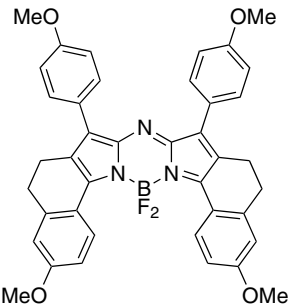

346
$CHCl_3$, Φ 0.29
$\lambda_{max\ abs}$ 736 nm
ε 157000 M^{-1} cm^{-1}
$\lambda_{max\ emiss}$ 748 nm

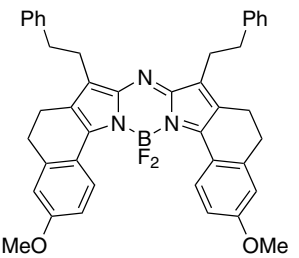

347
$CHCl_3$, Φ 0.31
$\lambda_{max\ abs}$ 721 nm
ε 162000 M^{-1} cm^{-1}
$\lambda_{max\ emiss}$ 732 nm

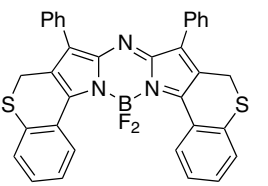

348
$CHCl_3$, Φ 0.11
$\lambda_{max\ abs}$ 706 nm
ε 115000 M^{-1} cm^{-1}
$\lambda_{max\ emiss}$ 730 nm

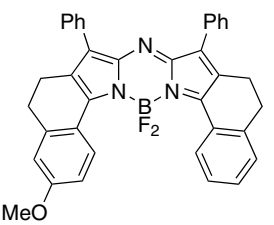

349
$CHCl_3$, Φ 0.32
$\lambda_{max\ abs}$ 723 nm
ε 157000 M^{-1} cm^{-1}
$\lambda_{max\ emiss}$ 734 nm

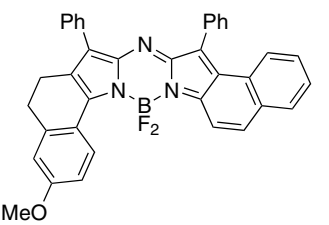

350
$CHCl_3$, Φ 0.11
$\lambda_{max\ abs}$ 715 nm
ε 141000 M^{-1} cm^{-1}
$\lambda_{max\ emiss}$ 730 nm

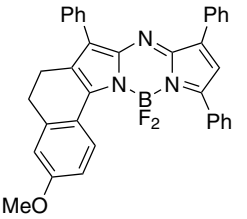

351
$CHCl_3$, Φ 0.44
$\lambda_{max\ abs}$ 688 nm
ε 108000 M^{-1} cm^{-1}
$\lambda_{max\ emiss}$ 710 nm

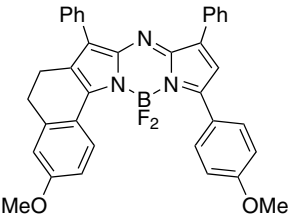

352
$CHCl_3$, Φ 0.38
$\lambda_{max\ abs}$ 708 nm
ε 96200 M^{-1} cm^{-1}
$\lambda_{max\ emiss}$ 732 nm

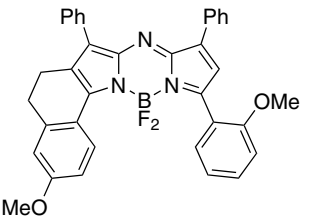

353
$CHCl_3$, Φ 0.38
$\lambda_{max\ abs}$ 678 nm
ε 83900 M^{-1} cm^{-1}
$\lambda_{max\ emiss}$ 713 nm

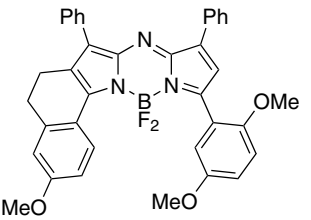

354
$CHCl_3$, Φ 0.24
$\lambda_{max\ abs}$ 681 nm
ε 66500 M^{-1} cm^{-1}
$\lambda_{max\ emiss}$ 728 nm

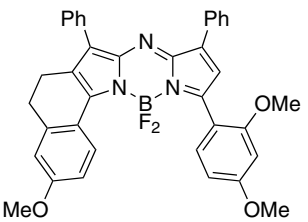

355
$CHCl_3$, Φ 0.18
$\lambda_{max\ abs}$ 707 nm
ε 78000 M^{-1} cm^{-1}
$\lambda_{max\ emiss}$ 735 nm

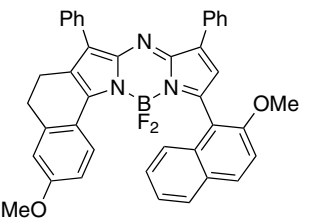

356
$CHCl_3$, Φ 0.46
$\lambda_{max\ abs}$ 668 nm
ε 113000 M^{-1} cm^{-1}
$\lambda_{max\ emiss}$ 692 nm

intense (high ε) absorption bands at long wavelengths. In comparison to the "non-constrained" tetraaryl-azaBODIPY **335**, there is a bathochromic shift of up to 52 nm and a concomitant halving of the fwhm (27 nm for **347** vs. 52 nm for **335**). The novel dyes were reported to possess excellent chemical and photostability. Furthermore, the fluorescence is insensitive to solvent polarity.[291,292]

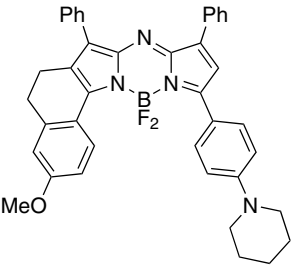

357
$CHCl_3$, Φ 0.05
$\lambda_{max\ abs}$ 774 nm
ε 70300 M^{-1} cm^{-1}
$\lambda_{max\ emiss}$ 815 nm

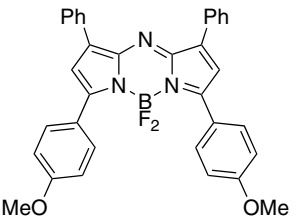

335
$CHCl_3$, Φ 0.36
$\lambda_{max\ abs}$ 688 nm
ε 78500 M^{-1} cm^{-1}
$\lambda_{max\ emiss}$ 715 nm

There are also several details regarding the spectral properties of the dyes in this series. Substitution at the 3-position of the core does not affect the ε-value of the dyes (compare **345**–**347**). Introduction of electron-donating groups results in a small blue-shift and a slightly higher fluorescence quantum yield (**345** vs. **346**). Shorter λ_{abs}, lower ε, broader absorption band, and lower fluorescence quantum yield were associated with the sulfur-containing dye **348**. The dehydrogenated carbocyclic restricted ring in system **350** decreases its quantum yield relative to **345**. Aza-BODIPYs with only one side restricted have much lower extinction coefficients (**351**–**357** vs. **345**). The quantum yields of non-symmetric aza-BODIPY dyes are highly dependent on the substituents on the aromatic ring. Electron donating *para*-substituents give higher quantum yields (**351** and **352**), with shorter λ_{abs} indicating that the phenyl rings are twisted. *ortho*-Electron donating groups (e.g. in **353**) result in short λ_{abs}, low ε, and broad absorption bands, indicating that the phenyl rings in **353** are twisted. Unexpectedly shorter λ_{abs}, low ε, broader absorption bands and lower quantum yields were observed when two methoxy groups were present (**354** and **355**). The sharp and intense absorption, high quantum yield obtained in the special case of **356** wherein a 2-methoxy-1-naphthyl substituent is present indicates that the naphthyl ring is distorted so that electron transfer is suppressed.

2. *Dyes Based on Benz[c,d]indole*

Synthesis of compound **359** involves refluxing 2-benz[*c*,*d*]indolamine hydroiodide with 2-(methylthio)benz[*c*,*d*]indole-hydroiodide in 1,2-dichlorobenzene in presence of triethylamine gives the amine **358**. Subsequent treatment with boron trifluoride etherate affords the desired product **359** (Chart 39).[293]

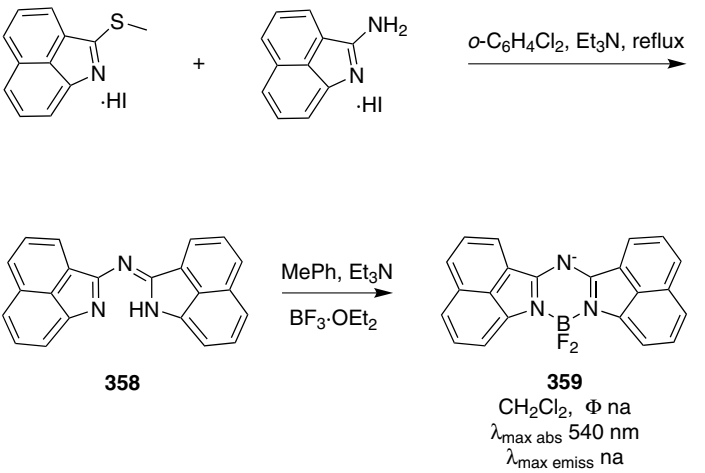

Chart 39.

While the benz[*c,d*]indole based BODIPY dye **313** displays a red-shifted absorption and fluorescence, the aza-BODIPY analog **359** shows a blue-shifted absorption at 540 nm. Unfortunately, no fluorescence properties have been reported.

C. Cyclized Aza-BODIPY Systems

As for BODIPYs, near-IR derivatives of aza-BODIPYs could be obtained via intramolecular B-O ring formation. Thus, systems like **361** were obtained via two complementary routes (Scheme 27).[294] Scheme 27a outlines the route developed for BODIPY by Burgess where upon treatment with boron tribromide, demethylation of the methoxy groups to the corresponding bisphenols occurs followed by spontaneous cyclization. Surprisingly, bromination of the pyrrole ring was also observed for **361b** leading to the products **361e** and **f**. When strong electron-donating groups were used in the *para*-position of the 3- and 5-aryl ring, e.g. **360c** and **d**, the desired product could be formed (as evidenced by UV) but not isolated, as they decomposed rapidly upon exposure to air. Thus, a complementary route (Scheme 27b) was developed by O'Shea and coworkers[294] to allow inclusion of strong electron donating substituent. Fluorophores **361g–h** were obtained in a one-pot BF_2 chelation and intramolecular phenolic oxygen-fluorine displacement from dipyromethene ligands **362g–h**.

As for BODIPY, restriction caused by the B-O bonds in **361** lead to bathochromic shifts for both the absorption (86 nm) and emission (56 nm) maxima and over a 7-fold increase in the quantum yield from 0.07 to 0.51 (**332** to **361a**). Interestingly,

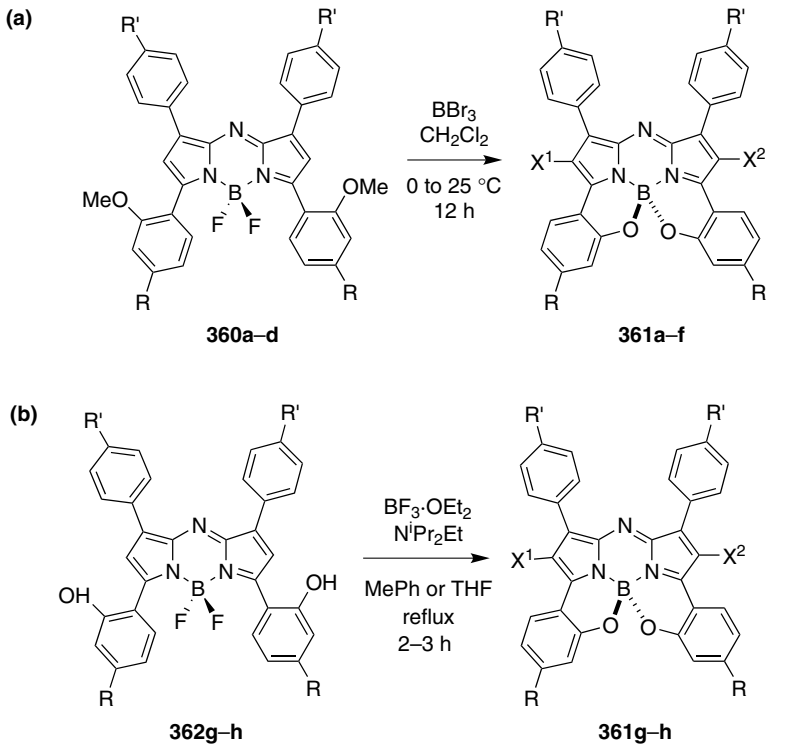

	R	R'	X^1	X^2	λ_{abs}	λ_{emiss}	Φ
a	H	H	H	H	728	746	0.51
b	H	Br	H	H	745	760	0.46
c	OMe	Br	H	H	unstable, decomposed		
d	NMe_2	Br	H	H	unstable, decomposed		
e	H	Br	Br	H	747	769	0.35
f	H	Br	Br	Br	755	776	0.36
g	OMe	H	H	H	765	782	0.18
h	H	OMe	H	H	728	742	0.17

Scheme 27. Synthesis of cyclized aza-BODIPYs via (**a**) demethylation and cyclization; and (**b**) intramolecular phenolic oxygen-fluoride displacement.

the tetrabromo derivative **361f** also has red-shifted absorption and emission maxima and introduction of bromines onto the pyrrole did not result in a significant quenching of fluorescence.

D. Other Metals

Tricoordinate Cu(I), Ag(I), and Au(I) complexes of the tetraphenylazadipyrromethene **363** have recently been described (Chart 40).[295] All complexes exhibit an intense absorption band centered around 600 nm. In the case of the silver based complex, the extinction coefficient is twice that of the copper ones. All complexes are weakly luminescent at room temperature (Φ = 0.0024–0.0039 compared to 0.0014 for **363**).

Aza-BODIPY complexes **365a–d** of Co(II), Ni(II), Cu(II) and Zn(II) were easily prepared from the aza-dipyrrin **332** by heating with the corresponding metal acetate salt in butanol (Chart 41). They all have 1:2 metal:ligand stoichiometries. The complexes absorb around 600 nm, with the exception of the Cu(II) one which shows a splitting with λ values of 566–640 nm, similar to the free ligand **332**

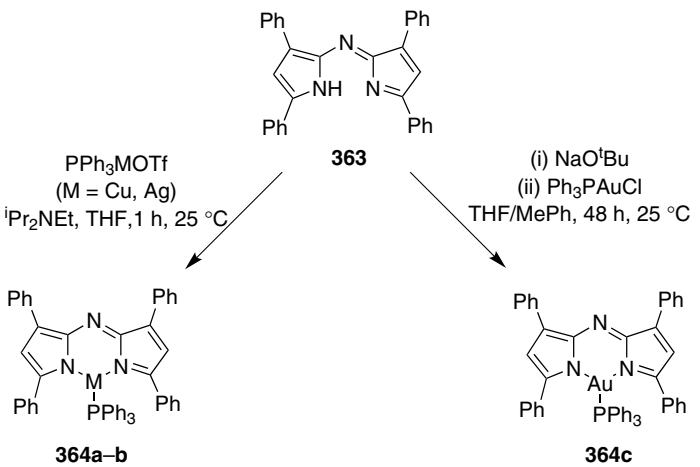

in $CHCl_3$

	M	λ_{abs}	ε M^{-1} cm^{-1}	λ_{emiss}	Φ
a	Cu	597	38 000	642	0.0025
b	Ag	615	65 000	647	0.0039
c	Au	600	45 000	645	0.0024

Chart 40.

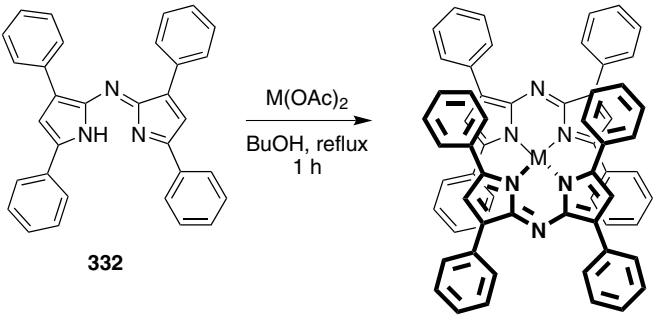

332 **365a–d**

in CH_2Cl_2

	M	λ_{abs}	ε M^{-1} cm^{-1}
a	Co(II)	602	94 000
b	Ni(II)	603	142 000
c	Cu(II)	640/567	65 700/62 800
d	Zn(II)	593	78 6 00

Chart 41.

(λ_{abs} 593 nm), suggesting that the absorption is primarily ligand centered with band broadening upon metal chelation. In contrast to the BF_2 chelates, these complexes were non-fluorescent.[296]

XIII. Other Analogs of the BODIPYs

A. GFP-Chromophore Analogs

Compounds **371** were synthesized as mimics of the green fluorescent protein (GFP) fluorophore.[297] Synthetic analogues **H**–**K** of the GFP chromophore (**G**) have been prepared and studied, [298,299] but they fluoresce at shorter wavelengths and are not fluorescent primarily because of free rotation about the aryl-alkene bond (Figure 11). Steric and electronic factors prevent free rotation of the aryl substituents and isomerization of the alkene when the chromophore is encapsulated within the β-barrel protein structure; hence, the molecule is strongly fluorescent. To block free rotation around the aryl-alkene bond, inclusion of boron into compounds **370** to give compounds **371** was performed.

Synthesis of compounds **370** was first attempted following the known method, e.g. condensation of hippuric or aceturic acid derivatives with aldehydes

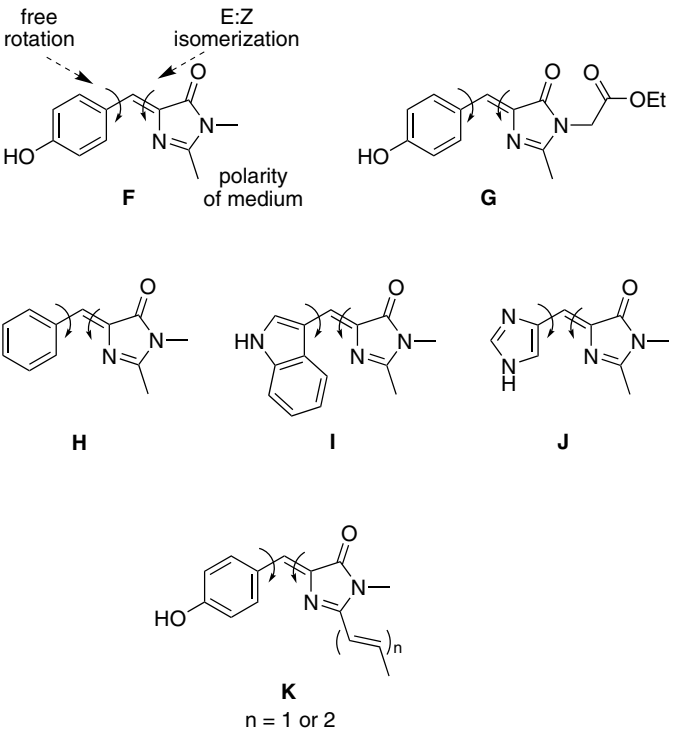

Figure 11. The GFP chromophore (**F**) and some synthetic analogues (**G–K**).

(Scheme 28a), but these conditions did not work well for pyrrole-2-carbaldehyde. Consequently, the targets compounds **370** were prepared via the route described in Scheme 28b. This new route involves preparation of an imidazolinone **367**, condensation of this with pyrrole-2-carbaldehyde to give compounds **368**, followed by addition of boron. In the last step, compound **368** isomerizes to form **369** and **370**. *E,Z*-Isomerization of compounds **368** did not significantly impact the syntheses of products **370** since the isomers interconvert in the chelation step. When *E*-**368c** (prepared via condensation mediated by HBr/TFA (condition ii in Scheme 28b)) was converted to the boron-containing products, both compounds **369c** and **370c** were formed, in a ca. 2:1 ratio, respectively. Similarly, when a 1:1 mixture of *E*-**368c** and *Z*-**368c** were treated with $BF_3{\cdot}OEt_2$, **369c** and **370c** were formed in a ratio of approximately 2:1. Therefore, it appears that formation of **370c** from **368c** is a stereorandom process.

Compounds **371** are neutral, uncharged, highly fluorescent molecules that absorb and emit around 520–530 nm. Addition of BF_2 to the open-chain intermediates **369** greatly increased the quantum yields of compounds **370** providing more evidence that GFP chromophores within the protein are highly fluorescent due to

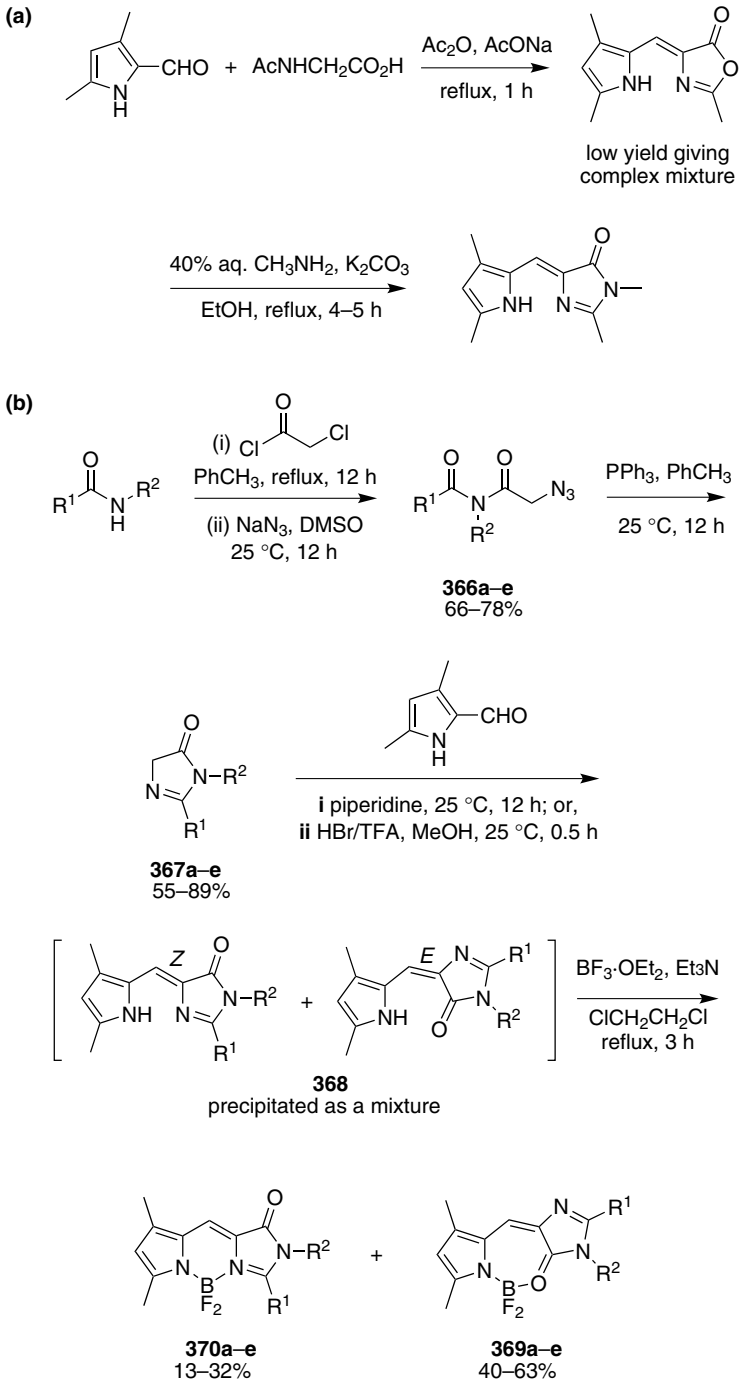

Scheme 28. Synthesis of compounds **370** from (**a**), hippuric acid and pyrrole-2-carbaldehyde; (**b**) imidazolinone **367** and pyrrole-2-carbaldehydes.

the conformational locking within the β-barrel cocoon. The absorption and fluorescence maxima of **370a–e** are red-shifted by up to 20 nm in less polar media like CH_2Cl_2 (data not shown). Among the series, **370f** has the lowest fluorescence quantum yield, probably due to d-PeT. Compounds **370** can easily be sulfonated and modified to include a point of attachment to biomolecules while maintaining their strong fluorescence.

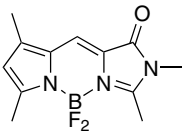

370a
MeOH, Φ 0.89
$\lambda_{max\ abs}$ 477 nm
$\lambda_{max\ emiss}$ 485 nm

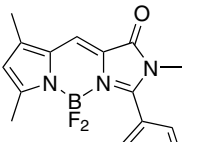

370b
MeOH, Φ 0.87
$\lambda_{max\ abs}$ 490 nm
$\lambda_{max\ emiss}$ 521 nm

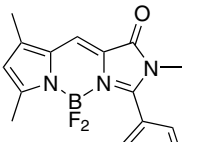

370c
MeOH, Φ 0.86
$\lambda_{max\ abs}$ 492 nm
$\lambda_{max\ emiss}$ 532 nm

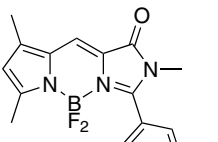

370d
MeOH, Φ 0.85
$\lambda_{max\ abs}$ 493 nm
$\lambda_{max\ emiss}$ 521 nm

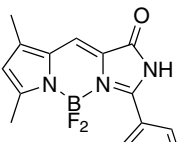

370e
MeOH, Φ 0.80
$\lambda_{max\ abs}$ 495 nm
$\lambda_{max\ emiss}$ 531 nm

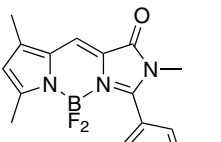

370f
Hexanes, Φ 0.53
$\lambda_{max\ abs}$ 498 nm
$\lambda_{max\ emiss}$ 587 nm

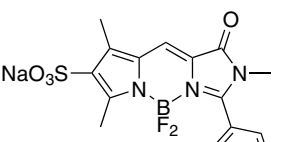

370g
PBS pH 7.4, Φ 0.87
$\lambda_{max\ abs}$ 481 nm
$\lambda_{max\ emiss}$ 518 nm

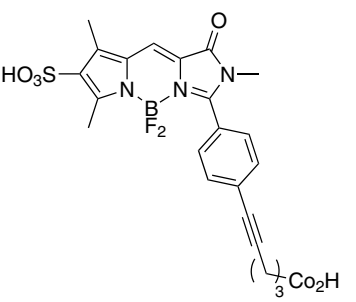

370h
PBS pH 7.4, Φ 0.82
$\lambda_{max\ abs}$ 482 nm
$\lambda_{max\ emiss}$ 526 nm

B. Fused Perylene Tetracarboxylic Diimide and BODIPY Analog

Perylene tetracarboxylic diimides (PDIs) are commonly modified by introducing side groups either to the imide nitrogen atoms or at the bay positions. Substitution at the imide nitrogen can improve their solubilities in organic solvents, while substituents at the bay positions can change their photophysical properties depending on their withdrawing or donating abilities and their steric hindrance. Electron donating groups can red-shift both the absorption and emission maxima, but induce a significant loss of fluorescence. To change the absorption and emission of PDIs without loss of fluorescence, compounds **374** an **375** were designed.[300] They combine PDI and BODIPY units. Compounds **374** and **375** were prepared from the corresponding PDIs **371** and **372** by condensation with 2-methylquinoline, followed by complexation with boron (Scheme 29).

The photophysical properties of the PDIs derivatives **373**–**375** were studied and compared to **376**. The new probes have good solubility in conventional organic solvents. Introduction of the quinoline unit resulted in a 6 and 11 nm red shift for the absorption maxima of **373a** and **b**, respectively, compared to **376**. The absorption maxima for **374** and **375** were further shifted to the red to 616 and 650 nm, respectively, upon complexation with boron. This is because coordination with boron has driven the quinoline to take a precisely coplanar conformation with PDI, therefore extending the conjugation of the aromatic system. Similarly, the

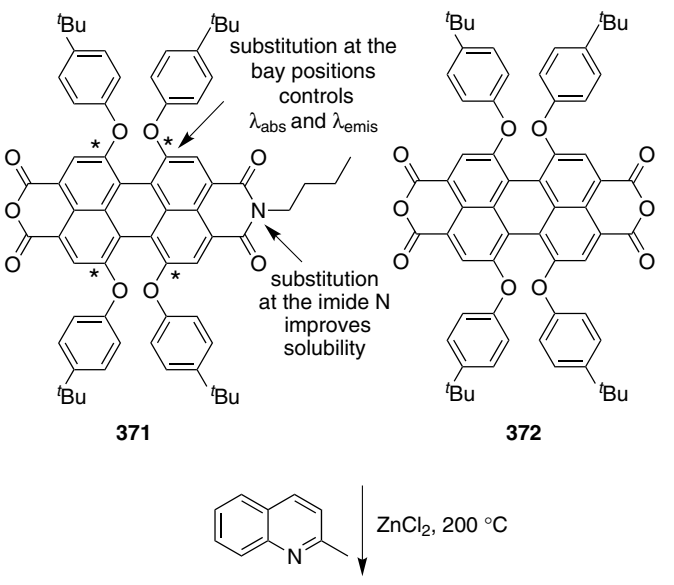

Scheme 29. Synthesis of compounds **374** and **375**.

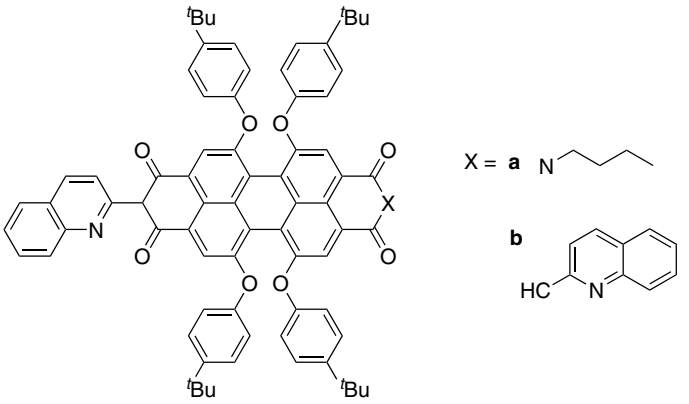

373a
CH_2Cl_2, Φ 0.66
λ_{abs} 582 nm
λ_{emiss} 620 nm

373b
CH_2Cl_2, Φ 0.59
λ_{abs} 588 nm
λ_{emiss} 632 nm

$BF_3{\cdot}OEt_2$
$^iPr_2NEt$
PhMe, 80 °C

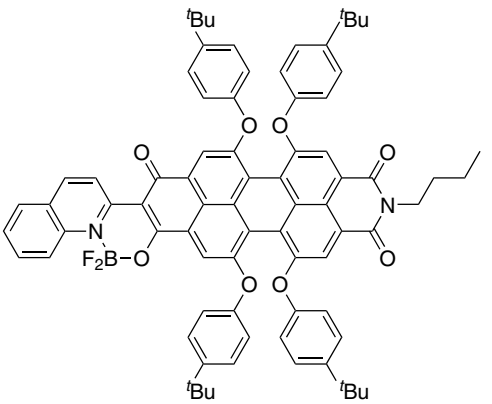

374 72%
CH_2Cl_2, Φ 0.50
$\lambda_{max\ abs}$ 616 nm
$\lambda_{max\ emiss}$ 655 nm

Scheme 29. (*Continued*)

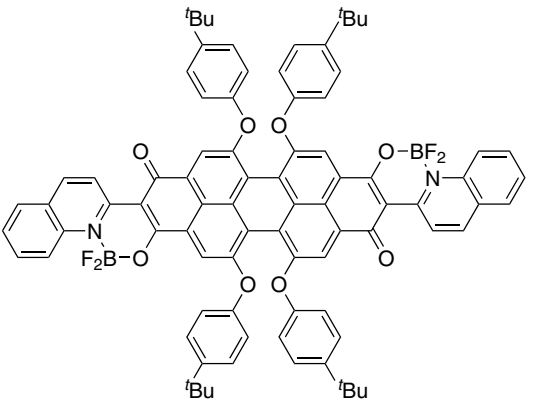

375 68%
CH_2Cl_2, Φ 0.35
$\lambda_{max\ abs}$ 650 nm
$\lambda_{max\ emiss}$ 689 nm

Scheme 29. (*Continued*)

emission of **373a**–**b**, **374** and **375** were red-shifted relative to **376**. The fluorescence quantum yields and fluorescence lifetimes of **373a**–**b**, **374** and **375** are almost half of that of **376**. This might be caused by the increased flexibility of the molecule upon introduction of the quinoline, which induces mass nonradioactive decay.

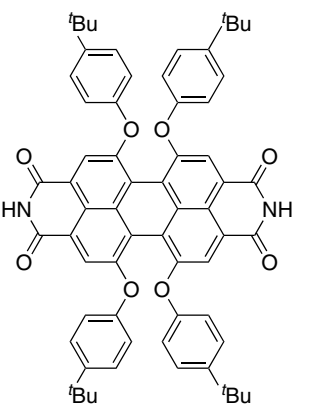

376
CH_2Cl_2, Φ 1.00
λ_{abs} 576 nm
λ_{emiss} 607 nm

C. Biimidazol-2-yl-BF_2 Complexes

Biimidazol-2-yls difluoroborate complexes **377** have been obtained by: (i) reacting glyoxal bisulfite, 2,3-butanedione and concentrated aqueous NH_3 (Scheme 30a)[301,302]; (ii) condensation of 1,2-cyclohexanedione with 40% aqueous glyoxal in ethanol saturated with dry ammonia gas[302]; and, (iii) condensation of oxamide with *o*-phenylenediamine in refluxing ethylene glycol (Scheme 30c).[303,304] It would

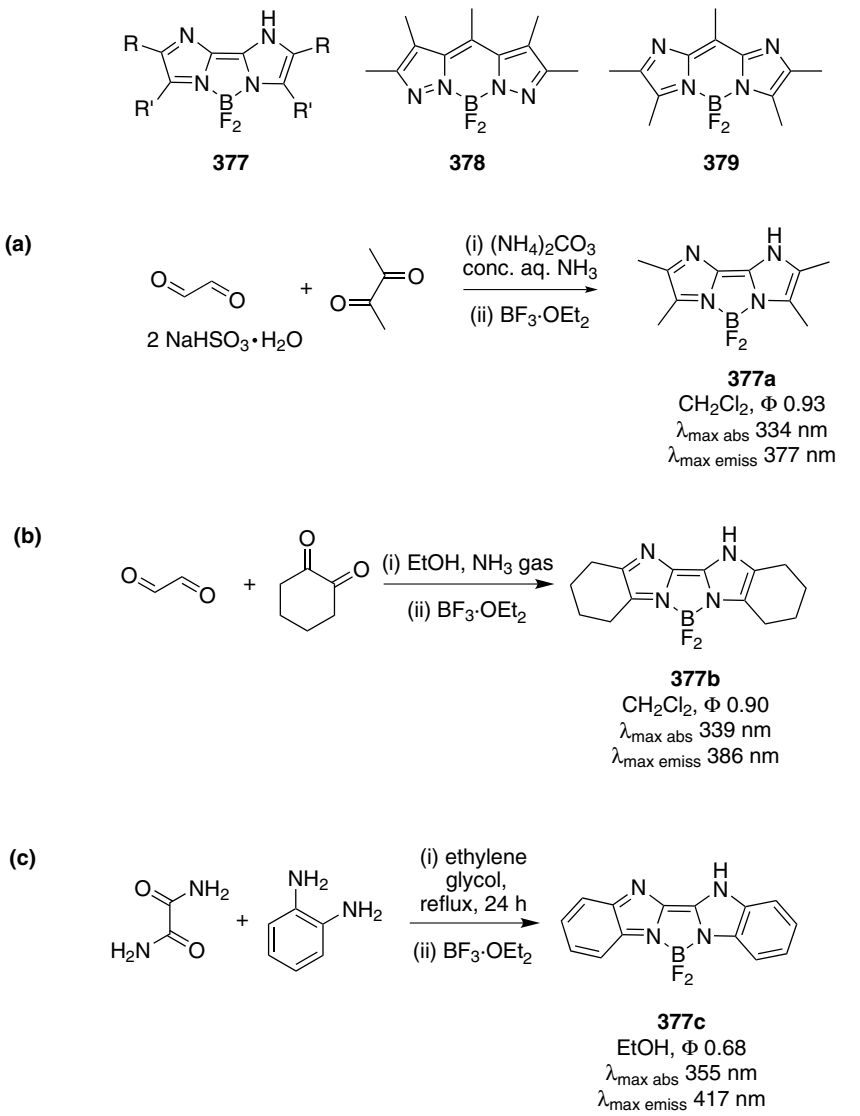

Scheme 30. Synthesis of biimidazol-2-yls BF_2 complexes.

seem logical that similar dyes of the type **378** and **379** could be prepared, but attempts to do so have been reported as unsuccessful.[305]

The parent, non-*B*-coordinated heterocyclic systems for molecules **377** are not significantly fluorescent, but the BF_2 complexes display strong fluorescence. Predictably, red shifts for both the absorption and emission maxima, and increased extinction coefficients are observed with increased conjugation and rigidity.

D. Pyridine-Based Systems

The dipyridyl-2-yl-boron complexes **380–384** have been prepared from reactions of bipyridines with boron electrophiles.[306] They absorb between 302–322 nm, with the exception of the complex **383**, which absorbs at 371 nm. No fluorescence was detected for these complexes.

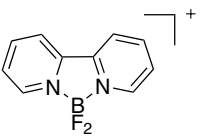

380

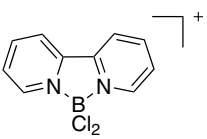

381

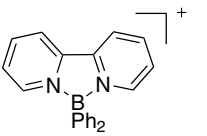

382

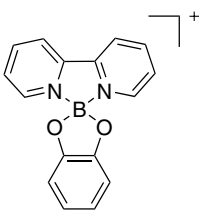

383

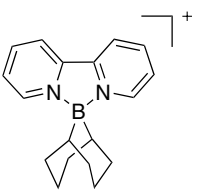

384

The pyridomethene-BF_2 complex **385** was synthesized as shown in Chart 42 from the 2,2′-dipyridylmethane by fusion with sodium borohydride.[307] The product shows a strong absorption at 468 nm, with a extinction coefficient of 17,783 $M^{-1}cm^{-1}$ in chloroform, but does not fluoresce.

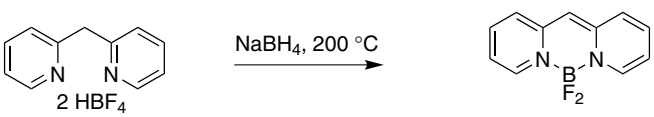

385

Chart 42.

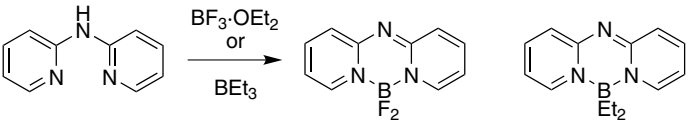

386a
EtOH, Φ 0.81
$\lambda_{max\ abs}$ 382 nm
$\lambda_{max\ emiss}$ 422 nm

386b
no UV/Flu data

Chart 43.

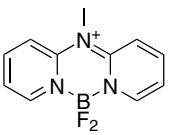

387
EtOH, Φ 0.36
$\lambda_{max\ abs}$ 325 nm
$\lambda_{max\ emiss}$ 362 nm

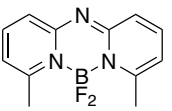

388
EtOH, Φ 0.40
$\lambda_{max\ abs}$ 396 nm
$\lambda_{max\ emiss}$ 416 nm

The 10-azapyridomethene-BF_2 complex **386a** was obtained via condensation between dipyrid-2-ylamine and boron trifluoride.[280] Similarly, 10-azapyridomethene-$B(Et)_2$ **386b** was obtained by condensation with triethylboron (Chart 43). Complex **386a** absorbs at 382 nm (log ε = 4.47) in ethanol, and strongly fluoresces at 422 nm (Φ = 0.81).

Treatment of dipyrid-2-ylamine with methyl iodide gives the methyldipyrid-2-ylamine, which can be converted to the 10-methyl-10-azapyridomethene-BF_2 complex **387** by treatment with boron trifluoride. The homologous complex **388** was obtained by condensation between 2-amino-6-methylpyridine and 2-chloro-6-methylpyridine, and subsequent treatment with boron trifluoride. Both these complexes are fluorescent, but the neutral one, **388**, fluoresces at longer wavelength.

E. 2-Ketopyrrole Complexes

The 2-ketopyrrole complexes **389–393** were isolated as minor byproducts (less than 5%) in the synthesis of the corresponding BODIPY analogs.[308] The yield of **389–393** could be improved by increasing the amount of acid chloride used in the synthesis. 2-Ketopyrrole complexes are less conjugated than BODIPY dyes, hence their absorption, extinction coefficients and emission wavelengths are shorter/smaller. The Stokes' shifts for these compounds, however, are greater than for BODIPY systems (48 nm to 154 nm, *cf* approximately 10–15 nm for BODIPY dyes).

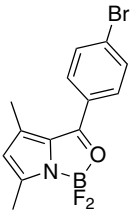

389
$CHCl_3$, Φ na
$\lambda_{max\ abs}$ 321 nm
ε 19 000
$\lambda_{max\ emiss}$ 475 nm

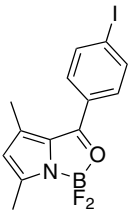

390
$CHCl_3$, Φ na
$\lambda_{max\ abs}$ 322 nm
ε 16 000
$\lambda_{max\ emiss}$ 475 nm

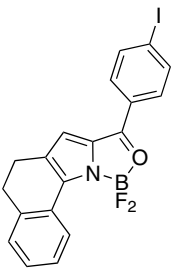

391
$CHCl_3$, Φ 0.89
$\lambda_{max\ abs}$ 468 nm
ε 48 000
$\lambda_{max\ emiss}$ 516 nm

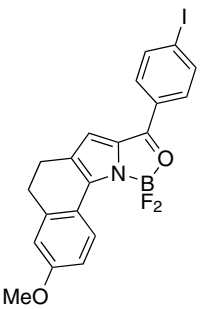

392
$CHCl_3$, Φ 0.52
$\lambda_{max\ abs}$ 488 nm
ε 43 000
$\lambda_{max\ emiss}$ 544 nm

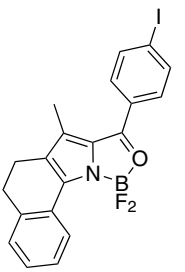

393
$CHCl_3$, Φ 0.58
$\lambda_{max\ abs}$ 445 nm
ε 46 000
$\lambda_{max\ emiss}$ 504 nm

F. Azobenzene Derivatives

Azobenzenes are the most common chromophores in commercial dyes and, because of photoinduced isomerization, they are used as photoresponsive molecular switches. A consequence of facile photoisomerization is that quantum yields for these compounds are so low that fluorescence tends only to be observed in a rigid matrix at low temperature. A recent innovation in this field is fixation of the π-conjugate systems using boryl-entities to give the fluorescent compounds **394**–**396** (Chart 44).[309]

Azobenzene dyes **394** and **395** display a remarkable red shifted absorbance (386 nm and 439 nm, respectively) relative to unsubstituted (*E*)-azobenzene (λ = 315 nm). Irradiation of **394** and **395** with a super-high-pressure mercury lamp did not cause photoisomerization. The azobenzene derivative **396**, bearing a fluorinated substituent on the boron atom, showed almost no fluorescence. We speculate that this could be due to intramolecular charge transfer from the least electron rich aryl substituent into the excited state of the complexed azobenzene system.

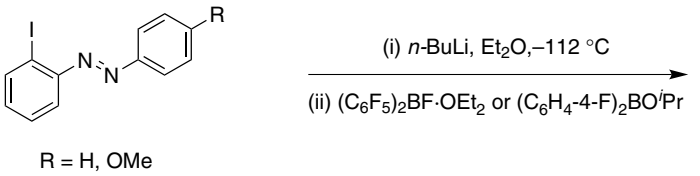

R = H, OMe

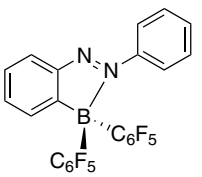

394
hexanes; Φ 0.23
$\lambda_{max\ abs}$ 386 nm
$\lambda_{max\ emiss}$ 503 nm

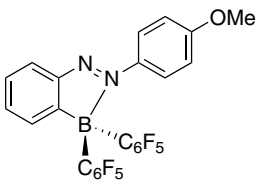

395
hexanes; Φ 0.76
$\lambda_{max\ abs}$ 439 nm
$\lambda_{max\ emiss}$ 524 nm

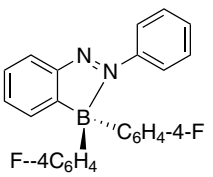

396
no fluorescence

Chart 44.

G. Miscellaneous *N,N*-Bidentate Diphenyl Boron Chelates

Luminescent *N,N*-bidentate diphenylboron chelates **397**–**409**[310,311] have emission maxima that vary with the nature of the parent organic system. Limited information was provided regarding the spectroscopic properties of these molecules, but the data presented are interesting because some of the dyes have high quantum yields and/or fluorescence emissions around 600 nm. These systems perhaps warrant further attention.

A variety of methods were used to produce the parent heterocycles for the dyes shown above (Scheme 31). The 2-(2′-pyridyl)indole and 2-(2′-thiazolyl)indole based ligands were synthesized by a two-step Fischer synthesis (Scheme 31a

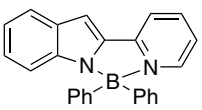

397
$\lambda_{max\ emiss}$ 516 nm
Φ 0.29

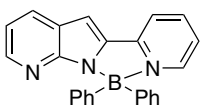

398
$\lambda_{max\ emiss}$ 476 nm
Φ 0.61

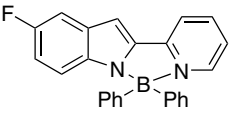

399
$\lambda_{max\ emiss}$ 490 nm
Φ 0.33

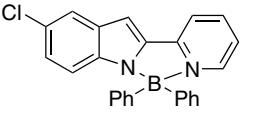

400
$\lambda_{max\ emiss}$ 487 nm
Φ 0.22

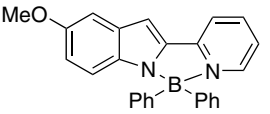

401
$\lambda_{max\ emiss}$ 532 nm
Φ 0.036

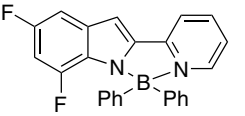

402
$\lambda_{max\ emiss}$ 481 nm
Φ 0.32

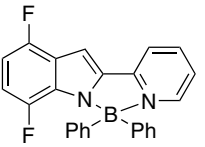

403
$\lambda_{max\ emiss}$ 482 nm
Φ 0.31

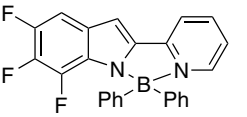

404
$\lambda_{max\ emiss}$ 469 nm
Φ 0.65

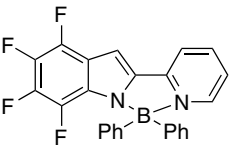

405
$\lambda_{max\ emiss}$ 467 nm
Φ 0.60

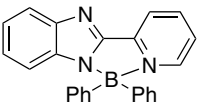

406
$\lambda_{max\ emiss}$ 445 nm
Φ 0.46

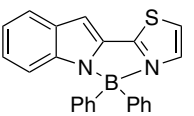

407
$\lambda_{max\ emiss}$ 470 nm
Φ 0.14

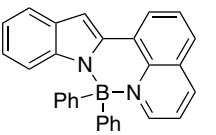

408
$\lambda_{max\ emiss}$ 611 nm
Φ na

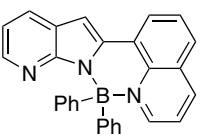

409
$\lambda_{max\ emiss}$ 583 nm
Φ na

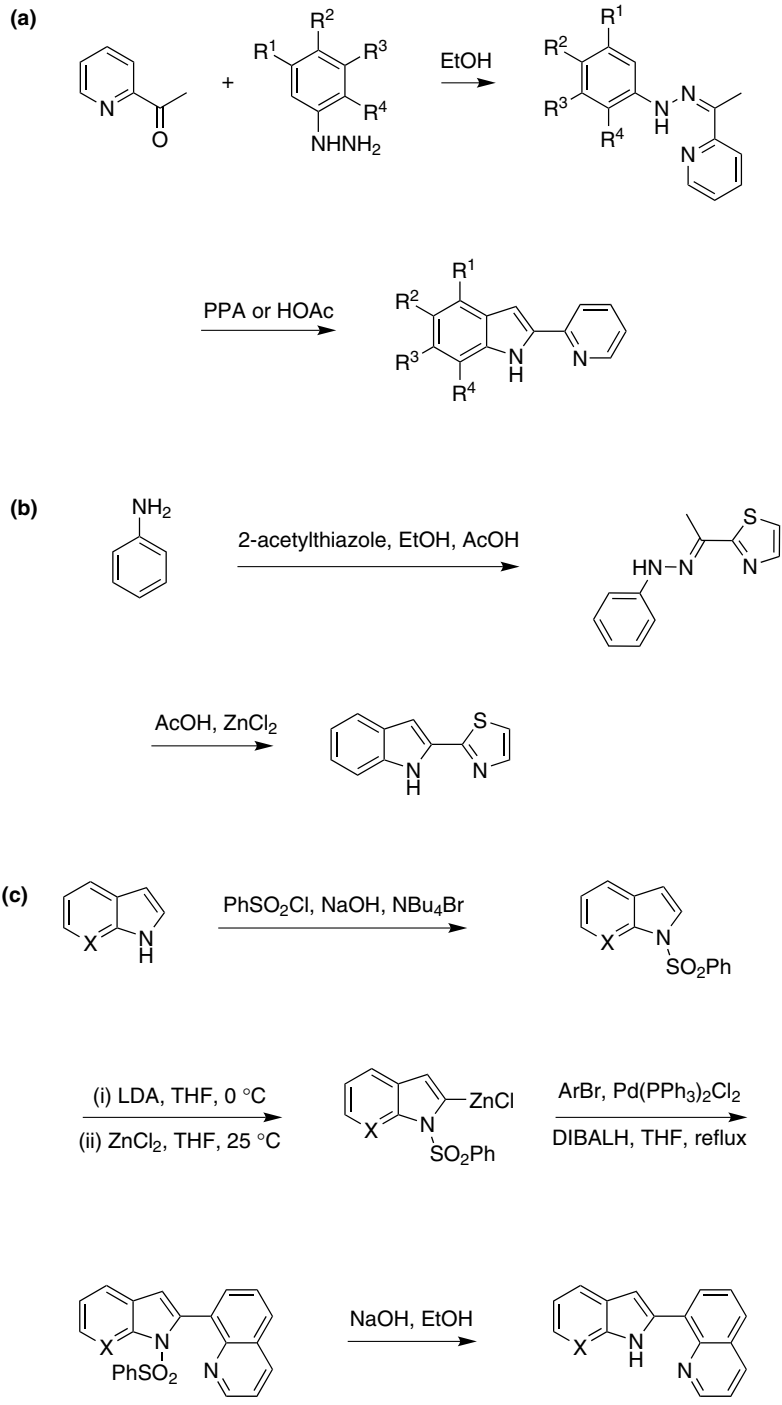

Scheme 31. Two-step Fischer synthesis of (**a**) 2-(2′-pyridyl)indole; (**b**) 2-(2′-thiazolyl)indole; (**c**) synthesis of 2-(8′-quinolyl)indole or aza-indole via Negishi coupling.

and b, respectively). Scheme 31c illustrates how a Negishi coupling[312] was used for the synthesis of the 2-(8′-quinolyl)indole or -azaindole. Treatment of the product heterocycles shown in Scheme 30 with triphenylboron (1:1 ratio) in toluene afforded the boron complexes **397**–**409** in good yields.

H. Boryl-Substituted Thienylthiazoles

Finally, there are compounds that are even less closely related to the BODIPY core, formed by intramolecular B-N coordination in *N*-heteroaromatic systems. This new concept is illustrated for the development of new electronic materials. The interaction between the Lewis acid (boron) and Lewis base (nitrogen) not only constrain the π-conjugated framework in a coplanar fashion, but also lower the LUMO level (Figure 12). Thus, (3-boryl-2-thienyl)-2-thiazole **410** was synthesized from (3-bromo-2-thienyl)-2-thiazole as shown in Scheme 32.[313]

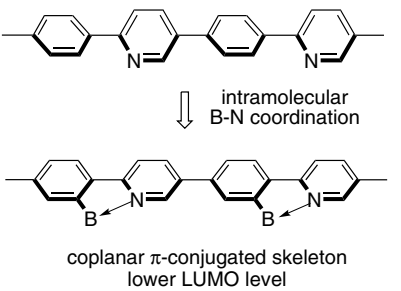

Figure 12. Intramolecular B-N Coordination of *N*-heteroaromatic systems.

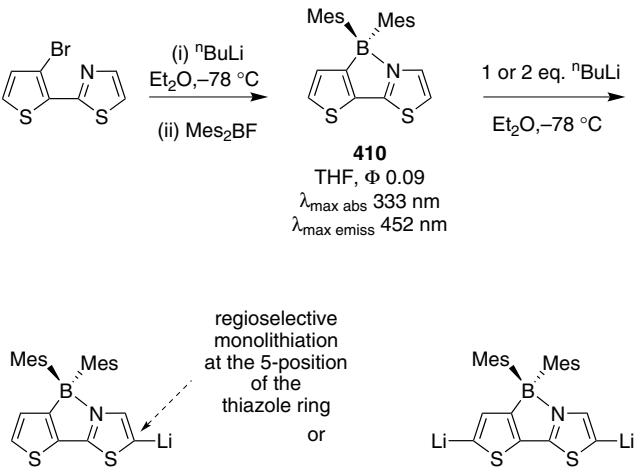

Scheme 32. Synthesis of the dimesityl-boryl substituted thienylthiazole **410**.

Compound **410** can easily be functionalized to the tin **411** or iodo **412** derivatives via the lithiated intermediates. Lithiation occurs regioselectively at the 5-position of the thiazole ring.

The corresponding tin and iodo derivatives can be used as building blocks in metal-catalyzed coupling reactions to prepare extended π-electron systems such as the head-to-head (H-H), head-to-tail (H-T), and tail-to-tail (T-T) dimers **413–415** (Scheme 33). The dimers display red-shifted absorption and emission relative to the monomer. The boryl-substituted thienylthiazoles **410** and **413–415** show weak fluorescence emission in the range 452–492 nm.[313]

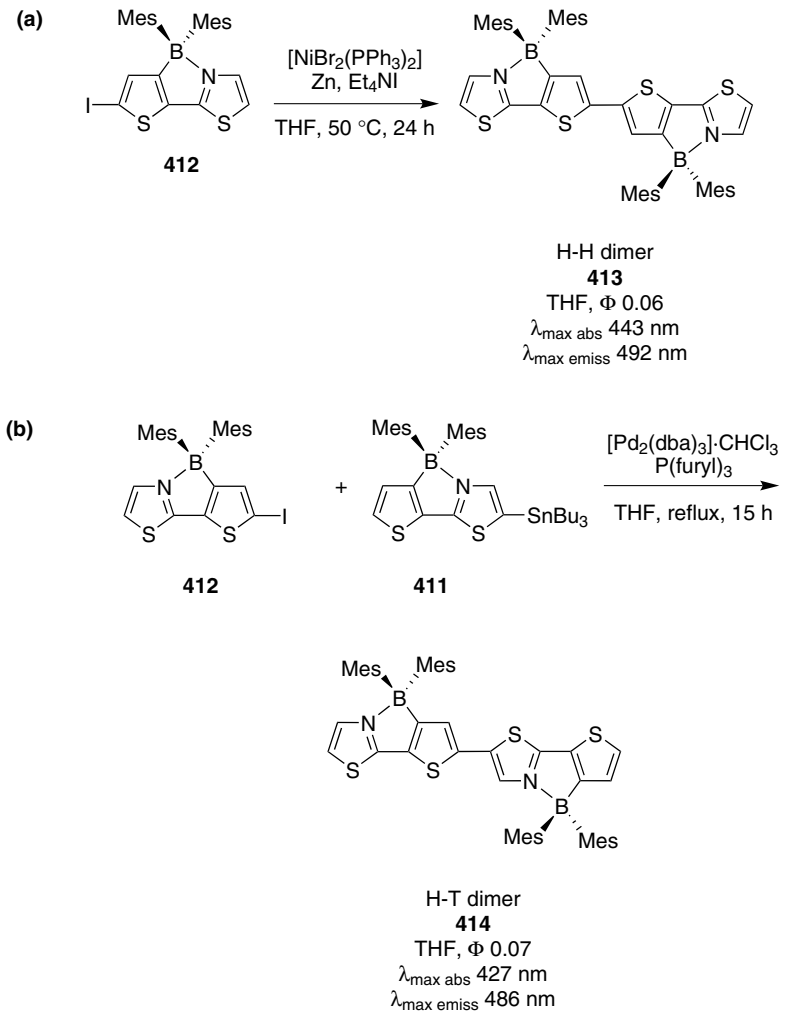

Scheme 33. Synthesis of (**a**), head-to-head; (**b**), head-to-tail, and (**c**), tail-to-tail dimers.

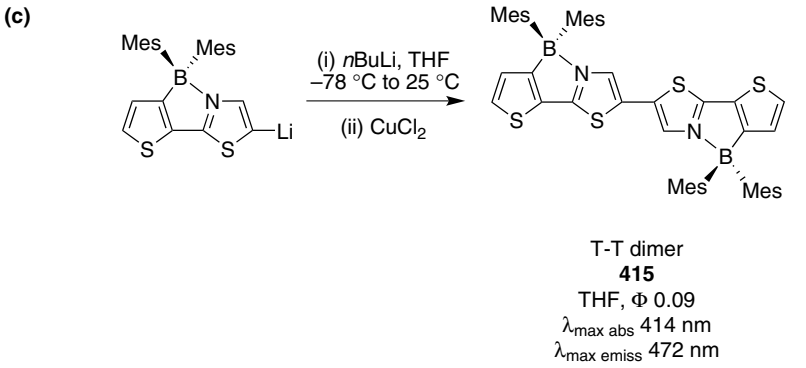

Scheme 33. (*Continued*)

XIV. Conclusion

Modifications of the BODIPY core have reached an advanced stage of development, and there has been tremendous activity in the area even since our 2007 review.[77] The area of BODIPY-syntheses now resembles a jig-saw puzzle that is perhaps 95% complete, but with a few important pieces that have yet to be added. For instance, synthetic methods for BODIPY syntheses were previously dominated by condensation reactions of pyrroles with carboxylic acid or aldehyde derivatives. This situation has shifted markedly due to the emergence of some useful BODIPY synthons that can be elaborated to give dyes that would not be conveniently accessible via condensation processes. These key synthons include derivatives that have: *meso*-*S*-alkyl substituents **G**; 3,5-*S*-alkyl groups **H**; boronate esters **I** and **J**; and, 2,6- and 3,5-halogenated systems **K** and **L**, respectively; 3,5-dichloro substituents **M**. The halogenated systems, for instance, may be functionalized via S_NAr reactions, transition-metal mediated couplings, or directly attached to proteins.

Recent insights into the ways in which BODIPY dyes can react have also broadened the range of speciality dyes that can be prepared. Notable examples of this include modification of the BF_2 substituents, particularly by Ziessel and coworkers who have added many different *C*-substituents,[216,217,314] and cyclic systems incorporating the boron atom as illustrated by work from our laboratories.[315] Similarly, Akkaya's group[160,167] and others[157] have shown the value of Knoevanagel condensations of Me-substituted BODIPY dyes, particularly for syntheses of lipophilic probes that fluoresce in the near-IR region.

Access to near-IR fluorophores has been a long-standing objective in the field, particularly for applications in biotechnology. Significant contributions in this area come from incorporation of extended heterocyclic systems, one excellent example being the "Keio" fluors, e.g. **300h**[262,263] and another is the isoindole-based

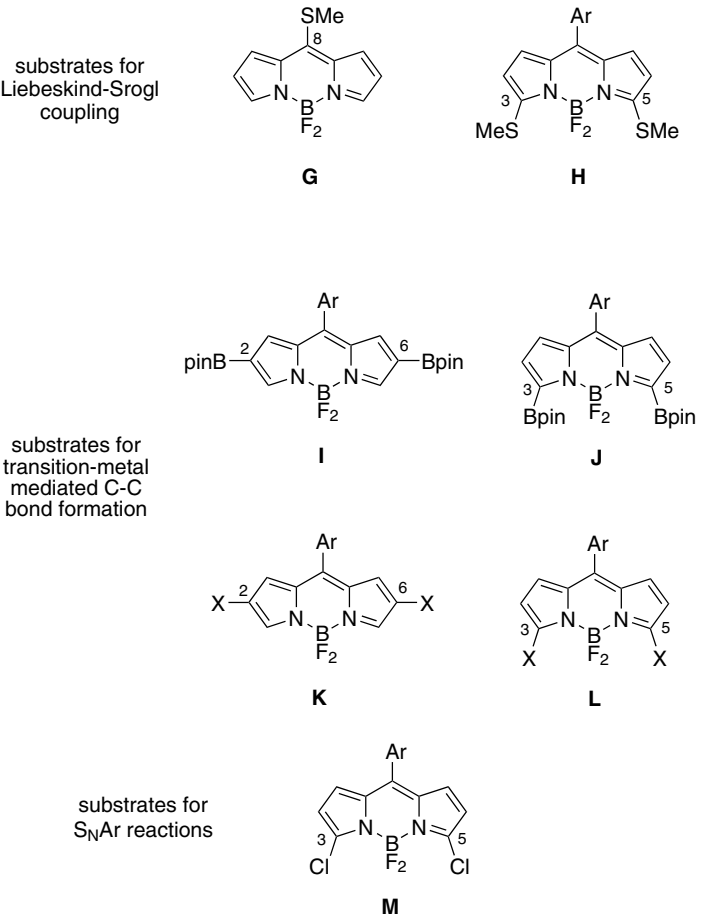

systems **258**. O'Shea and coworkers have rejuvenated interest in the aza-BODIPY dyes, which are extremely interesting for the near-IR emission properties.

So, what are the remaining synthetic challenges in the area? Even though there have been some significant breakthroughs in syntheses of *water-soluble* BODIPY dyes (e.g. **104**, **110, 112** and **114**) all the one prepared so far tend to emit well below 600 nm. There is a significant demand in biotechnology for water-soluble dyes that fluoresce brilliantly in the near-IR region, and the BODIPY community had not yet addressed this issue directly. Similarly, there is an unmet need for conveniently accessible, water-soluble cassettes for multiplexing, i.e. that can be excited at one wavelength but fluoresce at conspicuously different wavelengths.

Short wavelength light has poor tissue permeability, may cause photodamage, and is easily swamped by background fluorescence. Conversely, two-photon methods enable of deeper imaging in tissue with minimal photodamage and induction of peripheral cell autofluorescence. However, only a few conventional

fluorescent dyes, such as rhodamines and fluorescein,[316] exhibit satisfactory two-photon cross-sections (TPAs) for practical applications. Efforts to design fluorophores with higher TPAs have not embraced BODIPYs systems as a means to generate probes with higher TPAs than endogenous compounds in cells.[317–323] A recent article by Qian[324] reports the novel long-wavelength BODIPY derivatives **416** and **417** which have considerable TPA cross-sections and strong red emissions. Efficient internal charge transfer processes and donor–acceptor arrangements are important in designing two-photon absorbing molecules. We envisage this could be an area of some interest in the next decade.

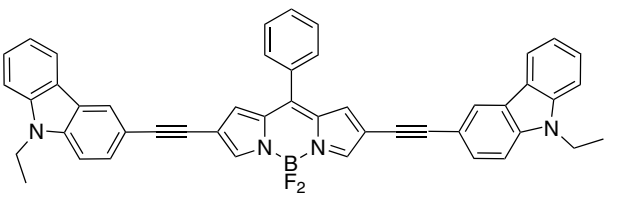

416
THF, Φ 0.36
$\lambda_{max\ abs}$ 597 nm
$\lambda_{max\ emiss}$ 653 nm
$\lambda_{max\ emiss\ TPE}$ 670 nm
σ 46 GM

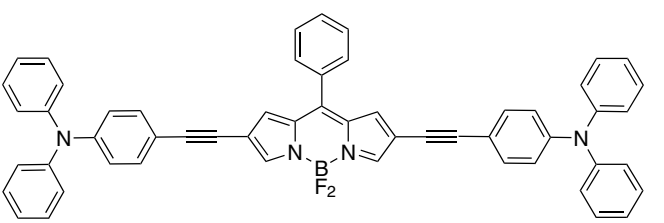

417
THF, Φ 0.31
$\lambda_{max\ abs}$ 593 nm
$\lambda_{max\ emiss}$ 659 nm
$\lambda_{max\ emiss\ TPE}$ 687 nm
σ 60 GM

Compounds **418–419** are two more examples of BODIPY based systems in which the TPA properties have been studied. The TPA (σ) for these were found to be 48 and 75 GM at 990 nm, corresponding to about 2.4 and 3.7 times that of a reference compound **104** (σ = 20 GM at 920 nm).[318]

Materials research and some aspects of *in vivo* imaging might also motivate more interest in polymer systems based on, or incorporating BODIPY dyes. Several inroads into this type of research have already been made, but the contributions so far lack direct illustration of potential applications of these substances.

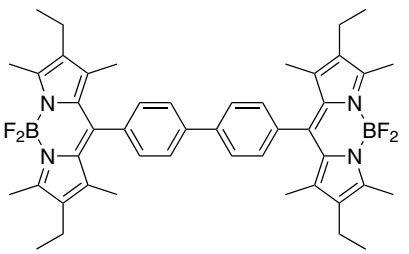

418
PhMe, Φ 0.72
$\lambda_{max\ abs}$ 527 nm
$\lambda_{max\ emiss}$ 542 nm
$\sigma_{at\ 700\ nm}$ 57 GM
$\sigma_{at\ 990\ nm}$ 48 GM

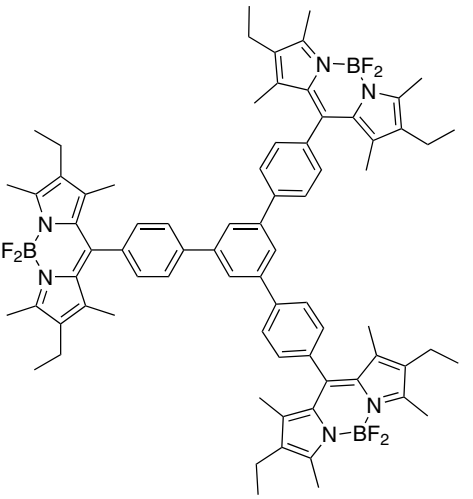

419
PhMe, Φ 0.72
$\lambda_{max\ abs}$ 527 nm
$\lambda_{max\ emiss}$ 542 nm
$\sigma_{at\ 700\ nm}$ 82 GM
$\sigma_{at\ 990\ nm}$ 75 GM

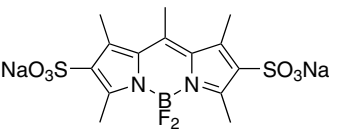

104
H_2O, Φ 0.83
$\lambda_{max\ abs}$ 491 nm
$\lambda_{max\ emiss}$ 519 nm
$\sigma_{at\ 700\ nm}$ - GM
$\sigma_{at\ 990\ nm}$ 9 GM

This could be another area of interest. Similarly, dendritic systems such as **419**, seems to be at an early stage of development.

Finally, we envisage that research on BODIPY dyes is set to move into a second era. This will feature syntheses of tailor-made probes to explore issues in biotechnology and materials research that are more sophisticated than simple sensing applications. For instance, we can imagine specialized applications in genomics, directed *in vivo* diagnostics, and synthetic biology that may come to the fore.

XV. References

1. Karolin, J.; Johansson, L. B.-A.; Strandberg, L.; Ny, T. *J. Am. Chem. Soc.* **1994**, *116*, 7801–7806.

2. Haugland, R. P. *Handbook of Fluorescent Probes and Research Chemicals*; 6th ed.; Molecular Probes: Eugene, OR, **1996**.
3. Tan, K.; Jaquinod, L.; Paolesse, R.; Nardis, S.; Di Natale, C.; Di Carlo, A.; Prodi, L.; Montalti, M.; Zaccheroni, N.; Smith, K. M. *Tetrahedron* **2004**, *60*, 1099–1106.
4. Yee, M.-C.; Fas, S. C.; Stohlmeyer, M. M.; Wandless, T. J.; Cimprich, K. A. *J. Biol. Chem.* **2005**, *280*, 29053–29059.
5. Wagner, R. W.; Lindsey, J. S. *Pure Appl. Chem.* **1996**, *68*, 1373–1380.
6. Metzker, M. L. Substituted 4,4-difluoro-4-bora-3a, 4a-diaza-s-indacene compounds for 8-color DNA sequencing. WO Patent 2003066812, February 5,2003.
7. Fa, M.; Bergstrom, F.; Hagglof, P.; Wilczynska, M.; Johansson, L. B. A.; Ny, T. *Structure* **2000**, *8*, 397–405.
8. Bergstrom, F.; Hagglof, P.; Karolin, J.; Ny, T.; Johansson, L. B. A. *Proc. Natl. Acad. Sci. USA* **1999**, *96*, 12477–12481.
9. Wagner, R. W.; Lindsey, J. S. *Pure Appl. Chem.* **1996**, *68*, 1373–1380.
10. Katayama, M.; Nakane, R.; Matsuda, Y.; Kaneko, S.; Hara, I.; Sato, H. *Analyst* **1998**, *123*, 2339–2342.
11. Karolin, J.; Johansson, L. B. A.; Strandberg, L.; Ny, T. *J. Am. Chem. Soc.* **1994**, *116*, 7801–7806.
12. Drummen, G. P. C.; van Liebergen, L. C. M.; Op den Kamp, J. A. F.; Post, J. A. *Free Radical Biol. Med.* **2002**, *33*, 473–490.
13. Johnson, I. D.; Kang, H. C.; Haugland, R. P. *Anal. Biochem.* **1991**, *198*, 228–237.
14. Kurata, S.; Kanagawa, T.; Yamada, K.; Torimura, M.; Yokomaku, T.; Kamagata, Y.; Kurane, R. *Nucleic Acids Res.* **2001**, *29*, e34/31–e34/35.
15. Luo, Y.; Prestwich, G. D. *Bioconjugate Chem.* **1999**, *10*, 755–763.
16. Yamada, K.; Toyota, T.; Takakura, K.; Ishimaru, M.; Sugawara, T. *New J. Chem.* **2001**, *25*, 667–669.
17. Pagano, R. E.; Chen, C.-S. *Ann. NY Acad. Sci.* **1998**, *845*, 152–160.
18. Samsonov, A. V.; Mihalyov, I.; Cohen, F. S. *Biophys. J.* **2001**, *81*, 1486–1500.
19. Boldyrev, I. A.; Molotkovsky, J. G. *Russian J. Bioorg. Chem.* **2006**, *32*, 78–83.
20. Tahtaoui, C.; Parrot, I.; Klotz, P.; Guillier, F.; Galzi, J.-L.; Hibert, M.; Ilien, B. *J. Med. Chem.* **2004**, *47*, 4300–4315.
21. Shute, T. S.; Matsushita, M.; Dickerson, T. J.; La Clair, J. J.; Janda, K. D.; Burkart, M. D. *Bioconjugate Chem.* **2005**, *16*, 1352–1355.
22. Rostron, J. P.; Ulrich, G.; Retailleau, P.; Harriman, A.; Ziessel, R. *New J. Chem* **2005**, *29*, 1241–1244.
23. Lawrie, G.; Grondahl, L.; Battersby, B.; Keen, I.; Lorentzen, M.; Surawski, P.; Trau, M. *Langmuir* **2006**, *22*, 497–505.
24. Merino, E. J.; Weeks, K. M. *J. Am. Chem. Soc.* **2005**, *127*, 12766–12767.
25. Fang, Y.; Peng, J.; Ferrie, A. M.; Burkhalter, R. S. *Anal. Chem.* **2006**, *78*, 149–155.
26. Worthington, A. S.; Burkart, M. D. *Org. Biomol. Chem.* **2006**, *4*, 44–46.
27. Li, J.; Kim, I. H.; Roche, E. D.; Beeman, D.; Lynch, A. S.; Ding, C. Z.; Ma, Z. *Bioorg. Med. Chem. Lett.* **2006**, *16*, 794–797.
28. Li, Z.; Mintzer, E.; Bittman, R. *J. Org. Chem.* **2006**, *71*, 1718–1721.
29. Toyota, T.; Tsuha, H.; Yamada, K.; Takakura, K.; Yasuda, K.; Sugawara, T. *Langmuir* **2006**, *22*, 1976–1981.
30. Rose, T. M.; Prestwich, G. D. *ACS Chem. Biol.* **2006**, *1*, 83–92.

31. Meng, Q.; Kim, D. H.; Bai, X.; Bi, L.; Turro, N. J.; Ju, J. *J. Org. Chem.* **2006**, *71*, 3248–3252.
32. Ferguson, C. G.; Bigman, C. S.; Richardson, R. D.; Van Meeteren, L. A.; Moolenaar, W. H.; Prestwich, G. D. *Org. Lett.* **2006**, *8*, 2023–2026.
33. Sculimbrene, B. R.; Imperiali, B. *J. Am. Chem. Soc.* **2006**, *128*, 7346–7352.
34. Peters, C.; Billich, A.; Ghobrial, M.; Hoegenauer, K.; Ullrich, T.; Nussbaumer, P. *J. Org. Chem.* **2007**, *72*, 1842–1845.
35. Golovkova, T. A.; Kozlov, D. V.; Neckers, D. C. *J. Org. Chem.* **2005**, *70*, 5545–5549.
36. Trieflinger, C.; Rurack, K.; Daub, J. *Angew. Chem., Int. Ed.* **2005**, *44*, 2288–2291.
37. Turfan, B.; Akkaya, E. U. *Org. Lett.* **2002**, *4*, 2857–2859.
38. Gee, K. R.; Rukavishnikov, A.; Rothe, A. *Comb. Chem. High Throughput Screening* **2003**, *6*, 363–366.
39. Zhang, X.; Wang, H.; Li, J.-S.; Zhang, H.-S. *Anal. Chim. Acta* **2003**, *481*, 101–108.
40. DiCesare, N.; Lakowicz, J. R. *Tetrahedron Lett.* **2001**, *42*, 9105–9108.
41. Rurack, K.; Kollmannsberger, M.; Daub, J. *Angew. Chem. Int. Ed.* **2001**, *40*, 385–387.
42. Baki, C. N.; Akkaya, E. U. *J. Org. Chem.* **2001**, *66*, 1512–1513.
43. Kollmannsberger, M.; Rurack, K.; Resch-Genger, U.; Rettig, W.; Daub, J. *Chem. Phys. Lett.* **2000**, *329*, 363–369.
44. Rurack, K.; Kollmannsberger, M.; Resch-Genger, U.; Daub, J. *J. Am. Chem. Soc.* **2000**, *122*, 968–969.
45. Cha, N. R.; Moon, S. Y.; Chang, S.-K. *Tetrahedron Lett.* **2003**, *44*, 8265–8268.
46. Werner, T.; Huber, C.; Heinl, S.; Kollmannsberger, M.; Daub, J.; Wolfbeis, O. S. *Fresenius' J. Anal. Chem* **1997**, *359*, 150–154.
47. Kollmannsberger, M.; Gareis, T.; Heinl, S.; Breu, J.; Daub, J. *Angew. Chem., Int. Ed.* **1997**, *36*, 1333–1335.
48. Knaus, H. G.; Moshammer, T.; Kang, H. C.; Haugland, R. P.; Glossmann, H. *J. Biol. Chem.* **1992**, *267*, 2179–2189.
49. Kalai, T.; Hideg, K. *Tetrahedron* **2006**, *62*, 10352–10360.
50. Kalai, T.; Hideg, E.; Jeko, J.; Hideg, K. *Tetrahedron Lett.* **2003**, *44*, 8497–8499.
51. Moon, S. Y.; Cha, N. R.; Kim, Y. H.; Chang, S.-K. *J. Org. Chem.* **2004**, *69*, 181–183.
52. Gabe, Y.; Urano, Y.; Kikuchi, K.; Kojima, H.; Nagano, T. *J. Am. Chem. Soc.* **2004**, *126*, 3357–3367.
53. Li, M.; Wang, H.; Zhang, X.; Zhang, H.-S. *Spectrochim. Acta, Part A* **2004**, *60A*, 987–993.
54. Koutaka, H.; Kosuge, J.-I.; Fukasaku, N.; Hirano, T.; Kikuchi, K.; Urano, Y.; Kojima, H.; Nagano, T. *Chem. Pharm. Bull.* **2004**, *52*, 700–703.
55. Martin, V. V.; Rothe, A.; Diwu, Z.; Gee, K. R. *Bioorg. Med. Chem. Lett.* **2004**, *14*, 5313–5316.
56. Zhang, X.; Zhang, H.-S. *Spectrochim. Acta, Part A* **2005**, *61A*, 1045–1049.
57. Martin, V. V.; Rothe, A.; Gee, K. R. *Bioorg. Med. Chem. Lett.* **2005**, *15*, 1851–1855.
58. Wu, Y.; Peng, X.; Guo, B.; Fan, J.; Zhang, Z.; Wang, J.; Cui, A.; Gao, Y. *Org. Biomol. Chem.* **2005**, *3*, 1387–1392.
59. Baruah, M.; Qin, W.; Basaric, N.; De Borggraeve Wim, M.; Boens, N. *J. Org. Chem.* **2005**, *70*, 4152–4157.
60. Yamada, K.; Nomura, Y.; Citterio, D.; Iwasawa, N.; Suzuki, K. *J. Am. Chem. Soc.* **2005**, *127*, 6956–6957.
61. Coskun, A.; Akkaya, E. U. *J. Am. Chem. Soc.* **2005**, *127*, 10464–10465.
62. Basaric, N.; Baruah, M.; Qin, W.; Metten, B.; Smet, M.; Dehaen, W.; Boens, N. *Org. Biomol. Chem.* **2005**, *3*, 2755–2761.

63. Malval, J.-P.; Leray, I.; Valeur, B. *New J. Chem* **2005**, *29*, 1089–1094.
64. Baruah, M.; Qin, W.; Vallee, R. A. L.; Beljonne, D.; Rohand, T.; Dehaen, W.; Boens, N. *Org. Lett.* **2005**, *7*, 4377–4380.
65. Bricks, J. L.; Kovalchuk, A.; Trieflinger, C.; Nofz, M.; Bueschel, M.; Tolmachev, A. I.; Daub, J.; Rurack, K. *J. Am. Chem. Soc.* **2005**, *127*, 13522–13529.
66. Coskun, A.; Deniz, E.; Akkaya, E. U. *Org. Lett.* **2005**, *7*, 5187–5189.
67. Zeng, L.; Miller, E. W.; Pralle, A.; Isacoff, E. Y.; Chang, C. J. *J. Am. Chem. Soc.* **2006**, *128*, 10–11.
68. Meallet-Renault, R.; Herault, A.; Vachon, J.-J.; Pansu, R. B.; Amigoni-Gerbier, S.; Larpent, C. *Photochem. Photobiol.* **2006**, *5*, 300–310.
69. Mei, Y.; Bentley, P. A.; Wang, W. *Tetrahedron Lett.* **2006**, *47*, 2447–2449.
70. Qi, X.; Jun, E. J.; Xu, L.; Kim, S.-J.; Hong, J. S. J.; Yoon, Y. J.; Yoon, J. *J. Org. Chem.* **2006**, *71*, 2881–2884.
71. Wang, J.; Qian, X. *Org. Lett.* **2006**, *8*, 3721–3724.
72. Li, J.-S.; Wang, H.; Huang, K.-J.; Zhang, H.-S. *Anal. Chim. Acta* **2006**, *575*, 255–261.
73. Kim, H. J.; Kim, J. S. *Tetrahedron Lett.* **2006**, *47*, 7051–7055.
74. Gabe, Y.; Ueno, T.; Urano, Y.; Kojima, H.; Nagano, T. *Anal. Biochem.* **2006**, *386*, 621–626.
75. Arbeloa, T. L.; Arbeloa, F. L.; Arbeloa, I. L.; Garcia-Moreno, I.; Costela, A.; Sastre, R.; Amat-Guerri, F. *Chem. Phys. Lett.* **1999**, *299*, 315–321.
76. http://probes.invitrogen.com In *Molecular Probes, pH Indicators-Chapter 20* Invitrogen Corporation, 2006.
77. Loudet, A.; Burgess, K. *Chem. Rev.* **2007**, *107*, 4891–4832.
78. Dixon, H. B. F.; Cornish-Bowden, A.; Liebecq, C.; Loening, K. L.; Moss, G. P.; Reedijk, J.; Velick, S. F.; Venetianer, P.; Vliegenthart, J. F. G.; *et al*. *Pure Appl. Chem.* **1987**, *59*, 779–832.
79. Treibs, A.; Kreuzer, F. H. *Liebigs Ann. Chem.* **1968**, *718*, 208–223.
80. Tram, K.; Yan, H.; Jenkins, H. A.; Vassiliev, S.; Bruce, D. *Dyes Pigm.* **2009**, *82*, 392–395.
81. Arroyo, I. J.; Hu, R.; Merino, G.; Tang, B. Z.; Pena-Cabrera, E. *J. Org. Chem.* **2009**, *74*, 5719–5722.
82. Van Koeveringe, J. A.; Lugtenburg, J. *Recl. Trav. Chim. Pays-Bas* **1977**, *96*, 55–58.
83. Vos de Wael, E.; Pardoen, J. A.; Van Koeveringe, J. A.; Lugtenburg, J. *Recl. Trav. Chim. Pays-Bas* **1977**, *96*, 306–309.
84. Vos de Wael, E.; Pardoen, J. A.; Van Koeveringe, J. A.; Lugtenburg, J. *Recl. Trav. Chim. Pays-Bas* **1977**, *96*, 306–309.
85. Bandichhor, R.; Thivierge, C.; Bhuvanesh, N. S. P.; Burgess, K. *Acta Chrystallogr. Sect. E* **2006**, *E62*, o4310–o4311.
86. Schmitt, A.; Hinkeldey, B.; Wild, M.; Jung, G. *J. Fluoresc.* **2009**, *19*, 755–758.
87. Plater, M. J.; Aiken, S.; Bourhill, G. *Tetrahedron* **2002**, *58*, 2405–2413.
88. Shah, M.; Thangaraj, K.; Soong, M. L.; Wolford, L.; Boyer, J. H.; Politzer, I. R.; Pavlopoulos, T. G. *Heteroat. Chem.* **1990**, *1*, 389–399.
89. Boyer, J. H.; Haag, A. M.; Sathyamoorthi, G.; Soong, M. L.; Thangaraj, K.; Pavlopoulos, T. G. *Heteroat. Chem.* **1993**, *4*, 39–49.
90. Goud, T. V.; Tutar, A.; Biellmann, J.-F. *Tetrahedron* **2006**, *62*, 5084–5091.
91. Nicolaou, K. C.; Claremon, D. A.; Papahatjis, D. P. *Tetrahedron Lett.* **1981**, *22*, 4647–4650.
92. Tahtaoui, C.; Thomas, C.; Rohmer, F.; Klotz, P.; Duportail, G.; Mely, Y.; Bonnet, D.; Hibert, M. *J. Org. Chem.* **2007**, *72*, 269–272.
93. Wu, L.; Burgess, K. *Chem. Commun.* **2008**, 4933–4935.

94. Sun, Z.-N.; Wang, H.-L.; Liu, F.-Q.; Chen, Y.; Tam, P. K. H.; Yang, D. *Org. Lett.* **2009**, *11*, 1887–1890.
95. Sekiya, M.; Umezawa, K.; Sato, A.; Citterio, D.; Suzuki, K. *Chem. Commun.* **2009**, 3047–3049.
96. Oleynik, P.; Ishihara, Y.; Cosa, G. *J. Am. Chem. Soc.* **2007**, *139*, 1842–1843.
97. Krumova, K.; Oleynik, P.; Karam, P.; Cosa, G. *J. Org. Chem.* **2009**, *74*, 3641–3651.
98. Matsui, M.; Funabiki, K.; Nakaya, K.-I. *Bull. Chem. Soc. Japan* **2005**, *78*, 464–467.
99. Huh, J. O.; Do, Y.; Lee, M. H. *Organometallics* **2008**, *27*, 1022–1025.
100. de Silva, A. P.; Gunaratne, H. Q. N.; Gunnlaugsson, T.; Huxley, A. J. M.; McCoy, C. P.; Rademacher, J. T.; Rice, T. E. *Chem. Rev.* **1997**, *97*, 1515–1566.
101. Tanaka, K.; Miura, T.; Umezawa, N.; Urano, Y.; Kikuchi, K.; Higuchi, T.; Nagano, T. *J. Am. Chem. Soc.* **2001**, *123*, 2530–2536.
102. Ueno, T.; Urano, Y.; Setsukinai, K.; Takakusa, H.; Kojima, H.; Kikuchi, K.; Ohkubo, K.; Fukuzumi, S.; Nagano, T. *J. Am. Chem. Soc.* **2004**, *126*, 14079–14085.
103. Sunahara, H.; Urano, Y.; Kojima, H.; Nagano, T. *J. Am. Chem. Soc.* **2007**, *129*, 5597–5604.
104. Rehm, D.; Weller, A. *Isr. J. Chem.* **1970**, *8*, 259–271.
105. Ueno, T.; Urano, Y.; Kojima, H.; Nagano, T. *J. Am. Chem. Soc.* **2006**, *128*, 10640–10641.
106. Pavlopoulos, T. G.; Boyer, J. H.; Shah, M.; Thangaraj, K.; Soong, M. L. *Appl. Opt.* **1990**, *29*, 3885–3886.
107. Boyer, J. H.; Thangaraj, K.; Soong, M. L.; Sathyamoorthi, G.; Ross, T. M.; Haag, A. M. *Proc. Int. Conf. Lasers* **1991**, 739–741.
108. Pavlopoulos, T. G. *Proc. SPIE-Int. Soc. Opt. Eng.* **1999**, *3613*, 112–118.
109. Suzuki, T.; Tanaka, T.; Higashiguchi, I.; Oda, A. Organic electroluminescent device elements. JP Patent 11176572, 1999.
110. Takuma, K.; Misawa, T.; Sugimoto, K.; Nishimoto, T.; Tsukahara, H.; Tsuda, T.; Imai, G.; Kogure, H. Visible light-curable resin compositions and their use in inks. JP Patent 10273504, January 29, 1998.
111. Imai, G.; Kogure, H.; Ogiso, A.; Misawa, T.; Nishimoto, T.; Tsukahara, H.; Takuma, K. Visible light-curable resin compositions and their use in electrophotographic material. JP Patent 2000001509, 2000.
112. Imai, G.; Kogure, H.; Ogiso, A.; Misawa, T.; Nishimoto, T.; Tsukahara, H.; Takuma, K. Visible light-curable resin compositions and their use in electrophotographic material. JP Patent 2000001510, 2000.
113. Imai, G.; Kogure, H.; Ogiso, A.; Misawa, T.; Nishimoto, T.; Tsukahara, H.; Takuma, K. Positive-working visible ray-sensitive resin composition containing pyrromethene boron complex sensitizer and its usage. JP Patent 2000039715, 2000.
114. Imai, G.; Kogure, H.; Ogiso, A.; Misawa, T.; Nishimoto, T.; Tsukahara, H.; Takuma, K. Positive-working visible ray-sensitive resin composition containing pyrromethene boron complex sensitizer and its usage. JP Patent 2000039716, 2000.
115. Haugland, R. P.; Kang, H. C. Reactive fluorescent dipyrrometheneboron difluoride dyes as molecular probes for biopolymers. US Patent 4774339, 1988.
116. Yogo, T.; Urano, Y.; Ishitsuka, Y.; Maniwa, F.; Nagano, T. *J. Am. Chem. Soc.* **2005**, *127*, 12162–12163.
117. Rohand, T.; Baruah, M.; Qin, W.; Boens, N.; Dehaen, W. *Chem. Commun.* **2006**, 266–268.
118. Baruah, M.; Qin, W.; Vallee, R. A. L.; Beljonne, D.; Rohand, T.; Dehaen, W.; Boens, N. *Org. Lett.* **2005**, *7*, 4377–4380.

119. Li, L.; Nguyen, B.; Burgess, K. *Bioorg. Med. Chem. Lett.* **2008**, *18*, 3112–3116.
120. Dilek, O.; Bane, S. L. *Tetrahedron Lett.* **2008**, *49*, 1413–1416.
121. Qin, W.; Leen, V.; Rohand, T.; Dehaen, W.; Dedecker, P.; Van der Auweraer, M.; Robeyns, K.; Van Meervelt, L.; Beljonne, D.; Van Averbeke, B.; Clifford, J. N.; Driesen, K.; Binnemans, K.; Boens, N. *J. Phys. Chem. A* **2009**, *113*, 439–447.
122. Amat-Guerri, F.; Liras, M.; Carrascoso, M. L.; Sastre, R. *Photochem. Photobiol.* **2003**, *77*, 577–584.
123. Tian, M.; Peng, X.; Feng, F.; Meng, S.; Fan, J.; Sun, S. *Dyes Pigm.* **2009**, *81*, 58–62.
124. Rieth, R. D.; Mankad, N. P.; Calimano, E.; Sadighi, J. P. *Org. Lett.* **2004**, *6*, 3981–3983.
125. Bowie, A. L.; Hughes, C. C.; Trauner, D. *Org. Lett.* **2005**, *7*, 5207–5209.
126. Beck, E. M.; Grimster, N. P.; Hatley, R.; Gaunt, M. J. *J. Am. Chem. Soc.* **2006**, *128*, 2528–2529.
127. Thivierge, C.; Bandichhor, R.; Burgess, K. *Org. Lett.* **2007**, *9*, 2135–2138.
128. Chen, J.; Mizumura, M.; Shinokubo, H.; Osuka, A. *Chem.-Eur. J.* **2009**, *15*, 5942–5949.
129. Treibs, A.; Kreuzer, F.-H. *Liebigs Ann. Chem.* **1968**, *718*, 208–223.
130. Sathyamoorthi, G.; Boyer, J. H.; Allik, T. H.; Chandra, S. *Heteroat. Chem.* **1994**, *5*, 403–407.
131. Allik, T. H.; Hermes, R. E.; Sathyamoorthi, G.; Boyer, J. H. *Proc. SPIE-Int. Soc. Opt. Eng.* **1994**, *2115*, 240–248.
132. Wories, H. J.; Koek, J. H.; Lodder, G.; Lugtenburg, J.; Fokkens, R.; Driessen, O.; Mohn, G. R. *Recl. Trav. Chim. Pays-Bas* **1985**, *104*, 288–291.
133. Morgan, L. R.; Boyer, J. H. Boron difluoride compounds useful in photodynamic therapy and production of laser light. US Patent 5,189,029, 1995.
134. Morgan, L. R.; Boyer, J. H. Heterocyclic compounds and their use in photodynamic therapy. WO Patent 9419355, February 18, 1994.
135. Urano, T.; Nagasaka, H.; Tsuchiyama, M.; Ide, H. Photopolymerizable composition. US Patent 5498641, April 7, 1994.
136. Boyer, J. H.; Morgan, L. R. Preparation of difluoroboradiaza-s-indacene compounds and methods for using them. US Patent 5189029, 1993.
137. Boyer, J. H.; Morgan, L. R. Fluorescent chemical compositions useful as laser dyes and photodynamic therapy agents, and methods for their use. US Patent 361936, 1990.
138. Li, L.; Han, J.; Nguyen, B.; Burgess, K. *J. Org. Chem.* **2008**, *73*, 1963–1970.
139. Niu, S. L.; Ulrich, G.; Ziessel, R.; Kiss, A.; Renard, P.-Y.; Romieu, A. *Org. Lett.* **2009**, *11*, 2049–2052.
140. Yang, H.; Li, H.; Wittenberg, R.; Egi, M.; Huang, W.; Liebeskind, L. S. *J. Am. Chem. Soc.* **2007**, *129*, 1132–1140.
141. Pena-Cabrera, E.; Aguilar-Aguilar, A.; Gonzalez-Dominguez; Lager, E.; Zamudio-Vazquez, R.; Godoy-Vargas, J.; Villanueva-Garcia, F. *Org. Lett.* **2007**, *9*, 3985–3988.
142. Yakubovskyi, V. P.; Shandura, M. P.; Kovtun, Y. P. *Eur. J. Org. Chem.* **2009**, 3237–3243.
143. Bonardi, L.; Ulrich, G.; Ziessel, R. *Org. Lett.* **2008**, *10*, 2183–2186.
144. Thoresen, L. H.; Kim, H.; Welch, M. B.; Burghart, A.; Burgess, K. *Synlett* **1998**, 1276–1278.
145. Burghart, A.; Kim, H.; Welch, M. B.; Thoresen, L. H.; Reibenspies, J.; Burgess, K.; Bergström, F.; Johansson, L. B.-A. *J. Org. Chem.* **1999**, *64*, 7813–7819.
146. Miyaura, N.; Yanagi, T.; Suzuki, A. *Tetrahedron Lett.* **1981**, *11*, 513–519.
147. Boukou-Poba, J. P.; Farnier, M.; Guilard, R. *Tetrahedron Lett.* **1979**, *20*, 1717–1720.
148. Katrizky, A. R.; Li, J.; Gordeev, M. F. *Synthesis* **1994**, 93–96.
149. Trofimov, B. A. *Adv. Heterocycl. Chem.* **1990**, *51*, 177–301.

150. Rettig, W. *Angew. Chem. Int. Ed.* **1986**, *98*, 969–986.
151. Wakamiya, A.; Sugita, N.; Yamaguchi, S. *Chem. Lett.* **2008**, *37*, 1094–1095.
152. Bergstroem, F.; Mikhalyov, I.; Haeggloef, P.; Wortmann, R.; Ny, T.; Johansson, L. B. A. *J. Am. Chem. Soc.* **2002**, *124*, 196–204.
153. Mikhalyov, I.; Gretskaya, N.; Bergstroem, F.; Johansson, L. B. A. *Phys. Chem. Chem Phys.* **2002**, *4*, 5663–5670.
154. Marushchak, D.; Kalinin, S.; Mikhalyov, I.; Gretskaya, N.; Johansson, L. B. A. *Spectrochim. Acta, Part A* **2006**, *65A*, 113–122.
155. Zaitsev, A. B.; Meallet-Renault, R.; Schmidt, E. Y.; Mikhaleva, A. I.; Badre, S.; Dumas, C.; Vasil'tsov, A. M.; Zorina, N. V.; Pansu, R. B. *Tetrahedron* **2005**, *61*, 2683–2688.
156. Meallet-Renault, R.; Clavier, G.; Dumas-Verdes, C.; Badre, S.; Shmidt, E. Y.; Mikhaleva, A. I.; Laprent, C.; Pansu, R.; Audebert, P.; Trofimov, B. A. *Russ. J. Gen. Chem.* **2008**, *78*, 2247–2256.
157. Rurack, K.; Kollmannsberger, M.; Daub, J. *New J. Chem.* **2001**, *25*, 289–292.
158. Coskun, A.; Akkaya, E. U. *Tetrahedron Lett.* **2004**, *45*, 4947–4949.
159. Yu, Y.-H.; Descalzo, A. B.; Shen, Z.; Rohr, H.; Liu, Q.; Wang, Y.-W.; Spieles, M.; Li, Y.-Z.; Rurack, K.; You, X.-Z. *Chem. Asian J.* **2006**, *1*, 176–187.
160. Dost, Z.; Atilgan, S.; Akkaya, E. U. *Tetrahedron* **2006**, *62*, 8484–8488.
161. Baruah, M.; Qin, W.; Flors, C.; Hofkens, J.; Vallee, R. A. L.; Beljonne, D.; Van der Auweraer, M.; De Borggraeve, W. M.; Boens, N. *J. Phys. Chem. A* **2006**, *110*, 5998–6009.
162. Rurack, K.; Kollmannsberger, M.; Daub, J. *Angew. Chem., Int. Ed.* **2001**, *40*, 385–387.
163. Deniz, E.; Isbasar, G. C.; Bozdemir, O. A.; Yildirim, L. T.; Siemiarczuk, A.; Akkaya, E. U. *Org. Lett.* **2008**, *10*, 3401–3403.
164. Ozlem, S.; Akkaya, E. U. *J. Am. Chem. Soc.* **2009**, *131*, 48–49.
165. Dahim, M.; Mizuno, N. K.; Li, X.-M.; Momsen, W. E.; Momsen, M. M.; Brockman, H. L. *Biophys. J.* **2002**, *83*, 1511–1524.
166. Saki, N.; Dinc, T.; Akkaya, E. U. *Tetrahedron* **2006**, *62*, 2721–2725.
167. Buyukcakir, O.; Bozdemir, O. A.; Kolemen, S.; Erbas, S.; Akkaya, E. U. *Org. Lett.* **2009**.
168. Rohand, T.; Qin, W.; Boens, N.; Dehaen, W. *Eur. J. Org. Chem.* **2006**, 4658–4663.
169. Qin, W.; Rohand, T.; Dehaen, W.; Clifford, J. N.; Driesen, K.; Beljonne, D.; Van Averbeke, B.; Van der Auweraer, M.; Boens, N. *J. Phys. Chem. A* **2007**, *111*, 8588–8597.
170. Leen, V.; Braeken, E.; Luckermans, K.; Jackers, C.; Van der Auweraer, M.; Boens, N.; Dehaen, W. *Chem. Commun.* **2009**, 4515–4517.
171. Kusturin, C.; Liebeskind, L. S.; Rahman, H.; Sample, K.; Schweitzer, B.; Srogl, J.; Neumann, W. L. *Org. Lett.* **2003**, *5*, 4349–4352.
172. Han, J.; Gonzalez, O.; Aguilar-Aguilar, A.; Pena-Cabrera, E.; Burgess, K. *Org. Biomol. Chem.* **2009**, *7*, 34–36.
173. Metzker, M. L.; Lu, J.; Gibbs, R. A. *Science* **1996**, *271*, 1420–1422.
174. Kolb, H. C.; Finn, M. G.; Sharpless, K. B. *Angew. Chem. Int. Ed.* **2001**, *40*, 2004–2021.
175. Yilmaz, M. D.; Bozdemir, O. A.; Akkaya, E. U. *Org. Lett.* **2006**, *8*, 2871–2873.
176. Shiragami, T.; Tanaka, K.; Andou, Y.; Tsunami, S.-I.; Matsumoto, J.; Luo, H.; Araki, Y.; Ito, O.; Inoue, H.; Yasuda, M. *Photochem. Photobiol.* **2005**, *170*, 287–297.
177. Liu, J.-Y.; Ermilov Eugeny, A.; Roder, B.; Ng Dennis, K. P. *Chem. Commun.* **2009**, 1517–1519.
178. D'Souza, F.; Smith, P. M.; Zandler, M. E.; McCarty, A. L.; Itou, M.; Araki, Y.; Ito, O. *J. Am. Chem. Soc.* **2004**, *126*, 7898–7907.

179. Koepf, M.; Trabolsi, A.; Elhabiri, M.; Wytko, J. A.; Paul, D.; Albrecht-Gary, A. M.; Weiss, J. *Org. Lett.* **2005**, *7*, 1279–1282.
180. Paul, D.; Wytko, J. A.; Koepf, M.; Weiss, J. *Inorg. Chem.* **2002**, *41*, 3699–3704.
181. Leray, I.; Valeur, B.; Paul, D.; Regnier, E.; Koepf, M.; Wytko, J. A.; Boudon, C.; Weiss, J. *Photochem. Photobiol.* **2005**, *4*, 280–286.
182. Azov, V. A.; Schlegel, A.; Diederich, F. *Angew. Chem., Int. Ed.* **2005**, *44*, 4635–4638.
183. Holten, D.; Bocian, D.; Lindsey, J. S. *Acc. Chem. Res.* **2002**, *35*, 57–69.
184. Wagner, R. W.; Lindsey, J. S. *J. Am. Chem. Soc.* **1994**, *116*, 9759–9760.
185. Wagner, R. W.; Lindsey, J. S.; Seth, J.; Palaniappan, V.; Bocian, D. F. *J. Am. Chem. Soc.* **1996**, *118*, 3996–3997.
186. Li, F.; Yang, S. I.; Ciringh, Y.; Seth, J.; Martin, C. H.; Singh, D. L.; Kim, D.; Birge, R. R.; Bocian, D. F.; Holten, D.; Lindsey, J. S. *J. Am. Chem. Soc.* **1998**, *120*, 10001–10017.
187. Kumaresan, D.; Agarwal, N.; Gupta, I.; Ravikanth, M. *Tetrahedron* **2002**, *58*, 5347–5356.
188. Kumaresan, D.; Gupta, I.; Ravikanth, M. *Tetrahedron Lett.* **2001**, *42*, 8547–8550.
189. Ravikanth, M.; Agarwal, N.; Kumaresan, D. *Chem. Lett.* **2000**, 836–837.
190. Li, F.; Yang, S. I.; Ciringh, Y.; Seth, J.; Martin, C. H., III; Singh, D. L.; Kim, D.; Birge, R. R.; Bocian, D. F.; Holten, D.; Lindsey, J. S. *J. Am. Chem. Soc.* **1998**, *120*, 10001–10017.
191. Ulrich, G.; Ziessel, R. *Tetrahedron Lett.* **2004**, *45*, 1949–1953.
192. Ulrich, G.; Ziessel, R. *J. Org. Chem.* **2004**, *69*, 2070–2083.
193. Goze, C.; Ulrich, G.; Charbonniere, L.; Cesario, M.; Prange, T.; Ziessel, R. *Chem.-Eur. J.* **2003**, *9*, 3748–3755.
194. Ulrich, G.; Ziessel, R. *Synlett* **2004**, 439–444.
195. Galletta, M.; Campagna, S.; Quesada, M.; Ulrich, G.; Ziessel, R. *Chem. Commun.* **2005**, 4222–4224.
196. Galletta, M.; Puntoriero, F.; Campagna, S.; Chiorboli, C.; Quesada, M.; Goeb, S.; Ziessel, R. *J. Phys. Chem. A* **2006**, *110*, 4348–4358.
197. Odobel, F.; Zabri, H. *Inorg. Chem.* **2005**, *44*, 5600–5611.
198. Harriman, A.; Rostron, J. P.; Cesario, M.; Ulrich, G.; Ziessel, R. *J. Phys. Chem. A* **2006**, *110*, 7994–8002.
199. Ziessel, R.; Diring, S.; Retailleau, P. *J. Chem. Soc. Dalton Trans.* **2006**, 3285–3290.
200. Wan, C.-W.; Burghart, A.; Chen, J.; Bergstroem, F.; Johansson, L. B.-A.; Wolford, M. F.; Kim, T. G.; Topp, M. R.; Hochstrasser, R. M.; Burgess, K. *Chem. Eur. J.* **2003**, *9*, 4430–4441.
201. Kim, T. G.; Castro, J. C.; Loudet, A.; Jiao, J. G.-S.; Hochstrasser, R. M.; Burgess, K.; Topp, M. R. *J. Phys. Chem.* **2006**, *110*, 20–27.
202. Ziessel, R.; Goze, C.; Ulrich, G.; Cesario, M.; Retailleau, P.; Harriman, A.; Rostron, J. P. *Chem.-Eur. J.* **2005**, *11*, 7366–7378.
203. Diring, S.; Puntoriero, F.; Nastasi, F.; Campagna, S.; Ziessel, R. *J. Am. Chem. Soc.* **2009**, *131*, 6108–6110.
204. Zrig, S.; Remy, P.; Andrioletti, B.; Rose, E.; Asselberghs, I.; Clays, K. *J. Org. Chem.* **2008**, *73*, 1563–1566.
205. Han, J.; Loudet, A.; Barhoumi, R.; Burghardt, R.; Burgess, K. *J. Am. Chem. Soc.* **2009**, 1642–1643.
206. Wu, L.; Loudet, A.; Barhoumi, R.; Burghardt, R. C.; Burgess, K. *J. Am. Chem. Soc.* **2009**, *131*, 9156–9157.
207. Morris, M. C.; Depollier, J.; Mery, J.; Heitz, F.; Divita, G. *Nature Biotech.* **2001**, *19*, 1173–1176.

208. Loudet, A.; Han, J.; Barhoumi, R.; Pellois, J.-P.; Burghardt, R. C.; Burgess, K. *Org. Biomol. Chem.* **2008**, *6*, 4516–4522.
209. Albota, M.; Beljonne, D.; Bredas, J.-L.; Ehrlich, J. E.; Fu, J.-Y.; Heikal, A. A.; Hess, S. E.; Kogej, T.; Levin, M. D.; Marder, S. R.; McCord-Maughon, D.; Perry, J. W.; Rockel, H.; Rumi, M.; Subramaniam, G.; Webb, W. W.; Wu, X.-L.; Xu, C. *Science* **1998**, *281*, 1653–1656.
210. Nalwa, H. S. *Adv. Mater. (Weinheim, Fed. Repub. Ger.)* **1993**, *5*, 341–358.
211. Zhu, M.; Jiang, L.; Yuan, M.; Liu, X.; Ouyang, C.; Zheng, H.; Yin, X.; Zuo, Z.; Liu, H.; Li, Y. *J. Polym. Sci., Part A: Polym. Chem.* **2008**, *46*, 7401–7410.
212. Cakmak, Y.; Akkaya, E. U. *Org. Lett.* **2009**, *11*, 85–88.
213. Meng, G.; Velayudham, S.; Smith, A.; Luck, R.; Liu, H. *Macromolecules* **2009**, *42*, 1995–2001.
214. Cihaner, A.; Algi, F. *React. Funct. Polym.* **2009**, *69*, 62–67.
215. Ulrich, G.; Goze, C.; Guardigli, M.; Roda, A.; Ziessel, R. *Angew. Chem., Int. Ed.* **2005**, *44*, 3694–3698.
216. Ziessel, R.; Goze, C.; Ulrich, G. *Synthesis* **2007**, *6*, 936–949.
217. Ziessel, R.; Ulrich, G.; Harriman, A. *New J. Chem.* **2007**, *31*, 496–501.
218. Nagai, A.; Miyake, J.; Kokado, K.; Nagata, Y.; Chujo, Y. *J. Am. Chem. Soc.* **2008**, *130*, 15276–15278.
219. Kee, H. L.; Kirmaier, C.; Yu, L.; Thamyongkit, P.; Youngblood, W. J.; Calder, M. E.; Ramos, L.; Noll, B. C.; Bocian, D. F.; Scheidt, W. R.; Birge, R. R.; Lindsey, J. S.; Holten, D. *J. Phys. Chem. B* **2005**, *109*, 20433–20443.
220. Goze, C.; Ulrich, G.; Mallon, L. J.; Allen, B. D.; Harriman, A.; Ziessel, R. *J. Am. Chem. Soc.* **2006**, *128*, 10231–10239.
221. Harriman, A.; Izzet, G.; Ziessel, R. *J. Am. Chem. Soc.* **2006**, *128*, 10868–10875.
222. Goze, C.; Ulrich, G.; Ziessel, R. *Org. Lett.* **2006**, *8*, 4445–4448.
223. Goze, C.; Ulrich, G.; Ziessel, R. *J. Org. Chem.* **2007**, *72*, 313–322.
224. Harriman, A.; Mallon, L.; Ziessel, R. *Chem.-Eur. J.* **2008**, *14*, 11461–11473.
225. Kang, H. C.; Haugland, R. P. Dibenzopyrromethene boron Difluoride Dyes. US Patent 5,433,896, July 18, 1995.
226. Goeb, S.; Ziessel, R. *Tetrahedron Lett.* **2008**, *49*, 2569–2574.
227. Goeb, S.; Ziessel, R. *Org. Lett.* **2007**, *9*, 737–740.
228. Hudnall, T. W.; Gabbai, F. P. *Chem. Commun.* **2008**, 4596–4597.
229. Bonnier, C.; Piers, W. E.; Parvez, M.; Sorensen, T. S. *Chem. Commun.* **2008**, 4593–4595.
230. Fischer, H.; Schubert, M. *Ber. Dtsch. Chem. Ges.* **1924**, *57B*, 610–617.
231. Fischer, H.; Klarer, J. *Ann.* **1926**, *448*, 178–193.
232. Corwin, A. H.; Melville, M. H. *J. Am. Chem. Soc.* **1955**, *77*, 2755–2759.
233. Motekaitis, R. J.; Martell, A. E. *Inorg. Chem.* **1970**, *9*, 1832–1839.
234. Corwin, A. H.; Sydow, V. L. *J. Am. Chem. Soc.* **1953**, *75*, 4484–4486.
235. Porter, C. R. *J. Chem. Soc.* **1938**, 368–372.
236. Fergusson, J. E.; March, F. C.; Couch, D. A.; Emerson, K.; Robinson, W. T. *J. Chem. Soc. A* **1971**, 440–448.
237. March, F. C.; Fergusson, J. E.; Robinson, W. T. *J. Chem. Soc. Dalton Trans.* **1972**, 2069–2076.
238. Fergusson, J. E.; Ramsay, C. A. *J. Chem. Soc.* **1965**, 5222–5225.
239. Murakami, Y.; Sakata, K.; Harada, K.; Matsuda, Y. *Bull. Chem. Soc. Japan* **1974**, *47*, 3021–3024.
240. Murakami, Y.; Sakata, K. *Bull. Chem. Soc. Japan* **1974**, *47*, 3025–3028.
241. Murakami, Y.; Matsuda, Y.; Sakata, K.; Harada, K. *Bull. Chem. Soc. Japan* **1974**, *47*, 458–462.

242. Murakami, Y.; Matsuda, Y.; Sakata, K. *Inorg. Chem.* **1971**, *10*, 1728–1734.
243. Murakami, Y.; Matsuda, Y.; Sakata, K. *Inorg. Chem.* **1971**, *10*, 1734–1738.
244. Murakami, Y.; Matsuda, Y.; Iiyama, K. *Chem. Lett.* **1972**, 1069–1072.
245. Murakami, Y.; Sakata, K. *Inorg. Chim. Acta* **1968**, *2*, 273–279.
246. Murakami, Y.; Kohno, Y.; Matsuda, Y. *Inorg. Chim. Acta* **1969**, *3*, 671–675.
247. Murakami, Y.; Matsuda, Y.; Sakata, K.; Martell, A. E. *J. Chem. Soc. Dalton Trans.* **1973**, 1729–1734.
248. Murakami, Y.; Matsuda, Y.; Kobayashi, S. *J. Chem. Soc. Dalton Trans.* **1973**, 1734–1737.
249. Murakami, Y.; Matsuda, Y.; Kanaoka, Y. *Bull. Chem. Soc. Japan* **1971**, *44*, 409–415.
250. Cotton, F. A.; DeBoer, B. G.; Pipal, J. R. *Inorg. Chem.* **1970**, *9*, 783–788.
251. Johnson, A. W.; Kay, I. T.; Markham, E.; Price, R.; Shaw, K. B. *J. Chem. Soc.* **1959**, 3416–3424.
252. Ferguson, J.; West, B. O. *J. Chem. Soc. A* **1966**, 1565–1568.
253. Ferguson, J.; West, B. O. *J. Chem. Soc. A* **1966**, 1569–1572.
254. Yu, L.; Muthukumaran, K.; Sazanovich, I. V.; Kirmaier, C.; Hindin, E.; Diers, J. R.; Boyle, P. D.; Bocian, D. F.; Holten, D.; Lindsey, J. S. *Inorg. Chem.* **2003**, *42*, 6629–6647.
255. Sazanovich, I. V.; Kirmaier, C.; Hindin, E.; Yu, L.; Bocian, D. F.; Lindsey, J. S.; Holten, D. *J. Am. Chem. Soc.* **2004**, *126*, 2664–2665.
256. Thoi, V. S.; Stork, J. R.; Magde, D.; Cohen, S. M. *Inorg. Chem.* **2006**, *45*, 10688–10697.
257. Maeda, H.; Hasegawa, M.; Hashimoto, T.; Kakimoto, T.; Nishio, S.; Nakanishi, T. *J. Am. Chem. Soc.* **2006**, *128*, 10024–10025.
258. Chen, J.; Burghart, A.; Derecskei-Kovacs, A.; Burgess, K. *J. Org. Chem.* **2000**, *65*, 2900–2906.
259. Li, J. J. *Name Reactions in Heterocyclic Chemistry*; Wiley, **2005**.
260. Kim, H.; Burghart, A.; Welch, M. B.; Reibenspies, J.; Burgess, K. *Chem. Commun.* **1999**, 1889–1890.
261. Ikeda, C.; Maruyama, T.; Nabeshima, T. *Tetrahedron Lett.* **2009**, *50*, 3349–3351.
262. Umezawa, K.; Nakamura, Y.; Makino, H.; Citterio, D.; Suzuki, K. *J. Am. Chem. Soc.* **2008**, *130*, 1550–1551.
263. Umezawa, K.; Matsui, A.; Nakamura, Y.; Citterio, D.; Suzuki, K. *Chem.-Eur. J.* **2009**, *15*, 1096–1106.
264. Hemetsberger, H.; Knittel, D. *Monatsh. Chem.* **1972**, *103*, 194–204.
265. Gribble, G. W. *J. Chem. Soc., Perkin Trans. 1* **2000**, 1045–1180.
266. Wada, M.; Ito, S.; Uno, H.; Murashima, T.; Ono, N.; Urano, T.; Urano, Y. *Tetrahedron Lett.* **2001**, *42*, 6711–6713.
267. Shen, Z.; Röhr, H.; Rurack, K.; Uno, H.; Spieles, M.; Schulz, B.; Reck, G.; Ono, N. *Chem. Eur. J.* **2004**, *10*, 4853–4871.
268. Ito, S.; Murashima, T.; Ono, N.; Uno, H. *Chem. Commun.* **1998**, 1661–1662.
269. Wu, Y.; Klaubert, D. H.; Kang, H. C.; Zhang, Y.-Z. Long-wavelength dyes for infrared tracing and their use. US Patent 6005113, 1999.
270. Kotali, A.; Tsoungas, P. G. *Tetrahedron Lett.* **1987**, *28*, 4321–4322.
271. Vasilenko, N. P.; Mikhailenko, F. A.; Rozhinskii, Y. I. *Dyes Pigm.* **1981**, *2*, 231–237.
272. Posokh, S. V.; Gavrilov, O. D.; Mikhailenko, F. A.; Ryl'kov, V. V.; Slominskii, Y. L.; Stepanov, A. I. *Zh. Prikl. Khim.* **1984**, *40*, 218–222.
273. Descalzo, A. B.; Xu, H.-J.; Xue, Z.-L.; Hoffmann, K.; Shen, Z.; Weller, M. G.; You, X.-Z.; Rurack, K. *Org. Lett.* **2008**, *10*, 1581–1584.
274. Ventura, B.; Marconi, G.; Broering, M.; Kruger, R.; Flamigni, L. *New J. Chem.* **2009**, *33*, 428–438.

275. Broring, M.; Kruger, R.; Link, S.; Kleeberg, C.; Kohler, S.; Xie, X.; Ventura, B.; Flamingi, L. *Chem.-Eur. J.* **2008**, *14*, 2976–2983.
276. Broering, M.; Bregier, F.; Krueger, R.; Kleeberg, C. *Eur. J. Inorg. Chem.* **2008**, 5505–5512.
277. Rogers, M. A. T. *J. Chem. Soc.* **1943**, 590–596.
278. Davies, W. H.; Rogers, M. A. T. *J. Chem. Soc.* **1944**, 126–131.
279. Knott, E. B. *J. Chem. Soc.* **1947**, 1196–1201.
280. Sathyamoorthi, G.; Soong, M. L.; Ross, T. W.; Boyer, J. H. *Heteroat. Chem.* **1993**, *4*, 603–608.
281. Killoran, J.; Allen, L.; Gallagher, J.; Gallagher, W.; O'Shea, D. *Chem. Commun.* **2002**, 1862–1863.
282. Gorman, A.; Killoran, J.; O'Shea, C.; Kenna, T.; Gallagher, W. M.; O'Shea, D. F. *J. Am. Chem. Soc.* **2004**, *126*, 10619–10631.
283. McDonnell, S. O.; O'Shea, D. F. *Org. Lett.* **2006**, *8*, 3493–3496.
284. Loudet, A.; Bandichhor, R.; Wu, L.; Burgess, K. *Tetrahedron* **2008**, *64*, 3642–3654.
285. Gallagher, W. M.; Allen, L. T.; O'Shea, C.; Kenna, T.; Hall, M.; Gorman, A.; Killoran, J.; O'Shea, D. F. *Br. J. Cancer* **2005**, *92*, 1702–1710.
286. McDonnell, S. O.; Hall, M. J.; Allen, L. T.; Byrne, A.; Gallagher, W. M.; O'Shea, D. F. *J. Am. Chem. Soc.* **2005**, *127*, 16360–16361.
287. Hall, M. J.; Allen, L. T.; O'Shea, D. F. *Org. Biomol. Chem.* **2006**, *4*, 776–780.
288. Killoran, J.; O'Shea, D. F. *Chem. Commun.* **2006**, 1503–1505.
289. Coskun, A.; Yilmaz, M. D.; Akkaya, E. U. *Org. Lett.* **2007**, *9*, 607–609.
290. Gawley, R. E.; Mao, H.; Haque, M. M.; Thorne, J. B.; Pharr, J. S. *J. Org. Chem.* **2007**, *72*, 2187–2191.
291. Zhao, W.; Carreira, E. M. *Angew. Chem., Int. Ed.* **2005**, *44*, 1677–1679.
292. Zhao, W.; Carreira, E. M. *Chem.-Eur. J.* **2006**, *12*, 7254–7263.
293. Vasilenko, N. P.; Mikhailenko, F. A. *Ukr. Khim. Zh. (Russ. Ed.)* **1986**, *52*, 308–311.
294. Burgess, K.; Loudet, A.; Bandichhor, R.; Palma, A.; McDonnell, S.; Hall, M. *Org. Lett.* **2008**, *10*, 4771–4774.
295. Teets, T. S.; Partyka, D. V.; Esswein, A. J.; Updegraff, J. B., III; Zeller, M.; Hunter, A. D.; Gray, T. G. *Inorg. Chem.* **2007**, *46*, 6218–6220.
296. Palma, A.; Gallagher, J. F.; Muller-Bunz, H.; Wolowska, J.; McInnes, E. J. L.; O'Shea, D. F. *Dalt. Trans.* **2009**, 273–279.
297. Wu, L.; Burgess, K. *J. Am. Chem. Soc.* **2008**, *130*, 4089–4096.
298. Dong, J.; Solntsev, K. M.; Poizat, O.; Tolbert, L. M. *J. Am. Chem. Soc.* **2007**, *129*, 10084–10085.
299. Chen, K.-Y.; Cheng, Y.-M.; Lai, C.-H.; Hsu, C.-C.; Ho, M.-L.; Lee, G.-H.; Chou, P.-T. *J. Am. Chem. Soc.* **2007**, *129*, 4510–4511.
300. Feng, J.; Liang, B.; Wang, D.; Xue, L.; Li, X. *Org. Lett.* **2008**, *10*, 4437–4440.
301. Ronzio, A. R.; Waugh, T. D. In *Org. Synth*, 1955; Vol. 3.
302. Bernarducci, E. E.; Bharadwaj, P. K.; Lalancette, R. A.; Krogh-Jespersen, K.; Potenza, J. A.; Schugar, H. J. *Inorg. Chem.* **1983**, *22*, 3911–3920.
303. Lane, E. S. *J. Chem. Soc.* **1953**, 2238–2240.
304. Fieselmann, B. F.; Hendrickson, D. N.; Stucky, G. D. *Inorg. Chem.* **1978**, *17*, 2074–2084.
305. Ross, T. W.; Sathyamoorthi, G.; Boyer, J. H. *Heteroat. Chem.* **1993**, *4*, 609–612.
306. Huenig, S.; Wehner, I. *Heterocycles* **1989**, *28*, 359–363.
307. Douglass, J. E.; Barelski, P. M.; Blankenship, R. M. *J. Heterocycl. Chem.* **1973**, *10*, 255–257.
308. Chen, J.; Burghart, A.; Wan, C.-W.; Thai, L.; Ortiz, C.; Reibenspies, J.; Burgess, K. *Tetrahedron Lett.* **2000**, *41*, 2303–2307.

309. Yoshino, J.; Kano, N.; Kawashima, T. *Chem. Commun.* **2007**, 559–561.
310. Liu, S.-F.; Wu, Q.; Schmider, H. L.; Aziz, H.; Hu, N.-X.; Popovic, Z.; Wang, S. *J. Am. Chem. Soc.* **2000**, *122*, 3671–3678.
311. Liu, Q.-D.; Mudadu, M. S.; Thummel, R.; Tao, Y.; Wang, S. *Adv. Funct. Mater.* **2005**, *15*, 143–154.
312. Zeng, X.; Qian, M.; Hu, Q.; Negishi, E. *Angew. Chem., Int. Ed.* **2004**, *43*, 2259–2263.
313. Wakamiya, A.; Taniguchi, T.; Yamaguchi, S. *Angew. Chem. Int. Ed.* **2006**, *45*, 3170–3173.
314. Ulrich, G.; Ziessel, R.; Harriman, A. *Angew. Chem. Int. Ed.* **2008**, *47*, 1184–1201.
315. Kim, H.; Burghart, A.; Welch, M. B.; Reibenspies, J.; Burgess, K. *Chem. Commun.* **1999**, *18*, 1889–1890.
316. Xu, C.; Webb, W. W. *J. Opt. Soc. Am. B* **1996**, *13*, 481–491.
317. Xu, C.; Zipfel, W.; Shear, J. B.; Williams, R. M.; Webb, W. W. *Proc. Natl. Acad. Sci. USA* **1996**, *93*, 10763–10768.
318. Porres, L.; Monging, O.; Blanchard-Desce, M. *Tetrahedron Lett.* **2006**, *47*, 1913–1917.
319. Nicolini, C.; Baranski, J.; Schlummer, S.; Palomo, J.; Lumbierres-Burgues, M.; Kahms, M.; Kuhlmann, J.; Sanchez, S.; Gratton, E.; Waldmann, H.; Winter, R. *J. Am. Chem. Soc.* **2006**, *128*, 192–201.
320. Zheng, Q.; Xu, G.; Prasad, P. N. *Chem.-Eur. J.* **2008**, *14*, 5812–5819.
321. Meltola, N. J.; Wahlroos, R.; Soini, A. E. *J. Fluoresc.* **2004**, *14*, 635–647.
322. Meltola, N. J.; Soini, A. E.; Haenninen, P. E. *J. Fluoresc.* **2004**, *14*, 129–138.
323. Bouit, P.-A.; Kamada, K.; Feneyrou, P.; Berginc, G.; Toupet, L.; Maury, O.; Andraud, C. *Adv. Mater.* **2009**, *21*, 1151–1154.
324. Zhang, D.; Wang, Y.; Xiao, Y.; Qian, S.; Qian, X. *Tetrahedron* **2009**, *65*, 8099–8103.

38 Supramolecular Chemistry of Pyrrole-Based π-Conjugated Acyclic Anion Receptors

Hiromitsu Maeda

College of Pharmaceutical Sciences, Institute of Science and Engineering, Ritsumeikan University, Kusatsu 525-8577, Japan

PRESTO, Japan Science and Technology Agency (JST), Kawaguchi 332-0012, Japan

I. Introduction

Dimension-controlled organized structures consisting of organic molecules[1–7] have attracted considerable attention, due to their ability to act as potential soft materials[8] such as supramolecular gels[9–12] and liquid crystals.[13–15] Among a variety of noncovalent interactions to form supramolecular assemblies,[16] the electrostatic interaction is a fundamental interaction to form ionic pairs and salts of inorganic and organic species in solution as well as in the bulk (solid and liquid) states. Salts are used as utility materials in biotic systems and in industry. For example, some minerals are essential for life, whereas ionic liquids are used as nonvolatile utility solvents for various reactions. One of the advantages afforded by salts is the combination of numerous positive- and negative-charged species; this is a crucial factor for controlling their properties, such as stability, solubility, and conductivity. Furthermore, the structures and constituents of ionic species also play an important role in determining the properties of ion pairs. In the case of inorganic salts, the number of possible combinations is fairly large, but it is limited because there is less diversity in inorganic species. However, organic ionic species can afford various ion pairs and salts because of the varieties of organic molecules. One of the significant challenges to obtain utility salts consisting of organic ions is in the preparation of fairly stable charged organic species. The charge in organic molecules is usually delocalized and dispersed to several appropriate sites. Charged sites often behave as nucleophilic and electrophilic reaction sites for the corresponding cation and anion species. Based on this background, one of the most efficient strategies to prepare "organic ions" is to combine appropriate receptor molecules with inorganic ions such as spherical metal cations to halide anions. The combination of receptors and inorganic ions can afford a variety of fairly stable organic charged species as receptor–ion complexes.

Of the distinct charged species, cations and anions, the latter negative-charged ions are less "available" than cations. Metal coordination and electrostatic hydrogen bonding are efficient means by which organic molecules and related species can "capture" anions. Metal coordination, however, is often used to compensate for the positive charge(s) of metal cations so as to prevent them from yielding organic anionic species; in addition, the coordinated products are fairly stable because of the characteristic nature of the covalent bond. On the other hand, electrostatic hydrogen-bonding interactions that occur between anions and polarized hydrogen-bonding donor sites are useful for forming various receptor–anion

complexes that exhibit an anion exchange process in equilibrium. For example, in biotic systems, the ClC chloride channels catalyze the selective flow of Cl^- ions across cell membranes, thereby regulating electrical excitation in skeletal muscle and the flow of salt and water across epithelial barriers.[17,18] In 2002, MacKinnon and coworkers presented X-ray structures of two prokaryotic ClC Cl^- channels, wherein the antiparallel subunit defines a selectivity filter in which a Cl^- ion is stabilized by electrostatic interactions with α-helix dipoles and by chemical interaction with NH and OH sites.[19] The antibiotic ristocetin has been known to efficiently and selectively bind amino acid carboxylates.[20,21] At the same time, considerable efforts have been devoted to the development of artificial anion receptors and carriers, and various binding motifs have been synthesized in recent years.[22–37] Among the various artificial host molecules reported thus far, electronically neutral π-conjugated planar receptors form "planar anions" with spherical halide anions; negative-charged planar units are essential building units for supramolecular assemblies and functional materials by combination with appropriate countercations.

Among the building subunits of planar anion receptors, pyrrole is well-known as a π-conjugated aromatic heterocyclic molecule[38] present not only in biotic dyes such as heme and chlorophyll but also in artificial porphyrin derivatives.[39] In contrast to the relatively "inert" benzene, pyrrole has an excess of electrons (six) as compared to the number of atoms (five) in the framework. Therefore, pyrrole moieties are reactive and are stabilized by, for example, incorporation into aromatic macrocycles such as porphyrins or substitution by electron-withdrawing moieties. Pyrrole exhibits "duality" from its nitrogen moiety, which behaves both as a hydrogen-bonding acceptor or a metal coordination ligand due to the N site (Figure 1a) and as a hydrogen-bonding donor due to the NH site (Figure 1b). As the π-planes of the pyrrole unit also enable effective interactions that yield stacking assemblies and metal complexes as π-ligands (Figure 1c), pyrrole rings can act as potential building subunits forming supramolecular nanoscale structures. However, pyrrole rings are often observed as components of the preorganized macrocycles, porphyrins, and their analogs, wherein pyrrole N sites are located on the inside of fairly rigid closed rings and consequently cannot exhibit their potential as interaction sites. Therefore, new aspects of pyrrole rings can be revealed by the synthesis of new *acyclic* oligopyrrolic systems which form functional supramolecular materials and realize new properties and phenomena.

The pyrrole NH site acts as an efficient hydrogen-bonding donor. In fact, thus far, macrocycles consisting of pyrroles have been particularly attractive because they behave as essential binding units due to the presence of polarized NH sites, as seen in calixpyrroles (e.g. calix[4]pyrrole **1**)[40–43] and expanded porphyrins[44–47] including diprotonated sapphyrins (e.g. β-alkyl-substituted sapphyrin **2**)[48–50] and

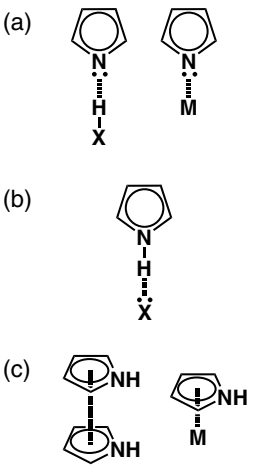

Figure 1. Possible interactions of pyrrole as (a) a hydrogen-bonding acceptor and a metal coordination site, (b) a hydrogen-bonding donor, and (c) a π-plane for stacking and metal coordination. The structures with an "aromatic circle" are used to represent various types of pyrrole units.

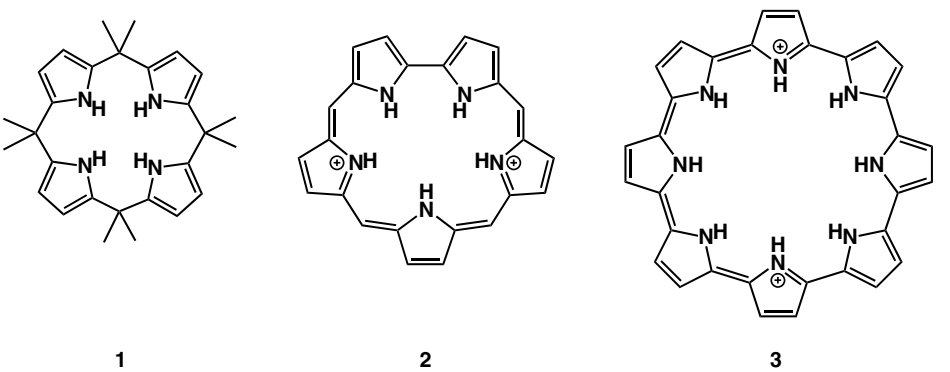

Figure 2. Representative cyclic oligopyrrole-based anion receptors: calix[4]pyrrole **1**, protonated sapphyrin **2**, and cyclooctapyrrole **3**. Expanded porphyrins **2** and **3** are represented as their skeleton forms.

cyclooligopyrroles (e.g. cyclooctapyrrole **3**)[51] (Figure 2). Multiple NH sites in the macrocycles cooperatively and efficiently bind a desired anion to form receptor–anion complexes. Although less extensively studied, acyclic pyrrole derivatives have potentially even greater advantages.[28,32,52,53] This is because they can form complexes with anions via the synthetic attachment of additional recognition units for hydrogen bonding, metal coordination, and van der Waals interaction, or simply because they easily form various macrocyclic systems. The receptors with

linear geometries are often required to change their conformation and to fit the volume and shape of the negatively charged species. Therefore, in the case of linear receptors, the essential factors that determine the binding affinities for guest species would be the existence of temporal preorganization along with other factors such as the strength of the induced effect required to polarize the association site(s) and the steric and electrostatic repulsions by the peripheral substituents. The balance between flexibility and rigidity is a key issue for controlling the anion-binding behavior of acyclic oligopyrroles — essentially, to form supramolecular structures with and without associated anions. The variety of linear oligopyrroles available may provide potential materials in the realm of supramolecular chemistry.

On the basis of the above chemistry, this chapter describes the behavior and properties of linear oligopyrrole systems as anion-binding receptors and the study of their supramolecular and materials chemistry which has recently been initiated. In sharp contrast to closed systems such as regular porphyrins, the characteristics of open-chain oligopyrroles that constitute the building subunits of supramolecular assemblies are significantly correlated with the nature of the pyrrole ring itself. As a postscript to this introductory section, acyclic receptors comprising indole moieties, which are "analogs" of pyrrole rings, are also fascinating and are being actively investigated; however, this chapter does not discuss the chemistry of indole-based anion receptors, because they were recently reviewed by Gale.[54]

II. Guanidinocarbonyl- and Amidopyrrole-Based Anion Receptors

The pyrrole ring itself acts as an anion receptor because of its polarized NH site (Figure 3). Obviously, it is not an efficient anion receptor in solution, wherein the binding constant (K_a) of 2,5-dimethylpyrrole for F^- in CD_2Cl_2 was estimated to be *ca*. 9 M^{-1},[40] due to the absence of supplementary interaction sites and cooperative binding sites of multiple pyrrole rings. However, pyrrole can form an anion complex in the crystal state; Gale and coworkers reported the first single-crystal X-ray structure of a pyrrole–anion complex, based on single crystals fabricated by the

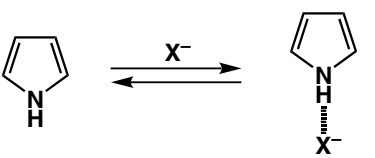

Figure 3. Anion-binding mode of pyrrole.

addition of a tetramethylammonium salt of Cl^- to pyrrole as a solvent.[55] Although anion-responsive monomeric pyrrole derivatives are interesting, this chapter focuses on the details of oligopyrrolic systems.

A. Guanidinocarbonylpyrrole-Based Anion Receptors

The representatives of "supplementary" interaction sites for pyrrole rings are guanidine and amide NH moieties; guanidine has positively charged and polarized NH sites,[35,56,57] whereas the amide NH is well-known as a polarized hydrogen-bonding donor site due to the neighboring carbonyl unit.[32,34] In 1999, Schmuck reported 2-(guanidinocarbonyl)pyrrole **4**, which shows the selective binding of *N*-acetyl-α-amino acid carboxylates in aqueous media (Figure 4a).[58] In DMSO-d_6, **4** associates with acetate ($CH_3CO_2^-$) with a binding constant (K_a) > 10^6 M^{-1}. Even in 40% water/DMSO-d_6, **4** binds $CH_3CO_2^-$ and *N*-acetyl-L-alanine carboxylate at 2790 and 770 M^{-1}, respectively. The corresponding phenylalanine carboxylate is bound much stronger (1700 M^{-1}) than the carboxylates including alanine, tryptophan (810 M^{-1}), and lysine (360 M^{-1}) because of effective π-stacking between the phenyl group of phenylalanine and the acylguanidinium unit of **4**.[58] On the basis of the carboxylate binding of guanidinocarbonylpyrrole derivatives, the receptors bearing a carboxylate unit would self-assemble to form dimer and oligomer structures. In fact, 5-(guanidinocarbonyl)-1*H*-pyrrole-2-carboxylate **5** (Figure 4b) is converted to an intermolecular self-assembled dimer, without the formation of dispersed oligomers, in DMSO. The dimer is very stable, as it shows the expected

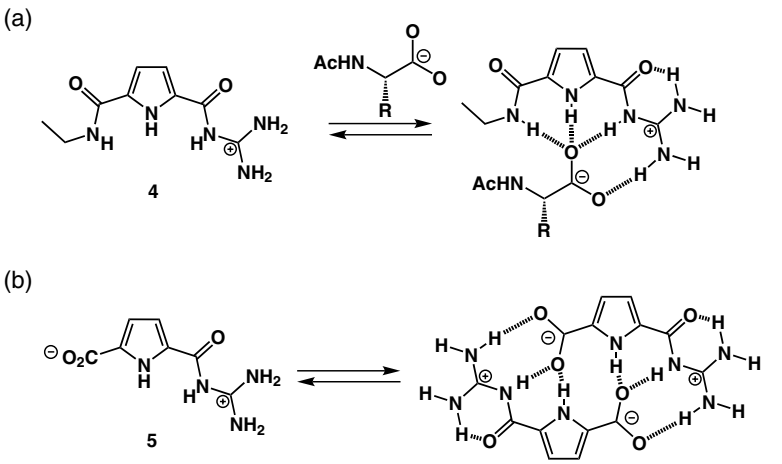

Figure 4. (a) Amino acid carboxylate binding of guanidinocarbonylpyrrole **4**[58]; (b) self-assembled dimerization of guanidinocarbonylpyrrole **5**.[59]

dimerization constant of *ca*. 10^{12} M^{-1}.[59] Schmuck summarized the various derivatives composed of the guanidinocarbonylpyrrole moiety in a review in 2006,[60] and therefore this section covers only oligopyrrolic systems bearing the guanidinocarbonyl moiety.

Schmuck *et al*. reported that self-assembled molecules formed with bispyrrole zwitterions bearing both carboxylate and guanidinium moieties (**6–8**, Figure 5a).[61,62] In DMSO, the zwitterion **6** forms a specifically folding monomer in which the carboxylate group on one end of the molecule interacts with the guanidinocarbonylpyrrole moiety on the other end (Figure 5b). In sharp contrast, the zwitterion **7**, which has a shorter spacer than **6**, cannot form such a folding structure. The concentration-independent behavior of **6** excludes the possibility of dimerization and higher oligomerization by self-assembly.[61] Another zwitterion, **8**, also forms a self-folding structure in methanol.[62]

Apart from zwitterions such as **6–8**, in DMSO-d_6 and DMSO-d_6/D_2O mixtures (0.5–50 mM), bis-zwitterion **9** (Figure 6a), which has a long oxyethylene spacer, exhibits the formation of a self-folding monomer and a self-assembled dimer in concentration-dependent equilibrium (Figure 6b). This is the first example of a homodimerization based solely on a hydrogen-bond-enforced ion pair formation, which leads to stable nanometer-sized discrete particles in DMSO–water mixtures

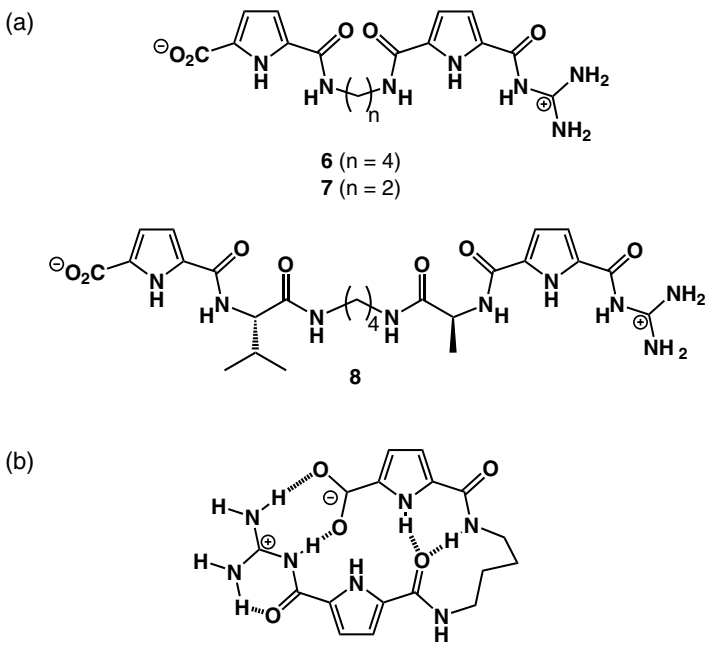

Figure 5. (a) Guanidinocarbonylpyrrole-based zwitterions **6–8**[61,62]; (b) self-folding mode of **6**.[61]

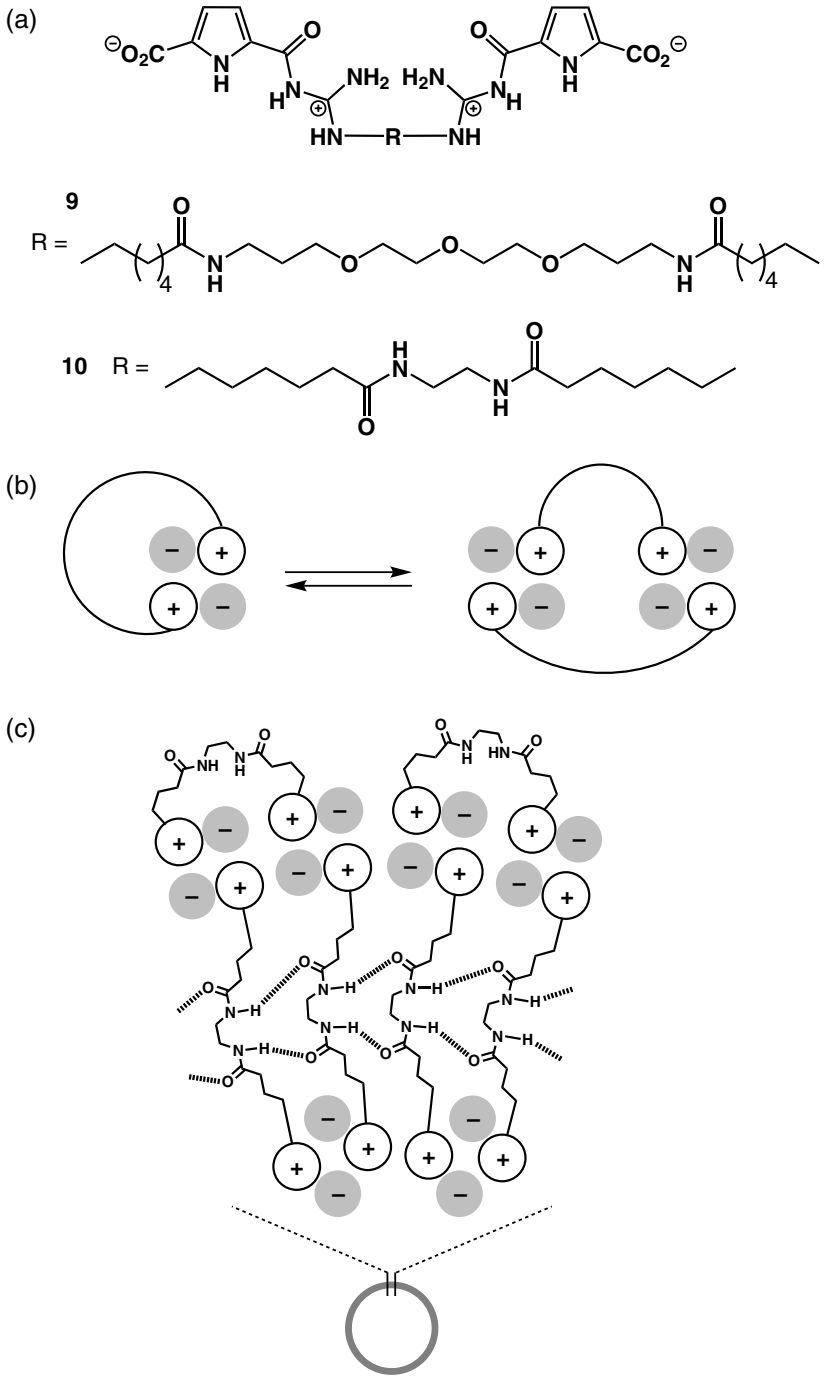

Figure 6. (a) Guanidinocarbonylpyrrole-based bis-zwitterions **9** and **10**[63,64]; (b) schematic representation of the self-folding monomer and self-assembled dimer of bis-zwitterions[63,64]; (c) schematic representation of self-assemblies to form vesicles.[64]

even without any structural bias within the molecule. The formation of nanometer-sized discrete particles by self-assembly was confirmed by DOSY NMR, FAB-MS, dynamic light scattering (DLS), and small-angle neutron scattering (SANS) studies.[63] Furthermore, in DMSO (0.5–50 mM), bis-zwitterion **10** (Figure 6a), wherein two charged binding sites are bridged by a bisamide lipophilic spacer, forms larger vesicular structures of *ca*. 150 nm under concentrated conditions (Figure 6c) along with a monomer and a dimer. The formation of larger aggregates is verified by atomic force microscopy (AFM) as well as DLS and SANS.[64]

One of the efficient binding motifs for guest species, especially trianions, is a tripodal host molecule based on 1,3,5-trisubstituted benzene.[65] Schmuck and Schwegmann also prepared a tripodal guanidinocarbonylpyrrole receptor **11** (Figure 7a), which binds trianionic species such as trimesic acid tricarboxylate and citrate with unprecedented high association constants of $>10^5$ M^{-1} in pure aqueous solutions.[66] This result suggests that the receptor **11** is one of the most efficient tricarboxylate receptors in aqueous media ($K_a = 3.4 \times 10^5$ and 1.6×10^5 M^{-1} for

(a)

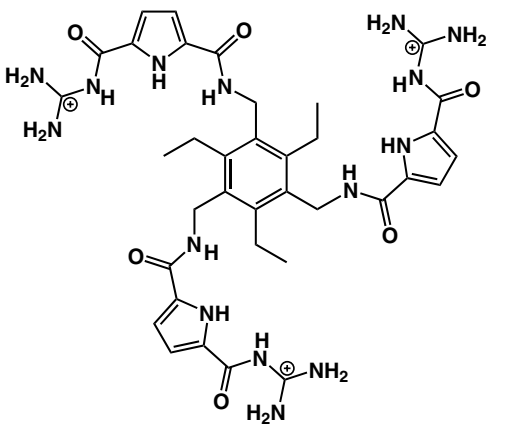

11

(b)

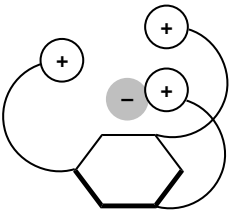

Figure 7. (a) Guanidinocarbonylpyrrole trimer **11**[66]; (b) anion-binding mode like a "molecular flytrap."[66]

trimesic acid tricarboxylate and citrate, respectively, as indicated by UV-visible spectral changes), because of the formation of an anion-binding complex like a "molecular flytrap," as elucidated from ^{1}H NMR and theoretical studies (Figure 7b).[66] Furthermore, Schmuck and Schwegmann used the tripodal receptor **11** as a "naked eye" sensor assembly for an indicator displacement assay with carboxyfluorescein for the selective detection of citrate.[67]

Zwitterionic guanidinocarbonylpyrrole can form supramolecular polymers[2,5] using additional metal coordination interactions.[68–70] Schmuck and coworkers reported the assembly behavior of terpyridyl-appended zwitterion **12** (Figure 8a)[71]; **12** dimerizes into hydrogen-bonding ion pairs in aqueous solution and, upon the addition of Fe(II), forms single-stranded supramolecular polymers in DMSO (Figure 8b). Polymerization by Fe(II) complexation was initially detected from DOSY NMR spectral changes and also from AFM; on a highly oriented pyrolytic graphite (HOPG) substrate, highly ordered molecular adlayers of individual polymer strands with a length of several hundred nanometers were observed.[71]

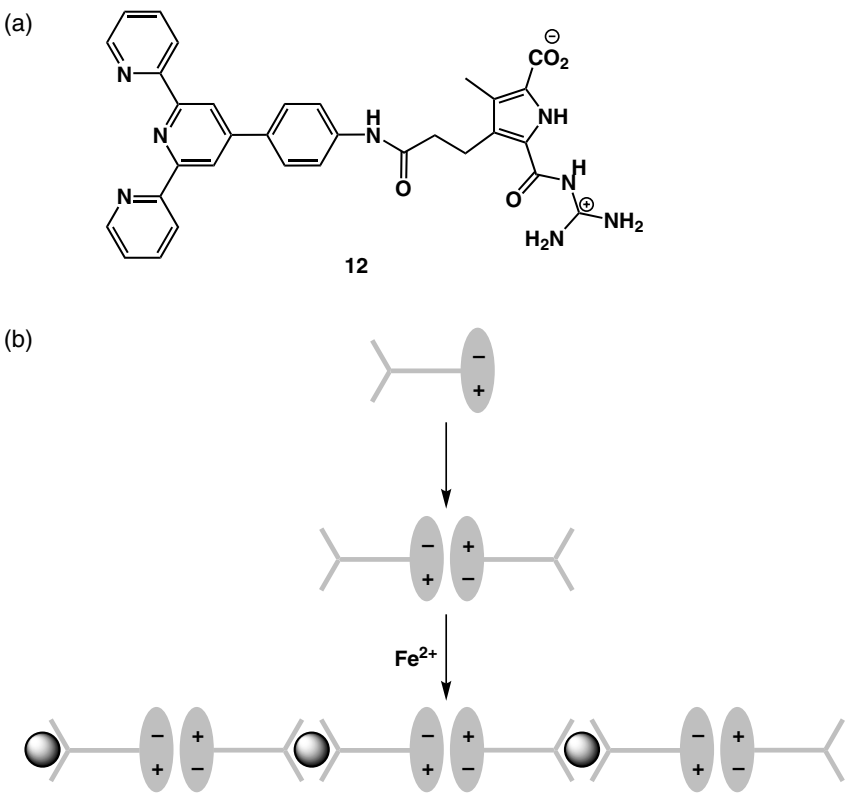

Figure 8. (a) Terpyridine-guanidinocarbonylpyrrole hybrid **12**[71]; (b) formation pathway for supramolecular polymers by self-assembled dimerization and metal coordination.[71]

B. Amidopyrrole-Based Anion Receptors

In 2001, Gale *et al*. reported 2,5-diamidopyrroles and 2-amidopyrroles (**13**–**16**, Figure 9a) as simple anion-binding receptors.[72,73] Amidopyrroles provide convergent binding sites (Figure 9b), which enable them to efficiently bind anions, especially oxoanions, in CD_3CN and 0.5% H_2O/DMSO. For example, **13** shows a K_a value of 2500 M^{-1} for benzoate in CD_3CN (Table 1).[72,73] Because Gale has summarized the various derivatives composed of the amidopyrrole moiety,[74] this section focuses mainly on the amidopyrrole-based oligopyrroles.

Gale *et al*. prepared phenylene-bridged amidopyrrole dimers **17** and **18** (Figure 10a), which have chlorine moieties at β positions to enhance the polarity of the pyrrole NH.[75] Crystals of **17** and **18**, which were obtained by slow evaporation of CH_3CN solutions in the presence of excess tetrabutylammonium fluoride (TBAF), exhibit the formation of interlocked chains of deprotonated **17** and **18**

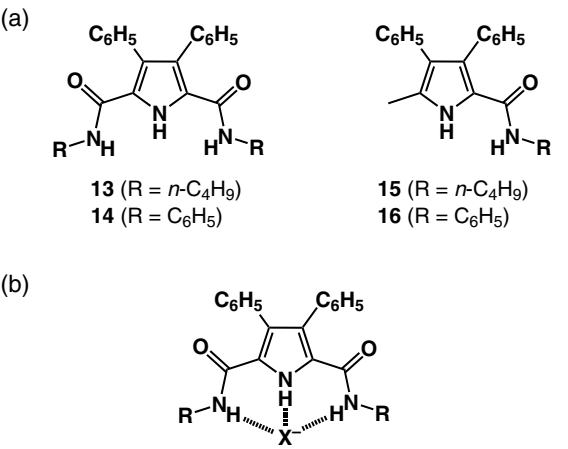

Figure 9. (a) Amidopyrroles **13**–**16**[72,73]; (b) anion-binding mode of amidopyrroles **13** and **14**.[72,73]

Table 1. Anion-binding constants (K_a, M^{-1}) of **13**–**15** upon the addition of anions as TBA salts in CD_3CN (**13** and **15**) and 0.5% H_2O/DMSO (**14**). Data taken from Refs. 72 and 73.

Anion	**13**	**14**	**15**
F^-	85	74	134
Cl^-	138	11	28
Br^-	<10	<10	<10
$H_2PO_4^-$	357	1450	89
$C_6H_5CO_2^-$	2500	560	202

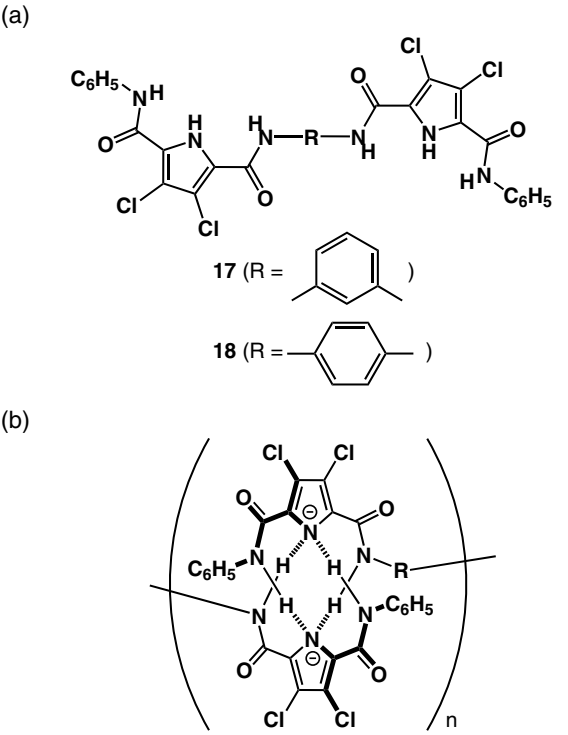

Figure 10. (a) Phenylene-bridged amidopyrrole dimers **17** and **18**[75]; (b) schematic representation of hydrogen-bonding chain structures of deprotonated **17** and **18**.[75]

anions via N–H···N hydrogen bonds (Figure 10b). In the solid state, the two half molecules are essentially planar, while the complete molecule is twisted such that the angle between the pyrrole rings is 61.79(5)°.[75] Furthermore, single-crystal X-ray analysis of the Cl^- complex of *p*-phenylene-bridged **18** as a TBA salt shows a [1 + 2]-type binding mode.[76] The molecular structures of protonated and Cl^- complexes were also supported by theoretical studies by Navakuhn and Ruangpornvisuti.[77,78]

Incorporation of additional pyrrole NH units to the monomeric amidopyrroles **13** and **14** would enhance the affinity of anion binding and modify the binding selectivity. Sessler *et al*. prepared amide-bridged tripyrrolyl derivative **19** (Figure 11a).[79] In the solid state, tripyrrolyl **19** forms intermolecular hydrogen bonds as elucidated from single-crystal X-ray analysis. In DMSO-d_6, **19** shows anion binding for $H_2PO_4^-$ and $C_6H_5CO_2^-$ with K_a values of 5500 and 10 300 M^{-1}, which are augmented compared to those of **14** (1450 and 560 M^{-1}, respectively), whereas **19** shows no binding behavior for Cl^-, Br^-, and HSO_4^-.[79] Sessler *et al*. also replaced the core pyrrole ring of **19** with pyridyl and phenyl moieties to afford

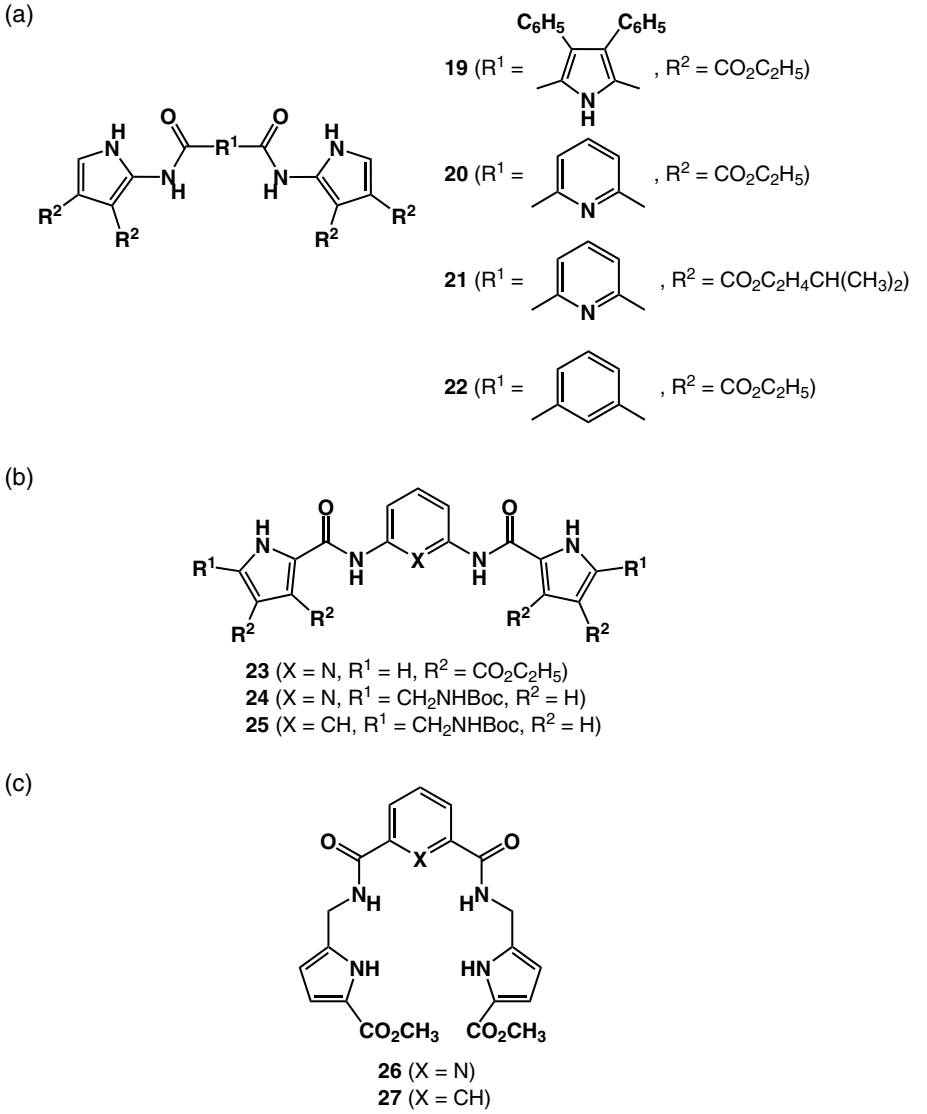

Figure 11. (a–c) Bisamidopyrrole-based anion receptors **19**–**27**.[79–81]

bispyrrole derivatives **20**–**22** (Figure 11b).[80] The solid-state structure of **20** shows a slightly distorted conformation with intramolecular hydrogen bonding, for example between the pyrrole-NH and amide-C=O. The bispyrroles **20**–**22** exhibit anion binding in nonpolar solvents such as CH_2ClCH_2Cl (Table 2), wherein **20** binds $CH_3CO_2^-$ ($K_a = 19\,000\ M^{-1}$), while these receptors show no interactions with Cl^- and Br^-. On the other hand, **23**, an isomeric form of **20** by changing the amide

Table 2. Anion-binding constants (K_a, M^{-1}) of **20**–**23** upon the addition of anions as TBA salts in CH_2ClCH_2Cl. Data taken from Ref. 80.

Anion	**20**	**21**	**22**	**23**
$C_6H_5CO_2^-$	43 000	NB[a]	WB[b]	NB[a]
$CH_3CO_2^-$	19 000	13 900	WB[b]	NB[a]
NO_2^-	13 000	WB[b]	WB[b]	NB[a]
CN^-	5600	WB[b]	WB[b]	WB[b]
NO_3^-	NB [a]	NB[a]	NB[a]	WB[b]
Cl^-	NB [a]	NB[a]	NB[a]	805
Br^-	NB [a]	NB[a]	NB[a]	WB[b]
HSO_4^-	NB [a]	NB[a]	NB[a]	NB[a]

[a]NB = No binding interaction observed. [b]WB = Evidence consistent with weak binding was observed; however, it was not possible to fit the data adequately to a 1:1, 1:2, or 2:1 binding profile.

Table 3. Anion-binding constants (K_a, M^{-1}) of **24**–**27** upon the addition of anions as TBA salts in DMSO-d_6. Data taken from Ref. 81.

Anion	**24**	**25**	**26**	**27**
F^-	102	73	1266	138
$H_2PO_4^-$	147	129	448	459
$CH_3CO_2^-$	74	75	380	262
Cl^-	65	52	75	75
HSO_4^-	<10	a	21	<10

[a]No significant shift in NMR.

linkages, binds Cl^- ($K_a = 805\ M^{-1}$) under similar conditions (Table 2).[80] Furthermore, Cheng and coworkers reported the similar receptors **24** and **25** as reference molecules of **26** and **27** (Figure 11c), which have sp^3 CH_2 moieties between pyrrole rings.[81] Among **24**–**27**, **26** binds anions more efficiently in DMSO-d_6, wherein K_a values for F^- are 102 (**24**), 73 (**25**), 1266 (**26**), and 138 (**27**) M^{-1}. In the cases of **24** and **25**, bulky Boc groups at the terminal positions inhibit the formation of U-type structures, which are appropriate for efficient anion binding (Table 3).[81]

In 2004, Cheng and coworkers prepared 1,2-pheylene-bridged bisamidopyrrole **28** (Figure 12), which, using intermolecular hydrogen bonding, forms a CH_3OH-assisted helical assembly in the crystal from CH_3OH/EtOAc and a knot-like dimer structure in the crystal from $CHCl_3$/DMSO or H_2O/DMSO.[82] In DMSO-d_6, **28** binds anions with K_a values of 320, <10, and 100 M^{-1} for F^-, Cl^-, and $H_2PO_4^-$, respectively.[82] Sun and coworkers modified the skeleton structure of **28** to provide the derivatives **29**–**33** from pyrrole-2-carbonyl chloride and various

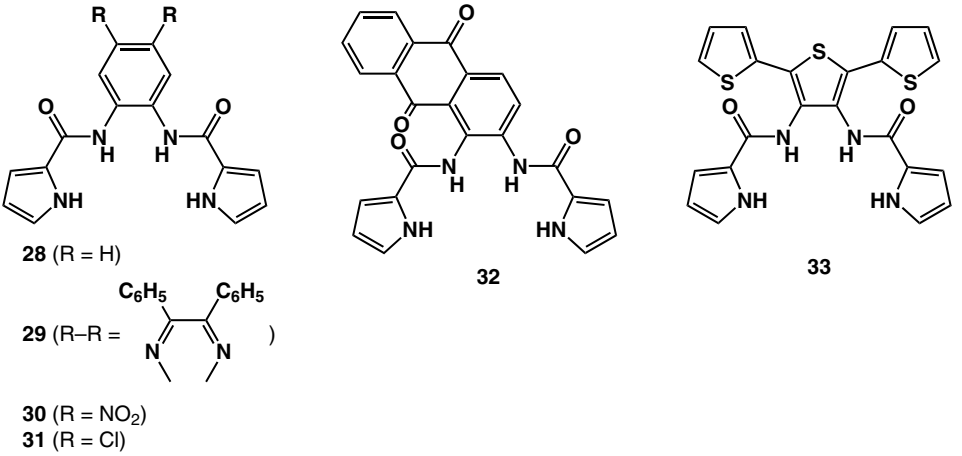

Figure 12. Bisamidopyrrole-based anion receptors **28**–**33**.[82–84]

diamino-substituted aryl units.[83] In CH_3CN/H_2O (9:1, v/v), both **29** and **30** respond to only CN^- among the 12 anions, including F^-, Cl^-, Br^-, I^-, NO_3^-, $CH_3CO_2^-$, $C_6H_5CO_2^-$, $HP_2O_7^{3-}$, $H_2PO_4^-$, HSO_4^-, and ClO_4^-. Upon addition of CN^-, the absorption bands of **29** at 291 and 378 nm decrease while three new bands at 299, 372, and 428 nm appear. Concomitantly, the fluorescence maximum at 425 nm is shifted to 554 nm. The binding constant for [1 + 2]-type stoichiometry was estimated as log $K = 5.91$.[83] Similarly, **30** shows absorption spectral changes with log $K = 9.20$. The colorimetric response of **30** to CN^- persists up to 50% water content. As seen in the ^1H NMR spectral changes of **30** in DMSO-d_6, formation of a CN^- adduct, a cyanohydrin, enables it to exhibit the sensing behavior to this anion. On the other hand, **29** shows an interaction between pyrrole moieties and CN^-.[83] A detailed examination of the receptors **29**–**33** for interaction with anions in CH_3CN or DMSO suggests efficient sensing behaviors for anions due to association, deprotonation, and cyanohydrin formation (Table 4).[84]

In 2007, Anzenbacher and coworkers demonstrated that the tripodal sensor molecules **34**–**37**, based on 1,3,5-triaminomethylbenzene (Figure 13), can bind and sense anions in hydrophilic polymer matrices, despite their inability to bind anions in water.[85] ^1H NMR titration suggests the formation of [1 + 1] complexes with C_3 symmetry. The anion-binding affinities of **35**–**37** follow the order of $H_2PO_4^- > HP_2O_7^{3-} > CH_3CO_2^- \gg Cl^- > Br^-$ due to the K_a (M^{-1}) range of 3.8–5.0 × 10^6 for F^-, 10–100 for Cl^-, 1.0–5.0 × 10^6 for $CH_3CO_2^-$, 2.3–5.0 × 10^6 for $H_2PO_4^-$, and 1.0–5.0 × 10^6 for $HP_2O_7^{3-}$ in DMSO. Less selectivity of these receptors **35**–**37** for anions compelled an examination of the possibility of sensor arrays including other anion receptors; the arrays detect the changes in the fluorescence intensity

Table 4. Equilibrium constants (K_a, K_d, and K_c,[a] M^{-1}) of **29**–**33** upon the addition of anions as TBA salts in CH_3CN (**29**, **30**, and **33**) or DMSO (**31** and **32**). Data taken from Ref. 84.

Anion	**29**	**30**	**31**	**32**	**33**
F^-	$K_a = 1.2 \times 10^4$ $K_d = 4.5 \times 10^7$	$K_a = 6.4 \times 10^4$ $K_d = 1.2 \times 10^7$	c	$K_a = 4.7 \times 10^3$ $K_d = 6.4 \times 10^4$	$K_a = 5.8 \times 10^3$
Cl^-	$K_a = 100$	$K_a = 60$	$K_a = 20$	$K_a = 110$	$K_a = 90$
$CH_3CO_2^-$	$K_d = 8.2 \times 10^5$	$K_a = 1.7 \times 10^3$ $K_d = 1.1 \times 10^6$	$K_a = 4.4 \times 10^4$	$K_a = 4.7 \times 10^4$	$K_a = 190$
$H_2PO_4^-$	$K_a = 2.3 \times 10^4$	$K_a = 7.7 \times 10^3$	$K_a = 3.3 \times 10^3$	$K_a = 250$	$K_a = 270$
CN^-	$K_c > 1.0 \times 10^{8b}$	$K_c > 1.0 \times 10^{8b}$	$K_d = 1.8 \times 10^6$	$K_d = 4.8 \times 10^4$	$K_d = 1.9 \times 10^4$
OH^-	$K_d = 7.2 \times 10^5$	$K_d = 1.1 \times 10^6$	$K_d = 4.8 \times 10^4$	$K_d = 1.2 \times 10^4$	$K_a = 9.9 \times 10^4$ $K_d = 3.2 \times 10^5$

[a]K_a, K_d, and K_c represent the association constant of the anion-receptor hydrogen-bonded complex, the proton dissociation constant for the receptor molecule, and the formation constant of the cyanohydrin complex, respectively.
[b]A 1:2 receptor-CN^- binding stoichiometry was found.
[c]The equilibrium constants did not satisfactorily fit the simple hydrogen-bonding or deprotonation process.

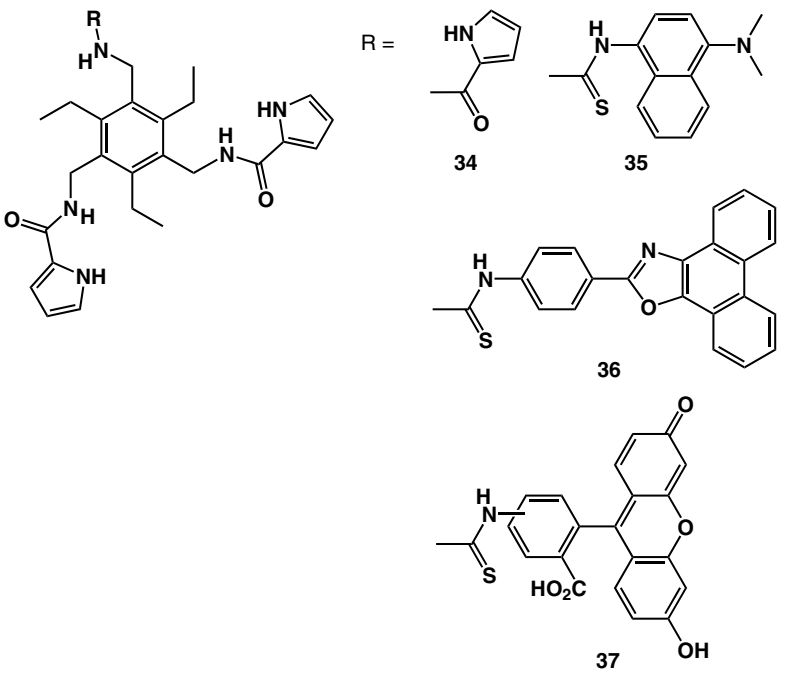

Figure 13. Amidopyrrole-based tripodal receptors **34**–**37**.[85]

of the sensor-polyurethane films upon the addition of aqueous solutions of anions.[85]

III. Dipyrrins and Their Analogs as Anion Receptors

A. Dipyrrin- and Dipyrromethane-Based Anion Receptors

Dipyrrins (dipyrromethenes) **38**, which are half-structures of porphyrins, are well-known as partial structures of bile pigments consisting of two pyrroles with an sp^2-*meso* position; they are essential π-conjugated bidentate monoanionic ligands for metal ions in natural and artificial systems.[86,87] Dipyrrins have only one pyrrole NH; therefore, the protonated form of dipyrrins can act as an anion receptor (Figure 14a). As observed in the pioneering work by Fischer and Orth, β-alkyl-substituted dipyrrins were prepared and were "stored" as hydrohalogenated salts[38]; however, there have been few examples of protonated dipyrrins as anion receptors, whose anion complexes are usually observed in solid-state structures. In 1978, Sheldrick and coworkers reported the first crystal structure of a protonated dipyrrin, which was characterized as a Br^- salt **39** (Figure 14b).[88] Sessler *et al*. demonstrated a similar anion complex as a Cl^- salt of protonated **40**[89]; in CH_3CN, the K_a values of **40** and **41**, which are protonated by HI, for Cl^- as a TBA salt are 8.8×10^5 and 3.0×10^5 M^{-1}, respectively, as determined from isothermal titration calorimetry (ITC) titrations (Figure 14c).[89] Dolphin and coworkers reported anion complexes of *meso*-aryl-substituted dipyrrin as protonated forms **42** and **43**.[90] Based on the conformation with two pyrrole rings facing the "outside," perfluorophenyl dipyrrin forms [2 + 1 (= receptors + anion)] complexes with dianion $ZnBr_4^{2-}$ and $ZnCl_4^{2-}$ (**42**) in the solid state, whereas the dipyrrin forms 1D supramolecular chain structure with Br^- (**43**) (Figure 14d). This is in sharp contrast to the cases of **39** and **40**, where two pyrrole NHs in the corresponding dipyrrin molecule cooperatively bind an anion.[90]

The flexibility observed in the pyrrole inversion upon protonation might be one of the reasons that the anion-binding chemistry of dipyrrins has not been well investigated. In contrast to dipyrrins, dipyrrinones such as **44**, where one of the pyrrole α positions is oxidized (Figure 15), can behave as neutral bidentate anion receptors. The dipyrrinone **44** binds anions with the binding constants (K_a) of 122, <10, 94, and 1680 M^{-1} for Cl^-, Br^-, NO_3^-, and HSO_4^-, respectively, in $CDCl_3$.[91] The preference for HSO_4^-, as compared to other anions, is due to the additional interaction of the amide-oxygen of **44** and protonic OH of the anion; this is also revealed by single-crystal X-ray analysis of **44**·HSO_4^-.[91]

Dipyrromethanes comprising two pyrrole rings bridged by an sp^3-*meso* carbon can be used as building units for π-conjugated porphyrin-related macrocycles

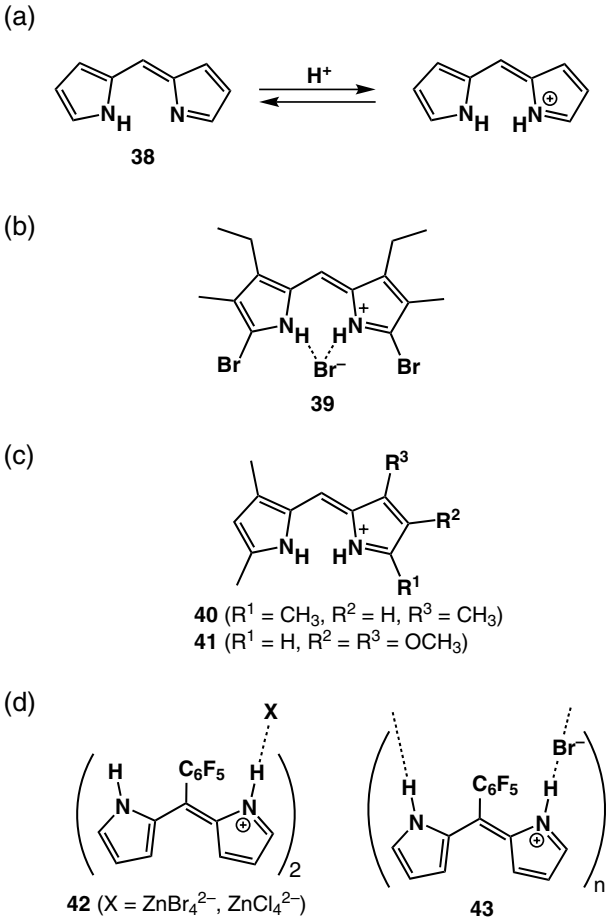

Figure 14. (a) Skeleton structure of dipyrrin (dipyrromethene) **38**; (b) first structure-solved Br^- complex of protonated dipyrrin **39**[88]; (c) protonated dipyrrins **40** and **41**[89]; (d) anion complexes of *meso*-perfluorophenyl dipyrrin in a protonated form (**42** and **43**).[90]

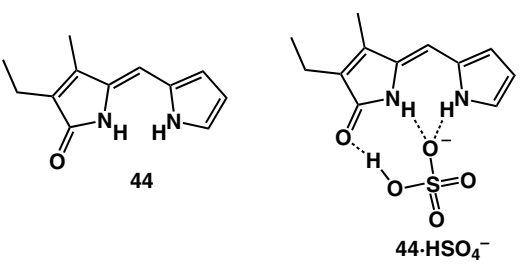

Figure 15. Dipyrrinone **44** and HSO_4^- complex.[91]

as well as dipyrrins, as discussed above. Dipyrromethanes can also be considered as half-structures of calix[4]pyrroles; from the weak cooperative interactions of pyrrole NH, due to the open-chain structures, the anion-binding properties of dipyrromethane seem fairly less significant. However, supplementary interaction sites would enhance the binding affinities for anions, as observed in the monopyrrolic anion receptor systems. Gale and coworkers reported the synthesis of 2,2-bisamidodipyrrolylmethanes: less stable **45** and **46** and relatively stable **47**–**49** and hemiamide derivative **50** (Figure 16).[92,93] Single-crystal X-ray analysis of **45**–**49** and hemiamide **50** reveals the formation of various hydrogen-bonding assemblies using pyrrole- and amide-NH sites and amide-CO moieties. Compounds **45**–**50** can bind, for example, F^- with K_a values of 8990, 7560, 124, 89, and 429 M^{-1}, respectively, in 5% H_2O/DMSO-d_6 and 1450 M^{-1} in 0.5% H_2O/DMSO-d_6 (Table 5).

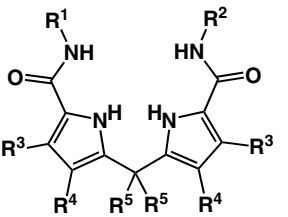

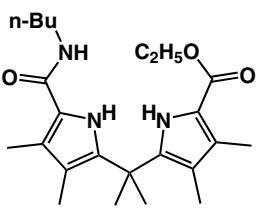

45 ($R^1 = R^2 =$ Ph, $R^3 = CH_3$, $R^4 = CH_2CH_3$, $R^5 =$ H)
46 ($R^1 = R^2 =$ n-Bu, $R^3 = CH_3$, $R^4 = CH_2CH_3$, $R^5 =$ H)
47 ($R^1 = R^2 =$ Ph, $R^3 = R^4 = R^5 = CH_3$)
48 ($R^1 = R^2 =$ n-Bu, $R^3 = R^4 = R^5 = CH_3$)
49 (R^1 = Ph, R^2 = n-Bu, $R^3 = R^4 = R^5 = CH_3$)

50

Figure 16. Amide-substituted dipyrromethanes **45**–**50**.[92,93]

Table 5. Anion-binding constants (K_a, M^{-1}) of **45**–**50** upon the addition of anions as TBA salts in 5% water/DMSO-d_6 (**45**–**49**) and 0.5% water/DMSO-d_6 (**50**). Data taken from Refs. 92 and 93.

Anion	**45**	**46**	**47**	**48**	**49**	**50**
F^-	8990	7560	124	89	429	1450
Cl^-	43	23	<15	a	a	<15
Br^-	10	13	—	—	—	—
$H_2PO_4^-$	b	b	1092	81	307	83
HSO_4^-	128	44	—	—	—	—
$C_6H_5CO_2^-$	424	354	41	20	33	41
F^{-c}	114	11	—	—	—	—
$H_2PO_4^{-c}$	234	20	—	—	—	—

[a]No significant shift.
[b]An adequate fit could not be obtained.
[c]Measured in 25% water/DMSO-d_6.

Significantly, **45** shows F^- and $H_2PO_4^-$ binding (114 and 234 M^{-1}) even in the extremely competitive solvent mixture 25% H_2O/DMSO-d_6.[92,93] Efficient binding for $H_2PO_4^-$ is also supported by DFT geometry optimization to show that the receptor adopts a cleft conformation wherein the receptor binds to two oxygen atoms in $H_2PO_4^-$, each by hydrogen-bonding with the pyrrole- and amide-NH sites.[92,93]

Another strategy to enhance the binding affinities of dipyrromethanes is formation of charge transfer (CT) complexes. Jiang and coworkers examined the complexation between dipyrromethanes **51**–**55** (Figure 17a) and TCNQ in CH_3CN/H_2O (1:1, v/v)[94]; TCNQ complexes of **52**–**55** do not show any changes in color and absorption spectra from the addition of anions, whereas **51**·TCNQ can serve as a highly selective colorimetric sensor, from blue to pale purple, for anions, especially PO_4^{3-} and CO_3^{2-}. In this case, anion-binding and sensing motifs are quite different — presumably *meso*-hydroxymethyl units for binding and electron-rich properties, essential to formation of CT complexes, for sensing.[94] On the other hand, Sessler *et al*. examined the anion-binding properties of **52** in a nonpolar solvent without electron-deficient components[95]; the K_a values in CD_2Cl_2 are 2100, 110, 19, <10, <10, 310, 11, and <10 M^{-1} for F^-, Cl^-, Br^-, I^-, HSO_4^-, $H_2PO_4^-$, NO_3^-, and ClO_4^-.[95] Furthermore, the incorporation of bulky units at the *meso* position would hinder the rotational mobility of the pyrrole moieties and thus increase the stability of anion complexes. In fact, Mlinarić-Majerski and coworkers prepared adamantane-based dipyrromethanes **56**–**59** (Figure 17b), which show greater K_a values for anions (e.g. 80 M^{-1} for Cl^- with **56**) than *meso*-phenyldipyrromethane **60** (e.g. 22 M^{-1} for Cl^-) in $CDCl_3$.[96] F^- binding of, especially, "dimers" **57** and **59** includes slightly complicated [2 + 1], [1 + 1], and [1 + 2] modes (Table 6).[96] Attachment of a chromogenic moiety to dipyrromethane is another method for exhibiting anion sensing. Chauhan *et al*. prepared 1-arylazo-substituted dipyrromethanes (**61**–**64**, Figure 17c), which bind anions with K_a values of, for example, $>10^6$ M^{-1} for F^- with **64** in DMSO (Table 7).[97] Compound **64** shows a dramatic color change from orange to blue by F^- binding corresponding to the absorption changes from λ_{max} = 438 nm to λ_{max} = 575 nm.[97]

Denekamp, Suwinska, Eichen, and coworkers reported anion-binding behavior of simple tripyrrole molecule **65** (Figure 18).[98] Tripyrrolemethane **65** shows efficient [1 + 1] and [1 + 2] F^- binding in CD_3CN (K_1 = 41 000 M^{-1} and K_2 = 17 000 M^{-1}) and wet DMSO-d_6 (K_1 = 5000 M^{-1} and K_2 = 2000 M^{-1} in 0.25% D_2O/DMSO-d_6; K_1 = 1400 M^{-1} and K_2 = 1000 M^{-1} in 1% D_2O/DMSO-d_6; K_1 = 220 M^{-1} and K_2 = 200 M^{-1} in 5% D_2O/DMSO-d_6). Compound **65** exhibits [1 + 1] binding for $H_2PO_4^-$ with K_a values of 300, 60, <50, and <50 M^{-1} in CD_3CN, 0.25%, 1%, and 5% D_2O/DMSO-d_6. The addition of halide anions as TBA salts to **65** result in

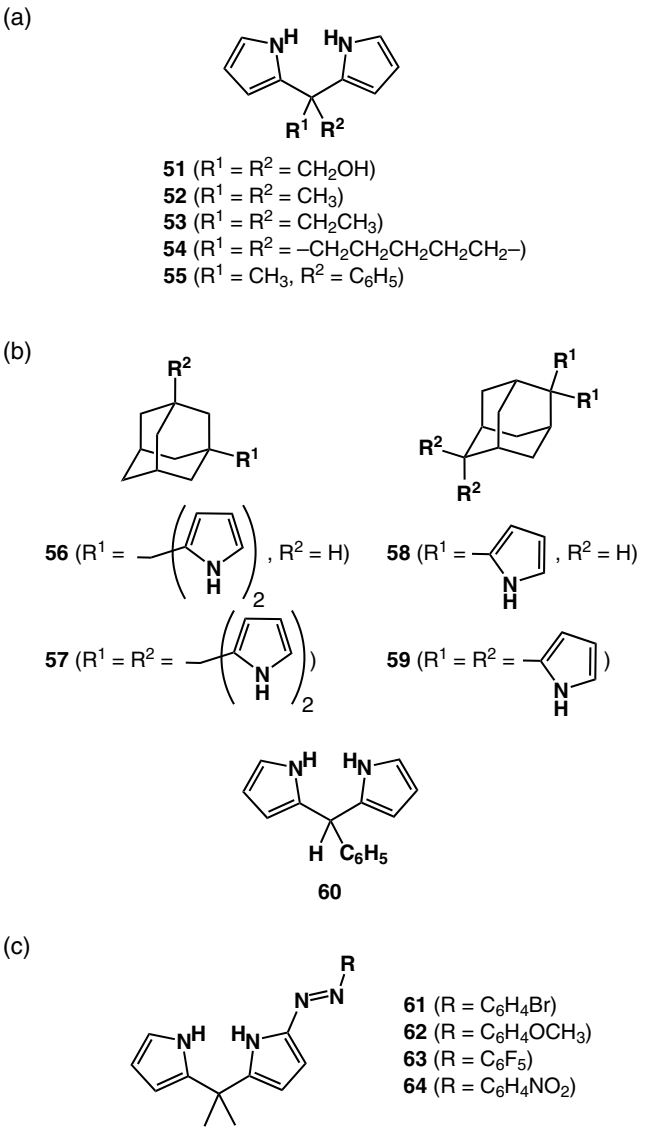

Figure 17. (a) *Meso*-disubstituted dipyrromethanes **51**–**55**[94,95]; (b) adamantane-based dipyrromethanes **56**–**59** and *meso*-phenyldipyrromethane **60** as a reference[96]; (c) 1-arylazo-substituted dipyrromethanes **61**–**64**.[97]

significantly smaller guest-induced shifts in the ^{1}H NMR spectra. Furthermore, single-crystal X-ray analysis of the Br^- complex of **65** reveals the formation of six crystallographically independent structures, some of which use the pyrrole β-CH site for Br^- binding.[98]

Table 6. Anion-binding constants (K_a, M^{-2}, M^{-1}, and M^{-2}, for 2:1, 1:1, and 1:2 binding) of **56–60** upon the addition of anions as TBA salts in $CDCl_3$ (F^-, Cl^-, Br^-, and $H_2PO_4^-$) and CD_3CN (HSO_4^-). Data taken from Ref. 96.

Anion	**56**	**57**	**58**	**59**	**60**
F^-	1×10^4 (2:1)	4.4×10^3 (2:1)	4.8×10^5 (2:1) or 1×10^4 (2:1) 1×10^3 (1:1)	150 (1:1) 3.3×10^3 (1:2)	170 (1:1) 2.3×10^4 (2:1)
Cl^-	80 (1:1)	68 (1:1)	NB[a]	NB[a]	22 (1:1)
Br^-	22 (1:1)	38 (1:1)	NB[a]	NB[a]	4.8 (1:1)
HSO_4^-	65 (1:1)	22 (1:1)	1.4×10^3 (1:1)	NB[a]	6 (1:1)
$H_2PO_4^-$	150 (1:1)	182 (1:1)	NB[a]	74 (1:1)	32 (1:1)

[a]No binding was observed.

Table 7. Anion-binding constants (K_a, M^{-1}) of **61–64** upon the addition of anions as TBA salts in DMSO. Data taken from Ref. 97.

Anion	**61**	**62**	**63**	**64**
F^-	1235	1934	$>10^5$	$>10^6$
Cl^-	<50	121	185	209
Br^-	ND[a]	ND[a]	219	386
I^-	ND[a]	ND[a]	ND[a]	ND[a]
HSO_4^-	ND[a]	ND[a]	ND[a]	1730
$H_2PO_4^-$	ND[a]	ND[a]	2420	82 400
$CH_3CO_2^{-c}$	ND[a]	ND[a]	9825	96 600

[a]Not determined.

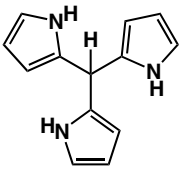

65

Figure 18. Tripyrrolemethane **65**.[98]

B. Dipyrrin- and Bipyrrole-Based π-Conjugated Systems

The anion-binding properties of a directly bridged bispyrrole, bipyrrole **66** (Figure 19a), were also examined by Sessler *et al.*[99] Bipyrrole **66** shows K_a values of 246, 4090, and 3650 M^{-1} for Cl^-, $C_6H_5CO_2^-$, and $CH_3CO_2^-$ by ITC (30 °C) and 53 and 35 M^{-1} for Br^- and HSO_4^- by ^1H NMR titrations (25 °C) in CH_3CN.[99] Also,

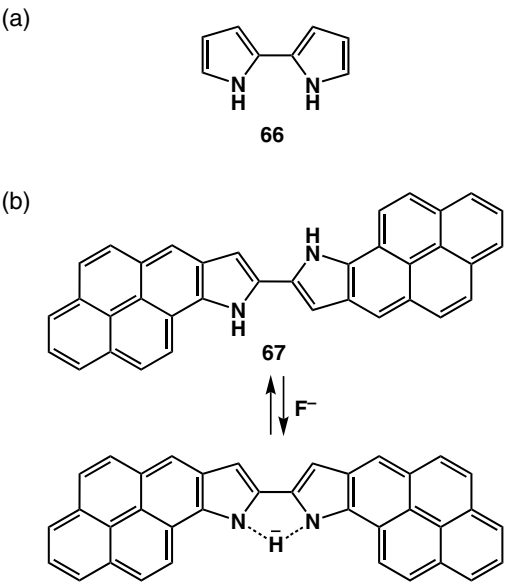

Figure 19. (a) Bipyrrole **66**[99]; (b) bispyrenopyrrole **67**.[100]

bis(pyreno[2,1-*b*]pyrrole) (**67**, Figure 19b), as one of the derivatives including π-fused "pyrrole" rings, displays excellent selectivity and sensitivity for detection of F^- in comparison with other anions such as Cl^-.[100] Excess F^- as a TBA salt deprotonates one of the pyrrole NH of **67** in DMSO, resulting in remarkable colorimetric and fluorescent changes in the visible region. ^{1}H NMR spectral changes using 2,2′-bisindole instead of **67** suggest that the *anti* form twisted conformation with and without the presence of 1 equivalent of F^- is transformed into *syn* conformation with presumably planar structure by deprotonation.[100]

One of the naturally occurring oligopyrroles is prodigiosin **68** (Figure 20a), which was first isolated from *Serratia marcescens* in 1929 and is characterized by a common pyrrolylpyrromethene skeleton consisting of dipyrrin and bipyrrole.[101] The prodigiosins and their analogs exhibit several biological activities. Kataoka and coworkers reported that prodigiosin acidified cellular organelles and vesicles by transporting HCl across membranes.[102,103] On the other hand, Sessler, Magda, and coworkers examined anion-binding properties of prodigiosin analogs **69–71** (Figure 20b)[89]; Cl^- binding constants (K_a) in CH_3CN using a TBA salt for **69–71** protonated by HI are 5.9×10^5, 1.1×10^5, and 1.1×10^5 M^{-1}, respectively, determined by ITC. The efficiency of Cl^- transport was determined by monitoring their efflux across a 200 nm liposome membrane as a function of time; the order of transport efficiency of prodigiosin analogs was found to be **69** > **70** > **71**. The order of anticancer activity *in vitro* was found to be similar: **69** > **70** > **71**.[89]

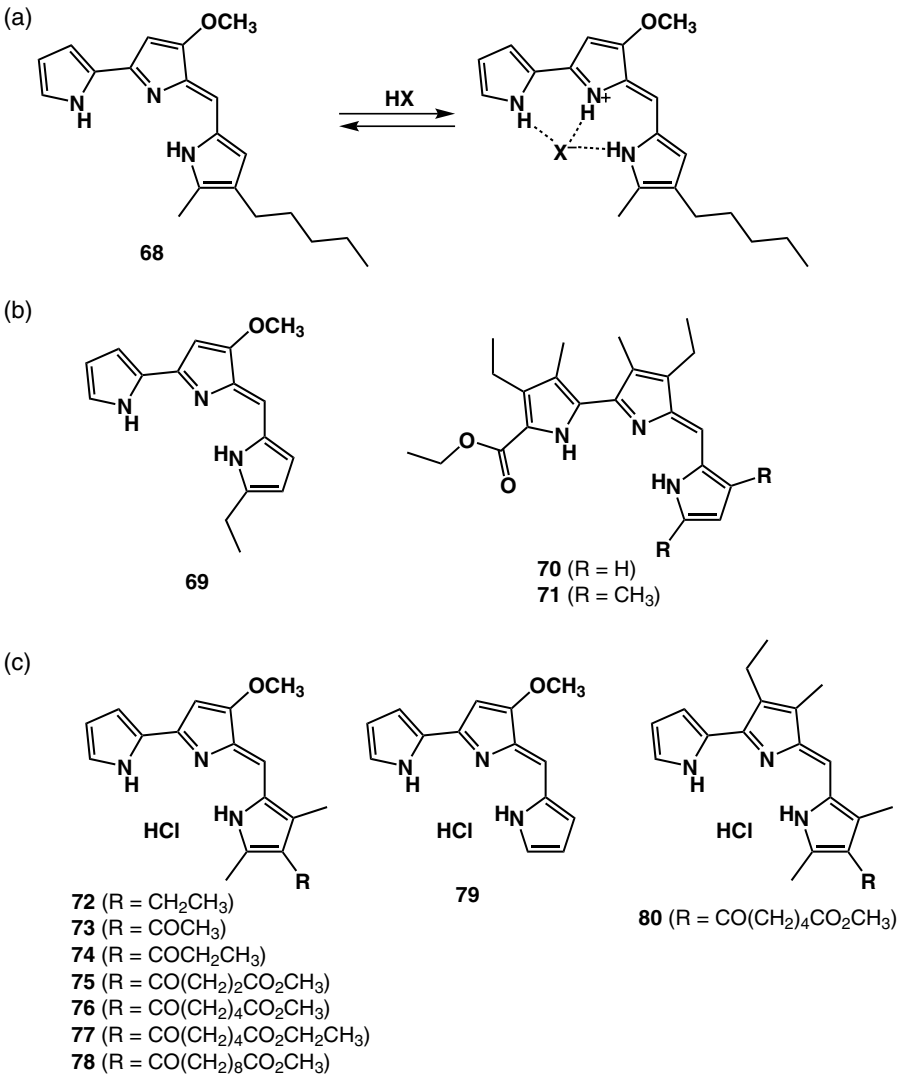

Figure 20. (a) Prodigiosin **68** and anion-binding mode[101,104]; (b, c) artificial prodigiosin derivatives **69**–**80** [protonated form in (c)].[89,105]

Seganish and Davis showed that prodigiosin **68** acts as a Cl^- carrier (H^+/Cl^- symporter) in phospholipid vesicles and demonstrated that **68** is able to exchange Cl^- for NO_3^- as an antiporter.[104] Furthermore, Thompson and coworkers prepared a series of prodigiosin derivatives **72**–**80** (Figure 20c) and demonstrated Cl^- transport through liposomal membranes.[105] The order of transport efficiency was found to be **72** ≥ **78**~**74** > **80**~**75**~**79** > **77** > **73** > **76**, with all prodigiosin analogs exhibiting significant Cl^- transport ability at relatively low ligand-to-lipid

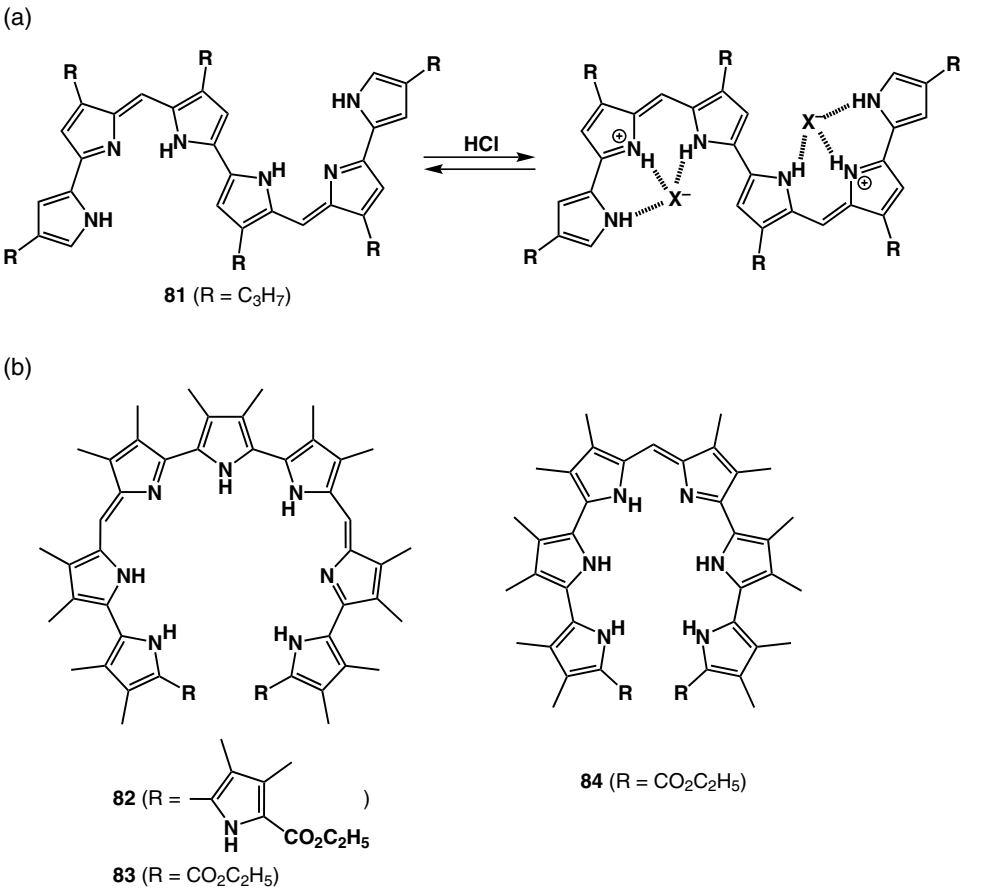

Figure 21. (a) Hexapyrrin **81** and anion-binding mode in protonated form[106]; (b) nona-, hepta-, and hexapyrrolic open-chain systems **82**–**84**.[107]

concentrations (0.1 mol % relative to lipid). Essentially, this result suggests that the prodigiosin core can be functionally altered without losing the ability to transport Cl^- across phospholipid membranes.[105]

As a π-conjugated pyrrole oligomer that has methine bridges and direct α–α linkages, hexapyrrolic "prodigiosin dimer" **81**, which is protonated by HCl, was reported by Sessler *et al*. (Figure 21a).[106] Single-crystal X-ray analysis of a Cl^- complex of the hexapyrrin **81** in protonated form reveals the formation of a fairly planar [1 + 2]-type complex with an S-shaped conformation. NOE experiments support the S-shaped conformation in the solution state.[106] Sessler and coworkers also prepared higher linear oligopyrroles **82**–**84** (Figure 21b), which show absorption maxima in the visible region like that of **81**.[107] The oligopyrroles **82**–**84** exhibit absorption spectral changes in the adduct forms with acetic acid.[107]

IV. Dipyrrolylquinoxalines and Related Aryl-Bridged Bispyrroles

A. Dipyrrolylquinoxalines

Among the open-chain pyrrole derivatives, 2,3-dipyrrol-2-ylquinoxaline (**85**, Figure 22a), a fluorescent dye directly connected to the pyrrole ring, was first synthesized by Oddo and Dainotti in 1911 by the acid-catalyzed condensation of 1,2-dipyrrol-2-ylethanedione (**86**, Figure 22b) and *o*-phenylenediamine,[108] and the process was much later refined by Behr *et al*.[109] Since the first synthesis, the anion-binding properties of dipyrrolylquinoxaline (DPQ) have not been investigated for a long time. In 1999, Sessler and coworkers found that DPQ **85** undergoes a change of color and quenching of emission in the presence of certain anions.[110] It contains two pyrrole NH groups that can function as anion-binding moieties and a built-in quinoxaline ring that might serve as a colorimetric receptor of anions. As illustrated in Figure 22a, this putative sensing system is expected to operate through a combination of electronic and conformational effects. DPQ **85** shows binding affinities (K_a), estimated from UV-visible absorption spectral changes upon the addition of anions, at 18 200, 50, and 60 M^{-1} for F^-, Cl^-, and $H_2PO_4^-$ as TBA salts in CH_2Cl_2, respectively, which are comparable to those of **86** at 23 000, 170, and <50 M^{-1}, respectively.[110] Even though DPQ is an electronically neutral acyclic oligopyrrole system, attachment of the electron-withdrawing quinoxaline moiety enhances the polarity of the pyrrole NH to efficiently bind anions.[110,111]

Replacement of the building blocks of DPQ **85** by other pyrrole and quinoxaline moieties affords the derivatives **87–93**, which possess various

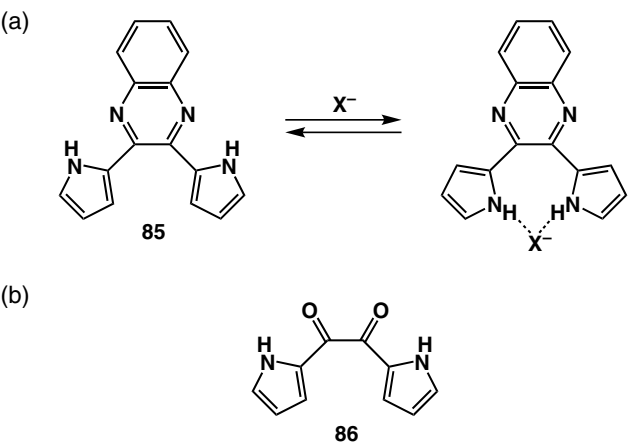

Figure 22. (a) Skeleton structure of dipyrrolylquinoxaline (DPQ) **85** and the anion-binding mode[110]; (b) 1,2-dipyrrol-2-ylethanedione **86**.[110]

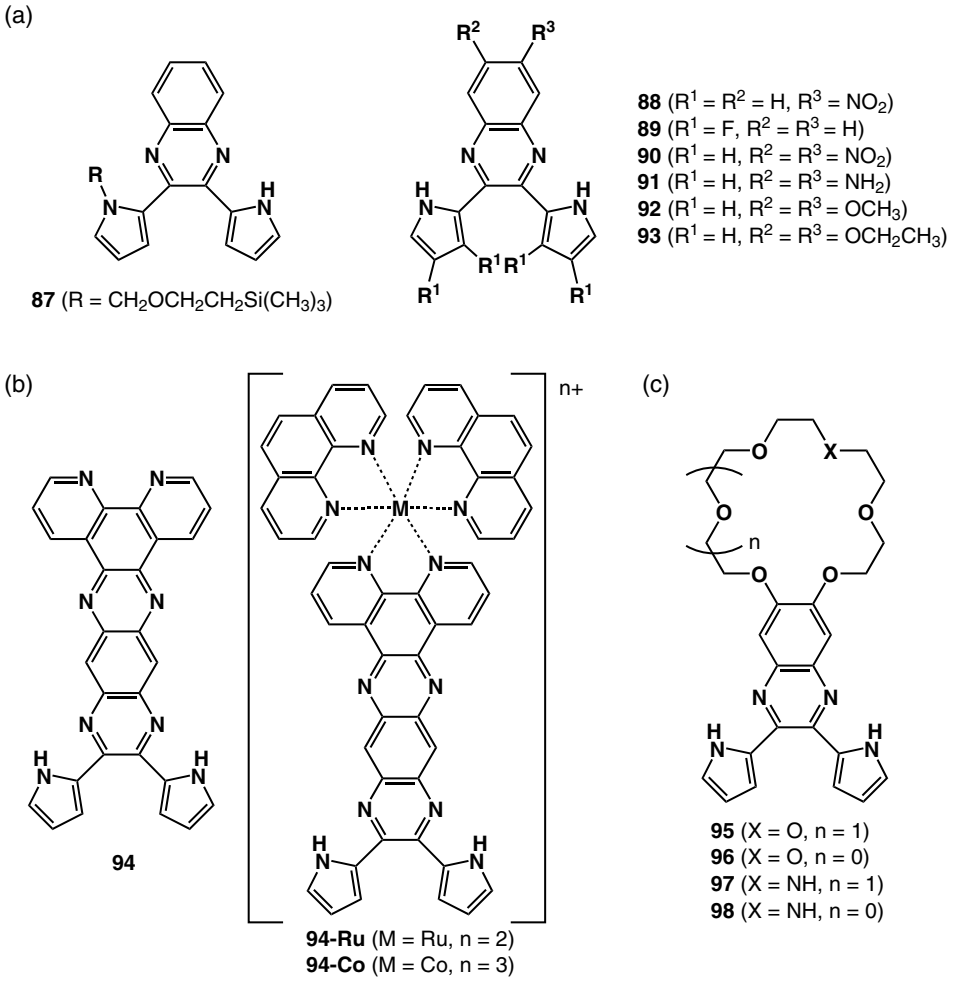

Figure 23. (a) DPQ derivatives **87**–**93**[110,112–114]; (b) phenanthroline-substituted DPQ **94** and metal complexes (**94-Ru**, **94-Co**)[113]; (c) crown-appended DPQs **95**–**98**.[114]

electron-withdrawing or electron-donating groups (Figure 23a).[110,112–114] For example, mono-N-substituted **87** shows smaller K_a values of 120, <50, and <50 M^{-1} for F^-, Cl^-, and $H_2PO_4^-$. 6-Nitroquinoxaline-containing **88** exhibits a higher K_a value (118 000 M^{-1} in CH_2Cl_2) for F^- and comparable values (50 and 65 M^{-1}) for Cl^- and $H_2PO_4^-$,[110] whereas 3,4-difluoropyrrole-substituted **89** shows higher anion binding (61 600, 180, and 17 300 M^{-1} for F^-, Cl^-, and $H_2PO_4^-$ in CH_2Cl_2) than **85**.[112] Diamino-substituted **91**, prepared from dinitro **90**, can be transformed into phenanthroline derivative **94** by condensation with 1,10-phenanthroline-5,6-diketone. Ru(II) and Co(III) complexes (**94-Ru**, **94-Co**) as ClO_4^- salts (Figure 23b)

Table 8. Anion-binding constants (K_a, M^{-1}) of **85**, **89**, **94**, **94-Ru**, and **94-Co** upon the addition of anions as TBA salts in DMSO. Data taken from Ref. 113.

Anion	**85**	**89**	**94**	**94-Ru**	**94-Co**
F^-	<100	59 000	440	12 000	54 000
Cl^-	ND[a]	ND[a]	ND[a]	10	20
$H_2PO_4^-$	ND[a]	5000	ND[a]	40	50

[a]Not determined.

show the higher K_a values for F^- (12 000 and 54 000 M^{-1} in DMSO) than **85** (<100 M^{-1}) and **94** (440 M^{-1}). The trend for the K_a values observed in **94**, **94-Ru**, and **94-Co** correlates with the increasing total charge of the receptor (Table 8). The redox properties of the metal complex can be used to detect the anion-binding behavior of **94-Co**[113]; differential pulse voltammetry (DPV) of **94-Co** in DMSO shows the reversible redox signal at 160 mV (vs. SHE) assignable to Co^{III}/Co^{II}, which disappears (or significantly shifts) by the addition of F^-. Addition of Cl^- and $H_2PO_4^-$ also shifts the higher reduction signals because of the "electron-donating" properties of bound anions.[113] As extended derivatives of dialkoxy-substituted **92** and **93**, "crowned" DPQs **95**–**98** (Figure 23c) were also reported.[114] Single-crystal X-ray structures of **92**, **95**, and **96** show the hydrogen-bonding molecular assemblies; in particular, the pyrrole NH sites of **92** and **96** form hydrogen bonds with methoxy- and crown-oxygen moieties. The cation-binding properties of **95**–**98** were examined, and a K^+-bridged dimer structure was also observed in the solid state of **96**. At present, although it has not yet been successful, the crown-substituted anion receptors are potential motifs for cooperatively binding cations and anions.[114]

The modification of pyrrole α positions also provides utility anion receptor molecules. Several α-formyl-substituted derivatives **99**–**101** (Figure 24a), prepared from **85**, **92**, and **93**, were converted to [2 + 2]-type Schiff base macrocycles **102**–**104** (Figure 24b) by condensation with 1,8-diaminoanthracene.[115] These macrocycles have two "pseudo" cavities; **102** exhibits homotropic positive allosteric effects for F^- and $H_2PO_4^-$ binding in CH_2Cl_2. The binding constants log K and the Hill coefficients are estimated to be 11.0 and 2.2 for F^- and 3.8 and 1.9 for $H_2PO_4^-$. This is the first example of an artificial allosteric system for $H_2PO_4^-$; once an anion is captured in one cavity, the other cavity "shrinks" to the point where its size is better-optimized for anion binding.[115] Furthermore, tetrapyrrole and hexapyrrole derivatives **105** and **106** (Figure 24c) were obtained by acid-catalyzed condensation of the biscarbinol form of **99** and **99** itself with excess pyrrole.[116] The receptors **105** and **106** have claw-like multiple binding NH sites; they show higher K_a values, 32 000, 550, and 4300 M^{-1} (**105**) and >1 000 000, 5800, and 300 000 M^{-1} (**106**) in CH_2Cl_2, for F^-, Cl^-, and $H_2PO_4^-$.[116]

(a)

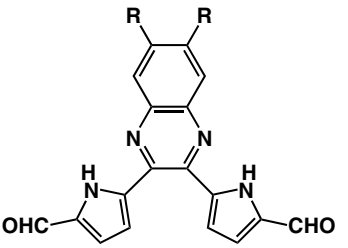

99 (R = H)
100 (R = OCH_3)
101 (R = OCH_2CH_3)

(b)

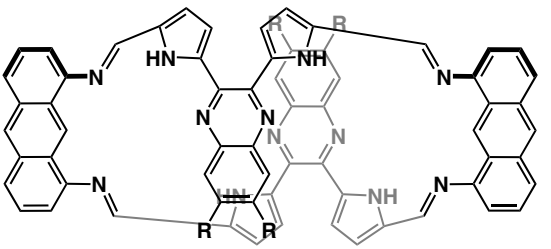

102 (R = H)
103 (R = OCH_3)
104 (R = OCH_2CH_3)

(c)

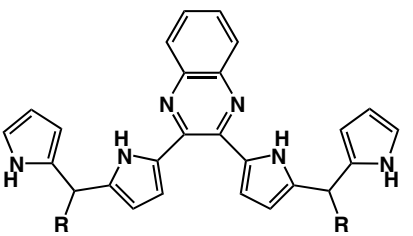

105 (R = H)

106 (R = )

Figure 24. (a) Formyl-substituted DPQs **99**–**101**[115]; (b) DPQ-bridged macrocycles **102**–**104**[115]; (c) oligopyrrolyl-substituted DPQs **105** and **106**.[116]

Pyrazine analogs **107**–**112** (Figure 25a) were also prepared from dipyrrolyldiketone and diaminomalonitrile and subsequent formylation of **108** and **109**.[117] A similar synthetic protocol for **105** and **106** affords oligopyrrolic **110**–**112**; **112** shows higher K_a values for Cl^-, 48 000 M^{-1}, than **106**. The hexapyrrolic analogous receptors **106**

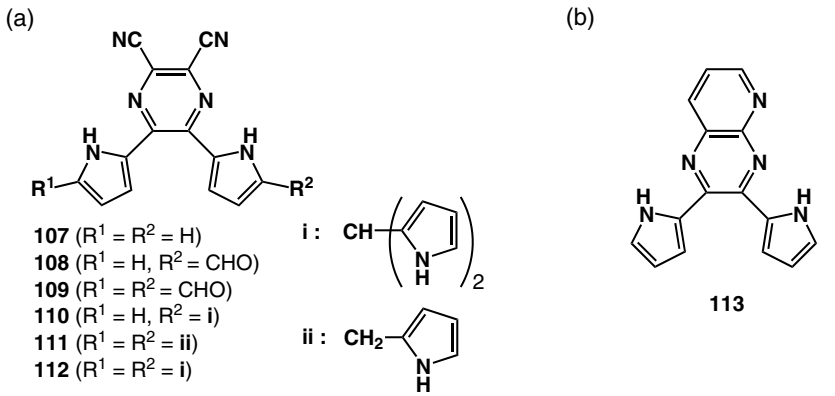

Figure 25. (a) Dipyrrolylpyrazine derivatives **107**–**112**[117]; (b) dipyrrolyl-substituted pyrido[2,3-*b*]pyrazine **113**.[118]

Table 9. Anion-binding constants (K_a, M^{-1}) of **106** and **112** upon the addition of anions as TBA salts in CH_2Cl_2. Data taken from Ref. 117.

Anion	**106**	**112**
Cl^-	5800	48 000
$H_2PO_4^-$	300 000	30 000
$CH_3CO_2^-$	46 000	175 000
oxalate	30 000	24 000
malonate	21 000	2100
succinate	53 000	2000[a]

[a]The equilibrium constant for the second binding for the [2 + 1] complex is 1.4 M^{-1}.

and **112** also efficiently bind dicarboxylates such as oxalate, malonate, and succinate as TBA salts in CH_2Cl_2 [e.g. 30 000 (**106**) and 24 000 (**112**) M^{-1} for oxalate] (Table 9).[117] In addition, Smanta and coworkers reported dipyrrolyl-substituted pyrido[2,3-*b*]pyrazine **113** (Figure 25b); the receptor **113**, which has both anion-binding and metal coordination sites, is responsive to F^- (4900 M^{-1} in CH_3CN) in the metal-free form.[118]

Formation of utility materials based on a DPQ structure has also been examined. In order to enhance and tune the fluorescence output, Anzenbacher and coworkers introduced aryl moieties at the 5- and 8-positions of the DPQ skeleton.[119,120] 5,8-Diaryl-substituted receptors **115**–**120** were prepared by Stille coupling or Suzuki coupling from dibromo derivative **114** (Figure 26a). The presence of 5,8-diaryl substituents results in both a dramatic increase in emission intensity

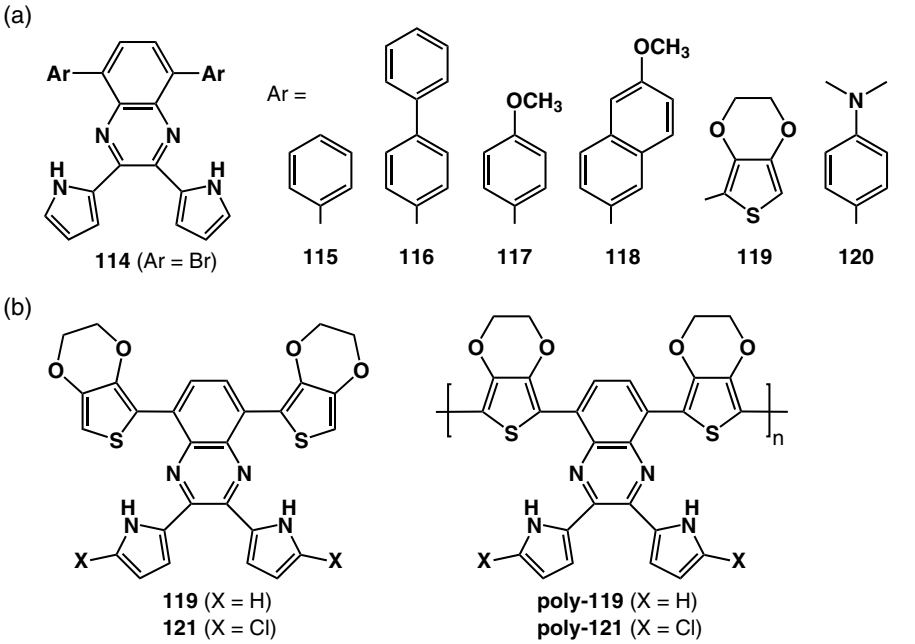

Figure 26. (a) 5,8-Dibromo- and 5,8-diaryl-substituted dipyrrolylquinoxalines **114–120**[119,120]; (b) thienyl-substituted dipyrrolylquinoxalines **119** and **121** and their polymers.[121]

Table 10. Anion-binding constants (K_a, M^{-1}) of **85** and **115–120** upon the addition of anions as TBA salts in CH_2Cl_2. Data taken from Refs. 119 and 120.

Anion	**85**	**115**	**116**	**117**	**118**	**119**	**120**
F^-	18 200	51 300	~12 200	24 700	10 200	25 600	27 500
Cl^-	<50	<100	<100	<100	<100	<100	<50
$HP_2O_7^{3-}$	14 300	93 700	~30 000	58 900	24 300	57 300	39 000
$H_2PO_4^-$	<100	<200	<100	<100	<100	<100	<50

and a shifted emission maximum compared to parent **85** (λ_{em} = 490 nm, Φ_F = 0.15 in CH_2Cl_2). That is to say, λ_{em} = 500 nm, Φ_F = 0.25 for **115**; λ_{em} = 506 nm, Φ_F = 0.38 for **116**; λ_{em} = 514 nm, Φ_F = 0.24 for **117**; λ_{em} = 520 nm, Φ_F = 0.13 for **118**; λ_{em} = 595 nm, Φ_F = 0.22 for **119**; and λ_{em} = 610 nm, Φ_F = 0.26 for **120**. The K_a values of **115–120** in CH_2Cl_2 are in the range of 10 200 (**118**) to 51 300 (**115**) M^{-1} for F^- and 24 300 (**118**) to 93 700 (**115**) M^{-1} for $HP_2O_7^{3-}$ (14 300 M^{-1} for **85**) (Table 10).[119,120] Significant changes in color and fluorescence emission are observed by the addition of F^- and $HP_2O_7^{3-}$. Therefore, polyurethane-embedded sensors exhibit color response in the presence of aqueous solutions of specific

Table 11. Anion-binding constants (K_a, M^{-1}) for **119** and **121** and apparent anion-binding constants (M^{-1}) for poly-**119** and poly-**121** upon the addition of anions as TBA salts in 0.1% H_2O/DMSO. Data taken from Ref. 121.

Anion	**119**	Poly-**119** [a]	**121**	Poly-**121**[a]
F^-	$>10^6$	48 000	$>10^6$	24 000
Cl^-	<100	<100	2000	<100
$HP_2O_7^{3-}$	$>10^6$	61 100	$>10^6$	11 000
$H_2PO_4^-$	<100	3800	$>10^6$	90 000

[a]Apparent binding constants were calculated with unknown concentration of the receptor in the material surface using the equation for 1:1 stoichiometry.

anions.[119,120] Furthermore, thienyl-substituted **119** and α-chloro **121** yielded conductive materials poly-**119** and poly-**121**, whose band gaps were estimated at 1.39 and 1.36 eV, respectively (Figure 26b).[121,122] Upon treatment with aqueous solutions of anions as TBA salts (the corresponding binding constants are summarized in Table 11), the sensor films resulted in gradual changes in the vis-NIR absorption spectra from $HP_2O_7^{3-}$ due to anion binding, which was also supported by the electrochemical quartz crystal microbalance (EQCM) method. Using sensing devices of poly-**121** with an interdigitated ITO electrode, the addition of anion ($HP_2O_7^{3-}$) results in dramatic changes in both visible-NIR spectra and drain current. The low level p-doping and a corresponding positive charge in the polymer results in a dramatic increase in the anion affinity.[121,122]

Pyrene-attached **122** and **123** (Figure 27a) exhibit fluorescence quenching through efficient binding for F^- and $HP_2O_7^{3-}$, 17 300 and 18 000 M^{-1} (**122**) and 19 600 and 29 500 M^{-1} (**123**), respectively, comparable to parent **85**.[123] The sensor **123** achieves signal amplification through effective excited state localization, whereas **122** shows Förster resonance energy transfer (FRET)–based light harvesting from the pyrene moieties to the DPQ moiety. Excitation of **122** at 320 nm, i.e. absorption of pyrene moieties, results in a ten-fold amplification of fluorescence compared to **85**. This means that **122** can be easily used for anion sensing for amounts that are ten times lower than **85**.[123] Anzenbacher *et al*. also reported that sensors **124** and **125** constitute a chromophore capable of undergoing an intensive change in color and a redox-active quinone moiety to generate strong colorimetric and electrochemical signals (Figure 27b).[124] According to UV-visible absorption spectral changes, **124** and **125** show efficient binding for F^- and $HP_2O_7^{3-}$, 482 200 and 316 000 M^{-1} (**124**) and 150 700 and 626 000 M^{-1} (**125**), respectively, in 0.5% H_2O/CH_3CN (Table 12). Electrochemical reduction waves of

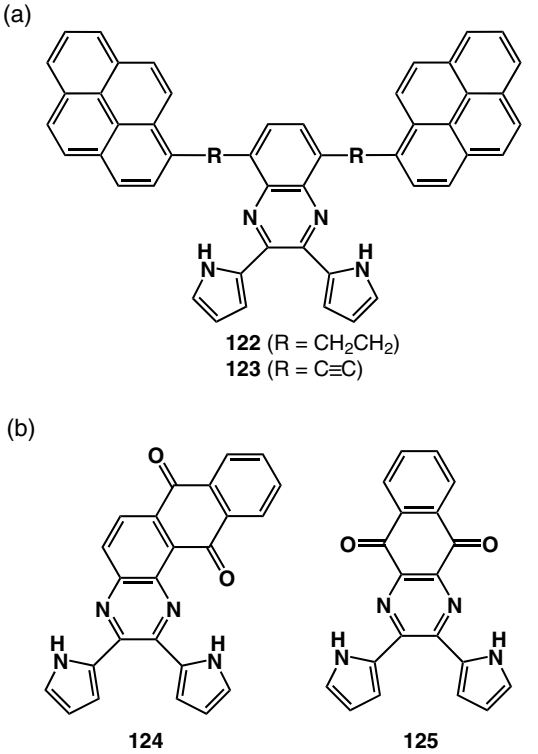

Figure 27. (a) Pyrene-substituted dipyrrolylquinoxalines **122** and **123**[123]; (b) quinone-substituted dipyrrolylquinoxalines **124** and **125**.[124]

Table 12. Anion-binding constants (K_a, M^{-1}) of **124** and **125** upon the addition of anions as TBA salts in 0.5% water/CH_3CN. *Data taken from Ref. 124.*

Anion	**124**	**125**
F^-	482 200	150 700
CN^-	6630	16 800
$HP_2O_7^{3-}$	316 000	626 000
$CH_3CO_2^-$	1200	3800
$H_2PO_4^-$	<100	525
$C_6H_5CO_2^-$	100	400
Cl^-	<50	<50

124 and **125** in square wave voltammetry (SWV) show cathodic shifts because the electron-rich sensor–anion complex is difficult to reduce. Binding constants estimated from SWV show considerable agreement with those from UV-visible absorption spectral changes.[124] In addition, Anzenbacher and coworkers used

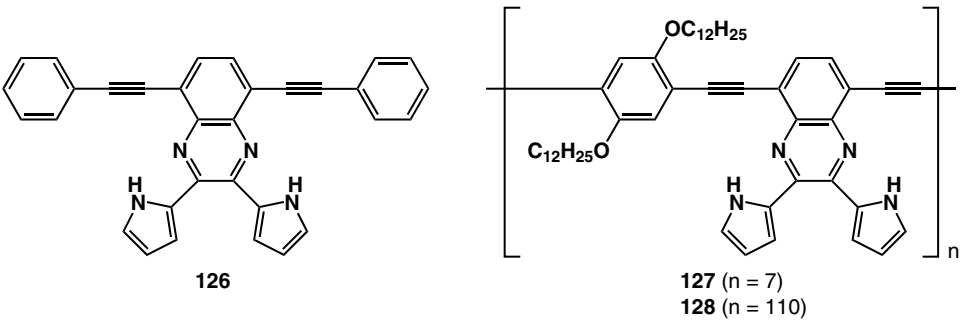

126 **127** (n = 7)
128 (n = 110)

Figure 28. Monomeric and polymeric forms of phenylethynyl-substituted dipyrrolylquinoxalines **126**–**128**.[127]

receptor **124** as one of the sensor molecules of the arrays detectable for anions in aqueous solutions.[125] Wong and coworkers also examined optical and electrochemical sensing for anion binding and conducted a theoretical study of **107** and **124**.[126]

Other extended and polymeric systems, **126**–**128** (Figure 28), have been reported by Sun and coworkers.[127] Monomer **126** exhibits F^- and $HP_2O_7^{3-}$ "binding" (2520 and 1440 M^{-1}), which are larger than those for CN^- (310 M^{-1}), $CH_3CO_2^-$ (50 M^{-1}), and other anions such as Cl^- and $H_2PO_4^-$ (<10 M^{-1}), in CH_2Cl_2; here, F^- and $HP_2O_7^{3-}$ are associated with a pyrrole NH while the other pyrrole NH is deprotonated under ambient conditions. The sensitivity of the DPQ-based chemosensor can be easily enhanced by incorporation into conjugated polymers **127** and **128**. The quenching constants derived from the Stern–Volmer plots, 16 800 (**126**), 70 200 (**127**), and 52 000 (**128**) M^{-1} for F^- and 11 200 (**126**), 49 300 (**127**), and 38 000 (**128**) M^{-1} for $HP_2O_7^{3-}$, respectively, demonstrated that the conjugated polymer with about ten repeating recognition sites is able to induce a substantial quenching effect with a 34-fold increase in the sensitivity as compared to the corresponding monomeric sensor.[127]

Other oligomer systems are achieved by incorporation into macrocycles such as **102**–**104**. Andrioletti and coworkers synthesized peralkyl-substituted DPQs **129**–**131**, which, however, cannot be converted to further modified derivatives.[128] Therefore, from the precursory diketone of **129**, tetrapyrrole derivatives **132** and **133**, similar to **104**, were obtained; **133** is a good starting material for macrocycles such as **134** and **135** (Figure 29). π-Conjugated **135** can be considered as a quinoxaline-bridged dipyrrin cyclic oligomer; single-crystal X-ray analysis of **135** shows a boat-like conformation with quinoxaline moieties almost facing each other, providing a rigid-wall cavity.[128]

On the other hand, Lee, Sessler, and coworkers reported DPQ-strapped calix[4]pyrrole **134**, which is prepared from **136** via dipyrromethane derivative

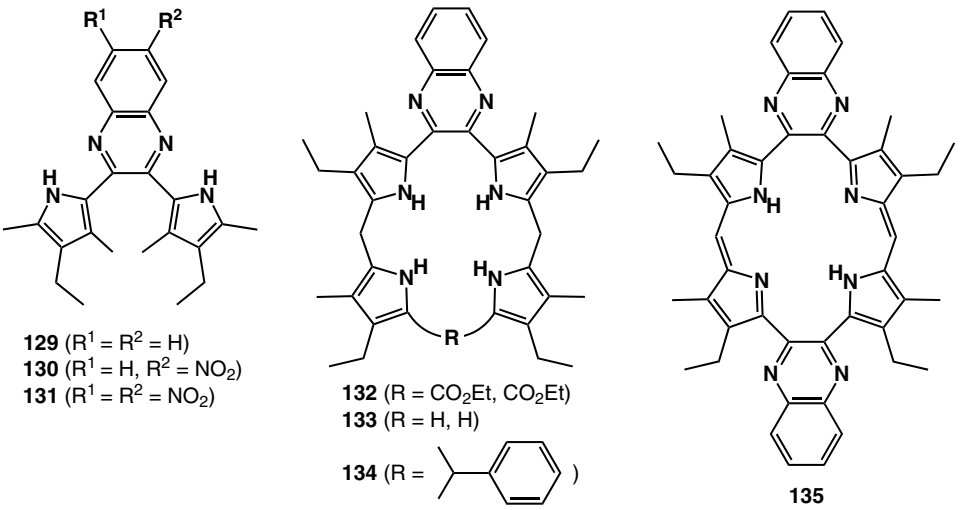

Figure 29. Alkyl-substituted DPQs **129**–**133** and macrocycles **134** and **135**.[128]

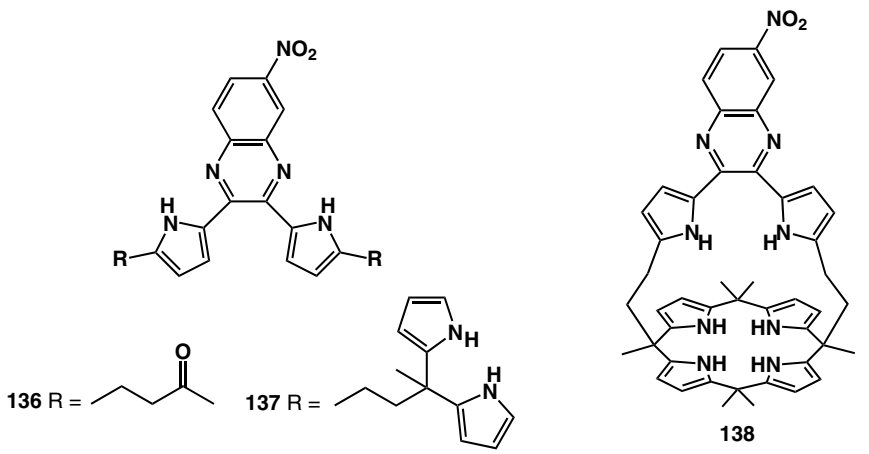

Figure 30. DPQ-calix[4]pyrrole hybrid **138** and starting **136** along with intermediate **137**.[129]

137 (Figure 30).[129] As seen from the ^{1}H NMR spectra (CD_3CN/DMSO-d_6 9:1, v/v) of **138**, with added TBAF, NH protons of the pyrroles on the strap, shifted from 5.99–5.96 to 5.57–5.54 ppm, do not interact with the added anions via simple NH–anion hydrogen bonds. This is derived from an anion–π interaction,[130,131] also supported by the downfield shifts of β-pyrrole CH from 6.54–6.49 and 5.80–5.74 to 6.85–6.80 and 5.92–5.90 ppm. ITC measurements (CD_3CN/DMSO-d_6 97:3, v/v) suggest multiple binding modes, [1 + 1] and [1 + 2], for F^- with K_a

values of 3.72×10^8 and 5.0×10^5 M^{-1}, and regular [1 + 1] binding for Cl^-, $CH_3CO_2^-$, and $H_2PO_4^-$ with K_a values of 1.94×10^4, 1.89×10^4, and 1.33×10^3 M^{-1}, respectively.[129]

B. Anion-Responsive Aryl-Bridged Bispyrroles

In addition to quinoxaline-bridged bispyrroles, there are several reports on aryl-bridged oligopyrroles that show anion binding. For example, 1,3-bis(pyrrol-2-yl)-benzenes **139–141** (Figure 31), which are an essential building unit of macrocycles, exhibit anion-binding behavior[95]; **139** shows K_a values at, for example, 2300, 4300, 1100, 190, 290, 1300, 280, and 32 M^{-1} for F^-, Cl^-, Br^-, I^-, HSO_4^-, $H_2PO_4^-$, NO_3^-, and ClO_4^-, respectively, estimated from ^1H NMR spectral changes in CD_2Cl_2. The K_a values are larger than those of dimethyldipyrromethane **52**, possibly because the bite angle present in **139** provides a better structural match to Cl^- (and likely most other anions).[95] Eichen and coworkers reported 1,3-dipyrrol-2-ylazulene **142** (Figure 31), which exhibits anion-binding properties for F^- (11 000 M^{-1}), Cl^- (110 M^{-1}), Br^- (100 M^{-1}), and I^- (50 M^{-1}) in CH_2Cl_2 and F^- (>1000 M^{-1}) in DMSO.[132] F^- enhances the fluorescence more than ten-fold in DMSO; this result presumably originates from the conformational changes from the fairly coplanar structure of core azulene and two pyrrole rings, elucidated by single-crystal X-ray analysis, to that with the partially disrupted π-conjugation between azulene and pyrroles.[132]

Sun, Hsu, Chow, and coworkers reported maleimide-bridged bispyrrole **143** (Figure 32a), which shows interaction with anions with K_a values of 18 500 and 36 300 M^{-1} for F^- and CN^- in CH_2Cl_2.[133] The significant fluorescence quenching and red-shift caused by F^- and CN^- are derived from deprotonation of a pyrrole NH.[133] Terpyrrole isomer **144** (Figure 32b), an analog of **143** and DPQs, was reported by Sessler and coworkers[134]; it shows color changes upon addition of anions such as F^- and $H_2PO_4^-$ in CH_2Cl_2. The K_a values of **144** are estimated as

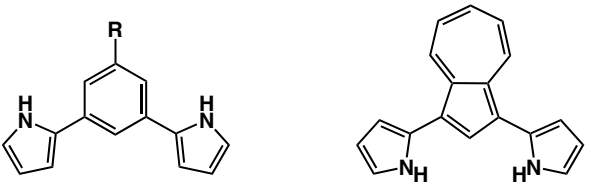

139 (R = H)
140 (R = *t*-Bu)
141 (R = OC_6H_{13})

142

Figure 31. Aryl-bridged bispyrrole derivatives **139–142**.[95,132]

(a)

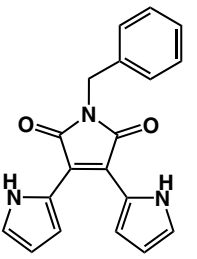

143

(b)

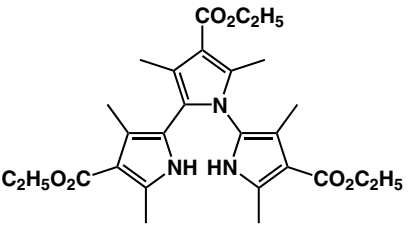

144

Figure 32. Pentacycle-bridged bispyrrole derivatives (a) **143**[133] and (b) **144**.[134]

182 000, 160, 60, and 17 500 M^{-1} for F^-, Cl^-, Br^-, and $H_2PO_4^-$, respectively, which are augmented compared to DPQ **85**.[134]

Metal-mediated changes to the preorganized conformation are observed in the metal complexes of bipyridine-bridged bispyrrole **145**.[135] Ru(II) and Rh(III) complexes **145-Ru** and **145-Rh** (Figure 33a) prepared by Sessler and coworkers, exhibit anion binding in DMSO, e.g. 7000, 370, and 104 000 M^{-1} for F^-, Cl^-, and $H_2PO_4^-$, respectively, in the case of **145-Ru** (Table 13). In particular, the K_a value for $H_2PO_4^-$ is *ca*. 2600-fold greater than for the DPQ-Ru(II) complex **94-Ru**. Higher affinities of triply charged **145-Rh** (870 M^{-1} for Cl^-) compared to **145-Ru** lead to precipitates upon $H_2PO_4^-$ binding. Single-crystal X-ray structures of Cl^- complexes of **145-Ru** and **145-Rh** elucidate C–H···Cl interactions (C···Cl: 3.65 and 3.59 Å on average for **145-Ru** and **145-Rh**) along with N–H···Cl interactions.[135] On the other hand, monomeric pyrrole building subunits can be incorporated into metal complexes by substitution of the metal ligand moiety. Gale and coworkers prepared Pt(II) complexes **146** and **147** (Figure 33b) from 3- and 4-(pyrrol-2-yl)pyridines.[136] The single-crystal X-ray structure of **146** as a BF_4^- salt elucidates the 1,2-alternate conformation and binding of two BF_4^- anions via N–H···F and C–H···F hydrogen bonds. The anion-binding behavior of **146** and **147** upon the addition of TBA salts in DMSO-d_6 reflects 1:1 stoichiometry except for $CH_3CO_2^-$ binding of **146** with K_2 (2400 M^{-1}) > K_1 (216 M^{-1}) (Table 14).[136] This

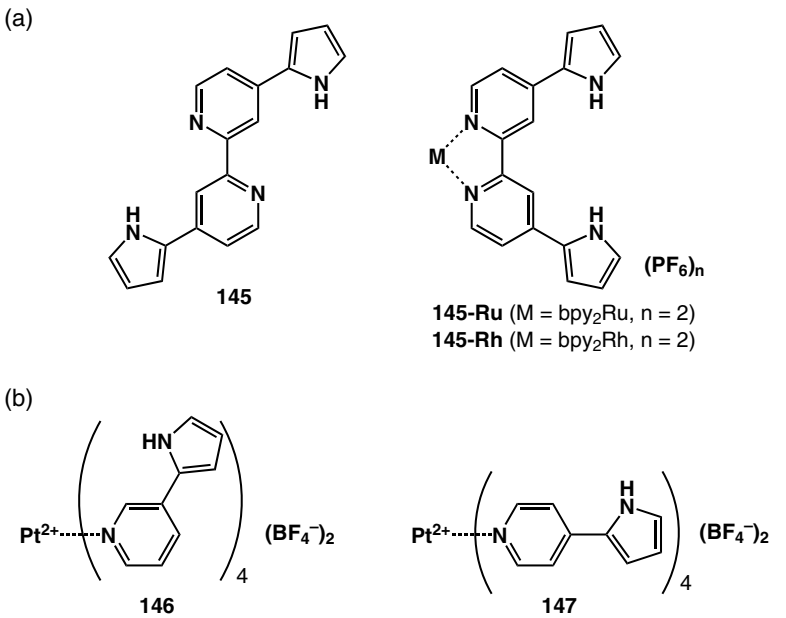

Figure 33. (a) Bipyridine-bridged bispyrrole **145** and metal complexes[135]; (b) Pt(II)-bridged pyrrole-based anion receptors **146** and **147**.[136]

Table 13. Anion-binding constants (K_a, M^{-1}) of **145-Ru** and **145-Rh** upon the addition of anions as TBA salts in DMSO. Data taken from Ref. 135.

Anion	**145-Ru**	**145-Rh**
F^-	7000	a
Cl^-	370	870
Br^-	70	100
CN^-	500	a
C6H5CO2$^-$	2140	5090
H2PO4$^-$	104 000	b

[a]Nonspecific binding profile.
[b]Precipitation occurred during ^{1}H NMR titration.

suggests that an allosteric effect is operating that preorganizes the second binding site upon complexation of the first equivalent of $CH_3CO_2^-$. In DMSO, compared to **147**, which binds anions using pyridyl *o*-CH sites and not pyrrole NH, **146** uses pyrrole β-CH and not NH to show large K_a values, e.g. 960 (**146**) and 216 (**147**) M^{-1} for Cl^- and 1115 (**146**) and <10 (**147**) M^{-1} for $CH_3SO_3^-$. In contrast to the binding mode in solution, **146** forms the $CH_3SO_3^-$ complex via an N–H···O hydrogen

Table 14. Anion-binding constants (K_a, M^{-1}) of **146** and **147** upon the addition of anions as TBA salts in DMSO-d_6. Data taken from Ref. 136.

Anion	**146**	**147**
Cl^-	960	216
Br^-	796	211
I^-	462	113
$CH_3CO_2^-$	$K_1 = 216$ $K_2 = 2400$	117
$C_6H_5CO_2^-$	a	111
$CH_3SO_3^-$	1115	<10
NO_3^-	29	<10
HSO_4^-	837	<10

[a]Precipitation during the titration; however, shifts of protons suggest a strong interaction of **146** with $C_6H_5CO_2^-$.

bond; this result suggests that the hydrogen-bonding acceptor DMSO molecules drive the pyrrole rings to invert and face the "outside."[136]

C. Dipyrrolylpyrazoles Derived from Dipyrrolyldiketones

In 2005, Maeda and Kusunose found that the key starting molecule to afford utility acyclic oligopyrrole derivatives was 1,3-dipyrrolyl-1,3-propanedione (dipyrrolyldiketone) **148** (Figure 34),[137] which was first reported by Oddo and Dainotti in 1912[138] and was refined by Battersby and coworkers in 1984.[139] This diketone is an analog of the precursory diketone of DPQ. Dipyrrolyldiketone **148** can be obtained from pyrrole by treatment with malonyl chloride. Therefore, dipyrrolyldiketone derivatives can be prepared from the corresponding substituted pyrroles. On the basis of the "pyrrole library," thus far, Maeda and coworkers have synthesized various dipyrrolyldiketone derivatives.[137,140–148]

One type of molecule derived from dipyrrolyldiketones is the pyrazole-bridged bispyrrole; pyrazoles can interact electrostatically or via hydrogen bonds with anionic or polar substrates as partially or fully protonated forms. In accordance with the first example reported by Oddo and Dainotti,[138] dipyrrolylpyrazoles (DPPs, **149**–**153**, Figure 35a) were synthesized by Maeda *et al*. by the condensation of excess hydrazine monohydrate with the corresponding dipyrrolyldiketones in refluxing acetic acid for 3–4 days.[149] *N*-Methyl-substituted **154**–**156** were obtained similarly from diketones or from the methylation of the corresponding DPPs. Based on the anion-binding ability of the pyrrole NH sites as observed in **155** and **156** (K_a = 1600 and 28 000 M^{-1} for $CH_3CO_2^-$ in CH_2Cl_2, respectively), the

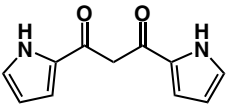

148

Figure 34. 1,3-Dipyrrolyl-1,3-propanedione **148**.[137]

(a)

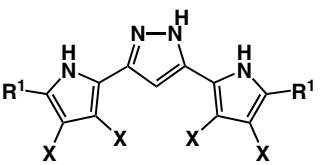

149 (R^1 = X = H)
150 (R^1 = CH_3, X = H)
151 (R^1 = $CH_2C(CH_3)_3$, X = H)
152 (R^1 = $C_{16}H_{33}$, X = H)
153 (R^1 = H, X = F)

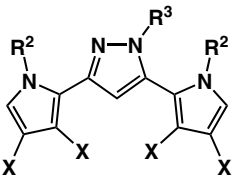

154 (R^2 = CH_3, R^3 = X = H)
155 (R^2 = H, R^3 = CH_3, X = H)
156 (R^2 = H, R^3 = CH_3, X = F)

(b) (i) (ii) (iii)

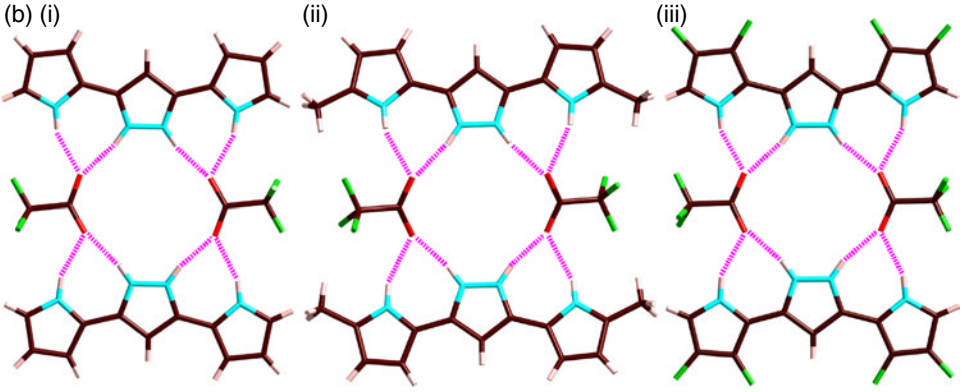

Figure 35. (a) Dipyrrolylpyrazoles **149**–**156**[149]; (b) solid-state [2 + 2] assemblies of (i) $\mathbf{149}_2$·TFA_2, (ii) $\mathbf{150}_2$·TFA_2, and (iii) $\mathbf{153}_2$·TFA_2.[149]

planar [2 + 2]-binding structures[150] with TFA were elucidated by single-crystal X-ray analyses of $\mathbf{149}_2$·TFA_2, $\mathbf{150}_2$·TFA_2, and $\mathbf{153}_2$·TFA_2 complexes (Figure 35b).[149] Complexation with an acid provides the planar geometry of DPP, which is required for the formation of micrometer- and nanometer-scale morphologies using intermolecular interactions such as π–π stacking. In fact, by casting the TFA complexes of DPP in CH_2Cl_2 on a silicon substrate, organized structures have been observed by SEM analysis. In sharp contrast to unsubstituted $\mathbf{149}_2$·TFA_2 and α-methyl $\mathbf{150}_2$·TFA_2, which yield crystalline objects, TFA complexes $\mathbf{150}_2$·TFA_2 and

151$_2$·TFA$_2$ with neopentyl and hexadecyl chains provide petal-like objects with widths of *ca*. 500 nm and assembled sheet structures with thicknesses <100 nm. Furthermore, β-fluorinated **153**$_2$·TFA$_2$ exhibits rod-like morphologies with widths of *ca*. 100–200 nm and small amounts of microcrystals.[149]

V. Boron Complexes of Dipyrrolyldiketones as Acyclic Anion Receptors with Planar Geometries

A. Synthesis and Properties of Boron Complexes of Dipyrrolyldiketones

Assemblies of π-conjugated molecules, mainly because of stacking interactions, are the basis of the dimension-controlled organized structures,[1–7] including soft materials. As π-conjugated molecules often have an optical absorption in the visible region, their assemblies behave as utility photonic and electronic materials. In addition, supramolecular assemblies comprising planar pyrrole-based anion receptors exhibit potential anion-responsive behavior and, under the appropriate conditions, form the functional organized structures comprising cations and anions, as described in the introduction. Therefore, initially, it is essential to design and synthesize promising fairly planar π-conjugated systems comprising pyrrole rings to efficiently bind anions.

As a candidate for a π-conjugated acyclic anion receptor to fabricate stacking structures, in 2005 Maeda and Kusunose reported the BF_2 complex **157** of dipyrrolyldiketone **148** (Figure 36).[137] Molecule **157** consists of two pyrrole rings and a boron-bridged 1,3-propanedione moiety. The pyrrole rings, which exist even in the acyclic structure, are stabilized by the neighboring electron-withdrawing carbonyl unit; therefore, the skeletal structure could be appropriate for various uses, such as sensors and materials. The absorption and emission maxima of receptor **157** are observed at 432 and 451 nm in CH_2Cl_2, respectively; these electronic properties of a single molecule could be applied to potential photonic and electronic materials such as supramolecular assemblies. The solid-state assembly of **157** is revealed by single-crystal X-ray analyses; planar **157**, wherein the pyrrole nitrogens are on opposite sides of the molecule as observed in solution, forms stacking structures with offset arrangement (Figure 37).[137,151] Observation of this stacking structure of parent **157** in the solid state is an impetus for supramolecular chemistry based on small molecules (*vide infra*).

The BF_2 complex **157** does not form a preorganized conformation, because the two pyrrole NH groups are not located at the appropriate positions for anion binding.[137] Upon the addition of anions, receptor **157** exhibits an inversion of the two pyrrole rings and binds anions using the pyrrole NH and bridging CH to form a planar receptor–anion complex (Figure 38). The BF_2 complex **157** can be considered

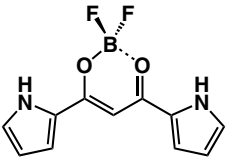

157

Figure 36. BF_2 complex of dipyrrolyldiketone **157**.[137]

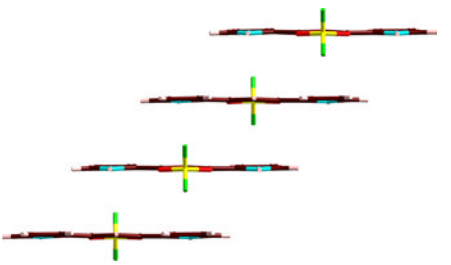

Figure 37. Solid-state molecular assembly of acyclic anion receptor **157**.

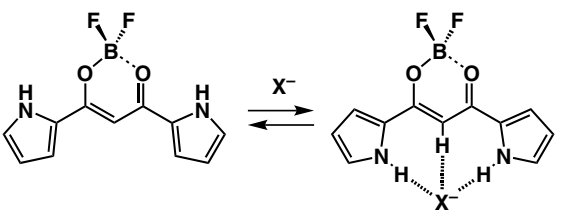

Figure 38. Anion-binding mode of BF_2 complex of dipyrrolyldiketone **157**.[137]

as a "molecular flipper" that enables space control between two planar states (free receptor and receptor–anion complex) by external chemical stimuli (anion). N–H···X^- and bridging C–H···X^- interactions are suggested from the ^{1}H NMR chemical shifts of other molecular flippers (instead of **157**, *vide infra*) upon the addition of anions as TBA salts. Furthermore, the discrete resonances of the two species — free receptor and anion complex — suggest that the equilibrium between these forms is too slow to be detected on the NMR time scale, possibly because of the requirement for pyrrole inversions to allow binding of the anion. The absorption and emission of **157** are adjusted by the addition of anions as TBA salts, suggesting its potential as a colorimetric anion sensor. UV-visible absorption spectral changes of **157** in CH_2Cl_2 by anion binding afford K_a values of 15 000,

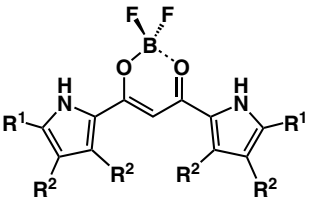

158-n ($R^1 = C_nH_{2n+1}$ (n = 1–16), R^2 = H)
159 ($R^1 = CH_2C(CH_3)_3$, R^2 = H)
160 (R^1 = H, $R^2 = C_2H_5$)
161 (R^1 = H, $R^2 = CH_3$)
162 (R^1 = H, R^2 = F)

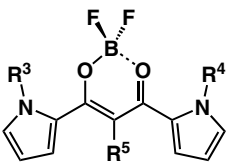

163 ($R^3 = R^4 = CH_3$, R^5 = H)
164 ($R^3 = CH_3$, $R^4 = R^5$ = H)
165 ($R^3 = R^4$ = H, $R^5 = C_2H_5$)

Figure 39. BF_2 complexes of dipyrrolyldiketones **158–165**.[140–142,144,146]

2100, 930 000, and 270 000 M^{-1} for Cl^-, Br^-, $CH_3CO_2^-$, and $H_2PO_4^-$, respectively.[137,144] Receptor **157** exhibits an efficient anion-binding property compared to DPQ **85**[110] and 1,3-bis(pyrrol-2-yl)benzene **139** (in CH_2ClCH_2Cl).[135]

On the basis of the library of pyrrole derivatives reported to date, the introduction of substituents to the receptor framework of **157** has yielded a variety of molecular flippers, **158–165** (Figure 39). Maeda *et al*. reported the α-alkyl-substituted receptors **158-n** and **159** from α-alkylpyrroles.[137,144] They also prepared β-alkyl- and β-fluorine-substituted receptors **160–162**, which can be considered as building blocks to form covalently linked oligomers due to the free α positions.[140,142,146] In addition, receptor molecules **163–165**, whose binding sites are (partially) protected, were also synthesized.[141] Furthermore, single-crystal X-ray analysis of some receptors revealed stacking structures similar to **157** (Figure 40). α-alkyl-substituted **158-1**,**4**,[144] **159**,[141] β-methyl-substituted **161**,[146] and β-fluorinated **162**[140] form 1D stacking structures, wherein core π-planes are partially overlapped, whereas α-ethyl-substituted **158-2** forms a dimer structure.[144] In contrast to these receptors, β-ethyl-substituted **160** shows no stacking structures and only N–H···F–B hydrogen-bonding interaction.[146] In the solid state, the interaction between NH and BF, which is essential for forming specific assembling modes such as the hydrogen-bonding dimer, is observed in other receptors, including parent **157**.

The anion-binding properties of the BF_2 complexes were examined from the UV-visible absorption spectral changes upon the addition of anions (Cl^-, Br^-, $CH_3CO_2^-$, $H_2PO_4^-$, and HSO_4^-) as TBA salts in CH_2Cl_2. The binding constants (K_a) of **157**, **158-16**, and **159–162** are summarized in Table 15[137,140,142,144,146]; enhanced values are obtained for unsubstituted **157** because of less sterical hindrance at the pyrrole α-positions and for β-fluorinated derivative **162** because of the polarized NH and CH binding sites. The K_a values of α-alkyl-substituted receptors **158-n** are

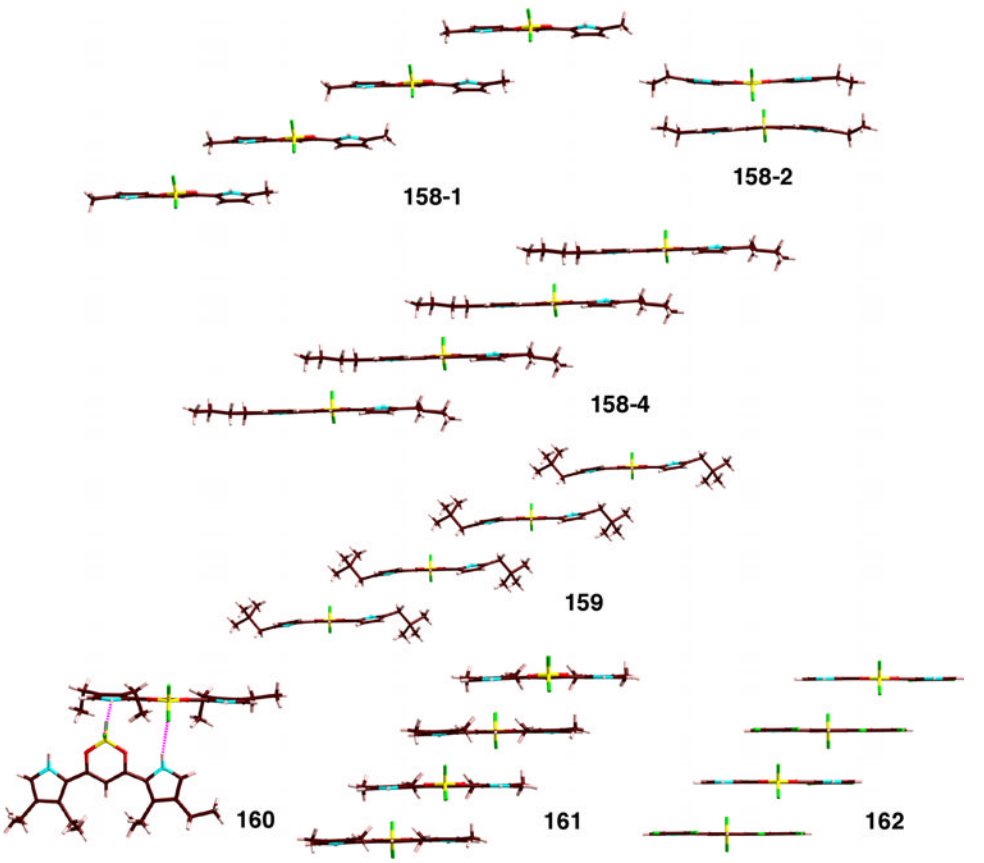

Figure 40. Selected solid-state molecular assemblies of acyclic anion receptors **158-1**,**2**,**4** and **159**–**162**.[137,140,142,144,146]

smaller in receptors with longer alkyl chains and their binding kinetics are also dependent on the alkyl chain lengths. All of the receptors **157**–**162** shown here except for **161** bind $CH_3CO_2^-$ more efficiently than the other anions. Upon the addition of $CH_3CO_2^-$ to **162** (2×10^{-3} M) in CD_2Cl_2 at −50 °C, both the NH and CH peaks (at 9.02 and 6.65 ppm, respectively) in ^{1}H NMR spectra disappear and new signals appear in the downfield region at 12.09 and 8.23 ppm, respectively. Similar downfield shifts are observed upon the addition of other anions to these acyclic receptors. The anion-binding behaviors of the "blocked" derivatives **163**–**165** suggest the essential role of the bridging CH site for anion binding.

The above observations, in which the anion-binding behavior of these acyclic receptors can be correlated with the effects of the peripheral substituents, can be explained from DFT calculations at the B3LYP/6-31G(d,p) level.[137,140,142,144,146] Consistent with experimental results such as from NMR analysis, molecular

Table 15. Anion-binding constants (K_a, M^{-1}) of **157**, **158-16**, and **159–162** upon the addition of anions as TBA salts in CH_2Cl_2. The values in the parentheses are the ratios to the K_a values of **157**. Data taken from Refs. 137, 140, 142, 144, and 146.

Anion	**157**	**158-16**	**159**	**160**	**161**	**162**
Cl^-	15 000	4000 (0.27)	2000 (0.13)	6800 (0.45)	4900 (0.33)	26 000 (1.7)
Br^-	2100	680 (0.32)	330 (0.16)	1200 (0.57)	680 (0.32)	1700 (0.81)
$CH_3CO_2^-$	930 000	110 000 (0.12)	110 000 (0.12)	210 000 (0.23)	61 000 (0.066)	960 000 (1.0)
$H_2PO_4^-$	270 000	20 000 (0.07)	13 000 (0.048)	91 000 (0.34)	87 000 (0.32)	190 000 (0.70)
HSO_4^-	ND[a]	ND[a] (— [b])	80 (— [b])	1200 (— [b])	ND[a] (— [b])	1100 (— [b])

[a]Not determined yet.
[b]Not given due to the absence of the K_a value of **157** for HSO_4^-.

simulations for the receptors **157–162** have suggested that the most stable conformations of the free receptors with intramolecular interactions between pyrrole NH and oxygen (the left side structure for **157** in Figure 38) are unsuitable for anion recognition, and therefore pyrrole inversions are required to bind anions. The relative energies of the "preorganized" structures (the right side structure for **157** in Figure 38) of **157–162** compared to each stable conformation are estimated at 9.08, 9.10 (**158-8** as an example), 8.96, 4.98, 6.94, and 15.04 kcal/mol, respectively, suggesting that the β-alkyl-substituted receptors **160** and **161** show stronger preferred preorganized geometries than those of **157–159** and **162**. From the experimental and theoretical data, the affinities for anions can be determined from the following factors: (i) electronic effects of the peripheral substituents, (ii) steric effects of the α substituents, and (iii) relative stabilities of the preorganized conformation.

The solid-state structures of the receptor–anion complexes have also been revealed by single-crystal X-ray analyses (Figure 41).[137,140,144] The receptor–anion complexes are dispersed in good solvents and, in some cases, are crystallized in poor solvents such as hydrocarbons to give single crystals obtained by using TBA salts of anions. In the case of the Cl^- complex of unsubstituted **157**, for a 1:1 mixture of the receptor and TBACl, the CH proton and one of the two pyrrole NH protons are associated with the Cl^- anion. The other NH proton turns to the opposite side and binds to another Cl^- anion to form an anion-bridged 1D hydrogen-bonding infinite chain (Figure 41a).[137] The β-fluorinated **162** utilizes only the NH interaction site to form the supramolecular 1D chains bridged by Cl^-, possibly

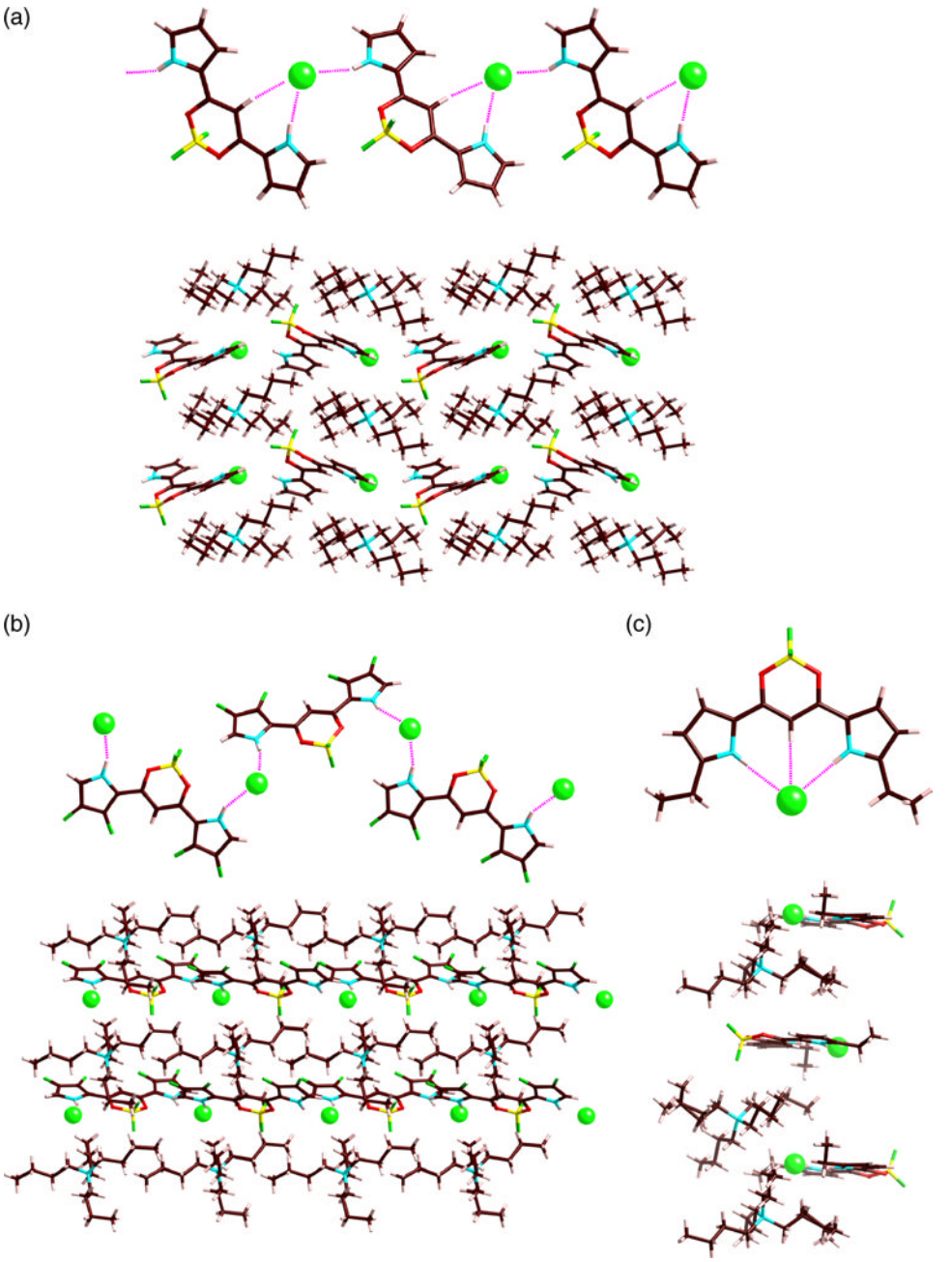

Figure 41. Solid-state chain structures or single-molecule and packing diagrams of receptor–anion complexes: (a) **157**·Cl^-, (b) **162**·Cl^-, (c) **158-2**·Cl^-. TBA cations are omitted for clarity in the top views.[137,140,144]

because of the more polarized NH as compared to NH sites of the β-H derivative (Figure 41b).[140] In both cases, countercations (TBA) are located between the 1D receptor–anion chains, quite different from the binding modes in the solution state, to form alternatively stacked structures. In contrast to the α-unsubstituted **157** and **162**, α-ethyl **158-2** has shown a similar binding mode, as observed in the solution state with the inversion of two pyrrole rings (Figure 41c).[144]

B. Aryl-Substituted Anion Receptors

In order to extend the π-conjugation of the molecular flippers for tunable electronic properties and stacking abilities, Maeda *et al*. attempted to synthesize α-aryl-substituted derivatives of dipyrrolyldiketone BF_2 complexes.[143] Initially, α-aryl-substituted **166–169** (Figure 42) were obtained from the α-aryl-substituted pyrroles, which were synthesized by cross-coupling reactions, via the corresponding α-aryl-substituted dipyrrolyldiketones. The absorption maxima (λ_{max}) of **166**, **167**, and **169** in CH_2Cl_2 appear at 500, 480, and 516 nm in CH_2Cl_2, respectively, which are red-shifted as compared to **157** (432 nm), **158-16** (457 nm), **159** (457 nm), **160** (452 nm), **161** (449 nm), and **162** (421 nm). Conversely, λ_{max} for **168** appears at 456 nm, which is blue-shifted by 46, 24, and 60 nm as compared to **166**, **167**, and **169**, respectively, as a result of the distortion of the aryl rings.[143]

Maeda and Eifuku also prepared the receptors bearing mono-alkoxy-substituted phenyl moieties **170–175** (Figure 43).[147] The UV-visible absorption maxima (λ_{max}) of **170**, **171**, and **172** in CH_2Cl_2 were observed at 513, 501, and 518 nm, respectively, suggesting that alkoxy substitution at the *ortho* and *para* positions affords a red-shift and that at the *meta* position has almost no effect in comparison with the λ_{max} value of α-phenyl **166** (500 nm), while the length of the alkoxy chains has almost no effect on the electronic state.[147]

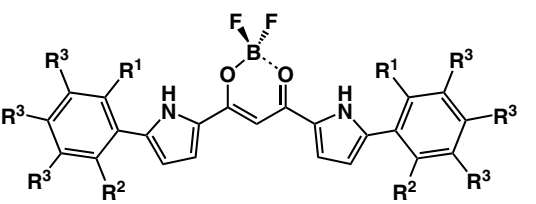

166 ($R^1 = R^2 = R^3 = H$)
167 ($R^1 = H$, $R^2 = CH_3$, $R^3 = H$)
168 ($R^1 = R^2 = CH_3$, $R^3 = H$)
169 ($R^1 = R^2 = H$, $R^3 = OCH_3$)

Figure 42. Aryl-substituted derivatives **166–169**.[143]

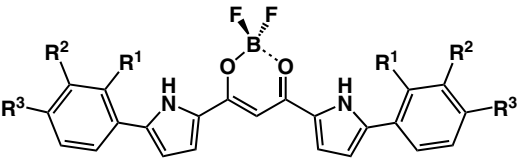

170 ($R^1 = OCH_3$, $R^2 = R^3 = H$)
171 ($R^1 = H$, $R^2 = OCH_3$, $R^3 = H$)
172 ($R^1 = R^2 = H$, $R^3 = OCH_3$)
173 ($R^1 = OC_8H_{17}$, $R^2 = R^3 = H$)
174 ($R^1 = H$, $R^2 = OC_8H_{17}$, $R^3 = H$)
175 ($R^1 = R^2 = H$, $R^3 = OC_8H_{17}$)

Figure 43. Aryl-substituted derivatives **170–175**.[147]

Single-crystal X-ray analysis of α-aryl-substituted receptors also demonstrates the stacking structures (Figure 44).[143,147] Phenyl- **166** and *o*-tolyl-substituted **167** form stacking assemblies, wherein the slightly distorted aryl rings in **167** produce less effective stacking, whereas 2,6-dimethylphenyl-substituted **168** has shown no stacking structures because of steric hindrance. X-ray analysis of **169** shows one trimeric and two tetrameric stacking structures as the various slipped assemblies in the solid state.[143] Like **166** and **167**, methoxy-substituted **170–172** also form stacking structures: compared with **171** and **172**, *o*-methoxy **170** has edge-to-edge–like stacking assemblies. α-Aryl-substituted receptors **166**, **167**, **171**, and **172** form hydrogen-bonding dimers using N–H···F–B interactions. On the other hand, *o*-methoxy **170** shows intramolecular N–H···O hydrogen bonds as observed in solution, whereas 2,6-dimethyl **168** is not incorporated in the assemblies using hydrogen-bonding interactions.[147]

The synthetic route for **166–175** based on aryl-substituted pyrroles is useful but is applied to a limited number of the derivatives. Therefore, the design of more efficient routes is required in order to introduce various aryl rings to the molecular flippers. In fact, selective iodination at the α-pyrrole positions of β-ethyl-substituted **160** by treatment with 2.7 and 1.1 equivalents of *N*-iodosuccinimide (NIS) in CH_2Cl_2 has been found to be a key step toward affording mono- **176** and bis-iodinated derivative **177** as essential starting materials of the coupling reactions for various utility molecules and covalently linked oligomer systems.[152] Bromination by *N*-bromosuccinimide (NBS) gives complicated mixtures containing species with a bromo-substituent at the fairly reactive bridging carbon. Suzuki cross-coupling reaction of **176** and phenylboronic acid (1.2 equivalents) affords monophenyl-substituted **178**, while a similar procedure using bis-iodinated derivative **177** and phenylboronic acid (2.2 equivalents) affords bisphenyl derivative **179**.[152] Under similar conditions using the corresponding aryl boronic acids, the

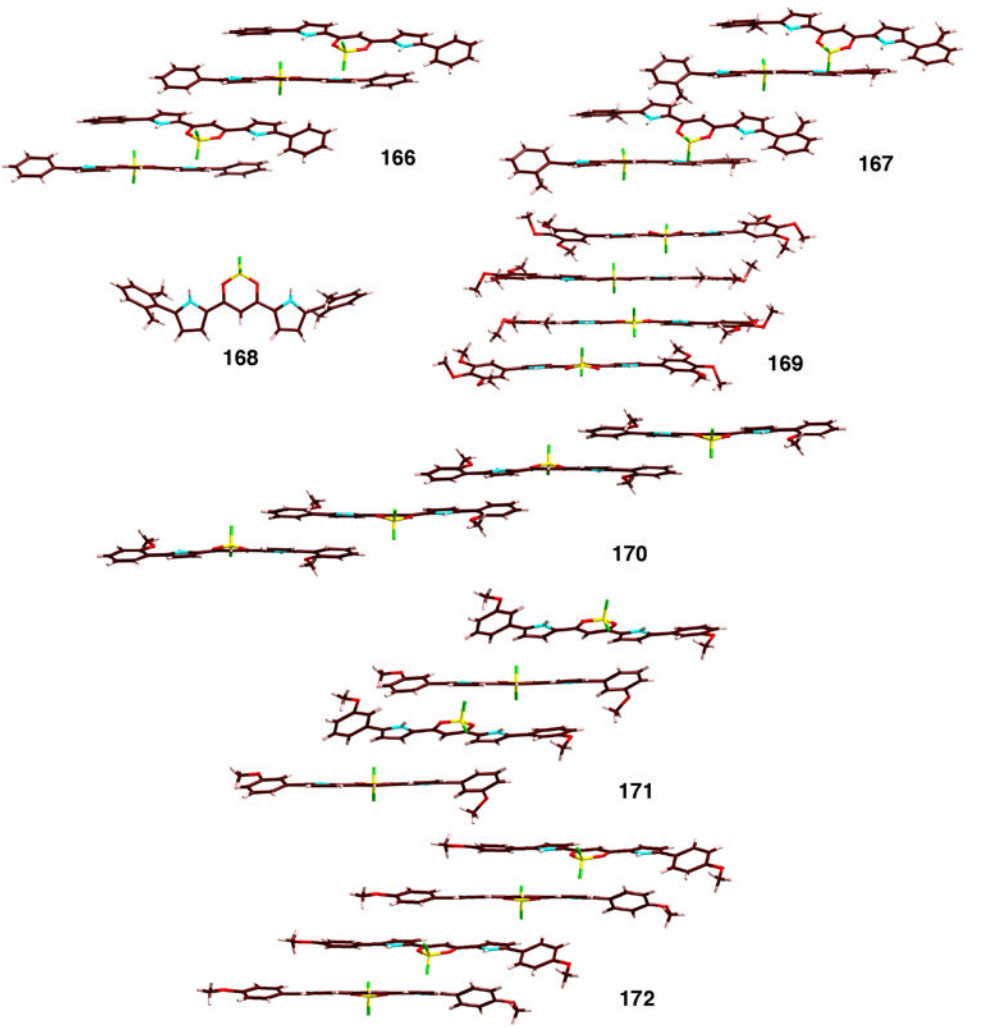

Figure 44. Solid-state molecular assemblies of acyclic anion receptors **168**–**172**. In the case of **169**, one of the three stacking modes is represented.[143,147]

bis-iodinated derivative **177** can be transformed into pyrrolyl-, furyl-, and thienyl-substituted derivatives **180**–**182** (Figure 45a).[153] Mono-iodinated **176** and bis-iodinated **177** are also converted to receptors **183**–**186** possessing a formyl functionality.[154] The covalently linked dimer **187** (Figure 45b) was synthesized by the coupling reaction of mono-iodinated **176** with 1,3-benzenediboronic acid bis(pinacol)ester (0.5 equivalents). Further iodination of phenylene-bridged dimer **187** affords bis-iodinated and mono-iodinated dimers (**188** and **189**).[152] The UV-visible absorption bands of **179**–**182** in CH_2Cl_2 are observed at 499, 551, 538,

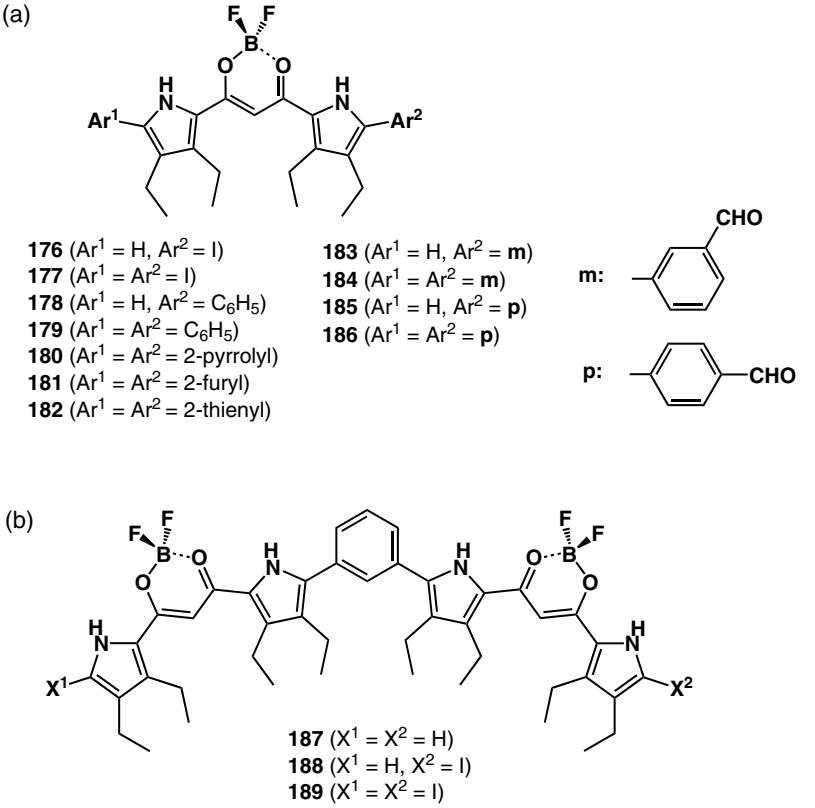

Figure 45. (a) Iodinated **176** and **177** and β-ethyl-substituted aryl-substituted receptors **178**–**186**[152–154]; (b) phenylene-bridged dimers **187**–**189**.[152]

and 527 nm, respectively, suggesting red-shifts that are comparable to that of α-unsubstituted **160** (451 nm).[152,153] Those of formyl-substituted **183**–**186** in CH_2Cl_2 are observed at 474, 495, 482, and 510 nm, respectively.[154] Dimer **187**, whose λ_{max} value is 489 nm due to the incomplete π-conjugation at the *meta*-phenylene linkage, and its iodinated derivatives can be potential subunits for forming anion-responsive oligomers.[152]

In the solid state, receptors **177** and **179**–**186** form stacked dimers or higher-stacked structures (Figure 46).[152–154] Compounds **177**, **179**–**182**, and **185** form the stacking dimers because of sterical β-ethyl-substituents, whereas formyl **183** and **184** exhibit a more tightly stacked structure comprising more than two units in these derivatives because of supporting van der Waals interactions between ethyl moieties and between ethyl units and the π-plane. In contrast, there are no stacked structures in **186**. In most structures, through intermolecular N–H···F–B hydrogen bonds, complicated 3D networks are formed along with stacking interactions. For

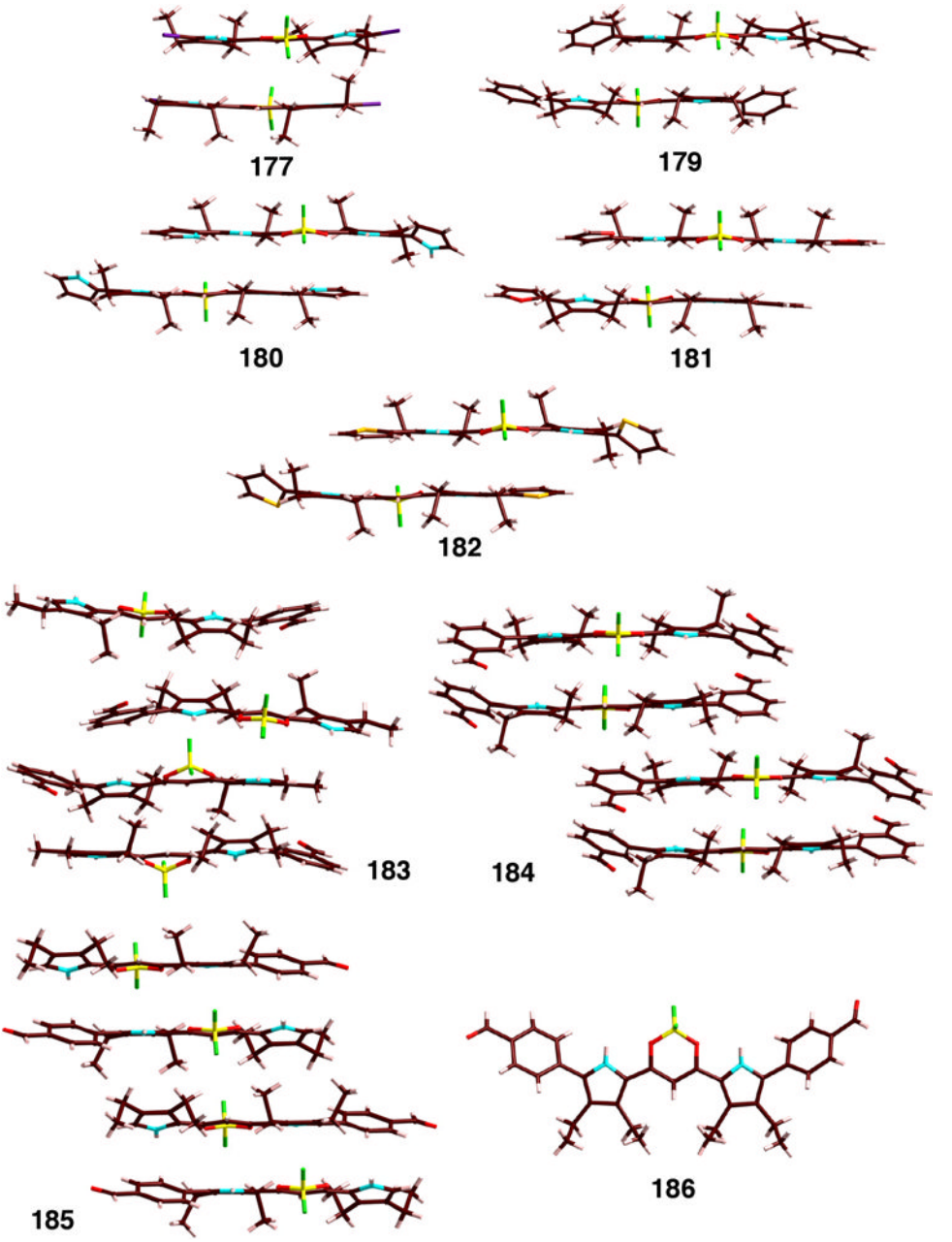

Figure 46. Solid-state molecular assemblies of acyclic anion receptors **177** and **179–186**.[152–154]

example, receptors **177** and **179–182** form dimeric structures using N–H···F and aryl-C(N)–H···F interactions,[152,153] while **183–186** fabricate more complicated hydrogen-bonding assemblies using the CHO moiety, along with pyrrole NH and BF units.[154] In these solid-state structures along with those of other receptors (Figures 40 and 44), the acyclic anion receptors exist as dispersed monomer forms in good solvents, while they form ordered 3D organized structures, i.e. crystals, in poor solvents.

The anion affinities of the β-unsubstituted α-aryl-substituted receptors and β-ethyl **179** were estimated from changes in the UV-visible absorption spectra in the presence of increasing concentrations of the respective anions (Table 16).[143,147,152] Compared to unsubstituted **157**,[142] α-phenyl **166** shows augmented K_a values, especially for halides (*ca.* 2.0- and 1.3-fold enhancement for Cl^- and Br^-, respectively), possibly due to pentacoordination (Figure 47), in contrast to oxoanion binding.[143] In contrast, doubly and totally *o*-C-blocked **167** and **168** exhibit K_a values less than those of **166** (*ca.* 1/10 and 1/30 for Cl^- binding), possibly due to sterical hindrance and electrostatic repulsion of the anions by the π-plane.[143] The K_a values of *meta*-substituted **171** and **172** and *para*-substituted **174** and **175** are almost comparable to those of **166**. There are no significant differences between methoxy- and octyloxy-substituted receptors. In contrast, the intramolecular hydrogen bonding in *ortho*-substituted **170** and **173** affords complicated binding modes with low affinities for anions; this result suggests that *ortho*-substituents can interfere with anion binding.[147] Furthermore, compared to **166**, β-ethyl **179** shows similar and smaller K_a values for oxoanions and halides, respectively.[152] ^{1}H NMR spectral changes of α-aryl-substituted receptors upon anion binding provide valuable insights into the binding behaviors of aryl-*o*-CH along with those of core pyrrole NH and bridging CH. For example, upon the addition of 1.5 equivalents of Cl^- as a TBA salt to a CD_2Cl_2 solution of **166** (1×10^{-3} M) at 20 °C, the signals due to **166** at 7.68 (*o*-CH), 9.73 (pyrrole NH), and 6.23 (bridging CH) ppm decreased in intensity with the concurrent appearance of new signals at 8.19, 12.27, and 9.04 ppm, respectively.[143] Furthermore, at lower temperatures with a small amount of Cl^-, a new NH signal between that of the free receptor and the [1 + 1] complex is attributed to the [2 + 1] binding complex $\mathbf{166}_2 \cdot Cl^-$. Formation of the [2 + 1] complex is also supported by DOSY NMR and electrospray ionization time-of-flight mass spectrometry (ESI-TOF-MS).[143] Furthermore, the signals of the aryl-substituted receptors and the pentacoordinated receptor–anion complexes can be observed independently, suggesting that a slow exchange takes place between these species on the NMR time scale. Rate constants k for the F^-, Cl^-, and Br^- binding of, for example, **166** using TBA salts in CH_2Cl_2 at 25 °C are estimated to be 7.2×10^4, 13.0×10^4, and 6.0×10^4 $M^{-1}s^{-1}$, respectively, by stopped-flow measurements. While the order of k ($Cl^- > Br^-$) is consistent with that of the binding

Table 16. Anion-binding constants (K_a, M^{-1}) of **166**–**168**, **171**, **172**, **174**, **175**, and **178** upon the addition of anions as TBA salts in CH_2Cl_2. The values in the parentheses are the ratios to the K_a value of unsubstituted **157**. Data taken from Refs. 143, 147, and 152.

Anion	**166**	**167**	**168**	**171**	**172**	**174**	**175**	**179**	**157**
Cl^-	30 000 (2.0)	2500 (0.17)	1000 (0.067)	57 000 (3.8)	25 000 (1.7)	26 000 (1.7)	24 000 (1.6)	6800 (0.45)	15 000
Br^-	2800 (1.3)	300 (0.14)	20 (0.0095)	5100 (2.4)	2100 (1.0)	2600 (1.2)	2400 (1.1)	1200 (0.57)	2100
$CH_3CO_2^-$	210 000 (0.23)	150 000 (0.16)	150 (0.00016)	490 000 (0.53)	420 000 (0.45)	140 000 (0.15)	330 000 (0.35)	210 000 (0.23)	930 000
$H_2PO_4^-$	72 000 (0.27)	8000 (0.029)	1400 (0.0052)	38 000 (0.14)	38 000 (0.14)	27 000 (0.10)	28 000 (0.10)	91 000 (0.34)	270 000
HSO_4^-	540 (— [b])	35 (— [b])	14 (— [b])	270 (— [b])	150 (— [b])	240 (— [b])	180 (— [b])	ND[a]	ND[a]

[a]Not determined yet.
[b]Not given due to the absence of the K_a value of **157** for HSO_4^-.

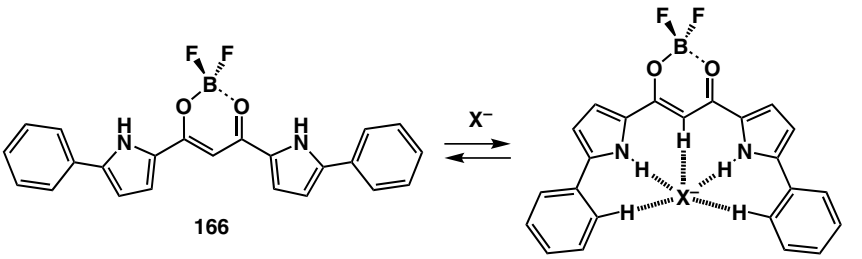

Figure 47. Anion-binding mode of aryl-substituted receptor **166**.[143]

Table 17. Anion-binding constants (K_a, M^{-1}) of **179–182** upon the addition of anions as TBA salts in 0.5% EtOH/$CHCl_3$. The values in the parentheses are the ratios to the K_a values of β-ethyl-substituted **160**. K_a values provided in Table 3 are those of solvated receptors, solvated anions, and receptor–anion complexes. Data taken from Ref. 153.

Anion	**179**	**180**	**181**	**182**	**160**
Cl^-	120 (0.12)	1 200 000 (1200)	360 (0.36)	1100 (1.1)	990
Br^-	30 (0.18)	180 000 (1100)	68 (0.40)	150 (0.88)	170
$CH_3CO_2^-$	410 (0.076)	3 000 000 (560)	500 (0.093)	1000 (0.19)	5400
$H_2PO_4^-$	130 (0.0086)	1 800 000 (120)	810 (0.054)	880 (0.059)	15 000
HSO_4^-	3 (0.014)	170 000 (810)	180 (0.85)	15 (0.071)	210

constants (K_a), the more associated F^- (240 000 M^{-1}) exhibits an intermediate value between those of Cl^- and Br^-; this suggests that thermodynamic stability is not always correlated with the kinetic properties.[143]

The K_a values of β-ethyl-substituted **179–182** (Table 17) are determined from UV-visible absorption spectral changes induced by the addition of appropriate anions as TBA salts in $CHCl_3$ containing 0.5% EtOH, which suppresses the binding affinities because of the higher K_a values of **180** in CH_2Cl_2.[153] For example, pyrrolyl **180** shows considerably larger K_a values, $>10^6$ M^{-1} for Cl^-, $H_2PO_4^-$, and $CH_3CO_2^-$, than those of **179**, **181**, and **182** and α-unsubstituted **160** because of the presence of multiple polarized NH sites. Upon the addition of 1 equivalent of Cl^- to $CDCl_3$ solution of **180** (1×10^{-3} M) at 20 °C, the signals of the "inner" NH and "outer" (terminal) NH are shifted from 9.29 and 8.77 ppm to 11.04 and 11.16 ppm, respectively, suggesting that the anions are bound more tightly to the terminal pyrrole NH.[153] The anion-binding behavior of formyl-substituted **183–186** was

Table 18. Anion-binding constants (K_a, M^{-1}) of **183–186** upon the addition of anions as TBA salts in CH_2Cl_2. The values in the parentheses are the ratios to the K_a values of β-ethyl-substituted **160**. Data taken from Ref. 154.

Anion	**183**	**184**	**185**	**186**
Cl^-	13 000 (1.9)	27 000 (4.0)	20 000 (2.9)	65 000 (9.6)
Br^-	2000 (1.7)	2700 (2.3)	2200 (1.8)	3900 (3.3)
$CH_3CO_2^-$	120 000 (0.57)	200 000 (0.95)	250 000 (1.2)	320 000 (1.5)
$H_2PO_4^-$	9700 (0.11)	71 000 (0.78)	74 000 (0.81)	37 000 (0.41)
HSO_4^-	400 (0.33)	870 (0.73)	420 (0.35)	320 (0.27)

also examined from the UV-visible absorption spectral changes (Table 18).[154] In contrast to the smaller K_a values in accord with an increase in the number of phenyl-substituents in **160**, **178**, and **179** because of the steric hindrance between the α-phenyl and β-ethyl moieties, bisformyl-substituted receptor **184** exhibits augmented K_a values compared to those of the corresponding monoformyl **183**. On the other hand, receptor **186** shows larger K_a values for halide and $CH_3CO_2^-$ anions than that for **185**.[154] This tendency of anion-binding behavior in formylphenyl-substituted receptors **183–186** may be derived from the increased affinity of the *o*-CH sites due to the electron-withdrawing formyl moiety.[152,154]

Maeda *et al*. reported single-crystal X-ray structures of the anion complexes of α-aryl-substituted receptors, **166**·Cl^-, **169**·Cl^-, and **180**·Cl^-, which form penta-coordinated geometries as the building components of the electrostatically mediated, alternatively stacking structures consisting of "planar anions (receptor–anion complexes)" and tetra-alkylammonium cations (Figure 48).[143,153] Based on the "charge-by-charge" columnar structures, which are observed only in the crystal states as 3D organized structures at present, dimension-controlled organic salts can be fabricated by using planar anions under appropriate conditions.

C. Anion-Responsive Supramolecular Gels Consisting of Acyclic Anion Receptors

Modification at the periphery of the receptors makes it possible to stabilize the stacked structures not only in the solid state but also in the solution state; for example, the introduction of various additional interactive moieties at the α-aryl rings enables the formation of molecular assemblies as soft materials that exhibit

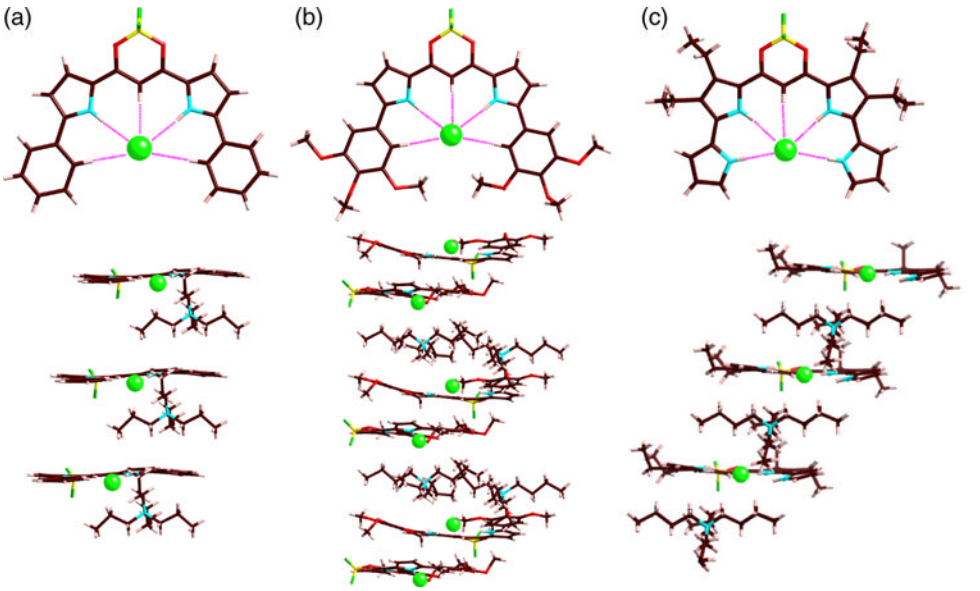

Figure 48. Solid-state single molecules and "charge-by-charge" assemblies of receptor–anion complexes: (a) **166**·Cl^-, (b) **169**·Cl^-, (c) **180**·Cl^-. Tetraalkylammonium cations are omitted for clarity in the top views.[143,153]

specific properties such as anion-responsive organized structures. Among the self-assembled oligomeric systems based on low-molecular-weight π-conjugated molecules, the gel materials — especially those susceptible to the influence of external stimuli — are of interest and play a crucial role as potential soft materials.[9–12,155,156] Supramolecular gels consist of nanoscale fibers, tubes, and sheets, formed by organized molecular assemblies. In contrast to physical stimuli, the structural modification of supramolecular gels under chemical control is very attractive because a large variety of potential additives are available.[157,158]

Maeda *et al*. prepared derivatives with aliphatic chains at the aryl rings (**190–192**, Figure 49) by procedures similar to those used for **166–175**.[143] These anion receptors **190–192** gelate octane (10 mg/mL); the transition temperatures between the gel and solution states are −8.5 (**190**), 4.5 (**191**), and 27.5 °C (**192**, Figure 50a), suggesting that the longer alkyl chains afford more stable gels. An octane gel of hexadecyloxy-substituted **192** (10 mg/mL) exhibits split absorption bands with absorption maxima at 525 and 555 nm along with a shoulder at 470 nm due to the formation of stacked structures; this is in contrast to the single peak at 493 nm exhibited in a diluted solution containing the dispersed monomers. The octane gel exhibits emission at 654 nm (excited at 470 nm), which is red-shifted as compared to that ($\lambda_{em} = 533$ nm; $\lambda_{ex} = 493$ nm) in the diluted condition (1×10^{-5} M).

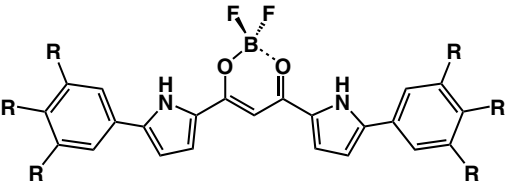

190 (R = OC_8H_{17})
191 (R = $OC_{12}H_{25}$)
192 (R = $OC_{16}H_{33}$)

Figure 49. BF_2 complexes **190**–**192** with 3,4,5-trialkoxy-substituted aryl rings.[143]

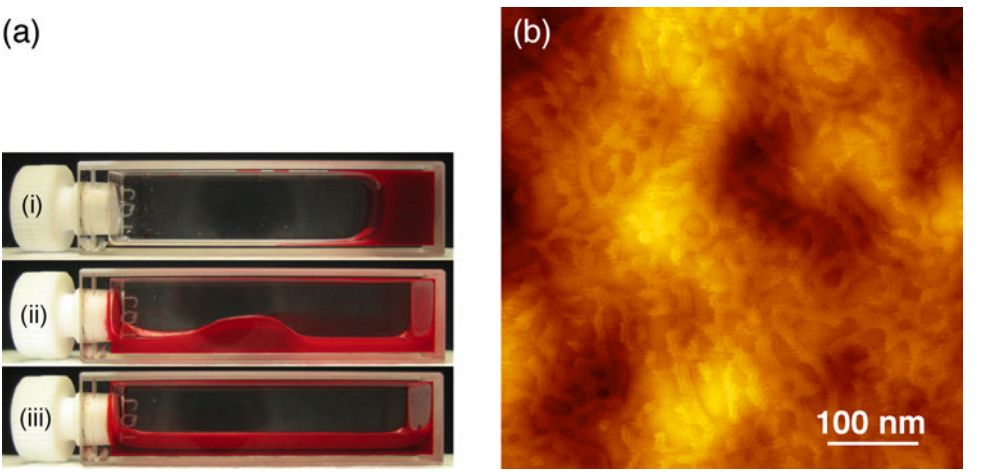

Figure 50. (a) Phase transition of **192** in octane (10 mg/mL) between solution and gel at (i) 25.0, (ii) 27.5, and (iii) 30.0 °C[143]; (b) AFM 2D image in a tapping mode of **192** (from octane gel) cast by spin-coating on a silicon substrate.[143]

Supramolecular organogel formation is achieved for the ordered structures based on the noncovalent interactions between the π-conjugated moieties and their substituents; this is supported by AFM (Figure 50b), SEM, and XRD observations.[143]

The addition of TBA salts of anions (10 equivalents) in the solid form to the fluorescent octane gel results in the transition to the solution state; the gels are gradually transformed into solutions beginning from areas close to where the solid salts have been added (Figure 51).[143] In this process, once the receptor (gelator) molecules in the gel bind to the anions, the counter TBA cations concertedly approach the receptor–anion complexes to form soluble ion pairs and afford the octane solution. These transitions in the case of the gel of **192** are quite distinct from the crystal states mentioned previously (e.g. **169**·Cl^-; Figure 48b), which are

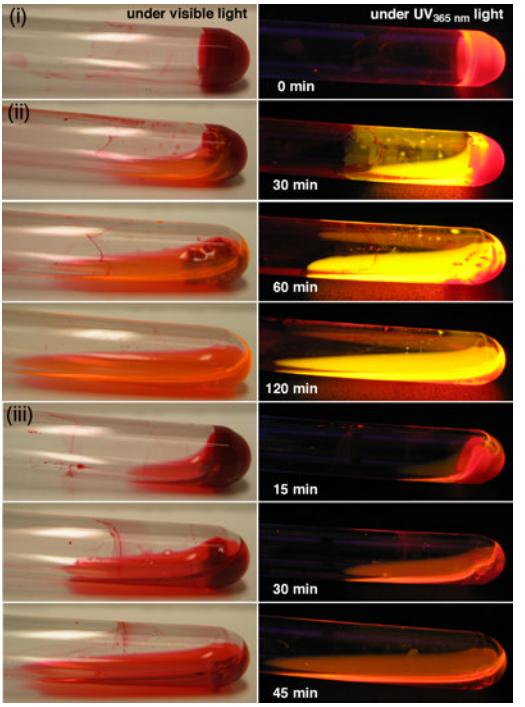

Figure 51. Transition of supramolecular organogel of **192** in octane (10 mg/mL, (i)) at 20 °C upon the addition of (ii) Cl^- (10 equiv.) and (iii) F^- (10 equiv.) added as solid TBA salts.[143]

due to the insolubility of the TBA salt of **169**·Cl^- in apolar hydrocarbon solvents. In contrast, the absorption and emission spectra of the gel from **192** that are changed by the addition of anions suggest that the transitions occur from the molecular assemblies to the dispersed monomeric states.[143,159]

The formyl group is well known to be transformed into an imine (Schiff base) moiety by treatment with a primary amine. Condensation of **183**–**186** with hexadecylamine or 3,4,5-trihexadecyloxyaniline and following reduction by $NaBH(OAc)_3$ afforded **193**–**200** (Figure 52).[154] In contrast to **192**, bis-substituted **198** and **200** in octane (10 mg/mL) appear to have fairly dispersed, and not gel-like, states at room temperature. When the solutions are cooled, **198** and **200** show opaque solutions below *ca.* 1 and *ca.* −10 °C, respectively, and form gel-like materials below *ca.* −10 and *ca.* −30 °C, respectively (Figure 53). The variable temperature (VT) UV-visible spectral changes in **198** at 1×10^{-3} M between 60 and −50 °C indicate the formation of stacked structures at lower temperatures. Formation of assembled structures is also supported by NMR analysis in octane-d_{18} and DLS. In these systems, connection of three π-conjugated moieties — a core π-plane and two side aryl units, by sp^3 methylene bridges provides supramolecular

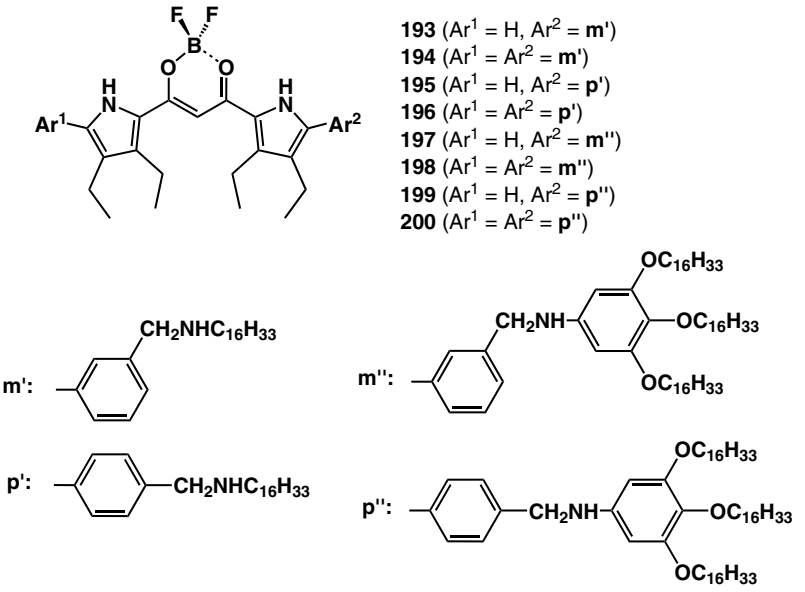

Figure 52. BF_2 complexes **193**–**200** derived from formyl-substituted receptor molecules.[154]

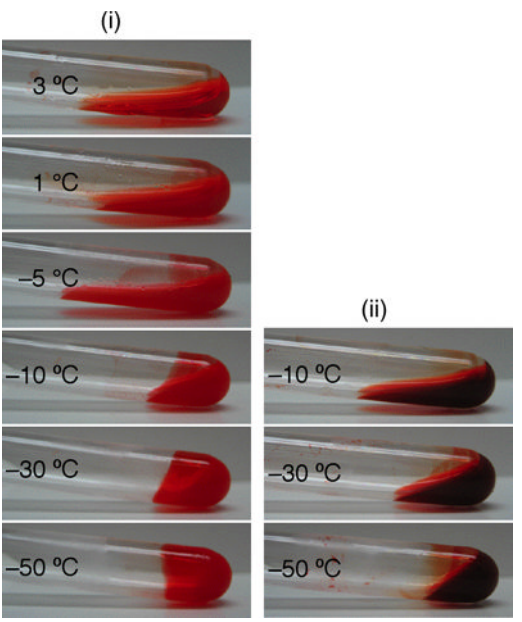

Figure 53. Photographs of the gel-like materials of (i) **198** and (ii) **200** in octane (10 mg/mL).[154]

assemblies, which are not very rigid but yield soft materials by fairly ordered organization under the appropriate conditions. Furthermore, addition of 1 equivalent of Cl^- as a TBA salt can modulate the assembled structures, along with the optical and electronic properties.[154]

D. Solvent-Assisted Organized Structures from Amphiphilic Anion Receptors

Supramolecular assemblies in an aqueous solution are ubiquitous in biotic systems such as folded proteins, DNA double helices, and membranes consisting of lipid bilayers. These organized structures can be formed by using the interactions between hydrophobic moieties inside the assemblies and the association of hydrophilic sites with water molecules.[8,16] Organized structures that can be modulated by external stimuli provide versatile actuators activated in aqueous solutions and related solvents.[160–162] Maeda *et al*. synthesized the poly(ethylene glycol) (PEG)-substituted amphiphilic π-conjugated acyclic oligopyrroles (type A — **201**–**204**; type B — **205**–**208**; Figure 54) by procedures similar to those for **166**–**175** and **190**–**192**.[145] While amphiphiles **201**, **207**, and **208** exhibit precipitation in water, derivatives **202**–**206** are soluble in the same solvent, wherein their λ_{max} values are observed at 460, 496, 506, 462, and 481 nm (1×10^{-5} M), respectively, which are blue-shifted as compared to those in MeOH (498, 510, 512, 510, and 512 nm), suggesting the formation of H-aggregates in aqueous solutions. The fluorescence spectra of **202**–**206** in aqueous solutions are observed as the fluorescence of each monomer at 546, 571, 572, 672, and 671 nm with low-emission quantum yields (Φ_F, determined at λ_{ex} values that are equal to the respective λ_{max} values) of 0.01, 0.01, 0.09, 0.02, and 0.02, respectively, which are characteristic aspects of H-aggregates. The solid films cast from the aqueous solutions of **202**–**206** exhibit almost the same red-shifted UV-visible absorption profiles (λ_{max} = 526, 540, 530, 548, and 531 nm, respectively) as those cast from CH_2Cl_2 solutions;

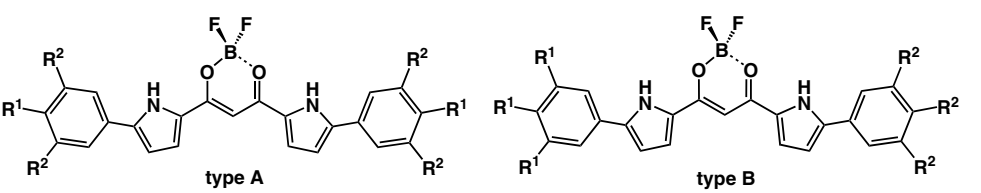

201 (R^1 = TEG, R^2 = H)
202 (R^1 = H, R^2 = TEG)
203 (R^1 = R^2 = TEG)
204 (R^1 = R^2 = HEG)

205 (R^1 = OC_8H_{17}, R^2 = TEG)
206 (R^1 = OC_8H_{17}, R^2 = HEG)
207 (R^1 = $OC_{16}H_{33}$, R^2 = TEG)
208 (R^1 = $OC_{16}H_{33}$, R^2 = HEG)

Figure 54. Amphiphilic derivatives of acyclic anion receptors **201**–**208**.[145]

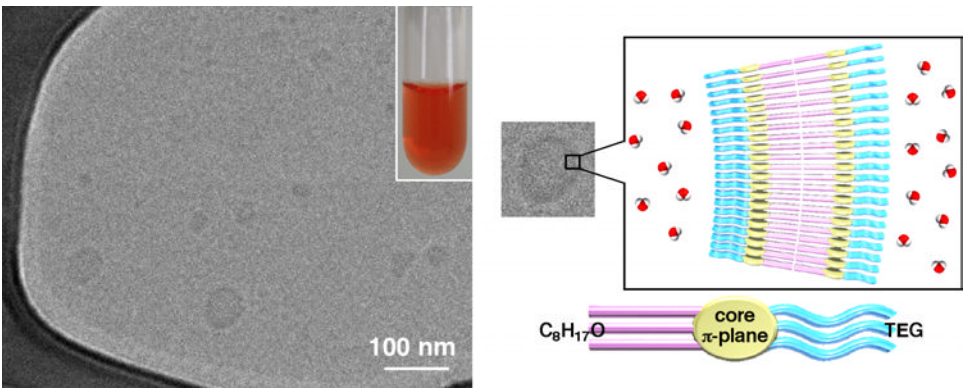

Figure 55. Image of cryo-TEM of **205** from an aqueous solution (1×10^{-5} M) without staining, photograph of the aqueous solution (1×10^{-4} M; inset), and possible assembling mode of **205** in vesicles.[145]

this result suggests that the removal of water molecules by slow evaporation at room temperature or by a freeze-drying process disrupts the H-aggregate formations, which are supported by water molecules, and instead forms other assembled structures (J-type aggregates).[145]

The morphologies of the transformed organized structures from the aqueous solutions were examined: only larger assemblies without specific shapes are observed by TEM analyses of the aqueous solutions (1×10^{-5} M) of **202–204** with $UO_2(OAc)_2$ staining, while under the same conditions **205** and **206** exhibit the formation of capsules, with diameters within the range of 50–150 nm, and cylindrical aggregates, respectively, as transformed objects from the removal of water molecules around the hydrophilic moieties.[145] Furthermore, cryo-TEM analysis of **205** (1×10^{-5} M) shows vesicular structures[163] with diameters of 30–80 nm (Figure 55), which are consistent with the result of the DLS measurements. The wall thickness (dark part) of capsules is estimated to be *ca*. 5 nm, indicating hydrophobic segments which consist of bilayers of amphiphilic molecules (*ca*. 3.9 nm from AM1 calculation). In contrast to the amphiphiles with only hydrophilic chains (type A), possibly **205** (type B) forms bilayers like biotic lipids by using hydrophobic interactions of the aliphatic chains and locates the hydrophilic TEG chains outside the layers to obtain water-soluble vesicles.[145]

E. Modifications around Boron Units of Acyclic Anion Receptors

The replacement of fluorine substituents in a boron moiety of molecular flippers by 1,2-diol units such as catechol derivatives enables the attachment of acyclic

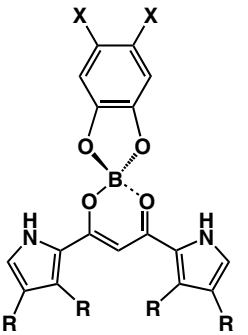

209 (R = H, X = H)
210 (R = C_2H_5, X = H)
211 (R = H, X = NO_2)
212 (R = C_2H_5, X = NO_2)

Figure 56. Catechol-substituted boron complexes of dipyrrolyldiketones **209**–**212**.[164]

anion receptors to the π-conjugated "backbone." Maeda *et al*. synthesized catechol-substituted receptors **209**–**212** (Figure 56) from the corresponding dipyrrolyldiketones[137,142] by treatment with BCl_3 and then with excess catechol derivatives in refluxing CH_2Cl_2.[164] The UV-visible absorption spectra of "BO_2" complexes **209** and **210** in CH_2Cl_2 exhibit absorption maxima (λ_{max}) at 435 and 454 nm, respectively, which are red-shifted by 2–3 nm in comparison with the maxima of the corresponding BF_2 complexes: unsubstituted **157** (432 nm) and β-ethyl **160** (452 nm). Furthermore, compared with the high-intensity fluorescence of **160** at 471 nm (λ_{em} excited at 420 nm; emission quantum yield — $\Phi_F = 0.98$), the weak fluorescent emission of **210** observed at 474 nm (λ_{em} excited at 420 nm; $\Phi_F = 0.001$)[165] can be attributed to the quenching path of the intramolecular electron transfer involved in HOMO and HOMO–1, which are localized at the catechol moiety. The binding constants (K_a) of **210** (and the ratios to the K_a values of **160**) for anions in CH_2Cl_2 are 2300 (0.34) (Cl^-), 270 (0.23) (Br^-), 33 000 (0.10) ($CH_3CO_2^-$), 67 000 (0.74) ($H_2PO_4^-$), and 80 (0.07) (HSO_4^-) M^{-1} due to the electronegativity of catechol oxygens (**210**), which is lower than that of fluorines (**160**). The K_a values of **212** for anions are higher [46 000 (Cl^-), 5400 (Br^-), 1 300 000 ($CH_3CO_2^-$), 150 000 ($H_2PO_4^-$), and 2300 (HSO_4^-) M^{-1}] than those of **210** because of the electron-withdrawing effect of the nitro groups.[164]

The substitution at a boron unit by vicinal hydroxyl groups of various functional units enables the formation of covalently linked dimers. Maeda *et al*. prepared ditopic receptors **213** and **214** (Figure 57a) by the treatment of intermediate BCl_2 complexes with *p*-phenylene-bridged dicatechol.[164] These receptors are extended systems bridged by "spacer" moieties between the acyclic anion receptor; single-crystal X-ray analysis of **214** suggests that the two receptor units are oriented in the same direction so that a Π-shaped *syn* conformation is generated with an intramolecular B–B distance of 8.68–9.17 Å (Figure 57b). Because of the

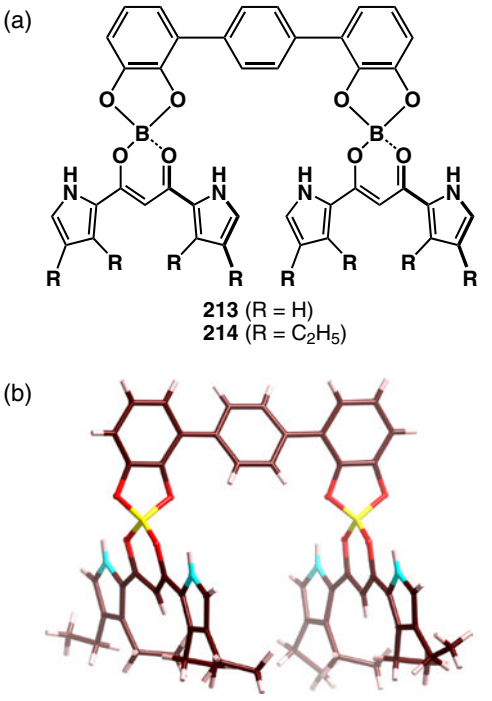

Figure 57. (a) Terphenyl-bridged dimers **213** and **214**[164]; (b) single-crystal X-ray structure of **214**.[164]

appropriate locations of the two receptor units, **214** has shown [1 + 1] binding for linear dicarboxylates [$^{-}O_2C(CH_2)_nCO_2^{-}$, $n = 2$–6]; the K_a values for succinate ($n = 2$), glutarate ($n = 3$), adipate ($n = 4$), pimelate ($n = 5$), and suberate ($n = 6$) as their TBA salt forms in CH_2Cl_2 are 19 000, 72 000, 810 000, 2 600 000, and 440 000 M^{-1}, respectively. This observation suggests that the distance between the receptor units (*ca.* 9 Å) is crucial in the determination of the selectivity of the dianions. In contrast to the α-linked oligomers,[152] the systems based on the BO_2 complexes behave as genuine multitopic receptors that can be incorporated in various macromolecules.[164,166]

VI. Summary

In this chapter, progress in the guest-binding and supramolecular chemistry of anion-responsive acyclic oligopyrroles has been described. Acyclic oligopyrrole systems are advantageous because they exhibit dynamic conformation changes and can be incorporated into various macromolecules and complexes as building subunits by means of covalent and noncovalent interactions such as metal coordination,

hydrogen bonding, and π–π stacking. The formation mechanisms and styles of nanoscale structures such as supramolecular assemblies depend on the molecular structures of the building subunits. Therefore, modifications to the receptor molecules result in versatile, unique organized architectures and stimulus-responsive soft materials with various utilities. Furthermore, anion binding by π-conjugated acyclic oligopyrroles is fascinating from the viewpoint of forming planar anionic species. The interaction of suitable negative-charged planar units with the appropriate cations will make it possible to form novel supramolecular assemblies and to tune and control the structures and properties of these materials, thereby making them practical. The use of appropriate molecular design and definitive synthetic procedures for the subunits will allow the formation of soft materials such as gels, liquid crystals, colloids, and micelles, consisting of both negative- and positive-charged species as the building components.

VII. Acknowledgments

The contribution from the Maeda group reported herein has been supported by Grants-in-Aid for Young Scientists (B) (Nos. 17750137, 19750122, 21750155) and Scientific Research in a Priority Area "Super-Hierarchical Structures" (Nos. 18039038, 19022036) from the Ministry of Education, Culture, Sports, Science and Technology (MEXT), Izumi Science and Technology Foundation, Iketani Science Technology Foundation, Mitsubishi Chemical Corporation Fund, Kumagai Foundation for Science and Technology, Nissan Science Foundation, Saneyoshi Scholarship Foundation, Japan Securities Scholarship Foundation, Science and Technology Foundation of Japan, Shorai Foundation for Science and Technology, and Kao Foundation for Arts and Sciences, the matching fund subsidies for private universities from the MEXT (2003–2008 and 2009–2014), and the Ritsumeikan Global Innovation Research Organization (R-GIRO) project (2008–2013).

VIII. References

1. Tsoucaris, G., Ed. *Current Challenges on Large Supramolecular Assemblies*, NATO Science Series, Kluwer: Dordrecht, **1999**.
2. Ciferri, A., Ed. *Supramolecular Polymers*; Marcel Dekker: New York, **2000**.
3. Würthner, F., Ed. *Supramolecular Dye Chemistry*; Topics in Current Chemistry, Springer-Verlag: Berlin, **2005**; Vol. 258, p. 324.
4. Atwood, J. L.; Steed, J. W., Eds. *Organic Nanostructures*; Wiley-VCH Verlag: Weinheim, **2007**.
5. Brunsveld, L.; Folmer, B. J. B.; Meijer, E. W.; Sijbesma, R. P. *Chem. Rev.* **2001**, *101*, 4071.
6. Shimizu, T.; Matsuda, M.; Minamikawa, H. *Chem. Rev.* **2005**, *105*, 1401.

7. Hoeben, F. J. M.; Jonkheijm, P.; Meijer, E. W.; Schenning, A. P. H. J. *Chem. Rev*. **2005**, *105*, 1491.
8. Hamley, I. W. *Introduction to Soft Matter: Polymers, Colloids, Amphiphiles and Liquid Crystals*; John Wiley & Sons: Chichester, **2000**.
9. Terech, P.; Weiss, R. G. *Chem. Rev.* **1997**, *97*, 3133.
10. Abdallah, D. J.; Weiss, R. G. *Adv. Mater.* **2000**, *12*, 1237.
11. Fages, F., Ed. *Low Molecular Mass Gelators*; Topics in Current Chemistry, Springer-Verlag: Berlin, **2005**; Vol. 256, p. 283.
12. Weiss, R. G.; Terech, P., Eds. *Molecular Gels: Materials with Self-Assembled Fibrillar Networks*; Springer: Dordrecht, **2006**.
13. Dierking, I. *Textures of Liquid Crystals*; Wiley-VCH Verlag: Weinheim, **2003**.
14. Kato, T.; Mizoshita, N.; Kishimoto, K. *Angew. Chem. Int. Ed.* **2006**, *45*, 38.
15. Kato, T., Ed. *Liquid Crystalline Functional Assemblies and Their Supramolecular Structures*; Structure and Bonding; Springer-Verlag: Berlin, **2008**, Vol. 128, p. 237.
16. Israelachvili, J. N. *Intermolecular and Surface Forces*; Academic: London, **1992**.
17. Miller, C. *Nature* **2006**, *440*, 484.
18. Pusch, M. In *Ion Channels from Structure and Function*; Kew, J.; Davies, C., Eds.; Oxford University Press: New York, **2010**; pp. 172–182 and references therein.
19. Dutzler, R.; Campbell, E. B.; Cadene, M.; Chait, B. T.; MacKinnon, R. *Nature* **2002**, *415*, 287.
20. Williams, D. H.; Cox, J. P. L.; Doig, A. J.; Gardner, M.; Gerhard, U.; Kaye, P. T.; Lal, A. R.; Nicholls, I. A.; Salter, C. J.; Mitchell, R. C. *J. Am. Chem. Soc.* **1991**, *113*, 7020.
21. Searle, M. S.; Williams, D. H.; Gerhard, U. *J. Am. Chem. Soc.* **1992**, *114*, 10697.
22. Bianchi, A.; Bowman-James, K.; García-España, E., Eds. *Supramolecular Chemistry of Anions*; Wiley-VCH: New York, **1997**.
23. Singh, R. P.; Moyer, B. A., Eds. *Fundamentals and Applications of Anion Separations*; Kluwer Academic/Plenum: New York, **2004**.
24. Stibor, I., Ed. *Anion Sensing*; Topics in Current Chemistry, Springer-Verlag: Berlin, **2005**; Vol. 255, p. 238.
25. Sessler, J. L.; Gale, P. A.; Cho, W.-S. *Anion Receptor Chemistry*; RSC: Cambridge, **2006**.
26. Vilar, R., Ed. *Recognition of Anions*; Structure and Bonding, Springer-Verlag: Berlin, **2008**; Vol. 129, p. 252.
27. Schmidtchen, F. P.; Berger, M. *Chem. Rev.* **1997**, *97*, 1515.
28. Beer, P. D.; Gale, P. A. *Angew. Chem. Int. Ed.* **2001**, *40*, 486.
29. Sessler, J. L.; Camiolo, S.; Gale, P. A. *Coord. Chem. Rev.* **2003**, *240*, 17.
30. Martínez-Máñez, R.; Sancenón, F. *Chem. Rev.* **2003**, *103*, 4419.
31. Gale, P. A. *Chem. Commun.* **2005**, 3761.
32. Gale, P. A. *Acc. Chem. Res.* **2006**, *39*, 465.
33. Gale, P. A.; Quesada, R. *Coord. Chem. Rev.* **2006**, *250*, 3219.
34. Kang, S. O.; Begum, R. A.; Bowman-James, K. *Angew. Chem. Int. Ed.* **2006**, *45*, 7882.
35. Bolondeau, P.; Segura, M.; Perez-Fernandez, R.; de Mendoza, J. *Chem. Soc. Rev.* **2007**, *36*, 198.
36. Gale, P. A.; García-Garrido, S. E.; Garric, J. *Chem. Soc. Rev.* **2008**, *37*, 151.
37. Caltagirone, C.; Gale, P. A. *Chem. Soc. Rev.* **2009**, *38*, 520.
38. Fischer, H.; Orth, H. *Die Chemie des Pyrrols*; Akademische Verlagsgesellschaft M. B. H.: Leipzig, **1934**.
39. Kadish, K. M.; Smith, K. M.; Guilard, R., Eds. *The Porphyrin Handbook*; Academic: San Diego, **2000**; Vols. 1–10.

40. Gale, P. A.; Sessler, J. L.; Král, V.; Lynch, V. *J. Am. Chem. Soc.* **1996**, *118*, 5140.
41. Gale, P. A.; Sessler, J. L.; Král, V. *Chem. Commun.* **1998**, 1.
42. Sessler, J. L.; Gross, D. E.; Cho, W.-S.; Lynch, V. M.; Schmidtchen, F. P.; Bates, G. W.; Light, M. E.; Gale, P. A. *J. Am. Chem. Soc.* **2006**, *128*, 12281.
43. Lee, C.-H.; Miyaji, H.; Yoon, D.-W.; Sessler, J. L. *Chem. Commun.* **2008**, 24.
44. Jasat, A.; Dolphin, D. *Chem. Rev.* **1997**, *97*, 2267.
45. Sessler, J. L.; Seidel, D. *Angew. Chem. Int. Ed.* **2003**, *42*, 5134.
46. Chandrashekar, T. K.; Venkatraman, S. *Acc. Chem. Res.* **2003**, *36*, 676.
47. Shimizu, S.; Osuka, A. *Eur. J. Inorg. Chem.* **2006**, 1319.
48. Sessler, J. L.; Cyr, M. J.; Lynch, V.; McGhee, E.; Ibers, J. A. *J. Am. Chem. Soc.* **1990**, *112*, 2810.
49. Shionoya, M.; Furuta, H.; Lynch, V.; Harriman, A.; Sessler, J. L. *J. Am. Chem. Soc.* **1992**, *114*, 5714.
50. Sessler, J. L.; Davis, J. *Acc. Chem. Res.* **2001**, *34*, 989.
51. Seidel, D.; Lynch, V.; Sessler, J. L. *Angew. Chem. Int. Ed.* **2002**, *41*, 1422.
52. Maeda, H. *Eur. J. Org. Chem.* **2007**, 5313.
53. Maeda, H. *J. Incl. Phenom.* **2009**, *64*, 193.
54. Gale, P. A. *Chem. Commun.* **2008**, 4525 and references therein.
55. Coles, S. J.; Gale, P. A.; Hursthouse, M. B. *CrystEngComm* **2001**, *53*, 1.
56. Best, M. D.; Tobey, S. L.; Anslyn, E. V. *Coord. Chem. Rev.* **2003**, *240*, 3.
57. Houk, R. J. T.; Tobey, S. L.; Anslyn, E. V. In *Anion Sensing*; Stibor, I. Ed.; Topics in Current Chemistry; Springer-Verlag: Berlin, **2005**, Vol. 255, pp. 119–229.
58. Schmuck, C. *Chem. Commun.* **1999**, 843.
59. Schmuck, C. *Eur. J. Org. Chem.* **1999**, 2397.
60. Schmuck, C. *Coord. Chem. Rev.* **2006**, *250*, 3053.
61. Schmuck, C. *J. Org. Chem.* **2000**, *65*, 2432.
62. Schmuck, C.; Dudaczek, J. *Eur. J. Org. Chem.* **2007**, 3326.
63. Schmuck, C.; Rehm, T.; Gröhn, F.; Reinhold, F. *J. Am. Chem. Soc.* **2006**, *128*, 1430.
64. Schmuck, C.; Rehm, T.; Klein, K.; Gröhn, F. *Angew. Chem. Int. Ed.* **2007**, *46*, 1693.
65. Gunther, H.; Anslyn, E. V. *Chem. Eur. J.* **2002**, *8*, 2218.
66. Schmuck, C.; Schwegmann, M. *J. Am. Chem. Soc.* **2005**, *127*, 3373.
67. Schmuck, C.; Schwegmann, M. *Org. Biomol. Chem.* **2006**, *4*, 836.
68. Sauvage, J.-P., Ed. *Transition Metals in Supramolecular Chemistry*; John Wiley & Sons: Chichester, **1999**.
69. Manners, I. *Synthetic Metal-Containing Polymers*; Wiley-VCH: Weinheim, **2004**.
70. Schubert, U. S.; Newkome, G. R.; Manners, I., Eds. *Metal-Containing and Metallosupramolecular Polymers and Materials*; ACS: Washington DC, **2006**.
71. Gröger, G.; Stepanenko, V.; Würthner, F.; Schmuck, C. *Chem. Commun.* **2009**, 698.
72. Gale, P. A.; Camiolo, S.; Chapman, C. P.; Light, M. E.; Hursthouse, M. B. *Tetrahedron. Lett.* **2001**, *42*, 5095.
73. Gale, P. A.; Camiolo, S.; Tizzard, G. J.; Chapman, C. P.; Light, M. E.; Coles, S. J.; Hursthouse, M. B. *J. Org. Chem.* **2001**, *66*, 7849.
74. Gale, P. A. *Chem. Commun.* **2005**, 3761.
75. Gale, P. A.; Navakhun, K.; Camiolo, S.; Light, M. E.; Hursthouse, M. B. *J. Am. Chem. Soc.* **2002**, *124*, 11228.
76. Light, M. E.; Gale, P. A.; Navakhun, K. *Acta Cryst. E* **2005**, *61*, o1300.

77. Navakhun, K.; Ruangpornvisuti, V. *J. Mol. Struct.* (*Theochem*) **2006**, *772*, 23.
78. Navakhun, K.; Ruangpornvisuti, V. *J. Mol. Struct.* (*Theochem*) **2009**, *907*, 131.
79. Sessler, J. L.; Pantos, G. D.; Gale, P. A.; Light, M. E. *Org. Lett.* **2006**, *8*, 1593.
80. Sessler, J. L.; Barkey, N. M.; Pantos, G. D.; Lynch, V. M. *New J. Chem.* **2007**, *31*, 646.
81. Zhang, Y.; Yin, Z.; Li, Z.; Hea, J.; Cheng, J.-P. *Tetrahedron* **2007**, *63*, 7560.
82. Yin, Z.; Li, Z.; Yu, A.; He, J.; Cheng, J.-P. *Tetrahedron Lett.* **2004**, *45*, 6803.
83. Chen, C.-L.; Chen, Y.-H.; Chen, C.-Y.; Sun, S.-S. *Org. Lett.* **2006**, *8*, 5053.
84. Chen, C.-L.; Lin, T.-P.; Chen, Y.-S.; Sun, S.-S. *Eur. J. Org. Chem.* **2007**, 3999.
85. Zyryanov, G. V.; Palacios, M. A.; Anzenbacher, P., Jr. *Angew. Chem. Int. Ed.* **2007**, *46*, 7849.
86. Falk, H. *The Chemistry of Linear and Oligopyrroles and Bile Pigments*; Springer-Verlag: Vienna, **1989**.
87. Wood, T. E.; Thompson, A. *Chem. Rev.* **2007**, *107*, 1831.
88. Becker, W.; Sheldrick, W. S.; Engel, J. *Acta Cryst. B* **1978**, *34*, 1021.
89. Sessler, J. L.; Eller, L. R.; Cho, W.-S.; Nicolaou, S.; Aguilar, A.; Lee, J. T.; Lynch, V. M.; Magda, D. J. *Angew. Chem. Int. Ed.* **2005**, *44*, 5989.
90. Shin, J.-Y.: Dolphin, D.; Patrick, B. O. *Cryst. Grow. Des.* **2004**, *4*, 659.
91. Huggins, M. T.; Musto, C.; Munro, L.; Catalano, V. J. *Tetrahedron* **2007**, *63*, 12994.
92. Vega, I. E. D.; Camiolo, S.; Gale, P. A.; Hursthouse, M. B.; Light, M. E. *Chem. Commun.* **2003**, 1686.
93. Vega, I. E. D.; Gale, P. A.; Hursthouse, M. B.; Light, M. E. *Org. Biomol. Chem.* **2004**, *2*, 2935.
94. Guo, Y.; Shao, S.-J.; Xu, J.; Shi, Y.-P.; Jiang, S.-X. *Inorg. Chem. Commun.* **2004**, *7*, 333.
95. Sessler, J. L.; An, D.; Cho, W.-S.; Lynch, V.; Marquez, M. *Chem. Eur. J.* **2005**, *11*, 2001.
96. Renić, M.; Basarić, N.; Mlinarić-Majerski, K. *Tetrahedron Lett.* **2007**, *48*, 7873.
97. Chauhan, S. M. S.; Bisht, T.; Garg, B. *Sens. Act. B* **2009**, *141*, 116.
98. Denekamp, C.; Suwinska, K.; Salman, H.; Abraham, Y.; Eichen, Y.; Ben Ari, J. *Chem. Eur. J.* **2007**, *13*, 657.
99. Sessler, J. L.; An, D.; Cho, W.-S.; Lynch, V. *J. Am. Chem. Soc.* **2003**, *125*, 13646.
100. Lin, C.-I.; Selvi, S.; Fang, J.-M.; Chou, P.-T.; Lai, C.-H.; Cheng, Y.-M. *J. Org. Chem.* **2007**, *72*, 3537.
101. Fürstner, A. *Angew. Chem. Int. Ed.* **2003**, *42*, 3582.
102. Kataoka, T.; Muroi, M.; Ohkuma, S.; Waritani, T.; Magae, J.; Takatsuki, A.; Kondo, S.; Yamasaki, M.; Nagai, K. *FEBS Lett*. **1995**, *359*, 53.
103. Sato, T.; Konno, H.; Tanaka, Y.; Kataoka, T.; Nagai, K.; Wasserman, H. H.; Ohkuma, S. *J. Biol. Chem.* **1998**, *273*, 21455.
104. Seganish, J. L.; Davis, J. D. *Chem. Commun.* **2005**, 5781.
105. Díaz, R. I. S.; Regourd, J.; Santacroce, P. V.; Davis, J. D.; Jakeman, D. L.; Thompson, A. *Chem. Commun.* **2007**, 2701.
106. Sessler, J. L.; Weghorn, S. J.; Lynch, V.; Fransson, K. *J. Chem. Soc. Chem. Commun.* **1994**, 1289.
107. Morosini, P.; Scherer, M.; Meyer, S.; Lynch, V.; Sessler, J. L. *J. Org. Chem.* **1997**, *62*, 8848.
108. Oddo, B.; Dainotti, C. *Gazz. Chim. Ital.* **1911**, *41*, 248.
109. Behr, D.; Brandänge, S.; Lindström, B. *Acta Chem. Scand.* **1973**, *27*, 2411.
110. Black, C. B.; Andrioletti, B.; Try, A. C.; Ruiperez, C.; Sessler, J. L. *J. Am. Chem. Soc.* **1999**, *121*, 10438.
111. Sessler, J. L.; Andrioletti, B.; Anzenbacher, P., Jr.; Black, C.; Eller, L.; Furuta, H.; Jursíkova, K.; Maeda, H.; Marquez, M.; Mizuno, T.; Try, A. In *Fundamentals and Applications of Anion*

Separations; Singh, R. P.; Moyer, B. A., Eds.; Kluwer Academic/Plenum: New York, **2004**; pp. 71–85.
112. Anzenbacher, P., Jr.; Try, A. C.; Miyaji, H.; Jursíková, K.; Lynch, V. M.; Marquez, M.; Sessler, J. L. *J. Am. Chem. Soc.* **2000**, *122*, 10268.
113. Mizuno, T.; Eller, L.; Wei, W.-H.; Sessler, J. L. *J. Am. Chem. Soc.* **2002**, *124*, 1134.
114. Kirkovits, G. J.: Zimmerman, R. S.; Huggins, M. T.; Lynch, V. M.; Sessler, J. L. *Eur. J. Org. Chem.* **2002**, 3768.
115. Sessler, J. L.; Maeda, H.; Mizuno, T.; Lynch, V. M.; Furuta, H. *Chem. Commun.* **2002**, 862.
116. Sessler, J. L.; Maeda, H.; Mizuno, T.; Lynch, V. M.; Furuta, H. *J. Am. Chem. Soc.* **2002**, *124*, 13474.
117. Sessler, J. L.; Pantos, G. D.; Katayev, E.; Lynch, V. M. *Org. Lett.* **2003**, *5*, 4141.
118. Ghosh, T.; Maiya, B. G.; Smanta, A. *Dalton Trans.* **2006**, 795.
119. Aldakov, D.; Anzenbacher, P., Jr. *Chem. Commun.* **2003**, 1394.
120. Aldakov, D.; Palacios, M. A.; Anzenbacher, P., Jr. *Chem. Mater.* **2005**, *17*, 5238.
121. Aldakov, D.; Anzenbacher, P., Jr. *J. Am. Chem. Soc.* **2004**, *126*, 4752.
122. Anzenbacher, P., Jr.; Jursikova, K.; Aldakov, D.; Marquez, M.; Pohl, R. *Tetrahedron* **2004**, *60*, 11163.
123. Pohl, R.; Aldakov, D.; Kubát, P.; Jursíková, K.; Marquez, M.; Anzenbacher, P., Jr. *Chem. Commun.* **2004**, 1282.
124. Anzenbacher Jr., P.; Palacios, M. A.; Jursíková, K.; Marquez, M. *Org. Lett.* **2005**, *7*, 5027.
125. Palacios, M. A.; Nishiyabu, R.; Marquez, M.; Anzenbacher, P., Jr. *J. Am. Chem. Soc.* **2007**, *129*, 7538.
126. Ghosh, T.; Maiya, B. G.; Wong, M. W. *J. Phys. Chem. A* **2004**, *108*, 11249.
127. Wu, C.-Y.; Chen, M.-S.; Lin, C.-A.; Lin, S.-C.; Sun, S.-S. *Chem. Eur. J.* **2006**, *12*, 2263.
128. Szydlo, F.; Andrioletti, B.; Rose, E. *Org. Lett.* **2006**, *8*, 2345.
129. Yoo, J.; Kim, M.-S.; Hong, S.-J.; Sessler, J. L.; Lee, C.-H. *J. Org. Chem.* **2009**, *74*, 1065.
130. Balleter, P. In *Recognition of Anions*; Vilar, R., Ed.; *Structure and Bonding*, Springer-Verlag: Berlin, **2008**; Vol. 129, pp. 127–174.
131. Schottel, B. L.; Chifotides, H. T.; Dunbar, K. R. *Chem. Soc. Rev.* **2008**, *37*, 68.
132. Salman, H.; Abraham, Y.; Tal, S.; Meltzman, S.; Kapon, M.; Tessler, N.; Speise, S.; Eichen, Y. *Eur. J. Org. Chem.* **2005**, 2207.
133. Lin, Z.; Chen, H. C.; Sun, S.-S.; Hsu, C.-P.; Chow, T. J. *Tetrahedron* **2009**, *65*, 5216.
134. Shevchuk, S. V.; Lynch, V. M.; Sessler, J. L. *Tetrahedron* **2004**, *60*, 11283.
135. Plitt, P.; Gross, D. E.; Lynch, V. M.; Sessler, J. L. *Chem. Eur. J.* **2007**, *13*, 1374.
136. Vega, I. E. D.; Gale, P. A.; Light, M. E.; Loeb, S. J. *Chem. Commun.* **2005**, 4913.
137. Maeda, H.; Kusunose, Y. *Chem. Eur. J.* **2005**, *11*, 5661.
138. Oddo, B.; Dainotti, C. *Gazz. Chim. Ital.* **1912**, *42*, 716.
139. Stark, W. M.; Baker, M. G.; Leeper, F. J.; Raithby, P. R.; Battersby, A. R. *J. Chem. Soc. Perkin Trans. 1* **1988**, 1187.
140. Maeda, H.; Ito, Y. *Inorg. Chem.* **2006**, *45*, 8205.
141. Fujimoto, C.; Kusunose, Y.; Maeda, H. *J. Org. Chem.* **2006**, *71*, 2389.
142. Maeda, H.; Kusunose, Y.; Mihashi, Y.; Mizoguchi, T. *J. Org. Chem.* **2007**, *72*, 2621.
143. Maeda, H.; Haketa, Y.; Nakanishi, T. *J. Am. Chem. Soc.* **2007**, *129*, 13661.
144. Maeda, H.; Terasaki, M.; Haketa, Y.; Mihashi, Y.; Kusunose, Y. *Org. Biomol. Chem.* **2008**, *6*, 433.
145. Maeda, H.; Ito, Y.; Haketa, Y.; Eifuku, N.; Lee, E.; Lee, M.; Hashishin, T.; Kaneko, K. *Chem. Eur. J.* **2009**, *15*, 3709.

146. Maeda, H.; Haketa, Y.; Bando, Y.; Sakamoto, S. *Synth. Met.* **2009**, *159*, 792.
147. Maeda, H.; Eifuku, N. *Chem. Lett.* **2009**, *38*, 208.
148. Maeda, H.; Kusunose, Y.; Terasaki, M.; Ito, Y.; Fujimoto, C.; Fujii, R.; Nakanishi, T. *Chem. Asian J.* **2007**, *2*, 350.
149. Maeda, H.; Ito, Y.; Kusunose, Y.; Nakanishi, T. *Chem. Commun.* **2007**, 1136.
150. As one of the other examples: Sanchez-Queseda, J.; Seel, C.; Prados, P.; de Mendoza, J. *J. Am. Chem. Soc.* **1996**, *118*, 277.
151. Maeda *et al*. discovered the formation of multicrystalline systems of **157** and have been investigating the photophysical and electric conductive properties of the single-crystal states, which would exhibit unique properties due to the ordered assembled structures consisting of π-conjugated molecules: Maeda, H.; Bando, Y.; Haketa, Y.; Honsho, Y.; Seki, S.; Nakajima, H.; Tohnai, N., submitted.
152. Maeda, H.; Haketa, Y. *Org. Biomol. Chem.* **2008**, *6*, 3091.
153. Maeda, H.; Mihashi, Y.; Haketa, Y. *Org. Lett.* **2008**, *10*, 3179.
154. Maeda, H.; Fujii, R.; Haketa, Y. *Eur. J. Org. Chem.* **2010**, 1469.
155. Ishi-i, T.; Shinkai, S. In *Supramolecular Dye Chemistry*; Würthner, F., Ed.; Topics in Current Chemistry; Springer-Verlag: Berlin, **2005**; Vol. 258, pp. 119–160.
156. Smith, D. K. In *Organic Nanostructures*; Atwood, J. L.; Steed, J. W., Eds.; Wiley-VCH Verlag: Weinheim, **2007**, pp. 111–154.
157. Maeda, H. *Chem. Eur. J.* **2008**, *14*, 11274.
158. Lloyd, G. O.; Steed, J. W. *Nature Chem.* **2009**, *1*, 437.
159. Anions as additives may not always act as inhibitors but also the building units of soft materials. From this point of view, structural modifications of the anion receptors and the choice of appropriate combinations of anions, cations, receptors, and solvents are currently being investigated in order to harness the fascinating properties of supramolecular gels that are sensitive to chemical stimuli: Maeda, H.; Haketa, Y.; Sasaki, S.; Masunaga, H.; Ogawa, H.; Mizuno, N.; Araoka, F.; Takezoe, H (to be submitted).
160. McCormick, C. L., Ed. *Stimuli-Responsive Water Soluble and Amphiphilic Polymers*; ACS: Washington DC, **2001**.
161. Urban, M. W., Ed. *Stimuli-Responsive Polymeric Films and Coating*; ACS: Washington, DC, **2005**.
162. For example: Aathimanikandan, S. V.; Savariar, E. N.; Thayumanavan, S. *J. Am. Chem. Soc.* **2005**, *127*, 14922.
163. Luisi, P. L.; Walde, P., Eds. *Giant Vesicles*; Wiley-VCH: Chichester, **2000**.
164. Maeda, H.; Fujii, Y.; Mihashi, Y. *Chem. Commun.* **2008**, 4285.
165. Emission quantum yield (Φ_F) of **210** is under further validation. See also Ref. 166.
166. Other elements instead of fluorine and oxygen can be introduced at boron moiety: Maeda, H.; Takayama, M.; Kobayashi, K.; Shinmori, H., submitted.

This page intentionally left blank

39 The Synthesis and Properties of Dipyrrins

Tabitha E. Wood, Md. Imam Uddin and Alison Thompson

Department of Chemistry, Dalhousie University, Halifax,
Nova Scotia, B3H 4J3, Canada

List of Abbreviations

Ac	acetyl
acac	acetylacetonato
bipy	2,2′-bipyridine
BODIPY	boron difluoride dipyrrinato
CAN	ammonium cerium(IV) nitrate
CDMT	2-chloro-4,6-dimethoxy-1,3,5-triazine
DAT	diaminotriazinyl
DCC	*N,N*′-dicyclohexylcarbodiimide
DDQ	2,3-dichloro-5,6-dicyano-1,4-benzoquinone
DIBAL-H	diisobutylaluminum hydride
DIEA	*N,N*-diisopropylethylamine
DMAP	*N,N*-dimethylaminopyridine
DMF	*N,N*-dimethylformamide
DMSO	dimethylsulfoxide
DTT	dithiothreitol
ESR	electron spin resonance
Et	ethyl
hfacac	hexafluoroacetylacetonato
HPLC	high performance liquid chromatography
*i*Pr	*iso*-propyl
IR	infrared
*m*CPBA	3-chloroperbenzoic acid
Me	methyl
MOF	metal-organic framework
*n*Bu	*n*-butyl
NMR	nuclear magnetic resonance
Ph	phenyl
salen	bis(salicylidene)ethylenediamine
p-TSA	*p*-toluenesulfonic acid
Tf	trifluoromethanesulfonyl
TFA	trifluoroacetic acid
THF	tetrahydrofuran

I. Dipyrrins

A. Nomenclature of Dipyrrins

In 1987 an IUPAC Commission established guidelines for the nomenclature of dipyrrins, and many other oligopyrrolic molecules.[1] The recommended numbering scheme for dipyrrins is shown in Figure 1. Occasionally the 1- and 9-positions are referred to as the α-positions, and the 5-position as the *meso*-position, which are terms borrowed from historic pyrrole and porphyrin nomenclature, respectively. Structural isomers of dipyrrins are named according to their connectivity, such as 2,2′-, 2,3′- and 3,3′-dipyrrins, although the actual usage of numbers to describe the connectivity in bis(dipyrrin)s is far from standardized.[2,3] 2,2′-Dipyrrins constitute the vast majority of structures being described when the generic term "dipyrrin" is used, and this convention will be followed in this chapter.

B. Syntheses of Dipyrrins

1. *Introduction*

Research interest regarding dipyrrins originated in experiments conducted by early twentieth century chemists who pursued extensive research on these compounds as intermediates in the synthesis of porphyrins. At this time, dipyrrins were commonly referred to as dipyrromethenes. A particularly important publication was Hans Fischer and Hans Orth's *Die Chemie Des Pyrrols*,[4] a compilation of physical data and preparative strategies for known dipyrrins (although many of them circuitous by today's standards) published in 1937. The required knowledge of techniques for the synthesis and handling of pyrrole derivatives towards the "messy and often ruinous manipulation"[5] of dipyrrins resulted in the relatively esoteric characterization of these compounds for many decades. After

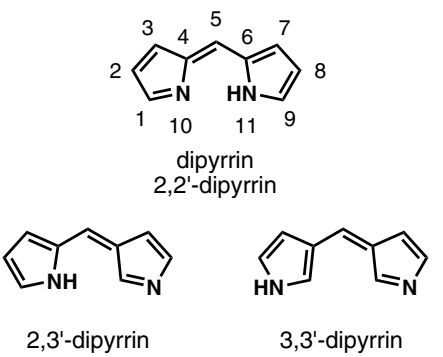

Figure 1. Dipyrrin numbering scheme.

languishing in relative obscurity, dipyrrins have now returned to the forefront of chemical research in the capacity of ligands that can be prepared from readily available reagents, and are often capable of forming crystalline charge-neutral complexes with desirable optical properties using an ever-growing variety of cations.

After a short history of the development of dipyrrin synthesis, Part I of this chapter describes the finite number of methods commonly used to synthesize dipyrrins. This is followed by a discussion of some of the physical properties of these molecules, as well as the applications that they have found. Part II focuses upon the synthesis, properties, and applications of cation-coordinated dipyrrinato complexes, which is where the majority of modern research interest seems to lie.

The aim of this chapter is to provide a brief summary of the historical background and current trends in the burgeoning field of dipyrrin and dipyrrinato complex research. The objective is therefore a representation of all modern dipyrrin research. A full appreciation of modern applications of dipyrrins is best achieved by reading this chapter in conjunction with Chapter 37 (by Burgess and Loudet) in the current volume in this Handbook on the synthesis and spectroscopic properties of BODIPY dyes, as well as Chapter 41 (by Broering) and Chapter 40 (by Balch and Garcia) concerning oligomeric dipyrrins and their dipyrrinato complexes.

Methods for the synthesis of dipyrrins vary according to the required symmetry in the product as well as the number and nature of substituents. The presence of a substituent in the 5-position is especially decisive with regard to a suitable synthetic strategy. Generally, methods that involve condensation of two different pyrrolic compounds are well-suited to the preparation of unsymmetric 5-unsubstituted dipyrrins. Conversely, methods involving the oxidation of dipyrromethanes, which are also known as 5,10-dihydrodipyrrins by IUPAC guidelines,[1] are more suited for the preparation of symmetric, especially 1,2,3,7,8,9-unsubstituted-5-substituted dipyrrins. Substituents on the skeleton of the dipyrrin generally reduce the possibility of oligomerization and increase the stability of the product to attack from a variety of nucleophiles.[6–10] The preparation of fully unsubstituted dipyrrin has been reported; however, the compound was unstable in solution above –40 °C due to its susceptibility to attack by both electrophiles and nucleophiles,[11] though it has also been known to be stable when isolated as its boron difluoride complex.[12,13] The preparation of 5-aryldipyrrins represents a shift in research interest from alkyl-substituted dipyrrins that are suitably disposed as precursors of naturally-occuring oligopyrroles towards dipyrrins that are capable of forming stable radical cations for optoelectrochemical applications.[14]

2. *Synthesis of Dipyrrins by Condensation of Pyrroles*

The procedures for synthesizing dipyrrins by the acid-catalyzed condensation of two pyrrole reagents have remained relatively unchanged from the time of Hans Fisher. In this class of reactions there are three general strategies, depending upon the nature of substitution about the target dipyrrin. The procedure for unsymmetric, 5-unsubstituted dipyrrins is described in the following section, that of symmetric, 5-unsubstituted dipyrrins in Section I.B.2.b and that of symmetric, 5-substituted dipyrrins in Section I.B.2.c.

a. *Unsymmetric 5-unsubstituted dipyrrins*

The acid-catalyzed condensation of a pyrrole-2-carboxaldehyde with a pyrrole that is unsubstituted in the 2-position yields a 5-unsubstituted dipyrrin[15] as shown in Figure 2, and is capable of providing unsymmetrically substituted products. Reports show that bacteria are capable of utilizing supplemented pyrrole-2-carboxaldehyde and 2-unsubstituted pyrrole substrates in the enzymatic synthesis of dipyrrin compounds using an analogous reaction.[16,17]

The choice of acid catalyst for this condensation is open to variation: hydrobromic acid is commonly used, as the corresponding hydrobromide salts of dipyrrins tend to be more crystalline than salts of many other anions,[4] but phosphorus(V) oxychloride has also seen usage.[18,19] In one report, the use of a 2,5-diunsubstituted pyrrole to prepare a 1-unsubstituted bis(dipyrrin) was made possible through the use of phosphorus(V) oxychloride when mineral acids failed.[20] Generally, the yield for this reaction is high, and is limited only by purification of the product from the reaction mixture, although this aspect is not to be assumed facile. Isolation is usually achieved by precipitation of the dipyrrin salts, as they are generally more stable than the free-base, especially in the case of 5-unsubstituted dipyrrins.[15] A limitation to this reaction is that low yields are obtained for dipyrrins prepared from 2-unsubstituted pyrroles with electron-withdrawing groups, resulting from competing self-condensation of the 5-formyl pyrrole with elimination of one carboxaldehyde group.[15] This can be avoided by planning the synthesis such that of the two pyrrole precursors, the less nucleophilic

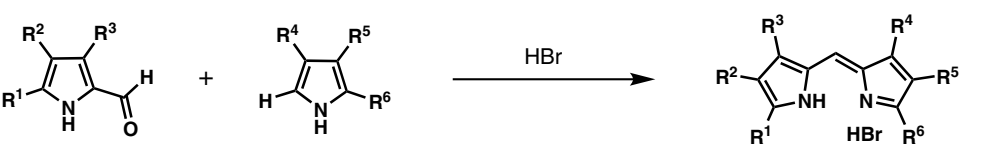

Figure 2. Synthesis of unsymmetric, 5-unsubstituted dipyrrins by acid-catalyzed condensation reactions.

pyrrole moiety bears the carboxaldehyde functional group. The 2-unsubstituted pyrrole reactant can be prepared *in situ* by decarboxylation of pyrrole-2-carboxylic acids in the presence of strong acid.[21,22]

b. *Symmetric 5-unsubstituted dipyrrins*

Symmetric dipyrrins that bear a hydrogen substituent at the 5-position can be prepared using two equivalents of a 2-unsubstituted pyrrole. This preparation generally involves combining the pyrrole reactant with a mixture of formic acid and a strong mineral acid, such as hydrobromic acid,[4] hydrochloric acid,[23] or perchloric acid,[24] or with a mixture of an orthoformate and trifluoroacetic acid,[25,26] as depicted in Figure 3. In the most popular variations of this method the 2-unsubstituted pyrrole is prepared *in situ* from a pyrrole bearing a functional group that can be eliminated under strongly acidic conditions, such as a carboxylic acid group, or a carboxylic ester (usually the ethyl ester). It has been shown that a moderate reaction temperature of 20 to 40 °C is critical for the preparation of the 2,8-di(carbethoxy)-substituted symmetric dipyrrin (**3** in Figure 4) using the *tert*-butyl ester derivative **1** as a precursor for *in situ* generation of the 2-unsubstituted pyrrole reagent.[26]

c. *Symmetric 5-substituted dipyrrins*

The condensation of two equivalents of a 2-unsubstituted pyrrole with an acid chloride,[27,28] as shown in Figure 5, provides a synthetic route to 5-substituted

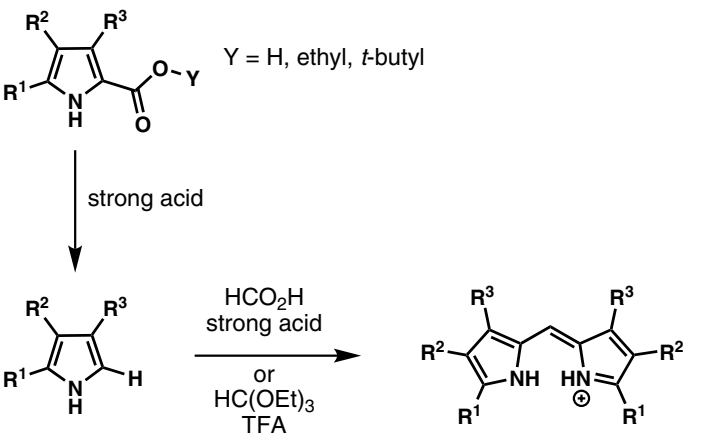

Figure 3. Synthesis of unsymmetric, 5-unsubstituted dipyrrins by acid-catalyzed condensation reactions.

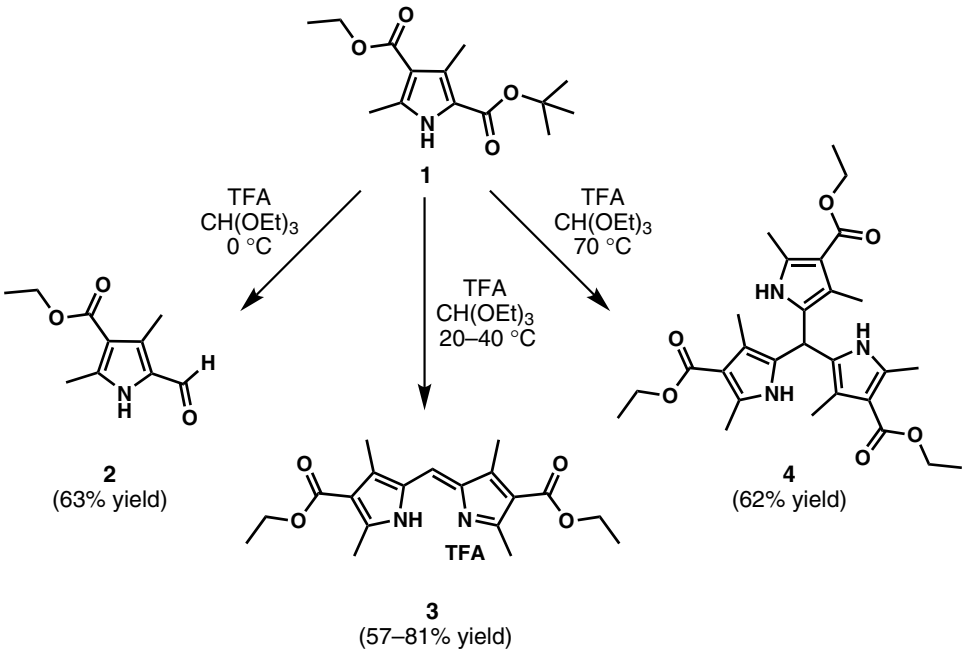

Figure 4. Temperature dependence for the condensation of *tert*-butyl 3,5-dimethyl-4-carbethoxypyrrole-2-carboxylate with triethylorthoformate.

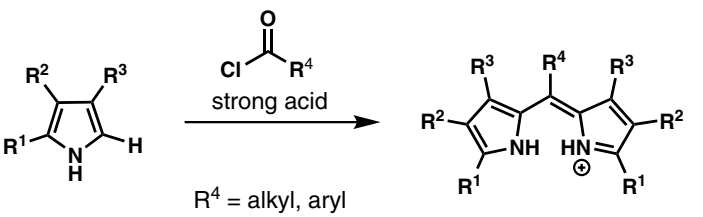

Figure 5. Synthesis of symmetric, 5-substituted dipyrrins by acid-catalyzed condensation reactions.

dipyrrins. Similar to the reaction with formic acid described in **b**, the 2-unsubstituted pyrrole may be prepared *in situ* from an appropriate precursor. It is reasonable to propose that these reactions proceed by a similar mechanism to that for the analogous reactions with formic acid, i.e. an acylated pyrrole intermediate is attacked by a second equivalent of the 2-unsubstituted pyrrole.[23] One report compares the preparation of a symmetric 5-aryldipyrrin by either the reaction of 4-iodobenzoyl chloride with an excess of 2-unsubstituted pyrrole, or the reaction of the 2-ketopyrrole product of 4-iodobenzoyl chloride and a 2-unsubstituted pyrrole, and a second equivalent of the 2-unsubstituted pyrrole in the presence of

phosphorous(V) oxychloride, and notes that the overall yield was higher for the two-step procedure.[29]

3. *Synthesis of Dipyrrins by Oxidation of Dipyrromethanes*

The preparation of 5-aryldipyrrins by the oxidation of dipyrromethanes (as outlined in Figure 6) has become a very popular synthetic route, though this method has thus far been less successful for the preparation of 5-alkyl and 5-unsubstituted dipyrrins.[30] This transformation can be effected using a variety of different oxidizing agents, the most popular of which is 2,3-dichloro-5,6-dicyano-1,4-benzoquinone (DDQ), although *p*-chloranil is occasionally seen when a more mild oxidizing agent is desired.[31,32] The dipyrrin products of this reaction are generally isolated in their free-base form, as 5-aryl dipyrrin bases are generally stable, unlike 5-unsubstituted dipyrrins. Chromatography and crystallization techniques are typically employed for the purification of free-base dipyrrins, and vacuum sublimation has been used to produce very pure samples.[33,34] One report details the isolation of dicyanovinyl-di(5-aryl)dipyrrins upon attempting to oxidize 5-(2,6-dichlorophenyl)dipyrromethane with DDQ, and fluoro-substituted derivatives behaved similarly.[35] Evidently the DDQ underwent an addition reaction with the pyrrolic moieties of the dipyrromethane. Treatment of the adducts under acidic or basic conditions promoted partial elimination and the creation of novel bis- and mono-dipyrrins bearing remnants of DDQ at the 2-positions of the dipyrrins.

Dipyrromethanes can be prepared from reactions analogous to those described earlier in this chapter for dipyrrins, with the *meso*-carbon precursor one oxidation state lower. For example, the acid-catalyzed reaction of a 2-acyl substituted pyrrole with a 2-unsubstituted pyrrole allows for the preparation of unsymmetrically substituted dipyrromethanes, and the reaction of two equivalents of a 2-unsubstituted pyrrole reagent with an aldehyde yields symmetric dipyrrolic products. Figure 7 shows a synthetic route to 5-unsubstituted dipyrromethanes involving the self-condensation of an appropriate pyrrole carbinyl cation precursor under acidic conditions[36] (e.g. Montmorillonite K-10 clay[37] or *p*-toluenesulfonic acid,[38] *p*-TSA), or

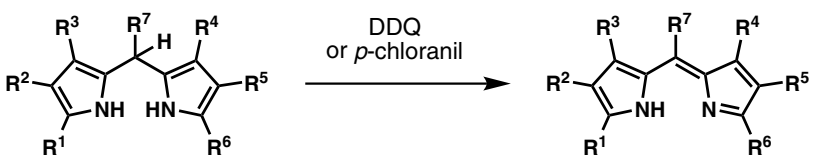

Figure 6. Synthesis of dipyrrins by oxidation of dipyrromethanes.

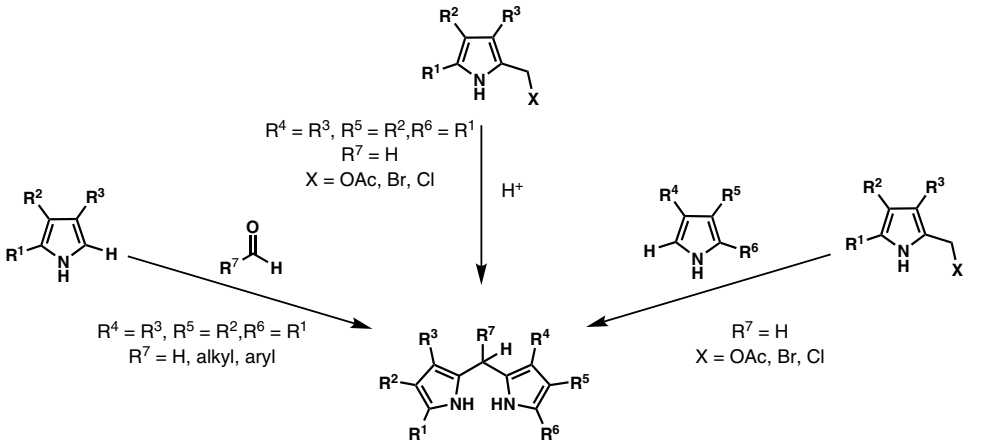

Figure 7. Synthesis of dipyrromethanes from condensation of pyrroles.

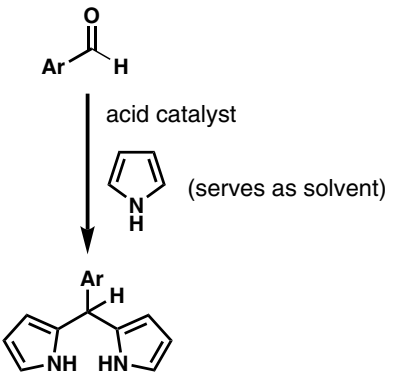

Figure 8. Synthesis of 5-substituted dipyrromethanes using excess pyrrole.

via the reaction of the same precursor species with a 2-unsubstituted pyrrole if unsymmetric dipyrromethanes are desired.[15]

One of the most important advances for opening the field of dipyrrin chemistry to researchers not specialized in the synthesis of pyrrole derivatives has been the development of procedures for preparing 5-aryldipyrrins from 5-aryldipyrromethanes, with pyrrole and an aromatic aldehyde, or the corresponding dimethyl acetal,[39] as starting materials.[40–46] Pyrrole is readily available commercially and can be purified by a non-rigorous distillation procedure, and the excess amount used in this reaction can be easily recycled. The optimal conditions for reactions of this type, shown in Figure 8, are highly generalizable: the reaction of an aromatic aldehyde with 100 equivalents of pyrrole in the presence of a mild

Lewis acid catalyst (such as $InCl_3$) at room temperature in the absence of air for a few hours. The dipyrromethane products are often isolated with high purity by chromatography or crystallization, with yields generally greater than 50%, and the reactions are scalable.[44] Methods for the preparation of dipyrromethanes that bear substituents on the pyrrole rings have also been developed. These procedures use only two equivalents of the precursor 2-unsubstituted pyrrole as oligomerization side-reactions are not as prominent.[32,47–52] Moreover, the use of 5-alkylthio-protected pyrroles precludes the use of excess pyrrole reagent by preventing oligomerization during dipyrromethane synthesis.[53]

C. Properties and Reactions of Dipyrrins

The Chemistry of Linear Oligopyrroles and Bile Pigments[24] describes some physical properties of dipyrrins (e.g. structure, solubility, NMR characteristics, fluorescence spectra, and light absorbance spectra). Thermal decomposition data, as well as solvation and light absorption characteristics, for dipyrrin and bis(dipyrrin) hydrobromide salts and dipyrrinato metal complexes have also been reported elsewhere.[2,3,54–57]

Dipyrrins as their free-bases are relatively strong bases.[15] Spectrophotometric titrations have been used to measure the pK_a of the N–H proton for a series of dipyrrins: electron-withdrawing and electron-donating effects of substituents were observed to have a definite effect upon the acidity of the dipyrrinato proton.[58] The solvolytic dissociation and deprotonation of dipyrrin hydrobromide salts by organic solvents such as DMSO, DMF, and pyridine (accelerated in dilute solution, $< 10^{-4}$ M) have been investigated, and these studies enabled the observation of a correlation between the proton affinity of a dipyrrin and its thermodynamic constant of complexation with zinc(II) ion.[3,56,57,59] The solvation effect upon the electronic absorption is less dramatic with solvents such as benzene, CCl_4, $CHCl_3$, CH_2Cl_2, and alcohols.[59]

For this part of the discussion, 2,2′- and 3,3′-dipyrrins are referred to specifically by their numbering system, whereas in all other parts of this article the default term "dipyrrin" implies a 2,2′-dipyrrin as mentioned previously. The physical and chemical properties of 2,2′- and 3,3′-dipyrrins largely depend upon the effects of the substituents attached to the dipyrrin skeleton, as well as upon the nature of the linkage in the case of bis(dipyrrin)s. 2,2′-Dipyrrins often have physical and chemical behaviors distinct from those of 3,3′-dipyrrins (Figure 9), and the electronic absorption properties of a series of 2,2′- and 3,3′-dipyrrins and related bis(dipyrrin)s have been extensively studied and compared.[59] In particular, dipyrrin HBr salts behave as weak electrolytes, partially dissociating to the protonated dipyrrin and bromide ion in polar organic solvents. In polar aprotic solvents,

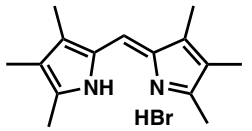

dipyrrin · HBr
ν_{N-H} 3415 cm^{-1}, δ_{N-H} 1601 cm^{-1}

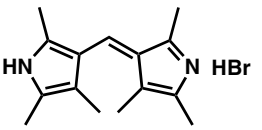

3,3'-dipyrrin · HBr
ν_{N-H} 3415 cm^{-1}, δ_{N-H} 1618 cm^{-1}

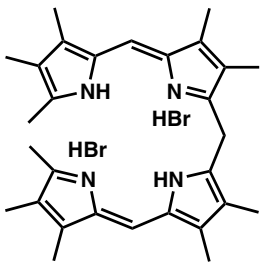

1,1'-bis(dipyrrin) · HBr
ν_{N-H} 3417 cm^{-1}, δ_{N-H} 1609 cm^{-1}

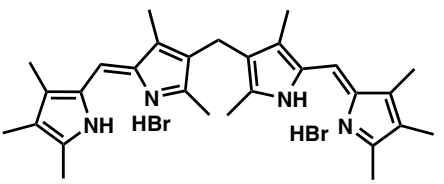

2,2'-bis(dipyrrin) · HBr
ν_{N-H} 3480 cm^{-1}, δ_{N-H} 1611 cm^{-1}

Figure 9. 2,2′- and 3,3′-Dipyrrins and bis(dipyrrin)s.

the equilibrium moves further towards the ionic forms as the bromide anion is better solvated. Solvolytic dissociation of the salts to generate free-bases in solution occurs in polar protic solvents. Such electrolytic and/or solvolytic behavior can be detected using absorption spectroscopy through the presence of shoulders representing the protonated dipyrrin or free-base dipyrrin, respectively, and/or through the gradual transformation of spectra of salts into spectra of free-base dipyrrins in polar protic solvents. Comparatively, the HBr salts of 3,3′-dipyrrins and 3,3′-linked bis(dipyrrin)s are less stable than their 2,2′-analogs (i.e. dissociation occurs more readily for 3,3′-dipyrrins and 3,3′-bis(dipyrrin)s than for 2,2′-dipyrrins), and the decreased stability was estimated from the long wave shift of the N–H stretching vibration band in the IR spectra (Figure 9).[59] The dissymmetry and planarity of a 2,2′-dipyrrin was examined using an X-ray crystal structure of the corresponding HBr and carboxylate salts.[25] In contrast 3,3′-isomeric salts were found to be weakly distorted from planarity, resulting in considerable bathochromic shifts of the most intense bands in the electronic spectra.[59]

In studies relating to the antioxidant properties of dipyrrins and other oligopyrrolic compounds, a significant difference between isomeric dipyrrins was observed. The 2,2′-dipyrrin, which mimics the linkage of natural linear tetrapyrrolic compounds, was found to be an excellent antioxidant whereas the 3,3′-linked isomer was found to be inactive in this regard.[60] To be an effective antioxidant, it was found that the N–H group of the 2,2′-linked dipyrrins should

be unprotected: the *N*-methylated compounds were not active antioxidants.[61] Additionally, the antioxidant property was found to drop dramatically in methanol due to hydrogen bonding at the pyrrolic N–H. Further to the electronic properties of dipyrrins, some oxidation potentials of linear hexapyrroles and the guest recognition abilities of cyclic oligopyrroles including metal complexes of Cs^+, Rb^+, and K^+ have been reported.[62,63]

The types of substituents attached to the dipyrrin have significant effect on the physical and chemical properties of the dipyrrin, particularly with respect to stability and biological properties. It was observed that dipyrrins bearing alkyl and benzyl substituents at the *meso*-position, and thus possessing an allylic acidic proton, undergo base-promoted isomerization to give the corresponding dipyrrinylethane as shown in Figure 10.[64] As previously noted,[34,65] dipyrrins bearing aryl and heteroaryl substituents at the 5-position enjoy increased stability over their 5-unsubstituted analogs, thereby facilitating easier handling and storage of the former under aerobic conditions, even as their free-bases.

A pyrrole attached through its 2-position to a 2,2′-dipyrrin gives the skeleton of the prodigiosin class of natural products, some of which possess important biological properties such as anticancer, antimicrobial, and immunosuppressive properties.[66] Analogs of prodigiosin such as phenolic A-ring derivatives (Figure 11) structurally resemble 2-(2′-hydroxyphenyl)benzimidazole, and other related systems, that can exist in *syn*- and *anti*-enol conformational forms. The *syn*-enol undergoes photochemical tautomerization to the keto form, accompanied by a large Stokes-shifted fluorescence. Indeed, such tautomerization to the keto form occurs in the ground-state for the A-ring *o*-phenolic prodigiosin derivative shown in Figure 11, in polar, protic solvents. Such proton transfer demonstrates yet another route by which to alter the conjugation of the dipyrrolic moiety.[67] As part of studies to investigate the light vs. dark cytotoxicity of derivatives of prodigiosin, a buffered aqueous solution of an A-ring phenyl analog (Figure 11) was photoirradiated in the presence of thioglycolic acid. Mono-, di-, and tri- conjugates of the dipyrrin and the thiol were subsequently isolated, thus supporting the intermediacy of a dipyrrin-centered radical cation and providing a route to functionally elaborated dipyrrins.[68]

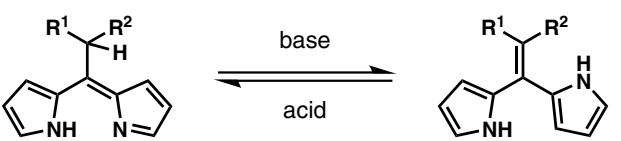

Figure 10. Tautomerization of dipyrrin bearing an allylic-H to the corresponding vinylic dipyrrole.

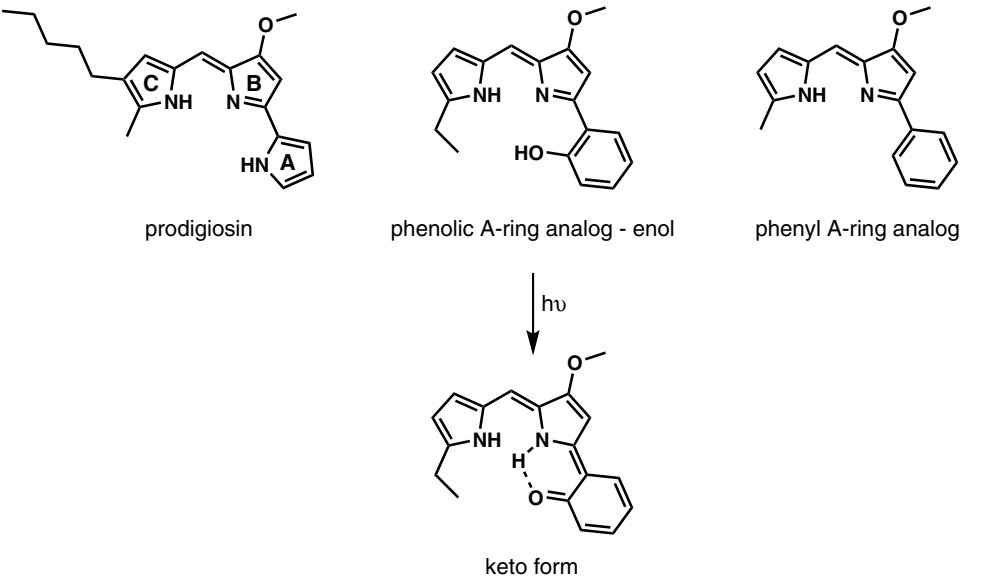

Figure 11. Dipyrrin-containing prodigiosin and two synthetic analogs.

The ^{15}N NMR chemical shifts for dipyrromethanes, dipyrrins, and dipyrrinato complexes have been found to be diagnostic of gross structure concerning the oxidation and complexation states of the dipyrrolic compounds, although such values do not reveal information about the effect that substituents might have upon the bonding environment of the nitrogen atom.[69] This general method has found use in reported ^{15}N chemical shifts of numerous pyrrolic compounds, with generally diagnostic values maintained.[64,70–73]

II. Dipyrrinato Complexes

A. Syntheses of Dipyrrinato Complexes

Popular procedures employed for the synthesis of dipyrrinato metal complexes vary mostly in whether the dipyrrin ligand is isolated before complexation, or prepared *in situ*. Generally, dipyrrins prepared by the condensation of pyrrolic reagents are isolated before complexation, whereas the general procedure for the oxidation of dipyrromethanes to dipyrrins is amenable to one-pot dipyrrin formation and complexation. The complexes formed can be classified according to the nature of the cation complexed, whether the complex is homoleptic or heteroleptic, as well as whether the complex exists as a discrete molecular unit or as part of a supramolecular complex.

1. *Complexation Geometries*

Dipyrrinato ligands bind cations in a chelating κ^2 manner in the vast majority of dipyrrinato complexes. As such, depending on the charge of the cation in the complex, ML, ML_2, and ML_3 dipyrrinato complexes are isolable. The coordination geometry of the metal center in these complexes is influenced not only by the nature of the metal ion, but also by steric interactions between substituents at the 1- and 9-positions of multiple ligands brought into close proximity by complex formation.[74] The vast majority of homoleptic ML_2 dipyrrinato complexes adopt tetrahedral, or distorted tetrahedral, coordination geometry. The distorted tetrahedral complex bis(5-phenyldipyrrinato) copper(II)[31] shows that interactions between 1- and 9-substituents as small as hydrogen atoms result in the preferential formation of non-square-planar coordination geometry about the complexed metal ion, although this is not the typical coordination geometry adopted by copper(II) complexes. Another interesting example is the diamagnetic low-spin complex bis(5-phenyldipyrrinato) nickel(II) (compound **5** in Figure 12).[31]

Octahedral coordination geometry is observed for ML_3 dipyrrinato complexes as seen for iron(III) tris(5-phenyldipyrrinato), compound **6** in Figure 13.[75] One report describes the auto-oxidation in air of an unstable tetrahedral bis(5-phenyldipyrrinato) cobalt(II) complex to the octahedral tris(5-phenyldipyrrinato) cobalt(III) complex, and observes that the same product could be prepared from

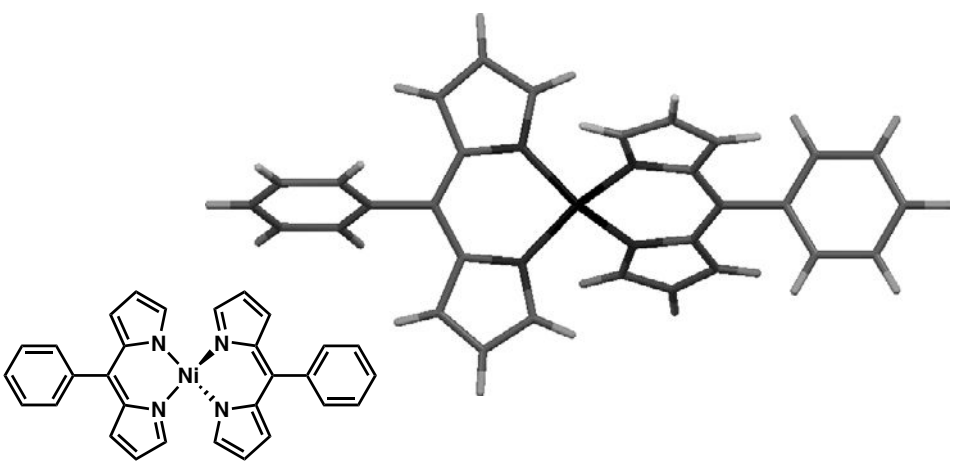

5

Figure 12. Tetrahedral coordination geometry in a nickel(II) dipyrrinato complex, adapted from Ref. 31.

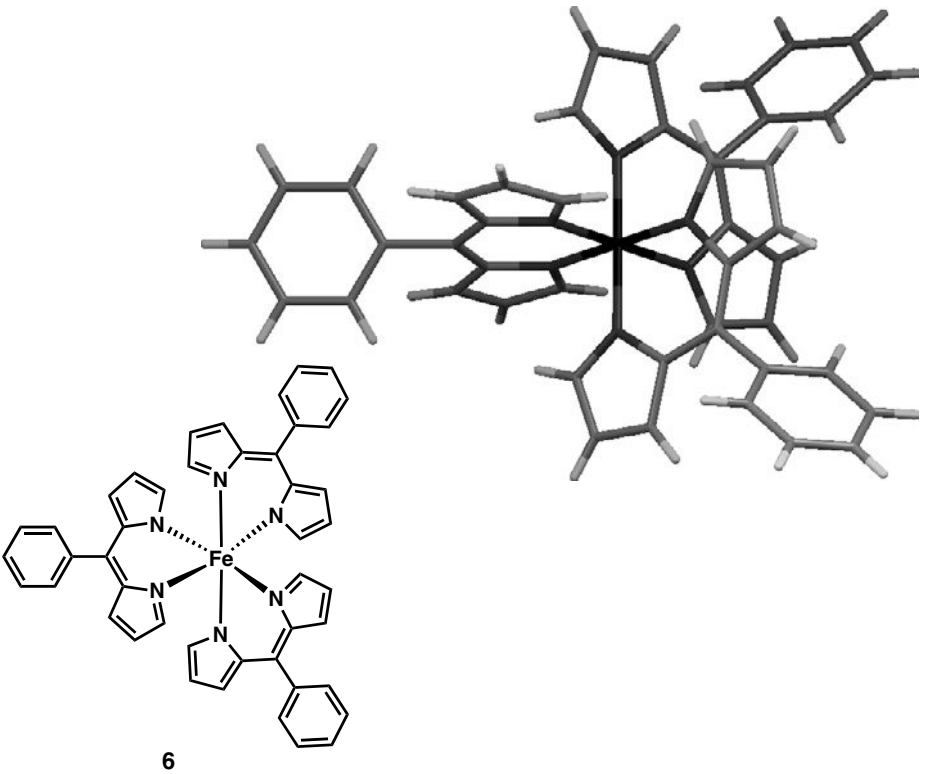

6

Figure 13. Octahedral coordination geometry in an iron(III) dipyrrinato complex, adapted from Ref. 76.

complexation of the dipyrrin ligand with an appropriate cobalt(III) salt.[76] In the ^{1}H NMR spectrum of the cobalt(III) complex, the relatively shielded chemical shift of the 1- and 9-hydrogen substituents is somewhat diagnostic for octahedral complex formation, as it results from these atoms being shielded by two adjacent aryl dipyrrinato systems.[76] Octahedral tris(dipyrrinato) complexes of iron(III), cobalt(III), gallium(III), and indium(III) have been extensively studied for use in the formation of metal-organic frameworks.[34,75,77–84]

Some exceptions to the κ^2 binding behavior of dipyrrinato ligands have been noted. The first example of a pyrrolic unit of a dipyrrin binding a metal ion in an η^5 manner, analogous to pyrrole in azaferrocene,[85] was reported by Bröring and coworkers (Figure 14).[86] It was demonstrated that the reaction of a bis(dipyrrin) with $Ru_3(CO)_{12}$ produced a ruthenium-dipyrrin cluster (**7**) in which one of the pyrrole rings was bound in an η^5 manner to a ruthenium ion. An example of a silver ion bound in an η^2 manner to one of the pyrrolic units in a dipyrrin complex (**8** in Figure 14) was reported by Hosseini and coworkers,[87] and was followed by the

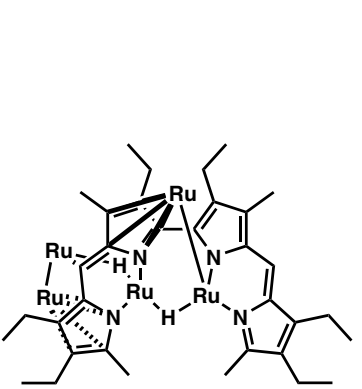

7
$Ru_5H[b(dpme)](CO)_{11}$
(carbonyl ligands removed for clarity)

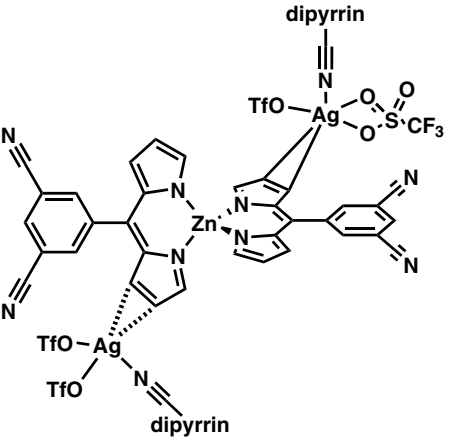

8

Figure 14. Example of η^5- and η^2-binding of dipyrrin, adapted from Refs. 86 and 87.

report of a related structure.[88] Indeed, the number of reports of complexes and macrocycles of dipyrrins involving coordination to silver has been increasing.

Although there are multiple conformations that dipyrrins can possibly adopt,[24,88] one conformation is observed in the vast majority of dipyrrinato complexes. Reported complexes of dipyrrins in which the pyrrolic units have adopted a conformation such that the nitrogen atoms are oriented in the same direction as the 5-substituent are very rare. One report presented solid state structures of dipyrrin complexes such as **9** in which protonated dipyrrins in an *E-syn* conformation formed supramolecular structures with tetrahalozinc anions (Figure 15).[89] A report has described the solid-state structure of a dimeric Ag(I) complex of 5-(4-cyanophenyl)dipyrrin in which the dipyrrin ligands adopt an *E-anti* conformation.[88]

2. *Scope of Metal Ions in Homoleptic Dipyrrinato Complexes*

The variety of metal ions with which dipyrrins are known to form isolable complexes is extensive. Upon deprotonation, the monoanionic dipyrrinato ligands generally form neutral homoleptic (bearing two or more identical ligands on a metal center) complexes. However, heteroleptic (bearing two or more different ligands on a metal center) complexes have also been observed. Dipyrrinato ligands are known to form homoleptic complexes with magnesium(II),[90] calcium(II),[91,92] chromium(III),[93] manganese(II),[91,94,95] manganese(III),[94] iron(II),[96] iron(III),[75,76,79–81,96] cobalt(II),[97–106] cobalt(III),[76,80–82,107] nickel(II),[31,91,92,97–99,101–106,108–110] copper(II),[30,31,54,55,78,79,84,90–92,97,98,101–106,108,111–113]

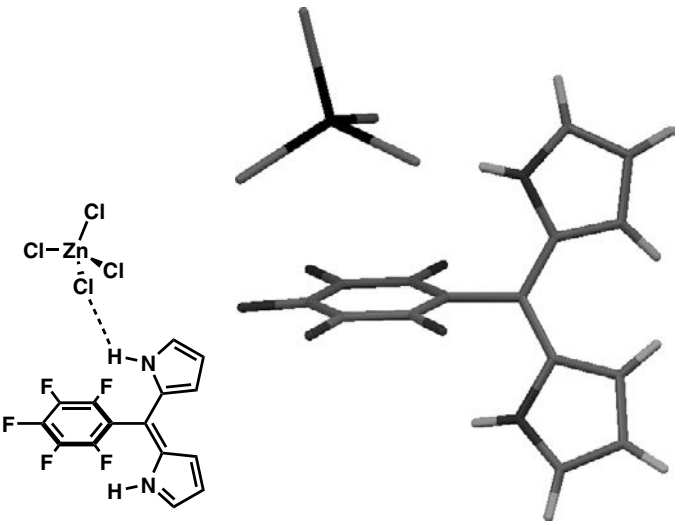

9

Figure 15. Rotation about the 5-position in dipyrrins, adapted from Ref. 89.

zinc(II),[30,31,54,55,82,91,97–99,101,102,105,106,108,114–119] gallium(III),[34,84] ruthenium(II),[120] rhodium(II),[121] palladium(II),[30,99,105,109,122] cadmium(II),[99,105] indium(III),[34,84] mercury(II),[99,105] thallium(I),[123] and thallium(III).[123] The synthesis of a lithium(I) dipyrrin complex was described in which the lithium ion was unsupported by coordinated solvent molecules in the solid-state structure,[119] and other lithium complexes were prepared and used *in situ*.[39,124]

3. *Dipyrrinato Complexes of Boron*

Chapter 37 in this volume is dedicated to a discussion of the syntheses and properties of boron difluoride complexes of dipyrrins (BODIPYs, Figure 16). Briefly, these extremely important fluorescent molecules were first reported in 1968.[125] Even in this earliest of reports the researchers described the intense fluorescence of complexes of this type and this has become recognized as their signature property. The effect of molecular structure upon the spectroscopic properties of boron difluoride dipyrrinato complexes has received a great deal of attention in the literature,[19,24,27–29,33,58,70,114,126–155] and continues to be a vibrant research theme.

4. *Heteroleptic Dipyrrinato Complexes*

Although the most commonly described dipyrrinato complexes are of a homoleptic nature, the isolation of heteroleptic complexes is becoming increasingly

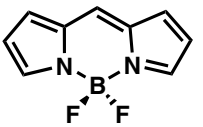

Figure 16. General structure of a boron difluoride dipyrrinato complex.

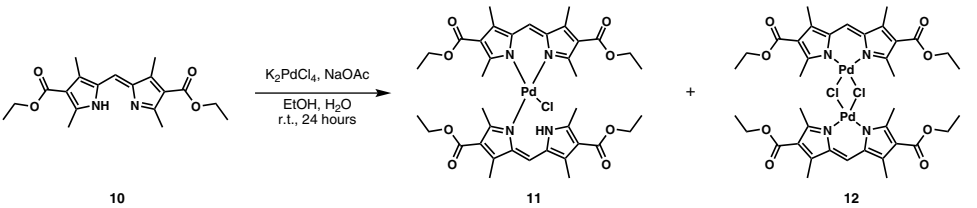

Figure 17. Formation of heteroleptic and bridged dimer palladium(II) dipyrrinato complexes.[99]

frequent. A variety of studies have shown heteroleptic complexes in solution as intermediates preceding the formation of homoleptic complexes.[56,156–159] Absorption spectroscopy solution studies of the complexation of copper(II) chloride or zinc(II) acetate with dipyrrin ligands have been reported to exhibit an isosbectic point, whereas those involving copper(II) acetate do not.[158] The somewhat broad absorption profile for the dipyrrinato unit, as well as overlapping signals for ligand, homoleptic, and heteroleptic complexes, creates a serious complication in the analysis of electronic absorption spectra corresponding to complexation reactions. With a number of heteroleptic species being possible along the reaction pathway, the clarifications afforded by ^{1}H NMR spectroscopy have made this a useful technique for detecting the presence of these species.[159]

One factor that may promote the formation of isolable heteroleptic dipyrrinato complexes is the resulting facilitation of a square planar coordination geometry about the complexed cation, while the steric requirements of 1- and 9-substituents force tetrahedral or octahedral coordination geometry in homoleptic complexes. Examples of this are the proposed products from the attempted formation of a homoleptic palladium(II) complex of dipyrrin **10**: the heteroleptic complex **11** and a bridged dimeric complex **12** (Figure 17).[99] The structure of heteroleptic **11** was later confirmed using X-ray analysis, with the dipyrrinato unit coordinated as a monoanionic bidentate ligand and the dipyrrin coordinated as a neutral unidentate ligand.[122] To date, there are very few reports of homoleptic palladium(II) dipyrrinato complexes.[30,160]

Complexation reaction conditions have been shown to affect the formation of heteroleptic dipyrrinato complexes. These variables include stoichiometry,[119] the

presence of non-dipyrrin species to coordinate with the metal ion,[22,73] the choice of solvent,[22] the ionic radius of the metal ion,[22] and the temperature utilized for the reaction. As an example, in the preparation of mercury(II) dipyrrinato complexes, the constitution of the product complex was shown to depend upon the salt used: mercury(II) nitrate gave a homoleptic dipyrrinato mercury(II) complex, while mercury(II) chloride gave a heteroleptic chlorodipyrrinato mercury(II) complex.[99] Similarly, it has been shown that conducting complexation reactions in DMF, a strongly coordinating solvent, promotes the formation of heteroleptic products.[22] Dipyrrinato lithium(I) complexes have been used successfully as starting materials in the preparation of several heteroleptic complexes.[39,119]

The scope of dipyrrinato complexation has recently been extended by reports of aluminum complexes of the N_2O_2 type, whereby dipyrrins substituted in the 1- and 9-positions with phenols, such as dipyrrin **13** in Figure 18, form tetradentate complexes, such as **14**, with aluminum(III).[161] The aluminum complexes are reminiscent of BODIPYs in that they are fluorescent. The addition of $ZnCl_2$ to the aluminum complexes results in a change of absorption properties with the concurrent formation of a heterometallic Al-dipyrrinato-Zn adduct, such as **15**, courtesy of the phenolic moieties binding to both aluminum and zinc.

Along a similar vein, a divalent tin complex has recently been reported.[124] In this example a lithium dipyrrinato complex was generated *in situ* by reacting a dipyrrin free-base with *n*-BuLi at −78 °C, followed by the addition of $SnCl_2$. The dipyrrinato-Sn-Cl species thus generated exhibited similar fluorescence properties to BODIPYs.[124]

Strongly-coordinating ligands, such as bidentate 2,2′-bipyridine (bipy),[120] *N,N′*-bis(salicylidene)ethylenediamine (salen),[88] acetylacetonato (acac),[162,163] or its hexafluoro-derivative (hfacac),[78] are frequently the ancilliary ligand in heteroleptic dipyrrinato metal complexes. Another feature that makes acac and hfacac excellent ancilliary ligands is the minimal steric encumbrance that they create near the metal center (unlike the 1- and 9-substituents of dipyrrins).[163] Thus,

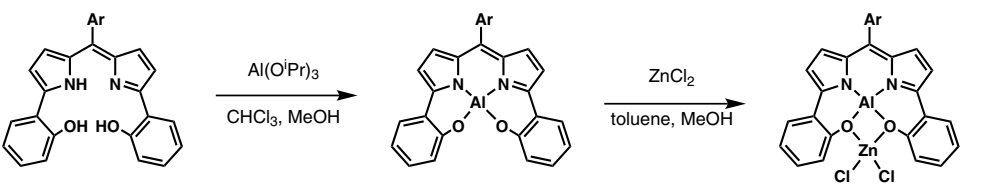

13a,b
Ar = Ph (**13a**)
mesityl (**13b**)

14a,b

15a,b

Figure 18. Formation of an aluminum(III) dipyrrinato complex.

heteroleptic dipyrrinato complexes of this type can accommodate square planar coordination geometry, such as for copper(II) and palladium(II).[99] Heteroleptic complexes of rhodium(I) have been reported to form upon the reaction of $[Rh(CO)_2Cl]_2$ with dipyrrins in the presence of sodium acetate[121] or potassium carbonate.[164] These complexes each contain a bidentane dipyrrinato ligand and two CO ligands. Heteroleptic iridium(III), ruthenium(III) and rhodium(III) dipyrrinato complexes have also been reported, with the latter two having been investigated as catalysts for transfer hydrogenolysis.[165,166] In a rare example of a heteroleptic complex in which the non-identical ligands are simply differently-substituted dipyrrins, the preparation of [5-(cyanophenyl)-1-methoxydipyrrinato]bis[5-(cyanophenyl)dipyrrinato] cobalt(III) complex was reported as a mixture with the homoleptic complex tris[5-(cyanophenyl)dipyrrinato] cobalt(III).[82]

In another example, heteroleptic zinc(II) halide complexes **17** were prepared from 5-(1-methylimidazol-2-yl)dipyrrin, **16**, by reaction with zinc halides and ammonia, while the homoleptic complex **18** could be prepared from zinc acetate (Figure 19).[73] The complexes **17** also serve as examples in which substituents on the dipyrrinato ligand coordinate with the complexed metal ion. This mode of chelation can result in the formation of discrete structures as in the case of the 5-(2-pyridyl)dipyrrinato zinc(II) halide dimeric complexes,[167] and monomeric

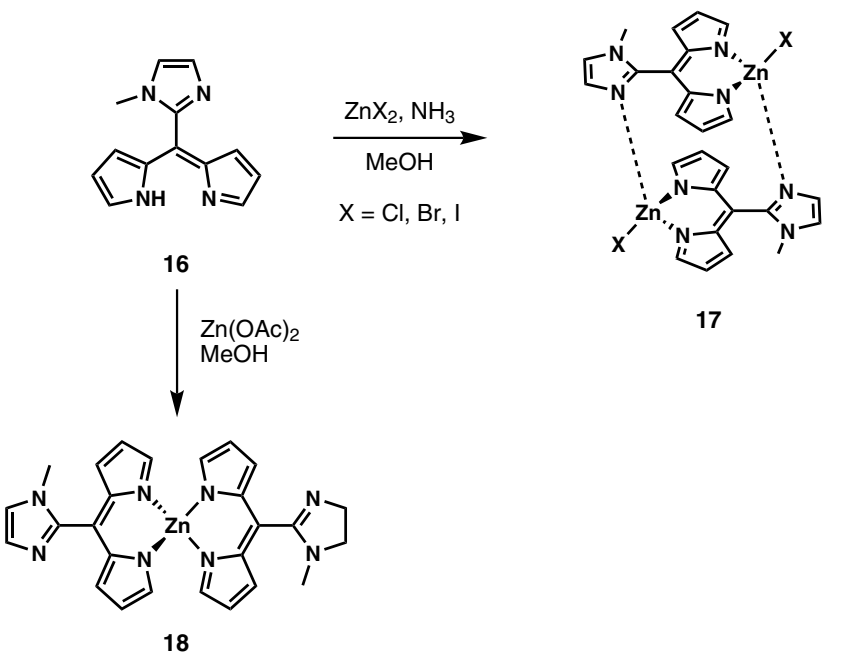

Figure 19. Formation of a discrete heteroleptic dipyrrinato complex.

nickel(II) and copper(II) diamidodipyrrinato complexes.[168] However, this may also result in the formation of vast coordination polymer networks.[169]

5. *Demetalation of Homoleptic Dipyrrinato Complexes*

Demetalation of dipyrrinato complexes can be achieved using several methods. Treatment of the homoleptic 5-phenyldipyrrinato zinc(II) complex with excess trifluoroacetic acid or methanolic hydrochloric acid was observed to result in incomplete demetalation,[30] which is somewhat surprising as many complexes are labile under acidic conditions. Dithiothreitol (DTT, threo-1,4-dimercapto-2,3-butanediol) has been used[30] to effect complete demetalation of a variety of dipyrrinato complexes when similar treatment with ethylene glycol proved unsatisfactory. As an alternative method for demetalation, reduction of the homoleptic 5-phenyldipyrrinato zinc(II) complex with sodium borohydride was shown to give the corresponding dipyrromethane,[30] akin to the well-documented reduction of dipyrrins to give dipyrromethanes.[170] The treatment of dipyrrinato rhodium(I) complexes with bromine or chlorine has been observed to result in demetalation of the complexes, generating the hydrobromide or hydrochloride salts, respectively, of the dipyrrin ligands.[121] Furthermore, the treatment of dimeric dipyrrinato copper(II) complexes with potassium cyanide resulted in complete demetalation.[79,84] This method of demetalation allowed for the preparation of gallium(III) and indium(III) dipyrrinato complexes (**22a**, **b** in Figure 20) that were not obtainable using standard one-pot procedures starting from dipyrromethanes.[84] As a consequence of reacting a copper(II) bis(dipyrrinato) complex with artemisinin, a 1,2,4-trioxane natural product, cleavage of the peroxidic O–O bond in the antimalarial compound was accompanied by concomitant cleavage of the Cu–N bonds and thus liberation of the metal and free-base/artemisinin adduct: the same effect was observed with iron(III) dipyrrinato complexes.[171]

6. *Supramolecular Dipyrrinato Metal Complexes*

The versatility of dipyrrins has made them a popular ligand in the design of supramolecular metal coordination complexes. Tetradentate bis(dipyrrin) ligands, in which two dipyrrin units are connected by a variable tether, have been shown to form an array of discrete supramolecular complexes whose interesting geometries can be controlled by factors such as the number of degrees of freedom and the location of the linking points of the tether unit. An outline of the nomenclature for bis(dipyrrin)s is shown in Figure 21, but the literature is rife with commonplace numbering for bis(dipyrrin)s. Dipyrrinato ligands that are substituted with

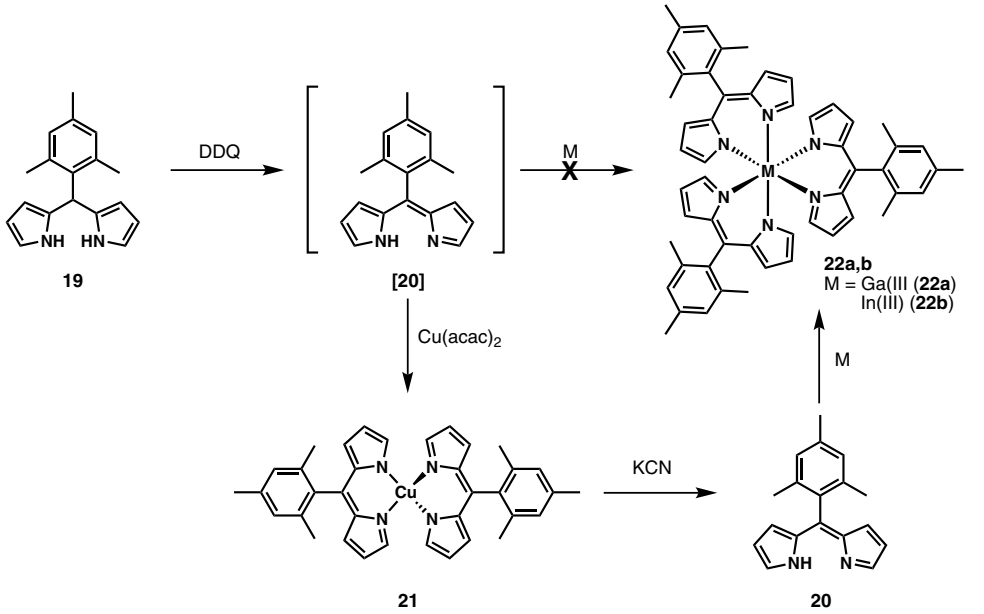

Figure 20. Demetalation of Cu(II) dipyrrinato metal complex using potassium cyanide.

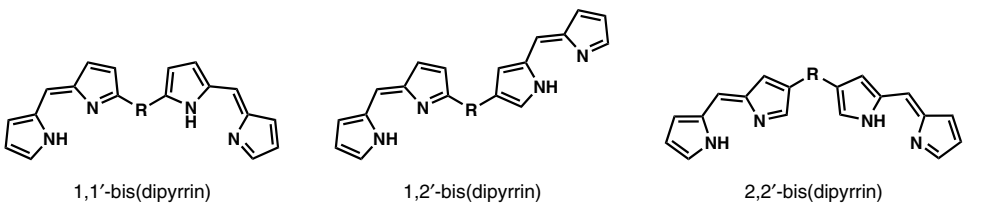

Figure 21. Bis(dipyrrin) numbering scheme.

metal-coordinating functional groups are finding utility in the formation of extended coordination polymers or metal-organic frameworks.

a. *Discrete helical complexes*

Metal ion complexation products of bis(dipyrrin)s adopt helicate (chiral) or mesocate (non-chiral) structures, arising from the approximately perpendicular arrangement of two bidentate dipyrrinato units to a single metal center as shown in Figure 22. Even in complexes with non-tetrahedral coordination geometries, the steric demands of the 1,9-positions of the dipyrrin force the two dipyrrinato units out of plane, creating a helical twist in the ligand backbone. It

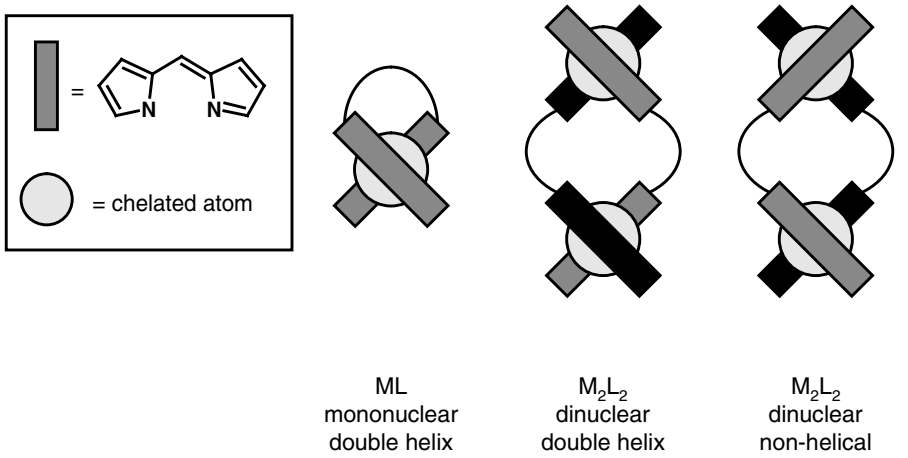

Figure 22. Helical conformation of metal complexes of bis(dipyrrin)s, adapted from Ref. 65.

has been demonstrated that these complexes can be formed stereoselectively,[21,172] as discussed in Section 8.

As with dipyrrins themselves, bis(dipyrrin)s were originally synthesized for the intended use as precursors in the preparation of macrocyclic tetrapyrroles,[173–189] and also of strapped porphyrins.[190] An account of the syntheses of palladium(II) complexes of 1,12-bis(dipyrrin)s was reported by Fisher and Stachel in 1939,[173] work that was reproduced 20 years later, showing that these complexes could be used to prepare oxacorrole palladium(II) complexes by oxidative cyclization.[174] Further investigations demonstrated the utility of nickel(II) complexes of bis(dipyrrin)s for the synthesis of tetrahydrocorrins and corroles.[182–186] It was during these studies that it was first noted how a combination of factors including reaction conditions, the nature of the coordinated metal ion, and the structure of the bis(dipyrrin) ligand affected the shape and size of the metal complex formed.[185,186,191,192]

As an example, bis(dipyrrin) ligand **23** (Figure 23) has been shown to form dimeric complexes **24a**, **b** when the metalation reactions were conducted in methanol with cobalt(II) or zinc(II) ions. However, monomeric complexes **25a**, **b** were formed with nickel(II) and copper(II) favoring the formation of mononuclear complexation products under these conditions.[191,192] A similar bis(dipyrrin) ligand had been shown to form monomeric complexation products with cobalt(II) when metalation was conducted in ethanol, but dimeric products when the reaction was conducted in methanol.[185,186] Triple-stranded helicates and mesocates (non-chiral) have been obtained using the same bis(dipyrrinato) ligand and cobalt(III) and iron(III), i.e. both forms isolated from the same reaction mixture.[193]

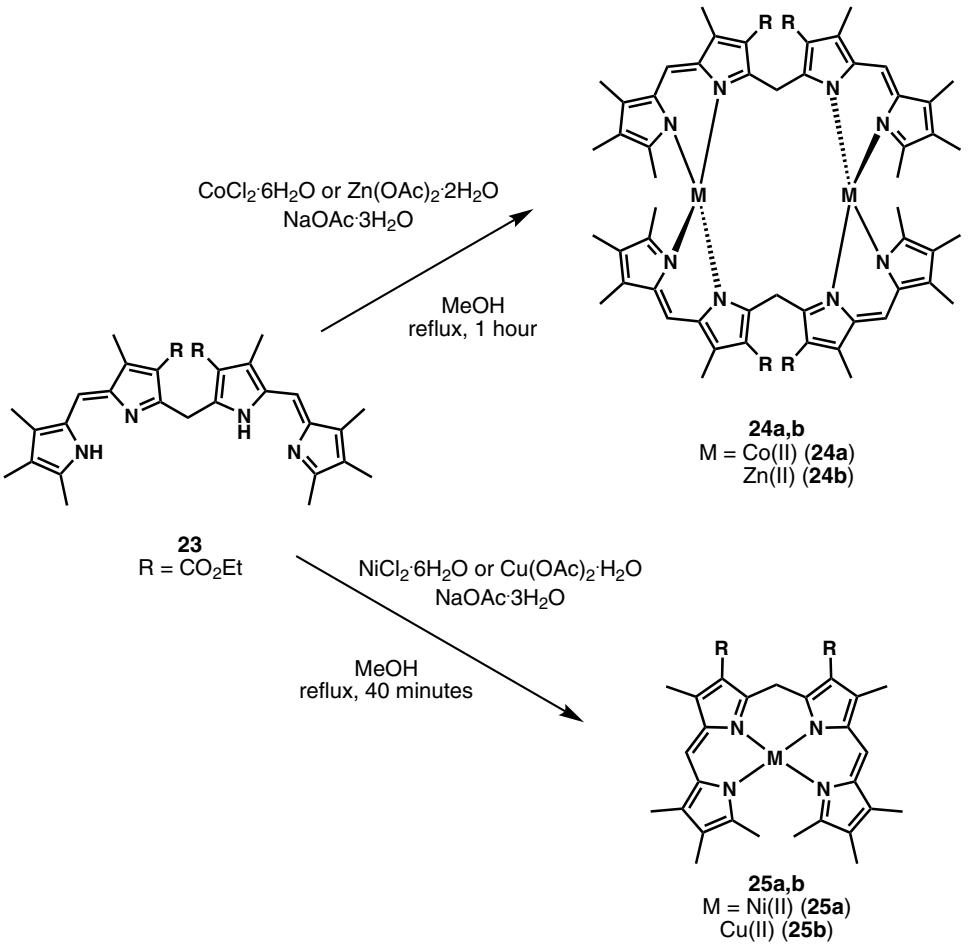

Figure 23. Dependence of bis(dipyrrin) complexation product upon reaction conditions.

It has further been shown that steric demands of the 1,9-substituents[20,194] affect the helicity of bis(dipyrrin) complexes, and that the points of connection between the two dipyrrin units, and the number of degrees of freedom in the tether, have an impact upon the metal-to-ligand ratio of the complexation products.[195–201] The demonstrated ability to influence the shape of bis(dipyrrin) metal complexes has created interest in their use to demonstrate metal-ion assisted self-assembly, and in their potential as supramolecular building blocks.[108,202] The solid state structures of a number of 1:1, and 2:2 metal ion-to-bis(dipyrrin) complexes have been reported, as well as the solid-state structures of a 3:3 zinc(II):1,1′-bis(dipyrrin) molecular triangle[196] and a zinc(II) 1,2′-bis(dipyrrinato) molecular rectangle.[203]

b. *Metal-organic frameworks (MOFs)*

Tris(dipyrrinato) iron(III), cobalt(III), indium(III), and gallium(III) complexes of 5-(4-pyridyl)dipyrrin self-assemble into heterobimetallic metal-organic frameworks[204] in the presence of silver(I) salts.[34,80,81] X-Ray crystallography reveals that each silver(I) ion is coordinated to three pyridyl ligands in the extended framework generating two dimensional (6,3) networks (Schläfli symbol 6^3, vertex symbol $6\cdot6\cdot6$) or three dimensional (10,3) networks (Schläfli symbol 10^3, vertex symbol $10_2\cdot10_4\cdot10_4$),[205] depending on the choice of silver salt (Figure 24).[34,81] MOFs prepared with AgOTf reliably formed three-dimensional (10,3) networks, whereas the use of $AgSbF_6$ produced two-dimensional (6,3) honeycomb-like networks. In the two-dimensional networks each silver(I) ion is coordinated to three different dipyrrinato complexes (through intermolecular interactions with substituents at the 5-position) and also coordinated by a solvent molecule (e.g. MeCN) rather than the SbF_6^- anion. On the other hand, the use of $AgPF_6$ gave two-dimensional networks with tris(dipyrrinato) iron(III) and cobalt(III) complexes and three-dimensional networks with tris(dipyrrinato) indium(III) and gallium(III) complexes. Networks prepared with salts of $AgBF_4$ reliably formed three-dimensional (10,3) networks with iron(III) or cobalt(III) complexes. The use of larger metalloligands such as cobalt(III) tris[5-(4-[pyridin-4-ethynyl]phenyl)dipyrrinato] and iron(III) tris[5-(4-quinolynyl)dipyrrinato] overrode the anion templating effect, and this is consistent with analogous organic systems.[34,81] Given their facile synthesis, the use of dipyrrinato ligands within such networks allows the possibility to tune optical, magnetic, and fluorescence properties within the framework, as well as to develop porous materials with interesting photophysical properties.

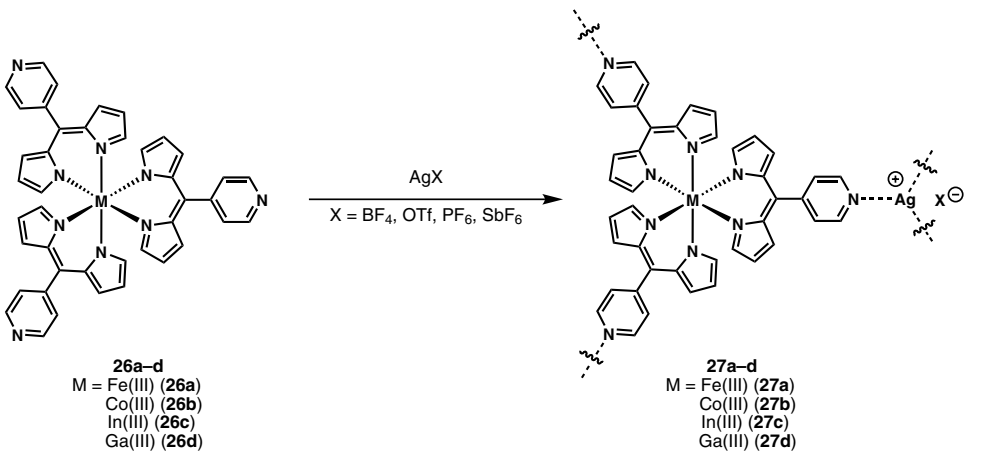

Figure 24. Synthesis of M(III)[5-(4-pyridyl)dipyrrinato]$_3$AgX metal-organic frameworks (MOFs).

Furthermore, the octahedral coordination geometry of central metal ions provides an opportunity to create homochiral extended solids.[81] Carboxylate-functionalized tris(dipyrrinato) *rac*-cobalt(III) complexes generated two-dimensional and three-dimensional MOFs with infinite and trinuclear zinc(II) secondary-building units.[77] However, under identical reaction conditions enantiopure metalloligands produced amorphous solids.[77]

Dipyrrins bearing suitable heterocyclic systems at the 5-position are also capable of non-covalent interactions such as hydrogen bonding (Figure 25) and metal coordination in the neutral and/or deprotonated forms.[87,88] This strategy for preparing extended networks of various types has seen extensive development, and now dipyrrins with additional coordinated functional groups at the 5-position are routinely used for the preparation of metallotectons, metallamacrocycles, and heterometallic MOFs.[81,88]

Tectons are molecular subunits that engage in multiple reliable directional intermolecular interactions as supramolecular synthons and can therefore serve as building blocks for the rational construction of crystals and material in the solid state. Enantiomerically pure and racemic cobalt(III) tris(dipyrrinato) complexes bearing three trigonally directed substituents such as aryl-CO_2H and diaminotriazinyl (DAT) groups in the 5-position, compounds **30a** and **b** in Figure 26, are able to generate molecular networks, building through hydrogen bonding within the metallotectons.[107,206] In essence, the complexed dipyrrinato units assemble via an

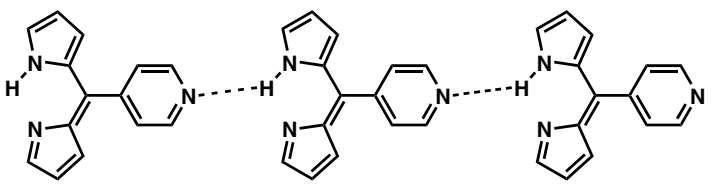

28

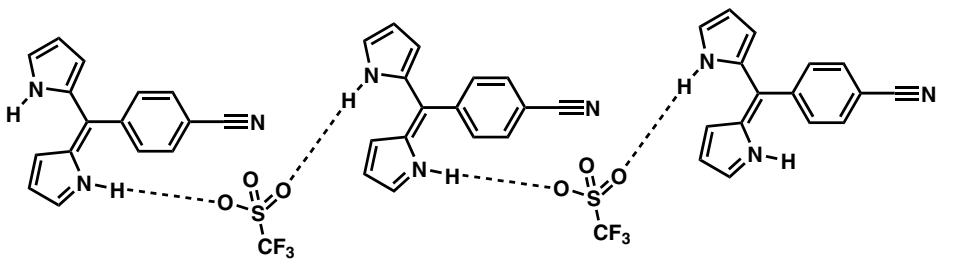

29

Figure 25. Hydrogen-bonded networks of substituted dipyrrins.

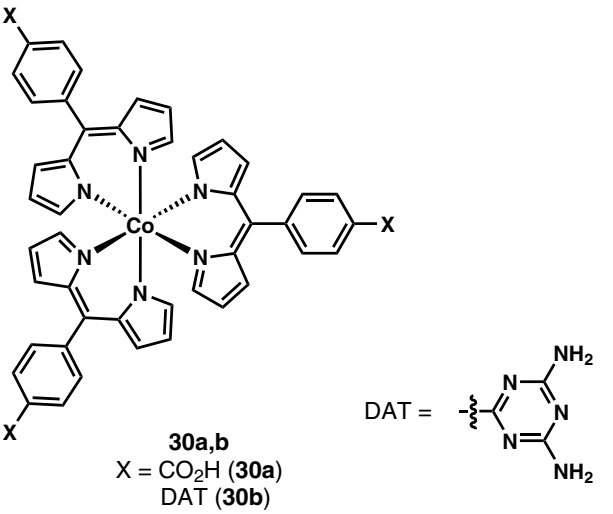

Figure 26. Intermolecular hydrogen bonding involving CO_2H and DAT groups in metallotectons.

additional mode of bonding, through intermolecular interactions such as hydrogen bonding at moieties peripheral to the dipyrrinato heterocyclic core. In general, but not always, crystalline complexes of the enantiomerically pure form pack less efficiently than their racemic counterparts, and the crystallization of racemic mixtures tends to produce racemic crystals rather than conglomerates of crystals composed of single enantiomers.[206] Metallotectons formed via the intermolecular interactions of carboxyl groups apparently prefer to adopt one-dimensional zig-zag chains through intertectonic hydrogen bonding, whereas those involving DAT groups are hydrogen bonded to three neighbors with each DAT group participating in four hydrogen bonds, and thus generating highly porous and robust networks.[107,206]

Mono- and dicyanophenyl substituted homo- and heteroleptic zinc(II) and copper(II) dipyrrinato metalloligands combined with silver salts to generate Ag(I)–C=C double bond interactions with one- and two-dimensional networks.[87] Interestingly, 5-(4-cyanophenyl)dipyrrin free-base **31** combined with $AgBF_4$ to generate metallamacrocycle **32**, whereas the heteroleptic (salen) Co(III) dipyrrinato **33** complex formed metallamacrocycle **34** with $Ag(SbF_6)$ after slow evaporation from benzene and benzene/acetonitrile respectively (Figure 27).[88] The average distance for Ag–C bonds in these complexes was within the usual range for η^1 and η^2 arene–silver complexes (2.39–2.63 Å), and the complex was determined to be unsymmetrical with one Ag–C contact longer than the other.[87,88]

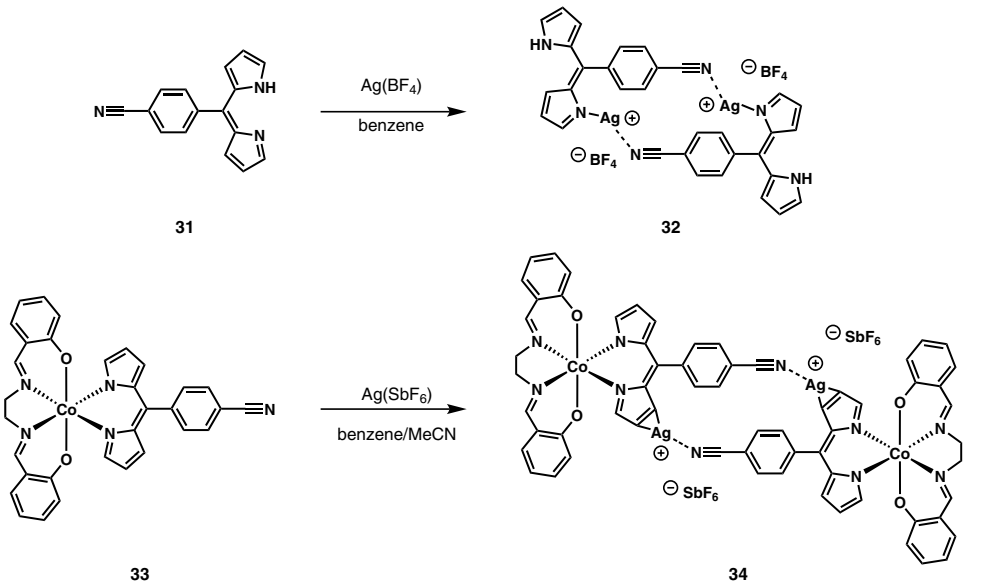

Figure 27. Formation of metallamacrocycles **32** and **34** using slow evaporation technique.[88]

Dipyrrins act as planar building blocks for self-assembled coordination oligomers in combination with various spacer units.[202] These interesting properties of dipyrrins make it possible to create well-defined micro- and nanometer-sized architectures of various shapes and sizes (Figure 28).[202,207] Another approach to linear short oligomeric chains of repeating dipyrrinato complexes involved the synthesis of a bis(dipyrrin) with one of the dipyrrin units complexed with BF_2.[208] Such capped bis(dipyrrin)s were then used as terminating units in oligomerization complexation reactions involving free-base bis(dipyrrin)s linked by an aryl group.

Dipyrrins with a catecholyl group attached to the 5-position (**35**) react with boron trichloride and produce self-assembled boron–dipyrrin macrocyclic oligomers of trimeric **36**, tetrameric **37**, and pentameric **38** nature (Figure 29).[137] The ^{11}B NMR spectrum of such oligomers showed a broad singlet at around 7.51 to 7.64 ppm, reflecting the formation of a tetrahedral boron complex with a 5-(catecholyl)dipyrrinato N_2O_2 ligand. Macrocycle **36**, having a cavity at the core of the molecule, can act as a supramolecular host with a binding site surrounded by oxygen atoms.[137] Thus, the introduction of K^+, Rb^+, and Cs^+ to complex **36** caused considerable spectral changes in the ^1H NMR spectra as a consequence of titration studies, and indicated the formation of 1:1 host:guest complexes. The Na^+ ion, with its ionic radius (0.97 Å) smaller than the radius of the cavity of complex **36** (1.4 Å), showed no interaction. The self-assembled square boron–dipyrrinato complex **37** generated one-dimensional channels filled with solvent molecules.[137]

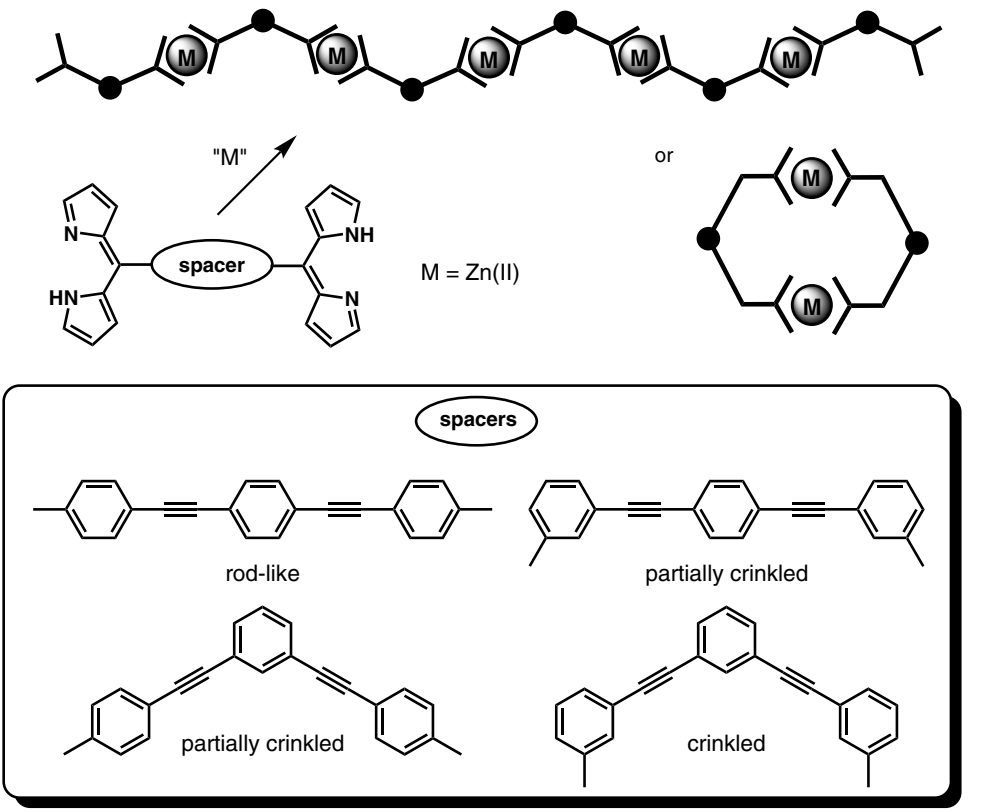

Figure 28. Formation of micro- and nanometer-sized architectures based on bis(dipyrrin)s with various spacer units, adapted from Ref. 207.

Heteroleptic dipyrrinato complexes have proven useful in the construction of extended networks and coordinative polymers. While homoleptic complexes of copper(II) were observed to form when 0.4 equivalents of copper(II) acetylacetonate was used in the complexation reaction,[113] heteroleptic complexes were more likely to be formed in the presence of stoichiometric, or excess, amounts of the metal salt, as expected. This coordination is responsible for the formation of many of the extended networks reported. For example, 5-(4-cyanophenyl)dipyrrin formed a discrete heteroleptic complex with copper(II) acetylacetonate but the 5-(4-pyridyl)dipyrrin heteroleptic complex formed a coordination polymer.

The discrete head-to-tail cyclic dimer **40** is formed upon reaction of one equivalent quantity of $Cu(hfacac)_2$ with two equivalents of 5-[3-(methylthio) phenyl]dipyrrin, formed *in situ* from the corresponding dipyrromethane (**39** in Figure 30).[78] The dimer is held together by two weak sulfur–copper(II) interactions between the thioether moiety of one dipyrrinato ligand and the copper(II)

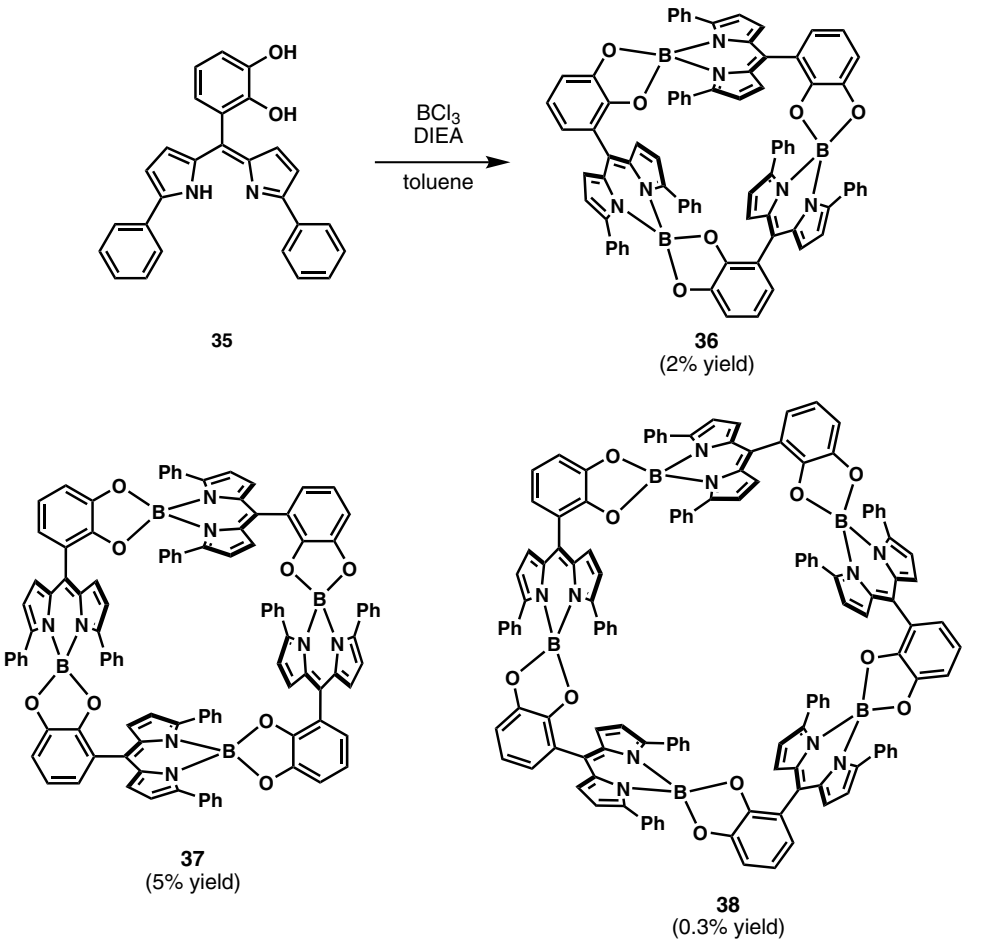

Figure 29. Synthesis of nano-porous materials based on boron–dipyrrin oligomers.[137]

center bound to the other dipyrrinato ligand. The isomeric dipyrrin **41** (Figure 30) gives extended helical copper(II) coordination polymers upon reaction with Cu(hfacac)$_2$, whereby the thioether moiety weakly binds to the axial position of a square pyramidal copper(II) center in a neighboring unit. The trifluoromethyl groups are oriented in the solid state with self-aggregation, reminiscent of phase-separation in fluoroalkanes. This interaction is extremely important to the stability of the polymer as complexation of copper(II) acetylacetonate with **41** gave a heteroleptic complex that decomposed during isolation to give the homoleptic dipyrrinato complex. Such disproportionation is common between solution and solid-state dipyrrin chemistry, and between pre- and post-work-up procedures.[159] Fluorine–fluorine interactions dominated the tendency of 5-quinolinyl substituted dipyrrins

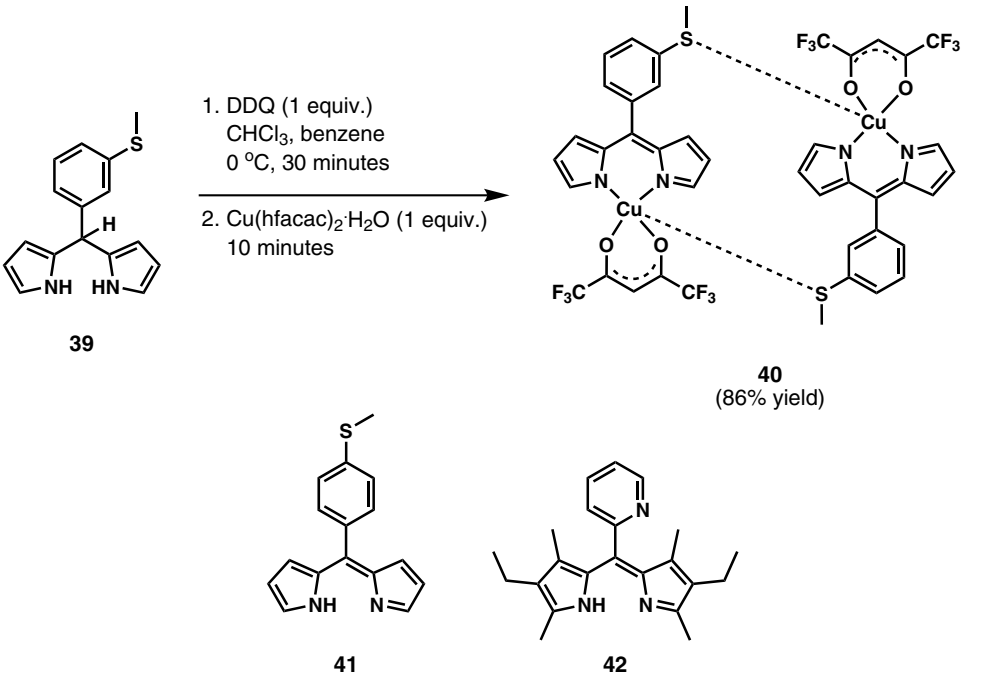

Figure 30. Heteroleptic head-to-tail copper(II) dipyrrinato(hfacac) complex dimer.[113]

to self-assemble into extended heteroleptic coordination polymers.[209] Another discrete heteroleptic head-to-tail cyclic dimer, $Zn_2(dipyrrinato)_2Cl_2$, was formed when 5-pyridyl substituted dipyrrin (**42**) was reacted with zinc(II) chloride. The dimer was found to be held together by each tetrahedral zinc(II) being coordinated to one bidentate dipyrrinato ligand and the pyridyl moiety of the other dipyrrinato ligand.[167]

This work has been extended to include dipyrrins substituted in the 5-position by aryl rings with appended 4-methanoate, 4-amido, and 4-nitro groups, and the magnetic and thermal properties of complexes formed from such ligands have been studied.[210] Upon the formation of square-planar heteroleptic complexes containing copper(II), the amido and nitro groups enabled the formation of polymeric chains in the solid state through hydrogen bonding and coordinative contacts, respectively. The ester functional group was used to immobilize a dipyrrin onto Wang resin, and subsequent reaction with stoichiometric amounts of copper(II) acetylacetonate gave immobilized heteroleptic Zn(dipyrrinato)(acac) complexes. An interesting feature of such immobilized complexes lies in the ability of the swollen polymer to react reversibly with pyridine.

In the quest for efficient light-harvesting systems and linear arrays capable of efficiently transferring the energy from absorbed photons through multiple

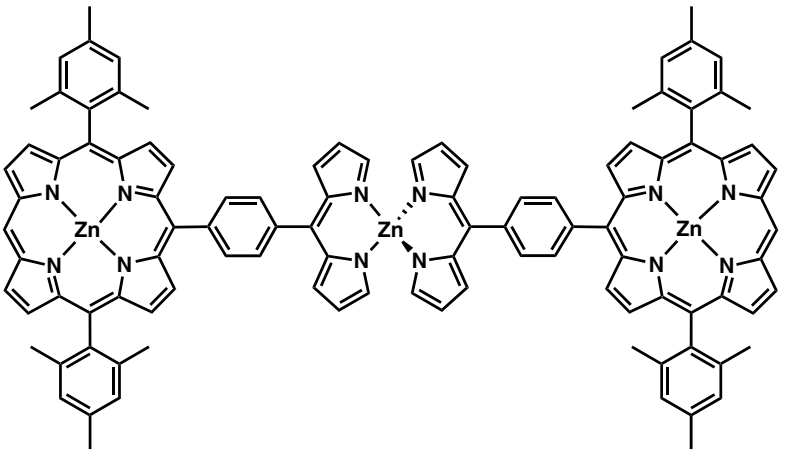

43

Figure 31. Porphyrin–zinc(II) dipyrrinato–porphyrin light-harvesting triad.

chromophores, dipyrrins have been used as auxiliary pigments and linkers in multiporphyrin structures. Typically, porphyrins have strong absorption profiles in the blue region but weak absorption throughout the rest of the visible spectrum limits their potential usefulness in light-harvesting arrays.[30] The incorporation of auxiliary pigments that absorb in complementary regions has the potential to increase the efficiency of the light-harvesting array in porphyrin–zinc(II) dipyrrinato–porphyrin triads such as **43** in Figure 31.[30] In essence, the dipyrrinato metal complex links the two porphyrin units together and simultaneously provides essential light-collection capabilities.

Fluorescence studies have indicated efficient energy transfer from the dipyrrinato moiety to the porphyrin, making such triads promising leads in the quest for efficient light-harvesting systems.[30] The ready self-assembly of homoleptic dipyrrinato complexes, and thus the linking role of the unit, renders such complexes advantageous over boron difluoride dipyrrinato complexes despite the longer excited-state decay of the latter. However, it is interesting to note that triads linked via dimeric dipyrrinato zinc(II) complexes were found to be unstable to silica, and decomposition to the corresponding free-base ensued.[30] Furthermore, it was postulated from results of electrochemical studies that oxidation of both porphyrin–zinc(II) dipyrrinato–porphyrin triads and homoleptic dipyrrinato zinc(II) complexes leads to demetalation.[30] One approach[30] used to prepare such triads involved the Suzuki coupling of 5-(4-iodophenyl)dipyrrinato palladium(II) and a porphyrin appended with a boronic-ester at a *meso*-position. Analogous arrays involve boron difluoride dipyrrinato–porphyrin–boron difluoride dipyrrinato triads such as **45a** (Figure 32), or the corresponding rhodium(I) complex **45b**.[211]

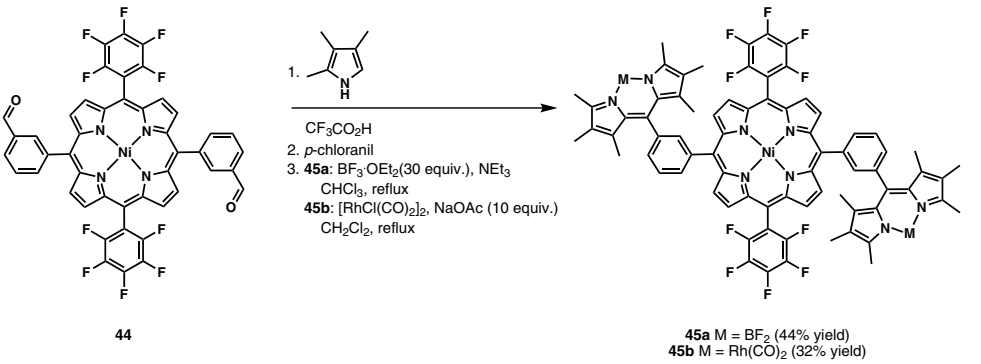

Figure 32. Dipyrrinato complex–porphyrin–dipyrrinato complex triad.[211]

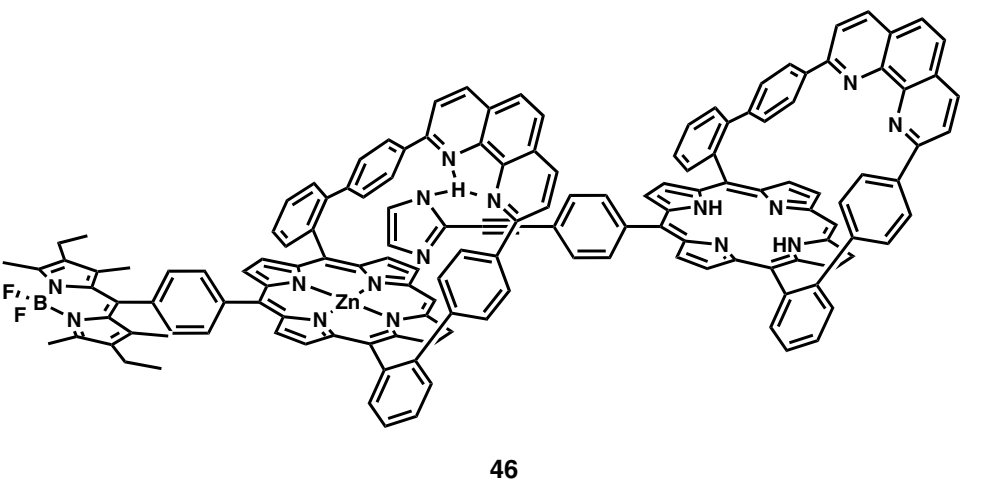

Figure 33. Boron difluoride dipyrrinato–porphyrin–porphyrin triad.[212]

A system involving a boron difluoride dipyrrinato–porphyrin–porphyrin architecture, **46** in Figure 33, was reported as a suitable building block for incorporation into light-harvesting arrays designed as linear coordination polymers.[212] Self-assembly of this system resulted from the affinity of imidazole for zinc(II) porphyrins, and so an imidazole-appended porphyrin and a boron difluoride dipyrrinato complex-appended zinc(II) porphyrin strapped with a phenanthroline unit were brought into close proximity. The boron difluoride dipyrrinato moiety absorbs energy that efficiently migrates to the porphyrin units. This self-assembled approach to light-harvesting arrays presents an attractive synthetic alternative to the use of covalent bonds to link appropriate absorbers and emitters. During attempts to form corroles, a phlorin–dipyrrin conjugate was isolated as a low-yield

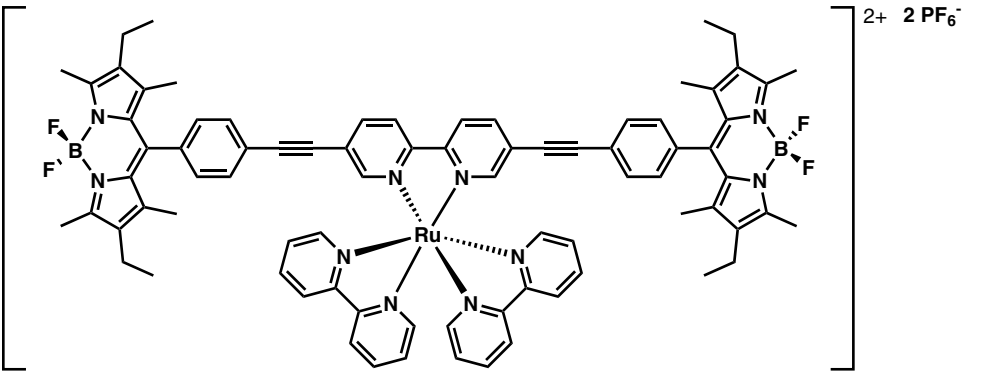

47

Figure 34. Boron difluoride dipyrrinato–ruthenium(II)tris(bipyridyl) multichromophoric system.

side-product from the condensation/oxidation of perfluorinated benzaldehyde and 5-mesityldipyrrin.[213]

Multichromophoric systems containing ruthenium(II) tris(bipyridyl) complexes and boron difluoride dipyrrinato units (Figure 34) allow electron-rich metal centers, effective energy absorbing dipyrrinato complexes and electron-accepting bipyridyl ligands to be united in a single structure (**47**).[169] The twisted nature of the structure, courtesy of methyl substituents on the dipyrrinato units, renders the dipyrrinato and bipyridyl chromophores non-planar and so conjugation of the two is prevented. In addition to efficient intercomponent energy transfer processes and rich reversible redox behavior, the complexes exhibit phosphorescence assigned to the boron difluoride dipyrrinato units. The latter is believed to be an effective decay process due to the presence of the heavy ruthenium(II) center surrounded by bipyridyl ligands.

7. *Chemical Manipulations of Dipyrrinato Complexes*

Chemical transformations to produce elaboration or diversification of dipyrrin structures are rarely performed using dipyrrins in their free-base or salt form.[82,154] Typically, these transformations are performed on the synthetic precursors to dipyrrins, or on dipyrrinato complexes. These compounds are frequently more stable and easier to isolate than the dipyrrin free-bases and salts. The complexes have an added advantage during purification, being generally less polar, more visible, and less prone to streaking during chromatography. Manipulations of functional groups on the 5-aryl substituents of dipyrrins are employed most frequently. This provides minimal disruption to the electronic environment of the binding unit of

the dipyrrinato ligand and capitalizes on the diversity of substituted aromatic aldehydes readily available for use in dipyrrin synthesis. There are an ever-increasing variety of reactions that are being performed using dipyrrinato complexes as substrates. The only apparent limitation is the requisite avoidance of strongly acidic and/or reductive conditions so as to prevent demetalation of the dipyrrinato complex, as discussed in Section II.A.5.

There are many examples of dipyrrinato complexes successfully used as reactants in metal-catalyzed cross-coupling reactions. One article describes the use of a boron difluoride dipyrrinato complex bearing an alkene attached by an alkyl tether as a successful substrate for an alkene cross-metathesis reaction catalyzed by Grubbs' second generation catalyst.[148] The Sonagashira reaction, or modifications thereof, has found particular success in application to coupling dipyrrinato complexes.[19,49,50,79,146,214–219] This reaction can be used to substitute both positions on the 5-aryl ring substituents and on the rings of the dipyrrin. Macromolecular light-harvesting arrays are commonly prepared by the coupling of boron difluoride dipyrrinato units with porphyrins by means of the Sonagashira reaction.[215,216] A cautionary note was provided in a report demonstrating that palladium-catalyzed Suzuki couplings are poisoned by free-base dipyrrins and zinc(II) and copper(II) complexes of dipyrrins, and this was attributed to the sequestration of palladium from the catalyst.[30] The corresponding palladium(II) dipyrrinato complex **48** is compatible with Suzuki coupling as shown in Figure 35, a method used for the synthesis of the porphyrin–zinc(II) dipyrrinato–porphyrin triad **50**.[30]

Dipyrrinato complexes have proven amenable to a variety of substitution reactions both via aromatic substitution at positions on the dipyrrin unit or otherwise on appended groups. The first reported substitution reaction of metal dipyrrinato complexes was the sulfonation of boron difluoride dipyrrinato complexes for the preparation of water-soluble fluorescent probes and laser dyes, as shown in Figure 36.[220,221] The increased nucleophilicity of the 2,8-positions over the 5-position of complex **51** results in selective substitution to give disulfonate **52** in acceptable yields. Recent investigations into the sulfonation of similar boron difluoride dipyrrinato complexes by this method noted that considerable experimentation was required to elucidate the optimal conditions for isolating high yields of pure sodium sulfonate salt products.[143]

In a rare example of a chemical transformation performed upon a free-base dipyrrin, as opposed to a dipyrrinato complex, 5-aryl-1,9-unsubstituted dipyrrins have been shown to undergo metal-mediated alkoxy monosubstitution using several different examples of alcohols.[82] The partially optimized reaction conditions showed that an oxidant, such as DDQ, was necessary for the alkoxy substitution to occur, and that product yields were highest when weakly- or noncoordinating solvents were employed.[82] In the presence of an oxidant, such as ammonium

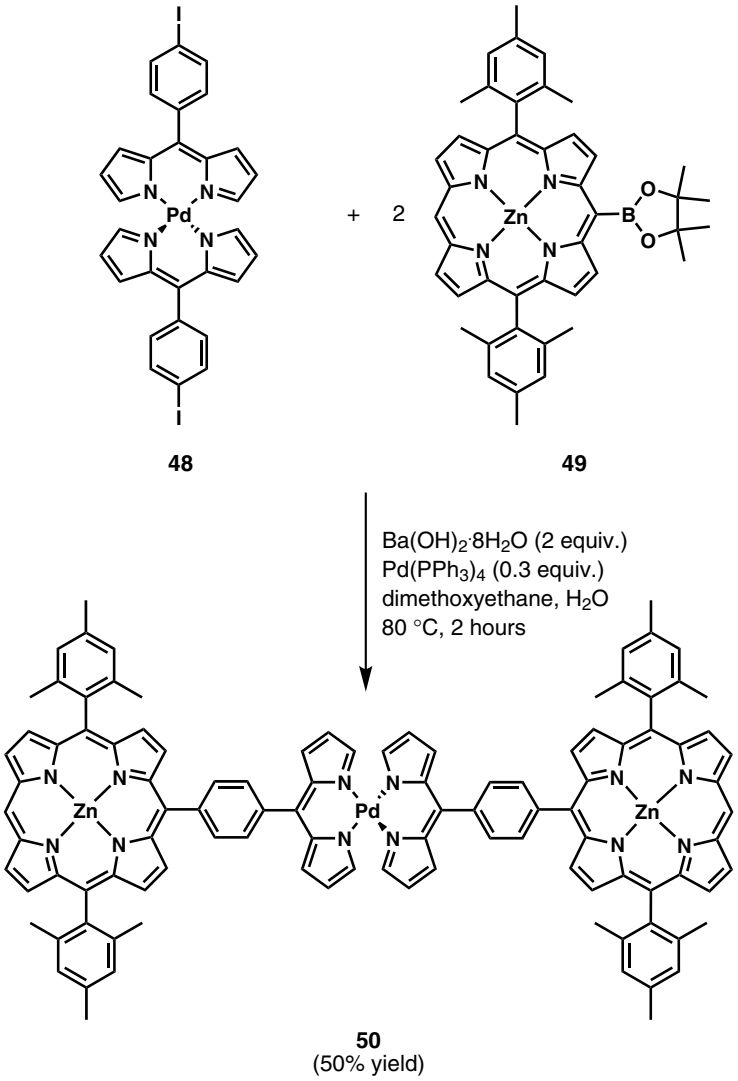

Figure 35. Suzuki cross-coupling reaction involving a palladium(II)dipyrrinato complex.[30]

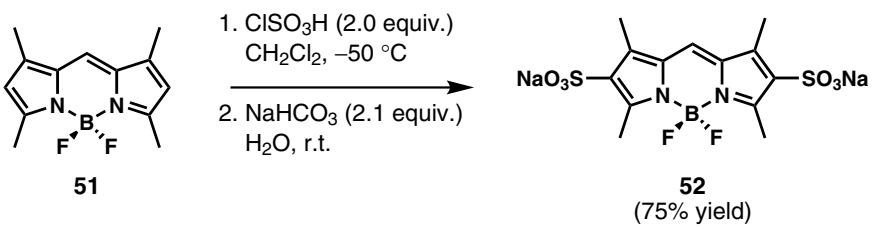

Figure 36. Sulfonation of dipyrrinato complex.

cerium(IV) nitrate (CAN), and a 2-unsubstituted pyrrole, a nickel(II) bis(dipyrrin) complex was found to undergo pyrrole exchange and pyrrylation at the newly formed 5-position.[20] Unsubstituted positions on the pyrrolic rings of boron difluoride dipyrrinato substrates have been successfully shown to undergo halogenation with bromine[153] and iodine.[222] However, 1,9-dichlorodipyrrinato complexes have previously been prepared from the corresponding dichlorodipyrromethane.[133] Additionally, a study demonstrating bromination reactions illustrated the regioselectivity of this reaction wherein the first equivalent of bromine yielded a tentatively assigned 1,9-dibromodipyrrinato complex, followed by the second and third equivalent adding at the 2,8-positions to yield a cleanly isolable tetrabromo product and a 1,2,3,7,8,9-hexabromodipyrrinato product, respectively.[153] These halogen-substituted dipyrrinato complexes can undergo subsequent substitution of the halogen substituents by nucleophiles such as cyanide, sulfides, and various amines.[133] A 5-thiomethyl-dipyrrinato boron difluoride complex, an example of an unusual 5-heteroatom-substituted dipyrrin, is known to undergo substitution of the thiomethyl substituent with aniline to yield the corresponding 5-anilino-dipyrrinato complex.[131] Based upon the absorbance spectrum and its non-fluorescence, the structure of this 5-aniline-substituted dipyrrinato ligand is thought to be more closely represented as an *N*-phenyl-dipyrrolic iminium species.[131]

Other examples of substitution reactions include those in which the derivatization transformation occurs at a substituent on the dipyrrin ring. Reports in the literature have described the esterification of a hydroxy substituent on a dipyrrinato complex with an acrylate group, for subsequent polymerization reactions,[223] and the substitution of the chlorine in a 5-chloromethyl-dipyrrinato complex with dipicolylamine to form a tertiary amine.[224] Motivated partly by the popularity of fluorescent biomarkers, it has been demonstrated that boron difluoride dipyrrinato complexes are compatible for use with the amide coupling reagent 2-chloro-4,6-dimethoxy-1,3,5-triazine (CDMT)[225] and carbodiimide reagents such as *N,N′*-dicyclohexylcarbodiimide (DCC).[132,226]

Manipulations of functional groups on 5-aryl substituents of complexed dipyrrinato ligands are also known: for example, hydroxy groups on 5-phenol substituted dipyrrins undergo alkylation.[154] Boron difluoride dipyrrinato complexes are amenable to tetrakis(triphenylphosphine) palladium(0)-mediated deprotection of allyl-protected hydroxy substituents on 5-aryl substituents.[145] The hydrogenation of the nitro-group of 5-(4-nitrophenyl)dipyrrin complexes to yield 5-(4-aminophenyl) dipyrrin complexes is a particularly useful transformation (Figure 37).[51,76,225] It has been demonstrated that primary amino groups present on 5-aryl substituents of dipyrrinato complexes can be transformed into azide groups[143] or, quantitatively, into isocyanate or isothiocyanate groups which can subsequently undergo transformations to give ureas and thioureas respectively by reaction with amines.[51,135]

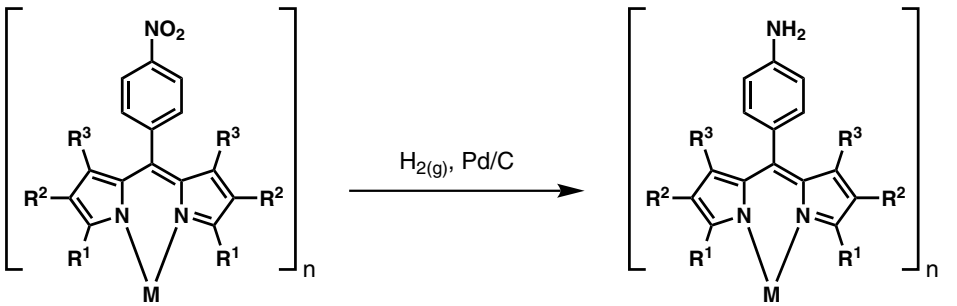

Figure 37. Derivatization of 5-substituted amino-aromatic dipyrrinato complexes.

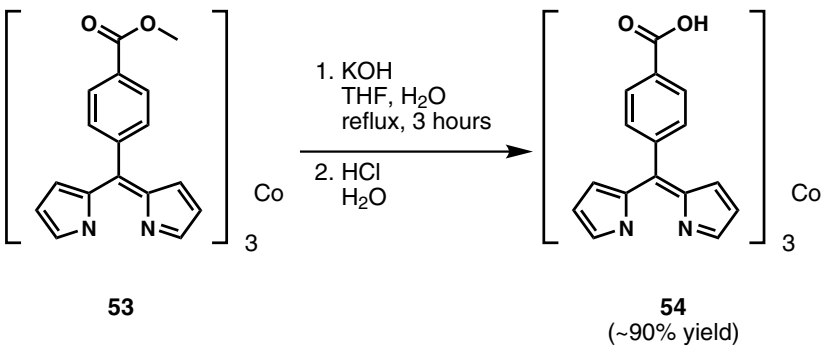

Figure 38. Derivatization of 5-substituted carboxy-aromatic dipyrrinato complexes.[76]

The azide products have been shown to successfully participate in copper-mediated azide–alkyne cycloaddition reactions, the so-called "click" reactions.[143,150] In addition, diamino-substituted 5-aryl substituents can be transformed into polyimine derivatives.[51]

In an interesting demonstration of the ability to perform manipulations of the functional groups present in dipyrrinato metal complexes, the methyl ester of **53** (Figure 38) was saponified and then reformed through a series of organic procedures.[76] Further functional group interconversions performed using the optically pure Δ and Λ enantiomers of cobalt(III) complex **54** showed that the carboxamide derivative could be dehydrated to give the cyano derivative, which could be transformed into the diaminotriazine derivative by reaction with dicyandiamide and potassium hydroxide without any loss of stereochemical purity throughout the procedures.[107]

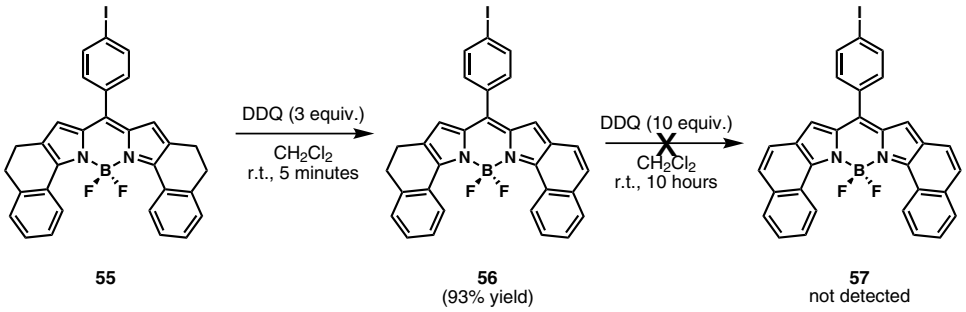

Figure 39. Dehydrogenation of dipyrrin substituents.[228]

Efforts to dehydrogenate rings attached to dipyrrins, in an attempt to increase conjugation to the dipyrrin rings, have not been very successful.[227,228] In one example, the attempted DDQ dehydrogenation of the methylene groups in compound **55** to prepare boron difluoride complex **57** resulted in **56**, in which only one side of **55** had undergone dehydrogenation (Figure 39).[228] Increasing the number of molar equivalents of DDQ failed to provide the desired product and increasing the temperature of the reaction resulted in decomposition of the starting material.[227] Computational modeling of the reaction revealed that the activation energy required to transform **56** to **57** was prohibitively high as a result of the strong steric interactions created between the hydrogen atoms of the aryl rings and the fluorine atoms when the dipyrrin ligand of the product is made planar upon dehydrogenation.[228] In a related example a symmetric dipyrrinato boron difluoride complex was reacted with 10 molar equivalents of DDQ in an attempt to dehydrogenate 1,2-butadiyl substituents and give a 1,2-butenyl product. However, an α-ketone derivative was the only product isolated.[227] This ketone product formed via a proposed mechanism of hydride abstraction, subsequent trapping of the carbocation with water, followed by oxidation.[227]

Oxidations of methyl groups on the dipyrrin rings of boron difluoride dipyrrinato complexes can be performed as shown in Figure 40.[223,227] In one example of this reaction, the 1-methyl group of the dipyrrinato complex **58** was oxidized to a formyl group using DDQ.[223] Hydrogenation of aldehyde **59**, catalyzed by palladium on activated charcoal, yielded the corresponding alcohol with the formation of two side-products: the formyldipyrromethane (with concomitant demetalation), and regenerated **58**.[223] Alternately, methyl substituents have been shown to undergo oxidation by lead(IV) tetra-acetate exemplified by the transformation of dipyrrinato complex **58** into **60**, a reaction traditionally used for the oxidation of α-methyl groups of pyrroles.[227]

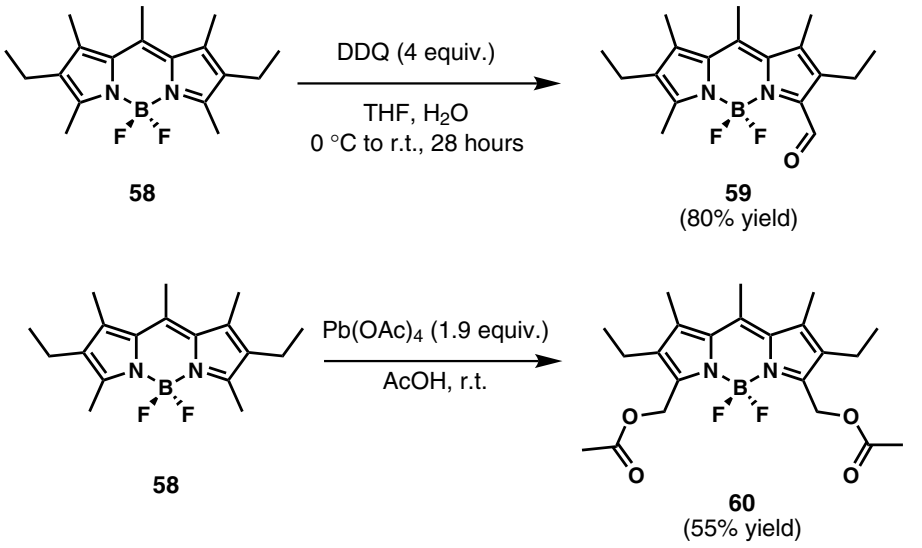

Figure 40. Examples of 1-methyl oxidations in dipyrrinato complexes.

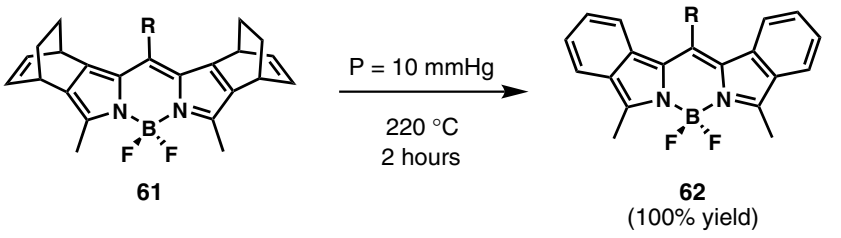

Figure 41. Retro Diels-Alder reaction performed upon a substituted boron difluoride dipyrrinato complex.

An examination of the sulfoxidation of 5-thienyldipyrrinato complexes showed a disparity between the boron difluoride complex in comparison to the corresponding iron(III), cobalt(III), nickel(II), and copper(II) complexes.[153] Under the conditions examined, namely titration to 100 equivalents of *m*CPBA in acetonitrile, a variety of boron difluoride derivatives cleanly undergo sulfoxidation of the 5-thienyl substituent. However, the iron(III), cobalt(III), and copper(II) complexes largely resist oxidation, while the nickel(II) complex undergoes extensive degradation, presumably due to oxidation of the metal center.[153]

A particularly unique example of the chemistry of dipyrrinato complexes is the retro Diels-Alder reaction to prepare the benzo-fused boron difluoride dipyrrinato product **62**, as shown in Figure 41.[229] The reactant dipyrrinato complex **61**

was prepared by condensing two equivalents of the corresponding tricyclic pyrrole precursor with one equivalent of an alkyl or aryl acid chloride. This was followed by boron complexation.[229]

Only a small fraction of the wealth of organic transformations is represented in this review of chemical reactions performed upon dipyrrinato complex substrates. There is much emphasis placed upon the manipulations of dipyrrinato complexes of boron difluoride in the literature. This undoubtedly stems from the great interest in modification of these complexes to fine-tune their optical properties, or to attach selective binding receptors. There remains a great opportunity to explore the potential diversity of chemical transformations of dipyrrinato complexes.

8. *Stereochemistry of Dipyrrinato Metal Complexes*

Due to their bidentate binding mode, dipyrrinato ligands have potential to form chiral homoleptic metal complexes with tetrahedral and octahedral coordination geometries. Tetrahedral homoleptic bis(dipyrrinato) complexes of unsymmetrical ligands are chiral as shown in Figure 42. Similarly, tetrahedral complexes of bis(dipyrrin) ligands (in which two dipyrrin units are attached by a linker) form *M* (left) and *P* (right) helical enantiomers. Octahedral homoleptic tris(dipyrrinato) complexes are propellor-shaped and therefore exhibit Λ and Δ chirality (Figure 42). Several

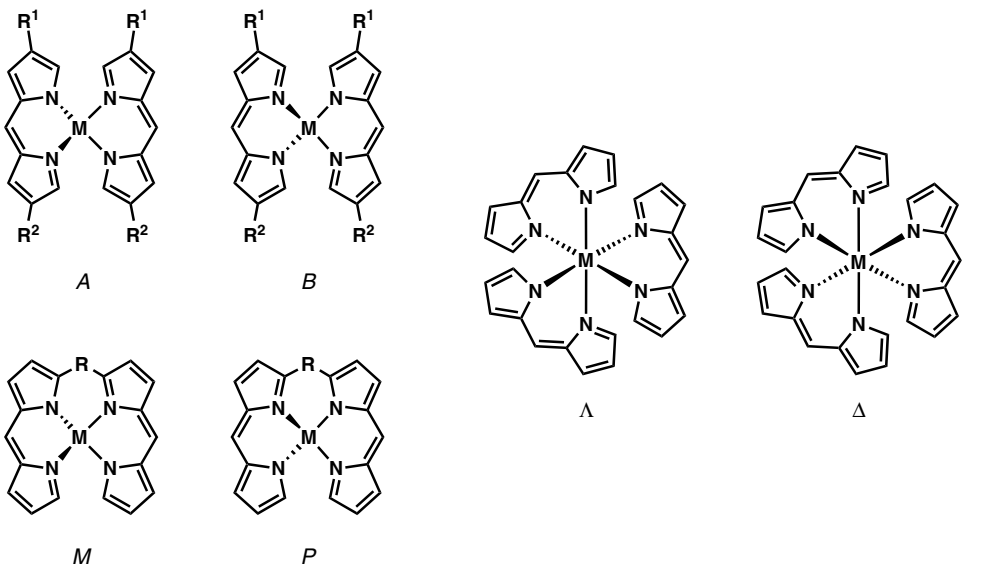

Figure 42. Chiral tetrahedral and octahedral dipyrrinato complexes.

studies have shown that optically pure dipyrrinato complexes are stable to racemization.[203] Enantiopure cobalt(III) tris(dipyrrinato) complexes were subjected to reaction conditions for further chemical manipulation of functional groups on the ligand with no observed loss of stereochemical purity.[107,172,230,231]

In the absence of any chiral influence the dipyrrinato metal complexes described above form as racemic mixtures of enantiomers. There has been a great deal of research interest focused on the preparation of optically pure dipyrrinato metal complexes either by resolving racemates, or by chiral templating and chiral induction during synthesis. Several examples have been reported of the successful resolution of *M* and *P* helical bis(dipyrrinato) complexes achieved using HPLC and a chiral stationary phase.[21,172,194,230] The precipitation of diastereomeric salts formed with (−)-cinchonidine has been demonstrated as a method to resolve the Λ and Δ enantiomers of tris[5-(4-carboxyphenyl)dipyrrinato] cobalt(III).[107]

High levels of stereoselectivity have been reported for the preparation of metal complexes of chiral-templated dipyrrinato ligands.[107] Characterization using HPLC, ^{1}H NMR spectroscopy, circular dichroism, and X-ray structure analysis supported the formation of a helical zinc(II) complex of a homochiral binol-linked bis(dipyrrinato) ligand with a diastereomeric ratio of > 99:1.[21,172] It has been shown that the stereoselectivity of the complexation process, as well as the ratio of ligand to metal ions, and the degree of helicity of the formed complex is influenced by structural features of the bis(dipyrrin) ligand such as the degrees of freedom provided by the linker group, and the points of connection, that is to say 2,2′- versus 3,3′-connection.[232] The use of chiral reagents to induce stereoselective dipyrrinato complex formation has shown some success.[21,194] In some examples distant point chiral auxiliaries substituted on a dipyrrinato ligand achieved small amounts of diastereoselectivity during zinc(II) complexation.[114,231,234] In another example, the use of copper(II) salts of either enantiopure *R*- or *S*-mandelic acid were shown to induce a modest degree of stereoselectivity in the formation of helical copper(II) complexes of dipyrrin-containing cyclooctapyrroles.[233] The same report demonstrated that diastereoselectivity for the formation of complexes of these cyclooctapyrroles from copper(II) chloride could be induced through the use of *R*-α-methylbenzylamine as an enantiopure base.[233] An interesting report described the preparation of metal-coordinated macrocycles from the phenylethynyl-linked bis(dipyrrin) ligand **63** as seen in Figure 43.[202] The space within the macrocycle cavity is large enough to allow rotation of the zinc(II) bis(dipyrrinato) units, resulting in the transition between chiral (ΔΔ- and ΛΛ-**64**) and achiral (*meso*) isomers.

Despite the popularity of BODIPY compounds, the synthesis of chiral boron difluoride dipyrrinato complexes is a relatively unexplored area of research.[155] Enantiopure atropisomeric binaphthyl auxiliaries attached through the 5-position

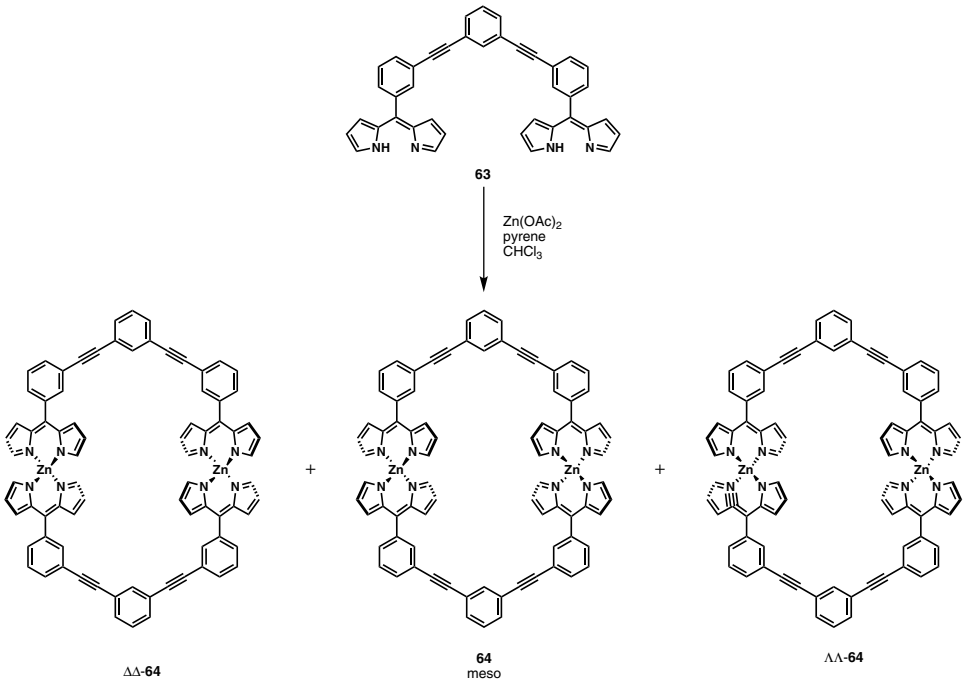

Figure 43. Preparation of achiral and chiral zinc(II) bis(dipyrrinato) complexes.

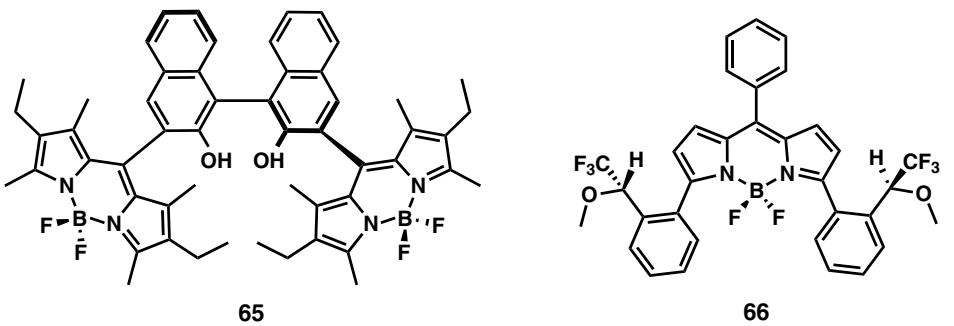

Figure 44. Chiral boron difluoride dipyrrinato complexes.

of the dipyrrinato ligand were the source of chirality in one boron difluoride complex, **65** in Figure 44.[236,237] Analysis of the rate of fluorescence quenching of the chiral boron difluoride dipyrrinato complex **65** by amines revealed differential quenching by enantiomers of chiral amines.[236,237] It was proposed that the observed differential quenching rates could be exploited for chiral discriminations. In another report regarding chiral boron difluoride dipyrrinato complexes such as **66**

in Figure 44, aryl substituents bearing a stereogenic center serve as the source of chirality at either the 5- or the 1,9-positions of the dipyrrinato ligand.[238]

B. Properties and Reactions of Dipyrrinato Complexes

The steric interactions between 1,9-substituents of dipyrrins,[99] even substituents as small as hydrogen atoms, were found to distort the geometry of coordination about the metal ions, as discussed in Section II.A.1. Even those metal(II) ions that usually prefer square planar coordination geometry were found to adopt pseudo-tetrahedral coordination geometry with dipyrrinato ligands.[239,240] These observations prompted the study of conductivities,[241] magnetic susceptibility,[94,96,102,105] ligand field parameters,[94,104,110] X-ray crystal structures,[92,105,122,239,240] and spectroscopic behavior from absorption spectra,[91,94,96,102–106,110,115,122] X-ray powder spectra,[102,106] IR spectra,[91,94,96,103,104,106,115] ^{1}H NMR spectra,[91,105,115,121,122,242] and ESR spectra[106,112] for a wide variety of dipyrrinato metal complexes, as previously summarized.[24]

The complexation of dipyrrinato ligands has recently been studied using absorption spectroscopy, calorimetry, and ^{1}H NMR spectroscopy. All revealed the intermediacy of heteroleptic dipyrrinato metal complexes in the complexation process to form homoleptic complexes as seen in Figure 45 and discussed in Section II.4.[159,243] Thermodynamic data such as equilibrium constants have been reported[55,157,244–246] for the complexation process, although the intermediate heteroleptic complexes were not accounted for in the calculations. More recent publications confirm the observation of the heteroleptic intermediates,[162,247] and reveal that the equilibria moves towards the formation of homoleptic dipyrrin complexes by alteration of factors such as basicity[243] and the coordination preferences of the metal salt anion.[162] For example, metal chlorides do not form heteroleptic dipyrrin complexes as readily as metal acetates, acetylacetonates or valinates.

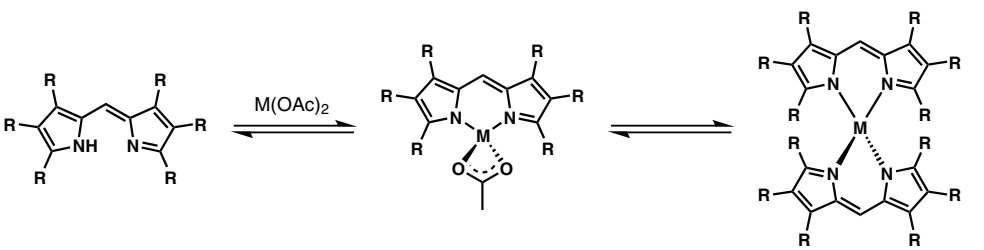

Figure 45. Formation of homoleptic dipyrrinato metal complexes through a heteroleptic intermediate.

1. *Fluorescent Dipyrrinato Metal Complexes*

Dipyrrinato complexes of BF_2 (BODIPYs) are strongly fluorescent, having a high fluorescence quantum yield, whereas the corresponding dipyrrin free-bases are generally not strongly fluorescent (with some exceptions). BODIPYs are currently in the midst of a substituent revival, with the fluoride substituents on the boron atom being replaced by a number of alternative substituents. The chemistry of BODIPYs is not extensively covered in the current chapter, but some select examples are included here as they exemplify the ability of the dipyrrinato ligand to support the boron atom as it is cajoled into compromising bonding environments. In one case,[70] a borenium cation was generated through mono-fluoride extraction of a BODIPY (**67** in Figure 46) using the triethylsilylium ion. The stabilization of the planar three-coordinate borenium ion usually requires a bulky ligand set, yet the dipyrrinato ligand and a single fluoro ligand were able to effect such stabilization in this case. A borenium hydride, **69**, was subsequently prepared via treatment with DIBAL-H, and the hydride was then converted into the corresponding tetrahedrally coordinated boronium ion, **70**, through treatment with DMAP. The incorporation of a dipyrrinato ligand into a sensor for fluoride ions through the use of boronium ions has also been reported, again exploiting the excellent capacity

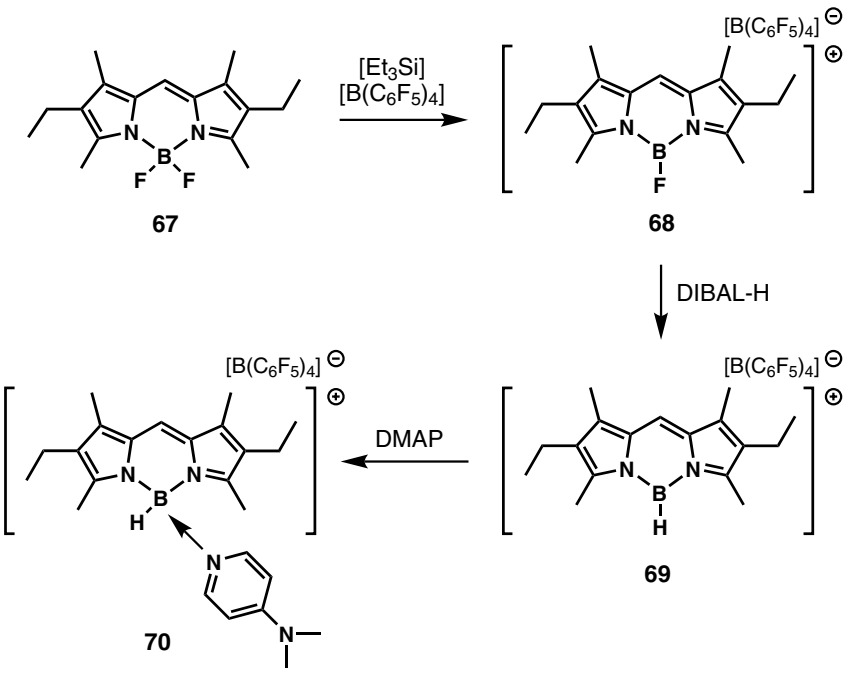

Figure 46. Generation of borenium cations from BODIPY dyes.[70]

of the dipyrrinato ligand to support novel bonding environments for the boron atom.[249] Perfluoroaryl-substituted BODIPYs have also been reported, whereby the boron atom was coordinated to one or two perfluorophenyl groups or a perfluorodiphenyl moiety. Borenium ions were generated via fluoride abstraction from a complex with one perfluorophenyl and one fluoro substituent on the boron atom.[248]

Although it was traditionally believed that homoleptic dipyrrinato metal complexes were nonfluorescent, it was reported that the zinc(II) dipyrrinato complex **71** in Figure 47, bearing a mesityl substituent at the 5-position of the dipyrrinato unit, is highly fluorescent.[116] Furthermore, 5-phenyl and 5-(4-*tert*-butylphenyl) substitution results in very weak emitters, as seen for **72a** and **b**. Presumably the 2,6-methyl groups of the mesityl group within **71** prohibit internal rotation, and so dramatically enhance the excited-state lifetime of complexes involving 5-mesityldipyrrinato ligands. These types of emitting dipyrrinato complexes would be ideally suited to applications for which intense absorption and fluorescence attributes in the visible region are desirable. As dipyrrinato ligands facilitate self-assembly, they are also valuable synthetic linking tools for supramolecular chemistry applications (see Section II.A.6). Homoleptic gallium(III) and indium(III)

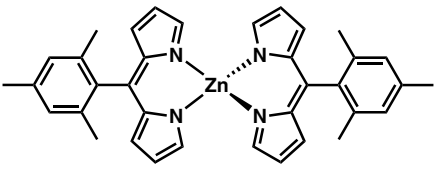

71
Fluorescence quantum yield (Φ_f) = 0.36 in toluene

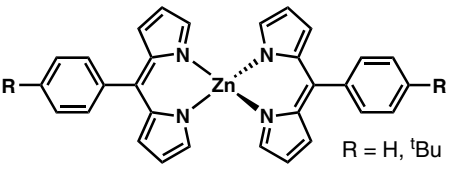

72a,**b**
Φ_f = ~0.006 in toluene

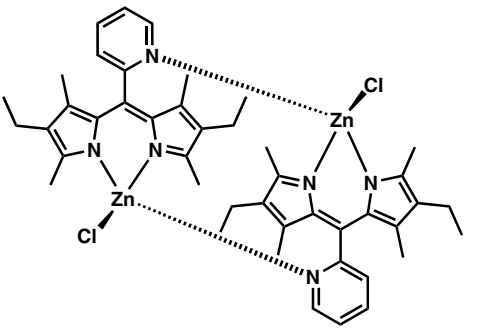

73
Φ_f = 0.057 in dichloromethane

Figure 47. Fluorescent and nonfluorescent zinc(II) dipyrrinato complexes.

analogs of **71** exhibit decreased levels of fluorescence.[84] Increased fluorescence as a result of inhibition of the rotation of an aryl group in the 5-position is also seen for a 5-(2-pyridyl)dipyrrinato ligand which forms a head-to-tail cyclic dimer, **73** in Figure 47, in the zinc(II) complex prepared using zinc(II) chloride.[167] The heteroleptic dimer contains two zinc(II) centers, two tridentate ligands and two coordinated chloride ions. The nitrogen atom of the pyridyl group satisfies tetrahedral zinc(II) coordination, and so rotation of the pyridyl group relative to the dipyrrinato unit is prohibited.

Bis-fullerenes coupled through a homoleptic dipyrrinato zinc motif have been reported.[250] In this case, dipyrrins appended with a substituent at the *meso*-position enabled the attachment of a fullerene. Coupling of such fullerene-appended dipyrrins via reaction with zinc(II) gave a bis(dipyrrinato) complex and thus brought together two fullerenes into the same molecule. The complex was studied for its fluoresence and energy-transfer properties, and was of special interest due to its two different constituent chromophores. A similar strategy using copper(II) was used to bring two 1,4-benzoquinine-containing triazoles into the same molecule.[251]

2. *Electrochemical Studies of Dipyrrinato Complexes*

Dipyrrins and their metal complexes exhibit intense ligand $\pi \rightarrow \pi^*$ transition afforded by electronic conjugation of the dipyrrinato system. Electrochemical studies of dipyrrinato complexes reveal consistent behavior for ligand-centered oxidations and reductions, although some variances due to molecular structure have been observed. The redox behavior of free-base dipyrrins is similar[128,230,252,253] to that of their protonated forms, although lower oxidation potentials are observed for the free-bases and this can be rationalized by the reduced electron availability in the protonated systems.[253] Of course, the electrochemical properties of dipyrrinato complexes also differ with respect to the nature and oxidation state of the complexed metal ion.[230,252,254] For dipyrrins with aryl substituents in the 5-position, the Hammett constants for the various aromatic substituents have been shown to directly correlate to the redox potentials of the corresponding nickel(II) dipyrrinato complex.[230]

Nickel(II),[230] copper(II),[252,254] and palladium(II)[254] complexes of 1,1′-bis(5-aryldipyrrin)s exhibit two reversible redox couples, although verification of the second reduction is sometimes limited by the electrolytic discharge limit.[230] Iron(III) complexes of 5-aryl dipyrrins display one quasi-reversible one-electron oxidation, with little variance upon the nature of aryl substituents at the 5-position.[75,79] The electronic absorptions for the heteroleptic iron complexes **74**, **75**, and **76** are observed in the range 460–518 nm, much like for their porphyrin congeners. Cyclic voltametry disclosed their fully reversible one electron $Fe^{III/II}$ redox

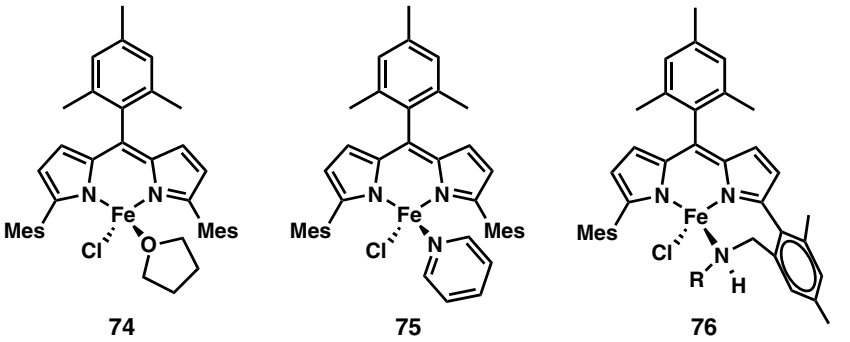

Figure 48. Heteroleptic iron–dipyrrinato complexes.

wave centered at –400 mV vs. an internal ferrocene reference (Figure 48).[39] The high-spin iron(II) dipyrrinato complexes **74** and **75** were reacted with organic azides ($R–N_3$) to expel nitrogen (N_2) and produce amination products (**76**), via C–H activation of a neighboring methyl group of an α-mesityl substituent, presumably induced by the Fe–dipyrrinato center.

Zinc(II) complexes of dipyrrins substituted with aryl groups at the 5-position undergo two highly irreversible one-electron oxidations,[30] the irreversibility having been attributed to demetalation of the complex upon formation of the mono- or dication.[30] The electrochemical behavior of BODIPYs[14,18,48,50,51,169,216,225,228,229,236,255–264] is often used to calculate HOMO–LUMO gaps for energy diagrams.[169,230] Generally, BODIPYs undergo one reversible one-electron oxidation, and one reversible one-electron reduction,[255] although scanning at more positive and negative potentials than are routinely used has revealed additional irreversible redox reactions.[256] Effecting increased conjugation by substitution with, for example, electron-donating groups has been found to stabilize the radical cation formed upon electrochemical oxidation and therefore make the oxidation potential of the corresponding substituted BODIPYs less positive. However, substitution with electron-withdrawing groups has been found to make the oxidation potential more positive.[49,51,145,169,259,260,265] Substituents with a higher HOMO energy level than the BODIPY unit diminish the fluorescence properties of BODIPYs (Figure 49).[145,152] Chemical modification of such substituents to give derivatives with a comparatively lower HOMO energy level would generate strongly fluorescent compounds. This strategy has been used as a probe for the detection of the oxidant hypochlorous acid (HOCl).[145]

The position at which groups conjugated to dipyrrins are situated has been shown to have little effect upon the redox potentials of BODIPYs.[18,265] For example, **77** and **78** (Figure 50) have essentially the same redox profile.[18] Some BODIPYs of dipyrrins substituted with pyridyl moieties at the 5-position have

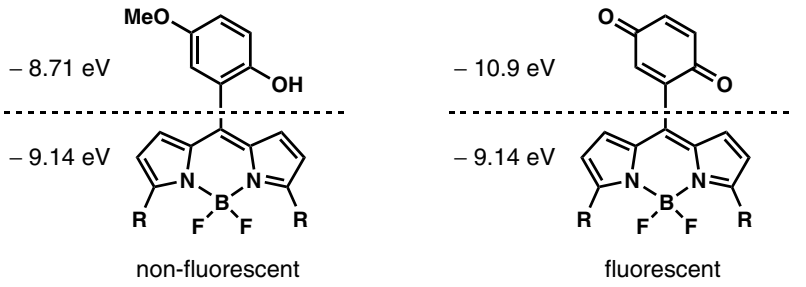

Figure 49. Dependence of fluorescence upon the HOMO energy levels of BODIPYs and their substituents, adapted from Ref. 145.

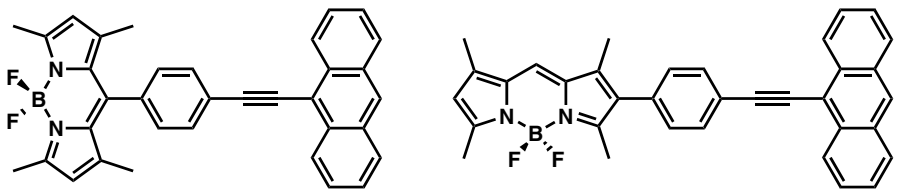

Figure 50. Differently substituted boron difluoride dipyrrinato complexes with similar redox behaviors.

been shown to possess electrochemical properties that are quite different to those of typical complexes in dichloromethane.[49] This observation, presumably due to reaction of the radical cation (formed upon oxidation) with the solvent, was found to be eliminated by recording the cyclic voltammograms in acetonitrile.[49] In compounds that contain more than one boron difluoride dipyrrinato unit, it has been observed that the two (or more) units undergo reduction at different potentials, indicating that the units are electronically isolated.[169,258]

III. Concluding Remarks

Dipyrrins and complexes thereof have interesting features to offer to many fields of research. The variable structure and functionalizations afforded by these molecules determine many useful biological, optical, electrochemical, and stereochemical properties. The increasing number of methods available for preparing increasingly diversely functionalized dipyrrins, and the expanding ability to characterize the properties of these molecules promise a dynamic and exciting future for dipyrrin research. Hopefully this chapter has provided a reference to where dipyrrin research has ventured in exploring the potential of these interesting and

adaptable molecules. Hopefully, it will also provide some new directions for exploration.

IV. References

1. Dixon, H. B. F.; Cornish-Bowden, A.; Liébecq, C.; Loening, K. L.; Moss, G. P.; Reedijk, J.; Velick, S. F.; Venetianer, P.; Vliegenthart, J. F. G. *Pure Appl. Chem.* **1987**, *59*, 779–832.
2. Berezin, M. B.; Semeikin, A. S.; Antina, E. V.; Pashanova, N. A.; Lebedeva, N. S.; Bukushina, G. B. *Russ. J. Gen. Chem.* **1999**, *69*, 1949–1955.
3. Rumyantsev, E. V.; Guseva, G. B.; Antina, E. V.; Berezin, M. B.; Sheinin, V. B.; V'Yugin, A. I. *Russ. J. Gen. Chem.* **2006**, *76*, 141–147.
4. Fischer, H.; Orth, H. *Die Chemie des Pyrrols*; Akademische Verlagsgesellschaft: Leipzig, 1937.
5. Eaton, S. S.; Eaton, G. R.; Chang, C. K. *J. Am. Chem. Soc.* **1985**, *107*, 3177–3184.
6. Brunings, K. J.; Corwin, A. H. *J. Am. Chem. Soc.* **1942**, *64*, 593–600.
7. Jain, A. C.; Kenner, G. W. *J. Chem. Soc.* **1959**, 185–189.
8. Booth, H.; Johnson, A. W.; Johnson, F.; Langdale-Smith, R. A. *J. Chem. Soc.* **1963**, 650–661.
9. Treibs, A.; Zimmer-Galler, R. *Ann.* **1963**, *664*, 140–145.
10. Bamfield, P.; Johnson, A. W.; Leng, J. *J. Chem. Soc.* **1965**, 7001–7005.
11. Van Koeveringe, J. A.; Lugtenburg, J. *Recl. Trav. Chim. Pays-Bas* **1977**, *96*, 55–58.
12. Tram, K.; Yan, H. B.; Jenkins, H. A.; Vassiliev, S.; Brucec, *D. Dyes Pigm*. **2009**, *82*, 392–395.
13. Arroyo, I. J.; Hu, R. R.; Merino, G.; Tang, B. Z.; Pena-Cabrera, E. *J. Org. Chem.* **2009**, *74*, 5719–5722.
14. Kollmannsberger, M.; Gareis, T.; Heinl, S.; Breu, J.; Daub, J. *Angew. Chem., Int. Ed. Engl.* **1997**, *36*, 1333–1335.
15. Paine, J. B., III. In *The Porphyrins*; Dolphin, D., Ed.; Academic Press: New York, **1978**; Vol. 1.
16. Chawrai, S. R.; Williamson, N. R.; Salmond, G. P. C.; Leeper, F. J. *Chem. Commun.* **2008**, 1862–1864.
17. Haynes, S. W.; Sydor, P. K.; Stanley, A. E.; Song, L.; Challis, G. L. *Chem. Commun.* **2008**, 1865–1867.
18. Wan, C.-W.; Burghart, A.; Chen, J.; Bergström, F.; Johansson, L. B.-Å.; Wolford, M. F.; Kim, T. G.; Topp, M. R.; Hochstrasser, R. M.; Burgess, K. *Chem. Eur. J.* **2003**, *9*, 4430–4441.
19. Hornillos, V.; Carrillo, E.; Rivas, L.; Amat-Guerri, F.; Acuña, A. U. *Bioorg. Med. Chem. Lett.* **2008**, *18*, 6336–6339.
20. Bröring, M.; Link, S.; Cordes, M.; Brandt, C. D. *Z. Anorg. Allg. Chem.* **2007**, *633*, 211–218.
21. Al-Sheikh Ali, A.; Benson, R. E.; Blumentritt, S.; Cameron, T. S.; Linden, A.; Wolstenholme, D.; Thompson, A. *J. Org. Chem.* **2007**, *72*, 4947–4952.
22. Antina, E. V.; Zakharova, S. P.; Rumyantsev, E. V. *Russ. J. Gen. Chem.* **2006**, *76*, 1157–1164.
23. Tu, B.; Wang, C. Q.; Ma, J. S. *Org. Prep. Proced. Int.* **1999**, *31*, 349–352.
24. Falk, H. *The Chemistry of Linear Oligopyrroles and Bile Pigments*; Springer-Verlag: New York, 1989.
25. Datta, S.; Lightner, D. A. *Monatsh. Chem.* **2008**, *139*, 1113–1117.
26. Wang, H.; Chen, M.; Wang, L. *Chem. Pharm. Bull.* **2007**, *55*, 1439–1441.
27. Lee, P. H. *Bull. Korean Chem. Soc.* **2008**, *29*, 261–264.
28. Goeb, S.; Ziessel, R. *Tetrahedron Lett.* **2008**, *49*, 2569–2574.
29. Tahtaoui, C.; Thomas, C.; Rohmer, F.; Klotz, P.; Duportail, G.; Mély, Y.; Bonnet, D.; Hibert, M. *J. Org. Chem.* **2007**, *72*, 269–272.

30. Yu, L.; Muthukumaran, K.; Sazanovich, I. V.; Kirmaier, C.; Hindin, E.; Diers, J. R.; Boyle, P. D.; Bocian, D. F.; Holten, D.; Lindsey, J. S. *Inorg. Chem.* **2003**, *42*, 6629–6647.
31. Brückner, C.; Karunaratne, V.; Rettig, S. J.; Dolphin, D. *Can. J. Chem.* **1996**, *74*, 2182–2193.
32. Wagner, R. W.; Lindsey, J. S. *J. Am. Chem. Soc.* **1994**, *116*, 9759–9760.
33. Falk, H.; Hofer, O.; Lehner, H. *Monatsh. Chem.* **1974**, *105*, 169–178.
34. Stork, J. R.; Thoi, V. S.; Cohen, S. M. *Inorg. Chem.* **2007**, *46*, 11213–11223.
35. Shin, J.-Y.; Patrick, B. O.; Dolphin, D. *Org. Biomol. Chem.* **2009**, *7*, 2032–2035.
36. Lash, T. D.; Chen, S. *Tetrahedron* **2005**, *61*, 11577–11600.
37. Jackson, A. H.; Pandey, R. K.; Rao, K. R. N.; Roberts, E. *Tetrahedron Lett.* **1985**, *26*, 793–796.
38. Bari, S. E.; Iturraspe, J.; Frydman, B. *Tetrahedron* **1995**, *51*, 2255–2266.
39. King, E. R.; Betley, T. A. *Inorg. Chem.* **2009**, *48*, 2361–2363.
40. Rao, P. D.; Dhanalekshmi, S.; Littler, B. J.; Lindsey, J. S. *J. Org. Chem.* **2000**, *65*, 7323–7344.
41. Lee, C.-H.; Lindsey, J. S. *Tetrahedron* **1994**, *50*, 11427–11440.
42. Littler, B. J.; Miller, M. A.; Hung, C.-H.; Wagner, R. W.; O'Shea, D. F.; Boyle, P. D.; Lindsey, J. S. *J. Org. Chem.* **1999**, *64*, 1391–1396.
43. Clausen, C.; Gryko, D. T.; Yasseri, A. A.; Diers, J. R.; Bocian, D. F.; Kuhr, W. G.; Lindsey, J. S. *J. Org. Chem.* **2000**, *65*, 7371–7378.
44. Laha, J. K.; Dhanalekshmi, S.; Taniguchi, M.; Ambroise, A.; Lindsey, J. S. *Org. Process Res. Dev.* **2003**, *7*, 799–812.
45. Gryko, D.; Lindsey, J. S. *J. Org. Chem.* **2000**, *65*, 2249–2252.
46. Boyle, R. W.; Brückner, C.; Posakony, J.; James, B. R.; Dolphin, D. *Org. Synth.* **1999**, *76*, 287–293.
47. Turfan, B.; Akkaya, E. U. *Org. Lett.* **2002**, *4*, 2857–2859.
48. Goze, C.; Ulrich, G.; Charbonnière, L.; Cesario, M.; Prange, T.; Ziessel, R. *Chem. Eur. J.* **2003**, *9*, 3748–3755.
49. Ulrich, G.; Ziessel, R. *J. Org. Chem.* **2004**, *69*, 2070–2083.
50. Ulrich, G.; Ziessel, R. *Tetrahedron Lett.* **2004**, *45*, 1949–1953.
51. Ziessel, R.; Bonardi, L.; Retailleau, P.; Ulrich, G. *J. Org. Chem.* **2006**, *71*, 3093–3102.
52. Stępień, M.; Simkowa, I.; Latos-Grażyński, L. *Eur. J. Org. Chem.* **2008**, 2601–2611.
53. Thamyongkit, P.; Bhise, A. D.; Taniguchi, M.; Lindsey, J. S. *J. Org. Chem.* **2006**, *71*, 903–910.
54. Lebedeva, N. S.; Antina, E. V.; Berezin, M. B.; Semeikin, A. S.; Bukushina, G. B. *Zh. Fiz. Khim.* **2000**, *74*, 1165–1170.
55. Pashanova, N. A.; Semeikin, A. S.; Berezin, M. B. *Russ. J. Gen. Chem.* **1999**, *69*, 1477–1480.
56. Guseva, G. B.; Antina, E. V.; Berezin, M. B.; Semeikin, A. S.; V'Yugin, A. I. *Russ. J. Gen. Chem.* **2002**, *72*, 126–130.
57. Guseva, G. B.; Rumyantsev, E. V.; Antina, E. V.; Berezin, M. B.; Vyugin, A. I. *Russ. J. Coord. Chem.* **2004**, *30*, 371–374.
58. Falk, H.; Leodolter, A. *Monatsh. Chem.* **1978**, *109*, 883–897.
59. Guseva, G. B.; Dudina, N. A.; Antina, E. V.; V'Yugin, A. I.; Semeikin, A. S. *Russ. J. Gen. Chem.* **2008**, *78*, 1215–1224.
60. Chepelev, L. L.; Beshara, C. S.; MacLean, P. D.; Hatfield, G. L.; Rand, A. A.; Thompson, A.; Wright, J. S.; Barclay, L. R. C. *J. Org. Chem.* **2006**, *71*, 22–30.
61. MacLean, P. D.; Chapman, E. E.; Dobrowolski, S. L.; Thompson, A.; Barclay, L. R. C. *J. Org. Chem.* **2008**, *73*, 6623–6635.
62. Iordache, A.; Melfi, P.; Bucher, C.; Buda, M.; Moutet, J.-C.; Sessler, J. L. *Org. Lett.* **2008**, *10*, 425–428.
63. Ikeda, C.; Sakamoto, N.; Nabeshima, T. *Org. Lett.* **2008**, *10*, 4601–4604.

64. Al-Sheikh Ali, A.; Cipot-Wechsler, J.; Cameron, T. S.; Thompson, A. *J. Org. Chem.* **2009**, *74*, 2866–2869.
65. Wood, T. E.; Thompson, A. *Chem. Rev.* **2007**, *107*, 1831–1861.
66. Fürstner, A. *Angew. Chem., Int. Ed.* **2003**, *42*, 3582–3603.
67. La, J. Q. H.; Michaelides, A. A.; Manderville, R. A. *J. Phys. Chem. B* **2007**, *111*, 11803–11811.
68. Tomlinson, J. T.; Park, G.; Misenheimer, J. A.; Kucera, G. L.; Hesp, K.; Manderville, R. A. *Org. Lett.* **2006**, *8*, 4951–4954.
69. Wood, T. E.; Berno, B.; Beshara, C. S.; Thompson, A. *J. Org. Chem.* **2006**, *71*, 2964–2971.
70. Bonnier, C.; Piers, W. E.; Parvez, M.; Sorensen, T. S. *Chem. Commun.* **2008**, 4593–4595.
71. Strong, E. T. J.; Cardile, S. A.; Brazeau, A. L.; Jennings, M. C.; McDonald, R.; Jones, N. D. *Inorg. Chem.* **2008**, *47*, 10575–10586.
72. Dogutan, D. K.; Zaidi, S. H. H.; Thamyongkit, P.; Lindsey, J. S. *J. Org. Chem.* **2007**, *72*, 7701–7714.
73. Maeda, H.; Hashimoto, T.; Fujii, R.; Hasegawa, M. *J. Nanosci. Nanotechnol.* **2009**, *9*, 240–248.
74. Brunings, K. J.; Corwin, A. H. *J. Am. Chem. Soc.* **1944**, *66*, 337–342.
75. Cohen, S. M.; Halper, S. R. *Inorg. Chim. Acta* **2002**, *341*, 12–16.
76. Brückner, C.; Zhang, Y.; Rettig, S. J.; Dolphin, D. *Inorg. Chim. Acta* **1997**, *263*, 279–286.
77. Garibay, S. J.; Stork, J. R.; Wang, Z.; Cohen, S. M.; Telfer, S. G. *Chem. Commun.* **2007**, 4881–4883.
78. Do, L.; Halper, S. R.; Cohen, S. M. *Chem. Commun.* **2004**, 2662–2663.
79. Halper, S. R.; Cohen, S. M. *Chem. Eur. J.* **2003**, *9*, 4661–4669.
80. Halper, S. R.; Cohen, S. M. *Inorg. Chem.* **2005**, *44*, 486–488.
81. Halper, S. R.; Do, L.; Stork, J. R.; Cohen, S. M. *J. Am. Chem. Soc.* **2006**, *128*, 15255–15268.
82. Halper, S. R.; Stork, J. R.; Cohen, S. M. *Dalton Trans.* **2007**, 1067–1074.
83. Murphy, D. L.; Malachowski, M. R.; Campana, C. F.; Cohen, S. M. *Chem. Commun.* **2005**, 5506–5508.
84. Thoi, V. S.; Stork, J. R.; Magde, D.; Cohen, S. M. *Inorg. Chem.* **2006**, *45*, 10688–10697.
85. Chadwick, D. J. In *Pyrroles*; Jones, R. A., Ed.; John Wiley & Sons: Toronto, **1990**; Vol. 1.
86. Bröring, M.; Pfister, A.; Ilg, K. *Chem. Commun.* **2000**, 1407–1408.
87. Salazar-Mendoza, D.; Baudron, S. A.; Hosseini, M. W. *Chem. Commun.* **2007**, 2252–2254.
88. Salazar-Mendoza, D.; Baudron, S. A.; Hosseini, M. W. *Inorg. Chem.* **2008**, *47*, 766–768.
89. Shin, J.-Y.; Dolphin, D.; Patrick, B. O. *Cryst. Growth Des.* **2004**, *4*, 659–661.
90. Corwin, A. H.; Melville, M. H. *J. Am. Chem. Soc.* **1955**, *77*, 2755–2759.
91. Motekaitis, R. J.; Martell, A. E. *Inorg. Chem.* **1970**, *9*, 1832–1839.
92. Clarke, E. T.; Squattrito, P. J.; Rudolf, P. R.; Motekaitis, R. J.; Martell, A. E.; Clearfield, A. *Inorg. Chim. Acta* **1989**, *166*, 221–231.
93. Murakami, Y.; Matsuda, Y.; Iiyama, K. *Chem. Lett.* **1972**, 1069–1072.
94. Murakami, Y.; Sakata, K.; Harada, K.; Matsuda, Y. *Bull. Chem. Soc. Jpn.* **1974**, *47*, 3021–3024.
95. Matsuda, Y.; Murakami, Y. *Bull. Chem. Soc. Jpn.* **1977**, *50*, 2321–2324.
96. Murakami, Y.; Matsuda, Y.; Sakata, K.; Harada, K. *Bull. Chem. Soc. Jpn.* **1974**, *47*, 458–462.
97. Fischer, H.; Schubert, M. *Ber.* **1924**, *57B*, 610–617.
98. Fischer, H.; Halbig, P.; Walach, B. *Ann.* **1927**, *452*, 268–302.
99. Porter, C. R. *J. Chem. Soc.* **1938**, 368–372.
100. West, B. *J. Chem. Soc.* **1952**, 3115–3122.
101. Johnson, A. W.; Kay, I. T.; Markham, E.; Price, R.; Shaw, K. B. *J. Chem. Soc.* **1959**, 3416–3424.
102. Fergusson, J. E.; Ramsay, C. A. *J. Chem. Soc.* **1965**, 5222–5225.

103. Murakami, Y.; Sakata, K. *Inorg. Chim. Acta* **1968**, *2*, 273–279.
104. Murakami, Y.; Matsuda, Y.; Sakata, K. *Inorg. Chem.* **1971**, *10*, 1728–1734.
105. Fergusson, J. E.; March, F. C.; Couch, D. A.; Emerson, K.; Robinson, W. T. *J. Chem. Soc. A* **1971**, 440–448.
106. Murakami, Y.; Matsuda, Y.; Sakata, K.; Martell, A. E. *J. Chem. Soc., Dalton Trans.* **1973**, 1729–1734.
107. Telfer, S. G.; Wuest, J. D. *Chem. Commun.* **2007**, 3166–3168.
108. Maeda, H.; Hashimoto, T. *Chem. Eur. J.* **2007**, *13*, 7900–7907.
109. Mellor, D. P.; Lockwood, W. H. *J. Proc. R. Soc. NSW* **1940**, *74*, 141–148.
110. Ferguson, J.; West, B. O. *J. Chem. Soc. A* **1966**, 1565–1568.
111. Rogers, M. A. T. *J. Chem. Soc.* **1943**, 596–597.
112. Murakami, Y.; Matsuda, Y.; Sakata, K. *Inorg. Chem.* **1971**, *10*, 1734–1738.
113. Halper, S. R.; Malachowski, M. R.; Delaney, H. M.; Cohen, S. M. *Inorg. Chem.* **2004**, *43*, 1242–1249.
114. Beshara, C. S.; Pearce, B. M.; Thompson, A. *Can. J. Chem.* **2008**, *86*, 951–957.
115. Murakami, Y.; Sakata, K. *Bull. Chem. Soc. Jpn.* **1974**, *47*, 3025–3028.
116. Sazanovich, I. V.; Kirmaier, C.; Hindin, E.; Yu, L.; Bocian, D. F.; Lindsey, J. S.; Holten, D. *J. Am. Chem. Soc.* **2004**, *126*, 2664–2665.
117. Badger, G. M.; Jones, R. A.; Laslett, R. L. *Aust. J. Chem.* **1964**, *17*, 1028–1035.
118. Hill, C. L.; Williamson, M. M. *J. Chem. Soc., Chem. Commun.* **1985**, 1228–1229.
119. Cipot-Wechsler, J.; Al-Sheikh Ali, A.; Chapman, E. E.; Cameron, T. S.; Thompson, A. *Inorg. Chem.* **2007**, *46*, 10947–10949.
120. Smalley, S. J.; Waterland, M. R.; Telfer, S. G. *Inorg. Chem.* **2009**, *48*, 13–15.
121. Roomi, M. W. *Tetrahedron Lett.* **1974**, 1131–1132.
122. March, F. C.; Fergusson, J. E.; Robinson, W. T. *J. Chem. Soc., Dalton Trans.* **1972**, 2069–2076.
123. Hsieh, A. T. T.; Rogers, C. A.; West, B. O. *Aust. J. Chem.* **1976**, *29*, 49–54.
124. Kobayashi, J.; Kushida, T.; Kawashima, T. *J. Am. Chem. Soc.* **2009**, *131*, 10836–10837.
125. Treibs, A.; Kreuzer, F. H. *Justus Liebigs Ann. Chem.* **1968**, *718*, 208–223.
126. Falk, H.; Gergely, S.; Hofer, O. *Monatsh. Chem.* **1974**, *105*, 1004–1018.
127. Falk, H.; Hofer, O. *Monatsh. Chem.* **1975**, *106*, 97–113.
128. Falk, H.; Leodolter, A.; Schade, G. *Monatsh. Chem.* **1978**, *109*, 183–192.
129. Falk, H.; Neufingerl, F. *Monatsh. Chem.* **1979**, *110*, 987–1001.
130. Falk, H.; Grubmayr, K.; Neufingerl, F. *Monatsh. Chem.* **1979**, *110*, 1127–1146.
131. Goud, T. V.; Tutar, A.; Biellmann, J.-F. *Tetrahedron* **2006**, *62*, 5084–5091.
132. Li, J.-S.; Wang, H.; Cao, L.-W.; Zhang, H.-S. *Talanta* **2006**, *69*, 1190–1199.
133. Li, L.; Nguyen, B.; Burgess, K. *Bioorg. Med. Chem. Lett.* **2008**, *18*, 3112–3116.
134. Choi, S. H.; Kim, K.; Lee, J.; Do, Y.; Churchill, D. G. *J. Chem. Crystallogr.* **2007**, *37*, 315–331.
135. Malatesti, N.; Hudson, R.; Smith, K.; Savoie, H.; Rix, K.; Welham, K.; Boyle, R. W. *Photochem.* **2006**, *82*, 746–749.
136. Choi, S. H.; Pang, K.; Kim, K.; Churchill, D. G. *Inorg. Chem.* **2007**, *46*, 10564–10577.
137. Ikeda, C.; Nabeshima, T. *Chem. Commun.* **2008**, 721–723.
138. Alexandrova, L. A.; Jasko, M. V.; Belobritskaya, E. E.; Chudinov, A. V.; Mityaeva, O. N.; Nasedkina, T. V.; Zasedatelev, A. S.; Kukhanova, M. K. *Bioconjugate Chem.* **2007**, *18*, 886–893.
139. Bröring, M.; Krüger, R.; Link, S.; Kleeberg, C.; Köhler, S.; Xie, X.; Ventura, B.; Flamingi, L. *Chem. Eur. J.* **2008**, *14*, 2976–2983.

140. Broering, M.; Krueger, R.; Kleeberg, C. *Z. Anorg. Allg. Chem.* **2008**, *634*, 1555–1559.
141. Bandhuvula, P.; Li, Z.; Bittman, R.; Saba, J. D. *Biochem. Biophys. Res. Commun.* **2009**, *380*, 366–370.
142. Ventura, B.; Marconi, G.; Bröring, M.; Krüger, R.; Flamigni, L. *New J. Chem.* **2009**, *33*, 428–438.
143. Li, L.; Han, J.; Nguyen, B.; Burgess, K. *J. Org. Chem.* **2008**, *73*, 1963–1970.
144. Liras, M.; Prieto, J. B.; Pintado-Sierra, M.; Arbeloa, F. L.; García-Moreno, I.; Costela, Á.; Infantes, L.; Sastre, R.; Amat-Guerri, F. *Org. Lett.* **2007**, *9*, 4183–4186.
145. Sun, Z.-N.; Liu, F.-Q.; Chen, Y.; Tam, P. K. H.; Yang, D. *Org. Lett.* **2008**, *10*, 2171–2174.
146. Parhi, A. K.; Kung, M.-P.; Ploessl, K.; Kung, H. F. *Tetrahedron Lett.* **2008**, *49*, 3395–3399.
147. Ueno, T.; Urano, Y.; Kojima, H.; Nagano, T. *J. Am. Chem. Soc.* **2006**, *128*, 10640–10641.
148. Peters, C.; Billich, A.; Ghobrial, M.; Högenauer, K.; Ullrich, T.; Nussbaumer, P. *J. Org. Chem.* **2007**, *72*, 1842–1845.
149. Blakemore, J. D.; Chitta, R.; D'Souza, F. *Tetrahedron Lett.* **2007**, *48*, 1977–1982.
150. Yilmaz, M. D.; Bozdemir, O. A.; Akkaya, E. U. *Org. Lett.* **2006**, *8*, 2871–2873.
151. Alamiry, M. A. H.; Benniston, A. C.; Copley, G.; Elliott, K. J.; Harriman, A.; Stewart, B.; Zhi, Y.-G. *Chem. Mater.* **2008**, *20*, 4024–4032.
152. Cihaner, A.; Algi, F. *Electrochim. Acta* **2008**, *54*, 786–792.
153. Choi, S. H.; Kim, K.; Jeon, J.; Meka, B.; Bucella, D.; Pang, K.; Khatua, S.; Lee, J.; Churchill, D. G. *Inorg. Chem.* **2008**, *47*, 11071–11083.
154. Wilson, C. J.; James, L.; Mehl, G. H.; Boyle, R. W. *Chem. Commun.* **2008**, 4582–4584.
155. Ulrich, G.; Ziessel, R.; Harriman, A. *Angew. Chem. Int. Ed.* **2008**, *47*, 1184–1201.
156. Thompson, A.; Bennett, S.; Gillis, H. M.; Wood, T. E. *J. Porphyrins Phthalocyanines* **2008**, *12*, 918–931.
157. Guseva, G. B.; Antina, E. V.; Berezin, M. B. *Russ. J. Coord. Chem.* **2003**, *29*, 690–693.
158. Jaumà, A.; Farrera, J. A.; Ribó, J. M. *Monatsh. Chem.* **1996**, *127*, 935–946.
159. Amiri, A.; Comeau, I. M.; Thompson, A. *J. Heterocycl. Chem.* **2006**, *43*, 431–435.
160. Muthukumaran, K.; Zaidi, S. H. H.; Yu, L. H.; Thamyongkit, P.; Calder, M. E.; Sharada, D. S.; Lindsey, J. S. *J. Porphyrins Phthalocyanines* **2005**, *9*, 745–759.
161. Ikeda, C.; Ueda, S.; Nabeshima, T. *Chem. Commun.* **2009**, 2544–2546.
162. Guseva, G. B.; Antina, E. V.; V'Yugin, A. I.; Mamardashvili, G. M.; Petrov, V. V. *Russ. J. Coord. Chem.* **2006**, *32*, 116–120.
163. Halper, S. R.; Cohen, S. M. *Angew. Chem., Int. Ed.* **2004**, *43*, 2385–2388.
164. Setsune, J.; Toda, M.; Yoshida, T. *Chem. Commun.* **2008**, 1425–1427.
165. Yadav, M.; Singh, A. K.; Maiti, B.; Pandey, D. S. *Inorg. Chem.* **2009**, *48*, 7593–7603.
166. Yadav, M.; Singh, A. K.; Pandey, D. S. *Organometallics* **2009**, *28*, 4713–4723.
167. Sutton, J. M.; Rogerson, E.; Wilson, C. J.; Sparke, A. E.; Archibald, S. J.; Boyle, R. W. *Chem. Commun.* **2004**, 1328–1329.
168. Thoi, V. S.; Stork, J. R.; Niles, E. T.; Depperman, E. C.; Tierney, D. L.; Cohen, S. M. *Inorg. Chem.* **2008**, *47*, 10533–10541.
169. Galletta, M.; Puntoriero, F.; Campagna, S.; Chiorboli, C.; Quesada, M.; Goeb, S.; Ziessel, R. *J. Phys. Chem. A* **2006**, *110*, 4348–4358.
170. Gossauer, A.; Engel, J. In *The Porphyrins*; Dolphin, D., Ed.; Academic Press: New York, **1978**; Vol. 2.
171. Bousejra-El Garah, F.; Pitie, M.; Vendier, L.; Meunier, B.; Robert, A. *J. Biol. Inorg. Chem.* **2009**, *14*, 601–610.

172. Al-Sheikh Ali, A.; Cameron, K. S.; Cameron, T. S.; Robertson, K. N.; Thompson, A. *Org. Lett.* **2005**, *7*, 4773–4775.
173. Fischer, H.; Stachel, A. *Z. Physiol. Chem.* **1939**, *258*, 121–136.
174. Johnson, A. W.; Price, R. *J. Chem. Soc.* **1960**, 1649–1653.
175. Mironov, A. F.; Rumyantseva, V. D.; Rozynov, B. V.; Evstigneeva, R. P. *Russ. J. Org. Chem.* **1971**, *7*, 164–166.
176. Clezy, P. S.; Lim, C. L.; Shannon, J. S. *Aust. J. Chem.* **1974**, *27*, 2431–2437.
177. Clezy, P. S.; Fookes, C. J. R.; Prashar, J. K. *Aust. J. Chem.* **1989**, *42*, 775–786.
178. Minnetian, O. M.; Morris, I. K.; Snow, K. M.; Smith, K. M. *J. Org. Chem.* **1989**, *54*, 5567–5574.
179. Clezy, P. S.; Jenie, U.; Prashar, J. K. *Aust. J. Chem.* **1990**, *43*, 839–856.
180. Clezy, P. S.; Mirza, A. H.; Prashar, J. K. *Aust. J. Chem.* **1990**, *43*, 857–866.
181. May, D. A. J.; Lash, T. D. *J. Org. Chem.* **1992**, *57*, 4820–4828.
182. Johnson, A. W.; Kay, I. T. *Proc. Chem. Soc.* **1964**, 89–90.
183. Dolphin, D.; Harris, R. L. N.; Johnson, A. W.; Kay, I. T. *Proc. Chem. Soc.* **1964**, 359–360.
184. Johnson, A. W.; Kay, I. T. *J. Chem. Soc.* **1965**, 1620–1629.
185. Dolphin, D.; Harris, R. L. N.; Huppatz, J. L.; Johnson, A. W.; Kay, I. T. *J. Chem. Soc. C* **1966**, 30–40.
186. Dolphin, D.; Harris, R. L. N.; Huppatz, J. L.; Johnson, A. W.; Kay, I. T.; Leng, J. *J. Chem. Soc. C* **1966**, 98–106.
187. Sheldrick, W. S.; Engel, J. *J. Chem. Soc. Chem. Commun.* **1980**, 5–6.
188. Sheldrick, W. S.; Engel, J. *Acta Crystallogr. B* **1981**, *B37*, 250–252.
189. Mwakwari, C.; Fronczek, F. R.; Smith, K. M. *Chem. Commun.* **2007**, 2258–2260.
190. Diekmann, H.; Chang, C. K.; Traylor, T. G. *J. Am. Chem. Soc.* **1971**, *93*, 4068–4070.
191. Murakami, Y.; Kohno, Y.; Matsuda, Y. *Inorg. Chim. Acta* **1969**, *3*, 671–675.
192. Murakami, Y.; Matsuda, Y.; Kanaoka, Y. *Bull. Chem. Soc. Jpn.* **1971**, *44*, 409–415.
193. Zhang, Z.; Dolphin, D. *Chem. Commun.* **2009**, 6931–6933.
194. Bröring, M.; Brandt, C. D. *Monatsh. Chem.* **2002**, *133*, 623–630.
195. Zhang, Y.; Thompson, A.; Rettig, S. J.; Dolphin, D. *J. Am. Chem. Soc.* **1998**, *120*, 13537–13538.
196. Thompson, A.; Rettig, S. J.; Dolphin, D. *Chem. Commun.* **1999**, 631–632.
197. Thompson, A.; Dolphin, D. *J. Org. Chem.* **2000**, *65*, 7870–7877.
198. Zhang, Y.; Wang, Z.; Yan, C.; Li, G.; Ma, J. *Tetrahedron Lett.* **2000**, *41*, 7717–7721.
199. Zhang, Y.; Ma, J. S. *Org. Prep. Proced. Int.* **2001**, *33*, 81–86.
200. Yang, L.; Zhang, Y.; Yang, G.; Chen, Q.; Ma, J. S. *Dyes Pigm.* **2004**, *62*, 27–33.
201. Shan, X.; Yang, L.; Li, W.; Chen, Q.; Wang, Z.; Hu, J.; Ma, J. S. *J. Chem. Crystallogr.* **2004**, *34*, 433–439.
202. Maeda, H.; Hasegawa, M.; Hashimoto, T.; Kakimoto, T.; Nishio, S.; Nakanishi, T. *J. Am. Chem. Soc.* **2006**, *128*, 10024–10025.
203. Yang, L.; Zhang, Y.; Chen, Q.; Ma, J. S. *Monatsh. Chem.* **2004**, *135*, 223–229.
204. Yaghi Omar, M.; O'Keeffe, M.; Ockwig Nathan, W.; Chae Hee, K.; Eddaoudi, M.; Kim, J. *Nature* **2003**, *423*, 705–714.
205. Öhrström, L.; Larsson, K. *Molecule Based Materials: The Structural Network Approach*; Elsevier: Boston, **2005**.
206. Telfer, S. G.; Wuest, J. D. *Cryst. Growth Des.* **2009**, *9*, 1923–1931.
207. Maeda, H. *Eur. J. Org. Chem.* **2007**, 5313–5325.
208. Miao, Q.; Shin, J.-Y.; Patrick, B. O.; Dolphin, D. *Chem. Commun.* **2009**, 2541–2543.

209. Halper, S. R.; Cohen, S. M. *Inorg. Chem.* **2005**, *44*, 4139–4141.
210. Heinze, K.; Reinhart, A. *Inorg. Chem.* **2006**, *45*, 2695–2703.
211. Maeda, H.; Ito, M. *Chem. Lett.* **2005**, *34*, 1150–1151.
212. Keopf, M.; Trabolsi, A.; Elhabiri, M.; Wytko, J. A.; Paul, D.; Albrecht-Gary, A. M.; Weiss, J. *Org. Lett.* **2005**, *7*, 1279–1282.
213. Gryko, D. T.; Koszarna, B. *Eur. J. Org. Chem.* **2005**, 3314–3318.
214. Ravikanth, M.; Agarwal, N.; Kumaresan, D. *Chem. Lett.* **2000**, 836–837.
215. Ambroise, A.; Kirmaier, C.; Wagner, R. W.; Loewe, R. S.; Bocian, D. F.; Holten, D.; Lindsey, J. S. *J. Org. Chem.* **2002**, *67*, 3811–3826.
216. Li, F.; Yang, S. I.; Ciringh, Y.; Seth, J.; Martin, C. H., III; Singh, D. L.; Kim, D.; Birge, R. R.; Bocian, D. F.; Holten, D.; Lindsey, J. S. *J. Am. Chem. Soc.* **1998**, *120*, 10001–10017.
217. Burghart, A.; Thoresen, L. H.; Chen, J.; Burgess, K.; Bergström, F.; Johansson, L. B.-Å. *Chem. Commun.* **2000**, 2203–2204.
218. Ulrich, G.; Goze, C.; Guardigli, M.; Roda, A.; Ziessel, R. *Angew. Chem. Int. Ed.* **2005**, *44*, 3694–3698.
219. Ulrich, G.; Ziessel, R. *Synlett* **2004**, 439–444.
220. Wories, H. J.; Koek, J. H.; Lodder, G.; Lugtenburg, J.; Fokkens, R.; Driessen, O.; Mohn, G. R. *Recl. Trav. Chim. Pays-Bas* **1985**, *104*, 288–291.
221. Shah, M.; Thangaraj, K.; Soong, M. L.; Wolford, L.; Boyer, J. H.; Politzer, I. R.; Pavlopoulos, T. G. *Heteroat. Chem.* **1990**, *1*, 389–399.
222. Yogo, T.; Urano, Y.; Ishitsuka, Y.; Maniwa, F.; Nagano, T. *J. Am. Chem. Soc.* **2005**, *127*, 12162–12163.
223. Chen, T.; Boyer, J. H.; Trudell, M. L. *Heteroat. Chem.* **1997**, *8*, 51–54.
224. Wu, Y.; Peng, X.; Guo, B.; Fan, J.; Zhang, Z.; Wang, J.; Cui, A.; Gao, Y. *Org. Biomol. Chem.* **2005**, *3*, 1387–1392.
225. Imahori, H.; Norieda, H.; Yamada, H.; Nishimura, Y.; Yamazaki, I.; Sakata, Y.; Fukuzumi, S. *J. Am. Chem. Soc.* **2001**, *123*, 100–110.
226. Martin, R. J.; Kusel, J. R.; Robertson, S. J.; Minta, A.; Haugland, R. P. *Parasitol. Res.* **1992**, *78*, 341–348.
227. Sathyamoorthi, G.; Wolford, L. T.; Haag, A. M.; Boyer, J. H. *Heteroat. Chem.* **1994**, *5*, 245–249.
228. Chen, J.; Burghart, A.; Derecskei-Kovacs, A.; Burgess, K. *J. Org. Chem.* **2000**, *65*, 2900–2906.
229. Wada, M.; Ito, S.; Uno, H.; Murashima, T.; Ono, N.; Urano, T.; Urano, Y. *Tetrahedron Lett.* **2001**, *42*, 6711–6713.
230. Bröring, M.; Brandt, C. D.; Lex, J.; Humpf, H.-U.; Bley-Escrich, J.; Gisselbrecht, J.-P. *Eur. J. Inorg. Chem.* **2001**, 2549–2556.
231. Wood, T. E.; Dalgleish, N. D.; Power, E. D.; Thompson, A.; Chen, X.; Okamoto, Y. *J. Am. Chem. Soc.* **2005**, *127*, 5740–5741.
232. Al-Sheikh-Ali, A.; Cameron, K. S.; Cameron, T. S.; Robertson, K. N.; Thompson, A. *Org. Lett.* **2005**, *7*, 4773–4775.
233. Setsune, J.; Tsukajima, A.; Okazaki, N.; Lintuluoto, J. M.; Lintuluoto, M. *Angew. Chem., Int. Ed.* **2009**, *48*, 771–775.
234. Wood, T. E.; Ross, A. C.; Dalgleish, N. D.; Power, E. D.; Thompson, A.; Chen, X.; Okamoto, Y. *J. Org. Chem.* **2005**, *70*, 9967–9974.
235. Kim, H.; Burghart, A.; Welch, M. B.; Reibenspies, J.; Burgess, K. *Chem. Commun.* **1999**, 1889–1890.

236. Beer, G.; Niederalt, C.; Grimme, S.; Daub, J. *Angew. Chem. Int. Ed.* **2000**, *39*, 3252–3255.
237. Beer, G.; Rurack, K.; Daub, J. *Chem. Commun.* **2001**, 1138–1139.
238. Gossauer, A.; Nydegger, F.; Kiss, T.; Sleziak, R.; Stoeckli-Evans, H. *J. Am. Chem. Soc.* **2004**, *126*, 1772–1780.
239. Elder, M.; Penfold, B. R. *J. Chem. Soc. A* **1969**, 2556–2559.
240. Cotton, F. A.; DeBoer, B. G.; Pipal, J. R. *Inorg. Chem.* **1970**, *9*, 783–788.
241. Eley, D. D.; Spivey, D. I. *Trans. Faraday Soc.* **1962**, *58*, 405–410.
242. Eaton, D. R.; LaLancette, E. A. *J. Chem. Phys.* **1964**, *41*, 3534–3539.
243. Jaumà, A.; Farrera, J. A.; Ribó, J. M. *Monatsh. Chem.* **1996**, *127*, 927–933.
244. Guseva, G. B.; Antina, E. V.; Semeikin, A. S.; Berezin, M. B.; V'Yugin, A. I. *Russ. J. Gen. Chem.* **2002**, *72*, 1306–1310.
245. Guseva, G. B.; Antina, E. V.; Berezin, M. B.; V'Yugin, A. I. *Russ. J. Coord. Chem.* **2004**, *30*, 30–33.
246. Guseva, G. B.; Antina, E. V.; Berezin, M. B.; V'Yugin, A. I. *Russ. J. Gen. Chem.* **2004**, *74*, 1282–1285.
247. Guseva, G. B.; Antina, E. V. *Russ. J. Coord. Chem.* **2005**, *31*, 164–165.
248. Bonnier, C.; Piers, W. E.; Al-Sheikh Ali, A.; Thompson, A.; Parvez, M. *Organometallics* **2009**, *28*, 4845–4851.
249. Hudnall, T. W.; Gabbai, F. P. *Chem. Commun.* **2008**, 4596–4597.
250. Rio, Y.; Sánchez-García, D.; Seitz, W.; Torres, T.; Sessler, J. L.; Guldi, D. M. *Chem. Eur. J.* **2009**, *15*, 3956–3959.
251. Algi, F.; Balci, M. *Synthesis* **2009**, 1341–1347.
252. Gill, H. S.; Finger, I.; Bozidarevic, I.; Szydlo, F.; Scott, M. J. *New J. Chem.* **2005**, *29*, 68–71.
253. Tabba, H. D.; Cavaleiro, J. A. S.; Jeyakumar, D.; Graça, M.; Neves, P. M. S.; Smith, K. M. *J. Org. Chem.* **1989**, *54*, 1943–1948.
254. Bröring, M.; Brandt, C. D.; Bley-Escrich, J.; Gisselbrecht, J.-P. *Eur. J. Org. Chem.* **2002**, 910–917.
255. Goze, C.; Ulrich, G.; Ziessel, R. *J. Org. Chem.* **2007**, *72*, 313–322.
256. D'Souza, F.; Smith, P. M.; Zandler, M. E.; McCarty, A. L.; Itou, M.; Araki, Y.; Ito, O. *J. Am. Chem. Soc.* **2004**, *126*, 7898–7907.
257. Shiragami, T.; Tanaka, K.; Andou, Y.; Tsunami, S.-i.; Matsumoto, J.; Luo, H.; Araki, Y.; Ito, O.; Inoue, H.; Yasuda, M. *J. Photochem. Photobiol. A* **2005**, *170*, 287–297.
258. Galletta, M.; Campagna, S.; Quesada, M.; Ulrich, G.; Ziessel, R. *Chem. Commun.* **2005**, 4222–4224.
259. Kollmannsberger, M.; Rurack, K.; Resch-Genger, U.; Rettig, W.; Daub, J. *Chem. Phys. Lett.* **2000**, *329*, 363–369.
260. Gabe, Y.; Urano, Y.; Kikuchi, K.; Kojima, H.; Nagano, T. *J. Am. Chem. Soc.* **2004**, *126*, 3357–3367.
261. Jones, G., II; Kumar, S.; Klueva, O.; Pacheco, D. *J. Phys. Chem. A* **2003**, *107*, 8429–8434.
262. Harriman, A.; Rostron, J. P.; Cesario, M.; Ulrich, G.; Ziessel, R. *J. Phys. Chem. A* **2006**, *110*, 7994–8002.
263. Ulrich, G.; Goze, C.; Goeb, S.; Retailleau, P.; Ziessel, R. *New J. Chem.* **2006**, *30*, 982–986.
264. Goze, C.; Ulrich, G.; Mallon, L. J.; Allen, B. D.; Harriman, A.; Ziessel, R. *J. Am. Chem. Soc.* **2006**, *128*, 10231–10239.
265. Burghart, A.; Kim, H.; Welch, M. B.; Thoresen, L. H.; Reibenspies, J.; Burgess, K.; Bergström, F.; Johansson, L. B.-Å. *J. Org. Chem.* **1999**, *64*, 7813–7819.

This page intentionally left blank

40 Coordination Chemistry of Verdohemes and Open-Chain Oligopyrrole Systems Involved in Heme Oxidation and Porphyrin Destruction

Alan L. Balch and Faye L. Bowles

Department of Chemistry, University of California, Davis, California 95616, USA

List of Abbreviations

OEP	dianion of octaethylporphyrin
TPP	dianion of tetraphenylporphyrin
OEOP	monoanion of octaethyloxaporphyrin
OEPO	trianion of octaethyloxophlorin
OEB	trianion of ocatethylbilindione
py	pyridine

I. Introduction

This article focuses on the coordination chemistry of a closely related set of tetrapyrrole ligands whose fundamental skeletons are shown in Scheme 1. These tetrapyrrole ligands are formed during the process of heme destruction and this chapter will emphasize the interrelationships of these ligands as heme degradation products and as ligands that impart distinctive chemical and physical properties to their complexes. The well-known porphyrin macrocycle provides a nearly planar array of four nitrogen atoms and usually coordinates as a dianion through the loss of the two N–H protons. The oxaporphyrin macrocycle found in verdoheme has an oxygen atom replacing one of the *meso* carbon atoms and usually coordinates metal ions as a monoanion. The two open-chain tetrapyrroles shown in Scheme 1

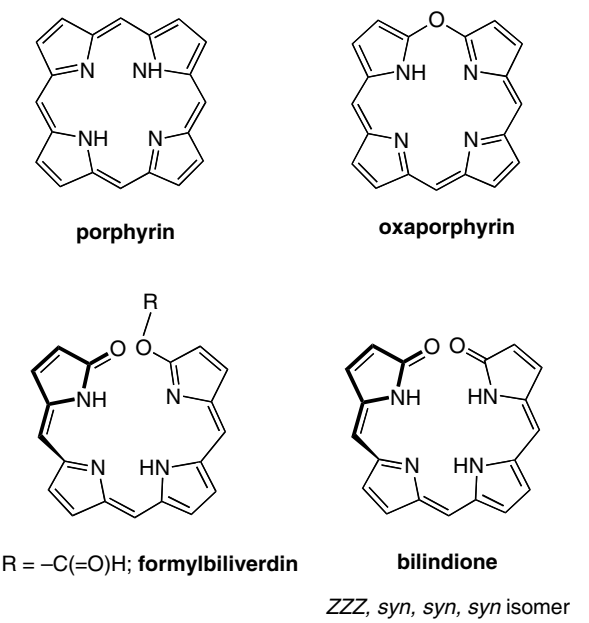

Scheme 1. Ring skeletons of tetrapyrrole ligands.

differ from the macrocycles in that they have helical structures that are produced in order to avoid contact of the terminal substitutents. The formylbiliverdin ligand coordinates as a dianion, while the bilindione ligand can lose three protons to form a trianion. There are a number of other open-ring tetrapyrrole ligands, such as the products of nucleophilic attack on verdohemes, that are related to the formylbiliverdin ligand and coordinate metal ions as a dianion. These different tetrapyrrole ligands are linked through a series of oxidation reactions of metalloporphyrins, as explained below.

A. Heme Catabolism

The enzyme heme oxygenase binds heme as the substrate and utilizes dioxygen to carry out a regiospecific opening of heme at the α-methine position, as shown in Scheme 2.[1–3] In the process, the α-methine carbon is converted to carbon monoxide, and iron is eventually released to give biliverdin as the final product. A second enzyme, biliverdin reductase, subsequently reduces biliverdin to bilirubin, the yellow pigment responsible for jaundice in humans. The regiospecificity of the

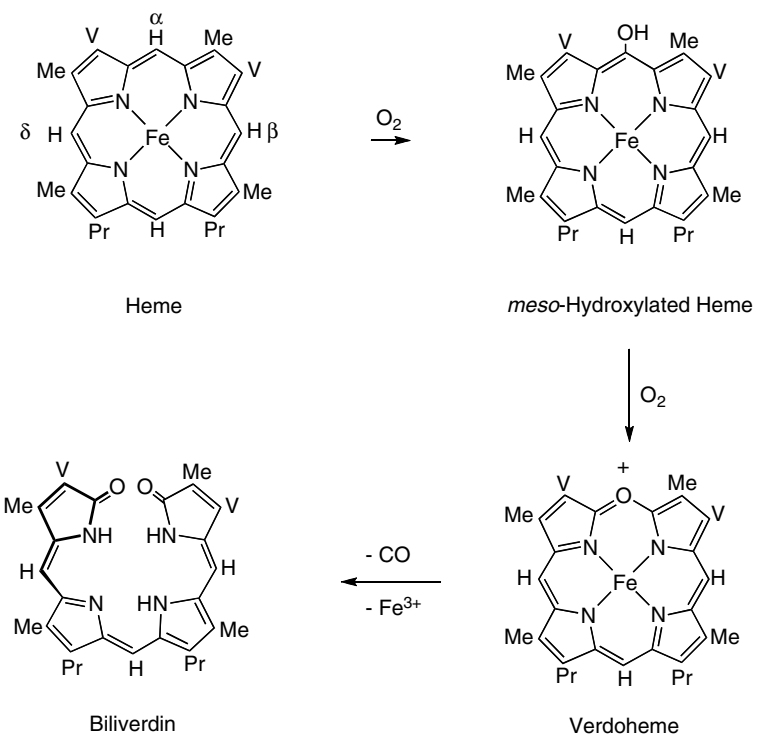

Scheme 2. Heme cleavage by heme oxygenase. Me, methyl; V, vinyl; Pr, propionate.

oxidation is introduced in the initial step of the process, which produces a *meso*-hydroxylated heme as a detectable intermediate in the reaction.[4] The coordination chemistry of *meso*-hydroxylated porphyrins or oxophlorins has been reviewed elsewhere.[5] A green heme, verdoheme, is a second intermediate that is formed during the heme-oxygenase-catalyzed oxidation.[6] The crystal structures of verdoheme bound to human heme oxygenase and to rat heme oxygenase 1 have been reported.[7,8]

B. Coupled Oxidation

Heme and other iron porphyrins are also converted into biliverdin, carbon monoxide and free iron ion by the purely chemical process of coupled oxidation.[9] In this procedure, the iron porphyrin is subjected to aerial oxidation in solution in the presence of an excess of axial ligands (pyridine or cyanide ion) and a reducing agent (ascorbic acid or hydrazine).[10,11] This reaction also produces *meso*-hydroxylated heme and verdoheme as intermediates. However, coupled oxidation of unsymmetrical hemes does not induce the regiospecific opening of heme that is characteristic of the heme oxygenase reaction. Thus, it is the protein, not the porphyrin alone, that guides this hydroxylation step. Coupled oxidation can also be used to oxidize heme proteins.[12–14] This process also results in heme cleavage and the eventual release of biliverdin. Similar intermediates, *meso*-hydroxylated heme and verdoheme, are involved. Coupled oxidation of myoglobin and an active site variant of myoglobin results in cleavage that occurs exclusively at the α-*meso* carbon.[15]

Finally, we note that open-chain oligopyrroles are utilized as pigments in chemistry and biology.[16] As a particularly relevant example, zinc biliverdin complexes have been found to be pigments in the eggshells of birds.[17,18]

II. Verdohemes

A. Verdoheme Formation by Porphyrin Oxidation

Verdohemes are produced chemically by the process of coupled oxidation, as described above.[19,20] Scheme 3 summarizes the results of detailed studies of the verdoheme products from coupled oxidation of $(py)_2Fe^{II}(OEP)$ (py is pyridine and OEP is the dianion of octaethylporphyrin) in pyridine solution with hydrazine as the reducing agent.[21,22] As seen in this scheme, the iron center can undergo a set of reactions that include changes in the oxidation state, axial ligation, and spin state without disruption of the oxaporphyrin ring. The oxaporphyrin ring resembles a porphyrin. However, the oxaporphyrin ligand bears a 1– charge, whereas a corresponding

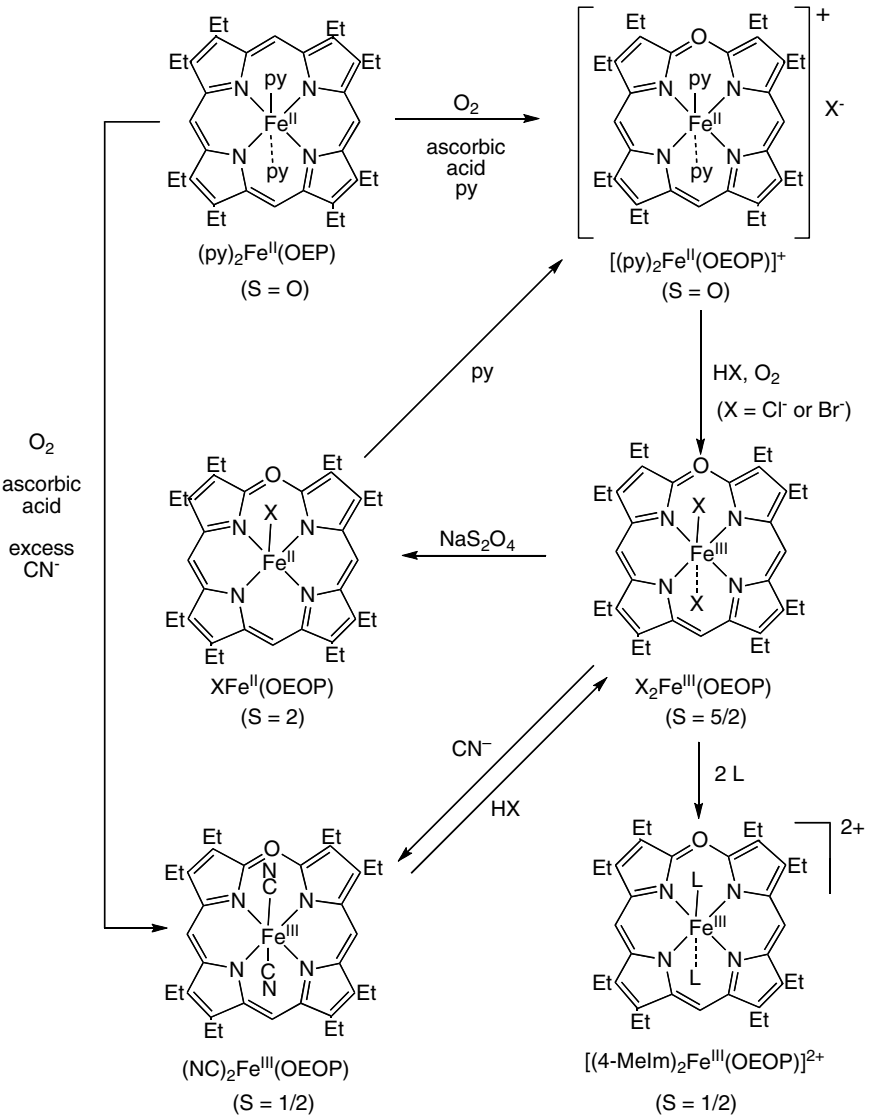

Scheme 3. Verdohemes produced by coupled oxidation.

porphyrin carries a 2– charge. The coupled oxidation of $(py)_2Fe^{II}(OEP)$ in the presence of pyridine results in the formation of green, diamagnetic $[(py)_2Fe^{II}(OEOP)](PF_6)$, which has been isolated as a somewhat air-sensitive solid. The structure of the cation, $[(py)_2Fe^{II}(OEOP)]^+$, is shown in Figure 1. The oxaporphyrin ligand is planar and the iron is six-coordinate. Treatment of $[(py)_2Fe^{II}(OEOP)](PF_6)$ with hydrochloric acid or hydrobromic acid in air results in the formation of paramagnetic $X_2Fe^{III}(OEOP)$ (X = Cl or Br). Structural studies by

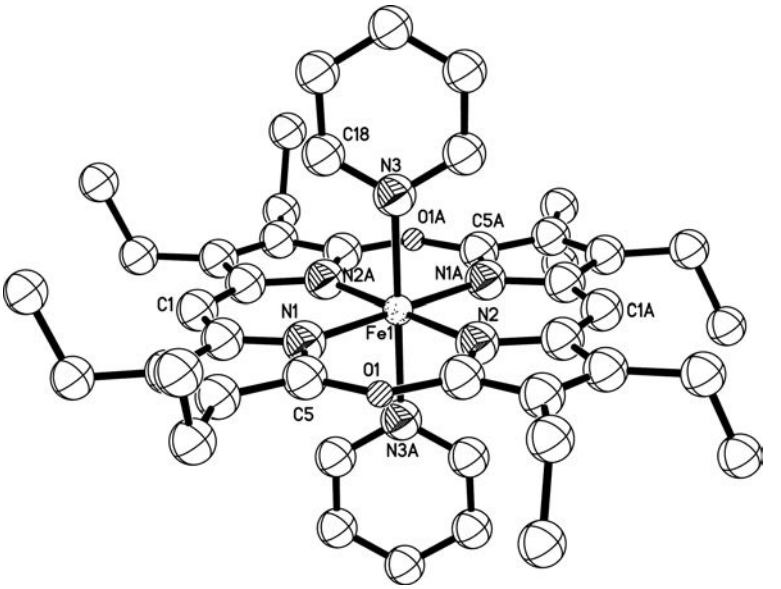

Figure 1. A drawing of $[(py)_2Fe^{II}(OEOP)]^+$ with uniform spherical atoms. Hydrogen atoms are not shown. As is usual with structures of oxaporphyrins, there is disorder in the position of the oxygen atom. The two sites labeled O1 and O1A are occupied equally by an oxygen atom and by a carbon atom. For clarity, the counter anion, $(PF_6)^-$, is not shown. Drawn from data in Balch, A. L.; Koerner, R.; Olmstead, M. M. *J. Chem. Soc., Chem. Commun.* **1995**, 873–874.

^{1}H NMR spectroscopy and X-ray crystallography reveal that the iron in $X_2Fe^{III}(OEOP)$ is six-coordinate and high-spin (S = 5/2). As seen in Figure 2, the iron in $Br_2Fe^{III}(OEOP)$ resides in the plane of the oxaporphyrin and is coordinated by two equivalent axial bromide ligands. Treatment of $X_2Fe^{III}(OEOP)$ with strong-field ligands, CN^- or 4-methylimidazole (4-MeIm), results in the substitution of the axial anionic ligands and the formation of low-spin, six-coordinate complexes, as seen in Scheme 3. Reduction of $X_2Fe^{III}(OEOP)$ with sodium dithionite yields air-sensitive $XFe^{II}(OEOP)$, whose oxidative chemistry is discussed in Section E. Paramagnetic $XFe^{II}(OEOP)$ contains a five-coordinate iron, which is also high-spin (S = 2). The structure of $ClFe^{II}(OEOP)$ as determined by single crystal X-ray diffraction is shown in Figure 3. The oxaporphyrin ligand is not planar but domed. The iron is 0.69 Å out of the porphyrin plane and bound to a single axial bromide ion. The average Fe–N distance increases from 1.964 Å in the iron(III) complex to 2.094 Å in the iron(II) complex. When $XFe^{II}(OEOP)$ is dissolved in pyridine, $[(py)_2Fe^{II}(OEOP)]Cl$ is produced.

Conducting the coupled oxidation of $Fe^{II}(OEP)$ in the presence of a large excess of potassium cyanide results in the formation of low-spin, six-coordinate

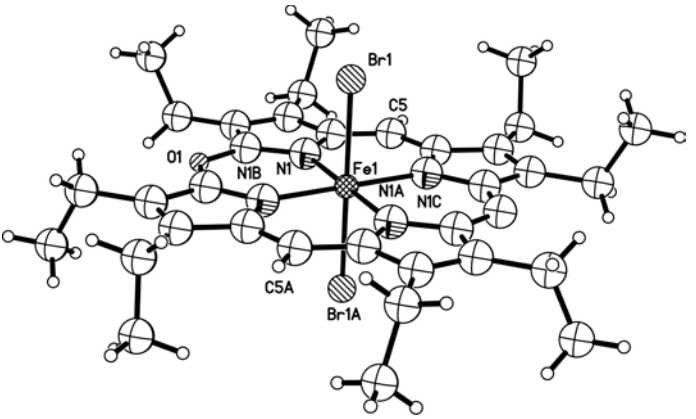

Figure 2. A drawing of Br_2Fe^{III}(OEOP) with uniform spherical atoms. There is disorder in the position of the oxygen atom but this is not shown. Drawn using data in Balch, A. L.; Grazynski, L. L.; Noll, B.; Olmstead, M. M.; Szterenberg, L. Safari, N. *J. Am. Chem. Soc.* **1993**, *115*, 1422–1429.

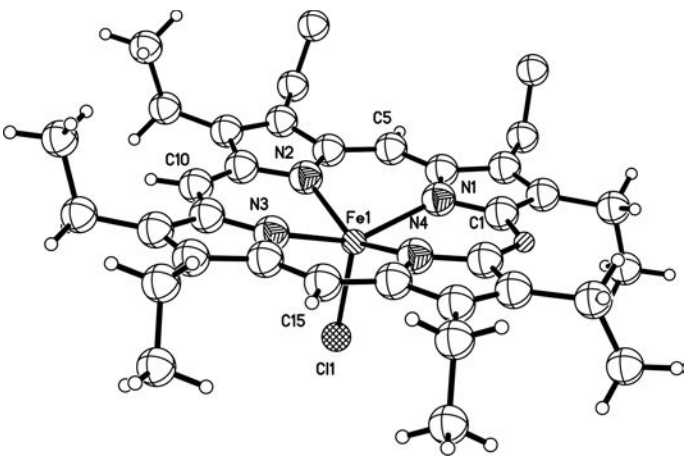

Figure 3. A drawing of $ClFe^{II}$(OEOP) with uniform spherical atoms. There is disorder in the position of the oxygen atom but this is not shown. Drawn utilizing data in Balch, A. L.; Grazynski, L. L.; Noll, B.; Olmstead, M. M.; Szterenberg, L.; Safari, N. *J. Am. Chem. Soc.* **1993**, *115*, 1422–1429.

$(NC)_2Fe^{III}$(OEOP), as seen in Scheme 3.[11] $(NC)_2Fe^{III}$(OEOP) can be reduced to air-sensitive $[(NC)_2Fe^{II}(OEOP)]^-$ by reaction with sodium dithionite.

The reaction of $[(py)_2Fe^{II}(OEOP)]Cl$ with an excess of ammonium hexafluorophosphate and hydrofluoric acid produces the high-spin, five-coordinate complex $(PF_6)Fe^{II}$(OEOP), which may be subsequently converted into

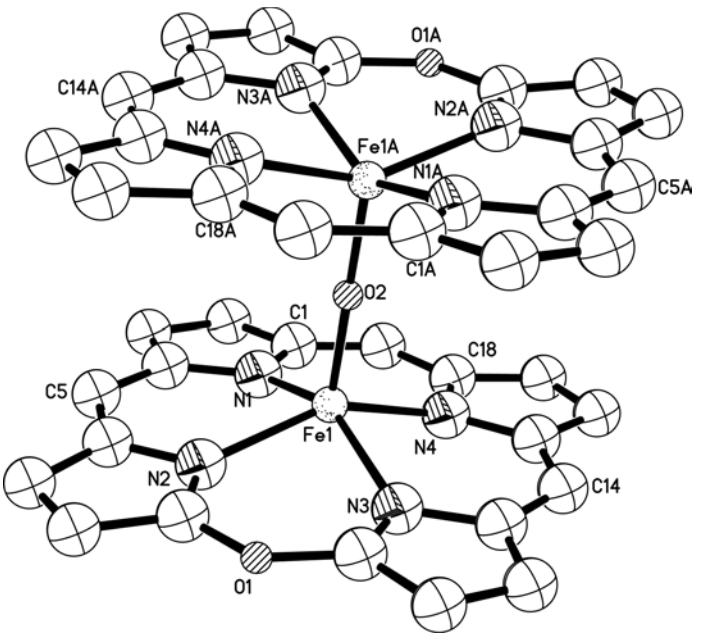

Figure 4. A drawing of the dication in the salt $[\mu\text{-O}\{Fe^{III}(OEOP)\}_2](PF_6)_2$ with uniform spherical atoms. For clarity the ethyl groups are not shown. Drawn from data in Khorasani-Motlagh, M.; Safari, N.; Noroozifar, M.; Saffari, J.; Biabani, M.; Reboucas, J. S.; Partick, B. *Inorg. Chem.* **2005**, *44*, 7762–7769.

$[\mu\text{-O}\{Fe^{III}(OEOP)\}_2](PF_6)_2$ by reaction with dioxygen.[23–25] The structure of the dication in $[\mu\text{-O}\{Fe^{III}(OEOP)\}_2](PF_6)_2$ is shown in Figure 4. The dication $[\mu\text{-O}\{Fe^{III}(OEOP)\}_2]^{2+}$ is the analog of the well-known porphyrin μ-oxo-dimer, e.g. $(\mu\text{-O})\{Fe^{III}(OEP)\}_2$.[26]

Exposure of the novel dimer, $\{Fe^{III}(\mu\text{-OEPO})\}_2$, to dioxygen after the addition of an isocyanide (RNC), which may be xylyl isocyanide or *t*-butylisocyanide, offers a route to the formation of diamagnetic, six-coordinate $(RNC)_2Fe^{II}(OEOP)$, as shown in Scheme 4.[27] Crystallographic characterization of $(xylylNC)_2Fe^{II}(OEOP)$ indicates that the structure is similar to that of $[(py)_2Fe^{II}(OEOP)]^+$ (see Figure 1) and that the oxaporphyrin ring is planar.

Coupled oxidation has also been utilized with $Fe^{II}(TPP)$ (TPP is the dianion of tetraphenylporphyrin) as the substrate.[28] No evidence of the formation of verdohemes was reported in this reaction. However, several iron-free, open-chain tetrapyrroles were isolated as products.[28]

Although the coupled oxidation procedure is usually performed with iron porphyrins, it can be modified to utilize cobalt porphyrins as well. For example, it is possible to convert $Co^{II}(OEP)$ into a number of products including the verdohemes

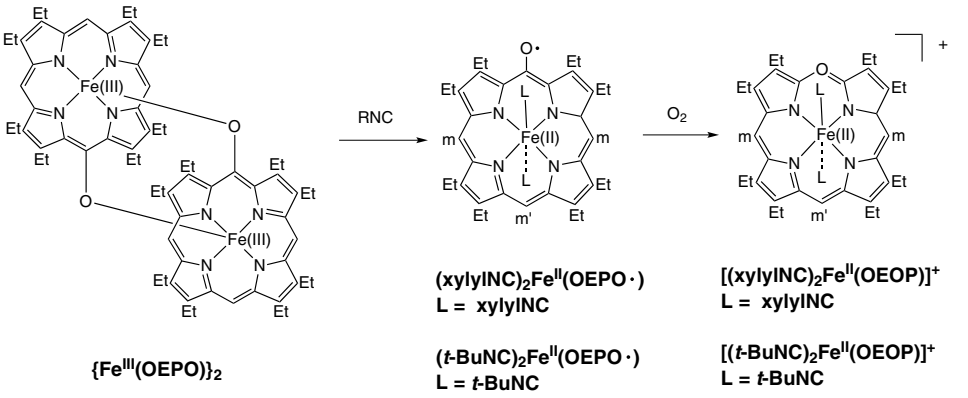

Scheme 4. Verdoheme formation by oxidation of a *meso*-hydroxylated heme.

Cl_2Co^{III}(OEOP) and $[Co^{II}(OEOP)](PF_6)$ through oxidation, as shown in Scheme 5.[29,30] Treatment of Co^{II}(OEP) with air in pyridine did not produce evidence of the formation of the corresponding verdoheme or biliverdin, but by changing the solvent to an 8:1 ratio of dichloromethane:tetrahydrofuran and cooling it was possible to observe the formation of a green suspension from which the various products shown in Scheme 5 were obtained. The crystallographically determined structures of six-coordinate, diamagnetic Cl_2Co^{III}(OEOP) and four-coordinate, S = 1/2 $[Co^{II}(OEOP)]^+$ are shown in Figure 5.

B. Verdoheme Formation by Dehydration of a Bilindione

Verdohemes can also be obtained by dehydration of the corresponding bilindione (biliverdin). Scheme 6 shows a prototypical reaction of this sort — the conversion of a bilindione to zinc verdoheme through reaction with a zinc(II) salt.[31] The structure of the product with a five-coordinate zinc ion and a slightly domed oxaporphyrin ligand is shown in Figure 6.

III. Open-Chain Tetrapyrroles from Ring Opening of Verdohemes

Verdohemes are subject to ring opening through the attack of external nucleophiles. This reaction has been widely employed to produce a variety of stable zinc(II) complexes with helical structures. These zinc(II) complexes are diamagnetic and readily characterized by UV-visible and ^{1}H NMR spectroscopy.

Addition of methoxide, methanethiolate, or dimethylamide to zinc verdoheme, $[Zn^{II}(OEOP)](O_2CCH_3)$, proceeds in a good yield to produce helical complexes of

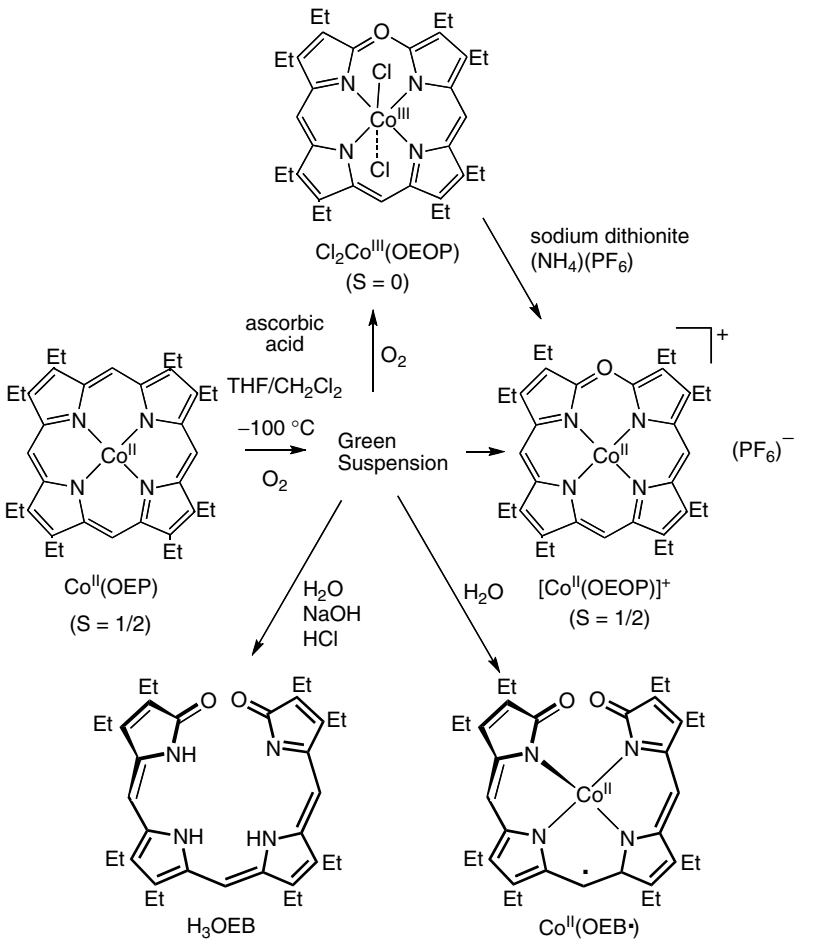

Scheme 5. Coupled oxidation of Co^{II} (OEP).

the open-ring tetrapyrroles, as shown in Scheme 7.[32,33] Presumably, these ring-opening reactions proceed through nucleophilic attack on a carbon atom adjacent to the oxygen atom of the verdoheme. Each of the products, Zn^{II}(OEBOMe), Zn^{II}(OEBSMe), and Zn^{II}(OEBNMe_2), has been isolated and characterized by single crystal X-ray diffraction. Figures 7 and 8 show the structures of Zn^{II}(OEBOMe) and Zn^{II}(OEBNMe_2), respectively. The ligands in Zn^{II}(OEBOMe), Zn^{II}(OEBSMe), and Zn^{II}(OEBNMe_2) all adopt a helical geometry that is characteristic of the geometry of H_3OEB and many complexes of other open-chain tetrapyrrole ligands. In each complex, the four-coordinate zinc ion has a geometry that is best described as a flattened tetrahedron. Generally, the Zn–N distance to the pyrrole ring bearing the added nucleophile is the longest of the four Zn–N

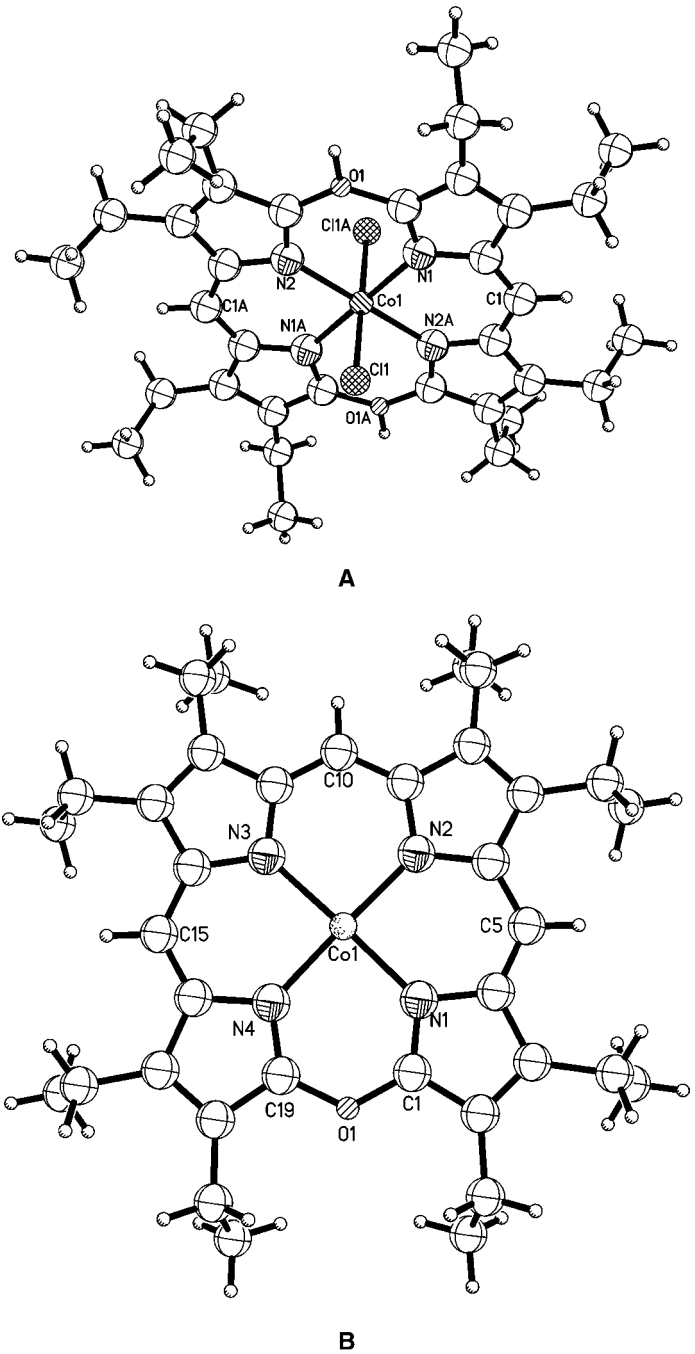

Figure 5. **A**, a drawing of Cl_2Co^{III}(OEOP) with uniform spherical atoms from data in Balch, A. L.; Mazzanti, M.; Olmstead, M. M. *J. Chem. Soc., Chem. Commun.* **1994**, 269–270. **B**, a drawing of the cation in the salt $[Co^{II}(OEOP)](PF_6)$ with uniform spherical atoms from data in Balch, A. L.; Mazzanti, M.; St. Claire, T.; Olmstead, M. M. *Inorg. Chem.* **1995**, *34*, 2194.

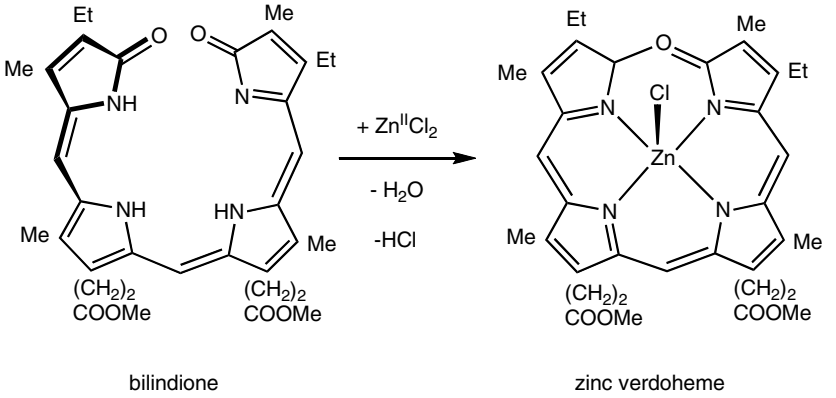

Scheme 6. Formation of a zinc verdoheme by dehydration of a bilindione.

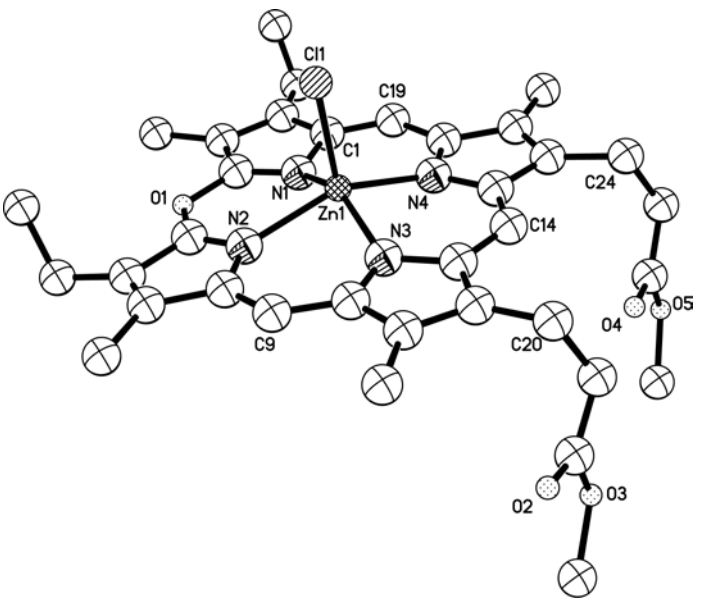

Figure 6. A drawing of chloro-(5-oxonia-mesoporphinato-dimethyl ester)-zinc(II) with uniform spherical atoms. Drawn using data from Fuhrhop, J.; Krüger, P.; Sheldrick, W. S. *Liebigs Ann. Chem.* **1977**, *3*, 339–359.

distances. For example, in $Zn^{II}(OEBNMe_2)$, the Zn–N(1) distance is 2.184(5) Å, which is the longest of the four Zn–N distances. The other Zn–N distances fall in the range 2.002(5)–2.022(5) Å and are slightly shorter than those found in zinc porphyrins, where the Zn–N distances fall in the range of 2.06–2.07 Å.[34] In $Zn^{II}(OEBNMe_2)$, the environment about N(5) of the dimethylamide group is planar.

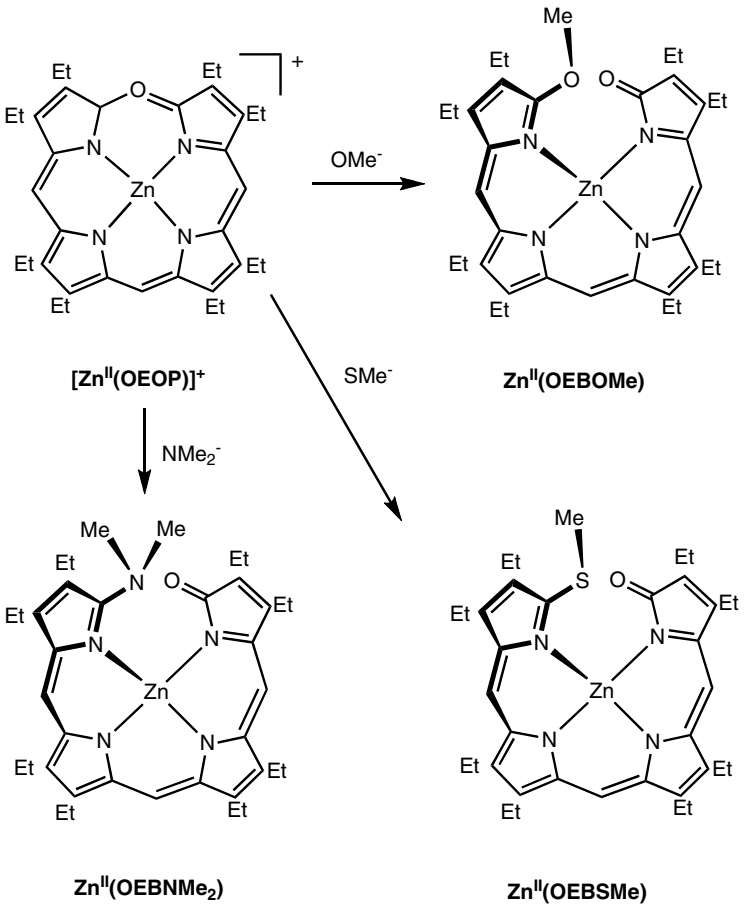

Scheme 7. Reactivity of zinc verdoheme with nucleophiles.

The C–N(5)–C bond angles, C(1)–N(5)–C(37), 122.0 (6)°, C(1)–N(5)–C(38), 123.5 (6)°, and C(37)–N(5)–C(38), 114.4 (5)°, are near 120°, and the sum of these three angles is 359.9°. The dimethylamide unit is also nearly coplanar with the adjacent pyrrole ring. The dihedral angle between these two units is only 16.6°. The planarity of N(5) and the orientation of the dimethylamide unit suggest that conjugation within the tetrapyrrole ligand extends out into this functionality.

Computational studies have examined the mechanism of the addition of nucleophiles to zinc verdohemes.[35]

The addition of cyanide ion to $[Zn^{II}(OEOP)](O_2CCH_3)$ is a more complex process than that observed when methoxide, methanethiolate, or dimethylamide is added to the same zinc verdoheme. When cyanide reacts with $[Zn^{II}(OEOP)](O_2CCH_3)$, ring opening is accompanied by a degree of substitution at the *meso* positions, as seen in Scheme 8.[36] The reaction of cyanide with $[Zn^{II}(OEOP)]$

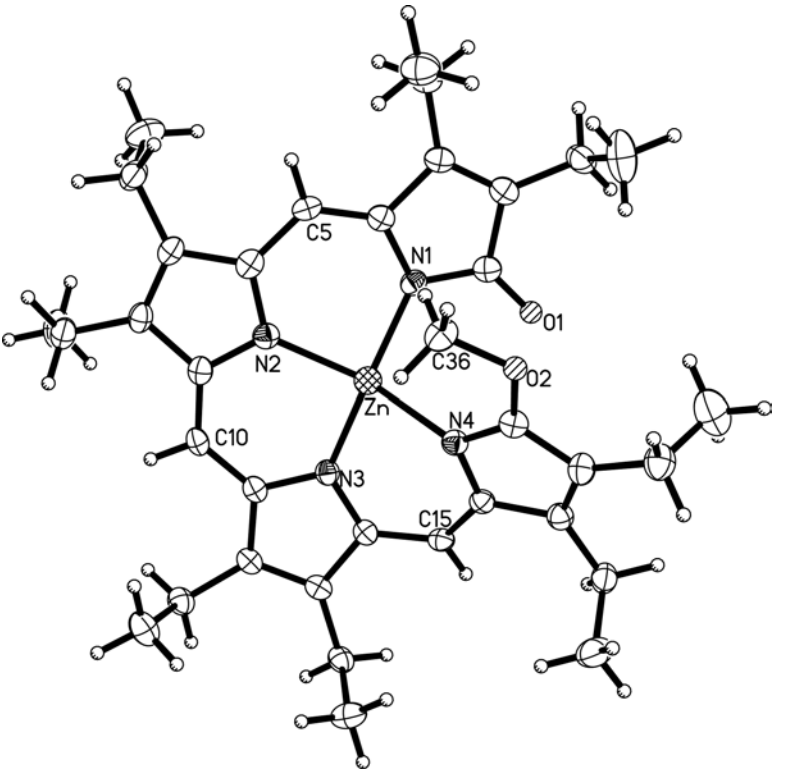

Figure 7. A drawing of Zn^{II}(OEBOMe) with 50% thermal ellipsoids. Drawn from data in Latos-Grazynski, L.; Johnson, J.; Attar, S.; Olmstead, M. M.; Balch, A. L. *Inorg. Chem.* **1998**, *37*, 4493–4499.

(O_2CCH_3) was challenging to control, and three products, H_2(OEB-15,19-$(CN)_2$), Zn^{II}(OEB-15,19-$(CN)_2$), and Zn^{II}(OEB-10,15,19-$(CN)_3$), have been isolated and identified crystallographically and spectroscopically, despite the fact that a clean separation of these products was difficult to accomplish. The reactions shown in Scheme 8 are somewhat reminiscent of the reaction of cyanide with H_3OEB, which also results in *meso* substitution and the formation of H_3OEB-10-CN.[37]

When Zn^{II}(OEB-15,19-$(CN)_2$) and Zn^{II}(OEB-10,15,19-$(CN)_3$) were crystallized from acetone/water, the unusual binuclear complexes μ-H_2O-{Zn^{II}(OEB-10,19-$(CN)_2$)}$_2$ and μ-H_2O-{Zn^{II}(OEB-10,15,19-$(CN)_3$)}$_2$ were obtained.[36] These complexes involve five-coordinate zinc ions rather than the four-coordinate zinc ions found in Zn^{II}(OEBOMe), Zn^{II}(OEBSMe), and Zn^{II}(OEBNMe_2) (see Scheme 7). The structure of μ-H_2O-{Zn^{II}(OEB-10,15,19-$(CN)_3$)}$_2$ is shown in Figure 9. Both μ-H_2O-{Zn^{II}(OEB-10,19-$(CN)_2$)}$_2$ and Zn^{II}(OEB-10,15,19-$(CN)_3$)

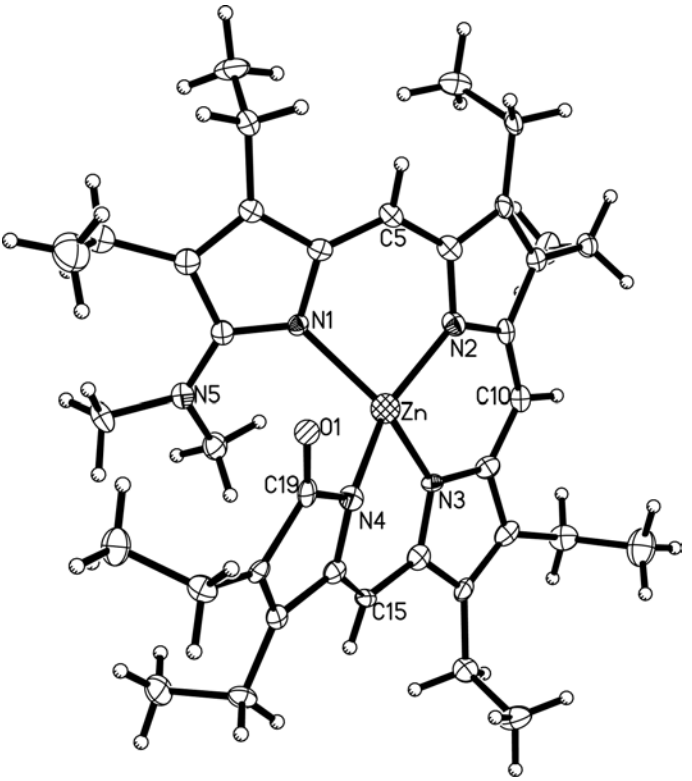

Figure 8. A drawing of $Zn^{II}(OEBNMe_2)$ with 50% thermal ellipsoids. Drawn with data from Johnson, J. A.; Olmstead, M. M.; Balch, A. L. *Inorg. Chem.* **1999**, *38*, 5379–5383.

have helical structures in which the chirality of each tetrapyrrole is the same in any one molecule. A bridging water molecule, which is hydrogen-bonded to both tetrapyrrole ligands and coordinated to two zinc ions, serves as an effective linker to transfer the helical sense of one tetrapyrrole to the adjoining tetrapyrrole.

The chiral nature of the helical zinc complexes shown in Scheme 7 has been utilized in a number of studies of molecular recognition involving chiral molecules as axial ligands.[38–50]

IV. Biliverdin and Its Metal Complexes

A. Free Ligand

The conformational aspects of metal-free biliverdins have been reviewed.[50] Briefly, the *ZZZ*, *syn*, *syn*, *syn* isomer shown in Scheme 1 is the favored geometry, as demonstrated by computational studies and experimental studies.[51] Several biliverdins have been crystallized and their structures determined by X-ray

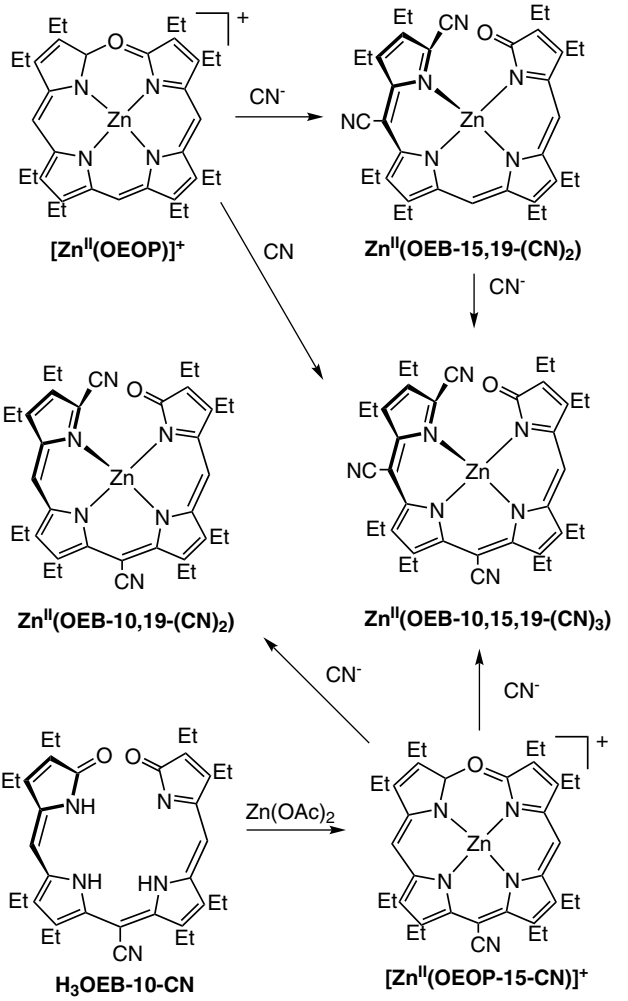

Scheme 8. Reactivity of zinc verdoheme with cyanide ion.

crystallography. Figure 10 shows the structure of an example.[52] Notice that the free ligand adopts a helical structure with the two terminal oxygen atoms separated by 3.4 Å. Several other bilindiones, including biliverdin dimethyl ester, have been examined by X-ray crystallography and shown to have very similar structures.[53,54]

Octaethylbiliverdin undergoes a two-electron oxidation to form $[H_2OEBox]^+$ when treated with diiodine, as shown in Scheme 9.[55] The oxidation product, a diamagnetic aquamarine cation, has been isolated as a triiodide salt and crystallized. The structure of the product reveals that the helical structure is retained after

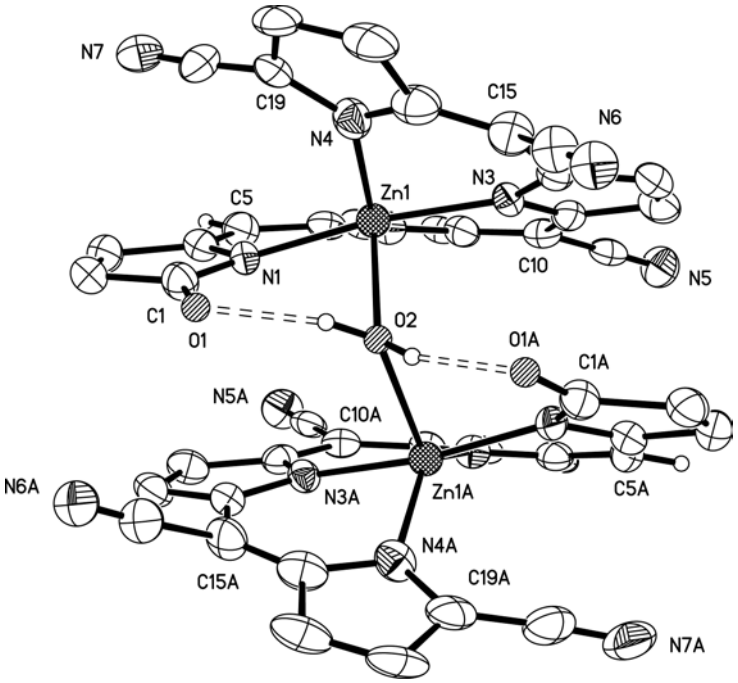

Figure 9. A drawing of μ-H_2O-{Zn^{II}(OEB-10,15,19-$(CN)_3$)}$_2$ with 50% thermal ellipsoids. For clarity the ethyl groups have been omitted. The dashed lines show the hydrogen bonding. Drawn from data in Johnson, J. A.; Olmstead, M. M.; Stolzenberg, A. M.; Balch, A. L. *Inorg. Chem.* **2001**, *40*, 5585–5595.

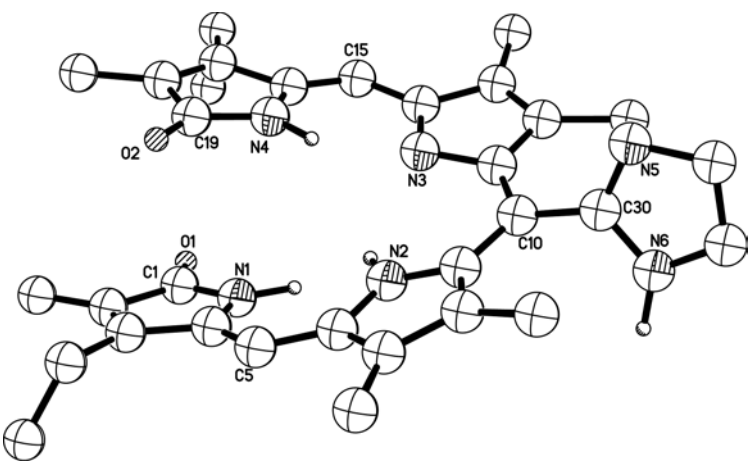

Figure 10. A drawing of a typical biliverdin or bilindione, (meso-substituted arylbilatriene-abc, 2-imidazolylderivative) with uniform spherical atoms. Drawn using data in Wagner, U.; Kratky, C.; Falk, H.; Woss, H. *Monatsh. Chem.* **1991**, *122*, 749–758.

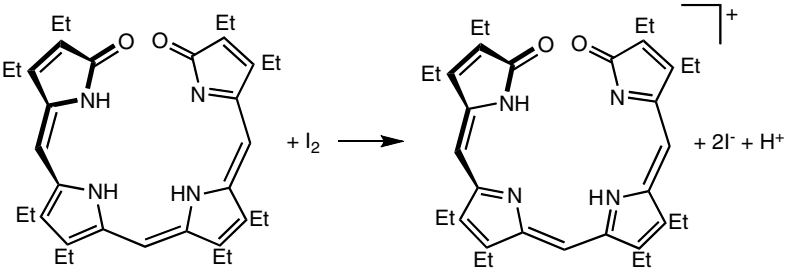

Scheme 9. Two-electron oxidation of octaethylbilindione.

oxidation but the nonbonded O···O separation in the product (2.98 Å) is less than that in a bilindione (3.34 Å). A computational analysis of the oxidation product and its dimerization through hydrogen bonding is available.[56]

B. Dimeric Complexes; The Case of $\{Mn^{III}(\mu\text{-OEB})\}_2$

Treatment of H_3OEB with various metal salts, including manganese acetate, produced metal complexes with the general formula M(OEB),[57–59] but these early studies did not provide insight into the diverse physical and electronic structures of these complexes, which may exist as monomers or dimers. The manganese complex, which forms olive green solutions, has a dimeric structure, $\{Mn^{III}(\mu\text{-OEB})\}_2$, as shown in Figure 11.[60] The manganese ions are five-coordinate with bonds to the four nitrogen atoms of one OEB ligand, with the fifth bond supplied by the oxygen atom of the other OEB ligand. Each dimer has C_2 symmetry and is chiral, but the compound crystallized as a racemate in the space group *C*2/*c*, where an inversion center relates a pair of dimers. The dimer, $\{Mn^{III}(\mu\text{-OEB})\}_2$, dissolves in pyridine to form intensely green solutions from which crystals of monomeric, five-coordinate $(py)Mn^{III}(OEB)$ have been obtained.[60] The structure of $(py)Mn^{III}(OEB)$ is shown in Figure 12. The manganese ion in $(py)Mn^{III}(OEB)$ is five-coordinate, with the tetrapyrrole ligand assuming a helical arrangement. The manganese ion has a distorted trigonal prismatic coordination. The N(l)-Mn-N(3) unit with a bond angle of 177.1(2)° forms the axis, while the equatorial plane contains the pyrrole nitrogen atoms, N(2) and N(3), and the pyridine nitrogen atom, N(5).

The magnetic moments of these manganese complexes are indicative of the presence of high-spin Mn(III) (d^4) ions.[60] In pyridine solution, $(py)Mn^{III}(OEB)$ has a magnetic moment of 4.8(3) μ_β at 23 °C. In chloroform solution at 21 °C,

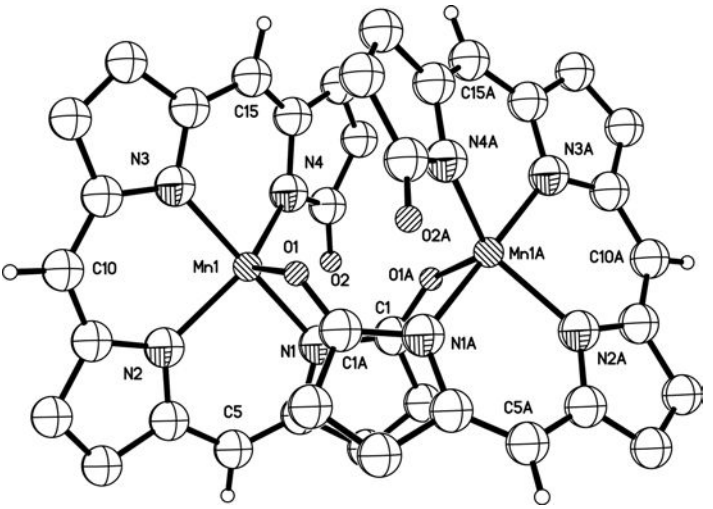

Figure 11. A drawing of $\{Mn^{III}(\mu\text{-OEB})\}_2$ with uniform spherical atoms. For clarity, all ethyl groups have been removed. Drawn from data in Balch, A. L.; Mazzanti, M.; Noll, B. C.; Olmstead, M. M. *J. Am. Chem. Soc.* **1994**, *116*, 9114–9122.

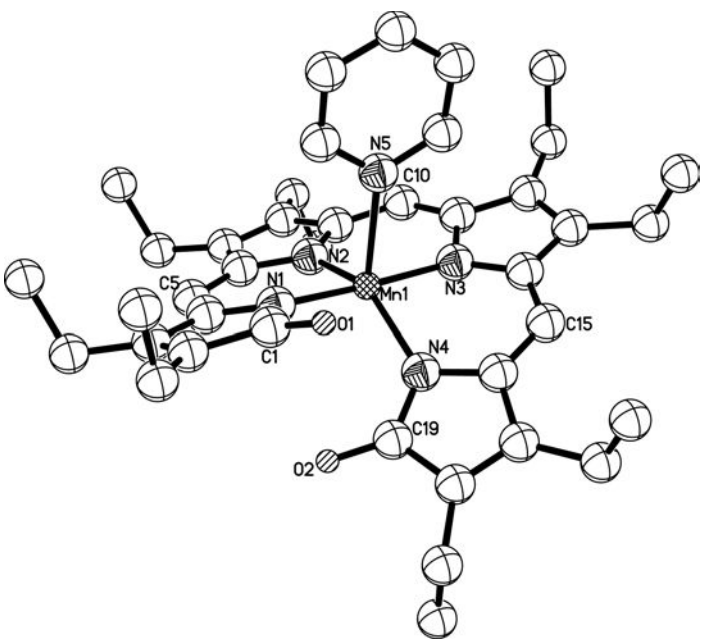

Figure 12. A drawing of (py)Mn^{III}(OEB) with uniform spherical atoms. Drawn with data from Balch, A. L.; Mazzanti, M.; Noll, B. C.; Olmstead, M. M. *J. Am. Chem. Soc.* **1994**, *116*, 9114–9122.

$\{Mn^{III}(\mu\text{-OEB})\}_2$ has a magnetic moment of 4.7(3) μ_β for each Mn ion, and this value is unchanged over the temperature range from −50 to +21 °C. Hence, it appears that any magnetic coupling between the two Mn(III) ions is small, as is expected since the nonbonded Mn–Mn distance is large, 4.430 (1) Å, and the covalent path between the two Mn(III) ions is long.[60] Due to the paramagnetic nature of the high-spin Mn(III) ions, no ^{1}H NMR spectrum could be detected for $(py)Mn^{III}(OEB)$ or $\{Mn^{III}(\mu\text{-OEB})\}_2$.

Solutions of either $\{Mn(\mu\text{-OEB})\}_2$ in chloroform or $(py)Mn^{III}(OEB)$ in pyridine are air-sensitive, but the products of oxidation have not been identified.[60] The biliverdin ligand system has also been utilized to develop a catalytic scavenger of superoxide that employs the Mn(III)/Mn(IV) redox couple.[61]

C. Monomeric Biliverdin Complexes, $M^{II}(OEB\bullet)$

A series of monomeric complexes are formed by reaction of H_3OEB with cobalt, nickel, palladium, or copper. Spectroscopic studies (*vide infra*) all point to the fact that these complexes involved an oxidized ligand radical, which requires them to be formulated as $M^{II}(OEB\bullet)$ rather than $M^{III}(OEB)$.

Crystals of the products — $Co^{II}(OEB\bullet)$,[60] $Ni^{II}(OEB\bullet)$,[59] $Pd^{II}(OEB\bullet)$,[62] and $Cu^{II}(OEB\bullet)$[63] — are isostructural. Figure 13 shows the structure of a representative example, $Pd^{II}(OEB\bullet)$. To prevent contact between the terminal oxygen atoms, the tetrapyrrole ligand assumes a helical geometry. The constraints of this arrangement require that the palladium ion should not have truly planar geometry. Thus, the PdN_4 unit shows the following deviations from planarity: Pd, 0.00; N(1), +0.22; N(2), –0.23 Å. Selected bond distances and angles for the set of $M^{II}(OEB\bullet)$ complexes are given in Table 1. These data show that cobalt, nickel, and copper complexes have similar bond distances while the palladium complex, as expected, has longer metal–nitrogen bond lengths. The C(1)–O(1) bond distances, which fall in the range of 1.20–1.25 Å, are consistent with the presence of a C=O group at the end of the ligand.

Evidence for the presence of ligand free radicals in this series comes from spectroscopic measurements that are also supported by computational studies.[64,65] Both $Ni^{II}(OEB\bullet)$ and $Pd^{II}(OEB\bullet)$ display EPR resonances that are indicative of ligand-based spins (g = 2.03 for Ni, 2.08 for Pd) and show only very broad, unassigned resonances in the 0–3 ppm region of the NMR spectrum.[62] In contrast, $Cu^{II}(OEB\bullet)$ does not produce an EPR spectrum, but shows a well-resolved ^{1}H NMR spectrum that extends from 135 to −90 ppm.[63] The eight methylene resonances (at 92, 87, 66, 48, 28, 20, 6, and −1 ppm) show linewidth variations with the resonances, with the largest hyperfine shifts showing the greatest linewidths. These variations result from local dipolar

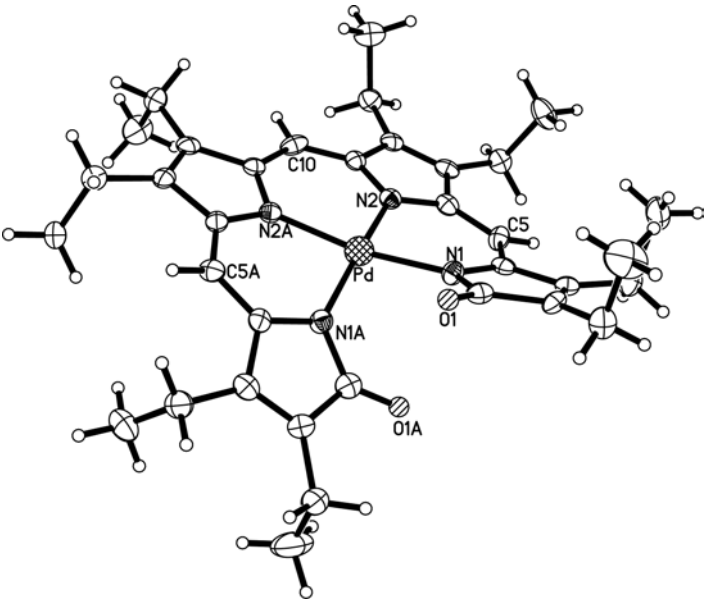

Figure 13. A drawing of Pd^{II}(OEB•) with 50% thermal ellipsoids. Co^{II}(OEB•), Ni^{II}(OEB•), and Cu^{II}(OEB•) have been crystallographically characterized and have similar structures. Drawn from data in Lord, P. A.; Olmstead, M. M.; Balch, A. L. *Inorg. Chem.* **2000**, *39*, 1128–1134.

Table 1. Selected bond distances and angles for M^{II}(OEB•).

	Co^{II}(OEB•)[a]	Ni^{II}(OEB•)[b]	Pd^{II}(OEB•)[c]	Cu^{II}(OEB•)[d]
Bond distances (Å)				
M–N(1)	1.873(3)	1.875(7)	2.012(4)	1.954(2)
M–N(2)	1.909(3	1.897(7)	2.011(4)	1.962(2)
C(1)–O(1)	1.209(4)	1.248(9)	1.223(6)	1.216(3)
Bond angles (deg.)				
N(1)–M–N(2)	90.2(1)	90.0(2)	89.42(15)	90.3(1)
N(1)–M–N(1′)	93.1(2)	92.7(3)	93.5(2)	96.2(1)
N(2)–M–N(2′)	92.0(2)	92.7(3)	90.6(2)	91.1(1)
N(1)–M–N(2′)	162.0(2)	162.3(2)	167.03(16)	158.6(1)

Data from: [a]Ref. 60; [b]Ref. 59; [c]Ref. 62; [d]Ref. 63.

relaxation due to the delocalized spin density that resides on the tetrapyrrole ligand.

Co^{II}(OEB•), Ni^{II}(OEB•), Pd^{II}(OEB•), and Cu^{II}(OEB•) are members of four series of complexes that are related by reversible redox reactions. Scheme 10 summarizes relevant information. For palladium, the three-membered electron

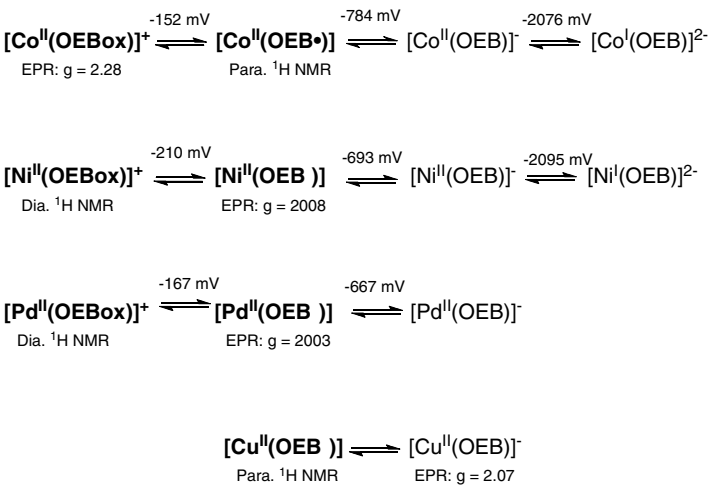

Scheme 10. Redox reactions of monomeric M^{II} (OEB•). Key: **Boldface,** complex isolated and characterized by X-ray diffraction; EPR, solution *g* value given; Dia. ^{1}H NMR, diamagentic ^{1}H NMR spectrum; Para. ^{1}H NMR, paramagnetically broadened and shifted ^{1}H NMR spectrum analyzed. Above each redox process the average electrochemical E_p(ox) and E_p(red) are given in mV for a dichloromethane solution vs. ferrocene/ferrocinium.

transfer series involving $[Pd^{II}(OEBox)]^+$, $Pd^{II}(OEB•)$, and $[Pd^{II}(OEB)]^-$ has been characterized electrochemically, while for nickel the four compounds — $[Ni^{II}(OEBox)]^+$, $Ni^{II}(OEB•)$, $[Ni^{II}(OEB)]^-$, and $[Ni^{I}(OEB)]^{-2}$ — have been detected electrochemically.[62] The most highly oxidized members of these series have been isolated in the form of their diamagnetic tri-iodide salts. $[Ni^{II}(OEBox)]I_3$ and $[Pd^{II}(OEBox)]I_3$ have been characterized spectroscopically and by X-ray diffraction. Figure 14 shows the structure of $[Pd^{II}(OEBox)]I_3$. A compilation of relevant bond distances and angles for $[Ni^{II}(OEBox)]I_3$ and $[Pd^{II}(OEBox)]I_3$ and related compounds is given in Table 2. These two compounds are isomorphic and isostructural. Their structures again involve helical coordination of the open-chain tetrapyrrole ligand about the metal. The triiodide ion is not coordinated to the metal but sits over one of the *meso* carbon atoms of the tetrapyrrole. Reduction of $[M^{II}(OEBox)]I_3$ causes a slight elongation of the M–N bonds, as seen in the data in Tables 1 and 2.

$Co^{II}(OEB•)$ has a magnetic moment of 1.9 μ_β at 25 °C, which decreases with decreasing temperature so that it is 1.4 μ_β at −173 °C.[60] The ^{1}H NMR spectrum of $Co^{II}(OEB•)$ shows paramagnetically shifted resonances that do not obey the Curie law. Thus, the complex may be formulated as $Co^{II}(OEB•)$ with a reduced, paramagnetic cobalt(II) ion and an oxidized ligand, which is present as a coordinated radical. Temperature variations in the coupling between the two paramagnetic

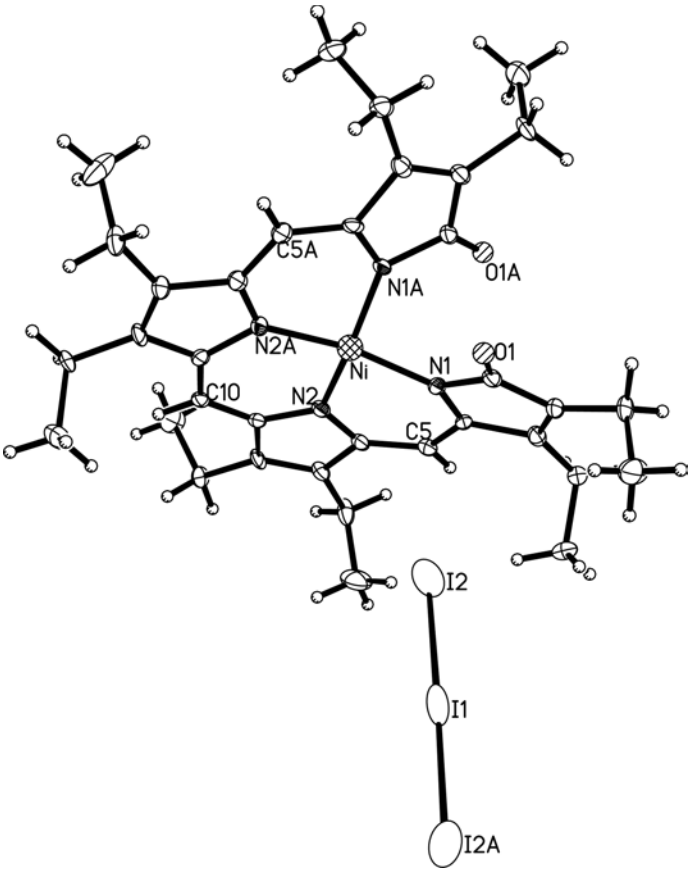

Figure 14. A drawing of both ions in the salt $[Pd^{II}(OEBox)]I_3$ with 50% thermal ellipsoids. $[Ni^{II}(OEBox)]I_3$ is isostructural. Drawn utilizing data in Lord, P. A.; Olmstead, M. M.; Balch, A. L. *Inorg. Chem.* **2000**, *39*, 1128–1134.

centers could produce the changes that are seen in the magnetic properties. Alternatively, there may be a thermal equilibrium between a diamagnetic $Co^{III}(OEBox)$ state and a paramagnetic $Co^{II}(OEB\bullet)$ state or there may be an equilibrium between a diamagnetic $Co^{III}(OEBox)$ state and a triplet $Co^{III}(OEBox)$ state. Cyclic voltammetry of $Co^{II}(OEB\bullet)$ shows that this complex is also part of a four-membered electron transfer series that includes $[Co^{II}(OEBox)]^+$, $Co^{II}(OEB\bullet)$, $[Co^{II}(OEB)]^-$, and $[Co^{I}(OEB)]^{-2}$.[66] Oxidation by diiodine produces $[Co^{II}(OEBox)]I_3$, which has been isolated and crystallized. The structure is shown in Figure 15. While one of the iodine atoms of the triiodide ion lies above the cobalt, the triiodide ion is disordered so that there are three different Co–I distances — 2.875(10), 2.818(4), and 2.798(14) Å — that are considerably longer than a typical Co–I_3 bond distance of 2.589 Å. Consequently, the triiodide ion is

Table 2. Selected bond distances and angles for $[M^{II}(OEBox)]^{+}$

	$[Ni^{II}(OEBox)]I_3$ (Ref. a)	$[Pd^{II}(OEBox)]I_3$ (Ref. a)	$[Co^{II}(OEBox)]I_3$ (Ref. b)	$[(py)_2Co^{II}(OEBox)]I_3$ (Ref. c)
Bond distances (Å)				
M–N(1)	1.867(5)	1.983(2)	1.916(7)	1.950(5)
M–N(2)	1.879(5)	1.986(2)	1.910(7)	1.956(4)
M–N(3)			1.926(7)	1.997(5)
M–N(4)			1.898(7)	
C(1)–O(1)	1.198(7)	1.204(3)	1.196(10)	1.216(7)
Bond angles (deg.)				
N(1)–M–N(2)	90.0(2)	88.61(10)	90.3(3)	89.8(2)
N(1)–M–N(1′) or N(1)–M–N(4)	92.7(3)	93.79(14)	92.0(3)	91.3(3)
N(2)–M–N(2′) or N(3)–M–N(4)	92.7(3)	91.59(14)	89.0(3)	92.0(3)
N(1)–M–N(2′) or N(2)–M–N(4)	162.3(2)	167.72(10)	158.6(3)	167.2(2)
N(1)–M–N(3)			173.4(3)	85.6(2)
N(2)–M–N(3)			91.1(3)	94.6(2)
N(3)–M–N(3′)				174.5(3)

Data from: [a]Ref. 62; [b]Ref. 66; [c]Ref. 67.

only loosely associated with the cation. The NMR spectrum $[Co^{II}(OEBox)]I_3$ complex in dichloromethane solution indicates that the anion is dissociated and the cobalt ion is four-coordinate. The EPR spectrum of $[Co^{II}(OEBox)]I3$ (solution: g, 2.28; solid: g_1, 2.23; g_2, 2.42; and g_3, 2.01) and the magnetic moment of 1.8 μ_β indicate that it is a low-spin Co(II) complex.

Changes in the axial ligation of this cobalt complex can alter the electronic distribution between the metal and the ligand. Addition of pyridine to a sample of $[Co^{II}(OEBox)]I_3$ results in the formation of $[[(py)_2Co^{III}(OEB\bullet)]I_3$, as indicated by a marked alteration in the EPR spectrum.[67] In a frozen solution the new spectrum shows a sharp, slightly anisotropic signal ($g_{x,y}$ = 1.996, g_z = 2.018) near the free electron g value, with none of the cobalt hyperfine coupling that is seen for $[Co^{II}(OEBox)]I_3$. The salt $[(py)_2Co^{III}(OEB\bullet)]I_3$ has been isolated in crystalline form, and the cation has been shown to involve a six-coordinate cobalt ion with two axial pyridine ligands, as seen in Figure 16.

Solutions of $Cu^{II}(OEB\bullet)$ and $Co^{II}(OEB\bullet)$ are sensitive to air, which causes their conversion into tetrahedral complexes containing two monoanionic tetraethyl-propentdyopent (TEPD) ligands, as shown in Scheme 11.[63,68] In addition to forming $Co^{II}(TEPD)_2$ in a 40% yield, aerial oxidation of $Co(OEB\bullet)$ produces both carbon monoxide and carbon dioxide, which were detected by infrared-spectroscopic

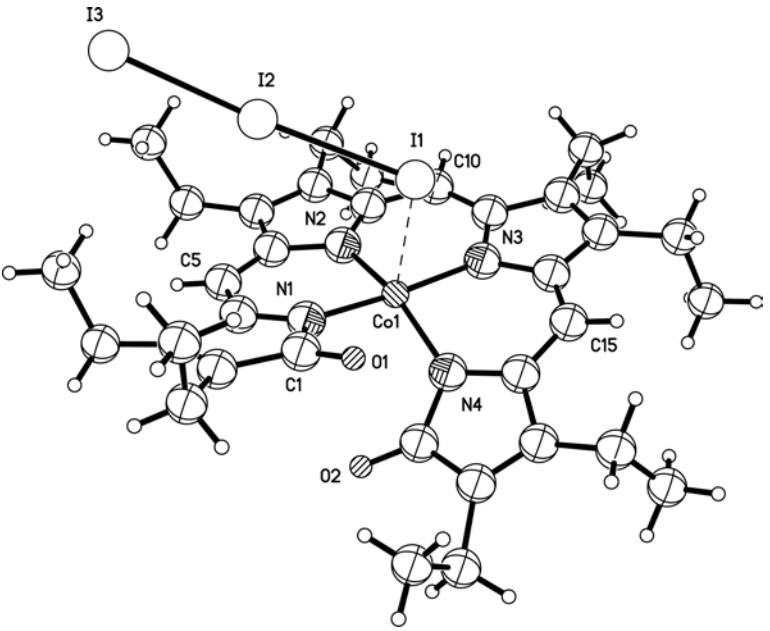

Figure 15. A drawing of $[Co^{II}(OEBox)]I_3$ with uniform spherical atoms. Only one of the three orientations of the triiodide ion is shown. Drawn from data in Attar, S.; Balch, A. L.; Ozarowski, A.; Van Calcar, P.; Winkler, K. *J. Am. Chem. Soc.* **1997**, *119*, 3317–3323.

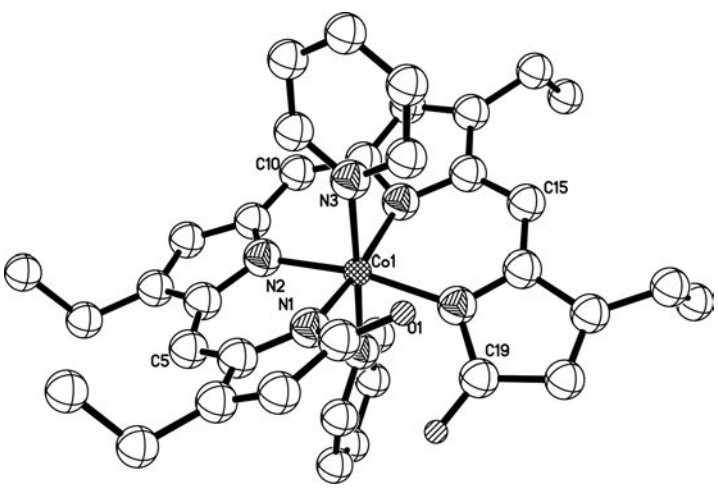

Figure 16. A drawing of the cation, $[(py)_2Co^{III}(OEB\cdot)]^+$, with uniform spherical atoms. For simplicity the triiodide ion is not shown. Drawn using data from Attar, S.; Ozarowski, A.; Van Calcar, P. M.; Winkler, K.; Balch, A. L. *Chem. Commun.* **1997**, *12*, 1115–1116.

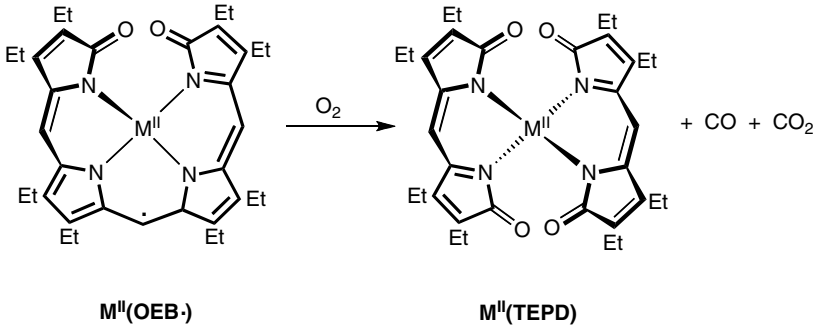

Scheme 11. Air oxidation of M^{II} (OEB), M = Co or Cu.

analysis of the gases above the reaction mixture. This behavior has a certain analogy to the oxidation of porphyrins that leads to the formation of biliverdins with the release of carbon monoxide, as shown earlier in Scheme 2. The structure of $Co^{II}(TEPD)_2$ with nearly tetrahedral coordination of the cobalt ion is shown in Figure 17. $Cu^{II}(TEPD)_2$ has a very similar structure. In chloroform-*d* solution the magnetic susceptibility of $Co^{II}(TEPD)_2$ is 3.9 μ_β at 23 °C.[68] This value is consistent with the presence of high-spin (S = 3/2) cobalt(II) in the complex.

D. Dimeric Complexes Revisited; The Curious Case of $\{Pd_2(\mu\text{-OEB})\}_2$

In addition to forming $Pd^{II}(OEB\bullet)$, the reaction of palladium salts with H_3OEB can produce a novel, diamagnetic dimer, $\{Pd_2(\mu\text{-OEB})\}_2$, whose remarkable structure is shown in Figure 18.[69] $\{Pd_2(\mu\text{-OEB})\}_2$ consists of two helical $Pd^{II}(OEB)$ units that are joined through a $(Pd^{I}_2)^{2+}$ unit. The coordination geometry within the two $Pd^{II}(OEB)$ portions of the tetranuclear complex is similar to that in $Pd^{II}(OEB\bullet)$ (see Figure 13) and $[Pd^{II}(OEBox)]^+$ (see Figure 14). While complexes of the type $[Pd^{I}_2L_6]^{2+}$ (L is a neutral, two-electron donor) are a well-established part of palladium chemistry,[70] the environment of the central $(Pd^{I}_2)^{2+}$ unit which is suspended between the two $Pd^{II}(OEB)$ moieties has several novel features. Each palladium atom of the $(Pd^{I}_2)^{2+}$ unit is coordinated to an olefinic bond of one of the two $Pd^{II}(OEB)$ units. Such η^2 coordination of a transition metal center to the π system at one of the *meso* carbon atoms of the OEB ligand is unusual for the chemistry of porphyrins or open-chain tetrapyrroles. One nitrogen atom from each tetrapyrrole ligand is also coordinated to one of the palladium ions in the central $(Pd^{I}_2)^{2+}$ unit. Thus, N8 bridges Pd4 and Pd3, while N4 bridges Pd2 and Pd1. The Pd–N distances that involve the bridging nitrogen atoms [Pd1–N4, 2.082(9); Pd2–N4, 2.107(8); Pd3–N8, 2.091(8); Pd4–N8, 2.094(8) Å] are longer than the strictly terminal Pd–N distances [2.007(10), 2.051(8) Å]. Such bridging by pyrrole

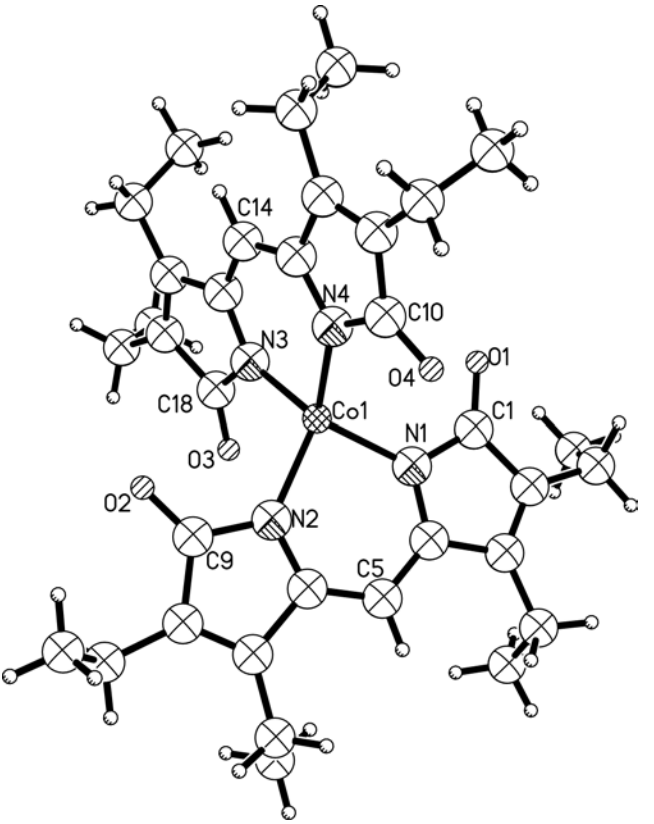

Figure 17. A drawing of $Co^{II}(TEPD)_2$ with uniform spherical atoms. Drawn with data from Koerner, R.; Olmstead, M. M.; Van Calcar, P. M.; Winkler, K.; Balch, A. L. *Inorg. Chem.* **1998**, *37*, 982–988.

nitrogen atoms in transition metal complexes of porphyrins and related tetrapyrroles is uncommon. The coordination of the $(Pd^{I}_2)^{2+}$ portion is completed by Pd–O bonds to each of the Pd^{II}(OEB) units.

$\{Pd_2(\mu\text{-OEB})\}_2$ undergoes several interesting reactions, as shown in Scheme 12.[71] Treatment of $\{Pd_2(\mu\text{-OEB})\}_2$ with pyridine results in the formation of Pd^{II}(OEB•), which has been described previously.[62] More remarkably, the reaction of diiodine with $\{Pd_2(\mu\text{-OEB})\}_2$ in pyridine solution produces the rearranged complex **1** (in Scheme 12), in which one of the *meso* carbon atoms of the ligand has been incorporated into one of the pyrrole rings to produce a pyridine-like ring and *trans*-$Pd(py)_2I_2$. This process of bilindione rearrangement and oxidation occurs as a direct consequence of the π-coordination of the palladium. The reaction results in the migration of a nitrogen atom from a pyrrole carbon atom to what was formerly a *meso* carbon atom to transform a former pyrrole ring into a

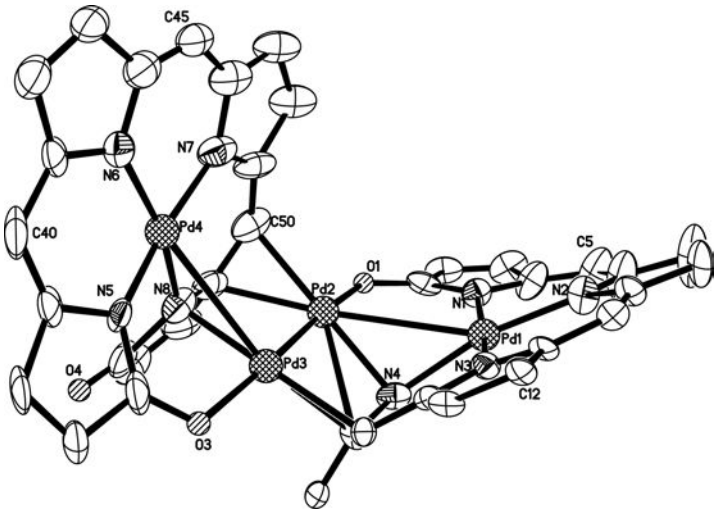

Figure 18. A drawing of $\{Pd_2(\mu\text{-OEB})\}_2$ with 50% thermal ellipsoids. For clarity, the ethyl groups are not shown. Drawn with data in Lord, P.; Olmstead, M. M.; Balch, A. L. *Angew. Chem. Int. Ed.* **1999**, *38*, 2761–2763.

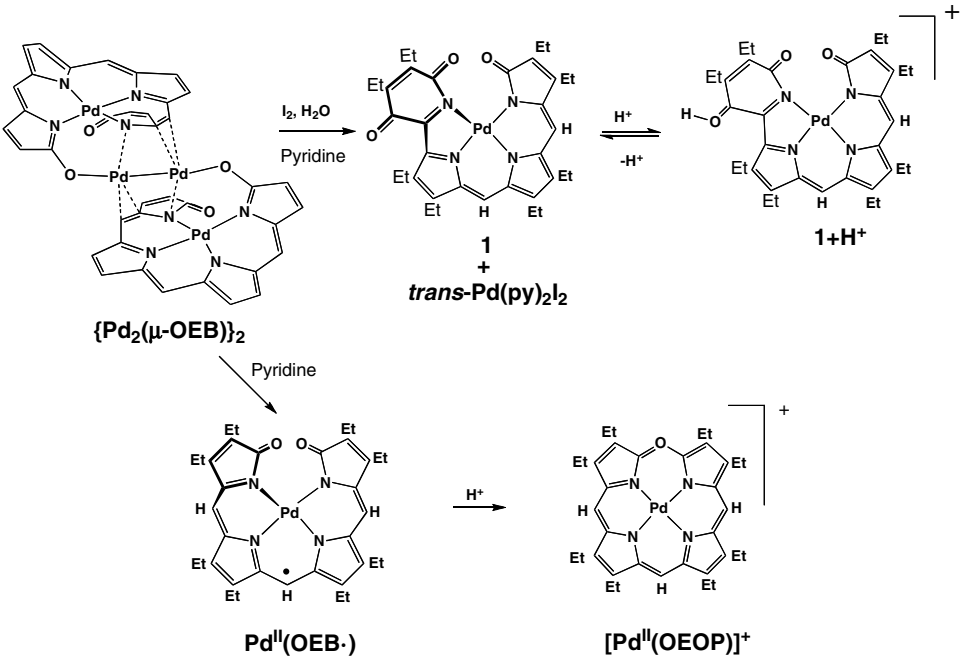

Scheme 12. Reactions of $\{Pd_2(\mu\text{-OEB})\}_2$.

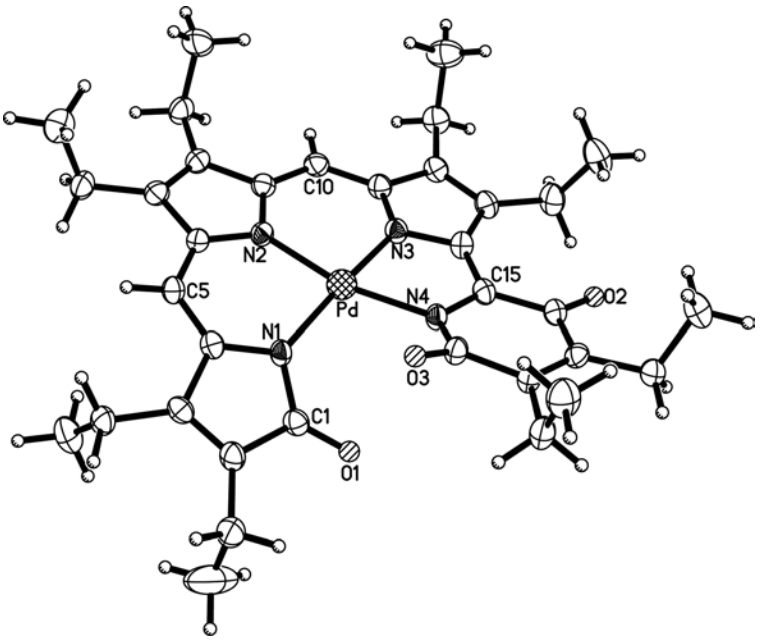

Figure 19. A drawing of the rearranged complex **1** of Scheme 12 with 50% thermal ellipsoids. Drawn from data in Lord, P. A.; Noll, B. C.; Olmstead, M. M.; Balch, A. L. *J. Am. Chem. Soc.* **2001**, *123*, 10554–10559.

six-membered ring. Additionally, this process results in cleavage of the Pd–Pd and Pd–C bonds, oxidation of palladium, and introduction of an oxygen atom from water, but not necessarily in this particular sequence. The helical structure of **1** is shown in Figure 19. The overall structure is similar to the structures of Pd^{II}(OEB•) and $[Pd^{II}(OEBox)]^{+}$.

E. Iron Biliverdin Complexes

Iron biliverdin complexes play an integral role in the process of heme cleavage and have been detected as relatively stable intermediates in the enzymatic and purely chemical paths of heme oxidation. However, the formation of an iron biliverdin complex by direct metalation of a biliverdin has not been reported. Despite many attempts in the Balch laboratory, where many other metals have been coordinated to produce biliverdin metal complexes, direct metalation using iron salts has not been observed. In contrast, iron biliverdin and related complexes are available from oxidation of porphyrins and from verdohemes. The study of the reactions leading to the formation of iron biliverdin complexes has involved complementary studies in solution utilizing UV-visible spectroscopy and especially

^{1}H NMR spectroscopy and X-ray crystallographic studies of individual isolated compounds. Many of the compounds involved are paramagnetic; yet, clearly resolved ^{1}H NMR spectra have been obtained and analyzed for these compounds.

The coupled oxidation process generally produces a verdoheme in only ~40% yield and this low yield suggests that there are other products. Careful examination of the coupled oxidation of $(py)_2Fe^{II}(OEP)$ in pyridine solution resulted in the isolation of $[(py)_2Fe^{II}(OEOP)]Cl$ as a diamagnetic green solid in a 50% yield along with a previously unknown, paramagnetic iron complex that was identified as $\{Fe^{III}(\mu\text{-OEB})\}_2$ in a 32% yield.[72] $\{Fe^{III}(\mu\text{-OEB})\}_2$ was identified by a combination of ^{1}H NMR and X-ray crystallographic studies. Figure 20 shows the structure of the dimer. In this dimer, each iron is coordinated to four nitrogen atoms from one OEB trianion and an oxygen donor from another OEB ligand. The structure of $\{Fe^{III}(\mu\text{-OEB})\}_2$ is related to that of $\{Mn^{III}(\mu\text{-OEB})\}_2$, which was shown previously in Figure 11. For a dimer of this sort, a centrosymmetric (and hence achiral) dimer is formed when the two monomeric units that combine have opposite helicity (opposite chirality), as shown in Scheme 13. The initially reported data showed that $\{Fe^{III}(\mu\text{-OEB})\}_2$ has such a centrosymmetric structure.[72] However, if the two monomeric units that combine have the same helicity, then a chiral dimer with C_2 symmetry will form. Scheme 13 shows schematic diagrams of the enantiomeric pair of C_2 dimers for $\{M^{III}(\mu\text{-OEB})\}_2$. $\{Mn^{III}(\mu\text{-OEB})\}_2$ has the C_2 structure in the solid state.[60]

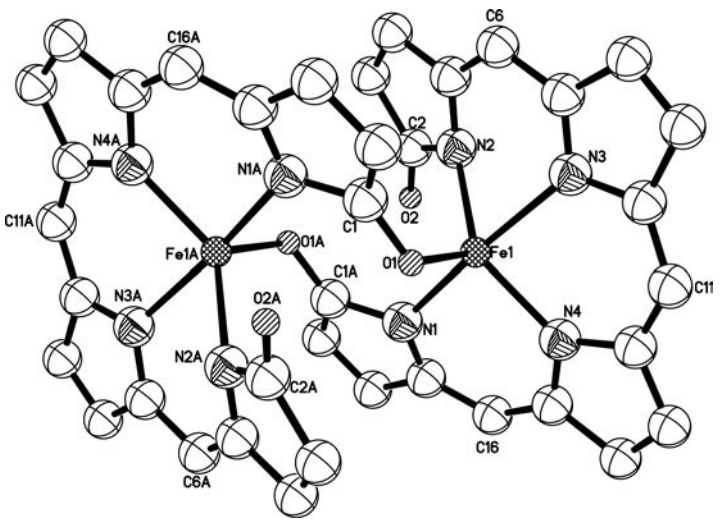

Figure 20. A drawing of $\{Fe^{III}(\mu\text{-OEB})\}_2$ with 50% thermal ellipsoids. For clarity the ethyl groups are not shown. Drawn using data from Balch, A. L.; Latos-Grazynski, L.; Noll, B. C.; Olmstead, M. M.; Safari, N. *J. Am. Chem. Soc.* **1993**, *115*, 9056–9061.

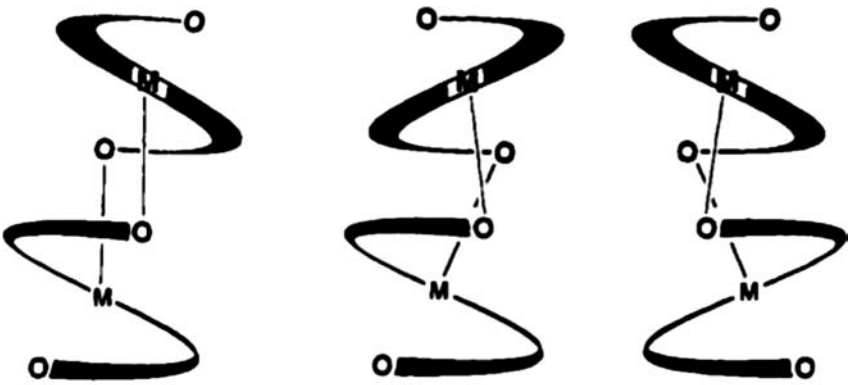

Scheme 13. Isomers of dimeric $\{M^{III}(OEB)\}_2$.

Treatment of $\{Fe^{III}(\mu\text{-OEB})\}_2$ with hydrochloric acid releases the blue bilindione H_3OEB in a 91% yield.[72] In pyridine-d_5 solution, ^1H NMR studies have shown that $\{Fe^{III}(\mu\text{-OEB})\}_2$ undergoes cleavage of the Fe–O bond when the dimer is dissolved in pyridine to form monomeric $(py)_2Fe^{III}(OEB)$. This process is reversible and is related to similar disruption of $\{Mn^{III}(\mu\text{-OEB})\}_2$ by coordination of pyridine. The ease with which $\{Fe^{III}(\mu\text{-OEB})\}_2$ undergoes loss of iron is one of its notable characteristics. Indeed, the crystal structure of $\{Fe^{III}(\mu\text{-OEB})\}_2$, shown in Figure 20, suffers from partial occupancy of the iron sites. The ease of loss of iron from $\{Fe^{III}(\mu\text{-OEB})\}_2$ and the difficulty of inserting iron into biliverdin may be an important consideration in the process of heme destruction.[72]

In pyridine solution, $(py)_2Fe^{III}(OEB)$ is air-sensitive, and upon exposure to the atmosphere it is converted into a tripyrrole, as shown in Scheme 14.[73] The oxidative process is apparently related to the previously discussed oxidation of $Cu^{II}(OEB\bullet)$ and $Co^{II}(OEB\bullet)$ by air, which results in oxidation of a *meso* C–H unit to produce complexes containing two dipyrrole ligands, as shown in Scheme 11.[63,68] Oxidation of $(py)_2Fe^{III}(OEB)$ seems to select one of the two equivalent C–H groups rather than the unique C–H group in the middle of the ligand. The structure of the product, $[ClFe^{III}(HETP)]^-$, is shown in Figure 21. The Fe–N distances in the two independent anions in the crystal are 1.990(7) [2.049(8)], 2.077(8) [2.077(9)], and 2.001(7) [2.001(6)] Å, and the Fe–Cl distances are 2.251(3) and [2.253(3)] Å. These distances are similar to those of five-coordinate iron(III) complexes such as $ClFe^{III}(OEP)$, which has an Fe–N distance of 2.073(8) Å and are Fe–Cl distance of 2.235(9) Å.[74]

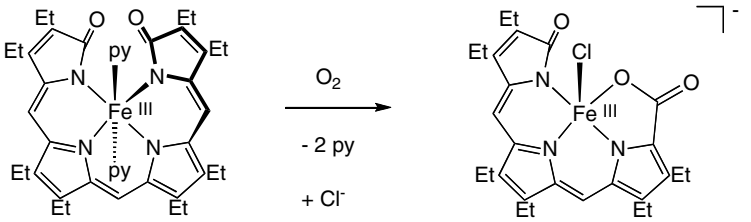

Scheme 14. Oxidative formation of an iron tripyrrole complex.

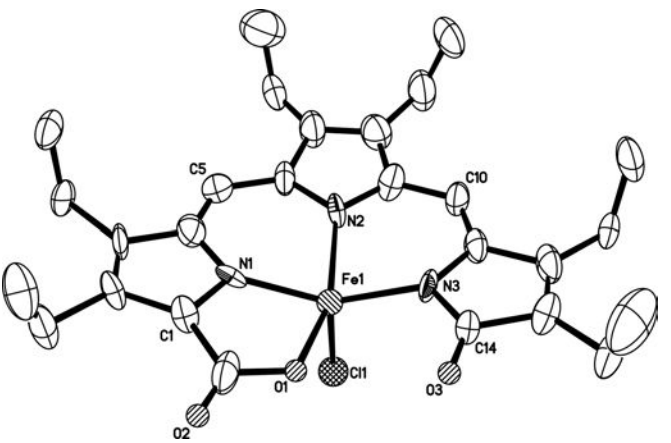

Figure 21. A drawing of the anion in (n-Bu_4N)[$ClFe^{III}$(HETP)] with 50% thermal ellipsoids. Drawn with data from Rath, S. P.; Olmstead, M. M. Latos-Grazynski, L.; Balch, A. L. *J. Am. Chem. Soc.* **2003**, *125*, 12678–12679.

Related helical iron complexes have been obtained by various reactions of verdohemes, as shown in Scheme 15. For example, studies of the reaction of 5-oxaporphyrin iron complexes with methoxide ion were undertaken to provide models for the initial step in hydrolysis of verdohemes.[75,76] Treatment of both low-spin [$(py)_2Fe^{II}$(OEOP)]Cl and high-spin $ClFe^{II}$(OEOP) with the methoxide ion in either pyridine or methanol solution with careful exclusion of dioxygen caused ring opening and addition of methoxide to one end of the tetrapyrrole in reactions that are analogous to those of zinc verdohemes shown in Scheme 7. Black {Fe^{II}(μ-OEBOMe)}$_2$ was isolated in crystalline form from the reaction of $ClFe^{II}$(OEOP) with methoxide in methanol and studied by single-crystal X-ray diffraction. The structure of the dimer is shown in Figure 22. The molecule has a centrosymmetric, dimeric structure composed of two helical Fe(μ-OEBOMe) units with FeN_4

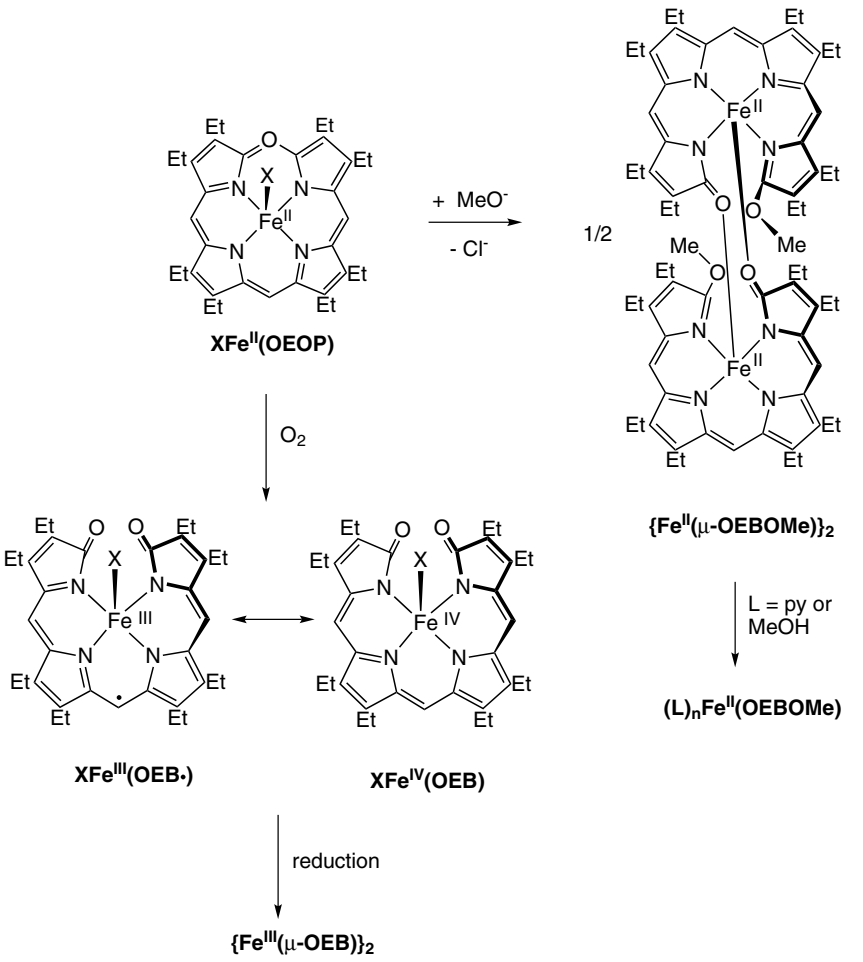

Scheme 15. Ring opening reactions of XFe^{II}(OEOP).

coordination that are connected by a pair of Fe–O bonds. Thus, each iron ion has approximately trigonal bipyramidal geometry. Black crystals of $\{Fe^{II}(\mu\text{-OEBOMe})\}_2$ dissolve in dichloromethane in the presence of methanol or pyridine to form high-spin $\{(MeOH)_nFe^{II}(OEBOMe)\}$ or $\{(py)_nFe^{II}(OEBOMe)\}$ (n = 1 or 2) through rupture of the Fe–O bonds in the dimer.[75] The electronic absorption spectra of these open-chain complexes show characteristic low-energy features at *ca.* 720 and 810 nm. At 23 °C, the paramagnetically shifted ^{1}H NMR spectrum of $\{Fe^{II}(\mu\text{-OEBOMe})\}_2$ shows a characteristic upfield methoxy resonance, 16 methylene resonances in the 47–5 ppm region, and *meso* resonances in the 51–29 ppm region. The temperature dependence of these spectra shows marked deviations from the Curie law that are consistent with a dimeric structure.

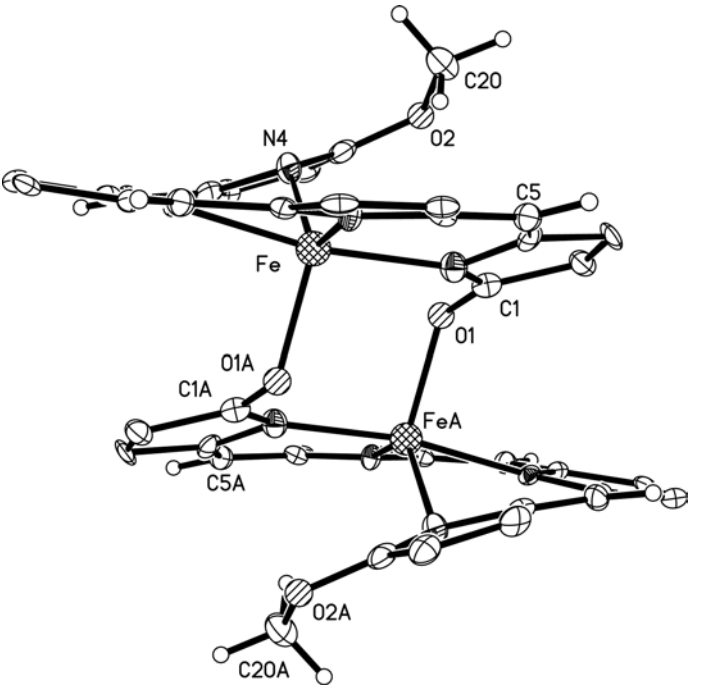

Figure 22. A drawing of $\{Fe^{II}(\mu\text{-OEBOMe})\}_2$ with 50% thermal ellipsoids. For clarity the ethyl groups are not shown. Drawn from data in Koerner, R.; Latos-Grazynski, L.; Balch, A. L. *J. Am. Chem. Soc.* **1998**, *120*, 9245–9255.

The process of hydrolysis of verdoheme and its conversion into biliverdin has also been the subject of some computational studies.[77,78]

High-spin, five-coordinate XFe^{II}(OEOP) (X = Cl or Br) is unusually reactive toward dioxygen. In contrast, the six-coordinate iron(III) verdoheme, Cl_2Fe^{III}(OEOP), is not affected by exposure to dioxygen. Treatment of a green solution of XFe^{II}(OEOP) (X = Cl or Br) with dioxygen results in the formation of a new paramagentic complex, which may be formulated as an iron(IV) complex [XFe^{IV}(OEB)] or as a complex with an oxidized ligand and iron(III) [XFe^{III}(OEB•)], in a matter of minutes, as seen in Scheme 15.[79] The reaction was initially monitored by ^{1}H NMR spectroscopy. The formation of XFe^{IV}(OEB)/XFe^{III}(OEB•) was signaled by the growth of eight new methylene resonances in the upfield −20 to −70 ppm region, with the other eight methylene resonances in the downfield region from 70 to 10 ppm and with dispersed *meso* proton resonances at 35, −28, and −167 ppm. XFe^{IV}(OEB)/XFe^{III}(OEB•) has been isolated in crystalline form and its structure has been determined by X-ray crystallography. Figure 23 shows the structure of this five-coordinate monomer, which has the iron bound to four pyrrole nitrogen atoms and the chloride ligand.[79] The tetrapyrrole ligand assumes the helical shape that is characteristic of the other

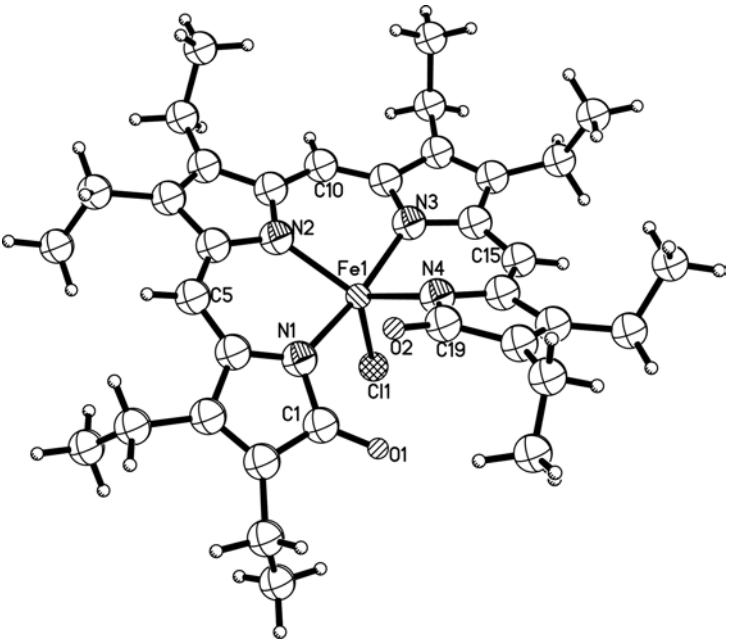

Figure 23. A drawing of Fe^{IV}(OEB)/Fe^{III}(OEB•) with uniform spherical atoms. Drawn with data from Nguyen, K.; Rath, S. P.; Grazynski, L. L.; Olmstead, M. M.; Balch, A. L. *J. Am. Chem. Soc.* **2004**, *126*, 6210–6211.

bilindione complexes described above. The Fe–N distances for the terminal pyrrole groups [Fe–N1, 2.018(2); Fe–N4, 2.016(2) Å] are somewhat shorter than those for the inner two pyrrole rings [Fe–N2, 2.049(2); Fe–N3, 2.070(2) Å]. For comparison, the Fe–N distances in high-spin, five-coordinate iron(III) porphyrins fall in the range of 2.06–2.09 Å.[80] The Fe–Cl distance, 2.2694(8) Å, is similar to those found in a number of five-coordinate iron(III) porphyrins.

The structure of rat heme oxygenase-1 with an iron biliverdin complex bound at the active site has been determined by single-crystal X-ray diffraction.[81] Figure 24 compares the structure of the synthetically prepared XFe^{IV}(OEB)/XFe^{III}(OEB•)[79] with that of the protein-bound iron biliverdin complex in the heme oxygenase.[81] The two structures show considerable similarity. Both utilize helical bilindione ligands with similar pitches. However, the protein structure involves an axial imidazole ligand from a histidine residue of the protein. The chloride ligand in synthetic XFe^{IV}(OEB)/XFe^{III}(OEB•) occupies a similar position. Unfortunately, there are no experimental data that definitively determine the oxidation state of the iron in the protein-bound iron biliverdin complex.

Pyridine solutions of $ClFe^{III}$(*meso*-NH_2-OEP) or $(py)_2Fe^{II}$(*meso*-NH_2-OEP) undergo oxidative ring opening when exposed to dioxygen, as shown in

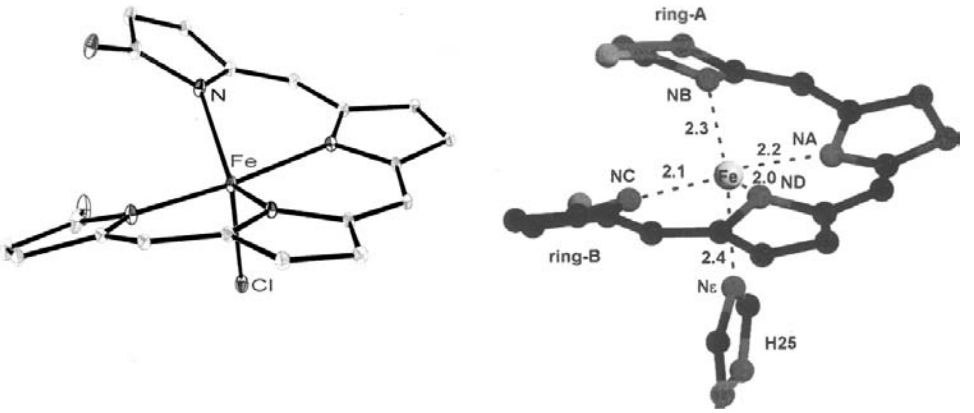

Figure 24. A comparison of the structure of Fe^{IV}(OEB)/Fe^{III}(OEB•) with that of rat heme oxygenase-1 bound iron biliverdin complex. Drawn using data from Nguyen, K.; Rath, S. P.; Grazynski, L. L.; Olmstead, M. M.; Balch, A. L. *J. Am. Chem. Soc.* **2004**, *126*, 6210-6211 and from Sugushima, M.; Sakamoto, H.; Higashimoto, Y.; Noguchi, M.; Fukuyama, K. *J. Biol. Chem.* **2003**, *278*, 32352–32358.

Scheme 16.[82,83] In pyridine-d_5 solutions of ClFe^{III}(*meso*-NH_2-OEP), there is a temperature-dependent equilibrium between the high-spin (S = 5/2), six-coordinate complex, {(py)ClFe^{III}(*meso*-NH_2-OEP)}, and the six-coordinate, low-spin [S = 1/2 with the less common $(d_{xz}d_{yz})^4(d_{xy})^1$ ground state] complex, [$(py)_2$Fe^{III}(*meso*-NH_2-OEP)]$^+$. Such pyridine solutions are air-sensitive, and the remarkable degradation reactions have been monitored by ^{1}H NMR spectroscopy. These studies revealed conversion of $(py)_2$Fe^{II}(*meso*-NH_2-OEP) into a green intermediate that was not isolated and then into a new open-chain tetrapyrrole complex **2** in Scheme 16, in which the original amino group and the attached *meso* carbon atom have been converted into a nitrile group. Additional oxidation at an adjacent *meso* carbon occurs to produce a ligand that binds iron by three pyrrole nitrogen atoms and the oxygen atom introduced at a *meso* carbon. This open-chain tetrapyrrole complex itself is sensitive to attack by dioxygen and is converted into a tripyrrole complex that is stable to further oxidation and has been isolated as set out earlier in Scheme 14. Compound **2** has been isolated with a molecule of ethanol acting as an axial ligand. The structure of **2**-ethanol is shown in Figure 25.

V. Metal Complexes of Formylbiliverdin and Related Tetrapyrroles

The coordination complexes of octaethylformylbiliverdin (H_2OEFB) are helical molecules that have much in common with the products of ring opening of verdohemes by nucleophiles. Transmetalation of Mg^{II}(OEFB), which can be

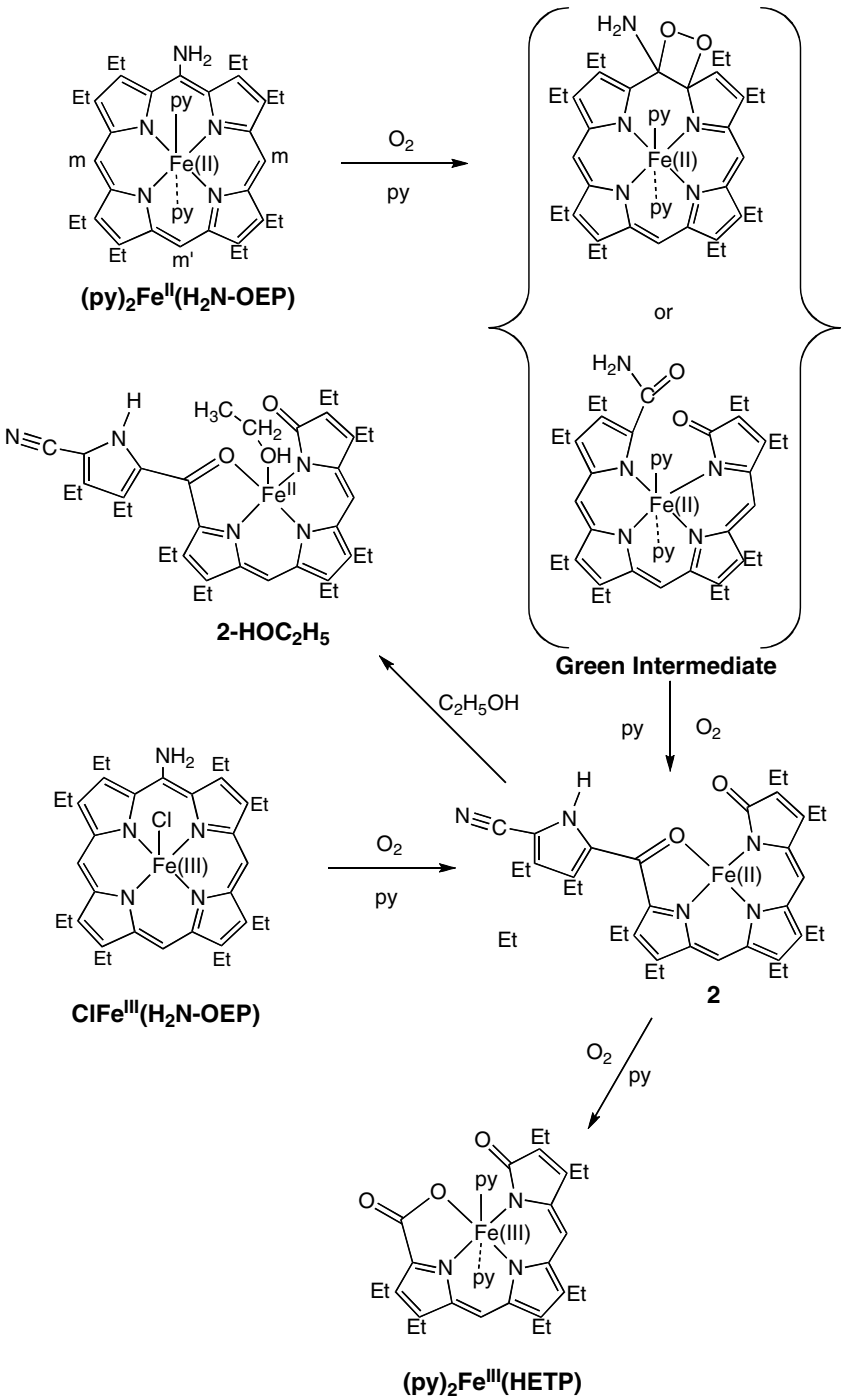

Scheme 16. Oxidation of $(py)_2Fe^{II}(H_2N\text{-}OEP)$.

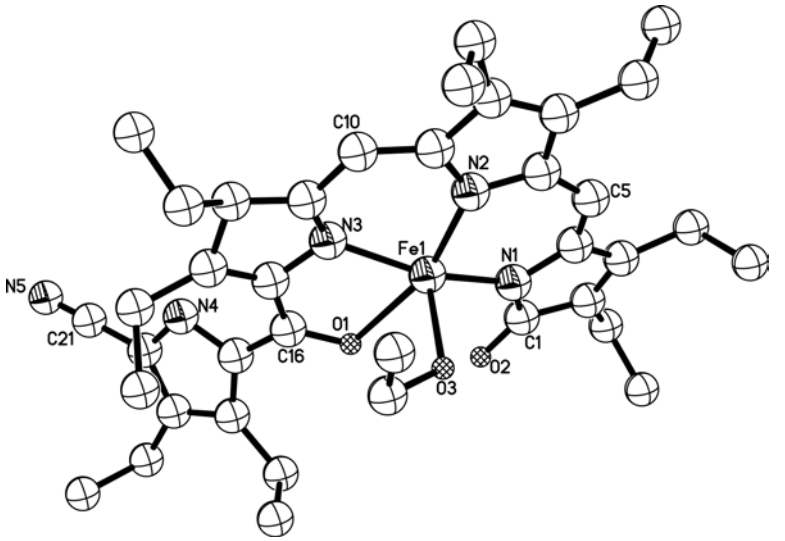

Figure 25. A drawing of the ring opened complex **2**-ethanol obtained by oxidation of $(py)_2$FeII(*meso*-NH2-OEP) with uniform spherical atoms. Notice that the pyrrole ring containing N4 is twisted out of the plane of the FeN_3O unit. Drawn with data from Kalish, H.; Lee, H. M.; Olmstead, M. M.; Grazynski, L. L.; Rath. S. P.; Balch, A. L. *J. Am. Chem. Soc.* **2003**, *125*, 4674–4675.

obtained by photooxidation of Mg^{II}(octaethylporphyrin) in air,[84] with a metal(II) acetate yielded the low-spin, monomeric complexes Cu^{II}(OEFB), Ni^{II}(OEFB), and Co^{II}(OEFB), as shown in Eq. 1 of Scheme 17.[85] Single crystal X-ray diffraction of Cu^{II}(OEFB) revealed that it consists of a four-coordinate copper(II) center that is bonded to the four nitrogen atoms of the tetrapyrrole ligand to produce a distorted planar coordination, as shown in Figure 26. The tetrapyrrole ligand has a helical geometry. The structure of the solid is complicated by the existence of three molecules in the asymmetric unit and C–H···O hydrogen bonding between pairs of these. Both Cu^{II}(OEFB) and Co^{II}(OEFB) can be converted to the verdoheme analogs, $[Cu^{II}(OEOP)]^+$ and $[Co^{II}(OEOP)]^+$, through oxidation with hydrogen peroxide. Additionally, $[Cu^{II}(OEOP)]^+$ was produced by heating a toluene solution Cu^{II}(OEFB) in the presence of trifluoroacetic acid under an atmosphere of dioxygen. Carbon monoxide is produced when Cu^{II}(OEFB) is converted to $[Cu^{II}(OEOP)]^+$ by either procedure. The product, $[Cu^{II}(OEOP)](PF_6)$, has been isolated and characterized by single-crystal X-ray diffraction. The cation has a planar, porphyrin-like structure. The ^{1}H NMR spectrum of diamagnetic Ni^{II}(OEFB) was shown to be consistent with the helical structure through the use of lanthanide and chiral lanthanide shift reagents. The EPR spectrum of Co^{II}(OEFB) shows that it forms a low-spin adduct with pyridine and that this adduct acts as a reversible dioxygen carrier.[84]

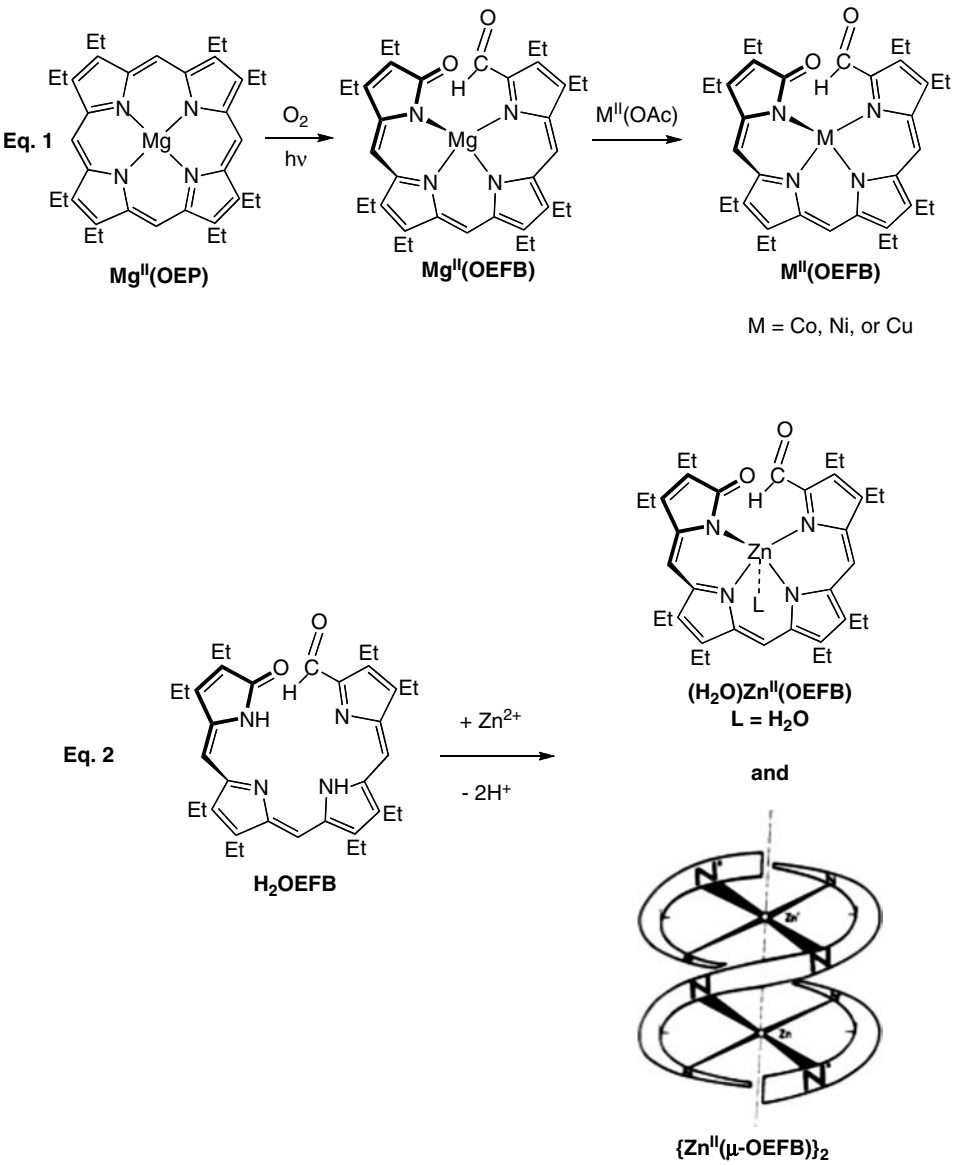

Scheme 17. Formation of formylbiliverdin complexes.

As shown in Eq. 2 of Scheme 17, introduction of Zn(II) into H_2OEFB resulted in the formation of two products: brown, monomeric, five-coordinate $(H_2O)Zn^{II}$(OEFB) and the unusual dimeric $\{Zn^{II}(\mu\text{-OEZB})\}_2$, which is green.[86,87] Both products were characterized by X-ray crystallography. The structure of brown $(H_2O)Zn^{II}$(OEFB) is similar to those of many of the other helical biliverdin-based complexes discussed

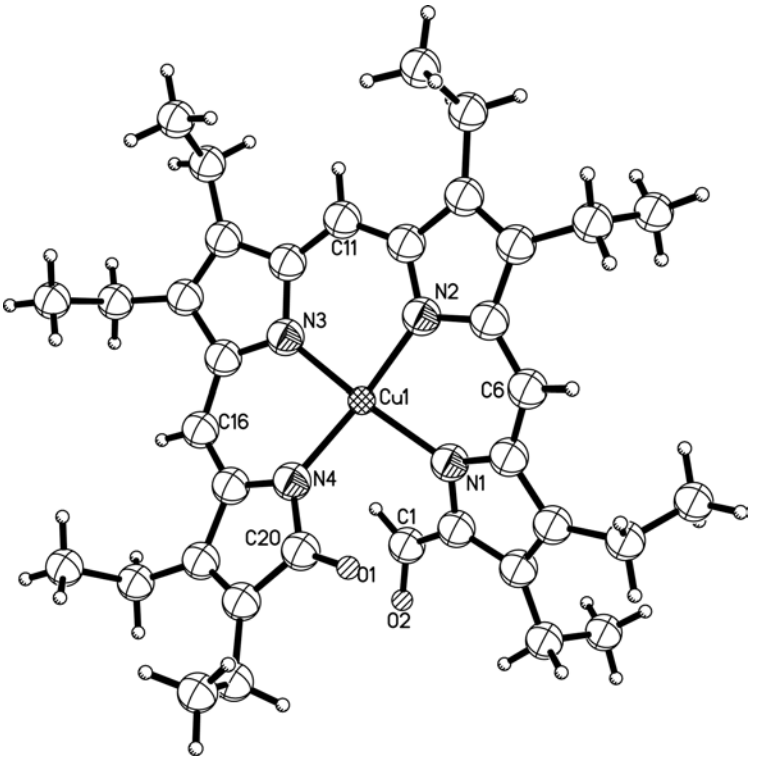

Figure 26. A drawing of Cu^{II}(OEFB) with 50% thermal ellipsoids. Drawn from data in Koerner, R.; Olmstead, M. M.; Ozarowski, A.; Phillips, S. L.; Van Calcar, P. M.; Winkler, K.; Balch, A. L. *J. Am. Chem. Soc.* **1998**, *120*, 1274–1284.

in this chapter, e.g. Cu^{II}(OEFB) shown in Figure 26. The structure of the green complex is unusual since it involves the formylbiliverdin ligands acting as bridging ligands with two nitrogen atoms of one ligand bound to one zinc ion, and the other two nitrogen atoms coordinated to a second zinc ion, as illustrated in schematic form in Scheme 17. The resulting molecule has a helical structure nature that is quite distinct from that of $\{Mn^{III}(\mu\text{-OEB})\}_2$ (shown in Figure 11) and $\{Fe^{III}(\mu\text{-OEB})\}_2$ (shown in Figure 20). In particular, the oxygen atoms of the OEB ligands do not coordinate the zinc ions. It was reported that the conversion of brown $(H_2O)Zn^{II}$(OEFB) into green $\{Zn^{II}(\mu\text{-OEFB})\}_2$ was promoted by acid, but the role of acid in this conversion is unclear.[86,87] This system might profit from further investigation, particularly since the crystallographic coordinates of $(H_2O)Zn^{II}$(OEFB) and green $\{Zn^{II}(\mu\text{-OEFB})\}_2$ are not in the Cambridge Crystallographic Database.

Open-chain tetrapyrrole ligands can also form dinuclear complexes. Photooxidation of magnesium tetraphenylporphyrin induces ring cleavage and the

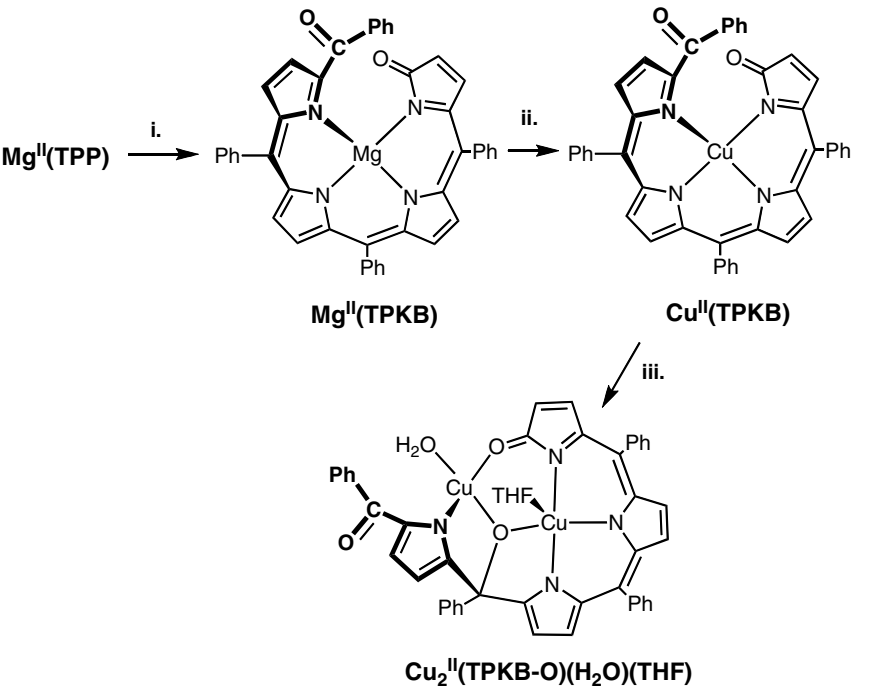

i. hν/air; ii. Cu(OAc)$_2$•4H$_2$O; iii. Cu(OAc)$_2$•4H$_2$O/D/Acetone/18hr.

Scheme 18. Formation of a dinuclear copper complex.

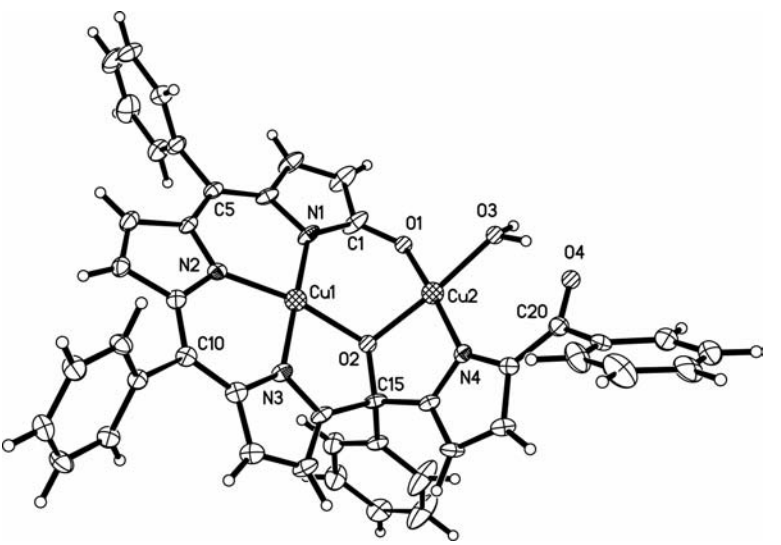

Figure 27. A drawing of Cu$^{II}_2$(TPKB-O)(H$_2$O)(THF) with 50% thermal ellipsoids. For clarity, the tetrahydrofuran molecule coordinated to Cu1 has not been shown. Drawn using data from Koerner, R.; Olmstead, M. M.; Ozarowski, A.; Balch, A. L. *Inorg. Chem.* **1999**, *38*, 3262–3263.

formation of magnesium tetraphenylketobiliverdin, Mg^{II}(TPKB),[88] which has been transmetalated with $Cu^{II}(OAc)_2 \cdot H_2O$ in methanol to produce two new complexes, brown–yellow Cu^{II}(TPKB) and blue Cu^{II}_2(TPKB-O)(H_2O)(THF), as shown in Scheme 18.[89] The yield of blue Cu^{II}_2(TPKB-O)(H_2O)(THF) was greatly improved by treating Cu^{II}(TPKB) with excess $Cu^{II}(OAc)_2 \bullet H_2O$ in boiling acetone for 18 h. This reaction occurs either under normal atmospheric conditions or under an atmosphere of purified dinitrogen. Thus, dioxygen is not necessary for the formation of Cu^{II}_2(TPKB-O)(H_2O)(THF). Figure 27 shows the structure of the dinuclear complex, Cu^{II}_2(TPKB-O)(H_2O)(THF).

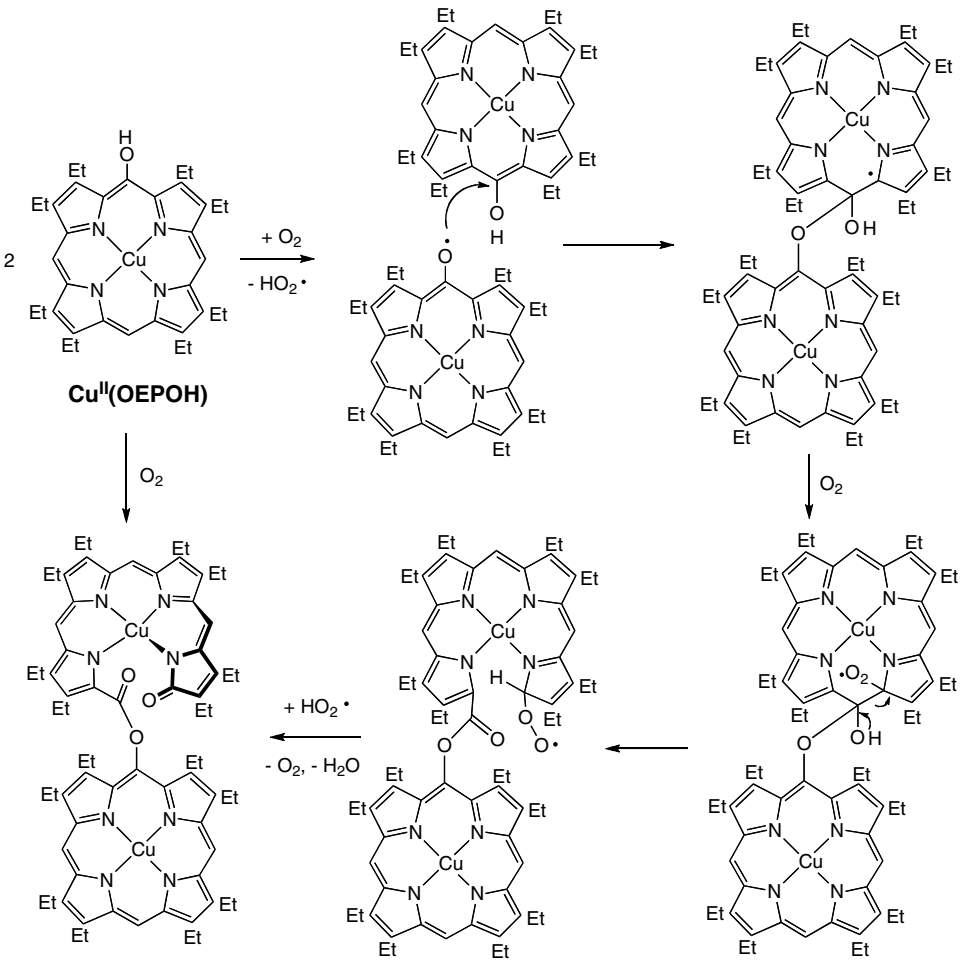

Scheme 19. Formation of dinuclear {Cu^{II}(μ-OEPOC(O)OEB)Cu^{II}}.

VI. Some Other Interesting Open-Chain Complexes that Do Not Fit the Above Classification

As shown in Scheme 19, Cu^{II}(OEPOH) undergoes oxidation by dioxygen to form the novel dinuclear copper complex, {Cu^{II}(μ-OEPOC(O)OEB)Cu^{II}}, whose structure has been determined by X-ray crystallography.[90] Figure 28 shows a drawing of the neutral dinuclear complex. This remarkable compound is composed of a copper(II) *meso*-substituted porphyrin portion (with a planar CuN_4 unit) that is attached through an ester linkage to a helical copper(II) complex of an open-chain tetrapyrrole. The ring-opened portion must have been provided by oxidative cleavage of a second molecule of Cu^{II}(OEPOH). A speculative mechanism suggested for this process is shown on the right hand side of Scheme 19.

In related chemistry, oxidation of Ni^{II}(OEPNH$_2$) with ferric chloride in a mixture of chloroform and ethanol results in the formation of two products, as shown in Scheme 20.[91] The structure of one of these, Ni^{II}(OEB-CO_2Et), is shown in Figure 29. Ni^{II}(OEB-CO_2Et) has a helical structure that resembles those of many of the other biliverdin complexes discussed in this chapter. Despite the distortion from planarity of the nickel ion, the complex displays a conventional ^{1}H NMR spectrum.[91]

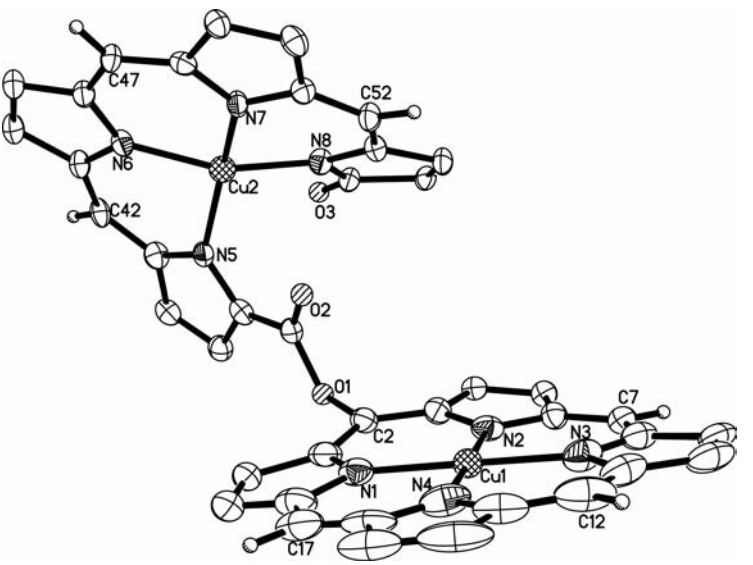

Figure 28. A drawing of {Cu^{II}(μ-OEPOC(O)OEB)Cu^{II}} with 50% thermal ellipsoids. For clarity, ethyl groups have been omitted. Drawn from data from Phillips, S.; Noll, B. C.; Olmstead, M. M.; Balch, A. L. *Can. J. Chem.* **2001**, *79*, 922–929.

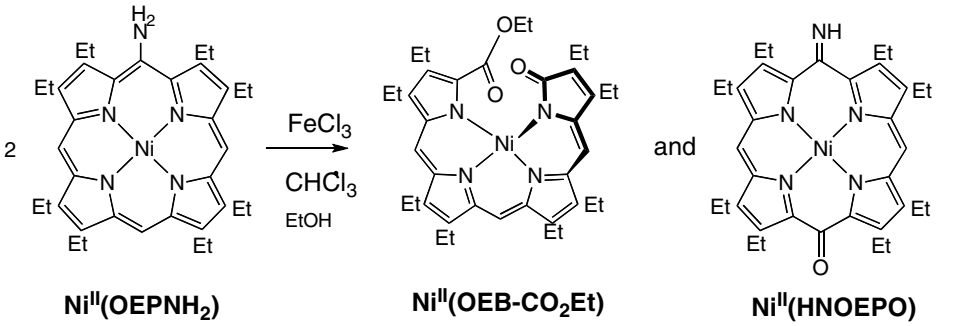

Scheme 20. Oxidation of $Ni^{II}(OEPNH_2)$.

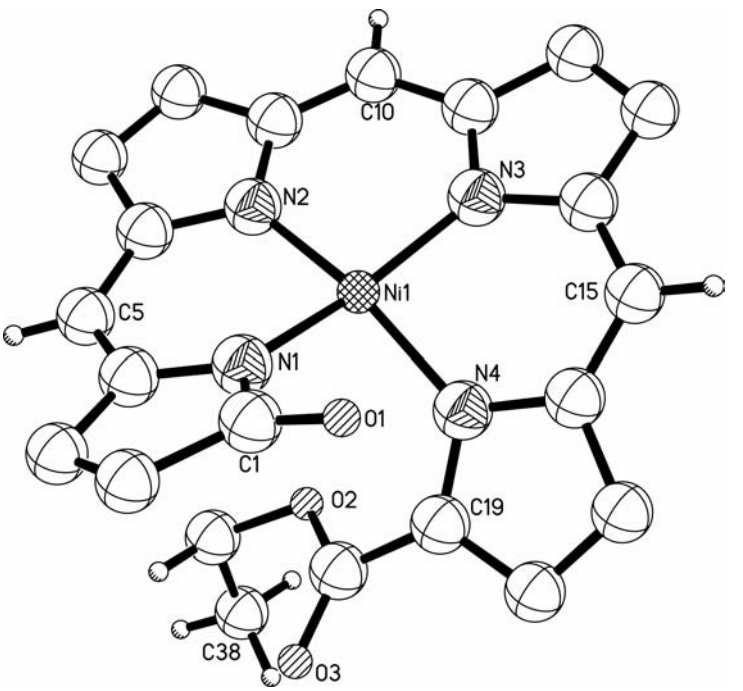

Figure 29. A drawing of the $Ni^{II}(OEB\text{-}CO_2Et)$ with uniform spherical atoms. For clarity, the eight ethyl groups on the pyrrole rings have been omitted. Drawn using data from Sprutta, N.; Rath, S. P.; Olmstead, M. M.; Balch, A. L. *Inorg. Chem.* **2005**, *44*, 1452–1459.

Some unusual open-chain tetrapyrrole complexes have been obtained by photooxidation of the phlorin complex **3** shown in Scheme 21.[92] The phlorin **3** was obtained by addition of *n*-butyl lithium to H_2TPP. Photooxidation of the phlorin **3** produced the open-ring compounds **4** and **5**. Treatment of **4** and **5** with $Ni^{II}(acetylacetonate)_2$

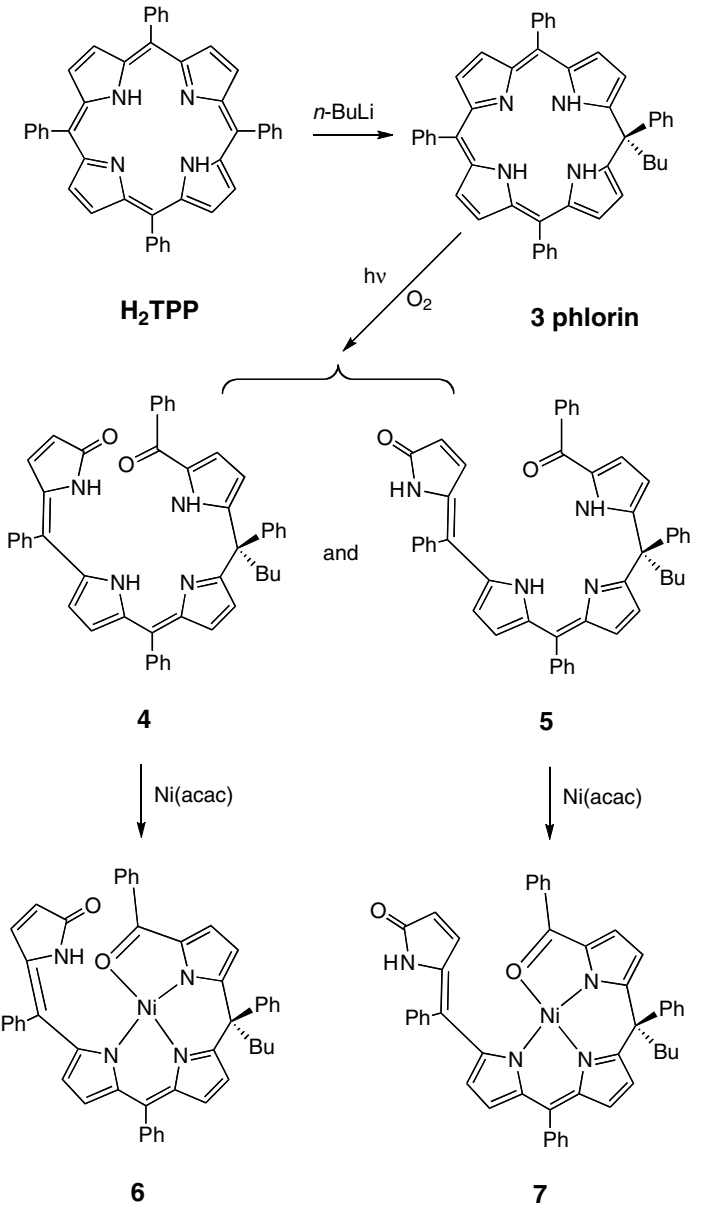

Scheme 21. Formation of phlorin-derived open-chain nickel complexes.

produced the four-coordinate nickel(II) complexes **6** and **7**, shown in Scheme 21. The structures of **6** and **7**, are shown in Figures 30 and 31, respectively. Despite the rather crowded nature of these complexes, the nickel ions in both compounds have a nearly planar geometry.

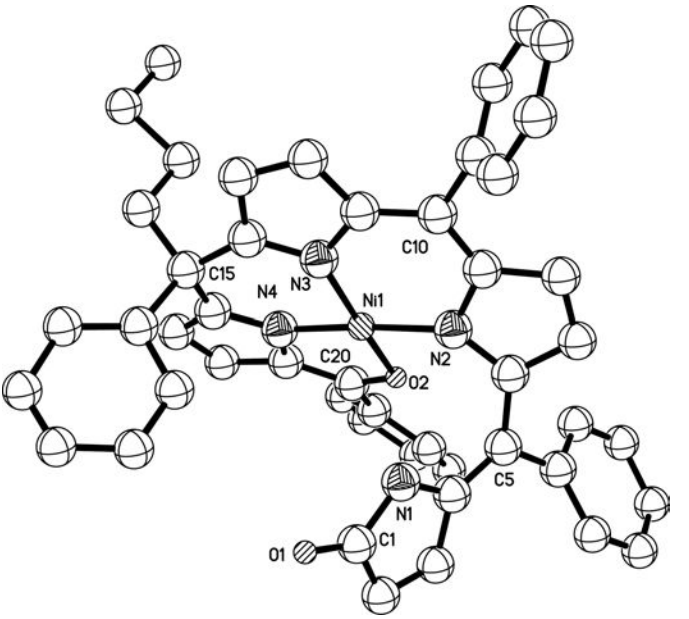

Figure 30. A drawing of **6**, (5,10,15,20-tetraphenyl-15-*n*-butylbiladiene-ab-1,20(21H)-dione-N,N′,N″,O)-nickel(II) with uniform spherical atoms. Hydrogen atoms were omitted. Drawn with data in Jeandon, C.; Krattinger, B.; Ruppert, R.; Callot, H. J. *Inorg. Chem.* **2001**, *40*, 3149–3153.

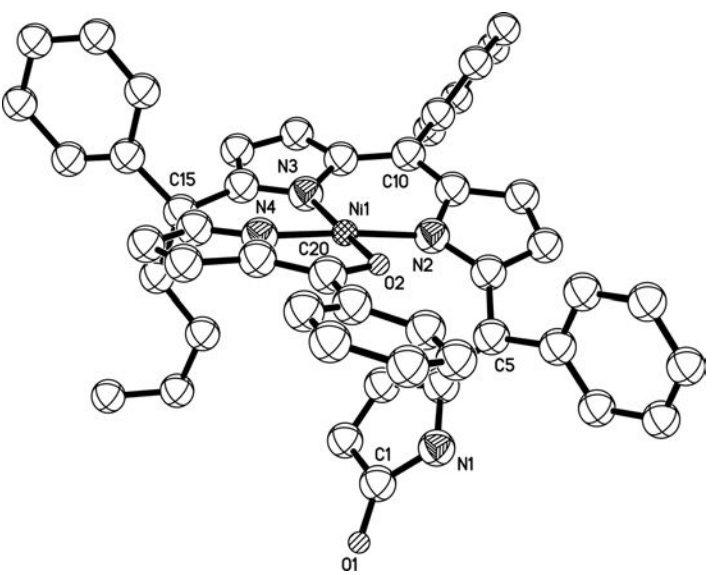

Figure 31. A drawing of **7**, (5,10,15,20-tetraphenyl-15-*n*-butylbiladiene-ab-1,20(21H)-dione-N,N′,N″,O)-nickel(II) with uniform spherical atoms. Hydrogen atoms were omitted. Drawn utilizing data from Jeandon, C.; Krattinger, B.; Ruppert, R.; Callot, H. J. *Inorg. Chem.* **2001**, *40*, 3149–3153.

VII. Conclusions

This article has reviewed the structural chemistry of verdohemes and open-chain oligopyrroles that are formed as the products of porphyrin degradation, generally by oxidative processes. The results have shown that the verdohemes usually have planar structures that are similar to the corresponding porphyrins. One rather characteristic aspect of the open-chain compounds and their metal complexes is the helical nature of their structures. Despite their nonplanarity, the complexes of bilindiones undergo facile, reversible redox reactions that are ligand-based. The chiral nature of the biliverdin chelates offers an interesting aspect that deserves further study. So far, the only explicit use of the chiral nature of these chelated complexes has employed axial ligand binding to the type of zinc complexes shown in Scheme 7 to selectively coordinate chiral ligands.[38–50]

VIII. Acknowledgment

Research conducted in the Balch laboratory at U. C. Davis was supported by Grant GM 26226 from the U.S. National Institutes of Health.

IX. References

1. Maines, M. D. *Heme Oxygenase: Clinical Applications and Functions*; CRC Press: Boca Raton, **1992**.
2. Ortiz de Montellano, P. R. *Acc. Chem. Res*. **1998**, *31*, 543–549.
3. Ortiz de Montellano, P. R.; Wilks, A. *Adv. Inorg. Chem*. **2001**, *51*, 359–407.
4. Liu, Y.; Moënne-Loccoz, P.; Loehr, T. M.; Ortiz de Montellano, P. R. *J. Biol. Chem*. **1997**, *272*, 6909–6917.
5. Balch, A. L. *Coord. Chem. Rev*. **2000**, *200–202*, 349–377.
6. Matera,K. M.; Takahashi, S.; Fujii, H.; Zhou, H.; Ishikawa, K.; Yoshimura, T.; Rousseau, D. L.; Yoshida, T.; Ikeda-Saito, M. *J. Biol. Chem.* **1996**, *271*, 6618–6624.
7. Ladd, L.; Ortiz de Montellano, P. R.; Poulos, T. K. *J. Inorg. Biochem.* **2004**, *98*, 1686–1695.
8. Sato, H.; Sugishima, M.; Sakamoto, H.; Higshimoto, Y.; Shimokawa, C.; Fukuyama, K.; Palmer, G.; Noguchi, M. *Biochem. J.* **2009**, *419*, 339–345.
9. O'Carra, P. In *Porphyrins and Metalloporphyrins;* Smith, K. M., Ed.; Elsevier: New York, **1975**; pp. 123–153.
10. St. Claire, T. N.; Balch, A. L. *Inorg. Chem*. **1999**, *38*, 684–691.
11. Balch, A. L.; Koerner, R.; Latos-Grazynski, L.; Lewis, J. E.; St. Claire, T. N.; Zovinka, E. P. *Inorg. Chem*. **1997**, *36*, 3892.
12. O'Carra, P.; Colleran, E. *FEBS Lett.* **1969**, *5*, 295–297.
13. Rice, J. K.; Fearnley, I. M.; Barker, P. D. *Biochemistry*, **1999**, *38*, 16847–16856.
14. Avila, L.; Huang, H.; Damaso, C. O.; Lu, S.; Moënne-Loccoz, P.; Rivera, M. *J. Am. Chem. Soc.* **2003**, *125*, 4103–4110.
15. Hildebrand, D. P.; Tang, H.; Luo, Y.; Hunter, C. L.; Smith, M.; Brayer, G. D.; Mauk, A. G. *J. Am. Chem. Soc.* **1996**, *118*, 12909–12915.

16. Mizutani, T.; Yagi, S. *J. Porphyrins Phthalocyanines* **2004**, *8*, 226–237.
17. Kennedy, G. Y.; Vevers, H. G. *Comp. Biochem. Physiol*. **1973**, *44*, 11–25.
18. Miksik, I.; Holan, V.; Deyl, Z. *Comp. Biochem. Physiol. B Biochem. Mol. Biol.* **1996**, *113*, 107–612.
19. Warburg, O; Negelein, E. *Chem. Ber.* **1930**, *63,* 1816–1816.
20. Masuoka, N.; Itano, H. A. *Biochemistry* **1987**, *26*, 3672–3680.
21. Balch, A. L.; Latos- Grazynski, L.; Noll, B. C.; Olmstead, M. M.; Safari, N. *J. Am. Chem. Soc.* **1993**, *115*, 1422–1429 and references therein.
22. Balch, A. L.; Koerner, R.; Olmstead, M. M. *J. Chem. Soc. Chem. Commun.* **1995**, 873–874.
23. Khorasani-Motlagh, M.; Safari, N.; Noroozifar, M.; Saffari, J.; Biabani, M.; Reboucas, J. S.; Partick, B. *Inorg. Chem.* **2005**, *44*, 7762–7769.
24. Khorasani-Motlagh, M.; Safari, N.; Noroozifar, M.; Shahroosvand, H.; Paraii, Z.; Partick, B. *Inorg. Chim. Acta* **2007**, *360*, 2331–2338.
25. Khorasani-Motlagh, M.; Safari, N.; Noroozifar, M.; Shahroosvand, H.; Parsa, A. *J. Coord. Chem.* **2008**, *21*, 3458–3466.
26. Lee, H. M.; Olmstead, M. M.; Gross, G. G.; Balch, A. L. *Cryst. Growth Des*. **2003**, *3*, 691–697.
27. Rath, S. P.; Olmstead, M. M.; Balch, A. L. *Inorg. Chem.* **2004**, *43*, 7648–7655.
28. Yamauchi, T.; Mizutani, T.; Wada, K.; Horii, S.; Furukawa, H.; Masaoka, S.; Chang, H.-C.; Kitagawa, S. *Chem. Commun*. **2005**, 1309–1311.
29. Balch, A. L.; Mazzanti, M.; Olmstead, M. M. *J. Chem. Soc. Chem. Commun.* **1994**, 269–270.
30. Balch, A. L.; Mazzanti, M.; St. Claire, T.; Olmstead, M. M. *Inorg. Chem.* **1995**, *34*, 2194–2200.
31. Fuhrhop, J.; Krüger, P.; Sheldrick, W. S. *Liebigs Ann. Chem.* **1977**, *3*, 339–359.
32. Latos-Grazynski, L.; Johnson, J.; Attar, S.; Olmstead, M. M.; Balch, A. L. *Inorg. Chem.* **1998**, *37*, 4493–4499.
33. Johnson, J. A.; Olmstead, M. M.; Balch, A. L. *Inorg. Chem.* **1999**, *38*, 5379–5383.
34. Scheidt, W. R. In *The Porphyrins*, Dolphin, D., Ed.; **1978**, Vol. 3, pp. 463–511.
35. Bahrami, H.; Zehedi, M.; Safari, N. *J. Inorg. Biochem.* **2006***, 100*, 1449–1461.
36. Johnson, J. A.; Olmstead, M. M.; Stolzenberg, A. M.; Balch, A. L. *Inorg. Chem.* **2001**, *40*, 5585–5595.
37. Falk, H.; Schlederer, T. *Monat. Chem.* **1978**, *109*, 1013–1015.
38. Mizutani, T.; Yagi, S.; Honmaru, A.; Ogoshi, H. *J. Am. Chem. Soc.* **1996**, *118*, 5318–5319.
39. Mizutani, T.; Yagi, S.; Honmaru, A.; Murakami, S.; Furusyo, M.; Takagishi, T.; Ogoshi, H. *J. Org. Chem.* **1998**, *63*, 8769–8784.
40. Mizutani, T.; Yagi, S.; Morinaga, T.; Nomura, T.; Takagishi, T.; Kitagawa, S.; Ogoshi, H. *J. Am. Chem. Soc.* **1999**, *121*, 754–759.
41. Yagi, S.; Yamada, R.; Takagishi, T.; Sakai, N.; Takahashi, H.; Mizutani, T.; Kitagawa, S.; Ogoshi, H. *Chem. Commun.* **1999**, 911–912.
42. Mizutani, T.; Yagi, S.; Honmaru, A.; Goldacker, T.; Kitagawa, S.; Furusyo, M.; Takagishi, T.; Ogoshi, H. *Supramol. Chem.* **1999**, *10*, 297–308.
43. Mizutani, T.; Sakai, N.; Yagi, S.; Takagishi, T.; Kitagawa, S.; Ogoshi, H. *J. Am. Chem. Soc.* **2000**, *122*, 748–749.
44. Yagi, S.; Sadachi, H.; Kashiwagi, Y.; Takagishi, T.; Mizutani, T.; Kitagawa, S.; Ogoshi, H. *Chem. Lett*. **2000**, *29*, 1054–1055.
45. Yagi, S.; Morinaga, T.; Nomura, T.; Takagishi, T.; Mizutani, T.; Kitagawa, S.; Ogoshi, H. *J. Org. Chem.* **2001**, *66*, 3848–3853.

46. Hamakubo, K.; Yagi, S.; Nakazumi, H.; Mizutani, T.; Kitagawa, S. *Tetrahedron Lett*. **2005**, *46*, 7151–7154.
47. Hamakubo, K.; Yagi, S.; Nakazumi, H.; Mizutani, T.; Kitagawa, S. *Tetrahedron* **2006**, *62*, 3619–3628.
48. Yagi, S.; Hamakubo, K.; Ikawa, S.; Nakazumi, H.; Mizutani, T. *Tetrahedron* **2008**, *64*, 10598–10604.
49. Shimizu, T.; Asano, N.; Mizutani, T.; Chang, H.-C.; Kitagawa, S. *Tetrahedron Lett.* **2009**, *50*, 536–539.
50. Mizutani, T.; Yagi, S. *J. Porphyrins Phthalocyanines* **2004**, *8*, 226–237.
51. Braslavsky, S. E.; Holzwarth, A. R.; Schaffner, K.; *Angew. Chem. Int. Ed.* **1983***, 22*, 656–658.
52. Wagner, U.; Kratky, C.; Falk, H.; Woss, H. *Monatsh. Chem.* **1991**, *122*, 749–758.
53. Sheldrick, W. *J. Chem. Soc. Perkins 2*, **1976**, *13*, 1457–1462.
54. Paolesse, R.; Froiio, A.; Nardis, S.; Mastroianni, M.; Russo, M.; Nurco, D. J.; Smith, K. M. *J. Porphyrins Phthalocyanines* **2003**, *7*, 585–591.
55. Balch, A. L.; Koerner, R.; Olmstead, M. M.; Mazzanti, M.; Safari, N.; St. Claire, T. *J. Chem. Soc. Chem. Commun.* **1995**, 643–644.
56. Zehedi, M.; Safari, N.; Haddadpuor, S. *J. Mol. Struct. (Theochem)* **2000**, *531*, 79–88.
57. Fuhrhop, J.-H.; Salek, A.; Subramanian, J.; Mengenen, C.; Besecke, S. *Liebigs Ann. Chem.* **1975**, 1131–1147.
58. Bonnett, R.; Buckley, D. G.; Hamzetash, D. *J. Chem. Soc*. *Perkin Trans. 1* **1981**, 322–325.
59. Bonfiglio, J. V.; Bonnett, R.; Buckley, D. G.; Hamzetash, D.; Hursthouse, K. M.; Malik, K. M. A.; McDonagh, A. F.; Trotter, J. *Tetrahedron* **1983**, *39*, 1865–1874.
60. Balch, A. L.; Mazzanti, M.; Noll, B. C.; Olmstead, M. M. *J. Am. Chem. Soc.* **1994**, *116*, 9114–9122.
61. Spasojević, I.; Batinić-Haberle, I.; Stevens, R. D.; Hambright, P.; Thorpe, A. N.; Grodkowski, J.; Neta, P.; Fridovich, I. *Inorg. Chem.* **2001**, *40*, 726–739.
62. Lord, P. A.; Olmstead, M. M.; Balch, A. L. *Inorg. Chem.* **2000**, *39*, 1128–1134.
63. Balch, A. L.; Mazzanti, M.; Noll, B. C.; Olmstead, M. M. *J. Am. Chem. Soc.* **1993**, *115*, 12206–12207.
64. Szterenberg, L.; Latos-Grazynski, L.; Wojaczynski, J. *ChemPhysChem* **2002**, *3*, 575–583.
65. Wasbotten I.; Ghosh, A. *Inorg. Chem*. **2006**, *45*, 4914–4921.
66. Attar, S.; Balch, A. L.; Ozarowski, A.; Van Calcar, P.; Winkler, K. *J. Am. Chem. Soc.* **1997**, *119*, 3317–3323.
67. Attar, S.; Ozarowski, A.; Van Calcar, P. M.; Winkler, K.; Balch, A. L. *Chem. Commun.* **1997**, *12*, 1115–1116.
68. Koerner, R.; Olmstead, M. M.; Van Calcar, P. M.; Winkler, K.; Balch, A. L. *Inorg. Chem.* **1998**, *37*, 982–988.
69. Lord, P.; Olmstead, M. M.; Balch, A. L. *Angew. Chem. Int. Ed.* **1999**, *38*, 2761–2763.
70. Balch, A. L. *Comments Inorg. Chem*. **1984**, *3*, 51–67.
71. Lord, P. A.; Noll, B. C.; Olmstead, M. M.; Balch, A. L. *J. Am. Chem. Soc.* **2001**, *123*, 10554–10559.
72. Balch, A. L.; Latos-Grazynski, L.; Noll, B. C.; Olmstead, M. M.; Safari, N. *J. Am. Chem. Soc.* **1993**, *115*, 9056–9061.
73. Rath, S. P.; Olmstead, M. M. Latos-Grazynski, L.; Balch, A. L. *J. Am. Chem. Soc.* **2003**, *125*, 12678–12679.
74. Olmstead, M. M.; Costa, D. A.; Maitra, K.; Noll, B. C.; Phillips, S. L.; Van Calcar, P. M.; Balch, A. L. *J. Am. Chem. Soc*. **1999**, *121*, 7090–7097.

75. Koerner, R.; Latos-Grazynski, L.; Balch, A. L. *J. Am. Chem. Soc.* **1998**, *120*, 9245–9255.
76. Latos-Grazynski, L.; Wojaczynski, J.; Koerner, R.; Johnson, J. J.; Balch, A. L. *Inorg. Chem.* **2001**, *40*, 4971–4977.
77. Gheidi, M.; Safari, N.; Bahrami, H.; Zehedi, M. *J. Inorg. Biochem.* **2007**, *101*, 385–395.
78. Davari, M. D.; Bahrami, H.; Zehedi, M.; Safari, N. *J. Mol. Model.* **2009**, *15*, 1299–1315.
79. Nguyen, K.; Rath, S. P.; Grazynski, L. L.; Olmstead, M. M.; Balch, A. L. *J. Am. Chem. Soc.* **2004**, *126*, 6210–6211.
80. Scheidt, W. R.; Reed, C. A. *Chem. Rev.* **1981**, *81*, 543–555.
81. Sugushima, M.; Sakamoto, H.; Higashimoto, Y.; Noguchi, M.; Fukuyama, K. *J. Biol. Chem.* **2003**, *278*, 32352–32358.
82. Kalish, H.; Lee, H. M.; Olmstead, M. M.; Grazynski, L. L.; Rath. S. P.; Balch, A. L. *J. Am. Chem. Soc.* **2003**, *125*, 4674–4675.
83. Rath, S. P.; Kalish, H.; Grazynski, L. L.; Olmstead, M. M.; Balch, A. L. *J. Am. Chem. Soc.* **2004**, *126*, 646–654.
84. Wasser, P. K. W.; Fuhrhop, J.-H. *Ann. N.Y. Acad. Sci.* **1973**, *206*, 533–548.
85. Koerner, R.; Olmstead, M. M.; Ozarowski, A.; Phillips, S. L.; Van Calcar, P. M.; Winkler, K.; Balch, A. L. *J. Am. Chem. Soc.* **1998**, *120*, 1274–1284.
86. Fuhrhop, J.-H.; Wasser, P. K. W.; Subramanian, J.; Schrader, U. *Justus Liebigs Ann. Chem*. **1974**, 1450–1466.
87. Struckmeier, G.; Thewalt, U.; Fuhrhop, J.-H. *J. Am. Chem. Soc.* **1976**, *98*, 278–279.
88. Matsuura, T.; Inoue, K.; Ranade, A. C.; Saito, I. *Photochem. Photobiol*. **1980**, *31*, 23–26.
89. Koerner, R.; Olmstead, M. M.; Ozarowski, A.; Balch, A. L. *Inorg. Chem.* **1999**, *38*, 3262–3263.
90. Phillips, S.; Noll, B. C.; Olmstead, M. M.; Balch, A. L. *Can. J. Chem.* **2001**, *79*, 922–929.
91. Sprutta, N.; Rath, S. P.; Olmstead, M. M.; Balch, A. L. *Inorg. Chem.* **2005**, *44*, 1452–1459.
92. Jeandon, C.; Krattinger, B.; Ruppert, R.; Callot, H. J. *Inorg. Chem.* **2001**, *40*, 3149–3153.

41 Beyond Dipyrrins: Coordination Interactions and Templated Macrocyclizations of Open-Chain Oligopyrroles

Martin Bröring

Technische Universität Carolo-Wilhelmina zu Braunschweig,
Institut für Anorganische und Analytische Chemie,
Hagenring 30, Braunschweig, Germany

List of Abbreviations

[G-0]	zeroth generation
[G-1]	first generation
[G-2]	second generation
1D	one-dimensional
2D	two-dimensional
3D	three-dimensional
3-Mebpi	bis(3-methylpyridylimino)isoindoline anion
3,6-Me_2bpi	bis(3,6-dimethylpyridylimino)isoindoline anion
4-Mebpi	bis(4-methylpyridylimino)isoindoline anion
4,6-Me_2bpi	bis(4,6-dimethylpyridylimino)isoindoline anion
5-Mebpi	bis(5-methylpyridylimino)isoindoline anion
6-Mebpi	bis(6-methylpyridylimino)isoindoline anion
acac	acetylacetonate anion
$acac^F$	1,1,1-trifluoroacetylacetonate anion
Am	amyl

A^{Me}	methyl-2-acetate
an	acetonitrile ligand
Aryl	any (hetero)aromatic substituent
bai	bis(arylimino)isoindoline anion
BAr^F	tetrakis[3,5-bis(trifluoromethyl)phenyl]boranate
Bn	benzyl
BODIPY	borondipyrrin
bop	bis(oxazolinyl)pyrrole anion
bpi	bis(2-pyridylimino)isoindoline anion
bpmi	bis(2-pyrimidylimino)isoindoline anion
bsi	bis(2-selenazolylimino)isoindoline anion
bti	bis(2-thiazolylimino)isoindoline anion
cat	catalyst
CD	circular dichroism
cod	cyclooctadiene
dca	dicyanamide
dcm	dichloromethane host
DDQ	dichlorodicyanoquinone
dmf	dimethylformamide ligand
DMF	dimethylformamide
dppe	bis(diphenylphosphino)ethane
dppm	bis(diphenylphosphino)methane
EPR	electron paramagnetic resonance
Et	ethyl
fla	flavonolate
GC–MS	coupled gas chromatography/mass spectrometry
GO	galactose oxidase
H(2-Iphti)	(2-iodophenylimino)(6-methylpyridylimino)isoindoline
H(2-tolti)	(2-methylphenylimino)(4-methylthiazolylimino)isoindoline
H(3-Mebpi)	bis(3-methylpyridylimino)isoindoline
H(3,6-Me_2bpi)	bis(3,6-dimethylpyridylimino)isoindoline
H(4-Mebpi)	bis(4-methylpyridylimino)isoindoline
H(4-tBubti)	bis(4-*tert*-butylthiazolylimino)isoindoline
H(4,6-Me_2bpi)	bis(4,6-dimethylpyridylimino)isoindoline
H(5-Mebpi)	bis(5-methylpyridylimino)isoindoline
H(6-Mebpi)	bis(6-methylpyridylimino)isoindoline
Hal	halogene
H(bai)	bis(arylimino)isoindoline
H(bop)	bis(oxazolinyl)pyrrole
H(bpi)	bis(2-pyridylimino)isoindoline

H(bpmi)	bis(2-pyrimidylimino)isoindoline
H(bsi)	bis(2-selenazolylimino)isoindoline
H(bti)	bis(2-thiazolylimino)isoindoline
Hex	*n*-hexyl
H(fla)	flavonole
HO	heme oxygenase
H_3(oeb)	octaethylbilindione
H(phpi)	(phenylimino)(6-methylpyridylimino)isoindoline
HRMS	high-resolution mass spectrometry
H_2(salen)	bis(salicylimino)ethan
H(trpy)	tripyrrin
im	imidazolyl
iPr	*iso*-propyl
LDA	lithium diisopropylamide
mCPBA	3-chloroperbenzoic acid
Me	methyl
NADPH	reduced form of nicotinamide adenine dinucleotide phosphate
nBu	*n*-butyl
NLO	nonlinear optics
NMR	nuclear magnetic resonance
OAc	acetate
OAc^F	trifluoroacetate
O-bs	O-benzoylsalicylate
oefb	octaethylformylbilinone dianion
oeb	octaethylbilindione trianion
oebOX	octaethylbilindione anion
OTf	trifluoromethylsulfonate/triflate
ox	oxalate
P	3-propionate
Ph	phenyl
P^{Me}	methyl-3-propionate
Pr	*n*-propyl
py	pyridine
r.t.	room temperature
sal	salicylate
salen	bis(salicylimino)ethan dianion
sBu	*sec*-butyl
SOD	superoxide dismutase
SQUID	superconducting quantum interference device
tBu	*tert*-butyl

tcm	tricyanmethanide
tfa	trifluoroacetic acid
thf	tetrahydrofuran ligand
THF	tetrahydrofuran
TIPS	tri-*iso*-propylsilyl
tol	4-methylphenyl
trpy	tripyrrin anion
VE	valence electron
VT	variable temperature
XRD	X-ray diffraction

I. Introduction

A. Introductory Remarks and Scope of This Chapter

The coordination chemistry of open-chain oligopyrroles has long been a heterogeneous and peripheral area of porphyrin chemistry.[1–3] In most of the early instances the description of open-chain tri- and tetrapyrrole coordination compounds appeared only within the context of tetrapyrrole synthesis or analysis, and systematic studies of such species in their own right were not to be found until Fuhrhop and coworkers worked on bilin analogs in the 1970s. Due to their ubiquitous occurrence in nature and their biological importance, linear oligopyrroles have mainly been studied as purely organic entities in biological dyes, or as intermediates in heme and corrin biosyntheses, degradation, and phytochrome formation.[4] Those aspects remain important issues of this chemistry. Nevertheless, some reports on the importance of transition metal complexes of such ligands have been known for quite some time. The peculiar lability of iron biliverdin complexes which occur as intermediates in the biological heme degradation process[5–10] was recognized early,[11,12] and the use of divalent zinc ions in the analysis of phytochromes belongs to the standard repertoire of today's photobiologists and biochemists.[13–15] A further example is the early development of an accurate and relatively simple method for the determination of bilirubin in urine based on the formation of a strong copper(II) complex with azobilirubin.[16,17] As can be seen from these examples, the linear tetrapyrroles clearly dominate the field compared with the tripyrroles. This is certainly due to the fact that even the better-known groups of tripyrrolic compounds, the biopyrrins[18] and the prodigiosens,[19–21] still await detailed studies as ligands in coordination compounds.

Besides the tri- and tetrapyrrolic derivatives, some related oligopyrroles with two or with more than four pyrrole moieties have been reported as ligands. Work on shorter dipyrrolic species, the so-called dipyrrins, has recently been

reviewed[22,23] and is the topic of another chapter in this volume.[24] Reports on metal or anion complexes of longer or of branched oligopyrroles are rather rare,[25–30] which may well relate to the restricted number of easily accessible or naturally occurring examples of this class.[31–45] Several types of hybrid (oligo)pyrrole/Schiff base ligands and some intriguing transition metal chelates thereof have also been described, often employing the molecular achitecture of the H_2(salen) ligand family.[46–55] The tripyrrolic compounds have also found mimics which have been introduced very successfully into modern coordination chemistry. These are the bis(arylimino)isoindoline [H(bai)] ligands related to the phthalocyanines, and most recently the bis(oxazolinyl)pyrroles [H(bop)], which show much promise in catalysis (Figure 1). This article will concentrate on tripyrrolic and longer chain entities, including the H(bai) and H(bop) ligand classes. Dipyrrins and salen-like pyrrole hybrid ligands, as well as the technically important polypyrrole, [56,57] are considered to be beyond the scope of this review.

B. Types of Open-Chain Tri- and Tetrapyrrolic Species

In principle, a plethora of different open-chain tri- and tetrapyrroles can be derived from a simple building system using pyrroles and several bridging units at either the pyrrolic α- or β-positions, although only a minor number of these have been prepared and studied to date.[58] As mentioned above, two classes of linear tripyrroles are naturally occurring. These are prodigiosin **1** and the related prodigiosenes; and two biopyrrins of the tripyrrindione type — biotripyrrin a **2** and the regioisomeric biotripyrrin b **3** (Figure 1). Prodigiosenes are red pigments which are produced from microorganisms such as *Streptomyces* or *Serratia*.[19,59,60] They are much-studied substances in medicine, as the natural and many synthetic derivatives show promise as immunosuppressive and as anticancer drugs.[61–69] Little is known with respect to the coordination properties of prodigiosenes. The biopyrrins have been isolated very early from urine and urate sediments, but their molecular structures were unknown for a long time.[70–75] Biotripyrrin a **2** as the more stable *endo*-vinyl isomer was identified first and initially named "uroerythrin". The elusive *exo*-vinyl isomer **3** was later found and named "biotripyrrin b".[18] Both species are products from the antioxidative action of biliverdin IXα (Figure 2), and their level in human urine is a medicinal indicator of stress and inflammation under a multitude of different conditions, like schizophrenia, depression, sepsis, heart failure, or after surgery.[76–91] The first synthetic tripyrrindiones were known prior to the structure elucidation of **2** and **3**,[92–95] and simple model systems like hexaethyl derivative **4** have been prepared.[96–99] Related degradation products of modified metal porphyrins with the tripyrrin-1-one framework **5** were detected under several nonbiological oxidative conditions, usually as

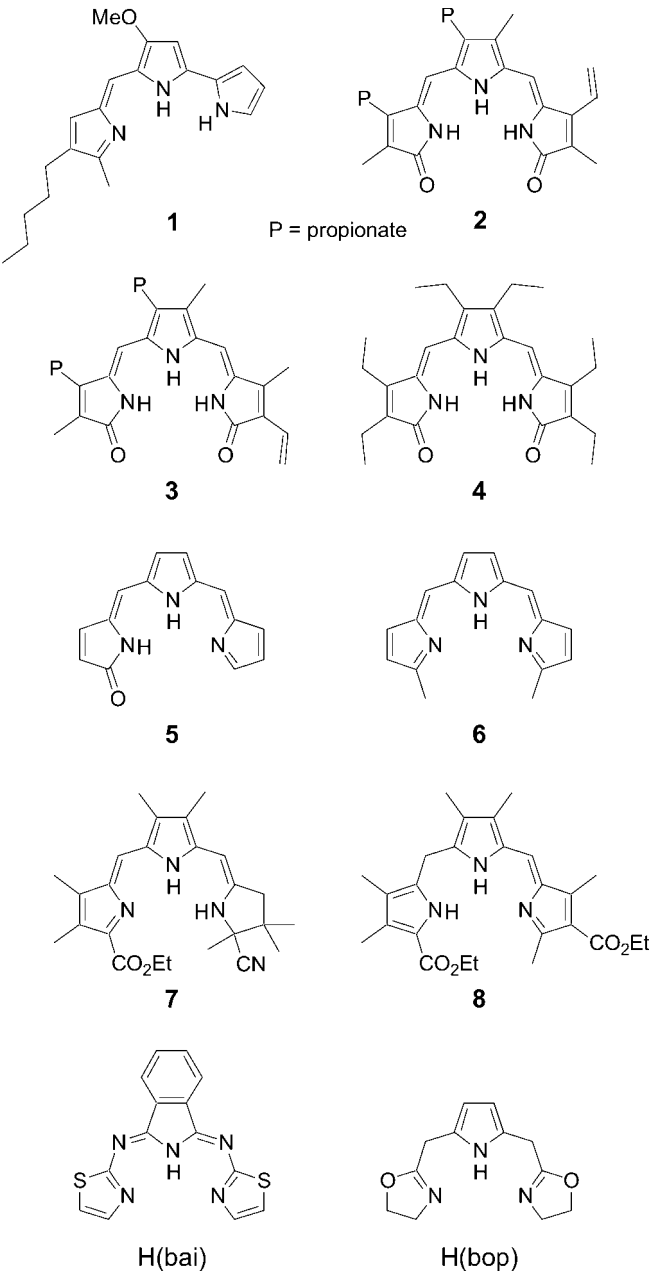

Figure 1. Selected examples for linear tripyrrolic ligands **1**–**8**, for bis(arylimino)isoindolines [H(bai)], and for bis(oxazolinyl)pyrroles [H(bop)].

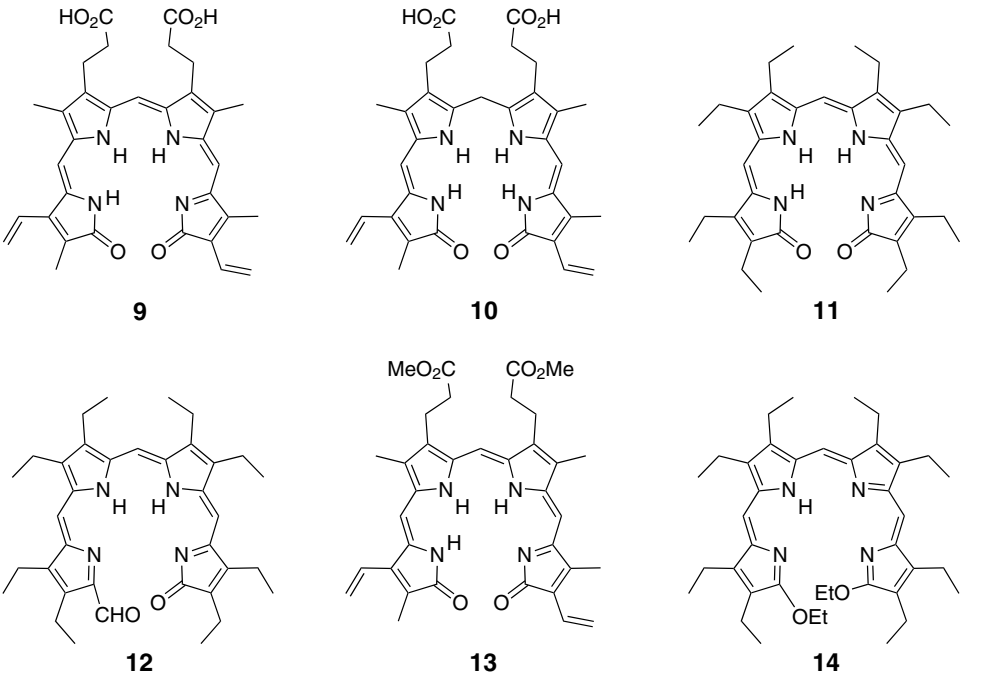

Figure 2. Some natural and artificial bilindione-type ligands: biliverdin-IXα **9**, bilirubin-IXα **10**, octaethylbilindione H_3(oeb) **11**, formyl-octaethylbilinone **12**, dimethyl biliverdin-IXα **13**, and diethoxybilatriene **14**.

metal complexes,[100–103] and several related species have been synthesized by design.[96–98,104–118] Finally, the synthetic alkyl- or alkoxy-substituted tripyrrins **6**,[98,117,119–123] the partially hydrogenated tripyrrin **7**,[124,125] and many tripyrrenes such as **8**[126–134] are known tripyrrolic ligands and belong to this class of compounds.

The natural linear tetrapyrroles comprise many intermediates in syntheses of biological porphyrin, chlorin, corrin, and phytochrome compounds, as well as of the respective degradation processes, of which only biliverdin IXα **9** and bilirubin IXα **10** have been studied as ligands in coordination compounds (Figure 2). Such oxoterminated species, the so-called bilindione-type ligands, provide several model ligands with simplified preparations and peripheral substitution such as **11** or **12**, or with protected carboxylate and/or terminal oxo groups such as **13**[135] and **14**, respectively. These model compounds overcome the typical drawbacks of the natural materials, i.e. solubility problems in nonaqueous solutions and formation of carboxylate salts in the presence of metal ions. Bilindiones have been employed as ligands in many studies of the biological importance of iron biliverdins, and a number of other applications of these chelate complexes have been made in the more recent past.

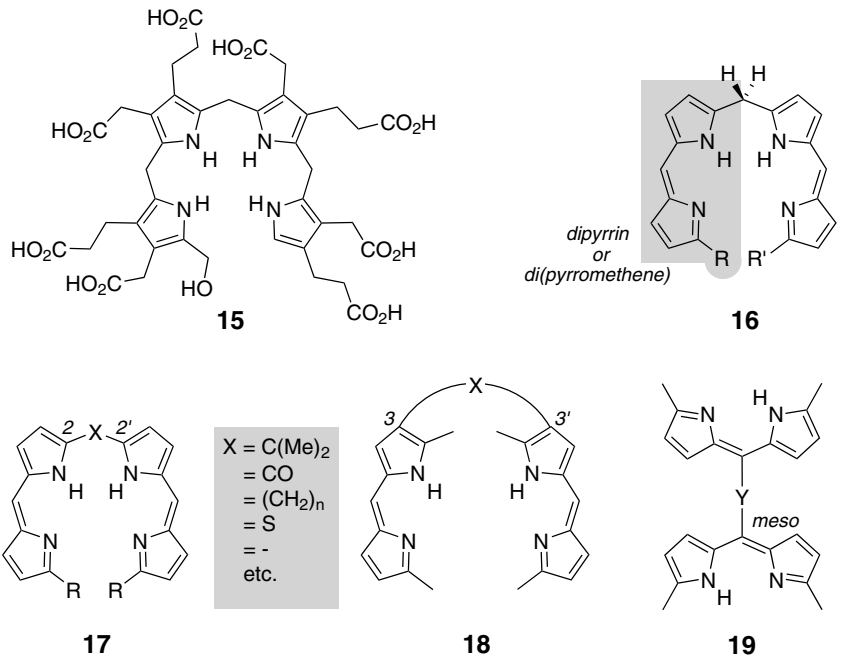

Figure 3. Examples for bilane and bis(dipyrrin)-type tetrapyrroles: preuroporphyrinogen **15**, methylenebis(dipyrrin) or *a,c*-biladiene **16**, 2,2′-bis(dipyrrin) **17**, 3,3′-bis(dipyrrin) **18**, and *meso*-bridged bis(dipyrrin) **19**.

The central tetrapyrrolic intermediate of heme biosynthesis is preuroporphyrinogen **15**, a typical bilane devoid of stabilization by electron-withdrawing groups at the terminal pyrrole rings.[136] The tetrapyrrolic core of this biomolecule is very reactive with respect to hydrolytic as well as oxidative processes, but may be stabilized through twofold dehydrogenation and formation of methylene-bridged bis(dipyrrin)s **16**, often called *a,c*-biladienes (Figure 3).[137,138] Artificial species derived from **16** may carry different residues (R and R′) at the terminal position which alter their reactivity, and the nature and position of the bridging unit may be changed to allow the construction of a large number of tetrapyrrolic bisdipyrrin ligands such as **17** or **18**. Coordination compounds of such engineered ligands have been used as precursors for the syntheses of many corrinoid and porphyrinoid compounds, and have found entry into the construction of supramolecular systems. Several examples of oligo(dipyrrin)s connected via the bridging methine group (C-6) **19** have been prepared and used in the latter field as well as in photochemistry. Other artificial tetrapyrroles containing one or no dipyrrin subunit are also well known,[139–147] but have only rarely been employed in coordination compounds to date.[148–150] Partly hydrogenated species, on the other hand,[151–153]

have been studied in much detail within the context of research toward the synthesis of cobalamins and hydroporphyrins.

II. Preparation of Open-Chain Oligopyrrole Ligands

A. Tripyrroles: Prodigiosenes and Related Species

The basic framework of prodigiosenes contains three pyrrole nuclei which are connected to each other via the α-positions, one pair directly and one pair with a methine bridge. Three general approaches are to be found in the scientific literature on prodigiosene syntheses. The retrosynthetic analysis leading to these three synthetic pathways, A–C, is shown in Figure 4. In most of the reported cases, the formation of the prodigiosene follows the biosynthesis of these molecules and proceeds by the acid condensation of a monoformyl bipyrrole with a pyrrole, as displayed on pathway A.[32] For simple alkyl-substituted derivatives, the alternative approach employing a bipyrrole and a formylpyrrole as in path B is advantageous, as the precursors are often easier available.[154] However, pathway C, i.e. the formation of the direct pyrrole–pyrrole bond in the final step is somewhat ponderous and has been used so far only for one partially hydrogenated derivative[140] and for the total synthesis of several natural species and their analogs. Since no reports on the coordinating properties of these latter species are available, this issue will not be discussed here, and only some key references for the structure elucidation and total

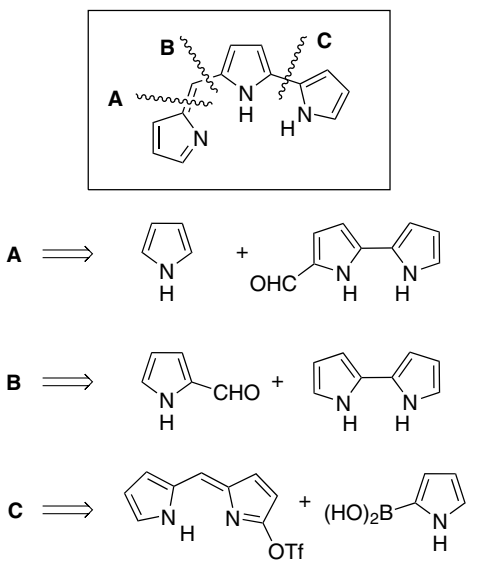

Figure 4. Retrosynthetic analysis of the prodigiosene chromophore.

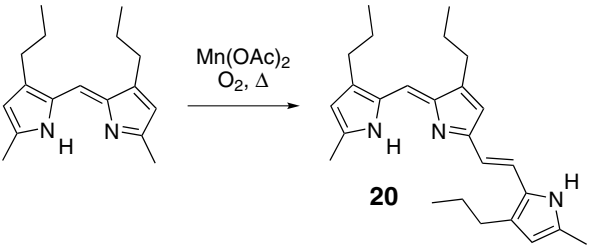

Figure 5. Formation of **20**.

syntheses of natural or biomimetic prodigiosenes are given here for the interested reader.[21,155–171] A vinylogous derivative, the tripyrrole **20**, has been described as the unexpected product of an unusual oxidation reaction of a tetraalkyldipyrrin.[172] No metal chelates of this novel species were reported (Figure 5).

B. Tripyrroles: Tripyrrinones, Tripyrrins, and Related Tripyrroles

The basic skeleton of the major group of linear tripyrrolic ligands contains two one-carbon bridges, thus preorganizing the three C_4N heterocycles for a meridional N,N,N coordination to a metal center. These ligands may be ordered by the functionalities occupying the α-terminal positions, and by the degree of hydrogenation, into the above-described groups. The major reaction leading to these compounds is the basic or acidic condensation of pyrrolic aldehydes. Symmetric tripyrrindiones such as **4** or **21** form under enforced basic conditions from a pyrrolic dialdehyde and two pyrridinone moieties, as depicted in Figure 6. The reaction is not complete, and significant amounts of dipyrrolic compounds **22** and **23** form as byproducts.[99] Symmetric tripyrrins **6** with some variation in their substitution have been described to form under strongly acidic conditions in boiling trifluoroacetic acid.[119–123] Again, one equivalent of a pyrrole dialdehyde is used in combination with two equivalents of an α-free pyrrole. These tripyrrins are stable as protonated moieties but decompose quickly in the presence of nucleophiles. The nucleophilic attack occurs presumably at the α-terminal positions, as the sterically protected *tert*-butyl derivative **24** can easily be obtained from its protonated form by the action of the base (Figure 6).[123] Unprotected tripyrrins may be obtained by the decomplexation reaction of nickel(II) tripyrrins with excess cyanide (see later in this section). In the neutral form, tripyrrins are much less prone to nucleophilic attack and consecutive decay, and may be used for coordination studies. These free base tripyrrins were fully characterized, while protonated species have only been incompletely analyzed by ^{1}H NMR spectroscopy (after condensation in deuterated trifluoroacetic acid) and by HRMS.[119]

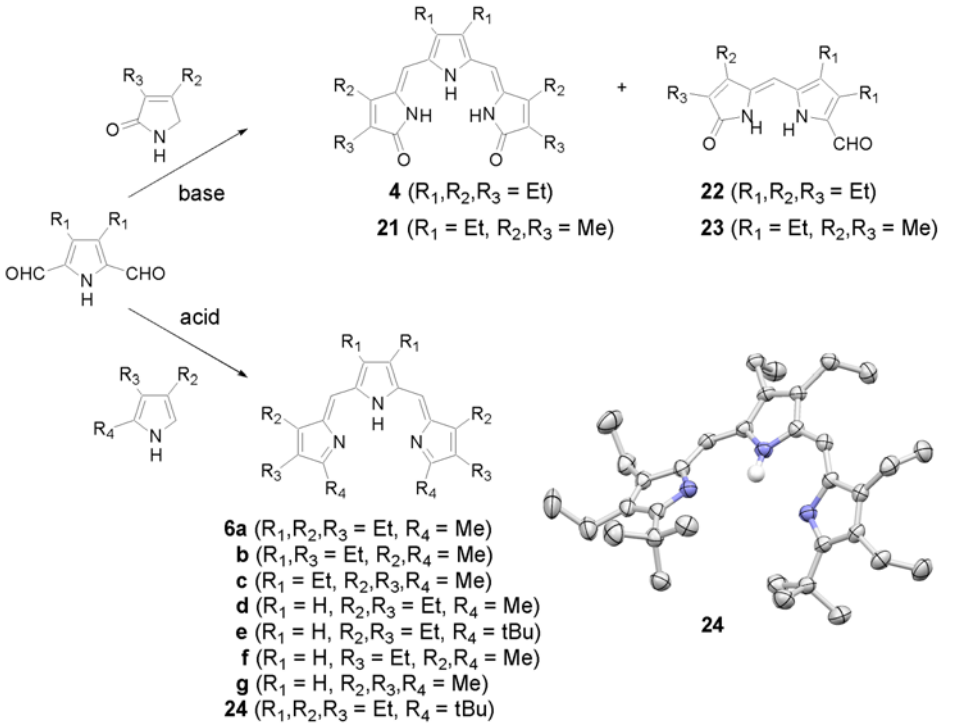

Figure 6. Stepwise condensation reactions for the preparation of symmetric tripyrrindiones and tripyrrins, and molecular structure of *tert*-butyl terminated tripyrrin **24** (crystallographic figure adapted from Ref. 123).

Tripyrrin-1-ones **25** with different terminal substituents R have been obtained by the basic condensation of a formylpyrrole with a hydrogen- or halogen-terminated dipyrrinone **26**, as shown in Figure 7.[98,105,110] Water-soluble sulfonic acid derivatives have also been obtained from hydrogen-terminated tripyrrin-1-ones by the action of sulfuric acid,[113] and unsymmetric tripyrrindiones such as **27** are readily available from the bromo-substituted tripyrrin-1-ones by hydrolysis with aqueous acetate.[97] In addition, the basic condensation is not restricted to pyrrolic aldehydes but allows the preparation of a number of analogs **28** by the use of different aromatic aldehydes (Figure 7).[107,109,173,174]

A related acidic condensation strategy using an unsymmetric dipyrromethane **29** and a formylpyrrole is the key to the synthesis of most of the known tripyrrenes **8** (Figure 8).[126–132] Tripyrrenes have rarely been described in coordination compounds and are mainly used as precursors for the synthesis of unsymmetrically substituted porphyrins or linear tetrapyrroles. An alternative approach has been described in the acidic condensation of a dipyrrinone **26** with an acetoxymethyl-activated pyrrole **30** to give the tripyrrene **31**.[134] Unsymmetric tripyrrin **7** was

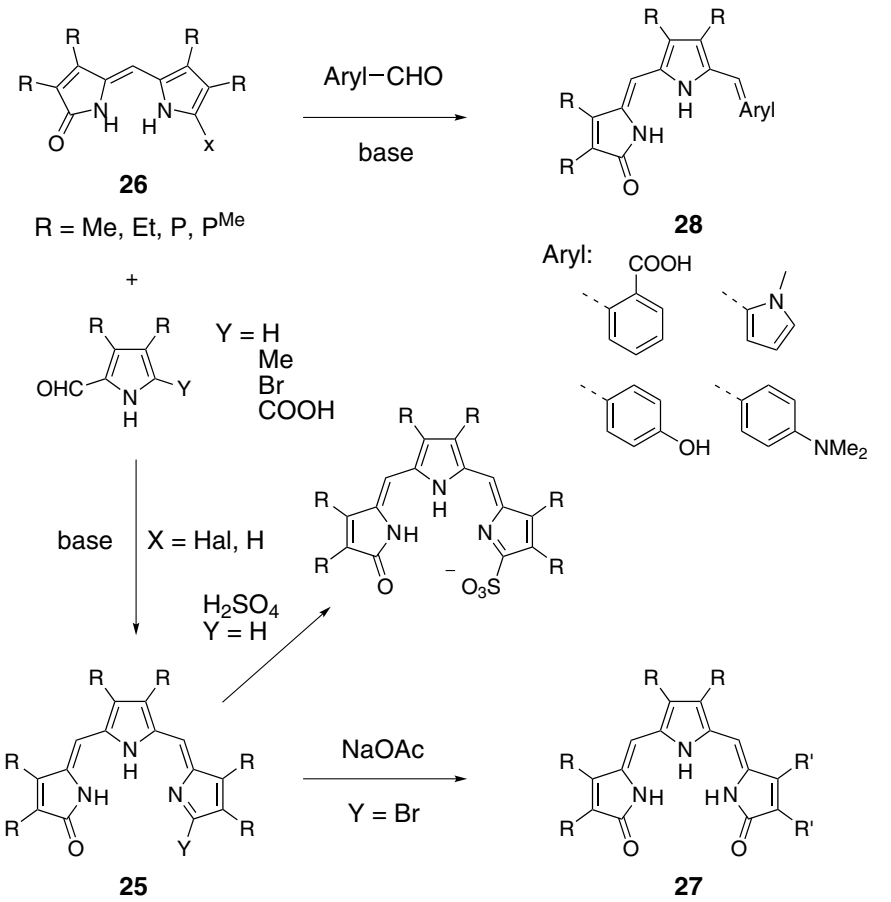

Figure 7. 2 + 1 Condensation reaction for the preparation of tripyrrin-1-ones and related derivatives.

prepared as a precursor for the synthesis of hydroporphyrins by a different strategy, employing the coupling of a dipyrrinthione **32** and the hydrogenated bromomethylpyrrole **33** and consecutive sulfur extrusion.[124,125]

Besides the condensation-reaction-based approaches described above, only little work is reported for tripyrroles using different strategies. The oxidative degradation of natural linear tetrapyrroles results *inter alia* in tripyrrolic products.[175] A multistep photooxidation of biliverdins and other bilatrienes in the presence of Tl(III) or Pb(IV) reagents has been found to produce mainly formyltripyrrin-1-ones,[106,108,111] and a different one-step strategy for the synthesis of these tripyrroles from bilatrienes has been communicated.[115] Bromination of α-methyldipyrrinone **34** also results in the formation of formyltripyrrin-1-one **35**, presumably via a bilatriene intermediate **36** (Figure 9).[112] A seemingly more

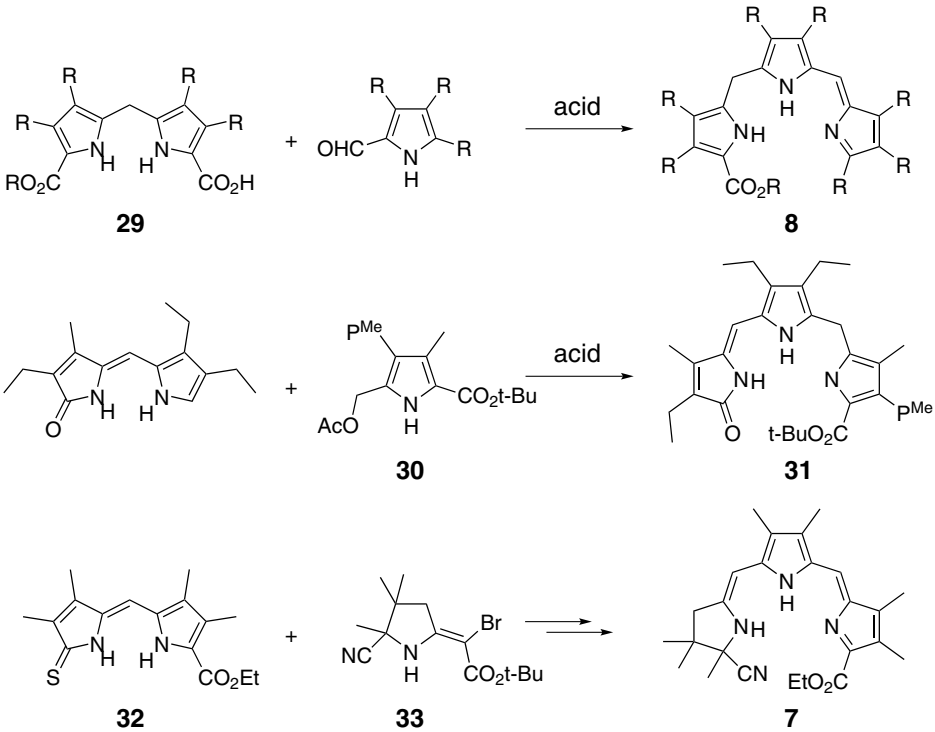

Figure 8. 2 + 1 Condensation reactions for the preparation of partly hydrogenated tripyrroles.

conventional approach to tripyrrins, the oxidative dehydrogenation of tripyrranes **37** and **40** under different conditions, has been reported by two groups (Figure 9).[117,118] No simple tripyrrins were isolated, but tripyrrin-1-ones **38** and **41**, along with methoxytripyrrin **39** and tripyrrin-2-one **42**, respectively, were obtained.

Finally, tripyrrolic compounds **43**–**46** have been isolated and characterized as byproducts from condensation reactions for the preparation of dipyrrins[96] and porphyrins (Figure 10).[116,133]

C. Tripyrroles: Bis(arylimino)isoindolines [H(bai)]

In the course of investigations into the reactivity and properties of heterocyclic amines, Linstead prepared the first bis(arylimino)isoindolines [H(bai)] in 1952.[173–175] The simple preparation and advantageous chemical stability of the H(bai) dyes have led to continual development of novel derivatives ever since. H(bai) ligands contain only one central pyrrole unit, but as their molecular

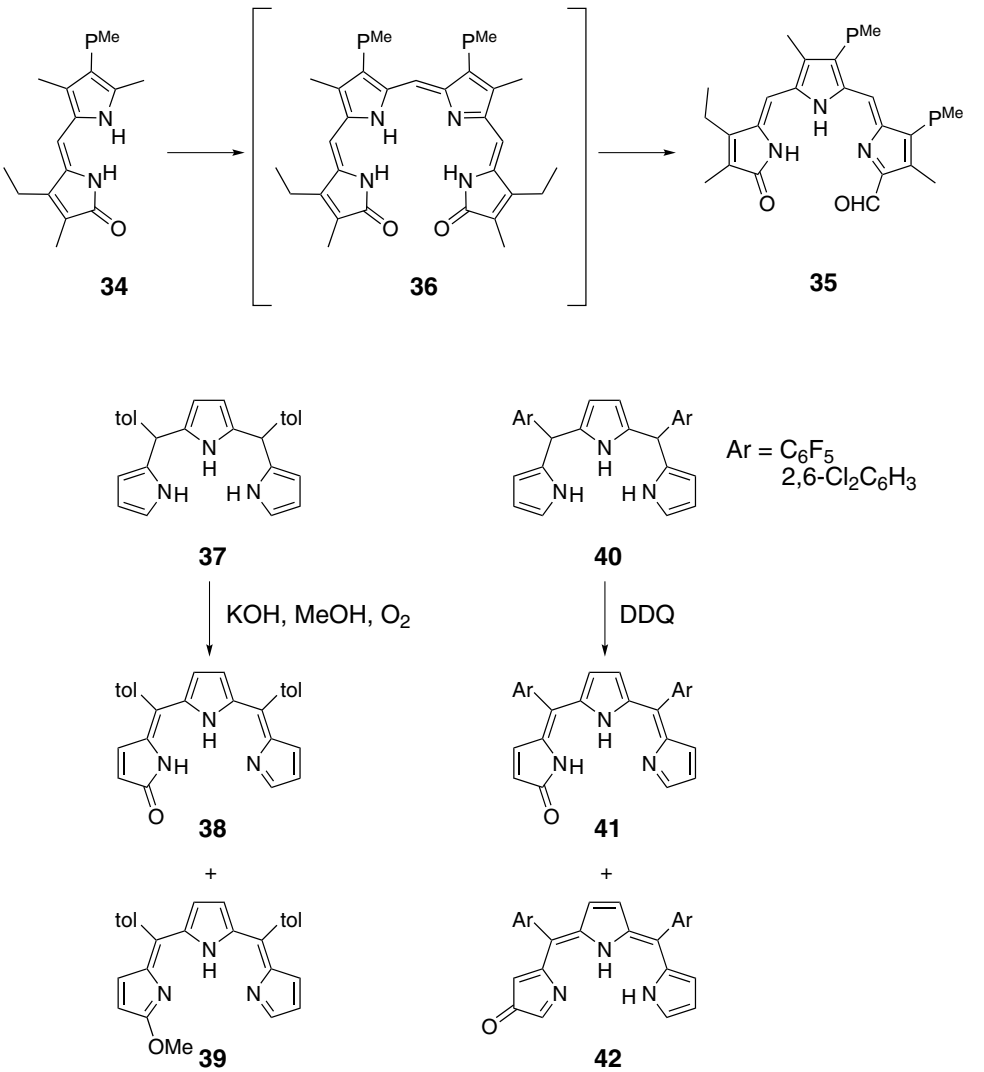

Figure 9. Selected oxidative transformations leading to tripyrrolic ligands.

framework and coordination properties are closely related to phthalocyanines and tripyrrins, respectively, they will be introduced in this section. Linstead's H(bai) synthesis is generally a condensation reaction of the 1,3-di-iminoisoindoline **47** and a heterocyclic amine in an alcoholic solvent, as generalized in Figure 11. In most cases, the heterocyclic endgroups consist of (substituted) pyridyl or thiazolyl moieties. Other terminal groups are possible; however, the investigation of such H(bai) dyes has mainly been driven so far by their optical properties, as these chromophores are bright yellow to red in color.[176–179] Another early investigation

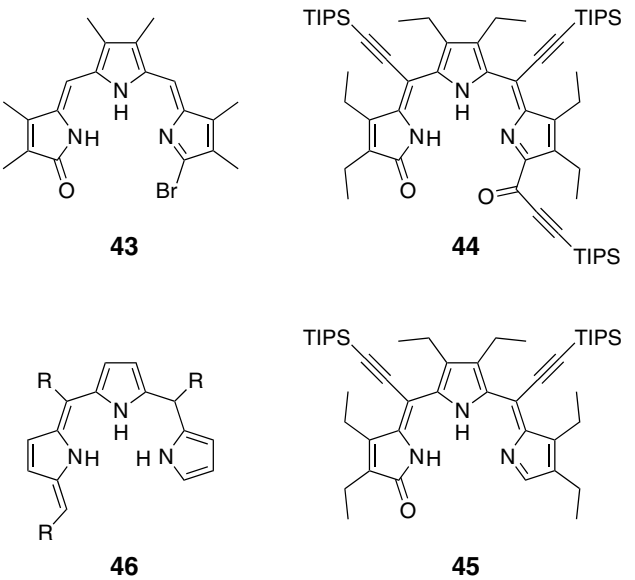

Figure 10. Tripyrroles as isolated byproducts from different condensation/oxidation reactions.

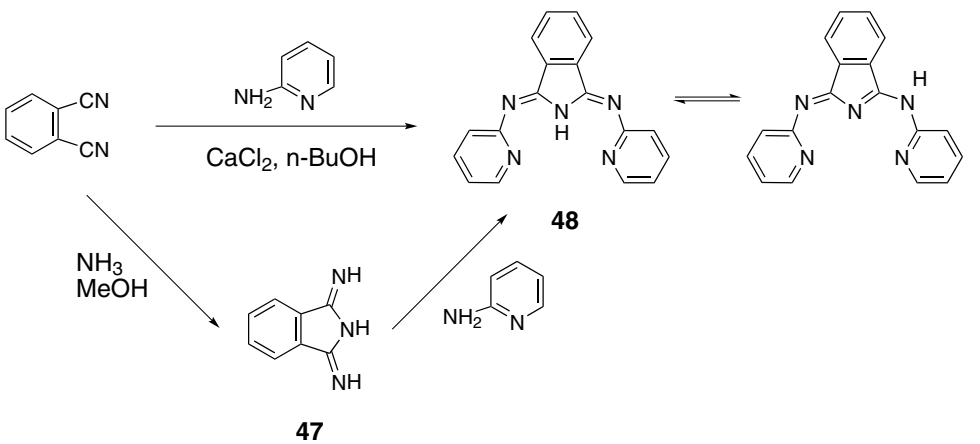

Figure 11. General preparation and tautomers of bis(pyridylimino)isoindoline **48** as an example for symmetric H(bai) ligands.

is the issue of N–H···N tautomeric forms which are present depending on the end groups.[180–185] In this context, several aryl- and alkyl-terminated H(bai) species as well as some monocondensation products have been prepared and studied.[186–188] The substitution of the imino groups of **47** proceeds in a stepwise manner,[173–175] and the role of the alcoholic solvent in the formation of acetale intermediates has

been assumed, similar to the synthesis of phthalocyanines. A broader use of H(bai) compounds as ligands for transition metal ions has been documented in the literature after the development of a one-step synthesis from phthalonitrile and amino heterocycles in the presence of a metal salt, by Siegl (Figure 11).[189–191] Depending on the cation, either the free base ligand (Ca^{2+}, Mg^{2+}) or the respective transition metal–bai complexes form under these usually forcing conditions, in varying yields. Although initally favored over the two-step synthesis, the one-step scheme has been found to be less economical in most reported studies.

H(bai) ligands have been prepared with a number of different end groups and substituents on both the central isoindoline and the terminal heterocycles.[192–202] Several chiral ligands have been prepared.[203,204] Figure 12 provides an overview of the reported derivatives relevant to coordination studies. For some bis(pyridylimino)isoindolines (bpi), functionalization strategies have been worked out, based on either nucleophilic aromatic substitution[190] or palladium-catalyzed coupling reactions.[195]

While several protocols for the preparation of symmetric H(bai) species are known, unsymmetric H(bai) ligands have so far been prepared mainly as mixtures.[186–188] On the base of known preparations of symmetrical H(bai)s, a two-step strategy and a mixed one-step synthesis with separation have recently been proposed and reported for the successful preparation of unsymmetric H(bai)s. In cases with one terminal phenyl and one terminal heteroaryl functionality, the two-step strategy was found advantageous due to tautomerization issues. The introduction of two different heterocycles, however, is usually accompanied by a significant amount of scrambling, so that a one-step process and control of the products by the stoichiometry of the heteroaromatic amines is favored.[205,206] Figure 13 shows the examples prepared to date.

D. Tripyrroles: Bis(oxazolinyl)pyrroles [H(bop)]

Oxazolines and their derivatives, in particular as part of the pybox family of ligands, have been attracting much attention in asymmetric catalysis. Transition metal complexes of the tridentate pybox manifold and of related meridional coordinating N,N,N and N,C,N donor ligands have been intensively studied and have found a wide range of applications. Bis(oxazolinyl) derivatives with a central pyrrole unit show a structurally tight relation to natural tripyrroles and will be discussed in this section. In general, two types of such bis(oxazolinyl)pyrroles [H(bop)] exist: one group with directly linked heterocycles, as in **54**[207,208]; and a second group with two dangling oxazolinyl groups connected via methylene bridges, as in **55**.[209,210] The latter group has a rigidified subgroup with twofold benzo annelation **56**.[211,212] All H(bop) derivatives have been prepared using

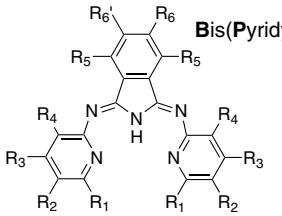

Bis(**P**yridylimino)**I**soindolin
H(bpi)

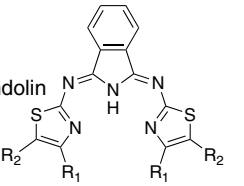

Bis(**T**hiazolylimino)**I**soindolin
H(bti)

	R_1	R_2
	H	H
	Me	H
	Me	iPr
	tBu	H

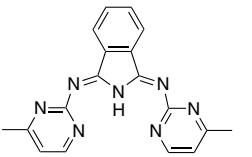

Bis(**P**yrimidylimino)**I**soindolin
H(bpmi)

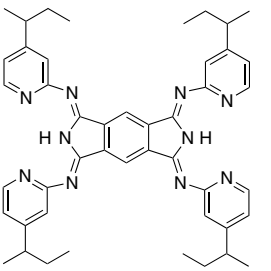

	R_1	R_2	R_3	R_4	R_5	R_6	R_6'
48	H	H	H	H	H	H	H
6-Mebpi	Me	H	H	H	H	H	H
5-Mebpi	H	Me	H	H	H	H	H
	H	Cl	H	H	H	H	H
	H	Br	H	H	H	H	H
	H	NO_2	H	H	H	H	H
	H	$CCSiMe_3$	H	H	H	H	H
	H	$CCSiPh_3$	H	H	H	H	H
	H	CCPh	H	H	H	H	H
4-Mebpi	H	H	Me	H	H	H	H
	H	H	Et	H	H	H	H
	H	H	Pr	H	H	H	H
	H	H	sBu	H	H	H	H
	H	H	tBu	H	H	H	H
	H	H	Am	H	H	H	H
3-Mebpi	H	H	H	Me	H	H	H
	H	H	H	H	H	Me	H
	H	H	H	H	H	OR*	H
4,6-Me_2bpi	Me	H	Me	H	H	H	H
3,6-Me_2bpi	Me	H	H	Me	H	H	H
	Me	H	H	Me	OMe	H	H
	H	Me	H	H	H	Me	H
	H	Cl	H	H	H	Cl	Cl
	H	H	Me	H	H	Me	H
	H	H	tBu	H	H	Me	H
	H	H	tBu	H	H	NO_2	H
	H	H	tBu	H	H	Me	Me
	H	H	tBu	H	H	Hex	Hex
	H	H	tBu	H	H	Cl	Cl

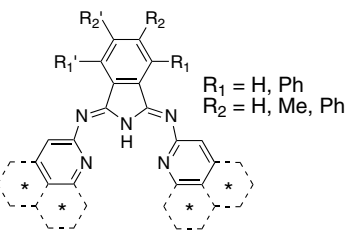

R_1 = H, Ph
R_2 = H, Me, Ph

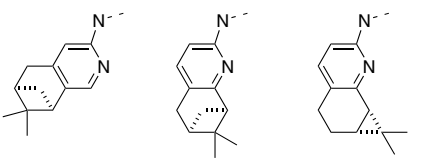

* dendritic compounds, s. chapter 8.2

myrbpi pinbpi carbpi

Figure 12. Overview of different symmetric H(bai) ligands and selected abbreviations.

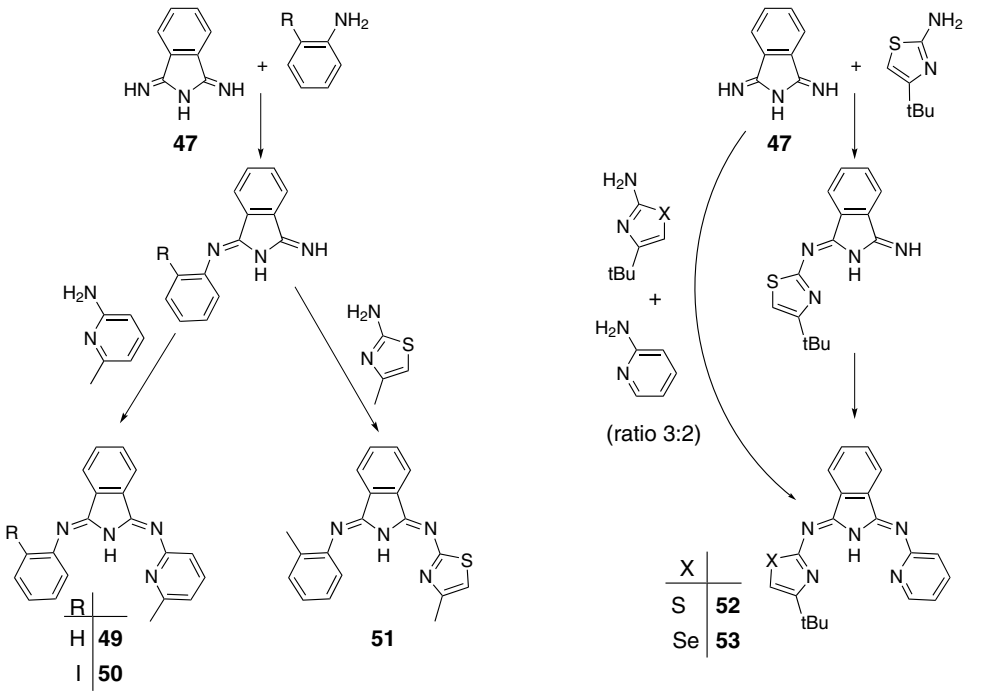

Figure 13. One- and two-step strategies for the preparation of unsymmetric H(bai)s **49**–**53**.

the same strategy by a two-step double condensation of a pyrrole dinitrile or di(carboxylic ester) derivative and an amino alcohol (Figure 14). Most derivatives have been prepared from chiral pool amino alcohols and are thus available as enantiomerically pure chiral ligands.

E. Tetrapyrroles: Model Ligands Prepared from Natural Biliverdin and Bilirubin

Chemically simplified bilin derivatives obtained from natural sources have been known for some time,[135,137,138,213,214] as three major drawbacks are associated with the use of natural biliverdin **9** and bilirubin **10** in chemical studies and, in particular, as ligands for coordination compounds. All three issues are correlated with the peripheral substitution of the tetrapyrrole core. The presence of two propionate side chains renders the natural bilines almost insoluble in most organic solvents and provides additional reactive sites for metal ions as well as for hydrogen bridging. This problem is usually overcome by the introduction of methyl or other alkyl esters, as shown for biliverdin derivative **13** in Figure 2. Additional reactivity stems from the vinyl substituents. Substitution by ethyl instead of the sensitive

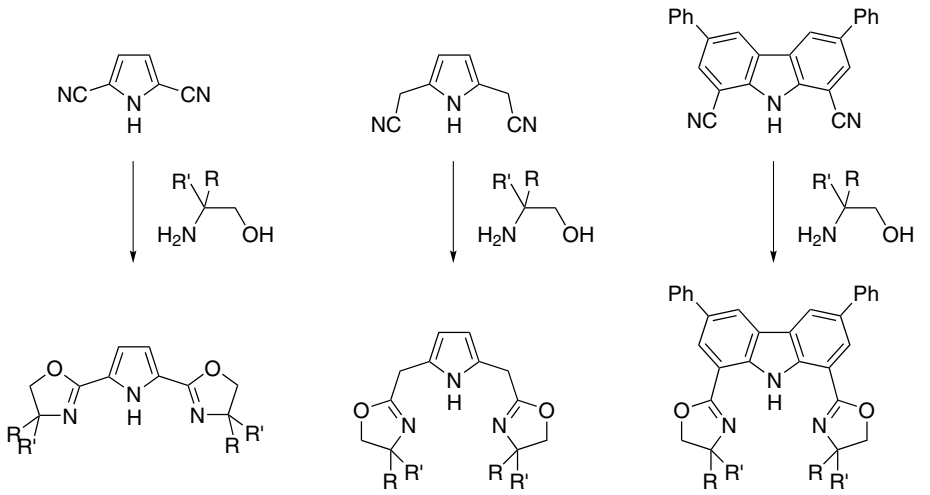

Figure 14. Preparation of the bis(oxazolinyl)pyrrole [H(bop)] ligands **54**–**56**.

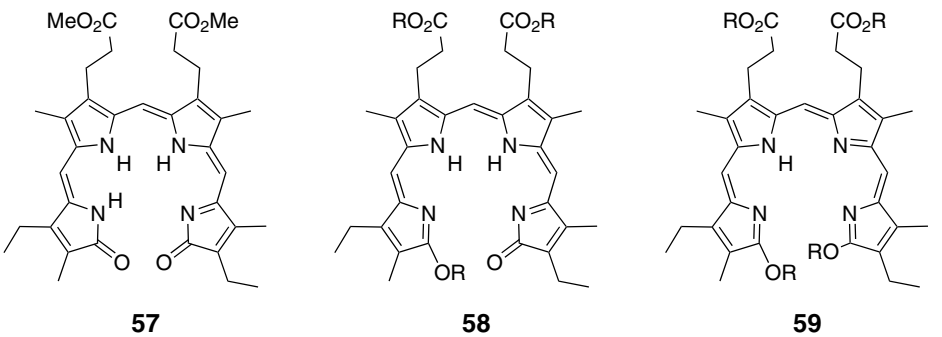

Figure 15. Mesobiliverdin dimethyl ester **57** and O-lactim-ethers derived therefrom.

vinyl groups results in the so-called *meso* forms, which are also of biological origin. These mesobilins are often used as the methyl- or ethyl-esters, thus directing the site of interaction with metal ions exclusively toward the porphyrinoid N_4 cavity (see **57** in Figure 15). The third problem is associated with the terminal oxo groups and relates to different tautomeric forms of the biological species. Figure 15 illustrates that this prototropic dynamic can result in three different protonation states for the same ligand. This ambiguity can be overcome by O-alkylation of one or both oxo groups, thus resulting in ligands **57**–**59** with distinct charges of (3-), (2-), and (1-) in the fully N–H deprotonated states.

F. Tetrapyrroles: Oxidative Ring-Opening of Tetrapyrrole Macrocycles

The naturally occurring degradation processes of heme and chlorophyll are initiated by oxidative ring-opening transformations. Biomimetic and chemical variations of such transformations have been developed and have led to the preparation of a number of different artificial tetrapyrroles. Two protocols — the coupled oxidation of iron porphyrins and the photooxidation of porphyrins and chlorins bound to magnesium, zinc, and other ions — dominate this approach and have also attracted scientific interest in their own right.

Many metal porphyrins undergo the coupled oxidation reaction to give *meso*-oxygenated porphyrinoids,[215] but only for iron porphyrins have the ring-opening and formation of open-chain tetrapyrrolic products been reported. The reaction occurs either under biomimetic conditions with dioxygen and ascorbic acid, or as a shunt reaction in the presence of hydrogen peroxide. Both variants require pyridine as solvent or cosolvent. Iron β-alkylporphyrins **60** (Figure 16) yield bilindiones **61** exclusively with loss of one *meso* carbon atom. For nonsymmetric derivatives, all possible regioisomers are formed in different ratios.[216] Iron complexes of *meso*-arylporphyrins **62** are less selective and react in two steps via a hydrated product **63**.[217,218] This intermediate can be dehydrated to form tetrapyrroles of the aroylbilinone type **64**. Bilindiones **65** form in a side reaction as minor byproducts. The absence of β-situated alkyl groups allows the rotation of the terminal C_4H_2NO unit(s), which results in the presence of conformational isomers **a** and **b** for **63**–**65** (Figure 16).

Photooxidative porphyrin cleavage occurs simply upon irradiation of a porphyrin in the presence of dioxygen. Porphyrins with magnesium, zinc, and cadmium central atoms have been employed mainly for this reaction; however, other metals such as copper, iron, nickel, or thallium may also be used.[219] Two differences are characteristic with respect to the coupled oxidation approach. First, all products are still in the metalated form except for iron derivatives, and free base porphyrins as well as an N-alkylated species have also been shown to undergo the reaction.[220] Second, no carbon atom is expelled during the reaction, so that formylbilinones or aroylbilinones are formed throughout. Mechanistic studies on magnesium tetraphenylporphyrin have shown that initially an intermediate with a four-membered C_2O_2 ring is formed, which then ring-opens to give the observed products (Figure 17).[221,222]

With *meso*-arylporphyrins as substrates, hydrated forms **63** and aroylbilinones **64** are the only products.[223–225] No regioisomers of **64** have been described in the product mixture. Coincidentally, the successive reaction of tetraphenylporphyrin with butyl lithium and O_2/hν has provided a *meso*-butylated aroylbiladienone with the same regiochemistry.[226]

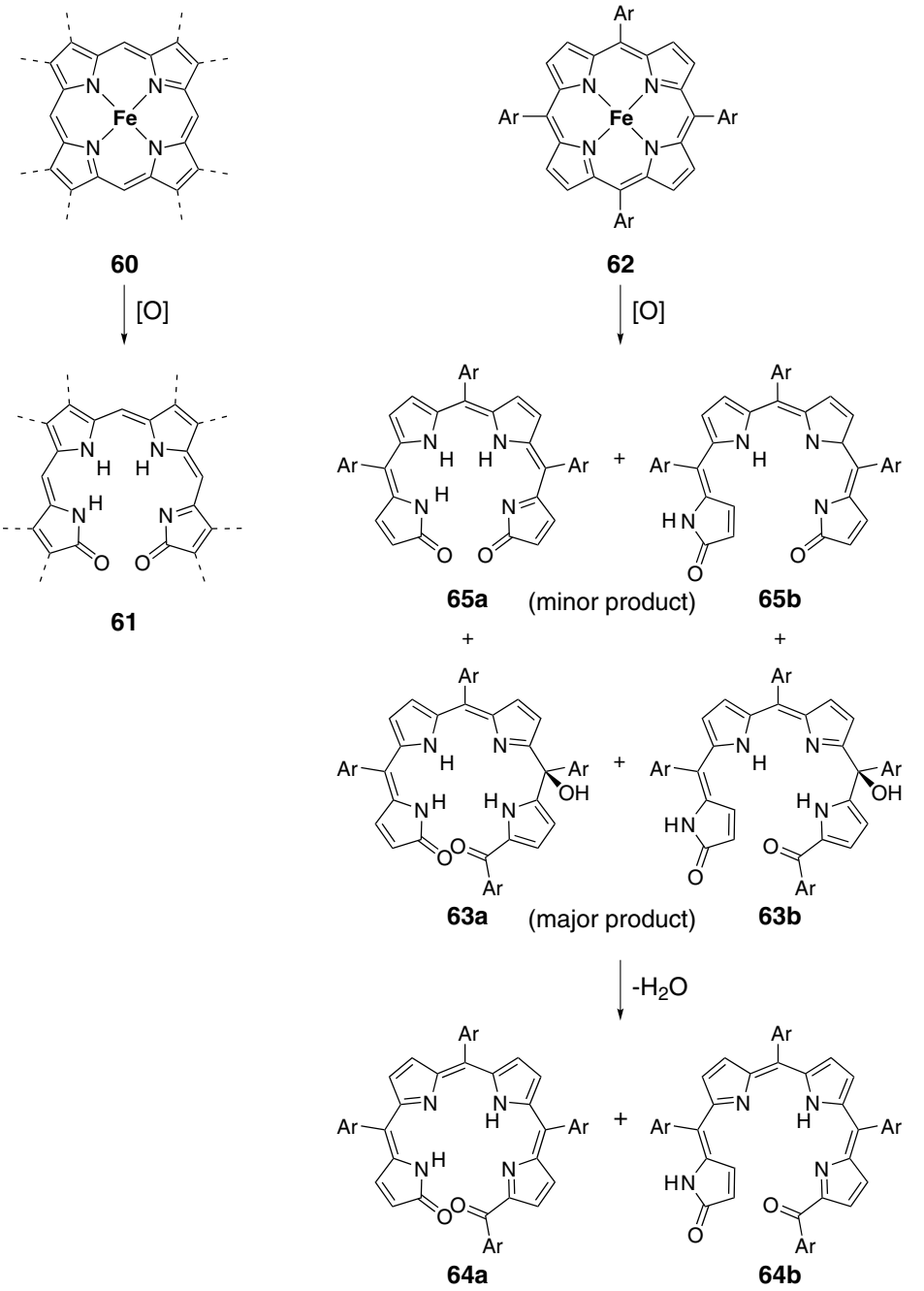

Figure 16. Coupled oxidation of iron porphyrins with β-alkyl- (left) and *meso*-aryl (right) substituents.

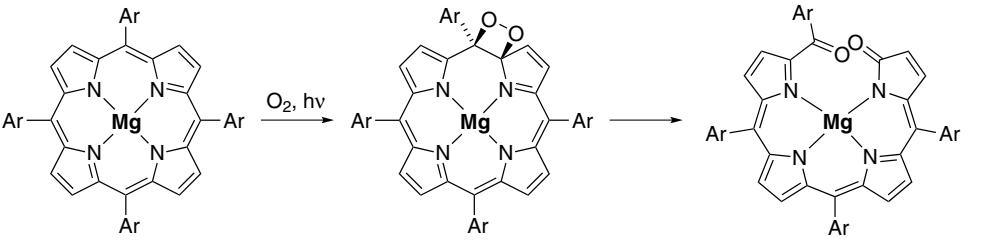

Figure 17. Proposed mechanism for the photooxidation of magnesium tetraphenylporphyrin.

β-Alkylporphyrins form exclusively formylbilinones such as **12** and no hydrated species.[219] The reaction shows a high degree of regioselectivity. In magnesium and zinc complexes of protoporphyrin IX dimethylester **66**, the oxygenation is directed to the position between the two vinylpyrrole moieties. Zinc, copper, and nickel complexes of the partially hydrogenated β-alkylporphyrin **67** (a chlorin) are exclusively opened next to the reduced five-membered ring.[219] For pheophorbide **68** an intriguing dependency of the site of oxygenation from the metal atom (zinc vs. cadmium) has been observed (Figure 18).[227,228] This reaction was also studied mechanistically.[229]

Some further oxygenation protocols leading to ring-opened tetrapyrroles and/or their corresponding metal chelates have been reported. A sterically encumbered octaalkyltetraphenylporphyrin has been successfully oxygenated by sodium nitrite/tfa or by *m*-CPBA/pyridine, resulting in the respective zinc, copper, or nickel chelates of the persubstituted aroylbilinone.[230] Trivalent thallium has occasionally been reported as a powerful oxidant for the ring-opening of chlorins, although overoxidation is a problem here.[231,232] Early work on vitamin B_{12} analogs revealed selective macrocycle opening with ozone,[233,234] and a monoarylcorrole was ring-opened at the direct pyrrole–pyrrole junction by molecular dioxygen to give a biliverdin analog.[235] This latter reaction has, however, not yet found practical application.

G. Tetrapyrroles: Coupling of Dipyrrolic Building Blocks

The coupling methodologies of oligopyrroles differ with respect to the precursor nuclearity and the desired bridges. Coupling reactions of two dipyrroles have been achieved by direct coupling, by coupling through a one-carbon bridge, and by coupling through different functionalized bridges, all using different methods. The direct linkage of dipyrroles on the more reactive α-positions of pyrroles was first observed in 1939 as a serendipitous finding during a debromination study on 1-bromo-9-methoxydipyrrin **71** with elemental zinc.[236] In the same year, the action

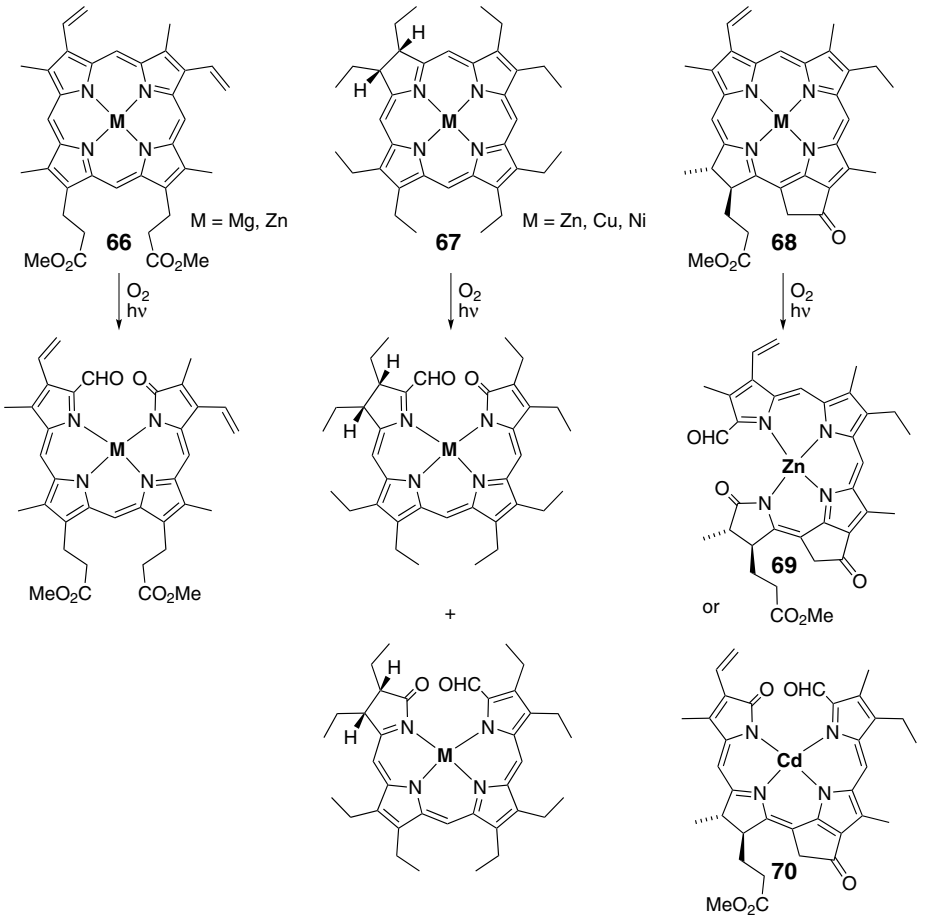

Figure 18. Photooxygenation of different β-alkylporphyrins and chlorins.

of lead(IV) acetate on a nonbrominated dipyrrinone **73** was found to result in the formation of a similar artificial tetrapyrrole, the so-called 2,2′-bidipyrrinone **74** (Figure 19).[237] Twenty years later, a similar reductive coupling of 1,9-dibromodipyrrins **75** with palladium on a solid support was observed[238] and further developed as a method for the preparation of a series of β-substituted 2,2′-bidipyrrins.[239] Three more decades later, the oxidative coupling of dipyrrinone **79** was investigated with a large number of oxidants, leading to products **80** and **81** in different oxidation states (Figure 19).[240]

Meso-aryl-2,2′-bidipyrrins are also available from dipyrrolic precursors. A first example, **82**, was found as a byproduct from a corrole-forming reaction and was structurally characterized.[241] A more directed approach uses the template action of divalent nickel to produce complexes **83**, from which the desired

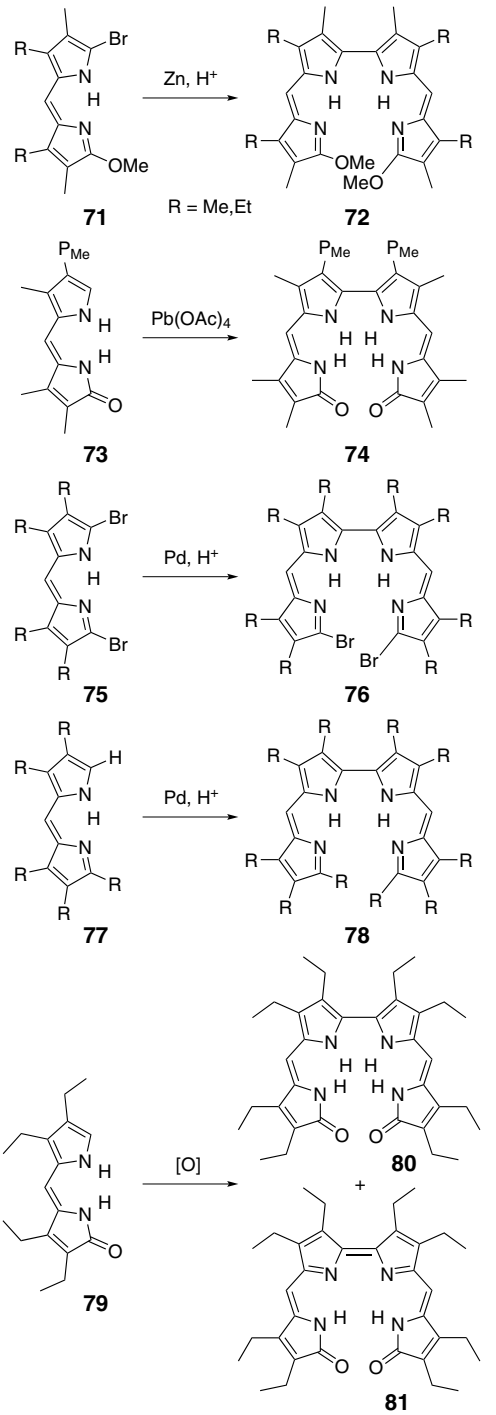

Figure 19. 2,2′-Bidipyrrins from direct couplings of dipyrrolic precursors.

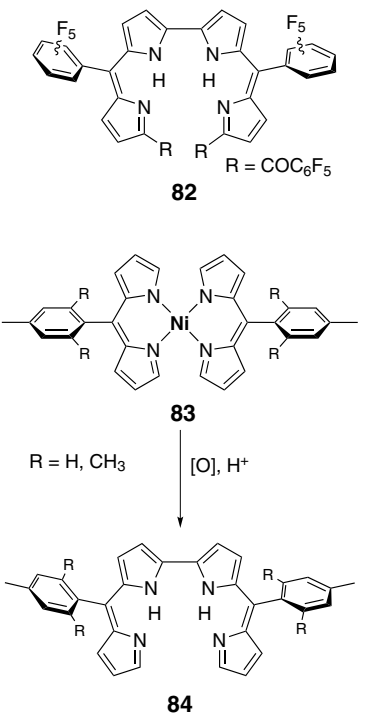

Figure 20. *Meso*-aryl-2,2′-bidipyrrins.

tetrapyrroles **84** could be obtained after oxidative coupling and hydrolytic release (Figure 20).[242]

The introduction of a central CH bridge during the coupling of dipyrrolic precursors has been achieved by the use of trialkylorthoformiate reagents under acidic conditions. Octaethylbilindione **11** has been prepared from the respective dipyrrinone by this method,[243] and chlorin **85** has been described earlier to form under similar conditions (Figure 21).[244] With careful choice of conditions the same reagent was successfully applied to the coupling of the sensitive 2,2′-bipyrrole to give bisnorbilin **86**.[143]

Octaalkylbilindione **88** has been prepared from methylated dipyrrinone **87** by direct oxidation with loss of one carbon atom. Two different protocols employing air and strong alkali[245] or chloranil[246] have been reported for this transformation (Figure 22).

In order to form unsymmetric derivatives and differentiate between the two dipyrrolic precursors, several coupling strategies leading to different types of C_1 bridges have been reported. Methylene bridges can be introduced by coupling a dipyrrole with a bromomethyl or chloromethyl group, e.g. **89**, and an unsubstituted derivative such as **90** under acidic conditions.[247,248] The introduction of a keto

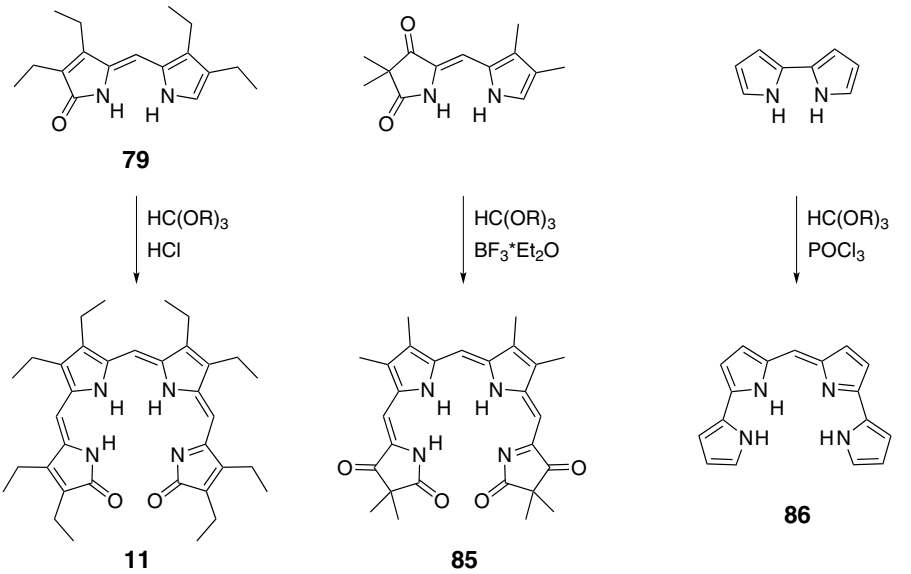

Figure 21. Application of trialkylorthoformiate as C_1-synthon for methine-bridged open-chain tetrapyrroles.

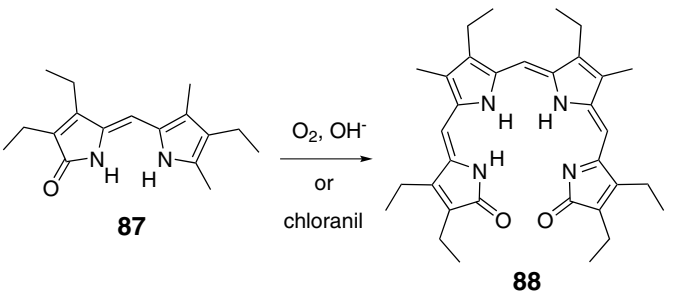

Figure 22. Direct oxidative coupling of α-methyldipyrrinone **87**.

bridge in **91** was achieved by using a dimethylamido terminal group under Vilsmeier conditions (Figure 23).[248]

The most frequently used and most widely applicable method for the coupling of dipyrroles is the acidic coupling of a dipyrrolic aldehyde **92** with an α-free dipyrrole **93** (Figure 24). This reaction typically results in the formation of a stable methine bridge. In many cases, the sensitive α-free dipyrrole is formed *in situ* from an acid labile precursor, especially from a carboxylic acid or *tert*-butyl ester **95** or **96**, respectively. The approach allows the construction of many symmetric and unsymmetric derivatives of the so-called *b*-bilene type **94**.[33,249–251]

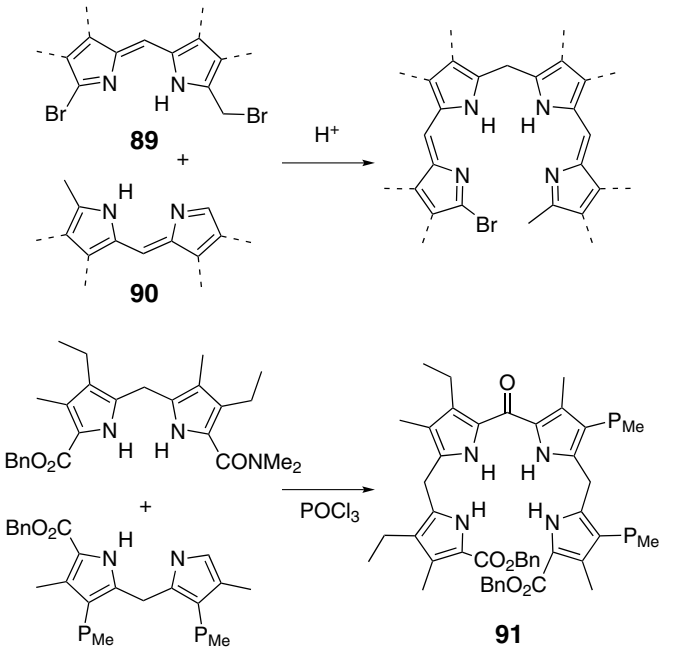

Figure 23. Examples of unsymmetric coupling of dipyrroles through methylene and keto bridges.

Ring-annelated species such as **97** have been accessed from suitable precursors,[252,253] as have been partially hydrogenated tetrapyrroles **98**[153] and **99**,[254] and several bipyrrole-containing species, such as **100**[139,141] or **101**[147] (Figure 24).

A special coupling strategy has been reported in the context of vitamin B_{12} synthesis. This approach couples two dipyrroles **102** and **103** carrying a cyanovinyl group and a lactim-ether, respectively, under alkaline conditions to give tetrapyrrole **104** (Figure 25).[151]

A series of artificial tetrapyrroles with a longer chain central bridge and an (often) extended π system has been prepared from dipyrrinone precursors **105** (Figure 26). Different reagents have been exploited in order to obtain the desired compounds.[255–259] For some of the species the presence of different stable oxidation states has been confirmed. BODIPYs (BOron DIPYrrins) **106** have been used as luminescent building blocks and introduced as functional units in a number of large molecule constructions (Figure 27).[23] Bis(dipyrrins) **107** with the dipyrroles connected to each other at the *meso* position via a large spacer have been built from dialdehyde **108** using the same synthetic strategy as for dipyrrins (Figure 28).[260] A similar approach was successfully applied to the preparation of "Pacman" biscorroles.[261]

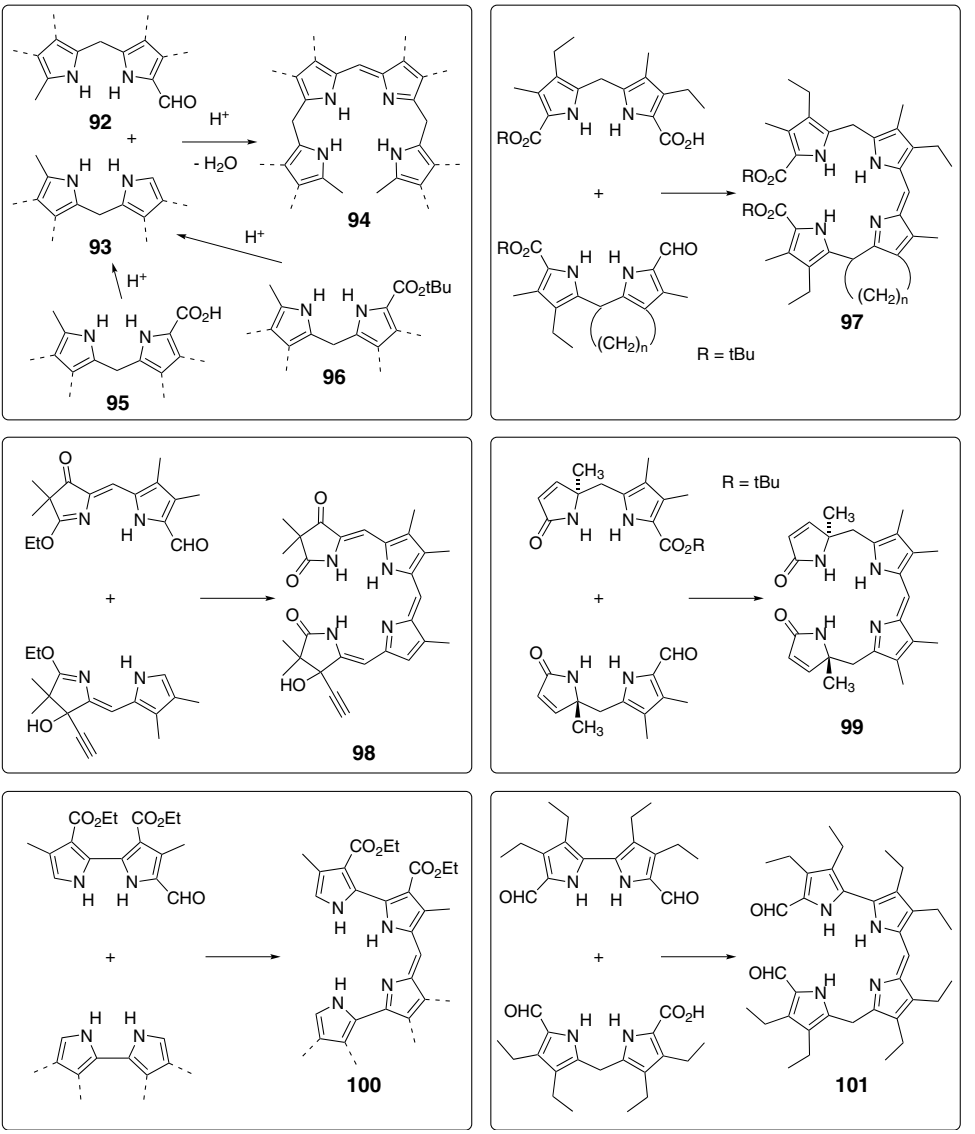

Figure 24. Overview of tetrapyrroles formed by the coupling of a dipyrrole aldehyde with an α-free dipyrrole or related precursor.

H. Tetrapyrroles: Coupling Two Pyrrole Units with a Dipyrrole

This is the most important method for preparing open-chain tetrapyrroles. The coupling of a dipyrrolic center to two pyrrole termini shows the largest number of applications in the literature and allows the construction of numerous variants of all important as well as many less usual tetrapyrrole architectures. The major

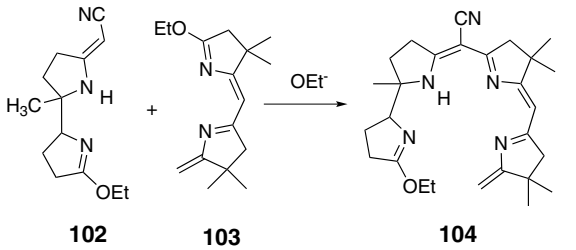

Figure 25. Coupling strategy in the context of vitamin B_{12} synthesis.

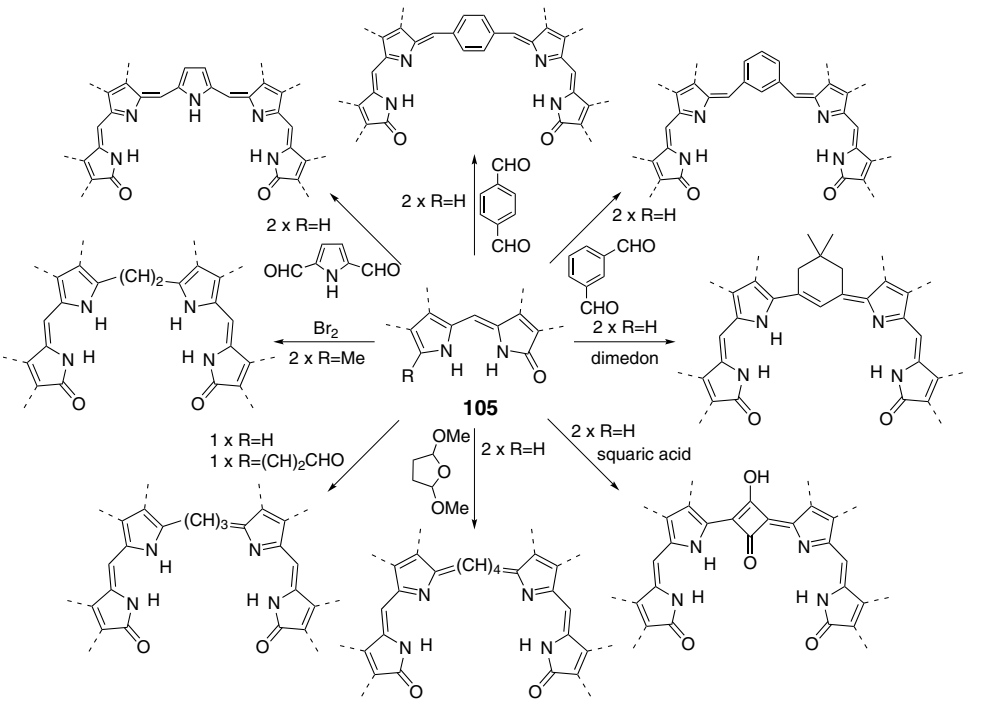

Figure 26. Dipyrrinone-based tetrapyrroles with extended central bridges.

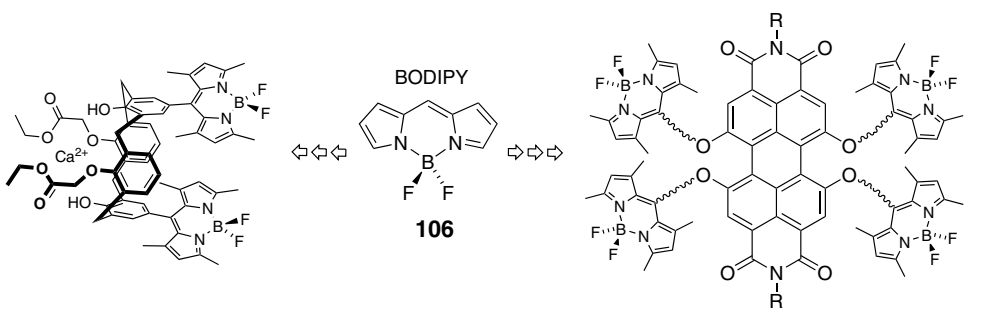

Figure 27. Examples for BODIPY-based photofunctional oligomers.

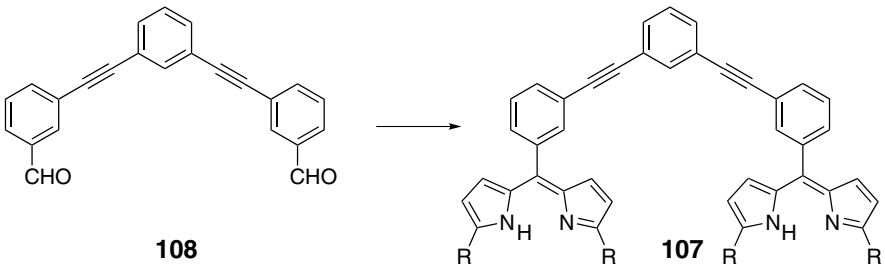

Figure 28. *Meso*-bridged bis(dipyrrin)s **107**.

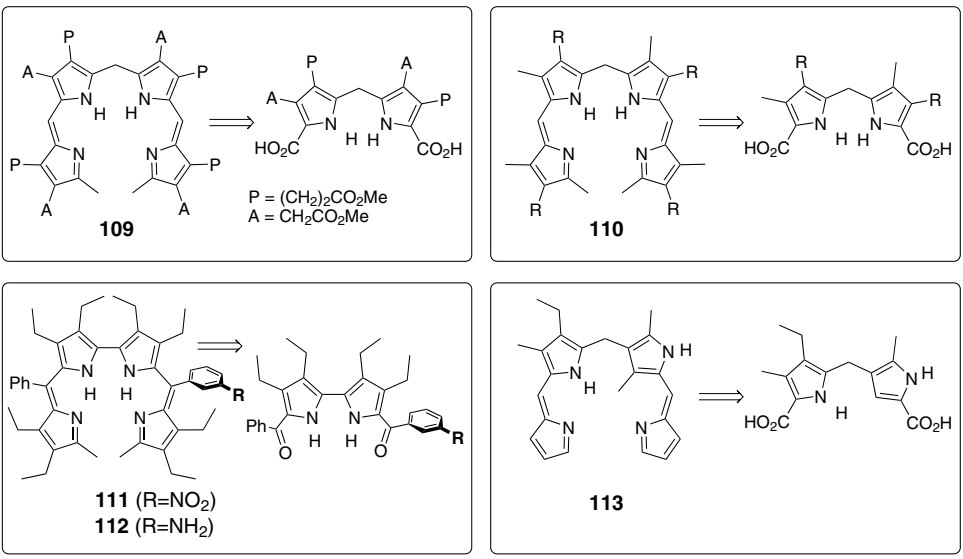

Figure 29. Unsymmetric tetrapyrroles from condensation reactions of one dipyrrolic and two pyrrolic units.

drawback of this approach is found in the necessity to produce C_2-symmetric products. In part, this symmetry constraint can be broken by the use of unsymmetric dipyrroles, as shown by several examples in the past (Figure 29).[129,262–264]

Usually, the coupling is achieved in one step through twofold condensation of an aldehyde with an unsubstituted pyrrole or with a carboxylate, as described above. The aldehyde function may be located on the pyrrolic or the dipyrrolic precursor; however, in some cases different yields have been reported. Only two cases employing different strategies have been described.[265,266] Many derivatives can be found in the literature which are best organized by the type of the central dipyrrole moiety.

2,2′-Bipyrroles have been used extensively as the central building block for tetrapyrroles, and the preparation of many simple alkyl-substituted

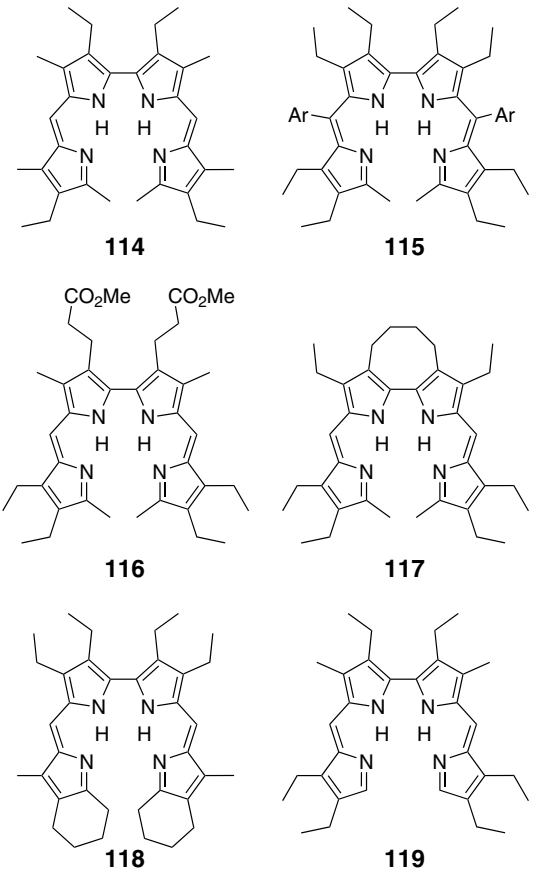

Figure 30. 2,2′-Bidipyrrins **114**–**119** prepared from 2,2′-bipyrrole dialdehydes or diketones.

2,2′-bidipyrrins **114** has been reported from this group of precursors.[27,263,267] Persubstituted derivatives with different *meso*-aryl groups **115** are available under forcing conditions,[263,267] and some functionalized species with biomimetic propionate side chains **116**[268] and with annelated carbocyclic rings **117** and **118**[269–271] are known (Figure 30). Bipyrroles undergo the double condensation reaction only if the keto function is localized at the dipyrrolic precursor. If the terminal positions are free, as in **119**,[270] particularly smooth reaction conditions have to be applied, and several byproducts form from oxidative scrambling reactions.[271]

Due to the biomimetic, bilirubin-like bridging pattern of the tetrapyrrolic products, the so-called *a*,*c*-biladienes, a central dipyrromethane unit, have most often been applied to open-chain tetrapyrrole preparations with this approach. Different alkyl, acetate, propionate, alkoxy, and carboxylic ester side chains are present at the β-positions of these derivatives, and hydrogen atoms,[273,275,281,284]

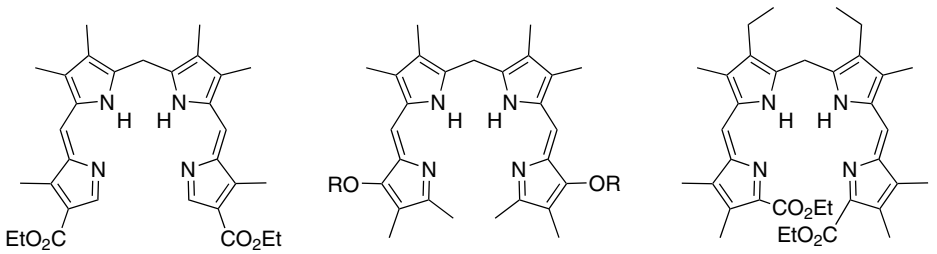

Figure 31. Typical *a,c*-biladienes with different terminal groups.

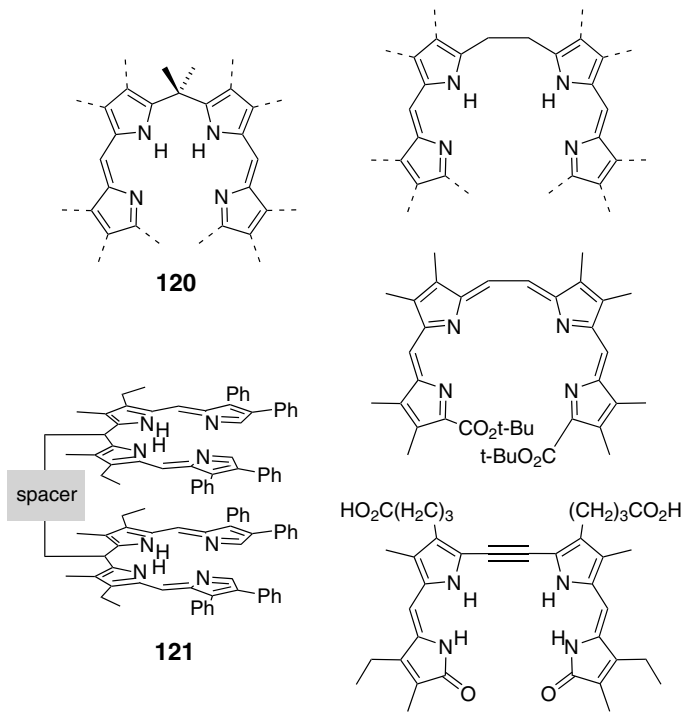

Figure 32. Preparation of *meso*-substituted *a,c*-biladienes **120** and **121**, and an overview of extended biladienes.

methyl groups,[32,128,272–274,276–280,283,284] or carboxylic esters[276,282,283] may be used as terminating entities, as shown in selected examples in Figure 31.

Two types of higher functionalized dipyrromethane building blocks have been described: *meso*,*meso*-dimethyl compounds **120**[239,285,286] and bridged bis-*a*,*c*-biladienes **121**[261] (Figure 32). Both species were prepared in excellent yields using the above methodology. Tetrapyrroles with other extended bridges have only occasionally been synthesized by this approach. In all known cases so far, dicarbon units in different oxidation states constitute the central bridge (Figure 32).[239,287–290]

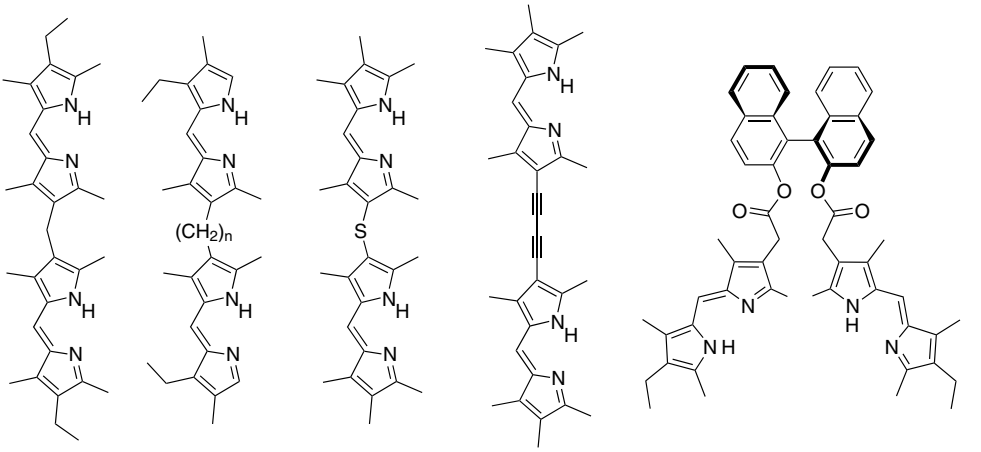

Figure 33. Typical examples for β-bridged bis(dipyrrins) **122**–**126**.

Unique to this approach is the preparation of tetrapyrroles with a central bridge between pyrrolic β-positions (Figure 33). Most studies use a methylene bridge at this position, as in **122**. Both possible options with the aldehyde located at the pyrrolic as well as the dipyrrolic unit have been successfully applied.[291–295] Some further reports deal with similar constructions using longer flexible alkane linkers (C_2–C_8) as found in **123**,[291,296,297] a sulfur bridge as in **124**,[28] or rigid diacetylenes such as **125**.[298] A chiral derivative **126** with the dipyrrins connected by a binaphthyl bridge has been reported.[299] These ligands are often referred to as bis(dipyrrins), as their coordination behavior is more reminiscent of the single dipyrrin subunits than of the bilins.

Functionality has occasionally been introduced with the terminal pyrrole moieties or by a posterior modification. Chiral tetrapyrroles were obtained by the use of enantiomerically pure pyrrole propionates.[300] An *a*,*c*-biladiene with two terminal nickel porphyrin moieties has been described.[40] Benzyl, acetyl, and propionyl substituents have been introduced at the terminal α-positions of *a*,*c*-biladienes as probes for a macrocyclization reaction to porphyrins.[301] Two oxidative protocols have been reported for the introduction of terminal formyl groups in fully substituted 2,2′-bidipyrrins.[302] None of these reports has, however, found any generalization in the preparation of tetrapyrroles to date.

I. Tetrapyrroles: Stepwise Coupling of Pyrrolic Precursors

Further developments in the preparation of unsymmetric open-chain tetrapyrroles have targeted the application of sequences that build the desired compounds from

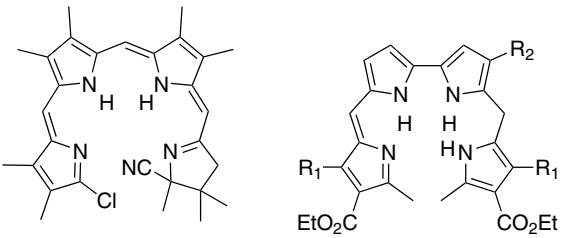

127

Figure 34. Partially hydrogenated unsymmetric tetrapyrroles **127** and **128**.

single pyrroles in a linear strategy. Several of such approaches have been published, and in some cases relevant material for coordination studies has been reported. In most of the reports, unsymmetric *a*,*c*-biladienes have been prepared for templated macrocyclization studies to yield metal porphyrins.[130,132,301,303–305] In general, the applied method involves an orthogonal protecting group strategy in order to condense a dipyrrole with pyrrole A, and after deprotection with pyrrole B to form the desired product. A hydrogenated chlorin precursor **127** could be prepared by a similar approach,[152] and two early reports confirm the accessibility of a class of unsymmetric, *meso*-hydrogenated 2,2′-bidipyrrins **128** (Figure 34).[141,239]

III. Coordination Behavior and Complex Properties

A. Interaction of Prodigiosenes with Metal Ions

Despite the strong biomedical interest in the prodigiosene group of linear tripyrroles, little is known about the coordination properties of these entities. Early studies on an ethoxycarbonyl-terminated, partially hydrogenated ligand gave analytical data in agreement with a 2:1 complex **129** for Ni^{II} and a hydrolyzed 1:1 species with Cu^{II} **130**.[140] The hydrolysis occurred in the second case only, and the carboxylate anion was assumed to fill the coordination sphere of the copper ion (Figure 35). Several studies suggested a functional role of prodigiosenes as ligands by a measured reactivity such as ion transport[154] or nuclease activity,[150,306] in the presence of certain ions. Divalent copper appears to be the ion of choice in all these studies. Only recently have the first crystallographic analyses of prodigiosene copper and zinc chelates appeared in the literature and confirmed the suggested stoichiometries of the compounds.[307] While zinc(II) chelate **131** was found to reside in the expected tetrahedral arrangement and with two protonated, pendant pyrroles, copper(II) complex **132** contains a N,N,N-bound two-electron oxidized tripyrrole ligand, regioselectively hydrated at the dipyrrin α-position. This hydroxy group is believed to originate from the redox cycling of molecular

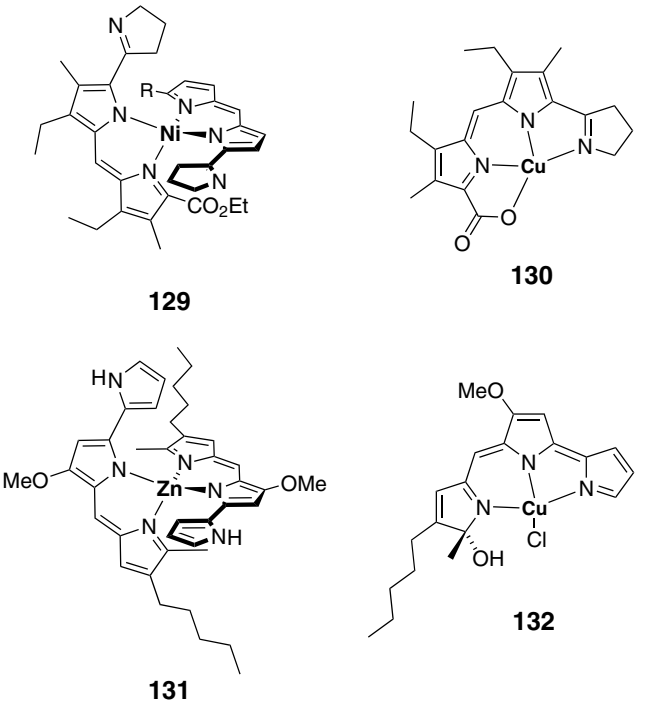

Figure 35. Metal complexes with prodigiosene ligands.

oxygen and Cu^{I} ions, producing hydrogen peroxide, with copper(I) being formed in an initial step by partial copper oxidation of the prodigiosene ligand. A similar Cu^{I}/O_2 driven redox cycling is presumably responsible for the DNA strand scission, i.e. nuclease activity, of this and related species.

B. Tripyrrinone and Tripyrrin Metal Chelates

Although natural tripyrroles with a tripyrrindione core, biopyrrins **3** and **4**, have been known to coordinate to ions, metal chelates of these or artificial tripyrrindiones have not yet been isolated. Some description of the optical properties of zinc and copper derivatives may be found in the literature,[98] but neither crystallographic nor analytical data have so far been reported. Copper and iron complexes of tripyrrin-1-ones **133**–**135** and **136** have been found occasionally as oxidative degradation products of metal chelates of N-confused porphyrin,[100,101] carbaporphyrin,[102] and *meso*-aminoporphyrin (Figure 36).[103] Copper chelates **133**–**135** were investigated in more detail with respect to the regiochemistry of the ring-opening,[103] and to demetalation/remetalation possibilities, and several examples of tripyrrin-1-one complexes with a N,N,N-bound zinc(II), nickel(II), palladium(II), and platinum(II)

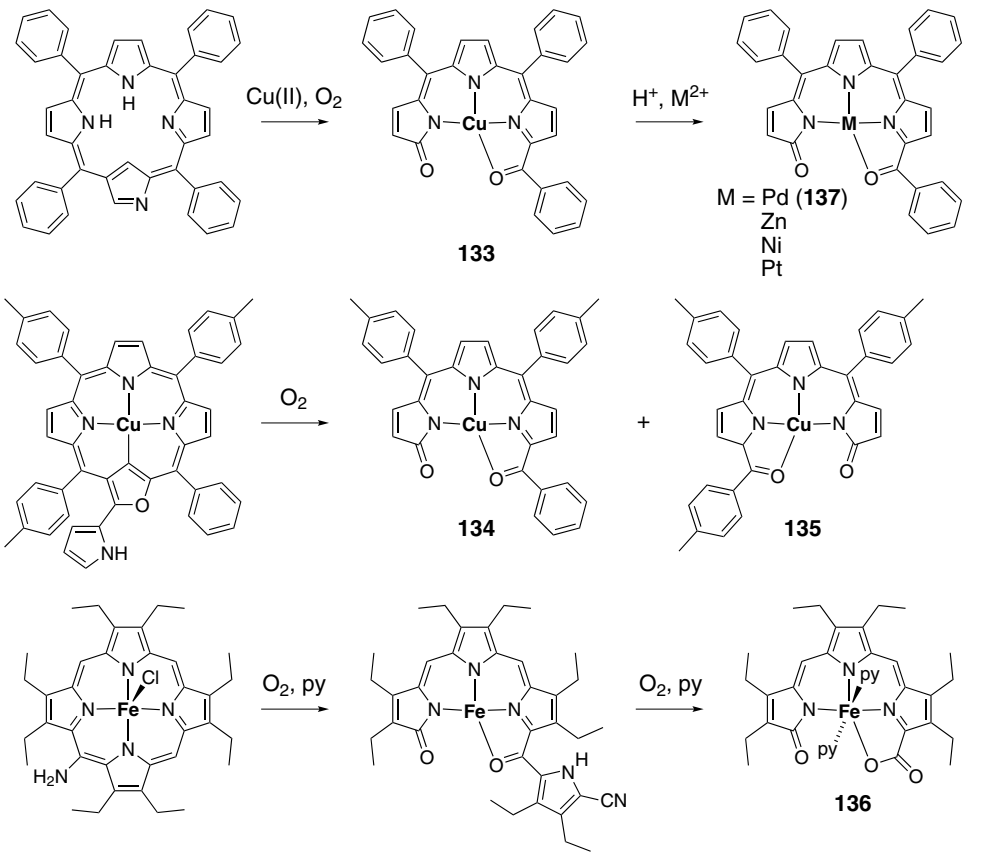

Figure 36. Oxidative degradation processes leading to metal tripyrrin-1-ones.

ion were obtained.[101] Structural characterization has been performed for the iron (see Section V.A), copper, and palladium derivatives. Another structural analysis is available for nickel chelate **138**, which was prepared from **44** (Figure 37).[116] The basic structures of **138** and the palladium example **137** deviate mainly by the different degrees of tripyrrole nonplanarity, which appears to be of sterical origin.

Tripyrrin-1-one carboxylic acids **139** have been found to form a variety of metal derivatives **140** which are insoluble in water (Figure 38).[92,93,95] Further work revealed two distinct groups of species. With iron(II), cobalt(II), rhodium(III), iridium(IV), nickel(II), palladium(II), platinum(II), copper(II), zinc(II), cadmium(II), mercury(II), tin(II), lead(II), and UO_2^{2+} ions, typical transition metal complexes were described, the transformation being accompanied by extensive changes in the IR and UV-visible spectra. NH_4^+, alkali, and alkali earth ions, on the other hand, react with **139** to give sparingly water-soluble compounds, for which a helical arrangement of several tripyrrinone acid molecules around the

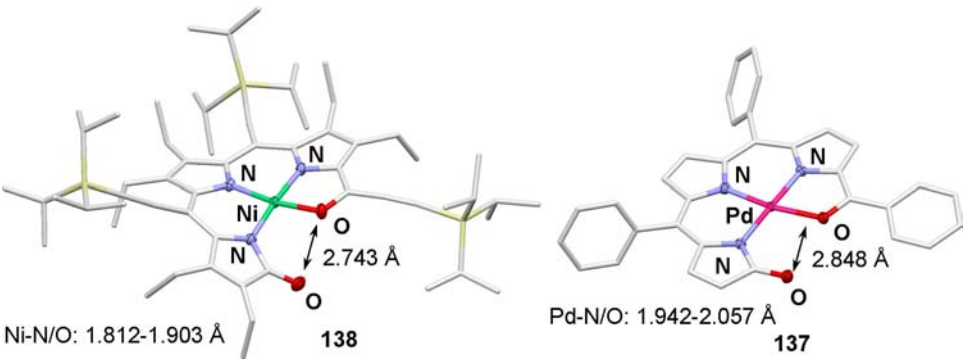

Figure 37. Molecular structures and selected data for nickel and palladium tripyrrin-1-ones **138** and **137**. (Adapted from Refs. 101 and 116.)

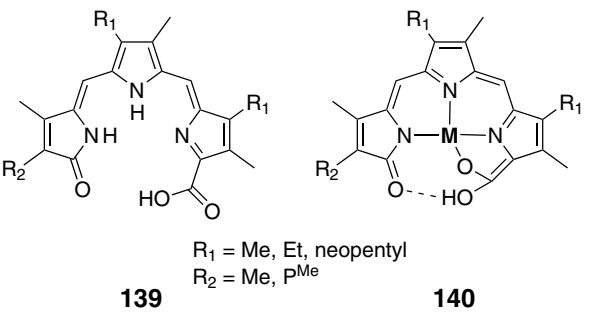

Figure 38. Schematic view of tripyrrin-1-one carboxylic acid **139**, and assumed structure of its metal chelates **140**.

metal ion was proposed.[104,105] No crystallographic analysis has been reported, and details of the aggregation process have not been unraveled. A UV-visible titration study later revealed L_1M_1 stoichiometries for transition metal and alkali metal chelates, and a L_2M_1 stoichiometry for the calcium(II) compound.[110]

The copper(II) and zinc(II) chelates **141**–**147** of several tripyrrin-1-ones with carboxylate, sulfonate, and/or alkyl substitution have been prepared by the extraction of the corresponding ions from aqueous solutions (Figure 39). The products have been described as rather labile, and in the case of copper were found to be very sensitive to oxidation by excess copper(II) and by air. The chelates show L_1M_1 stoichiometry and the expected structures for NH dideprotonated tripyrrin-1-one ligands chelating the metal ion in a N,N,N mode. For zinc derivative **148**, however, the tripyrrole is only monodeprotonated, and the lactam ring resides preferentially in the tautomeric hydroximino form. The pH dependence of this tautomeric equilibrium was determined by a spectrophotometric titration.[113] Such

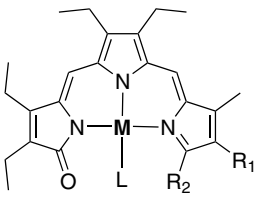

	R_1	R_2	M
141	H	Me	Cu
142	Me	H	Zn
143	Me	H	Cu
144	SO_3^-	Me	Zn
145	SO_3^-	Me	Cu
146	Me	SO_3^-	Zn
147	Me	SO_3^-	Cu

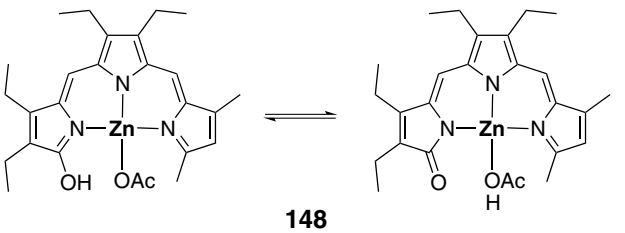

148

Figure 39. Zinc and copper chelates of tripyrrin-1-ones **141**–**148**.

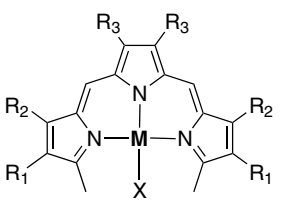

ligand	R_1	R_2	R_3
L1	Et	Et	Et
L2	Et	Et	H
L3	Et	Me	Et
L4	Et	Me	H
L5	Me	Me	Et
L6	Me	Me	H

Figure 40. Schematic view of metal tripyrrins with different coligands X; for details see Table 1.

tripyrrin-1-ones and related aryl-substituted dipyrrinones have also been studied in the context of their ability to function as ion transporters for a large number of metal cations.[308–311]

Tripyrrins with terminal alkyl substitution were studied in coordination compounds in some detail. Fully protonated tripyrrin moieties, as formed under the condensation conditions in neat trifluoroacetic acid, decompose very quickly in the presence of nucleophiles and base. The successful preparation of the first examples involved the divalent palladium, zinc, and copper derivatives, which with the corresponding acetate salts gave trifluoracetato complexes **149**–**154**, **167**–**170**, and **176**, **177** (Figure 40 and Table 1).[119–122] Ni(II) could be introduced by the same approach, but the intermediate nickel chelate required an exchange of the anionic ligand (presumably trifluoracetate) with a cyanate ion to give **186/187** in order to gain sufficient stability for the necessary chromatographic separation.[312,313] Nickel isocyanates may be cleanly demetalated using excess cyanide

Table 1. Metal, ligand, and coligand of known four-coordinate metal tripyrrins from Figure 40.

	M	X	L	Ref.
149	Pd	OAc^F	L1	119
150	Pd	OAc^F	L2	120
151	Pd	OAc^F	L3	318
152	Pd	OAc^F	L4	121
153	Pd	OAc^F	L5	121
154	Pd	OAc^F	L6	121
155	Pd	tcm	L3	316
156	Pd	tcm	L6	316
157	Pd	dca	L1	316
158	Pd	dca	L6	316
159	Pd	OAc	L1	120
160	Pd	Cl	L1	120
161	Pd	Br	L1	120
162	Pd	I	L1	120
163	Pd	N_3	L1	120
164	Pd	NCO	L1	120
165	Pd	NCS	L1	120, 316
166	Pd	NCSe	L1	316
167	Zn	OAc^F	L1	121, 122
168	Zn	OAc^F	L2	122
169	Zn	OAc^F	L3	122
170	Zn	OAc^F	L5	121
171	Zn	tcm	L1	122
172	Zn	dca	L3	122
173	Zn	N_3	L1	122
174	Zn	NCS	L1	122
175	Zn	NCSe	L1	122
176	Cu	OAc^F	L1	121, 122
177	Cu	OAc^F	L3	122
178	Cu	tcm	L3	122
179	Cu	dca	L3	122
180	Cu	Cl	L1	122, 317
181	Cu	NCSe	L1	122
182	Ni	Cl	L1	312, 319
183	Ni	Cl	L3	319
184	Ni	Br	L1	312
185	Ni	I	L1	312
186	Ni	NCO	L1	313
187	Ni	NCO	L3	313
188	Ni	CN	L1	313
189	Ni	NO_3	L3	319
190	Ni	sal	L3	313
191	Ni	ox	L1	319
192	Mn	NCO	L3	314
193	Mn	NCS	L3	314

(*Continued*)

Table 1. (*Continued*)

	M	X	L	Ref.
194	Mn	OAc	L3	314
195	Fe	NCO	L3	314
196	Fe	NCS	L3	314
197	Fe	OAc	L3	314
198	Co	OAc^F	L1	121
199	Co	Cl	L1	314, 317
200	Co	I	L1	314
201	Co	NCO	L3	314
202	Co	NCS	L3	314
203	Co	OAc	L1	314
204	Co	OAc	L3	314
205	Co	NO_3	L1	314
206	Cd	OAc	L1	315
207	Cd	OAc	L3	315
208	Cd	sal	L1	315
209	Cd	$acac^F$	L3	315

and have been used as the only source of free base tripyrrin ligands. Remetalation with acetate salts of divalent manganese, iron, cobalt, and cadmium proceeds smoothly and allows access to metal tripyrrins **194**, **197**, **203/204**, and **206/207** as the acetato complexes.[314,315] The diversity of the metal tripyrrins described to date is mainly based on the large variety of axial ligands which may be introduced by simple extraction with an aqueous solution of the appropriate alkali salt.[122,314–316] By this means, halide, pseudohalide, and a variety of oxo anions have been introduced as coligands to metal tripyrrins. For palladium halide derivatives, two alternative routes for ligand exchange have been reported to give advantageous results. Iodopalladium tripyrrin **162** was made under Finkelstein conditions with sodium iodide in dichloromethane, and the chloro and bromo derivatives **160/161** were obtained using the corresponding trimethylsilylhalide at low temperature (Figure 40 and Table 1).[120] All these compounds contain metal ions only in the +2 oxidation state. Electrochemical data are available for a set of chloro complexes with Pd(II), Ni(II), Zn(II), Cu(II), and Co(II). Only copper ions may be reduced to the monovalent state within the tripyrrin environment. Spectroelectrochemical studies revealed exclusively ligand-centered oxidation and reduction steps for all other compounds.[317]

The tripyrrin molecule is formally derived from the macrocyclic parent porphyrin by the loss of one of the four C_4N rings. Chemically, however, the trpy ligand differs largely from the porphyrin with respect to ligand stability and the open *cis*-situated coordination site at the central ion. With regard to the meridional N,N,N coordination and the monoanionic nature, the tripyrrin ligand is closely

related to the class of pincer ligands. The major difference with the tripyrrin systems studied so far appears to be the presence of two terminal methyl moieties which shield the one coordination site situated in the N_3M plane of a given complex. Neutral palladium(II) complexes of such α,ω-dimethyltripyrrin ligands are typically characterized by the steric repulsion which is present between the anionic coligand (in particular the donor atom of that coligand) and the two methyl groups situated at the termini of the open-chain tripyrrole (methyl termini). The steric overcrowding at the open site of the linear tripyrrole leads to strained, nonplanar structures, and in one case even fluxional behavior has been observed, i.e. a dynamic interconversion process between two different nonplanar conformations **210**-I and **210**-II (Figure 41).[119–121,318] These two limiting conformations have so far been the only ones observed for neutral palladium tripyrrin species, and they have been named *strained pseudoplanar* and *helical*, in accordance with the corresponding tripyrrole conformation. In the pseudoplanar conformation, the Pd^{2+} ion is bound in an intermediate situation between distorted square-planar and distorted tetrahedral, while for the helical form a planar coordination of the

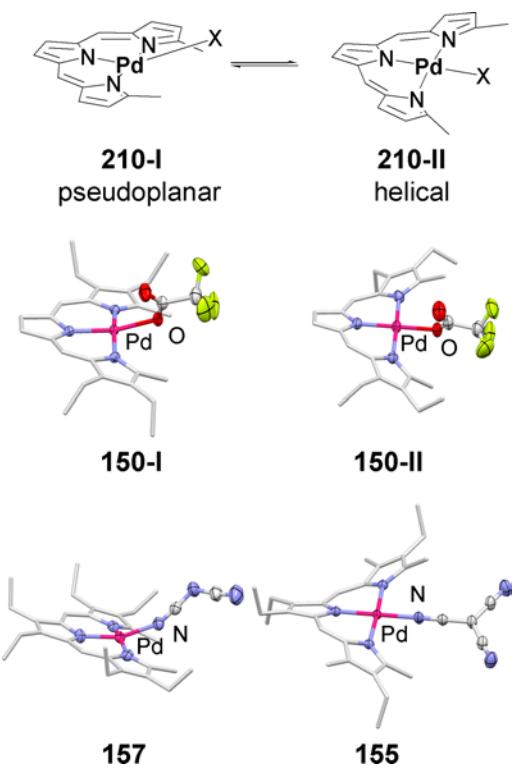

Figure 41. Structural aspects and dynamics of neutral palladium tripyrrins (crystallographic figures adapted from Refs. 120 and 316).

palladium(II) ion results. The pseudoplanar scenario is present in the majority of compounds,[120] while the helical form has mainly been observed with the trifluoracetato ligand. In addition, a linear coligand containing a small donor atom increases the chance to observe (trpy)Pd species in the helical conformation. The N-donor pseudohalides thiocyanate and tricyanomethanide have been used successfully for this purpose. The related dicyanamido ligand, on the other hand, produces palladium tripyrrins which reside exclusively in the pseudoplanar form.[316] The inner strain of palladium tripyrrins supports ligand exchange processes and has been used to prepare a variety of cationic derivatives (see Section IV.A).

In contrast to the situation with palladium, nickel(II) tripyrrins usually contain a high-spin-configurated d^8 ion in solution and in the solid state, with a structure described as unstrained pseudoplanar, as demonstrated for cyanato derivative **186** in Figure 42. The coordination environment of the nickel ion in these species is strongly distorted toward a tetrahedron.[312,313,319] The only known exceptions are cyano complexes **188** and **211**, in which low-spin nickel(II) ions are present. In both species strained pseudoplanar conformations with distorted square-planar coordination of the nickel ions are realized, regardless of the terminal or the bridging binding mode of the cyano ligand (Figure 42).[319] A typical probe for distinguishing between the strained and the unstrained pseudoplanar forms, besides the spin-state-dependent Ni–N distances, is the distance between the methyl termini of the tripyrrin ligands and the donor atoms of the coligand. For example, this distance is 3.406–3.503 Å for the unstrained cyanato derivative **186**, but only

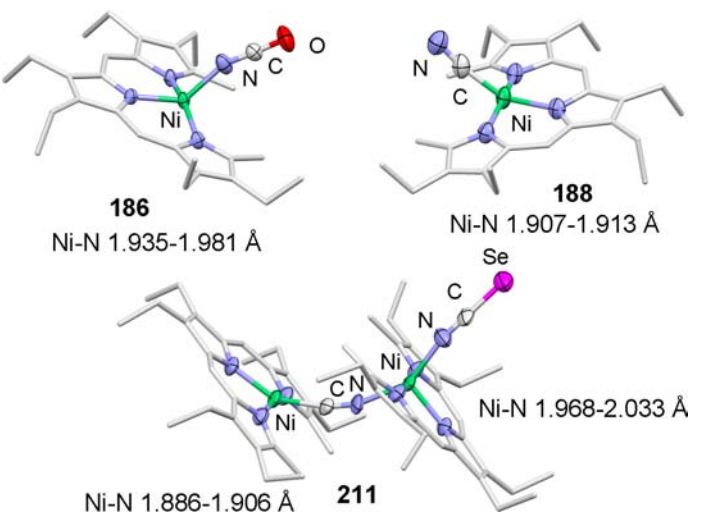

Figure 42. Structural aspects of high-spin and low-spin nickel(II) tripyrrins. (Adapted from Ref. 319.)

2.993–3.018 Å for the strained cyano complex **188**. Another marked difference in this regard is the finding that metal tripyrrins in the strained pseudoplanar conformation do not accept a fifth donor atom (for an exception see Section IV.A), while unstrained pseudoplanar examples readily bind to one, but not two, additional donor or solvent molecules, and form products with five-coordinate nickel. Thermodynamic data are available for the binding of pyridine N-oxide to a chloronickel tripyrrin.[312]

Four-coordinate complexes of the tripyrrin ligand with divalent cobalt, copper, and zinc centers also tend to form unstrained pseudoplanar molecules. Examples are the halide and pseudohalide species **173**, **180**, **184**, and **200**, summarized in Figure 43. As for the nickel chelates, these complexes tend to bind a

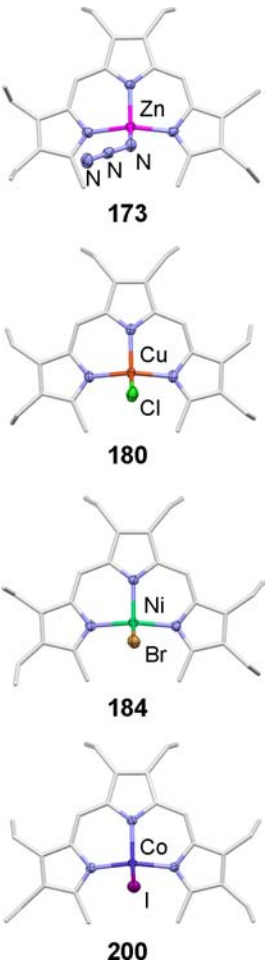

Figure 43. Four-coordinate tripyrrin (pseudo)halide complexes with different 3d metal centers. (Adapted from Refs. 122, 312 and 314.)

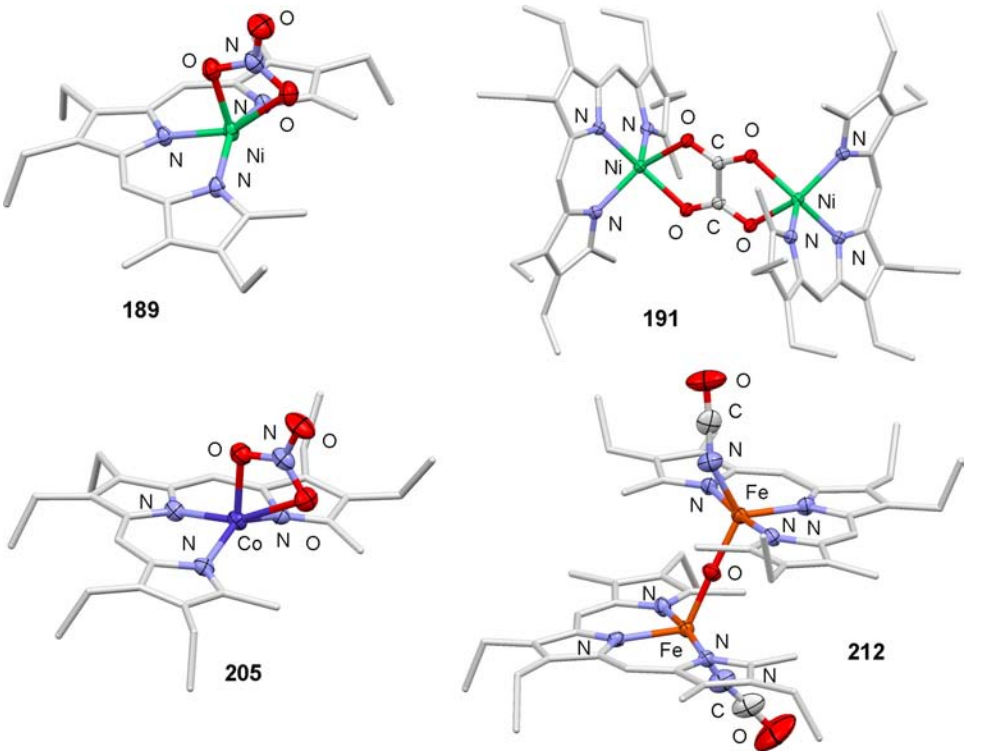

Figure 44. Metal tripyrrins of iron, cobalt, and nickel in different trigonal bipyramidal forms. (Adapted from Refs. 314 and 319.)

fifth donor atom. This tendency, however, is less pronounced for the smaller copper and zinc ions. If bidentate ligands such as nitrate, salicylate, oxalate, or acetate are employed, nickel and cobalt tripyrrins prefer a chelating η^2-coordination and formation of five-coordinate species with a strained trigonal pyramidal structure, as in **189**, **191**, and **205** (Figure 44). Linear or stretched polydentate ligands, on the other hand, yield 1D coordination polymers with the metal tripyrrin building block in an unstrained trigonal bipyramidal situation (see Section VIII.A).[121,122]

Attempts to crystallize simple iron or manganese tripyrrins have not been successful so far. These compounds are reported to be extremely sensitive with respect to dissociation as well as oxidation, so long-term crystallization attempts usually resulted in the decomposition of the material. In one instance, however, the slow crystallization of an iron tripyrrin with isocyanate coordination yielded a small amount of very sensitive dark violet crystals that were shown by XRD to consist of the μ-oxo derivative **212** (Figure 44). Compound **212** is so far the only

example of a metal tripyrrin with the metal in an oxidation state other than +2. Further spectroscopic data of **212** were not reported.[314]

Ligand exchange experiments on cadmium tripyrrins disclosed a marked tendency toward pentacoordination, which is achieved by the formation either of chelates or of 1D coordination polymers arising from the size of the central metal. The attempted introduction of chloro, iodo, or cyanato ligands, instead, led mainly to decomposed material, while the use of 1,1,1-trifluoracetylacetonate, salicylate, and acetate ligands resulted in stable, pentacoordinate, and monomeric complexes such as **208** or **209**, with the external ligand bound as a four- or six-membered O,O-chelate ring (Figure 45).[315] With the pseudohalogenido ligands thiocyanate, selenocyanate, and azide as well as with the weakly coordinating trifluoroacetate, 1D coordination polymers with a variety of chain structures were obtained (see Section VIII.A). Treatment with fluoride and other basic anions like hydroxide, phenoxide, or *tert*-butoxide does not result in the expected formation of the ligand exchange product or in the breakdown of the sensitive tripyrrolic ligand framework, but yields the sterically congested 2:1 product, bis(tripyrrinato)cadmium(II) **213**, as the only isolated compound in an almost quantitative yield. Compound **213** is the only tripyrrinate with a hexacoordinate metal center observed so far. The compound is very stable and was characterized by means of solution spectroscopy and single crystal X-ray diffraction (Figure 45). The result of the X-ray crystallographic analysis demonstrates the chiral nature of single molecules of **213** in the solid state. This chirality stems from the helical distortion of both tripyrrin ligands, which in turn is the structural answer to the presence of a steric constraint at the open face of this ligand. In solution, however, the compound was reported to racemize rapidly.[320]

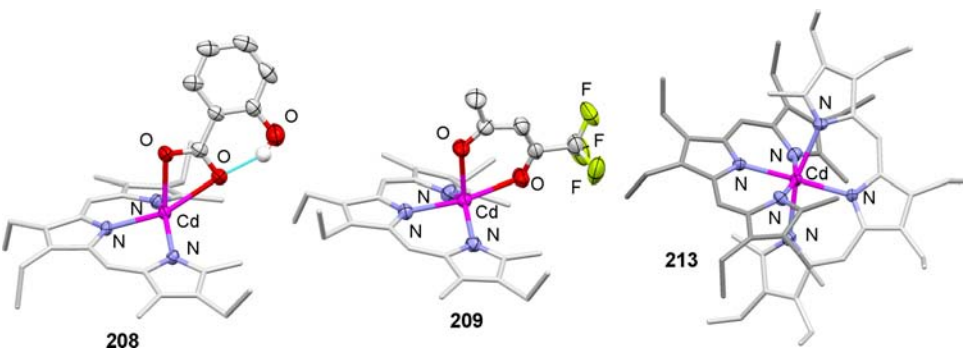

Figure 45. Examples of five- and six-coordinate cadmium tripyrrins **208**, **209**, and **213**. (Adapted from Refs. 315 and 320.)

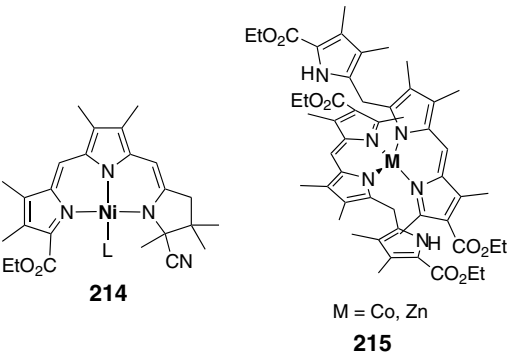

Figure 46. Coordination compounds of partially hydrogenated tripyrroles **7** and **8**.

A small number of reports have appeared concerning coordination compounds of other tripyrroles. Two types of partially hydrogenated tripyrrins were employed as ligands. Nickel(II) complex **214** (Figure 46) was reported to function as a stabilized storage form of the corresponding, highly sensitive free base tripyrrin **7**, which is used as an intermediate for the preparation of sophisticated, functionalized chlorins.[124,125] Tetrahedral cobalt(II) and zinc(II) complexes were prepared from *meso*-hydrogenated tripyrrene **8**, a precursor for unsymmetric porphyrins, and characterized in solution as the L_2M_1 species **215**.[128]

Several examples of tri- and tetrapyrrolic ligands with N,N,N,O coordination have been reported. This coordination is known for carbonyl, carboxylate, and sulfonate terminated tripyrrin-1-one complexes. Structural proof beyond these species has been obtained accidentally in those cases summarized in Figure 47. Nickel(II) salts react with biladien-5-ones to give tripyrrin chelates **216** and **217**.[321] Both compounds show evidence of an oxidative introduction of a hydroxo or methoxo group, respectively, during the metalation process, as seen above for the copper chelate of prodigiosene **132**. Metal chelates of a *meso*-alkylated tetrapyrrole were obtained, and two stereoisomers **218** and **219** were characterized.[226] A copper(II) complex of a *meso*-oxotripyrrin **220** forms from the tripyrrane precursor under oxidative conditions. Demetalation/remetalation allows the preparation of isostructural zinc(II) and cobalt(II) chelates of this new ligand.[114]

A hybrid dipyrrin/pyrrole/Schiff base ligand was observed as a square-planar nickel(II) complex **221** from an unexpected hydration/condensation sequence and was analyzed by structural means (Figure 48).[322]

C. Bis(arylimino)isoindoline Complexes

Middle and late transition metal ions as well as most noble metals have been employed in general studies concerning the preparation and properties of bai

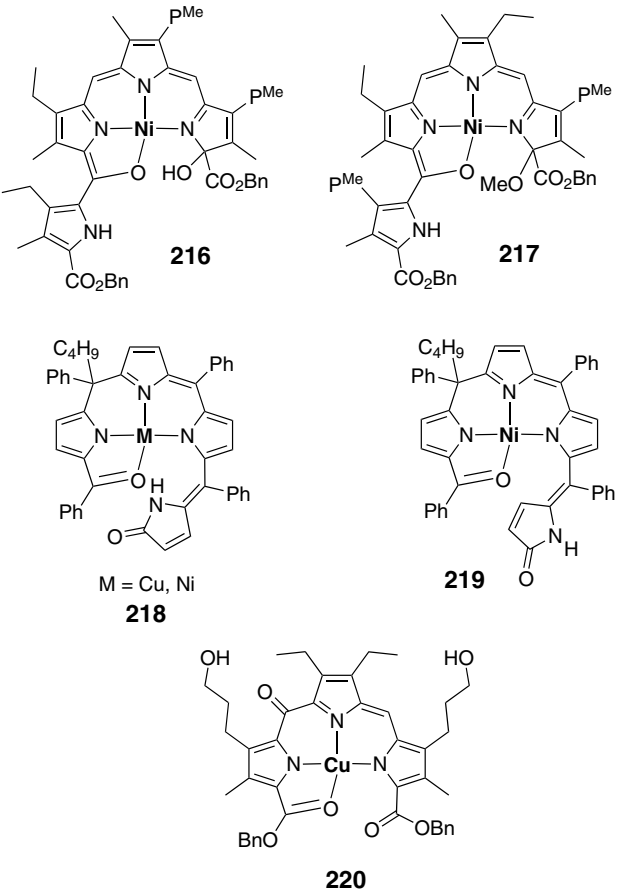

Figure 47. Coordination compounds of tri- and tetrapyrroles with N,N,N,O coordination.

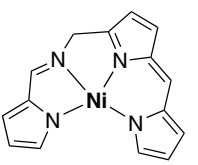

Figure 48. Unexpected formation of tripyrrole imine complex **221**.

complexes. Many of these studies are strongly focussed on an application such as catalysis or bioinorganic modeling. Most of the compounds described so far are of either the L_1M_1 or the L_2M_1 stoichiometry. The first metal chelates of unsubstituted parent ligand H(bpi) **48** were described by Elvidge and Linstead in 1952.[173]

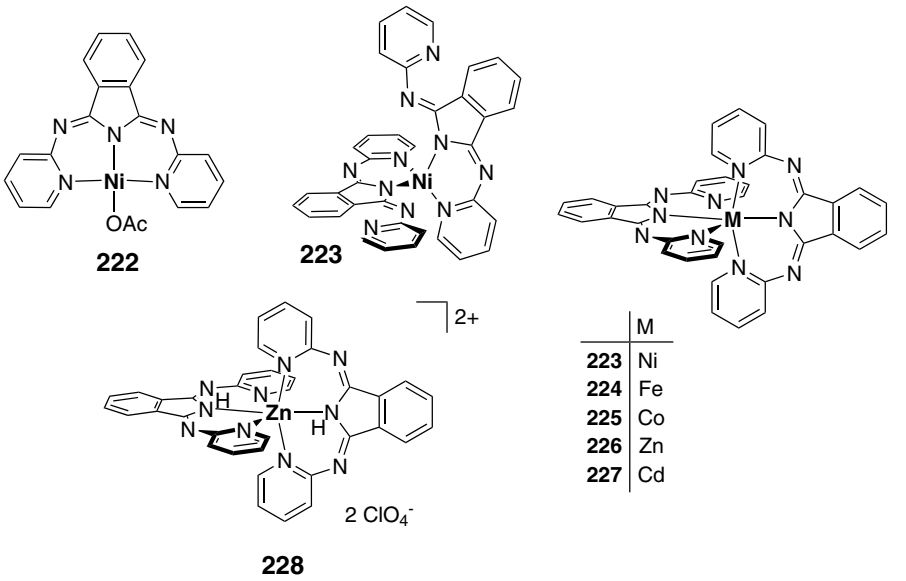

Figure 49. Early assignments of metal chelates **222**–**228** with the bpi and H(bpi) ligands.

Two species were obtained by the action of nickel(II) acetate on **48** and assigned to L_1M_1 and L_2M_1 compounds **222** and **223**, respectively, on the basis of analytical data. The tetracoordinate structure of **223** was later corrected in favor of the octahedral species (Figure 49).[184] In this second report about metal bai compounds, further L_2M_1 compounds [M = Fe(II), Co(II), Zn(II), and Cd(II)] **224**–**227** were discussed, and characterized by optical, magnetic, and analytical methods. At ambient temperature, octahedral coordination and high-spin configurations were found throughout the series, and double protonation was observed if perchlorate salts and no additional base were employed in the coordination of H(bpi) **48**. Results from optical and vibrational spectroscopy on these protonated complexes pointed to the presence of two NH groups per molecule. The location of these protons was first assumed at the central pyrrole nitrogen of the ligands, as depicted for **228** in Figure 49, since this is the most basic site of the bpi anion.[184] Later work provided crystallographic proof for the protonation of the bridging imino groups (see below).[323]

Detailed analyses of the electronic and magnetic structures of L_2M_1-type bpi complexes **223**–**225** and **229** with the divalent ions of nickel, iron, cobalt, and manganese, respectively, and of several simple alkylated bpi derivatives have been performed, and the room temperature susceptibility data as well as optical spectra of these series of compounds proved the presence of high-spin species throughout. Electrochemical data were provided for compounds with the 4-Mebpi ligand.[183]

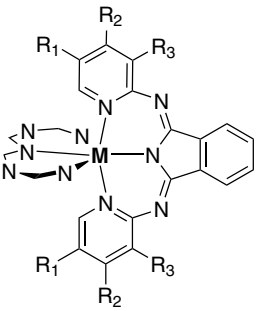

Figure 50. General view of simple L_2M_1 compounds (see Table 2 for metal ions and substituents).

Table 2. Metal ion and substitution pattern of known L_2M_1 complexes **229**–**243** with bpi and alkylated bpi ligands (see Figure 50).

	M	R_1	R_2	R_3
229	Mn	H	H	H
230	Mn	H	H	Me
231	Fe	Me	H	H
232	Fe	H	Me	H
234	Fe	H	tBu	H
235	Fe	H	H	Me
236	Co	Me	H	H
237	Co	H	Me	H
238	Co	H	tBu	H
239	Co	H	H	Me
240	Ni	Me	H	H
241	Ni	H	Me	H
242	Ni	H	tBu	H
243	Ni	H	H	Me

Paramagnetic NMR spectra could be fully assigned on the basis of data obtained by high-field, high-resolution ^{2}H NMR experiments. $(bpi)_2Zn$ **226** was studied as a diamagnetic reference compound for corrections, and EPR data were obtained for cobalt derivative **225** (Figure 50 and Table 2). In addition, the first crystallographic analysis of a L_2M_1 bai chelate, $(3\text{-Mebpi})_2Mn$ **230**, was reported. The geometry about the metal center is a distorted octahedron. Because the two 3-methylpyridyl groups of a single bpi unit are unable to span the metal, their average *trans* angle is reduced from 180° to about 160°, and the planarity of the conjugated π system of **230** is lost in favor of a slightly helical conformation due to steric congestion.[324]

$(bpi)_2Fe$ **224** and a derivative (**244**) carrying a methyl group at the isoindoline backbone were later characterized structurally.[194,325] Both derivatives showed

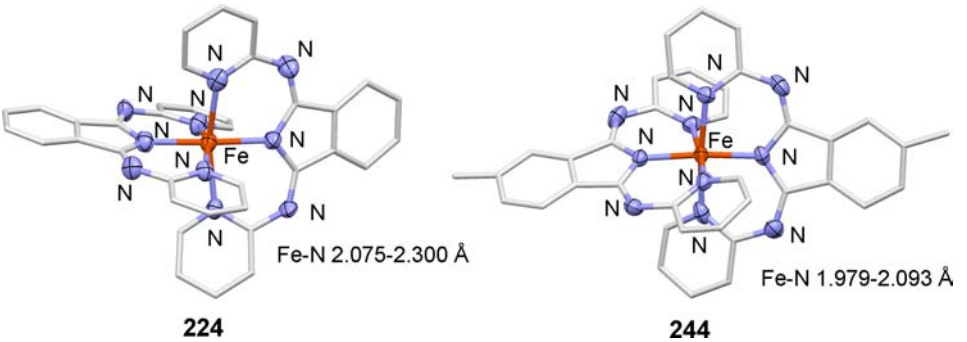

Figure 51. Molecular structures of $(bai)_2Fe$ compounds **224** and **244**. (Adapted from Refs. 194 and 325.)

iron–nitrogen bond lengths of about 2.0–2.3 Å, characteristic of high-spin Fe(II). A Mössbauer study on **224** confirmed this assignment (Figure 51).

Acetatonickel(II) complex **222** of the L_1M_1 type, already described in the first report of metal bai chelates, had been obtained again as a byproduct of $(bpi)_2Ni$ synthesis, and was characterized electronically as a high-spin species at ambient temperature.[184] Further L_1M_1 chelates **245**–**247** with the acetate coligand and M = Co(II), Cu(II), and Zn(II) have been described as isolated products from the template synthesis of bpi (Figure 52).[191] Ni(II), Co(II), and Cu(II) proved to be good template ions and gave good yields in this transformation, while for Zn(II) only 20% of the product could be obtained. Divalent nickel was also successfully used in the template syntheses of several other bai ligands from 2-amino-3-methylpyridine, 2-amino-4-methylpyridine, 2-amino-5-methylpyridine, 2-amino-5-chloropyridine, and 2-aminothiazole, but was unsuccessful with 2-amino-6-methylpyridine, 2-amino-4,6-dimethylpyridine, 2-amino-4-methylthiazole, aniline, 3-aminopyridine, 4-aminopyridine, and 2-aminopyrimidine. The diversity of metal bai complexes was further increased by the description of successful ligand exchange reactions of acetate against azide for the simple nickel and copper chelates **248** and **249**.[191] In later work, ligand exchange was undertaken on (bpi)Ni(OAc) **222**, and new halide, pseudohalide, and cyanamide compounds were reported as well-studied products. The latter cyanamides, such as **250**, were reported to contain a low-spin Ni(II) ion, which is easily solvated to form five-coordinate high-spin species (Figure 52). Thermodynamic parameters have been measured for this association process, and the results suggest that both electronic and steric factors play important roles in determining the stability of the solvated complexes.[326]

The chemistry of copper bai complexes was developed mainly in the context of bioinorganic mimicking of redox enzymes and of the interaction of Cu(I) with dioxygen. Acetato complex **251** was prepared from the components by a

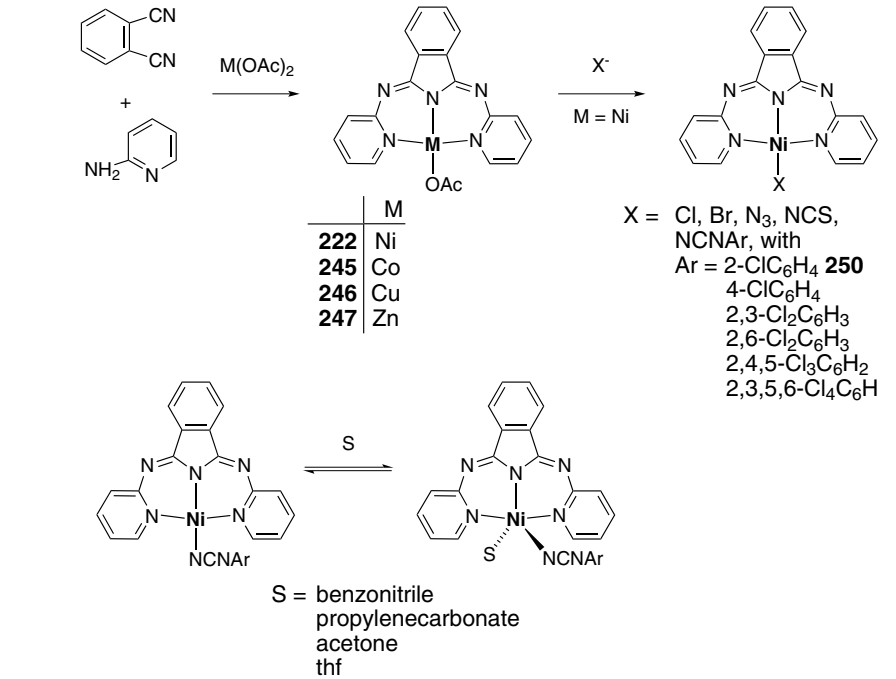

Figure 52. Template synthesis of acetato metal bai complexes, and ligand exchange chemistry on [(bpi)Ni(OAc)] **222**.

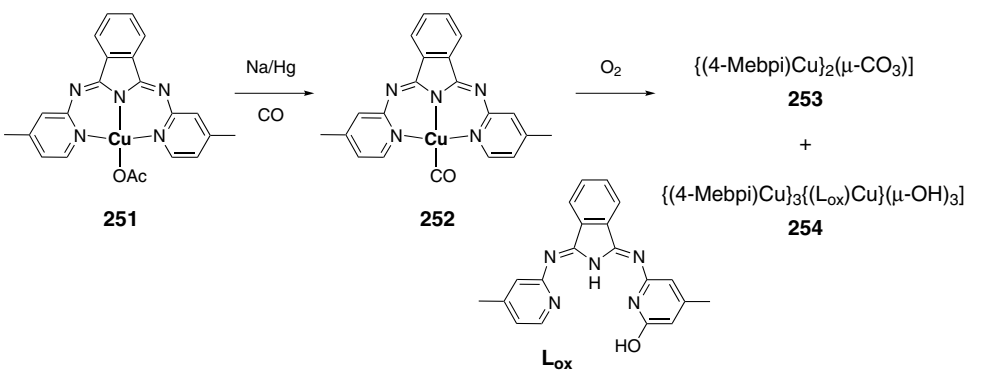

Figure 53. Cu(I)/O_2 reactivity in the 4-Mebpi system.

stoichiometric reaction, and gave carbonyl copper(I) species **252** upon reduction with sodium amalgam in the presence of CO (Figure 53). **252** reacts with dioxygen under the formation of two products: a carbonato-bridged dimer **253** and a tetranuclear hydroxo cluster **254** with the partially oxygenated bpi ligand.[327] Both products were identified by single-crystal analyses.

Two different bai-based model systems for galactose oxidase (GO), a fungal H_2O_2-producing enzyme, have been reported. A structural model **255** containing a distorted pentacoordinate copper(II) ion in a N_3O_2 ligand field was prepared from 5-Mebpi and a deprotonated dibenzoylmethane ligand. EPR analysis of a microcrystalline sample of this compound showed a dipolar spin coupling, which was explained by the formation of weakly associated dimers in the crystal lattice.[328] Acetato complex **251** with the 4-Mebpi ligand could be crystallized with one additional water ligand in a different five-coordinate N_3O_2 environment. This compound has been studied as a spectroscopic model of the GO active site with respect to the influence of cyanide and other anion binding on EPR and optical spectra.[329] For quercetin dioxygenase, another copper-dependent oxidoreductase, a functional model complex **256**, was reported.[330] Compound **256** formed upon treatment of mesitylcopper(I) with flavonol H(fla) in the presence of H(bpi) **48** as a diamagnetic complex, which on reaction with molecular oxygen underwent oxidative splitting of the C2–C3 bond of the pyranone ring of the flavonolate ligand to give the copper(I) chelate [(H(bpi))Cu(O-bs)] (O-bs = O-benzoylsalicylate) and carbon monoxide. The reaction of $[Cu(an)_4]ClO_4$ (an = acetonitrile), H(fla), and H(bpi) with dioxygen at room temperature affords the paramagnetic copper(II) complex $[(H(bpi))Cu(fla)]ClO_4$, and after elimination of $HClO_4$, [(bpi)Cu(fla)] **257** is formed. The latter undergoes cleavage of the pyranone ring upon oxygenation at 80 °C to give [(bpi)Cu(O-bs)] and carbon monoxide. [(bpi)Cu(fla)] and its perchloric acid adduct serve as good catalysts for the oxygenation of flavonol to O-benzoylsalicylic acid. Figure 54 provides an overview of the different oxygenase models.

More structural information on copper bai species is available through an acetato copper(II) complex with a benzoannelated ligand,[331] a chiral polysubstituted example,[203] and a twofold hydrated pentacoordinate cation as perchlorate.[332] Another, quite instructive study compares the conformation and catalytic performance of two simple acetato copper(II) complexes with a bpi- and a thiazole-based bti ligand, **258** and **259**, respectively (Figure 55).[196] Both species are selective catalysts for the allylic peroxidation of cyclohexene, with bpi derivative **258** showing the higher activity. Structurally, this derivative is characterized by a significant nonplanar distortion of the conjugated heterocyclic ligand framework, while bti derivative **259** is essentially planar, due to reduced steric encumbrance at the site of the anionic coligand. This effect is even more pronounced for bai ligands with terminal methyl substituents and has been observed in palladium complexes **260** and **261** (Figure 55).[199] However, whether an increased ligand exchange reactivity of bpi vs. bti complexes is accompanied by this increase in intramolecular strain has so far remained unexplored.

The conformational flexibility of bai ligands and their possible presence in protonated and deprotonated states have become particularly obvious in studies of

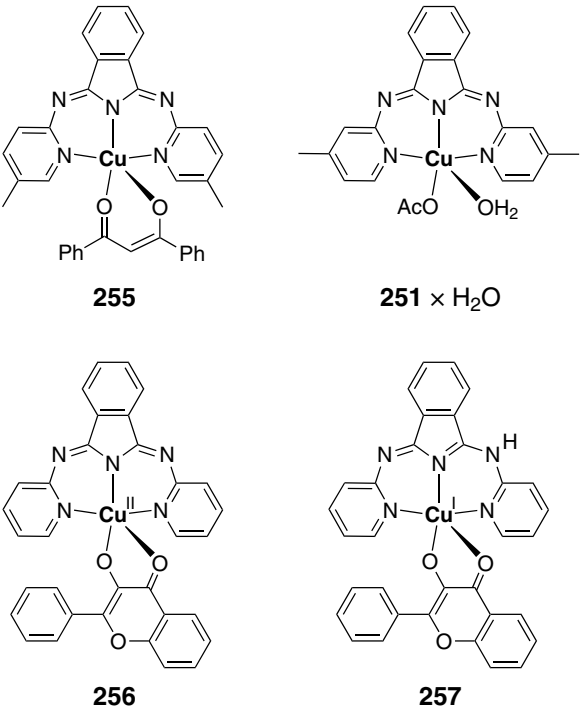

Figure 54. (bpi)Cu-based model compounds for different oxidoreductases.

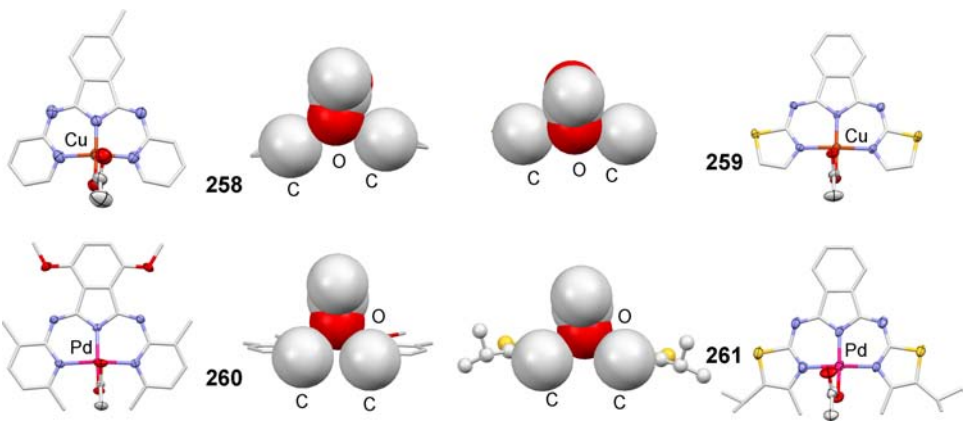

Figure 55. Conformative differences of [(bpi)Cu(OAc)] **258** and [(bti)Cu(OAc)] **259**, and of the methyl-terminated palladium analogs **260** and **261**. (Adapted from Refs. 196 and 199.)

zinc and cadmium chelates. The reaction of Cd(II) and Zn(II) perchlorates with H(4-Mebpi) produced series of L_2M_1-type complexes with zero, one, and two additional protons **262**–**267** (Figure 56).[323,332] Complexes (4-Mebpi)$_2$Cd **262**, (4-Mebpi)$_2$Zn **263**, and [(H(4-Mebpi)(4-Mebpi)Cd]ClO_4 **264** were characterized

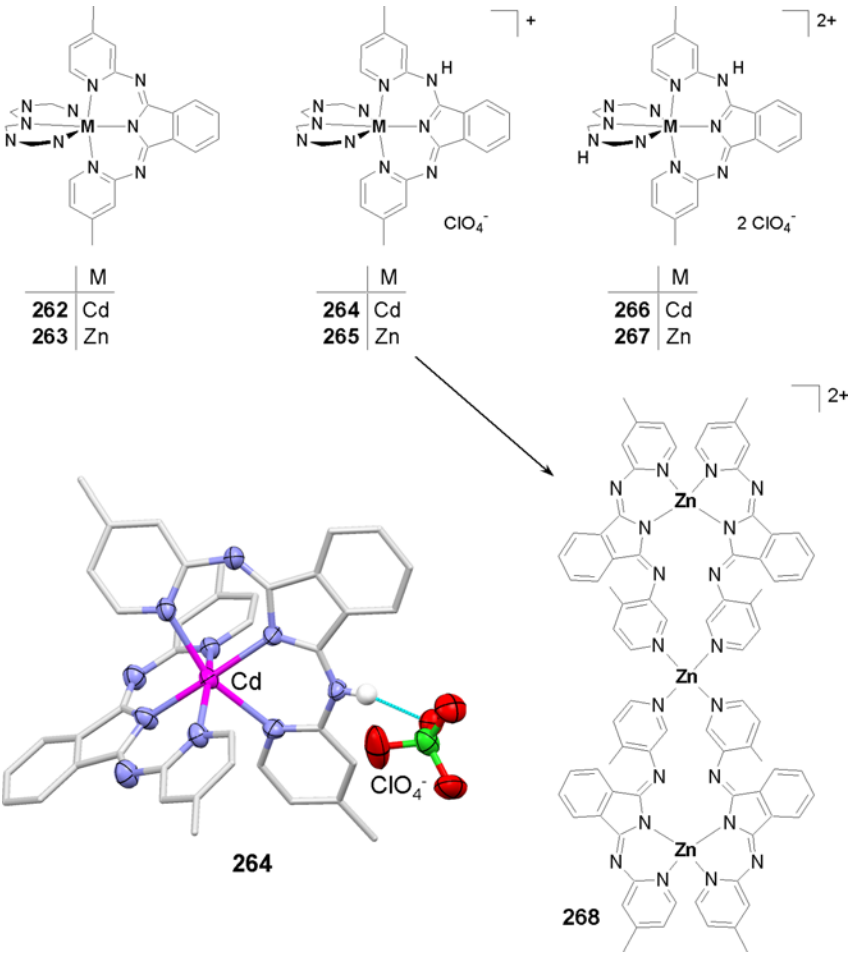

Figure 56. Structures and reactivity of zinc and cadmium chelates of 4-Mebpi in different protonation states. (Adapted from Ref. 323.)

crystallographically, with the additional proton of the latter being located at one of the bridging imino groups. Whereas $[(H(4\text{-Mebpi})(4\text{-Mebpi})Cd]ClO_4$ **264** is stable in solution, $[(H(4\text{-Mebpi})(4\text{-Mebpi})Zn]ClO_4$ **265** converts to the tetrahedrally coordinated, trinuclear complex $[(4\text{-Mebpi})_4Zn_3](ClO_4)_2$ **268** with a linear zinc backbone. All protonated complexes were reported to be tautomeric in solution because of the shuffling of the iminium protons between imine nitrogen atoms.

Besides the protonated $(4\text{-Mebpi})_2M_1$ complexes discussed above, the synthesis and structure of L_1M_1 complex $[(4\text{-Mebpi})Cd(NO_3)_2]$ **269** with a seven-coordinate cadmium ion have been reported (Figure 57).[180] As before, this compound is tautomeric in solution as the NH proton moves between the bridging

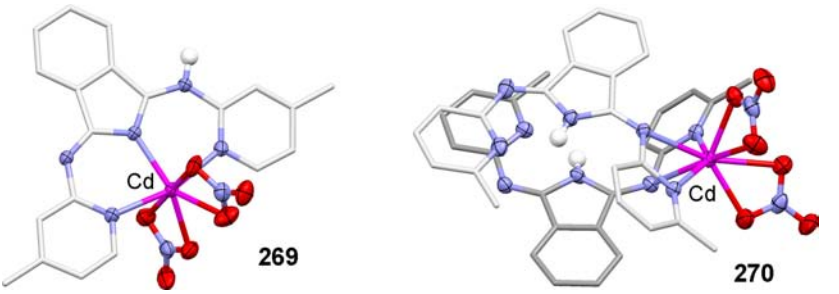

Figure 57. Cadmium H(bpi) chelates with high coordination numbers. (Adapted from Refs. 180 and 197.)

imine nitrogen atoms. If the sterically encumbered 6-Mebpi ligand is employed, cadmium and zinc atoms bind in a different N,N coordination mode using one bridging imine and one pyridine nitrogen atom. Cadmium(II) forms the eight-coordinate fluxional complex **270** with two protonated 6-Mebpi units and two chelating nitrate ligands, while in the presence of zinc(II) the ligand hydrolyzes with loss of one of the pyridylamine subunits.[197]

An extension of the chemistry of bai ligands was achieved by the advent of binucleating ligand **271**. Dinuclear species **272–275** were obtained by the reaction of **271** with mononuclear acetato metal(II) compounds of the 4-Mebpi ligand of manganese, iron, cobalt, and nickel (Figure 58). Magnetic, optical, and electrochemical investigations have revealed that the two metal ions in **272–275** are only very weakly coupled, and an application of these and related dinuclear or polynuclear compounds as multielectron catalysts was discussed.[183]

Dinuclear ruthenium complexes were prepared in which the metal atoms are bridged by bis(bpi) ligand **271** and terminated by 4-Mebpi.[182] Mixed valence (Ru(II)/Ru(III)) **276** and mixed metal complexes were prepared and their spectroscopical and electrochemical properties studied in the context of electron transfer mechanisms. Mononuclear ruthenium complex **277** was found to contain a protonated H(4-Mebpi) unit and three chloride anions as ligands, thus residing in the oxidation state +3 (Figure 59). This complex catalyzes the autoxidation and electrochemical oxidation of alcohols in basic alcoholic solution. The reaction is general, resulting in the oxidation of primary and secondary alcohols, with the principal products being aldehydes and ketones. More than 200 turnovers were observed in the oxidation of ethanol at the ambient temperature, with little or no loss of catalytic activity. Possible pathways for the catalytic autoxidation and electrochemical oxidation were discussed.[181]

Dinuclear molybdenum(II) complexes **278–288** with a variety of different bai ligands have been reported to form upon exchange of one of the acetato ligands

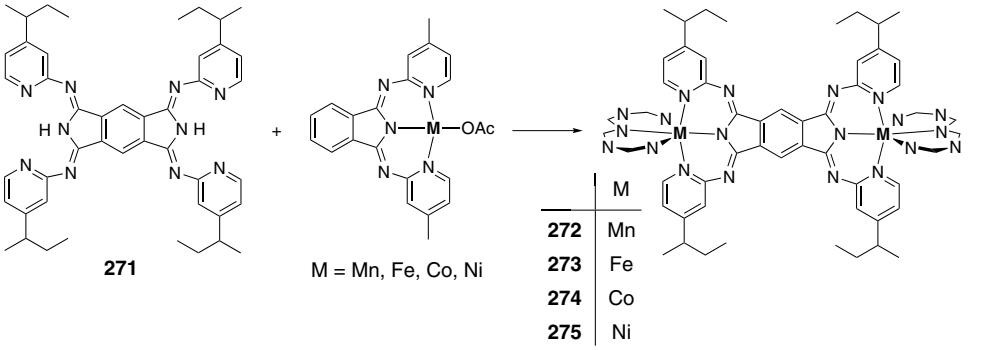

Figure 58. Preparation of homodinuclear bis(bpi) complexes **272**–**275**.

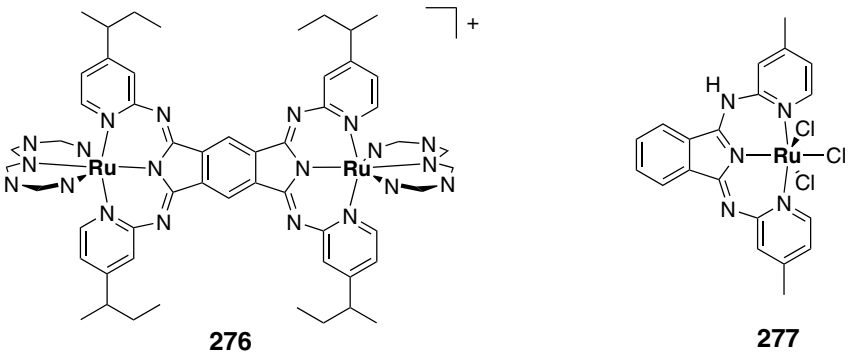

Figure 59. Dinuclear and mononuclear ruthenium complexes **276** and **277**.

from $Mo_2(OAc)_4$ with one deprotonated bai ligand.[333] The structure of the parent bpi compound **278** has been determined,[334] and it consists of a quadruply bonded dimolybdenum unit which is bound to three bridging acetates and one bridging bai ligand. The bai ligand is bound to one molybdenum by an imino nitrogen and to the other molybdenum by the isoindoline nitrogen and a pyridyl nitrogen. The pyridyl nitrogen is bound in a position approximately coaxial with the metal–metal bond (Figure 60). The Mo–Mo bond distance is 2.109 Å, and it has been found that the d–d* transition of the quadruple bond is influenced by the different heterocyclic end groups of the bai ligands in a complex fashion.[335]

Several studies concerning bai complexes with low-spin d^8 metal ions have been reported. Such ions tend to form square-planar or square-pyramidal coordination compounds for electronic reasons and are thus well suited for the preparation of L_1M_1-type species. Rhodium(I) **289**–**292** and iridium(I) complexes **293**–**297** have been reported with a variety of different bai ligands, mainly with the bpi framework (Figure 61).[185] Different neutral coligands have been used to

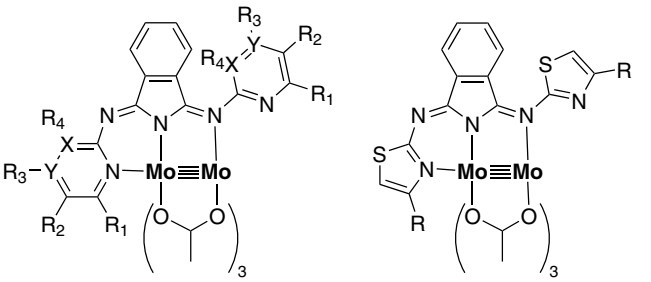

	R_1	R_2	R_3	R_4	X	Y
278	H	H	H	H	H	H
279	H	H	Me	H	C	C
280	Me	H	Me	H	C	C
281	H	Cl	H	H	C	C
282	H	Br	H	H	C	C
283	H	I	H	H	C	C
284	H	Cl	H	Cl	C	C
285	H	H	H	H	N	C
286	H	H	H	H	C	N

	R
287	H
288	Me

Figure 60. Dimolybdenum bai chelates **278**–**288**.

stabilize these compounds, with CO being the best choice in both cases. For rhodium(I) derivative **289** the oxidative addition of methyl iodide was studied. The expected product **298** undergoes insertion reactions to acyl complexes **299** and **300** upon addition of further CO, or $P(OMe)_3$, respectively.

Divalent palladium also forms neutral square-planar complexes with an anionic coligand occupying the fourth coordination site. Species with bpi- and bti-type ligands have been reported, and several crystallographic studies provided insight into metal–ligand interactions and crystal-packing phenomena.[195,199,204,336] Figure 62 presents selected examples **301**–**304** of such crystallographic analyses. For some of these palladium chelates, catalytic activity was reported in the hydrogenation of alkenes[195] and in C–C coupling reactions (see Section IV.C).

The cobalt-catalyzed oxidation of hydrocarbons by molecular oxygen represents one of the largest-scale applications of homogeneous catalysis and is widely used in industry, such as for the synthesis of adipic acid from cyclohexane. A significant increase in selectivity in the decomposition of cyclohexyl hydroperoxide to cyclohexanol and cyclohexanone in the presence of transition metal (particularly cobalt) complexes of bai derivatives was reported repeatedly in the patent literature[337–340] and set off significant activity in the field of bai-based oxidation catalyses that continues today. In the original reports it was stated that cobalt bpi catalysts are very active and long-lived, allowing cyclohexylhydroperoxide to be

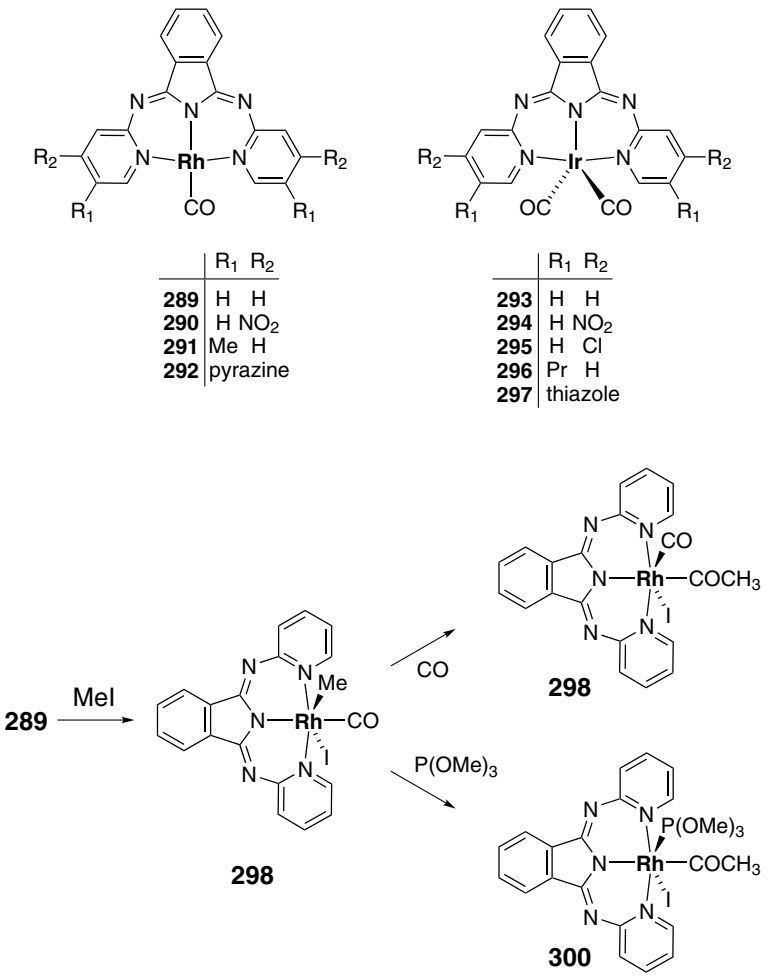

Figure 61. Chemistry of iridium and rhodium bai species.

converted in a selective, low-temperature process. The structure of one of the precatalysts, the L_2M_1 derivative [(3-Mebpi)$_2$Co], had been determined crystallographically. Under reaction conditions, it was assumed that the active form of the catalyst has lost one bpi ligand.[341] This assumption was later confirmed by the synthesis and characterization of active cobalt(III) alkylperoxide species (Figure 63 and Table 3).[194,342] An X-ray structure was obtained of one *tert*-butylperoxo derivative, **306**. This analysis revealed a distorted octahedral environment with a chelating carboxylate moiety and an apically bonded *tert*-butylperoxo group. The reactivity of cobalt(III) alkylperoxo complexes toward hydrocarbons was found to be dependent on their thermal decomposition rate, with bpi complexes being the most reactive. In addition, the activity of the cobalt bpi catalysts proved to

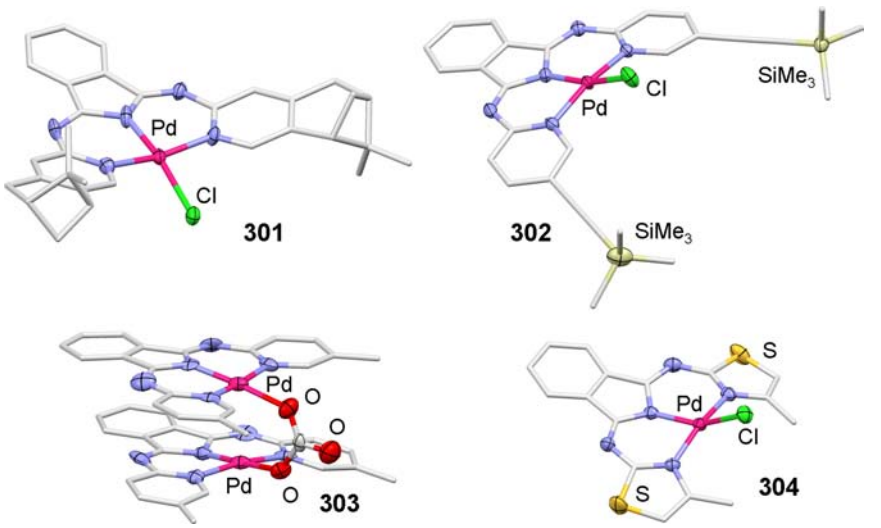

Figure 62. Selected molecular structures of neutral palladium bai complexes **301**–**304**. (Adapted from Refs. 195, 204, and 336.)

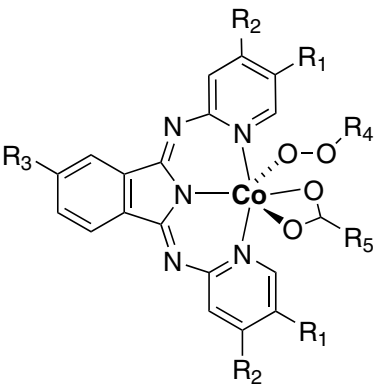

Figure 63. General view of cobalt(III) alkylperoxo complexes for the catalytic oxidation of hydrocarbons (for substituents see Table 3).

be essentially independent of the substitution pattern in the ligand. Saturated hydrocarbons are oxidized by Co(III) *tert*-butylperoxo complexes into alcohols, ketones, and *tert*-butylperoxo products. The hydroxylation reaction preferentially occurs at the more nucleophilic C–H bonds with extensive epimerization at the hydroxylated carbon atom. Hydrocarbons having labile allylic or benzylic C–H bonds react already at room temperature to give a large amount of allylic or benzylic *tert*-butyl peroxide. Olefins having no allylic hydrogen atom are

Table 3. Substituent pattern of known cobalt(III) alkylperoxo complexes **305–319** (see Figure 63).

	R_1	R_2	R_3	R_4	R_5
305	H	H	H	tBu	Me
306	H	H	H	tBu	Me
307	H	H	H	CMe_2Ph	Me
308	H	H	H	CMe_2Ph	Ph
309	H	Me	H	tBu	Me
310	H	Me	H	tBu	Ph
311	H	Me	H	tBu	tBu
312	H	Me	H	CMe_2Ph	tBu
313	Cl	H	H	tBu	Me
314	Br	H	H	tBu	Me
315	Me	H	H	tBu	Me
316	Br	H	Me	tBu	Me
317	H	H	Me	tBu	Me
318	H	Me	Me	tBu	Me
319	H	tBu	Me	tBu	Me

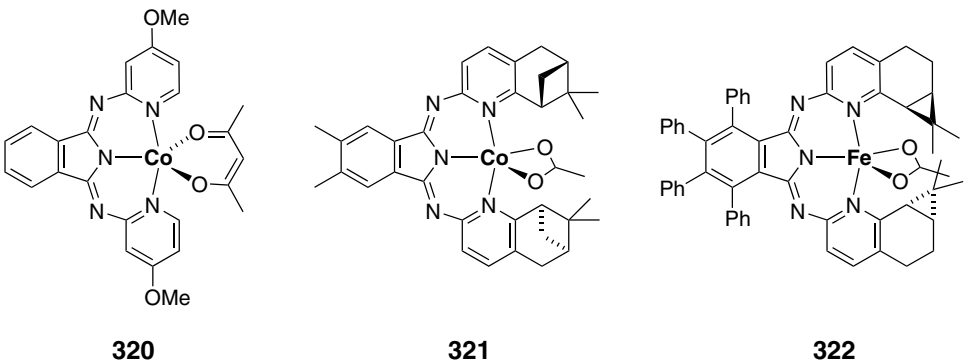

320 **321** **322**

Figure 64. Selected cobalt and iron bpi catalysts **320**–**322**.

preferentially transformed into epoxides. The catalytic hydroxylation of alkanes by *tert*-BuOOH in the presence of cobalt(III) bpi complexes has the same characteristics as the stoichiometric reaction. The homolytic decomposition and reactivity of cobalt(III) alkylperoxo complexes were discussed in the context of the Haber–Weiss mechanism of alkyl hydroperoxide decomposition and of hydrocarbon hydroxylation by first-row transition metal peroxides. A photochemical variant of this reaction has also been worked out.[343] Figure 63 and Table 3 show typical cobalt(III) catalysts.

Besides their use in the technical process described here, achiral and chiral cobalt and iron bpi chelates such as **320**, **321**, and **322** (Figure 64) have most recently been investigated as useful and selective catalysts for the living radical

polymerization of acrylates,[202] the stereoselective cyclopropanation of alkenes, and the stereoselective hydrosilylation.[203] These results demonstrate the great potential of this group of complexes in modern catalysis research.

D. Complexes of Bis(oxazolinyl)pyrroles

Bis(oxazolinyl)pyrroles [H(bop)] are the most recent extension to the tripyrrin class of ligands in coordination chemistry. These ligands allow the relatively simple introduction of chirality at the terminal positions and are therefore particularly valuable in molecular catalysis. Three slightly different types of H(bop) ligands have been reported. Ligands **54a** and **54b** consist of a pyrrole center with two directly attached oxazoline moities, and have been studied in the coordination to divalent palladium. A dinuclear complex **323** was obtained from achiral ligand **54a**, demonstrating that for steric reasons only two of the three nitrogen donors can bind to the same metal ion (Figure 65).[207,208] As the dinuclear species forms a double-helical structure, the use of the chiral ligands (*R*,*R*)- and (*S*,*S*)-**54b** yields

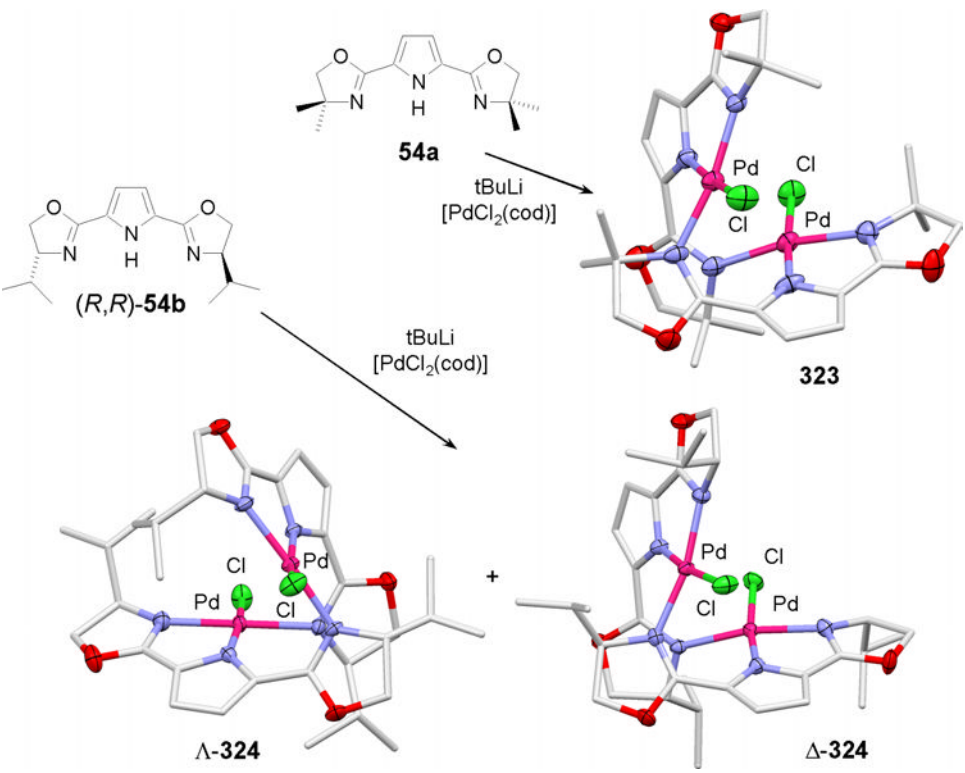

Figure 65. Molecular structures of dinuclear palladium complexes with achiral and chiral bop ligands (crystallographic figures adapted from Refs. 207 and 208).

mixtures of double-stranded helicate diastereomers **324** which have been separated and investigated in detail with respect to structure and dynamics. In addition, dinuclear complex **323** was found active in the catalytic Suzuki cross-coupling reaction (see Section IV.C).

H(bop) ligands **55**, which contain bridging methylene groups between the heterocyclic components, have been described as complexes with palladium, zinc, and rhodium. Chloro palladium(II) chelates **325** form from the respective ligand after deprotonation and treatment with [$PdCl_2$(cod)] in fair-to-acceptable yields. Peculiar dehydrogenation and formation of the complexes with conjugated ligands **326** has been observed in this system. The transformation occurs in the presence of oxygen or of excess palladium and is highly chemoselective. Crystallographic analyses of members of nonconjugated and of conjugated complexes confirm significant planarization and rigidification during this process (Figure 66).[209] If zinc is coordinated to **55a**, complex **327** with a conjugated ligand is formed immediately. Other than **326**, however, **327** is not an oxidized but rather a rearranged form of the original framework. A similar rearrangement was found in the palladium series.[344]

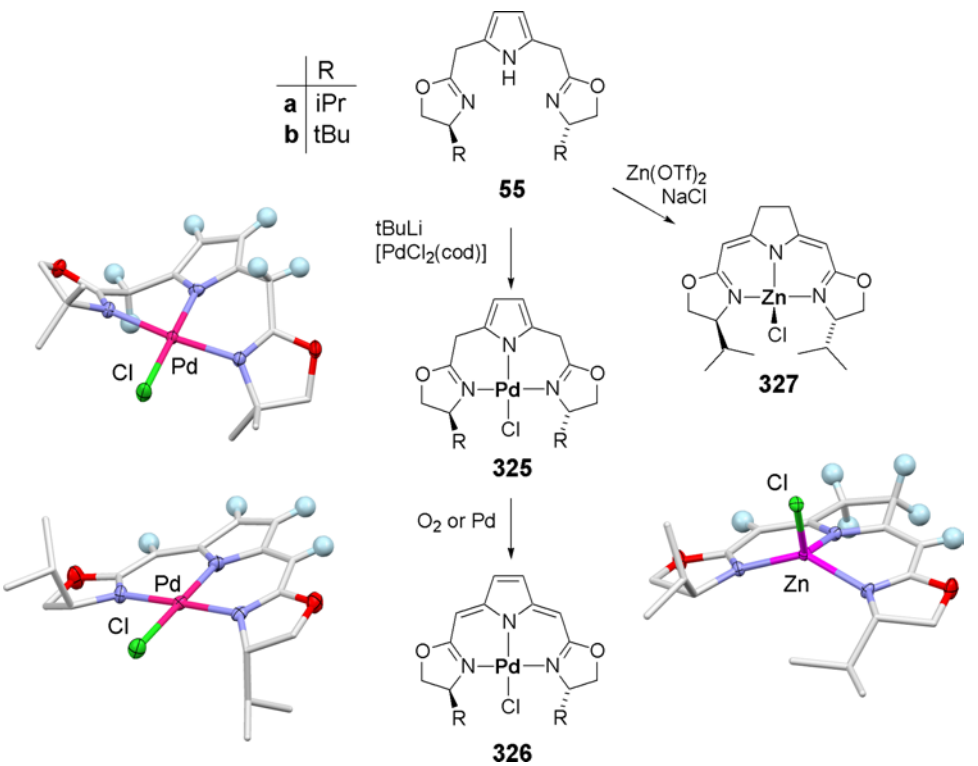

Figure 66. Planarization of palladium and zinc bop species (crystallographic figures adapted from Refs. 209 and 344).

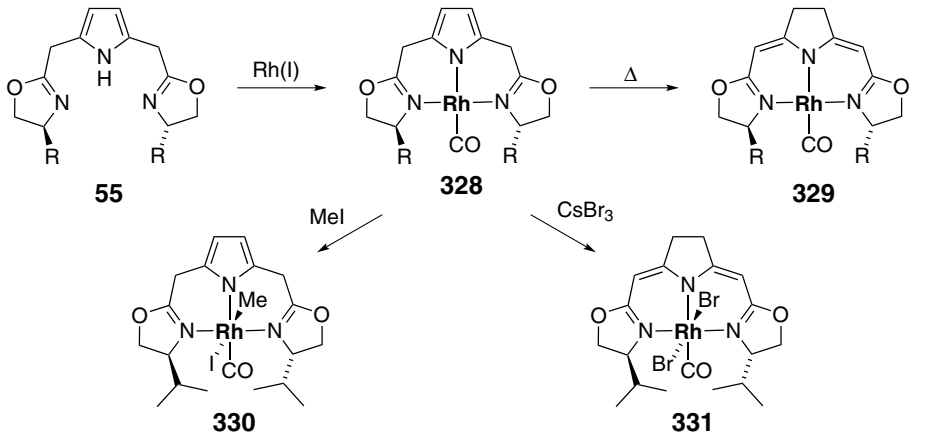

Figure 67. Chemistry of rhodium bop complexes.

Rhodium(I) complexes **328** have been prepared analogously from deprotonated ligands and $[RhCl(CO)_2]_2$ or $[Rh(acac)(CO)_2]$, for a number of different derivatives (Figure 67). Upon heating the compounds at 100 °C in toluene over several hours, a rearrangement to isomeric species **329** occurs, similar to that described above for zinc complex **327**. Compound **328** (R = iPr) reacts with methyl iodide in the expected way by oxidative addition to rhodium(III) complex **330**. $CsBr_3$, on the other hand, converts **328** (R = iPr) into dibromo rhodium(III) compound **331** with a rearranged bop ligand.[210]

The third subgroup of H(bop) ligands are the chiral, twofold benzoannelated species **56** (Figure 14). With respect to the rigidity of the conjugated backbone, these ligands are closely related to the rearranged and even closer to the oxidized derivatives mentioned above. Pincer ligands **56** have so far been described only in the context of chromium-catalyzed asymmetric Nozaki–Hiyama allylation and related processes.[211,212,345]

E. Behavior of Bilirubin and Biliverdin Toward Metal Ions

A role of the natural bile pigments biliverdin **9** and bilirubin **10** in the secretion of trace metals was assumed early on the basis of changes in the optical spectra of medicinal preparations. Later on, numerous attempts to quantify the interactions of bile pigments with different transition metal ions and to clarify the unknown structures of these complexes were undertaken. Zn^{2+} was the first ion for which a distinct binding to bilirubin **10** and mesobilirubin in a biomimetic buffer was confirmed spectrophotometrically.[346] Many other di- and trivalent 3d and 4f cations also led to marked changes in the optical spectra under similar conditions.

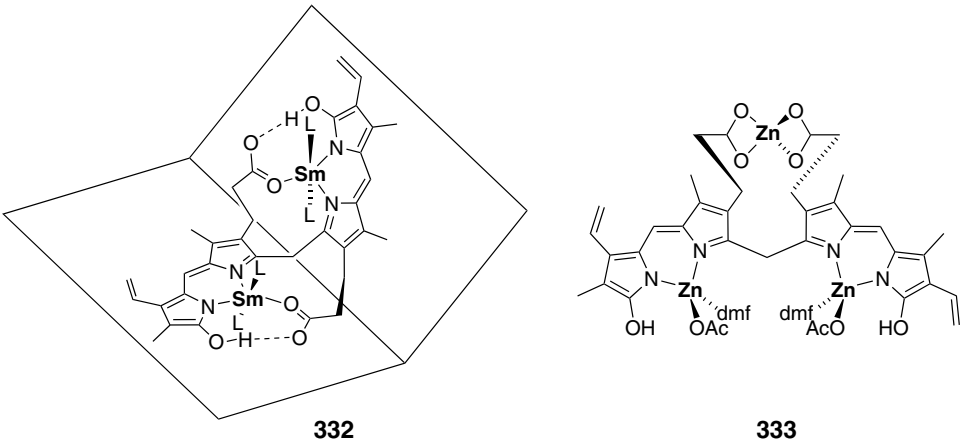

332 **333**

Figure 68. Assumed folded structures of dinuclear samarium complex of bilirubin **332** formed in protic media and trinuclear zinc species **333** formed in DMF solution.

However, the complexes formed were unstable in most cases.[347] Sm^{3+} was found to form a stable adduct with bilirubin **10**, and the first structural assignment of a L_1M_2 complex of this ion, **332** was deduced from the results of a spectrophotometric titration of **10** with samarium acetate (Figure 68).[348] Subsequently the 1:2 stoichiometry of **332** was confirmed and similar chelates with Zn^{2+}, Cd^{2+}, and Fe^{2+} ions were identified. Stability constants were obtained by spectrophotometric titrations, and a quite small stability window of around pH 8 was found to be a typical feature of these compounds.[349–352] In aprotic media, however, the interaction patterns are obviously different due to intramolecular hydrogen bridges of **332** and similar chelates, and bilirubin **10** has been found to form stable trinuclear species such as **333** with Zn^{2+}, Cd^{2+}, and Co^{2+} under these conditions (Figure 68).[353]

In a surface-confined state, however, the coordination behavior of bilirubin **10** differs markedly from the above findings. Raman studies of **10** absorbed on silver (SERS method) indicate the formation of L_1M_1 complexes in the presence of excess metal cations. In the case of the divalent Fe^{2+}, Co^{2+}, Ni^{2+}, and Cu^{2+} ions, bilirubin acts as a tetradentate nitrogen donor like in **334**, while for Ag^{+} and Au^{3+} an open conformation as in **335** and binding to only two nitrogen atoms is reported (Figure 69).[354,355]

In addition, the former species displays a pronounced sensitivity toward redox transformations, and in the copper case the reversible oxidation to a complex of biliverdin **9** was reported. Copper(II) was indeed found earlier to oxidize bilirubin **10** to biliverdin **9** in aqueous solution as well as in DMSO,[352] and a spectrophotometric titration of bilirubin **10** with the tetrachloroaurate anion also confirmed the initial formation of biliverdin **9**. Further addition of $[AuCl_4]^{-}$, however, resulted in

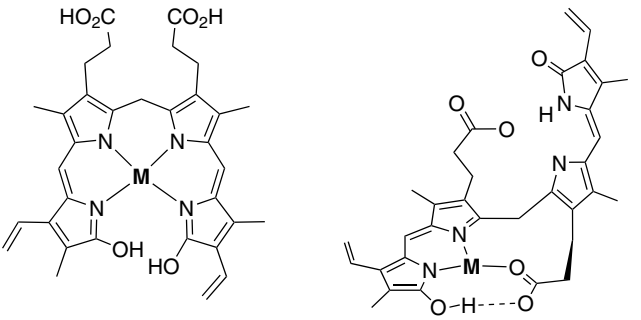

334 **335**

Figure 69. Assumed structures of mononuclear bilirubin complexes **334** and **335** on a silver surface.

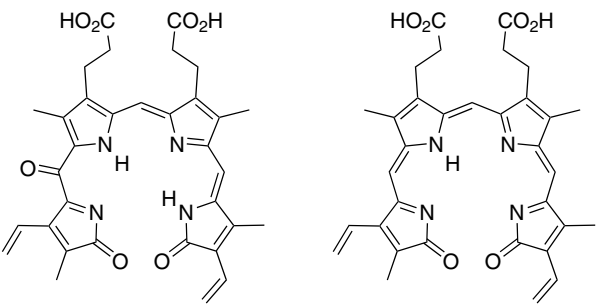

336 **337**

Figure 70. Bilipurpurin **336** and biliviolin **337**.

a new spectral pattern which was assigned to a gold(III) complex of the oxygenated bilipurpurin **336** (Figure 70).[356] Bilipurpurin **336** and biliviolin **337** are the two most important natural degradation products of biliverdin **9** and bilirubin **10**, and have long been known to exist as metal-binding dyes in oxidized bile.[111,357,358]

Bile extracts show a characteristic fluorescence in the present of zinc cations. In 1934, Lemberg prepared the first pure zinc and copper complexes of biliverdin dimethyl ester **13** and proved that the zinc derivative is in fact not fluorescent under inert conditions.[359] Fluorescence occurs upon aerial oxidation of chelate **338** and has been assigned from the optical spectra to the 2 e^-, 2 H^+ oxidized biliviolin species **339** (Figure 71). This assignment was later confirmed by the preparation and investigation of model compounds.[111,358]

Metal complexes of biliverdin **9** itself were described rather late for Zn^{2+}, Cd^{2+}, and Cu^{2+} ions, and spectrophotometric titrations have confirmed the expected 1:1 stoichiometry in all cases.[352] Biliverdin dimethyl ester **13**, the corresponding diethyl

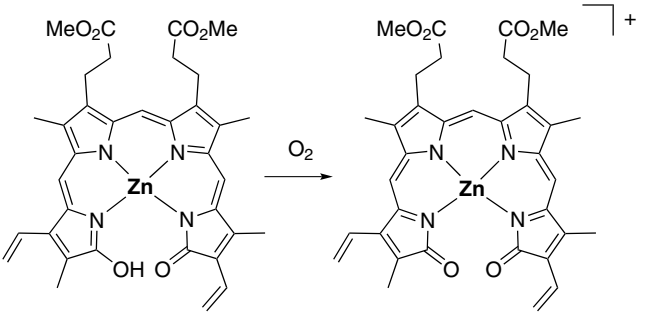

Figure 71. Aerial oxidation of zinc biliverdin dimethyl ester **338** to the fluorescent biliviolin complex **339**.

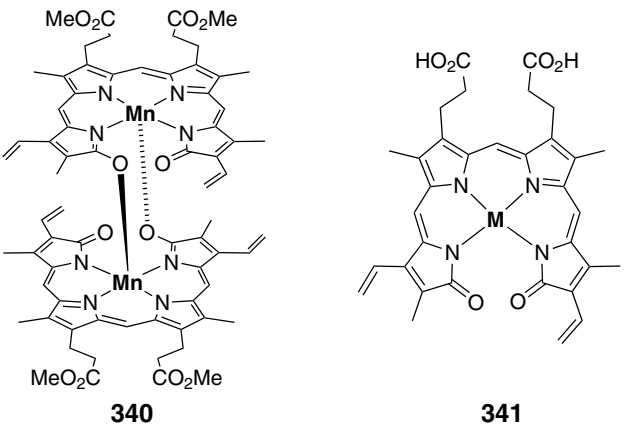

Figure 72. Di- and mononuclear complexes **340** and **341** of biliverdin ligands.

ester, and respective *meso* forms such as **57** were used instead in order to establish complexes of this ligand framework with the divalent transition metal ions Mn^{2+}, Co^{2+}, Ni^{2+}, Cu^{2+}, and Zn^{2+}, and detailed studies of the electronic structures of these species have been reported. In addition to these investigations, a related O-lactim ether derivative was shown to be capable of coordinating to divalent copper and zinc ions.[214,360,361] Iron was found to form unstable material only under forcing conditions. While the metalated species with divalent metal ions are usually monomeric in solution, a dimeric structure is reported for the Mn^{3+} derivative **340** (Figure 72).[362,363] This compound has recently found application as a superoxide dismutase (SOD) mimetic. As the most recent additions, palladium and platinum complexes of biliverdin **9** were obtained and investigated by spectrophotometric

titrations. The compounds were assigned to species **341** with the metal ions in the oxidation state +3.[364,365] Results from model studies (*vide infra*), however, give rise to the assumption that these species are better understood as complexes of divalent metal ions with a biliverdin radical ligand.

F. Mononuclear Tetrapyrrole L_1M_1 Complexes and Associates

As described in the foregoing section, biliverdin and its carboxylic ester and lactim ether derivatives bind to transition metal ions to form complexes with a simple L_1M_1 composition. Structural information about complexes with this ligand framework was obtained from model studies using bilindione ligands such as octaethylbilindione [H_3(oeb)] **11** with simpler alkyl substituents. Bonnett and coworkers described the first transition metal chelates (manganese, cobalt, nickel, copper, and zinc) with this ligand (Figure 73). An iron derivative could not be obtained.[243,366,367] Nickel derivative [(oeb)Ni] **342** was characterized crystallographically and a more detailed investigation toward the electronic structure was performed. The oeb ligand was found to bind in a noninnocent, radical dianionic fashion to a nickel(II) ion, and only a minor contribution of a nickel(III) state was deduced from EPR spectra. The same conclusions had been drawn earlier by

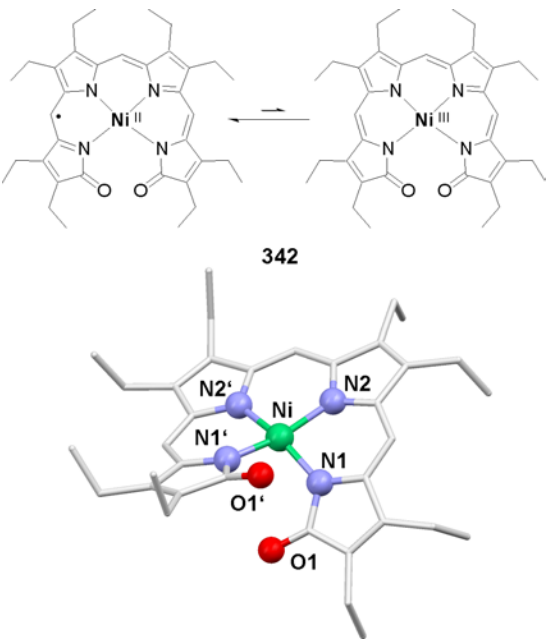

Figure 73. Assumed resonance structure and molecular structure of [(oeb)Ni] **342** (crystallographic figure adapted from Ref. 366).

Fuhrhop and coworkers based on spectroscopic investigations into related nickel complexes of mesobiliverdin diethylester and biliverdin diethylester.[361] An X-ray diffraction study on **342** revealed steric interactions between the terminal oxo groups and a helical distortion of the tetrapyrrole ligand. The nickel ion binds to the four nitrogen atoms in a slightly distorted square-planar fashion with small Ni–N distances of 1.875 and 1.897 Å, indicating a low-spin character of the metal ion. The radical character of the ligand, however, cannot be extracted from the structural parameters of the ligand backbone.

In later studies further transition metal complexes of oeb **11** and related bilindiones were investigated in more detail, mainly by the group of Balch.[10] Manganese derivatives usually contain an intact trianionic ligand and a five-coordinate, trivalent manganese ion, with the fifth coordination site being occupied either by the keto terminus of a second complex moiety **343** or by a solvent molecule (methanol, pyridine **344**). Several examples have been structurally characterized.[368,369] A manganese(II) complex **345** of a biliverdin ester had been described before to change its optical spectra with the pH of the solution. This observation was interpreted in terms of a conformational change of the ligand and of the metal binding, as depicted in Figure 74.[243]

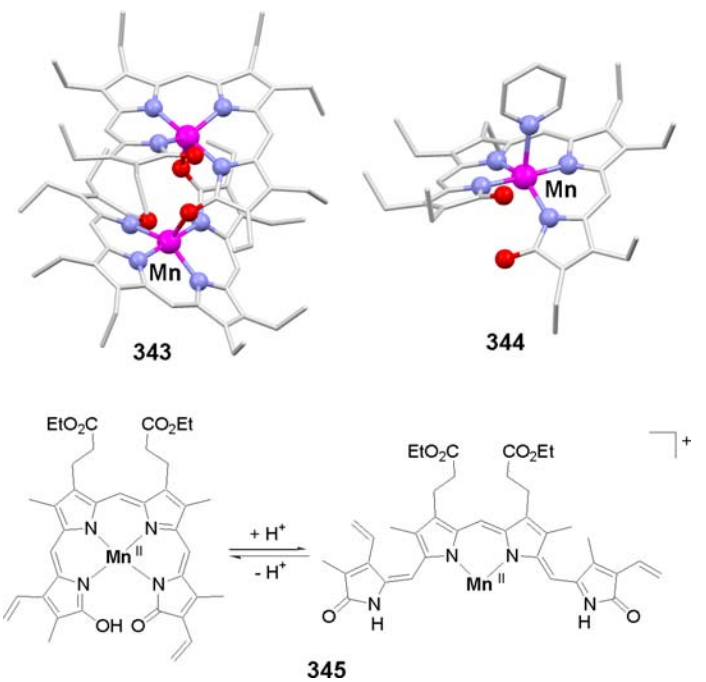

Figure 74. Structures and dynamics of manganese complexes **343**–**345** with bilindione ligands (crystallographic figures adapted from Refs. 368 and 369).

Several reports dealing with iron derivatives can be found in the literature, and the first isolated complexes have more recently been reinvestigated. The iron chemistry of open-chain tetrapyrrole ligands relates directly to the heme degradation process and poses a special challenge due to the sensitivity of the compounds. Section V discusses biological findings and the model chemistry of open-chain iron tetrapyrroles related to iron biliverdin IXα.

Cobalt complexes of oeb **11** have been prepared by careful hydrolysis of the respective verdoheme analogs, as shown in Figure 75.[368,370] The primary product [(oeb)Co] **346** displays a thermal spin equilibrium with a singlet ground state and a triplet excited state. These states have been assigned to the formulations *low-spin*-Co^{III}-oeb^{3-} and *low-spin*-Co^{II}-oeb^{2-}, respectively, the latter with the radical dianionic oeb ligand seen earlier in nickel complex **342**. The complex redox behavior of **346** has been investigated in some detail, and an oxidized species [(oeb)Co(I_3)] **347** with a two-electron-oxidized, monoanionic tetrapyrrole ligand (so-called oebOX) and a weakly bound triiodide ligand at the divalent cobalt atom

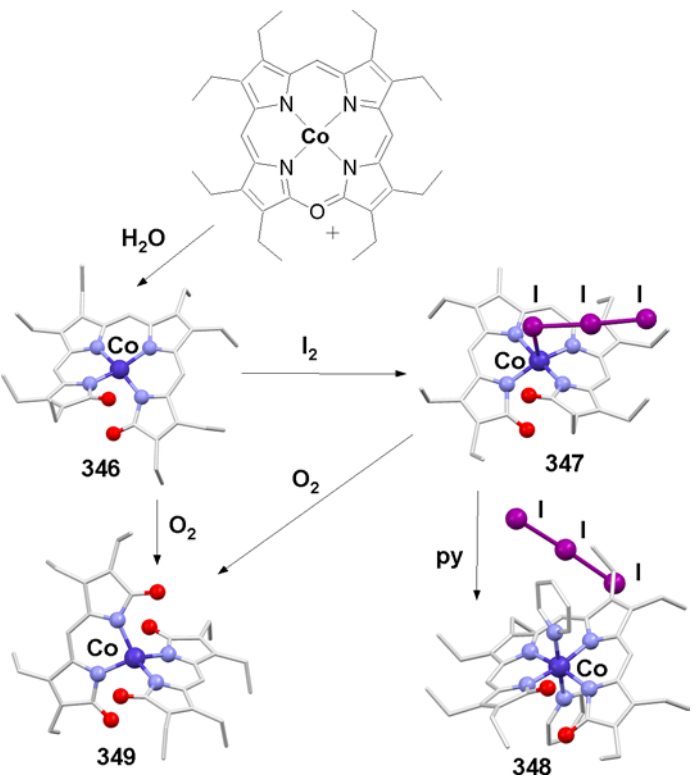

Figure 75. Structures and oxidation characteristics of oeb cobalt complexes (crystallographic figures adapted from Refs. 368 and 371–373).

was analyzed spectroscopically and crystallographically.[371] This ligand may be regarded as a model for biliviolin **337** (Figure 75). Compound **347** accepts two pyridine ligands to form the six-coordinate cobalt(III) complex **348** with the oeb radical dianion.[372] Oxidation of **346** or **347** in the presence of dioxygen leads to ligand degradation, and a cobalt complex with two propentdyopent ligands **349** was isolated as the final product.[373]

The identification of nickel(II)octaethylbilindione **342** as a compound with a radical ligand, which was discussed earlier, was confirmed by later work, and a similar electronic structure has been found for a related palladium derivative, **350**. As for cobalt chelate **346**, the nickel and palladium derivatives are easily oxidized and reduced at the ligand to form anionic $[(oeb)M]^-$ and cationic $[(oebOX)M]^+$ species. The latter are again stabilized by triiodide anions which are, however, not bound to the metal centers in these cases. Both of the species **351** (Ni) and **352** (Pd) form isostructural assemblies with the triiodide anion and were structurally investigated in the solid state (Figure 76).[374] No significant bond length or angle changes were found between the neutral and the cationic [(oeb)M] complexes of each metal ion, which points to ligand-centered redox processes.

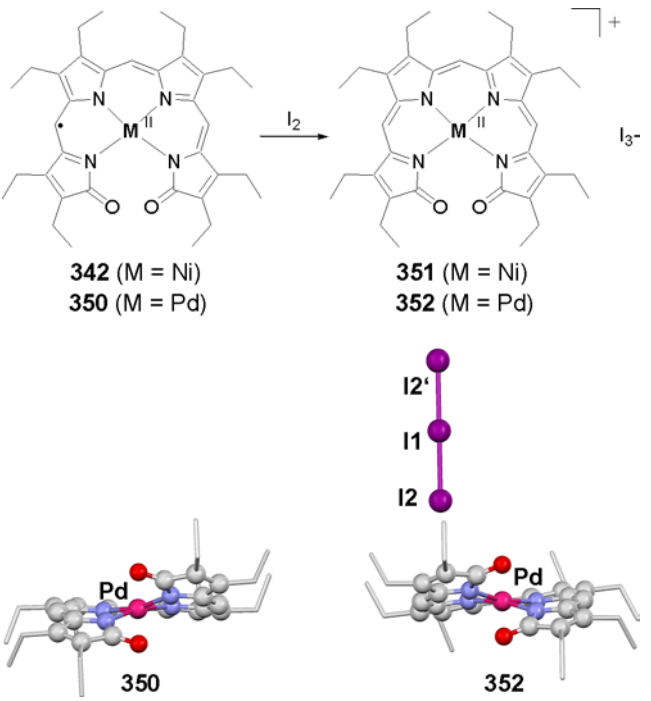

Figure 76. Iodine oxidation of nickel and palladium complexes of oeb **342** and **350**, and comparison of structures for palladium derivatives **350** and **352** (crystallographic figures adapted from Ref. 374).

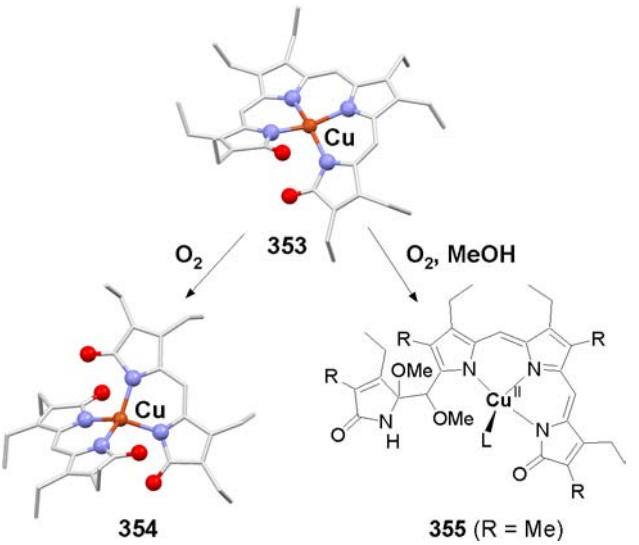

Figure 77. Structure and redox behavior of copper bilindiones (crystallographic figures adapted from Ref. 375).

[(oeb)Cu] **353** also constitutes a complex with the bilindione radical dianion.[369,375] A similar tetraethyl-tetramethyl-substituted compound has been electro-oxidized and -reduced at the ligand, while an oxidation state of +2 was maintained at the copper atom.[376] Structural data of these species are, however, not available. In the presence of dioxygen, **353** forms propentdyopent derivative **354**,[375] while a twofold methoxylation at a terminal *meso* methine group of **355** was observed under slightly different conditions in methanol.[369] A similar dimethoxy derivative has been described to form upon controlled oxidation of a thallium(III) bilindione with dioxygen in methanolic solution.[106] Figure 77 summarizes the findings on copper bilindiones.

Zinc complexes such as **356** and **357** have been described with different octa-alkylbilindiones and with the corresponding monolactim ethers. Different from most of the known chelate complexes, the tetrapyrrole ligand of **356** binds in a nonradical and twofold deprotonated state. The third proton is believed to be situated in a hydrogen-bridging position between the terminal oxygen atoms. Therefore, monolactim ethers as in **357** are preferred for the coordination to zinc(II) and find broad application in this chemistry.[246,369] An early report describes pH-dependent changes in the optical spectra of a zinc(II) bilindione **358** and explains this feature by reversible formation of a zinc complex with an open and a closed tetrapyrrole ligand, similar to the findings described above for divalent manganese (Figure 78).[243] Two DFT studies have been reported on metal bilindione species, confirming the above findings that bilindione is a

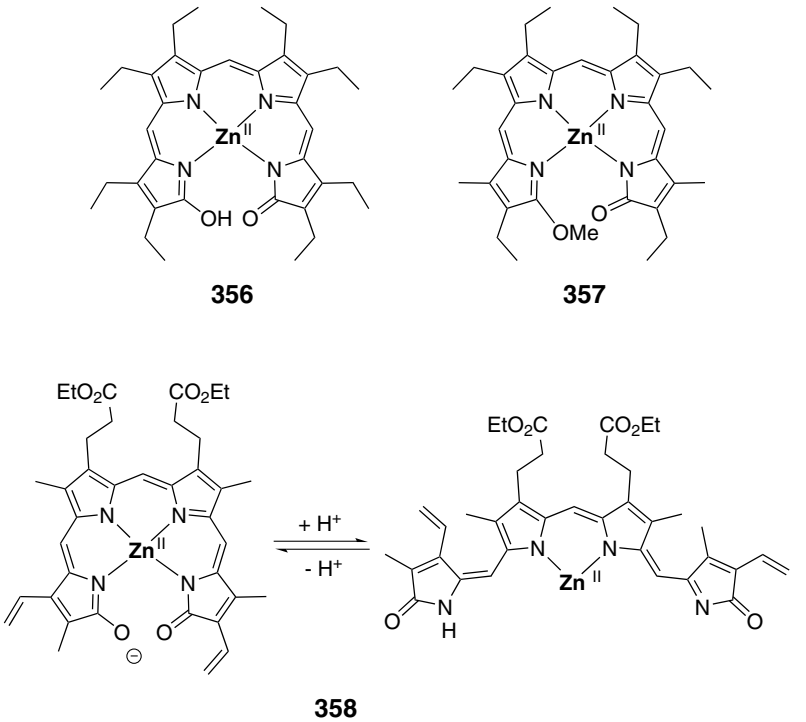

356 **357** **358**

Figure 78. Typical structures and assumed dynamics of zinc bilindiones.

redox active ligand and exists in a radical form in simple Co, Ni, Pd, and Cu chelates.[377,378]

A large number of coordination compounds of open-chain tetrapyrroles have been obtained as products from the photooxidation or related oxygenation protocols of metalloporphyrinoids. The ligands of these products are terminated by one oxo and one formyl or aroyl group and thus serve as dianionic ligands. A non-innocent behavior or electronic ambiguity which is typical of bilindiones is unknown for metal chelates of this group, so that a discussion ordered after different originating porphyrinoids is more instructive in this case.

Zinc and magnesium chelates of the ring-opened formylbilinone from protoporphyrin IX dimethyl ester have been described.[219] Some preference has been found with respect to the site of the ring-opening, and the two isomers with the oxygenated termini opposite to the propionate side chains have been reported. The model system octaethylporphyrin has been used coordinated to a number of different divalent metal ions, and photooxidation of these complexes led to the formation of the respective metal octaethylformylbilinones (oefb) with magnesium(II), cobalt(II) **359**, nickel(II), copper(II) **360**, and zinc(II) **361** centers (Figure 79). The compounds have been carefully characterized, and their

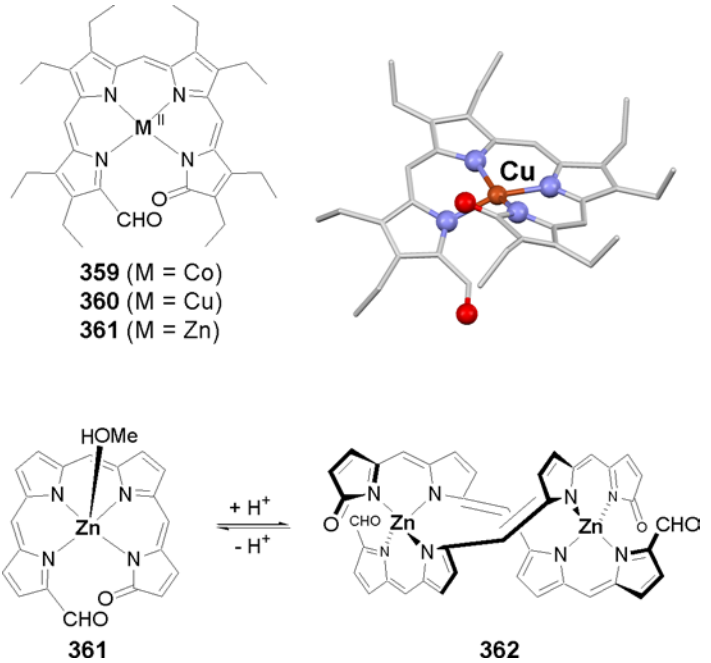

Figure 79. Selected metal octaethylformylbilinones [(oefb)M] (crystallographic figure adapted from Ref. 379).

magnetism as well as their redox behavior has been studied. A structural characterization has been achieved for the copper and the zinc derivatives **360** and **361**.[219,243,379] The first preparation of an iron derivative of an open-chain tetrapyrrole ligand was also achieved by this route (Section IV). Some special observations have been made with the cobalt, copper, and zinc derivatives of oefb **359–361**. [(oefb)Co] **359** is capable of binding molecular dioxygen in pyridine solution in a reversible process. [(oefb)Cu] **360**, on the other hand, decarbonylates in the presence of dioxygen and yields a copper verdoheme analog.[379] The zinc chelate has been reported to change its optical spectra with pH. This feature was interpreted in terms of a reversible change of the ligand conformation and metal-binding mode, as shown above for zinc and manganese(II) chelates of bilindione ligands.[219] An X-ray diffraction study, however, proved that a pH-dependent dimerization/monomerization equilibrium between the forms **361** × MeOH and **362** is responsible for the observation (Figure 79).[380]

Metal chelates of carbonyl-terminated bilinones obtained by oxidizing metal porphyrinoids have occasionally been reported from other oxygenation protocols. Nickel and copper complexes of a dodecasubstituted porphyrin open to give benzoylbilinone derivatives **363** with mCPBA in pyridine.[230] The oxidative ring-opening of nickel *meso*-amino-octaethylporphyrin with iron(III) in alcoholic

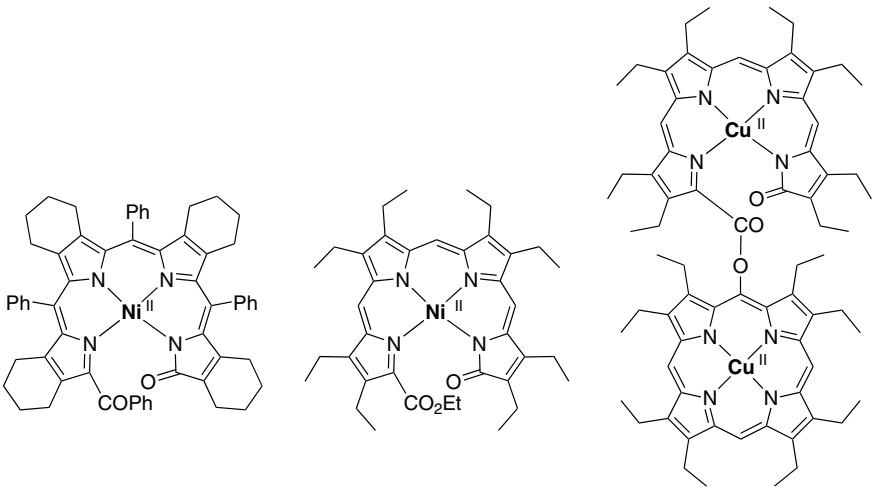

363 **364** **365**

Figure 80. L_1M_1 chelates **363–365** of open-chain tetrapyrroles from alternative porphyrin ring-opening procedures.

solution results in the formation of ethoxycarbonylbilinone **364**.[381] In a similar way, the ring-opening of copper *meso*-hydroxy-octaethylporphyrin and its trifluoroacetate was reported to yield dinuclear complex **365** (Figure 80).[382] All these products were identified by X-ray crystallographic studies.

While the photooxidation protocol has been widely applied to β-substituted metalloporphyrins, the transfer of this method to tetraarylporphyrins and in particular to metal tetraphenylporphyrins [(tpp)M] has been reported in only a limited number of cases. [(tpp)Mg] opens photooxidatively to give the corresponding benzoylbilinone **366**. The magnesium ion is labile, and **366** was shown to undergo transmetalation with copper(II) to give copper chelate **367**.[383] If the metalloporphyrin is activated by nucleophilic addition of n-BuLi at a *meso* position, the subsequent photooxidative ring-opening occurs at a neighboring methine group in a regiospecific fashion. The products **218** and **219** from this transformation now employ the benzoyl oxgen atom as the fourth donor for the nickel(II) or copper(II) ion rather than the fourth N atom from the pendant pyrrolinone moiety (Figure 81).[226] This behavior is presumably a result of protonation and electroneutrality issues.

The zinc complex of tpp has been found to yield a hydrated product **368** after photooxidation which dimerizes by several hydrogen-bonding interactions, as shown in Figure 82.[384] Compound **368** is capable of reversibly losing a molecule of water under different conditions (heat, solvent change), and the first applications of the associated coordination, thermo- and solvato-chromic features of the

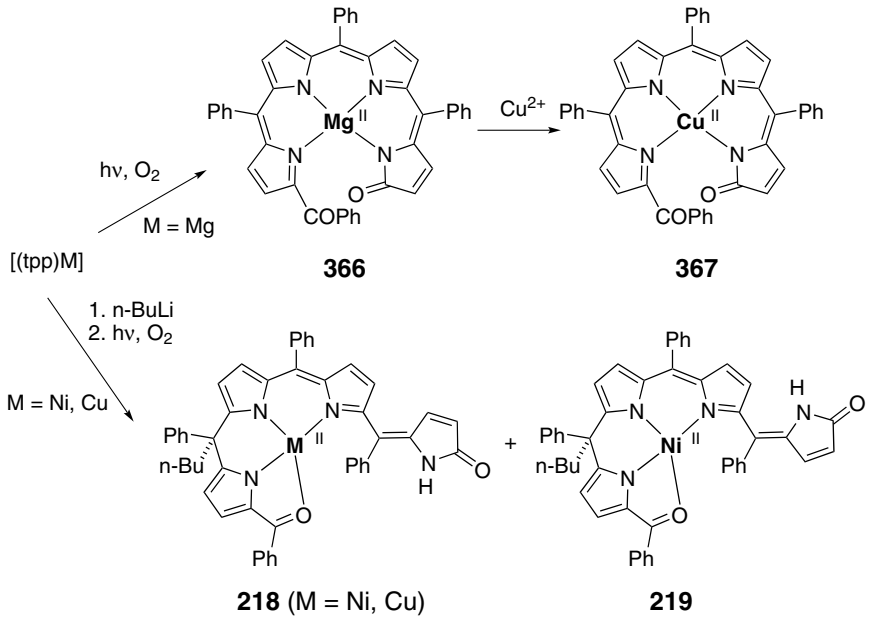

Figure 81. Formation of copper(II) and nickel(II) complexes of ring-opened tetraphenylporphyrins.

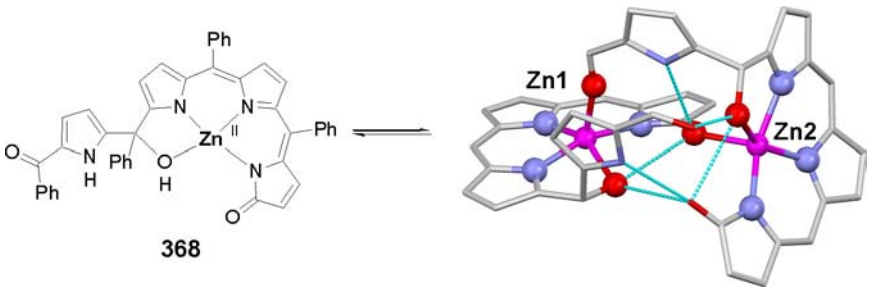

Figure 82. Hydrated zinc benzoylbilinone **368** in monomeric and dimeric form, with hydrogen-bonding network (aryl groups omitted for clarity; crystallographic figure adapted from Ref. 384).

compound as sensoric moments,[385] as well as its use as a conductivity switch,[386] have been reported.

Another group of metal complexes with open-chain tetrapyrrole ligands is available from the attack of different nucleophiles on verdoheme analogs. Verdoheme is an intermediate in the natural heme degradation process and differs from heme by the exchange of one *meso*-situated CH group with an O^+ function. The positive charge thus located at the porphyrin perimeter directs the attack of nucleophiles toward a position adjacent to the oxonium bridge. Consequently,

metalated bilinones with a heterofunctionality as the second terminus result after ring-opening. Mainly zinc(II) complexes have been reported so far from this approach. First examples were obtained by the nucleophilic attack of ammonia and of simple amines on zinc verdoheme dimethyl ester and on the corresponding *meso* form.[387,388] Products **369** are mixtures of two regioisomers, as expected from the unsymmetric substitution pattern of the starting material. A systematic exploration of the action of different O-, N-, and S- nucleophiles on zinc(II) and cobalt(II) complexes of an octaethyl-substituted ligand has been reported in a series of papers. Alkoxide addition results in the formation of monolactim ethers of zinc(II) and cobalt(II) bilinones.[389] A similar *S*-lactim ether and a dimethylamino derivative were obtained with zinc as the central ion.[390] Then again, cyanide addition to zinc derivative **370** did not produce a single product but rather a complex mixture of mono-, di- and trisubstituted species.[391] Some of the products could be isolated and characterized. Figure 83 summarizes results from these studies.

Occasionally, partially hydrogenated or reduced bilindione ligands related to the chlorins have been described as metal complexes. The examples known to date have, however, not been investigated in much detail, and structural information is absent. A stercobilin type ligand **371** has been shown by spectroscopic means to coordinate to copper and zinc ions in an unknown fashion.[392] The nickel and palladium complexes **372** of a threefold deprotonated tetraoxo derivative have been reported to reside in the metal(II)–ligand radical form.[243] Zinc and copper(II) chlorins have been ring-opened to hydrogenated formylbilinones **373**.[219] Zinc oxochlorin **374** loses the metal ion after thallium trifluoroacetate treatment with spontaneous oxidative ring-opening. A similar benzoannelated nickel chelate **375** yields methoxybilinone **376** if oxidized with the same reagent and further by a coupled oxidation with O_2 and ascorbate.[232] Figure 84 provides an overview of these investigations.

While oxo-terminated open-chain tetrapyrroles of the biliverdin type are characterized by a conjugated ligand backbone and thus by a certain conformational rigidity, the π-system of twofold methyl- or alkoxycarbonyl-terminated species is always discontinued at the central *b*-position, thus forming ligands composed of two methylene-linked and electronically decoupled dipyrrin subunits. The additional flexibility gained by this change in the framework results in the observation of coordination compounds in different binding modes and stoichiometries, similar to the chemistry of the bilirubin chromophore discussed above. Hydrogen-terminated *a*,*c*-biladienes tend to form macrocyclic metal corroles by oxidative ring closure reactions in the presence of transition metal ions. Dehydrogenated *a*,*b*,*c*-bilatrienes with methyl termini are also very reactive with respect to a variety of different electrocyclic ring closure transformations and cannot be obtained as metal chelates (see Section VII). *b*-Bilenes, on the other hand, react

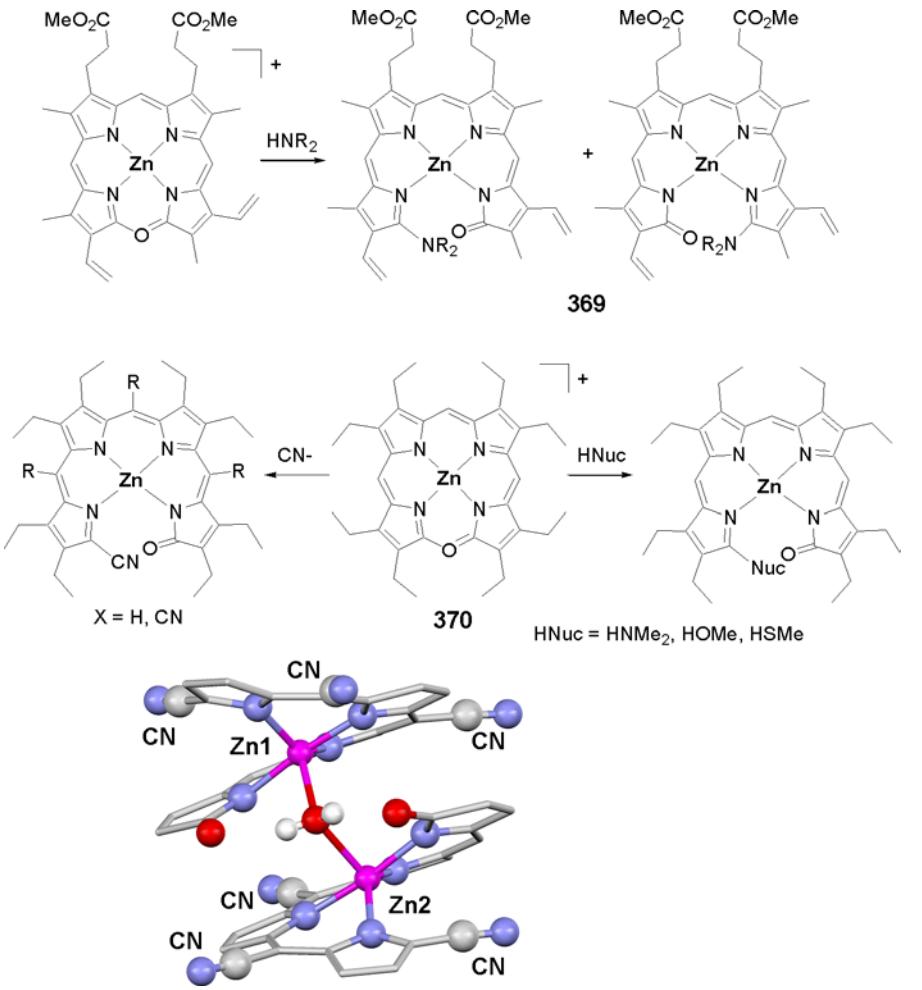

Figure 83. Products from addition/substitution reactions on zinc verdoheme analogs, and molecular structure of a water-bridged zinc bilinone dimer with several cyano groups (alkyl substituents omitted; crystallographic figure adapted from Ref. 391).

similarly to substituted dipyrrins in the presence of metals, and the formation of distorted tetrahedral zinc(II) and cobalt(II) chelates **377** in a L_2M_1 stoichiometry has been reported (Figure 85).[128,272]

a,*c*-Biladiene derivatives with methyl termini have occasionally been investigated as ligands in coordination compounds in order to study possible intermediates in the templated macrocyclization of such compounds to porphyrinoids under oxidizing conditions. The binding of one or two metal ions to *a*,*c*-biladienes in the stretched or in the coiled conformation, respectively, is mainly conducted by the coordinative preferences of the metal ion. The thermodynamics of the metalation

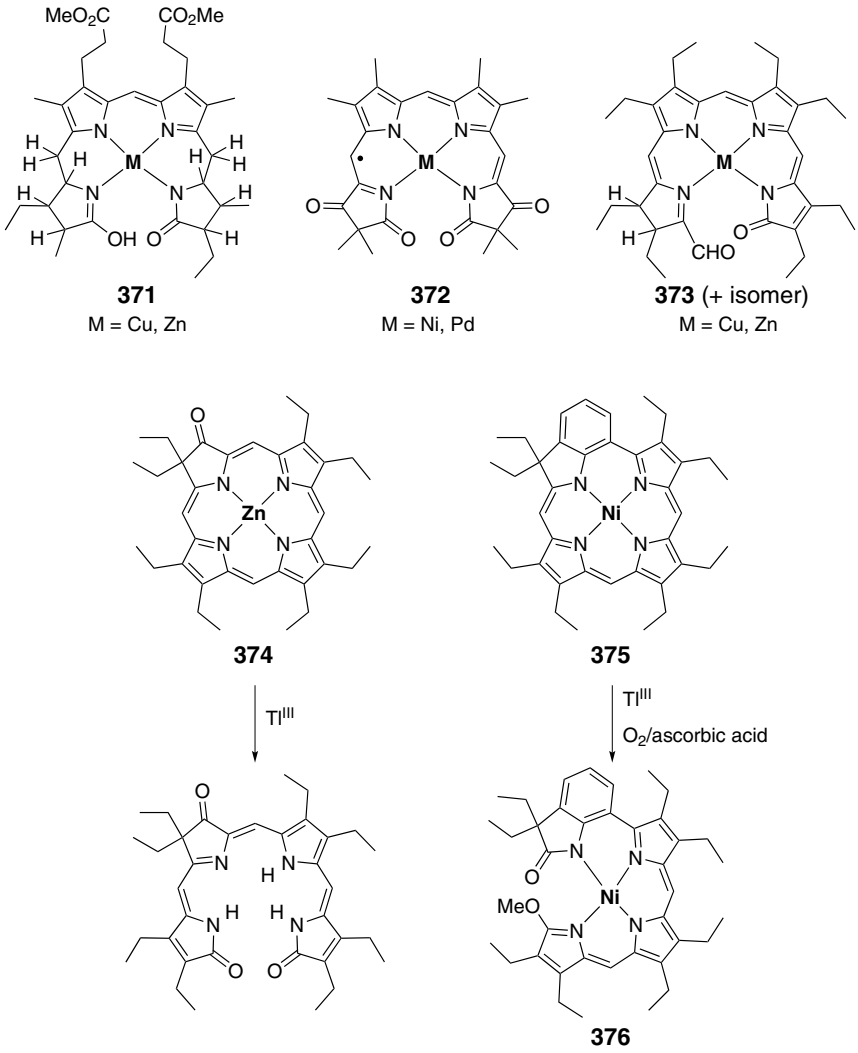

Figure 84. Known compounds from investigations toward metal chelates of partially reduced bilindiones.

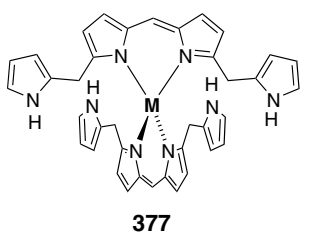

Figure 85. Coordination mode of *b*-bilenes.

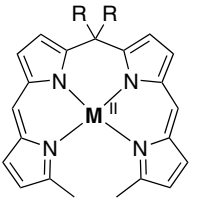

M = Ni, Cu
R = H, Me

378

Figure 86. Mononuclear nickel(II) and copper(II) complexes of *a,c*-biladienes **378**.

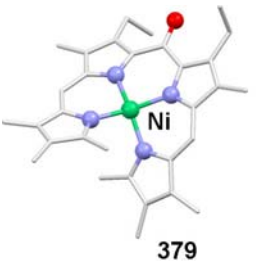

379

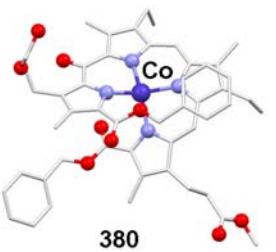

380

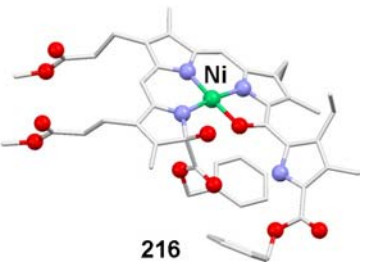

216

Figure 87. Structures of selected mononuclear L_1M_1 complexes of tetrapyrroles with *meso* oxo functionality. (Adapted from Ref. 321.)

reaction and the influence of the metal ions on the stoichiometry of the products have been investigated in DMF solutions on decamethyl-*a*,*c*-biladiene for divalent ions of nickel, copper, zinc, cadmium, and mercury by a combined calorimetric and spectroscopic study.[393] Nickel(II) and copper(II) bind to these ligands in a L_1M_1 mode, while for zinc(II) and cobalt(II) L_2M_2 species have been reported[276,394] (see Section III.H for more examples). The twofold methylation of the central *b*-position, on the other hand, has no significant influence on the coordination properties of *a*,*c*-biladienes (Figure 86).[239]

Linear tetrapyrroles carrying a *meso*-situated oxo functionality at either the central or a side position have been employed occasionally in coordination studies. The readily accessible bilane precursors have been used and oxidized *in situ* to the respective biladienes before addition of the metal ion carrier. The divalent ions of cobalt, nickel, palladium, and copper form L_1M_1 complexes such as **379** and **380** with the expected N_4 coordination.[321,395] Exceptions are found for nickel chelate **216**, in which the metal binds to a side-oxygenized and hydrated biladiene ligand in a N_3O fashion, and for an analogous methanol solvate (Figure 87).[321]

Formally, the removal of the central methylene bridge of biladienes yields 2,2′-bidipyrrins, a nonnatural class of linear tetrapyrroles for which many coordination compounds have been reported. L_1M_1 complexes of these ligands are

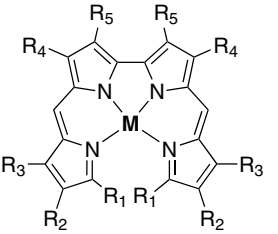

M = Ni, Pd, Cu
R_1 = H, Me, Cl, Br, OMe
R_2 = Me, CO_2Et
R_3 = Me, Et, P_{Me}, P_{Et}
R_4 = Me, Et, P_{Me}, P_{Et}
R_5 = H, Me

Figure 88. Early metalated 2,2′-bidipyrrins of the L_1M_1 type.

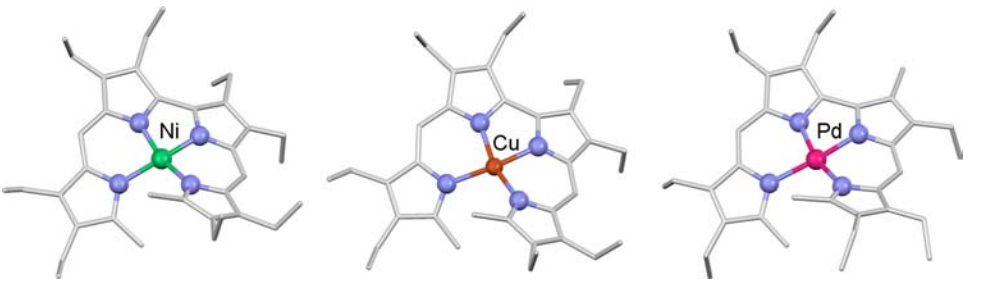

Figure 89. Molecular structures of nickel, palladium, and copper octaethyl-10,10′-dimethyl-2,2′-bidipyrrins. (Adapted from Refs. 396 and 397.)

less prone to oxidative macrocyclization reactions, because the termini of 2,2′-bidipyrrins in metal complexes are further apart from each other than in related *a*,*c*-biladiene chelates. Metalated 2,2′-bidipyrrins have a long history. The first examples were reported in the 1930s in the context of reduction experiments with halogenated dipyrrins.[236,238] Johnson and Price developed the chemistry of 2,2′-bidipyrrins systematically, with the goal of producing corroles from these tetrapyrroles by a metal-templated oxidative macrocyclization. Work from the Johnson group described a number of L_1M_1 coordination compounds with the divalent ions of nickel, palladium, and copper and with 2,2′-bidipyrrins carrying a range of different substituents and termini (Figure 88). A cyclization in the desired way, however, could not be realized.[239]

The first crystallographic investigations and the proof of stable, noninverting helical structures in solution were reported only during the 1990s. Methyl-terminated nickel, palladium, and copper chelates of symmetric and unsymmetric 2,2′-bidipyrrins with alkyl and mixed alkyl/aryl substitution were investigated and shown to display helical solid state structures throughout (Figure 89). The ethyl substituents of diamagnetic nickel and palladium chelates display diastereotopically split signals in solution ^{1}H NMR spectra up to 370 K, indicating static helices even for the large palladium ion. Spectroelectrochemical investigations have shown that two oxidation and two reduction processes occur. All processes are

purely ligand-centered and reversible, although some variation has been observed in the reduction steps of copper derivatives. Other than for *a*,*c*-biladienes, however, an electrochemical ring closure reaction within the group of methyl-terminated 2,2′-bidipyrrin chelates has not been observed.[271,396,397]

The molecular geometry of these simple 2,2′-bidipyrrin complexes has been fine-tuned by the choice of the termini as well as by additional carbocyclic substituents which serve as clamps and restrict intramolecular movement. H-terminated 2,2′-bidipyrrin complexes such as **381** are characterized by small helical distortions and a fast helix inversion in solution, while all alkyl-terminated dervatives investigated so far are rigid under the same conditions (Figure 90). *Tert*-Butyl groups at the terminal positions of a 2,2′-bidipyrrin have been reported to inhibit metal coordination entirely, so that neither L_1M_1 nor dinuclear L_1M_2 or L_2M_2 species were obtained from this tetrapyrrole.[243,270] Besides the obvious strain imposed by the *tert*-butyl substituents in the binding event, these groups seem to reduce the accessibility of the dipyrrin N-donor atoms and thus kinetically prevent the binding of metal ions. A similar stability or an enforced CH activation of the *tert*-butyl substituent has been reported for several related heterocyclic N-donor chelate ligands.[123,201,398–400] In a different approach, an eight-membered carbocycle has been employed as a central clamp. This restraint tears the terminal methyl groups apart from each other and thus results in a slight planarization of the overall structure. A palladium derivative of this ligand, **382**, has been reported.[269] As above, a precedent oligoheterocyclic species with a similar restraint is known.[401]

Complexes with ligand frameworks other than those of the *a*,*c*-biladienes and 2,2′-bidipyrrins have scarcely been reported to date. A copper complex of an

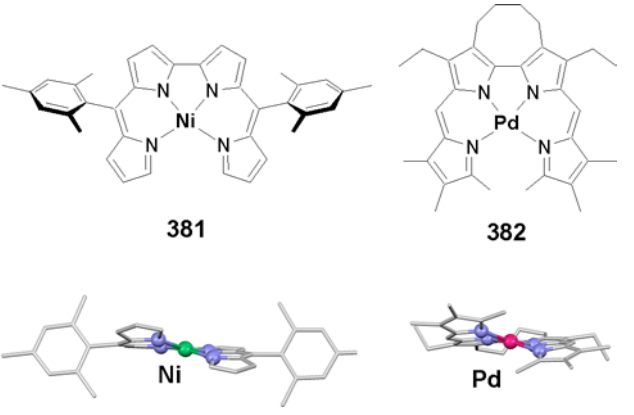

Figure 90. Helical distortions of the H-terminated nickel-2,2′-bidipyrrin complex **381** and the clamp-restrained palladium derivative **382** (end-on views; crystallographic figures adapted from Refs. 241 and 269).

ethylene-bridged bis(dipyrrin) has been mentioned,[239] as has been a zinc chelate of a partially hydrogenated *a*-norbilene.[140] Little spectroscopic evidence and no structural data are available for either species. A study concerning copper nuclease activity of the naturally occurring tetrapyrrole **383** in the presence of copper ions has appeared, but nothing is mentioned with respect to the coordination mode or stoichiometry of the active species.[150] A similar ligand framework, however, is present as a partial structure in palladium derivative **384**, the only structurally characterized metal complex of a hexapyrrolic ligand (Figure 91).[30]

Several transition metal chelates of strongly hydrogenated open-chain tetrapyrrolic ligands have been reported in the context of vitamin B_{12} research. A protocol for the reversible ring-opening and closure of some similar neutral $Co(CN)_2$ and positively charged Ni species yields open-chain derivatives **385** and **386** (Figure 92).[233,234] Divalent nickel provided a good template ion for the cyclization of another open-chain B_{12} precursor, **387**, and has been structurally characterized.[151,402] Yet another ligand framework is present in the Ni, Pd, and Pt complexes **388**, which were also structurally characterized and discussed in the context of the influence of the metal ion size on the magnitude of helical distortion.[403]

The helical molecular structure of all these mononuclear tetrapyrrole complexes and the issue of stereochemistry have been the topic of a number of different studies on open-chain tetrapyrrole coordination chemistry. The central question concerning the stability of the helical form and the rate of helix inversion has been discussed in several contributions. H-terminated 2,2′-bidipyrrin complexes of nickel and of trivalent iron (see Section V.B) have been shown by qualitative VT ^{1}H NMR studies to invert fast on the time scale of the NMR experiment, and no coalescence could be observed for these species. Alkyl-terminated derivatives, on the other hand, are rigid and show no dynamics up to the upper temperature limit of the experiment.[270,396,397] A nickel-2,2′-bidipyrrin with alkyl

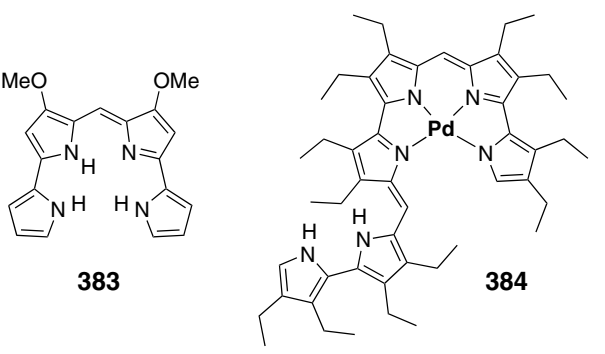

383 **384**

Figure 91. Dipyrrolyldipyrrin derivatives **383** and **384**.

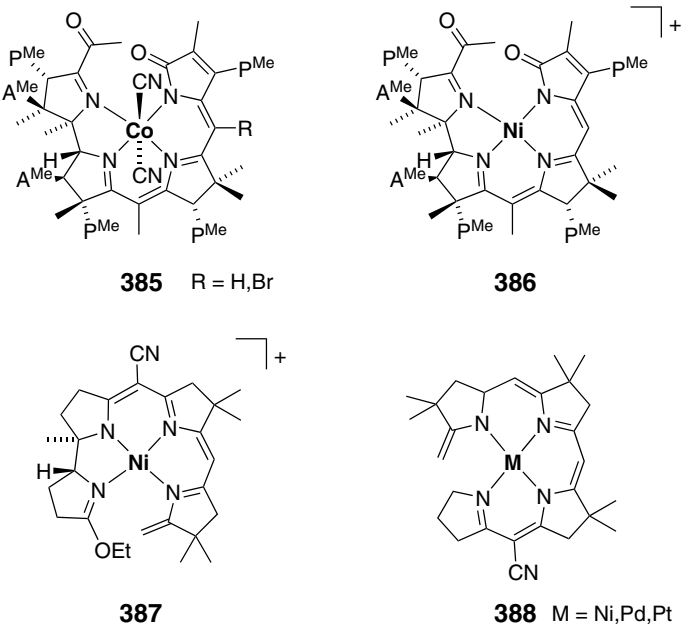

Figure 92. Metal chelates of linear tetrapyrroles **385**–**388** related to vitamin B_{12}.

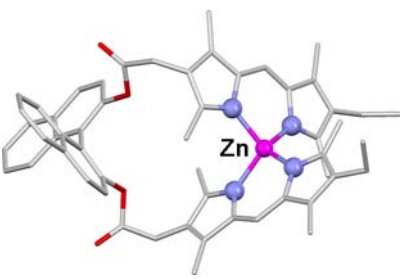

Figure 93. Molecular structure of the enantiomerically pure zinc bis(dipyrrin) **389**. (Adapted from Ref. 299.)

and aryl substitution has been separated into its enantiomers chromatographically, and CD spectra were obtained from the chiral material.[396] Enantiopure material was subjected to prolonged heating in high-boiling solvents, but no signs of helix inversion have been found below the decomposition temperature. Stereoselective synthesis of a helical chiral metal complex with an open-chain tetrapyrrole ligand has been achieved by using a set of β-bridged bis(dipyrrin)s with a chiral binaphthyl-type strap such as **126**. Zinc chelates of such ligands, e.g. **389**, form enantiomerically pure with up to 99% ee, depending on the lengths and flexibility of the bridging linker (Figure 93).[299]

Conformational dynamics were studied in depth on zinc bilinone **357** and related species with different substituents at the pyrrole rings. A slow inversion of the helix was found by variable ^{1}H NMR spectroscopy at low temperature (223 K). The rate of the process can be lowered with the size of the terminal pyrrole substituents (reorganization effect). More interestingly, the inversion rate can also be accelerated by the addition of donor ligands, particularly amines and amino acid esters. Further quantitative investigations confirmed that this acceleration is catalytic in the external donor, and a kinetic model has been proposed (Figure 94). This finding is an important issue in the context of the use of such tetrapyrrole complexes as sensor molecules.[246,404]

Chiral discrimination has been observed to occur during the coordinative binding of chiral guests to dynamic zinc bilinone hosts such as **390**. Using amino acid esters or chiral aliphatic amines, the point chirality of the guest is effectively transferred to the helical chirality of the host in a diastereospecific way. The degree of chiral induction has been quantified by CD spectroscopy and depends largely on the nature and binding capability of the guest.[405,406] In addition, the choice of solvent was found to vary the efficiency of the chirality transfer in a predictable fashion.[407] Some covalent dimers and trimers of zinc bilinones, such as **391** (Figure 95), have been prepared and used in related binding studies. It has been found that the conformations of the monomeric forms tend to form homohelical structures upon binding of a small molecule. The synchronous alignment of the helices enhances the sensoric moment, i.e. the change in CD effect upon binding. Consequently, these compounds have been discussed in terms of model systems for allosteric binding of small N donor molecules.[408,409] In another

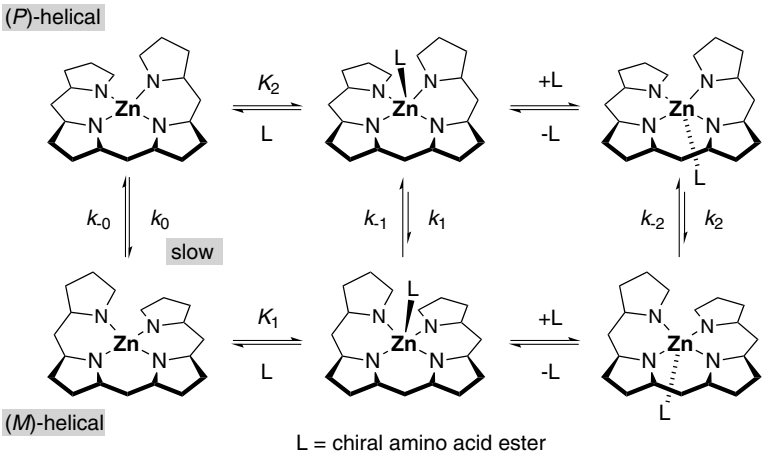

Figure 94. Schematic view of the kinetic model for the catalytic enhancement of the rate of helix inversion on zinc bilinone **390**.

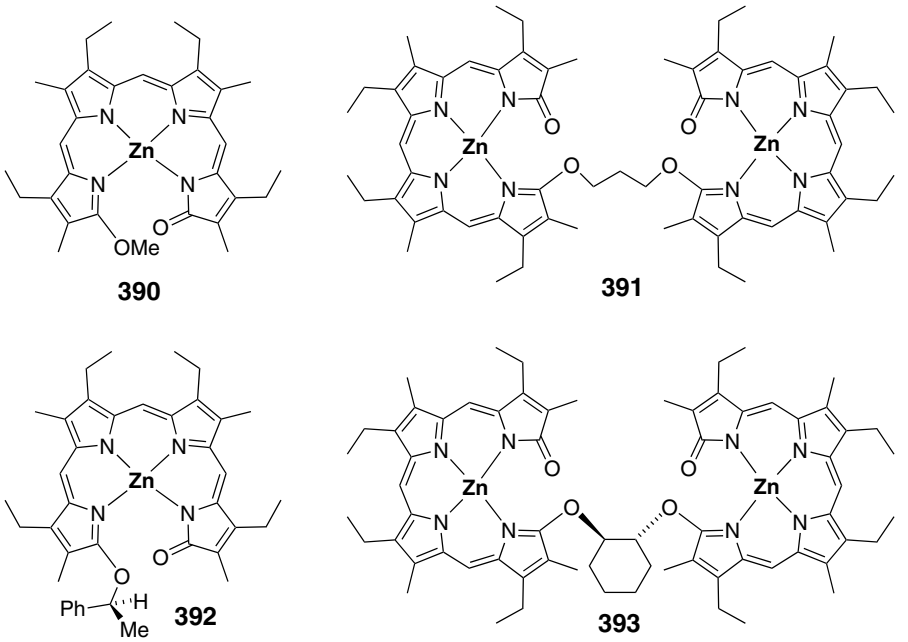

Figure 95. Monomeric and dimeric zinc bilinones **390**–**393** as dynamic multifunctional sensor molecules.

contribution, several chiral substituents were introduced as the alkoxy moiety of the zinc bilinone (e.g. **392** in Figure 95). The substituents were found to induce a significant chiral discrimination on the helical structure in solution.[410] The effect is even stronger if an allosteric enhancement is used,[411] and a number of compounds with chiral bridges between two zinc bilinone subunits, such as **393**, have been prepared and studied. These compounds have found applications in sensing and molecular recognition of the chirality of amino acid esters,[412,413] as well as in liquid crystals.[414]

G. Dinuclear Tetrapyrrole L_2M_2 Complexes

The capability of bilirubin to bind simultaneously to more than one metal cation has been discussed earlier, and related species have been reported for several artificial *a*,*c*-biladiene and 2,2′-bidipyrrin ligands, mainly with zinc ions.[236,273] As for the natural species, the coordination mode and structural details were speculative at the beginning, and a L_2Zn_2 binding mode has been proposed based on combustion and optical data. In-depth studies on the distinction between the L_1M_1 and the L_2M_2 binding modes were undertaken on an α,ω-dimethyl-*a*,*c*-biladiene derivative using vapor pressure osmometry, ligand field spectroscopy, NMR and powder

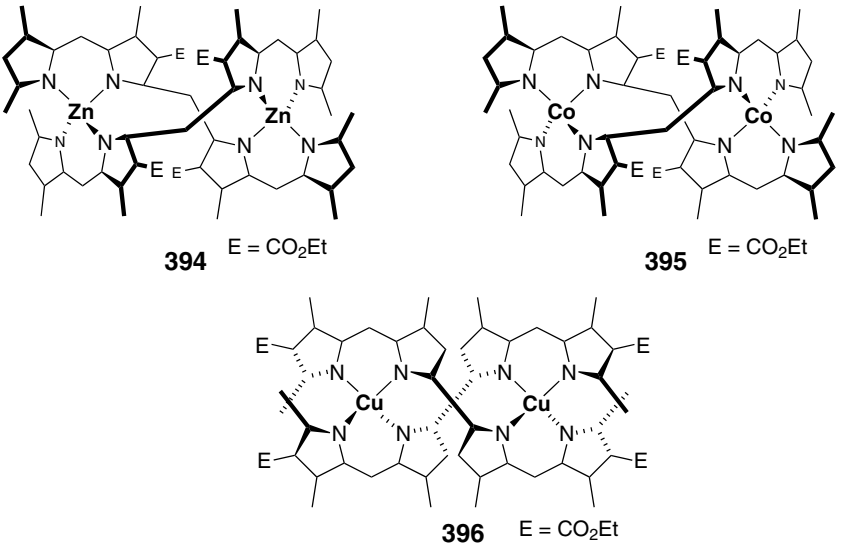

Figure 96. Early dinuclear L_2M_2 derivatives **394**–**396**.

X-ray diffraction techniques, and zinc and cobalt(II) dervatives **394** and **395** were found to exist in the L_2M_2 mode in solution as well as in the solid state.[277,394] At about the same time, copper ions were observed to bind to a 2,2′-bidipyrrin ligand in either a L_1Cu_1 or a L_2Cu_2 mode **396**, depending on the pH of the reaction mixture.[239] Similar 3D molecular structures were proposed for these compounds, as depicted in Figure 96.

A pH-dependent dynamic process similar to the findings on **396** has also been observed spectroscopically with manganese(II) and zinc complexes of bilindione ligands such as **345** or **358** (Figures 74 and 78). This dynamic, however, has not been interpreted in terms of dimer formation. Instead, a conformational change of the ligand and concomitant reduction of the coordination number is reportedly responsible.[214,219] The first single-crystal X-ray diffraction analysis on a dinuclear L_2M_2 species was reported in 1976 and proved the often-stated pH-dependent equilibrium of zinc bilins for formylbilinone complexes **361** and **362** (Figure 79).[380] During the last decade several single-crystal X-ray diffraction studies on dinuclear metal bilins have appeared in the scientific literature and have supported the general formation of a bis-helical conformation. Dimeric zinc decamethyl-*a*,*c*-biladiene **397** has been characterized crystallographically, and the two dipyrrin subunits of each tetrapyrrole ligand were found to reside in an almost orthogonal arrangement. This relaxed conformation results in a zinc···zinc distance of 4.38 Å (Figure 97).[415,416] A very similar, but less symmetric, molecular structure with a metal···metal distance of 4.33 Å has been observed for a cobalt(II) *a*,*c*-biladiene derivative **398**.[27] A dinuclear zinc

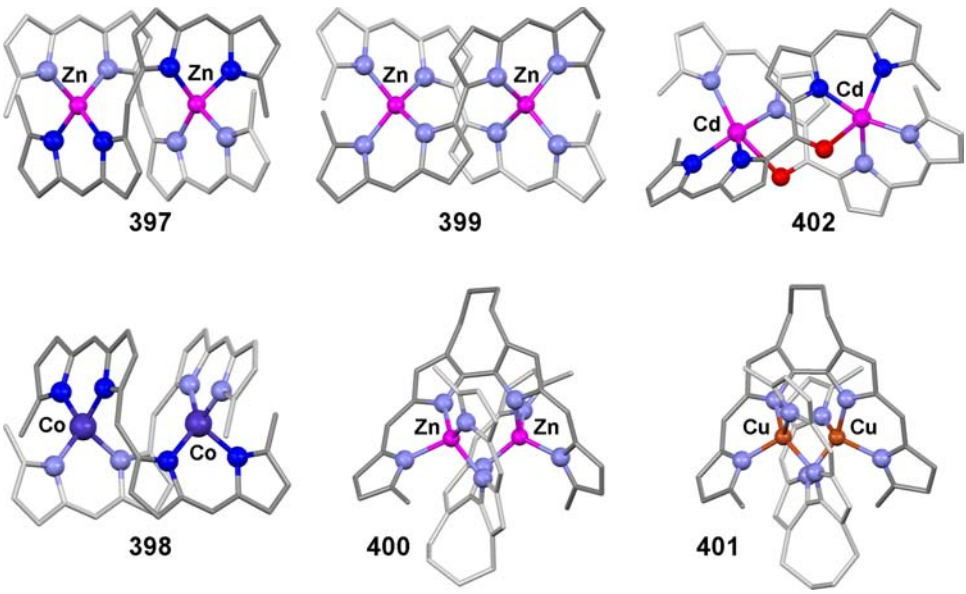

Figure 97. Molecular structures of dinuclear bis(dipyrrin) helicates **397**–**402** (peripheral substituents omitted; adapted from Refs. 27, 269, 395, and 415).

2,2′-bidipyrrin complex **399** with a smaller bridge between the dipyrrin subunits was found to crystallize in a stretched conformation with a zinc···zinc distance of 4.89 Å.[27] An annelated carbocyclic ring at the bipyrrolic unit of 2,2′-bidipyrrins serves as a clamp and results in reduced flexibility of the ligand. A zinc complex of such a ligand, **400**, has been reported to form a compressed helicate (zinc···zinc distance of 3.44 Å). This effect is even larger with the corresponding copper chelate **401**, where a copper···copper distance of only 3.01 Å has been found.[269] This value is below the van der Waals distance for copper but is still too large for covalent Cu–Cu bonding interactions. On the other hand, the introduction of a fifth donor atom such as in the 10-oxobiladienes can lead to stretched conformations. This has been demonstrated for cadmium chelate **402**, where pentacoordinate metal ions in a distance of 5.12 Å are present (Figure 97).[395]

While α-bridged bis(dipyrrin) ligands tend to form L_1M_1 complexes with most transition metal ions, β-bridged tetrapyrroles such as **122**–**126** (Figure 33) are much more prone to bind to two ions in either a L_1M_2 or a L_2M_2 fashion.[295] Attempts to develop tetrapyrrole-based helicates have therefore turned more recently to this latter group of ligands. In β-bridged (bis)dipyrrins, the two chelating dipyrrin units coordinate to the same or two different metals, depending on the size and flexibility of the bridge. As a rule, short- and medium-length bridges result in exclusive formation of dinuclear helicates while longer and more flexible

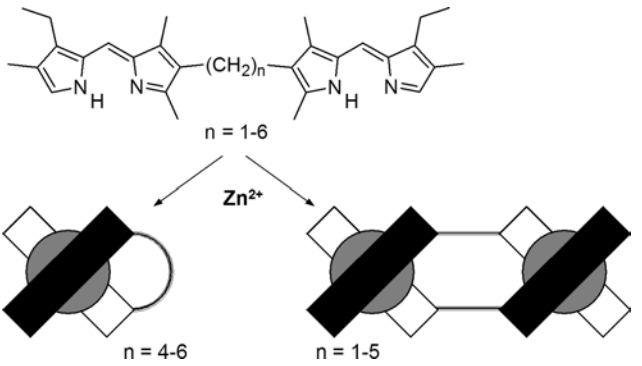

Figure 98. Formation of mono- and dinuclear coordination compounds from β-bridged bis(dipyrrin)s as a function of the lengths of the bridging unit.

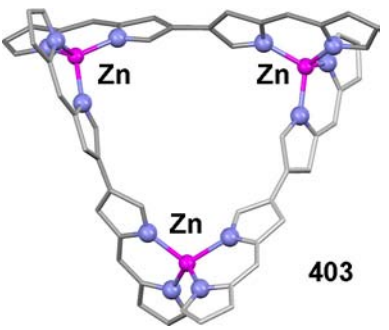

Figure 99. Molecular structure of trinuclear zinc chelate **403**. (Adapted from Ref. 417.)

bridges yield mixtures of mono- and dinuclear coordination compounds. These results were obtained in a study on zinc, copper(II), and cobalt(II) chelates, as sketched in Figure 98.[291] For binap-bridged ligands the aspect of flexibility has been found to be of major importance. Methylene derivative **126** forms a clean L_1M_1 compound **389**, while more rigid as well as a more flexible forms with zero and four CH_2 units in the bridges, respectively, produce mixtures of mono- and dinuclear species.[299] In the case of a directly connected 3,3′-bidipyrrin ligand (i.e. for $n = 0$ in Figure 98), a trinuclear species L_3Zn_3 **403** was reported (Figure 99).[417]

Methylene-bridged members have been employed in most of the reported coordination studies on β-bridged bis(dipyrrin)s, and crystallographic analyses were obtained on dinuclear nickel(II),[418] cobalt(II),[419] and zinc(II)[292,293,419] chelates such as **404**–**406** (Figure 100). In addition, optical and vibrational spectra have been recorded, and detailed TD-DFT calculations have been undertaken to elucidate the physicochemical properties of these new materials.[420] A triple helicate/mesocate system was described, and the zinc chelate **407** of an unsymmetric methylene

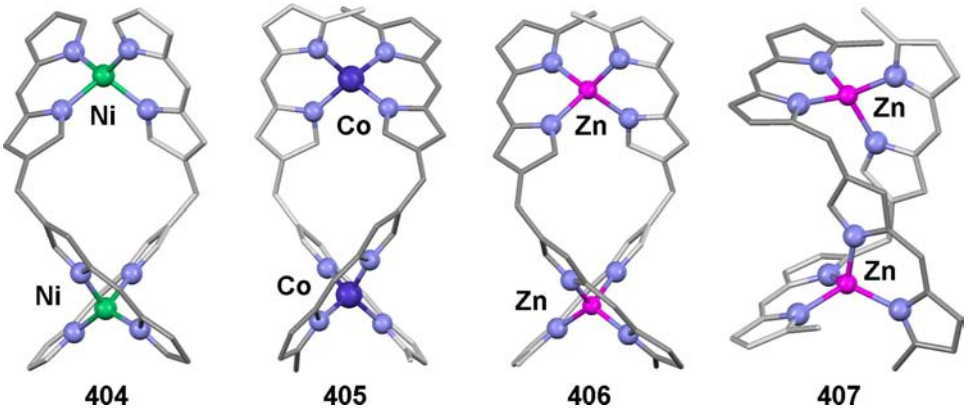

Figure 100. Results from X-ray crystallographic studies (peripheral substituents omitted) on dinuclear helicates with β- and α,β-bridged bis(dipyrrin) ligands **404**–**407**. (Adapted from Refs. 264, 292, 418 and 419.)

α,β-bridged ligand has been found to crystallize in only one of the two possible conformations.[264,421]

Two reports can be found in which bridges other than the simple saturated hydrocarbon have been used (Figure 33). A sulfur atom connected (bis)dipyrrin ligand **124** was used in the coordination to zinc ions.[28] The resulting complex displays a molecular structure similar to that of methylene derivative **406**. In another instance, several rigid bridges based on oligoacetylenes such as **125** were used and the tetrapyrroles coordinated to zinc and cobalt(II) ions.[298] Dimeric cobalt chelates similar to **405** result for bent bridges, and a trimeric zinc compound similar to **403** (Figure 99) has been found for linear ligand **125** (Figure 33). These elongated bridges leave hollows in the crystal lattice, thus giving hope for an application in supramolecular materials (see Section VIII).

Stereochemical aspects of the dinuclear helicates formed from zinc ions and methylene-bridged bis(dipyrrins) have been discussed in three contributions. The presence of helical chiral molecules in solution has been proven in one case by NMR spectroscopy using lanthanide shift reagents.[422] For a series of β-bridged bis(dipyrrin) ligands carrying chiral peripheral groups such as tetra-amide **408** (Figure 101), the diastereoselectivity of the helicate formation upon the addition with zinc ions was investigated,[300] and the stereochemical stability of the products was established in solution by separation using chiral HPLC.[423]

H. Oligonuclear Noble Metal Species

The coordination of tetrapyrrolic ligands to noble metal atoms may be expected to yield helical chiral porphyrinoids. Such derivatives would be intriguing

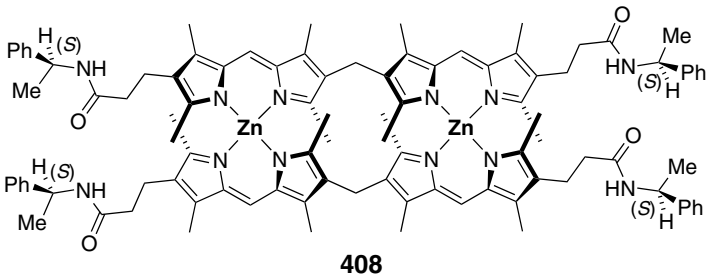

408

Figure 101. Stereochemically stable dinuclear double helicate **408**.

bioorganometallic compounds with perspectives in enantioselective catalysis, and several attempts to obtain species of this class have been undertaken in the past. The coordination chemistry of these metals, however, and in particular the observed coordination modes, have been found to differ largely from those of the 3d metals. With the exception of examples for divalent palladium and platinum, no simple noble metal compounds with N_4 coordination have so far been obtained, and even with palladium some unexpected behavior was reported.

Rhodium(I) and iridium(I) are well known to prefer square-planar coordination. Both ions have been employed in coordination studies with 2,2′-bidipyrrin ligands.[424–426] Mononuclear complexes HL_1M_1 and dinuclear species L_1M_2 have been observed and isolated. Figure 102 summarizes the formation and reactivity of rhodium and iridium 2,2′-bidipyrrin coordination compounds, and Figure 103 gives molecular structures of two examples of the L_1M_2 type.

Rhodium(I) and iridium(I) form mono- and dinuclear complexes with 2,2′-bidipyrrins in which the metal ions are always coordinated in a distorted square-planar geometry. Mononuclear HL_1M_1 species **409** of rhodium and iridium form exclusively upon the use of particular metal precursors, i.e. $[Rh(cod)Cl]_2$ and $[Ir(cod)OMe]_2$, respectively. If the combination of metal and anionic coligand is switched, i.e. if $[Rh(cod)OMe]_2$ and $[Ir(cod)Cl]_2$ are used, dinuclear species **410** are obtained as the only isolated products. No rationale has been provided so far for this peculiarity. The exchange of the cod ligands in **409** and **410** for two CO is generally possible and results in very robust dinuclear and very labile mononuclear products. Dinuclear rhodium carbonyl derivative **411a** may also be obtained directly by the use of $[Rh(CO)_2Cl]_2$ in the presence of a solid base. All dinuclear complexes with either cod or CO coligands, such as iridium derivative **411b**, display a *syn* conformation with short M···M contacts in solution and in the solid state (Figure 103).

Rhodium carbonyl complex **411a** has been used as starting material for ligand exchange studies with different monophosphanes and diphosphanes. Excess triphenylphosphine displaces the sterically less hindered CO ligand on both rhodium

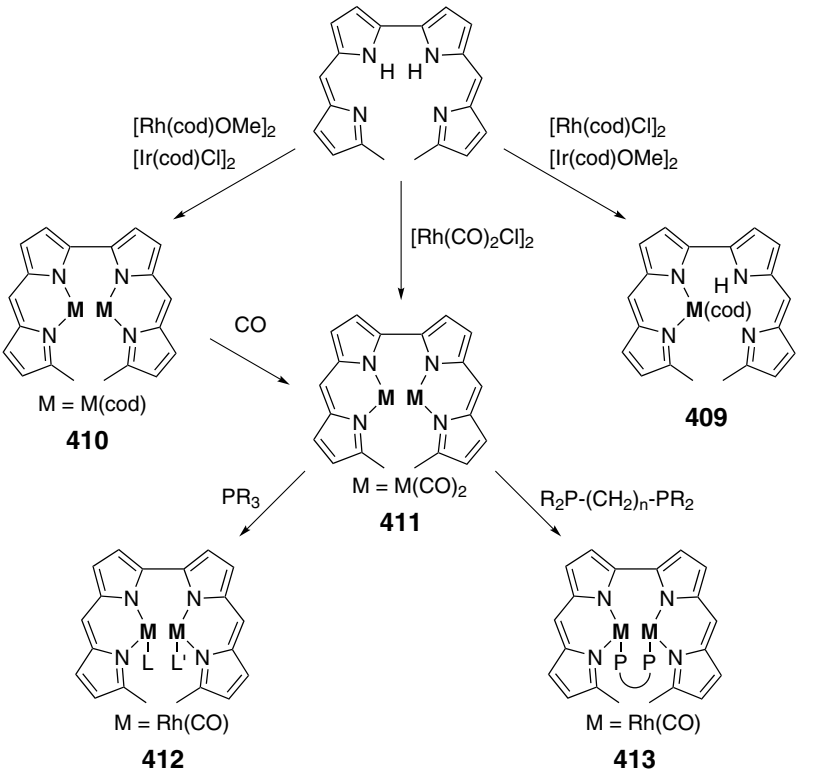

Figure 102. Rhodium and iridium complexes with 2,2′-bidipyrrin ligands.

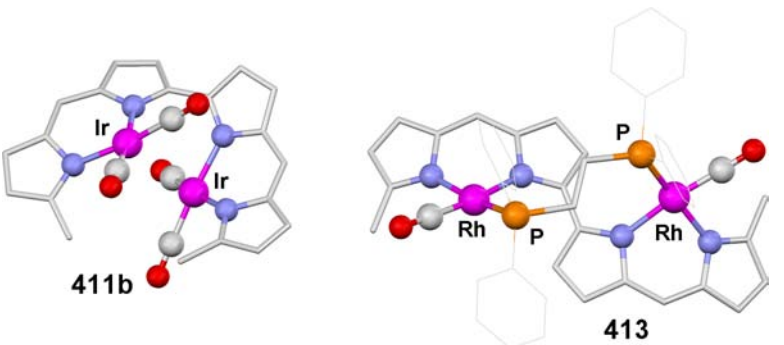

Figure 103. Molecular structures of dinuclear iridium and rhodium 2,2′-bidipyrrins **411b** and **413** in the *syn* and *anti* conformations. (Adapted from Refs. 425 and 426.)

atoms to give symmetric derivative **412**, while the more basic trimethylphosphane and tri-isopropylphosphane can only be used in stoichiometric amounts and form inseparable mixtures of derivatives of **412** with one and two phosphane ligands (Figure 102; L = PR_3, L′ = CO). 2D correlation NMR studies have confirmed a *syn*

conformation of the tetrapyrrole in all cases. If chelating diphosphanes such as dppm or dppe are employed, the tetrapyrrole switches to an *anti* conformation. As the X-ray crystallographic analysis on **413** shows, the 2,2′-bidipyrrin is now stretched out and the two rhodium atoms are bridged over the same side of the tetrapyrrole by the diphosphane clamp. Again, only the less hindered CO ligand has been exchanged. All attempts to form simple L_1M_1 species with N_4 coordination to monovalent or trivalent rhodium and iridium ions have failed so far, despite the fact that the transformation of L_1M_2 to L_1M_1 is well established in the chemistry of the related porphyrins.

While the compounds with rhodium and iridium ions still follow the general principles of the chemistry of these ions with porphyrinoid ligands, several other cases have been reported in which the coordination mode has been entirely unpredictable. One such case was observed during a study of the synthesis of copper complex **367** (Figure 81). In the presence of excess copper(II) ions and water this complex is hydrated at a *meso* position, and a second copper atom binds to the hydrated ligand to form the new dinuclear species with a Cu_2O_2 core. Upon crystallization, this dinuclear complex dimerizes via an additional, but weak, Cu_2O_2 interaction to give tetranuclear species **414** (Figure 104).[383] A similarly hydrated aroylbilinone ligand has been reported for a mononuclear zinc chelate. This species, however, dimerizes directly via multiple H-bonding interactions to give **368** (Figure 82).

Another tetranuclear cluster was observed as a byproduct during the synthesis of (oeb)Pd **350**. Mixed-valence species **415** contains two divalent and two monovalent palladium ions, the latter being connected to each other by a covalent

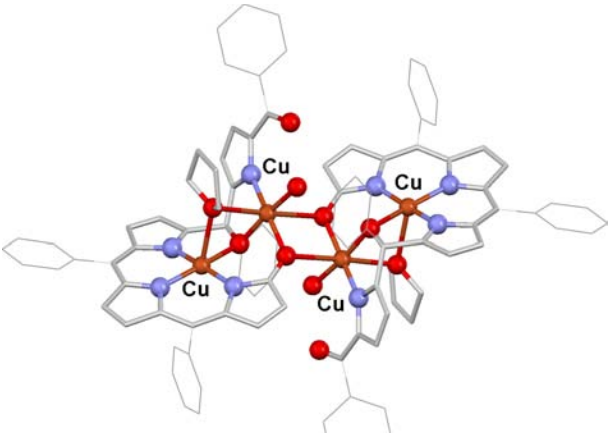

Figure 104. Molecular structures of tetranuclear dimer **414**. (Adapted from Ref. 383.)

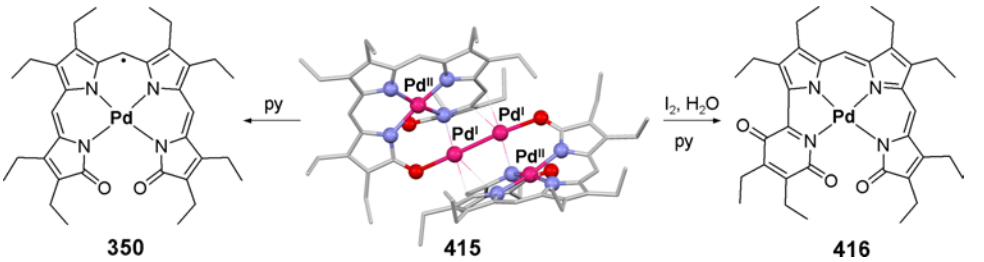

Figure 105. Structure and reactivity of tetranuclear palladium chelate **415** (crystallographic figure adapted from Ref. 427).

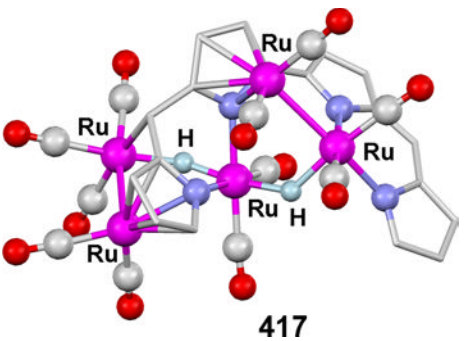

Figure 106. Molecular structure of pentanuclear ruthenium carbonyl cluster **417** (alkyl groups omitted; adapted from Ref. 429).

bond.[427] Compound **415** is remarkably stable and survives even chromatographic conditions, presumably because the $(Pd^{I})_2$ subunit is perfectly shielded by the two tetrapyrrole π systems. The reactivity of **415** was studied in some detail and revealed further peculiarities (Figure 105).[428] In the presence of pyridine, **415** was found to decompose with the formation of the radical palladium(II) oeb complex **350**. If iodine and water are present, however, the oeb tetrapyrrole framework undergoes an unprecedented rearrangement, yielding the novel palladium chelate **416**.

The coordination compound of a linear tetrapyrrole with the highest nuclearity has been isolated from the reaction of a 2,2′-bidipyrrin with $[Ru_3(CO)_{12}]$ in boiling toluene. After chromatographic workup a red compound was isolated in a 13% yield, which was identified by single-crystal X-ray diffraction as pentanuclear ruthenium carbonyl complex **417** (Figure 106).[429] As for Pd_4 derivative **415**, the remarkable stability of the cluster compound arises from an efficient shielding of the linear Ru_5H_2 core, which in this case is affected by the tetrapyrrole and the 11 CO coligands. Two features of **417** deserve special attention. First, this complex comprises three different types of metal–tetrapyrrole interactions, i.e. four

classical Ru–N coordinative bonds, two Ru–C_4N–η^5 bonds, and one organometallic Ru–C(sp^3) bond. In addition, the ruthenium atoms are in different formal oxidation states, i.e. 2 × Ru(0) at the ends and 3 × Ru(II) in the center. Second, the NH protons of the ligand have remained in the cluster framework as bridging hydride ligands. These hydrides were unambigously identified by NMR spectroscopy and confirm that NH activation processes occur during ruthenium complexation.

IV. Pincer-Like Palladium Complexes

A. Cationic Species

Cationic N donor chelate complexes and organometallics of divalent palladium have found many uses in academic as well as applied chemistry. Prominent examples are found in the polymerization or oligomerization of alkenes and in alkene/CO copolymerization reactions which are successfully catalyzed by activated palladium complexes with diimine or other N,N chelate ligands, and which yield a plethora of functional polymers with specialized and commercially interesting properties. In addition, many stoichiometric and catalytic C–C and C–E bond-forming and isomerization reactions and a vast number of C–H activation processes and cyclopalladation reactions have been investigated within this class of transition metal complexes, and several of these transformations have been proven valuable in the syntheses of small molecules. More fundamental studies, concerning e.g. functionalization strategies, ligand exchange processes, structure/reactivity correlations, fluxional behavior, or electron transfer issues, are also well documented in the scientific literature, particularly for cationic bipy, terpy, and pincer-type palladium(II) species. In the series of tripyrroles, cationic palladium complexes have become available with methyl-terminated tripyrrin and bti ligands. Transition metal complexes of α,ω-dimethyltripyrrin or bti ligands are characterized by the steric repulsion which is present between an anionic coligand (in particular the donor atom of that coligand) and the two methyl groups situated at the termini of the open-chain tripyrrole. The steric overcrowding at the open site of the linear tripyrrole leads to strained, nonplanar structures, as shown for some neutral derivatives above, and eases the formation of cationic species.

The formation of cationic palladium(II) tripyrrin complexes by salt metathesis of the respective trifluoroacetates **149** and **150** with different salts of weakly coordinating anions was reported.[430] With nonhydrolizable counterions, cationic mono- and dinuclear complexes **418**–**421** are observed, depending on the nature of the anion and the solvent (Figure 107). Mononuclear cations **420** and **421**, which are formed only with the BAr^F anion [= tetrakis(3,5-bis(trifluoromethyl)phenyl)boranate], were

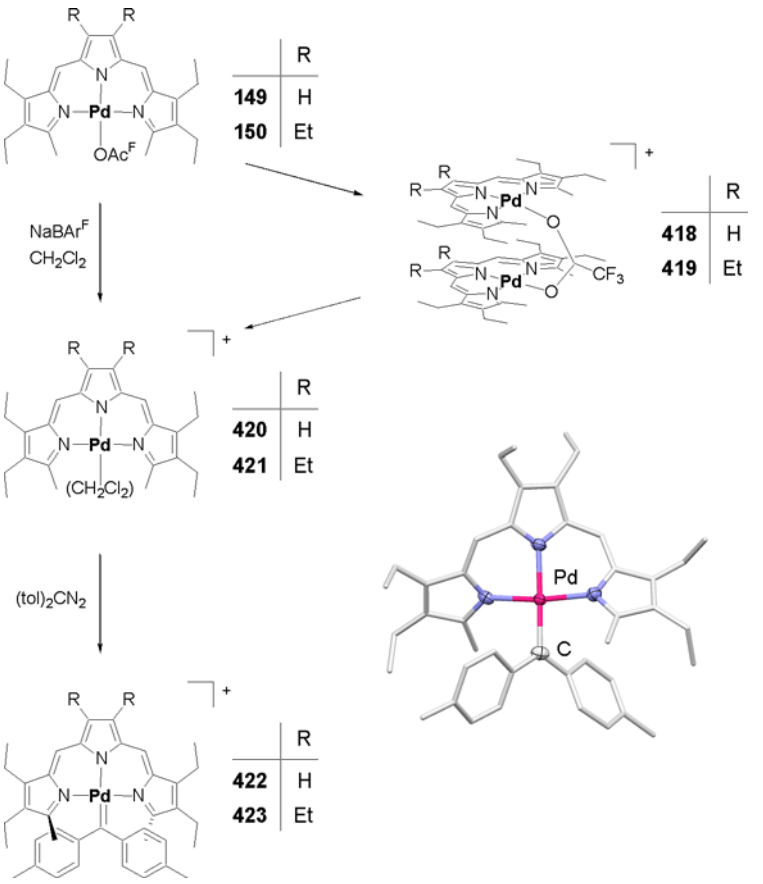

Figure 107. Salt metathesis and carbene complex formation on palladium tripyrrins (crystallographic figure adapted from Ref. 431).

assumed to carry a weakly bound molecule of dichloromethane at the fourth coordination site. When treated with diazoalkanes, these cations are sufficiently reactive to form carbene complexes **422** and **423** (Figure 107).[431] Coordination compounds of alkylidene ligands with the d^8 transition metal ions Rh(I) and Ir(I) have become available in recent years, and the structural and spectroscopic properties as well as reactivity patterns are known for several examples. In addition, a large and constantly growing number of Pd(II) and Pt(II) complexes of Fischer- and Arduengocarbenes have been reported in much detail. Surprisingly, though, Pd(II) complexes of non-heteroatom-stabilized carbene ligands have remained unknown so far, with the exception of **422** and **423**. Pd(II) carbenes have, however, been postulated as the reactive intermediates in the Pd(II)-catalyzed cyclopropanation of alkenes.

Four-coordinate Lewis base adducts with CH_3NC, *t*$BuNH_2$, PMe_3, PEt_3, and P*i*Pr_3 **424**–**432** have been prepared from mononuclear cations **420** and **421** and

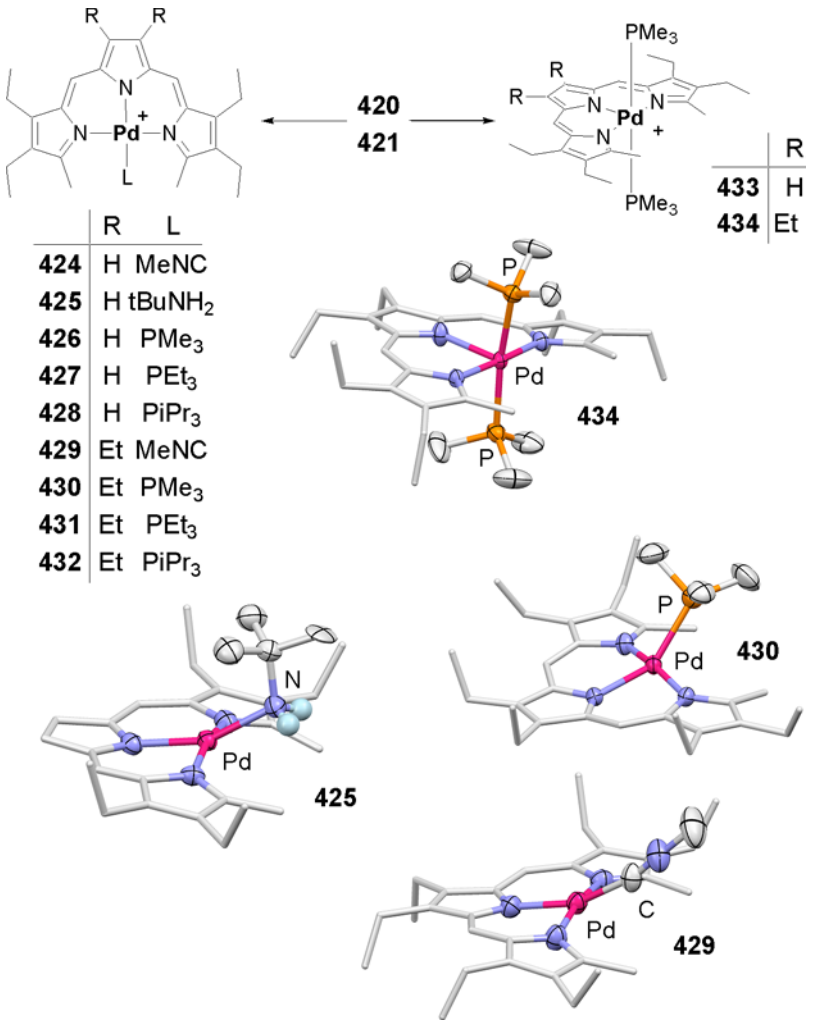

Figure 108. Molecular structures of four- and five-coordinate palladium tripyrrin complexes (crystallographic figures adapted from Refs. 430 and 432).

were analyzed by X-ray diffraction.[430] With two equivalents of PMe_3, five-coordinate 18 VE (valence electron) complexes **433** and **434** were obtained; these are stable in the solid and in solution (Figure 108).[432] The square-pyramidal coordination of **433** and **434** results in an unstrained molecular structure and in elongation of the apical Pd–N bond to about 2.3 Å. Pd(II) ions usually form very stable square-planar 16 VE complexes, due to a high-energy nonoccupied $4d(x^2–y^2)$ orbital. Ligand exchange reactions on these tetracoordinate complexes always proceed via an associative mechanism, with a square-pyramidal or trigonal-bipyramidal 18 VE species being the reactive intermediate. As shown

by electrochemical methods, anionic 18 VE complexes play a major role in all important palladium-catalyzed C–C coupling reactions. In the past, many such five-coordinate Pd(II) species have been characterized in the solid state by X-ray diffraction. In solution, however, these compounds are mainly dissociated, and only four-coordinate 16 VE species could be observed directly. Again, tripyrrin derivatives **433** and **434** are the only exceptions to this rule. In addition, the exclusive formation of a stable five-coordinate complex seems to be characteristic of the PMe_3 ligand and was observed also in a series of cationic cobalt tripyrrines.[433]

With one half equivalent of $NaBAr^F$, only every second trifluoracetato ligand of **149** and **150** is exchanged, and the system stabilizes in dimeric double-decker trifluoracetates **418** and **419** with attractive structures (Figure 109). From these, dichloromethane complexes **420** and **421** can be obtained simply by adding the remaining equivalents of the reagent.[430] bti palladium complexes, on the other hand, are less reactive, and always form the chlorobridged double-decker compound **435** from a neutral precursor, regardless of the stoichiometry of the reaction.[434] A cationic mononuclear palladium bti species has been obtained from this double-decker with acetonitrile and additional $NaBAr^F$, while harder O donor ligands failed in this reaction. The ultrasoft $TeMe_2$ ligand, on the other hand, was

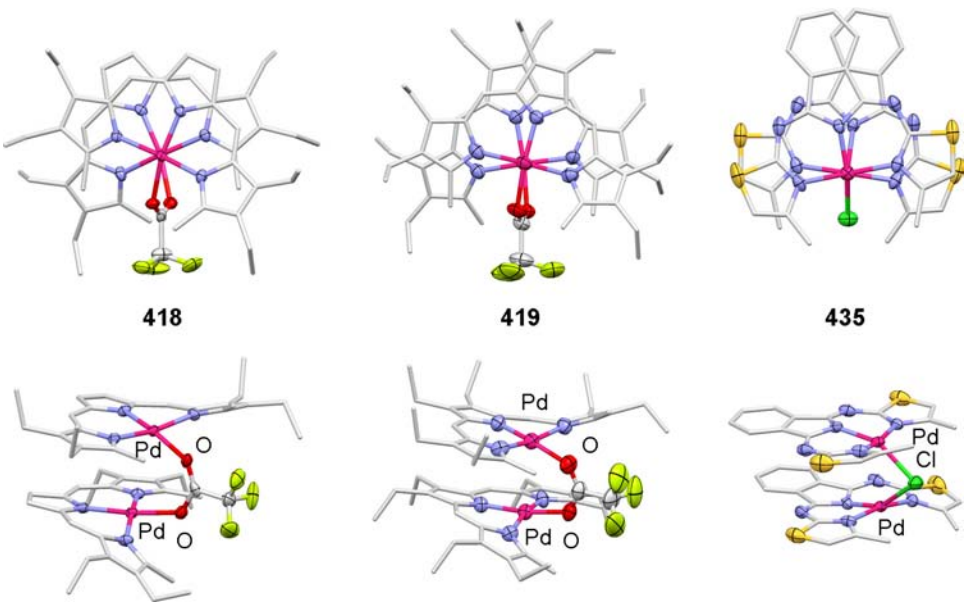

Figure 109. Selected representations from X-ray crystallographic analyses of cationic palladium tripyrrin and bti complexes with double-decker structures. (Adapted from Refs. 430 and 434).

reported to displace the bti ligand and form a cationic complex $[PdCl(TeMe_2)_3]^+$ under these conditions.[435]

B. Intramolecular CH Activation

Palladacycles constitute an important class of organometallic species. Despite their historical role in the development of organometallic chemistry, cyclometalated palladium(II) compounds have found entry in many different fields, such as organic synthesis, catalysis, and materials science. In addition, many of the nowadays-indispensable palladium-promoted organic transformations are considered to proceed via palladacyclic intermediates. A cyclopalladation reaction was reported to occur yielding square-planar 6-Mebpi complex **436**, in which a deprotonated isoindoline anion coordinates as a tridentate pyridinium C,N,N pincer ligand (Figure 110).[197] The finding is in contrast with the classical N,N,N coordination observed with sterically hindered bti ligands and indicates an increase in intramolecular strain in going from the bti or tripyrrin to the bpi ligand framework. The related reaction of H(6-Mebpi) with palladium acetate results in the high-yield formation of the cyclometalated and insoluble tetranuclear dimer **437**.[198] This latter transformation was monitored by ^{1}H NMR spectroscopy and was found to proceed stepwise via a classical Werner-type N,N,N chelate and a mononuclear cyclometalated C,N,N chelate species.

An H(4,6-Me_2bpi) ligand was studied in which the steric encumbrance of the N,N,N and the C,N,N coordination scenario is of comparable strength. Both of the forms **438** and **439** could be isolated and characterized crystallographically.[436] It was reported that the addition of a second equivalent of palladium acetate to **438** resulted in irreversible formation of cyclometalated dimer **439**. Further studies with bai ligands with different degrees of intramolecular strain gave classical Werner-type compounds **440**, **441**, and **442**. Neither unstrained complex **440** nor pyrazine derivative **442** could be triggered to bind a second Pd(II) ion, and it was concluded that the second metalation step supports the C–H activation but does not induce it. In addition, compound **441** showed that the reactivity of the system is not sufficient for C–C activation (Figure 111).[198]

These findings on cyclometalated palladium bai complexes led to the development of a strategy for the preparation of unsymmetric C,N,N pincer complexes by a stepwise condensation to bis(arylimino)isoindolines and successive cyclopalladation. Several new species from this class were prepared, characterized, and visualized by X-ray crystallographic analyses.[205] The simple phenylimino-substituted bai ligand H(phpi) reacts with palladium(II) acetate upon cyclopalladation to yield the expected complex **443**, but is subject to side reactions. As a product from one such side reaction, a dimetalated species **444** was detected

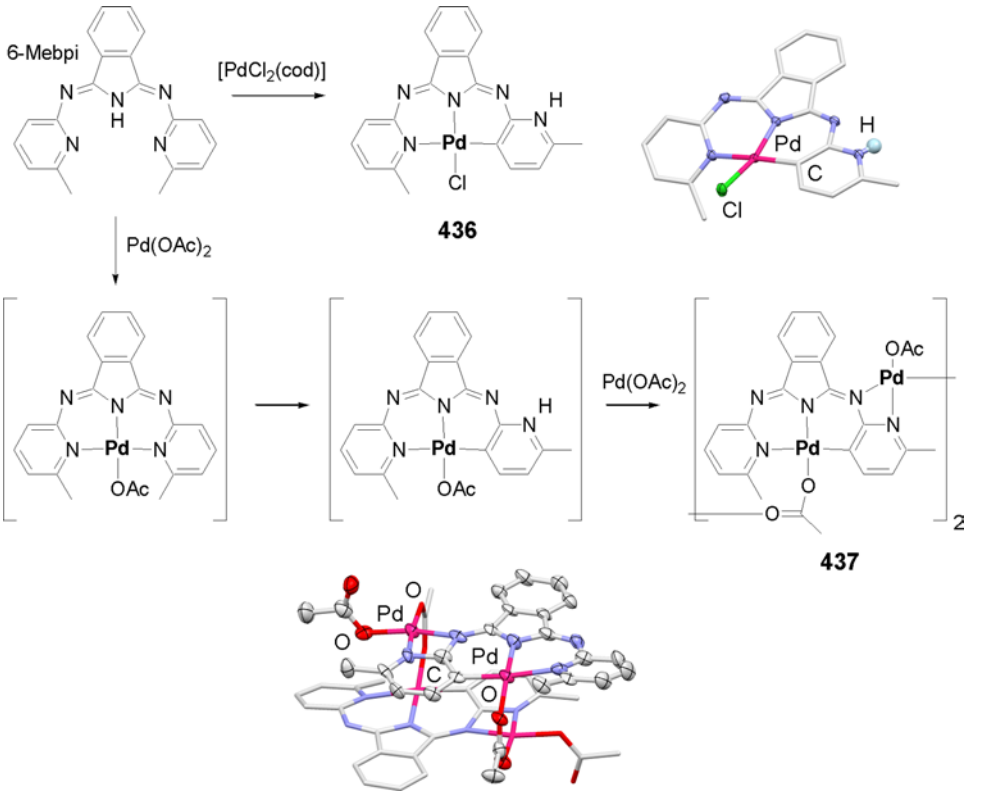

Figure 110. Cyclopalladation reactions with the H(6-Mebpi) ligand (crystallographic figures adapted from Refs. 197 and 198).

crystallographically. If the coordination site for a second palladium atom, i.e. the 2-position of the phenyl group, is substituted by methyl or even by iodo, the respective ligands H(2-tolti) and H(2-Iphti) react cleanly and produce the desired mononuclear products **445** and **446** in acceptable yields. In this system, the iodophenyl group is not attacked by palladium(II) acetate but can easily be used for oxidative addition to the zerovalent palladium precursor $[Pd(PPh_3)_4]$ to yield an *exo* complex **447** (Figure 112).

The use of a H(bti) ligand with methyl groups at terminal positions led to the Werner-type compound **304** only. When these methyl groups were exchanged for *tert*-butyl substituents, however, the reaction took a different course, and a new compound **448** with C(sp^3)–H-activated *tert*-butyl group and S-coordinated thiazole donor in the *cis*-position was isolated (Figure 113).[201] The reaction was carried out using three equivalents of palladium acetate and was reported to proceed smoothly in a range of different solvents (acetonitrile, toluene, methanol, dichloromethane, etc.) at ambient temperature without any detected side products.

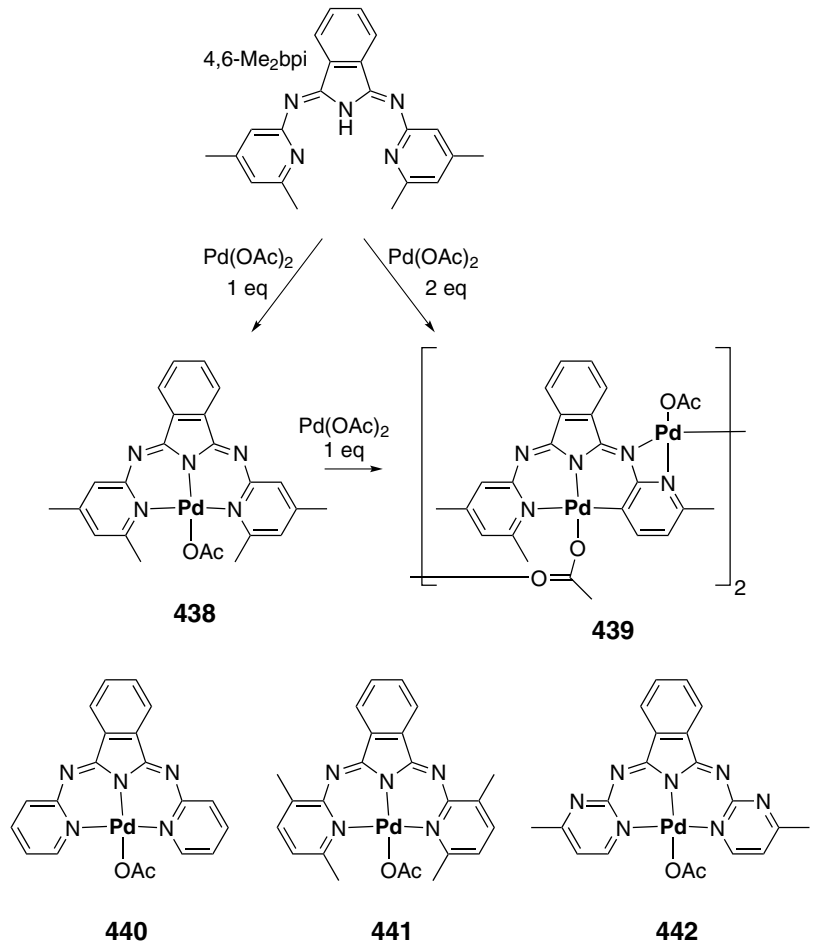

Figure 111. C–H activation and dimer formation studies on different bai ligands.

Both the C(sp^3)–H activation and the S(thiazole) coordination at palladium(II) are rare features in palladium chemistry. The thiazole was found to be bound only very weakly, and clean exchange of this donor with CO and pyridine to give **449** and **450**, respectively, has been observed.

C. Active Catalysts

Pincer complexes of palladium(II) are of general interest in the context of catalytic C–C coupling reactions. While so far no reports on catalytic properties of palladium chelates with "real" tripyrrole ligands have appeared, the more robust bai and bop systems have been the subjects of a number of reports. Compound **323**

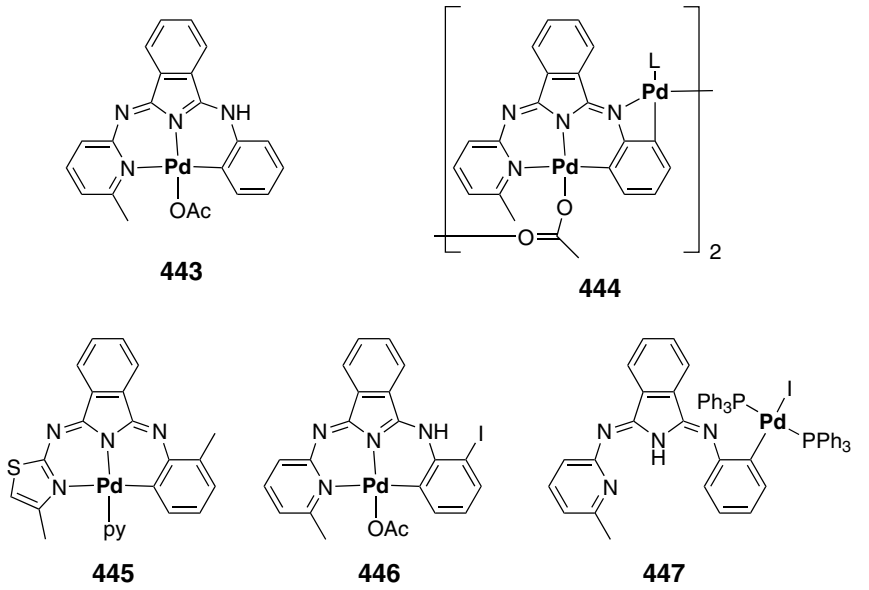

Figure 112. Cyclometalated palladium chelates **443**–**447** from unsymmetric bai ligands.

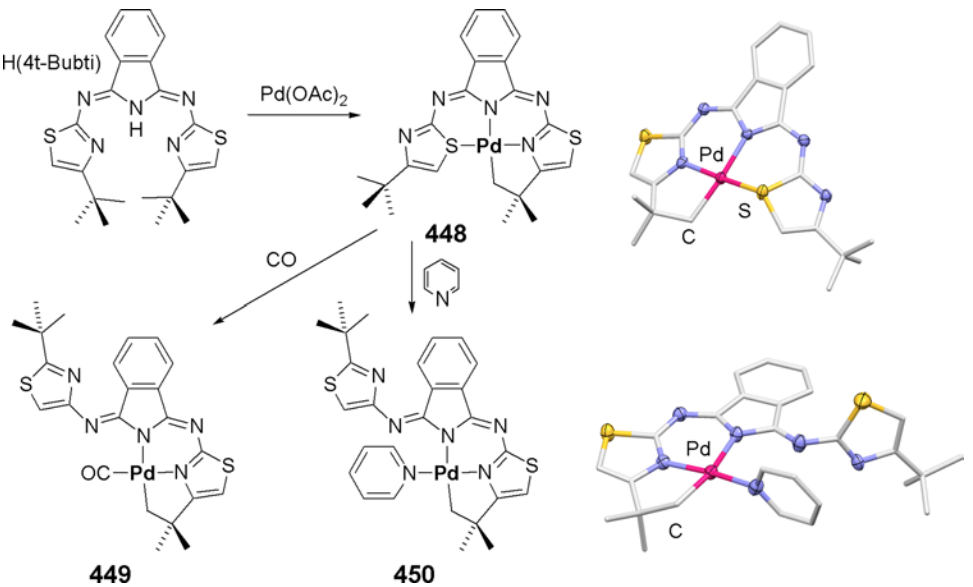

Figure 113. C(sp^3)–H activation and chemistry of hemilabile cyclometalated palladium bti **448** (crystallographic figures adapted from Ref. 201).

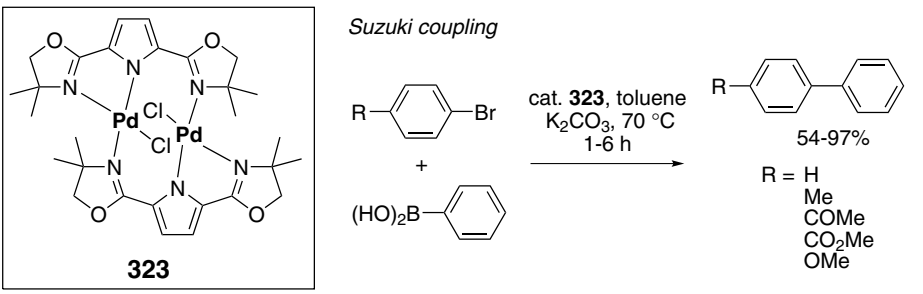

Figure 114. Catalytic performance of palladium bop dimer **323**.

was found to be a highly active catalyst in the Suzuki-type coupling of phenylboronic acid with aryl bromides at relatively moderate temperature (Figure 114). The new catalyst was found to be very stable under the conditions of the Suzuki coupling, and no palladium black was formed during the reaction. The catalytic reaction was followed by GC-MS, and 100% conversion was obtained with both activated and deactivated bromides after 1–6 hours. Decrease of the catalyst/substrate ratio to 10^{-5} still gave an 82% isolated yield of 4-bromoacetophenone and 54% 4-methoxyacetophenone after 4 hours, amounting to turnover numbers of 82,000 and 54,000, respectively. In contrast to the reactivity toward aryl bromides, the catalyst proved to possess only very low activity toward the corresponding chlorides, with the reaction effectively stopping after a few cycles at 110 °C.[437]

Compound **445** has been used as a precatalyst for Heck and Stille-type coupling reactions, as depicted in Figure 115. The catalytic performance was studied as a function of electronic and steric factors of the substrate. In the Heck reaction, the reactivity decreases as expected in the order iodoaryl > bromoaryl > chloroaryl, whereas an increase in steric repulsion has only a minor effect on the outcome of the reaction. The activity of **445** as a precatalyst is higher compared to palladium acetate, but does not reach the performance of some other palladium complexes that have been studied earlier. A similar picture is provided by the attempts to catalyze Stille coupling reactions. In this case, however, the influence of steric bulk was reported to be much more pronounced than for the Heck reaction. In all cases, the reaction mixtures turned dark upon heating, and the addition of mercury stopped the transformations immediately, indicating that the active species throughout is elemental palladium.[205]

The activity of **451** in the catalytic hydrogenation of C=C double bonds was tested for the reaction with styrene, 1-octene, and cyclohexene. As expected, the reaction proceeds fast for styrene and very slowly for the internal alkene, cyclohexene. A mechanistic scheme taking into account the possibility of imino N protonation during the cycle has been proposed (Figure 116). The stability of the palladium

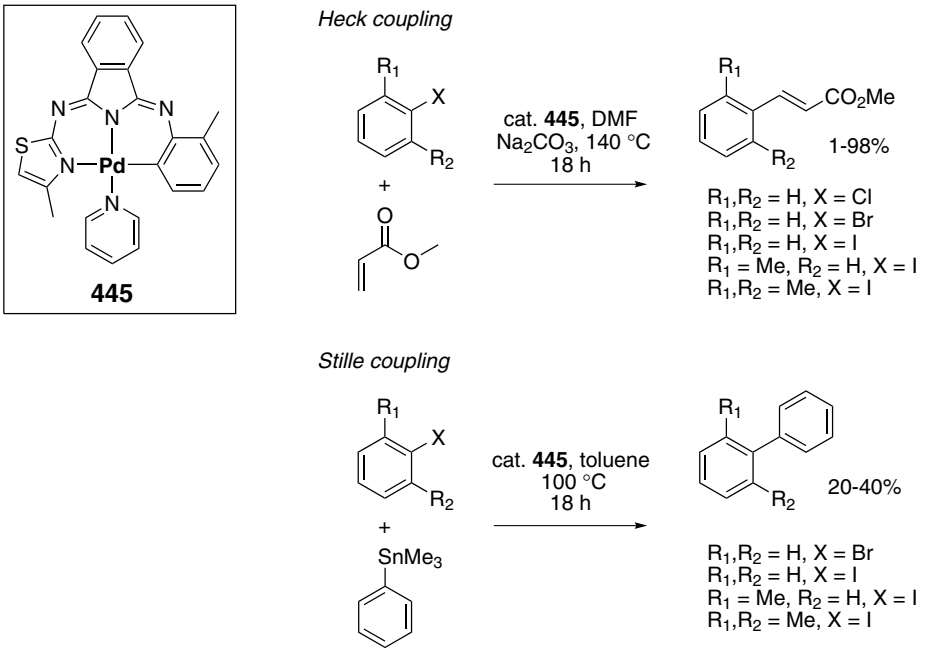

Figure 115. Catalytic performance of cyclometalated palladium bai **445**.

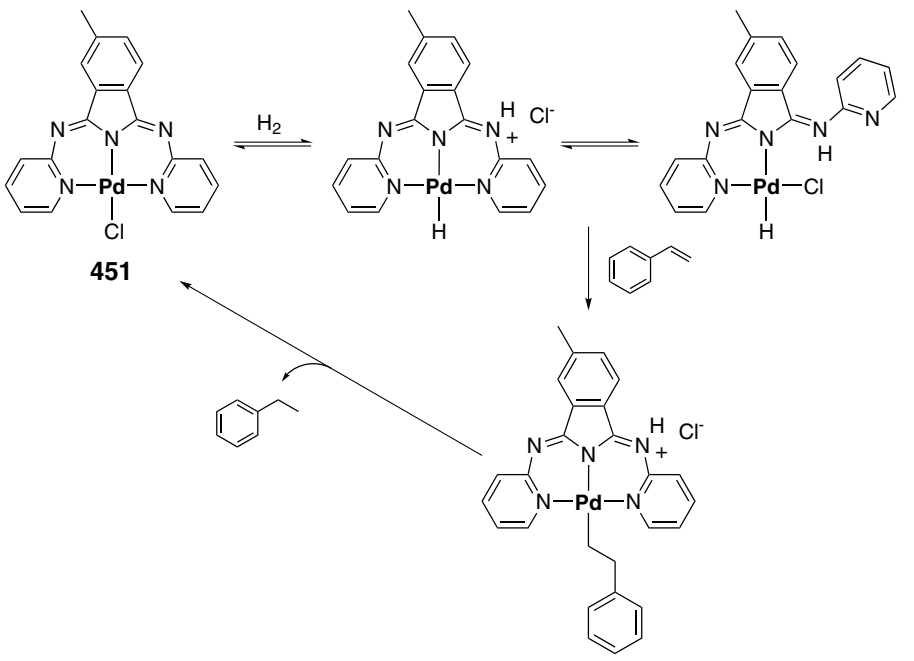

Figure 116. Mechanistic proposal for the catalytic hydrogenation of styrene by **451**.

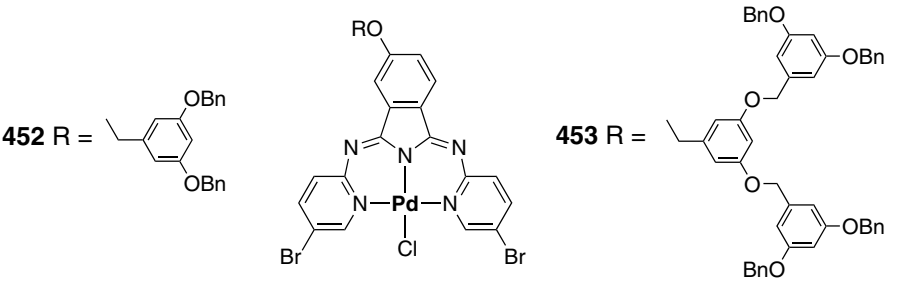

Figure 117. Dendritic palladium bpi hydrogenation catalysts **452** and **453**.

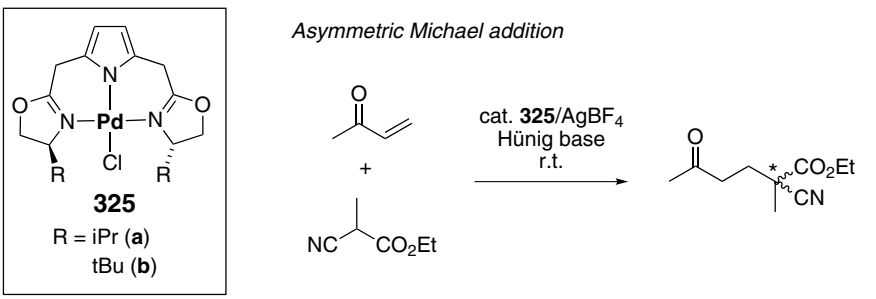

Figure 118. Asymmetric Michael addition catalyzed by chiral palladium bop complexes **325**.

complex, the reproducibility of the reaction kinetics, the different behavior toward the three olefins chosen as substrates, as well as the possibility of isolating the non-decomposed catalyst after several catalytic runs, provide circumstantial evidence for molecular catalysis with the bpi–palladium complexes in this case.[438]

Similar results were obtained with dendron-substituted complexes **452** and **453** (Figure 117).[439] A remarkable feature of these catalysts carrying dendritic wedges is the rapid isomerization of 1-octene to 2-octene, which for the second generation dendrimer catalyst **453** leads initially to an almost complete shift of the C=C double bond (> 80%) before the hydrogenation of the olefin(s) sets in.

Finally, bop complexes **325a** and **325b** were tested in catalytic asymmetric Michael addition of ethyl 2-cyanopropionate to methyl vinylketone (catalyst loading: 1 mol%) and were found to give maximum ee values of 43% and 21%, respectively, at low conversions (Figure 118).[209]

V. Biomimetic Iron Complexes

A. Intermediates and Products from Ring-Opening Reactions

Heme oxygenases (HOs) are a family of enzymes which catalyze the oxygen-dependent degradation of heme to biliverdin IX **9**, CO, and iron. Three molecules

of O_2 and seven reducing equivalents are required for this transformation. In mammals, HO has a key function in physiological heme metabolism, whereas in certain pathogenic bacteria it is used for iron uptake from heme obtained from the host. In contrast, in higher plants, cyanobacteria, and algae, HO functions in the biosynthesis of linear tetrapyrroles such as the phytochrome chromophore, or phycocyanobilin. More recently, an additional role of certain HOs in the production of CO as a neurotransmitter has been speculated on. This natural heme degradation process is still one of the major driving forces for linear tetrapyrrole research, in particular with respect to their coordination properties. The mechanism of the transformation of heme to biliverdin IXα **9** is complex and has been studied ever since the enzymatic nature of the reaction was unraveled in 1963. The current proposal for vertebrate HO action consists of three distinct oxygenation steps and is shown in Figure 119.[5,8,9] Several details of this scheme are, however, still a topic of lively debate.[440]

An iron biliverdin intermediate has been proposed as the direct precursor to biliverdin,[12] but all initial attempts to prepare such iron bilindione derivatives or related tetrapyrrole iron complexes failed because of the remarkable and unexpected instability of the products.[214,219] Recent protein crystallographic studies

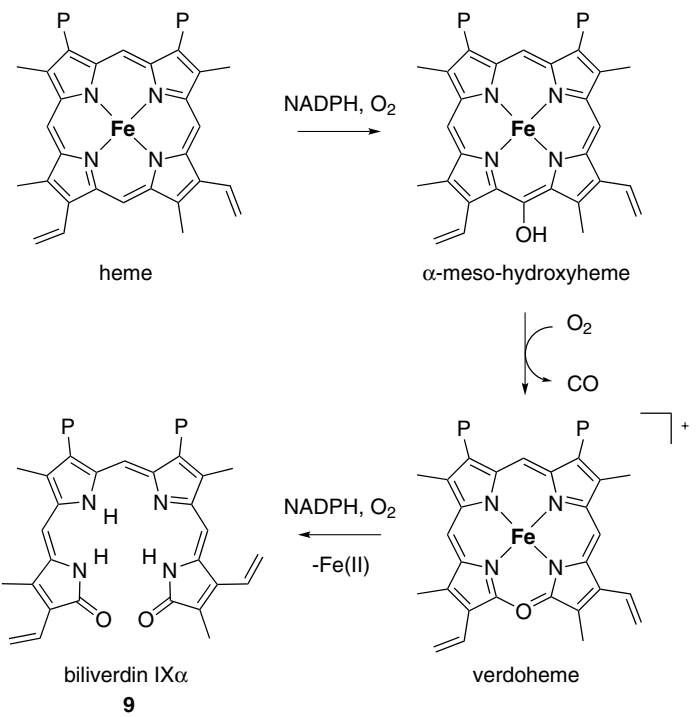

Figure 119. Distinct steps of HO action.

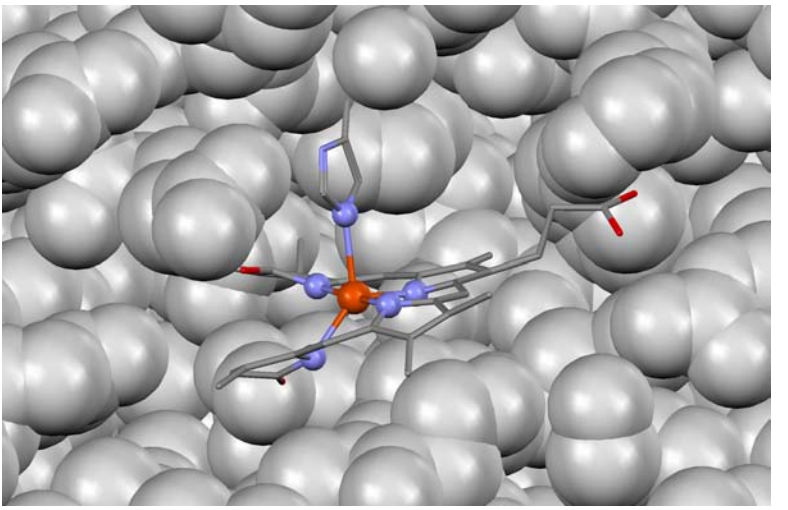

Figure 120. Iron biliverdin IXα embedded in the active site of rat HO-1 (PDB code 1J2C; adapted from Ref. 6).

have now established the presence of iron biliverdin IXα and free biliverdin IXα in the protein matrix at different stages of the reaction.[6,7] Details of these studies show the influence of the increase of required space for the ring-opened compounds upon the flexibility of the protein pocket and suggest a stepwise mechanism in which iron is released from the complex before dissociation of the biliverdin. An iron biliverdin moiety bound in the protein pocket of rat HO-1 is shown in Figure 120.

Whereas all attempts to prepare iron biliverdins directly by the coordination of iron to linear bilindiones or formylbilinones failed, the biomimetic oxidative ring-opening of a verdoheme analog was successful and led to the observation of iron bilin model compounds with the oeb ligand. Figure 121 summarizes the results obtained on products of iron(II) octaethylporphyrin **453**. Upon treatment of the intact porphyrin **453** with O_2 and a reductant (ascorbate, hydrazine) in pyridine, an immediate reaction to oxophlorin **454**[441] and a further reaction with concomitant CO extrusion to verdohemochrome **455** occur.[442] Compound **455** has been characterized as a diamagnetic, low-spin iron(II) complex. NMR investigations of the reaction mixture, however, indicated the presence of a paramagnetic contaminant which was identified as iron(III) bilindione complex **456**. If the pyridine-containing solvent is removed from solutions of **456** *in vacuo*, the compound is found to undergo a dimerization to bilindione complex **457**. Dimer **457** was the first-ever crystallographically characterized iron bilindione species.[442]

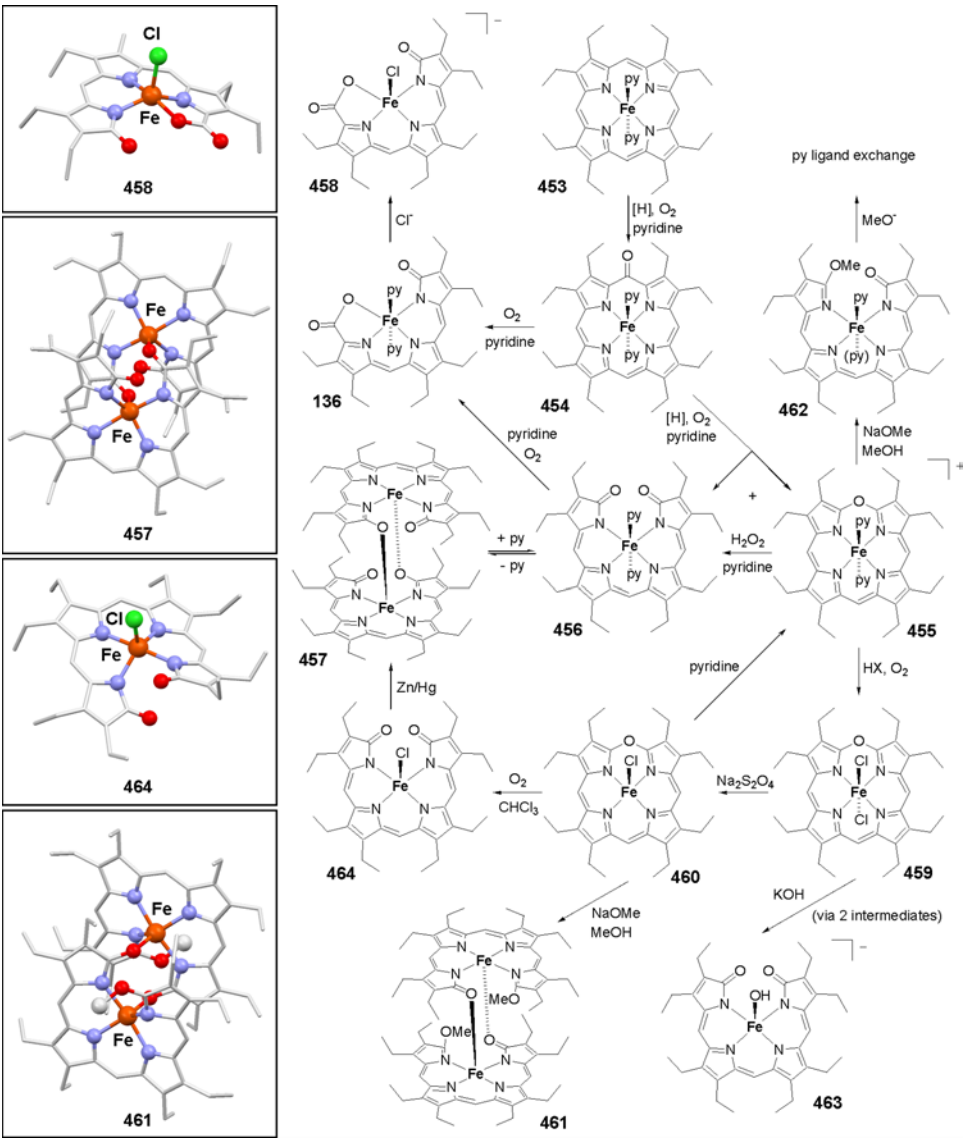

Figure 121. Reactivity scheme and structures of crystallographically characterized products of coupled oxidation processes starting from iron octaethylporphyrin **453** (crystallographic figures adapted from Refs. 442–444 and 446).

Iron(III) derivatives **456** and **457** turned out to be very labile and sensitive to O_2. The oxidative decomposition of **456** and **457** in the absence of excess reduction equivalents splits off one of the terminal pyrrole subunits and leads to tripyrrinone carboxylate species **136**.[443] Tripyrrinone **136** is also formed directly

from oxophlorin **454** under the same conditions. Upon exchange of the pyridine coligands with chloride anions, anionic iron chelate **458** formed, and was analyzed by means of X-ray crystallography.

When iron(II) verdohemochrome **455** was treated with O_2 in the presence of chloride or bromide anions, dichloroiron(III) verdohemochrome complex **459** or the corresponding bromo derivative was isolated. These iron(III) species were readily reduced, with loss of one halogen atom to chloro (or bromo) iron(II) derivative **460**.[444] Treatment of **460** with pyridine recovers the starting pyridine adduct **455**, while the addition of sodium methoxide in methanol yields an inert and insensitive Fe(II)–monolactim ether complex, which was isolated and crystallographically characterized as dimer **461**. The reaction of verdohemochrome **455** with sodium methoxide and of **459** with potassium hydroxide have been studied in more detail by proton NMR spectroscopy.[445] Compound **455** has been found to open its macrocycle upon treatment with the methoxide nucleophile to yield monolactim ether **462**, which is then subject to pyridine ligand exchange processes. Iron(III) derivative **459** reacts with the hydroxide ion via two intermediate steps (ligand exchange and deprotonation) to give anionic hydroxoiron(III) bilindione **463**. The exchange of chloro vs. hydroxo ligands at the iron center was reported to occur with a large change in the resonance spectra, indicating a change in the electronic fine structure of the compound during this process.

Finally, if chloroiron(II) verdohemochrome **460** is treated with dioxygen in chloroform solution, the macrocycle opens spontaneously to give oxidized bilindione chelate **464**.[446] Compound **464** is stable and insensitive to oxidation and was characterized crystallographically. Upon reduction with a zinc amalgam a new species is formed, which was isolated and analyzed as dimer **457**.

Apparently, the reactivity of the iron(II) porphyrin is markedly enhanced after the first oxygenation step to afford oxophlorin **454**. Further products then form, following different decomposition and ring-opening cascades, depending on the respective conditions. Oxophlorin **454** thus plays the role of the activated species in the decomposition processes, similar to α-*meso*-hydroxyheme in the natural HO-catalyzed reaction (Figure 119). The activation of the porphyrin macrocycle may also be achieved by the introduction of a *meso*-situated amino functionality, as in **465**. Under simple aerobic conditions, **465** cleaves its macrocycle with remarkable ease.[447] Detailed NMR investigations have led to a proposed pathway for this decomposition, as depicted in Figure 122. Tripyrrinone complex **136** was identified as the final product, and a tetrapyrrolic N_3O coordinated species **466** was trapped and analyzed crystallographically.[103]

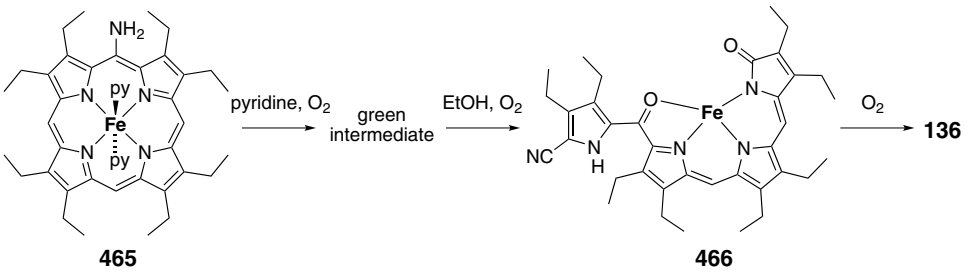

Figure 122. Intermediates of the aerobic ring cleavage of iron *meso*-aminoporphyrin **465**.

B. Direct Metalation of 2,2′-Bidipyrrins

Other than for the bilinones and related formylbilinones which cannot be metalated directly to give the iron chelate species, iron(III) complexes of hydrogen-terminated 2,2′-bidipyrrins were obtained from a metal insertion reaction, as shown in Figure 123. However, a successful preparation was achieved only if the ligand was prepared *in situ* from mono- and dipyrrolic components directly before the addition of a mixture of iron(II) and iron(III) precursors. This scheme was first developed for the synthesis of chloroiron derivative **467** of octaethyl-2,2′-bidipyrrin. In the reaction mixture, **467** is rather unstable and decomposes quickly in an aerobic and protic environment. The crucial point in the preparation turned out to be a quick crystallization step. As a clean compound and in the absence of protons and oxygen, **467** was reported to be a well-behaved complex which could be characterized in depth and employed in a number of reactivity studies. Anion exchange and introduction of the axial ion fluoride, bromide, and iodide ligands have been achieved using typical reagents and conditions for such transformations. The preparation of the complete series of halide complexes **467**–**470** is summarized in Figure 123.[448]

Results from single–crystal X-ray diffraction studies and powder diffraction data provide evidence for the presence of two crystal morphologies for the chloro, bromo, and iodo derivatives **467**, **469**, and **470**, respectively. In both forms, the molecules organize in weakly associated and slipped π-stacked dimers. These dimers, however, pack in either one (iodo complex **470**) or two orientations (chloro complex **467**), resulting in a triclinic or monoclinic crystal system, respectively, as depicted in Figure 124. Bromo derivative **469** was found to crystallize in either structure. Intriguingly, the molecular parameters of the FeN_4Br subunit differ significantly for these two isomorphs, as does the crystal density.[448,449] The different packing pattern thus appears to depend on the different steric requirements of the halide ligands.

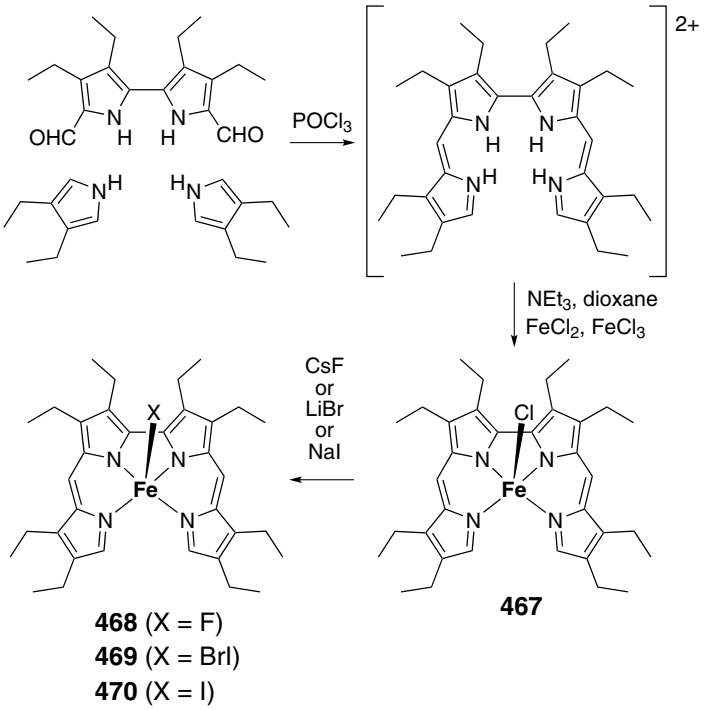

Figure 123. Preparation of chloroiron 2,2′-bidipyrrin **467** and salt metatheses to give halogen derivatives **468**–**470**.

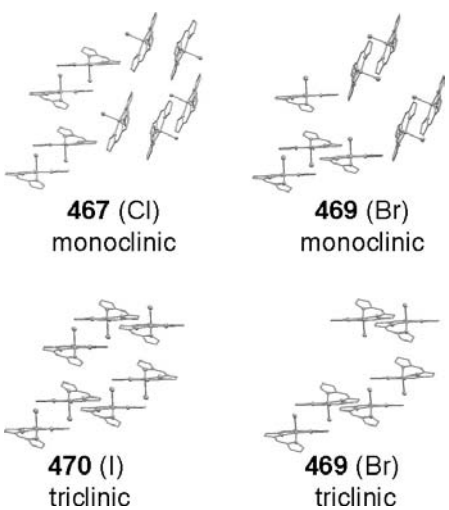

Figure 124. Representations of the crystal packing in monoclinic and triclinic crystals of halogenoiron 2,2′-bidipyrrins **467**, **469**, and **470** (ethyl substituents omitted; adapted from Refs. 448 and 449).

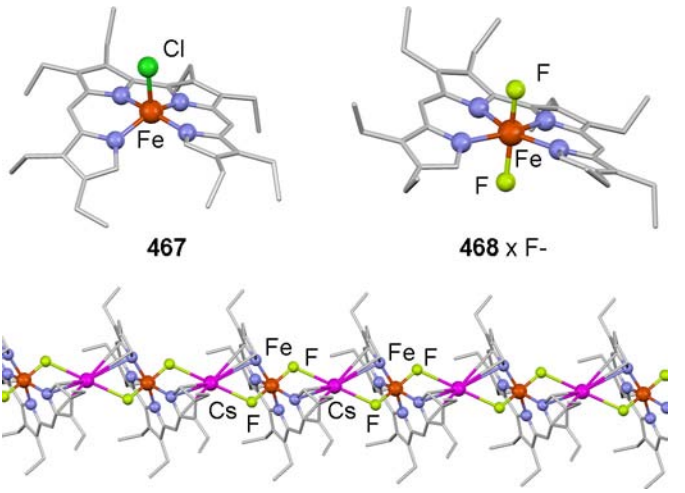

Figure 125. Selected molecular structures for mono- and polymeric iron 2,2′-bidipyrrin complexes. (Adapted from Ref. 448.)

The molecular structures of **467**, **469**, and **470** are very similar and are generally characterized by very short iron–nitrogen distances, in combination with elongated iron-halide bonds as compared to other iron porphyrinoids (Figure 125). Mössbauer and SQUID measurements performed on microcrystalline samples revealed the presence of an unexpected intermediate-spin ground state (S = 3/2) and a thermal excitation to a high-spin state (S = 5/2), and showed that the amount of high-spin admixture at a given temperature decreases with increasing size of the axial halide ligand. In solution, however, only a high-spin state (S = 5/2) can be observed for all species over the whole temperature range.

Fluoro derivative **468** was reported to be extremely sensitive to hydrolytic decomposition and could be crystallized only in the presence of excess reagent, i.e. CsF. Compound **468** forms 1D chains composed of Cs^+ ion-bridged anionic difluoroiron 2,2′-bidipyrrin moieties and some solvate molecules (Figure 125). The six-coordinate iron(III) atom in **468** × CsF now displays significantly elongated Fe–N bond lengths, and a Mössbauer analysis provided evidence for the expected high-spin ground state (S = 5/2). The compound slowly transforms in solution, as shown by ^{1}H NMR spectroscopy. This transformation yields a single new species with twice the number of resonance signals, and a comparison with the NMR spectra of the other halogen species **467**, **469**, and **470** indicated the dissociation of one of the fluoride anions and the formation of a pentacoordinate iron species.[448]

By treatment of the halogen derivatives with hydroxide ions, or simply by using a stronger base during the workup of the iron insertion step, μ-oxodiiron

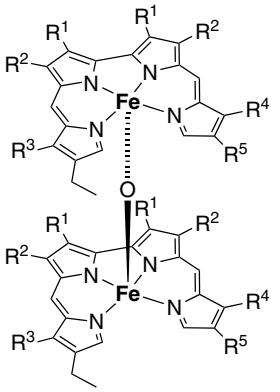

471 (R^1-R^5 = Et)
472 (R^1,R^3-R^5 = Et, R^2 = Me)
473 (R^3-R^5 = Et, R^1,R^2 = Me)
474a (R^1,R^2,R^5 = Et, R^3,R^4 = Me)
474b (R^1,R^2,R^4 = Et, R^3,R^5 = Me)

Figure 126. Overview of known μ-oxo di(iron 2,2′-bidipyrrin) complexes **471**–**474**.

derivatives have been obtained.[450] These species are well known in porphyrin and salen chemistry but have not been observed so far with bilindione ligands. With respect to the sensitive halogen derivatives **467**–**470**, such oxo-bridged dinuclear chelates are reported to be less labile and allowed the preparation of alkyl-substituted iron 2,2′-bidipyrrins beyond the octaethyl derivative. The known examples **471**–**474** are summarized in Figure 126. All compounds are weakly paramagnetic at ambient temperature, as expected for dinuclear high-spin (S = 5/2) iron(III) complexes with antiferromagnetic exchange and an exchange coupling constant in the order of –120 cm^{-1} (for the spin Hamiltonian $\hat{\mathbf{H}} = -2J\hat{\mathbf{S}}_1 \times \hat{\mathbf{S}}_2$). Compounds **471**–**474** thus show behavior analogous to those of iron porphyrins and iron salens.

Figure 127 provides an overview of the structural complexity of the μ-oxo dimers of iron 2,2′-bidipyrrins.[450,451] The most intriguing structural details are the different relative arrangements of the two tetrapyrrole helices of each molecule. In all cases pockets of different size and shape are formed close to the briding oxygen atom. These pockets are filled with guests, either solvent molecules (dichloromethane, water, pyrrole) or an ethyl side chain of a neighboring complex molecule. In two cases a hydrogen bridge between the guest and the host-oxygen atom was observed. For such hydrogen-bridged species elongated Fe–O bonds and reduced Fe–O–Fe angles result.

Chloro compound **467** and oxo-bridged dimer **471** were studied to probe the possible influence of steric strain on the lability of the bound iron atom in linear tetrapyrrole complexes. In the presence of air, the iron chelates react stepwise with nucleophiles (methanol or imidazolate) at the tetrapyrrole terminal α,ω-positions, presumably through the hexacoordinate species $[Fe(bdp)MeOH)_2]^+$ and $[Fe(im)_2(bdp)]^-$, respectively. The successive increase of strain at these positions is

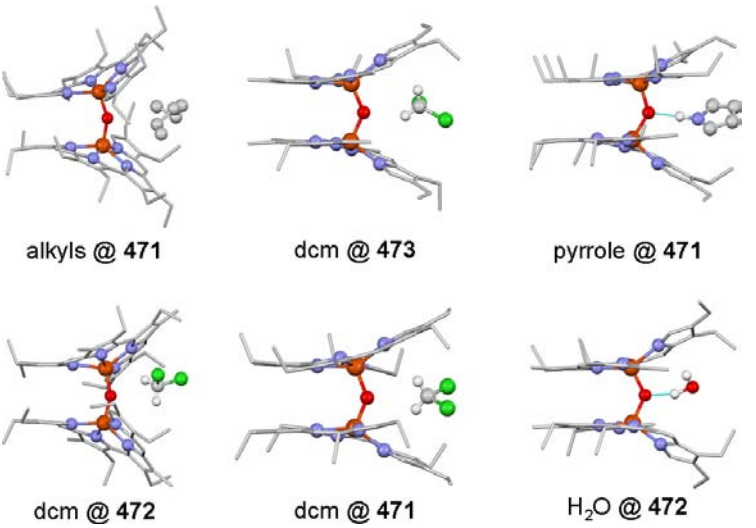

Figure 127. Molecular structures of μ-oxo di(iron 2,2′-bidipyrrin) complexes **471**–**473** with different hosts (dcm = dichloromethane; adapted from Refs. 450 and 451).

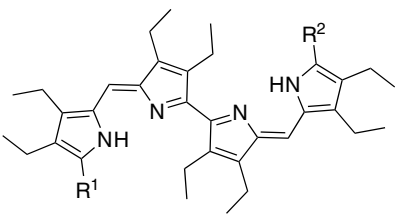

475 (R^1 = OMe, R^2 = H)
476 (R^1,R^2 = OMe)
477 (R^1 = im, R^2 = H)
478 (R^1,R^2 = im)

Figure 128. Products **475**–**478** from oxidative demetalation of iron 2,2′-bidipyrrins.

proposed to result in increasingly labile intermediates that spontaneously release the iron ion from the mono- or disubstituted tetrapyrrole ligands. In both cases, the respectively substituted free ligands **475**–**478** were isolated and characterized as the major products of the decomposition step (Figure 128).

VI. Fluorescent Boron Derivatives (OligoBODIPYs)

Boron dipyrrins (BODIPYs, also called boron dipyrromethenes or boraindacenes) constitute a class of boron chelates with a dipyrrin ligand (usually with a BF_2 subunit) that are currently attracting increased interest in many research areas owing to their advantageous photophysical properties.[23,452,453] BODIPYs are very versatile and have found use as light-stable functional dyes in a variety of different applications, such as laser dyes, fluorescence switches, or biomolecular labels. While many simple BODIPY derivatives are known and numerous compounds

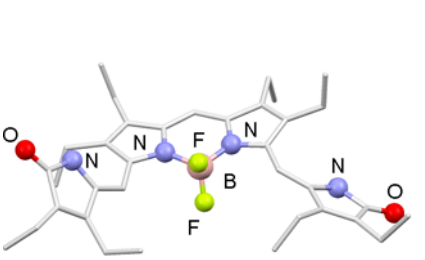

479

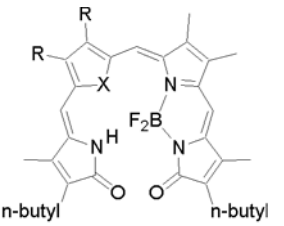

480a (X = NH, R = Me)
480b (X = NMe, R = H)
480c (X = O, R = H)
480d (X = S, R = H)

Figure 129. BF_2 chelates of bilindione ligands **479** and **480** (crystallographic figure adapted from Ref. 367).

are even commercially available, only a limited number of BF_2 complexes with linear tetrapyrroles have been described so far. The first such complex was the difluoroboron derivative of octaethylbilindione ligand **479**, which forms as a strongly fluorescent species upon treatment of H_3oeb **11** with boron trifluoride etherate and triethylamine.[367] A crystallographic analysis was performed and revealed that the central dipyrrin unit of the tetrapyrrole ligand **479** is borylated (Figure 129). A series of other bilindiones as well as some partially hydrogenated species of the urobilin type have also been used in coordination studies with boron trifluoride.[254,454] These reports discuss the formation of two isomeric forms, one with a central BF_2 unit and one unsymmetric, in which one pyrrole and one lactam ring are coordinated. This new coordination mode leads to complete fluorescence quenching and has been enforced by the exchange of one NH vs. a NMe, O, or S functionality. Examples **480a**–**480d** are shown in Figure 129. As a useful property, these compounds show characteristic through-space ^{19}F–^{1}H couplings in the ^{1}H NMR spectra which have allowed analysis of different solution structures in some depth.

While bilindiones have been found to bind exclusively to one BF_2 unit, two such entities may be introduced into artificial linear tetrapyrroles of the 2,2′-bidipyrrin type. Species such as **481** (Figure 130) may also be regarded as covalent dimers of the basic BODIPY luminophore and have therefore been named BisBODIPYs. The solid state molecular structure of these dimers and the relative orientation of the subunits have been illustrated by several X-ray diffraction studies which showed that the BODIPY subunits of the molecules are conformationally restricted in a chiral, almost orthogonal arrangement.[455] Two of the fluorine atoms are found in close contact with each other and a ^{19}F NMR experiment has shown a characteristic through-space coupling between these atoms in solution. Further ^{19}F–^{1}H and ^{19}F–^{13}C through-space couplings are found

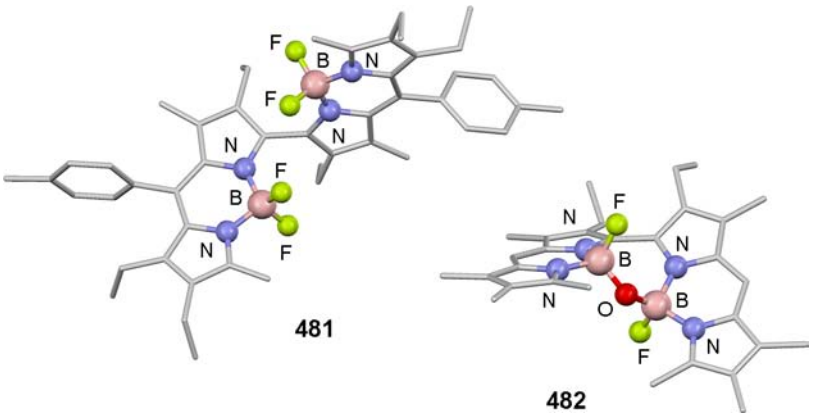

Figure 130. Molecular structures of BisBODIPY **481** and hydrolysis product **482** based on 2,2′-bidipyrrin ligands. (Adapted from Refs. 268 and 455.)

in other spectra and have been investigated in detail and used for a solution structure determination.[456,457] All BisBODIPYs exhibit a clear exciton splitting in the absorpiton spectra with maxima at about 490 and 560 nm, and are highly luminescent with an intense emission band at around 640 nm. The Stokes shift, which is the difference between the maximum of the lowest-energy absorption band and the maximum of the emission band, has a typical value of 5–15 nm for simple BODIPYs, whereas this value increases to 80 nm or more for the dimers, along with a slight decrease in fluorescence quantum yields and lifetimes. In addition, some triplet state is excited in the dimers while only singlet photophysics is known for simple BODIPYs.[458] A derivative with biomimetic di(methylpropionate) substitution has also been described. Hydrolysis of the ester groups does not, however, result in the desired dicarboxylate but in slow decomposition. The formation of an oxo-bridged species **482** as an early intermediate in this process has been made probable by a crystallographic study (Figure 130).[268]

Dinuclear boron species with 2,2′-bidipyrrin ligands consist of electronically decoupled but exitonically correlated BODIPY units and may be regarded as intermediate between linear tetrapyrrolic and functionally bridged bis- and oligoBODIPY dyes. The latter class employs the robust BODIPY unit as a building block in different molecular architectures. The designed combination of two or more of these chromophors allows one to tune special properties for a number of topical fields of application, such as sensors, energy transfer, or light-emitting polymers. Bis(BODIPY)s on the basis of binaphthyl bridges **483** were developed as dyes for optoelectronics and have been investigated as chirality sensors.[459,460] A related architecture with a bridging 2,2′-bipyridine subunit **484** has been reported to act as a photometric sensor for metal cations.[461] BisBODIPY **485** contains a

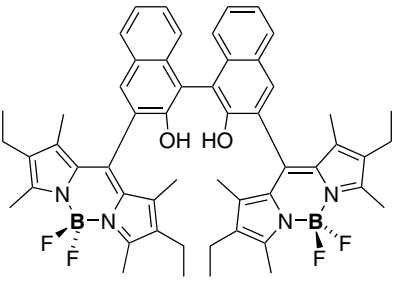

483

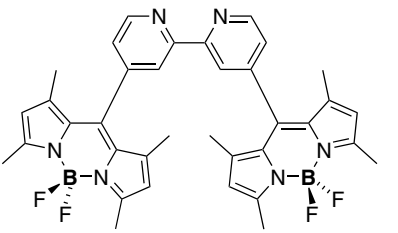

484

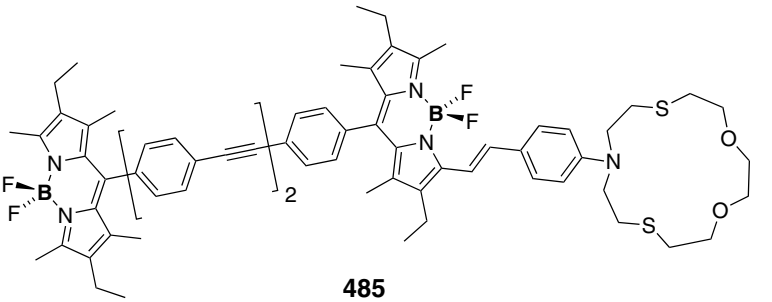

485

Figure 131. *Meso*-bridged BisBODIPY dyes **483–485** for sensor applications.

long and rigid di(phenylacetylene)-type linker and has been employed as a radiometric sensor for mercury.[462] Figure 131 gives selected examples for this class of tetrapyrroles.

The relatively simple preparation of monofunctionalized BODIPYs and their strong photoluminescence have led to different oligomeric architectures for the study of intramolecular energy transfer. Such compounds have often been called energy transfer cassettes and may be divided into two classes: through-space energy transfer cassettes[463–467] and through-bond energy transfer cassettes.[468–478] The former class has been used mainly in studies toward an understanding of the geometrical requirements for multiple dye antenna systems, while the latter class is currently discussed as being particularly valuable for applications in biosensing. Figure 132 summarizes examples from both groups of functional dyes.

Several studies describing the use of BODIPY units in the backbone of homo- and copolymers have appeared in the scientific literature. Poly(aryleneethynylene)s co-containing BODIPYs were synthesized and studied with respect to NLO properties.[479] Transition-metal-catalyzed polycondensation reactions were used to prepare similar homo- and copolymeric BODIPYs from a di-iodinated monomer. Depending on the bridging units, these polymers show very similar or slightly different photophysical properties with respect to the monomer, and the fluorescence quantum yields remain remarkably high upon polymerization.[480–483] Three

Through-space energy transfer cassettes

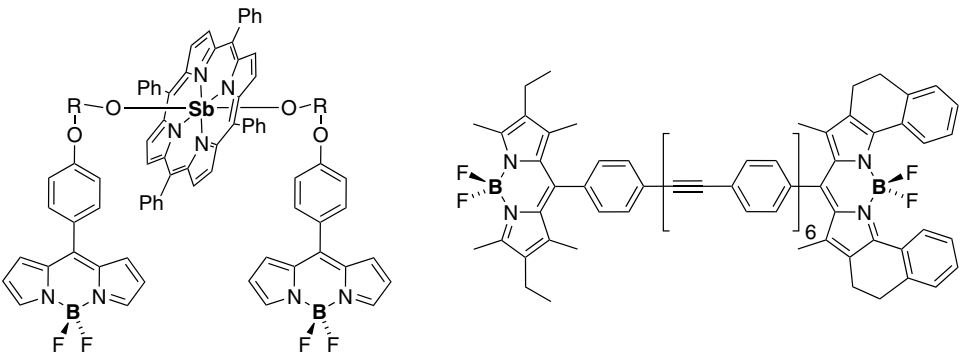

Through-bond energy transfer cassettes

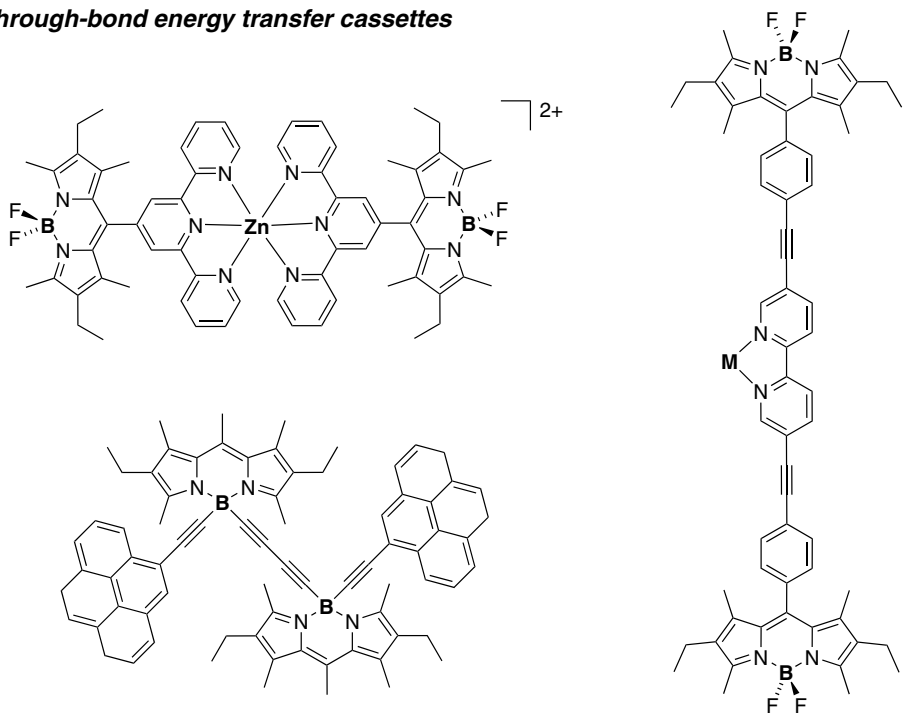

Figure 132. Selected examples for bis(BODIPY) dyes used in energy transfer studies.

examples of alternating fluorene and BODIPY-containing polymers were prepared under Suzuki conditions and studied for their optical properties. These polymers were found to display a sensitive fluorescent response to fluoride and cyanide anions, while no interaction with chloride, bromide, or iodide anions could be

monitored.[484] Copolymers of BODIPYs and dithiophene units have been prepared and were tested for application in OLEDs.[485,486] Polymers with BODIPY units as side chains have also been reported,[487,488] and one example of a polymer with the boron atom in the main chain is known.[489]

VII. Macrocyclization Reactions

A. To Give Porphyrins

The formation of porphyrins upon metal ion insertions in methyl-terminated linear tetrapyrroles was reported as early as 1961.[272] This transformation, which originally led to copper porphyrins, has found multifaceted interest as a highly variable and reliable preparative entry to tailor-made porphyrins, and the systematic exploration of the scope and limitations of tetrapyrrole cyclization to porphyrins has been documented in many publications over about 40 years. As a general view the macrocyclization way to porphyrins proceeds by either the *a*,*c*-biladiene route or the *b*-bilene route (Figure 133). The two approaches give equally good results and have been extensively reviewed in the past.[490–493] Therefore, only the basic concepts and findings will be summarized here.

The cyclization of β-substituted α,ω-dimethyl-*a*,*c*-biladienes and α,ω-dimethyl-*b*-bilenes occurs spontaneously at ambient temperature upon treatment with excess Cu(II) ions and air in solution.[33,129,132,249,266,494–498] For all simple tetrapyrrole precursors copper porphyrins form and may be demetalated in a second step to give the free base porphyrins. The second methyl group is generally lost during the reaction and does not remain in the product under standard conditions. Terminal alkylacetate, alkylpropionate, or benzyl groups have been employed, and several intermediates as well as rearrangement products could be isolated from these attempts.[301,499,500] Some of these compounds, **486–488**, are shown in Figure 134 and point to particular reaction pathways during the porphyrin formation process. The reaction is very smooth and allows the introduction

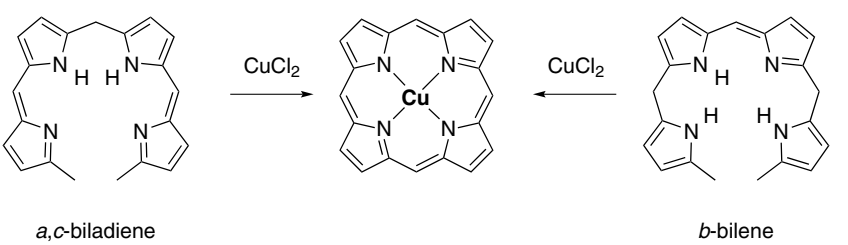

Figure 133. Schematic view of the *a,c*-biladiene and the *b*-bilene routes to copper porphyrins.

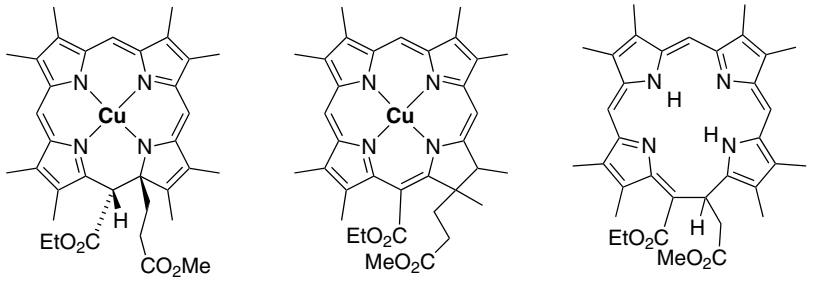

486 **487** **488**

Figure 134. Selected examples **486–488** of isolated intermediates and rearrangement products from the copper(II)-mediated ring closure of *a,c*-biladienes.

of a large number of different β-substituents and patterns. Only side chains with an increased sensitivity to oxidation processes such as vinyl groups may not be used. In addition, chlorin derivatives have been prepared from partially reduced precursors by this methodology.[252,501]

The course of the macrocyclization reaction depends strongly on the choice of the metal ion. Porphyrins form exclusively if copper(II) is used, while with nickel(II) only corrin-type products are isolated (see below). Trivalent ions of rhodium and chromium have been reported to perform well in the transformation to porphyrins, although for the latter the products do not contain a metal ion.[502,503] Oxidative conditions of any sort appear to be vital for a successful porphyrin synthesis. Remarkably, the ring closure of an α,ω-dimethyl-*a,c*-biladiene has been achieved without any metal ion present by electrochemical means.[504] This points to the role of the metal ion as a supporting template, which is not necessarily required.[505]

^{13}C isotope labeling studies have been undertaken in order to gain insight into the mechanism of the ring closure reaction.[506,507] The results prove that only one of the terminal methyl groups remains in the porphyrin as a *meso* methine moiety. From these studies and in agreement with the isolated intermediates from above, the mechanistic scheme in Figure 135 was proposed. In a first step a bilatriene **489** with a fully conjugated backbone forms upon oxidation of both *a,c*-biladiene and *b*-bilene precursors. The two routes thus meet very early in the reaction sequence, which explains the similar performance of the two linear tetrapyrroles. The bilatriene is proposed to exist in a helical conformation even without metal ion coordination. Such a templating action does not appear necessary but would certainly help to put the methyl termini in close contact. This bilatriene should also be very prone to one electron oxidation, and after deprotonation of the oxidized form an activated methylene-terminated π-system **490** is formed, which is proposed to undergo a fast electrocyclic ring closure. Further oxidation and dehydrogenation

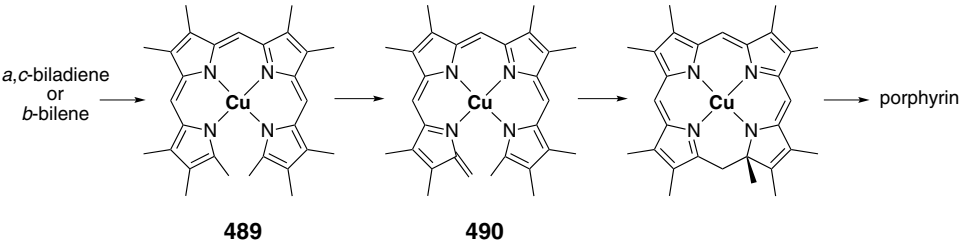

Figure 135. Mechanistic proposal for the formation of porphyrins from methyl terminated *a,c*-biladienes.

steps as well as a nucleophilic substitution at the pending methyl group finally result in the observed porphyrin.

B. To Give Corroles and Other Porphyrinoids with a Direct Pyrrole–Pyrrole Bond

Due to the unsymmetric C_{19} perimeter of the corrole macrocycle, there are generally two different linear tetrapyrroles which may serve as precursors for macrocyclization reactions to give this ligand: the methyl-terminated 2,2′-bidipyrrins and the hydrogen- or halogen-terminated *a*,*c*-biladienes. The first successful synthesis of a corrole followed the second route and used copper(II) ions as template and as oxidant.[273] As for the porphyrin synthesis, the choice of the metal ion is vital and dictates the outcome of the reaction. Nickel and palladium ions gave products with unclear constitution, while for copper, cobalt, and iron corroles **491** were obtained in good yields (Figure 136).[508,509] Cobalt corroles played a major role in the early development of this chemistry due to their relevance to potential vitamin B_{12} syntheses.

The strategy to form macrocycles by the oxidative formation of the direct pyrrole–pyrrole bond starting from a templated tetrapyrrole ligand has been reported as a successful strategy also for the syntheses of corrphycenes such as **492**. Two protocols are known to fulfill this task, both using copper(II) ions as the template and redox active reagent.[287,288] A macrocyclic nickel complex without a fully conjugated ligand backbone, 10,10′-dimethylisocorrole **493**, could be prepared by the same strategy (Figure 137).[285,286] This example indicates that electrocyclic reactions may be of lesser importance in this chemistry than is usually believed. All the above reactions proceed in minutes and at ambient temperature, and an open-chain metal complex or related intermediate could be isolated for any of the linear tetrapyrrole precursors.

Early attempts to prepare metal corroles from α,ω-dibromo-2,2′-bidipyrrin complexes and formaldehyde failed, and instead gave the first metal chelates of

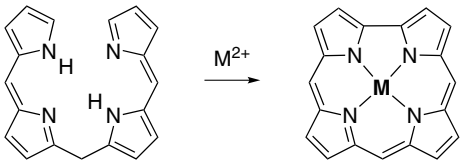

491

Figure 136. Formation of metal corrole **491** from *a,c*-biladienes.

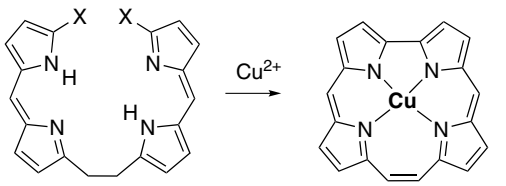

492

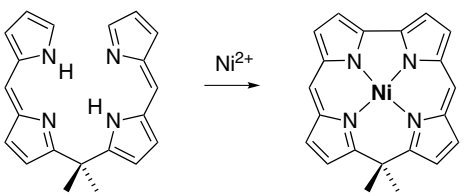

493

Figure 137. Formation of metal porphyrinoids **492** and **493** from 1,2-ethylene- and 2,2-propylene bridged bis(dipyrrin)s.

10-oxacorroles.[273,510] A study devoted to the preparation of related heterocorroles **494** succeeded in the syntheses of 10-oxa-, 10-aza-, and 10-thia-corroles, as shown in Figure 138. Treatment of α,ω-dimethyl-2,2′-bidipyrrins with divalent metal ions of zinc, copper, nickel, and palladium under the conditions used for the porphyrin synthesis from *a*,*c*-biladienes left the methyl termini untouched and yielded only the metal complexes of the linear tetrapyrroles.

The failure of metal corrole formation from methyl-terminated 2,2′-bidipyrrins was later related to the reaction conditions. Under more forcing conditions, i.e. at >150 °C and in the presence of air, manganese corroles **495** were obtained as the only nonpolymeric products (Figure 139).[511] Octa- and decasubstituted species form in yields of about 20% and were structurally characterized as the iodo manganese(IV) complexes.[512,513] The reaction has been applied also to the preparation of a biomimetic corrole with propionate substitution, albeit with a

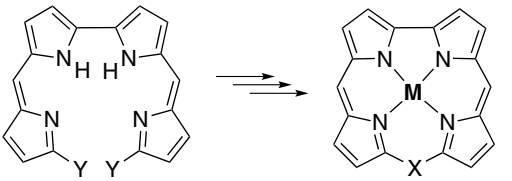

494

Figure 138. Single- and multistep formation of metalated heterocorroles **494** from halogenated 2,2′-bidipyrrins.

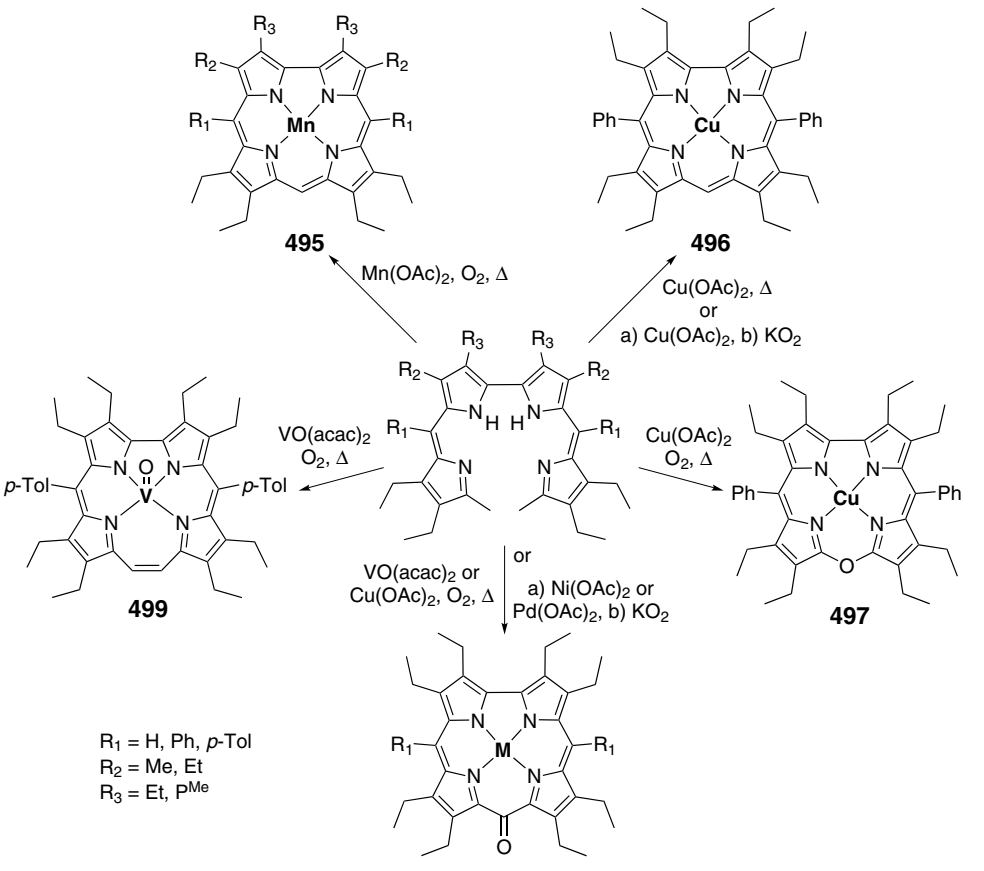

495 **496** **499** **497** **498**

Figure 139. Porphyrinoid macrocycles **495–499** obtained from α,ω-dimethyl-2,2′-bidipyrrins.

reduced yield.[268] Besides the manganese(II)/air system, copper(II) salts are also active in the formation of copper corroles **496** at elevated temperatures. Here, the absence of air is crucial; otherwise overoxidation products such as oxacorroles **497** and oxocorroles **498** form (Figure 139).[514] The superoxide anion may be used as an alternative oxidant at ambient temperature. The copper, nickel, and palladium complexes of the decasubstituted 2,2′-bidipyrrin react with superoxide to form copper corrole and nickel as well as palladium 10-oxocorrole **498**, respectively.[302] A 10-oxocorrole product also forms if vanadyl(IV) acetylacetonate is used as the templating agent at 150 °C in air. For this template, a second product was found and characterized structurally as vanadyl corrphycene **499**.[515] As both methyl carbon atoms are still present in **499**, this finding points to a difference in the reaction mechanism in terms of a twofold redox activation step for vanadium(IV).

The corrole formation from α,ω-dimethyl-2,2′-bidipyrrins was proposed to proceed via a mechanism similar to that accepted for the porphyrin formation discussed above. Other than in this case, however, a templating ion is necessary because 2,2′-bidipyrrins exist in a linear, stretched conformation and will not form macrocycles but rather polymers upon oxidation. In addition, the fully conjugated bidipyrrin chromophore is less prone to oxidation compared with the bilatriene moiety, so that higher temperatures or very strong oxidants are required to activate the tetrapyrrole. As for the porphyrin synthesis, the final step in the M/O_2-induced corrole-forming reaction is the loss of one of the methyl termini and aromatization of the tetrapyrrole. If rhodium or iridium ions are used as templates, this methyl group remains untouched and has been found in product complexes **500** (Figure 140).[424–426]

First attempts to form macrocycles from the hydrogen-terminated 2,2′-bidipyrrin complex **467** of iron have been reported (Figure 141). When **467** is treated with excess iodide in air, **470** is formed first by ligand exchange, followed by a slow oxidative ring closure to give norcorrole **501**. Compound **501** itself tends to dimerize and forms the mixed valence species **502** as the final,

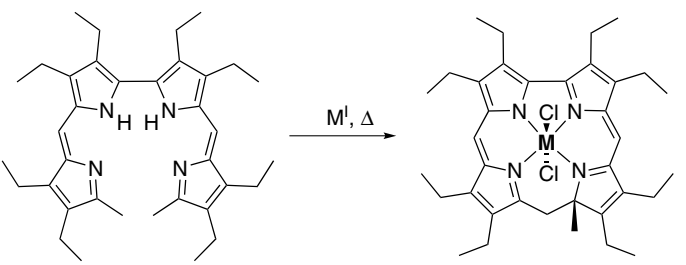

500

Figure 140. Macrocyclic rhodium(III) and iridium(III) chelates **500** from 2,2′-bidipyrrins.

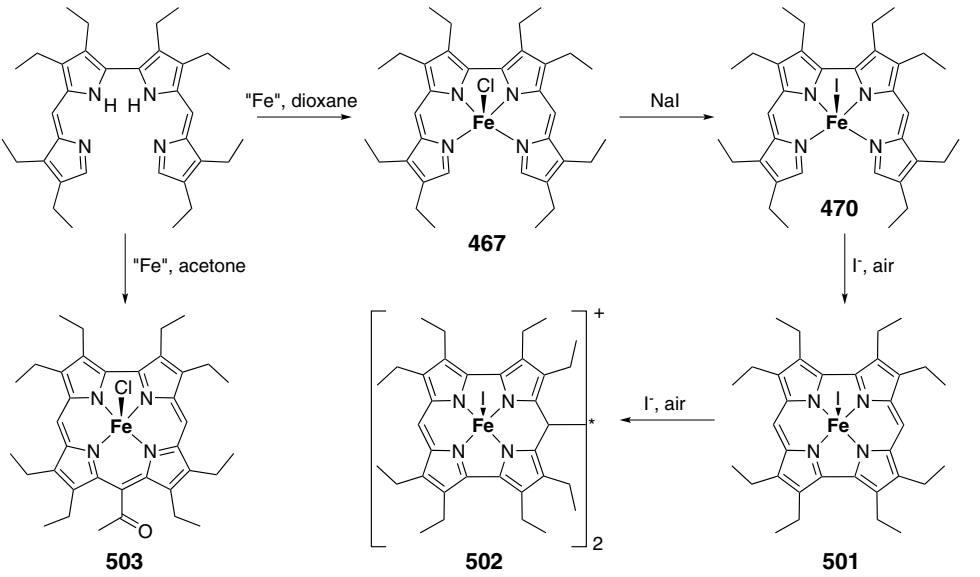

Figure 141. Macrocycle formation starting from iron 2,2′-bidipyrrin **467**.

crystallographically characterized product.[516] In a different example, 10-acetylcorrole complex **503** of iron was found if the iron insertion reaction of an *in-situ*-formed 2,2′-bidipyrrin was carried out in the presence of acetone. A multistep mechanistic scheme was proposed for this transformation; however, no proof has so far been given for it.[517]

Besides bilatriene- and bidipyrrin-based linear tetrapyrroles, a third class of tetrapyrroles, the bisnorbilins of basic structure **86** (Figure 21), have been reported to undergo metal-induced ring closure reactions to afford porphyrinoid products. Crucial to this reaction is the presence of one or two vinylogous aldehydes as terminal groups. As before, the employment of different metal ions results in the formation of different porphyrinoids, as depicted in Figure 142. Divalent copper and nickel ions transform monoformyl derivative **504** into formylisocorrole complexes of which copper derivative **506** could be isolated.[148] Palladium acetate instead induces a condensation to a rare porphyrinoid isomer, isoporphycene **507**. Similar metal isoporphycenes **508** with one additional formyl group form during the action of copper acetate, palladium acetate, or nickel acetate on disubstituted bisnorbilen **505**.[146,149]

C. To Give Corrins and Hydroporphyrins

One of the key transformations during the total synthesis of vitamin B_{12} is the ring closure to the corrin system, which was finally realized in the way shown for

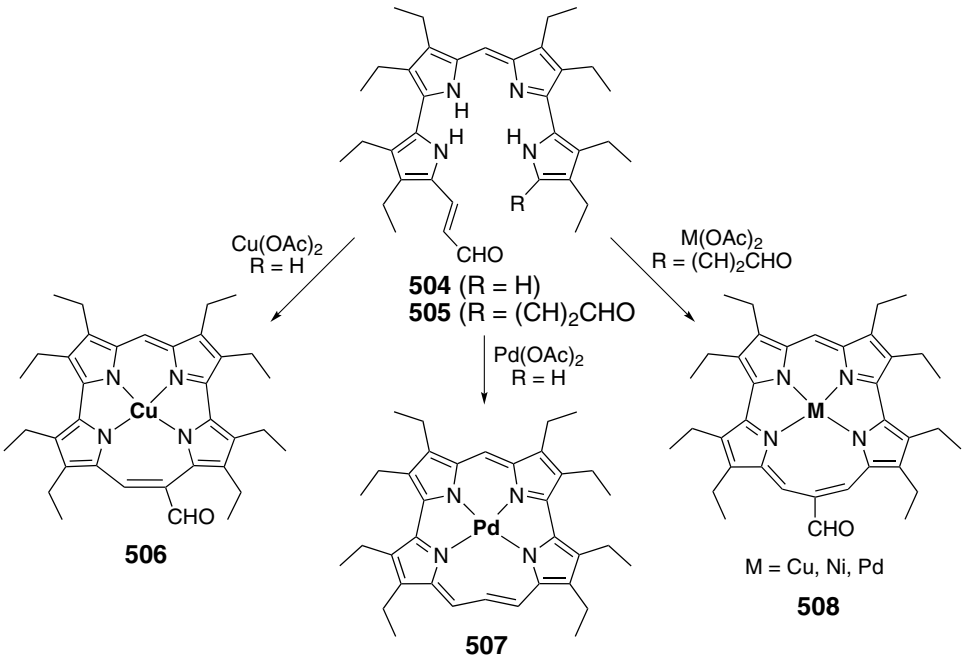

Figure 142. Bisnorbilin-originated macrocyclic complexes **504–508**.

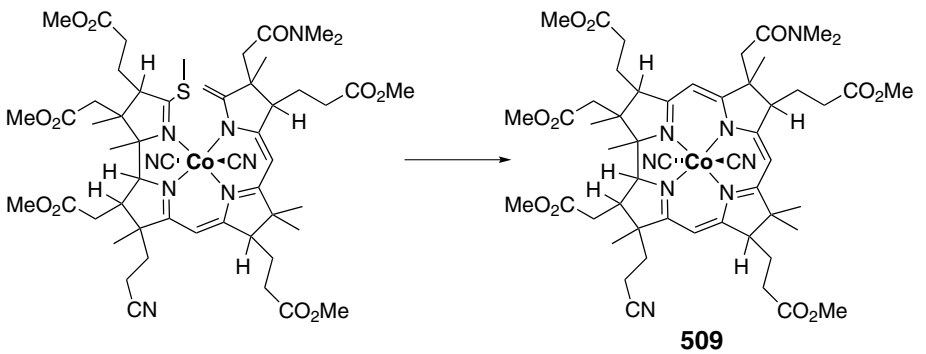

Figure 143. Cobalt-templated macrocyclization to bisnorcobyrinic acid **509**.

bisnorcobyrinic acid derivative **509** in Figure 143. As a biomimetic approach to this step, different ring closure alternatives starting from metal chelates of linear tetrapyrroles have been investigated in great detail. The employment of different metal ions and reaction conditions has allowed the preparation of the highly reduced macrocycle of vitamin B_{12} as well as of a wealth of related corrinoids with different degrees of reduction. The total synthesis of vitamin B_{12} including the many model studies performed during the process of it,[518–521] as well as a set of

model reactions starting from *a*,*c*-biladiene precursors, have been comprehensively and repeatedly reviewed,[492,493,522] and a summary of related work toward the preparation of hydroporphyrinoid systems has also appeared in the literature.[523]

The first strategy, similar to the successful approach described above, was to use an ethoxy instead of a methylthio derivative with the same regiochemistry. The ready cyclization of such a precursor had been demonstrated in a much-cited paper as early as 1964,[151] wherein the cationic nickel complex **387** of a reduced tetrapyrrole forms corrin **510** if treated under strongly alkaline conditions (Figure 144).

At about the same time, several reports of model studies on *b*-bilene- and *a*,*c*-biladiene-type tetrapyrroles started to influence the field. Most remarkably, the direct pyrrole–pyrrole junction was formed by this new approach, including the introduction of one or two stereocenters (Figure 145). Divalent nickel and cobalt ions served as template ions and allowed a straightforward and high-yield cyclization of mono- and dimethyl-terminated tetrapyrroles to give the corresponding corrins **511**–**513**.[274,276,283,494,524–526] The substituent pattern of the tetrapyrroles was widely varied, including such substituents as propionate and acetate esters or acids, or alkoxy groups, in order to find suitable derivatives which react selectively in later hydrogenation steps.[262,278–280,527,528] Most recently, this chemistry has been extended to benzopyrrolic species and zinc, copper, and lanthane template ions.[529] The

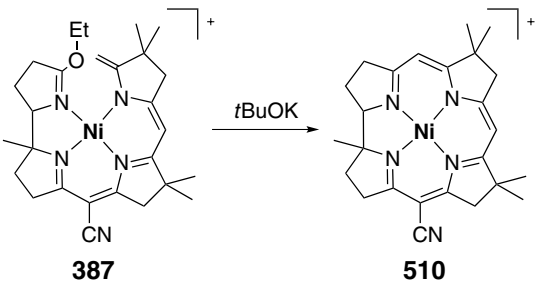

387 **510**

Figure 144. Nickel-templated macrocyclization to vitamin B_{12} model complex **510**.

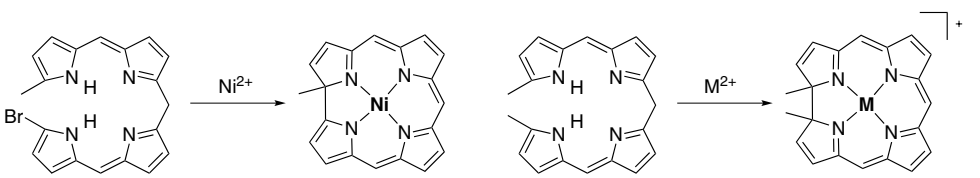

511 **512** (M = Ni)
513 (M = Co)

Figure 145. Nickel- and cobalt-templated ring closure of *a,c*-biladienes to corrin analogs **511–513**.

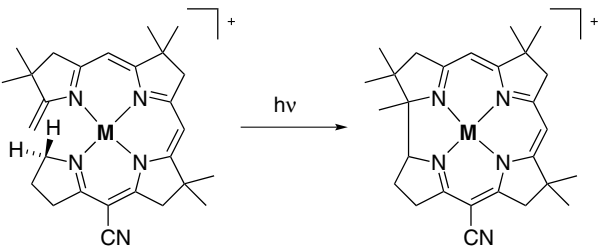

388

Figure 146. Photochemical ring closure of metal chelates **388**.

attempted hydrogenation chemistry, however, did not result in the desired products.[305,530] As a second transformation, methylations were attempted on a simple nickel bilin of this class, and the formation of a ring-opened product carrying one or two methyl substituents at the central *meso* position was reported.[531]

Apart from these drawbacks, a photochemical variation of this new ring closure strategy was successfully applied to partially reduced linear tetrapyrroles such as **388** (Figure 146).[532] Further research with similar systems was reported and revealed possibilities for exchange of the photochemical trigger with a redox step, with a proton-catalyzed reaction, or with a complex metalation/rearrangement process.[533–535] Different hydrocorrinoids were obtained from these studies. Furthermore, the isolation and characterization of a chlorin as a byproduct in one case led to the development of synthetic entries to hydroporphyrins.[152]

The templated macrocyclization reaction is not restricted to alkyl-terminated precursors and has been developed further toward alkoxy-terminated species. Such compounds can easily be obtained from natural bilirubin by simple peralkylation, and were cyclized to give the corresponding corrins with cobalt and nickel template ions.[213] A second important extension was found for ethoxycarbonyl-terminated *a*,*c*-biladienes. Unlike most alkyl- or hydrogen-terminated *a*,*c*-biladienes, helical complexes of ester-terminated linear tetrapyrroles can be obtained and isolated. Thus, besides nickel and cobalt derivatives, palladium and platinum chelates have been obtained and transformed into the corresponding macrocycles.[282,536,537] From this class of tetrapyrroles several β-hydroxylated and β-oxygenated derivatives related to the corrins were be obtained.[538]

VIII. Supramolecular Assemblies

A. Tripyrrin- and Bai-Based Coordination Polymers

Polymeric supramolecular assemblies of metalloporphyrins and metallophthalocyanines have had a significant impact in the field of metal-organic functional

materials. Well-established examples can be found, for example, in ferromagnetic and ferrimagnetic 1D coordination polymers of iron and manganese porphyrins with radical bridging ligands, or in π-stacked metallophthalocyanines which exhibit anisotropic electric conductivity after doping with iodine. The field of coordination polymers and metal-organic frameworks (MOFs) has seen a tremendous increase in research activity. Much of this research was motivated by crystal engineering and the preparative access to new functional materials with potential applications in gas storage (especially for dihydrogen) and drug delivery, and as single-chain magnets or conductors. These novel approaches have involved a number of porphyrin ligands so far, but artificial porphyrinoids have not been taken into account at all for this purpose. Two noteworthy exceptions to this rule can be found in the literature: the chemistry of coordination polymers from metalated dipyrrins and the chemistry of polymeric metallotripyrrins.[539,540]

The first indication of the formation of coordination polymers from tripyrrins came from a paramagnetic ^{1}H NMR study of homologous pseudohalide complexes of a nickeltripyrrin, **186**, **514**, and **515**. The spectral widths observed for the thio- and selenocyanate homologs **514** and **515** were markedly reduced with respect to NCO derivative **186**, while the line-broadening developed in the opposite direction. The signal pattern, however, appeared almost identical in all three spectra. Magnetic susceptibility measurements undertaken in dilute solutions by the Evans method indicated the expected temperature-independent behavior and magnetic moment for **186**, while for **514** a reduced magnetic moment in combination with an unexpected temperature dependence was found. These findings were attributed to the beginning of an oligomerization process of **514** and **515** in solution. The formation of coordination oligo- and polymers from thio- and selenocyanato derivatives of nickel tripyrrins was confirmed by the results of X-ray crystallographic work on **514** (Figure 147).[313] While isocyanato complex **186** crystallizes monomeric in an unstrained pseudoplanar geometry, the thiocyanate ligand in **514** is bound in a bridging μ(N,S) mode and connects the nickel tripyrrins to give one-dimensional strands with pentacoordinate nickel ions. The monomeric units are from an unstrained trigonal-bipyramidal geometry, which appears ideally suited for the formation of such chain structures. It was, however, noted that the Ni–N bond appears much stronger than the Ni–S bond according to structural parameters. A similar coordination mode of the $NCSe^-$ anion had been observed for **211**.

While the helical polymeric chains of **514** pack densely in the crystal lattice and leave little free space between the strands, the employment of other pseudohalide-bridging ligands results in the stabilization of functionalized inner surfaces. Dicyanamido and tricyanmethanido ligands, called dca and tcm, respectively, have been proven to be particularly useful in this regard. The treatment of

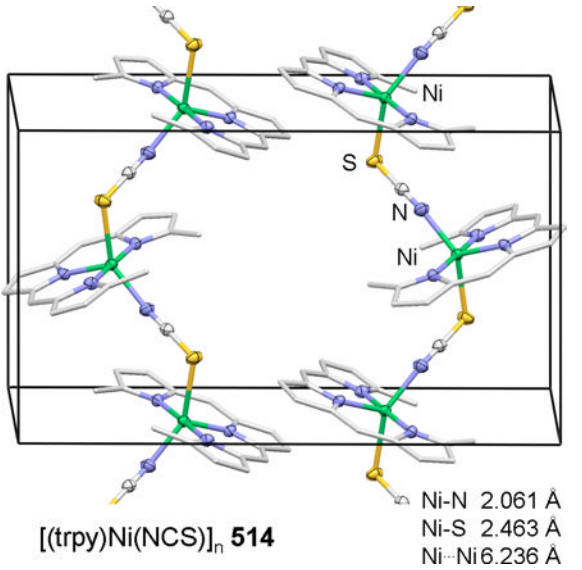

Figure 147. Crystallographic unit cell with strands of coordination polymer $[(trpy)NiNCS]_n$ **514** (β-ethyl groups omitted for clarity; adapted from Ref. 313).

cyanato derivative **187** with the sodium or potassium salt of either of these anions results in the immediate formation of a solid which can be filtered and washed to yield analytically clean material. Redissolution of the microcrystalline or amorphous material is possible in methanol, and careful crystallization yielded highly crystalline nickel(II)-based coordination polymers. Figure 148 presents two structurally distinct examples for a dicyanamido derivative **516** and a tricyanmethanido species **517**.[313] Both materials are characterized by functionalized inner surfaces, which differ from each other by both the functionalization and the dimensionality. The monomeric subunits of **516** and **517** show structural parameters typical of *high-spin* nickel(II) species. Unlike before, however, the binding between the nickel ion and the two external donors is of comparable strength. The dca and tcm bridges lead to large Ni···Ni separations of about 8.4 Å, and the tripyrrolic ligands of adjacent nickel tripyrrin subunits are separated by about 8 Å. The nickel tripyrrin planes in tricyanmethanido derivative **517** are arranged in a coplanar fashion and without any torsion, whereas in **516** a tilt of 10° and a torsion angle of 40° are observed. This difference can be explained by the steric influence of the third, noncoordinating cyano group of **517**. These rather small differences between the intrastrand structures of **516** and **517** markedly influence the relative arrangement of the pillars. The empty space between adjacent nickel tripyrrin planes in a single chain of **516** is partially filled by two nearby pillars that come very close and whose nickel tripyrrin units interdigitate at interstrand π–π

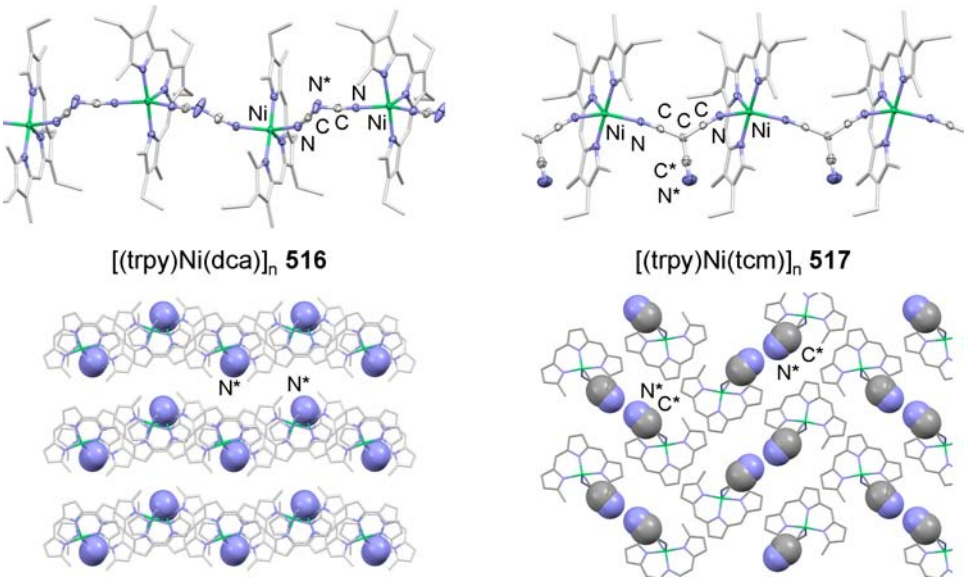

Figure 148. Organization of polymeric chains of tripyrrin nickel dca and tcm complexes **516** and **517**. (Adapted from Ref. 313.)

distances of about 3.4 Å. As the next pillars are significantly further away, a 2D-layered pillar structure results. Interestingly, the divalent central nitrogen atoms of the dicyanamido bridges are oriented toward the gaps between these layers, thus producing a functionalized cleft. Complex **517** instead forms a structure with almost isolated polymer chains in which six pillars arrange to form a trapezoid pore with dimensions of about 6.2 × 4.7 Å. The noncoordinated cyano group of two of these pillars points directly into this pore, resulting in functionalization of the pore with N···N distances of 5.8 Å. The potential of such arrangements in the field of anisotropic ion conductors is evident from Figure 148.

Hydrogen bridges are another bonding scheme found within the class of nickel-tripyrrin-based coordination polymers. The constitutionally most simple example was observed for the aqua complex of a chloro nickel tripyrrin **182** which forms 1D strands by H-bridges between the water ligand of one complex unit and the chloro ligand of an adjacent one.[319] Interestingly, the so-formed supramolecular structure is isostructural with the arrangement of isothiocyanate polymer **514** (Figure 149). A second, more complex example has been found during attempts to use cyanometalate anions as bridging ligands in a brick-and-mortar approach. Thus, a 2:1 mixture of **518** and sodium tetracyanonickelate crystallizes from a methanol/toluene mixture as the pentanuclear dication $[\{(trpy)Ni(MeOH)\}_4\{Ni(CN)_4\}]^{2+}$, which is connected to four adjacent $[Ni(CN)_4]^{2-}$ dianions via hydrogen bonds and forms a 3D coordination network in the crystal (Figure 149).[313]

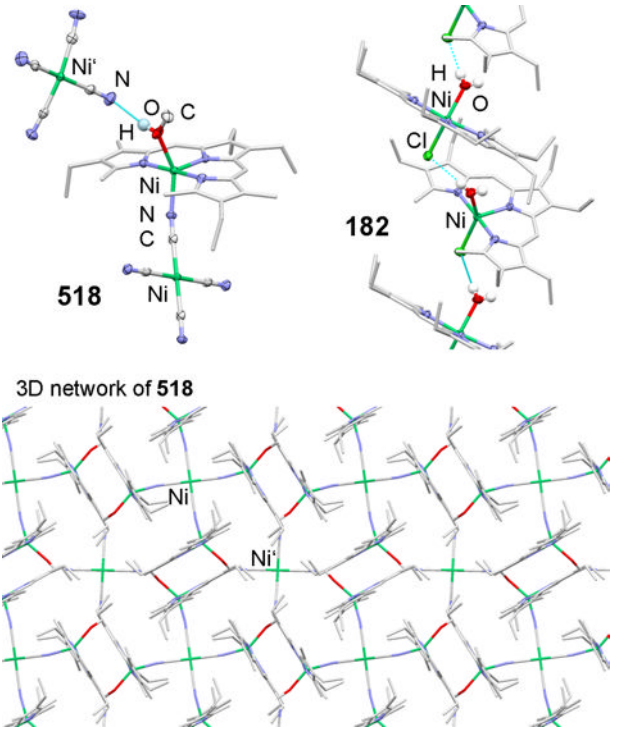

Figure 149. 1D and 3D nickel tripyrrin polymers of **182** and **518** with hydrogen bridges. (Adapted from Refs. 313 and 319.)

The approach using bidentate pseudohalides and cyanometalates — in particular, the favorable dicyanamide and tricyanmethanide anions — in combination with metal tripyrrin precursors was also investigated with other divalent metal ions. Zinc and copper ions show a tendency to form predominantly tetracoordinate species in the tripyrrin environment, in the unstrained pseudoplanar type, regardless of the external ligand (tricyanmethanido, dicyanamido, NCSe, N_3). UV-visible spectroscopic investigations, however, indicate some weak association of methanol in this solvent and the formation of pentacoordinate species from both transition metal ions. Coordination polymers have indeed been found by single-crystal X-ray diffraction in two cases: a dicyanamido derivative of zinc **519** and a heterodinuclear chain of a dicyanoargentate copper(II) species **520**. The spatial relation of the (trpy)M subunits and the arrangement of the polymeric chains in the crystal lattices are shown in Figure 150. The zinc ion in **519** is coordinated by five nitrogen atoms in a distorted trigonal-bipyramidal geometry with the two imino type donors of the trpy ligand occupying the apical positions. The (trpy)Zn fragment is almost planar with the zinc ion only 0.0007 Å above the tripyrrin N,N,N plane. The polymeric chain of **519** is formed by a torsionless and coplanar

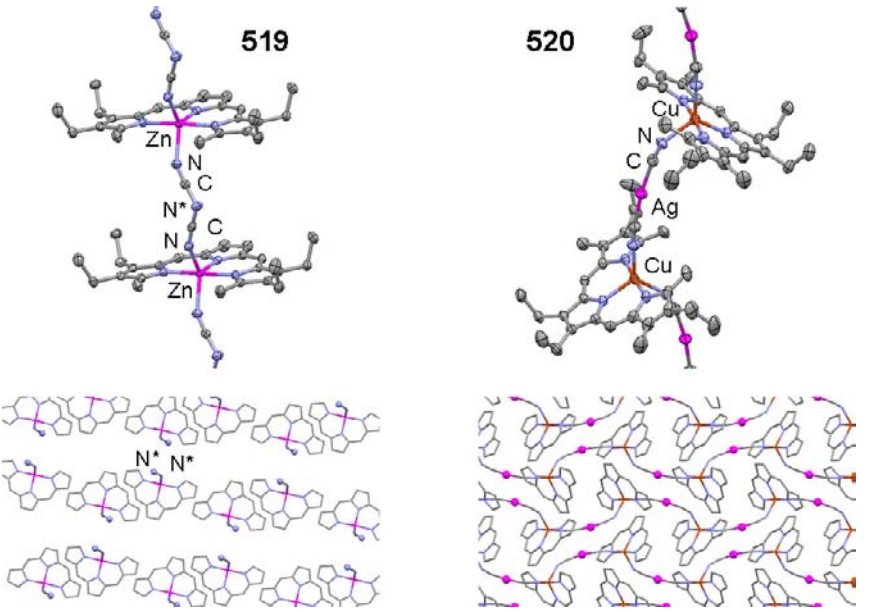

Figure 150. 1D coordination polymers of zinc and copper tripyrrins **519** and **520**. (Adapted from Ref. 122.)

arrangement of the (trpy)Zn subunits. The dicyanamido ligand is μ-1,5-bridging two subunits in such a way that the central nitrogen atom appears turned to the side. The space which is formed between opposite (trpy)Zn plates is filled by adjacent polymeric columns, similar to that observed for dicyanamido nickel derivative **516**. The alkyl side chains of the (trpy)Zn subunits of the next two neighboring strands are interdigitating with the (trpy)Zn plates, thus forming layers of pillars, which show clefts in the crystal. Interestingly, and as indicated in Figure 150, the central nitrogen atoms of the dicyanamido bridges are localized on the surfaces of these clefts. The coordination environment of the copper(II) ion in polymeric **520** is very similar to that for zinc(II) in **519**. Five N donor atoms form a slightly distorted trigonal bipyramide around the copper center, and the out-of-plane deviation of the copper ion from the tripyrrin N,N,N plane is negligible at 0.0301 Å. The unsymmetric bridging mode of the $[Ag(CN)_2]^-$ ligand is documented in the unequal N–Cu–N angles of the triangular base, and in the difference of the Cu–N bond lengths of 2.085 and 2.149 Å. Each copper(II) ion has two intrachain Ag(I) neighbors within a distance of 5.064 and 5.242 Å. The dicyanargentato ligand is not linear but is slightly bent, and the two ends bind with different angles and lengths to the copper centers of the trpyCu units. Adjacent trpyCu planes of each copper(II) ion in **520** are arranged without torsion, but not in a

coplanar fashion. Different from **519**, the steric demand of the tripyrrin backbone of **520** thus leads to densely packed zigzag chains without open spaces.[122]

As described above, the advent of free-base tripyrrins has led to the availability of further metallotripyrrin subunits as potential monomers for supramolecular aggregates. Ethereal solutions of free-base tripyrrins were prepared by treatment of nickel isocyanate complexes [(trpy)Ni(NCO)] with excess cyanide. From these solutions sensitive metallotripyrrins with cobalt(II), iron(II), and manganese(II) ions [(trpy)MX] and with a choice of external ligands X could be obtained in pure, crystalline form. [(trpy)Fe(NCO)] undergoes a redox transformation to μ-oxoiron(III) species **212** upon crystallization, and was structurally characterized as such with an almost linear Fe–O–Fe subunit (Figure 44).[314] A very similar coordination and association has been described for dinuclear chloro iron(III) bpi derivative **521** (Figure 151), albeit with tilted Fe–O–Fe bonding.[541]

Donor association was studied by UV-visible spectroscopy employing different solvents, and showed that all manganese(II) and iron(II) species are very prone to the formation of pentacoordinate species, whereas the cobalt(II)-containing compounds have an intermediate tendency to do so. Nevertheless, complex fragments of all three metal ions form 1D coordination polymers with dicyanamido ligands, and were investigated by means of IR and SQUID measurements.

The introduction of the large cadmium(II) ion into the tripyrrin N,N,N coordination site was accomplished by the use of cadmium acetate as the metal precursor. Ligand exchange experiments using sodium salts of different anions disclose a marked tendency toward pentacoordination, which is achieved by the formation either of chelates or of 1D coordination polymers arising from the size of the central metal.[315] Thus, attempted introduction of chloro, iodo, or cyanato ligands leads mainly to decomposed material, while the use of 1,1,1-trifluoracetylacetonate, salicylate, and acetate ligands results in stable, pentacoordinate, and monomeric complexes. With the pseudohalogenido ligands thiocyanate, selenocyanate, and azide as well as with the weakly coordinating trifluoroacetate, trigonal bipyramidal species form as 1D coordination polymers

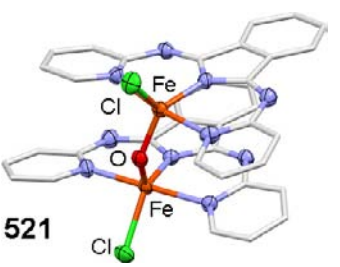

521

Figure 151. Molecular structure of μ-oxo-di[(bpi)chloroiron(III)] **521**. (Adapted from Ref. 541.)

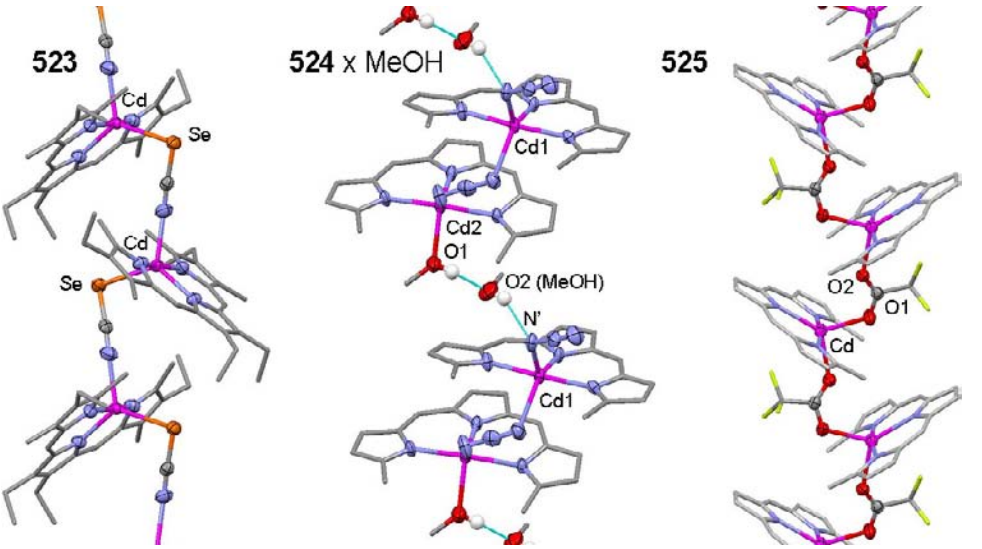

Figure 152. Different 1D chain structures of cadmium tripyrrin polymers with bridging selenocyanate **523**, azide **524**, and trifluoroacetate ligands **525**. (Adapted from Ref. 315.)

522–**525**, respectively, with a variety of chain structures (Figure 152). The most interesting compound in this series is azido derivative **524**, which is present in crystal as a coordinatively and hydrogen-bonded methanol adduct with a dimeric repeating subunit.

In addition to the tripyrrin-based aggregates, three examples of bai-based coordination polymers are found in the literature. The polymeric copper bti with acetate bridges crystallizes together with monomer **259**.[196] In contrast to the almost ideally planar four-coordinate structure of monomeric **259**, the copper atoms in the polymeric chains display fivefold coordination and a ligand polyhedron which is an intermediate form between a trigonal-bipyramidal and a square-pyramidal geometry. While the arrangement of the three heterocycles of the bti ligand remains almost planar, the acetato ligand is tilted out of this plane, therefore making space for the coordination of the second acetato oxygen atom of a neighboring coordination unit. Significantly, the Cu–O bond lengths of 2.08 and 2.23 Å are longer than in the square-planar monomer **259**, and indicate substantial intermolecular bonding, leading to the polymeric assembly (Figure 153). A related cobalt(II) bpi complex **526** aggregates as a coordination polymer in which each Co atom is coordinated by two bridging acetate groups and one bpi ligand (Co–O = 2.043, 2.022 Å). The polymeric nature of **526** was reported to be responsible for the low solubility of bpi cobalt acetato complexes in general.[202] The polymer chains of both bai-based polymers adopt folded structures similar to cadmium tripyrrin **525**, and as represented in Figure 153.

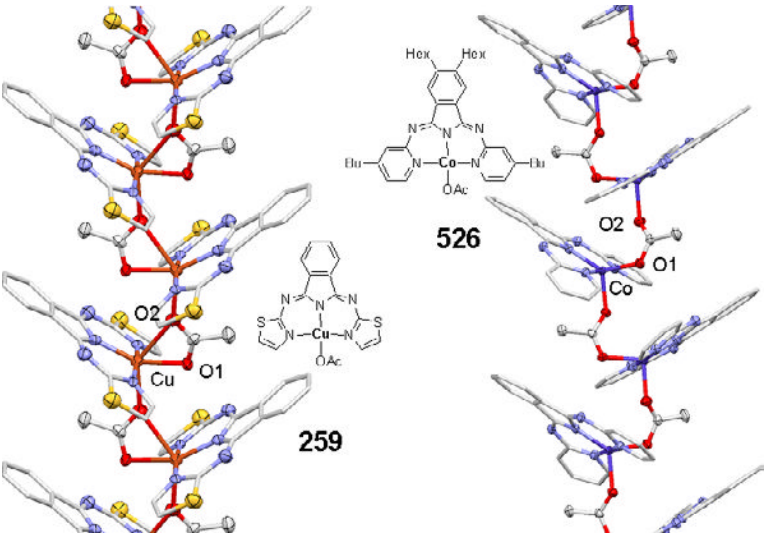

Figure 153. Polymeric acetato complexes of copper bti **259** and cobalt bpi **526** (crystallographic figures adapted from Refs. 196 and 202).

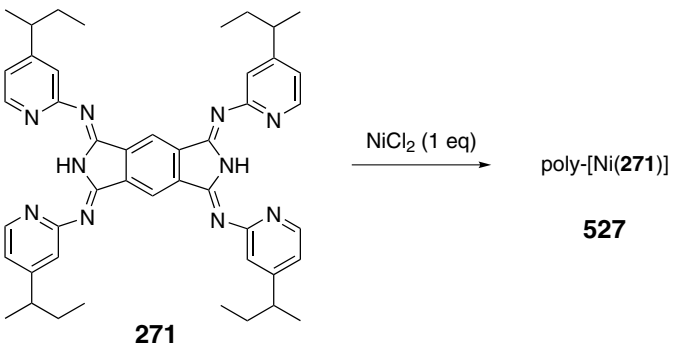

Figure 154. Coordination polymer **527**, formed from bischelating bpi ligand **271** and nickel(II).

A different approach to coordination polymers was briefly reported in one instance. The reaction of bischelating ligand **271** with nickel chloride in a 1:1 ratio results in the formation of a metal-organic polymer **527** (Figure 154).[192] Only the optical spectrum of this new coordination polymer was reported.

B. Bis(arylimino)isoindolines in Dendrimers

Many ligands and catalytically active metal complexes have been immobilized on the inside or outside of dendrimers. The aim of these research activities has been the development of catalysts which combine the advantages of homogeneous

catalysis (high activity and selectivity; directed catalyst design) with those of heterogeneous catalysts (e.g. facile catalyst separation and recycling). In principle, the position of the catalytic sites in high density at the periphery of dendritic macromolecules may significantly alter the activity and selectivity when compared with the respective mononuclear catalysts. Three approaches to organization of bpi ligands and palladium complexes by dendritic hosts have been reported. They differ generally by the type of the chemical linker and by the order of steps during the assembly of the supermolecules.

A successful approach to dendritic bpi ligands employed the highly efficient coupling of alkynyl linker units to carbosilane dendrimers and dendrons. The suitably functionalized bpi ligands **528a** and **528b** were prepared by nucleophilic substitution of 4-nitrophthalodinitrile with 4-butynol, followed by double condensation with 2-aminopyridines. Lithiation of **528a** with LDA and reaction with Si–Cl or Si–OTf (OTf = triflate) end groups in core or peripheral positions of dendritic carbosilanes gave *endo* or *exo* bpi functionalized dendrimers, respectively, such as **529** (Figure 155), **530** (Figure 156), and others.[542] All functional

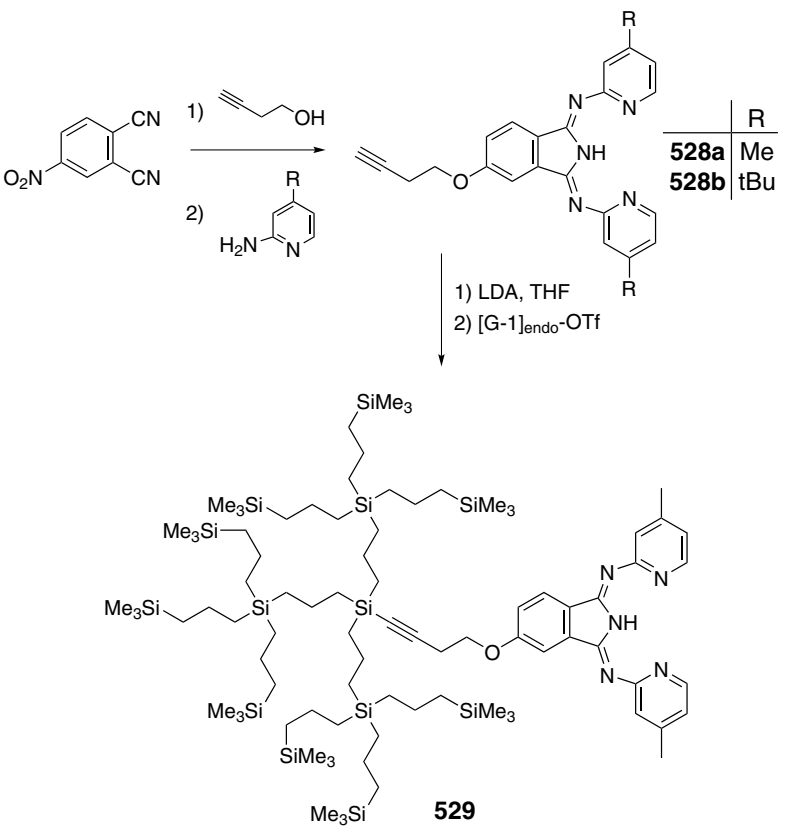

Figure 155. Preparation of alkinyl-bpi appended [G-1]-carbosilane dendrimer **529**.

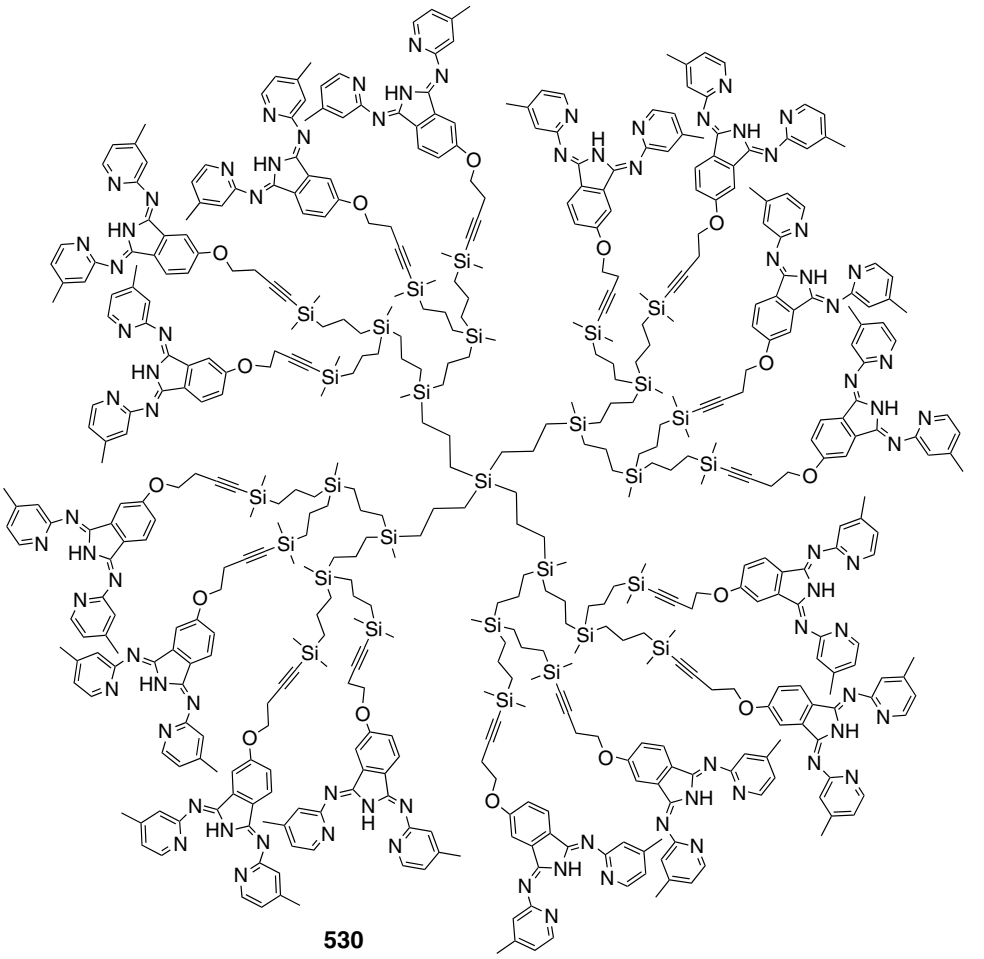

Figure 156. [G-2]-Carbosilane dendrimer **530** with 16 H(4-Mebpi) ligands.

dendrimers were metalated by reaction with $[(PhCN)_2PdCl_2]$ in dichloromethane to give the corresponding pallada-dendrimers.

A related alternative was reported using ethyleneglycol-modified bpi ligands for the immobilization in carbosilane dendrimers.[543] The fixation of the linker was again carried out at the stage of the phthalodinitrile precursor by nucleophilic *ipso*-substitution. Following the condensation with the aminopyridine, the ethylene-glycol-functionalized H(bpi) derivative **531** was treated with the zero-generation carbosilane dendrimer [G-0]4-exo-Cl **532** and yielded the functionalized dendrimer **533** (Figure 157). Palladium(II) was again successfully introduced by reaction of the ligands with $[(PhCN)_2PdCl_2]$ in benzene using triethylamine as auxiliary base.

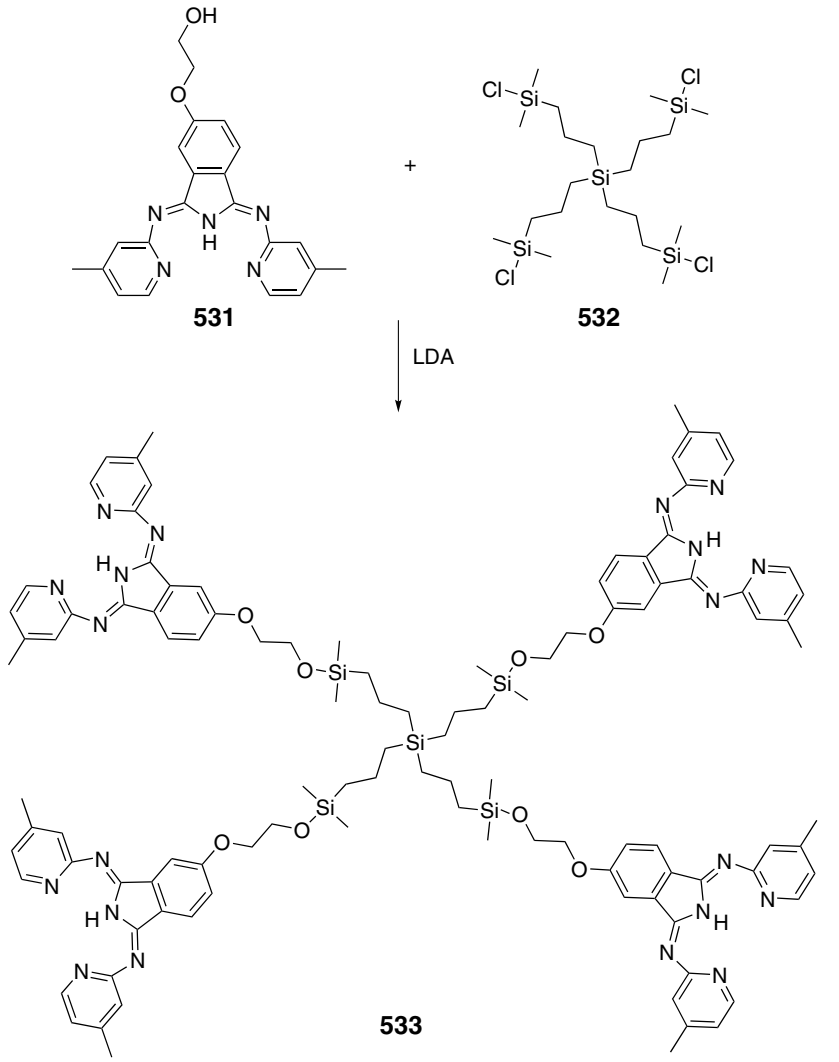

Figure 157. [G-0]-Carbosilane dendrimer with four bpi units by ethylene glycol linkage.

In the third report, polyether dendritic wedges — the so-called Fréchet wedges — were attached to bpi ligands, and the corresponding Pd(II) complexes were synthesized and studied as hydrogenation catalysts (see Section IV.C). The fixation of dendrons at the ligand framework was carried out at the stage of the phthalodinitrile precursor of the bpi ligands, again by nucleophilic substitution of 4-nitrophthalodinitrile, with the *in-situ*-generated alcoholates. The reaction of 1,3-dibenzyloxy-2-propanol [G-1] **534** and the coupling of Fréchet's first and second generation arylether dendrons [(3,5)-G-1]-OH **535**, [*t*-bu-(3,5)-G-1]-OH **536**, and

[(3,5)-G-2]-OH **537** gave the corresponding O-coupled phthalodinitrile derivatives **538**–**541**. The synthesis of bpi ligands **542**–**545** was then achieved in the last step by reaction with two molar equivalents of 2-amino-5-bromopyridine (Figure 158). All the ligands were cleanly metalated to give the corresponding palladium(II) complexes. In contrast to the unsubstituted complexes, the dendrimer-functionalized derivatives **452** and **453** hydrogenate styrene and 1-octene without decomposition (see Section IV.C), and catalyst **453**, carrying the second generation dendron, displayed sufficient stability to be isolated and reused several times.[439]

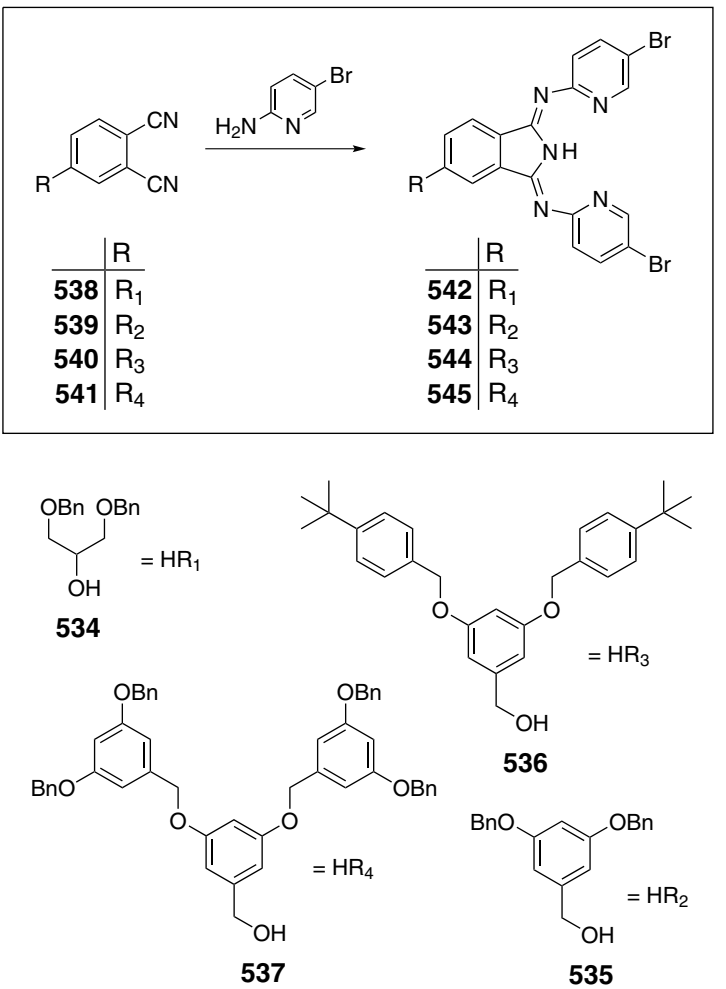

Figure 158. Preparation of bpi ligands **542**–**545** carrying Fréchet wedges.

C. Tetrapyrroles in Supramolecular Assemblies

Attempts to use tetrapyrrolic entities for supramolecular engineering started with the finding of tetrapyrrole-based helicates and have been reported so far only for di- and trinuclear metal complexes of three different classes of bis(dipyrrin)s. A dinuclear copper helicate **401** with a sterically restricted 2,2′-bidipyrrin ligand was reported to pack in a peculiar fashion and form solvent

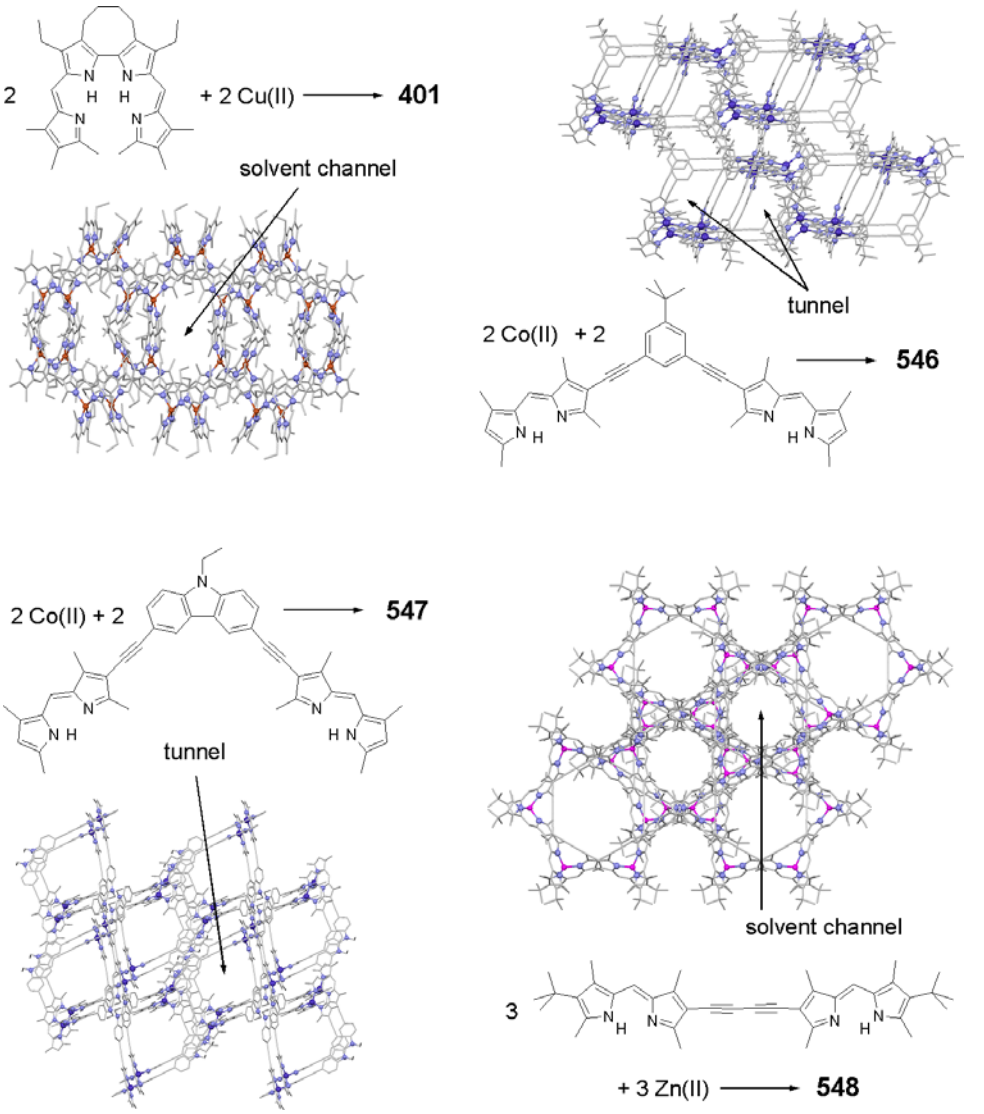

Figure 159. Di- and trinuclear tetrapyrrole species **401** and **546**–**548**, and selected views of their crystal structures (crystallographic figures adapted from Refs. 269 and 298).

channels in the crystalline state.[269] Di- and trinuclear zinc and cobalt chelates of expanded, β-bridged bis(dipyrrin)s **546**, **547**, and **548** show similar behavior and have been analyzed crystallographically in some detail. In these cases porous solids with tunnels or with solvent-filled channels result from the packing of molecules (Figure 159).[298]

A set of *meso*-bridged bis(dipyrrin)s with expanded bridges **107** and **549–551** has been prepared, and the metal complexes of these ligands were tested in supramolecular assemblies and nanostructures. A dinuclear zinc(II) chelate **552** was found to reside in either of two stereochemically distinct forms: a *rac* and a *meso* form. NMR analyses provide evidence for slow exchange of the stereochemistry by the independent rotation of each of the bis(dipyrrinato)zinc subunits

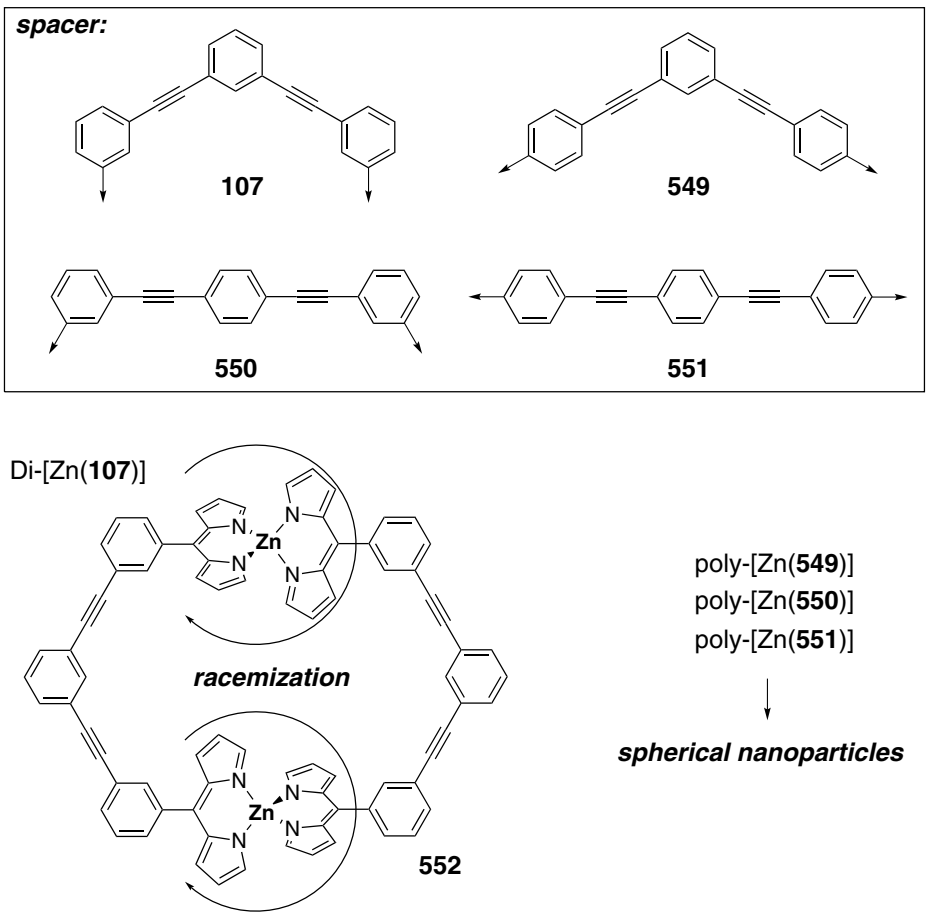

Figure 160. Molecular and supramolecular behavior of di- and polymeric zinc chelates of stretched tetrapyrroles.

within the nanoring.[260] For ligands with a more stretched architecture, such as **549–551**, the formation of spherical nanoparticles from 1D polymeric coordination compounds has been detected (Figure 160).[544] First coordination oligomers of this type have most recently been isolated by a statistic approach using a linking bis(dipyrrin) and an end group.[545] Albeit only little is known so far about such and other tetrapyrrole-based nanostructures, there seems to be much potential for controlling the fabrication and morphology of such nano-objects through this coordination chemistry approach in the future.

IX. Concluding Remarks

The coordination chemistry of linear open-chain tri- and tetrapyrrole ligands is currently developing into a very broad area ranging from biomedical and microbiological applications through synthetic improvements in macrocycle preparations and luminescent material for modern photophysics to catalysis and nanoscience. The basics of the coordination chemistry of such ligands are well-understood for the most important examples only — the tripyrrins, bais, bilins, and the bidipyrrins — but still not sufficiently developed for most of the many possible ligand architectures. Furthermore, most of the many linear tetrapyrroles known from preparative studies have not been or have only been little investigated within coordination compounds. This is particularly true for the natural tripyrroles and for tetrapyrroles designed using the bis(dipyrrin) concept. The possibilities still to open up in the field of linear oligopyrrole metal chelates leave much space for future work on stereochemically and electronically interesting species with unforeseen reactivity, and the opportunity to use these compounds in life science, materials, and nanotechnology will be the topic of interdisciplinary studies in the near future.

X. Acknowledgments

I thank Anne Scheja for her help in accessing obscure papers, and Dr. Klaus Harms for his support in mining crystallographic data.

XI. References

1. Subramanian, J.; Fuhrhop, J.-H. In *The Porphyrins*; Dolphin, D., Ed.; Academic Press: New York, **1978**.
2. McDonagh, A. F. In *The Porphyrins*; Dolphin, D., Ed.; Academic Press: New York, **1978**.
3. Gossauer, A.; Engel, J. In *The Porphyrins*; Dolphin, D., Ed.; Academic Press: New York, **1978**.
4. *The Porphyrin Handbook*; Kadish, K. M.; Smith, K. M.; Guilard, R., Eds.; Academic Press: New York, **2003**, Vols. 12 and 13.

5. Liu, Y.; Ortiz de Montellano, P. R. *J. Biol. Chem.* **2000**, *275*, 5297–5307.
6. Sugishima, M.; Sakamoto, H.; Higashimoto, Y.; Noguchi, M.; Fukuyama, K. *J. Biol. Chem.* **2003**, *278*, 32352–32358.
7. Lad, L.; Friedman, J.; Li, H. Y.; Bhaskar, B.; Ortiz de Montellano, P. R.; Poulos, T. L. *Biochemistry* **2004**, *43*, 3793–3801.
8. Ortiz de Montellano, P. R. *Curr. Opin. Chem. Biol.* **2000**, *4*, 221–227.
9. Ortiz de Montellano, P. R.; Wilks, A. *Adv. Inorg. Chem.* **2001**, *51*, 359–407.
10. Balch, A. L.; Bowles, F. In *Handbook of Porphyrin Science*; Kadish, K. M.; Smith, K. M.; Guilard, R., Eds.; World Scientific: Singapore, **2010**, Vol. 8.
11. Granick, S.; Mauzerall, D. In *Metabolic Pathways*; Greenberg, D. M., Ed.; Academic Press: New York, **1961**, Vol. 2.
12. Kondo, T.; Nicholson, D. C.; Jackson, A. H.; Kenner, G. W. *Biochem. J.* **1971**, *121*, 601–607, and citations therein.
13. Berkelman, T. R.; Lagarias, J. C. *Anal. Biochem.* **1986**, *156*, 194–201.
14. Cheng, L.-J.; Ma, J.-S.; Chiang, L.-C. *Photochem. Photobiol.* **1990**, *52*, 1071–1076.
15. Dekok, J. *Photochem. Photobiol.* **1985**, *42*, 663–668.
16. Heirwegh, K.; Van Roy, F. *Clin. Chim. Acta* **1965**, *12*, 684–689.
17. Michaelsson, M. *Scand. J. Clin. Lab. Invest.* **1961**, *13*, 56.
18. Yamaguchi, T.; Shioji, I.; Sugimoto, A.; Komoda, Y.; Nakajima, H. *J. Biochem.* **1994**, *116*, 298–303.
19. Gerber, N. N. *Crit. Rev. Microbiol.* **1974**, *3*, 469–485.
20. Bennett, J. W.; Bentley, R. *Adv. Appl. Microbiol.* **2000**, *47*, 1–32.
21. Fürstner, A. *Angew. Chem. Int. Ed.* **2003**, *42*, 3582–3603.
22. Wood, T. E.; Thompson, A. *Chem. Rev.* **2007**, *107*, 1831–1861.
23. Loudet, A.; Burgess, K. *Chem. Rev.* **2007**, *107*, 4891–4932.
24. Wood, T. E.; Uddin, I. MD.; Thompson, A. In *Handbook of Porphyrin Science*; Kadish, K. M.; Smith, K. M.; Guilard, R., Eds.; World Scientific: Singapore, **2010**, Vol. 8.
25. Falk, H.; Flödl, H. *Monatsh. Chem.* **1986**, *117*, 57–67.
26. Sessler, J. L.; Weghorn, S. J.; Lynch, V.; Fransson, K. *J. Chem. Soc. Chem. Commun.* **1994**, 1289–1290.
27. Zhang, Y.; Thompson, A.; Rettig, S. J.; Dolphin, D. *J. Am. Chem. Soc.* **1998**, *120*, 13537–13538.
28. Chen, Q.-Q.; Zhang, Y.; Dolphin, D. *Tetrahedron Lett.* **2002**, *43*, 8413–8416.
29. Sessler, J. L.; Camiolo, S.; Gale, P. A.; *Coord. Chem. Rev.* **2003**, *240*, 17–55.
30. Bröring, M.; Link, S.; Köhler, S.; Cónsul Tejero, E. *Z. Anorg. Allg. Chem.* **2004**, *630*, 817–820.
31. Fischer, H.; Reinecke, H. *Hoppe-Seyler's Z. Physiol. Chem.* **1938**, *251*, 204–217.
32. Bullock, E.; Grigg, R.; Johnson, A. W.; Wasley, J. F. W. *J. Chem. Soc.* **1963**, 2326–2335.
33. Clezy, P. S.; Liepa, A. J. *J. Chem. Soc. Chem. Commun.* **1969**, 767–768.
34. Clezy, P. S.; Liepa, A. J.; Webb, N. W. *Aust. J. Chem.* **1972**, *25*, 1991–2001.
35. Bringmann, G.; Franck, B. *Liebigs Ann. Chem.* **1982**, 1261–1271.
36. Bringmann, G.; Franck, B. *Liebigs Ann. Chem.* **1982**, 1272–1279.
37. Falk, H.; Flödl, H. *Monatsh. Chem.* **1985**, *116*, 1177–1187.
38. Wagner, U. G.; Kratky, C.; Falk, H.; Flödl, H. *Monatsh. Chem.* **1987**, *118*, 1185–1194.
39. Falk, H.; Flödl, H. *Monatsh. Chem.* **1989**, *120*, 45–51.
40. Maravin, G. B.; Tauer, A. Y.; Mironov, A. F. *Synlett*. **1993**, 355–356.
41. Morosini, P.; Scherer, M.; Meyer, S.; Lynch, V.; Sessler, J. L. *J. Org. Chem.* **1997**, *62*, 8848–8853.

42. Chen, Q.-Q.; Dolphin, D. *Can. J. Chem.* **2002**, *80*, 1668–1675.
43. Sessler, J. L.; Berthon-Gelloz, G.; Gale, P. A.; Camiolo, S.; Anslyn, E. V.; Anzenbacher Jr., P.; Furuto, H.; Kirkovits, G. J.; Lynch, V. M.; Maeda, H.; Morosini, P.; Scherer, M.; Shriver, J.; Zimmerman, R. S. *Polyhedron* **2003**, *22*, 2963–2983.
44. Iordache, A.; Melfi, P.; Bucher, C.; Buda, M.; Moutet, J.-C.; Sessler, J. L. *Org. Lett.* **2008**, *10*, 425–428.
45. Shin, J. Y.; Hepperle, S. S.; Dolphin, D. *Tetrahedron Lett.* **2009**, *50*, 6909–6912.
46. Vickovic, I.; Suste, A.; Falk, H.; Kosutic Hulita, N.; Tonejic, A. M. *Monatsh. Chem.* **1995**, *126*, 971–982.
47. Reid, S. D.; Blake, A. J.; Köckenberger, W.; Wilson, C.; Love, J. B. *Dalton Trans.* **2003**, 4387–4388.
48. Wu, Z.; Chen, Q.; Xiong, S.; Xin, B.; Zhao, Z.; Jiang, L.; Ma, J. S. *Angew. Chem. Int. Ed.* **2003**, *42*, 3271–3274.
49. Yang, L. Y.; Chen, Q.-Q.; Li, Y.; Xiong, S.; Li, G.; Ma, J. S. *Eur. J. Inorg. Chem.* **2004**, 1478–1487.
50. Wu, Z.; Yang, G.; Chen, Q.-Q.; Liu, J.; Yang, S.; Ma, J. S. *Inorg. Chem. Commun.* **2004**, *7*, 249–252.
51. Munro, O. Q.; Joubert, S. D.; Grimmer, C. D. *Chem. Eur. J.* **2006**, *12*, 7987–7999.
52. Reid, S. D.; Blake, A. J.; Wilson, C.; Love, J. B. *Inorg. Chem.* **2006**, *45*, 636–643.
53. Reid, S. D.; Wilson, C.; De Matteis, C. I.; Love, J. B. *Eur. J. Inorg. Chem.* **2007**, 5286–5293.
54. Shan, X.-F.; Wu, L.-Z.; Liu, X.-Y.; Zhang, L.-P.; Tung, P.-H. *Eur. J. Inorg. Chem.* **2007**, 3315–3319.
55. Thoi, V. S.; Stork, J. R.; Niles, E. T.; Depperman, E. C.; Tierney, D. L.; Cohen, S. M. *Inorg. Chem.* **2008**, *47*, 10533–10541.
56. Miller, J. S.; Epstein, A. J. *Synthesis and Properties of Low-Dimensional Materials*; The New York Academy of Science: New York, **1978**, Part III.
57. Bloor, D. In *Introduction to Molecular Electronics*; Petty, M. C.; Bryce, M. R.; Bloor, D., Eds.; Edward Arnold: London, **1995**.
58. An attempt at a systematic description of linear oligopyrroles can be found in: Falk, H. *The Chemistry of Linear Oligopyrroles and Bile Pigments*; Springer: Vienna, **1989**.
59. Williams, R. P.; Hearn, W. R. *Antibiotics* **1967**, *2*, 410–432.
60. Williams, R. P. *Appl. Microbiol.* **1973**, *25*, 396–402.
61. Castro, A. J. *Nature* **1967**, *213*, 903–904.
62. Songia, S.; Mortellaro, A.; Taverna, S.; Fornasiero, C.; Schreiber, E. A.; Erba, E.; Colotta, F.; Mantovani, A.; Isetta, A.-M.; Golay, J. *J. Immunol.* **1997**, *158*, 3987–3995.
63. Lee, M. H.; Yamashita, M.; Tsuji, R. F.; Kataoka, T.; Magae, J.; Nagai, K. *J. Antibiot.* **1998**, *51*, 92–94.
64. Sato, T.; Konno, H.; Tanaka, Y.; Kataoka, T.; Nagai, K.; Wasserman, H. H.; Ohkuma, S. *J. Biol. Chem.* **1998**, *273*, 21455–21462.
65. Yamamoto, C.; Takemoto, H.; Kuno, K.; Yamamoto, D.; Tsubura, A.; Kamata, K.; Hirata, H.; Yamamoto, K.; Kano, H.; Seki, T.; Inoue, K. *Hepatology* **1999**, *30*, 894–904.
66. Mortellaro, A.; Songia, S.; Gnocchi, P.; Ferrari, M.; Fornasiero, C.; D'Alessio, R.; Isetta, A.; Colotta, F.; Golay, J. *J. Immunol.* **1999**, *162*, 7102–7109.
67. Manderville, R. A. *Curr. Med. Chem. Anti-Cancer Agents* **2001**, *1*, 195–218.
68. Montaner, B.; Pérez-Tomás, R. *Curr. Cancer Drug Targets* **2003**, *3*, 57–65.
69. Pérez-Tomás, R.; Montaner, B.; Llagostera, E.; Soto-Cerrato, V. *Biochem. Pharm.* **2003**, *66*, 1447–1452.

70. Proust, L. *Ann. Chem.* **1800**, *36*, 265.
71. Simon, A. *Anthropochemie* **1842**, 343.
72. Pane, N. *J. Am. Med. Assoc.* **1916**, *66*, 1433–1434.
73. Borrien, V. *J. Pharm. Chemie* **1917**, *16*, 45–51.
74. Weiss, M. *Deut. Arch. Klin. Med.* **1930**, *166*, 331–348.
75. Berüter, J.; Colombo, J.-P.; Schlunegger, U. P. *Eur. J. Biochem.* **1975**, *56*, 239–244.
76. Vítek, L. *Pediatrics* **2005**, *115*, 1411–1412.
77. Hiroshi, I.; Matsumoto, T.; Morita, Y.; Hirano, A.; Okada, M.; Hashizume, N.; Shioji, I.; Yoshimura, H. *J. Clin. Lab. Anal.* **2007**, *21*, 1–6.
78. Otani, K.; Shimizu, S.; Chijiiwa, K.; Yamaguchi, K.; Kuroki, S.; Tanaka, M. *J. Surg. Res.* **2001**, *96*, 44–49.
79. Tsukahara, H.; Shibata, R.; Ohshima, Y.; Todoroki, Y.; Sato, S.; Ohta, N.; Hiraoka, M.; Yoshida, A.; Nishima, S.; Mayumi, M. *Life Sci.* **2003**, *72*, 2509–2516.
80. Tsujinaka, T.; Fujita, J.; Morimoto, T.; Ogawa, A.; Ebisui, C.; Yano, M.; Shiozaki, H.; Monden, M.; Yamaguchi, T.; Nakajima, H. *Surg. Today* **1998**, *28*, 1119–1123.
81. Kozaki, N.; Shimizu, S.; Chijiiwa, K.; Yamaguchi, K.; Kuroki, S.; Shimoharada, K.; Yamaguchi, T.; Nakajima, H.; Tanaka, M. *HPB Surg.* **1999**, *11*, 241–248.
82. Yamaguchi, T.; Shioji, I.; Sugimoto, A.; Yamaoka, M. *Biochem. Biophys. Res. Commun.* **2002**, *293*, 517–520.
83. Shimoharada, K.; Inoue, S.; Nakahara, M.; Kanzaki, N.; Shimizu, S.; Kang, D.; Namasaki, N.; Kinoshita, S. *Clin. Chem.* **1998**, *44*, 2554–2555.
84. Yasukawa, R.; Miyaoka, T.; Yasuda, H.; Hayashida, M.; Inagaki, T.; Horiguch, J. *Psychiatry Res.* **2007**, *153*, 203–207.
85. Miyaoka, T.; Yasukawa, R.; Yasuda, H.; Shimizu, M.; Mizuno, S.; Sukegawa, T.; Inagaki, T.; Horiguchi, J. *Eur. Neuropsychopharmacol.* **2005**, *15*, 249–252.
86. Vítek, L.; Kráslová, I.; Muchová, L.; Novotny, L.; Yamaguchi, T. *J. Gastroenterol. Hepatol.* **2007**, *22*, 841–845.
87. Hiraoka, A.; Sasaki, S.; Yamada, T.; Shinohara, A.; Chiba, M. *J. Health Sci.* **2006**, *52*, 817–820.
88. Suefuji, H.; Nishikawa, H.; Arai, H.; Hokamaki, J.; Kajawara, I.; Kugiyama, K.; Yoshimura, M. *Am. J. Cardiol.* **2002**, *90*, 108–111.
89. Hokamaki, J.; Kawano, H.; Yoshimura, M.; Soejima, H.; Miyamoto, S.; Kajiwara, I.; Kojima, S.; Sakamoto, T.; Sugiyama, S.; Hirai, N. *J. Am. Coll. Cardiol.* **2004**, *43*, 1880–1885.
90. Morita, Y.; Takahashi, H.; Kamihata, H.; Yamamoto, Y.; Hara, K.; Iwasaka, T. *Int. J. Cardiol.* **2001**, *80*, 243–250.
91. Yamaguchi, T.; Terakado, M.; Horio, F.; Aoki, K.; Tanaka, M.; Nakajima, H. *Biochem. Biophys. Res. Commun.* **1996**, *223*, 129–135.
92. Fischer, H.; Adler, E. *Hoppe-Seyler's Z. Physiol. Chem.* **1931**, *200*, 209–231.
93. Fischer, H.; Reinecke, H. *Hoppe-Seyler's Z. Physiol. Chem.* **1939**, *259*, 83–96.
94. Fischer, H.; Reinicke, H. *Hoppe-Seyler's Z. Physiol. Chem.* **1940**, *265*, 9–21.
95. Plieninger, H.; Lichtenwald, H. *Hoppe-Seyler's Z. Physiol. Chem.* **1942**, *273*, 206–224.
96. von Dobeneck, H.; Schnierle, F. *Tetrahedron Lett.* **1966**, 5327–5330.
97. von Dobeneck, H.; Messerschmitt, T.; Brunner, E.; Wunderer, U. *Liebigs Ann. Chem.* **1971**, *751*, 40–49.
98. von Dobeneck, H.; Sommer, U.; Brunner, E.; Lippacher, E.; Schnierle, F. *Liebigs Ann. Chem.* **1973**, 1934–1942.
99. Roth, S. D.; Shkindel, T.; Lightner, D. A. *Tetrahedron* **2007**, *63*, 11030–11039.

100. Furuta, H.; Maeda, H.; Osuka, A. *Org. Lett.* **2002**, *4*, 181–184.
101. Furuta, H.; Maeda, H.; Osuka, A. *Inorg. Chem. Commun.* **2003**, *6*, 162–164.
102. Pawlicki, M.; Kanska, I.; Latos-Grazynski, L. *Inorg. Chem.* **2007**, *46*, 6575–6584.
103. Rath, S. P.; Kalish, H.; Latos-Grazynski, L.; Olmstead, M. M.; Balch, A. L. *J. Am. Chem. Soc.* **2004**, *126*, 646–654.
104. Plieninger, H.; Stumpf, K. *Chem. Ber.* **1970**, *103*, 2562–2570.
105. Khan, S. A.; Plieninger, H. *Chem. Ber.* **1975**, *108*, 2475–2477.
106. Eivazi, F.; Hudson, M. F.; Smith, K. M. *Tetrahedron Lett.* **1976**, *42*, 3837–3840.
107. Falk, H.; Grubmayr, K. *Monatsh. Chem.* **1977**, *108*, 625–645.
108. Cullen, D. L.; Meyer, E. F.; Eivazi, F.; Smith, K. M. *J. Chem. Soc. Perkin 2* **1978**, 259–263.
109. Falk, H.; Leodolter, A. *Monatsh. Chem.* **1978**, *109*, 883–897.
110. Munder, S.; Pfaff, E.; Plieninger, H.; Sander, W. *Liebigs Ann. Chem.* **1980**, 2031–2038.
111. Acero, C.; Ribò, J. M.; Solé, R.; Trull, F. R. *Monatsh. Chem.* **1993**, *124*, 401–417.
112. Ma, J. S.; Chen, Q. Q.; Wang, C. Q.; Liu, Y. Y.; Yan, F.; Cheng, L. J.; Jin, S.; Falk, H. *Monatsh. Chem.* **1995**, *126*, 201–209.
113. Jaumà, A.; Farrera, J. A.; Ribò, J. M. *Monatsh. Chem.* **1996**, *127*, 935–946.
114. Sessler, J. L.; Gebauer, A.; Král, V.; Lynch, V. *Inorg. Chem.* **1996**, *35*, 6636–6637.
115. Wang, P.; Zhang, Y.; Chen, Q.-Q.; Ma, J.-S. *Org. Prep. Proced. Int.* **2002**, *34*, 182–187.
116. Krivokapic, A.; Cowley, A. R.; Anderson, H. L. *J. Org. Chem.* **2003**, *68*, 1089–1096.
117. Galezowski, M.; Jazwinski, J.; Lewtak, J. P.; Gryko, D. T. *J. Org. Chem.* **2009**, *74*, 5610–5613.
118. Shin, J.-Y.; Hepperle, S. S.; Patrick, B. O.; Dolphin, D. *Chem. Commun.* **2009**, 2323–2325.
119. Bröring, M.; Brandt, C. D. *Chem. Commun.* **2001**, 499–500.
120. Bröring, M.; Brandt, C. D. *J. Chem. Soc. Dalton Trans.* **2002**, 1391–1395.
121. Bröring, M.; Brandt, C. D.; Prikhodovski, S. *J. Porphyrins Phthalocyanines* **2003**, *7*, 17–24.
122. Bröring, M.; Prikhodovski, S.; Brandt, C. D.; Cónsul Tejero, E.; Köhler, S. *Dalton Trans.* **2007**, 200–208.
123. Bröring, M.; Prikhodovski, S.; Cónsul Tejero, E. *Chem. Commun.* **2007**, 876–877.
124. Montforts, F.-P. *Angew. Chem. Int. Ed. Engl.* **1981**, *20*, 778–779.
125. Montforts, F.-P.; Schwarz, U. M. *Liebigs Ann. Chem.* **1985**, 1228–1253.
126. Atkinson, J. H.; Johnson, A. W.; Raudenbusch, W. *J. Chem. Soc. C* **1966**, 1155–1165.
127. Jackson, A. H.; Kenner, G. W.; Sach, G. S. *J. Chem. Soc. C* **1967**, 2045–2059.
128. Murakami, Y.; Matsuda, Y.; Kobayashi, S.-I. *J. Chem. Soc. Dalton Trans.* **1973**, 1734–1737.
129. de Almeida, J. A. P. B.; Kenner, G. W.; Rimmer, J.; Smith, K. M. *Tetrahedron* **1976**, *32*, 1793–1799.
130. Engel, J.; Gossauer, A. *Liebigs Ann. Chem.* **1976**, 1637–1658.
131. Sheldrick, W. S.; Borkenstein, A. *Acta Cryst. B* **1978**, *34*, 2055–2058.
132. Smith, K. M.; Craig, G. W. *J. Org. Chem.* **1983**, *48*, 4302–4306.
133. Hidalgo, F. J.; Zamora, R. *J. Biol. Chem.* **1993**, *268*, 16190–16197.
134. Tipton, A. K.; Lightner, D. A. *Monatsh. Chem.* **1999**, *130*, 425–440.
135. Lemberg, R. *Liebigs Ann. Chem.* **1932**, *499*, 25–40.
136. Jordan, P. M. *New Compr. Biochem.* **1991**, *19*, 1–66.
137. Nomenclature of oligopyrroles: Dixon, H. B. F.; Cornish-Bowden, A.; Liebecq, C.; Loening, K. L.; Moss, G. P.; Reedijk, J.; Velick, S. F.; Venetianer, P.; Vliegenthart, J. F. G. *Pure Appl. Chem.* **1987**, *59*, 779–832.
138. An alternative nomenclature system: Lemberg, R.; Legge, J. W. *Hematin Compounds and Bile Pigments*; Interscience: New York, **1949**.

139. Grigg, R.; Johnson, A. W. *J. Chem. Soc.* **1964**, 3315–3322.
140. Atkinson, J. H.; Johnson, A. W. *J. Chem. Soc.* **1965**, 2614–2621.
141. Dolphin, D.; Grigg, R.; Johnson, A. W.; Leng, J. *J. Chem. Soc.* **1965**, 1460–1467.
142. Wasserman, H. H.; Friedland, D. J.; Morrison, D. A. *Tetrahedron Lett.* **1968**, 641–644.
143. Sepulveda-Boza, S.; Breitmaier, E. *Liebigs Ann. Chem.* **1983**, 894–896.
144. Paul, V. J.; Lindquist, N.; Fenical, W. *Mar. Ecol. Prog. Ser.* **1990**, *59*, 109–118.
145. Ikeda, H.; Sessler, J. L. *J. Org. Chem.* **1993**, *58*, 2340–2342.
146. Vogel, E.; Bröring, M.; Erben, C.; Demuth, R.; Lex, J.; Nendel, M.; Houk, K. N. *Angew. Chem. Int. Ed. Engl.* **1997**, *36*, 353–357.
147. Vogel, E.; Bröring, M.; Weghorn, S. J.; Scholz, P.; Deponte, R.; Lex, J.; Schmickler, H.; Schaffner, K.; Braslavsky, S. E.; Müller, M.; Pörting, S.; Fowler, C. J.; Sessler, J. L. *Angew. Chem. Int. Ed. Engl.* **1997**, *36*, 1651–1654.
148. Vogel, E.; Binsack, B.; Hellwig, Y.; Erben, C.; Heger, A.; Lex, J.; Wu, Y.-D. *Angew. Chem. Int. Ed. Engl.* **1997**, *36*, 2612–2615.
149. Vogel, E.; Scholz, P.; Demuth, R.; Erben, C.; Bröring, M.; Schmickler, H.; Lex, J.; Hohleichner, G.; Bremm, D.; Wu, Y.-D. *Angew. Chem. Int. Ed.* **1999**, *38*, 2919–2923.
150. Melvin, M. S.; Wooton, K. E.; Rich, C. C.; Saluta, G. R.; Kucera, G. L.; Lindquist, N.; Manderville, R. A. *J. Inorg. Biochem.* **2001**, *87*, 129–135.
151. Bertele, E.; Boos, H.; Dunitz, J. D.; Elsinger, F.; Eschenmoser, A.; Felner, I.; Gribi, H. P.; Gschwend, H.; Meyer, E. F.; Pesaro, M.; Scheffold, R. *Angew. Chem. Int. Ed. Engl.* **1964**, *3*, 490–496.
152. Montforts, F.-P.; Bats, J. W. *Helv. Chim. Acta* **1987**, *70*, 402–411.
153. Inhoffen, H. H.; Petrovicki, W.; Gossauer, A. *Liebigs Ann. Chem.* **1973**, 1067–1074.
154. Eichinger, D.; Falk, H. *Monatsh. Chem.* **1987**, *118*, 255–260.
155. Wrede, F.; Rothhase, A. *Hoppe-Seyler's Z. Physiol. Chem.* **1934**, *226*, 95–107.
156. Wasserman, H. H.; McKeon, J. E.; Smith, L.; Forgione, P. *J. Am. Chem. Soc.* **1960**, *82*, 506–507.
157. Rapoport, H.; Holden, K. G. *J. Am. Chem. Soc.* **1962**, *84*, 635–642.
158. Hearn, W. R.; Elson, M. K.; Williams, R. H.; Medina-Castro, J. *J. Org. Chem.* **1970**, *35*, 142–146.
159. Berner, H.; Schulz, G.; Reinshagen, H. *Monatsh. Chem.* **1977**, *108*, 233–242.
160. Berner, H.; Schulz, G.; Reinshagen, H. *Monatsh. Chem.* **1977**, *108*, 285–297.
161. Berner, H.; Schulz, G.; Reinshagen, H. *Monatsh. Chem.* **1977**, *108*, 915–927.
162. Berner, H.; Schulz, G.; Reinshagen, H. *Monatsh. Chem.* **1978**, *109*, 137–145.
163. Boger, D. L.; Patel, M. *Tetrahedron Lett.* **1987**, *28*, 2499–2502.
164. Boger, D. L.; Patel, M. *J. Org. Chem.* **1988**, *53*, 1405–1415.
165. Wasserman, H. H.; Lombardo, L. J. *Tetrahedron Lett.* **1989**, *30*, 1725–1728.
166. D'Alessio, R.; Rossi, A. *Synlett*. **1996**, 513–514.
167. Fürstner, A.; Szillat, H.; Gabor, B.; Mynott, R. *J. Am. Chem. Soc.* **1998**, *120*, 8305–8314.
168. Wasserman, H. H.; Petersen, A. K.; Xia, M.; Wang, J. *Tetrahedron Lett.* **1999**, *40*, 7587–7589.
169. Fürstner, A.; Grabowski, J.; Lehmann, C. W. *J. Org. Chem.* **1999**, *64*, 8275–8280.
170. Fürstner, A.; Krause, H. *J. Org. Chem.* **1999**, *64*, 8281–8286.
171. Fürstner, A.; Grabowski, J.; Lehmann, C. W.; Kataoka, T.; Nagai, K. *ChemBioChem* **2001**, *2*, 60–68.
172. Bröring, M.; Penno, D.; Krüger, R. *J. Porphyrins Phthalocyanines* **2007**, *11*, 755–760.
173. Elvidge, J. A.; Linstead, R. P. *J. Chem. Soc.* **1952**, 5000–5007.
174. Elvidge, J. A.; Linstead, R. P. *J. Chem. Soc.* **1952**, 5008–5012.

175. Clark, P. F.; Elvidge, J. A.; Linstead, R. P. *J. Chem. Soc.* **1953**, 3593–3601.
176. Baumann, F. US 2945861.
177. Baumann, F. DE 1151335 19630711.
178. Lon, M. PL 44432 19610405.
179. Forter, W.; Kehrer, F. CH 379670 19640831.
180. Anderson, O. P.; la Cour, A.; Dodd, A.; Garrett, A. D.; Wicholas, M. *Inorg. Chem.* **2003**, *42*, 4513–4515.
181. Gagné, R. R.; Marks, D. N. *Inorg. Chem.* **1984**, *23*, 65–74.
182. Marks, D. N.; Siegl, W. O.; Gagné, R. R. *Inorg. Chem.* **1982**, *21*, 3140–3147.
183. Gagné, R. R.; Marritt, W. A.; Marks, D. N.; Siegl, W. O. *Inorg. Chem.* **1981**, *20*, 3260–3267.
184. Robinson, M. A.; Trotz, S. I.; Hurley, T. J. *Inorg. Chem.* **1967**, *6*, 392–394.
185. Siegl, W. O. *J. Organomet. Chem.* **1976**, *107*, C27–C30.
186. Spiessens, L. I.; Anteunis, M. J. O. *Bull. Soc. Chim. Belg.* **1984**, *93*, 459–477.
187. Spiessens, L. I.; Anteunis, M. J. O. *Bull. Soc. Chim. Belg.* **1988**, *97*, 431–451.
188. Sato, R.; Nakayama, M.; Yuzawa, Y.;Goto, T.; Saito, M. *Chem. Lett.* **1985**, 1887–1902.
189. Siegl, W. O. *J. Org. Chem.* **1977**, *42*, 1872–1878.
190. Siegl, W. O. *J. Heterocyclic Chem.* **1981**, *18*, 1613–1618.
191. Siegl, W. O. *Inorg. Nucl. Chem. Lett.* **1974**, *10*, 825–829.
192. Siegl, W. O. *Inorg. Chim. Acta* **1977**, *25*, L65–L66.
193. Zhang, Y.; Thompson, L. K.; Bridson, J. N.; Bubenik, M. *Inorg. Chem.* **1995**, *34*, 5870–5877.
194. Meder, M. B.; Siggelkow, B. A.; Gade, L. H. *Z. Anorg. Allg. Chem.* **2004**, *630*, 1962–1968.
195. Siggelkow, B. A.; Meder, M. B.; Galka, C. H.; Gade, L. H. *Eur. J. Inorg. Chem.* **2004**, 3424–3435.
196. Meder, M. B.; Gade, L. H. *Eur. J. Inorg. Chem.* **2004**, 2716–2722.
197. Dietrich, B. L.; Egbert, J.; Morris, A. M.; Wicholas, M.; Anderson, O. P.; Miller, S. M. *Inorg. Chem.* **2005**, *44*, 6476–6481.
198. Bröring, M.; Kleeberg, C.; Cónsul Tejero, E. *Eur. J. Inorg. Chem.* **2007**, 3208–3216.
199. Bröring, M.; Kleeberg, C. *Inorg. Chim. Acta* **2007**, *360*, 3281–3286.
200. Bröring, M.; Kleeberg, C. *J. Porphyrins Phthalocyanines* **2008**, *12*, 839–844.
201. Bröring, M.; Kleeberg, C. *Chem. Commun.* **2008**, 2777–2778.
202. Langlotz, B. K.; Fillol, J. L.; Gross, J. H.; Wadepohl, H.; Gade, L. H. *Chem. Eur. J.* **2008**, *14*, 10267–10279.
203. Langlotz, B. K.; Wadepohl, H.; Gade, L. H. *Angew. Chem. Int. Ed.* **2008**, *47*, 4670–4674.
204. Bröring, M.; Kleeberg, C. *Inorg. Chim. Acta* **2009**, *362*, 1065–1070.
205. Bröring, M.; Kleeberg, C.; Köhler, S. *Inorg. Chem.* **2008**, *47*, 6404–6412.
206. Kleeberg, C.; Bröring, M. *Polyhedron* **2010**, *29*, 507–513.
207. Mazet, C.; Gade, L. H. *Organometallics* **2001**, *20*, 4144–4146.
208. Mazet, C.; Gade, L. H. *Chem. Eur. J.* **2002**, *8*, 4308–4318.
209. Gade, L. H.; Mazet, C. *Chem. Eur. J.* **2003**, *9*, 1759–1767.
210. Konrad, F.; Fillol, J. L.; Wadepohl, H.; Gade, L. H. *Inorg. Chem.* **2009**, *48*, 8523–8535.
211. Inoue, M.; Suzuki, T.; Nakada, M. *J. Am. Chem. Soc.* **2003**, *125*, 1140–1141.
212. Suzuki, T.; Kinoshita, A.; Kawada, H.; Nakada, M. *Synlett*. **2003**, 570–572.
213. Inhoffen, H. H.; Maschler, H.; Gossauer, A. *Liebigs Ann. Chem.* **1973**, 141–145.
214. Fuhrhop, J.-H.; Salik, A.; Subramanian, J.; Mengersen, C.; Besecke, S. *Liebigs Ann. Chem.* **1975**, 1131–1147.
215. Bonnett, R.; Dimsdale, M. J. *J. Chem. Soc. Perkin 1* **1972**, 2540–2548.

216. Crusats, J.; Suzuki, A.; Mizutani, T.; Ogoshi, H. *J. Org. Chem.* **1998**, *63*, 602–607.
217. Yamauchi, T.; Mizutani, T.; Wada, K.; Horii, S.; Furukawa, H.; Masoka, S.; Chang, H.-C.; Kitagawa, S. *Chem. Commun.* **2005**, 1309–1311.
218. Asano, N.; Uemura, S.; Kinugawa, T.; Akasaka, H.; Mizutani, T. *J. Org. Chem.* **2007**, *72*, 5320–5326.
219. Fuhrhop, J.-H.; Wasser, P. K. W.; Subramanian, J.; Schrader, U. *Liebigs Ann. Chem.* **1974**, 1450–1466.
220. Setsune, J.-I.; Kashihara, K.; Wada, K. *Chem. Lett.* **2001**, 72–73.
221. Smith, K. M.; Brown, S. B.; Troxler, R. F.; Lai, J.-J. *Tetrahedron Lett.* **1980**, *21*, 2763–2766.
222. Smith, K. M.; Brown, S. B.; Troxler, R. F.; Lai, J.-J. *Photochem. Photobiol.* **1982**, *36*, 147–152.
223. Cavaleiro, J. A. S.; Hewlins, M. J. E.; Jackson, A. H.; Neves, M. G. P. M. S. *Tetrahedron Lett.* **1992**, *33*, 6871–6874.
224. Cavaleiro, J. A. S.; Neves, M. G. P. S.; Hewlins, M. J. E.; Jackson, A. H. *J. Chem. Soc. Perkin Trans. 1* **1990**, 1937–1943.
225. Cavaleiro, J. A. S.; Hewlins, M. J. E.; Jackson, A. H.; Neves, G. P. M. S. *J. Chem. Soc. Chem. Commun.* **1986**, 142–144.
226. Jeandon, C.; Krattinger, B.; Ruppert, R.; Callot, H. J. *Inorg. Chem.* **2001**, *40*, 3149–3153.
227. Iturraspe, J.; Gossauer, A. *Tetrahedron* **1992**, *48*, 6807–6812.
228. Iturraspe, J.; Gossauer, A. *Helv. Chim. Acta* **1991**, *74*, 1713–1717.
229. Curty, C.; Engel, N.; Iturraspe, J.; Gossauer, A. *Photochem. Photobiol.* **1995**, *61*, 552–556.
230. Ongayi, O.; Vicente, M. G. H.; Ou, Z.; Kadish, K. M.; Kumar, M. R.; Fronczek, F. R.; Smith, K. M. *Inorg. Chem.* **2006**, *45*, 1463–1470.
231. Cavaleiro, J. A. S.; Smith, K. M. *J. Chem. Soc. Perkin 1* **1973**, 2149–2155.
232. Isaac, M.; Senge, M. O.; Smith, K. M. *J. Chem. Soc. Perkin Trans. 1* **1995**, 705–714.
233. Hinze, R.-P.; Schiebel, H. M.; Laas, H.; Heise, K.-P.; Gossauer, A.; Inhoffen, H. H. *Liebigs Ann. Chem.* **1979**, 811–828.
234. Holze, G.; Inhoffen, H. H. *Angew. Chem. Int. Ed. Engl.* **1985**, *24*, 867–869.
235. Tardieux, C.; Gros, C. P.; Guilard, R. *J. Heterocycl. Chem.* **1998**, *35*, 965–970.
236. Fischer, H.; Stachel, A. *Hoppe-Seyler's Z. Physiol. Chem.* **1939**, *258*, 121–136.
237. Siedel, W.; Möller, H. *Hoppe-Seyler's Z. Physiol. Chem.* **1939**, *113*, 113–136.
238. Johnson, A. W.; Price, R. *J. Chem. Soc.* **1960**, 1649–1653.
239. Dolphin, D.; Harris, R. L. N.; Huppatz, J. L.; Johnson, A. W.; Kay, I. T.; Leng, J. *J. Chem. Soc. C* **1966**, 98–106.
240. Falk, H.; Flödl, H.; Wagner, U. G. *Monatsh. Chem.* **1988**, *119*, 739–749.
241. Simkhovich, L.; Goldberg, I.; Gross, Z. *Org. Lett.* **2003**, *5*, 1241–1244.
242. Gill, H. S.; Finger, I.; Bozidarevic, I.; Szydlo, F.; Scott, M. J. *New J. Chem.* **2005**, *29*, 68–71.
243. Bonnett, R.; Buckley, D. G.; Hamzetash, D. *J. Chem. Soc. Perkin Trans. 1* **1981**, 322–325.
244. Gossauer, A.; Inhoffen, H. H.; *Liebigs Ann. Chem.* **1970**, *738*, 18–30.
245. Lightner, D. A.; Quistad, G. B.; Pak, C. S. *Synthesis* **1976**, 335–336.
246. Mizutani, T.; Yagi, S.; Honmaru, A.; Goldacker, T.; Kitagawa, S.; Furusyo, M.; Takagishi, T.; Ogoshi, H. *Supramol. Chem.* **1999**, *10*, 297–308.
247. Wijesekera, T. P.; Dolphin, D. *Synlett.* **1990**, *5*, 235–244.
248. Jackson, A. H.; Kenner, G. W.; McGillivray, G.; Sach, G. S. *J. Am. Chem. Soc.* **1965**, *87*, 676–677.
249. Clezy, P. S.; Liepa, A. J. *Aust. J. Chem.* **1971**, *24*, 1027–1040.

250. Conlon, J. M.; Elix, J. A.; Feutrill, G. I.; Johnson, A. W.; Roomi, M. W.; Whelan, J. *J. Chem. Soc. Perkin Trans. 2* **1974**, 713–721.
251. Smith, K. M.; Kishore, D. *Tetrahedron* **1983**, *29*, 1841–1847.
252. Li, W.; Lash, T. D. *Tetrahedron Lett.* **1998**, *39*, 8571–8574.
253. Lash, T. D.; Catarello, J. J. *Tetrahedron* **1993**, *49*, 4159–4172.
254. Gossauer, A.; Fehr, F.; Nydegger, F.; Stöckli-Evans, H. *J. Am. Chem. Soc.* **1997**, *119*, 1599–1608.
255. Chen, Q.-Q.; Falk, H. *Monatsh. Chem.* **1995**, *126*, 1097–1107.
256. Falk, H.; Chen, Q.-Q.; Micura, R. *Monatsh. Chem.* **1996**, *127*, 77–83.
257. Chen, Q.-Q.; Falk, H. *Monatsh. Chem.* **1995**, *126*, 1323–1329.
258. Chen, Q.-Q.; Falk, H. *Monatsh. Chem.* **1995**, *126*, 1233–1244.
259. Nogales, D. F.; Anstine, T. D.; Lightner, D. A. *Tetrahedron* **1994**, *50*, 8579–8596.
260. Maeda, H.; Hashimoto, T. *Chem. Eur. J.* **2007**, *13*, 7900–7907.
261. Guilard, R.; Jêrome, F.; Barbe, J.-M.; Gros, C. P.; Ou, Z.; Shao, J.; Fischer, J.; Weiss, R.; Kadish, K. M. *Inorg. Chem.* **2001**, *40*, 4856–4865.
262. Engel, J.; Gossauer, A. *J. Chem. Soc. Chem. Commun.* **1975**, 570–571.
263. Bröring, M.; Griebel, D.; Hell, C.; Pfister, A. *J. Porphyrins Phthalocyanines* **2001**, *5*, 708–714.
264. Yang, L.; Zhang, Y.; Chen, Q.; Ma, J. S. *Monatsh. Chem.* **2004**, *135*, 223–229.
265. Sessler, J. L.; Brucker, E. A.; Weghorn, S. J.; Kisters, M.; Schäfer, M.; Lex, J.; Vogel, E. *Angew. Chem. Int. Ed. Engl.* **1994**, *33*, 2308–2312.
266. Badger, G. M.; Jones, R. A.; Harris, R. L. N. *Aust. J. Chem.* **1964**, *17*, 1013–1021.
267. Bröring, M. *Synthesis* **2000**, 1291–1294.
268. Bröring, M.; Brégier, F.; Krüger, R.; Kleeberg, C. *Eur. J. Inorg. Chem.* **2008**, 5505–5512.
269. Bröring, M.; Link, S.; Brandt, C. D.; Cónsul Tejero, E. *Eur. J. Inorg. Chem.* **2007**, 1661–1670.
270. Bröring, M.; Brandt, C. D. *Monatsh. Chem.* **2002**, *133*, 623–630.
271. Bröring, M.; Link, S.; Cordes, M.; Brandt, C. D. *Z. Anorg. Allg. Chem.* **2007**, *633*, 211–218.
272. Johnson, A. W.; Kay, I. T. *J. Chem. Soc.* **1961**, 2418–2423.
273. Johnson, A. W.; Kay, I. T. *J. Chem. Soc.* **1965**, 1620–1629.
274. Johnson, A. W.; Overend, W. R. *J. Chem. Soc. Perkin 1* **1972**, 2681–2691.
275. Dolphin, D.; Johnson, A. W.; Leng, J.; van den Broek, P. *J. Chem. Soc. C* **1966**, 880–884.
276. Dolphin, D.; Harris, R. L. N.; Huppatz, J. L.; Johnson, A. W.; Kay, I. T. *J. Chem. Soc. C* **1966**, 30–40.
277. Murakami, Y.; Kohno, Y.; Matsuda, Y. *Inorg. Chim. Acta* **1969**, *3*, 671–675.
278. Inhoffen, H. H.; Schwarz, N.; Heise, K.-P. *Liebigs Ann. Chem.* **1973**, 146–160.
279. Inhoffen, H. H.; Fattinger, F.; Schwarz, N. *Liebigs Ann. Chem.* **1974**, 412–438.
280. Pekel, N. D.; Melenteva, T. A. *Zh. Obshc. Chem.* **1979**, *49*, 2706–2716.
281. Murakami, Y.; Matsuda, Y.; Sakata, K.; Yamada, S.; Tanaka, Y.; Aoyama, Y. *Bull. Chem. Soc. Jpn.* **1981**, *54*, 163–169.
282. Pekel, N. D.; Melenteva, T. A. *Zh. Obshc. Chem.* **1982**, *52*, 106–108.
283. Liu, C.-J.; Thompson, A.; Dolphin, D. *J. Inorg. Biochem.* **2001**, *83*, 133–138.
284. Rumyantsev, E. V.; Antina, E. V. *Russ. J. Gen. Chem.* **2007**, *77*, 1441–1447.
285. Vogel, E.; Michels, M.; Zander, L.; Lex, J.; Tuzun, N. S.; Houk, K. N. *Angew. Chem. Int. Ed.* **2003**, *42*, 2857–2862.
286. Hohlneicher, G.; Bremm, D.; Wytko, J.; Bley-Escrich, J.; Gisselbrecht, J.-P.; Gross, M.; Michels, M.; Lex, J.; Vogel, E. *Chem. Eur. J.* **2003**, *9*, 5636–5642.
287. Falk, H.; Chen, Q.-Q. *Monatsh. Chem.* **1996**, *127*, 69–75.

288. Neya, S.; Nishinaga, K.; Ohyama, K.; Funasaki, N. *Tetrahedron Lett.* **1998**, *39*, 5217–5220.
289. Chen, Q.; Chen, B.; Li, X. *Synth. Commun.* **2000**, *30*, 383–396.
290. Tu, B.; Ghosh, B.; Lightner, D. A. *J. Org. Chem.* **2003**, *68*, 8950–8963.
291. Thompson, A.; Dolphin, D. *J. Org. Chem.* **2000**, *65*, 7870–7877.
292. Zhang, Y.; Wang, Z.; Yan, C.; Li, G.; Ma, J. *Tetrahedron Lett.* **2000**, *41*, 7717–7721.
293. Zhang, Y.; Ma, J. S. *Org. Prep. Proced. Int.* **2001**, *33*, 81–86.
294. Guseva, G. B.; Dudina, N. A.; Antina, E. V.; V'yugin, A. I.; Semeikin, A. S. *Russ. J. Gen. Chem.* **2008**, *78*, 1215–1224.
295. Guseva, G. B.; Dudina, N. A.; Antina, E. V.; V'yugin, A. I.; Semeikin, A. S. *Russ. J. Coord. Chem.* **2009**, *35*, 65–72.
296. Paine III, J. B.; Dolphin, D. *Can. J. Chem.* **1978**, *56*, 1710–1712.
297. Dolphin, D.; Hiom, J.; Paine, J. B. *Heterocycles* **1981**, *16*, 417–447.
298. Ma, L.; Shin, J. Y.; Patrick, B. O.; Dolphin, D. *CrystEngComm* **2008**, *10*, 1531–1533.
299. Ali, A. A.-S.; Benson, R. E.; Blumentritt, S.; Cameron, T. S.; Linden, A.; Wolstenholme, D.; Thompson, A. *J. Org. Chem.* **2007**, *72*, 4947–4952.
300. Wood, T. E.; Ross, A. C.; Dalgleish, N. D.; Power, E. D.; Thompson, A.; Chen, X.; Okamoto, Y. *J. Org. Chem.* **2005**, *70*, 9967–9974.
301. Lin, J. J.; Gerzevske, K. R.; Liddell, P. A.; Senge, M. O.; Olmstead, M. M.; Khoury, R. G.; Weeth, B. E.; Tsao, S. A.; Smith, K. M. *J. Org. Chem.* **1997**, *62*, 4266–4276.
302. Bröring, M.; Hell, C.; Brandt, C. D.; Cónsul Tejero, E. *J. Porphyrins Phthalocyanines* **2003**, *7*, 214–219.
303. Harris, R. L. N.; Johnson, A. W.; Kay, I. T. *Chem. Commun.* **1965**, 232–234.
304. Bamfield, P.; Harris, R. L. N.; Johnson, A. W.; Kay, I. T.; Shelton, K. W. *J. Chem. Soc. C* **1966**, 1436–1443.
305. Dicker, I. D.; Grigg, R.; Johnson, A. W.; Pinnock, H.; Richardson, K.; van den Broek, P. *J. Chem. Soc. C* **1971**, 536–547.
306. Melvin, M. S.; Tomlinson, J. T.; Saluta, G. R.; Kucera, G. L.; Lindquist, N.; Manderville, R. A. *J. Am. Chem. Soc.* **2000**, *122*, 6333–6334.
307. Park, G.; Tomlinson, J. T.; Melvin, M. S.; Wright, M. W.; Day, C. S.; Manderville, R. A. *Org. Lett.* **2003**, *5*, 113–116.
308. Falk, H.; Leodolter, A. *Monatsh. Chem.* **1978**, *109*, 883–897.
309. Eichinger, D.; Falk, H. *Monatsh. Chem.* **1982**, *113*, 355–364.
310. Eichinger, D.; Falk, H. *Monatsh. Chem.* **1987**, *118*, 91–103.
311. Eichinger, D.; Falk, H. *Monatsh. Chem.* **1987**, *118*, 261–271.
312. Bröring, M.; Prikhodovski, S.; Brandt, C. D. *J. Chem. Soc. Dalton Trans.* **2002**, 4213–4218.
313. Bröring, M.; Prikhodovski, S.; Brandt, C. D.; Cónsul Tejero, E. *Chem. Eur. J.* **2007**, *13*, 396–406.
314. Bröring, M.; Prikhodovski, S.; Brandt, C. D.; Cónsul Tejero, E.; Köhler, S.; Pietzonka, C. *Inorg. Chem.* **2007**, *46*, 917–925.
315. Bröring, M.; Prikhodovski, S.; Cónsul Tejero, E.; Köhler, S. *Eur. J. Inorg. Chem.* **2007**, 1010–1019.
316. Bröring, M.; Prikhodovski, S.; Brandt, C. D.; Cónsul Tejero, E. *Z. Anorg. Allg. Chem.* **2007**, *633*, 458–464.
317. Bley-Escrich, J.; Prikhodovski, S.; Brandt, C. D.; Bröring, M.; Gisselbrecht, J.-P. *J. Porphyrins Phthalocyanines* **2003**, *7*, 220–226.

318. Bröring, M.; Prikhodovski, S.; Köhler, S. *Acta Cryst. C* **2007**, *63*, m68–m70.
319. Bröring, M.; Prikhodovski, S.; Brandt, C. D. *Inorg. Chim. Acta* **2004**, *357*, 1733–1738.
320. Bröring, M.; Prikhodovski, S.; Cónsul Tejero, E. *Inorg. Chim. Acta* **2007**, *360*, 2905–2910.
321. Khoury, R. G.; Senge, M. O.; Colchester, J. E.; Smith, K. M. *J. Chem. Soc. Dalton Trans.* **1996**, 3937–3950.
322. Brückner, C.; Mar, E. K.; Rettig, S. J.; Dolphin, D. *Chem. Ber.* **1996**, *129*, 1195–1198.
323. Wicholas, M.; Garrett, A. D.; Gleaves, M.; Morris, A. M.; Rehm, M.; Anderson, O. P.; La Cour, A. *Inorg. Chem.* **2006**, *45*, 5804–5811.
324. Domaille, P. J.; Harlow, R. L.; Ittel, S. D.; Peet, W. G. *Inorg. Chem.* **1983**, *22*, 3944–3952.
325. Balogh-Hergovich, E.; Speier, G.; Réglier, M.; Giorgi, M.; Kuzmann, E.; Vértes, A. *Inorg. Chem. Commun.* **2005**, *8*, 457–459.
326. Letcher, R. J.; Zhang, W.; Bensimon, C.; Crutchley, R. J. *Inorg. Chim. Acta* **1993**, *210*, 183–191.
327. Gagné, R. R.; Gall, R. S.; Lisensky, G. C.; Marsh, R. E.; Speltz, L. M. *Inorg. Chem.* **1979**, *18*, 771–781.
328. Addison, A. W.; Burke, P. J.; Henrick, K. *Inorg. Chem.* **1982**, *21*, 60–63.
329. Bereman, R. D.; Shields, G. D.; Dorfman, J. R.; Bordner, J. *J. Inorg. Biochem.* **1983**, *19*, 75–93.
330. Balogh-Hergovich, E.; Kaizer, J.; Speier, G.; Huttner, G.; Jacobi, A. *Inorg. Chem.* **2000**, *39*, 4224–4229.
331. Baird, D. M.; Maehlmann, W. P.; Bereman, R. D.; Singh, P. *J. Coord. Chem.* **1997**, *42*, 107–126.
332. Anderson, O. P.; la Cour, A.; Dodd, A.; Garrett, A. D.; Wicholas, M. *Inorg. Chem.* **2003**, *42*, 122–127.
333. Baird, D. M.; Hassan, R.; Kim, W. K. *Inorg. Chim. Acta* **1987**, *130*, 39–42.
334. Baird, D. M.; Shih, K. Y.; Welch, J. H.; Bereman, R. D. *Polyhedron* **1989**, *8*, 2359–2365.
335. Baird, D. M.; Shih, K. Y. *Polyhedron* **1991**, *10*, 229–235.
336. Bröring, M.; Kleeberg, C. *Z. Anorg. Allg. Chem.* **2007**, *633*, 2210–2216.
337. Druliner, J. D.; Ittel, S. D.; Krusic, P. J.; Tolman, C. A. US 4326084.
338. Ittel, S. D.; Peet, W. G. 48024 A1.
339. Hermolin, J. US 4499305.
340. Igersheim, F.; Costantini, M. EP 270468 A2.
341. Tolman, C. A.; Druliner, J. D.; Krusic, P. J.; Nappa, M. J.; Seidel, W. C.; Williams, I. D.; Ittel, S. D. *J. Mol. Catal.* **1988**, *48*, 129–148.
342. Saussine, L.; Brazi, E.; Robine, A.; Mimoun, H.; Fischer, J.; Weiss, R. *J. Am. Chem. Soc.* **1985**, *107*, 3534–3540.
343. Farinas, E. T.; Nguyen, C. V.; Mascharak, P. K. *Inorg. Chim. Acta* **1997**, *263*, 17–21.
344. Capacchione, C.; Wadepohl, H.; Gade, L. H. *Z. Anorg. Allg. Chem.* **2007**, *633*, 2131–2134.
345. Inoue, M.; Suzuki, T.; Kinoshita, A.; Nakada, M. *Chem. Rec.* **2008**, *8*, 169–181.
346. O'Carra, P. *Nature* **1962**, *195*, 899–900.
347. Velapoldi, R. A.; Menis, O. *Clin. Chem.* **1971**, *17*, 1165–1170.
348. Kuenzle, C. C.; Pelloni, R. R.; Weibel, M. H.; Hemmerich, P. *Biochem. J.* **1972**, *130*, 1147–1150.
349. Van Norman, J. D.; Szentirmay, R. *Bioinorg. Chem.* **1974**, *4*, 37–43.
350. Van Norman, J. D.; Humans, M. M. *Anal. Chem.* **1974**, *46*, 926–929.
351. Van Norman, J. D.; Yatsko, E. T. *Bioinorg. Chem.* **1978**, *9*, 349–353.

352. Sovago, I.; Harman, B.; Kolozsvari, I.; Matyuska, F. *Inorg. Chim. Acta* **1985**, *106*, 181–186.
353. Hutchinson, D. W.; Johnson, B.; Knell, A. J. *Biochem. J.* **1973**, *133*, 399–400.
354. Chen, J.; Hu, J.-M.; Xu, Z.-S.; Sheng, R.-S. *Spectrochimi. Acta A* **1994**, *50*, 929–936.
355. Hu, J.-M.; Liang, E.-J.; Duschek, F.; Kiefer, W. *Spectrochimi. Acta A* **1997**, *53*, 1431–1438.
356. Mintcheva, N.; Antonov, L.; Mitewa, M.; Ponticelli, G.; Cocco, M. T. *Trans. Met. Chem.* **2003**, *28*, 316–322.
357. Garner, R. J. *Nature* **1954**, *173*, 451–452.
358. Falk, H.; Gergely, S.; Grubmayr, K.; Hofer, O. *Z. Naturforsch. B* **1977**, *32*, 299–303.
359. Lemberg, R. *Biochem. J.* **1934**, *38*, 978–987.
360. Beringhelli, T.; Morazzoni, F.; Manitto, P.; Monti, D. *Spectrochim. Acta A* **1983**, *39*, 751–759.
361. Subramanian, J.; Fuhrhop, J.-H.; Salek, A.; Gossauer, A. *J. Magn. Res.* **1974**, *15*, 19–30.
362. Spasojevic, I.; Batinic-Haberle, I.; Stevens, R. D.; Hambright, P.; Thorpe, A. N.; Grodkowski, J.; Neta, P.; Fridovich, I. *Inorg. Chem.* **2001**, *40*, 726–739.
363. Spasojevic, I.; Batinic-Haberle, I. *Inorg. Chim. Acta* **2001**, *317*, 230–242.
364. Gencheva, G.; Bobev, S.; Mitewa, M. *Res. Chem. Intermed.* **1997**, *23*, 101–107.
365. Mitewa, M.; Gencheva, G.; Bobev, S.; Gochev, G.; Mehandjiev, D.; Wawer, I. *Res. Chem. Intermed.* **1999**, *25*, 431–439.
366. Bonfiglio, J. V.; Bonnett, R.; Hursthouse, M. B.; Malik, K. M. A. *J. Chem. Soc. Chem. Commun.* **1977**, 83–84.
367. Bonfiglio, J. V.; Bonnett, R.; Buckley, D. G.; Hamzetash, D.; Hursthouse, M. B.; Malik, K. M. A.; McDonagh, A. F.; Trotter, J. *Tetrahedron* **1983**, *39*, 1865–1874.
368. Balch, A. L.; Mazzanti, M.; Noll, B. C.; Olmstead, M. M. *J. Am. Chem. Soc.* **1994**, *116*, 9114–9122.
369. Jaumà, A.; Escuer, A.; Farrera, J.-A.; Ribó, J. M. *Monatsh. Chem.* **1996**, *127*, 1051–1062.
370. Balch, A. L.; Mazzanti, M.; St. Claire, T. N.; Olmstead, M. M. *Inorg. Chem.* **1995**, *34*, 2194–2200.
371. Attar, S.; Balch, A. L.; Van Calcar, P. M.; Winkler, K. *J. Am. Chem. Soc.* **1997**, *119*, 3317–3323.
372. Attar, S.; Ozarowski, A.; Van Calcar, P. M.; Winkler, K.; Balch, A. L. *Chem. Commun.* **1997**, 1115–1116.
373. Koerner, R.; Olmstead, M. M.; Van Calcar, P. M.; Winkler, K.; Balch, A. L. *Inorg. Chem.* **1998**, *37*, 982–988.
374. Lord, P. A.; Olmstead, M. M.; Balch, A. L. *Inorg. Chem.* **2000**, *39*, 1128–1134.
375. Balch, A. L.; Mazzanti, M.; Noll, B. C.; Olmstead, M. M. *J. Am. Chem. Soc.* **1993**, *115*, 12206–12207.
376. Anglada, M. C.; Farrera, J.-A.; Ribó, J. M. *Tetrahedron Lett.* **1997**, *38*, 669–672.
377. Szterenberg, L.; Latos-Grazynski, L.; Wojaczynski, J. *ChemPhysChem* **2003**, *4*, 691–698.
378. Wasbotten, I.; Ghosh, A. *Inorg. Chem.* **2006**, *45*, 4914–4921.
379. Koerner, R.; Olmstead, M. M.; Ozarowski, A.; Phillips, S. L.; Van Calcar, P. M.; Winkler, K.; Balch, A. L. *J. Am. Chem. Soc.* **1998**, *120*, 1274–1284.
380. Struckmeier, G.; Thewalt, U.; Fuhrhop, J.-H. *J. Am. Chem. Soc.* **1976**, *98*, 278–279.
381. Sprutta, N.; Rath, S. P.; Olmstead, M. M.; Balch, A. L. *Inorg. Chem.* **2005**, *44*, 1452–1459.
382. Phillips, S.; Noll, B. C.; Olmstead, M. M.; Balch, A. L. *Can. J. Chem.* **2001**, *79*, 922–929.
383. Koerner, R.; Olmstead, M. M.; Ozarowski, A.; Balch, A. L. *Inorg. Chem.* **1999**, *38*, 3262–3263.

384. Shimizu, T.; Asano, N.; Mizutani, T.; Chang, H.-C.; Kitagawa, S. *Tetrahedron Lett.* **2009**, *50*, 536–539.
385. Kita, K.; Tokuoka, T.; Monno, E.; Yagi, S.; Nakazumi, H.; Mizutani, T. *Tetrahedron Lett.* **2006**, *47*, 1533–1536.
386. Matsui, E.; Matsuzawa, N. N.; Harnack, O.; Yamauchi, T.; Hatazawa, T.; Yasuda, A.; Mizutani, T. *Adv. Mater.* **2006**, *18*, 2523–2528.
387. Fuhrhop, J.-H.; Krüger, P. *Liebigs Ann. Chem.* **1977**, 360–370.
388. Gerlach, B.; Montforts, F.-P. *Liebigs. Ann. Chem.* **1995**, 1509–1514.
389. Latos-Grazynski, L.; Johnson, J.; Attar, S.; Olmstead, M. M.; Balch, A. L. *Inorg. Chem.* **1998**, *37*, 4493–4499.
390. Johnson, J. A.; Olmstead, M. M.; Balch, A. L. *Inorg. Chem.* **1999**, *38*, 5379–5383.
391. Johnson, J. A.; Olmstead, M. M.; Stolzenberg, A. M.; Balch, A. L. *Inorg. Chem.* **2001**, *40*, 5585–5595.
392. Cole, W. J.; Gray, C. H.; Nicholson, D. C.; Norman, M. *J. Chem. Soc. C* **1966**, 1321–1326.
393. Makarova, S. P.; Rumyantsev, E. V.; Antina, E. V. *Russ. J. Phys. Chem. A* **2008**, *82*, 2030–2034.
394. Murakami, Y.; Matsuda, Y.; Kanaoka, Y. *Bull. Chem. Soc. Jpn.* **1971**, *44*, 409–415.
395. Khoury, R. G.; Jaquinod, L.; Smith, K. M. *Tetrahedron* **1998**, *54*, 2339–2346.
396. Bröring, M.; Brandt, C. D.; Lex, J.; Humpf, H.-U.; Bley-Escrich, J.; Gisselbrecht, J.-P. *Eur. J. Inorg. Chem.* **2001**, 2549–2556.
397. Bröring, M.; Brandt, C. D.; Bley-Escrich, J.; Gisselbrecht, J.-P. *Eur. J. Inorg. Chem.* **2002**, 910–917.
398. Zucca, A.; Cinellu, M. A.; Pinna, M. V.; Stoccoro, S.; Minghetti, G.; Manassero, M.; Sansoni, M. *Organometallics* **2000**, *19*, 4295–4304.
399. Seoccoro, S.; Chelucci, G.; Cinellu, M. A.; Zucca, A.; Minghetti, G. *J. Organomet. Chem.* **1993**, *450*, C15–C16.
400. Seoccoro, S.; Soro, B.; Minghetti, G.; Zucca, A.; Cinellu, M. A. *J. Organomet. Chem.* **2003**, *679*, 1–9.
401. Hegde, V.; Madhukar, P.; Madura, J. D.; Thummel, R. P. *J. Am. Chem. Soc.* **1990**, *112*, 4549–4550.
402. Dobler, M.; Dunitz, J. D. *Helv. Chim. Acta* **1971**, *54*, 90–98.
403. Currie, M.; Dunitz, J. D. *Helv. Chim. Acta* **1971**, *54*, 98–112.
404. Mizutani, T.; Yagi, S. *J. Porphyrins Phthalocyanines* **2004**, *8*, 226–237.
405. Mizutani, T.; Yagi, S.; Honmaru, A.; Ogoshi, H. *J. Am. Chem. Soc.* **1996**, *118*, 5318–5319.
406. Mizutani, T.; Yagi, S.; Honmaru, A.; Murakami, S.; Furusyo, M.; Takagishi, T.; Ogoshi, H. *J. Org. Chem.* **1998**, *63*, 8769–8784.
407. Yagi, S.; Morinaga, T.; Nomura, T.; Takagishi, T.; Mizutani, T.; Kitagawa, S.; Ogoshi, H. *J. Org. Chem.* **2001**, *66*, 3848–3853.
408. Mizutani, T.; Sakai, N.; Yagi, S.; Takagishi, T.; Kitagawa, S.; Ogoshi, H. *J. Am. Chem. Soc.* **2000**, *122*, 748–749.
409. Hamakubo, K.; Yagi, S.; Nakazumi, H.; Mizutani, T.; Kitagawa, S. *Tetrahedron Lett.* **2005**, *46*, 7151–7154.
410. Mizutani, T.; Yagi, S.; Morinaga, T.; Nomura, T.; Takagishi, T.; Kitagawa, S.; Ogoshi, H. *J. Am. Chem. Soc.* **1999**, *121*, 754–759.
411. Yagi, S.; Sakai, N.; Yamada, R.; Takahashi, H.; Mizutani, T.; Takagishi, T.; Kitagawa, S.; Ogoshi, H. *Chem. Commun.* **1999**, 911–912.

412. Yagi, S.; Sadachi, H.; Kashiwagi, Y.; Takagishi, T.; Mizutani, T.; Kitagawa, S.; Ogoshi, *Chem. Lett.* **2000**, 1054–1055.
413. Hamakubo, K.; Yagi, S.; Nakazumi, H.; Mizutani, T.; Kitagawa, S. *Tetrahedron* **2006**, *62*, 3619–3628.
414. Yagi, S.; Hamakubo, K.; Ikawa, S.; Nakazumi, H.; Mizutani, T. *Tetrahedron* **2008**, *64*, 10598–10604.
415. Sheldrick, W. S.; Engel, J. *J. Chem. Soc. Chem. Commun.* **1980**, 5–6.
416. Sheldrick, W. S.; Engel, J. *Acta Cryst. B* **1981**, *37*, 250–252.
417. Thompson, A.; Rettig, S. J.; Dolphin, D. *Chem. Commun.* **1999**, 631–632.
418. Shan, X.; Yang, L.; Li, W.; Chen, Q.; Wang, Z. *J. Chem. Crystallogr.* **2004**, *34*, 433–439.
419. Yang, L. Y.; Zhang, Y.; Yang, G. Q.; Chen, Q.-Q.; Ma, J. S. *Dyes Pigm.* **2004**, *62*, 27–33.
420. Li, W.; Wang, Y.-B.; Yang, L.-Y.; Shan, X.-F.; Cai, X.; Szeghalmi, A.; Ye, Y.; Ma, J.-S.; Luo, M.-D.; Hu, J.; Kiefer, W. *J. Phys. Chem. B* **2006**, *110*, 21958–21965.
421. Zhang, Z.; Dolphin, D. *Chem. Commun.* **2009**, 6931–6933.
422. Thompson, A.; Dolphin, D. *Org. Lett.* **2000**, *2*, 1315–1318.
423. Wood, T. E.; Dalgleish, N. D.; Power, E. D.; Thompson, A.; Chen, X.; Okamoto, Y. *J. Am. Chem. Soc.* **2005**, *127*, 5740–5741.
424. Bröring, M.; Cónsul Tejero, E.; Pfister, A.; Brandt, C. D.; Pérez Torrente, J. J. *Chem. Commun.* **2002**, 3058–3059.
425. Bröring, M.; Cónsul-Tejero, E. *J. Organomet. Chem.* **2005**, *690*, 5290–5299.
426. Bröring, M.; Brandt, C. D.; Cónsul-Tejero, E. *Z. Anorg. Allg. Chem.* **2005**, *631*, 1793–1798.
427. Lord, P. A.; Olmstead, M. M.; Balch, A. L. *Angew. Chem. Int. Ed.* **1999**, *38*, 2761–2763.
428. Lord, P. A.; Noll, B. C.; Olmstead, M. M.; Balch, A. L. *J. Am. Chem. Soc.* **2001**, *123*, 10554–10559.
429. Bröring, M.; Pfister, A.; Ilg, K. *Chem. Commun.* **2000**, 1407–1408.
430. Bröring, M.; Brandt, C. D.; Link, S. *Inorg. Chim. Acta* **2005**, *358*, 3122–3134.
431. Bröring, M.; Brandt, C. D.; Stellwag, S. *Chem. Commun.* **2003**, 2344–2345.
432. Bröring, M.; Brandt, C. D. *Chem. Commun.* **2003**, 2156–2157.
433. Bröring, M.; Brandt, C. D.; Köhler, S.; Sieber, M. *J. Porphyrins Phthalocyanines* **2005**, *9*, 683–690.
434. Bröring, M.; Kleeberg, C. *Z. Anorg. Allg. Chem.* **2008**, *634*, 2793–2798.
435. Bröring, M.; Kleeberg, C. *Z. Anorg. Allg. Chem.* **2008**, *634*, 946–949.
436. Bröring, M.; Kleeberg, C. *Dalton Trans.* **2007**, 1101–1103.
437. Mazet, C.; Gade, L. H. *Organometallics* **2001**, *20*, 4144–4146.
438. Siggelkow, B. A.; Meder, M. B.; Galka, C. H.; Gade, L. H. *Eur. J. Inorg. Chem.* **2004**, 3424–3435.
439. Siggelkow, B. A.; Gade, L. H. *Z. Anorg. Allg. Chem.* **2005**, *631*, 2575–2584.
440. Matsui, T.; Omori, K.; Jin, H.; Ikeda-Saito, M. *J. Am. Chem. Soc.* **2008**, *130*, 4220–4221.
441. St. Claire, T. N.; Balch, A. L. *Inorg. Chem.* **1999**, *38*, 684–691.
442. Balch, A. L.; Latos-Grazynski, L.; Noll, B. C.; Olmstead, M. M.; Safari, N. *J. Am. Chem. Soc.* **1993**, *115*, 9056–9061.
443. Rath, S. P.; Olmstead, M. M.; Latos-Grazynski, L.; Balch, A. L. *J. Am. Chem. Soc.* **2003**, *125*, 12678–12679.
444. Koerner, R.; Latos-Grazynski, L.; Balch, A. L. *J. Am. Chem. Soc.* **1998**, *120*, 9246–9255.
445. Latos-Grazynski, L.; Wojacynski, J.; Koerner, R.; Johnson, J. J.; Balch, A. L. *Inorg. Chem.* **2001**, *40*, 4971–4977.

446. Nguyen, K. T.; Rath, S. P.; Latos-Grazynski, L.; Olmstead, M. M.; Balch, A. L. *J. Am. Chem. Soc.* **2004**, *126*, 6210–6211.
447. Kalish, H.; Lee, H. M.; Olmstead, M. M.; Latos-Grazynski, L.; Rath, S. P.; Balch, A. L. *J. Am. Chem. Soc.* **2003**, *125*, 4674–4675.
448. Bröring, M.; Köhler, S.; Link, S.; Burghaus, O.; Pietzonka, C.; Kelm, H.; Krüger, H.-J. *Chem. Eur. J.* **2008**, *14*, 4006–4016.
449. Bröring, M.; Köhler, S. *Z. Anorg. Allg. Chem.* **2008**, *634*, 1469–1471.
450. Bröring, M.; Köhler, S.; Ostapowicz, T.; Funk, M.; Pietzonka, C. *Eur. J. Inorg. Chem.* **2009**, 3628–3635.
451. Bröring, M.; Ostapowicz, T.; Funk, M. *Z. Anorg. Allg. Chem.* **2010**, *636*, 775–778.
452. Ziessel, R.; Ulrich, G.; Harriman, A. *New J. Chem.* **2007**, *31*, 496–501.
453. Ulrich, G.; Ziessel, R.; Harriman, A. *Angew. Chem. Int. Ed.* **2008**, *47*, 1184–1201.
454. Borle, F.; Fehr, F.; Nesvadba, P.; Gossauer, A. *Photochem. Photobiol.* **1997**, *65*, 949–956.
455. Bröring, M.; Krüger, R.; Link, S.; Kleeberg, C.; Köhler, S.; Xie, X.; Ventura, B.; Flamigni, L. *Chem. Eur. J.* **2008**, *14*, 2976–2983.
456. Xie, X.; Yuan, Y.; Krüger, R.; Brégier, F.; Bröring, M. *Magn. Reson. Chem.* **2009**, *47*, 1024–1030.
457. Bröring, M.; Yuan, Y.; Krüger, R.; Kleeberg, C.; Xie, X. *Z. Anorg. Allg. Chem.* **2010**, *636*, 518–523.
458. Ventura, B.; Marconi, G.; Bröring, M.; Krüger, R.; Flamigni, L. *New J. Chem.* **2009**, *33*, 428–438.
459. Beer, G.; Niederalt, C.; Grimme, S.; Daub, J. *Angew. Chem. Int. Ed.* **2000**, *39*, 3252–3255.
460. Beer, G.; Daub, J.; Rurack, K. *Chem. Comm.* **2001**, 1138–1139.
461. Coskun, A.; Baytekin, B. T.; Akkaya, E. U. *Org. Lett.* **2002**, *4*, 2857–2859.
462. Coskun, A.; Akkaya, E. U. *J. Am. Chem. Soc.* **2006**, *128*, 14474–14475.
463. Kolb, H. C.; Finn, M. G.; Sharpless, K. B. *Angew. Chem. Int. Ed.* **2001**, *40*, 2004–2021.
464. Yilmaz, M. D.; Bozdemir, O. A.; Akkaya, E. U. *Org. Lett.* **2006**, *8*, 2871–2873.
465. Shiragami, T.; Tanaka, K.; Andou, Y.; Tsunami, S.-i.; Matsumoto, J.; Luo, H.; Araki, Y.; Ito, O.; Inoue, H.; Yasuda, M. *J. Photochem. Photobiol. A* **2005**, *170*, 287–297.
466. Azov, V. A.; Schlegel, A.; Diederich, F. *Angew. Chem. Int. Ed.* **2005**, *44*, 4635–4638.
467. Mula, S.; Ulrich, G.; Ziessel, R. *Tetrahedron Lett.* **2009**, *50*, 6383–6388.
468. Holten, D.; Bocian, D.; Lindsey, J. S. *Acc. Chem. Res.* **2002**, *35*, 57–69.
469. Li, F.; Yang, S. I.; Ciringh, Y.; Seth, J.; Martin, C. H.; Singh, D. L.; Kim, D.; Birge, R. R.; Bocian, D. F.; Holten, D.; Lindsey, J. S. *J. Am. Chem. Soc.* **1998**, *120*, 10001–10017.
470. Kumaresan, D.; Agarwal, N.; Gupta, I.; Ravikanth, M. *Tetrahedron* **2002**, *58*, 5347–5356.
471. Kumaresan, D.; Gupta, I.; Ravikanth, M. *Tetrahedron Lett.* **2001**, *42*, 8547–8550.
472. Ravikanth, M.; Agarwal, N.; Kumaresan, D. *Chem. Lett.* **2000**, 836–837.
473. Galletta, M.; Puntoriero, F.; Campagna, S.; Chiorboli, C.; Quesada, M.; Goeb, S.; Ziessel, R. *J. Phys. Chem. A* **2006**, *110*, 4348–4358.
474. Galleta, M.; Campagna, S.; Quesada, M.; Ulrich, G.; Ziessel, R. *Chem. Commun.* **2005**, 4222–4223.
475. Goze, C.; Ulrich, G.; Charbonniere, L.; Cesario, M.; Prange, T.; Ziessel, R. *Chem. Eur. J.* **2003**, *9*, 3748–3755.
476. Ulrich, G.; Ziessel, R. *Synlett*. **2004**, 439–444.
477. Harriman, A.; Rostron, J. P.; Cesario, M.; Ulrich, G.; Ziessel, R. *J. Phys. Chem. A* **2006**, *110*, 7994–8002.
478. Goze, C.; Ulrich, G.; Ziessel, R. *Org. Lett.* **2006**, *8*, 4445–4448.

479. Zhu, M.; Jiang, L.; Yuan, M.; Liu, X.; Ouyang, C.; Zheng, H.; Yin, X.; Zuo, Z.; Liu, H.; Li, Y. *J. Polym. Sci. A* **2008**, *46*, 7401–7410.
480. Alemdaroglu, F. E.; Alexander, S. C.; Ji, D.; Prusty, D. K.; Börsch, M.; Herrmann, A. *Macromolecules* **2009**, *42*, 6529–6536.
481. Donuru, V. R. R.; Vegesna, G. K.; Velayudham, S.; Meng, G.; Liu, H. *J. Polym. Sci. A* **2009**, *47*, 5354–5366.
482. Donuru, V. R.; Vegesna, G. K.; Velayudham, S.; Green, S.; Liu, H. *Chem. Mater.* **2009**, *21*, 2130–2138.
483. Cakmak, Y.; Akkaya, E. U. *Org. Lett.* **2009**, *11*, 85–88.
484. Meng, G.; Velayudham, S.; Smith, A.; Luck, R.; Liu, H. *Macromolecules* **2009**, *42*, 1995–2001.
485. Forgie, J. C.; Skabara, P. J.; Stibor, I.; Vilela, F.; Vobecka, Z. *Chem. Mater.* **2009**, *21*, 1784–1786.
486. Algi, F.; Cihaner, A. *Org. Electron.* **2009**, *10*, 453–458.
487. Nagai, A.; Kokado, K.; Miyake, J.; Chujo, Y. *Macromolecules* **2009**, *42*, 5446–5452.
488. Wang, D.; Miyamoto, R.; Shiraishi, Y.; Hirai, T. *Langmuir* **2009**, *25*, 13176–13182.
489. Nagai, A.; Miyake, J.; Kokado, K.; Nagata, Y.; Chujo, Y. *J. Am. Chem. Soc.* **2008**, *130*, 15276–15278.
490. Smith, K. M. In *The Porphyrin Handbook*; Kadish, K. M.; Smith, K. M.; Guilard R., Eds.; Academic Press: New York, **2003**, Vol. 1, pp. 1–43.
491. Clezy, P. S. *Aust. J. Chem.* **1991**, *44*, 1163–1193.
492. Johnson, A. W. *Chem. Soc. Rev.* **1975**, *4*, 1–26.
493. Evstigneeva, R. P. *Pure Appl. Chem.* **1981**, *53*, 1129–1140.
494. Grigg, R.; Johnson, A. W.; Kenyon, R.; Math, V. B.; Richardson, K. *J. Chem. Soc. C* **1969**, 176–182.
495. Almeida, J. A. P. B.; Kenner, G. W.; Smith, K. M.; Sutton, M. J. *J. Chem. Soc. Chem. Commun.* **1975**, 111–112.
496. Smith, K. M.; Minnetian, O. M. *Synth. Commun.* **1985**, *15*, 75–79.
497. Smith, K. M.; Minnetian, O. M. *J. Chem. Soc. Perkin Trans. 1* **1986**, 277–280.
498. Minnetian, O. M.; Morris, I. K.; Snow, K. M.; Smith, K. M. *J. Org. Chem.* **1989**, *54*, 5567–5574.
499. Liddell, P. A.; Gerzevske, K. R.; Lin, J. J.; Olmstead, M. M.; Smith, K. M. *J. Org. Chem.* **1993**, *58*, 6681–6691.
500. Liddell, P. A.; Olmstead, M. M.; Smith, K. M. *J. Am. Chem. Soc.* **1990**, *112*, 2038–2040.
501. Lash, T. D.; Li, W.; Quizon-Colquitt, D. M. *Tetrahedron* **2007**, *63*, 12324–12342.
502. Boschi, T.; Paolesse, R.; Tagliatesta, P. *Inorg. Chim. Acta* **1990**, *168*, 83–87.
503. Gerzevske, K. R.; Lin, J. J.; Smith, K. M. *Heterocycles* **1994**, *37*, 207–212.
504. Swanson, K. L.; Snow, K. M.; Jeyakumar, D.; Smith, K. M. *Tetrahedron* **1991**, *47*, 685–696.
505. Lin, J. J.; Holmes, R. T.; Smith, K. M. *J. Porphyrins Phthalocyanines* **1998**, *2*, 363–368.
506. Smith, K. M.; Kehres, L. A. *J. Chem. Soc. Perkin Trans. 1* **1983**, 2329–2335.
507. Smith, K. M.; Minnetian, O. M. *J. Org. Chem.* **1985**, *50*, 2073–2080.
508. Paolesse, R. In *The Porphyrin Handbook*; Kadish, K. M.; Smith, K. M.; Guilard R., Eds.; Academic Press: New York, **2003**, Vol. 2, pp. 201–232.
509. Erben, C.; Will, S.; Kadish, K. M. In *The Porphyrin Handbook*; Kadish, K. M.; Smith, K. M.; Guilard, R., Eds.; Academic Press: New York, **2003**, Vol. 2, pp. 233–300.
510. Johnson, A. W.; Kay, I. T. *J. Chem. Soc.* **1961**, 168–169.
511. Bröring, M.; Hell, C. *Chem. Commun.* **2001**, 2336–2337.

512. Bröring, M.; Hell, C.; Steiner, M.; Brandt, C. D. *Z. Anorg. Allg. Chem.* **2007**, *633*, 1082–1086.
513. Bröring, M.; Hell, C.; Brandt, C. D. *Chem. Commun.* **2007**, 1861–1862.
514. Bröring, M.; Brégier, F.; Cónsul Tejero, E., Hell, C.; Holthausen, M. C. *Angew. Chem. Int. Ed.* **2007**, *46*, 445–448.
515. Bröring, M.; Hell, C.; Brégier, F.; Burghaus, O.; Cónsul Tejero, E. *Inorg. Chem.* **2007**, *46*, 5477–5479.
516. Bröring, M.; Köhler, S.; Kleeberg, C. *Angew. Chem. Int. Ed.* **2008**, *47*, 5658–5661.
517. Bröring, M.; Köhler, S. *J. Porphyrins Phthalocyanines* **2008**, *12*, 1111–1117.
518. Eschenmoser, A. *Quart. Rev.* **1970**, *24*, 366–415.
519. Woodward, R. B. *Pure Appl. Chem.* **1973**, *33*, 145–177.
520. Eschenmoser, A. *Angew. Chem. Int. Ed. Engl.* **1988**, *27*, 5–39.
521. Blanche, F.; Cameron, B.; Crouzet, J.; Debussche, L.; Thibaut, D.; Vuilhorgne, M.; Leeper, F. J.; Battersby, A. R. *Angew. Chem. Int. Ed.* **1995**, *34*, 383–411.
522. Genokhova, N. S.; Melenteva, T. A.; Berezovskii, V. M. *Usp. Khim.* **1980**, *49*, 2132–2158.
523. Montforts, F.-P.; Gerlach, B.; Hoeper, F. *Chem. Rev.* **1994**, *94*, 327–347.
524. Harris, R. L. N.; Johnson, A. W.; Kay, I. T. *Chem. Commun.* **1965**, 355–356.
525. Grigg, R.; Johnson, A. W.; von den Broek, P. *J. Chem. Soc. Chem. Commun.* **1967**, 502–503.
526. Clarke, D. A.; Grigg, R.; Harris, R. L. N.; Johnson, A. W.; Kay, I. T.; Shelton, K. W. *J. Chem. Soc. C* **1967**, 1648–1656.
527. Engel, J.; Gossauer, A.; Johnson, A. W. *J. Chem. Soc. Perkin 1* **1978**, 871–875.
528. Melenteva, T. A.; Pekel, N. D.; Berezovskii, V. M. *Zh. Obshc. Khim.* **1970**, *40*, 165–171.
529. Galanin, N. E.; Yakubov, L. A.; Kudrik, E. V.; Shaposhnikov, G. P. *Russ. J. Org. Chem.* **2009**, *45*, 206–210.
530. Dicker, I. D.; Dolphin, D.; Grigg, R.; Johnson, A. W. *J. Chem. Soc. Chem. Commun.* **1967**, 560–561.
531. Inhoffen, H. H.; Buchler, J. W.; Puppe, L.; Rohbock, K. *Liebigs Ann. Chem.* **1971**, *747*, 133–150.
532. Yamada, Y.; Miljkovic, D.; Wehrli, P.; Golding, B.; Löliger, P.; Keese, R.; Müller, K.; Eschenmoser, A. *Angew. Chem. Int. Ed. Engl.* **1969**, *8*, 343–348.
533. Kräutler, B.; Pfaltz, A.; Nordmann, R.; Hodgson, K. O.; Dunitz, J. D.; Eschenmoser, A. *Helv. Chim. Acta* **1976**, *59*, 924–937.
534. Rasetti, V.; Kräutler, B.; Pfaltz, A.; Eschenmoser, A. *Angew. Chem. Int. Ed. Engl.* **1977**, *16*, 459–461.
535. Angst, C.; Kratky, C.; Eschenmoser, A. *Angew. Chem. Int. Ed. Engl.* **1981**, *20*, 263–265.
536. Gossauer, A.; Maschler, H.; Inhoffen, H. H. *Tetrahedron Lett.* **1974**, *15*, 1277–1278.
537. Engel, J.; Inhoffen, H. H. *Liebigs Ann. Chem.* **1977**, 767–771.
538. Inhoffen, H. H.; Maschler, H. *Liebigs Ann. Chem.* **1974**, 1269–1278.
539. Bröring, M. *J. Porphyrins Phthalocyanines* **2008**, *12*, 1242–1249.
540. Bröring, M.; Prikhodovski, S. *Z. Anorg. Allg. Chem.* **2008**, *634*, 2451–2458.
541. Balogh-Hergovich, E.; Speier, G.; Réglier, M.; Giorgi, M.; Kuzmann, E.; Vértes, A. *Eur. J. Inorg. Chem.* **2003**, 1735–1740.
542. Meder, M. B.; Haller, I.; Gade, L. H. *Dalton Trans.* **2005**, 1403–1415.
543. Meder, M.; Galka, C. H.; Gade, L. H. *Monatsh. Chem.* **2005**, *136*, 1693–1706.
544. Maeda, H.; Hasegawa, M.; Hashimoto, T.; Kakimoto, T.; Nishio, S.; Nakanishi, T. *J. Am. Chem. Soc.* **2006**, *128*, 10024–10025.
545. Miao, Q.; Shin, J.-Y.; Patrick, B. O.; Dolphin, D. *Chem. Commun.* **2009**, 2541–2543.

This page intentionally left blank

Index to Volume 8

C

D

E

F

G

H

I

P

R

S

T

U

V

W

Z

Handbook of Porphyrin Science

with Applications to Chemistry, Physics, Materials Science, Engineering, Biology and Medicine

Volume 9

Electronic Absorption Spectra – Phthalocyanines

Karl M. Kadish ▪ Kevin M. Smith ▪ Roger Guilard

Editors

World Scientific

Handbook of Porphyrin Science

with Applications to Chemistry, Physics, Materials Science, Engineering, Biology and Medicine

This page intentionally left blank

Handbook of Porphyrin Science

with Applications to Chemistry, Physics, Materials Science, Engineering, Biology and Medicine

Volume 9

Electronic Absorption Spectra – Phthalocyanines

Editors

Karl M. Kadish
University of Houston, USA

Kevin M. Smith
Louisiana State University, USA

Roger Guilard
Université de Bourgogne, France

World Scientific

NEW JERSEY • LONDON • SINGAPORE • BEIJING • SHANGHAI • HONG KONG • TAIPEI • CHENNAI

Published by

World Scientific Publishing Co. Pte. Ltd.

5 Toh Tuck Link, Singapore 596224

USA office: 27 Warren Street, Suite 401-402, Hackensack, NJ 07601

UK office: 57 Shelton Street, Covent Garden, London WC2H 9HE

British Library Cataloguing-in-Publication Data
A catalogue record for this book is available from the British Library.

HANDBOOK OF PORPHYRIN SCIENCE
with Applications to Chemistry, Physics, Materials Science, Engineering, Biology and Medicine (Volumes 6–10)

ISBN-13 978-981-4307-18-5 (Set)
ISBN-13 978-981-4307-22-2 (Vol. 9)

Typeset by Stallion Press
Email: enquiries@stallionpress.com

Printed in Singapore.

Contents

Preface

Although the porphyrin and tetrapyrrole research area was regarded as "fully matured" during the 20th century, as evidenced for example by the awarding of numerous Nobel Prizes to its principal researchers, new advances and accomplishments in the field still amaze us as editors. The area continues to blossom and to expand into new areas of science and applications that would probably never have occurred to our 20th century heroes. An earlier *Porphyrin Handbook* assembled the large amount of factual data that had been accumulated during the 20th century. Our new venture, the *Handbook of Porphyrin Science* takes a completely new look at our research area and comprehensively details the contemporary science now appearing in the scientific literature that would indeed have been hard to predict even 10 years ago. In particular, fundamentally new methodologies and potential commercial applications of the beautiful compounds that we all love are exemplified, fully recognizing the subtitle of the series — "with applications to chemistry, physics, materials science, engineering, biology and medicine".

The three of us have complementary expertise in physical chemistry, synthetic and bioorganic chemistry, and in synthetic and mechanistic organometallic chemistry; this has enabled us to cover the whole field of porphyrin science and applications, and to devise comprehensive volume and author content. As of the date of writing, between the three of us, we have published more than 1600 tetrapyrrole research articles, and hold 31 patents related to commercial applications of porphyrin science. So we do know our field, and this has enabled us to assemble a first-rate group of experts who have written comprehensive up-to-date chapters with accuracy and authority; we thank our authors for their cooperation and willingness to go along with our highly ambitious schedule for production of these volumes.

We look forward to comments from our readers, and to suggestions that might enable us to expand our basic interests and scientific coverage even further. Meanwhile, we hope that porphyrin researchers, old, new and of the future, will enjoy reading these volumes just as much as we enjoyed planning and, with the help of World Scientific Publishing Company, producing them from manuscript to published article, in a timely manner.

Karl M. Kadish (Houston, Texas, USA)
Kevin M. Smith (Baton Rouge, Louisiana, USA)
Roger Guilard (Dijon, Bourgogne, France)
January, 2010

This page intentionally left blank

Contributing Authors*

Hasrat Ali
Université de Sherbrooke
Sherbrooke, Québec, Canada
Chapter 16

Cristina Alonso
University of Hull
Kingston-upon-Hull, HU6 7RX, UK
Chapter 17

Edith Antunes
Rhodes University
Grahamstown, 6139, South Africa
Chapter 34

Naoki Aratani
Kyoto University
Kyoto 606-8502, Japan
aratani@kuchem.kyoto-u.ac.jp
Chapter 1

Teodor Silviu Balaban
Karlsruhe Institute of Technology
D-76021 Karlsruhe, Germany
Silviu.Balaban@int.fzk.de
Chapter 3

Alan L. Balch
University of California, Davis
Davis, CA 95616, USA
balch@chem.ucdavis.edu
Chapter 40

David P. Ballou
University of Michigan
Ann Arbor, MI 48109-5606, USA
Chapter 28

Faye Bowles
University of California, Davis
Davis, CA 95616, USA
Chapter 40

Ross W. Boyle
University of Hull
Kingston-upon-Hull, HU6 7RX, UK
r.w.boyle@hull.ac.uk
Chapter 17

Ozguncem Bozkulak
Childrens Hospital Los Angeles
Los Angeles, CA 90027, USA
Chapter 22

Martin Bröring
Technische Universität Carolo-Wilhelmina zu Braunschweig
Hagenring 30, Braunschweig, Germany
m.broering@tu-bs.de
Chapter 41

Kevin Burgess
Texas A&M University
College Station, TX 77842, USA
burgess@tamu.edu
Chapter 37

*Full contact information for authors can be found on the title page of each chapter.

José A.S. Cavaleiro
University of Aveiro
3810-193 Aveiro, Portugal
jcavaleiro@ua.pt
Chapter 9

Sung Cho
Yonsei University
Seoul, 120-747, Korea
Chapter 5

Daniel P. Collins
University of South Carolina
Columbia, SC 29208, USA
Chapter 28

John H. Dawson
University of South Carolina
Columbia, SC 29208, USA
dawson@mail.chem.sc.edu
Chapter 28

Ilia G. Denisov
The University of Illinois
Urbana, IL 61801, USA
Denisov@illinois.edu
Chapter 26

Charles Michael Drain
Hunter College of The City University of New York
New York, NY 10065, USA
cdrain@hunter.cuny.edu
Chapter 15

Francis D'Souza
Wichita State University
Wichita, KS 67260-0051, USA
Francis.DSouza@wichita.edu
Chapter 4

Florence Duclairoir
Institut Nanosciences et Cryogénie
38054 Grenoble cedex 9, France
Chapter 47

Manivannan Ethirajan
Roswell Park Cancer Institute
Buffalo, NY 14263, USA
Chapter 19

Alessandro Feis
University of Florence
I-50019 Sesto Fiorentino, Italy
Chapter 31

Angela Ferrario
Childrens Hospital Los Angeles
Los Angeles, CA 90027, USA
Chapter 22

Kimberly B. Fields
University of South Florida
Tampa, FL 33620, USA
Chapters 13, 43

Takamitsu Fukuda
Osaka University
Toyonaka 560-0043, Japan
tfukuda@chem.sci.osaka-u.ac.jp
Chapter 42

Shunichi Fukuzumi
Osaka University
Suita, Osaka 565-0871, Japan
fukuzumi@chem.eng.osaka-u.ac.jp
Chapter 46

Hiroyuki Furuta
Kyushu University
Fukuoka 819-0395, Japan
hfuruta@cstf.kyushu-u.ac.jp
Chapter 10

Jean-Paul Gisselbrecht
Université de Strasbourg
67000 Strasbourg, France
gissel@unistra.fr
Chapter 14

Charles J. Gomer
University of Southern California
Los Angeles, CA 90027, USA
Chapter 22

Bruno Grimm
Friedrich-Alexander-University Erlangen-Nuremberg
91058 Erlangen, Germany
Chapter 2

Dirk M. Guldi
Friedrich-Alexander-University Erlangen-Nuremberg
91058 Erlangen, Germany
dirk.guldi@chemie.uni-erlangen.de
Chapter 2

Anita Hausmann
Friedrich-Alexander-University Erlangen-Nuremberg
91058 Erlangen, Germany
Chapter 2

Takashi Hayashi
Osaka University
Suita 565-0871, Japan
thayashi@chem.eng.osaka-u.ac.jp
Chapter 23

Petra Hellwig
Université de Strasbourg
67000 Strasbourg, France
hellwig@chimie.u-strasbg.fr
Chapter 36

Yoshio Hisaeda
Kyushu University
Fukuoka 819-0395, Japan
yhisatcm@mail.cstm.kyushu-u.ac.jp
Chapter 48

Barry D. Howes
University of Florence
I-50019 Sesto Fiorentino, Italy
Chapter 31

Akira Ikezaki
Toho University
Ota-ku, Tokyo 143-8540, Japan
Chapter 32

Osamu Ito
Tohoku University
Sendai, 981-3215, Japan
Chapter 4

Anabella Ivancich
Centre Nationale de la Recherche Scientifique (URA 2096)
F-91191 Gif-sur-Yvette, France
Chapter 31

Christophe Jeandon
Université de Strasbourg
67000 Strasbourg, France
cjeandon@unistra.fr
Chapter 14

Norbert Jux
Universität Erlangen-Nürnberg
91054 Erlangen, Germany
norbert.jux@chemie.uni-erlanger.de
Chapter 20

Axel Kahnt
Friedrich-Alexander-University Erlangen-Nuremberg
91058 Erlangen, Germany
Chapter 2

David Kessel
Wayne State University School of Medicine
Detroit, MI 48201, USA
dhkessel@med.wayne.edu
Chapter 21

Dongho Kim
Yonsei University
Seoul, 120-747, Korea
dongho@yonsei.ac.kr
Chapters 5, 6

Kil Suk Kim
Yonsei University
Seoul, 120-747, Korea
Chapter 6

Nagao Kobayashi
Tohoku University
Sendai 980-8578, Japan
nagaok@mail.tains.tohoku.ac.jp
Chapters 33, 42

Lechosław Latos-Grażyński
University of Wrocław
Wrocław 50 383, Poland
llg@wchuwr.pl
Chapter 8

Genxi Li
Nanjing University
Nanjing 210093, PR China
genxili@nju.edu.cn
Chapter 27

Jong Min Lim
Yonsei University
Seoul, 120-747, Korea
Chapter 6

Aurore Loudet
Texas A&M University
College Station, TX 77842, USA
Chapter 37

Evgeny A. Lukyanets
Organic Intermediates and Dyes Institute
Moscow, 123995, Russia
rmeluk@niopik.ru
Chapter 11

Marian Luna
Childrens Hospital Los Angeles
Los Angeles, CA 90027, USA
Chapter 22

Hiromitsu Maeda
Ritsumeikan University
Kusatsu 525-8577, Japan
maedahir@ph.ritsumei.ac.jp
Chapter 38

Jean-Claude Marchon
Institut Nanosciences et Cryogénie
38054 Grenoble cedex 9, France
jean-claude.marchon@cea.fr
Chapter 47

M. Victoria Martínez-Díaz
Universidad Autónoma de Madrid
28049-Madrid, Spain
Chapter 45

Frederic Melin
Université de Strasbourg
67000 Strasbourg, France
Chapter 36

Shingo Nagano
Tottori University
Tottori 680-8552, Japan
Chapter 25

Mikio Nakamura
Toho University
Ota-ku, Tokyo 143-8540, Japan
mnakamu@med.toho-u.ac.jp
Chapter 32

Wonwoo Nam
Ewha Womans University
Seoul 120-750, South Korea
wwnam@ewha.ac.kr
Chapter 44

Victor N. Nemykin
University of Minnesota Duluth
Duluth, MN 55812, USA
vnemykin@d.umn.edu
Chapter 11

Maria G.P.M.S. Neves
University of Aveiro
3810-193 Aveiro, Portugal
Chapter 9

Tebello Nyokong
Rhodes University
Grahamstown, 6139, South Africa
t.nyokong@ru.ac.za
Chapter 34

Yoshiki Ohgo
Toho University
Ota-ku, Tokyo 143-8540, Japan
Chapter 32

Tetsuo Okujima
Ehime University
Matsuyama 790-8577, Japan
Chapter 7

Noboru Ono
Ehime University
Matsuyama 790-8577, Japan
ononbr@dpc.ehime-u.ac.jp
Chapter 7

Atsuhiro Osuka
Kyoto University
Kyoto 606-8502, Japan
osuka@kuchem.kyoto-u.ac.jp
Chapter 1

Ravindra K. Pandey
Roswell Park Cancer Institute
Buffalo, NY 14263, USA
ravindra.pandey@roswellpark.org
Chapter 19

Nayan J. Patel
Roswell Park Cancer Institute
Buffalo, NY 14263, USA
Chapter 19

Miłosz Pawlicki
University of Wrocław
Wrocław 50 383, Poland
Chapter 8

Sébastien Richeter
Université Montpellier 2
34095 Montpellier Cedex 5, France
sebastien.richeter@univ-montp2.fr
Chapter 14

Beate Röder
Humboldt-Universität zu Berlin
12489 Berlin, Germany
roeder@physik.hu-berlin.de
Chapter 20

Natalie Rucker
Childrens Hospital Los Angeles
Los Angeles, CA 90027, USA
Chapter 22

Joshua V. Ruppel
University of South Florida
Tampa, FL 33620, USA
Chapters 13, 43

Romain Ruppert
Université de Strasbourg
67000 Strasbourg, France
rruppert@unistra.fr
Chapter 14

Aoife Ryan
Trinity College Dublin
Dublin 2, Ireland
Chapter 12

Wolfgang Seitz
Friedrich-Alexander-University
Erlangen-Nuremberg
91058 Erlangen, Germany
Chapter 2

Mathias O. Senge
Trinity College Dublin
Dublin 2, Ireland
sengem@tcd.ie
Chapter 12

Natalia N. Sergeeva
Trinity College Dublin
Dublin 2, Ireland
Chapter 12

Hisashi Shimakoshi
Kyushu University
Fukuoka 819-0395, Japan
Chapter 48

Jae-Yoon Shin
Yonsei University
Seoul, 120-747, Korea
Chapter 6

Yoshitsugu Shiro
Harima Institute
Hyogo 679-5148, Japan
yshiro@riken.jp
Chapters 24, 25

Martha Sibrian-Vazquez
Portland State University
Portland, OR 97201, USA
Chapter 18

Sunaina Singh
Hunter College of The City University of
New York
New York, NY 10065, USA
Chapter 15

Stephen G. Sligar
The University of Illinois
Urbana, IL 61801, USA
s-sligar@uiuc.edu
Chapter 26

Giulietta Smulevich
University of Florence
I-50019 Sesto Fiorentino, Italy
giulietta.smulevich@unifi.it
Chapter 31

Nicole L. Snyder
Hamilton College
Clinton, NY 13323, USA
Chapters 13, 43

Fabian Spänig
Friedrich-Alexander-University Erlangen-Nuremberg
91058 Erlangen, Germany
Chapter 2

Tatyana Spolitak
University of Michigan
Ann Arbor, MI 48109-5606, USA
Chapter 28

Hiroshi Sugimoto
Harima Institute
Hyogo 679-5148, Japan
Chapter 24

Osamu Takikawa
National Center for Geriatrics and Gerontology
Obu, Aichi 474-8522, Japan
Chapter 24

Alison Thompson
Dalhousie University
Halifax, Nova Scotia, Canada
alison.thompson@dal.ca
Chapter 39

Motoki Toganoh
Kyushu University
Fukuoka 819-0395, Japan
Chapter 10

Augusto C. Tomé
University of Aveiro
3810-193 Aveiro, Portugal
Chapter 9

Tomas Torres
Universidad Autónoma de Madrid
28049-Madrid, Spain
tomas.torres@uam.es
Chapter 45

Paola Turano
University of Florence
I-50019 Sesto Fiorentino, Italy
turano@cerm.unifi.it
Chapter 30

Md. Imam Uddin
Dalhousie University
Halifax, Nova Scotia, Canada
Chapter 39

Johan E. van Lier
Université de Sherbrooke
Sherbrooke, Québec, Canada
Johannes.Van.Lier@USherbrooke.ca
Chapter 16

Maria da Graça H. Vicente
Louisiana State University
Baton Rouge, LA 70803, USA
vicente@lsu.edu
Chapter 18

Sam P. de Visser
The University of Manchester
Manchester M1 7DN, UK
sam.devisser@manchester.ac.uk
Chapter 44

F. Ann Walker
University of Arizona
Tucson, AZ 85721-0041, USA
awalker@email.arizona.edu
Chapter 29

Jacek Waluk
Polish Academy of Sciences
01-224 Warsaw, Poland
waluk@ichf.edu.pl
Chapter 35

Sam Wong
Childrens Hospital Los Angeles
Los Angeles, CA 90027, USA
Chapter 22

Tabitha E. Wood
Dalhousie University
Halifax, Nova Scotia, Canada
Chapter 39

Frank Xu
Childrens Hospital Los Angeles
Los Angeles, CA 90027, USA
Chapter 22

Hiroko Yamada
Ehime University
Matsuyama 790-8577, Japan
Chapter 7

Jaesung Yang
Yonsei University
Seoul, 120-747, Korea
Chapter 5

Hyejin Yoo
Yonsei University
Seoul, 120-747, Korea
Chapter 5

Min-Chul Yoon
Yonsei University
Seoul, 120-747, Korea
Chapter 6

Zin Seok Yoon
Yonsei University
Seoul, 120-747, Korea
Chapter 5

X. Peter Zhang
University of South Florida
Tampa, FL 33620, USA
pzhang@cas.usf.edu
Chapters 13, 43

Contents of Volumes 1–10

Volume 1 Supramolecular Chemistry

Volume 2 Synthesis and Coordination Chemistry

Volume 3 Synthetic Methodology

Volume 4 Phototherapy, Radioimmunotherapy and Imaging

Volume 5 Heme Proteins

Volume 6 NMR and EPR Techniques

Volume 7 Physicochemical Characterization

Volume 8 Open-Chain Oligopyrrole Systems

Volume 9 Electronic Absorption Spectra — Phthalocyanines

Volume 10 Catalysis and Bio-Inspired Systems — Part I

This page intentionally left blank

42 UV-Visible Absorption Spectroscopic Properties of Phthalocyanines and Related Macrocycles

Takamitsu Fukuda* and Nagao Kobayashi†

*Department of Chemistry, Graduate School of Medicine, Osaka University, Toyonaka 560-0043, Japan

†Department of Chemistry, Graduate School of Science, Tohoku University, Sendai 980-8578, Japan

List of Abbreviations

1-ClNp	1-chloronaphthalene
AcOEt	ethyl acetate
AcOH	acetic acid
BSA	bovine serum albumin
BuOH	1-butanol
CEL	cremophor EL
CTAC	cetyl trimethylammonium chloride
DCB	*o*-dichlorobenzene
DCM	dichloromethane
dib	diisocyanobenzene
DMA	*N,N*-dimethylacetamide
DMF	*N,N*-dimethylformamide
DMPA	*N,N*-dimethylpropianamide
DMSO	dimethyl sulfoxide
Et	ethyl
EtOH	ethanol
FCS	fetal calf serum
HMPA	hexamethylphosphoric triamide
Me	methyl
MeCN	acetonitrile
MeOH	methanol
$NHEt_2$	diethylamine
PBS	phosphate buffer saline
Ph	phenyl
PhCl	chlorobenzene
PhCN	benzonitrile
$PhNO_2$	nitrobenzene
PMMA	poly(methyl methacrylate)
Pr	propyl
PrOH	1-propanol
PVA	polyvinyl alcohol
py	pyridine
pyz	pyrazine

r. i.	relative intensity
SDS	sodium lauryl sulfate
$TBABF_4$	tetrabutylammonium tetrafluoroborate
TBAP	tetrabutylammonium perchlorate
t-Bu	*tert*-butyl
TFA	trifluoroacetic acid
THF	tetrahydrofuran
TMS	tetramethylsilyl
Ts	tosyl
tz	tetrazine
ε	molar extinction coefficient

I. Introduction

This chapter covers UV-vis absorption spectroscopic properties of phthalocyanines (Pcs) and related macrocycles, including tetraazaporphyrins (TAPs), naphthalocyanines (Ncs), and anthracocyanines (Acs). Pcs consist of four isoindole units, which are linked angularly by four *meso*-nitrogen bridges, leading to a macrocyclic aromatic molecule (Figure 1). Considering the aromatic skeleton of porphyrin as a reference, the replacement of four *meso*-carbons with nitrogen atoms generates a TAP. Therefore, Pcs, Ncs, and Acs are radially benzo-, naphtho-, and anthraco-ring-fused TAP analogs, respectively. Hereafter, the term "Pc" also includes these analogs. Since the chance discovery of an insoluble blue pigment in the early 20th century,[1] and the subsequent structural determination,[2,3] Pc-based dyestuffs, known today as phthalocyanine blue or phthalocyanine green, have been widely employed as robust coloring materials. In the late 20th century, the application of Pcs expanded into various advanced materials, such as dyes for read-write optical media, photosensitizers for photodynamic therapy (PDT), photovoltaic devices, and so forth.[4–18] These sophisticated molecular functionalities are ascribed to the versatile electronic structures of Pcs and as a consequence, Pcs have established a firm position as high-tech materials today.

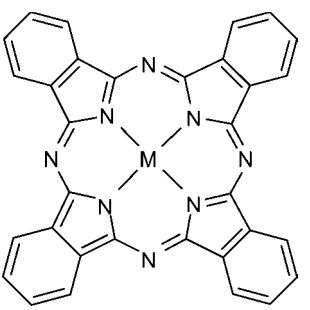

Figure 1. Molecular geometry of a metalloPc. M represents the central element.

More recently, chemists have been able to synthesize more complicated and more controlled Pc derivatives, thanks to the development of advanced synthetic strategies and purification techniques, leading to rapid progress of this academic field over the past decade. UV-vis absorption is one of the most important properties of Pc derivatives, because the spectral shape of an absorption spectrum is closely related to the molecular and electronic structure of the compound. It should also be noted that absorption spectroscopy is routinely used by chemists working in relevant fields, so that they can check their reactions quickly when synthesizing novel Pc derivatives. From this point of view, electronic absorption spectroscopy in Pc chemistry is equivalent to NMR and IR spectroscopy in general organic synthesis, since the appearance of the expected absorption signals provide a very powerful first evidence for formation of the Pc skeletons.

Figure 2 depicts the absorption spectrum of ZnPc in pyridine as an example of the typical spectral pattern of metalloPcs. The sharp, intense band observed in the lowest energy region (674 nm) is an *x*/*y*-polarized π–π^* transition, referred to as the Q band. The broad band in the 300–400 nm region consists of more than one component, including B_1 and B_2 bands, and is referred to as the Soret region.[19] Several less-intense components observed at the foot of the Q band are considered to be of vibronic origin.[20] Vapor phase absorption spectra of typical metalloPcs exhibit additional three-band components in the 200–300 nm region, which are referred to as N, L, and C bands in the order of increasing energy.[21] The characteristics of the B and N bands are sensitive to the central metal, and it is suggested that MLCT and LMCT transitions are involved in this spectral region.[22]

Figure 3 compares the absorption spectra of octaethyl-substituted NiTAP (solid line) and MgTAP (dashed line) in hexane.[23] Intense single Q bands appear at 590 and 596 nm for the nickel and magnesium complexes, respectively, while the near

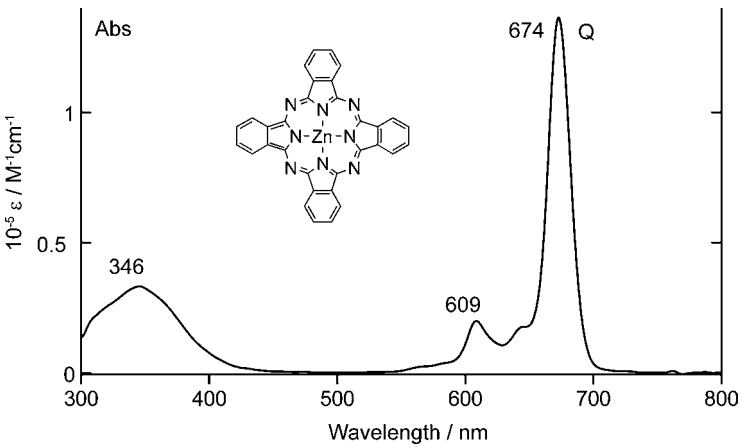

Figure 2. Absorption spectrum of ZnPc in pyridine.

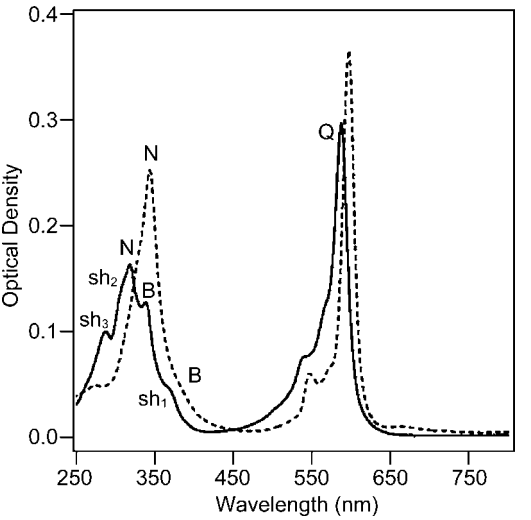

Figure 3. Absorption spectra of octaethyl-substituted NiTAP (solid line) and MgTAP (dashed line) in hexane at room temperature. Redrawn with permission from Rosa, A.; Ricciardi, G.; Baerends, E. J.; van Gisbergen, S. J. A. *J. Phys. Chem. A* **2001**, *105*, 3311–3327. Copyright 2001 American Chemical Society.

UV region shows different spectral shapes. More structure is seen in the near UV region for the nickel complex compared to the magnesium complex. Although not shown, the magnetic circular dichroism (MCD) signal corresponding to the Q band is a derivative-shaped Faraday A term, indicating that the Q band arises from a transition to an orbitrally degenerate excited state. Although the general absorption features of Pcs can be well-described by Gouterman's four-orbital model, various structural parameters such as the central metal and macrocyclic substituents affect the band energy and even the constituents of the observed bands. In this chapter, therefore, we have collected UV-vis absorption data of previously reported Pcs and related analogs, and summarize their spectral characteristics with respect to the molecular structures, central metals, and macrocyclic substituents.

As a general introduction, the theoretical background of the absorption spectral properties of Pcs is described in the first section, followed by a summary of their spectral characteristics. Pcs are classified with respect to their central metal (group), and the way in which the central metal affects the absorption spectral properties is discussed in detail. The relationship between the aromatic skeletal structures and the spectral features, as well as substituent effects will also be included. Although we will not go into detail in this chapter, MCD spectroscopy gives more information on the electronic structures of Pcs than absorption spectroscopy, and therefore, some conclusions based on results from MCD spectroscopy will also be cited where necessary. At the end of this chapter, comprehensive absorption data of the known Pc derivatives are compiled (Tables 1–13), which may assist the reader in designing and/or

characterizing new Pc derivatives during the course of their research. The abbreviations and nomenclatures used in these tables will be explained in the corresponding section. Details of the spectral properties of ring-oxidized or -reduced Pc species are omitted in this chapter, since this was covered in an earlier publication.[24] Finally, the authors would like to inform the reader that several excellent publications and review articles regarding the absorption properties of Pc derivatives are already available. In particular, a Russian book published in 1989 by Luk'yanets is all-inclusive and well-categorized, and was probably the only comprehensive database of absorption data for Pc compounds at that time.[25] The fundamental chemistry of Pcs, including their spectroscopic properties, has been reviewed by Lever.[20] Stillman and Nyokong gave a detailed account of the spectral properties of Pcs in 1989.[26] Detailed discussion on mono-, di-, and triazaporphyrin derivatives is omitted from this chapter, since the properties of these compounds have already been summarized.[27]

II. Basic Theoretical Description of the Absorption Properties of Phthalocyanines

Since the central element of neutral Pcs is formally divalent, the Pc skeleton can be regarded as a dianion. Typical metalloPcs with D_{4h} symmetry have an unsplit lowest-energy band (Q band) in the visible region (*ca.* 650–700 nm) and less-intense B bands in the 300–500 nm region (Soret region). Although charge transfer (CT) transitions are also relevant for metalloPcs having unsaturated transition metal ions at the center, most of the observed absorption bands in the UV-vis region can be ascribed to π–π* transitions. Therefore, a "particle on a ring" model, which often appears in basic quantum chemistry textbooks, is probably the simplest way to describe the electronic structures of Pcs. Historically, porphyrins took the lead in theoretical studies on the electronic structures and optical transitions of this type of macrocyclic molecule. Simpson assumed an 18-membered cyclic polyene having 18 π electrons, which means that the symmetry of the wavefunctions of the HOMO and LUMO are $e^{\pm i4\theta}$ and $e^{\pm i5\theta}$, respectively.[28] Assuming this model, one-electron transitions from the HOMO to LUMO generate four states with the symmetries of $e^{\pm i\theta}$ and $e^{\pm i9\theta}$. The former two states are allowed, and correspond to the Soret band of porphyrins, while the latter are forbidden, being consistent with the weak Q band of porphyrins. This model, however, is unable to sufficiently explain the energy difference between the Soret and Q bands (Figure 4a). Meanwhile, Platt and coworkers obtained porphyrin π-MOs using an LCAO technique.[29] On the basis of this model, the degeneracy of the HOMO obtained by Simpson's model is lifted due to symmetry lowering from the cyclic polyene to the D_{4h} porphyrin skeleton, to give two occupied MOs with a_{1u} and a_{2u} symmetries. The LUMO remains degenerate and has e_{g_x} and e_{g_y} symmetries. Although Platt's model is superior in terms of the energy difference between the Soret

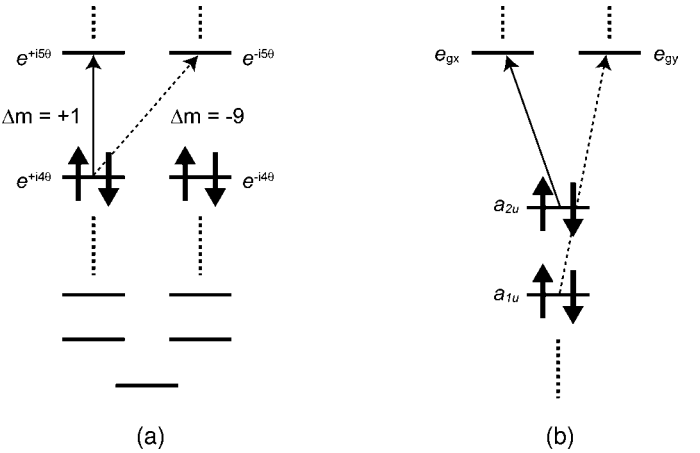

Figure 4. Early MO models of a porphyrin proposed by (a) Simpson[28] and (b) Platt and coworkers.[29]

and Q bands, it does not explain the observed intensity differences (Figure 4b). Therefore, it was necessary to combine these two models in order to understand the absorption spectra of porphyrin. In 1959, Gouterman demonstrated how Simpson's model is related to the LCAO MOs. This model is referred to today as "Gouterman's four-orbital model."[30] Gouterman's four-orbital model states that the two lowest singlet excited states, S_1 and S_2, of D_{4h} porphyrins consist mainly of a linear combination of the $^1(a_{2u}e_g)$ and $^1(a_{1u}e_g)$ configurations, where a_{2u}, a_{1u}, and e_g correspond to the HOMO, HOMO-1, and LUMO of porphyrin, respectively. In other words, one-electron excited states having the same symmetry possibly interact with each other. The degree of this type of configurational interaction depends on the relative energy difference of the related two one-electron excited states, i.e. two degenerate excited states with the same symmetry can interact most significantly. This relationship can be formulated for *y* polarized states as:

$$\left|S_{1y}\right\rangle \equiv \left|Q_y\right\rangle \equiv -\sin\nu\left|B_y^0\right\rangle + \cos\nu\left|Q_y^o\right\rangle, \tag{1}$$

$$\left|S_{2y}\right\rangle \equiv \left|B_y\right\rangle \equiv \cos\nu\left|B_y^0\right\rangle + \sin\nu\left|Q_y^o\right\rangle, \tag{2}$$

where $\left|B_y^0\right\rangle$ and $\left|Q_y^0\right\rangle$ are defined respectively as:

$$\left|B_y^0\right\rangle \equiv 2^{-\frac{1}{2}}\left[^1(a_{2u}e_{gy}) + {}^1(a_{1u}e_{gx})\right], \tag{3}$$

$$\left|Q_y^0\right\rangle \equiv 2^{-\frac{1}{2}}\left[^1(a_{2u}e_{gy}) - {}^1(a_{1u}e_{gx})\right]. \tag{4}$$

Readers should consult the original paper for the definition of tan 2ν.[30] In the case of porphyrin, $2\nu \leq 1$ due to the accidental degeneracy of the a_{1u} and a_{2u} orbitals, and $|Q_y\rangle$ and $|B_y\rangle$ can be approximated as:

$$|Q_y\rangle = |Q_y^0\rangle - \nu|B_y^0\rangle, \tag{5}$$

$$|B_y\rangle = |B_y^0\rangle + \nu|Q_y^0\rangle. \tag{6}$$

As a consequence, the corresponding transition energies E and dipole strengths q for the Q and B bands are:

$$\begin{aligned} E_Q &= \frac{1}{2}\left[E(a_{1u}e_{gx}) + E(a_{2u}e_{gy})\right] - (1+2\nu^2)\int (a_{1u}e_{gx})\mathbf{H}(a_{2u}e_{gy})dv, \\ q_Q^2 &= (\nu R - r)^2, \end{aligned} \tag{7}$$

and

$$\begin{aligned} E_B &= \frac{1}{2}\left[E(a_{1u}e_{gx}) + E(a_{2u}e_{gy})\right] + (1+2\nu^2)\int (a_{1u}e_{gx})\mathbf{H}(a_{2u}e_{gy})dv, \\ q_B^2 &= R^2 - \nu^2 R^2 + 2\nu Rr, \end{aligned} \tag{8}$$

respectively, where R and r are defined as:

$$\begin{aligned} R^2 &\equiv \frac{1}{2}\left(\langle a_{1u}e_{gx}|\mathbf{r}|S_0\rangle + \langle a_{2u}e_{gy}|\mathbf{r}|S_0\rangle\right)^2, \\ r^2 &\equiv \frac{1}{2}\left(\langle a_{1u}e_{gx}|\mathbf{r}|S_0\rangle - \langle a_{2u}e_{gy}|\mathbf{r}|S_0\rangle\right)^2. \end{aligned} \tag{9}$$

Since $\langle a_{1u}e_{gx}|\mathbf{r}|S_0\rangle \approx \langle a_{2u}e_{gy}|\mathbf{r}|S_0\rangle$, $R^2 \geq r^2$. Therefore, much smaller transition moments for the Q band than the B band of porphyrin are expected, which is consistent with the experimental results.

Gouterman confirmed the validity of these formulas by plotting oscillator strength vs. Q-band energy for various metallotetraphenylporphyrins. Figure 5 shows the agreement of experiment with the theoretical relationships, supporting the validity of Gouterman's four orbital model.[31] When the accidental degeneracy of the a_{1u} and a_{2u} orbitals is lifted, largely by changing the molecular structure, ν is no longer much less than 1. In this case, the Q transitions gain intensity, and the Q–B energy separation increases. Figure 6 shows the four frontier orbitals and their energies for TAP, calculated by ZINDO. Unlike porphyrin, the a_{2u} orbital (HOMO–1) is largely stabilized, and the accidental

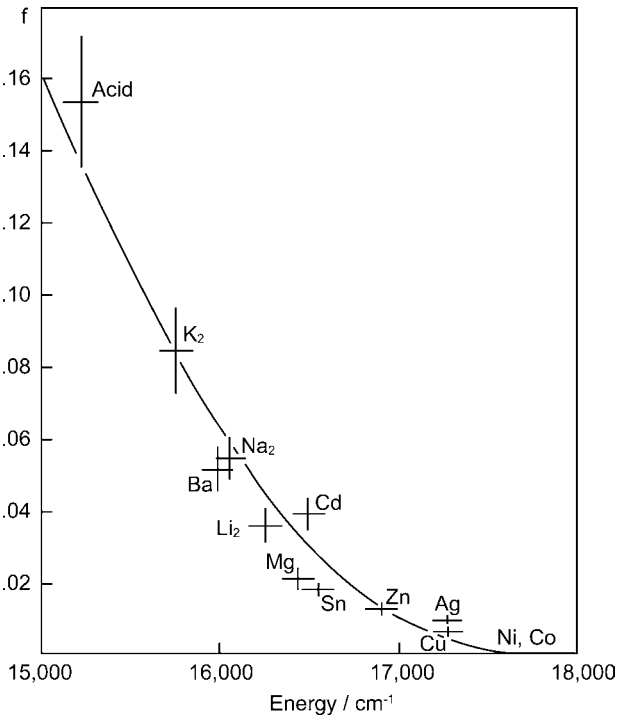

Figure 5. Oscillator strength vs. energy of Q(0–0) band in metallotetraphenylporphyrins. The line is theoretical. Redrawn from Gouterman, M. *J. Mol. Spectrosc.* **1961**, *6*, 138–163. Copyright 1961, with permission from Elsevier.[31]

degeneracy between the a_{1u} and a_{2u} orbitals is lost. The a_{1u} orbital has anti-nodes at the diagonal *meso*-atoms, while the a_{2u} orbital has significant MO amplitude on these four atoms. The large MO amplitude (electron density) at the electronegative atoms leads to stabilization of the corresponding MOs. Therefore, replacement of the four *meso*-carbons with nitrogen atoms, to give the TAP skeleton, results in the stabilization of the a_{2u} (HOMO−1) orbital relative to the a_{1u} orbital (HOMO). As a consequence, the interaction between the $^1(a_{1u}e_g)$ and $^1(a_{2u}e_g)$ configurations calculated for TAPs is not as significant as it is for the porphyrins. In the case of the Q transition of TAPs calculated by the Pariser-Parr-Pople (PPP)-SCF-MO method, the $^1(a_{1u}e_g)$ configuration accounts for *ca.* 72%, while only 57% of the HOMO–LUMO transition contributes to the Q transition for porphyrin.[32] The Q band also becomes purer, the larger the molecule, so that the $^1(a_{1u}e_g)$ configuration accounts for *ca.* 72, 87, 91, and 92% for TAP, Pc, Nc, and Ac, respectively.[32] These results justify Gouterman's four-orbital model for the Q bands, although it is known that higher-lying excited states are necessary to correctly describe the Soret region.

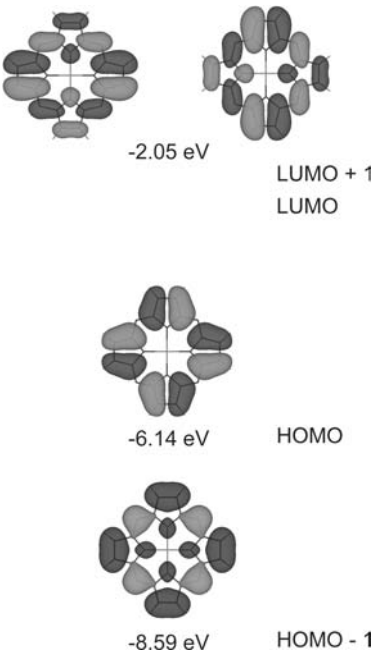

Figure 6. Four frontier MOs of ZnTAP calculated within the framework of the ZINDO method.

Higher-level calculations are able to estimate the effect of non-π electrons such as d electrons and lone pairs on the nitrogen atoms, which are ignored for the Gouterman model. Figure 7 shows energy level schemes for MgTAP, ZnTAP, and NiTAP obtained using DFT calculations (refer to Ref. 22 for details of the calculations). The hatched lines (the $4a_{2u}$, $1a_{1u}$, and $5e_g$ orbitals) indicate that these are the four Gouterman orbitals. The metal 3d orbitals and N_b lone pair orbitals are indicated by heavy lines and dashed lines, respectively. From the calculated results based on the TDDFT method, the Q transition (1^1E_u state) of NiTAP consists of 84% of $1a_{1u} \rightarrow 5e_g$ and 14% of $4a_{2u} \rightarrow 5e_g$ configurations, supporting Gouterman's interpretations (see Table 4 in Ref. 22). Although Gouterman's second-lowest transition corresponds to the $4a_{2u} \rightarrow 5e_g$ configuration-dominated transition, an additional two transitions (2^1E_u and 3^1E_u states) are predicted in between the so-called Q and B transitions, which consist of almost pure $2b_{2u} \rightarrow 5e_g$ and $3a_{2u} \rightarrow 5e_g$ configurations, respectively. Since the transition to the 3^1E_u state is predicted to be very low in intensity, the shoulder denoted as sh_1 in Figure 3 arises mainly from a transition to 2^1E_u. Contrary to the Gouterman model, the next-lowest state (4^1E_u), assigned as the B transition, contains only 38% of the $4a_{2u} \rightarrow 5e_g$ configuration, and instead $4e_g(d\pi) \rightarrow 2b_{1u}(\pi^*)$ and $12e_u(N_b(1one\ pair) \rightarrow 7_{1g}(d\sigma^*)$ configurations account for 44 and 14%, respectively, showing

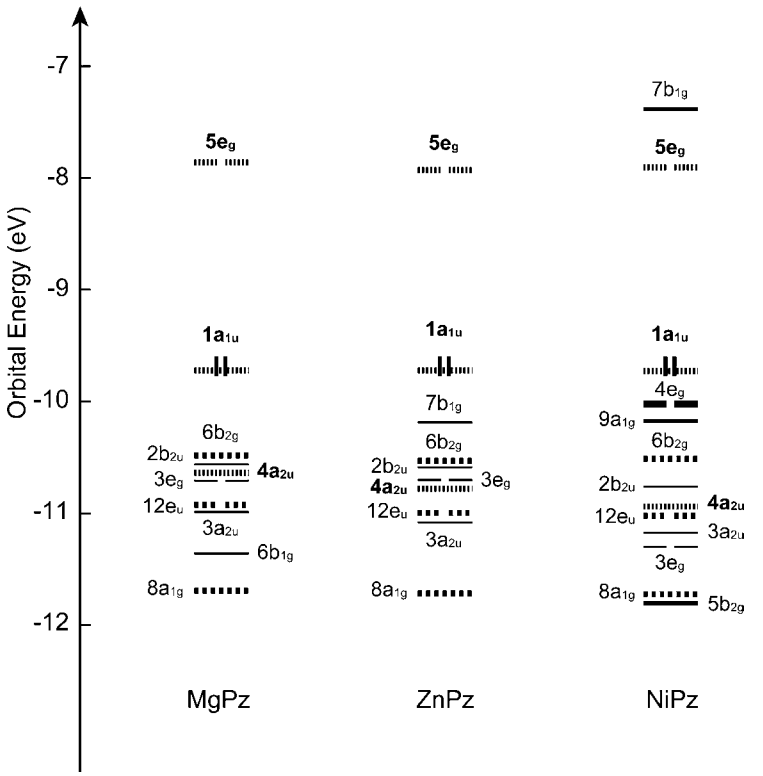

Figure 7. Energy level scheme for MgTAP, ZnTAP and NiTAP. Double occupancy is indicated for the HOMO only. The hatched lines, i.e. $4a_{2u}$, $1a_{1u}$, and $5e_g$ orbitals, indicate that these are the four Gouterman orbitals. The metal 3d orbitals and the N_b lone pair orbitals are indicated with heavy lines and dashed lines, respectively. Redrawn from Baerends, E. J.; Ricciardi, G.; Rosa, A.; van Gisbergen, S. J. A. *Coord. Chem. Rev.* **2002**, *230*, 5–27. Copyright 2002, with permission from Elsevier.

that the presence of MLCT and LMCT transitions cannot be ignored for interpretation of the bands in the near UV region for NiTAPs. The other combinations of these configurations generate an additional two excited states, 5^1E_u and 6^1E_u, of which the latter is assigned to the N transition. In the case of MgTAP and ZnTAP, metal-centered orbitals contribute less significantly to the absorption spectra (see Tables 4 and 5 in Ref. 22). As a result, fewer structures are seen in the absorption spectrum in the near UV region for octaethyl-substituted MgTAP (Figure 3). On the other hand, the $3a_{2u} \rightarrow 5e_g$ configuration is responsible for the B and N transitions in addition to Gouterman's configurations ($4a_{2u} \rightarrow 5e_g$ and 1 $a_{1u} \rightarrow 5e_g$), since ring deformations caused in the magnesium and zinc complexes increase the $4a_{2u}$ orbital energy. The same type of calculations for NiPc has been conducted by the same group, which clarified that the B band of NiPc can no longer be described

in terms of the four-orbital model.[23] In the B band region, seven excited states are predicted, of which the 4^1E_u, 7^1E_u, and 8^1E_u states have large oscillator strengths (see Table 5 in Ref. 23). These are of π–π^* origin, and the 4^1E_u, and 7^1E_u, and 8^1E_u states are assigned to B_1 and B_2 bands, respectively. MLCT and LMCT transitions are involved in the higher-lying excited states.

III. Absorption Spectra of Pcs

A. H_2Pc and HPc

Unsubstituted H_2Pc is sparingly soluble in most organic solvents, while the solubility increases remarkably for substituted H_2Pcs such as tetra-*tert*-butyl H_2Pc. Therefore, vapor-phase[21,33] or matrix-isolated[34–36] absorption spectra were reported in the early papers. Unsubstituted H_2Pc shows split Q band components at *ca.* 693 and 656 nm in $CHCl_3$, CCl_4, and DMF.[37–39] This splitting has been interpreted as due to the diagonally occupying two protons on the pyrrolic nitrogens reducing the molecular symmetry from D_{4h} to D_{2h}, thus lifting the degeneracy of the LUMO. Clear band splitting is not observed for the Soret region at room temperature. Although the solvent dependence of the Q band positions is small, the addition of a strong base to the solution causes deprotonation, to give an unsplit Q band. Whalley reported a coalesced Q band for H_2Pc dissolved in pyridine, suggesting that the two central protons of H_2Pc have some acidity, and are removed from the Pc skeleton in basic media.[40] Figure 8 shows the spectral changes in the Q-band region during the addition of NaOH/EtOH to a solution of H_2Pc in $PhCCl_3$. The initial spectrum exhibits two clear Q-band components, having approximately equal intensity (A). Upon addition of the base, these bands begin to coalesce to a single absorption band (B and C). It is claimed that the two central protons are replaced by sodium cations.[41] The spectral envelope for tetra-*tert*-butyl H_2Pc is practically identical with that of the unsubstituted derivative, as shown in Figure 9.[42] The lower energy Q band position depends slightly on the solvent, ranging from 694 to 703 nm. As a general trend, the Q bands shift to the red in the order of alkanes < oxygen-containing solvents < aromatic hydrocarbons < nitrogen-containing solvents < 1-chloronaphthalene.

The Q-band splitting energy is related to the Q-band energy, and the splitting decreases with increasing size of the aromatic skeleton. Figure 10 depicts the absorption spectra of tetra-*tert*-butyl H_2TAP, Pc, Nc, and Ac (from top to bottom).[43–45] The splitting reaches almost 2000 cm^{-1} for H_2TAP, and decreases to 733 cm^{-1} for H_2Pc. In the case of H_2Nc and H_2Ac, no splitting of the Q band is observed experimentally, although a small splitting can be observed for H_2Ac having a Q band above 950 nm if the conditions permit, as illustrated in Figure 11.[46]

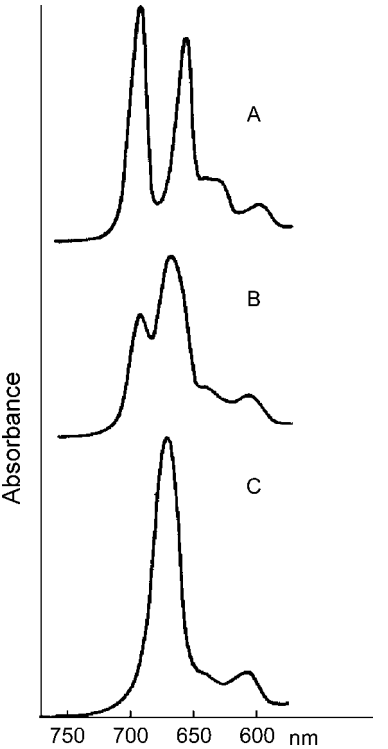

Figure 8. Q-band region of absorption spectra of H_2Pc. A: H_2Pc in $PhCCl_3$, B and C: after addition of NaOH/EtOH solution. Redrawn from Ledson, D. L.; Twigg, M. V. *Inorg. Chim. Acta* **1975**, *13*, 43–46. Copyright 1975, with permission from Elsevier.

A solvent dependency of the splitting energy is also observed for tetra-*tert*-butyl H_2Nc.[47] In *n*-octane, the Q band appears at 778 and 760 nm, while these coalesce to single absorption at 784 nm in $CHCl_3$. According to group theory, a molecule with D_{2h} symmetry has no degenerate excited states. Therefore, it is conceivable that the observed single absorption arises from two energetically-close merged bands. MCD spectroscopy also supports this assignment. In addition, this type of decrease of the splitting energy with respect to the Q-band energy is observed not only for aromatic ring-expanded series but also for Pcs having different substituents.[48]

Low symmetry H_2Pcs can have two tautomers depending on the location of the two central protons. Drobizhev *et al.* observed the two-photon induced photo-tautomerization of a mono-benzo-fused H_2Pc derivative.[49] As depicted in Figure 12, the sample film shows two strong, narrow absorption peaks at 706 and 753 nm at 77 K (T_1), indicating that the T_1 tautomer is the more stable of the two possible structures. A similar tautomerism was also observed by using resonant one-photon

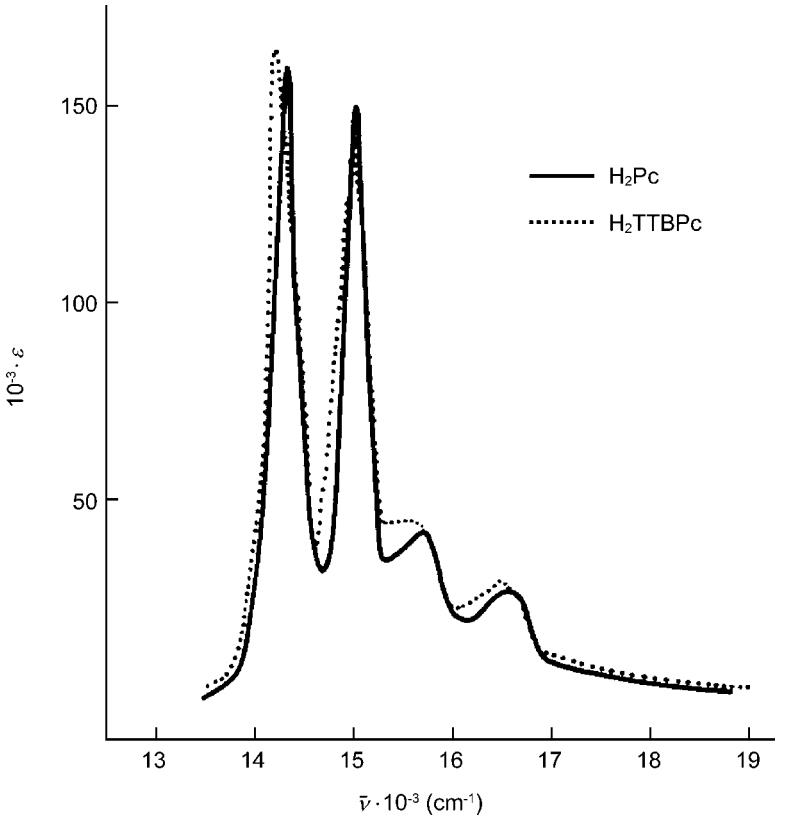

Figure 9. Q-band region of absorption spectra of H_2Pc (solid line) and tetra-*tert*-butyl H_2Pc (dotted line) in 1-chloronaphthalene. Redrawn from Jerwin, K.; Wasgestian, F. *Spectrochim. Acta A* **1984**, *40*, 159–163. Copyright 1984, with permission from Elsevier.

excitation.[50] The absorption spectral shapes of tautomeric isomers of low-symmetry H_2TAP derivatives were assigned by the combined use of MCD spectroscopy and MO calculations (Figure 13).[51] The spectral shapes of $1H_2$ and $3H_2$ in Figure 13 resemble that of the summation of T_1 and T_2 of Ref. 49 (Figure 12), indicating that the observed spectra arise from a mixture of the two tautomers. The MCD spectra show dispersion-type pseudo A-terms corresponding to the bands at 653 and 671 nm for $1H_2$ and $3H_2$, respectively. The calculations predict that these originate from $1H_2Y$ and $3H_2Y$, respectively. On the other hand, band peaks at 701 and 598 nm for $1H_2$, and 709 and 611 nm for $3H_2$ can be assigned to two split Q components, since oppositely-signed MCD signals were observed for these two coupled peaks. The calculations show that these spectra arise from $1H_2X$ and $3H_2X$, respectively. Since the two possible tautomeric structures are identical for $2AdH_2$, only one chemical species likely contributes to the spectrum. In the case of

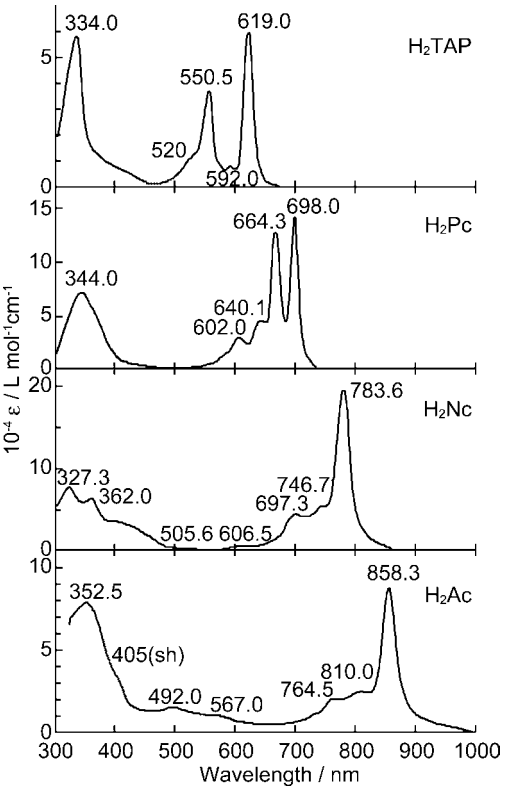

Figure 10. Absorption spectra of tetra-*tert*-butyl H_2TAP, H_2Pc, H_2Nc, and H_2Ac (from top to bottom) in pyridine. Redrawn from Kobayashi, N.; Nakajima, S.; Ogata, H.; Fukuda, T. *Chem. Eur. J.* **2004**, *10*, 6294–6312.

$2OpH_2$, spectral data suggest that only one of the possible two isomers, i.e. $2OpH_2X$, is likely to be present. These observations imply that the stability and equilibrium constants of tautomers depend significantly on the molecular structure.

Figure 14 gives another example of spectral observations demonstrating tautomeric isomers.[52] The thiophene-fused derivative shows three distinct bands in the Q-band region (Figure 14, top), indicating that the spectrum arises from a mixture of two tautomers. Similar spectral shapes were also reported for other thiophene-fused H_2Pcs.[53,54] On the other hand, absorption spectra of the dimethyl acetylenedicarboxylate adduct, and the derivative obtained therefrom (Figure 14, middle and bottom, respectively) appear to originate from one chemical species.

Sugimoto and coworkers prepared the stable free radical of Pc (HPc) by the reaction of Li_2Pc with iodine in acetone.[55] HPc is a dark brown solid, and is almost insoluble in most organic solvents. Figure 15 shows the reflectance spectra of LiPc, HPc, and Li_2Pc from top to bottom (see the subsequent section for LiPc and

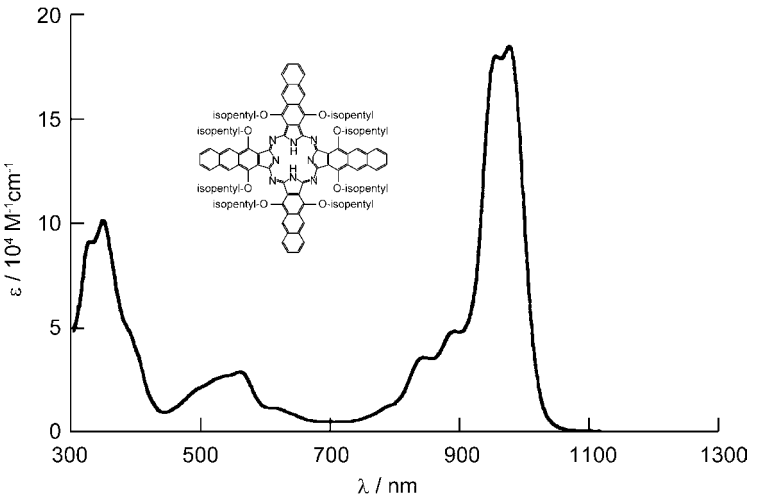

Figure 11. Absorption spectrum of symmetrically-substituted α-octa(isopentyloxy) H_2Ac in toluene. Bedworth, P. V.; Perry, J. W.; Marder, S. R. *Chem. Commun.* **1997**, 1353–1354. Redrawn by permission of The Royal Society of Chemistry.

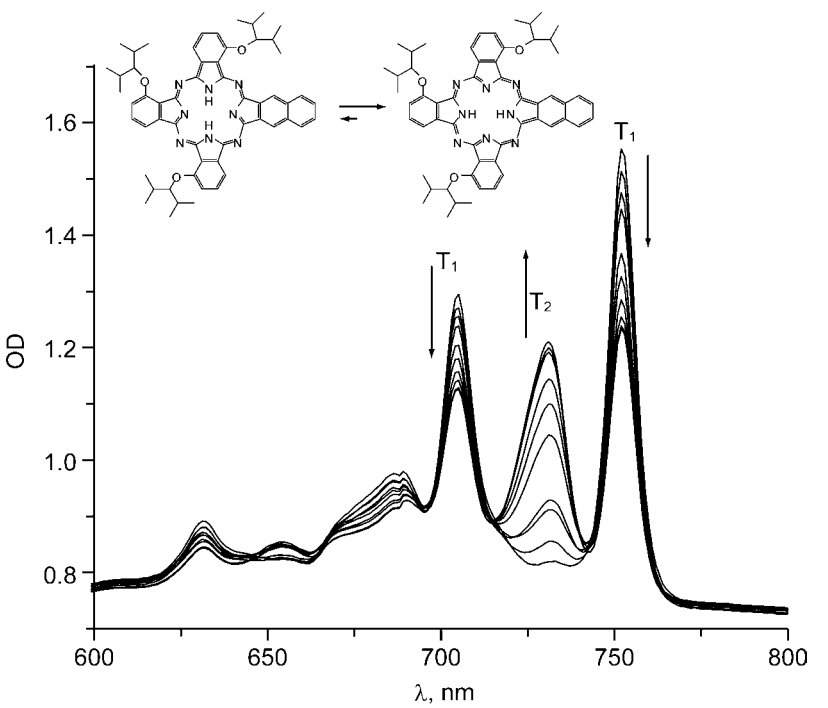

Figure 12. Spectral changes during two-photon induced photo-tautomerization of mono-benzo-fused H_2Pc derivative doped in polyethylene. The sample was irradiated off-resonantly with a femtosecond laser at 783 nm at 77 K. Redrawn from Drobizhev, M.; Makarov, N. S.; Rebane, A.; Wolleb, H.; Spahni, H. *J. Lumin.* **2008**, *128*, 217–222. Copyright 2008, with permission from Elsevier.

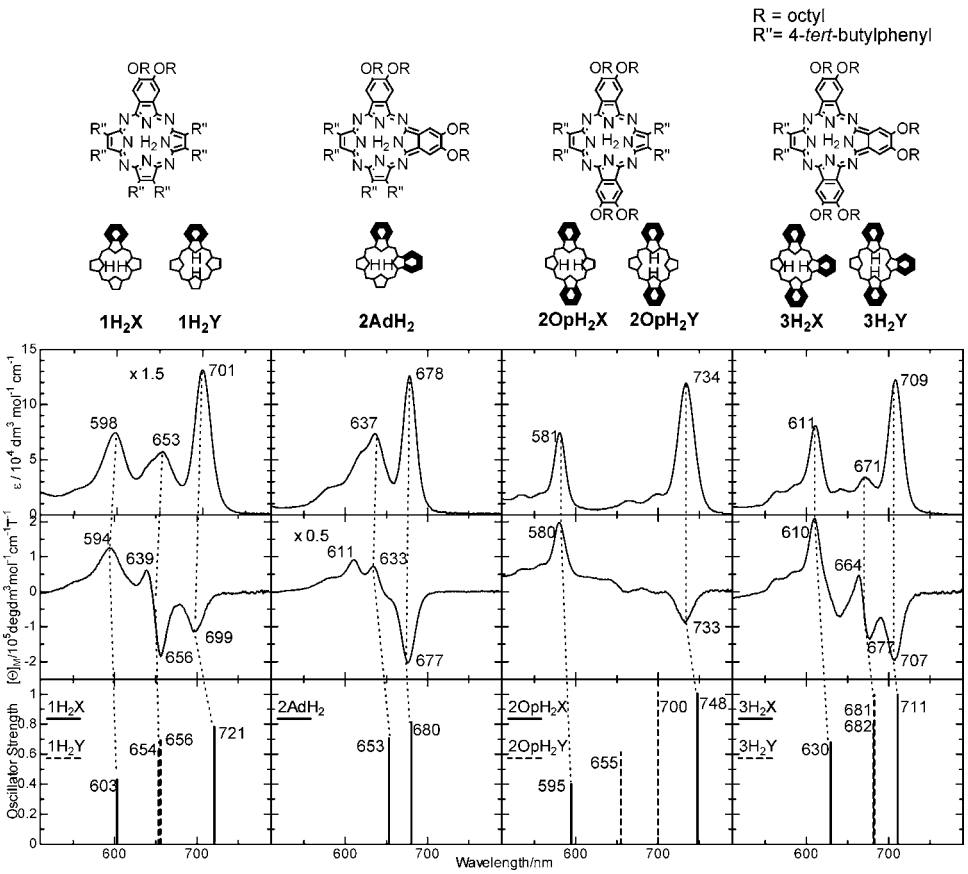

Figure 13. Absorption (top), MCD (middle) spectra, and calculated transition energies and oscillator strengths (bottom) of low-symmetry H_2TAP derivatives. Reproduced from Ishii, K.; Itoya, H.; Miwa, H.; Kobayashi, N. *Chem. Commun.* **2005**, 4586–4588.

Li_2Pc).[55] It can be seen from the spectra that new bands appear at 440 and 490 nm compared to Li_2Pc, in addition to broad band in the 550–800 nm region.

B. Group 1: Li_2Pc, LiHPc, LiPc, Na_2Pc and K_2Pc

Similar to metal-free Pcs, alkali metal Pcs can have two metal cations in the central cavity, since alkali metals are monovalent. The solubility of unsubstituted Li_2Pc in alcohols and acetone is much greater than that of H_2Pc.[56] However, an unsplit Q band is reported for Li_2Pc in acetone, where the absorption spectrum of Li_2Pc is similar to that of typical metalloPcs rather than H_2Pc.[20,57] Stillman and Thomson measured the absorption spectra of Li_2Pc dissolved in DMSO in the absence and presence of NaCN, and reported that unsplit Q bands appear at 15 350 cm^{-1} (651 nm) and

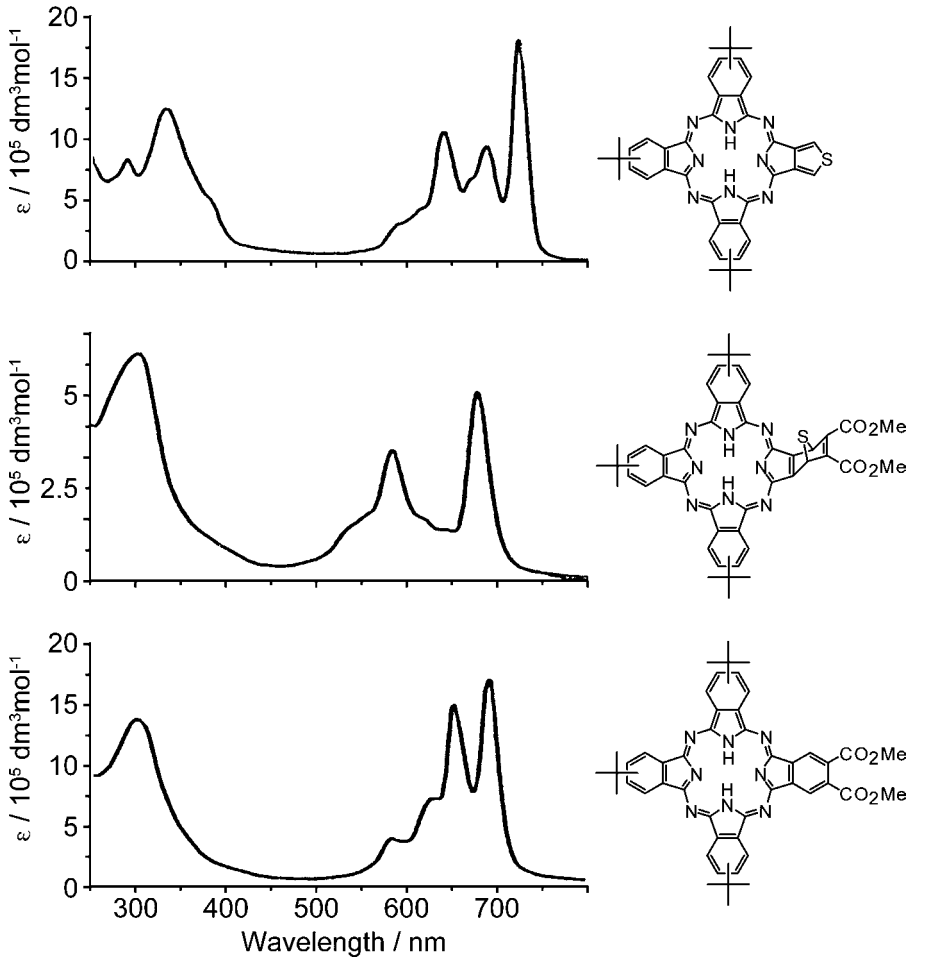

Figure 14. Absorption spectra of tribenzo[*b, g, l*]thiopheno[3,4-*q*]porphyrazine (top), its dimethyl acetylenedicarboxylate adduct (middle), and substituted tribenzo[*b, g, l*]porphyrazine (bottom). Nemykin, V. N.; Polshina, A. E.; Kobayashi, N. *Chem. Lett.* **2000**, 1236–1237. Redrawn by permission of The Chemical Society of Japan.

15 340 cm^{-1} (652 nm), respectively.[58] By combining the results of absorption and MCD spectroscopy, they commented that the lithium ions do not occupy the center of the ring in the same manner as protons. However, the MCD spectra discard the possibility that the lithium ions are not occupying the ring center. As a consequence, they concluded that in DMSO, Li_2Pc contains only one lithium ion in the center of the ring, or that two lithium ions are disposed, to preserve an axis of symmetry perpendicular to the D_{4h} ring plane. The absorption spectrum of Li_2Nc is very similar to that of Li_2Pc in shape, except that the Q band shifts to the red by *ca.* 80 nm.[59] A larger

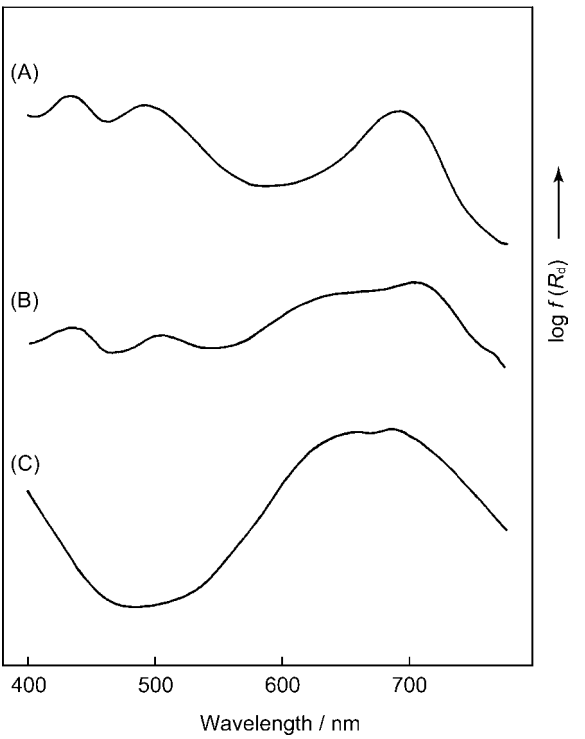

Figure 15. Reflectance spectra of LiPc (A), HPc (B), and Li_2Pc (C). Sugimoto, H.; Higashi, T.; Mori, M. *J. Chem. Soc. Chem. Commun.* **1983**, 622–623. Redrawn by permission of The Royal Society of Chemistry.

absorption coefficient is observed for the Q band of Li_2Nc (*ca.* 375 000 $M^{-1}cm^{-1}$) compared to Li_2Pc (*ca.* 150 000 $M^{-1}cm^{-1}$) in acetone. Li_2Pc is readily demetallated by protic solvents. Upon addition of a small amount of distilled water (pH = *ca.* 6) to a solution of Li_2Pc in weakly coordinating solvents (DMA or DMSO), the initial Q band at 658 nm collapses, while new bands appear at *ca.* 655 and 685 nm. These two bands diminish further, to give a single new Q band at 664 nm within 2 hours, suggesting that the solvent molecules are protonated and act as axial ligands above and below the Pc plane.[60] Upon heating this solution, the spectrum changes into that typical of H_2Pc with D_{2h} symmetry, with split Q bands at 685 and 658 nm being observed. The lithium-hydrogen complex, LiHPc, is formed by the reaction of excess of phthalonitrile with lithium amyloxide.[56] LiHPc is expected to be also formed as an intermediate during the demetalation process of Li_2Pc. On the other hand, LiHPc yields Li_2Pc on treatment with lithium amyloxide. LiHPc exhibits an unsplit Q band at 667 nm in pyridine, indicating that both the lithium cation and proton are eliminated, and presumably the observed spectrum arises from the Pc

dianion.[61] Homborg prepared several lithium Pc derivatives, including (tetraalkylammonium)LiPc, AgLiPc, and CuLiPc.[62] The absorption spectrum of (tri-*n*-dodecylbutyl)-ammonium LiPc in CH_2Cl_2 showing an unsplit intense principal band at 14 990 cm^{-1} (667 nm) is practically identical to that of LiHPc in pyridine, suggesting presumably that the observed spectra arise from $LiPc^-$ or Pc^{2-} species (not shown).[61,62] The double decomposition of (tri-*n*-dodecylbutyl)-ammonium LiPc with either a cuprous or silver complex in nonpolar aprotic solvents yields CuLiPc and AgLiPc, respectively, of which the former exhibits absorption peaks at 678, 648, and 610 nm in KBr at 10 K. In contrast, AgLiPc shows band peaks at 812, 482, and 435 nm in addition to the normal peaks at 672, 645, and 607 nm in KBr, indicating that the ring-oxidized species is involved in the spectrum.[63]

Mono-lithiated Pcs (LiPcs) and Ncs (LiNcs) are prepared by electrochemical oxidation or air oxidation of the corresponding di-lithiated complex.[64–73] Figure 16 shows the absorption spectra of LiPc (dashed line) and its aggregate (solid line) in 1-chloronaphthalene.[59] In Ref. 59, the authors claimed that the peaks at 945 and 693 nm for LiPc can be assigned to the aggregate form, since these disappear at low concentration, although this assignment is debatable. Substituted LiPc derivatives have also been prepared in a similar manner to the unsubstituted derivative. Figure 17 depicts the absorption spectra of α-OBu-substituted LiNc (solid line) and the corresponding H_2Nc (dashed line) in THF.[73] While H_2Nc exhibits a strong Q band at 865 nm, the LiNc derivative shows peaks at 1005, 857, 705, and 449 nm. These spectral features are similar to those observed for unsubstituted LiNc in various solvents.[70] Substituted LiPc derivatives also show similar spectral characteristics.[69]

Ledson and Twigg claimed that the chemical species generated by the addition of an NaOH/EtOH solution to H_2Pc in $PhCCl_3$ is Na_2Pc (Figure 8c). However,

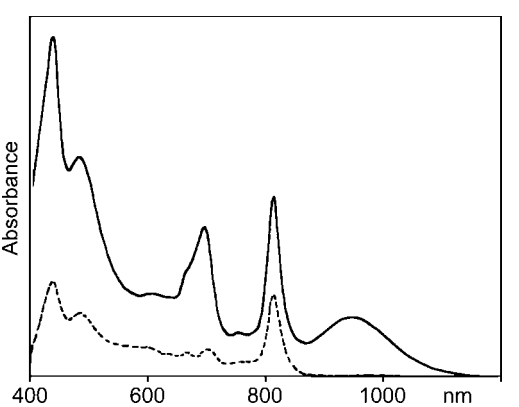

Figure 16. Absorption spectra of LiPc (dashed line) and its aggregate form (solid line) in 1-chloronaphthalene. Redrawn with permission from Gilat, S. L.; Ebbesen, T. W. *J. Phys. Chem.* **1993**, *97*, 3551–3554. Copyright 1993 American Chemical Society.

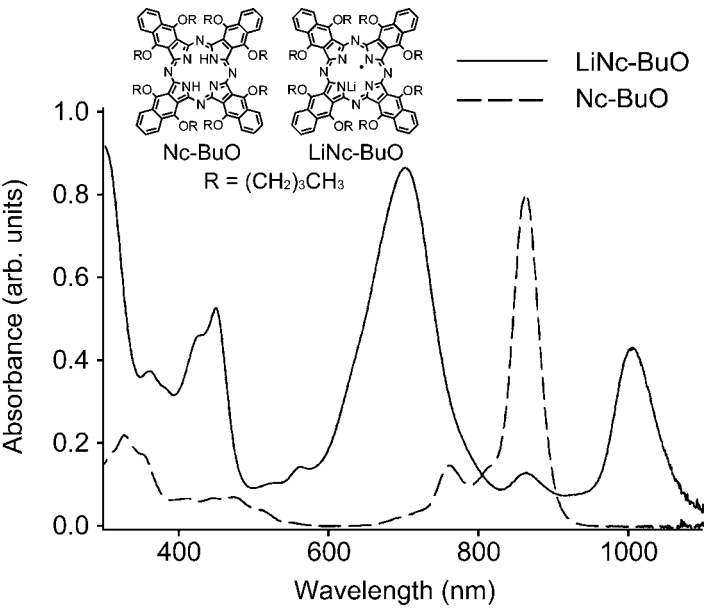

Figure 17. Absorption spectra of α-OBu substituted LiNc (solid line) and the corresponding H_2Nc derivative (dashed line) in THF. Pandian, R. P.; Kim, Y. I.; Woodward, P. M.; Zweier, J. L.; Manoharan, P. T.; Kuppusamy, P. *J. Mater. Chem.* **2006**, *16*, 3609–3618. Redrawn by permission of The Royal Society of Chemistry.

there is no evidence proving that the spectrum shown in Figure 8c really arises from Na_2Pc rather than the Pc dianion (Pc^{2-}).

Reaction of potassium amyloxide and phthalonitrile gives K_2Pc.[74] Crystals of K_2Pc(DMF)$_4$, K_2Pc(diglyme)$_2$, and K_2Pc(18-crown-6)$_2$ were grown from K_2Pc in DMF, in benzene containing excess 18-crown-6, or hot diglyme, respectively, and their X-ray structures solved.[75,76] The potassium cations are located out of the Pc plane, with the K–K axis being practically coincident with the principal axis of the Pc skeleton. K_2Pc in DMF shows an unsplit Q band at 667 nm.[75] The crystal structures of KPc have also been solved.[77]

C. Group 2: BePc, MgPc, CaPc and BaPc

Information on BePc is very limited, because particular caution is required due to the highly toxic nature of beryllium.[57,74,78–80] BePc dihydrate exhibiting a Q band at 692 nm in 1-chloronaphthalene has been reported,[57] although a recent study by Kubiak *et al.* has clarified from thermogravimetric measurements that anhydrous BePc is readily hydrated in moist air to give the monohydrate, BePc(H_2O), rather than the dihydrate.[80]

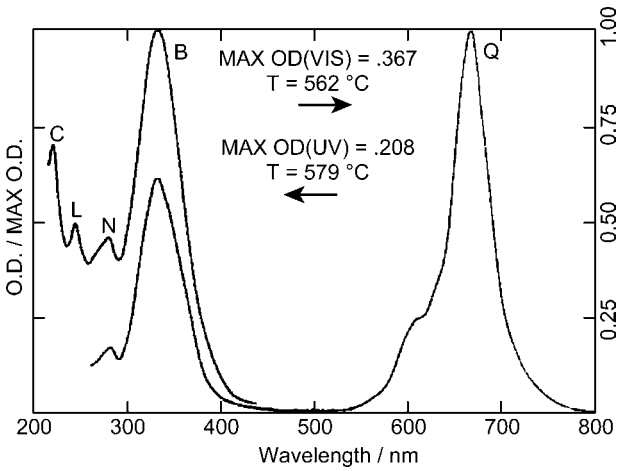

Figure 18. Vapor-phase absorption spectrum of MgPc. Redrawn from Edwards, L.; Gouterman, M. *J. Mol. Spectrosc.* **1970**, *33*, 292–310. Copyright 1970, with permission from Elsevier.

MgPc is an ideal species for investigating the optical absorption properties of metalloPcs, because MO mixing between the central metal and Pc ligand is negligible. Edward and Gouterman reported a vapor phase absorption spectrum, exhibiting the Q and B bands at 666 and 332 nm, respectively, in addition to N, L, and C bands in the 200–300 nm region (Figure 18).[21] Unsubstituted MgPc has a high solubility in various organic solvents, especially in N- or O-donor solvents, making possible the spectroscopic study of the unsubstituted species.[20,81] MgPc is able to coordinate two axial ligands, and Janczak reported the crystal structure of $MgPc(H_2O)$.[82] The Q-band energy depends little on the axial ligands. Thus, the Q bands of MgPc, $MgPc(im)_2$, $MgPc(meim)_2$, $MgPc(py)_2$, $MgPc(mepy)_2$, and $MgPc(CN^-)_2$ in CH_2Cl_2 appear at 670, 672, 672, 671, 671, and 671 nm, respectively, where im = imidazole, meim = methylimidazole, and mepy = 4-methylpyridine.[83] Figure 19 depicts the absorption spectrum of $MgPc(py)_2$ in pyridine.[84] The spectrum is similar in shape to that recorded in the vapor phase (Figure 18), although more well-resolved vibronic bands can be recognized to lie at higher energy to the Q band in pyridine. According to the band deconvolution analysis of the absorption and MCD spectral data performed by Stillman and coworkers (Figure 20), five degenerate transitions are identified for $MgPc(im)_2$ in CH_2Cl_2 at 672, 364, 339, 282, and 248 nm, which are assigned as the Q, B, N, L, and C transitions, respectively.[83]

A theoretical interpretation of the absorption spectrum of MgTAP based on TDDFT calculations has already been described earlier.[22] Ishikawa *et al.* performed *ab initio* calculations of the excited states of MgPc based on the HF/CIS/6-31G

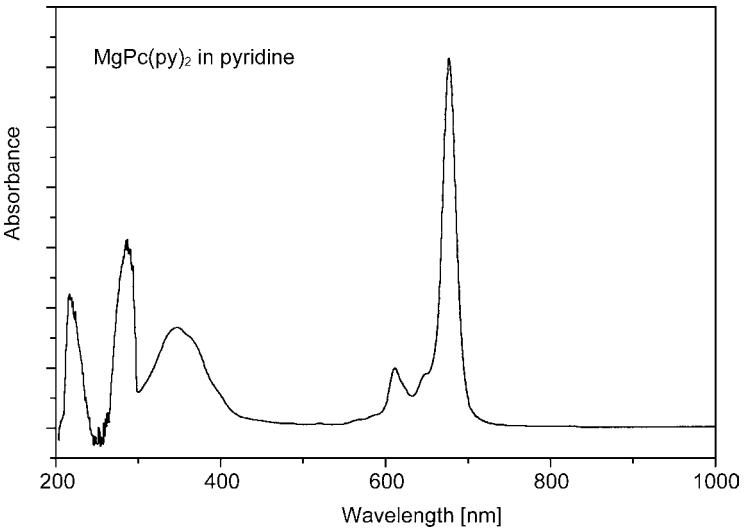

Figure 19. Absorption spectrum of $MgPc(py)_2$ in pyridine. Redrawn from Janczak, J.; Kubiak, R. *Polyhedron* **2002**, *21*, 265–274. Copyright 2002, with permission from Elsevier.

level.[85] The lowest state, assigned as the Q band ($1E_u$), is accounted for by 92% of the $2a_{1u} \rightarrow 6e_g$ (HOMO $\rightarrow$ LUMO) transition, while the $3E_u$ and $4E_u$ states are predicted at 5.36 and 5.74 eV with an oscillator strength (f) of 2.40 and 0.85, and therefore are assigned as the B_1 and B_2 transitions, respectively. In addition to these three excited states, another excited state having E_u symmetry ($2E_u$) with $f =$ 0.0054 is also predicted between the Q and B_1 transitions, which consists of 52% of $3b_{2u} \rightarrow 6e_g$ (HOMO–2 $\rightarrow$ LUMO) and 21% of $4a_{2u} \rightarrow 6e_g$ (HOMO–7 $\rightarrow$ LUMO) configurations.

MgPc films are known to have several polymorphic phases, which arise from different molecular stacking arrangements. The α-phase obtained by vacuum deposition has an optical absorption maximum at around 695 nm, while the x_1-phase prepared by thermal or solvent treatment of the α-phase has a stronger absorption peak at 830 nm (Figure 21).[86,87] Mizuguchi and coworkers has succeeded in growing two kinds of six-coordinate MgPc crystal, namely $MgPc/(H_2O)_2$(*N*-methyl-2-pyrrolidone)$_2$ and MgPc/(2-methoxyethanol)$_2$, and clarified that the former crystals exhibit a near-IR absorption around 830 nm.[88] By using the X-ray data for these crystals, the origin of the near-IR absorption is discussed in terms of exciton coupling.

CaPc was obtained by either the reaction of calcium oxide or ethoxide with phthalonitrile, or double decomposition between Li_2Pc and $CaCl_2$, and was reported to have a dull green color.[56,74] However, the absorption properties of CaPc have not been reported to date. Although BaPc is formed similarly by using baryta and phthalonitrile, no absorption data is available.[74]

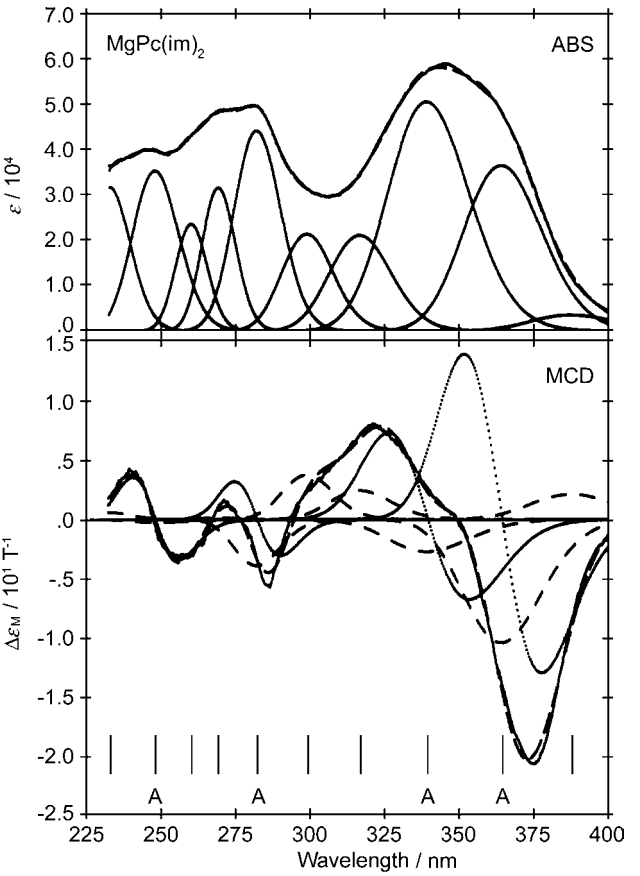

Figure 20. Results of band analysis for $MgPc(im)_2$ in CH_2Cl_2 for the UV region. The fitted data are shown by the dashed lines, and the experimental data by the solid line. Each Gaussian component is also shown, as well as the corresponding MCD signals. The vertical lines labeled 'A' correspond to the band centers of Faraday A terms. Redrawn with permission from Ough, E.; Nyokong, T.; Creber, K. A. M.; Stillman, M. J. *Inorg. Chem.* **1988**, *27*, 2724–2732. Copyright 1988 American Chemical Society.

D. Group 3: ScPc, $ScPc_2$, YPc_2 and Y_2Pc_3

Lapkina *et al.* prepared monomeric tetra(15-crown-5)phthalocyaninato(acetate) scandium, and reported that the absorption spectrum of this complex in $CHCl_3$ shows a Q band at 697 nm accompanied by a shoulder at *ca.* 680 nm.[89] The addition of 3 vol.% MeOH to the $CHCl_3$ solution results in a hypsochromic shift of the Q-band maximum to 681 nm. The absorption spectral shapes of the corresponding sandwich dimers, namely neutral $[Sc(R_4Pc)_2]^0$ and its reduced form $[Sc(R_4Pc)_2]^-$, are typical of those seen for lanthanide double-decker Pcs, and practically identical with those of unsubstituted $[ScPc_2]^0$ and $[ScPc_2]^-$,

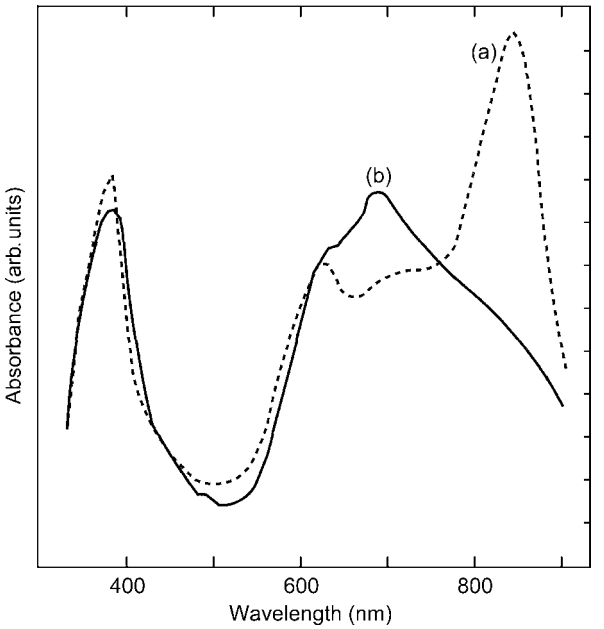

Figure 21. Absorption spectra of a MgPc film: curve (a), as-prepared; curve (b), after heat-treatment at 250 °C for 1 hour under vacuum. Redrawn from Kubota, H. G.; Muto, J.; Itoh, K. M. *J. Mater. Sci. Lett.* **1996**, *15*, 1475–1477 with kind permission from Springer Science and Business Media.

respectively.[90] Figure 22 shows the spectral changes observed in the course of the reduction of $[Sc(R_4Pc)_2]^0$ with hydrazine monohydrate in $CHCl_3$ to yield $[Sc(R_4Pc)_2]^-$.[89] The neutral form shows bands at 661, 466, and 365 nm in addition to bands at 919 and 1210 nm (not shown), which are characteristic of radical sandwich lanthanide diphthalocyanines. The most intense band at 661 nm is an analog of the prominent π–π^* transition (Q band). The band at 1210 nm has been assigned to an intervalence charge transfer transition. It is known that this band position depends largely on the metal ions. Upon addition of hydrazine monohydrate to give the anionic form, these bands lose their intensity, and instead, new bands at 724 and 619 nm appear. The intervalence transition that is prominent for the neutral species is absent for the reduced form. The crystal structure of a ($^nBu_4N$) complex of $[ScPc_2]^-$ with an orthorhombic unit cell indicates that the scandium ion is eight-coordinated by the eight isoindole nitrogen atoms in square antiprismatic coordination polyhedra. The rotational conformation of the two Pc moieties is staggered, and each Pc ring has a saddle-type deformation.[90]

Although the number of examples is limited, double- and triple-decker type yttrium Pcs, namely PcYPc (or YPc_2) and PcYPcYPc (or Y_2Pc_3), have also been

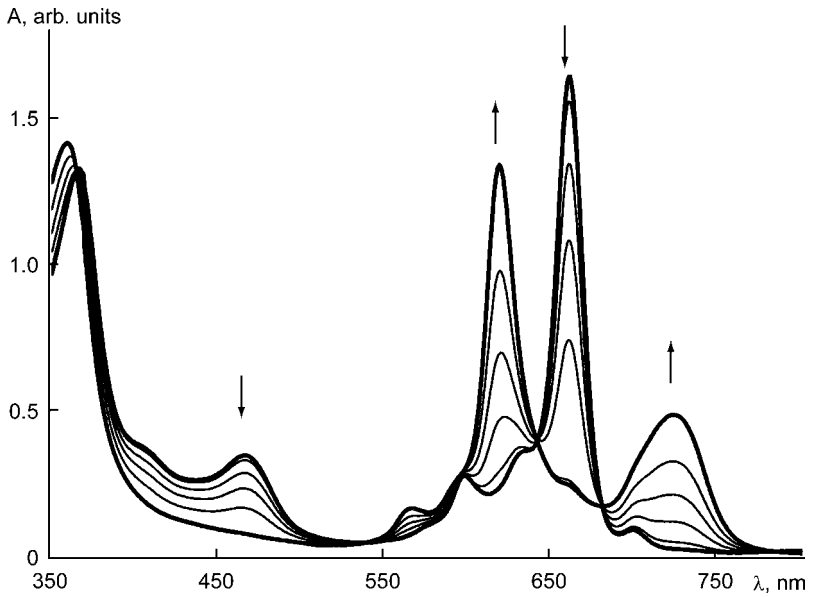

Figure 22. Spectrophotometric titration of a solution of $[Sc(R_4Pc)_2]^0$ in $CHCl_3$ with N_2H_4–H_2O to $[Sc(R_4Pc)_2]^-$. Redrawn from Lapkina, L. A.; Sakharov, S. G.; Konstantinov, N. Y.; Larchenko, V. E.; Gorbunova, Y. G.; Tsivadze, A. Y. *Russ. J. Inorg. Chem.* **2007**, *52*, 1758–1768 with kind permission from Springer Science and Business Media.

reported. In general, the closer the ring-to-ring separation, the stronger the π–π interactions are expected to be. The smaller ionic radius of yttrium compared to most of the lanthanide ions results in sandwich-type Pc dimer and trimer complexes containing yttrium ion(s) exhibiting profound effects of the π–π interactions on their absorption properties. Figure 23 depicts the absorption of $[Y(Pc)_2]^-$ (reduced form, top) and $[Y(Pc)_2]^0$ (neutral form, bottom) in CH_2Cl_2.[91] The latter shows bands at 663 (15 080 cm^{-1}), 598 (16 710 cm^{-1}), and 458 nm (21 810 cm^{-1}) in the visible region, and 1538 (6500 cm^{-1}), 1395 (7110 cm^{-1}), and 916 nm (10 950 cm^{-1}) in the near-IR region in $CHCl_3$.[92] The near-IR bands are blue-shifted compared to the corresponding lanthanide complexes such as $[Eu(Pc)_2]^0$ and $[Gd(Pc)_2]^0$, indicating a larger π–π interaction between the two Pc rings due to the smaller ionic radius of yttrium.[92] The reduced form has bands at 14 470 (691 nm) and 16 050 cm^{-1} (623 nm), of which the former is slightly blue-shifted compared to the corresponding scandium complex (724 nm), while the latter band appears at an approximately identical position (619 nm). The crystal structure of the ($^nBu_4N$) complex of $[YPc_2]^-$ is isostructural with that of $[ScPc_2]^-$.[90] The triple-decker, Pc_3Y_2, is synthesized from *o*-phthalonitrile and yttrium(III) acetate hexahydrate.[93] Figure 24 shows the spectral changes observed during the preparation of Pc_3Y_2. An absorption band which can be assigned as a monophthalocyanine

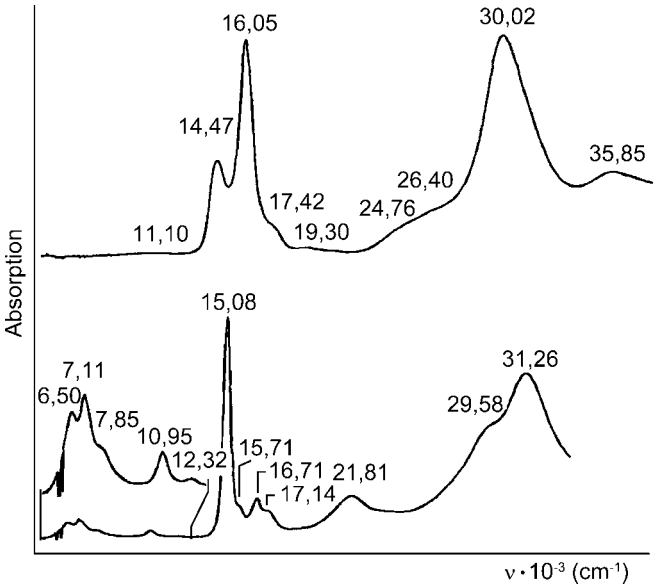

Figure 23. Absorption spectra of $[Y(Pc)_2]^-$ (top) and $[Y(Pc)_2]^0$ (bottom) in CH_2Cl_2. Redrawn from Ostendorp, G.; Homborg, H. *Z. Anorg. Allg. Chem.* **1996**, *622*, 1358–1364.

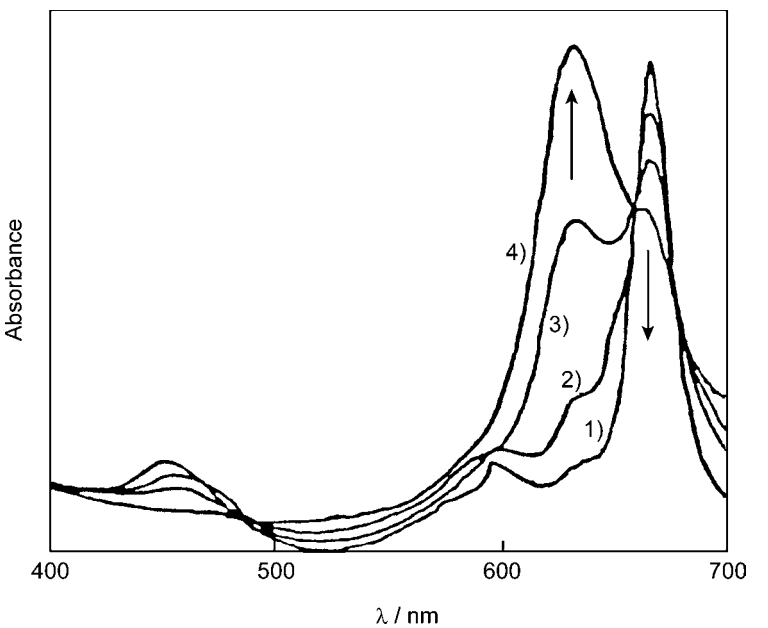

Figure 24. Spectral changes observed during the reaction of *o*-phthalonitrile and $Y^{III}(OAc)_3$ monohydrate at *ca.* 230 °C. Kasuga, K.; Ando, M.; Morimoto, H.; Isa, M. *Chem. Lett.* **1986**, 1095–1098. Redrawn by permission of The Chemical Society of Japan.

complex first appears at 665 nm (1), subsequently followed by the appearance of a band characteristic of the radical double-decker Pc_2 at 460 nm (2). After continuing the heating for several hours, the band at 665 nm shifts to 633 nm, which is assigned to Pc_3Y_2 (3 and 4).[93] The spectrum of Pc_3Y_2 is similar to that of $[YPc_2]^-$, with the Q band appearing at 633 nm and an accompanying weak band on the longer wavelength side (705 nm). Kasuga *et al.* observed that the Q-band position shifts to shorter wavelength with decreasing ionic radius for a series of Pc_3M_3 complexes, where M is Nd, Gd, Er, Y, and Lu.[93] On the other hand, the longer-wavelength band shifts to longer wavelength with decreasing ionic radius, being different from that observed for $[MPc_2]^-$ type complexes. The spectral properties of sandwich-type Pc dimers and trimers are interpreted in more detail in the subsequent section.

E. Complexes of the Lanthanide Elements

Although some monomer Pcs containing a lanthanide(III) ion (Ln^{III}) as the central metal have been synthesized and their absorption properties reported, these are more or less similar to the corresponding Pcs containing other central metals. However, as described briefly in the previous section, the absorption properties of double- and triple-decker Pc dimers and trimers are quite different from those of the original Pc monomers. Therefore, sandwich-type Pc dimers and trimers dominate the chemistry of Ln^{III}Pcs. In this section, the origin of the absorption bands of these sandwich-type complexes is interpreted on the basis of a series of studies by Ishikawa *et al.*[94] Double-decker Pc dimers are generally able to have three different oxidation states: a reduced form ($[Ln^{III}(Pc)_2]^-$), a neutral form ($[Ln^{III}(Pc)_2]^0$), and an oxidized form $[Ln^{III}(Pc)_2]^+$. Figure 25 shows absorption (top) and MCD (bottom) spectra of $[Lu^{III}(Pc)_2]^-$ (reduced form) in CH_2Cl_2/MeOH (4:1 v/v).[95] In this case, the formal charge of both Pc rings is 2–. Clear splitting of the Q-band is observed, of which the lower energy component has a smaller relative intensity. The maximum in the B band region shifts to higher energy compared to the typical Pc monomer, and shoulder-like weak bands appear in between the Q and B regions. The Q and B components both show an *A* term in the MCD spectrum, indicating that all of the excited states remain doubly degenerate. The simplest interpretations of what occurs on the interaction of two chromophores are based on the exciton-coupling theory, which predicts a hypsochromic shift of the Q band for a face-to-face dimer conformation.[96] However, the exciton model fails to explain the appearance of the lower energy Q-component. Ishikawa *et al.* took the electronic configuration of charge transfer (CT) between the Pc rings into consideration, and successfully interpreted the observed spectra theoretically.

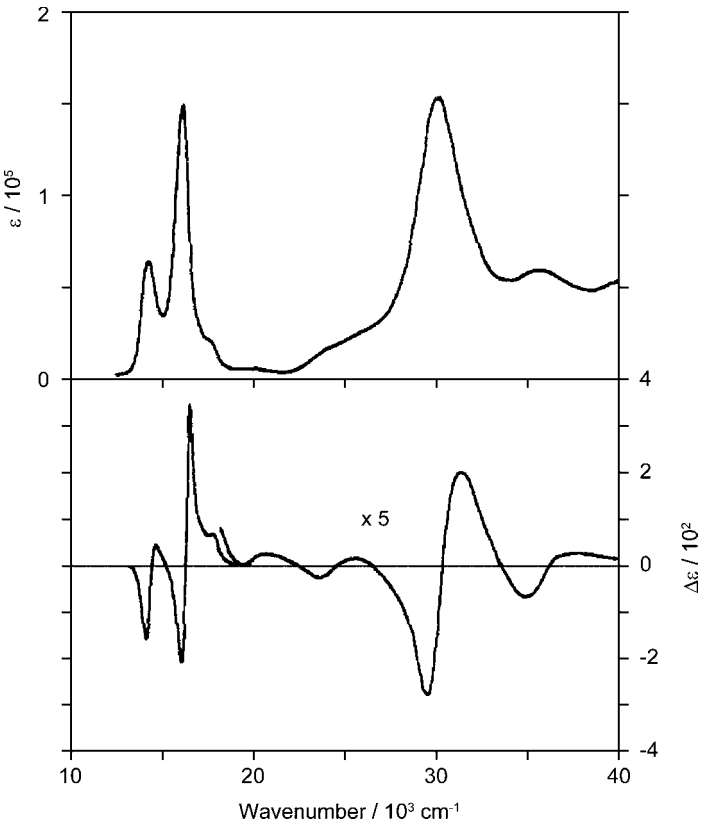

Figure 25. Absorption (top) and MCD (bottom) spectra of $[Lu(Pc)_2]^-$. Redrawn with permission from Ishikawa, N.; Ohno, O.; Kaizu, Y.; Kobayashi, H. *J. Phys. Chem.* **1992**, *96*, 8832–8839. Copyright 1992 American Chemical Society.

Let $|G\rangle = |\cdots a\bar{a}\cdots b\bar{b}|$ be the wavefunction for the ground state in accordance with Ishikawa's notation, and define the two constituting Pc rings as A and B. Local excitation (LE) within a Pc ring can be expressed as:

$$|\mathrm{LE^A}\rangle = |^1(j \leftarrow a)_\mathrm{A}\rangle = \frac{\{|\cdots j\bar{a}\cdots b\bar{b}| - |\cdots \bar{j}a\cdots b\bar{b}|\}}{\sqrt{2}}, \tag{10}$$

$$|\mathrm{LE^B}\rangle = |^1(k \leftarrow b)_\mathrm{B}\rangle = \frac{\{|\cdots a\bar{a}\cdots k\bar{b}| - |\cdots a\bar{a}\cdots \bar{k}b|\}}{\sqrt{2}}, \tag{11}$$

where the HOMOs and LUMOs of Pc(A) and Pc(B) are denoted as *a* and *b*, and *j* and *k*, respectively. These excitations take place only within each Pc ring, and no inter-Pc-ring excitation (charge transfer) is considered. The interaction

of these two configurations generates two new excited states (EC, exciton states):

$$\left|\mathrm{EC}^{+}\right\rangle = \frac{\left\{\left|\mathrm{LE}^{\mathrm{A}}\right\rangle + \left|\mathrm{LE}^{\mathrm{B}}\right\rangle\right\}}{\sqrt{2}}, \tag{12}$$

$$\left|\mathrm{EC}^{-}\right\rangle = \frac{\left\{\left|\mathrm{LE}^{\mathrm{A}}\right\rangle - \left|\mathrm{LE}^{\mathrm{B}}\right\rangle\right\}}{\sqrt{2}}, \tag{13}$$

of these, the former is allowed, while the latter is forbidden. As a consequence, a blue shift of the Q band is expected on the basis of the exciton model. Next, the charge transfer configuration (a one-electron excitation from one Pc ring to another) can be written as:

$$\left|\mathrm{CT}^{\mathrm{B}\leftarrow\mathrm{A}}\right\rangle = \left|{}^{1}(k \leftarrow a)_{\mathrm{B}\leftarrow\mathrm{A}}\right\rangle = \frac{\left\{\left|\cdots k\bar{a}\cdots b\bar{b}\right| - \left|\cdots \bar{k}a\cdots b\bar{b}\right|\right\}}{\sqrt{2}}, \tag{14}$$

$$\left|\mathrm{CT}^{\mathrm{A}\leftarrow\mathrm{B}}\right\rangle = \left|{}^{1}(j \leftarrow b)_{\mathrm{A}\leftarrow\mathrm{B}}\right\rangle = \frac{\left\{\left|\cdots a\bar{a}\cdots j\bar{b}\right| - \left|\cdots a\bar{a}\cdots \bar{j}b\right|\right\}}{\sqrt{2}}. \tag{15}$$

The interaction of these also yields two new excited states (CR, charge resonance states):

$$\left|\mathrm{CR}^{+}\right\rangle = \frac{\left\{\left|\mathrm{CT}^{\mathrm{B}\leftarrow\mathrm{A}}\right\rangle + \left|\mathrm{CT}^{\mathrm{A}\leftarrow\mathrm{B}}\right\rangle\right\}}{\sqrt{2}}, \tag{16}$$

$$\left|\mathrm{CR}^{-}\right\rangle = \frac{\left\{\left|\mathrm{CT}^{\mathrm{B}\leftarrow\mathrm{A}}\right\rangle - \left|\mathrm{CT}^{\mathrm{A}\leftarrow\mathrm{B}}\right\rangle\right\}}{\sqrt{2}}, \tag{17}$$

where both of these states are forbidden unless the orbitals of Pc(A) and Pc(B) overlap. However, the allowed $\left|\mathrm{EC}^{+}\right\rangle$ state possibly mixes with the $\left|\mathrm{CR}^{+}\right\rangle$ state, since these two configurations have identical irreducible representation along with a nonzero interaction between them. As a consequence of these discussions, the higher-energy bands in both Q and B band regions can be assigned to $\left|\mathrm{EC}^{+}\right\rangle$ states, and the lower-energy bands to $\left|\mathrm{CR}^{+}\right\rangle$ states. Quantum chemical calculations performed by Ishikawa *et al.* indicate that the lowest allowed excited state is $1\mathrm{E}_1$, in which the most dominant component is a charge resonance configuration, written as:

$$\left|6\mathrm{e}_{\mathrm{g}} \leftarrow 2\mathrm{a}_{1\mathrm{u}}\mathrm{CT}^{+}\right\rangle = \frac{\left\{\left|6\mathrm{e}_{\mathrm{g}}^{\mathrm{B}} \leftarrow 2\mathrm{a}_{1\mathrm{u}}^{\mathrm{A}}\right\rangle - \left|6\mathrm{e}_{\mathrm{g}}^{\mathrm{A}} \leftarrow 2\mathrm{a}_{1\mathrm{u}}^{\mathrm{B}}\right\rangle\right\}}{\sqrt{2}}. \tag{18}$$

The second allowed excited state is $2E_1$, in which the most dominant component is an exciton type configuration, written as:

$$\left|6e_g \leftarrow 2a_{1u}EC^+\right\rangle = \frac{\left\{\left|6e_g^A \leftarrow 2a_{1u}^A\right\rangle + \left|6e_g^B \leftarrow 2a_{1u}^B\right\rangle\right\}}{\sqrt{2}}. \tag{19}$$

Therefore, the two observed Q bands (14 000 and 16 000 cm^{-1}) can be safely assigned to $1E_1$ and $2E_1$, respectively. See the original papers for the corresponding MO-based interpretations.[94,95] It is known that the splitting of the Q band becomes smaller with increasing ionic radius of the Ln^{III} ion, in other words, with increasing ring-to-ring distance. Calculations conducted by varying the interplanar distances show that the energy of the CR configuration shifts rapidly to higher energy with increasing interplanar distance. The observed spectral shifts are consistently in agreement with the calculated results. For example, the relatively large splitting of the Q band observed for $[Y^{III}(Pc)_2]^-$ is consistent with the small ionic radius of Y^{III}.

The absorption characteristics of triple-decker Pc trimers can be interpreted in a similar manner, since the formal charge of all the Pc rings is 2–. Figure 26 shows absorption (top) and MCD (bottom) spectra of [PcLu(Crown-substituted Pc)LuPc] in $CHCl_3$.[97] Two distinct bands (Q bands) are observed at 15 800 and 14 000 cm^{-1} similarly to $[Lu^{III}(Pc)_2]^-$, although the relative intensity of the lower energy band is considerably weaker than the other band, compared to the dimer species. Dispersion-type MCD A terms appear, corresponding to both of these bands, indicating that the bands are associated with doubly degenerate states. Two shoulders (10 500 and 12 000 cm^{-1}) are detected on the lower energy side of these bands, although the intensities are very weak. In the near-IR region, a broad band is observed at 7400 cm^{-1}. Therefore, at least five bands exist on the lower energy side of the Q band. In the B-band region, a broad band at 30 300 cm^{-1} along with a shoulder at 27 000 cm^{-1} are reported. Similarly to the dimer case, three locally excited configurations are written as:

$$\left|LE^A\right\rangle = \left|{}^1(j \leftarrow a)_A\right\rangle, \quad \left|LE^B\right\rangle = \left|{}^1(k \leftarrow b)_B\right\rangle, \quad \left|LE^C\right\rangle = \left|{}^1(l \leftarrow c)_C\right\rangle.$$

By neglecting the interaction between Pc(A) and Pc(C), three diagonalized EC states are obtained as follows:

$$\left|EC^{+-+}\right\rangle = \frac{1}{\sqrt{2}}\left|LE^A\right\rangle - \frac{1}{\sqrt{2}}\left|LE^B\right\rangle + \frac{1}{\sqrt{2}}\left|LE^C\right\rangle, \tag{20}$$

$$\left|EC^{+-}\right\rangle = \frac{1}{\sqrt{2}}\left|LE^A\right\rangle - \frac{1}{\sqrt{2}}\left|LE^C\right\rangle, \tag{21}$$

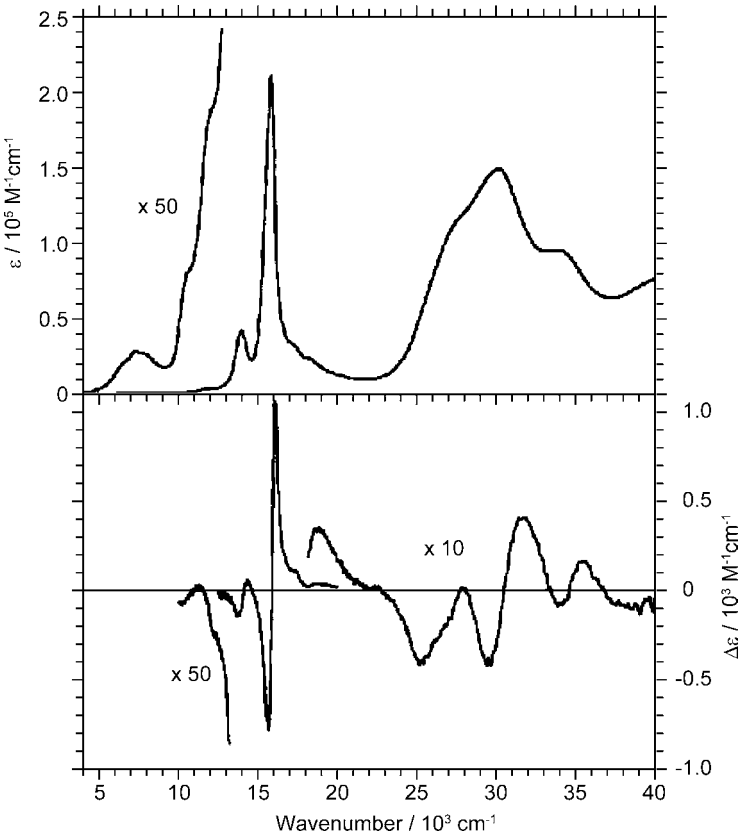

Figure 26. Absorption (top) and MCD (bottom) spectra of [PcLu(Crown-Pc)LuPc] in $CHCl_3$. Redrawn from Ishikawa, N.; Kaizu, Y. *Chem. Phys. Lett.* **1994**, *228*, 625–632. Copyright 1994, with permission from Elsevier.

$$\left|\mathrm{EC}^{+++}\right\rangle = \frac{1}{2}\left|\mathrm{LE}^{\mathrm{A}}\right\rangle + \frac{1}{\sqrt{2}}\left|\mathrm{LE}^{\mathrm{B}}\right\rangle + \frac{1}{2}\left|\mathrm{LE}^{\mathrm{C}}\right\rangle. \tag{22}$$

Under D_{4h} symmetry, only $|EC^{+-+}\rangle$ and $|EC^{+++}\rangle$ are allowed, and a much smaller transition dipole moment is expected for the former configuration (*ca.* 1/34). There are six possible charge transfers, and the possible allowed resonance states obtained therefrom are:

$$\left|\mathrm{CR}^{\mathrm{A}\rightarrow\mathrm{B}\leftarrow\mathrm{C}}\right\rangle = \frac{\left\{\left|\mathrm{CT}^{\mathrm{B}\leftarrow\mathrm{A}}\right\rangle + \left|\mathrm{CT}^{\mathrm{B}\leftarrow\mathrm{C}}\right\rangle\right\}}{\sqrt{2}}, \tag{23}$$

$$\left|\mathrm{CR}^{\mathrm{A}\leftrightarrow\mathrm{C}}\right\rangle = \frac{\left\{\left|\mathrm{CT}^{\mathrm{C}\leftarrow\mathrm{A}}\right\rangle + \left|\mathrm{CT}^{\mathrm{A}\leftarrow\mathrm{C}}\right\rangle\right\}}{\sqrt{2}}, \tag{24}$$

$$|\mathrm{CR}^{\mathrm{A}\leftarrow\mathrm{B}\rightarrow\mathrm{C}}\rangle = \frac{\{|\mathrm{CT}^{\mathrm{A}\leftarrow\mathrm{B}}\rangle + |\mathrm{CT}^{\mathrm{C}\leftarrow\mathrm{B}}\rangle\}}{\sqrt{2}}, \tag{25}$$

These CR configurations belong to the same irreducible representation as $|\mathrm{EC}^{+-+}\rangle$ and $|\mathrm{EC}^{+++}\rangle$, meaning that they can borrow transition intensity from the exciton coupling states. As a consequence, two EC type and three CR type bands are expected in the Q-band region of triple-decker Pc complexes. The most intense band at 15 800 cm^{-1} is safely assigned to the $|\mathrm{EC}^{+++}\rangle$ state. Ishikawa *et al.* pointed out that the second intense band at 14 000 cm^{-1} is not the $|\mathrm{EC}^{+-+}\rangle$ state, but can be assigned to one of the allowed charge resonance states, since the splitting energy between these two bands (1800 cm^{-1}) is much smaller than that expected for EC type splitting (*ca.* 6000–9000 cm^{-1}).[97] Therefore, the three weak bands in the 7000–12 000 cm^{-1} region are assigned to the $|\mathrm{EC}^{+--}\rangle$ state and two of the three allowed CR states. This description of the electronic states of the triple-decker Pc trimer are fully supported also by the results of quantum chemical CI calculations.

The absorption properties of neutral double-decker Pc complexes ($[\mathrm{Ln}^{\mathrm{III}}(\mathrm{Pc})_2]^0$) and the oxidized form ($[\mathrm{Ln}^{\mathrm{III}}(\mathrm{Pc})_2]^+$) are quite different from the reduced form shown above. Figure 27 compares the absorption of $[\mathrm{Lu}(\mathrm{Pc})_2]^0$ (broken line) and $[\mathrm{Lu}(\mathrm{Pc})_2]^+$ (solid line). The neutral form (broken line) shows absorption bands at 7000, 11 000, 15 200, and 22 000 cm^{-1} along with broad bands at around 30 000 cm^{-1}. Although this spectral shape resembles a superposition of the typical metalloPc monomer ($\mathrm{M}^{\mathrm{II}}\mathrm{Pc}^{2-}$, 15 200 and 30 000 cm^{-1}) and its π-radical cation ($\mathrm{M}^{\mathrm{II}}\mathrm{Pc}^{\bullet-}$, 11 000 and

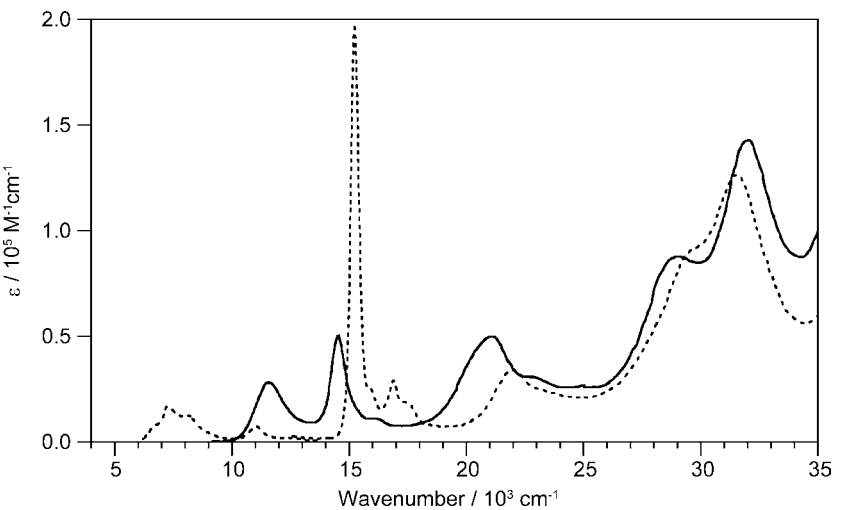

Figure 27. Absorption spectra of $[\mathrm{Lu}(\mathrm{Pc})_2]^0$ (broken line) and $[\mathrm{Lu}(\mathrm{Pc})_2]^+$ (solid line) in CH_2Cl_2. Redrawn from Ishikawa, N.; Kaizu, Y. *J. Porphyrin Phthalocyanines* **1999**, *3*, 514–521.

22 000 cm^{-1}), the band at 7000 cm^{-1} is unassignable to these. This feature, together with the results of NMR, ENDOR, and resonance Raman spectroscopy, suggests that the hole is delocalized over the two Pc rings for the neutral form.[98,99] A comparative study of the spectra of $[Lu(Pc)_2]^0$, $[LuPcNc]^0$, and $[Lu(Nc)_2]^0$ demonstrated that the spectral shapes of the hetero-dimer, $[LuPcNc]^0$, are neither identical to Pc nor Nc, i.e. the hole is not localized on one of the two Pc rings.[100] Upon oxidation of the neutral form, the Q band at 15 200 cm^{-1} shifts to lower energy by 700 cm^{-1} and decreases in intensity (Figure 27, solid line). The MCD signal corresponding to this band is a dispersion type A-term. The band at *ca.* 22 000 cm^{-1} shifts by 1000 cm^{-1} to 21 000 cm^{-1}. The NIR band at 7000 cm^{-1} disappears upon oxidation, and a new band accompanied by an MCD B-term appears at 11 500 cm^{-1}. Readers should refer to the original papers for further details and theoretical treatment of the spectral characteristics of the electron-deficient oxidized species.[94,101,102]

The electronic absorption spectra of $[Ln^{III}(Pc)_2]^-$, where Ln = Y, Pr, Nd, Sm–Lu, are compared in Figure 28. Each spectrum consists of a single Soret band

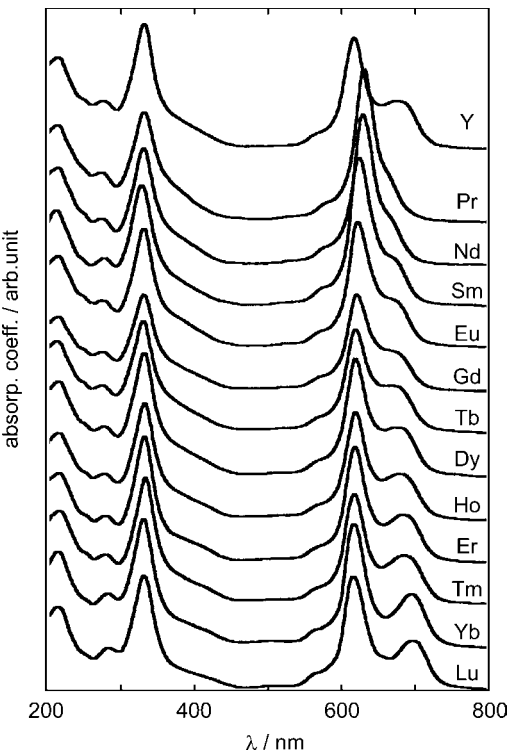

Figure 28. Electronic absorption spectra of a series of $[Ln^{III}(Pc)_2]^-$ complexes in $CHCl_3$. Redrawn from Kobayashi, N. *Coord. Chem. Rev.* **2002**, *227*, 129–152 with permission.

(*ca.* 300–350 nm) and one or two split Q bands. The extent of the Q-band splitting increases with decreasing ionic radius of the Ln^{III} ions, reflecting the extent of the π–π interaction between the two Pc rings. The splitting increases much more rapidly than anticipated from the variation of the radius, if exciton interactions only are taken into consideration. As described above, a rapid increase of electronic interactions via overlapping orbitals with decreasing Pc–Pc distance rationalizes the experimental results. The absorption spectra of $[Ln(Pc)_2]^0$ are different from those of neutral species, as shown in Figure 29. The spectra show intense bands at *ca.* 15 000 and 31 000 cm^{-1}, which shift to higher energy with decreasing Ln^{III}

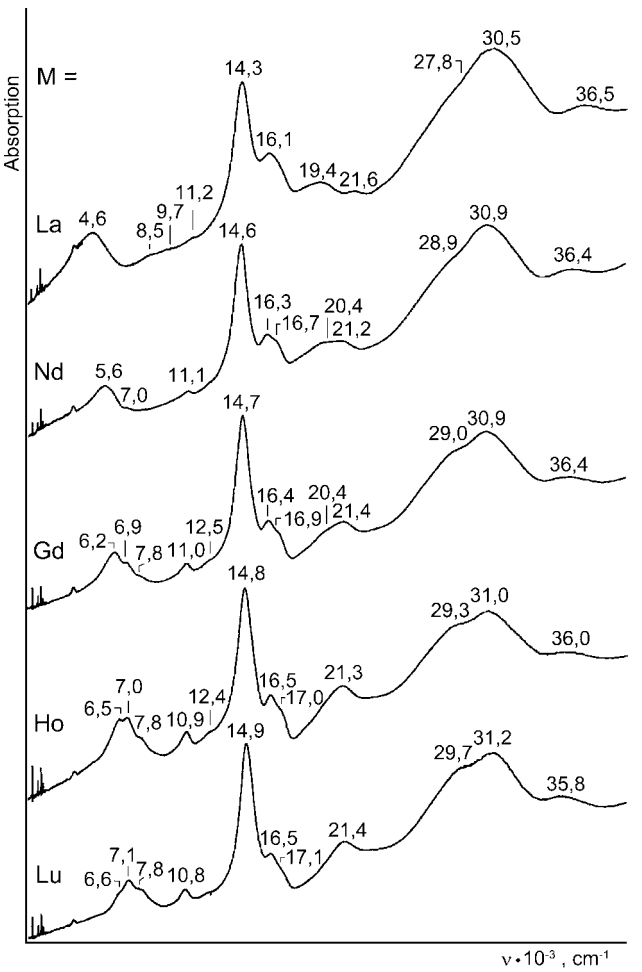

Figure 29. Electronic absorption spectra of $[Ln(Pc)_2]^0$ in KBr, where Ln = La, Nd, Gd, Ho, and Lu. Redrawn from Ostendorp, G.; Homborg, H. *Z. Anorg. Allg. Chem.* **1996**, *622*, 1222–1230.

radius. The bands have some similarity to those observed for monomer Pc^{2-}, while the bands at *ca.* 11 000 and 22 000 cm^{-1} are characteristic of a Pc^{-} π-radical, although it has been clarified that the hole is delocalized over two Pc rings as described above. The band at *ca.* 11 000 cm^{-1} shifts to lower energy with decreasing Ln^{III} radius. The NIR bands observed in the 4000–9000 cm^{-1} region show a distinct dependency on the metal size.[103] These bands are now assigned to an electronic transition from a bonding orbital constructed from the HOMO of each Pc ring to a half-occupied antibonding orbital.

A series of tetra-*tert*-butyl Nc Ln^{III} sandwich dimers has been reported.[104,105] Similar to the Pc series, both radical and reduced forms have been prepared. The main Q bands of the radical form (767–799 nm) and the π-radical anion band (593–648 nm) shift to the red with increasing metal size, while the B band region (328–334 nm) remains relatively unshifted (Figure 30).[106] A similar trend was also

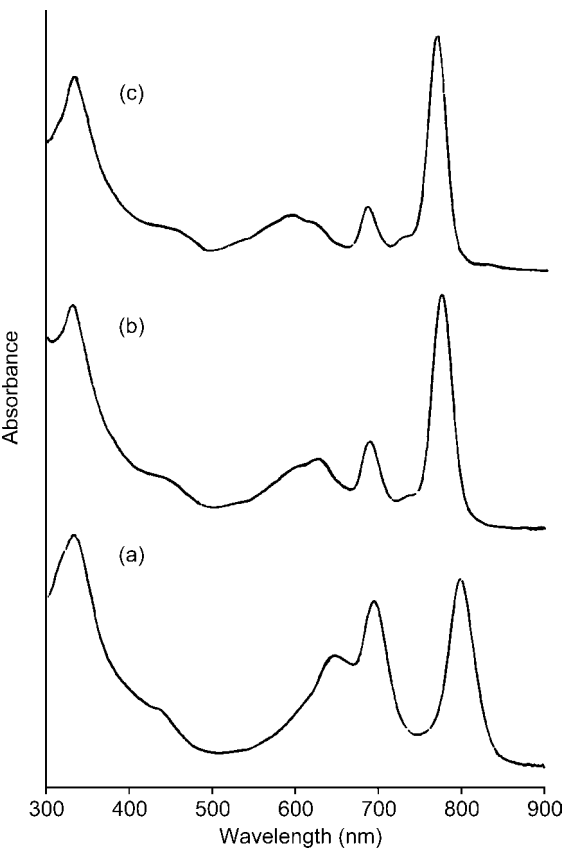

Figure 30. Absorption spectra of the radical form of (a) La[Nc(*tert*-Bu)$_4$]$_2$, (b) Eu[Nc(*tert*-Bu)$_4$]$_2$, and (c) Er[Nc(*tert*-Bu)$_4$]$_2$ in $CHCl_3$/EtOH = 1:1 (v/v). Redrawn from Jiang, J. Z.; Liu, W.; Poon, K. W.; Du, D. M.; Arnold, D. P.; Ng, D. K. P. *Eur. J. Inorg. Chem.* **2000**, 205–209.

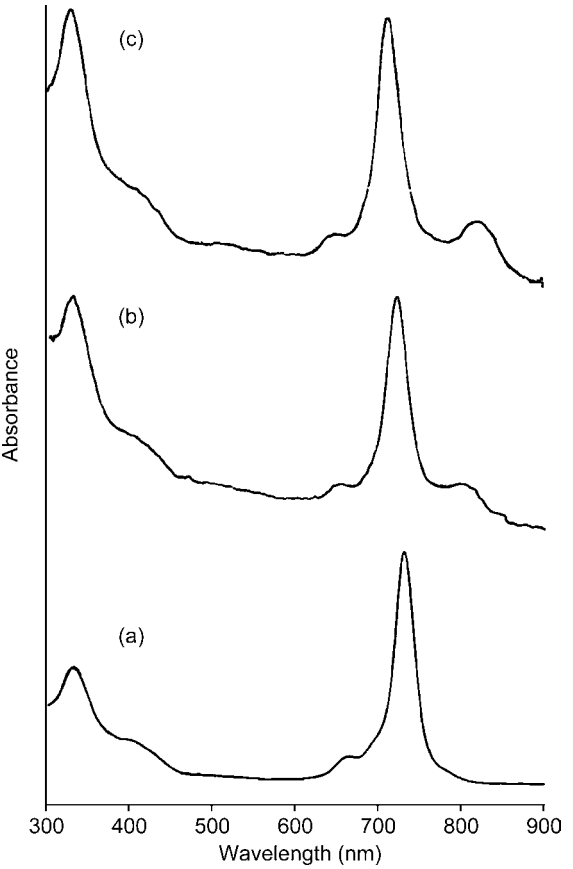

Figure 31. Absorption spectra of the reduced form of (a) La[Nc(*tert*-Bu)$_4$]$_2$, (b) Eu[Nc(*tert*-Bu)$_4$]$_2$, and (c) Er[Nc(*tert*-Bu)$_4$]$_2$ in $CHCl_3$/EtOH = 1:1 (v/v). Redrawn from Jiang, J. Z.; Liu, W.; Poon, K. W.; Du, D. M.; Arnold, D. P.; Ng, D. K. P. *Eur. J. Inorg. Chem.* **2000**, 205–209.

observed for the broad NIR band (1818–2346 nm, not shown). The band assignments appear to be the same as with the Pcs. In the reduced form, the Q band generally splits into two, to give an intense blue-shifted band (715–729 nm) and a weak band (782–821). Figure 31 depicts some examples of the reduced Nc dimer. The B-band region (328–333 nm) is virtually unshifted compared to the corresponding neutral form. The Q band of alkylthiosubstituted 2,3-Nc differs from that of tetra-*tert*-butyl 2,3-Nc in shape, but the spectral shape is similar in the other regions.[104]

F. Complexes of the Actinide Elements

A very limited number of actinide Pcs has been reported to date because of the radioactivity of the actinide elements. Guilard *et al.* reported the absorption

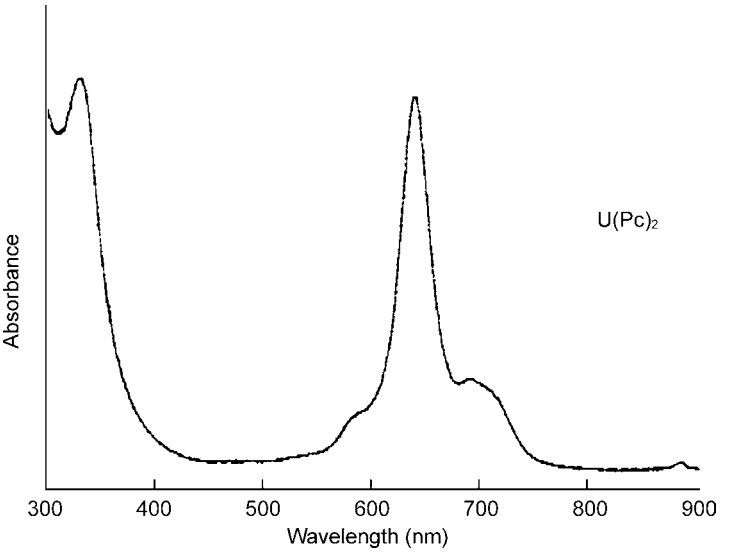

Figure 32. Absorption spectrum of UPc_2 in CH_2Cl_2. Redrawn with permission from Kadish, K. M.; Moninot, G.; Hu, Y.; Dubois, D.; Ibnlfassi, A.; Barbe, J. M.; Guilard, R. *J. Am. Chem. Soc.* **1993**, *115*, 8153–8166. Copyright 1993 American Chemical Society.

properties of $Th^{IV}Pc(acac)_2$ and $U^{IV}Pc(acac)_2$, where acac = acetyl acetonato.[107] The absorption spectra of these are similar to typical metalloPcs in shape, with the Q band appearing at 684 and 689 nm, respectively, in PhCN containing 0.2 M TBAP. Double-decker dimers have been reported for thorium,[108] protoactinium,[109,110] uranium,[108,111] neptunium,[112] and americium[113] complexes. PuPc appears in Ref. 108. No actinide-containing Nc sandwich has been reported. Figure 32 shows the absorption spectrum of $U(Pc)_2$ in CH_2Cl_2. The Soret band is located at 332 nm, which is blue shifted with respect to the corresponding band of $UPc(acac)_2$ (351 nm).[107] In the Q-band region, the intense band at 638 nm is accompanied by weaker bands positioned on both sides (593 and 700 nm).

The reaction of phthalonitrile with UO_2Cl_2 yields macrocyclic uranyl complexes, in which the UO_2 moiety is surrounded by five isoindole units linked by *meso*-nitrogen atoms, namely superphthalocyanine (superPc).[114–116] Only uranium is known to give this superPc structure up to the present date. The lowest-energy transition is red-shifted compared to typical metalloPcs. The unsubstituted superPc shows absorption bands at 912, 810 (shoulder), and 420 nm in toluene, while the pentamethyl-substituted congener has bands at 922, 810 (shoulder), and 420 nm (Figure 33).[114] Basic quantum chemical calculations within the framework of SCF-CI-PPP method indicate that superPc possesses a singly-degenerate HOMO and an essentially doubly-degenerate LUMO, similar to

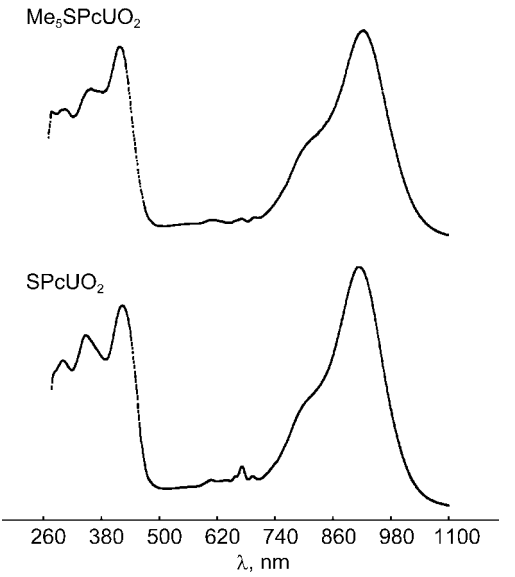

Figure 33. Absorption spectra of superPcs, with (top) and without (bottom) five methyl groups as peripheral substituents in benzene. Weak signals in the 620–740 nm region are due to trace amounts of metal-free Pcs. Redrawn with permission from Marks, T. J.; Stojakovic, D. R. *J. Am. Chem. Soc.* **1978**, *100*, 1695–1705. Copyright 1978 American Chemical Society.

metalloPcs.[115] Therefore, the bands located at 912 nm can be assigned to a π–π^* origin.

G. Group 4: TiPc, ZrPc, $ZrPc_2$ and HfPc

$Ti^{III}Pc$ and $Ti^{IV}Pc$ have been reported, of which only the latter has been the subject of an absorption study. Although TiPc described in Ref. 117 was handled as if it were a Ti^{II} complex, the description is ambiguous. Figure 34 shows the absorption spectra of TiOPc in 1-chloronaphthalene at various temperatures.[118] The spectra are typical in shape, with a Q band at *ca.* 699 nm, and show a slight hypsochromic shift accompanied with a reduction in intensity with increasing temperature. The Ti=O bond exhibits reactivity towards bidentate ligands such as catechol and its derivatives, to give axially-substituted TiPcs.[119] Barthel and Hanack investigated the effect of axial modification, and demonstrated that any effects are very limited.[120] $Ti(Pc)_2$ obtained by the reaction of $TiCl_2Pc$ and Na_2Pc has a unique structure.[121] The two Pc planes are 'stapled' by two carbon–carbon σ bonds, and accordingly, the Pc chromophore no longer exists in the resultant compounds (no absorption above 500 nm).

Cherian and Menon reported optical data of vacuum-deposited $TiCl_2Pc$ thin films (Figure 35).[122] The Q and B bands appear at 712 and 365 nm, respectively,

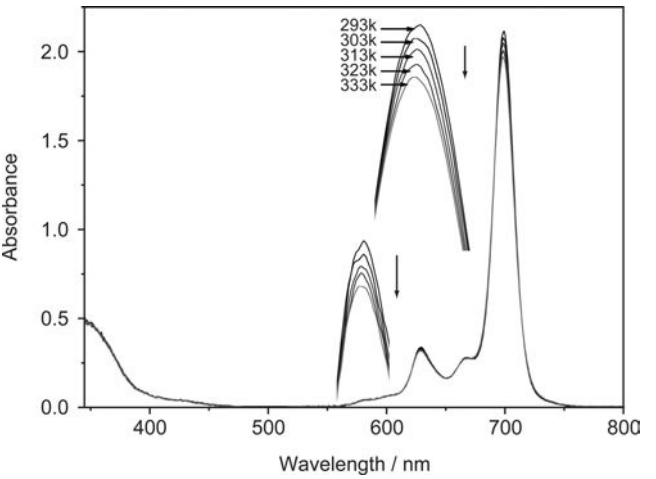

Figure 34. Absorption spectra of TiOPc in 1-chloronaphthalene at various temperatures. Redrawn from Ma, C. Y.; Ye, K. Q.; Yu, S. K.; Du, G. T.; Zhao, Y. F.; Cong, F. D.; Chang, Y. C.; Jiang, W. H.; Cheng, C. H.; Fan, Z. Q.; Yu, H. F.; Li, W. C. *Dyes Pigments* **2007**, *74*, 141–147. Copyright 2007, with permission from Elsevier.

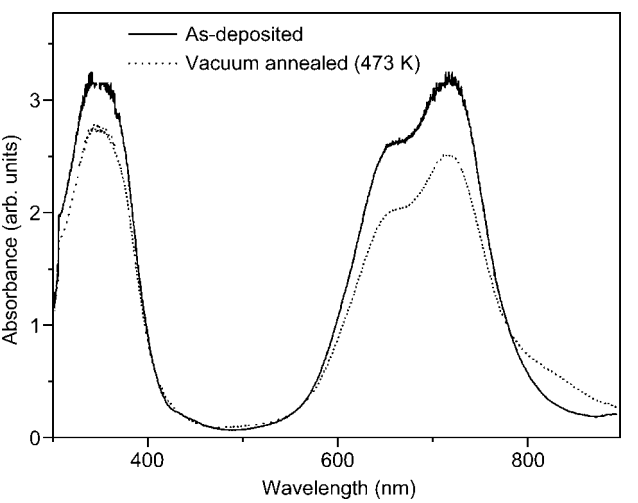

Figure 35. Optical absorption spectra of $TiCl_2Pc$ thin films. Redrawn from Cherian, R. C.; Menon, C. S. *J. Phys. Chem. Solids* **2008**, *69*, 2858–2863. Copyright 2008, with permission from Elsevier.

remaining unchanged by the annealing process. The solid-state absorption spectra of TiOPc differ significantly from those in solvent, and also depend on the crystal system. Despite the importance of solid-state Pcs, however, the analysis of solid-state spectra has been less than satisfactory until recently. Figure 36 (top right)

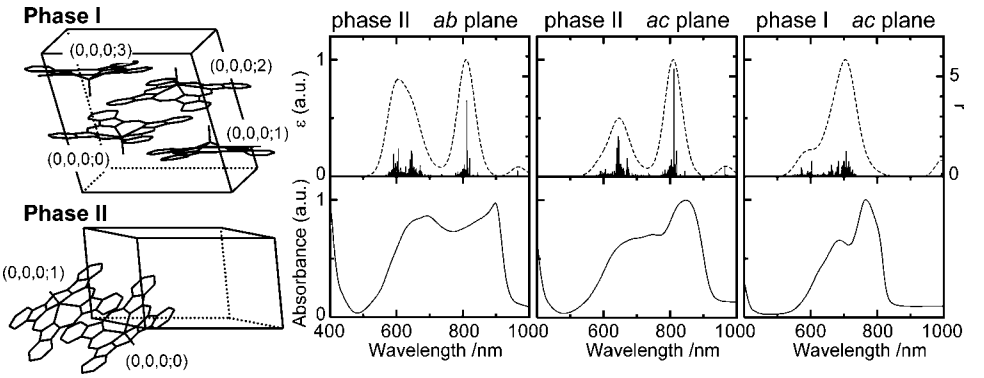

Figure 36. Calculated (broken line) and experimental (solid line) absorption spectra when the incident light direction is perpendicular to the crystallographic *ab* plane of phase II (top left), *ac* plane of phase II (top middle), and *ac* plane of phase I (top right) with molecular structures in the unit cell of phase I (top left) and phase II (bottom left). Solid bars in the calculated spectra denote the products of oscillator strengths and coefficients of CT configurations, ρ. Redrawn with permission from Nakai, K.; Ishii, K.; Kobayashi, N.; Yonehara, H.; Pac, C. *J. Phys. Chem. B* **2003**, *107*, 9749–9755. Copyright 2003 American Chemical Society.

depicts the calculated solid-state absorption spectra of TiOPc, in which exciton and charge-transfer (CT) interactions, and molecular distortions are taken into consideration.[123] The results reproduce fairly well the experimental results (bottom right), where the characteristics of phase dependence, dependence on the incident light direction, and the absorption profiles are rationalized. Readers should consult the original paper for the calculation details.[123] The calculations also clarified that the large red shift and high CT character originate from large exciton interactions and large intermolecular resonance integrals, respectively. In addition, it has been revealed that the photoconductive properties correlate well with the intermolecular resonance integrals. These considerations are important for investigating applications of the Pcs.

As a result of the large ionic radius and high valent nature of zirconium (Zr^{IV}), the metal center of ZrPc is located out of the Pc plane, and ZrPcs are able to have a variety of axial substituents. Figure 37 shows the absorption spectrum of ZrPc possessing two octanoato ($C_7H_{15}COO$) groups as axial substituents in DMSO.[124] The spectrum is similar in shape to a general metalloPc, with no additional bands being observed. The Q band at 688 nm is barely sensitive to the axial substituents, and the Q-band positions for the chloro adduct ($ZrCl_2Pc$) and β-diketonate adducts are observed at 688 and 682–692 nm, respectively.[124–126] Tomachynski *et al.* reported that the shape of the spectrum does not change dramatically in various solvents, with only a small shift of the Q-band position being observed. The lowest value of molar extinction coefficient is observed in DMSO, while the largest

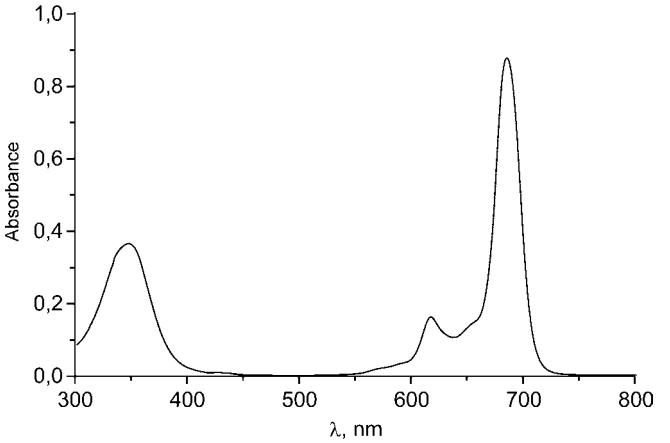

Figure 37. Absorption spectrum of ZrPc possessing two $C_7H_{15}COO$ groups as axial substituents in DMSO. Redrawn from Tretyakova, I. N.; Chernii, V. Y.; Tomachynski, L. A.; Volkov, S. V. *Dyes Pigments* **2007**, *75*, 67–72. Copyright 2007, with permission from Elsevier.

value is estimated in toluene. The double-decker form, $Zr(Pc)_2$, is also possible. Since the zirconium center is tetravalent, unlike the tervalent state of lanthanide ions, the neutral form can be described as Pc(2–)ZrPc(2–). Therefore, the absorption properties of neutral $Zr(Pc)_2$ resemble those of $Sn(Pc)_2$ rather than $[Ln(Pc)_2]^0$.[127] Figure 38 illustrates the absorption spectra of $Zr(Pc)_2$ (1), and its one-electron (2) and two-electron (3) electro-oxidized species.[128] The figure clearly demonstrates that the neutral, oxidized, and double-oxidized forms correspond to the reduced, neutral, and oxidized forms of the lanthanide congeners. Silver *et al.* also investigated the electrochromic behavior of $Zr(Pc)_2$.[127]

The spectroscopic behavior of HfPcs is very similar to ZrPc.[124–127] The Q-band position of $HfCl_2Pc$ is reported to be at 684 and 688 nm in DMSO and toluene, respectively.[124]

H. Group 5: VPc, NbPc and TaPc

Similar to TiOPc, vanadium(IV) (V^{IV}) is the stable oxidation state for VPc, and as a result, vanadyl (V=O) Pc complexes have been the most commonly studied. The crystal structure of VIPc is also available, although the absorption properties are absent.[129] The crystal structures of VOPc indicate that the molecule takes a dome-type deviated form, to give C_{4v} molecular symmetry.[130,131] Kobayashi *et al.* reported that Q bands of tetra-*tert*-butyl VOTAP, VOPc, and VONc were observed at 594.0, 698.0, and 809.6 nm, respectively, and that the dipole strength increases in this order.[43] Compared to the corresponding copper derivatives, the Q band of

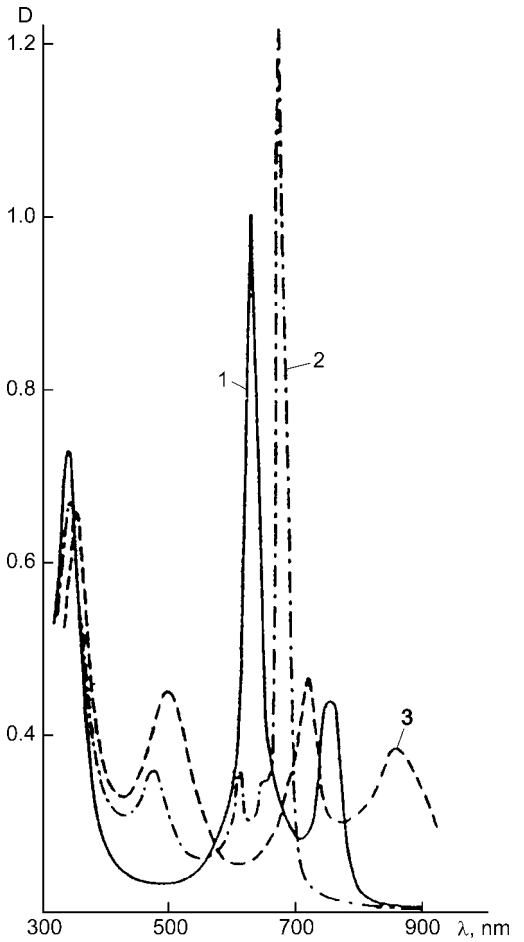

Figure 38. Absorption spectra of $[Zr(Pc)_2]$ (1), and its one-electron (2) and two-electron (3) electro-oxidized species in *o*-dichlorobenzene containing 0.2 M TBAP. Redrawn from Tomilova, L. G.; Ovchinnikova, N. A.; Lukyanets, E. A. *Zh. Obshch. Khim.* **1987**, *57*, 2100–2104.

the VO complexes lies at longer wavelength, with an intensity which is always lower. Huang and Sharp mentioned that any peculiarities of the electronic properties of VOPc compared with other Pcs are related to the axial ligand and the unpaired electron of the vanadyl ion.[132] Unsubstituted VOPc shows absorption peaks at 700.8 and 630 nm, with a shoulder at 670 nm in 1-chloronaphthalene, while a slight blue shift is observed in CH_2Cl_2.[132] Figure 39 shows the absorption data of $VOPcF_{16}$ in (a) acetone and (b) benzene.[133] The acetone solution of the complex exhibits a Q band at 640 nm, while the Q band appears at 709 nm in benzene. Polar solvents such as DMF, pyridine, and CH_2Cl_2 also give a Q-band

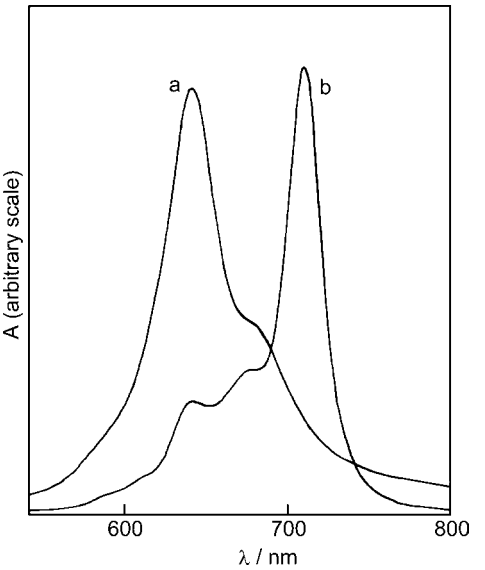

Figure 39. Absorption spectra of $VOPcF_{16}$ in acetone (a) and benzene (b). Redrawn from Handa, M.; Suzuki, A.; Shoji, S.; Kasuga, K.; Sogabe, K. *Inorg. Chim. Acta* **1995**, *230*, 41–44. Copyright 1995, with permission from Elsevier.

position of *ca.* 640 nm. On the other hand, the Q-band appears at 709 nm in non-polar solvents such as *o*-DCB. Tetra-*tert*-butyl VOPc does not exhibit such a strong solvent dependence. The band at 709 nm originates from the monomer species, while the band at *ca.* 640 nm can be ascribed to the dimer species. The ESR data also support these assignments.[133] The Q band of α-$(SC_5H_{11})_8$ substituted VOPc appears beyond 830 nm (830, 834, 841, and 850 nm in toluene, THF, $CHCl_3$, and CH_2Cl_2, respectively).[134]

In the case of niobium, $Nb^{IV}Pc$ and $Nb^{V}Pc$ are possible and, accordingly, $NbPcCl_2$ and $NbPcCl_3$ have been synthesized.[135] Various derivatives are obtained by elimination of the chlorides in $NbPcCl_2$ in the presence of nucleophiles, to yield Nb^{IV}(cat)Pc, Nb^{IV}(oxal)Pc, $Nb^{IV}(SO_4)$Pc, $Nb^{IV}Cl_2$IPc, and Nb^{V}(cat)IPc, where cat = catecolato and oxal = oxalato.[135] $NbCl_2Pc$ shows absorption bands at 690 (Q band), 625, 340, and 272 nm in CH_2Cl_2 (Figure 40, dotted line).[136] Niobium shows some similarities to titanium regarding Pc formation. The structure of $Nb(Pc)_2$ is isostructural, and the two Pc planes are "stapled" by two carbon–carbon σ bonds. The resultant compound exhibits no absorption above 500 nm (Figure 40).[136–139]

$Ta^{V}Cl_3Pc$ was synthesized by Gingl and Strähle,[140,141] and the absorption spectrum was reported recently.[142] Due to the large ionic radius of Ta^{V}, the three axial ligands take on *cis* conformations. The Q and B bands appear at 697 and 342 nm

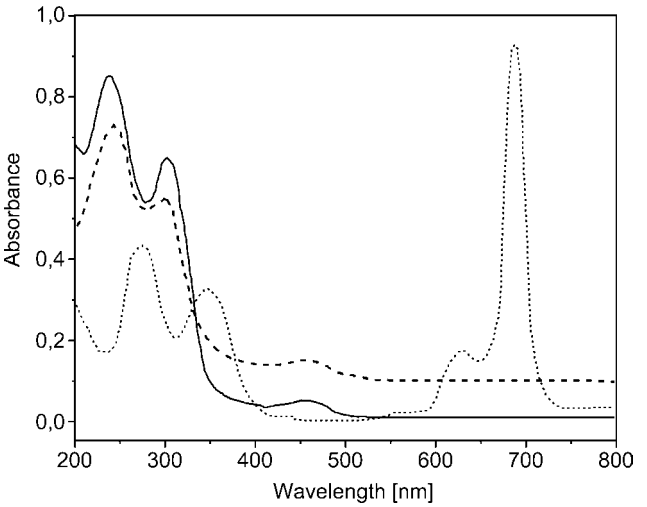

Figure 40. UV-vis spectra in CH_2Cl_2 solution of $[NbPc_2]IBr_2$ (solid line), $[NbPc_2]IBr_2 \cdot I_2$ (dashed line) and $NbPcCl_2$ (dotted line). Redrawn from Janczak, J.; Kubiak, R. *Polyhedron* **2003**, *22*, 313–322. Copyright 2003, with permission from Elsevier.

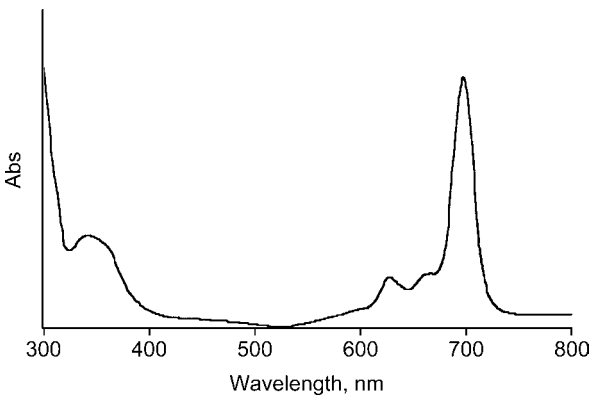

Figure 41. Electronic absorption spectrum of $TaPcCl_3$ in $CHCl_3$. Redrawn from Tau, P.; Nyokong, T. *J. Porphyrins Phthalocyanines* **2006**, *10*, 69–75 with permission from the Society of Porphyrins and Phthalocyanines.

in $CHCl_3$, respectively (Figure 41). Although the crystal structures of $^{cis}[Ta^{V}F_4Pc]^-$ and $^{cis}[Ta^{IV}F_3Pc]^-$ have also been reported, their absorption data are not given.[143]

I. Group 6: CrPc, MoPc and WPc

The Cr^{II} and Cr^{III} Pc complexes have been isolated. The absorption spectra are typical in that the most intense band is in the visible region at 670–690 nm, with

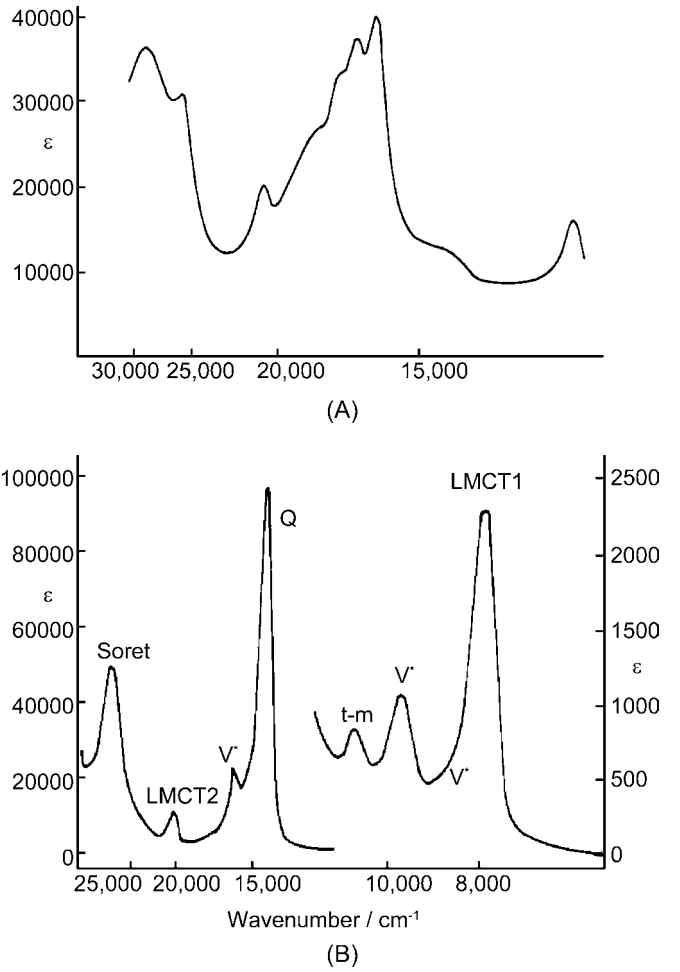

Figure 42. Electronic spectra of electrochemically-prepared tetrasulfonato $Cr^{II}Pc$ in DMF (A) and Na_3(tetrasulfonato)$Cr^{III}Pc$ (B). Redrawn with permission from Lever, A. B. P.; Pickens, S. R.; Minor, P. C.; Licoccia, S.; Ramaswamy, B. S.; Magnell, K. *J. Am. Chem. Soc.* **1981**, *103*, 6800–6806. Copyright 1981 American Chemical Society.

the second most intense band at 330–350 nm. For example, $Cr^{II}Pc(py)_2$ shows band peaks at 687, 632, 560, 525, 500, and 345 nm in pyridine, while $Cu^{III}PcOH$ exhibits peaks at 689, 621, 502, and 347 nm in methanol.[144] The spectra of tetrasulfonato $Cr^{II}Pc$ (A) and Na_3(tetrasulfonato)$Cr^{III}Pc$ (B) are shown in Figure 42.[145] Additional absorption bands are observed both in the near-IR region and at energies lying between the Soret and Q bands. The Cr^{III} species has a hole in the $e_g(d_\pi)$ orbital. The bands at 7900 and 20 080 cm^{-1}, designated as LMCT1 and LMCT2 in Figure 42B respectively, are assigned to $a_{1u}(\pi) \rightarrow e_g(d_\pi)$ and $a_{2u}(\pi) \rightarrow e_g(d_\pi)$

transitions, respectively, by careful analysis of the redox potentials of the compound. Since the a_{1u} orbital has a node at the chelating nitrogen atoms, the orbital overlap associated with the LMCT1 is small. As a consequence, LMCT1 is expected theoretically to be less intense than LMCT2, which is consistent with the experimental result. In the case of the Cr^{II} species, the LMCT1 transition (11 850 cm^{-1}) is remarkably intense compared with the Cr^{III} complex, while the Q band lies at a high energy (16 300 cm^{-1}) and is weak. Lever *et al.* mentioned that it seems probable there is extensive mixing between the Q and LMCT1 transitions in the Cr^{II} species, because they lie fairly close together, producing both the blue shift of the Q band and the unusual intensity distribution.[145] It is conceivable that the band at 19 650 cm^{-1} might be assigned to the $a_{2u}(\pi) \rightarrow a_{1g}(d_{z^2})$ transition (LMCT3). It is possible for the Cr^{III} complex to yield a μ-oxo dimer species, CrPc–O–CrPc, by the reaction of tetra-*tert*-butyl $CrCl_2HPc$ with 2 N NaOH in benzene.[146] The resulting compound shows absorption peaks at 629, 495, and 340 nm in toluene.

MoPc,[147] MoOPc,[148] MoO_2Pc,[149] and $MoClPc_2$[150] were reported in the early studies. The structure of MoOPc is similar to that of VOPc, and the molybdenum coordination is square pyramidal, where the molybdenum atom is located 69 pm above the plane generated from the four coordinating nitrogens.[151,152] The nature of the oxidation state of molybdenum in MoOPc had been the subject of discussion, and the oxidation state of molybdenum in MoOPc prepared from the reaction of phthalonitrile and molybdenum trichloride was shown to be +5 from ESR study,[153] while the reaction of ammonium molybdate and phthalonitrile was reported to give $Mo^{IV}OPc$.[152] The absorption spectrum of $Mo^{IV}OPc$ in 1,2,4-trichlorobenzene shows a prominent peak at 703 nm and a weaker peak at 643 nm, while VOPc exhibits the corresponding peaks at 700 and 630 nm.[152] Successive washing of MoOPc with 0.1 N NaOH, water, and acetone yields $Mo^{V}O(OH)Pc$.[154] Figure 43 shows the Q-band region absorption data of $Mo^{V}O(OH)Pc$ (c) and its electro-oxidized or reduced species (a and b, respectively). The initial state (Mo^{V}) exhibits a Q band at 700 nm. Upon oxidation/reduction, the Q band shifts to longer/shorter wavelength without any reduction in intensity, which are assigned to the Mo^{VI} and Mo^{IV} species, respectively.[154,155] Nitrido-MoPc complexes, namely MoNPcs, have also been also successfully synthesized.[156,157] The Q band of octa-β-alkyl-substituted MoNPc appears at 709–716 nm in toluene.[156] Gorsch and Homborg reported the absorption properties of a $(MoPc)_2$ dimer having a Mo–Mo direct bond (Figure 44).[158]

The number of reports on WPc is very limited.[156,157,159–161] Tungsten has an oxidation state of +5 in WCl_3Pc[159] and W(O)OH(PcCl).[161] The maximum of the Q band for W(O)OH(PcCl) is at 730 nm. The nitride complex, WNPc, shows a red shift of the Q-band maximum to 751.0 nm in 1-chloronaphthalene. In this case, the

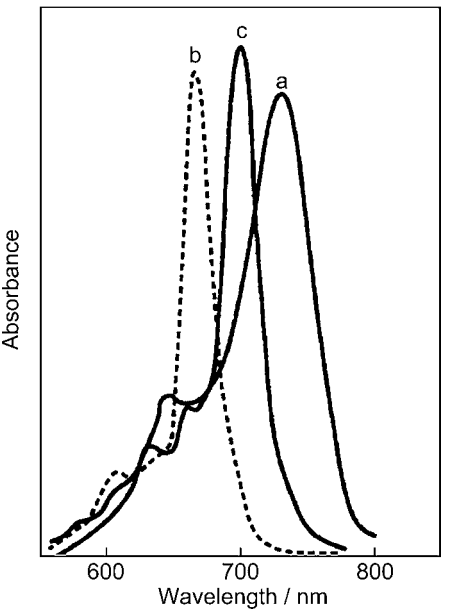

Figure 43. Spectral changes observed during: (a) electrochemical oxidation of $Mo^{V}O(OH)Pc$ at 0.55 V dissolved in 1-chloronaphthalene containing 0.1 M TBAP; and (b) electrochemical reduction of $Mo^{V}O(OH)Pc$ at –0.5 V dissolved in DMSO containing 0.1 M TEAP. Spectrum (c) corresponds to the $Mo^{V}O(OH)Pc$ complex in 1-chloronaphthalene before electrolysis. Redrawn from Nyokong, T. *Polyhedron* **1994**, *13*, 215–220. Copyright 1994, with permission from Elsevier.

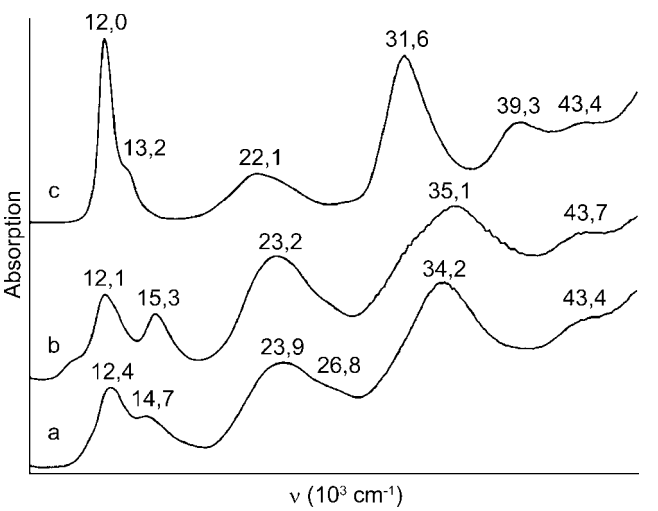

Figure 44. Absorption spectra of a $(MoPc)_2$ dimer (a: fresh solution, and b: 1 day later), and MoOPc (c) in conc. H_2SO_4. Redrawn from Gorsch, M.; Homborg, H. *Z. Anorg. Allg. Chem.* **1998**, *624*, 634–641.

Q band is broadened and shows two shoulders at 699.5 and 673.5 nm.[156] The substituted derivatives, WN(*tert*-Bu_4Pc) and WN((C_5H_{11})$_8$Pc), show broad Q bands at 745.0 and 770.5 nm in toluene, respectively.[156]

J. Group 7: MnPc, TcPc, RePc and $RePc_2$

The manganese ion in MnPc exists in several stable oxidation states, ranging from Mn^{I} to Mn^{IV} depending on the number and nature of the axial ligand, while the transition energies also depend on both the metal oxidation state and spin state. Figure 45 shows the absorption spectrum of $Mn^{II}Pc$ dissolved in pyridine.[162] $Mn^{II}Pc$ is considered to have fifth and sixth ligands in a coordinating solvent, and thus the spectrum shown in Figure 45 arises from the dipyridinated Pc species, $Mn^{II}Pc(py)_2$, which was confirmed also by X-ray crystallography.[163] In addition to the intense principal band at 660 nm, the spectrum is characterized by a less intense absorption in the 800–900 nm region. Furthermore, several bands in the 500–600 nm region are characteristic of MnPc, which do not appear for metalloPcs containing a main-group metal such as magnesium and zinc. Elvidge and Lever,[164] and Rutter and McQueen[165] reported that the main absorption band appears respectively at 712.5 and 620 nm. However, Engelsma *et al.* confirmed that these bands originate from oxidized species.[162] Of the possible ground states for a d_5 ion (Mn^{II}) in a D_{4h} crystal field, the $^4A_{2g}$ [166–170] and ^4E_g [171] states have been suggested for the ground state of $Mn^{II}Pc$. Williamson *et al.* measured the absorption and MCD spectra of $Mn^{II}Pc$ isolated in an Ar matrix, and concluded that the obtained data are consistent with a $^4E_g(e_g^3\, b_{2g}\, a_{1g})$ ground state term.[172] Figure 46 shows absorption (bottom) and MCD (top) spectra of Ar-matrix-isolated $Mn^{II}Pc$ obtained at *ca.* 5 K. Compared to the spectrum shown in Figure 45, the bands observed for the matrix-isolated

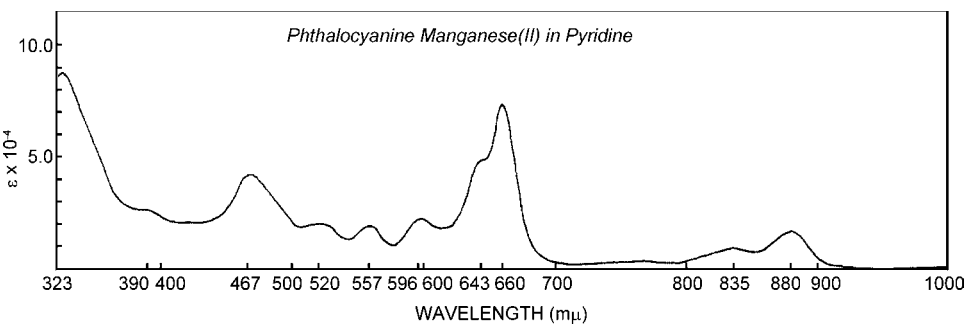

Figure 45. Absorption spectrum of $Mn^{II}Pc$ in pyridine. Redrawn with permission from Engelsma, G.; Yamamoto, A.; Markham, E.; Calvin, M. *J. Phys. Chem.* **1962**, *66*, 2517–2531. Copyright 1962 American Chemical Society.

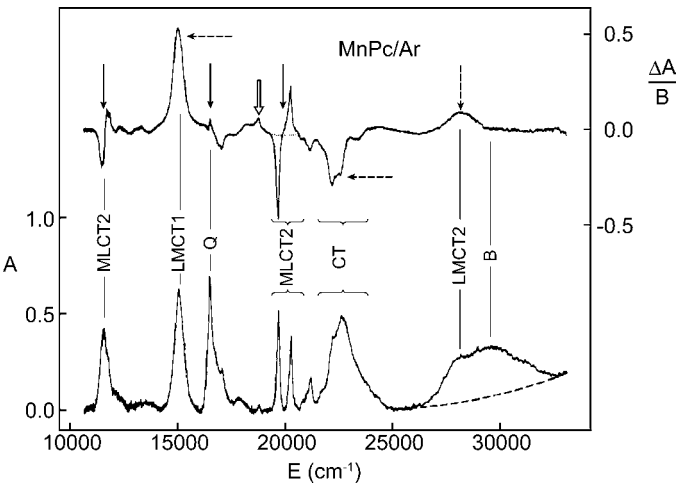

Figure 46. Absorption (bottom) and MCD (top) spectra of Ar matrix-isolated $Mn^{II}Pc$ obtained at *ca.* 5 K and B = 0.15 T. Redrawn with permission from Williamson, B. E.; VanCott, T. C.; Boyle, M. E.; Misener, G. C.; Stillman, M. J.; Schatz, P. N. *J. Am. Chem. Soc.* **1992**, *114*, 2412–2419. Copyright 1992 American Chemical Society.

$Mn^{II}Pc$ are sharper, and some additional bands which are not seen in Figure 45 can be recognized. The strong MCD signals seen in Figure 46 indicate the presence of Faraday C terms based on ground-state degeneracy, which is confirmed by the saturation measurements. The MCD signals corresponding to the bands at *ca.* 11 600, 16 500, and 20 000 cm^{-1} are pairs of oppositely-signed C terms (bisignated C terms, solid arrows in Figure 46), while the dashed arrows at *ca.* 15 000, 22 500, and 28 200 cm^{-1} indicate that these are assigned as single-signed C terms. Given that the ground state is $^4A_{2g}(b_{2g}^2\ e_g^2\ a_{1g})$, the only *x*,*y*-polarized spin-allowed transitions are of the type $^4A_{2g} \rightarrow {}^4E_u$. The ^{4}Eu excited terms are split by first-order spin-orbit (SO) interactions into four Kramers doublets, each of which is split further by an externally applied magnetic field. See Figure 4 in Ref. 172, where an energy level diagram for the transitions $^4A_{2g}(b_{2g}^2\ e_g(d_\pi)^2\ a_{1g}) \rightarrow {}^4E_u(b_{2g}^2\ e_g\ a_{1g}\ b_{1u}(\pi^*))$ designated as MLCT2 by Lever *et al.* is shown as an example.[145] In this case, at very low temperature, bisignated MCD C terms with a sign which is negative at lower energy and positive at higher energy are expected. Similarly, bisignated C terms are expected for the other $^4A_{2g} \rightarrow {}^4E_u$ transitions including LMCT1 ($a_{1u}(\pi) \rightarrow e_g(d_\pi)$), although the MCD signal observed at 15 000 cm^{-1} is apparently single-singed and therefore inconsistent with this assumption. In the case of $^4E_g(e_g^3\ a_{1g}\ b_{2g})$ as the ground state, the MLCT2 excitation corresponds to $^4E_g \rightarrow {}^4A_{1u}$, $^4A_{2u}$, $^4B_{1u}$, and $^4B_{2u}$ (see Figure 5 in Ref. 172). At the low-temperature limit in this case, $^4E_g \rightarrow {}^4A_{1u}$ and $^4A_{2u}$ transitions are expected to be associated with

negative C terms, and $^4E_g \rightarrow {}^4B_{1u}$ and $^4B_{2u}$ transitions to be associated with positive C terms, while weak bisignated C terms are expected for $\pi \rightarrow \pi^*$ excitations due to small interactions between the π-skeleton and metal orbitals. Since these theoretical expectations are fully consistent with the experimental data, the ground state of $Mn^{II}Pc$ is determined to be ^4E_g ($e_g^3\ b_{2g}\ a_{1g}$). As a consequence, LMCT1 ($a_{1u}(\pi) \rightarrow e_g(d\pi)$) and LMCT2 ($a_{2u}(\pi) \rightarrow e_g(d_\pi)$), giving rise to $^4B_{2u}$ and $^4B_{1u}$ terms, respectively, are assigned as the bands at *ca.* 15 000 and 28 200 cm^{-1}, since positive-signed C terms are expected for these transitions. The weak bisignated C term at *ca.* 16 500 cm^{-1} implies that the corresponding absorption band originates from π–π^* transitions, namely the Q band. In the case of MLCT2 ($e_g(d_\pi) \rightarrow b_{1u}(\pi^*)$), four transitions, of which two corresponding to $^4B_{1u}$ and $^4B_{2u}$ terms show positive C terms, and the other two corresponding to $^4A_{1u}$ and $^4A_{2u}$ show negative C terms, are expected. Therefore, the bands at *ca.* 11 600 and 20 000 cm^{-1} can be assigned to these, of which the former band contains two overlapping transitions. DFT study also predicts that the ground state of unligated $Mn^{II}Pc$ is ^4E_g.[173] For the six-coordinated adducts with two pyridine ligands, an intermediate-spin state was assigned experimentally,[163] which, however, has been doubted theoretically.[173] According to the DFT calculations, the axial coordinations raise the energy of the d_{z^2}-orbital. Therefore, $Mn^{II}Pc(py)_2$ adopts a low-spin $^2A_{1g}$ ($a_{1g}^1\ b_{3g}^2\ b_{2g}^2 = d_{xy}^1\ d_\pi^4$) state.

In the case of $Mn^{III}Pc$ derivatives (high-spin d^4 species), LMCT transitions corresponding to the $a_{1u}(HOMO) \rightarrow e_g(d_\pi)$ and $a_{2u}(HOMO–1) \rightarrow e_g(d_\pi)$ transitions are observed in the near infrared (*ca.* 7600 cm^{-1}) and visible (*ca.* 20 100 cm^{-1}) regions, respectively (Figure 47).[145] The weaker bands observed between the Q and lower energy LMCT bands were assigned as either vibronic or trip-multiplet transitions by Lever *et al.* When charge-transfer (CT) transitions lie close to either the Q or B bands, quite significant changes take place in the bandwidth, band energy, and band intensity. Thus, the Q band of MnPc is often observed in a lower energy region compared to other metalloPcs, since configuration interactions between the π–π^* and CT one-electron transitions lowers the Q band energy. The Leznoff and Nyokong groups described some substituted $Mn^{III}Pc$ derivatives, such as $Mn^{III}Pc$ substituted by hexadecaalkoxy groups, and $Mn^{II}Pc$ having eight alkylthio groups.[174,175] Since the Q band of these compounds appears beyond the visible region (for example, $Mn^{III}Pc(SC_5H_{11})_8(OAc)$ shows a Q band at 893 nm in CH_2Cl_2), contributions of the Q band to the "color" of the compounds are less significant. Instead, the color appearance is affected by the LMCT transition observed between 450 and 650 nm. As a result, $Mn^{III}Pc$ derivatives with electron-donating substituents are brown or red in color. The spectra of $Mn^{IV}Pc$ species have been rarely reported. Mbambisa *et al.* generated the $Mn^{IV}Pc(2–)$ species electrochemically, and observed the lowest energy band at 920 nm in CH_2Cl_2 containing

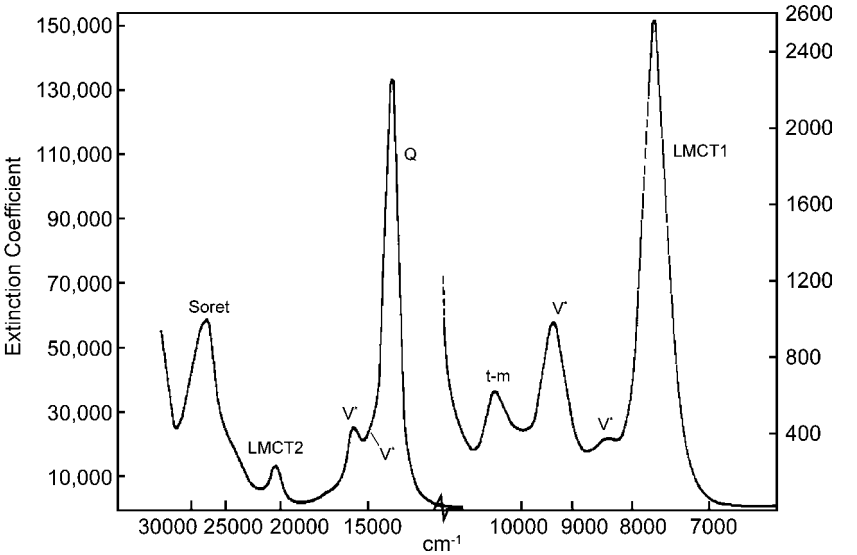

Figure 47. Absorption spectrum of (*tert*-Bu)$_4$Mn^{III}Pc(OAc) in DMF. Redrawn with permission from Lever, A. B. P.; Pickens, S. R.; Minor, P. C.; Licoccia, S.; Ramaswamy, B. S.; Magnell, K. *J. Am. Chem. Soc.* **1981**, *103*, 6800–6806. Copyright 1981 American Chemical Society.

0.1 M $TBABF_4$.[175] The Mn^VPc analog was first achieved by employing the triazacorrole (corrolazine) skeleton as a Mn^V-oxo complex, which shows moderately intense bands at 634 and 418 nm.[176]

Yoshihara *et al.* concluded that the oxidation state of the technetium ion in TcPc obtained using a recoil implantation technique is +4.[177] Synthesis of a Tc^V complex was also reported as nitrido-Tc^VPc.[178] El-Tamer *et al.* prepared ^{99m}TcPc tetrasulfonate, and illustrated its blue color using a picture.[179] However, no detailed absorption study is available on TcPc.

Soluble RePcs were first reported by Ziener *et al.*[180,181] The absorption spectrum of (*tert*-Bu)$_4$ReNPc and (*tert*-Bu)$_4$ReO(OEt)Pc exhibits band maxima at 698 and 363 nm, and 726 and 368 nm, respectively, in CH_2Cl_2. The μ-oxo dimer, [(*tert*-Bu)$_4$ReO(OEt)Pc]$_2$O, exhibits a Q band at 688 nm, which is blue-shifted by *ca.* 40 nm relative to the monomeric species. In addition, the dimer species shows a small band at 747 nm in CH_2Cl_2.[181] The BBr_3 adduct of the nitride complex, (*tert*-Bu)$_4$ReN(BBr_3)Pc, shows a Q band red-shifted from 698 to 725 nm due to the electron-withdrawing effect of the BBr_3 group.[102] Frick *et al.* claimed that [(*tert*-Bu)$_4$Re(O)Pc]$_2$ forms a rhenium–rhenium bond. Figure 48 compares the absorption spectra of [(*tert*-Bu)$_4$Re(O)Pc]$_2$ (top) and [(C_5H_{11})$_8$Re(O)Pc]$_2$O in chloroform or as a KBr pellet.[156] The Q band of [(*tert*-Bu)$_4$Re(O)Pc]$_2$ is blue-shifted (652.5 nm in $CHCl_3$) relative to (*tert*-Bu)$_4$ReNPc (698 nm in CH_2Cl_2),

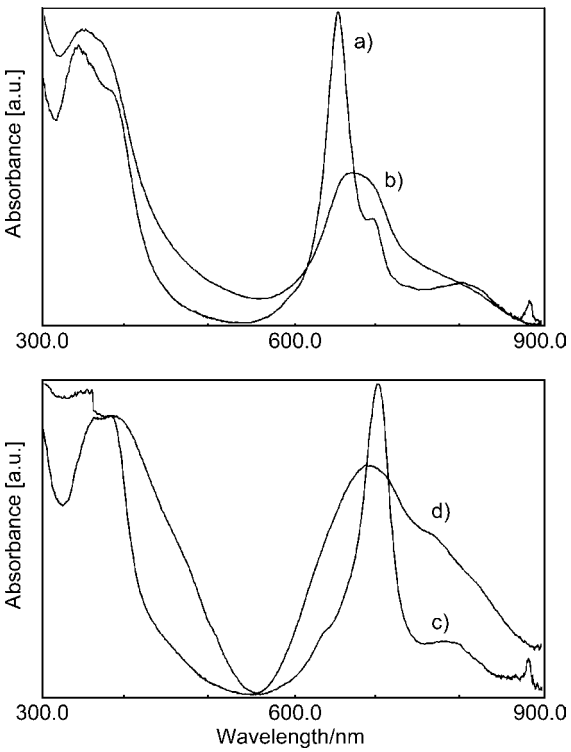

Figure 48. Absorption spectra of [(*tert*-Bu)$_4$Re(O)Pc]$_2$ (top) and [(C$_5$H$_{11}$)$_8$Re(O)Pc]$_2$O (bottom) in chloroform (a and c) and as a KBr pellet (b and d). Redrawn from Frick, K.; Verma, S.; Sundermeyer, J.; Hanack, M. *Eur. J. Inorg. Chem.* **2000**, 1025–1030.

while that of [(C$_5$H$_{11}$)$_8$Re(O)Pc]$_2$O (701.5 nm in $CHCl_3$) is approximately identical, indicating that larger exciton type π–π interactions are involved for [(*tert*-Bu)$_4$Re(O)Pc]$_2$ due to the closer ring-to-ring distance. The weak bands in the longer wavelength region of the Q band are also indicative of the formation of a face-to-face dimer structure as described in Section E. Figure 49 exhibits another example of the absorption data of (RePc)$_2$, having a rhenium–rhenium bond whose structure has been unambiguously determined by crystallography.[182] The spectrum reveals the principal absorptions at 15 800 (Q region), 29 500/33 100 (B1/B2 region), and 36 600 cm^{-1} (N region). On the other hand, the dissolved complex shows a splitting of the Q region into two strong bands of comparable intensity at 14 100 and 16 500 cm^{-1} (Figure 49b). The band at 8950 cm^{-1} for the monomer species (Figure 49c) was assigned as a trip-doublet transition, resulting from spin–spin coupling of the triplet state of the Pc ligand with the $^2T_{2g}$ ground state of low-spin Re^{II} which is assumed to have a pseudo-O$_h$ symmetry.[182,183]

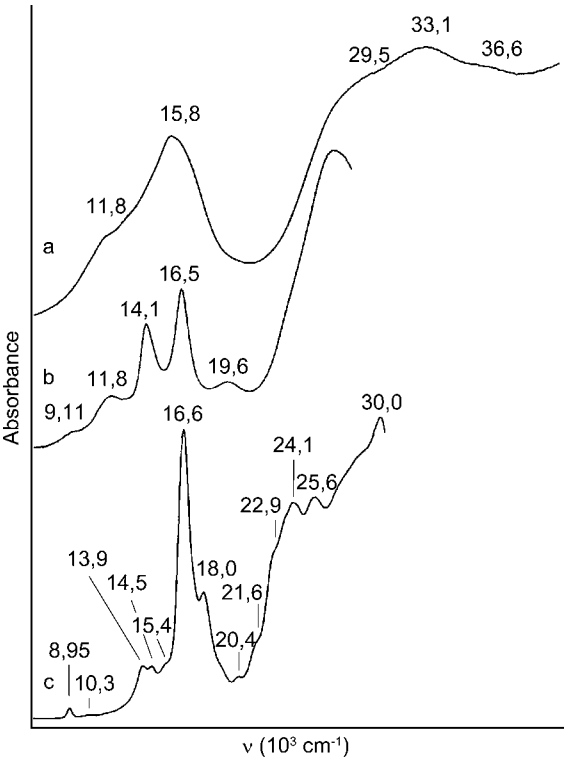

Figure 49. Absorption spectra of $(RePc)_2$ dispersed in a KBr pellet (a), $(RePc)_2$ dissolved in 1-chloronaphthalene (b), and $^{trans}[Re(PPh_3)_2Pc]$ dissolved in pyridine (c). Redrawn from Göldner, M.; Hückstädt, H.; Murray, K. S.; Moubaraki, B.; Homborg, H. *Z. Anorg. Allg. Chem.* **1998**, *624*, 288–294.

K. Group 8: FePc, RuPc and OsPc

The oxidation state of the iron ion in FePc can vary from Fe^{I} to Fe^{IV}, depending on the number and the nature of the axial ligands. Edwards and Gouterman compared the absorption data of $Fe^{II}Pc$, both in vapor-phase and in DMSO, and found that a large blue shift was observed in the Q band on going from vapor (676 nm) to DMSO (655.5 nm), indicating that the principal species in DMSO differs from that in vapor.[21] A large number of bisaxially coordinated low-spin $Fe^{II}Pcs$ has been studied.[184–203] Dale estimated the effect of axial ligands on the absorption spectrum of $Fe^{II}L_2Pc$, where L represents a ligand at one of the axial positions.[200] Figure 50 depicts the absorption spectra of $Fe^{II}Pc$, $Fe^{II}(py)_2Pc$, $Fe^{II}(NH_3)_2Pc$, and $Fe^{II}(CN)_2Pc$ in DMSO (from top to bottom). In the presence of axial ligands, the magnitudes of the resultant shifts in the absorption bands appear to be related to the σ-donor strength of the axial ligands. The spectrum of $Fe^{II}(py)_2Pc$ is similar to that of

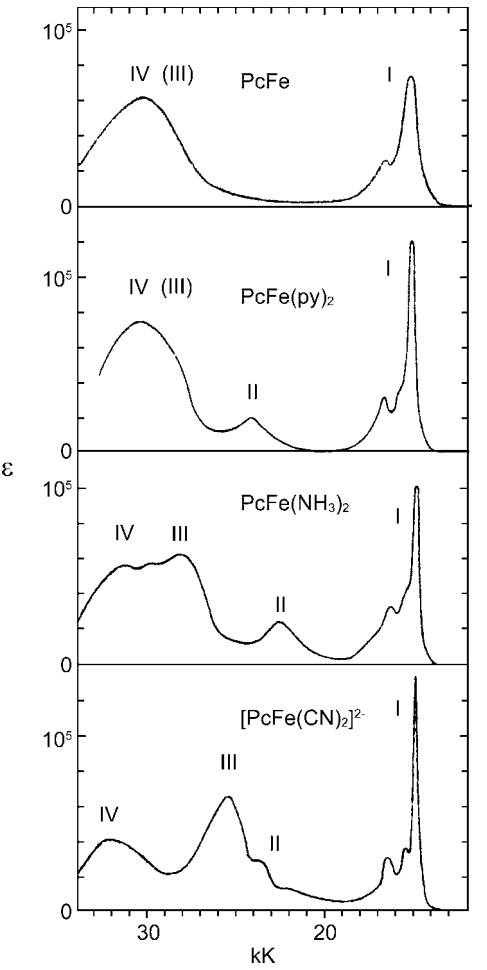

Figure 50. Absorption spectra of $Fe^{II}Pc$, $Fe^{II}Pc(py)_2$, $Fe^{II}Pc(NH_3)_2$, and $Fe^{II}Pc(CN)_2$ in DMSO (from top to bottom). Dale, B. W. *Trans. Faraday Soc.* **1969**, *65*, 331–339. Redrawn by permission of The Royal Society of Chemistry.

$Fe^{II}Pc$, although an additional band at 24 100 cm^{-1} is recognized. A small shoulder on the low-energy side of the band at 30 300 cm^{-1} is also characteristic. In the case of $Fe^{II}(NH_3)_2Pc$, the band at *ca.* 30 000 cm^{-1} splits into at least two components. A similar trend was also observed for $Fe^{II}(im)_2Pc$, $Fe^{II}(n\text{-}Bu)_2Pc$, and $Fe^{II}(pip)_2Pc$ (not shown). In the case of $Fe^{II}(CN)_2Pc$, two, clearly separated bands are observed in the UV region. The bands labeled as I in Figure 50 (Q band) vary by less than 400 cm^{-1}. On the other hand, the bands labeled as II–IV deviate progressively from $Fe^{II}Pc$ as the π-donor strength of the axial ligands is increased. Dale tentatively assigned band II to a CT transition, and later, Stillman and Thomson

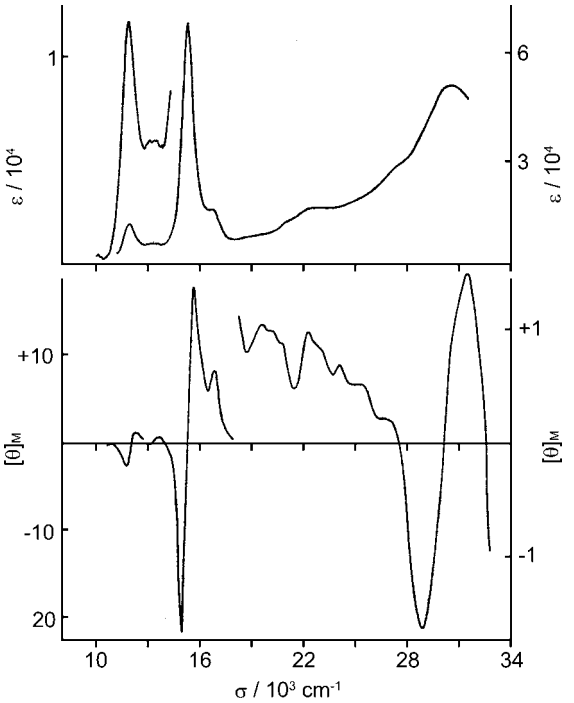

Figure 51. Absorption (top) and MCD (bottom) spectra of $Fe^{II}Pc$ in *o*-DCB. Stillman, M. J.; Thomson, A. J. *J. Chem. Soc. Faraday Trans. 2* **1974**, *70*, 790–804. Redrawn by permission of The Royal Society of Chemistry.

claimed that this assignment is not overturned by the MCD data.[204] However, it has been claimed that the spectrum of $Fe^{II}(CN)_2Pc$ has a resemblance to that of $Co^{III}(CN)_2Pc$ which is devoid of CT transitions.[204] See the following section and Figure 63 on $Co^{III}(CN)_2Pc$. In a weekly coordinating solvent, $Fe^{II}Pc$ exhibits a new absorption band close to 12 000 cm^{-1}, which is absent in the spectra shown in Figure 50, while the corresponding MCD signal is a dispersion type A-term, as depicted in Figure 51. Stillman and Thomson proposed that a satisfactory interpretation of these results can be obtained if a spin state other than S = 0 is assumed for the iron ion, and concluded that the ground state of $Fe^{II}Pc$ in *o*-DCB is $^3A_{2g}$.[204] In this case, the e_g orbitals must be the highest occupied d-orbitals, and the transition $^3A_{2g} \rightarrow {}^3E_u$ is expected to give rise to the lowest energy band. Of the two possible excited configurations, $(e_g b_{1u})$ and $(e_g b_{2u})$, the latter possibly corresponds to the lowest-energy band.[145,204] Nemykin *et al.* prepared a series of $Fe^{II}L_2Pcs$, and demonstrated that the experimental MLCT band positions are well-correlated with the theoretical results obtained by a semi-empirical AM1 method and the cone angle concept.[201] Ough and Stillman classified the axial ligands into three groups

on the basis of the spectral features, according to the σ donor and π acceptor strengths, i.e. (1) strong σ donors and weak π acceptors, (2) strong σ and π donors, and (3) weak σ donors and strong π acceptors. The authors performed a detailed analysis of the absorption and MCD spectra of the corresponding $Fe^{II}L_2Pc$ species.[202] Accordingly, (1) an increase of the σ donor strength of the axial ligands decreases the energy of the degenerate transitions; (2) an increase of the π acceptor strength of the axial ligand decreases the separation between the B1-B2 and MLCT1-MLCT2 transitions; and (3) an increase of the π donor strength of the axial ligands increases the separation between the B1–B2 and MLCT1–MLCT2 transitions. Fukuda *et al.* demonstrated that a highly-deformed 1,4,8,11,15,18,22, 25-octaphenyl $Fe(py)_2Pc$ with a saddle-type D_{2d} aromatic symmetry shows broad absorption bands of medium intensity on the lower energy side of the Q band.[205] These bands have been assigned to MLCT transitions which are forbidden for normal planar $Fe^{II}Pcs$ with D_{4h} symmetry. Hanack *et al.* compared the absorption spectra of tetra-*tert*-butyl $Fe^{II}L_2Pc$, $Fe^{II}L_2Nc$, and $Fe^{II}L_2Ac$, where L = Me_2PhNC (Figure 52).[206] The spectra show a bathochromic shift of the Q band with linear annulation of the benzene units (658, 751, and 829 nm for Pc, Nc, and Ac, respectively), and the absorption coefficients of the Q bands increase on going from Pc to Ac. A series of bisaxially substituted FeNcs have also been synthesized by the same group.[207]

Lever and Wilshire reported the absorption spectrum of $(py)Fe^{I}Pc(2-)$ in py/LiCl (Figure 53).[208] The observation that the spectral envelope is quite different from that of normal metalloPcs indicates that the Fe^{I} ion interacts significantly with the π-system. The observed band peak positions are 30 615, 26 572sh, 19 405,

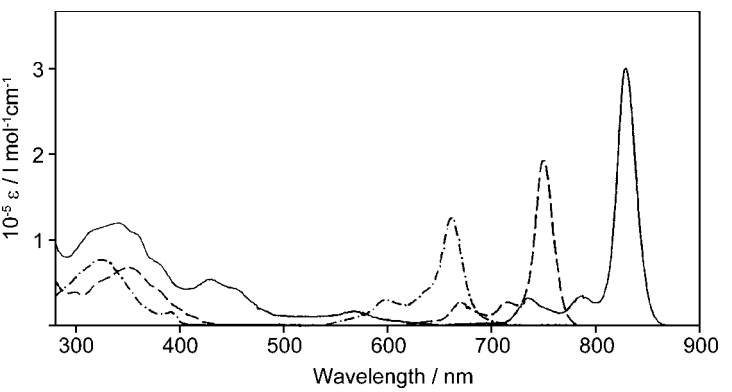

Figure 52. Absorption spectra of (*tert*-butyl)$_4Fe^{II}PcL_2$ (dashed-dotted line), (*tert*-butyl)$_4Fe^{II}NcL_2$ (dashed line), and (*tert*-butyl)$_4Fe^{II}AcL_2$ (solid line) in $CHCl_3$, where L = Me_2PhNC. Hanack, M.; Dieing, R.; Röhrig, U. *Chem. Lett.* **1993**, 399–402. Redrawn by permission of The Chemical Society of Japan.

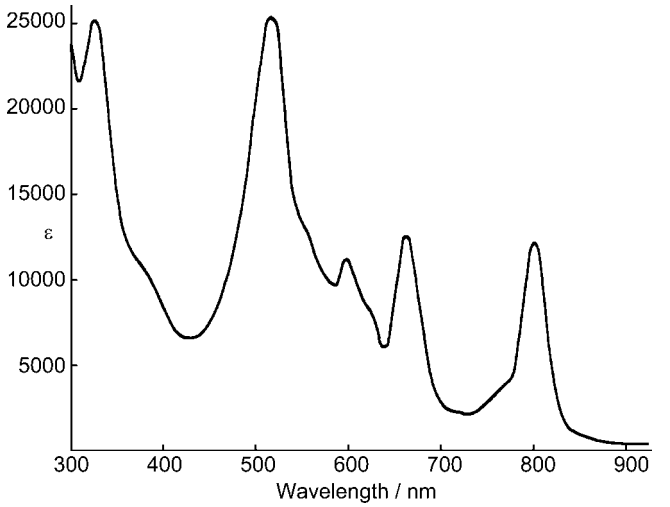

Figure 53. Absorption spectrum of (py)Fe^{I}Pc(–2) in py/LiCl. Redrawn with permission from Lever, A. B. P.; Wilshire, J. P. *Inorg. Chem.* **1978**, *17*, 1145–1151. Copyright 1978 American Chemical Society.

16 800, 16 250sh, 15 130, 13 890sh, and 12 480 cm^{-1}. The authors also claimed that $Fe^{II}Pc$ in *N,N*-dimethylacetamide containing LiCl is oxidized by air (oxygen), to give the stable Fe^{III} complex. Kennedy *et al.* reported a detailed investigation of the spectral properties of a range of six- and five-coordinated $Fe^{III}Pcs$.[209] Anionic six-coordinate species, B^+–[$Fe^{III}L_2$(Pc(2–))]$^-$ (B^+ = bulky cation; L = OH^-, OPh^-, NCO^-, NCS^-, N_3^-, CN^-), display low-spin d^5 characteristics. The absorption spectra of these species (Figure 54, part a top, and part b a–c) can be distinguished from those of five-coordinate complexes (Figure 54, part a c–f). The six-coordinate species show a Q band at *ca.* 690 nm with a weak band at *ca.* 775 nm, while the Q band of the five-coordinate species appears at *ca.* 660 nm with shoulders on each side at *ca.* 590 and 710 nm. Weak LMCT bands are also observed at 465 and 840 nm. The Q band at *ca.* 660 nm indicates that the complex has a high-spin d^5 configuration. Kobayashi *et al.* reported that the spin state of iron in 1,2,8,9,15,16,22,23-octadecyloxycarbonyl $Fe^{III}Pc$ dissolved in CH_2Cl_2 or $CHCl_3$ changes from a high-spin to a low-spin state by the addition of tetrabutylammonium chloride and/or bromide (Figure 55).[210] In the absence of an electrolyte, the complex exhibits peaks at 817, 738, 650, and 337 nm. When tetrabutylammonium chloride is added, the spectrum changes with a set of isosbestic points, and the final spectrum shows new peaks at 690, 617, 552, 410, and 329 nm, which corresponds to a change of the electronic configuration from the high-spin to low-spin state. Reports on $Fe^{IV}Pc$ species are limited.[211,212] Bottomley *et al.* observed spectral changes obtained during the electrolysis of a μ-nitrido FePc dimer, $(FePc)_2N$, in pyridine (Figure 56).[212] The neutral

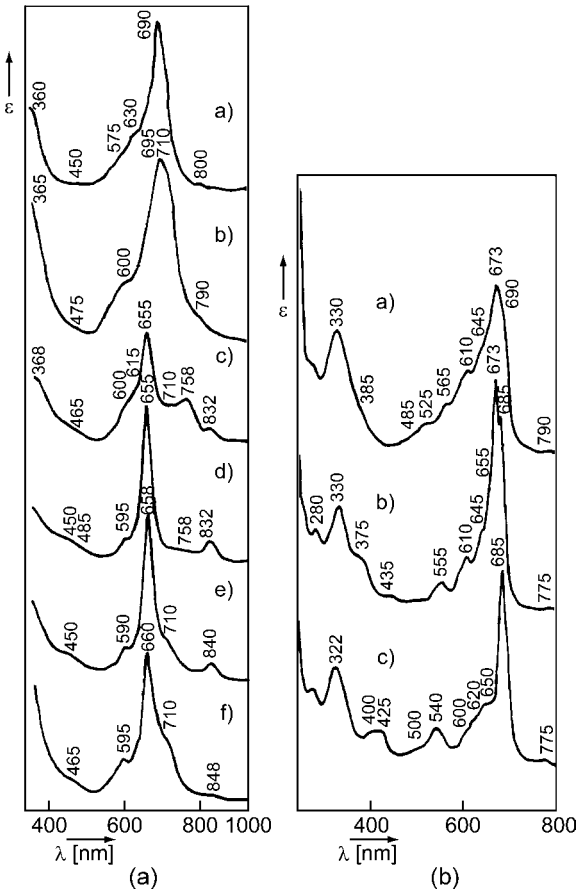

Figure 54. Part (a) (left): Electronic spectra of (a) (PNP)[Fe(OH)$_2$Pc], (b) (FePc)$_2$O, (c) FeFPc, (d) FeClPc, (e) FeBrPc, and (f) FeIPc in 1-chloronaphthalene. Part (b) (right): Electronic spectra of (a) (TBA)[Fe(NCS)$_2$Pc], (b) (PNP[Fe(NCO)$_2$Pc], and (c) (PNP)[Fe(CN)$_2$Pc] in CH_2Cl_2. Redrawn with permission from Kennedy, B. J.; Murray, K. S.; Zwack, P. R.; Homborg, H.; Kalz, W. *Inorg. Chem.* **1986**, *25*, 2539–2545. Copyright 1986 American Chemical Society.

complex is considered to have an $Fe^{III1/2}$–$Fe^{III1/2}$ (or Fe^{IV}–Fe^{III}) mixed valence state, and the spectrum before electrolysis shows a strong band at 626 nm, with two shoulders at 573 and 658 nm. After electrolysis at an applied potential of +0.300 V vs. SCE, the final spectrum shows a prominent band at 637 nm, with two shoulders at 578 and 677 nm. The authors assigned this species as $(Fe^{IV}Pc)_2N$. A similar experiment was also performed for a μ-oxo FePc dimer, $(FePc)_2O$, in pyridine (Figure 57).[211] The initial spectrum shows an intense band at 622 nm and two shoulders at 569 and 653 nm, while the intense band shifts to 652 nm in addition to new shoulders appearing at 624 and 692 nm after electrolysis at +0.59 V vs. SCE. The generated species is speculated to be an Fe^{IV}–Fe^{III} complex.

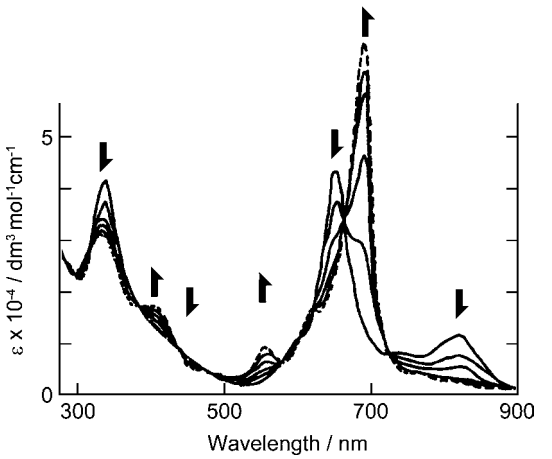

Figure 55. Absorption spectral changes observed upon addition of tetrabutylammonium chloride to a 1.75×10^{-5} M solution of 1,2,8,9,15,16,22,23-octadecyloxycarbonyl $Fe^{III}Pc$ in CH_2Cl_2. Kobayashi, N.; Koshiyama, M.; Ishikawa, Y.; Osa, T.; Shirai, H.; Hojo, N. *Chem. Lett.* **1984**, 1633–1636. Redrawn by permission of The Chemical Society of Japan.

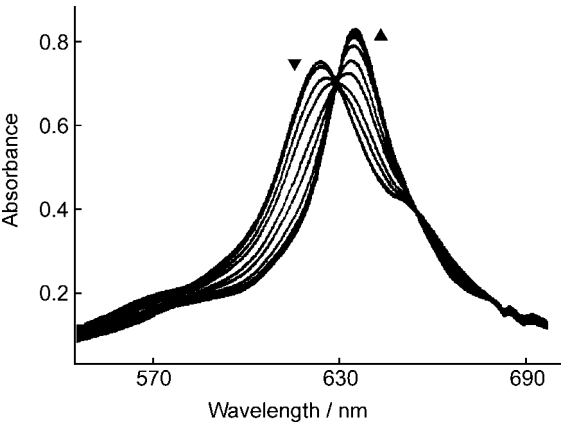

Figure 56. Absorption spectral changes obtained during the electrolysis of $(FePc)_2N$ in pyridine at +0.300 V vs. SCE, generating the dimeric cation. Redrawn with permission from Bottomley, L. A.; Gorce, J. N.; Goedken, V. L.; Ercolani, C. *Inorg. Chem.* **1985**, *24*, 3733–3737. Copyright 1985 American Chemical Society.

The synthesis, properties, and applications of RuPcs have been reviewed by Rawling and McDonagh.[213] The absorption properties of RuPcs are relatively sensitive to axial ligands. Although nitrogen-containing aromatic heterocycles, amines, and phosphanes appear not to have a significant effect on the Soret band, the coordination of a carbonyl ligand (CO) leads to a profound hypsochromic shift of the Soret band, along with a significant increase in the molar

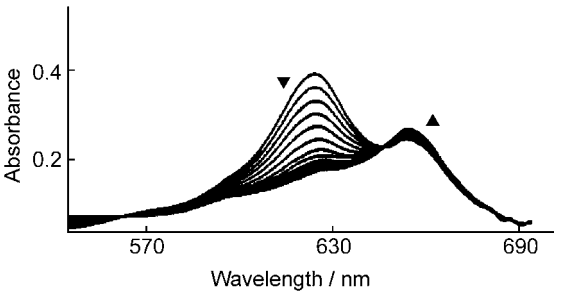

Figure 57. Absorption spectral changes obtained during the electrolysis of $(FePc)_2O$ in pyridine at +0.59 V vs. SCE. Redrawn with permission from Bottomley, L. A.; Ercolani, C.; Gorce, J. N.; Pennesi, G.; Rossi, G. *Inorg. Chem.* **1986**, *25*, 2338–2342. Copyright 1986 American Chemical Society.

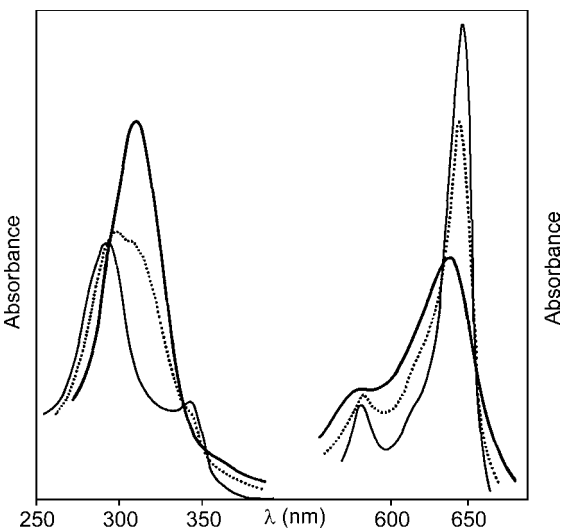

Figure 58. Visible spectral changes during photolysis of Ru(4-Mepy)(CO)Pc in CH_3CN (thin solid line), to give $Ru(CH_3CN)_2Pc$ (thick solid line). Redrawn with permission from Dolphin, D.; James, B. R.; Murray, A. J.; Thornback, J. R. *Can. J. Chem.* **1980**, *58*, 1125–1132.

extinction coefficient of the Q band.[214–216] A variety of RuL_2Pc complexes have been prepared by photolysis of RuL'(CO)Pc complexes in the presence of excess L, where L represents pyridine derivatives, imidazole, DMF, DMSO, and acetonitrile.[214,217] Figure 58 shows the spectral changes seen during photolysis of Ru(4-Mepy)(CO)Pc in CH_3CN to give $Ru(CH_3CN)_2Pc$. The mono carbonyl complexes, Ru(py)(CO)Pc, Ru(4-Mepy)(CO)Pc, Ru(4-*tert*-Bupy)(CO)Pc, Ru(dmf)(CO)Pc, and Ru(dmso)(CO)Pc, show an intense, sharp Q band in the 637–645 nm region, which is characteristic of typical metalloPcs. Absorption

bands in the 340–380 nm region are also distinctive for this type of complexes. Upon photolysis, the Q band shifts slightly to the blue, broadens, and loses the intensity. Thus, the molar extinction coefficient of $Ru(CH_3CN)_2Pc$ is half as large as that of the monocarbonyl complexes. Although the absorption band in the 340–380 nm region disappears for $Ru(CH_3CN)_2Pc$, further photolysis in pyridine, to give $Ru(py)_2Pc$, generates an absorption band at *ca.* 370 nm again.[214] Tetra-15-crown-5 appended $Ru^{II}Pc$ also shows a similar spectral trend.[216] Gutierrez observed that $Ru^{II}(CO)(py)Pc$ exhibits splitting of the Q band in a glassy matrix at 5 K, which is likely to be attributed to the polar electronic influence of solvents on the microenvironment around the complex.[218] Stuzhin *et al.* reported a series of $Ru^{II}L_2(OPTAP)$ complexes, where OPTAP = octaphenyl TAP (Figure 59).[219] For the N-base adducts (L = NH_3, pyridine (py), pyrazine (pyz), and *s*-tetrazine (tz)), the decrease of the σ-donor and increase of the π-acceptor properties of the axial ligands leads to a slight hypsochromic

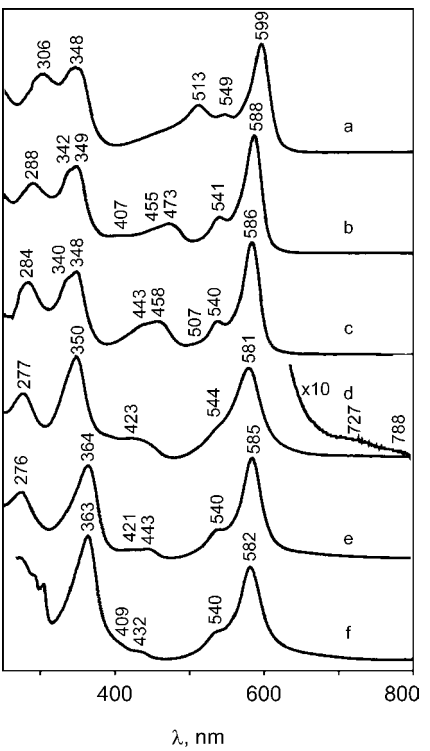

Figure 59. Absorption spectra of $Ru(NH_3)_2(OPTAP)$ (a), $Ru(py)_2(OPTAP)$ (b), $Ru(pyz)_2(OPTAP)$ (c), $Ru(tz)_2(OPTAP)$ (d), $Ru(tert\text{-}BuNC)_2(OPTAP)$ (e), and $Ru(did)_2(OPTAP)$ (f) in THF (a) and CH_2Cl_2 (b–f). Redrawn with permission from Stuzhin, P. A.; Vagin, S. I.; Hanack, M. *Inorg. Chem.* **1998**, *37*, 2655–2662. Copyright 1998 American Chemical Society.

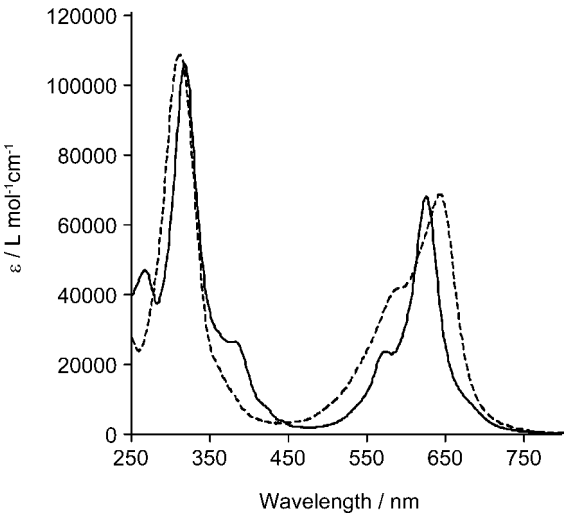

Figure 60. Absorption spectra of tetra-*tert*-butyl $Ru^{II}Pc$ having either 4-(*N,N*-dimethylamino) pyridine (solid line) or 4-nitropyridine (dashed line) as axial ligands in CH_2Cl_2. Redrawn with permission from Rawling, T.; Xiao, H.; Lee, S. T.; Colbran, S. B.; McDonagh, A. M. *Inorg. Chem.* **2007**, *46*, 2805–2813. Copyright 2007 American Chemical Society.

shift of the $\pi \rightarrow \pi^*$ transitions. In particular, the Q, B, and L bands for $Ru(NH_3)_2$(OPTAP) are shifted to lower energy because of the pure σ-donor properties of NH_3. In the case of isocyanides (*tert*-BuNC and *p*-diisocyanodurole (did)) as axial ligands, the B band is shifted considerably to the red, while the Q band remains at the same position, similarly to py, pyz,, and tz adducts. The origin of these observations is attributed to the strong π-accepting and σ-donating properties of isocyanides. Medium-intensity absorption bands between the Q and B bands are assigned to CT transitions.[220] The CT band of $Ru(NH_3)_2$(OPTAP) appears at 513 nm, since coordinated NH_3 ligands have only σ-donor properties. In the case of π-accepting ligands, the CT band shifts to the blue in the order L = py (473 nm), pyz (458 nm), and tz (423 nm). However, the assignments of these CT transitions have not been fully understood. Rawling *et al.* compared the effects of the electron-donating/withdrawing properties of axial substituents. Figure 60 shows the absorption spectra of tetra-*tert*-butyl $Ru^{II}Pc$ having either 4-(*N,N*-dimethylamino)pyridine (solid line) or 4-nitropyridine (dashed line) as axial ligands.[221] The spectrum of the electron donating 4-(*N,N*-dimethylamino)pyridine complex shows Q and Soret bands at 626 and 318 nm, respectively, in CH_2Cl_2, while these bands shift to 645 (Q) and 318 nm (Soret) for the 4-nitropyridine adduct. A dimeric RuPc, in which two ruthenium atoms are bonded directly, has also been proposed,[222–224] and the absorption data have been reported.[222]

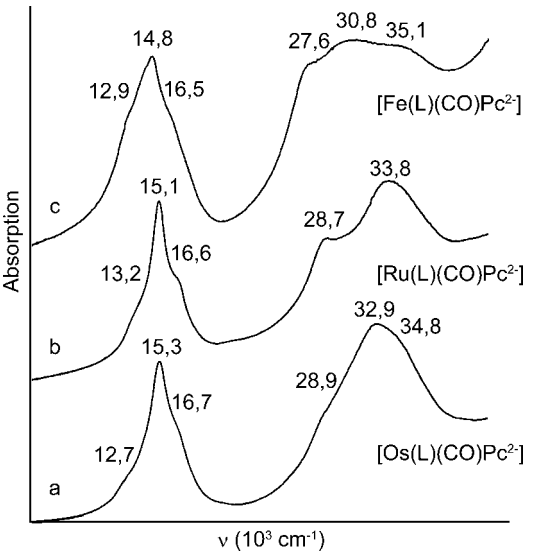

Figure 61. Absorption spectra of M(L)(CO)Pc in a KBr pellet. (a) M = Os, L = THF, (b) M = Ru, L = H_2O, (c) M = Fe, L = CH_3OH. Redrawn from Weidemann, M.; Homborg, H. *Z. Anorg. Allg. Chem.* **1996**, *622*, 2095–2098.

Several OsPc complexes have been described in the literature, although spectroscopic investigations of these are limited.[217,225–237] However, the spectroscopic properties of OsPcs have a general resemblance to those of RuPcs. $Os^{II}(py)_2Pc$ exhibits absorption bands at 616, 563, 369, and 308 nm in chloroform, while the corresponding bands of $Ru(py)_2Pc$ appear at 625, 573, 377, and 313 nm, respectively.[214,229] Of these, the bands at 377 and 369 nm for the ruthenium and osmium complexes, respectively, have been assigned to CT transitions between the metal and axial ligands.[200] The corresponding transition for $Fe(4\text{-pic})_2Pc$ is observed at 410 nm. Figure 61 compares absorption spectra of M(L)(CO)Pc, where M = Os, Ru, and Fe.[235] A bathochromic shift of the Q band is observed in the order Fe (14.8 kcm^{-1}), Ru (15.1 kcm^{-1}), and Os (15.3 kcm^{-1}) complexes, and all of these exhibit shoulders on both sides of the Q band. The Soret region shows different spectral shapes. The iron complex shows a featureless spectrum in this region, while the ruthenium and osmium complexes have prominent band components at 33.8 and 32.9 kcm^{-1}, respectively. Additional bands are observed in the lower-energy region of the Soret region, implying the presence of CT transitions. However, it is claimed that the presence of CT transitions for OsPc is not readily confirmed.[235] Hanack and Vermehren reported that the Q and Soret bands of $Os(dmso)_2Pc \cdot dmso$, $Os(pyz)_2Pc$, and $Os(\textit{tert}\text{-}BuNC)_2Pc$ are shifted to shorter wavelength compared with the corresponding ruthenium complexes.[229]

L. Group 9: CoPc, RhPc and IrPc

The oxidation state of the cobalt ion in CoPc can vary from Co^{I} to Co^{III}. Unsubstituted Co^{II}Pc shows absorption peaks at 658, 597, and 332 nm in pyridine, while slight red shifts are observed for tetra-*tert*-butyl Co^{II}Pc (662, 600, and 330 nm).[238] Kobayashi *et al.* compared the absorption data of tetra-*tert*-butyl Co^{II}TAP, Co^{II}Pc, Co^{II}Nc, and Co^{II}Ac (Figure 62, solid lines).[43] The Q band shifts to longer wavelength, but with an extent diminishing with increasing size of ligand. The Q bands appear at 579, 672, 759, and 839 nm for Co^{II}TAP, Co^{II}Pc, Co^{II}Nc, and Co^{II}Ac, respectively. In Figure 62, the spectra of the corresponding first reduction products are also drawn using dotted lines. The Q band of the Co^{I} species always appears in the longer wavelength region compared with the corresponding Co^{II}

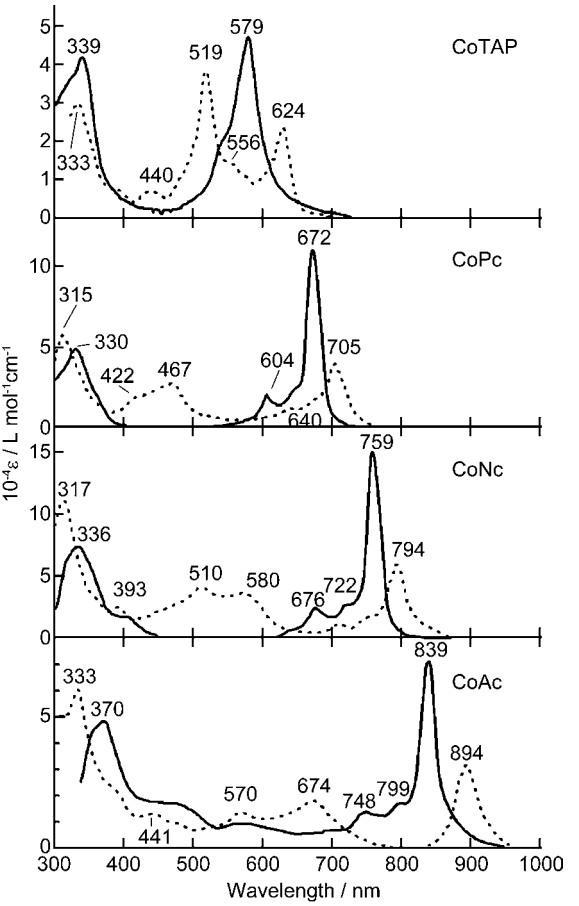

Figure 62. Electronic absorption data of Co^{II} (solid lines) and electrochemically-reduced Co^{I} complexes of tetra-*tert*-butyl TAP, Pc, Nc, and Ac (from top to bottom) in *o*-DCB. Redrawn from Kobayashi, N.; Nakajima, S.; Ogata, H.; Fukuda, T. *Chem. Eur. J.* **2004**, *10*, 6294–6312.

species. It is known that the Q band shifts to longer wavelength with concomitant decrease in intensity upon reduction of $Co^{II}Pc$ to form $Co^{I}Pc$. A new absorption band thus developed between the Q and B bands in the 400–500 nm region is assigned to the MLCT transition from $e_g(d_\pi)$ to ligand b_{1u} and b_{2u} orbitals.[204,239–242] Similar behavior is observed on reduction of all the complexes in Figure 62 (dotted lines). The energy differences of the two MLCT peaks in each species (422 and 467 nm for CoPc, 510 and 580 nm for CoNc, and 570 and 674 nm for CoAc) increases with molecular size on going from CoPc (2280 cm^{-1}), to CoNc (2380 cm^{-1}), and further to CoAc (2710 cm^{-1}), indicating an increased energy difference between the ligand b_{1u} and b_{2u} orbitals in this order. Assuming that the energy of the $e_g(d_\pi)$ orbital is insensitive to the size of the ligand, then the longer-wavelength shift of the MLCT bands with increasing molecular size indicates that the energy difference between the cobalt $e_g(d_\pi)$ and ligand b_{1u} and b_{2u} orbitals becomes smaller the larger the ligand. In the case of CoTAP, two prominent bands appear upon reduction (519 and 624 nm), of which the former appears to be an MLCT transition. However, the assignments of these bands have not been fully understood. Stillman and Thomson performed an MCD experiment on chemically-reduced $Co^{I}Pc$ in DMSO, and observed more than one *A* term between the Q and Soret region, confirming the assignments of the MLCT transitions.[204] Addition of cyanide (CN^-) to a DMSO solution of $Co^{II}Pc$ generates $Co^{III}(CN)_2Pc$ (Figure 63).[204] The high-energy region of the spectra (19 000- cm^{-1}) contains at least three identifiable bands, and thus the spectral envelope is more complex in shape than that of $Co^{II}Pc$. The bands at *ca.* 22.5 kcm^{-1} are extra bands compared with $Zn^{II}(CN)_2Pc$ (not shown), so that these are likely to be CT bands. However, the only allowed CT transition is the $a_{2u} \rightarrow a_{1g}$ LMCT transition, which cannot give rise to an MCD *A* term. As a consequence, the extra band cannot be assigned as LMCT. It is suggested that all the bands in the near UV region arise from excited configurations of the Pc ring as a plausible alternative.[204] Nombona and Nyokong obtained spectral changes during the generation of electrochemically-oxidized α-tetraphenylthio- or β-tetraphenylthio-substituted $Co^{II}Pcs$.[243] The Co^{II} complexes have a Q band at 695 and 673 nm for the α and β derivatives, respectively. The oxidation results in a bathochromic shift of the Q band (709 and 686 nm for the α and β derivatives, respectively) with an increase in intensity.

$Rh^{II}(py)_2Pc$ exhibits absorption peaks at 661, 633, 598, 371, and 327 nm in DMF.[244] In contrast, a hypsochromic shift of these bands is observed for the Rh^{III} complex. Here, $Rh^{III}ClPc$ shows absorption peaks at 654, 625, 590, 341, and 280 nm in chloroform, which does not change significantly when the rhodium center is coordinated to pyridine, 4,4′-bipyridine, 1,4-diazabicyclo[2,2,2]octane (dabco), and 2-methylpyrazine (mepyz).[245] In addition, the chloride ligand has a small effect on the absorption energies, where the iodo congener, $Rh^{III}IPc$, shows

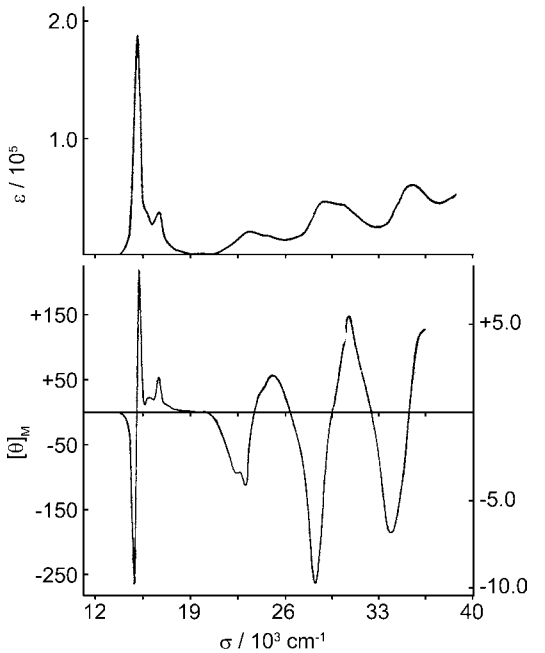

Figure 63. Absorption (top) and MCD (bottom) spectra of $Co^{III}(CN)_2Pc$. Stillman, M. J.; Thomson, A. J. *J. Chem. Soc. Faraday Trans. 2* **1974**, *70*, 790–804. Redrawn by permission of The Royal Society of Chemistry.

absorption peaks at 656, 632, 593, 573, and 556 nm in 1-chloronaphthalene.[246] Therefore, the effect of the oxidation state of rhodium on the absorption bands is opposite to that observed for CoPc. The spectra of Rh^{III} complexes are typical in shape of metalloPcs (Figure 64a). The absorption spectrum of $(^nBu_4N)[Rh^IPc^{2-}]$ in isopropanol indicates that the Q band of this complex is shifted slightly to longer wavelength compared with the Rh^{III} species (Figure 64c).[247] It is proposed that the intense band at *ca.* 40 000 cm^{-1} can be assigned to MLCT transitions. Gaffo *et al.* observed a pronounced, partially-reversible quenching of the Q-band absorption when an LB film of the RhPc complex is exposed to chlorine gas.[248] Balkus *et al.* reported absorption data of RhPc encapsulated in zeolites.[249] Photolysis of octaethyl Rh(Me)TAP in benzene ($\lambda > 350$ nm) results in the formation of $[(\text{octaethyl TAP})Rh]_2$, which has a direct Rh–Rh bond. The spectroscopic changes occurring during the photolysis are shown in Figure 65 (top).[250] Dissolution of $[(\text{octaethyl TAP})Rh]_2$ in pyridine gives a new species which shows a weak band at 750 nm (Figure 65, bottom). The generated species is proposed to be a π anion radical, i.e. $[(\text{octaethyl } Rh^{III}(py)_2TAP)]^{\bullet}$.

Several references are available on IrPc, although few of these include any absorption study.[246,247,251–260] $Ir^{III}ClPc$ exhibits absorption peaks at 648, 625, 586,

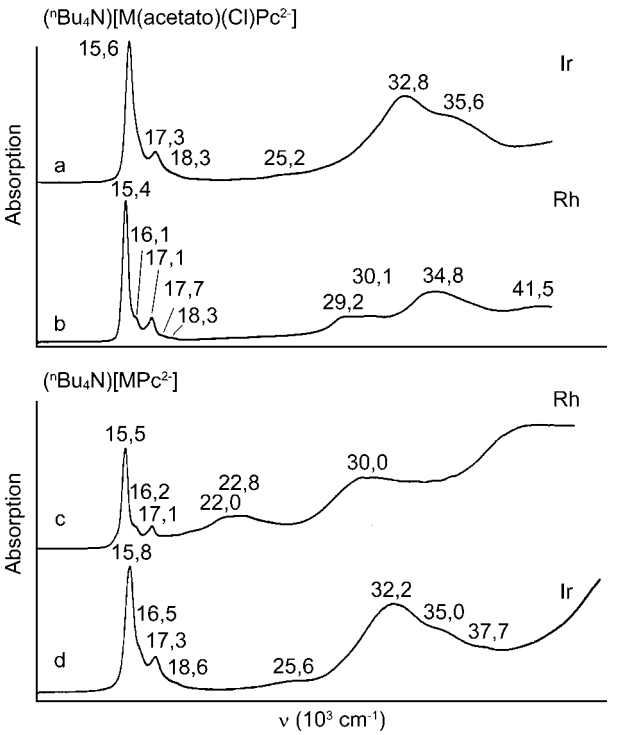

Figure 64. Absorption spectra of (^{n}Bu$_4$N)[M^{III}(acetate)(Cl)Pc^{2-}] in CH_2Cl_2 [M = Ir (a) and Rh (b)], and (^{n}Bu$_4$N)[M^{I}Pc^{2-}] in isopropanol [M = Rh (c) and Ir (d)]. Redrawn from Hückstädt, H.; Homborg, H. *Z. Anorg. Allg. Chem.* **1998**, *624*, 715–720 and Hückstädt, H.; Homborg, H. *Z. Anorg. Allg. Chem.* **1998**, *624*, 980–986.

567, 553, and 390 nm in 1-chloronaphthalene.[246] Examples of absorption spectra of Ir^{III} and Ir^I complexes are shown in Figures 64a and d, respectively.[247,258]

M. Group 10: NiPc, PdPc and PtPc

The spectral properties of NiPcs are, in a sense, featureless because no significant metal-ligand interactions, nor any axial ligands are expected. The first oxidation and reduction couples of general NiPc are ligand-centered. Unsubstituted Ni^{II}Pc shows absorption peaks at 651, 594, 327.5, 235, and 210 nm [Q, Q(1–0), B, L, and C band, respectively, Figure 66].[21] Fielding and MacKay observed weak bands at *ca.* 6400 cm^{-1} (1560 nm) for a crystalline thin film of NiPc, which they assigned to the d–d transition.[261] These bands, however, disappear in vapor-phase and solution spectra. Lever *et al.* commented that no LMCT transitions from the a_{1u} or a_{2u} levels of Pc are permitted, and no absorption other than the π–π^* transitions are observed at energies below the Soret band.[145] Indeed, although recent DFT

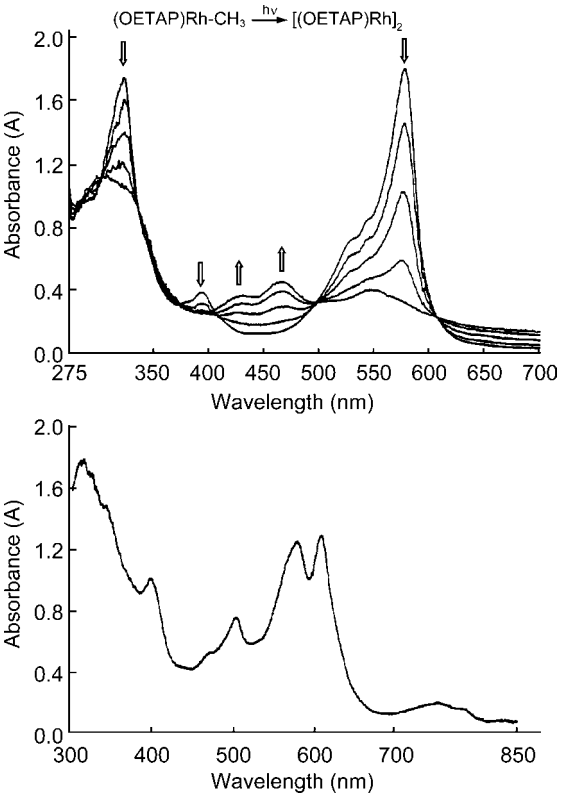

Figure 65. UV-vis spectral changes during the photolysis of octaethyl Rh(Me)TAP in benzene, to form [(octaethyl TAP)Rh]$_2$ (top), and absorption spectrum of a solution resulting from dissolving [(octaethyl TAP)Rh]$_2$ in pyridine at 295 K (bottom). Redrawn with permission from Ni, Y. P.; Fitzgerald, J. P.; Carroll, P.; Wayland, B. B. *Inorg. Chem.* **1994**, *33*, 2029–2035. Copyright 1994 American Chemical Society.

calculations predict that the $b_{1g}(d_{x^2-y^2})$ orbital lies at an energy below the $e_g(\pi^*)$ orbital,[262] no absorption bands have been observed in the corresponding region due to the symmetry-forbidden nature of the transition ($a_{1u}(\pi) \rightarrow b_{1g}(d_{x^2-y^2})$). The normalized Q-band region absorption spectra of NiPc (670 nm), NiNc (770 nm), α-octabutoxy NiPc (740 nm), and α-octabutoxy NiNc (845 nm) in 1-chloronaphthalene are shown in Figure 67.[262] The spectra show a red shift of the Q band upon substitution with either benzoannulation or octabutoxy. Since these two effects are both operative and independent, the Q band of α-octabutoxy NiNc is red-shifted by *ca.* 170 nm relative to that of NiPc. In addition, α-butoxy substitution of both the Pc and Nc rings also induces a substantial broadening of the Q bands.

PdPc exhibits absorption peaks at 660, 635, 595, 575, 560, 440, 420 nm in 1-chloronaphthalene. Figure 68 shows the absorption spectra of octaphenyl PdAc

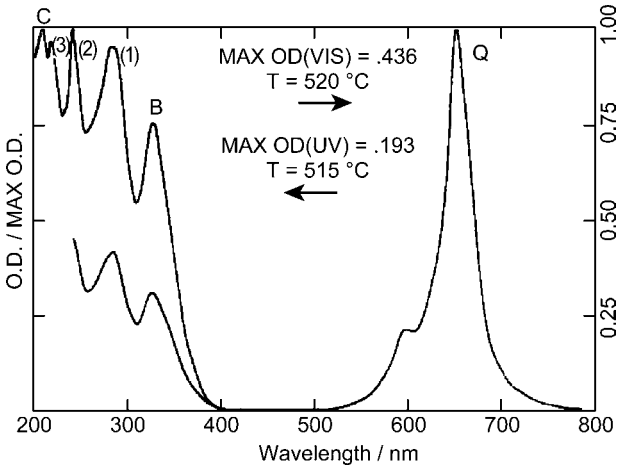

Figure 66. Vapor-phase absorption spectrum of NiPc. Redrawn from Edwards, L.; Gouterman, M. *J. Mol. Spectrosc.* **1970**, *33*, 292–310. Copyright 1970, with permission from Elsevier.

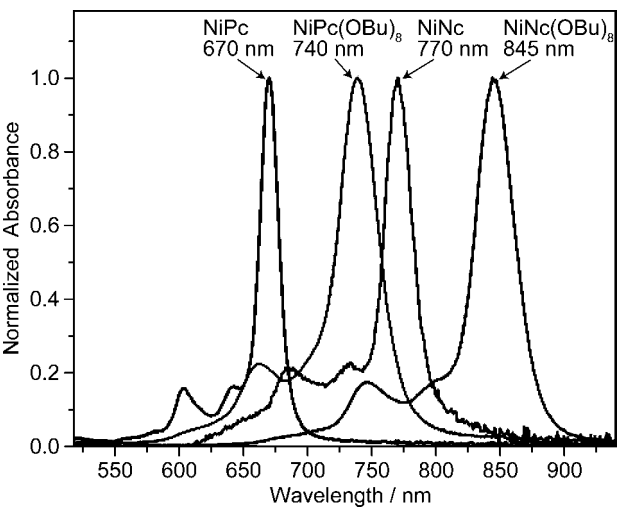

Figure 67. Normalized Q-band region absorption spectra of NiPc (670 nm), NiNc (770 nm), α-octabutoxy NiPc (740 nm), and α-octabutoxy NiNc (845 nm) in 1-chloronaphthalene at room temperature. Redrawn with permission from Soldatova, A. V.; Kim, J.; Peng, X. H.; Rosa, A.; Ricciardi, G.; Kenney, M. E.; Rodgers, M. A. J. *Inorg. Chem.* **2007**, *46*, 2080–2093. Copyright 2007 American Chemical Society.

(compound 1 in the figure) and its *trans*-annular endoperoxide (compound 2 in the figure) in benzene.[263,264] The photooxygenation of 1 in the presence of molecular oxygen generates 2. The spectral changes observed in the course of the photooxygenation unambiguously proved that the newly generated compound has an

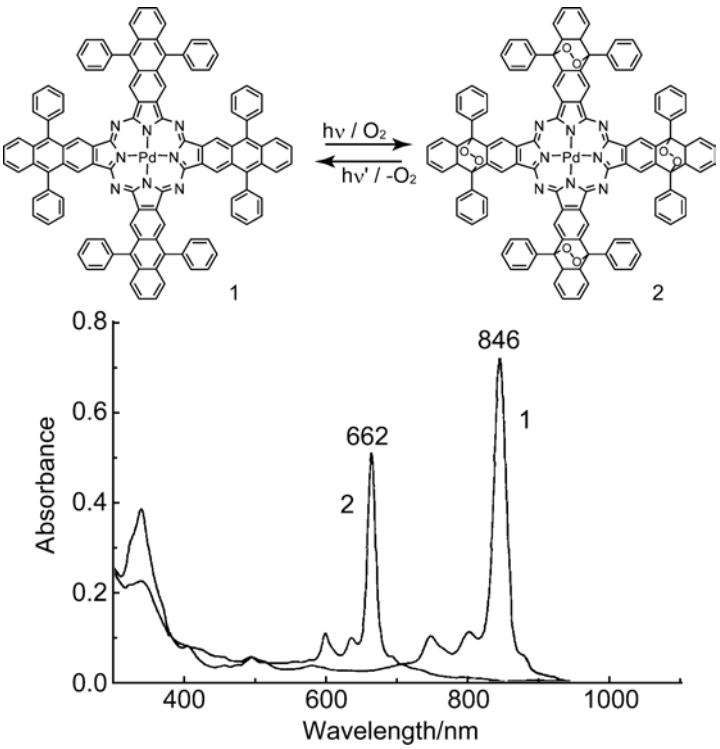

Figure 68. Absorption spectrum of octaphenyl PdAc in benzene. Redrawn from Freyer, W.; Flatau, S. *Tetrahedron Lett.* **1996**, *37*, 5083–5086. Copyright 1996, with permission from Elsevier.

aromatic structure identical to Pc. The Q band at 846 nm for 1 disappears during the photooxygenation, and a new band at 662 nm is generated instead. Excitation of the photoproduct 2 into higher excited electronic states by UV-laser light results in the release of molecular oxygen and the regeneration of the starting molecule 1. Miwa *et al.* synthesized a series of low-symmetry PdPc derivatives, and confirmed that the absorption spectra are analogous in shape with those of the corresponding zinc complexes (not shown).[265] The splitting energy of the Q band is also similar to that of the corresponding zinc derivatives, although the Q band shifts by 300–400 cm^{-1} to higher energy relative to the zinc complexes. This blue shift of the Q band is attributed to destabilization of the LUMO by interaction between the LUMO of the ligand and the dπ orbital of the palladium ion. The Soret bands of the palladium complexes (*ca.* 300–360 nm) also shift to the higher energy side. In addition, broad absorption bands are observed between the Soret and Q bands (400–500 nm). Presumably, this absorption can be assigned to an MLCT transition (d$\pi \rightarrow \pi^*$), because the corresponding MCD spectrum shows intense dispersion-type signals in this region.

Similarly to NiPc, the platinum in PtPc takes on a tetra-coordinated square planer structure. Therefore, PtPc is a four-coordinated planar complex, and thus no axial ligands are involved. In 1-chloronaphthalene, $Pt^{II}Pc$ shows absorption peaks at 650, 625, 586, 567, 550, and 455 nm. Spectroscopic studies on PtPc have been reported by Brown *et al.*[266]

N. Group 11: CuPc, AgPc and AuPc

$Cu^{II}Pc$ is the most common CuPc, and it has not been possible to isolate a Cu^{I} derivative.[267] Gardberg *et al.* reported the crystal structures of singly and doubly oxidized CuPc derivatives, $CuPc(ReO_4)$ and $CuPc(ReO_4)_2$, and demonstrated that both of these are compounds of Cu^{II}.[268] There have been very limited reports on the absorption data of unsubstituted $Cu^{II}Pc$, since it is sparingly soluble in most solvents. The best solvent for unsubstituted CuPc is probably 1-chloronaphthalene, although it is reported that CuPc forms light-scattering microcrystals at concentrations as low as 1×10^{-5} mol dm^{-3} even in this solvent.[58,269] Unsubstituted CuPc, shows absorption bands at 657.5 (Q), 600 (Q(0–1)), 325 (B), 276 (N), 240.5 (L), and 218 (C) nm in the vapor-phase (Figure 69),[21] and at 678, 648, 611, 588, 567, 526, 510 nm in 1-chloronaphthalene.[40,270] In a series of tetra-*tert*-butyl CuTAP, CuPc, and CuNc, the Q band shifts from 583 nm (CuTAP), to 676 nm (CuPc), and to 771 nm (CuNc).[43] No LMCT transitions are permitted from a_{1u} or a_{2u}. However, Schott reported a near-infrared absorption band for CuPc crystals, as shown in Figure 70.[271] At least nine bands can be recognized in the 800–1100 nm

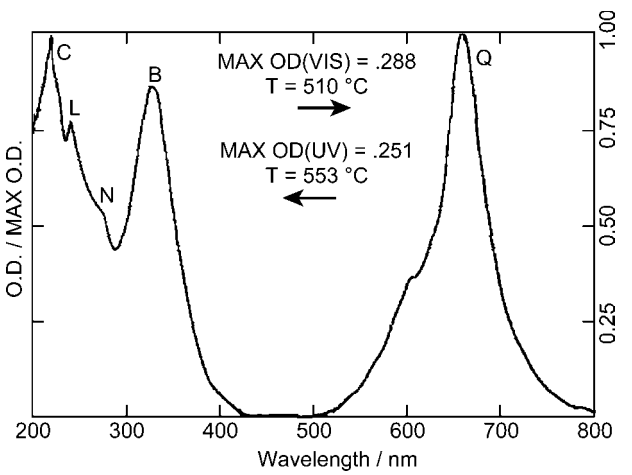

Figure 69. Vapor-phase absorption spectrum of CuPc. Redrawn from Edwards, L.; Gouterman, M. *J. Mol. Spectrosc.* **1970**, *33*, 292–310. Copyright 1970, with permission from Elsevier.

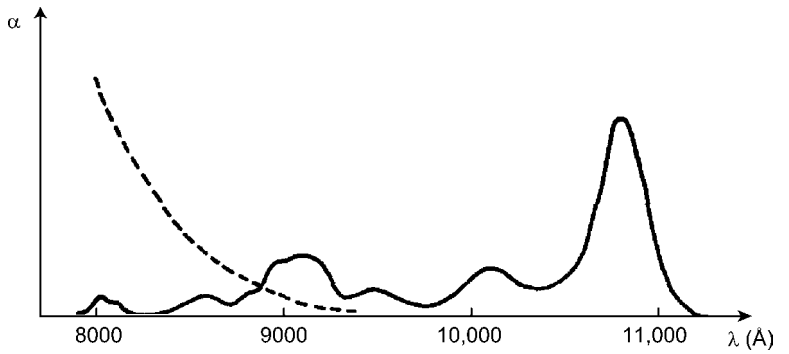

Figure 70. Near-infrared absorption of CuPc crystals. The dotted line shows the tail of the red band. Redrawn with permission from Schott, M. *J. Chem. Phys.* **1966**, *44,* 429–430. Copyright 1966 American Institute of Physics.

region, of which the band at *ca.* 1080 nm is the most intense. Lever *et al.* also succeeded in observing the corresponding absorption for tetrasulfonato CuPc in DMSO (not shown).[145] It is likely that these bands originate from trip-multiplet transitions, since no other options are available in this region. The absorption peaks of hexadecachloro CuPc (Pigment Green 7) in H_2SO_4 differ, depending on the reference. The reported values are 854, 813, 768, 469, and 350 nm in Ref. 272, 860, 815, 730, and 490 nm in Ref. 273, and 861, 816, 770, 729, 656, 584, and 465 nm in Ref. 274.

Barrett *et al.* synthesized a Pc complex containing one silver ion, which is soluble in 1-chloronaphthalene, but tends to decompose in the boiling solvent, with the formation of phthalocyanine and metallic silver.[56] However, they could not determine whether the structure of the complex is $Ag^{II}Pc$ or $Ag^{I}HPc$. It is known that the corresponding porphyrins are compounds of Ag^{II}.[275] Anderson *et al.* reported that this complex shows absorption bands at 675, 642.5, 605, 580, and 560 nm in 1-chloronaphthalene.[57] ESR studies performed by Kholmogorov and Glebovsky implied that the oxidation state of the silver is 1,[276,277] while MacCragh and Koski concluded that the oxidation state of the silver is 2.[278] The synthesis and spectroscopy of tetraneopentoxy $Ag^{II}Pc$ ($TNAg^{II}Pc$) have been reported.[279–281] Figure 71 shows the spectroelectrochemistry of $TNAg^{II}Pc$. Stepwise, controlled-potential first oxidation of a solution of the complex results in the spectroscopic changes shown in Figure 71 (top). The initial spectrum shows absorption peaks at 685, 618, 386, and 356 nm, with isosbestic points observed at 703, 557, and 395 nm in the course of the oxidation. The final spectrum, showing absorption bands at 722, 647, 424, and 361 nm, is consistent with that of a metalloPc(2–) species and not an oxidized Pc(1–) species. Therefore, the observed spectral changes can be ascribed to the oxidation of the metal from Ag^{II} to Ag^{III}, to give $[Ag^{III}TNPc(2–)]^{+}$. Both the Q and Soret bands

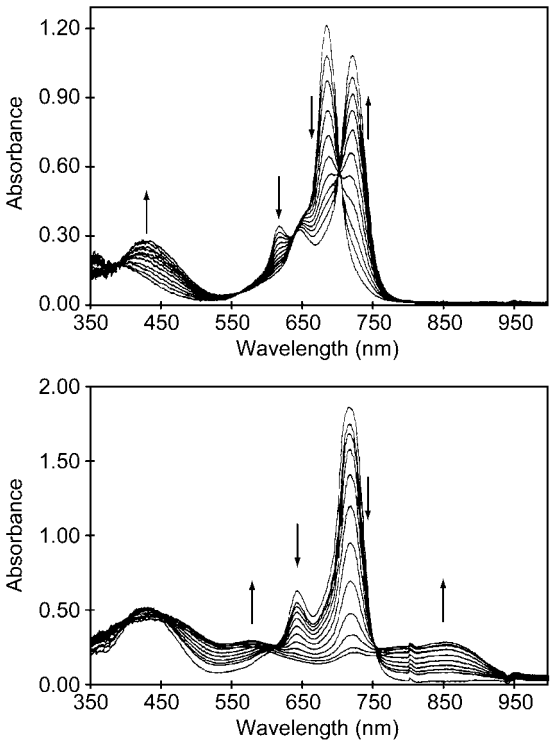

Figure 71. Stepwise, controlled-potential spectroelectrochemistry: (top) TNAg^{II}Pc in *o*-DCB solution, showing the development of [Ag^{III}Pc(2–)]$^{+}$ as the potential is stepped through the first oxidation wave from 0.55 to 0.9 V vs. SCE; (bottom) electrochemically generated [Ag^{III}Pc(2–)]$^{+}$ in *o*-DCB showing the development of the π radical cation [Ag^{III}Pc(1–)]$^{2+}$ as the potential is stepped through the second oxidation wave from 1.10 to 1.40 V vs. SCE. The solutions contain 0.2 M TBAPF_6. Redrawn with permission from Fu, G. Y.; Fu, Y. S.; Jayaraj, K.; Lever, A. B. P. *Inorg. Chem.* **1990**, *29*, 4090–4095. Copyright 1990 American Chemical Society.

shift to longer wavelength by *ca.* 40 nm for the Ag^{III} species compared with the Ag^{II} species. The spectral changes associated with the second oxidation potential, to exhibit absorption bands at 854, 721, 649, 574, and 439 nm (Figure 71, bottom) is characteristic of the formation of a radical Pc(1–) species.

MacCragh and Koski reported that Au^{II}Pc shows absorption peaks at 662, 633, 601, and 348 nm,[282] although it is still questionable whether gold Pc is a truly divalent gold complex or a tervalent complex.

O. Group 12: ZnPc, CdPc, Cd_2Pc_3 and HgPc

The Zn^{II} ion has a d^{10} configuration, so LMCT and d–d transitions should not appear in the UV-vis region. Therefore, Zn^{II}Pc is free from CT transitions, and is

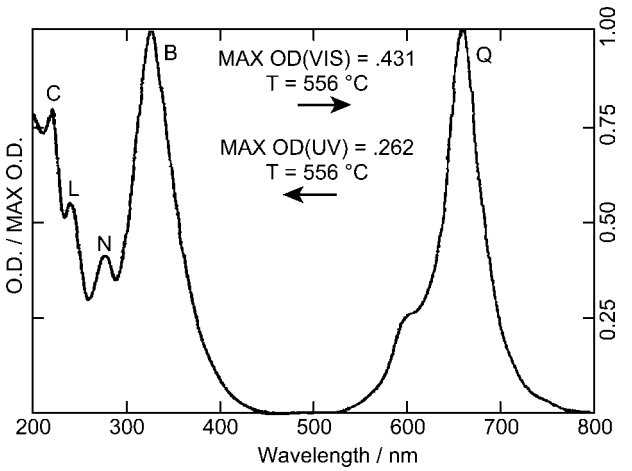

Figure 72. Vapor-phase absorption spectrum of ZnPc. Redrawn from Edwards, L.; Gouterman, M. *J. Mol. Spectrosc.* **1970**, *33*, 292–310. Copyright 1970, with permission from Elsevier.

well-suited for a spectroscopic study of the Pc ligand. Unsubstituted ZnPc shows absorption bands at 661 (Q), 600 (Q(0–1)), 326.5 (B), 276 (N), 240 (L), and 220 (C) nm in the vapor-phase (Figure 72),[21,33] at 680, 649, 616, 587.5, and 565 nm in 1-chloronaphthalene,[57] and at 672, 646, 607, and 347.5 nm in pyridine.[40] In coordinating solvents, a solvent molecule coordinates at the axial position of the zinc atom,[283] so that the actual species in pyridine solution is Zn^{II}(py)Pc.[284] Bajema *et al.* measured the absorption spectra of a matrix-isolated ZnPc at liquid hydrogen temperature by using argon, krypton, xenon, methane, nitrogen, and sulfur hexafluoride.[34] It was observed that the width of the absorption lines increases in the order of Ar < CH_4 < Kr < Xe < N_2 < SF_6. The absorption and MCD spectra of Zn^{II}Pc in DMSO with and without added cyanide (CN^-) are shown in Figure 73.[204] The band at *ca.* 29 kcm^{-1} in DMSO splits into two upon addition of CN^-. Nyokong *et al.* performed a band deconvolution analysis of both the MCD and absorption data for ZnPc and its π-cation-radical species,[19] of which the latter is omitted here, since another chapter of this handbook describes this species in detail.[24] Figure 74 shows the absorption and MCD spectra of Zn(CN^-)Pc in the Q-band (left) and B-band (right) regions. The MCD signal corresponding to the Q band at *ca.* 15 000 cm^{-1} (670 nm) is a Faraday A-term, reflecting the degenerated states of the Q band. On the other hand, the vibronic bands in the 15 200–17 500 cm^{-1} region give Faraday B type MCD signals, unlike the case for porphyrins. In the B-band region (23 000–38 000 cm^{-1}), three MCD A-terms are deconvoluted at 25 874, 30 213, and 36 505 cm^{-1}, which can be assigned to the B, N, and L bands, respectively. Coordination of imidazole instead of cyanide to the zinc changes the shape of the

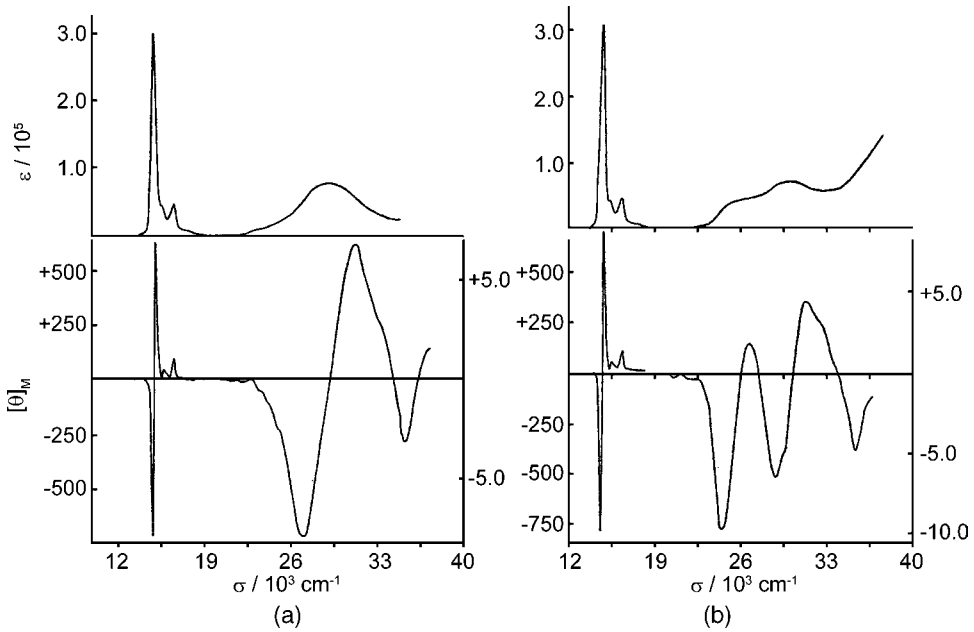

Figure 73. Absorption (top) and MCD (bottom) spectra of $Zn^{II}Pc$ in (a) DMSO and (b) DMSO plus NaCN. Stillman, M. J.; Thomson, A. J. *J. Chem. Soc. Faraday Trans. 2* **1974**, *70*, 790–804. Redrawn by permission of The Royal Society of Chemistry.

spectra slightly (not shown). In this case, the B-band region contains at least four MCD A-term components, which are deconvoluted at 27 150, 29 780, 35 440, and 40 650 cm^{-1}. These are assigned to the B, N, L, and C bands, respectively. Moment analysis of MCD data can estimate the value of the angular momentum associated with the photo-excitations. It has been proposed that the value of the angular momentum of the metalloPc is always less than that of the pure Pc ring, since the empty $1e_g(\pi^*)$ orbitals of the Pc can interact with the metal orbitals, reducing the value of angular momentum.[285] Nyokong *et al.* reported that the angular momentum of the ZnPc species follows the trend $Zn(CN^-)Pc > Zn(py)Pc > Zn(im)Pc$, and commented that the observed results can be rationalized on the basis of the effects of the π-acceptor and σ-donor strengths of the axial ligand.[19] The CN^- ion as an axial ligand is a good π acceptor, so that it lowers the energy of the metal d orbitals, which results in an increase in the angular momentum. On the other hand, imidazole is a strong σ donor, leading to a decrease in the angular momentum. Since pyridine is a weaker σ donor than imidazole, Zn(py)Pc gives an intermediate result. VanCott *et al.* measured the MCD and absorption spectra of ZnPc isolated in an argon matrix over the range 14 700–74 000 cm^{-1}.[35] The matrix spectra show sharper bands and much more structure than the gas-phase, thin-film, or

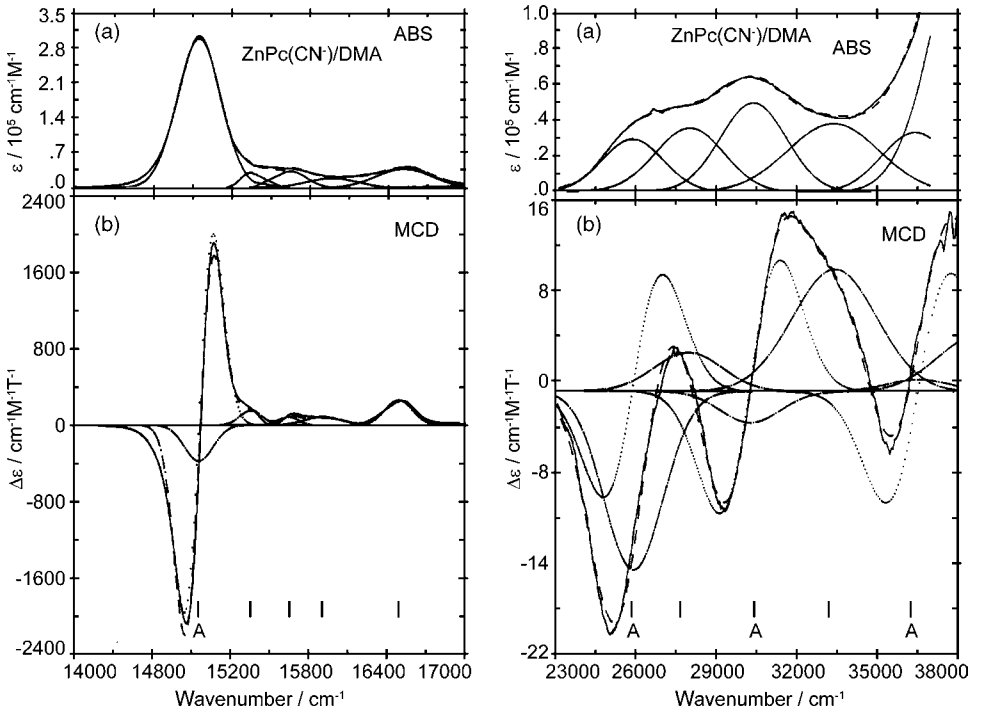

Figure 74. Band deconvolution analysis for ZnPc with added CN^- ligand in dimethylacetamide for the Q-band (left) and B-band (right) region: (a) absorption experimental data (solid line) and fitted result (dashed line) together with the deconvoluted individual bands; (b) MCD experimental data (solid line) and fitted result (dashed line) together with the individual *A* and *B* terms. Redrawn with permission from Nyokong, T.; Gasyna, Z.; Stillman, M. J. *Inorg. Chem.* **1987**, *26*, 1087–1095. Copyright 1987 American Chemical Society.

solution spectra. Figure 75 (top left) shows the Q(0–0)-region absorption and MCD spectra of ZnPc/Ar at *ca.* 5 K. At least 12 peaks and shoulders are observed in the absorption data in this region, each of which is associated with a maximum or minimum in the MCD. Interestingly, the individual MCD signals correspond to Faraday B-terms. This is due presumably to the existence of a crystal-field-stabilized Jahn-Teller effect, resulting in the splitting of a doubly degenerate excited state, to give rise to a pair of B terms of opposite sign but equal magnitude. The spectra of the other energy region are also summarized in Figure 75. Readers should see Ref. 35 for a detailed discussion.

There are very few reports on CdPcs in the literature.[74,286–293] α-Octa-*n*-hexyl CdPc exhibits a Q band at 708 nm in hexane, which is characteristic of a metalloPc substituted with alkyl chains at the α-positions (Figure 76, lower).[288,289] Recently, Chambrier *et al.* have reported the first example of a di-cadmium tris-Pc triple-decker sandwich complex, which shows absorption peaks at 867, 718, 646, 599,

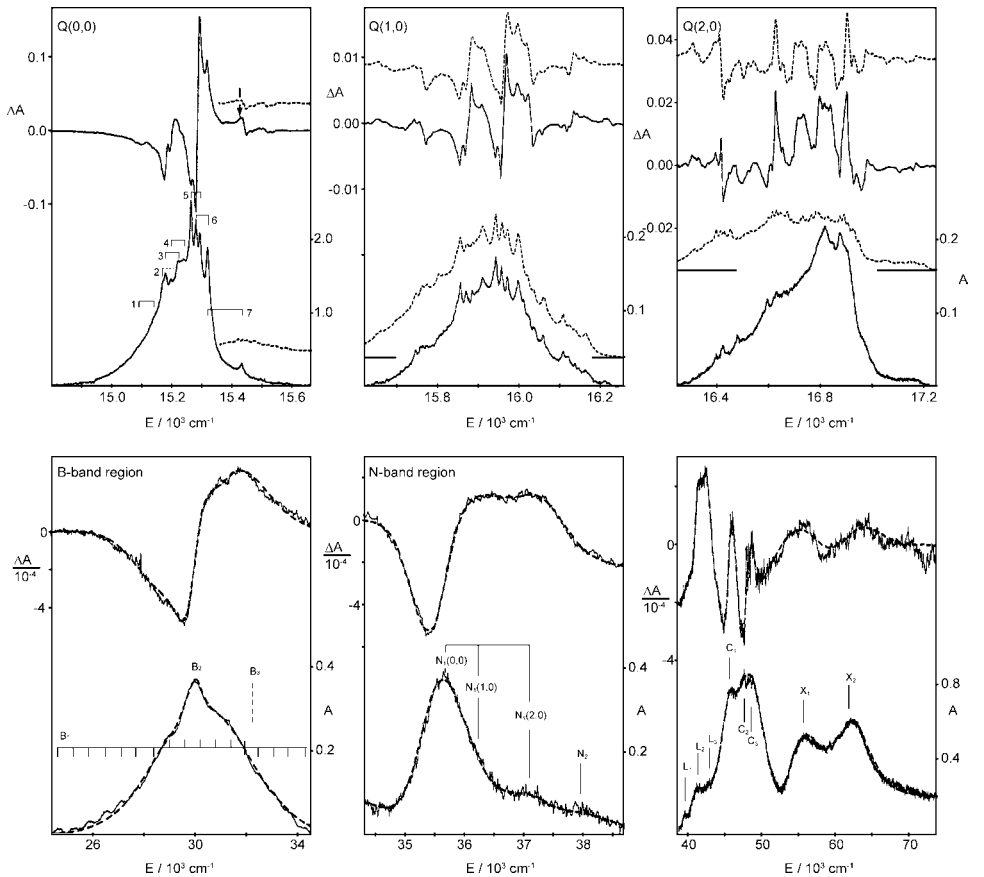

Figure 75. MCD (upper curve) and absorption spectra (lower curves) of ZnPc/Ar in the region of the Q(0,0) (top left), Q(1,0) (top center), Q(2,0) (top right), B-band (bottom left), N-band (bottom center), and vacuum ultraviolet (bottom right) envelope at *ca.* 5 K. *A* is absorbance and Δ*A* is the MCD per tesla. Redrawn with permission from Vancott, T. C.; Rose, J. L.; Misener, G. C.; Williamson, B. E.; Schrimpf, A. E.; Boyle, M. E.; Schatz, P. N. *J. Phys. Chem.* **1989**, *93*, 2999–3011. Copyright 1989 American Chemical Society.

and 483 nm in hexane (Figure 76, upper).[288,289] The relative intensities of some of these bands vary somewhat in other solvents.

Phthalocyaninatobis(methylmercury), $(CH_3Hg^{I})_2Pc$, and $Hg^{II}Pc$ have been reported,[56,286,294,295] of which the former shows absorption peaks at 721, 654, 440, 342, and 285 nm.[294]

P. Group 13: B-subPc, AlPc, GaPc, InPc and TlPc

In 1972, Meller and Ossko serendipitously found that reactions of phthalonitrile with boron complexes such as BBr_3, BCl_3, and $PhBCl_2$ yielded macrocyclic

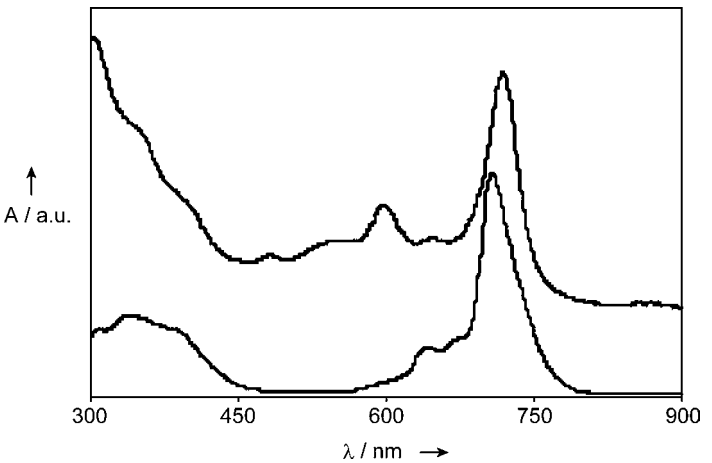

Figure 76. Absorption spectra of α-octa-*n*-hexyl CdPc (below) and the Cd_2Pc_3 type triple decker complex obtained therefrom (above) in hexane. Chambrier, I.; Hughes, D. L.; Swarts, J. C.; Isare, B.; Cook, M. J. *Chem. Commun.* **2006**, 3504–3506. Redrawn by permission of The Royal Society of Chemistry.

boron complexes, in which the boron is surrounded by three isoindole units linked by meso-nitrogen atoms, named subphthalocyanine (subPc).[296] There is a comprehensive review on subPcs by Torres and coworkers.[297] The boron atom in subPc has one axial ligand, and BBr-subPc and BCl-subPc show axial reactivity with nucleophiles, to yield axially-substituted subPcs. The corresponding boron Pc complex has not been reported to date. The absorption spectra of subPcs resemble that of typical metalloPcs in shape, irrespective of the ring contraction from the 18π-system of Pcs to the 14π-system, and the resultant cone-shaped aromatic ring deformation. The Q band generally appears at *ca.* 560–590 nm, while another band containing more than one transition is also observed in the Soret region. Compared with the Q band positions of the corresponding cyclic tetramers, namely TAPs, Pcs, and Ncs, the Q bands of subPcs shift to the blue by *ca.* 170–180, 120–130, and 100–120 nm, respectively. In addition, the molar extinction coefficients (ε) are smaller than those of the corresponding tetramers.[298] Figure 77 (dotted line) shows the absorption spectrum of BCl-subPc in $CHCl_3$.[299] An intense Q band appears at 565 nm, which is accompanied by an associated vibronic band at *ca.* 520 nm. In the Soret region, a peak at 305 nm was observed.[300] BF- and tri-*tert*-butyl BBr-subPcs exhibit Q bands at 570 and 567 nm, respectively.[296] BPh-subPc obtained from the reaction of phthalonitrile with triphenylboron (BPh_3) in the presence of DBU in naphthalene shows a Q band at 566 nm in toluene.[301] Thus, the effect of the axial ligand on the Q band position is relatively small. There are several reports on subazaporphyrins

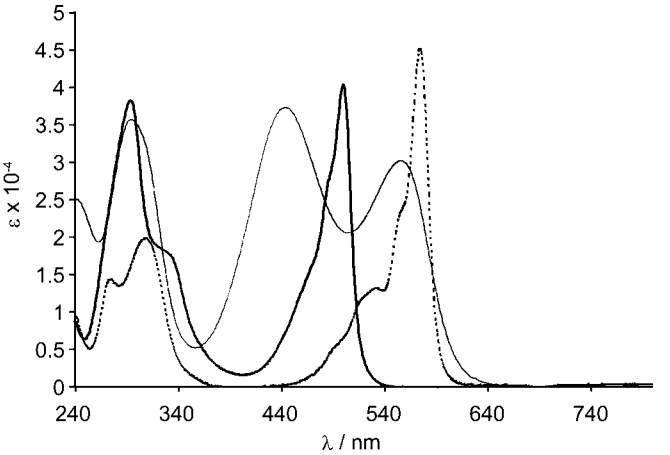

Figure 77. Absorption spectra of BCl-subPc (dotted line), BCl-(*n*-Pr)$_6$subAP (thick line), and BCl-($SC_{18}H_{37}$)subAP in $CHCl_3$. Redrawn from Rodríguez-Morgade, M. S.; Esperanza, S.; Torres, T.; Barberá, J. *Chem. Eur. J.* **2004**, *11*, 354–360.

(subAPs). Hanack mentioned that hexa-*p-tert*-butylphenyl BCl-subAP shows an absorption peak at 378 nm in toluene,[301] while Kobayashi tentatively assigned the Q band of a BBr-subAP derivative in $CHCl_3$ prepared from 1-(1,2,2-tricyanoethenyl)-2-trifluoromethylbenzne at 411 nm.[302] Torres and coworkers isolated a series of subAP derivatives. Figure 77 compares the absorption spectra of BCl-subPc (dotted line), BCl-(*n*-Pr)$_6$subAP (thick line), and BCl-($SC_{18}H_{37}$)subAP in $CHCl_3$.[299] The Q-band region of the former two complexes are very similar in shape. BCl-(*n*-Pr)$_6$subAP shows absorption peaks at 501 and 295 nm corresponding to the Q and Soret bands, respectively. On the other hand, the spectrum of BCl-($SC_{18}H_{37}$)subAP has a different shape to that of the other two derivatives, exhibiting a peak in the Soret region (298 nm) in addition to two broad bands at 444 and 559 nm. The band at 444 nm was assigned to $n \rightarrow \pi^*$ transitions from the peripheral sulfur lone-pair electrons to a π^* orbital of the macrocycle, while the band at 559 nm was assigned as the Q transitions. The peripheral thioalkyl groups shift the Q band to the red by *ca.* 60 nm. The same group also reported that fluoro subAP derivatives, namely BF-subAPs, exhibit a Q band in the *ca.* 500–570 nm region, depending on the peripheral substituents, although the introduction of a fluorine atom into the axial position itself has no significant effect on the Q band position.[303] The first X-ray structure of a subAP derivative was reported for BOH-Et$_6$subAP, which shows a Q band at 496 nm in hexane.[304] A comparative study of a series of ring-expanded subPc analogs clearly indicates a tendency for both the Soret and Q bands to shift to longer wavelengths and increase in intensity with increasing size of the π-system. Thus, the Q band

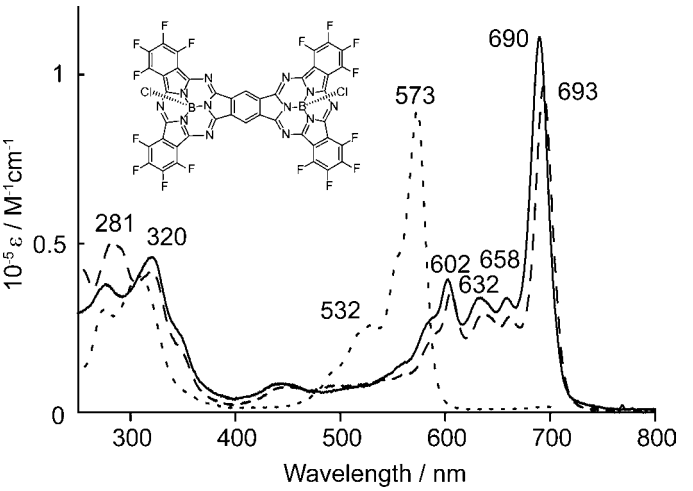

Figure 78. Absorption spectra of *cis* (solid line) and *trans* (dashed line) forms of dimeric BCl-F_{16}subPc in $CHCl_3$. The spectrum of the monomeric form, BCl-F_{12}subPc is also shown as a reference (dotted line). Redrawn from Fukuda, T.; Stork, J. R.; Potucek, R. J.; Olmstead, M. M.; Noll, B. C.; Kobayashi, N.; Durfee, W. S. *Angew. Chem. Int. Ed.* **2002**, *41*, 2565–2568.

of subnaphthalocyanines (subNcs) appears at 650 and 667 nm, for BPh-subNc and BBr-subNc, respectively.[298,301,302]

A binuclear subPc dimer which shares a central benzene ring was first prepared as a mixture of *cis* and *trans* isomers by Kobayashi in 1991.[305] A decade later, two groups have succeeded independently in separating these two isomers by using the fluoro-substituted dimer.[306,307] As shown in Figure 78, the absorption bands of the dimer species in the visible region are shifted to the red by *ca.* 120 nm and have more structure compared to the monomer species, BCl-F_{12}subPc, indicating an extension of the π-system. Both *cis* and *trans* isomers show similar-shaped spectra, although the Q band of the *trans* isomer appears at longer wavelength compared to the *cis* isomer, by *ca.* 3–4 nm, while the absorbance on the shorter-wavelength side of the Soret band is higher for the *trans* isomer.[307] As an extension, trinuclear subPc trimers have also been synthesized, and their absorption spectra reported.[308] The Q band of a μ-oxo dimer, (tri-*tert*-butyl subPc)$_2$O, shifts to the blue, while the position of the Soret band is virtually unchanged. The blue-shift of the Q band is explained on the basis of an exciton interaction.[302,309] On the other hand, Torres and coworkers claimed that the shape of the absorption spectrum of a subPc dimer having a direct B–B linkage is practically identical to that of the monomer species.[310]

AlPcs are of interest because of their possible application in the area of photodynamic therapy (PDT). The aluminum ion in AlPc is generally trivalent, and thus

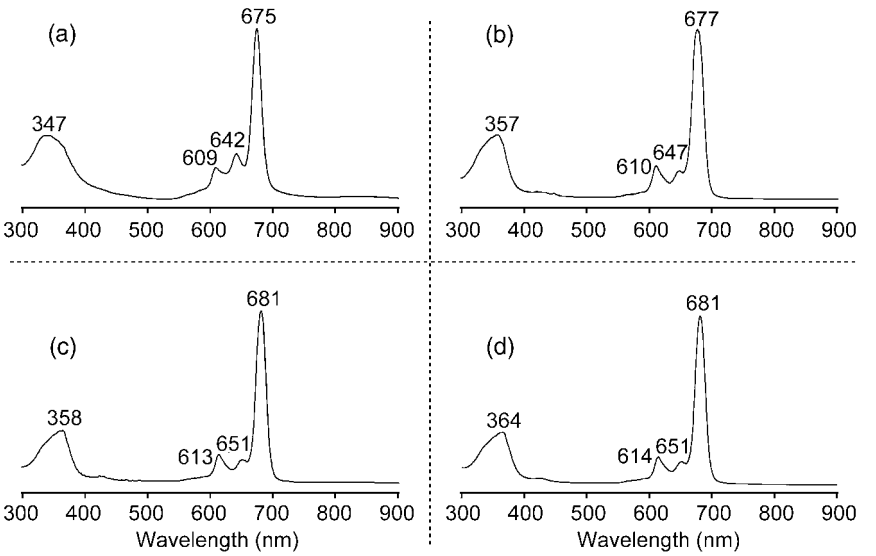

Figure 79. Absorption spectra of AlPcCl in (a) THF, (b) DMF, (c) DMSO, and (d) pyridine. Redrawn with permission from Ou, Z. P.; Shen, J.; Kadish, K. M. *Inorg. Chem.* **2006**, *45*, 9569–9579. Copyright 2006 American Chemical Society.

neutral AlPc has an axial ligand. As intuitively expected, and empirically and theoretically supported, the structure of typical $Al^{III}LPc$ takes on a dome-shaped C_{4v} symmetry.[311] Unsubstituted AlClPc and Al(OH)Pc show band peaks at 691, 665, 622, 597 and 576 nm in 1-chloronaphthalene, and 672 nm in DMF, respectively.[57,312] AlBrPc and AlIPc are also known.[313] The axial ligand can be replaced with various alcohols. For example, tri-*n*-hexylsiloxy-substituted AlPc is obtained by reacting tri-*n*-hexylchlorosilane with Al(OH)Pc, and has absorption band peaks appearing at 672, 638, 606, and 345 nm in THF.[314] Homborg and Murray isolated a $[AlF_2Pc]^{2-}$ species by treatment of AlClPc in dichloromethane with TBAF·$3H_2O$, which is subject to hydrolysis, to give $[(AlFPc)_2O]^{2-}$.[315] Figure 79 depicts the absorption spectra of AlClPc in THF, DMF, DMSO, and pyridine.[316] The spectral envelopes are typical of "normal" Pcs. An intense Q band appears at 675–681 nm depending on the solvent, accompanied by two additional bands between 609 and 651 nm. The B band is located in the 347–364 nm region. There is a correlation between the band energies and donor number of the solvent, where the B and Q bands shift bathochromically and show an increase in molar extinction coefficients (ε) upon changing from the low-donor THF to high-donor pyridine. Electrochemical study revealed that AlClPc(solvent) is the effective species. Addition of TBAF·$3H_2O$ to a THF solution of AlClPc produces a three-step spectral change, of which the first step (0–0.35 equivalent of F^-) can be attributed to the formation of the μ-oxo dimer, $(AlPc)_2O$.

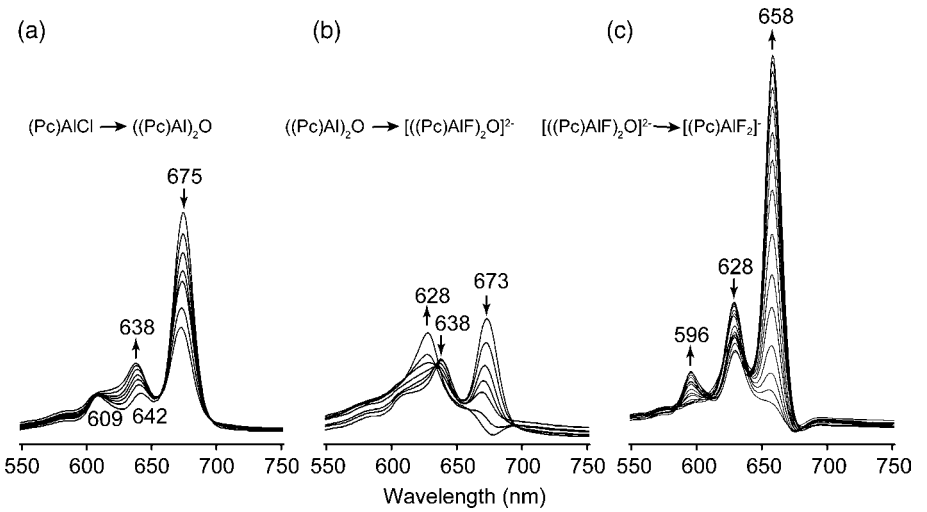

Figure 80. Spectroscopically monitored titration of AlPcCl with TBAF·3H_2O in THF: (a) first step (0–0.35 equiv of F^-), (b) second step (0.35–5.2 equiv of F^-), and (c) third step (5.2–86.4 equiv of F^-). Redrawn with permission from Ou, Z. P.; Shen, J.; Kadish, K. M. *Inorg. Chem.* **2006**, *45*, 9569–9579. Copyright 2006 American Chemical Society.

Accordingly, the initial Q band at 675 nm decreases in intensity and shifts slightly to the blue (673 nm) during the titration, while a new band appears at 638 nm. Further addition of TBAF·3H_2O (0.35–5.2 equivalent of F^-) causes the disappearance of the band at 673 nm, and the appearance of a single, new band at 628 nm, suggesting the formation of the $[(AlFPc)_2O]^{2-}$ species. The final step (5.2–86.4 equivalent of F^-) generates the six-coordinate fluoride complex, $[AlF_2Pc]^{2-}$, which is monitored by the appearance of an intense Q band at 658 nm (Figure 80). The spectrum of $[AlF_2Pc]^{2-}$ is similar to that of ZnPc and MgPc in shape. Similar spectral changes are also observed for a TBAOH titration, although there is no spectral evidence for the formation of a μ-oxo dimer nor six-coordinate $[Al(OH)_2Pc]^{2-}$. In the original paper, it was concluded that the final spectrum, exhibiting bands at 668, 638, and 601 nm, in a TBACN titration arises from Al(CN)Pc(THF). Reinot *et al.* described that the Q-band of AlPc splits into two components.[317] Although the formation of a dimer species and the presence of coordinated water molecules are possible reasons for the observed Q-band splitting, TDDFT calculations demonstrated that the origin of the splitting is largely related to a change in the N–C bonds caused by interaction between the surroundings and the molecule.[318] Reduction of AlClPc with 1.1 equivalents of Na/Hg in THF yields the stable radical $AlPc(THF)_2$, whose absorption peak appears at 649 nm.[319]

Similar to AlPcs, the gallium ion in GaPc is generally trivalent, and chlorogallium (GaCl) derivatives are the most common. No CT transitions are expected

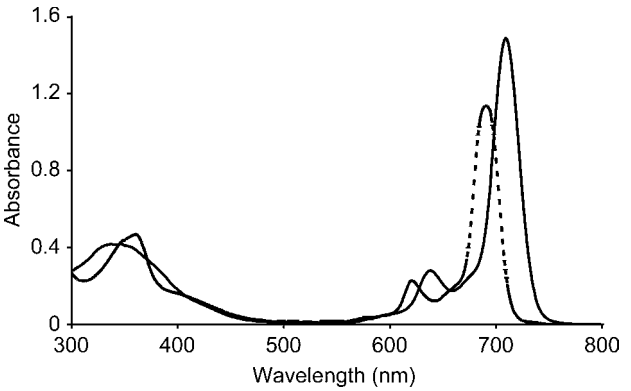

Figure 81. Absorption spectra of α-tetra-phenoxy GaClPc (solid line) and β-tetra-phenoxy GaClPc (dashed line) in DMSO. Redrawn from Durmuş, M.; Nyokong, T. *Tetrahedron* **2007**, *63*, 1385–1394. Copyright 2007, with permission from Elsevier.

for complexes of this category. Nyokong and coworkers have developed a variety of GaPc derivatives in anticipation of the application of these complexes to PDT,[320–324] while Hanack and coworkers are interested in GaPcs as optical limiting (OL) materials.[325–330] Unsubstituted Ga^{III}ClPc exhibits a Q band at 680, 678, and 677 nm in DMSO, DMF, and THF, respectively.[321] Figure 81 shows the absorption spectra of α-tetraphenoxy Ga^{III}ClPc (solid line) and β-tetraphenoxy Ga^{III}ClPc (dashed line) in DMSO.[323] The spectra have the general shape of metalloPcs, showing Q bands at 712 nm (α-derivative) and 691 nm (β-derivative). The α-substituted derivative has its Q band at slightly longer wavelength compared to the β-substituted derivative. In addition, some differences in spectral shape are observed in the 300–400 nm region between the α and β derivatives. Interestingly, the Q band of β-octaphenoxy GaClPc occurs at 687 nm in DMSO, which is an even shorter wavelength than that of the β-tetraphenoxy derivative (691 nm).[321] Figure 82 compares the absorption spectra of tetra-*tert*-butyl GaClPc (dashed line) and tetra-*tert*-butyl Ga(*p*-trifluoromethylphenyl)Pc (solid line).[326] As shown in the figure, both spectra resemble each other in shape, in particular, in the Q-band region, indicating that the electronic structure of Ga^{III}Pc is relatively independent of the axial ligand. The Q band position is not significantly changed by μ-oxo dimerization. For example, tetra-*tert*-butyl GaClPc and [tetra-*tert*-butyl GaPc]$_2$O show Q bands at 693 and 692 nm in toluene, respectively.[329,331]

The indium ion in InPc is also trivalent,[322,323,325,329,332–345] and the absorption properties of InPcs resemble those of GaPcs. The Q band of tetra-*tert*-butyl InClPc appears at 695 nm in toluene, while α-octathiohexyl InClPc extends to 836 nm in THF.[338] The axial chloride ligand can be replaced with an aryl or alkyl group by employing a Grignard reaction.[333] Figure 83 demonstrates how the absorption

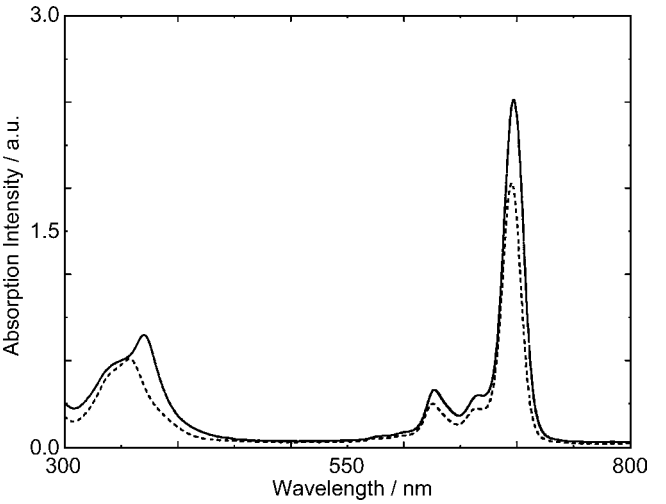

Figure 82. Absorption spectra of tetra-*tert*-butyl GaClPc (dashed line) and tetra-*tert*-butyl Ga(*p*-trifluoromethylphenyl)Pc (solid line) in $CHCl_3$. Redrawn from Chen, Y.; Subramanian, L. R.; Barthel, M.; Hanack, M. *Eur. J. Inorg. Chem.* **2002**, 1032–1034.

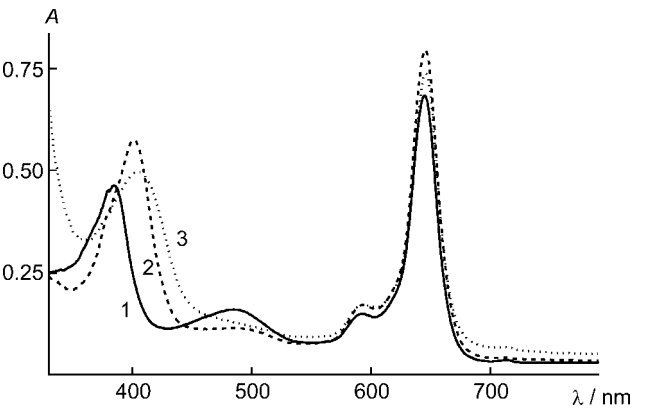

Figure 83. Absorption spectra of octaphenyl InClTAP (1), InPhTAP (2), and In(*n*-Bu)TAP (3) in benzene. Redrawn from Mal'chugina, O. V.; Stuzhin, P. A. *Russ. Chem. B* **2002**, *51*, 2261–2267 with kind permission from Springer Science and Business Media.

spectra of octaphenyl In(L)TAP differs in shape, depending on the axial ligand, where L = Cl, Ph, or *n*-Bu.[333] The main differences in the spectrum occur in the B band region, while the position of the Q band remains virtually unchanged (645 nm). The Q band can be assigned as the $a_{1u} \rightarrow e_g$ transitions. Since the a_{1u} orbital has zero coefficients at the coordinated pyrrole nitrogen atoms, the a_{1u} orbital does not influence the Q band position significantly. The formation of the μ-oxo dimer leads to a small blue shift of the Q band and a red shift of the

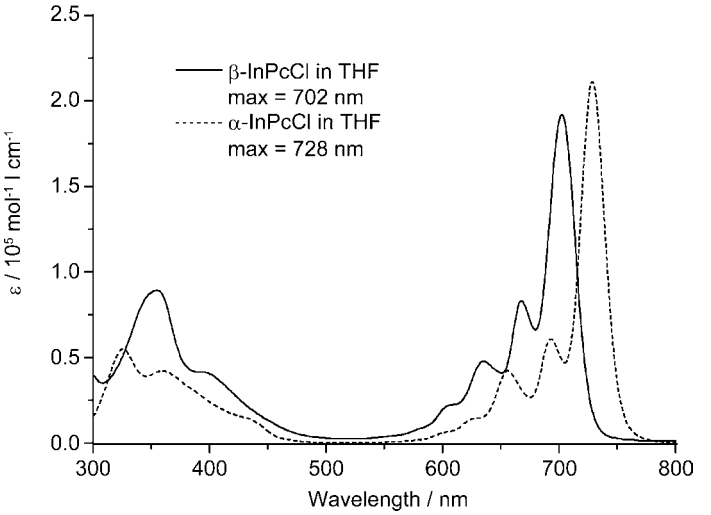

Figure 84. Absorption spectra of α-tetraalkoxy InClPc and β-tetraalkoxy InClPc in THF. The alkoxy group is $-OCH_2CH(CH_2CH_3)_2$. Redrawn from Wang, S. Q.; Gan, Q.; Zhang, Y. F.; Li, S. Y.; Xu, H. J.; Yang, G. Q. *ChemPhysChem* **2006**, *7*, 935–941.

B band.[325] The axially bridged In–In Pc dimer, namely [tetra-*tert*-butyl InPc]$_2$·2tmed (tmed = *N,N,N′,N′*-tetramethylethylenediamine), was first reported by Hanack and coworkers.[346] Spectroscopic studies clarified that the dimerization does not greatly affect the spectral profile, so that the main differences between the spectral features of the monomer and dimer are associated with changes of the molar extinction coefficients due to the different number of absorbing Pc rings per molecular unit.[341] Figure 84 compares the absorption spectra of tetra α- or β-alkoxy InClPcs as an example of representative absorption shapes of InPcs.

Barrett *et al.* reported that double-decomposition reactions between Li_2Pc and thallium hydroxide gave a bright green precipitate, presumably the TlPc complex.[56] However, no further spectroscopic investigations on TlPcs are found in the literature.

Q. Group 14: SiPc, GePc, SnPc, $SnPc_2$ and PbPc

SiPcs have two axial ligands above and below the Pc plane. Only the tetravalent species, $Si^{IV}Pc$, is known to date. Optical data for SiPcs are normal in shape, and are similar to that of MgPc (Figure 85, dashed line).[347,348] $SiCl_2Pc$ exhibits a Q band at 699 nm in pyridine, which is shifted to 671 nm when the two axial ligands are replaced with two hydroxyl groups. The axial ligands can be readily replaced with various substituents. For example, axial substitution by two $OSiMe_3$ groups

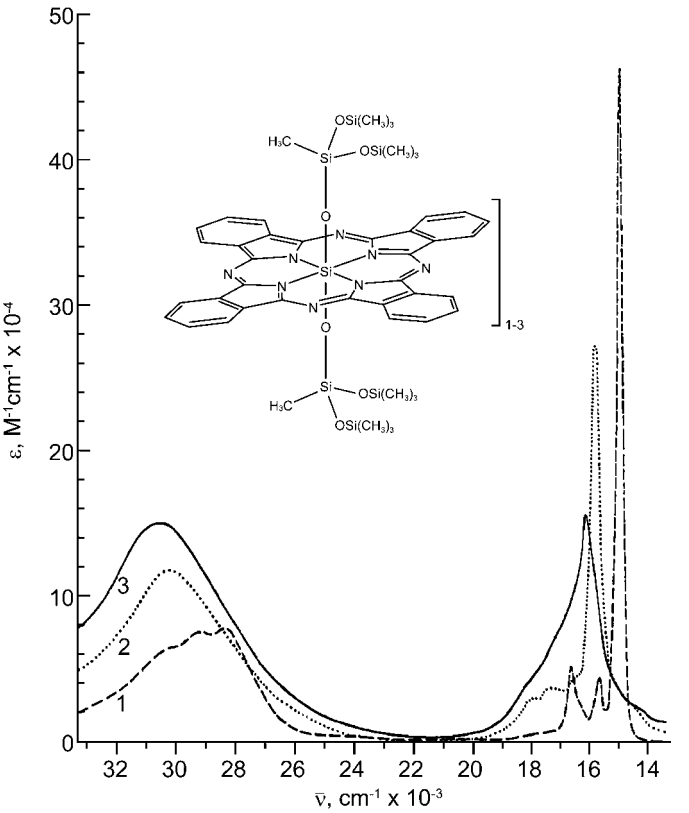

Figure 85. Absorption spectra of silicon Pc monomer (dashed line) and μ-oxo dimer (dotted line) and trimer (solid line). The axial ligands are $OSi(CH_3)(OSi(CH_3)_3)_2$. Redrawn with permission from Kane, A. R.; Sullivan, J. F.; Kenny, D. H.; Kenney, M. E. *Inorg. Chem.* **1970**, *9*, 1445–1448. Copyright 1970 American Chemical Society.

is achieved by reacting $SiPc(OH)_2$ with $(Me_3Si)_2NH$ in dry pyridine.[349] The resultant $SiPc(OSiMe_3)_2$ shows a Q band at 667 nm in benzene. Treatment of $SiPcCl_2$ with primary Grignard reagents in the dark gives the corresponding diorgano Pc derivatives, $SiPcR_2$.[350] A similar procedure using monoorgano-monochloro precursors, $SiPcR^1Cl$, gives unsymmetrical organo SiPcs, $SiPcR^1R^2$. The Q band of $SiPc(C_8H_{17})_2$ appears at 783 nm in cyclohexane. In the case of the bis(alkylcarboxylato)-substituted complex, $SiPc(OCOC_8H_{17})$, the Q band appears at 697 nm in $CHCl_3$. These examples indicate that the Q band position of SiPcs is relatively sensitive to their axial substituents. Thermal reaction of $SiPc(OH)_2$ yields a dimer, trimer, and oligomers having siloxane bonds. As shown in Figure 85, the spectral envelope is sensitive to the number of Pc rings per molecule. A blue shift of the Q and B bands with increasing chain length was observed, which was mainly attributed to exciton interactions between the constituted Pc rings. Thus, the Q band at

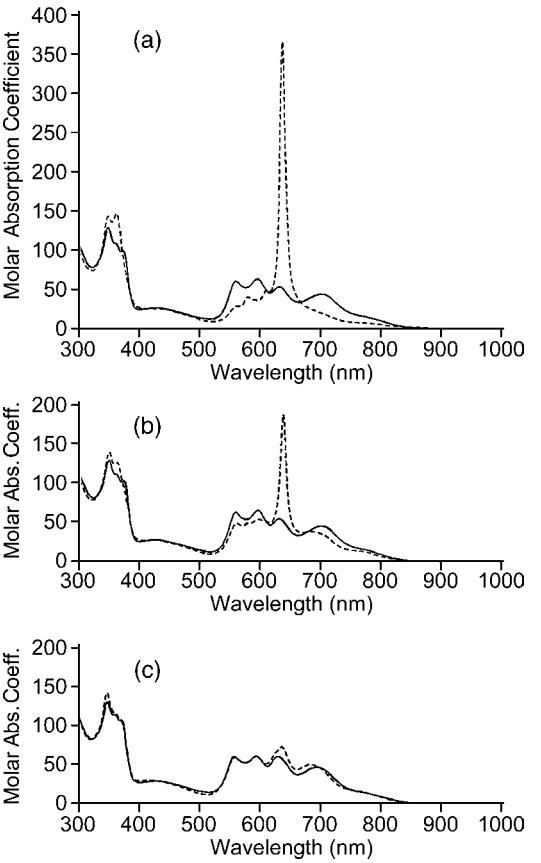

Figure 86. Absorption spectra of (a) $[(H_{17}C_8O)_8SiPc(OSiMe_2\text{-}tert\text{-}Bu)_2]_2O$, (b) $[(3,7\text{-}Me_2\text{-}C_8H_{15}O)_8SiPc(OSiMe_2\text{-}tert\text{-}Bu)_2]_2O$, and (c) $[(2\text{-}Et\text{-}C_6H_{12}O)_8SiPc(OSiMe_2\text{-}tert\text{-}Bu)_2]_2O$ in benzene (dashed lines) and CH_2Cl_2 (solid lines) at 25 °C. Redrawn with permission from Kleinwächter, J.; Hanack, M. *J. Am. Chem. Soc.* **1997**, *119*, 10684–10695. Copyright 1997 American Chemical Society.

15 040 cm^{-1} (665 nm) for the monomer shifts to 15 880 cm^{-1} (630 nm), 16 180 cm^{-1} (618 nm), and 16 270 cm^{-1} (615 nm) for dimer, trimer, and tetramer, respectively.[347] Kleinwächter and Hanack reported that the torsion angle between adjacent Pc rings in μ-oxo SiPcs depends on the choice of peripheral substituents.[351] Figure 86 demonstrates the solvatochromic behavior of octaalkoxy-substituted μ-oxo SiPc dimers. The spectra recorded in CH_2Cl_2 are quite different from those of typical metalloPcs, with all the dimer species showing a multiply split Q-band comprising at least five transitions between 500 and 900 nm in CH_2Cl_2 (Figure 86, solid lines). Nonaromatic solvents such as acetone, diethyl ether, THF, $CDCl_3$, and *n*-hexane also give similar results. In contrast, the spectral envelopes depend on the peripheral substituents (R) when recorded in benzene. When R = OC_8H_{17}, a

sharp Q band appears at 639 nm with accompanying tails on both sides (Figure 86a, dashed line), while no such clear Q band can be observed even in benzene when R = 2-Et-OC_6H_{12} (Figure 86c, dashed line). An intermediate result was obtained when R = 3,7-Me_2-OC_8H_{15} (Figure 86b, dashed line). The authors in Ref. 351 concluded that the torsion angle between the two Pc rings is *ca.* 20–30° in nonaromatic solvents. On the other hand, the species which gives a sharp Q band has a fully staggered or eclipsed conformation. Absorption data on silicon triazacorrole and silicon tetrabenzotriazacorrole have been reported independently by the Hanack and Kobayashi groups.[352–355]

The chemistry of GePcs is analogous to that of the SiPcs. $Ge^{IV}Cl_2Pc$ is synthesized by the reaction of germanium tetrachloride with H_2Pc,[356] 1,3-diiminoisoindoline,[357] or phthalonitrile.[358] The axial ligands can be replaced with dihydroxy and further by diphenoxy groups, to give $Ge^{IV}(OH)_2Pc$ and $Ge^{IV}(OPh)_2Pc$, respectively.[356] Unsubstituted $Ge(OH)_2Pc$ exhibits absorption peaks at 676, 645, 607, 415, 358, and 315 nm in pyridine.[358] $Ge(OSi(n\text{-}C_6H_{13})_2Pc$ shows a Q band at 673.7 nm (14 843 cm^{-1}) in toluene, which is red-shifted by *ca.* 120 cm^{-1} compared to the corresponding silicon derivative.[359] Figure 87 compares the absorption spectra of $Si(OH)_2Pc$ (dashed line), $Ge(OH)_2Pc$ (dotted line), and $Sn(OH)_2Pc$ (solid line) in pyridine.[358] The Q band shifts to the red in the order of SiPc → GePc → SnPc, which is attributed to the decrease in electronegativity of the central metal in this order. Lower electronegativity causes

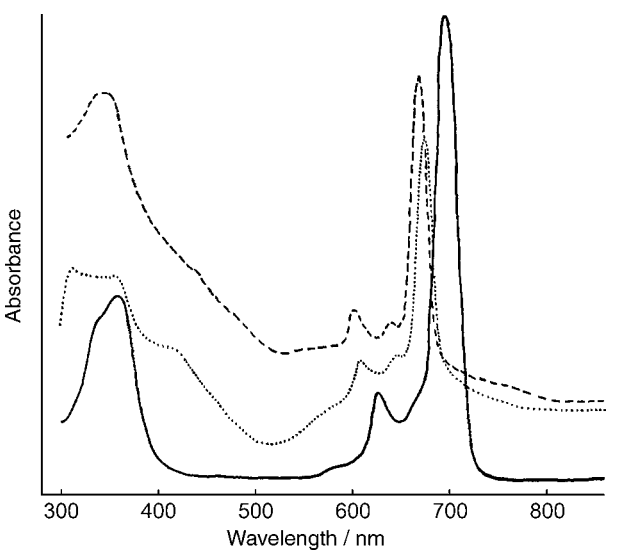

Figure 87. Absorption spectra of $Si(OH)_2Pc$ (dashed line), $Ge(OH)_2Pc$ (dotted line), and $Sn(OH)_2Pc$ (solid line) in pyridine. Redrawn with permission from Dirk, C. W.; Inabe, T.; Schoch, K. F.; Marks, T. J. *J. Am. Chem. Soc.* **1983**, *105*, 1539–1550. Copyright 1983 American Chemical Society.

a shift of charge on the metal onto the Pc ring, and as a consequence, the $a_{2u}(\pi)$ orbital increases in energy. GePcs are also able to form μ-oxo dimer, trimer, and oligomers, which show the same trend in spectral envelope shape as the silicon congeners. $\{[(CH_3)_3SiO]_2(CH_3)SiO\}(Ge^{IV}PcO)_2\{Si(CH_3)[OSi(CH_3)_3]_2\}$ exhibits a Q transition at 15 840 cm^{-1}, while the Q band of the corresponding monomer species appears at 14 970 cm^{-1}.[347,360] Hohol and Urban synthesized μ-oxo GePc polymers, $[GePcO]_n$, by irradiating a solution of $GeCl_2Pc$ with ultrasonic energy in the presence of a germanium chalcogenide.[357] Figure 88 shows the absorption spectral changes during the sonication of $GeCl_2Pc$. With increasing sonication time, a hypsochromic shift of the Q band from 690 to 640 nm is observed, demonstrating a general tendency observed for μ-oxo oligomerization of Pc derivatives.[357] Stover *et al.* reported that a reduction reaction of $Ge^{IV}Cl_2Pc$ with either $NaBH_4$ or $SnCl_2$ yielded $Ge^{II}Pc$.[361] This complex

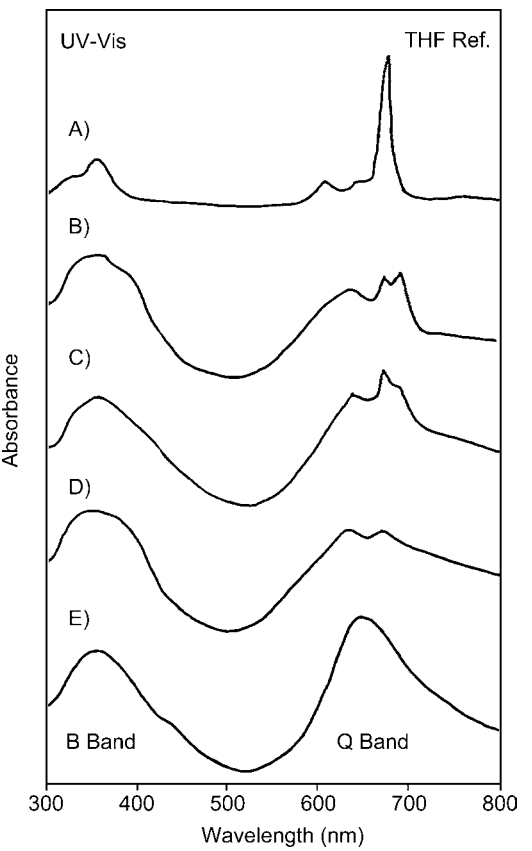

Figure 88. Absorption spectral changes of $GeCl_2Pc$ during the course of sonication in the presence of sodium telluride, for periods of: A, 0 minutes; B, 15 minutes; C, 30 minutes; D, 60 minutes; and E, 120 minutes. Redrawn from Hohol, M. D.; Urban, M. W. *Polymer* **1993**, *34*, 1995–2002. Copyright 1993, with permission from Elsevier.

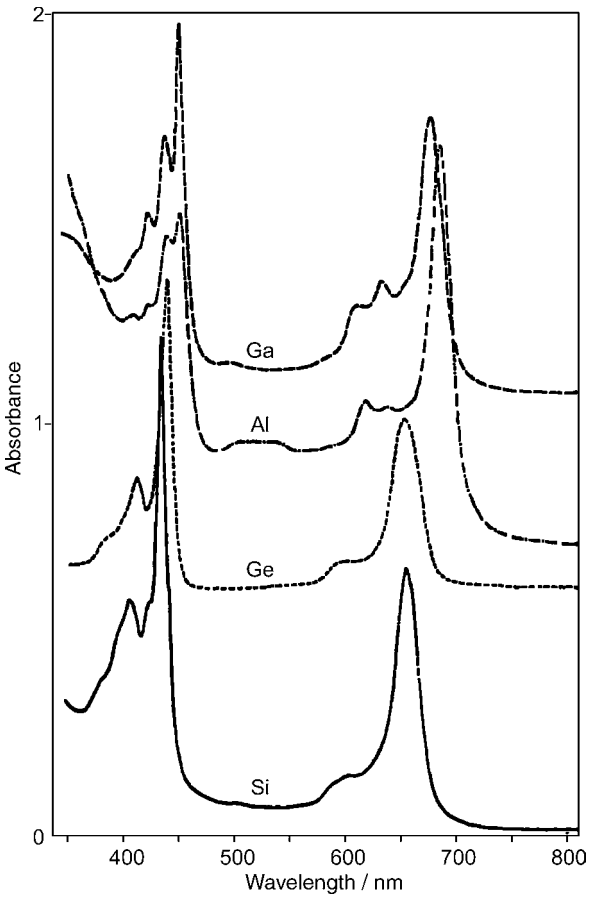

Figure 89. Absorption spectra of metalloid TBC derivatives in isopropyl alcohol. Redrawn with permission from Fujiki, M.; Tabei, H.; Isa, K. *J. Am. Chem. Soc.* **1986**, *108*, 1532–1536. Copyright 1986 American Chemical Society.

shows intense absorption bands at 445 and 330 nm, together with a shoulder at 415 nm in pyridine, in addition to intense bands and shoulders at 655, 602sh nm. However, the compound was later shown instead to be germanium triazatetrabenzocorrole hydroxide, Ge(OH)TBC.[362] Figure 89 exemplifies the absorption spectra of gallium, aluminum, germanium, and silicon complexes of the TBC derivatives. Recently, Cissell *et al.* reinvestigated the synthesis of $Ge^{II}Pc$, and reported that the reaction of $GeCl_2$(dioxane) with $K_2Pc(DMF)_4$ in THF gives a new germanium complex, which has a complicated-shaped absorption spectrum, suggesting that it has a 20-π electronic configuration, i.e. $Ge^{IV}Pc(4–)$, (Figure 90, black line).[363] After exposure to air, the complex shows clear Q-like bands in the 600–700 nm region (Figure 90, gray line).

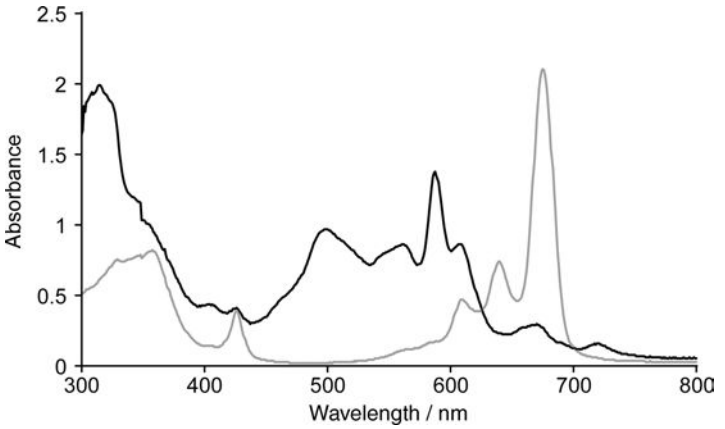

Figure 90. Absorption spectra of $Ge(py)_2Pc$ in pyridine (black line) and spectrum of the same sample in pyridine after exposure to air (gray line). Redrawn with permission from Cissell, J. A.; Vaid, T. P.; DiPasquale, A. G.; Rheingold, A. L. *Inorg. Chem.* **2007**, *46*, 7713–7715. Copyright 2007 American Chemical Society.

$Sn^{II}Pc$ and $Sn^{IV}Pc$ species have been reported to date, and their X-ray structures are also available.[364,365] $Sn^{IV}Cl_2Pc$ shows absorption peaks at 690, 625, and 270 nm in the vapor phase, with a spectral window in the 400–600 nm region (Figure 91).[21] $Sn^{IV}(OH)_2Pc$ and $Sn^{II}Pc$ exhibit absorption bands at 696, 665, 626, 360, and 340 nm in pyridine,[358] and at 682 and 359 nm in ethanol,[366] respectively. Similarly to SiPc and GePc, a hypsochromic shift of the Q transition is observed on formation of the μ-oxo oligomers, although the shift is quite small (695 nm for $[SnPcO]_n$, and 696 nm for the monomer).[358] A series of homo- and hetero- μ-oxo dimers, namely Si–O–Si, Si–O–Ge, and Si–O–Sn complexes, show a bathochromic shift of the Q band in this order.[359] Nyokong and coworkers have reported the spectroscopic properties of some substituted SnPc derivatives.[367–369] Sn^{IV} also forms a double-decker-type binuclear $Sn^{IV}Pc_2$.[40,74,370–372] X-ray crystallography clarified that the two Pc moieties are rotated by 42° with respect to each other.[371] Since the tin center is tetravalent, unlike the tervalent state of lanthanide ions, the neutral form can be described as Pc(2–)SnPc(2–). Therefore, the absorption properties of neutral $Sn(Pc)_2$ resemble those of $Zr(Pc)_2$ rather than $[Ln(Pc)_2]^0$. Figure 92 shows the absorption and MCD spectra of $Sn^{IV}Pc_2$.[372] A splitting of the Q band is observed, of which the lower energy component has a smaller intensity. The B band also shows a notable blue shift compared to the monomer species, with a longer wavelength tail extending to *ca.* 22 kcm^{-1}. The MCD spectrum shows dispersion type A-terms for the Q and B bands, indicating degenerate excited states corresponding to these bands. Importantly, A-terms are observed for both of the split Q bands. As described above (Section E), the exciton theory is insufficient to fully understand

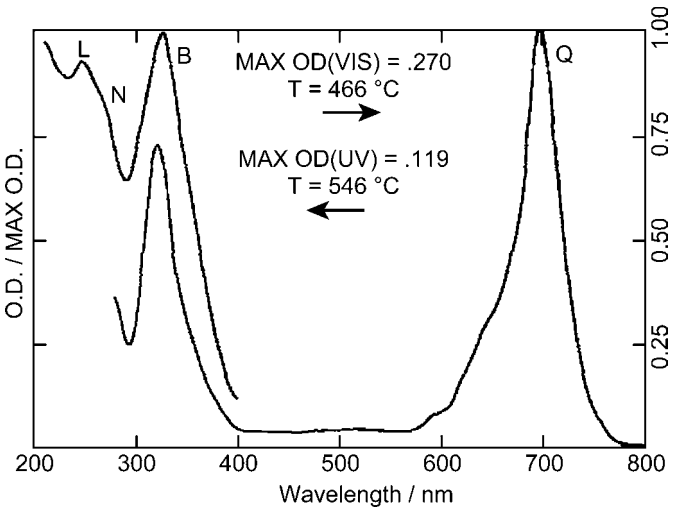

Figure 91. Vapor-phase absorption spectrum of $Sn^{IV}Cl_2Pc$. Redrawn from Edwards, L.; Gouterman, M. *J. Mol. Spectrosc.* **1970**, *33*, 292–310. Copyright 1970, with permission from Elsevier.

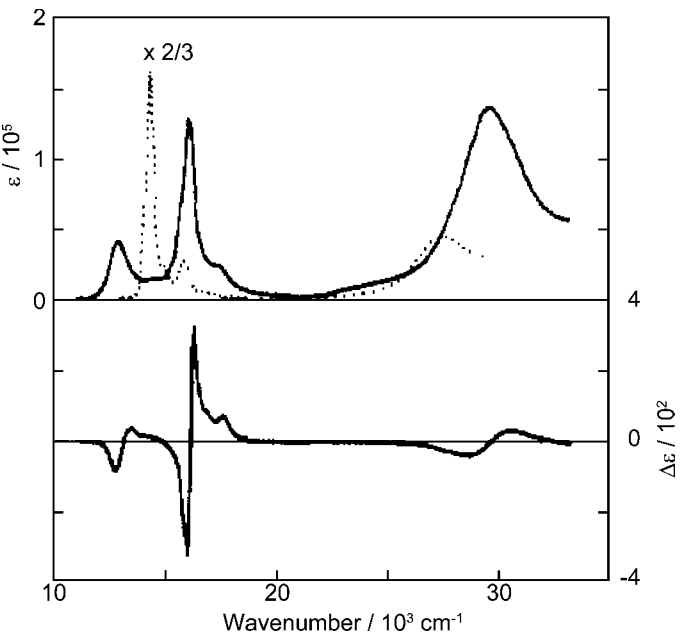

Figure 92. Absorption (top) and MCD (bottom) spectra of $SnPc_2$ in toluene (solid line). The absorption spectrum of monomeric $SnCl_2Pc$ in 1-chloronaphthalene is also shown as a dotted line. Redrawn with permission from Ohno, O.; Ishikawa, N.; Matsuzawa, H.; Kaizu, Y.; Kobayashi, H. *J. Phys. Chem.* **1989**, *93*, 1713–1718. Copyright 1989 American Chemical Society.

these spectral features, and the inclusion of charge resonance terms is inevitably necessary to theoretically reproduce the experimental results.

In the case of PbPc complexes, only $Pb^{II}Pc$ species have been isolated. X-ray crystallography clarified that the Pc ring in PbPc adopts a shuttlecock conformation, with the lead ion located above the convex side and displaced by 0.906 Å (monoclinic and tetragonal forms) or *ca.* 1.28 Å (triclinic form) from the mean-plane of the four pyrrole nitrogen atoms.[373–375] Unsubstituted PbPc shows absorption peaks at 698 (Q), 640 (Q(1–0)), 332.5 (B), 280 (N), 245 (L), and 207.5 (C) nm in the vapor phase (Figure 93).[21] Figure 94 shows the absorption spectrum of α-tetrapentoxy PbPc in $CHCl_3$.[376] The spectrum has a shape typical of metalloPcs for the B and Q band regions, with the B and Q bands appearing at 333 and 751 nm, respectively, as unsplit single bands. The authors in Ref. 376 assigned the weak absorption band at around 431–437 nm as an n-π^* transition due to the presence of the alkoxy groups. However, this assignment remains a matter of debate, because even unsubstituted PbPc shows similar spectral envelopes in this region (Figure 93). In addition, other substituted PbPc complexes, such as thioalkyl–,[338] phenyl–,[377] and nitro-substituted[378–380] derivatives, also exhibit weak absorption bands in this region, indicating that the band is inherent in PbPcs rather than originating from substituents. Zhang *et al.* performed time-dependent DFT calculations in order to calculate the electronic absorption spectra of metalloPcs of group 14, by employing a combination of the B3LYP functional and the LANL2DZ basis set.[381] According to their results, the band in the 400–500 nm region consists mainly of the HOMO–1 → LUMO transition, in which the HOMO–1 orbital of PbPc is mainly composed of the

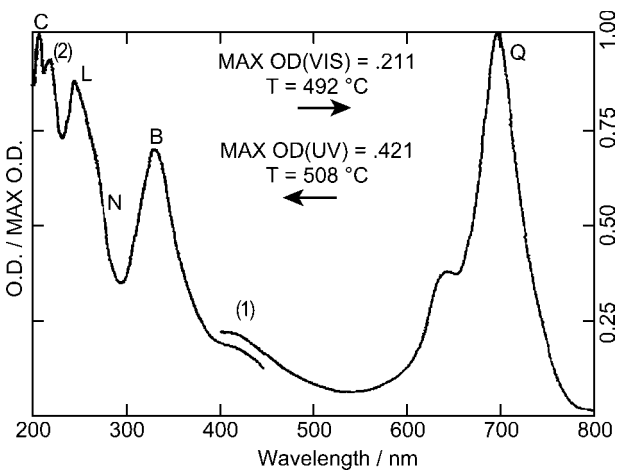

Figure 93. Vapor-phase absorption spectrum of PbPc. Redrawn from Edwards, L.; Gouterman, M. *J. Mol. Spectrosc.* **1970**, *33*, 292–310. Copyright 1970, with permission from Elsevier.

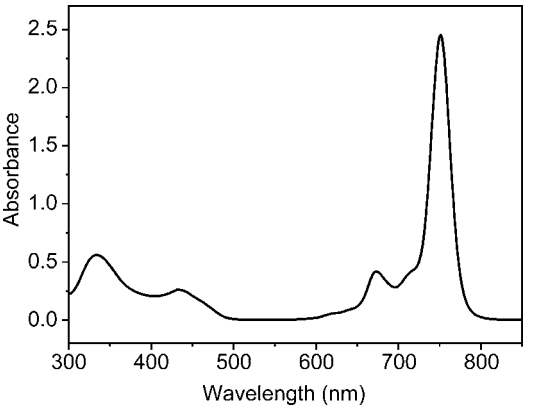

Figure 94. Absorption spectrum of α-tetrapentoxy PbPc in $CHCl_3$. Redrawn with permission from Bian, Y. Z.; Li, L.; Dou, J. M.; Cheng, D. Y. Y.; Li, R. J.; Ma, C. Q.; Ng, D. K. P.; Kobayashi, N.; Jiang, J. Z. *Inorg. Chem.* **2004**, *43*, 7539–7544. Copyright 2004 American Chemical Society.

d_{z^2} orbital of the lead with some subsidiary contribution from the p_z orbital of the nitrogen atoms, i.e. the band in this region has an MLCT character. Yaraşir *et al.* performed spectroelectrochemistry of octapropyl PbTAP, which revealed that the complex is demetalated during the controlled potential coulometry measurement after the first reduction couple of the complex (not shown).[382]

R. Group 15: PPc, AsPc, SbPc, BiPc, $BiPc_2$ and Bi_2Pc_3

In 1981, Gouterman *et al.* reported the synthesis of $P^{III}Pc$ and $P^{IV}Pc$ by the reaction of H_2Pc with py-PBr_3, and commented that the absorption spectrum of $P^{III}Pc$ shows an unusual sharp band at 442 nm.[366,383] However, Fujiki *et al.* pointed out later that the "$P^{III}Pc$" species is in fact a tetrabenzotriazacorrole (TBC) complex, P^{V}=O(TBC).[362] Figure 95 shows the absorption spectra of unsubstituted P^{V}=O(TBC) in pyridine (solid line) and in trifluoroacetic acid (TFA, dashed line).[384] In pyridine, at least five components can be recognized in the Q-band region, while a marked bathochromic shift is observed in TFA compared to pyridine. The sharp, intense bands at *ca.* 440 nm are characteristic features of the spectrum in pyridine. These spectral characteristics have similarities to those reported by Gouterman *et al.*[383] and to other references on TBC.[362,385–387] Examples of authentic phosphorus Pcs are rare.[384,388,389] The ionic $P^{V}Pc$ species, $[P^{V}(OH)_2Pc]^{+}(OH)^{-}$, shows a typical UV-vis absorption spectrum unlike TBC (669, 640, 602, 353 nm in pyridine). Upon addition of HCl to the complex dissolved in DMF, a bathochromic shift of the Q band is observed (not shown), which is presumably due to the formation of the $[P^{V}(OH)(OH_2)]^{2+}$ species.[384]

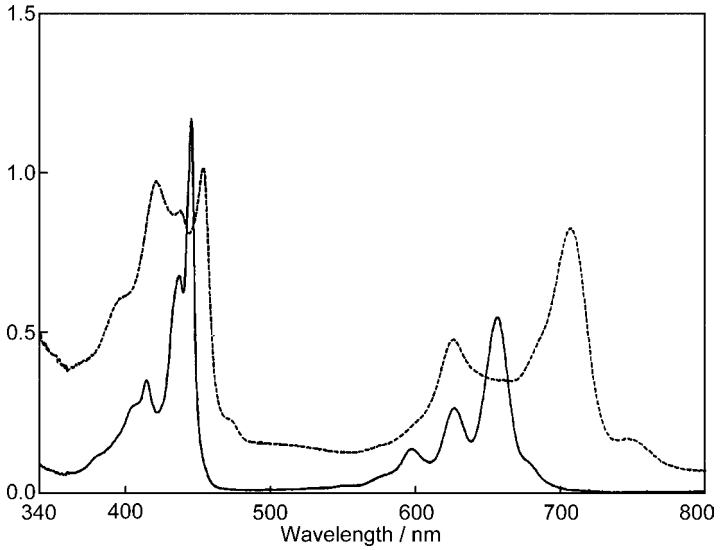

Figure 95. Absorption spectra of unsubstituted P^{V}=O(TBC) in pyridine (solid line) and in trifluoroacetic acid (dashed line). Redrawn from Li, J. Z.; Subramanian, L. R.; Hanack, M. *Eur. J. Org. Chem.* **1998**, 2759–2767.

Very few AsPc complexes have been described in the literature.[165,390–393] $As^{III}ClPc$ shows absorption bands at 580 and 340 nm in DMF.[165,366]

In analogy to PPcs, both Sb^{III} and Sb^{V} species are available for SbPcs. The low-valent $[Sb^{III}Pc]^{+}F^{-}$ can be easily converted to the high-valent species, $[Sb^{V}(OH)_2Pc]^{+}F^{-}$, by treatment of the low-valent complex with stoichiometric amounts of 30% hydrogen peroxide.[394] Figure 96 shows the absorption spectra of $[Sb^{III}Pc]^{+}F^{-}$ (top) and $[Sb^{V}(OH)_2Pc]^{+}F^{-}$ (bottom) in ethanol. In the case of the Sb^{III} complex, two prominent bands in the 300–500 nm region are assigned to the B and MLCT bands. In contrast, no MLCT transitions can be recognized for the Sb^{V} complex, indicating that all of the transitions are attributed to π–π^* transitions. Therefore, the absorption spectrum of the Sb^{V} species is typical in shape to that of metalloPcs. The Q band of the Sb^{III} complex appears at 729 nm, while that of the corresponding Sb^{V} complex is observed at 699 nm. The counter anions exert little effect on the absorption properties.[395] In contrast, the axial ligands have a moderate effect on the absorption spectra. Thus, the Q band of tetra-*tert*-butyl $[Sb^{V}L_2Pc]^{+}$ appears at 723.5, 739, and 742 nm in CH_2Cl_2 for L = OH, Cl, and Br species, respectively.[396] Isago reported that an unusual red shift of the Q band in nonaqueous media was observed for tetra-*tert*-butyl $[Sb^{III}Pc]^{+}$.[397]

A series of $Bi^{III}PcX$ complexes, where X = Cl^{-}, Br^{-}, I^{-}, and NO_3^{-}, were prepared by Isago and Kagaya.[398] The spectra of these are insensitive to X, and are

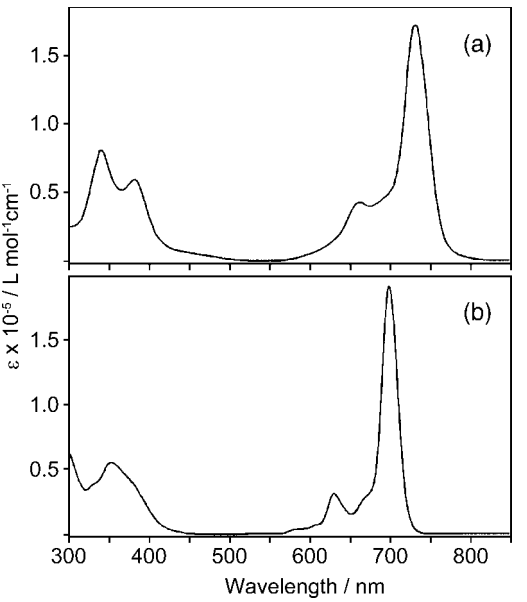

Figure 96. Absorption spectra of (a) $[Sb^{III}Pc]^+F^-$ and (b) $[Sb^{V}(OH)_2Pc]^+F^-$ in ethanol. Redrawn with permission from Knör, G. *Inorg. Chem.* **1996**, *35*, 7916–7918. Copyright 1996 American Chemical Society.

virtually identical to each other in shape. Thus, the band peaks are observed at 716.0, 645.0, 415sh, and 343.0 nm, and at 716.0, 645.0, 415sh, and 344.0 nm, and at 715.5, 645.0, 415sh, and 343.0 nm, and at 716.0, 645.0, 415sh, and 343.0 nm for X = Cl^-, Br^-, I^-, and NO_3^-, respectively in DMSO, indicating the ionic nature of the $Bi^{III}PcX$ species. The absorption spectrum of $Bi^{III}PcCl$ is displayed in Figure 97. The spectrum is characteristic of typical metalloPcs. The band at *ca.* 415 nm can be assigned to an MLCT band arising from a transition from the $a_{2u}(6p_z)$ orbital of the bismuth(III) to the $e_g(\pi^*)$ orbital of the Pc moiety. Double-decker[399,400] and triple-decker[401,402] BiPc complexes, namely $BiPc_2$ and Bi_2Pc_3, respectively, are also available. The reduced form of the dimer, $[BiPc(2-)_2]^-$ (Figure 98a), shows a spectral shape typical of this type of complex.[399] Two split Q bands appear at 13.33 and 15.59 kcm^{-1}, of which the latter is the exciton-dominated component. In the case of the neutral form (Figure 98b), the spectrum is also typical in shape of this type of complex. A sharp, most intense band was observed at 14.54 kcm^{-1} accompanied by two vibronic bands at 15.16 and 16.06 kcm^{-1}. The band at 21.01 kcm^{-1}, as well as a series of weak bands in the near-IR region, is indicative of the presence of the Pc radical moiety. Figure 99 shows the absorption spectra of Bi_2Pc_3.[402] The spectra in pyridine (a) and DMSO (c) are similar in shape, while that in DMF (b) is shifted hypsochromically by *ca.* 43 nm. In pyridine, two Q components lie at 718 and 644 nm, of which the former is

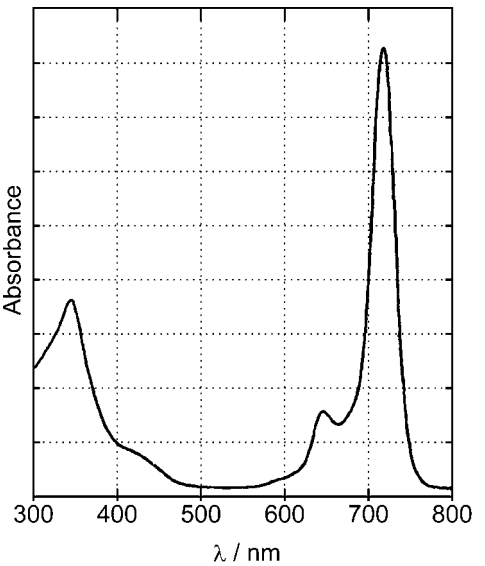

Figure 97. Absorption spectrum of $Bi^{III}PcCl$ in DMSO. Isago, H.; Kagaya, Y. *Bull. Chem. Soc. Jpn.* **1994**, *67*, 383–389. Redrawn by permission of The Chemical Society of Japan.

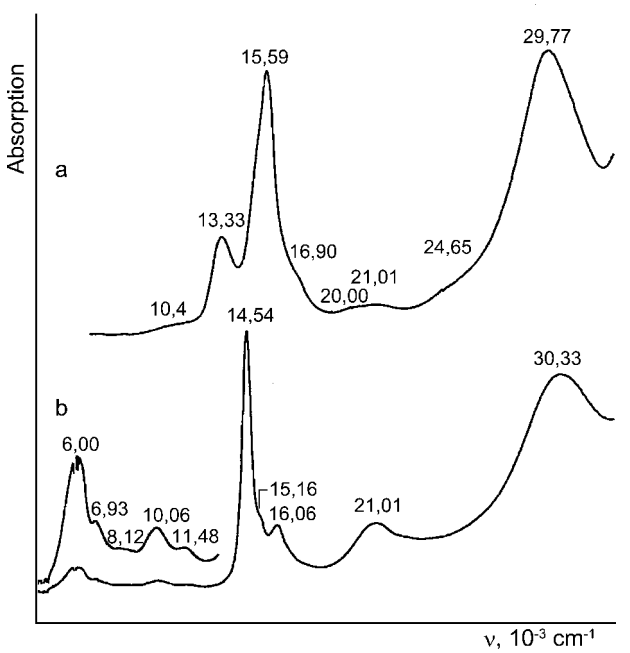

Figure 98. Absorption spectra of (a) $[BiPc(2-)_2]^-(^nBu_4N^+)$ and (b) $[Bi(Pc)_2]^0$ in CH_2Cl_2. Redrawn from Ostendorp, G.; Homborg, H. *Z. Anorg. Allg. Chem.* **1996**, *622*, 873–880.

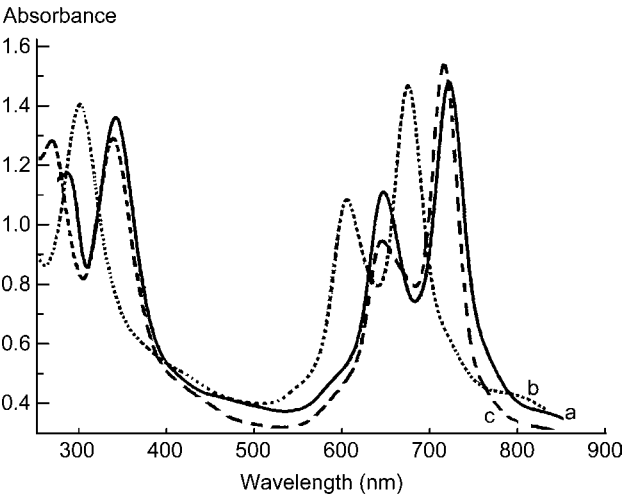

Figure 99. Absorption spectra of Bi_2Pc_3 in (a) pyridine, (b) DMF, and (c) DMSO. Redrawn from Benihya, K.; Mossoyan-Deneux, M.; Hahn, F.; Boucharat, N.; Terzian, G. *Eur. J. Inorg. Chem.* **2000**, 1771–1779.

more intense, being in disagreement with the spectra of Ln_2Pc_3 and In_2Pc_3.[403] The crystal structure of (1,24-bicyclophthalocyaninato)bismuth(III) was reported in 2001. As a result of disruption of the aromatic π-system, this complex shows no absorption bands in the Q-band region (not shown).[404]

IV. Collective Absorption Data Tables

The remainder of the chapter is devoted to a collective database of the absorption data for hitherto reported Pc and its derivatives and analogs. Abbreviations used throughout the database are summarized in List of Abbreviations. In this database, the covered compounds are grouped into 13 categories (13 tables). Since units used to represent transition energy vary from one paper to another, only the first transition energy of each compound is accompanied by the unit. Moreover, molar extinction coefficients or relative intensities are given in parentheses if available. Band shoulders are denoted using "sh." Thus, an example of the method of representing transition energies and intensities is: 698 nm (lg ε 5.21), 665sh, 638 (4.62), etc…

Table 1 summarizes the absorption data of unsubstituted Pcs. Central metal, solvent, transition energy and intensity, remarks, and reference number are given from the left column to the right. Since Table 1 treats unsubstituted species, no further structural information appears in this table.

Table 2 summarizes the absorption data of α- and/or β-substituted Pcs. Some of the so-called "low symmetry Pcs" are also included in this table.

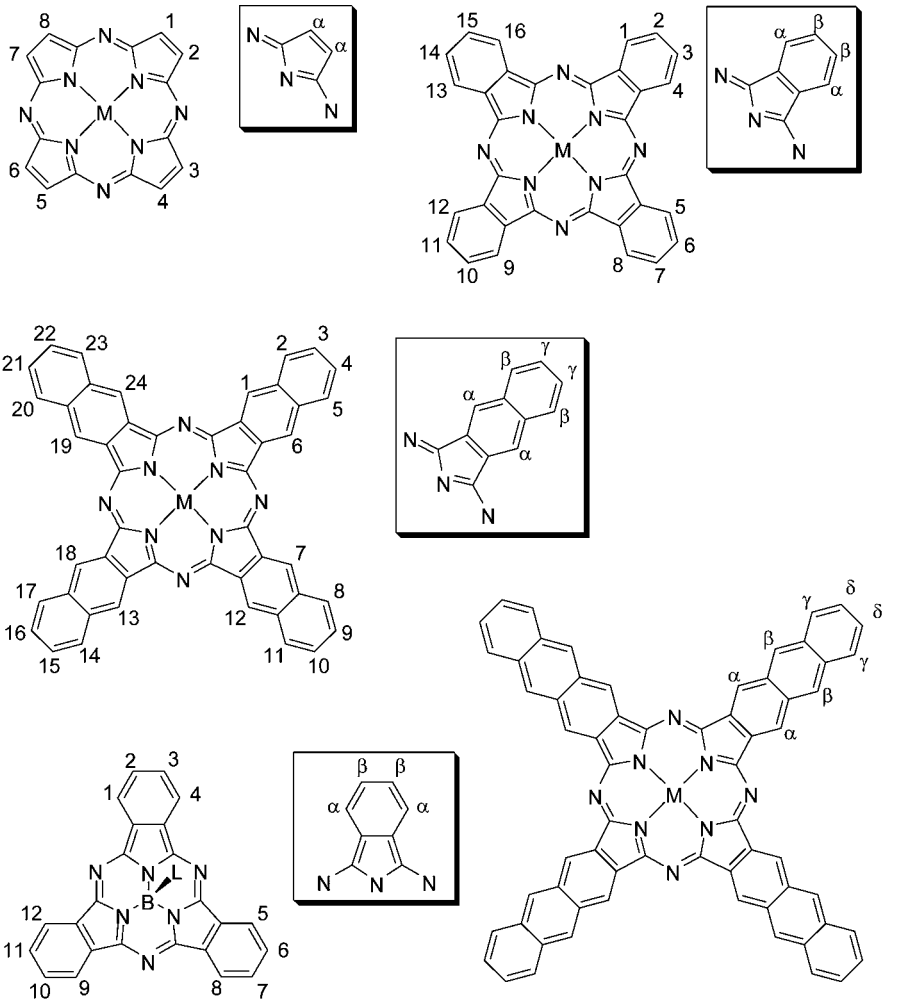

Figure 100. Numbering system, showing the positions of the substituents employed throughout the following absorption database in order to specify molecular structures.

Structures are represented by using the numbering system shown in Figure 100. For example, "R_2, R_3 = Me" and "R_2 = Me" stand for "2,3-bismethyl Pc" and "2-monomethyl Pc," respectively. If identical substituents are introduced into the four benzene rings around the Pc core, α and/or β symbols are used in order to simplify the notation. Thus, "$\alpha\alpha$ = Me", "$\beta\beta$ = Me" and "$\alpha\alpha\beta\beta$ = Me" are equivalent to "R_1, R_4, R_5, R_8, R_9, R_{12}, R_{13}, R_{16} = Me" and "R_2, R_3, R_6, R_7, R_{10},

R_{11}, R_{14}, R_{15} = Me", and "R_1, R_2, R_3 R_4, R_5, R_6, R_7 R_8, R_9, R_{10}, R_{11}, R_{12}, R_{13}, R_{14}, R_{15}, R_{16} = Me" respectively. Moreover, "α = Me" and "β = Me" stand for "R_1, $R_5(R_8)$, $R_9(R_{12})$, $R_{13}(R_{16})$ = Me" and "R_2, $R_6(R_7)$, $R_{10}(R_{11})$, $R_{14}(R_{15})$ = Me", respectively. Therefore, these two notations imply that the sample is a mixture of the possible structural isomers. The notation "$\alpha\beta$ = Me" is ambiguous because two structures, namely "R_1, R_2, … = Me" and "R_1, R_3, … = Me", are possible. In this case, for example, "$\alpha\beta$ (R_1, R_2) = Me" is used to specify the molecular structure. If different substituents are introduced at the two α or β positions and the sample contains structural isomers, "$\alpha\alpha'$ = Me, Et" and "$\beta\beta'$ = Me, Et" are used. Molecular structures are given directly in the table for more complex molecules.

Table 3 summarizes the absorption data of TAPs and mono-, di-, or triazaporphyrin analogs. The numbering system is shown in Figure 100. Thus, "α = Me" and "$\alpha\alpha$ = Me" correspond to "R_1, $R_3(R_4)$, $R_5(R_6)$, $R_7(R_8)$ = Me" and "R_1, R_2, R_3, R_4, R_5, R_6, R_7, R_8 = Me", respectively.

Table 4 summarizes the absorption data of Nc, Ac, and other ring-expanded Pc analogs. The numbering system is used to represent the structures of Ncs, as shown in Figure 100. The other skeletal structures are directly drawn in the table.

Table 5 summarizes the absorption data of sub- and super-Pcs. For subPcs, the axial ligand is denoted as L unless otherwise specified. The numbering system is shown in Figure 100.

Table 6 summarizes the absorption data of Pc analogs containing heteroatoms inside the aromatic skeleton. This category includes pyrazinoporphyrazines.

Table 7 summarizes the absorption data of Pc derivatives having crown-ether or related macrocycle units.

Table 8 summarizes the absorption data of tetraazachlorin derivatives.

Table 9 summarizes the absorption data of triazacorrole derivatives. The numbering system used is shown in the table.

Table 10 summarizes the absorption data of double decker and triple decker type Pc derivatives. This category includes hetero dimers consisting of Pc and porphyrin rings.

Table 11 summarizes the absorption data of dimers and oligomers. Sandwich-type structures are not included in this table, which appear in Table 10.

Table 12 summarizes the absorption data of Pc analogs containing triazole units.

Table 13 summarizes the absorption data of Pc polymers.

Table 1. UV-vis absorption data of unsubstituted Pcs.

M	Solvent	Transition Energy (Intensity)	Remark	Ref.
2H	$CHCl_3$	693 nm, 656, 637, 594		405
		692 nm (ε 166,000), 656 (140,000), 340 (96,800)		117
		703 nm (10^{-5} ε 2.07), 665 (1.68), 350 (1.32)		406
		692 nm, 656, 632sh, 603sh, 387sh , 347		407
		698 nm (10^{-3} ε 52.1), 665 (51.8), 638 (46.2), 602 (44.3), 350 (47.4)		408
	DCM	690 nm (ε 162,000), 654 (151,000), 340 (94,500)		117
	EtOH	668 nm (ε 155,500), 604 (26,000), 344 (51,000)		117
	CCl_4	693 nm, 656		38
	DMF	693.29 nm (A_{max} 0.19), 656.39 (0.18), 639.39 (0.088), 603.82 (0.06), 276.76 (2.45)		39
	THF	698.5 nm, 664.5		48
	py	694 nm, 658		409
		694 nm (lg ε 5.21), 659 (5.18), 640 (4.62), 602 (4.43)		410
		694 nm, 659		411
		694 nm, 659, 640, 630, 602		41
		672 nm, 644		40
	1-ClNp	698 nm (ε 162,000), 665 (151,500), 350 (55,000)		117
		6990 Å (lg ε 4.23), 6650 (4.19), 6450 (3.71), 6360 (3.71), 6170 (3.44), 6020 (3.54), 5760 (2.89), 5550 (2.59)		270
		698 nm (lg ε 5.21), 665 (5.18), 638 (4.62), 602 (4.43), 350 (4.74)		412
		698 nm (ε 160,000), 665 (150,000)		413
		698 nm (10^{-4} ε 16.2), 665 (15.1), 638 (4.17), 602 (2.69)		114
		698 nm, 663		414
		700 nm, 675, 664, 632.5, 600, 576, 550		57
		7030 Å (lg ε 5.23), 6680 (5.22), 6360 (4.75), 6040 (4.52), 5760 (4.02), 5560 (3.88)		415
		6980 Å (lg ε 5.21), 6650 (5.18), 6380 (4.62), 6020 (4.43), 5540 (3.57), 3500 (4.74)		40
		698 nm (lg ε 5.21), 665 (5.18), 638 (4.62), 602 (4.43), 350 (4.74)		416
		698 nm (10^{-3} ε 52.1), 665 (51.8), 638 (46.2), 602 (44.3), 350 (47.4)		417
	1,2,4-trichlorobenzene	697 nm, 659		152
	α,α,α-trichlorotoluene	692 nm, 655, 638, 628, 595		41
	benzene	693 nm, 656, 639, 630sh, 595, 574sh, 553sh, 376sh, 356, 342		418
		694 nm, 657, 639, 630, 597		41
	36 N H_2SO_4	722 nm (lg ε 4.870), 744 (4.765), 693 (4.309), 443 (4.346), 302 (4.715), 225 (4.642), 203 (4.642)		378
	$PhNO_2$	698 nm, 663, 644, 636, 602		41

(*Continued*)

Table 1. (*Continued*)

M	Solvent	Transition Energy (Intensity)	Remark	Ref.
	PhCl	696 nm, 658, 641, 632, 598		41
	p-xylene	694 nm, 656, 639, 629, 595		41
	dioxane	688 nm, 653, 635, 627, 596		41
	H_2SO_4	698 nm, 665		419
2Li	acetone	688 nm, 628, 595, 569, 550		57
Be(II)	1-ClNp	692 nm, 681.5, 655, 630.5, 614, 591, 570		57
2Na	py	694 nm, 658		409
Mg(II)	Vapor phase	666 nm		420
	DCM	670 nm, 642, 606, 345, 282		83, 421
		672 nm (ε 128,000), 608 (19,000), 344 (41,000)		117
		674 nm (10^{-3} ε 49.4), 647 (43.9), 610 (44.5), 347 (47.3)		408
		670 nm, 642, 606, 345, 282		422
	DMF	668 nm (ε 155,000), 604 (26,000), 344 (51,000)		117
	py	678 nm		411
		674 nm (10^{-3} ε 49.4), 647 (43.9), 610 (44.5), 347 (47.3)		417
		674 nm (lg ε 4.94), 644sh , 607 (4.12), 347 (4.36)		423
		674 nm (lg ε 4.94), 647 (4.39), 610 (4.45), 347 (4.73)		412
	1-ClNp	704.5 nm, 678, 662.5, 649, 630.5, 612.5, 597		57
		7020 Å (lg ε 4.15), 6800 (4.93), 6480 (4.08), 6110 (4.08)		415
Mg(II)L	DCM	672 nm, 643, 607, 345, 281	L = *trans*- 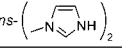	83
		672 nm, 643, 607, 345, 282	L = *trans*- 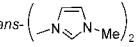	83
		671 nm, 642, 605, 345, 282	L = *trans*-py_2	83
		671 nm, 642, 607, 345, 282	L = *trans*-$(py(4\text{-}Me))_2$	83
		671 nm, 642, 606, 345, 282	L = *trans*-$(CN^-)_2$	83
	py	6745 Å (lg ε 4.94), 6470 (4.39), 6100 (4.45), 5870 (3.79), 5680 (3.59), 3470 (4.73)	L = OH_2	40
		674 nm, 347	L = OH_2	424
Al(III)OH	THF	674 nm, 644, 608		316
	DMF	672 nm		312
	H_2SO_4	810 nm		312
	py	677 nm		425
Al(III)Cl	THF	675 nm (10^{-1} ε 10.2), 642 (1.4), 609 (1.6), 347 (2.4)		316
		670 nm (lg ε 5.477), 638, 606, 336		314

(*Continued*)

Table 1. (*Continued*)

M	Solvent	Transition Energy (Intensity)	Remark	Ref.
	DMF	677 nm (10^{-1} ε 15.4), 647 (2.3), 610 (2.5), 357 (5.0)		316
	DMSO	681 nm (10^{-1} ε 16.8), 651 (2.2), 613 (2.6), 358 (5.1)		316
	py	681 nm (10^{-1} ε 18.5), 651 (2.5), 614 (3.0), 364 (5.7)		316
	1-ClNp	691 nm, 665, 622, 597, 576		57
		680 nm (ε 126,000)		413
	MeOH	670 nm, 643, 604, 582.5, 559		57
	quinoline	684 nm		273
	conc H_2SO_4	810 nm, 720, 460		273
Al(III)CN	THF	668 nm, 638, 601		316
Al(III)L	THF	672 nm (lg ε 5.535), 638 (4.832), 606 (4.792), 345 (5.033)	L = $OSi(C_6H_{13})_3$	314
		671 nm (lg ε 5.371), 638 (5.004), 606 (4.792), 336 (5.93)	L = 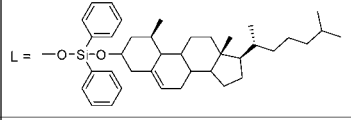	314
Si(IV)L	DMF	673 nm (lg ε 5.40), 644 (4.54), 606 (4.59), 356 (4.88)	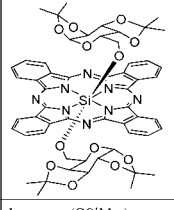	426
	C_6H_6	667 nm, 640, 606, 355	L = *trans*-$(OSiMe_3)_2$	349
	toluene	669 nm	L = *trans*-$(OSi(CH_3)_2(CH_2)_3SH)_2$	427
	toluene	680 nm	L = *trans*-$OSi(CH_3)_2(CH_2)_3SH$, OH	427
	toluene	668 nm	L = *trans*-$(OSi(CH_3)_2(CH_2)_3CH_3)_2$	427
	toluene	668 nm	L = *trans*-$(OSi(CH_3)_2\ (CH_2)_2C(CH_3)_3)_2$	427
	DMF	683 nm, 419.8	L = *trans*- 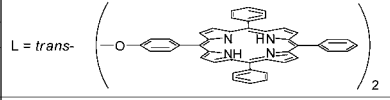	428
	toluene	682 nm, 421.8		428
		682 nm (lg ε 5.38), 651 (4.67), 613 (4.69), 551 (4.42), 516 (4.63), 421 (5.90)		429
	DMF	682.5 nm, 427.5		428

(*Continued*)

Table 1. (*Continued*)

M	Solvent	Transition Energy (Intensity)	Remark	Ref.
	toluene	682 nm (5.39), 652 (4.59), 613 (4.70), 551(4.61), 425 (5.92)	L = *trans*- 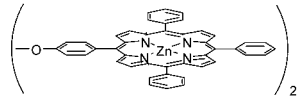	428
	DMF	673.5 nm, 356	L = *trans*-$(OH)_2$	428
	toluene	673 nm, 357	L = *trans*-$(OH)_2$	428
	$CHCl_3$	684 nm, 656, 615, 352, 330, 260	L = *trans*- 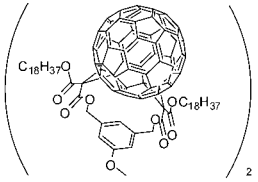	430
	$CHCl_3$	689 nm, 657, 618, 354, 318, 259	L = *trans*- 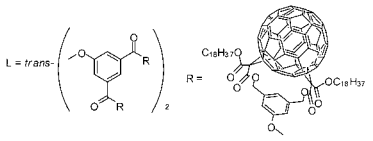	430
	$CHCl_3$	690 nm, 658, 619, 364, 356, 319, 259	L = *trans*- 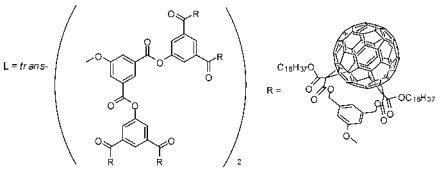	430
	$CHCl_3$	683 nm, 653, 613, 356	L = *trans*- 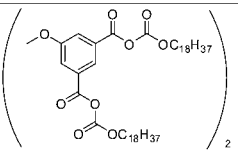	430
	DMF	674 (10^5 ε 2.06)		431

(*Continued*)

Table 1. (*Continued*)

M	Solvent	Transition Energy (Intensity)	Remark	Ref.
	H_2O + 0.1% DMF	722br	L = *trans*- 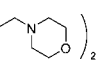	431
	DMF	678 (10^{-5} ε 2.00)	L = *trans*- 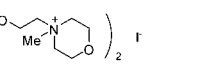	431
	H_2O	683 (10^{-5} ε 1.98)		431
	benzene	684 nm (10^{-4} ε 27.7), 653 (3.9), 613 (4.9), 359 (13.7)	L = *trans*- 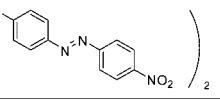	432
	DMF	674 nm (lg ε 5.45), 645 (4.56), 606 (4.63), 355 (4.93)	L = *trans*- 	433
		674 nm (lg ε 5.31), 644 (4.46), 606 (4.52), 355 (4.81)	L = *trans*- 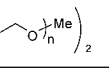	433
	$CHCl_3$	686 (r.i.1.00), 656 (0.13), 616 (0.15), 360 (0.28)	L = *trans*- 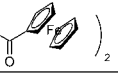	434
	DCM	678 nm, 650, 610, 354	L = *trans*- 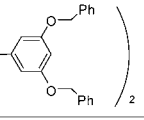	435
		680 nm, 650, 610, 354	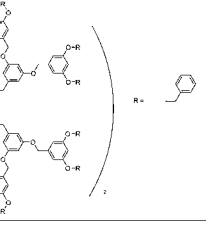	435

(*Continued*)

Table 1. (*Continued*)

M	Solvent	Transition Energy (Intensity)	Remark	Ref.
		680 nm, 650, 612, 348	L = *trans*- 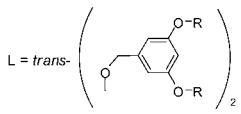 R = 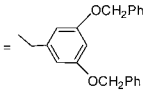	435
	py	671 nm, 640, 602, 445, 340	L = *trans*-$(OH)_2$	358
		685 nm	L = *trans*-$(OCOPh(4\text{-}t\text{-}Bu))_2$	436
		685 nm	L = *trans*-(3-thienyl)acetate	436
		685 nm	L = *trans*-$(OCOCH_2Ph(2\text{-}OMe))_2$	436
		685 nm	L = *trans*-$(OCOCH_2Ph(3\text{-}OMe))_2$	436
		686 nm	L = *trans*-$(OCOCH_2Ph(4\text{-}OMe))_2$	436
		688 nm	L = *trans*-$(OCOPh(3,4\text{-}(OMe)_2))_2$	436
		687 nm	L = *trans*-$(OCOCH_2Ph(3,4\text{-}(OMe)_2))_2$	436
		685 nm	L = *trans*-$(OCOCH_2CH_2Ph(3,4\text{-}(OMe)_2))_2$	436
		686 nm	L = *trans*-$(OCOCH_2CH_2CH_2Ph(3,4\text{-}(OMe)_2))_2$	436
		687 nm	L = *trans*-$(OCOCH_2Ph(2,5\text{-}(OMe)_2))_2$	436
		686 nm	L = *trans*-$(OCOCH_2Ph(3,4,5\text{-}(OMe)_3))_2$	436
	$CHCl_3$	686 nm (r.i 1.260), 654 (0.158), 616 (0.184), 360 (0.356)	L = *trans*- 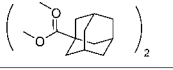	437
	1-ClNp	682 nm (r.i 1.268), 652 (0.156), 614 (0.183), 360 (0.323)	L = 2-[2-(methoxyethoxy)ethoxy]acetate	437
	cyclohexane	783 nm (lg ε 4.88), 653 (3.89), 617 (3.93), 325 (4.46), 243 (4.59)	L = *trans*-$(C_8H_{17})_2$	350
	DMSO	672 nm	L = *trans*-$(OH)_2$	438
	py	699 nm, 627, 367, 314	L = *trans*-Cl_2	439
		671 nm, 641.5, 604	L = *trans*-$(OH)_2$	439
	THF	667 nm, 636, 602, 377, 363, 318	L = *trans*-$(OH)_2$	439
	$CHCl_3$	674.5 nm, 644, 605, 357	L = *trans*-$(OH)_2$	439
	benzene	672 nm, 642, 605, 355	L = *trans*-$(OH)_2$	439
	py	670.5 nm, 640, 604	L = *trans*-$(Si[C(CH_3)_3](CH_3)_2)_2$	439
	$CHCl_3$	668 nm, 638, 602	L = *trans*-$(Si[C(CH_3)_3](CH_3)_2)_2$	439
	benzene	668.5 nm, 638, 604, 353, 330sh	L = *trans*-$(Si[C(CH_3)_3](CH_3)_2)_2$	439
	THF	665 nm, 634, 597, 574, 553, 352, 336, 287	L = *trans*-$(Si[OSiC(CH_3)_3]_2(CH_3))_2$	439
	$CHCl_3$	697 nm, 670, 653, 616, 370, 367, 325, 291	L = *trans*-$(OCOC_8H_{17})_2$	440
		702 nm, 676, 653, 615, 372, 365, 340, 292	L = *trans*-$(OCOC_{10}H_{21})_2$	440

(*Continued*)

Table 1. (*Continued*)

M	Solvent	Transition Energy (Intensity)	Remark	Ref.
		699 nm, 674, 654, 618, 367, 342, 330, 294	L = *trans*-$(OCOC_{11}H_{23})_2$	440
		702 nm, 672, 655, 620, 372, 369, 323, 297	L = *trans*-$(OCOC_{13}H_{27})_2$	440
		700 nm, 678, 652, 612, 368, 330, 295	L = *trans*-$(OCOC_{15}H_{29})_2$	440
		695 nm, 667, 653, 620, 372, 365, 322, 290	L = *trans*-$(OCOC_{21}H_{43})_2$	440
	DMF	677 nm (lg ε 5.19), 645 (4.33), 608 (4.39), 353 (4.68)	L = *trans*-$(OCH(CH_2NMe_2)_2)_2$	441
		676 nm (lg ε 5.48), 644 (4.61), 607 (4.68), 354 (4.98)	L = *trans*-$(OCH(CH_2NMe_2)_2)$, (OMe)	441
		675 nm (lg ε 5.85), 643 (5.00), 607 (5.08), 355 (5.37)	L = *trans*-$(OCH(CH_2NMe_2)_2)$, (OEt)	441
		675 nm (lg ε 5.32), 643 (4.47), 607 (4.54), 354 (4.82)	L = *trans*-$(OCH(CH_2NMe_2)_2)$, (OC_6H_{13})	441
		682 nm (lg ε 5.36), 612 (4.75), 356 (5.02)	L = *trans*-$(OCH(CH_2NMe_3)_2)$, (OMe), $[Pc]^{2+}2I^-$	441
		670 nm (lg ε 4.94), 604 (4.18), 329 (4.72)	L = *trans*-$(OCH(CH_2NMe_3)_2)_2$, $[Pc]^{4+}4I^-$	441
	DMF	680 nm (10^{-5} ε 2.3)	L = *trans*- 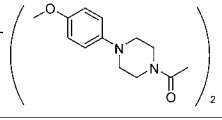	442
	H_2O + 0.5% v/v DMF	680–750br nm		442
	DMF	685 nm (10^{-5} ε 2.3)	L = *trans*- 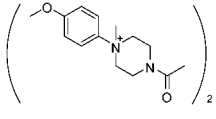 $[Pc]^{2+}2I^-$	442
	H_2O	690 nm (10^{-5} ε 1.9)		442
	DCM	685 nm	L = *trans*-(Ph), (OCOPh(4-*t*-Bu))	443
		688 nm	L =  L' = 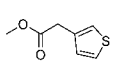	443
		685 nm	L = *trans*-(Ph), (OPh)	443
		685 nm	L = *trans*-$(OCOPh(4\text{-}t\text{-}Bu))_2$	443
		686 nm	L = *trans*- 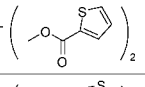	443
		684 nm	L = *trans*- 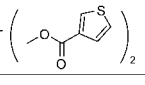	443

(*Continued*)

Table 1. (*Continued*)

M	Solvent	Transition Energy (Intensity)	Remark	Ref.
		685 nm	L = *trans*- 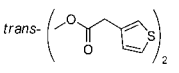	443
		685 nm	L = *trans*-$(OCOPh(3,5\text{-}Ph_2))_2$	443
		680 nm	L = *trans*-$(OPh(4\text{-}t\text{-}Bu))_2$	443
		691 nm	L = *trans*- 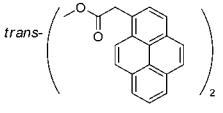	443
		684 nm	L = *trans*- 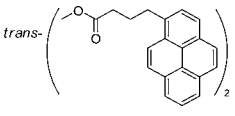	443
	toluene	670 nm (lg ε 5.4)	L = *trans*-$(OSi(Me)_2CH_2NMe_2)_2$	444
		668 nm (lg ε 5.4)	L = *trans*-$(OSi(Me)_2(CH_2)_2NMe_2)_2$	444
		668 nm (lg ε 5.5)	L = *trans*-$(OSi(Me)_2(CH_2)_3NMe_2)_2$	444
		668 nm (lg ε 5.5)	L = *trans*-$(OSi(Me)_2(CH_2)_4NMe_2)_2$	444
		668 nm (lg ε 5.5)	L = *trans*-$(OSi(Me)_2(CH_2)_5NMe_2)_2$	444
		668 nm (lg ε 5.5)	L = *trans*-$(OSi(Me)_2(CH_2)_6NMe_2)_2$	444
		669 nm (lg ε 5.4)	L = *trans*-$(OSi(Me)_2(CH_2)_3NEt_2)_2$	444
		669 nm (lg ε 5.5)	L = *trans*-$(OSi(Me)_2(CH_2)_3NPr_2)_2$	444
		669 nm (lg ε 5.5)	L = *trans*-$(OSi(Me)_2(CH_2)_3NBu_2)_2$	444
		669 nm (lg ε 5.5)	L = *trans*-$(OSi(Me)_2(CH_2)_3N(C_5H_{11})_2)_2$	444
		669 nm (lg ε 5.4)	L = *trans*-$(OSi(Me)_2(CH_2)_3N(C_6H_{13})_2)_2$	444
		668 nm (lg ε 5.4)	L = *trans*-$(OSi(Me)_2(CH_2)_3NH_2)_2$	444
	DCM	674 nm (ε 271,000)	L = *trans*-$(OCH_2C_3F_7)_2$	445
		672 nm (ε 258,000)	L = *trans*-$(O(CH_2)_2C_4F_9)_2$	445
		672 nm (ε 242,000)	L = *trans*-$(O(CH_2)_2C_6F_{13})_2$	445
		672 nm (ε 270,000)	L = *trans*-$(O(CH_2)_2C_{10}F_{21})_2$	445
		672 nm (ε 269,000)	L = *trans*-$(OCH_2CH_2(CF_2)_6CF(CF_3)_2)_2$	445
		671 nm (ε 238,000)	L = *trans*-$(OC_6H_{13})_2$	445
		672 nm (ε 259,000)	L = *trans*-$(OC_{12}H_{25})_2$	445
		691 nm (ε 293,000)	L = *trans*-$(OCOC_3F_7)_2$	445

(*Continued*)

Table 1. (*Continued*)

M	Solvent	Transition Energy (Intensity)	Remark	Ref.
	toluene	669 nm (lg ε 5.6)	L = *trans*-$(OSi(C_6H_{13})_3)_2$	446
	DMF	673 nm (lg ε 5.76), 644 (4.92), 606 (4.99), 356 (5.28)	L = *trans*- 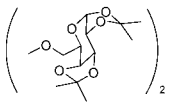	447
		672 nm (lg ε 5.40), 641 (4.53), 604 (4.61), 356 (4.90)	L = 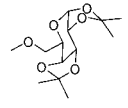 L' = OC_2H_5	447
		671 nm (lg ε 5.48), 641 (4.63), 604 (4.70), 354 (5.00)	L = 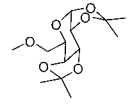 L' = OC_5H_{11}	447
		671 nm (lg ε 5.55), 641 (4.69), 604 (4.75), 352 (5.13)	L = 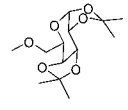 L' = OC_8H_{17}	447
	$CHCl_3$	684 nm (r.i 1.00), 652 (0.12), 614 (0.14), 360 (0.27)	L = *trans*-$(OCOC_{11}H_{23})_2$	437
		675 nm, 645, 607, 580, 563, 430, 354, 330, 259	L = *trans*- 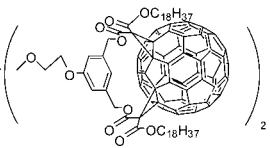	448
		676 nm, 647, 610, 580, 563, 381, 358, 277, 259	L = *trans*- 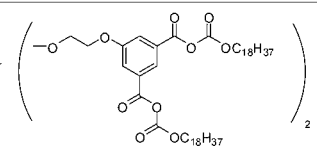	448

(*Continued*)

Table 1. (*Continued*)

M	Solvent	Transition Energy (Intensity)	Remark	Ref.
	toluene	678 nm (ε 250,000)	L = *trans*- 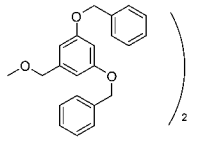	449
		680 nm (ε 250,000)	L = *trans*- 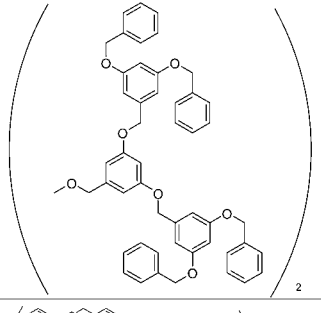	449
		680 nm (ε 250,000)	L = *trans*- 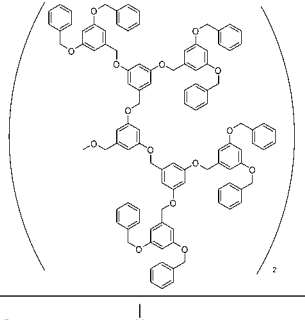	449
	DMF	668 nm (ε 230,000)	L = 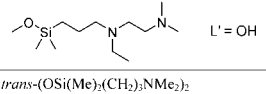 L' = OH	450
		668 nm (ε 220,000)	L = *trans*-$(OSi(Me)_2(CH_2)_3NMe_2)_2$	450

(*Continued*)

Table 1. (*Continued*)

M	Solvent	Transition Energy (Intensity)	Remark	Ref.
		668 nm (ε 230,000)	L = *trans*- 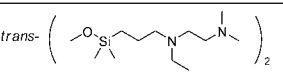	450
	toluene	668.5 nm	L = *trans*-$(OSi(C_6H_{13})_3)_2$	359
	$CHCl_3$	677 nm (10^{-4} ε 21.1084), 649 (2.9795), 610 (3.3731), 356 (6.9402), 288 (2.1438)	L = *trans*-$(OCH_2CH_2N(CH_2CH_2OH)_2)_2$	451
		674 nm (10^{-4} ε 17.9275), 645 (2.3412), 607 (2.7461), 353 (5.3799), 280 (1.7930)	L = *trans*-$(OCH_2CH_2OCH_2CH_2OCH_2CH_2OH)_2$	451
		677 nm (10^{-4} ε 12.8583), 638 (4.5367), 610 (2.7112), 355 (5.4310), 289 (2.2720)	L = *trans*-$(OCH_2CH_2N(CH_2CH_2OH)CO(4\text{-}py))_2$	451
		688 nm (Abs. 1.200), 656 (0.147), 618 (0.175), 348 (0.290), 334 (0.290)	L = *trans*- 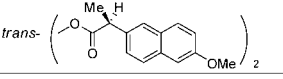	452
	EtOH	672 nm, 638, 604, 355	L = *trans*-$(O(CH_2CH_2O)_{16}Me)_2$	453
	DCM	678 nm, 650, 610, 352	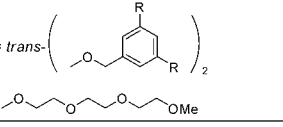	454, 455
	EtOH	677 nm		454, 455
	DCM	679 nm, 650, 610, 352	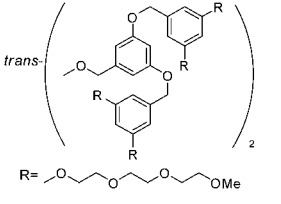	454, 455
	EtOH	679 nm		454, 455
	DCM	680 nm, 650, 610, 352		454, 455

(*Continued*)

Table 1. (*Continued*)

M	Solvent	Transition Energy (Intensity)	Remark	Ref.
	EtOH	680 nm	L = *trans*- 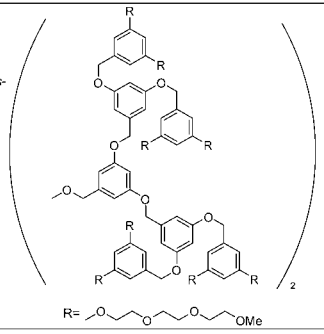	454, 455
	AcOEt	666 nm ($10^5\,\varepsilon$ 2)	L = *trans*-$(Osi(Me)_2C(Me)_2CHMe_2)_2$	456
P(IV)L	py	669 nm (r.i. 1.00), 640 (0.14), 602 (0.16), 353 (0.32)	$[Pc]^+OH^-$, L = *trans*-$(OH)_2$	384
2K	py	694 nm, 659		409
Ti(II)	$CHCl_3$	690 nm (ε 157,500), 626 (24,800), 356 (52,500)		117
	1-ClNp	698 nm (ε 138,000), 626 (26,100), 356 (46,600)		117
	EtOH	664 nm (ε 74,300), 600 (10,900), 340 (24,300)		117
Ti(IV)O	1-ClNp	699.0 nm, 629.0	293 K	118
		698.5 nm, 629.0	303 K	118
		698.5 nm, 628.5	313 K	118
		698.5 nm, 628.5	323 K	118
		698.0 nm, 628.0	333 K	118
Ti(IV)L	py	696.5 nm, 627.0	L = 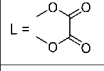	120
	$CHCl_3$	693.5 nm, 665.0, 627.0, 348.0	L = 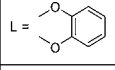	120
		693.5 nm, 665.0, 628.0, 347.0	L = 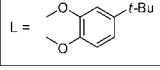	120

(*Continued*)

Table 1. (*Continued*)

M	Solvent	Transition Energy (Intensity)	Remark	Ref.
		694.5 nm, 661.0, 629.5, 348.5	L = 	120
		695.0 nm, 661.0, 630.0, 348.5	L = 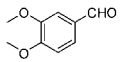	120
		696.0 nm, 660.0, 631.5	L = 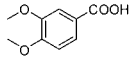	120
		695.0 nm, 660.0, 630.0, 352.0	L = 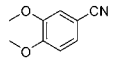	120
		696.0 nm, 661.0, 628.5, 348.5	L = 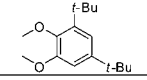	120
		696.0 nm, 663.0, 628.5, 348.5	L = 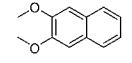	120
		696.0 nm, 656.0, 628.5, 348.5	L = 	120
V(IV)O	1-ClNp	704 nm, 632, 350		273
		719 nm, 695, 668, 633, 603.5, 581		57
	$CHCl_3$	694 nm		457
	DMF	696 nm		457
	py	688 nm		457
	conc H_2SO_4	810 nm, 718, 450		273
Cr(II)	1-ClNp	694 nm, 660, 621, 598, 576		57
Cr(III)OH	PhCl	689 nm (lg ε 4.92), 621 (4.14), 502 (3.91), 347 (4.62)		144
	MeOH	676 nm (lg ε 5.17), 610 (4.48), 502 (4.05), 477 (3.99), 344 (4.60), 268 (4.48)	[Pc]2H_2O	144
		670 nm (lg ε 5.11), 605 (4.40), 505 (3.82), 475 (3.79), 340 (4.55)	[Pc]2MeOH	144
	DMF	681 nm		312
	H_2SO_4	815 nm		312
Cr(III)L	MeOH	677 nm, 611, 515, 345, 321, 308, 271	$[Pc]^-K^+$, L = *trans*-(OH),(CN)	144
		675 nm, 615, 518, 490, 380, 345, 322, 309, 258	$[Pc]^-K^+$, L = *trans*-$(CN)_2$	144

(*Continued*)

Table 1. (*Continued*)

M	Solvent	Transition Energy (Intensity)	Remark	Ref.
		682 nm, 617, 511, 349, 298, 270	$[Pc]^-K^+$, L = *trans*-$(SCN)_2$	144
	MeOH + trace of HCl	682 nm (lg ε 5.15), 615 (4.30), 507 (4.03), 495 (3.93), 355 (4.70), 347 (4.71), 282 (4.57)	$[Pc]^-H^+$, L = *trans*-Cl_2	144
	MeOH + 0.25% NaOH	669 nm (lg ε 5.25), 604 (4.47), 475 (3.56), 337 (4.71), 278 (4.59), 268 (4.63)	$[Pc]^{2-}2Na^+$, L = *trans*-(OH),(O)	144
	py	687 nm (lg ε 4.85), 632 (4.20), 560 (3.70), 525 (3.86), 500 (3.70), 345 (4.59)	L = *trans*-py_2	144
Mn(II)	*conc* H_2SO_4	837 nm, 425		458
	DMF	708.5 nm, 642.0, 494.5		459
Mn(II)O_2	DMA	705 nm (lg ε 4.63), 678sh, 634 (3.98), 495 (3.74), 417 (3.94), 355 (4.02), 295 (3.90)		460
Mn(III)OH	DMA	717 nm (lg ε 4.69), 646 (4.01), 503.5 (3.78), 359 (4.18)		460
Fe(I)	THF	800 nm, 665, 596, 515, 326	$[Pc]^-$	461
Fe(I)L	py + LiCl	803 nm, 661 nm, 596, 512, 324	L = py, $[Pc]^-$	461
Fe(II)	H_2SO_4	785 nm		461
		796 nm, 698		405
		796 nm, 698		462
	1-ClNp	6580 Å (lg ε 4.70), 6320 (4.26), 5970 (4.20)		415
		660 nm, 595		57
	py + ether	6490 Å (lg ε 5.01), 6230 (4.46), 5900 (4.43)		415
	DCB	6560 Å (lg ε 4.84), 5950 (3.95), 3300 (4.68)		40
	vapor phase	676 nm		420
	quinoline	660 nm, 632, 593		57
	py	654 nm, 410, 324		461
		655 nm (r.i. 1.8), 595 (0.4), 415 (0.3), 333 (1.0)		238
	conc H_2SO_4	780 nm, 450		458
	DMSO	653 nm (lg ε 4.86), 594 (4.38)	L = *trans*-$(DMSO)_2$	463
		662 nm (lg ε 5.08), 598 (4.49), 426 (4.30)	L = *trans*-$(imidazole)_2$	463
		655 nm (lg ε 5.09), 593 (4.50), 425 (4.30)	L = *trans*-$(py(4\text{-}NH_2))_2$	463
		655 nm (lg ε 5.07), 593 (4.49), 413 (4.32)	L = *trans*-py_2	463
		652 nm		464
	DMF	657.5 nm, 627.5, 598.0, 424.5		459
Fe(II)Me	PhCl	707 nm (lg ε 4.96), 675 (4.76), 639 (4.75), 540 (4.75), 479 (4.94)		465
Fe(II)Et	PhCl	702 nm (lg ε 4.90), 677 (4.71), 657 (4.70), 550 (4.74), 479 (4.87)		465
Fe(II)L	$CHCl_3$	658 nm, 598, 325	L = $(PhCN)_2$	199
		661 nm, 597, 392sh, 323	L = $(Me_4dib)_2$	199
	PhCl	699 nm (lg ε 4.82), 676 (4.64), 651 (4.63), 545 (4.64), 479 (4.81)	L = $CHMe_2$	465

(*Continued*)

Table 1. (*Continued*)

M	Solvent	Transition Energy (Intensity)	Remark	Ref.
	DCM	664 nm, 602, 426, 394, 310	L = *trans*-$(CN)_2$, $[Pc]^{2-}2Na^{+}$	202
		664 nm, 602, 453, 394, 310	L = *trans*-$(CN^{-})_2$	201
		651 nm, 591, 412, 328	L = *trans*-py_2	202
		655 nm, 593, 411, 332		201
		652 nm, 592, 413, 331	L = *trans*-$(py(4\text{-}Me))_2$	202
		652 nm, 592, 411, 331		201
		657 nm, 596, 423, 339	L = *trans*- 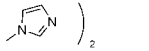	202
		657 nm, 596, 422, 339		201
		658 nm, 597, 423, 338	L = *trans*- 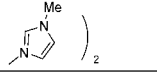	202
		658 nm, 597, 422, 338		201
		659 nm, 598, 425, 340	L = *trans*- 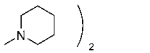	202
		663 nm, 636, 605, 424, 334		201
		661 nm, 601, 425, 332	L = *trans*-$(NH_3)_2$	202
		664 nm, 637, 604, 425, 335		201
		659 nm, 596, 363, 317, 288	L = *trans*-(NH_3), (CO)	202
	benzene	664 nm (r.i. 1.47), 637 (0.81), 605 (0.57), 427 (0.28), 334 (1)	L = *trans*-$(NH_2Pr)_2$	201
		663 nm (r.i. 1.64), 636 (0.7), 604 (0.64), 425 (0.28), 334 (1)	L = *trans*-$(NH_2(i\text{-}Pr))_2$	201
		664 nm (r.i. 1.58), 637 (0.71), 605 (0.6), 427 (0.35), 334 (1)	L = *trans*-$(NH_2Bu)_2$	201
		663 nm (r.i. 2.06), 636 (0.8), 604 (0.69), 425 (0.32), 334 (1)	L = *trans*-$(NH_2(s\text{-}Bu))_2$	201
		661 nm (r.i. 2.23), 634 (0.68), 600 (0.57), 422 (0.32), 331 (1)	L = *trans*-$(NH_2(t\text{-}Bu))_2$	201
		655 nm (r.i. 1.82), 628 (0.6), 595 (0.52), 416 (0.29), 330 (1)	L = *trans*-$(NH_2CH_2CF_3)_2$	201
		664 nm (r.i. 1.50), 637 (0.57), 604 (0.49), 426 (0.24), 330 (1)	L = *trans*- 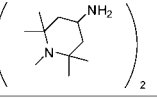	201
		664 nm (r.i. 1.91), 640 (0.64), 606 (0.55), 434 (0.36), 334 (1)	L = *trans*- 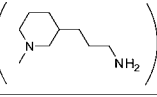	201

(*Continued*)

Table 1. (*Continued*)

M	Solvent	Transition Energy (Intensity)	Remark	Ref.
		665 nm (r.i. 1.44), 640 (0.66), 607 (0.58), 430 (0.29), 334 (1)	L = *trans*- 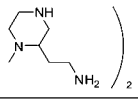	201
		665 nm (r.i. 1.72), 639 (0.75), 607 (0.69), 433 (0.32), 334 (1)	L = *trans*-$(NH(CH_2)_3NH_2)_2$	201
		666 nm (r.i. 1.84), 640 (0.81), 608 (0.71), 433 (0.35), 334 (1)	L = *trans*-$(NH(CH_2)_4NH_2)_2$	201
		665 nm (r.i. 2.51), 636 (0.78), 604 (0.66), 429 (0.37), 337 (1)	L = *trans*-$(NH(CH_2)_5NH_2)_2$	201
		664 nm (r.i. 2.89), 636 (0.82), 604 (0.72), 428 (0.39), 335 (1)	L = *trans*-$(NH(CH_2)_6NH_2)_2$	201
		664 nm (r.i. 3.41), 636 (1.0), 603 (0.87), 428 (0.43), 334 (1)	L = *trans*-$(NH(CH_2)_7NH_2)_2$	201
	benzene	660 nm (r.i. 2.05), 633 (0.82), 601 (0.66), 423 (0.28), 332 (1)	L = *trans*- 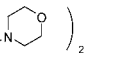	201
	benzene	655 nm (r.i. 1.48), 594 (0.38), 408 (0.27), 335 (1)	L = *trans*- 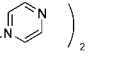	201
	benzene	654 nm (r.i. 1.71), 595 (0.45), 412 (0.23), 327 (1)	L = *trans*- 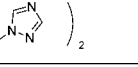	201
	$CHCl_3$	654 nm, 630, 595, 410	L = *trans*-$(py(4\text{-}CHO))_2$	201
		658 nm, 598, 387sh, 326	L = *trans*-$(CN(t\text{-}Bu))_2$	201
	DCM	659 nm, 596, 369, 317	L = *trans*-(NH_3), (CO)	201
	py	6540 Å (lg ε 5.03), 5930 (4.47), 4140 (4.29), 3295 (4.88)	L = *trans*-py_2	40
	$CHCl_3$	665 nm, 605, 394sh, 312	L = *trans*- 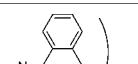	466
		792 nm, 669, 480sh, 403	L = *trans*- 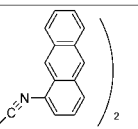	466
		665 nm, 601, 397sh, 323	L = *trans*-$(CNC_{12}H_{25})_2$	466
		658 nm, 598, 397sh, 326	L = *trans*-$(NCt\text{-}Bu)_2$	207

(*Continued*)

Table 1. (*Continued*)

M	Solvent	Transition Energy (Intensity)	Remark	Ref.
		658 nm, 598, 396sh, 325	L = *trans*- 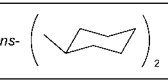	207
		658 nm, 595, 325	L = *trans*-(CH_2Ph)	207
	PhCl	655 nm, 630sh, 595, 410, 331	L = *trans*- 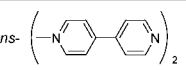	207
	py	644 nm, 595, 415, 333	L = *trans*- 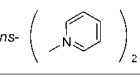	207
	$CHCl_3$	656 nm, 594, 410, 328	L = $(OCO(2\text{-py}))_2$	229
		658 nm	L = *trans*-$(CN(t\text{-Bu}))_2$	467
	DMSO	653 nm, 414	L = *trans*-py_2	464
		653 nm, 414	L = *trans*-$(py(3\text{-Me}))_2$	464
		654 nm, 413	L = *trans*-$(py(4\text{-Me}))_2$	464
		654 nm, 416	L = *trans*-$(py(3\text{-}CH_2OH))_2$	464
		654 nm, 416	L = *trans*-$(py(4\text{-}CH_2OH))_2$	464
		654 nm, 415	L = *trans*-$(py(3\text{-OH}))_2$	464
		656 nm, 421	L = *trans*-$(py(4\text{-OH}))_2$	464
		651 nm, 548, 409	L = *trans*-$(py(3\text{-Cl}))_2$	464
		681 nm, 550, 394	L = *trans*-$(py(4\text{-Cl}))_2$	464
		652 nm, 405	L = *trans*-$(py(3\text{-CHO}))_2$	464
		652 nm, 520, 407	L = *trans*-$(py(4\text{-CHO}))_2$	464
		650 nm, 460, 406	L = *trans*-$(py(3\text{-CN}))_2$	464
		651 nm, 502, 406	L = *trans*-$(py(4\text{-CN}))_2$	464
	$CHCl_3$	663 nm (10^{-4} ε 11.53), 599 (3.09), 320 (6.90)	L = *trans*-(ONPh), (NH_2Bu)	468
		663 nm (10^{-4} ε 11.47), 602 (3.29), 322 (7.37)	L = *trans*-(ONPh(4-Me)), (NH_2Bu)	468
		663 nm (10^{-4} ε 11.45), 600 (3.49), 322 (8.07)	L = *trans*-$(ONPh(4\text{-}CHMe_2))$, (NH_2Bu)	468
		660 nm (10^{-4} ε 10.25), 598 (2.90), 320 (6.36)	L = *trans*- 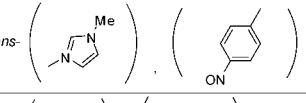	468
		655 nm (10^{-4} ε 10.86), 593 (1.12), 330 (6.92)	L = *trans*- 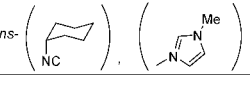	468

(*Continued*)

Table 1. (*Continued*)

M	Solvent	Transition Energy (Intensity)	Remark	Ref.
		658 nm (10^{-4} ε 8.19), 600 (2.81), 420 (0.90), 322 (5.79)	L = *trans*-($P(OPh)_3$), (NH_2Bu)	468
		661 nm (10^{-4} ε 12.89), 598 (3.10), 424 (1.72), 342 (6.17)	L = *trans*- 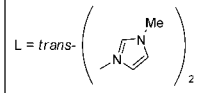	468
		664 nm (10^{-4} ε 9.81), 604 (2.78), 424 (1.63), 332 (5.76)	L = *trans*-(NH_2CH_2Ph)$_2$	468
		654 nm (10^{-4} ε 10.07), 595 (2.63), 413 (2.10), 332 (5.83)	L = *trans*-($P(OEt)_3$)$_2$	468
		662 nm (10^{-4} ε 12.05), 599 (3.62), 395 (1.69), 322 (7.52)	L = *trans*- 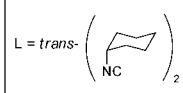	468
		662 nm (10^{-4} ε 12.10), 599 (3.55), 393 (1.66), 321 (7.57)	L = *trans*-($CNBu$)$_2$	468
		657 nm (10^{-4} ε 10.64), 604 (3.23), 412 (1.98), 320 (7.05)	L = *trans*- 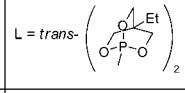	468
	py	654 nm	L = CNC_6H_{11}	205
Fe(III)Cl	DMSO	653 nm (lg ε 4.24), 597sh (3.89), 328 (4.28), 212 (3.95)		469
	DMF	657 nm (lg ε 4.04), 601sh (3.72), 422 (3.70), 323 (4.18), 211 (3.96)		469
	py	658 nm (lg ε 4.77), 594sh (4.15), 414 (4.15), 333 (4.78), 214 (4.14)		469
	1-ClNp	659 nm, 595		57
	quinoline	660 nm, 628, 591		57
Co(I)	THF	694 nm, 633, 467, 312	$[Pc]^-$	461
Co(II)	H_2SO_4	786 nm		461
		790 nm		312
		784 nm, 697, 425		462
		790 nm		470
		784 nm, 697, 425		405
	conc H_2SO_4	784 nm, 424		458
	py	659 nm, 333		424
		655 nm, 593		57
		658 nm (r.i. 1.8), 597 (0.3), 332 (1.0)		238
		6575 Å (lg ε 5.07), 5965 (4.51), 3300 (4.86)		40
	1-ClNp	6720 Å (lg ε 5.19), 6065 (4.53), 3480 (4.65)		40
		672 nm (lg ε 5.19), 606 (4.53), 348 (4.65)		416

(*Continued*)

Table 1. (*Continued*)

M	Solvent	Transition Energy (Intensity)	Remark	Ref.
		672 nm (ε 155,000)		413
		672 nm, 642, 604, 580, 561		57
	DMF	660 nm		312
		660 nm		470
		658.0 nm, 598.5		459
Co(III)Cl	py	656 nm (r.i. 1.9), 595 (0.4), 334 (1.0)		238
Co(III)L	py	675 nm, 346	L = *trans*-$(CN)_2$, $[Pc^-]K^+$	424
Ni(II)	H_2SO_4	775 nm, 683		405
		775 nm, 683		462
		778 nm		312
	Vapor phase	651 nm		420
	1-ClNp	669 nm		414
		671 nm (10^{-4} ε 21.6), 643 (2.95), 603 (3.24)		114
		670 nm (lg ε 5.32), 643 (4.54), 604 (4.51), 350 (4.57), 327 (4.29)		416
		671 nm (10^{-3} ε 51.0), 643 (44.7), 351 (45.7)		417
		6710 Å (lg ε 5.10), 6430 (4.47), 6030 (4.51), 5800 (3.82), 5600 (3.75), 3510 (4.57)		40
		671 nm (lg ε 5.10), 643 (4.51), 351 (4.57)		412
		676 nm, 641, 602.5, 580, 558		57
	DCM	671 nm (10^{-3} ε 51.0), 643 (44.7), 351 (45.7)		408
	DMF	671.0 nm, 624.0, 592.0		459
		667 nm		312
Cu(II)	DCM	678 nm (10^{-3} ε 53.4), 648 (45.1), 611 (45.6), 350 (47.6)		408
	H_2SO_4	791 nm, 699, 440		405
	$CHCl_3$	666 nm(lg ε 5.02), 637(4.19), 602(4.22), 343(4.50)		471
	heptane	29,950 cm^{-1}, 31,400, 32,800, 34,200, 36,750, 38,200, 39,600, 41,700, 43,250		472
	H_2O	29,800 cm^{-1}, 31,250, 32,750, 36,750, 38,200, 39,500, 41,750, 43,350		472
	1-ClNp	6780 Å (lg ε 5.1), 6480 (4.36), 6110 (4.39), 5880 (3.57), 5640 (3.37), 4560 (2.38), 4270 (3.0), 4140 (3.69)		270
		671 nm (lg ε 5.10), 643 (4.51), 351 (4.57)		412
		680 nm, 614, 346		273
		678 nm (lg ε 5.34), 648 (4.51), 611 (4.56)		473
		6830 Å (lg ε 5.36), 6480 (4.70), 6120 (4.77), 5820 (4.11), 5640 (4.00)		415
		6780 Å (lg ε 5.34), 6480 (4.51), 6110 (4.56), 5880 (4.06), 5670 (3.91), 5260 (3.57), 5100 (3.56), 3500 (4.76)		40

(*Continued*)

Table 1. (*Continued*)

M	Solvent	Transition Energy (Intensity)	Remark	Ref.
		678 nm (10^{-4} ε 21.9), 648 (3.24), 611 (3.63)		114
		680 nm, 648, 609, 585, 565		57
		679 nm (lg ε 5.34), 648 (4.51), 611 (4.56), 350 (4.76)		416
		678 nm (10^{-3} ε 53.4), 648 (45.1), 611 (45.6), 350 (47.6)		417
		678 nm (ε 219,000)		413
	py	672 nm		411
	1,2,4-trichlorobenzene	677 nm (lg ε 5.16), 648 (4.40), 610 (4.47), 345 (4.68)	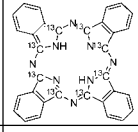	474
	DMF	668 nm		312
	conc H_2SO_4	794 nm, 700, 440		273
	H_2SO_4	794 nm		312
		791 nm		461
		791 nm, 699, 440		462
		790.0 nm, 700.5, 441.0		459
		792 nm, 702, 668, 639, 440		274
Zn(II)	$CHCl_3$	670 nm		475
		673 nm		286
	DCM	671 nm		286
		671 nm (10^{-4} ε 15.5), 645 (2.54), 606 (2.66)		476
	py	674 nm, 348		477
		674 nm (10^{-5} ε 1.35), 609 (0.20), 345 (0.33)		284
		672 nm, 644, 608, 344		478
		672 nm (ε 282,000), 607 (38,900), 347 (64,500)		117
		672 nm		411
		673 nm		475
		672 nm (lg ε 5.45), 646 (4.56), 607 (4.59), 348 (4.81)		40, 412
	H_2SO_4	786 nm, 697, 418		405
		788 nm		312
		786 nm, 697, 418		462
		783 nm		461

(*Continued*)

Table 1. (*Continued*)

M	Solvent	Transition Energy (Intensity)	Remark	Ref.
	DMSO	672 nm (lg ε 5.38)		286
		673 (10^{-5} ε 1.5332)		124
		674 nm, 646, 608, 348		478
		672 nm (lg ε 5.14)		479
		672 nm		438
		672 nm (lg ε 5.38)		480
		670 nm		475
		672 nm		481
	EtOH	666 nm, 600, 342		482
	DMF	670 nm, 640, 602, 340		478
		668 nm (ε 103,500), 603 (16,500), 344 (28,500)		117
		669 nm (10^{-4} ε 14.6), 637 (2.28), 603 (2.39)		476
		680 nm (lg ε 4.80)		483
		670 nm		312
		668 nm		475
		670 nm (lg ε 5.37)		286
	THF	948 nm, 636, 562, 323	$[Pc]^-$	461
		666 nm		484
		666 nm		485
		670.5 nm		48
		666 nm		475
		668 nm (lg ε 5.48)		286
	PVA in DMSO	673 nm (10^{-4} ε 6.81)		486
	Vapor phase	661 nm		420
	1-ClNp	681 nm (ε 224.000)		413
		680 nm, 649, 616, 587.5, 565		57
	PhCN	673 nm		475
	1,4-dioxane	665 nm		475
	n-butylamine	668 nm		475
	triethylamine	664 nm		475
Zn(III)L	$CHCl_3$	671 nm (lg ε 5.37), 606 (4.57), 341 (4.80), 284 (4.35)	L = 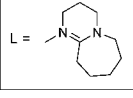	487

(*Continued*)

Table 1. (*Continued*)

M	Solvent	Transition Energy (Intensity)	Remark	Ref.
Ga(III)Cl	DMSO	680 nm		321
	DMF	678 nm		321
	THF	677 nm		321
	DMSO	680 nm (lg ε 5.15)		322
Ga(III)OH	DMF	684 nm		312
Ge(II)	$CHCl_3$	6600 Å, 6050, 4450, 4150, 3260, 2930		361
	py	6550 Å (lg ε 4.83), 6020 (4.21), 4450 (5.07), 4150 (5.63), 3300		361
Ge(IV)L	py	676 nm, 645, 607, 415, 358, 315	L = *trans*-$(OH)_2$	358
	DMSO	676 nm	L = *trans*-$(OH)_2$	438
	toluene	673.7 nm	L = *trans*-$(OSi(C_6H_{13})_3)_2$	359
Zr(IV)L	DMSO	688 (10^{-5} ε 1.1646)	L = *cis*-Cl_2	124, 125
		692 nm (lg ε 5.14), 621 (4.41), 345 (4.74)	L = *cis*-Cl_2	488
	toluene	688 (10^{-5} ε 0.8276)	L = *cis*-Cl_2	124
	toluene	688 (10^{-5} ε 0.8276)	L = *cis*- 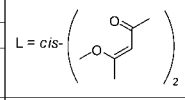	125
	DMSO	684 (10^{-5} ε 1.3140)		125
	THF	684 (10^{-5} ε 1.6225)		125
	toluene	688 (10^{-5} ε 1.9971)	L = *cis*- 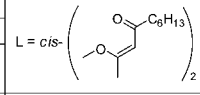	125
	DMSO	686 (10^{-5} ε 1.489)		125
	THF	682 (10^{-5} ε 2.1950)		125
	toluene	682 (10^{-5} ε 7.246)	L = *cis*- 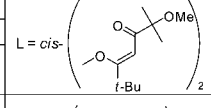	125
	DMSO	685 (10^{-5} ε 1.610)		125
	THF	683 (10^{-5} ε 2.356)		125
	toluene	686 (10^{-5} ε 2.871)	L = *cis*- 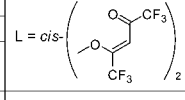	125
	DMSO	682 (10^{-5} ε 0.8995)		125
	THF	680 (10^{-5} ε 1.1300)		125
	toluene	686 (10^{-5} ε 4.942)	L = *cis*- 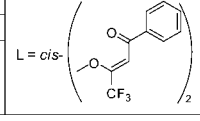	125
	DMSO	686 (10^{-5} ε 1.2360)		125
	THF	686 (10^{-5} ε 1.7725)		125

(*Continued*)

Table 1. (*Continued*)

M	Solvent	Transition Energy (Intensity)	Remark	Ref.
	toluene	686 (10^{-5} ε 3.083)	L = *cis*- 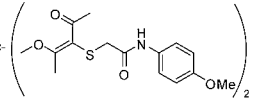	125
	DMSO	692 (10^{-5} ε 1.1005)		125
	THF	688 (10^{-5} ε 1.7750)		125
	toluene	691 (10^{-5} ε 4.323)	L = *cis*- 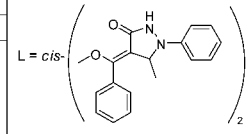	125
	DMSO	694 (10^{-5} ε 1.4995)		125
	THF	690 (10^{-5} ε 2.3065)		125
	DMSO	688 (10^{-5} ε 1.9971)	L = *cis*- 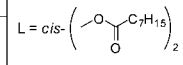	124
	toluene	684 (10^{-5} ε 1.5430)		124
	DMSO	684 (10^{-5} ε 2.4915)	L = *cis*- 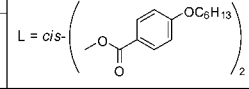	124
	toluene	684 (10^{-5} ε 1.9861)		124
	DMSO	686 (10^{-5} ε 2.0252)	L = *cis*- 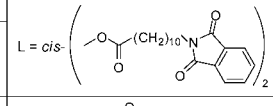	124
	toluene	684 (10^{-5} ε 7151)		124
	DMSO	688 nm (lg ε 5.21), 618 (4.52), 340 (4.94)	L = 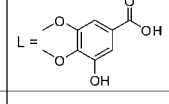	488
		686 nm (lg ε 5.18), 618 (4.44), 342 (4.72)	L = 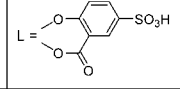	488

(*Continued*)

Table 1. (*Continued*)

M	Solvent	Transition Energy (Intensity)	Remark	Ref.
		688 nm (lg ε 5.28), 617 (4.54), 343 (4.88)	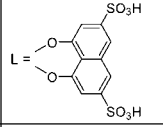	488
	H_2O	690 nm, 337	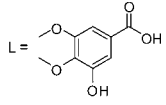	489
	MeOH	682 nm, 340		489
	EtOH	682 nm, 339		489
	DMSO	685 nm, 342		489
	DMF	681 nm, 341		489
	acetone	683 nm, 344		489
	DCM	688 nm, 341		489
	$CHCl_3$	689 nm, 341		489
	H_2O	696 nm, 343	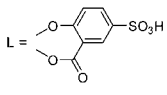	489
	MeOH	684 nm, 350		489
	EtOH	685 nm, 349		489
	DMSO	688 nm, 348		489
	DMF	684 nm, 347		489
	acetone	693 nm, 348		489
	DCM	686 nm, 348		489
	$CHCl_3$	693 nm, 349		489
	H_2O	692 nm, 338	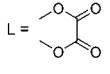	489
	MeOH	677 nm, 341		489
	EtOH	678 nm, 342		489
	DMSO	681 nm, 343		489
	DMF	676 nm, 340		489
	acetone	678 nm, 341		489
	DCM	683 nm, 342		489
	$CHCl_3$	683 nm, 342		489
	H_2O	700 nm, 343	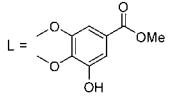	489
	MeOH	684 nm, 348		489
	EtOH	684 nm, 349		489
	DMSO	688 nm, 349		489
	DMF	682 nm, 446		489

(*Continued*)

Table 1. (*Continued*)

M	Solvent	Transition Energy (Intensity)	Remark		Ref.
	acetone	684 nm, 346			489
	DCM	690 nm, 348			489
	$CHCl_3$	692 nm, 349			489
	DMF	680 nm, 613sh, 343	L = $(OH)_2$, Cl		490
	DMSO	685 nm, 615sh, 345	L = $(OH)_2$, Cl		490
	DCM	680 nm, 635sh, 615sh, 345	L = $(OH)_2$, Cl		490
	DCB	687 nm, 640sh, 620sh, 340	L = $(OH)_2$, Cl		490
Zr(III)	$CDCl_3$	688.1 nm (lg ε 5.29), 684.9 (5.29), 617.2 (4.58), 344.6 (4.78)	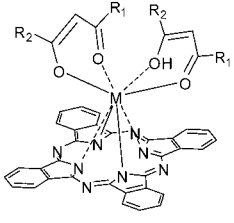	R_1, R_2 = Me	126
		685.5 nm (lg ε 5.16), 616.1 (4.42), 340.7 (4.75)		R_1 = Me, R_2 = Pr	126
		688.9 nm (lg ε 5.27), 681.6sh (5.25), 616.1 (4.52), 340.7 (4.85)		R_1 = Me, R_2 = C_6H_{13}	126
		687.9 nm (lg ε 5.46), 686.3sh (5.45), 618.4 (4.70), 335.4 (5.10)		R_1 = Me, R_2 = C_7H_{15}	126
		691.7sh nm (lg ε 5.07), 685.6 (5.11), 617.1 (4.37), 346.1sh (4.71)		R_1 = CF_3, R_2 = Me	126
		689.4 nm (lg ε 5.05), 682.2 (5.00), 618.8 (4.29), 336.1(4.63)		R_1, R_2 = CF_3	126
		689.4 nm (lg ε 5.16), 680.4sh (5.15), 616.6 (4.42), 346.5sh (4.74)		R_1 = CF_3, R_2 = $H(Et)_2$	126
		686.7 nm (lg ε 5.21), 682.0 (5.20) sh, 617.2 (4.45), 340.9 (4.90)		R_1 = CF_3, R_2 = CMe_3	126
		687.0 nm (lg ε 5.36), 685.8 (5.35), 618.4 (4.60), 335.5 (4.94)		R_1 = CF_3, R_2 = $C(OMe)(Me)_2$	126
		691.9 nm (lg ε 5.18), 684.1sh (5.16), 618.6 (4.45), 345.5sh (4.84)		R_1 = CF_3, R_2 = Ph	126
		686.4br nm (lg ε 5.13), 618.2 (4.30), 342.8 (4.58)		R_1 = Me, R_2 = Ph	126
		688.9 nm (lg ε 5.21), 682.6sh (5.19), 616.6 (4.43), 339.9 (4.73)		R_1 = *t*-Bu, R_2 = Pr	126
		685.0 nm (lg ε 5.31), 654.7sh (5.28), 617.1 (4.52), 341.7 (4.80)		R_1 = *t*-Bu, R_2 = $C(OMe)(Me)_2$	126
Zr(IV)L	$CDCl_3$	686.0 nm (lg ε 5.29), 618.2 (4.58), 342.5 (4.78)	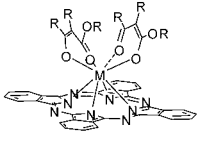	R = 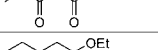	491
		687.1 nm — 685.6 (lg ε 5.16), 618.9 (4.42), 341.6 (4.75)		R = 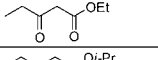	491
		686.9 nm (lg ε 5.27), 618.1 (4.52), 341.7 (4.85)		R = 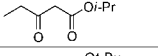	491
		686.3 nm (lg ε 5.45), 618.4 (4.70), 341.4 (5.10)		R = 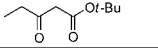	491
		686.6 nm (lg ε 5.07), 618.1 (4.37), 342.1 (4.71)		R = 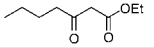	491
		686.4 nm (lg ε 5.00), 618.2 (4.29), 341.8 (4.63)		R = 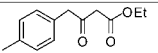	491

(*Continued*)

Table 1. (*Continued*)

M	Solvent	Transition Energy (Intensity)	Remark	Ref.
		686.3 nm (lg ε 5.21), 618.4 (4.45), 342.0 (4.72)	R = 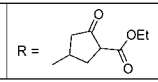	491
	DMSO	680.70 nm (10^{-4} ε 29.31), 613.90 (5.07), 345.07 (9.98)	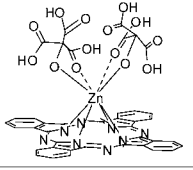	492
	H_2O	681.50 nm (10^{-4} ε 5.79), 610.50 (7.84), 344.45 (5.91)		492
	RPMI	682.50 nm (10^{-4} ε 5.20), 643.90 (7.02), 344.45 (5.43)		492
	RPMI with FCS	686.30 nm (10^{-4} ε 18.43), 618.40 (3.51), 350.07 (7.13)		492
	Tris	682.25 nm (10^{-4} ε 5.16), 627.35 (6.58), 334.45 (5.12)		492
Mo(IV)O	DMSO	670 nm, 640, 605, 385, 330		154
	1,2,4-trichlorobenzene	703 nm, 643		152
	py	710 nm, 676, 652		152
	DCM	775 nm	Generated by UV photolysis	154
		782 nm, 695, 380	Br_2 oxidation	154
		767 nm, 380	$FeCl_3$ oxidation	154
		760 nm	bulk electrolysis	154
	DCB	782 nm, 367	Generated by UV photolysis	154
		781 nm, 695, 375	Br_2 oxidation	154
		770 nm, 730	$FeCl_3$ oxidation	154
		778 nm, 730, 370	bulk electrolysis	154
Mo(V)N	1-ClNp	777.0 nm, 703.5, 664.5, 639.5, 602.5, 396.5		156
	KBr	791.5 nm, 732.0, 649.5, 609.5, 509.5, 365.0		156
Mo(V)O	DMSO	690 nm, 660, 625, 340	bulk electrolysis	154
	DCM	695 nm, 655, 633		154
	DCB	700 nm, 660, 633, 345		154
Ru(II)	H_2SO_4	764 nm, 680		462
		764 nm, 680		405
	acetone + imidazole	622.0 nm, 571.0		459
Ru(III)Cl	DMF	650 nm (lg ε 5.05), 587 (4.30), 346 (4.42)		493
	DCB	719 nm (lg ε 4.27), 569 (4.34)	$[Pc]^+$	493
		657 nm (lg ε 5.21), 594 (4.43), 349 (4.48)		493
Ru(II)L	$CHCl_3$	640 nm (ε 60,000), 573sh (27,600), 460sh (68,600), 444 (76,700), 368 (127,100), 325 (125,400)		494

(*Continued*)

Table 1. (*Continued*)

M	Solvent	Transition Energy (Intensity)	Remark	Ref.
	CS_2	633 nm (ε 67,200), 576 (25,500), 460 (41,600), 406sh (100,000)	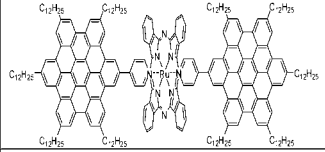	494
	DCM	622 nm (10^{-4} ε 6.7), 560 (2.8), 375 (2.8)	L = *trans*-(py(4-Me))$_2$	495
		640 nm (10^{-4} ε 15.2), 618 (4.5), 580 (4.1), 342 (2.9)	L = *trans*-(CO), (py(4-Me))	495
		622 nm (10^{-4} ε 7.4), 567 (2.9), 375 (2.6)	L = *trans*-py$_2$	495
		637 nm (10^{-4} ε 16.5), 614 (4.5), 578 (3.7), 342 (2.8)	L = *trans*-(CO), py	495
		621 nm (10^{-4} ε 6.5), 567 (2.8), 375 (2.7)	L = *trans*-(py(4-*t*-Bu))$_2$	495
		640 nm (10^{-4} ε 17.0), 615 (3.9), 579 (3.5), 345 (2.8)	L = *trans*-(CO), (py(4-*t*-Bu))	495
		640 nm (lg ε 4.8), 582sh (4.3), 402sh (3.9), 315 (4.8)	L = *trans*-(PH_2Ph)$_2$	496
		640 nm (lg ε 4.8), 580sh (4.3), 410sh (4.0), 291 (4.8)	L = *trans*-($PHPh_2$)$_2$	496
		637 nm (lg ε 4.8), 578sh (4.3), 403sh (3.9), 316 (4.8)	L = *trans*- 	496
		638 nm (lg ε 4.4), 579sh (3.8), 403sh (3.4), 316 (4.4)	L = *trans*-(PH_2*t*-Bu)$_2$	496
		640 nm (lg ε 4.3), 581sh (3.9), 438sh (3.3), 315 (4.4)	L = *trans*-($P(CH_2CH_2CN)_2Ph$)$_2$	496
		639 nm (lg ε 4.2), 581sh (3.8), 418sh (3.4), 297 (4.3)	L = *trans*-($P(CH_2CH_2CO_2Et)_2Ph$)$_2$	496
		641 nm (lg ε 4.5), 582sh (4.1), 418sh (3.5), 296 (4.6)	L = *trans*-($P(CH_2CH_2CN)Ph_2$)$_2$	496
		638 nm (lg ε 4.5), 578sh (4.1), 419sh (3.6), 296 (4.6)	L = *trans*-($P(CH_2CH_2COMe)Ph_2$)$_2$	496
		637 nm (lg ε 4.4), 582sh (4.2), 418sh (3.7), 298 (4.4)	L = *trans*-($P(CH_2CH_2PO(OEt)_2)Ph_2$)$_2$	496
		641 nm (lg ε 4.3), 580sh (3.8), 418sh (3.4), 295 (4.4)	L = *trans*-($P(CH_2CH_2SOOPh)Ph_2$)$_2$	496
		637 nm (lg ε 4.6), 582sh (4.3), 418sh (3.8), 302 (4.5)	L = *trans*-($P(CH_2CH(Me)COOMe)Ph_2$)$_2$	496
		643 nm (lg ε 4.7), 581sh (4.3), 416sh (3.7), 299 (4.7)	L = *trans*-($P(CH(COOMe)CH_2COOMe)Ph_2$)$_2$	496
		634 nm (lg ε 4.3), 580sh (3.8), 428sh (3.4), 306 (4.4)	L = *trans*-(PMe_2Ph)$_2$	496
		637 nm (lg ε 4.4), 579sh (4.0), 420sh (3.5), 296 (4.5)	L = *trans*-($PMePh_2$)$_2$	496
		639 nm (lg ε 4.5), 580sh (4.2), 421sh (3.7), 302 (4.5)	L = *trans*-($PBuPh_2$)$_2$	496
		640 nm (lg ε 4.4), 581 (3.9), 421 (3.4), 299 (4.5)	L = *trans*-($P(CH_2Ph)Ph_2$)$_2$	496
		639 nm (lg ε 4.3), 580sh (3.9), 420sh (3.5), 296 (4.5)	L = *trans*-($P(CH_2CHCH_2)Ph_2$)$_2$	496
		640 nm (lg ε 4.5), 581sh (4.0), 420sh (3.5), 296 (4.6)	L = *trans*-($P(CH_2CCMe)Ph_2$)$_2$	496
		642 nm (lg ε 4.5), 578sh (4.0), 415sh (3.7), 299 (4.6)	L = *trans*-($P(CHCCH_2)Ph_2$)$_2$	496
		643 nm ($\varepsilon \times 10^3$ 58), 584sh, 409sh, 303 (78)	L = *trans*-($AsPh_3$)$_2$	497

(*Continued*)

Table 1. (*Continued*)

M	Solvent	Transition Energy (Intensity)	Remark	Ref.
		626 nm, 565, 387, 316, 284	L = *trans*-py_2	219
		641 nm, 587, 442, 376sh, 314, 268	L = *trans*- 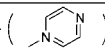	219
		641 nm, 582, 350sh, 312	L = *trans*-(CN*t*-Bu)	219
	PhCl	626 nm, 575sh, 446, 370, 314, 272	L = *trans*- 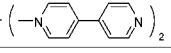	498
		641 nm, 587, 442, 376sh, 314, 268	L = *trans*- 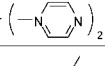	498
	$CHCl_3$	639 nm, 587, 436, 375sh, 313, 273	L = *trans*- 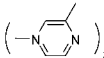	498
		636 nm, 587sh, 431, 313, 273	L = *trans*- 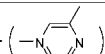	498
		638 nm, 587, 435, 314, 271	L = *trans*- 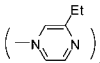	498
		637 nm, 588sh, 434, 315, 271	L = *trans*- 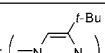	498
		641 nm, 585, 462, 315	L = *trans*- 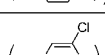	498
		634 nm, 585sh, 453, 375sh, 317	L = *trans*- 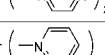	498
		627 nm, 573sh, 402sh, 369sh, 312	L = *trans*-py(3-F)	499
	PhCl	641 nm, 587, 376sh, 314	L = *trans*-$(pyz)_2$	216
	$CHCl_3$	626 nm, 573sh, 402, 363, 321	L = *trans*-$(py(3\text{-}Cl))_2$	500
		625 nm, 573, 377, 313	L = *trans*-py_2	501
		628 nm, 576sh, 371sh, 314	L = *trans*- 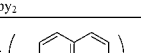	215
		628 nm, 576sh, 371sh, 314		216
	DCM	624 nm, 375, 316	L = *trans*-$(py(4\text{-}Me))_2$	502
	$CHCl_3$	632 nm, 586sh, 425, 377sh, 313	L = *trans*- 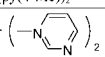	498

(*Continued*)

Table 1. (*Continued*)

M	Solvent	Transition Energy (Intensity)	Remark	Ref.
		625 nm, 573, 377, 313	L = py_2	229
		626 nm, 563.5, 408, 374, 314, 274.5	L = *trans*-(py(3-Cl))$_2$	503
Rh(III)Cl	1-ClNp	656 nm (lg ε 4.45), 633 (3.72), 593 (3.73), 573 (3.20), 555 (3.06), 420 (3.06)		246
	DMF	644 nm, 344		504
	acetone	679.5 nm, 648.0, 585.5		459
Rh(III)I	1-ClNp	656 nm (lg ε 4.33), 632 (3.59), 593 (3.58), 573 (2.96), 556 (2.80)		246
Rh(III)L	DMF	651 nm, 343	L = *trans*-$(CN)_2$, $[Pc]^-K^+$	504
		650 nm, 345	L = *trans*-(CN), $(NH_2C_4H_9)$	504
	$CHCl_3$	654 nm, 625, 590, 347	L = *trans*-Cl, py	505
	DCM	650 nm, 623, 585, 345	L = *trans*-Cl, py	505
	DMSO	653 nm, 625, 587, 348	L = *trans*-Cl, py	505
	DMF	647 nm, 620, 585	L = *trans*-Cl, py	505
	MeCN	648 nm, 617, 584, 340	L = *trans*-Cl, (DMSO)	505
	DMSO	653 nm, 625, 593, 345	L = *trans*-Cl, (DMSO)	505
	DMF	653 nm, 623, 588, 345	L = *trans*-Cl, (DMSO)	505
	acetone	646 nm, 620, 584, 400, 375	L = *trans*-$(CN)_2$, $[Pc]^-K^+$	505
	DMSO	655 nm, 625, 590, 405, 375, 345	L = *trans*-$(CN)_2$, $[Pc]^-K^+$	505
	DMF	650 nm, 623, 587, 403, 375, 342	L = *trans*-$(CN)_2$, $[Pc] K^+$	505
Pd(II)	H_2SO_4	797 nm, 692		405
	1-ClNp	660 nm		266
		660 nm (lg ε 4.77), 635 (3.98), 595 (4.04), 575 (3.48), 560 (3.37), 440 (3.48), 420 (3.69)		246
		6605 Å (lg ε 5.32), 6330 (4.51), 5955 (4.57), 5765 (4.07), 5570 (3.98), 3470 (4.69)		40
	H_2SO_4	797 nm, 692		462
		789.0 nm, 699.5, 440.0		459
Pd(III)Cl	1-ClNp	660 nm (lg ε 4.98), 635 (4.26), 595 (4.29), 575 (3.72), 557 (3.52), 440 (3.49), 420 (3.74)		246
Ag(II)	1-ClNp	675 nm, 642.5, 605, 580, 560		57
Cd(II)	DMSO	679 nm (lg ε 5.36)		286
	DMF	674 nm (lg ε 5.38)		286
In(III)Cl	DMF	681 nm		344
	THF	687 nm		344
	DMSO	700 nm, 689, 686		323
		686 nm (lg ε 4.46)		322
		686 nm		344
	$CHCl_3$	690.2 nm, 656.8sh, 622.5, 358.2, 337.9sh		332

(*Continued*)

Table 1. (*Continued*)

M	Solvent	Transition Energy (Intensity)	Remark	Ref.
Sn(IV)L	py	696 nm, 665, 626, 360, 340	L = *trans*-$(OH)_2$	358
	$CHCl_3$	692 nm (r.i 1.00), 666sh (0.18), 626 (0.21), 360 (0.40)	L = *trans*-$(OCOC_{11}H_{23})_2$	437
	1-ClNp	692 nm (r.i 2.34), 662 (0.34), 622 (0.40), 362 (0.71)	L = *trans*- 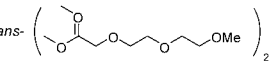	437
	toluene	680.0 nm	L = *trans*-$(OSi(C_6H_{13})_3)_2$	359
	DMSO	697 nm	L = *trans*-$(OH)_2$	438
Sb(III)	EtOH	729 nm (10^{-3} ε 171.7), 660 (42.6), 381 (59.8), 338 (81.4), 257 (66.1)	$[Pc]^+F^-$	394
Sb(V)L	EtOH	699 nm (10^{-3} ε 190.8), 628sh (32.6), 385 (37.7), 350 (56.5), 298 (64.0)	L = *trans*-$(OH)_2$, $[Pc]^+F^-$	394
	DCM	729 nm (lg ε 5.30), 370 (4.78), 258 (4.83)	L = $(Br)_2$, $[Pc]^+IBr_2^-$	396
		729 nm (lg ε 5.30), 370 (4.74)	L = $(Br)_2$, $[Pc]^+PF_6^-$	396
Hf(IV)L	DMSO	684 (10^{-5} ε 1.3831)	L = *cis*-Cl_2	124
		690 nm (lg ε 5.16), 618 (4.45), 348 (4.81)	L = *cis*-Cl_2	488
	toluene	688 (10^{-5} ε 1.1624)	L = *cis*-Cl_2	124
	DMSO	684 (10^{-5} ε 1.6773)	L = *cis*- 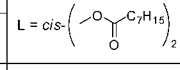	124
	toluene	684 (10^{-5} ε 1.4624)		124
	DMSO	684 (10^{-5} ε 1.7687)	L = *cis*- 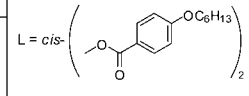	124
	toluene	684 (10^{-5} ε 1.5637)		124
	DMSO	684 (10^{-5} ε 1.7241)	L = *cis*- 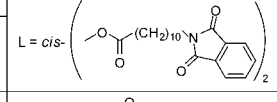	124
	toluene	684 (10^{-5} ε 1.5008)		124
	DMSO	688 nm (lg ε 5.19), 619 (4.48), 346 (4.84)	L = 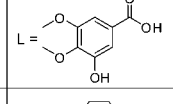	488
		688 nm (lg ε 5.19), 618 (4.38), 349 (4.70)	L = 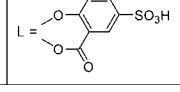	488

(*Continued*)

Table 1. (*Continued*)

M	Solvent	Transition Energy (Intensity)	Remark	Ref.
		690 nm (lg ε 5.28), 620 (4.56), 349 (4.89)	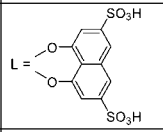	488
	H_2O	701 nm, 346	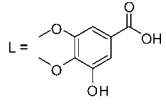	489
	MeOH	684 nm, 346		489
	EtOH	686 nm, 349		489
	DMSO	690 nm, 349		489
	DMF	688 nm, 347		489
	acetone	687 nm, 348		489
	DCM	696 nm, 349		489
	$CHCl_3$	693 nm, 348		489
	H_2O	689 nm, 341	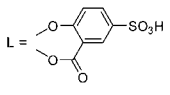	489
	MeOH	683 nm, 350		489
	EtOH	685 nm, 340		489
	DMSO	687 nm, 347		489
	DMF	681 nm, 346		489
	acetone	685 nm, 347		489
	DCM	689 nm, 347		489
	$CHCl_3$	691 nm, 346		489
	H_2O	682 nm, 334	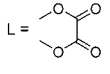	489
	MeOH	676 nm, 344		489
	EtOH	678 nm, 347		489
	DMSO	678 nm, 341		489
	DMF	675 nm, 341		489
	acetone	676 nm, 340		489
	DCM	683 nm, 342		489
	$CHCl_3$	686 nm, 343		489
	H_2O	699 nm, 343	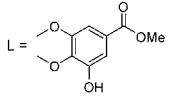	489
	MeOH	685 nm, 346		489
	EtOH	686 nm, 346		489
	DMSO	691 nm, 349		489
	DMF	687 nm, 348		489

(*Continued*)

Table 1. (*Continued*)

M	Solvent	Transition Energy (Intensity)	Remark		Ref.
	acetone	685 nm, 347			489
	DCM	692 nm, 349			489
	$CHCl_3$	695 nm, 349			489
	DMF	676 nm, 612sh, 342	L = $(OH)_2$, Cl		490
	DMSO	680 nm, 610sh, 343	L = $(OH)_2$, Cl		490
	DCM	678 nm, 617sh, 338	L = $(OH)_2$, Cl		490
	DCB	687 nm, 625sh, 345	L = $(OH)_2$, Cl		490
	$CDCl_3$	685.8 nm — 684.3 (lg ε 5.38), 616.9 (4.61), 340.5 (4.82)	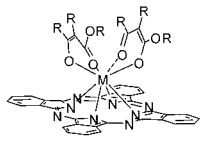	R = 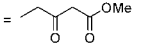	491
		684.6 nm (lg ε 5.21), 616.5 (4.48), 340.1 (4.79)		R = 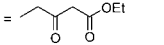	491
		684.1 nm (lg ε 5.22), 616.2 (4.42), 339.5 (4.78)		R = 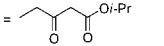	491
		685.2 nm (lg ε 5.45), 616.9 (4.67), 340.8 (4.98)		R = 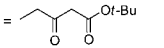	491
		684.4 nm (lg ε 5.38), 616.9 (4.26), 341.0 (4.58)		R = 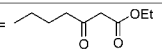	491
		684.9 nm (lg ε 5.08), 616.9 (4.40), 342.8 (4.74)		R = 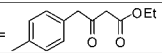	491
		684.8 nm (lg ε 5.34), 616.7 (4.58), 340.4 (4.90)		R = 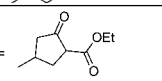	491
Hf(III)	$CDCl_3$	686.8 nm (lg ε 5.38), 684.2 (5.37), 616.7 (4.61), 340.9 (4.82)	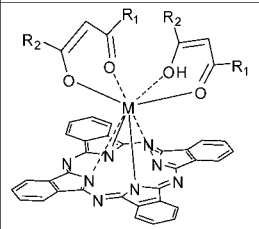	R_1, R_2 = Me	126
		687.8 nm (lg ε 5.23), 680.6sh (5.21), 615.5 (4.48), 342.7 (4.79)		R_1 = Me, R_2 = Pr	126
		686.2 nm (lg ε 5.24), 684.1sh (5.22), 618.2 (4.42), 334.5 (4.78)		R_1 = Me, R_2 = C_6H_{13}	126
		685.8 nm (lg ε 5.45), 684.4sh (5.44), 616.9 (4.67), 339.1 (4.98)		R_1 = Me, R_2 = C_7H_{15}	126
		692.2 nm (lg ε 5.40), 683.4sh (5.38), 617.9 (4.26), 349.0 (4.58)		R_1 = CF_3, R_2 = Me	126
		693.3 nm (lg ε 5.09), 682.1 (5.08), 619.4 (4.40), 345.0sh (4.74)		R_1, R_2 = CF_3	126
		687 nm (lg ε 5.35), 682.8sh (5.34), 616.7 (4.58), 340.9 (4.90)		R_1 = CF_3, R_2 = *t*-Bu	126
		688.9 nm (lg ε 5.13), 678.8sh (5.12), 615.0 (4.41), 338.9 (4.72)		R_1 = CF_3, R_2 = $CH(Et)_2$	126
		684.4 nm (lg ε 5.25), 654.2 (4.43), 615.3 (4.49), 334.2 (4.87)		R_1 = CF_3, R_2 = $C(OMe)(Me)_2$	126
		692.2 nm (lg ε 5.21), 683.4sh (5.19), 617.9 (4.48), 349.0 (4.83)		R_1 = CF_3, R_2 = Ph	126
		684.9 nm (lg ε 5.17), 616.9 (4.27), 342.8 (4.53)		R_1 = Me, R_2 = Ph	126
		688.3 nm (lg ε 5.17), 680.6sh (5.15), 615.6 (4.43), 343.3 (4.76)		R_1 = *t*-Bu, R_2 = Pr	126

(*Continued*)

Table 1. (*Continued*)

M	Solvent	Transition Energy (Intensity)	Remark	Ref.
		685.6 nm (lg ε 5.57), 683.7sh (5.57), 616.3 (4.61), 337.1 (4.87)	R_1 = *t*-Bu, R_2 = $C(OMe)(Me)_2$	126
Ta(V)L	$CHCl_3$	697 nm (lg ε 4.22), 625 (3.58), 342 (4.02)	L = Cl_4	142
W(V)N	1-ClNp	751.0 nm, 699.5, 673.5, 359.5		156
	KBr	753.0 nm, 704.0, 674.5, 622.5, 355.0		156
Re(V)N	nujol	750 nm, 697, 669, 375		181
Os(II)L	$CHCl_3$	618 nm, 570sh, 365, 305	L = tz_2	231
		616 nm, 563, 460, 436, 416, 369, 308	L = py_2	229
		620 nm, 580sh, 465, 440, 423, 375, 310	L = *trans*-py_2	231
		625 nm, 570sh, 420, 365sh, 310	L = *trans*-pyz_2	231
Ir(III)Cl	1-ClNp	648 nm (lg ε 4.75), 625 (4.06), 586 (4.06), 567 (3.56), 553 (3.38), 390 (3.55)		246
Pt(II)	H_2SO_4	784 nm, 693, 426		405
		784 nm, 693, 426		462
	1-ClNp	650 nm		266
		650 nm (lg ε 4.86), 625 (4.16), 586 (4.18), 567 (3.68), 550 (3.51), 455 (3.24)		246
		652 nm, 624, 588, 564.5, 545		57
Hg(I)	benzene	721 nm (lg ε 5.09), 654 (4.43), 440 (4.16), 342 (4.69), 285 (4.35)	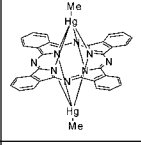	294
Hg(II)	DMSO	684 nm (lg ε 5.25)		286
	DMF	681 nm (lg ε 5.11)		286
Pb(II)	DMSO	705 nm (lg ε 4.905), 635 (4.139), 443 (3.826), 334 (4.451)		378
		705 nm (lg ε 4.945), 635 (4.226), 443 (3.878), 334 (4.532)		380
		705 nm, 635, 443, 334		379
	1-ClNp	685 nm, 642, 615, 591		57
	36 N H_2SO_4	722 nm (lg ε 4.937), 744 (4.935), 692 (4.383), 440 (4.398), 302 (4.764), 228sh (4.552)		378
Bi(III)Cl	DMSO	716.0 nm (10^{-5} ε 1.69), 645.0 (0.34), 415sh (*ca.* 0.17), 343.0 (0.71)		398
Bi(III)Br	DMSO	716.0 nm (10^{-5} ε 1.68), 645.0 (0.34), 415sh (*ca.* 0.17), 344.0 (0.71)		398
Bi(III)I	DMSO	715.5 nm (r.i. 1.00), 645.0 (0.20), 415sh (*ca.* 0.10), 343.0 (0.47)		398
Bi(III)NO_3	DMSO	716.0 nm (r.i. 1.00), 645.0 (0.24), 415sh (*ca.* 0.10), 343.0 (0.48)		398
Nd(III)(OAc)	DCM	680 nm, 639		506

(*Continued*)

Table 1. (*Continued*)

M	Solvent	Transition Energy (Intensity)	Remark	Ref.
Sm(III)L	DCM	820 (r.i.1.05), 717 (0.36), 675, 497 (1.0), 424 (0.89), 320sh, 292 (3.42)	L = *cis*- 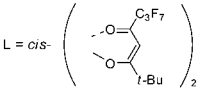	421
	benzene-amine = 1000: 1	675 (r.i.1), 640sh, 608 (0.15), 337 (0.64), 293 (0.32)	L = *cis*- 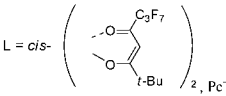 , Pc^-, reduced form	421
Eu(III)L	$CHCl_3$	679 nm (r.i 1.0), 614 (0.20), 335 (0.76), 318 (0.73)	L = 8-hydroxyquinoline	507
	DCM	821 (r.i.1.08), 716 (0.45), 674, 500 (1.0), 425 (0.9), 320sh, 292 (3.64)	L = *cis*- 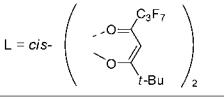	421
	benzene-amine = 1000: 1	674 (r.i.1), 643sh, 609 (0.2), 341 (0.67), 295 (0.36)	L = *cis*- 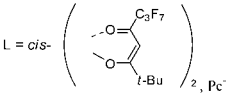 , Pc^-, reduced form	421
	DCM	821 (r.i.0.92), 717 (0.41), 692 (0.55), 675, 496 (1.0), 424 (0.95), 320sh, 292 (3.41)	L = *trans*- 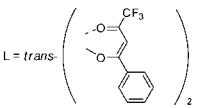	421
	benzene-amine = 1000: 1	675 (r.i.1), 642sh, 611 (0.17), 335 (0.65), 309 (0.38)	L = *trans*- 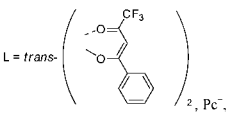 , Pc^-, reduced form	421
Gd(III)Cl	EtOH	671 nm, 606, 344		508
Gd(III)Br	EtOH	671 nm, 606, 344		508
Gd(III)OAc	EtOH	670 nm, 605, 343		508
Gd(III)L	DCM	821 (r.i.1.1), 714 (0.2), 694 (0.17), 499 (1.0), 424 (0.88), 320sh, 292 (3.96)	L = *cis*- 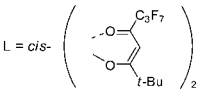	421

(*Continued*)

Table 1. (*Continued*)

M	Solvent	Transition Energy (Intensity)	Remark	Ref.
	benzene-amine = 1000: 1	676 (r.i.1), 641sh, 604 (0.16), 300 (0.72)	L = *cis*- 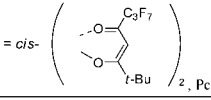 , Pc^-, reduced form	421
Dy(III)Cl	EtOH	671 nm, 604, 344		508
Dy(III)Br	EtOH	669 nm, 604, 342		508
Dy(III)OAc	EtOH	670 nm, 604, 342		508
Lu(III)OAc	DCM	712 nm, 626		506
	DCM + 3% MeOH	675 nm (10^{-4} ε 18.0), 343 (7.0)		509
	benzene	674 nm		510
Lu(III)L	DCM	821 (r.i.0.9), 717 (0.36), 675, 609, 501 (1.0), 424 (0.96), 320sh, 291 (4.47)	L = *cis*- 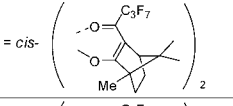	421
	benzene-amine = 1000: 1	675 (r.i.1), 645 (0.33), 609 (0.15), 328 (0.74), 292 (0.56)	L = *cis*- 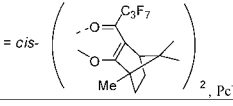 , Pc^-, reduced form	421
Th(IV)L	PhCN	684 nm (10^{-4} ε 20.7), 617 (4.0), 353 (6.3)	L = *cis*-$(acac)_2$	107
		679 nm (10^{-4} ε 4.1), 651 (4.6), 617 (3.2), 587 (5.3), 352 (3.5)	$[Pc]^-$, L = *cis*-$(acac)_2$	107
		649 nm (10^{-4} ε 2.2), 544 (5.6), 351 (2.2)	$[Pc]^{2-}$, L = *cis*-$(acac)_2$	107
U(IV)L	PhCN	689 nm (10^{-4} ε 16.6), 620 (3.4), 351 (5.7)	L = *cis*-$(acac)_2$	107
		677 nm (10^{-4} ε 3.7), 652 (4.1), 620 (3.2), 591 (5.0), 352 (3.5)	$[Pc]^-$, L = *cis*-$(acac)_2$	107
		646 nm (10^{-4} ε 2.3), 549 (5.3), 349 (2.9)	$[Pc]^{2-}$, L = *cis*-$(acac)_2$	107

Table 2. UV-vis absorption data of α- and/or β-substituted Pcs.

Structure	M	Solvent	Transition Energy (Intensity)	Remark	Ref.
R_2, R_3 = Me	2H	DMF	687 nm, 652, 627, 592, 337		511
β = Me	2H	toluene	696 nm, 659, 642, 632, 596		114
		1,2,4-Cl_3Np	700 nm, 665, 646, 635, 601		114
	Cu(II)	H_2SO_4	786 nm		461
	Zn(II)	$CHCl_3$	673.0 nm, 610.0, 348.0, 276.0		487
	Zn(III)L	$CHCl_3$	678.0 nm (lg ε 5.38), 611.0 (4.60), 348.0 (4.91), 275.0 (4.74)	L = DBU	487
		$CHCl_3$	676.0 nm (lg ε 5.29), 610.0 (4.49), 347.0 (4.80), 286.0 (4.35)	L = py	487
$\beta\beta$ = Me	2H	1,2,4-Cl_3Np	704 nm, 678, 658, 647, 612		114
	Fe(II)	py	662 nm (r.i. 1.3), 635sh (0.4), 600 (0.3), 418 (0.2), 337 (1.0)		238
		DMSO	658 nm		464
	Fe(II)L	DMSO	659 nm, 420	L = *trans*-py_2	464
		DMSO	660 nm, 417	L = *trans*-(py(3-Me))$_2$	464
		DMSO	659 nm, 422	L = *trans*-(py(4-Me))$_2$	464
		DMSO	659 nm, 418	L = *trans*-(py(3-CH_2OH))$_2$	464
		DMSO	661 nm, 422	L = *trans*-(py(4-CH_2OH))$_2$	464
		DMSO	661 nm, 422	L = *trans*-(py(3-OH))$_2$	464
		DMSO	662 nm, 430	L = *trans*-(py(4-OH))$_2$	464
		DMSO	658 nm, 558sh, 413	L = *trans*-(py(3-Cl))$_2$	464
		DMSO	690 nm, 558sh, 396	L = *trans*-(py(4-Cl))$_2$	464
		DMSO	660 nm, 404	L = *trans*-(py(3-CHO))$_2$	464
		DMSO	664 nm, 413	L = *trans*-(py(4-CHO))$_2$	464
		DMSO	656 nm, 556sh, 412	L = *trans*-(py(3-CN))$_2$	464
		DMSO	656 nm, 510sh, 410	L = *trans*-(py(4-CN))$_2$	464
	Ni(II)	1,2,4-Cl_3Np	674 nm (10^{-4} ε 28.1), 644 (0.94), 607 (0.96)		114
	Mo(V)N	DMF	710.0 nm, 344.0		157
	W(V)N	DMSO	764.5 nm, 367.5		157
	Re(V)N	DMSO	694.0 nm, 626.5, 363.5		157
$\alpha\alpha\beta\beta$ = Me	Fe(II)	py	716 nm, 686, 644, 620sh, 370sh, 336		512

(*Continued*)

Table 2. (*Continued*)

Structure	M	Solvent	Transition Energy (Intensity)	Remark	Ref.
β = Et	Ru(II)	toluene	630 nm, 571sh, 380sh, 338	L = *trans*-py_2	215
	Ru(II)L	toluene	630 nm, 571sh, 380sh, 338	L = *trans*-py_2	216
$\beta\beta$ = Et	2H	DCB	708 nm, 673, 644, 611, 347		513
	Eu(III)OAc	$CHCl_3$	688 nm, 621, 353		513
	Er (III)OAc	$CHCl_3$	687 nm, 618, 353		513
	Lu(III)OAc	$CHCl_3$	688 nm, 620, 352		513
$\beta\beta$ = Pr	P(V)L	py	684 nm (r.i. 1.00), 654 (0.15), 615 (0.16), 351 (0.31)	L = *trans*-$(OH)_2$, $[Pc]^+[OH]^-$	384
	Mo(V)N	toluene	709.0 nm, 672.5, 647.5, 348.5		156
	W(V)N	toluene	759.5 nm, 374		157
	Re(V)N	toluene	703.0 nm, 672.0, 633.0, 368.5, 351.5		157
β = Bu	V(IV)O	H_2SO_4	834 nm		461
$\beta\beta$ = Bu	2H	DCB	709 nm, 674, 645, 613, 348		513
		1,2,4-Cl_3Np	708 nm (10^{-4} ε 18.4), 673 (15.0), 653 (2.64), 641 (3.57), 609 (2.64)		114
	$P(OH)_2$	py	688 nm (r.i. 1.0), 658 (0.187), 620 (0.208), 356 (0.431)	$[Pc]^+[OH]^-$	514
	Ni(II)	1,2,4-Cl_3Np	679 nm (10^{-4} ε 24.2), 649 (3.82), 611 (4.11)		114
		toluene	675 nm, 645, 607		114
	Mo(V)N	toluene	711.5 nm, 673.0, 647.5, 614.5, 351.5		156
	W(V)N	toluene	763.0 nm, 373.5		157
	Re(II)N	toluene	705 nm, 673, 633, 369, 351		102
	Eu(III)OAc	$CHCl_3$	692 nm, 624, 354		513
	Er(III)OAc	$CHCl_3$	691 nm, 622, 353		513
	Lu(III)OAc	$CHCl_3$	690 nm, 621, 353		513

(*Continued*)

Table 2. (*Continued*)

Structure	M	Solvent	Transition Energy (Intensity)	Remark	Ref.
	Lu(III)	DCM	688(10^{-3} ε 183), 655 (25), 621 (25), 591 (4.6), 561 (6.3), 527 (7.7), 486 (4.4), 402 (7.8), 372 (19), 351 (60), 326 (38), 294 (28), 274 (32), 247 (52)	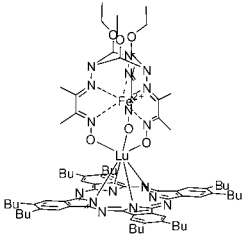	515
R_2 = *t*-Bu	2H	$CHCl_3$	695 nm (lg ε 5.17), 658 (5.13), 639 (4.71), 597 (4.47), 358sh, 339 (4.87)		516
		$CHCl_3$	695 nm (ε 147,910), 658 (134,896), 639 (51,286), 597 (29,512), 358sh, 339 (74,131)		517
α = *t*-Bu	Si(IV)L	$CHCl_3$	705 nm (lg ε 4.99), 632 (4.44), 359 (4.84), 300 (4.80)	L = *trans*- 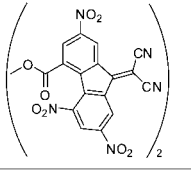	518
	V(IV)O	$CHCl_3$	700 nm		457
β = *t*-Bu	2H	pentane	695 nm (lg ε 5.21), 654 (5.04), 340 (4.86)		42
		benzene	700 nm (lg ε 5.26), 663 (5.18), 644 (4.72), 632 (4.71), 600 (4.49), 585sh (3.94), 565sh (3.67), 400sh (4.13), 364sh (4.85), 346 (4.89)		418
		benzene	700 nm (ε 180,000) 663		519
		hexane	695 nm (lg ε 5.33), 654 (5.11), 338 (4.90)		42
		heptane	696 nm (lg ε 5.34), 653 (5.11), 338 (4.90)		42
		octane	695 nm (lg ε 5.37), 656 (5.17), 340 (4.92)		42
		toluene	699 nm (lg ε 5.26), 662 (5.18), 345 (4.84)		42
		py	700 nm (lg ε 5.19), 665 (5.15), 345 (4.86)		42
		py	698.0 nm (lg ε 5.15), 664.3 (5.11), 640.1 (4.61), 602.0 (4.44), 344.0 (4.84)		43

(*Continued*)

Table 2. (*Continued*)

Structure	M	Solvent	Transition Energy (Intensity)	Remark	Ref.
		3,5-lutidine	700 nm (lg ε 5.16), 665 (5.10), 345 (4.78)		42
		2,6-lutidine	700 nm (lg ε 5.22), 663 (5.15)		42
		PrOH	697 nm (lg ε 4.93), 658 (4.92), 336 (4.82)		42
		BuOH	698 nm (lg ε 5.01), 660 (4.97), 338 (4.85)		42
		pentanol	698 nm (lg ε 5.10), 660 (5.01), 340 (4.86)		42
		AcOH	697 nm (lg ε 4.89), 660 (4.86), 338 (4.73)		42
		dimethylsulphone	698 nm (lg ε 5.02), 666 (5.02), 342 (4.76)		42
		2,2-dimethylbutane	695 nm (lg ε 5.07), 653 (4.94), 336 (4.85)		42
		2,2-dimethylpentane	695 nm (lg ε 5.16), 654 (5.02), 338 (4.82)		42
		2,2-dimethylheptane	695 nm (lg ε 5.26), 654 (5.09), 339 (4.87)		42
		pinacolone	696 nm (lg ε 5.15), 657 (5.10), 340 (4.87)		42
		4-*t*-butyl-*o*-xylene	699 nm (lg ε 5.26), 662 (5.14), 340 (4.82)		42
		t-butanol	694 nm (lg ε 4.79), 655 (4.78), 335 (4.74)		42
		t-butylacetate	696 nm (lg ε 5.15), 657 (5.10), 340 (4.88)		42
		t-butylmethylether	694 nm (lg ε 5.19), 655 (5.11), 340 (4.90)		42
		4-*t*-butylpyridine	700 nm (lg ε 5.23), 663 (5.17), 342 (4.87)		42
		1-ClNp	703 nm (lg ε 5.22), 668 (5.16), 345 (4.84)		42
		$CHCl_3$	701 nm (lg ε 5.23), 664 (5.17), 645 (4.75), 602 (4.50), 367sh, 341 (4.96)		407
		toluene	699 nm, 662		520
		CCl_4	700 nm, 661		38
	Mg(II)	benzene	679 nm (ε 200,000)		519
	Mg(II)	MeOH	675 nm, 610, 348		521
	Al(III)OAc	DCM	693 nm (lg ε 5.38), 343 (4.92)		522
	Al(III)OTMS	DCM	689 nm (lg ε 5.42), 342 (4.95)		522
	Al(III)$OSiPh_3$	DCM	692 nm (lg ε 5.43), 343 (4.92)		522
	Al(III)Et	$CHCl_3$	696 nm, 627, 369		523
	Al(III)OEt	$CHCl_3$	693 nm, 623, 340		523
	Si(IV)L	benzene	678 nm (10^{-1} ε 32.5), 648 (4.3), 610 (4.6), 358 (10.6)	L = *trans*-$(OH)_2$	432

(*Continued*)

Table 2. (*Continued*)

Structure	M	Solvent	Transition Energy (Intensity)	Remark	Ref.
		DCM	695 nm (lg ε 5.31), 664 (4.43), 624 (4.51), 360 (4.98), 334 (5.04), 255 (5.40)	L = *trans*- 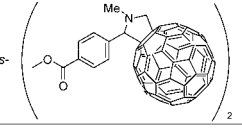	524
	P(V)L	py	677 nm (r.i. 1.00), 648 (0.15), 609 (0.16), 353 (0.40)	L = *trans*-$(OH)_2$	384
	$P(OH)_2$	py	677 nm (r.i. 1.0), 648 (0.160), 609 (0.185), 353 (0.395)	$[Pc]^+[OH]^-$	514
	Ti(IV)O	DCM	696 nm, 628, 347		525
		$CHCl_3$	699.0 nm, 629.5, 347.0		526
	Ti(IV)L	DCM	701 nm (lg ε 5.16), 632 (4.49), 343 (4.83), 275 (4.79)	L= 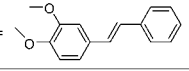	525
		DCM	701 nm (lg ε 5.14), 632 (4.48), 356 (4.96), 291 (4.87)	L= 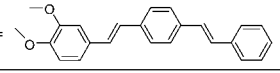	525
		DCM	701 nm (lg ε 5.14), 632 (4.48), 356 (4.96), 291 (4.87)	L= 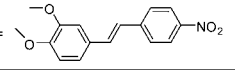	525
		$CHCl_3$	702.0 nm, 633.0, 347.5	L = 	526
		$CHCl_3$	697.0 nm, 631.0, 497.0, 347.0	L = 	526
		$CHCl_3$	703.0 nm, 634.0, 352.5	L = 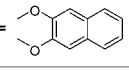	526
		$CHCl_3$	695.5 nm, 631.0, 347.5	L = 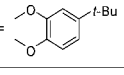	526
		$CHCl_3$	702.0 nm, 635.0, 354.0	L = 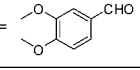	526

(*Continued*)

Table 2. (*Continued*)

Structure	M	Solvent	Transition Energy (Intensity)	Remark	Ref.
		$CHCl_3$	702.0 nm, 634.5, 347.0	L = 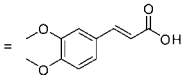	526
		$CHCl_3$	701.5 nm, 633.0, 348.5	L = 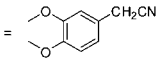	526
		$CHCl_3$	724.0sh nm, 705.0, 639.0, 371.0	L = 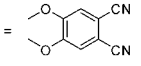	526
		$CDCl_3$	726.0sh nm, 707.5, 639.5, 359.5	L = 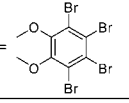	526
		THF	697 nm ($10^{-4}\varepsilon$ 7.9), 631 (1.6), 341 (5.0)	L = 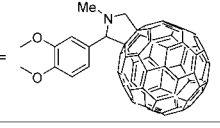	527
	V(IV)O	py	698.0 nm (lg ε 5.01), 630.0 (4.32), 350.0 (4.70)		43
	Cr(III)L	THF	686 nm (lg ε 5.41), 656 (4.54), 618 (4.58), 497 (4.06), 483 (4.03), 353 (4.79)	L = *trans*-Cl_2, $[Pc]^-H^+$	146
		toluene	715sh nm, 696, 660sh, 618, 520, 509, 490, 360	L = *trans*-Cl_2, $[Pc]^-H^+$	146
		py	684 nm (lg ε 5.28), 655 (4.65), 616 (4.66), 484 (4.54), 370 (4.74), 351 (4.80)	L = *trans*-Cl_2, $[Pc]^-H^+$	146
		py	697 nm (lg ε 5.24), 670 (4.66), 627 (4.66), 509 (4.55), 503 (4.57), 371 (4.80), 359 (4.84)	L = *trans*-Cl_2, [Pc] H^+, 90 °C	146
		toluene	693 nm (lg ε 5.21), 670 (4.55), 623 (4.55), 507 (4.36), 500 (4.41), 372 (4.69), 359 (4.75)	L = Cl, $[Pc]py_2$	146
		benzene	787 nm (lg ε 4.24), 735sh, 706 (4.33), 543 (4.44), 442 (4.29), 382sh, 352 (4.49)	L = *trans*-Cl_2	146
	Mn(III)	benzene	680 nm, 350		528
	Mn(III)Cl	$CHCl_3$	729 nm, 657, 532, 370, 279		529
		benzene	725 nm (lg ε 4.92)		530

(*Continued*)

Table 2. (*Continued*)

Structure	M	Solvent	Transition Energy (Intensity)	Remark	Ref.
		benzene	725 nm (lg ε 5.06), 518 (4.23), 351 (4.72)		528
	Mn(III)L	py	621 nm (lg ε 5.08), 340 (4.98)	L = py	528
	Fe(II)	py	657 nm (r.i. 1.2), 630sh (0.4), 597 (0.3), 416 (0.3), 331 (1.0)		238
	Co(II)	py	662 nm (r.i. 1.6), 600 (0.3), 330 (1.0)		238
		py	666.0 nm (lg ε 5.04), 599.0 (4.49), 332.0 (4.73)		43
		DMF	664 nm		531
		MeOH	667 nm, 603, 330		521
	Co(III)L	DMF	676 nm	L = *trans*-$(CN)_2$, $[Pc]^-K^+$	531
	Cu(II)	hexane	670 nm, 606, 334		521
		py	676.0 nm (lg ε 5.17), 609.0 (4.37), 345.0 (4.59)		43
		H_2SO_4	808 nm		461
	Zn(II)	benzene	678 nm (ε 200,000)		519
		benzene	678 nm (lg ε 5.30), 648 (4.41), 610 (4.48), 584sh (3.73), 567sh (3.57), 349 (4.76)		532
		PVA in DMSO	691 nm (10^{-4} ε 8.97)		486
		DMF	675 nm, 609, 346		533
		MeOH	673 nm, 608, 345		521
	Zn(III)L	$CHCl_3$	678.0 nm (lg ε 5.08), 612.0 (4.28), 348.0 (4.59), 287.0 (4.15)	L = DBU	487
	Ga(III)Cl	$CHCl_3$	695.0 nm, 664.0, 625.5, 357.0, 338.0		345
		$CHCl_3$	695 nm, 664.5sh, 625, 336		331
		$CHCl_3$	695 nm, 664.5sh, 625, 356		325, 326
		$CHCl_3$	695.5 nm, 664.5sh, 625, 356		326
		toluene	693 nm		329
	Ga(III)L	toluene	696 nm	L = $PhCF_3$	329
		$CHCl_3$	692 nm, 664sh, 624, 356	L = OPh(4-Cl)	328
		$CHCl_3$	696.5 nm, 666sh, 626.5, 369.5	L = Ph(4-CF_3)	326
	Zr(IV)Cl_2	DMF	688 nm		534
		H_2SO_4	826 nm		534
	Ru(II)CO	benzene	651 nm (10^{-1} ε 0.117), 588 (2.49), 345sh, 298 (7.21)		224
	Ru(II)L	$CHCl_3$	648 nm, 586sh, 314	L = *trans*-$(CN(t\text{-}Bu))_2$	500

(*Continued*)

Table 2. (*Continued*)

Structure	M	Solvent	Transition Energy (Intensity)	Remark	Ref.
		benzene	630 nm (10^{-4} ε 5.97), 575sh, 437, 370sh, 314 (10.3)	L = *trans*- 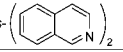	224
		$CHCl_3$	641 nm (lg ε 4.72), 585 (4.36), 312 (4.96), 285 (4.85)	L = *trans*-$(PhCN)_2$	535
		MeCN	625 nm (lg ε 4.80), 575 (4.32), 383 (4.32), 318 (5.00)	L = *trans*-$(py)_2$	535
		DCM	627 nm (ε 68,000), 576sh, 378sh, 317 (110,000)	L = *trans*-$(4\text{-}Mepy)_2$	221
		DCM	627 nm (ε 71,000), 573sh, 382sh, 318 (110,000), 243	L = *trans*-$(4\text{-}NH_2py)_2$	221
		DCM	626 nm (ε 66,000), 573sh, 382sh, 318 (105,000), 267	L = *trans*-$(4\text{-}NMe_2py)_2$	221
		DCM	645 nm (ε 69,000), 591sh, 382sh, 312 (109,000)	L = *trans*-$(4\text{-}NO_2py)_2$	221
		$CHCl_3$	648 nm, 591sh, 450, 315, 266sh	L = *trans*-$(pyz)_2$	536
		$CHCl_3$	630 nm, 578sh, 380, 316	L = *trans*- 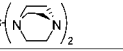	536
		$CHCl_3$	632 nm, 584sh, 452, 365, 319	L = *trans*-$(bpy)_2$	536
		$CHCl_3$	652 nm (lg ε 5.18), 627sh , 590 (4.42), 569 (3.80), 552 (3.50), 345 (4.53), 330 (4.56)296 (5.01)	L = CO	537
		$CHCl_3$	633 nm, 585sh, 410, 364, 313	L = *trans*-$(py(3\text{-}Cl))_2$	500
			633 nm, 586, 413, 360, 313		503, 538
	Ru(IV)L	py	651 nm (10^{-4} ε 21.5)	L = *trans*-CO, py	539
		py	630 nm (10^{-4} ε 8.20)	L = *trans*-py_2	539
	Cd(II)	DCM	683 nm, 660, 635		289
	In(III)Cl	$CHCl_3$	697.3 nm, 667.1sh, 628.2, 359.5, 339.7sh		332
		$CHCl_3$	697.3 nm, 667.1sh, 628.2, 359.5, 339.7sh		343
		$CHCl_3$	697.3 nm, 667.1, 628.2, 359.5, 339.7		345
		toluene	695 nm		341
		toluene	695 nm		329
		$CHCl_3$	697 nm, 667sh, 628, 359.5		325
	In(III)Br	$CHCl_3$	697.7 nm, 666.8sh, 628.4, 362.2, 342.0sh		332
	In(III)I	$CHCl_3$	698.7 nm, 667.9sh, 629.3, 366.3, 342.2sh		332
	In(III)C_6F_5	$CHCl_3$	697.8 nm, 665.7sh, 628.7, 365.6, 341.9sh		343
	In(III)L	DCM	700 nm, 663, 602	L = OC(Me)CHCOMe	540
		$CHCl_3$	698.0 nm, 667.3sh, 628.6, 369.3, 340.9sh	L = Ph(4-CF_3)	332
		$CHCl_3$	697.8 nm, 666.5sh, 628.5, 368.6, 341.4sh	L = Ph(3-CF_3)	332
		$CHCl_3$	697.4 nm, 666.6sh, 628.2, 368.5, 341.0sh	L = Ph(4-F)	332
		$CHCl_3$	697.9 nm, 666.5sh, 628.6, 366.2, 341.6sh	L = Ph(3,5-F_2)	332

(*Continued*)

Table 2. (*Continued*)

Structure	M	Solvent	Transition Energy (Intensity)	Remark	Ref.
		$CHCl_3$	698.0 nm, 667.0sh, 628.8, 368.9, 341.9sh	L = Ph(2,3,5,6-F_4)	332
		$CHCl_3$	697.8 nm, 665.7sh, 628.7, 365.6, 341.9sh	L = C_6F_5	332
		$CHCl_3$	698.2 nm, 667.4sh, 628.9, 366.4, 341.1sh	L = Ph(4-Br)(2,3,5,6-F_4)	332
		$CHCl_3$	696.7 nm, 666.2sh, 627.7, 368.0, 343.5sh	L = Me	332
		$CHCl_3$	698.0 nm, 667.3sh, 628.6, 369.3, 340.9sh	L = Ph(4-CF_3)	343
		$CHCl_3$	697.8 nm, 666.5sh, 628.5, 368.6, 341.4sh	L = Ph(3-CF_3)	343
		$CHCl_3$	697.4 nm, 666.0sh, 628.2, 368.5, 341.0sh	L = Ph(4-F)	343
		toluene	696 nm	L = $PhCF_3$	329
	Sn(IV)L	DCM	700 nm (ε 5.20), 632 (4.21), 366 (4.75)	L = *trans*-$(OH)_2$	541
		DCM	702 nm (ε 5.11), 633 (4.40), 592 (4.00), 552 (4.04), 517 (4.32), 418 (5.76), 361 (4.83)	L = *trans*- 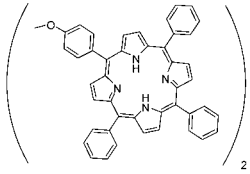 2	541
		DCM	701 nm (ε 4.43), 632 (3.76), 595 (3.46), 553 (3.76), 423 (5.33), 358 (4.16)	L = *trans*- 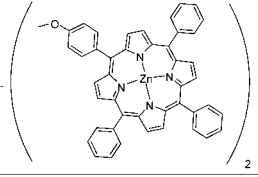 2	541
	Sb(V)L	DCM	742 nm (lg ε 5.19), 369 (4.65), 256 (4.99)	L = *trans*-$(I)_2$, $[Pc]^+I^-$	396
		DCM	723.5 nm	L = *trans*-$(OH)_2$, $[Pc]^+$	396
		$CHCl_3$	739 nm, 663, 437sh, 403, 351, 312	L = *trans*-Cl_2, $[Pc]^+ClO_4^-$	542
	Hf(IV)Cl_2	DMF	687 nm		534
		H_2SO_4	831 nm		534
	W(V)N	toluene	745.0 nm, 677.0, 365.0		156
	W(IV)O	toluene	725.0 nm, 674.5, 611.0, 356.5		156
	Re(II)L	DCM	775 nm, 725, 382	L = $NBBr_3$	102

(*Continued*)

Table 2. (*Continued*)

Structure	M	Solvent	Transition Energy (Intensity)	Remark	Ref.
	Re(III)L	DCM	695 nm (lg ε 5.08), 626 (4.40), 601 (3.83), 579 (3.58), 557 (3.06), 356 (4.79), 286 (4.47), 270 (4.54), 246 (4.70)	L = *trans*-NC(Me)$_2$CH$_2$COMe, OH	102
	Re(V)N	DCM	698 nm (lg ε 5.553), 363 (5.099)		181
		nujol	750 nm, 697, 669, 375		181
	Re(V)L	DCM	726 nm (lg ε 4.854), 368 (4.847)	L = *trans*-O, (OEt)	181
		DCM	676.0 nm, 360.5	L = NBF_3	157
		toluene	719.5 nm, 696.5, 667.0, 627.0, 365.0	L = $NBCl_3$	157
		DCM	721.0 nm, 356.0	L = $NBCl_3$	157
		DCM	733.5 nm, 371.5	L = $NBCl_2Ph$	157
		DCM	715.5 nm, 681.5, 352.5	L = $NB(C_6F_5)_3$	157
		DCM, glass plate	695.5 nm, 664.0, 344.5	L = $NBPh_3$	157
		DCM, glass plate	696.0 nm, 657.5, 341.5	L = $NBEt_3$	157
		DCM, glass plate	696.0 nm, 366.0	L = $NAlCl_3$	157
		DCM	720.5 nm, 350.5	L = $NGaCl_3$	157
		DCM	721.5 nm, 691.0, 350.5	L = $NGaBr_3$	157
		DCM, glass plate	694.5 nm, 349.5	L = $NInCl_3$	157
		toluene, glass plate	725.5 nm, 696.0, 666.0, 369.0	L = NSi(*t*-Bu)Me$_2$, [Pc]$^+$Cl$^-$	157
	Er(III)L	$CHCl_3$	845 nm (lg ε 3.60), 670 (7.45), 615 (4.18), 452 (3.70), 335 (4.59), 330 (4.62)	L = acac	543
$R_2(R_3)$, $R_6(R_7)$, $R_{10}(R_{11})$ = *t*-Bu	2H	DCB	700 nm, 668, 643, 610, 363sh, 345		302
α = C_5H_{11}	Pb(II)	$CHCl_3$	751 nm (lg ε 5.39), 673 (4.62), 432 (4.42), 333 (4.75)		376
$\alpha\alpha$ = C_5H_{11}	Ti(IV)O	toluene	730.5 nm, 696sh, 655.5, 359.0, 315.5sh		544
β = C_5H_{11}	Sn(IV)L	DCM	760 nm	L = *trans*-Cl_2	545
		DCM	752 nm	L = *trans*-$(OH)_2$	545
$\beta\beta$ = C_5H_{11}	2H	$CHCl_3$	701 nm (lg ε 5.28), 677 (5.14), 647 (4.76), 617 (4.46), 377sh, 347 (4.90)		407
		$CHCl_3$	701 nm (lg ε 5.28), 677 (5.14), 647 (4.76), 617 (4.46), 377sh, 347 (4.90)		407
	P(V)L	py	685 nm (lg ε 1.00), 654 (0.14), 615 (0.16), 351 (0.29)	L = *trans*-$(OH)_2$	384
	W(V)N	toluene	770.5 nm, 695.5, 376.0		156
	Mo(V)N	toluene	716.0 nm, 679.0, 649.5, 353.5		156
	In(III)Cl	$CHCl_3$	706.2 nm, 675.4sh, 635.4, 361.3, 342.2sh		332

(*Continued*)

Table 2. (*Continued*)

Structure	M	Solvent	Transition Energy (Intensity)	Remark	Ref.
		$CHCl_3$	706.2 nm, 675.4sh, 635.4, 361.3, 342.2sh		343
	In(III)C_6F_5	$CHCl_3$	707.5 nm, 675.7sh, 636.6, 370.1, 349.3sh		343
	In(III)Ph	$CHCl_3$	706.6 nm, 676.2sh, 635.8, 375.9, 353.6sh		343
	In(III)L	$CHCl_3$	707.2 nm, 675.6sh, 636.4, 375.3, 353.7sh	L = Ph(4-CF_3)	332
		$CHCl_3$	707.3 nm, 675.9sh, 636.2, 374.9, 354.0sh	L = Ph(3-CF_3)	332
		$CHCl_3$	706.7 nm, 674.9sh, 635.8, 375.0, 354.6sh	L = Ph(4-F)	332
		$CHCl_3$	707.5 nm, 675.7sh, 636.3, 370.1, 349.3sh	L = C_6F_5	332
		$CHCl_3$	706.6 nm, 676.2sh, 635.8, 375.9, 353.6sh	L = Ph	332
		$CHCl_3$	707.2 nm, 675.6sh, 636.4, 375.3, 353.7sh	L = Ph(4-CF_3)	343
		$CHCl_3$	707.3 nm, 675.9sh, 636.2, 374.9, 354.0sh	L = Ph(3-CF_3)	343
		$CHCl_3$	706.7 nm, 674.9sh, 635.8, 375.0, 354.6sh	L = Ph(4-F)	343
	W(V) L	toluene	731.5 nm, 367.0	L = $NGeMe_3$	157
		toluene	725.5 nm, 358.5	L = NSi(*t*-Bu)Me_2	157
		THF	723.0 nm, 357.5	L = NSi(*t*-Bu)Me_2	157
		THF	725.0 nm	L = $NSiPh_3$	157
	Re(II)N	DCM	708 nm, 676, 638, 361, 347		102
	Re(II)L	DCM	738 nm, 702, 668, 380	L = $NBBr_3$	102
$\alpha\alpha$ = *i*-C_5H_{11}	2H	toluene	731 nm		546
	Cu(II)	THF	705 nm (10^{-5} ε 0.6)		546
	Zn(II)	toluene	703 nm (10^{-5} ε 2.2)		546
	Pb(II)	THF	744 nm (lg ε 5.2)		547
		THF	744 nm (10^{-5} ε 1.6)		546
$\alpha\alpha$ = C_6H_{13}	2H	toluene	733 nm		546
	Si(IV)L	THF	703.5 nm (10^{-5} ε 2.4)	L = *trans*-$(OH)_2$	546
	Ti(IV)O	toluene	730.5 nm, 696.0sh, 656.0, 409sh, 362.0, 316.0sh		544
	Ni(II)	toluene	702 nm		546
	Zn(II)	toluene	705 nm		546
	Pd(II)	cyclohexane	690 nm (10^{-5} ε 1.0)		546
	Cd(II)	hexane	709 nm, 643		289
	In(III)Cl	toluene	729 nm (10^{-5} ε 2.2)		546
	In(III)L	THF	728 nm (10^{-5} ε 2.2)	L = Ph(4-F)	546

(*Continued*)

Table 2. (*Continued*)

Structure	M	Solvent	Transition Energy (Intensity)	Remark	Ref.
	Sn(IV)L	THF	735 nm (log ε 5.34), 699 (4.65), 660 (4.73), 364 (4.89)	L = *trans*-Cl_2	367
		toluene	736 nm	L = *trans*-Cl_2	367
	Pb(II)	THF	741 nm (lg ε 5.23)		547
		toluene	746 nm (10^{-5} ε 1.4)		546
$\beta\beta = C_6H_{13}$	2H	THF	704.5 nm, 666.5		289
	Cd(II)	THF	686 nm, 619		289
		hexane	678 nm, 642, 480, 329		289
	Re(II)N	toluene	704 nm, 671, 634, 369, 350		102
	W(V)N	toluene	762.0 nm, 374.0		157
$\alpha = C_7H_{15}$	Mn(III)OAc	$CHCl_3$	733 nm, 685, 531, 358, 271		529
$\alpha\alpha = C_7H_{15}$	Mn(III)OAc	$CHCl_3$	769 nm, 693, 549, 395sh, 364, 282		529
	Fe(II)L	$CHCl_3$	683 nm	L = *trans*-$(CN(t\text{-}Bu))_2$	467
	Co(II)	DMF	700 nm, 666sh, 634, 329, 304		531
	Co(III)L	DMF	708 nm, 637, 440, 349, 289	L = *trans*-$(CN)_2$, $[Pc]^-Na^+$	531
$\beta\beta = C_7H_{15}$	2H	$CHCl_3$	708 nm, 672, 644, 610, 344		548
	Ti(IV)O	$CHCl_3$	710 nm (lg ε 5.27), 680 (4.42), 639 (4.48), 347 (4.80)		549
	Ti(IV)O	$CHCl_3$	710 nm (lg ε 5.27), 680 (4.42), 639 (4.48), 347 (4.80)		119
	Ti(IV)L	$CHCl_3$	712 nm (lg ε 5.17), 642 (4.49), 349 (4.76)	L = 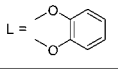	119
	Mn(III)OAc	$CHCl_3$	743 nm, 669, 534, 385, 278		529
	Fe(II)L	$CHCl_3$	675 nm	L = *trans*-$(CN(t\text{-}Bu))_2$	467
	Co(II)	$CHCl_3$	679 nm, 651sh, 610, 329, 290		531
	Co(III)L	DMF	683 nm, 648sh, 615, 435, 363, 344sh, 291	L = *trans*-$(CN)_2$, $[Pc]^-Na^+$	531
	W(V)N	toluene	763.0 nm, 373.5		157
	Re(II)N	DCM	708 nm, 676, 638, 361, 347		102
$\alpha\alpha = C_8H_{17}$	2H	cyclohexane	728 nm, 694		550
	Ru(II)CO	petroleum ether	669 nm (lg ε 4.62)		551
	Ru(II)L	DCM	658 nm (lg ε 4.34)	L = *trans*-$(NCPh)_2$	551
		DCM	645 nm (lg ε 4.53)	L = *trans*-$(py(4\text{-}Me))_2$	551
		DCM	643 nm (lg ε 4.7)	L = *trans*-$(py(4\text{-}NMe_2))_2$	551

(*Continued*)

Table 2. (*Continued*)

Structure	M	Solvent	Transition Energy (Intensity)	Remark	Ref.
		DCM	671 nm, 604, 551, 516, 419	L = *trans*-(CO)(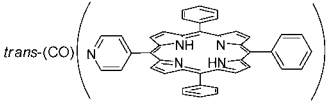)	551
		DCM	662 nm (lg ε 4.25), 646 (4.26), 591 (4.12), 554 (4.01), 515 (4.15), 419 (5.35), 366 (4.40)	L = *trans*-(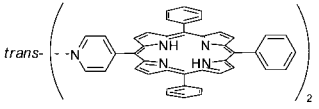)$_2$	551, 552
	Cd(II)	THF	707 nm, 642		289
ββ = 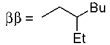	2H	THF	706 nm, 669		289
	Cd(II)	THF	688 nm, 621		289
		DCM	697 nm, 605		289
$\alpha\alpha = C_{10}H_{21}$	2H	toluene	730 nm		546
	Ni(II)	toluene	702 nm		546
	Zn(II)	THF	700 nm		367
		toluene	704 nm		367
		toluene	705 nm		546
		toluene	703 nm, 634		553
		toluene	707 nm (log ε 4.720), 635		554
	Ru(II)CO	THF	676 nm		551
	Ru(II)L	DCM	671 nm (lg ε 5.04)	L = *trans*-(CO)(py)	551
		DCM	667 nm (lg ε 4.79)	L = *trans*-(CO)(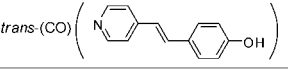)	551
		DCM	671 nm (lg ε 4.22)	L = *trans*-(CO)(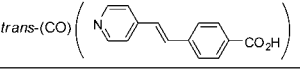)	551
		DCM	667 nm (lg ε 4.35)	L = *trans*-(CO)(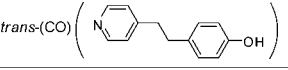)	551

(*Continued*)

Table 2. (*Continued*)

Structure	M	Solvent	Transition Energy (Intensity)	Remark	Ref.
		DCM	671 nm (lg ε 4.18)	L = *trans*-(CO)(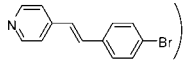)	551
	Cd(II)	THF	708 nm, 641		289
	Sn(IV)L	THF	735 nm (log ε 5.34), 701 (4.64), 661 (4.68), 429.6 (4.46), 365 (4.80), 324, (4.78)	L = *trans*-Cl_2	367
		toluene	736 nm	L = *trans*-Cl_2	367
$\beta\beta$ = $C_{12}H_{25}$	2H	$CHCl_3$	707 nm (lg ε 5.0), 672, 645, 610		473
	Cu(II)	$CHCl_3$	687 nm (lg ε 5.2), 657, 618		473
β = $(CH_2)_3N(Et)_2$	Co(II)	DCB	672 nm (lg ε 5.16), 650 (4.63), 610 (4.48), 332 (4.76), 292 (4.47)		555
	Cu(II)	DCB	682 nm (lg ε 5.14), 658 (4.60), 650 (4.52), 616 (4.53), 346 (4.70), 292 (4.18)		555
β = $(CH_2)_3N^+(Et)_2Me$	Co(II)	H_2O	670 nm (lg ε 4.77), 626 (4.82), 320 (4.82), 292 (4.88), 226 (5.14)	$[Pc]^{4+}4I^-$	555
		MeCN	660 nm (lg ε 5.26), 598 (4.61), 326 (4.98), 287 (4.86), 244 (5.10)	$[Pc]^{4+}4I^-$	555
	Cu(II)	H_2O	670 nm (lg ε 4.57), 630 (4.75), 334 (4.73), 225 (5.01)	$[Pc]^{4+}4I^-$	555
		MeCN	670 nm (lg ε 5.24), 607 (4.39), 338 (4.84), 245 (4.89)	$[Pc]^{4+}4I^-$	555
β = CF_3	Ti(IV)O	PhCl	689.0 nm, 621.0		544
$\alpha\alpha$ = $(CH_2)_6CH{=}CH_2$	2H	DCM	727 nm (10^{-5} ε 0.63), 700 (0.52)		289
	Cd(II)	THF	707 nm		289
		DCM	712 nm		289
R_3, R_7, R_{11} = $CC(CH_2)_3COOH$	Zn(II)	THF	678 nm (lg ε 5.34), 612 (4.62)		556
		0.1 N NaOH	623 nm	broad	556
R_3, R_7, R_{11} = $CC(CH_2)_8COOH$	Zn(II)	THF	679 nm (lg ε 5.33), 612 (4.61)		556
		0.1 N NaOH	633 nm	broad	556
R_2, R_3, R_6, R_7, R_{10}, R_{11} = $CC(CH_2)_3COOH$	Zn(II)	THF	687 nm (lg ε 5.33)		556
		0.1 N NaOH	632 nm	broad	556
β = CCH	2H	DMSO	689 nm (lg ε 4.49), 292 (5.07)		557
	Ni(II)	DMSO	682 nm (lg ε 4.63), 292 (5.17)		557
	Zn(II)	DMSO	697 nm (lg ε 4.46), 359 (4.35), 291 (4.39)		557
$\beta\beta$ = CCH	2H	THF	708 nm (r.i. 0.86), 636 (0.26), 364 (0.40), 261 (0.60)		558

(*Continued*)

Table 2. (*Continued*)

Structure	M	Solvent	Transition Energy (Intensity)	Remark	Ref.
	Zn(II)	THF	698 nm (r.i. 1.20), 664 (0.26), 628 (0.24), 252 (0.47), 366 (0.54)		558
$\beta\beta$ = CCPr	2H	THF	728 nm (lg ε 5.03), 694 (5.00), 628 (4.55), 363 (4.27)		559
	Zn(II)	THF	706 nm (lg ε 5.45), 638 (4.74), 368 (5.14)		559
$\beta\beta$ = CCBu	2H	THF	730 nm (lg ε 5.22), 694 (5.19), 366 (5.04)		559
	Zn(II)	THF	708 nm (lg ε 5.52), 634 (4.73), 370 (5.12)		559
β = CC(*t*-Bu)	2H	$CHCl_3$	712 nm (lg ε 5.28), 674 (5.25), 645 (4.78), 615 (4.57), 399 (4.60), 349 (4.91)		407
$\alpha\beta$ (R_1, R_2) = CC(*t*-Bu)	2H	$CHCl_3$	734 nm (lg ε 5.32), 698 (5.27), 666 (4.72), 632 (4.59), 418 (4.65), 368 (5.03), 314 (4.89)		558
$\beta\beta$ = CC(*t*-Bu)	2H	$CHCl_3$	734 nm (lg ε 5.32), 694 (5.27), 666 (4.72), 632 (4.59), 368 (5.03)		559
	Zn(II)	$CHCl_3$	714 nm (lg ε 5.40), 640 (4.61), 370 (5.00)		559
$\beta\beta$ = CCC_5H_{11}	2H	THF	730 nm (lg ε 5.47), 694 (5.35), 636 (4.92), 364 (5.32)		559
	Zn(II)	THF	706 nm (lg ε 5.54), 636 (4.77), 370 (5.12)		559
$\beta\beta$ = CCC_6H_{13}	2H	THF	730 nm (lg ε 5.44), 694 (5.38), 636 (4.89), 364 (5.29)		559
	Zn(II)	THF	708 nm (lg ε 5.57), 636 (4.81), 370 (5.21)		559
β = $CCCMe_2OH$	2H	THF	708 nm (lg ε 5.30), 675 (5.33), 350 (5.17)		557
	Ni(II)	THF	679 nm (lg ε 5.04), 338 (4.76)		557
	Zn(II)	THF	684 nm (lg ε 5.02), 358 (4.51)		557
$\beta\beta$ = $CCSi(Me)_2$(*t*-Bu)	2H	THF	732 nm (r.i. 2.16), 698 (2.03), 668 (0.59), 636 (0.48), 424 (0.51), 372 (1.44), 314 (1.44), 258 (0.85)		558
	Zn(II)	THF	710 nm (r.i. 0.64), 678 (0.08), 638 (0.09), 374 (0.24)		558
β = CC-TMS	Ni(II)	$CHCl_3$	683 nm (lg ε 5.09)		557
$\beta\beta$ = CCPh(4-*t*-Bu)	2H	py	726 nm, 656, 398,316		560
β = CCPh(4-OCH_2(*t*-Bu))	2H	THF	716 nm (lg ε 6.08), 678 (6.19), 390 (6.18), 330 (6.41), 258 (6.14), 216 (6.23)		560
	2Li	THF	720 nm (lg ε 6.89), 686 (6.04), 648 (6.07), 398 (6.52), 316 (6.40), 282 (6.35), 212 (6.40)		560
ββ = 	Zn(II)	THF	737 nm (lg ε 5.24), 702sh, 661 (4.55), 378 (4.97)		561

(*Continued*)

Table 2. (*Continued*)

Structure	M	Solvent	Transition Energy (Intensity)	Remark	Ref.
ββ = 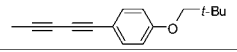	2Li	THF	738 nm, 660, 408, 304, 214		560
R_1 = 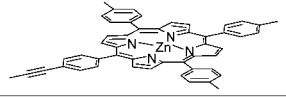	Zn(II)	$CHCl_3$	676 nm (lg ε 5.47), 652 (4.93), 610 (4.80), 555 (4.67), 426 (5.95)		562
α = 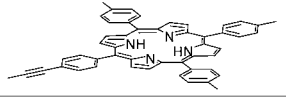	2H	$CHCl_3$	718 nm (lg ε 4.91), 687 (4.85), 650 (4.57), 594 (4.40), 554 (4.59), 517 (4.79), 422 (6.09)		562
α = 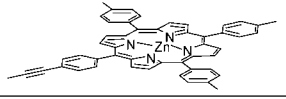	Zn(II)	$CHCl_3$	695 nm (lg ε 5.19), 628 (4.76), 603 (4.70), 558 (4.86), 426 (6.11)		562
β = CN	Cr(III)Cl	DMF	689 nm		534
		H_2SO_4	744 nm, 712		534
	Zr(IV)Cl_2	DMF	693 nm		534
		H_2SO_4	759 nm, 730		534
	In(III)Cl	DMF	694 nm, 617		534
$\beta\beta$ = CN	HLi(I)	DMF	697 nm, 647, 407, 332		563
	Fe(II)	DMF	683 nm, 620sh, 475, 383, 319		564
		DMF	692 nm, 629sh, 557, 469, 380, 327sh		565
	Fe(II)L	DMF	708 nm, 489, 340, 326	L = *trans*-pyz_2	565
	Co(II)	HMPA	685, 617sh, 501		565
	Co(II)L	HMPA	682 nm, 612, 494, 334	L = *trans*-pyz_2	565
	Cu(II)	H_2SO_4	728 nm		461
	Zn(II)	*conc* H_2SO_4	737 nm, 700, 667, 639, 395, 344, 318		563
		H_2SO_4	756 nm		461
R_1, R_4 = Ph	Zn(II)	py	682 nm (10^{-5} ε 1.82), 616 (0.29), 345 (0.48)		284
R_1, R_4, R_9, R_{12} = Ph	Zn(II)	py	699 nm (10^{-5} ε 1.29), 683 (1.10), 642 (0.22), 623 (0.21), 378 (0.42), 343 (0.47)		284

(*Continued*)

Table 2. (*Continued*)

Structure	M	Solvent	Transition Energy (Intensity)	Remark	Ref.
R_1, R_4, R_5, R_8 = Ph	Zn(II)	py	704 nm (10^{-5} ε 1.92), 636 (0.35), 343 (0.54)		284
R_1, R_4, R_5, R_8, R_9, R_{12} = Ph	Zn(II)	py	732 nm (10^{-5} ε 1.33), 656 (0.27), 394 (0.28), 340 (0.43)		284
α = Ph	2H	$CHCl_3$	713 nm, 681		566
	Ni(II)	$CHCl_3$	692 nm		566
$\alpha\alpha$ = Ph	2H	$CHCl_3$	788 nm (lg ε 4.96), 699sh (4.37), 414sh (4.39), 336 (4.58), 281sh (4.91)		567
		toluene	790 nm, 393sh		377
	Fe(II)L	py	694 nm, 435, 380	L = *trans*-py_2	205
	Ni(II)	toluene	758 nm, 681sh		377
	Zn(II)	toluene	780 nm		377
		py	786 nm (10^{-5} ε 0.83), 697 (0.21), 429 (0.26)		284
	Sn(IV)L	toluene	837sh nm, 796, 710sh, 485, 352	L = *trans*-$(OH)_2$	377
	Pb(II)	toluene	861sh, 831, 455		377
β = Ph	2H	$CHCl_3$	710 nm, 675		566
	Ni(II)	1-ClNp	688 nm		566
$\beta\beta$ = Ph	2H	1-ClNp	724 nm, 691		414
	Ti(IV)O	$CHCl_3$	703 nm (lg ε 5.19), 632 (4.32), 350 (4.75), 296 (4.61)		568
	Ni(II)	1-ClNp	695 nm		414
α = Ph(2-Me)	2H	$CHCl_3$	703 nm, 669		566
	Ni(II)	$CHCl_3$	675 nm		566
β = Ph(2-Me)	2H	$CHCl_3$	704 nm, 668		566
	Ni(II)	$CHCl_3$	674 nm		566
$\beta\beta$ = Ph(2-Me)	2H	1-ClNp	717 nm, 683		414
	Ni(II)	1-ClNp	689 nm		414
α = Ph(2-OMe)	2H	$CHCl_3$	703 nm, 669		566
β = Ph(2-OMe)	2H	$CHCl_3$	708 nm, 673		566
	Ni(II)	$CHCl_3$	679 nm		566
$\beta\beta$ = Ph(2-CF_3)	2H	1-ClNp	712 nm, 678		414
	Ni(II)	1-ClNp	679 nm		414
α = Ph(2-Cl)	Mn(III)	benzene	725nm		530
	Mn	benzene	680 nm, 350		528

(*Continued*)

Table 2. (*Continued*)

Structure	M	Solvent	Transition Energy (Intensity)	Remark	Ref.
	Mn(III)OH	benzene	725 nm (lg ε 4.92), 515 (4.08), 360 (4.53)		528
α = Ph(3-Me)	2H	$CHCl_3$	721 nm, 689		566
	Ni(II)	$CHCl_3$	693 nm		566
β = Ph(3-Me)	2H	$CHCl_3$	711 nm, 676		566
	Ni(II)	1-ClNp	688 nm		566
$\beta\beta$ = Ph(3-CF_3)	2H	$CHCl_3$ + 1% THF	713 nm (lg ε 5.32), 677 (5.25), 648 (4.75), 614 (4.58), 355 (5.06)		340
	Mg(II)	py	695 nm (r.i. 1.000), 626 (0.173), 367 (0.387)		340
	In(III)Cl	$CHCl_3$ + 1% THF	710 nm (lg ε 5.56), 679 (4.68), 639 (4.75)		340
α = Ph(4-Me)	2H	$CHCl_3$	725 nm, 693		566
	Ni(II)	$CHCl_3$	694 nm		566
β = Ph(4-Me)	2H	$CHCl_3$	713 nm, 678		566
	Ni(II)	1-ClNp	690 nm		566
$\beta\beta$ = Ph(4-Me)	2H	1-ClNp	726 nm, 694		414
	Ni(II)	1-ClNp	697 nm		414
$\beta\beta$ = Ph(4-*t*-Bu)	2H	1-ClNp	728 nm, 696		414
	Ti(IV)O	$CHCl_3$	706 nm (lg ε 5.34), 634 (4.53), 348 (4.80), 298 (4.73)		568
	Ni(II)	1-ClNp	699 nm		414
$\alpha\alpha$ = Ph(4-OMe)	2H	py	826 nm (lg ε 5.09), 728sh, 496sh, 402sh, 308 (5.09)		569
	Zn(II)	py	814 nm (lg ε 5.02), 728sh, 480sh, 423 (4.40), 309 (5.06)		569
$\beta\beta$ = Ph(4-OCH_2Ph)	Ti(IV)O	$CHCl_3$	705 nm (lg ε 5.44), 636 (4.87), 349 (5.09), 299 (4.93)		568
$\beta\beta$ = Ph(4-CF_3)	2H	1-ClNp	723 nm, 690		414
	Ni(II)	1-ClNp	693 nm		414
β = Ph(4-SO_3H)	Co(II)	DMF	682 nm (lg ε 5.14), 621, 334 (4.99)		570
		H_2O	694 nm, 638		570
		0.5% NaOH	680 nm, 649		570
	Cu(II)	DMF	690 nm (lg ε 5.04), 621 (4.46), 356 (4.72)		570
		H_2O	627 nm		570
		0.5% NaOH	608 nm		570
β = Ph(2,5-$(OMe)_2$)	2H	DCM	705 nm, 671, 645, 611, 343		571

(*Continued*)

Table 2. (*Continued*)

Structure	M	Solvent	Transition Energy (Intensity)	Remark	Ref.
	Zn(II)	DCM	683 nm, 618, 349		571
β= 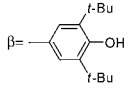	2H	DCM	715 nm, 683, 652, 620, 344		572
	Zn(II)	DMSO	698 nm (lg ε 5.57), 628 (4.81), 369 (5.09)		573
		PBS	706 nm (lg ε 4.02), 653 (3.96), 373 (3.99)		573
R_1, R_5, R_9 = 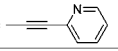	Zn(II)	DMF	686 nm (lg ε 5.27)		556
R_1, R_5, R_9 = 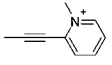	Zn(II)	DMF	691 nm, 679sh		556
		H_2O	628 nm	broad	556
R_1, R_5, R_9 = 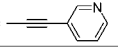	Zn(II)	DMF	691 nm (lg ε 5.33), 620 (4.59)		556
R_1, R_5, R_9 = 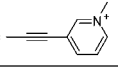	Zn(II)	DMF	698 nm, 684sh		556
R_3, R_7, R_{11} = 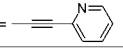	Zn(II)	DMF	681nm (lg ε 5.31), 617 (4.57)		556
R_3, R_7, R_{11} = 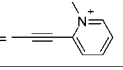	Zn(II)	DMF	712sh nm (lg ε 5.31), 695		556
		H_2O	636 nm	broad	556
R_3, R_7, R_{11} = 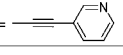	Zn(II)	DMF	687 nm (lg ε 5.28), 622 (4.57)		556
R_3, R_7, R_{11} = 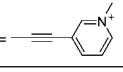	Zn(II)	DMF	696 nm, 682		556
		H_2O	628 nm	broad	556
$R_2, R_3, R_6, R_7, R_{10}, R_{11}$ = 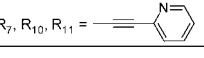	Zn(II)	DMF	696 nm (lg ε 5.31)		556
$R_2, R_3, R_6, R_7, R_{10}, R_{11}$ = 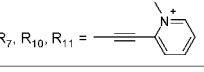	Zn(II)	DMF	736sh nm, 703		556
		H_2O	644 nm	broad	556
$R_2, R_3, R_6, R_7, R_{10}, R_{11}$ = 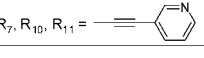	Zn(II)	DMF	702 nm (lg ε 5.30)		556

(*Continued*)

Table 2. (*Continued*)

Structure	M	Solvent	Transition Energy (Intensity)	Remark	Ref.
$R_2, R_3, R_6, R_7, R_{10}, R_{11}$ = 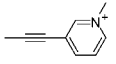	Zn(II)	DMF	726sh nm, 700		556
		H_2O	648 nm	broad	556
β = 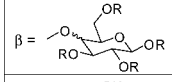	Zn(II)	DMSO	680 nm (r.i. 100), 612sh (19), 354 (42)	R = CH_2Ph	574
β = 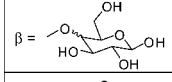	Zn(II)	DMSO	681 nm (r.i. 100), 613sh (17), 354 (41)		574
ββ = 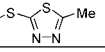	Zn(II)	py	705 nm(ε 90000), 665(37000), 375(60000)		575
$\beta\beta = CH_2OC_5H_{11}$	Ti(IV)O	$CHCl_3$	700 nm (lg ε 5.28), 665 (4.60), 631 (4.55), 352 (4.90)		549
$\beta\beta = CH_2OC_6H_{13}$	Co(II)	py	665.0 nm		576
$\beta\beta = CH_2OC_8H_{17}$	Pd(II)	$CHCl_3$	664 nm, 637, 598, 334, 283		577
	Pt(II)	$CHCl_3$	654 nm, 628, 591, 350sh, 286		577
$\beta\beta = O(CH_2)_{10}O(CH_2CH_2O)_3Me$	Si(IV)L	DCM	680 nm (lg ε 5.39), 358 (5.10)	L = *trans*-$(OH)_2$	578
β = 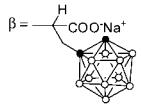	Co(II)	H_2O	636 nm (lg ε 5.4), 290 (5.6), 192 (5.8)	● C ○ BH	579
β = 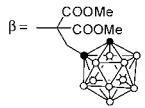	Co(II)	DCM	670 nm (lg ε 4.3), 630 (3.6), 602 (3.6), 328 (3.9), 266 (3.9)	● C ○ BH	579
β = 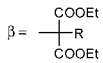	Co(II)	$CHCl_3$	671 nm, 329, 287	R = 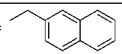	580
	Cu(II)	$CHCl_3$	681 nm, 343, 287		580
	Pd(II)	$CHCl_3$	663 nm, 334, 284		580
	Co(II)	$CHCl_3$	671 nm, 330	R = 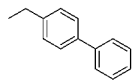	581
	Cu(II)	$CHCl_3$	681 nm, 344		581
	Pd(II)	$CHCl_3$	662 nm, 333		581

(*Continued*)

Table 2. (*Continued*)

Structure	M	Solvent	Transition Energy (Intensity)	Remark	Ref.
β = 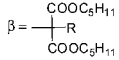	Pb(II)	$CHCl_3$	718 nm, 350	R = $CH_2COOC_5H_{11}$	582
		$CHCl_3$	720 nm, 347	R = 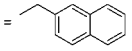	582
	Pd(II)	$CHCl_3$	662 nm, 329, 276	R = 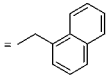	580
	Pb(II)	$CHCl_3$	721 nm, 344		582
β = 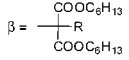	Co(II)	$CHCl_3$	671 nm (ε 11,400), 617 (4,800), 329 (11,600)	R = H	583
	Cu(II)	$CHCl_3$	676 nm (ε 12,400), 614 (5,500), 346 (9,800)	R = H	583
	Pd(II)	$CHCl_3$	657 nm (ε 10,610), 628 (3,940), 594 (2,460), 332 (4,230)	R = H	583
		$CHCl_3$	662 nm (ε 8,700), 630 (3,840), 598 (3,990), 348 (6,200)	R = C_6H_{13}	583
α = $(CH_2)_3COOH$	Zn(II)	MeOH	678 nm (lg ε 4.83), 649 (4.16), 613 (4.15), 353 (4.35)		584
$\beta\beta$ = $(CH_2)_2COOH$	Zn(II)	MeOH	677 nm (lg ε 4.72), 631 (4.35), 343 (4.56)		584
α = $(CH_2)_4COOC_5H_{11}$	Zn(II)	THF	684 nm, 616, 348		584
$\beta\beta$ = $(CH_2)_2COOCH_2Ph$	Zn(II)	THF	682 nm, 654, 615, 350		584
$\beta\beta$ = $CH_2CH(Me)COOH$	Zn(II)	MeOH	679 nm (lg ε 4.73), 614 (3.92), 350 (4.32)		584
$\beta\beta$ = $CH_2CH(Me)COOCH_2Ph$	Zn(II)	$CHCl_3$	683 nm, 616, 351		584
β = 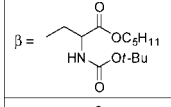	Zn(II)	THF	673 nm, 644, 608, 347		584
β = 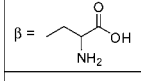	Zn(II)	MeOH	674 nm (lg ε 4.31), 634 (4.30), 337 (4.40)		584
ββ = 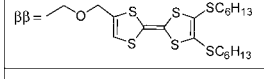	2H	toluene	700.0 nm (ε 33,459), 664.5 (42,654), 636.0 (45,037), 324.5 (133,580)		585
ββ = 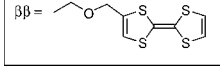	2H	DMF	677 nm (ε 13,300), 647 (13,400), 336 (27,900), 272 (56,500)	measured at 25 °C	586
			670 nm (ε 8,645), 638 (8,589), 330sh (15,500)	measured at 0 °C	586

(*Continued*)

Table 2. (*Continued*)

Structure	M	Solvent	Transition Energy (Intensity)	Remark	Ref.
ββ = 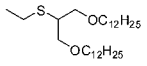	2H	$CHCl_3$	708.5 nm (10^{-4} ε 16.56), 673 (13.84), 653.5sh (4.62), 620.5 (2.85), 348.5 (7.49)		587
	Ni(II)	$CHCl_3$	679.5 nm (10^{-4} ε 21.65), 651sh (3.54), 611.5 (3.38), 462.5 (0.23), 336.5 (4.79)		587
β = 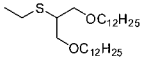	2H	$CHCl_3$	705.5 nm (10^{-4} ε 29.00), 669.5 (25.60), 650.5sh (9.09), 618.0 (5.44), 345.5 (14.77)		587
	Ni(II)	$CHCl_3$	676.5 nm (10^{-4} ε 21.54), 648 (3.98), 609.5sh (3.68), 334.5 (5.38)		587
α = COOH	Al(III)OH	DMF	682 nm		312
		DMSO	686 nm		312
		H_2SO_4	718 nm		312
	Cr(III)OH	DMF	684 nm		312
		DMSO	685 nm		312
		H_2SO_4	737 nm		312
	Co(II)	DMF	674 nm		312
		DMSO	670 nm		312
		H_2SO_4	714 nm		312
	Cu(II)	H_2SO_4	722 nm		461
		DMF	678 nm		312
		DMSO	679 nm		312
		H_2SO_4	717 nm		312
	Zn(II)	DMF	679 nm		312
		DMSO	679 nm		312
		H_2SO_4	728 nm		312
	Ga(III)OH	DMF	681 nm		312
		DMSO	680 nm		312
		H_2SO_4	716 nm		312
αβ(R_1, R_3) = COOH	Al(III)OH	py	709.5 nm		425
		DMF	688 nm		312
		H_2SO_4	728 nm		312
	Cr(III)OH	DMF	701 nm		312
		DMSO	699 nm		312

(*Continued*)

Table 2. (*Continued*)

Structure	M	Solvent	Transition Energy (Intensity)	Remark	Ref.
		H_2SO_4	724 nm		312
	Co(II)	DMF	674 nm		312
		DMSO	670 nm		312
		H_2SO_4	700 nm		312
	Ni(II)	DMF	687 nm		312
		DMSO	685 nm		312
		H_2SO_4	723 nm		312
	Cu(II)	DMF	693 nm		312
		DMSO	690 nm		312
		H_2SO_4	720 nm		312
	Zn(II)	DMF	696 nm		312
		DMSO	685 nm		312
		H_2SO_4	729 nm		312
	Ga(III)OH	DMF	705 nm		312
		DMSO	705 nm		312
		H_2SO_4	718 nm		312
β= COOH	Al(III)OH	DMF	684 nm		312
		DMSO	690 nm		312
		H_2SO_4	785 nm		312
	Cr(III)OH	DMF	691 nm		312
		DMSO	694 nm		312
		H_2SO_4	798 nm		312
	Co(II)	DMF	668 nm		312
		DMSO	668 nm		312
		H_2SO_4	762 nm		312
		H_2SO_4	756 nm		461
	Ni(II)	DMF	687 nm		312
		DMSO	687 nm		312
		H_2SO_4	767 nm		312
	Cu(II)	H_2SO_4	780 nm		461

(*Continued*)

Table 2. (*Continued*)

Structure	M	Solvent	Transition Energy (Intensity)	Remark	Ref.
		DMF	685 nm		312
		DMSO	687 nm		312
		H_2SO_4	778 nm		312
	Zn(II)	DMF	688 nm		312
		DMSO	687 nm		312
		H_2SO_4	778 nm		312
	Ga(III)OH	DMF	694 nm		312
		DMSO	696 nm		312
		H_2SO_4	761 nm		312
$\beta\beta$ = COOH	Al(III)OH	py	706.1 nm		425
		DMF	693 nm		312
		DMSO	699 nm		312
		H_2SO_4	753 nm		312
	Cr(III)OH	DMF	704 nm		312
		DMSO	702 nm		312
		H_2SO_4	762 nm		312
	Co(II)	py	684.0 nm		588, 576
		DMF	687 nm		312
		DMSO	689 nm		312
		H_2SO_4	751 nm		312
	Cu(II)	DMF	690 nm		312
		DMSO	694 nm		312
		H_2SO_4	746 nm		312
	Zn(II)	*conc* H_2SO_4	745 nm, 710, 674, 413, 345		563
		DMF	696 nm, 626, 357		563
β = COO^-	Al(III)Cl	DMSO	690 nm (lg ε 5.21)		589
	Zn(II)	DMSO	688 nm (lg ε 5.00)		589
$\beta\beta$ = COO^-	Al(III)Cl	DMSO	707 nm (lg ε 5.20)		589
	Zn(II)	DMSO	700 nm (lg ε 5.18)		589
	Co(II)	H_2O	678 nm, 255	$[Pc]^{8-}8Na^-$	590
		CCl_4	620 nm, 445	$[Pc]^8$ 8Na	590
β = COONa	Fe(II)	DMSO	659 nm		464

(*Continued*)

Table 2. (*Continued*)

Structure	M	Solvent	Transition Energy (Intensity)	Remark	Ref.
	Fe(II)L	DMSO	666 nm, 429	L = *trans*-py_2	464
		DMSO	666 nm, 424	L = *trans*-$(py(3\text{-}Me))_2$	464
		DMSO	666 nm, 427	L = *trans*-$(py(4\text{-}Me))_2$	464
		DMSO	667 nm, 424	L = *trans*-$(py(3\text{-}CH_2OH))_2$	464
		DMSO	668 nm, 426	L = *trans*-$(py(4\text{-}CH_2OH))_2$	464
		DMSO	667 nm, 424	L = *trans*-$(py(3\text{-}OH))_2$	464
		DMSO	668 nm, 430	L = *trans*-$(py(4\text{-}OH))_2$	464
		DMSO	665 nm, 555sh, 420	L = *trans*-$(py(3\text{-}Cl))_2$	464
		DMSO	689 nm, 555, 405	L = *trans*-$(py(4\text{-}Cl))_2$	464
		DMSO	666 nm, 421	L = *trans*-$(py(3\text{-}CHO))_2$	464
		DMSO	666 nm, 420	L = *trans*-$(py(4\text{-}CHO))_2$	464
		DMSO	665 nm, 520sh, 420	L = *trans*-$(py(3\text{-}CN))_2$	464
		DMSO	662 nm, 552sh, 412	L = *trans*-$(py(4\text{-}CN))_2$	464
$\beta\beta$ = COONa	Al(III)OH	H_2O	690 nm (r.i. 2.22), 650sh (0.45), 614 (0.40), 361 (1)		591
	Fe(II)	H_2O	682 nm (r.i. 1.50), 612 (0.35), 340 (1)		591
	Cu(II)	H_2O	685 nm (r.i. 2.25), 655sh (0.45), 615 (0.45), 348 (1)		591
	Zn(II)	H_2O	686 nm (r.i. 2.20), 656sh (0.45), 618 (0.40), 354 (1)		591
β = COOMe	Cu(II)	DMF	676 nm, 610		592
β = COOEt	Cu(II)	DMF	676 nm, 611		592
		benzene	681 nm, 608		592
$\beta\beta$ = COOEt	Zn(II)	DCM	687 nm, 617, 352		593
$\beta\beta$ = $COOCH_2CH_2Cl$	Al(III)OH	$CHCl_3$	695 nm (r.i. 2.30), 657 (0.74), 625 (0.52), 353 (1)		594
	Fe(II)	$CHCl_3$	680sh nm (r.i. 0.50), 651 (1.1), 337 (1)		594
	Co(II)	$CHCl_3$	677 nm, 600, 332		594
	Zn(II)	$CHCl_3$	688 nm (r.i. 2.65), 362 (1)		594
β = COOPr	Cu(II)	DMF	676 nm, 604		592
		benzene	685 nm, 617		592
		$CHCl_3$	683 nm, 615		592
		CCl_4	687 nm, 598		592
β = COOBu	Cu(II)	DMF	674 nm, 605		592
		benzene	683 nm, 614		592
		$CHCl_3$	683 nm, 614		592

(*Continued*)

Table 2. (*Continued*)

Structure	M	Solvent	Transition Energy (Intensity)	Remark	Ref.
		CCl_4	683 nm, 600		592
β= $COOC_8H_{13}$	Cu(II)	benzene	681 nm, 604		592
β= $COOC_7H_{15}$	Cu(II)	benzene	683 nm, 614		592
		$CHCl_3$	683 nm, 615		592
		CCl_4	685 nm, 608		592
β= $COOC_9H_{19}$	Cu(II)	benzene	685 nm, 614		592
		$CHCl_3$	683 nm, 615		592
		CCl_4	682 nm, 612		592
β= $COOC_{10}H_{21}$	Cu(II)	benzene	681 nm, 616		592
		$CHCl_3$	683 nm, 617		592
		CCl_4	681 nm, 606		592
β= $COOC_{11}H_{23}$	Cu(II)	benzene	681 nm, 613		592
		$CHCl_3$	683 nm, 618		592
		CCl_4	682 nm, 612		592
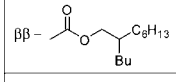	Zn(II)	DCM	687 nm (10^{-4} ε 27.9), 617 (4.65), 352 (8.81)		593
β= $COOC_{16}H_{33}$	Cu(II)	benzene	685 nm, 617		592
		$CHCl_3$	683 nm, 618		592
		CCl_4	682 nm, 614		592
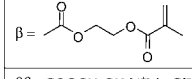	Cu(II)	THF	679 nm, 619, 345		595
$\beta\beta$= $COOCH_2CH_2N^+Me_3Cl^-$	Al(III)OH	H_2O	675sh nm, 640	$[Pc]^{8-}8Cl^-$	594
		DMSO	687 nm, 654	$[Pc]^{8-}8Cl^-$	594
	Fe(II)	H_2O	634 nm	$[Pc]^{8-}8Cl^-$	594
		EtOH	636br nm	$[Pc]^{8-}8Cl^-$	594
		DMSO	672 nm, 636sh	$[Pc]^{8-}8Cl^-$	594
	Co(II)	H_2O	636 nm, 449, 310	$[Pc]^{8-}8Cl^-$	594
		anhydrous EtOH	656 nm, 449, 322	$[Pc]^{8-}8Cl^-$	594
	Zn(II)	H_2O	641 nm, 344	$[Pc]^{8-}8Cl^-$	594
		DMSO	684 nm, 623	$[Pc]^{8-}8Cl^-$	594
β= $COONCH_2COONa$	Al(III)OH	H_2O	688 nm (r.i. 1.42), 650sh (0.48), 618 (0.55), 360 (1)		591

(*Continued*)

Table 2. (*Continued*)

Structure	M	Solvent	Transition Energy (Intensity)	Remark	Ref.
	Fe(II)	H_2O	678 nm (r.i. 1.25), 610 (0.30), 335 (1)		591
	Co(II)	H_2O	674 nm (r.i. 0.85), 600sh (0.45), 328 (1)		591
	Cu(II)	H_2O	674 nm (r.i. 1.05), 650sh (1.03), 356 (1)		591
	Zn(II)	H_2O	657 nm (r.i. 1.10), 654 (1.08), 358 (1)		591
β = COCl	Co(II)	DMF	678 nm (lg ε 4.55), 608 (1.10), 342 (1.37)		596
β = $CONHC_{18}H_{37}$	Ni(II)	$CHCl_3$	600 nm (10^{-4} ε 4.05), 335 (2.55)		597
β = 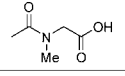	Co(II)	0.1% NaOH	670 nm, 630 (aggregated)		591
ββ = 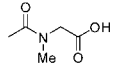	Co(II)	H_2O	675sh nm, 630		591
		0.1% NaOH	675 nm (r.i. 1.30), 618 (0.45), 330 (1)		591
		H_2O	675 nm (r.i. 1.05), 632 (0.65), 319 (1)	$[Pc]^{8+}8Cl^-$	591
	Cu(II)	H_2O	616.0 nm (r.i. 1.10), 340.5 (1)		591
		H_2O + NaOH	685 nm (r.i. 2.34), 617.5 (0.40), 349 (1)		591
		DMSO	683 nm (r.i. 3.45), 614 (0.80), 351 (1)		591
	Zn(II)	$CHCl_3$	695 nm (r.i. 1.95), 360.5 (1)		591
		H_2O	636 nm (r.i. 0.95), 344 (1)		591
		H_2O + NaOH	687 nm (r.i. 1.85), 635 (0.35), 618 (0.40), 353.5 (1)		591
		DMSO	683 nm (r.i. 2.09), 618 (0.63), 354 (1)		591
		H_2O	680sh nm, 643 (aggregated)		591
		0.1% NaOH	683 nm, 615, 354		591
ββ = 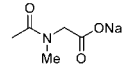	Co(II)	H_2O	675 nm (r.i. 1.50), 619 (0.45), 331 (1)		591
		0.01 M NaOH	675 nm (r.i. 1.35), 619 (0.40), 331 (1)		591
	Cu(II)	H_2O	685 nm (r.i. 2.34), 650sh (0.40), 617 (0.45), 349 (1)		591
	Zn(II)	H_2O	686 nm (r.i. 1.95), 655sh (0.45), 619 (0.40), 354 (1)		591
β = 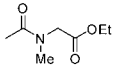	Co(II)	$CHCl_3$	670 nm, 619		591
β = 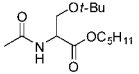	Zn(II)	$CHCl_3$	682.0 nm, 614.0, 348.0		584

(*Continued*)

Table 2. (*Continued*)

Structure	M	Solvent	Transition Energy (Intensity)	Remark	Ref.
β = 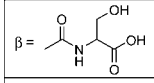	Zn(II)	MeOH	675.0 nm (lg ε 4.83), 634.5 (4.54), 344.5 (4.64)		584
ββ = 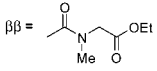	Co(II)	$CHCl_3$	673 nm (r.i. 1.55), 614 (0.60), 338 (1)		591
	Cu(II)	$CHCl_3$	679.5 nm (r.i. 2.08), 631.5 (0.32), 613.5 (0.43), 348.5 (1)		591
R_2 = OH	2H	50% DMF in MeOH	692 nm (lg ε 4.25), 664 (4.18), 348 (4.17)		598
α = OH	Al(III)OH	DMF	704 nm		534
		H_2SO_4	814 nm		534
	Cr(III)OH	DMF	710 nm		534
		H_2SO_4	817 nm		534
	Ga(III)OH	DMF	714 nm		534
β = OH	Ni(II)	H_2SO_4	753 nm (lg ε 4.53), 402 (4.11), 304 (4.67)		599
	Al(III)Cl	DMF	701 nm		534
		H_2SO_4	850 nm		534
	Cr(III)Cl	DMF	697 nm		534
		H_2SO_4	885 nm		534
	In(III)Cl	DMF	707 nm		534
	$Sn(IV)Cl_2$	DMF	714 nm		534
		H_2SO_4	841 nm		534
	$Hf(IV)Cl_2$	DMF	698 nm		534
		H_2SO_4	849 nm		534
$\beta\beta$ = OH	2H	DMF	712 nm, 678		600
	Zn(II)	DMF	685 nm		600
	Lu(III)OAc	DMF	681 nm		600
β = OMe	2H	py	705 nm (lg ε 4.73), 671 (4.67), 642 (4.31), 608 (4.17), 390sh (4.35), 346 (4.56)		410
		$CHCl_3$	702.61 nm (A_{max} 0.55), 666.18 (0.48), 642.18 (0.22), 607.78 (0.12), 392.04 (0.16), 344.03 (0.32), 288.79 (0.18)		39
	Zn(II)	toluene	678 nm, 611, 352		601
		THF	675 nm, 608, 347		601

(*Continued*)

Table 2. (*Continued*)

Structure	M	Solvent	Transition Energy (Intensity)	Remark	Ref.
		py	682 nm, 614, 358		601
		FCS 10% v/v in PBS	682 nm, 627, 339		601
$\beta\beta$ = OMe	2H	py	688 nm, 654		410
	Fe(II)	py	657 nm (r.i. 1.0), 632sh (0.3), 596 (0.3), 437sh (0.2), 406 (0.2), 342 (1.0)		238
	Co(II)	py	655 nm (r.i. 1.2), 597 (0.3), 400sh (0.1), 345sh (1.0), 330 (1.0)		238
$\alpha\alpha$ = OEt	2H	toluene	758 nm, 733		602
	Si(IV)L	toluene	747 nm	L = *trans*-$(OH)_2$	602
		toluene	746 nm	L = *trans*-$(OTMS)_2$	602
$\alpha\alpha$ = OEt	2H	toluene	758 nm (10^{-5} ε 1.38), 734 (1.16)		603
β = OEt	2H	py	707 nm (lg ε 4.71), 671 (4.66), 642 (4.32), 609 (4.21), 392sh (4.36), 346 (4.65)		410
$\alpha\alpha$ = OCH_2CF_3	Ti(IV)O	DCM	745.0 nm, 668.0sh, 345.5sh, 327.0		544
β = OCH_2CF_3	Mg(II)	benzene	698.0 nm (lg ε 4.84), 660.4 (4.79), 635.0 (4.56), 605.0 (4.40), 328.4 (5.02)		604
		DCM	694.6 nm (lg ε 4.83), 657.8 (4.84), 630.8 (4.70), 602.8sh (4.50), 323.6 (5.06)		604
		$CHCl_3$	696.8 nm (lg ε 4.86), 658.4 (4.83), 639.0 (4.65), 609.2sh (4.47), 324.8 (4.80)		604
		AcOEt	693.0 nm (lg ε 4.86), 656.0 (4.88), 631.2 (4.70), 603.4sh (4.57), 325.6 (4.98)		604
		acetone	691.8 nm (lg ε 4.69), 656.0 (4.74), 628.2 (4.69), 602.0sh (4.63), 322.8 (4.94)		604
		MeOH	685.8sh nm (lg ε 3.98), 593.8 (4.54), 320.0 (4.68)		604
	Al(III)Cl	AcOEt	675.6 nm (lg ε 4.84), 608.8 (4.19), 347.0 (4.60)		604
		acetone	676.6 nm (lg ε 4.68), 638.8 (4.37), 341.0 (4.70)		604
		MeOH	674.4 nm (lg ε 4.95), 608.6 (4.27), 356.8 (4.68)		604
	Ti(IV)O	DCM	695.5 nm, 627.0, 344.5, 280.0, 236.5		544
	Fe(III)Cl	benzene	699.6 nm (lg ε 4.40), 656.2 (4.53), 595.8 (3.98), 328.8 (4.56)		604

(*Continued*)

Table 2. (*Continued*)

Structure	M	Solvent	Transition Energy (Intensity)	Remark	Ref.
		DCM	696.4sh nm (lg ε 4.38), 656.4 (4.51), 608.6sh (4.10), 353.4 (4.54)		604
		$CHCl_3$	694.8 nm (lg ε 4.36), 663.0 (4.38), 600.4sh (4.21), 358.4 (4.42)		604
		AcOEt	695.6 nm (lg ε 4.50), 664.6sh (4.40), 598.2sh (4.25), 346.8 (4.55)		604
		acetone	688.0sh nm (lg ε 4.19), 662.8sh (4.29), 627.0 (4.33), 336.4 (4.57)		604
		MeOH	690.6sh nm (lg ε 4.47), 665.2 (4.77), 615.4sh (4.23), 331.6 (4.67)		604
	Co(II)	AcOEt	659.6 nm (lg ε 5.04), 612.5sh (4.55), 326.2 (4.85)		604
		acetone	659.0 nm (lg ε 5.02), 615.8sh (4.68), 325.6 (4.89)		604
		MeOH	654.6 nm (lg ε 4.72), 617.4 (4.69), 323.6 (4.75)		604
	Cu(II)	benzene	675.0 nm (lg ε 4.51), 612.6 (4.36), 338.2 (4.40)		604
		DCM	670.4 nm (lg ε 4.28), 608.0 (4.38), 327.4 (4.63)		604
		$CHCl_3$	673.8 nm (lg ε 4.15), 611.6 (4.10), 329.8 (4.17)		604
		AcOEt	667.8 nm (lg ε 4.45), 607.8 (4.49), 329.8 (4.55)		604
		acetone	665.7 nm (lg ε 4.32), 605.5 (4.48), 326.9 (4.54)		604
		MeOH	660.8sh nm (lg ε 4.18), 593.6 (4.40), 320.0 (4.45)		604
	Zn(II)	benzene	677.0 nm (lg ε 5.01), 609.0 (4.25), 356.6 (4.65)		604
		DCM	674.0 nm (lg ε 4.61), 608.6sh (4.26), 342.4 (4.50)		604
		$CHCl_3$	674.0 nm (lg ε 4.91), 608.8 (4.25), 346.8 (4.66)		604
		AcOEt	668.8 nm (lg ε 5.02), 603.4 (4.27), 346.6 (4.71)		604
		acetone	670.8 nm (lg ε 5.04), 603.8 (4.32), 349.2 (4.65)		604
		MeOH	669.2 nm (lg ε 4.70), 625.4 (4.42), 338.4 (4.66)		604
$\beta\beta = OCH_2CF_3$	Ti(IV)O	acetone-d_6	684.5 nm, 619.0,		544
$\beta = OCH_2CF_3$	2H	THF	732.6 nm, 705.7		48
		acetone	728.0 nm, 702.8		605
		benzene	736.8 nm, 708.9		605
		$CHCl_3$	736.4 nm, 704.1		605
		decanol	733.4 nm, 704.4		605
		1,4-dioxan	733.0 nm, 708.0		605
		DMF	731.2 nm, 709.0		605

(*Continued*)

Table 2. (*Continued*)

Structure	M	Solvent	Transition Energy (Intensity)	Remark	Ref.
		EtOH	726.1 nm, 699.0		605
		AcOEt	731.0 nm, 702.5		605
		hexane	734.1 nm, 701.5		605
		hexanol	731.0 nm, 701.8		605
		MeOH	726.0 nm, 698.3		605
		$PhNO_2$	736.5 nm, 709.0		605
		THF	730.7 nm, 705.0		605
	Zn(II)	THF	707.0 nm		48
		$CHCl_3$	710 nm, 677, 639, 362		512
		acetone	702.3 nm		605
		MeCN	701.4 nm		605
		benzene	710.8 nm		605
		$CHCl_3$	708.3 nm		605
		decanol	707.0 nm		605
		dioxan	707.3 nm		605
		DMF	704.8 nm		605
		EtOH	702.6 nm		605
		hexane	705.8 nm		605
		hexanol	705.7 nm		605
		MeOH	701.6 nm		605
		py	707.9 nm		605
		THF	703.7 nm		605
$\alpha\alpha$= OPr	2H	toluene	760 nm (10^{-5} ε 1.35), 737 (1.17)		603
β= OPr	2H	py	707 nm (lg ε 4.72), 672 (4.68), 642 (4.40), 609sh (4.31), 392sh (4.49), 346 (4.65)		410
α= O(*i*-Pr)	2H	$CHCl_3$	728.21 nm, 695.37, 316.92		606
β= O(*i*-Pr)	2H	DCM	706 nm (lg ε 4.64), 670 (4.58)		607
		$CHCl_3$	708 nm (lg ε 4.77), 672 (4.70), 644 (4.36), 610 (4.16), 388 (4.27), 338 (4.71)		387
		DMF	14200 cm^{-1} (lg ε 4.72), 14900 (4.74), 15500 (4.31), 16300 (4.17), 25500 (4.23), 29600 (4.67)		387
	P(V)L	py	14600 cm^{-1}, 25400	L = *trans*-$(OH)_2$, $[Pc]^+OH^-$	387

(*Continued*)

Table 2. (*Continued*)

Structure	M	Solvent	Transition Energy (Intensity)	Remark	Ref.
	Co(II)	H_2SO_4	815 nm		461
α = OBu	2H	THF	723.0 nm, 689.7		48
	Zn(II)	THF	696.0 nm		48
$\alpha\alpha$ = OBu	2H	THF	762.0 nm, 744.0		48
		toluene	758 nm (lg ε 5.13)		608
		DCM + 0.5% py	744 nm, 661		608
		EtOH	1055.8 nm		608
		toluene	760 nm (10^{-3} ε 132), 739 (113), 407 (24), 330 (54.9)		389
		toluene	761 nm (10^{-5} ε 1.34), 738 (1.13)		603
		toluene	761 nm (10^{-5} ε 1.1), 739 (0.95)		419, 609
		$CHCl_3$	764.68 nm , 751.26, 330.1		606
	Si(IV)L	toluene	749 nm	L = *trans*- 	602
		toluene	749 nm	L = *trans*-$(OH)_2$	609
		toluene	747 nm (10^{-5} ε 2.3)	L = *trans*-$(OSi(C_6H_{13})_3)_2$	609
	P(V)L	MeOH	889 nm (10^{-3} ε 91), 785 (25), 559 (14), 366 (31)	L = *trans*-$(OMe)_2$, $[Pc]^+OH^-$	389
	Ti(IV)O	$CHCl_3$	791 nm (lg ε 5.10), 704 (4.46), 479 (3.99), 340 (4.63)		549
	Co(II)	THF	718 nm		610
		DCM	730 nm (lg ε 4.88), 689.5		608
	Ni(II)	toluene	733 nm		611
	Zn(II)	DMF	739 nm		610
		py	758.0 nm		48
		PVA in DMSO	748 nm (10^{-4} ε 5.51)		486
		DCM + 0.5 vol % py	744 nm (lg ε 5.12), 327.0		608
		toluene	758 nm		419
β = OBu	2H	THF	703.1 nm, 666.3		48
	Zn(II)	H_2SO_4	827 nm		461
		THF	674.5 nm		48

(*Continued*)

Table 2. (*Continued*)

Structure	M	Solvent	Transition Energy (Intensity)	Remark	Ref.
$\beta\beta$ = OBu	2H	py	698 nm, 662, 603sh, 424, 346		410
		THF	698.3 nm, 660.2		48
		toluene	702 nm (10^{-5} ε 1.11), 662 (1.0)		419
	Co(II)	DCM	670 nm		410
	Cu(II)	DCM	676 nm, 611sh, 337		410
	Zn(II)	DCM	677 nm, 341		410
		DMF	673 nm, 644, 607, 370		533
		THF	674.5 nm		48
		DMF	678 nm		419
	Sn(II)	DCM	676 nm, 611sh, 408, 338		410
	Pb(II)	DCM	716 nm, 402		410
$\alpha\alpha\beta\beta$ = OBu	Co(II)	THF	714 nm		610
	Zn(II)	DMF	728 nm		610
β = O(*i*-Bu)	2H	DCM	706 nm (lg ε 5.02), 670 (4.97)		607
β = O(*t*-Bu)	Mn(III)	benzene	683 nm, 355		528
	Mn(III)Cl	benzene	729 nm (lg ε 4.90), 534 (4.08), 368 (4.60)		528
	Mn(III)L	py	634 nm, 350	L = py	528
$\beta\beta$ = O(*i*-Bu)	Zn(II)	toluene	675 nm (lg ε 5.53), 646 (4.67), 608 (4.71), 349 (4.94), 289 (4.81)		612
R_1, R_4 = OC_5H_{11}	Mg(II)	DMSO	673 nm (lg ε 4.74), 624 (4.06), 345 (4.41)		613
	Zn(II)	DMSO	673 nm (lg ε 5.02), 624 (4.84), 345 (4.23)		613
R_1, R_4, R_5, R_8, R_9, R_{12} = OC_5H_{11}	2H	benzene	759 nm (r.i. 1.87), 716 (1.49), 648 (0.58), 482 (0.41), 332 (1.76)		614
α = OC_5H_{11}	2H	$CHCl_3$	727 nm (lg ε 5.29), 696 (5.12), 663 (4.68), 631 (4.58), 387 (4.62), 353 (4.52)		407
	Ni(II)	py	700 nm		615
$\alpha\alpha\beta\beta$ = OC_5H_{11}	2H	$CHCl_3$	774 nm (lg ε 5.19), 753 (5.14), 705 (4.65), 676 (4.60), 406sh, 331 (4.88)		407
		$CHCl_3$	770.0 nm (lg ε 5.16), 694.0 (4.58), 458.0 (4.19), 419.0 (4.24), 331.5 (4.78)		616
		toluene	762 nm (lg ε 5.09), 739 (5.01), 695 (4.51), 667 (4.46), 402 (4.31), 329 (4.69)		617
		toluene	762 nm (10^{-5} ε 1.39), 738 (1.20)		603

(*Continued*)

Table 2. (*Continued*)

Structure	M	Solvent	Transition Energy (Intensity)	Remark	Ref.
		toluene	762 nm, 738		419
	Mg(II)	DMSO	696 nm (lg ε 4.96), 625 (4.82), 343 (4.43)		613
	Ni(II)	toluene	734 nm (10^{-5} ε 1.66)		603
		DCM	742 nm (10^{-5} ε 1.69)		603
		toluene	734 nm		419
	Zn(II)	DCM	748 nm (10^{-5} ε 1.32)		603
		DCM	748 nm		419
	Ru(II)L	$CHCl_3$	699 nm, 630, 405, 312	L = *trans*-(py(3-Cl))$_2$	499
β = OC_5H_{11}	2H	$CHCl_3$	707 nm (lg ε 5.11), 671 (5.04), 645 (4.62), 610 (4.41), 392 (4.45), 344 (4.85)		407
		$CHCl_3$	706.03 nm (A_{max} 0.65), 668.98 (0.55), 607.78 (0.14), 389.28 (0.18), 344.04 (0.36), 289.7 (0.21)		39
	Er(III)L	$CHCl_3$	920 nm (lg ε 3.54), 675 (4.78), 605 (4.30), 450 (4.10), 350 (4.64), 320 (4.65)	L = acac	543
$\beta\beta$ = OC_5H_{11}	2H	$CHCl_3$	704 nm (10^{-5} ε 1.21), 676 (1.02)		618
		THF	698 nm (10^{-5} ε 3.3), 660 (2.7), 644 (1.1), 598 (0.60), 426 (0.77), 348 (1.8), 295 (1.3)		619
		$CHCl_3$	700 nm (lg ε 5.23), 664 (5.16), 639 (4.77), 604 (4.48), 427 (4.64), 349 (4.99)		407
		$CHCl_3$	702 nm, 664, 636, 602, 348		548
	Li, H	THF	785 nm (10^{-5} ε 0.19), 699 (0.17), 661 (0.15), 506 (0.68), 418 (0.43), 342 (1.0), 284 (0.83)		619
	2Li	THF	661 nm (10^{-5} ε 2.7), 631 (0.39), 598 (0.40), 357 (1.1), 282 (0.62)		619
		$CHCl_3$	675 nm, 355		548
	Mg	THF	673 nm (10^{-5} ε 3.2), 644 (0.39), 609 (0.41), 409 (0.11), 363 (0.63), 347 (0.80), 289 (0.57)		619
	Al(II)	THF	682 nm (10^{-5} ε 0.22), 660 (0.21), 614 (0.38), 584 (0.48), 563 (0.25), 542 (0.17), 397 (0.35), 338 (0.43), 285 (0.36)		619
	Al(III)Cl	THF	684 nm (10^{-5} ε 0.91), 656 (0.14), 616 (0.13), 430 (0.092), 368 (0.38), 298 (0.15)		619

(*Continued*)

Table 2. (*Continued*)

Structure	M	Solvent	Transition Energy (Intensity)	Remark	Ref.
	Ti(IV)O	$CHCl_3$	702 nm (lg ε 5.12), 669 (4.28), 631 (4.28), 439 (4.37), 348 (4.68)		119
		$CHCl_3$	702 nm (lg ε 5.12), 669 (4.28), 631 (4.28), 439 (4.37), 348 (4.68)		549
	Ru(II)	$CHCl_3$	700sh nm, 632.5, 587sh, 420sh, 318		500
	Ru(II)L	$CHCl_3$	625 nm, 576sh, 366, 323	L = *trans*-(py(3-Cl))$_2$	500
		$CHCl_3$	647 nm, 587sh, 325	L = *trans*-(CN(*t*-Bu))$_2$	500
		$CHCl_3$	658 nm, 634, 594, 410, 320,300	L = CO	500
	Os(II)L	DCM	680 nm, 631, 355, 296	L = *trans*-(py)$_2$	230
	Pt(II)	$CHCl_3$	653 nm, 630, 591, 401, 312sh, 293		577
β = OCH_2(*t*-Bu)	2H	DCM	705 nm (lg ε 4.79), 670 (4.73)		607
	Mg(II)	THF	676 nm (lg ε 5.04), 656 (4.45)610 (4.37), 356 (4.76), 288 (4.40)		620
$\beta\beta$ = OCH_2(*t*-Bu)	Ni(II)	toluene	672 nm (lg ε 5.17), 640 (4.52), 604 (4.46), 416 (4.37), 336 (4.59), 314 (4.73), 288 (4.78)		621
$\alpha\alpha\beta\beta$ = OCH_2(*t*-Bu)	2H	THF	784 nm (lg ε 5.13), 764 (5.13), 686 (4.55), 398 (4.58), 328 (4.78)		174
	Mg(II)	THF	754 nm (lg ε 5.30), 672 (4.62), 366 (4.70), 330 (4.77)		174
	Mn(III)OAc	THF	827 nm (lg ε 4.8), 740 (4.2), 570 (4.15), 465sh, 413 (4.4)		174
$\alpha\alpha\beta\beta$ = OCH_2(*t*-Bu)	Ni(II)	toluene	758 nm (lg ε 5.19), 676 (4.51), 440 (4.25), 386 (4.44), 342 (4.46), 314 (4.69)		621
R_1, R_5, R_9, R_{13} = $OCHEt_2$	2H	$CHCl_3$	729 nm (lg ε 5.22), 696 (5.16), 664 (4.66), 624 (4.51), 358sh (4.65), 318 (4.82)		622
	Ni(II)	$CHCl_3$	699 nm (lg ε 5.36), 664sh (4.63), 628 (4.61), 404sh (4.16), 298 (4.75)		622
α = $OCHEt_2$	Mg(II)	$CHCl_3$	758 nm (lg ε 4.54), 705 (5.34), 674sh (4.60), 634 (4.59), 319 (4.70)		623
	Co(II)	$CHCl_3$	696 nm (lg ε 5.11), 662sh (4.51), 626 (4.45), 418sh (4.00), 310 (4.65)		623
	Ni(II)	$CHCl_3$	699 nm (lg ε 5.36), 664sh (4.63), 628 (4.61), 404sh (4.16), 298 (4.75)		623

(*Continued*)

Table 2. (*Continued*)

Structure	M	Solvent	Transition Energy (Intensity)	Remark	Ref.
	Cu(II)	$CHCl_3$	707 nm (lg ε 5.43), 634 (4.70), 415sh (4.16), 318 (4.76)		623
	Zn(II)	$CHCl_3$	760 nm (lg ε 4.63), 703 (5.39), 674sh (4.72), 633 (4.68), 412sh (4.41), 318 (4.78)		623
$\beta\beta = OCHEt_2$	2H	toluene	702 nm, 662		419
	Ni(II)	toluene	672 nm		419
$\alpha\alpha =$ 	Co(II)	cyclohexane	731 nm (10^{-4} ε 1.95)		624
		DCM	742 nm (10^{-4} ε 1.67), 667, 326		624
		$CHCl_3$	742 nm (10^{-4} ε 1.60)		624
		DMF	729 nm (10^{-4} ε 1.26)		624
		THF	723 nm (10^{-4} ε 1.35)		624
		2-ethoxyethanol	725 nm (10^{-4} ε 1.43)		624
	Ni(II)	cyclohexane	734 nm (10^{-4} ε 2.04)		624
		DCM	747 nm (10^{-4} ε 1.74), 671, 331		624
		$CHCl_3$	748 nm (10^{-4} ε 1.68)		624
		DMF	749 nm (10^{-4} ε 1.36)		624
		THF	741 nm (10^{-4} ε 1.45)		624
		2-ethoxyethanol	744 nm (10^{-4} ε 1.56)		624
	Cu(II)	cyclohexane	743 nm (10^{-4} ε 2.09)		624
		DCM	755 nm (10^{-4} ε 1.77), 677, 335		624
		$CHCl_3$	758 nm (10^{-4} ε 1.70)		624
		DMF	749 nm (10^{-4} ε 1.49)		624
		THF	742 nm (10^{-4} ε 1.52)		624
		2-ethoxyethanol	746 nm (10^{-4} ε 1.57)		624
	Zn(II)	cyclohexane	740 nm (10^{-4} ε 2.15)		624
		DCM	753 nm (10^{-4} ε 1.87), 680, 336		624
		$CHCl_3$	756 nm (10^{-4} ε 1.83)		624
		DMF	739 nm (10^{-4} ε 1.53)		624
		THF	738 nm (10^{-4} ε 1.75)		624
		2-ethoxyethanol	740 nm (10^{-4} ε 1.72)		624
$\alpha = OC_6H_{13}$	2H	$CHCl_3$	729 nm, 696, 664, 630, 420sh, 354, 316		512
		MeOH	690 nm, 664, 631, 400sh, 313		512

(*Continued*)

Table 2. (*Continued*)

Structure	M	Solvent	Transition Energy (Intensity)	Remark	Ref.
$\alpha = OCH_2CHEt_2$	In(III)Cl	THF	728 nm (10^{-5} ε 2.11)		342
$\beta = OCH_2CHEt_2$	In(III)Cl	THF	702 nm (10^{-5} ε 1.92)		342
$\alpha = OC_7H_{15}$	2H	$CHCl_3$	730 nm (lg ε 5.18), 700 (5.10), 666 (4.60), 634 (4.49), 389 (4.62), 353 (4.53)		407
	Pb(II)	$CHCl_3$	755 nm (lg ε 5.33), 676 (4.57), 437 (4.39), 333 (4.70)		376
$\beta\beta = OCH(i\text{-}Pr)_2$	Zn(II)	EtOH	707 nm (10^{0} ε = 1.00)		625
		UDL	707 nm (10^{-6} ε = 1.16)	UDL = ultradeformable liposomes	625
R_2, $R_3 = OC_8H_{17}$	2H	$CHCl_3$	695 nm (lg ε 5.21), 659 (5.13), 640 (4.74), 599 (4.51), 431 (4.30), 339 (4.91)		516
		$CHCl_3$	695 nm (ε 162,181), 659 (134,896), 640 (54,954), 599 (32,359), 431 (19,952), 339 (81,283)		517
$\alpha\alpha = OC_8H_{17}$	2H	toluene	740 nm, 762		419
		toluene	762 nm (10^{-5} ε 1.42), 740 (1.22)		603
		DCM	767 nm (10^{-5} ε 1.38)		603
	Cu(II)	DCM	752 nm		419
		DCM	752 nm (10^{-5} ε 1.91)		603
$\beta = OC_8H_{17}$	2H	$CHCl_3$	705.80 nm (A_{max} 0.81), 668.76 (0.69), 646.35 (0.29), 607.79 (0.17), 389.77 (0.22), 343.93 (0.44), 289.51 (0.25)		39
	Ni(II)	DCM	676 nm, 625sh, 381, 363, 328, 302sh, 280, 243		626
$\beta\beta = OC_8H_{17}$	Zn(II)	toluene + 1×10^{-2} M py	677 nm (10^{-4} ε 28.6), 648 (4.06), 611 (4.25), 364 (10.4), 295 (4.69)		265
		PVA in DMSO	690 nm (10^{-4} ε 10.12)		486
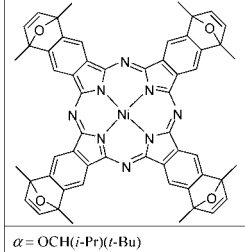	Ni(II)	DCM	884 nm, 867.50, 658.50, 373, 331		627
$\alpha = OCH(i\text{-}Pr)(t\text{-}Bu)$	2H	toluene	730.10 nm, 697.37		606

(*Continued*)

Table 2. (*Continued*)

Structure	M	Solvent	Transition Energy (Intensity)	Remark	Ref.
		DCM	731.67 nm, 702.13		606
		$CHCl_3$	732.64 nm, 700.85		606
		THF	731.93 nm, 699.25		606
		DMF	734.63 nm, 706.77		606
		DMSO	737.86 nm, 713.52		606
		py	735.83 nm, 708.71		606
R_1, R_8 = 	2H	toluene	679 nm, 714		628
α = OCH(*i*-Pr)(*t*-Bu)	V(IV)O	hexane	727 nm		457
		cyclohexane	730 nm		457
		toluene	739 nm		457
		DCM	742 nm		457
		$CHCl_3$	742 nm		457
		DMF	744 nm		457
		py	747 nm		457
$\beta\beta$ = $OCH_2CH(Et)Bu$	ln(III)L	DCM	696 nm, 627, 404	L = OC(Me)CHCOMe	540
β = $OCH(CH_2CHMe_2)_2$	2H	$CHCl_3$	726 nm, 693, 661, 627, 417sh, 349, 316		512
R_1, R_4, R_9, R_{12} = $OC_{10}H_{21}$	2H	$CHCl_3$	737.1 nm (lg ε 4.84), 712.3 (4.87), 644.5 (4.48), 434.4 (4.08), 337.7 (4.82)		616
$\alpha\alpha$ = $OC_{10}H_{21}$	2H	$CHCl_3$	775.0 nm (r.i. 1.579), 331.0 (1.397)		616
$\beta\beta$ = $OC_{10}H_{21}$	2H	CHCl3	704 nm, 667, 647, 604, 427, 350, 297		629
$\alpha\alpha$ = $OC_{12}H_{25}$	2H	DCM	768 nm (10^{-5} ε 1.45)		603
β = $OC_{12}H_{25}$	2H	$CHCl_3$	703 nm, 665, 604, 428, 349, 296		630
		$CHCl_3$	705.78 nm (A_{max} 0.90), 668.85 (0.76), 608.10 (0.20), 389.77 (0.26), 343.72 (0.50), 289.53 (0.31)		39
	Cu(II)	$CHCl_3$	678 nm, 612, 376, 340, 292		630
$\beta\beta$ = $OC_{12}H_{25}$	2H	$CHCl_3$	700 nm (lg ε 5.23), 660 (5.19), 640sh, 600 (4.46)		473
	Cu(II)	$CHCl_3$	675 nm (lg ε 5.66), 652-644sh, 610 (4.77)		473
$\beta\beta$ = $OC_{16}H_{33}$	2H	$CHCl_3$	702.77 nm (A_{max} 0.32), 665.23 (0.26), 648.02 (0.10), 603.86 (0.05), 425.04 (0.08), 348.44 (0.22), 295.62 (0.21)		39

(*Continued*)

Table 2. (*Continued*)

Structure	M	Solvent	Transition Energy (Intensity)	Remark	Ref.
$\beta\beta = OC_{18}H_{37}$	2H	$CHCl_3$	702.41 nm (A_{max} 0.67), 664.72 (0.54), 648.36 (0.24), 603.18 (0.11), 421.17 (0.11), 347.96 (0.49), 290.26 (0.65)		39
$\beta = O(CH_2CH_2O)_3CPh_3$	2H	toluene	704 nm, 668, 646, 608, 384, 344		631
$\alpha = OCH(CH_2OC_{12}H_{25})_2$	2H	$CHCl_3$	724 nm (lg ε 9.13), 692 (8.11) 661 (2.71), 626 (1.88), 351 (3.00)		632
	Ni(II)	$CHCl_3$	695 nm (lg ε 21.73), 665 (3.89), 624 (3.76), 406 (1.07), 335 (3.80)		632
	Zn(II)	$CHCl_3$	744 nm (lg ε 6.55), 704 (16.00), 671 (3.81), 635 (3.15), 412 (2.30), 350 (3.90)		632
$\beta = OCH(CH_2OC_{12}H_{25})_2$	2H	$CHCl_3$	705 nm (lg ε 9.66), 668 (7.97), 642 (2.93), 606 (1.82), 392 (2.31), 343 (5.02)		632
	Ni(II)	$CHCl_3$	675 nm (lg ε 19.95), 642 (3.54), 607 (3.73), 382 (2.80), 329 (4.60)		632
	Zn(II)	$CHCl_3$	682 nm (lg ε 15.50), 647 (2.33), 614 (2.97), 347 (7.21)		632
$\beta = OCH_2CH(C_8H_{17})(C_{10}H_{21})$	2H	toluene	705 nm (ε 132,000 ± 13,000), 671 (127,000 ± 13,000), 344 (114,000 ± 13,000)		633
$\beta = OCH_2CH(C_{10}H_{21})(C_{12}H_{25})$	2H	toluene	705 nm (ε 149,000 ± 15,000), 671 (146,000 ± 15,000), 344 (129,000 ± 15,000)		633
α = 	2H	$CHCl_3$	729 nm, 695, 663, 629, 317		634
	Ni(II)	$CHCl_3$	699 nm, 671, 628, 400, 375, 335, 298		634
	Cu(II)	$CHCl_3$	708 nm, 676, 635, 345, 318, 259		634
	Zn(II)	$CHCl_3$	695 nm, 666, 627, 372, 319		634
β = 	Ni(II)	$CHCl_3$	671 nm, 639, 605, 379, 328		634
β = 	2H	$CHCl_3$	723 nm, 690, 658, 624, 353, 319		634
	Cu(II)	$CHCl_3$	709 nm, 678, 635, 406, 345, 317, 260		634
ββ = 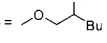	Mg(II)	DCM	679.0 nm (lg ε 5.31), 613.0sh (4.69), 360.0 (5.01)		330
	Ni(II)	DCM	670.0 nm, 604.0sh, 410.0, 310.0		635
	Cu(II)	DCM	679.0 nm, 611.5sh, 418.0, 339.5		635
	Ga(III)Cl	DCM	694.5 nm (lg ε 5.24), 625.0sh (4.62), 441.0 (4.38), 357.5 (4.96)		330

(*Continued*)

Table 2. (*Continued*)

Structure	M	Solvent	Transition Energy (Intensity)	Remark	Ref.
	Ru(II)L	$CHCl_3$	658 nm, 634, 594, 410, 320, 300sh	L = CO	500
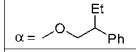	Ni(II)	$CHCl_3$	697 nm, 670, 627, 400, 336, 299		634
α = OPh	Ti(IV)O	$CDCl_3$	728 nm (lg ε 5.41), 651 (4.71), 348 (4.88)		636
	Ga(III)Cl	toluene	716 nm, 334		323
		DCM	717 nm, 336		323
		THF	707 nm, 330		323
		$CHCl_3$	723 nm, 333		323
		DMSO	712 nm (lg ε 5.34), 639 (4.69), 344 (4.80)		323
	Cd(II)	DMSO	698 nm (lg ε 5.26), 631 (4.56), 351 (4.73)		287
		toluene	694 nm (lg ε 5.21)		287
		THF	693 nm (lg ε 5.14)		287
		$CHCl_3$	700 nm (lg ε 5.23)		287
		DMF	694 nm (lg ε 5.25)		287
	In(III)Cl	DMSO	712 nm (lg ε 5.13), 639 (4.69), 331 (4.89)		323
	Sn(IV)L	DMSO	733 nm (lg ε 5.03), 652 (4.47), 339 (4.78)	L = *trans*-Cl_2	369
		THF	727nm, 357, 333	L = *trans*-Cl_2	369
		$CHCl_3$	737 nm, 347	L = *trans*-Cl_2	369
		DCM	732 nm, 345	L = *trans*-Cl_2	369
		toluene	730 nm, 357, 332	L = *trans*-Cl_2	369
	Pb(II)	DMSO	723 nm (lg ε 5.33), 652 (4.65), 460 (4.41), 347 (4.77)		637
		DMF	722 nm		637
		toluene	732 nm		637
		THF	724 nm		637
		$CHCl_3$	740 nm		637
β = OPh	2H	py	703 nm (lg ε 4.73), 669 (4.68), 638 (4.30), 609sh (4.17), 340 (4.55)		410
		$CHCl_3$	701 nm (lg ε 5.22), 666 (5.15), 639 (4.75), 607 (4.46), 393sh, 344 (4.86)		407
		PhCl	701 nm (lg ε 5.16), 665 (5.09)		607
		THF	696 nm (lg ε 5.06), 661		607
	Ti(IV)O	$CDCl_3$	702 nm (lg ε 5.21), 630 (4.50), 400 (4.43), 347 (4.77), 290 (4.57)		636

(*Continued*)

Table 2. (*Continued*)

Structure	M	Solvent	Transition Energy (Intensity)	Remark	Ref.
	Zn(II)	$CHCl_3$	742 nm (lg ε 5.24), 698 (5.23), 628 (4.44), 338 (4.61)		638
	Ga(III)Cl	toluene	696 nm, 353		323
		DCM	698 nm, 353, 290		323
		THF	691 nm, 364		323
		$CHCl_3$	699 nm, 353, 282		323
		DMSO	691 nm (lg ε 5.29), 621 (4.61), 361 (4.89)		323
	Cd(II)	DMSO	681 nm (lg ε 5.22), 613 (4.61), 350 (4.83)		287
		toluene	681 nm (lg ε 5.15)		287
		THF	677 nm (lg ε 5.13)		287
		$CHCl_3$	681 nm (lg ε 5.18)		287
		DMF	677 nm (lg ε 5.22)		287
	In(III)Cl	DMSO	696 nm (lg ε 5.09), 625 (4.65), 364 (5.02)		323
	Sn(IV)L	DMSO	709 nm (lg ε 5.03), 639 (4.39), 356 (4.80)	L = *trans*-Cl_2	369
		THF	701 nm, 354	L = *trans*-Cl_2	369
		$CHCl_3$	709 nm, 366	L = *trans*-Cl_2	369
		DCM	707 nm, 359	L = *trans*-Cl_2	369
		toluene	706 nm, 357	L = *trans*-Cl_2	369
	Pb(II)	DMSO	708 nm (lg ε 4.95), 638 (4.26), 346 (4.52)		637
		DMF	706 nm		637
		toluene	715 nm		637
		THF	708 nm		637
		$CHCl_3$	721 nm		637
$\beta\beta$ = OPh	Si(IV)L	unknown	678 nm (lg ε 5.31), 649 (4.50), 609 (4.52), 364 (4.92), 344 (4.76)	L = *trans*-Cl_2	639
		unknown	678 nm (lg ε 5.17), 642 (4.25), 609 (4.39), 364 (4.72), 343 (4.55)	L = *trans*-$(OH)_2$	639
		unknown	695 nm (lg ε 5.32), 661 (4.51), 626 (4.53), 366 (4.86), 346 (4.76)	L = *trans*- 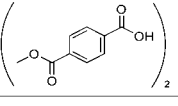	639
		unknown	697 nm (lg ε 5.09), 662 (4.35), 626 (4.46), 364 (4.71), 346 (4.65)	L = *trans*- $(OCO(4\text{-py}))_2$	639

(*Continued*)

Table 2. (*Continued*)

Structure	M	Solvent	Transition Energy (Intensity)	Remark	Ref.
		unknown	690 nm (lg ε 5.07), 660 (4.42), 621 (4.42), 367 (4.78), 347 (4.70)	L = *trans*-$(OCOEt)_2$	639
		unknown	696 nm (lg ε 5.06), 665 (4.38), 625 (4.30), 365 (4.68), 337 (4.77)	L = *trans*-$(OPh(4\text{-}NO_2))_2$	639
		unknown	683 nm (lg ε 5.39), 650 (4.53), 614 (4.59), 362 (4.93), 341 (4.78)	L = *trans*-$(OCH_2CH_2N(Me)_2)_2$	639
	Ti(IV)O	1-ClNp	709 nm (log ε 5.08), 636 (4.34), 356 (4.58)		640
	Ga(III)Cl	DMSO	687 nm (lg ε 5.10), 616 (4.56), 370 (4.90)		321
		DMF	689 nm		321
		toluene	697 nm		321
		THF	688 nm		321
		$CHCl_3$	700 nm		321
	In(III)Cl	DMSO	691 nm (lg ε 5.23), 622 (3.59), 368 (4.08)		344
		DMF	686 nm		344
		toluene	698 nm		344
		THF	696 nm		344
		$CHCl_3$	700 nm		344
		EtOH	683 nm (lg ε 5.4), 612, 346		641
	Pb(II)	DMSO	707 nm (lg ε 5.18), 637 (4.41), 348 (4.65)		637
		DMF	706 nm		637
		toluene	716 nm		637
		THF	709 nm		637
		$CHCl_3$	720 nm		637
β = OPh(2-CH_2CHCH_2)	2H	toluene	703 nm, 667, 639, 605, 350		642
	Pb(II)	toluene	721 nm, 650, 346		642
$\beta\beta$ = OPh(2-NH_2)	Ni(II)	DMF	673 nm (10^{-4} ε 7.96), 616 (3.22), 425 (2.84), 325 (14.0)		643
	Zn(II)	DMF	683 nm (10^{-4} ε 8.53), 645 (3.88), 390 (8.17)		643
β = 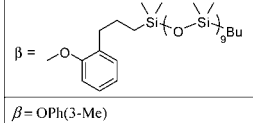	2H	toluene	703 nm, 666, 638, 605, 346		642
	Pb(II)	toluene	721 nm, 648, 365		642
β = OPh(3-Me)	Ni(II)	THF	668 nm (lg ε 5.50), 606 (4.77)	0.57×10^{-6} mol dm^{-1}	644

(*Continued*)

Table 2. (*Continued*)

Structure	M	Solvent	Transition Energy (Intensity)	Remark	Ref.
β = OPh(3-CF_3)	2H	THF	696 nm (lg ε 5.19), 660 (5.15), 638 (4.69), 603 (4.50)	0.51×10^{-6} mol dm^{-1}	644
	Co(II)	THF	661 nm (lg ε 5.06), 597 (4.42)	0.53×10^{-6} mol dm^{-1}	644
	Ni(II)	THF	668 nm (lg ε 5.35), 602 (4.67)	0.80×10^{-6} mol dm^{-1}	644
	Zn(II)	THF	670 nm (lg ε 5.24), 603 (4.58)	0.55×10^{-6} mol dm^{-1}	644
$\beta\beta$ = OPh(3-CF_3)	2H	$CHCl_3$ + 1% THF	698 nm (lg ε 5.26), 662 (5.18), 644 (4.72), 601 (4.50), 349 (4.96)		340
	Mg(II)	$CHCl_3$	678 nm (lg ε 5.47), 650 (4.61), 612 (4.65), 359 (5.07)		340
	In(III)Cl	$CHCl_3$	696 nm (lg ε 5.45), 667 (4.64), 627 (4.65), 365 (4.99)		340
$\beta\beta$ = OPh(3-$C_{15}H_{31}$)	2H	$CHCl_3$	703 nm, 667, 640, 606		645
	Ni(II)	$CHCl_3$	672 nm, 607		645
	Cu(II)	$CHCl_3$	684 nm, 615		645
	Zn(II)	$CHCl_3$	677 nm, 613		645
	Pd(II)	$CHCl_3$	665 nm, 599		645
α = 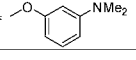	Zn(II)	DMF	694 nm (ε 202,000), 625, 386, 320		646
α = 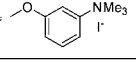	Zn(II)	DMF	690 nm (ε 196,000), 621, 388, 331	$[Pc]^{4+}4I^-$	646
β = 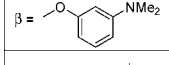	Zn(II)	DMF	681 nm, 612, 356		646
β = 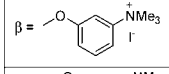	Zn(II)	DMF	677 nm (ε 161,000), 609, 353	$[Pc]^{4+}4I^-$	646
ββ = 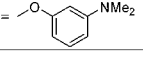	Zn(II)	DMF	680 nm (ε 374,000), 613, 364		646
ββ = 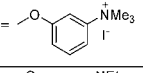	Zn(II)	DMF	677 nm (ε 297,000), 610, 362	$[Pc]^{8+}8I^-$	646
α = 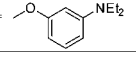	Zn(II)	DMF	696 nm (ε 261,000), 627, 378, 321, 263		646

(*Continued*)

Table 2. (*Continued*)

Structure	M	Solvent	Transition Energy (Intensity)	Remark	Ref.
α = 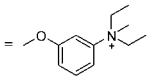	Zn(II)	DMF	688 nm (ε 195,100), 620, 380, 326	$[Pc]^{4+}4I^-$	646
β = 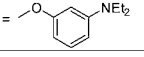	Zn(II)	DMF	680 nm (ε 223,000), 612, 356		646
β = 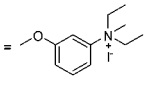	Zn(II)	DMF	676 nm (ε 185,000), 609, 353	$[Pc]^{4+}4I^-$	646
ββ = 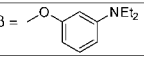	Zn(II)	DMF	680 nm (ε 261,000), 613, 362		646
ββ = 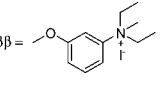	Zn(II)	DMF	676 nm (ε 236,000), 611, 361	$[Pc]^{8+}8I^-$	646
β = OPh(4-Me)	2H	$CHCl_3$	701 nm (lg ε 5.20), 668 (5.15)		607
$\beta\beta$ = OPh(4-Me)	Zn(II)	DMSO	679 nm (lg ε 5.12), 652 (4.30), 613 (4.63), 368 (4.56)		647, 480
R_2 = OPh(4-*t*-Bu)	2H	DMF	688 nm, 652, 633, 593, 334		511
	Zn(II)	DMF	667 nm, 602, 341		511
		DMF	675 nm (lg ε 5.09), 609 (3.71), 348 (3.96)		648
		DMSO	675 nm		648
R_2, R_3 = OPh(4-*t*-Bu)	Zn(II)	DMF	678 nm (lg ε 4.47), 611 (3.74), 359 (4.00)		648
		DMSO	678 nm		648
$R_5(R_3)$, $R_6(R_7)$, $R_{10}(R_{11})$ = OPh(4-*t*-Bu)	Zn(II)	DMF	669 nm (lg ε 4.57), 604 (3.82), 335 (4.24)		648
		DMSO	669 nm		648
R_2, R_3, R_6, R_7, R_{10}, R_{11} = OPh(4-*t*-Bu)	Zn(II)	DMF	670 nm (lg ε 4.75), 605 (3.91), 342 (4.09)		648
		DMSO	670 nm		648
α = OPh(4-*t*-Bu)	2H	$CHCl_3$	724 nm (lg ε 5.14), 690 (5.09), 660 (4.58), 626 (4.42), 323 (4.85)		638
	Ti(IV)O	$CDCl_3$	730 nm (lg ε 5.29), 653 (4.53), 348 (4.66)		636
	Ni(II)	$CHCl_3$	694 nm (lg ε 5.28), 624 (4.53), 330 (4.60)		638

(*Continued*)

Table 2. (*Continued*)

Structure	M	Solvent	Transition Energy (Intensity)	Remark	Ref.
	Zn(II)	$CHCl_3$	744 nm (lg ε 5.26), 713 (5.05), 670 (4.65), 645 (4.56), 416 (4.50), 323 (4.65)		638
	Ga(III)Cl	toluene	721 nm, 333		323
		DCM	723 nm, 338, 264		323
		THF	714 nm, 334		323
		$CHCl_3$	726 nm, 337		323
		DMSO	717 nm (lg ε 5.31), 644 (4.60), 348 (4.72)		323
	Cd(II)	DMSO	698 nm (lg ε 5.48), 629 (4.78), 329 (4.96)		287
		toluene	694 nm (lg ε 5.39)		287
		THF	693 nm (lg ε 5.36)		287
		$CHCl_3$	700 nm (lg ε 5.44)		287
		DMF	694 nm (lg ε 5.46)		287
	In(III)Cl	$CHCl_3$	725 nm, 354		649
		DMSO	714 nm (lg ε 5.20), 641 (4.60), 340 (4.77)		323
	Sn(IV)L	DMSO	737 nm (lg ε 5.01), 657 (4.41), 343 (4.71)	L = *trans*-Cl_2	369
		THF	730 nm, 356, 331	L = *trans*-Cl_2	369
		$CHCl_3$	737 nm, 347	L = *trans*-Cl_2	369
		DCM	733 nm, 349	L = *trans*-Cl_2	369
		toluene	732 nm, 359, 331	L = *trans*-Cl_2	369
	Pb(II)	DMSO	724 nm (lg ε 5.22), 652 (4.64), 460 (4.34), 347 (4.67)		637
		DMF	724 nm		637
		toluene	734 nm		637
		THF	726 nm		637
		$CHCl_3$	742 nm		637
β = OPh(4-*t*-Bu)	2H	py	704 nm (lg ε 5.14), 670 (5.11), 640 (4.66), 608 (4.51), 348 (4.84)		410
	Ti(IV)O	$CDCl_3$	704 nm (lg ε 5.40), 632 (4.71), 410 (4.82), 348 (4.96), 290 (4.59)		636
	Zn(II)	$CHCl_3$	682 nm (lg ε 5.30), 615 (4.42), 357 (4.53)		650
		DMSO	681 nm (lg ε 5.15)		480
	Ga(III)Cl	toluene	697 nm, 348		323
		DCM	698 nm, 352, 292		323
		THF	691 nm, 363		323

(*Continued*)

Table 2. (*Continued*)

Structure	M	Solvent	Transition Energy (Intensity)	Remark	Ref.
		$CHCl_3$	700 nm, 352, 291		323
		DMSO	697 nm (lg ε 5.32), 623 (4.65), 358 (4.90)		323
	In(III)Cl	DMSO	696 nm (lg ε 5.14), 626 (4.64), 363 (4.99)		323
	Sn(IV)L	DMSO	711 nm (lg ε 5.10), 637 (4.42), 349 (4.82)	L = *trans*-Cl_2	369
		THF	704 nm, 356	L = *trans*-Cl_2	369
		$CHCl_3$	710 nm, 363	L = *trans*-Cl_2	369
		DCM	709 nm, 358	L = *trans*-Cl_2	369
		toluene	707 nm, 359	L = *trans*-Cl_2	369
	Pb(II)	DMSO	709 nm (lg ε 5.00), 638 (4.37), 347 (4.42)		637
		DMF	707 nm		637
		toluene	716 nm		637
		THF	709 nm		637
		$CHCl_3$	722 nm		637
$\beta\beta$ = OPh(4-*t*-Bu)	Ti(IV)O	1-ClNp	710 nm (log ε 5.35), 638 (4.59), 354 (4.80)		640
	Zn(II)	DMF	670 nm (lg ε 4.73), 605 (4.20), 335 (4.48)		648
		DMSO	670 nm		648
		$CHCl_3$	683 nm (lg ε 5.16), 655 (4.31), 615 (4.34), 357 (4.61)		647
	Ga(III)Cl	DMSO	690 nm (lg ε 5.31), 620 (3.82), 347 (4.15)		321
		DMF	688 nm		321
		toluene	697 nm		321
		THF	689 nm		321
		$CHCl_3$	701 nm		321
	In(III)Cl	DMSO	692 nm (lg ε 5.10), 622 (3.59), 367 (4.22)		344
		DMF	686 nm		344
		toluene	698 nm		344
		THF	697 nm		344
		$CHCl_3$	701 nm		344
	Pb(II)	DMSO	709 nm (lg ε 4.94), 638 (4.17), 358 (4.41)		637
		DMF	707 nm		637
		toluene	717 nm		637
		THF	711 nm		637
		$CHCl_3$	723 nm		637

(*Continued*)

Table 2. (*Continued*)

Structure	M	Solvent	Transition Energy (Intensity)	Remark	Ref.
β = 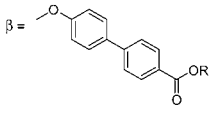	2H	DMSO	700 nm (lg ε 4.40), 668 (4.41), 340 (4.36), 288 (4.77)	R = H	651
		u	699 nm (lg ε 4.68), 668 (4.66), 338 (4.55), 287 (4.75)	R = C_6H_{13}	651
	Co(II)	DMSO	664 nm (lg ε 4.41), 343 (4.40), 289 (4.68)	R = H	651
	Zn(II)	DMSO	679 nm (lg ε 4.51), 347 (4.47), 289 (4.78)	R = H	651
$\beta\beta$ = OPh(4-CHO)	2H	$CHCl_3$	699 nm (lg ε 4.67), 663 (4.65), 637 (4.37), 608 (4.20), 348 (3.99), 275 (4.25)		652
	Zn(II)	DMSO	679 nm (lg ε 4.35), 651 (3.74), 618 (3.66), 352 (4.32)		647
R_2, R_3 = OPh(4-COOH)	Zn(II)	DMF	671 nm (lg ε 6.05), 606 (4.32), 357 (3.71), 284 (4.57)		648
		DMSO	671 nm		648
ββ= 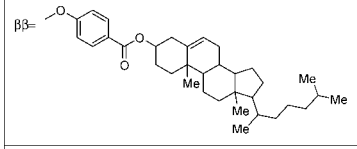	Zn(II)	$CHCl_3$	678 nm (lg ε 4.89), 647 (4.53), 632 (4.54), 351 (4.77)		647
ββ = 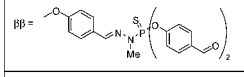	2H	$CHCl_3$	701 nm (lg ε 4.71), 667 (4.66), 643 (4.27), 607 (4.07), 259 (5.71)		652
ββ = 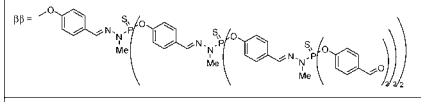	2H	$CHCl_3$	704 nm (lg ε 5.02), 672 (4.97), 643 (4.52), 611 (4.36), 274 (6.16), 264 (6.16)		652
ββ = 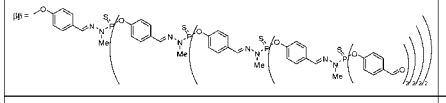	2H	$CHCl_3$	704 nm (lg ε 5.11), 672 (5.07), 643 (4.62), 611 (4.46), 277 (6.48), 263 (6.48)		652
β = OPh(4-OH)	Zn(II)	DMF	681 nm, 612, 350		653
$\beta\beta$ = OPh(4-OMe)	2H	$CHCl_3$	701 nm (lg ε 5.20), 650sh, 623 (4.78), 602sh, 422sh, 341 (4.76)		407
β = OPh(4-OMe)	2H	py	705 nm (lg ε 4.70), 672 (4.66), 640 (4.36), 608 (4.25), 396sh (4.43), 344 (4.64)		410
$\beta\beta$ = OPhO(CH_2)Ph	Ti(IV)O	1-ClNp	712 nm (lg ε 5.38), 639 (4.71), 354 (4.97)		640
β = OPh(4-SO_3H)	Zn(II)	DMF	678 nm, 610, 358, 278		646

(*Continued*)

Table 2. (*Continued*)

Structure	M	Solvent	Transition Energy (Intensity)	Remark	Ref.
β = OPh(4-NH_2)	Zn(II)	DMF	672 nm, 606, 343		653
$\beta\beta$ = OPh(4-NH_2)	Zn(II)	DMSO	683 nm (lg ε 5.23), 651 (4.73), 618 (4.69), 345 (5.03)		647
β = OPh(4-NO_2)	2H	py	699 nm (lg ε 4.68), 666 (4.64), 640 (2.22), 606 (4.09), 341 (4.54)		410
	Zn(II)	THF	672 nm, 607, 350		653
$\beta\beta$ = OPh(4-NO_2)	Zn(II)	DMSO	678 nm (lg ε 5.31), 639 (4.73), 616 (4.63), 346 (5.04)		647
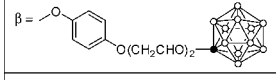	Zn(II)	DMF	677 nm, 612	○= BH ●= B $[Pc]^{-}8N(Bu)_4^{+}$	654
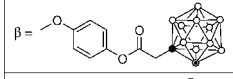	Zn(II)	DMF	680 nm, 612, 350	●= C ⊙= CH ○= BH	653
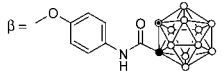	Zn(II)	DMF	680 nm, 612, 350	●= C ⊙= CMe ○= BH	653
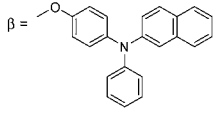	2H	DCM	702 nm (10^{-5} ε 2.01), 668 (1.73), 641, 608, 322 (1.95), 280 (1.58)		655
	Si(IV)L	DCM	684 nm (10^{-5} ε 2.33), 615, 356 (1.14), 322 (1.24), 281 (1.13)	L = *trans*-$(OSi(i\text{-}Pr)_3)_2$	655
	Ti(IV)O	DCM	704 nm (10^{-5} ε 2.32), 633, 348 (1.25), 320 (1.49), 280 (1.39)		655
	Cu(II)	DCM	682 nm (10^{-5} ε 1.99), 614, 322 (1.50), 280 (1.38)		655
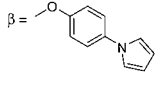	2H	DMF	700 nm (ε 10^{-4} 4.88), 670 (8.85), 637, 609, 344		656
	Mn(III)Cl	DMF	720 nm (ε 10^{-4} 6.36), 649, 497, 380		656
	Fe(II)	DMF	701 nm, 660, 628 nm (ε 10^{-4} 2.4), 457, 327		656
	Ni(II)	DMF	671 nm (ε 10^{-4} 2.84), 621, 329		656
	Co(II)	DMF	665 nm (ε 10^{-4} 7.5), 603, 328		656
	Zn(II)	DMF	678 nm (ε 10^{-5} 1.1), 609, 352		656
β = OPh(2-CH_2CHCH_2)(3-$C_{15}H_{31}$)	Cu(II)	$CHCl_3$	684 nm, 615		645
β = OPh(2,4-$(Me)_2$)	2H	$CHCl_3$	700 nm (lg ε 5.18), 667 (5.13)		607
α = OPh(2,4-(t-Bu)$_2$)	V(IV)O	hexane	724 nm		457
		cyclohexane	727 nm		457

(*Continued*)

Table 2. (*Continued*)

Structure	M	Solvent	Transition Energy (Intensity)	Remark	Ref.
		toluene	733 nm		457
		DCM	736 nm		457
		$CHCl_3$	738 nm		457
		DMF	731 nm		457
		py	737 nm		457
	Cu(II)	cyclohexane	704 nm		457
		toluene	705 nm		457
		DCM	708 nm		457
		$CHCl_3$	709 nm		457
		DMF	703 nm		457
		py	706 nm		457
	Pd(II)	cyclohexane	686 nm		457
		toluene	689 nm		457
		DCM	690 nm		457
		$CHCl_3$	692 nm		457
		DMF	692 nm		457
		py	694 nm		457
β= OPh(2,4-(*t*-Bu)$_2$)	Co(II)	$CHCl_3$	675 nm (10^{-4} ε 4.17), 609 (3.57)		657
	Ni(II)	$CHCl_3$	677 nm (10^{-4} ε 4.28), 609 (3.73)		657
	Cu(II)	$CHCl_3$	685 nm (10^{-4} ε 4.21), 616 (3.59), 339 (3.89)		657
	Zn(II)	DMF	680 nm (10^{-4} ε 4.09), 612 (3.40), 358 (3.68)		657
$\beta\beta$= OPh(2,4-(*t*-Bu)$_2$)	Mg(II)	$CHCl_3$	681 nm(lg ε 5.10), 650(4.25), 614(4.30), 365(4.68)		658
	Ni(II)	$CHCl_3$	765 nm(lg ε 4.53), 676(5.12), 608(4.57), 304(5.03)		658
	Cu(II)	$CHCl_3$	680 nm(lg ε 5.28), 651(4.51), 612(4.54), 350(4.76)		658
	Zn(II)	$CHCl_3$	680 nm(lg ε 5.38), 651(4.54), 613(4.59), 368(4.88)		658
		$CHCl_3$	686 nm (lg ε 4.84), 657 (3.93), 619 (3.97), 346 (4.33)		647
α= OPh(2-*i*-Pr)(5-Me)	2H	1-ClNp	729 nm, 699, 665, 631, 344		118
		1-ClNp	729.0 nm, 699.0, 665.0, 631.0	293K	118
		1-ClNp	729.5 nm, 698.0, 665.0, 633.0	303K	118
		1-ClNp	729.5 nm, 698.5, 664.5, 631.0	313K	118
		1-ClNp	729.5 nm, 699.5, 665.0, 632.5	323K	118
		1-ClNp	730.5 nm, 699.5, 665.0, 633.0	333K	118

(*Continued*)

Table 2. (*Continued*)

Structure	M	Solvent	Transition Energy (Intensity)	Remark	Ref.
	Ti(IV)O	1-ClNp	738 nm, 661, 428, 350		118
	In(III)Cl	1-ClNp	738 nm, 661, 359		118
β= OPh(2-*i*-Pr)(5-Me)	2H	1-ClNp	710 nm, 676, 646, 612, 343		118
	Ti(IV)O	1-ClNp	712 nm, 639, 397, 349		118
	In(III)Cl	1-ClNp	710 nm, 638, 359		118
	Zn(II)	$CHCl_3$	683 nm (lg ε 4.52), 615 (3.82), 352 (4.28), 348 (4.28)		659, 660
$\beta\beta$= OPh(2,6-$(Me)_2$)	2H	toluene	701 nm (ε 14,250), 664 (15,050), 647 (15,450), 636 (15,700), 601 (16,650), 353 (28,350)		661
		THF	704 nm (10^{-5} ε 1.65), 667 (1.39), 648 (0.47), 605 (0.28), 420 (0.41), 350 (0.86)		662
	2Li	PhCl	800 nm (ε 13000), 517 (52000), 400 (35000), 345, (78000)		663
	Zn(II)	THF	674 nm (10^{-5} ε 3.38), 644 (0.42), 608 (0.47), 355 (1.06)		662
		THF	674 nm (ε 338000), 644 (42000), 608 (47000), 355, (106000)		663
α= OPh(2,6-(i-Pr)$_2$)	2H	DCM	712 nm, 679, 648, 612, 343		664
β= OPh(2,6-(i-Pr)$_2$)	2H	DCM	704 nm, 669, 641, 608, 343		664
α= OPh(2,6-Ph_2)	2H	DCM	712 nm, 680, 649, 615, 352		664
		$CHCl_3$	723 nm, 690, 658, 624, 413sh, 352, 317		512
β= OPh(2,6-Ph_2)	2H	DCM	705 nm, 669, 641, 606, 352		664
β = 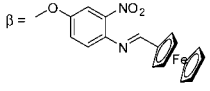	2H	DMSO	705 nm (lg ε 4.252), 676 (4.344), 643 (4.247), 618sh (4.154), 410 (4.647)		665
	Co(II)	DMSO	660 nm (lg ε 4.670), 620 (4.750), 610 (4.400), 410 (4.810)		665
β = 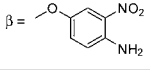	2H	DMSO	709 nm (lg ε 4.011), 676 (4.130), 610sh (3.953), 422 (4.335)		665
	Co(II)	DMSO	665 nm (lg ε 4.800), 610sh (4.400), 350 (4.815)		665
α= OPh(3,5-(t-Bu)$_2$)	2H	DCM	712 nm, 680, 649, 615, 352		664
β= OPh(3,5-(t-Bu)2)	2H	DCM	701 nm, 667, 639, 607, 342		664
		DCM	701 nm, 667, 639, 607, 342		572
	Ti(IV)O	DCM	705 nm (lg ε 5.39), 672 (sh), 634 (4.59), 420 (4.53), 348(4.84), 298(4.76)		525

(*Continued*)

Table 2. (*Continued*)

Structure	M	Solvent	Transition Energy (Intensity)	Remark	Ref.
	Ti(IV)L	DCM	709 nm (lg ε 5.16), 640 (sh), 420 (4.65), 326 (4.92), 299 (sh)	L= 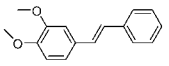	525
		DCM	707 nm (lg ε 5.17), 637 (sh), 421 (sh), 340 (4.85), 300 (4.83)	L= 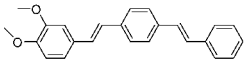	525
	Ni(II)	DCM	676.5 nm, 645.5sh, 608.5, 382.5, 332.0, 299.5, 285.5, 253.0		626
β= OPh(3,5-$(Me)_2$)	Zn(II)	DMSO	682 nm (lg ε 5.39), 613 (4.64), 360 (4.98)		573
		PBS	692 nm (lg ε 3.07), 645 (3.06), 360 (3.06)		573
$\beta\beta$= OPh(3,5-(t-$Bu)_2$)	Ni(II)	DCM	674.0 nm (lg ε 5.40), 648.0sh, 608 (4.66), 391.0 (4.62), 305 (5.06)		666
	In(III)Cl	EtOH	703 nm (lg ε 5.3), 633, 356		641
β= OPh(3-$C_{15}H_{31}$)(6-t-Bu)	Pd(II)	$CHCl_3$	667 nm, 601		645
β= OPh(3-$C_{15}H_{31}$)(6-CH_2CHCH_2)	Cu(II)	$CHCl_3$	681 nm, 615		645
β = 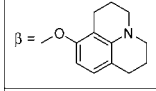	Zn(II)	DMF	682 nm (ε 188,000), 614, 356		646
β = 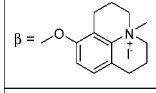	Zn(II)	DMF	678 nm (ε 174,000), 610, 357	$[Pc]^{4+}4I^-$	646
β= OPh(2,6-(t-$Bu)_2$)(4-Me)	2H	DCM	704 nm, 669, 641, 608, 343		664
	Ni(II)	DCM	670.0 nm, 643.0sh, 604.0, 365.0sh, 336.0, 297.5, 274.0, 246.5		626
α= OPh(3,5-(t-$Bu)_2$)(4-OH)	2H	DCM	728 nm, 694, 655, 623, 344		664
β= OPh(3,5-(t-$Bu)_2$)(4-OH)	2H	DCM	715 nm, 683, 652, 620, 344		664
ββ′ = 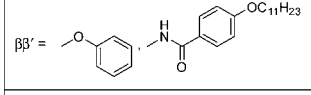	Co(II)	DMF	681 nm (lg ε 4.89), 627 (4.35), 335 (4.86)		667
		$CHCl_3$	678 nm, 634, 333		667
		H_2SO_4	794 nm		667
R_1, R_4 = 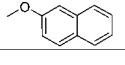	Mg(II)	DMSO	696 nm (lg ε 4.92), 673 (4.29), 606 (4.45), 347 (4.53)		613

(*Continued*)

Table 2. (*Continued*)

Structure	M	Solvent	Transition Energy (Intensity)	Remark	Ref.
$R_1, R_2 =$ 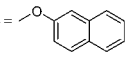	Zn(II)	DMF	670 nm (lg ε 4.97), 605 (4.24), 335 (4.69)		648
		DMSO	670 nm		648
$\beta =$ 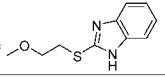	Mg(II)	DMSO	695 nm (lg ε 4.18), 622 (3.62), 356 (4.15)		668
$\alpha =$ 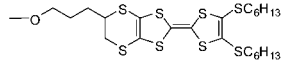	Mg(II)	$CHCl_3$	708.0 nm, 642.0, 318.0		669
		DCM	777.0 nm, 713.0, 321.0		669
$\beta\beta =$ 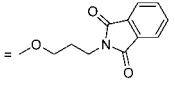	Zn(II)	THF	674 nm (10^{-5} ε 1.2)		670
$\alpha\alpha = OCH_2Ph(4\text{-}t\text{-}Bu)$	Mg(II)	$CHCl_3$	807 nm (lg ε 4.28), 745 (5.33), 660 (4.62), 470sh (4.23), 332 (4.77)		671
	Ni(II)	$CHCl_3$	742 nm (lg ε 5.28), 660 (4.62), 453sh (4.11), 327 (4.72)		671
	Cu(II)	$CHCl_3$	753 nm (lg ε 5.37), 665 (4.67), 455sh (4.16), 330 (4.86)		671
$\beta = O(CH_2)_2N(Me)_2$	2H	$CHCl_3$	704 nm (lg ε 3.8), 667 (3.8), 342 (3.7), 288 (3.5)		672
	Ni(II)	$CHCl_3$	672 nm (lg ε 3.8), 365 (3.4), 280 (3.8)		672
	Zn(II)	$CHCl_3$	679 nm (lg ε 3.9), 616 (3.5), 359 (3.9), 283 (3.6)		672
$\beta = O(CH_2)_2N^+(Me)_3I^-$	2H	H_2O	632 nm (lg ε 3.7), 328 (3.8)		672
	Ni(II)	H_2O	622 nm (lg ε 3.7), 276 (3.8)		672
	Zn(II)	H_2O	633 nm (lg ε 3.9), 337 (3.9)		672
		buffer Tris	702.5 nm (10^{-4} ε 2.2)		625
$\beta = OCH(CH_2N(Me)_2)_2$	Ni(II)	$CHCl_3$	673 nm (lg ε 3.9), 609 (3.6), 383 (3.5), 300 (3.9)		672
$\beta = OCH(CH_2N^+(Me)_3I^-)_2$	Ni(II)	H_2O	667 nm (lg ε 4.2), 168 (3.9)		672
	Zn(II)	DMF	679 nm (ε 169,810), 613, 354		673
$\beta = OCH(CH_2N(Me)_2)_2$	Zn(II)	DMF	678 nm (ε 63,250), 613, 354		673
$\beta = O(CH_2)_2NH\text{-}Boc$	Zn(II)	DMF	679 nm (lg ε 5.10), 612 (4.42), 354 (4.76)	Boc = COO(*t*-Bu)	674
$\beta = O(CH_2)_2NH_3^+Cl^-$	Zn(II)	DMF	683 nm (lg ε 4.91), 631 (4.54), 354 (4.79)		674
$\beta\beta = O(CH_2)_3NH_2$	Zn(II)	H_2O	680 nm (10^{-5} ε 1.0)		670

(*Continued*)

Table 2. (*Continued*)

Structure	M	Solvent	Transition Energy (Intensity)	Remark	Ref.
β-$O(CH_2)_3N(Me)_2$	Zn(II)	DMF	680 nm, 612, 356		533
β-$O(CH_2)_3N^+(Me)_3$	Zn(II)	DMF	680 nm, 612, 355		533
		H_2O + 5% SDS	684 nm, 651, 350		533
α-$OCH(CH_2O(C_{12}H_{25}))_2$	Zn(II)	DMF	701 nm (lg ε 5.20)		675
		toluene	744 nm (lg ε 4.13), 701 (5.20)		675
β-$OCH(CH_2O(C_{12}H_{25}))_2$	Zn(II)	DMF	681 nm (lg ε 5.19)		675
		toluene	682 nm (lg ε 5.03)		675
$\beta\beta$-OCH(Et)Bu	Mg(II)	DCM	679.0 nm (lg ε 5.31), 613.0sh (4.69), 360.0 (5.01)		676
	In(III)Cl	DCM	698.5 nm (lg ε 5.20), 629.5sh (4.59), 446.0 (4.34), 362.5 (4.91)		676
R_1, R_5, R_9, R_{13} = OCH(*i*-Pr)$_2$	Mn(III)Cl	$CHCl_3$	775 nm (lg ε 4.67), 693 (3.93), 550 (3.85), 337 (4.18)		677
	Co(II)	$CHCl_3$	702 nm (lg ε 4.31), 631 (3.66), 313 (3.86)		677
	Zn(II)	$CHCl_3$	711 nm (lg ε 5.13), 638 (4.37), 322 (4.54)		677
	Pd(II)	$CHCl_3$	694 nm (lg ε 5.10), 664 (4.08), 623 (4.36), 314 (4.31)		677
R_1, R_5, R_{12}, R_{16} = OCH(*i*-Pr)$_2$	Zn(II)	$CHCl_3$	709 nm (lg ε 5.14), 638 (4.41), 323 (4.59)		677
	Pd(II)	$CHCl_3$	696 nm (lg ε 5.19), 671 (4.44), 625 (4.46), 314 (4.44)		677
$\beta\beta$-OCH_2CH_2OEt	2H	benzene	699.99 nm (10^{-3} ε 25.1), 660.7 (26.3), 391.5 (11.4), 344.2 (29.0)		678
	Zn(II)	benzene	675.6 nm (10^{-3} ε 42.4), 350.9 (36.8)		678
$\beta\beta$-$OCH_2CH_2OCH_2CH_2OMe$	2H	benzene	699.99 nm (10^{-3} ε 37.5), 660.7 (35.9), 391.5 (11.5), 350.9 (33.7)		678
	Ni(II)	benzene	666.0 nm (10^{-3} ε 38.9), 618.7 (38.0), 391.5 (20.1), 286.0 (73.9)		678
	Zn(II)	benzene	676.9 nm (10^{-3} ε 110.9), 350.9 (68.1), 291.4 (54)		678
$\beta\beta$-$O(CH_2)_6O(CH_2CH_2O)_3Me$	2H	$CHCl_3$	702 nm (lg ε 5.21), 665 (5.11), 646sh (4.67), 602 (4.41)		679
α-OCH_2-TMS	Pd(II)	$CHCl_3$	693 nm (lg ε 5.36), 623 (4.65), 316 (4.66), 281 (4.56)		680
$\alpha\alpha$-OCH_2-TMS	2H	$CHCl_3$	775 nm (lg ε 4.67), 745 (4.64), 707 (4.14), 670 (4.08), 333 (4.38)		680
	Ni(II)	$CHCl_3$	753 nm (lg ε 5.19), 676 (4.59), 464 (4.18), 332 (4.70), 309 (4.61)		680
α-$O(CH_2)_2$-TMS	Pd(II)	$CHCl_3$	692 nm (lg ε 5.32), 621 (4.61), 314 (4.63), 281 (4.51)		680
α-OCH(Me)-TMS	Cu(II)	$CHCl_3$	716 nm (lg ε 5.28), 643 (4.57), 333 (4.71)		680

(*Continued*)

Table 2. (*Continued*)

Structure	M	Solvent	Transition Energy (Intensity)	Remark	Ref.
	Pd(II)	$CHCl_3$	698 nm (lg ε 5.38), 628 (4.68), 317 (4.69), 281 (4.59)		680
β = 	Ni(II)	DCM	676 nm, 613sh, 385, 364, 328, 301sh, 283,244		626
ββ = 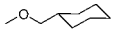	2H	$CHCl_3$	702 nm, 663, 414, 354		681
	2Li	$CHCl_3$	635 nm, 592, 360		681
	Dy(III)OCH_3	$CHCl_3$	686 nm, 620, 352		681
αααββ = 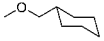	2H	THF	766 nm (lg ε 5.0), 682 (4.4), 390 (4.4), 324 (4.6)		174
	Mg(II)	THF	742 nm (lg ε 4.9), 676 (4.3), 364 (4.7), 328 (4.7)		174
	Mn(III)OAc	THF	808 nm		174
β = 	2H	DCM	707.0 nm, 672.0, 644.0, 610.5, 394.5, 344.0, 291.0		626
	Ni(II)	DCM	677.5 nm, 610.5sh, 386.0, 327.5, 301.5, 286.0, 244.5		626
β = 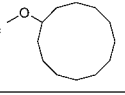	Ni(II)	DCM	678.0 nm, 625.0sh, 610.5, 386.5, 328.5, 302.0sh, 244.5		626
αααββ = 	Mg(II)	DCM	752 nm (lg ε 4.91), 672 (4.12), 364 (4.19)		682
	Ni(II)	DCM	750 nm (lg ε 4.93), 672 (4.43), 386 (4.55), 314 (4.77)		682
αααββ = 	Mg(II)	DCM	744 nm (lg ε 4.93), 668 (4.09), 328 (4.10)		682
	Ni(II)	DCM	736 nm (lg ε 4.85), 660 (4.25), 372 (4.40), 340 (4.48), 312 (4.61)		682
β = 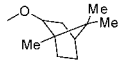	2H	DCM	707.0 nm, 671.5, 645.5, 610.5, 395.0, 343.0, 292.0, 256.0		626
	Ni(II)	DCM	677.5 nm, 610.0, 388.5, 328.0, 302.5, 280.0, 241.0		626
	Cu(II)	$CHCl_3$	704 nm, 668, 635, 346, 319		512
R_2, R_6, R_{10}, R_{14} = 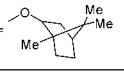	2H	benzene	707.2 nm, 670.1, 650.8, 607.7, 395.0sh, 352.5		626
	Ni(II)	DCM	676.0 nm, 609.3, 385.2, 328.0, 307.6		626
R_2, R_7, R_{10}, R_{15} = 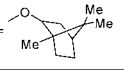	2H	benzene	711.0 nm, 670.3, 641.3, 608.6, 390.0, 348.5		626
	Ni(II)	DCM	685.3 nm, 668.3, 608.3, 388.9, 328.2, 302.9		626

(*Continued*)

Table 2. (*Continued*)

Structure	M	Solvent	Transition Energy (Intensity)	Remark	Ref.
R_2, R_6, R_{11}, R_{15} = 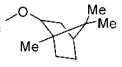	2H	benzene	706.7 nm, 672.1, 646.3, 610.8, 398.1, 345.1, 290.5		626
	Ni(II)	DCM	677.5 nm, 609.9, 385.2, 327.8, 305.2		626
R_2, R_6, R_{10}, R_{15} = 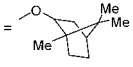	2H	benzene	706.9 nm, 672.1, 646.3, 611.4, 397.9, 345.3, 290.6		626
	Ni(II)	DCM	677.5 nm, 609.9, 385.2, 327.8, 305.2		626
ββ = 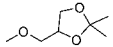	Zn(II)	DMF	673 nm (lg ε 5.65), 644 (4.81), 607 (4.84), 359 (5.23)		433
α = 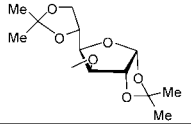	2H	$CHCl_3$	724 nm (lg ε 5.11), 690 (5.06), 660 (4.59), 626 (4.43), 353 (4.65), 315 (4.68)		683
	Zn(II)	$CHCl_3$	698 nm (lg ε 5.20), 669 (4.41), 629 (4.49), 350 (4.56), 319 (4.57)		683
β = 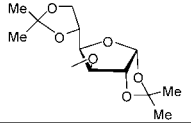	Zn(II)	$CHCl_3$	680 nm (lg ε 5.09), 648 (4.31), 612 (4.38), 350 (4.82)		683
R_1 = 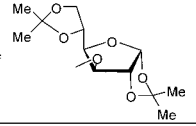	Zn(II)	$CHCl_3$	673 nm (lg ε 5.40), 645 (4.62), 607 (4.65), 343 (4.88)		683
R_2 = 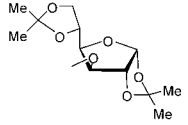	Zn(II)	$CHCl_3$	667 nm (lg ε 5.38), 640 (4.53), 603 (4.59), 344 (4.85)		683
α = 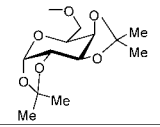	2H	$CHCl_3$	724 nm (lg ε 5.10), 691 (5.05), 659 (4.56), 626 (4.42), 352 (4.59), 315 (4.68)		683
	Zn(II)	$CHCl_3$	699 nm (lg ε 5.31), 667 (4.44), 629 (4.54), 350 (4.58), 319 (4.56)		683

(*Continued*)

Table 2. (*Continued*)

Structure	M	Solvent	Transition Energy (Intensity)	Remark	Ref.
β = 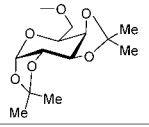	Zn(II)	$CHCl_3$	679 nm (lg ε 5.15), 647 (4.43), 613 (4.48), 351 (4.89)		683
R_1 = 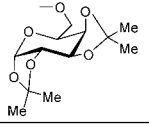	Zn(II)	$CHCl_3$	672 nm (lg ε 5.28), 645 (4.49), 608 (4.53), 341 (4.76)		683
R_2 = 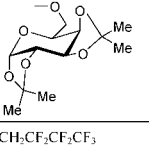	Zn(II)	$CHCl_3$	667 nm (lg ε 5.42), 639 (4.59), 603 (4.65), 344 (4.92)		683
$\beta = OCH_2CF_2CF_2CF_3$	Zn(II)	benzene	674.4 nm (lg ε 5.24), 609.4 (4.59), 356.0 (4.60)		604
		DCM	671.2 nm (lg ε 4.47), 609.6 (3.99), 341.8 (4.38)		604
		$CHCl_3$	672.4 nm (lg ε 5.04), 607.2 (4.46), 346.6 (4.84)		604
		AcOEt	667.0 nm (lg ε 5.24), 603.6 (4.59), 346.4 (4.90)		604
		acetone	665.6 nm (lg ε 5.24), 603.6 (4.53), 338.0 (4.86)		604
		MeOH	667.4 nm (lg ε 4.90), 628.2 (4.76)		604
$\alpha = OCH_2CF_2CF_2CF_2CHF_2$	Fe(III)OH	py	670 nm		615
	Ni(II)	py	687 nm		615
	Zn(II)	py	693 nm		615
$\beta = OCH_2CF_2CF_2CF_2CHF_2$	Fe(III)OH	py	657 nm		615
	Ni(II)	py	670 nm		615
$\beta = OCH_2CHCH_2$	Ni(II)	$CHCl_3$	672 nm, 618.5, 380, 328		334
	In(III)Cl	$CHCl_3$	701 nm, 631, 403, 358		334
$\beta = O(CH_2)_4CHCH_2$	In(III)Cl	$CHCl_3$	701 nm, 631, 403, 358		334
$\beta = O(CH_2)_8CHCH_2$	2H	$CHCl_3$	704 nm, 667.5, 646, 607, 388, 341		334
	Zn(II)	$CHCl_3$	680.5 nm, 613.5, 350.5		334

(*Continued*)

Table 2. (*Continued*)

Structure	M	Solvent	Transition Energy (Intensity)	Remark	Ref.
β = 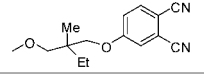	2H	DCM	720 nm (lg ε 4.64), 668 (4.57), 644 (4.22), 608 (4.13), 486sh (3.75), 344 (4.45)		684
	Zn(II)	DCM	686 nm (lg ε 5.13), 672 (5.00), 614 (4.63), 346 (4.91)		684
α = OCH_2Ph	Ti(IV)O	$CHCl_3$	728 nm (lg ε 5.38), 648 (4.67), 350 (4.78)		568
		DMF + 0.1 M $TBABF_4$	728 nm (lg ε 5.38)		568
β = OCH_2Ph	Ti(IV)O	$CHCl_3$	703 nm (lg ε 5.21), 633 (4.61), 347 (4.88), 294 (4.71)		568
		DMF + 0.1 M $TBABF_4$	703 nm (lg ε 5.21)		568
β = 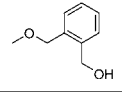	2H	THF	703 nm (lg ε 4.89), 666 (4.71), 342 (3.82)		685
	Zn(II)	THF	677 nm (lg ε 4.93), 612 (1.45), 350 (3.18)		685
β = 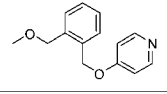	2H	THF	703 nm (lg ε 4.91), 667 (4.35), 344 (2.97)		685
	Zn(II)	THF	676 nm (lg ε 4.92), 611 (1.22), 352 (2.45)		685
β = 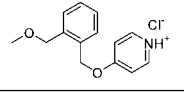	2H	H_2O	611 nm, 324	$[Pc^{4+}]4Cl^-$	685
	Zn(II)	H_2O	636 nm, 343	$[Pc^{1+}]4Cl$	685
α = $OCH_2Ph(4\text{-}COOC_5H_{11})$	Zn(II)	THF	696 nm		686
α = $OCH_2Ph(4\text{-}COOH)$	Zn(II)	0.1 M KOH aq	656 nm		686
β = $OCH(Ph(4\text{-}OMe))_2$	2H	THF	708 nm (lg ε 5.06), 672 (4.99), 644 (4.55), 610 (4.39), 392 (4.50), 344 (4.78)		620
	Zn(II)	THF	684 nm (lg ε 5.04), 614 (5.02), 352 (4.58), 286 (4.04), 272 (4.20), 238 (4.78)		620
β = 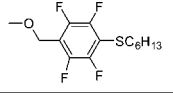	Co(II)	$CHCl_3$	674 nm (lg ε 4.42), 326 (4.22)		687
	Ni(II)	$CHCl_3$	675 nm (lg ε 4.53), 340 (4.43)		687
	Zn(II)	$CHCl_3$	685 nm (lg ε 4.53), 356 (4.35)		687

(*Continued*)

Table 2. (*Continued*)

Structure	M	Solvent	Transition Energy (Intensity)	Remark	Ref.
$\beta = OCH_2C_6F_5$	2H	$CHCl_3$	701 nm (lg ε 4.95), 663 (4.75), 343 (4.75)		688
		DCM	696 nm (lg ε 2.30), 662 (2.63), 630 (2.60), 333 (3.32), 287 (3.30), 235 (2.50)		689
	Ni(II)	$CHCl_3$	672 nm (lg ε 4.19), 332 (3.98)		688
	Co(II)	$CHCl_3$	669 nm (lg ε 4.34), 319 (4.40)		688
		DCM	668 nm (lg ε 3.57), 608 (2.30), 325 (3.12), 287 (3.66), 240 (4.20)		689
	Zn(II)	$CHCl_3$	678 nm (log ε 5.12), 351 (4.80)		688
		DCM	720 nm (lg ε 0.70), 674 (4.78), 611 (1.32), 352 (3.03), 279 (1.93)		689
$\beta = OCH(C_6F_5)_2$	2H	DMSO	700 nm (lg ε 4.72), 674 (4.75), 650 (4.67), 326 (5.03)		690
	Co(II)	DMSO	675 nm (lg ε 4.77), 320 (4.99)		690
	Zn(II)	DMSO	698 nm (lg ε 4.84), 641 (4.35), 356 (4.78)		690
β = 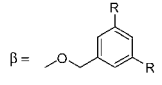	2H	DCM	705 nm, 670	R = $O(CH_2CH_2O)_3CH_3$	454, 455
		EtOH	610 nm	R = $O(CH_2CH_2O)_3CH_3$	454, 455
		spin-coated film	705 nm, 670	R = $O(CH_2CH_2O)_3CH_3$	691
β = 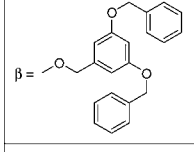	2H	DCM	718 nm, 682, 654, 620, 422, 346		692
		DCM	718 nm, 682, 654, 620, 422, 346		435
		spin-coated film	718 nm, 682		691
β = 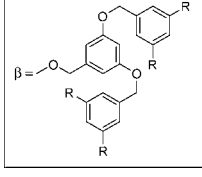	2H	DCM	705 nm, 670, 655, 620, 422, 346	R = $O(CH_2CH_2O)_3CH_3$	454, 455
		EtOH	625 nm	R = $O(CH_2CH_2O)_3CH_3$	454, 455
		spin-coated film	705 nm, 670	R = $O(CH_2CH_2O)_3CH_3$	691

(*Continued*)

Table 2. (*Continued*)

Structure	M	Solvent	Transition Energy (Intensity)	Remark	Ref.
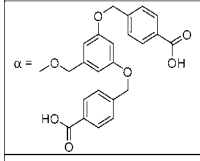	Zn(II)	0.1 M KOH aq	705 nm		686
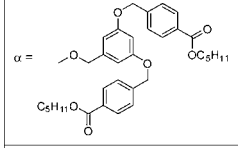	Zn(II)	THF	698 nm		686
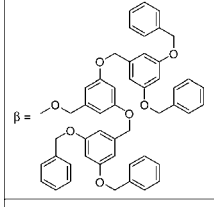	2H	DCM	716 nm, 680, 654, 620, 422, 346		692
		DCM	716 nm, 680, 654, 620, 422, 346		435
		spin-coated film	716 nm, 680		691
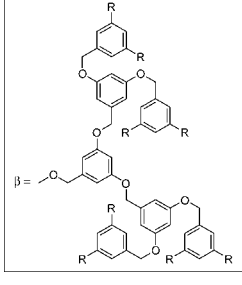	2H	DCM	705 nm, 670, 655, 620, 422, 346	R = $O(CH_2CH_2O)_3CH_3$	454, 455
		EtOH	635 nm	R = $O(CH_2CH_2O)_3CH_3$	454, 455
		spin-coated film	704 nm, 668	R = $O(CH_2CH_2O)_3CH_3$	691

(*Continued*)

Table 2. (*Continued*)

Structure	M	Solvent	Transition Energy (Intensity)	Remark	Ref.
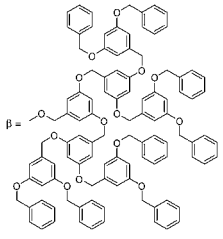	2H	DCM	715 nm, 680, 654, 620, 422, 346		435
		spin-coated film	715 nm, 679		691
		DCM	715 nm, 680, 654, 620, 422, 346		692
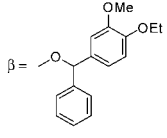	2H	THF	706 nm (lg ε 5.13), 668 (5.03), 638 (4.54), 610 (4.38), 388 (4.50), 344 (4.80)		620
	Zn(II)	THF	673 nm (lg ε 5.10), 656 (4.49), 612 (4.38), 352 (4.74), 290 (4.61)		620
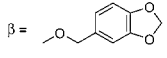	Mg(II)	$CHCl_3$	685 nm (lg ε 5.27), 616 (4.68), 354 (5.10)		693
	Co(II)	DMF	673 nm (lg ε 5.06)		693
	Cu(II)	DMF	659 nm (lg ε 5.04)		693
	Zn(II)	$CHCl_3$	689 nm (lg ε 5.26), 619 (4.66), 355 (5.11)		693
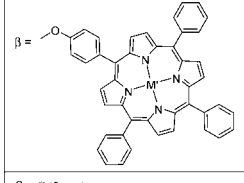	2H	$CHCl_3$	702 nm (lg ε 4.51), 668 (4.44), 638 (4.22), 603 (4.12), 558 (4.42), 421 (5.66), 339 (4.89)	M′ = Zn(II)	694
	Co(II)	DMSO	659 nm (lg ε 4.62), 594 (4.16), 540 (4.19), 419 (5.15), 331 (4.74)	M′ = Co(II)	695
	Zn(II)	DMSO	682 nm (lg ε 5.04), 602 (4.10), 561 (4.63), 429 (5.59), 365 (4.83)	M′ = Zn(II)	694
β = O(2-py)	Zn(II)	DMSO	680 nm (lg ε 5.36), 615 (4.32), 340 (4.50)		286
		DMF	673 nm (lg ε 5.18)		286
		$CHCl_3$	674 nm		286
		DCM	673 nm		286
		THF	672 nm		286
	Cd(II)	DMSO	685 nm (lg ε 5.30), 618 (4.52), 355 (4.70)		286
		DMF	682 nm (lg ε 5.11)		286

(*Continued*)

Table 2. (*Continued*)

Structure	M	Solvent	Transition Energy (Intensity)	Remark	Ref.
		$CHCl_3$	673 nm		286
		DCM	672 nm		286
		THF	677 nm		286
	Hg(II)	DMSO	690 nm (lg ε 5.17), 623 (4.06), 340 (4.55)		286
		DMF	685 nm (lg ε 5.08)		286
		$CHCl_3$	697 nm, 661		286
		DCM	697 nm, 661		286
		THF	697 nm, 661		286
β = 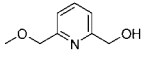	2H	py	683 nm (10^{-5} ε 5.05), 617 (4.96), 592 (4.60), 350 (5.02), 255 (5.09)		696
	Co(II)	py	674 nm (10^{-5} ε 5.08), 617 (4.63), 381 (5.13), 310 (5.15)		696
	Ni(II)	py	677 nm (10^{-5} ε 4.80), 616 (4.56), 485 (4.59), 332 (4.79), 295 (4.87)		696
	Cu(II)	py	689 nm (10^{-5} ε 5.18), 614 (4.71), 361 (5.10), 241 (5.14)		696
	Zn(II)	py	689 nm (10^{-5} ε 4.85), 615 (4.40), 375 (4.72), 323 (4.54)		696
α = O(3-py)	Ga(III)Cl	DMSO	705 nm (lg ε 5.08)		320
		DMSO	706 nm		324
β = O(3-py)	2H	py	666 nm (10^{-5} ε 1.06)		697
		py	700 nm (lg ε 4.90), 666 (4.85), 636 (4.49), 608 (4.33), 346 (4.72)		410
	Zn(II)	py	678 nm (10^{-5} ε 1.84)		697
		DMF	676 nm (ε 182,000), 609, 353		698
	Ga(III)Cl	DMSO	688 nm		324
		DMSO	687 nm (lg ε 5.09)		320
$\beta\beta$ = O(3-py)	Si(IV)L	DMSO	677 nm (lg ε 3.83)	L = *trans*-Cl_2	699
		DMSO	677 nm (lg ε 4.11), 609 (3.64), 364 (3.94)	L = *trans*-$(OH)_2$	699
		DCM	674 nm (lg ε 5.34), 644 (4.54), 607 (4.60), 360 (4.92)	L = *trans*-$(OSi(Pr)_3)_2$	699
		DCM	677 nm (lg ε 5.13), 646 (4.21), 609 (4.28), 359 (4.63)	L = *trans*-$(OSi(i\text{-}Pr)_2)_3)_2$	699
		DMF	680 nm (lg ε 5.09), 650 (4.29), 612 (4.36), 363 (4.59)	L = *trans*-$(OSi(C_6H_5)_2t\text{-}Bu)_2$	699
	Zn(II)	DMSO	678 nm (lg ε 4.08)		699

(*Continued*)

Table 2. (*Continued*)

Structure	M	Solvent	Transition Energy (Intensity)	Remark	Ref.
		DMF	675 nm (ε 219,000), 609, 362		698
α = O(3-py$^+$(*N*-Me))	Ga(III)Cl	DMSO	696 nm (lg ε 5.27)	$[Pc]^{4+}2SO_4^{2-}$	320
		H_2O	693 nm (lg ε 5.20)	$[Pc]^{4+}2SO_4^{2-}$	320
		DMSO	697 nm	$[Pc]^{4+}2SO^{2-}$	324
		H_2O	693 nm	$[Pc]^{4+}2SO^{2-}$	324
β = O(3-py$^+$)(*N*-Me)	Zn(II)	DMF	674 nm (ε 112,000), 608, 348	$[Pc]^{4+}$	698
	Ga(III)Cl	DMSO	683 nm	$[Pc]^{4+}2SO^{2-}$	324
		H_2O	681 nm	$[Pc]^{4+}2SO^{2-}$	324
		DMSO	683 nm (lg ε 5.25)	$[Pc]^{4+}2SO_4^{2-}$	320
		H_2O	681 nm (lg ε 5.29)	$[Pc]^{4+}2SO_4^{2-}$	320
$\beta\beta$ = O(3-py$^+$(*N*-Me))	Si(IV)L	DMSO	676 nm, 608, 360	L = *trans*-(OSi(CH$_2$CH$_2$CH$_3$)$_3$)$_2$, $[Pc]^{4+}$	699
		MeOH	670 nm, 603, 359	L = *trans*-(OSi(CH$_2$CH$_2$CH$_3$)$_3$)$_2$, $[Pc]^{4+}$	699
		H_2O (pH 6.0)	674 nm, 608, 357	L = *trans*-(OSi(CH$_2$CH$_2$CH$_3$)$_3$)$_2$, $[Pc]^{4+}$	699
		H_2O (pH 7.0)	674 nm, 608, 357	L = *trans*-(OSi(CH$_2$CH$_2$CH$_3$)$_3$)$_2$, $[Pc]^{4+}$	699
		H_2O (pH 8.0)	674 nm, 608, 357	L = *trans*-(OSi(CH$_2$CH$_2$CH$_3$)$_3$)$_2$, $[Pc]^{4+}$	699
		DMSO	678 nm, 610, 360	L = *trans*-(OSi(CH$_2$(CH$_3$)$_2$)$_3$)$_2$, $[Pc]^{4+}$	699
		MeOH	672 nm, 606, 358	L = *trans*-(OSi(CH$_2$(CH$_3$)$_2$)$_3$)$_2$, $[Pc]^{4+}$	699
		H_2O	677 nm (lg ε 4.84), 648 (4.05), 610 (4.07), 356 (4.45)	L = *trans*-(OSi(CH$_2$(CH$_3$)$_2$)$_3$)$_2$, $[Pc]^{4+}$	699
		H_2O (pH 6.0)	677 nm, 610, 356	L = *trans*-(OSi(CH$_2$(CH$_3$)$_2$)$_3$)$_2$, $[Pc]^{4+}$	699
		H_2O (pH 7.0)	677 nm, 610, 356	L = *trans*-(OSi(CH$_2$(CH$_3$)$_2$)$_3$)$_2$, $[Pc]^{4+}$	699
		H_2O (pH 8.0)	677 nm, 610, 357	L = *trans*-(OSi(CH$_2$(CH$_3$)$_2$)$_3$)$_2$, $[Pc]^{4+}$	699
		DMSO	681 nm, 612, 359	L = *trans*-(OSi(C$_6$H$_5$)$_2$C(CH$_3$)$_3$)$_2$, $[Pc]^{4+}$	699
		MeOH	675 nm, 607, 355	L = *trans*-(OSi(C$_6$H$_5$)$_2$C(CH$_3$)$_3$)$_2$, $[Pc]^{4+}$	699
		H_2O	679 nm (lg ε 4.81), 649 (3.96), 612 (4.01), 352 (4.29)	L = *trans*-(OSi(C$_6$H$_5$)$_2$C(CH$_3$)$_3$)$_2$, $[Pc]^{4+}$	699
		H_2O (pH 6.0)	680 nm, 612, 353	L = *trans*-(OSi(C$_6$H$_5$)$_2$C(CH$_3$)$_3$)$_2$, $[Pc]^{4+}$	699
		H_2O (pH 7.0)	680 nm, 612, 353	L = *trans*-(OSi(C$_6$H$_5$)$_2$C(CH$_3$)$_3$)$_2$, $[Pc]^{4+}$	699
		H_2O (pH 8.0)	680 nm, 612, 352	L = *trans*-(OSi(C$_6$H$_5$)$_2$C(CH$_3$)$_3$)$_2$, $[Pc]^{4+}$	699
	Zn(II)	DMF	674 nm (ε 177,000), 608, 354	$[Pc]^{8+}8I^-$	698
		DMSO	677 nm (lg ε 4.84), 611 (4.21), 359 (4.48)	$[Pc]^{4+}$	699
		MeOH	670 nm, 349	$[Pc]^{4+}$	699
		H_2O (pH 6.0)	667 nm, 632, 346	$[Pc]^{4+}$	699
		H_2O (pH 7.0)	667 nm, 632, 346	$[Pc]^{4+}$	699

(*Continued*)

Table 2. (*Continued*)

Structure	M	Solvent	Transition Energy (Intensity)	Remark	Ref.
		H_2O (pH 8.0)	668 nm, 632, 347	$[Pc]^{4+}$	699
		DMF	671 nm (10^{-5} ε 0.94)	$[Pc]^{4+}$	700
$\beta\beta$ = O(3-py)(N-C_6H_{13})	Zn(II)	DMF	675 nm (10^{-5} ε 0.53)	$[Pc]^{4+}$	700
$\beta\beta$ = O(3-py)(N-$C_{12}H_{25}$)	Zn(II)	DMF	673 nm (10^{-5} ε 1.08)	$[Pc]^{4+}$	700
$\beta\beta$ = O(3-py$^+$(N ($CH_2CH_2O)_3$Me))	Si(IV)L	DMSO	680 nm, 612, 359	L = *trans*-(OSi(C_6H_5)$_2$C(CH_3)$_3$)$_2$, $[Pc]^{4+}$	699
		MeOH	675 nm, 608, 356	L = *trans*-(OSi(C_6H_5)$_2$C(CH_3)$_3$)$_2$, $[Pc]^{4+}$	699
		H_2O	678 nm (lg ε 4.76), 649 (3.90), 610 (3.96), 353 (4.25)	L = *trans*-(OSi(C_6H_5)$_2$C(CH_3)$_3$)$_2$, $[Pc]^{4+}$	699
		H_2O (pH 6.0)	678 nm, 611, 353	L = *trans*-(OSi(C_6H_5)$_2$C(CH_3)$_3$)$_2$, $[Pc]^{4+}$	699
		H_2O (pH 7.0)	678 nm, 611, 353	L = *trans*-(OSi(C_6H_5)$_2$C(CH_3)$_3$)$_2$, $[Pc]^{4+}$	699
		H_2O (pH 8.0)	678 nm, 611, 353	L = *trans*-(OSi(C_6H_5)$_2$C(CH_3)$_3$)$_2$, $[Pc]^{4+}$	699
	Zn(II)	DMF	675 nm (lg ε 4.74), 609 (4.10), 354 (4.36)	$[Pc]^{4+}$	699
		DMSO	677 nm, 611, 356	$[Pc]^{4+}$	699
		MeOH	671 nm, 607, 351	$[Pc]^{4+}$	699
		H_2O	674 nm (lg ε 4.56), 611 (3.94), 351 (4.27)	$[Pc]^{4+}$	699
		H_2O (pH 6.0)	675 nm, 351	$[Pc]^{4+}$	699
		H_2O (pH 7.0)	676 nm, 350	$[Pc]^{4+}$	699
		H_2O (pH 8.0)	676 nm, 352	$[Pc]^{4+}$	699
β = 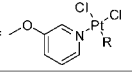	Zn(II)	DMSO	680 nm (lg ε 5.21), 640sh, 615 (4.66), 350 (5.01)	R = NH_3	701
		DMSO	679 nm (lg ε 5.23), 640sh, 613 (4.62), 349 (4.99)	R = $SOMe_2$	701
β = O(4-py)	Zn(II)	MeOH	670 nm (ε 95,300), 340 (60,300)		702
		DMF	681 nm, 614, 369		533
		DMF	680 nm, 613, 369		703
		MeOH	671 nm, 607, 353		703
β = O(4-py$^+$(*N*-Me))	Zn(II)	DMF	678 nm, 612, 374	$[Pc]^{4+}4I^-$	703
		MeOH	669 nm, 605, 351	$[Pc]^{4+}4I$	703
		H_2O + 5 % SDS	680 nm, 631, 354	$[Pc]^{4+}$	533
β = OCH_2(4-py)	2H	DMSO	705 nm(lg ε 4.15), 674(4.21), 344(4.10)		704
	Co(II)	DMSO	668 nm(lg ε 4.39), 332(4.40)		704
	Zn(II)	DMSO	682 nm(lg ε 4.43), 614(3.86), 357(4.16)		704
		DMF	679 nm, 610, 353		533
β = OCH_2(4-py$^+$(*N*-Me))	Zn(II)	H_2O	632 nm(lg ε 4.45), 337(4.58)	$[Pc]^{4+}4I^-$	704

(*Continued*)

Table 2. (*Continued*)

Structure	M	Solvent	Transition Energy (Intensity)	Remark	Ref.
		DMF	676 nm, 612, 353	$[Pc]^{4+}$	533
		H_2O + 5% SDS	682 nm, 645, 342	$[Pc]^{4+}$	533
$\beta\beta$ = OCH_2CH_2OEt	2H	benzene	700 nm (lg ε 4.40), 661 (4.42)		607
$\beta\beta$ = $OCH_2CH_2OCH_2Ph$	Cu(II)	$CHCl_3$	676.6 nm, 610.2		705
$\alpha\alpha$ = $OCH(CH_2OC_{12}H_{25})_2$	Ni(II)	$CHCl_3$	732 nm (lg ε 4.99), 657 (4.37), 340 (4.35), 300 (4.48)		706
		toluene	731 nm, 348, 300		706
		DCM	732 nm, 344, 302		706
		THF	732 nm, 343, 300		706
$\alpha\alpha$ = 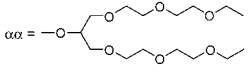	Ni(II)	$CHCl_3$	734 nm (lg ε 5.18), 659 (4.56), 346 (4.57), 303 (4.69)		706
		toluene	734 nm, 346, 303		706
		DCM	731 nm, 344, 301		706
		THF	734 nm, 351, 303		706
		DMSO	742 nm, 346, 305		706
		DMF	738 nm, 350, 304		706
		MeOH	734 nm, 351, 304		706
$\beta\beta$ = $O(CH_2CH_2O)_2Me$	Zn(II)	DCM	678 nm, 608, 356		707
$\beta\beta$ = $O(CH_2CH_2O)_3Me$	Zn(II)	DCM	679 nm, 608, 356		707
β = $O(CH_2CH_2O)_3Me$	2H	DMSO	706 nm (lg ε 3.5), 676 (3.5)		708
	Mg(II)	DMSO	682 nm (lg ε 5.5)		708
	Ni(II)	THF	671 nm (lg ε 5.1)		708
	Cu(II)	DMSO	681 nm (lg ε 5.1)		708
	Zn(II)	DMSO	681 nm (lg ε 5.5)		708
β = 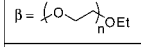	2H	$CHCl_3$	703 nm (lg ε 5.00), 670 (4.94)		607
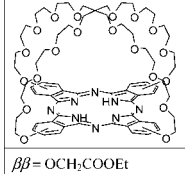	2H	$CHCl_3$	706 nm (lg ε 4.40), 670 (4.40)		607
$\beta\beta$ = OCH_2COOEt	Cu(II)	$CHCl_3$	707 nm (lg ε 4.89), 678 (5.09), 605 (4.74), 385 (4.11), 346 (4.51), 278 (4.73)255 (4.19)		709

(*Continued*)

Table 2. (*Continued*)

Structure	M	Solvent	Transition Energy (Intensity)	Remark	Ref.
β = 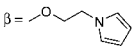	2H	DCM	701 nm, 666, 640, 338, 287, 230		710
	Co(II)	DCM	671 nm, 617, 326, 288, 226		710
	Ni(II)	DCM	671 nm, 619, 329, 279, 227		710
	Zn(II)	DCM	682 nm, 615, 348, 264, 232		710
β = 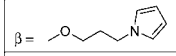	2H	DCM	703 nm, 665, 641, 608, 341, 288		710
β = 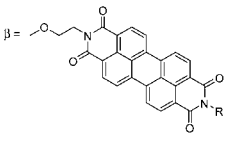	Mg(II)	1-methylpyrolidone	740 nm, 678, 526, 490,461, 257	R = 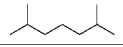	711
		1-methylpyrolidone	739 nm, 677, 525, 489, 458, 259	R = 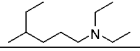	711
		1-methylpyrolidone	738 nm, 639, 527, 491, 460, 258	R = Ph(2,4,6-(*t*-Bu)$_3$)	711
		H_2O	761 nm, 529, 511, 223	R = 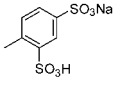	711
		H_2O/EtOH v/v = 1/1	731 nm, 526, 491, 463		711
β= OCOPh	Cu(II)	DMF	671 nm (r.i. 1.00), 610 (0.63)		712
		$CHCl_3$	672 nm (r.i. 1.00), 616 (0.75)		712
β= OCOPh(4-OC_9H_{19})	Ni(II)	DMF	666 nm (r.i. 1.00), 622 (0.70)		712
		$CHCl_3$	665 nm (r.i. 1.00), 631 (0.76)		712
	Cu(II)	DMF	670 nm (r.i. 1.00), 617 (0.74)		712
		$CHCl_3$	671 nm (r.i. 1.00), 611 (1.26)		712
β= OCOPh(4-$OC_{10}H_{21}$)	Cu(II)	DMF	610 nm (r.i. 1.00), 671 (1.65)		712
		$CHCl_3$	672 nm (r.i. 1.00), 613 (0.79)		712
β= OCOPh(4-$COOC_{11}H_{23}$)	Cu(II)	DMF	690 nm (r.i. 1.00), 621 (0.45)		712
		$CHCl_3$	672 nm (r.i. 1.00), 616 (0.51)		712
β= OCOPh(4-COOPh(4-C_7H_{15}))	Cu(II)	DMF	671 nm (r.i. 1.00), 618 (0.72)		712
		$CHCl_3$	672 nm (r.i. 1.00), 614 (0.96)		712
β= OCOPh(4-COOPh(4-C_8H_{17}))	Ni(II)	DMF	664 nm (r.i. 1.00), 613 (0.97)		712
		$CHCl_3$	664 nm (r.i. 1.00), 622 (0.82)		712
	Cu(II)	DMF	670 nm (r.i. 1.00), 616 (0.85)		712
		$CHCl_3$	672 nm (r.i. 1.00), 617 (0.93)		712
β= OCOPh(4-NO_2)	Cu(II)	DMF	689 nm (r.i. 1.00), 625 (0.69)		712

(*Continued*)

Table 2. (*Continued*)

Structure	M	Solvent	Transition Energy (Intensity)	Remark	Ref.
β = 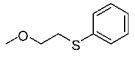	2H	$CHCl_3$	707 nm (10^{-5} ε 5.11), 671 (5.10), 644 (4.93), 392 (4.82), 335 (5.20), 287 (5.21)		713
	Co(II)	py	677 nm (10^{-5} ε 5.18), 611 (4.59), 345 (5.16), 275 (5.14)		713
	Ni(II)	py	677 nm (10^{-5} ε 5.17), 620 (4.60), 389 (4.83), 329 (5.18), 295 (5.17)		713
	Cu(II)	py	686 nm (10^{-5} ε 5.20), 617 (4.52), 334 (5.17), 265 (5.15)		713
	Zn(II)	$CHCl_3$	686 nm (10^{-5} ε 5.23), 617 (4.64), 353 (5.19), 270 (5.22)		713
β = 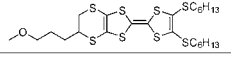	Mg(II)	$CHCl_3$	695.0 nm, 342.0		714
	Zn(II)	$CHCl_3$	685.0 nm, 344.0, 322.0		714
β = 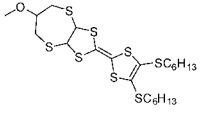	2H	$CHCl_3$	702.6 nm, 666.6, 639.4, 336.4, 287.6		715
	Mg(II)	$CHCl_3$	693.0 nm, 627.0, 361.0, 295.0		715
	Zn(II)	$CHCl_3$	686.0 nm, 317.0		715
β = 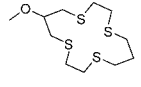	2H	$CHCl_3$	700 nm (10^{-4} ε 28.64), 670 (24.62), 637sh (11.30), 600 (7.13), 385sh (8.44), 340 (15.5), 287 (8.54), 240 (8.79)		716
	Co(II)	$CHCl_3$	675 nm (10^{-4} ε 11.48), 608sh (3.22), 330 (4.83), 293 (5.00), 222 (5.00)		716
	Ni(II)	$CHCl_3$	674 nm (10^{-4} ε 16.48), 607sh (3.93), 328 (5.15), 297 (5.00), 220 (5.00)		716
	Cu(II)	$CHCl_3$	680 nm (10^{-4} ε 22.85), 610sh (2.85), 334 (8.57), 282 (8.85), 232 (9.14)		716
	Zn(II)	$CHCl_3$	680 nm (10^{-4} ε 11.88), 612 (2.28), 332 (5.71), 280 (3.31), 240 (5.14)		716
$\beta\beta$ = SEt	Mg(II)	toluene	702 nm (lg ε 5.04), 670sh, 632 (4.33), 368 (4.61)		423, 717
α = SBu	2H	THF	733.5 nm, 710.0		48
	Zn(II)	THF	708.6 nm		48
$\alpha\alpha$ = SBu	2H	THF	804.5 nm		48
	Zn(II)	THF	779.6 nm		48
β = SBu	2H	MeOH	630 nm, 432, 350		512

(*Continued*)

Table 2. (*Continued*)

Structure	M	Solvent	Transition Energy (Intensity)	Remark	Ref.
		$CHCl_3$	715 nm, 683, 654, 622, 427, 345		512
		THF	713.5 nm, 681.5		48
	Zn(II)	THF	687.4 nm		48
$\beta\beta$ = SBu	2H	THF	729.0 nm, 699.5		48
	Fe(II)	DMSO	676 nm (lg ε 4.97), 348 (5.88)		718
		DMF	684 nm (lg ε 5.06), 620 (4.61), 449 (4.59), 356 (5.08)		718
	Fe(II)L	DMSO	686 nm (lg ε 5.10), 620, 468, 445, 408, 368	L = trans-$(CN)_2$, $[Pc]^{2-}2K^+$	718
		DMF	686 nm (lg ε 5.08), 620, 468, 445, 408, 366	L = trans-$(CN)_2$, $[Pc]^{2-}2K^+$	718
	Zn(II)	THF	707.0 nm		48
		$CHCl_3$	708 nm (lg ε 5.36), 637 (4.64), 363 (4.89), 328 (4.73)		719
β = S(*t*-Bu)	Mn(II)	benzene	685 nm, 355		528
	Mn(III)OH	benzene	731 nm (lg ε 4.86), 516 (4.04), 352 (4.57)		528
	Mn(III)L	py	635 nm, 355	L = py	528
$\beta\beta$ = S(*t*-Bu)	2H	py	719 nm (ε 119,500), 695 (119,100), 636 (29,000), 356 (64,700)		720
	Mg(II)	py	705 nm (ε 275,000), 636 (48,800), 371 (93,400)		720
	Zn(II)	py	692 nm (ε 273,400), 625 (44,700), 360 (83,500)		720
		THF	685 nm (ε 275,000)		721
$\alpha\alpha$ = SC_5H_{11}	Ti(IV)O	DCM	808 (lg ε 3.9), 718 (3.3), 352 (3.5), 290 (3.9)		175
	Ti(II)	DCM	769 nm		175
	V(IV)O	DCM	850 nm (lg ε 4.24), 754 (3.46), 344 (3.96)		134
		$CHCl_3$	841 nm		134
		THF	834 nm		134
		toluene	830 nm		134
	Mn(III)OAc	DCM	893 (lg ε 4.8), 794 (4.3), 553 (4.0), 363 (4.5), 285 (5.0)		175
	Mn(II)	DCM	795 nm		175
$\alpha\alpha$ = SC_6H_{13}	Cu(II)	THF	783 nm		338
	Zn(II)	THF	781 nm		338
	In(III)Cl	THF	836 nm		338
	Pb(II)	THF	818 nm		338
β = SC_6H_{13}	Ti(IV)O	$CHCl_3$	720 nm (lg ε 5.34), 349 (4.86)		722

(*Continued*)

Table 2. (*Continued*)

Structure	M	Solvent	Transition Energy (Intensity)	Remark	Ref.
	Ti(IV)L	$CHCl_3$	721 nm (lg ε 5.12), 342 (4.64)	L = 	722
$\beta\beta = SC_6H_{13}$	2H	$CHCl_3$	740 nm (10^{-4} ε 13.44), 700 (12.75), 670 (5.20), 636 (3.39), 448 (3.44), 360 (6.70), 330 (7.36)		723
	Ti(IV)O	$CHCl_3$	739 nm (lg ε 5.35), 336 (5.00)		722
	Ti(IV)L	$CHCl_3$	741 nm (lg ε 5.36), 335 (5.07)	L = 	722
	Co(II)	$CHCl_3$	704 nm (10^{-4} ε 12.24), 630 (4.00), 423 (2.62), 327 (11.76)		723
	Ni(II)	$CHCl_3$	702 nm (10^{-4} ε 11.10), 675 (6.46), 634 (4.09), 432 (2.70), 364sh (2.20), 325 (9.77)		723
	Cu(II)	$CHCl_3$	711 nm (10^{-4} ε 12.93), 675 (5.58), 643 (4.35), 440 (2.73), 327 (8.10)		723
	Zn(II)	$CHCl_3$	710 nm (10^{-4} ε 18.75), 675sh (2.86), 638 (3.40), 364 (6.55), 325 (5.10)		723
$\beta = SC_8H_{17}$	2H	$CHCl_3$	732 nm, 700, 668, 450, 330		630
	Ni(II)	$CHCl_3$	685 nm (lg ε 5.0), 660sh, 625sh, 393 (4.4), 306 (4.8), 257 (4.7)		724
	Cu(II)	$CHCl_3$	711 nm, 440, 325, 265		630
		$CHCl_3$	693 nm (lg ε 5.0), 630sh, 418sh, 342 (4.7), 299 (4.7)		724
$\beta\beta = SC_8H_{17}$	2H	py	733 nm (ε 115,000), 707 (140,200), 638 (21,600), 366 (40,000)		720
		$CHCl_3$	730 nm (lg ε 5.30), 699 (5.13), 679 (4.72), 660 (4.53), 451sh, 362 (4.86)		407
	Mg(II)	py	711 nm (ε 346,900), 639 (59,600), 376 (114,800)		720
	Ni(II)	$CHCl_3$	702 nm (lg ε 5.0), 675sh, 432 (4.4), 324 (5.0)		724
	Cu(II)	$CHCl_3$	713 nm (lg ε 4.6), 640sh, 440 (4.0), 325 (3.6)		724
	Zn(II)	py	712 nm (ε 278,800), 638 (47,400), 376 (79,300)		720
$\beta = SC_{12}H_{25}$	2H	$CHCl_3$	716 nm (lg ε 5.12), 682 (5.12), 655 (4.58), 621sh, 422 (4.56), 346 (4.89)		407
	Mn(II)Ac	DCM	698 nm		175

(*Continued*)

Table 2. (*Continued*)

Structure	M	Solvent	Transition Energy (Intensity)	Remark	Ref.
	Mn(III)OAc	DCM	749 nm (lg ε 4.9), 528 (4.6), 450 (4.3)		725
$\beta\beta = SC_{12}H_{25}$	2H	$CHCl_3$	716 nm (10^{-4} ε 12.20), 682 (10.62), 652sh (3.80), 615 (2.50), 410 (2.30), 346 (5.90)		726
		$CHCl_3$	732.2 nm (lg ε 5.16), 699.6 (5.14), 669.6 (4.76), 636.8 (4.56), 448.0 (4.57), 359.3 (4.85), 329.5 (4.89)		473
	Ni(II)	$CHCl_3$	702 nm (10^{-4} ε 13.95), 670 (7.09), 636 (3.86), 434 (3.27), 360sh (2.96), 326 (11.05)		723
		$CHCl_3$	687 nm (10^{-4} ε 19.60), 653sh (5.60), 621 (4.50), 402 (3.50), 305 (11.90)		726
		$CHCl_3$	680sh nm (10^{-4} ε 2.63), 643 (7.98)	$[Pc]2PdCl_2$	726
		$CHCl_3$	680sh nm (10^{-4} ε 1.93), 634 (6.28), 400 (2.10)	$[Pc]2AgNO_3$	726
	Cu(II)	$CHCl_3$	711.9 nm (lg ε 5.21), 680sh, 642.6 (4.68)		473
$\beta\beta = SC_{16}H_{33}$	Ni(II)	$CHCl_3$	686 nm (10^{4} ε 19.60), 646 (4.20), 618 (4.10), 399 (2.60), 306 (3.93)		726
$\beta\beta = SC_{18}H_{37}$	Ti(IV)O	$CHCl_3$	738 nm (lg ε 5.55), 705 (4.73), 661 (4.76), 468 (4.69), 337 (5.04)		727
β = 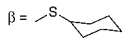	Ni(II)	DCM	683.0 nm, 650.5sh, 622.5sh, 412.5sh, 364.0sh, 334.0, 301.5, 261.5		626
ββ = 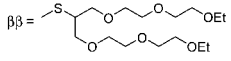	2H	$CHCl_3$	730 nm (10^{-4} ε 12.60), 700.5 (11.16), 673.5sh, 635.5 (2.68), 432.0 (2.78), 359.5 (5.64), 266.0 (3.68)		728
	Ni(II)	$CHCl_3$	702.0 nm (10^{-4} ε 20.68), 669.5sh, 630.5 (0.92), 422.0 (3.22), 322.5 (10.06), 272.0 (6.12)		728
β = 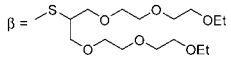	2H	$CHCl_3$	711.5 nm (10^{-4} ε 16.42), 678.0 (13.84), 651.0sh, 616.0 (3.24), 411.5 (2.96), 345.5 (7.68), 297.0 (5.66)		728
	Ni(II)	$CHCl_3$	682.0 nm (10^{-4} ε 22.54), 650.0sh, 615.0 (4.10), 392.0 (2.60), 303.0 (8.26), 260.0 (4.94)		728
$\beta = SCH(CH_2OC_{12}H_{25})_2$	Zn(II)	DCM + 0.2 M TBAP	687 nm (lg ε 4.80), 620 (4.01), 357 (4.01)		729
$\beta\beta = SCH_2CH_2NEt_2$	2H	THF	731 nm (10^{-4} ε 0.480), 701 (0.450), 668 (0.147), 636 (0.105), 337 (0.250)		730
	Co(II)	THF	690 nm, 635, 331		730
		H_2O	651 nm, 319	$[Pc]^{8+}8I^-$	730
	Zn(II)	THF	701 nm, 632, 342		730

(*Continued*)

Table 2. (*Continued*)

Structure	M	Solvent	Transition Energy (Intensity)	Remark	Ref.
		H_2O	666 nm, 420, 322	$[Pc]^{8+}8I^-$	730
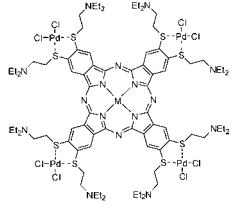	Co(II)	DMSO	701 nm, 336		730
	Zn(II)	DMSO	706 nm, 329		730
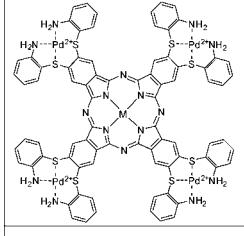	Co(II)	DMF	687 nm (10^{-4} ε 7.84), 629 (4.83), 330 (10.06)	M' = Pd, $[Pc]^{8+}8Cl^-$	643
	Ni(II)	DMF	695 nm (10^{-4} ε 6.66), 637 (5.20), 302 (14.22)	M' = Pd, $[Pc]^{8+}8Cl^-$	643
	Zn(II)	DMF	691 nm (10^{-4} ε 8.75), 628 (3.12), 367 (3.87)	M' = Pd, $[Pc]^{8+}8Cl^-$	643
α = SPh	Ti(IV)O	DCM	747 nm (lg ε 5.36), 669 (4.68), 344 (4.94), 265(4.87)		731
		THF	741 nm, 344		731
		$CHCl_3$	704 nm, 352		731
		DMSO	741 nm, 721, 342		731
	Mn(II)	DMF	764 nm (lg ε 5.02), 681 (4.47), 511 (3.36), 360 (2.37)		732
	Mn(III)	benzene	700 nm, 403, 350		528
	Mn(III)Cl	benzene	769 nm (lg ε 5.03), 530 (4.20), 480 (4.20), 360 (4.70)		528
	Mn(III)L	py	735 nm, 345	L = py	528
	Co(II)	DMF	693 nm (lg ε 4.71), 626 (4.56), 326 (4.15)		243
	Zn(II)	THF	706.7 nm		48
β = SPh	2H	py	713 nm (lg ε 4.77), 684 (4.73), 646 (4.40), 620sh (4.34), 420sh (4.42), 345 (4.63)		410
		$CHCl_3$	714 nm (lg ε 5.26), 681 (5.11), 651 (4.78), 618 (4.56), 423sh, 342 (4.90)		407
		$CHCl_3$	694 nm (lg ε 5.24), 627 (4.61), 414 (4.33), 343 (4.91)		733

(*Continued*)

Table 2. (*Continued*)

Structure	M	Solvent	Transition Energy (Intensity)	Remark	Ref.
		THF	709.5 nm, 677.7		48
	Ti(IV)O	DCM	692 nm	peripheral	175
		DCM	706 nm	nonperipheral	175
		DCM	714 nm (lg ε 5.06), 645 (3.47), 351 (4.68), 305 (4.57), 256 (4.62)		731
		THF	710 nm, 344		731
		$CHCl_3$	699 nm, 355		731
		DMSO	700 nm, 368		731
	Mn(II)	benzene	769 nm		530
	Co(II)	DMF	671 nm (lg ε 4.66), 608 (4.51), 331 (4.03)		243
	Zn(II)	THF	684.5 nm		48
		PVA in DMSO	680 nm (10^{-4} ε 13.11)		486
$\beta\beta$ = SPh	2H	$CHCl_3$	735 nm (lg ε 5.20), 709 (5.12), 672 (4.76), 643 (4.50), 435 (4.60), 348 (4.91)		407
	Ti(IV)O	1-ClNp	712 nm (log ε 5.29), 639 (4.56), 354 (4.83)		640
	Co(II)	DMF	688 nm		734
		$CHCl_3$	694 nm		734
	Cu(II)	DMF	699 nm		734
		$CHCl_3$	707 nm		734
		1-ClNp	748 nm		735
	Zn(II)	THF	707.8 nm		48
	In(III)Cl	EtOH	735 nm (lg ε 5.16), 659, 357		641
$\alpha\alpha\beta\beta$ = SPh	Cu(II)	DMSO	783 nm		736
	Zn(II)	DMSO	759 nm		736
$\beta\beta$ = SPh(4-Me)	Zn(II)	$CHCl_3$	715 nm (lg ε 5.30), 640 (4.60), 363 (4.85), 328 (4.68)		719
$\beta\beta$ = SPh(2-NH_2)	Co(II)	DMF	694 nm (10^{-4} ε 12.82), 630 (6.86), 370 (15.91), 340 (4.06)		643
	Ni(II)	DMF	711 nm (10^{-4} ε 11.39), 639 (3.68), 425 (4.43), 325 (12.65)		643
	Zn(II)	DMF	699 nm (10^{-4} ε 9.44), 640 (4.86), 365 (6.12), 320 (3.77)		643
@@R_2 = SPh(4-Me)	2H	$CHCl_3$	700 nm (lg ε 5.00), 663 (5.00), 641 (4.70), 610 (4.49), 424sh, 340 (4.87)		516

(*Continued*)

Table 2. (*Continued*)

Structure	M	Solvent	Transition Energy (Intensity)	Remark	Ref.
$R_2(R_3)$ = SPh(4-Me)	2H	$CHCl_3$	700 nm (ε 100,000), 663 (100,000), 641 (50,118), 610 (30,902), 424sh, 340 (74,131)		517
β = SPh(4-Me)	2H	$CHCl_3$	701 nm (lg ε 5.09), 665 (5.03), 645 (4.67), 638 (4.66), 605 (4.47), 346 (4.85)		516
α = SCH_2Ph	Ti(IV)O	DCM	746 nm (lg ε 5.10), 675 (4.66), 342 (4.84), 264 (4.88)		731
		THF	741 nm, 341		731
		$CHCl_3$	708 nm, 349		731
		DMSO	747 nm, 705, 342		731
	Ti(II)	DCM	687 nm		175
β = SCH_2Ph	Ti(IV)O	DCM	714 nm (lg ε 5.19), 645 (4.69), 349 (4.88), 306 (4.79), 264 (4.68)		731
		THF	711 nm, 355		731
		$CHCl_3$	700 nm, 355		731
		DMSO	708 nm, 359		731
	Ti(II)	DCM	694 nm		175
	Mn(II)Ac	DCM	701 nm		175
	Mn(III)OAc	DCM	745 nm (lg ε 5.1), 526 (4.8), 452 (4.4)		725
	Fe(I)	DMF	660 nm	$[Pc]^-$	737
	Fe(II)	DMF	720 nm (lg ε 4.06), 673 (4.25), 638 (4.45), 349 (4.57)		737
		DCM	670 nm		737
	Fe(III)	DMF	649 nm	$[Pc]^+$	737
	Co(I)	DMF	710 nm	$[Pc]^-$	737
	Co(II)	DMF	674 nm (lg ε 4.94), 613 (4.99), 325 (4.81)		737
		DCM	683 nm		737
	Co(III)	DMF	687 nm	$[Pc]^+$	737
	Zn(II)	DMF	689 nm (lg ε 5.22), 620 (4.99), 359 (4.81)		737
		DCM	690 nm		737
β = $SC_{13}H_{27}$	Fe(II)	DCM	682 nm	$[Pc]^-$	737
		DCM	712 nm (lg ε 4.66), 586 (4.99), 422 (3.97), 350 (5.00), 310 (5.00)		737
	Fe(III)	DCM	671 nm	$[Pc]^+$	737
	Co(I)	DCM	709 nm	$[Pc]^-$	737
	Co(II)	DCM	684 nm (lg ε 4.93), 623 (5.00), 310 (4.92)		737

(*Continued*)

Table 2. (*Continued*)

Structure	M	Solvent	Transition Energy (Intensity)	Remark	Ref.
	Co(III)	DCM	680 nm	$[Pc]^+$	737
	Zn(II)	DCM	691 nm (lg ε 5.4), 622 (4.99), 356 (4.97)		737
$\beta\beta$ = SCH_2Ph	Mg(II)	toluene	708 nm (lg ε 5.11), 676sh, 638 (4.40), 373 (4.73)		423
	Fe(II)	DMF	690 nm (lg ε 4.795), 623 (4.291), 451 (4.327), 359 (4.801)		738
	Co(II)	DMF	686 nm (lg ε 4.445), 619 (4.312), 327 (4.606)		738
$\beta\beta$ = SCH(Me)Ph	Mg(II)	toluene	710 nm (lg ε 5.24), 680sh, 638 (4.49), 378 (4.81)		739
$\beta\beta$ = $SCHPh_2$	Mg(II)	toluene	714 nm (lg ε 5.39), 682sh, 640 (4.63), 378 (4.99)		717
α = S(2-py)	Mn(III)OH	DMF	755 nm		740
α = S(2-py(*N*-Me))	Mn(III)OH	DMF	735 nm		740
$\beta\beta$ = $S(CH_2)_2OH$	Fe(III)Cl	DMF	657 nm (lg ε 5.32), 330(4.89)		741
β = $S(CH_2)_6OH$	Co(II)	THF	678 nm (12.08), 628 (6.34), 334 (16.11)		742
	Cu(II)	THF	684 nm (15.70), 622 (3.76), 582 (1.18), 351 (9.80)		742
	Zn(II)	THF	681 nm (6.00), 615 (1.22), 582sh (0.57), 345 (5.7)		742
$\beta\beta$ = $SCH(CH_2OC_{12}H_{25})_2$	Ti(IV)O	$CHCl_3$	727 nm (10^{-4} ε 28.0), 657 (7.13), 430 (7.7), 347 (16.0)		743
$\beta\beta$ = $S(CH_2CH_2O)_2Bu$	Zn(II)	THF	701 nm, 632, 366		744
$\beta\beta$ = $S(CH_2CH_2O)_3Me$	Ti(IV)O	$CHCl_3$	733 nm (10^{-4} ε 24.0), 659 (4.84), 451 (3.6), 337 (8.6)		743
β = 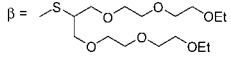	Ti(IV)O	hexane	705 nm (lg ε 4.81), 343		745
		THF	710 nm (lg ε 5.46), 352		745
		$CHCl_3$	715 nm (lg ε 5.52), 350, 307		745
		MeOH	708 nm (lg ε 4.96), 344		745
		DMSO	714 nm (lg ε 5.34), 353		745
	Zn(II)	DMSO	692 nm (lg ε 5.42)		479
ββ = 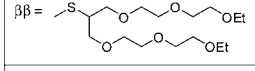	Zn(II)	DMSO	705 nm (lg ε 5.12)		479
ββ = 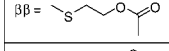	Ni(II)	$CHCl_3$	697(log ε 4.91), 317(4.86)		741
β = 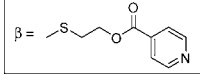	2H	$CHCl_3$	709 nm (lg ε 4.62), 676 (4.60), 345 (4.47)		746

(*Continued*)

Table 2. (*Continued*)

Structure	M	Solvent	Transition Energy (Intensity)	Remark	Ref.
β = 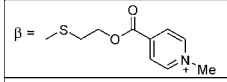	2H	DMSO	712 nm (lg ε 4.79), 688 (4.80), 346 (4.65)	$[Pc]^{+}4I^{-}$	746
β = 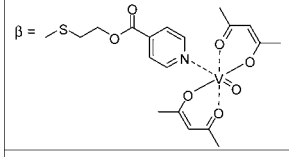	2H	$CHCl_3$	708 nm (lg ε 4.04), 676 (4.03), 343 (3.94)		746
ββ = 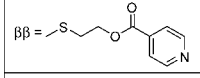	2H	$CHCl_3$	726(lg ε 4.88), 696(4.86), 354(3.97), 271(4.54)		741
ββ = 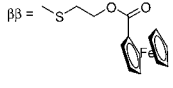	Fe(III)Cl	THF	690(log ε 5.10), 380(4.13)		741
	Zn(II)	$CHCl_3$	705(lg ε 3.85), 365(3.02), 309(2.96)		741
β = 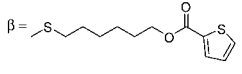	2H	THF	714 nm, 682, 655sh, 620sh, 344, 296 (thiophene)		747
	Co(II)	THF	676 nm, 609, 401, 325		748
	Cu(II)	THF	688 nm, 416, 342		747
	Zn(II)	THF	688 nm, 660, 620, 355		748
β = $S(CH_2)_2NMe_2$	2H	$CHCl_3$	714 nm (lg ε 3.9), 680 (3.9), 421 (3.5), 342 (3.9), 299 (3.8)		672
	Zn(II)	$CHCl_3$	695 nm (lg ε 4.0), 631 (3.9), 364 (4.0)		672
	Ti(IV)O	$CHCl_3$	723 nm (lg ε 4.87), 652 (4.25), 344 (4.56)		749
	Ti(IV)L	$CHCl_3$	720 nm (lg ε 4.94), 650 (4.56), 331 (4.75)	L = 	749
		$CHCl_3$	720 nm (lg ε 4.94), 656 (4.64), 340 (4.77), 280 (4.63)	L = 	749
β = $SCH_2CH_2N^{+}(Me)_3I^{-}$	2H	H_2O	637 nm (lg ε 3.7), 331 (3.7)	$[Pc]^{+}4I^{-}$	672
	Zn(II)	H_2O	642 nm (lg ε 3.8), 344 (3.8)	$[Pc]^{+}4I^{-}$	672
	Ti(IV)O	H_2O	680 nm (lg ε 4.85), 350 (4.59)	$[Pc]^{+}4I^{-}$	749
$\beta\beta$ = $S(CH_2)_2NMe_2$	2H	$CHCl_3$	731 nm (ε 23,490), 700 (22,340), 330 (12,620)		750
	Ti(IV)O	$CHCl_3$	739 nm (lg ε 4.90), 658 (4.32), 338 (4.76)		749

(*Continued*)

Table 2. (*Continued*)

Structure	M	Solvent	Transition Energy (Intensity)	Remark	Ref.
	Ti(IV)L	$CHCl_3$	729 nm (lg ε 4.92), 658 (4.69), 328 (4.57)	L = 	749
		$CHCl_3$	741 nm (lg ε 4.87), 656 (4.61), 334 (4.84), 280 (4.61)	L = 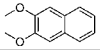	749
	Co(II)	$CHCl_3$	710 nm (ε 15,200), 364 (14,710)		750
	Zn(II)	$CHCl_3$	715 nm (lg ε3.9), 676 (3.8), 365 (4.0), 328 (3.8)		672
		$CHCl_3$	715 nm (ε 11,930), 371 (10,640)		750
$\beta\beta$ = $S(CH_2)_2N^+Me_3$	2H	H_2O	669 nm (ε 20,300), 321 (15.820)	$[Pc]^{8+}8I^-$	750
	Ti(IV)O	DMSO	722 nm (lg ε 4.91), 648 (4.34), 378 (4.75)	$[Pc]^{4+}8I^-$	749
	Co(II)	H_2O	678 nm (ε 15,340), 370 (7,970)	$[Pc]^{8+}8I^-$	750
	Zn(II)	H_2O	668 nm (ε 11,100), 365 (14,500)	$[Pc]^{8+}8I^-$	750
		H_2O	715 nm (lg ε 3.9), 676 (3.8), 365 (4.0).	$[Pc]^{8+}8I^-$	672
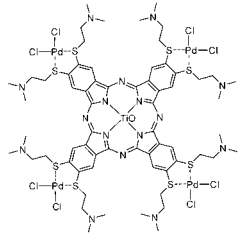	Ti(IV)O	$CHCl_3$	722 nm (lg ε 4.89), 648 (4.47), 335 (4.76)		749
β = $SCH_2CH_2N(Et)_2$	2H	$CHCl_3$	712 nm (lg ε 4.0), 680 (4.0), 340 (4.1), 302 (4.0)		672
	Zn(II)	$CHCl_3$	755 nm (lg ε 3.7), 690 (3.7), 656 (3.8), 362 (3.9)		672
β = 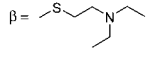	Co(II)	THF	675 nm (lg ε 3.94), 613 (3.36), 327 (3.77)		751
	Cu(II)	THF	689 nm (lg ε 3.40), 622 (2.71), 349 (2.90)		751
	Zn(II)	THF	687 nm (lg ε 4.27), 620 (3.45), 356 (3.75)		751
β = 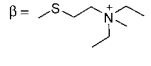	2H	H_2O	638 nm (lg ε 3.8), 331 (3.8)	$[Pc]^{4+}I^4$	672
	Co(II)	DMSO	672 nm (lg ε 4.35), 610 (3.90), 335 (4.22)	$[Pc]^{4+}I^{4-}$	751
	Cu(II)	DMSO	689 nm (lg ε 4.35), 620 (3.61), 356 (3.79)	$[Pc]^{4+}I^{4-}$	751
	Zn(II)	H_2O	656 nm (lg ε 3.9), 353 (3.78)	$[Pc]^{4+}I^{4-}$	672
		DMSO	690 nm (lg ε 4.26), 621 (3.48), 372 (3.79)	$[Pc]^{4+}I^4$	751
$\beta\beta$ = $SCH_2CH_2NMe_2$	Zn(II)	$CHCl_3$	780 nm (lg ε 3.7), 676 (3.8), 364 (3.9)		672

(*Continued*)

Table 2. (*Continued*)

Structure	M	Solvent	Transition Energy (Intensity)	Remark	Ref.
		DMF	705 nm (10^{-5} ε 2.0)		752
$\beta\beta$ = $SCH_2CH_2N^+Me_3I^-$	Zn(II)	H_2O	657 nm (lg ε 4.0), 354 (3.9)		672
β = $SCH_2CH_2NHCH_2CH_2CN$	2H	DMSO	712 nm (10^{-5} ε 4.47), 686 (4.49), 650 (4.39), 338 (4.7)		753
	Co(II)	DMSO	691 nm (10^{-5} ε 4.39)		753
	Zn(II)	DMSO	694 nm (10^{-5} ε 4.87), 361 (4.65)		753
$\beta\beta$ = 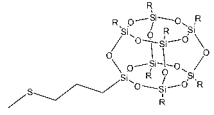	Co(II)	$CHCl_3$	686 (lg ε 4.247), 621 (3.804), 307 (4.511)	R = *i*-Bu	754
	Cu(II)	$CHCl_3$	697 (lg ε 4.630), 663 (4.284), 415 (4.062), 342 (4.489), 308 (4.547)	R = *i*-Bu	754
	Zn(II)	$CHCl_3$	697 (lg ε 4.315), 665 (3.690), 623 (3.649), 336 (4.346)	R = *i*-Bu	754
β = SO_2H	Co(II)	py	688.5 nm, 649.0, 354.0, 213.0		588, 576
β = SO_2Pr	Co(II)	$CHCl_3$	667 nm (lg ε 4.9), 602 (4.4), 328 (4.8)		755
	Zn(II)	$CHCl_3$	679 nm (lg ε 5.5), 609 (4.7), 345 (4.9)		755
$\beta\beta$ = SO_2Pr	Ni(II)	$CHCl_3$	674 nm (lg ε 5.2), 607sh (4.4), 348 (4.7)		756
	Zn(II)	$CHCl_3$	686 nm (lg ε 5.6), 617sh (4.7), 376 (4.9)		756
	Pd(II)	$CHCl_3$	665 nm (lg ε 5.36), 639 (4.6), 601 (4.63), 347 (4.84), 281 (4.74), 257 (4.81)		757
β = $SO_2C_8H_{17}$	Cu(II)	$CHCl_3$	678 nm (lg ε 5.0), 609 (4.4), 345 (4.7)		724
	Ni(II)	$CHCl_3$	668 nm (lg ε 4.8), 604 (4.2), 339 (4.5)		724
$\beta\beta$ = $SO_2C_8H_{17}$	Ni(II)	$CHCl_3$	676 nm (lg ε 4.4), 609 (3.6), 350 (3.9)		724
		$CHCl_3$	676 nm (lg ε 5.97)		758
	Cu(II)	$CHCl_3$	685 nm (lg ε 4.5), 615 (3.6), 355 (3.9)		724
α = SO_2Ph	Mn(II)	benzene	676 nm (lg ε 4.86), 342 (4.42)		528
		DMPA	706 nm		530
	Mn(III)OAc	AcOH	705 nm, 504, 360		528
	Mn(III)L	py	632 nm, 360	L = py	528
	Zn(II)	THF	664.0 nm		48
β = SO_2Ph	Mn(II)	$CHCl_3$	726 nm		530
		benzene	685 nm, 350		528
	Mn(III)Cl	$CHCl_3$	726 nm, 514, 360		528
	Mn(III)L	py	625 nm (lg ε 5.07), 350 (5.00)	L = py	528

(*Continued*)

Table 2. (*Continued*)

Structure	M	Solvent	Transition Energy (Intensity)	Remark	Ref.
	Zn(II)	THF	676.6 nm		48
$\alpha\beta(R_1, R_3) = SO_2Ph$	Mn(II)	benzene	694 nm (lg ε 4.88), 355 (4.58)		528
	Mn(III)OAc	AcOH	702 nm, 504, 358		528
	Mn(III)L	py	647 nm, 330	L = py	528
R_2 = Ts	2H	$CHCl_3$	687 nm (lg ε 5.11), 661 (5.13), 637 (4.84), 608 (4.64), 341 (4.75)		516
		$CHCl_3$	687 nm (ε 128,824), 661 (134,896), 637 (69,183), 608 (43,651), 341 (56,234)		517
β= Ts	2H	$CHCl_3$	701 nm (lg ε 5.09), 664 (5.00), 647 (4.55), 636 (4.54), 602 (4.35), 349 (4.76)		516
β= $SO_2NHC_8H_{17}$	Ni(II)	DMF	672 nm (10^{-3} ε 137.5), 604 (21.6), 336 (37.7)		759
	Fe(III)OH	MeOH	664 nm (10^{-3} ε 30.2), 608 (8.9), 326 (34.6)		759
	Co(II)	DMF	672 nm (10^{-3} ε 97.7), 608 (24.4), 336 (44.7)		759
	Cr(III)OH	MeOH	684 nm, 622, 496, 348		759
β= $SO_2NHC_{20}H_{41}$	Co(II)	MeOH	662 nm (10^{-3} ε 93.6), 607 (26.0), 329 (57.2)		759
$\alpha\beta(R_1, R_3) = SO_2NHC_{18}H_{37}$	Co(II)	$CHCl_3$	677 nm, 610sh		760
		DMF	674 nm, 630		760
$\alpha\beta(R_1, R_3) = SO_2N(Et)_2$	Co(II)	$CHCl_3$	668 nm, 605sh		760
		DMF	663 nm, 605sh		760
β= $SO_2N(C_8H_{17})_2$	Co(II)	MeOH	656 nm (10^{-3} ε 117.6), 606 (34.0), 324 (80.2)		759
$\alpha\beta(R_1, R_3) = SO_2N(C_8H_{17})_2$	Co(II)	$CHCl_3$	671 nm, 607sh		760
		DMF	667 nm, 607sh		760
β = 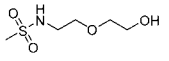	Zn(II)	MeOH	668 nm (ε 83,200), 344 (48,300)		702
β = 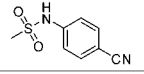	Zn(II)	MeOH	670 nm (ε 52,800), 604 (12,800), 340 (33,300)		702
β = 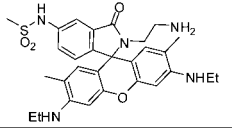	2H	$CHCl_3$	700 nm (r.i. 1.88), 663 (1.67), 645 (0.68), 637 (0.67), 346 (1)		761
		10% EtOH in $CHCl_3$	700 nm (r.i. 0.44), 663 (0.60), 637 (0.58), 602 (0.38), 528 (1.95), 349 (1)	salt	761
	Al(III)Cl	acetone	686 nm (r.i. 2.22), 617 (0.55), 355 (1)		761

(*Continued*)

Table 2. (*Continued*)

Structure	M	Solvent	Transition Energy (Intensity)	Remark	Ref.
		10% EtOH in $CHCl_3$	681 nm (r.i. 1.20), 618 (0.25), 530 (2.59), 350 (1)	salt	761
β = 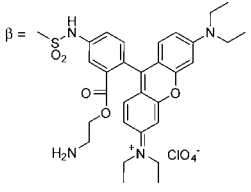	2H	DMSO	694 nm (r.i. 1.02), 674 (1.05), 640 (0.65), 566 (1.42), 341 (1)		761
	Al(III)Cl	DMSO	691 nm (r.i. 1.68), 683 (1.67), 650 (0.88), 618 (0.59), 565 (2.82), 357 (1)		761
$\beta = SO_2Cl$	Cr(III)Cl	DMF / H_2O	690 nm (10^{-3} ε 61.6), 658 (32.0), 630 (18.6), 492 (7.4), 347 (44.1)		759
$\beta = SO_3$	Zn(II)	DMSO	680 nm (lg ε 4.54)	$[Pc]^4$	480
$\beta = SO_3H$	Al(III)OH	DMF	680 nm (10^{-5} ε 2)		762
	Fe(II)	H_2SO_4	770 nm		461
	Ni(II)	pH 11 buffer	665 nm, 336		763
		H_2SO_4	747 nm (lg ε 5.00), 675 (4.26), 402 (4.21), 308 (4.92), 257 (4.79)		599
	Cu(II)	H_2SO_4	771 nm		461
$\alpha = SO_3Na$	Cu(II)	H_2SO_4	884 nm, 703, 668, 630, 440		274
$\beta = SO_3Na$	2H	H_2O	668 nm, 632, 335		764
		EtOH + H_2O = 1:1 v/v	693 nm, 658, 604, 340		764
	Al(III)Cl	H_2O	676 nm, 608, 342		764
		EtOH + H_2O = 1:1 v/v	674 nm, 609, 345		764
	Si(IV)L	PBS	679 nm (lg ε 4.96), 636	L = *trans*-Cl_2	765
		PBS + CEL	679 nm	L = *trans*-Cl_2	765
		DMSO	679 nm (lg ε 4.44)	L = *trans*-Cl_2	765
	Co(II)	H_2O	657 nm, 626, 318		764
		EtOH + H_2O = 1 :1 v/v	661 nm, 600, 326		764
	Cu(II)	H_2O	668 nm, 631, 327		764

(*Continued*)

Table 2. (*Continued*)

Structure	M	Solvent	Transition Energy (Intensity)	Remark	Ref.
		EtOH + H_2O = 1 :1 v/v	672 nm, 605, 341		764
	Zn(II)	H_2O	669 nm, 636, 337		764
		EtOH + H_2O = 1 :1 v/v	676 nm, 610, 344		764
	Ge(IV)L	PBS	680 nm (lg ε 4.83), 646	L = *trans*-Cl_2	765
		PBS + CEL	681 nm	L = *trans*-Cl_2	765
		DMSO	683 nm (lg ε 4.32)	L = *trans*-Cl_2	765
β= SO_3^- $^+NMe_2(C_{18}H_{37})_2$	Cr(III)Cl	DCM	686 nm (10^{-3} ε 44.4), 349 (48.2)		759
	Fe(III)Cl	DCM	684 nm (10^{-3} ε 48.0), 648 (32.7), 602 (17.3), 348 (48.4)		759
	Co(II)	DCM	672 nm (10^{-3} ε 103.3), 610 (32.9), 330 (79.9)		759
	Ni(II)	DCM	672 nm (10^{-3} ε 136.8), 640 (34.4), 602 (28.7), 338 (47.9)		759
β= SO_3^- $^+NBu_4$	Cr(III)Cl	DCM	686 nm (10^{-3} ε 6.0), 618 (1.1), 494 (0.9)		759
		H_2O	686 nm (10^{-3} ε 7.1), 656 (1.3), 620 (1.2), 496 (0.8), 340 (11.5)		759
	Co(II)	DCM	670 nm (10^{-3} ε 101.9), 604 (28.1), 330 (61.1)		759
		H_2O	660 nm (10^{-3} ε 60.0), 636 (47.7), 322 (59.5)		759
β = 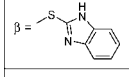	Mg(II)	DMF	687 nm (lg ε 4.25), 360 (4.11)		668
β = 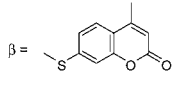	2H	DMF	685 nm (lg ε 4.46), 642 (4.37), 338 (4.82)		766
	Co(II)	DMF	686 nm (lg ε 4.46), 620 (4.10), 338 (4.57)		766
	Cu(II)	DMF	685 nm (lg ε 4.90), 615 (4.36), 317 (4.99)		766
	Zn(II)	DMF	688 nm (lg ε 5.08), 617 (4.38), 340 (4.78)		766
β = 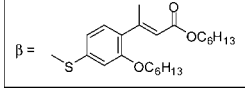	Zn(II)	DMF	690 nm (lg ε 5.08), 625 (4.40), 344 (4.79)		766

(*Continued*)

Table 2. (*Continued*)

Structure	M	Solvent	Transition Energy (Intensity)	Remark	Ref.
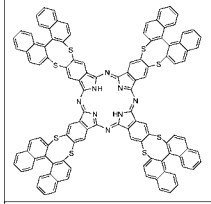	2H	THF	734 nm, 704, 670, 637, 431, 369, 332, 240, 218		767
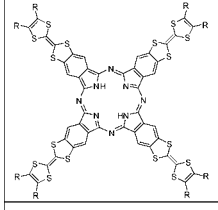	2H	DCM	615.7 nm (10^{-3} ε 51.9), 356.79 (76.3), 305.79 (71.2)	R = $SC_{10}H_{21}$	768
		DCM	627.0 nm (10^{-3} ε 56.1), 358.64 (79.2), 308.70 (68.3)	R = $SCH_2(CH_2OCH_2)Me$	768
$R_7 = NH_2$	2H	DMF	665 nm (lg ε 5.20), 614 (3.14), 346 (3.70)		769
$\alpha = NH_2$	Al(III)OH	DMF	778 nm		534
		H_2SO_4	743 nm, 715		534
	Ti(IV)O	DMF	830 nm (lg ε 3.83), 740 (3.47), 525 (2.83), 330 (4.0)		770
	Cr(III)OH	DMF	790 nm		534
		H_2SO_4	732 nm, 705		534
	Mn(III)OH	DMF	871 nm (lg ε 4.89), 763 (3.49), 547 (4.45), 354 (4.73)		770
	Co(II)	DMF	751.126 nm, 463.932, 330.057, 264.508		771
		H_2SO_4	738 nm		461
	Ni(II)	DMF	771.000 nm, 487.348, 311.0		771
	Cu(II)	DMF	775.568 nm, 436.539, 332.279, 272.0		771
	Zn(II)	DMF	766.0 nm, 478.070, 335.0, 200.0		771
	Ga(III)OH	DMF	805 nm		534
		H_2SO_4	717 nm, 693		534
	$Hf(IV)(OH)_2$	DMF	771 nm		534
		H_2SO_4	757 nm		534
$\beta = NH_2$	Al(III)OH	DMF	735 nm, 705		534

(*Continued*)

Table 2. (*Continued*)

Structure	M	Solvent	Transition Energy (Intensity)	Remark	Ref.
		H_2SO_4	762 nm, 748		534
	Ti(IV)O	DMF	755 nm (lg ε 5.24), 455 (4.02), 335 (4.91)		772
	Cr(III)OH	DMF	728 nm, 704		534
		H_2SO_4	778 nm, 763		534
	Co(II)	DMF	707.797 nm, 421.518, 321.169		771
		DMF	730 nm		773
		H_2SO_4	755 nm		773
		15 M H_2SO_4	740 nm, 380, 302, 210		774
	Ni(II)	DMF	721.129 nm, 433.796, 320.058, 304.504		771
		H_2SO_4	738 nm (lg ε 4.50), 380 (4.23), 302 (4.61), 212 (4.61)		599
		MeCN + TBAP	726 nm, 310		763
		15 M H_2SO_4	742 nm, 380, 302, 212		774
	Cu(II)	15 M H_2SO_4	740 nm, 375, 302, 216		774
		DMF	723.000 nm, 430.796, 338.0, 305.0		771
		H_2SO_4	749 nm		461
	Zn(II)	DMF	716.0 nm, 424.610, 354.0, 300.0		771
		DMF	715.0 nm, 643.0, 423.0, 354.0, 299.5		775
		H_2SO_4	742 nm		461
	Hf(IV)$(OH)_2$	DMF	731 nm, 705		534
		H_2SO_4	769 nm, 740		534
	Pb(II)	DMSO	735 nm (lg ε 4.313), 337 (4.454)		380
		36N H_2SO_4	785 nm (lg ε 4.146), 462 (4.152), 299sh (4.488), 260sh (5.598), 219 (4.776)		378
		DMSO	735 nm (lg ε 4.184), 337 (4.522)		378
$\beta\beta = NH_2$	Ni(II)	H_2SO_4	724 nm (10^{-3} ε 2.18), 709 (2.21), 676 (1.31), 647 (1.07), 366 (1.09), 303 (1.99)		776
		DMSO	717 nm (10^{-3} ε 2.50), 501 (0.62), 324 (1.92)		776
$\beta\beta = NHCOC_5H_{11}$	Ni(II)	$CHCl_3$	686 nm (10^{-3} ε 16.05), 639 (21.83), 350 (23.75)		776
$R_2 = NHCOC_{17}H_{35}$	2H	$CHCl_3$	696 nm (lg ε 5.03), 660 (5.00), 640sh, 607sh, 335 (5.00)		769
$\beta\beta = NHCOC_{11}H_{23}$	Ni(II)	$CHCl_3$	676 nm (10^{-3} ε 11.90), 618 (22.30), 344 (19.78)		776
$\beta = NHCOC_{18}H_{37}$	Ni(II)	$CHCl_3$	603 nm (10^{-4} ε 3.05), 330 (1.95)		597
$\alpha\alpha = NHCOPh$	Co(II)	DMF	708 nm		667

(*Continued*)

Table 2. (*Continued*)

Structure	M	Solvent	Transition Energy (Intensity)	Remark	Ref.
		$CHCl_3$	809 nm		667
β= NHCOPh	Cu(II)	DMF	690 nm (r.i. 1.00), 626 (0.41)		712
$\beta\beta$= NHCOPh	Co(II)	DMF	708 nm		777
		conc H_2SO_4	809 nm		777
β= NHCOPh(4-NO_2)	Cu(II)	DMF	693 nm (r.i. 1.00), 627 (0.74)		712
β= NHCOPh(4-OC_9H_{19})	Ni(II)	DMF	686 nm (r.i. 1.00), 625 (0.71)		712
		$CHCl_3$	625 nm		712
	Cu(II)	DMF	692 nm (r.i. 1.00), 626 (0.86)		712
		$CHCl_3$	624 nm		712
β= NHCOPh(4-$OC_{10}H_{21}$)	Cu(II)	DMF	692 nm (r.i. 1.00), 638 (0.72)		712
		$CHCl_3$	625 nm		712
β= NHCOPh(4-$COOC_{11}H_{23}$)	Cu(II)	DMF	690 nm (r.i. 1.00), 621 (0.53)		712
		$CHCl_3$	695 nm (r.i. 0.60), 616 (1.00)		712
β= NHCOPh(4-COOPh(4-C_7H_{15}))	Cu(II)	DMF	700 nm (r.i. 0.90), 643 (1.00)		712
		$CHCl_3$	696 nm (r.i. 0.70), 615 (1.00)		712
β= NHCOPh(4-COOPh(4-C_8H_{17}))	Ni(II)	DMF	687 nm (r.i. 1.00), 639 (0.86)		712
		$CHCl_3$	626 nm		712
	Cu(II)	DMF	690 nm (r.i. 1.00), 627 (0.52)		712
		$CHCl_3$	692 nm (r.i. 1.00), 644 (0.97)		712
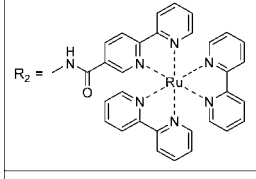	Zn(II)	THF	677 nm (lg ε 5.15), 611, 350 (4.78), 289 (4.86), 213 (4.98)		778
$\beta\beta$= NHTs	2H	$CHCl_3$	686 nm, 637		779
		benzene	687 nm, 639		779
		toluene	687 nm, 639		779
		nitromethane	681 nm, 637		779
		1,4-dioxane	717 nm		779
		acetone	708 nm, 682		779
		AcOEt	708 nm, 678		779

(*Continued*)

Table 2. (*Continued*)

Structure	M	Solvent	Transition Energy (Intensity)	Remark	Ref.
		MeOH	710 nm		779
		THF	710 nm, 681		779
		py	722 nm		779
		DMF	734 nm		779
		DMSO	740 nm		779
	Ni(II)	$CHCl_3$	673 nm, 638		779
		benzene	674 nm, 639		779
		toluene	673 nm, 639		779
		nitromethane	674 nm, 637		779
		1,4-dioxane	683 nm		779
		acetone	681 nm		779
		AcOEt	681 nm		779
		MeOH	694 nm		779
		THF	683 nm		779
		py	712 nm		779
		DMF	727 nm		779
		DMSO	730 nm		779
	Zn(II)	$CHCl_3$	682 nm, 640		779
		benzene	685 nm, 643		779
		toluene	684 nm, 643		779
		nitromethane	685 nm, 643		779
		1,4-dioxane	688 nm		779
		acetone	686 nm		779
		AcOEt	686 nm		779
		MeOH	696 nm		779
		THF	687 nm		779
		py	710 nm		779
		DMF	721 nm		779
		DMSO	721 nm		779
β = N-py	Mn(III)	benzene	705 nm, 370		528
	Mn(III)Cl	$CHCl_3$	798 nm (lg ε 4.30), 470 (4.00), 360 (4.30)		528
	Mn(III)L	py	732 nm, 360	L = py	528

(*Continued*)

Table 2. (*Continued*)

Structure	M	Solvent	Transition Energy (Intensity)	Remark	Ref.
$\alpha\beta$ (R_1, R_3) = NCHPh	Co(II)	1 M H_2SO_4	725 nm (lg ε 4.68), 636 (4.68), 305 (5.45), 213 (4.88)		780
	Ni(II)	1 M H_2SO_4	720 nm (lg ε 4.67), 674 (5.42), 316 (3.52), 218 (2.77)		780
	Cu(II)	1 M H_2SO_4	732 nm (lg ε 4.68), 640 (4.68), 325 (5.45), 215 (4.88)		780
	Zn(II)	1 M H_2SO_4	725 nm (lg ε 3.07), 671 (3.30), 306 (3.40), 208 (2.79)		780
α = NMe_2	V(IV)O	DMSO	828 nm, 740		781
	Cu(II)	DMF	778 nm, 700sh		781
β = NMe_2	2H	DMF	738 nm, 660, 440, 312		781
	V(IV)O	DMF	775 nm, 510,		781
	Co(II)	DMF	709 nm, 640, 322		781
	Cu(II)	DMF	730 nm, 654		781
$\beta\beta$ = NMe_2	V(IV)O	PhCl	744 nm, 710sh, 664, 470, 338sh, 324		781
	Cu(II)	benzene	708 nm, 670, 634, 465, 340sh, 322		781
β = 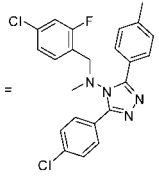	Co(II)	py	703(10^{-5} ε 5.12), 633(4.56), 300(5.03)		782
	Ni(II)	py	701(10^{-5} ε 5.00), 641(4.50), 271(5.04)		782
	Cu(II)	py	704(10^{-5} ε 5.08), 637(4.54), 293(5.01)		782
	Zn(II)	py	709(10^{-5} ε 5.04), 643(4.50), 357(4.92), 280(5.08)		782
β = 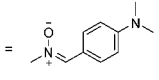	Co(II)	H_2SO_4	779 nm (lg ε 5.038), 696 (4.523), 418 (4.357), 292 (4.871), 208 (4.821)		783
	Ni(II)	H_2SO_4	760 nm (lg ε 4.960), 685 (4.494), 385 (4.376523), 306 (4.768), 248 (4.620), 205 (4.764)		783
	Cu(II)	H_2SO_4	740 nm (lg ε 4.793), 670 (4.443), 396 (4.339), 304 (4.646), 248 (4.588), 217 (4.803)		783
β = N-py	V(IV)O	DMF	766 nm, 690sh, 530, 520sh, 460		781
	Co(II)	DMF	708 nm, 645sh		781
β = 	Mn(II)	$CHCl_3$	798 nm		530

(*Continued*)

Table 2. (*Continued*)

Structure	M	Solvent	Transition Energy (Intensity)	Remark	Ref.
β = 	Zn(II)	DMF	676 nm, 612, 348		784
β = 	Zn(II)	DMF	678 nm, 612, 349		784
β = 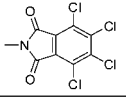	Zn(II)	DMF	679 nm, 638, 343		784
β = 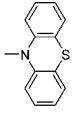	2H	$CHCl_3$	704 nm (10^{-1} ε 20.09), 665 (11.17), 338 (16.72), 257 (29.31)		785
	Ni(II)	$CHCl_3$	674 nm (10^{-1} ε 11.52), 608 (3.48), 335 (9.78), 296 (10.49), 257 (21.15)		785
	Co(II)	$CHCl_3$	680 nm (10^{-4} ε 2.28), 614 (1.14), 380 (2.35), 302 (6.57), 233 (21.97)		785
	Cu(II)	$CHCl_3$	686 nm (10^{-4} ε 11.94), 620 (3.74), 341 (9.90), 260 (13.69)		785
	Zn(II)	$CHCl_3$	680 nm (10^{-4} ε 17.56), 617 (3.68), 350 (8.40), 254 (19.25)		785
β = 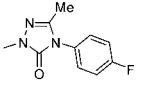	2H	$CHCl_3$	706 nm, 673, 267		786
	Ni(II)	$CHCl_3$	682 nm, 638sh, 256		786
	Co(II)	$CHCl_3$	682 nm, 648sh, 257		786
	Cu(II)	$CHCl_3$	685 nm, 634sh, 283		786
	Zn(II)	$CHCl_3$	689 nm, 655sh, 351, 288		786
$R_2 = NO_2$	Zn(II)	DMF	670 nm (lg ε 4.00), 605 (3.50), 343 (4.10)		648
		DMSO	670 nm		648
$R_2(R_3)$, $R_{10}(R_{11}) = NO_2$	2H	1-ClNp	704 nm, 683		787
		H_2SO_4	791 nm, 755		787
	Co(II)	1-ClNp	714 nm, 668		787
		H_2SO_4	812 nm, 760		787

(*Continued*)

Table 2. (*Continued*)

Structure	M	Solvent	Transition Energy (Intensity)	Remark	Ref.
	Cu(II)	1-ClNp	723 nm, 673		787
		H_2SO_4	810 nm, 758		787
$\alpha = NO_2$	2H	THF	694.0 nm, 659.0		48
		1-ClNp	701 nm (r.i. 3.20), 668 (2.58), 640 (0.84), 607 (0.56), 354 (1.00)		788
		H_2SO_4	747 nm (r.i. 3.64), 711 (2.93), 675sh (1.57), 630sh (1.00)		788
	Al(III)OH	py	679 nm		789
	Al(III)Cl	DMF	675 nm		534
		H_2SO_4	742 nm, 726		534
	Cr(III)Cl	DMF	682 nm		534
		H_2SO_4	745 nm, 730		534
	Mn(II)	H_2SO_4	845.0 nm, 799.0, 752.0, 721.5, 628.0		459
	Fe(II)	H_2SO_4	747.5 nm, 667.5, 517.5, 360, 298.5		272
	Co(I)	DCM	708 nm, 675sh, 643, 600sh, 520sh, 471, 313	[Pc]	461
	Co(II)	H_2SO_4	711.5 nm, 648, 391, 310		272
		H_2SO_4	715 nm		461
		DCM	678 nm, 645sh, 612, 380, 330		461
		1-ClNp	670 nm (r.i. 1.54), 602 (0.36), 345 (1.00)		788
		DMSO	654 nm (4.95), 598sh (4.36), 584sh (4.33), 410sh (3.69), 336 (4.64)		788
		H_2SO_4	709 nm		788
		DMF	653.36 nm		790
	Ni(II)	1-ClNp	670 nm (r.i. 2.00), 642sh (0.41), 600 (0.35), 343 (1.00)		788
		H_2SO_4	724 nm (r.i. 4.52), 652 (1.00)		788
		H_2SO_4	727.5 nm, 706, 652, 392, 310		272
		DMF	669 nm		790
	Cu(II)	H_2SO_4	727 nm, 715, 643.5, 400, 307		272
		H_2SO_4	728 nm		461
		1-ClNp	680 nm (r.i. 1.50), 650sh (0.26), 610 (0.24), 345 (1.00)		788
		$PhNO_2$	672 nm (r.i. 7.25), 642 (1.45), 602 (1.00)		788

(*Continued*)

Table 2. (*Continued*)

Structure	M	Solvent	Transition Energy (Intensity)	Remark	Ref.
		H_2SO_4	727 nm (r.i. 4.20), 717 (4.13), 642 (1.00)		788
		H_2SO_4	764 nm, 740, 705, 668, 613, 422		274
		DMF	669 nm		790
	Zn(II)	1-ClNp	680 nm (r.i. 2.23), 644sh (0.55), 612 (0.37), 390sh (0.56), 345(1.00)		788
		H_2SO_4	729 nm (r.i. 4.97), 714sh (4.00), 658 (1.00)		788
		DMF	671 nm		790
		THF	669.2 nm		48
	Ga(III)Cl	DMF	673 nm		534
		H_2SO_4	740 nm, 728		534
	Zr(IV)Cl_2	DMF	691 nm		534
		H_2SO_4	747 nm		534
	Pd(II)	H_2SO_4	720 nm, 706, 652, 392, 304		272
	In(III)Cl	DMF	680 nm		534
	Hf(IV)Cl_2	DMF	688 nm		534
		H_2SO_4	748 nm		534
$\beta = NO_2$	2H	THF	712.5 nm, 675.0		48
		py	684 nm, 662, 618, 349		410
		1-ClNp	720 nm (r.i. 2.07), 684 (1.63), 652 (0.57), 618 (0.38), 349 (1.00)		788
		H_2SO_4	780 nm (r.i. 2.85), 738 (2.65), 700sh (1.63), 660sh (1.00)		788
	Al(III)Cl	DMF	699 nm, 682		534
		H_2SO_4	775 nm, 750		534
	Al(III)OH	H_2SO_4	685 nm		791
		py	685 nm		789
		H_2SO_4	745.7 nm	$[Pc]^+$	791
	Ti(IV)O	DMF	705 nm (lg ε 5.09), 343 (4.87)		772
	Cr(III)Cl	DMF	694 nm, 685		534
		H_2SO_4	778 nm, 759		534
	Co(II)	DMF	682 nm, 623		790
		py	677 nm (r.i. 2.2), 614 (0.5), 457sh (0.2), 425sh (0.1), 375sh (0.5), 342 (1.0)		238

(*Continued*)

Table 2. (*Continued*)

Structure	M	Solvent	Transition Energy (Intensity)	Remark	Ref.
		1-ClNp	691 nm (r.i. 1.74), 620 (0.47), 346 (1.00)		788
		DMF	690 nm (r.i. 1.11), 684 (1.12), 640sh (0.64), 620 (0.59), 420sh (0.32), 340 (1.00)		788
		H_2SO_4	749 nm (r.i. 2.36), 660sh (1.00)		788
		15 M H_2SO_4	752 nm, 680, 385, 301, 202		774
	Ni(II)	H_2SO_4	746 nm (lg ε 4.50), 680sh (4.38), 408 (4.16), 302 (4.89), 204 (4.79)		599
		DMF	688 nm, 622		790
		1-ClNp	691 nm (r.i. 1.89), 620 (0.46), 345 (1.00)		788
		H_2SO_4	755 nm (r.i. 4.25), 670 (1.00)		788
		15 M H_2SO_4	757 nm, 675, 385, 303, 200		774
	Cu(II)	DMF	695 nm, 626.8		790
		H_2SO_4	776 nm		461
		DMF	669 nm		791
		H_2SO_4	727 nm	$[Pc]^{-}$	791
		H_2SO_4	760 nm	$[Pc]^{2-}$	791
		1-ClNp	704 nm (r.i. 1.40), 694 (1.35), 624 (0.30), 344 (1.00)		788
		$PhNO_2$	702 nm (r.i. 3.11), 682 (2.89), 650sh (1.56), 620sh (1.00)		788
		H_2SO_4	763 nm (r.i. 3.25), 739 (3.18), 705 (1.03), 663 (1.00)		788
		15 M H_2SO_4	764 nm, 740, 668, 385, 303, 200		774
	Zn(II)	DMF	687 nm, 648		790
		DMSO	682 nm (lg ε 4.87), 645 (4.67)		480
		1-ClNp	708 nm (r.i. 2.22), 696 (2.17), 630 (0.49), 370sh (0.59), 345 (1.00)		788
		H_2SO_4	763 nm (r.i. 4.74), 740sh (2.89), 672sh (1.00)		788
		THF	671.0 nm		48
	Ga(III)Cl	DMF	709 nm, 691		534
		H_2SO_4	783 nm, 741		534
	Zr(IV)Cl_2	DMF	715 nm, 698		534
		H_2SO_4	782 nm, 756		534
	In(III)Cl	DMF	714 nm, 695		534
	Hf(IV)Cl_2	DMF	716 nm, 696		534

(*Continued*)

Table 2. (*Continued*)

Structure	M	Solvent	Transition Energy (Intensity)	Remark	Ref.
		H_2SO_4	785 nm, 758		534
	Pb(II)	DMSO	715 nm (lg ε 4.725), 654 (4.411), 465 (3.956), 302 (4.515)		378, 380
		36 N H_2SO_4	782 nm (lg ε 5.004), 740 (4.880), 708sh (4.662),673sh (4.423), 382sh (4.352), 302 (4.802), 242 (4.621)		378
$\alpha\beta$(R_1, R_3 = NO_2)	2H	THF	712.5 nm, 675.0		48
	Mn(III)	benzene	684 nm, 673, 340		528
	Mn(III)OAc	AcOH	712 nm, 505, 350		528
	Mn(III)L	py	645 nm, 333	L = py	528
	Fe(II)	unknown	695 nm (lg ε 4.12), 612 (4.72), 460 (4.04), 318 (4.10), 216 (4.24)		792
	Co(II)	1-ClNp	695 nm (r.i. 1.14), 644sh (0.38), 626 (0.37), 353 (1.00)		788
		DMF	682 nm (r.i. 2.84), 672 (2.89), 612sh (0.49), 420sh (0.51), 330 (1.00)		788
		acetone	675 nm (r.i. 1.52), 665 (1.60), 610sh (0.74), 425 (0.23), 352 (1.00)		788
		H_2SO_4	695 nm		788
		unknown	680 nm (lg ε 3.64), 450 (3.79), 281 (4.26), 216 (3.96)		792
	Co(II)L	acetone	683 nm (r.i. 1.61), 667 (1.50), 608sh (0.29), 468 (0.36), 326 (1.00)	L = HBr	788
	Ni(II)	unknown	690 nm (lg ε 4.03), 468 (4.20), 318 (4.41), 257 (4.48), 214 (4.12)		792
	Cu(II)	1-ClNp	707 nm (r.i. 2.53), 630 (0.63), 351 (1.00)		788
		$PhNO_2$	699 nm (5.16), 683 (5.13), 620 (4.48)		788
		acetone	686 nm (r.i. 2.10), 672 (2.18), 630sh (0.82), 610sh (0.66), 350sh (0.84), 328 (1.00)		788
		unknown	682 nm (lg ε 4.05), 470 (4.14), 304 (4.40), 217 (4.04)		792
		H_2SO_4	711 nm (r.i. 5.12), 699 (4.56), 630 (1.00)		788
	Zn(II)	THF	674.0 nm		48
		unknown	680 nm (lg ε 4.11), 468 (4.04), 316 (4.11), 214 (4.20)		792
$\alpha\beta$ = NO_2	Cu(II)	1-ClNp	707 nm		735
β = F	Ni(II)	15 M H_2SO_4	746 nm (lg ε 4.24), 400sh (4.06), 305 (4.71)		793

(*Continued*)

Table 2. (*Continued*)

Structure	M	Solvent	Transition Energy (Intensity)	Remark	Ref.
	Zn(II)	THF	660 nm		484
$\beta\beta$ = F	V(IV)O	DMF	642 nm		133
		py	643 nm		133
		acetone	640 nm		133
		THF	686 nm, 639		133
		DCM	641 nm		133
		$CHCl_3$	643 nm		133
		benzene	709 nm		133
		DCB	709 nm		133
	Zn(II)	DMF	656 nm, 626, 594, 338		478
		DMSO	660 nm, 616, 340		478
		py	660 nm, 630, 604, 340		478
		THF	652 nm		484
$\alpha\beta$(R_1, R_3) = F	Co(II)	H_2SO_4	715 nm (lg ε 2.99), 444 (3.25), 243 (3.78)		794
	Ni(II)	H_2SO_4	620 nm (lg ε 2.84), 479 (3.09), 260 (3.48)		794
	Cu(II)	H_2SO_4	735 nm (lg ε 3.16), 647 (3.14), 473 (3.36), 326 (3.77)		794
	Zn(II)	H_2SO_4	616 nm (lg ε 3.00), 555 (3.15), 254 (3.49)		794
$\alpha\alpha\beta\beta$ = F	Ti(IV)O	1-ClNp	716 nm, 680, 646, 364		337
	V(IV)O	1-ClNp	716 nm, 685, 645, 368		337
	Cu(II)	py	679 nm, 647sh, 614sh		795
		H_2SO_4	821 nm		461
	Zn(II)	THF	668 nm		484
		PVA in DMSO	638 nm (10^{-4} ε 6.05)		486
		THF	672 nm (lg ε 5.173), 642 (4.698), 610 (4.505), 356 (4.690), 320 (4.612)		314
	Zr(IV)L	1-ClNp	704 m,. 660, 637, 370	L = *cis*-$(OH)_2$	337
	Ru(II)	THF	632 nm (10^{-3} ε 18.9), 314 (33.9)		796
		PhCN + 0.1 M TBAP	650sh nm, 549 (10^{-3} ε 8.2), 304 (29.1)	$[Pc]^+$	796
		PhCN + 0.1 M TBAP	633 nm (10^{-3} ε 18.9), 567sh, 395sh, 313 (33.9)		795
		PhCN + 0.1 M TBAP	656 nm (10^{-3} ε 14.9), 562 (11.9), 383sh, 313 (27.2)	$[Pc]^-$	795

(*Continued*)

Table 2. (*Continued*)

Structure	M	Solvent	Transition Energy (Intensity)	Remark	Ref.
	In(III)Cl	1-ClNp	715 nm, 685, 642, 593sh, 367		337
R_2 = Cl	Si(IV)	DMF	675 nm (lg ε 5.34), 606 (4.58), 356 (4.89)	L = *trans*- 	426
R_2, R_3 = Cl	Si(IV)	DMF	678 nm (lg ε 5.25), 607 (4.51), 356 (4.89)	L = *trans*- 	426
$R_2(R_3)$, $R_{10}(R_{11})$ = Cl	2H	1-ClNp	693 nm, 674		787
		H_2SO_4	842 nm, 790		787
	Co(II)	1-ClNp	672 nm		787
		H_2SO_4	788 nm		787
	Cu(II)	1-ClNp	681 nm		787
		H_2SO_4	796 nm		787
α = Cl	Al(III)Cl	DMF	680 nm		534
		H_2SO_4	832 nm, 792		534
	Al(OH)	py	691 nm		789
	V(IV)O	1-ClNp	709 nm, 644		273
		conc H_2SO_4	845 nm, 765, 465		273
		quinoline	714 nm, 645		273
	Cr(III)Cl	DMF	682 nm		534
		H_2SO_4	840 nm, 797		534
	Fe(III)Cl	DMSO	659 nm (lg ε 4.00), 597sh (3.79), 413 (3.92), 336 (4.28), 215 (3.91)		469
		DMF	662 nm (lg ε 3.98), 596sh (3.78), 408 (3.97), 273 (4.42), 212 (4.04)		469
		py	660 nm (lg ε 4.58), 597sh (4.06), 410 (4.19), 343 (4.58), 215 (4.08)		469
	Co(II)	DMSO	677 nm (lg ε 4.42), 609 (4.09), 324 (4.35), 206 (3.72)		797

(*Continued*)

Table 2. (*Continued*)

Structure	M	Solvent	Transition Energy (Intensity)	Remark	Ref.
	Ni(II)	DMSO	664 nm (lg ε 4.42), 623 (3.98), 323 (4.14), 305 (4.25), 208 (3.66)		797
	Cu(II)	DMSO	672 nm (lg ε 4.62), 631 (3.75), 334 (4.22), 208 (3.52)		797
		quinoline	690 nm, 620		273
		PhCl	686 nm, 619, 335		273
		conc H_2SO_4	830 nm, 730, 460		273
	Zn(II)	DMSO	675 nm (lg ε 4.52), 608 (4.03), 342 (4.36), 206 (4.28)		797
	Ga(III)Cl	DMF	687 nm		534
		H_2SO_4	840 nm, 800		534
	Zr(IV)Cl_2	DMF	693 nm		534
		H_2SO_4	841 nm, 796		534
	In(III)Cl	DMF	689 nm		534
	Hf(IV)Cl_2	DMF	691 nm		534
		H_2SO_4	839 nm, 794		534
$\alpha\alpha$ = Cl	V(IV)O	quinoline	720 nm		273
		conc H_2SO_4	880 nm, 840, 800, 520		273
		1-ClNp	736 nm, 660		273
	Cu(II)	quinoline	705 nm		273
		conc H_2SO_4	870 nm, 810, 770, 525		273
		1-ClNp	705 nm, 632		273
β = Cl	Al(OH)	py	683 nm		789
	Al(III)Cl	DMF	674 nm		534
		H_2SO_4	813 nm, 770		534
	V(IV)O	quinoline	705 nm		273
		conc H_2SO_4	820 nm, 730, 445		273
		PhCl	698 nm, 630, 343		273
	Cr(III)Cl	DMF	678 nm		534
		H_2SO_4	823 nm		534
	Fe(III)Cl	DMSO	681 nm (lg ε 4.15), 619sh (3.98), 340 (4.34), 215 (3.94)		469
		DMF	687 nm (lg ε 4.09), 625sh (3.98), 404 (4.01), 274 (4.47), 212 (4.10)		469

(*Continued*)

Table 2. (*Continued*)

Structure	M	Solvent	Transition Energy (Intensity)	Remark	Ref.
		py	681 nm (lg ε 4.26), 616sh (3.99), 348 (4.40), 215 (3.98)		469
	Ni(II)	15 M H_2SO_4	744 nm (lg ε 4.31), 400sh (4.13), 305 (4.74)		793
	Cu(II)	quinoline	682 nm, 630		273
		conc H_2SO_4	802 nm, 710, 435		273
		1-ClNp	679 nm, 610		273
		H_2SO_4	803 nm		461
	Ga(III)Cl	DMF	676 nm		534
		H_2SO_4	816 nm, 775		534
	Zr(IV)Cl_2	DMF	685 nm		534
		H_2SO_4	817 nm		534
	In(III)Cl	DMF	682 nm		534
	Hf(IV)Cl_2	DMF	685 nm		534
		H_2SO_4	814 nm		534
$\beta\beta$-Cl	Si(IV)	DMF	679 nm (lg ε 5.53), 649 (4.65), 611 (4.72), 357 (4.86)	L = *trans*- 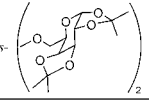	426
	Si(IV)L	DMF	679 nm, 650, 611, 358	L =  axial; average molecular weight 750	798
		EtOH	678 nm, 646, 609, 358	L = *trans*-$(O(CH_2CH_2O)_{16}Me)_2$	453
	V(IV)O	quinoline	650 nm		273
		conc H_2SO_4	825 nm, 735, 460		273
		1-ClNp	712 nm, 645		273
	Mn(II)	H_2SO_4	874.50 nm, 809.50, 764.0, 445.50		459
	Fe(II)	H_2SO_4	791.5 nm, 709.0, 511.0, 324.5		459
		H_2SO_4	790 nm, 709, 510, 325		272
	Co(II)	H_2SO_4	793.0 nm, 706.5, 434.5, 319.0		459
		H_2SO_4	795 nm, 708, 435, 319		272
	Ni(II)	H_2SO_4	795.0 nm, 705.5, 501.0, 323.5		459
		H_2SO_4	795 nm, 705, 500, 324		272
	Cu(II)	H_2SO_4	797.5 nm, 710.0, 444.5, 321.5		459

(*Continued*)

Table 2. (*Continued*)

Structure	M	Solvent	Transition Energy (Intensity)	Remark	Ref.
		H_2SO_4	798 nm, 710, 445, 320		272
		quinoline	695 nm, 635		273
		conc H_2SO_4	805 nm, 715, 440		273
		1-ClNp	695 nm, 630		273
	Zn(II)	H_2SO_4	797 nm, 707, 450, 318		272
		DMSO	683 nm, 641		480
$\alpha\beta$ = Cl	Co(II)	H_2SO_4	733 nm (lg ε 1.17), 649 (1.34), 479 (1.74), 265 (3.22)		799
	Ni(II)	H_2SO_4	725 nm (lg ε 1.65), 633 (1.70), 470 (1.66), 232 (3.06)		799
	Cu(II)	H_2SO_4	740 nm (lg ε 1.44), 642 (1.81), 483 (1.67), 241 (3.17)		799
	Zn(II)	H_2SO_4	750 nm (lg ε 1.55), 650 (1.79), 525 (1.72), 250 (3.14)		799
$\alpha\beta$ (R_1, R_2) = Cl	V(IV)O	quinoline	715 nm, 645		273
		conc H_2SO_4	835 nm, 800, 760, 470		273
		trichlorobenzene	714 nm, 645, 335		273
	Cu(II)	quinoline	692 nm, 625		273
		conc H_2SO_4	825 nm, 780, 740, 470		273
		1-ClNp	686 nm, 621		273
		H_2SO_4	838 nm, 794, 746, 709, 569, 661, 450		274
$\alpha\alpha\beta\beta$ = Cl	2H	1-ClNp	732 nm, 643		800
		DMF	724 nm (lg ε 4.490), 648 (4.721), 358 (4.636), 345 (4.769), 302 (4.666)		800
		1-methyl-2-pyrrolidinone	696 nm (lg ε 4.785), 656 (4.518), 412 (4.414), 332 (4.431)		800
	2Li	THF	684 nm (lg ε 5.22), 645 (4.49), 624 (4.44), 398 (4.66), 326 (4.60)		800
	Al(III)Cl	quinoline	715 nm, 645		273
		conc H_2SO_4	885 nm, 840, 500		273
		py	701 nm (lg ε 4.079), 370 (4.128)		800
		DMF	703 nm, 636, 365, 328		800
	Al(III)OH	1-methyl-2-pyrrolidinone	696 nm (lg ε 4.69), 342 (4.53)		800
		DMF	700br nm, 349		800
	Si(IV)L	py	708 nm, 353	L = *trans*-$(OH)_2$	800
		THF	698 nm, 343	L = *trans*-$(OH)_2$	800

(*Continued*)

Table 2. (*Continued*)

Structure	M	Solvent	Transition Energy (Intensity)	Remark	Ref.
		DMF	706 nm, 352	L = *trans*-$(OH)_2$	800
	V(IV)O	quinoline	720 nm		273
		conc H_2SO_4	885 nm, 840, 800, 510		273
		1-ClNp	745 nm, 680, 365		273
		H_2SO_4	862 nm		461
	Mn(II)	H_2SO_4	880.50 nm, 816.50, 773.0,443.0		459
	Fe(I)	DMF/LiCl	805 nm, 687, 654, 537, 400	$[Pc]^-$	461
	Fe(II)	py	679 nm (r.i. 1.3), 650sh (0.5), 618 (0.4), 437 (0.4), 357 (1)		238
		H_2SO_4	854 nm		461
		argon-purged DMF	678 nm, 619, 460, 361		461
		py	679 nm, 651, 617, 437, 357		272
	Co(I)	argon-purged DMF + hydrazine	701 nm, 656, 545sh, 480, 326	[Pc]	461
	Co(II)	1-ClNp	775 nm, 702, 630, 351		800
		H_2SO_4	854 nm, 813, 768, 469, 350		272
		H_2SO_4	832 nm		461
		argon-purged DMF	706sh nm, 641, 490sh, 360sh, 316		461
	Ni(II)	H_2SO_4	828 nm, 782, 745, 436, 353		272
	Cu(II)	H_2SO_4	853 nm, 794, 749, 504, 355		272
		quinoline	730 nm, 660		273
		conc H_2SO_4	860 nm, 815, 730, 490		273
		1-ClNp	720 nm, 660		273
		H_2SO_4	861 nm, 816, 770, 729, 656, 584, 465		274
	Zn(II)	DMF	692 nm (lg ε 4.38), 668 (4.39), 330.5 (4.22), 294.7 (4.17), 257 (4.38)		800
		1-methyl-2-pyrrolidinone	696 nm (lg ε 4.539), 654 (4.406), 386 (4.281), 344 (4.321)		800
		H_2SO_4	868 nm		461
		argon-purged DMF	711 nm, 660, 404sh, 378		461
		DMF + LiCl	928 nm, 894, 860sh, 830sh, 698, 625sh, 600, 474, 415	$[Pc]^-$	461
		DMF + LiCl	842 nm, 696, 553, 363	$[Pc]^{2-}$	461

(*Continued*)

Table 2. (*Continued*)

Structure	M	Solvent	Transition Energy (Intensity)	Remark	Ref.
		DMF	690 nm (lg ε 4.38), 668 (4.39), 330.5 (4.22), 294.7 (4.17), 257 (4.38)		314
	Ru(II)	MeCN	644 nm (10^{-3} ε 25.4), 414 (17.4), 342 (44.7)		796
		PhCN + 0.1 M TBAP	737sh nm, 656 (10^{-3} ε 13.0), 582sh, 332 (38.3)	$[Pc]^+$	796
		PhCN + 0.1 M TBAP	648 (10^{-3} ε 25.4), 590 (12.2), 400 (17.4), 339 (44.7)		796
		PhCN + 0.1 M TBAP	669 (10^{-3} ε 16.7), 583 (15.9), 395 (26.1), 342 (29.8)	$[Pc]^-$	796
$R_2(R_3)$, $R_{10}(R_{11})$ = Br	2H	H_2SO_4	836 nm, 784		787
	Co(II)	1-ClNp	673 nm		787
	Cu(II)	1-ClNp	681 nm		787
		H_2SO_4	799 nm		787
α = Br	Al(OH)	py	691 nm		789
	Fe(III)Cl	DMSO	661 nm (lg ε 4.47), 597sh (4.15), 445 (4.01), 343 (4.51), 214 (4.06)		469
		DMF	664 nm (lg ε 4.39), 620sh (4.01), 454 (3.94), 316 (4.43), 214 (4.16)		469
		py	660 nm (lg ε 4.50), 619sh (4.16), 437 (3.95), 358 (4.44), 215 (3.97)		469
	Zr(IV)Cl_2	DMF	691 nm		534
		H_2SO_4	846 nm, 817		534
	Hf(IV)Cl_2	DMF	693 nm		534
		H_2SO_4	842 nm, 796		534
β = Br	Al(III)Cl	DMF	678 nm		534
		H_2SO_4	820 nm, 775		534
	Al(OH)	py	683 nm		789
	Cr(III)Cl	DMF	682 nm		534
		H_2SO_4	831 nm		534
	Fe(III)Cl	DMSO	683 nm (lg ε 4.24), 612sh (4.01), 340 (4.43), 214 (4.05)		469
		DMF	691 nm (lg ε 4.12), 620sh (3.99), 408 (4.00), 273 (4.48), 213 (4.13)		469

(*Continued*)

Table 2. (*Continued*)

Structure	M	Solvent	Transition Energy (Intensity)	Remark	Ref.
		py	682 nm (lg ε 4.29), 614sh (4.00), 346 (4.40), 214 (3.96)		469
	Ni(II)	15 M H_2SO_4	743 nm (lg ε 4.34), 400 (4.23), 302 (4.78)		793
	Ga(III)Cl	DMF	678 nm		534
		H_2SO_4	821 nm, 781		534
	Zr(IV)Cl_2	DMF	687 nm		534
		H_2SO_4	825 nm		534
	In(III)Cl	DMF	685 nm		534
	Hf(IV)Cl_2	DMF	688 nm		534
		H_2SO_4	825 nm		534
$\beta\beta$ = Br	Si(IV)L	DMF	682 nm, 652, 613, 360	L = 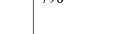 axial; average molecular weight 750	798
		EtOH	680 nm, 650, 612, 360	L = *trans*-$(O(CH_2CH_2O)_{16}Me)_2$	453
$\alpha\beta$ (R_1, R_3) = Br	Co(II)	H_2SO_4	615 nm (lg ε 2.39), 479 (2.39), 258 (2.77), 224 (3.80)		801
	Ni(II)	H_2SO_4	620 nm (lg ε 2.19), 475 (2.29), 249 (2.76), 225 (3.72)		801
	Cu(II)	H_2SO_4	647 nm (lg ε 2.13), 471 (2.40), 240 (2.79), 231 (3.81)		801
	Zn(II)	H_2SO_4	611 nm (lg ε 2.03), 482 (2.39), 242 (2.76), 227 (3.78)		801
R_1, R_5, R_9 = I	Zn(II)	THF	678 nm (lg ε 5.21), 611 (4.45), 339 (4.63)		556
R_2, R_7, R_{11} = I	Zn(II)	THF	671 nm (lg ε 5.37), 606 (4.59), 350 (4.88)		556
R_2, R_3, R_6, R_7, R_{10}, R_{11} = I	Zn(II)	THF	677 nm (lg ε 5.31), 612 (4.61), 355 (4.90)		556
α = I	Fe(III)Cl	DMSO	661 nm (lg ε 4.46), 597sh (4.06), 445 (4.09), 338 (4.46), 214 (4.04)		469
		DMF	664 nm (lg ε 4.41), 625sh (4.00), 454 (3.92), 316 (4.41), 213 (4.17)		469
		py	660 nm (lg ε 4.58), 597sh (4.00), 445 (3.88), 361 (4.31), 215 (3.96)		469
	Zr(IV)Cl_2	DMF	696 nm		534
		H_2SO_4	856 nm, 811		534
	Hf(IV)Cl_2	DMF	696 nm		534
		H_2SO_4	855 nm, 809		534
β = I	2H	H_2SO_4	883 nm (lg ε 5.17), 822 (5.23), 297 (5.17)		557

(*Continued*)

Table 2. (*Continued*)

Structure	M	Solvent	Transition Energy (Intensity)	Remark	Ref.
	Fe(III)Cl	DMSO	685 nm (lg ε 4.35), 613sh (4.10), 338 (4.53), 214 (4.13)		469
		DMF	694 nm (lg ε 4.34), 625sh (4.18), 410 (4.20), 275 (4.66), 213 (4.30)		469
		py	682 nm (lg ε 4.59), 613sh (4.22), 450 (4.07), 350 (4.58), 215 (4.16)		469
	Ni(II)	H_2SO_4	808 nm (lg ε 5.18), 295 (4.90)		557
		15 M H_2SO_4	740 nm (lg ε 4.32), 404 (4.16), 304 (4.78)		793
	Zn(II)	H_2SO_4	822 nm (lg ε 5.24), 296 (4.69)		557
	Zr(IV)Cl_2	DMF	693 nm		534
		H_2SO_4	838 nm		534
	Hf(IV)Cl_2	DMF	693 nm		534
		H_2SO_4	833 nm		534
β= P(O)$(OEt)_2$	2H	DCM	696 nm (ε 95,000), 660 (84,000), 632 (30,000), 600 (19,000), 340 (48,000), 288 (20,000), 246 (21,000)		802
	Ni(II)	DCM	695 nm (ε 106,000), 661 (110,000), 634 (34,000), 600 (16,000), 338 (63,000), 290 (32,000), 286sh (15,000), 246 (31,000)		802
	Cu(II)	DCM	676 nm (ε 126,000), 643sh (30,000), 608 (31,000), 342 (57,000), 285 (26,000), 252 (44,000), 229 (58,000)		802
	Zn(II)	DCM	687 nm (ε 108,000), 676 (105,000), 620 (25,000), 600 (19,000), 349 (45,000), 288sh (16,000), 275 (17,000), 245 (33,000), 222 (47,000)		802
β= P(O)(OEt)Ph	2H	DCM	699 nm (ε 132,000), 663 (120,000), 636 (42,000), 603 (27,000), 346 (63,000), 291 (27,000), 278sh (25,000), 225 (59,000)		802
	Ni(II)	DCM	699 nm (ε 143,000), 663 (136,000), 635 (49,000), 603 (31,000), 347 (69,000), 291 (39,000), 226 (76,000)		802
	Cu(II)	DCM	680 nm (ε 141,000), 649sh (35,000), 611 (37,000), 347 (61,000), 290 (32,000), 254 (63,000), 230 (79,000)		802
	Zn(II)	DCM	690 nm (ε 157,000), 680 (156,000), 622 (40,000), 351 (65,000), 245sh (62,000), 228 (88,000)		802

(*Continued*)

Table 2. (*Continued*)

Structure	M	Solvent	Transition Energy (Intensity)	Remark	Ref.
β= $P(O)Ph_2$	2H	DCM	700 nm (ε 113,000), 665 (130,000), 637 (51,000), 604 (31,000), 341 (75,000), 293 (45,000), 273 (42,000), 224 (115,000)		802
	Ni(II)	DCM	700 nm (ε 113,000), 665 (130,000), 637 (51,000), 604 (31,000), 341 (75,000), 293 (45,000), 273 (42,000), 224 (115,000)		802
	Cu(II)	DCM	680 nm (ε 204,000), 651 (41,000), 611 (47,000), 344 (95,000), 287 (33,000), 247 (72,000), 223 (126,000)		802
	Zn(II)	DCM	683 nm (ε 150,000), 619 (34,000), 369sh (55,000), 349 (64,000), 271sh (34,000), 248 (56,000), 225 (117,000)		802
$R_5(R_7)$, $R_6(R_7)$, $R_{10}(R_{11})$ = TMS	Ru(III)L	DCM	631 nm, 584, 410.5, 372.5, 315.5	L = *trans*-$(py(3\text{-}Cl))_2$	503
β= TMS	Ru(III)L	DCM	633.5 nm, 578.5sh, 411, 375, 317.5	L = *trans*-$(py(3\text{-}Cl))_2$	503
		$CHCl_3$	739 nm, 649.5, 589.5, 361, 315.5, 276	L = *trans*-$(CN(t\text{-}Bu))_2$	503
R_2, R_3 = Me, $R_6(R_7)$, $R_{10}(R_{11})$, $R_{14}(R_{15})$ = *t*-Bu	2H	$CHCl_3$	701 nm (lg ε 5.10), 664 (5.04), 644 (4.57), 603 (4.28), 342 (4.80)		516
		$CHCl_3$	701 nm (ε 125,892), 664 (109,647),664 (37,153) 603 (19,054), 342 (63,095)		517
R_1 = Me, R_4 = $(CH_2)_3OH$, R_5, R_8, R_9, R_{12}, R_{13}, R_{16} = C_8H_{17}	2H	cyclohexane	727 nm (10^{-5} ε 1.3), 694 (1.1)		803
R_1 = Me, R_4 = $(CH_2)_4OH$, R_5, R_8, R_9, R_{12}, R_{13}, R_{16} = C_8H_{17}	2H	cyclohexane	727 nm (10^{-5} ε 1.11), 694 (1.02)		803
R_1 = Me, R_4 = $(CH_2)_5OH$, R_5, R_8, R_9, R_{12}, R_{13}, R_{16} = C_8H_{17}	2H	cyclohexane	728 nm (10^{-5} ε 1.4), 694 (1.14)		803
	Cu(II)	cyclohexane	704 nm, 635		803
R_1 = Me, R_4 = $(CH_2)_6OH$, R_5, R_8, R_9, R_{12}, R_{13}, R_{16} = C_8H_{17}	2H	cyclohexane	727 nm (10^{-5} ε 1.22), 691 (1.01)		803
	Cu(II)	cyclohexane	704 nm (10^{-5} ε 1.8), 634 (0.4)		803
R_1 = Me, R_4 = $(CH_2)_8OH$, R_5, R_8, R_9, R_{12}, R_{13}, R_{16} = C_8H_{17}	2H	cyclohexane	727 nm (10^{-5} ε 1.28), 692 (1.06)		803
R_1 = Me, R_4 = $C_{11}H_{22}OH$, R_5, R_8, R_9, R_{12}, R_{13}, R_{16} = C_6H_{13}	2H	toluene	727 nm (10^{-5} ε 1.32), 695 (1.12)		804
R_1 = Me, R_4 = $C_9H_{18}OH$, R_5, R_8, R_9, R_{12}, R_{13}, R_{16} = $C_{10}H_{21}$	2H	THF	726 nm (10^{-5} ε 1.08), 695 (0.96)		804
	Zn(II)	THF	699 nm (10^{-5} ε 2.31)		804
R_1, R_4 = C_3H_8OH, R_5, R_8, R_9, R_{12}, R_{13}, R_{16} = $C_{10}H_{21}$	Zn(II)	THF	700 nm		804
R_1, R_4 = $(CH_2)_6OH$, R_5, R_8, R_9, R_{12}, R_{13}, R_{16} = C_7H_{15}	2H	cyclohexane	727 nm (10^{-5} ε 1.13), 694 (1.00)		803
R_1, R_4 = $(CH_2)_6OH$, R_5, R_8, R_9, R_{12}, R_{13}, R_{16} = C_8H_{17}	2H	cyclohexane	727 nm (10^{-5} ε 1.21), 694 (1.09)		803
	Cu(II)	cyclohexane	705 nm (10^{-5} ε 1.7), 635 (0.4)		803
R_1, R_4 = $C_6H_{12}OH$, R_5, R_8, R_9, R_{12}, R_{13}, R_{16} = C_9H_{19}	2H	THF	727 nm (10^{-5} ε 1.18), 694 (1.03)		804

(*Continued*)

Table 2. (*Continued*)

Structure	M	Solvent	Transition Energy (Intensity)	Remark	Ref.
	Zn(II)	THF	700 nm (10^{-5} ε 1.78)		804
R_1, R_4 = $C_9H_{18}OH$, R_5, R_8, R_9, R_{12}, R_{13}, R_{16} = $C_{10}H_{21}$	2H	THF	728 nm (10^{-5} ε 1.16), 700 (1.03)		804
	Zn(II)	THF	700 nm (10^{-5} ε 2.45)		804
R_2 = $R_6(R_7)$, $R_{10}(R_{11})$, $R_{14}(R_{15})$ = *t*-Bu	Zn(II)	$CHCl_3$	678 nm(lg ε 5.11), 612(4.48), 350(4.81)		805
R_2 = 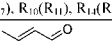 $R_6(R_7)$, $R_{10}(R_{11})$, $R_{14}(R_{15})$ = *t*-Bu	Zn(II)	$CHCl_3$	702 nm(lg ε 5.10), 675(5.05), 642(4.56), 353(4.86)		805
R_1, R_2, R_3, R_4 = 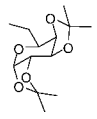	Zn(II)	$CHCl_3$	687 nm (lg ε 4.93), 630 (4.24), 343 (4.56)		806
R_1, R_2, R_3, R_4 = 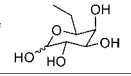	Zn(II)	DMSO	688 nm (lg ε 4.94), 620 (4.20), 345 (4.48)		806
		H_2O	631 nm (lg ε 4.41), 333 (4.37)		806
R_2 = $CHCH_2$, $R_6(R_7)$, $R_{10}(R_{11})$, $R_{14}(R_{15})$ = *t*-Bu	2H	$CHCl_3$	702 nm (lg ε 5.1), 668 (5.0), 647 (4.6), 607 (4.3), 344 (4.8)		807
	Cu(II)	DCB	683 nm (lg ε 5.20), 616 (4.56), 348 (4.86)		808
	Zn(II)	$CHCl_3$	718sh nm (lg ε 4.6), 682 (5.0), 616 (4.2), 354 (4.7)		807
R_2 = CHCHPh, R_6, R_7, R_{10}, R_{11}, R_{14}, R_{15} = OBu	Zn(II)	$CHCl_3$	691 nm (lg ε 5.2), 619 (4.49), 356 (4.93), 298 (4.71)		809
R_2 = CHCHPh, R_6, R_7, R_{10}, R_{11}, R_{14}, R_{15} = SO_2Pr	Ni(II)	$CHCl_3$	697 nm (lg ε 5.03), 672 (5.02), 615 (4.47), 344 (4.90), 296 (4.86), 261 (4.80)		809
R_2 = CHCHPh(4-NO_2), $R_6(R_7)$, $R_{10}(R_{11})$, $R_{14}(R_{15})$ = *t*-Bu	2H	$CHCl_3$	699 nm		810
		$CHCl_3$	717 nm (lg ε 4.90), 699 (5.13), 681 (5.12), 650 (4.76), 621 (4.55), 430sh, 347 (4.99)		811
	Co(II)	$CHCl_3$	688 nm		810
		$CHCl_3$	688 nm (lg ε 5.06), 672 (5.02), 637sh, 614 (4.50), 333 (4.84), 293 (4.68)		811
	Ni(II)	$CHCl_3$	688 nm		810
		$CHCl_3$	689 nm (lg ε 5.23), 672 (5.20), 639sh, 613 (4.66), 335 (4.95), 296 (4.87)		811
	Cu(II)	$CHCl_3$	697 nm		810

(*Continued*)

Table 2. (*Continued*)

Structure	M	Solvent	Transition Energy (Intensity)	Remark	Ref.
		$CHCl_3$	697 nm (lg ε 5.33), 681 (5.26), 643sh, 619 (4.75), 342 (5.11)		811
R_2 = CHCHPh(4-NO_2), R_5, R_8, R_9, R_{12}, R_{13}, R_{16} = C_8H_{17}	Ni(II)	$CHCl_3$	709 nm (lg ε 4.91), 692 (4.89), 660sh, 630 (4.26), 340 (4.54)		811
R_2 = CHCHPh(4-NO_2), R_5, R_8, R_9, R_{12}, R_{13}, R_{16} = OC_8H_{17}	Ni(II)	$CHCl_3$	737 nm (lg ε 5.11), 660 (4.47), 332 (4.66)		811
		$CHCl_3$	737 nm		810
R_2 = CHCHPh(4-CHO), R_6, R_7, R_{10}, R_{11}, R_{14}, R_{15} = OBu	Zn(II)	$CHCl_3$	692 nm (lg ε 5.1), 614 (4.36), 354 (4.70), 300 (4.86), 298 (4.63)		757
R_2 = CHCHCHCHPh(2-NO_2), R_6(R_7), R_{10}(R_{11}), R_{14}(R_{15}) = *t*-Bu	2H	$CHCl_3$	681 nm		810
R_2 = CHCH((4-py), R_6(R_7), R_{10}(R_{11}), R_{14}(R_{15}) = *t*-Bu	2H	$CHCl_3$	674 nm		810
R_2 = CHCH(Ph(4-NO_2)), R_6(R_7), R_{10}(R_{11}), R_{14}(R_{15}) = C_8H_{17}	Ni(II)	$CHCl_3$	709 nm		810
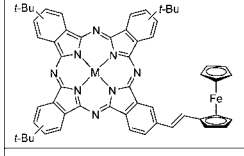	Co(II)	$CHCl_3$	681 nm (lg ε 5.18), 615 (4.60), 331 (4.97), 289 (4.86		812
	Zn(II)	$CHCl_3$	691 nm (lg ε 5.29), 621 (4.59), 350 (4.97)		812
R_2 = CCH, R_6(R_7), R_{10}(R_{11}), R_{14}(R_{15}) = *t*-Bu	Zn(II)	$CHCl_3$	684 nm (lg ε 5.4), 612 (4.7), 350 (5.1)		813
R_2, R_3 = CCH, R_6(R_7), R_{10}(R_{11}), R_{14}(R_{15}) = *t*-Bu	Zn(II)	$CHCl_3$	696 nm (lg ε 5.3), 672 (5.2), 612 (4.6), 353 (5.1)		814
R_2 = CCH, R_6(R_7), R_{10}(R_{11}), R_{14}(R_{15}) = *t*-Bu	Co(II)	$CHCl_3$	672 nm (lg ε 5.4), 607 (4.7), 328 (4.9)		755
	Ni(II)	$CHCl_3$	675 nm (lg ε 5.5), 607 (4.8), 337 (5.1)		755
	Zn(II)	$CHCl_3$	684 nm (lg ε 5.4), 612 (4.7), 350 (5.1)		755
R_2 = CCH, R_6, R_7, R_{10}, R_{11}, R_{14}, R_{15} = C_7H_{15}	2H	toluene	699 nm, 677, 657, 350		815
R_2 = CCH, R_6, R_7, R_{10}, R_{11}, R_{14}, R_{15} = C_7H_{15}	Mg(II)	toluene	695 nm, 681, 621, 357		815
R_2 = CCH, R_6, R_7, R_{10}, R_{11}, R_{14}, R_{15} = C_7H_{15}	Zn(II)	toluene	692 nm, 679, 616, 354		815
R_2 = CCH, R_6, R_7, R_{10}, R_{11}, R_{14}, R_{15} = OBu	Ni(II)	$CHCl_3$	672 nm (lg ε 5.4), 620 (5.0), 291 (5.4)		756
	Zn(II)	$CHCl_3$	681 nm (lg ε 4.9), 613 (4.3), 357 (4.7)		756
		$CHCl_3$	681 nm (lg ε 5.0), 613 (4.3), 356 (4.7)		814
R_2, R_3 = CCH, R_6, R_7, R_{10}, R_{11}, R_{14}, R_{15} = OBu	Zn(II)	$CHCl_3$	693 nm (lg ε 5.1), 668 (5.0), 608 (4.3), 358 (4.9)		814
R_2 = CCH, R_6, R_7, R_{10}, R_{11}, R_{14}, R_{15} = OC_8H_{17}	Zn(II)	$CHCl_3$	686 nm (lg ε 4.9), 615 (4.2), 357 (4.6), 289 (4.3)		816
R_2(R_3) = CH=CH_2, R_6(R_7), R_{10}(R_{11}), R_{14}(R_{15}) = SO_3Na	Ga(III)OH	DMF	685 nm		817
R_2(R_3) = CCBu, R_6(R_7), R_{10}(R_{11}), R_{14}(R_{15}) = SO_3Na	Ga(III)OH	DMF	683 nm		817
R_2 = CCC(Me)$_2$OH, R_6, R_7, R_{10}, R_{11}, R_{14}, R_{15} = C_7H_{15}	Mg(II)	toluene	695 nm, 682, 622, 357		815

(*Continued*)

Table 2. (*Continued*)

Structure	M	Solvent	Transition Energy (Intensity)	Remark	Ref.
R_2 = $CCC(Me)_2OH$, $R_6(R_7)$, $R_{10}(R_{11})$, $R_{14}(R_{15})$ = *t*-Bu	Co(II)	$CHCl_3$	673 nm (lg ε 5.2), 608 (4.6), 328 (4.9)		755
	Ni(II)	$CHCl_3$	676 nm (lg ε 5.0), 609 (4.4), 333 (4.7)		755
	Zn(II)	$CHCl_3$	684 nm (lg ε 5.1), 613 (4.5), 351 (4.9)		755
R_2 = $CCC(Me)_2OH$, R_6, R_7, R_{10}, R_{11}, R_{14}, R_{15} = C_7H_{15}	Zn(II)	toluene	693 nm, 680, 617, 354		815
R_2 = $CCC(Me)_2OH$, R_6, R_7, R_{10}, R_{11}, R_{14}, R_{15} = OBu	Ni(II)	$CHCl_3$	676 nm (lg ε 5.2), 610 (4.7), 291 (5.4)		756
	Zn(II)	$CHCl_3$	685 nm (lg ε 5.1), 613 (4.4), 356 (5.0)		756
		$CHCl_3$	685 nm (lg ε 5.1), 613 (4.4), 356 (5.0)		814
R_2 = $CCC(Me)_2OH$, R_6, R_7, R_{10}, R_{11}, R_{14}, R_{15} = OC_8H_{17}	Zn(II)	$CHCl_3$	672 nm (lg ε 5.0), 615 (4.6), 358 (4.8), 293 (4.7)		816
R_2 = 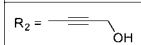 $R_6(R_7)$, $R_{10}(R_{11})$, $R_{14}(R_{15})$ = *t*-Bu	Zn(II)	$CHCl_3$	684 nm(lg ε 5.02), 614(4.28), 352(4.73)		805
R_2 = 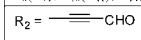 $R_6(R_7)$, $R_{10}(R_{11})$, $R_{14}(R_{15})$ = *t*-Bu	Zn(II)	$CHCl_3$	700 nm(lg ε 5.08), 672(5.04), 641(4.54), 612(4.40), 354(4.86)		805
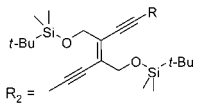 $R_6(R_7)$, $R_{10}(R_{11})$, $R_{14}(R_{15})$ = *t*-Bu	Co(II)	$CHCl_3$	683 nm (lg ε 4.9), 671 (4.9), 610 (4.4), 328 (5.3)	R = TMS	818
		$CHCl_3$	686 nm (lg ε 5.0), 612 (4.4), 330 (5.0)	R = H	818
	Zn(II)	$CHCl_3$	693 nm (lg ε 5.1), 679 (5.1), 616 (4.4), 352 (4.9)	R = TMS	818
		$CHCl_3$	694 nm (lg ε 5.1), 678 (5.1), 616 (4.4), 351 (4.9)	R = H	818
R_5, R_7, R_{11} = $CC(CH_2)_3COOH$, R_{15} = *t*-Bu	Zn(II)	THF	680 nm (lg ε 5.25)		556
		0.1 N NaOH	638 nm		556
R_5, R_7, R_{11} = $CC(CH_2)_8COOH$, R_{15} = *t*-Bu	Zn(II)	THF	683 nm (lg ε 5.33), 614 (4.60)		556
		0.1 N NaOH	623 nm		556
R_1, R_5, R_9 = $CC(CH_2)_3COOH$	Zn(II)	THF	679 nm (lg ε 5.29), 612 (4.60)		556
		0.1 N NaOH	640 nm		556
R_1, R_5, R_9 = $CC(CH_2)_3COOH$, R_{15} = *t*-Bu	Zn(II)	THF	681 nm (lg ε 5.28), 614 (4.54)		556
		0.1 N NaOH	643 nm		556
$R_2(R_3)$ = $CCCH_2CH_2OH$, $R_6(R_7)$, $R_{10}(R_{11})$, $R_{14}(R_{15})$ = SO_3Na	Ga(III)OH	DMF	683 nm		817
$R_2(R_3)$ = CHCHCOONa, $R_6(R_7)$, $R_{10}(R_{11})$, $R_{14}(R_{15})$ = SO_3Na	Ga(III)OH	DMF	691 nm		817
$R_2(R_3)$ = $CC(CH_2)_3COOH$, $R_6(R_7)$, $R_{10}(R_{11})$, $R_{14}(R_{15})$ = SO_3Na	Ga(III)OH	DMF	687 nm		817
$R_2(R_3)$ = $CCPh(4\text{-}NMe_2)$, $R_6(R_7)$, $R_{10}(R_{11})$, $R_{14}(R_{15})$ = SO_3Na	Zn(II)	DMF	685 nm		817
R_2 = $CCPh(4\text{-}N(Me)_2)$, R_6, R_7, R_{10}, R_{11}, R_{14}, R_{15} = SO_2Pr	Ni(II)	$CHCl_3$	701 nm (lg ε 4.3), 677 (4.4), 345 (4.4)		756
	Zn(II)	$CHCl_3$	711 nm (lg ε 5.3), 686 (5.3), 372 (5.1)		819

(*Continued*)

Table 2. (*Continued*)

Structure	M	Solvent	Transition Energy (Intensity)	Remark	Ref.
		$CHCl_3$	711 nm (lg ε 5.3), 686 (5.3), 372 (5.1)		756
R_2 = CCPh(4-NO_2), R_6, R_7, R_{10}, R_{11}, R_{14}, R_{15} = OBu	Zn(II)	$CHCl_3$	696 nm (lg ε 5.4), 677 (5.4), 357 (5.2)		819
R_2, R_3 = CCPh(4-NO_2), R_6, R_7, R_{10}, R_{11}, R_{14}, R_{15} = OBu	Zn(II)	$CHCl_3$	713 nm (lg ε 4.9), 672 (4.8), 361 (4.9)		819
R_2 = CCPh(4-NO_2), R_6, R_7, R_{10}, R_{11}, R_{14}, R_{15} = OBu	Ni(II)	$CHCl_3$	687 nm (lg ε 4.9), 668 (4.9), 313 (4.8)		756
	Zn(II)	$CHCl_3$	696 nm (lg ε 5.4), 677 (5.4), 615 (4.8), 357 (5.2)		756
R_2, R_3 = CCPh(4-NO_2), R_6, R_7, R_{10}, R_{11}, R_{14}, R_{15} = OBu	Zn(II)	$CHCl_3$	713 nm (lg ε 4.9), 672 (4.8), 610 (4.3), 361 (4.9)		756
R_2 = CCPh(4-NO_2), R_5, R_6, R_7, R_8, R_9, R_{10}, R_{11}, R_{12}, R_{13}, R_{14}, R_{15}, R_{16} = OCH_2CF_3	V(IV)O	1,4-dioxane	733.0 nm (lg ε 5.34), 658.0 (4.65), 350.0 (4.87), 226.0 (5.08)		820
R_2 = 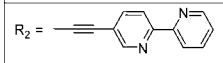 $R_6(R_7)$, $R_{10}(R_{11})$, $R_{14}(R_{15})$ = *t*-Bu	Zn(II)	THF	687 nm (lg ε 5.15), 671 (5.06), 633 (4.35), 610sh, 352 (4.89)		778
$R_2(R_3)$ = CC(4-py), $R_6(R_7)$, $R_{10}(R_{11})$, $R_{14}(R_{15})$ = SO_3Na	Ga(III)OH	DMF	683 nm		817
R_2 = 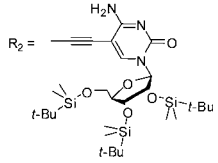 $R_6(R_7)$, $R_{10}(R_{11})$, $R_{14}(R_{15})$ = *t*-Bu	Zn(II)	DCM	679 nm (lg ε 5.12), 347 (5.03)		821
R_1, R_4 = CC-TMS, $R_6(R_7)$, $R_{10}(R_{11})$, $R_{14}(R_{15})$ = *t*-Bu	Ni(II)	$CHCl_3$	687 nm (lg ε 5.2), 672 (5.1), 610 (4.5), 297 (4.9), 270 (4.8)		822
R_1 = CC-TMS, $R_6(R_7)$, $R_{10}(R_{11})$, $R_{14}(R_{15})$ = *t*-Bu	Ni(II)	$CHCl_3$	677 nm (lg ε 5.2), 608 (4.4), 335 (4.7), 298 (4.8), 267 (4.7)		822
R_2, R_3 = CC-TMS, $R_6(R_7)$, $R_{10}(R_{11})$, $R_{14}(R_{15})$ = *t*-Bu	Zn(II)	DCM	699 nm (lg ε 4.4), 674 (4.3), 614 (3.6), 353 (4.3)		814
R_2, R_3 = CC-TMS, R_6, R_7, R_{10}, R_{11}, R_{14}, R_{15} = OBu	Zn(II)	1,4-dioxane	697 nm (lg ε 5.1), 670 (5.1), 610 (4.4), 360 (4.9)		814
R_2 = 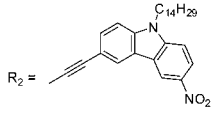 R_5, R_6, R_7, R_8, R_9, R_{10}, R_{11}, R_{12}, R_{13}, R_{14}, R_{15}, R_{16} = OCH_2CF_3	V(IV)O	1,4-dioxane	736.0 nm (lg ε 5.34), 660.5 (4.66), 354.5 (4.96), 229.0 (5.07), 210.5 (4.98)		823

(*Continued*)

Table 2. (*Continued*)

Structure	M	Solvent	Transition Energy (Intensity)	Remark	Ref.
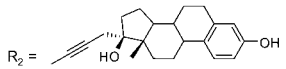 R_2 = $R_6(R_7)$, $R_{10}(R_{11})$, $R_{14}(R_{15})$ = Bu	Zn(II)	$CHCl_3$	680 nm		824
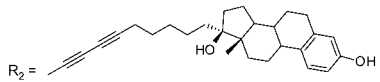 R_2 = $R_6(R_7)$, $R_{10}(R_{11})$, $R_{14}(R_{15})$ = Bu	Zn(II)	DMF	681 nm		824
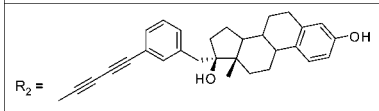 R_2 = $R_6(R_7)$, $R_{10}(R_{11})$, $R_{14}(R_{15})$ = Bu	Zn(II)	DMF	689 nm, 674		824
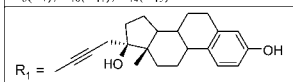 R_1 = $R_6(R_7)$, $R_{10}(R_{11})$, $R_{14}(R_{15})$ = Bu	Zn(II)	$CHCl_3$	691 nm		824
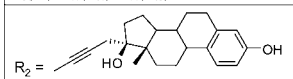 R_2 = $R_6(R_7)$, $R_{10}(R_{11})$, $R_{14}(R_{15})$ = SO_3Na	Zn(II)	MeOH	674 nm		824
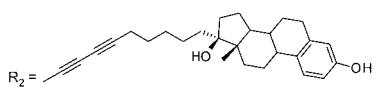 R_2 = $R_6(R_7)$, $R_{10}(R_{11})$, $R_{14}(R_{15})$ = SO_3Na	Zn(II)	MeOH	675 nm		824
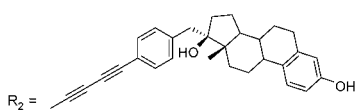 R_2 = $R_6(R_7)$, $R_{10}(R_{11})$, $R_{14}(R_{15})$ = SO_3Na	Zn(II)	MeOH	675 nm		824

(*Continued*)

Table 2. (*Continued*)

Structure	M	Solvent	Transition Energy (Intensity)	Remark	Ref.
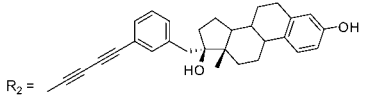 R_2 = $R_6(R_7)$, $R_{10}(R_{11})$, $R_{14}(R_{15})$ = SO_3Na	Zn(II)	MeOH	675 nm		824
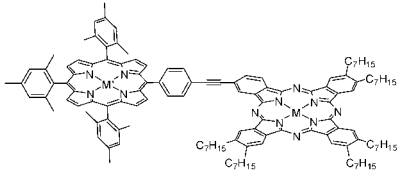	2H	toluene	719 nm, 700, 683, 652, 621, 550, 424, 353	M′ = Zn(II)	815
		toluene	719 nm, 700, 684, 652, 621, 550, 516, 421, 354	M′ = 2H	815
		toluene	719 nm, 700, 684, 652, 619, 566, 429, 352	M′ = Mg(II)	815
	Mg(II)	toluene	701 nm, 682, 566, 428, 356	M′ = Mg(II)	815
		toluene	699 nm, 680, 550, 516, 421, 357	M′ = 2H	815
		toluene	701 nm, 682, 656, 551, 424, 357	M′ = Zn(II)	815
	Zn(II)	toluene	699 nm, 681, 641, 618, 550, 423, 355	M′ = Zn(II)	815
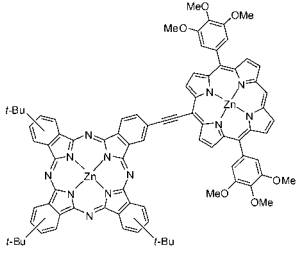	Zn(II)	toluene	710 nm (r.i. 0.55), 679 (0.45), 648 (0.17), 615 (0.14), 562 (0.09), 431 (1.0), 352 (0.35)		825
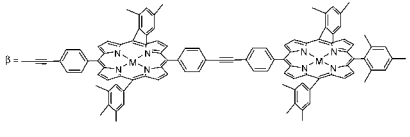	2H	toluene	723 nm (lg ε 5.4), 688 (5.3), 652 (5.0), 595 (4.8), 516 (5.3), 424 (6.4)		826
	Mg(II)	toluene	706 nm (lg ε 5.1), 636 (4.6), 610 (4.9), 566 (5.1), 429 (6.2)		826
	Zn(II)	toluene	701 nm (lg ε 5.5), 631 (4.7), 591 (4.6), 551 (5.3), 429 (6.4)		826
R_1, R_4, R_9, R_{12} = Ph, R_6, R_7, R_{14}, R_{15} = OMe	Zn(II)	$CHCl_3$	699 nm, 673, 640, 611, 350		827
R_1, R_4, R_9, R_{12} = Ph, $R_6(R_7)$, R_{14},(R_{15}) = *t*-Bu	Co(II)	DCB	697 nm (lg ε 5.01), 673 (5.01), 610 (4.47), 331 (4.86)		828
$R_2(R_3)$ = Ph(4-OCH_3), $R_6(R_7)$, $R_{10}(R_{11})$, $R_{14}(R_{15})$ = SO_3Na	Zn(II)	DMF	680 nm		817
	Ga(III)OH	DMF	693 nm		817
$R_2(R_3)$ = Ph(4-CHO), $R_6(R_7)$, $R_{10}(R_{11})$, $R_{14}(R_{15})$ = SO_3Na	Ga(III)OH	DMF	688 nm		817

(*Continued*)

Table 2. (*Continued*)

Structure	M	Solvent	Transition Energy (Intensity)	Remark	Ref.
$R_2(R_3)$ = Ph(4-COOH), $R_6(R_7)$, $R_{10}(R_{11})$, $R_{14}(R_{15})$ = SO_3Na	Ga(III)OH	DMF	690 nm		817
$R_2(R_3)$ = Ph(4-$COCH_3$), $R_6(R_7)$, $R_{10}(R_{11})$, $R_{14}(R_{15})$ = SO_3Na	Ga(III)OH	DMF	686 nm		817
$R_2(R_3)$ = Ph(4-OH), $R_6(R_7)$, $R_{10}(R_{11})$, $R_{14}(R_{15})$ = SO_3Na	Ga(III)OH	DMF	685 nm		817
$R_2(R_3)$ = Ph(4-C(Me_2)Et), $R_6(R_7)$, $R_{10}(R_{11})$, $R_{14}(R_{15})$ = SO_3Na	Ga(III)OH	DMF	685.5 nm		817
R_2, R_3 = Ph(4-COOH), R_6, R_7, R_{10}, R_{11}, R_{14}, R_{15} = *t*-Bu	2H	THF	714.5 nm, 681.0, 651.1, 619.4, 416.3, 357.9		829
	Zn(II)	THF	691.0 nm, 622.0, 364.5		829
R_2 = Ph(4-CH_2OH), $R_6(R_7)$, $R_{10}(R_{11})$, $R_{14}(R_{15})$ = *t*-Bu	Co(II)	THF	670 nm (ε 177,800), 604 (36,300), 341 (67,600)		830
R_2 = $(CH_2)_2$Ph(4-NO_2), $R_6(R_7)$, $R_{10}(R_{11})$, $R_{14}(R_{15})$ = *t*-Bu	2H	DCM	693 nm (lg ε 5.22)		831
R_2 = $(CH_2)_2$Ph(4-CHO), $R_6(R_7)$, $R_{10}(R_{11})$, $R_{14}(R_{15})$ = *t*-Bu	Zn(II)	$CHCl_3$	698 nm (lg ε 5.21), 683 (5.17), 622 (4.47), 357 (5.0), 293 (4.51)		832
R_2 = $(CH_2)_2$Ph(4-CHO), R_6, R_7, R_{10}, R_{11}, R_{14}, R_{15} = SO_2Pr	Pd(II)	$CHCl_3$	692 nm (lg ε 5.09), 661 (5.15), 644 (4.67), 600 (4.49), 345 (4.89), 256 (4.79)		832
R_2 = 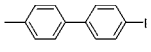 $R_6(R_7)$, $R_{10}(R_{11})$, $R_{14}(R_{15})$ = *t*-Bu	Zn(II)	$CHCl_3$	676 nm (lg ε 5.2), 610 (4.4), 351 (4.9)		833
R_2 = 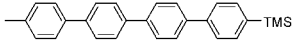 $R_6(R_7)$, $R_{10}(R_{11})$, $R_{14}(R_{15})$ = *t*-Bu	Zn(II)	$CHCl_3$	676 nm (lg ε 5.2), 610 (4.5), 347 (4.9)		833
R_3, R_7, R_{11} = (2-py), R_{15} = *t*-Bu	Zn(II)	DMF	696 nm (lg ε 5.32)		556
R_3, R_7, R_{11} = (2-py^+(N-Me)), R_{15} = *t*-Bu	Zn(II)	DMF	714 nm, 689,		556
R_3, R_7, R_{11} = (2-py^+(N-Me)), R_{15} = *t*-Bu	Zn(II)	H_2O	650 nm		556
R_3, R_7, R_{11} = (3-py), R_{15} = *t*-Bu	Zn(II)	DMF	700 nm (lg ε 5.34)		556
R_3, R_7, R_{11} = (3-py^+(N-Me)), R_{15} = *t*-Bu	Zn(II)	DMF	700 nm, 685sh,		556
		H_2O	648 nm		556
R_1, R_5, R_9 = (2-py), R_{15} = *t*-Bu	Zn(II)	DMF	685 nm (lg ε 5.29), 615 (4.58)		556
R_1, R_5, R_9 = (2-py^+(N-Me)), R_{15} = *t*-Bu	Zn(II)	DMF	700sh nm, 688		556
		H_2O	620 nm		556
R_1, R_5, R_9 = (3-py), R_{15} = *t*-Bu	Zn(II)	DMF	692 nm (lg ε 5.24), 622 (4.54)		556
R_1, R_5, R_9 = (3-py^+(N-Me)), R_{15} = *t*-Bu	Zn(II)	DMF	698sh nm, 689,		556
		H_2O	627 nm		556
R_2 = CHO, $R_6(R_7)$, $R_{10}(R_{11})$, $R_{14}(R_{15})$ = *t*-Bu	2H	$CHCl_3$	693 nm (lg ε 5.0), 680 (4.9), 643 (4.5), 621 (4.3), 344 (4.7)		807
	Cu(II)	DCB	682 nm (lg ε 5.21), 616 (4.62), 348 (4.85)		808

(*Continued*)

Table 2. (*Continued*)

Structure	M	Solvent	Transition Energy (Intensity)	Remark	Ref.
	Zn(II)	$CHCl_3$	698 nm (lg ε 5.0), 670 (5.0), 639 (4.4), 610 (4.3), 353 (4.8)		807
R_2 = COOH, $R_6(R_7)$, $R_{10}(R_{11})$, $R_{14}(R_{15})$ = *t*-Bu	Cu(II)	toluene	675 nm, 609, 346		595
	Zn(II)	THF	680 nm (ε 160,000), 668 (160,000), 606 (32000), 350 (80,000)		834
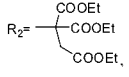 $R_6(R_7)$, $R_{10}(R_{11})$, $R_{14}(R_{15})$ = *t*-Bu	2H	DCM	674 nm (log ε 5.21), 611 (4.81)		835
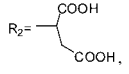 $R_6(R_7)$, $R_{10}(R_{11})$, $R_{14}(R_{15})$ = *t*-Bu	Zn(II)	EtOH	692 nm (log ε 5.28), 347 (4.85)		835
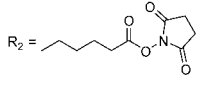	Zn(II)	THF	677 nm, 648, 611, 350	Ra = H, Rb = CH_2Ph	584
		THF	682 nm, 654, 615, 350	Ra = Me, Rb = CH_2Ph	584
		MeOH	677 nm (lg ε 4.62), 630 (4.18), 344 (4.41)	Ra = H, Rb = H	584
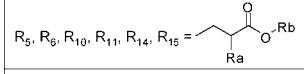		MeOH	679 nm (lg ε 4.89), 613 (4.20), 346 (4.70)	Ra = Me, Rb = H	584
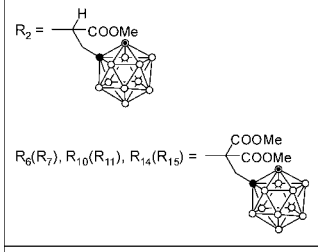	Co(II)	DCM	668 nm (lg ε 4.3), 604 (3.6), 328 (3.9), 206 (4.0)	● C ⊙CH ○BH	579
R_1, R_2 = CN, $R_6(R_7)$, $R_{10}(R_{11})$, $R_{14}(R_{15})$ = *t*-Bu	2H	$CHCl_3$	705 nm (lg ε 5.07), 679 (5.09), 648 (4.70), 616sh, 357 (4.82), 336sh		836
	Ni(II)	$CHCl_3$	700 nm (lg ε 4.84), 657 (4.77), 640sh, 590sh, 338 (4.67), 297 (4.87), 270 (4.89)		836

(*Continued*)

Table 2. (*Continued*)

Structure	M	Solvent	Transition Energy (Intensity)	Remark	Ref.
$\alpha\alpha = OC_6H_{13}$, $\beta = CN$	2H	toluene	772 nm, 752, 700, 678, 430, 340		837
$\alpha\alpha = C_{12}H_{25}$, $\beta = CN$	2H	toluene	743 nm, 707, 675, 642, 405, 370		837
	Cu(II)	toluene	724 nm, 643, 360		837
$\alpha\alpha = C_{12}H_{25}$, $\beta\beta = CN$	Cu(II)	toluene	732 nm, 680, 360		837
	Zn(II)	toluene	730 nm, 680, 410, 360		837
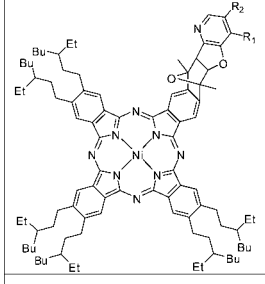	Ni(II)	DCM	673.50 nm, 608.50, 413.50, 330.50	$R_1 = H$, $R_2 = Me$	838
		DCM	670.50 nm, 600.50, 403	$R_1 = H$, $R_2 = H$	838
		DCM	669.50 nm, 601, 405.50, 324.50	$R_1 = CN$, $R_2 = H$	838
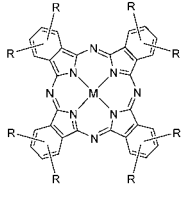	Al(III)Cl	H_2O	678 nm (ε 190,000)	R = 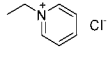	839
		MeOH	682 nm (ε 160,000)		839
		EtOH	685 nm (ε 145,000)		839
	Zn(III)	H_2O	677 nm (ε 180,000)		839
		MeOH	677 nm (ε 170,000)		839
		EtOH	677 nm (ε 140,000)		839
	Al(III)Cl	H_2O	684 nm (ε 190,000)	R = 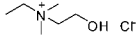	839
		MeOH	684 nm (ε 180,000)		839
		EtOH	686 nm (ε 180,000)		839
	Zn(III)	H_2O	680 nm (ε 190,000)		839
		MeOH	680 nm (ε 180,000)		839
		EtOH	681 nm (ε 185,000)		839
	Al(III)Cl	H_2O	680 nm (ε 170,000)	R = 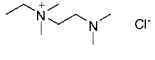	839
		MeOH	682 nm (ε 165,000)		839
		EtOH	685 nm (ε 110,000)		839
	Zn(III)	H_2O	677 nm (ε 175,000)		839
		MeOH	678 nm (ε 160,000)		839

(*Continued*)

Table 2. (*Continued*)

Structure	M	Solvent	Transition Energy (Intensity)	Remark	Ref.
		EtOH	678 nm (ε 110,000)		839
	Al(III)Cl	H_2O	685 nm (ε 100,000)	R = 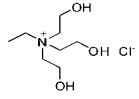	839
		MeOH	688 nm (ε 195,000)		839
		EtOH	688 nm (ε 185,000)		839
	Zn(III)	H_2O	638 nm (ε 66,000)		839
		MeOH	675 nm (ε 160,000)		839
		EtOH	676 nm (ε 150,000)		839
	Al(III)Cl	H_2O	680 nm (ε 170,000)	R = 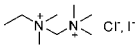	839
		MeOH	684 nm (ε 120,000)		839
	Zn(III)	H_2O	679 nm (ε 195,000)		839
		MeOH	680 nm (ε 130,000)		839
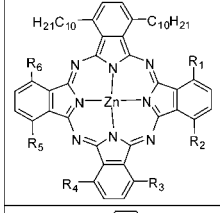	Zn(II)	DCM	715 nm (lg ε 190.48), 648 (40.73)	R_1, R_2, R_5, R_6 = $C_{10}H_{21}$, R_3, R_4 = 	840
		DCM	727 nm (lg ε 347.14), 665 (50.39)	R_1, R_2, R_5, R_6 =  R_3, R_4 = $C_{10}H_{21}$	840
		DCM	766 nm	R_1, R_2, R_3, R_4, R_5, R_6 = 	840
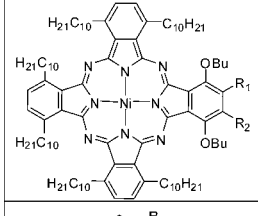	Ni(II)	toluene	716 nm (lg ε 5.10), 698 (5.03), 636 (4.39)	R_1, R_2 = Br	841, 842
		toluene	714 nm (lg ε 5.21), 694sh, 636 (4.57)	R_1 = Br, R_2 = OBu	841
		toluene	732 nm (lg ε 4.99), 702 (4.95)	R_1, R_2 = CC-TMS	841
		toluene	729 nm (lg ε 4.99), 698 (4.88), 666 (4.44), 628 (4.23)	R_1, R_2 = CCH,	841, 842
		toluene	714 nm (lg ε 5.10), 700sh, 635 (4.47)	R_1 = H, R_2 = Br,	841
		toluene	722 nm (lg ε 5.09), 700 (5.02), 640 (4.43), 346 (4.59)	R_1 = H, R_2 = CC-TMS	841
		toluene	721 nm (lg ε 5.07), 701 (5.01), 641 (4.39), 347 (4.54)	R_1 = H, R_2 = CCH,	841
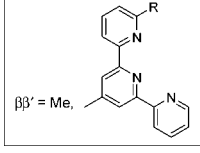	Zn(II)	DMF	684 nm (lg ε 5.32), 620 (4.52)	R = H	843
		DMF	688 nm (lg ε 5.28), 620 (4.53)	R = OCH_2(t-Bu)	843

(*Continued*)

Table 2. (*Continued*)

Structure	M	Solvent	Transition Energy (Intensity)	Remark	Ref.
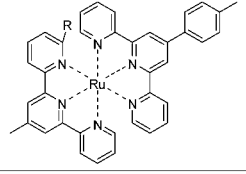 ββ′ = Me,	Zn(II)	DMF	692 nm (lg ε 5.42), 626 (4.77), 494 (5.07)	R = H, $[Pc]^{8+}$	843
		DMF	692 nm (lg ε 5.43), 626 (4.75), 496 (5.06)	R = OCH_2(*t*-Bu), $[Pc]^{8+}$	843
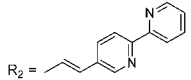 $R_6(R_7)$, $R_{10}(R_{11})$, $R_{14}(R_{15})$ = *t*-Bu	Zn(II)	THF	688 nm (lg ε 5.28), 677 (5.23), 613 (4.52), 352 (5.00), 225 (4.68)		778
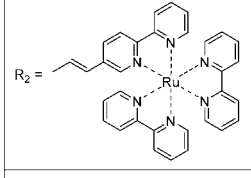	Zn(II)	THF	697 nm (lg ε 4.94), 674 (4.93), 645, 614, 355 (4.79), 289 (4.79), 211 (5.03)		778
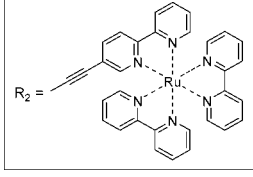	Zn(II)	THF	710 nm (lg ε 4.55), 676 (4.51), 646, 623, 355 (4.42), 289 (4.45), 218 (4.41)		778

(*Continued*)

Table 2. (*Continued*)

Structure	M	Solvent	Transition Energy (Intensity)	Remark	Ref.
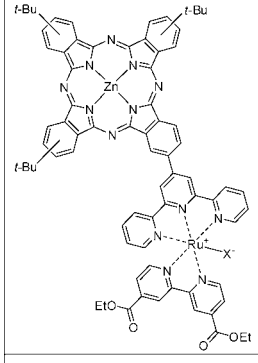	Zn(II)	DMF	705 nm (ε 87,000), 673 (73,300), 649 (36,000), 616 (22,000), 540 (14,000), 350 (57,600), 318 (60,000), 284 (40,000)	X = Cl	844
		DMF	704 nm (ε 91,000), 673 (78,000), 647 (34,400), 614 (23,000), 529 (13,900), 340 (58,000), 320 (63,000), 286 (44,200)	X = NCS	844
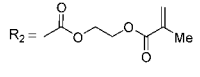 $R_6(R_7)$, $R_{10}(R_{11})$, $R_{14}(R_{15})$ = *t*-Bu	Cu(II)	toluene	695 nm, 670, 638, 342		595
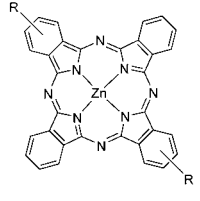	Zn(II)	MeOH	666 nm (ε 155,500), 340 (64,700)	R = 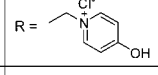	702
		MeOH	668 nm (ε 82,200), 334 (37,500)	R = 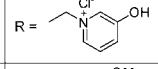	702
		MeOH	668 nm (ε 111,600), 340 (74,800)	R = 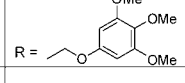	702
$R_2(R_3)$ = OH, $R_6(R_7)$, $R_{10}(R_{11})$, $R_{14}(R_{15})$ = *t*-Bu	2H	DCM	698 nm (lg ε 5.16), 664 (5.09), 644 (4.74), 604 (4.50), 342 (4.94), 290 (4.66)		598
R_2 = OH, R_6, R_7, R_{10}, R_{11}, R_{14}, R_{15} = Bu	Zn(II)	$CHCl_3$	685 nm, 614, 350		845
R_2 = OH, R_6, R_{10},R_{14} (R_7, R_{11}, R_{15}) = *t*-Bu	Zn(II)	$CHCl_3$	679 nm, 612, 349		845
$\alpha\alpha$ = $C_{12}H_{25}$, $\beta\beta$ = OMe	2H	spin-coated film	729 nm, 696		691
R_1 = OSO_2CF_3, $R_6(R_7)$, $R_{10}(R_{11})$, $R_{14}(R_{15})$ = *t*-Bu	2H	$CHCl_3$	707 nm (lg ε 5.1), 672 (5.1), 611 (4.4), 341 (4.8), 296 (3.5)		822

(*Continued*)

Table 2. (*Continued*)

Structure	M	Solvent	Transition Energy (Intensity)	Remark	Ref.
αα = OSO_2CF_3, ββ = 	2H	toluene	954.5 nm, 778 (lg ε 5.27)		608
		DCM	778 (lg ε 5.270), 684 (4.756), 338 (4.866)		608
	Co(II)	DCM	746 nm (lg ε 5.34), 670 (4.71), 304 (4.92)		608
	Zn(II)	DCM + 0.5 vol % py	758 nm (lg ε 5.42), 307.8		608
	Zn(II)	DCM	758 nm (lg ε 5.42), 678 (4.73), 370 (4.78)		608
αα = OBu, ββ = 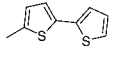	2H	toluene	932.0 nm, 794 (lg ε 5.31)		608
		DCM	794 (lg ε 5.316), 705 (4.663), 493 (4.554)		608
	Co(II)	DCM	762 nm (lg ε 5.43), 680 (4.71), 304 (4.92)		608
	Zn(II)	DCM + 0.5 vol % py	768 nm (lg ε 5.52), 287.7		608
		DCM	768 nm (lg ε 5.48), 686 (4.85), 332 (5.20)		608
αα = OC_8H_{17}, ββ = Me	2H	spin-coated film	763 nm, 735		691
		toluene	762 nm, 737		846
R_6, R_7, R_{10}, R_{11}, R_{14}, R_{15} = 	Ni(II)	DCM	670 nm, 604, 388, 309, 289	R_2 = 	847
		DCM	689 nm, 664, 633sh, 605sh, 394, 313, 289	R_2 = CHO	847
		DCM	682 nm, 617, 390, 309, 302, 293	R_1 = $CHNNMe_2$	847
		DCM	675 nm, 610, 412, 386, 312, 293	R_1 = CHO	847
R_2 = $R_6(R_7)$, $R_{10}(R_{11})$, $R_{14}(R_{15})$ = *t*-Bu	Zn(II)	$CHCl_3$	673 nm (lg ε 5.15), 610 (4.39), 352 (4.7)		848
$R_2(R_3)$ = $O(CH_2CH_2O)_3H$, R_6, R_7, R_{10}, R_{11}, R_{14}, R_{15} = $C_{16}H_{33}$	2H	toluene	706 nm, 670, 644, 606, 350,		631
R_2, $R_{10}(R_{11})$= $O(CH_2CH_2O)_3H$, R_6, R_7, R_{14}, R_{15} = $C_{16}H_{33}$	2H	toluene	708 nm, 672, 642, 610, 384, 344		631
R_2, $R_6(R_7)$ = $O(CH_2CH_2O)_3H$, R_{10}, R_{11}, R_{14}, R_{15} = $C_{16}H_{33}$	2H	DCM	706 nm, 670, 638, 608, 384, 344, 292		631
$R_2(R_3)$, $R_{10}(R_{11})$ = $(OCH_2CH_2)_4OH$, R_6, R_7, R_{14}, R_{15} = $C_{16}H_{33}$	2H	toluene	704 nm, 668, 642, 606, 394, 340		849
$R_2(R_3)$, $R_6(R_7)$ = $(OCH_2CH_2)_4OH$, R_{10}, R_{11}, R_{14}, R_{15} = $C_{16}H_{33}$	2H	toluene	706 nm, 670, 638, 608, 384, 344		849
$R_2(R_3)$, $R_6(R_7)$, $R_{10}(R_{11})$ = $(OCH_2CH_2)_4OH$, R_{14}, R_{15} = $C_{16}H_{33}$	2H	toluene	706 nm, 670, 638, 608, 384, 344		849
$R_2(R_3)$ = $O(CH_2CH_2O)_3CPh_3$, R_6, R_7, R_{10}, R_{11}, R_{14}, R_{15} = $C_{16}H_{33}$	2H	toluene	706 nm, 670, 644, 606, 350		631
R_2, $R_{10}(R_{11})$= $O(CH_2CH_2O)_3CPh_3$, R_6, R_7, R_{14}, R_{15} = $C_{16}H_{33}$	2H	toluene	706 nm, 670, 638, 608, 380, 292		631
R_2, $R_6(R_7)$ = $O(CH_2CH_2O)_3CPh_3$, R_{10}, R_{11}, R_{14}, R_{15} = $C_{16}H_{33}$	2H	DCM	706 nm, 670, 638, 608, 380, 344, 292		631
$R_2(R_3)$, $R_6(R_7)$, $R_{10}(R_{11})$ = $O(CH_2CH_2O)_3CPh_3$, R_{14}, R_{15} = $C_{16}H_{33}$	2H	toluene	707 nm, 671, 638, 610, 380, 344		631

(*Continued*)

Table 2. (*Continued*)

Structure	M	Solvent	Transition Energy (Intensity)	Remark	Ref.
R_2 = $OPhCH_2Ph(2\text{-}CH_2OH)$, R_6, R_7, R_{10}, R_{11}, R_{14}, R_{15} = Et	Zn(II)	$CHCl_3$	686 nm (lg ε 4.90), 617 (4.15), 352 (4.55)		850
R_2 = $OPhCH_2Ph(2\text{-}CH_2OH)$, R_6, R_7, R_{10}, R_{11}, R_{14}, R_{15} = Bu	Zn(II)	$CHCl_3$	686 nm (lg ε 4.94), 617 (4.21), 352 (4.61)		850
R_2 = $OPhCH_2(2\text{-}CH_2OH)$, $R_6(R_7)$, $R_{10}(R_{11})$, $R_{14}(R_{15})$ = *t*-Bu	Zn(II)	$CHCl_3$	680 nm (lg ε 4.96), 613 (4.18), 350 (4.56)		850
R_2, $R_6(R_7)$, $R_{10}(R_{11})$, $R_{14}(R_{15})$ = $O(CH_2CH_2O)_3H$	2H	DCM	704 nm, 670, 646, 608, 384, 344		631
$R_1(R_4)$, $R_9(R_{12})$ = OCH(*i*-Pr)(*t*-Bu)	2H	$CHCl_3$	714.87 nm, 680.89, 650.96, 618.21, 333.97		606
R_3, $R_{10}(R_{11})$ = 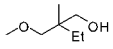 $R_6(R_7)$, $R_{14}(R_{15})$ = OCH_2(*t*-Bu)	2H	DCM	704 nm (lg ε 4.20), 670 (4.67), 656 (4.52), 614 (4.32), 390 (4.47), 342 (4.61)		684
R_2, $R_6(R_7)$, $R_{10}(R_{11})$ = 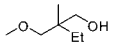 $R_{14}(R_{15})$ = OCH_2(*t*-Bu)	2H	DCM	702 nm (lg ε 4.61), 672 (4.64), 648 (4.54), 390sh, 340 (4.64)		684
$R_2(R_3)$ = 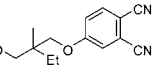 $R_6(R_7)$, $R_{10}(R_{11})$, $R_{14}(R_{15})$ = OCH_2(*t*-Bu)	2H	DCM	702 nm (lg ε 5.04), 666 (5.00), 648 (4.80), 606 (4.53), 390sh, 350 (4.83)		684
	Cu(II)	DCM	684 nm (lg ε 5.18), 672 (5.01), 614 (4.85), 340 (4.94)		684
		toluene	684 nm (lg ε 5.19), 672 (5.10), 612 (4.66), 348 (4.82)		684
	Zn(II)	DCM	684 nm (lg ε 5.36), 674 (5.27), 616 (4.72), 346 (5.15)		684
		toluene	686 nm (lg ε 5.06), 672 (5.00), 614 (4.56), 362 (4.85)		684
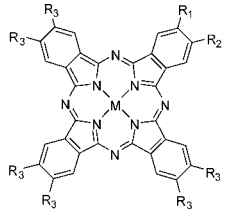	Zn(II)	$CHCl_3$	678 nm (lg ε 5.42), 355 (4.97)	R_1 = OMe, R_2 = OCH_2CH_2OH R_3 = 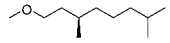	851
		$CHCl_3$	694 nm (lg ε 5.40), 678 (5.21), 355 (4.94)	R_1 = H, R_2 = 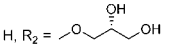 R_3 = 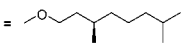	851
		$CHCl_3$	694 nm (lg ε 5.42), 678 (5.21), 355 (4.92)	R_1 = H, R_2 = 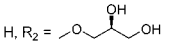 R_3 = 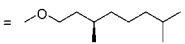	851
		$CHCl_3$	694 nm (lg ε 5.38), 678 (5.20), 355 (4.94)	R_1 = H, R_2 = 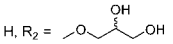 R_3 = 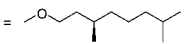	851

(*Continued*)

Table 2. (*Continued*)

Structure	M	Solvent	Transition Energy (Intensity)	Remark	Ref.
		$CHCl_3$	694 nm (lg ε 5.39), 678 (5.19), 355 (4.94)	R_1 = H, R_2 = 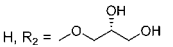 R_3 = 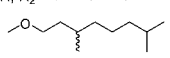	851
R_2=C(COOH)CH_2COOH, R_5, R_8, R_9, R_{12}, R_{13}, R_{16}=OBu	Zn(II)	EtOH	697 nm (lg ε 4.83), 636sh, 343 (4.69)		852
R_2 = OPhCH_2Ph(2-CH_2OH), R_6, R_7, R_{10}, R_{11}, R_{14}, R_{15} = OPr	Zn(II)	$CHCl_3$	680 nm (lg ε 4.65), 613 (3.94), 355 (4.32)		850
R_2, R_3 = OCH_2CH_2OH, R_6, R_7, R_{10}, R_{11}, R_{14}, R_{15} = OC_5H_{11}	2H	$CHCl_3$	704 nm (10^{-5} ε 1.21), 676 (1.02)		618
R_2=OC_6H_{13}, R_6(R_7), R_{10}(R_{11}), R_{14}(R_{15}) = $OC_{12}H_{25}$	Cu(II)	$CHCl_3$	672 nm, 612, 343		853
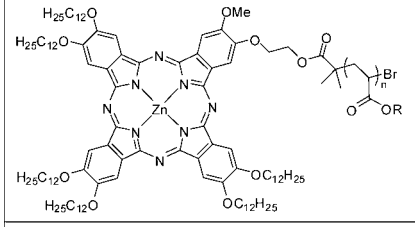	Zn(II)	DCM	678 nm, 331	R = Bu	854
		DCM	678 nm, 332	R = $(CH_2CH_2O)_3Me$	854
R_2 = $O(CH_2CH_2O)_2H$, R_6(R_7), R_{10}(R_{11}), R_{14}(R_{15}) = $O(CH_2CH_2O)_3Me$	2H	DMSO	706 nm (lg ε 3.4), 676 (3.5), 646 (3.4)		708
	Ni(II)	THF	671 nm (lg ε 4.3)		708
	Cu(II)	DMSO	681 nm (lg ε 4.8)		708
	Zn(II)	DMSO	680 nm (lg ε 4.9)		708
$\alpha\alpha$ = OC_6H_{13}, $\beta\beta$ = OPh(3,5-F_2)	Zn(II)	toluene	733 nm, 668		855
R_2, R_3 = OPh(4-$COOC_5H_{11}$), R_6, R_7, R_{10}, R_{11}, R_{14}, R_{15} = OC_5H_{11}	Zn(II)	$CHCl_3$	680 nm, 613, 356		856
R_2, R_3 = OPh(4-COOH), R_6, R_7, R_{10}, R_{11}, R_{14}, R_{15} = OC_5H_{11}	Zn(II)	$CHCl_3$	679 nm, 612, 365		856
R_2, R_3 = OPh(4-$COOC_5H_{11}$), R_6, R_7, R_{10}, R_{11}, R_{14}, R_{15} = OC_5H_{11}	Ru(II)L	$CHCl_3$	626 nm, 381, 324	L = *trans*-(py(4-Me))$_2$	856
R_2, R_3 = OPh(4-COOH), R_6, R_7, R_{10}, R_{11}, R_{14}, R_{15} = OC_5H_{11}	Ru(II)L	4-picoline	626 nm, 381, 324	L = *trans*-(py(4-Me))$_2$	856
R_2 = OPh(3-OH), R_6, R_7, R_{10}, R_{11}, R_{14}, R_{15} = OPh(3,5-(*t*-Bu)$_2$)	2H	DCM	702.0 nm (lg ε 5.35), 667.5 (5.28), 640.5 (4.81), 606.0 (4.65), 400sh, 345.0 (5.6), 291.5 (4.95)		666
	Ni(II)	DCM	673.5 nm (lg ε 5.40), 647.0sh, 606.5 (4.68), 382.5sh, 329.0sh, 305.5 (5.06)		666
R_2 = OPh(3-OC_6H_{12}Br), R_6, R_7, R_{10}, R_{11}, R_{14}, R_{15} = OPh(3,5-(*t*-Bu)$_2$)	2H	DCM	702.0 nm (lg ε 5.27), 668.0 (5.20), 639.5 (4.75), 607.0 (4.49), 400sh, 344.5 (4.99), 291.5 (4.88)		666
	Ni(II)	DCM	674.0 nm (lg ε 5.41), 646.0sh, 607.0 (4.71), 382.5sh, 329.0sh, 300.0 (5.12)		666

(*Continued*)

Table 2. (*Continued*)

Structure	M	Solvent	Transition Energy (Intensity)	Remark	Ref.
R_2 = OPh(4-CH_2OH), $R_6(R_7)$, $R_{10}(R_{11})$, $R_{14}(R_{15})$ = OPh(4-$CH_2OC_7H_{15}$)	Zn(II)	DMF	672 nm		857
R_1 = OPh(4-CH_2OH), $R_6(R_7)$, $R_{10}(R_{11})$, $R_{14}(R_{15})$ = OPh(4-$CH_2OC_7H_{15}$)	Zn(II)	DMF	689 nm		857
$\beta\beta$ = $OPhNO_2$, OPh(3,5-$(Me)_2$)	Cu(II)	DMF	682 nm, 631		667
		$CHCl_3$ + 0.5% NaOH aq	682 nm, 631		667
R_2 = OPh(4-*t*-Bu), $R_6(R_7)$, $R_{10}(R_{11})$, $R_{14}(R_{15})$ = OPh(4-COOH)	Zn(II)	DMF	682 nm (lg ε 4.97), 614 (4.24), 346 (4.69)		648
		DMSO	682 nm		648
R_2 = OPhR, $R_6(R_7)$, $R_{10}(R_{11})$, $R_{14}(R_{15})$ = 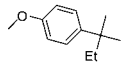	Zn(II)	DMF	676 nm (lg ε 5.33), 606 (4.66), 357 (4.99)	R = OEt	858
		DMF	680 nm (lg ε 5.13), 610 (4.65), 354 (4.85)	R = 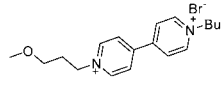	858
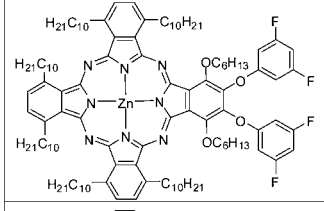	Zn(II)	toluene	719 nm, 655		855
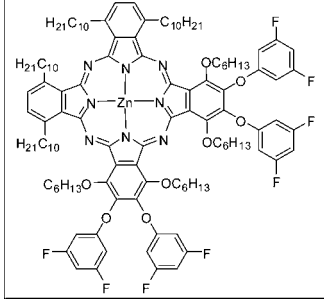	Zn(II)	toluene	726 nm, 665		855

(*Continued*)

Table 2. (*Continued*)

Structure	M	Solvent	Transition Energy (Intensity)	Remark	Ref.
$R_2 = O(CH_2)_{10}SH$, $R_6(R_7)$, $R_{10}(R_{11})$, $R_{14}(R_{15})$ = *t*-Bu	2H	$CHCl_3$	702 nm (lg ε 0.558), 665 (0.754), 643 (0.682), 339 (0.804)		859
R_2, $R_3 = OCH_2TMS$, $R_6(R_7)$, $R_{10}(R_{11})$, $R_{14}(R_{15})$ = *t*-Bu	2H	$CHCl_3$	712 nm (lg ε 4.98), 645 (4.41), 344 (4.71), 298 (4.46)		680
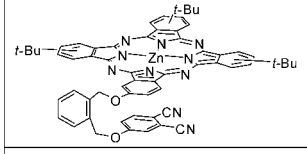	Zn(II)	$CHCl_3$	679 nm, 612, 348		860
R_1 = 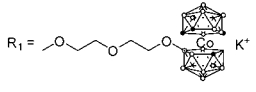 R_4 = OMe	Zn(II)	acetone	684 nm (lg ε 5.26), 618 (4.49)	● CH⊕ B ⊖BH	861
R_1, R_4 = 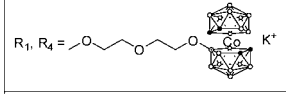	Zn(II)	acetone	686 nm (lg ε 5.36), 618 (4.62)	● CH⊕ B ⊖BH	861
R_2 = 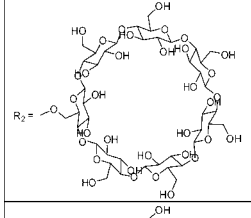	Zn(II)	DMSO	675 nm (lg ε 5.31), 350 (4.80)		862
R_2 = 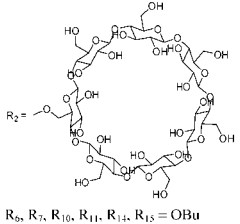 R_6, R_7, R_{10}, R_{11}, R_{14}, R_{15} = OBu	Zn(II)	DMSO	678 nm (lg ε 5.25), 360 (4.91)		862

(*Continued*)

Table 2. (*Continued*)

Structure	M	Solvent	Transition Energy (Intensity)	Remark	Ref.
$R_2 = O(CH_2)_{11}OPh(4\text{-}CHCH_2)$, R_6, R_7, R_{10}, R_{11}, R_{14}, $R_{15} = OC_{12}H_{25}$	2H	toluene	700 nm, 664, 646, 398, 342		863
	Zn(II)	toluene	679 nm, 612, 360		863
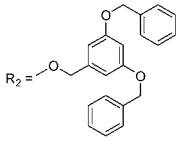 R_6, R_7, R_{10}, R_{11}, R_{14}, $R_{15} = OC_8H_{17}$	2H	DCM	700 nm, 664, 646, 398, 342		692
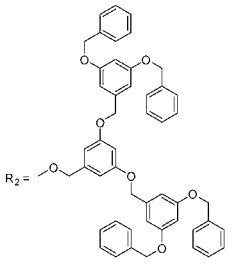 R_6, R_7, R_{10}, R_{11}, R_{14}, $R_{15} = OC_8H_{17}$	2H	DCM	700 nm, 664, 646, 398, 342		692
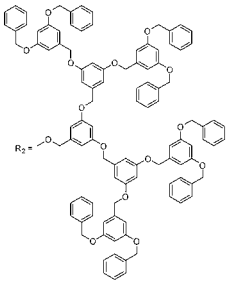 R_6, R_7, R_{10}, R_{11}, R_{14}, $R_{15} = OC_8H_{17}$	2H	DCM	702 nm, 664, 640, 400, 340		692

(*Continued*)

Table 2. (*Continued*)

Structure	M	Solvent	Transition Energy (Intensity)	Remark	Ref.
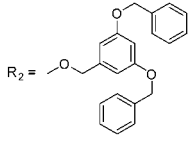 R_2 = R_{6}, R_7, R_{10}, R_{11}, R_{14}, R_{15} = $OCH_2CH_2OCH_2CH_2OMe$	2H	DCM	700 nm, 664, 646, 398, 342		435
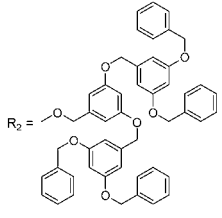 R_2 = R_{6}, R_7, R_{10}, R_{11}, R_{14}, R_{15} = $OCH_2CH_2OCH_2CH_2OMe$	2H	DCM	700 nm, 664, 646, 398, 342		435
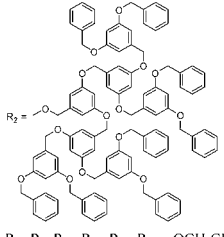 R_2 = R_{6}, R_7, R_{10}, R_{11}, R_{14}, R_{15} = $OCH_2CH_2OCH_2CH_2OMe$	2H	DCM	702 nm, 664, 640, 400, 340		435

(*Continued*)

Table 2. (*Continued*)

Structure	M	Solvent	Transition Energy (Intensity)	Remark	Ref.
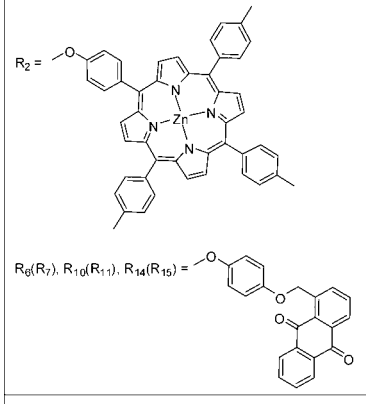	Zn(II)	DMF	680 nm (lg ε 4.30), 420 (4.74), 328 (3.82), 270 (4.91)		483
$R_2 = O(CH_2)_2NHBoc$, $R_6(R_7)$, $R_{10}(R_{11})$, $R_{14}(R_{15}) = t$-Bu	Zn(II)	DMF	677 nm (lg ε 5.35), 610 (4.59), 350 (4.90)	Boc = COO*t*-Bu	864
$R_2 = O(CH_2)_2NH_2$, $R_6(R_7)$, $R_{10}(R_{11})$, $R_{14}(R_{15}) = t$-Bu	Zn(II)	DMF	677 nm (lg ε 5.33), 610 (4.59), 350 (4.89)		864
$R_2 = O(CH_2)_2NH_3^+Cl^-$, $R_6(R_7)$, $R_{10}(R_{11})$, $R_{14}(R_{15}) = t$-Bu	Zn(II)	DMF	677 nm (lg ε 5.34), 610 (4.58), 350 (4.88)	$[Pc]^+[Cl]$	674
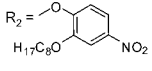 R_6, R_7, R_{10}, R_{11}, R_{14}, $R_{15} = SC_6H_{13}$	Co(II)	$CHCl_3$	697 nm (lg ε 5.4739), 629 (5.0012), 424 (4.7700), 327 (5.4681)		865
$R_2 = OPh(3\text{-}(NO_2)\text{-}4\text{-}(NH_2))$, R_6, R_7, R_{10}, R_{11}, R_{14}, $R_{15} = SC_6H_{13}$	Zn(II)	$CHCl_3$	710 nm (ε 28,632), 632 (4,700), 435 (10,256), 338 (26,709)		866
$R_2 = OPh(3,4\text{-}(NH_2)_2)$, R_6, R_7, R_{10}, R_{11}, R_{14}, $R_{15} = SC_6H_{13}$	Zn(II)	$CHCl_3$	709 nm (ε 30,185), 634 (5,544), 443 (6,160), 340 (21,766)		866
R_1, $R_4 = OSO_2CF_3$, $R_6(R_7)$, $R_{10}(R_{11})$, $R_{14}(R_{15}) = t$-Bu	Ni(II)	$CHCl_3$	686 nm (lg ε 5.2), 653 (5.2), 592 (4.6), 337 (4.9), 298 (5.0)		822
$R_1 = OSO_2CF_3$, $R_6(R_7)$, $R_{10}(R_{11})$, $R_{14}(R_{15}) = t$-Bu	Ni(II)	$CHCl_3$	677 nm (lg ε 5.1), 662 (5.1), 601 (4.5), 335 (4.7), 294 (4.8), 270 (4.7)		822

(*Continued*)

Table 2. (*Continued*)

Structure	M	Solvent	Transition Energy (Intensity)	Remark	Ref.
ββ′ = 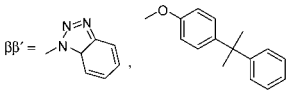	Co(II)	DMF	669 nm (lg ε 4.90), 605 (4.51)		867
		$CHCl_3$	675 nm (lg ε 4.90), 607 (4.25)		867
	Ni(II)	DMF	760 nm (lg ε 4.41), 679 (4.91), 600 (4.57)		867
		$CHCl_3$	771 nm (lg ε 4.36), 676 (4.96), 605 (4.46)		867
	Cu(II)	DMF	684 nm (lg ε 5.09), 613 (4.26)		867
		$CHCl_3$	771 nm (lg ε 3.57), 688 (5.17), 617 (4.46)		867
	Er(III)	DMF	689 nm (lg ε 4.87), 621 (4.16)		867
		$CHCl_3$	688 nm (lg ε 4.92), 618 (4.21)		867
R_2 = PDI, $R_6(R_7)$, $R_{10}(R_{11})$, $R_{14}(R_{15})$ = *t*-Bu	Zn(II)	DMF	679 nm (lg ε 5.17), 614 (4.41), 533 (4.72), 494 (4.46), 464 (4.10), 353 (4.82)	PDI = 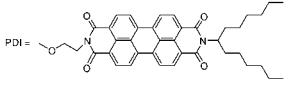	864
$\alpha\alpha$ = Et, $\beta\beta$ = SMe	2H	CHCl3	750 nm (lg ε 5.06)		868
	Ti(IV)O	CHCl3	760 nm (lg ε 5.15)		868
R_2, R_3 = CCPh, R_6, R_7, R_{10}, R_{11}, R_{14}, R_{15} = SC_6H_{13}	Co(II)	$CHCl_3$	711 nm (lg ε 4.00), 329 (4.19), 270 (3.98)		869
	Ni(II)	$CHCl_3$	703 nm (lg ε 4.83), 322 (4.89)		869
$\beta\beta$ = SC_6H_{13}, $CH(COOEt)_2$	Co(II)	$CHCl_3$	686 nm (10^{-4} ε 7.03), 319 (4.35)		870
	Cu(II)	$CHCl_3$	698 nm (10^{-4} ε 8.15), 344 (2.70)		870
	Zn(II)	$CHCl_3$	699 nm (10^{-4} ε 9.11), 363 (6.40)		870
$\beta\beta$ = SC_6H_{13}, $CH(COOC_6H_{13})_2$	2H	$CHCl_3$	718 nm (10^{-4} ε 9.88), 684 (8.54), 348 (4.01)		870
	Co(II)	$CHCl_3$	687 nm (10^{-4} ε 7.42), 317 (4.97)		870
	Cu(II)	$CHCl_3$	698 nm (10^{-4} ε 9.12), 345 (3.07)		870
	Zn(II)	$CHCl_3$	695 nm (10^{-4} ε 8.76), 358 (2.38)		870
$\beta\beta$ = SC_8H_{17}, OPh(3,5-$(OMe)_2$)	2H	$CHCl_3$	699 nm, 340, 232,		871
	Cu(II)	$CHCl_3$	696 nm, 290, 226,		871
	Zn(II)	$CHCl_3$	698 nm, 340, 231		871
$\beta\beta$ = $CH(COOC_6H_{13})_2$, $S(CH_2)_2N(Me)_2$	Co(II)	$CHCl_3$	685 nm (lg ε 5.08), 316 (4.91)		872
		H_2O	650 nm (lg ε 4.43), 319 (4.57)	$[Pc]^{+}4I$	872
		DMSO	680 nm (lg ε 4.98), 345 (4.81)	$[Pc]^{4+}4I^{-}$	872
	Zn(II)	$CHCl_3$	697 nm (lg ε 5.08), 372 (4.68)		872
R_2, R_3 = 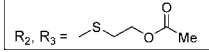	Co(II)	$CHCl_3$	699 nm (ε 14,200), 625 (5,000), 415 (3,100), 324 (13,300)		873

(*Continued*)

Table 2. (*Continued*)

Structure	M	Solvent	Transition Energy (Intensity)	Remark	Ref.
R_6, R_7, R_{10}, R_{11}, R_{14}, R_{15} = SC_6H_{13}	Ni(II)	$CHCl_3$	700 nm (ε 13,600), 660 (5,800), 620 (4,000), 421 (3,000), 319 (9,300)		873
	Zn(II)	$CHCl_3$	709 nm (ε 27,100), 675 (5,000), 635 (4,800), 440 (2,700), 364 (9,900)		873
$\alpha\beta$ (R_1 = SPh, R_3 = *t*-Bu)	2H	THF	738.5 nm, 710.5		48
	Mn(III)	benzene	704 nm, 350		528
	Mn(III)Cl	benzene	770 nm (lg ε 5.05), 525 (4.36), 365 (4.79)		528
	Mn(III)L	py	625 nm, 350	L = py	528
	Zn(II)	THF	709.5 nm		48
R_1, R_2, R_3, R_4 = Ph, R_6(R_7), R_{10}(R_{11}), R_{14}(R_{15}) = SPh	2H	$CHCl_3$	696 nm (lg ε 5.20), 627 (4.56), 414sh, 347 (4.82)		733
R_1, R_2, R_3, R_4, R_9, R_{10}, R_{11}, R_{12} = Ph, R_6(R_7), R_{14}(R_{15}) = SPh	2H	$CHCl_3$	696 nm (lg ε 5.23), 631 (4.74), 414sh, 347 (5.04)		733
R_1, R_2, R_3, R_4, R_5, R_6, R_7, R_8 = Ph, R_{10}(R_{11}), R_{14}(R_{15}) = SPh	2H	$CHCl_3$	715 nm (lg ε 5.08), 642 (4.40), 414sh, 343 (4.61)		733
R_2 = SPh, R_5, R_6, R_7, R_8, R_9, R_{10}, R_{11}, R_{12}, R_{13}, R_{14}, R_{15}, R_{16} = Ph	2H	$CHCl_3$	741 nm (lg ε 4.98), 666 (4.33), 348 (4.53)		733
$\beta\beta$ = SPh, OPh	Cu(II)	$CHCl_3$	694 nm		667, 734
		DMF	686 nm		734
		DMF	696 nm		667
$\beta\beta$ = SPh, OPh(4-*t*-Bu)	Co(II)	$CHCl_3$	699 nm		667, 734
		DMF	688 nm		667, 734
	Cu(II)	$CHCl_3$	708 nm		667, 734
		DMF	700 nm		667, 734
$\beta\beta$ = SPh, OPh(4-COOH)	Co(II)	DMF	697 nm		667, 734
	Cu(II)	DMF	709 nm		667, 734
$\alpha\alpha$ = Et, $\beta\beta$ = SCH_2Ph	2H	$CHCl_3$	755 nm (lg ε 5.1)		874
ββ′ = SC_6H_{13}, 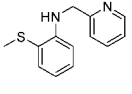	2H	$CHCl_3$	730 nm (10^{-1} ε 15.76), 700 (13.75), 667 (4.49), 359 (10.60)		875
	Co(II)	$CHCl_3$	702 nm (10^{-1} ε 8.30), 635 (2.61), 321 (5.09)		875
	Zn(II)	$CHCl_3$	713 nm (10^{-1} ε 14.73), 645 (4.20), 371 (9.26)		875
R_2, R_3 = OC_8H_{17}, R_6, R_7, R_{10}, R_{11}, R_{14}, R_{15} = $SO_2C_8H_{17}$	Ni(II)	$CHCl_3$	705 nm (lg ε 4.69), 664 (4.65), 599 (4.03), 342 (4.49), 293 (4.52)		758
$\alpha\beta$(R_1, R_3) = SO_2Ph, *t*-Bu	Mn(II)	benzene	715 nm		530
	Mn(III)	benzene	674 nm, 350		528
	Mn(III)Cl	benzene	715 nm (lg ε 4.93), 499 (3.94), 365 (4.53)		528
	Mn(III)L	py	639 nm, 341	L = py	528

(*Continued*)

Table 2. (*Continued*)

Structure	M	Solvent	Transition Energy (Intensity)	Remark	Ref.
	Zn(II)	THF	668.4 nm		48
R_2 = Ts, $R_6(R_7)$, $R_{10}(R_{11})$, $R_{13}(R_{15})$ = *t*-Bu	2H	$CHCl_3$	711sh nm, 687 (lg ε 5.00), 618 (4.33), 341 (4.59)		516
R_2, (R_3) = Ts, $R_6(R_7)$, $R_{10}(R_{11})$, $R_{14}(R_{15})$ = *t*-Bu	2H	$CHCl_3$	711sh nm, 687 (ε 100,000), 618 (21,379), 341 (38,904)		517
R_2, R_3 = NH(Ts), R_6, R_7, R_{10}, R_{11}, R_{14}, R_{15} = SC_6H_{13}	Ni(II)	$CHCl_3$	697.0 nm (10^{-4} ε 16.61), 413.0 (3.64), 322.5 (13.32)		876
R_2, R_3 = NH(Ts), R_6, R_7, R_{10}, R_{11}, R_{14}, R_{15} = $SC_{12}H_{25}$	Ni(II)	$CHCl_3$	697.5 nm (10^{-4} ε 15.82), 414.0 (3.22), 323.0 (13.00)		876
R_2, R_3 = NH(Ts), R_6, R_7, R_{10}, R_{11}, R_{14}, R_{15} = $SC_{16}H_{33}$	Ni(II)	$CHCl_3$	698.0 nm (10^{-4} ε 15.11), 413.5 (3.50), 323.5 (13.10)		876
R_2 = CCBu $R_6(R_7)$, $R_{10}(R_{11})$, $R_{14}(R_{15})$ = 	Zn(II)	$CHCl_3$	691 nm (lg ε 5.28), 676 (5.26), 613 (4.59), 361 (4.89)		877
R_2 = CCC_7H_{15} $R_6(R_7)$, $R_{10}(R_{11})$, $R_{14}(R_{15})$ = 	Zn(II)	$CHCl_3$	691 nm (lg ε 5.28), 677 (5.26), 614 (4.60), 362 (4.88)		877
R_2 = $CCC_{10}H_{21}$ $R_6(R_7)$, $R_{10}(R_{11})$, $R_{14}(R_{15})$ = 	Zn(II)	$CHCl_3$	692 nm (lg ε 5.27), 675 (5.25), 613 (4.59), 362 (4.90)		877
R_2 = $CCC_{13}H_{27}$ $R_6(R_7)$, $R_{10}(R_{11})$, $R_{14}(R_{15})$ = 	Zn(II)	$CHCl_3$	692 nm (lg ε 5.23), 676 (5.22), 614 (4.58), 362 (4.87)		877
R_2 = CCPh $R_6(R_7)$, $R_{10}(R_{11})$, $R_{14}(R_{15})$ = 	Zn(II)	$CHCl_3$	692 nm (lg ε 5.26), 676 (5.24), 614 (4.57), 359 (4.85)		877
R_2 = $CC(CH_2)_4OH$ $R_6(R_7)$, $R_{10}(R_{11})$, $R_{14}(R_{15})$ = 	Zn(II)	$CHCl_3$	691 nm (lg ε 5.21), 675 (5.19), 613 (4.49), 362 (4.49)		877

(*Continued*)

Table 2. (*Continued*)

Structure	M	Solvent	Transition Energy (Intensity)	Remark	Ref.
R_2 = CC–TMS $R_6(R_7)$, $R_{10}(R_{11})$, $R_{14}(R_{15})$ = 	Zn(II)	$CHCl_3$	690 nm (lg ε 5.26), 676 (5.26), 615 (4.65), 359 (4.90)		877
R_2 = CCBu, $R_6(R_7)$, $R_{10}(R_{11})$, $R_{14}(R_{15})$ = SO_3H	Zn(II)	MeOH	671 nm (lg ε 5.20), 607 (4.48), 344 (4.79)		877
R_2 = CCC_7H_{15}, $R_6(R_7)$, $R_{10}(R_{11})$, $R_{14}(R_{15})$ = SO_3H	Zn(II)	MeOH	671 nm (lg ε 5.31), 607 (4.52), 345 (4.82)		877
R_2 = $CCC_{10}H_{21}$, $R_6(R_7)$, $R_{10}(R_{11})$, $R_{14}(R_{15})$ = SO_3H	Zn(II)	MeOH	671 nm (lg ε 5.30), 607 (4.51), 345 (4.81)		877
R_2 = $CCC_{13}H_{27}$, $R_6(R_7)$, $R_{10}(R_{11})$, $R_{14}(R_{15})$ = SO_3H	Zn(II)	MeOH	678 nm (lg ε 5.14), 607 (4.36), 356 (4.68)		877
R_2 = CCPh, $R_6(R_7)$, $R_{10}(R_{11})$, $R_{14}(R_{15})$ = SO_3H	Zn(II)	DMF	677 nm (lg ε 5.15), 611 (4.41), 350 (4.70)		877
R_2 = $CC(CH_2)_4OH$, $R_6(R_7)$, $R_{10}(R_{11})$, $R_{14}(R_{15})$ = SO_3H	Zn(II)	DMF	678 nm (lg ε 5.21), 612 (4.46), 353 (4.77)		877
R_2 = CC-TMS, $R_6(R_7)$, $R_{10}(R_{11})$, $R_{14}(R_{15})$ = SO_3H	Zn(II)	MeOH	671 nm (lg ε 5.27), 607 (4.58), 344 (4.81)		877
$\beta\beta$ = SO_3H, COOH	Fe(III)OH	DMF	676 nm		312
		1% NH_4OH	679 nm		312
	Co(II)	DMF	684 nm		312
		1% NH_4OH	679 nm		312
	Cu(II)	DMF	684 nm		312
		1% NH_4OH	681 nm		312
	Zn(II)	DMF	679 nm		312
		1% NH_4OH	685 nm		312
$\beta\beta$ = COOH, SO_3H	Fe(III)OH	DMF	676 nm (r.i. 1), 613 (0.20), 345 (0.46)		878
		conc H_2SO_4	753 nm		878
		1% HCl	668 (r.i. 1), 613 (0.32)		878
		0.5% NaOH	678 (r.i. 1), 613 (0.24)		878
		1% NH_4OH	679 (r.i. 1), 613 (0.26)		878
	Co(II)	DMF	684 nm (r.i. 1), 615 (0.22), 350 (0.48)		878
		conc H_2SO_4	740 nm		878
		1% HCl	668 nm (r.i. 1), 610sh (0.32)		878
		0.5% NaOH	676 nm (r.i. 1), 608 (0.18)		878
		1% NH_4OH	679 nm (r.i. 1), 611 (0.20)		878
	Cu(II)	DMF	684 nm (r.i. 1), 620 (0.17), 353 (0.4)		878
		conc H_2SO_4	684 nm, 615, 350		878
		1% HCl	667sh nm (r.i. 0.71), 636 (1)		878
		0.5% NaOH	681 nm (r.i. 1), 613 (0.20)		878

(*Continued*)

Table 2. (*Continued*)

Structure	M	Solvent	Transition Energy (Intensity)	Remark	Ref.
		1% NH_4OH	681 nm (r.i. 1), 613 (0.21)		878
	Zn(II)	DMF	679 nm (r.i. 1), 617 (0.24)		878
		conc H_2SO_4	758sh nm (r.i. 0.82), 735 (1), 694sh (0.42), 667sh (0.30)		878
		1% HCl	685 nm (r.i. 1), 644 (0.75)		878
		0.5% NaOH	683 nm (r.i. 1), 617 (0.15)		878
		1% NH_4OH	685 nm (r.i. 1), 617 (0.16)		878
$\beta\beta$ = SO_3H, Cl	Co(II)	DMF	666 nm, 606sh		879
	Cu(II)	DMF	676 nm, 610		879
$\beta\beta$ = SO_3H, Br	Co(II)	DMF	664 nm, 606sh		879
	Cu(II)	DMF	678 nm, 611		879
R_1 = SO_3Na, $R_6(R_7)$, $R_{10}(R_{11})$, $R_{14}(R_{15})$ = *t*-Bu	Zn(II)	DMF	676 nm (lg ε 5.48), 608 (4.79), 345 (5.14)		880
		MeOH	675 nm (lg ε 5.36), 345 (5.03)		880
R_2 = SO_3Na, $R_6(R_7)$, $R_{10}(R_{11})$, $R_{14}(R_{15})$ = *t*-Bu	Cu(II)	DMF	675 nm (lg ε 5.56), 608 (4.82), 346 (5.11)		880
	Zn(II)	MeOH	674 nm (lg ε 5.5), 607 (4.8), 347 (5.16)		880
R_2 = NH_2, $R_6(R_7)$, $R_{10}(R_{11})$, $R_{14}(R_{15})$ = *t*-Bu	V(IV)O	1,4-dioxane	705.0 nm (lg ε 5.14), 637.5 (4.48), 488.0 (3.66), 443.5 (3.72), 347.5 (4.85), 297.5 (4.32), 220.5 (4.81)		881
	Zn(II)	$CHCl_3$	682 nm (lg ε 5.01), 617 (4.24), 351 (4.71)		778
R_2 = NH_2, $R_6(R_7)$, $R_{10}(R_{11})$, $R_{14}(R_{15})$ = OCH_2(*t*-Bu)	V(IV)O	1,4-dioxane	706.5 nm (lg ε 4.71), 641.5 (4.17), 397.0 (4.16), 347.0 (4.53), 276.5 (4.35), 235.0 (4.49), 210.0 (4.53)		881
$\alpha\beta$ (R_1, R_3) = NH_2, *t*-Bu	V(IV)O	PhCl	806 nm (r.i. 1.65), 709 (0.50), 500sh (0.30), 340 (1)		781
	Co(II)	PhCl	758 nm (r.i. 1.50), 680sh (0.50), 430sh (0.20), 328 (1)		781
	Cu(II)	unknown	770 nm (lg ε 5.25), 740sh (4.78), 683 (4.68), 450 (3.87), 331 (4.69)		781
R_2 = NH_2HCl, R_6, R_7, R_{10}, R_{11}, R_{14}, R_{15} = SC_6H_{13}	Zn(II)	$CHCl_3$	712 nm (lg ε 5.219), 640 (4.581), 439sh (4.507), 363 (4.892), 337 (4.911)		882
R_2 = NH_2HCl, $R_6(R_7)$, $R_{10}(R_{11})$, $R_{14}(R_{15})$ = $SCH_2CH_2N^+Me_3I^-$	2H	DMSO	687.5 nm (lg ε 3.60), 643.5 (2.58), 335 (3.73)	$[Pc]^{++}3I^-Cl^-$	883
	Co(II)	DMSO	680 nm (lg ε 3.46), 316 (3.72)	$[Pc]^{++}3I^-Cl^-$	883
	Zn(II)	DMSO	695 nm (lg ε 3.67), 653.5 (3.61), 356.5 (3.74)	$[Pc]^{+}3I\ Cl$	883
R_2 = NHC_6H_{13} $R_6(R_7)$, $R_{10}(R_{11})$, $R_{14}(R_{15})$ = 	Zn(II)	$CHCl_3$	710sh nm (lg ε 4.80), 688 (5.03), 630 (4.53), 355 (4.84)		877

(*Continued*)

Table 2. (*Continued*)

Structure	M	Solvent	Transition Energy (Intensity)	Remark	Ref.
R_2 = NHPh(4-OMe) $R_6(R_7)$, $R_{10}(R_{11})$, $R_{14}(R_{15})$ = 	Zn(II)	$CHCl_3$	710sh nm (lg ε 4.92), 689 (5.01), 628 (4.49), 353 (4.84)		877
R_2 = NHC_6H_{13}, $R_6(R_7)$, $R_{10}(R_{11})$, $R_{14}(R_{15})$ = SO_3H	Zn(II)	DMF	689 nm (lg ε 5.10), 626 (4.53), 346 (4.96)		877
R_2 = NHPh(4-OMe), $R_6(R_7)$, $R_{10}(R_{11})$, $R_{14}(R_{15})$ = SO_3H	Zn(II)	DMF	694 nm (lg ε 5.13), 627 (4.61), 346 (4.77)		877
$\beta\beta$ = SPh, NHCOMe	Cu(II)	$CHCl_3$	716 nm		667, 734
		DMF	712 nm		667, 734
$\beta\beta$ = SPh, $NHCOC_7H_{15}$	Cu(II)	$CHCl_3$	722 nm		667, 734
		DMF	718 nm		667, 734
$\beta\beta$ = OPh, NHCOMe	Co(II)	$CHCl_3$	688 nm, 623, 334		667
		DMF	682 nm (lg ε 4.87), 621 (4.34), 331 (4.82)		667
		H_2SO_4	822 nm		667
	Cu(II)	$CHCl_3$	690 nm, 625, 335		667
		DMF	687 nm (lg ε 4.89), 623 (4.35), 333 (4.82)		667
		H_2SO_4	825 nm		667
$\beta\beta$ = OPh, $NHCOC_7H_{15}$	Co(II)	$CHCl_3$	690 nm, 625, 333		667
		DMF	681 nm (lg ε 4.89), 624 (4.33), 332 (4.85)		667
		H_2SO_4	760 nm		667
	Cu(II)	$CHCl_3$	689 nm, 633, 335		667
		DMF	687 nm (lg ε 4.86), 625 (4.32), 336 (4.81)		667
		H_2SO_4	776 nm, 757		667
$\beta\beta$ = OPh, NHCOPh(4-$OC_{11}H_{23}$)	Cu(II)	$CHCl_3$	688 nm, 635, 336		667
		DMF	689 nm (lg ε 4.88), 629 (4.34), 338 (4.83)		667
		H_2SO_4	817 nm		667
R_2 = 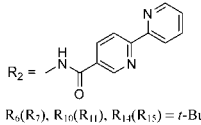 $R_6(R_7)$, $R_{10}(R_{11})$, $R_{14}(R_{15})$ = *t*-Bu	Zn(II)	THF	676 nm (lg ε 5.30), 611 (4.53), 350 (4.86), 289 (4.60), 212 (4.93)		778

(*Continued*)

Table 2. (*Continued*)

Structure	M	Solvent	Transition Energy (Intensity)	Remark	Ref.
R_2, R_3 = 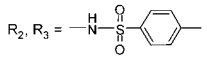 R_6, R_7, R_{10}, R_{11}, R_{14}, $R_{15} = SC_6H_{13}$	Ni(II)	$CHCl_3$	697.0 nm (10^{-4} ε 16.61), 413.0 (3.64), 322.5 (13.32)		876
R_2, R_3 = 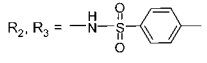 R_6, R_7, R_{10}, R_{11}, R_{14}, $R_{15} = SC_{12}H_{25}$	Ni(II)	$CHCl_3$	697.5 nm (10^{-4} ε 15.82), 414.0 (3.22), 323.0 (13.00)		876
R_2, R_3 = 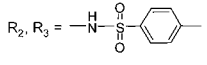 R_6, R_7, R_{10}, R_{11}, R_{14}, $R_{15} = SC_{16}H_{33}$	Ni(II)	$CHCl_3$	698.0 nm (10^{-4} ε 15.11), 413.5 (3.50), 323.5 (13.10)		876
$\alpha\beta$ (R_1, R_3) = NMe_2, *t*-Bu	2H	$CHCl_3$	770 nm (lg ε 5.05), 670sh (4.52), 440sh (4.20), 340 (4.84)		781
	V(IV)O	PhCl	821 nm (r.i. 1.25), 728 (0.40), 450sh (0.25), 337 (1.00)		781
	Mn(II)	benzene	840 nm		530
	Mn(III)	benzene	742 nm, 353		528
	Mn(III)Cl	benzene	845 nm (lg ε 4.60), 555 (4.30), 365 (4.57)		528
	Mn(III)L	py	756 nm, 365	L = py	528
	Co(II)	PhCl	770 nm, 684, 470sh		781
	Cu(II)	PhCl	782 nm (lg ε 5.08), 696 (4.46), 460sh (4.42), 385sh (4.47), 336 (4.89)		781
	Zn(II)	PhCl	786 nm (lg ε 5.03), 700sh (4.54), 450sh (4.09), 340 (4.83)		781
$R_2 = NO_2$, R_6, R_7, R_{10}, R_{11}, R_{14}, R_{15} = Et	Zn(II)	$CHCl_3$	713 nm (lg ε 4.49), 670 (4.43), 650 (4.15), 610 (3.83), 360 (4.31)		850
$R_2 = NO_2$, R_6, R_7, R_{10}, R_{11}, R_{14}, R_{15} = Bu	Zn(II)	$CHCl_3$	713 nm (lg ε 4.51), 672 (4.47), 648 (4.19), 610 (3.90), 356 (4.32)		850
$R_2 = NO_2$, $R_6(R_7)$, $R_{10}(R_{11})$, $R_{14}(R_{15})$ = *t*-Bu	2H	$CHCl_3$	692 nm (lg ε 5.00), 679 (5.01), 644 (4.70), 624 (4.64), 337 (4.80)		516, 517
	V(IV)O	1,4-dioxane	712.5 nm (lg ε 5.08), 685.5 (5.03), 484.0 (3.29), 352.5 (4.91), 210.5 (4.93)		881
$R_2(R_3)$, $R_{10}(R_{11}) = NO_2$, $R_6(R_7)$, $R_{14}(R_{15})$ = *t*-Bu	Zn(II)	DCM	677 nm (r.i. 1), 611 (0.16), 345 (0.23)		884

(*Continued*)

Table 2. (*Continued*)

Structure	M	Solvent	Transition Energy (Intensity)	Remark	Ref.
$R_2(R_3)$, $R_{10}(R_{11}) = NO_2$, $R_6(R_7) = t$-Bu	Zn(II)	DMF	692 nm (r.i. 0.98), 678 (1), 641 (0.29), 618 (0.2), 357 (0.42)		884
$R_2 = NO_2$, R_5, R_8, R_9, R_{10} R_{13}, $R_{16} = C_7H_{15}$	2H	$CHCl_3$	708 nm, 639, 359, 322		885
R_2, $R_{10}(R_{11}) = NO_2$, R_5, R_8, R_{13}, $R_{16} = C_7H_{15}$	2H	$CHCl_3$	720 nm, 690.5, 654, 333		885
$\beta\beta = NO_2$, COOMe	Cu(II)	DMF	714 nm		886
$\beta\beta$ = OH, NO_2	Al(III)OH	DMF	751 nm		667
		H_2SO_4	828 nm		667
	Cr(III)OH	DMF	750 nm		667
		H_2SO_4	850 nm		667
	Co(II)	DMF	716 nm		667
		H_2SO_4	833 nm		667
	Cu(II)	DMF	696 nm		667
		H_2SO_4	845 nm		667
	In(III)Cl	DMF	729 nm		667
$R_2 = NO_2$, R_6, R_7, R_{10}, R_{11}, R_{14}, R_{15} = OPr	Zn(II)	$CHCl_3$	708 nm (lg ε 4.50), 669 (4.45), 651 (4.14), 610 (3.86), 361 (4.32)		850
$\beta\beta = OC_{10}H_7$, NO_2	Cu(II)	$CHCl_3$	693 nm		667
		DMF	687 nm (lg ε 4.69), 612 (4.24), 344 (4.61)		667
		H_2SO_4	801		667
$R_2(R_3)$,$R_{10}(R_{11}) = NO_2$, $R_6(R_7)$, $R_{14}(R_{15}) = OCH_2CH(Me)_2$	2H	THF	696 nm (lg ε 4.27), 678 (4.38), 628 (4.49)	$M = 1.1 \times 10^{-5}$	887
		THF	700 nm (lg ε 4.43), 679 (4.53), 635 (4.53)	$M = 5.5 \times 10^{-6}$	887
		THF	703 nm (lg ε 4.77), 680 (4.86), 644 (4.62)	$M = 1.1 \times 10^{-7}$	887
$R_2 = NO_2$, $R_6(R_7)$, $R_{10}(R_{11})$, $R_{14}(R_{15}) = OCH_2(t$-Bu)	Zn(II)	1,4-dioxane	701.0 nm (lg ε 5.12), 667.5 (5.07), 640.0 (4.67), 606.0 (4.46), 354.0 (4.94), 275.0 (4.70), 211.5 (5.10)		881
$\beta\beta = NO_2$, OCOPh(4-$OC_{14}H_{29}$)	Cu(II)	$CHCl_3$	678 nm		667
		DMF	700 nm		667
R_2 = NO_2, R_5, R_6, R_7, R_8, R_9, R_{10}, R_{13}, R_{12}, R_{13}, R_{14}, R_{15}, R_{16} = OCH_2CF_3	V(IV)O	1,4-dioxane	730.0 nm (lg ε 5.23), 655.5 (4.58), 347.0 (4.76), 267.0 (4.52), 234.0 (4.73)		820
$\beta\beta$ = OPh, NO_2	2H	DMF	676 nm (lg ε 4.83), 610 (4.18), 361 (4.66)		667
		$CHCl_3$	702 nm, 678		667
		H_2SO_4	874 nm, 814		667
	Cr(III)OH	H_2SO_4	850 nm		667
	Co(II)	$CHCl_3$	681 nm		667

(*Continued*)

Table 2. (*Continued*)

Structure	M	Solvent	Transition Energy (Intensity)	Remark	Ref.
		DMF	678 nm (lg ε 4.79), 610 (4.25), 334 (4.62)		667
		DMF	678 nm		470
		H_2SO_4	786 nm		470, 667
	Cu(II)	$CHCl_3$	691 nm		667
		DMF	688 nm (lg ε 4.70), 610 (4.23), 340 (4.58)		667
		H_2SO_4	796 nm		667
$R_2(R_3)$,$R_{10}(R_{11})$ = NO_2, $R_6(R_7)$, $R_{14}(R_{15})$ = OPh(4-*t*-Bu)	2H	THF	693 nm (lg ε 4.66), 680 (4.73), 642 (4.53)	$M = 1.0 \times 10^{-5}$	887
		THF	694 nm (lg ε 4.77), 680 (4.84), 645 (4.54)	$M = 5.0 \times 10^{-6}$	887
		THF	703 nm (lg ε 4.77), 680 (4.86), 644 (4.62)	$M = 1.1 \times 10^{-7}$	887
		THF	696 nm (lg ε 4.94), 681 (5.00), 643 (4.53), 621sh (4.43)	$M = 1.0 \times 10^{-7}$	887
	Co(II)	THF	705 nm (lg ε 4.45), 661 (4.34), 641 (4.32), 597sh (4.00)	$M = 9.2 \times 10^{-6}$	887
	Cu(II)	THF	710 nm (lg ε 4.54), 665 (4.54), 643 (4.45), 604sh (4.18)	$M = 1.0 \times 10^{-5}$	887
		THF	710 nm (lg ε 4.61), 665 (4.59), 643 (4.46), 603sh (4.14)	$M = 5.0 \times 10^{-6}$	887
		THF	711 nm (lg ε 4.59), 665 (4.71), 645 (4.57), 602 (4.25)	$M = 1.0 \times 10^{-6}$	887
$\beta\beta$ = NO_2, OPh(4-*t*-Bu)	2H	$CHCl_3$	714 nm, 683		888
		$CHCl_3$	714 nm, 683, 624, 335		667
		DMF	694 nm		888
		DMF	694 nm (lg ε 4.88), 625 (4.32), 336 (4.82)		667
		H_2SO_4	817 nm, 789		667, 888
	Mg(II)	$CHCl_3$	714 nm		888
		DMF	694 nm		888
	Co(II)	$CHCl_3$	686 nm		888
		$CHCl_3$	686 nm, 626, 332		667
		DMF	677 nm		888
		DMF	677 nm (lg ε 4.88), 621 (4.35), 334 (4.83)		667
		H_2SO_4	784 nm		667, 888
	Cu(II)	$CHCl_3$	698 nm		888
		$CHCl_3$	698 nm, 627, 334		667
		DMF	686 nm		888

(*Continued*)

Table 2. (*Continued*)

Structure	M	Solvent	Transition Energy (Intensity)	Remark	Ref.
		DMF	686 nm (lg ε 4.87), 622 (4.33), 335 (4.84)		667
		H_2SO_4	808 nm		667, 888
$R_5(R_3)$,$R_{10}(R_{11}) = NO_2$, $R_6(R_7)$, $R_{14}(R_{15})$ = 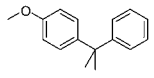	2H	THF	693 nm (lg ε 4.74), 680 (4.81), 643 (4.59)	$M = 8.8 \times 10^{-6}$	887
		THF	693 nm (lg ε 4.85), 681 (4.91), 645 (4.59)	$M = 4.4 \times 10^{-6}$	887
		THF	694 nm (lg ε 4.99), 681 (5.04), 645 (4.54), 621sh (4.45)	$M = 8.8 \times 10^{-7}$	887
$\beta\beta = NO_2$, OPh(4-COOH)	Co(II)	DMF	668 nm		888
		H_2SO_4	768 nm		667
		H_2SO_4	774 nm		888
		DMF	676 nm (lg ε 4.85), 621 (4.32), 332 (4.81)		667
	Cu(II)	DMF	688 nm (lg ε 4.83), 622 (4.30), 335 (4.81)		667
		H_2SO_4	774 nm		667
$\beta\beta = NO_2$, OPh(4-NO_2)	Co(II)	DMF	676 nm (lg ε 4.84), 621 (4.31), 332 (4.81)		667
		DMF	676 nm		888
		H_2SO_4	772 nm		667, 888
	Cu(II)	DMF	686 nm		888
		DMF	686 nm (lg ε 4.85), 625 (4.32), 334 (4.83)		667
		H_2SO_4	794 nm		667, 888
$\beta\beta' = NO_2$, 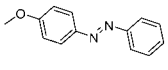	2H	$CHCl_3$	714 nm, 683		667
		DMF	702 nm (lg ε 4.79), 629 (4.27)		667
		H_2SO_4	813 nm, 772		667
	Co(II)	$CHCl_3$	695 nm		667
		DMF	685 nm (lg ε 4.81), 631 (4.22)		667
		H_2SO_4	774 nm		667
	Cu(II)	$CHCl_3$	694 nm		667
		DMF	687 nm (lg ε 4.87), 625 (4.31)		667
		H_2SO_4	791 nm		667
$R_5(R_3) = NO_2$, R_6,R_7, R_{10},R_{11}, R_{14},$R_{15} = SC_6H_{13}$	Zn(II)	$CHCl_3$	710 nm (lg ε 5.269), 638 (4.613), 440 (4.263), 363 (4.860), 337 (4.780)		889
$R_2 = NO_2$, $R_6(R_7)$, $R_{10}(R_{11})$, $R_{14}(R_{15}) = SCH_2CH_2NMe_2$	2H	DMSO	695 nm (lg ε 3.84), 630 (3.91), 343 (3.95)		883
	Co(II)	DMSO	676.5 nm (lg ε 3.61), 308.5 (4.29)		883
	Zn(II)	DMSO	694 nm (lg ε 3.81), 646 (3.63), 357.5 (3.81)		883

(*Continued*)

Table 2. (*Continued*)

Structure	M	Solvent	Transition Energy (Intensity)	Remark	Ref.
$R_2 = NO_2$, $R_6(R_7)$, $R_{10}(R_{11})$, $R_{14}(R_{15}) = SCH_2CH_2NMe_3I$	2H	DMSO	685 nm (lg ε 4.08), 621 (3.49), 356 (3.78)	$[Pc]^{3+}3I^-$	883
	Co(II)	DMSO	678.7 nm (lg ε 3.68), 303.5 (3.95)	$[Pc]^{3+}3I^-$	883
	Zn(II)	DMSO	691.5 nm (lg ε 3.63), 653 (3.47), 357.5 (3.61)	$[Pc]^{3+}3I^-$	883
$R_2 = NO_2$, R_6, R_7, R_{10}, R_{11}, R_{14}, $R_{15} = SC_6H_{13}$	Zn(II)	$CHCl_3$	710 nm (lg ε 5.269), 683 (4.613), 440sh (4.263), 363 (4.860), 337 (4.780)		882
$\beta\beta = NO_2$, SPh	2H	DMF	710 nm		734
	Co(II)	$CHCl_3$	704 nm (lg ε 4.81), 327 (4.64)		470
		$CHCl_3$	704 nm, 327		667
		DMF	698 nm (lg ε 4.52), 334 (4.48)		470
		DMF	694 nm (lg ε 4.52), 628 (4.12), 340 (4.48)		667
		benzene	706 nm (lg ε 4.83), 317 (4.81)		470
		H_2SO_4	844 nm		667
		H_2SO_4	846 nm (lg ε 4.99), 321 (4.90)		470
	Cu(II)	$CHCl_3$	718 nm, 342		667
		$CHCl_3$	718 nm (lg ε 4.82), 342 (4.97)		470
		DMF	710 nm (lg ε 4.86), 632 (4.18), 340 (4.81)		667
		DMF	710 nm (lg ε 4.81), 334 (4.86)		470
		benzene	716 nm (lg ε 4.82), 334 (4.99)		470
		H_2SO_4	846 nm		667
		H_2SO_4	853 nm (lg ε 4.74), 334 (4.64)		470
$\beta\beta = NO_2$, $SPhSO_3H$	Co(II)	DMF	694 nm		470
$\beta\beta = NH_2$, NO_2	Co(II)	DMF	766 nm, 694sh		667
		H_2SO_4	722 nm		667, 773
$\beta\beta = NO_2$, NH_2	Co(II)	DMF	766 nm		773
$\alpha = NC_5H_{10}$, $\beta = NO_2$	Cu(II)	1-ClNp	759 nm		735
$\beta\beta = NO_2$, NHCOMe	Co(II)	DMF	705 nm		773
		DMF	705 nm, 641sh		667
		H_2SO_4	725 nm		667, 773
$\beta\beta = NO_2$, $NHCOC_7H_{15}$	Co(II)	DMF	700 nm		773
		H_2SO_4	725 nm		773
$\beta\beta = NHCOPh$, NO_2	Co(II)	DMF	706 nm, 643sh		667
		DMF	706 nm		773

(*Continued*)

Table 2. (*Continued*)

Structure	M	Solvent	Transition Energy (Intensity)	Remark	Ref.
		H_2SO_4	725 nm		667, 773
$\beta\beta$ = NO_2, NHCOPh(4-$OC_{11}H_{23}$)	Co(II)	$CHCl_3$	695 nm, 628sh		667
		H_2SO_4	725 nm		667
	Cu(II)	$CHCl_3$	700 nm, 629sh		667
		H_2SO_4	725 nm		667
$\beta\beta$ = NO_2, Br	Co(II)	DMF	680 nm		470
		H_2SO_4	773 nm		470
	Cu(II)	H_2SO_4	686 nm		791
		H_2SO_4	743.7 nm	$[Pc]^+$	791
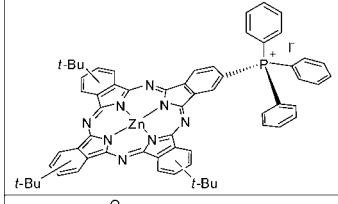	Zn(II)	$CHCl_3$	707 nm (ε 375,000), 665 (235,000), 642 (135,000), 602 (61,000), 358 (152,000)		890
αα = F, ββ = 	2H	DCM	734 nm (lg ε 4.02), 704 (4.01), 670 (3.51), 636 (3.40), 358 (3.63)		682
	Mg(II)	DCM	708 nm (lg ε 4.83), 636 (4.06), 364 (4.43), 318 (4.37)		682
	Ni(II)	DCM	708 nm (lg ε 4.91), 636 (4.23), 342 (4.34), 304 (4.47)		682
αα = F, ββ = 	Mg(II)	DCM	794 nm (lg ε 4.57), 708 (4.09), 478 (4.04), 358(4.34), 322 (4.34)		682
αα = F, ββ = F, 	Mg(II)	DCM	714 nm (lg ε 4.63), 646 (4.07), 362 (4.37)		682
$\alpha\alpha$ = F, $\beta\beta$ = $C(CF_3)_2F$	2H	acetone	690 nm (lg ε 5.15)		891
	Co(II)	acetone	668 nm (lg ε 4.05), 652 (3.90), 366 (3.91), 326 (4.13)	$F_{64}PcCo(acetone)_2$	892
		acetone	710 nm (lg ε 4.74), 582 (4.60), 476 (4.42), 422 (4.50), 330 (4.88)	$F_{64}PcCo(1\text{-triphenylphosphoranylidene-2-propanone})_2$	892

(*Continued*)

Table 2. (*Continued*)

Structure	M	Solvent	Transition Energy (Intensity)	Remark	Ref.
		acetone	710 nm (lg ε 4.76), 578 (4.62), 474 (4.45), 426 (4.48), 340 (4.77)	F_{64}PcCo(1-tributylphosphoranylidene-2-propanone)$_2$	892
R_2 = SO_3Na, R_5, R_6, R_7, R_8, R_9, R_{10}, R_{11}, R_{12}, R_{13}, R_{14}, R_{15}, R_{16} = F	Zn(II)	MeOH	633 nm, 344		880
		DMF	675 nm (lg ε 5.10), 356 (4.92)		880
$\beta\beta$ = Cl, NO_2	Co(II)	DMF	680 nm		667
		H_2SO_4	763 nm		667
	Cu(II)	DMF	683 nm, 640		667
		H_2SO_4	780 nm, 755		667
$\beta\beta$ = Cl, SO_3H	Co(II)	DMF	666 nm, 606sh		667
		$CHCl_3$	670 nm, 606		667
		H_2SO_4	781 nm, 417sh		667
	Cu(II)	DMF	676 nm, 610sh		667
		$CHCl_3$	676 nm, 602sh		667
		H_2SO_4	793 nm, 430sh		667
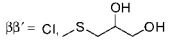	Co(II)	DMF	672 nm, 615, 350		893
	Ni(II)	DMF	688 nm, 635, 344		893
	Cu(II)	DMF	682 nm, 634, 322		893
	Zn(II)	DMF	679 nm, 637, 347		893
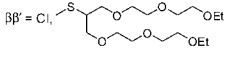	2H	$CHCl_3$	715.5 nm (10^{-4} ε 15.94), 682.5 (13.58), 651.5sh, 620.5 (3.28), 351.5 (7.84), 308.0 (5.28), 238.5 (3.80)		728
	Ni(II)	$CHCl_3$	688.5 nm (10^{-4} ε 21.70), 657.5sh, 619.5 (4.16), 402.5 (2.56), 312.5 (9.46), 261.5 (5.22)		728
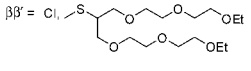	Ti(IV)O	hexane	713 nm (lg ε 4.46), 348, 307		745
		THF	716 nm (lg ε 5.24), 355, 313		745
		$CHCl_3$	720 nm (lg ε 5.27), 353, 316		745
		MeOH	712 nm (lg ε 4.70), 349, 314		745
		DMSO	716 nm (lg ε 5.11), 361, 309		745
	Zn(II)	DMSO	696 nm (lg ε 5.21)		479

(*Continued*)

Table 2. (*Continued*)

Structure	M	Solvent	Transition Energy (Intensity)	Remark	Ref.
ββ′ = Cl, 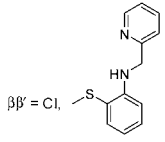	2H	DMF	719 nm (10^{-4} ε 10.12), 695 (12.53), 661 (8.68), 345 (13.29), 311 (14.70)		894
	Ni(II)	H_2SO_4	835 nm (10^{-4} ε 4.99), 741 (1.57), 392 (1.41), 311 (5.73)		894
	Zn(II)	DMF	699 nm (10^{-4} ε 6.12), 632 (1.51), 370 (3.35)		894
ββ′ = Cl, 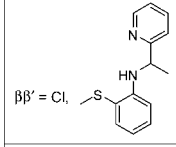	2H	DMF	718 nm (10^{-4} ε 13.19), 694 (15.02), 660 (7.36), 352 (10.78), 309 (11.38)		894
	Ni(II)	H_2SO_4	790 nm (10^{-4} ε 12.28), 701 (4.05), 401 (4.28), 308 (10.13)		894
	Zn(II)	DMF	699 nm (10^{-4} ε 12.39), 630 (2.65), 369 (5.31)		894
ββ′ = Cl, OPh(3,5-$(OMe)_2$)	2H	$CHCl_3$	699 nm, 666sh, 340, 291, 229		871
	Cu(II)	$CHCl_3$	679 nm, 624, 338, 230		871
	Zn(II)	$CHCl_3$	679 nm, 630, 344, 287		871
ββ′ = Cl, 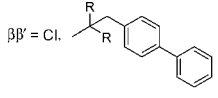	Co(II)	$CHCl_3$	673 nm (lg ε 5.38), 332 (5.01)	R=COOEt	895
	Cu(II)	$CHCl_3$	684 nm (lg ε 5.34), 344 (4.89)	R=$COOC_5H_{11}$	895
	Zn(II)	$CHCl_3$	682 nm (lg ε 5.49), 354 (4.92)	R=COOEt	895
	Pb(II)	$CHCl_3$	723 nm (lg ε 5.31), 357 (4.77)	R=$COOC_5H_{11}$	895
ββ′ = Cl, 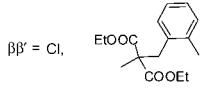	Co(II)	toluene	674 nm, 334		896
		THF	667 nm, 335		896
		$CHCl_3$	673 nm, 332		896
		DMF	668 nm, 335		896
		DMSO	666 nm, 338		896
	Cu(II)	toluene	683 nm, 351		896
		THF	678 nm, 352		896
		$CHCl_3$	683 nm, 345		896
		DMF	678 nm, 352		896
		DMSO	679 nm, 353		896
	Zn(II)	toluene	683 nm, 354		896
		THF	678 nm, 353		896
		$CHCl_3$	682 nm, 353		896

(*Continued*)

Table 2. (*Continued*)

Structure	M	Solvent	Transition Energy (Intensity)	Remark	Ref.
		DMF	680 nm, 351		896
		DMSO	682 nm, 354		896
	Pb(II)	toluene	720 nm, 355		896
		THF	712 nm, 351		896
		$CHCl_3$	722 nm, 355		896
		DMF	709 nm, 349		896
		DMSO	710 nm, 350		896
ββ′ = Cl, 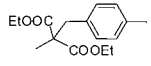	Co(II)	toluene	674 nm, 335		896
		THF	667 nm, 334		896
		$CHCl_3$	673 nm, 333		896
		DMF	667 nm, 335		896
		DMSO	666 nm, 338		896
	Cu(II)	toluene	683 nm, 351		896
		THF	677 nm, 351		896
		$CHCl_3$	683 nm, 345		896
		DMF	678 nm, 352		896
		DMSO	679 nm, 351		896
	Zn(II)	toluene	683 nm, 353		896
		THF	678 nm, 353		896
		$CHCl_3$	682 nm, 353		896
		DMF	680 nm, 353		896
		DMSO	682 nm, 354		896
	Pb(II)	toluene	720 nm, 355		896
		THF	712 nm, 352		896
		$CHCl_3$	722 nm, 355		896
		DMF	709 nm, 350		896
		DMSO	710 nm, 350		896
$\beta\beta$ = Cl, NO_2	Al(III)OH	H_2SO_4	678 nm		791
		H_2SO_4	738.2 nm	$[Pc]^{\cdot}$	791
		H_2SO_4	742.6 nm	$[Pc]^{2+}$	791
		py	678 nm		789

(*Continued*)

Table 2. (*Continued*)

Structure	M	Solvent	Transition Energy (Intensity)	Remark	Ref.
$\beta\beta$ = Cl, OPh(2-NH_2)	Ni(II)	DMF	670 nm (10^{-4} ε 6.85), 618 (3.06), 445 (3.04), 329 (11.24)		897
	Zn(II)	DMF	680 nm (10^{-4} ε 7.16), 638 (3.58), 367 (6.53)		897
$\beta\beta$ = Cl, SPh(2-NH_2)	Ni(II)	DMF	708 nm (10^{-4} ε 11.20), 643 (5.60), 440sh (4.45), 330 (14.04)		897
	Co(II)	DMF	687 nm (10^{-4} ε 7.14), 628 (3.20), 317 (8.65)		897
	Zn(II)	DMF	696 nm (10^{-4} ε 12.82), 642 (4.3), 355 (14.68)		897
$\beta\beta$ = Cl, CH$(COOEt)_2$	Co(II)	$CHCl_3$	669 nm (ε 10^{-4} 8.46), 331 (6.35)		898
	Cu(II)	$CHCl_3$	679 nm (ε 10^{-4} 8.88), 632 (7.04), 343 (8.46)		898
	Pd(II)	$CHCl_3$	662 nm (ε 10^{-4} 9.17), 335 (2.49)		898
$\beta\beta$ = Cl, CH$(COOC_6H_{13})_2$	2H	$CHCl_3$	700 nm (ε 10^{-4} 10.6), 663 (10.9), 632 (9.86), 340 (12.4)		898
$\beta\beta$ = Cl, CH_2COOH	Pd(II)	DMSO	660 nm (ε 10^{-4} 2.47), 603 (5.32), 335 (3.77)		898
$\alpha\alpha$ = Cl, $\beta\beta$ = OBu	Cu(II)	DCB	741 nm		736
	Zn(II)	DCM	723 nm		736
$\alpha\alpha$ = Cl, $\beta\beta$ = OPh	Co(II)	DMSO	690 nm		899
	Zn(II)	DMSO	695 nm		899
$\alpha\alpha$ = Cl, $\beta\beta$ = O(3-py)	Co(II)	DMSO	687 nm		899
	Zn(II)	DMSO	703 nm		899
$\alpha\alpha$ = Cl, $\beta\beta$ = SPh	Al(III)Cl	$CHCl_3$	750 nm		736
	Ti(IV)Cl_2	benzene	768 nm		736
	Cu(II)	DMSO	746 nm		736
	Zn(II)	DMSO	726 nm		736
$\alpha\alpha$ = Cl, $\beta\beta$ = $SC_{10}H_{21}$	Cu(II)	$CHCl_3$	734 nm		736
	Zn(II)	DCM	722 nm		736
$\alpha\alpha$ = Cl, $\beta\beta$ = NHPh, Cl ($\beta \neq \beta$)	Co(II)	DMF	703 nm		900
	Zn(II)	DMF	714 nm		900
$\alpha\alpha$ = Cl, $\beta\beta$ = NHC_8H_{17}, Cl ($\beta \neq \beta$)	Co(II)	benzene	708 nm		900
	Zn(II)	benzene	719 nm		900
$\alpha\alpha$ = Cl, $\beta\beta$ = $N(Et)_2$, Cl ($\beta \neq \beta$)	Co(II)	benzene	704 nm		900
	Zn(II)	benzene	714 nm		900
$\alpha\alpha$ = Cl, $\beta\beta$ = $N(Bu)_2$, Cl ($\beta \neq \beta$)	Co(II)	benzene	705 nm		900
	Zn(II)	benzene	716 nm		900

(*Continued*)

Table 2. (*Continued*)

Structure	M	Solvent	Transition Energy (Intensity)	Remark	Ref.
$\alpha\alpha$ = Cl, $\beta\beta$ = morpholino, Cl ($\beta \neq \beta$)	Co(II)	benzene	707 nm		900
	Zn(II)	benzene	718 nm		900
$\alpha\alpha$ = Cl, $\beta\beta$ = Cl, Oph	Co(II)	DMSO	679 nm		899
	Zn(II)	DMSO	690 nm		899
$\alpha\alpha$ = Cl, $\beta\beta$ = Cl, O(3-py)	Co(II)	DMSO	685 nm		899
	Zn(II)	DMSO	694 nm		899
$\alpha\alpha$ = Cl	Co(I)	DMF	682 nm (10^{-4} ε 3.03), 620sh, 492 (2.08), 318 (4.78)		901
	Co(II)	DMF	680 nm (10^{-1} ε 3.69), 625sh, 312 (4.80)		901
ββ' = Cl, 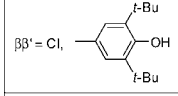	Co(III)	DMF	695 nm (10^{-4} ε 7.88), 625sh, 303 (5.17)		901
$\alpha\alpha$ = OBu, $\beta\beta$ = Cl	2H	DCM	769 nm (10^{-3} ε 128), 680 (52), 331 (61)		389
$\alpha\alpha$ = OMe, $\beta\beta$ = Cl	2H	toluene	736 nm, 711		603
$\alpha\alpha$ = OEt, $\beta\beta$ = Cl	2H	toluene	753 nm (10^{-5} ε 1.35), 726 (1.20)		603
$\alpha\alpha$ = OC_5H_{11}, $\beta\beta$ = Cl	2H	toluene	756 nm (10^{-5} ε 1.36), 735sh		603
	Cu(II)	toluene	739 nm (10^{-5} ε 1.35)		603
$\alpha\alpha'$ = Cl, OPh, $\beta\beta$ = OPh	Co(II)	DMSO	693 nm		899
	Zn(II)	DMSO	700 nm		899
$\alpha\alpha'$ = Cl, O(3-py), $\beta\beta$ = O(3-py)	Co(II)	DMSO	700 nm		899
	Zn(II)	DMSO	713 nm		899
$\alpha\alpha'$ = Cl, O(3-py), $\beta\beta$ = Cl, O(3-py)	Co(II)	DMSO	687 nm		899
	Zn(II)	DMSO	698 nm		899
$R_2(R_3)$, $R_{10}(R_{11})$ = Cl, $R_6(R_7)$, $R_{14}(R_{15})$ = NO_2	2H	1-ClNp	691 nm		787
		H_2SO_4	791 nm, 760		787
	Cu(II)	1-ClNp	708 nm, 685		787
		H_2SO_4	776 nm, 746		787
$R_1(R_4)$, $R_9(R_{12})$ = Cl, $R_6(R_7)$, $R_{14}(R_{15})$ = *t*-Bu	Cu(II)	benzene	683 nm		787
		H_2SO_4	822 nm		787
$R_1(R_4)$, $R_9(R_{12})$ = Cl, $R_6(R_7)$, $R_{14}(R_{15})$ = NO_2	2H	1-ClNp	702 nm, 693		787
		H_2SO_4	809 nm, 772		787
	Cu(II)	1-ClNp	714 nm, 681		787
		H_2SO_4	804 nm, 760		787
$R_2(R_3)$, $R_{10}(R_{11})$ = Cl, $R_6(R_7)$, $R_{14}(R_{15})$ = *t*-Bu	2H	benzene	689 nm, 670		787

(*Continued*)

Table 2. (*Continued*)

Structure	M	Solvent	Transition Energy (Intensity)	Remark	Ref.
		H_2SO_4	839 nm, 804		787
	Co(II)	benzene	668 nm		787
		H_2SO_4	799 nm		787
	Cu(II)	benzene	677 nm		787
		H_2SO_4	812 nm		787
α = Br, $\beta\beta$ = COOH, SO_3H ($\beta \neq \beta$)	Co(II)	DMF	682 nm		312
		1% NH_4OH	688 nm		312
R_1, R_4 = OBu, $R_2(R_3)$ = Br, R_5, R_8, R_9, R_{12}, R_{13}, R_{16} = C_6H_{13}	2H	THF	719 nm (10^{-5} ε 1.47)		902
	In(III)Cl	THF	741 nm (10^{-5} ε 2.25)		902
$R_2(R_3)$, $R_{10}(R_{11})$ = Br, $R_6(R_7)$, $R_{14}(R_{15})$ = *t*-Bu	2H	benzene	689 nm, 670		787
		H_2SO_4	839 nm, 801		787
	Co(II)	benzene	667 nm		787
	Cu(II)	benzene	679 nm		787
		H_2SO_4	807 nm		787
R_2, R_3 = Br, R_6, R_7, R_{10}, R_{11}, R_{14}, R_{15} = Ph(4-*t*-Bu)	Zn(II)	THF	688 nm (r.i. 1.00), 619 (0.169), 362 (0.393)		903
$\beta\beta$ = Br, NO_2	2H	DMF	683 nm, 630		667
		H_2SO_4	805 nm, 760, 720		667
	Al(III)OH	DMF	690 nm		667
		H_2SO_4	800 nm, 758, 730		667
	Cr(III)OH	DMF	688 nm		667
		H_2SO_4	800 nm, 767, 730		667
	Co(II)	DMF	680 nm		667
		H_2SO_4	773 nm		667
	Cu(II)	DMF	680 nm, 640		667
		H_2SO_4	783 nm, 758		667
	In(III)Cl	DMF	700 nm		667
$\beta\beta$= Br, NH_2	Cu(II)	DMF	714 nm, 646sh, 325		667
		H_2SO_4	778 nm		667
$\beta\beta$= Br, NHCOMe	2H	DMF	685 nm (lg ε 4.86), 618 (4.33), 320 (4.82)		667
		H_2SO_4	799 nm, 760		667
	Co(II)	DMF	679 nm (lg ε 4.85), 617 (4.32), 322 (4.81)		667
		H_2SO_4	776 nm		667

(*Continued*)

Table 2. (*Continued*)

Structure	M	Solvent	Transition Energy (Intensity)	Remark	Ref.
	Cu(II)	DMF	680 nm, 631sh, 321		667
		H_2SO_4	781 nm, 756		667
$\beta\beta$ = Br, NHCOPh	Co(II)	DMF	687 nm (lg ε 4.84), 624 (4.31), 324 (4.82)		667
		H_2SO_4	789 nm		667
	Cu(II)	DMF	688 nm, 639sh, 323		667
		H_2SO_4	776 nm, 750		667
$\beta\beta$ = Br, NHCOPh(4-$OC_{11}H_{23}$)	Co(II)	$CHCl_3$	695 nm, 634sh		667
		H_2SO_4	772 nm		667
	Cu(II)	$CHCl_3$	705 nm, 630sh		667
		H_2SO_4	774 nm, 752		667
$\beta\beta$ = Br, SO_3H	Co(II)	DMF	664 nm, 606sh		667
		$CHCl_3$	674 nm, 613		667
		H_2SO_4	791 nm, 417		667
	Cu(II)	DMF	678 nm, 611		667
		$CHCl_3$	667 nm, 611		667
		H_2SO_4	791 nm, 430sh		667
$\beta\beta$ = Br, COOH	Fe(II)	DMF	676 nm		904
		H_2O + 1% NH_4OH	689 nm		904
	Co(II)	DMF	676 nm, 638		904
		DMF	676 nm, 636		312
		H_2O +1% NH_4OH	683 nm, 622sh		904
		1% NH_4OH	683 nm		312
	Cu(II)	DMF	647 nm		312
		DMF	647 nm		904
		1% NH_4OH	650 nm		312
		H_2O + 1 % NH_4OH	650 nm		904
R_2 = I, $R_6(R_7)$, $R_{10}(R_{11})$, $R_{14}(R_{15})$ = *t*-Bu	Cu(II)	DCB	682 nm (lg ε 5.34), 613 (4.61), 346 (4.85)		808
	Zn(II)	$CHCl_3$	679 nm (lg ε 5.1), 612 (4.3), 351 (4.7)		755
$R_5(R_3)$, $R_{10}(R_{11})$ = NO_2, $R_6(R_7)$ = *t*-Bu, $R_{14}(R_{15})$ = I	Zn(II)	DMF	698 nm (r.i. 0.98), 680 (1), 644 (0.32), 620 (0.25), 358 (0.43), 280 (0.35)		884
R_2, $R_6(R_7)$, $R_{10}(R_{11})$, $R_{14}(R_{15})$ = I	Zn(II)	$CHCl_3$	679 nm (lg ε 5.2), 612 (4.5), 353 (4.8)		755
R_2 = SO_2Pr, $R_6(R_7)$, $R_{10}(R_{11})$, $R_{14}(R_{15})$ = I	Zn(II)	$CHCl_3$	683 nm (lg ε 5.3), 675 (5.3), 612 (4.7), 353 (5.0)		755

(*Continued*)

Table 2. (*Continued*)

Structure	M	Solvent	Transition Energy (Intensity)	Remark	Ref.
R_2 = *t*-Bu, $R_6(R_7)$, $R_{10}(R_{11})$ =SO_2Pr, $R_{14}(R_{15})$ = I	Co(II)	$CHCl_3$	666 nm (lg ε 5.1), 604 (4.6), 327 (4.9)		755
	Zn(II)	$CHCl_3$	682 nm (lg ε 5.3), 672 (5.3), 609 (4.5), 352 (4.8)		755
R_2 = I, R_3 = $CCC(CH_3)_2OH$, R_6, R_7, R_{10}, R_{11}, R_{14}, R_{15} = OBu	Zn(II)	THF	691 nm (lg ε 5.11), 669 (5.03), 358 (4.90)		905
R_2 = I, R_3 = $CCC(CH_3)_2OH$, $R_6(R_7)$, $R_{10}(R_{11})$, R_{14} (R_{15}) = *t*-Bu	Zn(II)	THF	688 nm (lg ε 5.14), 671 (5.06), 354 (4.86)		905
R_2 = I, R_3 = CCH, R_6, R_7, R_{10}, R_{11}, R_{14}, R_{15} = OBu	Zn(II)	THF	691 nm (lg ε 5.02), 669 (4.96), 358 (4.88)		905
R_2 = I, R_3 = CCH, $R_6(R_7)$, $R_{10}(R_{11})$, R_{14} (R_{15}) = *t*-Bu	Zn(II)	THF	688 nm (lg ε 5.05), 669 (4.99), 353 (4.81)		905
R_2 = I, $R_6(R_7)$, $R_{10}(R_{11})$, $R_{14}(R_{15})$ = *t*-Bu	2H	$CHCl_3$	695 nm (lg ε 5.0), 666 (5.1), 641 (4.6), 609 (4.4), 343 (4.9)		807
	Co(II)	$CHCl_3$	670 nm (lg ε 5.2), 606 (4.6), 329 (4.9)		818
	Zn(II)	THF	672 nm		906
		THF	672 nm		907
R_2 = I, R_6, R_7, R_{10}, R_{11}, R_{14}, R_{15} = SO_2Pr	2H	$CHCl_3$	705 nm (lg ε 5.33), 668 (5.26), 640 (4.1), 610 (4.5), 355 (4.88), 283 (4.36)		832
	Ni(II)	$CHCl_3$	686 nm (lg ε 5.6), 617sh (4.7), 376 (4.9)		756
	Zn(II)	$CHCl_3$	703 nm (lg ε 5.2), 669 (5.1), 643sh (4.6), 609sh (4.4), 368 (4.8)		756
R_2, $R_6(R_7)$, $R_{10}(R_{11})$ = I, R_{14}, R_{15} = SO_2Pr	Zn(II)	$CHCl_3$	689 nm (lg ε 5.2), 678 (5.1), 643 (4.7), 361 (4.9)		756
R_2, R_3 = I, R_6, R_7, R_{10}, R_{11}, R_{14}, R_{15} = OBu	Zn(II)	1,4-dioxane	688 nm (lg ε 5.1), 674 (5.1), 612 (4.4), 356 (4.9)		814
R_2, R_3 = I, $R_6(R_7)$, $R_{10}(R_{11})$, $R_{14}(R_{15})$ = *t*-Bu	Zn(II)	DCM	688 nm (lg ε 4.9), 674 (4.8), 611 (4.2), 352 (4.6)		814
R_2, R_6, R_{10} = I, R_{14} = *t*-Bu	Zn(II)	THF	673 nm (lg ε 5.31), 607 (4.56), 352 (4.89)		556
R_1, R_5, R_9 = I, $R_{13}(R_{15})$ = *t*-Bu	Zn(II)	THF	679 nm (lg ε 5.26), 611 (4.52), 339 (4.72)		556
$R_2(R_3)$, $R_{10}(R_{11})$ = *t*-Bu, $R_6(R_7)$, $R_{14}(R_{15})$ = NO_2	2H	1-ClNp	701 nm, 689		787
		benzene	691 nm, 681		787
	Cu(II)	1-ClNp	716 nm, 676		787
		benzene	701 nm, 670		787
R_2 = 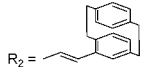 R_6, R_7, R_{10}, R_{11}, R_{14}, R_{15} = OBu	Zn(II)	$CHCl_3$	692 nm (lg ε 5.14), 622 (4.4), 355 (4.95), 291 (4.68)		908
R_2 = 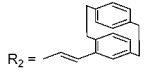 R_6, R_7, R_{10}, R_{11}, R_{14}, R_{15} = SO_2Pr	Ni(II)	$CHCl_3$	705 nm (lg ε 4.81), 677 (4.96), 615(4.37), 347 (4.79), 300 (4.66), 267 (4.63)		908

(*Continued*)

Table 2. (*Continued*)

Structure	M	Solvent	Transition Energy (Intensity)	Remark	Ref.
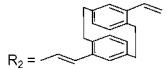 R_6, R_7, R_{10}, R_{11}, R_{14}, R_{15} = OBu	Zn(II)	$CHCl_3$	692 nm (lg ε 4.94), 620 (4.26), 356 (4.92), 276 (4.79)		908
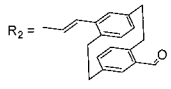 $R_6(R_7)$, $R_{10}(R_{11})$, $R_{14}(R_{15})$ = *t*-Bu	Zn(II)	$CHCl_3$	693 nm (lg ε 5.07), 620 (4.36), 351 (4.82), 293 (4.59)		909
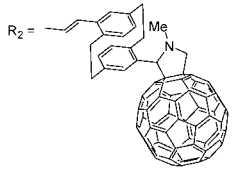 $R_6(R_7)$, $R_{10}(R_{11})$, $R_{14}(R_{15})$ = *t*-Bu	Zn(II)	$CHCl_3$	692 nm (lg ε 5.16), 621 (4.47), 435 (4.32),347 (5.04), 256 (5.23)		909
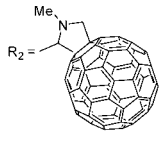 $R_6(R_7)$, $R_{10}(R_{11})$, $R_{14}(R_{15})$ = *t*-Bu	2H	$CHCl_3$	700 nm (lg ε 5.0), 668 (5.0), 648 (4.6), 607 (4.3), 426 (3.7), 339 (5.0)		807
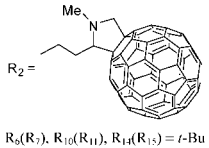 $R_6(R_7)$, $R_{10}(R_{11})$, $R_{14}(R_{15})$ = *t*-Bu	Zn(II)	$CHCl_3$	679 nm (lg ε 5.22), 613(4.45), 346(4.91), 256(5.10)		805

(*Continued*)

Table 2. (*Continued*)

Structure	M	Solvent	Transition Energy (Intensity)	Remark	Ref.
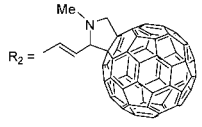 $R_6(R_7)$, $R_{10}(R_{11})$, $R_{14}(R_{15}) = t$-Bu	Zn(II)	$CHCl_3$	686 nm(lg ε 5.17), 617(4.51), 350(4.94), 257(5.12)		805
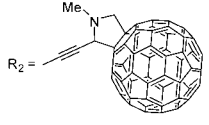 $R_6(R_7)$, $R_{10}(R_{11})$, $R_{14}(R_{15}) = t$-Bu	Zn(II)	$CHCl_3$	689 nm(lg ε 5.14), 678(5.12), 615(4.51), 351(4.96), 255(5.11)		805
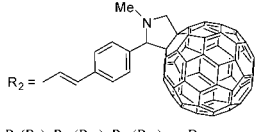 $R_6(R_7)$, $R_{10}(R_{11})$, $R_{14}(R_{15}) = t$-Bu	Zn(II)	$CHCl_3$	692 nm (lg ε 5.19), 621 (4.48),435 (4.32), 347 (5.04), 256 (5.20)		832
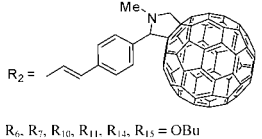 R_6, R_7, R_{10}, R_{11}, R_{14}, $R_{15} = OBu$	Zn(II)	$CHCl_3$	694 nm (lg ε 5.12), 622 (4.55), 435 (4.39), 357 (4.99), 257 (5.07)		757
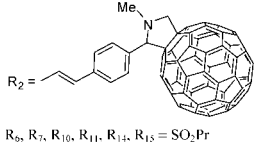 R_6, R_7, R_{10}, R_{11}, R_{14}, $R_{15} = SO_2Pr$	Pd(II)	$CHCl_3$	698 nm (lg ε 4.98), 665 (5.08), 644 (4.77), 605 (4.56), 432 (4.05), 342 (5.02), 257 (5.21)		832

(*Continued*)

Table 2. (*Continued*)

Structure	M	Solvent	Transition Energy (Intensity)	Remark	Ref.
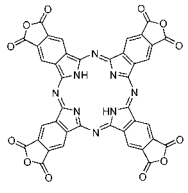	2H	DMF:DMSO = 9:1 v/v	713 nm (ε 148,000), 687 (135,500), 653 (63,100), 625 (46,800), 350 (85,400)		910
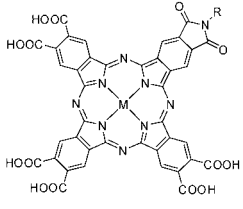	Al(III)OH	DMSO	708 nm (r.i. 1.80), 683 (0.45), 536 (0.25), 338 (1)	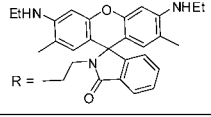	761
	Co(II)	DMSO	681 nm (r.i. 1.13), 610sh (0.60), 536 (0.37), 365 (1)	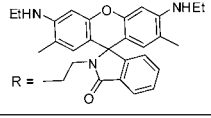	761
		DMSO	678 nm (r.i. 0.90), 561 (0.10), 329 (1)	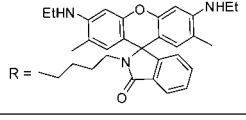	761
		DMSO	675 nm (r.i. 1), 566 (1.16), 337 (1)	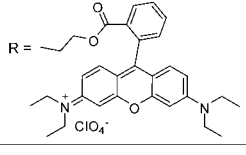	761

(*Continued*)

Table 2. (*Continued*)

Structure	M	Solvent	Transition Energy (Intensity)	Remark	Ref.
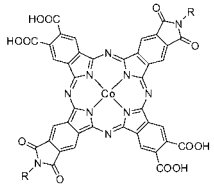	Co(II)	DMSO + AcOH	686 nm (r.i. 1.25), 630sh (1.06), 535 (0.42), 340 (1)	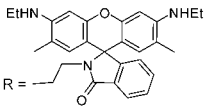	761
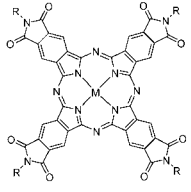	2H	DMSO:benzene = 1:4 v/v	644 nm (ε 13,300)	R = $C_{10}H_{21}$	910
	Al(III)OH	DMSO	701 nm (r.i. 2.89), 665sh (0.53), 625 (0.62), 374 (1)	R = $CH_2CH_2SO_3H$	594
		H_2O	698 nm (r.i. 1.90), 655sh (0.62), 625 (0.54), 356 (1)	R = $CH_2CH_2SO_3H$	594
		0.1M HCl	699 nm (r.i. 1.56), 665sh (0.76), 625 (0.59), 366 (1)	R = $CH_2CH_2SO_3H$	594
		0.01% NaOHaq	693 nm (lg ε 5.38), 650sh (4.73), 610 (4.80), 356 (4.91)	R = $CH_2CH_2SO_3H$	594
		DMSO	701 nm (r.i. 1.45), 657 (0.93), 362 (1)	R = $(CH_2)_2NEt_2$	911
	Fe(II)	DMSO	683 nm (r.i. 1.55), 615sh (0.70), 362 (1)	R = $CH_2CH_2SO_3H$	594
		H_2O	655 nm (r.i. 0.92), 345 (1)	R = $CH_2CH_2SO_3H$	594
		0.1M HCl	657 nm (r.i. 0.95), 347 (1)	R = $CH_2CH_2SO_3H$	594
		0.01% NaOHaq	677 nm (lg ε 5.01), 610sh (4.51), 346 (4.79)	R = $CH_2CH_2SO_3H$	594
		H_2O	676br nm	R = $CH_2CH_2SO_2N(Me)CH_2OCOH$	594
		0.01% NaOHaq	680 nm, 654sh	R = $CH_2CH_2SO_2N(Me)CH_2OCOH$	594
		$CHCl_3$	697sh nm, 655	R = $CH_2CH_2SO_2N(Me)CH_2OCOEt$	594
		acetone	598 nm	R = $CH_2CH_2SO_2N(Me)CH_2OCOEt$	594
		DMSO	686 nm (r.i. 1.05), 621 (0.70), 355 (1)	R = $(CH_2)_2NEt_2$	911
	Co(II)	DMSO	686 nm (r.i. 1.60), 623sh (0.70), 348 (1)	R = $CH_2CH_2SO_3H$	594
		H_2O	642 nm (r.i. 1.15), 325 (1)	R = $CH_2CH_2SO_3H$	594
		0.1M HCl	642 (r.i. 1.06), 333 (1)	R = $CH_2CH_2SO_3H$	594
		0.01% NaOHaq	672 nm (lg ε 5.04), 605sh (4.53), 330 (4.89)	R = $CH_2CH_2SO_3H$	594
		H_2O	641 nm	R = $CH_2CH_2SO_2N(Me)CH_2OCOH$	594
		0.01% NaOHaq	670 nm, 655sh	R = $CH_2CH_2SO_2N(Me)CH_2OCOH$	594
		DMSO	684 nm (r.i. 2.00), 615 (0.65), 354 (1)	R = $(CH_2)_2NEt_2$	911
		$CHCl_3$	676 nm	R = $CH_2CH_2SO_2N(Me)CH_2OCOEt$	594

(*Continued*)

Table 2. (*Continued*)

Structure	M	Solvent	Transition Energy (Intensity)	Remark	Ref.
		acetone	673 nm	R = $CH_2CH_2SO_2N(Me)CH_2OCOEt$	594
	Zn(II)	$CHCl_3$	697 nm (10^{-4} ε 14.0), 630 (2.7), 395sh, 365 (3.6)	R = $C_{10}H_{21}$	912
		DCM	696 nm (10^{-4} ε 7.2), 645 (4.0), 396sh, 361 (4.1)	R = $C_{10}H_{21}$	912
		CCl_4	695 nm (10^{-4} ε 5.2), 643 (2.9), 400sh, 362 (3.7)	R = $C_{10}H_{21}$	912
		ethylacetate	687 nm (10^{-4} ε 3.7), 643 (4.3), 399sh, 357 (4.1)	R = $C_{10}H_{21}$	912
		MeCN	712 nm (10^{-4} ε 2.8), 645 (2.9), 402sh, 359 (3.4)	R = $C_{10}H_{21}$	912
		DMF	697 nm (10^{-4} ε 4.9), 652 (4.4), 400sh, 357 (3.2)	R = $C_{10}H_{21}$	912
		DMSO	632 nm (10^{-4} ε 2.4), 401sh, 355 (3.1)	R = $C_{10}H_{21}$	912
		THF	690 nm (10^{-4} ε 6.0), 643 (3.9), 397sh, 360 (4.2)	R = $C_{10}H_{21}$	912
		toluene	697 nm (10^{-4} ε 9.0), 665 (2.8), 632 (2.5) 397sh, 359 (4.1)	R = $C_{10}H_{21}$	912
		benzene	695 nm (10^{-4} ε 5.4), 645 (3.3), 393sh, 358 (3.6)	R = $C_{10}H_{21}$	912
		$PhNO_2$	705 nm (10^{-4} ε 14.0), 635 (2.4)	R = $C_{10}H_{21}$	912
		PhCl	701 nm (10^{-4} ε 11.1), 632 (2.5), 397sh, 366 (3.9)	R = $C_{10}H_{21}$	912
		DCB	703 nm (10^{-4} ε 15.6), 632 (2.5), 397sh, 368 (4.2)	R = $C_{10}H_{21}$	912
		bromobenzene	703 nm (10^{-4} ε 13.5), 633 (2.6), 397sh, 367 (3.9)	R = $C_{10}H_{21}$	912
		py	702 nm (10^{-4} ε 9.1), 650 (3.1), 400sh, 365 (3.7)	R = $C_{10}H_{21}$	912
		1,4-dioxane	691 nm (10^{-4} ε 8.0), 643 (3.2), 397sh, 363 (4.4)	R = $C_{10}H_{21}$	912
		DMSO	695 nm (r.i. 1.60), 649sh (0.70), 352 (1)	R = $CH_2CH_2SO_3H$	594
		H_2O	690sh nm (r.i. 0.69), 648 (1.18), 356 (1)	R = $CH_2CH_2SO_3H$	594
		0.1M HCl	690sh nm (r.i. 0.65), 649 (1.11), 357 (1)	R = $CH_2CH_2SO_3H$	594
		0.01% NaOHaq	682 nm (lg ε 5.25), 612 (4.61), 350 (4.95)	R = $CH_2CH_2SO_3H$	594
		DMSO	703 nm (r.i. 2.75), 657 (1.05), 360 (1)	R = $(CH_2)_2NEt_2$	911
	2H	DMSO:benzene = 1:4 v/v	644 nm (ε 13,300)	R = 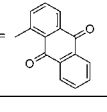	910

(*Continued*)

Table 2. (*Continued*)

Structure	M	Solvent	Transition Energy (Intensity)	Remark	Ref.
		DMF	693 nm (ε 42,800), 650 (35,500), 519 (29,000), 418 (412,000)	R = 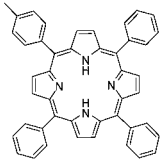	910
		DMSO:benzene = 1:4 v/v	648 nm (ε 13,500)	R = 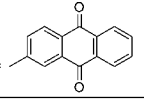	910
	Co(II)	DMSO	683 nm (r.i. 0.60), 565 (3.90), 354 (1)	R = 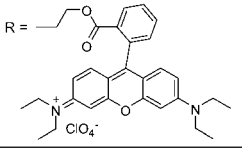	761
	Al(III)OH	H_2O + NaOH	688 nm (r.i. 1.45), 618 (0.55), 360 (1)	R = 	591
	Fe(II)	H_2O + NaOH	678 nm (r.i. 1.25), 335 (1)		591
	Co(II)	H_2O + NaOH	674 nm (r.i. 0.95), 330 (1)		591
	Cu(II)	H_2O + 1% NH_4OH	681 nm (r.i. 1.41), 611 (0.85), 347 (1)		591
		H_2O	633 nm (r.i. 1.08), 350 (1)		591
		H_2O + 0.5% NaOH	674 nm (r.i. 1.06), 633 (1), 355 (1)		591
	Zn(II)	H_2O	646 nm (r.i. 0.90), 352 (1)		591
		H_2O + 1% NH_4OH	689 nm (r.i. 2.23), 620.5 (0.41), 352 (1)		591
		H_2O + NaOH	680sh nm (r.i. 1.15), 657 (0.95), 358 (1)		591
	Al(III)OH	$CHCl_3$	704 nm (r.i. 1.80), 611 (0.50), 353 (1)	R = 	591
	Fe(II)	$CHCl_3$: MeOH = 20:1	695 nm (r.i. 1.55), 628 (0.90), 335 (1)		591
	Co(II)	$CHCl_3$	689 nm (r.i. 1.10), 334 (1)		591
	Cu(II)	$CHCl_3$	694.5 nm (r.i. 1.95), 360.5 (1)		591
	Zn(II)	$CHCl_3$	699 nm (r.i. 1.80), 646 (0.60), 357 (1)		591

(*Continued*)

Table 2. (*Continued*)

Structure	M	Solvent	Transition Energy (Intensity)	Remark	Ref.
$\beta\beta$ = $CONCH_3R$	Co(II)	DMSO	684 nm (r.i. 1.66), 610 (0.45), 348 (1)	R = 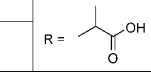	591
		0.1% NaOH	674 nm (r.i. 1.34), 610 (0.43), 332 (1)		591
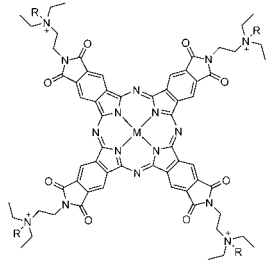	Al(III)OH	DMSO	699 nm (r.i. 1.45), 625 (0.63), 365 (1)	R = Me, $[Pc]^{4+}4I^-$	911
		H_2O	697 nm (r.i. 1.07), 659 (0.90), 358 (1)	R = Me, $[Pc]^{4+}4I^-$	911
		EtOH	699 nm (r.i. 1.25), 650 (0.52), 622 (0.43), 361 (1)	R = Me, $[Pc]^{4+}4OSO_2Ph(4\text{-}Me)^-$	911
		DMSO	700 nm (r.i. 1.82), 628 (0.50), 367 (1)	R = Me, $[Pc]^{4+}4OSO_2Ph(4\text{-}Me)^-$	911
		H_2O	699 nm (r.i. 0.75), 657 (0.67), 358 (1)	R = Me, $[Pc]^{4+}4OSO_2Ph(4\text{-}Me)^-$	911
		EtOH	697 nm (r.i. 3.73), 626 (0.60), 359 (1)	R = Me, $[Pc]^{4+}4PO_2(OMe)_2$	911
		DMSO	699 nm (r.i. 4.71), 624 (0.40), 374 (1)	R = Me, $[Pc]^{4+}4PO_2(OMe)_2$	911
		H_2O	698 nm (r.i. 1.48), 660 (0.98), 625sh (0.23), 361 (1)	R = Me, $[Pc]^{4+}4PO_2(OMe)_2$	911
		EtOH	698 nm (r.i. 1.55), 655 (0.65), 623 (0.53), 362 (1)	R = Et, $[Pc]^{4+}4OSO_3Et^-$	911
		DMSO	704 nm (r.i. 1.75), 631 (0.55), 367 (1)	R = Et, $[Pc]^{4+}4OSO_3Et^-$	911
		H_2O	690 nm (r.i. 0.75), 655 (0.73), 355 (1)	R = Et, $[Pc]^{4+}4OSO_3Et^-$	911
	Fe(II)	EtOH	690 nm (r.i. 0.77), 618 (0.20), 352 (1)	R = Et, $[Pc]^{4+}4OSO_3Et$	911
		DMSO	689 nm (r.i. 0.95), 618 (0.45), 360 (1)	R = Et, $[Pc]^{4+}4OSO_3Et^-$	911
		H_2O	650 nm (r.i. 0.50), 350 (1)	R = Et, $[Pc]^{4+}4OSO_3Et^-$	911
	Co(II)	DMSO	684 nm (r.i. 1.85), 615 (0.50), 354 (1)	R = Me, $[Pc]^{4+}4I^-$	911
		H_2O	655 nm (r.i. 0.98), 330 (1)	R = Me, $[Pc]^{4+}4I$	911
		H_2O	624 nm (r.i. 0.70), 325 (1)	R = Me, $[Pc]^{4+}4OSO_3Me^-$	911
		EtOH	685sh nm (r.i. 0.57), 610 (0.73), 325 (1)	R = Me, $[Pc]^{4+}4OSO_2Ph(4\text{-}Me)^-$	911
		DMSO	685 nm (r.i. 1.76), 618 (0.63), 354 (1)	R = Me, $[Pc]^{4+}4OSO_2Ph(4\text{-}Me)^-$	911
		H_2O	624 nm (r.i. 0.70), 325 (1)z	R = Me, $[Pc]^{4+}4OSO_2Ph(4\text{-}Me)$	911
		EtOH	681 nm (r.i. 1.00), 620 (0.50), 331 (1)	R = Me, $[Pc]^{4+}4PO_2(OMe)_2$	911
		DMSO	684 nm (r.i. 1.43), 623 (0.63), 339 (1)	R = Me, $[Pc]^{4+}4PO_2(OMe)_2$	911
		H_2O	657 nm (r.i. 0.83), 326 (1)	R = Me, $[Pc]^{4+}4PO_2(OMe)_2$	911
		EtOH	679 nm (r.i. 1.55), 655 (0.57), 327 (1)	R = Et, $[Pc]^{4+}4OSO_3Et^-$	911
		DMSO	683 nm (r.i. 1.75), 615 (0.68), 354 (1)	R = Et, $[Pc]^{4+}4OSO_3Et^-$	911
		H_2O	627 nm (r.i. 0.60), 325 (1)	R = Et, $[Pc]^{4+}4OSO_3Et^-$	911
	Zn(II)	DMSO	704 nm (r.i. 3.50), 630 (0.63), 359 (1)	R = Me, $[Pc]^{4+}4I^-$	911
		H_2O	655 nm (r.i. 1.10), 356 (1)	R = Me, $[Pc]^{4+}4I^-$	911
		EtOH	687 nm (r.i. 1.13), 655 (1.10), 356 (1)	R = Me, $[Pc]^{4+}4OSO_2Ph(4\text{-}Me)^-$	911

(*Continued*)

Table 2. (*Continued*)

Structure	M	Solvent	Transition Energy (Intensity)	Remark	Ref.
		DMSO	704 nm (r.i. 2.54), 635 (0.64), 356 (1)	R = Me, $[Pc]^{4+}4OSO_3Ph(4\text{-}Me)^-$	911
		H_2O	658 nm (r.i. 0.93), 354 (1)	R = Me, $[Pc]^{4+}4OSO_3Ph(4\text{-}Me)^-$	911
		EtOH	691 nm (r.i. 2.40), 655 (2.14), 356 (1)	R = Me, $[Pc]^{4+}4PO_2(OMe)_2$	911
		DMSO	706 nm (r.i. 2.67), 635 (0.77), 357 (1)	R = Me, $[Pc]^{4+}4PO_2(OMe)_2$	911
		H_2O	690sh nm (r.i. 1.00), 656 (1.35), 358 (1)	R = Me, $[Pc]^{4+}4PO_2(OMe)_2$	911
		EtOH	695 nm (r.i. 1.20), 653 (1.15), 360 (1)	R = Et, $[Pc]^{4+}4OSO_3Et^-$	911
		DMSO	704 nm (r.i. 3.05), 635 (0.61), 355 (1)	R = Et, $[Pc]^{4+}4OSO_3Et^-$	911
		H_2O	660 nm (r.i. 0.85), 357 (1)	R = Et, $[Pc]^{4+}4OSO_3Et^-$	911
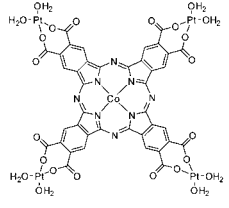	Co(II)	CCl_4	725 nm, 483, 420		590
		H_2O	683 nm, 239		590
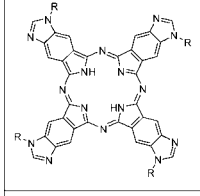	2H	DMF	713 nm, 638, 271, 225, 217, 210, 192	R = Me	913
		DMF	734 nm, 715, 266	R = Ph	913
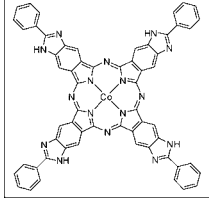	Co(II)	DMF	714 nm		777
		conc H_2SO_4	806 nm		777

(*Continued*)

Table 2. (*Continued*)

Structure	M	Solvent	Transition Energy (Intensity)	Remark	Ref.
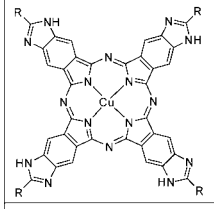	Cu(II)	H_2SO_4	761 nm, 310	R = Me	914
		DMF	711 nm, 650	R = C_5H_{11}	914
		H_2SO_4	802 nm, 426, 310		914
		DMF	694 nm, 643	R = Pr	914
		H_2SO_4	786 nm, 426, 310		914
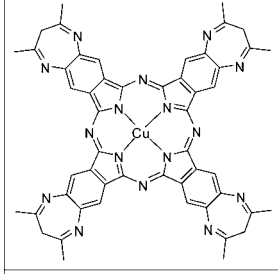	Cu(II)	H_2SO_4	798 nm, 772, 310		914
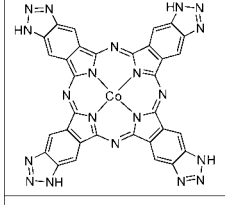	Co(II)	DMF	753 nm		915
		NaOH (5%)	748 nm		915
		H_2SO_4	807 nm		915
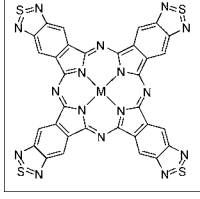	Co(II)	H_2SO_4	840 nm		915
	Cu(II)	H_2SO_4	830 nm (ε 76,400), 740 (16,800), 580 (2,800), 420 (10,200), 340 (65,200)		916

(*Continued*)

Table 2. (*Continued*)

Structure	M	Solvent	Transition Energy (Intensity)	Remark	Ref.
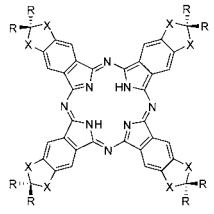	2H	DCM	700 nm, 660, 638, 580, 340, 285	X = CH_2, R = C_6H_{13}	917
		DCM	700 nm, 660, 638, 580, 340, 285	X = CH_2, R = C_7H_{15}	917
		DCM	700 nm, 660, 638, 580, 340, 285	X = CH_2, R = C_8H_{17}	917
		DCM	700 nm, 660, 638, 580, 340, 285	X = CH_2, R = C_9H_{19}	917
		DCM	700 nm, 660, 638, 580, 340, 285	X = CH_2, R = $C_{10}H_{21}$	917
		DCM	700 nm, 660, 638, 580, 340, 285	X = CH_2, R = $C_{11}H_{23}$	917
		DCM	700 nm, 660, 638, 580, 340, 285	X = CH_2, R = $C_{12}H_{25}$	917
		toluene	691 nm, 651, 645, 590, 429, 348	X = O, R = C_2H_5	917
		toluene	690 nm, 653, 645, 595, 430, 350	X = O, R = C_5H_{11}	917
		toluene	690 nm, 653, 645, 595, 430, 350	X = O, R = C_6H_{13}	917
		toluene	690 nm, 653, 645, 595, 430, 350	X = O, R = C_7H_{15}	917
		toluene	690 nm, 653, 645, 595, 430, 350	X = O, R = C_8H_{17}	917
		toluene	692 nm, 651, 645, 595, 430, 350	X = O, R = C_9H_{19}	917
		toluene	691 nm, 651, 645, 595, 430, 350	X = O, R = $C_{10}H_{21}$	917
		toluene	691 nm, 651, 645, 595, 430, 350	X = O, R = $C_{11}H_{23}$	917
		toluene	692 nm, 651, 638, 591, 428, 349	X = O, R = $C_{12}H_{25}$	917
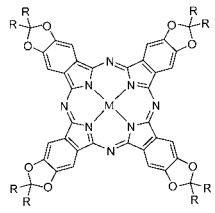	2H	$CHCl_3$	693 nm, 653, 593, 421, 348	R = Me	600
		DMF	692 nm, 658	R = Me	600
		spin-coated film	620 nm	R = C_5H_{11}	691
		spin-coated film	699 nm, 658	R = C_6H_{13}	691
		spin-coated film	699 nm, 658	R = C_7H_{15}	691
		spin-coated film	699 nm, 658	R = C_8H_{17}	691
		spin-coated film	699 nm, 658	R = C_9H_{19}	691
		spin-coated film	699 nm, 658	R = $C_{10}H_{21}$	691
		spin-coated film	635 nm	R = $C_{11}H_{23}$	691
		spin-coated film	635 nm	R = $C_{12}H_{25}$	691
	Zn(II)	$CHCl_3$	665 nm, 638, 600, 363	R = Me	600
		DMF	670 nm	R = Me	600
	Sm(III)OAc	$CHCl_3$	676 nm, 610, 420, 357	R = Me	600
	Eu(III)OAc	$CHCl_3$	671 nm, 602, 410, 359	R = Me	600
	Tb(III)OAc	$CHCl_3$	677 nm, 606, 417, 353	R = Me	600
	Dy(III)OAc	$CHCl_3$	675 nm, 604, 418, 358	R = Me	600

(*Continued*)

Table 2. (*Continued*)

Structure	M	Solvent	Transition Energy (Intensity)	Remark	Ref.
	Yb(III)Oac	$CHCl_3$	677 nm, 607, 410, 360	R = Me	600
	Lu(III)OAc	$CHCl_3$	676 nm, 605, 410, 355	R = Me	600
		DMF	668 nm	R = Me	600
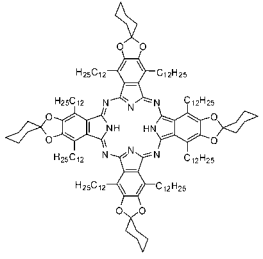	2H	spin-coated film	744 nm, 711		691
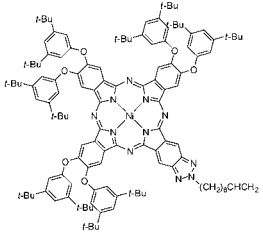	Ni(II)	DCM	707 nm (r.i.1.00), 675 (0.957), 651 (0.322), 610 (0.230), 319 (0.645), 308 (0.653)		918
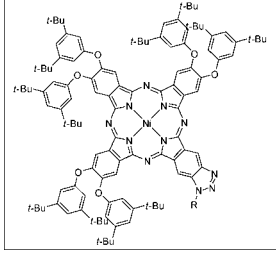	Ni(II)	DCM	692 nm (r.i.1.00), 675 (0.928), 612 (0.237), 309 (0.650)	R = H	918
		DCM	694 nm (r.i.1.00), 677 (0.941), 613 (0.225), 309 (0.604)	R = $(CH_2)_6CHCH_2$	918
		DCM	694 nm (r.i.1.00), 677 (0.937), 645sh, 613 (0.227), 385sh, 308 (0.604)	R = $(CH_2)_8SCOMe$	918

(*Continued*)

Table 2. (*Continued*)

Structure	M	Solvent	Transition Energy (Intensity)	Remark	Ref.
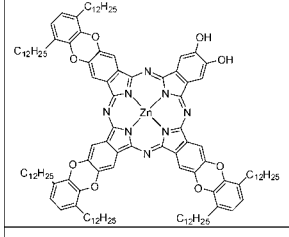	Zn(II)	THF	686 nm, 628, 360		919
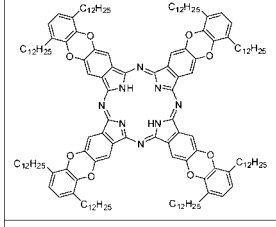	2H	unknown	703 nm, 668, 638, 492		920
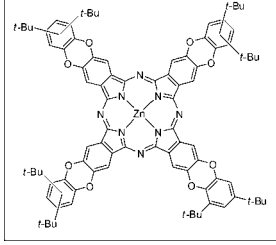	Zn(II)	unknown	680 nm		920

(*Continued*)

Table 2. (*Continued*)

Structure	M	Solvent	Transition Energy (Intensity)	Remark	Ref.
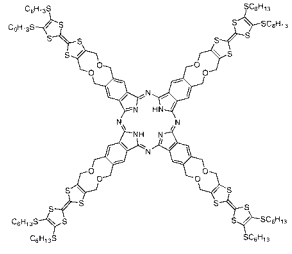	2H	toluene	709.0 nm (ε 43,894), 674.5 (49,320), 648.5 (39,303), 333.0 (85,493)		585
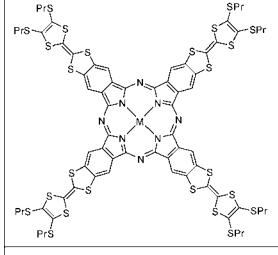	2H	py	691 nm (ε 22,000), 617 (27,000), 355 (45,000)		921
	Co(II)	py	687 nm (ε 42,000), 641 (40,000), 473sh (23,000), 333 (114,000)		921
	Ni(II)	py	620 nm (ε 26,000), 328 (99,000)		921
	Zn(II)	py	706 nm (ε 75,000), 655 (70,000), 367 (125,000)		921
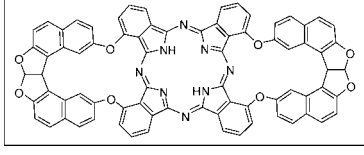	2H	THF	704 nm (lg ε 5.053), 671 (5.004), 644 (4.673), 613 (4.486), 337 (4.971)		922

(*Continued*)

Table 2. (*Continued*)

Structure	M	Solvent	Transition Energy (Intensity)	Remark	Ref.
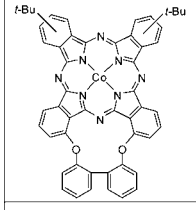	Co(II)	toluene	672 nm (lg ε 5.26), 647 (4.58), 607 (4.53), 328 (4.78)		828
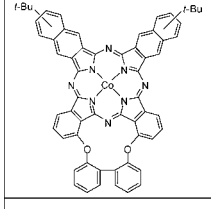	Co(II)	toluene	712 nm (lg ε 5.28), 682 (4.60), 639 (4.56), 412 (4.05), 335 (4.87)		828
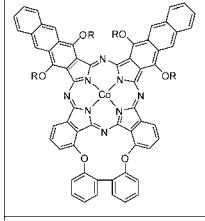	Co(II)	toluene	789 nm (lg ε 5.17), 706 (4.52), 495 (4.20), 350 (4.84), 330 (4.82)		828
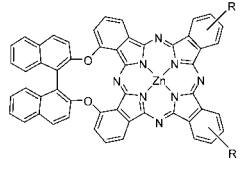	Zn(II)	DMSO	691 nm (lg ε 5.04), 621 (4.36), 338 (4.63)	R = OPh	481, 923
		DMSO	688 nm (lg ε 5.22), 619 (4.55), 354 (4.80)	R = OPh(4-*t*-Bu)	481, 923
		$CHCl_3$	691 nm	R = OPh(4-COOH)	481
		benzene	690 nm	R = OPh(4-COOH)	481
		DMF	688 nm	R = OPh(4-COOH)	481
		DMSO	693 nm (lg ε 5.25), 624 (4.60), 339 (5.10)	R = OPh(4-COOH)	481
		THF	687 nm	R = OPh(4-COOH)	481
		DMSO	694 nm (lg ε 5.18), 626 (4.58), 328 (5.07)	R = OPh(4-SO_3Na)	923

(*Continued*)

Table 2. (*Continued*)

Structure	M	Solvent	Transition Energy (Intensity)	Remark	Ref.
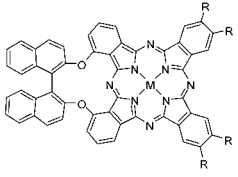	2H	$CHCl_3$	708 nm, 675	R = OPh(4-COOH)	924
		MeOH	623 nm	R = OPh(4-COOH)	924
		DMSO	677 nm (lg ε 5.2), 630 (4.7), 327 (5.0)	R = OPh(4-COOH)	924
		H_2O	633 nm (5.17)	R = OPh(4-COOH)	924
		BSA	632 nm	R = OPh(4-COOH)	924
		CTAC	702 nm, 670	R = OPh(4-COOH)	924
		TritonX	711sh nm, 687sh, 628	R = OPh(4-COOH)	924
		DMSO	686sh nm, 630, 327	R = OPh(4-COOH)	925
	Zn(II)	DMSO	687 nm (lg ε 5.08), 615 (5.04), 326 (4.63)	R = OPh	481
		DMSO	683 nm (lg ε 5.30), 613 (4.58), 354 (5.07)	R = OPh(4-*t*-Bu)	481
		$CHCl_3$	690 nm	R = OPh(4-COOH)	481
		DMF	686 nm	R = OPh(4-COOH)	481
		DMSO	691 nm (lg ε 5.21), 618 (4.55), 360sh, 335 (4.80)	R = OPh(4-COOH)	481
		THF	685 nm	R = OPh(4-COOH)	481
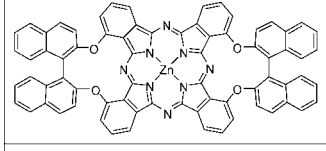	Zn(II)	DMF	686 nm, 677sh, 615, 395sh, 337		767
		DMSO	699 nm (lg ε 5.20), 630 (4.53), 321 (5.02), 294 (5.45)		481, 923
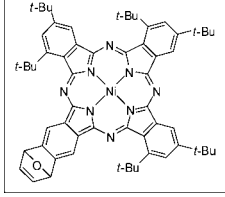	Ni(II)	$CHCl_3$	678.0 nm (ε 78,500), 669.0 (81,000), 604.5 (15,500), 364.5sh (15,500), 340.5 (22,500), 298.5 (28,500), 271.0 (22,500)		926

(*Continued*)

Table 2. (*Continued*)

Structure	M	Solvent	Transition Energy (Intensity)	Remark	Ref.
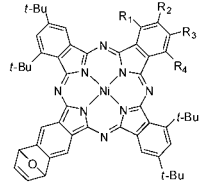	Ni(II)	$CHCl_3$	679.5 nm (ε 139,666), 669.5sh (127,333), 607.5 (26,000), 368.5sh (29,000), 337.5 (45,333), 299.0 (55,600), 271.5 (44,666)	$R_1(R_2)$, $R_3(R_4)$ = *t*-Bu	926
		$CHCl_3$	677.0 nm (ε 47,250), 671.0 (48,250), 640.0sh (9250), 605.5 (9000), 369.0sh (8500), 337.5 (13,500), 297.5 (16,500), 271.0 (12,500)	R_1, R_3 = *t*-Bu	926
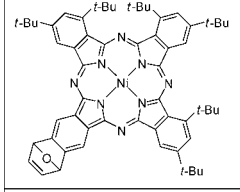	Ni(II)	$CHCl_3$	688.0 nm (ε 86,400), 618.5 (16,600), 369.0sh (17,600), 338.0 (27,800), 302.0 (33,800), 271.0 (27,800)		926
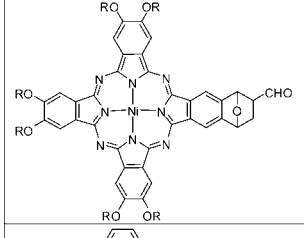	Ni(II)	DCM	668 nm, 602, 392, 308	R = 	927
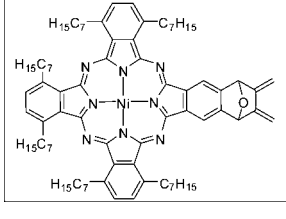	Ni(II)	toluene	689 nm, 619, 352, 301		928

(*Continued*)

Table 2. (*Continued*)

Structure	M	Solvent	Transition Energy (Intensity)	Remark	Ref.
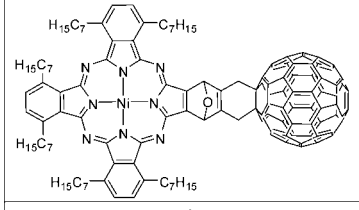	Ni(II)	toluene	699 nm, 679, 618, 436, 336, 305		928
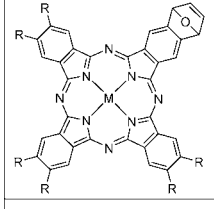	Ni(II)	$CHCl_3$	671 nm, 604, 400, 328sh, 310, 288	R = OC_8H_{17}	929
		DCM	667.5 nm, 611, 394	R = $OC_{10}H_{21}$	929
		DCM	665 nm, 601, 401, 309	R = 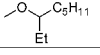	929
	Zn(II)	DCM +1% EtOH	677 nm (lg ε 5.38), 646sh, 610 (4.62), 354 (5.01), 288 (4.80)	R = OPh(3,5-(*t*-Bu)$_2$)	903
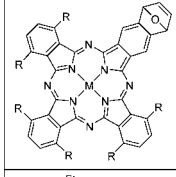	Ni(II)	toluene	688 nm, 618, 340, 299	R = C_7H_{15}	930
		$CHCl_3$	725 nm, 651, 448, 332, 305	R = OBu	929
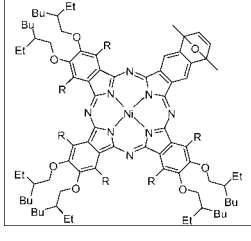	Ni(II)	DCM	884 nm, 666.50, 601.50, 403.50, 310.50, 287	R = H	627
		DCM	883.50 nm, 716.50, 379.50, 308.50	R = 	627

(*Continued*)

Table 2. (*Continued*)

Structure	M	Solvent	Transition Energy (Intensity)	Remark	Ref.
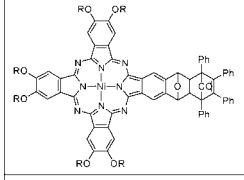	Ni(II)	$CHCl_3$	672 nm, 605, 393, 327sh, 309, 289	R = C_8H_{17}	929
		DCM	669.5 nm, 605.5, 388.5	R = $C_{10}H_{21}$	929
		DCM	670 nm, 603, 391	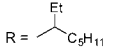	929
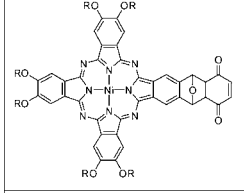	Ni(II)	DCM	666 nm, 603, 390, 309, 288	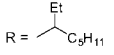	929
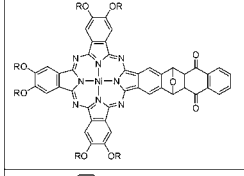	Ni(II)	DCM	668 nm, 603, 390.5, 309.5, 288.5	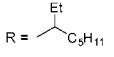	929
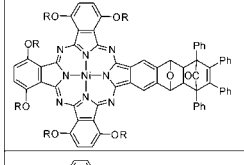	Ni(II)	$CHCl_3$	728 nm, 653, 452, 331, 304	R = Bu	929
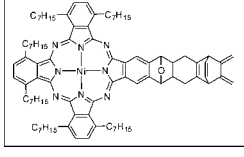	Ni(II)	toluene	688 nm, 619, 343, 299		930

(*Continued*)

Table 2. (*Continued*)

Structure	M	Solvent	Transition Energy (Intensity)	Remark	Ref.
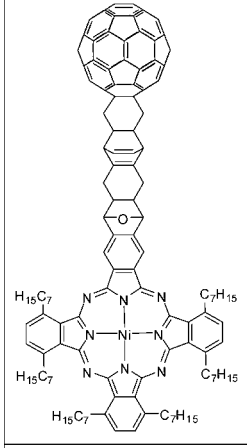	Ni(II)	toluene	693 nm, 625, 435, 333, 299		930
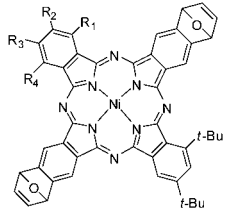	Ni(II)	$CHCl_3$	683.5 nm (ε 96,666), 657.0 (109,000), 627.0 (28,333), 595.0 (21,666), 370.5 (24,666), 334.0 (38,666), 295.5 (47,666), 270.5 (43,333)	$R_1(R_2)$, $R_3(R_4)$ = *t*-Bu	926

(*Continued*)

Table 2. (*Continued*)

Structure	M	Solvent	Transition Energy (Intensity)	Remark	Ref.
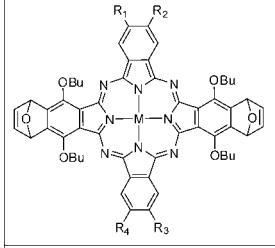	2H	$CHCl_3$	746 nm, 706.5, 662.5, 350.5	R_1, R_2, R_3, $R_4 = C_6H_{13}$	885
	Ni(II)	$CHCl_3$	694 nm, 658, 396, 324	R_2, $R_3(R_4) = NO_2$	885
	Zn(II)	$CHCl_3$	725 nm, 698, 666.5, 634, 355	R_2, $R_3(R_4) = NO_2$	885
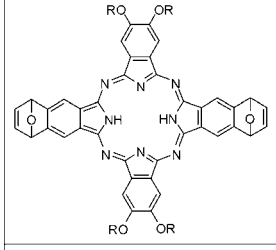	2H	DCM	695 nm, 657, 641, 349	R = 	540
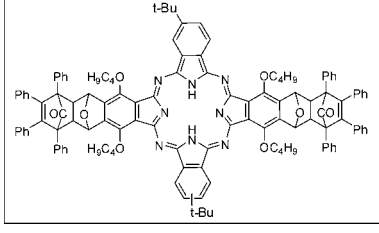	2H	$CHCl_3$	742 nm, 703, 669, 633.5, 336		885

(*Continued*)

Table 2. (*Continued*)

Structure	M	Solvent	Transition Energy (Intensity)	Remark	Ref.
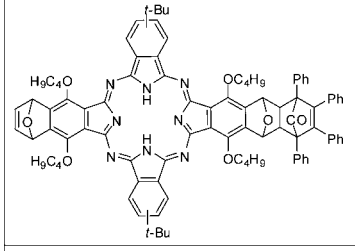	2H	$CHCl_3$	743.5 nm, 703, 661, 633, 605.5, 340.5		885
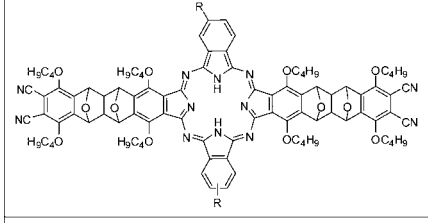	2H	$CHCl_3$	720 nm, 647.5, 406, 337.5	R = NO_2	885
		$CHCl_3$	741 nm, 702, 665, 633, 339	R = *t*-Bu	885
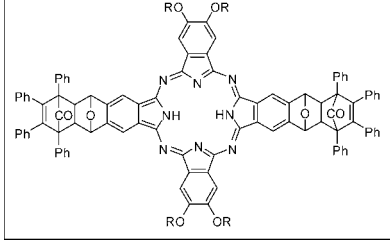	2H	DCM	696 nm, 661, 346	R = 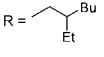	540

(*Continued*)

Table 2. (*Continued*)

Structure	M	Solvent	Transition Energy (Intensity)	Remark	Ref.
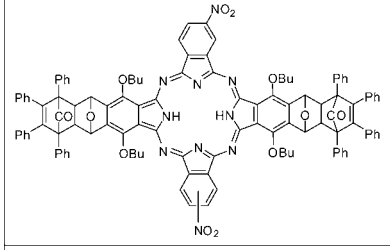	2H	$CHCl_3$	720 nm, 652, 407, 339.5		931
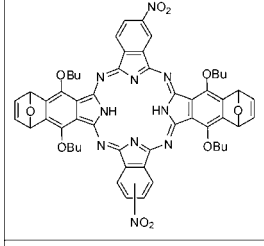	2H	$CHCl_3$	723.5 nm (lg ε 4.89), 662 (4.40), 425.5 (4.34), 336.5 (4.56)		931
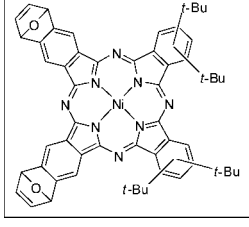	Ni(II)	$CHCl_3$	671.0 nm (ε 159,000), 641.0 (34,333), 604.0 (26,666), 371.0sh (26,666), 335.5 (44,333), 301.0 (53,000), 272.0 (51,000)		926

(*Continued*)

Table 2. (*Continued*)

Structure	M	Solvent	Transition Energy (Intensity)	Remark	Ref.
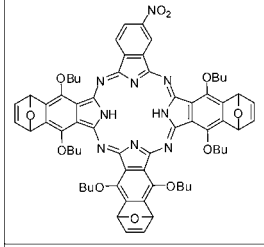	2H	$CHCl_3$	734.5 nm (lg ε 4.94), 714.5, 671 (4.36), 405.5 (4.38), 338 (4.56)		931
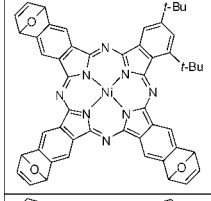	Ni(II)	$CHCl_3$	663.5 nm (ε 148,444), 630.5sh (41,333), 597.5 (32,000), 375.0 (30,888), 334.0 (57,111), 301.5 (67,111), 270.5 (70,000)		926
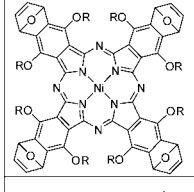	Ni(II)	$CHCl_3$	713 nm, 642, 383, 338, 311	R = Bu	929
		$CHCl_3$	714 nm, 643, 385, 336, 313	R = C_6H_{13}	929
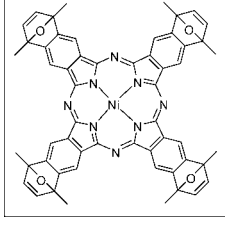	Ni(II)	DCM	884 nm, 867.5, 658.5, 373, 331		627

(*Continued*)

Table 2. (*Continued*)

Structure	M	Solvent	Transition Energy (Intensity)	Remark	Ref.
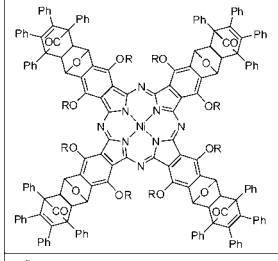	Ni(II)	$CHCl_3$	724 nm, 651, 422sh, 360, 339, 306	R = Bu	929
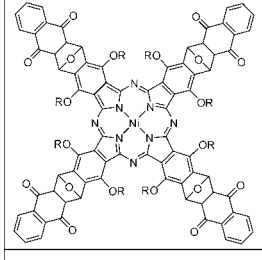	Ni(II)	$CHCl_3$	728 nm, 655, 425sh, 360, 308	R = Bu	929
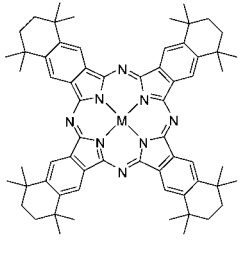	2H	benzene	712 nm (lg ε 5.40), 678 (5.34), 648 (4.83), 616 (4.67), 400sh (4.38), 348 (5.10)		932, 933
		methacrylate	709 nm (r.i 2.0), 675 (1.80), 647 (0.56), 612 (0.37), 343 (1)		932
	V(V)O	benzene	716 nm (lg ε 5.37), 683 (4.53), 643 (4.57), 390sh (4.43), 353 (4.91)		932, 933
	Co(II)	benzene	682 nm (lg ε 5.34), 653 (4.64), 615 (4.59), 380sh (4.11), 335 (4.94)		932, 933
	Cu(II)	benzene	691 nm (lg ε 5.47), 660 (4.62), 622 (4.68), 347 (4.96)		932, 933
		methylmethacrylate	688 nm (lg ε 5.44), 657 (4.65), 619 (4.65), 342 (4.99)		932
		H_2SO_4	844 nm (r.i. 2.75), 743 (0.40), 468 (0.50), 280 (1)		932
	Zn(II)	benzene	691 nm (lg ε 5.36), 660 (4.47), 623 (4.54), 351 (4.90)		932, 933

(*Continued*)

Table 2. (*Continued*)

Structure	M	Solvent	Transition Energy (Intensity)	Remark	Ref.
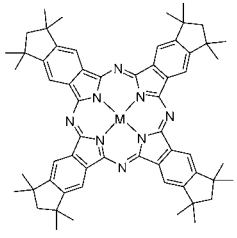	2H	benzene	703 nm (lg ε 5.15), 667 (5.08), 638 (4.53), 604 (4.34), 386sh (4.43), 349 (4.77)		932
	Cu(II)	benzene	681 nm (lg ε 5.41), 646 (4.48), 613 (4.59), 348 (4.86)		932
		H_2SO_4	824 nm (r.i 2.60), 726 (0.40), 457 (0.31), 279 (1)		932
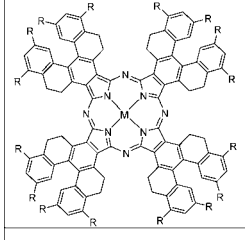	2H	toluene	748 nm, 715, 442, 383, 344	R = H	934
	Zn(II)	$CHCl_3$	728 nm, 370, 292, 244	R = Me	934
		toluene	752 nm, 707, 384, 343	R = H	934
	Pb(II)	toluene	796 nm, 384, 343	R = H	934
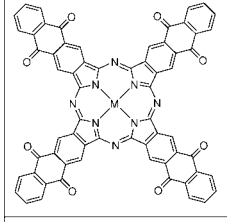	Al(III)	DMF	684 nm		935
	Co(III)	DMF	679 nm		935
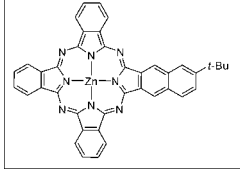	Zn(II)	DMF	700sh nm, 685, 619, 340		511

(*Continued*)

Table 2. (*Continued*)

Structure	M	Solvent	Transition Energy (Intensity)	Remark	Ref.
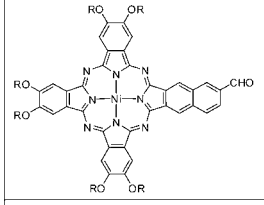	Ni(II)	DCM	692 nm, 632, 393, 331	R = 	927
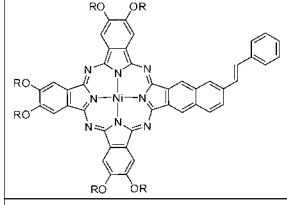	Ni(II)	DCM	694 nm, 628, 398, 326	R = 	927
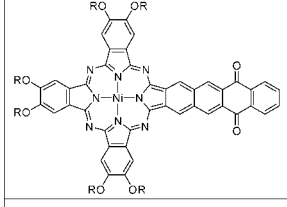	Ni(II)	DCM	708.5 nm, 680sh, 422, 329	R = 	929
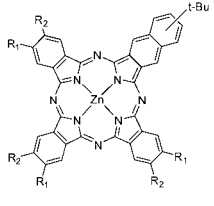	Zn(II)	DMF	707 nm (ε 115,000), 686 (130,000), 621, 350	$R_1(R_2)$ = H, $R_2(R_1)$ = 	698
		DMF	708 nm (ε 82,000), 683 (96,000), 619, 348	$R_1(R_2)$ = H, $R_2(R_1)$ = 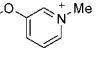 $[Pc]^{3+}$	698
		DMF	710 nm (ε 117,000), 684 (122,000), 620, 355	R_1, R_2 = 	698
		DMF	714 nm (ε 62,000), 682 (64,000), 618, 348	R_1, R_2 = 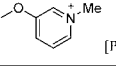 $[Pc]^{6+}$	698

(*Continued*)

Table 2. (*Continued*)

Structure	M	Solvent	Transition Energy (Intensity)	Remark	Ref.
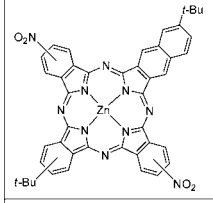	Zn(II)	DMF	724sh nm, 699 (r.i. 1), 684sh, 645 (0.47), 620sh, 357 (0.54)		884
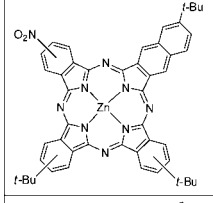	Zn(II)	DMF	696 nm (r.i. 1), 628 (0.2), 348 (0.45)		884
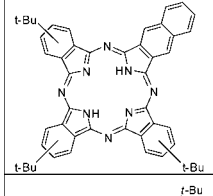	2H	DCB	729 nm, 688, 667, 620, 454, 346		302
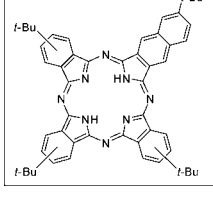	2H	benzene	729 nm (lg ε 4.93), 684 (4.91), 664 (4.72), 634 (4.34), 616 (4.41), 569sh (3.69), 404sh (4.19), 347 (4.79)		418

(*Continued*)

Table 2. (*Continued*)

Structure	M	Solvent	Transition Energy (Intensity)	Remark	Ref.
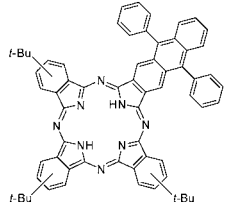	2H	benzene	757 nm (lg ε 4.59), 710 (4.62), 687 (4.39), 636 (4.12), 600sh (3.50), 464 (3.25), 348 (4.47)		418
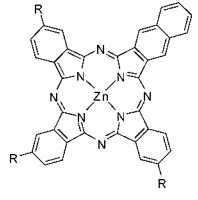	Zn(II)	THF	713 nm (lg ε 5.00), 688 (5.07)	R = $CC(CH_2)_3COOH$	556
		0.1 N NaOH	643 nm	R = $CC(CH_2)_3COOH$	556
		THF	716 nm (lg ε 5.09), 689 (5.16)	R = $CC(CH_2)_8COOH$	556
		0.1 N NaOH	628 nm	R = $CC(CH_2)_8COOH$	556
		DMF	727 nm (lg ε 4.99), 693 (5.05), 627 (4.51)	R = (2-py)	556
		DMF	742 nm, 702	R = (2-py^+(N-Me))	556
		H_2O	636 nm	R = (2-py^+(N-Me))	556
		DMF	732 nm (lg ε 5.07), 699 (5.13), 632 (4.53)	R = (3-py)	556
		DMF	730 nm, 695	R = (3-py^+(N-Me))	556
		H_2O	633 nm	R = (3-py^+(N-Me))	556
		THF	708 nm (lg ε 4.93), 680 (5.00), 650 (4.50), 616 (4.39), 349 (4.71)	R = I	556
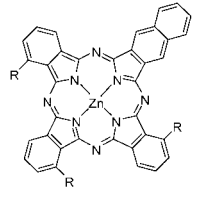	Zn(II)	THF	717 nm (lg ε 4.99), 689 (5.01)	R = $CC(CH_2)_3COOH$	556
		0.1 N NaOH	631 nm	R = $CC(CH_2)_3COOH$	556
		DMF	717 nm (lg ε 4.94), 689 (4.99)	R = (2-py)	556
		DMF	722 nm, 691	R = (2-py^+(N-Me))	556
		H_2O	636 nm	R = (2-py^+(N-Me))	556
		DMF	724 nm (lg ε 5.00), 695 (5.02)	R = (3-py)	556
		DMF	718 nm, 689,	R = (3-py^+(N-Me))	556
		H_2O	623 nm	R = (3-py^+(N-Me))	556
		THF	708 nm (lg ε 5.01), 680 (5.08), 650 (4.54), 616 (4.44), 349 (4.80)	R = I	556

(*Continued*)

Table 2. (*Continued*)

Structure	M	Solvent	Transition Energy (Intensity)	Remark	Ref.
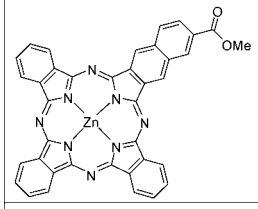	Zn(II)	DMSO	694 nm, 624, 342		482
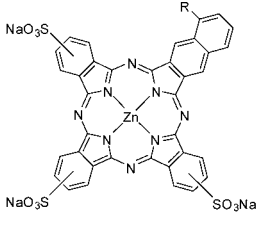	Zn(II)	MeOH	694 nm	R = 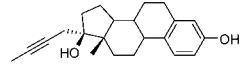	824
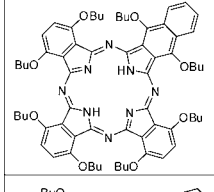	2H	toluene	802 nm (10^{-5} ε 0.66), 756 (0.82)		419, 609
	Si(IV)L	toluene	793 nm, 762	L = *trans*-$(OH)_2$	609
		toluene	794 nm (10^{5} ε 1.5), 761 (2.2)	L = *trans*-$(OSi(C_6H_{13})_3)_2$	609
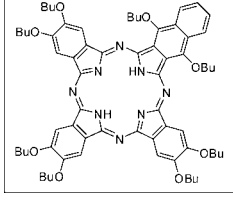	2H	toluene	742 nm (10^{-5} ε 1.41), 697 (1.48)		419

(*Continued*)

Table 2. (*Continued*)

Structure	M	Solvent	Transition Energy (Intensity)	Remark	Ref.
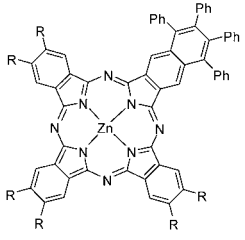	Zn(II)	THF	708sh nm, 697 (lg ε 5.36), 629 (4.68), 354 (5.10)	R = OPh(3,5-(*t*-Bu)$_2$)	903
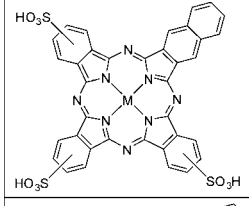	Al(III)OH	DMF	692 nm (10^{-4} ε 9.1), 626 (2.5), 353 (6.2)		762
	Zn(II)	DMF	704 nm (10^{-4} ε 8.1), 687 (8.7), 621 (2.4), 347 (5.5)		762
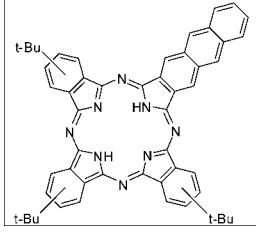	2H	DCB	757 nm, 708, 670sh, 642, 462, 347		302

(*Continued*)

Table 2. (*Continued*)

Structure	M	Solvent	Transition Energy (Intensity)	Remark	Ref.
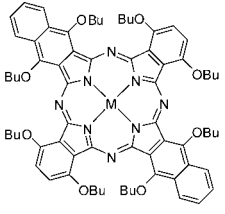	2H	toluene	852 nm (10^{-5} ε 0.75), 750 (0.98)		419, 609
	Si(IV)L	toluene	859 nm, 763	L = *trans*-$(OH)_2$	609
		toluene	851 nm (10^{-5} ε 1.2), 760 (1.5)	L = *trans*-$(OSi(C_6H_{13})_3)_2$	609
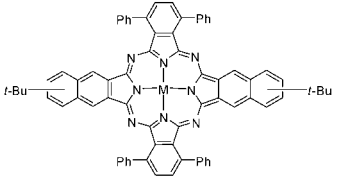	2H	$CHCl_3$	792 nm (lg ε 4.44), 740 (4.15), 691 (4.29), 353 (4.19)		936
	Co(II)	DCB	763 nm (lg ε 4.96), 705 (4.89), 688 (4.95), 631 (4.53), 323 (4.86)		828
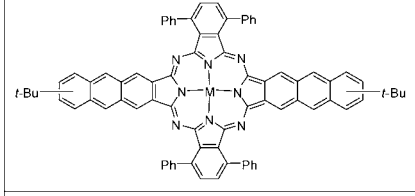	2H	$CHCl_3$	855 nm (lg ε 4.31), 784 (4.31), 728 (4.62), 662 (4.20), 357 (4.65)		936
	Co(II)	DCB	825 nm (lg ε 4.67), 719 (4.89), 658 (4.49), 372 (4.76), 323 (4.85)		828
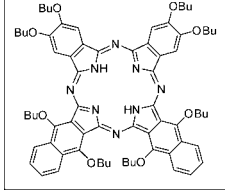	2H	toluene	770 nm (10^{-5} ε 1.33)		419

(*Continued*)

Table 2. (*Continued*)

Structure	M	Solvent	Transition Energy (Intensity)	Remark	Ref.
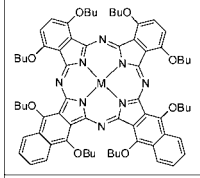	2H	toluene	807 nm (10^{-5} ε 1.90)		419, 609
	Si(IV)L	toluene	805 nm	L = *trans*-$(OH)_2$	609
		toluene	804 nm (10^{-5} ε 1.9)	L = *trans*-$(OSi(C_6H_{13})_3)_2$	609
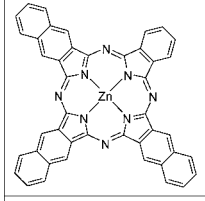	Zn(II)	DMF	672 nm (lg ε 4.76), 607 (4.07), 344 (4.69)		648
		DMSO	672 nm		648
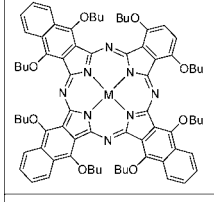	2H	toluene	851 nm (10^{-5} ε 0.89), 814 (0.99)		609
	Si(IV)L	toluene	861 nm, 825	L = *trans*-$(OH)_2$	609
		toluene	857 nm (10^{-5} ε 1.3), 820 (1.6)	L = *trans*-$(OSi(C_6H_{13})_3)_2$	609
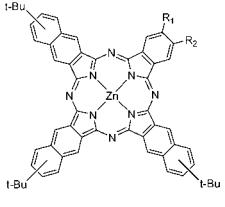	Zn(II)	DMF	750 nm (ε 119,000), 729 (128,000), 656, 344	$R_1(R_2)$ = H, $R_2(R_1)$ = 	698
		DMF	753 nm (ε 67,000), 726 (71,000), 653, 343	$R_1(R_2)$ = H, $R_2(R_1)$ = 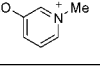 $[Pc]^+$	698
		DMF	753 nm (ε 123,000), 725 (131,000), 653, 346	R_1, R_2 =	698
		DMF	757 nm (ε 65,000), 722 (71,000), 650, 344	R_1, R_2 =  $[Pc]^{2-}$	698

(*Continued*)

Table 2. (*Continued*)

Structure	M	Solvent	Transition Energy (Intensity)	Remark	Ref.
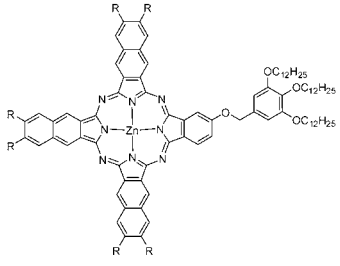	Zn(II)	THF	763 nm (lg ε 5.35), 733 (4.82), 681 (4.61), 363 (5.04)	R = 	561
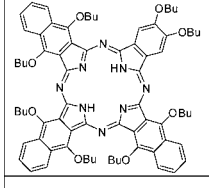	2H	toluene	817 nm (10^{-5} ε 1.40), 794 (1.51)		419
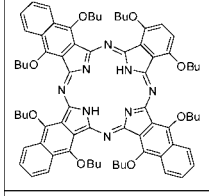	2H	toluene	851 nm (10^{-5} ε 0.89), 814 (0.99)		419
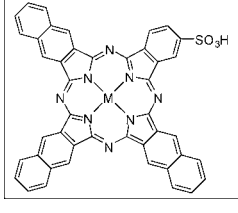	Al(III)OH	DMF	762 nm (10^{-4} ε 7.4), 738 (8.7), 347 (6.9)		762
	Zn(II)	DMF	746 nm (10^{-4} ε 4.2), 727 (4.8), 654 (1.7), 338 (4.1)		762

(*Continued*)

Table 2. (*Continued*)

Structure	M	Solvent	Transition Energy (Intensity)	Remark	Ref.
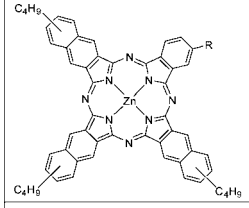	Zn(II)	DMF	759.2 nm, 726.5	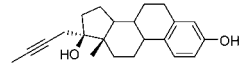	824
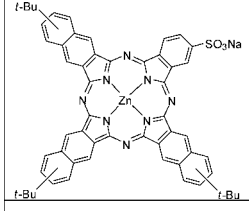	Zn(II)	DMF	751 nm (lg ε 5.20), 733 (5.21), 658 (4.56), 343 (4.92)		880
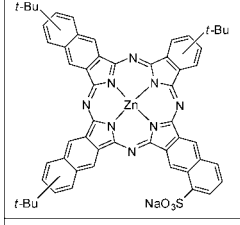	Zn(II)	DMF	698 nm (lg ε 5.48), 628 (4.8), 348 (5.12)		880
		MeOH	693 nm (lg ε 5.45), 343 (5.23)		880
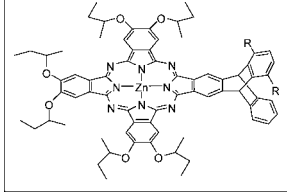	Zn(II)	toluene	682 nm (lg ε 5.40), 613 (4.64), 356 (4.93), 291 (4.76)	R = H	612
		toluene	681 nm (lg ε 5.32), 613 (4.56), 356 (4.86), 290 (4.72)	R = OMe	612
		toluene	682 nm (lg ε 5.39), 613 (4.62), 356 (4.90), 290 (4.73)	R = OCH_2Ph	612

(*Continued*)

Table 2. (*Continued*)

Structure	M	Solvent	Transition Energy (Intensity)	Remark	Ref.
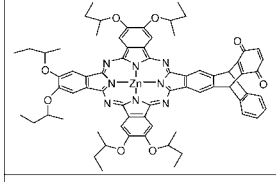	Zn(II)	toluene	688 nm (lg ε 5.20), 675 (5.20), 612 (4.51), 356 (4.87), 291 (4.71)		612
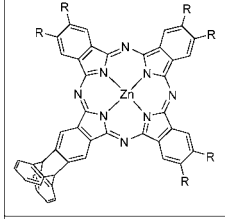	Zn(II)	THF	677 nm (lg ε 5.46), 648 (4.61), 611 (4.66), 357 (5.05)	R = OPh(3,5-(*t*-Bu)2)	903
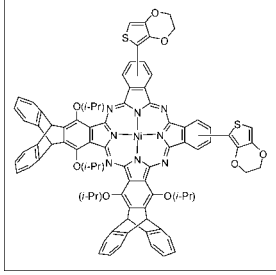	Ni(II)	DCM	718 nm (lg ε 4.73), 318 (4.42)		937

(*Continued*)

Table 2. (*Continued*)

Structure	M	Solvent	Transition Energy (Intensity)	Remark	Ref.
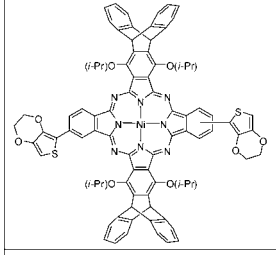	Ni(II)	DCM	715 nm (lg ε 5.05), 325 (4.65)		937
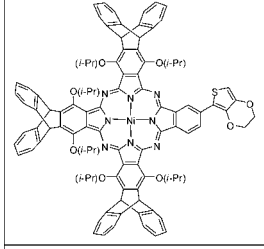	Ni(II)	DCM	730 nm (lg ε 4.94), 319 (4.71)		937
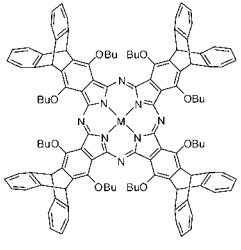	2H	toluene	758 nm, 731		602
	Si(IV)L	toluene	755 nm	L = *trans*-$(F)_2$	602
		toluene, 1.8 μM	745 nm (10^{-5} ε 2.7)	L = *trans*-$(OH)_2$	602
		toluene, 2.0 μM	741 nm (10^{-5} ε 2.9)	L = *trans*-$(OSi(C_6H_{13})_3)_2$	602
		toluene, 2.2 μM	745 nm (10^{-5} ε 2.7)	L = *trans*- 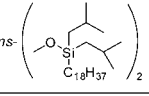	602
		toluene, 4.9 μM	748 nm (10^{5} ε 2.8)	L = *trans*- 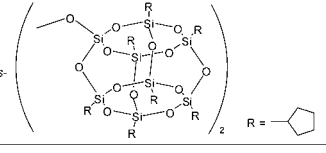	602

(*Continued*)

Table 2. (*Continued*)

Structure	M	Solvent	Transition Energy (Intensity)	Remark	Ref.
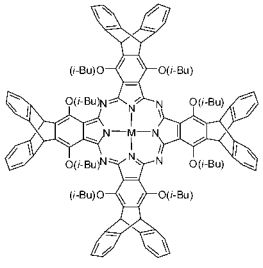	2H	toluene	764 nm, 737		602
	Si(IV)L	toluene	750 nm	L = *trans*-$(OH)_2$	602
		toluene	748 nm	L = *trans*-$(OSi(C_6H_{13})_3)_2$	602
		toluene, 2.9 μM	749 nm (10^{-5} ε 2.6)	L = *trans*- 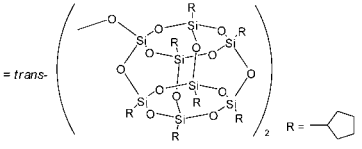	602
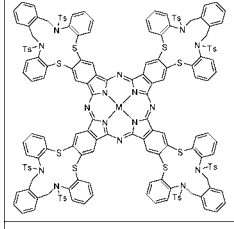	Ni(II)	$CHCl_3$	684 nm (10^{-4} ε 12.4), 643 (4.3), 609 (3.8), 335 (11.2)		938
	Co(II)	$CHCl_3$	690 nm (10^{-4} ε 7.6), 626 (5.4), 612 (2.2), 330 (9.7)		938
	Cu(II)	$CHCl_3$	694 nm (10^{-4} ε 12.5), 652 (3.2), 626 (3.1), 327 (7.1)		938
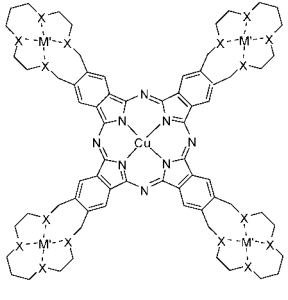	Cu(II)	$CHCl_3$	685 nm (10^{-4} ε 13.49), 617sh (3.00), 347 (7.58), 243 (14.28)	M′ = 2H, X = N(Ts)	939
		$CHCl_3$	678 nm (10^{-4} ε 8.67), 616 (3.33), 342 (5.27), 249 (4.78)	M′ = 2H, X = NH	939
		H_2O	669sh nm (10^{-4} ε 4.31), 639 (5.46), 332 (5.27), 220 (6.47)	M′ = 2H, X = NH	939
		H_2O	692sh nm (10^{-4} ε 1.68), 632 (2.09), 335 (2.95), 219 (7.54)	M′ = 2H, X = NH_2^+ 1/2(SO_4^{2-})	939
		H_2O	659sh nm (10^{-4} ε 7.34), 628 (7.88), 328 (8.31), 211 (10.68)	M′ = 2H, X = NMe_2^+ $MeOSO_3^-$	939
		H_2O	660 nm (10^{-4} ε 7.35), 628 (7.68), 329 (8.07), 211 (10.08)	M′ = 2H, X = NMe_2^+ ClO_4^-	939
		H_2O	669 nm (10^{-4} ε 7.84), 629sh (3.81), 330 (5.16), 220 (10.03)	M′ = Co(II), X = NH, $[Pc]^{8-}$ $8Cl^-$	939

(*Continued*)

Table 2. (*Continued*)

Structure	M	Solvent	Transition Energy (Intensity)	Remark	Ref.
		H_2O	660 nm (10^{-4} ε 5.69), 630sh (5.42), 330 (6.02), 218 (10.74)	M′ = Co(II), X = NH, $[Pc]^{8-}8ClO_4^-$	939
		H_2O	668 nm (10^{-4} ε 18.89), 637sh (4.13), 602sh (3.68), 333 (7.30), 215 (7.63)	M′ = Ni(II), X = NH, $[Pc]^{8+}$ $8Cl^-$	939
		H_2O	676 nm (10^{-4} ε 8.62), 637 (5.46), 339 (6.46), 216 (8.16)	M′ = Ni(II), X = NH, $[Pc]^{8+}8ClO_4^-$	939
		H_2O	667 nm (10^{-4} ε 6.28), 627 (5.34), 330 (5.70), 248sh (6.16), 211 (6.97)	M′ = Cu(II), X = NH, $[Pc]^{8-}$ $8Cl^-$	939
		H_2O	667 nm (10^{-4} ε 8.20), 625 (5.60), 328 (6.26), 236 (6.64), 214 (7.35)	M′ = Cu(II), X = NH, $[Pc]^{8-}8ClO_4$	939
		H_2O	670 nm (10^{-4} ε 10.39), 629 (5.07), 330 (6.19), 212 (7.12)	M′ = Zn(II), X = NH, $[Pc]^{8+}8Cl^-$	939
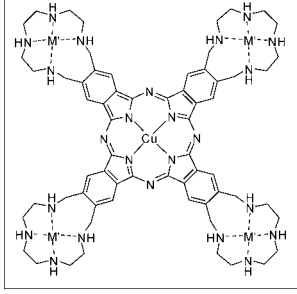	Cu(II)	EtOH	674 nm (lg ε 4.75), 634 (4.49), 342 (4.59)	M′ = –	940
		H_2O	670 nm (lg ε 4.60), 644 (4.62), 338 (4.61)	M′ = Ni(II), $[Pc]^{8+}8Cl^-$	940

(*Continued*)

Table 2. (*Continued*)

Structure	M	Solvent	Transition Energy (Intensity)	Remark	Ref.
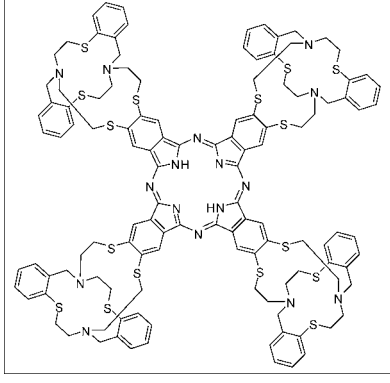	2H	py	734 nm (lg ε 11.44), 704 (10.15), 348 (6.70), 285 (10.74)		941

Table 3. UV-vis absorption data of TAPs and Mono-, Di- or triaza porphyrin analogs.

Structure	M	Solvent	Transition Energy (Intensity)	Remark	Ref.
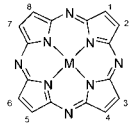	2H	$CHCl_3$	615 nm (lg ε 4.70), 542 (4.58), 331		942
		$CHCl_3$	615 nm (lg ε 4.70), 542 (4.57)		943
		$CHCl_3$	615 nm (lg ε 4.70), 542 (4.59), 331		944
		DCM	617 nm (10^{-3} ε 47.5), 545 (46.0), 333 (47.0)		408
		Benzene	615 nm, 590, 582, 563, 543, 534, 518sh, 373, 333		418
		PhCl	617 nm (10^{-3} ε 47.5), 545 (46.0), 333 (47.0)		417
		PhCl	617 nm (lg ε 4.75), 545 (4.60), 333 (4.70)		416
		py	576 nm, 530, 332		40
		py	613 nm (lg ε 4.71), 542 (4.57), 333 (4.79)		943
	Mg(II)	DCM	584 nm (10^{-3} ε 50.3), 536 (41.7), 326 (47.9)		408
		MeOH	584 nm (10^{-3} ε 50.3), 536 (41.7), 326 (47.9)		417
	Ni(II)	DCM	577 nm (10^{-3} ε 47.7), 530 (41.4), 345 (45.0)		408
		DCB	577 nm (lg ε 4.85), 530 (4.20), 345 (4.57), 314 (4.44)		416, 945
		DCB	577 nm (10^{-3} ε 47.7), 530 (41.4), 345 (45.0)		417
	Cu(II)	DCM	578 nm (10^{-3} ε 49.8), 531 (41.3), 334 (45.7)		408
		DCB	578 nm (lg ε 4.98), 531 (4.13), 334 (4.57)		416, 945
		DCB	578 nm (10^{-3} ε 49.8), 531 (41.3), 334 (45.7)		417
		py	574 nm (lg ε 4.81), 529 (4.03), 331 (4.57)		943
$\alpha\alpha$ = Me	2H	py	595 nm, 547		40
$\alpha\alpha$ = Et	Mg(II)	DCM	600 nm, 550, 346		422
	Fe(II)L	Benzene	590 nm, 574sh, 550sh, 491, 333, 315sh	L = *trans*- 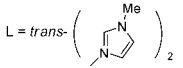	946
		1% py / benzene	586 nm, 564sh, 541, 458, 332	L = *trans*-py_2	946
	Fe(III)L	$CHCl_3$	581 nm, 532, 488sh, 348, 331	L = *trans*- 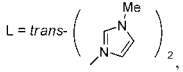 , $[Pc]^-Cl$	946
	Fe(III)Cl	$CHCl_3$	684 nm, 566, 446, 370, 316		946
		DCM	680 nm, 564, 444, 369, 315		947
		THF	670 nm, 554, 431, 366, 315		947
		Toluene	672 nm, 555, 436, 364, 318		947

(*Continued*)

Table 3. (*Continued*)

Structure	M	Solvent	Transition Energy (Intensity)	Remark	Ref.
	Fe(III)ClO_4	DCM	713sh nm, 683, 561, 502, 372, 310		947
		THF	696 nm, 565, 485, 382, 328		947
		Toluene	711 nm, 582, 497, 375, 312		947
	Fe(III)PF_6	DCM	715 nm, 560sh, 505, 372, 305		947
		THF	693 nm, 566sh, 487, 381, 326		947
		Toluene	687 nm, 588sh, 505, 372, 312		947
	Fe(III)SbF_6	DCM	722 nm, 558sh, 506, 372, 313		947
		THF	695 nm, 618, 568sh, 487, 374, 326		947
		Toluene	722 nm, 588sh, 509, 372, 322		947
	Fe(III)$OCOCF_3$	DCM	689 nm, 570, 446, 372, 308		947
		THF	676 nm, 560, 444, 372, 310sh		947
		Toluene	684 nm, 566, 445, 371, 310sh		947
$\alpha\alpha$ = Pr	Pb(II)	$CHCl_3$	625 nm (lg ε 4.01), 576 (1.26), 355 (3.24)		382
R_1, R_2, R_3, R_4, R_5, R_6 = Pr	2H	DCM	617 nm (lg ε 4.57), 559 (4.38), 338 (4.67)		948
	Mg(II)	DCM	600 nm (lg ε 4.80), 592sh, 560sh, 346 (4.83)		948
α = Me	2H	py	581 nm, 546		40
α = *t*-Bu	2H	$CHCl_3$	622 nm (lg ε 5.23), 553 (5.11), 520 (4.48), 336 (5.28)		407
		$CHCl_3$	623 nm (10^{-1} ε 6.50), 553 (4.03), 337 (6.73)		949
		$CHCl_3$	622 nm, 553, 336		950
		CCl_4	623 nm, 522		38
		Thin film	628 nm, 556		38
		Benzene	622 nm (lg ε 4.93), 597 (3.67), 579sh (3.66), 569sh (4.16), 553 (4.70), 534sh (4.12), 370sh (3.88), 338 (4.88)		418
		py	619 nm, 551, 331		951
	Mg(II)	py	592 nm, 545, 335		951
	Ti(IV)L	Toluene	603 nm (10^{-5} ε 0.60), 345 (0.41)	L = 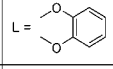	952
	Ti(IV)O	Toluene	597 nm (10^{-5} ε 1.51), 344 (0.83)		952
	V(IV)O	py	594 nm, 343		951
	Co(II)	Toluene	573 nm (lg ε 4.59), 338 (4.46), 319 (4.47)		828
	Ni(II)	$CHCl_3$	584 nm (lg ε 4.79), 341 (4.61), 314 (4.56)		950

(*Continued*)

Table 3. (*Continued*)

Structure	M	Solvent	Transition Energy (Intensity)	Remark	Ref.
	Cu(II)	py	583 nm, 337		951, 953
	Pd(II)	$CHCl_3$	577 nm (lg ε 4.77), 529 (4.11), 337 (4.56), 302 (4.42)		950
	Pb(II)	$CHCl_3$	622 nm (lg ε 4.87), 345 (4.62), 259 (4.26)		950
$\alpha\alpha$ = *t*-Bu	2H	py	619.0 nm (lg ε 4.79), 592.0 (3.84), 550.5 (4.59), 520.0 (4.02), 334.0 (4.79)		43
	Mg(II)	py	592.0 nm (lg ε 4.66), 543.0 (3.82), 335.0 (4.41)		43
	V(IV)O	py	594.0 nm (lg ε 4.68), 542.0 (3.96), 343.0 (4.57)		43
	Co(II)	py	570.0 nm (lg ε 4.61), 530.0 (4.16), 313.0 (4.52)		43
	Cu(II)	py	583.4 nm (lg ε 4.87), 535.5 (4.09), 337.0 (4.63)		43
α = CH_2OH	2H	Benzene	640 nm (lg ε 4.83), 575 (4.65), 347 (4.76)		943
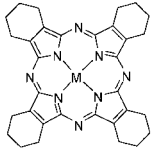	2H	py	595 nm, 548		40
	Co(II)	DCB	5890 Å, 5395, 3515		40
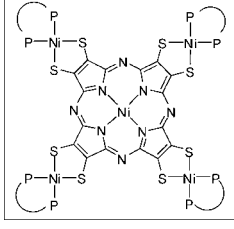	Ni(II)	DMSO	706 nm, 544, 395, 326sh, 291	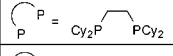	954
		DMSO	716 nm, 558, 412, 330sh, 300	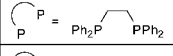	954
		DMSO	714 nm, 556, 388, (~330sh), 309	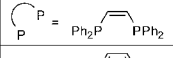	954
		DMSO	713 nm, 553, 410, (~330sh), 302	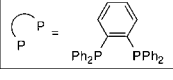	954

(*Continued*)

Table 3. (*Continued*)

Structure	M	Solvent	Transition Energy (Intensity)	Remark	Ref.
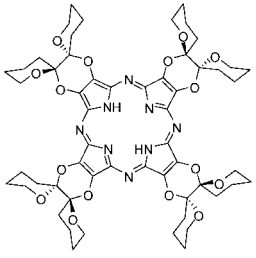	2H	$CHCl_3$	632 nm (lg ε 3.83), 554 (3.75), 427 (3.68), 338 (4.20)		955
α = Ph	2H	$CHCl_3$	660 nm (lg ε 4.11), 590 (4.02), 357 (4.32)		944
$\alpha\alpha$ = Ph	2H	$CHCl_3$	666 nm (lg ε 4.48), 599 (4.32), 368 (4.63)		944
	Mg(II)	THF	636 nm, 378		956
		py	636 nm, 460, 378		951
	Al(III)L	DCM	626 nm (r.i. 1), 572 (0.34), 374 (1.06)	L = *trans*-F_2, $[TAP]^-$	339
	Al(III)F	DCM	637 nm (r.t. 1), 587 (0.68), 370 (1.54)		339
	Al(III)Cl	DCM	636 nm (r.i. 1), 584 (0.67), ~448 (0.53), 348 (0.87)		339
	Al(III)Br	DCM	636 nm (r.i. 1), 582 (0.27), 452 (0.38), 371 (0.81)		339
	Co(II)	Toluene	615 nm (lg ε 3.83), 566sh (1.42), 354 (2.69)		957
	Zn(II)	Toluene + 1×10^{-2} M py	637 nm (10^{-1} ε 14.1), 585 (2.46), 383 (9.97)		265
	Ga(III)F	DCM	636 nm (r.i. 1), 583 (0.20), 466 (0.27), 367 (0.71)		339
	Ga(III)L	DCM	628 nm (r.i. 1), 575 (0.29), 375 (0.85)	L = *trans*-F_2, $[TAP]^-$	339
	Ga(III)Cl	DCM	636 nm (lg ε 4.98), 583 (4.22), 465 (4.37), 368 (4.90)		339
	Ga(III)Br	DCM	636 nm (r.i. 1), 583 (0.27), ~450 (0.39), 371 (0.98)		339
	Ru(II)L	DCM	585 nm (lg ε 5.00), 540 (4.47), 443 (4.07), 421 (4.05), 364 (4.97), 276 (4.80)	L = *trans*-(CN*t*-Bu)$_2$	958
		DCM	599 nm, 549, 513, 348, 306, 268sh	L = *trans*-$(NH_3)_2$	219
		DCM	588 nm (lg ε 4.98), 541 (4.49), 473 (4.41), 455sh, 407 (4.21), 349 (4.86), 342sh, 288 (4.79)	L = *trans*-py$_2$	219
		DCM	588 nm (lg ε 4.98), 541 (4.49), 473 (4.41), 407 (4.21), 349 (4.86), 288 (4.79)	L = *trans*-py$_2$	958
		DCM	585 nm (lg ε 5.02), 538 (4.50), 448 (4.25), 354 (4.93), 277 (4.79)	L = *trans*-py, (CN*t*-Bu)	958
		DCM	586 nm, 540, 507sh, 458, 443sh, 348, 340sh, 284	L = *trans*-pyz$_2$	219

(*Continued*)

Table 3. (*Continued*)

Structure	M	Solvent	Transition Energy (Intensity)	Remark	Ref.
		Uvasole	598 nm, 545, 507sh, 472, 450sh, 362, 345sh, 292	L = *trans*-py_2	219
		$CHCl_3$	588 nm, 542, 445, 421, 365	L = *trans*- 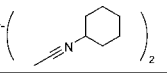	958
		DCM	587 nm (lg ε 4.91), 541 (4.41), 470 (4.50), 349 (4.79), 286 (4.76)	L = *trans*- 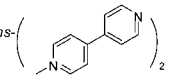	958
		DCM	594 nm (lg ε 4.89), 546 (4.43), 503 (4.55), 349 (4.86), 301 (4.82)	L = *trans*- 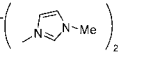	958
		$CHCl_3$	588 nm, 542, 450, 359	L = *trans*- 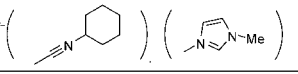	958
		$CHCl_3$	588 nm (lg ε 5.01), 541 (4.48), 449 (4.25), 358 (4.91)	L = *trans*- 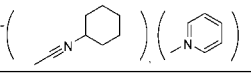	958
		DCM	788sh, 727sh, 581, 544sh, 423, 350, 277	L = *trans*- 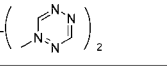	219
		DCM	585 nm (lg ε 5.00), 540 (4.47), 443 (4.07), 421 (4.05), 364 (4.97), 346sh, 276 (4.80)	L = *trans*-$(CN(t\text{-}Bu))_2$	219
		DCM	582 nm, 540sh, 432sh, 409sh, 363	L = *trans*- 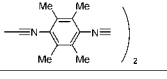	219
	In(III)F	DCM	642 nm (lg ε 4.93), 592 (4.25), 470 (4.27), 379 (4.87)		339
	In(III)L	DCM	642 nm (r.i. 1), 590 (0.21)	L = *trans*-F_2, $[TAP]^-$	339
	In(III)Cl	DCM	642 nm (lg ε 4.81), 591 (4.14), 475 (4.20), 377 (4.74)		339
		DCM	642 nm (r.i. 1.00), 590 (0.218), 475 (0.227), 378 (0.773)		336
		Benzene	645 nm (lg ε 4.73), 593 (4.12), 384 (4.62)		333
	In(III)Br	DCM	642 nm (lg ε 4.88), 592 (4.25), 478 (4.28), 382 (4.79)		339
	$In(III)NO_2$	DCM	642 nm (r.i. 1), 590 (0.22), –473 (0.22), 378 (0.77)		339
	In(III)Ph	Benzene	645 nm (lg ε 5.24), 593 (4.58), 401 (5.23)		333
	In(III)L	DCM	643 nm (lg ε 5.15), 591 (4.39), 483 (4.16), 395 (5.01)	L = Ph(4-CF_3)	336

(*Continued*)

Table 3. (*Continued*)

Structure	M	Solvent	Transition Energy (Intensity)	Remark	Ref.
		DCM	643 nm (lg ε 5.13), 591 (4.38), 481 (4.19), 392 (5.00)	L = Ph(3,5-F_2)	336
		DCM	641 nm (r.i. 1), 590 (0.21), ~458 (0.15), 378 (0.86)	L = 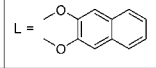 , $[TAP]^-$	339
	In(III)OPh	Benzene	644 nm (r.i. 1), 592 (0.22), 474 (0.24)		333
	In(III)Bu	Benzene	645 nm (lg ε 4.69), 594 (4.07), 406 (4.49)		333
	In(III)OCOBu	Benzene	645 nm, 594, 377		333
	In(III)OCOPh	Benzene	644 nm (lg ε 4.93), 592 (4.23), 378 (4.88)		333
$\alpha\alpha$ = Ph(4-*t*-Bu)	2H	DCM	656 nm (lg ε 4.81), 586 (4.63), 467 (4.37), 366 (4.84)		948
		Heptane	666 nm (lg ε 4.90), 595 (4.69), 562sh (4.34), 450 (4.51), 362 (4.97), 286 (4.53)		959
	Mg(II)	DCM	629 nm (lg ε 4.88), 591sh, 466, 372 (4.86)		948
		Heptane	646 nm (lg ε 4.98), 595sh (4.36), 460 (4.14), 380 (4.93)		959
	V(IV)O	Heptane	640 nm (lg ε 5.07), 585 (4.30), 470 (4.48), 364 (4.87)		959
	Fe(II)	Heptane	635 nm (lg ε 4.41), 595 (4.30), 455 (4.38), 345 (4.85)		959
	Fe(III)Cl	DCM	715 nm (lg ε 4.39), 565 (4.59), 457 (4.54), 316 (4.74)		960
	Fe(III)Br	DCM	724 nm (lg ε 4.25), 568 (4.58), 462 (4.53), 313 (4.71)		960
	Fe(III)I	DCM	731 nm (lg ε 4.08), 571 (4.60), 461 (4.53), 314 (4.71)		960
	Fe(III)L	DCM	622 nm (lg ε 4.77), 395 (4.84)	L = *trans*-CN_2, $[Pc]^-[NBu_4]^+$	960
		DCM	647 nm (lg ε 4.72), 577 (4.76), 389 (4.79)	L = *trans*-CN_2,	960
	Co(II)	Heptane	610 nm (lg ε 4.59), 562 (4.27), 437 (4.29), 382sh (4.39), 342 (4.69)		959
	Ni(II)	DCM	613 nm (lg ε 4.76), 564sh, 435 (4.25), 343 (4.74)		948
	Cu(II)	Heptane	625 nm (lg ε 5.00), 575 (4.36), 450 (4.40), 360 (4.88)		959
	Pd(II)	Heptane	615 nm (lg ε 4.61), 535 (4.20), 450 (4.17), 340 (4.70)		959
	In(III)Cl	DCM	653 nm (lg ε 5.07), 602 (4.42), 500 (4.50), 383 (4.94)		336
	In(III)L	DCM	653 nm (lg ε 5.10), 600 (4.41), 504 (4.31), 402 (4.98)	L = Ph(4-CF_3)	336
$\alpha\alpha$ = Ph(4-CF_3)	2H	Poly(chlorotrifluoroethylene)	680 nm, 610, 464, 376	solid state	336
	In(III)Cl	DCM	638 nm (lg ε 5.16), 585 (4.37), 457 (4.30), 379 (5.03)		336
	In(III)L	DCM	639 nm (lg ε 5.12), 587 (4.34), 393 (4.96)	L = Ph(4-CF_3)	336
$\alpha\alpha$ = Ph(3-CF_3)	2H	DCM	658 nm (lg ε 5.00), 590 (4.78), 552sh, 442sh, 365 (4.98)		336
		DCM	658 nm (lg ε 5.17), 589 (4.96), 364 (5.15)		961

(*Continued*)

Table 3. (*Continued*)

Structure	M	Solvent	Transition Energy (Intensity)	Remark	Ref.
	Mg(II)	DCM	631 nm (lg ε 5.24), 579 (4.48), 374 (5.16)		961
	Zn(II)	DCM	628 nm (lg ε 5.28), 576 (4.48), 372 (5.16)		961
	In(III)Cl	DCM	636 nm (lg ε 5.15), 584 (4.38), 458 (4.31), 378 (5.05)		336
	In(III)L	DCM	637 nm (lg ε 5.17), 585 (4.38), 394 (5.03)	L = Ph(4-CF_3)	336
$\alpha\alpha'$ = Ph(4-COOBu)	2H	DCM	668 nm (lg ε 4.84), 601 (4.63), 370 (4.82)		962
	Mn(III)Cl	DCM	665 nm (lg ε 4.84), 473 (4.50), 412 (4.66), 324 (4.73), 258 (4.91)		962
	Zn(II)	DCM	640 nm (lg ε 5.03), 374 (4.85)		962
$\alpha\alpha'$ = Ph(4-Cl)	Mg(II)	THF	640 nm, 380		956
α = Ph(4-Br)	2H	$CHCl_3$	660 nm (lg ε 4.63), 590 (4.43), 359 (4.65)		944
		py	658 nm, 596		944
$\alpha\alpha'$ = Ph(4-Br)	2H	$CHCl_3$	670 nm (lg ε 4.96), 602 (4.75), 372 (4.95)		944
	Mg(II)	THF	641 nm, 382		956
$\alpha\alpha'$ = Ph(4-SO_2Cl)	2H	$CHCl_3$	666 nm (lg ε 4.84), 599 (4.69), 369 (4.92)		944
$\alpha\alpha'$ = Ph(4-Ph)	Mg(II)	$CHCl_3$	652 nm (lg ε 4.64), 380 (4.86)		963
$\alpha\alpha'$ = 	Mg(II)	$CHCl_3$	644 nm (lg ε 3.15), 348 (3.46), 288 (3.70)		964
$\alpha\alpha'$ = (4-py)	2H	20% MeOH in $CHCl_3$	670 nm, 658 (10^3 ε 66), 590 (43), 366 (68)		965
	2H	Dilute aqueous HCl	690 nm, 674, 608, 376, 290, 258		965
	Mg(II)	20% MeOH in $CHCl_3$	650 nm, 634 (10^3 ε 125), 376 (99)		965
$\alpha\alpha'$ = (4-py$^+$)(N-Me)	2H	DMSO	723 nm, 680 (10^3 ε 86), 380 (50)	$[Pc]^{8+}8Cl$	965
	2H	H_2O pH 2.0	696 nm, 678, 616, 380, 266	$[Pc]^{8+}8Cl^-$, 2.0 M NaCl, 0.01 M phosphate	965
	2H	H_2O pH 4.0	676 nm (10^3 ε 55), 614 (40), 380 (62), 266 (45)	$[Pc]^{8+}8Cl^-$, 2.0 M NaCl, 0.01 M phosphate	965
	H	H_2O pH 8.0	686 nm, 672, 382, 332, 288	$[Pc]^{7+}7Cl^-$, 2.0 M NaCl, 0.01 M phosphate	965
	nil	H_2O pH 9.6	718 nm, 678, 385, 332, 287	$[Pc]^{6+}6Cl^-$, 2.0 M NaCl, 0.01 M phosphate	965
	Ni(II)	H_2O pH 4.0	642 nm (10^3 ε 72), 368 (62), 270 (38)	$[Pc]^{8+}8Cl^-$, 2.0 M NaCl, 0.01 M phosphate	965
	Cu(II)	H_2O pH 4.0	644 nm (10^{-3} ε 98), 382 (62), 322 (42), 266 (56)	$[Pc]^{8+}8Cl^-$, 2.0 M NaCl, 0.01 M phosphate	965
		H_2O pH 4.0	644 nm (10^3 ε 100), 382 (62), 266 (55)	$[Pc]^{8+}8[PF_6]^-$, 2.0 M NaCl, 0.01 M phosphate	965
$\alpha\alpha'$ = 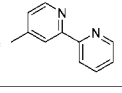	2H	DCM	660 nm, 593, 362, 283, 240		966

(*Continued*)

Table 3. (*Continued*)

Structure	M	Solvent	Transition Energy (Intensity)	Remark	Ref.
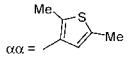	Mg(II)	$CHCl_3$	650 nm (10^{-5} ε 4.3), 365		967
		$CHCl_3$	650 nm (10^{-5} ε 1.81)		968
	Zn(II)	$CHCl_3$	651 nm (10^{-5} ε 3.48)		968
	Pd(II)	$CHCl_3$	635 nm, 493, 345		968
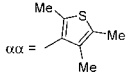	Pt(II)	$CHCl_3$	613 nm (10^{-5} ε 3.2), 574, 322		967
	Mg(II)	$CHCl_3$	643 nm, 588, 369		967
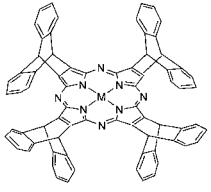	2H	DCM	634 nm (lg ε 4.85), 558 (4.68), 412 (4.39), 346 (4.82)		969
	Mg(II)	Unknown	595 nm (lg ε 4.92), 547 (4.07), 371 (4.80)		969
	Fe(II)	Toluene	646 nm (lg ε 4.25), 588 (4.60), 554 (4.56), 496 (4.42), 418sh, < 300		969
	Fe(II)L	Toluene	590 nm (lg ε 4.98), 570 (4.63), 548 (4.50), 496 (4.35), 356 (4.88)	L = *trans*-py_2	969
		Toluene	654 nm (lg ε 3.82), 572 (4.93), 530sh, 430sh, 368 (4.69)	L = CO	969
		Unknown	746 nm (lg ε 4.05), 646 (4.13), 572 (4.59), 520 (4.65), 414sh, < 300	L = quinoline	969
	Fe(III)Cl	DCM	672 nm (lg ε 4.22), 640sh, 516 (4.46), 432 (4.48), 324 (4.66)		969
	Fe(III)OH	Toluene	672 nm (lg ε 3.86), 618 (4.65), 506 (4.20), 432 (4.45), 324 (4.63)		969
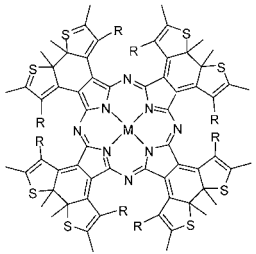	Mg(II)	$CHCl_3$	725 nm	R = H	967
	Mg(II)	$CHCl_3$	703 nm, 627, 364	R = Me	967
	Pt(II)	$CHCl_3$	665 nm		967

(*Continued*)

Table 3. (*Continued*)

Structure	M	Solvent	Transition Energy (Intensity)	Remark	Ref.
α = OH	2H	Acetone/AcOH	636 nm, 603		943
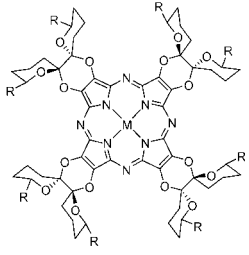	2H	$CHCl_3$	632 nm (lg ε 3.83), 554 (3.75), 427 (3.68), 338 (4.20)	R = H	970
	Mg(II)	$CHCl_3$	599 nm (lg ε 4.62), 551 (3.94), 455 (3.77), 347 (4.79)		970
	Mn(III)Cl	$CHCl_3$	635 nm (lg ε 4.22), 497 (4.23), 450 (4.32), 386 (4.38), 330 (4.44), 272 (4.43)		970
	2H	$CHCl_3$	632 nm (lg ε 4.55), 553 (4.45), 429 (4.37), 338 (4.89)	R = Ph	970
	Mn(III)Cl	$CHCl_3$	633 nm (lg ε 4.28), 491 (4.23), 448 (4.34), 388 (4.41), 330 (4.45), 230 (4.32)		970
$\alpha\alpha$ = SMe	2H	DCM	709 nm (10^{3} ε 35.0), 637 (25.5), 515 (20.0), 367 (42.3)		408
		PhCl	709 nm (10^{-3} ε 35.0), 637 (25.5), 515 (20.0)		417
	Mg(II)	DCM	669 nm, 506, 376		422
		DCM	668.5 nm (lg ε 4.46), 374.0 (4.69)		971
		DCM	672 nm (10^{-3} ε 75.2), 620 (26.5), 500 (12.9), 382 (68.9)		408
		PhCl	672 nm (10^{-3} ε 75.2), 620 (26.5), 500 (12.9), 375 (68.9)		417
	Ni(II)	DCM	660 nm (10^{-3} ε 42.2), 620 (21.7), 482 (18.6), 347 (39.9)		408
		PhCl	660 nm (10^{-3} ε 42.2), 482 (18.6), 347 (39.9)		417
	Cu(II)	DCM	667 nm (10^{-3} ε 48.4), 610 (19.9), 497 (14.8), 363 (36.2)		408
		PhCl	667 nm (10^{-3} ε 48.4), 610 (19.9), 497 (14.8), 363 (36.2)		417
R_2, R_3, R_4, R_5, R_6, R_7, R_8 = SEt	2H	DCM	704 nm (lg ε 4.34), 636 (4.21), 608sh (4.09), 472 (3.97), 354 (4.42)		972
	Mn(III)Cl	DCM	1137 nm (lg ε 2.83), 970 (2.55), 956 (2.63), 825sh (2.85), 720 (4.22), 585 (4.00), 505 (4.04), 446 (4.03), 335 (4.17)		972
	Ni(II)	DCM	673 nm (lg ε 3.68), 588sh (3.45), 467 (3.36), 327 (3.69)		972

(*Continued*)

Table 3. (*Continued*)

Structure	M	Solvent	Transition Energy (Intensity)	Remark	Ref.
	Cu(II)	DCM	665 nm (lg ε 5.52), 624sh (4.26), 471 (4.07), 355 (4.51), 342sh (4.49)		972
$\alpha\alpha$ = SEt	2H	$CHCl_3$	714 nm (lg ε 4.59), 637 (4.45), 498 (4.31), 354 (4.66)		972
		$CHCl_3$	504 nm (lg ε 4.38), 354 (4.18)	$[TAP^{4}]2H^{-}$	972
		DCM	715 nm (lg ε 4.81), 655 (4.60), 670sh (4.56), 632 (4.58), 520 (4.18), 490 (4.17), 360 (4.67)		973
	Mn(II)	EtOH	720 nm (lg ε 4.09), 640 (4.18), 590 (4.40), 450 (3.92), 420 (3.96), 345 (4.37), 280 (4.28)		973
	Mn(III)Cl	DCM	1104 nm (lg ε 2.95), 931 (2.87), 800 (3.00), 714 (3.95), 590sh (3.60), 512 (3.96), 432sh (3.53), 368 (3.90), 328sh (3.99)		972
	Fe(III)O	DCM	660 nm (lg ε 3.00), 644 (3.10), 624 (3.00), 416sh (4.08), 384 (4.37), 320sh (3.96), 292 (4.11), 248 (4.30)		973
	Ni(II)	DCM	663 nm (lg ε 4.40), 484 (4.05), 344sh (4.33), 325 (4.37)		972
	Cu(II)	DCM	669 nm (lg ε 4.66), 619sh (4.28), 492 (4.17), 355 (4.58), 339sh (4.56)		972
$\alpha\alpha$ = $S(CH_2)_2CH(Me)_2$	2H	$CHCl_3$	711 nm (lg ε 3.95), 641 (3.80), 348 (4.01)		974
	Mg(II)	$CHCl_3$	669 nm (lg ε 4.90), 343 (4.94)		974
	Co(II)	$CHCl_3$	674 nm (lg ε 4.85), 376 (4.56)		974
	Ni(II)	$CHCl_3$	666 nm (lg ε 4.89), 326 (4.62)		974
	Zn(II)	$CHCl_3$	673 nm (lg ε 4.90), 374 (4.65)		974
$\alpha\alpha$ = SC_6H_{13}	Ni(II)	Dichloroethane + 0.1 M TBAP	670 nm (10^{-1} ε 3.75), 490 (1.38), 335 (3.75)		975
	Cu(II)	Dichloroethane + 0.1 M TBAP	675 nm (10^{-1} ε 6.83), 495 (2.28), 360 (5.53)		975
R_2, R_3, R_4, R_5, R_6, R_7, R_8 = SC_8H_{17}	2H	$CHCl_3$	712 nm (lg ε 4.19), 640 (4.14), 610sh (4.03), 472 (3.94), 442sh (3.85), 354 (4.35)		976
$\alpha\alpha$ = SC_8H_{17}	2H	$CHCl_3$	713 nm (lg ε 4.48), 639 (4.36), 510 (4.24), 363 (4.52)		976
		DCM	710 nm (lg ε 4.08), 636 (3.05), 502 (2.23), 356 (4.66)		977
$\alpha\alpha$ = $S(CH_2)_2CHCH_2$	2H	$CHCl_3$	715 nm (lg ε 4.82), 648 (4.63), 635sh (4.62), 510 (4.43), 360 (4.85), 340sh (4.85)		978
	Co(II)	$CHCl_3$	645 nm (lg ε 4.71), 483 (4.16), 440 (4.16), 330 (4.69)		978

(*Continued*)

Table 3. (*Continued*)

Structure	M	Solvent	Transition Energy (Intensity)	Remark	Ref.
	Ni(II)	$CHCl_3$	720sh nm (lg ε 4.26). 665 (4.58), 650sh (4.55), 630sh (4.40), 570sh (4.06), 485 (4.13), 325 (4.58)		978
	Cu(II)	$CHCl_3$	675 nm (lg ε 4.87), 636sh (4.54), 500 (4.29), 355 (4.70), 340 (4.72)		978
$\alpha\alpha' = S(CH_2)_3CHCH_2$	2H	$CHCl_3$	713 nm (lg ε 4.41), 643 (4.24), 512 (4.10), 362 (4.41), 352 (4.41)		978
	Co(II)	$CHCl_3$	646 nm (lg ε 4.59), 600sh (4.34), 491 (4.10), 450 (4.02), 331 (4.54)		978
	Ni(II)	$CHCl_3$	670 nm (lg ε 4.03), 619sh (3.90), 489 (3.73), 341sh (4.00), 325 (4.03)		978
	Cu(II)	$CHCl_3$	672 nm (lg ε 4.65), 629sh (4.30), 499 (4.13), 356 (4.50)		978
$\alpha\alpha' = S(CH_2)_4CHCH_2$	2H	$CHCl_3$	713 nm (lg ε 4.01), 643 (3.86), 616sh (3.77), 530sh (3.72), 508 (3.74), 365 (4.00), 338 (4.00)		978
	Co(II)	$CHCl_3$	652 nm (lg ε 3.97), 624sh (3.88), 597sh (3.68), 484 (3.30), 448 (3.30), 347sh (3.91), 330 (3.94)		978
	Ni(II)	$CHCl_3$	667 nm (lg ε 3.96), 622sh (3.81), 490 (3.59), 345sh (3.94), 324 (3.99)		978
	Cu(II)	$CHCl_3$	678 nm (lg ε 3.82), 630sh (3.66), 504 (3.54), 358sh (3.77), 337 (3.78)		978
$\alpha\alpha' = S(CH_2)_6CHCH_2$	2H	$CHCl_3$	714 nm (lg ε 4.46), 654sh (4.27), 647 (4.30), 634sh (4.27), 514 (4.06), 364sh (4.41), 349sh (4.41), 344 (4.43)		978
	Co(II)	$CHCl_3$	664sh nm (lg ε 4.36). 649 (4.38), 489sh (3.70), 389sh (4.02) 344 (4.31)		978
	Ni(II)	$CHCl_3$	680sh nm (lg ε 4.39), 666 (4.41), 641sh (4.33), 619sh (4.26), 509sh (3.97), 490 (4.06), 347sh (4.37), 320 (4.42)		978
	Cu(II)	$CHCl_3$	674 nm (lg ε 4.65), 619sh (4.23), 504 (4.01), 489sh (3.99), 359sh (4.39), 344 (4.48)		978
$\alpha\alpha' = SCH_2CH_2OH$	Mg(II)	$CHCl_3$	666 nm, 370		979
$\alpha\alpha' = S(CH_2CH_2O)_3H$	2H	DCM	710 nm (lg ε 4.15), 630 (4.26), 506 (4.26), 336 (4.64)		980
	Mg(II)	H_2O	668 nm, 502, 372		980
	Mn(II)	$CHCl_3$	641 nm, 580sh, 469sh, 349		981
	Co(II)	$CHCl_3$	641 nm, 580sh, 469sh, 349		981

(*Continued*)

Table 3. (*Continued*)

Structure	M	Solvent	Transition Energy (Intensity)	Remark	Ref.
	Zn(II)	$CHCl_3$	668 nm, 617sh, 506sh, 374		981
α = $S(CH_2CH_2O)_2Me$	2H	THF	708 nm (lg ε 4.59), 636 (4.46), 504 (4.35), 356 (4.71)		982
	Co(II)	THF	643 nm (lg ε 4.67), 455 (4.08), 355 (4.69)		982
	Ni(II)	THF	661 nm (lg ε 4.62), 482 (4.26), 326 (4.65)		982
	Cu(II)	THF	664 nm (lg ε 4.65), 496 (4.19), 352 (4.62)		982
	Zn(II)	THF	672 nm (lg ε 4.84), 375 (4.81)		982
α = $S(CH_2CH_2O)_3Me$	2H	THF	704 nm (lg ε 4.59), 634 (4.49), 501 (4.37), 357 (4.75)		982
		H_2O	623 nm (lg ε 4.15), 508 (4.14), 335 (4.54)		982
	Co(II)	THF	645 nm (lg ε 4.68), 456 (4.09), 354 (4.69)		982
		H_2O	634 nm (lg ε 4.41), 430 (4.09), 334 (4.53)		982
	Ni(II)	THF	661 nm (lg ε 4.63), 483 (4.28), 327 (4.65)		982
		H_2O	623 nm (lg ε 4.31), 486 (4.18), 320 (4.54)		982
	Cu(II)	THF	662 nm (lg ε 4.66), 496 (4.20), 351 (4.63)		982
		H_2O	652 nm (lg ε 4.38), 502 (4.19), 338 (4.57)		982
	Zn(II)	THF	668 nm (lg ε 4.84), 372 (4.83)		982
		H_2O	661 nm (lg ε 4.59), 364 (4.69)		982
$\alpha\alpha$ = $S(CH_2)_3COOH$	2H	Phosphate buffer	700 nm (lg ε 2.94), 660 (2.75), 340 (4.21)		983
$\alpha\alpha$ = $S(CH_2)_3COOPr$	2H	DCM	709 nm (lg ε 3.99), 638 (3.01), 498 (2.23), 356 (4.66)		983
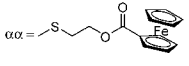	2H	$CHCl_3$	705 nm, 637 490, 349		979
	Mg(II)	$CHCl_3$	669 nm, 376		979
	Co(II)	$CHCl_3$	641 nm, 348		979
	Cu(II)	$CHCl_3$	667 nm, 345		979
	Zn(II)	$CHCl_3$	671 nm, 378		979
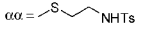	2H	$CHCl_3$	705 nm (lg ε 4.69), 638 (4.64), 356 (4.9)		984
	Mg(II)	$CHCl_3$	670 nm (lg ε 5.02), 374 (5.12)		984
	Co(II)	$CHCl_3$	647 nm (lg ε 4.5), 344 (4.6)		984
	Ni(II)	$CHCl_3$	657 nm (lg ε 4.76), 343 (4.9)		984
	Mg(II)	$CHCl_3$	656 nm (lg ε 4.26), 366 (4.59)		984
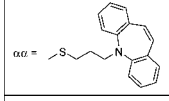	2H	$CHCl_3$	717 nm (lg ε 4.38), 659 (4.34), 506 (3.94), 350 (4.52), 273 (3.97), 240 (4.37)		985
	Mg(II)	$CHCl_3$	674 nm (lg ε 3.86), 623 (3.22), 491 (3.12), 344 (3.82), 321 (3.79), 246 (3.74)		985
$\alpha\alpha$ = SCH_2Ph	2H	$CHCl_3$	667 nm (lg ε 4.41), 602 (4.35), 351 (4.77)		986

(*Continued*)

Table 3. (*Continued*)

Structure	M	Solvent	Transition Energy (Intensity)	Remark	Ref.
		DCM	716 nm (10^{-3} ε 34.7), 648 (25.7), 508 (19.9), 354 (42.7)		408
		PhCl	716 nm (lg ε 4.54), 648 (4.41), 508 (4.30), 354 (4.63)		408
	Mg(II)	DCM	680 nm (10^{3} ε 74.1), 620 (24.7), 500 (12.9), 375 (69.2)		408
		$CHCl_3$	680 nm (lg ε 4.87), 500 (4.11), 382 (4.84)		408
		$CHCl_3$	671 nm (lg ε 4.80), 370 (4.85)		986
		$CHCl_3$	651.7 nm (10^{-3} ε 18.0), 364.4 (31.7), 246.1 (108.0)		987
	Mn(II)	$CHCl_3$	662 nm (lg ε 3.96), 328 (4.73)		986
		$CHCl_3$	662 nm (lg ε 3.96), 328 (4.73)		988
	Co(II)	$CHCl_3$	624 nm (lg ε 4.32), 327 (4.66)		988
		$CHCl_3$	628 nm (lg ε 4.32), 327 (4.66)		986
		DCM	628 nm (lg ε 4.32), 327 (4.66)		989
	Ni(II)	$CHCl_3$	627 nm (lg ε 4.18), 320 (4.54)		986
		$CHCl_3$	625 nm (lg ε 4.18), 318 (4.54)		988
		DCM	672 nm (10^{3} ε 42.7), 620 (22.1), 490 (18.6), 334 (39.8)		408
		PhCl	672 nm (lg ε 4.63), 490 (4.27), 330 (4.60)		408
	Cu(II)	$CHCl_3$	670 nm (lg ε 4.07), 316 (4.60)		986
		$CHCl_3$	663 nm (lg ε 4.07), 316 (4.60)		988
		DCM	673 nm (10^{3} ε 72.8), 620 (27.4), 502 (19.2), 356 (43.5)		408
		PhCl	673 nm (lg ε 4.86), 620 (4.44), 502 (4.28), 356 (4.63)		408
	Zn(II)	$CHCl_3$	668 nm (lg ε 4.38), 355 (4.65)		986
		$CHCl_3$	668 nm (lg ε 4.38), 356 (4.65)		988
$\alpha\alpha$ = SCH_2Ph(4-*t*-Bu)	2H	DCM	714 nm (lg ε 3.88), 653 (3.75), 352 (3.97)		990
	Mg(II)	DCM	678 nm (lg ε 4.38), 380 (4.42)		990
	Co(II)	DCM	684 nm (lg ε 4.32), 352 (4.38)		990
	Cu(II)	DCM	674 nm (lg ε 4.26), 346 (4.24)		990
	Zn(II)	DCM	679 nm (lg ε 4.35), 340 (4.31)		990
$\alpha\alpha$ = SCH_2Ph(4-COOBu)	2H	$CHCl_3$	716 nm, 648, 508, 354		991
$\alpha\alpha$ = $S(CH_2)_2P(O)(OEt)_2$	Mg(II)	$CHCl_3$	668 nm, 368		992
$\alpha\alpha$ = $S(CH_2)_2P(O)(OH)_2$	Mg(II)	$CHCl_3$	706 nm, 638, 362		992

(*Continued*)

Table 3. (*Continued*)

Structure	M	Solvent	Transition Energy (Intensity)	Remark	Ref.
αα = 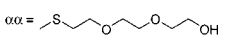	2H	DCM	709 nm, 642, 360		993
	Mg(II)	DCM	670 nm, 372		993
	Zn(II)	DCM	672 nm (lg ε 4.67), 378 (4.62)		993
αα = 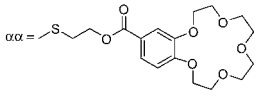	2H	$CHCl_3$	707 nm, 645, 357		994
	Mg(II)	$CHCl_3$	669 nm, 378		994
	Co(II)	$CHCl_3$	647 nm, 348		994
	Cu(II)	$CHCl_3$	664 nm, 346		994
	Zn(II)	$CHCl_3$	671 nm, 378		994
αα = 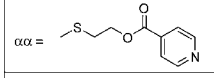	Mg(II)	$CHCl_3$	672 nm, 372		995
αα = 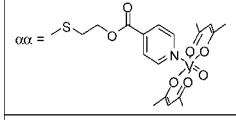	Mg(II)	$CHCl_3$	672 nm, 372		995
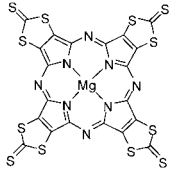	Mg(II)	DMF	646 nm, 382		996
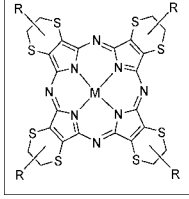	Fe(II)	H_2SO_4	672 nm, 437, 308.	R = Me	997
	2H	THF	699 nm (lg ε 3.97), 531 (4.10), 353 (4.27)	R = OEt	998
	Mg(II)	THF	660 nm (lg ε 4.53), 369 (4.54)		998
	Cu(II)	THF	659 nm (lg ε 4.09), 524 (3.85), 351 (4.23)		998
	Zn(II)	THF	661 nm (lg ε 4.26), 533 (3.70), 365 (4.27)		998

(*Continued*)

Table 3. (*Continued*)

Structure	M	Solvent	Transition Energy (Intensity)	Remark	Ref.
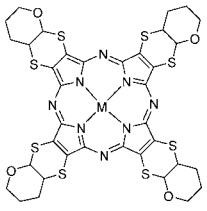	2H	THF	702 nm (lg ε 3.55), 622 (3.43), 517 (3.45), 357 (3.79)		998
	Mg(II)	THF	662 nm (lg ε 4.48), 522 (3.74), 370 (4.44)		998
	Cu(II)	THF	660 nm (lg ε 4.05), 517 (3.75), 353 (4.16)		998
	Zn(II)	THF	662 nm (lg ε 4.24), 528 (3.60), 366 (4.20)		998
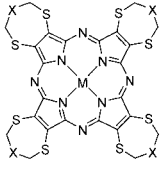	2H	DCM	700 nm (lg ε 3.98), 614 (3.99), 526 (4.02), 358 (4.37)	X = CH_2	412
	Mg(II)	DCM	664 nm (lg ε 4.15), 612 (3.82), 538 (3.69), 370 (4.30)		412
	Ni(II)	PhCl	640 nm (lg ε 4.61), 508 (4.55), 342 (4.85)		412
	Cu(II)	DMF	656 nm (lg ε 4.60), 536 (4.49), 352 (4.80)		412
	Zn(II)	DMF	666 nm (lg ε 4.56), 556 (4.20), 372 (4.73)		412
	2H	DMF	680 nm (lg ε 4.75), 610 (4.81), 518 (4.81), 346 (5.10)	X = S	412
	Mg(II)	DCM	656 nm (lg ε 4.29), 610 (4.15), 514 (4.10), 368 (4.50)		412
	2H	DMF	686 nm (lg ε 5.77), 616 (5.84), 514 (5.84), 346 (6.10)	X = O	412
	Mg(II)	DCM	656 nm (lg ε 4.15), 610 (3.99), 518 (3.93), 370 (4.32)		412
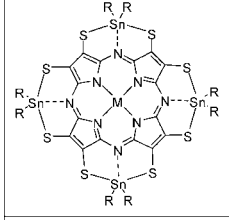	Ni(II)	cyclohexane	650 nm (lg ε 4.73), 414 (3.96), 342 (3.97), 284sh (4.20)	R = Bu	408
	Ni(II)	1,2-dichloroethane	675 nm (lg ε 4.81), 412 (3.96), 332 (3.97), 284 (4.20)		408
	Ni(II)	1,2-dichloroethane	676 nm (lg ε 4.73), 516sh, 438 (3.97), 336 (3.96), 304 (4.30), 260 (4.65)	R = *t*-Bu	408
	Cu(II)	1,2-dichloroethane	690 nm (lg ε 4.81), 424 (4.13), 308 (4.45), 256 (4.75)		408
α = SO_3H	2H	$CHCl_3$	641 nm (lg ε 4.73), 575 (4.58), 369 (4.80)		943
α = SO_3H	Cu(II)	py	629 nm (lg ε 4.86), 570 (4.22), 366 (4.56)		943
$\alpha\alpha$ = $N(Me)_2$	2H	DCM	679 nm (lg ε 4.02), 614sh, 528 (4.21), 334 (4.37)		948
		DCM	709 nm (lg ε 4.16), 531 (4.29), 334 (4.57)		999
	Mg(II)	DCM	752 nm (lg ε 4.33), 599 (4.27), 335 (4.81)		999
	Ni(II)	DCM	704 nm (lg ε 4.52), 561 (4.42), 360 (4.50), 325 (4.92)		966
	Zn(II)	DCM	718 nm (lg ε 4.46), 546 (4.32), 335 (4.69)		999
α = NH(*t*-Bu)	Mg(II)	DCM	708 nm (lg ε 4.29), 336 (4.59)		1000

(*Continued*)

Table 3. (*Continued*)

Structure	M	Solvent	Transition Energy (Intensity)	Remark	Ref.
$\alpha = N(Et)_2$	Mg(II)	DCM	714 nm (lg ε 4.3), 338 (4.5)		1000
$\alpha\alpha = N(CH_2CHCH_2)_2$	2H	$CHCl_3$	730 nm (lg ε 4.36), 526 (4.47), 333 (4.67)		966
$\alpha\alpha = N(CH_2Ph)_2$	Ni(II)	PhCl	674 nm (lg ε 4.00), 654 (4.04), 536 (3.95), 322 (4.71)		966
$\alpha\alpha = N(Me)(CH_2Ph)$	Mg(II)	PhCl	714 nm (lg ε 4.38), 544 (4.10), 350 (4.56)		966
$\alpha\alpha = N(CH_2CHCH_2)(CH_2Ph)$	2H	DCM	734 nm (lg ε 4.44), 536 (4.59), 330 (4.75)		966
	Ni(II)	DCM	688 nm (lg ε 4.49), 511 (4.53), 324 (4.72)		966
αα = 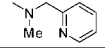	Mg(II)	$CHCl_3$	702 nm (lg ε 4.48), 531 (4.16), 352 (4.65), 258 (4.48)		1001
αα = 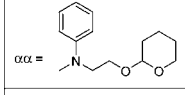	Mg(II)	$CHCl_3$	713 nm (lg ε 4.58), 569 (4.38), 516sh, 359 (4.77), 347sh		966
αα = 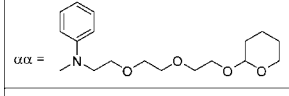	Mg(II)	DCM	711 nm (lg ε 4.57), 574 (4.47), 365 (4.75), 333 (4.69)		966
α = 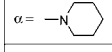	Mg(II)	DCM	705 nm (lg ε 4.28), 346 (4.60)		1000
α = (N-py)	Zn(II)	py	655 nm (lg ε 3.67), 560 (4.36), 360 (3.99)	$4Br^-$	943
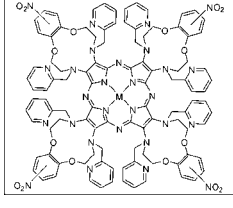	2H	$CHCl_3$	724 nm (lg ε 4.70), 665 (4.60), 578 (4.30), 348 (4.94)		1002
	Mg(II)	$CHCl_3$	666 nm (lg ε 4.52), 576 (4.18), 351 (4.79)		1002
	Zn(II)	$CHCl_3$	658 nm (lg ε 4.76), 583 (4.04), 354 (4.98)		1002

(*Continued*)

Table 3. (*Continued*)

Structure	M	Solvent	Transition Energy (Intensity)	Remark	Ref.
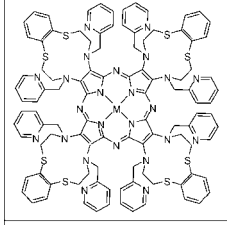	2H	$CHCl_3$	712 nm (lg ε 4.59), 670 (4.47), 575 (4.20), 345 (4.91)		1002
	Mg(II)	$CHCl_3$	662 nm (lg ε 4.83), 579 (4.28), 365 (4.96)		1002
	Zn(II)	$CHCl_3$	668 nm (lg ε 4.81), 580 (3.78), 350 (4.99)		1002
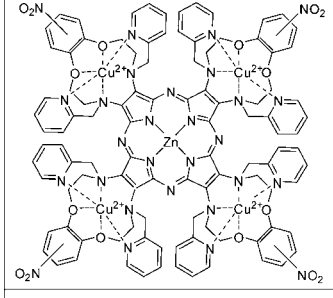	Zn(II)	py	657 nm (lg ε 4.78), 335 (4.88)	$[Pc]^{8+}([ClO_4]^-)_8$	1002
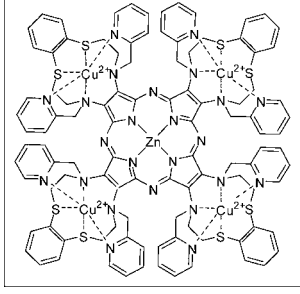	Zn(II)	$CHCl_3$	654 nm (lg ε 4.73), 317 (4.89)	$[Pc]^{8+}([ClO_4]^-)_8$	1002

(*Continued*)

Table 3. (*Continued*)

Structure	M	Solvent	Transition Energy (Intensity)	Remark	Ref.
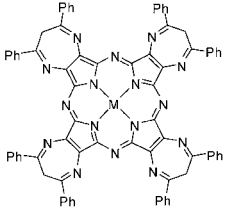	2H	py	677sh nm (lg ε 4.44), 639 (4.55), 490sh, 357 (4.86), 339sh		1003
	2Li	py	687 nm (lg ε 4.75), 640 (4.36), 394sh, 360 (4.84)		1004
	2Na	py	688 nm (lg ε 4.42), 643 (4.62), 359 (4.84)		1004
	Mg(II)	py	680 nm (lg ε 4.83), 639 (5.12), 589 (4.22), 374 (5.05), 351sh		1003
	Cu(II)	py	674 nm (lg ε 4.73), 628 (4.93), 577 (4.24), 365 (4.94), 323sh		1003
	Zn(II)	py	678 nm (lg ε 4.80), 637 (5.07), 585 (4.20), 384sh, 367 (5.02), 348sh		1003
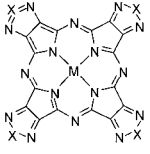	2H	py	682 nm (10^{-3} ε 44.38), 650sh (20.33), 619sh (11.23), 536 (4.23), 382 (36.14), 357 (49.08)	X = Se	1005
		py	682 nm		411
		H_2SO_4	710 nm, 346		1005
		TFA	665 nm, 308		1005
	Mg(II)	py	674 nm (10^{-3} ε 24.10), 648 (7.32), 618 (5.85), 356 (20.31), 319 (25.49)		1005
		py	674 nm		411
	Cu(II)	py	677 nm (10^{-3} ε 40.91), 651sh (16.14), 627sh (11.11), 361 (34.12), 321sh (25.60)		1005
		py	677 nm		411
		H_2SO_4	705 nm, 652, 611, 355		1005
		TFA	662 nm, 305		1005
	Zn(II)	py	681 nm		411
	2H	DCM	649 nm, 636, 604, 590sh, 413sh, 331, 275	X = S	1006
		DCM	649 nm, 636		411
		DCM	649 nm, 636		520
		PhCl	653 nm, 641, 607, 593, 415sh, 333		1006
		PhCl	658 nm, 641		411
		py	648 nm (10^{-4} ε 5.07), 622 (1.85), 591sh (0.98), 483 (0.49), 397sh (2.54), 375 (3.41), 318sh (4.29)	X = S , c = 2.05×10^{-5} M	1006
		py	648 nm	X = S	411
		TFA	642 nm, 624, 594, 575sh, 405sh, 319, 275		1006
		AcOH	642 nm, 624		411

(*Continued*)

Table 3. (*Continued*)

Structure	M	Solvent	Transition Energy (Intensity)	Remark	Ref.
		H_2SO_4	676 nm, 656sh, 626, 605sh, 327, 302, 272sh		1006
	Mg(II)	PhCl	647 nm, 620, 590, 410sh, 330		1006
		py	642 nm (10^{-1} ε 7.06), 615 (1.36), 585 (1.02), 398sh (1.79), 371 (3.23), 322 (3.32)	X = S, c = 2.35×10^{-5} M	1006
		py	642 nm	X = S	411
	Al(III)Cl	py	647 nm, 622, 590, 393sh, 364sh, 340		1007
		DMF	643 nm, 617, 586, 385sh, 355sh, 333		1007
		DMSO	649 nm, 623, 590, 340		1007
		TFA	648 nm, 642sh, 620, 583, 329		1007
		H_2SO_4	660 nm, 649sh, 600sh, 330		1007
	Al(III)Br	py	646 nm, 620, 586, 392sh, 364sh, 340		1007
		DMF	643 nm, 618, 586, 359sh, 331		1007
		DMSO	651 nm, 627, 592, 343		1007
		TFA	647 nm, 643sh, 622sh, 583, 329		1007
		H_2SO_4	660 nm, 649sh, 602sh, 330		1007
	Al(III)OH	py	648 nm, 620, 588, 392sh, 363sh, 340		1007
		DMF	643 nm, 618, 585, 351sh, 326		1007
		DMSO	652 nm, 629sh, 592, 342		1007
		TFA	647 nm, 643sh, 620sh, 583, 329		1007
		H_2SO_4	660 nm, 649sh, 602sh, 330		1007
	Mn(II)	DMSO	708sh nm, 653, 623sh, 599sh, 498sh, 466sh, 375sh, 352sh, 309		1008
		TFA	681 nm, 646, 618sh, 593sh, 513, 330		1008
		H_2SO_4	662 nm, 642sh, 601sh, 348sh, 316sh		1008
	Fe(II)	py	676 nm, 646sh, 603sh, 504, 443, 411, 344		1008
		TFA	684sh nm, 643, 627sh, 599sh, 577sh, 472, 320		1008
		H_2SO_4	693 nm, 667sh, 481, 306		1008
	Co(II)	py	639 nm, 605sh, 585sh, 445, 341		1008
		DMSO	664sh nm, 632, 605sh, 580sh, 458, 331		1008
		HCOOH	635 nm, 332		1008
		TFA	678sh nm, 632, 602sh, 578sh, 315		1008
		H_2SO_4	656 nm, 631sh, 593sh, 314		1008
	Ni(II)	py	631 nm, 605sh, 578, 365, 327sh, 311	X = S	1008
		DMSO	627 nm, 603, 571, 358, 305		1008

(*Continued*)

Table 3. (*Continued*)

Structure	M	Solvent	Transition Energy (Intensity)	Remark	Ref.
		HCOOH	638 nm, 613, 583, 331		1008
		TFA	635 nm, 597sh, 576sh, 390sh, 322		1008
		H_2SO_4	660 nm, 627sh, 601, 317		1008
	Cu(II)	PhCl	642 nm, 618, 584, 337		1006
		py	642 nm (10^4 ε 9.69), 618 (2.48), 586 (1.61), 439 (0.37), 363sh (2.73), 331 (4.47)	X = S, c = 1.61×10^5 M	1006
		py	642 nm	X = S	411
		TFA	631 nm, 609sh, 575, 457sh, 395sh, 325, 275		1006
		H_2SO_4	661 nm, 627sh, 598sh, 322, 306sh, 270		1006
	Zn(II)	py	645 nm, 619, 588, 396sh, 367, 336		1008
		py	645 nm		411
		DMSO	638 nm, 609sh, 585, 398sh, 353, 329		1008
		HCOOH	639 nm, 612sh, 589, 331		1008
		TFA	643 nm, 613sh, 583, 327		1008
		H_2SO_4	664 nm, 632sh, 603, 323		1008
	Ga(III)Cl	py	645 nm, 617, 585, 400sh, 367sh, 337		1007
		DMF	641 nm, 615, 584, 323sh		1007
		DMSO	647 nm, 624, 587, 338		1007
		TFA	645 nm, 640sh, 615, 582, 329		1007
		H_2SO_4	659 nm, 648sh, 597sh, 330		1007
	Ga(III)OH	py	646 nm, 618, 587, 393sh, 370sh, 342		1007
		DMF	640 nm, 615, 583, 331		1007
		DMSO	647 nm, 624, 589, 340		1007
		TFA	646 nm, 640sh, 616sh, 582, 329		1007
		H_2SO_4	659 nm, 649sh, 612sh, 599sh, 330		1007
	In(III)OAc	py	658 nm, 602, 390sh, 365sh, 321		1007
		DMF	654 nm, 598sh, 369		1007
		DMSO	658 nm, 636sh, 609, 357sh		1007
		TFA	646 nm, 629, 594, 371sh, 328		1007
		H_2SO_4	671 nm, 618sh, 390sh, 317		1007
α = F	2H	$CHCl_3$	636 nm, 576		943
α = Cl	2H	$CHCl_3$	638 nm (lg ε 4.71, 572 (4.57), 351 (4.81)		943
α = Br	2H	$CHCl_3$	639 nm (lg ε 4.71), 572 (4.57), 350 (4.81)		943
		$CHCl_3$	639 nm (lg ε 4.71), 574 (4.57), 350 (4.81)		942

t(*Continued*)

Table 3. (*Continued*)

Structure	M	Solvent	Transition Energy (Intensity)	Remark	Ref.
		$CHCl_3$	639 nm (lg ε 4.71), 572 (4.57), 350 (4.81)		944
	Cu(II)	py	620 nm (lg ε 4.86), 560 (4.36), 358 (4.90)		943
$\alpha\alpha' = N(CH_2Ph)(CH_2CH_2OH)$	2H	$CHCl_3$	725 nm (lg ε 4.32), 556 (4.32), 335 (4.63)		966
$\alpha\alpha' = N(CH_2Ph)((CH_2CH_2O)_3H)$	2H	$CHCl_3$	740sh nm, 661sh, 556 (lg ε 4.53), 348sh, 328 (4.62)		966
$\alpha\alpha' = N(CH_2Ph)((CH_2CH_2O)_3Me)$	2H	$CHCl_3$	741sh nm, 667sh, 556 (lg ε 4.60), 356 (4.60), 327 (4.60)		966
	Mg(II)	$CHCl_3$	708 nm (lg ε 4.51), 577 (4.36), 365 (4.66), 330 (4.63)		966
	Ni(II)	$CHCl_3$	680 nm (lg ε 4.38), 532 (4.46), 379sh, 312 (4.68)		966
$\alpha\alpha' = t$-Bu, NO_2	2H	$CHCl_3$	632 nm (lg ε 4.87), 604 (4.01), 563 (4.71), 530sh (4.17), 341 (4.85)		1009
		hexane	623 nm (r.i. 1.0), 591 (0.2), 564 (0.28), 545 (1.09), 514sh (0.32), 337 (1.04), 321 (0.79)		1009
	Co(II)	$CHCl_3$	577 nm (lg ε 4.84), 529sh (4.36), 317 (4.68)		1009
		hexane	576 nm (r.i. 1.0), 528sh (0.48), 315 (1.05)		1009
	Cu(II)	$CHCl_3$	588 nm (r.i. 1.0), 536 (0.2), 338 (0.53)		1009
	Zn(II)	$CHCl_3$	602 nm (r.i. 1.0), 584 (0.9), 538sh (0.2), 338 (0.78)		1009
$\alpha\alpha' = CN$, NH(t-Bu)	2H	DCM	774.7 nm, 748.3, 719.6, 683.5, 444.7, 403.4, 335		1000
$\alpha\alpha' = CN$, $N(Et)_2$	2H	DCM	802 nm, 742.5, 705, 670, 437.5, 425, 343		1000
	Zn(II)	DCM	745 nm (lg ε 4.5), 662 (3.8), 343 (4.3)		1000
$\alpha\alpha' = CN$, $NH(C_5H_{11})$	2H	DCM	754 nm, 670, 460, 406, 328		1000
	Zn(II)	DCM	728 nm (lg ε 4.20), 338, 332 (4.5)		1000
$\alpha\alpha' = CN$, 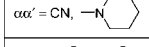	2H	DCM	816 nm, 753, 710, 660, 521, 371.5		1000
	Zn(II)	DCM	758 nm (lg ε 4.25), 686 (3.43), 346 (4.36)		1000
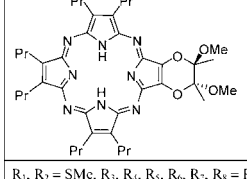	2H	DCM	627 nm (lg ε 4.99), 557 (4.74), 341 (5.09)		1010
R_1, R_2 = SMe, R_3, R_4, R_5, R_6, R_7, R_8 = Pr	2H	DCM	634 nm (lg ε 4.21), 584 (4.16), 550 (3.84), 348 (4.39)		1011
R_1, R_2 = SCH_2COOEt, R_3, R_4, R_5, R_6, R_7, R_8 = Pr	2H	DCM	632 nm (lg ε 4.11), 592 (4.04), 348 (4.20)		1011
R_1, R_2 = SCH_2COOEt, R_3, R_4, R_5, R_6, R_7, R_8 = Pr	Ni(II)	DCM	618 nm (lg ε 4.55), 600 (4.53), 385 (4.02), 325 (4.57)		1011

(*Continued*)

Table 3. (*Continued*)

Structure	M	Solvent	Transition Energy (Intensity)	Remark	Ref.
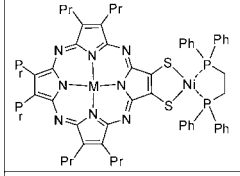	2H	DCM	661 nm (lg ε 4.34), 587 (4.44), 549 (4.38), 339 (4.68)		1011
	Zn(II)	DCM	668 nm (lg ε 3.93), 622 (4.41), 572 (4.03), 346 (4.48)		1011
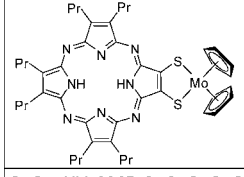	2H	DCM	636 nm (lg ε 3.56), 576 (3.76), 345 (3.87)		1011
R_1, R_2 = NMeCOCF$_3$, R_3, R_4, R_5, R_6, R_7, R_8 = Pr	2H	DCM	616 nm (lg ε 4.01), 586 (4.08), 546 (3.55), 340 (4.16)		1012
R_1 = NMe$_2$, R_2 = NHMe, R_3, R_4, R_5, R_6, R_7, R_8 = Pr	2H	Hexanes/AcOEt = 9:1	652 nm, 625, 595, 549, 338		1012
R_1 = NMe$_2$, R_2 = NMeCOMe, R_3, R_4, R_5, R_6, R_7, R_8 = Pr	2H	DCM	668 nm (lg ε 3.56), 617 (3.59), 591 (3.61), 549 (3.50), 342 (4.08)		1012
	Zn(II)	DCM	626 nm (lg ε 4.25), 508 (3.73), 342 (4.55)		1012
R_1 = NMe$_2$, R_2 = NMeCOCF$_3$, R_3, R_4, R_5, R_6, R_7, R_8 = Pr	2H	DCM	670 nm (lg ε 3.83), 595 (3.93), 540 (3.65), 344 (4.35)		1012
	Zn(II)	DCM	630 nm (lg ε 3.94), 490 (3.26), 342 (4.20)		1012
R_1 = NHMe, R_2 = NMeCOCF$_3$, R_3, R_4, R_5, R_6, R_7, R_8 = Pr	Zn(II)	DCM	644 nm (lg ε 4.29), 617 (4.46), 572 (4.05), 341 (4.62)		1012
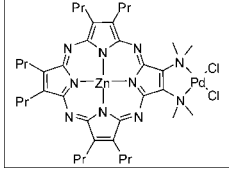	Zn(II)	DCM	605 nm (lg ε 4.83), 578 (4.65), 342 (4.81)		1013

(*Continued*)

Table 3. (*Continued*)

Structure	M	Solvent	Transition Energy (Intensity)	Remark	Ref.
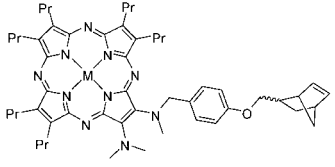	2H	DCM	638 nm (lg ε 4.03), 555 (4.14), 338 (4.53)		1014
	Mg(II)	DCM	650 nm (lg ε 4.34), 557 (4.09), 348 (4.66)		1014
	Zn(II)	DCM	602 nm (lg ε 4.43), 560 (4.34), 340 (4.80)		1014
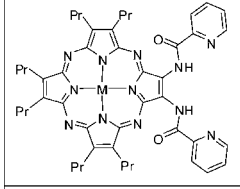	2H	DCM	631 nm (lg ε 4.18), 572 (4.48), 347 (4.74)		1015
	Ni(II)	DCM	600 nm (lg ε 4.64), 328 (4.67)		1015
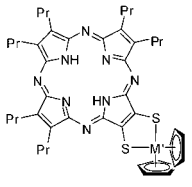	2H	$CHCl_3$	637 nm, 576, 346	M′ = Mo(IV)	1016
		DCM	627 nm, 601, 352	M′ = Mo(V)	1016
R_1, R_2 = SCH_2Ph(4-COOBu), R_3, R_4, R_5, R_6, R_7, R_8 = Pr	2H	$CHCl_3$	634 nm (lg ε 4.50), 596 (4.48), 346 (4.63)		1016
R_1, R_2 = NMe_2, R_3, R_4, R_5, R_6, R_7, R_8 = Pr	Zn(II)	DCM	597 nm (lg ε 4.48), 341 (4.82)		999

(*Continued*)

Table 3. (*Continued*)

Structure	M	Solvent	Transition Energy (Intensity)	Remark	Ref.
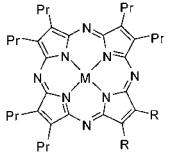	2H	DCM	640 nm (lg ε 4.23), 571 (4.37), 339 (4.70)	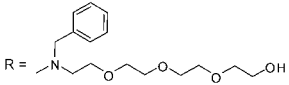	962
	Zn(II)	DCM	609 nm (lg ε 4.47), 345 (4.76)		962
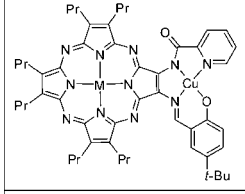	V(IV)O	DCM	634 nm (lg ε 4.52), 566 (4.47), 347 (4.80)		1017
	Mn(III)Cl	DCM	637 nm (lg ε 4.42), 595 (4.43), 366 (4.56)		1017
	Cu(II)	DCM	640 nm (lg ε 4.46), 607 (4.54), 344 (4.75)		1017
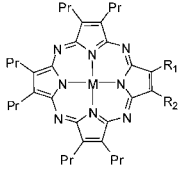	2H	DCM	636 nm (lg ε 4.26), 553 (4.36), 343 (4.78)	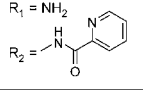	1017
	V(IV)O	DCM	605 nm (lg ε 4.29), 555 (4.23), 343 (4.61)		1017
	Mn(III)Cl	DCM	627 nm (lg ε 4.19), 557 (4.16), 366 (4.52)		1017
	Fe(III)Cl	DCM	564 nm, 375, 317		1018
	Zn(II)	DCM	604 nm, 345	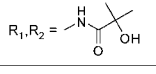	1018
		DCM	649 nm (lg ε 4.04), 612 (4.73), 596 (4.64), 346 (4.77)	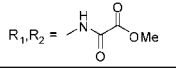	1018
		DCM: MeOH = 25:1	616 nm (lg ε 4.54), 350 (4.66), 239 (3.81)	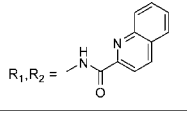	1018

(*Continued*)

Table 3. (*Continued*)

Structure	M	Solvent	Transition Energy (Intensity)	Remark	Ref.
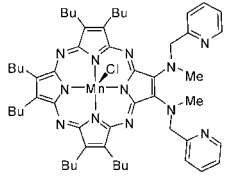	Mn(III)Cl	$CHCl_3$	737 nm (lg ε 4.48), 684sh, 521 (4.15), 381 (4.60), 367sh, 279 (4.70)		1001
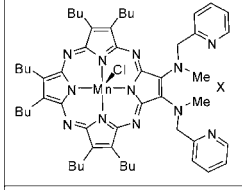	Mn(III)Cl	$CHCl_3$/MeOH = 3:1	733 nm (lg ε 4.60), 656 (4.43), 607sh, 390 (4.58), 367sh, 284sh, 267 (4.67)	X = $Cu(OAc)_2$	1001
		$CHCl_3$/MeOH = 1:1	735 nm (lg ε 4.74), 664 (4.57), 615sh, 386 (4.72), 373sh, 281 (4.77)	X = $CoCl_2$	1001
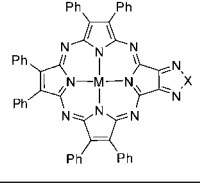	Mg(II	DCM	676 nm, 610, 565sh, 462, 373	X = Se	1019
		DCM	660 nm, 615, 561sh, 460, 369	X = S	1019
	Fe(II)L	py	655 nm (lg ε 4.47), 597 (4.24), 547 (3.97), 502 (4.04), 460 (4.08), 353 (4.75)	L = *trans*-py_2, X = Se	1019
		py	645 nm (lg ε 4.43), 598 (4.31), 551 (3.99), 465 (4.15), 351 (4.89)	L = *trans*-py_2, X = S	1019
R_1, R_2 = OH, R_3, R_4, R_5, R_6, R_7, R_8 = Ph(4-*t*-Bu)	Ni(II)	DCM	642 nm (lg ε 4.70), 607 (4.63), 448 (4.43), 337 (4.79)		1010
	Cu(II)	DCM	640 nm (lg ε 4.98), 610 (4.75), 458 (4.43), 354 (4.87)		1010
R_1, R_2 = $OSiMe_2$(*t*-Bu), R_3, R_4, R_5, R_6, R_7, R_8 = Ph(4-*t*-Bu)	2H	DCM	761 nm (lg ε 3.08), 657 (3.85), 629 (4.80), 601 (4.01), 558 (4.56), 342 (4.90)		1010

(*Continued*)

Table 3. (*Continued*)

Structure	M	Solvent	Transition Energy (Intensity)	Remark	Ref.
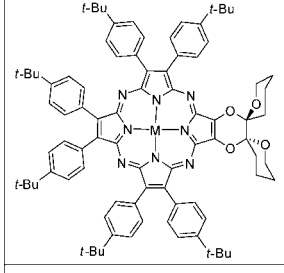	2H	DCM	675 nm (lg ε 4.60), 652 (4.64), 610 (4.61), 458 (4.50), 362 (4.87)		1010
	Ni(II)	DCM	632 nm (lg ε 4.78), 614 (4.75), 446 (4.51), 342 (4.87)		1010
	Cu(II)	DCM	634 nm (lg ε 5.03), 615 (4.95), 456 (4.56), 357 (5.03)		1010
	Zn(II)	DCM	640 nm (lg ε 4.88), 625 (4.81), 466 (4.26), 432 (4.30), 359 (4.89)		1010
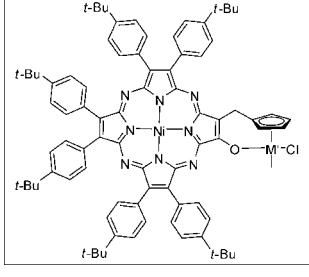	Ni(II)	DCM	667 nm (lg ε 4.42), 625 (4.49), 435 (4.31), 342 (4.70), 269 (4.71)	M′ = Ti	1010

(*Continued*)

Table 3. (*Continued*)

Structure	M	Solvent	Transition Energy (Intensity)	Remark	Ref.
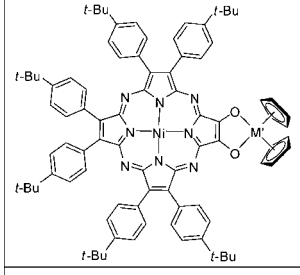	Ni(II)	DCM	624 nm (lg ε 4.61), 594 (4.65), 427 (4.34), 342 (4.77), 273 (4.77)	M′ = Ti	1010
		DCM	617 nm (lg ε 4.60), 597 (4.62), 440 (4.24), 342 (4.70)	M′ = Zr	1010
		DCM	624 nm (lg ε 4.49), 594 (4.52), 458 (4.25), 432 (4.22), 339 (4.71)	M′ = Hf	1010
R_1, R_4, R_6, $R_7(R_8)$ = *t*-Bu, R_2 = CHClPh	2H	Benzene	630 nm (lg ε 4.70), 562 (4.55), 340 (4.80)		1020
R_1, R_3, R_5, R_7 = *t*-Bu, R_2 = CN	Cu(II)	Benzene	602 nm (lg ε 4.92), 574 (4.77), 524sh (4.01), 336 (4.74)		1020
R_1, R_4, R_6, $R_7(R_8)$ = *t*-Bu, R_2 = OPh	2H	Benzene	627 nm (lg ε 4.81), 557 (4.44), 340 (4.80)		1020
R_1, R_4, R_6, $R_7(R_8)$ = *t*-Bu, R_2 = SPh	2H	Benzene	624 nm (r.i. 1.0), 584 (0.88), 332 (1.3)		1020
R_1, R_2 = $SCH_2PhCOOBu$, R_3, R_4, R_5, R_6, R_7, R_8 = Ph(4-*t*-Bu)	2H	$CHCl_3$	682 nm, 614, 474, 372		1021
	Ni(II)	$CHCl_3$	642 nm, 600, 462, 348	$[TAP]^{-2}$ $2[Na]^{+1}$	1021
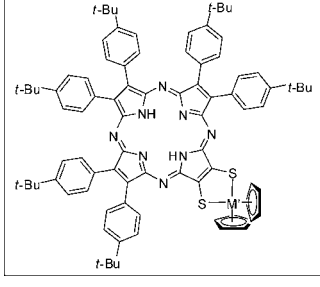	2H	$CHCl_3$	672sh nm (lg ε 4.44), 622 (4.95), 462 (4.35), 368 (4.85)	M′ = Mo(IV)	1016
		$CHCl_3$	684 nm, 609, 459, 371	M′ = V(IV)	1016
		DCM	672 nm, 622, 481, 371	M′ = Mo(V)	1016

(*Continued*)

Table 3. (*Continued*)

Structure	M	Solvent	Transition Energy (Intensity)	Remark	Ref.
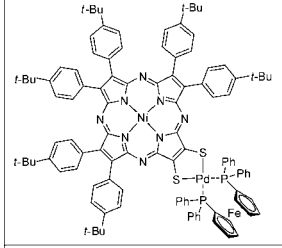	Ni(II)	$CHCl_3$	639 nm, 623, 481, 342		1021
R_1, R_2 = $SOCH_2$(*t*-Bu), R_3, R_4, R_5, R_6, R_7, R_8 = Ph(4-*t*-Bu)	Ni(II)	$CHCl_3$	636 nm, 451, 349		1021
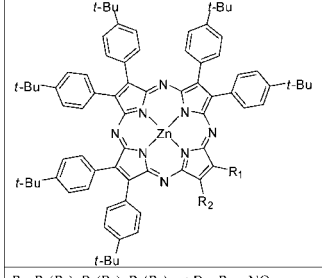	Zn(II)	DCM: MeOH = 50:1	641 nm (lg ε 4.85), 374 (4.82)	R_1,R_2 = 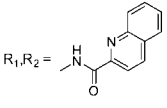	1018
R_1, R_3(R_4), R_5(R_6), R_7(R_8) = *t*-Bu, R_2 = NO_2	2H	$CHCl_3$	615 nm (lg ε 4.79), 574 (4.64), 536sh (4.18), 332 (4.81)		1009
		Hexane	610 nm (r.i. 1.0), 555 (0.69), 514 (0.29), 330 (1.02)		1009
R_1(R_2), R_3(R_4), R_5(R_6), R_7(R_8) = *t*-Bu, R_1(R_2), R_3(R_4), R_5(R_6) = NO_2 and R_1(R_2), R_3(R_4), R_5(R_6), R_7(R_8) = t-Bu, R_1(R_2), R_3(R_4), R_7(R_8) = NO_2	2H	$CHCl_3$	618 nm (lg ε 4.81), 569 (4.64), 528sh (4.11), 337 (4.82)		1009
		Hexane	612 nm (r.i. 1.0), 582sh (0.21), 555 (0.74), 518sh (0.28), 332 (1.03)		1009
	Co(II)	$CHCl_3$	568 nm (r.i. 1.0), 524sh (0.42), 316 (1.33)		1009
	Zn(II)	$CHCl_3$	608 nm (r.i. 1.0), 592 (0.94), 543sh (0.3), 333 (0.87)		1009
R_1, R_2 = NO_2, R_3, R_4, R_5, R_6, R_7, R_8 = Ph(4-*t*-Bu)	2H	DCM	657 nm (lg ε 4.66), 523 (4.49), 373 (4.64), 353sh		948
	Ni(II)	DCM	659 nm (lg ε 4.03), 582sh, 502 (3.87), 370 (4.15), 348 (4.14)		948
R_1, R_2 = NMe_2, R_3, R_4, R_5, R_6, R_7, R_8 = Ph(4-COOBu)	2H	DCM	594 nm (lg ε 3.83), 359 (4.00)		962

(*Continued*)

Table 3. (*Continued*)

Structure	M	Solvent	Transition Energy (Intensity)	Remark	Ref.
R_1, R_2 = 4-py, R_3, R_4, R_5, R_6, R_7, R_8 = NMe_2	2H	DCM	539 nm (lg ε 4.38), 339 (4.49)		966
	Zn(II)	DCM	593 nm (lg ε 4.46), 357 (4.77)		966
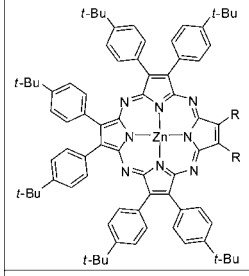	Zn(II)	THF	682 (r.i.1.00), 629 (0.770), 580 (0.236), 379 (0.802), 365 (0.840)	R′= 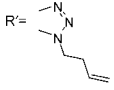	918
		THF	691 (r.i.1.00), 623 (0.742), 582sh, 383 (0.781), 364 (0.791)	R′= 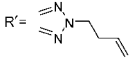	918
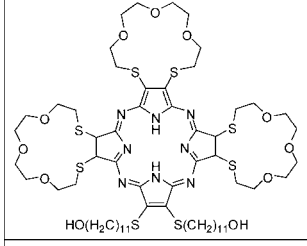	2H	$CHCl_3$	712 nm (lg ε 4.31), 644 (4.18), 504 (4.00), 346 (4.38)		1022
R_1, R_2 = SMe, $R_3(R_4)$, $R_5(R_6)$, R_7 (R_8) = OPh(4-C(Ph)$_3$)	2H	$CHCl_3$	703 nm (r.i. 0.90), 667 (0.69), 632 (0.56), 348 (1.00)		1023
R_1 = Br, R_2, R_3, R_4, R_5, R_6, R_7, R_8 = SC_8H_{17}	2H	$CHCl_3$	708 nm (lg ε 4.43), 639 (4.33), 522 (4.22), 355 (4.52)		976
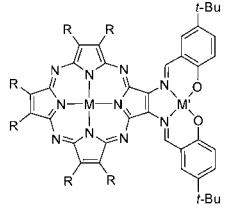	2H	DCM	688 nm (lg ε 4.39), 656 (4.40), 569 (4.21), 348 (4.71)	R = Pr, M′ = Ni(II)	1024
	Mn(III)Cl	DCM	694 nm, 656, 381, 344	R = Pr, M′ = Cu(II)	1024
		DCM	748 nm, 592, 367	R = Pr, M′ = Ni(II)	1024
		DCM	685 nm, 642, 573, 382, 337	R = Pr, M′ = V(IV)O	1025
	Ni(II)	DCM	696 nm (lg ε 4.06), 582 (3.89), 338 (4.32)	R = Pr, M′ = Ni(II)	1024
	Cu(II)	DCM	662 nm, 592, 341	R = Pr, M′ = Mn(III)Cl	1024
		DCM	690 nm, 660, 553, 352	R = 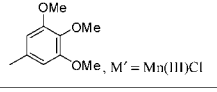 M′ = Mn(III)Cl	1024

(*Continued*)

Table 3. (*Continued*)

Structure	M	Solvent	Transition Energy (Intensity)	Remark	Ref.
		DCM	666 nm, 600, 346	R = Pr, M′ = Cu(II)	1025
		DCM	645 nm, 532, 349	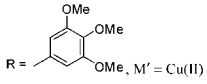 R = , M′ = Cu(II)	1025
		DCM	679 nm, 537, 348	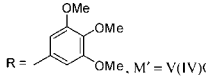 R = , M′ = V(IV)O	1025
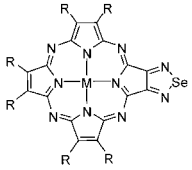	2H	DCM	653 nm (lg ε 4.87), 552 (4.60), 346 (4.81)	R = Pr	1026
	Mg(II)	DCM	650 nm (lg ε 4.12), 599 (4.19), 346 (4.52)		1026
	Mn(III)Cl	DCM	679 nm, 618, 361		1024
	Ni(II)	DCM	634 nm (lg ε 4.37), 578 (4.36), 346 (4.51), 332 (4.51)		1024
	Cu(II)	DCM	636 nm (lg ε 4.50), 593 (4.42), 581 (4.41), 354 (4.63), 339 (4.58)		1024
	Zn(II)	DCM	638 nm (lg ε 5.59), 595 (5.48), 354 (5.73), 341 (5.69)		1018
	2H	DCM	710 nm, 579, 535, 342	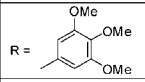 R =	1024
	Mg(II)	DCM	689 nm, 617, 362		1024
	Cu(II)	DCM	685 nm, 616, 550, 456, 342		1024
	Zn(II)	DCM: MeOH = 25:1	676 nm (lg ε 4.77), 611 (4.54), 366 (4.77)	R = Ph(4-*t*-Bu)	1018
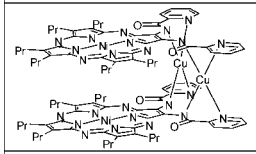	Ni(II)	DCM	590 nm (lg ε 4.85), 319 (5.04)		1015
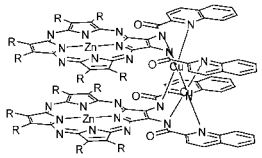	Zn(II)	DCM: MeOH = 10: 1	653 nm (lg ε 4.21), 608 (4.13), 345 (4.41), 318 (4.40), 251 (4.65)	R = Pr	1018
		DCM	696 nm, 576, 471, 390, 332	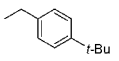 R =	1018

(*Continued*)

Table 3. (*Continued*)

Structure	M	Solvent	Transition Energy (Intensity)	Remark	Ref.
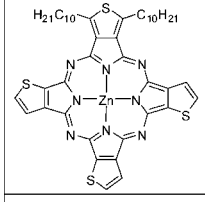	2H	Cyclohexane	740 nm, 701, 664, 631, 342		54
		THF	740 nm, 701, 664, 631, 342		54
R_1, R_3, R_5, R_7 = *t*-Bu, R_2, R_6 = CN	Cu(II)	Benzene	627 nm (lg ε 4.92), 563 (4.58), 341 (4.71)		1020
R_1, R_3, R_5, R_7 = *t*-Bu, R_2, R_4 = CN	Cu(II)	Benzene	598 nm (r.i. 1.0), 540 (0.16), 342 (0.62)		1020
R_1, R_4, R_6, R_7(R_8) = *t*-Bu, R_2, R_3(R_5) = SPh	2H	Benzene	624 nm (r.i. 1.0), 564 (0.7), 332 (1.27)		1020
R_1, R_2, R_3, R_4 = SMe, R_5 (R_6), R_7 (R_8) = OPh(4-C(Ph)$_3$)	2H	$CHCl_3$	683 nm (r.i. 1.00), 616 (0.31), 353 (0.70)		1023
R_1, R_2, R_5, R_6 = SMe, R_2 (R_3), R_7 (R_8) = OPh(4-C(Ph)$_3$)	2H	$CHCl_3$	700 nm (r.i. 0.63), 622 (0.53), 347 (1.00)		1023
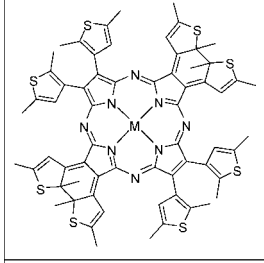	Mg(II)	$CHCl_3$	712 nm		968
	Zn(II)	$CHCl_3$	713 nm		968
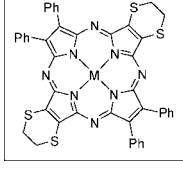	2H	Benzene	675 nm, 629, 598, 364		787
	Co(II)	Benzene	623 nm, 455, 335		787
		18 M H_2SO_4	670 nm		787
	Cu(II)	Benzene	636 nm, 454, 334		787
		18 M H_2SO_4	675 nm		787

(*Continued*)

Table 3. (*Continued*)

Structure	M	Solvent	Transition Energy (Intensity)	Remark	Ref.
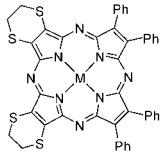	2H	Benzene	686 nm, 635, 598, 362		787
	Co(II)	Benzene	625 nm, 458, 342		787
		18 M H_2SO_4	673 nm		787
	Cu(II)	Benzene	642 nm, 461, 338		787
		18 M H_2SO_4	683 nm		787
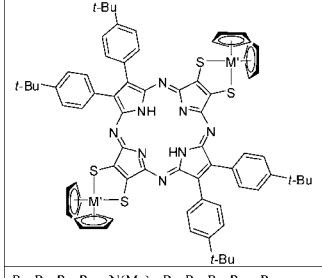	2H		742 nm (very broad), 667, 610, 399	M′ = V(IV)	1016
R_1, R_2, R_3, R_4 = N(Me)$_2$, R_5, R_6, R_7, R_8 = Pr	2H	DCM	563 nm (lg ε 4.14), 337 (4.53)		1013
	Zn(II)	DCM	625 nm (lg ε 4.17), 337 (4.54)		1013
R_1, R_2, R_5, R_6 = N(Me)$_2$, R_3, R_4, R_7, R_8 = Pr	2H	DCM	625sh nm, 537 (lg ε 4.46), 336 (4.71)		1013
	Zn(II)	DCM	628 nm (lg ε 4.40), 342 (4.77)		1013
$R_1(R_2)$, $R_3(R_4)$, $R_5(R_6)$, $R_7(R_8)$ = *t*-Bu, $R_1(R_2)$, $R_3(R_4)$ = NO_2 and $R_1(R_2)$, $R_3(R_4)$, $R_5(R_6)$, $R_7(R_8)$ = *t*-Bu, $R_1(R_2)$, $R_5(R_6)$ = NO_2	2H	$CHCl_3$	623 nm (lg ε 4.82), 593 (4.02), 556 (4.61), 526sh (4.17), 338 (4.83)		1009
		Hexane	617 nm (r.i. 1.0), 591 (0.17), 549 (0.67), 520 (0.17), 331 (0.96)		1009
	Co(II)	$CHCl_3$	573 nm (lg ε 4.88), 524sh (4.41), 336sh (4.79), 317 (4.68)		1009
	Zn(II)	$CHCl_3$	598 nm (r.i. 1.0), 548sh (0.27), 337 (0.7)		1009
$R_1(R_2)$, $R_3(R_4)$, $R_5(R_6)$, $R_7(R_8)$ = *t*-Bu, $R_1(R_2)$, $R_3(R_4)$, $R_5(R_6)$ = NO_2 and $R_1(R_2)$, $R_3(R_4)$, $R_5(R_6)$, $R_7(R_8)$ = *t*-Bu, $R_1(R_2)$, $R_3(R_4)$, $R_7(R_8)$ = NO_2	Cu(II)	$CHCl_3$	594 nm (r.i. 1.0), 576 (0.93), 548 (0.29), 534sh (0.23), 338 (0.87)		1009

(*Continued*)

Table 3. (*Continued*)

Structure	M	Solvent	Transition Energy (Intensity)	Remark	Ref.
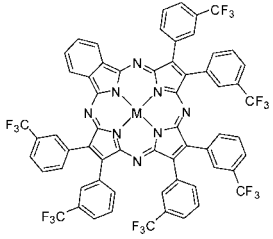	2H	DCM	690 nm (lg ε 4.97), 635 (4.65), 582 (4.73), 363 (4.90)		1027
		DCM + 1% THF	689 nm (lg ε 4.97), 635 (4.65), 581 (4.73), 363 (4.90)		961
	Mg(II)	DCM	665 nm (lg ε 5.04), 619 (4.94), 571 (4.35), 371 (5.02)		961, 1027
		THF	663 nm (r.i. 0.96), 619 (0.77), 573sh (0.22), 372 (1.00)		1028
	In(III)Cl	DCM	673 nm (r.i 1.000), 624 (0.771), 575 (0.211), 370 (0.909)		1027
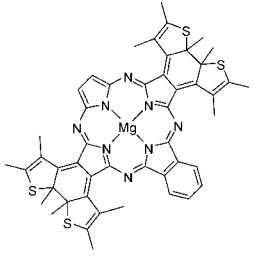	Mg(II)	$CHCl_3$	731 nm, 612, 365		967
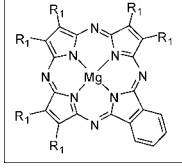	Mg(II)	$CHCl_3$	669 nm (10^{-5} ε 3.8), 630, 367	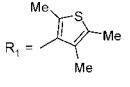	967

(*Continued*)

Table 3. (*Continued*)

Structure	M	Solvent	Transition Energy (Intensity)	Remark	Ref.
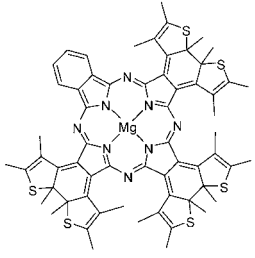	Mg(II)	$CHCl_3$	720 nm, 623, 372		967
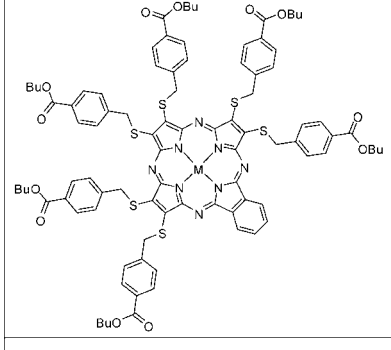	2H	$CHCl_3$	726 nm, 680, 624, 500, 356		991
	Ni(II)	$CHCl_3$	682 nm, 644, 326		991
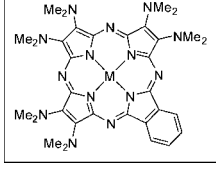	2H	DCM	696 nm (lg ε 4.41), 538 (4.53), 336 (4.75)		1029
	Mg(II)	DCM	707 nm (lg ε 4.59), 343 (4.80)		1029

(*Continued*)

Table 3. (*Continued*)

Structure	M	Solvent	Transition Energy (Intensity)	Remark	Ref.
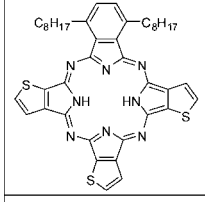	2H	Cyclohexane	697 nm (10^{-5} ε 1.43), 673 (0.89), 645 (0.81), 619 (1.08), 345 (0.97)		54
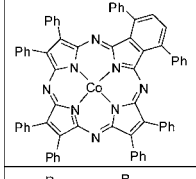	Co(II)	Toluene	655sh nm (lg ε 4.61), 634 (5.48), 574sh (2.36), 344 (5.09)		957
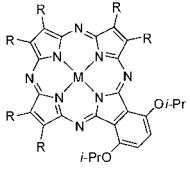	2H	DCM	743sh nm, 702, 654sh, 354	R = $S(CH_2CH_2O)_3H$	980
		DCM	744sh nm, 700 (lg ε 4.34), 656 (3.76), 346 (4.61)	R = $S(CH_2)_3COOMe$	977
		DCM	752sh nm, 703 (lg ε 4.65), 661sh, 488 (4.21), 346 (4.66)	R = SCH_2Ph	1030
		DCM	673 nm (lg ε 4.55), 600 (4.67), 568sh, 333 (4.77)	R = Pr	1030
		DCM	667 nm (lg ε 4.49), 591 (4.58), 447 (4.24), 331 (4.78), 230 (4.25)	R = 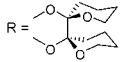	1030
		DCM	744sh nm, 700 (lg ε 4.34), 656 (3.77), 346 (4.61)	R = 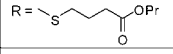	983
		Phosphate buffer (pH 8)	700 nm (lg ε 3.47), 666sh, 340 (4.30)	R = 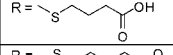	983
		DCM	744 nm, 700, 658, 346	R = 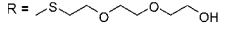	993
	Mg(II)	DCM	676 nm, 368		993
	Zn(II)	DCM	706sh nm, 676 (lg ε 4.69), 618sh, 368 (4.60)		993
	Ni(II)	DCM	709 nm (lg ε 4.50), 519 (4.31), 315 (4.68)	R = $N(Me)_2$	1030

(*Continued*)

Table 3. (*Continued*)

Structure	M	Solvent	Transition Energy (Intensity)	Remark	Ref.
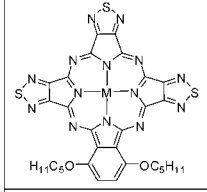	2H	DCM	715 nm (lg ε 4.80), 698sh, 680sh, 668sh, 655sh, 505 (4.19), 433sh, 384sh, 335 (4.83)		617
	Mg(II)	DMF	684 nm, 628sh, 374sh, 358		617
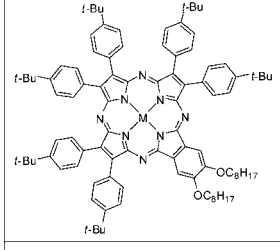	Zn(II)	Toluene + 1×10^{-2} M py	667 nm (10^{-4} ε 7.73), 625 (6.89), 577 (1.51), 377 (7.37)		265
	Pd(II)	Toluene + 1×10^{-2} M py	655 nm (10^{-4} ε 7.21), 613 (6.90), 562 (2.31), 450 (1.98), 343 (5.97)		265
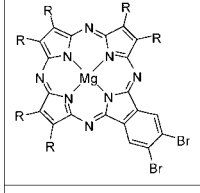	Mg(II)	THF	659 nm (r.i. 0.95), 625 (0.97), 574 (0.20), 374 (1.00)	R = Ph(3-CF_3)	1028
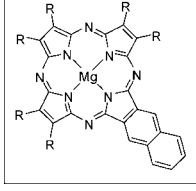	Mg(II)	THF	695 nm (r.i. 0.91), 624 (1.00), 580 (0.25), 362 (0.97)	R = Ph(3-CF_3)	1028

(*Continued*)

Table 3. (*Continued*)

Structure	M	Solvent	Transition Energy (Intensity)	Remark	Ref.
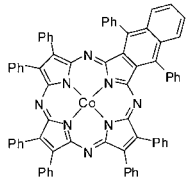	Co(II)	Toluene	687 nm (lg ε 3.35), 635 (5.01), 585sh (2.72), 351 (5.56)		957
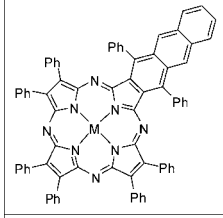	Co(II)	Toluene	726 nm (lg ε 1.88), 654 (3.68), 609sh (2.67), 361 (4.69)		957
	Ni(II)	Toluene	729 nm (lg ε 3.66), 645 (5.82), 598sh (2.66), 446 (1.49), 361 (5.68)		957
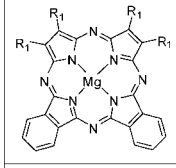	Mg(II)	$CHCl_3$	654 nm (10^{-5} ε 2.85), 594, 363	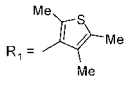	967
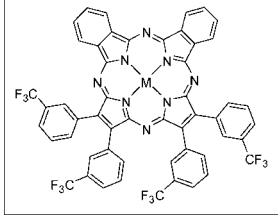	2H	DCM + 1% THF	663 nm (lg ε 5.03), 624 (4.84), 353 (4.93)		961, 1027
	Mg(II)	DCM	652 nm (lg ε 5.23), 588 (4.55), 367 (4.98)		961
		DCM + 1% THF	652 nm (lg ε 5.23), 588 (4.55), 367 (4.98)		1027
	In(III)Cl	DCM + 1% THF	661 nm (lg ε 5.11), 596 (4.66), 369 (4.89)		1027

(*Continued*)

Table 3. (*Continued*)

Structure	M	Solvent	Transition Energy (Intensity)	Remark	Ref.
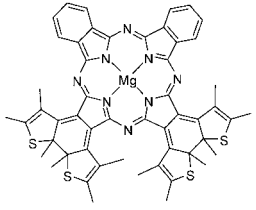	Mg(II)	$CHCl_3$	715 nm, 618, 373		967
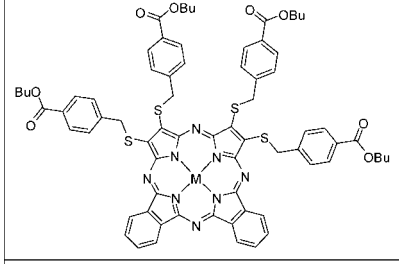	2H	DCM	692 nm, 652, 628, 352		991
	Mn(III)Cl	DCM	712 nm, 473, 357		991
	Ni(II)	DCM	659 nm, 602, 336		991
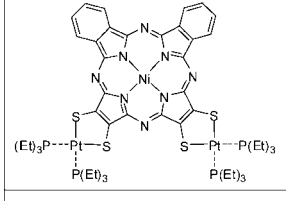	Ni(II)	DCM	680 nm, 604, 328		991
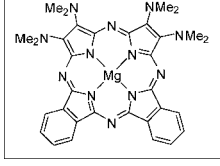	Mg(II)	DCM	684 nm (lg ε 4.43), 350 (4.65)		1029

(*Continued*)

Table 3. (*Continued*)

Structure	M	Solvent	Transition Energy (Intensity)	Remark	Ref.
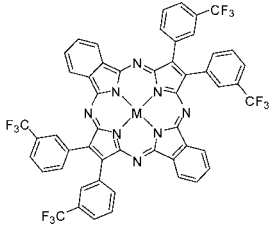	2H	DCM	730 nm (lg ε 5.09), 696 (4.32), 663 (4.15), 630 (3.85), 565 (4.90), 524 (4.25), 363 (4.84), 336 (4.83)		1027
		DCM + 1% THF	730 nm (lg ε 5.09), 565 (4.90), 363 (4.84), 336 (4.83)		961
	Mg(II)	DCM	711 nm (lg ε 5.09), 648 (4.26), 593 (4.83), 553 (4.19), 378 (4.84), 353 (4.84)		961
		DCM + 1% THF	711 nm (lg ε 5.09), 648 (4.26), 593 (4.83), 553 (4.19), 378 (4.84), 353 (4.84)		1027
	In(III)Cl	DCM	724 nm (lg ε 5.07), 659 (4.28), 601 (4.82), 559 (4.24), 384 (4.85), 352 (4.80)		1027
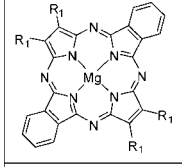	Mg(II)	$CHCl_3$	702 nm (10^5 ε 2.93), 609, 564, 362	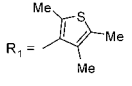	967
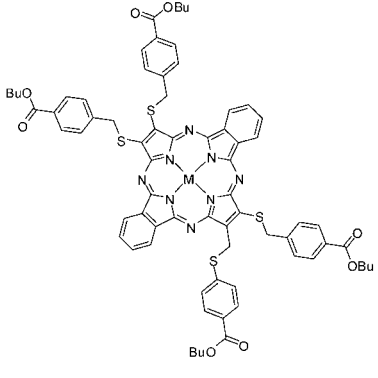	2H	DCM	747 nm, 708, 590, 350		991
	Mn(III)Cl	DCM	780 nm, 654, 382		991
	Ni(II)	DCM	722 nm, 605, 354		991

(*Continued*)

Table 3. (*Continued*)

Structure	M	Solvent	Transition Energy (Intensity)	Remark	Ref.
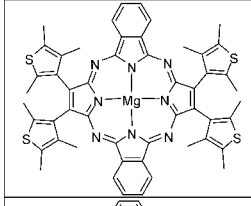	Mg(II)	$CHCl_3$	702 nm, 609, 564, 362		1031
		Net film	716 nm, 619, 585, 386		1031
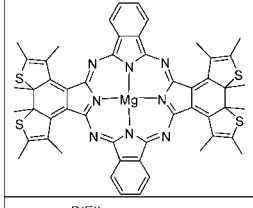	Mg(II)	$CHCl_3$	730 nm, 612, 365		1031
		Net film	759 nm, 621, 385		1031
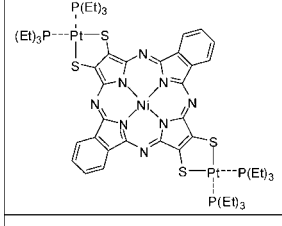	Ni(II)	DCM	676 nm, 600, 568, 330		991
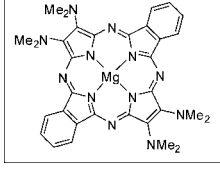	Mg(II)	DCM	694 nm (lg ε 4.42), 352 (4.71)		1029

(*Continued*)

Table 3. (*Continued*)

Structure	M	Solvent	Transition Energy (Intensity)	Remark	Ref.
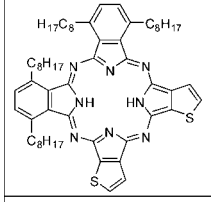	2H	Cyclohexane	695 nm (10^{-5} ε 1.65), 654 (1.00), 634 (0.54), 593 (0.30), 344 (0.62)		54
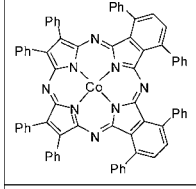	Co(II)	Toluene	676 nm (lg ε 7.27), 613sh (3.12), 338 (5.39)		957
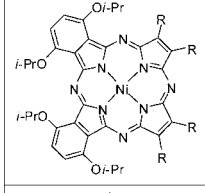	Ni(II)	DCM	718 nm (lg ε 4.65), 318 (4.70)	R = $N(Mc)_2$	1030
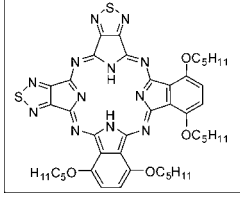	2H	DCM	735 nm (lg ε 4.98), 700sh, 658 (4.46), 514 (3.97), 336 (4.81)		617
		Toluene	728 nm (lg ε 5.06), 700sh, 657 (4.48), 506 (3.97), 425sh, 333 (4.72)		617

(*Continued*)

Table 3. (*Continued*)

Structure	M	Solvent	Transition Energy (Intensity)	Remark	Ref.
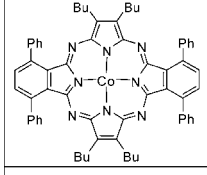	Co(II)	Toluene	639 nm (lg ε 4.92), 583 (4.45), 328 (4.76)		828
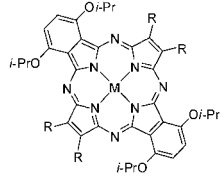	2H	DCM	747 nm (lg ε 4.63), 548 (4.68), 327 (4.75)	R = $N(Me)_2$	1030
	Ni(II)	DCM	727 nm (lg ε 4.68), 321 (4.75)		1030
	2H	DCM	798 nm (lg ε 4.72), 718 (4.36), 656 (4.70), 434 (4.23), 344 (4.72)	R = SCH_2Ph	1030
		DCM	718 nm (lg ε 4.59), 638 (4.88), 596 (4.59), 333 (4.85)	R = Pr	1030
		DCM	705 nm (lg ε 4.51), 632 (4.79), 586 (4.36), 451 (4.20), 380 (4.15), 327 (4.74), 230 (4.50)	R = 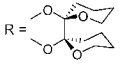	1030
	2H	DCM	794 nm (lg ε 4.54), 656 (4.67), 343 (4.64)	R = 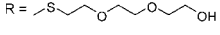	980
		DCM	796 nm, 654, 340		993
	Mg(II)	DCM	761 nm, 667, 354		993
	Zn(II)	DCM	761 nm (lg ε 4.64), 666 (4.73), 352 (4.64)		993
	2H	DCM	798 nm (lg ε 4.18), 712 (2.22), 654 (5.49), 422 (1.96), 340 (4.80)	R = 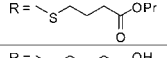	983
		Phosphate buffer (pH 8)	798 nm (lg ε 2.45), 658 (4.20), 334 (4.56)	R = 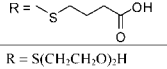	983
	Mg(II)	DCM	761 nm (lg ε 4.64), 666 (4.73), 352 (4.64)	R = $S(CH_2CH_2O)_2H$	977
	Zn(II)	DCM	761 nm (lg ε 4.64), 666 (4.73), 352 (4.64)	R = $S(CH_2CH_2O)_2H$	977
	2H	DCM	798 nm (lg ε 4.18), 712 (2.21), 656 (5.48), 422 (1.96), 340 (4.80)	R = $S(CH_2CH_2O)_3Me$	977
	Zn(II)	DCM	761 nm (lg ε 4.64), 666 (4.73), 352 (4.64)	R = $S(CH_2CH_2O)_3Me$	977

(*Continued*)

Table 3. (*Continued*)

Structure	M	Solvent	Transition Energy (Intensity)	Remark	Ref.
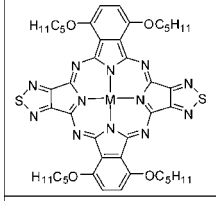	2H	DCM	721 nm (lg ε 4.81), 660sh, 506 (3.97), 429sh, 333 (4.80)		617
	Mg(II)	DCM	719 nm, 650sh, 510sh, 455sh, 346		617
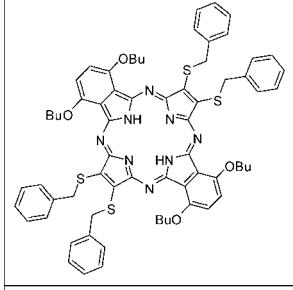	2H	DCM	796 nm (lg ε 5.34), 720 (5.10), 656 (5.42), 434 (4.99), 342 (5.37)		1016
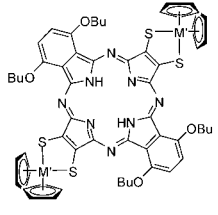	2H	DCM	670sh nm (lg ε 5.23), 622 (5.79), 344 (5.56), 312 (5.50)	M′ = Mo(IV)	1016
		Unknown	742 nm (very broad), 667, 610, 399	M′ = V(IV)	1016
		DCM	809 nm, 709, 625, 420	M′ = Mo(IV), Mo(V)	1016
		DCM	808 nm, 708, 642, 418, 368	M′ = Mo(V)	1016

(*Continued*)

Table 3. (*Continued*)

Structure	M	Solvent	Transition Energy (Intensity)	Remark	Ref.
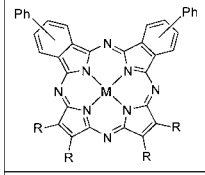	2H	Benzene	681 nm, 637, 591, 361	R = Ph	1032
	Cu(II)	Benzene	700sh nm, 657, 624, 570sh, 362		1032
	Co(II)	Benzene	655 nm, 456, 342		1032
		Benzene	655 nm, 456, 342		787
		18 M H_2SO_4	744 nm		787
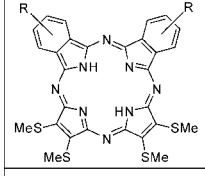	2H	$CHCl_3$	683 nm (r.i. 1.00), 616 (0.31), 353 (0.70)	R = OPh(4-CPh_3)	1023
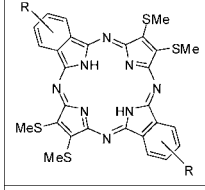	2H	$CHCl_3$	700 nm (r.i. 0.63), 622 (0.53), 347 (1.00)	R = OPh(4-CPh_3)	1023
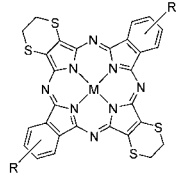	2H	1-ClNp	722 nm, 690sh, 654sh, 627, 565, 524	R = Cl	787
		H_2SO_4	679 nm		787
		1-ClNp	722 nm, 691sh, 654sh, 627, 565, 534	R = Br	787
		H_2SO_4	681 nm		787
		1-ClNp	716 nm, 656, 595, 545	R = NO_2	787
		H_2SO_4	681 nm		787
		Benzene	729 nm, 693, 668, 611, 554, 351	R = *t*-Bu	787
		H_2SO_4	691 nm		787
	Co(II)	1-ClNp	720sh nm, 655, 528	R = Cl	787
		H_2SO_4	733 nm		787
		1-ClNp	719sh nm, 658, 540	R = Br	787
		H_2SO_4	733 nm		787
		1-ClNp	672 nm, 530	R = NO_2	787

(*Continued*)

Table 3. (*Continued*)

Structure	M	Solvent	Transition Energy (Intensity)	Remark	Ref.
		H_2SO_4	727 nm		787
		Benzene	670 nm, 620, 530, 333	R = *t*-Bu	787
		H_2SO_4	732 nm		787
	Cu(II)	1-ClNp	690sh nm, 660, 595, 541	R = Cl	787
		H_2SO_4	737 nm		787
		1-ClNp	690sh nm, 661, 615, 540	R = Br	787
		H_2SO_4	735 nm		787
		1-ClNp	683 nm, 610sh, 550	R = NO_2	787
		H_2SO_4	716 nm		787
		Benzene	700 nm, 632, 580, 352	R = *t*-Bu	787
		H_2SO_4	730 nm		787
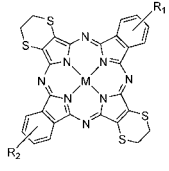	2H	Benzene	726 nm, 668, 612	R_1 = *t*-Bu, R_2 = Cl	787
		H_2SO_4	696 nm		787
		Benzene	727 nm, 687, 667, 611, 553	R_1 = *t*-Bu, R_2 = Br	787
		H_2SO_4	687 nm		787
		Benzene	720 nm, 680, 612, 520	R_1 = *t*-Bu, R_2 = NO_2	787
		H_2SO_4	685 nm		787
		H_2SO_4	678 nm	R_1 = Cl, R_2 = NO_2	787
	Co(II)	Benzene	680sh nm, 635	R_1 = *t*-Bu, R_2 = Br	787
		H_2SO_4	731 nm		787
		Benzene	650 nm	R_1 = *t*-Bu, R_2 = NO_2	787
		H_2SO_4	727 nm		787
	Cu(II)	benzene	698 nm, 634	R_1 = *t*-Bu, R_2 = Cl	787
		H_2SO_4	729 nm		787
		benzene	699 nm, 635, 580, 525	R_1 = *t*-Bu, R_2 = Br	787
		H_2SO_4	731 nm		787
		benzene	692 nm, 660	R_1 = *t*-Bu, R_2 = NO_2	787
		H_2SO_4	733 nm		787
		H_2SO_4	720 nm	R_1 = Cl, R_2 = NO_2	787

(*Continued*)

Table 3. (*Continued*)

Structure	M	Solvent	Transition Energy (Intensity)	Remark	Ref.
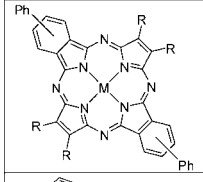	2H	benzene	710 nm, 679, 621, 590sh, 351	R = Ph	1032
	Cu(II)	benzene	654 nm, 595, 358		1032
	Co(II)	benzene	649 nm, 458, 340		1032
		benzene	649 nm, 458, 340		787
		18 M H_2SO_4	727 nm		787
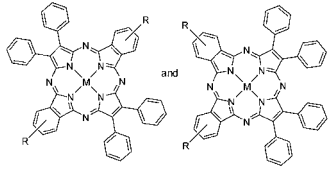	2H	benzene	696 nm, 675, 630, 615, 581, 357	R = Cl	787
	Co(II)	benzene	638br nm, 357		787
		18 M H_2SO_4	728 nm		787
	Cu(II)	benzene	685 nm, 562, 357		787
		18 M H_2SO_4	750 nm		787
	2H	benzene	696 nm, 675, 630, 615, 583, 357	R = Br	787
	Co(II)	benzene	640 nm, 358		787
		18 M H_2SO_4	735 nm		787
	Cu(II)	benzene	685 nm, 653, 358		787
		18 M H_2SO_4	759 nm		787
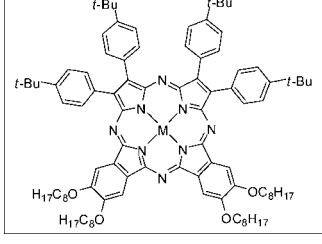	Zn(II)	toluene + 1×10^{-2} M py	654 nm (10^{-1} ε 16.7), 592 (3.12), 376 (10.2)		265
	Pd(II)	toluene + 1×10^{-2} M py	640 nm (10^{-1} ε 15.1), 581 (3.60), 440 (2.24), 338 (6.21), 305 (5.88)		265

(*Continued*)

Table 3. (*Continued*)

Structure	M	Solvent	Transition Energy (Intensity)	Remark	Ref.
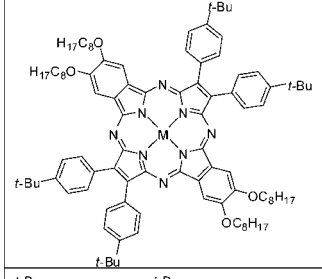	Zn(II)	toluene + 1×10^{-2} M py	708 nm (10^{-4} ε 10.0), 645 (1.49), 605 (6.60), 389 (5.95), 359 (5.90)		265
	Pd(II)	toluene + 1×10^{-2} M py	692 nm (10^{-4} ε 9.08), 632 (1.75), 593 (5.62), 547 (1.90), 453 (1.55), 310 (5.68)		265
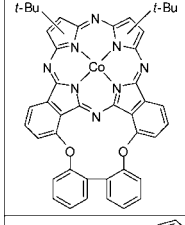	Co(II)	toluene	629 nm (lg ε 4.80), 570 (4.32), 319 (4.57)		828
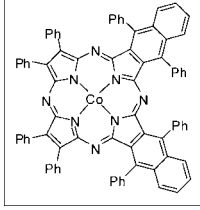	Co(II)	toluene	712 nm (lg ε 5.61), 639sh (2.46), 434sh (1.30), 344 (5.06), 312 (5.74)		957

(*Continued*)

Table 3. (*Continued*)

Structure	M	Solvent	Transition Energy (Intensity)	Remark	Ref.
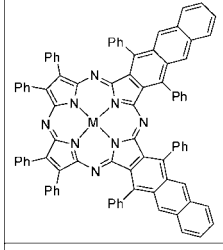	Co(II)	toluene	748 nm (lg ε 7.82), 669sh (3.06), 490 (1.48), 425sh (2.69), 355 (7.83)		957
	Ni(II)	toluene	745 nm (lg ε 16.8), 673 (5.44), 485 (2..87), 358 (12.1)		957
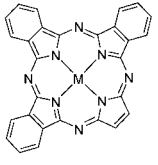	2H	py	663 nm, 626, 590		40
		PhCl	675 nm (lg ε 4.89), 594 (4.84), 566 (4.36), 349 (4.77)		416
	Co(II)	DCB	658 nm (lg ε 4.61), 625 (4.67), 567 (4.26), 319 (4.64)		416
	Ni(II)	DCB	655 nm (lg ε 4.84), 623 (4.90), 566 (4.31), 343 (4.64)		416
	Cu(II)	DCB	663 nm (lg ε 4.94), 630 (4.94), 574 (4.38), 349 (4.83)		416
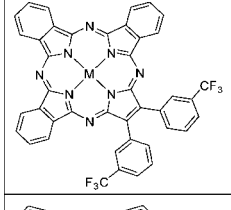	2H	THF	693 nm (r.i 1.000), 655 (0.289), 634 (0.270), 595 (0.733), 345 (0.918)		1027
	Mg(II)	DCM + 1% THF	689 nm (lg ε 5.12), 635 (4.78), 621 (4.89), 578 (4.37), 354 (4.91)		1027
	In(III)Cl	DCM + 5% THF	704 nm (lg ε 4.95), 633 (4.74), 587 (4.25), 357 (4.76)		1027
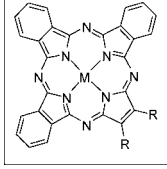	Pt(II)	$CHCl_3$	655 nm (10^{-5} ε 2.75), 618, 559, 285	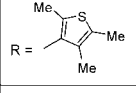	967
	Mg(II)	$CHCl_3$	687 nm (10^{-5} ε 3.7), 644, 585, 355		967
		$CHCl_3$	678 nm, 653, 353	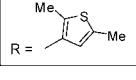	967

(*Continued*)

Table 3. (*Continued*)

Structure	M	Solvent	Transition Energy (Intensity)	Remark	Ref.
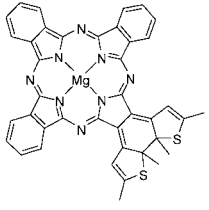	Mg(II)	$CHCl_3$	712 nm		967
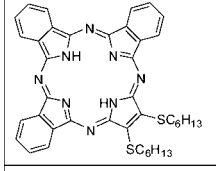	2H	$CHCl_3$	708 nm (ε 48,300), 676 (13,090), 654 (11,940), 616 (26,600), 346 (34,480)		1033
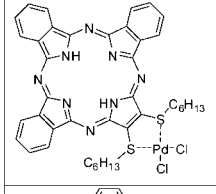	2H	$CHCl_3$	703 nm (ε 15,560), 684 (20,120), 637 (12,920), 579 (11,800), 344 (22,160)		1033
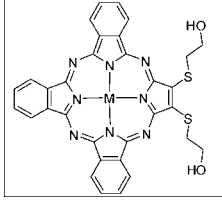	2H	THF	690 nm (lg ε 4.63), 653 (4.57), 339 (4.39)		1034
	Co(II)	THF	656 nm (lg ε 4.41), 326 (4.30)		1034
	Zn(II)	THF	666 nm (lg ε 4.84), 346 (4.42)		1034

(*Continued*)

Table 3. (*Continued*)

Structure	M	Solvent	Transition Energy (Intensity)	Remark	Ref.
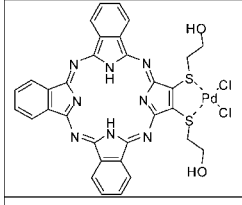	2H	THF	690 nm (lg ε 4.37), 654 (4.34), 331 (4.41)		1034
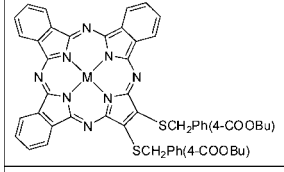	2H	$CHCl_3$	708 nm, 610, 346		1035
	Mg(II)	$CHCl_3$	696 nm, 652, 636, 358		1035
	Mn(III)Cl	$CHCl_3$	749 nm, 680, 496, 360		1035
	Ni(II)	$CHCl_3$	696 nm, 650, 638, 354		1035
	Cu(II)	$CHCl_3$	696 nm, 650, 638, 354		1035
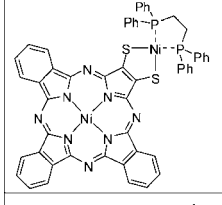	Ni(II)	$CHCl_3$	668 nm, 603, 333		1035
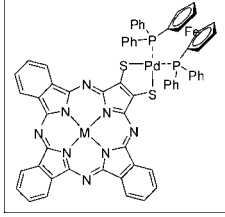	2H	$CHCl_3$	722 nm, 643, 592, 337		1035
	Ni(II)	$CHCl_3$	666 nm, 603, 333		1035
	Cu(II)	$CHCl_3$	679 nm, 606, 339		1035

(*Continued*)

Table 3. (*Continued*)

Structure	M	Solvent	Transition Energy (Intensity)	Remark	Ref.
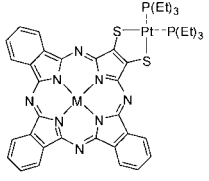	2H	$CHCl_3$	725 nm, 644, 591, 338		1035
	Mn(III)Cl	$CHCl_3$	712 nm, 656, 516, 352		1035
	Ni(II)	$CHCl_3$	669 nm, 602, 333		1035
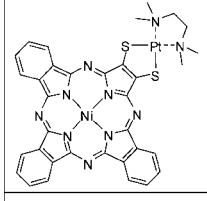	Ni(II)	$CHCl_3$	669 nm, 609, 335		1035
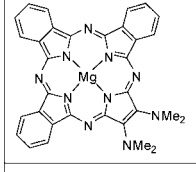	Mg(II)	DCM	670 nm (lg ε 4.61), 350 (4.73)		1029
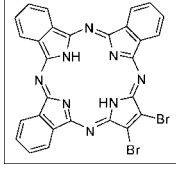	2H	DCB	682 nm (lg ε 4.82), 656 (4.65), 597 (4.62), 347 (4.80)		416

(*Continued*)

Table 3. (*Continued*)

Structure	M	Solvent	Transition Energy (Intensity)	Remark	Ref.
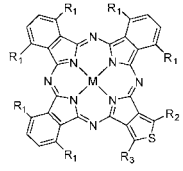	2H	cyclohexane	742 nm, 663	$R_1 = C_8H_{17}$, $R_2 = R_3 = H$	550
		cyclohexane	742 nm (10^5 ε 2.40), 705 (0.71), 687 (0.63), 663 (1.15), 333 (0.78)	$R_1 = C_8H_{17}$, $R_2 = R_3 = H$	53, 54
		cyclohexane	764 nm (10^{-5} ε 2.01), 727 (0.79), 706 (0.87), 674 (1.11), 336 (1.01), 306 (0.92)	$R_1 = C_8H_{17}$, $R_2 = R_3 = Me$	54
		cyclohexane	768 nm (10^{-5} ε 1.39), 729 (0.63), 708 (0.68), 677 (0.79), 337 (0.75), 307 (0.69)	$R_1 = R_2 = R_3 = C_8H_{17}$	53, 54
		cyclohexane	768 nm (10^{-5} ε 1.39), 731 (0.54), 709 (0.60), 678 (0.76), 340 (0.61), 309 (0.53)	$R_1 = C_8H_{17}$, $R_2 = Me$, $R_3 = C_6H_{12}OH$	54
	Ni(II)	cyclohexane	738 nm (10^{-5} ε 1.24), 693 (0.89), 675 (0.63), 622 (0.30), 337 (0.49), 300 (0.73)	$R_1 = C_8H_{17}$, $R_2 = Me$, $R_3 = C_6H_{12}OH$	54
	2H	cyclohexane	742 nm (10^{-5} ε 1.81), 705 (0.54), 687 (0.48), 662 (0.88), 386 (0.36), 336 (0.56)	$R_1 = C_6H_{13}$, $R_2 = R_3 = H$	53, 54
	Co(II)	cyclohexane	714 nm, 678, 283	$R_1 = C_6H_{13}$, $R_2 = R_3 = H$	54
	Ni(II)	cyclohexane	716 nm (10^{-5} ε 2.35), 681 (1.89), 614 (0.43), 333 (0.67), 298 (1.10)	$R_1 = C_6H_{13}$, $R_2 = R_3 = H$	54
		cyclohexane	716 nm (10^{-5} ε 2.35), 681 (1.89), 614 (0.43), 333 (0.6), 298 (1.1)	$R_1 = C_6H_{13}$, $R_2 = R_3 = H$	53
	Zn(II)	cyclohexane	726 nm (10^5 ε 1.38), 689 (1.25), 336 (0.67)	$R_1 = C_6H_{13}$, $R_2 = R_3 = H$	54
	Cu(II)	cyclohexane	722 nm (10^5 ε 1.14), 686 (1.04), 335 (0.71)	$R_1 = C_6H_{13}$, $R_2 = R_3 = H$	54
	2H	cyclohexane	764 nm (10^5 ε 1.57), 726 (0.61), 705 (0.67), 674 (0.87), 336 (0.69)	$R_1 = C_6H_{13}$, $R_2 = R_3 = Me$	54
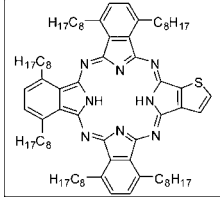	2H	cyclohexane	720 nm (10^5 ε 1.64), 700 (0.85), 679 (0.80), 648 (1.11), 347 (0.79)		53
		cyclohexane	720 nm (10^{-5} ε 1.64), 700 (0.85), 679 (0.80), 648 (1.11), 347 (0.79)		54
		cyclohexane	720 nm, 648		550

(*Continued*)

Table 3. (*Continued*)

Structure	M	Solvent	Transition Energy (Intensity)	Remark	Ref.
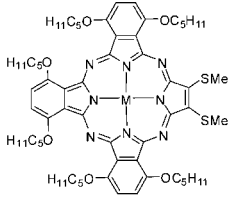	2H	benzene	710 nm (D 0.132), 666 (0.168), 506 (0.117)		614
	Ni(II)	unknown	664 nm (D 0.411), 486 (0.206)		614
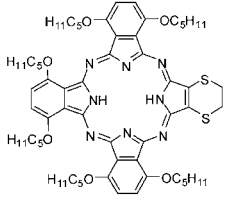	2H	benzene	767 nm, 722, 670, 513, 430, 339		614
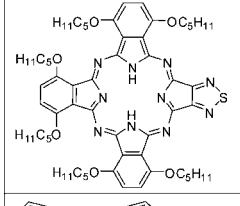	2H	DCM	766 nm (lg ε 5.21), 730 (5.02), 699sh, 663sh, 520sh, 458 (4.29), 408sh, 329 (4.96)		617
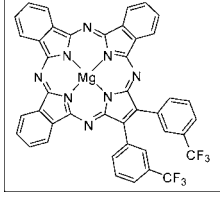	Mg(II)	DCM + 1% THF	689 nm (lg ε 5.12), 635 (4.78), 621 (4.89), 578 (4.37), 354 (4.91)		961
		THF	695 nm (r.i. 1.000), 596 (0.733), 345 (0.918)		961

(*Continued*)

Table 3. (*Continued*)

Structure	M	Solvent	Transition Energy (Intensity)	Remark	Ref.
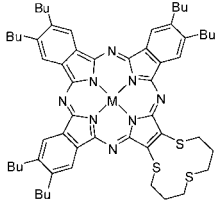	2H	$CHCl_3$	715 nm, 675, 617, 575sh, 355		1036
	Cu(II)	$CHCl_3$	707 nm, 652, 638, 589, 356		1036
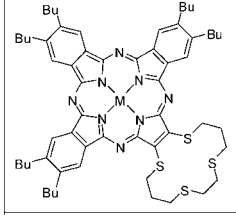	2H	$CHCl_3$ / MeOH = 4 : 1	718 nm (10^{-4} ε 7.72), 680 (3.63), 623 (5.25), 578 (1.74), 354 (6.63)		1036
	Ni(II)	$CHCl_3$ / MeOH = 4 : 1	696 nm (10^{-4} ε 6.03), 646 (4.71), 636 (4.80), 586 (2.05), 380sh, 338 (4.08)		1036
	Cu(II)	$CHCl_3$ / MeCN = 4 : 1	708 nm (10^{-4} ε 7.42), 658 (4.95), 644 (4.52), 596 (2.18), 348 (5.64)		1036
		$CHCl_3$ / MeOH = 4 : 1	708 nm (10^{-4} ε 6.10), 658 (3.90), 644 (3.80), 596 (2.15), 348 (4.98)		1036
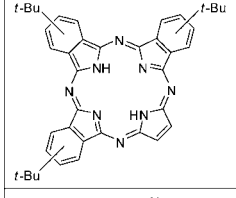	2H	benzene	680 nm (lg ε 4.58), 650sh (3.98), 619sh (4.12), 596 (4.54), 572sh (4.16), 565sh (4.12), 532sh (3.11), 354 (4.52)		418
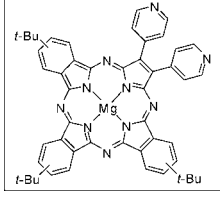	Mg(II)	$CHCl_3$	702 nm (lg ε 4.92), 642sh, 622 (4.69), 575sh, 376sh, 359 (4.76)		1037

(*Continued*)

Table 3. (*Continued*)

Structure	M	Solvent	Transition Energy (Intensity)	Remark	Ref.
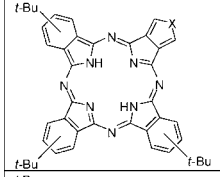	2H	$CHCl_3$	727 nm (lg ε 5.25), 692 (4.96), 648 (5.02), 337 (5.08)	X = S	52, 520
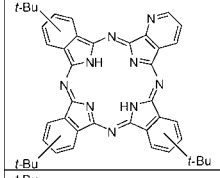	2H	DCM	688 nm (10^{-4} ε 11.70), 659 (8.28), 635 (3.10), 605 (2.15), 343 (5.24)		302, 520
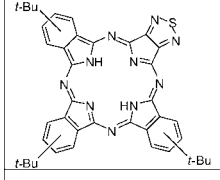	2H	DCM	693 nm (r.i. 1.00), 657 (0.59), 635sh, 630 (0.20), 598 (0.12), 353 (0.39), 295 (0.30)		520
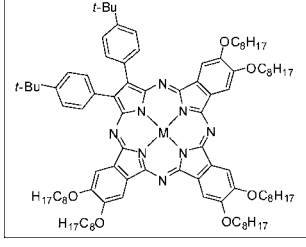	Zn(II)	toluene + 1×10^{-2} M py	690 nm (10^{-4} ε 11.6), 642 (6.66), 628 (6.51), 583 (1.98), 364 (7.68)		265
	Pd(II)	toluene + 1×10^{-2} M py	674 nm (10^{-4} ε 9.86), 629 (7.22), 617 (6.86), 573 (3.06), 408 (2.17), 300 (7.80)		265

(*Continued*)

Table 3. (*Continued*)

Structure	M	Solvent	Transition Energy (Intensity)	Remark	Ref.
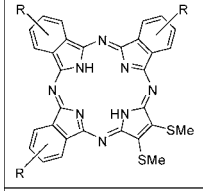	2H	$CHCl_3$	703 nm (r.i. 0.90), 667 (0.69), 632 (0.56), 348 (1.00)	R = 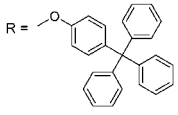	1023
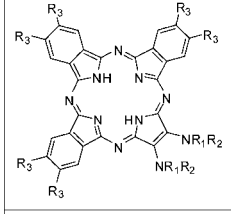	2H	$CHCl_3$	723 nm (lg ε 4.60), 688 (4.60), 649 (4.69), 577 (4.42), 528**sh**, 338 (4.83), 293 (4.46)	R_1, R_2 =  R_3 = H	966
	$CHCl_3$	727 nm (lg ε 4.61), 691 (4.56), 644 (4.57), 583 (4.46), 527**sh**, 341 (4.83), 292 (4.45)	R_1, R_2 =  R_3 = H	966
	$CHCl_3$	733 nm (lg ε 4.69), 691 (4.61), 656 (4.62), 577sh, 524 (4.25), 345 (4.89), 299 (4.56)	R_1, R_2 =  R_3 = Bu	966
	$CHCl_3$	734 nm (lg ε 4.74), 691 (4.62), 655 (4.64), 590sh, 517 (4.24), 347 (4.90), 298 (4.58)	R_1, R_2 =  R_3 = Bu	966
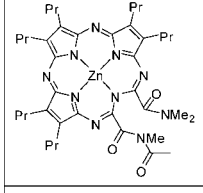	Zn(II)	DCM	651 nm (lg ε 3.98), 572 (3.86), 357 (4.09), 341 (4.10)		1012
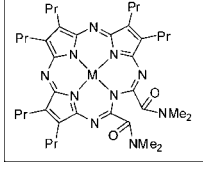	2H	DCM	693 nm (lg ε 4.49), 543 (4.39), 348 (4.75)		999
	Zn(II)	DCM	649 nm (lg ε 4.59), 565 (4.47), 356 (4.69), 339 (4.67)		999

(*Continued*)

Table 3. (*Continued*)

Structure	M	Solvent	Transition Energy (Intensity)	Remark	Ref.
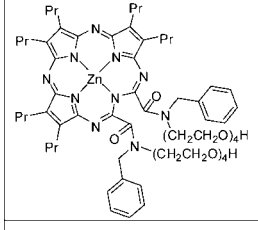	Zn(II)	DCM	654 nm, 565, 354, 338		962
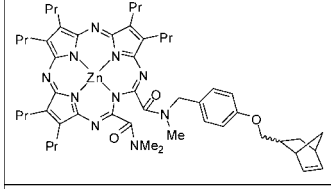	Zn(II)	DCM	650 nm (lg ε 4.40), 566 (4.30), 356 (4.53), 338 (4.53)		1014
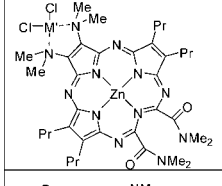	Zn(II)	DCM	631 nm (lg ε 4.51), 584 (4.61), 347 (4.79)	M′ = Pd(II)	1013
		DCM	619 nm (lg ε 4.47), 581 (4.60), 344 (4.72)	M′ = Pt(II)	1013
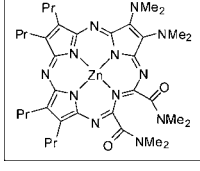	Zn(II)	DCM	671 nm, 580, 342		1013

(*Continued*)

Table 3. (*Continued*)

Structure	M	Solvent	Transition Energy (Intensity)	Remark	Ref.
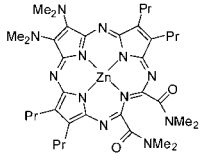	Zn(II)	DCM	661 nm (lg ε 3.93), 553 (4.15), 362 (4.35), 330 (4.38)		1013
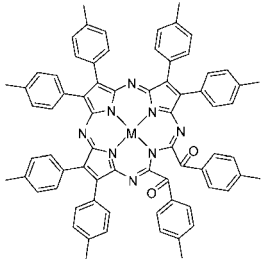	2H	$CHCl_3$	704 nm (lg ε 4.78), 632 (4.71), 488 (4.71), 376 (4.87)		1038
	Mg(II)	$CHCl_3$	644 nm (lg ε 4.91), 380 (4.82)		1038
	Co(II)	$CHCl_3$	644 nm (lg ε 4.86), 364 (4.80)		1038
	Cu(II)	$CHCl_3$	648 nm (lg ε 4.81), 372 (4.76)		1038
	Zn(II)	$CHCl_3$	640 nm (lg ε 4.83), 366 (4.74)		1038
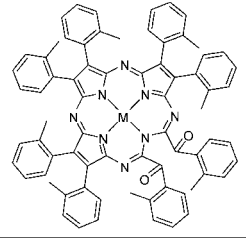	2H	$CHCl_3$	712 nm (lg ε 3.82), 636 (4.15), 484 (4.15), 352 (4.49)		1038
	Mg(II)	$CHCl_3$	648 nm (lg ε 4.70), 352 (4.91)		1038
	Co(II)	$CHCl_3$	648 nm (lg ε 4.36), 354 (4.46)		1038
	Cu(II)	$CHCl_3$	640 nm (lg ε 4.32), 356 (4.38)		1038
	Zn(II)	$CHCl_3$	644 nm (lg ε 4.38), 348 (4.42)		1038

(*Continued*)

Table 3. (*Continued*)

Structure	M	Solvent	Transition Energy (Intensity)	Remark	Ref.
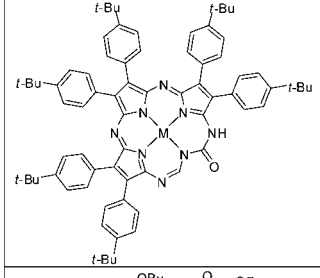	Ni(II)	DCM	768 nm (lg ε 4.65), 562 (4.44), 532 (4.33), 440 (4.32), 352 (4.40)		1039
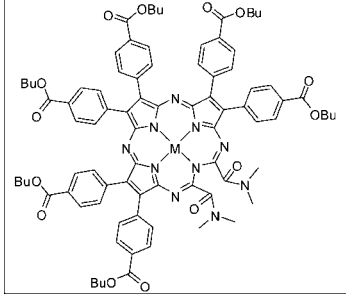	2H	DCM	743 nm (lg ε 4.27), 577 (4.02), 375 (4.39), 256 (4.38)		962
	Zn(II)	DCM	701 nm (lg ε 4.63), 593 (4.43), 387 (4.60), 359 (4.65)		962

(*Continued*)

Table 3. (*Continued*)

Structure	M	Solvent	Transition Energy (Intensity)	Remark	Ref.
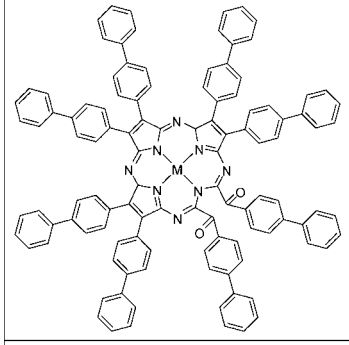	2H	$CHCl_3$	712 (lg ε 4.49), 650 (4.41), 368 (4.77)		963
	Co(II)	$CHCl_3$	656 (lg ε 4.56), 352 (4.84)		963
	Cu(II)	$CHCl_3$	658 (lg ε 4.58), 348 (4.82)		963
	Zn(II)	$CHCl_3$	654 (lg ε 4.60), 356 (4.80)		963
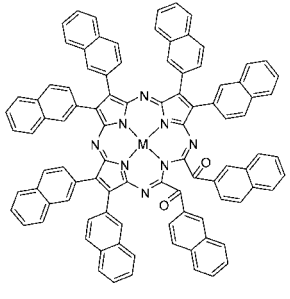	2H	$CHCl_3$	676 nm (lg ε 3.01), 620 (2.94), 348 (3.52), 284 (3.69)		964
	Co(II)	$CHCl_3$	640 nm (lg ε 3.17), 340 (3.52), 288 (3.64)		964
	Cu(II)	$CHCl_3$	632 nm (lg ε 3.16), 348 (3.55), 288 (3.68)		964
	Zn(II)	$CHCl_3$	644 nm (lg ε 3.35), 344 (3.58), 288 (3.67)		964
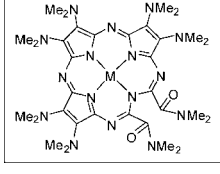	2H	DCM	783 nm (lg ε 4.46), 542 (4.53), 485 (4.47), 322 (4.76)		1040
		DCM	788 nm (lg ε 4.46), 542 (4.53), 323 (4.76)		999
	Zn(II)	DCM	747 nm (lg ε 4.46), 594 (4.46), 334 (4.80)		999

(*Continued*)

Table 3. (*Continued*)

Structure	M	Solvent	Transition Energy (Intensity)	Remark	Ref.
	Zn(II)	DCM	789 nm (lg ε 4.20), 579 (4.05), 470 (3.80), 363 (4.39), 314 (4.40)		999
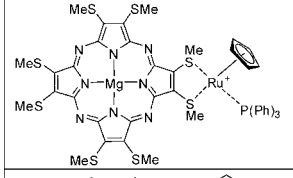	Mg(II)	DCM	672.0 nm (lg ε 4.48), 364.0 (4.68), 230.5 (4.79)	[TAP^{1}] [PF_6^-]	971
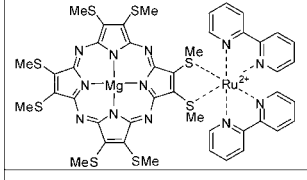	Mg(II)	DCM	664.5 nm (lg ε 4.59), 488.5 (4.27), 372.5 (4.73), 296.0 (4.82), 239.5 (4.69)	[TAP^{2+}] 2[PF_6^-]	971
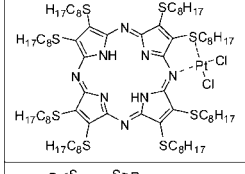	2H	$CHCl_3$	651 nm (lg ε 4.48), 517 (4.41), 368sh (4.34), 331 (4.43)		976
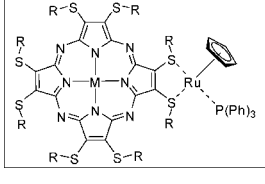	Mg(II)	$CHCl_3$	650.4 nm (10^{-3} ε 36.4), 370.0 (56.3), 320.0 (79.0), 270.0 (100.0)	R = CH_2Ph	987
	Co(II)	DCM	627 nm (lg ε 4.30), 325 (4.65), 273sh (4.69), 263 (4.69), 231 (4.90)	R = CH_2Ph	989

(*Continued*)

Table 3. (*Continued*)

Structure	M	Solvent	Transition Energy (Intensity)	Remark	Ref.
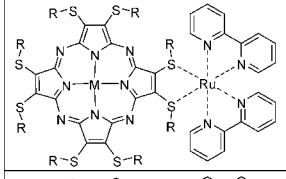	Co(II)	DCM	609 nm (lg ε 4.21), 470 (4.26), 358 (4.61), 296 (5.01), 238 (4.94)	R = CH_2Ph	989
	Ni(II)	DCM	634 nm (lg ε 4.71), 474 (4.68), 336 (5.08), 296 (5.32), 231 (5.31)	R = CH_2Ph	1041
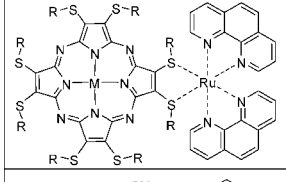	Mg(II)	$CHCl_3$	652.5 nm (10^3 ε 27.3), 365.0 (46.3), 322.2 (46.5), 266.2 (100.0)	R = CH_2Ph	987
	Co(II)	DCM	613 nm (lg ε 3.97), 448sh (4.25), 289 (4.72), 267 (5.00), 230 (4.97)	R = CH_2Ph	989
	Ni(II)	DCM	630 nm (lg ε 4.33), 442 (4.49), 311 (4.76), 266 (5.19), 231 (5.20)	R = CH_2Ph	1041
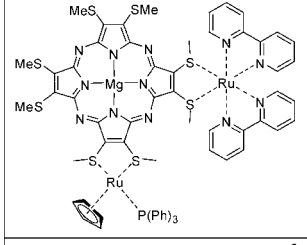	Mg(II)	DCM	669.0 nm (lg ε 4.33), 481.0 (4.15), 364.5 (4.57), 294.5 (4.77), 231.0 (4.78)		971
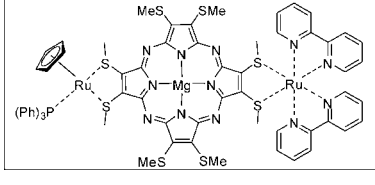	Mg(II)	DCM	660.0 nm (lg ε 4.37), 487.5 (4.24), 361.0 (4.64), 294.5 (4.83), 232.0 (4.77)		971

(*Continued*)

Table 3. (*Continued*)

Structure	M	Solvent	Transition Energy (Intensity)	Remark	Ref.
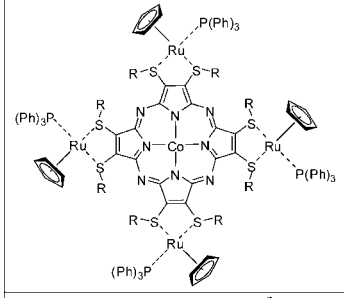	Co(II)	DCM	637 nm (lg ε 4.31), 331 (4.69), 273 (4.82), 265 (4.84), 233 (5.18)	R = CH_2Ph	989
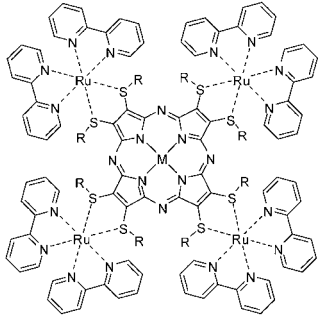	Co(II)	DCM	630 nm (lg ε 4.20), 480 (4.32), 345 (4.61), 295 (5.07), 239 (4.94)	R = CH_2Ph	989
	Ni(II)	DCM	637 nm (lg ε 4.64), 490 (4.76), 350 (5.04), 296 (5.50), 244 (5.30)		1041

(*Continued*)

Table 3. (*Continued*)

Structure	M	Solvent	Transition Energy (Intensity)	Remark	Ref.
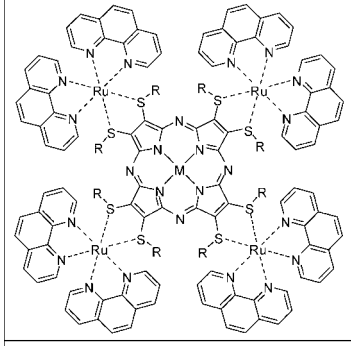	Co(II)	DCM	635 nm (lg ε 4.17), 448sh (4.30), 335sh (4.61), 268 (4.99), 233 (4.97)	R = CH_2Ph	989
	Ni(II)	DCM	640 nm (lg ε 4.52), 446 (4.67), 315 (4.94), 267 (5.39), 233 (5.37)		1041
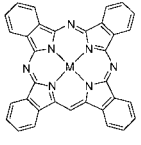	2H	1-ClNp	6940 Å (lg ε 5.19), 6520 (5.03), 6380 (4.75), 6220 (4.66), 5920 (4.43), 5700 (4.03), 4620 (4.03)		415
	Mg(II)	1-ClNp	7220 Å (lg ε 4.36), 6810 (4.96), 6580 (4.82), 6300 (4.30), 6150 (4.38), 6000 (4.18), 4480 (4.18)		415
	Fe(II)	1-ClNp	6570 Å (lg ε 4.74), 6350 (4.67), 5820 (4.23)		415
		py / ether	6460 Å (lg ε 4.98), 6250 (4.83), 5920 (4.46), 5710 (4.36)		415
	Cu(II)	1-ClNp	6840 Å (lg ε 5.21), 6550 (5.01), 6270 (4.58), 6140 (4.57), 6000 (4.49), 4460 (3.85)		415
	Zn(II)	1-ClNp	6780 Å (lg ε 5.23), 6540 (5.00), 6260 (4.43), 6130 (4.42), 5980 (4.38), 4440 (4.20), 4265 (4.51)		415
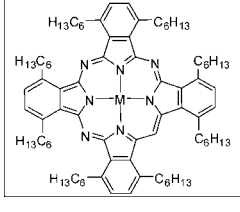	Sn(IV)L	THF	727 nm (log ε 5.15), 701 (4.95), 660 (4.63), 637 (4.62), 425 (4.71), 372 (4.83)	L = *trans*-Cl_2	367
		toluene	730 nm, 702	L = *trans*-Cl_2	367

(*Continued*)

Table 3. (*Continued*)

Structure	M	Solvent	Transition Energy (Intensity)	Remark	Ref.
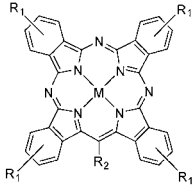	2H	THF	696 nm (ε 84,500), 652 (5,200), 624 (275,00), 386 (58,900), 364 (52,600)	$R_1 = OCH_2t$-Bu, $R_2 = C_{15}H_{31}$	1042
		THF	688 nm (ε 170,000), 648 (112,000), 630 (44,800), 620 (44,700), 590 (26,900), 440 (28,200), 388 (91,200), 364 (70,800)	$R_1 = t$-Bu, $R_2 = C_{15}H_{31}$	1042
		THF	690 nm (ε 168,000), 648 (104,000), 620 (50,600), 564 (30,000), 384 (82,000)	$R_1 = t$-Bu, R_2 = Ph	1042
	Mg(II)	THF	668 nm (ε 117,000), 648 (89,300), 618 (22,000), 594 (22,500), 446 (34,500), 400 (54,500)	R_1 = H, $R_2 = C_{15}H_{31}$	1042
		THF	670 nm (ε 157,000), 648 (110,000), 618 (22,800), 594 (25,500), 444 (27,800), 398 (68,200)	R_1 = H, R_2 = Ph	1042
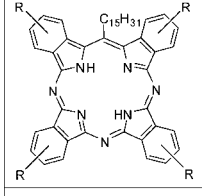	2H	THF	688 nm, 646, 620, 593, 386, 367, 280	R = t-Bu	1043
		THF	699 nm, 652, 622, 594, 383, 282	R = OCH_2t-Bu	1043
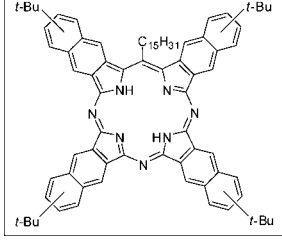	2H	THF	778 nm (ε 132,000), 746 (98,300), 674 (31,900), 430 (40,700), 374 (60,800), 346 (62,800)		1042
		THF	778 nm, 745, 713, 493, 430sh, 371, 343		1043

(*Continued*)

Table 3. (*Continued*)

Structure	M	Solvent	Transition Energy (Intensity)	Remark	Ref.
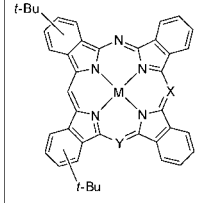	2H	benzene	670 nm (lg ε 4.96), 634 (4.91), 580 (4.21), 400 (4.75), 378 (4.77)	X = N, Y = CH	532
		benzene	690 nm (r.i 2.10), 670 (1.00), 646 (1.75), 634 (1.29), 586 (0.45), 378 (1.56)	X = CH, Y = N	532
	Zn(II)	benzene	672 nm (lg ε 4.13), 646 (5.15), 628 (4.84), 586 (4.17), 420 (5.00), 402 (4.78), 390sh (4.61)	X, Y = CH	532
		benzene	672 nm (lg ε 4.62), 646 (5.23), 584 (4.26), 422 (4.85), 416 (4.79), 404 (4.72), 384 (4.69)	X = N, Y = CH	532
		py	672 nm (r.i 0.27), 646 (1.0), 574 (0.14), 416 (0.54), 386 (0.42)	X = N, Y = CH	532
		benzene	670 nm (lg ε 5.32), 648 (5.16), 614 (4.43), 590 (4.47), 380 (4.78)	X, Y = N	532
		py	672 nm (r.i 1.0), 650 (0.65), 618 (0.18), 592 (0.12), 390 (0.29), 380 (0.29)	X, Y = N	532
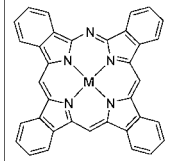	2H	1-ClNp	6900 Å (lg ε 4.45), 6690 (4.72), 6390 (4.34), 6260 (4.57), 6100 (4.40), 4390 (4.87), 4240 (4.89)		415
	Cu(II)	1-ClNp	6780 Å (lg ε 4.17), 6510 (5.01), 6300 (4.89), 5980 (4.25), 5740 (4.11), 4620 (3.75), 4220 (4.93)		415
	Zn(II)	1-ClNp	7020 Å, 6760, 6510, 6330, 6070, 5900, 5770, 4570, 4350		415
		py/ether	6630 Å (lg ε 4.72), 6400 (5.19), 6240 (4.98), 6120 (4.32), 5900 (4.18), 5830 (4.15), 5710 (4.08), 4240 (5.29), 4140 (5.18)		415
	Mg(II)	py/ether	6680 Å (lg ε 4.53), 6450 (5.28), 6290 (5.02), 6170 (4.30), 6010 (4.28), 5920 (4.26), 5820 (4.23), 5750 (4.11), 4320 (5.15), 4210 (5.34)		415
	Fe(II)	py/ether	6440 Å (lg ε 4.26), 6180 (4.68), 5980 (4.78), 4270 (4.92)		415
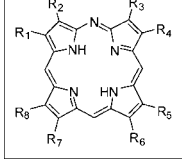	2H	DCM/TFA	592 nm (lg ε 4.65), 544 (4.26), 395 (5.16)	R_1, R_2, R_3, R_4, R_5, R_6, R_7, R_8 = Me	1044
		DCM/Et_3N	610 nm (lg ε 4.68), 557 (4.29), 532 (4.67), 500 (4.36), 372 (5.37)	R_1, R_3, R_4, R_5, R_6, R_7, R_8 = Me	1044
		DCM	609 nm (lg ε 4.62), 557 (4.16), 532 (4.60), 500 (4.15), 373 (5.33)	R_2, R_7 = Et, R_4, R_5 = CH_2COOMe, R_1, R_3, R_6, R_8 = Me	1044
		DCM	610 nm (lg ε 4.49), 558 (4.02), 534 (4.48), 503 (4.01), 374 (5.16)	R_2, R_4 = CH_2CH_2OCOPh, R_6, R_7 = CH_2COOMe, R_1, R_3, R_5, R_8 = Me	1044

(*Continued*)

Table 3. (*Continued*)

Structure	M	Solvent	Transition Energy (Intensity)	Remark	Ref.
		DCM	609 nm (lg ε 4.86), 557 (4.39), 533 (4.85), 501 (4.37), 373 (5.57)	R_1, R_2, R_5, R_7 = Et, R_3, R_4, R_6, R_8 = Me	1044
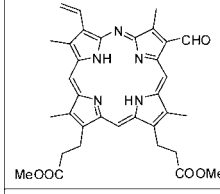	2H	$CHCl_3$	627 nm (ε 10,000), 573 (22,000), 564 (24,000), 411 (104,000)		1045
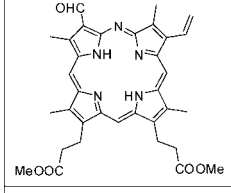	2H	$CHCl_3$	640 nm (ε 4,500), 624 (6,000), 567sh (8,500), 560 (10,000), 407 (48,000)		1045
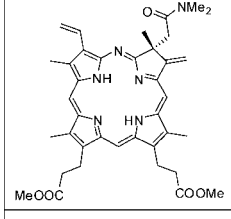	2H	$CHCl_3$	669 nm (ε 57,000), 611 (6,500), 538 (16,000), 501 (7,500), 398 (125,000)		1045
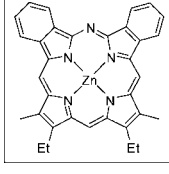	Zn(II)	THF	599 nm (10^{-4} ε 105), 587 (50), 559 (12), 406 (142), 312 (18)		1046

(*Continued*)

Table 3. (*Continued*)

Structure	M	Solvent	Transition Energy (Intensity)	Remark	Ref.
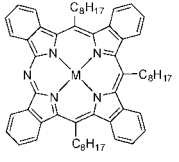	2H	$CHCl_3$	678 nm (r.i 0.07), 661 (0.23), 611 (0.22), 603 (0.27), 595 (0.28), 562 (0.01), 442 (0.26), 425 (1.00), 409 (0.94), 382 (0.36)		1047
	Zn(II)	$CHCl_3$	648 nm (r.i 0.11), 625 (0.33), 575 (0.13), 454 (0.33), 425 (1.00), 402 (0.38)		1047
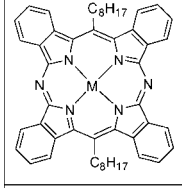	2H	$CHCl_3$	664 nm (r.i 0.57), 645 (0.30), 611 (0.27), 603 (0.30), 595 (0.30), 561 (0.17), 424 (0.93), 409 (1.00)		1047
	Zn(II)	$CHCl_3$	669 nm (r.i 0.21), 642 (0.23), 626 (0.38), 579 (0.17), 458 (0.37), 426 (1.00), 402 (0.56)		1047
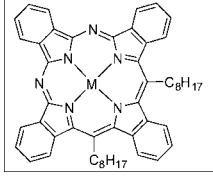	2H	$CHCl_3$	669 nm (r.i 1.00), 648 (0.36), 605 (0.42), 431 (0.93), 416 (0.94)		1047
	Zn(II)	$CHCl_3$	670 nm (r.i 0.12), 643 (0.17), 627 (0.62), 582 (0.13), 430 (1.00), 406 (0.34)		1047

Table 4. UV-vis absorption aata of Naphthalocyanine, Anthracocyanine, and other ring-expanded Pc analogs.

Structure	M	Solvent	Transition Energy (Intensity)	Remark	Ref.
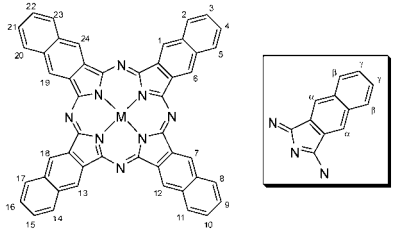	2H	1-ClNp	780 nm		45, 410
			785 nm, 745, 699, 349		47
	2Li	acetone	736 nm, 700, 660, 380, 318		1048
	Mg(II)	1-ClNp	776 nm		45
	Al(III)OH	1-ClNp	815 nm (lg ε 5.21), 720, 425		1049
		quinoline	795 nm		45
	Si(IV)L	$CHCl_3$	778 nm, 739, 691, 347	L = *trans*-$(OCH_2CH_2OMe)_2$	1050
		DMF	782 nm (10^{-5} ε 5.8)	L = *trans*-$(OCH_2CH_2OMe)_2$	1050
		benzene	782 nm	L = *trans*-$((OCH_2CH_2)_{17}OMe)_2$	1051
		MeOH	782 nm (10^{-1} ε 23), 747sh (3.9), 695 (3.9), 333 (7.6)	L = *trans*-$((OCH_2CH_2)_{43}OMe)_2$	1051
		EtOH	781 nm (10^{-1} ε 23), 743 (3.9), 694 (4.0), 333 (7.5)	L = *trans*-$((OCH_2CH_2)_{43}OMe)_2$	1051
		H_2O	805 nm	L = *trans*-$((OCH_2CH_2)_{43}OMe)_2$	1051
		benzene	781 nm (10^{-1} ε 27), 742 (4.1), 694 (4.4), 335 (7.4)	L = *trans*-$((OCH_2CH_2)_{43}OMe)_2$	1051
		DCM	782 nm	L = *trans*-$((OCH_2CH_2)_{26}OPh(4\text{-}C(Me)_2CH_2CMe_3))_2$	1051
		MeOH	781 nm	L = *trans*-$((OCH_2CH_2)_{26}OPh(4\text{-}C(Me)_2CH_2CMe_3))_2$	1051
		DMF	782 nm	L = *trans*-$((OCH_2CH_2)_{26}OPh(4\text{-}C(Me)_2CH_2CMe_3))_2$	1051
		benzene	781 nm	L = *trans*-$((OCH_2CH_2)_{26}OPh(4\text{-}C(Me)_2CH_2CMe_3))_2$	1051
		DCM	799 nm	L = *trans*-$((OPh(4\text{-}CO(OCH_2CH_2)_3OMe)_2$	1051
		DCM	789 nm	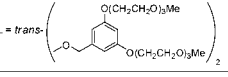	455
		EtOH	787 nm		455
		DCM	793 nm	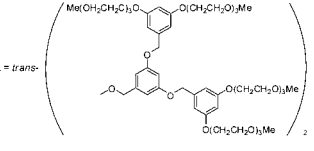	455
		EtOH	790 nm		455

(*Continued*)

Table 4. (*Continued*)

Structure	M	Solvent	Transition Energy (Intensity)	Remark	Ref.
		DCM	793 nm	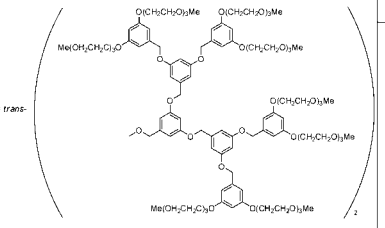	455
		EtOH	794 nm		455
		hexane	763 nm (10^{-5} ε 5.2)	L = *trans*-$(OSi(Me)_2(C_{18}H_{37}))_2$	456
		DMF	780 nm (10^{-5} ε 5)	L = *trans*-$(OSi(Me)_2C(Me)_2CHMe_2)_2$	456
		benzene	776 nm (10^{-1} ε 59), 737 (5.8), 690 (6.5), 336 (9.2)	L = *trans*-$(OSi(i\text{-}Bu)_2(C_{18}H_{37}))_2$	1051
		toluene	776 nm (10^{-1} ε 52), 736 (5.9), 690 (6.5), 333 (9.1)	L = *trans*-$(OSi(i\text{-}Bu)_2(C_{18}H_{37}))_2$	1051
		DCM	773 nm	L = *trans*-$(OSi(C_6H_{13})_3)_2$	1051
		DMF	777 nm	L = *trans*-$(OSi(C_6H_{13})_3)_2$	1051
		benzene	775 nm	L = *trans*-$(OSi(C_6H_{13})_3)_2$	1051
		acetone	770 nm (10^{5} ε 5)	L = *trans*-$(OSi(C_6H_{13})_3)_2$	456
		DCM	784 nm (ε 267,000)	L = *trans*-$(OCH_2CH_2(CF_2)_5CF_3)_2$	445
		DCM	775 nm (ε 400,000)	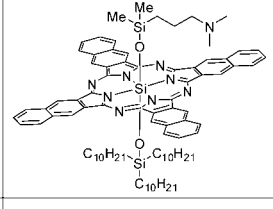	1052
	V(IV)O	1-ClNp	820 nm (r.i 5.3), 780 (1.1), 730 (1)		1053
	Mn(III)OAc	1-ClNp	855 nm		45
	Fe(II)L	Nujol	835 nm, 713sh, 500sh, 407, 278	L = *trans*- 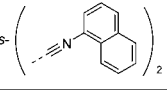	1054

(*Continued*)

Table 4. (*Continued*)

Structure	M	Solvent	Transition Energy (Intensity)	Remark	Ref.
		Nujol	925 nm, 726, 574, 447sh, 388, 279sh	L = *trans*- 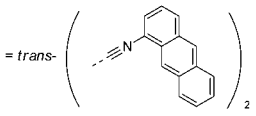	1054
		$CHCl_3$	750 nm	L = *trans*-$(CN(t\text{-}Bu))_2$	467
		$CHCl_3$	750 nm, 716sh, 670, 420sh, 359	L = *trans*- 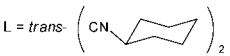	207
		$CHCl_3$	750 nm, 717sh, 670, 420sh, 359	L = *trans*-$(CN(t\text{-}Bu))_2$	207, 501
		$CHCl_3$	751 nm, 717sh, 670, 420sh, 355	L = *trans*-$(CN(CH)_2Ph)_2$	207
		py	745 nm, 667, 460, 380	L = *trans*-py_2	207
		$CHCl_3$	752 nm, 668, 454, 378	L = *trans*- 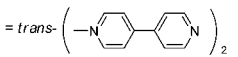	207
	Co(II)	py	748 nm, 714, 668		1055
		1-ClNp	764 nm		45
	Ni(II)	1-ClNp	768 nm		45
	Cu(II)	1-ClNp	776 nm (r.i 2.5), 695 (1)		45, 1053
	Zn(II)	DMSO	766 nm (lg ε 5.24)		480
		DMSO	767 nm (ε 160,000), 332 (42,000)		1056
	Zn(III)L	$CHCl_3$	765.0 nm (lg ε 4.93), 727.0 (4.18), 683.0 (4.20), 330.0 (4.42), 270.0 (4.62)	L = 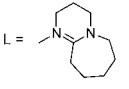	487
	Ga(III)L	benzene	795 nm	L = $OSi(C_6H_{13})_3$	1051
	Ru(II)	H_2SO_4	853 nm, 305, 235		501
	Ru(II)L	$CHCl_3$	722 nm, 690sh, 644, 439, 315	L = *trans*- 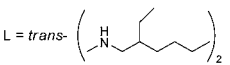	501
		$CHCl_3$	715 nm, 686, 641, 323	L = *trans*-$(CNCH_2Ph)_2$	536
		$CHCl_3$	714 nm, 684sh, 641, 325	L = *trans*-$(CNt\text{-}Bu)_2$	501
		DCM	714 nm, 641, 325	L = *trans*-$(CNt\text{-}Bu)_2$	219

(*Continued*)

Table 4. (*Continued*)

Structure	M	Solvent	Transition Energy (Intensity)	Remark	Ref.
		$CHCl_3$	717 nm, 688sh, 643, 429, 316	L = *trans*-py_2	501
		$CHCl_3$	718 nm, 688sh, 643, 423, 318	L = *trans*-$(py(3\text{-}Cl))_2$	501
		DCM	717 nm, 643, 429, 316	L = *trans*-py_2	219
		$CHCl_3$	721 nm, 690sh, 646, 416, 322	L = *trans*-$(pyz)_2$	501
		DCM	721 nm, 646, 416, 322	L = *trans*-$(pyz)_2$	219
		$CHCl_3$	718 nm, 688sh, 644, 423, 318	L = *trans*-$(bpy)_2$	536
		$CHCl_3$	717 nm, 688sh, 642, 430, 313	L = *trans*- 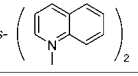	501
	Pd(II)	1-ClNp	752 nm		45
	Sn(II)L	benzene	788 nm	L = *trans*-$(OSi(C_6H_{13})_3)_2$	1051
$\alpha\alpha$ = Me	Zn(II)	THF	791 nm (lg ε 5.58), 754 (5.12), 709 (4.98), 331 (5.29)		1057
$\alpha\alpha = C_6H_{13}$	Zn(II)	THF	808 nm (lg ε 5.30), 722 (4.67)		1057
$\beta\beta = C_7H_{15}$	Fe(II)L	$CHCl_3$	760 nm, 724sh, 679, 414, 370	L = *trans*-$(CN(t\text{-}Bu))_2$	467
$\beta\beta = C_6H_{13}$	Ti(IV)O	$CHCl_3$	826 nm (lg ε 5.31), 782 (4.58), 734 (4.56), 451 (4.23), 337 (4.85)		549
	Zn(II)	THF	766 nm (lg ε 5.34), 729 (4.60), 684 (4.55), 338 (4.82)		1057
γ = *t*-Bu	2H	CCl_4	785 nm, 771		38
		CCl_4 (1.86×10^{-2} M)	760sh nm, 693		38
		benzene	781 nm (lg ε 5.27), 742 (4.52), 694 (4.52), 671sh (4.23), 650sh (3.82), 435sh (4.18), 385sh (4.47), 362 (4.72), 327 (4.75)		418
		PhCl	784 nm (lg ε 5.43), 751sh (4.70), 700 (4.66), 398sh (4.52), 365 (4.81), 326 (4.85)		1058
		octane	778 nm, 760, 356, 321		47
	Al(III)OH	py	794 nm (lg ε 5.37), 750 (4.62), 708 (4.62), 415sh (4.42), 360 (4.88), 340 (4.90)		1058
	Ti(IV)O	THF	801.5 nm, 714.5, 358.0, 349.5		544
	V(IV)O	DMSO	803 nm (r.i 6.1), 764 (0.9), 716 (1)		1053
		PhCl	815 nm (lg ε 5.49), 775 (4.64), 725 (4.69), 421sh (4.53), 448 (4.49), 360 (4.93)		1058
		quinoline	826 nm (r.i 7.25), 782 (0.9), 733 (1)		1053

(*Continued*)

Table 4. (*Continued*)

Structure	M	Solvent	Transition Energy (Intensity)	Remark	Ref.
	Mn(III)OAc	PhCl	855 nm (lg ε 5.05), 785 (4.44), 762sh (4.32), 600 (4.34), 470sh (4.17), 406sh (4.52), 370 (4.63)		1058
	Co(II)	PhCl	764 nm (lg ε 5.01), 680 (4.42), 408sh (4.22), 315 (4.87)		1058
		DMF	748 nm		531
	Co(III)L	DMF	768 nm	L = *trans*-CN), py	531
		DMF	765 nm	L = *trans*-$(CN)_2$, $[Pc]^-K^+$	531
	Ni(II)	PhCl	769 nm (lg ε 4.94), 732 (4.41), 683sh (4.28), 413sh (4.00), 339 (4.51), 330 (4.68)		1058
	Cu(II)	py	770 nm (lg ε 5.23), 730 (4.76), 685 (4.70), 650sh (4.27), 410sh (4.47), 335 (4.90)		1059
		PhCl	776 nm (lg ε 5.23), 738sh (4.72), 694 (4.68), 416sh (4.37), 366 (4.70), 329 (4.88)		1058
		quinoline	782 nm (r.i 3.4), 697 (1)		1053
	Zn(II)	DMF	762 nm (ε 157,000), 726, 681, 337		698
		toluene	770 nm (lg ε 5.25), 729 (4.40), 684 (4.47), 385 (4.62), 335 (4.78)		1058
	Ru(II)L	DCM	716 nm (10^{-3} ε 117), 644sh, 418sh, 340 (83)	L = trans-$(As(Ph)_3)_2$	497
		py	728.5 (10^{-1} ε 34.2)	L = *trans*- (CO), py	539
		py	717 (10^{-4} ε 21.9)	L = *trans*-py_2	539
		$CHCl_3$	723 nm, 690sh, 648, 322	L = *trans*-$(pyz)_2$	536
		$CHCl_3$	718 nm, 689sh, 640, 325	L = *trans*- 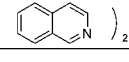	536
	Pd(II)	PhCl	754 nm (lg ε 5.01), 722sh (4.45), 672 (4.38), 405sh (4.21), 310 (4.85)		1058
	In(III)Cl	EtOH	793 nm (lg ε 5.93), 749, 706, 324		641
	In(III)(C_6F_5)	$CHCl_3$	806.0 nm, 764.5sh, 717.0, 449.0sh, 420.0sh, 365.0, 342.5		1060
	In(III)Ph(4-CF_3)	$CHCl_3$	804.5 nm, 763.5sh, 716.0, 447.0sh, 420.0sh, 363.0, 349.5		1060
	Sn(IV)L	PhCl	829 nm (r.i. 1.0), 785 (0.14), 732 (0.17), 480 (0.08), 449 (0.07), 367 (0.19), 345 (0.24)	L = *trans*-Cl_2	1058

(*Continued*)

Table 4. (*Continued*)

Structure	M	Solvent	Transition Energy (Intensity)	Remark	Ref.
	Pr(III)OAc	benzene	766 nm (lg ε 5.12), 740sh (4.41), 683 (4.41), 407sh (4.39), 360 (4.65), 345 (4.76), 333br (4.82)		1061
	Nd(III)Cl	benzene	766 nm, 739sh, 680, 410sh, 340, 333br		1061
	Sm(III)OAc	benzene	765 nm, 740sh, 681, 400sh, 349, 333br		1061
	Eu(III)Cl	benzene	768 nm, 740sh, 682, 410sh, 345, 329br		1061
	Eu(III)OAc	benzene	763 nm, 740sh, 682, 410, 334br		1061
	Gd(III)OAc	benzene	765 nm, 739sh, 681, 410sh, 345, 330br		1061
	Tb(III)OAc	benzene	765 nm, 740sh, 683, 411sh, 345, 331br		1061
	Ho(III)OAc	benzene	763 nm, 738sh, 681, 409sh, 333br		1061
	Er(III)OAc	benzene	763 nm, 740sh, 681, 410sh, 360sh, 345, 333br		1061
	Tm(III)OAc	benzene	769 nm (lg ε 5.19), 739sh (4.61), 685 (4.51), 409sh (4.38), 345 (4.80), 333br (4.79)		1061
		benzene	810 nm, 683	$[Pc]^-$	1061
	Lu(III)L	benzene	769 nm (lg ε 5.13), 740sh (4.46), 683 (4.42), 410sh (4.3), 340 (4.47), 333br (4.53)	L = 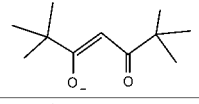	1061
		benzene	815 nm, 687	L = 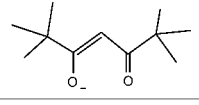 $[Pc]^-$	1061
	Lu(III)Cl	benzene	767 nm, 740sh, 683, 410sh, 345, 333br		1061
	Lu(III)OAc	benzene	770 nm, 740sh, 683, 410sh, 333br		1061
		benzene	820 nm, 693	$[Pc]^-$	1061
	Lu(III)acac	benzene	770 nm, 740sh, 684, 414sh, 349, 333br		1061
$\beta\gamma(R_2,R_4)$ = *t*-Bu	In(III)Cl	$CHCl_3$	812.5 nm, 772.5sh, 722.0, 688.7sh, 517.0sh, 468.5sh, 435.5sh, 367.5, 343.0		1060
	In(III)Ph(4-CF_3)	$CHCl_3$	809.0 nm, 769.5sh, 720.5, 687.3sh, 450.0sh, 365.7sh, 351.5		1060
	In(III)(C_6F_5)	$CHCl_3$	812.0 nm, 770.5sh, 720.5, 687.5sh, 663.0sh, 427.0sh, 367.5sh, 345.5		1060
γ= *t*-Bu	2H	$CHCl_3$	782 nm (lg ε 5.28), 737 (4.94), 699 (4.82), 412 (4.62), 360 (4.93), 324 (5.23)		407

(*Continued*)

Table 4. (*Continued*)

Structure	M	Solvent	Transition Energy (Intensity)	Remark	Ref.
		py	783.6 nm (lg ε 5.31), 697.5 (4.53), 746.7 (4.72), 606.5 (3.70), 362.0 (4.52), 505.6 (3.36), 327.3 (4.90)		43
	V(IV)O	py	809.6 nm (lg ε 5.10), 719.0 (4.35), 365.0 (4.79)		43
	Co(II)	py	752.0 nm (lg ε 5.18), 672.5 (4.47), 340.0 (4.89)		43
	Cu(II)	py	771.2 nm (lg ε 5.35), 684.5 (4.62), 336.0 (4.78)		43
$\gamma\gamma$ = 	Zn(II)	THF	789 nm (lg ε 5.40), 751 (4.77), 704 (4.76), 495 (4.43), 366 (5.10)		561
$\beta\beta\gamma\gamma$= Ph	Zn(II)	THF	766 nm (lg ε 5.07), 730 (4.26), 688 (4.31), 255 (4.91)		1062
$\gamma\gamma$= Ph(3-CF_3)	Mg(II)	THF	770 nm (lg ε 5.63), 733 (4.78), 687 (4.82), 351 (5.15)		335
	V(IV)O	THF	807 nm (lg ε 5.59), 765 (4.77), 718 (4.81), 364 (5.16), 346 (5.16)		335
		toluene	817 nm, 773, 725, 446, 368, 325		335
	Cu(II)	THF	777 nm, 733, 435sh, 338	Not isolated in pure state	335
	Zn(II)	THF	771 nm (lg ε 5.58), 733 (4.79), 688 (4.80), 344 (5.16)		335
		toluene	779 nm, 739, 694, 422, 350		335
	In(III)Cl	THF	808 nm, 769sh, 719, 367, 346	Not isolated in pure state	335
		toluene	812 nm, 771, 720, 457, 370, 348	Not isolated in pure state	335
β= $COONH_2$	V(IV)O	quinoline	832 nm (r.i 8.8), 791 (1.35), 740 (1)		1053
		DMSO	814 nm (r.i 9.7), 725 (1)		1053
$\beta\beta$= $CH_2OC_6H_{13}$	Zn(II)	THF	756 nm (lg ε 6.22), 721 (5.32), 676 (5.35), 336 (5.55)		1063
$\beta\beta$= $CH_2O(CH_2CH_2O)_2C_4H_9$	Zn(II)	THF	757 nm (lg ε 5.94), 722 (5.14), 678 (5.15), 336 (5.40)		1063
γ= COOH	Zn(II)	DMF	764 nm, 333		1064
γ= CN	2H	DMF	681sh nm, 263		1064
	Co(II)	DMF	744 nm, 324		1064
	Zn(II)	DMF	764 nm, 347		1064
$\gamma\gamma$= $CONHCH_2COOEt$	Co(II)	DMSO	~750 nm		591
γ= OH	Zn(II)	THF	772 nm, 726, 680, 335		1065
$\alpha\alpha$= OBu	2H	toluene	864 nm (lg ε 5.5)		1066
		toluene	862 nm (10^{-5} ε 2.0)		609
		toluene	863 nm (10^{-5} ε 2.05)		419
		toluene	862 nm (10^{-5} ε 1.81)		603
	Co(II)	toluene	830 nm (lg ε 4.6)		1066

(*Continued*)

Table 4. (*Continued*)

Structure	M	Solvent	Transition Energy (Intensity)	Remark	Ref.
	Ni(II)	toluene	844 nm (lg ε 5.5)		1066, 262, 611
	Zn(II)	toluene	846 nm (lg ε 4.9)		1066
	Cu(II)	toluene	850 nm (lg ε 5.4)		1066
	Pd(II)	benzene	827 nm		1067
$\alpha\alpha = OC_5H_{11}$	2H	$CHCl_3$	862 nm (lg ε 5.25), 814sh (4.62), 754 (4.57), 450 (4.47), 330 (4.85)		1059
		toluene	862 nm		419
	Cu(II)	$CHCl_3$	845 nm (lg ε 5.27), 810sh (4.68), 744 (4.66), 480 (4.43), 460 (4.39), 335 (4.94)		1059
		benzene	848 nm (lg ε 5.27), 810sh (4.66), 748 (4.66), 480 (4.44), 455sh (4.41), 335 (4.96)		1059
		toluene	849 nm		419, 603
		py	840 nm (lg ε 5.26), 784sh (4.65), 740 (4.65)		1059
$\alpha\alpha = O(i\text{-}C_5H_{11})$	2H				
	Co(II)	$CHCl_3$	838 nm, 745, 468, 444, 323		1068
	Cu(II)	$CHCl_3$	856 nm, 755, 475, 447, 331		1068
	Pd(II)	$CHCl_3$	829 nm, 731, 468, 438, 323		1068
$\alpha\alpha = OC_8H_{17}$	2H	toluene	862 nm (10^{-5} ε 1.82)		603
$\beta = OC_6H_{13}$	Fe(II)L	$CHCl_3$	758 nm, 725sh, 677, 360, 310	L = *trans*-(CN(*t*-Bu))$_2$	467
$\beta\gamma$ (R_2,R_4) = 	In(III)Cl	$CHCl_3$	825.5 nm, 786.2sh, 731.5, 502.5sh, 385.0sh, 350.0		1060
	In(III)Ph(4-CF_3)	$CHCl_3$	821.5 nm, 782.0sh, 728.5, 497.5sh, 449.0sh, 363.5		1060
	In(III)(C_6F_5)	$CHCl_3$	824.0 nm, 784.6sh, 730.0, 500.0sh, 452.5sh, 356.5		1060
$\gamma = OC_6H_{13}$	Fe(II)L	$CHCl_3$	755 nm, 727sh, 677, 351	L = *trans*-(CN(*t*-Bu))$_2$	467
$\gamma = OCH_2COOH$	Zn(II)	DMF	765 nm, 726, 682		1065
		$CHCl_3$	768 nm, 720, 678, 333		1065
$\gamma = OCH_2Ph$	Zn(II)	$CHCl_3$	765 nm, 720, 675, 330		1065
$\gamma\gamma = OC_5H_{11}$	2H	THF	782 nm		419
	Ni(II)	toluene	766 nm		419
$\gamma\gamma = OC_6H_{13}$	Fe(II)L	$CHCl_3$	752 nm, 722sh, 673, 358	L = *trans*-(CN(*t*-Bu))$_2$	467
$\gamma\gamma$ = OPh(3-CF_3)	V(IV)O	THF	796 nm (lg ε 5.57), 754 (4.77), 708 (4.80), 362 (5.07), 334 (5.06)		1069

(*Continued*)

Table 4. (*Continued*)

Structure	M	Solvent	Transition Energy (Intensity)	Remark	Ref.
$\gamma\gamma$= OPh(3,5-(*t*-Bu)$_2$)	In(III)Cl	toluene	806 nm (ε 145,731), 765 (20,214), 716 (22,164), 368 (41,855), 338 (53,888)		1070
		toluene	804 nm, 742, 711, 371		1069, 1071
	In(III)Br	toluene	809 nm (ε 250,394), 767 (41,364), 717 (45,452), 380 (71,692), 361 (65,153), 346 (70,875)		1070
	In(III)I	toluene	809 nm (ε 279,310), 767 (45,660), 718 (49,048), 381 (79,013), 361 (70,451), 346 (77,319)		1070
γ= OPh(2,6-(*i*-Pr)$_2$)	2H	DCM	784 nm, 740, 710, 330		664
γ= OPh(3,5-(*t*-Bu)$_2$)	2H	DCM	782 nm, 720, 330		664
γ= OPh(2.6-Ph$_2$)	2H	DCM	784 nm, 736, 620, 338		664
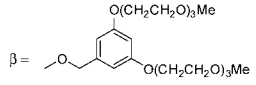	2H	DCM	785 nm		455
		EtOH	678 nm		455
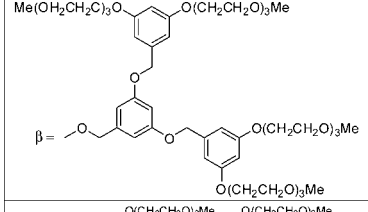	2H	DCM	786 nm		455
		EtOH	696 nm		455
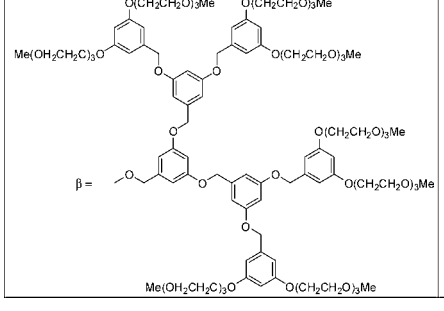	2H	DCM	786 nm		455
		EtOH	705 nm		455

(*Continued*)

Table 4. (*Continued*)

Structure	M	Solvent	Transition Energy (Intensity)	Remark	Ref.
γ= OPh(3-CF_3)	V(IV)O	THF	796sh nm, 736	Not isolated in pure state	335
$\gamma\gamma$= OPh(3-CF_3)	Mg(II)	THF	757 nm (lg ε 5.66), 721 (4.80), 677 (4.85), 357 (5.07)		335
	V(IV)O	THF	796 nm (lg ε 5.57), 754 (4.77), 708 (4.80), 362 (5.07), 334 (5.06)		335
		toluene	805 nm, 763, 715, 440sh, 369, 327		335
	Cu(II)	THF	761 nm, 715, 326	Not isolated in pure state	335
	Zn(II)	THF	758 nm (lg ε 5.59), 721 (4.81), 678 (4.83), 351 (5.13), 330 (5.16)		335
		toluene	767 nm, 729, 684, 351		335
	In(III)Cl	THF	796 nm, 757, 709, 366, 337	Not isolated in pure state	335
		toluene	800 nm, 760, 711, 448sh, 373, 339	Not isolated in pure state	335
$\gamma\gamma$= SPr	Zn(II)	THF	778 nm (lg ε 5.17), 745 (4.59), 693 (4.41), 355 (4.83)		1057
$\gamma\gamma$= SBu	Zn(II)	THF	778 nm, 745, 693, 355		744
$\gamma\gamma$= $SC_{12}H_{25}$	Zn(II)	THF	780 nm (lg ε 5.92), 743 (5.16), 697 (5.13), 347 (5.49)		1063
$\gamma\gamma$= $S(CH_2CH_2O)_2Bu$	Zn(II)	THF	777 nm, 740, 702, 354		744
$\gamma\gamma$= SPh	Zn(II)	THF	779 nm (lg ε 5.67), 741 (4.90), 694 (4.92), 353 (5.16)		335, 1057
β= NH_2	V(IV)O	quinoline	886 nm (r.i 9.17), 782 (1.95), 711 (1)		1053
		DMSO	846 nm		1053
β= NO_2	V(IV)O	quinoline	802 nm		1053
		1-ClNp	815 nm (r.i 1), 776 (1.05)		1053
	Cu(II)	quinoline	780 nm (r.i 1.4), 705 (1)		1053
γ= NH_2	V(IV)O	DMSO	833 nm		1053
		quinoline	870 nm		1053
γ= $NHCOC_5H_{11}$	Zn(II)	DMF	771 nm, 684, 340		1072
γ= $NHCOC_{11}H_{23}$	Zn(II)	DMF	770 nm, 686, 340		1072
γ= NHCOPh	Zn(II)	DMF	772 nm, 687, 334		1072
γ= NHCOPh(4-OMe)	Zn(II)	DMF	773 nm, 687, 334		1072
γ= NO_2	Zn(II)	DMF	768 nm, 328		1064
	V(IV)O	1-ClNp	825 nm (r.i 3.05), 781 (1.05), 736 (1)		1053
γ= Cl	Si(IV)L	benzene	774 nm	L = *trans*-$(OSi(C_6H_{13})_3)_2$	1051
γ= Br	Si(IV)L	benzene	775 nm	L = *trans*-$(OSi(C_6H_{13})_3)_2$	1051
	Cu(II)	quinoline	785 nm (r.i 1.95), 701 (1)		1053

(*Continued*)

Table 4. (*Continued*)

Structure	M	Solvent	Transition Energy (Intensity)	Remark	Ref.
$\beta\beta\gamma\gamma$= F	Ga(III)Cl	THF	765.0 nm, 718.0, 338.0		327
$\gamma\gamma$= Br	Cu(II)	quinoline	785 nm		1053
$\gamma\gamma$= Cl	Cu(II)	quinoline	782 nm		1053
	V(IV)O	1-ClNp	820 nm (r.i 1.65), 782 (1)		1053
$\alpha\alpha$= Me, $\beta\beta$= C_6H_{13}	Zn(II)	hexane	812 nm (lg ε 5.35), 727 (4.75)		1057
$R_3(R_4)$ = CN, $R_9(R_{10})$, $R_{15}(R_{16})$, $R_{21}(R_{22})$ = *t*-Bu	2H	$CHCl_3$	772 nm, 312		1064
$R_3(R_4)$ = NO_2, $R_9(R_{10})$, $R_{15}(R_{16})$, $R_{21}(R_{22})$ = *t*-Bu	2H	$CHCl_3$	778 nm, 328		1064
β = 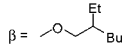 , γ = *t*-Bu	In(III)Cl	$CHCl_3$	823.0 nm, 781.4sh, 730.0, 694.3sh, 667.6sh, 526.9sh, 499.0sh, 453.5sh, 349.1		1060
	In(III)Ph(4-CF_3)	$CHCl_3$	820.0 nm, 780.0sh, 728.5, 490.0sh, 453.0sh, 360.0		1060
	In(III)(C_6F_5)	$CHCl_3$	822.5 nm, 783.5sh, 729.5, 493.0sh, 454.0sh, 355.0		1060
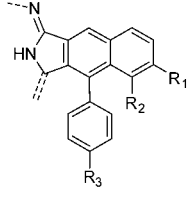	Ga(III)Br	$CHCl_3$	820 nm (lg ε 5.30), 776 (4.52), 726 (4.57), 421sh (4.44), 338 (4.87)	R_1, R_2, R_3 = H	1073
		$CHCl_3$	826 nm (lg ε 5.38), 782 (4.54), 732 (4.61), 434sh (4.42), 340 (4.87)	R_1, R_3 = *t*-Bu, R_2 = H	1073
		$CHCl_3$	825 nm (lg ε 5.31), 779 (4.36), 731 (4.36), 433sh (3.78), 342 (4.74)	R_1, R_2 = H, R_3 = *t*-Bu	1073
		$CHCl_3$	825 nm (lg ε 5.31), 782 (4.40), 730 (4.46), 435sh (3.95), 339 (4.04)	R_1 = *t*-Bu, R_2 R_3 = H	1073
		$CHCl_3$	826 nm (lg ε 5.30), 780 (4.58), 731 (4.56), 435sh (4.28), 336 (4.89)	R_1, R_2 = H, R_3 = Ph	1073
		$CHCl_3$	795 nm (lg ε 5.29), 756 (4.54), 707 (4.43), 406sh (4.56), 344 (4.84)	R_1,R_2 =  , R_3 = H	1073
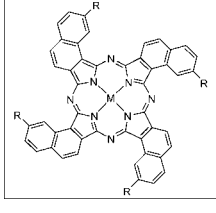	Mg(II)H_2O	py	688 nm, 383	R = H	424
	Co(II)	py	666 nm, 354	R = H	424
	Co(III)L	py	685 nm, 403	R = H, [Pc]$^-$K$^+$, L = *trans*-$(CN)_2$	424
	Fe(II)	py	668 nm, 606, 354	R = Me	1074
	Fe(II)	py	666 nm, 604, 353	R = *t*-Bu	1074
	Fe(II)	py	670 nm, 607, 364	R = Ph	1074
	Fe(II)	$CHCl_3$	662 nm, 602, 354	R = *t*-Bu, L = *trans*-(NC*t*-Bu)$_2$	1074

(*Continued*)

Table 4. (*Continued*)

Structure	M	Solvent	Transition Energy (Intensity)	Remark	Ref.
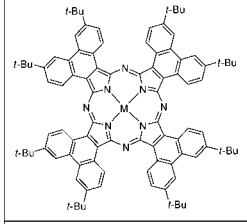	2H	$PhNO_2$	728 nm, 690, 665, 480		959
	Mg(II)	$CHCl_3$	697 nm (lg ε 5.30), 630 (4.59), 470 (4.24), 380 (4.89)		959
	Cu(II)	DCB	700 nm (lg ε 5.13), 635 (4.42), 477 (4.38), 360 (4.79)		959
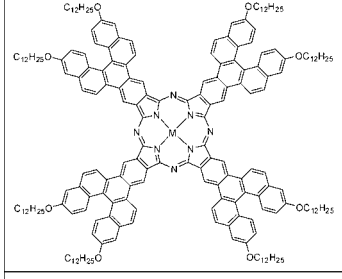	2H	toluene	793 nm, 708, 439, 322		1075
	Zn(II)	toluene	781 nm, 709, 430, 331		1075
	Pb(II)	toluene	831 nm, 731, 428, 337		1075
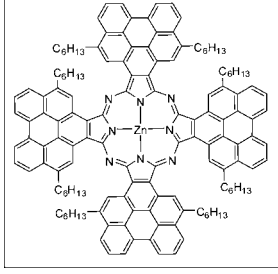	Zn(II)	THF	797 nm (10^{-5} ε 1.36)		1076

(*Continued*)

Table 4. (*Continued*)

Structure	M	Solvent	Transition Energy (Intensity)	Remark	Ref.
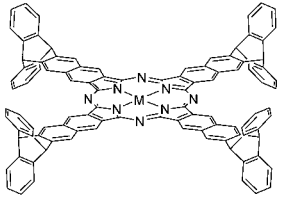	2H	$CHCl_3$	784 nm (lg ε 5.45), 736 (4.78), 698 (4.78), 370 (4.93), 326 (5.08)		1077
	Cu(II)	$CHCl_3$	774 nm (lg ε 508), 732 (4.48), 684 (4.48), 352 (4.69), 324 (4.73)		1077
	Mg(II)	$CHCl_3$	772 nm (lg ε 5.34), 730 (4.48), 684 (4.56), 376 (5.00)		1077
	Al(III)Cl	$CHCl_3$	792 nm (lg ε 5.23), 750 (4.66), 710 (4.60), 366 (4.71), 334 (4.72)		1077
	V(IV)O	$CHCl_3$	814 nm (lg ε 5.24), 768 (4.56), 722 (4.56), 378 (4.74), 326 (4.85)		1077
	Co(II)	$CHCl_3$	758 nm (lg ε 5.15), 724 (4.74), 676 (4.66), 336 (4.87), 324 (4.98)		1077
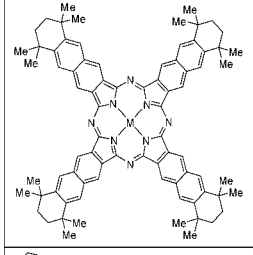	2H	benzene	795 nm (lg ε 5.41), 756 (4.64), 708 (4.63), 420sh (4.51), 369 (4.84), 331 (4.84)		932
	Cu(II)	benzene	788 nm (lg ε 5.31), 750sh (4.63), 700 (4.62), 432 (4.46), 404sh (4.44), 353 (4.89)		932
		methylmethacrylate	783 nm (r.i 2.60), 748sh (0.64), 697 (0.53), 425 (0.29), 400sh (0.32), 341 (1)		932
	Co(II)	benzene	771 nm (lg ε 4.80), 743 (4.61), 677 (4.44), 641 (4.48), 410sh (4.43), 334 (4.52)		932
	Zn(II)	1-ClNp	793 nm (lg ε 4.43), 708 (4.20), 435 (4.25), 368 (4.54)		932
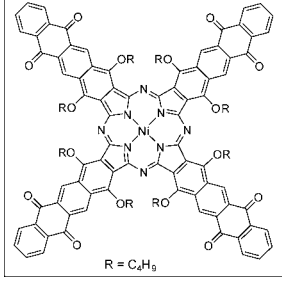	Ni(II)	toluene	855 nm, 758, 484, 327		929

(*Continued*)

Table 4. (*Continued*)

Structure	M	Solvent	Transition Energy (Intensity)	Remark	Ref.
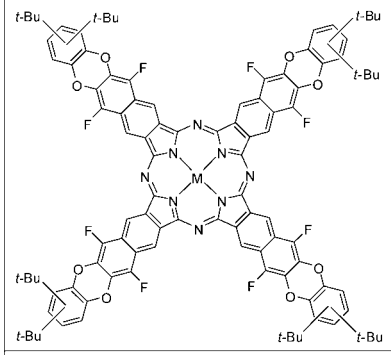	2Li(**I**)	hexane	741.0 nm, 704.0, 662.0, 398.0		1078
	Zn(II)	THF	774.0 nm, 717.0, 387.0		1078
		1-ClNp	773.0 nm, 440.0		1078
	In(III)Cl	THF	780.0 nm, 732.0, 380.0		1078
		1-ClNp	828.0 nm, 785.0, 732.0, 380.0		1078
	In(III)L	THF	799.0sh nm, 740.0, 402.0	L = Ph(4-CF_3)	1078
		1-ClNp	824.0 nm, 786.0, 729.0, 438.0sh	L = Ph(4-CF_3)	1078
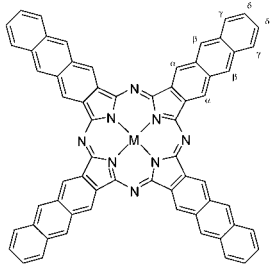	2H	DMF	777 nm		410
		toluene	980 nm, 954	$\alpha\alpha$ = O(*i*-C_5H_{11})	46
		CCl_4	904 nm, 884	$\beta\beta$ = Ph	38
		benzene	901 nm (lg ε 4.88), 879 (4.86), 816 (4.24), 782 (4.13), 740sh (3.76), 581sh (3.80), 535 (3.96), 507 (4.0), 404sh (4.43), 352 (4.75)	$\beta\beta$ = Ph	418
	Al(III)Cl	DMF	920 nm	$\beta\beta$ = Ph	1079
	VO(IV)	DMF	910 nm	$\beta\beta$ = Ph	1079
	Fe(II)	$CHCl_3$	829 nm, 786, 736, 568, 454, 430, 379, 360, 341, 316, 264	L = *trans*-(CNPh(2,6-$(Me)_2$)), δ = *t*-Bu	206
	Fe(II)	py	828 nm, 790, 733, 587, 527, 510, 454, 434, 344	L = *trans*-py_2, δ = *t*-Bu	206
	Cu(II)	py	630 nm (lg ε 5.44)	$\beta\beta$ = Ph	410
		benzene	878 nm (lg ε 5.30), 825 (4.52), 775 (4.48), 595 (4.08), 510 (4.27), 354 (5.00)	$\beta\beta$ = Ph	1059
		PhCl	887 nm (lg ε 5.31), 835 (4.55), 782 (4.55), 590 (4.25), 515 (4.37), 352 (5.07)	$\beta\beta$ = Ph	1059
		py	880 nm (lg ε 5.28), 827 (4.50), 777 (4.47), 592 (4.04), 515 (4.20), 368 (4.97)	$\beta\beta$ = Ph	1059
		DMF	870 nm	$\beta\beta$ = Ph	1079
	Pd(**II**)	benzene	846 nm		264

(*Continued*)

Table 5. UV-vis absorption data of sub- and super-Pcs.

Structure	M	Solvent	Transition Energy (Intensity)	Remark	Ref.
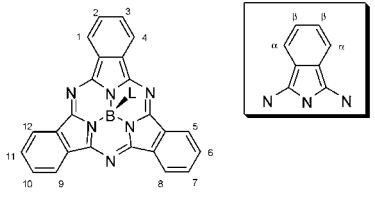	BF	unknown	570 nm		296
		unknown	563 nm (lg ε 4.8), 520sh, 307 (4.5), 268(4.5), 255(4.5)		303
	BCl	unknown	565 nm (lg ε 4.4), 529sh, 308 (4.1), 273 (4.1)		303
		$CHCl_3$	565 nm (lg ε 4.95), 524sh, 489sh, 305 (4.70)		300
		DMF	562 nm, 302		511
		DMF/H_2O(10%)/ HCl(1.2mM)	566 nm		1080
		DMSO	569 nm (10^{-4} ε 0.29)		1081
		unknown	560 nm, 300		1082
		toluene	565 nm (lg ε 4.80), 524sh, 305 (4.47)		1083
		unknown	565 nm		296
	BBr	$CHCl_3$	567 nm (lg ε 4.86), 543sh (4.60), 508sh (4.34), 303 (4.60), 271 (4.54), 255sh (4.48)		1084
	BPh	unknown	566 nm, 311		1082
		toluene	566 nm		301
	BL	DMF	561 nm (lg ε 4.88), 504 (4.32), 301 (4.60)	L = 	1085
		DMF	561 nm (lg ε 4.72), 505 (4.16), 301 (4.47)	L = 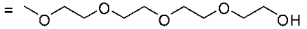	1085
		DMF	562 nm (lg ε 4.90), 505 (4.34), 302 (4.58)	L = 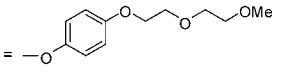	1085
		DMF	562 nm (lg ε 4.83), 505 (4.27), 302 (4.54)	L = 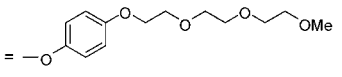	1085

(*Continued*)

Table 5. (*Continued*)

Structure	M	Solvent	Transition Energy (Intensity)	Remark	Ref.
		DCM	567 nm (ε 53,300)	L = 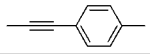	1086
		DCM	567 nm (ε 88,000)	L = 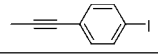	1086
		DCM	567 nm (ε 65,600)	L = 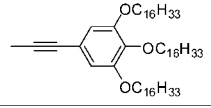	1086
		DCM	566 nm (ε 76,000)	L = 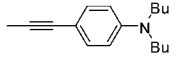	1086
		DCM	568 nm (ε 89,400), 340 (68,500)	L = 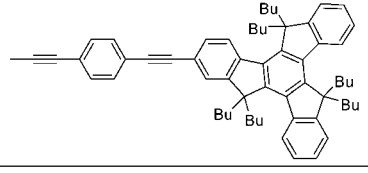	1086
		DCM	567 nm (ε 59,000), 414 (0.665)	L = 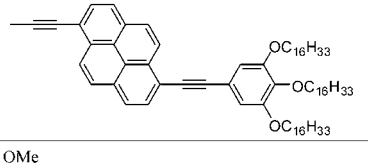	1086
		$CHCl_3$	561 nm (lg ε 4.87), 542sh (4.60), 507sh (4.30), 303 (4.57), 270 (4.48), 256sh (4.34)	L = OMe	1084
		$CHCl_3$	561 nm (lg ε 4.85), 541sh (4.57), 506sh (4.34), 302 (4.54), 270 (4.43), 256 (4.30)	L = OEt	1084
		unknown	561 nm, 302	L = OEt	1082

(*Continued*)

Table 5. (*Continued*)

Structure	M	Solvent	Transition Energy (Intensity)	Remark	Ref.
		$CHCl_3$	562 nm (lg ε 4.93), 542sh (4.65), 507sh (4.40), 303 (4.65), 271 (4.54), 255 (4.43)	L = O(*t*-Bu)	1084
		$CHCl_3$	562 nm (lg ε 4.91), 542sh (4.70), 506sh (4.40), 305 (4.60), 267 (4.57), 255 (4.51)	L = OPh	1084
		toluene	562 nm (10^{-5} ε 4.093), 524 (1.241), 302 (1.545)	L = OPh	1087
		unknown	563 nm (lg ε 5.0), 548sh, 529sh, 304 (4.7), 271 (4.7)	L = OPh(4-*t*-Bu)	303
		toluene	563 nm (lg ε 4.96), 502 (5.06)	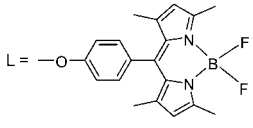	1088
		toluene	645 nm (lg ε 5.10), 562 (5.02)	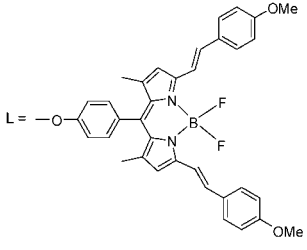	1088
		toluene	562 nm (10^{-5} ε 4.082), 524 (1.241), 385 (1.545), 302 (2.182)	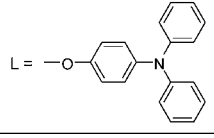	1087

(*Continued*)

Table 5. (*Continued*)

Structure	M	Solvent	Transition Energy (Intensity)	Remark	Ref.
		toluene	562 nm (10^{-3} ε 4.091), 523 (1.241), 431 (0.488), 300 (4.723)	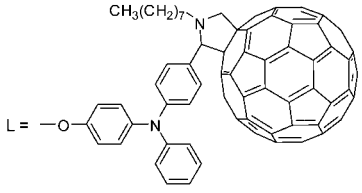	1087
		toluene	565 nm (10^{-5} ε 4.095), 528 (1.332), 435 (0.976), 301 (6.555)	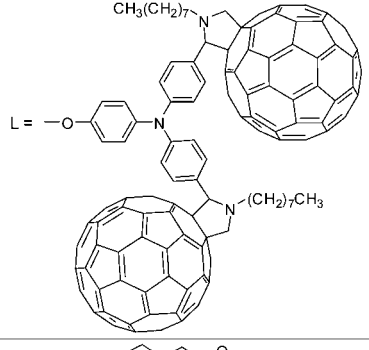	1087
		hexane	555 nm (lg ε 4.81), 513sh, 298 (4.49)	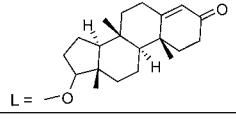	1089
		$CHCl_3$	565 nm (10^{-4} ε 7.88), 550sh, 526sh, 306 (3.69)	L = $OSi(C_6H_{13})_3$	1090
β = *t*-Bu	BBr	$CHCl_3$	567 nm, 556sh, 512, 305, 266		305
		unknown	567 nm, 305		1082
$\beta\beta$ = *n*-Bu	BCl	THF	575 nm (lg ε 4.76), 311 (4.56)		1091
	BL	THF	569 nm (lg ε 4.77), 308 (4.58)	L = OMe	1091
R_2 = CCPr	BCl	$CHCl_3$	573 nm (lg ε 4.5), 527sh, 308 (4.0), 273 (4.0)		816

(*Continued*)

Table 5. (*Continued*)

Structure	M	Solvent	Transition Energy (Intensity)	Remark	Ref.
β = CCH	BCl	unknown	583 nm, 345		1082
β = CCPr	BCl	$CHCl_3$	583 nm (lg ε 4.5), 530sh, 345 (4.2), 275 (4.5)		1092
β = $CCCH_2OMe$	BCl	$CHCl_3$	577 nm (lg ε 4.3), 530sh, 325 (4.2), 269 (4.5)		1092
β = CCPh(4-NO_2)	BCl	$CHCl_3$	590 nm (lg ε 4.6), 540sh, 355 (4.5), 285 (4.6)		1093, 1092
β = CCTMS	BCl	$CHCl_3$	583 nm (lg ε 4.6), 530sh, 345 (4.3), 276 (4.6)		1092
$\alpha\alpha$ = $OCH(Me)_2$	BBr	EtOH	546.8 nm (lg ε 3.3), 312 (3.4)		1094
β = $OCH(Me)_2$	BBr	EtOH	574.0 nm (lg ε 4.2), 302 (4.5)		1094
β = OCH_2(*t*-Bu)	BBr	EtOH	572.8 nm (lg ε 4.6), 334.6 (4.3)		1094
$\alpha\alpha$ = $O(CH_2)_4Me$	BBr	EtOH	548.8 nm (lg ε 3.4), 332.6 (3.5)		1094
β = 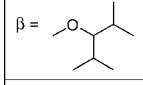	BBr	EtOH	585 nm (lg ε 4.5), 307 (4.2)		1095
β = —O— 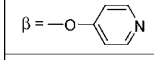	BCl	DMF/H_2O(10%)/ HCl (1.2mM)	569 nm		1080
β = —O— 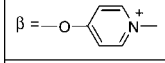	BCl	DMF/H_2O(10%)/ HCl (1.2mM)	569 nm		1080
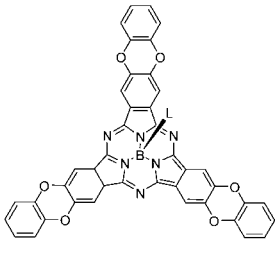	BL	$CHCl_3$	571 nm (lg ε 4.7), 555sh, 532sh, 401 (4.0), 287 (4.7)	L = OPh	1096
		MeCN	570 nm	L = OPh(4-*t*-Bu)	1097
		$CHCl_3$	572 nm (lg ε 4.6), 533sh, 403 (3.9), 288 (4.5)	L = OPh(3-CHO)	1096
		$CHCl_3$	573 nm (lg ε 4.6), 529sh, 430, 256 (5.0)	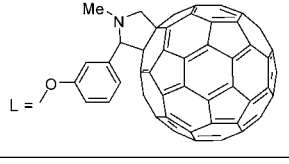	1096

(*Continued*)

Table 5. (*Continued*)

Structure	M	Solvent	Transition Energy (Intensity)	Remark	Ref.
$\beta\beta$ = SEt	BCl	toluene	592 nm (lg ε 4.77), 546sh, 362 (4.14), 296 (4.55)		1098, 1083
$\beta\beta$ = SPr	BL	MeCN	596 nm	L = OPh(4-*t*-Bu)	1097
R_2, R_6, R_{10} = SC_8H_{17}	BCl	$CHCl_3$	588 nm (lg ε 4.6), 540sh, 366 (4.2), 292 (4.6)		1099
R_3, R_6, R_{10} = SC_8H_{17}	BCl	$CHCl_3$	585 nm (lg ε 4.6), 540sh, 366 (4.2), 349 (4.2), 291 (4.6)		1099
β = SC_8H_{17}	BCl	$CHCl_3$	584 nm (lg ε 4.7), 540sh, 361 (4.2), 289 (4.6)		1093
	BOH	$CDCl_3$	574 nm (lg ε 4.2), 540sh, 353 (4.2), 287 (4.4)		1100
	BL	$CHCl_3$	599 nm (lg ε 5.0), 560sh, 406 (4.5), 389 (4.5), 298 (4.8)	L = OPh(4-*t*-Bu)	308
		$CHCl_3$	580 nm (lg ε 4.5), 540sh, 361 (4.0), 288 (4.4)	L = $OSi(C_6H_{13})_3$	1100
$\beta\beta$ = SC_8H_{17}	BCl	$CHCl_3$	603 nm (lg ε 4.9), 557 (4.4), 413 (4.5), 387 (4.5), 304 (4.8)		1093
	BOH	$CHCl_3$	597 nm (lg ε 4.9), 556sh, 421 (4.4), 371 (4.5), 296 (4.8)		1101
	BL	MeCN	596 nm	L = OPh(4-*t*-Bu)	1097
		$CHCl_3$	598 nm (lg ε 4.9), 556sh, 422 (4.4), 375 (4.5), 296 (4.8)	L = $OSiEt_3$	1101
$\beta\beta$ = $SC_{10}H_{21}$	BCl	$CHCl_3$	602 nm (lg ε 5.00), 558 (4.50), 415 (4.53), 389 (4.52), 306 (4.85)		1102
$\beta\beta$ = $SC_{16}H_{33}$	BCl	$CHCl_3$	602 nm (lg ε 4.9), 557 (4.4), 413 (4.5), 387 (4.5), 298 (4.8)		1101
	BOH	$CHCl_3$	602 nm (lg ε 4.9), 557 (4.4), 413 (4.5), 387 (4.5), 298 (4.8)		1101
	BL	$CHCl_3$	597 nm (lg ε 4.9), 557sh, 422 (4.4), 379 (4.5), 298 (4.8)	L = $OSiEt_3$	1101

(*Continued*)

Table 5. (*Continued*)

Structure	M	Solvent	Transition Energy (Intensity)	Remark	Ref.
$\beta\beta$ = SCH_2Ph	BCl	toluene	601 nm (lg ε 4.78), 555sh, 386 (4.21), 304 (4.52)		1098, 1083
$\beta\beta$ = SPh(4-Me)	BCl	$CHCl_3$	607 nm (lg ε 4.9), 550sh, 389 (4.3), 293 (4.6)		1093
β = $SO_2C_8H_{17}$	BCl	$CHCl_3$	570 nm (lg ε 4.5), 523sh, 307 (4.6)		1093
$\beta\beta$ = $SO_2C_8H_{17}$	BCl	$CHCl_3$	684 nm (lg ε 3.5), 579 (4.8), 532sh, 296 (4.7), 241 (4.8)		1093
$\beta\beta$ = SO_2Ph(4-Me)	BCl	$CHCl_3$	655 nm (lg ε 3.8), 586 (4.6), 533sh, 313 (4.4)		1093
R_2, R_6, R_{10} = NO_2	BCl	$CHCl_3$	581 nm (lg ε 4.7), 553sh, 306 (4.3)		1103
R_3, R_6, R_{10} = NO_2	BCl	$CHCl_3$	588 nm (lg ε 4.5), 569 (4.5), 532sh, 523sh, 302 (4.4)		1103
β = $N(Ph)_2$	BL	$CHCl_3$	623 nm (lg ε 4.5), 577sh, 426 (4.2), 303 (4.6), 255 (4.5)	L = OPh(2-CHO)	1104
		$CHCl_3$	624 nm (lg ε 4.6), 580sh, 428 (4.3), 301 (4.8)	L = OPh(3-CHO)	1096
		$CHCl_3$	626 nm (lg ε 4.4), 484 (3.8), 436 (3.9), 298 (4.5)	L = OPh(4-CHO)	1104
R_2, R_6, R_{10} = $N(Ph)_2$	BL	$CHCl_3$	622 nm (lg ε 4.6), 556sh, 437 (4.2), 400sh, 311 (4.6)	L = OPh	1096
		$CHCl_3$	629 nm (lg ε 4.5), 452 (4.1), 434 (4.1), 312 (4.8)	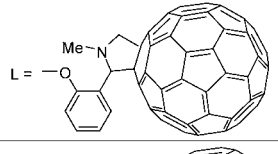	1104
		$CHCl_3$	626 nm (lg ε 4.6), 584sh, 433 (4.2), 308 (4.9), 258 (5.0)	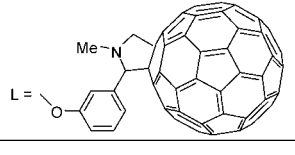	1096

(*Continued*)

Table 5. (*Continued*)

Structure	M	Solvent	Transition Energy (Intensity)	Remark	Ref.
		$CHCl_3$	624 nm (lg ε 4.4), 578sh, 433 (4.0), 308 (4.7), 260 (4.8)	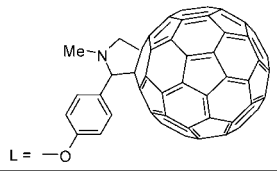	1104
R_3, R_6, R_{10} = $N(Ph)_2$	BL	$CHCl_3$	620 nm (lg ε 4.6), 554sh, 473 (4.2), 428 (4.2), 305 (4.7)	L = OPh	1096
		$CHCl_3$	629 nm (lg ε 4.5), 581sh, 436 (4.1), 401 (3.9), 306 (4.7), 259 (4.9)	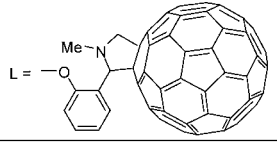	1104
		$CHCl_3$	626 nm (lg ε 4.6), 566sh, 432 (4.2), 308 (5.0), 258 (5.2)	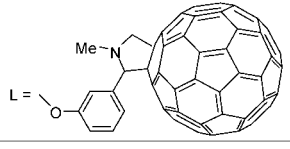	1096
		$CHCl_3$	624 nm (lg ε 4.5), 578sh, 433 (4.1), 308 (4.8), 260 (4.9)	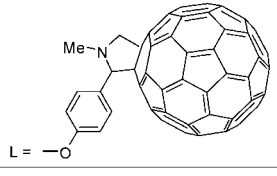	1104
R_2 = *t*-Bu, R_6(R_7), R_{10}(R_{11}) = NO_2	BCl	DCM	593 nm (r.i. 1), 564 (0.73), 518 (0.39), 427 (0.05)		884
R_2 = NO_2, R_6(R_7), R_{10}(R_{11}) = *t*-Bu	BCl	DCM	600 nm (r.i. 1), 567 (0.72), 542 (0.55), 520 (0.45), 342 (0.34)		884
R_1, R_5, R_9 = NO_2, R_3, R_7, R_{11} = *t*-Bu	BOH	$CHCl_3$	566 nm, 534, 515, 286		1105
R_2 = CCPr, R_6, R_7, R_{10}, R_{11} = SC_8H_{17}	BCl	$CHCl_3$	595 nm (lg ε 4.6), 580sh, 553sh, 422 (4.1), 363 (4.3), 305 (4.6)		816

(*Continued*)

Table 5. (*Continued*)

Structure	M	Solvent	Transition Energy (Intensity)	Remark	Ref.
R_2 = CCPr, $R_6(R_7)$, $R_{10}(R_{11})$ = NO_2	BCl	$CHCl_3$	596 nm (lg ε 4.6), 573 (4.5), 551 (4.3), 527 (4.2), 296 (4.4), 274 (4.5), 246 (4.4)		816
R_2 = I, R_6, R_7, R_{10}, R_{11} = SC_8H_{17}	BCl	$CHCl_3$	593 nm (lg ε 4.6), 577sh , 553sh, 429 (3.9), 357 (3.9), 309 (4.3)		816
R_2 = I, $R_6(R_7)$, $R_{10}(R_{11})$ = NO_2	BCl	$CHCl_3$	591 nm (lg ε 4.5), 569 (4.4), 546 (4.2), 524 (4.1), 300 (4.3)		816
R_2 = I, R_6, R_7, R_{10}, R_{11} = $SO_2C_8H_{17}$	BCl	$CHCl_3$	595 nm (lg ε 4.7), 564 (4.3), 552 (4.1), 516 (4.0), 356sh, 306 (4.3)		816
$\alpha\alpha\,\beta\beta$ = F	BL	MeCN	570 nm	L = OPh(4-*t*-Bu)	1097
	BF	unknown	571 nm (lg ε 4.9), 553sh, 529 (4.4), 490sh, 308 (4.6), 278sh, 267 (4.5)		303
	BCl	unknown	574 nm (lg ε 4.5), 556sh, 530sh, 311(4.1), 277(4.0)		303
		$CHCl_3$	573 nm (10^{-4} ε 8.96), 555sh, 532 (2.59), 309 (4.04), 275 (3.03)		307
		unknown	570 nm (ε 60,000), 555, 530, 495		1106
		unknown	570 nm, 310		1082
	BL	unknown	570 nm (lg ε 4.7), 555sh, 530 (4.2), 307(4.4)	L = OPh(4-*t*-Bu)	303
		$CHCl_3$	571 nm (lg ε 4.5), 531 (1.3), 307 (2.0), 268 (1.4), 241 (1.4)	L = OPh(3(4)-CHO)	1107
		$CHCl_3$	572 nm (lg ε 4.6), 554sh, 530sh, 308 (4.1), 275 (3.8)	L = 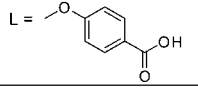	1108
		$CHCl_3$	571 nm (lg ε 4.6), 552sh, 531sh, 310 (4.4)	L= 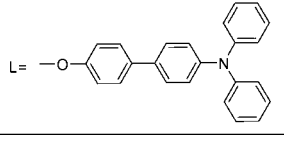	1109

(*Continued*)

Table 5. (*Continued*)

Structure	M	Solvent	Transition Energy (Intensity)	Remark	Ref.
		$CHCl_3$	573 nm (lg ε 4.6), 529sh, 430, 316 (4.5), 260 (4.8)	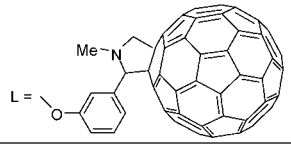	1096
β = I	BL	$CHCl_3$	572 nm (lg ε 4.5), 532sh, 325 (3.9), 273 (4.2)	L = OPh(2-CHO)	1104
		$CHCl_3$	571 nm (lg ε 4.6), 530sh, 326 (4.0), 273 (4.3)	L = OPh(3-CHO)	1096
		$CHCl_3$	572 nm (lg ε 4.5), 531sh, 326 (3.9), 274 (4.2)	L = OPh(4-CHO)	1104
		$CHCl_3$	573 nm (lg ε 4.1)	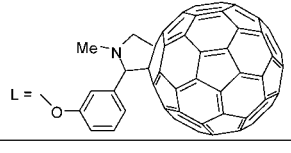	1110
		toluene	574 nm		1110
$\beta\beta$ = I	BBr	DCM	583 nm (lg ε 4.71)		556
R_2 = I	BCl	$CHCl_3$	570 nm (lg ε 4.5), 537sh, 523sh, 309 (4.2), 272 (4.1)		816
R_2, R_6, R_{10} = I	BCl	$CHCl_3$	571 nm (lg ε 4.5), 530sh, 318 (4.1)		308
R_3, R_6, R_{10} = I	BCl	$CHCl_3$	571 nm (lg ε 4.8), 530sh, 320 (4.4)		308
R_2, R_6, R_{10} = I	BL	$CHCl_3$	573 nm (lg ε 4.5), 558sh, 530sh, 340 (4.0), 317 (4.1), 277 (4.2)	L = OPh	1096
R_3, R_6, R_{10} = I	BL	$CHCl_3$	573 nm (lg ε 4.6), 558sh, 532sh, 342sh, 317 (4.2), 276 (4.3)	L = OPh	1096

(*Continued*)

Table 5. (*Continued*)

Structure	M	Solvent	Transition Energy (Intensity)	Remark	Ref.
R_2, R_6, R_{10} = I	BL	$CHCl_3$	573 nm (lg ε 4.5), 524sh, 432, 322, 260 (4.8)	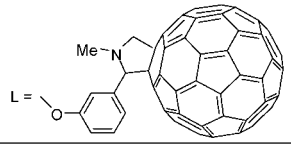	1096
R_3, R_6, R_{10} = I	BL	$CHCl_3$	573 nm (lg ε 4.5), 522sh, 431, 322 (4.4), 260 (4.8)		1096
R_2, R_6, R_{10} = I	BL	$CHCl_3$	575 nm (lg ε 4.4), 525sh, 430, 320 (4.2), 262 (4.6)	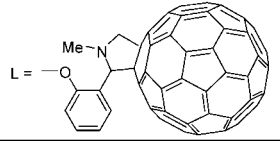	1104
R_3, R_6, R_{10} = I	BL	$CHCl_3$	575 nm (lg ε 4.4), 525sh, 430, 320 (4.2), 262 (4.6)		1104
R_2, R_6, R_{10} = I	BL	$CHCl_3$	572 nm (lg ε 4.4), 522sh, 432, 320 (4.2), 260 (4.6)	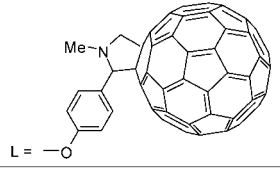	1104
R_3, R_6, R_{10} = I	BL	$CHCl_3$	572 nm (lg ε 4.5), 520sh, 432, 320 (4.3), 260 (4.7)		1104
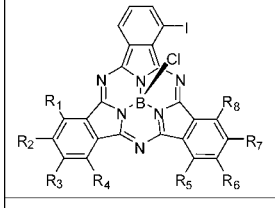	BCl	$CHCl_3$	584 nm (lg ε 4.6), 537sh, 397sh, 367sh, 287 (4.5), 260 (4.6)	R_3, R_6 = SC_8H_{17}	1099
		$CHCl_3$	584 nm (lg ε 4.6), 540sh, 409sh, 365 (3.9), 289 (4.6)	R_2, R_7 = SC_8H_{17}	1099
		$CHCl_3$	584 nm (lg ε 4.6), 539sh, 401sh, 366 (3.9), 291 (4.5)	(R_2, R_6), (R_3, R_7) = SC_8H_{17}	1099
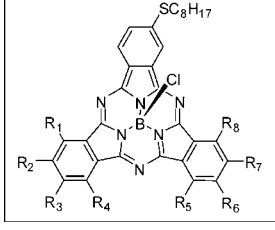	BCl	$CHCl_3$	578 nm (lg ε 4.8), 562sh, 538sh, 283 (4.8)	R_4, R_5 = I	1099
		$CHCl_3$	581 nm (lg ε 4.8), 563sh, 536sh, 405sh, 288 (4.7)	R_1, R_8 = I	1099
		$CHCl_3$	581 nm (lg ε 4.8), 563sh, 539sh, 400sh, 287 (4.7)	(R_4, R_8),(R_1, R_5) = I	1099

(*Continued*)

Table 5. (*Continued*)

Structure	M	Solvent	Transition Energy (Intensity)	Remark	Ref.
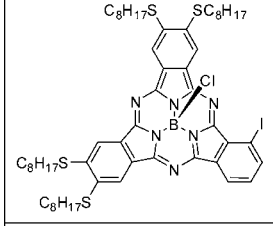	BCl	$CHCl_3$	594 nm (lg ε 4.6), 577sh, 555sh, 420 (4.2), 357 (4.2), 304 (4.6), 242 (4.5)		1099
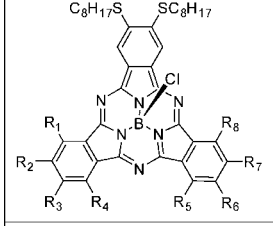	BCl	$CHCl_3$	586 nm (lg ε 4.7), 569sh, 544sh, 430 (4.2), 299 (4.6), 242 (4.6)	R_1, R_5 = I	1099
		$CHCl_3$	587 nm (lg ε 4.7), 570sh, 545sh, 420sh, 288 (4.7), 242 (4.7)	R_4, R_5 = I	1099
		$CHCl_3$	586 nm (lg ε 4.7), 570sh, 548sh, 434 (4.2), 297 (4.6), 243 (4.6)	R_1, R_8 = I	1099
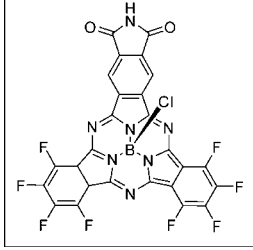	BCl	$CHCl_3$	586 nm (lg ε 4.7), 573 (4.6), 545 (4.3), 523 (4.2), 310 (4.5), 280sh, 241 (4.6)		308

(*Continued*)

Table 5. (*Continued*)

Structure	M	Solvent	Transition Energy (Intensity)	Remark	Ref.
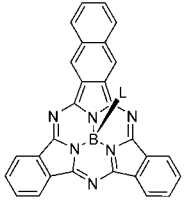	BL	$CHCl_3$	625sh, 599 (10^{-4} ε 2.13), 566 (3.61), 530sh, 313sh, 281 (3.29)	L = $OSi(C_6H_{13})_3$	1090
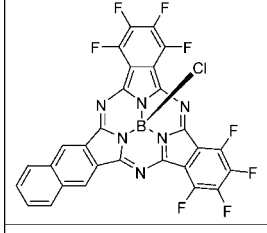	BCl	DCM	617 nm (ε 59,000), 584 nm (40,000), 560sh, 525 (30,000), 495sh, 300 (46,000)		1106
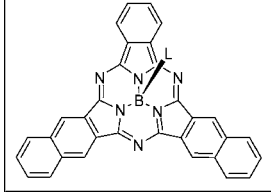	BL	$CHCl_3$	652 nm (10^{-4} ε 1.52), 626 (2.07), 325sh, 287 (3.09)	L = $OSi(C_6H_{13})_3$	1090

(*Continued*)

Table 5. (*Continued*)

Structure	M	Solvent	Transition Energy (Intensity)	Remark	Ref.
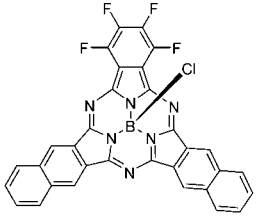	BCl	DCM	640 nm (ε 69,000), 605 (51,000), 580sh, 547 (34,000), 510sh, 319 (54,000)		1106
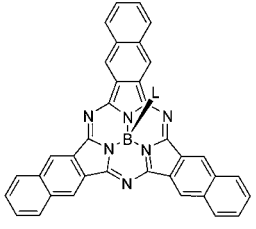	BCl	$CHCl_3$	650 nm		1090
		unknown	673 nm		1106
		DMSO	662 nm (10^{-4} ε 3.43)		1081
	BBr	DCB	667 nm (10^{-4} ε 6.26), 608 (2.06), 328 (3.09), 302 (4.62)		302
	BPh	toluene	650 nm		301
		toluene	654 nm	γ= *t*-Bu	301
	BL	$CHCl_3$	651 nm (10^{-4} ε 6.60), 601sh, 474 (0.47), 395 (0.56), 331sh, 292 (6.44)	L = $OSi(C_6H_{13})_3$	1090
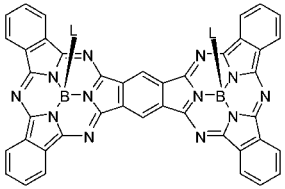	BL	$CHCl_3$	692 nm (lg ε 4.9), 662 (4.4), 636 (4.4), 605 (4.5), 592sh, 441 (3.9), 320 (4.5), 278 (4.4)	$\alpha\alpha\,\beta\beta$= F, L = Cl	308
		$CHCl_3$	706 nm (lg ε 4.8), 675 (4.3), 647 (4.3), 609 (4.4), 599sh, 441 (3.8), 339 (4.4)	β= I, L = O(4-*t*-BuPh)	308
		$CHCl_3$	718 nm, 596, 567sh, 537, 307	β= *t*-Bu, L = Br	305
		$CHCl_3$	739 nm (lg ε 5.0), 704 (4.6), 630sh, 605 (4.7), 421 (4.7), 294 (5.1)	$\beta\beta$= SC_8H_{17}, L = O(4-*t*-BuPh)	308
		$CHCl_3$	689 nm (lg ε 4.9), 657 (4.5), 633 (4.5), 601 (4.6), 589sh, 449 (3.9), 317 (4.6)	$\alpha\alpha\,\beta\beta$= F, L = O(4-*t*-BuPh)	308
		$CHCl_3$	689 nm (lg ε 4.9), 657 (4.4), 631 (4.4), 601 (4.5), 586sh, 441 (3.9), 319 (4.5), 273 (4.5)	$\alpha\alpha\,\beta\beta$ = F, L = OPh	308

(*Continued*)

Table 5. (*Continued*)

Structure	M	Solvent	Transition Energy (Intensity)	Remark	Ref.
		$CHCl_3$	691 nm (lg ε 5.0), 660 (4.4), 633 (4.5), 603 (4.5), 590sh, 490 (3.9), 450 (3.8), 319 (4.6)	L = 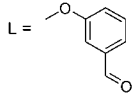 $\alpha\alpha\,\beta\beta$ = F ,	1111
		$CHCl_3$	689 nm (lg ε 4.9), 657 (4.4), 631 (4.4), 601 (4.5), 586sh, 441 (3.9), 319 (4.5), 273 (4.5)	L = OPh, $\alpha\alpha\beta\beta$ = F	306
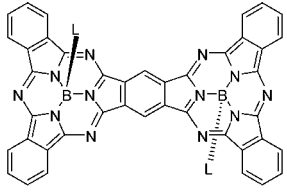	BCl	$CHCl_3$	704 nm (lg ε 4.9), 672 (4.6), 643 (4.5), 607 (4.6), 443 (4.0), 321 (4.6)	β = I, L = O(4-*t*-BuPh)	308
		$CHCl_3$	693 nm (lg ε 4.9), 661 (4.4), 635 (4.4), 604 (4.5), 592sh, 441 (3.7), 319 (4.5), 278 (4.4)	$\alpha\alpha\,\beta\beta$ = F	308, 1111
	BL	$CHCl_3$	736 nm (lg ε 5.0), 703 (4.6), 672 (4.5), 629 (4.6), 620sh, 430 (4.4), 336sh, 298 (4.8)	$\beta\beta$ = SC_8H_{17}, L = O(4-*t*-BuPh)	308
		$CHCl_3$	688 nm (lg ε 4.9), 657 (4.4), 631 (4.4), 600 (4.5), 587sh, 441 (3.7), 319 (4.4), 274 (4.3)	$\alpha\alpha\,\beta\beta$ = F, L = OPh	308
		$CHCl_3$	688 nm (lg ε 4.8), 656 (4.3), 631 (4.4), 600 (4.4), 588sh, 439 (3.8), 314 (4.5)	$\alpha\alpha\,\beta\beta$ = F, L = O(4-*t*-BuPh)	308
		$CHCl_3$	688 nm (lg ε 4.9), 657 (4.4), 631 (4.4), 600 (4.5), 587sh, 441 (3.7), 319 (4.4), 274 (4.3)	$\alpha\alpha\,\beta\beta$ = F, L = OPh	306

(*Continued*)

Table 5. (*Continued*)

Structure	M	Solvent	Transition Energy (Intensity)	Remark	Ref.
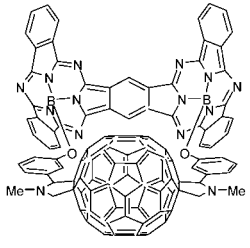	BL	$CHCl_3$	694 nm (lg ε 5.0), 659 (4.6), 634 (4.6), 606 (4.7), 590sh, 491 (4.2), 310 (4.9), 269 (5.1)	$\alpha\alpha\beta\beta$ = F	1111
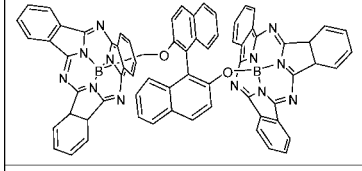	BL	DCM	562 nm (ε 140,000), 550sh, 525sh, 303 (85,000)		1112
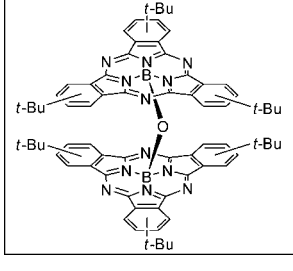	BL	$CHCl_3$	538 nm (10^{-4} ε 3.06), 307 (2.63), 264 (3.25)		302

(*Continued*)

Table 5. (*Continued*)

Structure	M	Solvent	Transition Energy (Intensity)	Remark	Ref.
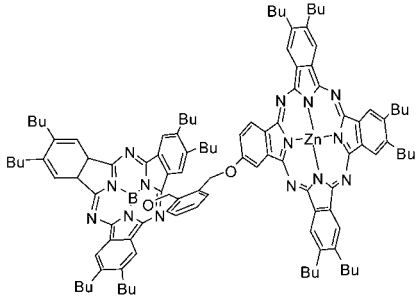	BL	THF	682 nm (lg ε 4.83), 615 (4.10), 572 (4.38), 349 (4.55)		1091
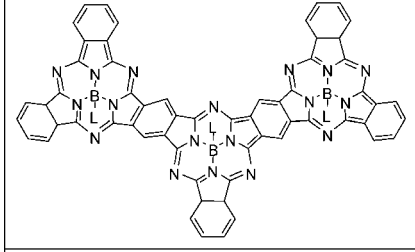	BL	$CHCl_3$	755 nm (lg ε 4.9), 697 (4.6), 661 (4.5), 637 (4.4), 585 (4.5), 317 (4.6), 280 (4.6)	$\alpha\alpha\,\beta\beta$ = F, L = Cl	308
		$CHCl_3$	807 nm (lg ε 5.0), 735 (4.9), 697 (4.8), 617 (4.7), 433 (4.6), 350sh, 298 (5.0)	$\beta\beta$ = SC_8H_{17}, L = O(4-*t*-BuPh)	308
		$CHCl_3$	570 nm (lg ε 4.7), 555sh, 530 (4.2), 307 (4.4)	$\alpha\alpha\,\beta\beta$ = F , L = O(4-*t*-BuPh)	308
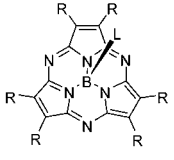	BL	unknown	496 nm (ε 40,000), 481sh, 324sh, 289 (35,000)	R = Et, L = OH	304
		$CHCl_3$	500 nm (lg ε 4.38), 327sh, 289 (4.45)	R = Pr, L = OH	299
		unknown	499 nm (lg ε 4.6), 324 (4.4), 282 (4.6)	R = Pr, L = F	303
		unknown	501 nm (lg ε 4.6), 335sh, 295 (4.6)	R = Pr, L = Cl	303
		unknown	499 nm (lg ε 4.6), 316 (4.4), 285 (4.6)	R = Pr , L = OPh	303
		toluene	378 nm	R = Ph(4-*t*-Bu), L = Cl	301
		$CHCl_3$	550 nm (lg ε 4.03), 430 (4.09), 288 (4.27)	R = SC_5H_{11}, L = OH	299
		$CHCl_3$	559 nm (lg ε 4.32), 444 (4.40), 299 (4.38)	R = SC_5H_{11}, L = Cl	299

(*Continued*)

Table 5. (*Continued*)

Structure	M	Solvent	Transition Energy (Intensity)	Remark	Ref.
		$CHCl_3$	559 nm (lg ε 4.12), 442 (4.18), 297 (4.18)	R = $SC_{12}H_{25}$, L = Cl	299
		$CHCl_3$	558 nm (lg ε 4.48), 446 (4.57), 298 (4.55)	R = $SC_{18}H_{37}$, L = Cl	299
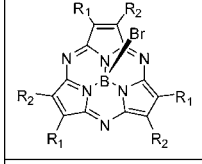	BBr	$CHCl_3$	411 nm (10^{-4} ε 1.22), 255 (2.70)	R_1, R_2 = CN, Ph(2-CF_3)	302
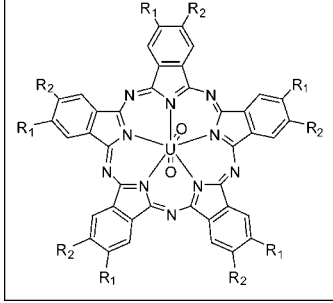	UO_2	toluene	912 nm (10^4 ε 6.67), 810sh, 420 (5.41)	R_1, R_2 = H	114
		1-ClNp	914 nm (10^4 ε 6.67), 810sh, 424 (5.02)	R_1, R_2 = H	114
		toluene	922 nm, 810sh, 420	R_1(R_2) = Me	114
		1-ClNp	935 nm, 820sh, 422	R_1, R_2 = Me	114
		toluene	938 nm (10^4 ε 6.98), 820sh, 417 (6.90)	R_1, R_2 = Bu	114
		1,2,4-trichlorobenzene	939 nm (10^4 ε 7.34), 820sh, 419 (7.26)	R_1, R_2 = Bu	114

Table 6. UV-vis absorption data of Pc analogs containing heteroatoms inside the aromatic skeleton.

Structure	M	Solvent	Transition Energy (Intensity)	Remark	Ref.
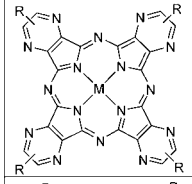	Al(III)OH	$CHCl_3$	632 nm	R = *t*-Bu	1113
	Ni(II)	$CHCl_3$	626 nm, 603, 570, 322	R = *t*-Bu	512
		MeOH	617 nm, 575, 306	R = *t*-Bu	512
	Lu(III)Cl	$CHCl_3$	639 nm, 584, 342	R = *t*-Bu	1114
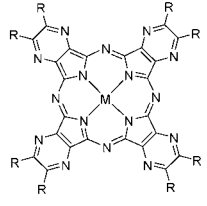	2H	py	675 nm (ε 66,600), 640 (46,500), 512 (63,800), 361 (117,000)	R = NHBu	1115
		py	673 nm (ε 124,500), 648 (113,800), 592 (24,600), 480 (42,100), 375 (107,700)	R = SBu	1115
		py	648 nm (ε 97,400), 606 (73,200), 556 (19,400), 425 (32,800), 346 (93,000)	R = OBu	1115
		DCB/AcOH = 1:1 v/v	676.5 nm (lg ε 4.47), 654.0 (4.40)	R = 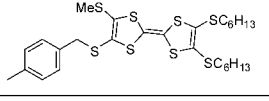	1116
		$CHCl_3$	655 nm, 616, 440, 352	R = SBu/OBu	1115
		DCM	648 nm (lg ε 5.11), 612 (4.82), 335	R = Me	410
		THF	679 nm (ε 87,500), 649 (64,100), 620sh, 595sh, 513 (56,700), 367 (96,800)	R = NEt_2	721
		THF	671 nm (ε 132,300), 640 (110,200)	R = S(*t*-Bu)	721
	Mg(II)	py	675 nm, 389	R = 	477
		py	659 nm, 373	R = py	477
		py	659 nm (ε 236,000), 629sh, 596 (33,000), 373 (130,000)	R = Ph	477
		py	677 nm, 390	R = 	477
		py	651 nm (ε 172,600), 595 (27,400), 510 (37,100), 373 (134,400)	R = NHBu	1115
		py	656 nm (ε 287,100), 594 (37,400), 386 (141,600)	R = SBu	1115
		py	626 nm (ε 208,400), 569 (27,200), 368 (115,300)	R = OBu	1115
		py	656 nm (ε 280,000), 594 (36,000), 385 (138,000)	R = SC_8H_{17}	1115

(*Continued*)

Table 6. (*Continued*)

Structure	M	Solvent	Transition Energy (Intensity)	Remark	Ref.
		THF	679 nm, 362	R = 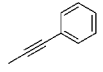	1117
		THF	676 nm, 389	R = 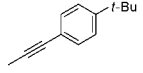	1117
		THF	676 nm (ε 338,000), 612 (44,000), 394 (205,000), 317 (87,000)	R = 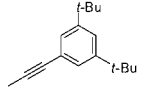	1117
		THF	677 nm (ε 157,000), 405 (194,000)	R = 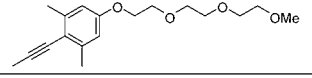	1117
		DMSO	684 nm (ε 320,000), 618 (49,000), 413 (189,000)	R = 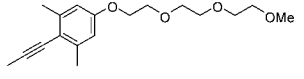	1117
	Al(III)OH	$CHCl_3$	636 nm	R = C_2H_5	1113
	Cu(II)	DCM	659 nm (lg ε 4.84)	R = 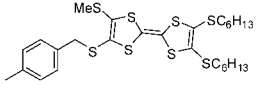	1116
	Zn(II)	py	651 nm (ε 82,300), 597 (17,700), 522 (23,200), 377 (109,000)	R = NHBu	1115
		py	655 nm (ε 251,100), 593 (32,400), 460 (24,900), 385 (134,200)	R = SBu	1115
		py	624 nm (ε 202,900), 567 (26,900), 368 (128,400)	R = OBu	1115
		THF	673 nm (ε 323,000), 611 (44,000), 387 (211,000), 289 (40,000)	R = 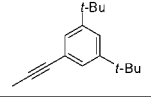	1117
		py	661 nm (ε 224,000), 599 (26,000), 385 (113,000)	R = 	1118

(*Continued*)

Table 6. (*Continued*)

Structure	M	Solvent	Transition Energy (Intensity)	Remark	Ref.
		py	664 nm (ε 187,000), 600 (37,000), 390 (91,000)	R = 	1118
		DMF	654 nm (ε 290,000)	R = S(*t*-Bu)	1119
		DMF	654 nm (ε 281,000), 390 (137,000)	R = S(*t*-Bu)	1120
		DMF	654 nm (lg ε 5.45)	R = S(*t*-Bu)	1121
		DMF/H_2O/HCl	654 nm (lg ε 5.45)	R = S(*t*-Bu)	1121
		$CHCl_3$	654 nm (ε 260,000)	R = $S(CH_2)_7CH_3$	1119
		DMF	659 nm (ε 136,000), 598 (18,900), 393 (35,100)	R = COOBu	1120
		DMF	655 nm (lg ε 5.38)	R = $SC_2H_4NEt_2$	1121
		py	657 nm (ε 241,800), 595 (33,000), 386 (136,600)	R = $SC_2H_4NEt_2$	1121
		DMF	655 nm (lg ε 5.33)	R = $SC_2H_4NEt_2$, HCl adduct	1121
		DMF/H_2O/HCl	657 nm (lg ε 5.38)	R = $SC_2H_4NEt_2$, HCl adduct	1121
		H_2O + HCl	650 nm (lg ε 5.32)	R = $SC_2H_4NEt_2$, HCl adduct	1121
		py	673 nm (ε 228,000), 609 (41,000), 394 (130,000)	R = 	477
		py	657 nm (ε 187,000), 596 (32,000), 377 (111,000)	R = py	477
		py	657 nm (ε 174,000), 628sh, 593 (36,000), 377 (123,000)	R = Ph	477
		py	677 nm (ε 166,000), 612 (29,000), 395 (89,000)	R = 	477
		THF	650 nm (ε 298,000)	R = S(*t*-Bu)	721
		THF	654 nm (ε 173,000), 626sh, 595sh, 501 (33,100), 373.5 (108,900)	R = NEt_2	721
		DCM	664 nm (lg ε 4.53)	R = 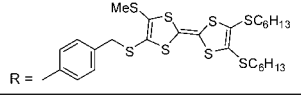	1116
	nil	py	664 nm (ε 139,600)	R = NEt_2, $[Pc]^{2-}$	721
		py	656 nm (ε 228,200)	R = S(*t*-Bu), $[Pc]^2$	721
	Mg(II)	DMF	654 nm	R = S(*t*-Bu)	1122
		py	658 nm (ε 298,000), 596 (36,400), 382 (145,000)		720, 1122
		THF	651 nm		1122
		DMF	646 nm	R = NHC_4H_9	1122

(*Continued*)

Table 6. (*Continued*)

Structure	M	Solvent	Transition Energy (Intensity)	Remark	Ref.
		py	651 nm (ε 172,600), 595 (27,400), 510 (37,100), 373 (134,400)		1115, 1122
		THF	641 nm		1122
	Zn(II)	DMF	654 nm	R = S(*t*-Bu)	1122
		py	657 nm (ε 298,000), 595 (33,600), 385 (146,000)		720, 1122
		THF	650 nm		1122
		py	655 nm (ε 106,000), 600 (25,000), 385 (88,000)	R = 	1123
		py	655 nm (ε 169,000), 595 (31,000), 385 (124,000)	R = 	1123
	Si(IV)L	DCM	647 nm, 598, 578, 356, 298, 258, 242	R = C_8H_{17}, L = *trans*-Cl_2	1124
		DCM	629.4 nm, 603.9, 580.0sh, 570.8, 350, 295.6, 251, 232	R = C_8H_{17}, L = *trans*-$(OH)_2$	1124
		DCM	624.4 nm, 597.6, 578, 566.6, 347.8, 296.4, 251, 231.9	R = C_8H_{17}, L = *trans*-$(OSi(Me)_2t\text{-}Bu)_2$	1124
		DCM	626.6 nm, 600.5, 578, 568.6, 348.1, 295.8, 250, 232.1	R =  , L = *trans*-$(OSi(Me)_2t\text{-}Bu)_2$	1124
		DCM	631.2 nm, 605.8, 582, 572.2, 350.9, 297.2	R =  , L = *trans*-$(OH)_2$	1124
		DCM	626.6 nm, 600.5, 578sh, 568.6, 348.1, 295.8, 250, 232.1	R = C_8H_{17}, L = *trans*-$(OSi(Me)_2t\text{-}Bu)$, (OH)	1124
		DCM	688.1 nm, 657.9, 618.4, 356.3, 341, 296.2, 284	R = C_9H_{19}, L = *trans*-$(OH)_2$	1124
	Mg(II)	py	660 nm (ε 160,350), 595 (23,900), 370 (97,200), 305 (127,900)	R = 2-py	1125
	Cu(II)	py	674 nm (ε 67,000), 605 (13,000), 390 (48,000)	R = 	1125
		py + NH_4OH	650 nm (ε 199,200), 587 (36,000), 375 (112,800), 305 (225,600)	R = 2-py	1125

(*Continued*)

Table 6. (*Continued*)

Structure	M	Solvent	Transition Energy (Intensity)	Remark	Ref.
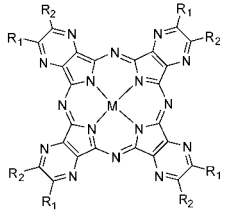	Zn(II)	py	670 nm (ε 179,000), 605 (47,000), 390 (132,000)	R_1, R_2 = 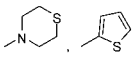	1123
		py	670 nm (ε 146,000), 610 (41,000), 390 (117,000)	R_1, R_2 = 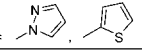	1123
	Cu(II)	$CHCl_3$	670 nm, 368	R_1, R_2 = 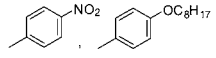	1126
		$CHCl_3$	670 nm, 368	R_1, R_2 = 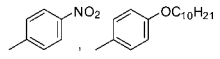	1126
		$CHCl_3$	670 nm, 368	R_1, R_2 = 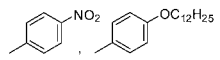	1126
		$CHCl_3$	664 nm, 368	R_1, R_2 = 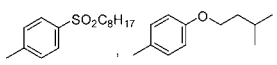	1126
		$CHCl_3$	664 nm, 368	R_1, R_2 = 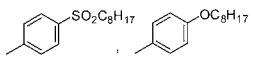	1126
		$CHCl_3$	664 nm, 368	R_1, R_2 = 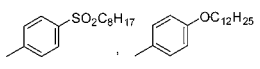	1126
	Mg(II)	DMF	662 nm	R_1, R_2 = S(*t*-Bu), $NH(CH_2)_5COOH$	1122
		py	666 nm		1122
		THF	655 nm (ε 138,600), 595 (29,200), 464 (24,100), 379 (124,300)		1122
	2H	THF	683 nm (ε 29,200), 645 (26,400), 501 (31,800), 363 (56,900)	R_1, R_2 = S(*t*-Bu), $NH(CH_2)_5COOH$	1122
	Zn(II)	DMF	667 nm (ε 62,800), 378 (101,800)	R_1, R_2 = S(*t*-Bu), $NH(CH_2)_5COOH$	1122
	Mg(II)	DMF	662 nm	R_1, R_2 = S(*t*-Bu), $NH(CH_2)_5COC_4H_6$	1122
		py	666 nm		1122
		THF	655 nm (ε 132,900), 595 (28,500), 462 (23,200), 378 (119,000)		1122

(*Continued*)

Table 6. (*Continued*)

Structure	M	Solvent	Transition Energy (Intensity)	Remark	Ref.
	2H	THF	682 nm (ε 33,600), 645 (32,000), 517 (47,200), 365 (74,900)	R_1, R_2 = S(*t*-Bu), $NH(CH_2)_5COC_4H_9$	1122
	Mg(II)	DMF	662 nm	R_1, R_2 = S(*t*-Bu), $NH(CH_2)_5CONEt_2$	1122
		py	666 nm		1122
		THF	655 nm (ε 138,900), 596 (28,500), 475 (22,800), 379 (128,000)		1122
	2H	DMF	683 nm, 659	R_1, R_2 = S(*t*-Bu), $NH(CH_2)_5CONEt_2$	1122
		py	684 nm, 660		1122
		THF	680 nm (ε 71,800), 650 (54,000), 487 (42,900), 365 (81,600)		1122
	Zn(II)	DMF	662 nm	R_1, R_2 = S(*t*-Bu), $NH(CH_2)_5CONEt_2$	1122
		py	664 nm		1122
		THF	652 nm (ε 112,400), 595 (30,500), 475 (28,500), 374 (116,700)		1122
		py	671 nm (ε 234,000), 605 (47,000), 395 (160,000)	R_1, R_2 =  , S(*t*-Bu)	1118
		py	675 nm (ε 208,000), 615 (49,000), 390 (172,000), 315 (191,000)	R_1, R_2 =  , 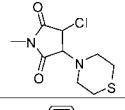	1118
		py	675 nm (ε 161,000), 610 (40,000), 395 (146,000)	R_1, R_2 =  , 	575
		py	675 nm (ε 183,000), 610 (43,000), 395 (143,000)	R_1, R_2 =  , 	575
		py	670 nm (ε 223,000), 605 (47,000), 395 (145,000)	R_1, R_2 =  , 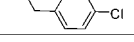	575

(*Continued*)

Table 6. (*Continued*)

Structure	M	Solvent	Transition Energy (Intensity)	Remark	Ref.
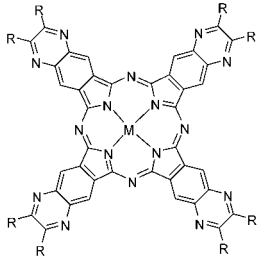	Mg(II)	THF	771 nm (ε 510,700), 731 (54,000), 703 (58,000), 553 (18,000), 389 (288,000), 255 (226,000), 249 (210,000), 244 (175,000)	R = Si(*i*Pr)$_3$	1127
		THF	770 nm (ε 516,800), 730 (59,400), 704 (59,400), 571 (26,100), 394 (305,500), 286 (139,000), 261 (200,000), 255 (244,000), 249 (232,000), 244 (196,000)	R = CCPh(3,5-(*t*-Bu)$_2$)	1127
		THF	772 nm (ε 411,000), 732 (46,000), 705 (45,000), 693 (43,000), 548 (22,000), 397 (264,000)	R = CCPh(4-OSi(*i*-Pr)$_3$)	1127
		DMSO	788 nm (ε 38,000), 584 (13,000), 287 (157,000), 273 (159,000), 266 (159,000)	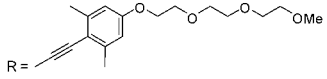	1127
		THF	735 nm (ε 431,000), 700 (50,400), 660 (52,500), 483 (7,300), 364 (133,100), 310 (79,400), 271 (81,500)	R = $C_{12}H_{25}$	1127
	Zn(II)	THF	770 nm (ε 507,000), 731 (56,000), 702 (58,000), 547 (27,000), 380 (249,000)	R = CCSi(*i*-Pr)$_3$	1127
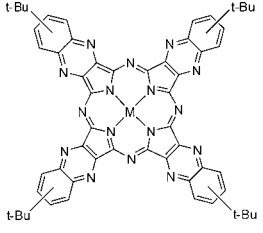	2H	DMF	707 nm (lg ε 4.61), 640 (4.32), 350 (4.78)		1128
		$CHCl_3$	712 nm (lg ε 4.78), 679 (4.41), 644 (4.32), 347 (4.72)		1128
		benzene	710 nm (lg ε 4.25), 665 (3.78), 347 (4.45)		1128
		H_2SO_4	750 nm (lg ε 4.21), 612 (4.08), 378 (4.86), 264 (4.78), 205 (4.93)		1128
	Co(II)	DMF	695 nm (lg ε 4.78), 648 (4.34), 348 (4.79)		1128
		$CHCl_3$	704 nm (lg ε 4.62), 660 (4.38), 342 (4.75)		1128
		benzene	698 nm (lg ε 4.08), 647 (3.54), 350 (4.28)		1128
		H_2SO_4	746 nm (lg ε 4.25), 603 (4.58), 535 (4.62), 402 (4.89), 268 (4.85)		1128
	Cu(II)	DMF	704 nm (lg ε 4.52), 670 (4.02), 647 (4.12), 352 (4.65)		1128

(*Continued*)

Table 6. (*Continued*)

Structure	M	Solvent	Transition Energy (Intensity)	Remark	Ref.
		$CHCl_3$	707 nm (lg ε 4.65), 664 (4.19), 344 (4.68)		1128
		benzene	708 nm (lg ε 4.12), 648 (3.63), 329 (4.38)		1128
		H_2SO_4	745 nm (lg ε 4.48), 544 (4.51), 395 (4.88), 251(4.91), 207 (4.89)		1128
	Zn(II)	DMF	707 nm (lg ε 4.32), 669 (4.11), 347 (4.41)		1128
		$CHCl_3$	704 nm (lg ε 4.58), 671 (4.25), 645 (4.15), 357 (4.78)		1128
		benzene	714 nm (lg ε 4.18), 667 (3.68), 650 (3.52), 348 (4.34)		1128
		H_2SO_4	768 nm (lg ε 4.72), 605 (4.63), 560 (4.52), 390 (5.12), 256 (4.93)		1128
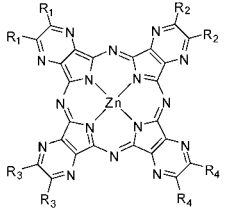	Zn(II)	DMF	655 nm (lg ε 5.27)	R_1, R_2, R_3 = S(*t*-Bu), R_4 = $SC_2H_4NEt_2$	1121
		py	657 nm (ε 186,500), 595 (25,600), 385 (102,300)		1121
		DMF	655 nm (lg ε 5.26)	R_1, R_2, R_3 = S(*t*-Bu), R_4 = $SC_2H_4NEt_2$, HCl adduct	1121
		DMF/water/HCl	657 nm (lg ε 5.26)		1121
		DMF	655 nm (lg ε 5.26)	R_1, R_2 = S(*t*-Bu), R_3, R_4 = $SC_2H_4NEt_2$	1121
		py	657 nm (ε 182,400), 595 (24,600), 385 (102,600)		1121
		DMF	655 nm (lg ε 5.26)	R_1, R_2 = S(*t*-Bu), R_3, R_4 = $SC_2H_4NEt_2$, HCl adduct	1121
		DMF/water/HCl	657 nm (lg ε 5.27)		1121
		DMF	655 nm (lg ε 5.27)	R_1, R_4 = S(*t*-Bu), R_2, R_3 = $SC_2H_4NEt_2$	1121
		py	657 nm (ε 179,700), 595 (24,000), 385 (105,700)		1121
		DMF	655 nm (lg ε 5.25)	R_1, R_4 = S(*t*-Bu), R_2, R_3 = $SC_2H_4NEt_2$, HCl adduct	1121
		DMF/water/HCl	657 nm (lg ε 5.26)		1121
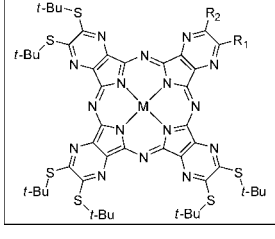	Mg(II)	DMF	659 nm (ε 151,400), 598 (30,400), 377 (132,000)	R_1 = S(*t*-Bu), R_2 = $NH(CH_2)_5COOH$	1129
		THF	655 nm (ε 165,400), 593 (30,000), 382 (130,200)	R_1 = S(*t*-Bu), R_2 = $NH(CH_2)_5COOH$	1129
	Zn(II)	DMF	658 nm (ε 135,600), 598 (25,700), 384 (105,700)	R_1 = S(*t*-Bu), R_2 = $NH(CH_2)_5COOH$	1129
		DMF	654 nm (ε 228,000), 594 (31,000), 387 (127,200)	R_1 = Me, R_2 = $S(CH_2)_2COOH$	1129

(*Continued*)

Table 6. (*Continued*)

Structure	M	Solvent	Transition Energy (Intensity)	Remark	Ref.
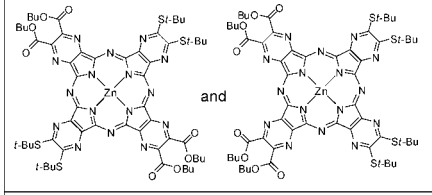	Zn(II)	DMF	660 nm (ε 194,300), 599 (23,100), 391 (83,000)		1120
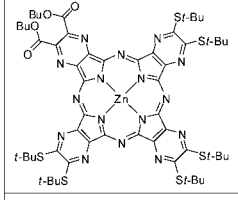	Zn(II)	DMF	656 nm (ε 174,500), 597 (21,100), 394 (92,000)		1120
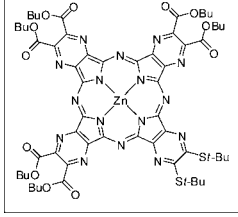	Zn(II)	DMF	660 nm (ε 159,500), 602 (20,700), 394 (55,500)		1120

(*Continued*)

Table 6. (*Continued*)

Structure	M	Solvent	Transition Energy (Intensity)	Remark	Ref.
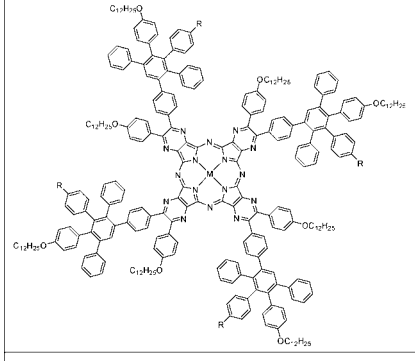	2H	$CHCl_3$	679 nm, 651, 377	R = Br	1130
		$CHCl_3$	679 nm, 651, 379	R = $O(CH_2)_{11}CH_3$	1130
	Mg(II)	$CHCl_3$	653 nm, 385	R = Br	1130
		$CHCl_3$	650 nm, 384	R = $O(CH_2)_{11}CH_3$	1130
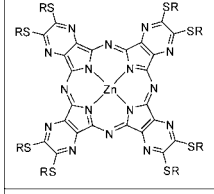	Zn(II)	py	665 nm (ε 171,000), 605 (36,000), 390 (103,000)	R = 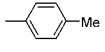	575
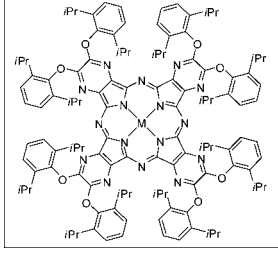	2H	THF	645 nm (ε 75,000), 607		1131
		$CHCl_3$	645 nm, 607, 348		1132
	Co(II)	THF	606 nm (ε 64,000)		1131
	Ni(II)	THF	615 nm (ε 170,000)		1131
	Zn(II)	THF	624 nm (ε 246,000)		1131, 1133

(*Continued*)

Table 6. (*Continued*)

Structure	M	Solvent	Transition Energy (Intensity)	Remark	Ref.
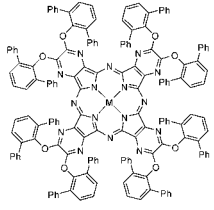	2H	THF	651 nm (ε106,000), 611		1131
	Co(II)	THF	608 nm (ε108,000)		1131
	Ni(II)	THF	619 nm (ε241,000)		1131
	Zn(II)	THF	626 nm (ε287,000)		1131
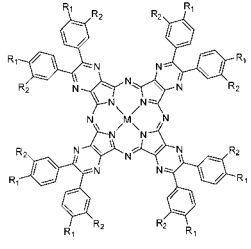	Ni(II)	$CHCl_3$	666 nm (lg ε5.53), 602 (4.64), 536 (4.54), 377 (4.92), 347 (4.92), 297 (4.83)	$R_1 = OC_{10}H_{21}$, R_2 = H	1134
		$CHCl_3$	653 nm (lg ε5.23), 602 (4.56), 492 (4.62), 378 (4.99), 296 (4.92)	$R_1 = OC_{12}H_{25}$, R_2 = H	1134
		$CHCl_3$	657 nm (lg ε5.28), 595 (4.59), 520 (4.53), 390 (4.88), 334 (4.91), 313 (4.92)	$R_1 = R_2 = OC_8H_{17}$	1134
		$CHCl_3$	657 nm (lg ε5.27), 595 (4.59), 521 (4.54), 391 (4.88), 330 (4.92), 313 (4.93)	$R_1 = R_2 = OC_{10}H_{21}$	1134
		$CHCl_3$	657 nm (lg ε5.22), 594 (4.53), 514 (4.49), 390 (4.83), 331 (4.87), 314 (4.89)	$R_1 = R_2 = OC_{12}H_{25}$	1134
	Cu(II)	$CHCl_3$	662 nm (lg ε4.77), 500 (4.52), 377 (5.06), 288 (4.79)	$R_1 = OC_{10}H_{21}$, R_2 = H	1134
		$CHCl_3$	662 nm (lg ε4.84), 500 (4.50), 377 (5.03), 290 (4.76)	$R_1 = OC_{12}H_{25}$, R_2 = H	1134
		$CHCl_3$	666 nm (lg ε5.31), 601 (4.64), 541 (4.55), 377 (4.92), 351 (4.91), 276 (4.83)	$R_1 = R_2 = OC_8H_{17}$	1134
		$CHCl_3$	666 nm (lg ε5.29), 602 (4.63), 542 (4.54), 377 (4.92), 346 (4.90), 276 (4.84)	$R_1 = R_2 = OC_{10}H_{21}$	1134
		$CHCl_3$	666 nm (lg ε5.33), 602 (4.64), 536 (4.54), 377 (4.92), 347 (4.92), 276 (4.83)	$R_1 = R_2 = OC_{12}H_{25}$	1134

(*Continued*)

Table 6. (*Continued*)

Structure	M	Solvent	Transition Energy (Intensity)	Remark	Ref.
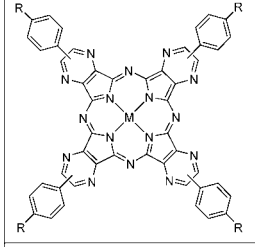	Al(III)OH	$CHCl_3$	651 nm	R = *i*-Bu	1113
		$CHCl_3$	651 nm	R = C_8H_{17}	1113
		$CHCl_3$	650 nm	R = $C_{12}H_{25}$	1113
		$CHCl_3$	650 nm	R = $C_{16}H_{33}$	1113
	V(IV)O	$CHCl_3$	647 nm	R = $C_{16}H_{33}$	1113
	Cu(II)	$CHCl_3$	640 nm	R = $C_{16}H_{33}$	1113
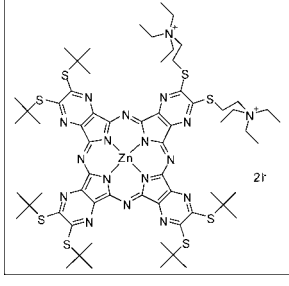	Zn(II)	DMF	655 nm (ε 152,100)	$[Pc]^{2+}[I]^{-}_{2}$	1119

(*Continued*)

Table 6. (*Continued*)

Structure	M	Solvent	Transition Energy (Intensity)	Remark	Ref.
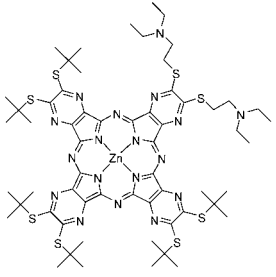	Zn(II)	DMF	655 nm (ε 178,600)		1119
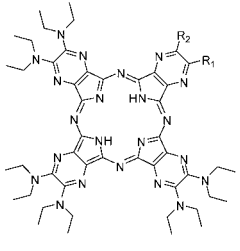	2H	THF	678 nm (ε 88,300), 647 (64,800), 618sh, 592sh, 507 (56,100), 364 (104,600)	R_1 = $NH(CH_2)_2OH$, R_2 = $N(C_2H_5)_2$	1135
		py	663 nm (ε 108,800)	R_1 = $NH(CH_2)_2OH$, R_2 = $N(C_2H_5)_2$	1135
		THF	678 nm (ε 95,300), 647 (69,500), 617sh, 591sh, 508 (58,400), 365 (108,000)	R_1 = $NH(CH_2)_2O(CH_2)_2OH$, R_2 = $N(C_2H_5)_2$	1135
		py	662 nm (ε 138,600)	R_1 = $NH(CH_2)_2O(CH_2)_2OH$, R_2 = $N(C_2H_5)_2$	1135
		THF	675 nm (ε 86,200), 644 (67,200), 618sh, 592sh, 510 (61,300), 363 (102,800)	R_1, R_2 = $NH(CH_2)_2O(CH_2)_2OH$	1135
		py	661 nm (ε 137,300)	R_1, R_2 = $NH(CH_2)_2O(CH_2)_2OH$	1135
		THF	679 nm (ε 93,700), 649 (68,600), 663 (131,500)	R_1, R_2 = NEt_2	1135
		py	663 nm (ε 131,500)	R_1, R_2 = NEt_2	1135

(*Continued*)

Table 6. (*Continued*)

Structure	M	Solvent	Transition Energy (Intensity)	Remark	Ref.
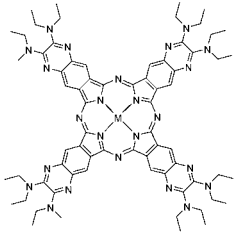	2H	DCM	763 nm (ε 182,000), 685 (48,000), 459 (51,200), 373 (115,600)		1136
	Zn(II)	THF	744 nm, 708, 665, 435, 372		1136
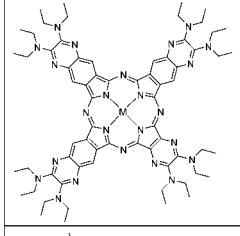	2H	DCM	752 nm (ε 170,000), 713 (165,000), 685 (65,000), 644 (40,000), 477 (53,200), 372 (140,000)		1136
	Zn(II)	THF	730 nm (ε 193,000), 709 (202,000), 668 (42,300), 638 (42,000), 435sh, 373 (147,500)		1136
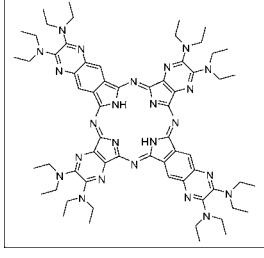	2H	DCM	750 nm (ε 134,500), 690sh, 668 (136,500), 636sh, 613(35,500), 517 (52,000), 373 (135,000)		1136
	Zn(II)	THF	720 nm (ε 142,200), 679 (159,000), 662 (75,400), 613 (37,300), 435 (40,500), 375 (130,000)		1136

(*Continued*)

Table 6. (*Continued*)

Structure	M	Solvent	Transition Energy (Intensity)	Remark	Ref.
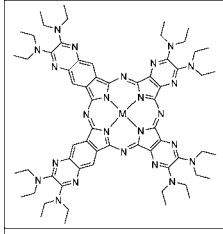	2H	DCM	718 nm (ε201,500), 652 (44,600), 495 (51,600), 374 (135,600)		1136
	Zn(II)	THF	694 nm (ε329,000), 664 (48,500), 626 (46,600), 373 (141,000)		1136
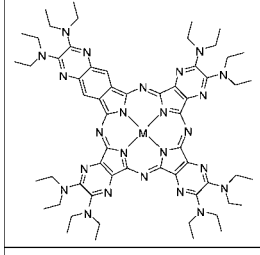	2H	DCM	715 nm (ε103,000), 674 (88,600), 653 (65,000), 529 (60,000), 372 (118,000)		1136
	Zn(II)	THF	683 nm (ε138,000), 665 (156,000), 633 (34,300), 604 (29,400), 463 (29,200), 374 (124,200)		1136
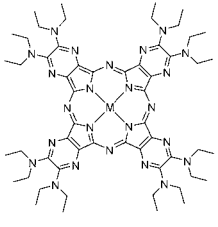	2H	DCM	686 nm (ε92,800), 657 (70,000), 528 (74,400), 370 (11,4000)		1136
	Zn(II)	THF	654 nm (ε173,000), 595 (29,900), 501 (33,200), 374 (108,900)		1136

(*Continued*)

Table 6. (*Continued*)

Structure	M	Solvent	Transition Energy (Intensity)	Remark	Ref.
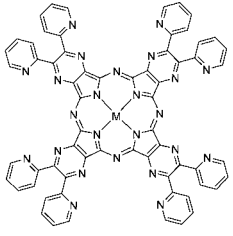	2H	$CHCl_3$	668 nm (lg ε 5.21), 635 (5.10), 618 (4.61), 609 (4.57), 582 (4.40), 400sh, 356 (5.05)		1137
		DCM	668 nm (lg ε 5.30), 635 (5.21), 618 (4.72), 609 (4.69), 583 (4.54), 400sh, 357 (5.16)		1137
		AcOH	666 nm (lg ε 5.31), 640 (5.21), 613 (4.74), 589 (4.60), 386sh, 355 (5.27)		1137
		PhCN	670 nm, 643, 623sh		1137
	Mg(II)	py	658 nm (lg ε 5.54), 631sh (4.64), 596 (4.65), 375 (5.23)		1138
		DMSO	653 nm (lg ε 5.34), 629sh (4.55), 594 (4.36), 566sh (3.96), 374 (5.08)		1138
		DMSO	658 nm (lg ε 5.54), 631sh, 596 (4.65), 375 (5.23)		1139
	Mn(II)	DMSO	783 nm (lg ε 3.98), 644 (4.28), 564 (4.54), 532 (4.54), 401sh, 346 (4.71)		1139
	Co(II)	py	635 nm (lg ε 4.94), 575sh (4.38), 441 (4.40), 364 (5.01)		1138
		DMSO	634 nm (lg ε 5.24), 586sh (4.71), 355 (5.23)		1138
		DMSO	635 nm (lg ε 4.94), 575sh, 441 (4.40), 364 (5.01)		1139
	Cu(II)	py	653 nm (lg ε 4.93), 591 (4.18), 379 (4.64)		1138
		py	653 nm (lg ε 4.93), 591 (4.18), 379 (4.64)		1139
		DMSO	648 nm (lg ε 5.18), 590 (4.44), 365 (4.91)		1138
	Zn(II)	py	658 nm (lg ε 5.18), 630sh (4.35), 598 (4.31), 378 (4.90)		1138
		py	658 nm (lg ε 5.18), 630sh, 598 (4.31), 378 (4.90)		1139
		DMSO	655 nm (lg ε 5.36), 629sh (4.61), 592 (4.54), 565sh (4.02), 372 (5.10)		1138

(*Continued*)

Table 6. (*Continued*)

Structure	M	Solvent	Transition Energy (Intensity)	Remark	Ref.
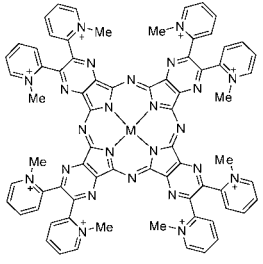	2H	H_2O	655 nm (lg ε 4.33), 632 (4.26), 353 (4.49)	$[Pc]^{8+}I^{8-}$	1140
		HCl 2N	684 nm (lg ε 4.74), 669 (4.71), 614sh (4.16), 610sh (4.12), 366 (4.55)	$[Pc]^{8+}I^{8-}$	1140
		H_2O (pH 11)	708 nm (lg ε 3.99), 666 (3.99), 613 (4.19), 475(3.87), 351 (4.75)	$[Pc]^{8+}I^{8-}$	1140
		py	675 nm (lg ε 4.70), 645 (4.60), 617sh, 362 (4.87)	$[Pc]^{8+}I^{8-}$	1140
		DMSO	671 nm (lg ε 4.97), 638sh (4.34), 618 (4.24), 464sh (4.14), 414sh (4.60), 358 (4.86)	$[Pc]^{8+}I^{8-}$	1140
		DMF	672 nm (lg ε 4.94), 635 (4.37), 610 (4.26), 474 (4.06), 402 (4.69), 359 (4.88)	$[Pc]^{8+}I^{8-}$	1140
		MeCN	665 nm, 630sh, 600, 470, 358	$[Pc]^{8+}I^{8-}$	1140
		PhCN	677 nm, 642sh, 609, 364	$[Pc]^{8+}I^{8-}$	1140
		MeOH	666 nm, 637sh, 610sh, 355	$[Pc]^{8+}I^{8-}$	1140
	Mg(II)	py	673 nm (lg ε 4.34), 642sh (3.66), 605 (3.59), 578sh (3.22), 410sh (3.81), 368 (4.06)	$[Pc]^{8+}I^{8-}$	1138
		DMSO	660 nm (lg ε 5.15), 630sh (4.33), 600 (4.33), 562sh (3.80), 415sh (4.56), 370 (4.83)	$[Pc]^{8+}I^{8-}$	1138
		H_2O (1.26×10^{-7}M)	657 nm (lg ε 5.94), 631sh (5.35), 601 (5.18), 366 (5.71)	$[Pc]^{8+}I^{8}$	1138
	Co(II)	py	656 nm (lg ε 5.03), 589 (4.55), 471sh (4.59), 364 (5.09)	$[Pc]^{8+}I^{8-}$	1138
		DMSO	642 nm (lg ε 4.97), 583sh (4.35), 462sh (4.36), 360 (5.02)	$[Pc]^{8+}I^{8-}$	1138
		H_2O	645 nm (lg ε 4.89), 590 (4.34), 445 (4.33), 354 (4.95)	$[Pc]^{8+}I^{8-}$	1138
	Cu(II)	py	662 nm (lg ε 5.00), 612sh (4.64), 372 (4.98)	$[Pc]^{8+}I^{8-}$	1138
		DMSO	655 nm (lg ε 5.18), 593 (4.46), 560sh (4.07), 359 (4.95)	$[Pc]^{8+}I^{8-}$	1138
		H_2O (1.01×10^{-7}M)	655 nm (lg ε 4.82), 596sh (4.24), 362 (4.77)	$[Pc]^{8+}I^{8-}$	1138

(*Continued*)

Table 6. (*Continued*)

Structure	M	Solvent	Transition Energy (Intensity)	Remark	Ref.
	Zn(II)	py	673 nm (lg ε 5.23), 640sh (4.48), 607 (4.38), 468sh (4.09), 373 (4.92)	$[Pc]^{8+}$ I^{8}	1138
		DMSO	666 nm (lg ε 4.74), 637sh (3.89), 600sh (3.86), 373 (4.37)	$[Pc]^{8+}$ I^{8}	1138
		H_2O (5.18×10^{-7}M)	654 nm (lg ε 4.70), 626 (4.69), 360 (4.89)	$[Pc]^{8+}$ I^{8-}	1138
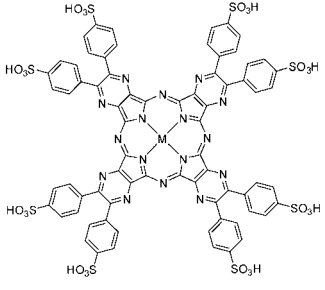	Fe(II)	H_2O	646 nm, 492, 352		1141
	Co(II)	H_2O	636 nm, 351		1141, 1142
	Ni(II)	H_2O	645 nm, 605		1141
	Cu(II)	H_2O	645 nm, 605, 360		1141

(*Continued*)

Table 6. (*Continued*)

Structure	M	Solvent	Transition Energy (Intensity)	Remark	Ref.
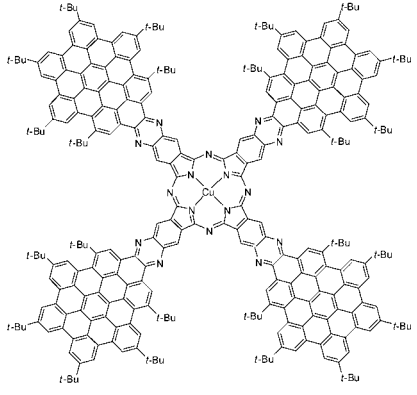	Cu(II)	$CHCl_3$	869 nm, 780, 379		1143
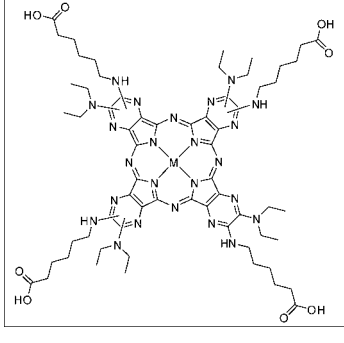	2H	py	681 nm (ε 76,000), 652 (58,000), 503 (50,000), 365 (109,000)		1144
	Mg(II)	py	659 nm (ε 111,000), 599 (25,000), 490 (21,000), 376 (106,000)		1144
	Zn(II)	py	658 nm (ε 110,000), 600 (29,000), 499 (25,000), 378 (121,000)		1144

(*Continued*)

Table 6. (*Continued*)

Structure	M	Solvent	Transition Energy (Intensity)	Remark	Ref.
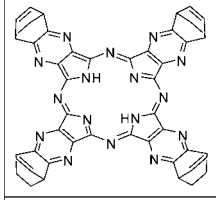	2H	DMF	631 nm (lg ε 5.21), 608sh (4.33), 575 (4.33), 344 (4.81)		1145
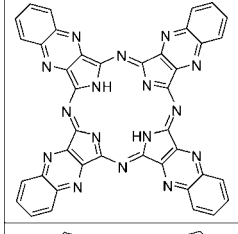	2H	DMF	706 nm (lg ε 4.72), 669 (4.40), 652 (4.39), 482 (4.38), 410 (4.84)		1145
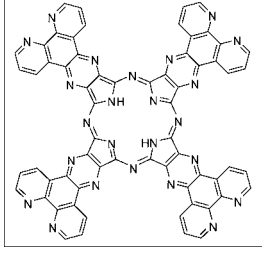	2H	CF_3COOD	689 nm, 623, 359, 303, 263		1146

(*Continued*)

Table 6. (*Continued*)

Structure	M	Solvent	Transition Energy (Intensity)	Remark	Ref.
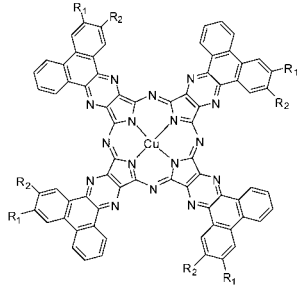	Cu(II)	DCM	693 nm (10^{5} ε 1.35), 376 (1.10)	R_1 = H, R_2 = COC_7H_{15}	1147
		DCM	706 nm (10^{-5} ε 1.21), 638 (0.93), 368 (0.82)	R_1 = COC_7H_{15}, R_2 = H	1147
		DCM	699 nm (10^{5} ε 1.15), 361 (0.72)	R_1 = H, R_2 = C_8H_{17}	1147
		DCM	704 nm (10^{-5} ε 0.95), 633 (0.79), 357 (0.65)	R_1 = C_8H_{17}, R_2 = H	1147
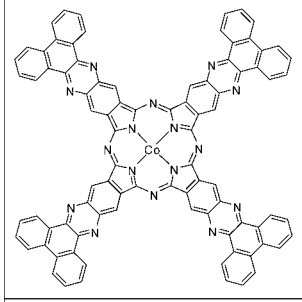	Co(II)	DMF	708 nm		915
		H_2SO_4	793 nm		915
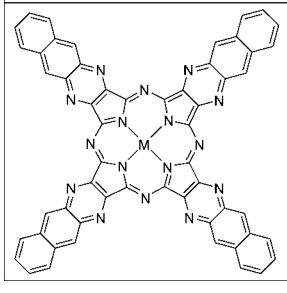	V (IV)O	Quinoline	830 nm, 750, 535		1148
	Co(II)	Quinoline	785 nm, 495		1148
	Cu(II)	Quinoline	810 nm, 540		1148
	Zn(II)	Quinoline	810 nm, 760, 545		1148

(*Continued*)

Table 6. (*Continued*)

Structure	M	Solvent	Transition Energy (Intensity)	Remark	Ref.
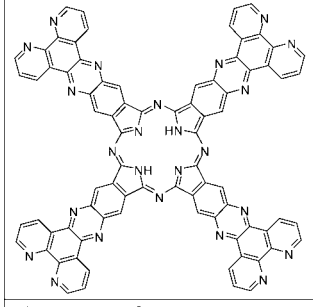	2H	TFA	822 nm, 750, 575, 450, 400		1149
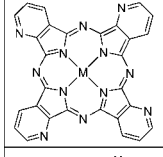	Si(IV)L	DMSO	645 nm	L = *trans*-$(OH)_2$	438
	Zn(II)	DMSO	647 nm		438
	Ge(IV)L	DMSO	641 nm (lg ε 4.71)	L = *trans*-$(OH)_2$	438
	Sn(IV)L	DMSO	648 nm	L = *trans*-$(OH)_2$	438
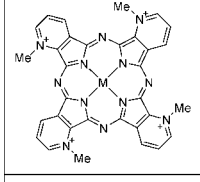	Si(IV)L	DMSO	653 nm, 640	L = *trans*-$(OH)_2$	438
	Zn(II)	H_2O	640 nm		1150
		DMSO	655 nm, 641		438
	Ge(IV)L	DMSO	687 nm	L = *trans*-$(OH)_2$	438
	Pd(II)	H_2O	619 nm (lg ε 4.5), 608 (4.2), 555 (3.6), 335 (4.0)		1151
	Sn(IV)L	DMSO	642 nm	L = *trans*-$(OH)_2$	438
	Pt(II)	H_2O	609 nm (lg ε 4.4), 599 (4.3), 549 (3.9)		1151
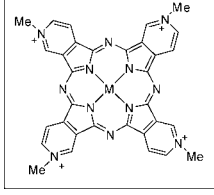	Pd(II)	H_2O	659 nm (lg ε 4.3), 643 (3.9), 594 (2.1), 322 (3.3)		1151
	Pt(II)	H_2O	685 nm (lg ε 4.4), 671 (4.4), 626 (3.8), 398 (3.5)		1151

(*Continued*)

Table 6. (*Continued*)

Structure	M	Solvent	Transition Energy (Intensity)	Remark	Ref.
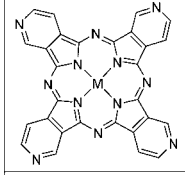	2H	TFA	684 nm (lg ε 5.2), 647 (5.1), 375 (4.7)		1152
	Cu(II)	TFA	673 nm (lg ε 5.0), 656 (5.0), 598 (4.4), 370 (4.6)		1152
	Co(II)	TFA	655 nm (lg ε 4.8), 601sh (4.4), 350 (4.6)		1152
	Ni(II)	TFA	665 nm (lg ε 4.8), 650 (4.8), 592 (4.3), 348 (4.5)		1152
	Zn(II)	py	675 nm (lg ε 4.243), 664, 603		553, 554
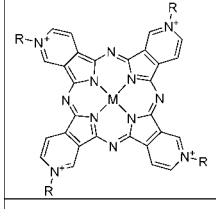	2H	$CHCl_3$	648 nm (lg ε 5.4), 364 (5.4)	R = $C_{12}H_{25}$	1152
	Co(II)	$CHCl_3$	692 nm (lg ε 4.3), 578 (4.3), 482 (4.4), 316 (4.6)		1152
	Ni(II)	$CHCl_3$	656 nm (lg ε 4.3), 394 (4.2), 275 (5)		1152
	Cu(II)	$CHCl_3$	669 nm (lg ε 4.5), 331 (4.5)		1152
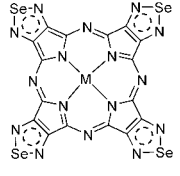	Mn(II)	DMSO	685nm, 626, 445, 347		1153
		TFA	668 nm, 613, 537, 339, 305, 294, 283		1153
		96% H_2SO_4	709 nm, 682, 657, 625, 341		1153
	Co(II)	1-ClNp	687 nm, 655, 620, 497, 469, 438, 358		1153
		py	673 nm, 645, 606, 473, 441, 396, 352, 334		1153
		DMSO	670 nm, 609, 476, 347, 331sh		1153
		TFA	664 nm, 631, 598, 319		1153
		96% H_2SO_4	700 nm, 667, 641, 604, 499, 430, 344		1153
	Ni(II)	1-ClNp	686 nm, 656, 620, 424, 356		1153
		py	661 nm, 631, 604, 357		1153
		DMSO	657 nm, 631, 602, 353		1153
		TFA	669 nm, 640, 610, 311		1153
		96% H_2SO_4	693 nm, 638, 601, 358, 335		1153
	Zn(II)	py	681 nm, 652, 624, 360, 313		1153
		DMSO	680 nm, 659, 626, 353, 320		1153
		TFA	667 nm, 641, 610, 340		1153
		96%, H_2SO_4	699 nm, 645, 607, 361, 332, 256		1153

(*Continued*)

Table 6. (*Continued*)

Structure	M	Solvent	Transition Energy (Intensity)	Remark	Ref.
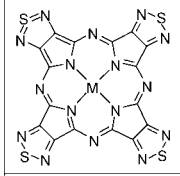	2H	PhCl	653 nm, 641, 607, 593, 415sh, 333		1154
		py	648 nm, 622sh, 591sh, 483, 397sh, 375, 318sh		1154
	Mg(II)H_2O	py	642 nm, 615, 585, 398sh, 371, 322		1154
	Cu(II)	py	642 nm, 618, 586, 440sh, 363sh, 331		1154
	Zn(II)	py	645 nm, 619, 588, 396sh, 367sh, 336		1154
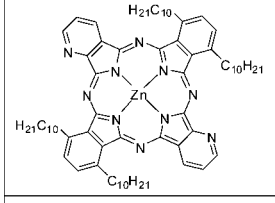	Zn(II)	Toluene	665 nm (lg ε 5.494)		1155
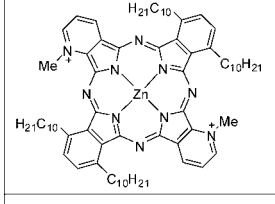	Zn(II)	py	746 nm, 673, 649, 606		1155
		Toluene	738 nm, 668, 641, 600		1155
		H_2O	723 nm, 676, 646		1155
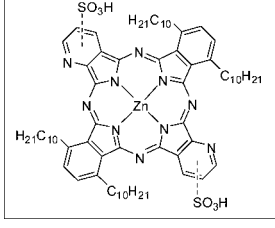	Zn(II)	py	693 nm, 658, 628, 597		1155
		Toluene	673 nm, 645, 605		1155
		H_2O	708 nm, 687, 652		1155

(*Continued*)

Table 6. (*Continued*)

Structure	M	Solvent	Transition Energy (Intensity)	Remark	Ref.
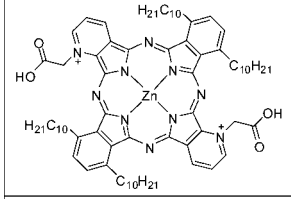	Zn(II)	py	679 nm, 650		1155
		Toluene	677 nm, 620		1155
		H_2O	687 nm, 647		1155
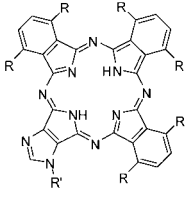	2H	Cyclohexane	701 nm (10^{-5} ε 1.34), 660 (1.17)	R = C_6H_{13}, R′ = C_4H_9	550
		Cyclohexane	701 nm (10^{-5} ε 1.08), 660 (0.89)	R = C_8H_{17}, R′ = C_4H_9	550
		THF	700 nm (10^{-5} ε 0.70), 663 (0.76)	R = $C_{10}H_{21}$, R′ = CH_3	550
		Cyclohexane	701 nm, 660	R = C_6H_{13}, R′ = $(CH_2)_6OH$	550
		Cyclohexane	701 nm, 660	R = C_8H_{17}, R′ = $(CH_2)_6OH$	550
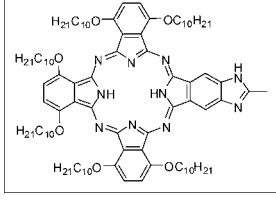	2H	$CHCl_3$	767 nm (r.i. 1.00), 724 (0.51), 689 (0.36), 426 (0.23), 334 (0.55)		1156
		$CHCl_3 + NHEt_2$	751 nm (r.i. 1.00), 674 (0.41), 463 (0.22), 330 (0.68)		1156
		$CHCl_3 + HCl$	864 nm (r.i. 1.00), 751 (0.68), 547 (0.34), 335 (0.77)		1156

(*Continued*)

Table 6. (*Continued*)

Structure	M	Solvent	Transition Energy (Intensity)	Remark	Ref.
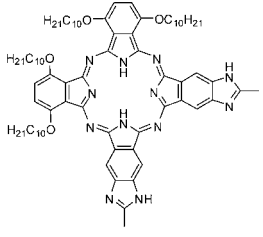	2H	$CHCl_3 + HCl$	859 nm (r.i. 1.00), 770 (0.91), 558 (0.52), 370 (1.55)		1156
		$CHCl_3$	754 nm (r.i. 1.00), 674 (0.31), 463 (0.18), 331 (0.49)		1156
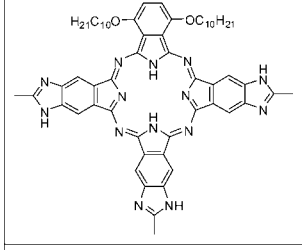	2H	$CHCl_3$	738 nm (r.i. 1.00), 708 (0.58), 669 (0.33) 401 (0.32), 331 (0.48)		1156
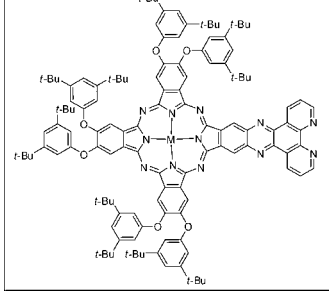	2H	$CHCl_3$	739 nm (lg ε 5.0), 694 (4.9), 673 (4.7), 625 (4.4), 412 (4.5), 358 (4.8), 292 (4.5)		1157
	Mg(II)	$CHCl_3$	727 nm (lg ε 5.0), 714 (5.0), 641 (4.5), 380 (5.0), 270 (4.9)		1157
	Co(II)	$CHCl_3$	698 nm (lg ε 4.9), 629 (4.4), 338 (4.8), 309 (4.8)		1157
	Zn(II)	$CHCl_3$	726 nm (lg ε 4.3), 708 (4.3), 638 (3.9), 377 (4.3)		1157

(*Continued*)

Table 6. (*Continued*)

Structure	M	Solvent	Transition Energy (Intensity)	Remark	Ref.
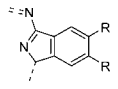	2H	THF	738 nm (lg ε 5.47), 713 (5.37), 676, 640, 376 (4.96), 342, 309	R = 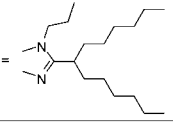	485
	Mg(II)	THF	713 nm (lg ε 5.61), 680, 640, 363 (5.14), 310		485
	Zn(II)	THF	713 nm (lg ε 5.58), 681, 640, 357 (5.03), 309		485
	2H	THF	740 nm (lg ε 5.38), 718 (5.31), 679, 648, 382 (4.96), 316	R = 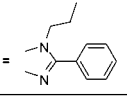	485
	Mg(II)	THF	717 nm (lg ε 5.53), 684, 643, 364 (5.12), 314		485
	Zn(II)	THF	717 nm (lg ε 5.59), 685, 643, 357 (5.08), 315		485
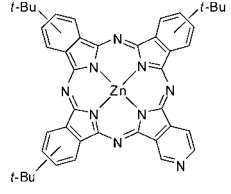	Zn(II)L	Decane	678 nm, 664	L=py	1158
		Decane	696sh nm, 690, 656	L = 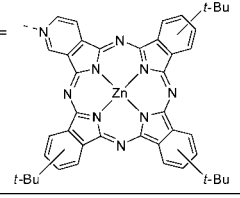	1158
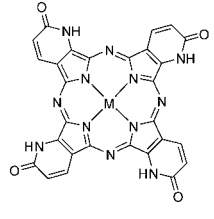	Co(II)	DMF	629 nm (Abs 1.07), 574 (0.24), 406sh (0.27), 329 (0.51)		1159
		DMF (anhydrous)	678 nm (Abs 0.201), 472 (0.234)		1159
		27% HCl	622 nm (Abs 0.79), 548 (0.23), 334 (0.45)		1159
		DMSO	627 nm (Abs 0.70), 571 (0.22), 334 (0.66)		1159
		H_2SO_4	643 nm (Abs 0.45), 617 (0.37), 583 (0.26), 323 (0.75)		1159
	Ni(II)	DMF	641 nm (Abs 1.10), 577 (0.21), 410sh (0.30), 330 (0.52)		1159
		27% HCl	645 nm (Abs 0.72), 578 (0.24), 331 (0.37)		1159
	Cu(II)	DMSO	643 nm (Abs 0.396), 582 (0.156), 332 (0.254)		1159
		27% HCl	628 nm (Abs 0.71), 577 (0.21), 330 (0.30)		1159
		H_2SO_4	663 nm (Abs 1.31), 635 (0.83), 596 (0.46), 332 (0.82)		1159

(*Continued*)

Table 6. (*Continued*)

Structure	M	Solvent	Transition Energy (Intensity)	Remark	Ref.
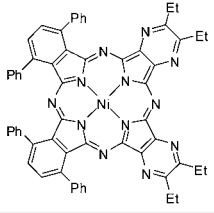	Ni(II)	DCM	680 nm (lg ε 110,000), 610 (25,000), 353sh, 312 (67,000)		1160
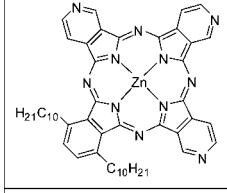	Zn(II)	Toluene	686 nm, 635, 617		553, 554
		PMMA film	675.2 nm		554
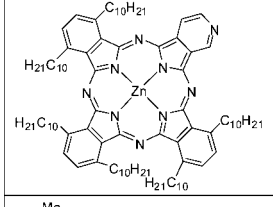	Zn(II)	Toluene	686 nm (lg ε 4.661), 635, 617		553, 554
		PMMA film	670.0 nm		554
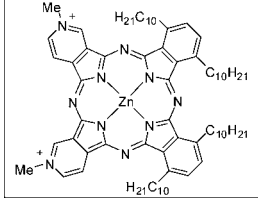	Zn(II)	Toluene	686 nm (lg ε 4.814), 636, 617		1161
		Toluene	681 nm	$[Pc]^{2+}$	1161
		py	689 nm	$[Pc]^{2+}$	1161
		H_2O	689 nm	$[Pc]^{2+}$	1161

(*Continued*)

Table 6. (*Continued*)

Structure	M	Solvent	Transition Energy (Intensity)	Remark	Ref.
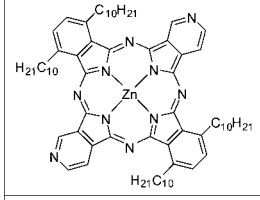	Zn(II)	Toluene	705 nm (lg ε 4.27), 690, 627		554
		PMMA film	728.2 nm, 681.6, 653.5		554
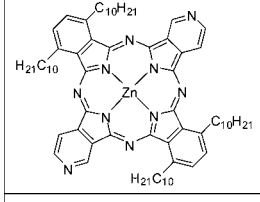	Zn(II)	toluene	708 nm, 673 (lg ε 4.19), 609		554
		PMMA film	670.0 nm		554
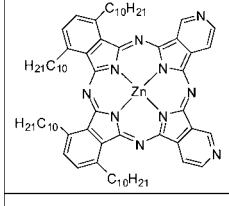	Zn(II)	Toluene	689 nm (lg ε 4.33), 619		554
		PMMA film	696.4 nm		554
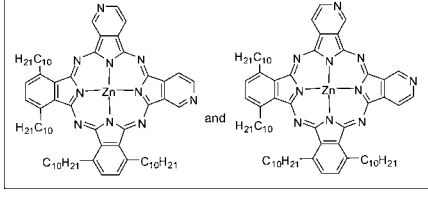	Zn(II)	Toluene	688 nm, 671 (lg ε 4.48), 638, 610		554
		PMMA film	665.5 nm		554

(*Continued*)

Table 6. (*Continued*)

Structure	M	Solvent	Transition Energy (Intensity)	Remark	Ref.
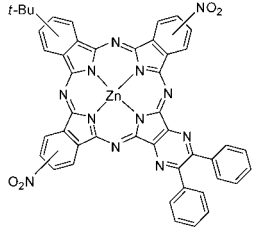	Zn(II)	DMF	697 (r.i. 1), 679 (0.92), 642s, 621s, 356 (0.64)		884
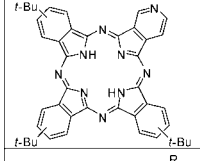	2H	DCB	688 nm, 659, 635, 605, 456sh, 343		302
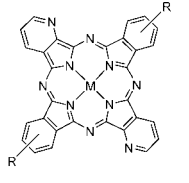	2H	DMF	640 nm	R = Cl	787
		H_2SO_4	743 nm, 692, 680	R = Cl	787
		DMF	646 nm	R = NO_2	787
		H_2SO_4	710 nm, 672	R = NO_2	787
		DMF	655 nm, 645	R = *t*-Bu	787
		benzene	670 nm, 657	R = *t*-Bu	787
	Cu(II)	DMF	652 nm	R = Cl	787
		H_2SO_4	760 nm, 692, 637	R = Cl	787
		DMF	650 nm	R = NO_2	787
		H_2SO_4	720 nm, 687, 660, 635	R = NO_2	787
		DMF	650 nm	R = *t*-Bu	787
		Benzene	655 nm	R = *t*-Bu	787
		H_2SO_4	697 nm, 663, 636	R = *t*-Bu	787

(*Continued*)

Table 6. (*Continued*)

Structure	M	Solvent	Transition Energy (Intensity)	Remark	Ref.
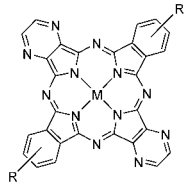	2H	DMF	650 nm	R = Cl	787
		H_2SO_4	766 nm, 652	R = Cl	787
		DMF	600-700 nm	R = NO_2	787
		H_2SO_4	722 nm, 672	R = NO_2	787
	Cu(II)	DMF	632 nm	R = Cl	787
		H_2SO_4	696 nm, 654	R = Cl	787
		DMF	654 nm	R = NO_2	787
		H_2SO_4	735 nm, 675, 653	R = NO_2	787
		DMF	647 nm	R = *t*-Bu	787
		H_2SO_4	704 nm, 660	R = *t*-Bu	787
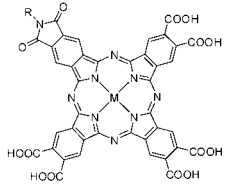	Al(III)OH	DMSO	708 nm (r.i. 1.80), 683 (0.45), 536 (0.25), 338 (1)	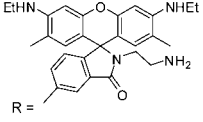	761
	Co(II)	DMSO	681 nm (r.i. 1.13), 610sh (0.60), 536 (0.37), 365 (1)		761
		DMSO	678 nm (r.i. 0.90), 561 (0.10), 329 (1)	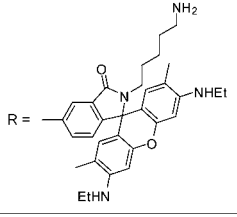	761
		DMSO	675 nm (r.i. 1), 566 (1.16), 337 (1)	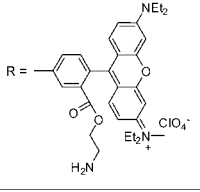	761

(*Continued*)

Table 6. (*Continued*)

Structure	M	Solvent	Transition Energy (Intensity)	Remark	Ref.
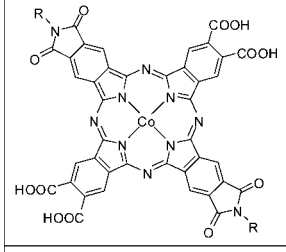	Co(II)	DMSO + AcOH	686 nm (r.i. 1.25), 630sh (1.06), 535 (0.42), 340 (1)	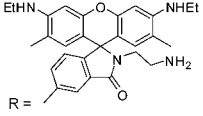	761
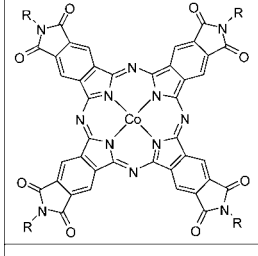	Co(II)	DMSO	683 nm (r.i. 0.60), 565 (3.90), 354 (1)	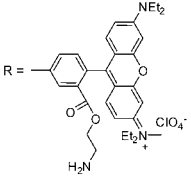	761
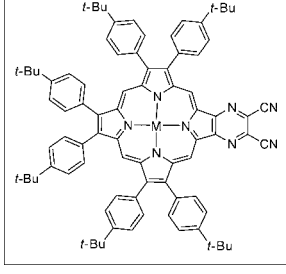	Ni(II)	DCM	660 nm (lg ε 5.10), 609 (4.73), 498 (4.55), 451 (4.48), 351 (5.06)		1010
	Cu(II)	DCM	660 nm (lg ε 4.89), 609 (4.31), 501 (4.26), 370 (4.78)		1010

(*Continued*)

Table 6. (*Continued*)

Structure	M	Solvent	Transition Energy (Intensity)	Remark	Ref.
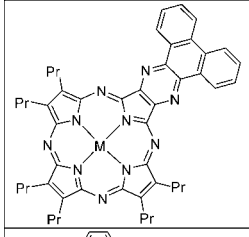	2H	DCM	634 nm (lg ε 4.71), 565 (4.57), 340 (4.74)		1026
	Mg(II)	DCM	627 nm (lg ε 4.59), 355 (4.75)		1026
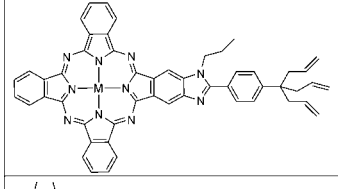	2H	THF	695 nm, 669, 651, 336		1162
	2Li	THF	671 nm, 663, 602		1162
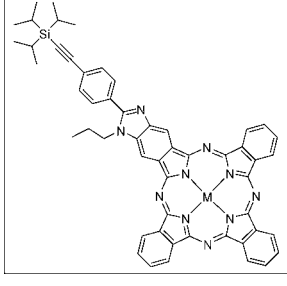	2H	THF	695 nm (lg ε 4.98), 669 (4.98), 649, 622, 337 (4.89)		485
	Zn(II)	THF	674 nm (lg ε 5.43), 611, 340 (5.10)		485

(*Continued*)

Table 6. (*Continued*)

Structure	M	Solvent	Transition Energy (Intensity)	Remark	Ref.
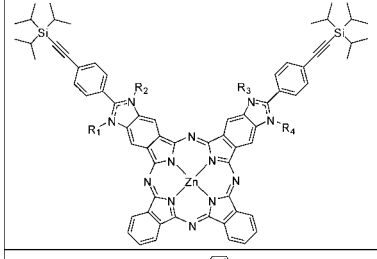	Zn(II)	THF	693 nm (lg ε 5.31), 623, 340 (4.95)	$R_1(R_2)$, $R_3(R_4)$ = Pr or $R_1(R_2)$, $R_4(R_3)$ = Pr	485
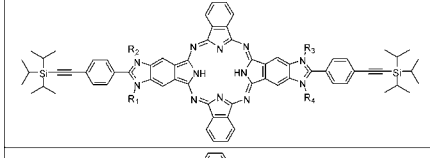	2H	THF	732 nm (lg ε 4.94), 703 (5.18), 681 (4.99), 662 (4.99), 631, 610, 340 (5.13)	$R_1(R_2)$, $R_3(R_4)$ = Pr or $R_1(R_2)$, $R_4(R_3)$ = Pr	485
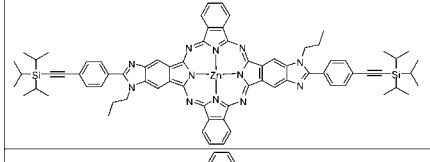	Zn(II)	THF	709 nm (lg ε 5.21), 679 (5.37), 648, 614, 338 (5.12)		485
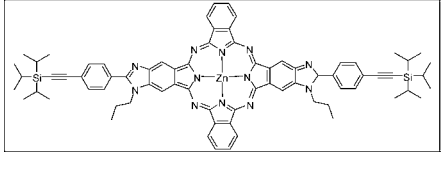	Zn(II)	THF	709 nm (lg ε 5.19), 679 (5.36), 648, 614, 338 (5.11)		485

Table 7. UV-vis absorption data of Pc derivatives having crown-ether units.

Structure	M	Solvent	Transition Energy (Intensity)	Remark	Ref.
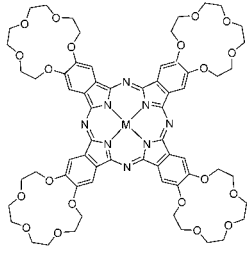	2H	$ClHCl_3$	701 nm (lg ε 5.10), 661 (4.01), 644 (4.66), 601 (4.38), 420 (4.48), 348 (4.88)		1163
		$ClHCl_3$	701 nm (lg ε 5.10), 661 (5.01), 644 (4.66), 601 (4.38), 420 (4.48), 348 (4.88)		1164
		$CHCl_3$	701 nm (10^4 ε 12.61), 661 (10.34), 644 (4.53), 601 (2.4), 420 (3.03), 348 (7.51)		1165
		$CHCl_3$	700 nm (ε 33,400), 662 (27,500), 645 (11,800), 601 (6,200), 421 (8,100), 347 (30,800)		1166
		$CHCl_3$	635 nm (10^{-4} ε 3.69), 410 (1.89), 340 (4.71)	[Pc]•2$NaClO_4$	1165
		$CHCl_3$	640 nm (10^{-4} ε 1.72), 332 (2.28)	[Pc]•2KSCN	1165
		$CHCl_3$	700 nm (10^{-4} ε 4.3), 660 (3.83), 352 (3.66)	[Pc]•2NH_4SCN	1165
	Fe(II)	$CHCl_3$	702 nm (10^{-4} ε 3.31), 682sh (2.48), 662sh (2.06), 606sh (0.7), 412 (2.27), 350 (3.83)		1165
	Co(II)	$CHCl_3$	698 nm (10^{-4} ε 2.69), 612sh (1.48), 360 (2.36)	[Pc]•4NaSCN	1165
		$CHCl_3$	675 nm (10^{-4} ε 2.16), 628 (2.16)	[Pc]•2KSCN	1165
		$ClHCl_3$	675 nm (10^{-4} ε 2.73), 620sh (2.00), 355 (2.67)	[Pc]•2NH_4SCN	1165
		$ClHCl_3$	668 nm (ε 59,400), 608 (19,800), 400 (13,400), 329sh, 297 (49,300)		1166
	Ni(II)	$CHCl_3$	669 nm (10^{-4} ε 12.38), 638 (3.51), 603 (2.7), 406 (2.21), 330 (4.13)		1165
		$CHCl_3$	667 nm (ε 70,000), 638 (22,300), 603 (17,700), 401 (14,900)		1166
	Cu(II)	$CHCl_3$	676 nm (ε 129,400), 610 (31,200), 409 (23,300), 338 (57,400), 292 (54,100)		1166
	Zn(II)	$CHCl_3$	677 nm (ε 96,700), 610 (17,300), 420sh, 352 (61,200)		1166
	Ru(II)L	$CHCl_3$	625 nm (lg ε 4.84), 573sh, 368 (4.57), 323 (5.13)	L = *trans*-$(py)_2$	215, 216
		$CHCl_3$	625 nm (lg ε 4.56), 573sh, 375 (4.26), 322 (4.80)	L = *trans*-$(NMe_3)_2$	216
		$CHCl_3$	625 nm (lg ε 4.88), 573sh, 368 (4.59), 324 (5.15)	L = *trans*-$(NEt_3)_2$	215, 216
		$CHCl_3$	625 nm (lg ε 4.42), 573sh, 368 (4.26), 324 (4.73)	L = *trans*- 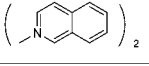	215, 216

(*Continued*)

Table 7. (*Continued*)

Structure	M	Solvent	Transition Energy (Intensity)	Remark	Ref.
		$CHCl_3$	631 nm (lg ε 4.79), 576sh, 362 (4.54), 322 (5.15)	L = *trans*-$(pyz)_2$	216
		$CHCl_3$	655 nm (lg ε 4.97), 593 (4.30), 313 (4.81)	L = *trans*-(CO), (CH_3OH)	215, 216
	Sc(III)OAc	$CHCl_3$	697 nm (lg ε 5.05), 623 (4.22), 405 (4.19), 352 (4.71), 294 (4.54)		89
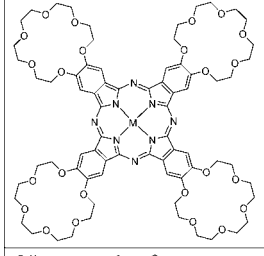	2H	$CHCl_3$	700 nm (lg ε 4.60), 660 (4.56), 640sh, 600 (3.92)		1167
		$CHCl_3$	700 nm (lg ε 4.60), 660 (4.56)		607
	Cu(II)	$CHCl_3$	675 nm (lg ε 4.63), 652–644sh, 610 (3.90)		1167
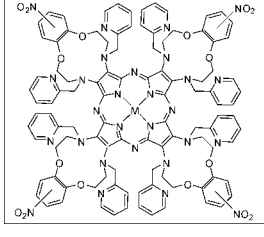	2H	$CHCl_3$	724 nm (lg ε 4.70), 665 (4.60), 578 (4.30), 348 (4.94)		1002
	Mg(II)	$CHCl_3$	666 nm (lg ε 4.52), 576 (4.18), 351 (4.79)		1002
	Zn(II)	$CHCl_3$	658 nm (lg ε 4.76), 583 (4.04), 354 (4.98)		1002

(*Continued*)

Table 7. (*Continued*)

Structure	M	Solvent	Transition Energy (Intensity)	Remark	Ref.
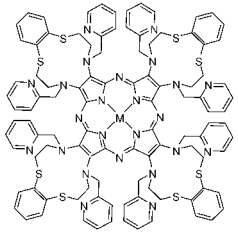	2H	$CHCl_3$	712 nm (lg ε 4.59), 670 (4.47), 575 (4.20), 345 (4.91)		1002
	Mg(II)	$CHCl_3$	662 nm (lg ε 4.83), 579 (4.28), 365 (4.96)		1002
	Zn(II)	$CHCl_3$	668 nm (lg ε 4.81), 580 (3.78), 350 (4.99)		1002
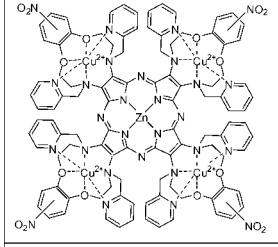	Zn(II)	py	657 nm (lg ε 4.78), 335 (4.88)		1002
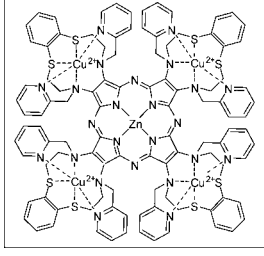	Zn(II)	$CHCl_3$	654 nm (lg ε 4.73), 317 (4.89)		1002

(*Continued*)

Table 7. (*Continued*)

Structure	M	Solvent	Transition Energy (Intensity)	Remark	Ref.
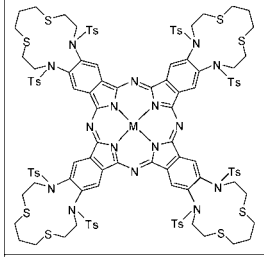	2H	$CHCl_3$	704 nm ($10^5\varepsilon$ 4.78), 644 (4.72), 350 (5.12), 293 (5.28)		1168
	Co(II)	$CHCl_3$	683 nm ($10^5\varepsilon$ 5.17), 626 (4.99), 290 (5.26)		1168
	Ni(II)	$CHCl_3$	692 nm ($10^{-5}\varepsilon$ 5.15), 620 (4.9), 296 (5.26)		1168
	Cu(II)	$CHCl_3$	692 nm ($10^{-5}\varepsilon$ 4.96), 626 (4.86), 380 (4.9), 293 (5.21)		1168
	Zn(II)	$CHCl_3$	689 nm ($10^{-5}\varepsilon$ 5.23), 635 (4.86), 353 (5.19), 290 (5.22)		1168
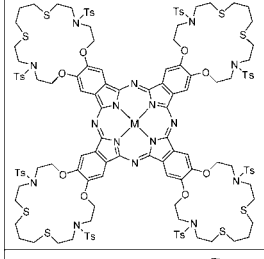	2H	$CHCl_3$	683 nm ($10^{-4}\varepsilon$ 4.28), 632 (5.10), 338 (5.03), 278 (5.21)		1169
	Co(II)	$CHCl_3$	677 nm ($10^{-4}\varepsilon$ 5.21), 614 (4.92), 284 (5.24)		1169
	Ni(II)	$CHCl_3$	674 nm ($10^{-4}\varepsilon$ 5.23), 629 (5.01), 395 (4.50), 278 (5.26)		1169
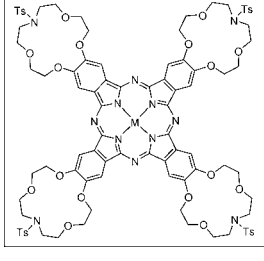	2H	$CHCl_3$	743 ($10^{-5}\varepsilon$ 5.16), 689 (5.14), 629 (4.64), 330 (5.14), 285 (5.12)		1170
	Co(II)	$CHCl_3$	671 ($10^{-5}\varepsilon$ 5.16), 617 (4.67), 335 (5.14), 291 (5.13)		1170
	Ni(II)	$CHCl_3$	677 ($10^{-5}\varepsilon$ 5.17), 620 (4.69), 328 (5.15), 290 (5.13)		1170
	Cu(II)	$CHCl_3$	689 ($10^5\varepsilon$ 5.18), 623 (4.62), 349 (5.15), 287 (5.13)		1170
	Zn(II)	$CHCl_3$	683 ($10^{-5}\varepsilon$ 5.19), 635 (4.74), 344 (5.19), 293 (5.14)		1170

(*Continued*)

Table 7. (*Continued*)

Structure	M	Solvent	Transition Energy (Intensity)	Remark	Ref.
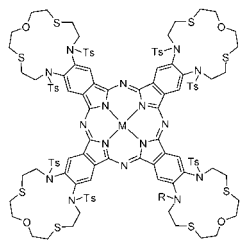	2H	DMSO	709 nm (10^{-1} ε 0.93), 649 (0.91), 609sh (0.83), 349 (1.76), 295 (3.25), 264 (3.69)		1171
	Fe(II)	DMSO	719sh nm (10^{-1} ε 1.52), 664 (1.90), 442 (1.20), 341 (2.29), 243 (3.92), 221 (6.20)		1171
	Co(II)	DMSO	680 nm (10^{-1} ε 3.12), 638 (2.83), 605sh (1.73), 348 (3.44), 259 (2.87), 243 (1.75)		1171
	Ni(II)	DMSO	694sh nm (10^{-1} ε 0.74), 612 (0.82), 404 (0.30), 243 (0.43)		1171
	Cu(II)	DMSO	677sh nm (10^{-1} ε 1.78), 621 (2.25), 337sh (2.36), 281 (3.84)		1171
	Zn(II)	DMSO	662 nm (10^{-1} ε 1.35), 628 (1.24), 336 (3.46), 269 (5.67), 238 (12.43)		1171
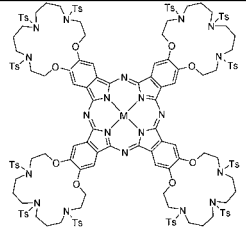	2H	$CHCl_3$	728 nm (10^{-5} ε 3.95), 682 (4.81), 654 (4.51), 592 (4.41), 404 (4.93), 340 (4.27) 294 (6.13), 243 (4.61)		1172
	Ni(II)	$CHCl_3$	711 nm (10^{-5} ε 4.06), 672 (4.85), 642 (4.59), 612 (4.53), 498 (4.19), 338 (5.42) 294 (4.91), 243 (6.24)		1172
	Co(II)	$CHCl_3$	714 nm (10^{-5} ε 3.91), 672 (4.98), 645 (4.56), 608 (4.51), 498 (4.34), 387 (5.08) 342 (5.73), 291 (6.26), 243 (5.48)		1172
	Cu(II)	$CHCl_3$	722 nm (10^{-5} ε 4.08), 681 (4.86), 644 (4.69), 624 (4.13), 417 (5.47), 384 (6.65) 342 (4.89), 294 (5.38), 243 (4.78)		1172
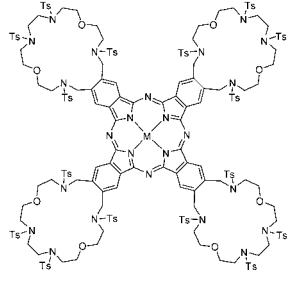	2H	$CHCl_3$	686sh nm (lg ε 5.86), 627 (4.09), 338sh (4.98), 288 (4.71), 263 (5.24)	$M = 10^{-4}$	1173
		$CHCl_3$	695 nm (lg ε 6.32), 635sh (4.31), 342 (5.19), 294 (5.04), 270 (5.37)	$M = 10^{-6}$	1173
	Ni(II)	$CDCl_3$	677 nm (lg ε 5.61), 617sh (3.52), 338 (5.17), 300sh (4.06), 273 (4.14), 244 (5.12)	$M = 10^{-4}$	1173
		$CDCl_3$	684 nm (lg ε 5.88), 629sh (3.74), 345 (5.32), 310sh (4.27), 276 (4.27), 250 (5.29)	$M = 10^{-6}$	1173
	Zn(II)	$CDCl_3$	691sh nm (lg ε 4.78), 629 (4.11), 342sh (4.20), 275 (4.49), 246 (5.26)	$M = 10^{-4}$	1173
		$CDCl_3$	697 nm (lg ε 4.96), 636sh (4.34), 347 (4.36), 278 (4.63), 254 (5.41)	$M = 10^{-6}$	1173

(*Continued*)

Table 7. (*Continued*)

Structure	M	Solvent	Transition Energy (Intensity)	Remark	Ref.
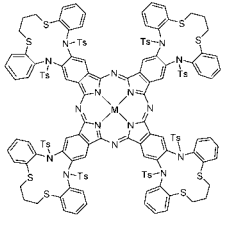	2H	py	749 nm (10^{5} ε 4.80), 695 (4.78), 485 (4.59), 340 (4.73), 315 (4.79), 293 (4.87)		1174
	Ni(II)	py	681 nm (10^{5} ε 4.73), 650 (4.24), 612 (4.40), 358 (4.60), 330 (4.82)		1174
	Cu(II)	py	692 nm (10^{-5} ε 4.83), 626 (4.30), 365 (4.48), 305 (4.71), 274 (4.81)		1174
	Zn(II)	py	686 nm (10^{-5} ε 4.82), 617 (4.40), 482 (4.21), 379 (4.72), 329 (4.54)		1174
	Co(II)	py	671 nm (10^{5} ε 4.90), 611 (4.32), 374 (4.49), 303 (4.77), 269 (4.88)		1174
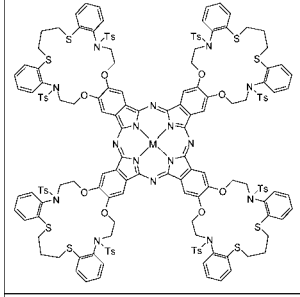	2H	$CHCl_3$	707 nm (10^{-5} ε 5.11), 689 (5.08), 334 (4.68), 281 (4.83)		1175
	Co(II)	$CHCl_3$	686 nm (10^{-5} ε 5.04), 617 (4.52), 351 (4.64), 276 (4.75)		1175
	Ni(II)	$CHCl_3$	680 nm (10^{-5} ε 5.16), 611 (4.58), 342 (4.76), 270 (4.88)		1175
	Cu(II)	$CHCl_3$	691 nm (10^{-5} ε 4.96), 622 (4.40), 354 (4.60), 282 (4.71)		1175
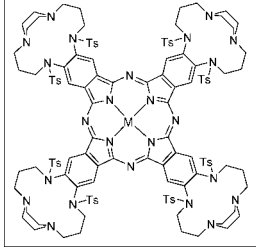	2H	py	686 nm (10^{-5} ε 4.72), 620 (4.61), 431 (4.56), 344 (4.75), 321 (4.88), 288 (4.96)		1176
	Ni(II)	py	687 nm (10^{-5} ε 4.68), 611 (4.45), 395 (4.68), 305 (4.74), 278 (4.87)		1176
	Zn(II)	py	686 nm (10^{-5} ε 4.94), 620 (4.53), 350 (4.84), 310 (5.01), 286 (5.15)		1176

(*Continued*)

Table 7. (*Continued*)

Structure	M	Solvent	Transition Energy (Intensity)	Remark	Ref.
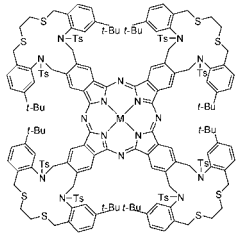	2H	$CHCl_3$	710 nm (lg ε 5.34), 672 (5.35), 656 (5.19), 624 (5.08), 376 (5.38), 310 (5.39)		1177
	Ni(II)	$CHCl_3$	694 nm (lg ε 5.38), 668 (4.85), 622 (4.59), 419 (4.90), 341 (5.41)		1177
	Cu(II)	$CHCl_3$	692 nm (lg ε 5.26), 655 (4.73), 611 (4.66), 466 (4.75), 394 (5.20), 355 (5.38)		1177
	Zn(II)	$CHCl_3$	690 nm (lg ε 5.45), 665 (4.90), 627 (4.83), 390 (4.96), 330 (5.07)		1177
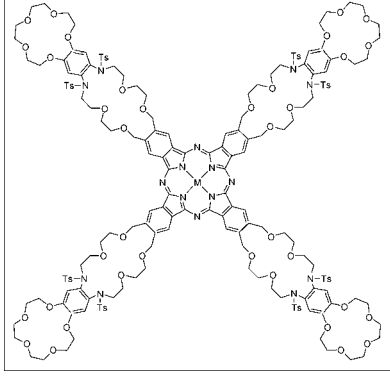	2H	$CHCl_3$	686 nm (lg ε 4.12), 639 (3.75), 620 (3.85), 586 (3.71), 335 (4.17), 272 (4.29), 240 (4.65)		1178
	Ni(II)	$CHCl_3$	677 nm (lg ε 4.86), 645 (4.38), 627 (4.26), 611 (4.30), 545 (3.91), 340 (4.25), 279 (3.98), 245 (4.43)		1178

(*Continued*)

Table 7. (*Continued*)

Structure	M	Solvent	Transition Energy (Intensity)	Remark	Ref.
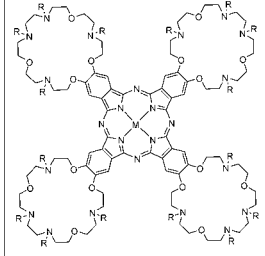	2H	$CHCl_3$	706 nm (10^{-1} ε 5.03), 672 (5.02), 642 (4.58), 610 (4.49), 392 (4.59), 344 (4.88)	R = Ts	1179
	Co(II)	$CHCl_3$	644 nm (10^{-1} ε 4.94), 612 (4.43), 598 (4.42), 392 (4.54)	R = Ts	1179
	Ni(II)	$CHCl_3$	670 nm (10^{-4} ε 4.90), 642 (4.46), 614 (4.39), 604 (4.38), 390 (4.56)	R = Ts	1179
	Cu(II)	$CHCl_3$	672 nm (10^{-4} ε 5.06), 646 (4.60), 610 (4.54), 406 (4.67), 340 (4.95)	R = Ts	1179
		$CHCl_3$	672 nm (10^{-4} ε 5.00), 656 (4.58), 638 (4.46), 608 (4.49), 412 (4.44), 344 (4.78)	R = H	1179
	Zn(II)	$CHCl_3$	672 nm (10^{-4} ε 5.03), 646 (4.23), 608 (4.22), 354 (4.63)	R = Ts	1179
	Pb(II)	$CHCl_3$	672 nm (10^{-4} ε 5.00), 650 (4.36), 638 (4.32), 608 (4.36), 410 (4.41), 344 (4.80)	R = Ts	1179
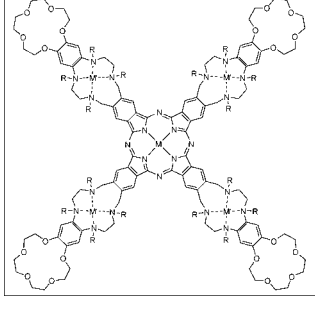	Ni(II)	$CHCl_3$	670 nm (10^{-4} ε 15.1), 640sh (5.2), 605 (5.3), 340 (8.9)	R = Ts	1180
	Cu(II)	$CHCl_3$	672 nm (10^{-4} ε 13.8), 640sh (2.6), 602 (2.8), 330 (5.3)	R = Ts	1180
		MeOH	678 nm (10^{-4} ε 8.9), 639sh (1.6), 607 (1.7), 335 (2.4)	R = H	1180
		H_2O	668 nm (10^{-4} ε 10.6), 637sh (3.8), 602 (4.1), 330 (6.2)	M′ = Ni, R = H, $8Cl^-$	1180

(*Continued*)

Table 7. (*Continued*)

Structure	M	Solvent	Transition Energy (Intensity)	Remark	Ref.
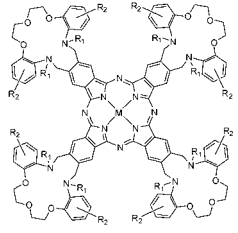	2H	$CHCl_3$	697 nm (10^{-1} ε 7.64), 675 (6.80), 354sh (3.54), 263 (28.08)	R_1 = Ts, R_2 = H	1181
	Co(II)	$CHCl_3$	670 nm (10^{-1} ε 18.36), 648sh (4.20), 602 (3.50), 320 (54.2), 271 (6.18), 227 (5.76)	R_1 = Ts, R_2 = H	1181
		H_2O	668 nm (10^{-1} ε 4.34), 630 (4.30), 307sh (6.96), 273sh (6.92)	R_1 = H, R_2 = SO_3Na	1181
	Ni(II)	DMSO	673 nm (10^{-1} ε 7.46), 650 (3.3), 602sh (3.1), 330sh (5.1), 263 (9.28)	R_1 = Ts, R_2 = H	1181
	Cu(II)	DMF	685 nm (10^{-1} ε 10.68), 600sh (3.2), 349 (8.4), 260 (12.7)	R_1 = Ts, R_2 = H	1181
		H_2O	635 nm (10^{-1} ε 4.2), 391 (0.88), 327 (4.76)	R_1 = H, R_2 = SO_3Na	1181
	Zn(II)	$CHCl_3$	717 nm (10^{-1} ε 3.02), 677 (11.98), 647sh (2.96), 607 (2.52), 420sh (0.88), 333 (4.3), 229 (6.12), 202 (5.24)	R_1 = Ts, R_2 = H	1181
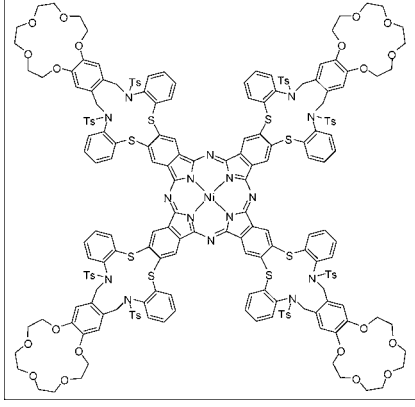	Ni(II)	$CHCl_3$	674 nm (10^{-1} ε 11.3), 635 (5.7), 605 (5.0), 342 (11.0)		938
		DMSO	677 nm (10^{-1} ε 7.0), 648 (2.3), 612 (2.5), 343 (6.9)	2KSCN	938

(*Continued*)

Table 7. (*Continued*)

Structure	M	Solvent	Transition Energy (Intensity)	Remark	Ref.
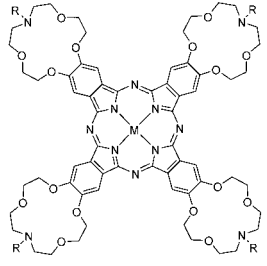	Ni(II)	$CHCl_3$	667 nm (10^{-1} ε 18.1), 603 (3.3), 312 (7.1)	R = 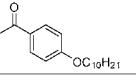	1182
	Zn(II)	$CHCl_3$	676 nm (10^{-4} ε 25.0), 610 (3.8), 355 (10.1)		1182
	Ni(II)	$CHCl_3$	668 nm (10^{-4} ε 18.2), 603 (3.3), 312 (7.2)	R = 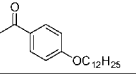	1182
	Zn(II)	$CHCl_3$	676 nm (10^{-4} ε 26.8), 609 (4.4), 356 (10.7)		1182
	Ni(II)	$CHCl_3$	668 nm (10^{-4} ε 19.3), 603 (3.6), 312 (7.8)	R = 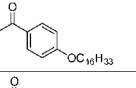	1182
	Zn(II)	$CHCl_3$	676 nm (10^{-4} ε 26.5), 610 (4.3), 355 (10.5)		1182
	Ni(II)	$CHCl_3$	668 nm (10^{-4} ε 20.4), 603 (3.4), 312 (8.3)	R = 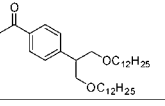	1182
	Zn(II)	$CHCl_3$	677 nm (10^{-4} ε 27.1), 609 (4.4), 356 (11.0)		1182
	Cu(II)	$CHCl_3$	677 nm (10^{-4} ε 10.4), 648 (2.8), 610 (2.5), 410 (2.0), 340 (5.3)	R = 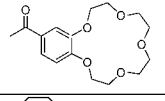	1183
	Cu(II)	DMF	677 nm (10^{-4} ε 14.32), 652 (7.2), 612 (6.0), 344 (14.72), 314 (4.4)	R = 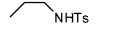	1183
	Cu(II)	DMF	683 nm (10^{-4} ε 8.75), 650 (4.25), 345 (5.87), 317 (3.5)	R = 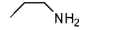	1183
	Cu(II)	DMSO	683 nm (10^{-4} ε 7.1), 640sh (3.78), 610 (3.25), 350 (6.9)	R = 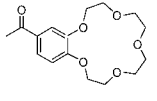 Pc・2KSCN	1183

(*Continued*)

Table 7. (*Continued*)

Structure	M	Solvent	Transition Energy (Intensity)	Remark	Ref.
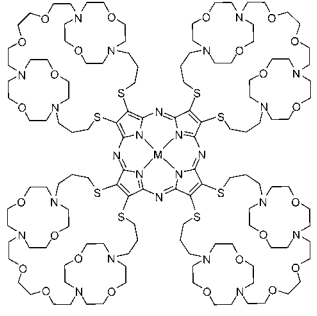	2H	$CHCl_3$	718 nm (lg ε 5.08), 639 (4.94), 512 (4.80), 360 (5.21), 339 (5.19)		1184
	Mg(II)	$CHCl_3$	683 nm (lg ε 5.21), 624 (4.65), 510 (4.67), 320 (5.28)		1184
	Zn(II)	$CHCl_3$	679 nm (lg ε 5.12), 620 (4.43), 508 (4.61), 325 (5.31)		1184
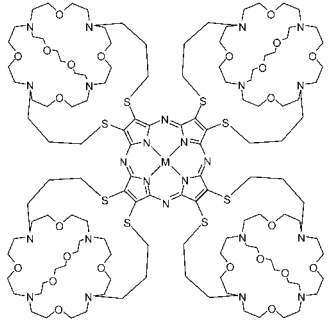	2H	$CHCl_3$	716 nm (lg ε 5.18), 648 (4.97), 510 (4.84), 349 (5.27)		1184
	Mg(II)	$CHCl_3$	678 nm (lg ε 5.28), 636 (4.86), 508 (4.52), 329 (5.34)		1184
	Zn(II)	$CHCl_3$	674 nm (lg ε 5.20), 632 (4.72), 510 (4.43), 320 (5.40)		1184

(*Continued*)

Table 7. (*Continued*)

Structure	M	Solvent	Transition Energy (Intensity)	Remark	Ref.
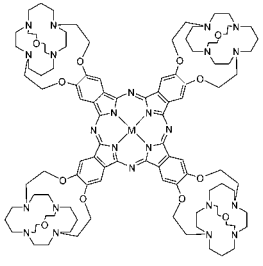	2H	$CHCl_3$	680 nm (10^5 ε 3.98), 668 (3.95), 620 (3.77), 410 (4.08), 308 (3.11)		1185
	Ni(II)	$CHCl_3$	670 nm (10^5 ε 3.21), 613 (3.14), 336 (4.02), 303 (3.33)		1185
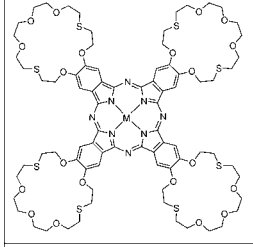	2H	$CHCl_3$	722 nm, 630, 579, 363, 308, 267		1186
	Ni(II)	$CHCl_3$	690 nm, 628, 578, 350, 288, 259		1186
	Cu(II)	$CHCl_3$	686 nm, 626, 574, 329, 287, 256		1186
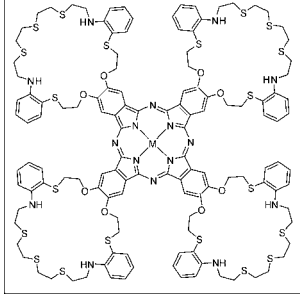	2H	$CHCl_3$	767 nm (lg ε 4.14), 707 (4.16), 671 (4.12), 446 (4.28), 362 (4.45), 314 (4.77), 250 (5.05)		1187
	Ni(II)	$CHCl_3$	677 nm (lg ε 4.46), 617 (4.15), 401 (4.38), 311 (4.83), 290 (4.86), 248 (5.03)		1187

(*Continued*)

Table 7. (*Continued*)

Structure	M	Solvent	Transition Energy (Intensity)	Remark	Ref.
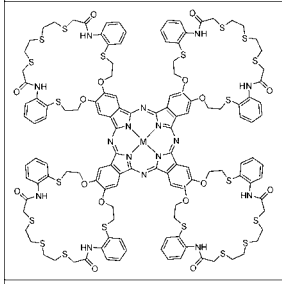	2H	$CHCl_3$:py = 1:1	686 nm (lg ε 3.84), 623 (3.40), 304 (4.99)		1187
	Ni(II)	py	671 nm (lg ε 4.34), 643 (4.08), 607 (4.09), 402 (4.44), 306 (4.80)		1187
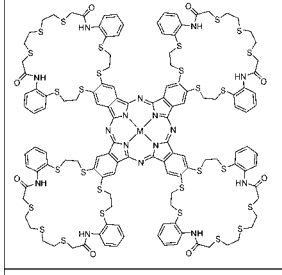	2H	DMF	707 nm (10^{-5} ε 4.18), 656 (4.17), 449 (4.18), 368 (4.43), 326 (4.49), 296 (4.62)		1188
	Ni(II)	DMF	701 nm (10^{-5} ε 4.35), 656 (4.20), 482 (4.41), 410 (4.58), 311 (4.93), 275 (5.05)		1188
	Zn(II)	DMF	713 nm (10^{-5} ε 4.65), 681 (4.30), 644 (4.21), 371 (4.73), 272 (5.03)		1188
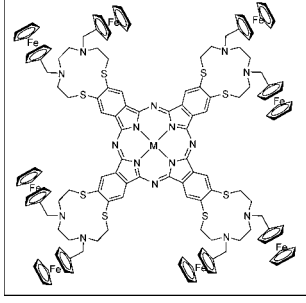	2H	$CHCl_3$	696 nm (10^{-5} ε 5.27), 676 (5.29), 630 (4.88), 355 (4.67), 270 (4.95), 243 (5.01)		1189
	Ni(II)	$CHCl_3$	693 nm (10^{-5} ε 5.17), 627 (4.92), 357 (4.70), 268 (4.93), 240 (4.97)		1189

(*Continued*)

Table 7. (*Continued*)

Structure	M	Solvent	Transition Energy (Intensity)	Remark	Ref.
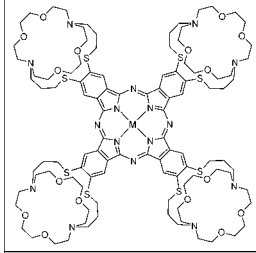	2H	$CHCl_3$	716 nm (lg ε 4.30), 668 (4.25), 510 (3.78), 350 (4.69), 248 (4.33)		1190
	Mg(II)	$CHCl_3$	673 nm (lg ε 4.28), 495 (3.27), 381 (4.21), 246 (3.94)		1190
	Zn(II)	$CHCl_3$	678 nm (lg ε 3.92), 384 (3.94), 254 (3.76)		1190
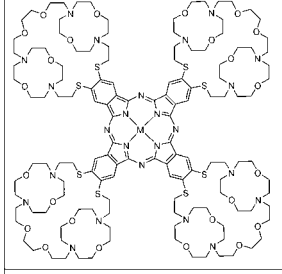	2H	$CHCl_3$	714 nm (10^{-5} ε 4.89), 681 (4.71), 635 (4.58), 353 (4.77), 298 (5.03), 271 (5.24)		1191
	Ni(II)	py	701 nm (10^{-5} ε 4.97), 630 (4.38), 348 (4.65), 302 (4.92), 285 (5.29)		1191
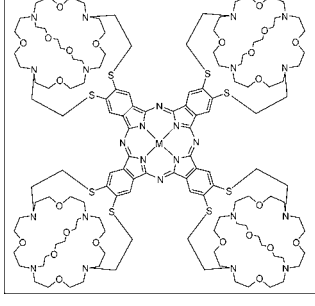	2H	$CHCl_3$	711 nm (10^{-5} ε 4.84), 673 (4.47), 640 (4.59), 367 (4.74), 306 (5.08), 275 (5.21)		1191
	Ni(II)	py	695 nm (10^{-5} ε 4.80), 665 (4.59), 628 (4.45), 363 (4.81), 303 (5.12), 273 (5.24)		1191

(*Continued*)

Table 7. (*Continued*)

Structure	M	Solvent	Transition Energy (Intensity)	Remark	Ref.
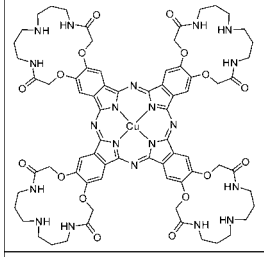	Cu(II)	$CHCl_3$	682 nm (lg ε 5.23), 611 (5.08), 432 (4.38), 379 (4.65), 342 (4.72, 284 (4.89), 251 (4.31)		709
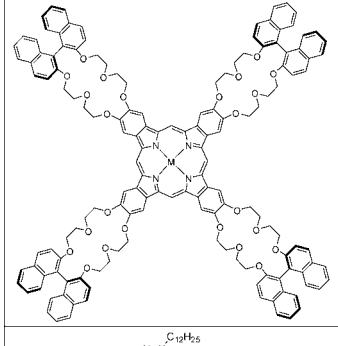	2H	$CHCl_3$	700 nm (ε 333,000), 662 (272,000), 640 (102,000), 602 (57,800), 425 (78,100), 340 (213,000), 294 (207,000)		1192
	Cu(II)	$CHCl_3$	678 nm (ε 337,000), 656 (61,300), 610 (63,600), 410 (71,700), 338 (221,000), 283 (278,000)		1192
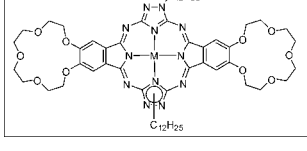	2H	$CHCl_3$	379 nm (lg ε 4.681), 358 (4.753), 340 (4.575), 293 (4.540), 259 (4.716)		1193
	Co(II)	$CHCl_3$	513 nm (lg ε 3.489), 479 (3.569), 433 (3.814), 385 (4.568), 364 (4.632), 352sh, 295 (4.666), 259 (4.733)		1193

(*Continued*)

Table 7. (*Continued*)

Structure	M	Solvent	Transition Energy (Intensity)	Remark	Ref.
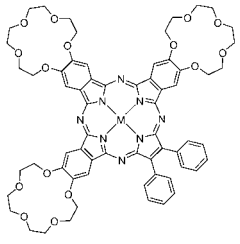	Cu(II)	$CHCl_3$	677 nm (10^{-4} ε 6.72), 641 (2.85), 624sh (2.51), 338 (4.08), 292 (3.45), 276 (3.40)		1194
	Zn(II)	$CHCl_3$	686 nm (10^{-4} ε 8.50), 638 (5.73), 625sh (5.22), 582 (1.76), 364sh (5.57), 353 (6.47), 303 (2.85), 273 (3.28)		1194
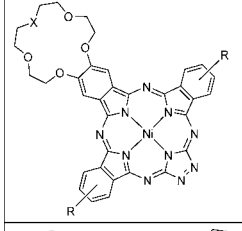	Ni(II)	$CHCl_3$	628 nm (lg ε 4.12), 530 (4.00), 370 (4.42), 259 (4.57)	R = H, X = O	1195
		$CHCl_3$	626 nm (lg ε 3.52), 562 (3.58), 517sh, 364 (3.99), 259 (4.23)	R = H, X = NCOOEt	1195
		$CHCl_3$	631 nm (lg ε 3.70), 576 (3.61), 530 (3.67), 435sh, 371 (4.10), 282 (4.30), 261 (4.30)	R = H, X = $NCOC_{17}H_{35}$	1195
		$CHCl_3$	619 nm (lg ε 3.54), 571sh, 355 (4.21), 260 (4.52)	R = H, X = $NCOOC_{18}H_{37}$	1195
		$CHCl_3$	637 nm (lg ε 3.22), 572 (3.40), 529 (3.50), 400sh, 366 (3.90), 279 (4.20)	R = OC_8H_{17}, X = O	1195
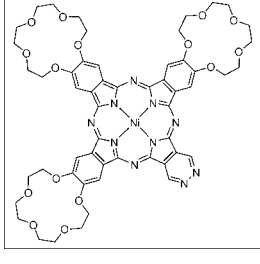	Ni(II)	$CHCl_3$	620 nm (lg ε 3.19), 590 (3.36), 490sh, 430sh, 335 (3.85), 280 (4.30)		1195

(*Continued*)

Table 7. (*Continued*)

Structure	M	Solvent	Transition Energy (Intensity)	Remark	Ref.
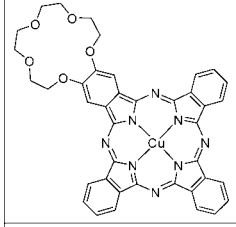	Cu(II)	$ClHCl_3$	673 nm (lg ε 4.87), 644 (4.26), 608 (4.24), 435 (3.62), 341 (4.55)		471
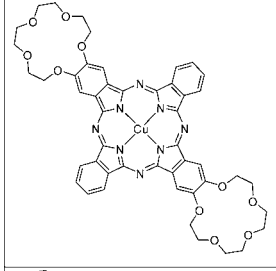	Cu(II)	$CHCl_3$	675 nm (lg ε 4.88), 646 (4.28), 610 (4.29), 423 (3.75), 340 (4.58)		471
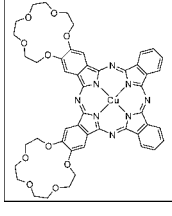	Cu(II)	$CHCl_3$	674 nm (lg ε 4.77), 646 (4.17), 609 (4.17), 424 (3.75), 340 (4.48)		471

(*Continued*)

Table 7. (*Continued*)

Structure	M	Solvent	Transition Energy (Intensity)	Remark	Ref.
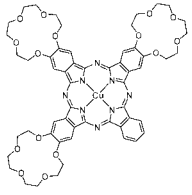	Cu(II)	$CHCl_3$	676 nm (lg ε 4.95), 647 (4.38), 611 (4.35), 414 (4.01), 341 (4.61)		471
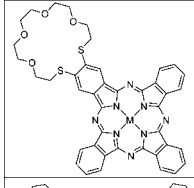	2H	$CHCl_3$	707 nm, 675, 614, 567sh, 344		1036
	Mg(II)	$CHCl_3$	694 nm, 652, 634, 594, 356		1036
	Ni(II)	$CHCl_3$	683 nm, 641, 580, 333, 293		1036
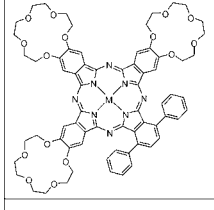	Cu(II)	$CHCl_3$	685sh nm (10^{-4} ε 6.25), 679 (6.85), 616 (1.75), 341 (3.81), 274 (4.50)		1194
	Zn(II)	$CHCl_3$	678 nm (10^{-4} ε 9.22), 613 (1.67), 353 (4.48), 292 (2.39), 279 (2.60)		1194
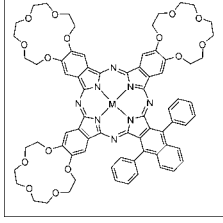	Cu(II)	$CHCl_3$	710sh nm (10^{-4} ε 12.58), 699 (13.78), 631 (3.94), 418 (2.25), 342 (5.59), 299 (6.44)		1194
	Zn(II)	$CHCl_3$	698 nm (10^{-4} ε 11.53), 628 (2.59), 351 (5.97), 296 (4.17)		1194

(*Continued*)

Table 7. (*Continued*)

Structure	M	Solvent	Transition Energy (Intensity)	Remark	Ref.
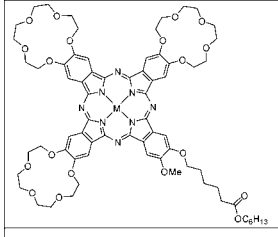	2H	$CHCl_3$	700 nm (ε 153,000), 662 (124,000), 644 (51,000), 600 (27,000), 422 (36,000), 349 (84,000), 295 (56,000)		1196
	Lu(III)OAc	$CHCl_3$	679 nm (ε 119,000), 614 (23,000), 356 (62,000), 291 (40,000)	Neutral form	1196
		$CHCl_3 + Br_2$	826 nm (ε 10,000), 728 (13,000), 537 (19,000), 403 (22,000), 355 (32,000), 284 (47,000)	Oxidized form	1196
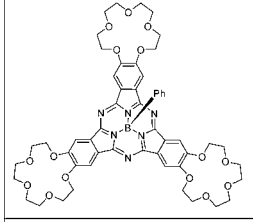	BPh	$CHCl_3$	569 nm (10^{-4} ε 5.32), 326 (3.56), 275 (4.72)		302
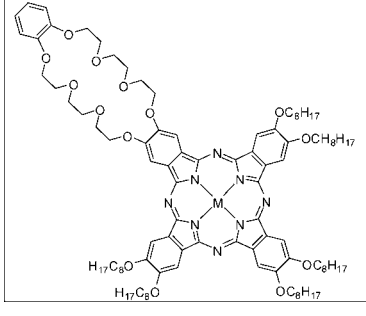	Ni(II)	$CHCl_3$	671 nm (lg ε 5.21), 643sh (4.45), 605 (4.39), 411 (4.36), 310 (4.78), 289 (4.89)		1197
	Co(II)	$CHCl_3$	678 nm (lg ε 4.79), 627 (4.66), 401 (4.68), 339 (4.85), 292 (4.87)		1197
	Zn(II)	$CHCl_3$	678 nm (lg ε 4.91), 656sh (4.15), 612 (4.11), 355 (4.56)		1197

(*Continued*)

Table 7. (*Continued*)

Structure	M	Solvent	Transition Energy (Intensity)	Remark	Ref.
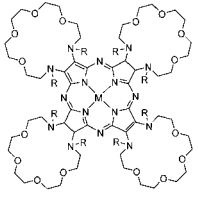	2H	$CHCl_3$	740sh nm, 668sh, 562 (lg ε 4.58), 358 (4.55), 326 (4.58)	R = 	1001
	Mg(II)	$CHCl_3$	709 nm (lg ε 4.58), 566 (4.37), 363 (4.71), 334 (4.67)	R = 	1001
		$CHCl_3$	664 nm (lg ε 4.29), 580 (4.25), 342 (4.58), 257 (4.54)	R = 	1001
	Ni(II)	$CHCl_3$	671 nm (lg ε 4.41), 541 (4.51), 380sh, 312 (4.69)	R = 	1001
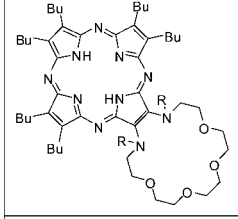	2H	$CHCl_3$	730 nm (lg ε 4.75), 685sh, 654 (4.67), 590sh, 519sh, 345 (4.92), 299 (4.60)	R = 	1001
		$CHCl_3$	733 nm (lg ε 4.69), 688sh, 658 (4.65), 602sh, 527sh, 345 (4.91), 299 (4.59)	R = 	1001
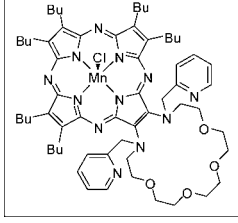	Mn(III)Cl	$CHCl_3$	730 nm (lg ε 4.50), 661sh, 524 (4.20), 381 (4.64), 367sh, 279 (4.74)		1001

(*Continued*)

Table 7. (*Continued*)

Structure	M	Solvent	Transition Energy (Intensity)	Remark	Ref.
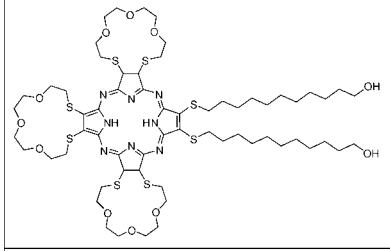	2H	$CHCl_3$	712 nm (lg ε 4.31), 644 (4.18), 504 (4.00), 346 (4.38)		1022
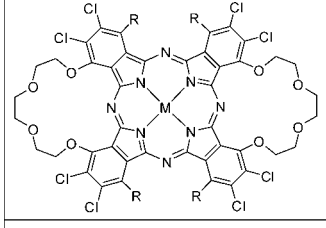	Cu(II)	$CHCl_3$	738 nm (lg ε 4.95), 664 (4.37), 347 (4.57), 327 (4.58)	R = OPr	1198
		$ClHCl_3$	738 nm (lg ε 4.99), 663 (4.41), 349 (4.58), 326 (4.59)	R = OC_5H_{11}	1198
		$CHCl_3$	739 nm (lg ε 4.87), 665 (4.29), 327 (4.55)	R = 	1198
		$CHCl_3$	739 nm (lg ε 4.93), 665 (4.35), 345 (4.58), 328 (4.58)	R = OC_8H_{17}	1198
	Co(II)	$CHCl_3$	719 nm (lg ε 4.92), 651 (4.41), 316 (4.68)	R = OC_5H_{11}	1198
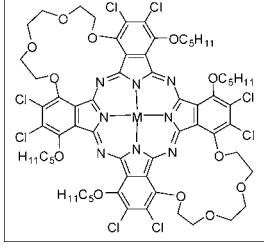	Cu(II)	$CHCl_3$	739 nm (lg ε 5.04), 663 (4.45), 348 (4.61), 327 (4.62)	R = OC_5H_{11}	1198
	Co(II)	$CHCl_3$	721 nm (lg ε 4.98), 651 (4.57), 318 (4.76)	R = OC_5H_{11}	1198

(*Continued*)

Table 7. (*Continued*)

Structure	M	Solvent	Transition Energy (Intensity)	Remark	Ref.
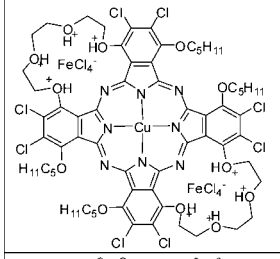	Cu(II)	$CHCl_3$	853 nm, 799, 513, 357, 324	$[Pc]^{8+}$,	1198
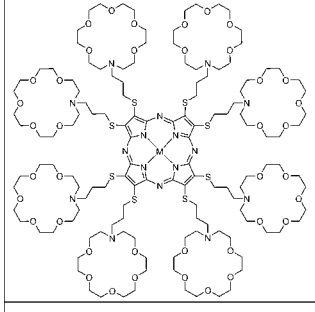	2H	$CHCl_3$	716 nm (lg ε 5.14), 677 (5.18), 346 (5.16), 245 (5.12)		1199
	Mg(II)	$CHCl_3$	677 nm (lg ε 4.92), 614 (4.38), 380 (4.83), 332 (4.63)		1199
	Zn(II)	$CHCl_3$	680 nm (lg ε 4.80), 383 (4.90), 295 (5.04)		1199
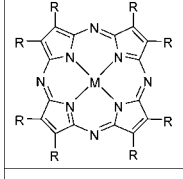	2H	$CHCl_3$	707 nm, 645, 357	R = 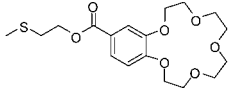	994
	Mg(II)	$CHCl_3$	669 nm, 378		994
	Co(II)	$CHCl_3$	647 nm, 348		994
β = 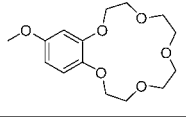	2H	THF	702 nm (10^{-4} ε 9.92), 668 (9.98), 636 (3.10), 610 (2.82), 341 (5.01)		1200
	Co(II)	THF	666 nm (10^{-4} ε 8.73), 604 (2.27), 332 (4.51)		1200
	Ni(II)	THF	675 nm (10^{-4} ε 6.21), 635 (1.55), 609 (1.41), 338 (3.85)		1200

(*Continued*)

Table 7. (*Continued*)

Structure	M	Solvent	Transition Energy (Intensity)	Remark	Ref.
	Zn(II)	$CHCl_3$	690 nm (10^{-1} ε 14.35), 616 (2.86), 351 (6.24)		1200
β = 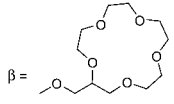	2H	$CHCl_3$	705 nm (lg ε 108,000), 668 (95,600), 476 (26,800), 330 (157,600)		1201
	Ni(II)	$CHCl_3$	674 nm (lg ε 109,200), 611 (33,400), 400 (25,800), 331 (39,000), 280 (60,000)		1201
	Zn(II)	$CHCl_3$	681 nm (lg ε 180,000), 614 (45,900), 354 (120,000), 287 (59,200)		1201
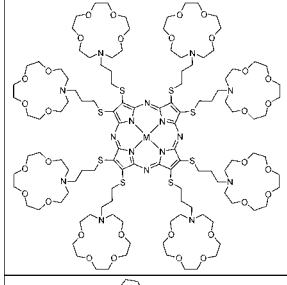	2H	$CHCl_3$	662 nm (lg ε 4.83), 347 (4.95), 278 (5.24)		1202
	Mg(II)	$CHCl_3$	674 nm (lg ε 5.26), 371 (5.17), 275 (5.21)		1202
	Co(II)	$CHCl_3$	650 nm (lg ε 5.16), 293 (5.24)		1202
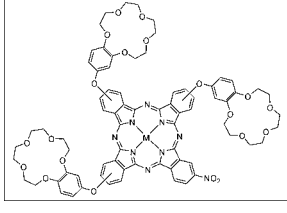	Co(II)	$CHCl_3$	678 nm (lg ε 4.87), 630 (4.26), 338 (4.62)		1203
	Ni(II)	$CHCl_3$	675 nm (lg ε 4.92), 624 (4.22), 338 (4.56)		1203
	Cu(II)	$CHCl_3$	679 nm (lg ε 4.83), 627 (4.82), 338 (4.81)		1203
	Zn(II)	$CHCl_3$	696 nm (lg ε 4.82), 675 (4.87), 377 (4.59)		1203

(*Continued*)

Table 7. (*Continued*)

Structure	M	Solvent	Transition Energy (Intensity)	Remark	Ref.
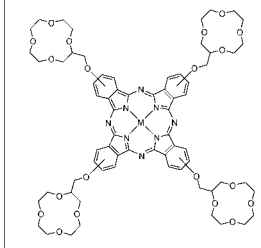	2H	$CHCl_3$	707 nm ($10^5\varepsilon$ 5.29), 671 (5.25), 647 (4.86), 614 (4.34), 389 (4.47), 341 (5.17), 290 (4.92)		1204
	Co(II)	$CHCl_3$	678 nm ($10^5\varepsilon$ 5.23), 618 (4.47), 328 (4.85), 280 (4.62)		1204
	Ni(II)	$CHCl_3$	678 nm ($10^{-5}\varepsilon$ 5.22), 616 (4.39), 382 (4.79), 328 (4.96), 275 (4.87)		1204
	Cu(II)	$CHCl_3$	689 nm ($10^{-5}\varepsilon$ 5.25), 620 (4.51), 338 (4.90), 288 (4.67)		1204
	Zn(II)	$CHCl_3$	686 nm ($10^{-5}\varepsilon$ 5.29), 617 (4.54), 353 (4.91), 281 (4.74)		1204
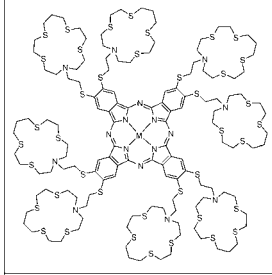	2H	py	716 nm (lg ε 4.72), 688 (4.71), 652 (4.34), 621 (4.15), 432 (4.40), 346 (4.85), 330 (4.83)		1205
	Ni(II)	py	685 nm (lg ε 5.44), 640 (5.42), 611 (5.33), 386 (5.39), 354 (5.52), 322 (5.51)		1205
	Cu(II)	py	703 nm (lg ε 4.87), 646 (4.26), 631 (4.20), 470 (4.11), 351 (4.82), 327 (4.80)		1205
	Zn(II)	py	695 nm (lg ε 5.43), 664 (5.38), 617 (5.22), 382 (5.42), 354 (5.57), 324 (5.60)		1205
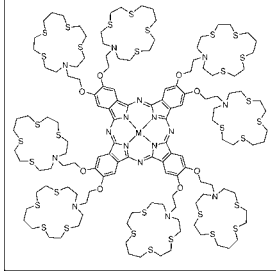	2H	$CHCl_3$	712 nm (lg ε 4.82), 672 (4.70), 649 (4.45), 611 (3.78), 369 (4.63), 332 (4.75)		1206
	Co(II)	py	692 nm (lg ε 4.66), 645 (3.93), 607 (3.86), 372 (4.62), 313 (4.80)		1206
	Ni(II)	py	695 nm (lg ε 4.77), 692 (4.02), 606 (3.88), 369 (4.41), 322 (4.84)		1206
	Cu(II)	py	687 nm (lg ε 4.73), 642 (4.06), 611 (3.93), 364 (4.59), 315 (4.75)		1206
	Zn(II)	$CHCl_3$	694 nm (lg ε 4.66), 652 (4.28), 624 (4.03), 366 (4.57), 325 (4.67), 292 (4.75)		1206

(*Continued*)

Table 7. (*Continued*)

Structure	M	Solvent	Transition Energy (Intensity)	Remark	Ref.
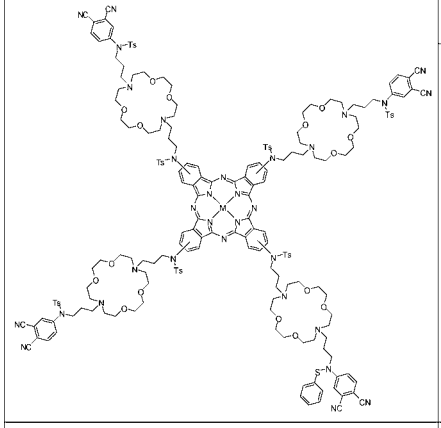	2H	$CHCl_3$	709 nm (lg ε 5.32), 678 (5.31), 650 (4.75), 610 (4.33), 365 (5.20), 325 (5.30)		1207
	2Li	$CHCl_3$	680 nm (lg ε 5.33), 620 (4.24), 395 (4.88), 344 (4.90), 312 (4.93)		1207
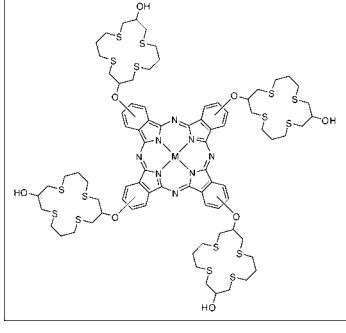	2H	$CHCl_3$	710 nm (10^{-5} ε 5.29), 674 (5.22), 647 (4.83), 614 (4.66), 345 (5.08), 295 (5.11)		1208
	Co(II)	$CHCl_3$	683 nm (10^{-5} ε 5.16), 614 (4.70), 357 (5.08), 302 (5.10)		1208
	Ni(II)	$CHCl_3$	683 nm (10^{-5} ε 5.15), 614 (4.67), 350 (5.05), 300 (5.07)		1208
	Cu(II)	$CHCl_3$	689 nm (10^{-5} ε 5.15), 617 (4.68), 361 (5.09), 295 (5.11)		1208
	Zn(II)	$CHCl_3$	689 nm (10^{-5} ε 5.19), 620 (4.63), 353 (5.13), 311 (5.15)		1208
	Pb(II)	$CHCl_3$	728 nm (10^{-5} ε 5.26), 653 (4.62), 365 (5.13), 299 (5.15)		1208

(*Continued*)

Table 7. (*Continued*)

Structure	M	Solvent	Transition Energy (Intensity)	Remark	Ref.
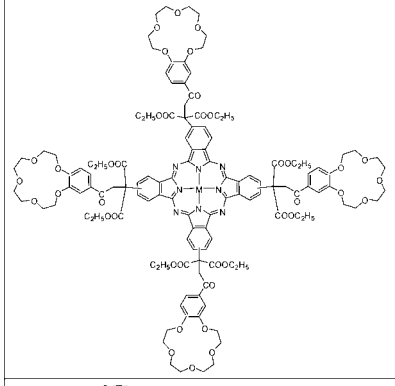	Cu(II)	$CHCl_3$	651 nm, 586, 340		1209
	Co(II)	$CHCl_3$	673 nm, 613, 345		1209
	Pb(II)	$CHCl_3$	661 nm, 596, 335		1209
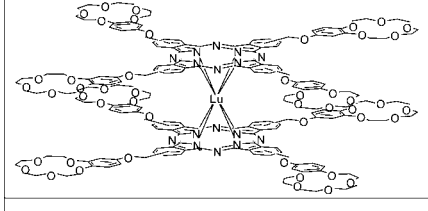	Lu(III)	$CHCl_3$	684 nm (ε 142,600), 614 (27,800), 349 (94,200)		1210
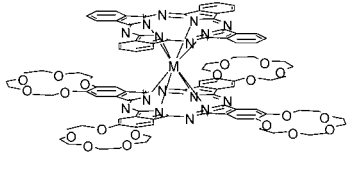	La(III)	$CHCl_3$	689 nm (lg ε 4.84), 612 (4.42), 508 (4.37), 335 (4.89), 289 (4.81)		1211
	Sm(III)	$CHCl_3$	675 nm (lg ε 5.06), 610 (4.41), 490 (4.49), 331 (4.97), 290 (4.92)		1211
	Dy(III)	$CHCl_3$	668 nm (lg ε 5.05), 605 (4.32), 481 (4.42), 326 (4.91), 289 (4.89)		1211
	Tm(III)	$CHCl_3$	666 nm (lg ε 5.22), 603 (4.55), 469 (4.63), 368 (5.17), 327 (5.15), 290 (5.04)		1211

(*Continued*)

Table 7. (*Continued*)

Structure	M	Solvent	Transition Energy (Intensity)	Remark	Ref.
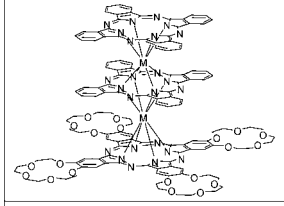	Sm(III)	$ClHCl_3$	682sh nm, 642, 338, 291		1212
	Dy(III)	$CHCl_3$	700 nm, 640, 338, 293		1212
	Tm(III)	$ClHCl_3$	712 nm, 631, 338, 291		1212
	Y(III)	$CHCl_3$	702 nm, 639, 338, 294		1212
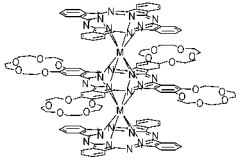	Sm(III)	$ClHCl_3$	682sh nm, 643, 334, 293		1213
	Tb(III)	$CHCl_3$	695 nm, 641, 333, 292		1213
	Dy(III)	$CHCl_3$	700 nm, 640, 333, 293		1213
	Tm(III)	$CHCl_3$	709 nm, 635, 333, 292		1213
	Y(III)	$CHCl_3$	702 nm, 639, 333, 294		1213
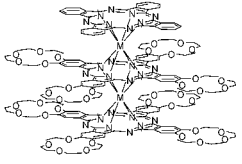	Sm(III)	$CHCl_3$	690sh nm, 644, 353, 292		1213
	Tb(III)	$CHCl_3$	696 nm, 642, 355, 292		1213
	Dy(III)	$CHCl_3$	702 nm, 640, 354, 291		1213
	Tm(III)	$CHCl_3$	713 nm, 636, 355, 292		1213
	Y(III)	$CHCl_3$	705 nm, 639, 355, 291		1213
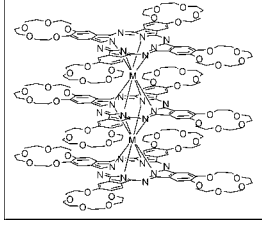	La(III)	$CHCl_3$	646 nm (r.i 1.00), 361 (0.48)		1163
	Pr(III)	$CHCl_3$	646 nm (lg ε 5.21), 358 (5.10), 291 (5.10)		1214
	Nd(III)	$CHCl_3$	646 nm (lg ε 5.33), 359 (5.16), 292 (5.16)		1214
	Gd(III)	$ClHCl_3$	695sh nm (lg ε 4.43), 644 (5.17), 590sh (4.17), 361 (5.02), 293 (4.94)		1215
	Yb(III)	$CHCl_3$	689 nm (lg ε 4.66), 636 (5.16), 359 (5.10), 290 (4.89)		1215
	Lu(III)	$CHCl_3$	718 nm (lg ε 4.33), 638 (5.07), 362 (5.01)		1215

(*Continued*)

Table 7. (*Continued*)

Structure	M	Solvent	Transition Energy (Intensity)	Remark	Ref.
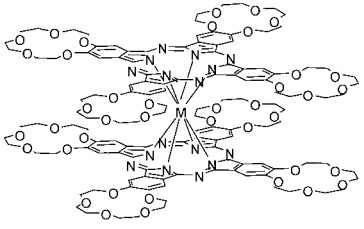	Sc(III)	$ClHCl_3$	1377sh nm, 1219 (lg ε 4.11), 926 (4.06), 661 (5.22), 466 (4.57), 365 (5.13)		89
		$ClHCl_3$	724 nm (lg ε 4.69), 619 (5.13), 359 (5.14)	$[(Pc)_2]$, reduced form	89
		$CHCl_3$	876 nm (lg ε 4.45), 691 (4.73), 485 (4.92), 383 (5.13)	$[(Pc)_2]^+$, oxidized form	89
	La(III)	$CHCl_3$	691 nm (lg ε 4.57), 623 (4.14), 508 (4.17), 375 (4.53), 343 (4.66), 291 (4.63)		1211
	Pr(III)	$CHCl_3$	684 nm (lg ε 5.01), 617 (4.46), 499 (4.56), 371 (4.95), 340 (5.00), 291 (5.01)		1214
		$CHCl_3$	640 nm (lg ε 5.36), 587 (4.34), 359 (5.16)	$[(Pc)_2]^-$, reduced form	1214
	Nd(III)	$CHCl_3$	682 nm (lg ε 4.85), 497 (4.35), 372 (4.77), 339 (4.80), 292 (4.83)		1214
		$CHCl_3$	638 nm (lg ε 5.14), 359 (4.98), 285	$[(Pc)_2]^-$, reduced form	1214
	Sm(III)	$ClHCl_3$	678 nm (lg ε 5.08), 613 (4.53), 492 (4.54), 371 (4.98), 337 (4.95), 292 (4.96)		1211
	Gd(III)	$CHCl_3$	675 nm (lg ε 5.08), 488 (4.53), 368 (5.00), 337 (4.93), 292 (4.96)		1215
	Dy(III)	$CHCl_3$	671 nm (lg ε 4.95), 607 (4.28), 484 (4.40), 368 (4.88), 335 (4.80), 291 (4.86)		1211
	Tm(III)	$CHCl_3$	668 nm (lg ε 5.21), 604 (4.48), 479 (4.61), 368 (5.12), 340sh, 291 (5.04)		1211
	Yb(III)	$CHCl_3$	670 nm (lg ε 5.18), 479 (4.60), 369 (5.12), 292 (5.06)		1215
	Lu(III)	$CHCl_3$	665 nm (lg ε 5.20), 476 (4.66), 367 (5.13)		1215
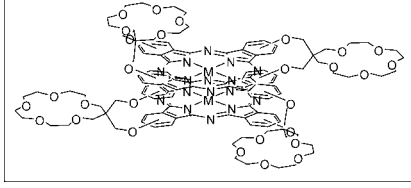	Co(II)	DMF	660 nm (lg ε 5.43), 602 (4.83), 333 (5.32)		1216
	Zn(II)	DMF	675 nm (lg ε 5.79), 638 (5.56), 348 (5.71)		1216

(*Continued*)

Table 7. (*Continued*)

Structure	M	Solvent	Transition Energy (Intensity)	Remark	Ref.
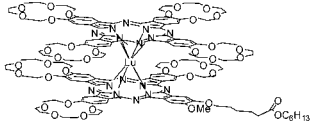	Lu(III)	$CHCl_3$	666 nm (ε 159,000), 603 (30,000), 476 (39,000), 367 (131,000), 291 (102,000)	Neutral form	1196
		$CHCl_3$ + 10% hydrazine	701 nm (ε 66,000), 627 (164,000), 360 (176,000)	Reduced form	1196
		$CHCl_3 + Br_2$	703 nm (ε 54,000), 498 (84,000), 385 (116,000), 336 (79,000), 293 (120,000)	Oxidized form	1196
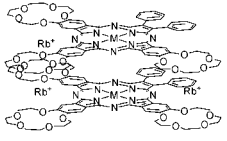	Cu(II)	$CHCl_3$	634 nm (10^{-4} ε 3.54), 332 (3.25), 287 (3.29), 274 (3.47)		1194
	Zn(II)	$CHCl_3$	641 nm (10^{-4} ε 5.08), 593 (2.66), 344 (6.28), 272 (4.34)		1194
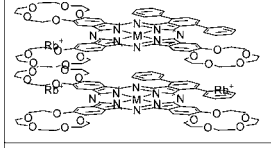	Cu(II)	$CHCl_3$	698sh nm (10^{-4} ε 2.36), 677 (2.83), 640 (2.93), 337 (3.03), 271 (4.47)		1194
	Zn(II)	$CHCl_3$	673 nm (10^{-4} ε 2.73), 637 (3.98), 342 (3.61), 290 (2.28), 278 (2.76)		1194
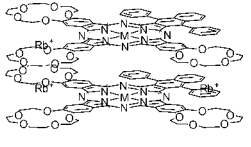	Cu(II)	$CHCl_3$	693 nm (10^{-4} ε 5.19), 650 (5.80), 415 (2.05), 339 (6.62), 297 (6.12)		1194
	Zn(II)	$CHCl_3$	694 nm (10^{-4} ε 3.57), 649 (4.27), 345 (5.53), 293 (4.45)		1194

(*Continued*)

Table 7. (*Continued*)

Structure	M	Solvent	Transition Energy (Intensity)	Remark	Ref.
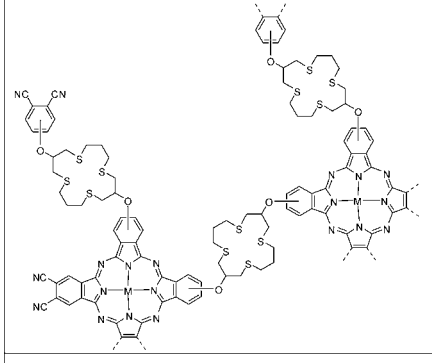	2H	py	703 nm (10^5 ε 5.11), 683 (5.09), 617 (4.57), 354 (5.02), 332 (4.99), 248 (5.13)		1217
	Co(II)	py	681 nm (10^5 ε 5.17), 614 (4.62), 373 (5.11), 318 (5.14), 261 (5.16)		1217
	Ni(II)	py	680 nm (10^5 ε 5.16), 611 (4.60), 362 (5.08), 340 (5.07), 240 (5.17)		1217
	Cu(II)	py	689 nm (10^5 ε 5.17), 617 (4.57), 361 (5.10), 320 (5.12), 249 (5.14)		1217
	Zn(II)	py	692 nm (10^5 ε 5.24), 620 (4.65), 344 (5.10), 321 (5.11), 254 (5.18)		1217
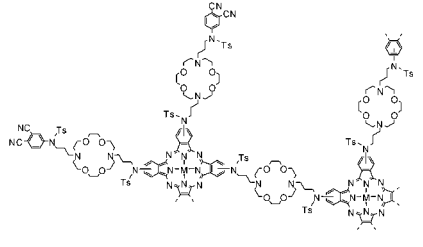	2H	py	704 nm (lg ε 4.38), 676 (4.36), 644 (4.19), 608 (3.95), 356 (4.45), 338 (4.54), 321 (4.31), 295 (4.30)		1207
		H_2SO_4	776 nm (lg ε 4.01), 731sh (3.75), 693 (3.28), 652 (2.96), 414 (3.40), 308 (4.22), 285 (4.27), 254 (4.26)		1207
	Co(II)	H_2SO_4	820 nm (lg ε 3.40), 759sh (3.17), 715 (2.70), 654 (2.38), 379 (4.38), 354 (4.57), 314 (4.60), 267 (4.64)		1207
	Ni(II)	H_2SO_4	857 nm (lg ε 4.26), 807sh (4.20), 731 (4.11), 651 (3.59), 512 (2.32), 416 (4.18), 397 (4.29), 315 (4.54), 277 (4.59)		1207
	Cu(II)	H_2SO_4	852 nm (lg ε 3.90), 756sh (3.98), 734 (3.81), 659 (2.75), 429 (3.91), 394 (4.06), 301 (4.49), 277 (4.58), 253 (4.60)		1207
	Zn(II)	H_2SO_4	835 nm (lg ε 3.73), 760sh (3.60), 726 (3.34), 671 (2.78), 418 (3.30), 354 (3.42), 325 (3.25), 267 (4.35)		1207

(*Continued*)

Table 7. (*Continued*)

Structure	M	Solvent	Transition Energy (Intensity)	Remark	Ref.
	2H	py	706 nm, 672, 640sh, 606, 389, 360, 320, 301, 285		1218
		H_2SO_4	810 nm, 720sh, 675, 608, 392, 345, 320, 274		1218
	Co(II)	H_2SO_4	816 nm, 755sh, 720, 663, 391, 377, 326, 292		1218
	Ni(II)	H_2SO_4	816 nm, 758sh, 719, 639, 460, 414, 378, 297		1218
	Cu(II)	H_2SO_4	832 nm, 775sh, 732, 617, 430, 412, 338, 304		1218
	Zn(II)	H_2SO_4	850 nm, 819sh, 736, 619, 458, 365, 327, 297		1218

Table 8. UV-vis absorption data of tetraazachlorin derivatives.

Structure	M	Solvent	Transition Energy (Intensity)	Remark	Ref.
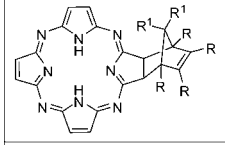	2H	DCB	678 nm (lg ε 4.90), 643 (4.00), 619 (4.05), 520(4.55), 349 (4.61), 333 (4.61)	R, R^1 = H	1219
		DCM	670 nm (lg ε 4.83), 640 (4.01), 614 (3.89), 582 (3.60), 517 (4.54), 343 (4.67), 329 (4.64)	R = Cl, R^1 = OMe	1219
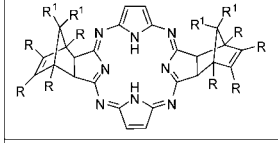	2H	DCM	762 nm (lg ε 4.82), 724 (4.07), 686 (3.51), 466 (4.37), 414 (3.89), 355 (4.56), 300 (4.47)	R = Cl, R^1 = OMe	1219
		DCM	756 nm (lg ε 4.86), 718 (4.18), 467 (4.45), 355 (4.60), 301 (4.51)	R, R^1 = Cl	1219
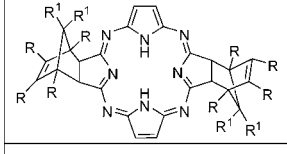	2H	DCM	765 nm (lg ε 4.85), 726 (4.09), 682 (3.47), 465 (4.38), 415 (3.80), 355 (4.57)	R = Cl, R^1 = OMe	1219
		DCM	755 nm (lg ε 4.84), 717 (4.09), 468 (4.37), 356 (4.63), 300 (4.49)	R, R^1 = Cl	1219
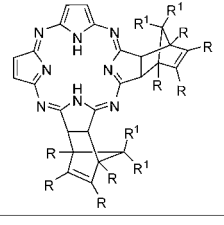	2H	DCM	618 nm (r.i 1.0), 591(1.05), 379sh, 367sh, 322 (1.30)	R = Cl, R^1 = OMe	1219
		DCM	614 nm (r.i 1.0), 591 (0.4), 514 (0.23), 499 (0.22), 366 (0.47)	R, R^1 = Cl	1219
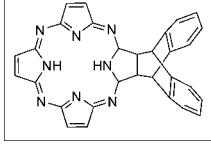	2H	$CHCl_3$	677 nm (10^{-4} ε 7.42), 519 (3.57), 346 (4.83)		949

(*Continued*)

Table 8. (*Continued*)

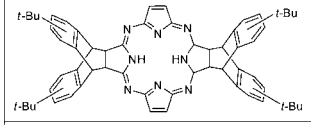	2H	$CHCl_3$	792 nm (10^{-4} ε 6.11), 463 (1.62), 353 (3.87)		949
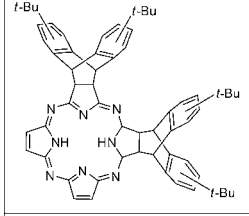	2H	$CHCl_3$	597 nm (10^{-4} ε 3.89), 310 (3.32)		949
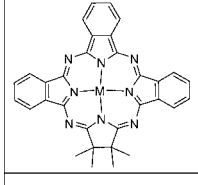	2H	PhCl	748 nm (10^{5} ε 0.95), 711 (0.16), 677 (0.13), 606 (0.37), 341 (0.68)		1220
	Ni(II)	PhCl	724 nm (10^{-5} ε 1.11), 663 (0.17), 592 (0.61), 414 (0.05), 325 (0.33)		1220
	V(IV)O	PhCl	765 nm (10^{-5} ε 1.03), 697 (0.21), 625 (0.40), 334 (0.49)		1220
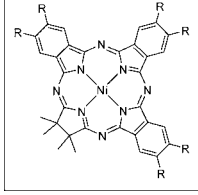	Ni(II)	$CHCl_3$	734 nm (10^{-5} ε 0.91), 597 (0.50), 366 (0.19), 333 (0.27)	R = OBu	1221
		$CHCl_3$	744 nm (10^{-5} ε 0.83), 599 (0.68), 325 (0.32)	R = SO_2Bu	1221

(*Continued*)

Table 8. (*Continued*)

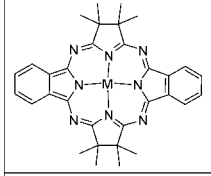	Ni(II)	PhCl	842 nm (10^{-5} ε 1.03), 797 (0.30), 756 (0.15), 538 (0.32), 497 (0.09), 331 (0.19)		1220
	V(IV)O	PhCl	901 nm (10^{-5} ε 0.59), 852 (0.34), 807sh (0.18), 575 (0.18), 536 (0.09), 338 (0.22)		1220
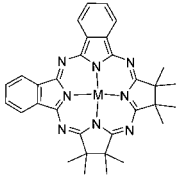	Ni(II)	PhCl	671 nm (10^{-5} ε 1.41), 645 (0.35), 576 (0.18), 313sh (0.23)		1220
	V(IV)O	PhCl	719 nm (10^{-5} ε 1.11), 324 (0.48)		1220
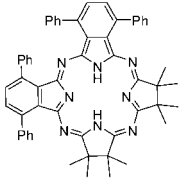	Ni(II)	Toluene	711 nm		1222
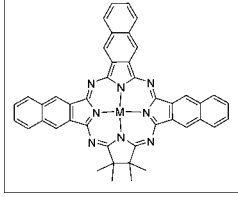	2H	PhCl	824 nm (10^{-5} ε 1.45), 768 (0.34), 725 (0.32), 679 (0.29), 347 (0.54)		1220
	Ni(II)	PhCl	806 nm (10^{-5} ε 1.13), 763 (0.21), 681 (0.38), 309 (0.83)		1220

(*Continued*)

Table 8. (*Continued*)

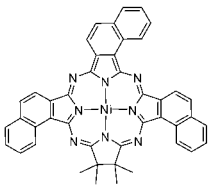	Ni(II)	PhCl	745 nm (10^{-5} ε 0.46), 675 (0.09), 596 (0.38), 551 (0.06), 444 (0.05), 375 (0.13), 302 (0.37)		1223
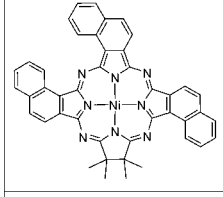	Ni(II)	PhCl	743 nm (10^{-5} ε 0.46), 675 (0.09), 597 (0.34), 551 (0.05), 448 (0.05), 352 (0.13), 301 (0.33)		1223
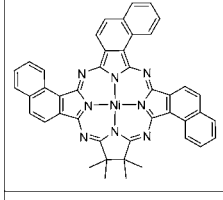	Ni(II)	PhCl	744 nm (10^{-5} ε 0.46), 673 (0.09), 598 (0.36), 548 (0.05), 450 (0.04), 378 (0.09), 347 (0.14), 304 (0.33)		1223
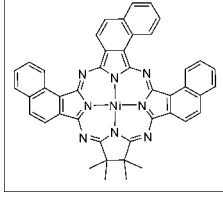	Ni(II)	PhCl	743 nm (10^{-5} ε 0.46), 670 (0.08), 599 (0.33), 553 (0.04), 451 (0.04), 377 (0.08), 348 (0.15), 303 (0.32)		1223

(*Continued*)

Table 8. (*Continued*)

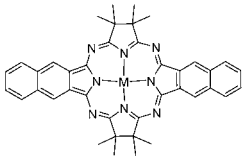	Ni(II)	PhCl	892 nm (10^{-5} ε 1.15), 844 (0.30), 793 (0.17), 646 (0.16), 601 (0.07), 463 (0.05), 304 (0.92)		1220
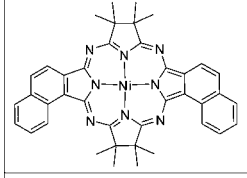	Ni(II)	PhCl	879 nm (10^{-5} ε 0.87), 823 (0.32), 783 (0.17), 513 (0.23), 478 (0.08), 348 (0.23), 329 (0.28), 303 (0.63)		1223
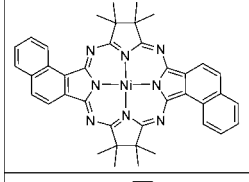	Ni(II)	PhCl	880 nm (10^{-5} ε 0.87), 825 (0.37), 780 (0.19), 513 (0.27), 473 (0.09), 347 (0.27), 330 (0.33), 304 (0.76)		1223
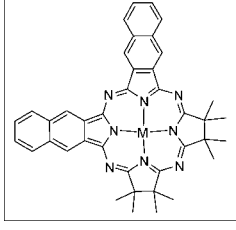	Ni(II)	PhCl	751 nm (10^{-5} ε 1.09), 716 (0.33), 634 (0.16), 498 (0.05), 301 (0.62)		1220

(*Continued*)

Table 8. (*Continued*)

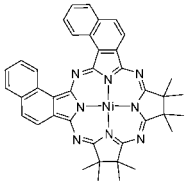	Ni(II)	PhCl	689 nm (10^{-5} ε 1.76), 660 (0.28), 630 (0.29), 569 (0.22), 356 (0.17), 299 (0.75)		1223
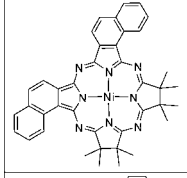	Ni(II)	PhCl	675 nm (10^{-5} ε 1.75), 649 (0.26), 626 (0.24), 569 (0.13), 373 (0.11), 307 (0.38)		1223
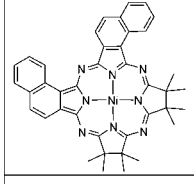	Ni(II)	PhCl	681 nm (10^{-5} ε 1.74), 653 (0.25), 625 (0.25), 569 (0.15), 385 (0.10), 297 (0.57)		1223
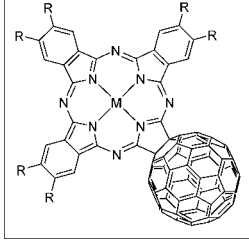	Ni(II)	$CHCl_3$	773 nm (10^{-5} ε 0.32), 699 (0.39), 618 (1.00), 322 (1.35)	R = OBu	1221
		$CHCl_3$	759 nm (10^{-5} ε 1.03), 694 (0.19), 612 (1.14), 327 (0.85)	R = SO_2Bu	1221

(*Continued*)

Table 8. (*Continued*)

	Ni(II)	$CHCl_3$	672 nm (10^{-5} ε 0.17), 566 (0.04), 321 (0.53)	R = OBu	1221
		$CHCl_3$	712 nm (10^{-5} ε 0.86), 682 (0.21), 661 (0.16), 609 (0.10), 325 (0.65)	R = SO_2Bu	1221
	Ni(II)	$CHCl_3$	907 nm (10^{-5} ε 0.30), 858 (0.09), 809 (0.06), 554 (0.20), 508 (0.12), 317 (1.03)		1221

Table 9. UV-vis absorption data of triazacorrole derivatives.

Structure	M	Solvent	Transition Energy (Intensity)	Remark	Ref.
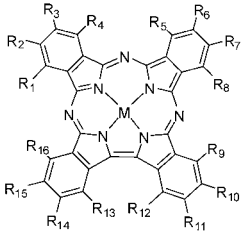	P(III)OH	DMF	15200 cm^{-1} (lg ε 4.64), 15800 (4.42), 16700 (4.03), 22300 (4.98), 22800 (4.62), 23900 (4.52)	$R_3(R_3)$, $R_6(R_7)$, $R_{10}(R_{11})$, $R_{14}(R_{15})$ = O(–Pr), $[Pc]^-H^+$	387
		py	658 nm (lg ε 4.62), 634 (4.39), 602 (4.04), 450 (4.95), 420 (4.49), 330 (4.47)		387
	P(V)OH	DCM	726 nm (10^{-3} ε 61), 690sh (35), 656sh (25), 526 (55), 490sh (43), 365 (34), 334 (39)	R_1, R_4, R_5, R_8, R_9, R_{12}, R_{13}, R_{16} = OBu, $[Pc]^+OH^-$	389
		DCM	722 nm (10^{-3} ε 57.8), 685 (25.7), 652 (16.7), 500 (61), 349 (28.9)	R_1, R_4, R_5, R_8, R_9, R_{12}, R_{13}, R_{16} = OBu, R_2, R_3, R_6, R_7, R_{10}, R_{11}, R_{14}, R_{15} = Cl, $[Pc]^-OH^-$	389
	P(V)O	py	656 nm (lg ε 0.47), 627 (0.22), 597 (0.12), 442 (1.00), 435 (0.58), 413(0.30)	R_1, R_2, R_3, R_4, R_5, R_6, R_7, R_8, R_9, R_{10}, R_{11}, R_{12}, R_{13}, R_{14}, R_{15}, R_{16} =H	384
		py	662 nm (lg ε 0.49), 636 (0.26), 604 (0.12), 447 (1.00), 417 (0.32)	R_2, R_3, R_6, R_7, R_{10}, R_{11}, R_{14}, R_{15} = Pr	384
		py	663 nm (r.i. 1.0), 637 (0.549), 606 (0.272), 448 (1.780), 418 (0.698)	R_2, R_3, R_6, R_7, R_{10}, R_{11}, R_{14}, R_{15} = Bu	514
		py	658 nm (r.i. 1.0), 632 (0.491), 601 (0.242), 445 (1.860), 438 (1.241), 416 (0.629)	$R_2(R_3)$, $R_6(R_7)$, $R_{10}(R_{11})$, $R_{14}(R_{15})$ = *t*-Bu	514
		py	658 nm (lg ε 0.49), 632 (0.25), 601 (0.12), 445 (1.00), 415 (0.31)		384
		py	662 nm (lg ε 0.48), 637 (0.26), 605 (0.11), 448 (1.00), 418 (0.31)	R_2, R_3, R_6, R_7, R_{10}, R_{11}, R_{14}, R_{15} = C_5H_{11}	384
	P(V)L	DMSO	656 nm	R_1, R_2, R_3, R_4, R_5, R_6, R_7, R_8, R_9, R_{10}, R_{11}, R_{12}, R_{13}, R_{14}, R_{15}, R_{16} = H, L = *trans*-$(OH)_2$	385
		DMF	655 nm		386
		DMSO	662 nm	R_1, R_2, R_3, R_4, R_5, R_6, R_7, R_8, R_9, R_{10}, R_{11}, R_{12}, R_{13}, R_{14}, R_{15}, R_{16} = H, L = *trans*-$(OH)_2$, $(SO_3^-)_n$	385
		DMF	657 nm		386
		Tris-HCl	658 nm		385
		DMF	677 nm	$R_2(R_3)$, $R_6(R_7)$, $R_{10}(R_{11})$, $R_{14}(R_{15})$ = O(*i*-Pr), L = *trans*-$(OH)_2$	386
		DCM	720 nm (10^{3} ε 73), 682 (37), 653 (23), 520 (64), 495 (52), 331 (29)	R_1, R_4, R_5, R_8, R_9, R_{12}, R_{13}, R_{16} = OBu, L = trans-$(OMe)_2$	389
	Si(IV)OH	$CHCl_3$	675 nm (r.i. 0.56), 620 (0.12), 448 (1.00), 434 (0.35), 416 (0.39), 342 (0.24), 295 (0.27)	R_2, R_3, R_6, R_7, R_{10}, R_{11}, R_{14}, R_{15} = C_5H_{11}	354
	Si(IV)L	Benzene	662 nm, 441	R_1, R_2, R_3, R_4, R_5, R_6, R_7, R_8, R_9, R_{10}, R_{11}, R_{12}, R_{13}, R_{14}, R_{15}, R_{16} = H, L = *trans*-$(OTMS)_2$	349

(*Continued*)

Table 9. (*Continued*)

Structure	M	Solvent	Transition Energy (Intensity)	Remark	Ref.
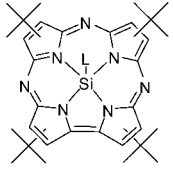	Si(IV)L	$CHCl_3$	591 nm, 407	$R_1(R_4)$, $R_5(R_8)$, $R_9(R_{12})$, $R_{13}(R_{16})$ = *t*-Bu, L = OTMS	353
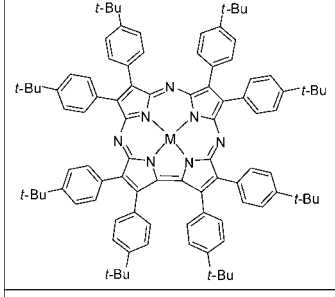	Mn(III)Cl	DCM	635 nm, 480, 435	$[Pc]^-NEt_4^+$	1224
	Co(III)L	DCM	738 nm (10^{-4} ε 1.5), 680 (1.6), 445 (4.6)	L = CN	1225
		DCM	778 nm (10^{-4} ε 0.8), 673 (1.6), 619 (1.3), 450 (4.0)	L = 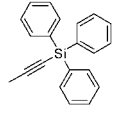	1225
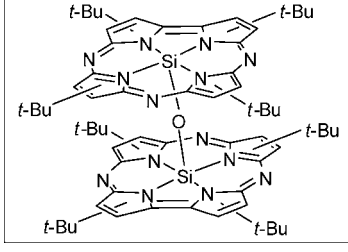	Si(IV)	$CHCl_3$	596 nm, 380		353

(*Continued*)

Table 10. UV-vis absorption data of sandwich-type Pcs.

Structure	M	Solvent	Transition Energy (Intensity)	Remark	Ref.
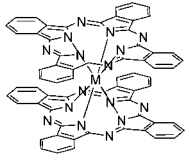	Y(III)	$CHCl_3$	1538 nm, 1395, 916, 663, 598, 458, 319	Neutral form	92
	Zr(IV)	DCB	746 nm (lg ε 4.67), 628 (5.21), 338 (5.03)	Neutral form	128
	La(III)	$CHCl_3$	689 nm (r.i 0.78), 612 (0.30), 486 (0.20), 451(0.16), 326 (1.00), 278 (0.47)	Neutral form	1211
	Pr(III)	$CHCl_3$	1784 nm, 899	Neutral form	1226
	Nd(III)	DCM	676 nm, 485~455	Neutral form	506
	Sm(III)	$CHCl_3$	673 nm (r.i 1.00), 606 (0.22), 458 (0.19), 322 (0.81), 280 (0.38)	Neutral form	1211
	Eu(III)	$CHCl_3$	1607 nm, 1406, 906, 671, 605, 461, 322	Neutral form	548
		$CHCl_3$	1601 nm (lg ε 3.82), 1399 (3.61), 908 (3.37), 671 (4.93), 605 (4.21), 459 (4.17), 342 (4.60), 322 (4.78)	Neutral form	1227
		$CHCl_3$	1599 nm (5.27), 907 (3.44), 671 (5.33), 604 (4.61), 587 (4.52), 461 (4.57), 344 (4.99), 321 (5.18)	Neutral form	1228
		toluene	669 nm, 637, 325	Neutral form	1229
		$CHCl_3$/MeOH = 3:1	681 nm (4.82), 635 (5.33), 583 (4.45), 359 (4.81), 333 (5.28), 283 (4.96)	Reduced form	1228
		Toluene	637 nm	Reduced form	1229
	Gd(III)	$CHCl_3$	1573 nm, 1410, 910, 670, 605, 459, 323	Neutral form	548
		$CHCl_3$	1573 nm, 1415sh, 909	Neutral form	1226
		DCM	668 nm, 459	Neutral form	506
	Tb(III)	DCM	665 nm, 459	Neutral form	506
	Dy(III)	DCM	1536sh nm (10^{-4} ε 1.3), 1404 (1.4), 1260sh (0.7), 900 (0.7), 790	Neutral form	1230
		$CHCl_3$	665 nm (r.i 1.00), 600 (0.19), 458 (0.21), 320 (0.76), 279 (0.42)	Neutral form	1211
		DCM	664 nm, 459	Neutral form	506
	Tm(III)	$CHCl_3$	661 nm (r.i 1.00), 596 (0.16), 458 (0.19), 320 (0.69), 281 (0.41)	Neutral form	1211
		DCM	1500sh nm (10^{-4} ε 1.1), 1392 (1.7), 1260 (1.1), 906 (0.8), 880 (0.4)	Neutral form	1230
	Yb(III)	DCM	1500sh nm (10^{-4} ε 1.7), 1386 (2.1), 1252 (1.5), 906 (1.0), 880 (0.4)	Neutral form	1230

(*Continued*)

Table 10. (*Continued*)

Structure	M	Solvent	Transition Energy (Intensity)	Remark	Ref.
		DCM	659 nm, 457	Neutral form	506
	Lu(III)	$CHCl_3$	1370 nm, 1261sh, 903	Neutral form	1226
		DCM	1500sh nm (10^{-1} ε 0.8), 1382 (1.6), 1248 (1.2), 906 (0.8), 880 (0.3)	Neutral form	1230
		DCM	914 nm (lg ε 3.72), 658 (5.12), 596 (4.36), 456 (4.45), 318 (5.04)	Neutral form	1048
		DCM	659 nm, 457	Neutral form	506
		DMF	669 nm, 625	Neutral form	510
		Benzene	658 nm	Neutral form	510
		DCB: MeCN = 1:1	659 nm	Neutral form	1231
		DCB	660 nm, 633sh, 596, 576sh, 459, 344	Neutral form	1232
		DCM/TBAP 0.03 M	660 nm (10^{-1} ε 18.2)	Neutral form	509
		DCB	702 nm, 618, 563sh, 336	Reduced form	1232
		DCB: MeCN = 1:1	690 nm, 616	Reduced form	1231
		DCB	699 nm, 487, 358	Oxidized form	1232
		DCB: MeCN = 1:1	693 nm, 477	Oxidized form	1231
		DCM + 0.03 M TBAP	700 nm (10^{-1} ε 6.7), 616 (12.8), 333 (14.8)	Reduced form	509
		DCM + 0.03 M TBAP	870 nm (10^{-1} ε 2.8), 692 (5.0), 475 (5.1)	Oxidized form	509
	Hf(IV)	benzene	744 nm (lg ε 4.51), 626 (5.01), 334 (4.84)	Reduced form	128
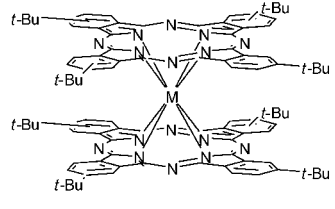	La(III)	MeOH	646 nm, 587, 337	Neutral form	521
		DCB + TBAP	686 nm (lg ε 4.80), 646 (4.63), 462 (4.12), 318 (4.90)	Neutral form	1233
	Ce(IV)	toluene	645 nm (r.i 1.00), 335 (0.85)	Reduced form	1234
		DCB + TBAP	646 nm (lg ε 4.96), 340 (4.85)	Reduced form	1233
	Pr(III)	toluene	686 nm (r.i 0.92), 614 (0.36), 487 (0.24), 351 (0.65), 326 (1.00)	Neutral form	1234
		DCB + TBAP	682 nm (lg ε 4.82), 644 (4.69), 610 (4.34), 480 (4.15), 324 (4.94)	Neutral form	1233
		toluene	649 nm (r.i 1.00), 342 (0.89)	Reduced form	1234
		DCB + TBAP	646 nm (lg ε 4.92), 340 (4.64)	Reduced form	1233
		$CHCl_3$	1789 nm, 906	Neutral form	1226
	Nd(III)	toluene	675 nm (r.i 0.93), 607 (0.34), 470 (0.22), 351 (0.68), 327 (1.00)	Neutral form	1234

(*Continued*)

Table 10. (*Continued*)

Structure	M	Solvent	Transition Energy (Intensity)	Remark	Ref.
		DCB + TBAP	682 nm (lg ε 4.80), 646 (4.59), 612 (4.31), 480 (4.22), 348 (4.51), 324 (4.67)	Neutral form	1233
		toluene	648 nm (r.i 1.00), 342 (0.86)	Reduced form	1234
		DCB + TBAP	644 nm (lg ε 4.96), 340 (4.82)	Reduced form	1233
	Sm(III)	toluene	678 nm (r.i 1.00), 652 (0.41), 612 (0.33), 476 (0.22), 344 (0.84), 327 (0.97)	Neutral form	1234
		DCB + TBAP	679 nm (lg ε 4.86), 644 (4.60), 502 (4.16), 340 (5.02), 330 (5.04)	Neutral form	1233
		toluene	648 nm (r.i 1.00), 342 (0.91)	Reduced form	1234
		DCB + TBAP	645 nm (lg ε 4.93), 338 (4.89)	Reduced form	1233
	Eu(III)	toluene	675 nm (r.i 1.00), 645 (0.56), 611 (0.40), 471 (0.28), 342 (0.91), 326 (1.00)	Neutral form	1234
		toluene	647 nm (r.i.1.00), 342 (0.92)	Reduced form	1234
		DCB + TBAP	644 nm (lg ε 4.73), 342 (4.69)	Reduced form	1233
	Gd(III)	$CHCl_3$	1586 nm, 1446sh, 920	Neutral form	1226
		toluene	674 nm (r.i 1.00), 645 (0.24), 607 (0.27), 469 (0.21), 345 (0.67), 325 (0.83)	Neutral form	1234
		DCB + TBAP	674 nm (lg ε 5.29), 644sh (4.61), 604 (4.64), 478 (4.72), 340 (5.15), 320 (5.15)	Neutral form	1233
		toluene	647 nm (r.i 0.97), 340 (1.00)	Reduced form	1234
	Tb(III)	MeOH	677 nm, 612, 345	Neutral form	521
		toluene	671 nm (r.i 1.00), 645 (0.35), 606 (0.26), 468 (0.20), 340 (0.71), 325 (0.80)	Neutral form	1234
		MeCN	672 nm	Neutral form	1231
		toluene	647 nm (r.i 0.95), 342 (1.00)	Reduced form	1234
		DCB + TBAP	690sh nm (lg ε 4.37), 643 (4.87), 340 (4.82)	Reduced form	1233
		MeCN	689 nm, 631	Reduced form	1231
		MeCN	709 nm, 491	Oxidized form	1231
	Dy(III)	toluene	670 nm (r.i 1.00), 644 (0.42), 605 (0.27), 466 (0.21), 340 (0.80), 324 (0.85)	Neutral form	1234
		DCB	667 nm, 454	Neutral form	1235
		DCB + TBAP	672 nm (lg ε 5.19), 642sh (4.60), 603 (4.55), 478 (4.72), 340 (4.91), 320 (4.97)	Neutral form	1233

(*Continued*)

Table 10. (*Continued*)

Structure	M	Solvent	Transition Energy (Intensity)	Remark	Ref.
		toluene	646 nm (r.i 0.93), 342 (1.00)	Reduced form	1234
		DCB	677 nm, 607	Reduced form	1235
		DCB + TBAP	692sh nm (lg ε 4.30), 642 (4.82), 340 (4.78)	Reduced form	1233
	Ho(III)	toluene	668 nm (r.i 1.00), 642 (0.36), 604 (0.30), 466 (0.26), 341 (0.73), 322 (0.85)	Neutral form	1234
		toluene	703 nm (r.i 0.26), 642 (0.91), 342 (1.00)	Reduced form	1234
		DCB + TBAP	701sh nm (lg ε 4.19), 640 (4.95), 342 (4.92)	Reduced form	1233
	Er(III)	$CHCl_3$	1420 nm (lg ε 3.81), 925 (3.80), 675 (4.81), 600 (4.10), 475 (4.24), 338 (4.81), 309 (4.86)	Neutral form	543
		toluene	667 nm (r.i 1.00), 641 (0.21), 603 (0.24), 465 (0.24), 343 (0.64), 321 (0.76)	Neutral form	1234
		DCB + TBAP	666 nm (lg ε 5.05), 638sh (4.26), 600 (4.35), 464 (4.54), 342 (4.82), 318 (4.87)	Neutral form	1233
		toluene	712 nm (r.i 0.18), 642 (0.88), 342 (1.00)	Reduced form	1234
		DCB + TBAP	704 nm (lg ε 4.17), 638 (4.92), 340 (4.87)	Reduced form	1233
	Tm(III)	toluene	666 nm (r.i 1.00), 639 (0.25), 601 (0.20), 465 (0.19), 344 (0.63), 322 (0.70)	Neutral form	1234
		toluene	713 nm (r.i 0.19), 637 (0.92), 342 (1.00)	Reduced form	1234
	Yb(III)	toluene	666 nm (r.i 1.00), 644 (0.17), 604 (0.21), 465 (0.22), 344 (0.60), 322 (0.74)	Neutral form	1234
		DCB + TBAP	664 nm (lg ε 5.17), 636sh (4.40), 599 (4.20), 464 (4.52), 342 (4.88), 322 (4.90)	Neutral form	1233
		toluene	716 nm (r.i 0.18), 637 (0.90), 342 (1.00)	Reduced form	1234
		DCB + TBAP	711 nm (lg ε 4.07), 635 (4.90), 340 (4.80)	Reduced form	1233
	Lu(III)	$CHCl_3$	1400 nm, 1264, 926	Neutral form	1226
		toluene	667 nm (r.i 1.00), 638 (0.17), 602 (0.18), 466 (0.20), 344 (0.60), 322 (0.68)	Neutral form	1234
		benzene	662 nm,	Neutral form	510
		MeCN	664 nm	Neutral form	1231
		DCB + TBAP	662 nm (lg ε 5.21), 634sh (4.57), 599 (4.20), 462 (4.49), 342 (4.99), 328 (5.02)	Neutral form	1233
		toluene	722 nm (r.i 0.18), 636 (0.96), 342 (1.00)	Reduced form	1234
		MeCN	702 nm, 624	Reduced form	1231

(*Continued*)

Table 10. (*Continued*)

Structure	M	Solvent	Transition Energy (Intensity)	Remark	Ref.
		DCB	706 nm (r.i. 1), 622 (1.94), 335 (2.48)	Reduced form	1235
		DCB + TBAP	714 nm (lg ε 4.05), 634 (4.84), 340 (4.81)	Reduced form	1233
		MeCN	697 nm, 485	Oxidized form	1231
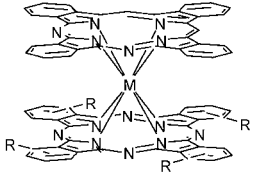	Sm(III)	$CHCl_3$	1855 nm (lg ε 4.80), 926 (5.21), 826 (5.07), 703 (5.09), 665 (5.07), 632 (5.12), 322 (5.24)	R = O(i-C_5H_{11}), Neutral form	1236
	Eu(III)	$CHCl_3$	1770 nm (lg ε 4.20), 1138 (3.59), 929 (3.62), 701 (5.03), 663 (4.98), 630 (5.01), 322 (5.16)	R = O(i-C_5H_{11}), Neutral form	1236
	Gd(III)	$CHCl_3$	1712 nm (lg ε 4.05), 930 (3.47), 698 (4.87), 661 (4.74), 628 (4.79), 323 (4.94)	R = O(i-C_5H_{11}), Neutral form	1236
	Zr(IV)	DMF	748 nm, 630	R = Cl, Neutral form	510
		benzene	750 nm, 628	R = Cl, Neutral form	510
		DMF	748 nm, 631	R = Br, Neutral form	510
		benzene	751 nm, 629	R = Br, Neutral form	510
		DMF	750 nm, 630	R = I, Neutral form	510
		benzene	751 nm, 629	R = I, Neutral form	510
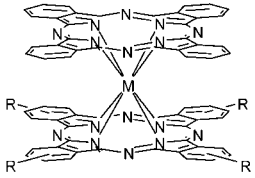	Y(III)	DMF	683 nm, 622	R = Cl, Neutral form	510
	Zr(IV)	DMF	750 nm, 630	R = Cl, Neutral form	510
		benzene	751 nm, 630	R = Cl, Neutral form	510
		DMF	751 nm, 629	R = Br, Neutral form	510
		benzene	753 nm, 630	R = Br, Neutral form	510
	Er(III)	DMF	682 nm, 620	R = Br, Neutral form	510
	Zr(IV)	DMF	747 nm, 629	R = I, Neutral form	510
		benzene	749 nm, 629	R = I, Neutral form	510
	Lu(III)	benzene	660 nm	R = t-Bu, Neutral form	510
		Toluene	676 nm, 612, 346	R = t-Bu, Neutral form	1237
		DMF	715 nm, 632	R = NO_2, Neutral form	510

(*Continued*)

Table 10. (*Continued*)

Structure	M	Solvent	Transition Energy (Intensity)	Remark	Ref.
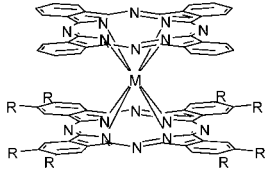	Y(III)	$CHCl_3$	1523 nm, 1424, 921, 672, 605, 485, 344sh, 323	R = C_7H_{15}, Neutral form	92
	Eu(III)	$CHCl_3$	1596 nm, 1443, 915, 679 (lg ε 5.01), 612 (4.35), 495 (4.33), 325 (4.88)	R = C_7H_{15}, Neutral form	1238
	Y(III)	$CHCl_3$	1549 nm, 1410, 916, 668, 604, 485, 366sh, 332	R = OC_5H_{11}, Neutral form	92
	Eu(III)	$CHCl_3$	1592 nm, 1414, 907, 676 (lg ε 4.82), 609 (4.17), 491 (4.32), 334 (4.77)	R = OC_5H_{11}, Neutral form	1238
		$CHCl_3$	1612 nm (lg ε 4.18), 1399 (3.94), 909 (3.70), 676 (5.27), 609 (4.63), 485 (4.54), 350 (5.02), 326 (5.15)	R = OPh, Neutral form	1239
	Ho(III)	$CHCl_3$	1609 nm (lg ε 3.93), 1410 (4.18), 917 (3.76), 669 (5.31), 604 (4.59), 472 (4.50), 349 (4.99), 323 (5.11)	R = OPh, Neutral form	1239
	Lu(III)	$CHCl_3$	1526 nm (lg ε 3.82), 1410 (4.19), 913 (3.85), 665 (5.34), 600 (4.57), 466 (4.52), 347 (5.02), 321 (5.11)	R = OPh, Neutral form	1239
	Eu(III)	$CHCl_3$	1858 nm (lg ε 3.87), 1658 (4.11), 924 (3.62), 694 (5.25), 624 (4.68), 452 (4.54), 327 (5.08)	R = SPh, Neutral form	1239
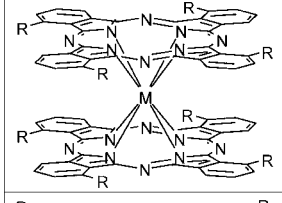	Y(III)	$CHCl_3$	1816 nm (lg ε 4.20), 945 (3.57), 713 (5.11), 632 (4.99), 454sh, 377sh, 306 (5.00)	R = 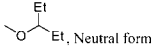	1240
	Eu(III)	$CHCl_3$	2052 nm (lg ε 4.17), 943 (3.40), 724 (5.00), 639 (5.03), 453sh, 382sh, 305 (4.98)	R = 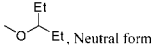	1240
	Lu(III)	$CHCl_3$	1666 nm (lg ε 4.21), 946 (3.72), 707 (5.19), 628 (4.96), 456sh, 370sh, 305 (5.02)	R = 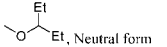	1240
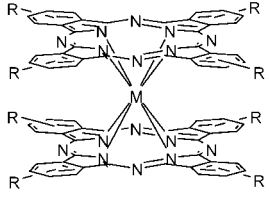	Lu(III)	DMF	720 nm, 650	R = NH_2, Neutral form	1231
		DMF	727 nm	R = NH_2, Reduced form	1231
	Er(III)	DMF	721 nm, 651	R = NH_2, Neutral form	1231
		DMF	726 nm	R = NH_2, Reduced form	1231
	Dy(III)	DMF	695 nm, 645	R = NH_2, Neutral form	1231
		DMF	696 nm	R = NH_2, Reduced form	1231
	Er(III)	DMF	693 nm, 634	R = NO_2, Neutral form	1231
		DMF	706 nm	R = NO_2, Reduced form	1231
		DMF	652 nm	R = NO_2, Oxidized form	1231
	Lu(III)	DMF	692 nm, 638	R = NO_2, Neutral form	1231
		DMF	705 nm	R = NO_2, Reduced form	1231

(*Continued*)

Table 10. (*Continued*)

Structure	M	Solvent	Transition Energy (Intensity)	Remark	Ref.
		DMF	645 nm	R = NO_2, Oxidized form	1231
	Er(III)	$CHCl_3$	1450 nm (lg ε 3.87), 955 (4.40), 678 (4.99), 600 (4.63), 450 (4.74), 360 (5.10), 310 (5.13)	R = OC_5H_{11}, Neutral form	543
	Pr(III)	THF	688 nm (10.2), 653 (2.2), 595 (3.0), 533 (3.5), 442 (2.80), 354 (8.2)	R = $SC_6H_{12}OH$, Neutral form	1241
	Yb(III)	THF	687 nm (8.54), 654 (3.2), 620 (3.4), 512 (3.2), 421 (3.0), 355 (5.3)	R = $SC_6H_{12}OH$, Neutral form	1241
	Lu(III)	THF	686 nm (11.6), 650 (3.1), 616 (2.3), 508 (1.7), 354 (8.0)	R = $SC_6H_{12}OH$, Neutral form	1241
		DMSO	705 nm (lg ε 4.82), 635 (4.23), 440 (4.33), 377 (4.74)	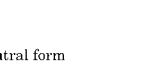 R = , Neutral form	1242
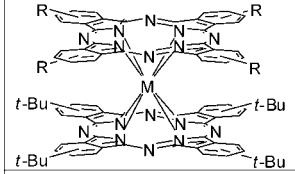	Er(III)	DMF	680 nm, 630	R = Cl, Neutral form	510
		benzene	667 nm	R = Cl, Neutral form	510
	Lu(III)	DCM	666 nm, 487, 342, 324	R = Cl, Neutral form	1243
	Er(III)	DMF	694 nm, 630	R = Br, Neutral form	510
		benzene	667 nm	R = Br, Neutral form	510
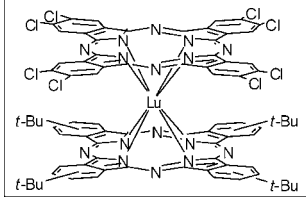	Lu(III)	DCM	670 nm, 602, 474	Neutral form	1243

(*Continued*)

Table 10. (*Continued*)

Structure	M	Solvent	Transition Energy (Intensity)	Remark	Ref.
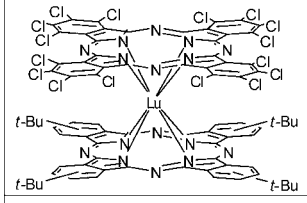	Lu(III)	DCM	694 nm, 500, 330	Neutral form	1243
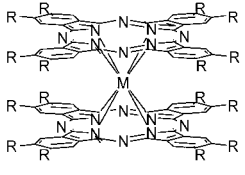	Eu(III)	toluene	680 nm, 647, 343	R = Me, Neutral form	1229
		toluene	647 nm	R = Me, Reduced form	1229
	Tb(III)	DCB	678 nm	R = Me, Neutral form	1231
		DCB	693 nm, 638	R = Me, Reduced form	1231
		DCB	714 nm, 503	R = Me, Oxidized form	1231
	Lu(III)	DCB	672 nm, 641sh, 606, 583sh, 473, 350	R = Me, Neutral form	1232
		DCB	672 nm	R = Me, Neutral form	1231
		DCB	702 nm, 632, 575sh, 343	R = Me, Reduced form	1232
		DCB	704 nm, 634	R = Me, Reduced form	1231
		DCB	704 nm, 636, 493, 359	R = Me, Oxidized form	1232
		DCB	704 nm, 494	R = Me, Oxidized form	1231
	Eu(III)	$CHCl_3$	687 nm, 617, 491, 355, 329	R = Et, Neutral form	1244
	Dy(III)	$CHCl_3$	681 nm, 612, 483, 354, 328	R = Et, Neutral form	1244
	Er(III)	$CHCl_3$	678 nm, 611, 480, 352, 327	R = Et, Neutral form	513
	Lu(III)	$CHCl_3$	675 nm, 608, 476, 350, 325	R = Et, Neutral form	1244
		DCB	673 nm, 644, 606, 584sh, 479, 351	R = Et, Neutral form	1232
		DCB	712 nm, 632, 575sh, 521, 344	R = Et, Reduced form	1232
		DCB	707 nm, 636, 493, 361	R = Et, Oxidized form	1232
	Ce(III)	DCM	584 nm (lg ε 4.87), 470 (4.12), 326 (5.01)	R = Pr, Neutral form	1245
	Eu(III)	DCM	783 nm (lg ε 3.31), 595 (4.52), 320 (4.96)	R = Pr, Neutral form	1245
	Lu(III)	DCM	789 nm (lg ε 3.57), 588 (4.77), 496 (4.03), 318 (5.16)	R = Pr, Neutral form	1245
	Eu(III)	$CHCl_3$	690 nm, 618, 494, 357, 330	R = Bu, Neutral form	1244
		DCB	691 nm, 661sh, 617, 602sh, 494, 357	R = Bu, Neutral form	1232
		DCB	698sh nm, 651, 587sh, 548, 347	R = Bu, Reduced form	1232
		DCB	732 nm, 648, 507, 366	R = Bu, Oxidized form	1232

(*Continued*)

Table 10. (*Continued*)

Structure	M	Solvent	Transition Energy (Intensity)	Remark	Ref.
	Dy(III)	$CHCl_3$	684 nm, 615, 485, 354, 328	R = Bu, Neutral form	1244
		DCB	684 nm, 652sh, 614, 595sh, 489, 355	R = Bu, Neutral form	1232
		DCB	707sh nm, 646, 585sh, 539, 345	R = Bu, Reduced form	1232
		DCB	721 nm, 644, 504, 365	R = Bu, Oxidized form	1232
	Er(III)	$CHCl_3$	680 nm, 612, 481, 353, 329	R = Bu, Neutral form	513
	Lu(III)	DCB	674 nm, 644sh, 608, 585sh, 478, 351	R = Bu, Neutral form	1232
		$CHCl_3$	677 nm, 610, 479, 352, 325	R = Bu, Neutral form	1244
		DCB	711 nm, 637, 578sh, 530, 345	R = Bu, Reduced form	1232
		DCB	709 nm, 636, 494, 361	R = Bu, Oxidized form	1232
	Y(III)	$CHCl_3$	1583 nm, 1449, 932, 682, 613, 486, 353, 328	R = C_7H_{15}, Neutral form	92
	Eu(III)	$CHCl_3$	1677br nm, 922br, 690 (lg ε 5.09), 618 (4.54), 497 (4.47), 357 (4.94), 331 (5.03)	R = C_7H_{15}, Neutral form	548
	Gd(III)	$CHCl_3$	1633br nm, 925br, 686 (lg ε 5.09), 616 (4.49), 492 (4.47), 355 (4.92), 329 (4.99)	R = C_7H_{15}, Neutral form	548
	Ce(IV)	Toluene	697 nm, 644, 472, 358	R = C_8H_{17}, Neutral form	1246
	Sm(III)	$CHCl_3$	680 nm	R = OPr, Neutral form	681
		DCB	674 nm, 643sh, 613, 586sh, 494, 374	R = OPr, Neutral form	1247
		DCB	684 nm, 634, 583sh, 365	R = OPr, Reduced form	1247
		DCB	724 nm, 640sh, 520, 391	R = OPr, Oxidized form	1247
	Tm(III)	DCB	666 nm, 640sh, 603, 581sh, 480, 369	R = OPr, Neutral form	1247
		DCB	700 nm, 626, 596sh, 363	R = OPr, [Reduced form	1247
		DCB	701 nm, 634sh, 502, 389	R = OPr, Oxidized form	1247
	Lu(III)	$CHCl_3$	660 nm	R = OPr, Neutral form	681
		DCB	664 nm, 634sh, 600, 576sh, 481, 367	R = OPr, Neutral form	1247
		DCB	702 nm, 624, 570sh,361	R = OPr, Reduced form	1247
		DCB	697 nm, 632sh, 499, 387	R = OPr, Oxidized form	1247
	Y(III)	$CHCl_3$	1578 nm, 1427, 916, 672, 608, 484, 369, 335	R = OC_5H_{11}, Neutral form	92
	Sm(III)	$CHCl_3$	675 nm	R = OC_5H_{11}, Neutral form	681
		DCB	675 nm	R = OC_5H_{11}, Neutral form	1231
		DCB	684 nm, 633	R = OC_5H_{11}, Reduced form	1231
		DCB	718 nm, 520	R = OC_5H_{11}, Oxidized form	1231
	Eu(III)	$CHCl_3$	1693br nm, 906br, 679 (lg ε 5.01), 613 (4.43), 492 (4.51), 371 (4.96), 337 (4.89)	R = OC_5H_{11}, Neutral form	548

(*Continued*)

Table 10. (*Continued*)

Structure	M	Solvent	Transition Energy (Intensity)	Remark	Ref.
	Gd(III)	$CHCl_3$	1674br nm, 911br, 677 (lg ε 5.09), 612 (4.47), 490 (4.54), 371 (5.02), 337 (4.95)	R = OC_5H_{11}, Neutral form	548
	Tm(III)	DCB	678 nm, 626	R = OC_5H_{11}, Reduced form	1231
		DCB	670 nm	R = OC_5H_{11}, Neutral form	1231
		DCB	702 nm, 504	R = OC_5H_{11}, Oxidized form	1231
	Lu(III)	$CHCl_3$	669 nm	R = OC_5H_{11}, Neutral form	681
		DCB	681 nm, 623	R = OC_5H_{11}, Reduced form	1231
		DCB	669 nm	R = OC_5H_{11}, Neutral form	1231
		DCB	701 nm, 502	R = OC_5H_{11}, Oxidized form	1231
	Er(III)	$CHCl_3$	682 nm, 612, 495, 370	R = $OC_{10}H_{21}$, Neutral form	629
	Ce(IV)	$CHCl_3$	1650 nm, 686, 650, 500, 357	R = $OC_{12}H_{25}$, Neutral form	1248
		$CHCl_3$/EtOH = 1:1	647 nm, 358	R = $OC_{12}H_{25}$, Reduced form	1248
		$CHCl_3$	1650 nm, 700, 648, 518, 361	R = $OC_{12}H_{25}$, Oxidized form	1248
	Eu(III)	$CHCl_3$	1654 nm (lg ε 4.05), 909 (3.79), 681 (5.34), 614 (4.76), 500 (4.58), 365 (5.17), 331 (5.20)	R = OPh, Neutral form	1239
	Ho(III)	$CHCl_3$	1617 nm (lg ε 4.07), 1410 (4.28), 917 (3.81), 674 (5.33), 608 (4.68), 492 (4.53), 362 (5.14), 328 (5.13)	R = OPh, Neutral form	1239
	Lu(III)	$CHCl_3$	1526 nm (lg ε 4.01), 1410 (4.28), 911 (3.92), 670 (5.39), 605 (4.69), 484 (4.58), 361 (5.18), 326 (5.15)	R = OPh, Neutral form	1239
	Nd(III)	DCB	676 nm, 646sh, 613, 587sh, 500, 374	R = OCH_2Ph, Neutral form	1249
		DCB	681 nm, 634, 583sh, 358	R = OCH_2Ph, Reduced form	1249
		DCB	719 nm, 644sh, 523, 390	R = OCH_2Ph, Oxidized form	1249
	Sm(III)	$CHCl_3$	675 nm	R = OCH_2Ph, Neutral form	681
		DCB	673 nm, 642sh, 610, 584sh, 493, 371	R = OCH_2Ph, Neutral form	1249
		DCB	684 nm, 632, 581sh, 360	R = OCH_2Ph, Reduced form	1249
		DCB	717 nm, 648sh, 520, 390	R = OCH_2Ph, Oxidized form	1249
	Dy(III)	DCB	665 nm, 635sh, 603, 576sh, 483, 369	R = OCH_2Ph, Neutral form	1249
		DCB	688 nm, 623, 574sh, 362	R = OCH_2Ph, Reduced form	1249
		DCB	702 nm, 636sh, 510, 388	R = OCH_2Ph, Oxidized form	1249
	Lu(III)	$CHCl_3$	662 nm	R = OCH_2Ph, Neutral form	681
		DCB	664 nm, 634sh, 602, 577sh, 476, 369	R = OCH_2Ph, Neutral form	1249
		DCB	705 nm, 623, 571sh, 359	R = OCH_2Ph, Reduced form	1249
		DCB	699 nm, 629sh, 500, 388	R = OCH_2Ph, Oxidized form	1249

(*Continued*)

Table 10. (*Continued*)

Structure	M	Solvent	Transition Energy (Intensity)	Remark	Ref.
	Sm(III)	$CHCl_3$	685 nm, 619, 495, 371	R =  , Neutral form	681
	Eu(III)	$CHCl_3$	683 nm, 617, 495, 371	R =  , Neutral form	681
	Dy(III)	$CHCl_3$	679 nm, 613, 489, 369	R =  , Neutral form	681
	Er(III)	$CHCl_3$	676 nm, 609, 485, 369	R =  , Neutral form	681
	Lu(III)	$CHCl_3$	673 nm, 603, 481, 368	R =  , Neutral form	681
		$CHCl_3$	675.8 nm (lg ε 5.35), 649.4 (4.76), 609.0 (4.70), 460.4 (4.64), 356.3 (5.18), 328.6 (5.19), 288.2 (5.21)	R = OPh(3,4-(OC_8H_{17})$_2$), Neutral form	1250
		$CHCl_3$	675.5 nm (lg ε 5.25), 646.1 (4.64), 609.3 (4.61), 460.7 (4.55), 355.7 (5.09), 330.4 (5.10), 288.1 (5.12)	R = OPh(3,4-(OC_9H_{19})$_2$), Neutral form	1250
		$CHCl_3$	675.6 nm (lg ε 5.25), 644.9 (4.63), 609.6 (4.60), 460.9 (4.55), 353.8 (5.08), 329.9 (5.10), 289.2 (5.11)	R = OPh(3,4-($OC_{10}H_{21}$)$_2$), Neutral form	1250
		$CHCl_3$	675.0 nm (lg ε 5.30), 646.1 (4.71), 610.3 (4.64), 460.9 (4.58), 355.2 (5.12), 329.6 (5.13), 288.8 (5.14)	R = OPh(3,4-($OC_{11}H_{23}$)$_2$), Neutral form	1250
		$CHCl_3$	674.0 nm (lg ε 5.30), 644.1 (4.71), 608.2 (4.65), 460.1 (4.60), 353.0 (5.13), 328.3 (5.14), 287.9 (5.16)	R = OPh(3,4-($OC_{12}H_{25}$)$_2$), Neutral form	1250
		$CHCl_3$	673.6 nm (lg ε 5.14), 644.4 (4.60), 609.2 (4.52), 460.1 (4.51), 350.9 (5.05), 327.6 (5.08), 287.9 (5.14)	R = OPh(3,4-($OC_{13}H_{27}$)$_2$), Neutral form	1250
		$CHCl_3$	675.2 nm (lg ε 5.27), 647.7 (4.65), 608.9 (4.63), 460.1 (4.57), 356.3 (5.11), 328.2 (5.11), 290.2 (5.14)	R = OPh(3,4-($OC_{14}H_{29}$)$_2$), Neutral form	1250
		$CHCl_3$	675.2 nm (lg ε 5.24), 647.4 (4.66), 610.2 (4.62), 461.3 (4.56), 352.9 (5.10), 329.5 (5.12), 289.6 (5.19)	R = OPh(3,4-($OC_{15}H_{31}$)$_2$), Neutral form	1250
		$CHCl_3$	674.8 nm (lg ε 5.20), 648.0 (4.63), 610.2 (4.59), 461.1 (4.53), 354.1 (5.09), 329.5 (5.08), 287.4 (5.16)	R = OPh(3,4-($OC_{16}H_{32}$)$_2$), Neutral form	1250
	Ce(III)	$CHCl_3$	687 nm (lg ε 5.2), 494 (4.7), 370 (5.0), 312 (5.2)	R = $SC_{18}H_{37}$, Neutral form	1251
	Eu(III)	$CHCl_3$	2030 nm (lg ε 4.12), 1847 (5.00), 949 (3.71), 715 (5.23), 646 (4.88), 450 (4.72), 341 (5.09), 311 (5.12)	R = SPh, Neutral form	1239

(*Continued*)

Table 10. (*Continued*)

Structure	M	Solvent	Transition Energy (Intensity)	Remark	Ref.
	Lu(III)	$CHCl_3$	717 nm (lg ε 4.221), 687 (4.295), 659 (4.022), 625 (3.859), 427 (3.783), 350 (4.193), 307 (4.171)	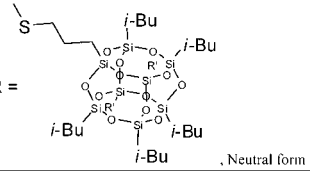 , Neutral form	1252
	Gd(III)	py	703 nm (lg ε 3.607), 656 (3.744), 420 (3.330), 352 (3.809)	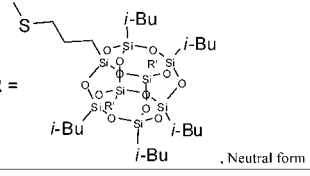 , Neutral form	1252
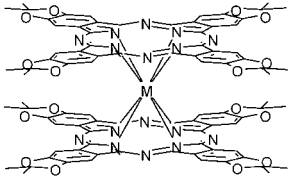	Nd(III)	$CHCl_3$	676 nm, 612, 486, 371, 338	Neutral form	1253
		DCB	900 nm, 672, 639sh, 607, 585sh, 485, 371	Neutral form	1253
	Eu(III)	$CHCl_3$	672 nm, 613, 478, 371, 342	Neutral form	1253
	Tb(III)	$CHCl_3$	671 nm (10^{-4} ε 9.8), 603, 476, 370, 333	Neutral form	1253
		DCB	896 nm, 667, 634sh, 604, 576sh, 475, 371	Neutral form	1253
	Dy(III)	$CHCl_3$	670 nm, 602, 472, 367, 332	Neutral form	1253
	Yb(III)	$CHCl_3$	668 nm, 602, 468, 365, 331	Neutral form	1253
	Lu(III)	$CHCl_3$	665 nm, 601, 465, 363, 330	Neutral form	1253
		DCB	895 nm, 664, 633sh, 602, 574sh, 473, 372	Neutral form	1253
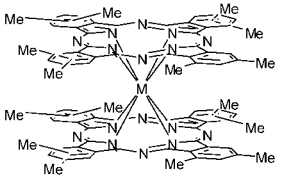	Er(III)	DMF	689 nm	Neutral form	1231
		DMF	703 nm, 639	Reduced form	1231
		DMF	736 nm, 515	Oxidized form	1231
	Tm(III)	DMF	687 nm	Neutral form	1231
		DMF	704 nm, 639	Reduced form	1231
		DMF	734 nm, 514	Oxidized form	1231
	Lu(III)	DMF	685 nm	Neutral form	1231
		DMF	708 nm, 637	Reduced form	1231
		DMF	730 nm, 510	Oxidized form	1231

(*Continued*)

Table 10. (*Continued*)

Structure	M	Solvent	Transition Energy (Intensity)	Remark	Ref.
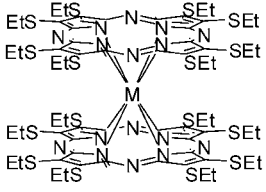	La(III)	$CHCl_3$	704 nm (lg ε 3.86), 658 (3.75), 618sh, 477 (3.4), 349 (4.01)	Neutral form	1254
	Nd(III)	$CHCl_3$	855 nm (lg ε 3.1), 669 (3.73), 617sh, 500 (3.2), 364 (4.40)	Reduced form	1254
	Eu(III)	$CHCl_3$	835 nm (lg ε 3.2), 668 (3.92), 619sh, 548 (3.3), 353 (4.05)	Reduced form	1254
	Dy(III)	$CHCl_3$	824 nm (lg ε 3.1), 662 (3.92), 611sh, 525 (3.4), 358 (4.15)	Reduced form	1254
	Yb(III)	$CHCl_3$	905 nm (lg ε 3.1), 676 (4.2), 629sh, 478 (3.26), 357 (4.33)	Reduced form	1254
	Lu(III)	$CHCl_3$	915 nm (lg ε 3.1), 676 (4.33), 611sh, 488 (3.52), 374 (4.31)	Reduced form	1254
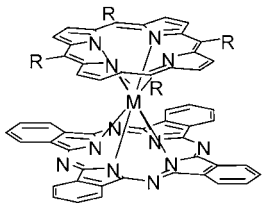	Y(III)	$CHCl_3$	692 nm (r.i. 0.39), 662 (0.58), 606 (0.26), 507 (0.31), 444 (1.00), 429 (0.79), 414 (0.71)	R = Me, Neutral form	1255
		DMF 1% H_2O_2	664 nm (r.i. 0.40), 613 (0.54), 428 (1.00), 413 (0.91)	R = Me, Neutral form	1255
	La(III)	$CHCl_3$	663 nm (r.i. 0.61), 609 (0.45), 443 (0.68), 428 (1.00), 409 (0.78)	R = Me, Neutral form	1255
		DMF 1% H_2O_2	688 nm (r.i. 0.50), 653 (0.56), 603 (0.36), 444 (0.73), 429 (1.00), 416 (0.72)	R = Me, Neutral form	1255
	Er(III)	$CHCl_3$	694 nm (r.i. 0.13), 663 (1.00), 634 (0.18), 599 (0.21), 457 (0.15), 432 (0.20)	R = Me, Neutral form	1255
		DMF 1% H_2O_2	688 nm (r.i. 0.48), 619 (1.00), 561 (0.20), 434 (0.23)	R = Me, Neutral form	1255
	Lu(III)	$CHCl_3$	693 nm (r.i. 0.36), 660 (1.00), 628 (0.21), 595 (0.21), 457 (0.29), 430 (0.24)	R = Me, Neutral form	1255
		DMF 1% H_2O_2	694 nm (r.i. 0.54), 613 (1.00), 562 (0.19), 427 (0.24)	R = Me, Neutral form	1255
		Acetone + 1% H_2O_2	997 nm (r.i. 0.53), 658 (1.00), 475 (0.56)	R = Me, Neutral form	1255
	La(III)	DCM	1535 nm (lg ε 3.38), 965 (3.24), 484 (4.15), 412 (5.37), 324 (4.65)	R = Ph, Neutral form	1256
	Pr(III)	DCM	1469 nm (lg ε 3.36), 968 (3.27), 480 (3.98), 410 (5.28), 325 (4.72)	R = Ph, Neutral form	1256
	Nd(III)	DCM	1434 nm (lg ε 3.43), 995 (3.31), 476 (4.07), 410 (5.39), 326 (4.66)	R = Ph, Neutral form	1256

(*Continued*)

Table 10. (*Continued*)

Structure	M	Solvent	Transition Energy (Intensity)	Remark	Ref.
	Sm(III)	DCM	1384 nm (lg ε 3.60), 996 (3.37), 473 (4.48), 406 (4.89), 324 (4.76)	R = Ph, Neutral form	1257
	Eu(III)	DCM	1375 nm (lg ε 3.53), 1011 (3.35), 473 (4.47), 403 (4.87), 319 (4.79)	R = Ph, Neutral form	1257
	Eu(III)	DCM	1350 nm (lg ε 3.41), 1002 (3.25), 476 (4.13), 408 (5.26), 326 (4.69)	R = Ph, Neutral form	1256
	Gd(III)	DCM	1350 nm (lg ε 3.54), 1020 (3.31), 473 (4.50), 402 (4.88), 316 (4.81)	R = Ph, Neutral form	1257
	Gd(III)	DCM	1321 nm (lg ε 3.39), 1005 (3.21), 472 (3.87), 406 (5.31), 327 (4.71)	R = Ph, Neutral form	1256
	Y(III)	DCM	1285 nm (lg ε 3.37), 1053 (3.23), 472 (4.21), 402 (5.18), 328 (4.65)	R = Ph, Neutral form	1256
	Er(III)	DCM	1255 nm (lg ε 3.35), 1057 (3.19), 470 (3.88), 400 (5.20), 328 (4.71)	R = Ph, Neutral form	1256
	Lu(III)	DCM	1211 nm (lg ε 3.38), 1067 (3.22), 468 (3.97), 396 (5.13), 328 (4.68)	R = Ph, Neutral form	1256
	Y(III)	DCM	843 nm (lg ε 3.64), 648 (3.59), 600 (3.80), 575 (3.73), 480 (4.20), 410 (5.66), 384 (4.48), 338 (4.86)	R = Ph, Reduced form $[NBu_4]^+$	1256
	La(III)	DCM	746 nm (lg ε 3.66), 630 (3.58), 602 (3.85), 576 (3.81), 482 (4.23), 418 (5.78), 380 (4.51), 336 (4.92)	R = Ph, Reduced form $[NBu_4]^+$	1256
	Pr(III)	DCM	770 nm (lg ε 3.64), 636 (3.71), 598 (3.89), 574 (3.80), 479 (4.31), 416 (5.81), 379 (4.58), 336 (4.97)	R = Ph, Reduced form $[NBu_4]^+$	1256
	Nd(III)	DCM	784 nm (lg ε 3.68), 644 (3.65), 604 (3.83), 577 (3.75), 483 (4.27), 414 (5.79), 382 (4.54), 337 (5.01)	R = Ph, Reduced form $[NBu_4]^+$	1256
	Eu(III)	DCM	785 nm (lg ε 3.74), 644 (3.68), 601 (3.81), 578 (3.77), 481 (4.21), 413 (5.68), 381 (4.49), 337 (4.84)	R = Ph, Reduced form $[NBu_4]^+$	1256
	Gd(III)	DCM	788 nm (lg ε 3.64), 638 (3.65), 603 (3.79), 577 (3.74), 478 (4.23), 410 (5.70), 388 (4.52), 335 (4.89)	R = Ph, Reduced form $[NBu_4]^+$	1256
	Er(III)	DCM	843 nm (lg ε 3.70), 649 (3.62), 602 (3.83), 574 (3.71), 479 (4.18), 409 (5.62), 382 (4.48), 336 (4.85)	R = Ph, Reduced form $[NBu_4]^+$	1256
	Lu(III)	DCM	850 nm (lg ε 3.65), 647 (3.69), 606 (3.78), 577 (3.69), 480 (4.21), 410 (5.60), 381 (4.41), 337 (4.80)	R = Ph, Reduced form $[NBu_4]^+$	1256
	La(III)	DCM	1183 nm (lg ε 3.77), 472 (4.39), 406 (5.13), 326 (5.20)	R = Ph, Oxidized form $[SbCl_6]^-$	1256

(*Continued*)

Table 10. (*Continued*)

Structure	M	Solvent	Transition Energy (Intensity)	Remark	Ref.
	Pr(III)	DCM	1140 nm (lg ε 3.81), 470 (4.45), 406 (5.08), 328 (5.12)	R = Ph, Oxidized form $[SbCl_6]^-$	1256
	Nd(III)	DCM	1140 nm (lg ε 3.83), 468 (4.42), 403 (5.10), 326 (5.18)	R = Ph, Oxidized form $[SbCl_6]^-$	1256
	Eu(III)	DCM	1080 nm (lg ε 3.73), 470 (4.36), 402 (5.13), 328 (5.14)	R = Ph, Oxidized form $[SbCl_6]^-$	1256
	Gd(III)	DCM	1072 nm (lg ε 3.70), 467 (4.31), 403 (4.98), 329 (5.08)	R = Ph, Oxidized form $[SbCl_6]^-$	1256
	Y(III)	DCM	1031 nm (lg ε 3.65), 467 (4.38), 400 (4.91), 332 (5.11)	R = Ph, Oxidized form $[SbCl_6]^-$	1256
	Er(III)	DCM	1027 nm (lg ε 3.68), 468 (4.36), 400 (4.94), 332 (5.03)	R = Ph, Oxidized form $[SbCl_6]^-$	1256
	Lu(III)	DCM	1006 nm (lg ε 3.64), 466 (4.37), 397 (4.93), 330 (5.12)	R = Ph, Oxidized form $[SbCl_6]$	1256
	Ce(III)	$CHCl_3$	911 nm, 685, 632, 479, 413, 323	R = Ph(4-*t*-Bu), Neutral form	1248
	Ce(III)	$CHCl_3$/EtOH = 1:1	840 nm, 679, 638, 481, 428, 388, 330	R = Ph(4-*t*-Bu), Reduced form	1248
	Ce(III)	$CHCl_3$	1088 nm, 922, 676, 621, 489, 408, 360	R = Ph(4-*t*-Bu), Oxidized form	1248
	Y(III)	$CHCl_3$	1656 nm (lg ε 3.49), 1238 (3.91), 1034 (3.79), 732 (3.55), 470 (4.70), 401 (5.03), 332 (4.92)	R = Ph(4-Cl), Neutral form	1258
	La(III)	$CHCl_3$	1418 nm (lg ε 3.47), 923 (3.64), 689 (3.47), 492 (4.38), 414 (5.00), 328 (4.77)	R = Ph(4-Cl), Neutral form	1258
	Pr(III)	$CHCl_3$	1376 nm (lg ε 3.68), 954 (3.70), 692 (3.62), 486 (4.53), 411 (5.08), 327 (4.87)	R = Ph(4-Cl), Neutral form	1258
	Nd(III)	$CHCl_3$	1693 nm (lg ε 3.37), 1377 (3.60), 969 (3.61), 725 (3.37), 482 (4.48), 411 (4.99), 328 (4.79)	R = Ph(4-Cl), Neutral form	1258
	Sm(III)	$CHCl_3$	1663 nm (lg ε 3.48), 1330 (3.76), 986 (3.67), 726 (3.41), 467 (4.57), 407 (5.01), 327 (4.83)	R = Ph(4-Cl), Neutral form	1258
	Eu(III)	$CHCl_3$	1662 nm, 1317, 1000, 728, 473, 409, 330	R = Ph(4-Cl), Neutral form	1259
	Eu(III)	$CHCl_3$	1662 nm (lg ε 3.30), 1317 (3.63), 1000 (3.49), 728 (3.31), 473 (4.45), 409 (5.13), 330 (4.73)	R = Ph(4-Cl), Neutral form	1258
	Eu(III)	$CHCl_3$	1311 nm (lg ε 3.43), 995 (2.95), 472 (4.38), 406 (4.76), 326 (4.62)	R = Ph(4-Cl), Neutral form	1260

(*Continued*)

Table 10. (*Continued*)

Structure	M	Solvent	Transition Energy (Intensity)	Remark	Ref.
	Gd(III)	$CHCl_3$	1697 nm (lg ε 3.27), 1282 (3.61), 1008 (3.50), 729 (3.27), 472 (4.44), 404 (4.85), 328 (4.68)	R = Ph(4-Cl), Neutral form	1258
	Tb(III)	$CHCl_3$	1667 nm (lg ε 3.36), 1258 (3.75), 1026 (3.62), 729 (3.39), 470 (4.55), 403 (4.93), 329 (4.77)	R = Ph(4-Cl), Neutral form	1258
	Tb(III)	$CHCl_3$	1273 nm (lg ε 4.76), 1018 (3.60), 470 (4.91), 402 (5.40), 329 (5.21)	R = Ph(4-Cl), Neutral form	1260
	Dy(III)	$CHCl_3$	1658 nm (lg ε 3.55), 1250 (3.95), 1031 (3.83), 730 (3.62), 470 (4.74), 402 (5.10), 331 (4.96)	R = Ph(4-Cl), Neutral form	1258
	Ho(III)	$CHCl_3$	1677 nm (lg ε 3.47), 1233 (4.00), 1042 (3.89), 732 (3.68), 469 (4.80), 402 (5.15), 333 (5.02)	R = Ph(4-Cl), Neutral form	1258
	Er(III)	$CHCl_3$	1637 nm (lg ε 3.45), 1228 (3.93), 1054 (3.84), 734 (3.59), 470 (4.70), 400 (5.04), 333 (4.92)	R = Ph(4-Cl), Neutral form	1258
	Tm(III)	$CHCl_3$	1631 nm (lg ε 3.37), 1211 (3.88), 1069 (3.81), 734 (3.54), 470 (4.64), 400 (4.97), 334 (4.86)	R = Ph(4-Cl), Neutral form	1258
	Yb(III)	$CHCl_3$	1623 nm (lg ε 3.40), 1161 (3.94), 1070 (3.87), 736 (3.60), 470 (4.68), 399 (4.99), 334 (4.89)	R = Ph(4-Cl), Neutral form	1258
	Lu(III)	$CHCl_3$	1587 nm (lg ε 3.40), 1148 (3.97), 1089 (3.95), 738 (3.61), 470 (4.69), 398 (4.99), 334 (4.90)	R = Ph(4-Cl), Neutral form	1258
	Ce(III)	$CHCl_3$	832 nm, 633, 526, 465, 438, 398, 331	R = 4-py, Neutral form	1248
	Ce(III)	$CHCl_3$/EtOH = 1:1	763 nm, 626, 583, 483, 419, 382, 334	R = 4-py, Reduced form	1248
	Ce(III)	$CHCl_3$	831 nm, 692, 673, 635, 497, 399, 332	R = 4-py, Oxidized form	1248
	Eu(III)	$CHCl_3$	1218 nm, 978, 467, 403, 324	R = 4-py, Neutral form	1261
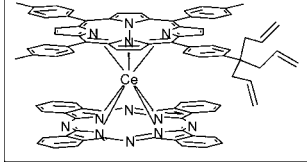	Ce(III)	Toluene	818 nm, 620, 569, 471, 403, 334	Neutral form	1162

(*Continued*)

Table 10. (*Continued*)

Structure	M	Solvent	Transition Energy (Intensity)	Remark	Ref.
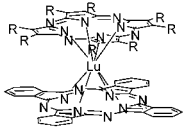	Lu(III)	DMF	679 nm, 613	R = OPh, Neutral form	510
		Benzene	662 nm, 649	R = OPh, Neutral form	510
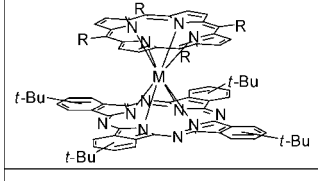	Ce(III)	Toluene	628 nm, 470, 403, 338	R = Ph(4-Me), Neutral form	1246
		Toluene	629 nm, 586, 469, 402, 336	R = C_5H_{11}, Neutral form	1246
	Lu(III)	1-methyl-2-pyrolidone	649 nm, 551, 515, 420	R = Ph(4-*t*-Bu), Neutral form	1262
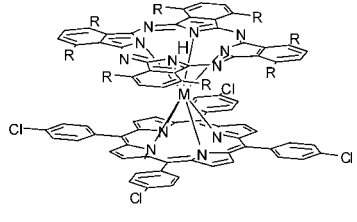	Y(III)	$CHCl_3$	1174 nm (lg ε 2.78), 1033 (2.94), 646 (3.25), 590 (3.48), 538 (3.49), 470 (3.56), 406 (4.09), 309 (3.90)	R = OC_5H_{11}, reduced form	1263
	Sm(III)	$CHCl_3$	1220 nm (lg ε 2.70), 989 (2.96), 679 (3.15), 596 (3.47), 551 (3.46), 469 (3.58), 410 (4.14), 310 (3.89)	R = OC_5H_{11}, reduced form	1263
	Eu(III)	$CHCl_3$	1211 nm (lg ε 2.71), 998 (2.94), 671 (3.17), 594 (3.46), 547 (3.46), 469 (3.57), 409 (4.11), 310 (3.88)	R = OC_5H_{11}, reduced form	1263
	Y(III)	$CHCl_3$	944 nm (lg ε 3.09), 849 (3.03), 617 (3.59), 576 (3.24), 490 (3.84), 413 (4.35), 315 (3.83)	R = OC_5H_{11}, $[Pc]^-H^+$	1263
	Sm(III)	$CHCl_3$	898 nm (lg ε 3.14), 849 (3.13), 613 (3.52), 567 (3.23), 492 (3.73), 416 (4.36), 315 (3.81)	R = OC_5H_{11}, $[Pc]^-H^+$	1263
	Eu(III)	$CHCl_3$	907 nm (lg ε 3.13), 849 (3.11), 614 (3.53), 569 (3.23), 492 (3.74), 415 (4.35), 315 (3.81)	R = OC_5H_{11}, $[Pc]^-H^+$	1263
	Y(III)	$CHCl_3$	954 nm (lg ε 4.20), 848sh, 627 (4.56), 571 (4.20), 498 (4.75), 418 (5.40), 323 (4.85)	R = OC_4H_9, Neutral form	1263
	Eu(III)	$CHCl_3$	928 nm, 623, 499, 419, 324	R = OC_4H_9, Neutral form	1264
		$CHCl_3$	624 nm, 499, 420, 324	R = OC_4H_9, Neutral form	1259

(*Continued*)

Table 10. (*Continued*)

Structure	M	Solvent	Transition Energy (Intensity)	Remark	Ref.
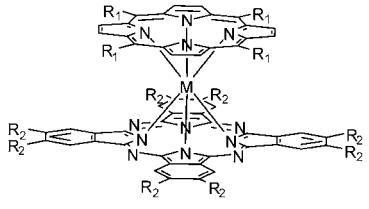	Eu(III)	$CHCl_3$	1307 nm (lg ε 3.65), 993 (3.44), 500 (4.46), 469 (4.45), 409 (4.84), 364 (4.70)	R_1 = Ph(4-$OC_{12}H_{25}$), R_2 = OC_8H_{17}, Neutral form	1260
		$CHCl_3$	1276 nm, 1003, 470, 407, 332	R_1 = Ph(4-Cl), R_2 = OPh(4-OMe) , Neutral form	1259
		$CHCl_3$	1857 nm, 1393, 1041, 715, 644, 491, 416, 328	R_1 = Ph(4-Cl), R_2 = SPh, Neutral form	1259
	Tb(III)	$CHCl_3$	1285 nm (lg ε 4.22), 1018 (3.66), 490 (4.69), 466 (4.67), 405 (5.02), 365 (4.93)	R_1 = Ph(4-$OC_{12}H_{25}$), R_2 = OC_8H_{17}, Neutral form	1260
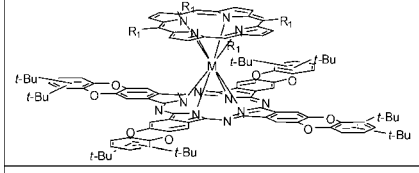	Eu(III)	$CHCl_3$	737 nm, 632, 495, 417, 381, 315	R_1 = Ph(4-Cl) , Neutral form	
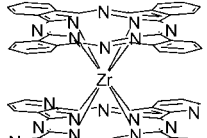	Zr(IV)	DMF	747 nm, 628	Neutral form	510
		Benzene	749 nm, 627	Neutral form	510
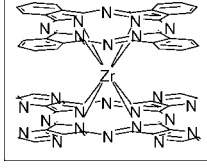	Zr(IV)	DMF	746 nm, 628	Neutral form	510
		Benzene	749 nm, 627	Neutral form	510

(*Continued*)

Table 10. (*Continued*)

Structure	M	Solvent	Transition Energy (Intensity)	Remark	Ref.
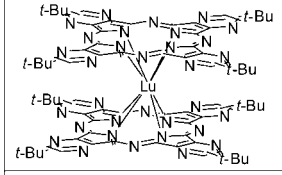	Lu(III)	$CHCl_3$	681 nm, 573, 333	Neutral form	1114
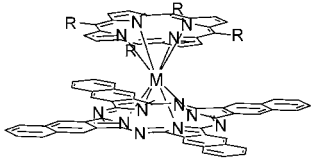	Y(III)	$CHCl_3$	1131 nm (lg ε 4.09), 614 (4.57), 552 (4.58), 479 (4.45), 419 (5.11), 326 (4.91)	R = Ph(4-*t*-Bu), Neutral form	1265
	La(III)	$CHCl_3$	1025 nm (lg ε 4.10), 635 (4.67), 583 (4.57), 482 (4.40), 424 (5.19), 323 (4.95)	R = Ph(4-*t*-Bu), Neutral form	1265
	Pr(III)	$CHCl_3$	1053 nm (lg ε 4.16), 630 (4.69), 579 (4.62), 480 (4.47), 421 (5.24), 329 (4.96)	R = Ph(4-*t*-Bu), Neutral form	1265
	Nd(III)	$CHCl_3$	1064 nm (lg ε 4.10), 628 (4.65), 574 (4.59), 481 (4.46), 419 (5.27), 327 (4.94)	R = Ph(4-*t*-Bu), Neutral form	1265
	Sm(III)	$CHCl_3$	1084 nm (lg ε 4.10), 622 (4.63), 563 (4.59), 481 (4.47), 419 (5.21), 325 (4.94)	R = Ph(4-*t*-Bu), Neutral form	1265
	Eu(III)	$CHCl_3$	1096 nm (lg ε 4.09), 621 (4.60), 561 (4.58), 480 (4.45), 417 (5.08), 326 (4.91)	R = Ph(4-*t*-Bu), Neutral form	1265
	Gd(III)	$CHCl_3$	1104 nm (lg ε 4.17), 620 (4.69), 558 (4.67), 481 (4.54), 417 (5.17), 327 (5.00)	R = Ph(4-*t*-Bu), Neutral form	1265
	Tb(III)	$CHCl_3$	1120 nm (lg ε 4.14), 617 (4.66), 555 (4.64), 489 (4.52), 417 (5.13), 323 (4.98)	R = Ph(4-*t*-Bu), Neutral form	1265
	Dy(III)	$CHCl_3$	1131 nm (lg ε 4.08), 616 (4.58), 555 (4.69), 480 (4.46), 417 (5.12), 327 (4.92)	R = Ph(4-*t*-Bu), Neutral form	1265
	Ho(III)	$CHCl_3$	1132 nm (lg ε 4.00), 615 (4.50), 553 (4.52), 480 (4.38), 416 (5.17), 327 (4.84)	R = Ph(4-*t*-Bu), Neutral form	1265
	Er(III)	$CHCl_3$	1139 nm (lg ε 4.06), 613 (4.55), 550 (4.56), 481 (4.44), 414 (5.03), 327 (4.90)	R = Ph(4-*t*-Bu), Neutral form	1265
	Tm(III)	$CHCl_3$	1146 nm (lg ε 4.10), 612 (4.55), 549 (4.58), 482 (4.44), 415 (5.01), 328 (4.89)	R = Ph(4-*t*-Bu), Neutral form	1265
	Eu(III)	$CHCl_3$	1084 nm, 893, 630, 488, 416, 324	R = 4-py, Neutral form	1261

(*Continued*)

Table 10. (*Continued*)

Structure	M	Solvent	Transition Energy (Intensity)	Remark	Ref.
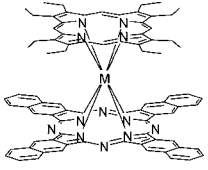	Y(III)	$CHCl_3$	1308 nm (lg ε 4.11), 772 (3.80), 658sh, 596 (4.67), 530 (4.23), 399 (4.93), 327 (4.99)	Neutral form	1266
	La(III)	$CHCl_3$	1816 nm (lg ε 3.46), 1091 (3.62), 745sh, 712sh, 612 (4.48), 554sh, 404 (4.80), 327 (4.73)	Neutral form	1266
	Ce(III)	$CHCl_3$	935 nm, 660, 610, 467, 392, 324	Neutral form	1248
		$CHCl_3$/EtOH = 1:1	853 nm, 741sh, 648, 601sh, 478, 406, 330	Reduced form	1248
		$CHCl_3$	1200 nm, 618, 452, 384, 322	Oxidized form	1248
	Pr(III)	$CHCl_3$	1719 nm (lg ε 3.72), 1139 (3.79), 743sh, 703sh, 607 (4.65), 547sh, 402 (4.92), 327 (4.91)	Neutral form	1266
	Nd(III)	$CHCl_3$	1642 nm (lg ε 3.76), 1157 (3.81), 749sh, 686 (4.07), 605 (4.66), 545sh, 403 (4.94), 327 (4.94)	Neutral form	1266
	Sm(III)	$CHCl_3$	1561 nm (lg ε 3.83), 1189 (3.98), 752sh, 694sh, 603 (4.78), 540sh, 401 (4.98), 328 (5.04)	Neutral form	1266
	Eu(III)	$CHCl_3$	1542 nm (lg ε 3.76), 1196 (3.85), 757sh, 684sh, 601 (4.68), 539 (4.36), 401 (4.89), 326 (4.98)	Neutral form	1266
	Gd(III)	$CHCl_3$	1522 nm (lg ε 3.87), 1208 (3.97), 754sh, 684sh, 677sh, 600 (4.76), 536 (4.47), 400 (4.98), 327 (5.04)	Neutral form	1266
	Tb(III)	$CHCl_3$	1480 nm (lg ε 3.87), 1223 (3.92), 760sh, 676sh, 598 (4.74), 535 (4.47), 400 (4.99), 326 (5.05)	Neutral form	1266
	Dy(III)	$CHCl_3$	1463 nm (lg ε 3.86), 1251 (3.90), 766 (3.64), 668 (4.19), 597 (4.63), 530 (4.42), 399 (4.93), 325 (4.97)	Neutral form	1266
	Ho(III)	$CHCl_3$	1287 nm (lg ε 4.06), 771 (3.83), 662 (4.35), 597 (4.76), 528 (4.57), 400 (5.06), 325 (5.10)	Neutral form	1266
	Er(III)	$CHCl_3$	1319 nm (lg ε 4.11), 772 (3.80), 658 (4.37), 595 (4.75), 525 (4.58), 399 (5.07), 324 (5.11)	Neutral form	1266
	Tm(III)	$CHCl_3$	1328 nm (lg ε 3.97), 775 (3.64), 657 (4.21), 594 (4.58), 525 (4.42), 398 (4.90), 324 (4.95)	Neutral form	1266
	Yb(III)	$CHCl_3$	1331 nm (lg ε 3.95), 778 (3.68), 655 (4.18), 595 (4.48), 524 (4.37), 400 (4.87), 324 (4.90)	Neutral form	1266
	Lu(III)	$CHCl_3$	1336 nm (lg ε 3.89), 779 (3.57), 654 (4.15), 591 (4.51), 522 (4.37), 398 (4.85), 324 (4.93)	Neutral form	1266

(*Continued*)

Table 10. (*Continued*)

Structure	M	Solvent	Transition Energy (Intensity)	Remark	Ref.
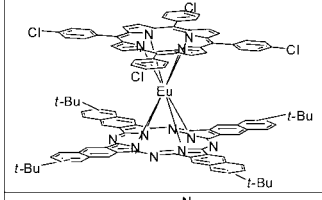	Eu(III)	$CHCl_3$	1072 nm (lg ε 4.24), 642 (4.67), 555 (4.52), 479 (4.52), 419 (5.20), 334 (4.97)	Neutral form	1265
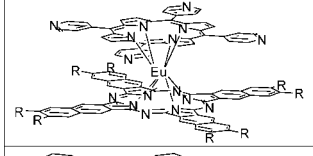	Eu(III)	$CHCl_3$	1094 nm, 899, 659, 497, 419, 352, 317	R = $SC_{12}H_{25}$, Neutral form	1261
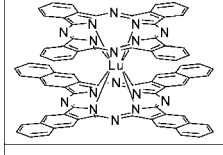	Lu(III)	DCM	987 nm (lg ε 3.91), 706 (4.96), 632 (4.63), 326 (5.05)	Neutral form	1048
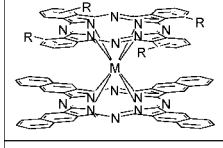	Y(III)	$CHCl_3$	1753 nm (lg ε 3.18), 1004 (2.75), 740 (4.17), 650 (3.86), 600 (3.63), 483 (3.48), 322 (4.13)	R = OC_5H_{11}, Neutral form	1267
	Sm(III)	$CHCl_3$	1965 nm (lg ε 2.54), 994 (2.57), 753 (4.01), 656 (3.95), 610 (3.67), 435 (3.48), 323 (4.08)	R = OC_5H_{11}, Neutral form	1267
	Eu(III)	$CHCl_3$	1917 nm (lg ε 3.16), 997 (2.62), 750 (4.09), 655 (3.95), 607 (3.68), 436 (3.50), 323 (4.12)	R = OC_5H_{11}, Neutral form	1267
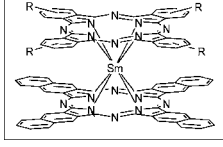	Sm(III)	$CHCl_3$	1709 nm (lg ε 4.01), 972 (3.63), 728 (4.93), 639 (4.72), 602 (4.56), 419 (4.56), 333 (5.04), 303 (4.92)	R = OC_5H_{11}, Neutral form	1267

(*Continued*)

Table 10. (*Continued*)

Structure	M	Solvent	Transition Energy (Intensity)	Remark	Ref.
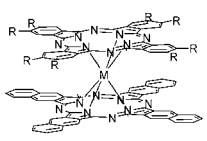	Sm(III)	$CHCl_3$	1760 nm (lg ε 4.45), 982 (4.03), 735 (5.35), 645 (5.22), 603 (4.94), 440 (4.79), 331 (5.47), 302 (5.30)	R = OC_8H_{17}, Neutral form	1267
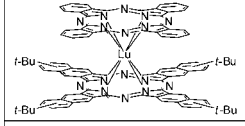	Sm(III)	$CHCl_3$	1667 nm (lg ε 4.25), 972 (3.99), 723 (5.38), 646 (5.21), 442 (4.64), 339 (5.31)	R_1, R_2 = H, R_3 = *t*-Bu, Neutral form	1267
	Lu(III)	Benzene	776 nm, 654	Neutral form	510
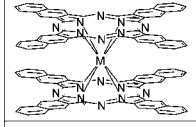	Lu(III)	DCM	1089 nm (lg ε 4.48), 760 (5.07), 680 (4.48), 572 (4.47), 328 (5.03)	Neutral form	1048
		Benzene	761 nm	Neutral form	510
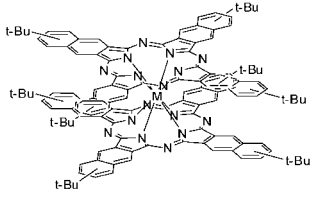	Y(III)	$CHCl_3$/EtOH = 1:1	1822sh nm, 1666, 1081, 769, 686, 597, 443sh, 330	Neutral form	105, 1268
		$CHCl_3$/EtOH = 1:1	821 nm, 719, 657sh, 401sh, 332	Reduced form	105
		$CHCl_3$: MeOH = 1:1	821 nm, 719, 657, 401sh, 332	Reduced form	1268
	La(III)	$CHCl_3$/EtOH = 1:1	2346 nm, 1052, 799, 694, 648, 437sh, 334	Neutral form	105
		$CHCl_3$: MeOH = 1:1	2280 nm, 1054, 799, 694, 649, 437sh, 334	Neutral form	1268
		$CHCl_3$/EtOH = 1:1	729 nm, 663, 400sh, 333	Reduced form	105, 1268
	Ce(III)	$CHCl_3$/EtOH = 1:1	2190 nm, 1055, 790, 691, 640, 435sh, 332	Neutral form	105
		$CHCl_3$/EtOH = 1:1	782sh nm, 727, 658, 410sh, 330	Reduced form	105
	Pr(III)	$CHCl_3$/EtOH = 1:1	2129 nm, 1057, 786, 691, 637, 437sh, 331	Neutral form	105, 1268
		$CHCl_3$/EtOH = 1:1	783sh nm, 726, 662, 417sh, 328	Reduced form	105
		$CHCl_3$: MeOH = 1:1	783 nm, 726, 662, 417sh, 328	Reduced form	1268
	Nd(III)	$CHCl_3$/EtOH = 1:1	2041 nm, 1681, 1062, 783, 690, 633, 438sh, 332	Neutral form	105, 1268
		$CHCl_3$/EtOH = 1:1	787sh nm, 725, 659, 419sh, 333	Reduced form	105
		$CHCl_3$: MeOH = 1:1	787 nm, 725, 659, 419sh, 333	Reduced form	1268
	Sm(III)	$CHCl_3$: MeOH = 1:1	1990 nm, 1678, 1164, 781, 689, 640, 450sh, 325	Neutral form	1268
		$CHCl_3$: MeOH = 1:1	795 nm, 724, 657, 418sh, 331	Reduced form	1268
	Eu(III)	$CHCl_3$/EtOH = 1:1	1928 nm, 1674, 1071, 776, 689, 627, 440sh, 331	Neutral form	105

(*Continued*)

Table 10. (*Continued*)

Structure	M	Solvent	Transition Energy (Intensity)	Remark	Ref.
		$CHCl_3$: MeOH = 1:1	1927 nm, 1673, 1071, 779, 688, 632, 441sh, 329	Neutral form	1268
		$CHCl_3$/EtOH = 1:1	799 nm, 721, 654, 413sh, 332	Reduced form	105, 1268
	Gd(III)	$CHCl_3$/EtOH = 1:1	1883 nm, 1674, 1072, 774, 688, 596, 439sh, 328	Neutral form	105
		$CHCl_3$: MeOH = 1:1	1883 nm, 1672, 1073, 772, 688, 590, 439sh, 325	Neutral form	1268
		$CHCl_3$/EtOH = 1:1	802 nm, 719, 649sh, 418sh, 329	Reduced form	105
		$CHCl_3$: MeOH = 1:1	802 nm, 719, 649, 418sh, 329	Reduced form	1268
	Tb(III)	$CHCl_3$/EtOH = 1:1	1864 nm, 1671, 1073, 772, 687, 622, 438sh, 331	Neutral form	105, 1268
		$CHCl_3$/EtOH = 1:1	808 nm, 718, 654sh, 405sh, 332	Reduced form	105
		$CHCl_3$: MeOH = 1:1	808 nm, 718, 654, 405sh, 332	Reduced form	1268
	Dy(III)	$CHCl_3$: MeOH = 1:1	1844sh nm, 1668, 1079, 773, 686, 628, 451sh, 327	Neutral form	1268
		Toluene	785 nm (r.i. 3.15), 742sh (0.74), 694 (0.59), 590 (1), 420sh (0.87), 356sh (1.42), 329 (2.49)	Neutral form	1235
		Toluene/Et_2NH	810 nm (r.i. 1), 741 (4.18), 328 (3.46)	Reduced form	1235
		$CHCl_3$: MeOH = 1:1	815 nm, 719, 652, 408sh, 332	Reduced form	1268
		Toluene/Br_2	825 nm (r.i. 1), 641 (4.88), 323 (12)	Oxidized form	1235
		HOAc/(O_2)	789 nm (r.i. 1), 687 (3.03), 345 (3.91), 323 (5.58)	Oxidized form	1235
	Ho(III)	$CHCl_3$: MeOH = 1:1	1788sh nm, 1664, 1086, 768, 686, 627, 450sh, 330	Neutral form	1268
		$CHCl_3$: MeOH = 1:1	821 nm, 717, 652, 417sh, 333	Reduced form	1268
	Er(III)	$CHCl_3$/EtOH = 1:1	1818sh nm, 1646, 1084, 767, 685, 593, 448sh, 330	Neutral form	105
		$CHCl_3$: MeOH = 1:1	1770sh nm, 1642, 1087, 767, 685, 595, 450sh, 330	Neutral form	1268
		$CHCl_3$/EtOH = 1:1	821 nm, 715, 647sh, 400sh, 333	Reduced form	105
		$CHCl_3$: MeOH = 1:1	821 nm, 715, 647, 400sh, 333	Reduced form	1268
	Tm(III)	$CHCl_3$: MeOH = 1:1	1755sh nm, 1634, 1080, 767, 685, 600, 450sh, 330	Neutral form	1268
		$CHCl_3$: MeOH = 1:1	823 nm, 712, 645, 417sh, 333	Reduced form	1268
	Yb(III)	$CHCl_3$: MeOH = 1:1	1733sh nm, 1623, 1087, 766, 687, 608, 455sh, 333	Neutral form	1268
		$CHCl_3$: MeOH = 1:1	828 nm, 714, 641, 421sh, 333	Reduced form	1268
	Lu(III)	$CHCl_3$: MeOH = 1:1	1719sh nm, 1600, 1062, 767, 685, 611, 452sh, 331	Neutral form	1268
		DCB	758 nm (r.i. 3.68), 720sh (0.73), 678 (1), 582 (1), 328 (2.56)	Neutral form	1235
		DCB	820 nm (r.i. 1), 704 (2.97), 326 (2.72)	Reduced form	1235
		$CHCl_3$: MeOH = 1:1	830 nm, 713, 640, 416sh, 336	Reduced form	1268

(*Continued*)

Table 10. (*Continued*)

Structure	M	Solvent	Transition Energy (Intensity)	Remark	Ref.
		DCB	808 nm (r.i. 1), 616 (1.49), 332 (1.76)	Oxidized form	1235
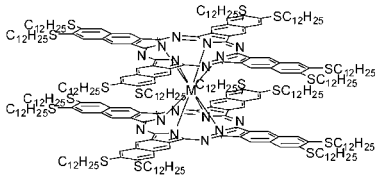	Y(III)	$CHCl_3$	1840 nm (lg ε 4.04), 1654 (4.38), 1093 (3.90), 786 (5.39), 702 (5.13), 366 (5.28)	Neutral form	1269
	Nd(III)	$CHCl_3$	2040 nm (lg ε 3.60), 1675 (3.70), 1054 (3.00), 802 (5.03), 712 (5.07), 358 (5.07)	Neutral form	1269
	Eu(III)	$CHCl_3$	1890 nm (lg ε 4.15), 1668 (4.15), 1070 (3.78), 794 (5.30), 708 (5.19), 360 (5.25)	Neutral form	1269
	Gd(III)	$CHCl_3$	1874 nm (lg ε 3.70), 1665 (3.78), 1070 (2.48), 792 (5.06), 708 (5.02), 342 (5.16)	Neutral form	1269
	Tb(III)	$CHCl_3$	1853 nm (lg ε 4.04), 1660 (4.30), 1074 (3.78), 790 (5.29), 706 (5.11), 362 (5.25)	Neutral form	1269
	Ho(III)	$CHCl_3$	1830 nm (lg ε 3.85), 1650 (4.23), 1092 (3.78), 786 (5.17), 702 (5.08), 366 (5.08)	Neutral form	1269
	Er(III)	$CHCl_3$	1844 nm (lg ε 3.70), 1660 (4.00), 1094 (3.78), 784 (5.18), 703 (5.08), 359 (5.15)	Neutral form	1269
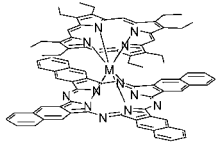	La(III)	$CHCl_3$	1816 nm (lg ε 3.46), 1091 (3.62), 745sh, 712sh, 612 (4.48), 554sh, 404 (4.80), 327 (4.73)	Neutral form	1266
	Ce(III)	$CHCl_3$	935 nm, 660, 610, 467, 392, 324	Neutral form	1248
		$CHCl_3$	*ca.* 1200 nm, 618, 452, 384, 322	Oxidized form	1248
		$CHCl_3$/EtOH = 1:1	853 nm, 741sh, 648, 601sh, 478, 406, 330	Reduced form	1248
	Pr(III)	$CHCl_3$	1719 nm (lg ε 3.72), 1139 (3.79), 743sh, 703sh, 607 (4.65), 547sh, 402 (4.92), 327 (4.91)	Neutral form	1266
	Nd(III)	$CHCl_3$	1642 nm (lg ε 3.76), 1157 (3.81), 749sh, 686 (4.07), 605 (4.66), 545sh, 403 (4.94), 327 (4.94)	Neutral form	1266
	Sm(III)	$CHCl_3$	1561 nm (lg ε 3.83), 1189 (3.98), 752sh, 694sh, 603 (4.78), 540sh, 401 (4.98), 328 (5.04)	Neutral form	1266
	Eu(III)	$CHCl_3$	1542 nm (lg ε 3.76), 1196 (3.85), 757sh, 684sh, 601 (4.68), 539 (4.36), 401 (4.89), 326 (4.98)	Neutral form	1266
	Gd(III)	$CHCl_3$	1522 nm (lg ε 3.87), 1208 (3.97), 754sh, 677sh, 600 (4.76), 536 (4.47), 400 (4.98), 327 (5.04)	Neutral form	1266

(*Continued*)

Table 10. (*Continued*)

Structure	M	Solvent	Transition Energy (Intensity)	Remark	Ref.
	Tb(III)	$CHCl_3$	1480 nm (lg ε 3.87), 1223 (3.92), 760sh, 676sh, 598 (4.74), 535 (4.47), 400 (4.99), 326 (5.05)	Neutral form	1266
	Dy(III)	$CHCl_3$	1463 nm (lg ε 3.86), 1251 (3.90), 766 (3.64), 668 (4.19), 597 (4.63), 530 (4.42), 399 (4.93), 325 (4.97)	Neutral form	1266
	Y(III)	$CHCl_3$	1308 nm (lg ε 4.11), 772 (3.80), 658sh, 596 (4.67), 530 (4.23), 399 (4.93), 327 (4.99)	Neutral form	1266
	Ho(III)	$CHCl_3$	1287 nm (lg ε 4.06), 771 (3.83), 662 (4.35), 597 (4.76), 528 (4.57), 400 (5.06), 325 (5.10)	Neutral form	1266
	Er(III)	$CHCl_3$	1319 nm (lg ε 4.11), 772 (3.80), 658 (4.37), 595 (4.75), 525 (4.58), 399 (5.07), 324 (5.11)	Neutral form	1266
	Tm(III)	$CHCl_3$	1328 nm (lg ε 3.97), 775 (3.64), 657 (4.21), 594 (4.58), 525 (4.42), 398 (4.90), 324 (4.95)	Neutral form	1266
	Yb(III)	$CHCl_3$	1331 nm (lg ε 3.95), 778 (3.68), 655 (4.18), 595 (4.48), 524 (4.37), 400 (4.87), 324 (4.90)	Neutral form	1266
	Lu(III)	$CHCl_3$	1336 nm (lg ε 3.89), 779 (3.57), 654 (4.15), 591 (4.51), 522 (4.37), 398 (4.85), 324 (4.93)	Neutral form	1266
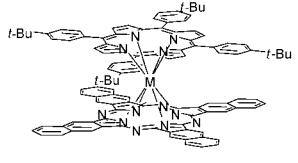	La(III)	$CHCl_3$	1025 nm (lg ε 4.10), 635 (4.67), 583 (4.57), 482 (4.40), 424 (5.19), 323 (4.95)	Neutral form	1265
	Pr(III)	$CHCl_3$	1053 nm (lg ε 4.16), 630 (4.69), 579 (4.62), 480 (4.47), 421 (5.24), 329 (4.96)	Neutral form	1265
	Nd(III)	$CHCl_3$	1064 nm (lg ε 4.10), 628 (4.65), 574 (4.59), 481 (4.46), 419 (5.27), 327 (4.94)	Neutral form	1265
	Sm(III)	$CHCl_3$	1084 nm (lg ε 4.10), 622 (4.63), 563 (4.59), 481 (4.47), 419 (5.21), 325 (4.94)	Neutral form	1265
	Eu(III)	$CHCl_3$	1096 nm (lg ε 4.09), 621 (4.60), 561 (4.58), 480 (4.45), 417 (5.08), 326 (4.91)	Neutral form	1265
	Gd(III)	$CHCl_3$	1104 nm (lg ε 4.17), 620 (4.69), 558 (4.67), 481 (4.54), 417 (5.17), 327 (5.00)	Neutral form	1265
	Tb(III)	$CHCl_3$	1120 nm (lg ε 4.14), 617 (4.66), 555 (4.64), 489 (4.52), 417 (5.13), 323 (4.98)	Neutral form	1265
	Dy(III)	$CHCl_3$	1131 nm (lg ε 4.08), 616 (4.58), 555 (4.69), 480 (4.46), 417 (5.12), 327 (4.92)	Neutral form	1265
	Y(III)	$CHCl_3$	1131 nm (lg ε 4.09), 614 (4.57), 552 (4.58), 479 (4.45), 419 (5.11), 326 (4.91)	Neutral form	1265

(*Continued*)

Table 10. (*Continued*)

Structure	M	Solvent	Transition Energy (Intensity)	Remark	Ref.
	Ho(III)	$CHCl_3$	1132 nm (lg ε 4.00), 615 (4.50), 553 (4.52), 480 (4.38), 416 (5.17), 327 (4.84)	Neutral form	1265
	Er(III)	$CHCl_3$	1139 nm (lg ε 4.06), 613 (4.55), 550 (4.56), 481 (4.44), 414 (5.03), 327 (4.90)	Neutral form	1265
	Tm(III)	$CHCl_3$	1146 nm (lg ε 4.10), 612 (4.55), 549 (4.58), 482 (4.44), 415 (5.01), 328 (4.89)	Neutral form	1265
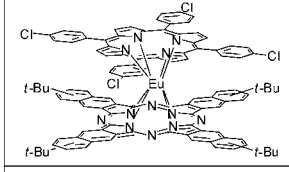	Eu(III)	$CHCl_3$	1072 nm (lg ε 4.24), 642 (4.67), 555 (4.52), 479 (4.52), 419 (5.20), 334 (4.97)	Neutral form	1265
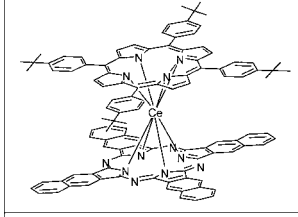	Ce(III)	$CHCl_3$	911 nm, 685, 632, 479, 413, 323	Neutral form	1248
		$CHCl_3$	1088 nm, 922, 676, 621, 489, 408, 360	Oxidized form	1248
		$CHCl_3$/EtOH = 1:1	840 nm, 679, 638, 481, 428, 388, 330	Reduced form	1248
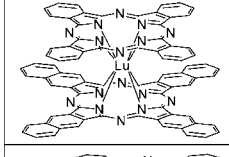	Lu(III)	DCM	987 nm (lg ε 3.91), 706 (4.96), 632 (4.63), 326 (5.05)	Neutral form	1048
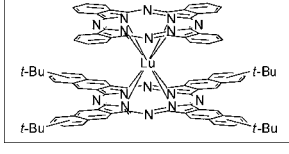	Lu(III)	benzene	776 nm, 654	Neutral form	510
	Lu(III)OAc	benzene	765 nm	Neutral form	510

(*Continued*)

Table 10. (*Continued*)

Structure	M	Solvent	Transition Energy (Intensity)	Remark	Ref.
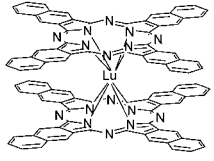	La(III)	$CHCl_3$/EtOH = 1:1	729 nm, 663, 400sh, 333	Reduced form Na^+,γ = *t*-Bu	105
	Ce(IV)	$CHCl_3$ / EtOH = 1:1	782sh nm, 727, 658, 410sh, 330	Na^+,γ = *t*-Bu	105
	Pr(III)	$CHCl_3$/EtOH = 1:11	783sh nm, 726, 662, 417sh, 328	Reduced form Na^+,γ = *t*-Bu	105
	Nd(III)	$CHCl_3$/EtOH = 1:11	787sh nm, 725, 659, 419sh, 333	Reduced form Na^+,γ = *t*-Bu	105
	Eu(III)	$CHCl_3$/EtOH = 1:11	799 nm, 721, 654, 413sh, 332	Reduced form Na^+,γ = *t*-Bu	105
	Gd(III)	$CHCl_3$/EtOH = 1:11	802 nm, 719, 649sh, 418sh, 329	Reduced form Na^+,γ = *t*-Bu	105
	Tb(III)	$CHCl_3$/EtOH = 1:11	808 nm, 718, 654sh, 405sh, 332	Reduced form Na^+,γ = *t*-Bu	105
	Er(III)	$CHCl_3$/EtOH = 1:11	821 nm, 715, 647sh, 400sh, 333	Reduced form Na^+,γ = *t*-Bu	105
	Y(III)	$CHCl_3$/EtOH = 1:11	821 nm, 719, 657sh, 401sh, 332	Reduced form Na^+,γ = *t*-Bu	105
	Lu(III)	DCM	1089 nm (lg ε 4.48), 760 (5.07), 680 (4.48), 572 (4.47), 328 (5.03)		1048
		Benzene	761 nm		510
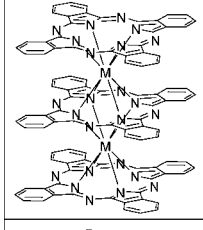	Gd(III)	THF	636 nm	R_1, R_2, R_3 = H	1270
	Y(III)	PhCl	705 nm, 633		93
	Lu(III)	DCM	13.9×10^3 cm^{-1}, 15.9×10^3, 17.5×10^3, 29.8×10^3		1271
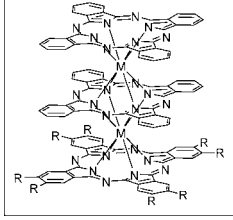	Gd(III)	$CHCl_3$	640 nm	R = OC_8H_{17}	1270

(*Continued*)

Table 10. (*Continued*)

Structure	M	Solvent	Transition Energy (Intensity)	Remark	Ref.
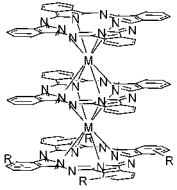	Sm(III)	$CHCl_3$	652 nm, 335, 294	R = O(*i*-C_5H_{11})	1272
	Gd(III)	$CHCl_3$	701 nm, 649, 336, 295	R = O(*i*-C_5H_{11})	1272
	Lu(III)	$CHCl_3$	723 nm, 643, 335, 296	R = O(*i*-C_5H_{11})	1272
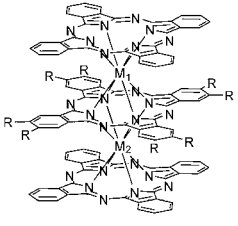	Y(III)	$CHCl_3$	703 nm, 641, 333	R = OC_8H_{17}	1273
	Nd(III)	$CHCl_3$	685sh nm, 644, 335	R = OC_8H_{17}	1273
	Sm(III)	$CHCl_3$	691sh nm, 644, 335	R = OC_8H_{17}	1273
	Eu(III)	$CHCl_3$	689sh nm, 643, 333	R = OC_8H_{17}	1273
	Gd(III)	$CHCl_3$	642 nm	R = OC_8H_{17}	1270
		$CHCl_3$	692 nm (lg ε 4.55), 643 (5.25), 333 (5.09), 295 (4.93)	R = OC_8H_{17}	1274
	Tb(III)	$CHCl_3$	698 nm (lg ε 4.51), 642 (5.23), 333 (5.08), 294 (4.93)	R = OC_8H_{17}	1274
		$CHCl_3$	694 nm, 642, 332	R = OC_8H_{17}	1273
	Dy(III)	$CHCl_3$	703 nm (lg ε 4.60), 640 (5.13), 333 (5.14), 295 (4.96)	R = OC_8H_{17}	1274
		$CHCl_3$	700 nm, 641, 335	R = OC_8H_{17}	1273
	Ho(III)	$CHCl_3$	707 nm (lg ε 4.56), 639 (5.18), 331 (5.11), 295 (4.92)	R = OC_8H_{17}	1274
		$CHCl_3$	704 nm, 640, 334	R = OC_8H_{17}	1273
	Er(III)	$CHCl_3$	711 nm (lg ε 4.58), 638 (5.22), 331 (5.12), 295 (4.93)	R = OC_8H_{17}	1274
		$CHCl_3$	705 nm, 639, 334	R = OC_8H_{17}	1273
	Tm(III)	$CHCl_3$	714 nm (lg ε 4.54), 637 (5.23), 332 (5.08), 296 (4.88)	R = OC_8H_{17}	1274
		$CHCl_3$	712 nm, 638, 334	R = OC_8H_{17}	1273
	Yb(III)	$CHCl_3$	720 nm (lg ε 4.45), 634 (5.12), 332 (5.00), 296 (4.81)	R = OC_8H_{17}	1274

(*Continued*)

Table 10. (*Continued*)

Structure	M	Solvent	Transition Energy (Intensity)	Remark	Ref.
	Lu(III)	$CHCl_3$	722 nm (lg ε 4.51), 634 (5.20), 331 (5.05), 296 (4.87)	R = OC_8H_{17}	1274
	M_1 = Lu(III), M_2 =Gd(III)	$CHCl_3$	706 nm (lg ε 4.58), 641 (5.18), 331 (5.18), 295 (4.97)	R = OC_8H_{17}	1274
	M_1 = Lu(III), M_2 =Tb(III)	$CHCl_3$	708 nm (lg ε 4.58), 640 (5.27), 332 (5.14), 295 (4.93)	R = OC_8H_{17}	1274
	M_1 = Lu(III), M_2 =Dy(III)	$CHCl_3$	711 nm (lg ε 4.51), 638 (5.23), 332 (5.08), 295 (4.88)	R = OC_8H_{17}	1274
	M_1 = Lu(III), M_2 =Ho(III)	$CHCl_3$	713 nm (lg ε 4.61), 635 (5.28), 333 (5.17), 296 (4.97)	R = OC_8H_{17}	1274
	M_1 = Lu(III), M_2 =Er(III)	$CHCl_3$	716 nm (lg ε 4.58), 635 (5.26), 332 (5.14), 296 (4.94)	R = OC_8H_{17}	1274
	M_1 = Lu(III), M_2 =Tm(III)	$CHCl_3$	718 nm (lg ε 4.53), 634 (5.22), 332 (5.08), 296 (4.88)	R = OC_8H_{17}	1274
	M_1 = Lu(III), M_2 =Yb(III)	$CHCl_3$	719 nm (lg ε 4.57), 632 (5.18), 332 (5.12), 296 (4.93)	R = OC_8H_{17}	1274
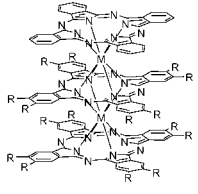	Y(III)	$CHCl_3$	705 nm, 641, 348	R = OC_8H_{17}	1273
	Pr(III)	$CHCl_3$	647 nm, 348	R = OC_8H_{17}	1273
	Nd(III)	$CHCl_3$	683sh nm, 645, 345	R = OC_8H_{17}	1273
	Sm(III)	$CHCl_3$	684sh nm, 644, 347	R = OC_8H_{17}	1273
	Eu(III)	$CHCl_3$	689sh nm, 644, 347	R = OC_8H_{17}	1273
	Gd(III)	$CHCl_3$	643 nm	R = OC_8H_{17}	1270
	Tb(III)	$CHCl_3$	696 nm, 642, 350	R = OC_8H_{17}	1273
	Dy(III)	$CHCl_3$	702 nm, 641, 348	R = OC_8H_{17}	1273
	Ho(III)	$CHCl_3$	707 nm, 640, 348	R = OC_8H_{17}	1273
	Er(III)	$CHCl_3$	709 nm, 639, 348	R = OC_8H_{17}	1273
	Tm(III)	$CHCl_3$	714 nm, 638, 348	R = OC_8H_{17}	1273

(*Continued*)

Table 10. (*Continued*)

Structure	M	Solvent	Transition Energy (Intensity)	Remark	Ref.
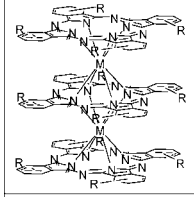	Cd(II)	Hexane	718 nm ($10^{-5}\varepsilon$ 1.3), 599 (0.6), 550, 484	R = C_6H_{13}	289
		Hexane	872 nm, 719, 644, 599, 547, 484	R = C_8H_{17}	289
		Hexane	718 nm, 647, 599, 550, 483	R = $C_{10}H_{21}$	289
		Hexane	719 nm, 600, 483	R = 	289
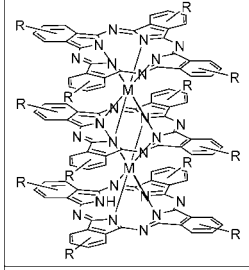	Cd(II)	Hexane	693 nm, 615, 495, 334	R = 	289
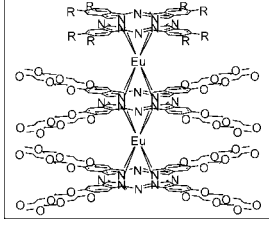	Eu(III)	Toluene	687 nm (lg ε 4.34), 644 (5.19), 364 (5.00), 334 (4.89)	R = C_6H_{13}	1275
		Toluene	689 nm (lg ε 4.30), 645 (5.17), 362 (4.94), 334 (4.84)	R = C_8H_{17}	1275
		Toluene	689 nm (lg ε 4.26), 645 (5.14), 362 (4.93), 335 (4.83)	R = $C_{10}H_{21}$	1275
		Toluene	689 nm (lg ε 4.23), 645 (5.14), 362 (4.89), 336 (4.80)	R = $C_{12}H_{25}$	1275

(*Continued*)

Table 10. (*Continued*)

Structure	M	Solvent	Transition Energy (Intensity)	Remark	Ref.
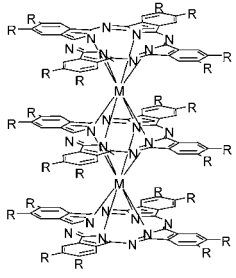	Eu(III)	$CHCl_3$	657 nm, 346	R = Et	513
	Er(III)	$CHCl_3$	705 nm, 645, 345	R = Et	513
	Lu(III)	$CHCl_3$	727 nm, 644, 347	R = Et	513
	Eu(III)	$CHCl_3$	670 nm, 590, 347	R = Bu	513
	Er(III)	$CHCl_3$	667 nm, 347	R = Bu	513
	Lu(III)	$CHCl_3$	726sh nm, 667, 348	R = Bu	513
	Gd(III)	Toluene	644 nm	R = OC_8H_{17}	1270
	Er(III)	$CHCl_3$	657 nm, 635, 415, 345	R = 	681
	Eu(III)	$CHCl_3$	663 nm, 579, 405, 346	R = 	681
	Lu(III)	$CHCl_3$	670.2 nm (lg ε 5.09), 393.4 (4.98), 336.3 (5.23), 290.1 (5.27)	R = OPh(3,4-$(OC_8H_{17})_2$)	1250
		$CHCl_3$	671.0 nm (lg ε 5.11), 391.8 (5.01), 324.9 (5.24), 289.3 (5.29)	R = OPh(3,4-$(OC_9H_{19})_2$)	1250
		$CHCl_3$	669.7 nm (lg ε 5.11), 393.0 (5.02), 333.8 (5.26), 290.6 (5.29)	R = OPh(3,4-$(OC_{11}H_{23})_2$)	1250
		$CHCl_3$	669.9 nm (lg ε 5.12), 392.4 (5.02), 337.8 (5.26), 289.0 (5.31)	R = OPh(3,4-$(OC_{12}H_{25})_2$)	1250
		$CHCl_3$	673.2 nm (lg ε 5.13), 391.8 (5.03), 335.6 (5.24), 288.7 (5.31)	R = OPh(3,4-$(OC_{14}H_{29})_2$)	1250
		$CHCl_3$	670.6 nm (lg ε 5.12), 394.0 (5.03), 336.1 (5.26), 289.6 (5.30)	R = OPh(3,4-$(OC_{16}H_{33})_2$)	1250
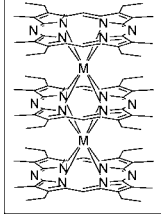	Ce(III)	$CHCl_3$	652 nm (lg ε 3.84), 572 (4.13), 534 (4.04), 354 (5.25)		1276
	Eu(III)	$CHCl_3$	682 nm (lg ε 3.63), 587 (4.05), 445 (4.03), 349 (5.07)		1276

(*Continued*)

Table 10. (*Continued*)

Structure	M	Solvent	Transition Energy (Intensity)	Remark	Ref.
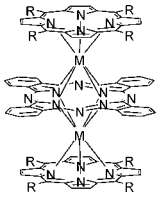	Sm(III)	DCM	605 nm (lg ε 4.31), 546 (4.09), 487 (4.51), 418 (5.29), 355 (5.02)	R = Ph	1257
	Eu(III)	DCM	605 nm (lg ε 4.33), 539 (4.10), 488 (4.56), 417 (5.35), 354 (5.09)	R = Ph	1257
	Gd(III)	DCM	604 nm (lg ε 4.36), 556 (4.14), 491 (4.61), 417 (5.36), 353 (5.08)	R = Ph	1257
	Eu(III)	Toluene	625 nm, 567, 502, 428, 362	R_1 = C_5H_{11}	1277
		Toluene	607 nm, 492, 421, 354	R = Ph(4-*t*-Bu)	1277
		$CHCl_3$	950 nm (lg ε 3.97), 603 (4.22), 551 (4.02), 491 (4.49), 419 (5.28), 354 (5.03)	R = Ph(4-Cl)	1260
	Tb(III)	$CHCl_3$	971 nm (lg ε 3.17), 603 (4.89), 493 (5.23), 419 (6.03), 354 (5.72)	R = Ph(4-Cl)	1260
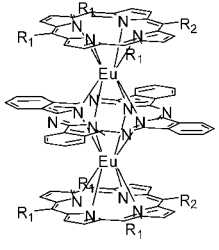	Eu(III)	Toluene	607 nm, 492, 421, 355	R_1 = Ph(4-Me) 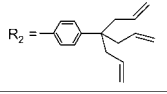	1162
	Ce(III)	Toluene	609 nm, 549, 484, 421, 362	R_1 = Ph(4-Me) 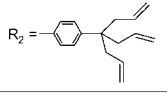	1162
	Eu(III)	Toluene	606 nm, 559, 493, 421, 355	R_1 = Ph(4-*t*-Bu) 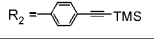	1277
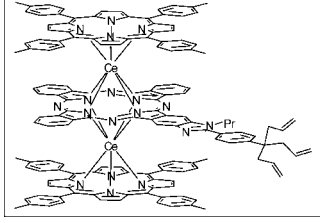	Ce(III)		608 nm, 549, 493, 419, 359		1162

(*Continued*)

Table 10. (*Continued*)

Structure	M	Solvent	Transition Energy (Intensity)	Remark	Ref.
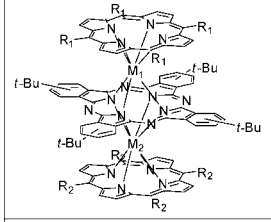	Ce(III)	Toluene	615 nm, 568, 497, 426, 354	R_1, $R_2 = C_5H_{11}$	1246
	Eu(III)	Toluene	626 nm, 566, 502, 427, 357	R_1, $R_2 = C_5H_{11}$	1277
	Ce(III)	Toluene	607 nm, 492, 422, 362	R_1, R_2 = Ph(4-Me)	1246
	Eu(III)	Toluene	608 nm, 493, 421, 362	R_1, R_2 = Ph(4-Me)	1277
	M_1 = Ce(III), M_2 = Eu(III)	Toluene	607 nm, 493, 421, 367, 360	$R_1 = C_5H_{11}$, R_2 = Ph(4-Me)	1246
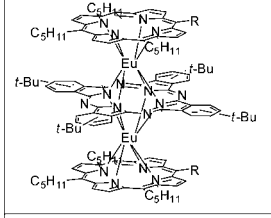	Eu(III)	Toluene	619 nm, 566, 502, 428, 358	R = 	1277
		Toluene	619 nm, 569, 501, 428, 359	R = Ph(4-I)	1277
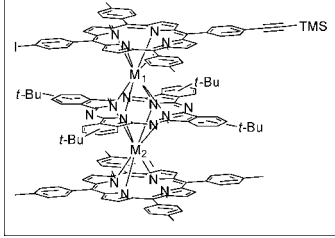	M_1 = Ce(III), M_2 = Eu(III)	Toluene	607 nm, 493, 420, 364		1246

(*Continued*)

Table 10. (*Continued*)

Structure	M	Solvent	Transition Energy (Intensity)	Remark	Ref.
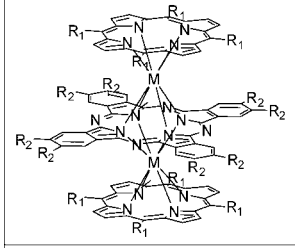	Eu(III)	Toluene	620 nm, 567, 500, 426, 347	$R_1 = C_5H_{11}$, R_2 = Me	1277
		Toluene	608 nm, 496, 420, 364	$R_1 = C_5H_{11}$, R_2 = Ph	1277
		Toluene	611 nm, 496, 419, 374	R_1 = Ph(4-Me), $R_2 = C_8H_{17}$	1277
		$CHCl_3$	938 nm (lg ε 3.61), 606 (4.07), 556 (3.96), 491 (4.28), 462 (4.31), 421 (5.31), 377 (4.87)	R_1 = Ph(4-$OC_{12}H_{25}$), $R_2 = OC_8H_{17}$	1260
	Tb(III)	$CHCl_3$	951 nm (lg ε 3.51), 608 (4.00), 563 (3.81), 498 (4.19), 467 (4.18), 420 (5.10), 376 (4.75)	R_1 = Ph(4-$OC_{12}H_{25}$), $R_2 = OC_8H_{17}$	1260
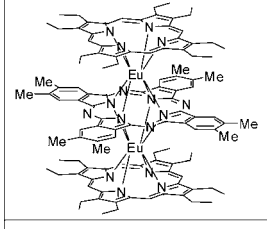	Eu(III)	Toluene	594 nm, 484, 404, 353		1277
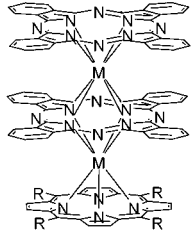	Eu(III)	Toluene	684 nm, 652, 631, 417, 351	$R = C_5H_{11}$	1277
	Sm(III)	DCM	719 nm (lg ε 4.52), 617 (4.79), 555 (4.33), 521 (4.40), 414 (4.94), 340 (5.16)	R = Ph	1257
	Eu(III)	DCM	722 nm (lg ε 4.49), 616 (4.80), 554 (4.33), 518 (4.42), 411 (4.97), 341 (5.18)	R = Ph	1257
	Gd(III)	DCM	728 nm (lg ε 4.46), 617 (4.80), 558 (4.29), 520 (4.38), 411 (4.92), 340 (5.16)	R = Ph	1257
	Eu(III)	Toluene	721 nm, 668, 619, 521, 419, 342	R = Ph(4-*t*-Bu)	1277
		$CHCl_3$	724 nm (lg ε 4.45), 616 (4.71), 557 (4.26), 522 (4.31), 413 (4.90), 342 (5.12)	R = Ph(4-Cl)	1260
	Tb(III)	$CHCl_3$	738 nm (lg ε 5.15), 618 (5.51), 521 (5.08), 412 (5.71), 344 (5.91)	R = Ph(4-Cl)	1260
	Nd(III)	$CHCl_3$	704 nm (lg ε 4.35), 620 (4.60), 550sh, 515sh, 418 (5.00), 338 (5.03)	R = Ph(4-OMe)	1278

(*Continued*)

Table 10. (*Continued*)

Structure	M	Solvent	Transition Energy (Intensity)	Remark	Ref.
	Eu(III)	$CHCl_3$	724 nm (lg ε 4.26), 617 (4.53), 545sh, 518sh, 418 (4.80), 340 (4.98)	R = Ph(4-OMe)	1278
	Gd(III)	$CHCl_3$	730 nm (lg ε 4.54), 618 (4.84), 538sh, 520sh, 417 (5.03), 340 (5.17)	R = Ph(4-OMe)	1278
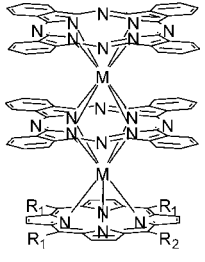	Eu(III)	Toluene	736 nm, 624, 581, 522, 439, 407, 341	$R_1 = C_5H_{11}$, $R_2 = (CH_2)_6Br$	1277
		Toluene	740 nm, 624, 583, 523, 440, 408, 341	$R_1 = C_5H_{11}$, $R_2 = (CH_2)_6SAc$	1277
		Toluene	733 nm, 624, 581, 524, 440, 406, 340	$R_1 = C_5H_{11}$, $R_2 = (CH_2)_6SCN$	1277
		Toluene	721 nm, 619, 553, 521, 415, 342	R_1 = Ph(4-Me), 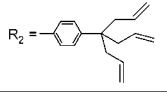	1162
		Toluene	721 nm, 618, 552, 522, 417, 342	R_1 =Ph(4-*t*-Bu), 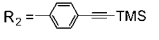	1277
		Toluene	722 nm, 618, 552, 522, 415, 343	R_1 =Ph(4-*t*-Bu), 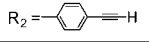	1277
		Toluene	721 nm, 618, 523, 419, 341	R_1 =Ph(4-*t*-Bu), 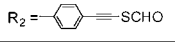	1277
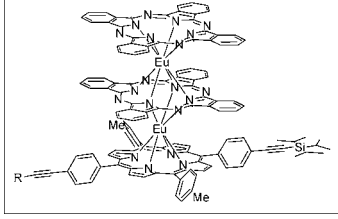	Eu(III)	Toluene	723 nm, 617, 522, 416, 342	R = TMS	1229
		Toluene	722 nm, 617, 522, 418, 342	R = H	1229

(*Continued*)

Table 10. (*Continued*)

Structure	M	Solvent	Transition Energy (Intensity)	Remark	Ref.
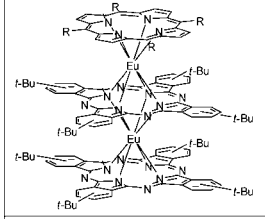	Eu(III)	Toluene	736 nm, 629, 583, 527, 413, 345	R = C_5H_{11}	1277
		Toluene	727 nm, 620, 526, 417, 346	R = Ph(4-Me)	1277
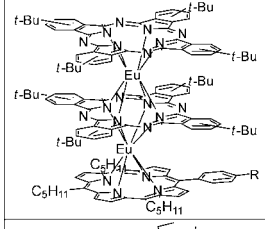	Eu(III)	Toluene	733 nm, 627, 583, 530, 419, 345	R = 	1277
		Toluene	732 nm, 627, 583, 529, 416, 345	R = 	1277
		Toluene	723 nm, 625, 577, 527, 415, 339	R = 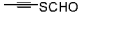	1277
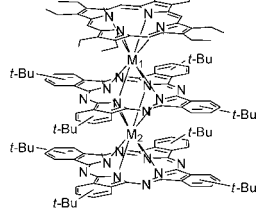	Eu(III)	Toluene	724 nm, 658, 623, 394, 342		1246
	M_1 = Ce(III), M_2 = Eu(III)	Toluene	712 nm, 628, 546, 400, 344		1246

(*Continued*)

Table 10. (*Continued*)

Structure	M	Solvent	Transition Energy (Intensity)	Remark	Ref.
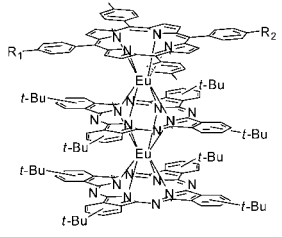	Eu(III)	Toluene	727 nm, 621, 526, 418, 347	R_1, R_2 = I	1246
		Toluene	729 nm, 621, 527, 418, 347	R_1 = CCTMS, R_2 = CCTIPS	1246
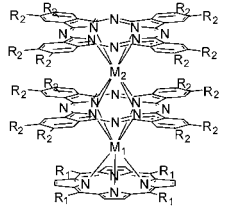	Eu(III)	Toluene	735 nm, 624,581, 522, 439, 406, 341	$R_1 = C_5H_{11}$, R_2 = H	1277
		Toluene	740 nm, 625, 535, 416, 352	$R_1 = C_5H_{11}$, R_2 = Me	1277
	M_1 = Ce(III), M_2 = Eu(III)	Toluene	714 nm, 624, 534, 421, 346	R_1 = Ph(4-Me), $R_2 = OC_8H_{17}$	1246
	Eu(III)	$CHCl_3$	728 nm (lg ε 4.58), 621 (4.81), 524 (4.47), 494 (4.44), 420 (5.16), 365 (5.18)	R_1 = Ph(4-$OC_{12}H_{25}$), $R_2 = OC_8H_{17}$	1260
	Tb(III)	$CHCl_3$	744 nm (lg ε 4.61), 626 (4.89), 526 (4.57), 423 (5.23), 368 (5.23)	R_1 = Ph(4-$OC_{12}H_{25}$), $R_2 = OC_8H_{17}$	1260
	M_1 = Eu(III), M_2 = Tb(III)	$CHCl_3$	735 nm (lg ε 4.51), 623 (4.73), 524 (4.42), 501 (4.36), 420 (5.10), 365 (5.13)	R_1 = Ph(4-$OC_{12}H_{25}$), $R_2 = OC_8H_{17}$	1260
	M1 = Tb(III), M2 = Eu(III)	$CHCl_3$	736 nm (lg ε 4.45), 621 (4.74), 522 (4.41), 499 (4.40), 419 (5.07), 366 (5.12)	R_1 = Ph(4-$OC_{12}H_{25}$), $R_2 = OC_8H_{17}$	1260
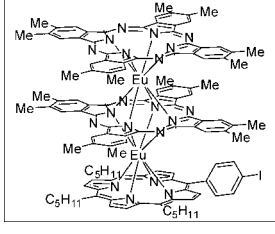	Eu(III)	Toluene	747 nm, 630, 533, 418, 350		1229

(*Continued*)

Table 10. (*Continued*)

Structure	M	Solvent	Transition Energy (Intensity)	Remark	Ref.
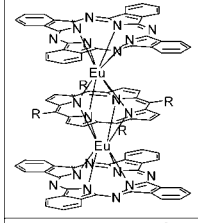	Eu(III)	Toluene	652 nm, 519, 406, 342	R = Ph(4-*t*-Bu)	1277
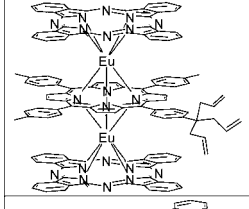	Eu(III)	Toluene	788 nm, 652, 517, 445, 343		1162
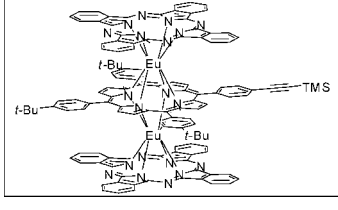	Eu(III)	Toluene	653 nm, 625, 519, 416, 343		1277

(*Continued*)

Table 10. (*Continued*)

Structure	M	Solvent	Transition Energy (Intensity)	Remark	Ref.
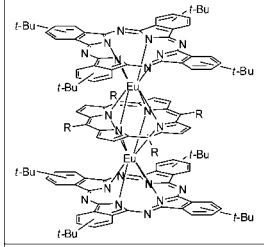	Eu(III)	Toluene	727 nm, 620, 526, 417, 346	R = 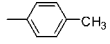	1277
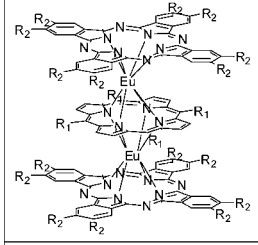	Eu(III)	Toluene	737 nm, 631, 540, 423, 373	R_1 = Ph(4-Me), R_2 = OC_8H_{17}	1277
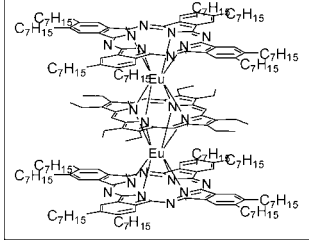	Eu(III)	Toluene	658 nm, 625, 504, 444, 344		1277

(*Continued*)

Table 10. (*Continued*)

Structure	M	Solvent	Transition Energy (Intensity)	Remark	Ref.
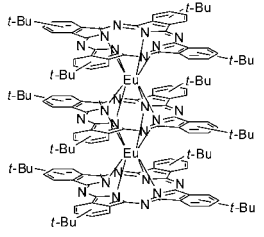	Eu(III)	Toluene	649 nm, 341		1277
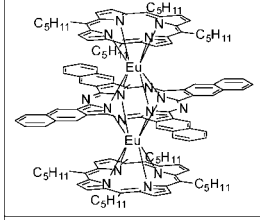	Eu(III)	Toluene	612 nm, 543, 429, 330		1277
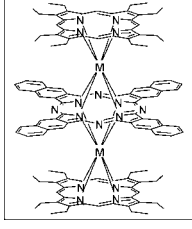	Nd(III)	$CHCl_3$	1021 nm (lg ε 4.27), 637 (4.41), 524 (4.39), 407 (5.41), 352 (5.17), 337 (5.18)		1266
	Eu(III)	$CHCl_3$	1101 nm (lg ε 3.93), 640 (4.41), 525 (4.21), 406 (5.22), 350 (5.07), 338 (5.08)		1266

(*Continued*)

Table 10. (*Continued*)

Structure	M	Solvent	Transition Energy (Intensity)	Remark	Ref.
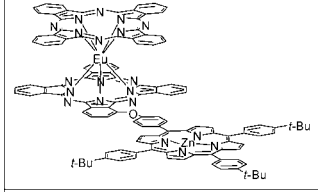	Eu(III)	$CHCl_3$	1618 nm (lg ε 4.23), 909 (3.70), 675 (5.29), 607 (4.68), 592 (4.65), 549 (4.62), 455 (4.57), 421 (5.87), 400 (4.89), 343 (5.01), 321 (5.18)		1228
		$CHCl_3$/MeOH = 3:1	682 nm (lg ε 4.84), 632 (5.35), 609 (4.81), 566 (4.55), 429 (5.87), 408 (4.89), 360 (4.86), 332 (5.27), 290 (5.01)	L = NH_2NH_2, Reduced form	1228
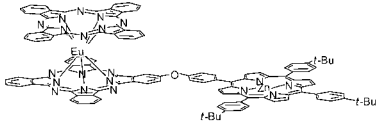	Eu(III)	$CHCl_3$	1602 nm (lg ε 14.21), 909 (3.73), 672 (5.31), 604 (4.63), 587 (4.59), 548 (4.61), 455 (4.59), 421 (5.90), 400 (4.89), 343 (5.04), 321 (5.20)		1228
		$CHCl_3$/MeOH = 3:1	683 nm (lg ε 4.92), 632 (5.41), 603 (4.77), 566 (4.56), 428 (5.90), 407 (4.89), 362 (4.87), 332 (5.28), 284 (5.03)	Reduced form	1228
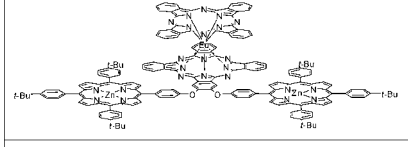	Eu(III)	$CHCl_3$	1595 nm (lg ε 3.94), 909 (3.49), 672 (5.35), 604 (4.65), 587 (4.67), 549 (4.86), 466 (4.61), 422 (6.08), 401 (5.18), 344 (5.10), 320 (5.24)		1228
		$CHCl_3$/MeOH = 3:1	683 nm (lg ε 4.84), 631 (5.34), 603 (4.94), 564 (4.83), 429 (6.08), 408 (5.21), 360 (5.06), 333 (5.39), 284 (5.21)	Reduced form	1228
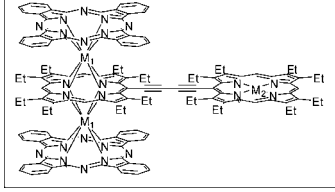	M_1 = Eu(III), M_2 = Ni(II)	DCM	798 nm (lg ε 4.10), 659 (4.94), 634 (4.93), 518br (4.83), 447 (5.10), 341 (5.25)		1279

(*Continued*)

Table 10. (*Continued*)

Structure	M	Solvent	Transition Energy (Intensity)	Remark	Ref.
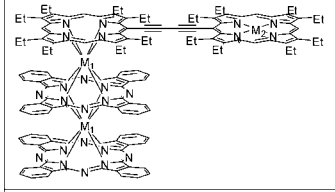	Eu(III)	DCM	730sh nm (lg ε 4.32), 630 (5.02), 513sh (4.89), 476 (5.04), 458sh (5.02), 432 (5.00), 341 (5.25)		1279
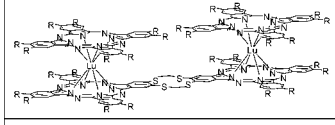		$CHCl_3$	703 nm (10^{-1} ε 29.20), 634 (67.00), 547 (47.29), 390 (15.71), 322 (19.97)	$R = SC_6H_{13}$	1280
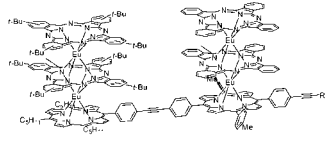	M_1 = Eu(III), M_2 = Ni(II)	Toluene	725 nm, 623, 526, 420, 345	R = 	1229
		Toluene	725 nm, 669, 623, 526, 423, 344	R = H	1229
		Toluene	725 nm, 622, 526, 422, 344	R = 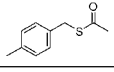	1229
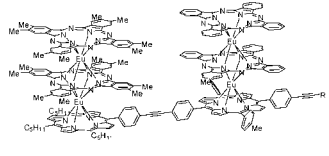	Eu(III)	Toluene	725 nm, 621, 528, 422, 346	R = 	1229
		Toluene	725 nm, 666, 622, 528, 423, 347	R = H	1229
		Toluene	724 nm, 621, 527, 420, 347	R = 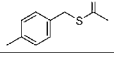	1229

(*Continued*)

Table 10. (*Continued*)

Structure	M	Solvent	Transition Energy (Intensity)	Remark	Ref.
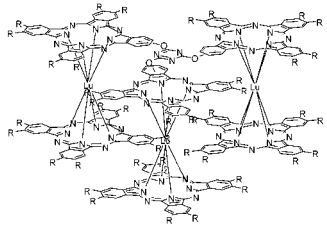	Lu(III)OAc	$CHCl_3$	724 nm (lg ε 6.69), 692 (6.83), 662 (6.81), 430 (6..50)	$R = SC_6H_{13}$	1281
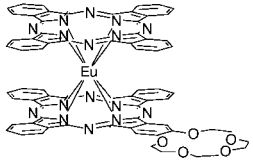	Eu(III)	$CHCl_3$	1606 nm (lg ε 3.82), 908 (3.37), 672 (4.93), 606 (4.21), 588 (4.10), 476 (4.17), 458 (4.18), 345sh, 324 (4.78)		1227
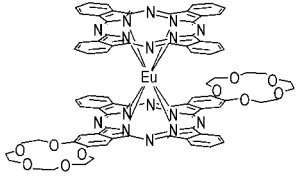	Eu(III)	$CHCl_3$	1604 nm (lg ε 4.02), 908 (3.61), 672 (5.16), 607 (5.46), 588 (4.37), 481 (4.45), 454 (4.40), 346sh, 325 (5.03)		1227
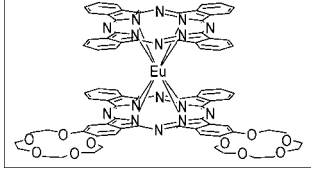	Eu(III)	$CHCl_3$	1604 nm (lg ε 4.09), 908 (3.63), 672 (5.17), 607 (4.46), 587 (4.37), 480 (4.44), 455 (4.41), 346sh, 324 (5.02)		1227

(*Continued*)

Table 10. (*Continued*)

Structure	M	Solvent	Transition Energy (Intensity)	Remark	Ref.
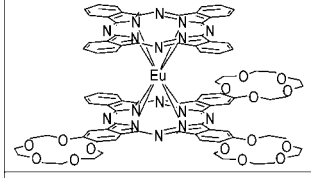	Eu(III)	$CHCl_3$	1606 nm (lg ε 3.96), 908 (3.58), 673 (5.13), 607 (4.43), 588 (4.32), 485 (4.45), 449 (4.36), 364sh, 326 (4.98)		1227
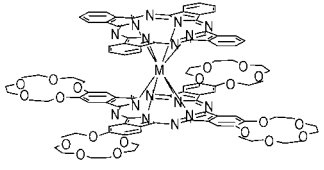	La(III)	$CHCl_3$	689 nm (lg ε 4.84), 612 (4.42), 508 (4.37), 335 (4.89), 289 (4.81)		1211
	Sm(III)	$CHCl_3$	675 nm (lg ε 5.06), 610 (4.41), 490 (4.49), 331 (4.97), 290 (4.92)		1211
	Eu(III)	$CHCl_3$	1606 nm (lg ε 3.91), 906 (3.55), 674 (5.06), 609 (4.38), 588 (4.27), 489 (4.46), 369 (4.75), 331 (4.92)		1227
	Dy(III)	$CHCl_3$	668 nm (lg ε 5.05), 605 (4.32), 481 (4.42), 326 (4.91), 289 (4.89)		1211
	Tm(III)	$CHCl_3$	666 nm (lg ε 5.22), 603 (4.55), 469 (4.63), 368 (5.17), 327 (5.15), 290 (5.20)		1211
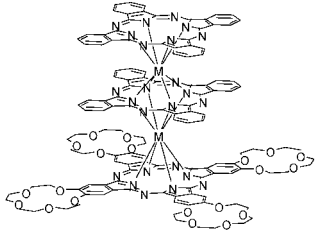	Y(III)	$CHCl_3$	702 nm, 639, 338, 294		1212
	Sm(III)	$CHCl_3$	682sh nm, 642, 338, 291		1212
	Dy(III)	$CHCl_3$	700 nm, 640, 338, 293		1212
	Tm(III)	$CHCl_3$	712 nm, 631, 338, 291		1212

(*Continued*)

Table 10. (*Continued*)

Structure	M	Solvent	Transition Energy (Intensity)	Remark	Ref.
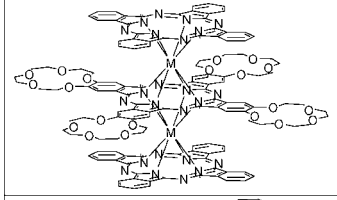	Y(III)	$CHCl_3$	702 nm, 639, 333, 294		1213
	Sm(III)	$CHCl_3$	682sh nm, 643, 334, 293		1213
	Tb(III)	$CHCl_3$	695 nm, 641, 333, 292		1213
	Dy(III)	$CHCl_3$	700 nm, 640, 333, 293		1213
	Tm(III)	$CHCl_3$	709 nm, 635, 333, 292		1213
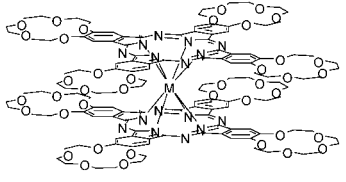	Sc(III)	$CHCl_3$	1377sh nm, 1219 (lg ε 4.11), 926 (4.06), 661 (5.22), 466 (4.57), 365 (5.13)		89
		$CHCl_3$	724 nm (lg ε 4.69), 619 (5.13), 359 (5.14)	Reduced form	89
		$CHCl_3$	876 nm (lg ε 4.45), 691 (4.73), 485 (4.92), 383 (5.13)	Oxidized form	89
	La(III)	$CHCl_3$	691 nm (lg ε 4.57), 623 (4.14), 508 (4.17), 375 (4.53), 343 (4.66), 291 (4.63)		1211
	Pr(III)	$CHCl_3$	684 nm (lg ε 5.01), 617 (4.46), 499 (4.56), 371 (4.95), 340 (5.00), 291 (5.01)		1214
		$CHCl_3$	640 nm (lg ε 5.36), 587 (4.34), 359 (5.16)	Reduced form	1214
	Nd(III)	$CHCl_3$	682 nm (lg ε 4.85), 497 (4.35), 372 (4.77), 339 (4.80), 292 (4.83)		1214
		$CHCl_3$	638 nm (lg ε 5.14), 359 (4.98), 285	Reduced form	1214
	Sm(III)	$CHCl_3$	678 nm (lg ε 5.08), 613 (4.53), 492 (4.54), 371 (4.98), 337 (4.95), 292 (4.96)		1211
	Eu(III)	$CHCl_3$	1610 nm (lg ε 4.14), 907 (3.62), 677 (5.22), 612 (4.56), 590 (4.41), 491 (4.64), 371 (5.08), 335 (5.06)		1227
	Gd(III)	$CHCl_3$	675 nm (lg ε 5.08), 488 (4.53), 368 (5.00), 337 (4.93), 292 (4.96)		1215
	Dy(III)	$CHCl_3$	671 nm (lg ε 4.95), 607 (4.28), 484 (4.40), 368 (4.88), 335 (4.80), 291 (4.86)		1211
	Tm(III)	$CHCl_3$	668 nm (lg ε 5.21), 604 (4.48), 479 (4.61), 368 (5.12), 340sh, 291 (5.04)		1211
	Yb(III)	$CHCl_3$	670 nm (lg ε 5.18), 479 (4.60), 369 (5.12), 292 (5.06)		1215
	Lu(III)	$CHCl_3$	665 nm (lg ε 5.20), 476 (4.66), 367 (5.13)		1215

(*Continued*)

Table 10. (*Continued*)

Structure	M	Solvent	Transition Energy (Intensity)	Remark	Ref.
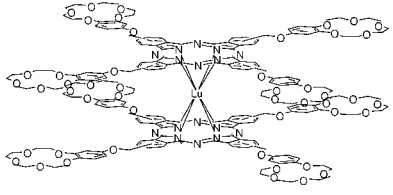	Lu(III)	$CHCl_3$	684 nm (ε 142,600), 614 (27,800), 349 (94,200)		1210
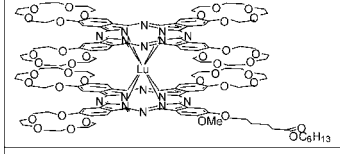	Lu(III)	$CHCl_3$	666 nm (ε 159,000), 603 (30,000), 476 (39,000), 367 (131,000), 291 (102,000)	Neutral form	1196
		$CHCl_3$ + 10% hydrazine	701 nm (ε 66,000), 627 (164,000), 360 (176,000)	Reduced form	1196
		$CHCl_3 + Br_2$	703 nm (ε 54,000), 498 (84,000), 385 (116,000), 336 (79,000), 293 (120,000)	Oxidized form	1196
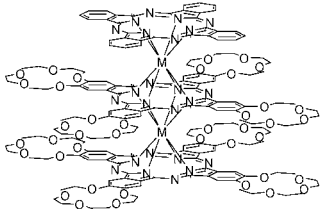	Y(III)	$CHCl_3$	705 nm, 639, 355, 291		1213
	Sm(III)	$CHCl_3$	690sh nm, 644, 353, 292		1213
	Tb(III)	$CHCl_3$	696 nm, 642, 355, 292		1213
	Dy(III)	$CHCl_3$	702 nm, 640, 354, 291		1213
	Tm(III)	$CHCl_3$	713 nm, 636, 355, 292		1213

(*Continued*)

Table 10. (*Continued*)

Structure	M	Solvent	Transition Energy (Intensity)	Remark	Ref.
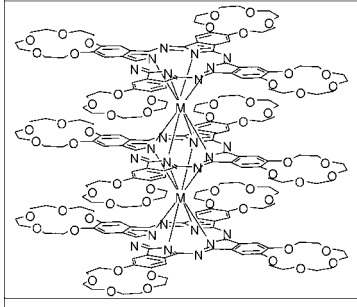	La(III)	$CHCl_3$	646 nm (r.i 1.00), 361 (0.48)		1163
	Pr(III)	$CHCl_3$	646 nm (lg ε 5.21), 358 (5.10), 291 (5.10)		1214
	Nd(III)	$CHCl_3$	646 nm (lg ε 5.33), 359 (5.16), 292 (5.16)		1214
	Gd(III)	$CHCl_3$	695sh nm (lg ε 4.43), 644 (5.17), 590sh (4.17), 361 (5.02), 293 (4.94)		1215
	Yb(III)	$CHCl_3$	689 nm (lg ε 4.66), 636 (5.16), 359 (5.10), 290 (4.89)		1215
	Lu(III)	$CHCl_3$	718 nm (lg ε 4.33), 638 (5.07), 362 (5.01)		1215
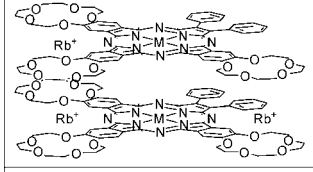	Zn(II)	$CHCl_3$	641 nm (10^{-4} ε 5.08), 593 (2.66), 344 (6.28), 272 (4.34)		1194
	Cu(II)	$CHCl_3$	634 nm (10^{-4} ε 3.54), 332 (3.25), 287 (3.29), 274 (3.47)		1194
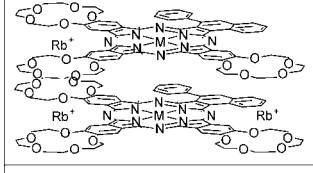	Zn(II)	$CHCl_3$	673 nm (10^{-4} ε 2.73), 637 (3.98), 342 (3.61), 290 (2.28), 278 (2.76)		1194
	Cu(II)	$CHCl_3$	698sh nm (10^{-4} ε 2.36), 677 (2.83), 640 (2.93), 337 (3.03), 271 (4.47)		1194
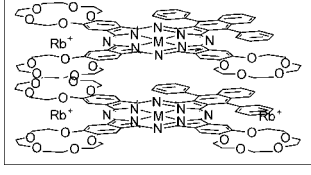	Zn(II)	$CHCl_3$	694 nm (10^{-4} ε 3.57), 649 (4.27), 345 (5.53), 293 (4.45)		1194
	Cu(II)	$CHCl_3$	693 nm (10^{-4} ε 5.19), 650 (5.80), 415 (2.05), 339 (6.62), 297 (6.12)		1194

(*Continued*)

Table 10. (*Continued*)

Structure	M	Solvent	Transition Energy (Intensity)	Remark	Ref.
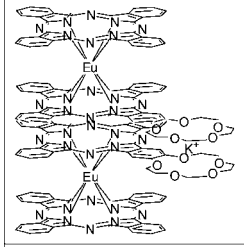	Eu(III)	$CHCl_3$/MeOH	1604 nm (lg ε 3.82), 904 (3.32), 672 (4.88), 607 (4.21), 588sh, 476 (4.16), 460 (5.35), 345sh, 324 (4.78)		1227
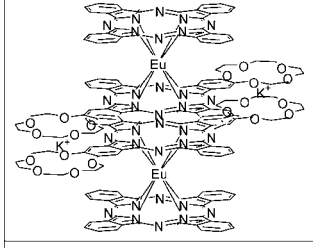	Eu(III)	$CHCl_3$/MeOH	1606 nm (lg ε 3.99), 904 (3.56), 671 (4.90), 633 (4.76), 588sh, 478 (4.22), 456sh, 345sh, 327 (4.96)		1227
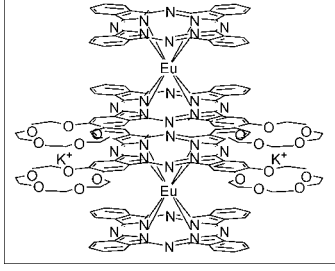	Eu(III)	$CHCl_3$/MeOH	1604 nm (lg ε 4.05), 904 (3.64), 672 (4.99), 636 (4.55), 610sh, 587sh, 478 (4.31), 454sh, 346sh, 325 (4.95)		1227

(*Continued*)

Table 10. (*Continued*)

Structure	M	Solvent	Transition Energy (Intensity)	Remark	Ref.
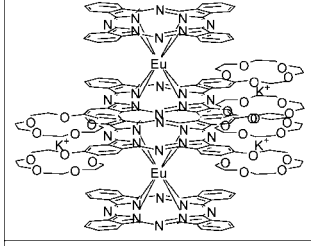	Eu(III)	$CHCl_3$/MeOH	1594 nm (lg ε 3.94), 904 (3.53), 664 (4.77), 637 (4.64), 584sh, 484 (4.14), 354sh, 322 (4.89)		1227
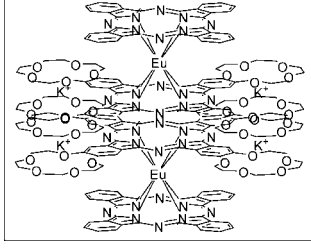	Eu(III)	$CHCl_3$/MeOH	1592 nm (lg ε 3.92), 898 (3.41), 661 (4.82), 590sh, 491 (4.27), 354sh, 324 (4.93)		1227

Table 11. UV-vis absorption data of Pc dimers and oligomers.

Structure	M	Solvent	Transition Energy (Intensity)	Remark	Ref.
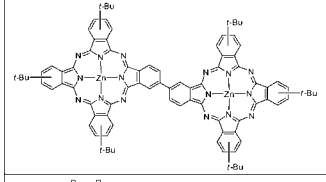	Zn(II)	THF	703 nm, 671		906
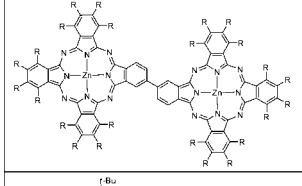	Zn(II)	THF	704 nm	R = OCH_2CF_3	906
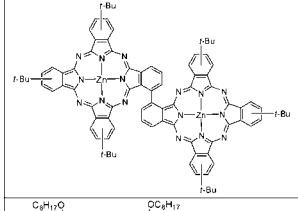	Zn(II)	THF	691 nm, 668		906
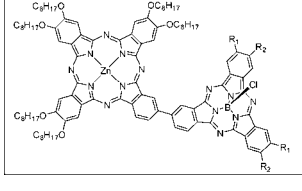	M_1 = Zn(II), M_2 = BCl	$CHCl_3$	698 nm (lg ε 4.8), 677 (4.8), 641 (4.2), 617 (4.2), 578 (4.5), 528sh, 357 (4.7), 298 (4.6)	R_1, R_2 = H	816
		$CHCl_3$	701 nm (lg ε 4.9), 677 (4.9), 656 (4.4), 597 (4.6), 426sh, 357 (4.8), 296 (4.7)	R_1, R_2 = SC_8H_{17}	816

(*Continued*)

Table 11. (*Continued*)

Structure	M	Solvent	Transition Energy (Intensity)	Remark	Ref.
		$CHCl_3$	702 nm (lg ε 4.9), 678 (5.0), 654sh, 594 (4.6), 586sh, 557sh, 538sh, 361 (4.8), 298 (4.8)	$R_1 = H$, $R_2 = NO_2$	816
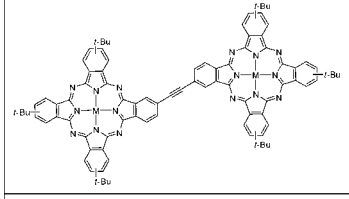	Zn(II)	THF	705 nm, 671		907
		$CHCl_3$	710 nm (lg ε 4.7), 678 (4.7), 344 (4.6)		755
	Ni(II)	$CHCl_3$	678 nm (lg ε 4.3), 336 (4.0)		755
	Co(II)	$CHCl_3$	700 nm (lg ε 4.4), 676 (4.6), 622 (4.3), 329 (4.4)		755
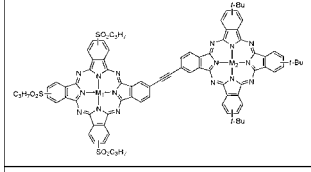	M_1 = Zn(II) M_2 = Zn(II)	$CHCl_3$	677 nm (lg ε 4.2), 343 (4.3)		755
	M_1 = Zn(II), M_2 = Ni(II)	$CHCl_3$	671 nm (lg ε 4.2), 627 (4.18), 331 (4.2)		755
	M_1 = Co(II), M_2 = Zn(II)	$CHCl_3$	690 nm (lg ε 4.3), 672 (4.4), 638 (4.2), 330 (4.2)		755
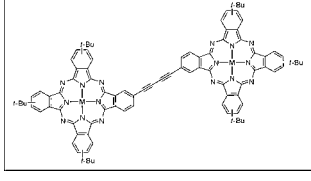	Zn(II)	$CHCl_3$	709 nm (lg ε 4.7), 675 (4.7), 350 (4.6)		755, 813
	Ni(II)	$CHCl_3$	671 nm (lg ε 4.6), 332 (4.6)		755

(*Continued*)

Table 11. (*Continued*)

Structure	M	Solvent	Transition Energy (Intensity)	Remark	Ref.
	Co(II)	$CHCl_3$	672 nm (lg ε 4.8), 326 (4.8)		755
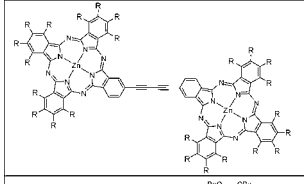	Zn(II)	$CHCl_3$	707 nm, 363	R = OCH_2CF_3	1282
		$CHCl_3$	708sh nm, 677 (lg ε 4.4), 344 (4.7)	R = OBu	814
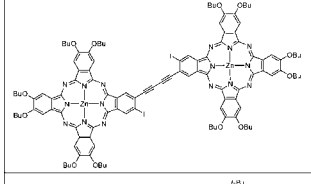	Zn(II)	THF	717 nm (lg ε 4.99), 670 (5.02), 358 (5.09)		905
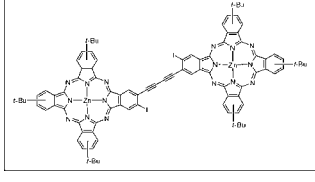	Zn(II)	THF	714 nm (lg ε 5.46), 670 (5.34), 356 (5.23)		905

(*Continued*)

Table 11. (*Continued*)

Structure	M	Solvent	Transition Energy (Intensity)	Remark	Ref.
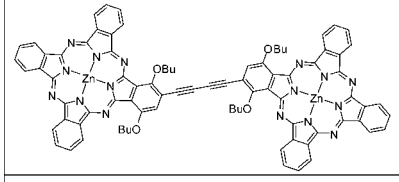	Ni(II)	toluene	752 nm (lg ε 5.43), 702 (5.27), 634 (4.71), 438 (4.52), 353 (4.95), 307 (5.06)		841
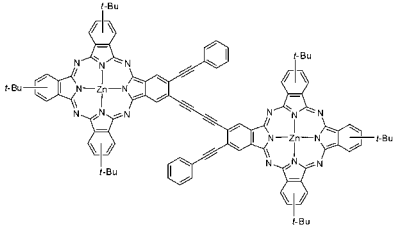	Zn(II)	THF	721 nm (lg ε 5.57), 674 (5.33), 357 (5.22)		905
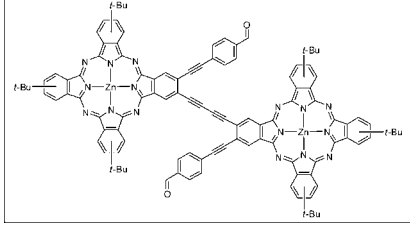	Zn(II)	THF	724 nm (lg ε 5.41), 672 (5.23), 609 (4.66), 356 (5.18)		1283

(*Continued*)

Table 11. (*Continued*)

Structure	M	Solvent	Transition Energy (Intensity)	Remark	Ref.
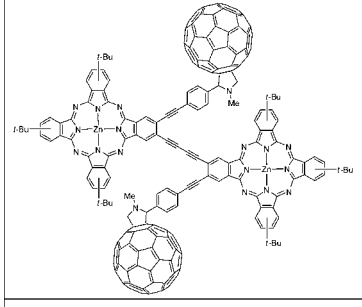	Zn(II)	THF	721 nm (lg ε 5.26), 674 (5.14), 352 (5.15)		1283
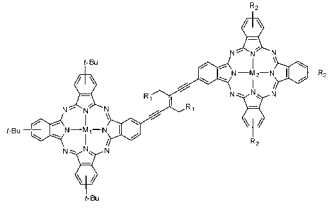	Co(II)	$CHCl_3$	694sh nm (lg ε 4.2), 670 (4.3), 611sh (3.8)	R_1 = —O—Si(Me)(Me)—*t*-Bu; R_2 = *t*-Bu	818
	Zn(II)	$CHCl_3$	680 nm (lg ε 4.7), 618 (4.1), 348 (4.6)	R_1 = —O—Si(Me)(Me)—*t*-Bu; R_2 = *t*-Bu	818
	M_1 = Zn(II), M_2 = Co(II)	$CHCl_3$	679 nm (lg ε 4.5), 614 (3.8), 314 (4.3)	R_1 = —O—Si(Me)(Me)—*t*-Bu; R_2 = *t*-Bu	818
	M_1 = Zn(II), M_2 = Co(II)	$CHCl_3$	680 nm (lg ε 4.6), 616sh (4.2), 329 (4.6)	R_1 = —O—Si(Me)(Me)—*t*-Bu; R_2 = SO_2Pr	818
	Co(II)	$CHCl_3$	676 nm (lg ε 4.5), 639sh (4.0), 608sh (4.1), 336 (4.6)	R_1 = —O—Si(Me)(Me)—*t*-Bu; R_2 = SO_2Pr	818

(*Continued*)

Table 11. (*Continued*)

Structure	M	Solvent	Transition Energy (Intensity)	Remark	Ref.
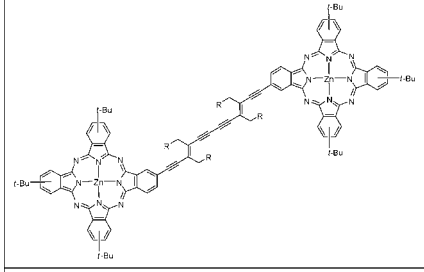	Zn(II)	$CHCl_3$	696 nm (lg ε 4.1), 678 (4.1), 644sh (3.6), 616sh (3.5), 350 (4.0)	R = —O—Si(Me)(Me)—*t*-Bu	818
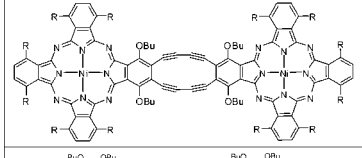	Ni(II)	toluene	822 nm (lg ε 5.32), 691 (4.93)	R = $C_{10}H_{21}$	841
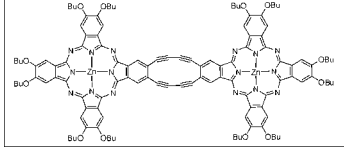	Zn(II)	$CHCl_3$	717sh nm, 671 (lg ε 4.5), 624sh, 355 (4.6)		814

(*Continued*)

Table 11. (*Continued*)

Structure	M	Solvent	Transition Energy (Intensity)	Remark	Ref.
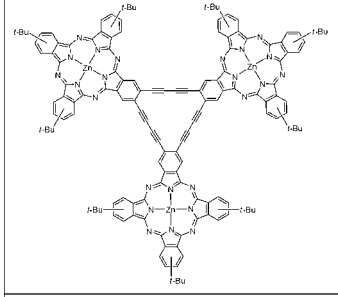	Zn(II)	$CHCl_3$	720sh nm. 680 (lg ε 4.7). 350 (4.8)		814
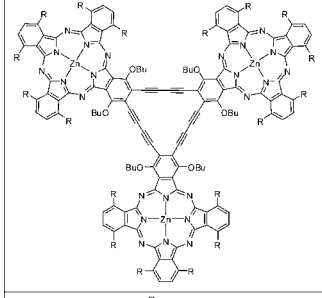	Ni(II)	toluene	780 nmn. 698	R = $C_{10}H_{21}$	841
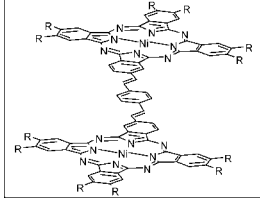	Ni(II)	DCM	675 nm. 414. 313. 290	R = 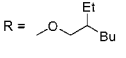	847

(*Continued*)

Table 11. (*Continued*)

Structure	M	Solvent	Transition Energy (Intensity)	Remark	Ref.
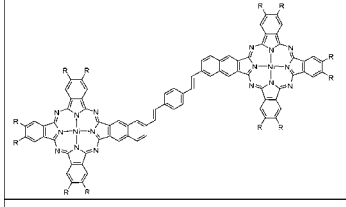	Ni(II)	DCM	693 nm, 648, 388, 328	R = 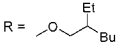	927
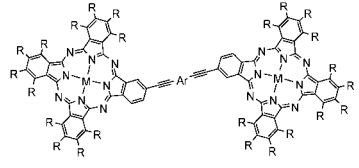	V(IV)O	1,4-dioxane	735.5 nm (lg ε 5.61), 659.0 (4.90), 354.0 (5.16), 229.5 (5.19)	R = OCH_2CF_3 Ar = 	823
		1,4-dioxane	734.0 nm (lg ε 5.61), 658.0 (4.90), 354.5 (5.13), 229.5 (5.16)	R = OCH_2CF_3 Ar = 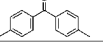	823
		1,4-dioxane	738.5 nm (lg ε 5.59), 662.0 (4.90), 358.0 (5.18), 319.5 (4.99), 231.0 (5.29)	R = OCH_2CF_3 Ar = 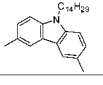	823
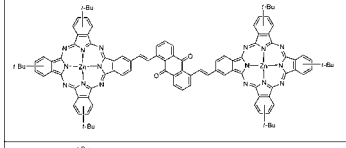	Zn(II)	THF	690 nm (lg ε 5.15), 674 (5.08), 350 (4.93)		1284
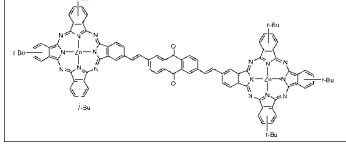	Zn(II)	THF	696 nm (lg ε 5.18), 675 (5.10), 352 (4.94)		1285, 1284

(*Continued*)

Table 11. (*Continued*)

Structure	M	Solvent	Transition Energy (Intensity)	Remark	Ref.
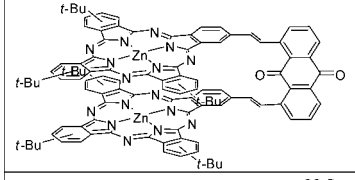	Zn(II)	THF	683 nm (lg ε 5.0), 348 (4.90)		1284
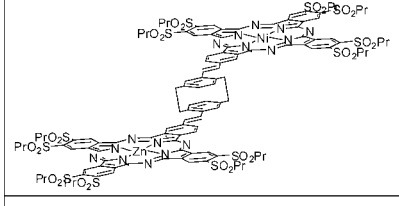	Ni(II), Zn(II)	$CHCl_3$	679 nm (lg ε 5.15), 639 (5.02), 347 (5.05), 298 (4.99)		908
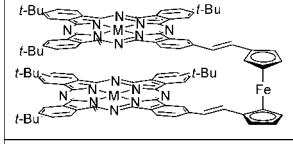	Zn(II)	$CHCl_3$	679 nm (lg ε 4.93), 649 (4.92), 341 (5.00)		812
	Co(II)	$CHCl_3$	672 nm (lg ε 4.48), 643 (4.42), 325 (4.56), 292 (4.59)		812
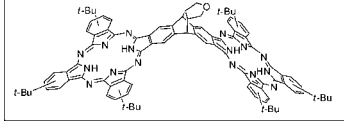	2H	$CHCl_3$	701 nm, 665, 645, 605, 344, 291		1286

(*Continued*)

Table 11. (*Continued*)

Structure	M	Solvent	Transition Energy (Intensity)	Remark	Ref.
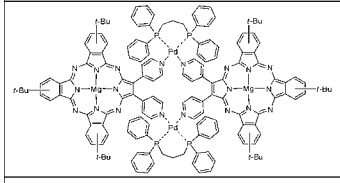	Mg(II)	$CHCl_3$	727 nm (lg ε 5.12), 666sh, 610 (4.76), 554sh, 361 (4.99), 266 (4.95)		1037
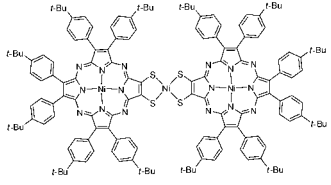	Ni(II)	$CHCl_3$	676 nm, 640, 596, 476, 365		1021
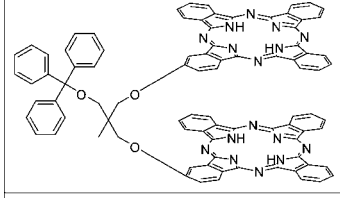	2H	DCM	694 nm (lg ε 4.71), 656 (4.66), 602 (4.22), 338 (4.66), 278 (4.75)		598
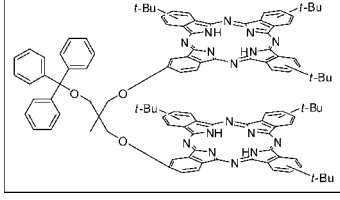	2H	DCM	640 nm (lg ε 4.99), 338 (5.07), 290 (4.99)		598

(*Continued*)

Table 11. (*Continued*)

Structure	M	Solvent	Transition Energy (Intensity)	Remark	Ref.
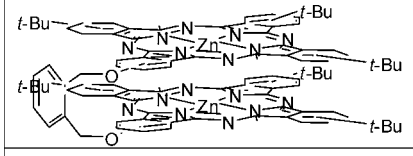	Zn(II)	$CHCl_3$	676 nm, 639, 340		860
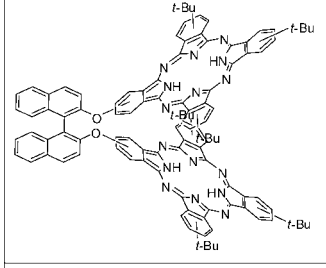	2H	$CHCl_3$	700sh nm, 660sh, 637 (ε 132.000), 337 (144.000), 289 (107.000)		1287
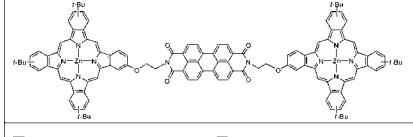	Zn(II)	DMF	677 nm (lg ε 5.28), 617 (4.59), 543 (4.70), 501 (4.27), 350 (5.03)		864
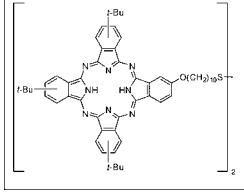	2H	$CHCl_3$	702 nm (lg ε 0.859), 665 (1.214), 643 (1.135), 339 (1.328)		859

(*Continued*)

Table 11. (*Continued*)

Structure	M	Solvent	Transition Energy (Intensity)	Remark	Ref.
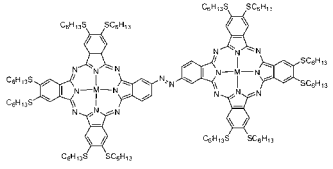	Co(II)	$CHCl_3$	710 nm (lg ε 4.770), 640sh (4.356), 330 (4.836), 280 (4.883)		1288
	Zn(II)	$CHCl_3$	705 nm (lg ε 4.809), 635sh (4.256), 360 (4.583), 275 (4.914)		1288
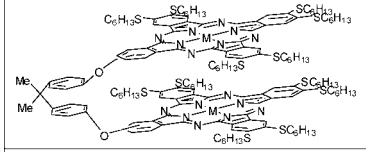	Zn(II)	$CHCl_3$	701 nm (lg ε 4.88), 630 (4.34), 361 (4.88)		1289
	Co(II)	$CHCl_3$	682 nm (lg ε 4.95), 624 (4.64), 325 (5.02)		1289
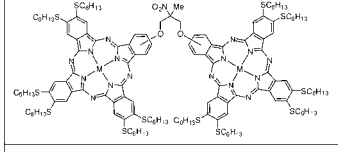	Zn(II)	$CHCl_3$	712 nm (lg ε 4.59), 322 (4.57)		1290
	Co(II)	$CHCl_3$	715 nm (lg ε 4.42), 639sh (4.27), 315 (4.61)		1290
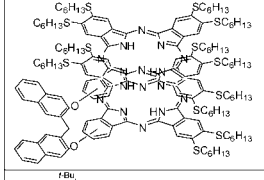	2H	DCM	730 nm (lg ε 5.149), 690 (5.406), 645 (5.470), 330 (5.733)		1291
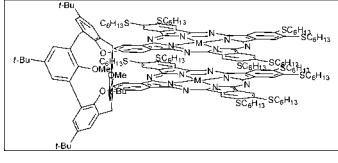	Zn(II)	$CHCl_3$	694 nm (lg ε 4.650), 632 (4.406), 360 (4.675)		1292

(*Continued*)

Table 11. (*Continued*)

Structure	M	Solvent	Transition Energy (Intensity)	Remark	Ref.
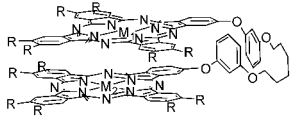	2H	DCM	701.5 nm (lg ε 5.16), 667.5 (5.20), 640.5 (5.02), 611.0sh, 393.5sh, 339.5 (5.10), 293.0 (5.00)	R = 	666
	Ni(II)	DCM	670.5 nm (lg ε 5.15), 628.5 (5.11), 577.0sh, 383.0sh, 299.5 (5.26)	R = 	666
	M_1 = 2H, M_2 = Ni(II)	DCM	699sh nm, 671.0 (lg ε 5.18), 644.0 (5.07), 392.0sh, 331.0sh, 300.5 (5.17)	R = 	666
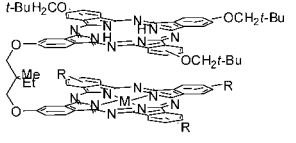	2H	DCM	692 nm (lg ε 4.71), 656 (4.68), 638 (4.34), 600 (4.12), 338 (4.52)	R = H	684
		THF	692 nm (lg ε 4.92), 656 (4.94), 636 (4.57), 596 (4.35), 338 (4.75)	R = H	684
		DCM	638 nm (lg ε 5.01), 338 (5.07)	R = *t*-Bu	684
		Toluene	638 nm (lg ε 5.01), 340 (5.04)	R = *t*-Bu	684
	Cu(II)	DCM	672 nm (lg ε 4.87), 638 (4.91), 336 (4.98)	R = OCH_2(*t*-Bu)	684
		Toluene	704sh nm, 674 (lg ε 4.99), 638 (5.01), 400sh, 340 (5.05)	R = OCH_2(*t*-Bu)	684
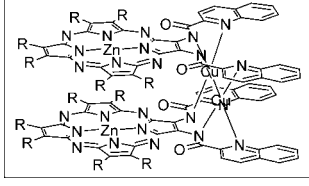	Zn(II)	DCM: MeOH = 10: 1	601 (4.38), 335 (4.63), 240 (4.66), 215 (4.56)	R = Pr	1018
		DCM: MeOH = 25: 1	630 (4.16), 338 (4.33), 240 (4.76)	R = Ph(4-*t*-Bu)	1018

(*Continued*)

Table 11. (*Continued*)

Structure	M	Solvent	Transition Energy (Intensity)	Remark	Ref.
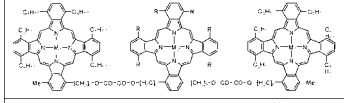	2H	Toluene or cyclohexane	728 nm (10^{-5} ε 1.85), 695 (2.03)	n = 6, R = C_8H_{17}	803
	Cu(II)	Toluene or cyclohexane	705 nm (10^{-5} ε 2.2), 646 (1.54)	n = 6, R = C_8H_{17}	803
	M_1 = Cu(II), M_2 = 2H	Toluene or cyclohexane	700 nm, 651	n = 5, R = C_7H_{15}	803
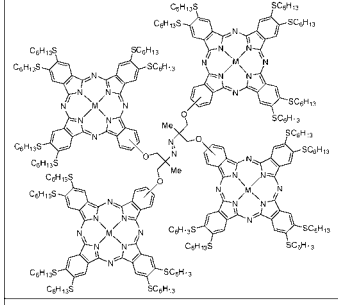	Zn(II)	DMF	697 nm (lg ε 4.63), 634sh (4.03), 367 (4.30)		1290
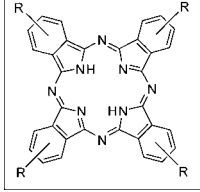	Cu(II)	DCM	698sh nm (lg ε 4.64), 662sh (4.73), 636 (4.78), 336 (4.81)	R = 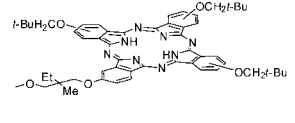	684

(*Continued*)

Table 11. (*Continued*)

Structure	M	Solvent	Transition Energy (Intensity)	Remark	Ref.
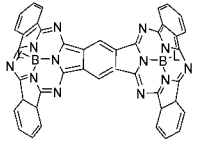	BCl	$CHCl_3$	692 nm (lg ε 4.9), 662 (4.4), 636 (4.4), 605 (4.5), 592sh, 441 (3.9), 320 (4.5), 278 (4.4)	$\alpha\alpha\beta\beta$ = F	308, 306
		$CHCl_3$	693 nm (lg ε 4.9), 661 (4.4), 635 (4.4), 604 (4.5), 592sh, 441 (3.7), 319 (4.5), 278 (4.4)	$\alpha\alpha\beta\beta$ = F	1111
		$CHCl_3$	690 nm (10^{-4} ε 11.1), 658 (3.39), 602 (3.94), 443 (0.86), 320 (4.61), 275 (3.81)	$\alpha\alpha\beta\beta$ = F	307
	BBr	$CHCl_3$	718 nm, 596, 567sh, 537, 305	β = *t*-Bu	305
	BL	$CHCl_3$	706 nm (lg ε 4.8), 675 (4.3), 647 (4.3), 609 (4.4), 599sh, 441 (3.8), 339 (4.4)	β = H L = OPh(4-*t*-Bu)	308
		$CHCl_3$	739 nm (lg ε 5.0), 704 (4.6), 676 (4.5), 630sh, 605 (4.7), 421 (4.7), 294 (5.1)	$\beta\beta$ = SC_8H_{17} L = OPh(4-*t*-Bu)	308
		$CHCl_3$	689 nm (lg ε 4.9), 657 (4.4), 631 (4.4), 601 (4.5), 586sh, 441 (3.9), 319 (4.5), 273 (4.5)	$\alpha\alpha\beta\beta$ = F L = OPh	308, 306
		$CHCl_3$	689 nm (lg ε 4.9), 657 (4.5), 633 (4.5), 601 (4.6), 589sh, 449 (3.9), 317 (4.6)	$\alpha\alpha\beta\beta$ = F L = OPh(4-*t*-Bu)	308
		$CHCl_3$	691 nm (lg ε 5.0), 660 (4.4), 633 (4.5), 603 (4.5), 590sh, 490 (3.9), 450 (3.8), 319 (4.6)	$\alpha\alpha\beta\beta$ = F L = 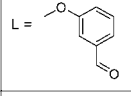	1111
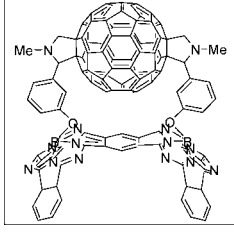	BL	$CHCl_3$	694 nm (lg ε 5.0), 659 (4.6), 634 (4.6), 606 (4.7), 590sh, 491 (4.2), 310 (4.9), 269 (5.1)	$\alpha\alpha\beta\beta$ = F	1111

(*Continued*)

Table 11. (*Continued*)

Structure	M	Solvent	Transition Energy (Intensity)	Remark	Ref.
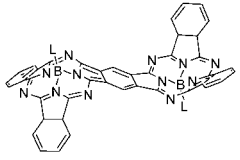	BCl	$CHCl_3$	693 nm (lg ε 4.9), 661 (4.4), 635 (4.4), 604 (4.5), 592sh, 441 (3.7), 319 (4.5), 278 (4.4)	$\alpha\alpha\beta\beta$ = F	306, 308
		$CHCl_3$	692 nm (lg ε 4.9), 662 (4.4), 636 (4.4), 605 (4.5), 592sh, 441 (3.9), 320 (4.5), 278 (4.4)	$\alpha\alpha\beta\beta$ = F	1111
		$CHCl_3$	693 nm (10^{-4} ε 6.43), 662 (1.90), 636 (1.96), 605 (2.39), 448 (0.51), 320 (2.78), 281 (3.35)	$\alpha\alpha\beta\beta$ = F	307
	BL	$CHCl_3$	704 nm (lg ε 4.9), 672 (4.6), 643 (4.5), 607 (4.6), 443 (4.0), 321 (4.6)	β = 1 L = OPh(4-*t*-Bu)	308
		$CHCl_3$	736 nm (lg ε 5.0), 703 (4.6), 672 (4.5), 629 (4.6), 620sh, 430 (4.4), 336sh, 298 (4.8)	$\beta\beta = SC_8H_{17}$, L = OPh(4-tBu)	308
		$CHCl_3$	688 nm (lg ε 4.9), 657 (4.4), 631 (4.4), 600 (4.5), 587sh, 441 (3.7), 319 (4.4), 274 (4.3)	$\alpha\alpha\beta\beta$ = F, L = OPh	306, 308
		$CHCl_3$	688 nm (lg ε 4.8), 656 (4.3), 631 (4.4), 600 (4.4), 588sh, 439 (3.8), 314 (4.5)	$\alpha\alpha\beta\beta$ = F, L = OPh(4-tBu)	308
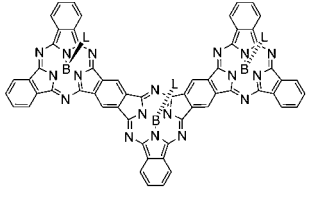	BCl	$CHCl_3$	755 nm (lg ε 4.9), 697 (4.6), 661 (4.5), 637 (4.4), 585 (4.5), 317 (4.6), 280 (4.6)	$\alpha\alpha\beta\beta$ = F	306, 308
	BL	$CHCl_3$	807 nm (lg ε 5.0), 735 (4.9), 697 (4.8), 617 (4.7), 433 (4.6), 350sh, 298 (5.0)	$\beta\beta = SC_8H_{17}$, L = OPh(4-tBu)	308
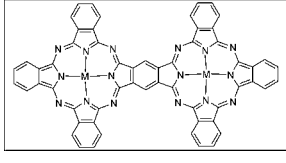	2H	$CHCl_3$	686 nm (10^{-5} ε 1.78), 347 (1.92)		406
	Zn(II)	DMSO	692 nm, 668, 640, 603, 340		1293
		DMF	830 nm, 700-670, 638-606, 340		478
		DMSO	834 nm, 698-670, 646-610, 362		478
		py	834 nm, 696-678, 648-614, 344		478

(*Continued*)

Table 11. (*Continued*)

Structure	M	Solvent	Transition Energy (Intensity)	Remark	Ref.
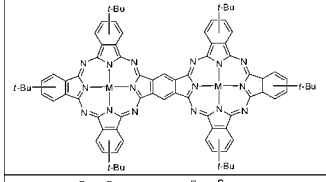	2H	THF	835 nm (lg ε 4.79), 687 (4.98), 343 (5.11)		1294
	Mg(II)	THF	848 nm (lg ε 4.99), 725 (4.51), 364 (4.76)		1294
	Zn(II)	THF	835 nm (lg ε 5.01), 717 (4.45), 358 (4.64)		1294
	Dy(III)(OAc)	THF	837 nm, 707, 674, 353		1295
	Yb(III)(OAc)	THF	837 nm, 706, 673, 356		1295
	Lu(III)(OAc)	THF	834 nm, 704, 670, 358		1295
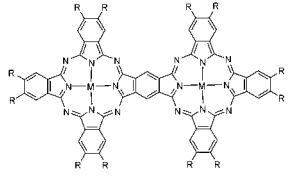	2H	$CHCl_3$	838 nm (10^{-5} ε 2.38), 748 (1.18), 664 (0.43), 447 (0.60), 354 (1.76), 301 (1.01)	R = 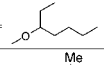	1296
		toluene	853 nm (ε 11.750), 830 (12.050), 745 (13.400), 358 (27.800)	R = 	661
	2H.i	PhCl	1151 nm (ε 95.000), 1074 (43.000), 996 (31.000), 694 (40.000), 507 (46.000), 338 (114.000)	R = 	663
	Cu(II)	$CHCl_3$	847 nm (10^{-5} ε 2.57), 773 (1.26), 736 (1.00), 452 (0.48), 350 (1.76), 288 (1.42)	R = 	1296
	Zn(II)	THF	847 nm (lg ε 4.93), 703 (4.59), 356 (4.79)	R = Et	1294
		THF	847 nm (lg ε 4.92), 704 (4.62), 359 (4.85)	R = Bu	1294
		THF	842 nm (lg ε 4.90), 716 (4.62), 360 (4.73)	R = OPr	1294
		DMF	658 nm, 638-602, 340	R = F	478
		DMSO	626 nm, 568, 342	R = F	478
		py	660 nm, 626-604, 344	R = F	478
		THF	840 nm (ε 470.000), 363 (187.000)	R = 	1297
		THF	840 nm (ε 470.000), 794 (62.000), 748 (93.900), 722 (108.000), 587sh (24.000), 363 (187.000)	R = 	663
		THF	840 nm (10^{-5} ε 4.70), 794 (0.61), 748 (0.93), 722 (1.08), 363 (1.87)	R = 	662

(*Continued*)

Table 11. (*Continued*)

Structure	M	Solvent	Transition Energy (Intensity)	Remark	Ref.
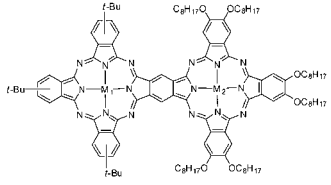	Ni(II)	$CHCl_3$	700 nm (lg ε 4.98), 660 (4.97), 640sh, 590sh, 335sh, 292 (5.08), 271 (5.09)		836
	M_1 = Ni(II), M_2 = Zn(II)	$CHCl_3$	703 nm (lg ε 5.01), 661 (5.01), 640sh, 590sh, 343 (4.94), 296 (5.02), 270 (5.03)		836
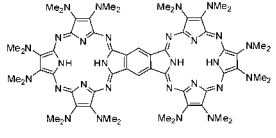	2H	DCM	839 nm (lg ε 4.90), 548 (4.64), 346 (4.93)		1029
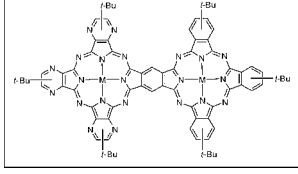	2H	THF	841 nm, 715, 337, 294		1298

(*Continued*)

Table 11. (*Continued*)

Structure	M	Solvent	Transition Energy (Intensity)	Remark	Ref.
	Zn(II)	THF	824 nm, 695, 644, 356, 285		1298
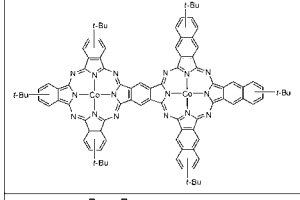	Co(II)		819 nm, 692, 334		1299
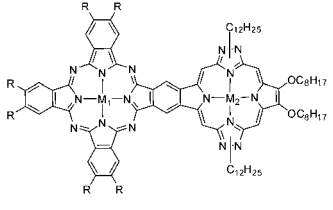	Ni(II)	$CHCl_3$	732 nm (lg ε 3.97), 672 (3.98), 617sh, 370 (4.25), 277 (4.57)	$R = OC_8H_{17}$	1300
	M_1 = Zn(II), M_2 = Ni(II)	$CHCl_3$	730 nm (lg ε 4.73), 680 (4.54), 660sh, 615sh, 450sh, 362 (4.82), 290 (4.82), 273 (4.84)	$R = OC_8H_{17}$	1300
	Zn(II)	$CHCl_3$	730 nm (lg ε 4.79), 685 (4.72), 660sh, 362 (5.00), 282sh, 265 (4.98)	$R = OC_8H_{17}$	1300
	M_1 = Ni(II), M_2 = Zn(II)	$CHCl_3$	721 nm (lg ε 4.56), 666 (4.63), 670sh, 367 (4.89), 285 (5.13), 278 (5.13)	$R = OC_8H_{17}$	1300
	Ni(II)	$CHCl_3$	698 nm (lg ε 4.96), 398sh, 345 (4.82), 284 (4.99)	$R = SO_2C_8H_{17}$	1300
	Ni(II)	$CHCl_3$	699 nm (lg ε 4.56), 688, 669 (4.26)	$R = SO_2C_8H_{17}$	758
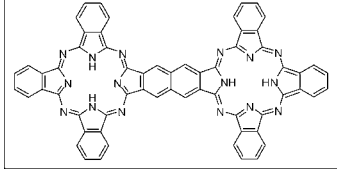	2H	$CHCl_3$	720 nm (10^{-5} ε 1.07), 694 (1.24), 341 (1.53)		406

(*Continued*)

Table 11. (*Continued*)

Structure	M	Solvent	Transition Energy (Intensity)	Remark	Ref.
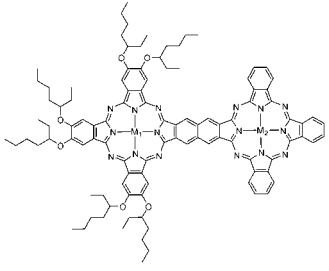	2H	DCM	688.0 nm (lg ε 4.28), 673.0 (4.35), 667.0sh (4.27), 358.0 (4.45)		330, 676
	Mg(II)	DCM	706.0sh nm (lg ε 4.78), 676.0 (4.89), 652.0sh (4.79), 432.5 (4.73), 362.0 (4.90)		330, 676
	Ni(II),	DCM	697.5 nm, 669.0, 640.0sh, 321.0		635
	M_1 = Ni(II), M_2 = Cu(II)	DCM	699.5 nm, 661.0, 638.0sh, 326.0		635
	Ga(III)Cl	DCM	718.5sh nm (lg ε 4.61), 687.5 (4.85), 654.5 (4.65), 344.0 (4.85)		330
	In(III)Cl	DCM	724.0sh nm (lg ε 4.46), 689.0 (4.69), 663.0 (4.49), 353.0 (4.70)		676
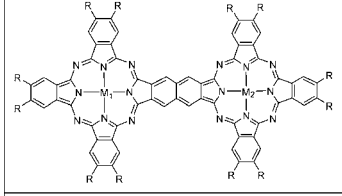	Ni(II),	DCM	664.5 nm, 626.0sh, 398.5, 370.5, 312.5	R = 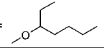	635
	M_1 = Ni(II), M_2 = Cu(II)	DCM	672.5 nm, 631.0sh, 304.0	R = 	635
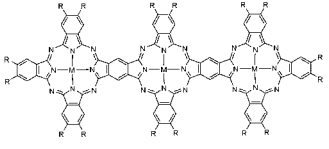	2H	THF	944 nm (ε 400.000), 890 (89.000), 836 (100.000), 754 (85.000), 660sh (45.000), 608 (41.000), 418sh (72.000), 356 (215.000)	R = 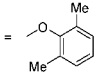	1297
		toluene	944 nm (ε 10.600), 887 (11.300), 833 (12.000), 760 (13.150), 362 (27.600)		661
	Zn(II)	THF	942 nm (ε 680.000), 885 (86.000), 832 (115.000), 746 (102.000), 709sh (62.000), 648 (48.000), 607 (48.000), 365 (253.000)		1297
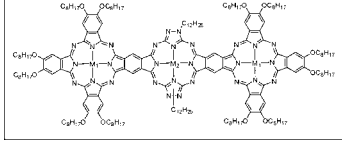	M_1 = Zn(II), M_2 = Ni(II)	$CHCl_3$	755 nm (lg ε 4.15), 679 (4.11), 364 (4.50), 252 (4.75)		836

(*Continued*)

Table 11. (*Continued*)

Structure	M	Solvent	Transition Energy (Intensity)	Remark	Ref.
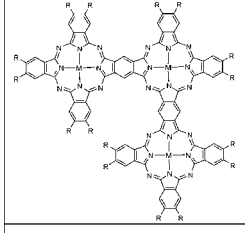	2H	THF	907 nm (ε 288.000), 860 (209.000), 810 (118.000), 773sh (102.000), 729 (107.000), 668sh (66.000), 420sh (84.000), 357 (232.000)	R = 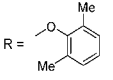	1297
	Zn(II)	THF	894 nm (ε 364.000), 849 (239.000), 787 (118.000), 715 (83.000), 664sh (64.000), 364 (251.000)		1297
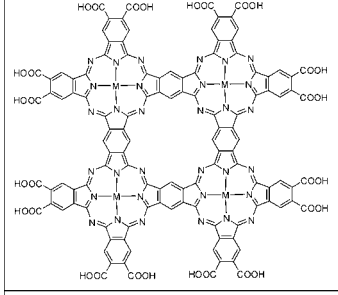	2H	H_2SO_4	492 nm, 434, 416, 321, 242		1301
	Cr(II)	H_2SO_4	751 nm, 490, 411, 322, 289, 230		1301
	Fe(II)	H_2SO_4	811 nm, 672, 413, 385, 324, 246, 222		1301
	Co(II)	H_2SO_4	792 nm, 744, 709, 679, 409, 320, 233		1301
	Cu(II)	H_2SO_4	764 nm, 712, 430, 411, 370, 322, 244		1301
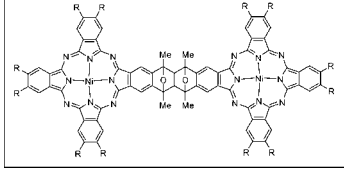	Ni(II)	DCM	668 nm, 396	R = 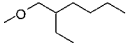	627

(*Continued*)

Table 11. (*Continued*)

Structure	M	Solvent	Transition Energy (Intensity)	Remark	Ref.
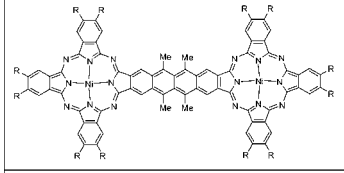	Ni(II)	DCM	690.5 nm, 673.5, 302, 286	R = 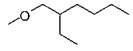	627
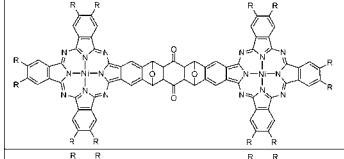	Ni(II)	DCM	660 nm, 629, 440sh, 392, 288	R = 	929
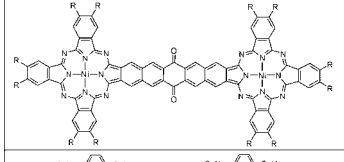	Ni(II)	DCM	730sh nm, 681, 333, 287	R = 	929
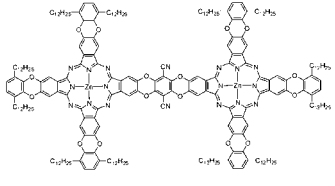	Zn(II)	THF	680 nm, 625, 358		919

(*Continued*)

Table 11. (*Continued*)

Structure	M	Solvent	Transition Energy (Intensity)	Remark	Ref.
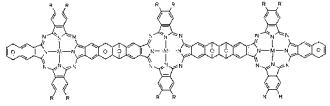	2H	DCM	699 nm, 661, 645, 343	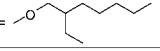	540
	In(III)L	DCM	686 nm, 350	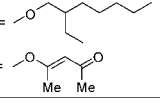	540
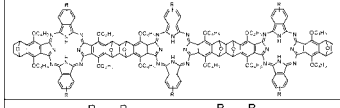	2H	$CHCl_3$	750 nm, 704, 663.5, 339	R = *t*-Bu	885
		Poly(chlorotrifluoroethylene)	745 nm, 684	R = NO_2	885
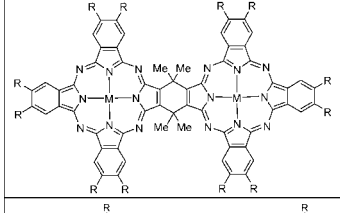	2H	$CHCl_3$	708 nm (10^{-5} ε 3.22), 675 (2.57), 654 (0.93), 611 (0.50), 394 (0.72), 349 (1.57)		662
	Zn(II)	THF	682 nm (10^{-5} ε 6.9), 652 (0.85), 615 (0.83), 356 (2.2)		662
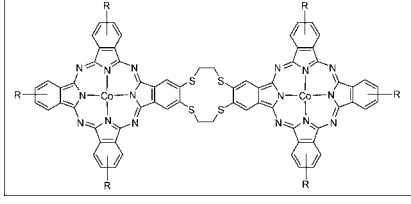	Co(II)	DMSO	682 nm (lg ε 4.77), 642sh (4.61), 430sh (4.08), 337 (5.09)	R = NO_2	889
		DMSO	716 nm (lg ε 4.897), 643 (4.710), 358 (4.952)	R = NH_2	889

(*Continued*)

Table 11. (*Continued*)

Structure	M	Solvent	Transition Energy (Intensity)	Remark	Ref.
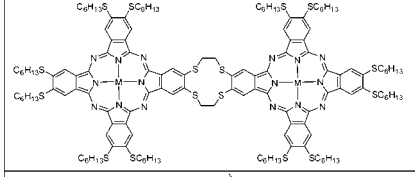	Lu(III)L	$CHCl_3$	715 nm (10^{-4} ε 14.41), 642 (29.75), 365 (73.81), 289 (91.19)	L = OAc	1280
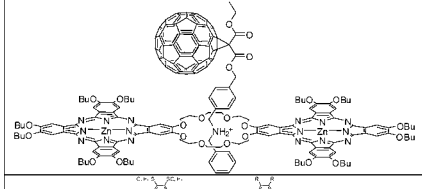	Zn(II)	$CHCl_3$	677 nm (lg ε 4.98), 629 (4.92), 343 (4.99), 293 (4.93)		1302
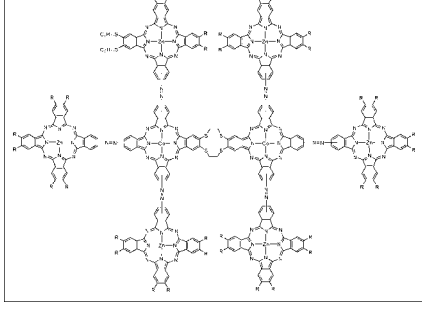	Co(II), Zn(II)	DMSO	700 nm (lg ε 4.968), 364 (4.473), 290 (5.039)	R = SC_6H_{13}	889

(*Continued*)

Table 11. (*Continued*)

Structure	M	Solvent	Transition Energy (Intensity)	Remark	Ref.
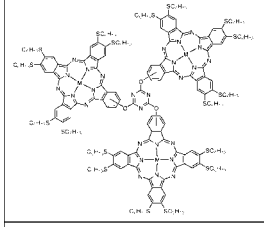	Zn(II)	$CHCl_3$	730 nm (lg ε 5.733), 702 (5.725), 390 (5.339), 344 (5.336)		1303
	Co(II)	$CHCl_3$	690 nm (lg ε 4.997), 674 (4.937), 612sh (4.413), 370 (4.655), 276 (4.979)		1303
	Cu(II)	$CHCl_3$	690 nm (lg ε 5.785), 616sh (5.170), 354 (5.472)		1303
	Lu(III)OAc	$CHCl_3$	706 nm (lg ε 7.15), 636sh (6.49), 378 (7.63)		1281
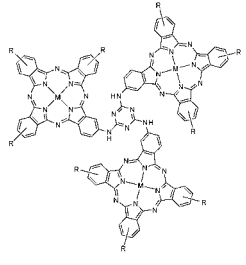	2H	DMSO	688 nm (lg ε 4.35), 634 (4.41), 334 (4.55)	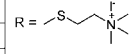	883
	Zn(II)	DMSO	694 nm (lg ε 4.43), 654 (4.15), 356.5 (4.31)		883
	Co(II)	DMSO	675.5 nm (lg ε 4.23), 322.5 (4.45)		883
	2H	DMSO	688.5 nm (lg ε 4.35), 646.5 (4.30), 335.5 (4.45)	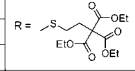	883
	Zn(II)	DMSO	690 nm (lg ε 4.43), 653 (4.24), 355.5 (4.39)		883
	Co(II)	DMSO	678.5 nm (lg ε 4.32), 313.5 (4.58)		883
	2H	DMSO	681.5 nm (lg ε 5.41), 635 (5.13), 358.5 (5.33)	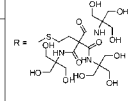	883
	Zn(II)	DMSO	691.5 nm (lg ε 5.37), 657 (5.15), 355 (5.32)		883
	Co(II)	DMSO	692.5 nm (lg ε 5.19), 316 (5.34)		883
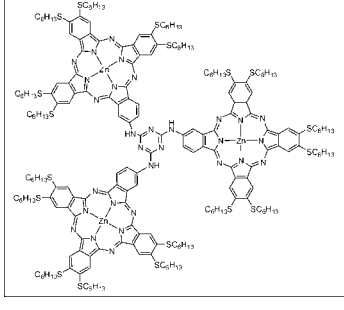	Zn(II)	$CHCl_3$	710 nm (lg ε 5.221), 638 (4.568), 439sh (4.272), 363 (4.816), 335 (4.750)		882

(*Continued*)

Table 11. (*Continued*)

Structure	M	Solvent	Transition Energy (Intensity)	Remark	Ref.
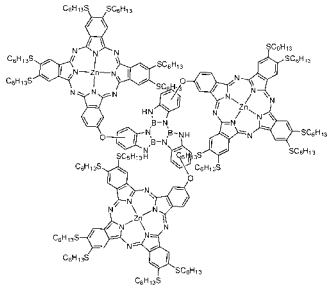	Zn(II)	$CHCl_3$	706 nm (ε 122.608), 629 (31.304), 434 (33.913), 321 (120.869)		866
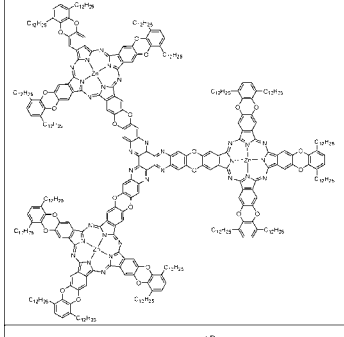	Zn(II)	THF	686 nm, 628, 360		919
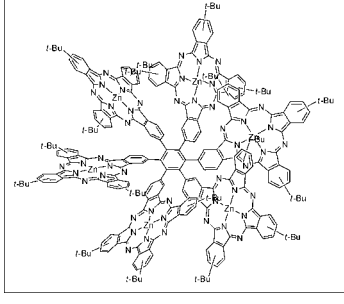	Zn(II)	THF	676 nm		907

(*Continued*)

Table 11. (*Continued*)

Structure	M	Solvent	Transition Energy (Intensity)	Remark	Ref.
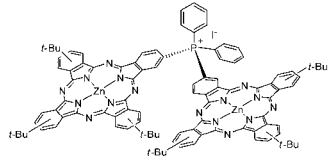	Zn(II)	THF	678 nm (ε 172.000), 666 (83.000), 643 (51.000), 603 (13.000), 358 (63.000)		890
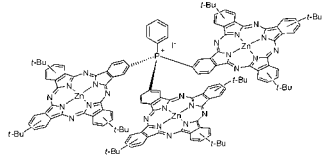	Zn(II)	THF	678 nm (ε 229.000), 348 (178.000)		890
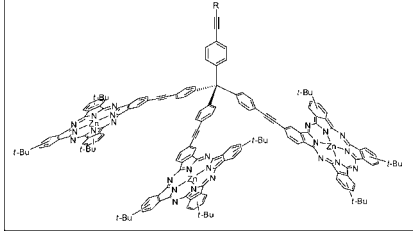	Zn(II)	THF	686 nm (lg ε 5.57), 673 (5.54), 348 (5.39)	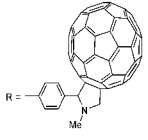	1304
		THF	686 nm (lg ε 5.5), 673 (5.5), 348 (5.3)	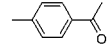	1304

(*Continued*)

Table 11. (*Continued*)

Structure	M	Solvent	Transition Energy (Intensity)	Remark	Ref.
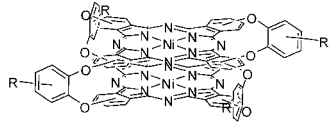	Ni(II)	DCM	670 nm	R = H	1305
		DCM	673 nm	R = *t*-Bu	1305
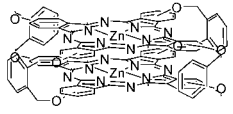	Zn(II)	$CHCl_3$	680 nm, 613, 352		860
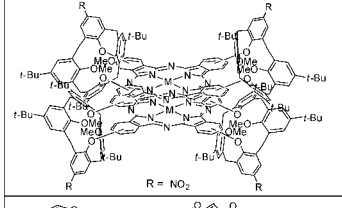	Zn(II)	AcOH	726 nm (lg ε 4.492), 692 (4.627), 634 (4.237), 304 (4.760)	R = NO_2	1306
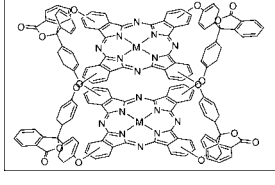	Co(II)	THF	669 nm (lg ε 4.929), 602 (4.568), 324 (4.734)		1307
	Zn(II)	THF	674 nm (lg ε 5.236), 609 (4.544), 351 (4.878)		1307

(*Continued*)

Table 11. (*Continued*)

Structure	M	Solvent	Transition Energy (Intensity)	Remark	Ref.
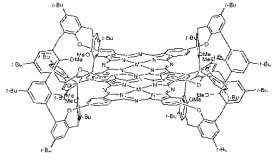	2H	MeOH	710 nm (lg ε 4.042), 674 (3.968), 626 (3.303), 336 (3.924)		1292
	Zn(II)	$CHCl_3$	688 nm (lg ε 4.706), 620 (4.117), 350 (4.575)		1292
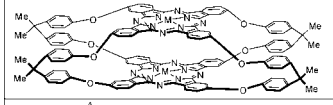	Co(II)	$CHCl_3$	675 nm (lg ε 4.70), 613 (4.32), 330 (4.67)		1289
	Zn(II)	$CHCl_3$	682 nm (lg ε 4.56), 613 (3.88), 337 (4.33), 307 (4.49)		1289
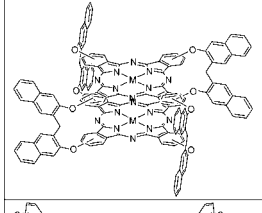	2H	DMSO	710 nm (lg ε 5.174), 680 (5.336), 630 (5.398), 325 (5.693)		1291
	Co(II)	DCM	690 nm (lg ε 5.632), 627 (5.033), 343 (5.556)		1291
	Zn(II)	DCM	730 nm (lg ε 5.545), 700 (5.488), 635 (5.100), 375 (5.362), 325 (5.510)		1291
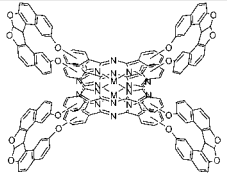	2H	THF	704 nm (lg ε 4.085), 672 (4.172), 643 (4.119), 335 (4.511)		922
	Co(II)	DMF	705 nm (lg ε 3.799), 674 (3.843), 646 (3.901), 620sh (3.801), 339 (4.248)		1308
	Zn(II)	DMF	684 nm (lg ε 3.358), 620 (2.818), 339 (3.390)		1308

(*Continued*)

Table 11. (*Continued*)

Structure	M	Solvent	Transition Energy (Intensity)	Remark	Ref.
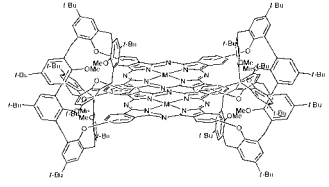	Zn(II)	$CHCl_3$	688 nm (lg ε 4.538), 620 (3.996), 342 (3.455)		1309
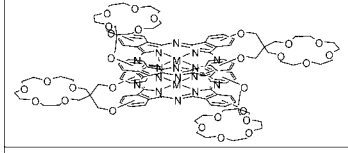	Co(II)	DMF	660 nm (lg ε 5.43), 602 (4.83), 333 (5.32)		1216
	Zn(II)	DMF	675 nm (lg ε 5.79), 638 (5.56), 348 (5.71)		1216
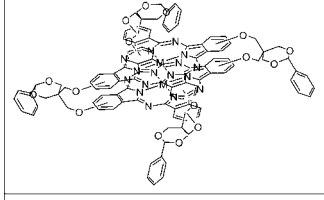	Co(II)	DMF	665 nm (lg ε 5.03), 625 (4.88), 330 (5.10), 278 (4.99)		1310
	Zn(II)	DMF	680 nm (lg ε 5.29), 638 (4.92), 353 (5.12)		1310
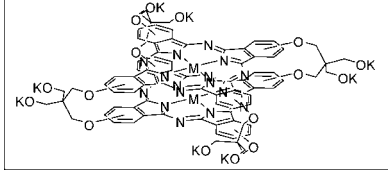	Co(II)	DMF	674 nm (lg ε 5.13), 610 (4.69), 336 (4.88)		1310
		H_2O	685 nm (lg ε 4.36), 623 (4.47), 279 (4.67)		1310
	Zn(II)	DMF	680 nm (lg ε 5.08), 639 (5.02), 344 (5.11)		1310
		H_2O	687 nm (lg ε 4.62), 637 (4.70), 338 (4.53)		1310

(*Continued*)

Table 11. (*Continued*)

Structure	M	Solvent	Transition Energy (Intensity)	Remark	Ref.
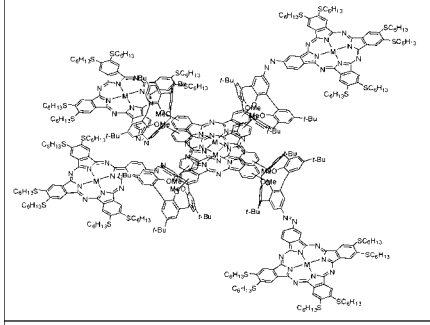	Zn(II)	THF	694 nm (lg ε 4.617), 630 (4.067), 360 (4.388)		1306
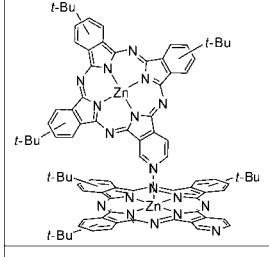	Zn(II)	decane	696sh nm, 690, 656		1158
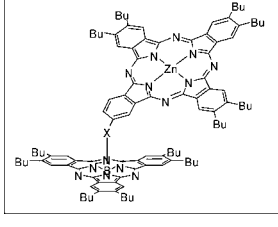	Zn(II)	THF	681 nm (lg ε 4.85), 614 (4.14), 573 (4.42), 348 (4.59)	X = —O—	845
		THF	682 nm (lg ε 4.83), 615 (4.10), 572 (4.38), 349 (4.55)	X = 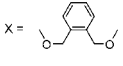	1091

(*Continued*)

Table 11. (*Continued*)

Structure	M	Solvent	Transition Energy (Intensity)	Remark	Ref.
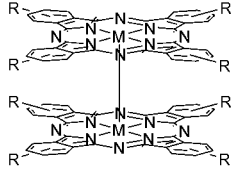	Rh(II)	DMF	629 nm (lg ε 4.68), 573 (4.20), 372 (4.31), 308 (4.80)	R = H	493
		DCB	633 nm (lg ε 4.80), 578 (4.34), 372 (4.68)	R = H	493
	Ru(II)L	Benzene	630 nm, 567, 444, 339	R = *t*-Bu L = 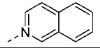	224
	In(III)L	Toluene	697 nm	R = *t*-Bu L = 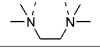	341
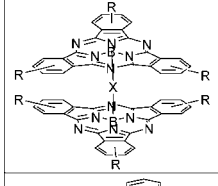	B	DCM	562 nm (ε 140,000), 550sh, 525sh, 303 (85,000)	R = H X = 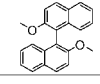	1112
		$CHCl_3$	538 nm (10^{-4} ε 3.06), 307 (2.63), 264 (3.25)	R = *t*-Bu X = —O—	302
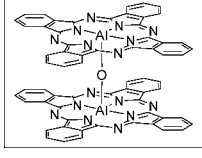	Al(III)	THF	673 nm, 638		316

(*Continued*)

Table 11. (*Continued*)

Structure	M	Solvent	Transition Energy (Intensity)	Remark	Ref.
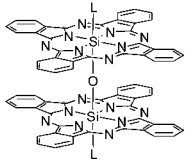	Si(IV)	$CHCl_3$	635 nm (10^{-1} ε 33.158), 587 (5.5765), 561 (3.9954), 331 (16.8562), 284 (11.4221)	L = 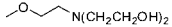	451
		$CHCl_3$	635 nm (10^{-1} ε 72.5280), 588 (1.9195), 561 (1.4425), 330 (43.1991), 285 (3.3188)	L = 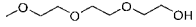	451
		$CHCl_3$	636 nm (10^{-1} ε 20.1947), 587 (4.1231), 562 (3.0501), 331 (11.2921), 284 (6.9204)	L = 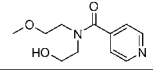	451
		py	636 nm, 580, 560, 332	L = OH	439
		THF	630 nm, 600, 575, 555, 328		439
		DCM	634 nm, 605, 577, 557, 331.5, 282		439
		py	635 nm, 608sh, 574, 555, 332	L = 	439
		THF	630 nm, 603sh, 574, 554, 331		439
		DCM	634 nm, 605sh, 574, 554, 330		439
		Benzene	633 nm, 606sh, 574, 554, 332		439
		THF	628 nm, 604sh, 574, 554, 331, 282.5	L = 	439
		Toluene	632.0 nm	L = $OSi(C_6H_{13})_3$	359
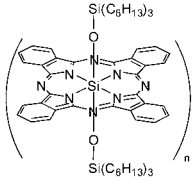	Si(IV)	Toluene	632.0 nm (lg ε 5.5)	n = 2	446
		Toluene	620.0 nm (lg ε 5.4)	n = 3	446
		Toluene	616.0 nm (lg ε 5.3)	n = 4	446

(*Continued*)

Table 11. (*Continued*)

Structure	M	Solvent	Transition Energy (Intensity)	Remark	Ref.
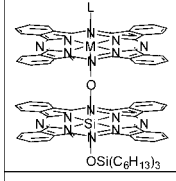	Ge(IV)	Toluene	635.1 nm	L = $OSi(C_6H_{13})_3$	359
	Sn(IV)	Toluene	642.4 nm	L = OH	359
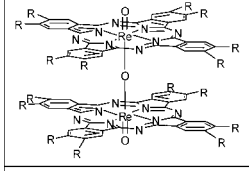	Re(V)	$CHCl_3$	778.5 nm, 701.5, 637.0, 380.5, 363.5	R = C_5H_{11}	156
		KBr	818.5 nm, 768.0, 691.0, 383.0	R = C_5H_{11}	156
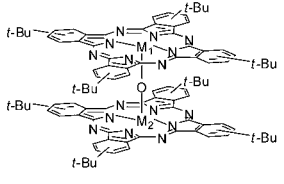	Cr(III)	Toluene	629 nm (lg ε 4.47), 495 (3.86), 340 (4.65)		146
	Ga(III)	$CHCl_3$	693.0 nm, 662.5, 623.5, 357.5, 341.5		345
		$CHCl_3$	693 nm, 662.5sh, 623.5, 357.5		325
		Toluene	692 nn		329
	In(III)	$CHCl_3$	697.0 nm, 665.5, 628.0, 360.0, 343.0		345
		$CHCl_3$	696 nm, 665sh, 627.5, 360		325
		Toluene	694 nm		329, 341
	M_1 = Ga(III), M_2 = In(III)	$CHCl_3$	695.5 nm, 664.5, 626.0, 358.0, 340.0		345
	Mn(III)L	py	621 nm (lg ε 5.08), 340 (4.98)	L = py	528

(*Continued*)

Table 11. (*Continued*)

Structure	M	Solvent	Transition Energy (Intensity)	Remark	Ref.
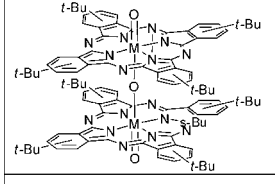	Re(V)	DCM	747 nm (lg ε 4.715), 688 (5.437), 374 (5.220)		181
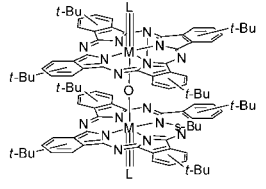	Re(II)	DCM	659 nm (lg ε 4.85), 634 (4.14), 603 (3.91), 575 (3.57), 554 (3.50), 353 (4.52), 340 (4.48), 289 (4.48), 257 (4.65)	L = 	102
	Mn(III)L	py	632 nm, 360	R = SO_2Ph, L = py	528
		py	735 nm, 345	R = SPh, L = py	528
	Fe(III)	$CHCl_3$	711 nm, 590sh, 360, 331, 300, 271sh	R = C_5H_{15}	1311
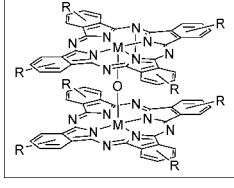	Sn(IV)OH	DCM	750 nm	R = C_5H_{11}	545
	Fe(III)	$CHCl_3$	692 nm, 600sh, 361, 289	R = C_5H_{11}	1311
	Mn(III)L	py	625 nm (lg ε 5.07), 350 (5.00)	R = SO_2Ph, L = py	528
		py	634 nm, 350	R = O(*t*-Bu), L = py	528
		py	635 nm, 335	R = S(*t*-Bu), L = py	528
		py	732 nm, 360	R = 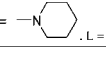 , L = py	528

(*Continued*)

Table 11. (*Continued*)

Structure	M	Solvent	Transition Energy (Intensity)	Remark	Ref.
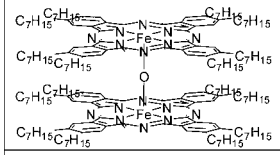	Fe(III)	$CHCl_3$	701 nm, 597sh, 362, 293		1311
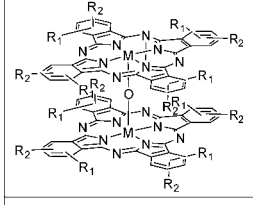	Mn(III)L	py	639 nm, 341	$R_1 = SO_2Ph$, $R_2 = t$-Bu, L = py	528
		py	625 nm, 350	$R_1 = SPh$, $R_2 = t$-Bu, L = py	528
		py	756 nm, 365	$R_1 = NMe_2$, $R_2 = t$-Bu, L = py	528
		py	645 nm, 333	R_1, $R_2 = NO_2$, L = py	528
		py	647 nm, 330	R_1, $R_2 = SO_2Ph$, L = py	528
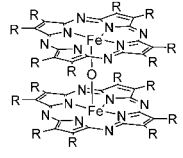	Fe(III)	$CHCl_3$	612 nm, 579sh, 351	R = Et	946
		DCM	660 nm (lg ε 5.00), 644 (5.10), 624 (5.00), 416sh (4.08), 384 (4.37), 320sh (3.96), 292 (4.11), 248 (4.30)	R = SEt	973
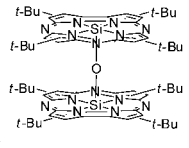	Si(IV)	$CHCl_3$	596 nm, 380		353

(*Continued*)

Table 11. (*Continued*)

Structure	M	Solvent	Transition Energy (Intensity)	Remark	Ref.
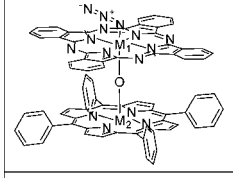	M_1 = Cr(III), M_2 = Mn(III)	DCM	1197 nm (lg ε 3.39), 1105 (2.76), 989 (3.02), 869 (3.92), 689 (4.91), 619 (4.34), 595sh (4.25), 474 (4.81), 395sh (4.77), 365sh (4.82), 342 (4.95)		1312
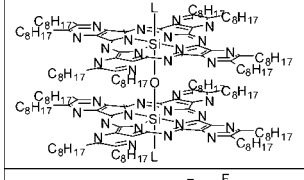	Si(IV)	DCM	611sh nm, 595, 570sh, 552sh, 342, 304sh, 252sh, 234	L = 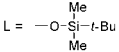	1124
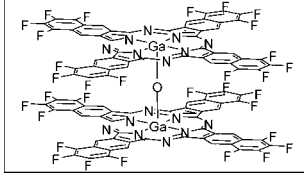	Ga(III)Cl	1-ClNp	805.0 nm, 763.0, 716.0, 339.0		327

(*Continued*)

Table 11. (*Continued*)

Structure	M	Solvent	Transition Energy (Intensity)	Remark	Ref.
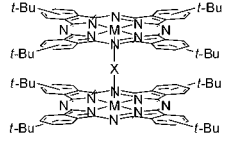	Ga(III)	Toluene	692 nm	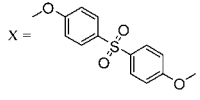	329
		$CHCl_3$	693 nm, 664.5sh, 624, 356.5		328
	In(III)	Toluene	694 nm	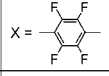	329
	In(III)Cl	Toluene	692 nm	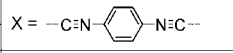	329
	In(III)(4-$PhCF_3$)	Toluene	694 nm		329
	Ru(II)CO	$CHCl_3$	651 nm (lg ε 5.43), 588 (4.76), 565 (4.68), 523 (4.40), 486sh, 410 (3.89), 347 (4.78), 329 (4.83), 300 (5.19), 247 (4.97)	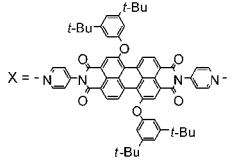	537
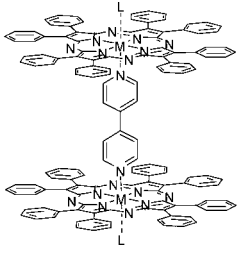	Ru(II)L	DCM	583 nm (lg ε 5.26), 538 (4.78), 431 (4.63), 353 (5.27), 276 (5.16)	L = --C≡N—*t*-Bu	958
		$CHCl_3$	587 nm, 541, 449, 357	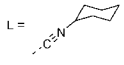	958

(*Continued*)

Table 11. (*Continued*)

Structure	M	Solvent	Transition Energy (Intensity)	Remark	Ref.
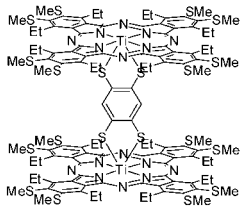	Ti(IV)	$CHCl_3$	757 nm (lg 5.05)		868
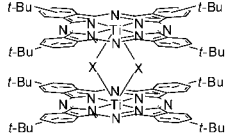	Ti(IV)	$CHCl_3$	697 nm	X = 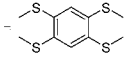	868
		$CHCl_3$	699.5 nm, 630.5, 346.0	X = 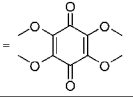	526
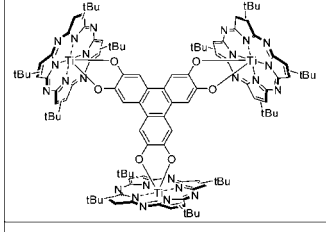	Ti(IV)	Toluene	601 nm (10^{-5} ε 1.86), 344 (1.28)		952
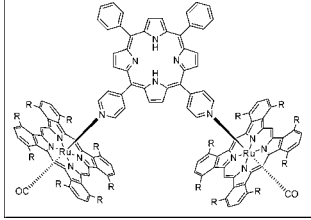	Ru(II)	DCM	671 nm (lg ε 5.07), 606 (4.46), 542 (3.90), 517 (4.01), 421 (5.11)	R = C_8H_{17}	551
		DCM	671 nm (lg ε 5.07), 606 (4.46), 542sh (3.90), 517 (4.01), 421 (5.11), 356 (4.55)	R = C_8H_{17}	552

(*Continued*)

Table 11. (*Continued*)

Structure	M	Solvent	Transition Energy (Intensity)	Remark	Ref.
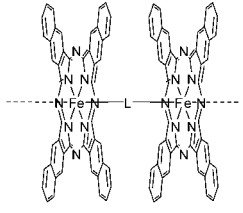	Fe(II)	Nujol	797 nm. 703sh. 485sh. 387. 276sh	L = 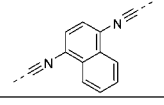	1054
		Nujol	787 nm. 694sh. 613. 432sh. 383. 264	L = 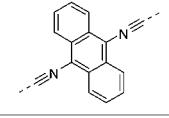	1054
		Nujol	1028 nm. 787. 695sh. 395. 278	L = 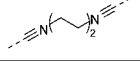	1054
		Nujol	786 nm. 697sh. 500sh. 378. 276	L = 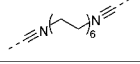	1054
		Nujol	796 nm. 695sh. 432sh. 408. 278	L = 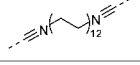	1054
		Nujol	811 nm. 697sh. 427sh. 392. 278	L = 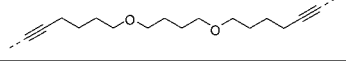	1054

(*Continued*)

Table 11. (*Continued*)

Structure	M	Solvent	Transition Energy (Intensity)	Remark	Ref.
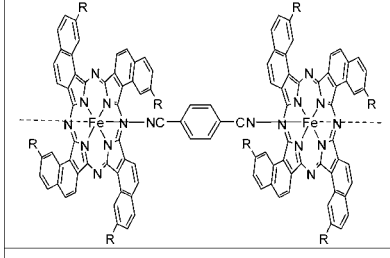	Fe(II)	Nujol	682 nm, 620, 383, 357, 252	R = *t*-Bu	1074
		Nujol	720 nm, 637, 390, 329	R = Me	1074
		Nujol	695 nm, 629, 377, 363, 274	R = Ph	1074
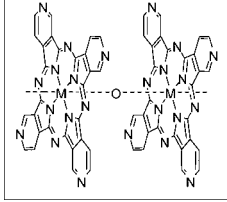	Si(IV)	DMF	615 nm (lg ε 5.5), 314 (5.2)		1313

Table 12. UV-vis absorption data of Pc analogs containing triazole units.

Structure	M	Solvent	Transition Energy (Intensity)	Remark	Ref.
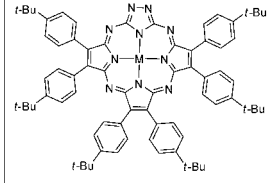	2H	$CHCl_3$	530 nm (lg ε 4.32), 486 (4.29), 417 (4.48), 323 (4.55), 242 (4.81)		1314
	Co(II)	$CHCl_3$	609 nm (lg ε 4.61), 564 (4.56), 500 (4.62), 378 (4.91), 331 (4.81), 247 (5.04)		1314
	Ni(II)	DCM	602 nm (lg ε 4.50), 579 (4.47), 472 (4.54), 374 (4.80), 325 (4.73), 250 (5.03)		1314
	Cu(II)	$CHCl_3$	630 nm (lg ε 4.44), 578 (4.40), 520 (4.48), 395 (4.74), 339 (4.66), 245 (4.83)		1314
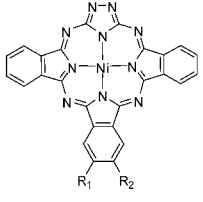	Ni(II)	TFA	582 nm (lg ε 3.54), 487 (3.86), 397 (4.38), 310sh, 293sh, 258 (4.56)	R_1, R_2 = H	1315
		$CHCl_3$	625 nm (lg ε 4.29), 572 (4.04), 531 (4.06), 497 (4.05), 374 (4.51), 313 (4.31), 259 (4.66)	R_1 = *t*-Bu, R_2 = H	1315
		d-TFA	580 nm (lg ε 3.84), 544 (3.90), 490sh, 400 (4.58), 318sh, 291sh, 258 (4.78)	R_1 = *t*-Bu, R_2 = H	1315
		$CHCl_3$	629 nm (lg ε 3.97), 572 (3.84), 531 (3.90), 497 (3.87), 369 (4.26), 260 (4.49)	$R_1 = OC_8H_{17}$, R_2 = H	1315
		$CHCl_3$	627 nm (lg ε 4.32), 574 (4.21), 533 (4.22), 497 (4.24), 371 (4.68), 288sh, 259 (4.83)	R_1, $R_2 = OC_{12}H_{25}$	1315
		TFA	580 nm (lg ε 3.50), 538 (3.75), 448sh, 390 (4.43), 291 (4.46), 258 (4.58)	$R_1 = NO_2$, R_2 = H	1315
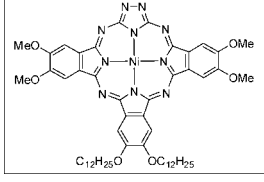	Ni(II)	$CHCl_3$	632 nm (lg ε 4.20), 575 (4.12), 534 (4.18), 430 (4.43), 365 (4.62), 290 (4.94)		1316

(*Continued*)

Table 12. (*Continued*)

Structure	M	Solvent	Transition Energy (Intensity)	Remark	Ref.
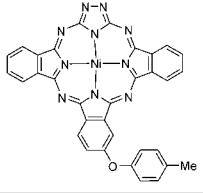	Ni(II)	$CHCl_3$	627 nm (lg ε 3.83), 364 (4.25)		1317
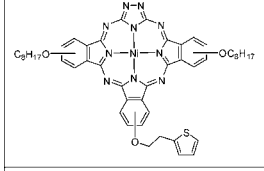	Ni(II)	$CHCl_3$	637 nm (lg ε 4.08), 529 (4.02), 516 (4.11), 421 (4.28), 363 (4.42), 274 (4.72)		1316
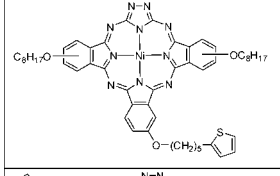	Ni(II)	$CHCl_3$	638 nm (lg ε 3.05), 423sh (3.15), 365 (3.79), 274 (4.39)		1318
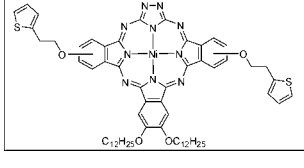	Ni(II)	$CHCl_3$	636 nm (lg ε 3.83), 572sh, 475sh, 367 (4.34), 292 (4.68)		1316

(*Continued*)

Table 12. (*Continued*)

Structure	M	Solvent	Transition Energy (Intensity)	Remark	Ref.
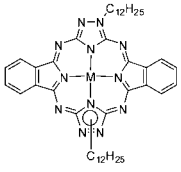	Mn(II)	$CHCl_3$	665 nm (lg ε 2.6), 590 (2.9), 545 (3.0), 505 (3.1), 460sh, 385 (4.6), 368 (4.6), 350sh, 290sh, 242 (4.7)		1319
	Fe(II)	$CHCl_3$	655 nm (lg ε 3.3), 595 (2.8), 480sh, 420sh, 385 (4.2), 365 (4.3), 345 (4.4), 335 (4.4), 270sh, 242 (4.7)		1319
	Co(II)	$CHCl_3$	665 nm (lg ε 3.7), 640 (3.6), 610 (3.5), 550 (3.5), 520 (3.6), 475 (3.9), 435 (4.2), 390sh, 365 (4.6), 352 (4.6), 340sh, 290 (4.6), 270sh, 242 (4.7)		1319
	Ni(II)	$CHCl_3$	665 nm (lg ε 2.5), 605 (2.9), 555 (3.0), 515 (3.0), 475 (2.9), 425 (4.6), 400 (4.5), 380 (4.5), 365 (4.5), 358 (4.5), 335 (4.6), 285sh, 242 (5.1)		1319
	Cu(II)	$CHCl_3$	645 nm (lg ε 2.8), 585 (3.0), 540 (3.2), 500 (3.2), 470 (3.2), 385 (4.6), 368 (4.6), 350sh, 290sh, 242 (4.7)		1319
	Zn(II)	$CHCl_3$	675 nm (lg ε 2.4), 580sh, 540sh, 500 (3.2), 470 (3.2), 385 (4.6), 368 (4.6), 350 (4.6), 290 (4.6), 242 (4.7)		1319
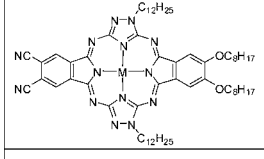	2H	$CHCl_3$	407 nm (lg ε 4.60), 383 (4.76), 363 (4.75), 282 (4.74), 261 (4.79), 228 (4.73)		1300
	Ni(II)	$CHCl_3$	451 nm (lg ε 4.34), 423 (4.29), 365 (4.57), 291 (4.77), 271 (4.79), 252 (4.78)		1300
	Zn(II)	$CHCl_3$	429 nm (lg ε 4.44), 402 (4.58), 380 (4.65), 367sh, 285 (4.74), 263 (4.76), 242 (4.73)		1300
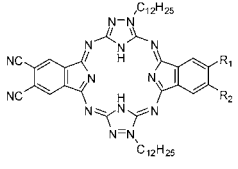	2H	$CHCl_3$	425 nm (lg ε 4.53), 397 (4.70), 376 (4.73), 364sh, 244 (4.92)	R_1, R_2 = CN	1320
		$CHCl_3$	406 nm (lg ε 4.62), 379 (4.85), 360 (4.85), 345sh, 279 (4.68), 243 (4.97)	R_1 = *t*-Bu, R_2 = H	1320
		$CHCl_3$	405 nm (lg ε 4.72), 382 (4.88), 362sh, 282sh, 251 (4.93)	$R_1 = OC_8H_{17}$, R_2 = H	1320
		$CHCl_3$	419 nm (lg ε 4.42), 391 (4.67), 369 (4.72), 361sh, 247 (4.84)	$R_1 = NO_2$, R_2 = H	1320
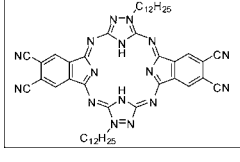	2H	$CHCl_3$	426 nm (lg ε 4.46), 398 (4.62), 375 (4.63), 359 (4.58), 244 (4.86)		1320

(*Continued*)

Table 12. (*Continued*)

Structure	M	Solvent	Transition Energy (Intensity)	Remark	Ref.
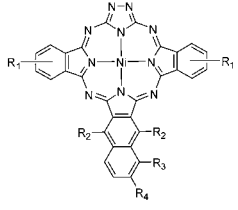	Ni(II)	$CHCl_3$	685 nm (lg ε 3.68), 627 (3.64), 561 (3.75), 516 (3.91), 472 (3.96), 385 (4.13), 299 (4.51)	R_1, R_4 = *t*-Bu	1321
		$CHCl_3$	631 nm (lg ε 5.23), 576 (5.12), 530 (5.09), 488 (5.08), 459 (5.06), 366 (5.35), 317 (5.49), 292 (5.50), 259 (5.64), 241 (5.62)	R_1 = H, R_4 = *t*-Bu, R_2, R_3 = H	1321
		$CHCl_3$	638 nm (lg ε 3.99), 554 (4.11), 522 (4.15), 488 (4.18), 351 (4.40), 244 (4.67)	R_1 = H, R_2 = OC_6H_{13}, R_3, R_4 = H	1321
		$CHCl_3$	643 nm (lg ε 4.52), 589 (4.33), 554 (4.25), 521 (4.22), 374 (4.52), 314 (4.60), 298 (4.60), 258 (4.75)	R_1 = H, R_3 = OC_6H_{13}, R_2, R_4 = H	1321
		$CHCl_3$	636 nm (lg ε 4.04), 579 (4.01), 513 (4.01), 354 (4.32), 274 (5.23)	R_1 = H, R_2 = OC_7H_{15}, R_3, R_4 = H	1321
		$CHCl_3$	638 nm (lg ε 4.19), 577 (4.18), 517 (4.22), 475 (4.26), 360 (4.41), 320 (4.55), 273 (4.76)	R_1 = OC_8H_{17}, R_4 = *t*-Bu, R_2, R_3 = H	1321
		$CHCl_3$	649 nm (lg ε 3.68), 590 (3.72), 473 (3.92), 399 (4.11), 365 (4.19), 260 (4.66)	R_1 = OC_8H_{17}, R_2 = OC_6H_{13}, R_3, R_4 = H	1321
		$CHCl_3$	646 nm (lg ε 4.21), 589 (4.09), 549 (4.12), 502 (4.17), 364 (4.38), 268 (4.79)	R_1 = OC_8H_{17}, R_3 = OC_6H_{13}, R_2, R_4 = H	1321
		$CHCl_3$	635 nm (lg ε 4.09), 590 (4.17), 537 (4.21), 400 (4.39), 366 (4.40), 270 (4.74)	R_1 = OC_8H_{17}, R_2 = OC_7H_{15}, R_3, R_4 = H	1321
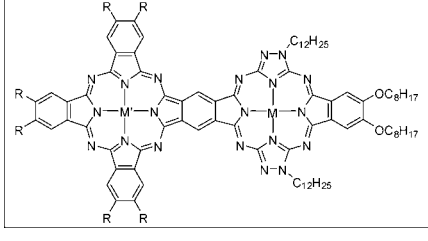	Ni(II)	$CHCl_3$	732 nm (lg ε 3.97), 672 (3.98), 617sh, 370 (4.25), 277 (4.57)	R = OC_8H_{17}, M′ = Ni(II)	1300
		$CHCl_3$	730 nm (lg ε 4.73), 680 (4.54), 660sh, 615sh, 450sh, 362 (4.82), 290 (4.82), 273 (4.84)	R = OC_8H_{17}, M′ = Zn(II)	1300
		$CHCl_3$	698 nm (lg ε 4.96), 398sh, 345 (4.82), 284 (4.99)	R = $SO_2C_8H_{17}$, M′ = Ni(II)	1300
	Zn(II)	$CHCl_3$	721 nm (lg ε 4.56), 666 (4.63), 670sh, 367 (4.89), 285 (5.13), 278 (5.13)	R = OC_8H_{17}, M′ = Ni(II)	1300
		$CHCl_3$	730 nm (lg ε 4.79), 685 (4.72), 660sh, 362 (5.00), 282sh, 265 (4.98)	R = OC_8H_{17}, M′ = Zn(II)	1300

(*Continued*)

Table 12. (*Continued*)

Structure	M	Solvent	Transition Energy (Intensity)	Remark	Ref.
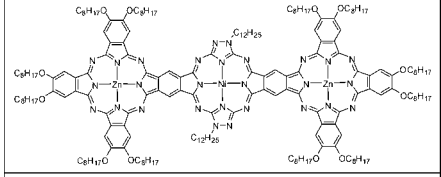	Ni(II) Zn(II)	$CHCl_3$	755 nm (lg ε 4.15), 679 (4.11), 364 (4.50), 252 (4.75)		836
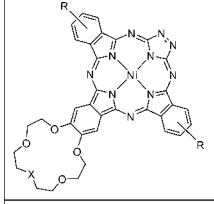	Ni(II)	$CHCl_3$	628 nm (lg ε 4.12), 530 (4.00), 370 (4.42), 259 (4.57)	R = H, X = O	1195
		$CHCl_3$	626 nm (lg ε 3.52), 562 (3.58), 517sh, 364 (3.99), 259 (4.23)	R = H, X = NCOOEt	1195
		$CHCl_3$	631 nm (lg ε 3.70), 576 (3.61), 530 (3.67), 435sh, 371 (4.10), 282 (4.30), 261 (4.30)	R = H, X = $NCOC_{17}H_{35}$	1195
		$CHCl_3$	619 nm (lg ε 3.54), 571sh, 355 (4.21), 260 (4.52)	R = H, X = $NCOOC_{18}H_{37}$	1195
		$CHCl_3$	637 nm (lg ε 3.22), 572 (3.40), 529 (3.50), 400sh, 366 (3.90), 279 (4.20)	R = OC_8H_{17}, X = O	1195
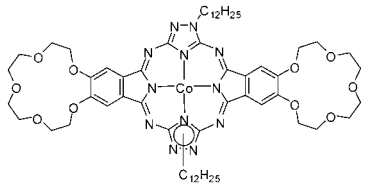	Co(II)	$CHCl_3$	513 nm (lg ε 3.489), 479 (3.569), 433 (3.814), 385 (4.568), 364 (4.632), 352sh, 295 (4.666), 259 (4.733)		1193
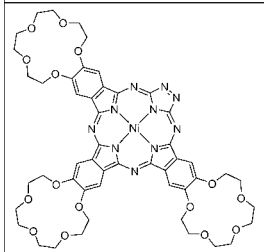	Ni(II)	$CHCl_3$	620 nm (lg ε 3.19), 590 (3.36), 490sh, 430sh, 355 (3.85), 280 (4.30)		1195

(*Continued*)

Table 12. (*Continued*)

Structure	M	Solvent	Transition Energy (Intensity)	Remark	Ref.
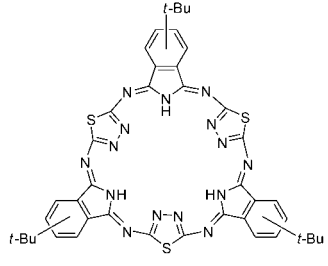	3H	$CHCl_3$	501 nm (lg ε 4.10), 463 (4.25), 413 (4.89), 392 (4.88), 278 (4.71)		1322
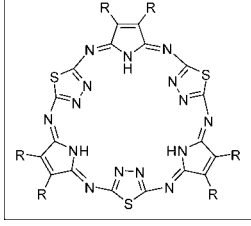	3H	$CHCl_3$	552 nm (lg ε 3.73), 515sh, 452 (4.69), 428 (4.69), 328 (4.28), 265 (4.45)	R = Ph(4-*t*-Bu)	1322

Table 13. UV-vis absorption data of Pc polymers.

Structure	M	Solvent	Transition Energy (Intensity)	Remark	Ref.
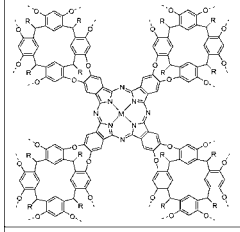	Co(II)	DMF	693 nm, 294	R = CH_3	1323
	Ni(II)	DMF	693 nm, 294	R = CH_3	1323
	Cu(II)	DMF	710 nm, 293	R = CH_3	1323
	Zn(II)	DMF	699 nm, 294	R = CH_3	1323
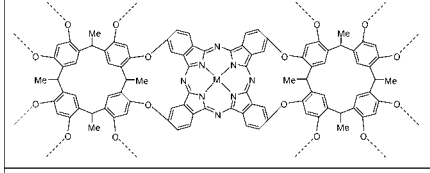	Co(II)	H_2SO_4	755 nm, 342	R = CH_3	1323
	Ni(II)	H_2SO_4	755 nm, 342	R = CH_3	1323
	Cu(II)	H_2SO_4	750 nm, 342	R = CH_3	1323
	Zn(II)	H_2SO_4	750 nm, 342	R = CH_3	1323
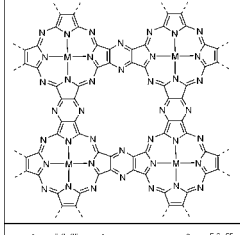	Fe(II)	H_2SO_4	700 nm		1324
		DMSO	656 nm		1324
	Co(II)	H_2SO_4	690 nm		1324
		DMSO	641 nm		1324
	Cu(II)	H_2SO_4	690 nm		1324
		DMSO	658 nm		1324
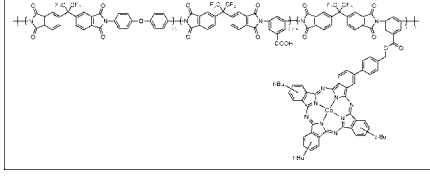	Co(II)	THF	671 nm (ε 74,100), 606 (24,500), 266 (182,000)		830

(*Continued*)

Table 13. (*Continued*)

Structure	M	Solvent	Transition Energy (Intensity)	Remark	Ref.
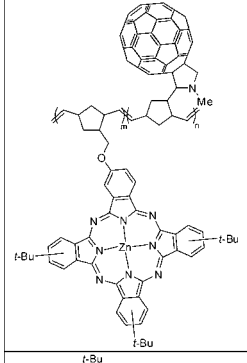	Zn(II)	$CHCl_3$	677 nm (ε / mL mg ^{1} cm ^{1} 67.6), 632 (30.8), 343 (56)	m/n = 3: 2s	848
		$CHCl_3$	677 nm (ε / mL mg ^{1} cm ^{1} 83.3), 632 (40.4), 343 (61.3)	m/n = 4: 1	848
		$CHCl_3$	677 nm (ε / mL mg^{-1} cm^{-1} 91.2), 632 (47.6), 345 (66.3)	n = 0	848
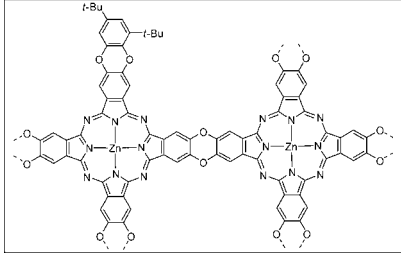	Zn(II)	Unknown	680 nm, 640		920

(*Continued*)

Table 13. (*Continued*)

Structure	M	Solvent	Transition Energy (Intensity)	Remark	Ref.
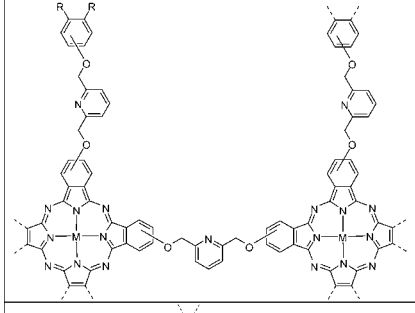	2H	py	707 nm (10^5 ε 5.14), 683 (5.11), 618 (4.56), 325 (5.07), 243 (5.10)	R = —C≡N or 	1325
	Co(II)	py	689 nm (10^5 ε 5.19), 623 (4.50), 365 (5.13), 252 (5.15)		1325
	Ni(II)	py	689 nm (10^{-5} ε 5.15), 623 (4.63), 392 (5.10), 305 (5.14), 235 (5.16)		
	Cu(II)	py	688 nm (10^{-5} ε 5.16), 618 (4.48), 348 (5.02), 275 (5.06)		1325
	Zn(II)	py	692 nm (10^{-5} ε 5.13), 632 (4.52), 368 (4.92), 313 (4.98)		
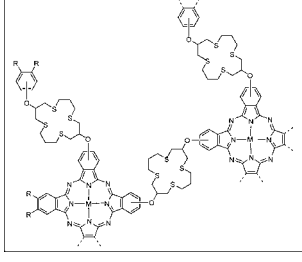	2H	py	703 nm (10^{-5} ε 5.11), 683 (5.09), 617 (4.57), 354 (5.02), 332 (4.99), 248 (5.13)	R = —C≡N or 	1217
	Co(II)	py	681 nm (10^{-5} ε 5.17), 614 (4.62), 373 (5.11), 318 (5.14), 261 (5.16)		1217
	Ni(II)	py	680 nm (10^{-5} ε 5.16), 611 (4.60), 362 (5.08), 340 (5.07), 240 (5.17)		1217
	Cu(II)	py	689 nm (10^{-5} ε 5.17), 617 (4.57), 361 (5.10), 320 (5.12), 249 (5.14)		1217
	Zn(II)	py	692 nm (10^{-5} ε 5.24), 620 (4.65), 344 (5.10), 321 (5.11), 254 (5.18)		

(*Continued*)

Table 13. (*Continued*)

Structure	M	Solvent	Transition Energy (Intensity)	Remark	Ref.
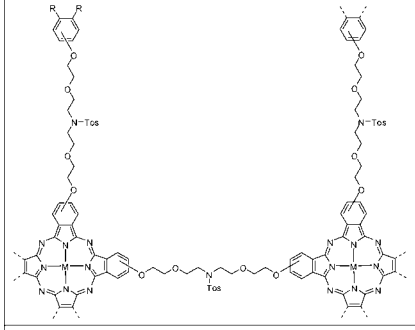	2H	$CHCl_3$	704 nm (10^5 ε 5.14), 674 (5.13), 644 (4.68), 326 (5.10), 285 (5.13)	R = —C≡N	1326
	Co(II)	$CHCl_3$	680 nm (10^5 ε 5.16), 623 (4.49), 341 (5.06), 280 (5.08)		1326
	Ni(II)	$CHCl_3$	680 nm (10^{-5} ε 5.16), 629 (4.50), 317 (5.07), 292 (5.09)		1326
	Cu(II)	$CHCl_3$	692 nm (10^{-5} ε 5.20), 635 (4.54), 377 (5.08), 275 (5.07)		1326
	Zn(II)	$CHCl_3$	689 nm (10^{-5} ε 5.22), 629 (4.57), 345 (5.09), 295 (5.13)		1326
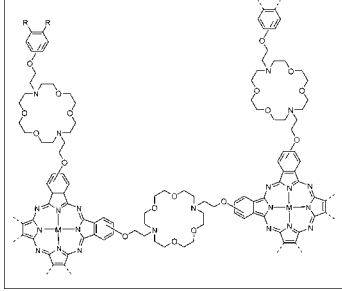	2H	py	706 nm, 672, 640sh, 606, 389, 360, 320, 301, 285	R = —C≡N	1218
		H_2SO_4	810 nm, 720sh, 675, 608, 392, 345, 320, 274		1218
	Co(II)	H_2SO_4	816 nm, 755sh, 720, 663, 391, 377, 326, 292		1218
	Ni(II)	H_2SO_4	816 nm, 758sh, 719, 639, 460, 414, 378, 297		1218
	Cu(II)	H_2SO_4	832 nm, 775sh, 732, 617, 430, 412, 338, 304		1218
	Zn(II)	H_2SO_4	850 nm, 819sh, 736, 619, 458, 365, 327, 297		1218

(*Continued*)

Table 13. (*Continued*)

Structure	M	Solvent	Transition Energy (Intensity)	Remark	Ref.
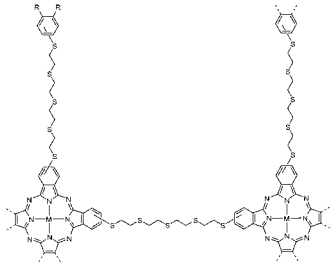	2H	py	715 nm (lg ε 2.72), 687 (2.71), 655 (2.34), 624 (2.14), 420 (2.41), 372 (2.69), 318 (2.73), 306 (2.35), 290 (2.83)	R = —C≡N	1327
		H_2SO_4	812 nm (lg ε 3.27), 719 (3.23), 674 (2.90), 607 (2.78), 393 (3.01), 344 (3.34), 319 (3.38), 271 (3.47)		1327
	Fe(II)	H_2SO_4	791 nm (lg ε 3.51), 729 (3.40), 656 (3.26), 612 (2.04), 378 (3.71), 315 (3.91), 265 (3.88)	R = 	1327
	Co(II)	H_2SO_4	842 nm (lg ε 3.64), 720 (3.34), 647 (3.10), 617 (2.95), 430 (3.51), 307 (3.81), 285 (3.89)		1327
	Ni(II)	H_2SO_4	856 nm (lg ε 3.53), 741 (3.04), 612 (2.72), 456 (3.36), 360 (3.48), 310 (3.68), 268 (3.72)		1327
	Cu(II)	H_2SO_4	875 nm (lg ε 3.73), 796 (3.56), 645 (3.41), 603 (3.06), 440 (3.67), 314 (3.86), 259 (3.96)		1327
	Zn(II)	H_2SO_4	883 nm (lg ε 3.84), 788 (3.56), 652 (3.23), 620 (2.97), 495 (3.32), 415 (3.65), 305 (3.94), 264 (3.76)		1327
	Pb(II)	H_2SO_4	874 nm (lg ε 2.93), 817 (2.75), 726 (3.14), 640 (3.75), 606 (2.13), 473 (3.46), 325 (3.87), 287 (3.94), 263 (4.10)		1327
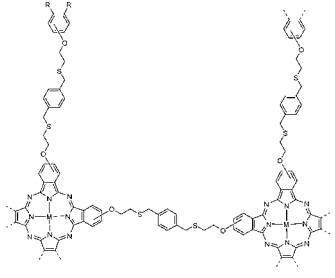	2H	py	706 nm (lg ε 3.32), 673 (3.29), 645 (3.01), 609 (2.84), 402 (2.89), 341 (3.37), 326 (3.82), 309 (3.81), 268 (3.62)	R = —C≡N	1328
		H_2SO_4	794 nm (lg ε 4.58), 698 (4.32), 634 (4.28), 610 (4.46), 388 (5.68), 304 (6.28), 292 (6.05), 258 (6.36)		1328
	Fe(II)	H_2SO_4	810 nm (lg ε 6.18), 733 (6.24), 618 (6.25), 386 (6.60), 318 (7.01), 270 (6.79)	R = 	1328
	Co(II)	H_2SO_4	800 nm (lg ε 5.89), 712 (5.39), 646 (4.75), 612 (4.88), 416 (5.45), 304 (6.19), 298 (6.08)		1328
	Ni(II)	H_2SO_4	796 nm (lg ε 6.65), 706 (6.12), 616 (4.42), 496 (5.74), 306 (6.72), 252 (6.82)		1328
	Cu(II)	H_2SO_4	834 nm (lg ε 5.37), 706 (3.90), 622 (5.85), 362 (5.91), 302 (6.24), 254 (6.23), 236 (6.85)		1328
	Zn(II)	H_2SO_4	824 nm (lg ε 6.40), 726 (5.73), 664 (4.81), 614 (4.97), 502 (5.52), 490 (5.50), 352 (6.12), 308 (6.47), 256 (6.49)		1328

(*Continued*)

Table 13. (*Continued*)

Structure	M	Solvent	Transition Energy (Intensity)	Remark	Ref.
	Pb(II)	H_2SO_4	883 nm (lg ε 3.93), 833 (3.85), 739 (4.74), 632 (4.89), 610 (3.83), 485 (4.57), 334 (4.95), 291 (5.26), 278 (5.24)		1328
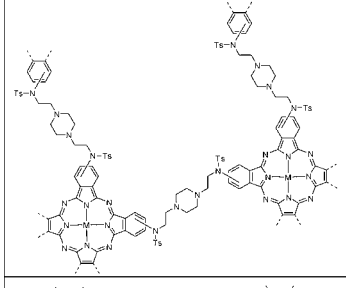	2H	DMSO	747 nm (10^{-3} ε 23.5), 675 (25.1), 645sh (20.3), 332sh (53.2), 262 (65.1)		1329
	Co(II)	H_2SO_4	739 nm (10^{-3} ε 119), 652sh (20.9), 381sh (16.5), 296 (54.1)		1329
	Ni(II)	DMSO	679 nm (10^{-3} ε 60.1), 647sh (36.5), 615sh (28.7), 463sh (21.0), 340sh (53.9), 276 (88.3)		1329
	Cu(II)	DMSO	675 nm (10^{-3} ε 12.1), 646 (6.0), 613sh (3.8), 583sh (1.8), 334sh (9.3), 264 (15.4)		1329
	Zn(II)	DMSO	682 nm (10^{-3} ε 123.9), 651sh (27.3), 616 (23.9), 355 (51.6), 261 (57.8)		1329
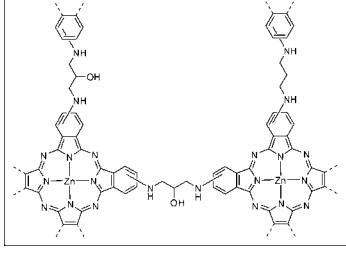	Zn(II)	MeOH	711.0 nm, 647.0, 500.0, 350.0, 267.0, 224.0		775

(*Continued*)

Table 13. (*Continued*)

Structure	M	Solvent	Transition Energy (Intensity)	Remark	Ref.
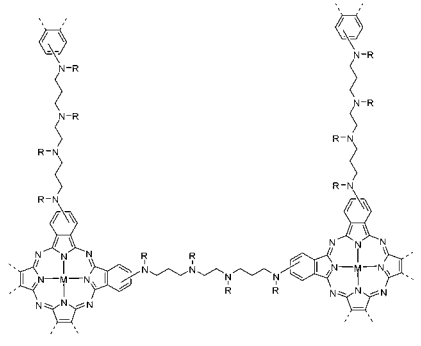	2H	$CHCl_3$	759 nm (1.68 $g^{-1}cm^{-1}$ L), 701 (19.76), 667 (16.96), 644 (7.84), 612sh (4.88), 343 (15.36), 241 (61.28)	R = Ts	1330
	Fe(II)	$CHCl_3$	759 nm (0.72 $g^{-1}cm^{-1}$ L), 684 (9.84), 615sh (3.20), 340 (9.44)	R = Ts	1330
	Co(II)	DMSO	760 nm (2.88 $g^{-1}cm^{-1}$ L), 690 (3.92), 650 (3.84), 625sh (3.28), 327 (6.00)	R = Ts	1330
		DMSO	732 nm (60.00 $g^{-1}cm^{-1}$ L), 640 (24.00), 370 (40.00), 280 (260.00)	R = H	1330
	Ni(II)	$CHCl_3$	760 nm (2.08 $g^{-1}cm^{-1}$ L), 672 (19.44), 607sh (5.36), 274 (28.48)	R = Ts	1330
	Cu(II)	$CHCl_3$	760 nm (0.08 $g^{-1}cm^{-1}$ L), 681 (25.44), 615sh (6.00), 345 (11.68), 260 (23.00)	R = Ts	1330
		DMSO	733 nm (25.44 $g^{-1}cm^{-1}$ L), 650 (16.00), 350 (20.00), 281 (208.00)	R = H	1330
	Zn(II)	$CHCl_3$	759 nm (1.60 $g^{-1}cm^{-1}$ L), 684 (12.24), 618sh (2.08), 330 (7.60), 242 (63.12)		1330
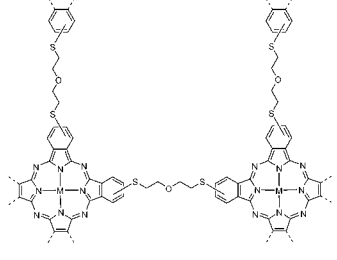	2H	DMSO	690 nm (391 $g^{-1}cm^{-1}$ L), 632 (373), 297 (2,337), 260 (1,361), 228 (3,760)		1331
	Fe(II)	H_2SO_4	850 nm (685 $g^{-1}cm^{-1}$ L), 760 (430), 410 (1,840), 384 (2,060), 257 (3,100), 224 (4,160)		1331
	Co(II)	H_2SO_4	830 nm (880 $g^{-1}cm^{-1}$ L), 753 (530), 369 (2,173), 284 (3,820), 252 (4,288), 231 (4,320)		1331
	Ni(II)	DMSO	770 nm (1,600 $g^{-1}cm^{-1}$ L), 731 (1,100), 406 (800), 360 (1,210), 298 (4,000), 265 (4,030), 248 (4,200)		1331
	Cu(II)	DMSO	759 nm (319 $g^{-1}cm^{-1}$ L), 683 (329), 592 (326), 459 (333), 398 (1,341), 227 (1,210)		1331
	Zn(II)	H_2SO_4	860 nm (1,576 $g^{-1}cm^{-1}$ L), 764 (1,325), 401 (1,713), 303 (3,215), 282 (3,300), 226 (4,580)		1331

(*Continued*)

Table 13. (*Continued*)

Structure	M	Solvent	Transition Energy (Intensity)	Remark	Ref.
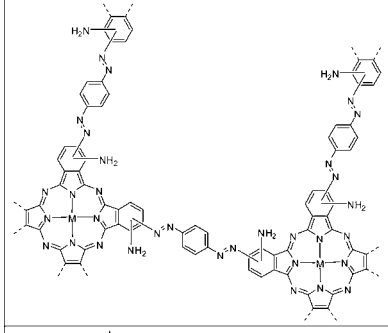	Co(II)	THF	650 nm, 593, 411, 315, 292		1332
	Ni(II)	THF	650 nm, 580, 415, 378, 305, 295		1332
	Cu(II)	THF	660 nm, 399, 298		1332
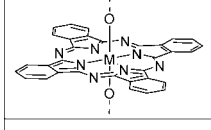	Si(IV)L	Nujol mulls	625 nm, 335, 285, 203		358
	Ge(IV)L	Nujol mulls	645 nm, 350, 285		358
	Sn(IV)L	Nujol mulls	695 nm, 655, 365, 290, 205		358
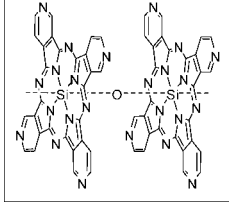	Si(IV)	DMF	615 nm (lg ε 3.5), 314 (3.2)		1313

(*Continued*)

Table 13. (*Continued*)

Structure	M	Solvent	Transition Energy (Intensity)	Remark	Ref.
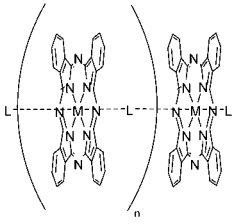	Fe(II)	Solid state	734 nm, 643, 402, 359	L = --C≡N—$(CH_2)_2$—N≡C--	466
		Solid state	689 nm, 623, 398, 333	L = --C≡N—$(CH_2)_6$—N≡C--	466
		Solid state	701 nm, 612, 401, 353	L = --C≡N—$(CH_2)_{12}$—N≡C--	466
		Solid state	722 nm, 627, 404, 366	L = --C≡N—$(CH_2)_3O(CH_2)_4O(CH_2)_3$—N≡C--	466
		Solid state	684 nm, 610, 397, 330	L = 	466
		Nujol	750sh nm, 680, 393, 330	L = 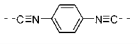	199
		$BaSO_4$	670 nm, 575, 440sh, 390, 331	L = 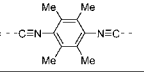	199
		$BaSO_4$	675 nm, 575sh, 385, 335	L = 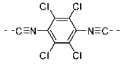	199
		Nujol	787sh nm, 710, 394, 350	L = 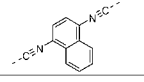	199
		Nujol	715 nm, 460, 400, 340	L = 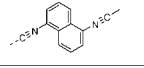	199
		Nujol	713, 633, 435, 394, 331, 275	L = 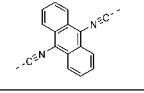	199
	Os(II)	PhCl	632 nm, 580sh, 420sh	L = 	231
	Ru(II)	py	639 nm, 582, 388sh, 358sh, 308	L = 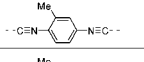	1333
		py	639 nm, 582, 385sh, 356sh, 309	L = 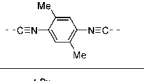	1333
		py	640 nm, 584, 387, 358sh, 308	L = 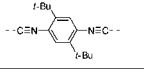	1333

(*Continued*)

Table 13. (*Continued*)

Structure	M	Solvent	Transition Energy (Intensity)	Remark	Ref.
		$CHCl_3$	641 nm, 621sh, 585sh, 307	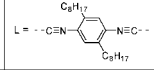	1333
		$CHCl_3$	639 nm, 618sh, 582, 392, 360sh, 306	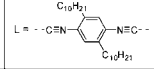	1333
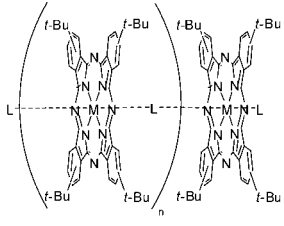	Co(II)	DMF	675 nm	L = - -C≡N- -	531
	Ru(II)	$CHCl_3$	645 nm, 588sh, 465, 308	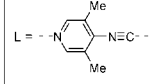	536
		$CHCl_3$	645 nm, 590, 405, 310	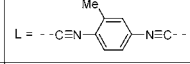	1333
		$CDCl_3$	645 nm, 590, 415, 404	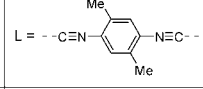	1333
		$CHCl_3$	648 nm, 592, 414, 314	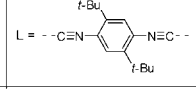	1333
		$CHCl_3$	647 nm, 589, 549, 415, 310, 295	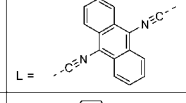	536
		$CHCl_3$	645 nm, 590, 305	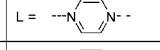	536
		$CHCl_3$	622 nm, 578sh, 368, 310	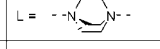	536
		$CHCl_3$	631 nm, 580sh, 492, 370, 315	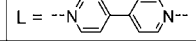	536

(*Continued*)

Table 13. (*Continued*)

Structure	M	Solvent	Transition Energy (Intensity)	Remark	Ref.
		$CHCl_3$	1315 nm, 640, 590, 302	L = 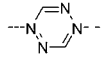	536
		$CHCl_3$	1180 nm, 644, 589, 303	L = 	536
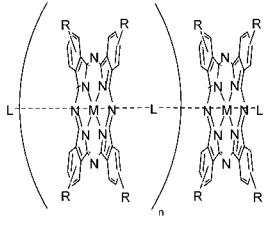	Fe(III)	$CHCl_3$	667 nm, 610, 400, 345, 300, 285	L = 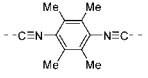 R = 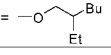	1334
	Fe(III)	Fluorolube	671 nm, 606, 432, 391	L = 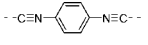 R = C_5H_{11}	1311
	Ru(II)	Toluene	704 nm, 645, 590sh, 410sh, 315	L = 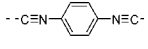 R = Et	1333
		Toluene	702 nm, 645, 589, 400, 313	L = 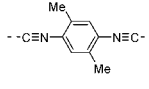 R = Et	1333
		$CHCl_3$	703 nm, 648, 593, 410, 314	L = 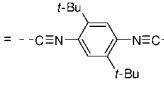 R = Et	1333
		$CHCl_3$	704 nm, 645, 590, 395, 315	L = 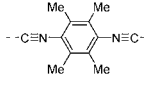 R = Et	1333

(*Continued*)

Table 13. (*Continued*)

Structure	M	Solvent	Transition Energy (Intensity)	Remark	Ref.
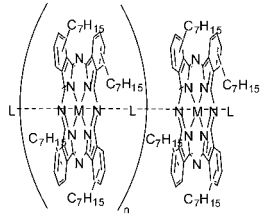	Fe(III)	$CHCl_3$	671 nm, 607, 394, 312	L = 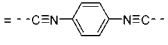	1311
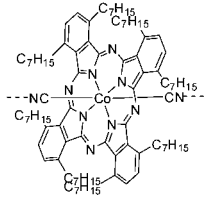	Co(II)	DMF	710 nm, 640, 445, 355, 289		531
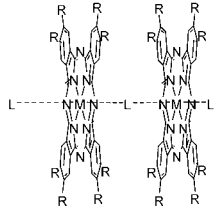	Fe(II)	DMF	693 nm, 631, 488, 392	L =  R = CN	565
		DCM	668 nm, 580, 408	L =  R = OC_5H_{11}	230
		DMF	688 nm, 624sh, 476, 382, 320	L = 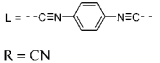 R = CN	564
		DCM	684 nm, 612, 462, 404	L = 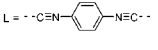 R = C_5H_{11}	230
	Fe(III)	$CHCl_3$	680 nm, 612sh, 459, 331, 302	L = 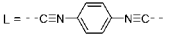 R = C_7H_{15}	1311

(*Continued*)

Table 13. (*Continued*)

Structure	M	Solvent	Transition Energy (Intensity)	Remark	Ref.
		DCM	682 nm, 604, 342, 304	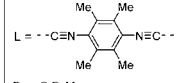 R = OC_5H_{11}	230
		$CHCl_3$	677 nm, 615, 430, 345, 310	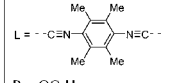 R = OC_8H_{17}	1334
		$CHCl_3$	666 nm, 610, 400, 345, 310, 295	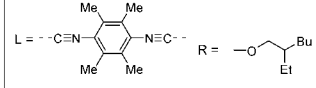	1334
	Co(II)	HMPA	701 nm, 650, 493, 395	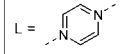 R = CN	565
		DMF	683 nm, 655sh, 615, 362, 341sh, 292	L = - -C≡N- - R = C_7H_{15}	531
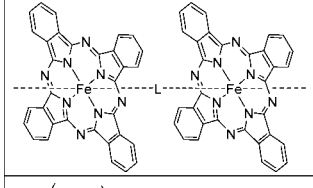	Fe(II)	Nujol	721 nm, 639, 524, 365	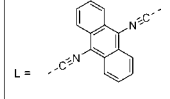 ααββ = Cl	466
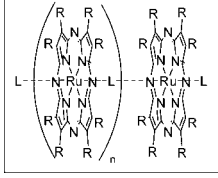	Ru(II)L	Uvasole	614 nm, 550sh, 445, 379, 287	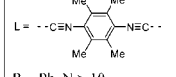 R = Ph, N > 10	219
		Uvasole	599 nm, 547sh, 462, 361, 349sh, 292	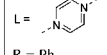 R = Ph	219

(*Continued*)

Table 13. (*Continued*)

Structure	M	Solvent	Transition Energy (Intensity)	Remark	Ref.
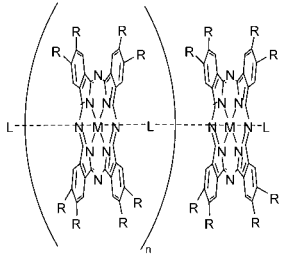	Ru(II)L	$CHCl_3$	658 nm, 600, 400, 325, 300	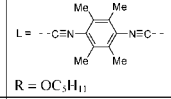	500
		$CHCl_3$	655 nm, 600, 410, 330, 310	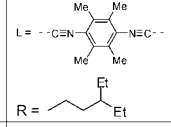	500
		$CHCl_3$	652 nm, 597sh, 320sh, 297	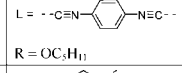	500
	Fe(III)	Pellets	1280 nm, 1080, 795, 718, 630, 559, 398, 363	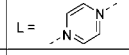	1335
		Pellets	1240 nm, 1100, 760, 625, 573, 402, 358	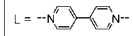	1335
		Pellets	1235 nm, 1060, 700, 624, 538, 404, 360	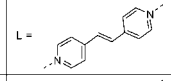	1335
		Pellets	1260 nm, 1050, 715, 614, 556, 410, 365	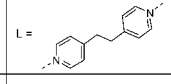	1335
		Pellets	1215 nm, 1030, 680, 606, 570, 415, 368	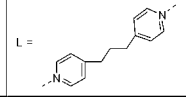	1335

(*Continued*)

Table 13. (*Continued*)

Structure	M	Solvent	Transition Energy (Intensity)	Remark	Ref.
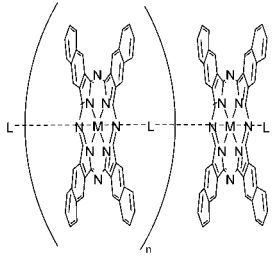	Fe(II)	Nujol	797 nm, 703sh, 485sh, 387, 276sh	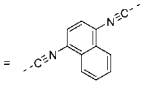	1054
		Nujol	787 nm, 694sh, 613, 432sh, 383, 264	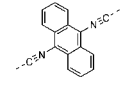	1054
		Nujol	1028 nm, 787, 695sh, 395, 278	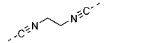	1054
		Nujol	786 nm, 697sh, 500sh, 378, 276	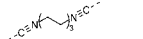	1054
		Nujol	796 nm, 695sh, 432sh, 408, 278	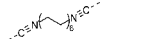	1054
		Nujol	811 nm, 697sh, 427sh, 392, 278	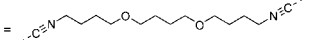	1054
		Nujol	802 nm, 698sh, 484sh, 391, 279	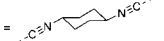	1054
	Ru(II)	Fluorolube	726 nm, 657, 429, 369, 318, 245	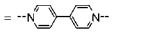	536
		$CHCl_3$	740 nm, 670sh, 330	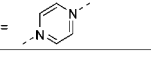	501
		Flurolublc	740 nm, 670sh, 420, 330		501
		Fluorolube	737 nm, 666, 440, 373, 315	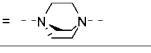	536
		Fluorolube	756 nm, 680sh, 335	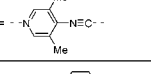	536
		Fluorolube	734 nm, 665sh, 346, 271	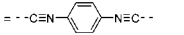	536
		Fluorolube	734 nm, 652sh, 351	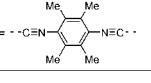	536

(*Continued*)

Table 13. (*Continued*)

Structure	M	Solvent	Transition Energy (Intensity)	Remark	Ref.
		Fluorolube	746 nm, 670sh, 356, 264	L = 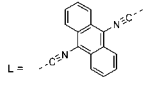	536
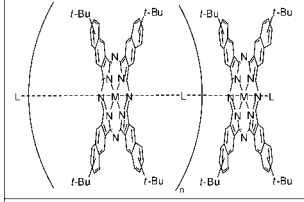	Co(II)	DMF	767 nm, 732sh, 687, 325	L = – –C≡N– –	531
	Ru(II)	Fluorolube	724 nm, 653, 426, 370, 320, 249	L = 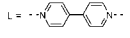	536
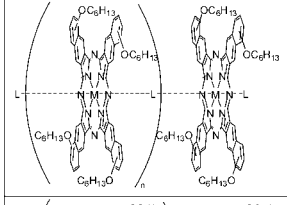	Fe(III)	Fluorolube	771 nm, 690sh, 346		1311
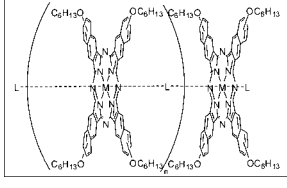	Fe(III)	Fluorolube	778 nm, 692sh, 356		1311

(*Continued*)

Table 13. (*Continued*)

Structure	M	Solvent	Transition Energy (Intensity)	Remark	Ref.
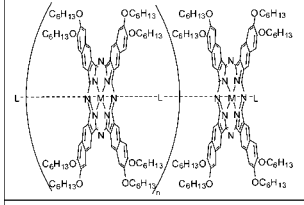	Fe(III)	Fluorolube	765 nm, 686, 359		1311
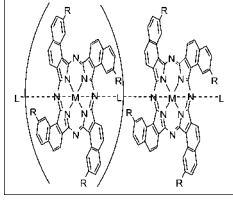	Fe(II)	Nujol	682 nm, 620, 383, 357, 252	R = *t*-Bu	1074
		Nujol	720 nm, 637, 390, 329	R = Me	1074
		Nujol	695 nm, 629, 377, 363, 274	R = Ph	1074

V. Acknowledgment

The authors would like to thank their students, T. Biyajima, N. Hashimoto, R. Hiramatsu, Y. Kikukawa, A. Miura, K. Oniwa, I. Sugita, S. Takaishi, and R. Tsuruya for collecting data for the tables.

VI. References

1. Braun, A.; Tcherniac, J. *Ber. Dtsch. Chem. Ges.* **1907**, *40*, 2709–2714.
2. Dent, C. E.; Linstead, R. P.; Lowe, A. R. *J. Chem. Soc.* **1934**, 1033–1039.
3. Robertson, J. M. *J. Chem. Soc.* **1935**, 615–621.
4. Leznoff, C. C.; Lever, A. B. P. *Phthalocyanines: Properties and Applications*; VCH, New York, **1989**.
5. McKeown, N. B. *Phthalocyanine Materials: Synthesis, Structure, and Function*; Cambridge University Press, Cambridge, **1998**.
6. Kadish, K. M.; Smith, K. M.; Guilard, R. *The Porphyrin Handbook*; Vols. 1–20; Academic Press, San Diego, **2000**, **2003**.
7. de la Torre, G.; Claessens, C. G.; Torres, T. *Chem. Commun.* **2007**, 2000–2015.
8. Nyokong, T. *Coord. Chem. Rev.* **2007**, *251*, 1707–1722.
9. Chen, Y.; Hanack, M.; Araki, Y.; Ito, O. *Chem. Soc. Rev.* **2005**, *34*, 517–529.
10. Inabe, T. *Bull. Chem. Soc. Jpn.* **2005**, *78*, 1373–1383.
11. de la Torre, G.; Vázquez, P.; Agulló-López, F.; Torres, T. *Chem. Rev.* **2004**, *104*, 3723–3750.
12. Inabe, T.; Tajima, H. *Chem. Rev.* **2004**, *104*, 5503–5533.
13. O'Flaherty, S. M.; Hold, S. V.; Cook, M. J.; Torres, T.; Chen, Y.; Hanack, M.; Blau, W. J. *Adv. Mater.* **2003**, *15*, 19–32.
14. Tsushima, M.; Ikeda, N.; Yonehara, H.; Etori, H.; Pac, C.; Ohno, T. *Coord. Chem. Rev.* **2002**, *229*, 3–8.
15. Hanack, M.; Dini, D.; Barthel, M.; Vagin, S. *Chem. Rec.* **2002**, *2*, 129–148.
16. Cook, M. J. *Chem. Rec.* **2002**, *2*, 225–236.
17. Hanack, M.; Schneider, T.; Barthel, M.; Shirk, J. S.; Flom, S. R.; Pong, R. G. S. *Coord. Chem. Rev.* **2001**, *219*, 235–258.
18. de la Torre, G.; Vázquez, P.; Agulló-López, F.; Torres, T. *J. Mater. Chem.* **1998**, *8*, 1671–1683.
19. Nyokong, T.; Gasyna, Z.; Stillman, M. J. *Inorg. Chem.* **1987**, *26*, 1087–1095.
20. Lever, A. B. P. *Adv. Inorg. Radiochem.* **1965**, *7*, 27–114.
21. Edwards, L.; Gouterman, M. *J. Mol. Spectrosc.* **1970**, *33*, 292–310.
22. Baerends, E. J.; Ricciardi, G.; Rosa, A.; van Gisbergen, S. J. A. *Coord. Chem. Rev.* **2002**, *230*, 5–27.
23. Rosa, A.; Ricciardi, G.; Baerends, E. J.; van Gisbergen, S. J. A. *J. Phys. Chem. A* **2001**, *105*, 3311–3327.
24. Mack, J.; Stillman, M. J. *The Porphyrin Handbook*: Kadish, K. M.; Smith, K. M.; Guilard, R. Eds.; Academic Press, San Diego, **2003**, Vol. 16, Chapter 103, pp. 43–116.
25. Luk'yanets, E. A. *Electronic Spectra of Phthalocyanine and Related Compounds*; NIOPIK, Moscow, 1989.
26. Stillman, M. J.; Nyokong, T. *Phthalocyanines — Properties and Applications*: Leznoff, C. C.; Lever, A. B. P. Eds.; VCH, **1989**, Vol. 1, Chapter 3, pp. 133–289.

27. Kobayashi, N. In *The Porphyrin Handbook*: Kadish, K. M.; Smith, K. M.; Guilard, R. Eds.; Academic Press, San Diego, **2000**, Vol. 2, Chaptre 13, pp. 301–360.
28. Simpson, W. T. *J. Chem. Phys.* **1949**, *17*, 1218–1221.
29. Longuet-Higgins, H. C.; Rector, C. W.; Platt, J. R. *J. Chem. Phys.* **1950**, *18*, 1174–1181.
30. Gouterman, M. *J. Chem. Phys.* **1959**, *30*, 1139–1161.
31. Gouterman, M. *J. Mol. Spectrosc.* **1961**, *6*, 138–163.
32. Kobayashi, N.; Konami, H. *J. Porphyr. Phthalocyan.* **2001**, *5*, 233–255.
33. Eastwood, D.; Edwards, L.; Gouterman, M.; Steinfeld, J. *J. Mol. Spectrosc.* **1966**, *20*, 381–390.
34. Bajema, L.; Gouterman, M.; Meyer, B. *J. Mol. Spectrosc.* **1968**, *27*, 225–235.
35. VanCott, T. C.; Rose, J. L.; Misener, G. C.; Williamson, B. E.; Schrimpf, A. E.; Boyle, M. E.; Schatz, P. N. *J. Phys. Chem.* **1989**, *93*, 2999–3011.
36. Douglas, I. N.; Grinter, R.; Thomson, A. J. *Mol. Phys.* **1974**, *28*, 1377–1388.
37. Sheinin, V. B.; Ivanova, Y. B. *Russ. J. Phys. Chem. A* **2007**, *81*, 1250–1255.
38. Freyer, W. F.; Neacsu, C. C.; Raschke, M. B. *J. Lumin.* **2008**, *128*, 661–672.
39. Chauhan, S. M. S.; Agarwal, S.; Kumari, P. *Synthetic Commun.* **2007**, *37*, 2917–2925.
40. Whalley, M. *J. Chem. Soc.* **1961**, 866–869.
41. Ledson, D. L.; Twigg, M. V. *Inorg. Chim. Acta* **1975**, *13*, 43–46.
42. Jerwin, K.; Wasgestian, F. *Spectrochim. Acta A* **1984**, *40*, 159–163.
43. Kobayashi, N.; Nakajima, S.; Ogata, H.; Fukuda, T. *Chem. Eur. J.* **2004**, *10*, 6294–6312.
44. Pop, D.; Winter, B.; Freyer, W.; Hertel, I. V.; Widdra, W. *J. Phys. Chem. B* **2003**, *107*, 11643–11647.
45. Mikhalenko, S. A.; Luk'yanets, E. A. *J. Gen. Chem. Ussr* **1969**, *39*, 2495–2498.
46. Bedworth, P. V.; Perry, J. W.; Marder, S. R. *Chem. Commun.* **1997**, 1353–1354.
47. Arabei, S. M.; Galaup, J. P.; Solovyov, K. N.; Donyagina, V. F. *Chem. Phys.* **2005**, *311*, 307–319.
48. Kobayashi, N.; Ogata, H.; Nonaka, N.; Luk'yanets, E. A. *Chem. Eur. J.* **2003**, *9*, 5123–5134.
49. Drobizhev, M.; Makarov, N. S.; Rebane, A.; Wolleb, H.; Spahni, H. *J. Lumin.* **2008**, *128*, 217–222.
50. Renge, I.; Wolleb, H.; Spahni, H.; Wild, U. P. *J. Phys. Chem. A* **1997**, *101*, 6202–6213.
51. Ishii, K.; Itoya, H.; Miwa, H.; Kobayashi, N. *Chem. Commun.* **2005**, 4586–4588.
52. Nemykin, V. N.; Polshina, A. E.; Kobayashi, N. *Chem. Lett.* **2000**, 1236–1237.
53. Cook, M. J.; Jafari-Fini, A. *J. Mater. Chem.* **1997**, *7*, 5–7.
54. Cook, M. J.; Jafari-Fini, A. *Tetrahedron* **2000**, *56*, 4085–4094.
55. Sugimoto, H.; Higashi, T.; Mori, M. *J. Chem. Soc. Chem. Commun.* **1983**, 622–623.
56. Barrett, P. A.; Frye, D. A.; Linstead, R. P. *J. Chem. Soc.* **1938**, 1157–1163.
57. Anderson, J. S.; Bradbrook, E. F.; Cook, A. H.; Linstead, R. P. *J. Chem. Soc.* **1938**, 1151–1156.
58. Stillman, M. J.; Thomson, A. J. *J. Chem. Soc. Faraday Trans. 2* **1974**, *70*, 805–814.
59. Gilat, S. L.; Ebbesen, T. W. *J. Phys. Chem.* **1993**, *97*, 3551–3554.
60. Martin, K. A.; Stillman, M. J. *Inorg. Chem.* **1980**, *19*, 2473–2475.
61. Homborg, H.; Kalz, W. *Z. Anorg. Allg. Chem.* **1984**, *514*, 115–119.
62. Homborg, H.; Kalz, W. *Z. Naturforsch B* **1978**, *33*, 968–975.
63. Homborg, H.; Kalz, W. *Z. Naturforsch B* **1978**, *33*, 1063–1066.
64. Tarasevich, M. R.; Akhundov, E. A. *J. Appl. Chem.-Ussr* **1983**, *56*, 300–303.
65. Turek, P.; Petit, P.; André, J. J.; Simon, J.; Even, R.; Boudjema, B.; Guillaud, G.; Maitrot, M. *J. Am. Chem. Soc.* **1987**, *109*, 5119–5122.

66. Ilangovan, G.; Zweier, J. L.; Kuppusamy, P. *J. Phys. Chem. B* **2000**, *104*, 9404–9410.
67. Ilangovan, G.; Zweier, J. L.; Kuppusamy, P. *J. Phys. Chem. B* **2000**, *104*, 4047–4059.
68. Ilangovan, G.; Pal, R.; Zweier, J. L.; Kuppusamy, P. *J. Phys. Chem. B* **2002**, *106*, 11929–11935.
69. Pandian, R. P.; Dolgos, M.; Dang, V.; Sostaric, J. Z.; Woodward, P. M.; Kuppusamy, P. *Chem. Mater.* **2007**, *19*, 3545–3552.
70. Manivannan, A.; Yanagi, H. *Chem. Lett.* **2001**, 568–569.
71. Manivannan, A.; Yanagi, H.; Ilangovan, G.; Kuppusamy, P. *J. Magn. Magn. Mater.* **2001**, *233*, L131–L135.
72. Ilangovan, G.; Manivannan, A.; Li, H. Q.; Yanagi, H.; Zweier, J. L.; Kuppusamy, P. *Free Radical Biol. Med.* **2002**, *32*, 139–147.
73. Pandian, R. P.; Kim, Y. I.; Woodward, P. M.; Zweier, J. L.; Manoharan, P. T.; Kuppusamy, P. *J. Mater. Chem.* **2006**, *16*, 3609–3618.
74. Barrett, P. A.; Dent, C. E.; Linstead, R. P. *J. Chem. Soc.* **1936**, 1719–1736.
75. Ziolo, R. F.; Extine, M. *Inorg. Chem.* **1981**, *20*, 2709–2711.
76. Ziolo, R. F.; Günther, W. H. H.; Troup, J. M. *J. Am. Chem. Soc.* **1981**, *103*, 4629–4630.
77. Margadonna, S.; Prassides, K.; Iwasa, Y.; Taguchi, Y.; Craciun, M. F.; Rogge, S.; Morpurgo, A. F. *Inorg. Chem.* **2006**, *45*, 10472–10478.
78. Linstead, R. P.; Robertson, J. M. *J. Chem. Soc.* **1936**, 1736–1738.
79. Sidorov, A. N. *Opt. Spektrosk.* **1962**, *13*, 668–672.
80. Kubiak, R.; Waśkowska, A.; Śledź, M.; Jezierski, A. *Inorg. Chim. Acta* **2006**, *359*, 1344–1350.
81. Kasuga, K.; Tsutsui, M. *Coord. Chem. Rev.* **1980**, *32*, 67–95.
82. Janczak, J.; Idemori, Y. M. *Acta Crystallogr. C* **2002**, *58*, m549–m550.
83. Ough, E.; Nyokong, T.; Creber, K. A. M.; Stillman, M. J. *Inorg. Chem.* **1988**, *27*, 2724–2732.
84. Janczak, J.; Kubiak, R. *Polyhedron* **2002**, *21*, 265–274.
85. Ishikawa, N.; Maurice, D.; HeadGordon, M. *Chem. Phys. Lett.* **1996**, *260*, 178–185.
86. Kubota, H. G.; Muto, J.; Itoh, K. M. *J. Mater. Sci. Lett.* **1996**, *15*, 1475–1477.
87. Hor, A. M.; Loutfy, R. O. *Thin Solid Films* **1983**, *106*, 291–301.
88. Endo, A.; Matsumoto, S.; Mizuguchi, J. *J. Phys. Chem. A* **1999**, *103*, 8193–8199.
89. Lapkina, L. A.; Sakharov, S. G.; Konstantinov, N. Y.; Larchenko, V. E.; Gorbunova, Y. G.; Tsivadze, A. Y. *Russ. J. Inorg. Chem.* **2007**, *52*, 1758–1768.
90. Hückstädt, H.; Tutaβ, A.; Göldner, M.; Cornelissen, U.; Homborg, H. *Z. Anorg. Allg. Chem.* **2001**, *627*, 485–497.
91. Ostendorp, G.; Homborg, H. *Z. Anorg. Allg. Chem.* **1996**, *622*, 1358–1364.
92. Jiang, J. Z.; Xie, J. L.; Choi, M. T. M.; Yan, Y.; Sun, S. X.; Ng, D. K. P. *J. Porphyr. Phthalocyan.* **1999**, *3*, 322–328.
93. Kasuga, K.; Ando, M.; Morimoto, H.; Isa, M. *Chem. Lett.* **1986**, 1095–1098.
94. Ishikawa, N. *J. Porphyr. Phthalocyan.* **2001**, *5*, 87–101.
95. Ishikawa, N.; Ohno, O.; Kaizu, Y.; Kobayashi, H. *J. Phys. Chem.* **1992**, *96*, 8832–8839.
96. Kasha, M.; Rawls, H. R.; Ashraf El-Bayoumi, M. *Pure Appl. Chem.* **1965**, *11*, 371–392.
97. Ishikawa, N.; Kaizu, Y. *Chem. Phys. Lett.* **1994**, *228*, 625–632.
98. Buchler, J. W.; Hüttermann, J.; Löffler, J. *Bull. Chem. Soc. Jpn.* **1988**, *61*, 71–77.
99. Donohoe, R. J.; Duchowski, J. K.; Bocian, D. F. *J. Am. Chem. Soc.* **1988**, *110*, 6119–6124.
100. Ishikawa, N.; Ohno, O.; Kaizu, Y. *Chem. Phys. Lett.* **1991**, *180*, 51–56.
101. Fryer, J. R. *J. Porphyr. Phthalocyan.* **1999**, *3*, 672–678.

102. Frick, K.; Ziener, U.; Hanack, M. *Eur. J. Inorg. Chem.* **1999**, 1309–1313.
103. Ostendorp, G.; Homborg, H. *Z. Anorg. Allg. Chem.* **1996**, *622*, 1222–1230.
104. Nyokong, T.; Furuya, F.; Kobayashi, N.; Du, D. M.; Liu, W.; Jiang, J. Z. *Inorg. Chem.* **2000**, *39*, 128–135.
105. Jiang, J. Z.; Liu, W.; Poon, K. W.; Du, D. M.; Arnold, D. P.; Ng, D. K. P. *Eur. J. Inorg. Chem.* **2000**, 205–209.
106. Liu, W.; Jiang, J. Z.; Du, D. M.; Arnold, D. P. *Aust. J. Chem.* **2000**, *53*, 131–135.
107. Guilard, R.; Dormond, A.; Belkalem, M.; Anderson, J. E.; Liu, Y. H.; Kadish, K. M. *Inorg. Chem.* **1987**, *26*, 1410–1414.
108. Lux, F.; Ammentor, F. *Radiochim. Acta* **1965**, *4*, 112.
109. Lux, F.; Dempf, D.; Graw, D. *Angew. Chem. Int. Ed.* **1968**, *7*, 819.
110. Lux, F.; Ammentor, F.; Dempf, D.; Graw, D.; Hagenber, W. *Radiochim. Acta* **1970**, *14*, 57–61.
111. Kadish, K. M.; Moninot, G.; Hu, Y.; Dubois, D.; Ibnlfassi, A.; Barbe, J. M.; Guilard, R. *J. Am. Chem. Soc.* **1993**, *115*, 8153–8166.
112. Msadak, M.; Roncali, J.; Garnier, F. *J. Electroanal. Chem.* **1985**, *189*, 99–111.
113. Moskalev, P. N.; Shapkin, G. N. *Radiokhimiya* **1977**, *19*, 356–359.
114. Cuellar, E. A.; Marks, T. J. *Inorg. Chem.* **1981**, *20*, 3766–3770.
115. Marks, T. J.; Stojakovic, D. R. *J. Am. Chem. Soc.* **1978**, *100*, 1695–1705.
116. Silver, J.; Jassim, Q. A. A. *Inorg. Chim. Acta* **1988**, *144*, 281–288.
117. Chahraoui, D.; Valat, P.; Kossanyi, J. *Res. Chem. Intermediat.* **1992**, *17*, 219–232.
118. Ma, C. Y.; Ye, K. Q.; Yu, S. K.; Du, G. T.; Zhao, Y. F.; Cong, F. D.; Chang, Y. C.; Jiang, W. H.; Cheng, C. H.; Fan, Z. Q.; Yu, H. F.; Li, W. C. *Dyes Pigments* **2007**, *74*, 141–147.
119. Law, W. F.; Liu, R. C. W.; Jiang, J. H.; Ng, D. K. P. *Inorg. Chim. Acta* **1997**, *256*, 147–150.
120. Barthel, M.; Hanack, M. *J. Porphyr. Phthalocyan.* **2000**, *4*, 635–638.
121. Ercolani, C.; Paoletti, A. M.; Pennesi, G.; Rossi, G.; Chiesivilla, A.; Rizzoli, C. *J. Chem. Soc. Dalton* **1990**, 1971–1977.
122. Cherian, R. C.; Menon, C. S. *J. Phys. Chem. Solids* **2008**, *69*, 2858–2863.
123. Nakai, K.; Ishii, K.; Kobayashi, N.; Yonehara, H.; Pac, C. *J. Phys. Chem. B* **2003**, *107*, 9749–9755.
124. Tretyakova, I. N.; Chernii, V. Y.; Tomachynski, L. A.; Volkov, S. V. *Dyes Pigments* **2007**, *75*, 67–72.
125. Tomachynski, L. A.; Tretyakova, I. N.; Chernii, V. Y.; Volkov, S. V.; Kowalska, M.; Legendziewicz, J.; Gerasymchuk, Y. S.; Radzki, S. *Inorg. Chim. Acta* **2008**, *361*, 2569–2581.
126. Tomachynski, L. A.; Chernii, V. Y.; Volkov, S. *J. Porphyr. Phthalocyan.* **2002**, *6*, 114–121.
127. Silver, J.; Lukes, P. J.; Hey, P. K.; Oconnor, J. M. *Polyhedron* **1989**, *8*, 1631–1635.
128. Tomilova, L. G.; Ovchinnikova, N. A.; Luk'yanets, E. A. *Zh. Obshch. Khim.* **1987**, *57*, 2100–2104.
129. Ejsmont, K.; Kubiak, R. *Acta Crystallogr. C* **1998**, *54*, 1844–1846.
130. Ziolo, R. F.; Griffiths, C. H.; Troup, J. M. *J. Chem. Soc. Dalton* **1980**, 2300–2302.
131. Griffiths, C. H.; Walker, M. S.; Goldstein, P. *Mol. Cryst. Liq. Cryst.* **1976**, *33*, 149–170.
132. Huang, T. H.; Sharp, J. H. *Chem. Phys.* **1982**, *65*, 205–216.
133. Handa, M.; Suzuki, A.; Shoji, S.; Kasuga, K.; Sogabe, K. *Inorg. Chim. Acta* **1995**, *230*, 41–44.
134. Mbambisa, G.; Nyokong, T. *Polyhedron* **2008**, *27*, 2799–2804.

135. Cellucci, L.; Ercolani, C.; Lukes, P. J.; Chiesi-Villa, A.; Rizzoli, C. *J. Porphyr. Phthalocyan.* **1998**, *2*, 9–19.
136. Donzello, M. P.; Ercolani, C.; Lukes, P. J. *Inorg. Chim. Acta* **1997**, *256*, 171–172.
137. Donzello, M. P.; Ercolani, C.; Chiesi-Villa, A.; Rizzoli, C. *Inorg. Chem.* **1998**, *37*, 1347–1351.
138. Bauer, E. M.; Donzello, M. P.; Ercolani, C.; Masetti, E.; Panero, S.; Ricciardi, G.; Rosa, A.; Chiesi-Villa, A.; Rizzoli, C. *Inorg. Chem.* **2003**, *42*, 283–293.
139. Janczak, J.; Kubiak, R. *Polyhedron* **2003**, *22*, 313–322.
140. Gingl, F.; Strähle, J. *Z. Kristallogr.* **1988**, *182*, 97–98.
141. Gingl, F.; Strähle, J. *Z. Naturforsch B* **1988**, *43*, 445–448.
142. Tau, P.; Nyokong, T. *J. Porphyr. Phthalocyan.* **2006**, *10*, 69–75.
143. Schweiger, K.; Hückstädt, H.; Homborg, H. *Z. Anorg. Allg. Chem.* **1997**, *623*, 1853–1854.
144. Elvidge, J. A.; Lever, A. B. P. *J. Chem. Soc.* **1961**, 1257–1265.
145. Lever, A. B. P.; Pickens, S. R.; Minor, P. C.; Licoccia, S.; Ramaswamy, B. S.; Magnell, K. *J. Am. Chem. Soc.* **1981**, *103*, 6800–6806.
146. Bode, M.; Wasgestian, F. *Inorg. Chim. Acta* **1994**, *224*, 185–188.
147. Boas, J. F.; Fielding, P. E.; Mackay, A. G. *Aust. J. Chem.* **1974**, *27*, 7–19.
148. Hill, H. A. O.; Norgett, M. M. *J. Chem. Soc. A* **1966**, 1476–1478.
149. Zhukov, Y. A.; Shylapora, L. N.; Sokolova, I. N.; Berezin, B. D. *Tr. Ivanov. Khim.-Tekhnol. Inst.* **1969**, *11*, 52.
150. Federov, M. I.; Shorin, V. A.; Federov, L. M. *Izv. Vyssh. Uchebn. Zaved., Fiz.* **1978**, *21*, 158.
151. Borschel, V.; Strähle, J. *Z. Naturforsch B* **1984**, *39*, 1664–1667.
152. Edmondson, S. J.; Mitchell, P. C. H. *Polyhedron* **1986**, *5*, 315–317.
153. Galindo, S.; González-Tovany, L.; Guía-García, M. A. *Rev. Mex. Fis.* **1986**, *32*, 435–453.
154. Nyokong, T. *Polyhedron* **1994**, *13*, 215–220.
155. Ferraudi, G.; Nyokong, T.; Feliz, M.; Perkovic, M.; Rillema, D. P. *Inorg. Chim. Acta* **1994**, *215*, 27–32.
156. Frick, K.; Verma, S.; Sundermeyer, J.; Hanack, M. *Eur. J. Inorg. Chem.* **2000**, 1025–1030.
157. Verma, S.; Hanack, M. *Z. Anorg. Allg. Chem.* **2003**, *629*, 880–892.
158. Gorsch, M.; Homborg, H. *Z. Anorg. Allg. Chem.* **1998**, *624*, 634–641.
159. Shishkin, V. G.; Al'yanov, M. I.; Snegireva, F. P. *Khim. Khim. Tekhnol.* **1976**, *19*, 1348–1351.
160. Al'yanov, M. I.; Snegireva, F. P.; Shishkin, V. G.; Borodkin, V. F. *Otkrytiya. Izobret. Prom. Obraztsy. Tovarnye Znaki* **1975**, *52*, 56.
161. Padilla, J.; Litter, M. I.; Campero, A. *An. Quim.* **1993**, *89*, 177–180.
162. Engelsma, G.; Yamamoto, A.; Markham, E.; Calvin, M. *J. Phys. Chem.* **1962**, *66*, 2517–2531.
163. Janczak, J.; Kubiak, R.; Śledź, M.; Borrmann, H.; Grin, Y. *Polyhedron* **2003**, *22*, 2689–2697.
164. Elvidge, J. A.; Lever, A. B. P. *P. Chem. Soc. London* **1959**, 195–195.
165. Rutter, H. A.; Mcqueen, J. D. *J. Inorg. Nucl. Chem.* **1960**, *12*, 361–363.
166. Barraclough, C. G.; Martin, R. L.; Mitra, S.; Sherwood, R. C. *J. Chem. Phys.* **1970**, *53*, 1638–1642.
167. Barraclough, C. G.; Gregson, A. K.; Mitra, S. *J. Chem. Phys.* **1974**, *60*, 962–968.
168. Miyoshi, H. *Bull. Chem. Soc. Jpn.* **1974**, *47*, 561–565.
169. Mitra, S.; Gregson, A. K.; Hatfield, W. E.; Weller, R. R. *Inorg. Chem.* **1983**, *22*, 1729–1732.
170. Labarta, A.; Molins, E.; Tejada, J. *Z. Phys. B Con. Mat.* **1985**, *58*, 299–304.
171. Schaffer, A. M.; Gouterman, M.; Davidson, E. R. *Theor. Chim. Acta* **1973**, *30*, 9–30.
172. Williamson, B. E.; VanCott, T. C.; Boyle, M. E.; Misener, G. C.; Stillman, M. J.; Schatz, P. N. *J. Am. Chem. Soc.* **1992**, *114*, 2412–2419.

173. Liao, M. S.; Watts, J. D.; Huang, M. J. *Inorg. Chem.* **2005**, *44*, 1941–1949.
174. Leznoff, C. C.; Black, L. S.; Hiebert, A.; Causey, P. W.; Christendat, D.; Lever, A. B. P. *Inorg. Chim. Acta* **2006**, *359*, 2690–2699.
175. Mbambisa, G.; Tau, P.; Antunes, E.; Nyokong, T. *Polyhedron* **2007**, *26*, 5355–5364.
176. Mandimutsira, B. S.; Ramdhanie, B.; Todd, R. C.; Wang, H. L.; Zareba, A. A.; Czemuszewicz, R. S.; Goldberg, D. P. *J. Am. Chem. Soc.* **2002**, *124*, 15170–15171.
177. Yoshihara, K.; Wolf, G. K.; Baumgartner, F. *Radiochim. Acta* **1974**, *21*, 96–100.
178. Rummel, S.; Hermann, M.; Schmidt, K. *Z. Chem.* **1985**, *25*, 152–153.
179. El-Tamer, M.; Saouaf, R.; Wang, T.; Fawwaz, R. *Ann. Surg. Oncol.* **2003**, *10*, 323–329.
180. Ziener, U.; Hanack, M. *Chem. Ber.* **1994**, *127*, 1681–1685.
181. Ziener, U.; Dürr, K.; Hanack, M. *Synthetic Met.* **1995**, *71*, 2285–2286.
182. Göldner, M.; Hückstädt, H.; Murray, K. S.; Moubaraki, B.; Homborg, H. *Z. Anorg. Allg. Chem.* **1998**, *624*, 288–294.
183. Göldner, M.; Kienast, A.; Homborg, H. *Z. Anorg. Allg. Chem.* **1998**, *624*, 141–146.
184. Dale, B. W.; Williams, R. J. P.; Edwards, P. R.; Johnson, C. E. *Trans. Faraday Soc.* **1968**, *64*, 620–629.
185. Ouédraogo, G. V.; More, C.; Richard, Y.; Benlian, D. *Inorg. Chem.* **1981**, *20*, 4387–4393.
186. Grenoble, D. C.; Drickamer, H. G. *J. Chem. Phys.* **1971**, *55*, 1624–1633.
187. Kostromina, N. A.; Chernii, V. Y.; Nemykin, V. N.; Komarov, I. V. *Zh. Neorg. Khim.* **1995**, *40*, 1491–1495.
188. Choy, C. K.; Mooney, J. R.; Kenney, M. E. *J. Magn. Reson.* **1979**, *35*, 1–12.
189. Taube, R.; Drevs, H.; Fluck, E.; Kuhn, P.; Brauch, K. F. *Z. Anorg. Allg. Chem.* **1969**, *364*, 297–315.
190. Taube, R. *Pure Appl. Chem.* **1974**, *38*, 427–438.
191. James, B. R.; Sams, J. R.; Tsin, T. B.; Reimer, K. J. *J. Chem. Soc. Chem. Commun.* **1978**, 746–747.
192. Calderazzo, F.; Pampaloni, G.; Vitali, D.; Pelizzi, G.; Collamati, I.; Frediani, S.; Serra, A. M. *J. Organomet. Chem.* **1980**, *191*, 217–242.
193. Dale, B. W.; Williams, R. J. P.; Edwards, P. R.; Johnson, C. E. *Trans. Faraday Soc.* **1968**, *64*, 3011–3013.
194. Calderazzo, F.; Frediani, S.; James, B. R.; Pampaloni, G.; Reimer, K. J.; Sams, J. R.; Serra, A. M.; Vitali, D. *Inorg. Chem.* **1982**, *21*, 2302–2306.
195. Valenti, V.; Fantucci, P.; Cariati, F.; Micera, G.; Petrera, M.; Burriesci, N. *Inorg. Chim. Acta* **1988**, *148*, 191–197.
196. Hanack, M.; Hirsch, A. *Synthetic Met.* **1989**, *29*, F9–F13.
197. Hudson, A.; Whitfield, H. J. *Inorg. Chem.* **1967**, *6*, 1120–1123.
198. Keppeler, U.; Deger, S.; Lange, A.; Hanack, M. *Angew. Chem. Int. Ed.* **1987**, *26*, 344–345.
199. Hanack, M.; Ryu, H. *Synthetic Met.* **1992**, *46*, 113–126.
200. Dale, B. W. *Trans. Faraday Soc.* **1969**, *65*, 331–339.
201. Nemykin, V. N.; Polshina, A. E.; Chernii, V. Y.; Polshin, E. V.; Kobayashi, N. *J. Chem. Soc. Dalton* **2000**, *7*, 1019–1025.
202. Ough, E. A.; Stillman, M. J. *Inorg. Chem.* **1994**, *33*, 573–583.
203. Nyokong, T. *J. Chem. Soc. Dalton* **1993**, 3601–3604.
204. Stillman, M. J.; Thomson, A. J. *J. Chem. Soc. Faraday Trans. 2* **1974**, *70*, 790–804.
205. Fukuda, T.; Homma, S.; Kobayashi, N. *Chem. Commun.* **2003**, 1574–1575.
206. Hanack, M.; Dieing, R.; Röhrig, U. *Chem. Lett.* **1993**, 399–402.

207. Deger, S.; Hanack, M. *Israel J. Chem.* **1986**, *27*, 347–351.
208. Lever, A. B. P.; Wilshire, J. P. *Inorg. Chem.* **1978**, *17*, 1145–1151.
209. Kennedy, B. J.; Murray, K. S.; Zwack, P. R.; Homborg, H.; Kalz, W. *Inorg. Chem.* **1986**, *25*, 2539–2545.
210. Kobayashi, N.; Koshiyama, M.; Ishikawa, Y.; Osa, T.; Shirai, H.; Hojo, N. *Chem. Lett.* **1984**, 1633–1636.
211. Bottomley, L. A.; Ercolani, C.; Gorce, J. N.; Pennesi, G.; Rossi, G. *Inorg. Chem.* **1986**, *25*, 2338–2342.
212. Bottomley, L. A.; Gorce, J. N.; Goedken, V. L.; Ercolani, C. *Inorg. Chem.* **1985**, *24*, 3733–3737.
213. Rawling, T.; McDonagh, A. *Coord. Chem. Rev.* **2007**, *251*, 1128–1157.
214. Dolphin, D.; James, B. R.; Murray, A. J.; Thornback, J. R. *Can. J. Chem.* **1980**, *58*, 1125–1132.
215. Gorbunova, Y. G.; Enakieva, Y. Y.; Sakharov, S. G.; Tsivadze, A. Y. *J. Porphyr. Phthalocyan.* **2003**, *7*, 795–800.
216. Gorbunova, Y. G.; Enakieva, Y. Y.; Sakharov, S. G.; Tsivadze, A. Y. *Russ. Chem. B* **2004**, *53*, 74–79.
217. Omiya, S.; Tsutsui, M.; Meyer, E. F.; Bernal, I.; Cullen, D. L. *Inorg. Chem.* **1980**, *19*, 134–142.
218. Gutiérrez, A. R. *Chem. Phys. Lett.* **1980**, *74*, 293–297.
219. Stuzhin, P. A.; Vagin, S. I.; Hanack, M. *Inorg. Chem.* **1998**, *37*, 2655–2662.
220. Stuzhin, P. A.; Migalova, I. S.; Berezin, B. D. *Zh. Neorg. Khim.* **1993**, *38*, 2004–2010.
221. Rawling, T.; Xiao, H.; Lee, S. T.; Colbran, S. B.; McDonagh, A. M. *Inorg. Chem.* **2007**, *46*, 2805–2813.
222. Capobianchi, A.; Paoletti, A. M.; Pennesi, G.; Rossi, G.; Caminiti, R.; Ercolani, C. *Inorg. Chem.* **1994**, *33*, 4635–4640.
223. Bertagnolli, H.; Weber, A.; Hörner, W.; Ertel, T. S.; Reinöhl, U.; Hanack, M.; Hees, M.; Polley, R. *Inorg. Chem.* **1997**, *36*, 6397–6400.
224. Dudnik, A. S.; Ivanov, A. V.; Tomilova, L. G.; Zefirov, N. S. *Russ. J. Coord. Chem.* **2004**, *30*, 110–114.
225. Herr, W. *Z. Naturforsch B* **1952**, *7*, 201–207.
226. Berezin, B. D.; Sosnikova, N. I. *Dokl. Akad. Nauk. Sssr* **1962**, *146*, 604–607.
227. Keen, I. M.; Malerbi, B. W. *J. Inorg. Nucl. Chem.* **1965**, *27*, 1311–1319.
228. Zakharov, A. N.; Gabrielov, A. G.; Romanovskii, B. V.; Sokolov, V. I. *Vestn. Mosk. U. Khim.* **1989**, *30*, 234–238.
229. Hanack, M.; Vermehren, P. *Inorg. Chem.* **1990**, *29*, 134–136.
230. Subramanian, L. R.; Gül, A.; Hanack, M.; Mandal, B. K.; Witke, E. *Synthetic Met.* **1991**, *42*, 2669–2673.
231. Hanack, M.; Gül, A.; Subramanian, L. R. *Inorg. Chem.* **1992**, *31*, 1542–1544.
232. Sievertsen, S.; Schlehahn, H.; Homborg, H. *Z. Anorg. Allg. Chem.* **1993**, *619*, 1064–1072.
233. Sievertsen, S.; Schlehahn, H.; Homborg, H. *Z. Naturforsch B* **1994**, *49*, 50–56.
234. Schlehahn, H.; Homborg, H. *Z. Anorg. Allg. Chem.* **1995**, *621*, 1558–1566.
235. Weidemann, M.; Homborg, H. *Z. Anorg. Allg. Chem.* **1996**, *622*, 2095–2098.
236. Sekota, M.; Nyokong, T. *Electroanal.* **1997**, *9*, 1257–1261.
237. Caminiti, R.; Donzello, M. P.; Ercolani, C.; Sadun, C. *Inorg. Chem.* **1998**, *37*, 4210–4213.
238. Metz, J.; Schneider, O.; Hanack, M. *Inorg. Chem.* **1984**, *23*, 1065–1071.

239. Nevin, W. A.; Liu, W.; Greenberg, S.; Hempstead, M. R.; Marcuccio, S. M.; Melnik, M.; Leznoff, C. C.; Lever, A. B. P. *Inorg. Chem.* **1987**, *26*, 891–899.
240. Kobayashi, N.; Lam, H.; Nevin, W. A.; Janda, P.; Leznoff, C. C.; Lever, A. B. P. *Inorg. Chem.* **1990**, *29*, 3415–3425.
241. Clack, D. W.; Yandle, J. R. *Inorg. Chem.* **1972**, *11*, 1738–1742.
242. Nevin, W. A.; Liu, W.; Melnik, M.; Lever, A. B. P. *J. Electroanal. Chem.* **1986**, *213*, 217–234.
243. Nombona, N.; Nyokong, T. *Dyes Pigments* **2009**, *80*, 130–135.
244. Münz, X.; Hanack, M. *Chem. Ber.-Recl.* **1988**, *121*, 235–238.
245. Münz, X.; Hanack, M. *Chem. Ber.-Recl.* **1988**, *121*, 239–242.
246. Menzel, E. R.; Rieckhof, KE.; Voigt, E. M. *J. Chem. Phys.* **1973**, *58*, 5726–5734.
247. Hückstädt, H.; Homborg, H. *Z. Anorg. Allg. Chem.* **1998**, *624*, 715–720.
248. Gaffo, L.; Couto, O. D. D.; Giro, R.; Brasil, M. J. S. P.; Galvão, D. S.; Cerdeira, F.; de Oliveira, O. N.; Wohnrath, K. *Solid State Commun.* **2004**, *131*, 53–56.
249. Balkus, K. J.; Welch, A. A.; Gnade, B. E. *J. Inclusion Phenom. Macrocyclic Chem.* **1991**, *10*, 141–151.
250. Ni, Y. P.; Fitzgerald, J. P.; Carroll, P.; Wayland, B. B. *Inorg. Chem.* **1994**, *33*, 2029–2035.
251. Chen, W. H.; Rieckhoff, K. E.; Voigt, E. M. *Can. J. Phys.* **1988**, *66*, 86–92.
252. Chen, M. J.; Rathke, J. W. *Organometallics* **1994**, *13*, 4875–4880.
253. Hückstädt, H.; Homborg, H. *Z. Naturforsch B* **1997**, *52*, 1003–1010.
254. Hückstädt, H.; Homborg, H. *Z. Naturforsch B* **1997**, *52*, 728–734.
255. Hückstädt, H.; Homborg, H. *Z. Anorg. Allg. Chem.* **1997**, *623*, 369–378.
256. Hückstädt, H.; Homborg, H. *Z. Anorg. Allg. Chem.* **1997**, *623*, 292–298.
257. Hückstädt, H.; Homborg, H. *J. Porphyr. Phthalocyan.* **1998**, *2*, 269–272.
258. Hückstädt, H.; Homborg, H. *Z. Anorg. Allg. Chem.* **1998**, *624*, 980–986.
259. Hückstädt, H.; Homborg, H. *J. Porphyr. Phthalocyan.* **1999**, *3*, 169–171.
260. Stuzhin, P. A.; Kabesheva, E. V.; Khelevina, O. G. *Russ. J. Coord. Chem.* **2003**, *29*, 352–356.
261. Fielding, P. E.; Mackay, A. G.; Day, P.; Scregg, G.; Williams, R. J. P. *J. Chem. Phys.* **1963**, *38*, 2777–2778.
262. Soldatova, A. V.; Kim, J.; Peng, X. H.; Rosa, A.; Ricciardi, G.; Kenney, M. E.; Rodgers, M. A. J. *Inorg. Chem.* **2007**, *46*, 2080–2093.
263. Freyer, W.; Flatau, S. *Tetrahedron Lett.* **1996**, *37*, 5083–5086.
264. Freyer, W.; Leupold, D. *J. Photochem. Photobiol., A* **1997**, *105*, 153–158.
265. Miwa, H.; Ishii, K.; Kobayashi, N. *Chem. Eur. J.* **2004**, *10*, 4422–4435.
266. Brown, R. J. C.; Kucernak, A. R.; Long, N. J.; Mongay-Batalla, C. *New. J. Chem.* **2004**, *28*, 676–680.
267. Watt, G. W.; Dawes, J. W. *J. Inorg. Nucl. Chem.* **1960**, *14*, 32–34.
268. Gardberg, A. S.; Doan, P. E.; Hoffman, B. M.; Ibers, J. A. *Angew. Chem. Int. Ed.* **2001**, *40*, 244–246.
269. Mcvie, J.; Sinclair, R. S.; Truscott, T. G. *J. Chem. Soc. Faraday Trans. 2* **1978**, *74*, 1870–1879.
270. Assour, J. M.; Harrison, S. E. *J. Am. Chem. Soc.* **1965**, *87*, 651–652.
271. Schott, M. *J. Chem. Phys.* **1966**, *44*, 429–430.
272. Safari, N.; Jamaat, P. R.; Pirouzmand, M.; Shaabani, A. *J. Porphyr. Phthalocyan.* **2004**, *8*, 1209–1213.
273. Mikhalenko, S. A.; Korobkova, E. V.; Luk'yanets, E. A. *J. Gen. Chem. Ussr* **1970**, *40*, 367–369.
274. Seelan, S.; Agashe, M. S.; Srinivas, D.; Sivasanker, S. *J. Mol. Catal. A: Chem.* **2001**, *168*, 61–68.

275. Haurowitz, F. *Ber. Dtsch. Chem. Ges.* **1935**, *68*, 1795–1806.
276. Kholmogorov, V. E.; Glebovsky, D. N. *Opt. Spektrosk.* **1962**, *12*, 728–732.
277. Kholmogorov, V. E. *Opt. Spektrosk.* **1963**, *14*, 303–304.
278. Maccragh, A.; Koski, W. S. *J. Am. Chem. Soc.* **1963**, *85*, 2375–2376.
279. Fu, G. Y.; Fu, Y. S.; Jayaraj, K.; Lever, A. B. P. *Inorg. Chem.* **1990**, *29*, 4090–4095.
280. Ouyang, J. A.; Lever, A. B. P. *J. Phys. Chem.* **1991**, *95*, 2101–2103.
281. Fu, Y. S.; Lever, A. B. P. *J. Phys. Chem.* **1991**, *95*, 6979–6984.
282. Maccragh, A.; Koski, W. S. *J. Am. Chem. Soc.* **1965**, *87*, 2496–2497.
283. Kobayash.T; Ashida, T.; Uyeda, N.; Suito, E.; Kakudo, M. *Bull. Chem. Soc. Jpn.* **1971**, *44*, 2095–2103.
284. Fukuda, T.; Homma, S.; Kobayashi, N. *Chem. Eur. J.* **2005**, *11*, 5205–5216.
285. Stephens, P. J.; Suëtaak, W.; Schatz, P. N. *J. Chem. Phys.* **1966**, *44*, 4592–4602.
286. Chidawanyika, W.; Ogunsipe, A.; Nyokong, T. *New. J. Chem.* **2007**, *31*, 377–384.
287. Chidawanyika, W.; Antunes, E.; Nyokong, T. *J. Photochem. Photobiol., A* **2008**, *195*, 183–190.
288. Chambrier, I.; Hughes, D. L.; Swarts, J. C.; Isare, B.; Cook, M. J. *Chem. Commun.* **2006**, 3504–3506.
289. Chambrier, I.; White, G. F.; Cook, M. J. *Chem. Eur. J.* **2007**, *13*, 7608–7618.
290. Yoshihara, K.; Kudo, H. *Nature* **1969**, *222*, 1060–1061.
291. Kudo, H.; Yoshihara, K. *J. Inorg. Nucl. Chem.* **1970**, *32*, 2845–2851.
292. Kudo, H. *J. Inorg. Nucl. Chem.* **1972**, *34*, 453–460.
293. Harbour, J. R.; Dietelbach, B.; Duff, J. *J. Phys. Chem.* **1983**, *87*, 5456–5460.
294. Clare, P.; Glockling, F. *Inorg. Chim. Acta* **1975**, *14*, L12–L12.
295. George, R. D.; Snow, A. W.; McMillan, P. F.; Burrows, V. A. *J. Am. Chem. Soc.* **1992**, *114*, 8286–8287.
296. Meller, A.; Ossko, A. *Monatsh. Chem.* **1972**, *103*, 150–155.
297. Claessens, C. G.; González-Rodríguez, D.; Torres, T. *Chem. Rev.* **2002**, *102*, 835–853.
298. Kobayashi, N. *J. Porphyr. Phthalocyan.* **1999**, *3*, 453–467.
299. Rodríguez-Morgade, M. S.; Esperanza, S.; Torres, T.; Barberá, J. *Chem. Eur. J.* **2004**, *11*, 354–360.
300. Díaz-García, M. A.; Agulló-López, F.; Sastre, A.; Torres, T.; Torruellas, W. E.; Stegeman, G. I. *J. Phys. Chem.* **1995**, *99*, 14988–14991.
301. Rauschnabel, J.; Hanack, M. *Tetrahedron Lett.* **1995**, *36*, 1629–1632.
302. Kobayashi, N.; Ishizaki, T.; Ishii, K.; Konami, H. *J. Am. Chem. Soc.* **1999**, *121*, 9096–9110.
303. Rodríguez-Morgade, M. S.; Claessens, C. G.; Medina, A.; González-Rodríguez, D.; Gutiérrez-Puebla, E.; Monge, A.; Alkorta, I.; Elguero, J.; Torres, T. *Chem. Eur. J.* **2008**, *14*, 1342–1350.
304. Stork, J. R.; Brewer, J. J.; Fukuda, T.; Fitzgerald, J. P.; Yee, G. T.; Nazarenko, A. Y.; Kobayashi, N.; Durfee, W. S. *Inorg. Chem.* **2006**, *45*, 6148–6151.
305. Kobayashi, N. *J. Chem. Soc. Chem. Commun.* **1991**, 1203–1205.
306. Claessens, C. G.; Torres, T. *Angew. Chem. Int. Ed.* **2002**, *41*, 2561–2565.
307. Fukuda, T.; Stork, J. R.; Potucek, R. J.; Olmstead, M. M.; Noll, B. C.; Kobayashi, N.; Durfee, W. S. *Angew. Chem. Int. Ed.* **2002**, *41*, 2565–2568.
308. Iglesias, R. S.; Claessens, C. G.; Torres, T.; Herranz, M. A.; Ferro, V. R.; de la Vega, J. M. G. *J. Org. Chem.* **2007**, *72*, 2967–2977.
309. Geyer, M.; Plenzig, F.; Rauschnabel, J.; Hanack, M.; del Rey, B.; Sastre, A.; Torres, T. *Synthesis-Stuttgart* **1996**, 1139–1151.

310. Eckert, A. K.; Rodríguez-Morgade, M. S.; Torres, T. *Chem. Commun.* **2007**, 4104–4106.
311. Strenalyuk, T.; Samdal, S.; Volden, H. V. *J. Phys. Chem. A* **2008**, *112*, 9075–9082.
312. Shaposhnikov, G. P.; Maizlish, V. E.; Kulinich, V. P. *Russ. J. Gen. Chem.* **2005**, *75*, 1480–1488.
313. Linsky, J. P.; Paul, T. R.; Nohr, R. S.; Kenney, M. E. *Inorg. Chem.* **1980**, *19*, 3131–3135.
314. Decréau, R.; Richard, M. J.; Julliard, M. *J. Porphyr. Phthalocyan.* **2001**, *5*, 390–396.
315. Homborg, H.; Murray, K. S. *Z. Anorg. Allg. Chem.* **1984**, *517*, 149–160.
316. Ou, Z. P.; Shen, J.; Kadish, K. M. *Inorg. Chem.* **2006**, *45*, 9569–9579.
317. Reinot, T.; Hayes, J. M.; Small, G. J.; Zerner, M. C. *Chem. Phys. Lett.* **1999**, *299*, 410–416.
318. Liu, K.; Wang, Y. H.; Yao, J. N.; Luo, Y. *Chem. Phys. Lett.* **2007**, *438*, 36–40.
319. Cissell, J. A.; Vaid, T. P.; Rheingold, A. L. *Inorg. Chem.* **2006**, *45*, 2367–2369.
320. Ogunsipe, A.; Nyokong, T.; Durmuş, M. *J. Porphyr. Phthalocyan.* **2007**, *11*, 635–644.
321. Chauke, V.; Ogunsipe, A.; Durmuş, M.; Nyokong, T. *Polyhedron* **2007**, *26*, 2663–2671.
322. Durmuş, M.; Nyokong, T. *Polyhedron* **2007**, *26*, 3323–3335.
323. Durmuş, M.; Nyokong, T. *Tetrahedron* **2007**, *63*, 1385–1394.
324. Durmuş, M.; Nyokong, T. *Inorg. Chem. Commun.* **2007**, *10*, 332–338.
325. Chen, Y.; Subramanian, L. R.; Fujitsuka, M.; Ito, O.; O'Flaherty, S.; Blau, W. J.; Schneider, T.; Dini, D.; Hanack, M. *Chem. Eur. J.* **2002**, *8*, 4248–4254.
326. Chen, Y.; Subramanian, L. R.; Barthel, M.; Hanack, M. *Eur. J. Inorg. Chem.* **2002**, 1032–1034.
327. Yang, G. Y.; Hanack, M.; Lee, Y. W.; Chen, Y.; Lee, M. K. Y.; Dini, D. *Chem. Eur. J.* **2003**, *9*, 2758–2762.
328. Chen, Y.; O'Flaherty, S. M.; Hanack, M.; Blau, W. J. *J. Mater. Chem.* **2003**, *13*, 2405–2408.
329. Chen, Y.; Araki, Y.; Fujitsuka, M.; Hanack, M.; Ito, O.; O'Flaherty, S. M.; Blau, W. J. *Solid State Commun.* **2004**, *131*, 773–778.
330. Calvete, M. J. F.; Dini, D.; Hanack, M.; Sancho-García, J. C.; Chen, W. Z.; Ji, W. *J. Mol. Model.* **2006**, *12*, 543–550.
331. Chen, Y.; He, N.; Doyle, J. J.; Liu, Y.; Zhuang, X. D.; Blau, W. J. *J. Photochem. Photobiol., A* **2007**, *189*, 414–417.
332. Chen, Y.; Hanack, M.; Blau, W. J.; Dini, D.; Liu, Y.; Lin, Y.; Bai, J. R. *J. Mater. Sci.* **2006**, *41*, 2169–2185.
333. Mal'chugina, O. V.; Stuzhin, P. A. *Russ. Chem. B* **2002**, *51*, 2261–2267.
334. Görlach, B.; Dachtler, M.; Glaser, T.; Albert, K.; Hanack, M. *Chem. Eur. J.* **2001**, *7*, 2459–2465.
335. Vagin, S.; Hanack, M. *Eur. J. Org. Chem.* **2003**, 2661–2669.
336. Vagin, S.; Barthel, M.; Dini, D.; Hanack, M. *Inorg. Chem.* **2003**, *42*, 2683–2694.
337. Dini, D.; Yang, G. Y.; Hanack, M. *J. Chem. Phys.* **2003**, *119*, 4857–4864.
338. Burnham, P. M.; Cook, M. J.; Gerrard, L. A.; Heeney, M. J.; Hughes, D. L. *Chem. Commun.* **2003**, 2064–2065.
339. Ivanova, S. S.; Stuzhin, P. A. *Russ. J. Coord. Chem.* **2004**, *30*, 765–773.
340. Vagin, S.; Hanack, M. *Eur. J. Org. Chem.* **2004**, 600–606.
341. Chen, Y.; Araki, Y.; Dini, D.; Liu, Y.; Ito, O.; Fujitsuka, M. *Mater. Chem. Phys.* **2006**, *98*, 212–216.
342. Wang, S. Q.; Gan, Q.; Zhang, Y. F.; Li, S. Y.; Xu, H. J.; Yang, G. Q. *ChemPhysChem* **2006**, *7*, 935–941.
343. Hanack, M.; Heckmann, H. *Eur. J. Inorg. Chem.* **1998**, 367–373.

344. Chauke, V.; Durmuş, M.; Nyokong, T. *J. Photochem. Photobiol., A* **2007**, *192*, 179–187.
345. Liu, Y.; O'Flaherty, S. M.; Chen, Y.; Araki, Y.; Bai, J. R.; Doyle, J.; Blau, W. J.; Ito, O. *Dyes Pigments* **2007**, *75*, 88–92.
346. Chen, Y.; Barthel, M.; Seiler, M.; Subramanian, L. R.; Bertagnolli, H.; Hanack, M. *Angew. Chem. Int. Ed.* **2002**, *41*, 3239–3242.
347. Kane, A. R.; Sullivan, J. F.; Kenny, D. H.; Kenney, M. E. *Inorg. Chem.* **1970**, *9*, 1445–1448.
348. Hush, N. S.; Woolsey, I. S. *Mol. Phys.* **1971**, *21*, 465–474.
349. Myakov, V. N.; Kurskii, Y. A.; Sedel'nikova, V. N.; Makhrova, T. V.; Lopatin, M. A. *Russ. J. Coord. Chem.* **2008**, *34*, 522–526.
350. Tamao, K.; Akita, M.; Kato, H.; Kumada, M. *J. Organomet. Chem.* **1988**, *341*, 165–179.
351. Kleinwächter, J.; Hanack, M. *J. Am. Chem. Soc.* **1997**, *119*, 10684–10695.
352. Kobayashi, N.; Furuya, F.; Yug, G. C.; Wakita, H.; Yokomizo, M.; Ishikawa, N. *Chem. Eur. J.* **2002**, *8*, 1474–1484.
353. Kobayashi, N.; Yokoyama, M.; Muranaka, A.; Ceulemans, A. *Tetrahedron Lett.* **2004**, *45*, 1755–1758.
354. Li, J. Z.; Subramanian, L. R.; Hanack, M. *Chem. Commun.* **1997**, 679–680.
355. Li, J. Z.; Subramanian, L. R.; Hanach, M. *J. Porphyr. Phthalocyan.* **2000**, *4*, 739–741.
356. Joyner, R. D.; Kenney, M. E. *J. Am. Chem. Soc.* **1960**, *82*, 5790–5791.
357. Hohol, M. D.; Urban, M. W. *Polymer* **1993**, *34*, 1995–2002.
358. Dirk, C. W.; Inabe, T.; Schoch, K. F.; Marks, T. J. *J. Am. Chem. Soc.* **1983**, *105*, 1539–1550.
359. Pelliccioli, A. P.; Henbest, K.; Kwag, G.; Carvagno, T. R.; Kenney, M. E.; Rodgers, M. A. J. *J. Phys. Chem. A* **2001**, *105*, 1757–1766.
360. Janson, T. R.; Kane, A. R.; Sullivan, J. F.; Knox, K.; Kenney, M. E. *J. Am. Chem. Soc.* **1969**, *91*, 5210–5124.
361. Stover, R. L.; Thrall, C. L.; Joyner, R. D. *Inorg. Chem.* **1971**, *10*, 2335–2337.
362. Fujiki, M.; Tabei, H.; Isa, K. *J. Am. Chem. Soc.* **1986**, *108*, 1532–1536.
363. Cissell, J. A.; Vaid, T. P.; DiPasquale, A. G.; Rheingold, A. L. *Inorg. Chem.* **2007**, *46*, 7713–7715.
364. Friedel, M. K.; Hoskins, B. F.; Martin, R. L.; Mason, S. A. *J. Chem. Soc. D Chem. Commun.* **1970**, 400–401.
365. Rogers, D.; Osborn, R. S. *J. Chem. Soc. D Chem. Commun.* **1971**, 840–841.
366. Sayer, P.; Gouterman, M.; Connell, C. R. *Acc. Chem. Res.* **1982**, *15*, 73–79.
367. Khene, S.; Cammidge, A. N.; Cook, M. J.; Nyokong, T. *J. Porphyr. Phthalocyan.* **2007**, *11*, 761–770.
368. Khene, S.; Geraldo, D. A.; Togo, C. A.; Limson, J.; Nyokong, T. *Electrochim. Acta* **2008**, *54*, 183–191.
369. Idowu, M.; Nyokong, T. *J. Photochem. Photobiol., A* **2008**, *199*, 282–290.
370. Kroenke, W. J.; Kenney, M. E. *Inorg. Chem.* **1964**, *3*, 251–254.
371. Bennett, W. E.; Broberg, D. E.; Baenziger, N. C. *Inorg. Chem.* **1973**, *12*, 930–936.
372. Ohno, O.; Ishikawa, N.; Matsuzawa, H.; Kaizu, Y.; Kobayashi, H. *J. Phys. Chem.* **1989**, *93*, 1713–1718.
373. Ukei, K. *Acta Crystallogr. B* **1973**, *B 29*, 2290–2292.
374. Ukei, K. *J. Phys. Soc. Jpn.* **1976**, *40*, 140–143.
375. Iyechika, Y.; Yakushi, K.; Ikemoto, I.; Kuroda, H. *Acta Crystallogr. B* **1982**, *38*, 766–770.
376. Bian, Y. Z.; Li, L.; Dou, J. M.; Cheng, D. Y. Y.; Li, R. J.; Ma, C. Q.; Ng, D. K. P.; Kobayashi, N.; Jiang, J. Z. *Inorg. Chem.* **2004**, *43*, 7539–7544.

377. Fukuda, T.; Ono, K.; Homma, S.; Kobayashi, N. *Chem. Lett.* **2003**, *32*, 736–737.
378. Kumar, T. M. M.; Achar, B. N. *J. Phys. Chem. Solids* **2006**, *67*, 2282–2288.
379. Kumar, T. M. M.; Achar, B. N. *J. Organomet. Chem.* **2006**, *691*, 331–336.
380. Achar, B. N.; Kumar, T. M. M.; Lokesh, K. S. *J. Porphyr. Phthalocyan.* **2005**, *9*, 872–879.
381. Zhang, Y. X.; Cai, X.; Zhang, X. X.; Xu, H.; Liu, Z. Q.; Jiang, J. Z. *Int. J. Quantum Chem.* **2007**, *107*, 952–961.
382. Yaraşir, M. N.; Koca, A.; Kandaz, M.; Salih, B. *J. Phys. Chem. C* **2007**, *111*, 16558–16563.
383. Gouterman, M.; Sayer, P.; Shankland, E.; Smith, J. P. *Inorg. Chem.* **1981**, *20*, 87–92.
384. Li, J. Z.; Subramanian, L. R.; Hanack, M. *Eur. J. Org. Chem.* **1998**, 2759–2767.
385. Huang, L.; Zhao, P.; Li, Z. Y.; Zhang, F. S.; Tung, C. H. *J. Phys. Chem. A* **2008**, *112*, 4165–4169.
386. Huang, L.; Li, Z. Y.; Zhang, F. S.; Tung, C. H.; Kasatani, K. Z. *Opt. Commun.* **2008**, *281*, 1275–1279.
387. Liu, J. B.; Zhang, F. S.; Zhao, F. Q.; Tang, Y. W.; Song, X. Q.; Yao, G. Q. *J. Photochem. Photobiol., A* **1995**, *91*, 99–104.
388. Kasuga, K.; Lin, L.; Handa, M.; Sugimori, T.; Isa, K.; Matsuura, K.; Takinami, Y. *Inorg. Chem.* **1999**, *38*, 4174–4176.
389. Fox, J. P.; Goldberg, D. P. *Inorg. Chem.* **2003**, *42*, 8181–8191.
390. Janczak, J.; Kubiak, R.; Jezierski, A. *Inorg. Chem.* **1999**, *38*, 2043–2049.
391. Janczak, J.; Idemori, Y. M. *Acta Crystallogr. E* **2002**, *58*, M36–M38.
392. Janczak, J.; Kubiak, R. *Acta Crystallogr. C* **2003**, *59*, M70–M72.
393. Janczak, J.; Perpetuo, G. J. *Acta Crystallogr. C* **2006**, *62*, M45–M47.
394. Knör, G. *Inorg. Chem.* **1996**, *35*, 7916–7918.
395. Kagaya, Y.; Isago, H. *Bull. Chem. Soc. Jpn.* **1997**, *70*, 2179–2185.
396. Isago, H.; Kagaya, Y. *Chem. Lett.* **2006**, *35*, 8–9.
397. Isago, H. *Chem. Commun.* **2003**, 1864–1865.
398. Isago, H.; Kagaya, Y. *Bull. Chem. Soc. Jpn.* **1994**, *67*, 383–389.
399. Ostendorp, G.; Homborg, H. *Z. Anorg. Allg. Chem.* **1996**, *622*, 873–880.
400. Janczak, J.; Kubiak, R.; Hahn, F. *Inorg. Chim. Acta* **1998**, *281*, 195–200.
401. Janczak, J.; Kubiak, R.; Richter, J.; Fuess, H. *Polyhedron* **1999**, *18*, 2775–2780.
402. Benihya, K.; Mossoyan-Déneux, M.; Hahn, F.; Boucharat, N.; Terzian, G. *Eur. J. Inorg. Chem.* **2000**, 1771–1779.
403. Janczak, J. *Pol. J. Chem.* **1998**, *72*, 1871–1878.
404. Benihya, K.; Mossoyan-Déneux, M.; Giorgi, M. *Eur. J. Inorg. Chem.* **2001**, 1343–1352.
405. Shaabani, A.; Maleki-Moghaddam, R.; Maleki, A.; Rezayan, A. H. *Dyes Pigments* **2007**, *74*, 279–282.
406. Yang, J.; Van De Mark, M. R. *Tetrahedron Lett.* **1993**, *34*, 5223–5226.
407. Li, R. J.; Zhang, X. X.; Zhu, P. H.; Ng, D. K. P.; Kobayashi, N.; Jiang, J. Z. *Inorg. Chem.* **2006**, *45*, 2327–2334.
408. Velázquez, C. S.; Fox, G. A.; Broderick, W. E.; Andersen, K. A.; Anderson, O. P.; Barrett, A. G. M.; Hoffman, B. M. *J. Am. Chem. Soc.* **1992**, *114*, 7416–7424.
409. Lokesh, K. S.; Uma, N.; Achar, B. N. *J. Non-Cryst. Solids* **2007**, *353*, 384–389.
410. Wöhrle, D.; Schnurpfeil, G.; Knothe, G. *Dyes Pigments* **1992**, *18*, 91–102.
411. Angeloni, S.; Ercolani, C. *J. Porphyr. Phthalocyan.* **2000**, *4*, 474–483.
412. Pullen, A. E.; Faulmann, C.; Cassoux, P. *Eur. J. Inorg. Chem.* **1999**, 269–276.
413. Lagorio, M. G.; Dicelio, L. E.; Roman, E. S. *J. Photochem. Photobiol., A* **1993**, *72*, 153–161.

414. Sugimori, T.; Torikata, M.; Nojima, J.; Tominaka, S.; Tobikawa, K.; Handa, M.; Kasuga, K. *Inorg. Chem. Commun.* **2002**, *5*, 1031–1033.
415. Barrett, P. A.; Linstead, R. P.; Rundall, F. G.; Tuey, G. A. P. *J. Chem. Soc.* **1940**, 1079–1092.
416. Elvidge, J. A.; Golden, J. H.; Linstead, R. P. *J. Chem. Soc.* **1957**, 2466–2472.
417. Schramm, C. J.; Hoffman, B. M. *Inorg. Chem.* **1980**, *19*, 383–385.
418. Freyer, W.; Mueller, S.; Teuchner, K. *J. Photochem. Photobiol., A* **2004**, *163*, 231–240.
419. Jin, S.; Cheng, G. Z.; Chen, G. Z.; Ji, Z. P. *J. Porphyr. Phthalocyan.* **2005**, *9*, 32–39.
420. Yuan, S. F.; Chen, Z. R. *J. Phys. Chem. A* **2005**, *109*, 2582–2585.
421. Nemykin, V. N.; Chernii, V. Y.; Volkov, S. V. *J. Chem. Soc. Dalton* **1998**, 2995–2999.
422. Ough, E. A.; Creber, K. A. M.; Stillman, M. J. *Inorg. Chim. Acta* **1996**, *246*, 361–369.
423. Adachi, K.; Watarai, H. *Bull. Chem. Soc. Jpn.* **2004**, *77*, 2011–2020.
424. Gacho, E. H.; Imai, H.; Tsunashima, R.; Naito, T.; Inabe, T.; Kobayashi, N. *Inorg. Chem.* **2006**, *45*, 4170–4176.
425. Sokolova, T. N.; Lomova, T. N.; Zaitseva, S. V.; Zdanovich, S. A.; Maizlish, V. E. *Russ. J. Inorg. Chem.* **2008**, *53*, 220–228.
426. Lo, P. C.; Fong, W. P.; Ng, D. K. P. *ChemMedChem* **2008**, *3*, 1110–1117.
427. Dayal, S.; Li, J.; Li, Y. S.; Wu, H. Q.; Samia, A. C. S.; Kenney, M. E.; Burda, C. *Photochem. Photobiol.* **2008**, *84*, 243–249.
428. Tannert, S.; Ermilov, E. A.; Vogel, J. O.; Choi, M. T. M.; Ng, D. K. P.; Röder, B. *J. Phys. Chem. B* **2007**, *111*, 8053–8062.
429. Ermilov, E. A.; Tannert, S.; Werncke, T.; Choi, M. T. M.; Ng, D. K. P.; Röder, B. *Chem. Phys.* **2006**, *328*, 428–437.
430. El-Khouly, M. E.; Kang, E. S.; Kay, K. Y.; Choi, C. S.; Aaraki, Y.; Ito, O. *Chem. Eur. J.* **2007**, *13*, 2854–2863.
431. Zhu, Y. J.; Huang, J. D.; Jiang, X. J.; Sun, J. C. *Inorg. Chem. Commun.* **2006**, *9*, 473–477.
432. Rodríguez-Redondo, J. L.; Sastre-Santos, A.; Fernández-Lázaro, F.; Soares, D.; Azzellini, G. C.; Elliott, B.; Echegoyen, L. *Chem. Commun.* **2006**, 1265–1267.
433. Hofman, J. W.; van Zeeland, F.; Turker, S.; Talsma, H.; Lambrechts, S. A. G.; Sakharov, D. V.; Hennink, W. E.; van Nostrum, C. F. *J. Med. Chem.* **2007**, *50*, 1485–1494.
434. Silver, J.; Sosa-Sánchez, J. L.; Frampton, C. S. *Inorg. Chem.* **1998**, *37*, 411–417.
435. Brewis, M.; Clarkson, G. J.; Helliwell, M.; Holder, A. M.; McKeown, N. B. *Chem. Eur. J.* **2000**, *6*, 4630–4636.
436. Farren, C.; FitzGerald, S.; Bryce, M. R.; Beeby, A.; Batsanov, A. S. *J. Chem. Soc. Perkin Trans. 2* **2002**, 59–66.
437. Silver, J.; Frampton, C. S.; Fern, G. R.; Davies, D. A.; Miller, J. R.; Sosa-Sánchez, J. L. *Inorg. Chem.* **2001**, *40*, 5434–5439.
438. Seotsanyana-Mokhosi, I.; Kuznetsova, N.; Nyokong, T. *J. Photochem. Photobiol., A* **2001**, *140*, 215–222.
439. Ciliberto, E.; Doris, K. A.; Pietro, W. J.; Reisner, G. M.; Ellis, D. E.; Fragala, I.; Herbstein, F. H.; Ratner, M. A.; Marks, T. J. *J. Am. Chem. Soc.* **1984**, *106*, 7748–7761.
440. Sosa-Sánchez, J. L.; Sosa-Sánchez, A.; Farfán, N.; Zamudio-Rivera, L. S.; López-Mendoza, G.; Flores, J. P.; Beltrán, H. I. *Chem. Eur. J.* **2005**, *11*, 4263–4273.
441. Lo, P. C.; Huang, J. D.; Cheng, D. Y. Y.; Chan, E. Y. M.; Fong, W. P.; Ko, W. H.; Ng, D. K. P. *Chem. Eur. J.* **2004**, *10*, 4831–4838.
442. Jiang, X. J.; Huang, J. D.; Zhu, Y. J.; Tang, F. X.; Ng, D. K. P.; Sun, J. C. *Bioorg. Med. Chem. Lett.* **2006**, *16*, 2450–2453.

443. Barker, C. A.; Findlay, K. S.; Bettington, S.; Batsanov, A. S.; Perepichka, I. F.; Bryce, M. R.; Beeby, A. *Tetrahedron* **2006**, *62*, 9433–9439.
444. Anula, H. M.; Berlin, J. C.; Wu, H. Q.; Li, Y. S.; Peng, X. Z.; Kenney, M. E.; Rodgers, M. A. J. *J. Phys. Chem. A* **2006**, *110*, 5215–5223.
445. Wang, M. X.; Funabiki, K.; Matsui, M. *Dyes Pigments* **2004**, *62*, 115–119.
446. Gunaratne, T.; Kennedy, V. O.; Kenney, M. E.; Rodgers, M. A. J. *J. Phys. Chem. A* **2004**, *108*, 2576–2582.
447. Lee, P. P. S.; Lo, P. C.; Chan, E. Y. M.; Fong, W. P.; Ko, W. H.; Ng, D. K. P. *Tetrahedron Lett.* **2005**, *46*, 1551–1554.
448. Kim, K. N.; Choi, C. S.; Kay, K. Y. *Tetrahedron Lett.* **2005**, *46*, 6791–6795.
449. Brewis, M.; Clarkson, G. J.; Goddard, V.; Helliwell, M.; Holder, A. M.; McKeown, N. B. *Angew. Chem. Int. Ed.* **1998**, *37*, 1092–1094.
450. He, J.; Larkin, H. E.; Li, Y. S.; Rihter, B. D.; Zaidi, S. I. A.; Rodgers, M. A. J.; Mukhtar, H.; Kenney, M. E.; Oleinick, N. L. *Photochem. Photobiol.* **1997**, *65*, 581–586.
451. Sinha, A. K.; Mandal, B. K. *Polym. J.* **1995**, *27*, 1079–1084.
452. Sosa-Sánchez, J. L.; Galindo, A.; Gnecco, D.; Bernès, S.; Fern, G. R.; Silver, J.; Sosa-Sánchez, A.; Enriquez, R. G. *J. Porphyr. Phthalocyan.* **2002**, *6*, 198–202.
453. Lo, P. C.; Wang, S. Q.; Zeug, A.; Meyer, M.; Röder, B.; Ng, D. K. P. *Tetrahedron Lett.* **2003**, *44*, 1967–1970.
454. Brewis, M.; Helliwell, M.; McKeown, N. B.; Reynolds, S.; Shawcross, A. *Tetrahedron Lett.* **2001**, *42*, 813–816.
455. Brewis, M.; Helliwell, M.; McKeown, N. B. *Tetrahedron* **2003**, *59*, 3863–3872.
456. Brasseur, N.; Nguyen, T. L.; Langlois, R.; Ouellet, R.; Marengo, S.; Houde, D.; van Lier, J. E. *J. Med. Chem.* **1994**, *37*, 415–420.
457. Jiang, Z.; Ou, Z. P.; Chen, N. S.; Wang, J. D.; Huang, J. L.; Shao, J. G.; Kadish, K. M. *J. Porphyr. Phthalocyan.* **2005**, *9*, 352–360.
458. Niño, M. E.; Giraldo, S. A.; Páez-Mozo, E. A. *J. Mol. Catal. A: Chem.* **2001**, *175*, 139–151.
459. Safari, N.; Jamaat, P. R.; Shirvan, S. A.; Shoghpour, S.; Ebadi, A.; Darvishi, M.; Shaabani, A. *J. Porphyr. Phthalocyan.* **2005**, *9*, 256–261.
460. Lever, A. B. P.; Wilshire, J. P.; Quan, S. K. *Inorg. Chem.* **1981**, *20*, 761–768.
461. Golovin, M. N.; Seymour, P.; Jayaraj, K.; Fu, Y. S.; Lever, A. B. P. *Inorg. Chem.* **1990**, *29*, 1719–1727.
462. Shaabani, A.; Rezayan, A. H. *J. Porphyr. Phthalocyan.* **2005**, *9*, 617–620.
463. Jones, J. G.; Twigg, M. V. *J. Chem. Soc. Dalton* **1978**, 1709–1714.
464. Bayo, K.; Saba, A.; Ouédraogo, G. V.; Terzian, G.; Benlian, D. *J. Mol. Struct.* **1992**, *271*, 19–26.
465. Tahiri, M.; Doppelt, P.; Fischer, J.; Weiss, R. *Inorg. Chem.* **1988**, *27*, 2897–2899.
466. Ryu, H.; Knecht, S.; Subramanian, L. R.; Hanack, M. *Synthetic Met.* **1995**, *72*, 289–296.
467. Polley, R.; Hanack, M. *J. Org. Chem.* **1995**, *60*, 8278–8282.
468. Watkins, J. J.; Balch, A. L. *Inorg. Chem.* **1975**, *14*, 2720–2723.
469. Somashekarappa, M. P.; Keshavayya, J.; Sherigara, S. *Spectrochim. Acta A* **2003**, *59*, 883–893.
470. Shishkina, O. V.; Maizlish, V. E.; Shaposhnikov, G. P. *Russ. J. Gen. Chem.* **2001**, *71*, 243–245.
471. Sheng, N.; Zhang, Y. X.; Xu, H.; Bao, M.; Sun, X.; Jiang, J. Z. *Eur. J. Inorg. Chem.* **2007**, 3268–3275.

472. Mikheev, Y. A.; Guseva, L. N.; Ershov, Y. A. *Russ. J. Phys. Chem. A* **2007**, *81*, 617–625.
473. Ban, K. Z.; Nishizawa, K.; Ohta, K.; Shirai, H. *J. Mater. Chem.* **2000**, *10*, 1083–1090.
474. Barrett, A. G. M.; Broderick, W. E.; Hoffman, B. M.; Velazquez, C. S. *J. Org. Chem.* **1989**, *54*, 3233–3234.
475. Ogunsipe, A.; Nyokong, T. *J. Mol. Struct.* **2004**, *689*, 89–97.
476. Kuwabara, T.; Teraguchi, M.; Kaneko, T.; Aoki, T.; Yagi, M. *J. Phys. Chem. B* **2005**, *109*, 21202–21208.
477. Mørkved, E. H.; Afseth, N. K.; Zimcik, P. *J. Porphyr. Phthalocyan.* **2007**, *11*, 130–138.
478. Bayo, K.; Mossoyan, J. C.; Ouédraogo, G. V. *Spectrochim. Acta A* **2004**, *60*, 653–657.
479. Atilla, D.; Durmuş, M.; Gürek, A. G.; Ahsen, V.; Nyokong, T. *Dalton Trans.* **2007**, 1235–1243.
480. Ogunsipe, A.; Chen, J. Y.; Nyokong, T. *New. J. Chem.* **2004**, *28*, 822–827.
481. Seotsanyana-Mokhosi, I.; Chen, J. Y.; Nyokong, T. *J. Porphyr. Phthalocyan.* **2005**, *9*, 316–325.
482. Pelisson, M. M. M.; Tomé, F. M.; Beltrame, M.; Simioni, A. R.; Tedesco, A. C. *J. Porphyr. Phthalocyan.* **2003**, *7*, 630–636.
483. Li, L.; Shen, S. Y.; Yu, Q.; Zhou, Q. F.; Xu, H. J. *J. Chem. Soc. Chem. Commun.* **1991**, 619–620.
484. Brinkmann, H.; Kelting, C.; Makarov, S.; Tsaryova, O.; Schnurpfeil, G.; Wöhrle, D.; Schlettwein, D. *Physica Status Solidi A — Applications and Materials Science* **2008**, *205*, 409–420.
485. Youngblood, W. J. *J. Org. Chem.* **2006**, *71*, 3345–3356.
486. Wróbel, D.; Boguta, A. *J. Photochem. Photobiol., A* **2002**, *150*, 67–76.
487. Del Sole, R.; De Luca, A.; Mele, G.; Vasapollo, G. *J. Porphyr. Phthalocyan.* **2005**, *9*, 519–527.
488. Tomachynski, L. A.; Chernii, V. Y.; Volkov, S. V. *J. Porphyr. Phthalocyan.* **2001**, *5*, 731–734.
489. Gerasymchuk, Y. S.; Volkov, S. V.; Chernii, V. Y.; Tomachynski, L. A.; Radzki, S. *J. Alloy. Compd.* **2004**, *380*, 186–190.
490. Nyokong, T. *Synthetic Met.* **1994**, *66*, 107–116.
491. Tomachynski, L. A.; Chernii, V. Y.; Kolotilova, Y. Y.; Chernega, A. N.; Howard, J. A. K.; Volkov, S. V. *Inorg. Chim. Acta* **2007**, *360*, 1493–1501.
492. Tomachynski, L. A.; Chernii, V. Y.; Gorbenko, H. N.; Filonenko, V. V.; Volkov, S. V. *Chem. Biodiversity* **2004**, *1*, 862–867.
493. Lever, A. B. P.; Tse, Y. H.; Manivannan, V.; Seymour, P.; Strelets, V. V.; Persand, L. S. *Inorg. Chem.* **1996**, *35*, 725–734.
494. Lucas, N. T.; Zareie, H. M.; McDonagh, A. M. *Acs Nano* **2007**, *1*, 348–354.
495. Farrell, N. P.; Murray, A. J.; Thornback, J. R.; Dolphin, D. H.; James, B. R. *Inorg. Chim. Acta* **1978**, *28*, L144–L146.
496. Huang, J. S.; Yu, G. A.; Xie, J.; Wong, K. M.; Zhu, N. Y.; Che, C. M. *Inorg. Chem.* **2008**, *47*, 9166–9181.
497. Rawling, T.; McDonagh, A. M.; Colbran, S. B. *Inorg. Chim. Acta* **2008**, *361*, 49–55.
498. Kobel, W.; Hanack, M. *Inorg. Chem.* **1986**, *25*, 103–107.
499. Weber, A.; Ertel, T. S.; Reinöhl, U.; Bertagnolli, H.; Leuze, M.; Hees, M.; Hanack, M. *Eur. J. Inorg. Chem.* **2000**, 2289–2294.
500. Hanack, M.; Hees, M.; Witke, E. *New. J. Chem.* **1998**, *22*, 169–172.

501. Hanack, M.; Polley, R. *Inorg. Chem.* **1994**, *33*, 3201–3204.
502. Yang, X. C.; Kritikos, M.; Åkermark, B.; Sun, L. C. *J. Porphyr. Phthalocyan.* **2005**, *9*, 248–255.
503. Dürr, K.; Hanack, M. *J. Porphyr. Phthalocyan.* **1999**, *3*, 224–229.
504. Hanack, M.; Münz, X. *Synthetic Met*. **1985**, *10*, 357–363.
505. Nyokong, T. *J. Chem. Soc. Dalton* **1994**, 1359–1365.
506. Clarisse, C.; Riou, M. T. *Inorg. Chim. Acta* **1987**, *130*, 139–144.
507. Ziminov, A. V.; Ramsh, S. M.; Yurre, T. A. *Russ. J. Gen. Chem.* **2008**, *78*, 510–511.
508. Lomova, T. N.; Andrianova, L. G. *Russ. J. Coord. Chem.* **2004**, *30*, 660–664.
509. Germain, A.; Ebbesen, T. W. *Chem. Phys. Lett.* **1992**, *199*, 585–589.
510. Kulinich, V. P.; Shaposhnikov, G. P. *Russ. J. Gen. Chem.* **2003**, *73*, 794–805.
511. Weitemeyer, A.; Kliesch, H.; Wöhrle, D. *J. Org. Chem.* **1995**, *60*, 4900–4904.
512. Ogata, H.; Higashi, R.; Kobayashi, N. *J. Porphyr. Phthalocyan.* **2003**, *7*, 551–557.
513. Pushkarev, V. E.; Breusova, M. O.; Shulishova, E. V.; Tomilov, Y. V. *Russ. Chem. B* **2005**, *54*, 2087–2093.
514. Breusova, M. O.; Pushkarev, V. E.; Tomilova, L. G. *Russ. Chem. B* **2007**, *56*, 1456–1460.
515. Voloshin, Y. Z.; Varzatskii, O. A.; Tomilova, L. G.; Breusova, M. O.; Magdesieva, T. V.; Bubnov, Y. N.; Krämer, R. *Polyhedron* **2007**, *26*, 2733–2740.
516. Sastre, A.; del Rey, B.; Torres, T. *J. Org. Chem.* **1996**, *61*, 8591–8597.
517. Sastre, A.; Díaz-García, M. A.; del Rey, B.; Dhenaut, C.; Zyss, J.; Ledoux, I.; Agulló-López, F.; Torres, T. *J. Phys. Chem. A* **1997**, *101*, 9773–9777.
518. Martín-Gomis, L.; Ohkubo, K.; Fernández-Lázaro, F.; Fukuzumi, S.; Sastre-Santos, A. *J. Phys. Chem. C* **2008**, *112*, 17694–17701.
519. Kuznetsova, N. A.; Okunchikov, V. V.; Derkacheva, V. M.; Kaliya, O. L.; Lukyanets, E. A. *J. Porphyr. Phthalocyan.* **2005**, *9*, 393–397.
520. Gaberkorn, A. A.; Donzello, M. P.; Stuzhin, P. A. *Russ. J. Org. Chem.* **2006**, *42*, 929–935.
521. Liu, L. C.; Lee, C. C.; Hu, A. T. *J. Porphyr. Phthalocyan.* **2001**, *5*, 806–807.
522. Kasuga, K.; Kabata, N.; Kato, T.; Sugimori, T.; Handa, M. *Inorg. Chim. Acta* **1998**, *278*, 223–225.
523. Kasuga, K.; Moriwaki, N.; Handa, M. *Inorg. Chim. Acta* **1996**, *244*, 137–139.
524. Martín-Gomis, L.; Ohkubo, K.; Fernández-Lázaro, F.; Fukuzumi, S.; Sastre-Santos, A. *Org. Lett.* **2007**, *9*, 3441–3444.
525. Lyubimtsev, A.; Misir, M. N.; Calvete, M.; Hanack, M. *Eur. J. Org. Chem.* **2008**, 3209–3214.
526. Barthel, M.; Dini, D.; Vagin, S.; Hanack, M. *Eur. J. Org. Chem.* **2002**, 3756–3762.
527. Ballesteros, B.; de la Torre, G.; Torres, T.; Hug, G. L.; Rahman, G. M. A.; Guldi, D. M. *Tetrahedron* **2006**, *62*, 2097–2101.
528. Dolotova, O. V.; Bundina, N. I.; Derkacheva, V. M.; Negrimovskii, V. M.; Minin, V. V.; Larin, G. M.; Kaliya, O. L.; Luk'yanets, E. A. *Zh. Obshch. Khim.* **1992**, *62*, 2064–2075.
529. Knecht, S.; Dürr, K.; Schmid, G.; Subramanian, L. R.; Hanack, M. *J. Porphyr. Phthalocyan.* **1999**, *3*, 292–298.
530. Dolotova, O. V.; Bundina, N. I.; Derkacheva, V. M.; Kaliya, O. L.; Luk'yanets, E. A. *Zh. Obshch. Khim.* **1988**, *58*, 2173.
531. Hanack, M.; Polley, R.; Knecht, S.; Schlick, U. *Inorg. Chem.* **1995**, *34*, 3621–3624.
532. Makarova, E. A.; Kopranenkov, V. N.; Shevtsov, V. K.; Luk'yanets, E. A. *Khim. Geterotsikl.* **1989**, 1385–1390.
533. Ganschow, M.; Wöhrle, D.; Schulz-Ekloff, G. *J. Porphyr. Phthalocyan.* **1999**, *3*, 299–309.

534. Shaposhnikov, G. P.; Maizlish, V. E.; Kulinich, V. P. *Russ. J. Gen. Chem.* **2005**, *75*, 1830–1839.
535. Rodríguez-Morgade, M. S.; Planells, M.; Torres, T.; Ballester, P.; Palomares, E. *J. Mater. Chem.* **2008**, *18*, 176–181.
536. Knecht, S.; Polley, R.; Hanack, M. *Appl. Organomet. Chem.* **1996**, *10*, 649–660.
537. Rodríguez-Morgade, M. S.; Torres, T.; Atienza-Castellanos, C.; Guldi, D. M. *J. Am. Chem. Soc.* **2006**, *128*, 15145–15154.
538. Hanack, M.; Knecht, S.; Polley, R. *Chem. Ber.* **1995**, *128*, 929–933.
539. Ishii, K.; Shiine, M.; Shimizu, Y.; Hoshino, S.; Abe, H.; Sogawa, K.; Kobayashi, N. *J. Phys. Chem. B* **2008**, *112*, 3138–3143.
540. Youssef, T. E.; O'Flaherty, S.; Blau, W.; Hanack, M. *Eur. J. Org. Chem.* **2004**, 101–108.
541. Giribabu, L.; Kumar, C. V.; Reddy, P. Y. *Chem. Asian J.* **2007**, *2*, 1574–1580.
542. Isago, H.; Kagaya, Y.; Nakajima, S. *Chem. Lett.* **2003**, *32*, 112–113.
543. Bo, S. H.; Tang, D. H.; Liu, X. H.; Zhen, Z. *Dyes Pigments* **2008**, *76*, 35–40.
544. Winter, G.; Heckmann, H.; Haisch, P.; Eberhardt, W.; Hanack, M.; Lüer, L.; Egelhaaf, H. J.; Oelkrug, D. *J. Am. Chem. Soc.* **1998**, *120*, 11663–11673.
545. Yi, R. P.; Yu, H. C.; Pei, F. C.; Xiao, X. H. *Chinese Chem. Lett.* **2008**, *19*, 273–276.
546. Auger, A.; Blau, W. J.; Burnham, P. M.; Chambrier, I.; Cook, M. J.; Isare, B.; Nekelson, F.; O'Flaherty, S. M. *J. Mater. Chem.* **2003**, *13*, 1042–1047.
547. Burnham, P. M.; Chambrier, I.; Hughes, D. L.; Isare, B.; Poynter, R. J.; Powell, A. K.; Cook, M. J. *J. Porphyr. Phthalocyan.* **2006**, *10*, 1202–1211.
548. Jiang, J. Z.; Liu, R. C. W.; Mak, T. C. W.; Chan, T. W. D.; Ng, D. K. P. *Polyhedron* **1997**, *16*, 515–520.
549. Law, W. F.; Lui, K. M.; Ng, D. K. P. *J. Mater. Chem.* **1997**, *7*, 2063–2067.
550. Bakboord, J. V.; Cook, M. J.; Hamuryudan, E. *J. Porphyr. Phthalocyan.* **2000**, *4*, 510–517.
551. Cammidge, A. N.; Berber, G.; Chambrier, I.; Hough, P. W.; Cook, M. J. *Tetrahedron* **2005**, *61*, 4067–4074.
552. Berber, G.; Cammidge, A. N.; Chambrier, I.; Cook, M. J.; Hough, P. W. *Tetrahedron Lett.* **2003**, *44*, 5527–5529.
553. Sakamoto, K.; Kato, T.; Cook, M. J. *J. Porphyr. Phthalocyan.* **2001**, *5*, 742–750.
554. Sakamoto, K.; Ohno-Okumura, E.; Kato, T.; Kawaguchi, T.; Cook, M. J. *J. Porphyr. Phthalocyan.* **2003**, *7*, 83–88.
555. Kobayashi, N.; Ojima, F.; Osa, T.; Vigh, S.; Leznoff, C. C. *Bull. Chem. Soc. Jpn.* **1989**, *62*, 3469–3474.
556. Sharman, W. M.; van Lier, J. E. *J. Porphyr. Phthalocyan.* **2005**, *9*, 651–658.
557. Maya, E. M.; Haisch, P.; Vázquez, P.; Torres, T. *Tetrahedron* **1998**, *54*, 4397–4404.
558. Leznoff, C. C.; Li, Z. P.; Isago, H.; D'Ascanio, A. M.; Terekhov, D. S. *J. Porphyr. Phthalocyan.* **1999**, *3*, 406–416.
559. Terekhov, D. S.; Nolan, K. J. M.; McArthur, C. R.; Leznoff, C. C. *J. Org. Chem.* **1996**, *61*, 3034–3040.
560. Leznoff, C. C.; Suchozak, B. *Can. J. Chem.* **2001**, *79*, 878–887.
561. Poon, K. W.; Liu, W.; Chan, P. K.; Yang, Q. C.; Chan, T. W. D.; Mak, T. C. W.; Ng, D. K. P. *J. Org. Chem.* **2001**, *66*, 1553–1559.
562. Zhao, Z. X.; Poon, C. T.; Wong, W. K.; Wong, W. Y.; Tam, H. L.; Cheah, K. W.; Xie, T. F.; Wang, D. J. *Eur. J. Inorg. Chem.* **2008**, 119–128.

563. Suchan, A.; Nackiewicz, J.; Hnatejko, Z.; Waclawek, W.; Lis, S. *Dyes Pigments* **2009**, *80*, 239–244.
564. Kim, S. J.; Matsumoto, M.; Shigehara, K. *Synthetic Met.* **1999**, *107*, 27–33.
565. Kim, S. J.; Matsumoto, M.; Shigehara, K. *J. Porphyr. Phthalocyan.* **2000**, *4*, 136–144.
566. Sugimori, T.; Okamoto, S.; Kotoh, N.; Handa, M.; Kasuga, K. *Chem. Lett.* **2000**, 1200–1201.
567. Kobayashi, N.; Fukuda, T.; Ueno, K.; Ogino, H. *J. Am. Chem. Soc.* **2001**, *123*, 10740–10741.
568. Tau, P.; Nyokong, T. *Electrochim. Acta* **2007**, *52*, 3641–3650.
569. Fukuda, T.; Ishiguro, T.; Kobayashi, N. *Tetrahedron Lett.* **2005**, *46*, 2907–2909.
570. Lutsenko, O. G.; Shaposhnikov, G. P.; Kulinich, V. P.; Lyubimtsev, A. V. *Russ. J. Gen. Chem.* **2004**, *74*, 446–450.
571. Aranyos, V.; Castano, A. M.; Grennberg, H. *Acta Chem. Scand.* **1999**, *53*, 714–720.
572. Clarkson, G. J.; Humberstone, P.; McKeown, N. B. *Chem. Commun.* **1997**, 1979–1980.
573. Seven, O.; Dindar, B.; Aydemir, S.; Cilli, F. *J. Porphyr. Phthalocyan.* **2008**, *12*, 953–963.
574. Alvarez-Mico, X.; Calvete, M. J. F.; Hanack, M.; Ziegler, T. *Tetrahedron Lett.* **2006**, *47*, 3283–3286.
575. Mørkved, E. H.; Pedersen, F. M.; Afseth, N. K.; Kjøsen, H. *Dyes Pigments* **2008**, *77*, 145–152.
576. Sakamoto, K.; Ohno, E. *Dyes Pigments* **1997**, *35*, 375–386.
577. Hanack, M.; Haisch, P.; Lehmann, H.; Subramanian, L. R. *Synthesis-Stuttgart* **1993**, 387–390.
578. Kimura, M.; Wada, K.; Iwashima, Y.; Ohta, K.; Hanabusa, K.; Shirai, H.; Kobayashi, N. *Chem. Commun.* **2003**, 2504–2505.
579. Kahl, S. B.; Li, J. *Inorg. Chem.* **1996**, *35*, 3878–3880.
580. Şener, M. K.; Gül, A.; Koçak, M. B. *Transition Met. Chem.* **2008**, *33*, 867–872.
581. Şener, M. K.; Koca, A.; Gül, A.; Koçak, M. B. *Polyhedron* **2007**, *26*, 1070–1076.
582. Dinçer, H. A.; Şener, M. K.; Koca, A.; Gül, A.; Koçak, M. B. *Electrochim. Acta* **2008**, *53*, 3459–3467.
583. Kandaz, M.; Özkaya, A. R.; Bekaroğlu, O. *Monatsh. Chem.* **2001**, *132*, 1013–1022.
584. Drechsler, U.; Pfaff, M.; Hanack, M. *Eur. J. Org. Chem.* **1999**, 3441–3453.
585. Wang, C. S.; Bryce, M. R.; Batsanov, A. S.; Stanley, C. F.; Beeby, A.; Howard, J. A. K. *J. Chem. Soc. Perkin Trans. 2* **1997**, 1671–1678.
586. Blower, M. A.; Bryce, M. R.; Devonport, W. *Adv. Mater.* **1996**, *8*, 63–65.
587. Atilla, D.; Aslıbay, G.; Gürek, A. G.; Can, H.; Ahsen, V. *Polyhedron* **2007**, *26*, 1061–1069.
588. Sakamoto, K.; Ohno, E. *Prog. Org. Coat.* **1997**, *31*, 139–145.
589. Idowu, M.; Ogunsipe, A.; Nyokong, T. *Spectrochim. Acta A* **2007**, *68*, 995–999.
590. Dolotova, O. V.; Kaliya, O. L. *Russ. J. Coord. Chem.* **2007**, *33*, 111–115.
591. Mikhalenko, S. A.; Solov'eva, L. I.; Luk'yanets, E. A. *Russ. J. Gen. Chem.* **2004**, *74*, 451–459.
592. Smirnova, A. I.; Maizlish, V. E.; Usol'tseva, N. V.; Bykova, V. V.; Anan'eva, G. A.; Kudrik, E. V.; Shirokov, A. V.; Shaposhnikov, G. P. *Russ. Chem. B* **2000**, *49*, 132–139.
593. Tylleman, B.; Gómez-Aspe, R.; Gbabode, G.; Geerts, Y. H.; Sergeyev, S. *Tetrahedron* **2008**, *64*, 4155–4161.
594. Mikhalenko, S. A.; Soloveva, L. I.; Luk'yanets, E. A. *Russ. J. Gen. Chem.* **2004**, *74*, 1775–1800.
595. Kutureva, V.; Baziakina, N.; Maximova, K.; Morozova, V.; Schnurpfeil, G.; Wöhrle, D.; Suvorova, O. *J. Porphyr. Phthalocyan.* **2008**, *12*, 832–838.

596. Mashazi, P. N.; Ozoemena, K. I.; Maree, D. A.; Nyokong, T. *Electrochim. Acta* **2006**, *51*, 3489–3494.
597. Fujiki, M.; Tabei, H.; Kurihara, T. *J. Phys. Chem.* **1988**, *92*, 1281–1285.
598. Leznoff, C. C.; Greenberg, S. *Tetrahedron Lett.* **1989**, *30*, 5555–5558.
599. Achar, B. N.; Jayasree, P. K. *Synthetic Met.* **1999**, *104*, 101–106.
600. Ivanov, A. V.; Svinareva, P. A.; Zhukov, I. V.; Tomilova, L. G.; Zefirov, N. S. *Russ. Chem. B* **2003**, *52*, 1562–1566.
601. Yslas, E. I.; Rivarola, V.; Durantini, E. N. *Bioorg. Med. Chem.* **2005**, *13*, 39–46.
602. Cheng, G.; Peng, X. Z.; Hao, G. L.; Kennedy, V. O.; Ivanov, I. N.; Knappenberger, K.; Hill, T. J.; Rodgers, M. A. J.; Kenney, M. E. *J. Phys. Chem. A* **2003**, *107*, 3503–3514.
603. Cook, M. J.; Dunn, A. J.; Howe, S. D.; Thomson, A. J.; Harrison, K. J. *J. Chem. Soc. Perkin Trans. 1* **1988**, 2453–2458.
604. Gao, L. D.; Qian, X. H. *Dyes Pigments* **2001**, *51*, 51–55.
605. Weitman, H.; Schatz, S.; Gottlieb, H. E.; Kobayashi, N.; Ehrenberg, B. *Photochem. Photobiol.* **2001**, *73*, 473–481.
606. Lin, M. J.; Wang, J. D. *J. Mol. Struct.* **2007**, *837*, 284–289.
607. Dominguez, D. D.; Snow, A. W.; Shirk, J. S.; Pong, R. G. S. *J. Porphyr. Phthalocyan.* **2001**, *5*, 582–592.
608. Muto, T.; Temma, T.; Kimura, M.; Hanabusa, K.; Shirai, H. *J. Org. Chem.* **2001**, *66*, 6109–6115.
609. Aoudia, M.; Cheng, G. Z.; Kennedy, V. O.; Kenney, M. E.; Rodgers, M. A. J. *J. Am. Chem. Soc.* **1997**, *119*, 6029–6039.
610. Shinohara, H.; Tsaryova, O.; Schnurpfeil, G.; Wöhrle, D. *J. Photochem. Photobiol., A* **2006**, *184*, 50–57.
611. Ricciardi, G.; Soldatova, A. V.; Rosa, A. *J. Inorg. Biochem.* **2008**, *102*, 406–413.
612. Lee, C. H.; Guo, H.; Chen, L. X.; Mandal, B. K. *J. Org. Chem.* **2008**, *73*, 8219–8227.
613. Maqanda, W.; Nyokong, T.; Maree, M. D. *J. Porphyr. Phthalocyan.* **2005**, *9*, 343–351.
614. Nikolaev, I. Y.; Kudrik, E. V.; Kulinich, V. P.; Shaposhnikov, G. P. *Russ. J. Gen. Chem.* **2005**, *75*, 468–472.
615. Sugimori, T.; Horike, S.; Handa, M.; Kasuga, K. *Inorg. Chim. Acta* **1998**, *278*, 253–255.
616. Kudrik, E. V.; Nikolaev, I. Y.; Shaposhnikov, G. P. *Russ. Chem. B* **2000**, *49*, 2027–2030.
617. Donzello, M. P.; Ercolani, C.; Gaberkorn, A. A.; Kudrik, E. V.; Meneghetti, M.; Marcolongo, G.; Rizzoli, C.; Stuzhin, P. A. *Chem. Eur. J.* **2003**, *9*, 4009–4024.
618. Ding, X. M.; Xu, H. J. *Dyes Pigments* **1998**, *39*, 223–229.
619. Deng, X. B.; Porter, W. W.; Vaid, T. P. *Polyhedron* **2005**, *24*, 3004–3011.
620. Leznoff, C. C.; D'Ascanio, A. M.; Yıldız, S. Z. *J. Porphyr. Phthalocyan.* **2000**, *4*, 103–111.
621. Bhardwaj, N.; Andraos, J.; Leznoff, C. C. *Can. J. Chem.* **2002**, *80*, 141–147.
622. Kasuga, K.; Kawashima, M.; Asano, K.; Sugimori, T.; Abe, K.; Kikkawa, T.; Fujiwara, T. *Chem. Lett.* **1996**, 867–868.
623. Kasuga, K.; Asano, K.; Lin, L.; Sugimori, T.; Handa, M.; Abe, K.; Kikkawa, T.; Fujiwara, T. *Bull. Chem. Soc. Jpn.* **1997**, *70*, 1859–1865.
624. Lin, M. J.; Wang, J. D.; Chen, N. S.; Huang, J. L. *Z. Anorg. Allg. Chem.* **2006**, *632*, 2315–2320.
625. Montanari, J.; Perez, A. P.; Di Salvo, F.; Diz, V.; Barnadas, R.; Dicelio, L.; Doctorovich, F.; Morilla, M. J.; Romero, E. L. *Int. J. Pharm.* **2007**, *330*, 183–194.

626. Sommerauer, M.; Rager, C.; Hanack, M. *J. Am. Chem. Soc.* **1996**, *118*, 10085–10093.
627. Youssef, T. E.; Hanack, M. *J. Porphyr. Phthalocyan.* **2002**, *6*, 571–577.
628. Wang, J. D.; Lin, M. J.; Wu, S. F.; Lin, Y. *J. Organomet. Chem.* **2006**, *691*, 5074–5076.
629. Sleven, J.; Görller-Walrand, C.; Binnemans, K. *Mat. Sci. Eng. C-Bio. S.* **2001**, *18*, 229–238.
630. Ooi, K.; Maeda, F.; Ohta, K.; Takizawa, T.; Matsuse, T. *J. Porphyr. Phthalocyan.* **2005**, *9*, 544–553.
631. Ali-Adib, Z.; Clarkson, G. J.; McKeown, N. B.; Treacher, K. E.; Gleeson, H. F.; Stennett, A. S. *J. Mater. Chem.* **1998**, *8*, 2371–2378.
632. Durmuş, M.; Lebrun, C.; Ahsen, V. *J. Porphyr. Phthalocyan.* **2004**, *8*, 1175–1186.
633. Tant, J.; Geerts, Y. H.; Lehmann, M.; De Cupere, V.; Zucchi, G.; Laursen, B. W.; Bjørnholm, T.; Lemaur, V.; Marcq, V.; Burquel, A.; Hennebicq, E.; Gardebien, F.; Viville, P.; Beljonne, D.; Lazzaroni, R.; Cornil, J. *J. Phys. Chem. B* **2005**, *109*, 20315–20323.
634. Rager, C.; Schmid, G.; Hanack, M. *Chem. Eur. J.* **1999**, *5*, 280–288.
635. Calvete, M.; Hanack, M. *Eur. J. Org. Chem.* **2003**, 2080–2083.
636. Tau, P.; Nyokong, T. *Polyhedron* **2006**, *25*, 1802–1810.
637. Modibane, D. K.; Nyokong, T. *Polyhedron* **2008**, *27*, 1102–1110.
638. Huang, X.; Zhao, F. Q.; Li, Z. Y.; Tang, Y. W.; Zhang, F. S.; Tung, C. H. *Langmuir* **2007**, *23*, 5167–5172.
639. Maree, M. D.; Nyokong, T. *J. Porphyr. Phthalocyan.* **2001**, *5*, 555–563.
640. Tau, P.; Nyokong, T. *J. Porphyr. Phthalocyan.* **2006**, *10*, 1040–1048.
641. Plater, M. J.; Jeremiah, A.; Bourhill, G. *J. Chem. Soc. Perkin Trans. 1* **2002**, 91–96.
642. Maya, E. M.; Shirk, J. S.; Snow, A. W.; Roberts, G. L. *Chem. Commun.* **2001**, 615–616.
643. Kandaz, M.; Bekaroğlu, O. *Chem. Ber.-Recl.* **1997**, *130*, 1833–1836.
644. Wei, S. H.; Huang, D. Y.; Li, L.; Meng, Q. H. *Dyes Pigments* **2003**, *56*, 1–6.
645. Attanasi, O. A.; Ciccarella, G.; Filippone, P.; Mele, G.; Spadavecchia, J.; Vasapollo, G. *J. Porphyr. Phthalocyan.* **2003**, *7*, 52–57.
646. Dei, D.; Chiti, G.; De Filippis, M. P.; Fantetti, L.; Giuliani, F.; Giuntini, F.; Soncin, M.; Jori, G.; Roncucci, G. *J. Porphyr. Phthalocyan.* **2006**, *10*, 147–159.
647. Maree, S. E.; Nyokong, T. *J. Porphyr. Phthalocyan.* **2001**, *5*, 782–792.
648. Matlaba, P.; Nyokong, T. *Polyhedron* **2002**, *21*, 2463–2472.
649. Yu, S.; Ma, C.; Cheng, C.; Wang, X.; Ji, D.; Fan, Z.; Xia, D.; He, W.; Chang, Y.; Du, G. *Dyes Pigments* **2008**, *76*, 492–498.
650. Ma, C. Y.; Du, G. T.; Cao, Y.; Yu, S. K.; Cheng, C. H.; Jiang, W. H.; Chang, Y. C.; Wang, X.; Cong, F. D.; Yu, H. F. *Dyes Pigments* **2007**, *72*, 267–270.
651. Kalkan, A.; Bayır, Z. A. *Polyhedron* **2006**, *25*, 39–42.
652. Leclaire, J.; Dagiral, R.; Fery-Forgues, S.; Coppel, Y.; Donnadieu, B.; Caminade, A. M.; Majoral, J. P. *J. Am. Chem. Soc.* **2005**, *127*, 15762–15770.
653. Tsaryova, O.; Semioshkin, A.; Wöhrle, D.; Bregadze, V. I. *J. Porphyr. Phthalocyan.* **2005**, *9*, 268–274.
654. Semioshkin, A.; Tsaryova, O.; Zhidkova, O.; Bregadze, V.; Wöhrle, D. *J. Porphyr. Phthalocyan.* **2006**, *10*, 1293–1300.
655. Ottmar, M.; Ichisaka, T.; Subramanian, L. R.; Hanack, M.; Shirota, Y. *Chem. Lett.* **2001**, 788–789.
656. Obirai, J.; Rodrigues, N. P.; Bedioui, F.; Nyokong, T. *J. Porphyr. Phthalocyan.* **2003**, *7*, 508–520.
657. Ağırtaş, M. S. *Dyes Pigments* **2007**, *74*, 490–493.

658. Ağırtaş, M. S. *Dyes Pigments* **2008**, *79*, 247–251.
659. Ma, C. Y.; Tian, D. L.; Hou, X. K.; Chang, Y. C.; Cong, F. D.; Yu, H. F.; Du, X. G.; Du, G. T. *Synthesis-Stuttgart* **2005**, 741–748.
660. Luo, Y.; Gao, J. S.; Cheng, C. W.; Sun, Y. F.; Du, X. G.; Xu, G. Y.; Wang, Z. L. *Org. Electron.* **2008**, *9*, 466–472.
661. Makarov, S.; Litwinski, C.; Ermilov, E. A.; Suvorova, O.; Röder, B.; Wöhrle, D. *Chem. Eur. J.* **2006**, *12*, 1468–1474.
662. Makarov, S. G.; Maksimova, K. N.; Baranov, E. V.; Fukin, G. K.; Suvorova, O. N.; Wöhrle, D.; Domrachev, G. A. *Russ. Chem. B* **2006**, *55*, 1748–1754.
663. Makarov, S. G.; Piskunov, A. V.; Suvorova, O. N.; Schnurpfeil, G.; Domrachev, G. A.; Wöhrle, D. *Chem. Eur. J.* **2007**, *13*, 3227–3233.
664. Brewis, M.; Clarkson, G. J.; Humberstone, P.; Makhseed, S.; McKeown, N. B. *Chem. Eur. J.* **1998**, *4*, 1633–1640.
665. Salan, U.; Altındal, A.; Bulut, M.; Bekaroğlu, O. *J. Porphyr. Phthalocyan.* **2006**, *10*, 1263–1270.
666. Lyubimtsev, A.; Vagin, S.; Syrbu, S.; Hanack, M. *Eur. J. Org. Chem.* **2007**, 2000–2005.
667. Shaposhnikov, G. P.; Maizlish, V. E.; Kulinich, V. P. *Russ. J. Gen. Chem.* **2007**, *77*, 138–146.
668. Ağırtaş, M. S.; Yıldıko, U.; Yılan, A. *J. Porphyr. Phthalocyan.* **2006**, *10*, 117–121.
669. Hu, Y. Y.; Lai, G. Q.; Shen, Y. J.; Li, Y. F. *J. Porphyr. Phthalocyan.* **2004**, *8*, 1042–1046.
670. Strassert, C. A.; Rodriguez, M. E.; Dicelio, L. E.; Awruch, J. *J. Porphyr. Phthalocyan.* **2005**, *9*, 361–367.
671. Kasuga, K.; Yashiki, K.; Sugimori, T.; Handa, M. *J. Porphyr. Phthalocyan.* **2005**, *9*, 646–650.
672. Zhang, L. X.; Huang, J.; Ren, L.; Bai, M. H.; Wu, L.; Zhai, B. P.; Zhou, X. *Bioorg. Med. Chem.* **2008**, *16*, 303–312.
673. De Filippis, M. P.; Dei, D.; Fantetti, L.; Roncucci, G. *Tetrahedron Lett.* **2000**, *41*, 9143–9147.
674. Sibrian-Vazquez, M.; Ortiz, J.; Nesterova, I. V.; Fernández-Lázaro, F.; Sastre-Santos, A.; Soper, S. A.; Vicente, M. G. H. *Bioconjugate Chem.* **2007**, *18*, 410–420.
675. Durmuş, M.; Ahsen, V.; Nyokong, T. *J. Photochem. Photobiol., A* **2007**, *186*, 323–329.
676. Calvete, M. J. F.; Dini, D.; Flom, S. R.; Hanack, M.; Pong, R. G. S.; Shirk, J. S. *Eur. J. Org. Chem.* **2005**, 3499–3509.
677. Liu, W.; Lee, C. H.; Chan, H. S.; Mak, T. C. W.; Ng, D. K. P. *Eur. J. Inorg. Chem.* **2004**, 286–292.
678. Foley, S.; Jones, G.; Liuzzi, R.; McGarvey, D. J.; Perry, M. H.; Truscott, T. G. *J. Chem. Soc. Perkin Trans. 2* **1997**, 1725–1730.
679. Kroon, J. M.; Koehorst, R. B. M.; van Dijk, M.; Sanders, G. M.; Sudhölter, E. J. R. *J. Mater. Chem.* **1997**, *7*, 615–624.
680. Kobayashi, N.; Higashi, R.; Tomura, T. *Bull. Chem. Soc. Jpn.* **1997**, *70*, 2693–2698.
681. Kalashnikova, L. P.; Nefedov, S. E.; Tomilova, L. G.; Zefirov, N. S. *Russ. Chem. B* **2007**, *56*, 2426–2432.
682. Causey, P. W.; Dubovyk, I.; Leznoff, C. C. *Can. J. Chem.* **2006**, *84*, 1380–1387.
683. Choi, C. F.; Huang, J. D.; Lo, P. C.; Fong, W. P.; Ng, D. K. P. *Org. Biomol. Chem.* **2008**, *6*, 2173–2181.
684. Leznoff, C. C.; Svirskaya, P. I.; Khouw, B.; Cerny, R. L.; Seymour, P.; Lever, A. B. P. *J. Org. Chem.* **1991**, *56*, 82–90.
685. Tolbin, A. Y.; Tomilova, L. G. *Russ. Chem. B* **2007**, *56*, 2433–2437.

686. Nishida, M.; Momotake, A.; Shinohara, Y.; Nishimura, Y.; Arai, T. *J. Porphyr. Phthalocyan.* **2007**, *11*, 448–454.
687. Özçeşmeci, M.; Hamuryudan, E. *Dyes Pigments* **2008**, *77*, 457–461.
688. Selçukoğlu, M.; Hamuryudan, E. *Dyes Pigments* **2007**, *74*, 17–20.
689. Koca, A.; Özkaya, A. R.; Selçukoğlu, M.; Hamuryudan, E. *Electrochim. Acta* **2007**, *52*, 2683–2690.
690. Özer, M.; Altındal, A.; Özkaya, A. R.; Bulut, M.; Bekaroğlu, O. *Polyhedron* **2006**, *25*, 3593–3602.
691. Brewis, M.; Hassan, B. M.; Li, H.; Makhseed, S.; McKeown, N. B.; Thompson, N. *J. Porphyr. Phthalocyan.* **2000**, *4*, 460–464.
692. Brewis, M.; Clarkson, G. J.; Holder, A. M.; McKeown, N. B. *Chem. Commun.* **1998**, 969–970.
693. Ağırtaş, M. S. *Inorg. Chim. Acta* **2007**, *360*, 2499–2502.
694. Zhao, Z. X.; Ogunsipe, A. O.; Maree, M. D.; Nyokong, T. *J. Porphyr. Phthalocyan.* **2005**, *9*, 186–197.
695. Zhao, Z. X.; Ozoemena, K. I.; Maree, D. M.; Nyokong, T. *Dalton Trans.* **2005**, 1241–1248.
696. Bıyıklıoğlu, Z.; Kantekin, H. *Transition Met. Chem.* **2007**, *32*, 851–856.
697. Oliver, S. W.; Smith, T. D. *Heterocycles* **1984**, *22*, 2047–2052.
698. Michelsen, U.; Kliesch, H.; Schnurpfeil, G.; Sobbi, A. K.; Wöhrle, D. *Photochem. Photobiol.* **1996**, *64*, 694–701.
699. Li, H. R.; Jensen, T. J.; Fronczek, F. R.; Vicente, M. G. H. *J. Med. Chem.* **2008**, *51*, 502–511.
700. Mantareva, V.; Petrova, D.; Avramov, L.; Angelov, I.; Borisova, E.; Peeva, M.; Wöhrle, D. *J. Porphyr. Phthalocyan.* **2005**, *9*, 47–53.
701. Nemykin, V. N.; Mytsyk, V. M.; Volkov, S. V.; Kobayashi, N. *J. Porphyr. Phthalocyan.* **2000**, *4*, 551–554.
702. Banfi, S.; Caruso, E.; Buccafurni, L.; Ravizza, R.; Gariboldi, M.; Monti, E. *J. Organomet. Chem.* **2007**, *692*, 1269–1276.
703. Scalise, N.; Durantini, E. N. *Bioorg. Med. Chem.* **2005**, *13*, 3037–3045.
704. Karaoğlu, H. R. P.; Gül, A.; Koçak, M. B. *Dyes Pigments* **2008**, *76*, 231–235.
705. Drager, A. S.; O'Brien, D. F. *J. Org. Chem.* **2000**, *65*, 2257–2260.
706. Durmuş, M.; Ayhan, M. M.; Gürek, A. G.; Ahsen, V. *Dyes Pigments* **2008**, *77*, 570–577.
707. Kimura, M.; Yamaguchi, Y.; Muto, T.; Hanabusa, K.; Shirai, H. *J. Porphyr. Phthalocyan.* **2000**, *4*, 123–128.
708. Erdem, S. S.; Nesterova, I. V.; Soper, S. A.; Hammer, R. P. *J. Org. Chem.* **2008**, *73*, 5003–5007.
709. Gök, Y.; Yıldız, S. Z. *Polyhedron* **1997**, *16*, 2335–2339.
710. Trombach, N.; Hild, O.; Schlettwein, D.; Wöhrle, D. *J. Mater. Chem.* **2002**, *12*, 879–885.
711. Liu, M. O.; Tai, C. H.; Hu, A. T. *J. Photochem. Photobiol., A* **2004**, *165*, 193–200.
712. Tararykina, T. V.; Maizlish, V. E.; Galanin, N. E.; Shaposhnikov, G. P.; Bykova, V. V.; Usol'tseva, N. V. *Russ. J. Org. Chem.* **2007**, *43*, 1719–1725.
713. Bıyıklıoğlu, Z.; Güner, E. T.; Topçu, S.; Kantekin, H. *Polyhedron* **2008**, *27*, 1707–1713.
714. Hu, Y. Y.; Lai, G. Q.; Shen, Y. J.; Li, Y. F. *Dyes Pigments* **2005**, *66*, 49–53.
715. Hu, Y. Y.; Lai, G. Q.; Shen, Y. J.; Li, Y. F. *Monatsh. Chem.* **2004**, *135*, 1167–1172.
716. Dabak, S.; Gürek, A. G.; Musluoğlu, E.; Ahsen, V. *New. J. Chem.* **2001**, *25*, 1583–1587.
717. Adachi, K.; Watarai, H. *J. Mater. Chem.* **2005**, *15*, 4701–4710.
718. Ozoemena, K.; Nyokong, T. *J. Chem. Soc. Dalton* **2002**, 1806–1811.

719. Ozoemena, K. I.; Nyokong, T. *Inorg. Chem. Commun.* **2003**, *6*, 1192–1195.
720. Kostka, M.; Zimcik, P.; Miletin, M.; Klemera, P.; Kopecky, K.; Musil, Z. *J. Photochem. Photobiol., A* **2006**, *178*, 16–25.
721. Petrik, P.; Zimcik, P.; Kopecky, K.; Musil, Z.; Miletin, M.; Loukotova, V. *J. Porphyr. Phthalocyan.* **2007**, *11*, 487–495.
722. Arslanoğlu, Y.; Sevim, A. M.; Hamuryudan, E.; Gül, A. *Dyes Pigments* **2006**, *68*, 129–132.
723. Gürek, A. G.; Bekaroğlu, O. *J. Chem. Soc. Dalton* **1994**, 1419–1423.
724. Nicolau, M.; del Rey, B.; Torres, T.; Mingotaud, C.; Delhaes, P.; Cook, M. J.; Thorpe, S. C. *Synthetic Met.* **1999**, *102*, 1462–1463.
725. Agboola, B.; Ozoemena, K. I.; Westbroek, P.; Nyokong, T. *Electrochim. Acta* **2007**, *52*, 2520–2526.
726. Gürol, I.; Ahsen, V.; Bekaroğlu, O. *J. Chem. Soc. Dalton* **1994**, 497–500.
727. Santiago, J.; Sugino, T.; Shimizu, Y. *Chem. Lett.* **1998**, 661–662.
728. Gürek, A. G.; Durmuş, M.; Ahsen, V. *New. J. Chem.* **2004**, *28*, 693–699.
729. Yılmaz, I.; Gürek, A.; Ahsen, V. *Polyhedron* **2005**, *24*, 791–798.
730. Bayır, Z. A. *Dyes Pigments* **2005**, *65*, 235–242.
731. Tau, P.; Nyokong, T. *Dalton Trans.* **2006**, 4482–4490.
732. Matemadombo, F.; Griveau, S.; Bedioui, F.; Nyokong, T. *Electroanal.* **2008**, *20*, 1863–1872.
733. Nemykin, V. N.; Kobayashi, N.; Nonomura, T.; Luk'yanets, E. A. *Chem. Lett.* **2000**, 184–185.
734. Balakireva, O. V.; Maizlish, V. E.; Shaposhnikov, G. P. *Russ. J. Gen. Chem.* **2003**, *73*, 292–296.
735. Negrimovskii, V. M.; Derkacheva, V. M.; Luk'yanets, E. A. *Zh. Obshch. Khim.* **1989**, *59*, 1688–1690.
736. Volkov, K. A.; Avramenko, G. V.; Negrimovskii, V. M.; Luk'yanets, E. A. *Russ. J. Gen. Chem.* **2007**, *77*, 1108–1116.
737. Agboola, B.; Ozoemena, K. I.; Nyokong, T. *Electrochim. Acta* **2005**, *51*, 4379–4387.
738. Matemadombo, F.; Maree, M. D.; Ozoemena, K. I.; Westbroek, P.; Nyokong, T. *J. Porphyr. Phthalocyan.* **2005**, *9*, 484–490.
739. Adachi, K.; Chayama, K.; Watarai, H. *Langmuir* **2006**, *22*, 1630–1639.
740. Sehlotho, N.; Durmuş, M.; Ahsen, V.; Nyokong, T. *Inorg. Chem. Commun.* **2008**, *11*, 479–483.
741. Akkurt, B.; Hamuryudan, E. *Dyes Pigments* **2008**, *79*, 153–158.
742. Yaraşir, M. N.; Kandaz, M.; Koca, A.; Salih, B. *Polyhedron* **2007**, *26*, 1139–1147.
743. Dündar, D.; Can, H.; Atilla, D.; Gürek, A. G.; Öztürk, Z. Z.; Ahsen, V. *Polyhedron* **2008**, *27*, 3383–3390.
744. Choi, M. T. M.; Li, P. P. S.; Ng, D. K. P. *Tetrahedron* **2000**, *56*, 3881–3887.
745. Atilla, D.; Durmuş, M.; Yılmaz, O.; Gürek, A. G.; Ahsen, V.; Nyokong, T. *Eur. J. Inorg. Chem.* **2007**, 3573–3581.
746. Özçesmeci, I.; Güner, S.; Okur, A. I.; Gül, A. *J. Porphyr. Phthalocyan.* **2007**, *11*, 531–536.
747. Yaraşir, M. N.; Kandaz, M.; Senkal, B. F.; Koca, A.; Salih, B. *Polyhedron* **2007**, *26*, 5235–5242.
748. Yaraşir, M. N.; Kandaz, M.; Senkal, B. F.; Koca, A.; Salih, B. *Dyes Pigments* **2008**, *77*, 7–15.
749. Arslanoğlu, Y.; Hamuryudan, E. *Dyes Pigments* **2007**, *75*, 150–155.
750. Gürsoy, S.; Cihan, A.; Koçak, M. B.; Bekaroğlu, O. *Monatsh. Chem.* **2001**, *132*, 813–819.
751. Öztürk, R.; Kalay, S.; Kalkan, A.; Türkan, A.; Abasıyanık, M. F.; Bayır, Z. A.; Gül, A. *J. Porphyr. Phthalocyan.* **2008**, *12*, 932–941.

752. Vittar, N. B. R.; Prucca, C. G.; Strassert, C.; Awruch, J.; Rivarola, V. A. *Int. J. Biochem. Cell B* **2008**, *40*, 2192–2205.
753. Ağırtaş, M. S.; Bekaroğlu, O. *J. Porphyr. Phthalocyan.* **2001**, *5*, 717–720.
754. Ceyhan, T.; Yüksek, M.; Yağlğoğlu, H. G.; Salih, B.; Erbil, M. K.; Elmali, A.; Bekaroğlu, O. *Dalton Trans.* **2008**, 2407–2413.
755. Maya, E. M.; Vázquez, P.; Torres, T. *Chem. Eur. J.* **1999**, *5*, 2004–2013.
756. Maya, E. M.; García, C.; García-Frutos, E. M.; Vázquez, P.; Torres, T. *J. Org. Chem.* **2000**, *65*, 2733–2739.
757. de la Escosura, A.; Martínez-Díaz, M. V.; Guldi, D. M.; Torres, T. *J. Am. Chem. Soc.* **2006**, *128*, 4112–4118.
758. Martín, G.; Martínez-Díaz, M. V.; de la Torre, G.; Ledoux, I.; Zyss, J.; Agulló-López, F.; Torres, T. *Synthetic Met.* **2003**, *139*, 95–98.
759. Sanchez, M.; Fache, E.; Bonnet, D.; Meunier, B. *J. Porphyr. Phthalocyan.* **2001**, *5*, 867–872.
760. Kulinich, V. P.; Shaposhnikov, G. P.; Gorelov, V. N.; Chernyaeva, E. A. *Russ. J. Gen. Chem.* **2006**, *76*, 1331–1336.
761. Derkacheva, V. M.; Mikhalenko, S. A.; Solov'eva, L. I.; Alekseeva, V. I.; Marinina, L. E.; Savina, L. P.; Butenin, A. V.; Luk'yanets, E. A. *Russ. J. Gen. Chem.* **2007**, *77*, 1117–1125.
762. Margaron, P.; Langlois, R.; van Lier, J. E.; Gaspard, S. *J. Photochem. Photobiol. B* **1992**, *14*, 187–199.
763. Berríos, C.; Marco, J. F.; Gutiérrez, C.; Ureta-Zañartu, M. S. *J. Phys. Chem. B* **2008**, *112*, 12644–12649.
764. Liu, M. O.; Tai, C. H.; Sain, M. Z.; Hu, A. T.; Chou, F. I. *J. Photochem. Photobiol. A* **2004**, *165*, 131–136.
765. Idowu, M.; Nyokong, T. *J. Photochem. Photobiol. A* **2008**, *197*, 273–280.
766. Esenpınar, A. A.; Bulut, M. *Dyes Pigments* **2008**, *76*, 249–255.
767. Kobayashi, N.; Higashi, R.; Titeca, B. C.; Lamote, F.; Ceulemans, A. *J. Am. Chem. Soc.* **1999**, *121*, 12018–12028.
768. Donders, C. A.; Liu, S. X.; Loosli, C.; Sanguinet, L.; Neels, A.; Decurtins, S. *Tetrahedron* **2006**, *62*, 3543–3549.
769. Sastre, A.; Torres, T.; Hanack, M. *Tetrahedron Lett.* **1995**, *36*, 8501–8504.
770. Nombona, N.; Tau, P.; Sehlotho, N.; Nyokong, T. *Electrochim. Acta* **2008**, *53*, 3139–3148.
771. Cong, F. D.; Ning, B.; Du, X. G.; Ma, C. Y.; Yu, H. F.; Chen, B. *Dyes Pigments* **2005**, *66*, 149–154.
772. Tau, P.; Nyokong, T. *J. Electroanal. Chem.* **2007**, *611*, 10–18.
773. Zharnikova, M. A.; Balakirev, A. E.; Maizlish, V. E.; Shaposhnikov, G. P. *Russ. J. Gen. Chem.* **2002**, *72*, 131–132.
774. Achar, B. N.; Lokesh, K. S. *J. Organomet. Chem.* **2004**, *689*, 3357–3361.
775. Shen, Y.; Xia, Y. B.; Chen, J. W.; Gu, F.; Jiao, F. H.; Zhang, J. C. *Chinese Phys. Lett.* **2004**, *21*, 1717–1719.
776. Yüksel, F.; Tuncel, S.; Ahsen, V. *J. Porphyr. Phthalocyan.* **2008**, *12*, 123–130.
777. Maizlish, V. E.; Shaposhnikov, G. P.; Balakireva, O. V.; Zharnikova, M. A.; Abramov, I. G.; Ivanovskii, S. A.; Smirnov, A. V. *Russ. J. Gen. Chem.* **2004**, *74*, 787–790.
778. González-Cabello, A.; Vázquez, P.; Torres, T.; Guldi, D. M. *J. Org. Chem.* **2003**, *68*, 8635–8642.
779. Yüksel, F.; Gürek, A. G.; Lebrun, C.; Ahsen, V. *New. J. Chem.* **2005**, *29*, 726–732.

780. Fasiulla; Khan, M. H. M.; Harish, M. N. K.; Keshavayya, J.; Reddy, K. R. V. *Dyes Pigments* **2008**, *76*, 557–563.
781. Mikhalenko, S. A.; Derkacheva, V. M.; Luk'yanets, E. A. *Zh. Obshch. Khim.* **1981**, *51*, 1650–1657.
782. Bekircan, O.; Bıyıklıoğlu, Z.; Acar, I.; Bektas, H.; Kantekin, H. *J. Organomet. Chem.* **2008**, *693*, 3425–3429.
783. Achar, B. N.; Kumar, T. M. M. *J. Porphyr. Phthalocyan.* **2007**, *11*, 42–49.
784. Cong, F. D.; Ning, B.; Ji, Y. P.; Wang, X. Y.; Ke, F. B.; Liu, Y. Y.; Cui, X. J.; Chen, B. *Dyes Pigments* **2008**, *77*, 686–690.
785. Şaşmaz, S.; Ağar, E.; Ağar, A. *Dyes Pigments* **1999**, *42*, 137–142.
786. Kahveci, B.; Özil, M.; Kantar, C.; Şaşmaz, S.; Işik, S.; Köysal, Y. *J. Organomet. Chem.* **2007**, *692*, 4835–4842.
787. Maizlish, V. E.; Kulinich, V. P.; Shaposhnikov, G. P. *Russ. J. Gen. Chem.* **2004**, *74*, 1801–1817.
788. Negrimovskii, V. M.; Derkacheva, V. M.; Kaliya, O. L.; Luk'yanets, E. A. *Zh. Obshch. Khim.* **1991**, *61*, 460–470.
789. Suslova, E. E.; Lomova, T. N. *Russ. J. Coord. Chem.* **2006**, *32*, 155–165.
790. Cong, F. D.; Ning, B.; Yu, H. F.; Cui, X. J.; Chen, B.; Cao, S. G.; Ma, C. Y. *Spectrochim. Acta A* **2005**, *62*, 394–397.
791. Sokolova, T. N.; Lomova, T. N.; Suslova, E. E.; Zaitseva, S. V.; Zdanovich, S. A.; Maizlish, V. E.; Shishkina, O. V.; Shaposhnikov, G. P. *Russ. J. Gen. Chem.* **2002**, *72*, 963–967.
792. Reddy, K. R. V.; Keshavayya, J.; Swamy, B. E. K.; Harish, M. N. K.; Mallikarjuna, H. R.; Sherigara, B. S. *Dyes Pigments* **2009**, *80*, 1–5.
793. Achar, B. N.; Jayasree, P. K. *Synthetic Met.* **2000**, *114*, 219–224.
794. Reddy, K. R. V.; Harish, M. N. K.; Fassiulla; Khan, M. H. M.; Keshavayya, J. *J. Fluorine Chem.* **2007**, *128*, 1019–1025.
795. Kol'tsov, E.; Basova, T.; Semyannikov, P.; Igumenov, I. *Mater. Chem. Phys.* **2004**, *86*, 222–227.
796. Christendat, D.; David, M. A.; Morin, S.; Lever, A. B. P.; Kadish, K. M.; Shao, J. G. *J. Porphyr. Phthalocyan.* **2005**, *9*, 626–636.
797. Somashekarappa, M. P.; Reddy, K. R. V.; Harish, M. N. K.; Keshavayya, J. *J. Mol. Struct.* **2005**, *753*, 190–194.
798. Huang, J. D.; Wang, S. Q.; Lo, P. C.; Fong, W. P.; Ko, W. H.; Ng, D. K. P. *New. J. Chem.* **2004**, *28*, 348–354.
799. Reddy, K. R. V.; Keshavayya, J.; Seetharamappa, J. *Dyes Pigments* **2003**, *59*, 237–244.
800. Decréau, R.; Chanon, M.; Julliard, M. *Inorg. Chim. Acta* **1999**, *293*, 80–87.
801. Reddy, K. R. V.; Keshavayya, J. *Dyes Pigments* **2002**, *53*, 187–194.
802. Märkl, G.; Gschwendner, K.; Rötzer, I.; Kreitmeier, P. *Helv. Chim. Acta* **2004**, *87*, 825–844.
803. Bryant, G. C.; Cook, M. J.; Ryan, T. G.; Thorne, A. J. *Tetrahedron* **1996**, *52*, 809–824.
804. Chambrier, I.; Cook, M. J.; Mayes, D. A.; MacDonald, C. *J. Porphyr. Phthalocyan.* **2003**, *7*, 426–438.
805. Quintiliani, M.; Kahnt, A.; Wölfle, T.; Hieringer, W.; Vázquez, P.; Görling, A.; Guldi, D. M.; Torres, T. *Chem. Eur. J.* **2008**, *14*, 3765–3775.
806. Ribeiro, A. O.; Tomé, J. P. C.; Neves, M. G. P. M. S.; Tomé, A. C.; Cavaleiro, J. A. S.; Iamamoto, Y.; Torres, T. *Tetrahedron Lett.* **2006**, *47*, 9177–9180.

807. Gouloumis, A.; Liu, S. G.; Sastre, A.; Vázquez, P.; Echegoyen, L.; Torres, T. *Chem. Eur. J.* **2000**, *6*, 3600–3607.
808. Guldi, D. M.; Zilbermann, I.; Gouloumis, A.; Vázquez, P.; Torres, T. *J. Phys. Chem. B* **2004**, *108*, 18485–18494.
809. de la Escosura, A.; Claessens, C. G.; Ledoux-Rak, I.; Zyss, J.; Martínez-Díaz, M. V.; Torres, T. *J. Porphyr. Phthalocyan.* **2005**, *9*, 788–793.
810. Rojo, G.; de la Torre, G.; García-Ruiz, J.; Ledoux, I.; Torres, T.; Zyss, J.; Agulló-López, F. *Chem. Phys.* **1999**, *245*, 27–34.
811. Torres, T.; de la Torre, G.; García-Ruiz, J. *Eur. J. Org. Chem.* **1999**, 2323–2326.
812. González, A.; Vázquez, P.; Torres, T. *Tetrahedron Lett.* **1999**, *40*, 3263–3266.
813. García-Frutos, E. M.; O'Flaherty, S. M.; Maya, E. M.; de la Torre, G.; Blau, W.; Vázquez, P.; Torres, T. S. *J. Mater. Chem.* **2003**, *13*, 749–753.
814. García-Frutos, E. M.; Fernández-Lázaro, F.; Maya, E. M.; Vázquez, P.; Torres, T. *J. Org. Chem.* **2000**, *65*, 6841–6846.
815. Yang, S. I.; Li, J. Z.; Cho, H. S.; Kim, D.; Bocian, D. F.; Holten, D.; Lindsey, J. S. *J. Mater. Chem.* **2000**, *10*, 283–296.
816. González-Rodríguez, D.; Claessens, C. G.; Torres, T.; Liu, S. G.; Echegoyen, L.; Vila, N.; Nonell, S. *Chem. Eur. J.* **2005**, *11*, 3881–3893.
817. Ali, H.; St-Jean, O.; Tremblay-Morin, J. P.; van Lier, J. E. *Tetrahedron Lett.* **2006**, *47*, 8275–8278.
818. Maya, E. M.; Vázquez, P.; Torres, T.; Gobbi, L.; Diederich, F.; Pyo, S.; Echegoyen, L. *J. Org. Chem.* **2000**, *65*, 823–830.
819. Maya, E. M.; García-Frutos, E. M.; Vázquez, P.; Torres, T.; Martín, G.; Rojo, G.; Agulló-López, F.; González-Jonte, R. H.; Ferro, V. R.; de la Vega, J. M. G.; Ledoux, I.; Zyss, J. *J. Phys. Chem. A* **2003**, *107*, 2110–2117.
820. Tian, M. Q.; Wada, T.; Kimura-Suda, H.; Sasabe, H. *J. Mater. Chem.* **1997**, *7*, 861–863.
821. Sessler, J. L.; Jayawickramarajah, J.; Gouloumis, A.; Pantos, G. D.; Torres, T.; Guldi, D. M. *Tetrahedron* **2006**, *62*, 2123–2131.
822. Nakai, K.; Usami, J.; Kobayashi, N. *J. Porphyr. Phthalocyan.* **2007**, *11*, 222–227.
823. Tian, M. Q.; Zhang, Y. D.; Wada, T.; Sasabe, H. *Dyes Pigments* **2003**, *58*, 135–143.
824. Khan, E. H.; Ali, H.; Tian, H. J.; Rousseau, J.; Tessier, G.; Shafiullah; van Lier, J. E. *Bioorg. Med. Chem. Lett.* **2003**, *13*, 1287–1290.
825. Sutton, J. M.; Boyle, R. W. *Chem. Commun.* **2001**, 2014–2015.
826. Li, J. Z.; Lindsey, J. S. *J. Org. Chem.* **1999**, *64*, 9101–9108.
827. Kobayashi, N.; Ashida, T.; Osa, T. *Chem. Lett.* **1992**, 2031–2034.
828. Kobayashi, N.; Miwa, H.; Nemykin, V. N. *J. Am. Chem. Soc.* **2002**, *124*, 8007–8020.
829. Eu, S.; Katoh, T.; Umeyama, T.; Matano, Y.; Imahori, H. *Dalton Trans.* **2008**, 5476–5483.
830. Maya, E. M.; de la Torre, G.; Lozano, A. E.; Torres, T.; de la Campa, J. G.; de Abajo, J. *Macromol. Rapid Comm.* **2006**, *27*, 1852–1858.
831. Drobizhev, M.; Makarov, N. S.; Rebane, A.; de la Torre, G.; Torres, T. *J. Phys. Chem. C* **2008**, *112*, 848–859.
832. de la Escosura, A.; Martínez-Díaz, M. V.; Barberá, J.; Torres, T. *J. Org. Chem.* **2008**, *73*, 1475–1480.
833. Dieu, L. Q.; Devaux, A.; López-Duarte, I.; Martínez-Díaz, M. V.; Brühwiler, D.; Calzaferri, G.; Torres, T. *Chem. Commun.* **2008**, 1187–1189.

834. Cid, J. J.; Yum, J. H.; Jang, S. R.; Nazeeruddin, M. K.; Ferrero, E. M.; Palomares, E.; Ko, J.; Grätzel, M.; Torres, T. *Angew. Chem. Int. Ed.* **2007**, *46*, 8358–8362.
835. Reddy, P. Y.; Giribabu, L.; Lyness, C.; Snaith, H. J.; Vijaykumar, C.; Chandrasekharam, M.; Lakshmikantam, M.; Yum, J. H.; Kalyanasundaram, K.; Grätzel, M.; Nazeeruddin, M. K. *Angew. Chem. Int. Ed.* **2007**, *46*, 373–376.
836. De la Torre, G.; Martínez-Díaz, M. V.; Torres, T. *J. Porphyr. Phthalocyan.* **1999**, *3*, 560–568.
837. Makhseed, S.; McKeown, N. B. *J. Porphyr. Phthalocyan.* **2003**, *7*, 125–130.
838. Youssef, T. E.; Hanack, M. *J. Porphyr. Phthalocyan.* **2005**, *9*, 28–31.
839. Makarov, D. A.; Yuzhakova, O. A.; Slivka, L. K.; Kuznetsova, N. A.; Negrimovsky, V. M.; Kaliya, O. L.; Lukyanets, E. A. *J. Porphyr. Phthalocyan.* **2007**, *11*, 586–595.
840. Al-Raqa, S. Y. *J. Porphyr. Phthalocyan.* **2006**, *10*, 55–62.
841. Cook, M. J.; Heeney, M. J. *Chem. Eur. J.* **2000**, *6*, 3958–3967.
842. Cook, M. J.; Heeney, M. J. *Chem. Commun.* **2000**, 969–970.
843. Kimura, M.; Hamakawa, T.; Hanabusa, K.; Shirai, H.; Kobayashi, N. *Inorg. Chem.* **2001**, *40*, 4775–4779.
844. Odobel, F.; Zabri, H. *Inorg. Chem.* **2005**, *44*, 5600–5611.
845. Tolbin, A. Y.; Tomilova, L. G. *Mendeleev Commun.* **2008**, *18*, 286–288.
846. McKeown, N. B.; Li, H.; Helliwell, M. *J. Porphyr. Phthalocyan.* **2005**, *9*, 841–845.
847. Schweikart, K. H.; Hanack, M. *Eur. J. Org. Chem.* **2000**, 2551–2556.
848. de la Escosura, A.; Martínez-Díaz, M. V.; Torres, T.; Grubbs, R. H.; Guldi, D. M.; Neugebauer, H.; Winder, C.; Drees, M.; Sariciftci, N. S. *Chem. Asian J.* **2006**, *1*, 148–154.
849. Treacher, K. E.; Clarkson, G. J.; Ali-Adib, Z.; McKeown, N. B. *Chem. Commun.* **1996**, 73–75.
850. Tolbin, A. Y.; Tomilova, L. G.; Zefirov, N. S. *Russ. Chem. B* **2005**, *54*, 2099–2103.
851. Kimura, M.; Kuroda, T.; Ohta, K.; Hanabusa, K.; Shirai, H.; Kobayashi, N. *Langmuir* **2003**, *19*, 4825–4830.
852. Giribabu, L.; Kumar, C. V.; Reddy, V. G.; Reddy, P. Y.; Rao, C. S.; Jang, S. R.; Yum, J. H.; Nazeeruddin, M. K.; Grätzel, M. *Sol. Energy Mat. Sol. Cells* **2007**, *91*, 1611–1617.
853. Yang, Z. L.; Pu, H. T.; Yuan, J. J.; Wan, D. C.; Liu, Y. S. *Chem. Phys. Lett.* **2008**, *465*, 73–77.
854. Kimura, M.; Ueki, H.; Ohta, K.; Hanabusa, K.; Shirai, H.; Kobayashi, N. *Chem. Eur. J.* **2004**, *10*, 4954–4959.
855. Al-Raqa, S. Y. *Dyes Pigments* **2008**, *77*, 259–265.
856. Yanagisawa, M.; Korodi, F.; Bergquist, J.; Holmberg, A.; Hagfeldt, A.; Åkermark, B.; Sun, L. C. *J. Porphyr. Phthalocyan.* **2004**, *8*, 1228–1235.
857. Cosimelli, B.; Roncucci, G.; Dei, D.; Fantetti, L.; Ferroni, F.; Ricci, M.; Spinelli, D. *Tetrahedron* **2003**, *59*, 10025–10030.
858. Liu, J. X.; Yu, Q.; Zhou, Q. F.; Xu, H. J. *J. Chem. Soc. Chem. Commun.* **1990**, 260–261.
859. Huang, X. B.; Liu, Y. Q.; Wang, S.; Zhou, S. Q.; Zhu, D. B. *Chem. Eur. J.* **2002**, *8*, 4179–4184.
860. Tolbin, A. Y.; Ivanov, A. V.; Tomilova, L. G.; Zefirov, N. S. *J. Porphyr. Phthalocyan.* **2003**, *7*, 162–166.
861. Li, H.; Fronczek, F. R.; Vicente, M. G. H. *Tetrahedron Lett.* **2008**, *49*, 4828–4830.
862. Ribeiro, A. O.; Tomé, J. P. C.; Neves, M. G. P. M. S.; Tomé, A. C.; Cavaleiro, J. A. S.; Serra, O. A.; Torres, T. *Tetrahedron Lett.* **2006**, *47*, 6129–6132.
863. Makhseed, S.; Cook, A.; McKeown, N. B. *Chem. Commun.* **1999**, 419–420.

864. Fukuzumi, S.; Ohkubo, K.; Ortiz, J.; Gutiérrez, A. M.; Fernández-Lázaro, F.; Sastre-Santos, A. *J. Phys. Chem. A* **2008**, *112*, 10744–10752.
865. Kulaç, D.; Bulut, M.; Altındal, A.; Özkaya, A. R.; Salih, B.; Bekaroğlu, O. *Polyhedron* **2007**, *26*, 5432–5440.
866. Özer, M.; Altındal, A.; Özkaya, A. R.; Bulut, M.; Bekaroğlu, O. *Synthetic Met.* **2005**, *155*, 222–231.
867. Znoiko, S. A.; Maizlish, V. E.; Shaposhnikov, G. P.; Abramov, I. G.; Voron'ko, M. N. *Russ. J. Gen. Chem.* **2007**, *77*, 1623–1627.
868. Kimura, T.; Kumasaka, J.; Namauo, T. *Eur. J. Org. Chem.* **2008**, 5079–5084.
869. Kalkan, A.; Koca, A.; Bayır, Z. A. *Polyhedron* **2004**, *23*, 3155–3162.
870. Dinçer, H. A.; Gül, A.; Koçak, M. B. *Dyes Pigments* **2007**, *74*, 545–550.
871. Kantar, C.; Akdemir, N.; Ağar, E.; Ocak, N.; Şaşmaz, S. *Dyes Pigments* **2008**, *76*, 7–12.
872. Dinçer, H. A.; Koca, A.; Gül, A.; Koçak, M. B. *Dyes Pigments* **2008**, *76*, 825–831.
873. Gürsoy, S.; Bayır, Z. A.; Hamuryudan, E.; Bekaroğlu, O. *Monatsh. Chem.* **2000**, *131*, 287–292.
874. Kimura, T.; Yomogita, A.; Matsutani, T.; Suzuki, T.; Tanaka, L.; Kawai, Y.; Takaguchi, Y.; Wakahara, T.; Akasaka, T. *J. Org. Chem.* **2004**, *69*, 4716–4723.
875. Hamuryudan, E.; Merey, S.; Bayır, Z. A. *Dyes Pigments* **2003**, *59*, 263–268.
876. Yüksel, F.; Atilla, D.; Ahsen, V. *Polyhedron* **2007**, *26*, 4551–4556.
877. Tian, H. J.; Ali, H.; van Lier, J. E. *Tetrahedron Lett.* **2000**, *41*, 8435–8438.
878. Lutsenko, O. G.; Kulinich, V. P.; Shaposhindkov, G. P.; Lyubomtsev, A. V. *Russ. J. Gen. Chem.* **2004**, *74*, 286–291.
879. Lutsenko, O. G.; Kulinich, V. P.; Shaposhnikov, G. P. *Russ. J. Gen. Chem.* **2003**, *73*, 1463–1467.
880. Kudrevich, S. V.; Ali, H.; van Lier, J. E. *J. Chem. Soc. Perkin Trans. 1* **1994**, 2767–2774.
881. Tian, M. Q.; Wada, T.; Sasabe, H. *Dyes Pigments* **2002**, *52*, 1–8.
882. Ozan, N.; Bekaroğlu, O. *Polyhedron* **2003**, *22*, 819–823.
883. Sülü, M.; Altındal, A.; Bekaroğlu, O. *Synthetic Met.* **2005**, *155*, 211–221.
884. Ali, H.; Sim, S. K.; van Lier, J. E. *J. Chem. Res.-S.* **1999**, 496–497.
885. Hanack, M.; Stihler, P. *Eur. J. Org. Chem.* **2000**, 303–311.
886. Balakirev, A. E.; Maizlish, V. E.; Shaposhnikov, G. P. *Russ. J. Gen. Chem.* **2002**, *72*, 1633–1635.
887. Young, J. G.; Onyebuagu, W. *J. Org. Chem.* **1990**, *55*, 2155–2159.
888. Balakirev, A. V.; Maizlish, V. V.; Shaposhnikov, G. P. *Russ. J. Gen. Chem.* **2002**, *72*, 307–310.
889. Abdurrahmanoğlu, S.; Altındal, A.; Bulut, M.; Bekaroğlu, O. *Polyhedron* **2006**, *25*, 3639–3646.
890. de la Torre, G.; Gouloumis, A.; Vázquez, P.; Torres, T. *Angew. Chem. Int. Ed.* **2001**, *40*, 2895–2898.
891. Lee, H. J.; Brennessel, W. W.; Lessing, J. A.; Brucker, W. W.; Young, V. G.; Gorun, S. M. *Chem. Commun.* **2003**, 1576–1577.
892. Bench, B. A.; Brennessel, W. W.; Lee, H. J.; Gorun, S. M. *Angew. Chem. Int. Ed.* **2002**, *41*, 750–754.
893. Kandaz, M.; Çetin, H. S.; Koca, A.; Özkaya, A. R. *Dyes Pigments* **2007**, *74*, 298–305.
894. Merey, S.; Bekaroğlu, O. *J. Chem. Soc. Dalton* **1999**, 4503–4510.
895. Dinçer, H. A.; Gonca, E.; Gül, A. *Dyes Pigments* **2008**, *79*, 166–169.
896. Bayar, S.; Dinçer, H. A.; Gonca, E. *Dyes Pigments* **2009**, *80*, 156–162.

897. Kandaz, M.; Yaraşir, M. N. U.; Koca, A.; Bekaroğlu, O. *Polyhedron* **2002**, *21*, 255–263.
898. Dinçer, H. A.; Gül, A.; Koçak, M. B. *J. Porphyr. Phthalocyan.* **2004**, *8*, 1204–1208.
899. Volkov, K. A.; Avramenko, G. V.; Negrimovskii, V. M.; Luk'yanets, E. A. *Russ. J. Gen. Chem.* **2007**, *77*, 1126–1133.
900. Volkov, K. A.; Avramenko, G. V.; Negrimovskii, V. M.; Luk'yanets, E. A. *Russ. J. Gen. Chem.* **2008**, *78*, 1787–1793.
901. Milaeva, E. R.; Speier, G. *Inorg. Chim. Acta* **1992**, *192*, 117–121.
902. Auger, A.; Burnham, P. M.; Chambrier, I.; Cook, M. J.; Hughes, D. L. *J. Mater. Chem.* **2005**, *15*, 168–176.
903. Vagin, S. I.; Frickenschmidt, A.; Kammerer, B.; Hanack, M. *Chem. Eur. J.* **2005**, *11*, 6568–6573.
904. Kuhnich, V. P.; Shaposhnikov, G. P.; Gorelov, V. N.; Doronina, E. A. *Russ. J. Gen. Chem.* **2005**, *75*, 970–974.
905. Quintiliani, M.; García–Frutos, E. M.; Vázquez, P.; Torres, T. *J. Inorg. Biochem.* **2008**, *102*, 388–394.
906. Ali, H.; Baillargeon, P.; van Lier, J. E. *Tetrahedron Lett.* **2008**, *49*, 7253–7255.
907. Bottari, G.; Torres, T. *Chem. Commun.* **2004**, 2668–2669.
908. de la Escosura, A.; Martínez-Díaz, M. V.; Thordarson, P.; Rowan, A. E.; Nolte, R. J. M.; Torres, T. *J. Am. Chem. Soc.* **2003**, *125*, 12300–12308.
909. Kahnt, A.; Guldi, D. M.; de la Escosura, A.; Martin-Diaz, M. V.; Torres, T. *J. Mater. Chem.* **2008**, *18*, 77–82.
910. Kobayashi, N.; Nishiyama, Y.; Ohya, T.; Sato, M. *J. Chem. Soc. Chem. Commun.* **1987**, 390–392.
911. Mikhalenko, S. A.; Solov'eva, L. I.; Luk'yanets, E. A. *Russ. J. Gen. Chem.* **2005**, *75*, 1489–1493.
912. Kobayashi, N.; Ohya, T.; Sato, M.; Nakajima, S. *Inorg. Chem.* **1993**, *32*, 1803–1808.
913. Pardo, C.; Yuste, M.; Elguero, J. *J. Porphyr. Phthalocyan.* **2000**, *4*, 505–509.
914. Balakirev, A. E.; Kudrik, E. V.; Shaposhnikov, G. P. *Russ. J. Gen. Chem.* **2002**, *72*, 1616–1619.
915. Balakirev, A. E.; Maizlish, V. E.; Shaposhnikov, G. P. *Russ. J. Gen. Chem.* **2002**, *72*, 311–314.
916. Mørkved, E. H.; Neset, S. M.; Bjørlo, O.; Kjøsen, H.; Hvistendahl, G.; Mo, F. *Acta Chem. Scand.* **1995**, *49*, 658–662.
917. McKeown, N. B.; Helliwell, M.; Hassan, B. M.; Hayhurst, D.; Li, H.; Thompson, N.; Teat, S. L. *Chem. Eur. J.* **2007**, *13*, 228–234.
918. Vagin, S. I.; Hanack, M. *J. Porphyr. Phthalocyan.* **2006**, *10*, 1309–1318.
919. Makhseed, S.; Bumajdad, A.; Ghanem, B.; Msayib, K.; McKeown, N. B. *Tetrahedron Lett.* **2004**, *45*, 4865–4868.
920. Msayib, K.; Makhseed, S.; McKeown, N. B. *J. Mater. Chem.* **2001**, *11*, 2784–2789.
921. Loosli, C.; Jia, C. Y.; Liu, S. X.; Haas, M.; Dias, M.; Levillain, E.; Neels, A.; Labat, G.; Hauser, A.; Decurtins, S. *J. Org. Chem.* **2005**, *70*, 4988–4992.
922. Odabaş, Z.; Altındal, A.; Salih, B.; Bulut, M.; Bekaroğlu, O. *Tetrahedron Lett.* **2007**, *48*, 6326–6329.
923. Seotsanyana-Mokhosi, I.; Nyokong, T. *J. Porphyr. Phthalocyan.* **2004**, *8*, 1214–1221.
924. Seotsanyana-Mokhosi, I.; Nyokong, T. *J. Porphyr. Phthalocyan.* **2005**, *9*, 476–483.
925. Seotsanyana-Mokhosi, I.; Kresfelder, T.; Abrahamse, H.; Nyokong, T. *J. Photochem. Photobiol., B* **2006**, *83*, 55–62.

926. Rodríguez-Morgade, S.; Hanack, M. *Chem. Eur. J.* **1997**, *3*, 1042–1051.
927. Jung, R.; Schweikart, K. H.; Hanack, M. *Eur. J. Org. Chem.* **1999**, 1687–1691.
928. Linssen, T. G.; Dürr, K.; Hanack, M.; Hirsch, A. *J. Chem. Soc. Chem. Commun.* **1995**, 103–104.
929. Hauschel, B.; Jung, R.; Hanack, M. *Eur. J. Inorg. Chem.* **1999**, 693–703.
930. Dürr, K.; Fiedler, S.; Linssen, T.; Hirsch, A.; Hanack, M. *Chem. Ber.-Recl.* **1997**, *130*, 1375–1378.
931. Stihler, P.; Hauschel, B.; Hanack, M. *Chem. Ber.-Recl.* **1997**, *130*, 801–806.
932. Mikhalenko, S. A.; Solov'eva, L. I.; Luk'yanets, E. A. *Zh. Obshch. Khim.* **1991**, *61*, 996–1003.
933. Mikhalenko, S. A.; Solov'eva, L. I.; Luk'yanets, E. A. *Zh. Obshch. Khim.* **1988**, *58*, 2618–2619.
934. Sooksimuang, T.; Behroozi, S. J.; Mandal, B. K. *J. Porphyr. Phthalocyan.* **2002**, *6*, 544–547.
935. Peng, Y. R.; Chen, K. Z.; Wen, J. B.; Shi, J. C.; Huang, B. Q. *Chinese Chem. Lett.* **2007**, *18*, 509–512.
936. Matsushita, O.; Muranaka, A.; Kobayashi, Y.; Kobayashi, N. *Heterocycles* **2007**, *74*, 321–329.
937. Kingsborough, R. P.; Swager, T. M. *Angew. Chem. Int. Ed.* **2000**, *39*, 2897–2900.
938. Kandaz, M.; Yılmaz, I.; Bekaroğlu, O. *Polyhedron* **2000**, *19*, 115–121.
939. Gürek, A.; Ahsen, V.; Gül, A.; Bekaroğlu, O. *J. Chem. Soc. Dalton* **1991**, 3367–3371.
940. Koçak, M.; Cihan, A.; Okur, A. I.; Bekaroğlu, O. *J. Chem. Soc. Chem. Commun.* **1991**, 577–578.
941. Gök, Y.; Kantekin, H.; Bilgin, A.; Mendil, D.; Değirmencioğlu, I. *Chem. Commun.* **2001**, 285–286.
942. Chizhova, N. V.; Khelevina, O. G.; Berezin, B. D. *Russ. J. Gen. Chem.* **2007**, *77*, 1455–1457.
943. Khelevina, O. G.; Chizhova, N. V.; Stuzhin, P. A. *J. Porphyr. Phthalocyan.* **2000**, *4*, 555–563.
944. Chizhova, N. V.; Migalova, I. S.; Stuzhin, P. A. *Russ. J. Gen. Chem.* **2004**, *74*, 292–294.
945. Linstead, R. P.; Whalley, M. *J. Chem. Soc.* **1952**, 4839–4846.
946. Fitzgerald, J. P.; Haggerty, B. S.; Rheingold, A. L.; May, L.; Brewer, G. A. *Inorg. Chem.* **1992**, *31*, 2006–2013.
947. Fitzgerald, J. P.; Yap, G. P. A.; Rheingold, A. L.; Brewer, C. T.; May, L.; Brewer, G. A. *J. Chem. Soc. Dalton* **1996**, 1249–1253.
948. Nie, H. L.; Barrett, A. G. M.; Hoffman, B. M. *J. Org. Chem.* **1999**, *64*, 6791–6796.
949. Miwa, H.; Makarova, E. A.; Ishii, K.; Luk'yanets, E. A.; Kobayashi, N. *Chem. Eur. J.* **2002**, *8*, 1082–1090.
950. Chen, Z. M.; Wu, Y. Q.; Zuo, X. *Dyes Pigments* **2007**, *73*, 245–250.
951. Kobayashi, N.; Nakajima, S.; Osa, T. *Chem. Lett.* **1992**, 2415–2418.
952. Muranaka, A.; Yoshida, K.; Akagi, Y.; Naka, H.; Uchiyama, M.; Kondo, Y.; Kobayashi, N. *Tetrahedron Lett.* **2008**, *49*, 5084–5086.
953. Kobayashi, N.; Miwa, H.; Isago, H.; Tomura, T. *Inorg. Chem.* **1999**, *38*, 479–485.
954. Velázquez, C. S.; Baumann, T. F.; Olmstead, M. M.; Hope, H.; Barrett, A. G. M.; Hoffman, B. M. *J. Am. Chem. Soc.* **1993**, *115*, 9997–10003.
955. Cook, A. S.; Williams, D. B. G.; White, A. J. P.; Williams, D. J.; Lange, S. J.; Barrett, A. G. M.; Hoffman, B. M. *Angew. Chem. Int. Ed.* **1997**, *36*, 760–761.

956. Gan, Q.; Xiong, F.; Li, S. Y.; Wang, S. Q.; Shen, S. Y.; Xu, H. J.; Yang, G. Q. *Inorg. Chem. Commun.* **2005**, *8*, 285–288.
957. Kobayashi, N.; Fukuda, T. *J. Am. Chem. Soc.* **2002**, *124*, 8021–8034.
958. Vagin, S.; Ziener, U.; Hanack, M.; Stuzhin, P. A. *Eur. J. Inorg. Chem.* **2004**, 2877–2884.
959. Marinina, L. E.; Mikhalenko, S. A.; Luk'yanets E. A. *Zh. Obshch. Khim.* **1973**, *43*, 2025–2029.
960. Ikeue, T.; Kurahashi, S.; Handa, M.; Sugimori, T.; Nakamura, M. *J. Porphyr. Phthalocyan.* **2008**, *12*, 1041–1049.
961. Khelevina, O. G.; Bubnova, A. S.; Makarova, O. N.; Lukina, S. A.; Vagin, S. I.; Stuzhin, P. A. *Russ. J. Coord. Chem.* **2006**, *32*, 451–457.
962. Sakellariou, E. G.; Montalban, A. G.; Beall, S. L.; Henderson, D.; Meunier, H. G.; Phillips, D.; Suhling, K.; Barrett, A. G. M.; Hoffman, B. M. *Tetrahedron* **2003**, *59*, 9083–9090.
963. Gonca, E.; Baklacı, U. G.; Dinçer, H. A. *Polyhedron* **2008**, *27*, 2431–2435.
964. Nazlı, A.; Gonca, E.; Gül, A. *J. Porphyr. Phthalocyan.* **2006**, *10*, 996–1002.
965. Anderson, M. E.; Barrett, A. G. M.; Hoffman, B. M. *Inorg. Chem.* **1999**, *38*, 6143–6151.
966. Fuchter, M. J.; Beall, L. S.; Baum, S. M.; Montalban, A. G.; Sakellariou, E. G.; Mani, N. S.; Miller, T.; Vesper, B. J.; White, A. J. P.; Williams, D. J.; Barrett, A. G. M.; Hoffman, B. M. *Tetrahedron* **2005**, *61*, 6115–6130.
967. Luo, Q. F.; Chen, B. Z.; Wang, M. Z.; Tian, H. *Adv. Funct. Mater.* **2003**, *13*, 233–239.
968. Tian, H.; Chen, B. Z.; Tu, H. Y.; Müllen, K. *Adv. Mater.* **2002**, *14*, 918–923.
969. Fitzgerald, J. P.; Lebenson, J. R.; Wang, G. B.; Yee, G. T.; Noll, B. C.; Sommer, R. D. *Inorg. Chem.* **2008**, *47*, 4520–4530.
970. Hachiya, S.; Cook, A. S.; Williams, D. B. G.; Montalban, A. G.; Barrett, A. G. M.; Hoffman, B. M. *Tetrahedron* **2000**, *56*, 6565–6569.
971. Kumar, R.; Kumar, A.; Prasad, R. *Transition Met. Chem.* **2007**, *32*, 1091–1095.
972. Belviso, S.; Ricciardi, G.; Lelj, F.; Scolaro, L. M.; Bencini, A.; Carbonera, C. *J. Chem. Soc. Dalton* **2001**, 1143–1150.
973. Ricciardi, G.; Bavoso, A.; Bencini, A.; Rosa, A.; Lelj, F.; Bonosi, F. *J. Chem. Soc. Dalton* **1996**, 2799–2807.
974. Erdoğmuş, A.; Koca, A.; Avcıata, U.; Gül, A. *Z. Anorg. Allg. Chem.* **2008**, *634*, 2649–2654.
975. Yu, B.; Zhou, Y. X.; Wang, D. K.; Wang, Z. X.; Sugiura, K.; Sakata, Y.; Levon, K. *J. Porphyr. Phthalocyan.* **2002**, *6*, 447–455.
976. Belviso, S.; Giugliano, A.; Amati, M.; Ricciardi, G.; Lelj, F.; Scolaro, L. M. *Dalton Trans.* **2004**, 305–312.
977. Sholto, A.; Lee, S.; Hoffman, B. M.; Barrett, A. G. M.; Ehrenberg, B. *Photochem. Photobiol.* **2008**, *84*, 764–773.
978. Belviso, S.; Ricciardi, G.; Lelj, F. *J. Mater. Chem.* **2000**, *10*, 297–304.
979. Akkus, H.; Gül, A. *Transition Met. Chem.* **2001**, *26*, 689–694.
980. Ehrlich, L. A.; Skrdla, P. J.; Jarrell, W. K.; Sibert, J. W.; Armstrong, N. R.; Saavedra, S. S.; Barrett, A. G. M.; Hoffman, B. M. *Inorg. Chem.* **2000**, *39*, 3963–3969.
981. Kandaz, M.; Özkaya, A. R.; Koca, A.; Salih, B. *Dyes Pigments* **2007**, *74*, 483–489.
982. Eichhorn, S. H.; Bruce, D. W.; Guillon, D.; Gallani, J. L.; Fischer, T.; Stumpe, J.; Geue, T. *J. Mater. Chem.* **2001**, *11*, 1576–1584.
983. Lee, S. W.; White, A. J. P.; Williams, D. J.; Barrett, A. G. M.; Hoffman, B. M. *J. Org. Chem.* **2001**, *66*, 461–465.

984. Uslu, R. Z.; Gül, A. *C. R. Acad. Sci. Paris, Série IIc* **2000**, *3*, 643–648.
985. Karadeniz, H.; Gök, Y. *Dyes Pigments* **2008**, *77*, 351–356.
986. Prasad, R.; Kumar, A. *Transition Met. Chem.* **2004**, *29*, 714–721.
987. Prasad, R.; Kumar, A.; Murguly, E.; Branda, N. *Inorg. Chem. Commun.* **2001**, *4*, 219–222.
988. Prasad, R.; Kumar, A. *J. Electroanal. Chem.* **2005**, *576*, 295–303.
989. Prasad, R.; Kumar, A. *Inorg. Chim. Acta* **2005**, *358*, 3201–3210.
990. Keskin, B.; Köseoğlu, Y.; Avcıata, U.; Gül, A. *Polyhedron* **2008**, *27*, 1155–1160.
991. Sibert, J. W.; Baumann, T. F.; Williams, D. J.; White, A. J. P.; Barrett, A. G. M.; Hoffman, B. M. *J. Am. Chem. Soc.* **1996**, *118*, 10487–10493.
992. Kemikli, N.; Öztürk, R. *Inorg. Chem. Commun.* **2008**, *11*, 338–340.
993. Lee, S. W.; Stackow, R.; Foote, C. S.; Barrett, A. G. M.; Hoffman, B. M. *Photochem. Photobiol.* **2003**, *77*, 18–21.
994. Sağlam, O.; Gül, A. *Polyhedron* **2001**, *20*, 269–275.
995. Öztürk, R.; Gül, A. *Tetrahedron Lett.* **2004**, *45*, 947–949.
996. Polat, M.; Gül, A. *J. Chem. Res. (S)* **1999**, 130–131.
997. Yang, C. J.; Sun, J.; Deng, K. J.; Wang, D. Y. *Catal. Commun.* **2008**, *9*, 321–326.
998. Sesalan, B. S.; Koca, A.; Gül, A. *Polyhedron* **2003**, *22*, 3083–3090.
999. Montalban, A. G.; Lange, S. J.; Beall, L. S.; Mani, N. S.; Williams, D. J.; White, A. J. P.; Barrett, A. G. M.; Hoffman, B. M. *J. Org. Chem.* **1997**, *62*, 9284–9289.
1000. Morgan, A. R.; Petousis, N. H.; van Lier, J. E. *Eur. J. Med. Chem.* **1997**, *32*, 21–26.
1001. Beall, L. S.; Mani, N. S.; White, A. J. P.; Williams, D. J.; Barrett, A. G. M.; Hoffman, B. M. *J. Org. Chem.* **1998**, *63*, 5806–5817.
1002. Bilgin, A.; Ertem, B.; Gök, Y. *Dyes Pigments* **2009**, *80*, 187–193.
1003. Donzello, M. P.; Ercolani, C.; Stuzhin, P. A.; Chiesi-Villa, A.; Rizzoli, C. *Eur. J. Inorg. Chem.* **1999**, 2075–2084.
1004. Donzello, M. P.; Dini, D.; D'Arcangelo, G.; Ercolani, C.; Zhan, R. Q.; Ou, Z. P.; Stuzhin, P. A.; Kadish, K. M. *J. Am. Chem. Soc.* **2003**, *125*, 14190–14204.
1005. Bauer, E. M.; Ercolani, C.; Galli, P.; Popkova, I. A.; Stuzhin, P. A. *J. Porphyr. Phthalocyan.* **1999**, *3*, 371–379.
1006. Stuzhin, P. A.; Bauer, E. M.; Ercolani, C. *Inorg. Chem.* **1998**, *37*, 1533–1539.
1007. Donzello, M. P.; Agostinetto, R.; Ivanova, S. S.; Fujimori, M.; Suzuki, Y.; Yoshikawa, H.; Shen, J.; Awaga, K.; Ercolani, C.; Kadish, K. M.; Stuzhin, P. A. *Inorg. Chem.* **2005**, *44*, 8539–8551.
1008. Bauer, E. M.; Cardarilli, D.; Ercolani, C.; Stuzhin, P. A.; Russo, U. *Inorg. Chem.* **1999**, *38*, 6114–6120.
1009. Kopranenkov, V. N.; Mundshtukova, I. D.; Luk'yanets, E. A. *Khim. Geterotsikl.* **1994**, 30–35.
1010. Bellec, N.; Montalban, A. G.; Williams, D. B. G.; Cook, A. S.; Anderson, M. E.; Feng, X. D.; Barrett, A. G. M.; Hoffman, B. M. *J. Org. Chem.* **2000**, *65*, 1774–1779.
1011. Fuchter, M. J.; Hoffman, B. M.; Barrett, A. G. M. *J. Org. Chem.* **2005**, *70*, 5086–5091.
1012. Fuchter, M. J.; Vesper, B. J.; Murphy, K. A.; Collins, H. A.; Phillips, D.; Barrett, A. G. M.; Hoffman, B. M. *J. Org. Chem.* **2005**, *70*, 2793–2802.
1013. Sakellariou, E. G.; Montalban, A. G.; Meunier, H. G.; Rumbles, G.; Phillips, D.; Ostler, R. B.; Suhling, K.; Barrett, A. G. M.; Hoffman, B. M. *Inorg. Chem.* **2002**, *41*, 2182–2187.
1014. Fuchter, M. J.; Hoffman, B. M.; Barrett, A. G. M. *J. Org. Chem.* **2006**, *71*, 724–729.
1015. Zhong, C.; Zhao, M.; Stern, C.; Barrett, A. G. M.; Hoffman, B. M. *Inorg. Chem.* **2005**, *44*, 8272–8276.

1016. Michel, S. L. J.; Goldberg, D. P.; Stern, C.; Barrett, A. G. M.; Hoffman, B. M. *J. Am. Chem. Soc.* **2001**, *123*, 4741–4748.
1017. Zhong, C.; Zhao, M.; Goslinski, T.; Stern, C.; Barrett, A. G. M.; Hoffman, B. M. *Inorg. Chem.* **2006**, *45*, 3983–3989.
1018. Goslinski, T.; Zhong, C.; Fuchter, M. J.; Stern, C. L.; White, A. J. P.; Barrett, A. G. M.; Hoffman, B. M. *Inorg. Chem.* **2006**, *45*, 3686–3694.
1019. Ul-Haq, A.; Donzello, M. P.; Stuzhin, P. A. *Mendeleev Commun.* **2007**, *17*, 337–339.
1020. Makarova, E. A.; Kopranenkov, V. N.; Shevtsov, V. K.; Luk'yanets, E. A. *Khim. Geterotsikl.* **1994**, 1206–1212.
1021. Baumann, T. F.; Barrett, A. G. M.; Hoffman, B. M. *Inorg. Chem.* **1997**, *36*, 5661–5665.
1022. Michel, S. L. J.; Barrett, A. G. M.; Hoffman, B. M. *Inorg. Chem.* **2003**, *42*, 814–820.
1023. Galanin, N. E.; Kudrik, E. V.; Shaposhnikov, G. P.; Aleksandriiskii, V. V. *Russ. J. Org. Chem.* **2004**, *40*, 723–728.
1024. Zhao, M.; Zhong, C.; Stern, C.; Barrett, A. G. M.; Hoffman, B. M. *Inorg. Chem.* **2004**, *43*, 3377–3385.
1025. Zhong, C.; Stern, C.; Barrett, A. G. M.; Hoffman, B. M. *J. Am. Chem. Soc.* **2005**, *127*, 9769–9775.
1026. Baum, S. M.; Trabanco, A. A.; Montalban, A. G.; Micallef, A. S.; Zhong, C.; Meunier, H. G.; Suhling, K.; Phillips, D.; White, A. J. P.; Williams, D. J.; Barrett, A. G. M.; Hoffman, B. M. *J. Org. Chem.* **2003**, *68*, 1665–1670.
1027. Vagin, S. I.; Hanack, M. *Eur. J. Org. Chem.* **2002**, 2859–2865.
1028. Vagin, S.; Hanack, M.; Kammerer, B.; Frickenschmidt, A. *Eur. J. Org. Chem.* **2004**, 4245–4250.
1029. Montalban, A. G.; Jarrell, W.; Riguet, E.; McCubbin, Q. J.; Anderson, M. E.; White, A. J. P.; Williams, D. J.; Barrett, A. G. M.; Hoffman, B. M. *J. Org. Chem.* **2000**, *65*, 2472–2478.
1030. Forsyth, T. P.; Williams, D. B. G.; Montalban, A. G.; Stern, C. L.; Barrett, A. G. M.; Hoffman, B. M. *J. Org. Chem.* **1998**, *63*, 331–336.
1031. Luo, Q. F.; Tian, H.; Chen, B. Z.; Huang, W. *Dyes Pigments* **2007**, *73*, 118–120.
1032. Kulinich, V. P.; Shaposhnikov, G. P. *Russ. J. Gen. Chem.* **2001**, *71*, 1632–1635.
1033. Sesalan, S. B.; Gül, A. *Monatsh. Chem.* **2000**, *131*, 1191–1195.
1034. Kalkan, A.; Bayır, Z. A. *Monatsh. Chem.* **2003**, *134*, 1555–1560.
1035. Baumann, T. F.; Nasir, M. S.; Sibert, J. W.; White, A. J. P.; Olmstead, M. M.; Williams, D. J.; Barrett, A. G. M.; Hoffman, B. M. *J. Am. Chem. Soc.* **1996**, *118*, 10479–10486.
1036. Lange, S. J.; Sibert, J. W.; Barrett, A. G. M.; Hoffman, B. M. *Tetrahedron* **2000**, *56*, 7371–7377.
1037. Kobayashi, N.; Muranaka, A.; Nemykin, V. N. *Tetrahedron Lett.* **2001**, *42*, 913–915.
1038. Gonca, E.; Baklacı, U. G.; Dinçer, H. A. *J. Porphyr. Phthalocyan.* **2008**, *12*, 116–122.
1039. Nie, H. L.; Stern, C. L.; Barrett, A. G. M.; Hoffman, B. M. *Chem. Commun.* **1999**, 703–704.
1040. Mani, N. S.; Beall, L. S.; White, A. J. P.; Williams, D. J.; Barrett, A. G. M.; Hoffman, B. M. *J. Chem. Soc. Chem. Commun.* **1994**, 1943–1944.
1041. Prasad, R.; Kumar, A. *J. Porphyr. Phthalocyan.* **2005**, *9*, 509–518.
1042. Leznoff, C. C.; Mckeown, N. B. *J. Org. Chem.* **1990**, *55*, 2186–2190.
1043. Mack, J.; Kobayashi, N.; Leznoff, C. C.; Stillman, M. J. *Inorg. Chem.* **1997**, *36*, 5624–5634.
1044. Singh, J. P.; Xie, L. Y.; Dolphin, D. *Tetrahedron Lett.* **1995**, *36*, 1567–1570.
1045. Gerlach, B.; Montforts, F. P. *Tetrahedron Lett.* **1993**, *34*, 6369–6370.
1046. Bonnett, R.; Martinez, G. *J. Porphyr. Phthalocyan.* **2000**, *4*, 544–550.

1047. Galanin, N. E.; Shaposhnikov, G. P. *Russ. J. Gen. Chem.* **2007**, *77*, 1951–1954.
1048. Guyon, F.; Pondaven, A.; Guenot, P.; L'Her, M. *Inorg. Chem.* **1994**, *33*, 4787–4793.
1049. Freyer, W.; Minh, L. Q. *J. Prakt. Chem.* **1987**, *329*, 365–373.
1050. Mantareva, V.; Shopova, M.; Spassova, G.; Wöhrle, D.; Müller, S.; Jori, G.; Ricchelli, F. *J. Photochem. Photobiol., B* **1997**, *40*, 258–262.
1051. Ford, W. E.; Rodgers, M. A. J.; Schechtman, L. A.; Sounik, J. R.; Rihter, B. D.; Kenney, M. E. *Inorg. Chem.* **1992**, *31*, 3371–3377.
1052. Soncin, M.; Busetti, A.; Biolo, R.; Jori, G.; Kwag, G.; Li, Y. S.; Kenney, M. E.; Rodgers, M. A. J. *J. Photochem. Photobiol., B* **1998**, *42*, 202–210.
1053. Kovshev, E. I.; Luk'yanets E. A. *Zh. Obshch. Khim.* **1972**, *42*, 1593–1597.
1054. Ryu, H.; Kang, Y. G.; Knecht, S.; Subramanian, L. R.; Hanack, M. *Synthetic Met.* **1997**, *87*, 69–73.
1055. Tsuchida, E.; Orihashi, Y.; Ohno, H.; Matsuda, H.; Nakanishi, H.; Kato, M.; Deger, S.; Behnisch, R.; Hanack, M. *Synthetic Met.* **1989**, *33*, 37–46.
1056. Vogler, A.; Kunkely, H. *Inorg. Chim. a-Lett.* **1980**, *44*, L209–L210.
1057. Yeung, Y. O.; Liu, R. C. W.; Law, W. F.; Lau, P. L.; Jiang, J. Z.; Ng, D. K. P. *Tetrahedron* **1997**, *53*, 9087–9096.
1058. Kovshev, E. I.; Luk'yanets E. A. *Zh. Obshch. Khim.* **1972**, *42*, 696–699.
1059. Freyer, W.; Stiel, H.; Teuchner, K.; Leupold, D. *J. Photochem. Photobiol., A* **1994**, *80*, 161–167.
1060. Schneider, T.; Heckmann, H.; Barthel, M.; Hanack, M. *Eur. J. Org. Chem.* **2001**, 3055–3065.
1061. Nemykin, V. N.; Kostromina, N. A.; Subbotin, N. B.; Volkov, S. V. *Russ. Chem. B* **1996**, *45*, 89–92.
1062. Lee, C. H.; Sooksimuang, T.; Mandal, B. K. *J. Porphyr. Phthalocyan.* **2006**, *10*, 135–139.
1063. Ng, D. K. P.; Yeung, Y. O.; Chan, W. K.; Yu, S. C. *Tetrahedron Lett.* **1997**, *38*, 6701–6704.
1064. Chen, P. L.; Wang, X. B.; Tang, D. H.; Zhen, Z.; Zhang, J. C.; Liu, X. H. *Dyes Pigments* **2001**, *48*, 85–92.
1065. Li, X. Y.; Long, N. J.; Clifford, J. N.; Campbell, C. J.; Durrant, J. R. *New J. Chem.* **2002**, *26*, 1076–1080.
1066. Soldatova, A. V.; Kim, J.; Rosa, A.; Ricciardi, G.; Kenney, M. E.; Rodgers, M. A. J. *Inorg. Chem.* **2008**, *47*, 4275–4289.
1067. Bucking, M.; Dickson, E. F. G.; Farahani, M.; Fischer, F.; Holmes, D.; Jori, G.; Kennedy, J. C.; Kenney, M. E.; Peng, X.; Pottier, R. H.; Weagle, G. *J. Photochem. Photobiol., B* **2000**, *58*, 87–93.
1068. Zuo, X.; Wang, B.; Wu, Y. Q. *Sensor Actuat. B-Chem.* **2007**, *123*, 94–100.
1069. Dini, D.; Calvete, M.; Vagin, S.; Hanack, M.; Eriksson, A.; Lopes, C. *J. Porphyr. Phthalocyan.* **2006**, *10*, 1165–1171.
1070. Sun, W. F.; Wang, G.; Li, Y. J.; Calvete, M. J. F.; Dini, D.; Hanack, M. *J. Phys. Chem. A* **2007**, *111*, 3263–3270.
1071. Dini, D.; Calvete, M. J. F.; Hanack, M.; Pong, R. G. S.; Flom, S. R.; Shirk, J. S. *J. Phys. Chem. B* **2006**, *110*, 12230–12239.
1072. Müller, S.; Mantareva, V.; Stoichkova, N.; Kliesch, H.; Sobbi, A.; Wöhrle, D.; Shopova, M. *J. Photochem. Photobiol., B* **1996**, *35*, 167–174.
1073. Donyagina, V. F.; Luk'yanets, E. A. *Russ. J. Gen. Chem.* **2005**, *75*, 795–799.
1074. Hanack, M.; Renz, G.; Strähle, J.; Schmid, S. *J. Org. Chem.* **1991**, *56*, 3501–3509.

1075. Sooksimuang, T.; Mandal, B. K. *J. Org. Chem.* **2003**, *68*, 652–655.
1076. Cammidge, A. N.; Gopee, H. *Chem. Eur. J.* **2006**, *12*, 8609–8613.
1077. Shatskaya, T. A.; Gal'pern, M. G.; Skvarchenko, V. R.; Luk'yanets, E. A. *Zh. Obshch. Khim.* **1987**, *57*, 2364–2368.
1078. Yang, G. Y.; Hanack, M.; Lee, Y. W.; Dini, D.; Pan, J. F. *Adv. Mater.* **2005**, *17*, 875–879.
1079. Kopranenkov, V. N.; Luk'yanets E. A. *Zh. Obshch. Khim.* **1971**, *41*, 2341.
1080. Spesia, M. B.; Durantini, E. N. *Dyes Pigments* **2008**, *77*, 229–237.
1081. Wróbel, D.; Boguta, A.; Mazurkiewicz, P. *Spectrochim. Acta A* **2003**, *59*, 2841–2854.
1082. Kipp, R. A.; Simon, J. A.; Beggs, M.; Ensley, H. E.; Schmehl, R. H. *J. Phys. Chem. A* **1998**, *102*, 5659–5664.
1083. Adachi, K.; Chayama, K.; Watarai, H. *Soft Matter.* **2005**, *1*, 292–302.
1084. Kasuga, K.; Idehara, T.; Handa, M.; Ueda, Y.; Fujiwara, T.; Isa, K. *Bull. Chem. Soc. Jpn.* **1996**, *69*, 2559–2563.
1085. Xu, H.; Jiang, X. J.; Chan, E. Y. M.; Fong, W. P.; Ng, D. K. P. *Org. Biomol. Chem.* **2007**, *5*, 3987–3992.
1086. Camerel, F.; Ulrich, G.; Retailleau, P.; Ziessel, R. *Angew. Chem. Int. Ed.* **2008**, *47*, 8876–8880.
1087. El-Khouly, M. E.; Shim, S. H.; Araki, Y.; Ito, O.; Kay, K. Y. *J. Phys. Chem. B* **2008**, *112*, 3910–3917.
1088. Liu, J. Y.; Yeung, H. S.; Xu, W.; Li, X. Y.; Ng, D. K. P. *Org. Lett.* **2008**, *10*, 5421–5424.
1089. Adachi, K.; Watarai, H. *Anal. Chem.* **2006**, *78*, 6840–6846.
1090. Zyskowski, C. D.; Kennedy, V. O. *J. Porphyr. Phthalocyan.* **2000**, *4*, 707–712.
1091. Tolbin, A. Y.; Breusova, M. O.; Pushkarev, V. E.; Tomiloval, L. G. *Russ. Chem. B* **2005**, *54*, 2083–2086.
1092. del Rey, B.; Torres, T. *Tetrahedron Lett.* **1997**, *38*, 5351–5354.
1093. del Rey, B.; Keller, U.; Torres, T.; Rojo, G.; Agulló-López, F.; Nonell, S.; Martí, C.; Brasselet, S.; Ledoux, I.; Zyss, J. *J. Am. Chem. Soc.* **1998**, *120*, 12808–12817.
1094. Cao, W. F.; Tu, H. Y.; Wang, J.; Tian, H.; Wang, Y.; Gu, D. H.; Gan, F. X. *Dyes Pigments* **2002**, *54*, 213–219.
1095. Chen, Z. M.; Xia, C. H.; Wu, Y. Q.; Zuo, X.; Song, Y. L. *Inorg. Chem. Commun.* **2006**, *9*, 187–191.
1096. González-Rodríguez, D.; Torres, T.; Guldi, D. M.; Rivera, J.; Herranz, M. A.; Echegoyen, L. *J. Am. Chem. Soc.* **2004**, *126*, 6301–6313.
1097. Diaz, D. D.; Bolink, H. J.; Cappelli, L.; Claessens, C. G.; Coronado, E.; Torres, T. *Tetrahedron Lett.* **2007**, *48*, 4657–4660.
1098. Adachi, K.; Watarai, H. *New. J. Chem.* **2006**, *30*, 343–348.
1099. Claessens, C. G.; Torres, T. *Chem. Eur. J.* **2000**, *6*, 2168–2172.
1100. Martínez-Díaz, M. V.; del Rey, B.; Torres, T.; Agricole, B.; Mingotaud, C.; Cuvillier, N.; Rojo, G.; Agulló-López, F. *J. Mater. Chem.* **1999**, *9*, 1521–1526.
1101. del Rey, B.; Martínez-Díaz, M. V.; Barberá, J.; Torres, T. *J. Porphyr. Phthalocyan.* **2000**, *4*, 569–573.
1102. Kang, S. H.; Kang, Y. S.; Zin, W. C.; Olbrechts, G.; Wostyn, K.; Clays, K.; Persoons, A.; Kim, K. *Chem. Commun.* **1999**, 1661–1662.
1103. Claessens, C. G.; González-Rodríguez, D.; Torres, T.; Martín, G.; Agulló-López, F.; Ledoux, I.; Zyss, J.; Ferro, V. R.; de la Vega, J. M. G. *J. Phys. Chem. B* **2005**, *109*, 3800–3806.
1104. González-Rodríguez, D.; Torres, T.; Herranz, M. A.; Echegoyen, L.; Carbonell, E.; Guldi, D. M. *Chem. Eur. J.* **2008**, *14*, 7670–7679.

1105. Kobayashi, N.; Nonomura, T. *Tetrahedron Lett.* **2002**, *43*, 4253–4255.
1106. Stork, J. R.; Potucek, R. J.; Durfee, W. S.; Noll, B. C. *Tetrahedron Lett.* **1999**, *40*, 8055–8058.
1107. Claessens, C. G.; González-Rodríguez, D.; del Rey, B.; Torres, T.; Mark, G.; Schuchmann, H. P.; von Sonntag, C.; MacDonald, J. G.; Nohr, R. S. *Eur. J. Org. Chem.* **2003**, 2547–2551.
1108. Palomares, E.; Martínez-Díaz, M. V.; Torres, T.; Coronado, E. *Adv. Funct. Mater.* **2006**, *16*, 1166–1170.
1109. Medina, A. S.; Claessens, C. G.; Rahman, G. M. A.; Lamsabhi, A. M.; Mó, O.; Yáñez, M.; Guldi, D. M.; Torres, T. *Chem. Commun.* **2008**, 1759–1761.
1110. González-Rodríguez, D.; Torres, T.; Guldi, D. M.; Rivera, J.; Echegoyen, L. *Org. Lett.* **2002**, *4*, 335–338.
1111. Iglesias, R. S.; Claessens, C. G.; Rahman, G. M. A.; Herranz, M. A.; Guldi, D. M.; Torres, T. *Tetrahedron* **2007**, *63*, 12396–12404.
1112. Fukuda, T.; Olmstead, M. M.; Durfee, W. S.; Kobayashi, N. *Chem. Commun.* **2003**, 1256–1257.
1113. Jaung, J. Y.; Matsuoka, M.; Fukunishi, K. *Dyes Pigments* **1999**, *40*, 73–81.
1114. Kobayashi, N.; Rizhen, J.; Nakajima, S.; Osa, T.; Hino, H. *Chem. Lett.* **1993**, 185–188.
1115. Zimcik, P.; Miletin, M.; Kostka, M.; Schwarz, J.; Musil, Z.; Kopecky, K. *J. Photochem. Photobiol., A* **2004**, *163*, 21–28.
1116. Wang, C. S.; Bryce, M. R.; Batsanov, A. S.; Howard, J. A. K. *Chem. Eur. J.* **1997**, *3*, 1679–1690.
1117. Mitzel, F.; FitzGerald, S.; Beeby, A.; Faust, R. *Eur. J. Org. Chem.* **2004**, 1136–1142.
1118. Zimcik, P.; Mørkved, E. H.; Andreassen, T.; Lenco, J.; Novakova, V. *Polyhedron* **2008**, *27*, 1368–1374.
1119. Zimcik, P.; Miletin, M.; Kopecky, K.; Musil, Z.; Berka, P.; Horakova, V.; Kucerova, H.; Zbytovska, J.; Brault, D. *Photochem. Photobiol.* **2007**, *83*, 1497–1504.
1120. Musil, Z.; Zimcik, P.; Miletin, M.; Kopecky, K.; Petrik, P.; Lenco, J. *J. Photochem. Photobiol., A* **2007**, *186*, 316–322.
1121. Zimcik, P.; Miletin, M.; Musil, Z.; Kopecky, K.; Kubza, L.; Brault, D. *J. Photochem. Photobiol., A* **2006**, *183*, 59–69.
1122. Musil, Z.; Zimcik, P.; Miletin, M.; Kopecky, K.; Link, M.; Petrik, P.; Schwarz, J. *J. Porphyr. Phthalocyan.* **2006**, *10*, 122–131.
1123. Mørkved, E. H.; Afseth, N. K.; Kjøsen, H. *J. Porphyr. Phthalocyan.* **2006**, *10*, 1301–1308.
1124. Kleinwächter, J.; Subramanian, L. R.; Hanack, M. *J. Porphyr. Phthalocyan.* **2000**, *4*, 498–504.
1125. Mørkved, E. H.; Ossletten, H.; Kjøsen, H.; Bjørlo, O. *J. Prakt. Chem.* **2000**, *342*, 83–86.
1126. Lee, B. H.; Jaung, J. Y.; Jang, S. C.; Yi, S. C. *Dyes Pigments* **2005**, *65*, 159–167.
1127. Mitzel, F.; FitzGerald, S.; Beeby, A.; Faust, R. *Chem. Eur. J.* **2003**, *9*, 1233–1241.
1128. Efimova, S. V.; Korzhenevskii, A. B.; Koifman, O. I. *Russ. J. Gen. Chem.* **2008**, *78*, 1447–1451.
1129. Zimcik, P.; Miletin, M.; Musil, Z.; Kopecky, K.; Slajsova, D. *Dyes Pigments* **2008**, *77*, 281–287.
1130. Jang, C. K.; Jaung, J. Y. *Mater. Lett.* **2008**, *62*, 3209–3212.
1131. Makhseed, S.; Samuel, J.; Ibrahim, F. *Tetrahedron* **2008**, *64*, 8871–8877.
1132. Makhseed, S.; Ibrahim, F.; Bezzu, C. G.; McKeown, N. B. *Tetrahedron Lett.* **2007**, *48*, 7358–7361.

1133. Makhseed, S.; Ibrahim, F.; Samuel, J.; Helliwell, M.; Warren, J. E.; Bezzu, C. G.; McKeown, N. B. *Chem. Eur. J.* **2008**, *14*, 4810–4815.
1134. Ohta, K.; Azumane, S.; Kawahara, W.; Kobayashi, N.; Yamamoto, I. *J. Mater. Chem.* **1999**, *9*, 2313–2320.
1135. Kopecky, K.; Zimcik, P.; Novakova, V.; Miletin, M.; Musil, Z.; Stribna, J. *Dyes Pigments* **2008**, *78*, 231–238.
1136. Musil, Z.; Zimcik, P.; Miletin, M.; Kopecky, K.; Lenco, J. *Eur. J. Org. Chem.* **2007**, 4535–4542.
1137. Donzello, M. P.; Ou, Z. P.; Monacelli, F.; Ricciardi, G.; Rizzoli, C.; Ercolani, C.; Kadish, K. M. *Inorg. Chem.* **2004**, *43*, 8626–8636.
1138. Bergami, C.; Donzello, M. P.; Monacelli, F.; Ercolani, C.; Kadish, K. M. *Inorg. Chem.* **2005**, *44*, 9862–9873.
1139. Donzello, M. P.; Ou, Z. P.; Dini, D.; Meneghetti, M.; Ercolani, C.; Kadish, K. M. *Inorg. Chem.* **2004**, *43*, 8637–8648.
1140. Bergami, C.; Donzello, M. P.; Ercolani, C.; Monacelli, F.; Kadish, K. M.; Rizzoli, C. *Inorg. Chem.* **2005**, *44*, 9852–9861.
1141. Shishkin, V. N.; Kudrik, E. V.; Shaposhnikov, G. P. *Russ. J. Coord. Chem.* **2005**, *31*, 516–520.
1142. Kudrik, E. V.; Theodoridis, A.; van Eldik, R.; Makarov, S. V. *Dalton Trans.* **2005**, 1117–1122.
1143. Fogel, Y.; Kastler, M.; Wang, Z. H.; Andrienko, D.; Bodwell, G. J.; Müllen, K. *J. Am. Chem. Soc.* **2007**, *129*, 11743–11749.
1144. Zimcik, P.; Miletin, M.; Ponec, J.; Kostka, M.; Fiedler, Z. *J. Photochem. Photobiol., A* **2003**, *155*, 127–131.
1145. Okujima, T.; Kikuchi, M.; Yamada, H.; Uno, H.; Ono, N. *J. Porphyr. Phthalocyan.* **2006**, *10*, 1197–1201.
1146. Du, X. G.; Ma, C. Y.; Hou, X. K.; Wang, G.; Li, W. C.; Du, G. T. *Heterocycles* **2003**, *60*, 2535–2542.
1147. Wen, T. C.; Chen, S. P.; Tsai, C. Y. *Synthetic Met.* **1998**, *97*, 105–112.
1148. Gal'pern, M. G.; Luk'yanets E. A. *Zh. Obshch. Khim.* **1971**, *41*, 2549–2552.
1149. Rusanova, J.; Pilkington, M.; Decurtins, S. *Chem. Commun.* **2002**, 2236–2237.
1150. Tempesti, T. C.; Stockert, J. C.; Durantini, E. N. *J. Phys. Chem. B* **2008**, *112*, 15701–15707.
1151. Sekota, M.; Nyokong, T. *J. Porphyr. Phthalocyan.* **1999**, *3*, 477–487.
1152. Nicolau, M.; Rojo, G.; Torres, T.; Agulló-López, F. *J. Porphyr. Phthalocyan.* **1999**, *3*, 703–711.
1153. Angeloni, S.; Bauer, E. M.; Ercolani, C.; Popkova, I. A.; Stuzhin, P. A. *J. Porphyr. Phthalocyan.* **2001**, *5*, 881–888.
1154. Donzello, M. P.; Ercolani, C.; Kadish, K. M.; Ricciardi, G.; Rosa, A.; Stuzhin, P. A. *Inorg. Chem.* **2007**, *46*, 4145–4157.
1155. Sakamoto, K.; Ohno-Okumura, E.; Kato, T.; Watanabe, M.; Cook, M. J. *Dyes Pigments* **2008**, *78*, 213–218.
1156. Galanin, N. E.; Kudrik, E. V.; Shaposhnikov, G. P. *Russ. J. Org. Chem.* **2008**, *44*, 225–230.
1157. Haas, M.; Liu, S. X.; Kahnt, A.; Leiggener, C.; Guldi, D. M.; Hauser, A.; Decurtins, S. *J. Org. Chem.* **2007**, *72*, 7533–7543.
1158. Ishii, K.; Iwasaki, M.; Kobayashi, N. *Chem. Phys. Lett.* **2007**, *436*, 94–98.
1159. Galanin, N. E.; Kudrik, E. V.; Maizlish, V. E.; Shaposhnikov, G. P. *Russ. J. Gen. Chem.* **2005**, *75*, 125–129.
1160. Fukuda, T.; Kobayashi, N. *Chem. Lett.* **2002**, 866–867.

1161. Sakamoto, K.; Kato, T.; Ohno-Okumura, E.; Watanabe, M.; Cook, M. J. *Dyes Pigments* **2005**, *64*, 63–71.
1162. Padmaja, K.; Youngblood, W. J.; Wei, L. Y.; Bocian, D. F.; Lindsey, J. S. *Inorg. Chem.* **2006**, *45*, 5479–5492.
1163. Martynov, A. G.; Nefedova, I. V.; Gorbunova, Y. G.; Tsivadze, A. Y. *Mendeleev Commun.* **2007**, *17*, 66–67.
1164. Arslanov, V. V.; Gorbunova, V. G.; Selektor, S. L.; Sheinina, L. S.; Tselykh, O. G.; Enakieva, Y. Y.; Tsivadze, A. Y. *Russ. Chem. B* **2004**, *53*, 2532–2541.
1165. Ahsen, V.; Yılmazer, E.; Ertas, M.; Bekaroğlu, O. *J. Chem. Soc. Dalton* **1988**, 401–406.
1166. Kobayashi, N.; Lever, A. B. P. *J. Am. Chem. Soc.* **1987**, *109*, 7433–7441.
1167. Sielcken, O. E.; van Tilborg, M. M.; Roks, M. F. M.; Hendriks, R.; Drenth, W.; Nolte, R. J. M. *J. Am. Chem. Soc.* **1987**, *109*, 4261–4265.
1168. Çelenk, E.; Kantekin, H. *Dyes Pigments* **2009**, *80*, 93–97.
1169. Kantekin, H.; Çelenk, E.; Karadeniz, H. *J. Organomet. Chem.* **2008**, *693*, 1353–1358.
1170. Kantekin, H.; Bıyıklıoğlu, Z.; Çelenk, E. *Inorg. Chem. Commun.* **2008**, *11*, 633–635.
1171. Agar, E.; Sasmaz, S.; Akdemir, N.; Keskin, I. *J. Chem. Soc. Dalton* **1997**, 2087–2090.
1172. Yıldız, S. Z.; Gök, Y. *New. J. Chem.* **1998**, *22*, 1365–1369.
1173. Gök, Y.; Yıldız, S. Z. *Polyhedron* **1997**, *16*, 113–117.
1174. Kantekin, H.; Bıyıklıoğlu, Z. *Dyes Pigments* **2008**, *77*, 98–102.
1175. Bıyıklıoğlu, Z.; Kantekin, H. *J. Organomet. Chem.* **2008**, *693*, 505–509.
1176. Bıyıklıoğlu, Z.; Kantekin, H.; Özil, M. *J. Organomet. Chem.* **2007**, *692*, 2436–2440.
1177. Bilgin, A.; Ertem, B.; Gök, Y. *Eur. J. Inorg. Chem.* **2007**, 1703–1712.
1178. Kantekin, H.; Değirmencioğlu, I.; Gök, Y. *Acta Chem. Scand.* **1999**, *53*, 247–252.
1179. Yıldız, S. Z.; Kantekin, H.; Gök, Y. *J. Porphyr. Phthalocyan.* **2001**, *5*, 367–375.
1180. Koçak, M.; Okur, A. I.; Bekaroğlu, O. *J. Chem. Soc. Dalton* **1994**, 323–326.
1181. Gümüs, G.; Öztürk, Z. Z.; Ahsen, V.; Gül, A.; Bekaroğlu, O. *J. Chem. Soc. Dalton* **1992**, 2485–2489.
1182. Atilla, D.; Ahsen, V. *J. Porphyr. Phthalocyan.* **2002**, *6*, 593–601.
1183. Kandaz, M.; Bekaroğlu, O. *J. Porphyr. Phthalocyan.* **1999**, *3*, 339–345.
1184. Bilgin, A.; Ertem, B. *Inorg. Chem. Commun.* **2008**, *11*, 1113–1116.
1185. Gök, Y.; Kantekin, H.; Kılıçaslan, M. B.; Alp, H. *Dyes Pigments* **2007**, *74*, 692–698.
1186. Değirmencioğlu, I.; Karaböcek, S.; Karaböcek, N.; Er, M.; Serbest, K. *Monatsh. Chem.* **2003**, *134*, 875–881.
1187. Gök, H. Z.; Kantekin, H.; Gök, Y.; Herman, G. *Dyes Pigments* **2007**, *74*, 699–705.
1188. Gök, H. Z.; Kantekin, H.; Gök, Y.; Herman, G. *Dyes Pigments* **2007**, *75*, 606–611.
1189. Mısır, M. N.; Gök, Y.; Kantekin, H. *J. Organomet. Chem.* **2007**, *692*, 1451–1456.
1190. Karadeniz, H.; Gök, Y.; Kantekin, H. *Dyes Pigments* **2007**, *75*, 498–504.
1191. Bilgin, A.; Ertem, B.; Gök, Y. *Polyhedron* **2005**, *24*, 1117–1124.
1192. Liu, H. W.; Chen, C. F.; Ai, M.; Gong, A. J.; Jiang, J.; Xi, F. *Tetrahedron: Asymmetry* **2000**, *11*, 4915–4922.
1193. Fernández-Lázaro, F.; Sastre, A.; Torres, T. *J. Chem. Soc. Chem. Commun.* **1995**, 419–420.
1194. Kobayashi, N.; Togashi, M.; Osa, T.; Ishii, K.; Yamauchi, S.; Hino, H. *J. Am. Chem. Soc.* **1996**, *118*, 1073–1085.
1195. Cabezón, B.; Quesada, E.; Esperanza, S.; Torres, T. *Eur. J. Org. Chem.* **2000**, 2767–2775.
1196. Pernin, D.; Haberroth, K.; Simon, J. *J. Chem. Soc. Perkin Trans. 1* **1997**, 1265–1266.

1197. Martínez-Díaz, M. V.; Fender, N. S.; Rodríguez-Morgade, M. S.; Gómez-López, M.; Diederich, F.; Echegoyen, L.; Stoddart, J. F.; Torres, T. *J. Mater. Chem.* **2002**, *12*, 2095–2099.
1198. Matsunami, M.; Takaki, A.; Maekawa, H.; Nishiguchi, I. *Sci. Technol. Adv. Mater.* **2005**, *6*, 172–180.
1199. Karadeniz, H.; Kantekin, H.; Gök, Y.; Çelenk, E. *Dyes Pigments* **2008**, *77*, 559–563.
1200. Hamuryudan, E. *Dyes Pigments* **2006**, *68*, 151–157.
1201. Gürol, I.; Ahsen, V. *J. Porphyr. Phthalocyan.* **2000**, *4*, 620–625.
1202. Kantekin, H.; Çelenk, E.; Bıyıklıoğlu, Z.; Karadeniz, H. *Transition Met. Chem.* **2008**, *33*, 189–193.
1203. Arslanoğlu, Y.; Koca, A.; Hamuryudan, E. *Polyhedron* **2007**, *26*, 891–896.
1204. Bıyıklıoğlu, Z.; Kantekin, H. *Dyes Pigments* **2009**, *80*, 17–21.
1205. Ertem, B.; Bilgin, A.; Gök, Y.; Kantekin, H. *Dyes Pigments* **2008**, *77*, 537–544.
1206. Ertem, B.; Bilgin, A.; Kantekin, H.; Gök, Y. *Polyhedron* **2008**, *27*, 2186–2192.
1207. Bilgin, A.; Yağcı, C.; Mendi, A.; Yıldız, U. *J. Appl. Polym. Sci.* **2008**, *110*, 2115–2126.
1208. Bıyıklıoğlu, Z.; Acar, I.; Kantekin, H. *Inorg. Chem. Commun.* **2008**, *11*, 630–632.
1209. Koçak, M.; Cihan, A.; Okur, A. I.; Gül, A.; Bekaroğlu, O. *Dyes Pigments* **2000**, *45*, 9–14.
1210. Koçak, M. *J. Porphyr. Phthalocyan.* **2000**, *4*, 742–744.
1211. Martynov, A. G.; Gorbunova, Y. G. *Inorg. Chim. Acta* **2007**, *360*, 122–130.
1212. Martynov, A. G.; Zubareva, O. V.; Gorbunova, Y. G.; Sakharov, S. G.; Tsivadze, A. Y. *Inorg. Chim. Acta* **2009**, *362*, 11–18.
1213. Martynov, A. G.; Zubareva, O. V.; Gorbunova, Y. G.; Sakharov, S. G.; Nefedov, S. E.; Dolgushin, F. M.; Tsivadze, A. Y. *Eur. J. Inorg. Chem.* **2007**, 4800–4807.
1214. Birin, K. P.; Gorbunova, Y. G.; Tsivadze, A. Y. *Russ. J. Inorg. Chem.* **2007**, *52*, 191–196.
1215. Lapkina, L. A.; Niskanen, E.; Ronkkomaki, H.; Larchenko, V. E.; Popov, K. I.; Tsivadze, A. Y. *J. Porphyr. Phthalocyan.* **2000**, *4*, 587–589.
1216. Özer, M.; Altındal, A.; Salih, B.; Bulut, M.; Bekaroğlu, O. *Tetrahedron Lett.* **2008**, *49*, 896–900.
1217. Kantekin, H.; Dilber, G.; Bıyıklıoğlu, Z. *J. Organomet. Chem.* **2008**, *693*, 1038–1042.
1218. Bilgin, A.; Yağcı, C.; Mendi, A.; Yıldız, U. *Polyhedron* **2007**, *26*, 617–625.
1219. Dudkin, S. V.; Makarova, E. A.; Luk'yanets, E. A. *Russ. J. Gen. Chem.* **2008**, *78*, 1441–1446.
1220. Fukuda, T.; Makarova, E. A.; Luk'yanets, E. A.; Kobayashi, N. *Chem. Eur. J.* **2004**, *10*, 117–133.
1221. Fukuda, T.; Masuda, S.; Kobayashi, N. *J. Am. Chem. Soc.* **2007**, *129*, 5472–5479.
1222. Fukuda, T.; Ogi, Y.; Kobayashi, N. *Chem. Commun.* **2006**, 159–161.
1223. Makarova, E. A.; Fukuda, T.; Luk'yanets, E. A.; Kobayashi, N. *Chem. Eur. J.* **2005**, *11*, 1235–1250.
1224. Lansky, D. E.; Sarjeant, A. A. N.; Goldberg, D. P. *Angew. Chem. Int. Ed.* **2006**, *45*, 8214–8217.
1225. Ramdhanie, B.; Telser, J.; Caneschi, A.; Zakharov, L. N.; Rheingold, A. L.; Goldberg, D. P. *J. Am. Chem. Soc.* **2004**, *126*, 2515–2525.
1226. Rodríguez-Méndez, M. L.; Gorbunova, Y.; de Saja, J. A. *Langmuir* **2002**, *18*, 9560–9565.
1227. Sheng, N.; Li, R. J.; Choi, C. F.; Su, W.; Ng, D. K. P.; Cui, X. G.; Yoshida, K.; Kobayashi, N.; Jiang, J. Z. *Inorg. Chem.* **2006**, *45*, 3794–3802.
1228. Bian, Y. Z.; Chen, X. H.; Wang, D. Y.; Choi, C. F.; Zhou, Y.; Zhu, P. H.; Ng, D. K. P.; Jiang, J. Z.; Weng, Y. X.; Li, X. Y. *Chem. Eur. J.* **2007**, *13*, 4169–4177.
1229. Lysenko, A. B.; Malinovskii, V. L.; Padmaja, K.; Wei, L. Y.; Diers, J. R.; Bocian, D. F.; Lindsey, J. S. *J. Porphyr. Phthalocyan.* **2005**, *9*, 491–508.

1230. Markovitsi, D.; Tranthi, T. H.; Even, R.; Simon, J. *Chem. Phys. Lett.* **1987**, *137*, 107–112.
1231. Magdesieva, T. V.; Zhukov, I. V.; Tomilova, L. G.; Korenchenko, O. V.; Kalashnikova, I. P.; Butin, K. P. *Russ. Chem. B* **2001**, *50*, 396–403.
1232. Zhukov, I. V.; Pushkarev, V. E.; Tomilova, L. G.; Zefirov, N. S. *Russ. Chem. B* **2005**, *54*, 189–194.
1233. Tomilova, L. G.; Dyumaev, K. M.; Tkachenko, O. P. *Russ. Chem. B* **1995**, *44*, 410–415.
1234. Battisti, D.; Tomilova, L.; Aroca, R. *Chem. Mater.* **1992**, *4*, 1323–1328.
1235. Nemykin, V. N.; Kostromina, N. A.; Volkov, S. V. *Russ. Chem. B* **1995**, *44*, 1883–1885.
1236. Bian, Y. Z.; Wang, R. M.; Jiang, J. Z.; Lee, C. H.; Wang, J. Z.; Ng, D. K. P. *Chem. Commun.* **2003**, 1194–1195.
1237. Liu, L. C.; Tai, C. H.; Hu, A. T.; Wei, T. H. *J. Porphyr. Phthalocyan.* **2004**, *8*, 984–988.
1238. Jiang, J. Z.; Liu, W.; Law, W. F.; Lin, J. M.; Ng, D. K. P. *Inorg. Chim. Acta* **1998**, *268*, 141–144.
1239. Lu, G.; Bai, M.; Li, R. J.; Zhang, X. X.; Ma, C. Q.; Lo, P. C.; Ng, D. K. P.; Jiang, J. Z. *Eur. J. Inorg. Chem.* **2006**, 3703–3709.
1240. Wang, R. M.; Li, R. J.; Bian, Y. Z.; Choi, C. F.; Ng, D. K. P.; Dou, J. M.; Wang, D. Q.; Zhu, P. H.; Ma, C. Q.; Hartnell, R. D.; Arnold, D. P.; Jiang, J. Z. *Chem. Eur. J.* **2005**, *11*, 7351–7357.
1241. Yaraşir, M. N.; Kandaz, M.; Koca, A.; Salih, B. *J. Porphyr. Phthalocyan.* **2006**, *10*, 1022–1033.
1242. Yağlğoğlu, H. G.; Arslan, M.; Abdurrahmanoğlu, S.; Ünver, H.; Elmali, A.; Bekaroğlu, O. *J. Phys. Chem. Solids* **2008**, *69*, 161–167.
1243. Mentec, A.; Pondaven, A.; Kerbaol, J. M.; L'Her, M. *Inorg. Chem. Commun.* **2006**, *9*, 810–813.
1244. Pushkarev, V. E.; Ivanov, A. V.; Zhukov, I. V.; Shulishov, E. V.; Tomilov, Y. V. *Russ. Chem. B* **2004**, *53*, 554–560.
1245. Montalban, A. G.; Michel, S. L. J.; Baum, S. M.; Vesper, B. J.; White, A. J. P.; Williams, D. J.; Barrett, A. G. M.; Hoffman, B. M. *J. Chem. Soc. Dalton* **2001**, 3269–3273.
1246. Gross, T.; Chevalier, F.; Lindsey, J. S. *Inorg. Chem.* **2001**, *40*, 4762–4774.
1247. Kalashnikova, I. P.; Zhukova, I. V.; Tomilova, L. G.; Zefirov, N. S. *Russ. Chem. B* **2003**, *52*, 1709–1714.
1248. Bian, Y. Z.; Jiang, J. Z.; Tao, Y.; Choi, M. T. M.; Li, R. J.; Ng, A. C. H.; Zhu, P. H.; Pan, N.; Sun, X.; Arnold, D. P.; Zhou, Z. Y.; Li, H. W.; Mak, T. C. W.; Ng, D. K. P. *J. Am. Chem. Soc.* **2003**, *125*, 12257–12267.
1249. Kalashnikova, I. P.; Zhukov, I. V.; Tomilova, L. G.; Zefirov, N. S. *Russ. Chem. B* **2005**, *54*, 2094–2098.
1250. Mukai, H.; Hatsusaka, K.; Ohta, K. *J. Porphyr. Phthalocyan.* **2007**, *11*, 846–856.
1251. Nekelson, F.; Monobe, H.; Shimizu, Y. *Chem. Commun.* **2006**, 3874–3876.
1252. Ceyhan, T.; Özdağ, M. A.; Salih, B.; Erbil, M. K.; Elmalı, A.; Özkaya, A. R.; Bekaroğlu, O. *Eur. J. Inorg. Chem.* **2008**, 4943–4950.
1253. Ivanov, A. V.; Svinareva, P. A.; Zhukov, I. V.; Tomilova, L. G.; Zefirov, N. S. *Russ. Chem. B* **2006**, *55*, 281–286.
1254. Ricciardi, G.; Belviso, S.; Lelj, F.; Ristori, S. *J. Porphyr. Phthalocyan.* **1998**, *2*, 177–188.
1255. Galanin, N. E.; Yakubov, L. A.; Shaposhnikov, G. P. *Russ. J. Org. Chem.* **2008**, *44*, 921–926.
1256. Chabach, D.; Tahiri, M.; Decian, A.; Fischer, J.; Weiss, R.; Bibout, M. E. *J. Am. Chem. Soc.* **1995**, *117*, 8548–8556.

1257. Jiang, J. Z.; Lau, R. L. C.; Chan, T. W. D.; Mak, T. C. W.; Ng, D. K. P. *Inorg. Chim. Acta* **1997**, *255*, 59–64.
1258. Lu, F. L.; Sun, X.; Li, R. J.; Liang, D. B.; Zhu, P. H.; Choi, C. F.; Ng, D. K. P.; Fukuda, T.; Kobayashi, N.; Bai, M.; Ma, C. Q.; Jiang, J. Z. *New. J. Chem.* **2004**, *28*, 1116–1122.
1259. Lu, F. L.; Cui, J. Z.; Yang, Q. H. *Inorg. Chim. Acta* **2007**, *360*, 2751–2757.
1260. Pan, N.; Jiang, J.; Cui, X.; Arnold, D. P. *J. Porphyr. Phthalocyan.* **2002**, *6*, 347–357.
1261. Jiang, J. Z.; Du, D. M.; Choi, M. T. M.; Xie, J. L.; Ng, D. K. P. *Chem. Lett.* **1999**, 261–262.
1262. Liu, M. O.; Hu, A. T. *J. Organomet. Chem.* **2004**, *689*, 2450–2455.
1263. Wang, R. M.; Li, R. J.; Li, Y.; Zhang, X. X.; Zhu, P. H.; Lo, P. C.; Ng, D. K. P.; Pan, N.; Ma, C. Q.; Kobayashi, N.; Jiang, J. Z. *Chem. Eur. J.* **2006**, *12*, 1475–1485.
1264. Liu, Q. Y.; Li, Y.; Liu, H. G.; Chen, Y. L.; Wang, X. Y.; Zhang, Y. X.; Li, X. Y.; Jiang, J. Z. *J. Phys. Chem. C* **2007**, *111*, 7298–7301.
1265. Jiang, J. Z.; Liu, W.; Cheng, K. L.; Poon, K. W.; Ng, D. K. P. *Eur. J. Inorg. Chem.* **2001**, 413–417.
1266. Jiang, J. Z.; Bian, Y. Z.; Furuya, F.; Liu, W.; Choi, M. T. M.; Kobayashi, N.; Li, H. W.; Yang, Q. C.; Mak, T. C. W.; Ng, D. K. P. *Chem. Eur. J.* **2001**, *7*, 5059–5069.
1267. Wang, R. M.; Li, Y.; Li, R. J.; Cheng, D. Y. Y.; Zhu, P. H.; Ng, D. K. P.; Bao, M.; Cui, X.; Kobayashi, N.; Jiang, J. Z. *Inorg. Chem.* **2005**, *44*, 2114–2120.
1268. Li, R. J.; Zhang, X. X.; Pan, N.; Zhu, P. H.; Kobayashi, N.; Jiang, J. Z. *J. Porphyr. Phthalocyan.* **2005**, *9*, 40–46.
1269. Zhang, Y.; Pan, N.; Xue, Q. B.; Bai, M.; Jiang, J. Z. *J. Porphyr. Phthalocyan.* **2006**, *10*, 1132–1139.
1270. Chen, Y. L.; Zhang, Y.; Zhu, P. H.; Fan, Y. J.; Bian, Y. Z.; Li, X. Y.; Jiang, J. Z. *J. Colloid. Interf. Sci.* **2006**, *303*, 256–263.
1271. Ishikawa, N.; Okubo, T.; Kaizu, Y. *Inorg. Chem.* **1999**, *38*, 3173–3181.
1272. Bian, Y. Z.; Li, L.; Wang, D. Q.; Choi, C. F.; Cheng, D. Y. Y.; Zhu, P. H.; Li, R. J.; Dou, J. M.; Wang, R. M.; Pan, N.; Ng, D. K. P.; Kobayashi, N.; Jiang, J. Z. *Eur. J. Inorg. Chem.* **2005**, 2612–2618.
1273. Liu, W.; Jiang, J. Z.; Pan, N.; Arnold, D. P. *Inorg. Chim. Acta* **2000**, *310*, 140–146.
1274. Zhu, P. H.; Pan, N.; Li, R. I. J.; Dou, J. M.; Zhang, Y.; Cheng, D. Y. Y.; Wang, D. Q.; Ng, D. K. P.; Jiang, J. Z. *Chem. Eur. J.* **2005**, *11*, 1425–1432.
1275. Li, R. J.; Ma, P.; Dong, S. H.; Zhang, X. Y.; Chen, Y. L.; Li, X. Y.; Jiang, J. Z. *Inorg. Chem.* **2007**, *46*, 11397–11404.
1276. Pan, N.; Bian, Y. Z.; Fukuda, T.; Yokoyama, M.; Li, R. J.; Neya, S.; Jiang, J. Z.; Kobayashi, N. *Inorg. Chem.* **2004**, *43*, 8242–8244.
1277. Gryko, D.; Li, J. Z.; Diers, J. R.; Roth, K. M.; Bocian, D. F.; Kuhr, W. G.; Lindsey, J. S. *J. Mater. Chem.* **2001**, *11*, 1162–1180.
1278. Moussavi, M.; Decian, A.; Fischer, J.; Weiss, R. *Inorg. Chem.* **1986**, *25*, 2107–2108.
1279. Arnold, D. P.; Jiang, J. Z. *Chem. Lett.* **1999**, 483–484.
1280. Abdurrahmanoğlu, S.; Özkaya, A. R.; Bulut, M.; Bekaroğlu, O. *Dalton Trans.* **2004**, 4022–4029.
1281. Ceyhan, T.; Korkmaz, M.; Erbil, M. K.; Bekaroğlu, O. *J. Porphyr. Phthalocyan.* **2005**, *9*, 423–429.
1282. Yoshiyama, H.; Shibata, N.; Sato, T.; Nakamura, S.; Toru, T. *Chem. Commun.* **2008**, 1977–1979.
1283. Kahnt, A.; Quintiliani, M.; Vázquez, P.; Guldi, D. M.; Torres, T. *ChemSusChem* **2008**, *1*, 97–102.

1284. Gouloumis, A.; González-Rodríguez, D.; Vázquez, P.; Torres, T.; Liu, S. G.; Echegoyen, L.; Ramey, J.; Hug, G. L.; Guldi, D. M. *J. Am. Chem. Soc.* **2006**, *128*, 12674–12684.
1285. Gouloumis, A.; Liu, S. G.; Vázquez, P.; Echegoyen, L.; Torres, T. *Chem. Commun.* **2001**, 399–400.
1286. Asano, Y.; Kobayashi, N. *Tetrahedron Lett.* **2004**, *45*, 9577–9580.
1287. Nemykin, V. N.; Koposov, A. Y.; Subbotin, R. I.; Sharma, S. *Tetrahedron Lett.* **2007**, *48*, 5425–5428.
1288. Yazıcı, A.; Ateş, D.; Bekaroğlu, O.; Kobayashi, N. *J. Porphyr. Phthalocyan.* **2006**, *10*, 1140–1144.
1289. Canlıca, M.; Altındal, A.; Özkaya, A. R.; Salih, B.; Bekaroğlu, O. *Polyhedron* **2008**, *27*, 1883–1890.
1290. Ceyhan, T.; Altındal, A.; Erbil, M. K.; Bekaroğlu, O. *Polyhedron* **2006**, *25*, 737–746.
1291. Odabaş, Z.; Altındal, A.; Özkaya, A. R.; Bulut, M.; Salih, B.; Bekaroğlu, O. *Polyhedron* **2007**, *26*, 695–707.
1292. Ceyhan, T.; Altındal, A.; Özkaya, A. R.; Çelikbiçak, O.; Salih, B.; Erbil, M. K.; Bekaroğlu, O. *Polyhedron* **2007**, *26*, 4239–4249.
1293. Bayo, K.; Bayo-Bangoura, M.; Mossoyan-Déneux, M.; Lexa, D.; Ouedraogo, G. V. *C. R. Chim.* **2007**, *10*, 482–488.
1294. Tolbin, A. Y.; Pushkarev, V. E.; Tomilova, L. G.; Zefirov, N. S. *Russ. Chem. B* **2006**, *55*, 1155–1158.
1295. Tolbin, A. Y.; Pushkarev, V. E.; Tomilova, L. G. *Mendeleev Commun.* **2008**, *18*, 94–95.
1296. Kobayashi, N.; Fukuda, T.; Lelièvre, D. *Inorg. Chem.* **2000**, *39*, 3632–3637.
1297. Makarov, S. G.; Suvorova, O. N.; Litwinski, C.; Ermilov, E. A.; Röder, B.; Tsaryova, O.; Dülcks, T.; Wöhrle, D. *Eur. J. Inorg. Chem.* **2007**, 546–552.
1298. Kobayashi, N.; Higashi, Y.; Osa, T. *J. Chem. Soc. Chem. Commun.* **1994**, 1785–1786.
1299. Kobayashi, N.; Ogata, H. *Eur. J. Inorg. Chem.* **2004**, 906–914.
1300. de la Torre, G.; Martínez-Díaz, M. V.; Ashton, P. R.; Torres, T. *J. Org. Chem.* **1998**, *63*, 8888–8893.
1301. Abd El-Ghaffar, M. A.; Youssef, E. A. M.; El-Halawany, N. R.; Ahmed, M. A. *Angew. Makromol. Chem.* **1998**, *254*, 1–9.
1302. Guldi, D. M.; Ramey, J.; Martínez-Díaz, M. V.; de la Escosura, A.; Torres, T.; Da Ros, T.; Prato, M. *Chem. Commun.* **2002**, 2774–2775.
1303. Ceyhan, T.; Korkmaz, M.; Kutluay, R.; Bekaroğlu, O. *J. Porphyr. Phthalocyan.* **2004**, *8*, 1383–1389.
1304. Quintiliani, M.; Kahnt, A.; Vázquez, P.; Guldi, D. M.; Torres, T. *J. Mater. Chem.* **2008**, *18*, 1542–1546.
1305. Blikova, Y. N.; Ivanov, A. V.; Tomilova, L. G.; Shvedene, N. V. *Russ. Chem. B* **2003**, *52*, 150–153.
1306. Ceyhan, T.; Altındal, A.; Özkaya, A. R.; Salih, B.; Erbil, M. K.; Bekaroğlu, O. *J. Porphyr. Phthalocyan.* **2007**, *11*, 625–634.
1307. Altun, S.; Altındal, A.; Özkaya, A. R.; Bulut, M.; Bekaroğlu, O. *Tetrahedron Lett.* **2008**, *49*, 4483–4486.
1308. Odabaş, Z.; Altındal, A.; Özkaya, A. R.; Bulut, M.; Salih, B.; Bekaroğlu, O. *Polyhedron* **2007**, *26*, 3505–3512.
1309. Ceyhan, T.; Altındal, A.; Özkaya, A. R.; Erbil, M. K.; Salih, B.; Bekaroğlu, Z. *Chem. Commun.* **2006**, 320–322.

1310. Özer, M.; Altındal, A.; Özkaya, A. R.; Salih, B.; Bulut, M.; Bekaroğlu, O. *Eur. J. Inorg. Chem.* **2007**, 3519–3526.
1311. Hanack, M.; Knecht, S.; Polley, R.; Subramanian, L. R. *Synthetic Met.* **1996**, *80*, 183–189.
1312. Donzello, M. P.; Bartolino, L.; Ercolani, C.; Rizzoli, C. *Inorg. Chem.* **2006**, *45*, 6988–6995.
1313. Nicolau, M.; Henry, C.; Martínez-Díaz, M. V.; Torres, T.; Armand, F.; Palacin, S.; Ruaudel-Teixier, A.; Wegner, G. *Synthetic Met.* **1999**, *102*, 1521–1522.
1314. Islyaikin, M. K.; Rodríguez-Morgade, M. S.; Torres, T. *Eur. J. Org. Chem.* **2002**, 2460–2464.
1315. Cabezón, B.; Rodríguez-Morgade, S.; Torres, T. *J. Org. Chem.* **1995**, *60*, 1872–1874.
1316. Armand, F.; Cabezón, B.; Martínez-Díaz, M. V.; Ruaudel-Teixier, A.; Torres, T. *J. Mater. Chem.* **1997**, *7*, 1741–1746.
1317. Romanenko, Y. V.; Danilova, E. A.; Khelevina, O. G.; Islyaikin, M. K. *Mendeleev Commun.* **2008**, *18*, 82–83.
1318. Martínez-Díaz, M. V.; Esperanza, S.; De la Escosura, A.; Catellani, M.; Yunus, S.; Luzzati, S.; Torres, T. *Tetrahedron Lett.* **2003**, *44*, 8475–8478.
1319. Díaz-García, M. A.; Ledoux, I.; Fernández-Lázaro, F.; Sastre, A.; Torres, T.; Agulló-López, F.; Zyss, J. *J. Phys. Chem.* **1994**, *98*, 4495–4497.
1320. de la Torre, G.; Torres, T. *J. Org. Chem.* **1996**, *61*, 6446–6449.
1321. Nicolau, M.; Cabezón, B.; Torres, T. *J. Org. Chem.* **2001**, *66*, 89–93.
1322. Islyaikin, M. K.; Danilova, E. A.; Yagodarova, L. D.; Rodríguez-Morgade, M. S.; Torres, T. *Org. Lett.* **2001**, *3*, 2153–2156.
1323. Kantar, C.; Ağar, E.; Şaşmaz, S. *Dyes Pigments* **2008**, *77*, 487–492.
1324. Korzhenevskii, A. B.; Markova, L. V.; Efimova, S. V.; Koifman, O. I.; Krylova, E. V. *Russ. J. Gen. Chem.* **2005**, *75*, 980–984.
1325. Kantekin, H.; Bıyıklıoğlu, Z. *Dyes Pigments* **2008**, *77*, 432–436.
1326. Bıyıklıoğlu, Z.; Kantekin, H. *Polyhedron* **2008**, *27*, 1650–1654.
1327. Bilgin, A.; Mendi, A.; Yıldız, U. *Polymer* **2006**, *47*, 8462–8473.
1328. Bilgin, A.; Yağcı, C.; Yıldız, U. *Macromol Chem. Phys.* **2005**, *206*, 2257–2268.
1329. Akdemir, N.; Ağar, E.; Şaşmaz, S.; Gümrükçüoğlu, I. E.; Çelebi, T. *Dyes Pigments* **2006**, *69*, 1–6.
1330. Ağar, E.; Şaşmaz, S.; Keskin, I.; Akdemir, N. *Dyes Pigments* **1998**, *36*, 249–258.
1331. Ağar, E.; Şaşmaz, S.; Keskin, I.; Karabulut, B. *Dyes Pigments* **1997**, *35*, 269–278.
1332. Alkan, C.; Aras, L.; Gündüz, G. *J. Appl. Polym. Sci.* **2007**, *106*, 378–385.
1333. Hanack, M.; Kamenzin, S.; Kamenzin, C.; Subramanian, L. R. *Synthetic Met.* **2000**, *110*, 93–103.
1334. Hanack, M.; Knecht, S.; Witke, E.; Haisch, P. *Synthetic Met.* **1993**, *55*, 873–878.
1335. Wei, H. H.; Shyu, H. L. *Polyhedron* **1985**, *4*, 979–981.

Index to Volume 9

T

U

V

W

Y

Z

Handbook of Porphyrin Science

with Applications to Chemistry, Physics, Materials Science, Engineering, Biology and Medicine

Volume 10

Catalysis and Bio-Inspired Systems

Karl M. Kadish ▪ Kevin M. Smith ▪ Roger Guilard

Editors

World Scientific

Handbook of Porphyrin Science

with Applications to Chemistry, Physics, Materials Science, Engineering, Biology and Medicine

This page intentionally left blank

Handbook of Porphyrin Science

with Applications to Chemistry, Physics, Materials Science, Engineering, Biology and Medicine

Volume 10

Catalysis and Bio-Inspired Systems

Part I

Editors

Karl M. Kadish
University of Houston, USA

Kevin M. Smith
Louisiana State University, USA

Roger Guilard
Université de Bourgogne, France

World Scientific

NEW JERSEY • LONDON • SINGAPORE • BEIJING • SHANGHAI • HONG KONG • TAIPEI • CHENNAI

Published by

World Scientific Publishing Co. Pte. Ltd.

5 Toh Tuck Link, Singapore 596224

USA office: 27 Warren Street, Suite 401-402, Hackensack, NJ 07601

UK office: 57 Shelton Street, Covent Garden, London WC2H 9HE

British Library Cataloguing-in-Publication Data
A catalogue record for this book is available from the British Library.

HANDBOOK OF PORPHYRIN SCIENCE
with Applications to Chemistry, Physics, Materials Science, Engineering, Biology and Medicine
(Volumes 6–10)

ISBN-13 978-981-4307-18-5 (Set)
ISBN-13 978-981-4307-23-9 (Vol. 10)

Typeset by Stallion Press
Email: enquiries@stallionpress.com

Printed in Singapore.

Contents

Preface

Although the porphyrin and tetrapyrrole research area was regarded as "fully matured" during the 20th century, as evidenced for example by the awarding of numerous Nobel Prizes to its principal researchers, new advances and accomplishments in the field still amaze us as editors. The area continues to blossom and to expand into new areas of science and applications that would probably never have occurred to our 20th century heroes. An earlier *Porphyrin Handbook* assembled the large amount of factual data that had been accumulated during the 20th century. Our new venture, the *Handbook of Porphyrin Science* takes a completely new look at our research area and comprehensively details the contemporary science now appearing in the scientific literature that would indeed have been hard to predict even 10 years ago. In particular, fundamentally new methodologies and potential commercial applications of the beautiful compounds that we all love are exemplified, fully recognizing the subtitle of the series — "with applications to chemistry, physics, materials science, engineering, biology and medicine".

The three of us have complementary expertise in physical chemistry, synthetic and bioorganic chemistry, and in synthetic and mechanistic organometallic chemistry; this has enabled us to cover the whole field of porphyrin science and applications, and to devise comprehensive volume and author content. As of the date of writing, between the three of us, we have published more than 1600 tetrapyrrole research articles, and hold 31 patents related to commercial applications of porphyrin science. So we do know our field, and this has enabled us to assemble a first-rate group of experts who have written comprehensive up-to-date chapters with accuracy and authority; we thank our authors for their cooperation and willingness to go along with our highly ambitious schedule for production of these volumes.

We look forward to comments from our readers, and to suggestions that might enable us to expand our basic interests and scientific coverage even further. Meanwhile, we hope that porphyrin researchers, old, new and of the future, will enjoy reading these volumes just as much as we enjoyed planning and, with the help of World Scientific Publishing Company, producing them from manuscript to published article, in a timely manner.

Karl M. Kadish (Houston, Texas, USA)
Kevin M. Smith (Baton Rouge, Louisiana, USA)
Roger Guilard (Dijon, Bourgogne, France)
January, 2010

This page intentionally left blank

Contributing Authors*

Hasrat Ali
Université de Sherbrooke
Sherbrooke, Québec, Canada
Chapter 16

Cristina Alonso
University of Hull
Kingston-upon-Hull, HU6 7RX, UK
Chapter 17

Edith Antunes
Rhodes University
Grahamstown, 6139, South Africa
Chapter 34

Naoki Aratani
Kyoto University
Kyoto 606-8502, Japan
aratani@kuchem.kyoto-u.ac.jp
Chapter 1

Teodor Silviu Balaban
Karlsruhe Institute of Technology
D-76021 Karlsruhe, Germany
Silviu.Balaban@int.fzk.de
Chapter 3

Alan L. Balch
University of California, Davis
Davis, CA 95616, USA
balch@chem.ucdavis.edu
Chapter 40

David P. Ballou
University of Michigan
Ann Arbor, MI 48109-5606, USA
Chapter 28

Faye Bowles
University of California, Davis
Davis, CA 95616, USA
Chapter 40

Ross W. Boyle
University of Hull
Kingston-upon-Hull, HU6 7RX, UK
r.w.boyle@hull.ac.uk
Chapter 17

Ozguncem Bozkulak
Childrens Hospital Los Angeles
Los Angeles, CA 90027, USA
Chapter 22

Martin Bröring
Technische Universität Carolo-Wilhelmina zu Braunschweig
Hagenring 30, Braunschweig, Germany
m.broering@tu-bs.de
Chapter 41

Kevin Burgess
Texas A&M University
College Station, TX 77842, USA
burgess@tamu.edu
Chapter 37

*Full contact information for authors can be found on the title page of each chapter.

José A.S. Cavaleiro
University of Aveiro
3810-193 Aveiro, Portugal
jcavaleiro@ua.pt
Chapter 9

Sung Cho
Yonsei University
Seoul, 120-747, Korea
Chapter 5

Daniel P. Collins
University of South Carolina
Columbia, SC 29208, USA
Chapter 28

John H. Dawson
University of South Carolina
Columbia, SC 29208, USA
dawson@mail.chem.sc.edu
Chapter 28

Ilia G. Denisov
The University of Illinois
Urbana, IL 61801, USA
Denisov@illinois.edu
Chapter 26

Charles Michael Drain
Hunter College of The City University of New York
New York, NY 10065, USA
cdrain@hunter.cuny.edu
Chapter 15

Francis D'Souza
Wichita State University
Wichita, KS 67260-0051, USA
Francis.DSouza@wichita.edu
Chapter 4

Florence Duclairoir
Institut Nanosciences et Cryogénie
38054 Grenoble cedex 9, France
Chapter 47

Manivannan Ethirajan
Roswell Park Cancer Institute
Buffalo, NY 14263, USA
Chapter 19

Alessandro Feis
University of Florence
I-50019 Sesto Fiorentino, Italy
Chapter 31

Angela Ferrario
Childrens Hospital Los Angeles
Los Angeles, CA 90027, USA
Chapter 22

Kimberly B. Fields
University of South Florida
Tampa, FL 33620, USA
Chapters 13, 43

Takamitsu Fukuda
Osaka University
Toyonaka 560-0043, Japan
tfukuda@chem.sci.osaka-u.ac.jp
Chapter 42

Shunichi Fukuzumi
Osaka University
Suita, Osaka 565-0871, Japan
fukuzumi@chem.eng.osaka-u.ac.jp
Chapter 46

Hiroyuki Furuta
Kyushu University
Fukuoka 819-0395, Japan
hfuruta@cstf.kyushu-u.ac.jp
Chapter 10

Jean-Paul Gisselbrecht
Université de Strasbourg
67000 Strasbourg, France
gissel@unistra.fr
Chapter 14

Charles J. Gomer
University of Southern California
Los Angeles, CA 90027, USA
Chapter 22

Bruno Grimm
Friedrich-Alexander-University Erlangen-Nuremberg
91058 Erlangen, Germany
Chapter 2

Dirk M. Guldi
Friedrich-Alexander-University Erlangen-Nuremberg
91058 Erlangen, Germany
dirk.guldi@chemie.uni-erlangen.de
Chapter 2

Anita Hausmann
Friedrich-Alexander-University Erlangen-Nuremberg
91058 Erlangen, Germany
Chapter 2

Takashi Hayashi
Osaka University
Suita 565-0871, Japan
thayashi@chem.eng.osaka-u.ac.jp
Chapter 23

Petra Hellwig
Université de Strasbourg
67000 Strasbourg, France
hellwig@chimie.u-strasbg.fr
Chapter 36

Yoshio Hisaeda
Kyushu University
Fukuoka 819-0395, Japan
yhisatcm@mail.cstm.kyushu-u.ac.jp
Chapter 48

Barry D. Howes
University of Florence
I-50019 Sesto Fiorentino, Italy
Chapter 31

Akira Ikezaki
Toho University
Ota-ku, Tokyo 143-8540, Japan
Chapter 32

Osamu Ito
Tohoku University
Sendai, 981-3215, Japan
Chapter 4

Anabella Ivancich
Centre Nationale de la Recherche Scientifique (URA 2096)
F-91191 Gif-sur-Yvette, France
Chapter 31

Christophe Jeandon
Université de Strasbourg
67000 Strasbourg, France
cjeandon@unistra.fr
Chapter 14

Norbert Jux
Universität Erlangen-Nürnberg
91054 Erlangen, Germany
norbert.jux@chemie.uni-erlanger.de
Chapter 20

Axel Kahnt
Friedrich-Alexander-University Erlangen-Nuremberg
91058 Erlangen, Germany
Chapter 2

David Kessel
Wayne State University School of Medicine
Detroit, MI 48201, USA
dhkessel@med.wayne.edu
Chapter 21

Dongho Kim
Yonsei University
Seoul, 120-747, Korea
dongho@yonsei.ac.kr
Chapters 5, 6

Kil Suk Kim
Yonsei University
Seoul, 120-747, Korea
Chapter 6

Nagao Kobayashi
Tohoku University
Sendai 980-8578, Japan
nagaok@mail.tains.tohoku.ac.jp
Chapters 33, 42

Lechosław Latos-Grażyński
University of Wrocław
Wrocław 50 383, Poland
llg@wchuwr.pl
Chapter 8

Genxi Li
Nanjing University
Nanjing 210093, PR China
genxili@nju.edu.cn
Chapter 27

Jong Min Lim
Yonsei University
Seoul, 120-747, Korea
Chapter 6

Aurore Loudet
Texas A&M University
College Station, TX 77842, USA
Chapter 37

Evgeny A. Lukyanets
Organic Intermediates and Dyes Institute
Moscow, 123995, Russia
rmeluk@niopik.ru
Chapter 11

Marian Luna
Childrens Hospital Los Angeles
Los Angeles, CA 90027, USA
Chapter 22

Hiromitsu Maeda
Ritsumeikan University
Kusatsu 525-8577, Japan
maedahir@ph.ritsumei.ac.jp
Chapter 38

Jean-Claude Marchon
Institut Nanosciences et Cryogénie
38054 Grenoble cedex 9, France
jean-claude.marchon@cea.fr
Chapter 47

M. Victoria Martínez-Díaz
Universidad Autónoma de Madrid
28049-Madrid, Spain
Chapter 45

Frederic Melin
Université de Strasbourg
67000 Strasbourg, France
Chapter 36

Shingo Nagano
Tottori University
Tottori 680-8552, Japan
Chapter 25

Mikio Nakamura
Toho University
Ota-ku, Tokyo 143-8540, Japan
mnakamu@med.toho-u.ac.jp
Chapter 32

Wonwoo Nam
Ewha Womans University
Seoul 120-750, South Korea
wwnam@ewha.ac.kr
Chapter 44

Victor N. Nemykin
University of Minnesota Duluth
Duluth, MN 55812, USA
vnemykin@d.umn.edu
Chapter 11

Maria G.P.M.S. Neves
University of Aveiro
3810-193 Aveiro, Portugal
Chapter 9

Tebello Nyokong
Rhodes University
Grahamstown, 6139, South Africa
t.nyokong@ru.ac.za
Chapter 34

Yoshiki Ohgo
Toho University
Ota-ku, Tokyo 143-8540, Japan
Chapter 32

Tetsuo Okujima
Ehime University
Matsuyama 790-8577, Japan
Chapter 7

Noboru Ono
Ehime University
Matsuyama 790-8577, Japan
ononbr@dpc.ehime-u.ac.jp
Chapter 7

Atsuhiro Osuka
Kyoto University
Kyoto 606-8502, Japan
osuka@kuchem.kyoto-u.ac.jp
Chapter 1

Ravindra K. Pandey
Roswell Park Cancer Institute
Buffalo, NY 14263, USA
ravindra.pandey@roswellpark.org
Chapter 19

Nayan J. Patel
Roswell Park Cancer Institute
Buffalo, NY 14263, USA
Chapter 19

Miłosz Pawlicki
University of Wrocław
Wrocław 50 383, Poland
Chapter 8

Sébastien Richeter
Université Montpellier 2
34095 Montpellier Cedex 5, France
sebastien.richeter@univ-montp2.fr
Chapter 14

Beate Röder
Humboldt-Universität zu Berlin
12489 Berlin, Germany
roeder@physik.hu-berlin.de
Chapter 20

Natalie Rucker
Childrens Hospital Los Angeles
Los Angeles, CA 90027, USA
Chapter 22

Joshua V. Ruppel
University of South Florida
Tampa, FL 33620, USA
Chapters 13, 43

Romain Ruppert
Université de Strasbourg
67000 Strasbourg, France
rruppert@unistra.fr
Chapter 14

Aoife Ryan
Trinity College Dublin
Dublin 2, Ireland
Chapter 12

Wolfgang Seitz
Friedrich-Alexander-University
Erlangen-Nuremberg
91058 Erlangen, Germany
Chapter 2

Mathias O. Senge
Trinity College Dublin
Dublin 2, Ireland
sengem@tcd.ie
Chapter 12

Natalia N. Sergeeva
Trinity College Dublin
Dublin 2, Ireland
Chapter 12

Hisashi Shimakoshi
Kyushu University
Fukuoka 819-0395, Japan
Chapter 48

Jae-Yoon Shin
Yonsei University
Seoul, 120-747, Korea
Chapter 6

Yoshitsugu Shiro
Harima Institute
Hyogo 679-5148, Japan
yshiro@riken.jp
Chapters 24, 25

Martha Sibrian-Vazquez
Portland State University
Portland, OR 97201, USA
Chapter 18

Sunaina Singh
Hunter College of The City University of
New York
New York, NY 10065, USA
Chapter 15

Stephen G. Sligar
The University of Illinois
Urbana, IL 61801, USA
s-sligar@uiuc.edu
Chapter 26

Giulietta Smulevich
University of Florence
I-50019 Sesto Fiorentino, Italy
giulietta.smulevich@unifi.it
Chapter 31

Nicole L. Snyder
Hamilton College
Clinton, NY 13323, USA
Chapters 13, 43

Fabian Spänig
Friedrich-Alexander-University Erlangen-Nuremberg
91058 Erlangen, Germany
Chapter 2

Tatyana Spolitak
University of Michigan
Ann Arbor, MI 48109-5606, USA
Chapter 28

Hiroshi Sugimoto
Harima Institute
Hyogo 679-5148, Japan
Chapter 24

Osamu Takikawa
National Center for Geriatrics and Gerontology
Obu, Aichi 474-8522, Japan
Chapter 24

Alison Thompson
Dalhousie University
Halifax, Nova Scotia, Canada
alison.thompson@dal.ca
Chapter 39

Motoki Toganoh
Kyushu University
Fukuoka 819-0395, Japan
Chapter 10

Augusto C. Tomé
University of Aveiro
3810-193 Aveiro, Portugal
Chapter 9

Tomas Torres
Universidad Autónoma de Madrid
28049-Madrid, Spain
tomas.torres@uam.es
Chapter 45

Paola Turano
University of Florence
I-50019 Sesto Fiorentino, Italy
turano@cerm.unifi.it
Chapter 30

Md. Imam Uddin
Dalhousie University
Halifax, Nova Scotia, Canada
Chapter 39

Johan E. van Lier
Université de Sherbrooke
Sherbrooke, Québec, Canada
Johannes.Van.Lier@USherbrooke.ca
Chapter 16

Maria da Graça H. Vicente
Louisiana State University
Baton Rouge, LA 70803, USA
vicente@lsu.edu
Chapter 18

Sam P. de Visser
The University of Manchester
Manchester M1 7DN, UK
sam.devisser@manchester.ac.uk
Chapter 44

F. Ann Walker
University of Arizona
Tucson, AZ 85721-0041, USA
awalker@email.arizona.edu
Chapter 29

Jacek Waluk
Polish Academy of Sciences
01-224 Warsaw, Poland
waluk@ichf.edu.pl
Chapter 35

Sam Wong
Childrens Hospital Los Angeles
Los Angeles, CA 90027, USA
Chapter 22

Tabitha E. Wood
Dalhousie University
Halifax, Nova Scotia, Canada
Chapter 39

Frank Xu
Childrens Hospital Los Angeles
Los Angeles, CA 90027, USA
Chapter 22

Hiroko Yamada
Ehime University
Matsuyama 790-8577, Japan
Chapter 7

Jaesung Yang
Yonsei University
Seoul, 120-747, Korea
Chapter 5

Hyejin Yoo
Yonsei University
Seoul, 120-747, Korea
Chapter 5

Min-Chul Yoon
Yonsei University
Seoul, 120-747, Korea
Chapter 6

Zin Seok Yoon
Yonsei University
Seoul, 120-747, Korea
Chapter 5

X. Peter Zhang
University of South Florida
Tampa, FL 33620, USA
pzhang@cas.usf.edu
Chapters 13, 43

Contents of Volumes 1–10

Volume 1 Supramolecular Chemistry

Volume 2 Synthesis and Coordination Chemistry

Volume 3 Synthetic Methodology

Volume 4 Phototherapy, Radioimmunotherapy and Imaging

Volume 5 Heme Proteins

Volume 6 NMR and EPR Techniques

Volume 7 Physicochemical Characterization

Volume 8 Open-Chain Oligopyrrole Systems

Volume 9 Electronic Absorption Spectra — Phthalocyanines

Volume 10 Catalysis and Bio-Inspired Systems — Part I

This page intentionally left blank

43 Metalloporphyrin-Catalyzed Asymmetric Atom/Group Transfer Reactions

Joshua V. Ruppel,* Kimberly B. Fields,* Nicole L. Snyder† and X. Peter Zhang*

*Department of Chemistry, University of South Florida, Tampa, FL 33620, USA
†Department of Chemistry, Hamilton College, Clinton, NY 13323, USA

I. Introduction

Metalloporphyrins have been shown to catalyze many fundamental and practically important chemical transformations in biological systems and in the chemical laboratory. The most notable examples have been accomplished using metalloporphyrin complexes inspired by biology. These complexes have been used to perform atom/group transfer reactions including oxene, nitrene, and carbene transfers, which in turn have provided chemists with direct access to complex and functionally diverse compounds from abundant and inexpensive alkenes and alkanes.

In an effort to improve the catalytic ability and specificity of these "synthetic enzymes", researchers have focused on the synthesis of "designed" complexes that are based on well-defined biological/chemical scaffolds. These complexes, which incorporate chiral peripheries into the metalloporphyrin framework, have provided researchers with scaffolds to directly manipulate the stereoselectivity of the reaction system. Three methodologies for synthesizing these derivatives have been developed: (1) porphyrins formed through the classical condensation of chiral aldehydes with pyrrole; (2) porphyrins formed through substitution of amino- and hydroxyl-substituted tetraphenylporphyrins with chiral building blocks; and (3) bridging of the enantiotropic faces of prochiral porphyrins to afford a chiral environment. The porphyrins prepared by these three methods have provided important information regarding the type of chiral environment required to induce enantioselectivity when used as catalysts. The trends indicate that the more rigid the chiral environment, the greater the catalytic stability and the slower the intramolecular decomposition. This in turn provides for a longer catalytic lifetime and higher turnover numbers (TON). On the other hand, more flexible substituents are more vulnerable to degradation, such as oxidation of the porphyrin periphery, and produce products with decreased enantioselectivity.

The chiral units' proximity to the active center constitutes an important observable trend. Chiral units that are far away provide less chiral induction as the approach of the incoming substrate is not substantially affected by the peripheral chiral environment. On the other hand, chiral units that are too close to the metal center often suffer from decomposition as the chiral environment itself becomes the substrate and is then compromised.

Chiral proximity also plays a role in the enantioselectivity observed with substrates of different sizes and shapes, although the specific requirements are not always as well defined or easy to define. This constraint has led some research groups to incorporate a modular design with steric environments that can be systematically modified to best suit each type of substrate.

The modification and design of porphyrin ligands to create chiral environments has led to a diverse array of catalysts. To categorize these chiral ligands, the

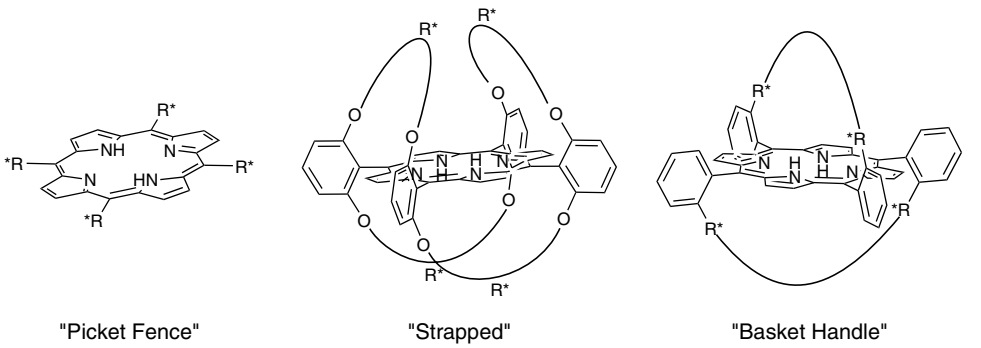

Figure 1. Examples of "picket fence", "strapped", and "basket handle" type porphyrin scaffolds.[1]

classification system outlined by Collman and coworkers in 1993 will be used.[1] In this system, chiral porphyrins (Por*) are categorized by class: "picket fence", "strapped", and "basket handle" (Figure 1).

The picket fence class contains porphyrin ligands with chiral units (R*) around the perimeter of the porphyrin ring, but without connections between adjacent or opposite functionalities. Chiral groups can be connected directly to the *meso*- or *beta*-positions or attached to the *meso*-aryl positions in a wide range of orientations.

The strapped and basket handle classes are categorized by the positions of the chiral units bridged around the porphyrin perimeter above and below the porphyrin plane. The major difference between the two classes is the orientation of the chiral bridge. Chiral bridges that connect adjacent positions (e.g., the 5,10-positions) are considered strapped. Chiral bridges connecting opposite positions (e.g., the 10,20-positions) are categorized as basket handle.

This chapter will review the major advancements in asymmetric atom/group transfer reactions utilizing metalloporphyrin catalysts, specifically the asymmetric epoxidation, cyclopropanation, and aziridination of alkenes. Several reports of various forms of C–H functionalization will also be discussed. These works will be organized by ligand class and the literature covers the period through July 2009.

II. Epoxidation

Early work on epoxidation was developed out of studies on cytochrome P-450, a heme-containing monooxygenase, which catalyzes the incorporation of oxygen from molecular dioxygen into organic substrates.[2] Simple mimics based on iron, manganese, chromium, and ruthenium metalloporphyrin frameworks have been

developed to convert alkenes, alkanes, and aromatic hydrocarbons into valuable commodity chemicals in a controlled and selective fashion.[3] A variety of oxidants have been employed for these systems; including molecular dioxygen, hydroperoxides, peroxyacids, NaOCl, N_2O, and iodosylbenzene (PhIO) and its derivatives.[3] These oxidants have been used to produce high-valent metal intermediates in an effort to replace existing auto-oxidation technologies[4] allowing for stereocontrol of the products.

In 1976, Ullrich and coworkers demonstrated that cytochrome P-450 could catalyze oxygenation reactions through an alternate pathway known as the "peroxide shunt".[5] This pathway allows for the use of exogenous oxygen sources such as PhIO which opened the door to the exploration of alternative oxidants. The mechanistic aspects of these processes will not be covered in this chapter, as they have been extensively addressed by others.[6–8]

Following Ullrich, Groves and coworkers showed that a number of single-oxygen donors, including hydroperoxides, peroxy acids, and PhIO could be used with metalloporphyrin enzyme mimics to perform oxygen transfer in a manner similar to the fully reconstituted enzyme system.[9,10] For example, the combination of 5,10,15,20-tetraphenylporphinatoiron(III) chloride [Fe(TPP)Cl], and PhIO was used to transfer oxygen to alkenes and alkanes to form epoxides and hydroxides, respectively. Groves and coworkers established that there were dramatic differences in both yield and selectivity between porphyrins with peripheral variations, suggesting that the ligand environment was as intimately involved in the oxygen transfer step as the transition metal ion. Their work provided a foundation for tuning the selectivity and reactivity of metalloporphyrin catalysts through alteration of the porphyrin periphery.[11] Subsequent work by Lindsay-Smith and coworkers illustrated the importance of having a sterically bulky porphyrin periphery to interrupt μ-oxo dimer formation while leaving the metal center open to the approach of the olefin into the active site.[12]

Although the capability of these metalloporphyrins to mimic the oxo-transferase ability of cytochrome P-450 using nonbiological oxidants was impressive, initial catalysts suffered from rapid decomposition of the macrocycle, particularly for porphyrins with open *meso*-positions.[3] Groves and coworkers typically reported TONs for epoxidation and hydroxylation of approximately 10 or less, prompting research into the production of catalysts with greater stability.[13] As a result, electron-withdrawing groups were incorporated onto the macrocycle to increase the stability of the porphyrin. Continued efforts by Chang and Ebina[14] and then later by Traylor and coworkers[15] eventually produced metalloporphyrin catalysts that were capable of effectively epoxidizing alkenes in up to 10,000 TON.

Additional insight for improving metalloporphyrin catalysis was provided by studies on metallosalens, close relatives of porphyrins. The salen architecture offers the advantage of two chiral sp^3-hybridized carbons at the periphery within close proximity to the active metal center.[1] Salens have been shown to be highly effective catalysts for asymmetric epoxidation. In addition to the use of iodosylarenes, the effective use of more practical, inexpensive, oxidants such as sodium hypochlorite (bleach) and molecular dioxygen have made these catalysts especially appealing.[16–27]

Several salens capable of providing greater than 90% enantiomeric excess of *cis*-substituted alkenes have been reported in the literature.[18,28] The major drawback of these complexes is based on the susceptibility of the catalyst to oxidative decomposition. As a consequence, metallosalens typically have low TON (<40). However, the degradation products are generally inactive, thus the products of the reaction remain uncompromised.[1] The development of a catalytic asymmetric epoxidation system that could match the selectivities of the reported salen systems with the stability and high TON typically reported for metalloporphyrin-catalyzed epoxidation systems would combine the best attributes of both systems to produce the "ideal" epoxidation catalyst.

This section will cover metalloporphyrin-catalyzed epoxidation reactions and, more specifically, investigations into the enantioselectivity of the products generated by these catalysts with a detailed overview of the major contributions to this field.

A. Chiral Picket Fence Porphyrins

Groves and Myers published the first metalloporphyrin-catalyzed asymmetric epoxidation system in 1983.[10] Utilizing a similar scaffold developed by Collman and coworkers for investigating the binding of molecular oxygen to ferrous porphyrinates,[29] Groves and Myers synthesized an $\alpha,\beta,\alpha,\beta$-atropisomer with chiral moieties directed toward the iron metal center (Figure 2). The resulting chiral iron porphyrin contained identical chiral faces, each consisting of two chiral groups. They evaluated the ability of this picket fence porphyrin **1** to epoxidize styrene using PhIO and found that styrene oxide was produced in 65% yield with a moderate enantioselectivity of 31% ee (entry 1, Table 1). The $\alpha,\alpha,\beta,\beta$-isomer **2** and the $\alpha,\alpha,\alpha,\alpha$-$\mu$-oxo-dimer **3** generated racemic products when evaluated under the same conditions (entries 2–3, Table 1).

These results prompted the use of a binaphthyl chiral appendage using the same porphyrin scaffold (Figure 3) in the hopes of generating a relatively large and rigid chiral cavity around the iron center. The resulting chiral porphyrin **4** was

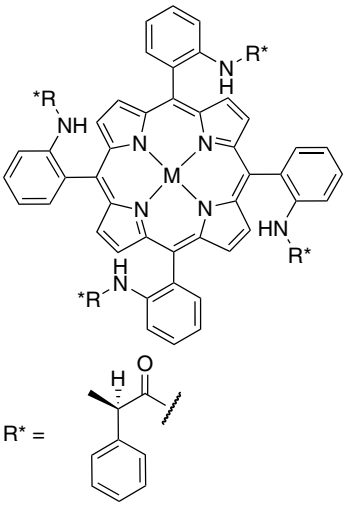

Figure 2. [Fe(HydPP)Cl].[10]

Table 1. Asymmetric epoxidation catalyzed by atropic isomers of [Fe(HydPP)Cl].[10]

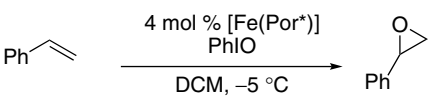

Entry[a]	[Fe(Por*)][b]	Yield (%)[c]	ee (%)
1	[Fe(**1**)Cl]	65	31(*R*)
2	[Fe(**2**)Cl]	99	0
3	[Fe(**3**)]$_2$O	93	0

[a] Reactions were performed using 4 mol % of [Fe(Por*)] with 1 equiv. of PhIO as oxidant and 3 equiv. of styrene in DCM. Over a period of 3 hours the oxidant was added at an average temperature of –5 °C and was stirred for an additional 45 mins; [b] See Figure 2; [c] Based upon consumed PhIO.

evaluated for epoxidation using iodosylmesitylene as the oxidant and as little as 0.625 mol % catalyst loading. The epoxidation of styrene, along with other olefins, proceeded in moderate yields (58–75%) and enantioselectivity (15–51% ee) (Table 2). However, Groves and Myers noted the activity of the metalloporphyrin diminished after 100 catalytic cycles. Presumably, the oxidation of the porphyrin

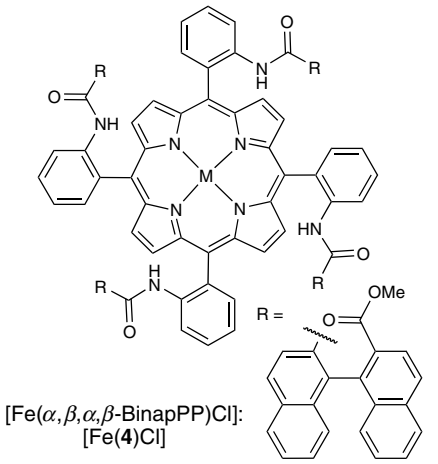

Figure 3. [Fe(**4**)Cl] picket fence catalyst.[10]

Table 2. Asymmetric epoxidation of aromatic olefins catalyzed by [Fe(**4**)Cl].[10]

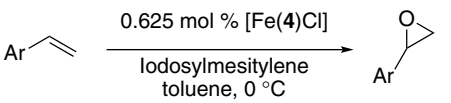

Entry[a]	Substrate	Yield (%)[b]	ee (%)
1	Styrene	67	48 (*R*)(+)
2[c]	4-Chlorostyrene	63	51 (+)
3	4-Methylstyrene	75	43 (+)
4	4-Nitrostyrene	—	36 (+)
5	2-Methylstyrene	58	15 (–)
6	2-Vinylnaphthalene	—	36 (+)

[a] Reactions were performed in a manner similar to that those described in Table 1; [b] Based upon consumed iodosylmesitylene; [c] Performed at –23 °C.

led to unfavorable changes in either the conformation or the electronic properties of the catalyst.

Several years after Groves and Myers seminal work on metalloporphyrin-catalyzed epoxidation, Paolesse and coworkers synthesized chiral porphyrin **5** containing camphanylamido groups on the *ortho*-positions of the *meso*-aryl groups (Scheme 1).[30] The subsequent catalyst [Fe(**5**)Cl] was used to generate

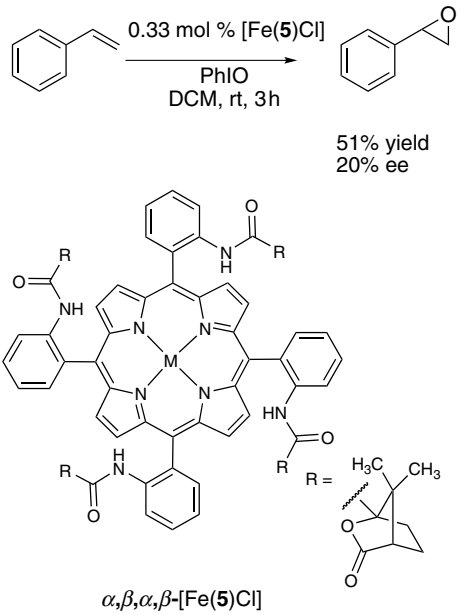

Scheme 1.[30]

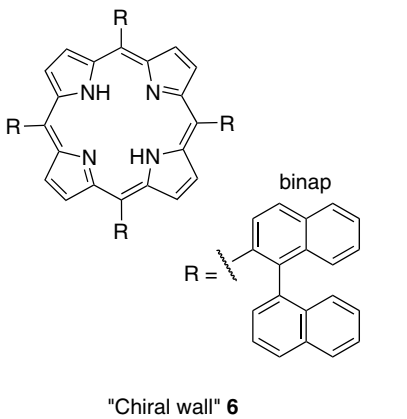

Figure 4. "Chiral wall" porphyrin.[31]

styrene oxide from styrene (5 equivalents) in moderate yields and 20% ee at room temperature in the presence of PhIO.

The binaphthyl group was also used as the chiral moiety by O'Malley and Kodadek in an effort to address catalytic stability.[31] Using the manganese complex of what they termed the "chiral wall" (**6**, Figure 4), the epoxidation of styrene and

Table 3. Asymmetric epoxidation of aromatic olefins catalyzed by [Mn(**6**)Cl].[31]

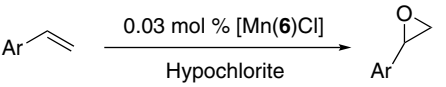

Entry[a]	Substrate	Catalytic efficiency[b]	ee (%)
1	Styrene	240	20
2	4-Chlorostyrene	160	20
3	2-Vinylnaphthalene	220	20
4	*trans*-β-Methylstyrene	190	15
5[c]	*cis*-β-Methylstyrene	200	40

[a] Reactions were performed with 0.03 mol % of catalyst with hypochlorite as oxidant; [b] Number of turnovers in 15 min; [c] 7:1 (*cis:trans*).

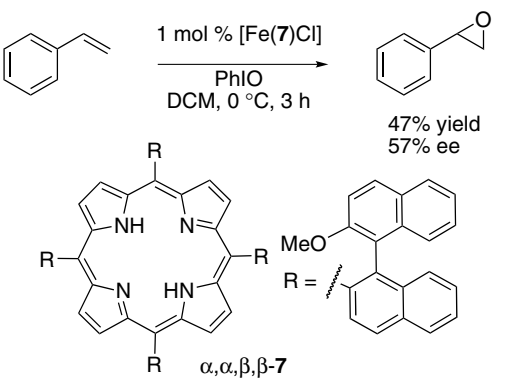

Scheme 2.[32]

several styrene derivatives was accomplished with moderate enantioselectivity (15–40% ee) using hypochlorite and only 0.03 mol % of catalyst to produce the corresponding styrene oxides (Table 3). "Chiral wall" porphyrin **6** was also shown to be quite stable, inducing the same enantioselectivities after several hundred catalytic turnovers (Table 3).

Several years after Kodadek's first report of the "chiral wall" catalyst, Salvadori and coworkers published results based on iron and manganese complexes of a similar ligand **7** (Scheme 2) for epoxidation.[32] The atropisomers of porphyrin **7** were prepared and evaluated for their ability to epoxidize styrene in an asymmetric fashion. Overall, the iron complex of the $\alpha,\alpha,\beta,\beta$-atropisomer [Fe(**7**)Cl] was found to provide the highest asymmetric induction (Scheme 2). It is also worth noting the differences in selectivities produced when different metals were

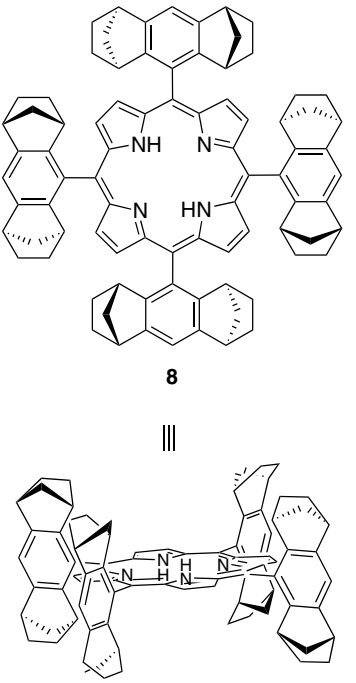

Figure 5. Halterman's D_4-symmetric porphyrin.[33]

used with $\alpha,\beta,\alpha,\beta$-porphyrin **7**: the resulting enantioselectivities of the manganese and iron complexes were 8 and 48% ee, respectively.

In 1991, Halterman and Jan published the synthesis and evaluation of a D_4-symmetric porphyrin **8** (Figure 5).[33] The Halterman porphyrin **8** has become one of the most investigated porphyrin-based catalyst not only for epoxidation but also for other atom/group transfer reactions that will be discussed later in this chapter. Halterman and coworkers reported the use of [Mn(**8**)Cl] with 4-*tert*-butylpyridine as an axial ligand for the epoxidation of styrene derivatives with Clorox® bleach.[34] Under these reaction conditions, high yields and moderate to good enantioselectivities were observed within hours (Table 4). Halterman and coworkers also reported the synthesis and evaluation of several derivatives of **8**. However, the reactivity and selectivity of these systems were either comparable to or lower than the manganese complex of **8**.[35]

One of the remarkable features of this reaction is the use of excess oxidant without adverse side reactions. In most oxidation systems, the oxidant is used as the limiting reagent and a large excess of substrate is used to consume the oxidant quickly to avoid poisoning the catalyst. Using commercially available Clorox® bleach, this catalyst performed well when a 3% sodium hypochlorite

Table 4. Asymmetric epoxidation of aromatic alkenes catalyzed by [Mn(**8**)Cl].[34]

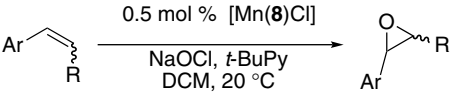

Entry[a]	Substrate	Time (h)	Yield (%)	ee (%)
1	Styrene	1	90	52 (*S*)
2	1,2-Dihydronaphthalene	1	97	56 (1*R*,2*S*)
3	Indene	1	98	41 (1*R*,2*S*)
4	*cis*-β-Methylstyrene	4	91 (*cis*)	76 (1*R*,2*S*)
			7 (*trans*)	34 (1*S*,2*S*)
5	*trans*-β-Methylstyrene	8	40	4 (1*R*,2*R*)
6	*trans*-β-Phenylstyrene	8	73	10 (1*S*,2*S*)
7	α-Methylstyrene	1	98	6 (*R*)

[a] Reactions were performed with 0.5 mol % of catalyst with 0.5 mol % of *t*-BuPy and 1 equiv. of substrate in a mixture of bleach (2.5 ml) and DCM (2 ml).

aqueous/DCM medium was employed in the presence of as little as 0.05 mol % of catalyst loading.

The use of the Mn(III) chloride complex of the Halterman porphyrin **8** was further studied by Chang and coworkers using Oxone® ($KHSO_5$) and *cis*-β-methylstyrene.[36] In their work, various axial ligands were employed to evaluate the potential *trans* effect on the yield and selectivity of the catalytic epoxidation reaction (Table 5). Although not as effective as Halterman's original catalytic system (entry 4, Table 4), a significant increase in enantiomeric excess was observed when DMAP was employed as the axial ligand (entry 13, Table 5).

Epoxidation employing [Ru(**8**)$(O)_2$] was first investigated by Che and coworkers for the stoichiometric epoxidation of styrene.[37] Moderate yields and enantioselectivities were obtained using styrene as the substrate (Scheme 3). The authors also reported the epoxidation reaction under catalytic conditions with dioxygen as the oxidant (8 atm), generating the desired product with low TON (10) and moderate enantioselectivity (70% ee) (Scheme 3). The authors commented that higher TON and enantioselectivity should be accessible with the optimization of these reaction conditions.

In a separate report, Che and coworkers explored the effects of solvent on the catalytic process with [Ru(**8**)(CO)].[38] The epoxidation of styrene derivatives in either benzene or dichloromethane using [Ru(**8**)(CO)] and PhIO was found to have little effect on the enantioselectivity of the catalytic process (entries 1 and 2, Table 6). Che and coworkers went on to evaluate both

Table 5. Effect of axial ligand on the asymmetric epoxidation of *cis*-β-methylstyrene catalyzed by [Mn(**8**)Cl].[36]

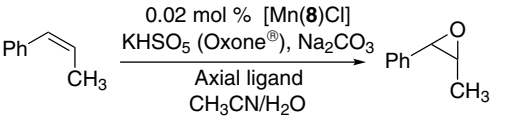

Entry[a]	Axial ligand	Conversion (%)	*cisl trans*	ee (%, cis)
1	—	60	21.3	43
2	Quinoline	24	18.9	25
3	3-Bromopyridine	24	29.6	29
4	4-Chloropyridine	28	10.6	31
5	4-Cyanopyridine	22	17.3	37
6	Pyridine	6	8.0	38
7	4-Phenylpyridine	50	14.0	61
8	4-*tert*-Butylpyridine	18	12.0	65
9	4-Methoxypyridine	30	12.8	69
10	Piperidine	7	25.2	71
11	1,2-Dimethylimidazole	24	10.3	72
12	Pyrrolidine	12	18.2	75
13	DMAP	79	6.4	81

[a] Procedure for oxidation: Oxone® (1 equiv.) and $NaHCO_3$ were dissolved in deionized water, followed by the substrate (1 equiv.), 0.1 mol % of axial ligand, and 0.02 mol % of catalyst in acetonitrile. The mixture was stirred overnight.

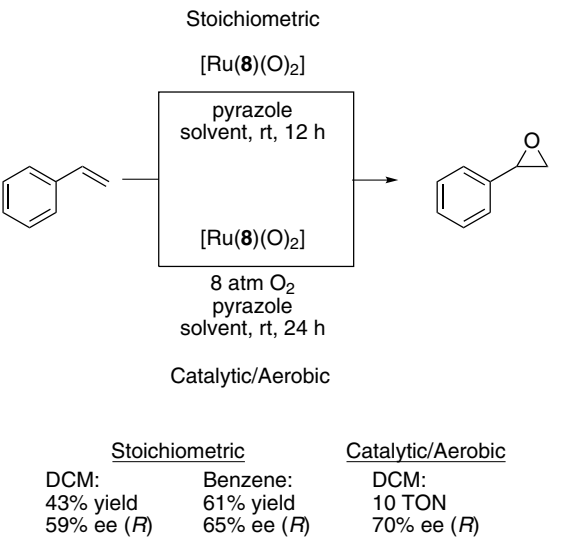

Scheme 3.[37]

Table 6. Asymmetric epoxidation of aromatic alkenes catalyzed by [Ru(**8**)(CO)] and [Ru(**8**)$(O)_2$].[38]

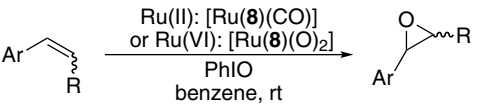

Entry	Substrate	Catalyst	Yield (%)	ee (%)
1	Styrene	Ru(II)	57	63 (*R*)
2	Styrene	Ru(II)[a]	71	55 (*R*)
3	Styrene	Ru(VI)[a]	52	51 (*R*)
4	4-Methylstyrene	Ru(II)	35	40
5	4-Methylstyrene	Ru(VI)[a]	41	38
6	4-Chlorostyrene	Ru(II)	66	51
7	3-Nitrostyrene	Ru(II)	40	52
8	*cis*-β-Methylstyrene	Ru(II)	52[b]	52 (1*R*,2*S*)
9	*cis*-β-Methylstyrene	Ru(VI)[a]	53[c]	55 (1*R*,2*S*)
10	1,2-Dihydronaphthalene	Ru(II)	46	62
11	*trans*-β-Methylstyrene	Ru(II)	41	17 *trans*
12	*trans*-β-Methylstyrene	Ru(VI)[a]	31	13 *trans*
13	Cyclohexenylbenzene	Ru(II)[a]	55	8
14	Cyclohexenylbenzene	Ru(VI)[a]	61	7

[a] Performed in DCM; [b] *cis:trans* = 6.3; [c] *cis:trans* = 11.

[Ru(**8**)(CO)] and [Ru(**8**)$(O)_2$] as catalysts for the epoxidation of styrene derivatives (Table 6). The [Ru(**8**)(CO)] was found to be slightly more selective than [Ru(**8**)$(O)_2$] (entries 2 and 3, Table 6), although this trend was not observed with all styrene derivatives.

In their continued effort to develop ruthenium complexes of the Halterman porphyrin **8**, Che and coworkers published the synthesis and evaluation of [Ru(**8**)Cl_2] in 2001.[39] For these reactions, 2,6-dichloropyridine-*N*-oxide (Cl_2pyNO) was used as oxidant with 1 mol % catalyst in benzene to generate moderate yields and enantioselectivities with high TON, typically greater than 800 (Table 7). This system was shown to be capable of catalyzing a wide range of substrates, including mono- and di-substituted olefins, having various steric and electronic properties (Table 7). To evaluate the stability of this catalytic system, [Ru(**8**)Cl_2] was reused in four consecutive runs, and it was observed that product conversion diminished with each consecutive run. Through characterization and the analysis of the catalyst after the reaction, it was determined that a new Ru(CO) complex, generated *in situ*, was suspected to be responsible for the decreased efficiency of the catalyst.

Another strategy employed to increase the catalytic turnover was the incorporation of the ruthenium porphyrin complex into sol-gel to produce a heterogeneous

Table 7. Asymmetric epoxidation of olefins catalyzed by [Ru(**8**)Cl_2].[39]

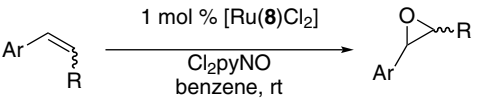

Entry[a]	Substrate	Time (h)	Yield (%)[b]	TON	ee (%)
1	Styrene	1.5	84 (100)	875	69
2	4-Chlorostyrene	4	88 (100)	930	65
3	*α*-Methylstyrene	5	80 (60)	790	24
4	*cis*-*β*-Methylstyrene	3	99 (100)	990	68
5	1,2-Dihydronaphthalene	3	78 (100)	890	80
6	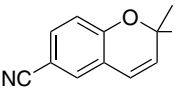	2	85 (90)	860	67
7	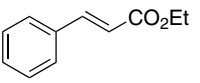	16	95 (18)	220	16

[a] Reactions were performed using 1 mol % of catalyst, 1 equiv. of substrate, and 1.1 equiv. of oxidant in benzene at room temperature; [b] Yields are based upon the amount of alkene consumed in the reaction. The value in parenthesis represents conversion of substrate.

matrix. Remarkably, the use of these immobilized catalysts not only increased the TON to more than 10,000 in some cases, but the observed selectivity was comparable to the homogenous catalytic system. This approach was further expanded in a later report by Che and coworkers through the use of mesoporous silica gel, generating TON in excess of 13,000 with comparable enantioselectivities.[40]

The [Ru(**8**)(CO)] complex was also evaluated by Berkessel and Frauenkrom for the epoxidation of olefins with 2,6-dichloropyridine-*N*-oxide.[41] [Ru(**8**)(CO)] proved to be an effective catalyst under the reported conditions, providing good to moderate yields and moderate enantioselectivities for the epoxidation of dihydronapthalene and styrene derivatives. As shown in Table 8, aliphatic and more hindered olefins were ineffective substrates for catalysis using this system.

Berkessel and coworkers published catalytic studies of ruthenium complexes of a variety of Halterman porphyrin derivatives in 2003.[42] Building on the complexes previously reported by Halterman's group,[43] they modified the *para*-position of the *meso*-aryl group by introducing various groups (Figure 6). The use of an electron-withdrawing trifluoromethyl group afforded a very effective catalyst when Cl_2pyNO was employed. This modification led to improved yields and enantioselectivities with a respectable turnover frequency (Table 9). Berkessel speculated that the electron-withdrawing trifluoromethyl group disfavored the oxidative poisoning/destruction of the catalyst by stabilizing the macrocycle.

Table 8. Asymmetric epoxidation of olefins catalyzed by [Ru(**8**)CO].[41]

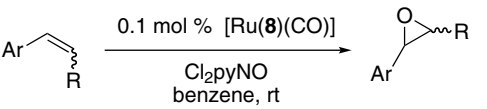

Entry[a]	Substrate	Conv. (%)	Yield (%)	ee (%)
1	1,2-Dihydronaphthalene	90	85	71
2[b]	1,2-Dihydronaphthalene	90	85	77
3	Styrene	100	79	70
4	Indene	65	55	54
5	1-Hexene	6	5	28
6	*trans*-Stilbene	6	5	0

[a] Reaction were performed using 0.1 mol % of catalyst with 1 equiv. of substrate and 1.1 equiv. of oxidant in benzene at room temperature for 48 h; [b] 1 mol % catalyst loading used.

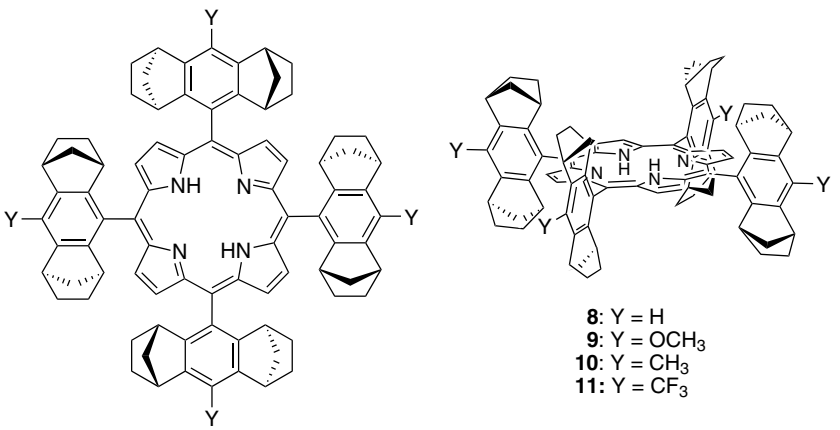

Figure 6. Halterman porphyrin **8** and its derivatives.[42]

Che and coworkers followed up on their previous catalytic work on ruthenium Halterman complexes by developing a molybdenum complex of **8**.[44] [Mo(**8**)(O)(OMe)] was used with *tert*-butylhydrogen peroxide (TBHP) for the epoxidation of aromatic alkenes. Although this molybdenum catalyst was fairly unique, the results as a whole provided low TON (4) and poor enantioselectivity (16% ee) (Scheme 4).

In 1997, Kodadek and coworkers reported the synthesis and catalytic activity of a new derivative of the D_4-symmetric Halterman porphyrin, **12** (Figure 7).[45] The manganese complex of **12** was used for the asymmetric epoxidation of a variety of olefins, including aliphatic olefins (Table 10). Moderate enantioselectivities and high TON were reported.

Table 9. Asymmetric epoxidation of olefins catalyzed by [Ru(**8**–**11**)(CO)].[42]

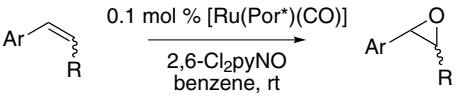

Entry[a]	Substrate	Por*[b]	Time (h)	Yield (%)	TOF (h^{-1})	ee (%)
1	Styrene	*ent*-**9**	2.5	82	328	76
2	Styrene	*ent*-**10**	2.5	78	312	76
3	Styrene	**11**	2.5	97	388	79
4	1,2-Dihydronaphthalene	**8**	48	85	—	71
5	1,2-Dihydronaphthalene	*ent*-**9**	7.5	66	88	80
6	1,2-Dihydronaphthalene	*ent*-**10**	7.5	70	94	78
7	1,2-Dihydronaphthalene	**11**	7.5	89	118	83
8	1-Hexene	**8**	45	10	2	21
9	1-Hexene	*ent*-**9**	45	8	2	36
10	1-Hexene	**10**	45	9	2	22
11	1-Hexene	**11**	45	16	4	18

[a] Reactions were performed with 0.1 mol % of catalyst, 1 equiv. of substrate, and 1.1 equiv. of oxidant in benzene at room temperature; [b] See Figure 6 for structure of porphyrin ligand.

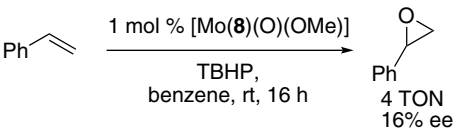

Scheme 4.[44]

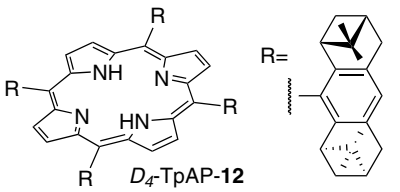

Figure 7. Kodadek's Halterman-like D_4-symmetric porphyrin.[45]

Higuchi and coworkers developed a D_4-symmetric chiral porphyrin **13** (Figure 8) related to Halterman porphyrin **8**.[46] The Fe(III) bromide complex of chiral porphyrin **13** was prepared and evaluated for the epoxidation of various aromatic olefins in the presence of PhIO. The results from this investigation are shown in Table 11. While the yields and enantiomeric excess are generally moderate, the selectivity ranged from 8% ee for *trans*-β-methylstyrene to 78% ee for

Table 10. Asymmetric epoxidation of olefins catalyzed by [Mn(**12**)Cl].[45]

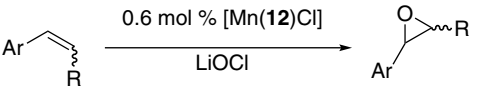

Entry[a]	Substrate	Yield (%)	TON	ee (%)
1	Styrene	70	2520	70
2	2-Vinylnaphthalene	46	2918	69
3	Indene	91	2110	24
4	*cis*-β-Methylstyrene	33	957	24
5	2,3,3-Trimethylpent-1-ene	nd	15000	85
6	3,3-Dimethylbut-1-ene	nd	130000	47

[a] Performed at 0 °C with 0.6 mol % of catalyst, 1 equiv. of substrate, in a bi-phasic solution of solvent and oxidant.

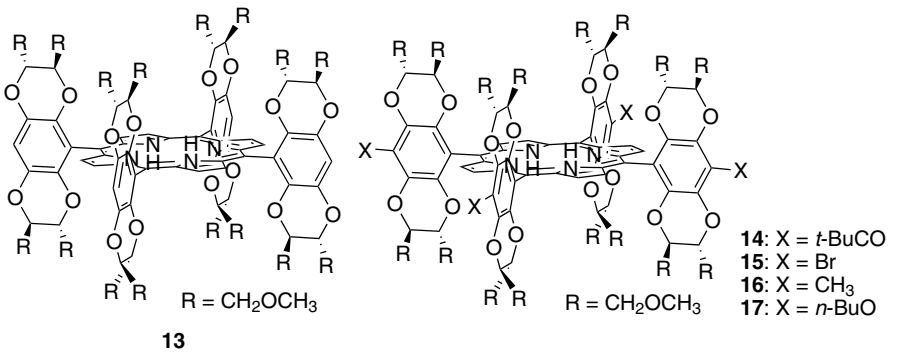

Figure 8. Higuchi's D_4-symmetric chiral porphyrins.[47]

Table 11. Asymmetric epoxidation of aromatic olefins catalyzed by [Fe(**13**)Br].[46]

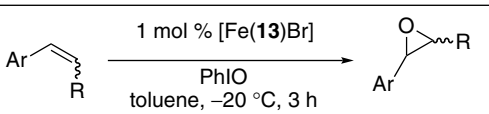

Entry[a]	Substrate	Yield (%)	TON	ee (%)
1	Styrene	68	68	47 (*S*)
2[b]	Styrene	64	638	45 (*S*)
3	1,2-Dihydronapthalene	73	73	31 (1*R*,2*S*)
4	2-Vinylnaphthalene	66	66	38 (*S*)
5	*cis*-β-Methylstyrene	70	70	8 (1*S*,2*R*)
6	*trans*-β-Methylstyrene	45	45	42 (1*S*,2*S*)
7	4-Fluorostyrene	59	59	52
8	3-Nitrostyrene	62	62	78

[a] Performed at –20 °C for 3 h with 1 mol % of [Fe(**13**)Br], 1 equiv. of oxidant, 10 equiv. of substrate; [b] Performed with 60 equiv. of substrate.

3-nitrostyrene (Table 11). As expected, when the substrate was increased from 10 equivalents to 60 equivalents, it was shown that the TON increased nearly ten-fold from 68 to 638 for the epoxidation of styrene. The authors attributed this to decreased poisoning of the catalyst by the oxidant.

The increase in enantioselectivity obtained for the epoxidation of electron-deficient styrene derivatives using the D_4-symmetric iron porphyrin complex [Fe(**13**)Br] led Higuchi and coworkers to further examine the electronic properties of this catalyst.[47] They were able to synthesize derivatives of **13** in which the *para*-position of the *meso*-aryl group was substituted with electron-donating or electron-withdrawing groups (Figure 8) to determine the effect of substitution on asymmetric induction. As presented in Table 12, no significant differences in enantioselectivity were observed; however, a slight trend of increased enantioselectivity was noted with the incorporation of electron-withdrawing substituents on the porphyrin.

Momenteau and coworkers developed a protocol for the preparation of iron and manganese glycosylated porphyrins (Figure 9) as catalysts for the epoxidation of olefins.[48] The atropisomers of these porphyrins were prepared and used to epoxidize

Table 12. Asymmetric epoxidation of aromatic olefins catalyzed by [Fe(**13**–**17**)Br].[47]

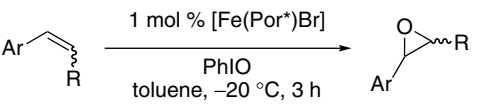

Entry[a]	Substrate	[Fe(Por*)][c]	Yield (%)	ee (%)
1	Styrene	**14**	72	42 (*S*)
2	Styrene	**15**	65	44 (*S*)
3	Styrene	**13**	68	47 (*S*)
4	Styrene	**16**	65	49 (*S*)
5	Styrene	**17**	66	52 (*S*)
6	*trans*-β-Methylstyrene[b]	**14**	48	39 (1*S*,2*S*)
7	*trans*-β-Methylstyrene[b]	**15**	43	40 (1*S*,2*S*)
8	*trans*-β-Methylstyrene[b]	**13**	45	42 (1*S*,2*S*)
9	*trans*-β-Methylstyrene[b]	**16**	46	44 (1*S*,2*S*)
10	*trans*-β-Methylstyrene[b]	**17**	49	45 (1*S*,2*S*)
11	3-Nitrostyrene	**14**	68	71
12	3-Nitrostyrene	**15**	70	74
13	3-Nitrostyrene	**13**	61	78
14	3-Nitrostyrene	**16**	70	78
15	3-Nitrostyrene	**17**	63	79

[a] Performed at –20 °C for 3 h with 1 mol % of [Fe(Por*)Br], 1 equiv. of oxidant, 10 equiv. of substrate; [b] The *cis*-epoxide was also obtained in 2–3% yield and 8–10% ee (1*S*,2*R*); [c] See Figure 8 for structures.

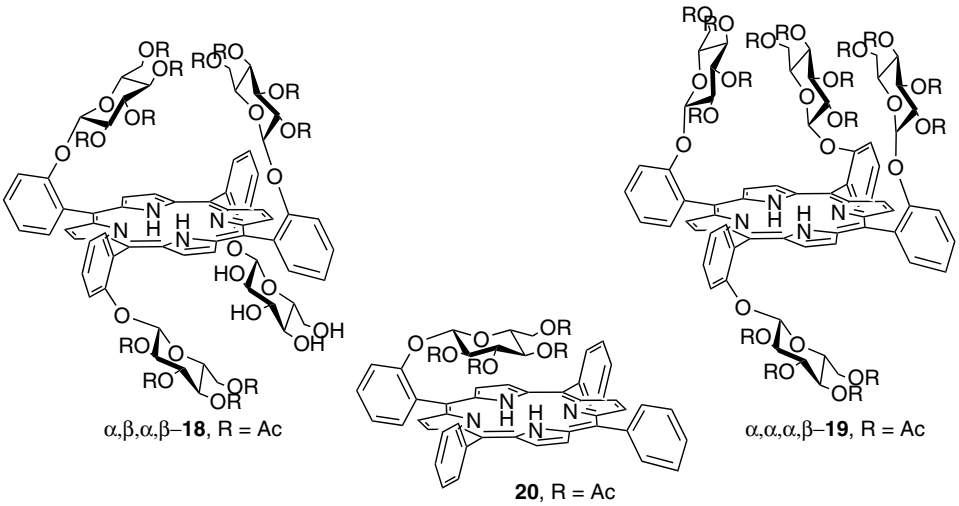

Figure 9. Glycosylated porphyrins.[48]

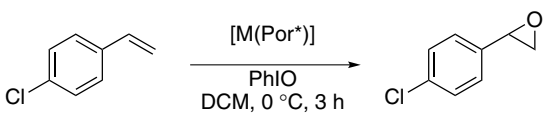

[Fe(**18**)Cl]: 60% yield, 57 TON, 33% ee
[Mn(**18**)Cl]: 53% yield, 50 TON, 27% ee
[Mn(**19**)Cl]: 34% yield, 32 TON, 23% ee
[Mn(**20**)Cl]: 6% yield, 24 TON, 0% ee

Scheme 5.[48]

4-chlorostyrene in the presence of PhIO. Moderate yields and enantioselectivities were reported using the Fe(III) chloride complex of the $\alpha,\beta,\alpha,\beta$-atropisomer which was shown to be the most effective catalyst (Scheme 5).

In a later report, Momenteau focused on 2-chloro, 6-glycosylated manganese porphyrins (Figure 10).[49] These glycosylated porphyrins were assessed using 4-chlorostyrene as the olefin substrate as in their previous work. Both PhIO and H_2O_2 were shown to be suitable for catalysis with [Mn(**21**–**23**)Cl] (Table 13). Although the manganese system was not as effective as the [Fe(**18**)Cl]-based system (Scheme 5) with respect to yield or enantioselectivity, the catalyst proved to be relatively more robust, yielding slightly higher TON.

Momenteau and coworkers continued to develop new glycosylated porphyrins via the incorporation of larger sugar units onto the *meta*-position of the *meso*-aryl

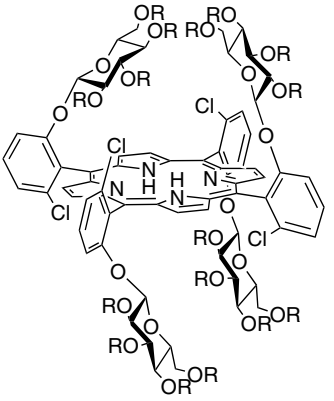

α,β,α,β – **21**, R = Ac

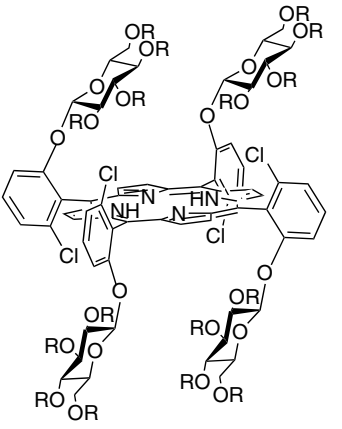

α,α,β,β – **22**, R = Ac

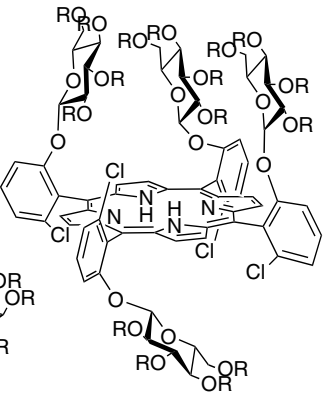

α,α,α,β – **23**, R = Ac

Figure 10. Atropisomers of glycoconjugated porphyrins containing electron-withdrawing groups.[49]

Table 13. Evaluation of glycoconjugated porphyrins **21–23** for the asymmetric epoxidation of 4-chlorostyrene with two different oxidants.[49]

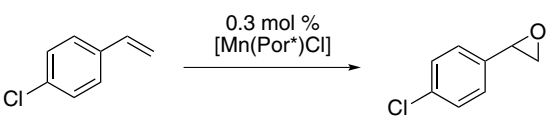

Entry	Oxidant	[Mn(Por*)][c]	Yield (%)	TON	ee (%)
1	PhIO[a]	**21**	25	49	20
2	PhIO[a]	**22**	26	49	19
3	PhIO[a]	**23**	45	57	16
4	H_2O_2[b]	**21**	24	64	23
5	H_2O_2[b]	**22**	31	62	22
6	H_2O_2[b]	**23**	29	58	22

[a] Performed at rt for 1 h with 1 equiv. of oxidant, 1.5 equiv. of 4-picoline, and 2.7 equiv. of substrate in DCM; [b] Performed at rt for 4 h with 1 equiv. of substrate, 4 equiv. oxidant, 2 equiv. of *t*-Bupy, and 2 equiv. of benzoic acid in DCM; [c] See Figure 10 for structures.

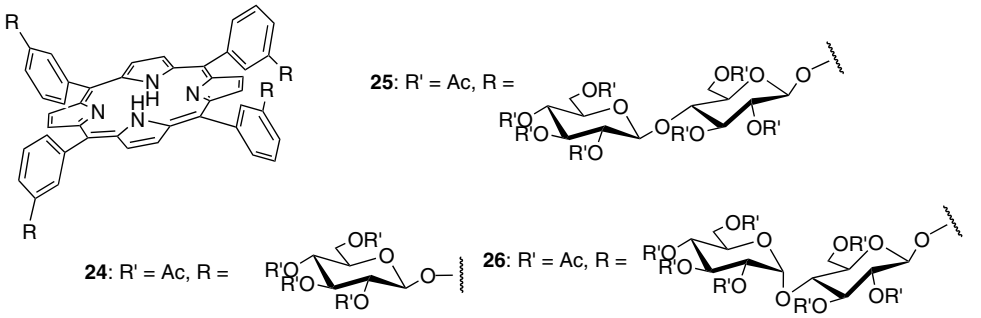

Figure 11. Glycoconjugated porphyrins with chiral substituents at the *meta*-position.[50]

Table 14. Asymmetric epoxidation of aromatic olefins catalyzed by [Mn(**21**–**26**)Cl].[50]

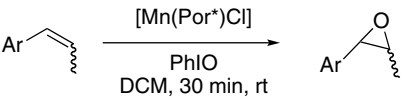

Entry[a]	Substrate	Por*[b]	Yield (%)	ee (%)
1	4-Chlorostyrene	**21**	5	24
2	4-Chlorostyrene	**22**	49	20
3	4-Chlorostyrene	**23**	42	29
4	4-Chlorostyrene	**24**	36	0
5	4-Chlorostyrene	**25**	33	0
6	4-Chlorostyrene	**26**	31	3
7	1,2-Dihydronaphthalene	**25**	62	8

[a] Performed for 30 min at room temperature with ~0.1 mol % catalyst 1.0 equiv. of oxidant, 2.5 equiv. of substrate, and 1.5 equiv. of 4-methylpyridine; [b] See Figures 10 and 11 for structures.

group, as shown in Figure 11.[50] Manganese complexes of these porphyrins, along with those presented earlier, were employed as catalyst to determine the efficacy of each complex in catalyzing the epoxidation of 4-chlorostyrene in the presence PhIO. The results, shown in Table 14, demonstrate that the sugar residues need to be in closer proximity to the metal center to induce asymmetry.

"Chiroporphyrins" **27**, developed by Marchon and coworkers, are porphyrins containing chiral cyclopropyl ester and amide moieties attached directly to the *meso*-positions of the porphyrin in an $\alpha,\beta,\alpha,\beta$-arrangement (Figure 12).[51] The manganese complexes of **27** were evaluated for their catalytic ability to epoxidize 1,2-dihydronaphthalene in the presence of the axial ligand pyridine. The results

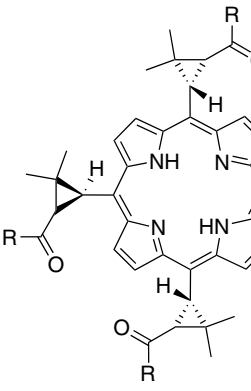

27

27a: R = OMe
27b: R = OEt
27c: R = OBn
27d: R = ONp
27e: R = OPh-*p*-NO_2
27f: R = OPh-*m*-NO_2
27g: R = *O*-(1*S*)-endo-bornyl
27h: R = O^{t}Bu
27i: R = N(Me)Ph
27j: R = N(Et)Ph
27k: R = N(Cy)C(O)NH(Cy)
27l: R = NH(Cy)

Figure 12. "Chiroporphyrins".[51]

revealed that when the *meso*-positions were functionalized with large cyclopropylamide groups, the catalyst afforded the corresponding epoxides with the highest enantioselectivities (Table 15).

With the success of their first generation of "chiroporphyrins", Marchon and coworkers envisioned using electron-withdrawing groups to enhance the activity of the catalytic system.[52] Their efforts led to the preparation of second generation "chiroporphyrins" with pentafluorophenyl groups occupying the 5,15-*meso*-positions of the porphyrin ring, and chiral cyclopropyl groups occupying the remaining 10,20-*meso*-positions (Figure 13). In most cases, these porphyrins were able to completely epoxidize the substrate in an hour or less (Scheme 6). Unfortunately, the enantioselectivities were generally lower in comparison to the first generation "chiroporphyrin" system.

Smith and Reginato developed chiral picket fence porphyrins (A_4-**31**, A_3B-**32**, A_2B_2-**33**, Figure 14) containing chiral ether moieties on the *ortho*-positions of the *meso*-aryl groups of the porphyrins.[53] The Fe(III) chloride complexes of A_4-**31** and A_2B_2-**33** were both evaluated for the epoxidation of styrene with PhIO in dichloromethane. The use of the more bulky [Fe(A_4-**31**)Cl] resulted in lower yields, as expected; the use of the [Fe(A_2B_2-**33**)Cl] provided a quantitative yield with similar enantioselectivity as compared to the A_4-complex **31** (Scheme 7). For the [Fe(A_2B_2-**33**)Cl]-catalyzed reaction, it was shown that lowering the temperature

Table 15. Asymmetric epoxidation of 1,2-dihydronaphthalene catalyzed by [Mn(**27**)Cl].[51]

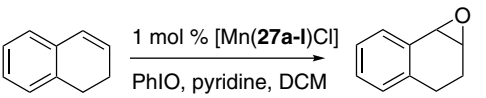

Entry[a]	R =	Catalyst	ee (%)
1	OMe	[Mn(**27a**)Cl]	60
2	OEt	[Mn(**27b**)Cl]	70
3	OBn	[Mn(**27c**)Cl]	65
4	ONp	[Mn(**27d**)Cl]	73
5	OPh-*p*-NO_2	[Mn(**27e**)Cl]	68
6	OPh-*m*-NO_2	[Mn(**27f**)Cl]	75
7	*O*-(1*S*)-endo-bornyl	[Mn(**27g**)Cl]	75
8	O^{t}Bu	[Mn(**27h**)Cl]	75
9	N(Me)Ph	[Mn(**27i**)Cl]	80
10	N(Et)Ph	[Mn(**27j**)Cl]	86
11	N(Cy)C(O)NH(Cy)	[Mn(**27k**)Cl]	83
12	NH(Cy)	[Mn(**27l**)Cl]	79

[a] Reactions performed for 1 h with 1 mol % catalyst, 1.0 equiv. of oxidant, 2.5 equiv. of pyridine, and 10 equiv. of olefin.

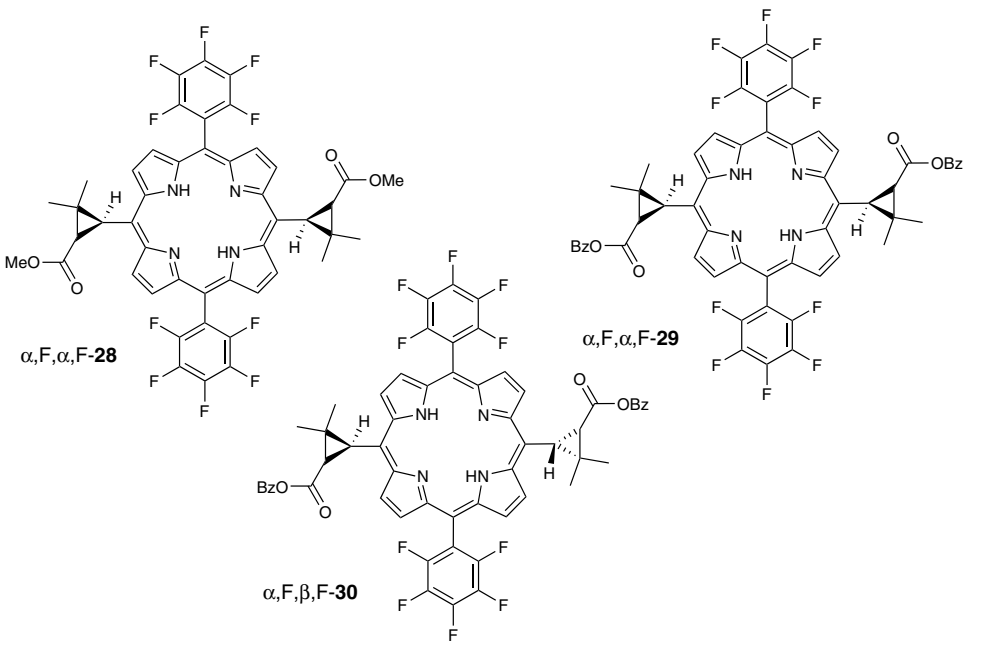

Figure 13. "Chiroporphyrins" with pentafluorophenyl groups.[52]

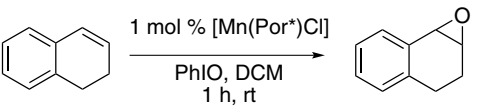

[Mn(α,F,α,F-MeCP)Cl] (**28**): 88% yield, 43% ee
[Mn(α,F,α,F-BzCP)Cl] (**29**): 96% yield, 35% ee
[Mn(α,F,β,F-BzCP)Cl] (**30**): 99% yield, 31% ee

Scheme 6.[52]

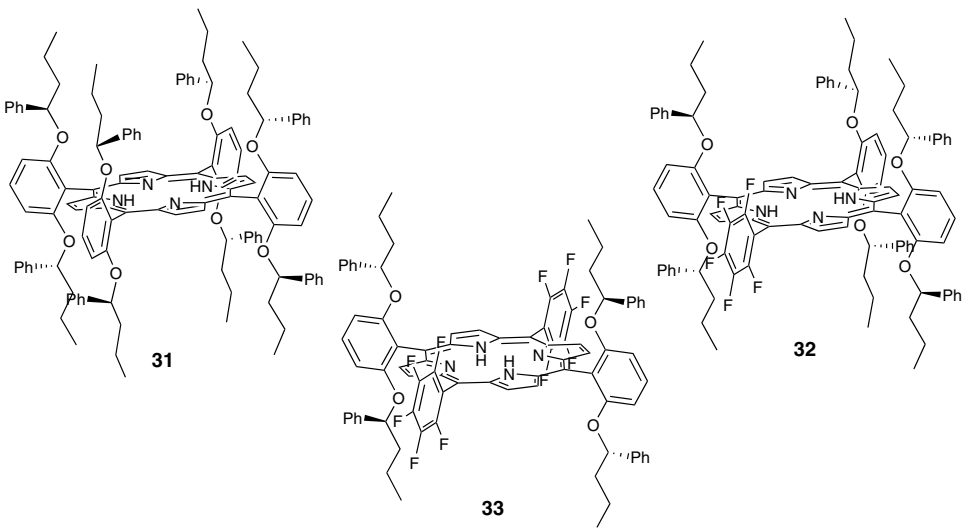

Figure 14. Chiral picket fence porphyrin-bearing chiral ether groups attached to the *ortho*-aryl position.[53]

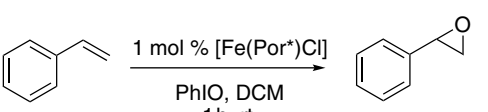

31: 48% yield, 16% ee
33: 91% yield, 16% ee
33, at 0 °C: 99% yield, 23% ee

Scheme 7.[53]

to 0 °C increased the enantioselectivity slightly without sacrificing yield. Although the porphyrin catalysts designed for this particular study were only moderately effective in inducing enantioselectivity, the results provided "proof of concept" that rigid and bulky chiral groups could be used to produce more effective catalysts.

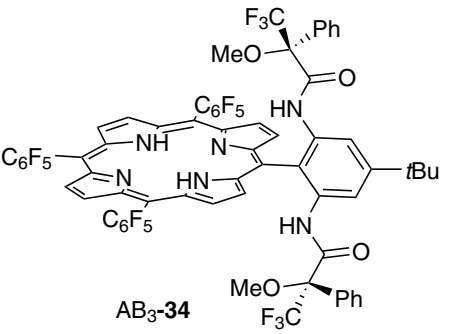

AB_3-**34**

Figure 15. Chiral picket fence porphyrin derived from Mosher's chiral amide.[55]

Prior to Smith and Reginato's work with chiral porphyrin ligands **31**–**33**, Rose and coworkers prepared a series of chiral porphyrins using Mosher's amide as the chiral moiety on the *ortho*-positions of the *meso*-aryl ring.[54] Among the different complexes examined for catalytic epoxidation, the Fe(III) bromide complex of AB_3-**34**, shown in Figure 15, gave the highest enantiomeric excess, albeit very low (6% ee).[55]

The research groups of Hevesi and Quici also developed porphyrins with chiral moieties on the *meso*-positions.[56,57] Although catalysts **35** and **36** (Figure 16) produced moderate yields and low enantioselectivities for epoxidation of styrene (Scheme 8), [Mn(**36**)Cl] exhibited respectable TON (195) for the reaction.

In an effort to mimic the chiral environment of the cytochrome P-450 enzyme, Ohkatsu and coworkers attached peptide chains to the *meso*-positions of the porphyrins using a modular approach, allowing them to tune the steric and electronic properties of the ligand environment to enhance asymmetric induction.[58] Epoxidation reactions of styrene with PhIO were initially performed using porphyrin derivatives containing three peptide chains (Figure 17). It was shown that varying the nature of the amino acid residues resulted in changes in yield and selectivity. For example, when γ-benzyl-L-glutamate (γ-BLG) was used in place of L-phenylalanine (L-Phe), the yield increased 15%; however, enantioselectivity decreased dramatically from 60% ee to 11% ee (Scheme 9). It was noted that lengthening the average peptide chain (n) decreased the yield of the epoxidation reaction as a result of increased hindrance. Several other biomimetic porphyrins with various side chains and compositions were also prepared. However, they provided no significant improvement in yield or enantioselectivity.

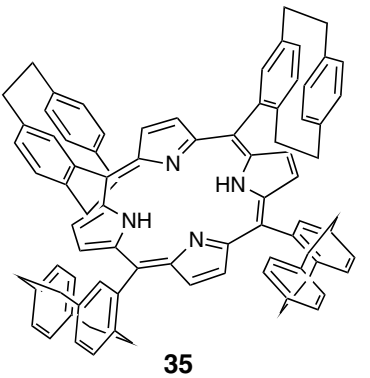

35

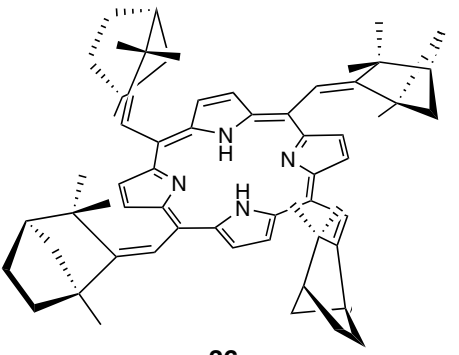

36

Figure 16. Chiral picket fence porphyrins.[56,57]

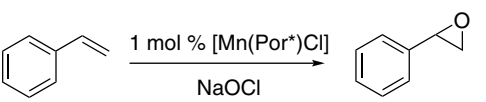

35: 78% yield, 10% ee
36: 65% yield, 25% ee

Scheme 8.[56,57]

B. Chiral Strapped Porphyrins

Naruta and coworkers developed one of the first examples of chiral strapped porphyrins incorporating binaphthyl groups for use in asymmetric epoxidation (Figure 18).[59,60] The binaphthyl group, which was used to bridge adjacent *meso*-aryl groups through an ether linkage, effectively blocked one face of the catalytic site thus establishing a sterically bulky chiral environment near the metal center. The use of the binaphthyl bridge is similar to the work discussed previously by

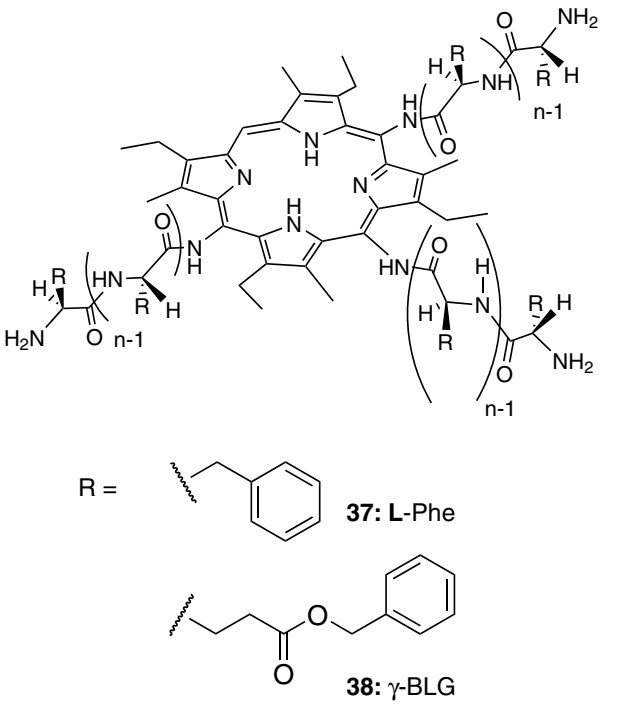

Figure 17. Peptide-bearing chiral picket fence porphyrins.[58]

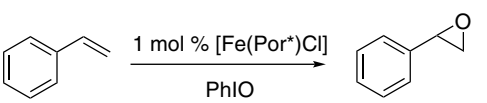

37: L-Phe-3PCs: n = 4.5, 45% yield, 60% ee
38: γ-BLG-3PCs: n = 4.6, 60% yield, 11% ee

n = average peptide chain length

Scheme 9.[58]

Groves and Myers[10] in 1983. These porphyrins, known as "twin-coronet" porphyrins, are classified by the arrangement of the "straps", which can be in either an eclipsed or staggered orientation, resulting in the generation of two unique ligand environments (Figure 18).

The difference in selectivity resulting from the two different conformations is showcased by the epoxidation of 2-nitrostyrene (Scheme 10). Based on an initial screening, the eclipsed [Fe(**39**)Cl] was further evaluated for the epoxidation of styrenes with PhIO (Table 16). Good enantioselectivities were observed for

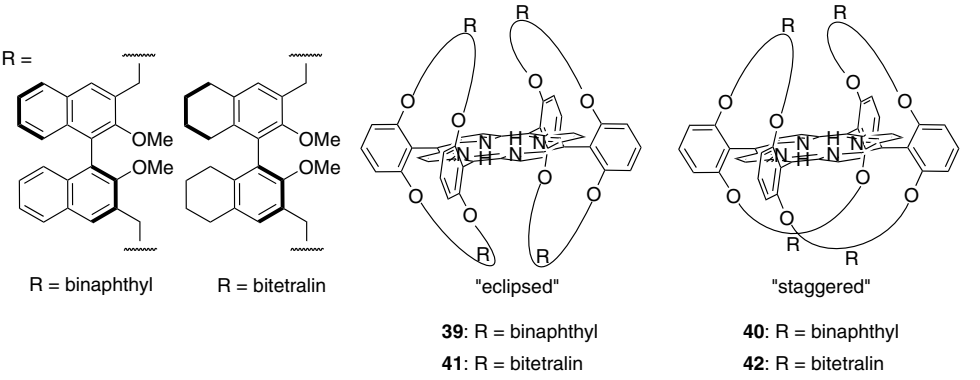

Figure 18. Binaphthyl and bitetralin "twin-coronet" porphyrins.[59–63]

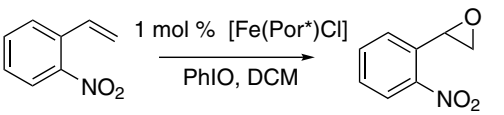

[Fe(**39**)Cl]: 26 TON, 80% ee
[Fe(**40**)Cl]: 26 TON, 54% ee

Scheme 10.[59,60]

Table 16. Asymmetric epoxidation of aromatic olefins catalyzed by [Fe(**39**)Cl].[59,60]

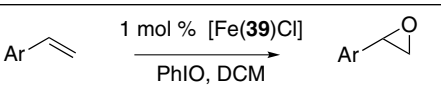

Entry[a]	Substrate	Time (h)	TON	ee (%)
1	Styrene	3.5	49	20 (*R*)
2	2-Nitrostyrene	3	26	80 (*R*)
3	3-Nitrostyrene	2	57	60 (*R*)
4	4-Nitrostyrene	2	38	54 (*R*)
5	3,5-Dinitrostyrene	2	20	74 (*R*)
6	Pentafluorostyrene	2	36	74 (*R*)
7	4-Trifluoromethylstyrene	3	42	41 (*R*)
8	4-Methylstyrene	5	48	11 (*R*)
9[b]	4-Methoxystyrene	1.5	0	—

[a]The reactions were performed with 1 mol % of catalyst, 1 equiv. of PhIO, and 5 equiv. of substrate in DCM; [b]Major product was aldehyde. Epoxidation product was not observed.

electron-poor styrene derivatives (entries 2–7, Table 16). Conversely, the more electron-rich substrates displayed lower enantioselectivities (entries 8 and 9, Table 16).

Naruta and coworkers continued their investigations with iron binaphthyl strapped porphyrin [Fe(**39**)Cl] and compared it to [Mn(**39**)Cl] for the epoxidation of styrene and its electron-deficient derivatives.[61] Differences in reactivity and selectivity between the manganese and iron complexes were observed for the epoxidation of *cis*-β-methylstyrene (entries 8–9, Table 17). It was shown that enantioselectivities could be marginally improved in select cases by the use of axial ligands and the electron-deficient oxidant iodosyl(pentafluorobenzene), C_6F_5IO.

Naruta and coworkers continued to develop "twin-coronet" porphyrins by producing bitetralin-strapped variations **41** and **42** (Figure 18).[60,62,63] The iron complexes of both the eclipsed **41** and staggered **42** forms were evaluated for the epoxidation of styrene with PhIO. The activity of the bitetralin-strapped version of the "twin-coronet" porphyrin correlated well with the binaphthyl-strapped version (Table 18). Additionally, the eclipsed and staggered Fe(III)Cl complexes of **41** and **42** were evaluated for the epoxidation of styrenes with PhIO; again the eclipsed version **41** was shown to be a better catalyst (entries 1 and 2, Table 18). The improved enantioselectivity generated with electron-poor styrene derivatives is highlighted by the 96% ee obtained with the use of 3,5-dinitrostyrene as substrate (entry 6, Table 18).

Table 17. Asymmetric epoxidation of aromatic olefins catalyzed by either [Fe(**39**)Cl] or [Mn(**39**)Cl].[61]

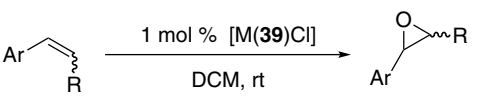

Entry[a]	Substrate	[M(39)Cl]	Oxidant	Axial ligand	Time (h)	TON	ee (%)
1	Styrene	[Fe(**39**)Cl]	PhIO	—	3.5	50	22 (*S*)
2	Styrene	[Mn(**39**)Cl]	PhIO	—	9	67	16 (*S*)
3	Styrene	[Mn(**39**)Cl]	C_6F_5IO	—	3	62	0
4[b]	Styrene	[Mn(**39**)Cl]	C_6F_5IO	AcPIm	6	67	23 (*S*)
5	2-Nitrostyrene	[Fe(**39**)Cl]	PhIO	—	3	26	80 (*S*)
6	2-Nitrostyrene	[Mn(**39**)Cl]	PhIO	—	9	22	66 (*S*)
7	*cis*-β-Methylstyrene	[Fe(**39**)Cl]	PhIO	—	2	38	19 (1*S*,2*R*)
8	*cis*-β-Methylstyrene	[Mn(**39**)Cl]	PhIO	—	4	28	61 (1*S*,2*R*)
9	*cis*-β-Methylstyrene	[Mn(**39**)Cl]	C_6F_5IO	—	1	23	47 (1*S*,2*R*)
10[b]	*cis*-β-Methylstyrene	[Mn(**39**)Cl]	C_6F_5IO	AcPIm	3	9	70 (1*S*,2*R*)

[a] Reactions were performed with 1 mol % of catalyst, 1 equiv. of oxidant, and 5 equiv. of substrate in DCM; [b] 5 mol % of AcPIm (4-imidazol-1-yl)acetophenone); [c] –20 °C.

Table 18. Asymmetric epoxidation of aromatic olefins catalyzed by [Fe(**41**–**42**)Cl].[62,63]

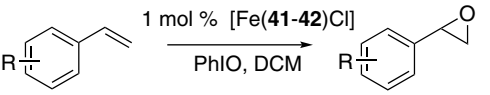

Entry[a]	R =	Catalyst	Time (h)	TON	ee (%)
1	H	**41**	8	84	54 (*S*)
2	H	**42**	7	44	28 (*S*)
3	2-NO_2	**41**	3	17	89 (*S*)
4	3-NO_2	**41**	2	26	74 (*S*)
5	4-NO_2	**41**	3	21	67 (*S*)
6	3,5-NO_2	**41**	4	36	96 (*S*)
7	F_5	**41**	3	10	83 (*S*)
8	4-Br	**41**	3	31	51 (*S*)
9	4-CH_3	**41**	3	30	27 (*S*)
10	3-OCH_3	**41**	2	33	73 (*S*)

[a] The reactions were performed with 1 mol % of catalyst, 1 equiv. of PhIO, and 5 equiv. of substrate in DCM; [b] See Figure 18 for structures.

Collman, Rose, and coworkers developed porphyrins analogous to Naruta's binaphthyl-strapped "twin-coronet" ligands.[64,65] The main difference between the two systems is the chiral bridge. Collman's catalysts are linked to the porphyrin via an amide linkage on the *ortho*-positions of the *meso*-aryl-groups, while Naruta's catalysts are linked through an ether linkage. The amide linkage provided for an open, accessible face (Figure 19) yielding higher reaction rates with a variety of olefin substrates, while decreasing oxidative poisoning of the catalyst (Table 19). For example, epoxidation of styrene with Collman's catalyst showed exceptional rate and stability with a TOF (turn over frequency) = 40/min and up to 5,500 turnovers. In addition, the amide linkage produced a more rigid structure, providing enantiomeric excesses of up to 83% for styrene (entry 1, Table 19).

Collman and coworkers observed an interesting change in enantioselectivity during the course of epoxidation catalyzed by [Fe(**43**)Cl]. They noted that the enantioselectivity increased initially but eventually decreased over the course of the reaction. Investigations into the cause for this observed phenomenon led to the discovery of the iron complex of a new porphyrin **44**, which was generated *in situ* from the oxidation of **43** (Figure 19), as a more selective catalyst. It was rationalized that the initial rise in enantioselectivity was attributed to the generation of **44**, and that subsequent decrease in enantioselectivity occurred as a result of the over oxidation of **44** to a less selective catalyst.

In a separate report, Roschmann and coworkers used Collman's catalyst for the epoxidation of allylic alcohols.[66] This report is especially noteworthy since it was the first example using porphyrins as catalysts for the asymmetric epoxidation

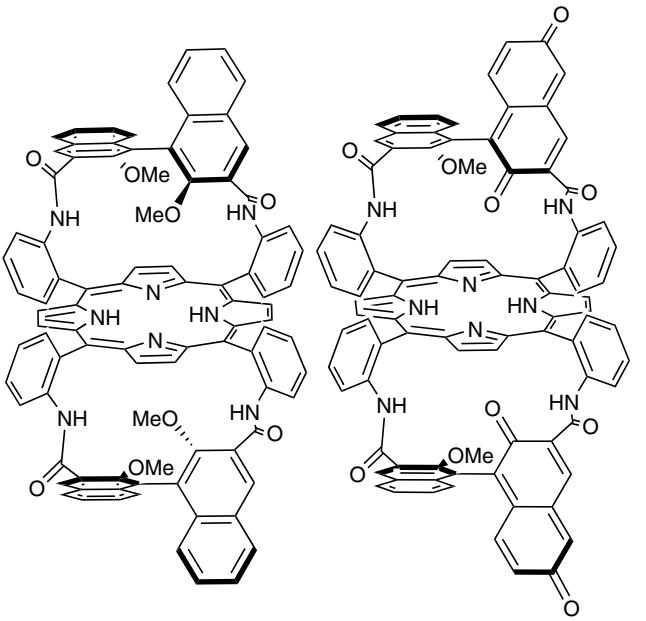

Figure 19. Binaphthyl-derived catalysts by Collman and Rose.[64,65]

Table 19. Asymmetric epoxidation of olefins catalyzed by [Fe(**43**)Cl].[64,65]

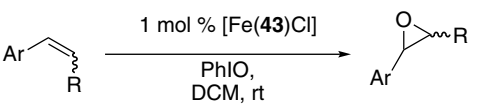

Entry[a]	Substrate	Yield (%)	ee (%)
1	Styrene	95	83 (*S*)
2[b]	Styrene	89	75 (*S*)
3	Pentafluorostyrene	75	88 (*S*)
4	3-Chlorostyrene	90	82 (*S*)
5	3-Nitrosytrene	78	72 (*S*)
6	1,2-Dihydronaphthalene	80	55 (1*S*,2*R*)
7	*cis*-*β*-Methylstyrene	78	49 (1*S*,2*R*)
8	3,3-Dimethyl-1-butene	85	82

[a] Reactions were performed using 1 mol % of catalyst, 10 equiv. of substrate, and 1.1 equiv. of oxidant in DCM at room temperature; [b] Oxidant is added in 10 portions.

of allylic alcohols. Previous work in this area focused almost exclusively on the use of established catalytic systems, such as the Sharpless system.[67–69]

Using the reaction conditions shown in Scheme 11, racemic allylic alcohols were subjected to catalytic oxidation with PhIO. The resulting epoxides were

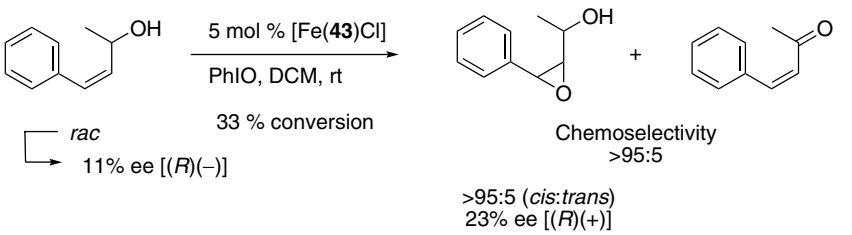

Scheme 11.[66]

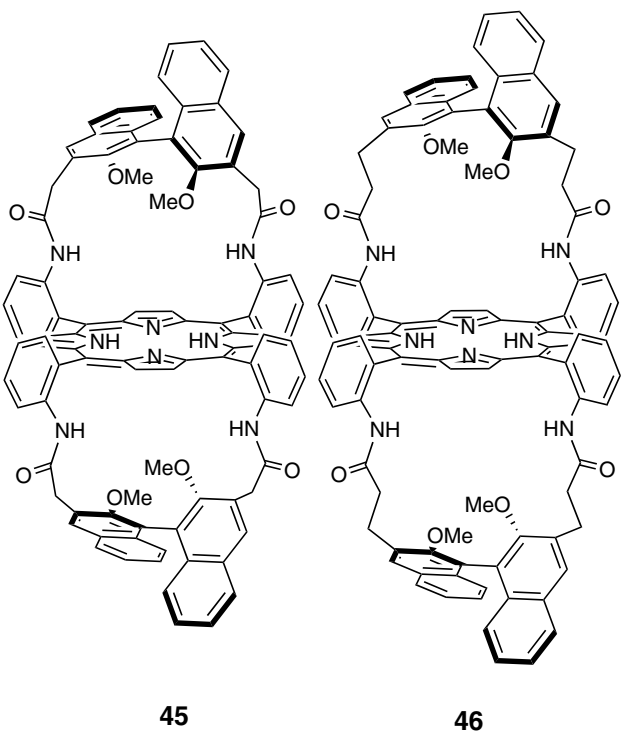

45 **46**

Figure 20. Rose's modified Collman catalyst.[70]

formed (33% conversion) in excellent diastereoselectivity and with modest enantioselectivity. The resolution of the allylic alcohol provided an enantiomeric purity of 11% ee. Other allylic olefins were examined using this system and similar results were obtained. The oxidation of allylic alcohols into α,β-unsaturated ketones was the only side reaction reported under the reaction conditions.

Rose and coworkers attempted to induce higher levels of enantioselectivity by extending the linkage on Collman's catalyst **43** to produce catalysts **45** and **46** with a flexible chiral pocket in close proximity to the metal center (Figure 20).[70]

Table 20. Asymmetric epoxidation of aromatic olefins catalyzed by [Fe(**45**)Cl].[70]

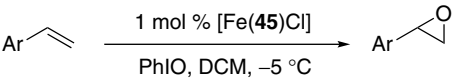

Entry[a]	Substrate	Yield (%)	ee (%)
1	Styrene	96	97 (*R*)
2	Pentafluorostyrene	80	96 (*R*)
3	3-Fluorostyrene	87	93 (*R*)
4	3-Chlorostyrene	90	88 (*R*)
5	3-Nitrostyrene	84	90 (*R*)
6	4-Chlorostyrene	75	84 (*R*)

[a] Reactions were performed with 1 mol % of catalyst, 1 equiv. of oxidant, and 10 equiv. of substrate in DCM at –5 °C.

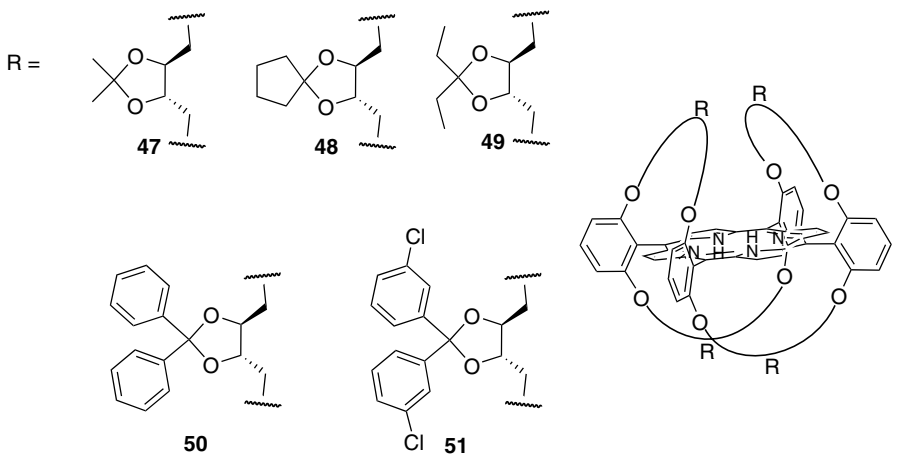

Figure 21. Homochiral threitol-strapped porphyrins.[72–76]

The iron chloride complex of **45** was used with PhIO to epoxidize several styrene derivatives (Table 20). The reported 96% yield and 97% ee for styrene is among the highest reported values for styrene epoxidation; not only for the Collman type catalysts, but also for any metalloporphyrin-based epoxidation system. In 2009, Ren and coworkers also examined the iron complexes of **45** and **46**, generating results similar to those communicated by Collman and Rose.[71]

Gross and coworkers also developed a series of porphyrin ligands based on the design of "twin-coronet" porphyrins.[72,73] Threitol derivatives were appended to adjacent *ortho*-aryl positions into an eclipsed orientation to produce the strapped ligands shown in Figure 21. Manganese, iron, and ruthenium complexes of these porphyrins were evaluated for their ability to serve as asymmetric catalysts in the

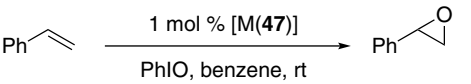

[Mn(**47**)Cl]: 77% yield, 10% ee
[Fe(**47**)Cl)]: 65% yield, 44% ee
[Ru(**47**)(CO)]: 47% yield, 42% ee

Scheme 12.[72,73]

Table 21. Asymmetric epoxidation of aromatic olefins catalyzed by iron and ruthenium complexes of **47** and **50**.[74,75]

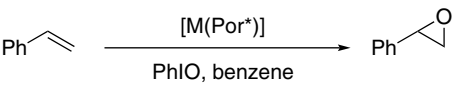

Entry	Substrate	[M(Por*)][e]	Temp (°C)	Yield (%)	ee (%)
1[a]	Styrene	[Fe(**47**)Cl]	25	76	44
2[a]	Styrene	[Fe(**50**)Cl]	23	75	59
3[b]	Styrene	[Fe(**50**)Cl]	–20	59	68
4[c]	Styrene	[Fe(**47**)CO]	25	39	48
5[d]	Styrene	[Ru(**47**)$(O)_2$]	25	29	54
6[a]	4-Fluorostyrene	[Fe(**47**)Cl]	25	68	56
7[a]	4-Fluorostyrene	[Fe(**50**)Cl]	23	70	65
8[b]	4-Fluorostyrene	[Fe(**50**)Cl]	–20	64	73
9[c]	4-Fluorostyrene	[Fe(**47**)CO]	25	39	51
10[d]	4-Fluorostyrene	[Ru(**47**)$(O)_2$]	25	9	53
11[a]	4-Chlorostyrene	[Fe(**47**)Cl]	25	55	53
12[a]	4-Chlorostyrene	[Fe(**50**)Cl]	23	65	63
13[b]	4-Chlorostyrene	[Fe(**50**)Cl]	–20	26	70
14[c]	4-Chlorostyrene	[Fe(**47**)CO]	25	15	45
15[d]	4-Chlorostyrene	[Ru(**47**)$(O)_2$]	25	2	57

[a] Reactions were performed with 0.01 mol % of catalyst, 1 equiv. of PhIO as oxidant, and 10 equiv. of substrate in benzene; [b] Toluene was used as solvent; [c] Reactions were performed with 1 mol % of catalyst, 1 equiv. of PhIO as oxidant, and 10 equiv. of substrate in benzene; [d] Reactions were performed with 0.3 mol % of catalyst, 1 equiv. of 2,6-dichloropyridine *N*-oxide as oxidant, and 1 equiv. of substrate in *m*-xylene for 5 h; [e] See Figure 21 for structures.

epoxidation of styrene (Scheme 12). In general, the Fe(III) chloride complex of **47** generated higher yields and enantiomeric excesses in comparison to the analogous magnesium and ruthenium derivatives.

Further exploration and development of the threitol-derived strapped homochiral porphyrin ligand system by Gross and coworkers led to the observation that lower reaction temperatures and higher catalyst loading could provide significant improvements over their previous system (Table 21).[74,75] An additional

Table 22. Asymmetric epoxidation of aromatic olefins catalyzed by [Ru(**51**)$(O)_2$].

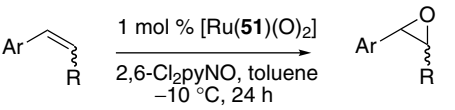

Entry[a]	Substrate	TON	ee (%)
1	Styrene	11	75
2[b]	Styrene	55	79
3	3-Chlorostyrene	135	74
4[b]	3-Chlorostyrene	226	81
5	4-Chlorostyrene	24	80
6[b]	4-Chlorostyrene	191	83
7	4-Bromostyrene	19	75
8	4-Fluorostyrene	86	75
9[b,c]	*cis*-β-Methylstyrene	487	69
10[b,d]	*trans*-β-Methylstyrene	242	38

[a] Performed for 1 mol % cat, 1.0 equiv. of oxidant and 1 equiv. of olefin in toluene for 24 h; [b] 48 h; [c] *cis*:*trans* = 15:1; [d] Only *trans*-olefin produced.

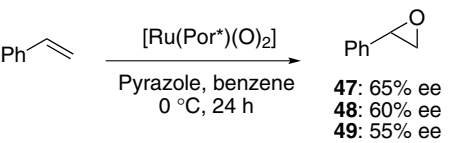

Scheme 13.[76]

development was the use of the ruthenium oxo complex [Ru(**51**)$(O)_2$] (Figure 21), which contains an electron-withdrawing chlorine atom on the aryl group. In many cases, the use of [Ru(**51**)$(O)_2$] resulted in increased enantioselectivities and TON (Table 22).

In addition to their report on catalytic olefin epoxidation by ruthenium complexes of the Halterman porphyrin **8,** Che and coworkers studied catalytic reactions of ruthenium complexes of **48** and **49** (Figure 21), which are derivatives of Gross's homochiral porphyrin **47**.[76] The complexes [Ru(**48**)$(O)_2$] and [Ru(**49**)$(O)_2$] were evaluated for the stoichiometric epoxidation of styrene, generating moderate enantioselectivities (Scheme 13).

Following their successful use of picket fence chiroporphyrin ligands, Marchon and coworkers synthesized a new strapped porphyrin variation consisting of different length cyclopropane moieties (Figure 22).[77] The manganese complexes of these new "bridled chiroporphyrins" were employed for the catalytic

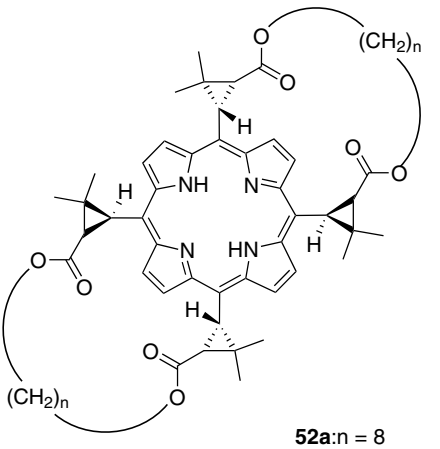

52a:n = 8
52b:n = 9
52c:n = 10
52 **52d**:n = 11
52e:n = 12
52f:n = 14
52g:n = 16

Figure 22. "Bridled chiroporphyrin".[77]

Table 23. Asymmetric epoxidation of 1,2-dihydronaphthalene catalyzed by [Mn(**52**)Cl].[77]

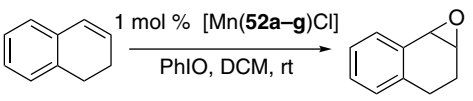

Entry[a]	n =	Yield (%)[b]	ee (%)[b]
1	**52a**:8	62	44
2	**52b**:9	63	51
3	**52c**:10	58	63
4	**52d**:11	54	61
5	**52e**:12	60	61
6	**52f**:12	48	53
7	**52g**:12	47	64

[a] The reactions were performed with 1 mol % of catalyst, 1 equiv. of PhIO, and 10 equiv. of substrate in DCM at room temperature; [b] Values reported represent an average from multiple runs.

epoxidation of 1,2-dihydronaphthalene (Table 23). It was shown that both yield and asymmetric induction were affected by the chain length of the catalyst.

Simonneaux and coworkers developed a homochiral porphyrin ligand system containing optically pure cyclohexane auxiliaries which were used to strap

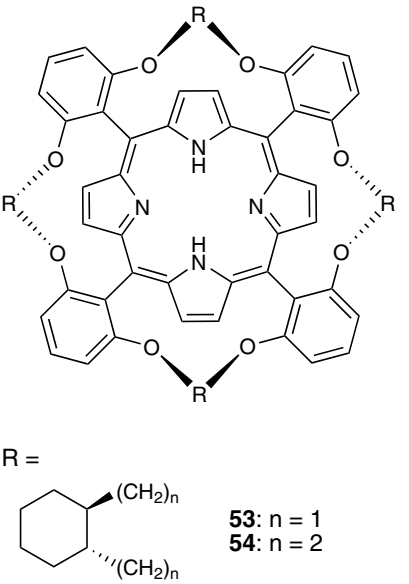

Figure 23. Homochiral-strapped porphyrin with chiral cyclohexane auxiliaries.[78]

Table 24. Asymmetric epoxidation of aromatic olefins catalyzed by [Ru(**54**)(O)$_2$].[78]

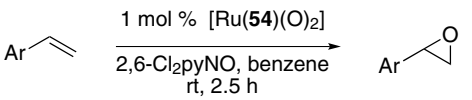

Entry[a]	Substrate	Yield (%)	TON	ee (%)
1	Styrene	84	276	23 (*R*)
2[b]	Styrene	62	204	7 (*R*)
3	2-Nitrostyrene	32	107	17 (*R*)
4	3-Nitrostyrene	15	50	30 (*R*)
5	2-Trifluoromethylstyrene	84	276	18 (*R*)
6	3-Trifluoromethylstyrene	74	244	32 (*R*)
7	4-Trifluoromethylstyrene	30	97	24 (*R*)
8	4-Methylstyrene	43	144	27 (*R*)
9	4-Bromostyrene	40	132	21 (*R*)
10	1,2-Dihydronaphtalene	2	33	73 (1*S*,2*R*)

[a] The reactions were performed with 1 mol % of catalyst, 1 equiv. of 2,6-dichloropyridine-*N*-oxide, and 1 equiv. of substrate in benzene; [b] [Ru(**53**)(O)$_2$] used as catalyst.

adjacent aryl positions (Figure 23).[78] This ligand system is similar to the threitol-strapped ligand derivatives reported by Gross and coworkers (Figure 21). [Ru(**54**)(O)$_2$] was able to reach an average TON greater than 200 for the epoxidation of several of the olefins in this study (Table 24). Unfortunately, the enantioselectivity

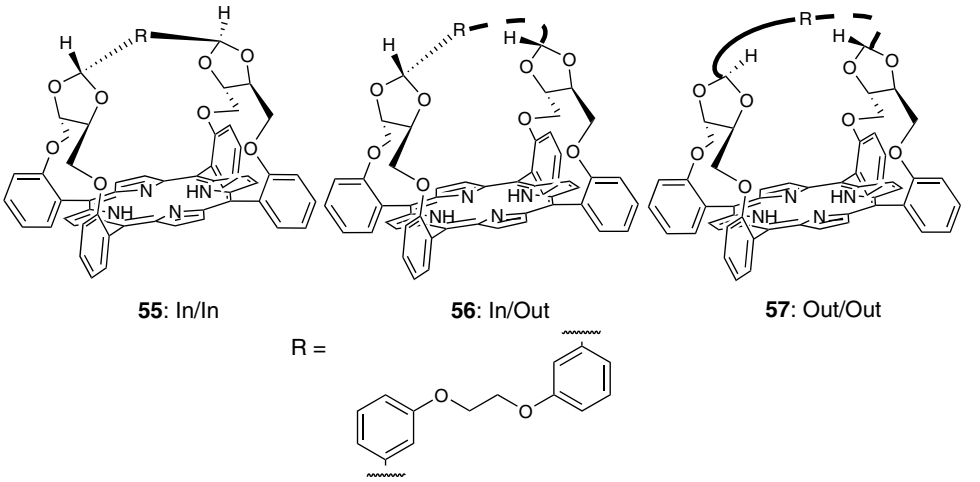

Figure 24. Threitol-strapped porphyrin.[79,80]

induced by these catalysts did not compare favorably with Gross's system (Tables 21 and 24).[72–75]

Collman and coworkers synthesized single-faced threitol-strapped porphyrins containing a bridge across the porphyrin plane connecting the two chiral moieties (**55**–**57**, Figure 24).[79,80] This system is analogous to basket handle porphyrin ligands, which will be discussed later in this chapter. The open-faced structure of porphyrins **55**–**57** (Figure 24) required an adequate axial ligand to block the achiral face of the catalyst from playing a role in the epoxidation process. The bulky 1,5-dicyclohexylimidazole (DiCyIm) was identified as a suitable axial ligand. The Mn(III) chloride complex of **57**, [Mn(**57**)Cl], was used as a catalyst for the epoxidation of several aromatic olefins in the presence of DiCyIm (Table 25). [Mn(**57**)Cl] was shown to be capable of epoxidation of a range of olefin substrates, including an example of an aliphatic olefin. Good yields and enantioselectivities were generally obtained.

Boitrel and coworkers synthesized and evaluated a series of Fe(III) chloride complexes of porphyrins as catalysts for asymmetric epoxidation. The ligand systems produced (including picket fence, strapped, and basket handle porphyrins) all contained chiral proline units, which served as chiral auxiliaries (Figure 25). The Fe(III) chloride complexes of these ligands were tested for their ability to epoxidize 4-chlorostyrene and 1,2-dihydronaphthalene.[81,82] The enantioselectivity of these reactions is summarized in Table 26. The only catalyst which displayed enhanced enantiomeric performance for both 4-chlorostyrene and 1,2-dihydronaphthalene was $\alpha,\alpha,\beta,\beta$-**61** (entry 7, Table 26).

Table 25. Asymmetric epoxidation of olefins catalyzed by [Mn(**57**)Cl].[79,80]

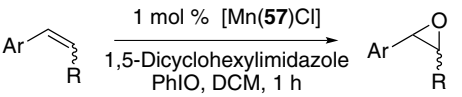

Entry[a]	Substrate	Temp (°C)	Yield (%)	ee (%)
1	Styrene	25	86	69 (*R*)
2	4-Chlorostyrene	25	83	70 (*R*)
3	2-Nitrostyrene	25	46	74
4	2-Methylstyrene	25	65	79
5	*cis*-β-Methylstyrene	25	89	78 (1*R*,2*S*)
6	*cis*-β-Methylstyrene	0	76	80 (1*R*,2*S*)
7	*trans*-β-Methylstyrene	25	81	21 (1*S*,2*S*)
8	1,2-Dihydronaphthalene	25	86	84 (1*R*,2*R*)
9	1,2-Dihydronaphthalene	0	67	87 (1*R*,2*R*)
10	1,2-Dihydronaphthalene	–10	26	88 (1*R*,2*R*)
11	Indene	25	84	74

[a] The reactions were performed with 1 mol % of catalyst, 1 equiv. of PhIO, and 100 equiv. of substrate in DCM.

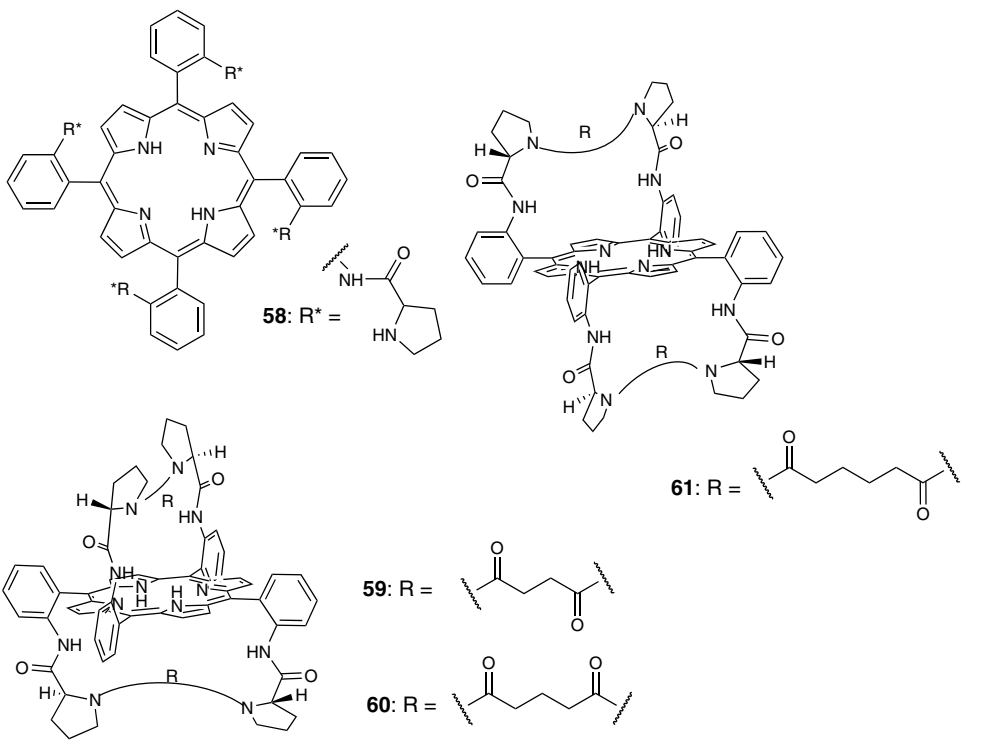

Figure 25. Proline-derived porphyrin ligands.[81,82]

Table 26. Asymmetric epoxidation of olefins by [Fe(**58–61**)Cl].[81,82]

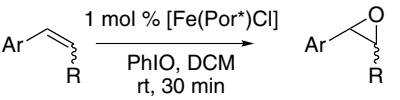

Entry[a]	Por*	4-Chlorostyrene (% ee)	1,2-Dihydronaphthalene (% ee)
1	*αβαβ*-**58**	16	34
2	*αααβ*-**58**	4	9
3	*αααβ*-**58**	10	14
4[b]	*αααα*-**58**	22	10
5	*αβαβ*-**59**	17	0
6	*αβαβ*-**60**	42	4
7	*αααβ*-**61**	31	26

[a] Reactions were performed with 1 mol % of catalyst, 1 equiv. of oxidant, and 10 equiv. of substrate in DCM at rt for 30 min; [b] 1-(*tert*-butyl)-5-phenylimidazole used as axial ligand (2.5 equiv.).

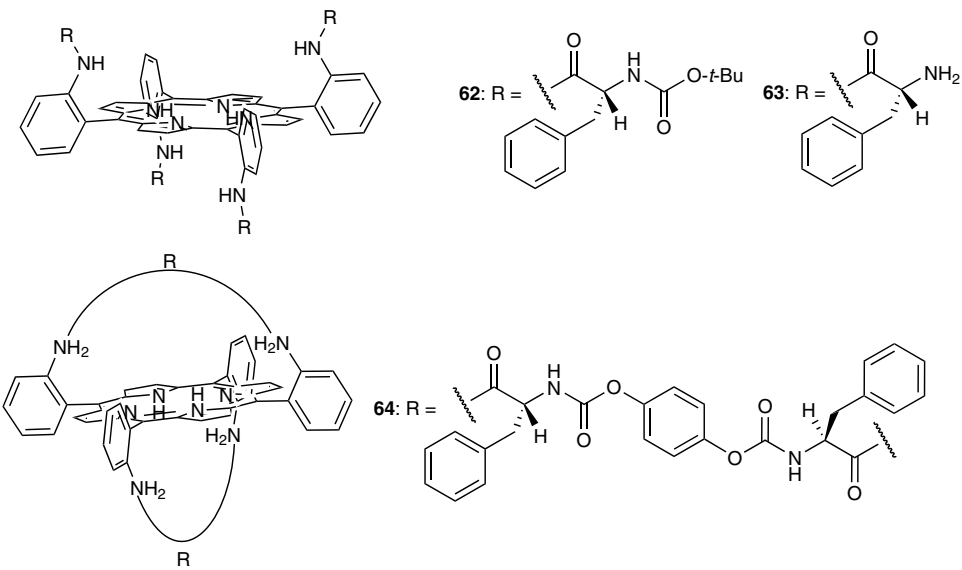

Figure 26. Picket fence and basket handle porphyrins bearing amino acids.[83]

C. Chiral Basket Handle Porphyrins

Mansuy and coworkers reported the first example of a basket handle porphyrin for the epoxidation of 4-chlorostyrene (**64**, Figure 26).[83] The rigid chiral environment was inspired by the desire to mimic the active site of cytochrome P-450. In the course of the development of **64**, precursors **62** and **63** (picket fence type ligands)

Table 27. Comparison of picket fence and basket handle porphyrins as catalysts for the asymmetric epoxidation of 4-chlorostyrene.[83]

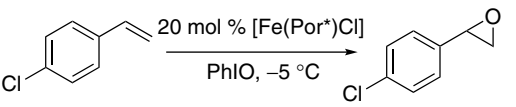

Entry[a]	Por*	Yield (%)	ee (%)
1	**62**	60	12 (*S*)
2	**63**	45	21 (*S*)
3	**64**	35	50 (*R*)

[a] Reactions were performed with 20 mol % of catalyst, 1 equiv. of oxidant, and 300 equiv. of substrate in DCM at –5 °C in a 1:1 ratio of DCM and benzene for 3 h.

were also evaluated for the epoxidation of 4-chlorostyrene (Table 27). In general, the iron basket handle porphyrin [Fe(**64**)Cl] was shown to be a superior catalyst in terms of selectivity when compared to the picket fence complexes [Fe(**62**)Cl] and [Fe(**63**)Cl]. However, it is noted that this system required high catalyst loadings (20 mol %) and generated only modest yields (35–50%) and enantioselectivities (12–50% ee).

Groves and Viski developed a basket handle derivative of their picket fence porphyrin using a binaphthyl bridge as shown in Figure 27.[84] Iron and manganese complexes of **65** were used as catalysts for the epoxidation of a number of different olefins (Table 28). This system was shown to be suitable for a range of aromatic and aliphatic olefins, generating low to moderate enantioselectivities. The low enantioselectivities reported were believed to result from the oxidative poisoning of the catalyst over the course of the reaction.[85] In the case of bulky substrates such as *cis*-β-methylstyrene, good asymmetric induction was achieved with the iron complex [Fe(**65**)Cl] (entry 6, Table 28).

Collman and coworkers also synthesized a basket handle porphyrin using binaphthyl groups. The iron complex of the "binap-capped" porphyrin **66**, shown in Figure 28, was used for the asymmetric epoxidation of mono- and di-substituted aromatic olefins to generate epoxides with moderate yields and enantioselectivities (Table 29).[86]

Inspired by the metalloenzyme cytochrome P-450, Inoue and coworkers synthesized a series of basket handle porphyrin ligands with optical antipodes, as shown in Figure 29. The iron complexes of these ligands were prepared and used as catalysts for the epoxidation of aromatic olefins as shown in Table 30.[87,88] Various axial ligands were used to coordinate to the open face of the porphyrin in

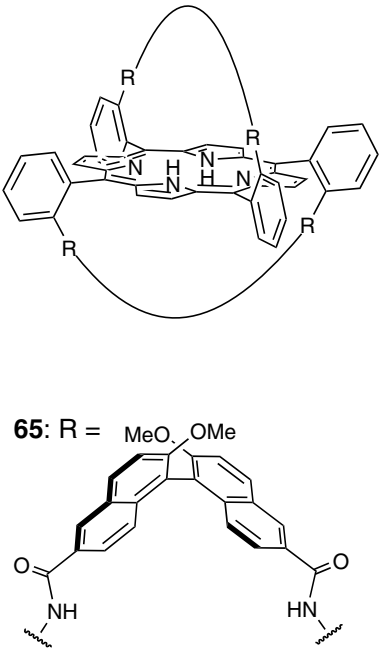

Figure 27. Vaulted binaphthyl porphyrins.[84]

Table 28. Asymmetric epoxidation of olefins catalyzed by [Fe(**65**)Cl].[84,85]

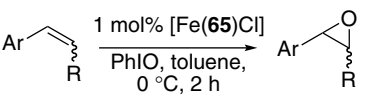

Entry[a]	Substrate	Yield (%)	ee (%)
1	Styrene	23	30 (*R*)
2[b]	Styrene	21	36 (*R*)
3	4-Chlorostyrene	39	38 (*R*)
4	*tert*-Butylethylene	14	40 (*S*)
5	*trans*-*β*-Methylstyrene	43	~1 (1*S*,2*S*)
6	*cis*-*β*-Methylstyrene	35	62 (1*S*,2*R*)
7[b]	*cis*-*β*-Methylstyrene	27	6 (1*S*,2*R*)
8	*trans*-2-Pentene	42	32 (1*S*,2*S*)
9	Indene	70	20 (1*S*,2*S*)
10	1,2-Dihydronaphthalene	61	42 (1*S*,2*S*)

[a] Reactions were performed with 1 mol % of catalyst, 1 equiv. of oxidant, and 10 equiv. of substrate in toluene (iodobenzene for low boiling point products) at 0 °C for 2 h; [b] [Mn(**65**)Cl] used as catalyst.

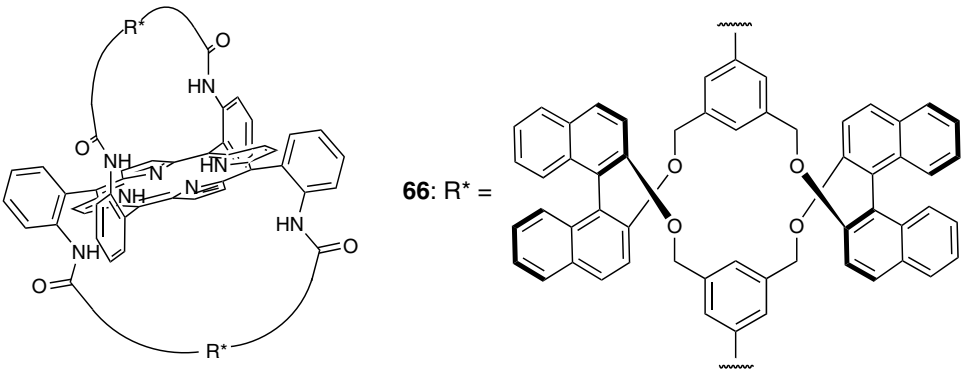

Figure 28. "Binap-capped" porphyrin.[86]

Table 29. Asymmetric epoxidation of aromatic olefins catalyzed by [Fe(**66**)Cl].[86]

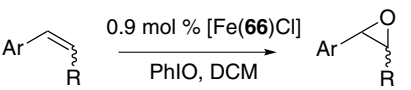

Entry[a]	Substrate	Yield (%)	ee (%)
1	Styrene	62	48 (*S*)
3	4-Chlorostyrene	64	50 (*S*)
4	4-Nitrostyrene	39	56 (*S*)
5	2-Vinylnaphthalene	36	63 (*S*)
6	*cis*-*β*-Methylstyrene	59	29 (1*S*,2*R*)
8	1,2-Dihydronaphthalene	45	21 (1*S*,2*R*)

[a] Reactions were performed with 0.9 mol % of catalyst, 1 equiv. of oxidant, and 27 equiv. of substrate in DCM.

an effort to prevent the generation of racemic products. As anticipated, both enantiomers of catalyst **67** gave similar results with opposite senses of asymmetric induction (entries 1–2, Table 30). The omission of the requisite axial ligand led to an increase in the overall product yield, but with a significant drop in enantiomeric excess as shown in entry 3 (Table 30).

III. Cyclopropanation

Metal-catalyzed cyclopropanation of olefins with diazo reagents has attracted interest due to the fundamental and practical importance of the resulting cyclopropyl units.[89–92] Cyclopropane rings are recurrent motifs in biologically important molecules and can serve as versatile precursors in organic synthesis.[93–96] Currently,

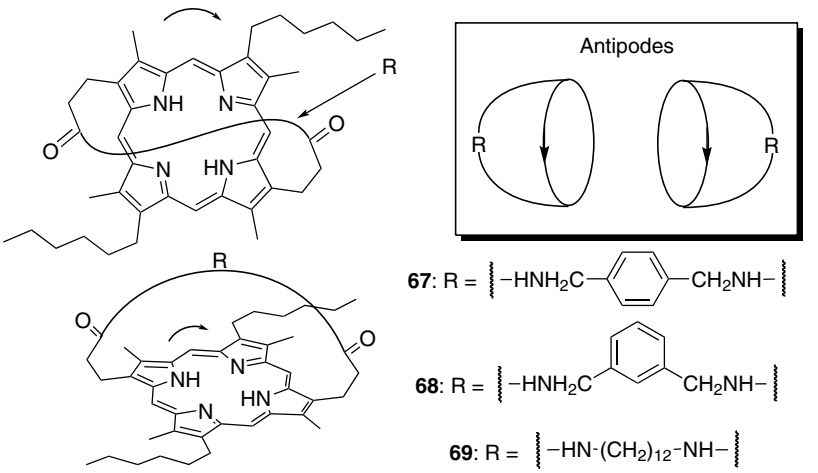

Figure 29. Basket handle type porphyrin antipodes.[87,88]

Table 30. Asymmetric epoxidation of aromatic olefins catalyzed [Fe(**67**–**69**)Cl].[87,88]

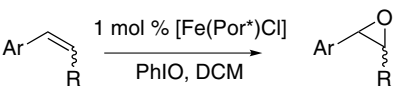

Entry[a]	Substrate	Por*[b]	Axial ligand	Yield (%)	ee (%)
1	Styrene	(+)-**67**	Imidazole	43	49 (*R*)
2	Styrene	(–)-**67**	Imidazole	45	48 (*S*)
3	Styrene	(+)-**67**	None	72	18 (*S*)
4	Styrene	(+)-**67**	1-Ethylimidazole	68	50 (*R*)
5	4-Chlorostyrene	(–)-**67**	Imidazole	41	42 (*S*)
6	4-Chlorostyrene	(–)-**67**	2-Methylimidazole	40	42 (*S*)
7	4-Chlorostyrene	(–)-**67**	2-Phenylimidazole	36	8 (*S*)
8	4-Methylstyrene	(+)-**67**	Imidazole	56	47 (*R*)
9	2-Vinylnaphthalene	(+)-**67**	Imidazole	65	42 (*R*)
10	Indene	(+)-**67**	Imidazole	58	58 (1*R*,2*S*)
11	1,2-Dihydronaphthalene	(+)-**67**	Imidazole	32	52 (1*R*,2*S*)
12	Styrene	(+)-**68**	1-Ethylimidazole	27	30 (*R*)
13	Styrene	(+)-**68**	None	18	16 (*S*)
14	Styrene	(+)-**69**	1-Ethylimidazole	33	17 (*R*)
15	Styrene	(+)-**69**	None	30	16 (*S*)

[a] Reactions were performed with 1 mol % of catalyst, 10 mol % of axial ligand, 1 equiv. of oxidant, and 5 equiv. of substrate in DCM for 3 h at –10 °C; [b] See Figure 29 for structures.

the metal-mediated decomposition of diazo reagents in the presence of olefins constitutes the most direct route to the synthesis of cyclopropanes. This approach provides the advantage of using achiral reagents with the induction of chirality occurring as a direct result of the chiral environment of the catalysts. Prior to the development of catalytic systems capable of decomposing diazo reagents, the Simmons–Smith reaction was the predominant method for cyclopropanation,[91] and chiral starting materials or chiral auxiliaries were required for asymmetric induction.

In the last 20 years, a number of metal-mediated asymmetric cyclopropanation systems incorporating copper, ruthenium, cobalt, rhodium, and various ligands have been developed.[97–104] Copper bisoxazoline and dirhodium complexes are examples of some of the more general and selective catalysts that have been prepared. For example, Doyle's use of dirhodium carboxamides as catalysts for the general and selective asymmetric intramolecular cyclopropanation with diazo reagents has achieved broad use in the chemical literature.[103–110]

Among the wide variety of catalytic systems, metalloporphyrin-based ligand designs are unique, owing to their excellent selectivities and high catalytic TON. Metalloporphyrins were first used as catalysts for cyclopropanation by Callot and coworkers.[111,112] Their initial reports on rhodium-catalyzed cyclopropanation were significantly expanded by Kodadek and coworkers.[113–119] Woo and coworkers showed that osmium porphyrins could also catalyze the cyclopropanation of alkenes, although with less efficiency.[120] Subsequently, Kodadek, Woo, and coworkers jointly reported that iron porphyrins were effective catalysts for the shape-selective and stereoselective cyclopropanation of alkenes.[121] These early works paved a solid foundation for the subsequent development of highly diastereoselective and enantioselective catalysts.

In the following sections, the asymmetric cyclopropanation of alkenes using metalloporphyrins will be discussed. This section will follow the same general outline as the epoxidation section. The robust Halterman porphyrin **8**, examined in various systems for the epoxidation of alkenes, has historically been one of the most widely studied chiral porphyrin ligands for cyclopropanation. More recently, the development of Co(II) complexes of a new family of D_2-symmetric chiral porphyrins capable of high levels of stereocontrol over an expansive substrate scope has broadened the use of metalloporphyrin-based catalysts for asymmetric cyclopropanation.

A. Chiral Picket Fence Porphyrins

Inspired by the previous reports of Doyle[105,106,110] and Callot[111,112] who used rhodium complexes for the cyclopropanation of olefins, O'Malley and Kodadek employed their "chiral wall" porphyrin (**6**, Figure 4, Section II.A) as a ligand for rhodium-catalyzed asymmetric cyclopropanation.[116,117,119] Based on Callot's work, they

believed that the use of the bulky "chiral wall" ligand would favor *cis* cyclopropane isomers, which are normally the minor products in most catalytic cyclopropanations. As anticipated, the *cis*-isomer was generated when the Rh(III) iodide complex of **6** was employed for the asymmetric cyclopropanation of styrene, *cis*-β-methylstyrene, and allyl benzene in the presence of ethyl diazoacetate (EDA). The TON for this catalytic system were outstanding with up to 4,500 TON obtained for the cyclopropanation of *cis*-β-methylstyrene. In all the cases examined, the *cis* isomer was favored over the *trans*, although the *trans* product exhibited significantly higher enantioselectivity (Table 31).

Kodadek and O'Malley designed and synthesized a new chiral porphyrin, termed the "chiral fortress" (**70**, Figure 30), incorporating bulkier aromatic rings

Table 31. Asymmetric cyclopropanation of olefins catalyzed by [Rh(**6**)I].[117,119]

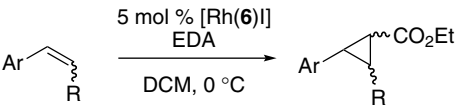

Entry[a]	Substrate	*cis*/*trans*	ee (%) *cis*	ee (%) *trans*	TON
1	Styrene	2.3	10	—	2000
2	*cis*-β-Methylstyrene	7.8	20	50	4500
3	Allylbenzene	4.3	45	60	550

[a] Reactions were performed with 5 mol % of catalyst, 1 equiv. of substrate, and 1 equiv. of EDA in DCM at 0 °C. EDA was added in 0.25 equiv. portions over the course of the reaction.

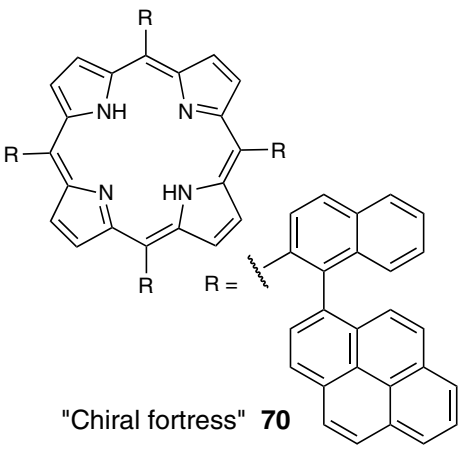

Figure 30. "Chiral fortress" porphyrin.[116]

Table 32. Asymmetric cyclopropanation of olefins catalyzed by [Rh(**70**)I].[116]

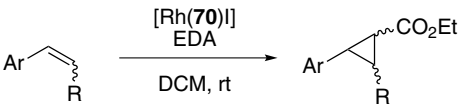

Entry[a]	Substrate	*cis*/*trans*	ee (%) *cis*	ee (%) *trans*	TON
1	Styrene	2.5	15	—	1600
2	*cis*-β-Methylstyrene	5.1	25	20	770
3	Allylbenzene	1.0	10	10	420
4	Ethoxyethane	0.83	15	10	130

[a] Reactions were performed with [Rh(**70**)I] as catalyst, 1 equiv. of substrate, and 1 equiv. of EDA in DCM at rt. EDA was added in 0.25 equiv. portions over the course of the reaction.

in an effort to enhance the formation of the *cis*-cyclopropanated products.[116] The rhodium complex of **70**, [Rh(**70**)I], was shown to be an active catalyst for the cyclopropanation of olefins. In comparison to the "chiral wall", [Rh(**6**)I], the *cis*:*trans* ratio was only slightly improved for styrene, and a decrease in diastereoselectivity was observed for all other substrates (Table 32). It was concluded that the active site was too sterically encumbered to induce similar levels of selectivity in comparison to the "chiral wall".

In 1997, Simonneaux and coworkers reported the successful use of ruthenium porphyrins such as [Ru(**71**)$(O)_2$] (Scheme 14) for the asymmetric cyclopropanation of olefins with EDA.[122] Previous studies using this system reported complex mixtures of products, with EDA dimerization identified as the major product of the reaction. The introduction of EDA over several hours minimized the formation of these side products and produced the desired cyclopropane derivatives with good diastereoselectivity albeit low enantioselectivity (Scheme 14). This technique ultimately proved useful for most rhodium, iron, and ruthenium systems.

Che and coworkers expanded their previous work on Halterman complexes by using ruthenium complexes, [Ru(**8**)(CO)] and [Ru(**8**)(CPh_2)] (Figure 5, Section II.A), as catalysts for the cyclopropanation of styrene derivatives with diazo reagents (Tables 33 and 34).[123,124] Overall, the [Ru(**8**)(CO)] complex generated higher yields and greater diastereo- and enantioselectivities over a range of aromatic olefins in comparison to [Ru(**8**)(CPh_2)]. In addition, the catalytic efficiency of both of these complexes were shown to be outstanding, providing TONs greater than 1,200.

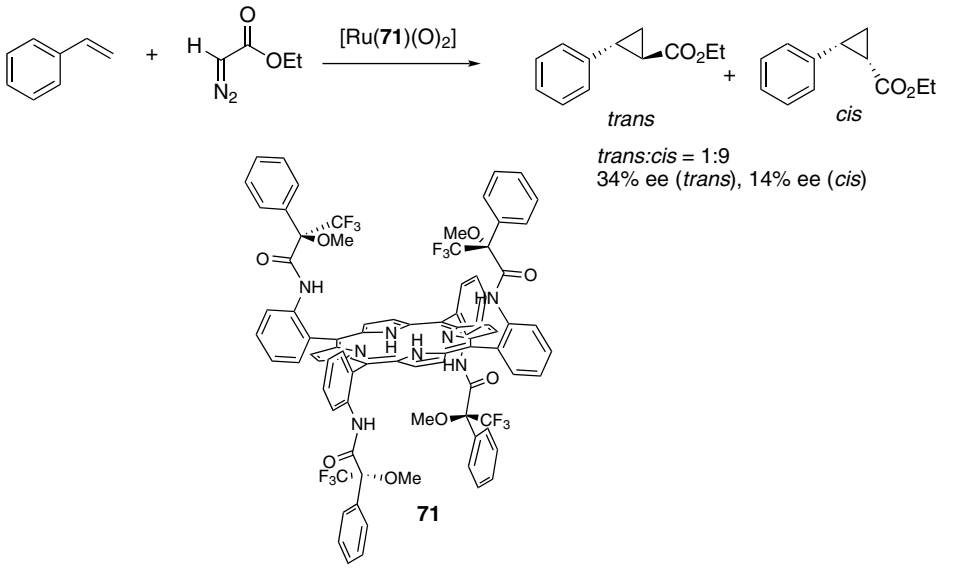

Scheme 14.[122]

Table 33. Asymmetric cyclopropanation of aromatic olefins catalyzed by [Ru(**8**)(CO)].[123,124]

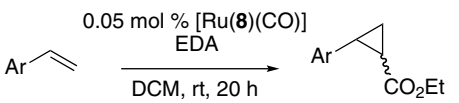

				ee (%)		
Entry[a]	Substrate	Yield (%)	*trans/cis*	*trans*	*cis*	TON
1	Styrene	83	18	87	4	1700
2	α-Methylstyrene	69	3.0	87	35	1400
2	4-Chlorostyrene	66	23	90	4	1300
3	4-Fluorostyrene	83	19	87	3	1700
4	4-Methylstyrene	78	18	81	9	1600
5	4-Methoxystyrene	61	15	85	8	1200

[a] Reactions were performed with 0.05 mol % of catalyst, 1 equiv. of EDA, and 5 equiv. of substrate in DCM at room temperature for 20 h.

The ruthenium carbonyl complex of the Halterman porphyrin, [Ru(**8**)(CO)], was also examined as a potential catalyst for intramolecular cyclopropanation to produce valuable cyclopropyl fused ring products (Table 35). Although the yields and enantioselectivities reported for these cyclopropanes are low to moderate, this represents one of the first reports of asymmetric intramolecular cyclopropanation catalyzed by a ruthenium porphyrin complex.

Table 34. Asymmetric cyclopropanation of aromatic olefins catalyzed by [Ru(**8**)(CPh_2)].[123,124]

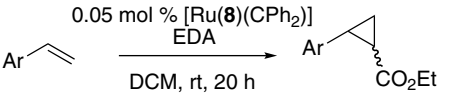

Entry[a]	Substrate	Yield (%)	*trans/cis*	ee (%) *trans*	ee (%) *cis*	TON
1	Styrene	36	11.0	83	7	720
2	α-Methylstyrene	72	5.6	66	25	1400
2	4-Chlorostyrene	61	5.2	88	40	1200
3	4-Fluorostyrene	71	8.4	85	12	1400
4	4-Methylstyrene	62	4.1	71	—	1200
5	4-Methoxystyrene	75	12	71	9	1500

[a] Reactions were performed with 0.05 mol % of catalyst, 1 equiv. of EDA, and 5 equiv. of substrate in DCM at room temperature for 20 h.

Table 35. Intramolecular asymmetric cyclopropanation catalyzed by [Ru(**8**)(CO)].[123,124]

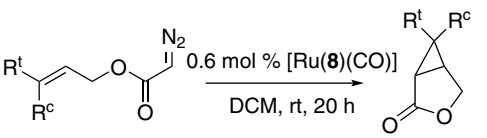

Entry[a]	R^t	R^c	Yield (%)	ee (%)
1	H	H	45	24 (1*R*,5*S*)
2	Me	Me	65	36 (1*R*,5*S*)
3	Me	H	65	28
4	Ph	H	60	85 (1*R*,5*R*)

[a] Reactions were performed with 0.6 mol % of catalyst and 1 equiv. of substrate in DCM at room temperature for 20 h.

Che and coworkers investigated ruthenium and rhodium complexes of the Halterman porphyrin **8** for both inter- and intramolecular asymmetric cyclopropanation.[125] As presented in Tables 36 and 37, for both inter- and intramolecular cyclopropanation systems, [Ru(**8**)(CO)] generated higher diastereo- and enantioselectivities. Despite using catalysts with the same ligand environment, an "enantiomeric switch" was observed for one of the substrates when the rhodium metal was exchanged with ruthenium (entry 4, Table 37). These results led to the assumption that these two metal complexes cyclopropanate via different mechanistic pathways, generating the two different enantiomers.

Table 36. Asymmetric cyclopropanation of aromatic olefins catalyzed by rhodium and ruthenium complexes of **8**.[125]

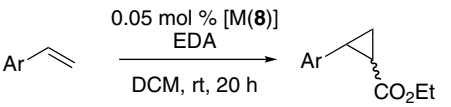

		[Rh(**8**)I]				[Ru(**8**)(CO)]			
				ee (%)				ee (%)	
Entry[a]	Substrate	Yield (%)	*trans/cis*	*trans*	*cis*	Yield (%)	*trans/cis*	*trans*	*cis*
1	Styrene	66	1.5	61	36	83	18	86	4
2	α-Methylstyrene	75	1.0	46	46	69	3.0	87	35
2	4-Chlorostyrene	81	1.2	62	20	66	23	90	4
3	4-Fluorostyrene	72	0.9	62	33	83	19	87	3
4	4-Methylstyrene	71	1.2	49	42	78	18	81	9
5	4-Methoxystyrene	83	1.6	68	44	61	15	85	8

[a] Reactions were performed with 0.05 mol % of catalyst, 1 equiv. of EDA, and 5 equiv. of substrate in DCM at room temperature for 20 h.

Table 37. Intramolecular asymmetric cyclopropanation catalyzed by rhodium and ruthenium complexes of **8**.[125]

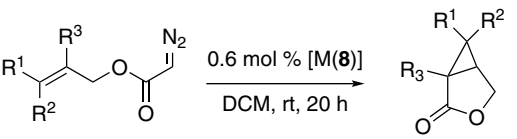

				[Rh(**8**)I]		[Ru(**8**)(CO)]	
Entry[a]	R1	R2	R3	Yield (%)	ee (%)	Yield (%)	ee (%)
1	H	H	H	23	20 (1*R*,5*S*)	48	24 (1*R*,5*S*)
2	Me	Me	H	81	37 (1*R*,5*S*)	65	36 (1*R*,5*S*)
3	Me	H	H	33	24 (1*R*,5*S*)	65	41 (1*R*,5*S*)
4	Ph	H	H	84	20 (1*R*,5*S*)	77	85 (1*S*,5*R*)
5	H	Ph	H	31	31 (1*R*,5*S*)	18	22 (1*R*,5*S*)

[a] Reactions were performed with 0.6 mol % of catalyst and 1 equiv. of substrate in DCM at room temperature for 20 h.

Che and coworkers also reported the use of ruthenium complex [Ru(**8**)(CO)] encapsulated in mesoporous molecular sieves for intramolecular cyclopropanation.[40] Although only one example was reported (Scheme 15), the catalytic system generated a respectable enantioselectivity (85% ee) and could be reused up to four times. The results from this heterogeneous system were comparable to the corresponding homogenous system (Table 37).

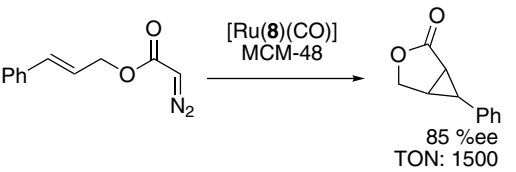

Scheme 15.[40]

Table 38. Asymmetric cyclopropanation of aromatic olefins catalyzed by [Fe(**8**)Cl].[126]

Entry[a]	Substrate	Yield (%)	*trans*:*cis*	trans ee (%)	TON
1	Styrene	71	12:1	80	368
2	4-Chlorostyrene	57	18:1	75	284
3	4-Methylstyrene	56	12:1	79	424
4	4-Methoxystyrene	65	13:1	74	416
5	α-Methylstyrene	68	3:1	81	390
6	1,1-Diphenylethane	72	—	83[b]	410

[a] Reactions were performed with 0.5 mol % of catalyst, 1 equiv. of EDA, and 5 equiv. of substrate in DCM at room temperature. 4 h slow addition of EDA is followed by 1 h of stirring in DCM; [b] *Z* isomer.

Iron complex [Fe(**8**)Cl] was also reported by Che and coworkers for asymmetric cyclopropanation with ethyl diazoacetate. The diastereo- and enantioselectivities reported were similar to those of the aforementioned rhodium and ruthenium complexes (Table 38).[126] However, the iron complex produced the cyclopropanes with lower TON in comparison to the ruthenium complex (Tables 38 and 33). Further investigation of the iron-catalyzed system showed that the use of nitrogen-based axial ligands could improve the diastereo- and enantioselectivity across a range of substrates as shown in Table 39. However, the use of an axial ligand resulted in even lower TON as shown in Table 39.

Berkessel and coworkers evaluated ruthenium complexes of the Halterman porphyrin **8** and its derivatives **9–11** (Figure 6, Section II.A)[42] as catalysts for the cyclopropanation of aromatic olefins using the slow addition method for the introduction of EDA (Table 40). Excellent diastereoselectivities and high enantioselectivities were observed with all ligand derivatives when styrene was used as the substrate (entries 1–5, Table 40). Results showed that the derivatization of the *para*-phenyl position of the *meso*-aryl group with electron-donating or -withdrawing groups did not have a pronounced effect on the diastereo- and enantioselectivity in comparison to the metal complexes of the Halterman porphyrin.

Table 39. Asymmetric cyclopropanation of styrene catalyzed by [Fe(**8**)L].[126]

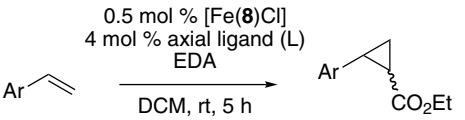

Entry[a]	Axial ligand (L)	*trans*:*cis*	*trans* ee (%)	TON
1	—	12:1	80	368
2	Pyridine	33:1	82	307
3	DMAP	24:1	81	321
4	1-Methylimidazole	26:1	83	275
5	1-Methylpyrrolidine	27:1	86	293
6	4-Phenylpyridine-*N*-oxide	23:1	83	209
7	DMSO	17:1	82	385

[a] Reactions were performed with 0.5 mol % of catalyst, 4 mol % of axial ligand (L), 1 equiv. of EDA, and 5 equiv. of substrate in DCM at room temperature for 4 h slow addition is followed by 1 h of stirring in DCM.

Table 40. Asymmetric cyclopropanation of olefins catalyzed by [Ru(**8**–**11**)(CO)].[42]

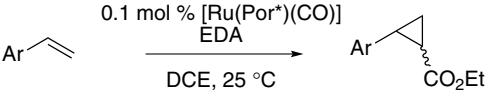

Entry[a]	Substrate	Por*[b]	Conversion (%)	*trans*:*cis*	ee *trans* (%)	ee *cis* (%)
1	Styrene	**8**	80	96:4	87 (1*S*,2*S*)	14 (1*S*,2*R*)
2	Styrene	*ent*-**9**	81	96:4	90 (1*R*,2*R*)	31 (1*R*,2*S*)
3	Styrene	*ent*-**10**	83	96:4	89 (1*R*,2*R*)	11 (1*R*,2*S*)
4	Styrene	**11**	94	97:3	89 (1*S*,2*S*)	<1
5	Styrene	**8**[c]	81	96:4	87 (1*S*,2*S*)	14 (1*S*,2*R*)
6	α-Methylstyrene	**8**	79	66:34	90 (1*S*,2*S*)	38 (1*S*,2*R*)
7	α-Methylstyrene	*ent*-**9**	76	68:32	91 (1*R*,2*R*)	43 (1*R*,2*S*)
8	α-Methylstyrene	*ent*-**10**	81	67:33	91 (1*R*,2*R*)	46 (1*R*,2*S*)
9	α-Methylstyrene	**11**	>98	69:31	91 (1*S*,2*S*)	36 (1*S*,2*R*)
10	α-Methylstyrene	**8**[c]	78	66:34	90 (1*S*,2*S*)	38 (1*S*,2*R*)
11	1-Hexene	**8**	20	86:14	46 (1*S*,2*S*)	9
12	1-Hexene	*ent*-**9**	15	85:15	40 (1*R*,2*R*)	<2
13	1-Hexene	*ent*-**10**	20	82:18	39 (1*R*,2*R*)	<2
14	1-Hexene	**11**	30	85:15	46 (1*S*,2*S*)	4
15	1-Hexene	**8**[c]	42	99.5:0.5	32 (1*S*,2*S*)	6

[a] Reactions were performed with 0.1 mol % of catalyst, 1 equiv. of substrate, and 1 equiv. of EDA in DCE at 0 °C. Diazo was added by means of a syringe pump over 2 h; [b] See Figure 6 for structures; [c] [Ru(**8**)PF_3] used as catalyst.

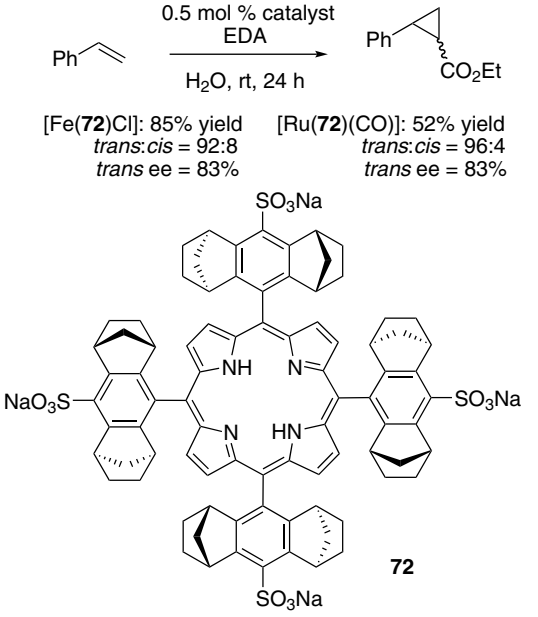

Scheme 16.[127]

Simonneaux and coworkers reported the synthesis of a water-soluble Halterman porphyrin derivative (**72**, Scheme 16) and the use of its iron and ruthenium complexes for the cyclopropanation of styrene with EDA.[127] While both [Fe(**72**)Cl] and [Ru(**72**)(CO)] catalysts displayed very similar diastereo- and enantioselectivities, the iron complex provided superior yields (Scheme 16). It was also noted that the iron complex was recyclable up to four times, with no significant decrease in enantioselectivity while retaining excellent diastereoselectivity. However, the enantioselectivity and yield of the cyclopropanated product generated by the ruthenium complex decreased significantly after the first cycle.

Continued development by Simonneaux and coworkers led to the introduction of heterogeneous catalytic systems for olefin cyclopropanation, and in 2005 they introduced the use of a heterogeneous polymer-supported Halterman porphyrin system as a catalyst for the cyclopropanation of olefins (Figure 31). Iron and ruthenium complexes of the Halterman porphyrin **8** were incorporated into the backbone of the polymer-based system,[128] and the use of an alternative diazo reagent, trifluorodiazoethane (Table 41), was employed for the first time.[129] The diastereoselectivities reported for this polymer-supported system were excellent, however, the yield and enantioselectivity were only moderate.

Following their use of trifluorodiazoethane, Simmonneaux and coworkers explored bulkier diazo reagents for asymmetric cyclopropanation. For example,

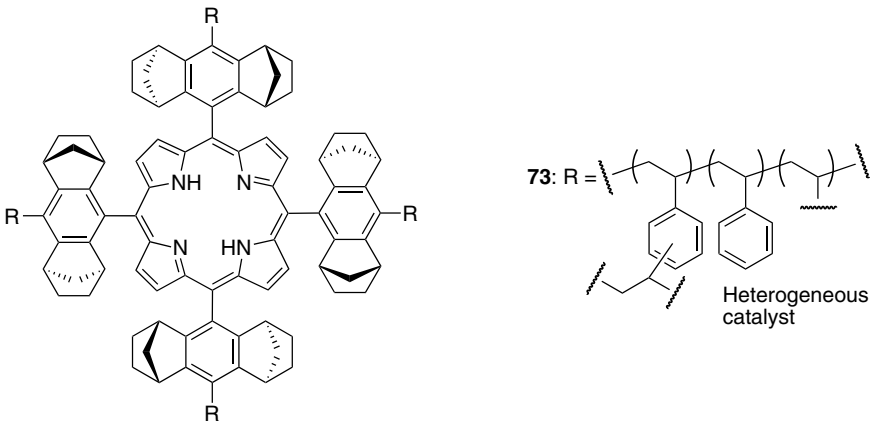

Figure 31. Polymer-supported Halterman ligand.[128]

Table 41. Asymmetric cyclopropanation with trifluorodiazoethane catalyzed by [Fe(**8**)Cl] and [Ru(**73**)(CO)].[128,129]

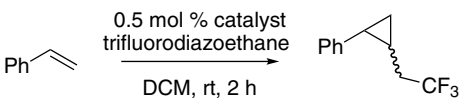

Entry[a]	Catalyst	Yield (%)	*trans:cis*	ee (%, *trans*)
1	[Fe(**8**)Cl]	50	99:1	61
2	[Ru(**8**)(CO)]	32	98:2	58
3	[Fe(**73**)Cl]	52	97:3	56
4	[Ru(**73**)(CO)]	33	99:1	61

[a] Reactions were performed with 0.5 mol % catalyst, 1 equiv. of diazo, and 5 equiv. of substrate in DCM at room temperature for 2 h.

the diazo reagent 2,6-di-*tert*-butyl-4-methylphenyl diazoacetate (Scheme 17) was employed in the cyclopropanation of styrene by [Ru(**8**)(CO)].[130] Although excellent diastereoselectivity was achieved with this system, the yield and enantioselectivity was relatively low. The authors speculated that the low yield and enantioselective outcome was a consequence of the formation of a stable carbene intermediate. Acquisition of a crystal structure of the carbene intermediate supported this claim.

Further studies on the expansion of diazo substrate scope led Simonneaux and coworkers to the use of the ruthenium Halterman complex for the asymmetric cyclopropanation of styrene with diisopropyl diazomethylphosphonate (DAMP).[131] The results, shown in Table 42, demonstrate that excellent diastereo- and

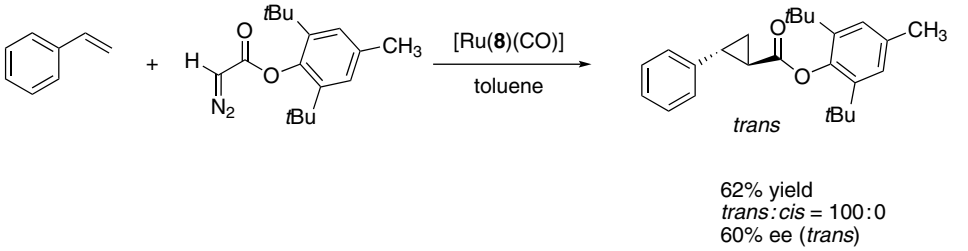

Scheme 17.[130]

Table 42. Asymmetric cyclopropanation of styrene with DAMP catalyzed by [Ru(**8**)(CO)].[131]

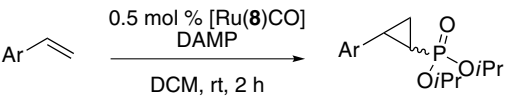

				ee (%)	
Entry[a]	Substrate	Yield (%)	*trans*:*cis*	*trans*	*cis*
1	Styrene	97	96:4	90	34
2	4-Methylstyrene	93	99:1	87	23
3	4-Methoxystyrene	96	97:3	90	23
4	4-Trifluoromethylstyrene	90	95:5	92	5
5	4-Chlorostyrene	92	97:3	88	27

[a] Reactions were performed with 0.5 mol % of catalyst, 1 equiv. of DAMP, and 5 equiv. of EDA in DCM at room temperature for 2 h.

enantioselectivities as well as high product yields could be achieved with this diazo reagent.

Simonneaux and coworkers also reported the design and synthesis of a new porphyrin ligand. The incorporation of a mixture of two types of rigid, bulky groups onto the meso positions of the porphyrin ring generated porphyrin ligands **74**–**76**, as shown in Figure 32. The ruthenium complexes of these Halterman-like porphyrins, bearing 1–4 chiral appendages (with 4 chiral appendages being the Halterman porphyrin **8**) were employed as catalysts for the cyclopropanation of styrene with EDA and DAMP (Table 43). Catalyst [Ru(**74**)(CO)] bearing three chiral groups displayed high levels of asymmetric induction, while ligands [Ru(**75**)(CO)] and [Ru(**76**)(CO)] having only one and two chiral groups, respectively, led to a significant reduction.

In 2006, Cenini and coworkers reported the use of porphyrin **77** for the ruthenium-catalyzed cyclopropanation of α-methylstyrene with EDA (Scheme 18).[132] In comparison to the Halterman porphyrin-based catalysts, this system produced

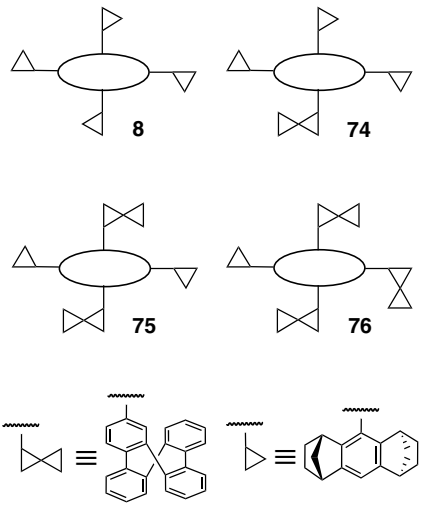

Figure 32. Schematic representation of the chiral porphyrin ligands **74**–**76**.[131]

Table 43. Asymmetric cyclopropanation of styrene with DAMP and EDA catalyzed by ruthenium complexes of Halterman porphyrin **8** and its derivatives **74**–**76**.[131]

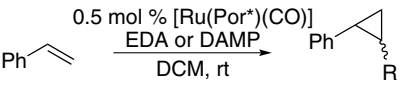

Entry[a]	Por*[b]	Diazo	Yield (%)	*trans*:*cis*	*trans* ee (%)
1	**8**	EDA	96	95:5	87
2	**8**	DAMP	97	96:4	90
3	**74**	EDA	95	93:7	65
4	**74**	DAMP	65	96:4	77
5	**75**	EDA	94	90:10	41
6	**75**	DAMP	55	95:5	66
7	**76**	EDA	96	90:10	25
8	**76**	DAMP	13	96:10	33

[a] Reactions were performed with 0.5 mol % of catalyst, 1 equiv. of diazo, and 5 equiv. of substrate in DCM at room temperature for 2 h (EDA) or 48 h (DAMP). R = CO_2Et from reaction with EDA and R = $P(O)(OiPr)_2$ for reactions with DAMP; [b] See Figure 32 for structures of ligands.

significantly lower selectivities. In the same report, a cobalt complex of **77** was used for the cyclopropanation of styrene with EDA. It was shown that [Co(**77**)] generated slightly greater diastereoselectivities (*trans*:*cis* = 4.4:1) than the ruthenium-catalyzed system. The enantioselectivities of the products generated from this cobalt-catalyzed system were not reported.

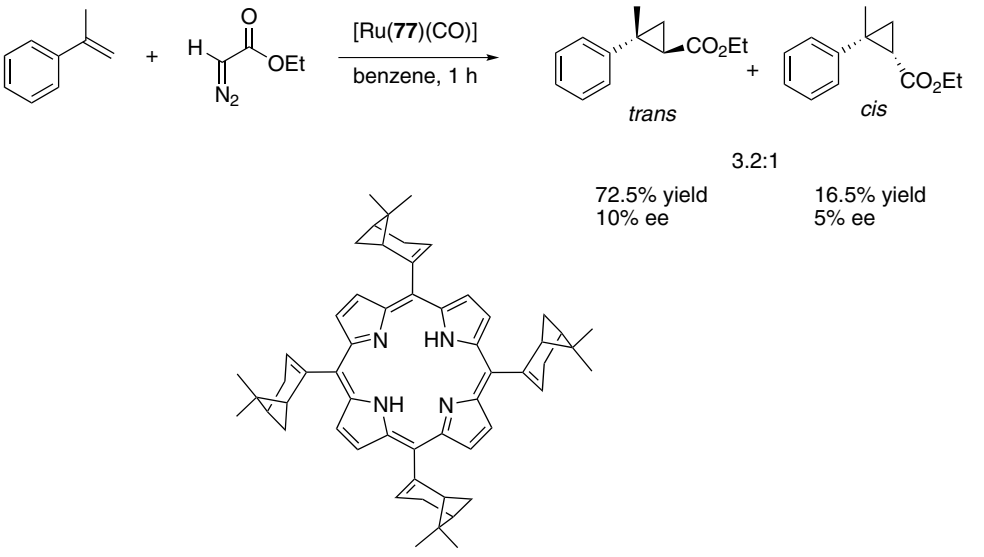

77

Scheme 18.[132]

Independently, Zhang and coworkers also reported some of the first examples of cobalt porphyrin-catalyzed asymmetric cyclopropanations.[133,134] One of the distinct advantages of using cobalt over the existing metal-catalyzed systems was that the slow addition of the diazo reagent was no longer required to inhibit dimer formation.

In the initial report by Zhang and coworkers, cobalt complexes of several chiral porphyrins (**78**–**82**, Figure 33) were prepared and evaluated for the asymmetric cyclopropanation of styrene with EDA (Table 44). Their initial results demonstrated that chiral groups directed toward the metal-center, as with complex **82**, provided the highest selectivities. Continued development of porphyrin ligand systems with chiral groups in close proximity to the metal center led to improved selectivities in Co(II)-catalyzed asymmetric cyclopropanation.

Based on this work, Zhang and coworkers designed and synthesized a series of D_2-symmetric chiral porphyrins for use in cobalt-catalyzed cyclopropanation (Figure 34).[135,136] One notable feature of these systems is the modular design of the porphyrin ligand. The synthetic strategy reported by Zhang and coworkers allows for the direct installation of select chiral amides using a palladium-catalyzed cross-coupling approach between brominated porphyrins and chiral amides. Through selection of the appropriate chiral groups, each of the four diastereomers of the cyclopropanated product could be accessed with excellent enantioselectivity (Scheme 19).

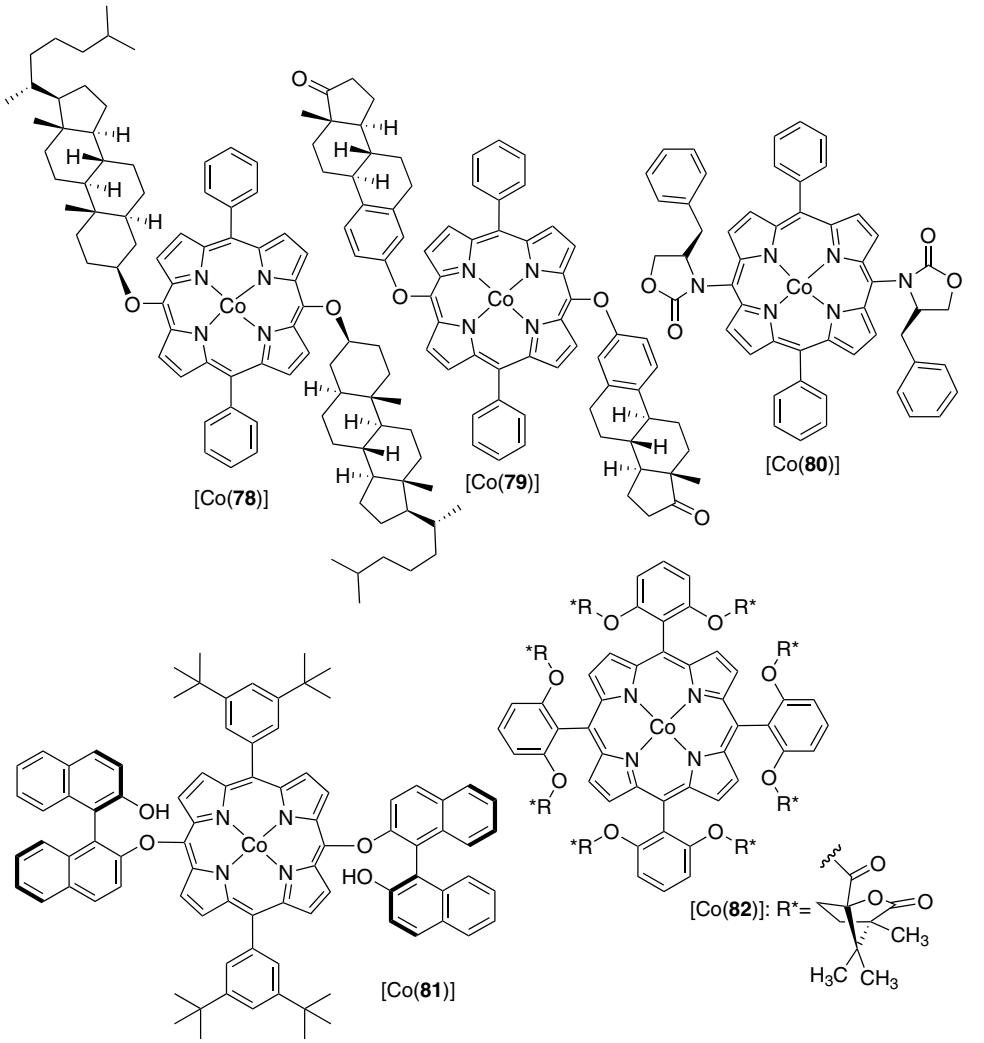

Figure 33. Chiral cobalt porphyrin complexes.[133,134]

The resulting chiral porphyrins (selected examples are shown in Table 45) were evaluated for the cobalt-catalyzed cyclopropanation of styrene with EDA and *tert*-butyl diazoacetate (*t*-BDA). Axial ligands, such as 4-*N*,*N*-dimethylaminopyridine (DMAP), were found to significantly increase diastereo- and enantioselectivity without diminishing the yields (entries 1 and 5, Table 45). Further improvements were achieved by lowering the reaction temperature (entries 8 and 9, Table 45). Given the low cost of cobalt, the "one-pot" process practicality, yield and enantioselectivity, chiral cobalt complexes

Table 44. Asymmetric cyclopropanation of styrene catalyzed by cobalt porphyrin complexes.[133,134]

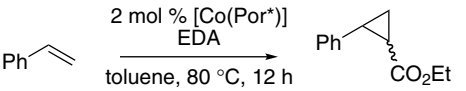

				% ee	
Entry[a]	Por*[b]	Yield (%)	*cis*:*trans*	*cis*	*trans*
1	**82**	73	64:36	77	62
2	**47**	84	48:52	31	10
3	**78**	97	28:72	1	9
4	**79**	99	32:68	1	1
5	**81**	79	36:64	1	1
6	**80**	80	34:66	6	6

[a] Reactions were performed with 2 mol % catalyst, 1.2 equiv. of diazo, and 1 equiv. of styrene at 80 °C for 12 h; [b] See Figures 21 and 33 for structures.

presented themselves as desirable alternatives to other cyclopropanation systems.[137]

Zhang and coworkers continued to focus their attention on increasing the substrate scope of their cobalt-based system (Table 46).[138] The cobalt D_2-symmetric porphyrin **87** was shown to be a suitable catalyst for the asymmetric cyclopropanation of aromatic olefins (entries 1–5, Table 46). However, the most notable feature of this catalytic system was its ability to cyclopropanate electron-deficient olefins, normally shown to be inactive in other cyclopropanation systems (entries 7–10, Table 46).[138]

In 2008, Zhang and coworkers reported the use of diazosulfones as diazo reagents for cobalt-catalyzed cyclopropanation.[139] During the course of this study, it was discovered that a new porphyrin ligand would be required to obtain high enantioselectivities (Figure 35). The results, shown in Table 47, demonstrated that the porphyrin complexes examined in the previous cyclopropanation system (**87**–**88**) did not produce adequate levels of enantioselectivity. Subsequently, ligands **89** and **92** were designed and synthesized in an effort to increase the rigidity and polarity of the chiral environment, thereby enhancing enantioselectivity. The more sterically demanding ligand **92** of the "group of six" (Figure 35) was shown to be the best for supporting cobalt-catalyzed cyclopropanation with diazosulfones (entry 7, Table 47).

With the cobalt complex of ligand **92** identified as the catalyst of choice, the substrate scope was examined (Table 48). Results showed that cobalt-catalyzed

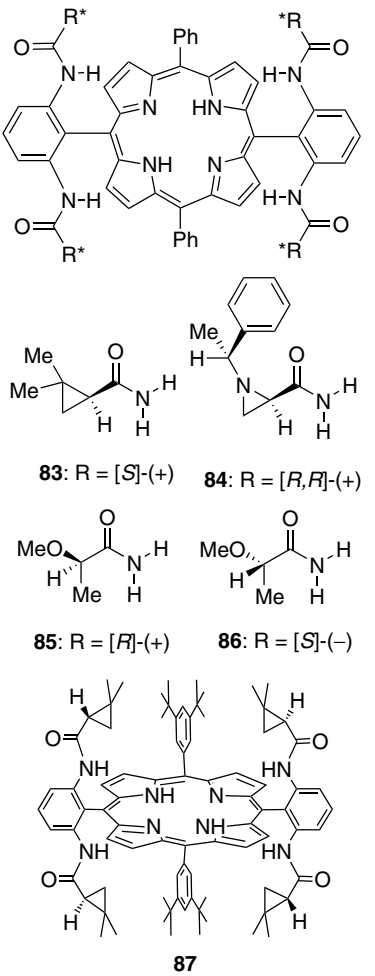

83: R = [*S*]-(+) **84**: R = [*R,R*]-(+)

85: R = [*R*]-(+) **86**: R = [*S*]-(–)

87

Figure 34. D_2-symmetric chiral porphyrins.[135]

cyclopropanation reactions with diazosulfones could be applied to a broad range of olefins, including aromatic and electron-deficient olefins, to generate the desired products with high levels of diastereo- and enantioselectivity.

The use of succinimidyl diazoacetate as a carbene source was examined by Zhang and coworkers for the cobalt-catalyzed cyclopropanation of both aromatic and electron-deficient olefins (Table 49).[140] Both ligands **87** and **90** from the "group of six" (Figure 35) provided excellent diastereo- and enantioselectivities. Although the yields associated with the cyclopropanation of electron-deficient olefins were diminished in this system, the stereoselectivities were still very high. The products of these reactions, cyclopropyl succinimidyl

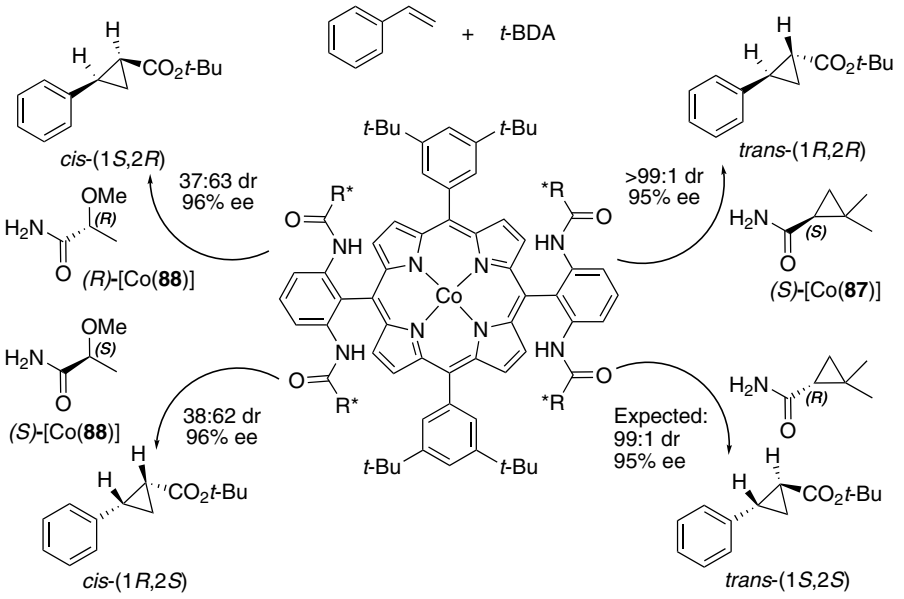

Scheme 19.[135]

Table 45. Asymmetric cyclopropanation of styrene catalyzed by [Co(**83**–**87**)].[135]

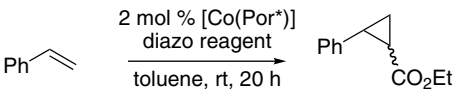

Entry[a]	Por*[c]	Diazo	Additive	Yield (%)	*trans*:*cis*	ee (%)
1	**83**	EDA	—	92	87:13	31
2	**84**	EDA	—	77	66:34	35
3	**85**	EDA	—	92	32:68	48
4	**86**	EDA	—	95	32:68	51
5	**83**	EDA	DMAP	91	96:04	67
6	**87**	EDA	—	89	88:12	43
7	**87**	EDA	DMAP	86	97:03	78
8	**87**	*t*-BDA	DMAP	88	99:01	95
9	**87**	*t*-BDA	DMAP	84	99:01	98

[a] Reactions were performed with 2 mol % catalyst, 1.2 equiv. of diazo, and 1 equiv. of styrene at room temperature for 20 h; [b] –20 °C; [c] See Figure 34 for structures.

esters, are valuable intermediates for the synthesis of cyclopropyl carboxamide derivatives.[140]

Zhang and coworkers also reported on the use of an acceptor/acceptor type diazo reagent, α-nitrodiazoacetate, which was shown to be a suitable diazo source

Table 46. Asymmetric cyclopropanation of olefins with *t*-BDA catalyzed by [Co(**87**)].[135–138]

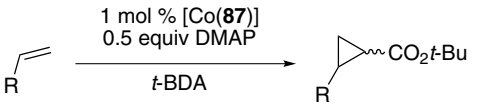

Entry[a]	Substrate	Yield (%)	*trans*:*cis*	ee (%, *trans*)
1	Styrene	84	>99:1	95
2	4-Chlorostyrene	69	98:2	91
3	4-Methoxystyrene	86	98:2	96
4	Pentafluorostyrene	74	97:3	84
5	2-Vinylnaphthalene	84	99:1	98
7[b]	Ethyl acrylate	92	99:1	91
8[b]	Acrylamide	77	99:1	97
9[b]	Pent-1-en-3-one	81	99:1	94
10[b]	Acrylonitrile	83	76:24	93

[a] Reaction conditions: 1 mol % of catalyst, 1.0 equiv. of olefin, 1.2 equiv. of *t*-BDA, and 0.5 equiv. of DMAP in toluene at 25 °C under N_2 for 20 h; [b] Chlorobenzene was used as solvent.

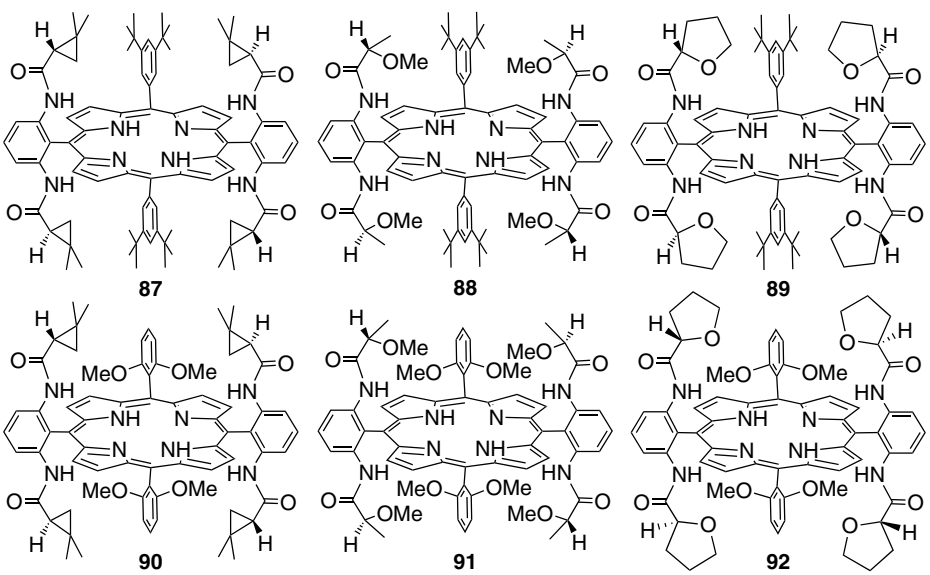

Figure 35. "Group of six" of D_2-symmetric chiral porphyrins.[139]

for use by many cobalt-catalyzed systems.[141,142] The results generated by the "group of six" (Figure 35) in the cyclopropanation of styrene with ethyl α-nitrodiazoacetate (ENDA) are shown in Table 50. Similar to other diazoacetate systems, **87** generated high diastereo- and enantioselectivities (Table 50). Among the solvents examined,

Table 47. Asymmetric cyclopropanation of styrene with diazosulfone catalyzed by Co(II) complexes of the "group of six" porphyrins.[139]

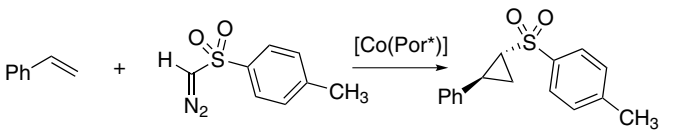

Entry[a]	[Co(Por*)][b]	Additive	Yield (%)	*trans*:*cis*	ee (%) *trans*
1	[Co(**87**)]	DMAP	–6	>99:01	3
2	[Co(**87**)]	—	86	>99:01	14
3	[Co(**88**)]	—	60	>99:01	23
4	[Co(**89**)]	—	30	>99:01	54
5	[Co(**90**)]	—	78	>99:01	56
6	[Co(**91**)]	—	99	>99:01	61
7	[Co(**92**)]	—	99	>99:01	92

[a] Reaction conditions: Performed at 25 °C for 48 h with DCM as solvent using 1 mol % [Co(Por*)] with 1.0 equiv. of styrene and 1.5 equiv. of N_2CHTs; [styrene] = 0.25 M; [b] See Figure 35 for structures.

Table 48. Asymmetric cyclopropanation of olefins with diazosulfone catalyzed by [Co(**92**)].[139]

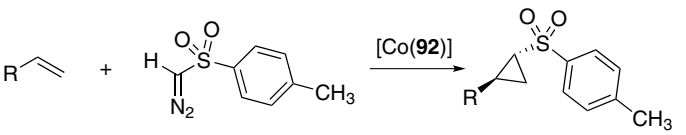

Entry[a]	Substrate	Yield (%)	*trans*:*cis*	ee (%) *trans*
1	Styrene	99	>99:01	92
2	4-*t*-Butylstyrene	57	>99:01	94
3	4-Methoxystyrene	80	>99:01	97
4	4-Trifluoromethylstyrene	72	>99:01	95
5	3-Nitrostyrene	77	>99:01	95
6	2-Vinylnaphthalene	81	>99:01	93
7	Methyl acrylate	96	96:04	89
8	Ethyl acrylate	72	>99:01	90
9	But-3-en-2-one	93	99:01	89
10	Acrylonitrile	81	79:21	61

[a] Reaction conditions: Performed at 25 °C for 48 h with DCM as solvent using 1 mol % [Co(**92**)] with 1.0 equiv. of styrene and 1.5 equiv. of N_2CHTs; [styrene] = 0.25 M.

n-hexane was found to be the preferred solvent, generating the highest enantioselectivity while maintaining high yield and diastereoselectivity (entry 2, Table 50). It was also shown that aromatic and electron-deficient olefins as well as aliphatic olefins were suitable substrates for cyclopropanation with ENDA (Table 51).

Table 49. Asymmetric cyclopropanation of olefins with succinimidyl diazoacetate catalyzed by [Co(**87**)] and [Co(**90**)].[140]

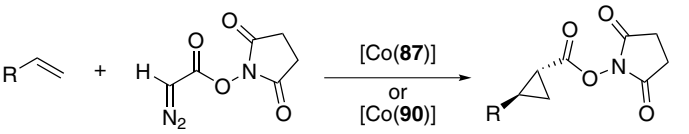

Entry[a]	Substrate	Yield (%)	*trans*:*cis*	ee (%) *trans*
1	Styrene	86	>99:01	92
2[b]	Styrene	70	>99:01	96
3	4-Methylstyrene	90	>99:01	95
4[b]	4-Methylstyrene	71	98:02	96
5	4-*t*-Butylstyrene	80	>99:01	97
6[b]	4-*t*-Butylstyrene	81	>99:01	98
7	4-Methoxystyrene	71	>99:01	95
8[b]	4-Methoxystyrene	75	99:01	97
9	4-Chlorostyrene	66	>99:01	90
10[b]	4-Chlorostyrene	48	>99:01	92
11	4-Trifluoromethylstyrene	77	>99:01	90
12[b]	4-Trifluoromethylstyrene	30	>99:01	94
13	4-Vinylphenyl acetate	71	>99:01	91
14	3-Nitrostyrene	50	>99:01	92
15	2-Vinylnaphthalene	33	99:01	91
16	Ethyl acrylate	57	>99:01	89
17	*N,N*-dimethylacrylamide	52	>99:01	96
18	But-3-en-2-one	55	>99:01	91

[a] Reaction conditions: Performed at 25 °C for 48 h with toluene as solvent using 5 mol % [Co(**87**)] with 1.0 equiv. of styrene and 1.5 equiv. of N_2CHCO_2Suc in the presence of 0.5 equiv. of DMAP; [styrene] = 0.25 M; [b] [Co(**90**)] used as catalyst.

B. Chiral Strapped Porphyrins

In 1998, Simonneaux and coworkers described the use of threitol-strapped ligand **47** (Figure 21), previously reported by Gross and coworkers for epoxidation[72,73] (Section II.B), for the ruthenium-catalyzed asymmetric cyclopropanation of aromatic olefins. The ruthenium complex [Ru(**47**)(CO)] was used with ethyl diazoacetate to generate cyclopropane products with excellent yields and moderate diastereo- and enantioselectivities (Table 52).[143]

In 2003, Simonneaux and coworkers reported on their work with threitol-strapped ruthenium catalysts for the cyclopropanation of styrene with diisopropyl diazomethylphosphonate (DAMP) as the carbene source.[144] The yield and diastereoselectivities (Scheme 20) produced with [Ru(**47**)(CO)] in the presence

Table 50. Asymmetric cyclopropanation of styrene with ENDA catalyzed by Co(II) complexes of the "group of six" porphyrins.[141]

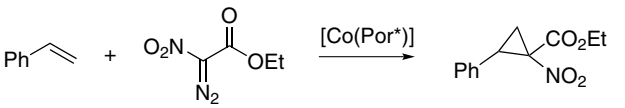

Entry[a]	Por*[b]	Solvent	Yield (%)	*Z*:*E*	ee (%) *Z*
1	[Co(**87**)]	CH_2Cl_2	99	91:09	81
2	[Co(**87**)]	*n*-C_6H_{14}	87	92:08	89
3	[Co(**88**)]	CH_2Cl_2	20	67:33	33
4	[Co(**89**)]	CH_2Cl_2	31	66:34	–23
5	[Co(**90**)]	CH_2Cl_2	99	91:09	58
6	[Co(**91**)]	CH_2Cl_2	69	81:19	47
7	[Co(**92**)]	CH_2Cl_2	<5	85:15	nd

[a] Reaction conditions: Performed at 25 °C for 48 h with DCM as solvent using 1 mol % [Co(Por*)] with 1.0 equiv. of styrene and 1.2 equiv. of ENDA; [styrene] = 0.25 M; [b] See Figure 35 for structures.

Table 51. Asymmetric cyclopropanation of olefins with α-nitrodiazoacetate catalyzed by [Co(**87**)].[141]

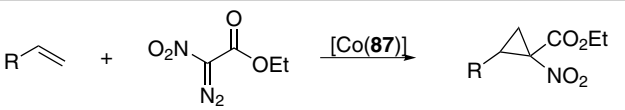

Entry[a]	Substrate	Yield (%)	*Z*:*E*	ee (%) *Z*
1	Styrene	93	92:08	92
2	4-Methylstyrene	86	93:07	90
3	4-Chlorostyrene	82	91:09	90
4	4-Trifluoromethylstyrene	88	92:08	90
5	3-Nitrostyrene	81	93:07	95
6[b]	Methyl acrylate	42	53:47	88
7[b]	Ethyl acrylate	62	56:44	88
8[b]	*N*,*N*-Dimethylacrylamide	92	63:37	75
9[c]	1-Hexene	45	92:08	80

[a] Reaction conditions: Performed at 25 °C for 24 h with hexane as solvent using 5 mol % [Co(**87**)] with 1.0 equiv. of styrene and 1.2 equiv. of ENDA; [styrene] = 0.25 M; [b] DCE used as solvent; [c] Reaction performed under neat conditions.

of DAMP were excellent, and comparable to the results generated by the ruthenium complex of the Halterman porphyrin **8** (Section III.A). However, unlike the Halterman system, the enantiomeric excess was shown to be significantly lower.

Table 52. Asymmetric cyclopropanation of aromatic olefins catalyzed by [Ru(**47**)(CO)].[143]

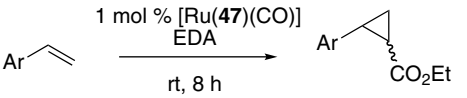

Entry[a]	Substrate	Yield (%)	*trans*:*cis*	ee (%) *trans*
1	Styrene	85	4:1	46
2	4-Methoxystyrene	95	6:1:1	47
3	4-Methylstyrene	82	9:9:1	46
4	4-Chlorostyrene	93	8:6:1	52
5	4-Bromostyrene	93	7:1:1	45
6	4-Fluorostyrene	92	11:0:1	50

[a] Reactions were performed with 1 mol % catalyst, 1 equiv. of diazo, and substrate neat at room temperature for 8 h.

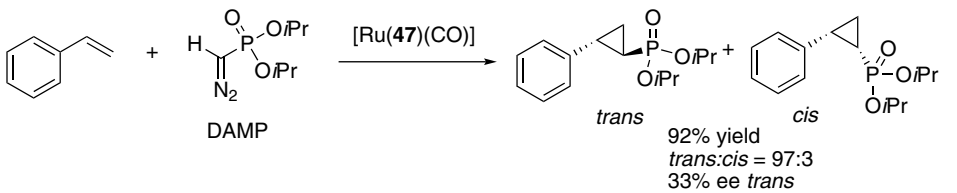

Scheme 20.[144]

The research groups of Rose and Cenini collaboratively developed an asymmetric cyclopropanation system utilizing cobalt complexes of the binaphthyl-strapped porphyrins **45** and **46** (Figure 20 in Section II.B).[145] These porphyrin complexes, first developed by Collman and Rose for asymmetric epoxidation, were evaluated for cobalt-catalyzed cyclopropanation of various styrene derivatives using EDA (Table 53). Although the yields were consistently excellent across a range of substrates, the diastereo- and enantioselectivities reported were not as high as the cobalt-catalyzed cyclopropanation systems developed by Zhang and coworkers.[135]

In 2002, Rose, Woo, and coworkers published a report using the Halterman porphyrin derivative **12** and Collman's bis-binaphthyl strapped ligand **43** for the Fe(II)-catalyzed asymmetric cyclopropanation of styrene with EDA.[146] The Fe(II) complex of the Halterman porphyrin derivative, [Fe(**12**)], generated excellent yields and diastereoselectivities. However, it afforded only a modest 45% ee (Scheme 21). The Fe(III) bis-binaphthyl strapped complex, [Fe(**43**)], showed decreased selectivities.

Table 53. Asymmetric cyclopropanation of aromatic olefins EDA catalyzed by [Co(**45**)] and [Co(**46**)].[145]

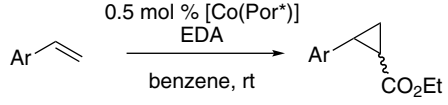

		[Co(**46**)][b]					[Co(**45**)][b]				
					ee (%)					ee (%)	
Entry[a]	Substrate	Time (h)	Yield (%)	*cis*:*trans*	*cis*	*trans*	Time (h)	Yield (%)	*cis*/*trans*	*cis*	*trans*
1	Styrene	36	92	27:33	60	10	48	96	25:75	57	42
2[c]	Styrene	60	89	16:84	50	46	60	93	18:82	66	31
3	α-Methylstyrene	20	95	27:33	76	31	16	94	28:72	39	22
4	4-Chlorostyrene	24	90	29:71	61	8	24	85	17:83	8	21
5	4-Methylstyrene	36	90	27:33	62	10	—	—	—	—	—
6	1,1-Diphenylethylene	72	93	—	56		72	93	—	22	

[a] Reactions were performed with 0.5 mol % of catalyst, 1 equiv. of EDA, and 10 equiv. of substrate in benzene at room temperature; [b] See Figure 20 for structures; [c] *N*-methylimidazole (20 equiv.) was added to reaction mixture.

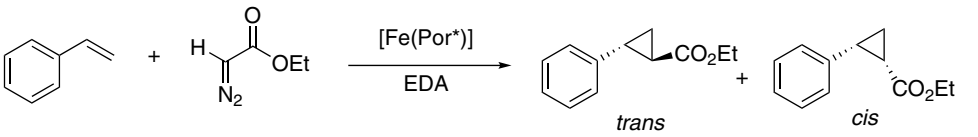

[Fe(**12**)]: 99% yield
21:1 *trans:cis*
45% ee (*trans*), 21% ee (*cis*)

[Fe(**43**)]: 95% yield
5.8:1 *trans:cis*
27% ee (*trans*), 25% ee (*cis*)

Scheme 21.[146]

IV. Aziridination

The fundamental and practical significance of aziridine derivatives in chemistry and biology has stimulated intensive research into their synthesis.[147–151] Among the most important routes for the preparation of aziridines, the metal-catalyzed aziridination of alkenes with nitrene sources has received significant attention as this method provides direct access to the desired products.

Despite the success of metalloporphyrins in other atom/group transfer reactions, their use in asymmetric aziridination has been limited.[152–155] Early important efforts in the development of asymmetric aziridination systems by Evans and Jacobsen were based on non-metalloporphyrin systems.[156,157] More recently, several research groups have made significant progress in the development of metalloporphyrin complexes capable of performing asymmetric aziridination. For example, Che and coworkers used manganese and ruthenium Halterman complexes for the asymmetric aziridination of a number of different olefins. In addition, Zhang and coworkers used cobalt complexes of their D_2-symmetric porphyrin catalysts for the aziridination of olefins using azides as nitrene sources. Finally, Marchon and coworkers employed the manganese complex of the "chiroporphyrin" ligand **27a** developed previously for epoxidation and cyclopropanation for use in asymmetric aziridination.

Traditionally, aziridination systems relied heavily on hypervalent iodine species, such as PhI=NTs and its derivatives.[158–163] Current investigations in the field have focused on the development of alternative nitrene sources, such as the *in-situ* generation of iminoiodane derivatives and azides.[164–172]

This section will review the current efforts in metalloporphyrin-catalyzed asymmetric aziridination, including recent developments concerning the use of new nitrene sources. As in previous sections, the reaction system will be categorized by the type of porphyrin ligand.

A. Chiral Picket Fence Porphyrins

Che and coworkers investigated the catalytic asymmetric aziridination of olefins by the manganese complex of the Halterman porphyrin **8**, [Mn(**8**)(OH)], using PhI=NTs as nitrene source.[173] Moderate yields and enantioselectivities were achieved with the manganese-catalyzed system, and modest TONs were reported (Table 54).

In a later report, Che and coworkers compared the ruthenium and manganese complexes of the Halterman porphyrin **8** (Table 55).[174] In the case of styrene, the manganese complex generated selectivity superior to that of its ruthenium counterpart (entries 1 and 2, Table 55). Comparisons between entries 3 and 4 in Table 55

Table 54. Asymmetric aziridination with PhI=NTs catalyzed by [Mn(**8**)(OH)].[173]

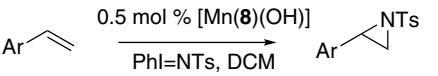

Entry[a]	Substrate	Yield (%)	TON	ee (%)
1	Styrene	71	130	49
2[b]	Styrene	73	142	55
3	4-Methylstyrene	66	132	44
4	4-Chlorostyrene	43	86	45
5	3-Chlorostyrene	49	98	49
6	2-Bromostyrene	44	88	62

[a] Reactions were performed with 0.5 mol % of catalyst, 20 equiv. of substrate, and 1 equiv. of PhI=NTs in DCM at 40 °C for 2 h; [b] 4-Phenylpyridine-*N*-oxide as additive.

Table 55. Asymmetric aziridination of aromatic olefins catalyzed by ruthenium and manganese complexes of **8**.[174]

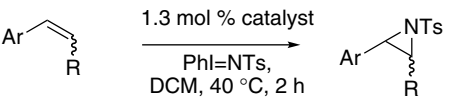

Entry[a]	Substrate	Catalyst	Yield (%)[b]	ee (%)
1	Styrene	[Mn(**8**)(OH)]	78 (99)	47
2	Styrene	[Ru(**8**)(CO)]	84 (71)	21
3	4-Methylstyrene	[Mn(**8**)(OH)]	76 (99)	44
4	4-Chlorostyrene	[Mn(**8**)(OH)]	93 (99)	50
5	2-Vinylnaphthalene	[Mn(**8**)(OH)]	94 (99)	56
6	Indene	[Ru(**8**)(CO)]	73 (99)	11

[a] Reactions were performed with 1.3 mol % of catalyst, 1 equiv. of substrate, and 3 equiv. of PhI=NTs in DCM at 40 °C for 2 h; [b] Yields are based upon the amount of alkene consumed in the reaction. The number in parenthesis represents conversion of substrate.

and those in Table 54 demonstrate that an improvement in yield could be achieved with higher catalyst loadings without sacrificing enantioselectivity.

Marchon and coworkers employed iron and manganese complexes of "chiroporphyrin" **27a** for the aziridination of aromatic olefins with PhI=NTs.[175] They reported that [Mn(**27a**)Cl] produced higher yields and greater enantioselectivities than [Fe(**27a**)Cl] when styrene was employed as a substrate (Scheme 22).

In their 2006 report on the use of the ruthenium complex of **77** for cyclopropanation using EDA, Cenini and coworkers also communicated the first report of the ruthenium porphyrin-catalyzed aziridination of olefins using aryl azides (Scheme 23).[132] They observed the formation of the aziridine product in low yield and enantioselectivity with the corresponding triazoline produced as the major side product.

The success of the D_2-symmetric chiral porphyrins developed for asymmetric cyclopropanation encouraged Zhang and coworkers to continue investigating other atom/group transfer reactions, including aziridination.[176] Their research focused not only on using the "group of six" porphyrins (Figure 35, Section III.A) as ligands for cobalt-catalyzed aziridination, but also on the use of nitrene sources other than hypervalent iodine reagents. They reported the use of diphenylphosphoryl azide (DPPA) for the asymmetric aziridination of aromatic olefins (Table 56).

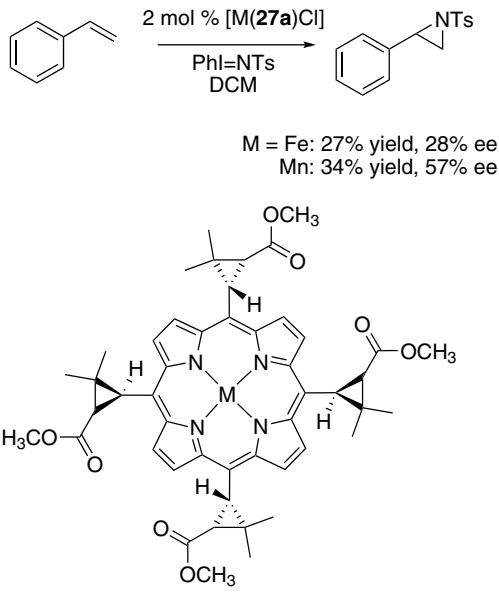

Scheme 22.[175]

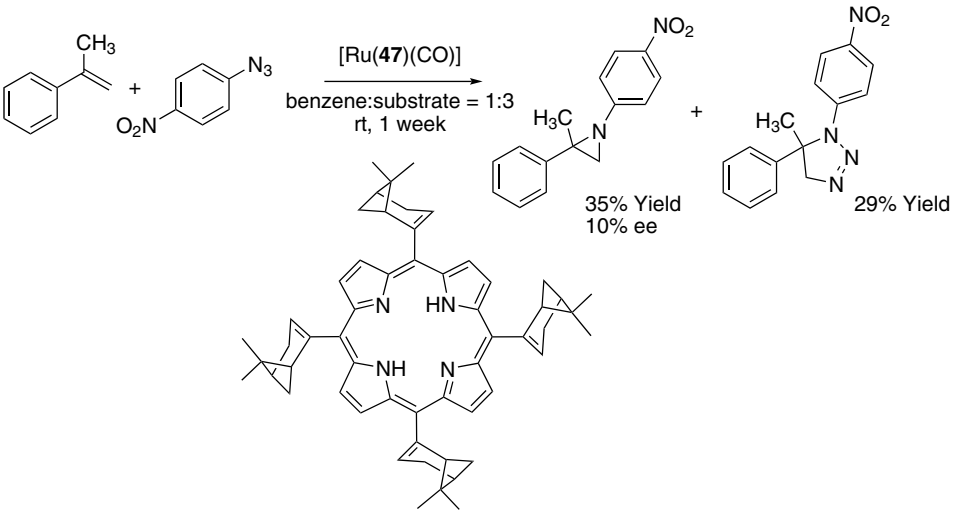

Scheme 23.[132]

Table 56. Asymmetric aziridination of aromatic olefins with DPPA catalyzed by [Co(**87**)].[176]

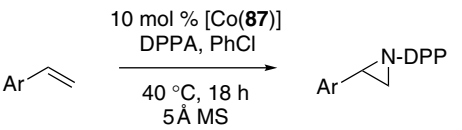

Entry[a]	Substrate	Yield (%)	ee (%)
1	Styrene	88	37
2	4-Methylstyrene	58	37
3	4-*tert*-Butylstyrene	77	53
4	4-Bromostyrene	65	28
5	4-Chlorostyrene	64	6
6	4-Trifluoromethylstyrene	64	44
7	3-Nitrostyrene	58	46

[a] Reactions were performed with 10 mol % of catalyst, 5 equiv. of substrate, and 1 equiv. of DPPA in PhCl at 40 °C for 18 h in the presence of 5 Å MS.

While their early attempt at cobalt-catalyzed asymmetric aziridination produced modest yields and enantioselectivities, their report is significant in that it presents one of the first uses of diphenylphosphoryl azide (DPPA) for asymmetric aziridination.

In their continued efforts to develop nitrene sources other than PhI=NTs and its derivatives, Zhang and coworkers synthesized and explored trichloroethoxysulfonyl

Table 57. Asymmetric aziridination of olefins with $TcesN_3$ catalyzed by [Co(**92**)].[177]

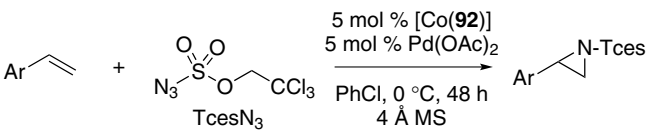

Entry[a]	Substrate	Yield (%)	ee (%)
1	Styrene	91	94
2[b]	Styrene	69	94
3	4-Methylstyrene	89	90
4	4-Chlorostyrene	93	91
5	4-Trifluoromethylstyrene	88	81
6	3-Nitrostyrene	82	88
7[c]	α-Methylstyrene	48	80
8[d]	Allylbenzene	42	91

[a] Reactions were performed with 5 mol % of catalyst, 5 equiv. of substrate, and 1 equiv. of $TcesN_3$ in PhCl at 0 °C for 48 h in the presence of 4 Å MS; [b] Without $Pd(OAc)_2$; [c] rt; [d] 24 h without $Pd(OAc)_2$.

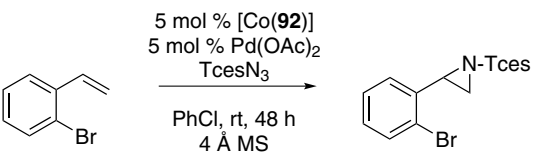

first cycle: 95% yield, 96% ee
second cycle: 89% yield, 94% ee
third cycle: 81% yield, 94% ee

Scheme 24.[177]

azide, $TcesN_3$.[177] The cobalt complex of the D_2-symmetric porphyrin **92** generated excellent yields and enantioselectivities for asymmetric aziridination of both aromatic and aliphatic olefins with $TcesN_3$ (Table 57). The importance of $Pd(OAc)_2$ as a co-catalyst was noted. The addition of sub-stoichiometric amounts of $Pd(OAc)_2$ improved yield without affecting the asymmetric induction (entries 1–2, Table 57). This effect is attributed to the potential activation of the olefin by $Pd(OAc)_2$ as a π-electrophilic Lewis acid.

The [Co(**92**)] catalyst was also demonstrated to be recyclable in the catalytic system. The cobalt catalyst could be precipitated onto molecular sieves with the addition of hexanes. After being filtered and dried, it was reused in subsequent reactions without significant loss of enantioselectivity over at least three cycles (Scheme 24).

V. Carbon–Hydrogen Bond Functionalization

Carbon–hydrogen bond functionalization via atom/group transfers represents a direct way to convert hydrocarbons into valuable intermediates.[52,154,178–184] This section will examine several examples of asymmetric carbon–hydrogen bond functionalization reactions, encompassing hydroxylation and amination, in addition to the analogous oxidation reactions including sulfoxidation and carbene insertion into thiols. Asymmetric catalytic systems that have been developed using chiral porphyrin catalysts, which were discussed previously in this chapter, will be briefly highlighted in these applications.

A. Chiral Picket Fence Porphyrins

1. *Hydroxylation*

In 1997, Halterman and coworkers reported on the use of the manganese complex of porphyrin **8**, [Mn(**8**)Cl], for the asymmetric hydroxylation of hydrocarbons.[34] Although reactions with ethylbenzene (entry 1, Table 58) gave rise to products in low yield and with poor enantioselectivity, reactions with indan and tetrahydronaphthalene resulted in improved yields and higher enantioselectivities (entries 2–3, Table 58). The authors noted that the reactions needed to be carefully monitored, as longer reaction times resulted in over-oxidation and the formation of a ketone side product.

The ruthenium complex of the Halterman porphyrin **8**, [Ru(**8**)(CO)], was also used by Che and coworkers in 1999 for asymmetric hydroxylation.[76,185] The use of the ruthenium carbonyl complex led to significant improvements in enantioselectivity when compared to the [Mn(**8**)Cl] prepared by Halterman. The ruthenium oxide complex [Ru(**8**)$(O)_2$] was also shown to be capable of performing hydroxylation under stoichiometric conditions, although with lower yield and enantioselectivities in comparison to [Ru(**8**)(CO)] (entries 1 and 2, Table 59).

Table 58. Asymmetric benzylic hydroxylation catalyzed by [Mn(**8**)Cl].[34]

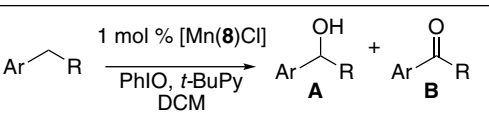

Entry[a]	Substrate	Time	Yield (%)	ee (%)	**A**:**B**
1	Ethylbenzene	16 h	27	9	1:1
2	Indan	20 m	50	53	5:1
3	Tetrahydronaphthalene	40 m	39	44	3:1
4	2-Ethylnaphthalene	14 h	24	40	2:1

[a] Reactions were performed using 1 mol % of catalyst, 10 equiv. of substrate, and 1 equiv. of PhIO with 20 mol % of *t*-BuPy as additive in DCM.

Table 59. Asymmetric benzylic hydroxylation catalyzed by [Ru(**8**)(CO)].[76,185]

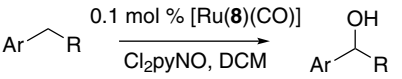

Entry[a]	Substrate	Time	Yield (%)[b]	ee (%)
1	Ethylbenzene	12	62 (13)	72
2[c]	Ethylbenzene	12	30	37
3	4-Ethyltoluene	30	72 (20)	76
4	1-Bromo-4-ethylbenzene	8	63 (14)	74
5	4-Ethylanisole	8	65 (15)	62
6	2-Ethylnaphthalene	20	62 (15)	75
7	Indan	6	65 (54)	12
8	Tetrahydronaphthalene	2	60 (42)	12

[a] Reactions were performed using 0.1 mol % of catalyst, 1 equiv. of substrate, and 1.1 equiv. of Cl_2pyNO as oxidant in benzene; [b] Yields are based upon the amount of alkene consumed in the reaction. The number in parenthesis represents conversion of substrate; [c] [Ru(**8**)$(O)_2$] used under stoichiometric condtitons.

Table 60. Asymmetric sulfoxidation catalyzed by [Mn(**8**)Cl].[34]

Entry[a]	Substrate	Yield A (%)	ee (%, A)	**A**:**B**
1	Thioanisole	93	55	44:1
2	Ethyl phenyl sulfide	82	42	13:1
3	2-Bromothioanisole	99	68	>95:1
4	4-Bromothioanisole	98	59	34:1
5	4-Methoxythioanisole	99	40	44:1
6	Thiochroman-4-one	99	47	>95:1

[a] Reactions were performed using 0.5 mol % of catalyst, 2 equiv. of substrate, and 1 equiv. of PhIO in DCM.

2. *Sulfoxidation*

In conjunction with their previous reports on epoxidation and hydroxylation using porphyrin **8**, Halterman and coworkers reported sulfoxidation of prochiral aromatic aryl alkyl sulfides.[34] Using the manganese complex [Mn(**8**)Cl], they demonstrated that the sulfoxide products **A** could be generated in high yields with moderate enantioselectivities (Table 60). Similar to the work on hydroxylation, minimal amounts of over-oxidized sulfone side products **B** were produced.

3. *Amination*

During the course of their study on the asymmetric aziridination of olefins with metal complexes of **8**, Che and coworkers reported the asymmetric amination of hydrocarbons.[174] The ruthenium complex [Ru(**8**)(CO)] was explored for catalytic amination of various benzylic substrates with PhI=NTs. Moderate to low enantioselectivities were produced (Table 61). Improvements were achieved through the *in-situ* generation of the nitrene from a sulfonyl amide in the presence of $PhI(OAc)_2$ (Table 62). These systems were able to achieve moderate enantioselectivities

Table 61. Asymmetric amination of benzylic hydrocarbons catalyzed by [Ru(**8**)(CO)].[174]

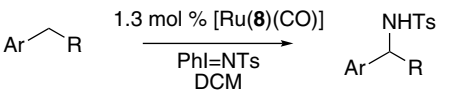

Entry[a]	Substrate	Yield (%)	ee (%)
1	4-Ethylanisole	82 (29)	22
2	Indan	92 (32)	3
3	Tetrahydronaphthalene	85 (22)	28
4	2-Ethylnaphthalene	84 (23)	47

[a] Reactions were performed using 1.3 mol % of catalyst, 2 equiv. of PhI=NTs, and 1 equiv. of substrate in DCM at 40 °C for 2 h; [b] Yields are based upon the amount of alkene consumed in the reaction. The number in parenthesis represents conversion of substrate.

Table 62. Asymmetric amination of benzylic hydrocarbons with *in-situ* generation of nitrene source catalyzed by [Mn(**8**)(OH)].[174]

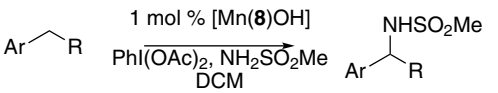

Entry[a]	Substrate	Yield (%)[b]	ee (%)
1	4-Ethylanisole	84 (26)	50
2	Tetrahydronaphthalene	84 (22)	46
3	2-Ethylnaphthalene	92 (21)	56
4[c]	2-Ethylnaphthalene	90 (34)	40

[a] Reactions were performed using 1 mol % of catalyst, 1 equiv. of $PhI(OAc)_2$, 1.25 equiv. of sulfonyl amide, and 1.5 equiv. of substrate in DCM at 40 °C for 2 h; [b] Yields are based upon the amount of alkene consumed in the reaction. The number in parenthesis represents conversion of substrate; [c] Catalyzed by [Ru(**8**)(CO)].

across a variety of benzylic substrates. It was also shown that [Mn(**8**)OH] was able to induce a higher level of asymmetry than the ruthenium complex [Ru(**8**)(CO)] (entries 3 and 4, Table 62).

B. Chiral-Strapped Porphyrins

1. *Hydroxylation*

In 1999, Gross and coworkers reported the use of the threitol-strapped porphyrin **51** (Figure 21) for the ruthenium-catalyzed hydroxylation of a racemic tertiary alkane.[75] The desired hydroxylation product was generated in 38% enantiomeric excess (Scheme 25). The result is remarkable since the asymmetric induction relies on the differentiation of the similar methyl and ethyl groups on the substrate by the active site of the catalyst (Scheme 25).

2. *Carbene Insertion*

In addition to using porphyrin ligand **47** for the ruthenium-catalyzed asymmetric cyclopropanation of olefins with EDA, Simonneaux and coworkers reported the ability of the catalyst to perform carbene insertion with thiols.[143] Although high yields were generated with this system, the resulting asymmetric induction was low (Scheme 26).

C. Chiral Basket Handle Porphyrins

1. *Hydroxylation*

Groves and coworkers employed both iron and manganese complexes of "vaulted" binaphthylporphyrin **65** (Figure 27) for studying the catalytic hydroxylation of hydrocarbons.[84] Several substrates were screened for hydroxylation with

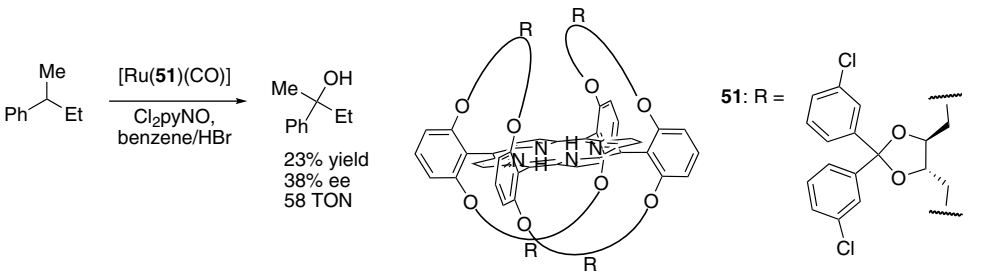

Scheme 25.[75]

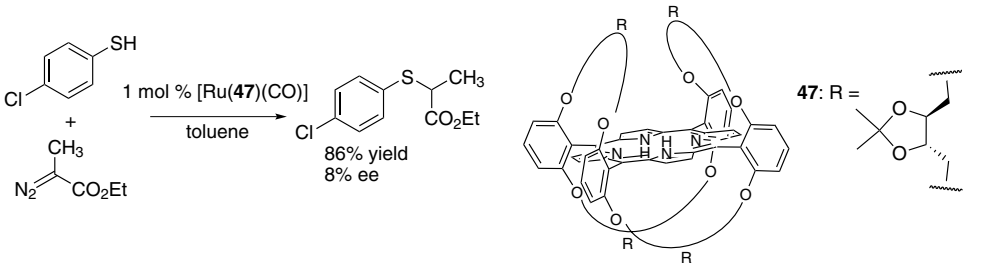

Scheme 26.[143]

Table 63. Asymmetric sulfoxidation catalyzed by iron and manganese complexes of ligand **65**.[84]

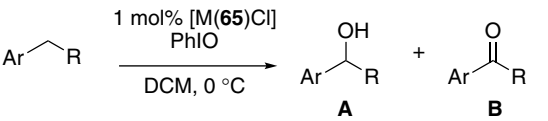

		[Fe(**65**)Cl]			[Mn(**65**)(Cl)]		
Entry[a]	Substrate	Yield (%)	ee (%)	A:B	Yield (%)	ee (%)	**A**:**B**
1	Ethylbenzene	40	40	2.3:1	77	26	1:3:1
2	1-Phenylpropane	32	44	5.0:1	98	16	1:4:1
3	Indan	72	54	7.2:1	82	18	4:5:1
4	Tetrahydronaphthalene	47	72	20.2:1	46	12	1:3:1

[a] Reactions were performed with 1 mol % of catalyst, 1 equiv. of PhIO, and 10 equiv. of substrate in DCM at 0 °C.

[Fe(**65**)Cl] and [Mn(**65**)Cl] as catalysts (Table 63). Although the yields generated by the manganese complex were typically higher, the iron-catalyzed system gave higher enantioselectivities. In addition to the desired hydroxylation products, ketones were observed as the side products, even in the presence of a tenfold excess of substrate.

2. *Sulfoxidation*

The iron complex of "vaulted" binaphthyl porphyrin **65** was also used by Groves and coworkers for asymmetric sulfoxidation of aryl sulfides.[84] Similar to the results by Halterman with [Mn(**8**)Cl] (Table 60), it was shown that the [Fe(**65**)Cl]-based sulfoxidation process could successfully generate the desired sulfoxide products **A** in good yields, but low enantioselectivities and with sulfones **B** as the over-oxidation side products (Table 64).

Table 64. Asymmetric sulfoxidation catalyzed by [Fe(**65**)Cl].[84]

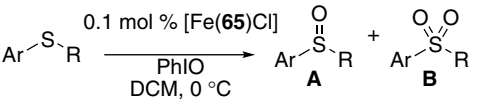

Entry[a]	Substrate	Yield (%)	ee (%)	**A**:**B**
1	Thioanisole	84	24	8.2:1
2	Ethyl phenyl sulfide	73	42	7.9:1
3	2-Bromothioanisole	74	48	8.4:1
4	4-Bromothioanisole	88	20	7.5:1
5	4-Methoxythioanisole	70	14	6.2:1
6	Thiochroman-4-one	67	28	8.9:1

[a] Reactions were performed using 0.5 mol % of catalyst, 1 equiv. of substrate, and 10 equiv. of PhIO in DCM at 0 °C.

VI. Conclusions

The use of chiral porphyrin ligands for asymmetric atom/group transfer reactions has significantly evolved since the first report by Groves and Myers in 1983. Various metal complexes of chiral porphyrins have been used for catalytic asymmetric epoxidation, cyclopropanation, aziridination, and in several reports of carbon–hydrogen bond functionalizations. The greatest efforts have been focused on the development of metalloporphyrin catalysts for asymmetric epoxidation. Much of the research in this area has been devoted to the synthesis and evaluation of metal complexes of Halterman porphyrin **8**. Catalytic systems based on this robust porphyrin have been shown to be capable of achieving several thousand TON for some catalytic processes. Complexes of Collman's binap-strapped porphyrins **43**–**44**, including its derivatives **45**–**46** prepared by Rose, have been demonstrated with the highest enantioselectivities for metalloporphyrin-catalyzed asymmetric epoxidation reactions.

The successes of both the Halterman porphyrin and Collman's binap-strapped porphyrins emphasize a balanced need for open access and steric hindrance of catalyst's active site where the approach of substrates and subsequent reactions take place. The desired balance of the two factors in these successful metalloporphyrin-catalyzed epoxidation processes has allowed for facilitation of reaction rates and reduction of catalyst degradation while reaching high selectivities.

Research activities on metalloporphyrin-catalyzed asymmetric cyclopropanation were also dominated by the use of metal complexes of Halterman porphyrin **8**. Similar to the development of metalloporphyrin-based asymmetric epoxidation, various metal complexes of the Halterman porphyrin have been employed as catalysts for asymmetric cyclopropanation. High diastereoselectivity and enantioselectivity,

along with high TON, have been achieved for some asymmetric cyclopropanation processes. The recent development of Co(II) complexes of the D_2-symmetic chiral porphyrins **87–92** by Zhang and coworkers has provided some of the most selective and practical cyclopropanation catalytic systems. These Co(II)-catalyzed cyclopropanation systems have been demonstrated to be effective for a wide range of alkene substrates and with different types of diazo reagents, providing the desired cyclopropane products in high yields with excellent diastereoselectivities and enantioselectivities.

The development of metalloporphyrin-catalyzed asymmetric aziridination has lagged behind in comparison to epoxidation and cyclopropanation reactions. Many of the same catalytic systems employed for asymmetric cyclopropanation have been extended to asymmetric aziridination. Although this direction of efforts have been further advanced by the recent publications from the research groups of Che, Zhang, and others, many challenging issues remain to be solved in the development of catalytic systems for asymmetric aziridination.

The demonstrated examples of asymmetric carbon–hydrogen bond functionalization processes, developed in conjunction with other atom/group transfer reactions, are another indication of the catalytic versatility of metalloporphyrin-based catalysts. Further development for these more challenging catalytic transformations is one of the most important on-going objectives in asymmetric catalysis by metalloporphyrins.

Finally, the diverse porphyrin ligand systems already developed and the great amount of progress achieved in epoxidation and cyclopropanation reactions ensure that the continued development of metalloporphyrin-based asymmetric atom/group transfer processes will remain an active goal for researchers around the world in the years to come.

VII. Acknowledgments

This chapter contains a number of contributions from our own research group. We would like to thank all of our coworkers and collaborators for their valuable contributions. We would also like to acknowledge the National Science Foundation, the American Chemical Society, and the University of South Florida for financial support.

VIII. References

1. Collman, J. P.; Zhang, X.; Lee, V. J.; Uffelman, E. S.; Brauman, J. I. *Science* **1993**, *261*, 1404.
2. Poulos, T. L. In *The Porphyrin Handbook*; Kadish, K. M., Smith, K. M., Guillard, R., Eds.; Academic Press: San Diego, CA, **2000**; Vol. 4, pp. 189–218.

3. Meunier, B.; Robert, A.; Pratviel, G.; Bernadou, J. In *The Porphyrin Handbook*; Kadish, K. M.; Smith, K. M.; Guillard, R., Eds.; Academic Press: San Diego, CA, **2000**; Vol. 4, pp. 119–188.
4. Sheldon, R. A.; Kochi, J. A. *Metal-Catalyzed Oxidations of Organic Compounds*; Academic Press: New York, **1981**.
5. Lichtenberger, F.; Nastainczyk, W.; Ullrich, V. *Biochem. Biophys. Res. Commun.* **1976**, *70*, 939.
6. Meunier, B.; de Visser, S. P.; Shaik, S. *Chem. Soc. Rev.* **2004**, *104*, 3947.
7. Rose, E.; Andrioletti, B.; Zrig, S.; Quelquejeu-Etheve, M. *Chem. Soc. Rev.* **2005**, *34*, 573.
8. Stephenson, N. A.; Bell, A. T. *J. Molec. Catal. A: Chem.* **2007**, *275*, 54.
9. Groves, J. T.; Nemo, T. E.; Myers, R. S. *J. Am. Chem. Soc.* **1979**, *101*, 1032.
10. Groves, J. T.; Myers, R. S. *J. Am. Chem. Soc.* **1983**, *105*, 5791.
11. Groves, J. T.; Shalyaev, K.; Lee, J. In *The Porphyrin Handbook*; Kadish, K. M.; Smith, K. M.; Guillard, R., Eds.; Academic Press: San Diego, CA, **2000**; Vol. 4, pp. 17–40.
12. Lindsay-Smith, J. R.; Sleath, P. R. *J. Chem. Soc., Perkin Trans. 2: Physical*, **1982**, *8*, 1009.
13. Groves, J. T.; Kruper, W. J., Jr.; Haushalter, R. C. *J. Am. Chem. Soc.* **1980**, *102*, 6375.
14. Chang, C. K.; Ebina, F. *J . Chem. Soc., Chem. Commun.* **1981**, 778.
15. Traylor, P. S.; Dolphin, D.; Traylor, T. G. *J . Chem. Soc., Chem. Commun.* **1984**, *5*, 279.
16. Zhang, W.; Loebach, J. L.; Wilson, S. R.; Jacobsen, E. N. *J. Am. Chem. Soc.* **1990**, *112*, 2801.
17. Zhang, W.; Jacobsen, E. N. *J. Org. Chem.* **1991**, *56*, 2296.
18. Jacobsen, E. N.; Zhang, W.; Guler, M. *J. Am. Chem. Soc.* **1991**, *113*, 6703.
19. Jacobsen, E. N.; Zhang, W.; Muci, A. R.; Ecker, J. R.; Deng, L. *J. Am. Chem. Soc.* **1991**, *113*, 7063.
20. Lee, N. H.; Jacobsen, E. N. *Tetrahedron Lett.* **1991**, *32*, 6533.
21. Lee, N. H.; Muci, A. R.; Jacobsen, E. N. *Tetrahedron Lett.* **1991**, *32*, 5055.
22. Jacobsen, E. N.; Deng, L. *J. Org. Chem.* **1992**, *57*, 4320.
23. Irie, R.; Noda, K.; Ito, Y.; Matsumoto, N.; Katsuki, T. *Tetrahedron Lett.* **1990**, *31*, 7345.
24. Irie, R.; Noda, K.; Ito, Y.; Matsumoto, N.; Katsuki, T. *Tetrahedron: Asymmetry* **1990**, *2*, 481.
25. Irie, R.; Noda, K.; Ito, Y.; Katsuki, T. *Tetrahedron Lett.* **1991**, *32*, 1055.
26. Yamada, T.; Imagawa, K.; Nagata, T.; Mukaiyama, T. *Chem. Lett.* **1992**, 2231.
27. Mukaiyama, T.; Yamada, T.; Nagata, T.; Imagawa, K. *Chem. Lett.* **1993**, 327.
28. McGarrigle, E. M.; Gilheany, D. G. *Chem. Rev.* **2005**, *105*, 1563.
29. Collman, J. P.; Gagne, R. R.; Reed, C. A.; Halbert, T. R.; Lang, G.; Robinson, W. T. *J. Am. Chem. Soc*. **1975**, *97*, 1427.
30. Licoccia, S.; Paci, M.; Tagliatesta, P.; Paolesse, R.; Antonaroli, S.; Boschi, T. *Magn. Res. Chem*. **1991**, *29*, 1084.
31. O'Malley, S.; Kodadek, T. *J. Am. Chem. Soc*. **1989**, *111*, 9116.
32. Reginato, G.; Di Bari, L.; Salvadori, P.; Guilard, R. *Eur. J. Org. Chem*. **2000**, 1165.
33. Halterman, R. L.; Jan, S.-T. *J. Org. Chem*. **1991**, *56*, 5253.
34. Halterman, R. L.; Jan, S.-T.; Nimmons, H. L.; Standlee, D. J.; Khan, M. A. *Tetrahedron* **1997**, *53*, 11257.
35. Halterman, R. L.; Jan, S.-J.; Abdulwali, A. H.; Standlee, D. J. *Tetrahedron* **1997**, *53*, 11277.
36. Lai, T.-S.; Ng, K.-H.; Liu, H.-Y.; Chang, C. K.; Yeung, L.-L. *Synlett* **2002**, 9, 1475.
37. Lai, T.-S.; Zhang, R.; Cheung, K.-K.; Kwong, H.-L.; Che, C.-M. *Chem. Commun*. **1998**, 1583.
38. Lai, T.-S.; Kwong, H.-L.; Zhang, R.; Che, C.-M. *Dalton Trans*. **1998**, 3559.
39. Zhang, R.; Yu, W.-Y.; Wong, K.-Y.; Che, C.-M. *J. Org. Chem*. **2001**, *66*, 8145.
40. Zhang, J.-L.; Liu, Y.-L.; Che, M.-C. *Chem. Commun.* **2002**, 2906.

41. Berkessel, A.; Frauenkrom, M. *J. Chem. Soc., Perkin Trans. 1* **1997**, 2265.
42. Berkessel, A.; Kaiser, P.; Lex, J. *Chem. Eur. J*. **2003**, *9*, 4746.
43. Halterman, R. L.; Jan, S.-J.; Abdulwali, A. H.; Standlee, D. J. *Tetrahedron* **1997**, *53*, 11277.
44. Liu, W.-S.; Zhang, R.; Huang, J.-S.; Che, M.-C.; Peng, S.-M. *J. Organomet. Chem.* **2001**, *634*, 34.
45. Barry, F.; Campbell, L.; Smith, D. W.; Kodadek, T. *Tetrahedron* **1997**, *53*, 7753.
46. Nakagawa, H.; Sei, Y.; Yamaguchi, K.; Nagano, T.; Higuchi, T. *J. Mol. Cat. A: Chem.* **2004**, *219*, 221.
47. Nakagawa, H.; Sei, Y.; Yamaguchi, K.; Nagano, T.; Higuchi, T. *Tetrahedron: Asymmetry* **2004**, *15*, 3861.
48. Maillard, P.; Guerquin-Kern, J. L.; Momenteau, M. *Tetrahedron Lett.* **1991**, *32*, 4901.
49. Vilain, S.; Maillard, P.; Momenteau, M. *J. Chem. Soc., Chem. Commun*. **1994**, 1697.
50. Vilain-Deshayes, S.; Robert, A.; Maillard, P.; Meunier, B.; Momenteau, M. *J. Mol. Cat. A: Chem.* **1996**, *113*, 23.
51. Perollier, C.; Pecaut, J.; Ramasseul, R.; Marchon, J.-C. *Inorg. Chem*. **1999**, *38*, 3758.
52. Liu, S.-Q.; Pecaut, J.; Marchon, J.-C. *Eur. J. Inorg. Chem*. **2002**, 1823.
53. Smith, J. R. L.; Reginato, G. *Org. Biomol. Chem.* **2003**, *1*, 2543.
54. Rose, E.; Kossanyi, A.; Quelquejeu, M.; Soleilhavoup, M.; Duwavran, F.; Bernard, N.; Lecas, A. *J. Am. Chem. Soc.* **1996**, *118*, 1567.
55. Rose, E.; Soleilhavoup, M.; Chirst-Tommasino, L.; Moreau, G.; Collman, J. P.; Quelquejeu, M.; Straumanis, A. *J. Org. Chem*. **1998**, *63*, 2042.
56. Proess, G.; Hevesi, L. *J. Mol. Cat. A: Chem.* **1993**, *80*, 395.
57. Banfi, S.; Manfredi, A.; Montanari, F.; Pozzi, G.; Quici, S. *J. Mol. Cat. A: Chem.* **1996**, *113*, 77.
58. Ohkatsu, Y.; Watanabe, T.; Gotto, T.; Wakita, M. *Bull. Chem. Soc. Jpn*. **1994**, *67*, 742.
59. Naruta, Y.; Tani, F.; Maruyama, K. *Chem. Lett.* **1989**, 1269.
60. Naruta, Y.; Tani, F.; Ishihara, N.; Maruyama, K. *J. Am. Chem. Soc*. **1991**, *113*, 6865.
61. Naruta, Y.; Tani, F.; Maruyama, K. *Tetrahedron Lett.* **1992**, *33*, 6323.
62. Naruta, Y.; Ishihara, N.; Tani, F.; Maruyama, K. *Chem. Lett.* **1991**, 1933.
63. Naruta, Y.; Ishihara, N.; Tani, F.; Maruyama, K. *Bull. Chem. Soc. Jpn.* **1993**, *66*, 158.
64. Collman, J. P.; Wang, Z.; Straumanis, A.; Quelquejeu, M.; Rose, E. *J. Am. Chem. Soc.* **1999**, *121*, 460.
65. Collman, J. P.; Wang, Z.; Linde, C.; Fu, L.; Dang, L.; Brauman, J. I. *Chem. Commun*. **1999**, 1783.
66. Adam, W.; Prikhodovski, S.; Roschmann, K. J.; Moller-Saha, C. R. *Tetrahedron: Asymmetry* **2001**, *12*, 2677.
67. Katsuki, T.; Sharpless, K. B. *J. Am. Chem. Soc.* **1980**, *102*, 5976.
68. Hanson, R. M.; Sharpless, K. B. *J. Org. Chem.* **1986**, *51*, 1922.
69. Johnson, R. A.; Sharpless, K. B. In *Comprehensive Organic Synthesis*; Trost, B. M.; Fleming, I. Eds.; Pergamon, New York, NY, **1991**; Vol. 7; pp. 389–436.
70. Rose, E.; Ren. Q.-Z.; Andriolett, B. *Chem. Eur. J.* **2004**, *10*, 224.
71. Ren, Q.; Wang, A.; Liu, S.; Ding, X. *Chinese J. Chem.* **2009**, *27*, 895.
72. Gross, Z.; Ini, S.; Kapon, M.; Cohen, S. *Tetrahedron Lett.* **1996**, *37*, 7325.
73. Gross, Z.; Ini, S. *J. Org. Chem.* **1997**, *62*, 5514.
74. Gross, Z.; Ini, S. *Inorg. Chem*. **1999**, *38*, 1446.
75. Gross, Z.; Ini, S. *Org. Lett*. **1999**, *1*, 2077.

76. Zhang, R.; Yu, W.-Y.; Lai, T.-S.; Che, C.-M. *Chem. Commun*. **1999**, 409.
77. Gazeau, S.; Pecaut, J.; Haddad, R.; Shelnutt, J.; Marchon, C. *Eur. J. Inorg. Chem*. **2002**, 2956.
78. Le Maux, P.; Lukas, M.; Simonneaux, G. *J. Mol. Cat. A: Chem.* **2003**, *206*, 95.
79. Collman, J. P.; Lee, V. J.; Kellen-Yuen, C. J.; Zhang, X.; Ibers, J. A.; Brauman, J. I. *J. Am. Chem. Soc.* **1995**, *117*, 692.
80. Collman, J. P.; Lee, V. J.; Zhang, X.; Ibers, J. A.; Brauman, J. I. *J. Am. Chem. Soc.* **1993**, *115*, 3834.
81. Boitrel, B.; Baveux-Chambenoit, V.; Richard, P. *Hel. Chim. Acta* **2004**, *87*, 2447.
82. Boitrel, B.; Baveux-Chambenoit, V. *New. J. Chem*. **2003**, *27*, 942.
83. Mansuy, D.; Battiono, P.; Renaud, J.-P.; Guerin, P. *J. Chem. Soc., Chem. Commun.* **1985**, 155.
84. Groves, J. T.; Viski, P. *J. Org. Chem*. **1990**, *55*, 3628.
85. Groves, J. T.; Crowley, S. J.; Shalyaev, K. V. *Chirality* **1998**, *10*, 106.
86. Collman, J. P.; Zhang, X.; Lee, V. J.; Brauman, J. I. *J. Chem. Soc., Chem. Commun.* **1992**, 1647.
87. Konishi, K.; Oda, K.; Nishida, K.; Aida, T.; Inoue, S. *J. Am. Chem. Soc*. **1992**, *114*, 1313.
88. Inoue, S.; Aida, T.; Konishi, K. *J. Mol. Cat. A: Chem.* **1992**, *72*, 121.
89. Doyle, M. P.; Forbes, D. C. *Chem. Rev*. **1996**, *98*, 911.
90. Lebel, H.; Marcoux, J. F.; Molinaro, C.; Charette, A. B. *Chem. Rev*. **2003**, *103*, 977.
91. Pellissier, H. *Tetrahedron* **2008**, *64*, 7041.
92. Zhang, Z.; Wang, J. *Tetrahedron* **2008**, *64*, 6577.
93. Donaldson, W. A. *Tetrahedron* **2001**, *57*, 8589.
94. Pietruszka, J. *Chem. Rev*. **2003**, *103*, 1051.
95. Salaun, J. *Chem. Rev*. **1989**, *89*, 1247.
96. Wessjohann, L. A.; Brandt, W. *Chem. Rev*. **2003**, *103*, 1625.
97. Miller, J. A.; Jin, W.; Nguyen, S. T. *Angew. Chem. Int. Ed. Engl*. **2002**, *41*, 2953.
98. Nishiyama, H.; Itoh, Y.; Matsumoto, H.; Park, S.-B.; Itoh, K. *J. Am. Chem. Soc*. **1994**, *116*, 2223.
99. Doyle, M. P.; Winchester, W. R.; Hoorn, J. A. A.; Lynch, V.; Simonsen, S. H.; Ghosh, R. *J. Am. Chem. Soc.* **1993**, *115*, 9968.
100. Hu, W.; Timmons, D. J.; Doyle, M. P. *Org. Lett*. **2002**, *4*, 901.
101. Lou, Y.; Horikawa, M.; Kloster, R. A.; Hawrylik, N. A.; Corey, E. J. *J. Am. Chem. Soc*. **2004**, *126*, 8916.
102. Evans, D. A.; Woerpel, K. A.; Hinnman, M. M.; Faul, M. M. *J. Am. Chem. Soc*. **1991**, *113*, 726.
103. Fritschi, H.; Leutenegger, U.; Pfaltz, A. *Angew. Chem. Int. Ed. Engl*. **1986**, *25*, 1005.
104. Lo, M. M.-C.; Fu, G. C. *J. Am. Chem. Soc*. **1998**, *120*, 10270.
105. Doyle, M. P.; Dorrow, R. L.; Terpstra, J. W.; Rodenhouse, R. A. *J. Org. Chem*. **1985**, *50*, 1663.
106. Doyle, M. P.; Loh, K.-L.; De Vries, K. M.; Chinn, M. M. *Tetrahedron Lett*. **1987**, *28*, 833.
107. Doyle, M. P.; Austin, R. E.; Bailey, S.; Dwyer, M. P.; Dyatkin, A. B.; Kalinin, A. V.; Kwan, M. M. Y.; Liras, S.; Oalmann, C. J.; Pieters, R. J.; Protopopova, M. N.; Raab, C. E.; Roos, G. H. P.; Zhou, Q.-L.; Martin, S. F. *J. Am. Chem. Soc*. **1995**, *117*, 5763.
108. Doyle, M. P.; Hu, W.; Weathers, T. M. *Chirality* **2003**, *15*, 369.
109. Doyle, M. P.; Kalinin, A. V. *J. Org. Chem*. **1996**, *61*, 2179.
110. Doyle, M. P.; Pieters, R. J. *J. Am. Chem. Soc.* **1991**, *113*, 1423.
111. Callot, H. J.; Piechocki, C. *Tetrahedron Lett*. **1980**, *21*, 3489.
112. Callot, H. J.; Metz, F.; Piechoski, C. *Tetrahedron Lett*. **1982**, *38*, 2365.
113. Bartely, D. W.; Kodadek, T. *J. Am. Chem. Soc*. **1993**, *115*, 1656.

114. Maxwell, J. L.; Brown, K. C.; Bartely, D. W.; Kodadek, T. *Science* **1992**, *256*, 1544.
115. Brown, K. C.; Kodadek, T. *J. Am. Chem. Soc*. **1992**, *114*, 8336.
116. O'Malley, S.; Kodadek, T. *Organometallics* **1992**, *11*, 2299.
117. Maxwell, J. L.; O'Malley, S. Brown, K. C.; Kodadek, T. *Organometallics* **1992**, *11*, 645.
118. Maxwell, J. L.; Kodadek, T. *Organometallics* **1991**, *10*, 4.
119. O'Malley, S.; Kodadek, T. *Tetrahedron Lett*. **1991**, *32*, 2445.
120. Smith, D. A.; Reynolds, D. N.; Woo, L. K. *J. Am. Chem. Soc*. **1993**, *115*, 2511.
121. Wolf, J. R.; Hamaker, C. G.; Djukic, J. P.; Kodadek, T.; Woo, L. K. *J. Am. Chem. Soc*. **1995**, *117*, 9194.
122. Galardon, E.; Le Maux, P.; Simonneaux, G. *Chem. Commun*. **1997**, 927.
123. Che, C.-M.; Huang, J.-S.; Lee, F.-W.; Li, Y.; Lai, T.-S.; Kwong, H.-L.; Tang, P.-F.; Lee, W.-S.; Lo, W.-C.; Peng, S.-M.; Zhou, Z.-Y. *J. Am. Chem. Soc*. **2001**, *132*, 4119.
124. Lo, W.-C.; Che, C.-M.; Chen, K.-F.; Mak, T. C. W. *Chem. Commun*. **1997**, 1205.
125. Teng, P.-F.; Lai, T.-S.; Kwong, H.-L.; Che, M.-C. *Tetrahedron: Asymmetry* **2003**, *14*, 837.
126. Lai, T.-S.; Chan, F.-Y.; So, P.-K.; Ma, D.-L.; Wong, K.-Y.; Che, C.-M. *Dalton Trans.* **2006**, 4845.
127. Nicolas, I.; Le Maux, P.; Simonneaux, G. *Tetrahedron Lett.* **2008**, *49*, 5793.
128. Ferrand, Y.; Le Maux, P.; Simonneaux, G. *Tetrahedron: Asymmetry* **2005**, *16*, 3829.
129. Le Maux, P.; Juillard, S.; Simonneaux, G. *Synthesis* **2006**, 1701.
130. Le Maux, P.; Roisnel, T.; Nicolas, I.; Simonneaux, G. *Organometallics* **2008**, *27*, 3037.
131. Ferrand, Y.; Le Maux, P.; Simonneaux, G. *Org. Lett*. **2004**, *6*, 3211.
132. Caselli, A.; Gallo, E.; Ragaini, F.; Ricatto, F.; Abbiati, G.; Cenini, S. *Inorg. Chim. Acta* **2006**, *359*, 2924.
133. Huang, L.; Chen, Y.; Gao, G.-Y.; Zhang, X. P. *J. Org. Chem*. **2003**, *68*, 8179.
134. Chen, Y.; Gao, G.-Y.; Zhang, X. P. *Tetrahedron Lett.* **2005**, *46*, 4965.
135. Chen, Y.; Fields, K. B.; Zhang, X. P. *J. Am. Chem. Soc*. **2004**, *126*, 14718.
136. Chen, Y.; Zhang, X. P. *Synthesis* **2006**, 1697.
137. Chen, Y.; Zhang, X. P. *J. Org. Chem*. **2007**, *72*, 5931.
138. Chen, Y.; Ruppel, J. V.; Zhang, X. P. *J. Am. Chem. Soc*. **2007**, *129*, 12074.
139. Zhu, S.; Ruppel, J. V.; Lu, H.; Wojtas, L.; Zhang, X. P. *J. Am. Chem. Soc*. **2008**, *130*, 5042.
140. Ruppel, J. V.; Gauthier, T. J.; Snyder, N. L.; Perman, J. A.; Zhang, X. P. *Org. Lett*. **2009**, *11*, 2273.
141. Zhu, S.; Perman, J. A.; Zhang, X. P. *Angew. Chem. Int. Ed*. **2008**, *47*, 8460.
142. Doyle, M. P. *Angew. Chem. Int. Ed*. **2009**, *48*, 850.
143. Galardon, E.; Roue, S.; Le Maux, P.; Simonneaux, G. *Tetrahedron Lett.* **1998**, *39*, 2333.
144. Paul-Roth, C.; De Montigny, F.; Rethore, G.; Simonneaux, G.; Gulea, M.; Masson, S. *J. Mol. Cat. A: Chem.* **2003**, *201*, 79.
145. Fantauzzi, S.; Gallo, E.; Rose, E.; Raoul, N.; Caselli, A.; Issa, S.; Ragaini, F.; Cenini, S. *Organometallics* **2008**, *27*, 6143.
146. Du, G.; Andrioletti, B.; Rose, E.; Woo, L. K. *Organometallics* **2002**, *21*, 4490.
147. Hu, X. E. *Tetrahedron* **2004**, *60*, 2701.
148. Pineschi, M. *Eur. J. Org. Chem*. **2006**, 4979.
149. Singh, G. S.; D'hooghe, M.; De Kimpe, N. *Chem. Rev*. **2007**, *107*, 2080.
150. Sweeny, J. B. *Chem. Soc. Rev*. **2002**, *31*, 247.
151. Tanner, D. *Angew. Chem., Int. Ed. Engl.* **1994**, *33*, 599.
152. Muller, P.; Fruit, C. *Chem. Rev*. **2003**, *103*, 2905.

153. Jacobsen, E. N. In *Comprehensive Asymmetric Catalysis*; Jacobsen, E. N.; Pfaltz, A.; Yamamoto, H., Eds.; Springer: Berlin, 1999; Vol. 2; p 607.
154. Halfen, J. A. *Curr. Org. Chem*. **2005**, *9*, 657.
155. Katsuki, T. *Chem. Lett.* **2005**, *34*, 1304.
156. Li, Z.; Conser, K. R.; Jacobsen, E. N. *J. Am. Chem. Soc*. **1993**, *115*, 5326.
157. Evans, D. A.; Faul, M. M.; Bilodeau, M. T.; Anderson, B. A.; Barnes, D. M. *J. Am. Chem. Soc*. **1993**, *115*, 5328.
158. Fantauzzi, S.; Gallo, E.; Caselli, A.; Piangiolino, C.; Ragaini, F.; Cenini, S. *Eur. J. Org. Chem.* **2007**, 6053.
159. Kawabata, H.; Omura, K.; Katsuki, T. *Tetrahedron Lett*. **2007**, *47*, 1571.
160. Omura, K.; Murakami, M.; Uchida, T.; Irie, R.; Katsuki, T. *Chem. Lett.* **2003**, *32*, 354.
161. Liang, C.; Peillard, F. R.; Fruit, C.; Muller, P.; Dodd, R. H.; Dauban, P. *Angew. Chem. Int. Ed*. **2006**, *45*, 4641
162. Fructos, M. R.; Trofimenko, S.; Diaz-Requejo, M. M.; Perez, P. J. *J. Am. Chem. Soc*. **2006**, *128*, 11784.
163. Sanders, C. J.; Gillespie, K. M.; Bell, D.; Scott, P. *J. Am. Chem. Soc*. **2000**, *122*, 7132.
164. Esteoule, A.; Duran, F.; Retailleau, P.; Dodd, R. H.; Dauban, P. *Synthesis* **2007**, 1251.
165. Guthikonda, K.; When, P. M.; Caliando, B. J.; Du Bois, J. *Tetrahedron* **2006**, *62*, 11331.
166. Li, Z.; Ding, X.; He, C. *J. Org. Chem*. **2006**, *71*, 5876.
167. Xu, Q.; Appella, D. H. *Org. Lett*. **2008**, *10*, 1497.
168. Yu, X.-Q.; Huang, J.-S.; Zhou, X.-G.; Che, C.-M. *Org. Lett.* **2000**, *2*, 2233.
169. Guthikonda, K.; Du Bois, J. *J. Am. Chem. Soc*. **2002**, *124*, 13672.
170. Dauban, P.; Saniere, L.; Tarrade, A.; Dodd, R. H. *J. Am. Chem. Soc.* **2001**, *123*, 7707.
171. Gao, G.-Y.; Jones, J. E.; Vyas, R.; Harden, J. D.; Zhang, X. P. *J. Org. Chem*. **2006**, *71*, 6665.
172. Ruppel, J. V.; Jones, J. E.; Huff, C. A.; Kamble, R. M.; Chen, Y.; Zhang, X. P. *Org. Lett.* **2008**, *10*, 1995.
173. Lai, T.-S.; Kwong, H.-L.; Che, C.-M.; Peng, S.-M. *Chem. Commun*. **1997**, 2373.
174. Liang, J.-L.; Huang, J.-S.; Yu, X.-Q.; Zhu, N.; Che, C.-M. *Chem. Eur. J*. **2002**, *8*, 1563.
175. Simonato, J.-P.; Pecaut, J.; Scheidt, W. R.; Marchon, J.-C. *Chem. Commun*. **1999**, 989.
176. Jones, J. E.; Ruppel, J. V.; Gao, G.-Y.; Moore, T. M.; Zhang, X. P. *J. Org. Chem*. **2008**, *73*, 7260.
177. Subbarayan, V.; Ruppel, J. V.; Zhu, S.; Perman, J. A.; Zhang, X. P. *Chem. Commun*. **2009**, 4266.
178. Johannsen, M.; Jorgensen, A. *Chem. Rev.* **1998**, *98*, 1689.
179. Muller, T. E.; Beller, M. *Chem. Rev.* **1998**, *98*, 675.
180. Racci, A., Ed. *Modern Amination Methods*; Wiley-VCH: Weinheim, 2000.
181. Salvatore, R. N.; Yoon, C. H.; Jung, K. W. *Tetrahedron* **2001**, *57*, 7785.
182. Davies, H. M. L.; Long, M. S. *Angew. Chem. Int. Ed.* **2005**, *44*, 3518.
183. Espino, C. G.; Du Bois, J. In *Modern Rhodium-Catalyzed Organic Reactions*; Evans, P. A., Ed.; Wiley-VCH; Weinheim, **2005**; pp. 379–416.
184. Davies, H. M. L. *Angew. Chem. Int. Ed.* **2006**, *45*, 6422.
185. Zhang, R.; Yu, W.-Y.; Che, C.-M. *Tetrahedron: Asymmetry* **2005**, *16*, 3520.

44 High-Valent Iron-Oxo Porphyrins in Oxygenation Reactions

Sam P. de Visser* and Wonwoo Nam†

*Manchester Interdisciplinary Biocentre and School of Chemical Engineering and Analytical Science, The University of Manchester, 131 Princess Street, Manchester M1 7DN, UK

†Department of Bioinspired Science, Department of Chemistry and Nano Science, Center for Biomimetic Systems, Ewha Womans University, Seoul 120–750, South Korea

I. Introduction

Cytochromes P450 (CYP 450s) are a superfamily of cysteine thiolate-ligated heme enzymes that catalyze the transfer of one oxygen atom from molecular oxygen into a wide variety of biological substrates (S), whereby the second oxygen

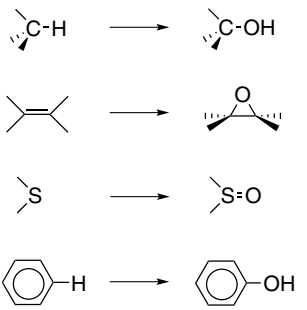

Scheme 1. Reactions catalyzed by CYP 450 enzymes.

atom is reduced by two electrons and two protons to a water molecule (Eq. 1).[1–7] They are therefore mono-oxygenase enzymes, as only one oxygen atom from molecular oxygen is incorporated into substrates. CYP 450s are widespread in nature and perform a vast array of oxidative transformation reactions of endogenous and exogenous molecules.[8–10] The most-often-encountered oxidation reactions by CYP 450s are the hydroxylation of saturated hydrocarbons, the epoxidation of olefins, the oxidation of heteroatoms, the oxidation of aromatic compounds, and heteroatom dealkylation (Scheme 1).[11–15] CYP 450s have a range of different functions in biosystems, varying from the biosynthesis of antibiotics in prokaryotes and hormones in eukaryotes to the biodegradation of drugs and xenobiotics.[16]

$$S + O_2 + 2e^- + 2H^+ \xrightarrow{\text{(Cytochrome P450)}} SO + H_2O \qquad (1)$$

Due to their versatility and efficiency in performing complicated hydroxylation reactions in regio- and stereoselective ways, they have attracted much attention in the communities of biological, bioinorganic, and oxidation chemistry. Moreover, templates of the active site have been created and investigated as biomimetics to gain insight into the fundamental properties of the CYP 450's active center. Most recently, computational chemists have become interested in CYP 450,[17–20] and the combination of experimental and computational studies with native and mutant enzymes and biomimetic complexes has given insights into the critical components of the CYP 450's active site. In this chapter, we will focus on biomimetic and computational research while paying special attention to reaction mechanisms of substrate monoxygenation by CYP 450.

The first X-ray crystal structure of CYP 450 was reported by Poulos and coworkers in 1985: the soluble bacterial CYP 450_{cam} isolated from the bacterium *Pseudomonas putida*.[21] Since then, many more crystal structures of catalytic cycle intermediates have been detected and characterized and, as a result, a

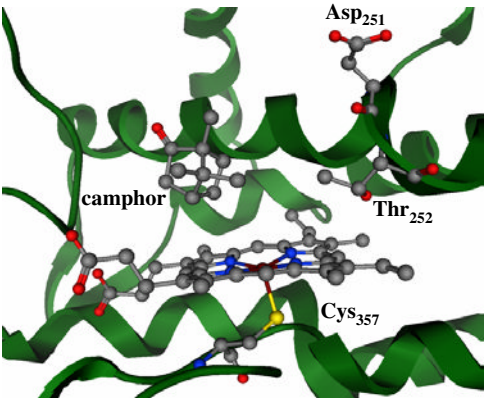

Figure 1. Active site structure of CYP 450 as taken from the 1DZ9 pdb file,[24] with key amino acids and substrate (camphor) highlighted.

protein databank[22] search on "P450" gives well over 300 different structures of various CYP 450 isozymes. These enzymes show considerable homology and all contain a central heme group, where the catalysis takes place. CYP 450 enzymes consist of a single polypeptide chain containing a heme *b* group (iron protoporphyrin IX) linked to a cysteine (Cys) amino acid via the axial ligand of the metal.[23] Figure 1 gives the active site structure of a typical CYP 450 isozyme, namely CYP 450_{cam}, as taken from the 1DZ9 protein databank structure.[24] This is a bacterial CYP 450 that regioselectively hydroxylates camphor at the C^5 position and is one of the most extensively studied CYP 450s.[25,26] The heme *b* group is bound to the protein via an iron-cysteinate bond that is deeply embedded in the hydrophobic interior of the enzyme to accommodate hydrophobic substrates, and the proximal Cys amino acid forms hydrogen bonds with neighboring amide protons of three amino acids,[27] which is believed to play a significant role in modulating the catalytic activity of CYP 450.[28–33] Indeed, the name "cytochrome P450" is derived from the fact that a red-shifted strong Soret band (high-energy π–π^* transition of the porphyrin ring) appears at 450 nm when CO binds to ferrous heme (Fe^{II}–CO), which is caused by the strong electron-donating character of the cysteinate proximal ligand.[34–36]

Since activation of inert C–H bonds is a holy grail of chemistry, mechanistic details of dioxygen activation and oxygen transfer reactions by CYP 450 have been intensively investigated in enzymes and biomimetic iron porphyrin complexes over the past four decades, thereby proposing the catalytic cycle of CYP 450 (Figure 2).[1–20,37,38] Recently, theoretical chemistry, and especially density functional theory (DFT) and quantum mechanics/molecular mechanics (QM/MM) techniques, have provided important clues to understanding structures, spin states,

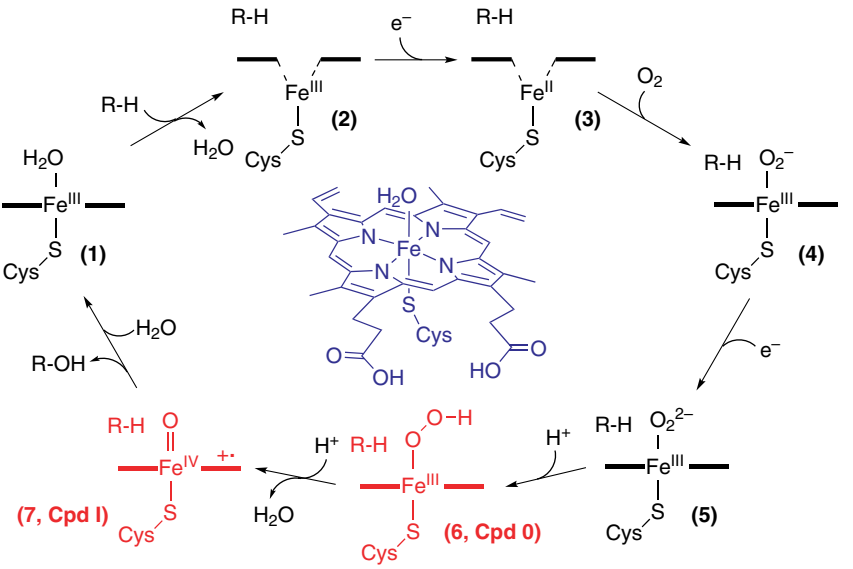

Figure 2. Proposed catalytic cycle of CYP 450.[14] Iron(III) protoporphyrin IX with a cysteinate as an axial ligand is shown in the center, and the two key intermediates, Cpd I and Cpd 0, are highlighted in red.

and chemical and physical properties of the unstable intermediates involved in the enzymatic and biomimetic oxidation reactions.[17–20,39] Since the topic of this review is not about the catalytic cycle of CYP 450 but is focused more on the reactivities of active oxidants in oxygenation reactions, only a bird's eye view of the overall catalytic reaction cycle is given and the interested reader is referred to the various detailed reviews of the catalytic cycle of CYP 450 enzymes.[17–20,39]

The catalytic cycle starts from the resting, substrate-free state, **1**, where CYP 450 contains a six-coordinate low-spin ferric state with water as the displaceable distal ligand (Figure 2). The binding of substrate into the substrate-binding pocket triggers a spin state crossing from low spin to high spin,[40] whereby the distal water molecule is expelled and a five-coordinate high-spin ferric state, **2**, is generated. In many CYP 450 isozymes, substrates bind in a very-tight-binding pocket where they are locked in position through electrostatic and hydrogen bonding interactions.[41] DFT and QM/MM calculations on model complexes indeed confirmed a different spin state ordering for **1** and **2**.[42–44] This spin state change triggers an electron transfer process from the reductase domain to reduce the ferric complex to a ferrous complex, **3**.[40] Dioxygen then binds to the ferrous heme to form the ferric-superoxo heme (Fe^{III}–O_2^-), **4**. Addition of the second electron to **4**, which is presumed to be the rate-limiting step in the catalytic cycle,[45] yields a ferric-peroxo species (Fe^{III}–O_2^{2-}), **5**, which is then protonated to

give a ferric-hydroperoxo complex, **6**, also known as compound 0 (Cpd 0). Recently, the ferric-peroxo and ferric-hydroperoxo intermediates were generated by radiolytic cryoreduction of the ferric-superoxo of CYP 450_{cam}, **4**, with gradual temperature annealing and characterized by EPR, ENDOR, and UV-vis spectroscopies.[24,46–48] The delivery of the second proton in the catalytic cycle onto the ferric-hydroperoxo species, **6**, results in heterolytic O–O bond cleavage to release a water molecule and generate a putative iron(IV)-oxo porphyrin π-cation radical intermediate, **7**, which is equivalent to compound I (Cpd I) of horseradish peroxidase (HRP). Although the intermediate **7** is believed to be the most likely candidate for the reactive species of CYP 450 that hydroxylates unactivated hydrocarbons, the characterization of the intermediate has not been successful, probably due to its high reactivity. Schlichting and coworkers reported that the ferric superoxo of CYP 450_{cam}, **4**, was converted by X-ray irradiation at cryogenic temperature into an intermediate that would be consistent with an iron(IV)-oxo species.[24] In different studies, the oxidation of CYP 450 by *m*-chloroperbenzoic acid (*m*-CPBA) generated intermediates with UV-vis spectral features characteristic of an iron(IV)-oxo porphyrin π-cation radical, **7**.[49,50] The final step of the CYP 450 reaction cycle is the transfer of an oxygen atom from **7** to the substrate to give the alcohol product, followed by the regeneration of the resting, water-bound state, **1**.

The catalytic cycle shown in Figure 2 is the consensus mechanism[2,3,5] for dioxygen activation by CYP 450. Among the short-lived intermediates in the catalytic cycle, the nature of active oxidants which are responsible for oxygen atom transfer to organic substrates attracted much attention in the bioinorganic and biological chemistry communities. It has been believed for a long time that iron(IV)-oxo porphyrin π-cation radicals, Cpd I, are generated via O–O bond heterolysis of ferric-hydroperoxo porphyrins, Cpd 0, and are the active oxidants that effect the oxygenation of organic substrates (Scheme 2, pathways A and B). Although Cpd I

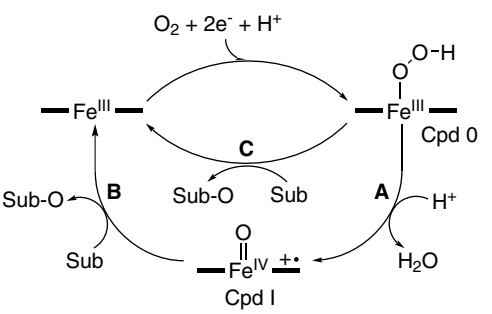

Scheme 2. Two intermediates, Cpd 0 and Cpd I, proposed[51] in the catalytic oxygenation of organic substrates by CYP 450.

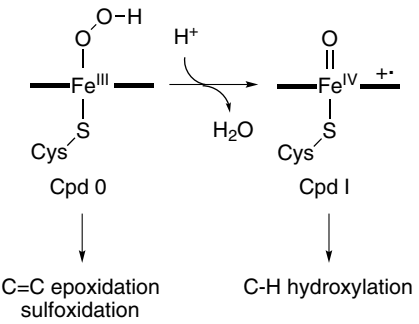

Scheme 3. Two-oxidant hypothesis of substrate monoxygenation by the CYP 450s.

has been poorly characterized in enzymatic reactions, probably due to high reactivity and instability in nature, a number of synthetic iron(IV)-oxo porphyrin π-cation radicals have been prepared and investigated in various oxygenation reactions, including alkane hydroxylation and olefin epoxidation.[14,15] Thus, there is no doubt that Cpd I is a strong oxidant capable of oxygenating various organic substrates. However, the nature of the active oxidant was thrown into doubt by site-directed mutagenesis studies that implicated the participation of Cpd 0 as a second electrophilic oxidant in substrate monoxygenation reactions, such as oxygenation of alkanes, olefins, sulfides, and *N*,*N*-dialkylanilines (Scheme 3).[51,52] The primary evidence for the second electrophilic oxidant derives from site-directed mutagenesis studies, in which different products and/or product distributions were observed in the reactions of CYP 450 and their mutants.[53–56] Thus, studies using so-called radical-clock substrates which distinguish between radical and cationic mechanisms implicated an ultrashort lifetime indicative of two active oxidants in the reaction mechanism.[52] Site-directed mutations were done that disrupted the proton relay machinery and supposedly blocked formation of Cpd I by termination of the catalytic cycle at Cpd 0. The key amino acids assigned to the proton transfer mechanisms in CYP 450_{cam} include the alcohol side-chain of Thr_{252} and the carboxylic acid group of Asp_{251} (see Figure 1). Indeed, the Thr252Ala mutation significantly decreased the activity of the enzyme and led to a substantial increase of decoupling whereby the ferric-hydroperoxo was converted into ferric-hydrogen peroxide and no hydroxylation took place.[57] Further studies showed that although the activity of the Thr252Ala mutant had sharply decreased toward aliphatic hydroxylation reactions, in fact double bond epoxidation reactions still proceeded and, in cases where epoxidation and hydroxylation mechanisms were competitive, a regioselectivity switch was observed.[53–56,58] Based on these studies, a two-oxidant scenario was hypothesized[51] wherein Cpd I is the oxidant for aliphatic hydroxylation reactions whereas Cpd 0 is responsible for double bond epoxidation (Scheme 3).

The two-oxidant hypothesis has created extensive discussion as a viable hypothesis, but was questioned by computational and biomimetic studies.[59–62] In particular, computational studies using DFT and combined QM/MM[59–62] have resulted in an alternative, namely the two-state reactivity (TSR) scenario,[19,63] wherein one oxidant, i.e. the iron(IV)-oxo heme π-cation radical (or Cpd I), is the active oxidant and reacts with substrates on several close-lying spin state surfaces. Later in this chapter a more detailed explanation of the TSR principle will be given. Biomimetic studies support the TSR scenario and have ruled out the ferric hydroperoxo as a potential oxidant of aliphatic and aromatic hydroxylation and sulfoxidation reactions.[64] Thus, *in situ* generated nonheme iron(III)-hydroperoxo complexes did not show any activity in nucleophilic and electrophilic reaction mechanisms, such as olefin epoxidation and sulfoxidation. The results derived from the direct reactivity studies of nonheme iron(III)-hydroperoxo intermediates imply that Cpd 0 is unlikely to be an oxidant of C=C epoxidation and sulfoxidation reactions as proposed by the two-oxidant model, and the experimental product distributions, therefore, originate from another oxidant.

To further ascertain that Cpd 0 is an unlikely oxidant, DFT and QM/MM calculations focused on the proton transfer step that converts Cpd 0 into Cpd I. These studies implicated that Cpd 0 and Cpd I are close in energy.[65–69] Recent QM/MM studies[69] showed that active site mutations, such as Thr252Ala, can give rise to extra water molecules in the substrate-binding pocket that promote distal protonation of Cpd 0 leading to hydrogen peroxide products (called uncoupling) rather than the formation of Cpd I. The intricate shape and size of the substrate-binding pocket and the availability of proton donors and acceptors, therefore, influence the protonation steps in the catalytic cycle and determine whether Cpd I or hydrogen peroxide is formed.

DFT calculations on the relative activity of ferryl-oxo versus ferric-hydroperoxo in C=C double bond epoxidation[59,60] found little evidence of activity of Cpd 0 and as such contradicted the experimental two-oxidant hypothesis. These studies used small model complexes and ignored the protein surroundings of enzymes. Nevertheless, as discussed above, the work was supported by experimental biomimetic studies on substrate epoxidation and hydroxylation by synthetic iron(IV)-oxo complexes versus their iron(III)-hydroperoxo analogs.[64] Thus, the sulfoxidation and epoxidation reactions of three different ferric-hydroperoxo oxidants, namely $[(N4Py)Fe^{III}(OOH)]^{2+}$, $[(Bn\text{-}tpen)Fe^{III}(OOH)]^{2+}$, and $[(TPA)Fe^{III}(OOH)]^{2+}$, with N4Py = *N*,*N*-bis(2-pyridylmethyl)-*N*-bis(2-pyridyl)-methylamine, Bn-tpen = *N*-benzyl-*N*,*N*′,*N*′-tris(2-pyridylmethyl)ethane-1,2-diamine and TPA = tris(2-pyridylmethyl)amine, were investigated in electrophilic and nucleophilic reactions. No reaction was observed between these ferric-hydroperoxo complexes and either thioanisole or cyclohexene (Scheme 4), thus supporting the DFT calculations.

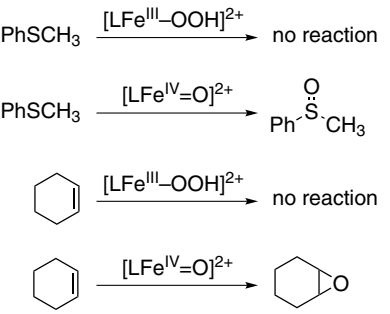

Scheme 4. Reactivities of nonheme $[LFe^{III}–OOH]^{2+}$ and $[LFe^{IV}=O]^{2+}$ complexes, where L = N4Py, Bn-tpen or TPA, in the oxidation of sulfides and olefins.

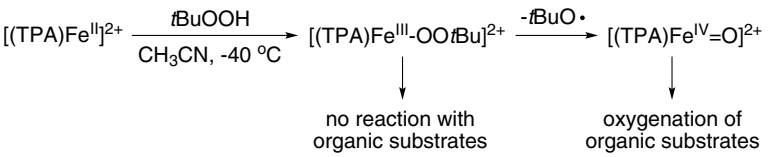

Scheme 5. Nonheme iron(III)-alkylperoxo and iron(IV)-oxo complexes in oxygenation reactions.

In addition to the lack of electrophilic oxidation by ferric-hydroperoxo, activity with respect to nucleophilic deformylation was not detected either.[64] By contrast, the analogous iron(IV)-oxo complexes reacted efficiently with olefins and sulfides to give epoxide and sulfoxide products.[64]

Similarly, reactivity and spectroscopic studies of a mononuclear nonheme iron(III)-alkylperoxo complex, $[(TPA)Fe^{III}(OOtBu)]^{2+}$ (*t*BuOOH = *tert*-butyl hydroperoxide), revealed that this intermediate is not capable of oxygenating substrates either and that a high-valent iron(IV)-oxo intermediate, $[(TPA)Fe^{IV}(O)]^{2+}$, which is generated via O–O bond homolysis of the $[(TPA)Fe^{III}(OOtBu)]^{2+}$ species,[70] is the active oxidant that effects the oxygenation of organic substrates, such as sulfides, olefins, and alcohols (Scheme 5).[71] These experimental results are strongly supported by DFT calculations, in which the energy barrier for the O–O bond activation of Fe(III)-OOR species is lower than that for the direct oxygen atom transfer from the intermediate to organic substrates.[71]

More recently, Woggon, van Eldik, and coworkers provided spectroscopic evidence for the formation of reactive intermediates, such as $(Porp)^{+\bullet}$ Fe^{IV}=O, and the involvement of the intermediate in oxygen atom transfer to substrates, such as *cis*-stilbene, in the reaction of an RSO_3^--substituted iron(III) porphyrin complex and *m*-CPBA.[72] In addition to the spectroscopic evidence for the formation of the

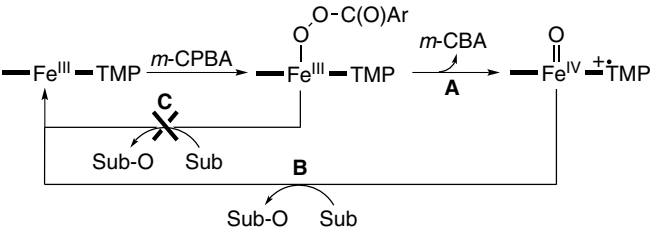

Scheme 6. High-valent iron(IV)-oxo porphyrin π-cation radical as an active oxidant in the oxygenation of organic substrates by Fe(TMP)Cl and *m*-CPBA.

iron(IV)-oxo porphyrin intermediate, rate constants for the formation and decay of intermediates formed in the catalytic reaction of the iron porphyrin complex and *m*-CPBA and for the oxygen atom transfer to the substrate were determined by using low-temperature rapid-scan stopped-flow techniques. Similarly, Nam and coworkers have provided strong evidence that a high-valent iron(IV)-oxo porphyrin π-cation radical is an active oxidant in the catalytic oxygenation of organic substrates by an iron(III) porphyrin complex and *m*-CPBA, whereas an iron(III)-oxidant porphyrin adduct is a sluggish oxidant in iron porphyrin model reactions.[73] In the study, the authors determined rate constants for the oxygenation of various substrates by $[(TMP)^{+\bullet}Fe^{IV}=O]^+$ (TMP = *meso*-tetramesitylporphyrin). Then, the reaction of Fe(TMP)Cl with *m*-CPBA was carried out in the presence of the substrates under catalytic reaction conditions. The formation of $[(TMP)^{+\bullet}Fe^{IV}=O]^+$ was observed, followed by the disappearance of the intermediate with rates identical to those observed in the reaction of $[(TMP)^{+\bullet}Fe^{IV}=O]^+$ and substrates under stoichiometric conditions. These results demonstrated that $[(TMP)^{+\bullet}Fe^{IV}=O]^+$, which is formed via O–O bond heterolysis of Fe^{III}(Porp)(*m*-CPBA) (Scheme 6, pathway A),[74,75] is an active oxidant that is responsible for the oxygenation of organic substrates at low and room temperatures (Scheme 6, pathway B). The results further implied that an iron(III) porphyrin-oxidant adduct, Fe^{III}(Porp)(*m*-CPBA), is a sluggish oxidant in oxygenation reactions (Scheme 6, pathway C).

II. Iron(IV)-Oxo Porphyrin π-Cation Radical Complexes

"High-valent iron-oxo porphyrins" is a description that refers to iron complexes with porphyrin ligands in which the oxidation state of the iron ion is higher than +3 and contains a terminal oxo group bound to the metal center. The first synthetic iron(IV)-oxo porphyrin π-cation radical complex, $[(TMP)^{+\bullet}Fe^{IV}=O]^+$, was reported by Groves and coworkers after reacting Fe(TMP)Cl with *m*-CPBA in a CH_2Cl_2/CH_3OH mixture at −78 °C.[76] The formation of $[(TMP)^{+\bullet}Fe^{IV}=O]^+$ occurs via O–O bond cleavage of the (TMP)Fe^{III}–OOC(O)Ar intermediate, as shown in

Scheme 6, pathway A.[74,75] The green species, formulated as $[(TMP)^{+\bullet}Fe^{IV}=O]^{+}$, was characterized by various spectroscopic techniques, such as UV-vis,[76] ^{1}H NMR,[76,77] EPR,[77] Mössbauer,[77,78] resonance Raman,[77,79] magnetic circular dichroism,[80] and EXAFS spectroscopies.[81] The $[(TMP)^{+\bullet}Fe^{IV}=O]^{+}$ complex was also prepared using other oxidants, such as ozone,[82] dimethyldioxirane,[83] and iodosylbenzene.[84] Since then, a number of iron(IV)-oxo porphyrin complexes have been synthesized with porphyrin ligands bearing electron-donating and -withdrawing substituents on the porphyrin ligand. The reactivities of the iron porphyrins were then investigated in various oxidation reactions under catalytic or stoichiometric conditions, to understand the electronic effect of porphyrin ligands on the chemical properties of the iron-oxo intermediates.[85–87] As electron-deficient iron(III) porphyrin complexes are better catalysts in catalytic oxygenation reactions,[85–87] iron(IV)-oxo porphyrin π-cation radicals bearing electron-deficient porphyrin ligands show high reactivities in hydrocarbon oxygenation.[88] This result indicates that the electronic nature of porphyrin ligands is an important factor that controls the oxidizing power of iron(IV)-oxo porphyrin π-cation radicals, and that iron-oxo species with electron-deficient porphyrins are more powerful oxidants in the electrophilic oxidation of organic substrates (Scheme 7).

Since the thiolate axial ligand in CYP 450 is believed to play a significant role in dioxygen activation and oxygen atom transfer reactions,[28–33,89,90] the effects of axial ligands bound *trans* to the iron-oxo moiety have also been investigated in various oxygenation reactions with iron(IV)-oxo porphyrin π-cation radical complexes bearing different axial ligands.[91–96] Gross and Nimri reported a pronounced axial ligand effect on the epoxidation of olefins by $(TMP)^{+\bullet}Fe^{IV}(O)(X)$, in which $(TMP)^{+\bullet}Fe^{IV}(O)(X)$ complexes bearing ligating anionic ligands (X = F^{-}, Cl^{-}, $CH_3CO_2^{-}$) showed a greater reactivity than those bearing nonligating anions (X = $CF_3SO_3^{-}$ and ClO_4^{-}) in the epoxidation of styrenes.[82] Subsequently, Nam and coworkers demonstrated that iron(IV)-oxo porphyrin π-cation radicals bearing

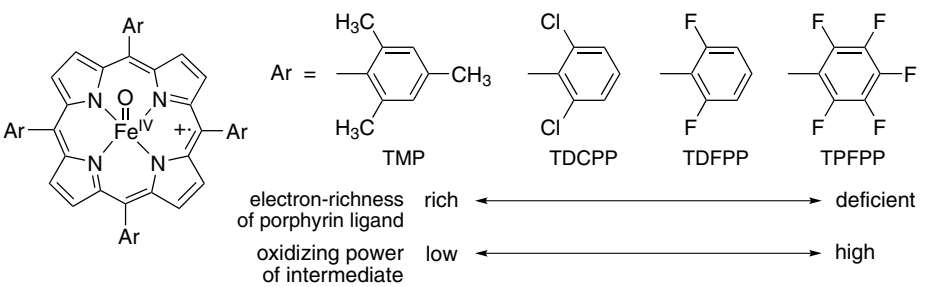

Scheme 7. Porphyrin ligand effect on the oxidizing power of iron(IV)-oxo porphyrin π-cation radicals in oxygenation reactions.[14,85]

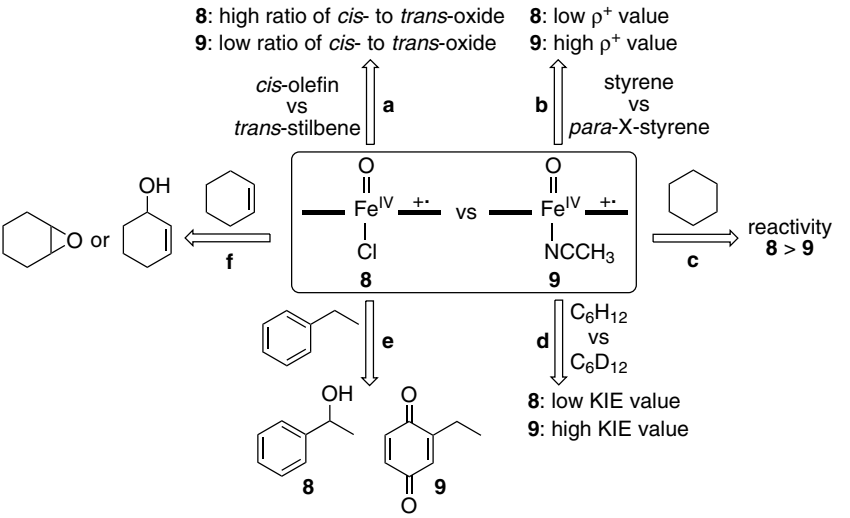

Scheme 8. Axial ligand effects on the reactivities of iron(IV)-oxo porphyrin π-cation radicals.[97]

different axial ligands such as chloride and acetonitrile, $(TPFPP)^{+\bullet}Fe^{IV}(O)(Cl)$ (**8**) and $(TPFPP)^{+\bullet}Fe^{IV}(O)(NCCH_3)$ (**9**) [TPFPP = *meso*-tetrakis(pentafluorophenyl) porphyrin] (Scheme 8), exhibit diverse reactivity patterns, such as in the selectivity of *cis*- versus *trans*-olefins (reaction *a*) and of styrene versus *para*-substituted styrenes (reaction *b*) in olefin epoxidation, the oxidizing power in alkane C–H activation (reaction *c*), the kinetic isotope effect (reaction *d*), the regioselectivity of aromatic ring oxidation versus C–H hydroxylation in ethylbenzene (reaction *e*) and of C=C epoxidation versus C–H hydroxylation (reaction *f*) in olefin oxygenation.[14,97] These results indicated that the axial ligands control not only the oxidizing power of the iron-oxo moiety but also the stereo- and regioselectivity change in substrate oxygenation reactions. The results further demonstrated that iron(IV)-oxo porphyrin π-cation radicals can exhibit diverse reactivity patterns under different circumstances, suggesting that one oxidant, not multiple oxidants, is involved in oxygenation reactions.[53–56] Very recently, theoretical calculations provided plausible explanations for the role of axial ligands in the change of the regioselectivity of aliphatic versus aromatic hydroxylation in ethylbenzene hydroxylation (reaction *e*)[98]; the change of the regioselectivity is proposed as a result of differences in orbital interactions between the axial ligand and the iron-oxo porphyrin system.

The effects of axial ligands on the reactivities of iron(IV)-oxo porphyrin π-cation radicals have also been studied with $[(TMP)^{+\bullet}Fe^{IV}(O)(para\text{-Y-PyO})]^{+}$ bearing *para*-substituted pyridine *N*-oxides (*para*-Y-PyO, Y = OCH_3, CH_3, H, Cl) as axial ligands in various oxygenation reactions, such as olefin epoxidation,

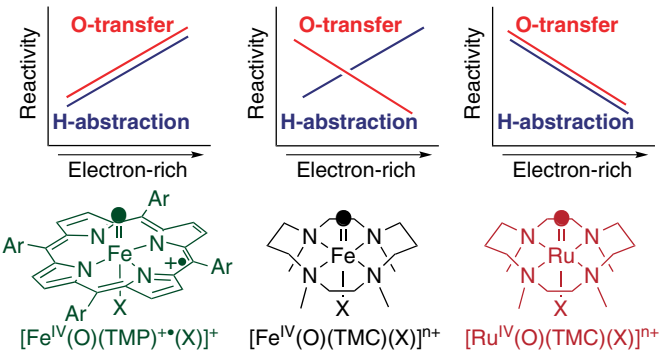

Figure 3. Schematic drawings showing the axial ligand effects on the reactivities of $[Fe(IV)(O)(TMP)^{+\bullet}(PyO)]^{+}$ (left), $[Fe(IV)(O)(TMC)(X)]^{n+}$ (middle), and $[Ru(IV)(O)(TMC)(X)]^{n+}$ (right) in oxo-transfer (red line) and H-atom abstraction (blue line) reactions.[99]

aromatic hydroxylation, alcohol oxidation, and alkane hydroxylation.[99] In all of the reactions, the reactivities of the iron-oxo porphyrin intermediate were found to depend on the axial ligands, giving negative Hammett ρ values of $-1.4 \sim -2.7$ when the reaction rates were plotted against σ_ρ of the substituents of *para*-Y-PyO. These results, as well as previous ones on the effect of anionic ligands,[82,97] show that iron(IV)-oxo porphyrin π-cation radicals bearing electron-donating axial ligands are more reactive in both oxo-transfer and hydrogen-atom abstraction reactions (Figure 3, left). Since iron(IV)-oxo porphyrin π-cation radicals are electrophilic species, the observed negative Hammett ρ values are counterintuitive. Thus, theoretical calculations of anionic and neutral ligands were attempted to elucidate the counterintuitive experimental findings.[99] In the case of anionic ligands, as the ligand becomes a better electron donor, it strengthens the FeO–H bond and enhances thereby H-abstraction activity. In addition, it weakens the Fe=O bond and encourages thereby oxo-transfer reactivity. Both are Bell–Evans–Polanyi effects.[100–102] However, in a series of neutral ligands like *para*-Y-PyO, there is a relatively weak trend that appears to originate in two-state reactivity (TSR).[19] This combination of experimental and theoretical studies provided rationales that shed light on the factors that control the reactivity patterns of iron(IV)-oxo porphyrin π-cation radicals in oxidation reactions either by TSR or by basicity of the iron-oxo reagent.[99]

As shown in Figure 3, the axial ligand effects have also been investigated systematically in nonheme iron(IV)- and ruthenium(IV)-oxo systems.[103–106] For example, the reactivity of a nonheme iron(IV)-oxo complex bearing different axial ligands, $[Fe(IV)(O)(TMC)(X)]^{n+}$ (TMC = 1,4,8,11-tetramethyl-1,4,8,11-tetraazacyclotetradecane; X = CH_3CN, $CF_3CO_2^-$, N_3^-, and RS^-), in oxo-transfer to PPh_3 and hydrogen atom abstraction from phenol O–H and alkylaromatic C–H bonds is

affected by the nature of anionic axial ligands (X^-) in opposite ways, depending on the reaction types (Figure 3, middle).[103,104] As can be seen in Figure 3 (middle), oxo-transfer reactivity correlates with the electrophilicity of the nonheme iron(IV) complex and is enhanced by the electron-withdrawing ligand, whereas H-atom abstraction reactivity follows an opposite trend and is enhanced by the electron-donating ligand. This dichotomy was theoretically interpreted based on the fact that nonheme iron(IV)-oxo reagents possess two close-lying spin states: a ground state with a triplet spin state (T) and a low-lying quintet spin state (Q).[104] As such, the inverted reactivity in H-atom abstraction was ascribed to the increased contribution of the more reactive quintet state (such as blending of the triplet and quintet states or faster spin crossover for the better donor ligand).[103,105,106] By contrast, in the analogous Ru(IV)-oxo complexes, $[Ru(IV)(O)(TMC)(X)]^{n+}$ (Figure 3, right), where the ground state is triplet and the quintet state is high-lying, it was observed that both reaction types were enhanced by electron-withdrawing ligands, in line with the increased electrophilicity of the Ru(IV)-oxo reagent.[106] Hence, the electrophilic reactivity trend in the nonheme Ru(IV)-oxo complexes was shown to be an outcome of a single-spin-state reactivity, which is quite different from the nonheme iron-oxo reagent that proceeds via TSR.[20,103,105]

Since the electron-donating property of the axial-thiolate ligand in CYP 450 is believed to be responsible for the strong oxidizing power of CYP 450 in the activation of C–H bonds,[28,89,90] continued extensive research is in progress to elucidate the axial ligand effects on the chemical and physical properties of iron(IV)-oxo intermediates in heme enzymes and the biomimetic heme and nonheme iron-oxo complexes.

III. Theoretical Modeling of CYP 450 Properties and Reactivities in Oxygenation Reactions

In recent years computational chemistry resources have improved significantly, and nowadays relatively large chemical systems (up to about 200 atoms) can be calculated with relative accuracy. As a consequence of that, there has been a substantial increase in computational studies focused on biomimetic and enzymatic systems. Many of these theoretical studies investigated the structure and function of heme enzymes. In this work, we will restrict ourselves to heme-based monoxygenase enzymes and biomimetics, and in particular focus on the mechanisms of substrate activation by their active oxidant.

As described in detail above, CYP 450s are heme-based monoxygenases that react with substrates efficiently. The reactions catalyzed by them include aliphatic C–H hydroxylation, C=C double bond epoxidation, aromatic C–H hydroxylation, sulfoxidation, dehydrogenation, and *N*-dealkylation.[5,11–13] In many substrates,

therefore, competing reaction mechanisms are possible, with multiple products formed; thus, the nature of the environment in the active site, such as the substrate-binding topology, plays in many cases a key role in determining the regioselectivity of a reaction.[11–13] By using combined experimental and theoretical modeling, mechanisms have been established for most of these reactions, which we will discuss in the following. Before discussing the reactivity patterns of CYP 450s in detail, let us first examine the active oxidant and its electronic properties and how these have an effect on its reactivity patterns.

There are many closely related heme enzymes, such as peroxidases and catalases, which have different functions and properties. Although their active site shows similarities to CYP 450s, including an iron(IV)-oxo species in the catalytic cycle, we will not look at these systems in depth. Studies on the mechanism and function of peroxidases and catalases have been reviewed elsewhere and therefore will not be dealt with in great detail here.[108–110]

A. Compound I

It is generally accepted that compound I (Cpd I) is the active species of CYP 450 that performs substrate monoxygenation, although there have been suggestions of alternative oxidants such as Cpd 0, which we will discuss later in this work. Cpd I of CYP 450 is elusive, but indirect experimental evidence through product distributions, kinetic isotope effects, and low-pressure mass-spectrometric studies has shown an iron(IV)-oxo porphyrin cation radical species to be the most likely candidate.[49,50,111] Further extensive theoretical modeling has made predictions on its electronic and spectroscopic properties, and confirmed it to be the most likely oxidant of CYP 450 enzymes. In this subsection we will describe the electronic properties of Cpd I and in particular the effect of the ligands on its chemical properties. Studies have been reported of many different Cpd I analogs, which essentially differ in the nature of the axial ligand used. To highlight the axial ligand used in the model, we will designate it in parentheses after Cpd I, i.e. Cpd I(SH^-) is a Cpd I mimic with SH^- in the axial ligand position.

Figure 4 displays the high-lying occupied and low-lying virtual molecular orbitals of [Fe^{IV}=O($Por^{+\bullet}$)Cl] or Cpd I(Cl^-), whereby the heme is abbreviated to iron(II) protoporphyrin IX and all side chains replaced by hydrogen atoms. Replacement of the axial ligand with another anionic ligand gives molecular orbitals with very similar shapes and energies. In this system the axial ligand is chloride, which is isoelectronic to thiolate (SH^-) and has been shown to produce similar electronic properties and molecular orbitals.[112] Experimental studies on biomimetic iron(IV)-oxo porphyrin complexes usually have trimethylphenyl or related groups on the *meso*-position (see Scheme 7).[14,15,104,113–115] Recent DFT

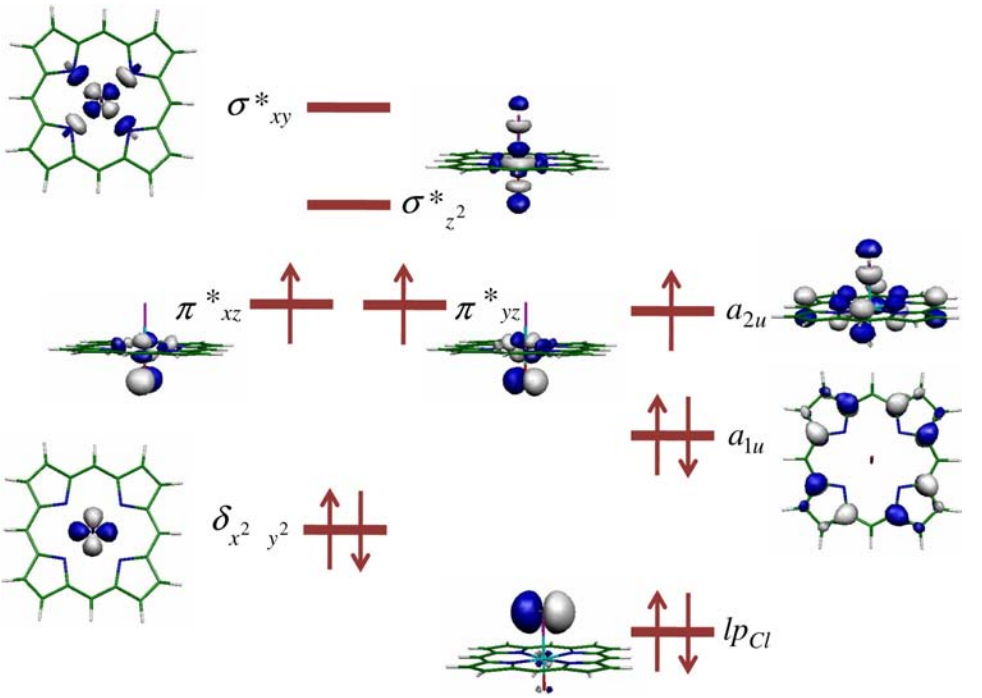

Figure 4. High-lying occupied and low-lying virtual orbitals of Cpd I(Cl^-).

studies with 2,6-dichlorophenyl groups on the four *meso*-positions of the porphyrin (TDCPP) implicated no change in the orbital occupation due to *meso*-substitution.[116] Although the stretch vibration for the Fe–O bond (ν_{Fe-O}) is decreased by 8 cm^{-1} upon addition of *meso*-substituents, as a matter of fact the bond distances are the same with respect to the unsubstituted porphyrin. However, the charge of the *meso*-carbon decreases from $Q = 0.21$ for the unsubstituted porphyrin to $Q = 0.09$ for TDCPP, which affects substrate binding.

The key molecular orbitals of Cpd I are divided into a set of metal-based 3*d* orbitals (left-hand side of Figure 4) and some high-lying heme- and ligand-based orbitals (right-hand side of Figure 4).[19,117,118] The metal 3*d*-type orbitals split into a nonbonding orbital (δ_{x2-y2}), a set of π^*_{FeO} orbitals (π^*_{xz} and π^*_{yz}) and a pair of σ^* orbitals (σ^*_{xy} and σ^*_{z2}). The lowest-lying of those is the nonbonding δ_{x2-y2} orbital, which, due to the symmetry in the heme ligand, cannot form favorable orbital interactions and is doubly occupied in Cpd I. Higher in energy are the two π^*_{FeO} antibonding orbitals built from $3d_{xz,yz}$ atomic orbitals on Fe with $2p_{x,y}$ on oxygen π^*_{xz} and π^*_{yz}, which are singly occupied in Cpd I. Two virtual metal-type orbitals in Cpd I are for the σ^* interactions of the metal with the porphyrin macrocycle (σ^*_{xy}) and for the metal with its distal and axial ligands (σ^*_{z2}). Thus, due to the

occupation of the metal 3*d*-type orbitals with four electrons, the oxidation state is Fe(IV) in Cpd I. The heme ligand has many π^*-type orbitals, and two of them are shown in Figure 4, namely the ones that in D_{4h} symmetry have the labels a_{1u} and a_{2u}.[117,119–122] The former is doubly occupied in Cpd I and although the a_{2u} orbital is expected at an energy similar to that for the a_{1u} orbital, in fact in Cpd I it is much higher in energy due to mixing of the a_{2u} orbital with a π orbital on the axial ligand.[123,124] Thus, the a_{2u} orbital is a mixed a_{2u} and π_{Cl} orbital in Cpd I(Cl^-) and is raised in energy, and as a consequence is also singly occupied.[119] Thiolate ligation has a similar effect, and also mixing of the a_{2u} and π_S orbital destabilizes the singly occupied orbital, although it is considerably smaller in peroxidase Cpd I models where an imidazole (ImH) group of a neutral histidine ligand binds to the axial position. Due to the fact that the a_{2u} and π^*_{FeO} orbitals are close in energy and the electrons in them interact little, Cpd I can exist in an overall quartet spin state or an overall doublet spin state, both with occupation $\delta_{x2-y2}^2\ \pi^*_{xz}{}^1\ \pi^*_{yz}{}^1\ a_{1u}{}^2\ a_{2u}{}^1$. As will be described in the next subsection, these two spin states will create TSR patterns on competing spin state surfaces.[63]

In many of the valence and virtual orbitals in Cpd I, the ligand *trans* to the oxo group, i.e. the axial ligand, plays a key role that determines its stability and electrophilicity.[125,126] For instance, the a_{2u} orbital mixes strongly with a lone-pair orbital on the axial ligand and hence is destabilized. As a consequence of these ligand interactions, the energies of the valence orbitals and also the optimized geometries vary, depending on the chosen model. Figure 5 depicts a selection of optimized geometries of different Cpd I systems with a variable axial ligand: Cpd

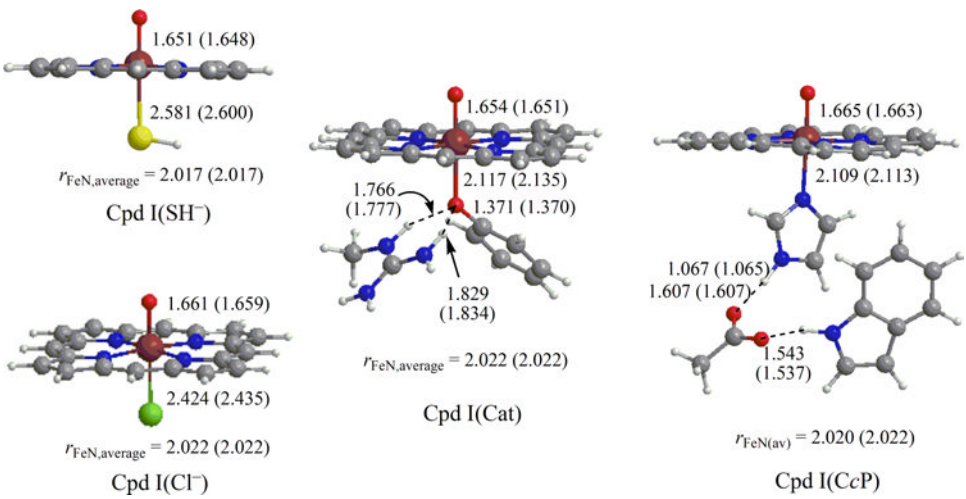

Figure 5. Optimized geometries of Cpd I models of P450, catalase, cytochrome *c* peroxidase, and a biomimetic iron(IV)-oxo porphyrin cation radical. Data taken from Refs. 127–131.

I(SH^-),[127] Cpd I(Cl^-),[112] Cpd I(Cat),[128] and Cpd I(C*c*P).[129–131] The latter two structures are mimics of the iron(IV)-oxo species of catalase and cytochrome *c* peroxidase (C*c*P) enzymes. In catalase a tyrosinate ligand binds in the axial ligand position that is held by hydrogen-bonding interactions with an arginine residue. In peroxidases, such as C*c*P, an axial histidine binds to the metal, which is involved in a triad of hydrogen-bonding interactions with a neighboring aspartic acid side chain that bridges also with a tryptophan group. This unique system has a tryptophan radical rather than a heme-based radical; however, addition of a point charge ($Q = +1$) at a distance of about 8 Å from the tryptophan group in the K^+ binding loop changed the system to a porphyrin radical instead.[129–132] Optimized geometries give only minor differences in the strength of the Fe–O bond, so that it does not appear to matter whether a neutral or anionic ligand binds to the metal in the axial position. This does not change when the axial ligand is replaced by one of the many other axial ligands tested so far.

The catalytic cycle of peroxidase enzymes is shown in Scheme 9 with C*c*P as an example. Thus, in C*c*P the heme is bound to an axial histidine residue (of His_{175}) that is part of a hydrogen-bonded triad with the acetic acid group of Asp_{235} and a proton from Trp_{191}. On the distal side several proton sources can be found, namely His_{52} and Arg_{48}. Hydrogen peroxide binds to the distal side, and the imidazole group of His_{52} abstracts one of its protons to give an Fe(III)-hydroperoxo species, i.e. Cpd 0. A subsequent proton transfer gives water and an Fe(IV)-oxo species, similarly to the catalytic cycle of CYP 450 shown above. This species abstracts an electron to give Cpd II, which is involved in the further reduction of the oxo group to a water molecule.

A closely related enzyme with a very similar active site to C*c*P is ascorbate peroxidase (APX), but despite its close resemblance to C*c*P in Cpd I(APX) the porphyrin is a cation radical and the tryptophan group in the axial binding site is neutral.[133] Further studies on the difference between Cpd I(APX) and Cpd I(C*c*P) with QM/MM methods revealed that the induced electric field due to the protein is responsible for the difference in orbital occupation: the electron affinity of the tryptophan and heme groups are influenced by perturbations of the protein and change Cpd I from [Fe^{IV}=O(Por)His---$Trp^{+\bullet}$] in C*c*P to [Fe^{IV}=O($Por^{+\bullet}$)His---Trp] in APX.[134] Indeed, DFT calculations on an active site model of Cpd I(C*c*P) with an additional point charge in the K^+ binding position gave a dramatic change in orbital occupation and hence electron distributions (Scheme 10).[128] Thus, without the point charge the group spin densities indicate a mixture between porphyrin cation radical and tryptophan radical, as also highlighted by Siegbahn and coworkers in earlier studies.[134] However, a positive charge in the K^+ binding site position changed the group spin densities and created a situation with a porphyrin cation radical and a closed shell tryptophan ($Por^{+\bullet}$ Trp). By contrast, the opposite

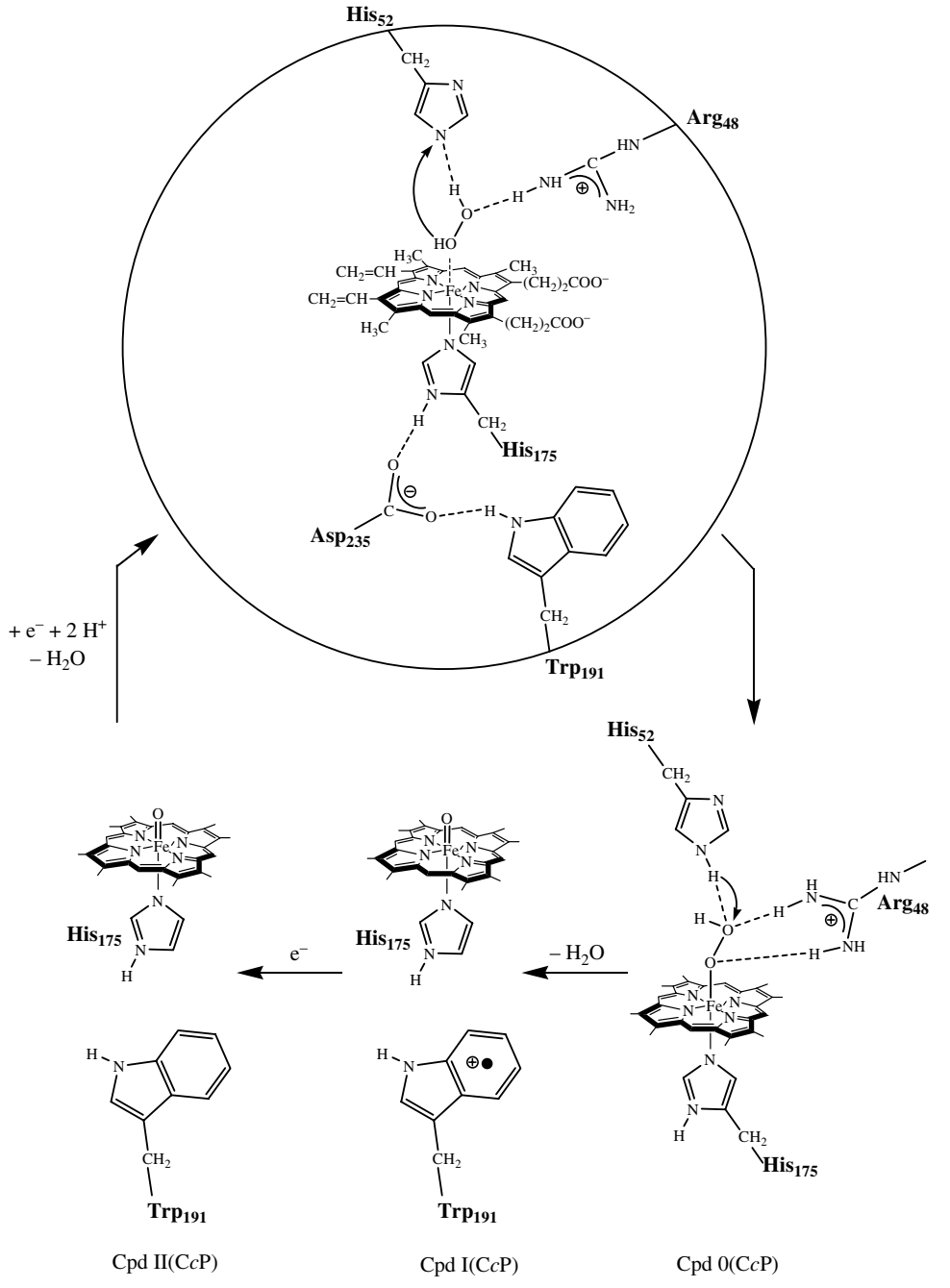

Scheme 9. Catalytic cycle of peroxidases, such as C*c*P.

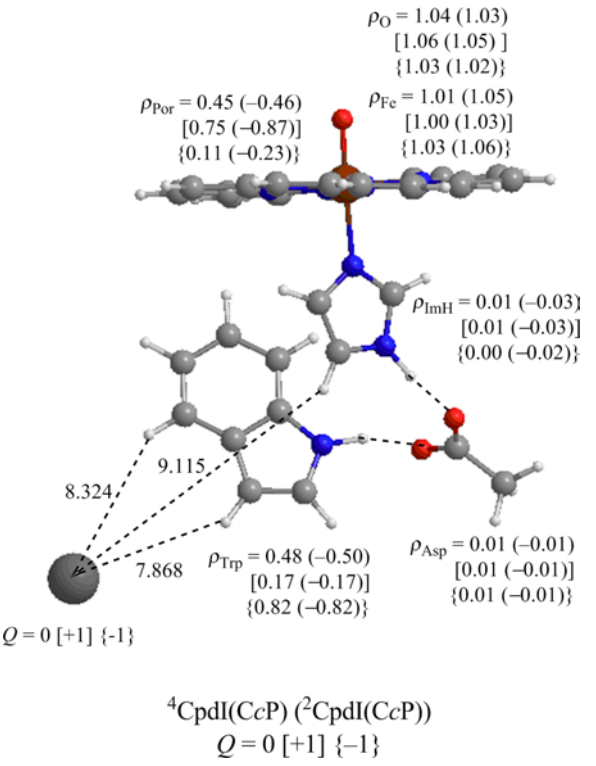

Scheme 10. Group spin densities of Cpd I(C*c*P) in the gas phase and with a point charge added.

was found with a negative point charge, where a tryptophan radical was created (Por Trp$^{\bullet}$). These studies support experimental work[135,136] and have confirmed a strong electronic change to the active species upon the addition of a point charge at a distance of almost 10 Å from the heme.

The differences in chemical properties between CYP 450s, heme peroxidases, and catalases were assigned to the axial ligand bound to the iron-heme, which is a cysteinate residue in CYP 450s, a histidine in peroxidases and a phenolate group of a tyrosine residue in catalases.[134,137] It was reasoned that cysteinate prompts a push effect of electrons, whereas histidine withdraws electrons from the active center and thereby changes the electronegativity of the iron(IV)-oxo oxidant. Quantum-chemical calculations have established two factors contributing to the push or pull effect of the axial ligand: (1) a quantum-chemical factor (ΔE_{QM}) due to orbital mixing between ligand and metal, and (2) an electric field effect (ΔE_{field}) from electrostatic interactions between the negatively charged ligand and the metal.[31] Figure 6 displays the estimated values of ΔE_{QM} and ΔE_{field}

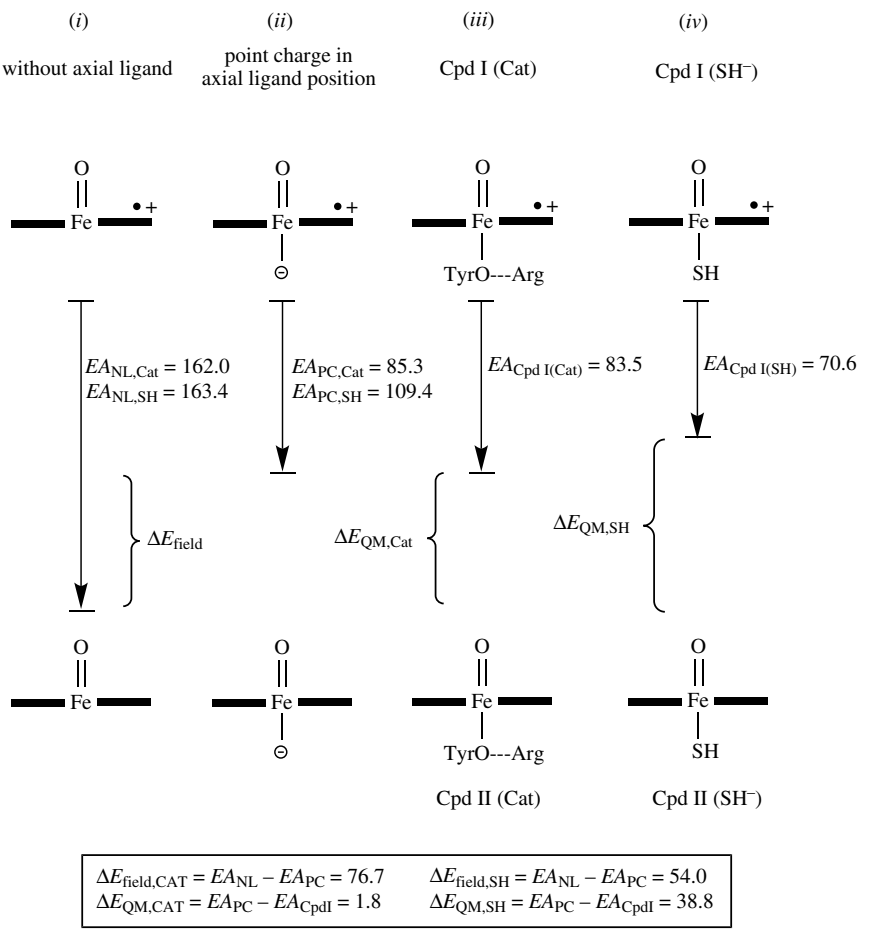

Figure 6. Quantum-chemical estimate of the push effect of anionic ligands on the iron(IV)-oxo moiety as calculated for Cpd I(Cat) and Cpd I(SH⁻), with values in kcal mol^{-1}.

for Cpd I(SH⁻) and Cpd I(Cat).[31,138] The electron affinity of Cpd I ($EA_{\text{Cpd I}}$) is calculated for Cpd I(SH⁻) and Cpd I(Cat). Subsequently, the ligand is removed from both systems and a single-point calculation of Cpd I and Cpd II provides EA_{NL}, the electron affinity of the iron(IV)-oxo porphyrin complex without ligand. Finally, the axial ligand of Cpd I and of Cpd II are replaced by a point charge, and single-point calculations give EA_{PC}. Subsequently, using the calculated values of EA_{NL}, EA_{PC}, and $EA_{\text{Cpd I}}$, the contributions of the field effect (ΔE_{field}) and the QM effect (ΔE_{QM}) are estimated (Figure 6). As follows, in Cpd I(Cat) the dominant contribution is the field effect, primarily because the distance between the ligand and the metal is small: $r_{\text{Fe–OPh}} = 2.117$ Å in ^{4}Cpd I(Cat), while $r_{\text{Fe–SH}} = 2.581$ Å in Cpd I(SH⁻). On the other hand, Cpd I(SH⁻) has a much larger QM effect due

to mixing of the a_{2u} orbital with a π_S orbital, which is much less when a tyrosinate group binds in the axial ligand position. As a consequence of the differences in ΔE_{field} and ΔE_{QM} between Cpd I(Cat) and Cpd I(SH^-), there is a 14.3 kcal mol^{-1} larger push effect in the thiolate ligated system, which will affect the electrophilicity of the oxo group.

DFT calculations on Cpd I(SH^-) that took environmental effects into consideration, such as a dielectric constant or hydrogen-bonding interactions toward the thiolate by additional ammonia molecules in the model, showed a shift of group spin densities away from the thiolate ligand onto the porphyrin macrocycle, as indicated in Figure 7.[124,139] Thus, the a_{2u} orbital is described as a mixture of two valence bond (VB) states, |a⟩ and |b⟩; |a⟩ reflects an Fe^{IV}=O(Por)($SH^{\bullet}$) configuration, whereas |b⟩ is an Fe^{IV}=O($Por^{+\bullet}$)(SH^-) state. Environmental effects, such as through

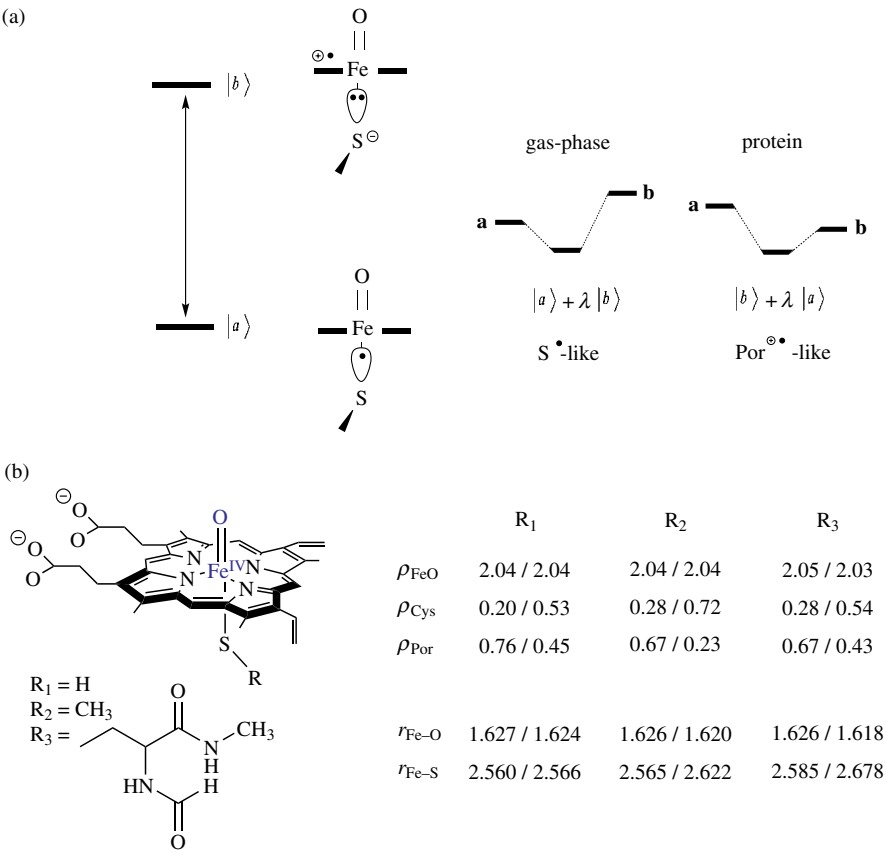

	R_1	R_2	R_3
ρ_{FeO}	2.04 / 2.04	2.04 / 2.04	2.05 / 2.03
ρ_{Cys}	0.20 / 0.53	0.28 / 0.72	0.28 / 0.54
ρ_{Por}	0.76 / 0.45	0.67 / 0.23	0.67 / 0.43
r_{Fe-O}	1.627 / 1.624	1.626 / 1.620	1.626 / 1.618
r_{Fe-S}	2.560 / 2.566	2.565 / 2.622	2.585 / 2.678

Figure 7. (a) VB diagram of mixing of porphyrin and thiolate states. (b) Effect of the local environment on the chemical description of the thiolate ligand using QM/MM versus DFT calculations on model complexes. Bond lengths are given in angstroms.

hydrogen-bonding interactions, change the charge of the thiolate ligand and make the system more[b)]-like.

To establish the electronic configuration of Cpd I of CYP 450 in its native environment, QM/MM calculations were performed on the complete enzyme with the active site in the QM region and the rest of the protein with solvent in the MM layer.[140] Figure 7(b) displays results of comparative QM/MM and gas phase DFT calculations on CYP 450_{cam} with three different Cpd I models deviating in the description of the axial ligand (SR) ranging from the smallest system SH^- via SCH_3^- to a full description of cysteinate and its neighboring peptide groups (SR_3). Only results for the quartet spin state structures are given in Figure 7(b), since the doublet spin data follow the same trends. The optimized geometries are all very much alike and the only differences obtained concern the Fe–S distance which is somewhat elongated in the gas phase models. The group spin densities give dramatic changes from a dominant thiolate-based radical in the gas phase to a porphyrin radical in an enzyme-mimicked environment. For the description of Cpd I of CYP 450, it is important, therefore, to take environmental perturbations into consideration since the gas phase distorts the orbital contributions. Further QM/MM calculations of Harvey and coworkers[141] on a selection of Cpd I structures of various CYP 450 isoforms showed only minor fluctuations in the electronic description of Cpd I, so that the actual size and shape of the protein are expected to have only minor effects.

B. Two-State Reactivity

As discussed above, the iron(IV)-oxo oxidant has close-lying doublet and quartet spin states with the same orbital occupation. Reaction mechanisms with substrates, as a consequence, proceed on both spin state surfaces, but not necessarily with the same barriers.[14–16,63] This has led to the experimental suggestion that two oxidants are active in the reaction mechanism, although it may be these two spin states that masquerade as two different oxidants. Figure 8 shows the potential energy profile of a typical TSR reaction starting from Cpd I(SH^-) for the aliphatic hydroxylation of propene. In the past this mechanism was shown for a range of different substrates irrespective of the axial ligand.[142–147] Thus, Cpd I is a chameleonic oxidant that behaves as multiple oxidizing species, but in fact is the same oxidant in a different spin state.[19] As a matter of fact, this appears a common phenomenon in bioinorganic chemistry that CYP 450s share with mononuclear nonheme iron(IV)-oxo complexes.[148–150]

Generally, hydroxylation reactions proceed with an initial hydrogen abstraction barrier ($\mathbf{TS}_H$) to form an iron-hydroxo complex ($\mathbf{I}_H$). Subsequently, a radical rebound step via a rebound transition state ($\mathbf{TS}_{reb}$) gives alcohol product complexes ($\mathbf{P}_H$).

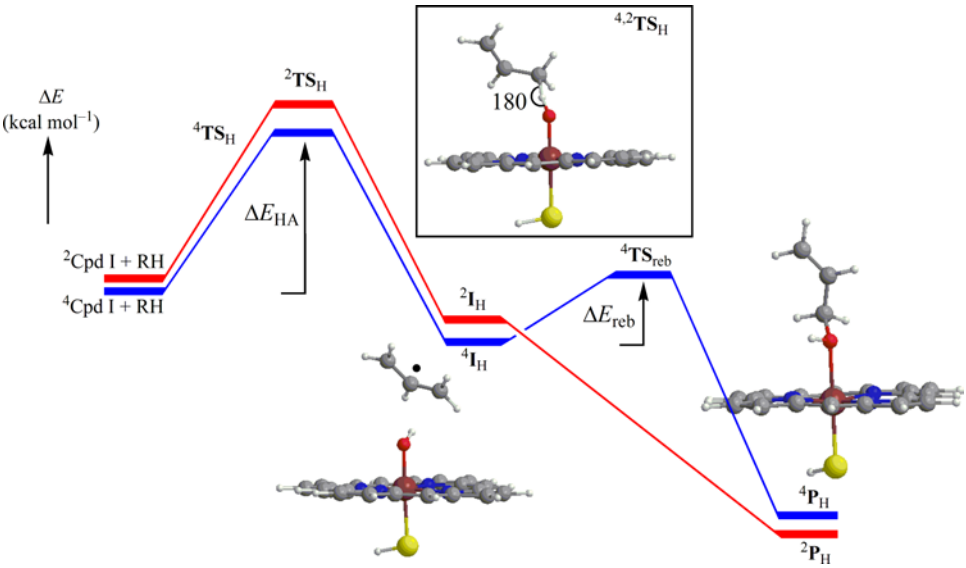

Figure 8. TSR potential energy profile for propene hydroxylation by Cpd I(SH^-).

On the doublet and quartet spin state surfaces, usually similar aliphatic hydrogen abstraction barriers and energies are encountered due to the same electron transfer processes in the reaction, namely electron donation into the a_{2u} orbital. As a result, $^4\mathbf{I}_H$ and $^2\mathbf{I}_H$ have the same orbital occupation, namely $\delta_{x2-y2}{}^2\,\pi^*_{xz}{}^1\,\pi^*_{yz}{}^1\,a_{1u}{}^2\,a_{2u}{}^2\,\phi_R{}^1$, and hence are degenerate. The radical rebound step, by contrast, undergoes different electron transfer processes. Namely, in the low spin state an electron is transferred from the substrate into the π^*_{xz} orbital, whereas in the high spin state it moves into a higher-lying σ^*_{z2} orbital.[151] Consequently, the high-spin process encounters a significant rebound barrier, whereas on the low-spin surface a virtually barrierless transition leads to alcohol products. The difference in rebound barrier between the high-spin and low-spin surfaces influences rearrangement reactions and product distributions. For instance, it was shown, using *trans*-2-phenylmethylcyclopropane as a radical-clock substrate, that rearrangement reactions are possible only on the quartet spin state surface and not on the doublet one, which influences product distributions as well as kinetic isotope effects.[152,153] There are cases where one of the two spin state surfaces is stabilized with respect to the other so that single-state reactivity (SSR) is encountered instead. Thus, aromatic hydroxylation generally proceeds on a dominant low-spin surface, whereas sulfoxidation does so on a high-spin surface. In the following subsections, therefore, we will discuss the various substrate monoxygenation reactions separately and discuss the differences and comparisons.

C. Aliphatic C–H Activation by Cpd I of CYP 450

As shown in the previous subsection, Cpd I reacts with aliphatic substrates via an initial hydrogen abstraction reaction, leading to a radical intermediate followed by a radical rebound of the hydroxyl group to the substrate rest group to form alcohol products. Thermodynamically, the hydrogen abstraction from substrate RH by Cpd I or [Fe^{IV}=O($Por^{+\bullet}$)L], with L the axial ligand to form the intermediate complex $\mathbf{I}_H$, has an exothermicity (ΔH_{HA}) dependent on the energies of reactants and products in Eq. 2.

$$[Fe^{IV}=O(Por^{+\bullet})L] + RH \rightarrow [Fe^{IV}(OH)(Por)L] + R^{\bullet} + \Delta H_{HA}. \quad (2)$$

The reaction enthalpy (ΔH_{HA}) for reaction 2 can be described as a function of the bond dissociation energy (BDE) of the C–H bond of the substrate and the BDE_{O-H} for the O–H bond of [Fe^{IV}(OH)(Por)L] through combination of Eqs. 2 and 3 to get Eq. 4.

$$RH \rightarrow R^{\bullet} + H^{\bullet} + BDE_{C-H}, \quad (3)$$

$$\Delta H_{HA} = BDE_{C-H} - BDE_{O-H}. \quad (4)$$

Since all hydrogen atom abstraction reactions using Cpd I(SH^-) have the same BDE_{O-H}, this means that the reaction exothermicity for formation of the intermediate complexes ($^{4,2}\mathbf{I}$) in Figure 8 should correlate linearly with BDE_{C-H} for a series of substrates RH. This correlation is shown in Figure 9 and indeed fits a straight line in agreement with Eq. 4. The standard deviation displayed in that figure is

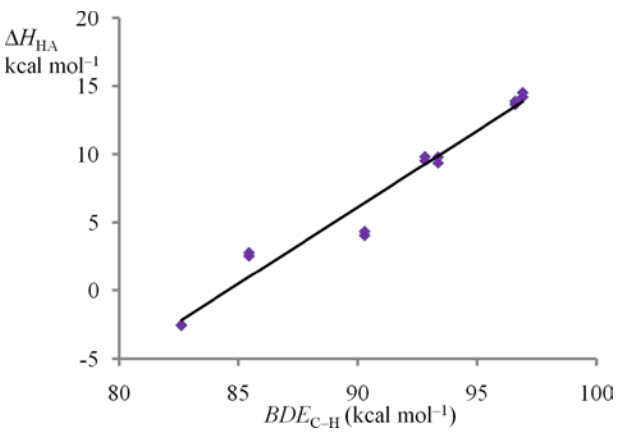

Figure 9. Correlation of the reaction energy of hydrogen abstraction (ΔH_{HA}) with BDE_{C-H}.

small and shows that the reproducibility of DFT calculations is quite good. Moreover, it appears that DFT-calculated exothermicities are within an error of a few kcal mol^{-1}. This is much smaller than the systematic error generally reported for DFT calculations of 3–5 kcal mol^{-1} with respect to experimentally determined enthalpies.[154–156]

The hydrogen abstraction mechanism has been further generalized by a valence bond (VB) curve crossing diagram, as shown in Figure 10.[147] Thus, the reaction starts on the bottom left of the figure with the reactant geometry, where the critical VB electrons are highlighted with dots. Thus, the Fe–O bond in Cpd I is described by the pairs of $\pi_{xz,yz}$ and $\pi^*_{xz,yz}$ molecular orbitals. The bonding pair is doubly occupied, whereas the antibonding pair has two unpaired electrons spread out over the iron(IV)-oxo group due to single occupation of two π^*_{FeO} orbitals, and hence six dots are drawn next to the Fe–O bond. In addition, Cpd I has a heme cation radical due to single occupation of the a_{2u} molecular orbital. The reaction finishes with the alcohol product complexes shown on the bottom right of the figure in red, which is the result of two-electron oxidation of our reactant species and transfer of one electron into the heme (a_{2u}) and one in a π^* orbital to give the metal oxidation state Fe(III). A VB curve crossing diagram is constructed by drawing a line from the reactant geometry, which has wave function Ψ_r, and connecting it to the product geometry with excited state wave function Ψ_p*. Similarly, starting from the product complexes with wave function Ψ_p,

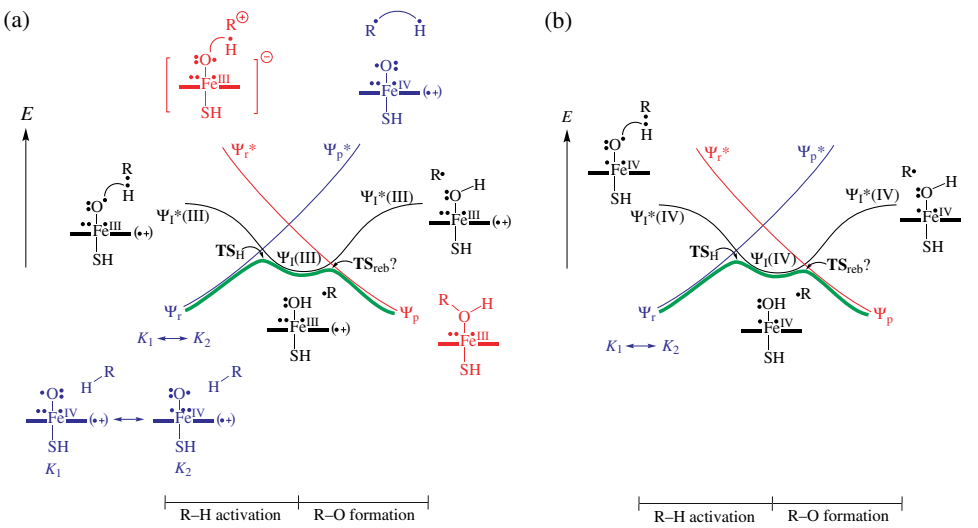

Figure 10. VB curve crossing model for the hydroxylation reaction of RH by Cpd I via an $Fe^{III}(Por^{+\bullet})(OH)$ intermediate [part (a)] or an $Fe^{IV}(Por)(OH)$ intermediate [part (b)]. Reproduced with permission from the American Chemical Society.[147]

a connection is made with the reactants via Ψ_r*. Thus, in Ψ_r* the system has the reactant geometry but the electronic configuration of the products, while for Ψ_p* it is the other way around. Crossing of these two VB curves will give rise to an avoided crossing and consequently a transition state for the reaction. Thus, a concerted reaction mechanism, such as ethylbenzene hydroxylation by iodosylbenzene, has only one barrier through the mixing of reactant and product curves.[157] However, in CYP 450 a third curve for the intermediate wave function bisects the reactant and product wave functions to give rise to two avoided crossings: one for hydrogen abstraction and one for radical rebound. This intermediate curve has either the metal in the oxidation state Fe(IV) together with a closed-shell heme, i.e. [Fe^{IV}(OH)(Por)L---R$^{\bullet}$], or the metal in the oxidation state Fe(III) combined with a cation radical on the heme to give [Fe^{III}(OH)($Por^{+\bullet}$)L---R$^{\bullet}$]. These two intermediate wave functions are identified with Ψ_I(IV) and Ψ_I(III), respectively, and give rise to the two distinctive radical intermediates in the reaction mechanism. Figure 10(a) displays the VB curve crossing mechanism that passes the Fe(III) intermediate, while the one passing the Fe(IV) intermediate is shown in Figure 10(b). Generally, gas-phase DFT calculations predict the Fe(IV) intermediates to be the lowest-lying,[146,158] but QM/MM seems to lower the Fe(III) intermediates.[140] Therefore, the relative ordering of the Fe(IV) and Fe(III) intermediates is dependent on polarized effects from, for example, the protein surroundings or through hydrogen-bonding interactions, and leads to multistate reactivity (MSR) patterns.

The intermediate curve crosses the reactant wave function and gives rise to an avoided crossing and hence a hydrogen abstraction transition state. This barrier leads to the corresponding radical intermediate but past the intermediate the wave function crosses the product wave function to give rise to a second avoided crossing and the radical rebound barrier. Thus, the VB curve crossing model explains why the reaction is stepwise via a radical intermediate. In VB terms, the hydrogen abstraction barrier ($\Delta E_H^{\ddagger}$) can be written in terms of the height of the crossing point (ΔE_c) minus the resonance energy (B):

$$\Delta E_H^{\ddagger} = \Delta E_c - B. \tag{5}$$

It was shown that the height of the crossing, in fact, is a fraction (f) of the promotion gap (G_H).[159] Since the electronic difference between the reactant configuration and the excited intermediate wave function (Ψ_I) is based on the singlet-to-triplet excitation energy of the C–H bond, this implies that the promotion gap is actually proportional to the strength of the C–H bond, i.e. the bond dissociation energy of the C–H bond (BDE_{C-H}), Eq. 6. In addition, the promotion gap contains electron transfer energies which for the Fe(IV) wave function reflect the energy

transfer from π^*_{OO} into the a_{2u} orbital, while for Fe(III) the electron transfer is into the π^*_{xz} orbital.

$$\Delta E_H^{\ddagger} = fG_H - B \propto \mathrm{BDE}_{CH}. \quad (6)$$

Indeed, DFT calculations of a series of hydrogen abstraction barriers by Cpd I(SH^-) and Cpd I(SCH_3^-) gave a linear correlation with BDE_{C-H}; one of these correlations is shown in Figure 11.[146,160] Further correction to the trend with resonance energy stabilization of the transition state structures gave the C–H bond strength D_{C-H}, which correlates perfectly with the barrier heights of C–H abstraction of nine aliphatic C–H bonds. Olsen and coworkers calculated 24 hydrogen abstraction barriers by Cpd I(SCH_3^-) and found correlations similar to those given

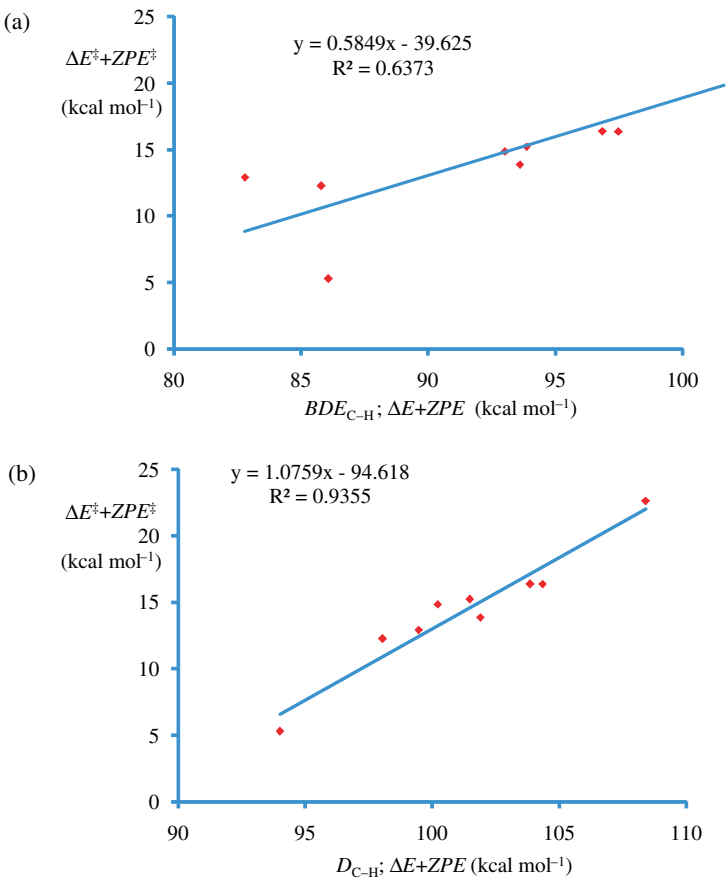

Figure 11. Correlation of the hydrogen abstraction barriers for a series of substrates with BDE_{C-H} and with D_{C-H}; data taken from Ref. 147.

in Figure 11.[160] In their paper the resonance energy is labeled "frozen BDE" and addition of this factor improves the correlation significantly. These studies confirm and rationalize experimental correlations of the logarithm of the rate constant with BDE as found for several mononuclear metal-oxo complexes.[161–164]

The subsequent step in the aliphatic hydroxylation mechanism is the radical rebound step which leads to alcohol product complexes. The general reaction for this is described by Eq. 7 for the process starting from the Fe(IV) intermediate, and by Eq. 8 for the Fe(III) intermediate. The reaction exothermicities for this reaction are ΔH_{rebIV} and ΔH_{rebIII}, respectively. Obviously, the two reactions lead to the same products, so that the overall exothermicity from Cpd I(L) and RH to form [Fe^{III}(Por)] and ROH products is identical.

$$[Fe^{IV}(OH)(Por)L] + R^{\bullet} \rightarrow [Fe^{III}(Por)] + ROH + \Delta H_{\text{rebIV}}, \quad (7)$$

$$[Fe^{III}(OH)(Por^{+\bullet})L] + R^{\bullet} \rightarrow [Fe^{III}(Por)] + ROH + \Delta H_{\text{rebIII}}. \quad (8)$$

The reaction energies given in Eqs. 7 and 8 reflect the OH transfer energies from the iron-porphyrin complexes to the radical R. Using the definition of the hydroxyl affinity (BDE_{C-OH}) as defined in Eq. 9, the reaction enthalpy for Eqs. 7 and 8 can be described in terms of differences in hydroxyl affinity between [Fe^{III}(Por)] and $R^{\bullet}$, as shown in Eqs. 10 and 11.

$$ROH \rightarrow R^{\bullet} + OH^{\bullet} + BDE_{C-OH}, \quad (9)$$

$$\Delta H_{\text{rebIV}} = BDE_{FeIV-OH} - BDE_{C-OH}, \quad (10)$$

$$\Delta H_{\text{rebIII}} = BDE_{FeIII-OH} - BDE_{C-OH}. \quad (11)$$

The overall reaction enthalpy (ΔH_r) for the reaction starting from Cpd I and substrate (RH) to give alcohol products and an Fe^{III}-porphyrin complex is therefore the sum of Eqs. 4 and 10 as given in Eq. 12:

$$\Delta H_r = \Delta H_{\text{HAIV}} + \Delta H_{\text{rebIV}} = BDE_{C-H} - BDE_{O-H} + BDE_{FeIV-OH} - BDE_{C-OH}. \quad (12)$$

For the radical rebound step, a VB curve crossing diagram was designed to explain the differences in rebound barriers between the high-spin and low-spin surfaces, as well as between the Fe^{IV} and Fe^{III} states. Figure 12 shows the VB curve crossing diagrams starting from [Fe^{IV}(OH)(Por)SH---$R^{\bullet}$], i.e. ^{4,2}**I**(IV).

As described in Eq. 6, the hydrogen abstraction barrier height ($\Delta E_H^{\ddagger}$) correlates with the excitation energy from the ground state wave function to the excitation

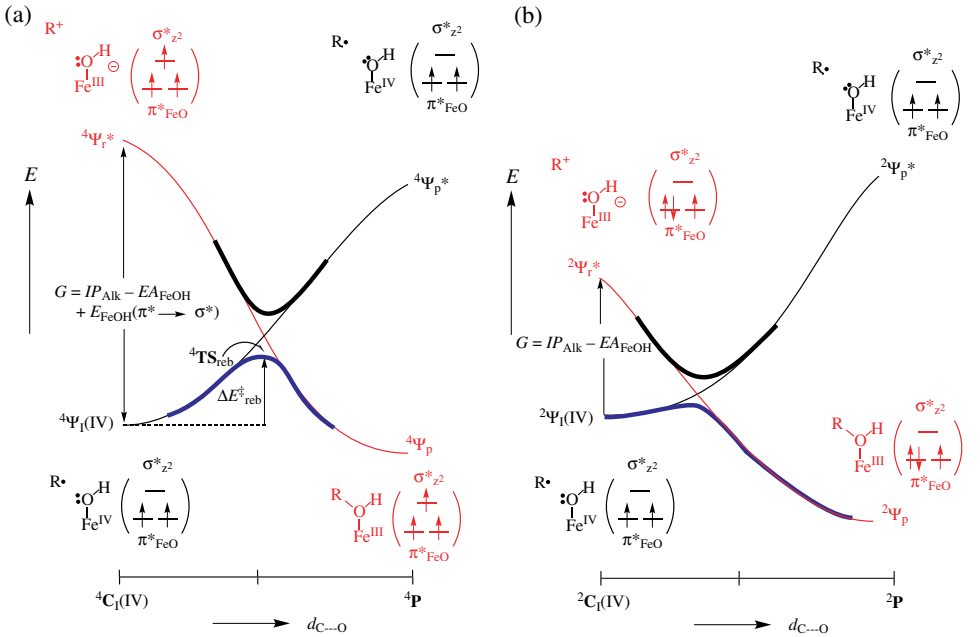

Figure 12. Rebound VB model in the high-spin (a) and low-spin (b) pathways, starting from the intermediate complexes in the Fe(IV) oxidation state. Reproduced with permission from the American Chemical Society.[147]

state wave function, G_H. The same is true for the radical rebound barrier ($\Delta E_{reb}^{\ddagger}$), which is proportional to the excitation energy from the ground state to the excitation state in the intermediate geometry, i.e. excitation from $^{4,2}\Psi_I(IV)$ to $^{4,2}\Psi_r^*$ for the Fe(IV)-type intermediates ^{4,2}**I**(IV) and from $^{4,2}\Psi_I(III)$ to $^{4,2}\Psi_r^*$ for the Fe(III)-type intermediates ^{4,2}**I**(III). Thus, ^{2}**I**(IV) has electronic configuration $\delta^2\ \pi^*_{xz}{}^1\ \pi^*_{yz}{}^1\ a_{2u}{}^2\ \phi_R{}^1$, whereas for the product complex ^{2}**P** and hence also $^2\Psi_r^*$ the configuration is $\delta^2\ \pi^*_{xz}{}^2\ \pi^*_{yz}{}^1\ a_{2u}{}^2$. In other words, the excitation energy involves ionizing the substrate rest group and reduction of the iron-hydroxo complex with one electron (EA_{FeIVOH}). The low-spin barrier will, therefore, correlate with the difference between the ionization potential of R (IP_R) and EA_{FeIVOH}:

$$\Delta E_{reb,LS}^{\ddagger} \propto IP_R - EA_{FeIVOH}. \tag{13}$$

The electron affinity of the iron-hydroxo complex leads to electron donation into the π^*_{xz} orbital to give ^{2}[Fe^{III}(OH)(Por)L]; however, excitation from $^4\Psi_I(IV)$ to $^4\Psi_r^*$ gives a quartet spin iron-hydroxo complex with occupation $\pi^*_{xz}{}^1\ \pi^*_{yz}{}^1\ \sigma^*_{z2}{}^1$. As a consequence of this, the excitation energy from $^4\Psi_I(IV)$ to $^4\Psi_r^*$ is larger than the difference between IP_R and $EA_{Fe}IV_{OH}$ by the excitation energy (E_{FeOH}) of an

electron from π^*_{xz} to σ^*_{z2}, (Eq. 14). This is the reason why a low-spin rebound is generally barrierless or small, whereas in high spin significant barriers are encountered that can cause reorganization of the radical leading to stereochemical scrambling or formation of by-products.

$$\Delta E_{\text{reb,HS}}^{\ddagger} \propto IP_{\text{R}} - EA_{\text{FeIVOH}} + E_{\text{FeOH}}(\pi^*_{xz} \rightarrow \sigma^*_{z2}). \quad (14)$$

In summary, electron transfer mechanisms, orbital occupations, and thermodynamic data explain why aliphatic hydroxylation reactions are stepwise via TSR scenarios on competing doublet and quartet spin state surfaces. Indeed, all calculated aliphatic hydroxylation reactions have so far been shown to proceed via the general mechanism shown in Figures 8 and 10. In the last few paragraphs of this subsection we will give some examples of aliphatic hydroxylation reactions studied by theoretical methods.

The first hydrogen abstraction reactions by CYP 450 model systems studied with DFT methods used methane as a substrate.[142,165,166] However, in the past 10 years, more realistic substrates have also been studied. Special emphasis always has been on camphor hydroxylation by CYP 450_{cam}, since it is the natural substrate hydroxylation reaction of this CYP 450 isozyme. Moreover, several crystal structures are available for this CYP 450 enzyme.[24,26] Initial studies used DFT methods, but later on complete enzyme studies with the QM/MM technique were reported.[145,167] Essentially, all these studies predict the same mechanistic trends that are described by the fundamental rules in this section: an initial hydrogen atom abstraction followed by a radical rebound. The regioselectivity of C^5 hydroxylation from camphor is determined by the substrate-binding site, where camphor is tightly bound and only the C^5 position approaches the heme close enough to enable hydroxylation.

Table 1 summarizes substrate hydroxylation reactions calculated with DFT or QM/MM methods for Cpd I(L).[112,133,147,160,168–181] Essentially, all calculations support the general mechanism shown in Figure 8, with a rate-determining hydrogen atom abstraction leading to an iron-hydroxo species that rebinds to the radical to give alcohol product complexes. Occasionally, however, the rebound step is replaced by *N*-dealkylation or dehydrogenation, but also in these cases the hydrogen atom abstraction is rate-determining. On average the low-spin states are below the high-spin ones by 0.9 ± 1.3 kcal mol^{-1}, irrespective of the axial ligand used. Clearly, substrate hydroxylation is a TSR phenomenon with competing spin state surfaces and reaction barriers. The close energy between $^4\mathbf{TS}_{\text{H}}$ and $^2\mathbf{TS}_{\text{H}}$ is evident from the electron transfer processes shown in Figure 10, where most substrates lead to an intermediate with the metal in the oxidation state Fe(IV). The only exceptions to this are methane hydroxylation which leads

Table 1. DFT-calculated hydrogen abstraction barriers (in kcal mol^{-1}) by Cpd I(L), as reported in the literature.

L	Substrate	$\Delta E_{H,HS}$	$\Delta E_{H,LS}$	Ref.	L	Substrate	$\Delta E_{H,HS}$	Ref.
SH^-	methane	22.9	22.3	147	SCH_3^-	methane	20.7	160
SH^-	methane	22.9	24.7	170	SCH_3^-	propane, 1° carbon	17.7	160
ImH	methane	25.8	25.0	170	SCH_3^-	propane, 2° carbon	14.8	160
PhO^-	methane	25.4	26.8	170	SCH_3^-	Isobutene	14.3	160
Cl^-	methane	24.7	25.1	170	SCH_3^-	propene	12.9	160
SH^-	ethane	17.4	15.3	147	SCH_3^-	propionaldehyde	11.4	160
SH^-	ethanol: from C1	11.7	10.3	175	SCH_3^-	toluene	13.0	160
SH^-	ethanol: from OH	12.3	12.7	175	SCH_3^-	ethylbenzene, 2°	12.1	160
SH^-	acetaldehyde	8.2	10.0	171	SCH_3^-	1-methylethyl-benzene	13.3	160
SH^-	propane, 2° carbon	15.8	13.9	147	SCH_3^-	dimethylether	12.2	160
SH^-	propane, 1° carbon	17.5	15.2	147	SCH_3^-	dimethylsulfane	11.0	160
SH^-	propane[c]	20.6	19.5	167	SCH_3^-	methylphenylsulfane	10.8	160
SH^-	propene	13.0	12.8	147	SCH_3^-	dimethylamine	7.6	160
ImH	propene	11.0	9.7	168	SCH_3^-	trimethylamine	6.7	160
Cl^-	propene	14.8	12.9	112	SCH_3^-	fluoroethane, 2°	18.4	160
Cat	propene	12.0	11.3	138	SCH_3^-	fluoroethane, 1°	14.7	160
CcP	propene	18.4	17.8	131	SCH_3^-	ethylbenzene, 1°	17.3	160
ImP	propene	19.1	13.0	174	SCH_3^-	2-fluoroprop-1-ene	13.2	160
$SO_3CH_3^-$	propene	11.9	11.4	169	SCH_3^-	prop-1-en-2-ol	11.7	160
OH^-	propene	5.7	3.9	181	SCH_3^-	*p*-xylene	12.7	160
SCH_3^-	trimethylamine	9.6	8.3	178	SCH_3^-	1-methyl-4-nitrosobenzene	11.8	160

(*Continued*)

Table 1. (*Continued*)

L	Substrate	$\Delta E_{H,HS}$	$\Delta E_{H,LS}$	Ref.	L	Substrate	$\Delta E_{H,HS}$	Ref.
SH^-	*N,N*-dimethylaniline	5.5	5.0	147	SCH_3^-	methoxybenzene	13.0	160
SH^-	toluene	12.4	12.1	147	SCH_3^-	*N*-methylaniline	7.6	160
SH^-	ethylbenzene	12.6	11.5	147	SCH_3^-	*N,N*-dimethylaniline	6.9	160
Cl^-	ethylbenzene	11.7	9.1	173				
SH^-	camphor	14.5	15.9	147				
$SCys^-$	camphor [c]	21.8	21.1	167				
SH^-	*trans*-2-phenyl-methylcyclopropane	14.5	13.1	147				
SH^-	*trans*-2-phenyl-isopropyl-cyclopropane	13.4	12.3	147				
SH^-	arginine	10.5	4.9	176				
SCH_3^-	morpholine	< 1	< 1	179				
OH^-	cyclohexane	2.2	1.0	172				
CH_3COO^-	cyclohexane	11.0	7.6	172				
Cl^-	cyclohexane	12.7	10.1	172				
$CF_3SO_3^-$	cyclohexane	15.4	12.9	172				
SH^-	*N*-cyclopropyl-*N*-methylaniline[a]	11.4	9.6	180				
SH^-	*N*-cyclopropyl-*N*-methylaniline[b]	11.2	9.2	180				
SH^-	testosterone-β1	13.0	11.4	177				
SH^-	testosterone- β2	8.2	9.7	177				
SH^-	testosterone- β6	6.1	5.3	177				
SH^-	testosterone- β15	11.6	9.7	177				

[a]Methyl group hydroxylation
[b]Cyclopropane ring hydroxylation
[c]QM/MM result

to an Fe(III) intermediate and substrate hydroxylation studied with QM/MM methods on enzymatic systems.

Three substrates (methane, propene, and cyclohexane) have been studied with a range of different Cpd I species with variable axial ligands. Thus, a phenolate ligand (PhO^-) as appears in catalase, for instance, destabilizes hydrogen abstraction barriers by a couple of kcal mol^{-1} with respect to Cpd I(SH^-), and therefore catalase is not a likely oxidant of hydroxylation reactions.[138,170] The theoretical studies on the effect of an imidazole ligand mimicking peroxidases such as horseradish peroxidase (HRP) or cytochrome *c* peroxidase (C*c*P) give conflicting results. Methane hydroxylation by an HRP mimic gave increased barrier heights with respect to those found for Cpd I(SH^-),[170] whereas in propene hydroxylation the opposite trend was observed.[168] Studies on propene hydroxylation by Cpd I of C*c*P using the model shown above in Figure 5, which includes the hydrogen-bonded axial triad, predicted sluggish activity of substrate hydroxylation reactions.[131] This is because Cpd I(C*c*P) is essentially [Fe^{IV}=O(Por)L---$Trp^{+\bullet}$] and has no heme cation radical, like all other Cpd I species. As a consequence the electron transfer processes take place over a larger distance and the barriers are higher. Recent experimental studies on biomimetic iron(IV)-oxo porphyrin complexes with imidazole, 2-methylimidazole, and 3-fluoro-4-nitrophenolate as axial ligands showed increased cyclooctene epoxidation rate constants for imidazole and phenolate ligated complexes as compared with a chloride axial ligand.[182] However, the nature of the oxidant in all these cases is Fe^{IV}=O($Por^{+\bullet}$)L with single occupation of the a_{2u} orbital.

Cyclohexane hydroxylation was studied with four different Cpd I(L) models, where L = OH^-, CH_3COO^-, Cl^-, and $CF_3SO_3^-$, as well as with a range of *para*-substituted pyridine *N*-oxides as axial ligand.[99,172] Thus, the hydrogen abstraction barrier of cyclohexane hydroxylation by Cpd I(L) was found to correlate linearly with both the electron affinity of Cpd I(L) and the Fe–O distance in the transition states. Moreover, calculations of second-order perturbation stabilization interaction energies between the transition state and reactants showed an increase with enhanced electron-donating ability of the oxidant. Therefore, the electron-donating ability of anionic axial ligands in iron(IV)-oxo complexes controls aliphatic hydroxylation reactions. The studies with *para*-substituted pyridine *N*-oxides as axial ligands showed that as the ligand becomes a better electron donor the FeO–H bond is strengthened and the Fe=O bond weakened to give more efficient hydrogen abstraction.

So far, all these DFT and QM/MM calculations have resulted from a hydrogen atom abstraction; however, technically, a hydride transfer is also possible as the first reaction step. As shown recently by Nam, Fukuzumi, and coworkers,[183,184] iron(IV)-oxo porphyrins are able to react with substrates with weak C–H bonds

via an initial hydride abstraction (Eq. 15), with exothermicity ΔH_{HT}, rather than the commonly observed hydrogen atom transfer:

$$[Fe^{IV}{=}O(Por^{+\bullet})L] + RH \rightarrow [Fe^{III}(OH)(Por)L]^{-} + R^{+} + \Delta H_{HT}. \quad (15)$$

In analogy with Eqs. 3 and 4, the exothermicity of Eq. 15 is written as a function of the hydride affinity of Cpd I ($HA_{Cpd\ I}$), the bond dissociation energy of the C–H bond in RH (BDE_{C-H}, Eq. 3), the ionization potential of the radical rest group R (IP_R), and the electron affinity of a hydrogen atom (EA_H):

$$\Delta H_{HT} = HA_{Cpd\ I} - BDE_{C-H} + IP_R - EA_H. \quad (16)$$

In the case where hydride transfer is a much more exothermic process than hydrogen atom abstraction by Cpd I, $\Delta H_{HT} > \Delta H_{HA}$, which can be rewritten by combining Eqs. 4 and 16:

$$HA_{Cpd\ I} - BDE_{O-H} > EA_H - IP_R. \quad (17)$$

Since the difference in energy between the hydride transfer and the hydrogen atom abstraction energies is roughly the difference between EA_H and $EA_{Fe}IV_{OH}$, this means that if $IP_R < EA_{Fe}IV_{OH}$ the hydride transfer is more exothermic, whereas the hydrogen atom transfer is more exothermic for $IP_R > EA_{Fe}IV_{OH}$. Most substrate rest groups have substantially larger ionization potentials than $EA_{Fe}IV_{OH}$; however, cofactor analogs such as 10-methyl-9,10-dihydroacridine ($AcrH_2$) have a very low ionization potential and as a consequence react via hydride transfer abstraction instead of the normal hydrogen atom abstraction.[185]

DFT studies of the reaction of Cpd I(Cl^-) with $AcrH_2$ predicted a hydride transfer mechanism via very low barriers ($^{4,2}\mathbf{TS}_{H,cat}$) of 5.6 and 6.1 kcal mol^{-1} for the quartet and doublet spin state surfaces, respectively (Figure 13).[185] These barriers are much lower than the hydrogen abstraction barriers of most substrates shown in Table 1. Moreover, an alternative hydrogen atom abstraction (via $^{4}\mathbf{TS}_{H,rad}$) was calculated and found to be higher in energy by 5.5 kcal mol^{-1}. The inset of Figure 13 shows the alternative hydroxylation mechanism starting from the one-electron reduced complex of Cpd I, namely compound II or Cpd II(Cl^-). This oxidant reacts with $AcrH_2$ via significantly higher barriers; furthermore, the reaction proceeds via hydrogen atom abstraction rather than hydride transfer. These calculations, therefore, show that Cpd II(Cl^-) is a possible oxidant of weak C–H bonds, but will not be as efficient and reactive as Cpd I(Cl^-), which can react via an alternative hydride transfer mechanism. The difference in energy between the hydrogen atom abstraction barriers by Cpd I and Cpd II in Figure 13

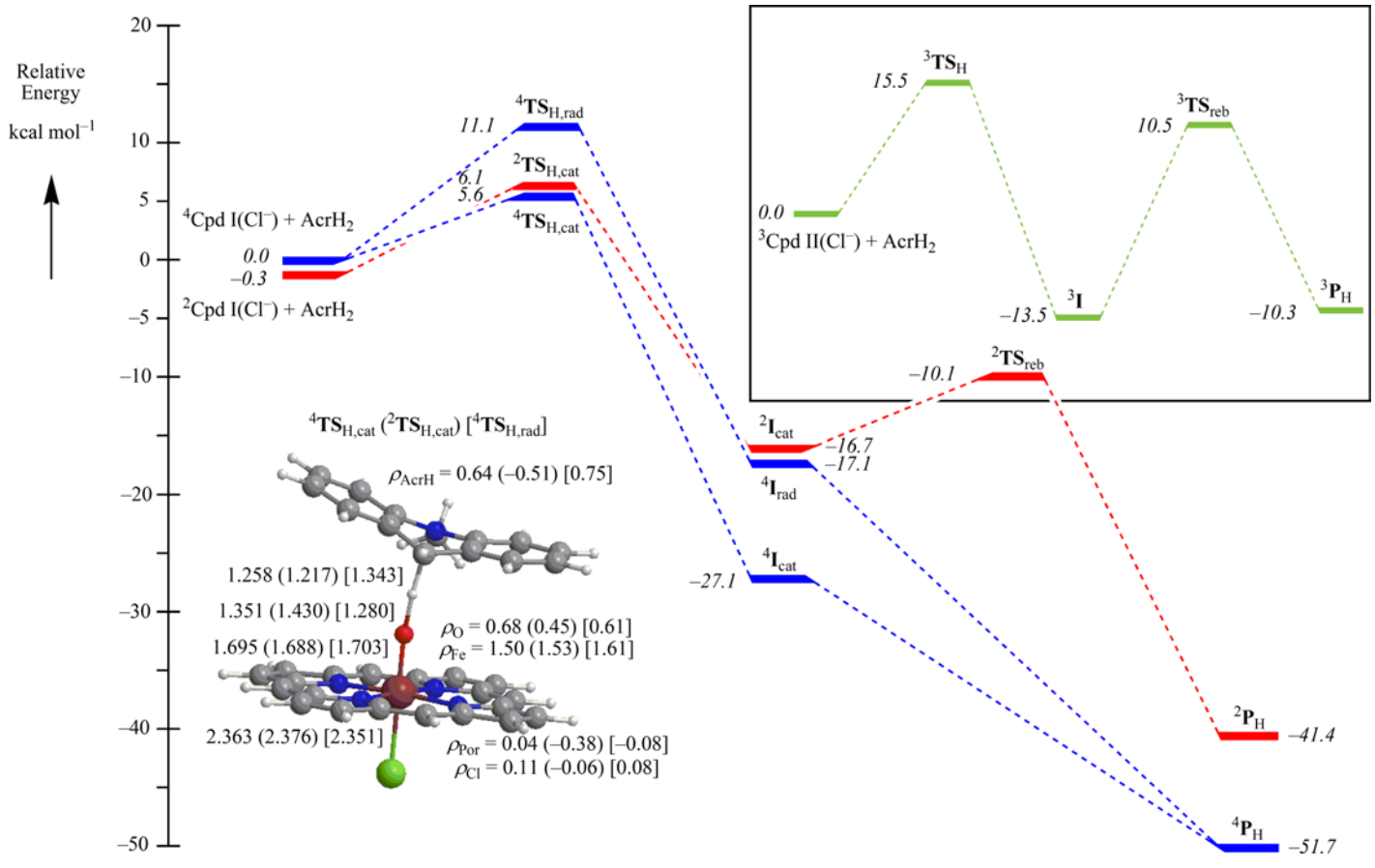

Figure 13. Potential energy profile of $AcrH_2$ hydroxylation by Cpd I(Cl^-) and Cpd II(Cl^-) as calculated by DFT. Energies are in kcal mol^{-1} relative to isolated reactants. Also shown are optimized geometries with group spin densities and bond lengths (in angstroms) of the hydrogen and hydride transfer transition states for Cpd I(Cl^-).

is 4.4 kcal mol^{-1}, which is close to the QM/MM difference of camphor hydroxylation by Cpd I and Cpd II of P450$_{cam}$.[186] This implies that the protein environment has little effect on the relative barriers and will not favor Cpd II over Cpd I. Although ^{4,2}**TS**$_{H,cat}$ appear to be transition states for a hydride transfer, in fact, looking at the group spin densities reveals that the hydride transfer is actually an initial hydrogen atom abstraction followed by a fast electron transfer prior to formation of the intermediate complex.

D. Aliphatic Hydroxylation Mechanisms with Byproduct Formation

The lifetime of the intermediate complexes (^{4,2}**I**) in the reaction mechanisms determines whether a substrate can undergo skeletal rearrangement and produce rearranged products. Experimentally, Ortiz de Montellano and Stearns[187] used bicyclo[2.1.0]pentane as a substrate to determine the lifetime of the radicals, i.e. ^{4,2}**I** in Figure 8. They measured the product ratio of un-rearranged (*U*) to rearranged (*R*) products, as well as the free radical rearrangement constant k_r (Figure 14). These studies established the lifetime of the radical: $\tau = 50$ ps. For a series of radical clock substrates, however,[53–56] it was shown that the lifetime of the radical is not realistic and the results pointed to carbocationic intermediates instead. Thus, it was suggested that radicals are not present and presumably two oxidants were active in the reaction mixture, which were assigned as ferric-hydroperoxo (Cpd 0) and Cpd I. To prove that these radical clock results are obtained through TSR patterns, a set of calculations on radical clock substrates, namely *trans*-2-phenyl-methylcyclopropane and *trans*-2-phenyl-isopropylcyclopropane, with Cpd I(SH$^-$) models were performed, and the highlights of those results are shown in Figure 15.[152,153,188]

Cpd I(SH$^-$) reacts with *trans*-2-phenylmethylcyclopropane via an initial and rate-determining hydrogen abstraction to give radical intermediates (^{4,2}**I**$_U$), as

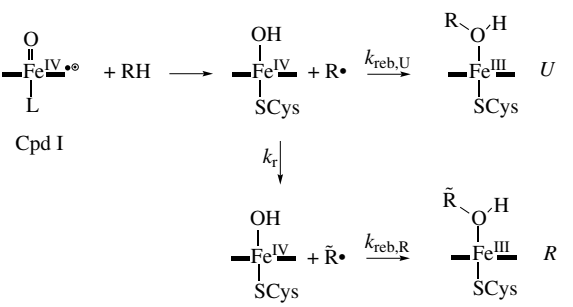

Figure 14. Reaction mechanism for formation of rearranged (*R*) and un-rearranged (*U*) products in the reaction of RH with Cpd I.

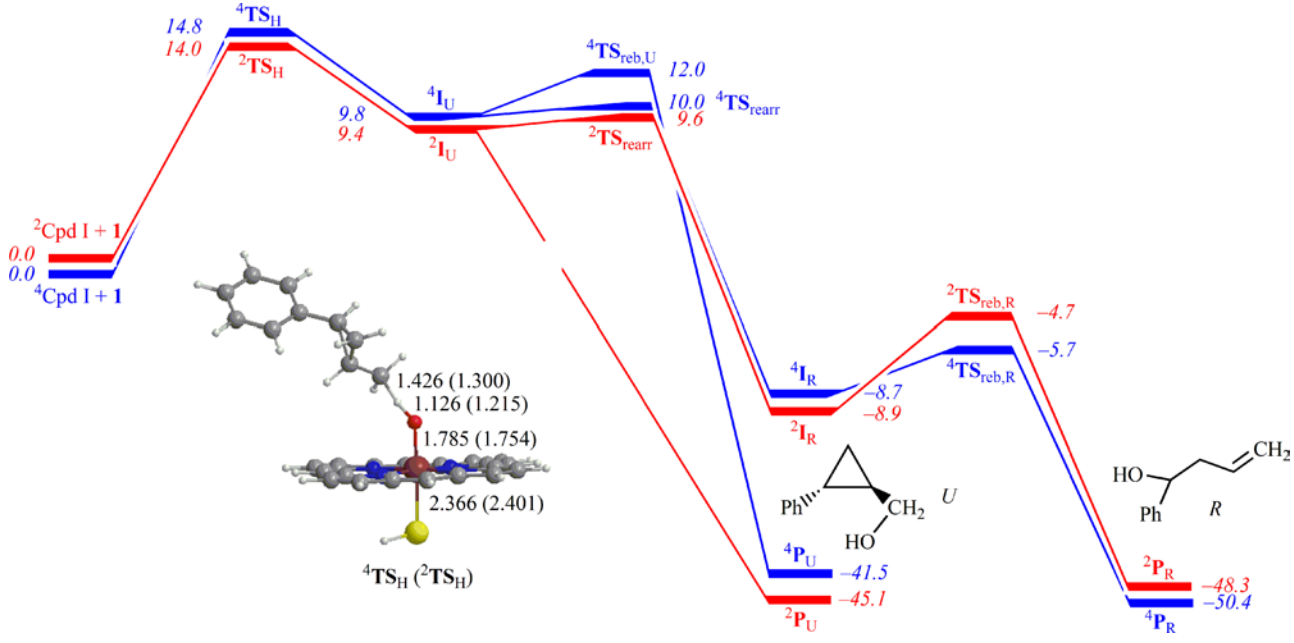

Figure 15. DFT-calculated reaction mechanism of *trans*-2-phenylmethylcyclopropane activation by Cpd I(SH^-) leading to un-rearranged (*U*) and rearranged (*R*) products. Energies in kcal mol^{-1}, with ZPE included taken from Ref. 153 and optimized geometries of hydrogen abstraction transition states from Ref. 147, with bond lengths in angstroms.

expected from the TSR discussion above. From these un-rearranged intermediates, the potential energy surface bifurcates, whereby one mechanism leads to a direct radical rebound and the formation of un-rearranged products ($^{4,2}\mathbf{P}_U$), whereas the alternative mechanism provides radical rearrangement via a barrier $^{4,2}\mathbf{TS}_{rearr}$ to give a rearranged radical intermediate ($^{4,2}\mathbf{I}_R$). A final rebound barrier from rearranged intermediates gives rearranged product complexes ($^{4,2}\mathbf{P}_R$). As follows from Figure 15, the rebound barrier of the un-rearranged intermediate on the doublet spin state is negligible, whereas a small barrier leads to rearranged intermediates, so that dominant un-rearranged products may be expected. On the other hand, on the quartet spin state surface, the rebound barrier of the un-rearranged intermediate is significant (2.2 kcal mol^{-1}), whereas the rearrangement costs only a few tenths of a kcal mol^{-1}, which implies that on the quartet spin state rearrangement will be the preferred mechanism. Accordingly, the product isotope effect (PIE) observed from the ratio of un-rearranged to rearranged products is in fact proportional to the kinetic isotope effect (KIE) ratio of the low-spin and high-spin structures (Eq. 18). Indeed, calculated PIE values were in excellent agreement with experimentally determined PIE data and hence proved the existence of a TSR scenario[153]:

$$\mathrm{PIE}(\mathbf{P}_U/\mathbf{P}_R) = \mathrm{KIE}_{LS}/\mathrm{KIE}_{HS}. \quad (18)$$

Subsequent studies tested the activity of Cpd 0 and ferric-hydrogen peroxide (Fe^{III}–H_2O_2) as possible oxidants of *trans*-2-phenylmethylcyclopropane.[189] These C–H hydroxylation barriers by Cpd 0 and Fe^{III}–H_2O_2 are 9.9 and 3.6 kcal mol^{-1} higher in energy than those obtained for Cpd I(SH^-) with environmental effects included. Moreover, the bond dissociation energy of the Fe–O bond in Fe^{III}–H_2O_2 is much lower in energy than the hydrogen abstraction barrier, so that predominant uncoupling reactions leading to free H_2O_2 are expected rather than C–H hydroxylation. In Cpd 0, the Fe–O bond is sufficiently strong and much higher in energy than the homolytic O–O bond breakage energy. Despite this, little C–H hydroxylation is expected from the Cpd 0 mechanism, due to a lower-lying barrier leading to *meso*-hydroxylation instead. These studies, therefore, have given theoretical evidence that neither Cpd 0 nor Fe^{III}–H_2O_2 can act as an alternative oxidant in C–H hydroxylation reactions in P450 enzymes.

Cpd I of CYP 450 enzymes often regioselectively hydroxylates a specific C–H bond of a substrate, such as the C^5 position in camphor by CYP 450_{cam}, whereby the substrate-binding topology determines the reactivity patterns. In many cases, therefore, gas phase DFT calculations on model complexes are insufficient to ascertain these regioselectivity preferences, and advanced methods such as QM/MM on the complete enzyme are required. In some cases,

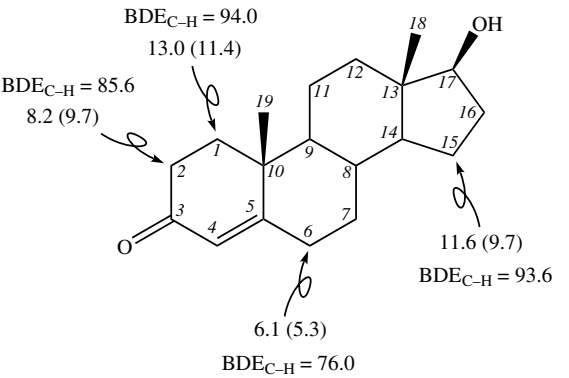

Figure 16. Testosterone hydroxylation at the β1, β2, β6, and β15 positions as calculated with DFT. Barriers and BDE$_{C-H}$ values are in kcal mol^{-1}, with low-spin data in parentheses.

however, the substrate-binding pocket is large and the regioselectivity is simply determined by the relative strengths of the available C–H bonds in the substrate. For instance, testosterone hydroxylation by CYP 450 can take place on many different positions, and experimentally determined product distributions yielded hydroxylated products at the β1, β2, β6, and β15 positions of testosterone (Figure 16). Gas phase DFT calculations[177] using a Cpd I(SH^-) oxidant on the hydroxylation of these four C–H bonds of testosterone showed that the product distributions and experimental rate constants correlate with the calculated hydrogen abstraction barrier heights and consequently with the strength of the C–H bond of the substrate.

Finally, a not-uncommon byproduct in aliphatic hydroxylation reactions is dehydrogenation of the substrate to give alkenes. Studies of C–H hydroxylation of the antiepileptic drug valproic acid by CYP 450 enzymes showed dehydrogenase-oxidase activity that originated from the same precursor as substrate monoxygenation, possibly an iron(IV)-oxo species.[190] Several studies, so far, have focused on substrate dehydrogenation by CYP 450 model complexes.[116,188] Figure 17 gives the general reaction scheme of competitive hydroxylation and dehydrogenation of a substrate $R_2CH_2CH_2R_1$, which may be a cycloalkane, with definitions of the reaction enthalpy of each individual step. Both investigations confirmed an initial and rate-determining hydrogen atom abstraction to form an iron-hydroxo complex. The reaction enthalpy $\Delta H_{r,1}$ for this is as described in Eq. 4 and will depend on the relative BDE values of the O–H and C–H bonds, i.e. $\Delta H_{r,1} = \Delta H_{HA}$. The intermediate rebound of the radical gives alcohol products with exothermicity $\Delta H_{r,2}$, i.e. $\Delta H_{r,2} = \Delta H_{rebIV}$ (Eq. 10). Instead of a radical rebound (Eqs. 7 and 8), a second hydrogen abstraction can form an Fe(III)–H_2O complex with a nearby alkene.

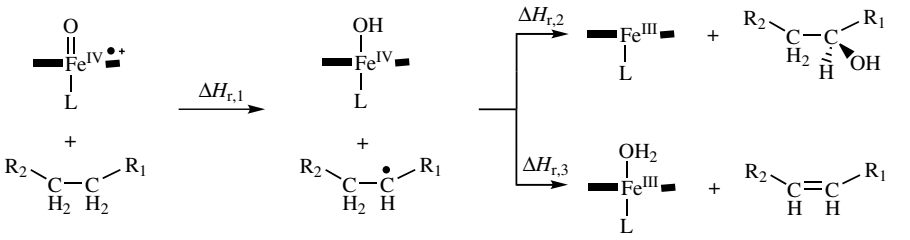

Figure 17. Reaction mechanism leading to substrate hydroxylation and dehydrogenation.

Table 2. DFT-calculated reaction enthalpies and BDE values (in kcal mol^{-1}) of selected substrates.

Substrate	BDE_{C-H}	$\Delta H_{r,1}$	BDE_{rad}	$\Delta H_{r,3}$	BDE_{C-OH}	$\Delta H_{r,2}$
ethane	96.2	9.5	36.7	–34.0	85.8	–55.5
trans-butane	92.6	5.9	33.5	–37.3	85.4	–55.2
cyclohexane	93.0	6.4	33.6	–37.2	85.8	–55.6
cyclohexene	77.7	–9.0	47.5	–23.3	69.1	–38.9
cyclohexadiene	69.0	–17.6	21.8	–49.0	59.7	–29.5

The reaction enthalpy $\Delta H_{r,3}$ for dehydrogenation of the radical, as with Eq. 4 is equal to the difference in bond dissociation energy of an O–H bond in [Fe^{III}–H_2O(Por)L] (designated BDE_{FeHO-H}) and the C–H bond of the radical complex (BDE_{rad}):

$$\Delta H_{r,3} = BDE_{rad} - BDE_{FeHO-H}. \quad (19)$$

To test the regioselectivity preference for a series of substrates, we did DFT calculations to obtain the reaction exothermicities $\Delta H_{r,1}$, $\Delta H_{r,2}$, and $\Delta H_{r,3}$ from BDE values; see Table 2.[116] As follows from the table, the C–H abstraction reaction exothermicity correlates linearly with the strength of the C–H bond, in agreement with the trend depicted in Figure 11. The dehydrogenation exothermicity is more or less constant for aliphatic hydrocarbons and sharply decreases for cyclohexadiene as the result of formation of resonance-stabilized benzene. An opposite trend is observed for the OH rebound to the radical, which is found to be constant and highly exothermic for aliphatic hydrocarbons and is less exothermic for cyclohexene and even more so for cyclohexadiene. As a consequence, the most exothermic reaction for cyclohexadiene is dehydrogenation rather than hydroxylation, which will be the preferred mechanism for all other substrates.

E. Aromatic C–H Activation by Cpd I of CYP 450

Aromatic hydroxylation deserves special attention, since its mechanism deviates significantly from aliphatic hydroxylation, described extensively above. As a matter of fact, aromatic hydroxylation does not start with an initial hydrogen abstraction, but with a C–O bond activation to give either a cationic or radicalar intermediate ($\mathbf{I}_{cat}$ or $\mathbf{I}_{rad}$). Figure 18 displays the aromatic hydroxylation of ethylbenzene by Cpd I(Cl^-).[173] The mechanism observed for aromatic hydroxylation of benzene and toluene by Cpd I(SH^-),[191,192] and benzene by Cpd I(SCH_3^-),[193–195] as well as that for ethylbenzene hydroxylation by Cpd I($NCCH_3$),[98] are the same as the mechanism shown in Figure 18. Moreover, combined experimental and theoretical studies using a nonheme iron(IV)-oxo oxidant showed the same mechanism for nonheme complexes, so that it appears to be universal.[196] The radical intermediate has the same orbital occupation as the aliphatic hydroxylation intermediate, namely $\delta_{x2-y2}^2\ \pi^*_{xz}{}^1\ \pi^*_{yz}{}^1\ a_{2u}{}^2\ \phi_R{}^1$, and hence the metal is in the oxidation state Fe(IV) and the substrate radical is smeared out over five neighboring carbon atoms of the substrate. This delocalized radical has a low ionization potential and, as a result of this, there is also a close-lying cationic intermediate with occupation $\delta_{x2-y2}{}^2\ \pi^*_{xz}{}^2\ \pi^*_{yz}{}^1\ a_{2u}{}^2\ \phi_R{}^0$ in the doublet spin state and $\delta_{x2-y2}{}^2\ \pi^*_{xz}{}^1\ \pi^*_{yz}{}^1\ \sigma^*_{z2}{}^1\ a_{2u}{}^2\ \phi_R{}^0$ in the quartet spin state; both have the metal in oxidation state Fe(III). The latter state is not shown in Figure 18 since it is higher in energy than the radical intermediate $^4\mathbf{I}_{rad}$. In the low spin state the ordering of the cationic and radical intermediates is reversed with a cationic ground state. From the intermediate complexes a proton shuttle takes place to one of the pyrrole nitrogen atoms of the porphyrin ring to form the proton transfer intermediate ($^{4,2}\mathbf{PT}$), which brings the aromaticity back into the substrate ring and consequently is an extremely exothermic process. Indeed, this process has been observed for iron(IV)-oxo porphyrin complexes as well as for nonheme iron(IV)-oxo oxidants.[196] From $^2\mathbf{I}_{cat}$, the proton shuttle to the heme is essentially barrierless, since the two structures have the same electronic configuration, whereas the process from the radical intermediates encounters a significant barrier ($\mathbf{TS}_{PT}$). Geometrically, the porphyrin ring is distorted in $^{4,2}\mathbf{PT}$ and one pyrrole ring bends downward due to protonation. A subsequent proton transfer to the oxo group gives *p*-ethylphenol products ($^{4,2}\mathbf{P}_{phenol}$) via negligible rebound barriers ($\mathbf{TS}_{reb}$). Alternatively, the proton can rebound to the *ortho*-carbon position to form 4-ethylcyclohexa-2,4-dienone ($^{4,2}\mathbf{P}_{keton}$) via a rearrangement barrier ($\mathbf{TS}_{rearr}$). This rearrangement barrier is considerable (>10 kcal mol^{-1}), so that the dominant products will be phenols rather than ketones. Furthermore, the mechanism shown in Figure 18 explains the experimentally detected "NIH" shift, which is the migration of protons from the hydroxylation site to the adjacent carbon atom.[197] Thus, crossing of $^{4,2}\mathbf{TS}_{rearr}$ from the proton

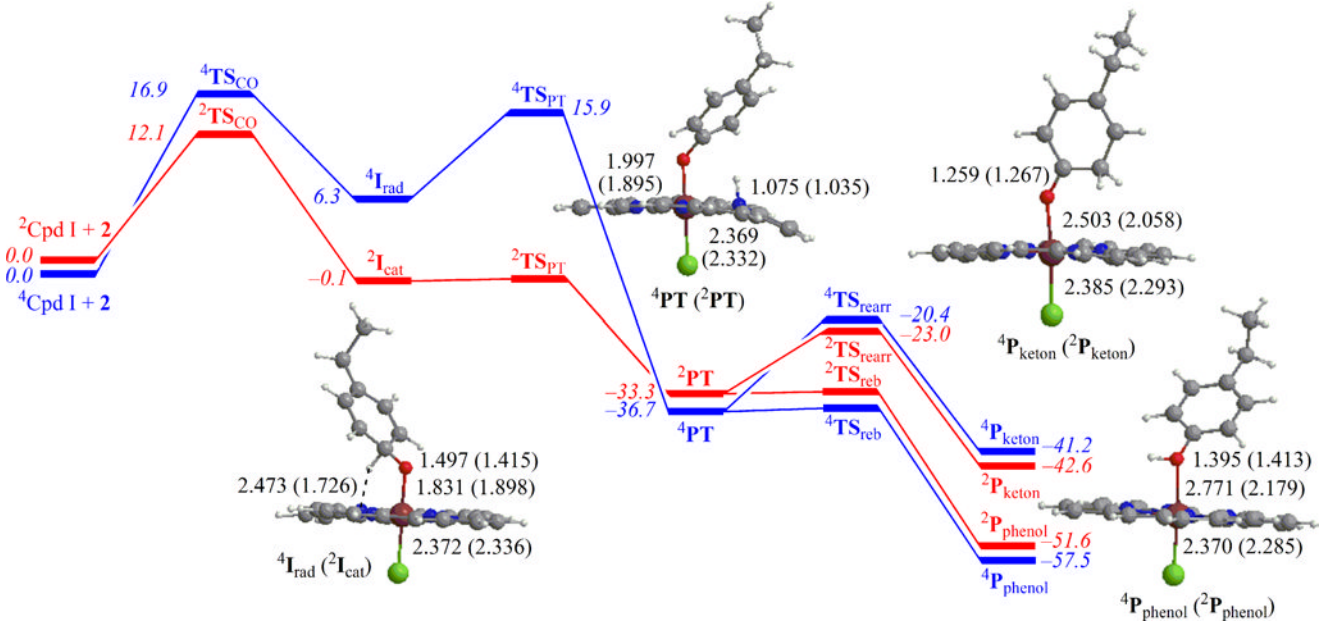

Figure 18. Aromatic hydroxylation of ethylbenzene by Cpd I(Cl^-) leading to phenol and ketone product complexes. All energies are in kcal mol^{-1} relative to isolated reactants, and bond lengths are in angstroms.

transfer intermediates gives cyclohexadienone products where one hydrogen atom has shifted to an adjacent carbon atom, in agreement with the NIH shift. Additionally, these studies prove that phenol and cyclohexadienone products originate from the same intermediate ($^2\mathbf{I}_{cat}$), which is of the cationic type. In contrast to aliphatic hydroxylation (discussed above), aromatic hydroxylation appears via single-state reactivity (SSR) on a dominant low-spin pathway, whereas the competing high-spin pathway has much higher barriers due to much less stable cationic intermediates. In addition to the mechanism shown in Figure 18, the process from $^2\mathbf{I}_{cat}$ also can lead to epoxide product complexes via a ring closure transition state ($\mathbf{TS}_{rc}$). This barrier in the case of benzene hydroxylation is much higher in energy than the proton shuttle barrier to form $^{4,2}\mathbf{PT}$.

As follows from the energy diagram in Figure 18 for ethylbenzene hydroxylation by Cpd I(Cl^-), the rate-determining step in the reaction is the C–O bond activation. Moreover, the reaction takes place on a dominant low-spin surface due to the difference in stability between $^4\mathbf{I}_{cat}$ and $^2\mathbf{I}_{cat}$. Since no hydrogen atoms migrate in the rate-determining step in the aromatic hydroxylation reaction, there is also no kinetic isotope effect for replacement of hydrogen atoms in the substrate by deuterium atoms. DFT studies of ethylbenzene-h_{10} and ethylbenzene-d_{10} hydroxylation by Cpd I(Cl^-) showed competing mechanisms via aromatic and aliphatic hydroxylation, whereby ethylbenzene-h_{10} gave dominant aliphatic hydroxylation, and the fully deuterated substrate aromatic hydroxylation.[173]

F. C=C Epoxidation by Cpd I of CYP 450

CYP 450s as well as biomimetic iron(IV)-oxo porphyrin complexes are known to catalyze C=C double bond epoxidation reactions very efficiently.[1,19,20] As a consequence many theoretical studies have been devoted to this process, as well as processes leading to byproducts of double bond epoxidation by Cpd I(SH^-).[60,143,144,158,198–201] As with the hydrogen abstraction reactions described above, C=C epoxidation proceeds by a stepwise mechanism via a radical intermediate. Thus, an initial C–C bond activation via barrier $^{4,2}\mathbf{TS}_E$ leads to formation of a C–O bond between oxo and substrate groups whereby the other carbon atom of the double bond remains as a radical center ($^{4,2}\mathbf{I}_E$). This radical attacks the oxo group and leads via a ring closure barrier ($\mathbf{TS}_{rc}$) to epoxide products. Figure 19 displays the calculated potential energy profiles of ethene, propene, and styrene epoxidation by Cpd I(SH^-), taken from Refs. 144, 198, and 201. The reactions proceed via TSR patterns on competing doublet and quartet spin states, where the doublet surface is essentially concerted, whereas the quartet spin intermediate has a significant lifetime due to the existence of a ring closure barrier. The rate-determining barrier, therefore, is the initial C–O bond activation via $^{4,2}\mathbf{TS}_E$ and is the lowest for styrene,

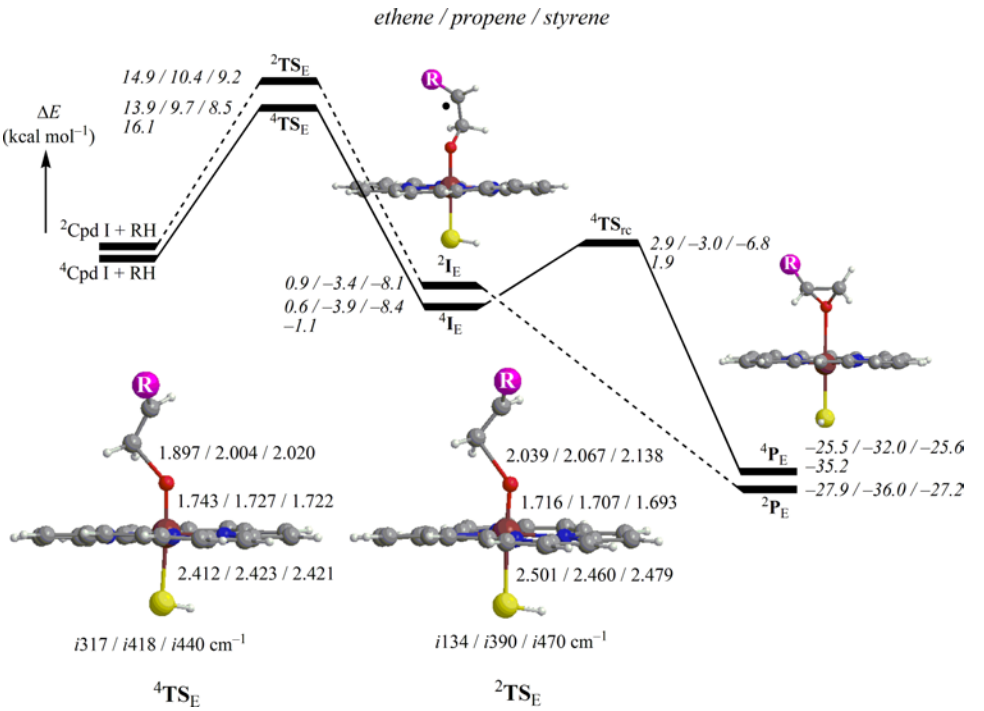

Figure 19. Potential energy profile of substrate (RH) epoxidation by CpdI(SH⁻). Energies are in kcal mol⁻¹ relative to isolated reactants in the quartet spin state. Also shown are optimized geometries of the rate-determining transition states for ethene, propene, and styrene epoxidation. The first line with data is taken from Refs. 144, 198, and 201 for ethene, propene, and styrene epoxidation, whereas the second line gives ethene epoxidation data for the quartet spin state from Ref. 60. The styrene data contain zero-point energies.

as expected from experimental observations. The calculated free energy of activation of styrene epoxidation by this CYP 450 model complex[201] of $\Delta G^{\ddagger}$ = 20.9 kcal mol^{-1} is in line with biochemical studies of CYP 450 enzymes that estimated a barrier of 24–25 kcal mol^{-1}.[52] The differences in barrier height lead to small differences in transition state geometries (Figure 19), where the lowest barriers correspond to early transition states with long C–O and short C–C and Fe–O distances.

Experimental studies on CYP 450$_{cam}$ and its T252A mutant showed that in the mutant C–H hydroxylation reactions were hampered, but not in the C=C epoxidation reactions.[51,52] It was concluded that this was due to the participation of two active oxidants in the reaction mixture, where Cpd I performs C–H hydroxylation reactions and Cpd 0 alkene epoxidation. To test this hypothesis, DFT calculations on competitive epoxidation of ethene by Cpd 0 and Cpd I were made.[59,60] However, DFT studies showed Cpd 0 to be a sluggish oxidant that reacts with alkenes via high reaction barriers, whereas the complementary reaction with Cpd I

encounters much lower barriers. Experimental studies on the reactivity differences of the iron(IV)-oxo porphyrin cation radical versus ferric-alkylperoxo with respect to C–H hydroxylation and epoxidation confirmed that Cpd 0 is a sluggish oxidant unable to compete with Cpd I.[64]

Finally, alkene epoxidation reactions in some cases produce byproducts; for instance, in enzymatic systems terminal olefins are known to give so-called suicidal complexes, which are dead-end products that destroy the activity of the enzyme.[202,203] In addition, byproducts have been reported as being due to stereochemical scrambling and hydrogen migration to form aldehydes. DFT calculations[158,200] established mechanisms for the formation of suicidal complexes ($^4\mathbf{P}_S$) and aldehyde ($^4\mathbf{P}_A$) byproducts, (Figure 20). Thus, both products originate from the intermediate ($\mathbf{I}_E$) in the epoxidation reaction mechanism and the amount of byproduct formation is therefore dependent on the lifetime of this complex. In the low-spin state the ring closure barrier to epoxide products is negligible, so that $^2\mathbf{I}_E$ (Figure 19) will have a very short lifetime. By contrast, a finite barrier for ring closure is found on the high-spin surface, which implies that $^4\mathbf{I}_E$ will have a finite lifetime during which rearrangement can occur. Hence, a manifestation of TSR, is the fact that byproducts are possible only on the high-spin surface and not on the low-spin surface since this is a pseudoconcerted reaction for C–H hydroxylation as well as epoxidation.

The intermediate complex $^4\mathbf{I}_E$(IV) is a radical intermediate with orbital occupation $\delta_{x2-y2}{}^2\,\pi^*_{xz}{}^1\,\pi^*_{yz}{}^1\,\phi_{St}{}^1$ and connects to the epoxide product complex $^4\mathbf{P}_E$ with configuration $\delta_{x2-y2}{}^2\,\pi^*_{xz}{}^1\,\pi^*_{yz}{}^1\,\sigma^*_{z2}{}^1$ via a ring closure transition state. It can react to form the suicidal complex ($^4\mathbf{P}_S$) through an attack of the radical on one of the nitrogen atoms of the porphyrin ring, whereby an N–C bond is formed and one of the pyrrole rings is lifted out of the plane of the heme. However, $^4\mathbf{P}_S$ has electronic configuration $\delta_{x2-y2}{}^2\,\pi^*_{xz}{}^1\,\pi^*_{yz}{}^1$, $\sigma^*_{xy}{}^1$, and a lower-lying mechanism for its formation from $^4\mathbf{I}_E$ is possible through an internal electron transfer and the formation of a cationic complex $^4\mathbf{I}_{cat}(xy)$ with configuration $\delta_{x2-y2}{}^2\,\pi^*_{xz}{}^1\,\pi^*_{yz}{}^1\,\sigma^*_{xy}{}^1$ that connects without barrier to the suicidal complex. The alternative cationic complex $^4\mathbf{I}_{cat}(z^2)$ with configuration $\delta_{x2-y2}{}^2\,\pi^*_{xz}{}^1\,\pi^*_{yz}{}^1\,\sigma^*_{z2}{}^1$ connects without barrier to the aldehyde product complex. The lifetime of the radical intermediates, i.e. either $^4\mathbf{I}_E$(IV) or $^4\mathbf{I}_E$(III), determines the amount of rearrangement to byproducts. Especially, mechanisms passing Fe(III) intermediates have high rebound barriers (as discussed above with VB curve crossing diagrams) and consequently are prone to the formation of suicidal inactivation and aldehyde byproducts.

G. Sulfoxidation by Cpd I of CYP 450

The final reaction catalyzed by CYP 450 enzymes and biomimetics that has received considerable attention is alkylsulfide sulfoxidation (Figure 21).[204–207] In

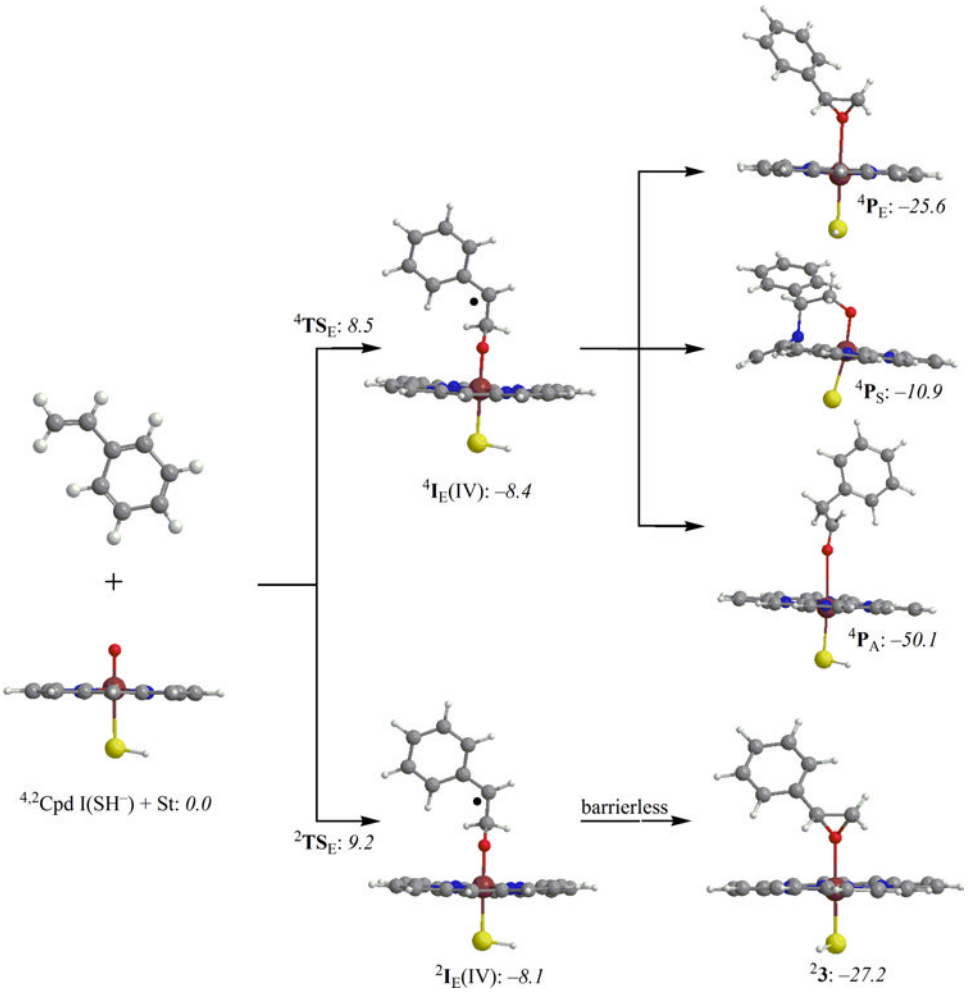

Figure 20. Double bond activation mechanisms of styrene (St) by Cpd I(SH^{-}) leading to products and byproducts. Energies are in kcal mol^{-1} relative to isolated reactants.

contrast to aliphatic and aromatic hydroxylation and C=C epoxidation reactions, this reaction is stepwise via a single transition state for the S–O bond formation (**TS**$_{SO}$), whereby two electrons are transferred from substrate to heme. These electron transfer processes are different in the doublet and quartet spin states, and hence considerably different barrier heights on the two spin state surfaces are encountered. In the low spin state the electron transfers are into the a_{2u} and π^*_{xz} orbitals, whereas in the high spin state they are into the a_{2u} and σ^*_{z2} molecular orbitals. As a consequence of these differences, the substrate attacks from the top in the quartet spin state to align the substrate with the σ^*_{z2} orbital, whereas the substrate attacks from the side in the doublet spin state for ideal overlap with

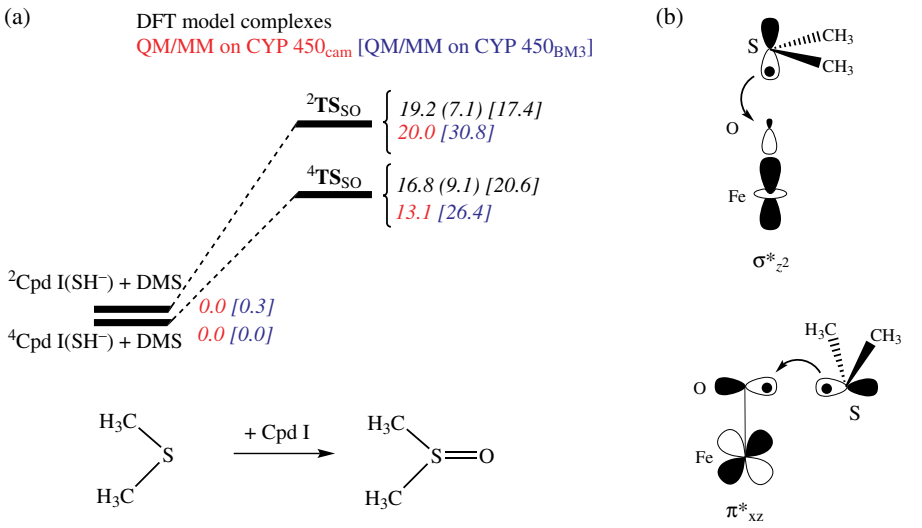

Figure 21. (a) DFT- and QM/MM-calculated sulfoxidation barriers of dimethylsulfide (DMS) by CYP 450 Cpd I models. The top line represents energies (in kcal mol^{-1}) from DFT model complexes of Cpd I(SH^-) or Cpd I(SCH_3^-) from Refs. 204, 207, and 206. The bottom line shows QM/MM-calculated energies of CYP 450_{cam} (in red) and CYP 450_{BM3} (in blue) from Ref. 62. (b) Electron transfer mechanisms in the high-spin (top) and low-spin (bottom) states.

the π^*_{xz} orbital. Due to these differences, the energy gap between ^{4}**TS**$_{SO}$ and ^{2}**TS**$_{SO}$ is considerable in some cases (6.9 kcal mol^{-1} for CYP 450_{cam}), but the DFT model complexes predict an energy gap of 2–3 kcal mol^{-1} although the ordering is reversed in Ref. 204. Nevertheless, all calculations give SSR patterns with preference for one spin state over the other; in three studies the quartet spin mechanism is the lowest, while in the remaining two studies the doublet spin is rate-determining. Clearly, more work is needed to establish what spin state is crucial for P450 sulfoxidation reactions.

IV. Conclusions

In the past two decades, significant understanding of the mechanistic functions of enzyme catalysis on a heme center has been achieved. These studies were focused on important and vital human heme enzymes such as CYP 450s which are involved in key metabolic and biosynthetic reactions, including drug metabolism and the biosynthesis of hormones. Different approaches have been used, ranging from enzymatic studies to experimental work on synthetic models (biomimetics) and, most recently, computational studies. The research has resulted in major breakthroughs in the understanding of the enzymatic processes. This

chapter has shown that the interplay of experimental and computational techniques on biomimetic models leads to advanced understanding of reaction mechanisms of iron-porphyrin complexes, which are correlated with enzymatic systems.

In this chapter, studies using biomimetic and computational methods have been reviewed. First of all, these studies established what the active oxidant of CYP 450 enzymes is. Many potential oxidants were tested, including Cpd 0 and Cpd II, but so far the iron(IV)-oxo porphyrin cation radical or Cpd I has been found to be the most efficient oxidant of substrate monoxygenation reactions. Alternative oxidants, such as the iron(III)-hydroperoxo complex, were tested and found to be poor oxidants of substrate epoxidation and sulfoxidation reactions. In principle, the reduced form of Cpd I, i.e. Cpd II, is able to react with substrates via hydrogen atom abstraction reactions and either dehydrogenate or hydroxylate substrates. Combined biomimetic and density functional studies showed that although Cpd II and its analogs can abstract hydrogen atoms from weak C–H bonds, its hydrogen abstraction barriers are much higher than those for Cpd I, especially in cases where a hydride abstraction is possible.

Further studies have shown how the intricate interplay of the ligands on the metal-oxo center influences the oxidative properties of the active species. Thus, an axial ligand induces either a push or a pull effect on the metal center and thereby changes the oxygen transfer ability of the oxidant. This ligand effect is attributed to two factors: a quantum-mechanical effect due to orbital interactions between the metal and the ligand, and an electric field effect due to charge–charge interactions between the ligand and the metal. These contributions are dependent on the nature of the axial ligand and determine the electrophilicity of the oxo group. In addition, Cpd I exists in close-lying doublet and quartet spin states with the same orbital occupation, and hence reactions on two spin state surfaces result, which has been termed “two-state reactivity” (TSR). As a consequence of TSR, there are barriers on two spin state surfaces and sometimes even different mechanisms on the doublet and quartet spin state surfaces. This makes interpretation of experimental data difficult, especially rate constants and product distributions.

The CYP 450 enzymes are versatile oxidants that catalyze a range of different reactions, including aliphatic and aromatic hydroxylation, dehydrogenation, epoxidation, sulfoxidation, etc. Most of these mechanisms have been studied with biomimetic and computational methods. General reaction schemes have been derived and factors that influence mechanisms are being identified. Nevertheless, the biomimetic and computational studies have shown that subtle changes to the models influence mechanisms, barriers, and product distributions, so that a universal mechanism is still lacking.

So what are the key questions that remain in the studies of CYP 450 and biomimetic analogs? First of all, there are still issues regarding the exact effects of the nature of the axial ligand and the porphyrin ring and its substituents. Why is it that with some biomimetic systems there is a regioselectivity preference for aromatic over aliphatic hydroxylation, whereas it is reversed with an alternative model? Furthermore, how does the protein environment influence the reaction mechanisms and regioselectivities? What happens if we replace the metal? The goal for the future will be to create biosynthetic systems of CYP 450 enzymes that have higher efficiency and turnover and regioselectively and stereospecifically monoxygenase substrates. Combination of experimental biomimetic and computational studies may provide the right tools for achieving this goal.

V. Acknowledgment

This work was supported by the National Research Foundation of Korea through the CRI and WCU (R31-2008-000-10010-0) Programs (W. N.).

VI. References

1. Dawson, J. H.; Sono, M. *Chem. Rev.* **1987**, *87*, 1255–1276.
2. Sono, M.; Roach, M. P.; Coulter, E. D.; Dawson, J. H. *Chem. Rev.* **1996**, *96*, 2841–2887.
3. Kadish, K. M.; Smith, K. M.; Guilard, R., Eds. *The Porphyrin Handbook*, Academic: San Diego, **2000**; Vol. 4.
4. Newcomb, M.; Toy, P. H. *Acc. Chem. Res.* **2000**, *33*, 449–455.
5. Ortiz de Montellano, P. R., Ed. *Cytochrome P450: Structure, Mechanism and Biochemistry*, 3rd ed.; Kluwer Academic/Plenum: New York, **2004**.
6. Watanabe, Y.; Nakajima, H.; Ueno, T. *Acc. Chem. Res.* **2007**, *40*, 554–562.
7. Watanabe, Y. In *The Porphyrin Handbook*; Kadish, K. M.; Smith, K. M.; Guilard, R., Eds., Academic: New York, **2000**; Vol. 4, Chapter 30, pp. 97–117.
8. Guengerich, F. P. *Chem. Res. Toxicol.* **2001**, *14*, 611–650.
9. Ortiz de Montellano, P. R.; De Voss, J. J. *Nat. Prod. Rep.* **2002**, *19*, 477–493.
10. Munro, A. W.; Girvan, H. M.; McLean, K. J. *Nat. Prod. Rep.* **2007**, *24*, 585–609.
11. Groves, J. T. Models and mechanisms of cytochrome P450 action. In *Cytochrome P450: Structure, Mechanism and Biochemistry*; 3rd ed. Ortiz de Montellano, P. R., Ed.; Kluwer Academic/Plenum: New York, **2005**; pp. 1–44.
12. Groves, J. T. *Proc. Natl. Acad. Sci. USA* **2003**, *100*, 3569–3574.
13. Groves, J. T.; Shalyaev, K.; Lee, J. In *The Porphyrin Handbook*; Kadish, K. M.; Smith, K. M.; Guilard, R., Eds.; Academic: New York, **2000**; Vol. 4, Chapter 27, pp. 17–40.
14 Nam, W. *Acc. Chem. Res.* **2007**, *40*, 522–531.
15. Nam, W. In *Comprehensive Coordination Chemistry II*; Que Jr., L.; Tolman, W. B., Eds.; Elsevier: New York, **2004**; Vol. 8, pp. 281–307.
16. Pylypenko, O.; Schlichting, I. *Annu. Rev. Biochem*. **2004**, *73*, 991–1018.
17. Loew, G. H.; Harris, D. L. *Chem. Rev.* **2000**, *100*, 407–419.

18. Meunier, B.; de Visser, S. P.; Shaik, S. *Chem. Rev*. **2004**, *104*, 3947–3980.
19. Shaik, S.; Kumar, D.; de Visser, S. P.; Altun, A.; Thiel, W. *Chem. Rev*. **2005**, *105*, 2279–2328.
20. Shaik, S.; Hirao, H.; Kumar, D. *Acc. Chem. Res.* **2007**, *40*, 532–542.
21. Poulos, T. L.; Finzel, B. C.; Gunsalus, I. C.; Wagner, G. C.; Kraut, J. *J. Biol. Chem.* **1985**, *260*, 16122–16130.
22. Berman, H. M.; Westbrook, J.; Feng, Z.; Gilliland, G.; Bhat, T. N.; Weissig, H.; Shindyalov, I. N.; Bourne, P. E. *Nucleic Acids Res*. **2000**, *28*, 235–242.
23. Denisov, I. G.; Makris, T. M.; Sligar, S. G.; Schlichting, I. *Chem. Rev.* **2005**, *105*, 2253–2277.
24. Schlichting, I.; Berendzen, J.; Chu, K.; Stock, A. M.; Maves, S. A.; Benson, D. E.; Sweet, R. M.; Ringe, D.; Petsko, G. A.; Sligar, S. G. *Science* **2000**, *287*, 1615–1622.
25. Poulos, T. L.; Finzel, B. C.; Howard, A. J. *Biochemistry* **1986**, *25*, 5314–5322.
26. Poulos, T. L.; Finzel, B. C.; Howard, A. J. *J. Mol. Biol*. **1987**, *195*, 687–700.
27. Raag, R.; Poulos, T. L. *Biochemistry* **1989**, *28*, 7586–7592.
28. Dawson, J. H. *Science* **1988**, *240*, 433–439.
29. Green, M. T.; Dawson, J. H.; Gray, H. B. *Science* **2004**, *304*, 1653–1656.
30. Green, M. T. *Curr. Opin. Chem. Biol.* **2009**, *13*, 84–88.
31. Ogliaro, F.; de Visser, S. P.; Shaik, S. *J. Inorg. Biochem.* **2002**, *91*, 554–567.
32. Stone, K. L.; Behan, R. K.; Green, M. T. *Proc. Natl. Acad. Sci. USA* **2005**, *102*, 16563–16565.
33. Dey, A.; Jiang, Y.; Ortiz de Montellano, P. R.; Hodgson, P. O.; Hedman, B.; Solomon, E. I. *J. Am. Chem. Soc*. **2009**, *131*, 7869–7878.
34. Klingenberg, M. *Arch. Biochem. Biophys.* **1958**, *75*, 376–386.
35. Omura, T.; Sato, R. *J. Biol. Chem.* **1962**, *237*, 1375–1376.
36. Omura, T.; Sato, R. *J. Biol. Chem.* **1964**, *239*, 2370–2378.
37. Rydberg, P.; Sigfridsson, E.; Ryde, U. *J. Biol. Inorg. Chem.* **2004**, *9*, 203–223.
38. Shaik, S.; de Visser, S. P. Computational approaches to cytochrome P450 function. In *Cytochrome P450*: *Structure, Mechanism and Biochemistry*, Ortiz de Montellano, P. R., Ed.; Kluwer Academic/Plenum: New York, **2004**; Chapter 2, pp. 45–85.
39. Shaik, S.; Hirao, H.; Kumar, D. *Nat. Prod. Rep.* **2007**, *24*, 533–552.
40. Sligar, S. G. *Biochemistry* **1976**, *15*, 5399–5406.
41. Swart, M.; Groenhof, A. R.; Ehlers, A. W.; Lammertsma, K. *Chem. Phys. Lett*. **2005**, *403*, 35–41.
42. Altun, A.; Thiel, W. *J. Phys. Chem. B* **2005**, *109*, 1268–1280.
43. Groenhof, A. R.; Swart, M.; Ehlers, A. W.; Lammertsma, K. *J. Phys. Chem. A* **2005**, *109*, 3411–3417.
44. Balding, P. R.; Porro, C. S.; McLean, K. J.; Sutcliffe, M. J.; Maréchal, J.-D.; Munro, A. W.; de Visser, S. P. *J. Phys. Chem. A* **2008**, *112*, 12911–12918.
45. Brewer, C. B.; Peterson, J. A. *J. Biol. Chem.* **1988**, *263*, 791–798.
46. Davydov, R.; Makris, T. M.; Kofman, V.; Werst, D. E.; Sligar, S. G.; Hoffman, B. M. *J. Am. Chem. Soc.* **2001**, *123*, 1403–1415.
47. Denisov, I. G.; Makris, T. M.; Sligar, S. G. *J. Biol. Chem.* **2001**, *276*, 11648–11652.
48. Denisov, I. G.; Hung, S.-C.; Weiss, K. E.; McLean, M. A.; Shiro, Y.; Park, S.-Y.; Champion, P. M.; Sligar, S. G. *J. Inorg. Biochem.* **2001**, *87*, 215–226.
49. Egawa, T.; Shimada, H.; Ishimura, Y. *Biochem. Biophys. Res. Commun.* **1994**, *201*, 1464–1469.
50. Kellner, D. G.; Hung, S.-C.; Weiss, K. E.; Sligar, S. G. *J. Biol. Chem.* **2002**, *277*, 9641–9644.
51. Vaz, A. D. N.; McGinnity, D. F.; Coon, M. J. *Proc. Natl. Acad. Sci. USA* **1998**, *95*, 3555–3560.

52. Newcomb, M.; Shen, R.; Choi, S.-Y.; Toy, P. H.; Hollenberg, P. F.; Vaz, A. D. N.; Coon, M. J. *J. Am. Chem. Soc*. **2000**, *122*, 2677–2686.
53. Jin, S.; Bryson, T. A.; Dawson, J. H. *J. Biol. Inorg. Chem.* **2004**, *9*, 644–653.
54. Nam, W.; Ryu, Y. O.; Song, W. J. *J. Biol. Inorg. Chem.* **2004**, *9*, 654–660.
55. Hlavica, P. *Eur. J. Biochem.* **2004**, *271*, 4335–4360.
56. Newcomb, M.; Hollenberg, P. F.; Coon, M. J. *Arch. Biochem. Biophys.* **2003**, *409*, 72–79.
57. Makris, T. M.; von Koenig, K.; Schlichting, I.; Sligar, S. G. *Biochemistry* **2007**, *46*, 14129–14140.
58. Vaz, A. D. N.; Pernecky, S. J.; Raner, G. M.; Coon, M. J. *Proc. Natl. Acad. Sci. USA* **1996**, *93*, 4644–4648.
59. Ogliaro, F.; de Visser, S. P.; Cohen, S.; Sharma, P. K.; Shaik, S. *J. Am. Chem. Soc*. **2002**, *124*, 2806–2817.
60. Kamachi, T.; Shiota, Y.; Ohta, T.; Yoshizawa, K. *Bull. Chem. Soc. Jpn*. **2003**, *76*, 721–732.
61. Sharma, P. K.; de Visser, S. P.; Shaik, S. *J. Am. Chem. Soc.* **2003**, *125*, 8698–8699.
62. Porro, C. S.; Sutcliffe, M. J.; de Visser, S. P. *J. Phys. Chem. A* **2009**, *113*, 11635–11642.
63. Shaik, S.; de Visser, S. P.; Ogliaro, F.; Schwarz, H.; Schröder, D. *Curr. Opin. Chem. Biol*. **2002**, *6*, 556–567.
64. Park, M. J.; Lee, J.; Suh, Y.; Kim, J.; Nam, W. *J. Am. Chem. Soc*. **2006**, *128*, 2630–2634.
65. Kumar, D.; Hirao, H.; de Visser, S. P.; Zheng, J.; Wang, D.; Thiel, W.; Shaik, S. *J. Phys. Chem. B* **2005**, *109*, 19946–19951.
66. Hirao, H.; Kumar, D.; Shaik, S. *J. Inorg. Biochem*. **2006**, *100*, 2054–2068.
67. Groenhof, A. R.; Ehlers, A. W.; Lammertsma, K. *J. Am. Chem. Soc*. **2007**, *129*, 6204–6209.
68. Wang, D.; Zheng, J.; Shaik, S.; Thiel, W. *J. Phys. Chem. B* **2008**, *112*, 5126–5138.
69. Altarsha, M.; Benighaus, T.; Kumar, D.; Thiel, W. *J. Am. Chem. Soc.* **2009**, *131*, 4755–4763.
70. Kaizer, J.; Costas, M.; Que Jr., L. *Angew. Chem. Int. Ed.* **2003**, *42*, 3671–3673.
71. Seo, M. S.; Kamachi, T.; Kouno, T.; Murata, K.; Park, M. J.; Yoshizawa, K.; Nam, W. *Angew. Chem. Int. Ed.* **2007**, *46*, 2291–2294.
72. Hessenauer-Ilicheva, N.; Franke, A.; Meyer, D.; Woggon, W.-D.; van Eldik, R. *J. Am. Chem. Soc.* **2007**, *129*, 12473–12479.
73. Han, A.-R.; Jeong, Y. J.; Kang, Y.; Lee, J. Y.; Seo, M. S.; Nam, W. *Chem. Commun.* **2008**, 1076–1078.
74. Groves, J. T.; Watanabe, Y. *J. Am. Chem. Soc.* **1988**, *110*, 8443–8452.
75. Yamaguchi, K.; Watanabe, Y.; Morishima, I. *J. Am. Chem. Soc.* **1993**, *115*, 4058.
76. Groves, J. T.; Haushalter, R. C.; Nakamura, M.; Nemo, T. E.; Evans, B. J. *J. Am. Chem. Soc*. **1981**, *103*, 2884–2886.
77. Jayaraj, K.; Terner, J.; Gold, A.; Roberts, D. A.; Austin, R. N.; Mandon, D.; Weiss, R.; Bill, E.; Müther, M.; Trautwein, A. X. *Inorg. Chem.* **1996**, *35*, 1632–1640.
78. Boso, B.; Lang, G.; McMurry, T. J.; Groves, J. T. *J. Chem. Phys.* **1983**, *79*, 1122–1126.
79. Hashimoto, S.; Mizutani, Y.; Tatsuno, Y.; Kitagawa, T. *J. Am. Chem. Soc.* **1991**, *113*, 6542–6549.
80. Jones, R.; Jayaraj, K.; Gold, A.; Kirk, M. L. *Inorg. Chem.* **1998**, *37*, 2842–2843.
81. Penner-Hahn, J. E.; Eble, K. S.; McMurry, T. J.; Renner, M.; Balch, A. L.; Groves, J. T.; Dawson, J. H.; Hodgson, K. O. *J. Am. Chem. Soc.* **1986**, *108*, 7819–7825.
82. Gross, Z.; Nimri, S. *Inorg. Chem.* **1994**, *33*, 1731–1732.
83. Wolowiec, S.; Latos-Grazynski, L. *Inorg. Chem.* **1998**, *37*, 2984–2988.
84. Nam, W.; Lim, M. H.; Oh, S.-Y. *Inorg. Chem.* **2000**, *39*, 5572–5575.

85. Fujii, H. *Coord. Chem. Rev*. **2002**, *226*, 51–60.
86. Dolphin, D.; Traylor, T. G.; Xie, L. Y. *Acc. Chem. Res.* **1997**, *30*, 251–259.
87. Meunier, B. *Chem. Rev.* **1992**, *92*, 1411–1456.
88. Goh, Y. M.; Nam, W. *Inorg. Chem.* **1999**, *38*, 914–920.
89. Behan, R. K.; Green, M. T. *J. Inorg. Biochem.* **2006,** *100*, 448–459.
90. Woggon, W.-D. *Acc. Chem. Res.* **2005**, *38*, 127–136.
91. Collman, J. P.; Groh, S. E. *J. Am. Chem. Soc.* **1982**, *104*, 1391–1403.
92. Higuchi, T.; Shimada, K.; Maruyama, N.; Hirobe, M. *J. Am. Chem. Soc.* **1993**, *115*, 7551–7552.
93. Urano, Y.; Higuchi, T.; Hirobe, M.; Nagano, T. *J. Am. Chem. Soc.* **1997**, *119*, 12008–12009.
94. Wagenknecht, H.-A.; Woggon, W.-D. *Angew. Chem. Int. Ed. Engl.* **1997**, *36*, 390–392.
95. Tani, F.; Matsu-ura, M.; Nakayama, S.; Ichimura, M.; Nakamura, N.; Naruta, Y. *J. Am. Chem. Soc.* **2001**, *123*, 1133–1142.
96. Tani, F.; Matsu-ura, M.; Nakayama, S.; Naruta, Y. *Coord. Chem. Rev.* **2002**, *226*, 219–226.
97. Song, W. J.; Ryu, Y. O.; Song, R.; Nam, W. *J. Biol. Inorg. Chem*. **2005**, *10*, 294–304.
98. de Visser, S. P.; Tahsini, L.; Nam, W. *Chem. Eur. J*. **2009**, *15*, 5577–5587.
99. Kang, Y.; Chen, H.; Jeong, Y. J.; Lai, W.; Bae, E. H.; Shaik, S.; Nam, W. *Chem. Eur. J.* **2009**, *15*, 10039–10046.
100. Bell, R. P. *Proc. R. Soc. London Ser. A* **1936**, *154*, 414–421.
101. Evans, M. G.; Polanyi, M. *Trans. Faraday Soc.* **1938**, *34*, 11–24.
102. Bordwell, F. G.; Cheng, J.-P.; Ji, G.-Z.; Satish, A. V.; Zhang, X. *J. Am. Chem. Soc.* **1991**, *113*, 9790–9795.
103. Sastri, C. V.; Lee, J.; Oh, K.; Lee, Y. J.; Lee, J.; Jackson, T. A.; Ray, K.; Hirao, H.; Shin, W.; Halfen, J. A.; Kim, J.; Que Jr., L.; Shaik, S.; Nam, W. *Proc. Natl. Acad. Sci. USA* **2007**, *104*, 19181–19186.
104. Rohde, J.-U.; Que Jr., L. *Angew. Chem. Int. Ed.* **2005**, *44*, 2255–2258.
105. de Visser, S. P. *Angew. Chem. Int. Ed.* **2006**, *45*, 1790–1793.
106. Hirao, H.; Que Jr., L.; Nam, W.; Shaik, S. *Chem. Eur. J*. **2008**, *14*, 1740–1756.
107. Dhuri, S. N.; Seo, M. S.; Lee, Y.-M.; Hirao, H.; Wang, Y.; Nam, W.; Shaik, S. *Angew. Chem. Int. Ed.* **2008**, *47*, 3356–3359.
108. Bikiel, D. E.; Boechi, L.; Capece, L.; Crespo, A.; De Biase, P. M.; Di Lella, S.; González Lebrero, M. C.; Martí, M. A.; Nadra, A. D.; Perissinotti, L. L.; Scherlis, D. A.; Estrin, D. A. *Phys. Chem. Chem. Phys*. **2006**, *8*, 5611–5628.
109. Hersleth, H.-P.; Ryde, U.; Rydberg, P.; Görbitz, C. H.; Andersson, K. K. *J. Inorg. Biochem.* **2006**, *100*, 460–476.
110. Degtyarenko, I.; Biarnés, X.; Nieminen, R. M.; Rovira, C. *Coord. Chem. Rev.* **2008**, 1497–1513.
111. Chiavarino, B.; Cipollini, R.; Crestoni, M. E.; Fornarini, S.; Lanucara, F.; Lapi, A. *J. Am. Chem. Soc.* **2008**, *130*, 3208–3217.
112. de Visser, S. P. *J. Biol. Inorg. Chem*. **2006**, *11*, 168–178.
113. Song, W. J.; Sun, Y. J.; Choi, S. K.; Nam, W. *Chem. Eur. J*. **2006**, *12*, 130–137.
114. Groves, J. T. *J. Inorg. Biochem*. **2006**, *100*, 434–447.
115. van Eldik, R. *Coord. Chem. Rev*. **2007**, *251*, 1649–1662.
116. Kumar, D.; Tahsini, L.; de Visser, S. P.; Kang, H. Y.; Kim, S. J.; Nam, W. *J. Phys. Chem. A* **2009**, *113*, 11713–11722.
117. Harris, D. L. *Curr. Opin. Chem. Biol.* **2001**, *5*, 724–735.

118. de Visser, S. P.; Shaik, S.; Sharma, P. K.; Kumar, D.; Thiel, W. *J. Am. Chem. Soc*. **2003**, *125*, 15779–15788.
119. Green, M. T. *J. Am. Chem. Soc*. **1999**, *121*, 7939–7940.
120. Green, M. T. *J. Am. Chem. Soc.* **2000**, *122*, 9495–9499.
121. Green, M. T. *J. Am. Chem. Soc.* **2001**, *123*, 9218–9219.
122. Hirao, H.; Shaik, S.; Kozlowski, P. M. *J. Phys. Chem. A* **2006**, *110*, 6091–6099.
123. Ghosh, A. *Acc. Chem. Res.* **1998**, *31*, 189–191.
124. Ogliaro, F.; de Visser, S. P.; Cohen, S.; Kaneti, J.; Shaik, S. *Chem. Bio. Chem* **2001**, *2*, 848–851.
125. Rietjens, I. M. C. M.; Osman, A. M.; Veeger, C.; Zakharieva, O.; Antony, J.; Grodzicki, M.; Trautwein, A. X. *J. Biol. Inorg. Chem.* **1996**, *1*, 372–376.
126. Kuramochi, H.; Noodleman, L.; Case, D. A. *J. Am. Chem. Soc.* **1997**, *119*, 11442–11451.
127. Ogliaro, F.; de Visser, S. P.; Groves, J. T.; Shaik, S. *Angew. Chem. Int. Ed*. **2001**, *40*, 2874–2878.
128. de Visser, S. P. *J. Phys. Chem. A* **2005**, *109*, 11050–11057.
129. de Visser, S. P. *Inorg. Chem*. **2006**, *45*, 9551–9557.
130. Menyhárd, D. K.; Náray-Szabó, G. *J. Phys. Chem. B* **1999**, *103*, 227–233.
131. de Visser, S. P. The axial ligand effect on substrate monoxygenation by the oxo-iron active species of heme enzymes: how does cytochrome *c* peroxidase compare to cytochrome P450? In *Inorganic Biochemistry: Research Progress*, Hughes, J. G.; Robinson, A. J., Eds.; Nova Science: New York, **2008**; Chapter 7, pp. 197–224.
132. Raven, E. L. *Nat. Prod. Rep.* **2003**, *20*, 367–381.
133. Harvey, J. N.; Bathelt, C. M.; Mulholland, A. J. *J. Comput. Chem.* **2006**, *27*, 1352–1362.
134. Wirstam, M.; Blomberg, M. R. A.; Siegbahn, P. E. M. *J. Am. Chem. Soc*. **1999**, *121*, 10178–10185.
135. Bhaskar, B.; Bonagura, C. A.; Li, H.; Poulos, T. L. *Biochemistry* **2002**, *41*, 2684–2693.
136. Dawson, J. H.; Holm, R. H.; Trudell, J. R.; Barth, G.; Linder, R. E.; Bunnenberg, E.; Djerassi, C.; Tang, S. C. *J. Am. Chem. Soc*. **1976**, *98*, 3707–3709.
137. Poulos, T. L. *J. Biol. Inorg. Chem*. **1996**, *1*, 356–359.
138. Wang, R.; de Visser, S. P. *J. Inorg. Biochem*. **2007**, *101*, 1464–1472.
139. Ogliaro, F.; Cohen, S.; de Visser, S. P.; Shaik, S. *J. Am. Chem. Soc*. **2000**, *122*, 12892–12893.
140. Schöneboom, J. C.; Lin, H.; Reuter, N.; Thiel, W.; Cohen, S.; Ogliaro, F.; Shaik, S. *J. Am. Chem. Soc.* **2002**, *124*, 8142–8151.
141. Bathelt, C. M.; Zurek, J.; Mulholland, A. J.; Harvey, J. N. *J. Am. Chem. Soc.* **2005**, *127*, 12900–12908.
142. Ogliaro, F.; Harris, N.; Cohen, S.; Filatov, M.; de Visser, S. P.; Shaik, S. *J. Am. Chem. Soc*. **2000**, *122*, 8977–8989.
143. de Visser, S. P.; Ogliaro, F.; Sharma, P. K.; Shaik, S. *Angew. Chem. Int. Ed.* **2002**, *41*, 1947–1951.
144. de Visser, S. P.; Ogliaro, F.; Sharma, P. K.; Shaik, S. *J. Am. Chem. Soc*. **2002**, *124*, 11809–11826.
145. Kamachi, T.; Yoshizawa, K. *J. Am. Chem. Soc.* **2003**, *125*, 4652–4661.
146. de Visser, S. P.; Kumar, D.; Cohen, S.; Shacham, R.; Shaik, S. *J. Am. Chem. Soc*. **2004**, *126*, 8362–8363.
147. Shaik, S.; Kumar, D.; de Visser, S. P. *J. Am. Chem. Soc*. **2008**, *130*, 10128–10140.
148. Hirao, H.; Kumar, D.; Que Jr., L.; Shaik, S. *J. Am. Chem. Soc*. **2006**, *128*, 8590–8606.

149. de Visser, S. P. *J. Am. Chem. Soc*. **2006**, *128*, 9813–9824.
150. de Visser, S. P. *J. Am. Chem. Soc*. **2006**, *128*, 15809–15818.
151. Shaik, S.; Cohen, S.; de Visser, S. P.; Sharma, P. K.; Kumar, D.; Kozuch, S.; Ogliaro, F.; Danovich, D. *Eur. J. Inorg. Chem*. **2004**, 207–226.
152. Kumar, D.; de Visser, S. P.; Shaik, S. *J. Am. Chem. Soc*. **2003**, *125*, 13024–13025.
153. Kumar, D.; de Visser, S. P.; Sharma, P. K.; Cohen, S.; Shaik, S. *J. Am. Chem. Soc*. **2004**, *126*, 1907–1920.
154. Becke, A. D. *J. Chem. Phys*. **1993**, *98*, 5648–5652.
155. Güell, M.; Luis, J. M.; Solà, M.; Swart, M. *J. Phys. Chem. A* **2008**, *112*, 6384–6391.
156. Neese, F. *Coord. Chem. Rev.* **2009**, *253*, 526–563.
157. Kim, S. J.; Latifi, R.; Kan, H. Y.; Nam, W.; de Visser, S. P. *Chem. Commun*. **2009**, 1562–1564.
158. de Visser, S. P.; Ogliaro, F.; Shaik, S. *Angew. Chem. Int. Ed*. **2001**, *40*, 2871–2874.
159. Shaik, S. S. *J. Am. Chem. Soc*. **1981**, *103*, 3692–3701.
160. Olsen, L.; Rydberg, P.; Rod, T. H.; Ryde, U. *J. Med. Chem.* **2006**, *49*, 6489–6499.
161. Mayer, J. M. *Acc. Chem. Res*. **1998**, *31*, 441–450.
162. Mayer, J. M. In *Biomimetic Oxidations Catalyzed by Transition Metal Complexes*; Meunier, B., Ed.; Imperial College Press: London, **1999**; pp. 1–43.
163. Kaizer, J.; Klinker, E. J.; Oh, N. Y.; Rohde, J.-U.; Song, W. J.; Stubna, A.; Kim, J.; Münck, E.; Nam, W.; Que Jr., L. *J. Am. Chem. Soc*. **2004**, *126*, 472–473.
164. Mader, E. A.; Manner, V. W.; Markle, T. F.; Wu, A.; Franz, J. A.; Mayer, J. M. *J. Am. Chem. Soc.* **2009**, *131*, 4334–4345.
165. Yoshizawa, K.; Kagawa, Y.; Shiota, Y. *J. Phys. Chem. B* **2000**, *104*, 12365–12370.
166. Harris, N.; Cohen, S.; Filatov, M.; Ogliaro, F.; Shaik, S. *Angew. Chem. Int. Ed*. **2000**, *39*, 2003–2005.
167. Schöneboom, J. C.; Cohen, S.; Lin, H.; Shaik, S.; Thiel, W. *J. Am. Chem. Soc.* **2004**, *126*, 4017–4034.
168. Kumar, D.; de Visser, S. P.; Sharma, P. K.; Derat, E.; Shaik, S. *J. Biol. Inorg. Chem*. **2005**, *10*, 181–189.
169. Kozuch, S.; Leifels, T.; Meyer, D.; Sbaragli, L.; Shaik, S.; Woggon, W.-D. *Synlett.* **2005**, *4*, 0675–0684.
170. Choe, Y.-K.; Nagase, S. *J. Comput. Chem.* **2005**, *26*, 1600–1611.
171. Wang, Y.; Wang, H.; Wang, Y.; Yang, C.; Yang, L.; Han, K. *J. Phys. Chem. B* **2006**, *110*, 6154–6159.
172. Kamachi, T.; Kouno, T.; Nam, W.; Yoshizawa, K. *J. Inorg. Biochem.* **2006**, *100*, 751–754.
173. de Visser, S. P. *Chem. Eur. J*. **2006**, *12*, 8168–8177.
174. de Visser, S. P. *J. Phys. Chem. B* **2007**, *111*, 12299–12302.
175. Wang, Y.; Yang, C.; Wang, H.; Han, K.; Shaik, S. *Chem. Bio. Chem.* **2007**, *8*, 277–281.
176. de Visser, S. P.; Tan, L. S. *J. Am. Chem. Soc*. **2008**, *130*, 12961–12974.
177. Zhang, Y.; Morisetti, P.; Kim, J.; Smith, L.; Lin, H. *Theor. Chem. Acc.* **2008**, *121*, 313–319.
178. Rydberg, P.; Ryde, U.; Olsen, L. *J. Chem. Theory Comput.* **2008**, *4*, 1369–1377.
179. Shaikh, A. R.; Sahnoun, R.; Broclawik, E.; Koyama, M.; Tsuboi, H.; Hatakeyama, N.; Endou, A.; Takaba, H.; Kubo, M.; Del Carpio, C. A.; Miyamoto, A. *J. Inorg. Biochem.* **2009**, *103*, 20–27.
180. Li, D.; Wang, Y.; Yang, C.; Han, K. *Dalton Trans.* **2009**, 291–297.
181. de Visser, S. P. *J. Am. Chem. Soc.* **2010**, *132*, 1087–1097.
182. Takahashi, A.; Kurahashi, T.; Fujii, H. *Inorg. Chem.* **2009**, *48*, 2614–2625.

183. Jeong, Y. J.; Kang, Y.; Han, A.-R.; Lee, Y.-M.; Kotani, H.; Fukuzumi, S.; Nam, W. *Angew. Chem. Int. Ed*. **2008**, *47*, 7321–7324.
184. Fukuzumi, S.; Kotani, H.; Lee, Y.-M.; Nam, W. *J. Am. Chem. Soc*. **2008**, *130*, 15134–15142.
185. Tahsini, L.; Bagherzadeh, M.; Nam, W.; de Visser, S. P. *Inorg. Chem.* **2009**, *48*, 6661–6669.
186. Altun, A.; Shaik, S.; Thiel, W. *J. Am. Chem. Soc*. **2007**, *129*, 8978–8987.
187. Ortiz de Montellano, P. R.; Stearns, R. A. *J. Am. Chem. Soc.* **1987**, *109*, 3415–3420.
188. Kumar, D.; de Visser, S. P.; Shaik, S. *J. Am. Chem. Soc*. **2004**, *126*, 5072–5073.
189. Derat, E.; Kumar, D.; Hirao, H.; Shaik, S. *J. Am. Chem. Soc.* **2006**, *128*, 473–484.
190. Rettie, A. E.; Boberg, M.; Rettenmeire, A. W.; Baillie, T. A. *J. Biol. Chem*. **1988**, *263*, 13733–13738.
191. de Visser, S. P.; Shaik, S. *J. Am. Chem. Soc*. **2003**, *125*, 7413–7424.
192. Hazan, C.; Kumar, D.; de Visser, S. P.; Shaik, S. *Eur. J. Inorg. Chem*. **2007**, 2966–2974.
193. Bathelt, C. M.; Ridder, L.; Mulholland, A. J.; Harvey, J. N. *J. Am. Chem. Soc.* **2003**, *125*, 15004–15005.
194. Bathelt, C. M.; Ridder, L.; Mulholland, A. J.; Harvey, J. N. *Org. Biomol. Chem.* **2004**, *2*, 2998–3005.
195. Bathelt, C. M.; Mulholland, A. J.; Harvey, J. N. *J. Phys. Chem. A* **2008**, *112*, 13149–13156.
196. de Visser, S. P.; Oh, K.; Han, A.-R.; Nam, W. *Inorg. Chem*. **2007**, *46*, 4632–4641.
197. Jerina, D. M.; Daly, J. W. *Science* **1974**, *185*, 573–582.
198. de Visser, S. P.; Ogliaro, F.; Harris, N.; Shaik, S. *J. Am. Chem. Soc*. **2001**, *123*, 3037–3047.
199. de Visser, S. P.; Ogliaro, F.; Shaik, S. *Chem. Commun*. **2001**, 2322–2323.
200. de Visser, S. P.; Kumar, D.; Shaik, S. *J. Inorg. Biochem*. **2004**, *98*, 1183–1193.
201. Kumar, D.; de Visser, S. P.; Shaik, S. *Chem. Eur. J*. **2005**, *11*, 2825–2835.
202. Ortiz de Montellano, P. R.; Mangold, B. L. K.; Wheeler, C.; Kunze, K. L.; Reich, N. O. *J. Biol. Chem*. **1983**, *258*, 4208–4213.
203. Tian, Z.-Q.; Richards, J.; Traylor, T. G. *J. Am. Chem. Soc*. **1995**, *117*, 21–29.
204. Sharma, P. K.; de Visser, S. P.; Ogliaro, F.; Shaik, S. *J. Am. Chem. Soc*. **2003**, *125*, 2291–2300.
205. Kumar, D.; de Visser, S. P.; Sharma, P. K.; Hirao, H.; Shaik, S. *Biochemistry* **2005**, *44*, 8148–8158.
206. Rydberg, P.; Ryde, U.; Olsen, L. *J. Chem. Theory Comput*. **2008**, *4*, 1369–1377.
207. Li, C.; Zhang, L.; Zhang, C.; Hirao, H.; Wu, W.; Shaik, S. *Angew. Chem. Int. Ed*. **2007**, *46*, 8168–8170.

This page intentionally left blank

45 On the Significance of Phthalocyanines in Solar Cells

M. Victoria Martínez-Díaz and Tomás Torres

Departamento de Química Orgánica,
Universidad Autónoma de Madrid, 28049-Madrid, Spain

List of Abbreviations

BCP	bathocuproine
BHJ	bulk heterojunction
CHENO	3α, 7α-dihydroxy-5β-cholic acid
D–A	donor–acceptor
DOTs	dendritic oligothiophenes
DSSCs	dye-sensitized solar cells
EBL	exciton blocking layer
EQE	external quantum efficiency
ERDS	energy relay dyes
IPCE	incident photon to current efficiency
ITO	indium tin oxide
MDMO-PPV	poly[2-methoxy-5-(3′,7′-dimethyloctyloxy)-1,4-phenylenevinylene]
Ncs	naphthalocyanines
OPVs	organic photovoltaics
PCBM	[6,6]-phenyl-C_{61}-butyric acid methyl ester
$PC_{71}BM$	phenyl-C_{71}-butyric acid methyl ester
Pcs	phthalocyanines
PEDOT:PSS	mixture of poly(3,4-ethylenedioxythiophene) and poly(styrenesulfonate)
P3HT	poly(3-hexylthiophene)
PPVs	poly(para-phenylenevinylenes)
PTs	polythiophenes
PTCBI	3,4,9,10-perylenetetracarboxylic bis(benzimidazole)
PyFs	pyrrolidinofullerenes
SubNcs	subnaphthalocyanines
SubPcs	subphthalocyanines
SWNTs	single walled carbon nanotubes

I. Introduction

During the last few decades, phthalocyanines (Pcs)[1–4] have found applications in different fields of technology. As a matter of fact, they have been successfully incorporated as active components of semiconductor and electrochromic devices, information storage systems and liquid crystal color displays, among others. More recently, they have received particular attention at the research level as building blocks for the construction of molecular materials due to their outstanding electronic and optical characteristics.[5–7] Numerous properties arise from their

electronic delocalization, which makes them valuable in different areas of science and technology.

Solar energy technologies are emerging as one of the most promising options for necessary sustainable energy production. In this connection, photosynthesis is the unavoidable example to be followed; it relies on the simple fact that sunlight constitutes the initial energy source of a complicated chain of events that take place in the photosynthetic process in living things. The ultimate goal, therefore, is to design and assemble artificial systems which can efficiently harvest, convert and store sunlight, replicating the natural analogs.[8–11] This is the reason why, during the last few decades, the development of artificial photosynthetic systems mimicking the natural process of solar energy conversion and the exploitation of molecular devices have attracted a great deal of interest.[12–17]

Porphyrinoids are typically employed as components of such photovoltaic and artificial photosynthetic devices.[18–30] However, synthetic porphyrin analogs such as phthalocyanines have the advantage, as photon harvesters, of exhibiting very high extinction coefficients in a wavelength range that extends to around 700 nm, where the maximum of the solar photon flux occurs.[31] Consequently, Pcs have emerged as excellent light-harvesting antennas for incorporation into donor–acceptor systems, mainly in connection with fullerenes as an acceptor moiety.[32–53] This overview is divided into two parts. The first is devoted to pure organic solar cells and the second to organic–inorganic hybrid or dye-sensitized solar cells.

II. Phthalocyanines in Organic Solar Cells

Organic materials, both small molecules and π-conjugated polymers, are real alternatives to silicon-based solar cells. In particular, they offer easy processing in thin films, by either vacuum evaporation or solution cast technologies, and the possibility of being adapted lo large-area substrates of complex shape.[54–63] Furthermore, organic thin films may show high optical absorption coefficients, which make them good chromophores for optoelectronic applications. Among organic molecules, semiconducting conjugated polymers — particularly poly(*para*-phenylenevinylenes) or PPVs and polythiophenes (PTs) — and fullerene derivatives have played a special role.[64,65]

In organic photovoltaic (OPV) devices, light absorption leads to the formation of excitons rather than free electron–hole pairs. Efficient exciton dissociation occurs under strong electric fields or at the interface between two materials of different electron affinities, i.e. donor–acceptor (D–A) interfaces. This concept has been extensively applied to the fabrication of organic D–A bilayer devices, commonly by vacuum deposition of the molecular components. The efficiency of OPV devices depends on the absorption efficiency of incident photons, which can be

simply increased by using thicker photoactive layers.[66] However, only excitons generated close to the D–A interface will generate free carriers, limiting the J_{sc} and the overall power conversion efficiencies. In order to improve the fraction of photogenerated excitons that diffuse to the D–A interface, the so-called bulk heterojunction (BHJ) solar cell configuration was proposed instead, in which an interpenetrating network of the donor and acceptor materials is used as a single active layer, thereby maximizing the interfacial area between donor and acceptors. The most effective BHJ organic solar cells currently reach power conversion efficiencies up to 6%, employing semiconducting conjugated polymer–fullerene composites as the active layer.[67–75]

A number of approaches have been explored for the optimization of organic solar cell,[76] starting from a better understanding of the mechanism of operation. It has been shown that the optimization of the solar cells is influenced by many different parameters, among which are fine-tuning of the electronic properties of the donor and acceptor components, active layer absorption properties, efficiency of the interfacial charge transfer process, and transport of the charges in the respective phases to the electrodes.

A common strategy for implementing these devices is to employ materials with a strong absorption in the red and near-infrared part of the solar spectrum, to harvest the photons where the maximal flux is located (approximately 700 nm). Despite significant progress in the synthesis of low-band-gap polymers capable of absorbing a broad range of solar photons in which alternating electron-rich and electron-poor units define the polymer backbone, only a few examples have achieved power conversion efficiencies comparable with those of devices fabricated from P3HT.[77–85] On the other hand, substitution of the typical acceptor component PCBM by the C_{70} derivative, with a significantly stronger absorption across the visible region, led to an improvement in the performance of a variety of polymer solar cells.[73,86]

Alternative routes would consist in introducing either on the polymer or in the acceptor counter-partner "colored" antenna groups, or just blending the polymer with small dye molecules or quantum dots. When one is selecting the chromophore, it is crucial to consider that its energy levels should lie between those of the polymer and the acceptor in order to avoid charge trapping on the dye.

Until very recently, solution-processable OPVs have always been related to soluble conjugated polymers because of their ability to form uniform films upon spin-coating. Solution-processable small molecule semiconductors have been proposed as new donor materials in BHJ solar cells as alternatives to conjugated polymers.[87–92] They offer some specific advantages, such as reproducible synthesis and easier purification, since they are intrinsically monodisperse. Moreover, molecular organic materials exhibit, in general, better charge transport properties

than polymeric semiconductors because they are more likely to exhibit long range order. However, they may lack the necessary viscosity for film casting and often present a poor solid state miscibility with the acceptor material. Until very recently, published results were quite poor.[87,93]

Together with fullerene derivatives, phthalocyanines are among the benchmark materials for photovoltaic heterojunctions based on small molecules. They exhibit very high extinction coefficients — typically higher than 100,000 $M^{-1}cm^{-1}$ at the Q band absorption (*ca*. 650–700 nm). In addition to their outstanding optical properties, Pcs have excellent thermal stability and a rich redox chemistry, which can be modulated by chemical synthesis.[1–6] Thus, it is possible to tune the physicochemical properties of synthetic phthalocyanines through introduction of specific substituents or central metals. Moreover, they exhibit a self-organization tendency which is reflected in high charge carrier mobility values. Usually Pcs play the double role of donor component and antenna. All of these properties make them especially suitable for integration into photovoltaic devices, as will be described in this review.

Unsubstituted Pcs possess remarkable limited solubility and a strong tendency to aggregate in most organic solvents, which makes it difficult to apply solution-processing techniques for the fabrication of solar cells. For this reason, phthalocyanine thin films are typically prepared via vapor deposition. Most of the success of phthalocyanines in the field of organic photovoltaics is based on unsubstituted Pc thin films incorporated as active layers in different types of architecture devices.

In contrast, chemically elaborate Pcs (including those with peripheral substituents to increase solubility in organic solvents or electroactive units to favor intramolecular photoinduced processes) are usually not stable for the application of high vacuum vapor deposition techniques. In these cases, photovoltaic device fabrication requires solution-processing techniques. Efficient solar cells based on solution-processed phthalocyanines are still scarce but have started to appear in the literature, as will be discussed in the following pages. Even rarer are the cases where efficient solar cells incorporate Pcs together with semiconducting polymers.

Depending on the production process, heterojunctions (both planar and bulk heterojunction solar cells) can be differentiated in vapor-deposited and solution-processed solar cells. However, mixtures of the two techniques are currently used in the preparation of single- and multilayered heterojunction solar cells. For the sake of schematizing the present overview, we have classified Pc-based organic solar cells into two types: (a) heterojunctions of any type in which phthalocyanines (or Pc analogs) have been processed by vapor deposition and (b) Pc-based organic solar cells in which these macrocycles have been solution-processed to be incorporated into the active film.

A. Incorporation of Phthalocyanines into Organic Photovoltaic Devices by Vapor Deposition

Pcs have been used in molecular organic solar cells since the first report by Tang in 1986.[94] In fact, a two-layer thin film photovoltaic cell was fabricated by vacuum evaporation of CuPc (donor) and the perylene derivative PTCBI (acceptor) (Figure 1), achieving a power conversion efficiency of *ca*. 1% under simulated AM2 illumination.

1. *Introduction of Exciton-Blocking Layers*

Device performance was significantly improved up to 2.4% by introduction of a large band gap (3 eV) and, hence, transparent exciton-blocking layer (EBL) of bathocuproine (BCP) between the photoactive organic layers and the metal cathode (Figure 2).[95] Inserting such a layer prevents damage of the active layer due to cathode evaporation and prohibits excitons from diffusing toward the Al electrode, where they would otherwise be quenched. Since the EBL provides a spacer between the photoactive region and the cathode, the optical intensity at the D–A interface is increased, thereby raising the light absorption efficiency.

2. *Hybrid Planar–Mixed Molecular Heterojunctions*

The device modification proposed by Hiramoto *et al.* in 1991 consisted in employing a three-layered organic solar cell with a photoactive interlayer of codeposited dyes, namely metal-free phthalocyanine and the perylene derivative PTCBI,

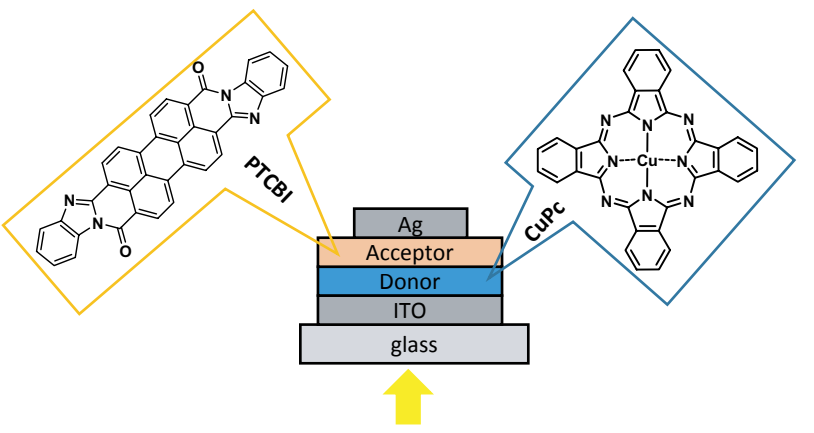

Figure 1. Planar donor–acceptor heterojunction made of CuPc and a perylene derivative.

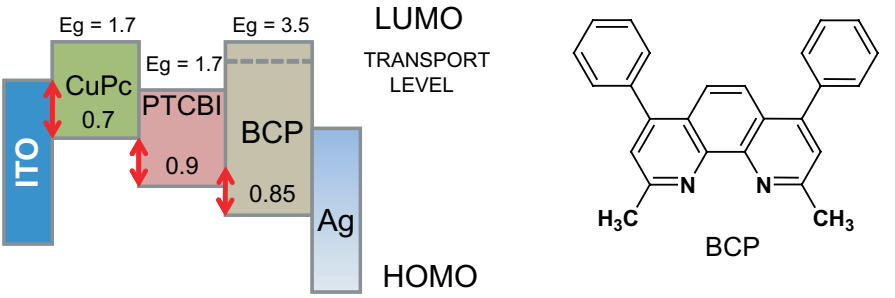

Figure 2. Energy level diagram of ITO/CuPc/PTCBI/BCP/Ag OPV cells, taken from Ref. 95.

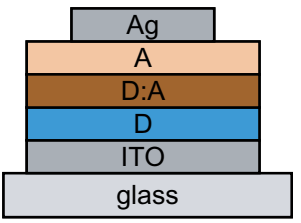

Figure 3. Schematic representation of hybrid planar–mixed molecular heterojunction (PM-HJ) devices.

between pristine donor and acceptor material layers (Figure 3).[96] This device architecture can be considered as a hybrid combination of planar and bulk heterojunction structures. However, the advantage of this configuration was not realized by the authors, due to the use of excessively thick layers.

The substitution of the acceptor material PTCBI with fullerene C_{60} by Forrest and coworkers in 2001 led to a substantial improvement in the cell efficiency (up to 3.6% when a BCP exciton-blocking layer was also employed).[97] The results were justified considering the longer exciton diffusion length of C_{60} (77 Å), which results in an enhanced transport of photogenerated carriers due to the spherical shape of the C_{60} molecules, in contrast to the planar perylene derivative.

Device implementation, namely fabrication of a hybrid planar–mixed heterojunction (PM–HJ) solar cell consisting of a 1:1 (by weight) mixed layer of CuPc and C_{60} sandwiched between a homogeneous layer of CuPc and C_{60} [ITO/CuPc/CuPc:C_{60}/C_{60}/BCP/Ag], gave rise to efficiencies up to 5% under 1–4 suns of simulated AM1.5G solar illumination.[98] The use of very thin layers turned out to be crucial for facilitating the diffusion of excitons across the entire heterojunction to the nearby D–A interface.

3. *Structural Modifications in the Phthalocyanines*

Other unsubstituted metallophthalocyanines, such as TiOPc and $(RuPc)_2$, have been incorporated in phototovoltaic devices[99–102] by high vacuum evaporation techniques, although the most relevant results were found with CuPc and ZnPc.[103–105]

Of special interest are metallophthalocyanines with strong absorption in the near IR. Among them, aluminum phthalocyanine chloride (AlPcCl) and tin phthalocyanine dichloride ($SnPcCl_2$) have attracted much attention. In addition to the work functions of the electrodes, most reports suggest that the V_{oc} value depends on the energy difference between the lowest unoccupied molecular orbital (LUMO) energy of the acceptor and the highest occupied molecular orbital (HOMO) energy of the donor.[106,107] As predicted on the bases of its HOMO energy (Figure 4), AlPcCl cells showed significantly higher open-circuit voltages than CuPc ones and therefore higher conversion efficiencies under the same experimental conditions (almost twice the values).[108,109] In addition, both AlPcCl and $SnPcCl_2$ extend the solar cell photoresponse into the near-IR region (between 755 and 1000 nm).[110] It seems that the main drawback of these long-wavelength absorbing-materials-based solar cells are the low open-circuit voltages obtained due to their small energy gaps and high dark currents. Recently, Forrest and coworkers have reported the benefit of incorporating an electron-blocking layer between the donor layer and the anode contact, which can help to reduce the dark current and subsequently increase the photovoltaic cell efficiency.[111] Thus, it was shown how the dark current of $SnPcCl_2/C_{60}$ heterojunction solar cells is decreased by two orders of magnitude compared to cells lacking the blocking layers, reaching overall efficiencies of 2.1% at 1 sun.

Among the phthalocyanines analogs, the boron chlorosubphthalocyanine derivative (SubPcCl) has been selected as a promising strongly absorbing donor material for C_{60}-based solar cells owing to its lower oxidation potential, which results in an increase of the V_{oc} as a consequence of a larger difference between

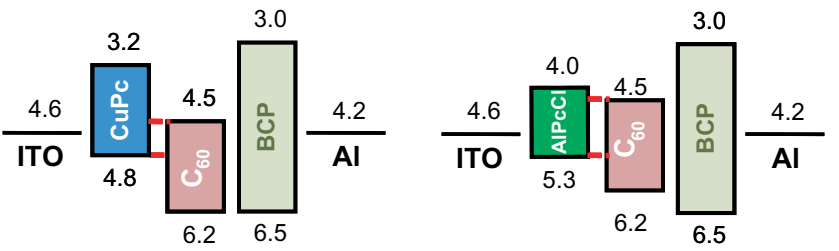

Figure 4. Schematic energy band diagrams of CuPc/C_{60}- and AlPc/C_{60}-based planar heterojunctions modified from Ref. 108.

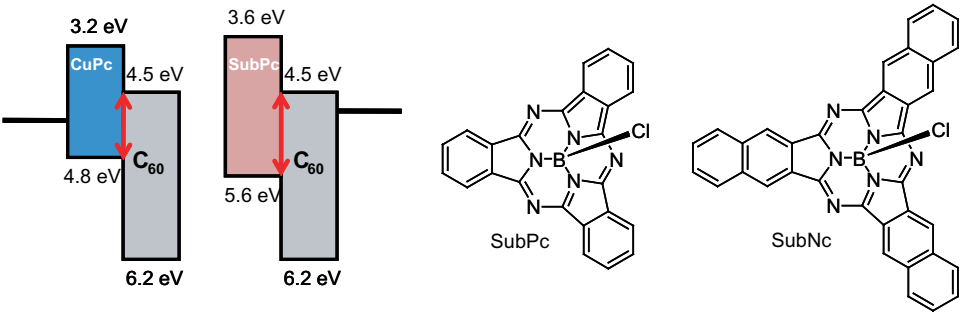

Figure 5. (a) Schematic energy level diagrams of CuPc/C_{60} and SubPc/C_{60} planar heterojunctions modified from Ref. 112. (b) Molecular structures of SubPc and SubNc macrocycles.

the LUMO of the acceptor and the HOMO of the donor (Figure 5).[112] Thus, it has been described that a double-heterostructure SubPc/C_{60} thin film solar cell has a more-than-doubled V_{oc} compared to a conventional CuPc/C_{60} cell under 1 sun AM1.5G simulated illumination. Power efficiencies of either 3% or 2.5% under 1 sun have been measured using SubPcCl or SubNcCl films, respectively, in combination with C_{60} in a planar bilayer donor/aceptor heterojunction.[113,114]

Very rarely, Pcs bearing electron-withdrawing substituents such as fluoro, namely $CuF_{16}Pc$, have played the role of acceptors blended with typical *p*-type materials, such as *p*-sexiphenyl.[115] However, the scope of Pcs as acceptor components has not been sufficiently studied yet.

In the same way, only very recently have perfluorinated SubPcs been employed as acceptors in bilayer organic solar cells in which unsubstituted SubPc played the expected role of donor material. Power conversion efficiencies of 0.96% and a remarkably high open-circuit voltage (as high as 940 mV) were achieved in devices with the following structure: ITO (100 nm)/SubPcCl (13 nm)/F_{12}SubPcF (33 nm)/BCP (10 nm)/Al (80 nm) under 1 sun simulated solar illumination.[116]

4. *Bilayer Heterojunctions Fabricated Using Two Different Processing Techniques*

Bilayer heterojunctions can also be fabricated using solution-processing techniques.[117] An innovative approach was proposed by Sariciftci and coworkers which consisted in donor–acceptor "diffused" bilayer solar cells formed by deposition of solutions of pyrrolidinofullerenes (PyFs) bearing chelating pyridyl groups on vacuum-evaporated films of ZnPc (Figure 6). The idea

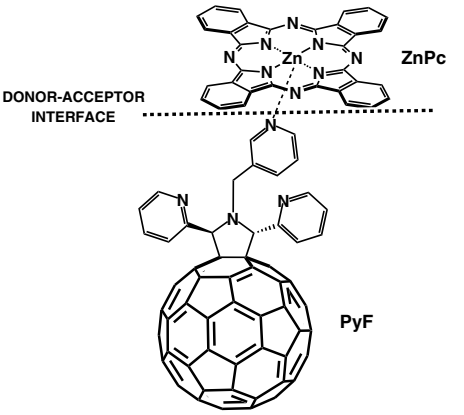

Figure 6. Py–Zn interaction at the donor–acceptor interface (from Ref. 118).

consisted in taking advantage of the coordination between the pyridyl groups attached to the fullerene component and the Zn(II) metal in the Pc cavity that would take place at the interface between the donor and the acceptor, thus facilitating the photoinduced charge separation process step. The devices exhibited conversion efficiencies of up to 1.5% under 100 nmW/cm^2 simulated AM1.5 illumination. Reference cells based on nonchelating fullerene derivatives (namely PCBM) as acceptor yielded significantly lower power conversion efficiencies (0.4–0.6%).[118]

5. *Tandem Solar Cells*

The number of photons that can be absorbed and collected in a single cell is limited by the maximum thickness of the active layer in regard to its transport properties. One way to bypass this limitation consists in tandem solar cells, which are stacks of different cells connected in series by a transparent intermediate layer. This layer ensures the recombination of electrons coming from one cell with the holes coming from the other cell in such a way that the resulting V_{oc} should be the sum of the single cells.[119] However, the overall efficiency is limited by the J_{sc}, which is the lowest of the individual cells. Highly efficient (η = 5.7%) tandem photovoltaic cells have been published by Forrest and coworkers by stacking two CuPc/C_{60} hybrid PM–HJs in series.[120]

Tandem solar cells have also been proposed as an alternative solution for overcoming the mismatch between the absorption spectra of the materials and the terrestrial solar spectrum which limits the efficiency of the photovoltaic devices.[121] In this case, each connected cell contains different active layers

which absorb in different spectral regions. Tandem solar cells based on the combination of P3HT:PCBM and CuPc/C_{60} subcells have been reported.[121–124] By using a highly transparent, high-work-function WO_3 layer as part of the interconnecting system for the two subcells, stacked devices with power conversion efficiencies as high as 4.6% are claimed.[124] The efficiency of the stacked devices is close to the sum of the efficiencies of the individual subcells. Organic connecting layers are highly desirable for simplifying the fabrication process (by lowering the sublimation temperature) and optimizing the cell performance. Namely, 3 nm each of $SnPcCl_2$ and F_{16}CuPc layers have recently been used for joining two identical ZnPc/C_{60} subcells with a hybrid planar–mixed heterostructure device configuration, shown in Figure 7.[125] Doubling of the V_{oc} was achieved for the tandem cell, whereas the overall efficiency increased from 1.11% of the single cell to 1.46%, showing that these Pc layers behave as good effective recombination centers for the electrons and holes photogenerated in the front and the back cell by a tunnel mechanism. The concept could be extended to tandem cells with different active layers wherein device performance is expected to be further increased.

To overcome the inherent problems of tandem solar cells — namely, the intercellular layer used to connect the subcells will reflect and absorb some light and hence will decrease the amount of transmitted light, new device architectures are being explored. Simple devices have been fabricated by spin-casting a P3HT:PCBM blend onto an evaporated thin layer of CuPc (Figure 8). In this way, two simultaneous bilayer heterojunctions are formed, achieving a power efficiency (2.79%) which is nearly the sum of those of the individual CuPc/PCBM and P3HT/PCBM cells with much less complex device architecture.[126] Optimization of these cells gave power conversion efficiency as high as 4.13%.[127]

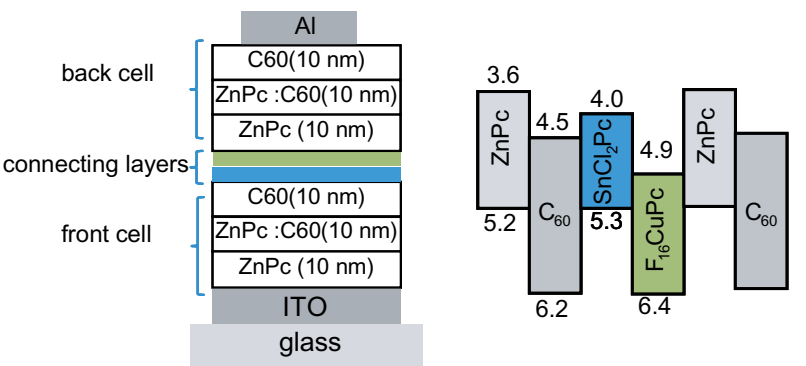

Figure 7. Device architecture and energy level diagram of tandem ZnPc/C_{60} cells incorporating thin $SnCl_2$Pc and F_{16}CuPc connecting layers, modified from Ref. 125.

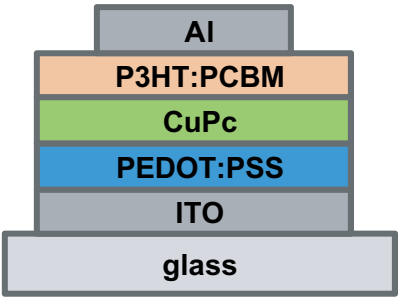

Figure 8. Device architecture of a P3HT:PCBM/CuPc bilayer heterojunction, modified from Ref. 126.

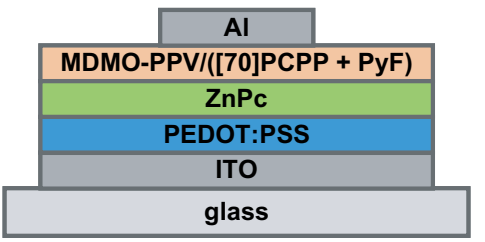

Figure 9. Multicomponent device mixture of bulk and bilayer heterojunctions, modified from Ref. 118.

Similarly, multicomponent devices made of spin-coated MDMO-PPV/[70]PCPP blends and bilayer ZnPc/PyF cells (Figure 9) yielded photovoltaic devices that showed power conversion efficiencies of up to 2.1%.[118]

Alternatively, OPV device performance enhancement can be based on the incorporation of absorbing dopants, aimed at extending the sensitivity of the device across the absorption of the three components. Absorbing dopants such as rubrene, $SnPcCl_2$ and SubPcCl have been tested independently as a second donor in well-established CuPc/C_{60} solar cells.[128–132] In all cases a remarkable enhancement of the power conversion efficiency has been observed as a consequence of the simultaneous formation of D_1/C_{60} and D_2/C_{60} nanoheterojunctions and/or the extended light-harvesting efficiency.

Another promising strategy consists in coupling an "antenna system" — which will not take part in the charge generation and transport steps but will donate the energy from photons absorbed in the blue and green spectral ranges — to the red absorbing solar cell materials.[133] The application of luminescent concentrators in organic solar cells based on ZnPc and C_{60} has been reported[134] wherein a photocurrent density increase from about 8.5 up to 10 mA/cm^2 was observed compared to a single solar cell of equal active area.

B. Incorporation of Phthalocyanines into Organic Photovoltaic Devices by Solution Processing

Solution process fabrication involving spin-coating techniques has attracted much attention, because they are suitable for producing low-cost large-area devices at ambient temperature and pressure. Moreover, these techniques are applicable to flexible devices.

Solution-processed Pc-based bulk heterojunction solar cells are rarely reported and almost ineffective.[135,136] In one report, the PV properties of cells containing soluble discotic liquid crystalline phthalocyanines and C_{60} as an active layer were discussed.[137] Highly ordered structures were obtained by thermal annealing of spin-coated thin films. However, efficiencies were only up to 0.08%.

Recently, bulk heterojunction devices made by spin-coating a blend containing rare earth phthalocyaninato double or triple deckers as electron donors and a perylenedi-imide derivative as electron acceptor have been published (Figure 10). These Pc derivatives offer unique optical electronic and optical properties, including a broad absorption which extends from the UV range to the near-IR, large exciton delocalization and high carrier mobility. The best cells (conversion efficiency of 1.3% under AM 1.5 solar illumination) were fabricated using a triple-decker Pc derivative and incorporating TiO_2 layers between the active layer and the electrodes.[138]

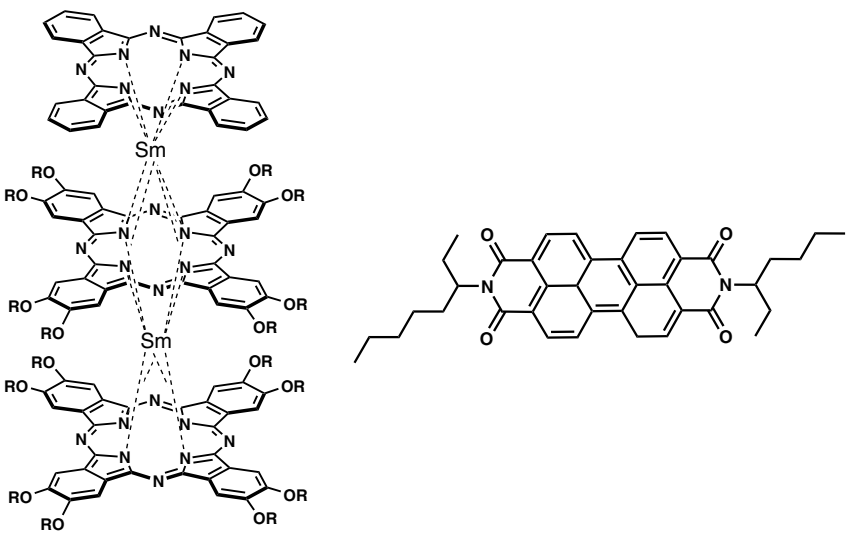

Figure 10. Molecular structures of the phthalocyaninato triple decker and perylenebisimide derivative active layer components of solar cells, described in Ref. 138.

In contrast with unsubstituted Pcs, the nonplanar structure of unsubstituted phthalocyanine boron analogs, so-called subnaphthalocyanine (SubNcCl) (Figure 5b), provides this macrocycle with distinctive physical properties such as high solubility and low tendency to aggregate, which makes feasible the fabrication of thin films via solution-processing techniques. A remarkable 1.5% power conversion efficiency has recently been reported by Frechet *et al.* with a planar heterojunction device made of a subnaphthalocyanine donor layer prepared by solution casting and a vapor-deposited C_{60} film.[139]

In addition, well-defined multilayered structures are difficult to construct using solvent-casting deposition techniques. New solution process techniques such as the layer-by-layer deposition method allow the fabrication of ultrathin films with a multilayered structure in the direction normal to the substrate and control of the thickness of each functional layer with nanometer precision.[140] This technique is based on the electrostatic adsorption of oppositely charged materials such as polycations or polyanions, and charged small molecules. Solution-processed thin film organic solar cells were developed by spin-coating deposition of a C_{60} film on top of PDDA/CuPcTS (tetrasodium tetrasulfonate CuPc derivative) films constructed by the layer-by-layer technique (Figure 11).[141] Although the reported efficiencies were very low compared with conventional CuPc-based solar cells fabricated by vacuum deposition, the approach seems useful for constructing solution-processed organic solar cells with a controlled multilayered structure.

In the field of OPVs, tandem solar cells have been shown to be the most successful option for catching as many photons of different energies as possible by connecting two cells in series whose active layers present complementary absorption. In any case, these multilayered devices are quite sophisticated. Ideally, simpler efficient solution-processed devices made of a single bulk heterojunction

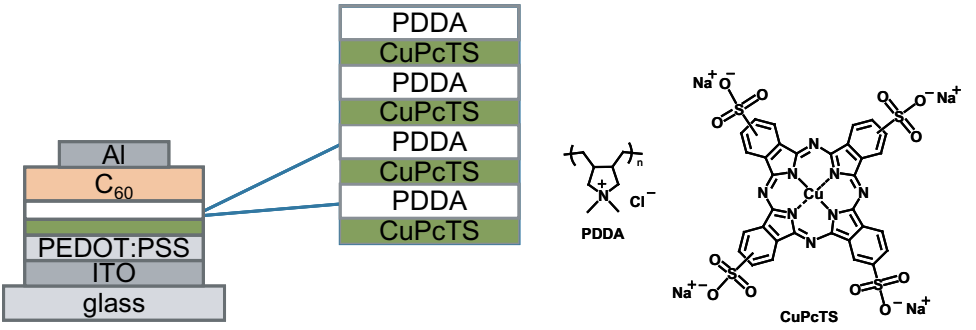

Figure 11. Molecular structures of the components PDDA and CuPcTS and device architecture, modified from Ref. 141.

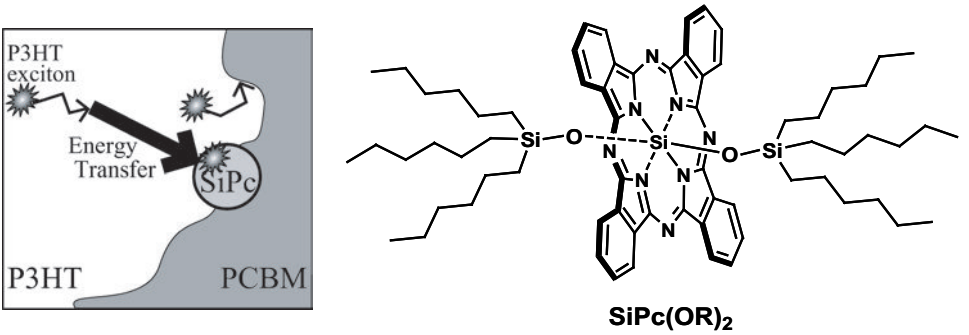

Figure 12. Schematic representation of a dye-sensitized P3HT/PCBM solar cell, taken from Ref. 145.

active layer consisting of a panchromatic mixture of donor and acceptors would be desired. Commonly, a dye molecule is introduced as the third component in a polymer/fullerene BHJ. Since mixing different active donor and acceptor molecules usually leads to phase segregation problems, this method rarely improves the device performance.[142–144] However, the introduction of a silicon phthalocyanine derivative [$SiPc(OR)_2$] as the third component in a P3HT/PCBM blend led to a substantial enhancement of the J_{sc} and hence the conversion efficiency by 20% compared with a P3HT/PCBM device.[145] To explain these results, the authors suggested a double role of the $SiPc(OR)_2$ molecule, as a light-harvesting photosensitizer and an energy funnel for the P3HT exciton, which implies that energy transfer from the P3HT to the $SiPc(OR)_2$ molecules is occurring at the P3HT/PCBM interface (Figure 12). The key point for this success is related to the use of a Pc dye molecule with a much-reduced tendency to form aggregates due to the axial substituents.

Covalent linkage of the active components has been proposed as a way to improve OPV performance avoiding phase segregation. Many Pc-based covalent donor–acceptor systems, like Pc–C_{60} dyads[32–53] (see one example in Figure 13), Pc-based polymers[146,147] and SWNT–Pc conjugates,[148–150] have been proposed as materials for photovoltaics but only a few of them have been tested in solar cells, although results are still very poor.[147,150,151]

The ZnPc–C_{60} dyad was used as a dye to improve the photocurrent around its maximum absorption (*ca.* 700 nm) as a third component in MDMO-PPV:PCBM cells.[152] Although a good matching of the device photocurrent spectrum and the solar emission spectrum is obtained, a reduction in the short-circuit current is observed, indicative of charge transfer problems.

The introduction of Pc–C_{60} dyad H_2Pc–C_{60}ee as a spin-coated film in a bilayer cell made of P3HT and C_{60} (or PTCDI) (Figure 14) leads to an enhancement in the

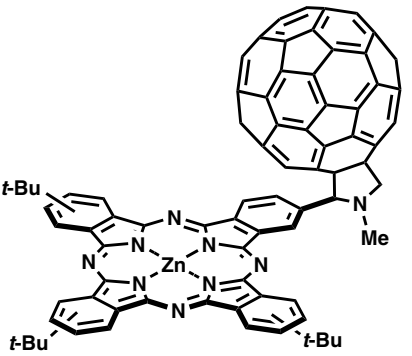

ZnPc-C_{60}

Figure 13. Molecular structure of the most representative ZnPc–C_{60} dyad.

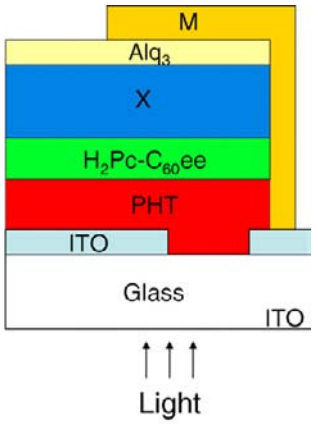

X = PTCDI, M = Au
X = C_{60}, M = Au
X = PTCDI, M = Al
X = C_{60}, M = Al

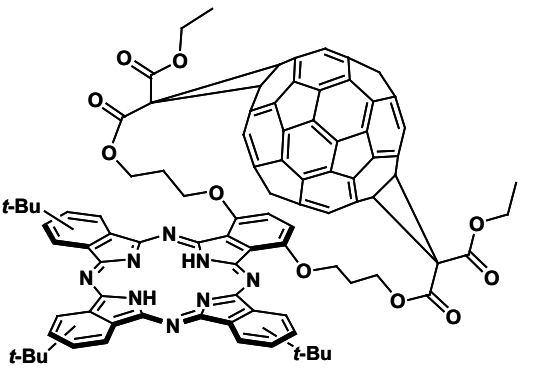

H_2Pc-C_{60}ee

Figure 14. Molecular structure of dyad H_2Pc–C_{60}ee and device configuration, taken from Ref. 153.

power conversion efficiency (between one- and-a-half and three times compared with the corresponding reference systems), as a consequence of an increase of the V_{oc}.[153] In other words, the dyad produces two different junctions in the cell (P3HT/dyad, and dyad/C_{60} or PTCDI) contributing to a more efficient charge transport toward the electrodes. Photoinduced electron transfer should take place in the

dyad layer, and subsequently the P3HT or acceptor layer would act as antenna and secondary electron donor, providing electron or holes to the dyad.

A promising approach would consist in the incorporation of relatively stable supramolecular systems in bulk heterojunctions. The great potential of RuPcs as platforms for the preparation of multifunctional materials has been proven.[154–158] Some examples of robust Pc assemblies have been reported based on the strong coordination of one or two pyridine axial ligands to the central Ru atom. Moreover, the strongly coordinated axial ligands dramatically decrease the natural tendency of Pcs to form aggregates and increase their solubility in organic solvents, which allow the processing of the molecules by spin-casting techniques.

Tetra-*tert*-butylRu(II)Pc has been self-assembled to different pyridine-functionalized chromophores, such as squaraines and dendritic oligothiophenes (DOTs) (Figure 15), yielding stable supramolecular systems[159] with enhanced light-harvesting ability. Furthermore, they have been incorporated into solution-processed BHJ cells blended with the suitable PCBM soluble acceptor. In particular, good efficiencies of up to 1.6% (when blended with $PC_{71}BM$ as acceptor) have been obtained for the DOT–RuPc hybrid molecules.

III. Phthalocyanines as Sensitizers of Dye-Sensitized Solar Cells

In the search for efficient, stable and low-cost alternatives to well-established but expensive silicon-based solar cells, dye-sensitized solar cells (DSSCs), mainly developed by the group of Grätzel, have been shown to be the most promising candidates.[160–163] In these devices, photons are collected by *organic dye* molecules which cover a layer of a wide-band-gap semiconducting material like *mesoporous* TiO_2. Anatase is a cheap material which can be processed in transparent flexible films which offer a huge interfacial area and high electron mobility. The third important component is the *redox electrolyte*, which interpenetrates the TiO_2 layer. Excitation of the dye leads to injection of electrons from the dye-excited state to the conduction band of the TiO_2 (Figure 16). The ground state of the dye is regenerated through reduction by the electrolyte (usually I^-/I_3^-) (Figure 16). The dyes employed should fulfill a number of requirements. The necessity of anchoring functions for attaching the dye to the semiconductor surface has been demonstrated. In particular, carboxylate groups have shown very good electronic coupling between the π^* orbital of the electronically excited complex and the 3d orbitals of the TiO_2 film. The LUMO level of the dye must be sufficiently high in energy for efficient charge injection in the TiO_2, and the HOMO level should allow efficient regeneration of the oxidized dye by the electrolyte. In contrast, the

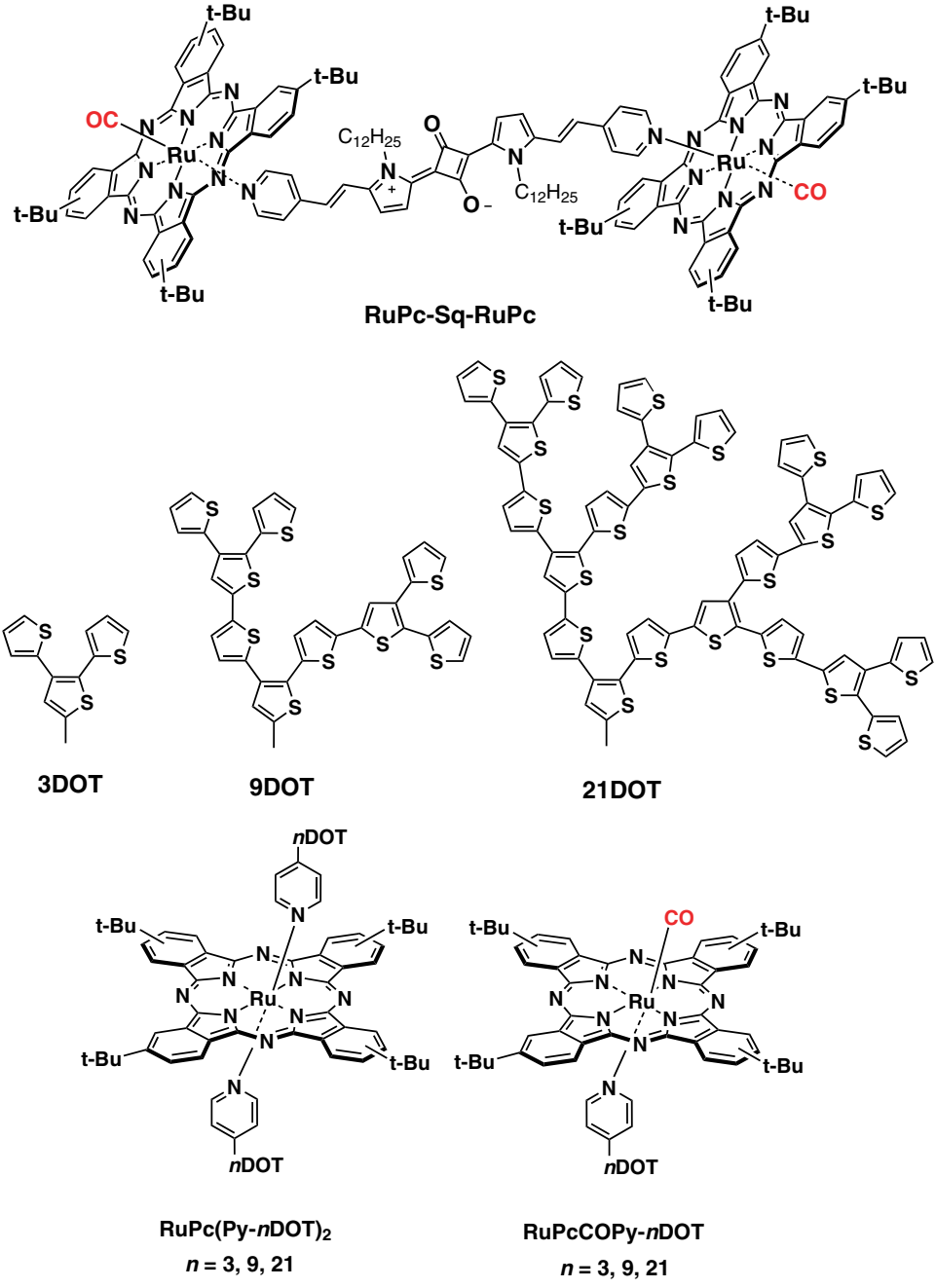

Figure 15. Molecular structures of multichromophoric Ru(II)Pc-based systems employed in BHJs, described in Refs. 158 and 159.

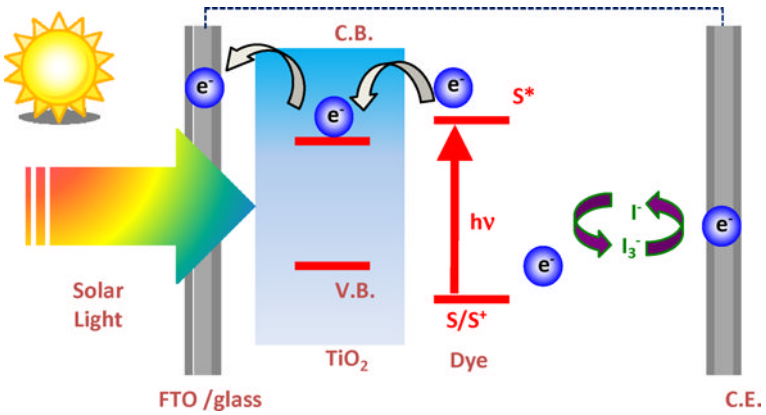

Figure 16. Schematic representation of fundamental processes in a DSSC.

redox mediator should not bind the semiconductor surface, since it should shuttle between the TiO_2 surface and the counterelectrode.

Energy conversion efficiencies of up to 11%, under AM 1.5 irradiation and small active solar cell area (0.2 cm^2), have been obtained using Ru-polypyridyl dyes, but commercial applications require further improvements in efficiency and stability. Despite extensive work in the development of dyes[164–168] for DSSCs, not very impressive progress has been reported. Improvement of the device performance has been limited by the light-harvesting capability of the state-of-the-art dyes, which lack strong absorption in the red/near-infrared region where the solar flux of photons is maximum. Dyes which have a high molar extinction coefficient in this spectral region would allow the preparation of thinner devices, minimizing charge recombination during the transport of charges to the electrode.[169]

A. Structural Optimization of Phthalocyanines

Pcs are also attractive sensitizers for DSSCs due to their intense red absorbance and robustness, as mentioned in Section II. Moreover, depending on the central metal and the peripheral substituents, they have appropriate redox properties for sensitization of the TiO_2 films and dye regeneration by the I^-/I_3^- electrolyte.

For a long time the applications of Pc dyes in DSSCs have been restricted due to problems associated with aggregation of the dye on the metal oxide surface, resulting in rapid deactivation of the dye-excited state and low sensitizing efficiency. Introduction of the required anchoring carboxy groups at the peripheral positions of Pcs usually leads to additional problems concerning poor solubility and aggregate formation.

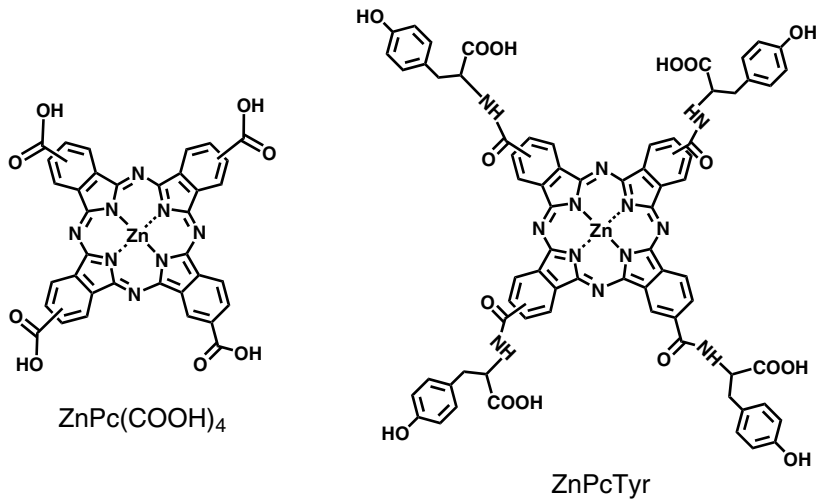

Figure 17. Molecular structures of tetracarboxy-ZnPcs tested in DSSCs.[170,175]

Efficient near-IR sensitization of nanocrystalline TiO_2 films by carboxy-zinc(II) and aluminum(III) phthalocyanines was first described by Grätzel, Wöhrle and coworkers in 1999.[170] Electron injection from the excited state of $ZnPc(COOH)_4$ (Figure 17) into the conduction band of TiO_2 was quite efficient in the near-IR region, displaying a maximum around 700 nm, where 45% of the photocurrent yield was obtained. The overall device efficiency was close to 1% under full AM 1.5 solar light.

The data were obtained employing CHENO and 4-*tert*-butylpyridine additives, which helped to reduce the inherent aggregation problem. While the role of the 4-*tert*-butylpyridine can be easily explained by weak axial coordination to the Zn(II) metal ion, the role of the cholic acid was not clear. In this work it was also shown that structural Pc modifications such as replacement of Zn(II) by Al(III)OH, or introduction of carboxyphenoxy substituents, lead to poorer efficiencies. Similar results were obtained with ZnPcs containing sulfonic acid groups, offering a new way for anchoring the Pc dye to the TiO_2.[171–174]

A few years later, solar cells based on ZnPcTyr-coated nanostructure TiO_2 electrodes were reported by Sun, Sundstrom and coworkers.[175] Introduction of peripheral bulky carboxy-containing tyrosine units (Figure 17) made the dye ethanol-soluble and considerably decreased its aggregation on the surface. However, monochromatic IPCE values of only 24% at 690 nm were achieved, while the overall conversion efficiency remained moderate (*ca*. 0.54%); it was, however, one of the best results reported at that time.

Introduction of axial ligands is by far the best way to avoid the natural behavior of Pcs toward aggregation. This strategy implies the incorporation of

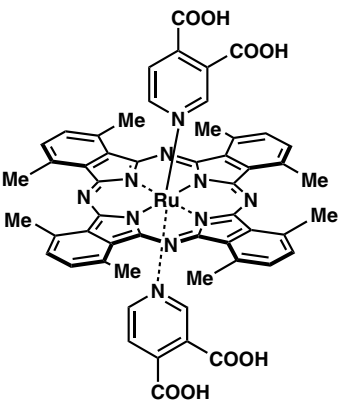

$RuPc[Py(COOH)_2]_2$

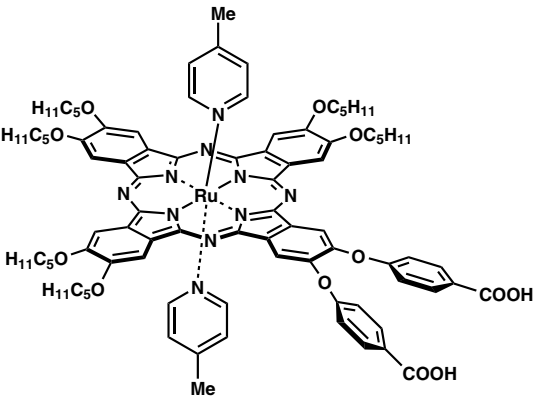

$RuPc(COOH)_2(PyMe)_2$

Figure 18. Molecular structures of carboxy-Ru(II)Pcs tested in DSSCs.[176,178]

metals able to form penta- or hexacoordinated complexes, such as Si(IV), Ti(IV) and Ru(II).

As early as 1998, $RuPc[Py(COOH)_2]_2$ (Figure 18) anchored to nanocrystalline TiO_2 films through axial pyridine 3,4-dicarboxylic acid ligands was already reported as an efficient near-IR sensitizer for photovoltaic injection cells.[176] Strikingly high photocurrent yields exceeding 60% in the near-IR region were obtained, demonstrating that efficient coupling of the dye-excited state to the conduction band could occur through space without involving the anchoring group. Other examples of RuPc bearing carboxylic groups, such as $RuPc(COOH)_2(PyMe)_2$ (Figure 18), came later,[177,178] but the results never went over 0.5% overall efficiencies.

Tetra-*tert*-butyl-substituted Pcs exhibit a good compromise between good solubility and reduced aggregation tendency. The Ti(IV)Pc derivative TiPc(COOH) bearing a carboxycatechol bidentate axial ligand (Figure 19) was efficiently anchored to nanocrystalline TiO_2 without the need for coadsorbents to prevent macrocycle aggregation.[179] However, photocurrent generation in the macrocycle Q band region was quite low, accounting for an inefficient electron injection from the LUMO level, which is close in energy to the TiO_2 conduction band.

Considering the rich electrochemistry of RuPcs, whose oxidation potential can be slightly tuned by changing the substituents at the pyridine axial ligands,[180] and in order to gain more insights into the possibilities of RuPcs as sentitizers of TiO_2, a family of tetra(*tert*-butyl)-RuPcs (RuPcA) bearing two different axial pyridine ligands were prepared by Torres and coworkers (Figure 19).[181] One ligand, 4-carboxypyridine, would play the role of the anchoring group and the

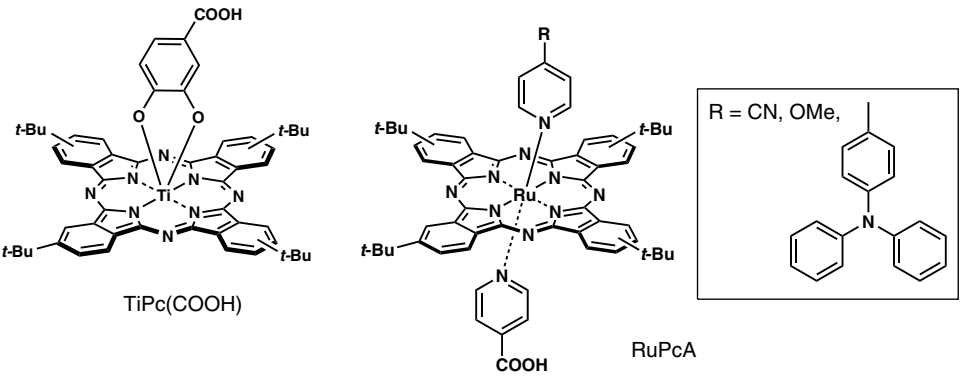

Figure 19. Molecular structures of tetra-*tert*-butyl-substituted TiPcs and RuPcs bearing carboxy groups at the axial ligand tested as TiO_2 film sensitizers, in Refs. 179 and 181.

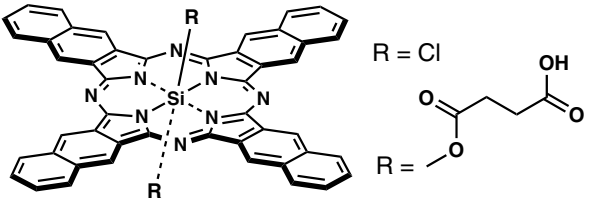

Figure 20. Silicon naphthalocyanine dyes tested in DSSCs.[182]

second one, bearing either an electron-withdrawing (e.g. CN) or an electron-donating (e.g. OMe, triphenylamine) substituent, can serve to modulate the electronic properties of the phthalocyanine. In DSSCs with suitable electrolytes, RuPcA were capable of efficient photocurrent generation, showing absorbed-photon-to-current efficiencies of up to 45%.

Very recently, silicon naphthalocyanine dyes (Figure 20) have been attached through the axial position to TiO_2 nanostructured photoelectrodes.[182] Si–O–Ti linkage resulted in being much more effective than the classical carboxy–TiO_2 interaction due to the high reactivity of $SiNcCl_2$ toward Si–O formation. Promising photovoltaic results were obtained, reaching a maximum IPCE of *ca.* 17% at 790 nm.

A major step forward for the application of Pcs in many fields, including DSSCs, came from the preparation of unsymmetrically functionalized, A_3B-type derivatives.[183] The introduction of *tert*-butyl groups at three of the isoindole units, leaving the fourth one for attaching the anchoring group, allowed the preparation of highly soluble carboxy–Zn(II)Pc derivatives PCH001 and TT-1 (Figure 21),

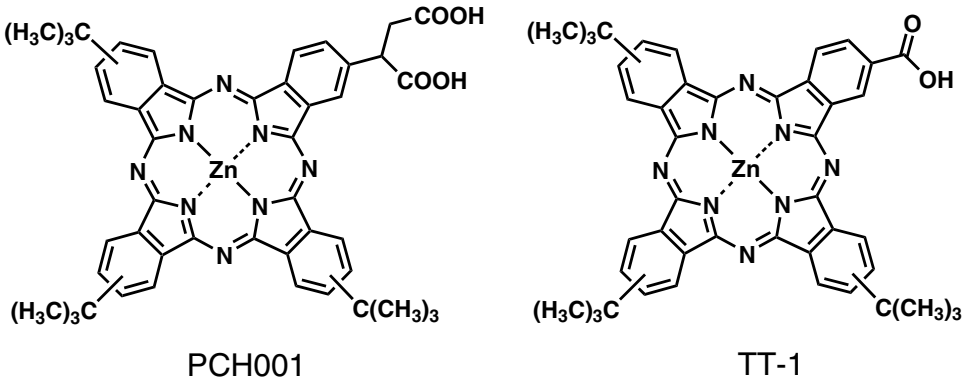

Figure 21. Molecular structures of unsymmetrically substituted carboxy–Zn(II)Pcs PCH001 and TT-1, reported in Refs. 184 and 185.

which had a low tendency toward aggregation.[184,185] In particular, TT-1 possesses a highly desirable "push–pull" structure with the carboxy group directly attached to the macrocycle, thus facilitating charge transfer from the LUMO orbital of the dye to the Ti 3d orbital and, therefore, optimizing the device performance to get overall efficiencies above 3.5% at 1 sun. This value, and the IPCE at the maximum absorption of the Q band of 80%, represented the best results ever reported for a PC–TiO_2 dye-sensitized solar cell.

Optimization of the dye component of the cell usually requires a systematic structural modification. In the case of phthalocyanine dyes, two approaches have been reported:

(1) *Peripheral modification* and preparation of new derivatives as single isomers with an enhanced *push–pull* character. Tri-*tert*-butyl-substituted Pcs PCH001 and TT-1 are, in fact, a mixture of regioisomers. However, by employing 3,6- or 4,5-disubstituted phthalonitrile precursors, this symmetry problem can be solved. Indeed, hexa-α-butoxy derivatives of PCH001 have been reported by Giribabu *et al.*[186] Neverthesless, when the new sensitizer PCH003 (Figure 22) was tested in DSSCs and compared with the parent molecule PCH001, the overall efficiency went down to *ca.* 1%, without any rational explanation. On the other hand, carboxy–ZnPc ZnPc($tBuC_6H_5$)$_6$($COOH$)$_2$ (Figure 22) bearing six bulky *t*-butylphenyl groups at the peripheral β position were also considered as sensitizers.[187] However, the corresponding cells displayed only 0.57% of conversion efficiency and 4.9% of IPCE at the Q band wavelength. It was demonstrated that, indeed, aggregation of Pcs was almost suppressed by introduction of the *t*-butylphenyl groups. However, the disappointing low

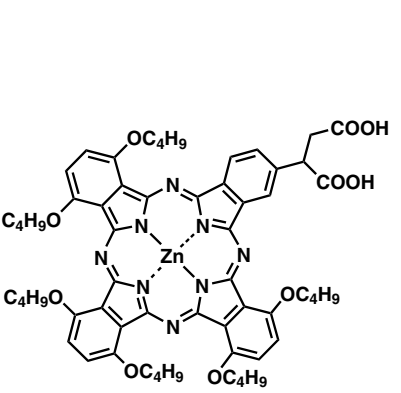

PCH003

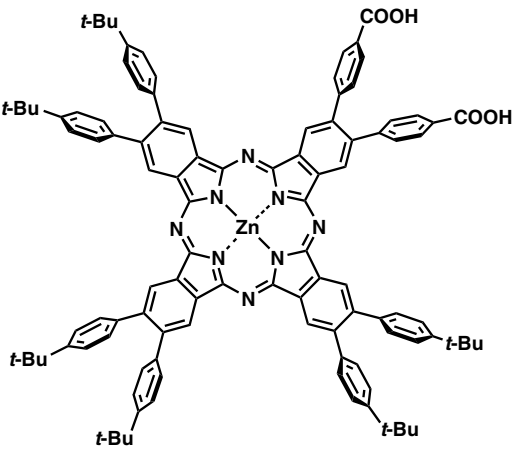

$ZnPc(tBuC_6H_5)_6(COOH)_2$

Figure 22. Molecular structures of ZnPcs PCH003 and $ZnPc(tBuC_6H_5)_6(COOH)_2$, described in Refs. 186 and 187.

device efficiencies were attributed to the inefficient coupling between the dye and the conduction band of TiO_2. Also remarkable is the absence of photocurrent response when the free-base derivative was employed, due to its low excited singlet state [the oxidation potential of the free base is 330 mV more positive than that of the Zn(II) derivative, whereas the HOMO–LUMO gaps remain similar].

(2) A different approach en route to dye optimization has been reported by Torres and coworkers.[188,189] TT-1 derivatives bearing different π-conjugated and non-conjugated linkers between the carboxy group and the Pc macrocycle have been systematically checked in DSSCs and compared with TT-1 sensitizers (Figure 23). This work has shown the influence of the location of the carboxy anchoring group on the device performance. A modification of the linker groups within the series TT1–TT5, TT-14 and TT-20 allows not only a variable distance between the dye and the photosensitized nanocrystalline TiO_2, but also a distinct orientation of the dye molecular plane with regard to the semiconductor surface which modifies the orbital coupling between the dyes and the semiconductor. In particular, a remarkable influence on the electron injection and the recombination steps has been demonstrated. Table 1 summarizes the photovoltaic results obtained. Under standard solar simulation conditions, TT2 and TT4 derivatives gave the poorest performance. As previously stated by Nazeeruddin *et al.*,[170] the IPCE values drop dramatically when the carboxy anchoring group is separated from the Pc by insulating alkoxy or

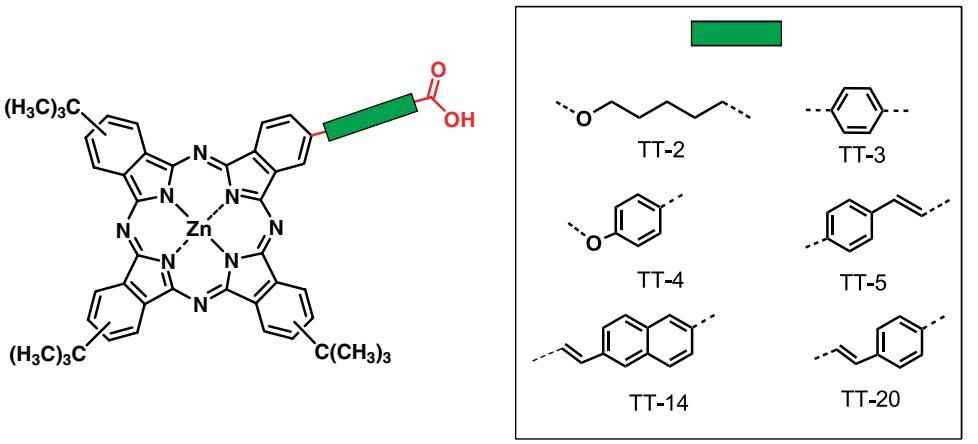

Figure 23. Molecular structures of TT-1 derivatives bearing different spacers between the macrocycle and the carboxylic anchoring group.[188,189]

Table 1. Comparative photovoltaic data[188,189] of tri-*tert*-butyl carboxy–PcZn dyes bearing different spacers between the Pc and the carboxy group.

Sensitizer	J_{sc} (mA/cm^2)	V_{oc} (mV)	η (%)
TT-1	7.6	617	3.52
TT-2	0.9	550	0.4
TT-3	4.8	610	2.20
TT-4	1.44	611	0.67
TT-5	6.8	613	3.10
TT-14	5.36	579	2.20
TT-20	4.36	587	1.87

aryloxy spacers. In constrast, rigid π-conjugated bridges do not interrupt electronic coupling between the Pc and the semiconductor surface, giving such derivatives (TT-3, TT-14 and TT-20) average power conversion efficiencies of 2%.

As in porphyrin derivatives,[190] conjugation of the carboxy anchoring group through an ethenyl spacer to the dye leads to superior photovoltaic responses in DSSCs. Thus, the TT-5 derivative, bearing a π-conjugated vinylenephenylene spacer, showed higher performance than the TT-20 derivative, which presents an opposite arrangement of the ethenyl and phenylene groups. In spite of this, the better results obtained with TT-1 suggest that the anchoring group should remain as close as possible to the chromophore so as to maximize the coupling between the Pc and the TiO_2.

The preparation of novel Pcs with better performance as DSSC sensitizers deserves much additional work. A hard synthetic effort is being developed in this connection, since there is convincing evidence that Pcs, among the plethora of red-light-absorbing molecules, can make a crucial contribution to the improvement of the current devices.

B. Insights into the Interfacial Electron Transfer Dynamics

After many years of research, numerous dyes have been tried and none have surpassed the best Ru–Bpy complexes.[160–169] In fact, the DSSC is a complicated system which is not yet fully understood. Besides systemic dye modification, new design rules are needed to guide new proposals focused on minimizing loss mechanisms and improving light harvesting. A better understanding of the physicochemical processes which underlie the function of DSSCs would also contribute to the optimization of these devices. In particular, there is a growing interest in studying the influence of dye structure on the interfacial electron transfer kinetics.[191] It can be said that "optimum" device performance will be observed when the recombination dynamics are as slow as possible while electron injection is sufficiently fast to compete with excited state decay.

As described above, upon excitation of the chromophore from its ground state to an excited state that is resonant with the TiO_2 conduction band, the electron is injected into the semiconductor surface. Electron injection is related to an efficient coupling between the dye and the TiO_2 conducting band. It can be monitored by following the formation of the corresponding electron transfer species. In the case of carboxy-substituted Zn(II)Pcs, it has been found that electron injection is very efficient (quantum yields higher than 90%) and very fast (around 200 ps). However, the question to answer is whether such a time scale of electron injection is necessary for achieving efficient DSSC function. It has been shown that efficient electron injection can also occur in systems where the dynamics are remarkably slower (up to three orders of magnitude). Ru(II) derivatives RuPcA (see Figure 29) exhibit electron injection rate constants of hundred of ns, and lower APCE values than Zn(II) derivatives.[181] The reason for the slow injection dynamics is that injection occurs more efficiently from the RuPcs triplet state. In other words, the relaxation of the singlet to the triplet excited state by intersystem crossing is faster (100 ps) than electron injection from the singlet excited state (600 ps to 30 ns). The long lifetime of this T_1 state (200 ns) enables electron injection into TiO_2 to be slow, in competition with the T_1 decay to the ground state.

Following efficient injection, the electron has to diffuse into the bulk and simultaneously relax to the bottom of the TiO_2 conduction band. If the relaxation inside the conduction band occurs faster than delocalization into the bulk, the electron

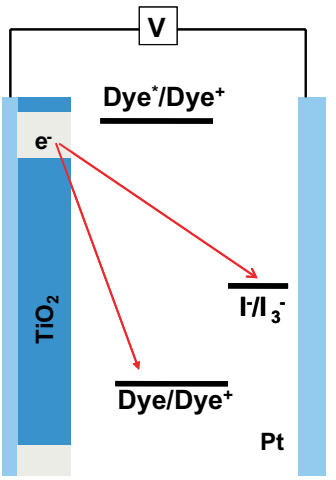

Figure 24. Schematic diagram representing recombination to the dye and dark current (recombination to the electrolyte) in a DSSC.

can be trapped at the surface. Since the electron is attracted by the positive charge remaining on the dye after injection, it can back-transfer and recombine with the hole of the chromophore ground state, thus short-circuiting the cell. By accepting the surface electron, the electrolyte can also short-circuit the cell.

From early studies it was already stated that very fast recombination to the dye (see Figure 24) was most likely responsible for the lower performance of Pc-sensitized solar cells[175] compared with highly efficient N3-sensitized TiO_2 films. Introduction of secondary donor groups could help to retard interfacial back electron transfer. However, this strategy was never reported.

O'Regan *et al.* have proposed that the bottleneck in Pc-sensitized cell performance could be related to the increased recombination rates to the I_2/I_3^- electrolyte, thus decreasing the resulting output voltage.[192] In fact, it was found that recombination is *ca.* 100 times faster for RuPc-sensitized cells than for the ones made of the N719 dye. This phenomenon, which it is claimed to be extrapolated to other organic dyes with an accessible aromatic surface, was rationalized considering that the reduction of iodine to tri-iodide could be mediated by the dye, through binding to the iodine, and therefore help to increase the iodine local concentration near the TiO_2 surface.

C. The Role of Coadsorbents

Coadsorbents are typically transparent compounds or ions which absorb together with the dye on the mesoporous semiconductor surface. They are used because

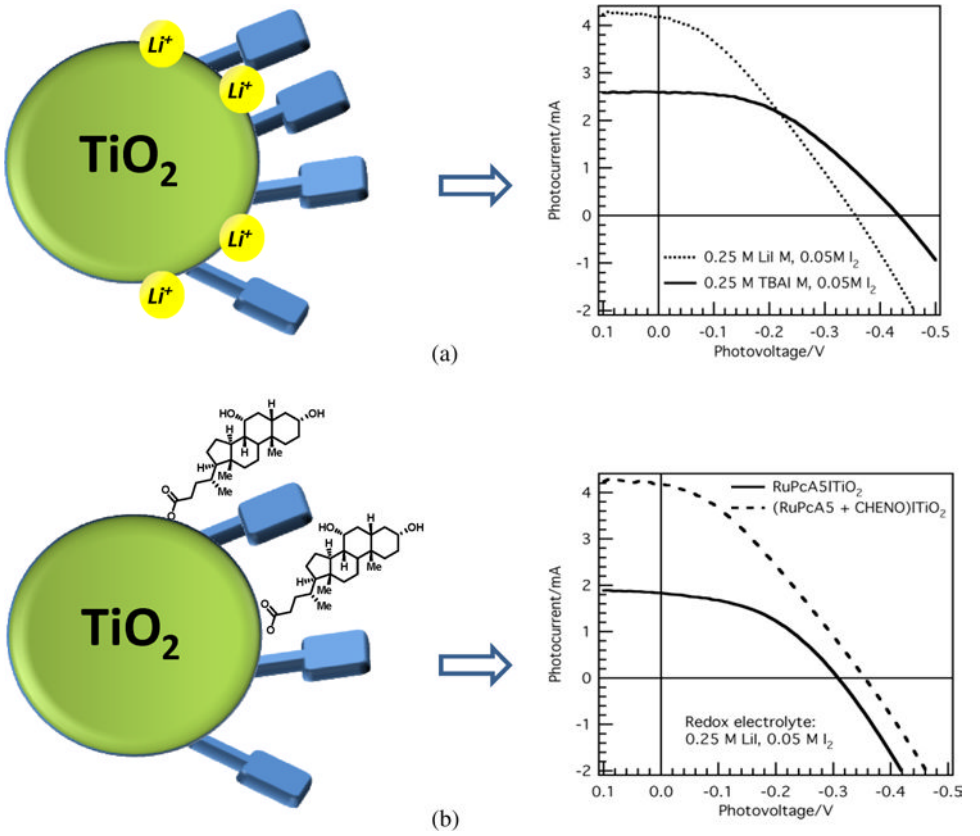

Figure 25. Schematic representation of a TiO_2 nanoparticle coated with both sensitizer and typical coadsorbents: (a) Li^+ and (b) CHENO. On the right side is represented how these coadsorbents affect the solar cell parameters (taken from Ref. 194).

their presence substantially improves the cell efficiency. However, the reason for this beneficial effect is not always well understood and their use is often empirical. Li^+ and CHENO are the most popular coabsorbents employed in DSSCs.

Li^+ cation acts directly on the TiO_2 surface, charging it positively. Its presence usually lowers the conduction band edge of TiO_2, therefore accelerating the electron injection and increasing the photocurrent in the device, although with concomitant decrease in photovoltage (see Figure 25a).

On the other hand, CHENO (see Figure 25b) bears a carboxylic acid functional group that allows its strong binding to the TiO_2 surface, in competition with the dye molecules. The addition of CHENO produced a remarkable increase in the photocurrent and to a lesser extent the photovoltage (Figure 25b). The increase in the photovoltage is usually attributed to the effect of CHENO breaking dye

aggregates.[167] In other cases, the beneficial effect of CHENO has been related to a decrease in recombination in the injected electrons with the redox electrolyte.[193]

Morandeira *et al.* have studied in detail the effect of these two coadsorbents on the device performance and photophysics of RuPcA-sensitized solar cells.[194] In the case of RuPcs the formation of aggregates is completely hindered by the presence of axial ligands. Indeed, the authors demonstrated that CHENO is not affecting the electron injection quantum yield, but the cation–TiO_2 (e^-) recombination and regeneration dynamics. In particular, the slower recombination of the dye cations with the TiO_2 electrons and the faster regeneration of the dye cations by the electrolyte are the reason claimed to be responsible for the enhanced photocurrent observed in the presence of CHENO coadsorbent molecules. A tentative explanation for that effect could be the change in the dye orientation induced by the presence of CHENO on the semiconductor surface, increasing the hole–electron distance. Anyway, the results suggest that the CHENO effect on DSSCs is more complex (and more beneficial) than what was previously assumed.

D. The Cosensitization Strategy

The possibility of combining different dyes with complementary absorbing spectra to achieve panchromatic sensitization of the TiO_2 films and increase device efficiency has always been a challenge in this field. Many "molecular cocktails" have been tried with limited success, due to the typical decrease in the sensitizing efficiency of the individual dyes upon mixing them.[195–201]

Pcs offer an optical window in the visible region that makes these molecules very appealing components of cosensitizer blends. $RuPc[Py(COOH)_2]_2$ (see Figure 18) was used together with Ru-bipyridyl dye N3 in a sophisticated device architecture which consisted in the deposition of a secondary Al_2O_3 layer between the N3-coated TiO_2 nanoparticles and the RuPc layer.[202] This approach avoided competition between the two dyes for absorption sites, and resulted in an interfacial electron transfer cascade in which the hole moved from the inner dye, closer to the TiO_2 surface, to the outer dye, thus retarding the interfacial charge recombination dynamics.

More recently, efficient cosensitized DSSCs have been prepared using the previously reported organic dyes, JK2 and TT-1 (see Figure 21). The photoresponse of the molecular cocktail was higher than those of the single dye-sensitized devices (Figure 26). The overall device efficiency, one day after the preparation of the device, was 7.74%.[181] The key point for this success was rationalized to be related to the high extinction coefficients of the dyes, which allow using low dye concentrations to achieve efficient absorption and therefore leave sufficient space on the TiO_2 surface to attach a second dye with a complementary absorption spectrum.[203]

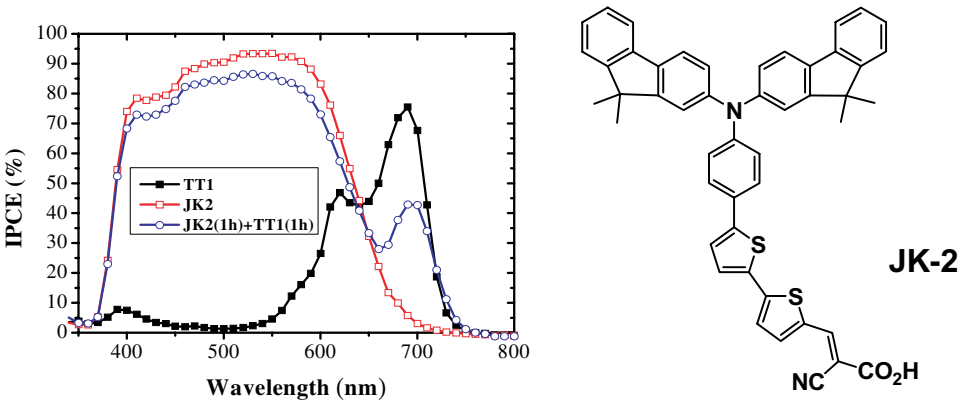

Figure 26. Molecular structure of JK2 dye and IPCE versus wavelength representation of the "TT-1/JK-2 molecular cocktail" in comparison with those of the individual cells, from Ref. 185.

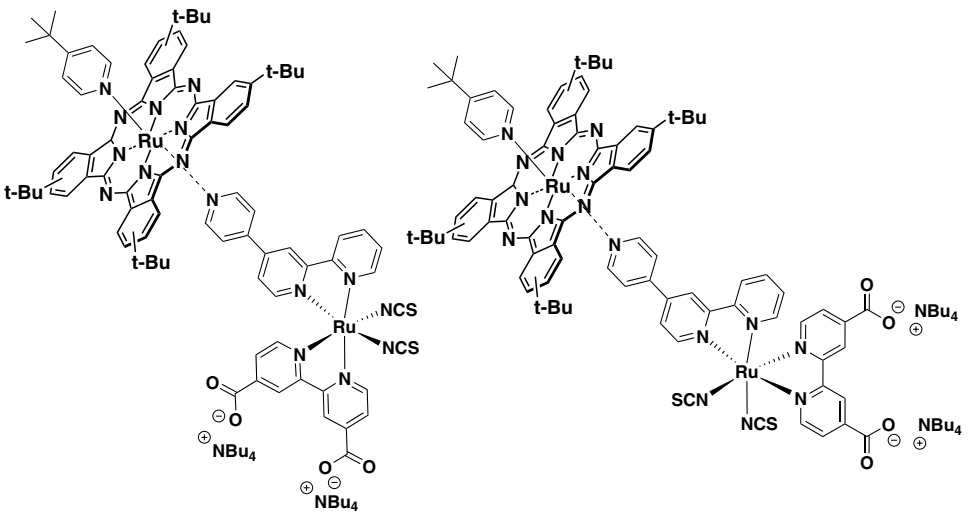

Figure 27. Molecular structures of the RuPc–Rubis(bipyrididyl) dyads tested in DSSCs.[204]

The cosensitization strategy possesses an obvious serious constraint concerning the number of sites on the titania surface that are available for dye attachment. Beyond that, it can be envisaged that molecular or covalent or supramolecular dyads constituted by two complementary absorbing dyes would positively contribute to the panchromatic sensitization of the TiO_2 films, avoiding the competition between the dyes for the binding sites in the TiO_2, since only one of the chromophoric units would bear the anchoring group to attach the whole molecule to the surface.[204] Up to now, only one example of a supramolecular dyad containing both RuPc and Ru bis(bipyridyl) chromophores (Figure 27) has been

published.[205] Unfortunately, solar cell efficiencies were not improved when compared with the reference N716 Ru bis(pipyridyl) dye. However, photocurrent generation *per molecule* was superior in the case of dyads. Indeed, the increased molecular size of the dyads is believed to be responsible for a concurrent decrease in dye coverage and DSSC performance.

A new concept for increasing light harvesting in DSSCs using energy relay dyes (ERDs) as cosensitizers has been proposed by Hardin *et al.*[206] In particular, a 26% increase in power conversion efficiency was achieved by incorporating an unattached highly luminescent PTCDI chromophore inside the liquid electrolyte in a TT-1 (see Figure 21) sensitized solar cell (Figure 28). The improvement in the device performance is attributed to the increase in the short-circuit photocurrent caused by an increase in the EQE in the 400–600 nm region, while the open-circuit voltage remained almost unchanged.

New sensitizers are being tested in DSSCs such as inorganic semiconducting materials that are so-called *quantum dots*. They possess ideal properties such as tunable band gaps. However, both quantum-dot-sensitized solar cells have shown lower efficiencies than initially expected, due to difficulties in finding appropriate redox couples and resolving stability issues.

Hybrid-sensitized solid cells combining PbS or CdS quantum dots with a near-IR-absorbing TT-1 have also been described. In this case, the TT-1 chromophore is added over the quantum-dot-deposited layer to strengthen the light-harvesting capabilities into the near-IR region.[207] Although the photocurrent decreased somewhat in the visible range compared to the original signal from PbS, photocurrents in the near-IR range increased at around 690 nm, where TT-1 dye absorbs strongly. A positive coctkail effect was obtained from a combination of CdS and sensitizer.

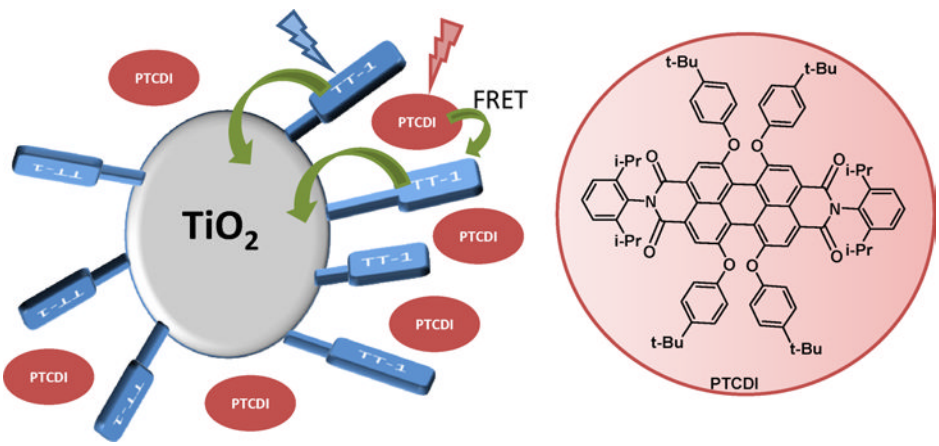

Figure 28. Schematic representation of a DSSC with energy relay dyes, reported in Ref. 206.

IV. Summary and Conclusions

Phthalocyanines, which possess intense absorption in the UV/blue and the red/near-IR region spectral regions, are materials especially suitable for integration in photovoltaic devices. In order to accomplish this function, specific requirements must be met, like collection of light energy, separation of charges, an appropriate active layer morphology that ensures charge migration, and stability, among others. Pcs usually play the double role of donor component and antenna.

Phthalocyanines are among the benchmark materials for photovoltaic heterojunctions based on small molecules. Thus, most of the success of Pcs in the organic photovoltaic field is based on unsubstituted Pc evaporated thin films incorporated as the active layer in different types of architecture devices; in this case efficiencies of *ca*. 6% have been reached. The use of Pc analogs in this area, like subphthalocyanines, is also very promising.

On the other hand, efficient solar cells based on solution-processed phthalocyanines are still scarce. The incorporation of phthalocyanines into polymeric photovoltaic devices is typically performed in blends together with semiconducting polymers and, usually, acceptor molecules such as fullerenes, obtaining only moderate (near 2%) efficiencies. Further developments using small molecules instead of polymers, or blends of conducting polymers and n-type Pcs instead of fullerenes, are worth of much attention.

The morphological problems of the so-called bulk heterojunctions have suggested the preparation of intrinsically bipolar materials, in which the donor and acceptor photoactive units are covalently linked within the same molecule, including the so-called "double-cable" approach with Pcs pending of conducting polymers. However, the efficiencies found in Pc-based solar cells fabricated exclusively with this kind of electroactive materials are still very low, and the field deserves further research.

On the other side, phthalocyanines are suitable to be applied as sensitizer dyes in dye-sensitized solar cells. DSSCs based on mesoporous TiO_2 have been an attractive alternative to the purely organic devices because of their huge interfacial area and high electron mobility in mesoporous titania. The efficiency of DSSCs has been limited by the low optical absorbance in the red/near-IR region of the dyes commonly used, such as ruthenium bipyridyl, as well as their low extinction coefficient. This is one of the points on which "colored" Pcs can be really useful in this area.

The applications of Pc dyes in DSSCs have been restricted due to problems associated with aggregation of the dye on the metal oxide surface, resulting in

rapid deactivation of the dye-excited state and low sensitizing efficiency. Recent development of red-absorbing Pc-based sensitizers with no dye aggregation on the TiO_2 surface has allowed efficient sensitization. Moreover, the modification of the spacer between the Pc core and the anchoring moiety has allowed not only a variable distance between the dye and the photosensitized nanocrystalline TiO_2, but also a distinct orientation of the dye molecular plane with regard to the semiconductor surface. Both axial and peripheral attachments of the Pc to the semiconductor have been shown to be effective, particularly the latter. Thus, efficient electron injection of a zinc phthalocyanine (TT-1), which yields 80% IPCE at 690 nm and an excellent efficiency (*ca.* 4%) under standard illumination conditions, have been described. Moreover, there has been illustrated the possibility of combining efficiently two dyes with complementary spectra and obtaining higher efficiencies, which could not be achieved separately by each of them, by taking advantage of the optical properties of the zinc phthalocyanine.

Very recently, a new design has been described, where high-energy photons are absorbed by an energy relay dye, unattached to the titania, which undergoes Förster resonant energy transfer to a Pc-sensitizing dye (TT-1). This novel architecture allows for broader spectral absorption and an increase in dye loading, and relaxes the design requirements for the phthalocyanine. This system offers a viable pathway for developing more efficient DSSCs.

The design of more efficient Pc-based sensitizers and their application to cosensitized and tandem solar cells, consisting of complementary absorbing dyes, energy relay dyes or "quantum dots," represent the trend in this area. The ultimate potential of Pcs for solar cell development can be hard to quantify, thus making predictions about the future very difficult. The results achieved to date, however, reveal that phthalocyanines must be considered seriously as photoactive components for future organic photovoltaic devices.

V. Acknowledgments

Funding from MEC and MICINN (CTQ2008-00418/BQU, CONSOLIDER-INGENIO 2010 CDS2007-00010 Nanociencia Molecular, FOTOMOL, PSE-120000-2009-008, PLE2009-0070), ESF-MEC (MAT2006-28180-E, SOHYDS), EU (Solar-N-type, MRTN-CT-2006-035533, ROBUST DSC, FP7-Energy-2007-1-RTD, No. 212792), COST Action D35 and CAM (MADRISOLAR, S2009/PPQ/1533) is gratefully acknowledged. We would also like to thank all coworkers and collaborators (Guldi, Durrant, Grätzel, Nazeeruddin and Palomares, among others) who have performed with us exciting research in the field of Pc-based organic photovoltaics.

VI. References

1. de la Torre, G.; Claessens, C. G.; Torres, T. *Chem. Commun.* **2007**, 2000–2015.
2. Claessens, C. G.; Hahn, U.; Torres, T. *Chem. Rec.* **2008**, *8*, 75–97.
3. Leznoff, C. C.; Lever, A. B. P., Eds. *Phthalocyanines: Properties and Applications*; VCH: Weinheim, **1989**, **1993**, **1996**; Vols. 1–4.
4. Kadish, K. M.; Smith, K. M.; Guilard, R., Eds. *The Porphyrin Handbook*; Academic: San Diego, **2003**, Vols. 15–20.
5. McKeown, N. B. *Phthalocyanine Materials: Synthesis, Structure and Function*; Cambridge University Press, **1998**.
6. de la Torre, T.; Nicolau, M.; Torres, T. In *Supramolecular Photosensitive and Electroactive Materials*; Nalwa, H. Ed.; Academic: New York, **2001**, pp. 1–111.
7. de la Torre, G.; Vázquez, P.; Agulló-López, F.; Torres, T. *Chem. Rev*. **2004**, *104*, 3723–3750.
8. Collings, A. F.; Critchley, C., Eds. *Artificial Photosynthesis: From Basic Biology to Industrial Application*; Wiley-VCH Verlag GmbH & Co. KGaA, Weinheim, **2005**, p. 313.
9. Thayyumanavan, S., Ed. *Artificial Mimicry of Photosynthesis*, in *Photosynth. Res.* **2006**, *87*(*1*), p. 150.
10. Deisenhofer, J.; Norris, J. R., Eds. *The Photosynthetic Reaction Center*; Academic: New York, **1993**.
11. Blankenship, R. E., Ed. *Molecular Mechanisms of Photosynthesis*; Blackwell Science, **2002**. (k) McEvoy, J. P.; Brudvig, G. W. *Chem. Rev.* **2006**, *106*, 4455–4483.
12. Balzani, V.; Clemente-León, M.; Credi, A.; Ferrer, B.; Venturi, M.; Flood, A. H.; Stoddart, J. F. *Proc. Natl. Acad. Sci. USA* **2006**, *103*, 1178–1183.
13. Wasielewski, M. R. *Chem. Rev.* **1992**, *92*, 435–461.
14. Gust, D.; Moore, T. A.; Moore, A. L. *Acc. Chem. Res.* **2001**, *34*, 40–48.
15. Arakawa, H. *et al*. *Chem. Rev.* **2001**, *101*, 953–996.
16. Chakraborty, S.; Wadas, T. J.; Hester, H.; Schmehl, R.; Eisenberg, R. *Inorg. Chem.* **2005**, *44*, 6865–6878.
17. Eisenberg, R.; Nocera, D. G. *Inorg. Chem.* **2005**, *44*, 6799–6801, and references therein.
18. Moore, G. F.; Hambourger, M.; Gervaldo, M.; Poluektov, O. G.; Rajh, T.; Gust, D.; Moore, T. A.; Moore, A. L. *J. Am. Chem. Soc.* **2008**, *130*, 10466–10467.
19. Rizzi, A. C.; van Gastel, M.; Liddell, P. A.; Palacios, R. E.; Moore, G. F.; Kodis, G.; Moore, A. L.; Moore, T. A.; Gust, D.; Braslavsky, S. E. *J. Phys. Chem. A* **2008**, *112*, 4215–4223.
20. Fukuzumi, S.; Kojima, T. *J. Mater. Chem.* **2008**, *18*, 1427–1439.
21. Kelley, R. F.; Lee, S. J.; Wilson, T. M.; Nakamura, Y. I.; Tiede, D. M.; Osuka, A.; Hupp, J. T.; Wasielewski, M. R. *J. Am. Chem. Soc.* **2008**, *130*, 4277–4284.
22. Benniston, A. C. *Phys. Chem. Chem. Phys.* **2007**, *9*, 5739–5747.
23. Satake, A.; Kobuke, Y. *Org. Biomol. Chem*. **2007**, *5*, 1679–1691.
24. Nakamura, Y.; Aratani, N.; Osuka, A. *Chem. Soc. Rev.* **2007**, *36*, 831–845.
25. Gadde, S.; Islam, D.-M. S.; Wijesinghe, C. A.; Subbaiyan, N. K.; Zandler, M. E.; Araki, Y.; Ito, O.; D'Souza, F. *J. Phys. Chem. C* **2007**, *111*, 12500–12503.
26. Schuster, D. I.; Li, K. E.; Guldi, D. M. *C. R. Chimie* **2006**, *9*, 892–908.
27. Langford, S. J.; Latter, M. J.; Woodward, C. P. *Photochem. Photobiol.* **2006**, *82*, 1530–1540.
28. Prodi, A.; Chiorboli, C.; Scandola, F.; Lengo, E.; Alessio, E.; Dobrawa, R.; Würthner, F. *J. Am. Chem. Soc.* **2005**, *127*, 1454–1562.
29. Imahori, H.; Fukuzumi, S. *Adv. Func. Mater*. **2004**, *14*, 525–536.

30. Imahori, H.; Mori, Y.; Matano, Y. *J. Photochem. Photobiol. C: Photochem. Rev.* **2003**, *4*, 51–83.
31. Rio, Y.; Rodríguez-Morgade, M. S.; Torres, T. *Org. Biomol. Chem.* **2008**, *6*, 1877–1894 and references therein.
32. Linssen, T. G.; Durr, K.; Hanack, M.; Hirsch, A. *J. Chem. Soc. Chem. Commun.* **1995**, 103–104.
33. Durr, K.; Fiedler, S.; Linssen, T.; Hirsch, A.; Hanack, M. *Chem. Ber.* **1997**, *130*, 1375–1378.
34. El-Khouly, M. E.; Ito, O.; Smith, P. M.; D'Souza, F. *J. Photochem. Photobiol. C* **2004**, *5*, 79–104.
35. Tian, Z.; He, C.; Liu, C.; Yang, W.; Yao, J.; Nie, Y.; Gong, Q.; Liu, Y. *Mater. Chem. Phys.* **2005**, *94*, 444–448.
36. Kim, K. N.; Choi, C. S.; Kay, K.-Y. *Tetrahed. Lett.* **2005**, *46*, 6791–6795.
37. Chen, Y.; El-Khouly, M. E.; Sasaki, M.; Araki, Y.; Ito, O. *Org. Lett.* **2005**, *7*, 1613–1616.
38. Isosomppi, M.; Tkachenko, N. V.; Efimov, A.; Vahasalo, H.; Jukola, J.; Vainiotalo, P.; Lemmetyinen, H. *Chem. Phys. Lett.* **2006**, *430*, 36–40.
39. El-Khouly, M. E.; Kang, E. S.; Kay, K.-Y.; Choi, C. S.; Aaraki, Y.; Ito, O. *Chem. Eur. J.* **2007**, *13*, 2854–286.
40. Loi, M. A.; Denk, P.; Hoppe, H.; Neugebauer, H.; Meissner, D.; Winder, C.; Brabec, C. J.; Lehtivuori, H.; Kumpulainen, T.; Efimov, A.; Lemmetyinen, H.; Kira, A.; Imahori, H.; Tkachenko, N. V. *J. Phys. Chem. C* **2008**, *112*, 9896–9902.
41. Niemi, M.; Tkachenko, N. V.; Efimov, A.; Lehtivuori, H.; Ohkubo, K.; Fukuzumi, S.; Lemmetyinen, H. *J. Phys. Chem. A* **2008**, *112*, 6884–6892.
42. Pinzón, J. R.; Cardona, C. M.; Herranz, M. A.; Plonska-Brzezinska, M. E.; Palkar, A.; Athans, A. J.; Fortea, N. M. A.; Poblet, J. M.; Bottari, G.; Torres, T.; Gayathri, S. S.; Guldi, D. M.; Echegoyen, L. *Chem. Eur. J.* **2009**, *15*, 864–877.
43. Kahnt, A.; Guldi, D. M.; de la Escosura, A.; Martinez-Diaz, M. V.; Torres, T. J. *Mater. Chem.* **2008**, *18*, 77–82.
44. Quintiliani, M.; Kahnt, A.; Vazquez, P.; Guldi, D. M.; Torres, T. *J. Mater. Chem.* **2008**, *18*, 1542–1546.
45. Kahnt, A.; Quintiliani, M.; Vazquez, P.; Guldi, D. M.; Torres, T. *ChemSusChem* **2008**, *1*, 97–102.
46. Quintiliani, M.; Kahnt, A.; Woeffle, T.; Hieringer, W.; Vazquez, P.; Goerling, A.; Guldi, D. M.; Torres, T. *Chem. Eur. J.* **2008**, *14*, 3765–3775.
47. Gouloumis, A.; de la Escosura, A.; Vazquez, P.; Torres, T.; Kahnt, A.; Guldi, D. M.; Neugebauer, H.; Winder, C.; Drees, M.; Sariciftci, N. S. *Org. Lett.* **2006**, *8*, 5187–5190.
48. Ballesteros, B.; de la Torre, G.; Torres, T.; Hug, G. L.; Rahman, G. M. A.; Guldi, D. M. *Tetrahedron* **2006**, *62*, 2097–2101.
49. Sessler, J. L.; Jayawickramarajah, J.; Gouloumis, A.; Dan Pantos, G.; Torres, T.; Guldi, D. M. *Tetrahedron* **2006**, *62*, 2123–2131.
50. de la Escosura, A.; Martinez-Diaz, M. V.; Guldi, D. M.; Torres, T. *J. Am. Chem. Soc.* **2006**, *128*, 4112–4118.
51. Guldi, D. M.; Ramey, J.; Martínez-Díaz, M. V.; de la Escosura, A.; Torres, T.; Da Ros, T.; Prato, M. *Chem. Commun.* **2002**, 2774–2775.
52. Guldi, D. M.; Gouloumis, A.; Vazquez, P.; Torres, T. *Chem. Commun.* **2002**, 2056–2057.
53. Sastre, A.; Gouloumis, A.; Vazquez, P.; Torres, T.; Doan, V.; Schwartz, B. J.; Wudl, F.; Echegoyen, L.; Rivera, J. *Org. Lett.* **1999**, *1*, 1807–1810.

54. Jacoby, M. *Chem. Eng. News* **2007**, 16.
55. Cunningham, A. *Sci. News* **2007**, *171*, 328.
56. Huynh, W. U.; Dittmer, J. J.; Alivisatos, A. P. *Science* **2002**, *295*, 2425.
57. Granstrom, M.; Petritsch, K.; Arias, A. C.; Lux, A.; Andersson, M. R.; Friend, R. H. *Nature* **1998**, *395*, 257.
58. Halls, J. J. M.; Walsh, C. A.; Greenham, N. C.; Marseglia, E. A.; Friend, R. H.; Moratti, S. C.; Holmes, A. B. *Nature* **1995**, *376*, 498.
59. Hoppe, H.; Sariciftci, N. S. *J. Mater. Res.* **2004**, *19*, 1924.
60. Winder, C.; Sariciftci, N. S. *J. Mater. Chem.* **2004**, *14*, 1077.
61. Sariciftci, N. S. *Mater. Today* **2004**, *7*, 36.
62. Wohrle, D.; Meissner, D. *Adv. Mater.* **1991**, *3*, 129–138.
63. Spanggaard, H.; Krebs, F. C. *Sol. Energ. Mater. Sol. Cells* **2004**, *83*, 125–146.
64. Brabec, C. J.; Sariciftci, N. S.; Hummelen, J. C. *Adv. Funct. Mater*. **2001**, *11*, 15.
65. Gnes, S.; Neugebauer, H.; Sariciftci, N. S. *Chem. Rev.* **2007**, *107*, 1324–1338.
66. Peumans, P.; Yakimov, A.; Forrest, S. R. *J. Appl. Phys.* **2003**, *93*, 3693.
67. Ma, W. L.; Yang, C. Y.; Gong, X.; Lee, K.; Heeger, A. J. *Adv. Funct. Mater.* **2005**, *15*, 1617.
68. Li, G.; Shrotriya, V.; Huang, J. S.; Yao, Y.; Moriarty, T.; Emery, K.; Yang, Y. *Nat. Mater.* **2005**, *4*, 864.
69. Reyes-Reyes, M.; Kim, K.; Carroll, D. L. *Appl. Phys. Lett.* **2005**, *87*, 083506.
70. Wienk, M. M.; Struijk, M. P.; Janssen, R. A. J. *Chem. Phys. Lett.* **2006**, *422*, 488.
71. Kim, J. Y.; Kim, S. H.; Lee, H. H.; Lee, K.; Ma, W.; Gong, X.; Heeger, A. J. *Adv. Mater*. **2006**, *18,* 572.
72. Kim, J. Y.; Lee, K.; Coates, N. E.; Moses, D.; Nguyen, T.-Q.; Dante, M.; Heeger, A. J. *Science* **2007**, *317*, 222.
73. Peet, J.; Kim, J. Y.; Coates, N. E.; Ma, W. L.; Moses, D.; Heeger, A. J.; Bazan, G. C. *Nat. Mater.* **2007**, *6*, 497.
74. Ma, C.; Fonrodona, M.; Schikora, M. C.; Wienk, M. M.; Janssen, R. A. J.; Bäuerle, P. *Adv. Funct. Mater.* **2008**, *18*, 3323–3331.
75. Park, S. H.; Roy, A.; Beaupre, S.; Cho, S.; Coates, N.; Moon, J. S.; Moses, D.; Leclerc, M.; Lee, K.; Heeger, A. J. *Nat. Photon.* **2009**, *3*, 297.
76. Thompson, B. C.; Frechet, J. M. *Angew. Chem. Int. Ed. Engl.* **2008**, *47*, 58–77.
77. Zhang, F.; Jespersen, K. G.; Bjorstrom, C.; Sevenssson, M.; Andersson, M. R.; Inganas, O. *Adv. Funct. Mater.* **2006**, *16*, 667–674.
78. Shi, C.; Yao, Y. M. Yang, Y.; Pei, Q. *J. Am. Chem. Soc.* **2006**, *128*, 8980–8986.
79. Wienk, M. M.; Turbiez, M. G. R.; Strujik, M. P.; Fonrodona, M.; Janssen, R. A. J. *Appl. Phys. Lett.* **2006**, *88*, 154511.
80. Muhlbacher, D.; Scharber, M.; Morana, M.; Zhu, Z.; Waller, D.; Gaudiana, R.; Brabec, C. *Adv. Mater.* **2006**, *18*, 2884–2889.
81. Bundgaard, E.; Krebs, F. C. *Sol. Energ. Mater. Sol. Cells* **2007**, *91*, 954–985.
82. Slooff, L. H.; Veenstra, S. C.; Kroon, J. M.; Moet, D. J. D.; Sweelssen, J.; Koetse, M. M. *Appl. Phys. Lett*. **2007**, *90*, 143506.
83. Li, Y.; Zou, Y. *Adv. Mater*. **2008**, *20*, 2952–2958.
84. Chen, C.-P.; Chan, S.-H.; Chao, T.-C.; Ting, C.; Ko, B.-T. *J. Am. Chem. Soc.* **2008**, *130*, 12828–12833.
85. Lee, J.-Y.; Shin, W.-S.; Haw, J.-R.; Moon, D.-K. *J. Mater. Chem.* **2009**, *19*, 4938–4945.
86. Wienk, M. M.; Kroon, J. M.; Verhees, W. J. H.; Knol, J.; Hummelen, J. C.; van Hal, P. A.; Janssen, R. A. J. *Angew. Chem. Int. Ed. Engl.* **2003**, *115*, 3371–3375.

87. Schmidt-Mende, L.; Fechtenkotter, A.; Mullen, K.; Moons, E.; Friend, R. H.; McKenzie, J. D. *Science* **2001**, *293*, 1119.
88. Peumans, P.; Uchida, S.; Forrest, S. R. *Nature* **2003**, *425*, 158–162.
89. Lloyd, M. T.; Anthony, J. E.; Malliaras, G. G. *Mater. Today* **2007**, *10*, 34.
90. Riede, M.; Mueller, T.; Tress, W.; Schueppel, R.; Leo, K. *Nanotechnology* **2008**, *19*, 424001.
91. Tamayo, A. B.; Dang, X.-D.; Walker, B.; Seo, J.; Kent, T.; Nguyen, T.-Q. *Appl. Phys. Lett.* **2009**, *94*, 103301.
92. Valentini, L.; Bagnis, D.; Marrocchi, A.; Seri, M.; Taticchi, A.; Kenny, J. M. *Chem. Mater.* **2008**, *20*, 32–34.
93. Sun, X. B.; Zhou, Y. H.; Wu, W. C.; Liu, Y. Q.; Tian, W. J.; Yu, G.; Qiu, W. F.; Chen, S. Y.; Zhu, D. B. *J. Phys. Chem. B* **2006**, *110*, 7702.
94. Tang, C. W. *Appl. Phys. Lett.* **1986**, *48*, 183–185.
95. Peumans, P.; Bulovic, V.; Forrest, S. R. *Appl. Phys. Lett.* **2000**, *76*, 2650–2652.
96. Hiramoto, M.; Fijiwara, H.; Yokoyama, M. *Appl. Phys. Lett.* **1991**, *58*, 1062–1064.
97. Peumans, P.; Forrest, S. R. *Appl. Phys. Lett.* **2001**, *79*, 126–128.
98. Xue, J.; Rand, B. P.; Uchida, S.; Forrest, S. R. *Adv. Mater.* **2005**, *17*, 66.
99. Tsuzuki, T.; Shirota, Y.; Rostalski, J.; Meissner, D. *Sol. Energ. Mater. Sol. Cells* **2000**, *61*, 1–8.
100. Pannemann, Ch.; Dyakonov, V.; Parisi, J.; Hild, O.; Wohrle, D. *Thin Solid Films* **2001**, *121*, 1585–1586.
101. Brousse, B.; Ratier, B.; Moliton, A. *Thin Solid Films* **2004**, *451–452*, 81–85.
102. Capobianchi, A.; Tucci, M. *Thin Solid Films* **2004**, *451–452*, 33–36.
103. Gebeyehu, D.; Pfeiffer, M.; Maennig, B.; Drechsel, J.; Werner, A.; Leo, K. *Thin Solid Films* **2004**, *451–452*, 29–32.
104. Pfuetzner, S.; Meiss, J.; Petrich, A.; Riede, M.; Leo, K. *Appl. Phys. Lett.* **2009**, *94*, 223307.
105. Pfuetzner, S.; Meiss, J.; Petrich, A.; Riede, M.; Leo, K. *Appl. Phys. Lett.* **2009**, *94*, 253303.
106. Brabec, C. J.; Cravino, A.; Meissner, D.; Sariciftci, N. S.; Fromherz, T. *Adv. Funct. Mater.* **2001**, *11*, 374–380.
107. Gadisa, A.; Svensson, M.; Andersson, M. R.; Inganas, O. *Appl. Phys. Lett.* **2004**, *84*, 1609–1611.
108. Kim, Y.; So, F.; Gao, Y. *Sol. Energ. Mater. Sol. Cells* **2009**, *93*, 1688–1691.
109. Bailey-Salzman, R. F.; Rand, B. P.; Forrest, S. R. *Appl. Phys. Lett.* **2007**, *91*, 013508/1–013508/3.
110. Rand, B. P.; Xue, J.; Yang, F.; Forrest, S. R. *Appl. Phys. Lett.* **2005**, *87*, 233508.
111. Li, N.; Lassiter, B. E.; Lunt, R. R.; Wei, G.; Forrest, S. R. *Appl. Phys. Lett.* **2009**, *94*, 023307.
112. Mutolo, K. L.; Mayo, E. I.; Rand, B. P.; Barry, P.; Forrest, S. R.; Thompson, M. E. *J. Am. Chem. Soc*. **2006**, *128*, 8108.
113. Gommans, H.; Cheyns, D.; Aernouts, T.; Girotto, C.; Poortmans, J.; Heremans, P. *Adv. Funct. Mater.* **2007**, 17, 2653.
114. Verreet, B.; Schols, S.; Cheyns, D.; Rand, B. P.; Gommans, H.; Aernouts, T.; Heremans, P.; Genoe, J. *J. Mater. Chem.* **2009**, *19*, 5295–5297.
115. Jiang, X.; Dai, J.; Wang, H.; Geng, Y.; Yan, D. *Chem. Phys. Lett.* **2007**, *446*, 329.
116. Gommans, H.; Aernouts, T.; Verreet, B.; Heremans, P.; Medina, A.; Claessens, C. G.; Torres, T. *Adv. Funct. Mater*. **2009**, *19*, 3435.
117. Koeppe, R.; Troshin, P. A.; Lyubovskaya, R. N.; Sariciftci, N. S. *Appl. Phys. Lett.* **2005**, *87*, 244102.
118. Troshin, P. A.; Koeppe, R.; Peregudov, A. S.; Peregudova, S. M.; Egginger, M.; Lyubovskaya, R. N.; Sariciftci, N. S. *Chem. Mater.* **2007**, *19*, 5363.

119. Gilot, J.; Wienk, M. M.; Janssen, R. A. J. *Appl. Phys. Lett.* **2007**, *90,* 143512.
120. Xue, J.; Uchida, S.; Rand, B. P.; Forrest, S. R. *Appl. Phys. Lett.* **2004**, *85*, 5757.
121. Kim, J. Y.; Lee, K.; Coates, N. E.; Moses, D.; Nguyen, T. Q.; Dante, M.; Heeger, A. J. *Science* **2007**, *317*, 222.
122. Colsmann, A.; Junge, J.; Kayser, C.; Lemmer U. *Appl. Phys. Lett.* **2006**, *89*, 203506.
123. Dennler, G.; Prall, H.-J.; Koeppe, R.; Egginer, M.; Autengruber, R.; Sariciftci, N. S. *Appl. Phys. Lett.* **2006**, *89*, 073502.
124. Janssen, A. G. F.; Riedl, T.; Hamwi, S.; Johannes, H.-H.; Kowalsky, W. *Appl. Phys. Lett.* **2007**, *91*, 073519.
125. Yu, B.; Zhu, F.; Wang, H.; Li, G.; Yan, D. *J. Appl. Phys.* **2008**, *104*, 114503.
126. Zhang, C.; Tong, S. W.; Jiang, C.; Kang, E. T.; Chan, D. S. H.; Zhu, C. *Appl. Phys. Lett.* **2008**, *92*, 083310.
127. Zhang, C.; Tong, S. W.; Jiang, C.; Kang, E. T.; Chan, D. S. H.; Zhu, C. *Appl. Phys. Lett.* **2008**, *93*, 043307.
128. Yang, F.; Lunt, R. R.; Forrest, S. R. *Appl. Phys. Lett.* **2008**, *92*, 53310.
129. Rand, B. P.; Xue, J.; Yang, F.; Forrest, S. R. *Appl. Phys. Lett.* **2005**, *87*, 233508.
130. Knoshita, Y.; Hasobe, T.; Murata, H. *Appl. Phys. Lett.* **2007**, *91*, 83518.
131. Kumar, H.; Kumar, P.; Bhardwaj, R.; Sharma, G. D.; Chand, S.; Jain, S. C.; Kumar, V. *J. Phys. D* **2009**, *42*, 015103.
132. Chang, M. Y.; Lai, S. L.; Fung, M. K.; Lee, C. S.; Lee, S. T. *Appl. Phys. Lett.* **2007**, *90*, 023504.
133. Koeppe, R.; Bossart, O.; Calzaferri, G.; Sariciftci, N. S. *Sol. Energ. Mater. Sol. Cells* **2007**, *91*, 986.
134. Koeppe, R.; Sariciftci, N. S.; Buchtemann, A. *Appl. Phys. Lett.* **2007**, *90*, 181126.
135. Hua, Y. L.; Petty, M. C.; Roberts, G. G.; Ahmad, M. M.; Hanack, M.; Rein, M. *Thin Solid Films* **1987**, *149*, 163.
136. Ding, H.; Zhang, X.; Ram, M. K.; Nicolini, C. *J. Colloid Interface Sci.* **2005**, *290*, 166.
137. Kippelen, B.; Yoo, S.; Haddock, J. A.; Domercq, B.; Barlow, S.; Minch, B. A.; Xia, W.; Marder, S. R.; Armstrong, N. R. In *Organic Photovoltaic Mechanisms, Materials, and Devices*; Sariciftci, S. R.; Sun, S., Eds.; CRC: Boca Raton, **2005**.
138. Wang, Q.; Li, Y.; Yan, X.; Rathi, M.; Ropp, M.; Galipeau, D.; Jiang, J. *Appl. Phys. Lett.* **2008**, *93*, 073303.
139. Ma, B.; Woo, C. H.; Miyamoto, Y.; Frechet, J. M. J. *Chem. Mater.* **2009**, *21*, 1413–1417.
140. Decher, G. *Science* **1997**, *277*, 1232.
141. Benten, H.; Kudo, N.; Ohkita, H.; Ito, S. *Thin Solid Films* **2009**, *517*, 2016–2022.
142. Peet, J.; Tamayo, A. B.; Dang, X.-D.; Seo, J. H.; Nguyen, T.-Q. *Appl. Phys. Lett.* **2008**, *93*, 163306.
143. Kaulach, I.; Muzikante, I.; Gerca, L.; Plotniece, M.; Roze, M.; Kalnachs, J.; Shlihta, G.; Shipkovs, P.; Kampars, V.; Tokmakov, A. *Eur. Phys. J. Appl. Phys.* **2007**, *40*, 169–173.
144. Dastoor, P. C.; McNeill, C. R.; Frohne, H.; Foster, C. J.; Dean, B.; Fell, C. J.; Belcher, W. J.; Campbell, W. M.; Officer, D. L.; Blake, I. M.; Thordarson, P.; Crossley, M. J.; Hush, N. S.; Reimers, J. R. *J. Phys. Chem. C* **2007**, *111*, 15415–15426.
145. Honda, S.; Nogami, T.; Ohkita, H.; Benten, H.; Ito, S. *Appl. Mater. Interfaces* **2009**, *1*, 804–810.
146. Martínez-Díaz, M. V.; Esperanza, S.; de la Escosura, A.; Catellani, M.; Yunus, S.; Luzzati, S.; Torres, T. *Tetrahedron Lett.* **2003**, *44*, 8475.
147. de la Escosura, A.; Martinez-Diaz, M. V.; Torres, T.; Grubbs, R. H.; Guldi, D. M.; Neugebauer, H.; Winder, C.; Drees, M.; Sariciftci, N. S. *Chem. Asian J.* **2006**, *1*, 148–154.

148. Ballesteros, B.; de la Torre, G.; Ehli, C.; Rahman, G. M. A.; Agullo-Rueda, F.; Guldi, D. M.; Torres, T. *J. Am. Chem. Soc.* **2007**, *129*, 5061–5068.
149. Ballesteros, B.; Campidelli, S.; de la Torre, G.; Ehli, C.; Guldi, D. M.; Prato, M.; Torres, T. *Chem. Commun.* **2007**, 2950–2952.
150. Campidelli, S.; Ballesteros, B.; Filoramo, A.; Diaz Diaz, D.; de la Torre, G.; Torres, T.; Rahman, G. M. A.; Ehli, C.; Kiessling, D.; Werner, F.; Sgobba, V.; Guldi, D. M.; Cioffi, C.; Prato, M.; Bourgoin, J.-P. *J. Am. Chem. Soc.* **2008**, *130*, 11503–11509.
151. Loi, M. A.; Denk, P.; Hoppe, H.; Neugebauer, H.; Winder, C.; Meissner, D.; Brabec, C.; Sariciftci, N. S.; Gouloumis, A.; Vazquez, P.; Torres, T. *J. Mater. Chem.* **2003**, *13*, 700–704.
152. Neugebauer, H.; Loi, M. A.; Winder, C.; Sariciftci, N. S.; Cerullo, G.; Gouloumis, A.; Vazquez, P.; Torres, T. *Sol. Energ. Mater. Sol. Cells* **2004**, *83*, 201–209.
153. Vivo, P.; Ojala, M.; Chukharev, V.; Efimov, A.; Lemmmetyinen, H. *J. Photochem. Photobiol. A* **2009**, *203*, 125–130.
154. Cammidge, A. N.; Berber, G.; Chambrier, I.; Hough, P. W.; Cook, M. J. *Tetrahedron* **2005**, *61*, 4067–4074.
155. Rodríguez-Morgade, M. S.; Torres, T.; Atienza-Castellanos, C.; Guldi, D. M. *J. Am. Chem. Soc.* **2006**, *128*, 15145.
156. Xu, H.; Ng, D. K. P. *Inorg. Chem.* **2008**, *47*, 7921–7927.
157. Rodríguez-Morgade, M. S.; Plonska-Brzezinska, M. E.; Athans, A. J.; Carbonell, E.; de Miguel, G.; Guldi, D. M.; Echegoyen, L.; Torres, T. *J. Am. Chem. Soc*. **2009**, *131*, 10484–10496.
158. Fischer, M. K. R.; López-Duarte, I.; Wienk, M. M.; Martínez-Díaz, M. V.; Janssen, R. A. J.; Bauerle, P.; Torres, T. *J. Am. Chem. Soc.* **2009**, *131*, 8669–8676.
159. Silvestri, F.; López-Duarte, I.; Seitz, W.; Beverina, L.; Martínez-Díaz, M. V.; Marks, T. J.; Guldi, D. M.; Pagani, G. A.; Torres, T. *Chem. Commun.* **2009**, 4500–4502.
160. Grätzel, M. *Inorg. Chem.* **2005**, *44*, 6841–6850.
161. Grätzel, M. *J. Photochem. Photobiol. C* **2003**, *4*, 145–153.
162. Grätzel, M. *J. Photochem. Photobiol. A* **2004**, *164*, 3–14.
163. Hagfeldt A.; Grätzel, M. *Acc. Chem. Res.* **2000**, *33*, 269–277.
164. Ooyama, Y.; Harima, Y. *Eur. J. Org. Chem.* **2009**, 2903–2934.
165. Robertson, N. *Angew. Chem. Int. Ed.* **2006**, *45*, 2338–2345.
166. Durrant, J. R.; Haque, S. A.; Palomares, E. *Chem. Commun.* **2006**, 3279–3289.
167. Rio, Y.; Vázquez, P.; Palomares, E. *J. Porphyrins Phthalocyanines* **2009**, *13*, 645–651.
168. Mishra, A.; Fischer, M. K. R.; Bäuerle, P. *Angew. Chem. Int. Ed.* **2009**, *48*, 2474–2499.
169. Imahori, H.; Umeyama, T.; Ito, S. *Acc. Chem. Res.* **2009**, *42*, 1809.
170. Nazeeruddin, M. K.; Humphry-Baker, R.; Grätzel, M.; Wöhrle, D.; Schnurpfeil, G.; Schneider, G.; Hirth, A.; Trombach, N. *J. Porphyrins Phthalocyanines* **1999**, *3*, 230.
171. Murrer, B. A.; Grätzel, M.; Nazeeruddin, M. K. PCT Int. Appl. **1999**, WO 9903868 A1.
172. Aranyos, V.; Hjelm, J.; Hagfeldt, A.; Grennberg, H. *J. Porphyrins Phthalocyanines* **2001**, *5*, 609.
173. He, J.; Hagfeldt, A.; Lindquist, S.-E.; Grennberg, H.; Korodi, F.; Sun, L.; Åkermark, B. *Langmuir* **2001**, *17*, 2743.
174. Huisman, C. L.; Goossens, A.; Schoonman, J. *J. Phys. Chem. B* **2002**, *106*, 10578.
175. He, J.; Benkö, G.; Korodi, F.; Polivka, T.; Lomoth, R.; Åkermark, B.; Sun, L.; Hagfeldt, A.; Sundstrom, V. *J. Am. Chem. Soc.* **2002**, *124*, 4922.
176. Nazeeruddin, M. K.; Humphry-Baker, R.; Grätzel, M.; Murrer, B. A. *Chem. Commun.* **1998**, 719.

177. Yanagisawa, M.; Korodi, F.; He, J.; Sun, L.; Sundstrom, V; Åkermark, B. *J. Porphyrins Phthalocyanines* **2002**, *6*, 217.
178. Yanagisawa, M.; Korodi, F.; Bergquist, J.; Holmberg, A.; Hagfeldt, A.; Åkermark, B.; Sun, L. *J Porphyrins Phthalocyanines* **2004**, *8*, 1228.
179. Palomares, E.; Martínez-Díaz, M. V.; Haque, S. A.; Torres, T.; Durrant, J. R. *Chem. Commun*. **2004**, 2112.
180. Rawling, T.; McDonald, A. *Coord. Chem. Rev.* **2007**, *251*, 1128–1157.
181. Morandeira, A.; López-Duarte, I.; Martínez-Díaz, M. V.; O'Regan, B.; Shuttle, C.; Haji-Zainulabidin, N. A.; Torres, T.; Palomares, E.; Durrant, J. R. *J. Am. Chem. Soc.* **2007**, *129*, 9250.
182. Macor, L.; Fungo, F.; Tempesti, T.; Durantini, E. N.; Otero, L.; Barea, E. M.; Fabregat-Santiago, F.; Bisquert, J. *Energ. Environ. Sci.* **2009**, *2*, 529.
183. Martínez-Díaz, M.V.; Díaz, D. D. *J. Porphyrins Phthalocyanines* **2009**, *13*, 397–407.
184. Reddy, Y.; Giribabu, L.; Lyness, C.; Snaith, H.; Vijaykumar, C.; Chandrasekharam, M.; Lakshmikantam, M.; Yum, J. H.; Kalyanasundaram, K.; Grätzel, M.; Nazeeruddin, M. K. *Angew. Chem. Int. Ed.* **2007**, *46*, 373.
185. Cid, J.-J.; Yum, J.-H.; Jang, S.-R.; Nazeeruddin, M. K.; Martínez-Ferrero, E.; Palomares, E.; Ko, J.; Grätzel, M.; Torres, T. *Angew. Chem. Int. Ed.* **2007**, *46*, 8358.
186. Giribabu, L.; Vijay Kumar, C.; Reddy, V. G.; Reddy, P. Y.; Rao, C. S.; Jang, S.-R.; Yum, J. H.; Nazeeruddin, M. K.; Grätzel, M. *Sol. Energ. Mater. Sol. Cells* **2007**, *91*, 1611–1617.
187. Eu, S.; Katoh, T.; Umeyama, T.; Matano, Y.; Imahori, H. *Dalton Trans.* **2008**, 5476–5483.
188. Cid, J. J.; García-Iglesias, M.; Yum, J.-H.; Forneli, A.; Albero, J.; Martínez-Ferrero, E.; Vázquez, P.; Gratzel, M.; Vázquez, P.; Nazeeruddin, M. K.; Palomares, E.; Torres, T. *Chem. Eur. J.* **2009**, *15*, 5130–5137.
189. Silvestri, F.; García-Iglesias, M.; Yum, J.-H.; Vázquez, P.; Martínez-Díaz, M. V.; Gratzel, M.; Nazeeruddin, M. K.; Torres, T. *J. Porphyrins Phthalocyanines* **2009**, *13*, 369–375.
190. Wang, Q.; Campbell, W. M.; Bonfantani, E. E.; Jolley, K. W.; Officer, D. L.; Walsh, P. J.; Gordon, K.; Humphry-Baker, R.; Nazeeruddin, M. K.; Gratzel, M. *J. Phys. Chem. B* **2005**, *109*, 15397–15409.
191. Prezhdo, O. V.; Duncan, W. R.; Prezhdo, V. V. *Acc. Chem. Res.* **2008**, *41*, 339–348.
192. O'Regan, B. C.; López-Duarte, I.; Martínez-Díaz, M. V.; Forneli, A.; Albero, J.; Morandeira, A.; Palomares, E.; Torres, T.; Durrant, J. R. *J. Am. Chem. Soc.* **2008**, *130*, 2906–2907.
193. Yum, J.-H.; Jang, S.-R.; Humphry-Baker, R.; Gratzel, M.; Cid, J.-J.; Torres, T.; Nazeeruddin, M. K. *Langmuir* **2008**, *24*, 5636–5640.
194. Morandeira, A.; López-Duarte, I.; O'Regan, B.; Martínez-Díaz, M. V.; Forneli, A.; Palomares, E.; Torres, T.; Durrant, J. R. *J. Mater. Chem.* **2009**, *19*, 5016.
195. Deng, H. H.; Lu, Z. H.; Shen, Y. C.; Mao, H. F.; Xu, H. J. *Chem. Phys*. **1998**, *231*, 95.
196. Zhao, W.; Hou, Y. J.; Wang, X. S.; Zhang, B. W.; Cao, Y.; Yang, R.; Wang W. B.; Xiao, X. R. *Sol. Energ. Mater. Sol. Cells* **1999**, *58*, 173.
197. Ehret, A.; Stuhi, L.; Spitler, M. T. *J. Phys. Chem. B* **2001**, *105*, 9960.
198. Sayama, K.; Tsukagoshi, S.; Mori, T.; Hara, K.; Ohga Shinpou, Y. A.; Abe, Y.; Suga, S.; Arakawa, H. *Sol. Energ. Mater. Sol. Cells* **2003**, *80*, 47.
199. Otaka, H.; Kira, M.; Yano, K.; Ito, S.; Mitekura, H.; Kawata, T.; Matsui, F. *J. Photochem. Photobiol. A: Chem.* **2004**, *164*, 67.
200. Perera, V. P. S.; Pitigala, P. K. D. D. P.; Senevirathne, M. K. I.; Tennakone, K. *Sol. Energ. Mater. Sol. Cells* **2005**, *85*, 91.

201. Siegers, C.; Würfel, U.; Zistler, M.; Gores, H.; Hohl-Ebinger, J.; Hinsch, A.; Rainer Haag, R. *Chem. Phys. Chem.* **2008**, *9*, 793–798.
202. Clifford, J. N.; Palomares, E.; Nazeeruddin, M. K.; Thampi, R.; Gratzel, M.; Durrant, J. R. *J. Am. Chem. Soc.* **2004**, *126*, 5670–5671.
203. Robertson, N. *Angew. Chem. Int. Ed. Engl.* **2008**, *47*, 1012–1014.
204. Siegers, C.; Hohl-Ebinger, J.; Zimmermann, B.; Würfel, U.; Mülhaupt, R.; Hinsch, A.; Haag, R. *Chem. Phys. Chem.* **2007**, *8*, 1548–1556.
205. Rawling, T.; Austin, C.; Buchholz, F.; Colbran, S. B.; McDonagh, A. M. *Inorg. Chem.* **2009**, *48*, 3215–3227.
206. Hardin, B. W.; Hoke, E. T.; Armstrong, P. B.; Yum, J.-H.; Comte, P.; Torres, T.; Frechet, J. M.; Nazeeruddin, M. K.; Grätzel, M.; McGehee, M. D. *Nat. Photon.* **2009**, *3*, 406–411.
207. Lee, H.; Leventis, H. C.; Moon, S.-J.; Chen, P.; Ito, S.; Haque, S. A.; Torres, T.; Nüesch, F.; Geiger, T.; Zakeeruddin, S. M.; Grätzel, M.; Nazeeruddin, M. K. *Adv. Funct. Mater.* **2009**, *19*, 2735–2742.

This page intentionally left blank

46 Artificial Photosynthetic Systems Composed of Porphyrins and Phthalocyanines

Shunichi Fukuzumi

Department of Materials and Life Sciences,
Graduate School of Engineering, SORST, JST,
Osaka University, Suita, Osaka 565-0871, Japan

Department of Bioinspired Science, Ewha Womans University,
Seoul 120-750, South Korea

I. Introduction

The food we eat and the fossil fuels we use are products of photosynthesis, which is the process that converts solar energy to chemical energy. The overwhelming part of our energy supply comes from the chemical energy which has been stored in the fossil fuels over several billions of years. The world's energy consumption rate of fossil fuels is expected to increase further in the next few decades, due to increase in demand from the developing countries. The rapid consumption of fossil fuels has caused unacceptable environmental problems such as greenhouse effects, which

are predicted to have disastrous climatic consequences.[1–3] Thus, renewable and clean energy resources are definitely required in order to maintain the quality of human life as well as the environment of the earth.[1–3] One of the most attractive strategies to stop global warming is the development of artificial systems that mimic natural photosynthesis in the conversion and storage of solar energy.[4–8]

Energy from sunlight is first captured by photosynthetic π-pigments such as chlorophylls and carotenoids, which cover a wide spectral range of solar irradiation.[9–11] The captured light energy is transferred to chlorophylls that are in a special protein environment where the actual energy conversion event starts via electron transfer processes.[9–11] Pigments and proteins involved in this actual primary electron transfer event together are called the reaction center.[9–11] A large number of π-pigment molecules (100–5000), collectively referred to as antennas, harvest light and transfer the light energy to the same reaction center.[9–11] The purpose of such antenna molecules is to maintain a high rate of electron transfer in the reaction center, even at lower light intensities.[9–11] The importance and the complexity of energy transfer and electron transfer processes in the photosynthetic reaction center have prompted the design and preparation of a variety of donor–acceptor covalently and noncovalently linked ensembles, including dyads, triads, tetrads and pentads, which are able to mimic the energy-transfer and electron transfer processes in the photosynthetic reaction center.[12–24]

This chapter presents an overview of development on artificial photosynthetic reaction center models using porphyrins, phthalocyanines and related maclocycles by focusing on a deeper understanding of the function of the photosynthetic reaction center and also applications of the functional models to develop low cost and efficient organic solar cells. First, a rational design of the photosynthetic reaction center models is described, based on the Marcus theory of electron transfer.[25,26] Then, the difference in the photoinduced electron transfer properties depending on the type of porphyrins (planar vs. nonpolar porphyrins and monomeric vs. dimeric porphyrins) is clarified in light of Marcus' theory. A variety of photosynthetic reaction center models composed of porphyrins or phthalocyanines linked with electron donors and acceptors by covalent and noncovalent bonding have been developed, including multicomponent systems, which undergo efficient charge separation, electron or hole migration and slow charge recombination. Finally, supramolecular porphyrin assemblies with electron donors and acceptors have been applied to develop porphyrin solar cells.

II. Rational Design of Photosynthetic Reaction Center Models

Rational design of the photosynthetic reaction center has been made possible based on the Marcus theory of electron transfer.[25,26] According to the theory, the

rate constant of nonadiabatic intramolecular electron transfer (k_{ET}) in an electron donor–acceptor-linked molecule at the fixed distance between the donor and acceptor moieties is given by Eq. (1)

$$k_{ET} = \left(\frac{4\pi^3}{h^2 \lambda k_B T}\right)^{\frac{1}{2}} V^2 \exp\left[-\frac{(\Delta G_{ET} + \lambda)^2}{4\lambda k_B T}\right], \quad (1)$$

where V is the electronic coupling matrix element, h is Planck's constant, T is the absolute temperature, ΔG_{ET} is the free energy change of electron transfer, and λ is the reorganization energy of electron transfer, which is the energy required to structurally reorganize the electron donor and acceptor and their solvation spheres upon electron transfer. According to Eq. 1, the logarithm of the rate constant (log k_{ET}) of electron transfer in an electron donor–acceptor dyad (D–A) in Figure 1a is given as a parabolic function of the driving force of electron transfer ($-\Delta G_{ET}$), as shown in Figure 1b. The parabolic dependence of log k_{ET} on $-\Delta G_{ET}$ is determined by two factors: one is the electronic coupling matrix element V, which determines the maximum k_{ET} value, and the other is the reorganization energy (λ). When the magnitude of the driving force of electron transfer becomes the same as the reorganization energy ($-\Delta G_{ET} \sim \lambda$), the k_{ET} value reaches a maximum, which is determined by the magnitude of electronic coupling (V) between the donor and

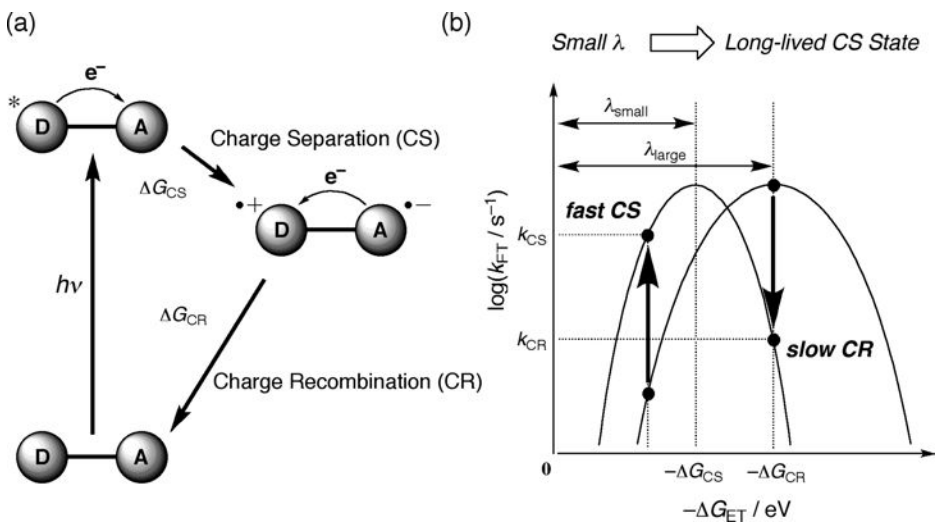

Figure 1. (a) Energy diagram of photoinduced electron transfer of an electron donor–acceptor dyad with photoexcitation of the donor moiety. (b) Driving force dependence of log k_{ET} of the CS and CR processes with different λ values.

acceptor moiety (Figure 1b). In the highly exothermic region of the parabola ($-\Delta G_{ET} > \lambda$), an increase in the driving force results in a decrease in the electron transfer rate. This highly exergonic range is generally referred to as the Marcus inverted region.[25–31] The smaller the reorganization energy, the faster the forward photoinduced charge separation (CS) process of an electron donor–acceptor dyad (D–A), but the charge recombination (CR) process becomes slower when the CR driving force ($-\Delta G_{CR}$) is larger than the reorganization energy (λ) of electron transfer, as shown in Figure 1b.

III. Planar vs. Nonplanar Porphyrins

Porphyrins normally have a planar π-core, which enables efficient electron transfer, because the uptake or release of electrons from porphyrins usually results in minimal structural change upon electron transfer.[31] Introduction of bulky substituents on a porphyrin macrocycle affords nonplanar conformations of porphyrins. For example, synthetic dodecaphenylporphyrin (H_2DPP), which contains a phenyl group at each β-pyrrole and *meso* position of the porphyrin macrocycle, adopts a saddle-shaped nonplanar conformation.[32–35] The doubly protonated porphyrin dication (H_4DPP^{2+}) is readily obtained due to the distortion and H_4DPP^{2+} can act as an electron acceptor.[36] How conformational distortions of the porphyrin ring affect the rates of intermolecular electron transfer reduction of diprotonated porphyrins in solution has been examined using a series of nonplanar porphyrins, hydrochloride salts of saddle-distorted dodecaphenylporphyrin ($[H_4DPP]Cl_2$), tetrakis(2,4,6-trimethylphenyl)porphyrin ($[H_4TMP]Cl_2$), tetraphenylporphyrin ($[H_4TPP]Cl_2$), and octaphenylporphyrin ($[H_4OPP]Cl_2$), in comparison with that of a planar porphyrin, (acetonitrile-κN)-(tetrakis(pentafluorophenyl)porphyrinato) zinc(II) ([Zn(F_{20}TPP)(MeCN)]), as electron acceptors.[35] The optimized structures of $[H_4DPP]Cl_2$, $[H_4OPP]Cl_2$, $[H_4TPP]Cl_2$, and $[H_4TMP]Cl_2$ exist in saddle-distorted structures — whereas [Zn(F_{20}TPP)(MeCN)] is planar, as shown in Figure 2[36] — together with the optimized structures of the one-electron-reduced species.[35]

The rate constants for photoinduced electron transfer from a series of analogous electron donors (ferrocene derivatives) to the triplet excited states of noplanar diprotonated porphyrins and planar [Zn(F_{20}TPP)(MeCN)] were determined by laser flash photolysis measurements.[35] The driving force dependence of the logarithm of the rate constants of the photoinduced electron transfer ($\log k_{et}$) is shown in Figure 3.[35] Intermolecular photoinduced electron transfer from an electron donor (D) to $^3\{[H_4DPP]Cl_2\}^*$ occurs as shown in Scheme 1, where k_{12} and k_{21} are the diffusion rate constant and the dissociation rate constant in the encounter

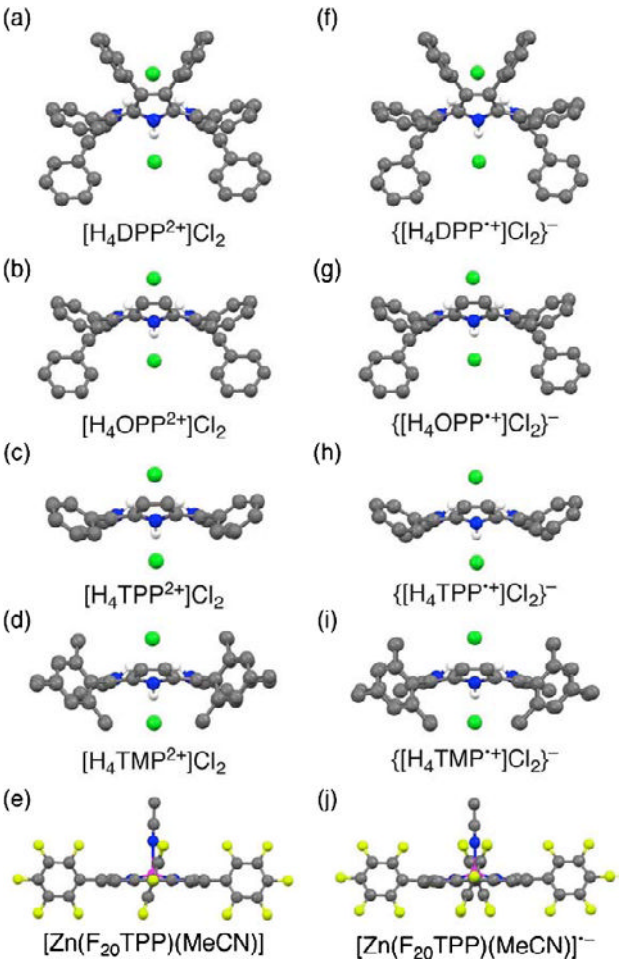

Figure 2. Optimized structures of (a) $[H_4DPP^{2+}]Cl_2$, (b) $[H_4OPP^{2+}]Cl_2$, (c) $[H_4TPP^{2+}]Cl_2$, (d) $[H_4TMP^{2+}]Cl_2$, (e) $[Zn(F_{20}TPP)(MeCN)]$, (f) $\{[H_4DPP^{\bullet+}]Cl_2\}^-$, (g) $\{[H_4OPP^{\bullet+}]Cl_2\}^-$, (h) $\{[H_4TPP^{\bullet+}]Cl_2\}^-$, (i) $\{[H_4TMP^{\bullet+}]Cl_2\}^-$, and (j) $[Zn(F_{20}TPP)(MeCN)]^{\bullet-}$ obtained by DFT calculations at the B3LYP/3-21G level of theory (adapted from Ref. 35). Hydrogen atoms of phenyl groups are omitted for clarity.

complex, respectively, and k_{ET} is the first-order rate constant of electron transfer in the encounter complex.[37]

The observed second-order rate constant of electron transfer (k_{et}) is given by Eq. 2. The dependence of k_{ET} on the driving force of electron transfer ($-\Delta G_{et}$) for

$$k_{et} = \frac{k_{ET}k_{12}}{k_{21} + k_{ET}} \tag{2}$$

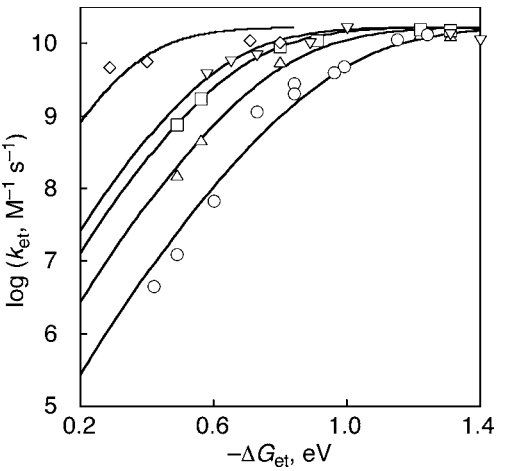

Figure 3. Driving force dependence of log k_{et} for electron transfer from electron donors to $^3\{[H_4DPP]Cl_2\}^*$ (○) and $^3[Zn(F_{20}TPP)(MeCN)]^*$ (◇) in MeCN at 298 K and $^3\{[H_4OPP]Cl_2\}^*$ (Δ), $^3\{[H_4TPP]Cl_2\}^*$ (□) and $^3\{[H_4TMP]Cl_2\}^*$ (▽) in MeCN containing *ca.* 30 equivalents of HCl at 298 K, and the fit of the curve based on the Marcus theory of electron transfer (Eq. 3) is shown by the solid line with λ = 1.69, 1.45, 1.29, 1.21, and 0.84 eV. (Adapted from Ref. 35.)

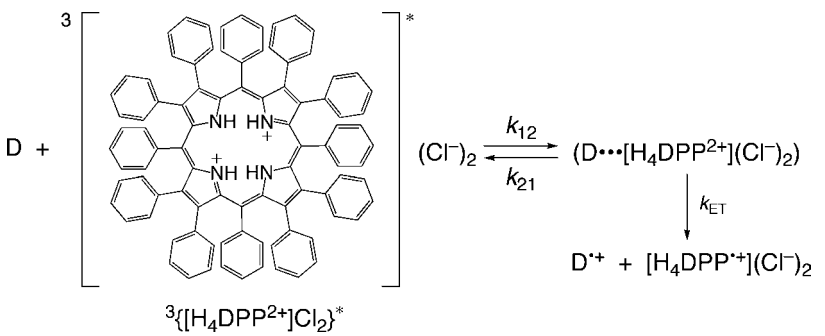

Scheme 1.

adiabatic outer-sphere electron transfer is given by Eq. 3,

$$k_{et} = \frac{k_{12} Z \exp\left[-\left(\frac{\lambda}{4}\right)\left(1+\frac{\Delta G_{et}}{\lambda}\right)^2 \Big/ k_B T\right]}{k_{12} + Z \exp\left[-\left(\frac{\lambda}{4}\right)\left(1+\frac{\Delta G_{et}}{\lambda}\right)^2 \Big/ k_B T\right]}, \quad (3)$$

where Z [= $(k_BT/h)(k_{12}/k_{21})$] is the collision frequency, which is taken as 1×10^{11} M^{-1} s^{-1}.[37,38] The k_{12} values is the diffusion rate constant in MeCN, which is

taken to be 2.0×10^{10} M^{-1} s^{-1}.[37] The driving force dependence of the log k_{et} values of photoinduced electron transfer from electron donors to $^3\{[H_4DPP]Cl_2\}^*$, $^3\{[H_4OPP]Cl_2\}^*$, $^3\{[H_4TPP]Cl_2\}^*$, and $[Zn(F_{20}TPP)(MeCN)]$ is well fitted by solid lines with the λ values of 1.69, 1.45, 1.29, and 0.84 eV, respectively.[35] Thus, the λ value becomes smaller as the porphyrin macrocycle becomes more planar.

A more quantitative analysis has been made by adopting root-mean-square out-of-plane displacement (ΔRMS), which is defined in Eq. 4,[39]

$$\Delta\mathrm{RMS} = \sqrt{\frac{1}{24}\sum_{i=1}^{24}\delta_i^2}, \tag{4}$$

where δ_i is the orthogonal displacement of atom *i* in the macrocycle from the mean plane. There is a good linear correlation between the λ and ΔRMS values, as shown in Figure 4.[35] The linear correlation between reorganization energy and distortion of the porphyrin ring (ΔRMS) indicates that the distortion governs the intramolecular term of the reorganization energy (λ_i) and the larger distortion gives rise to the larger λ_i, because the solvent term of reorganization energy may be the same. The differences in ΔRMS values of porphyrin dications before and after electron transfer are approximately the same, whereas the difference in the distance of hydrogen bonding among the pyrrole N–H protons and the chloride anions (N–H···Cl^-) becomes larger, with increase in ΔRMS values.[35] This suggests that the elongation of the hydrogen bond is the main factor in the increase of λ_i.

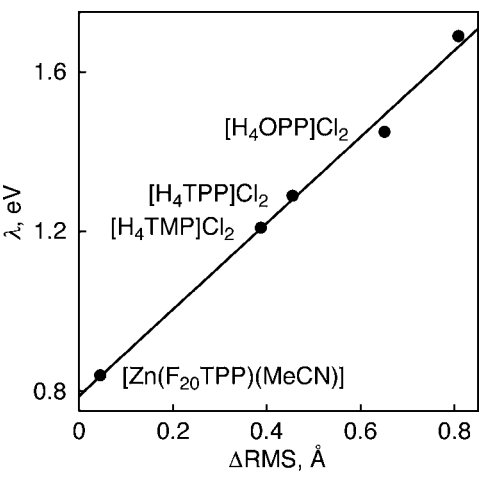

Figure 4. A relationship between λ values in photoinduced electron transfer reduction of diprotonated porphyrin dications in MeCN and root-mean-square out-of-plane displacements (ΔRMS). (Adapted from Ref. 35.)

This observation is similar to that in the oxidation of metalloporphyrins, which exhibit large reorganization energies due to the large changes in coordination bond lengths around metal centers before and after electron transfer.[40] The clarification of electron transfer properties of nonplanar vs. planar porphyrins provides invaluable information for utilizing their novel functions based on the saddle distortion of the porphyrin core, as will be discussed later.

IV. Monomer vs. Dimer Porphyrins

As described in the Introduction, a bacteriochlorophyll dimer, the so-called special pair, plays a pivotal role in initiating efficient multistep electron transfer reactions among photosynthetic pigments to attain the long-lived charge-separated state with a nearly 100% quantum yield.[9–11] High-resolution X-ray crystallographic studies have revealed that the mean plane distance of the bacteriochlorophylls in the special pair is around 3.5 Å.[41–43] Thus, it seems evident that a strong π–π interaction exists between the two macrocycles of the special pair, in particular when the special pair is oxidized to the radical cation. π-electron delocalization between discrete π-systems is well recognized in aromatic dimer radical cations which exhibit new charge resonance absorption bands in the electronic spectra and doubling of hyperfine splitting in the ESR spectra.[44–46] Porphyrins, which have similar macrocyclic frameworks to chlorophylls, are also known to form π-complexes with the radical cation to afford the dimer radical cations, the so-called "mixed valence" radical cations.[47,48] Extensive efforts have so far been devoted to mimicking the dimer structure and the redox properties of the special pair so as to understand the important role of the special pair in the photosynthetic reaction center.[49–55] In particular, the effects of π–π interaction in porphyrin dimer radical cations on the electron transfer dynamics of porphyrin dimers have been clarified in relation to the important role of the special pair in the photoinduced electron transfer dynamics in the photosynthetic reaction center, as described below.[55]

The intramolecular π–π interaction and the dynamics of photoinduced electron transfer reactions of porphyrin dimers were examined using cofacial porphyrin dimers linked with different spacers in comparison with a reference monomer porphyrin in Figure 5.[55] The mean plane distances between porphyrin rings of (DPB)Zn_2 and (DPO)Zn_2 are 3.8 Å and *ca.* 7.8 Å, respectively.[56,57] (DPOx)Zn_2 has a slipped conformation, because the porphyrin rings are linked by a flexible spacer, diphenyl oxide.[58]

The intramolecular π–π interaction in the one-electron oxidized species of (DPB)Zn_2, (DPOx)Zn, and (DPO)Zn_2 is recognized in Figures 6a–d, which show the cyclic voltammograms of ($Et_4Me_4Ph_1P$)Zn, (DPB)Zn_2, (DPOx)Zn_2, and

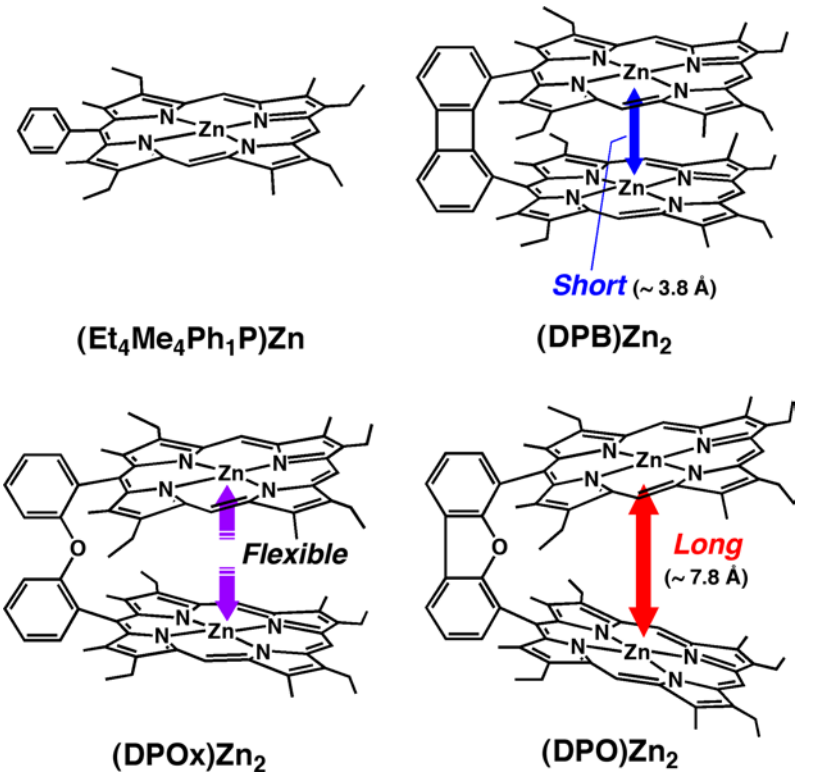

Figure 5. Chemical structures of zinc porphyrin monomer and dimers.

$(DPO)Zn_2$, respectively.[55] The oxidation process of $(DPB)Zn_2$ is split into four discrete one-electron steps. The first oxidation potential of $(DPB)Zn_2$ (0.58 V vs. SCE) is lower by 0.14 V than that of the reference porphyrin, $(Et_4Me_4Ph_1P)Zn$. This indicates that $(DPB)Zn_2^{\bullet+}$ is more stabilized than $(Et_4Me_4Ph_1P)Zn^{\bullet+}$ due to the π–π interaction between porphyrin rings. The second, third, and fourth oxidation potentials of $(DPB)Zn_2$ are higher than those of $(Et_4Me_4Ph_1P)Zn$, because the electrostatic repulsion becomes dominant rather than the attractive interaction. Such electrochemical oxidation of cofacial porphyrin dimers results in the geometrical change from the closed form of $(DPB)Zn_2^{\bullet+}$ to the open form of $(DPB)Zn_2^{2+}$.[51] Similar redox behavior is observed for the porphyrin dimer bearing a flexible spacer [$(DPOx)Zn_2$] (Figure 6c).[55] In the case of $(DPO)Zn_2$, the broadening of the redox wave suggests the existence of the weak interaction between porphyrins (Figure 6d).[55] A similar negative shift of the first oxidation potential of the natural special pair extracted from plants is observed as compared to the monomer counterpart.[59] Thus, the redox behavior of the porphyrin dimers, in particular $(DPB)Zn_2$, resembles that of the natural special pair in the photosynthetic reaction center.

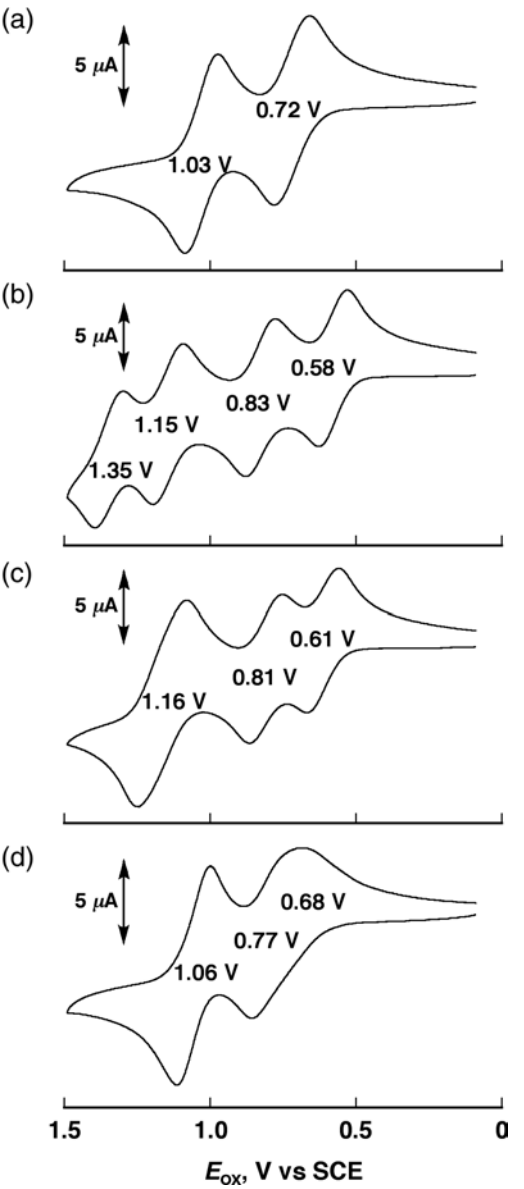

Figure 6. Cyclic voltammograms (0.1 V s^{-1}) of (a) $(Et_4Me_4Ph_1P)Zn$, (b) $(DPB)Zn_2$, (c) $(DPOx)Zn_2$, and (d) $(DPO)Zn_2$ at 1 mM in CH_2Cl_2 containing 0.1 M $TBAPF_6$. (Adapted from Ref. 55.)

New charge resonance absorption bands are observed in the vis-NIR spectral titration of cofacial porphyrin dimers with a one-electron oxidant $[Ru(bpy)_3]^{3+}$ (bpy = 2,2′-bipyridine), as shown in Figure 7.[55] Such charge resonance absorption bands in the NIR region are explained as the absorptions corresponding to the

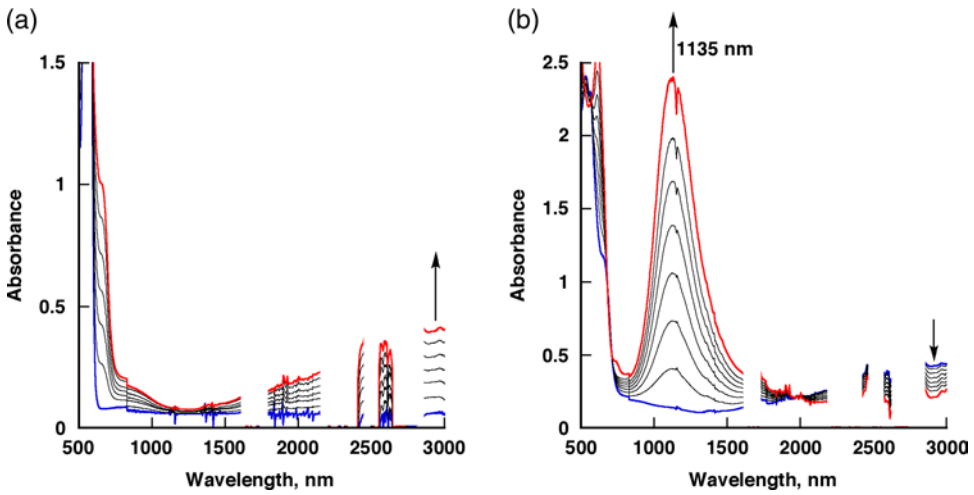

Figure 7. Vis-NIR spectral changes upon addition of $[Ru(bpy)_3]^{3+}$ ((a) 0–2.0×10^{-4} M; (b) 2.0×10^{-4} to 4.0×10^{-4} M) to a CH_2Cl_2 solution of $(DPB)Zn_2$ (2.0×10^{-4} M) at 298 K. The vibrational absorption due to the solvent is cut off. (Adapted from Ref. 55.)

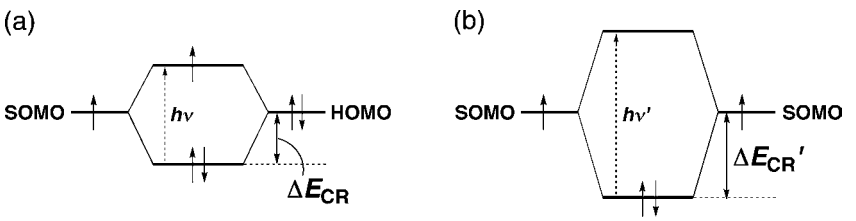

Figure 8. Molecular orbital diagrams for (a) the dimer radical cation and (b) the radical cation dimer.

electronic transition ($h\nu$) from the bonding to the antibonding π-orbital of the π-dimer radical cation (Figure 8a) and that of the π-radical cation dimer (Figure 8b).[55] Charge resonance absorption bands are also observed for the intermolecular formation of the π-dimer porphyrin radical cation and π-radical porphyrin cation.[60,61] The π-dimer radical cation $(DPB)Zn_2^{\bullet+}$ is stabilized by ΔE_{CR} due to π-bond formation between the porphyrin ring and the radical.[55] The π-radical cation dimer $(DPB)Zn_2^{2+}$ also gains bonding interactions between the porphyrin rings, and hence is stabilized by $\Delta E_{CR}'$.[55] The $\Delta E_{CR}'$ value of the dimer radical cation is larger than the ΔE_{CR} value of the radical cation dimer because of the lack of an electron in the antibonding π-orbital.[55] The larger $\Delta E_{CR}'$ value results in the blue shift of the absorption maximum of the radical cation dimer as compared to the dimer radical cation in Figure 7a.[55] The electrostatic repulsion in doubly charged dimeric units destabilizes $(DPB)Zn_2^{2+}$, leading to the higher oxidation potential as compared to

the first oxidation potential of $(Et_4Me_4Ph_1P)Zn$.[55] The ΔE_{CR} value estimated from the absorption maximum ($\lambda_{max} \cong 3000$ nm) is *ca.* 0.20 eV, which is consistent with the negative shift of the first oxidation potential of $(DPB)Zn_2$ (0.14 eV).[55] Similar spectral changes in the NIR region are observed when the other cofacial porphyrin dimers are oxidized by $[Ru(bpy)_3]^{3+}$.[55] The ΔE_{CR} value increases in the order $(DPO)Zn_2$ < $(DPOx)Zn_2$ < $(DPB)Zn_2$ as the mean plane distance between porphyrin rings decreases. In contrast to the case of the dimers, there is little change in the NIR region when $(Et_4Me_4Ph_1P)Zn$ is oxidized by $[Ru(bpy)_3]^{3+}$ under the same conditions.[55]

The photoinduced electron transfer dynamics of cofacial porphyrin dimers were compared with those of the reference porphyrin monomer using nitrobenzene derivatives and a series of benzoquinone compounds as electron acceptors.[55] The rate constants (k_{et}) of electron transfer from the triplet excited states of cofacial porphyrin dimers and the reference porphyrin monomer to electron acceptors were determined by laser flash photolysis measurements.[55] The k_{et} value increases with the degree of the interactions between porphyrin rings as mentioned above, i.e. $(DPO)Zn_2 < (DPOx)Zn_2 < (DPB)Zn_2$.[55] The k_{et} values of the porphyrin dimers are always larger than those of the monomer, $(Et_4Me_4Ph_1P)Zn$. The driving force of electron transfer from $^3(DPB)Zn_2^*$ to each acceptor is larger than that of $^3(Et_4Me_4Ph_1P)Zn^*$ by 0.10 eV, due to the stabilization of $(DPB)Zn_2^{\bullet+}$.[55]

As shown in Figure 9, the driving force dependence of log k_{et} cannot be fitted with one averaged λ value (Eq. 3) and the λ values of both monomer and dimers rise with increase in the driving force of photoinduced electron transfer.[55] Such an increase in the λ value may result from the elongation of the mean distances

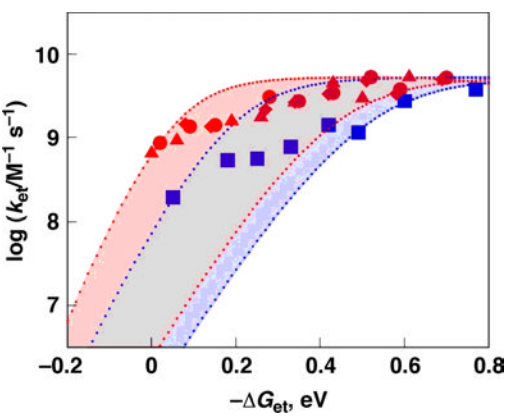

Figure 9. Dependence of log k_{et} on $-\Delta G_{et}$ for electron transfer from $(DPB)Zn_2$ (red circle), $(DPOx)Zn_2$ (red diamond), $(DPO)Zn_2$ (red triangle), and $(Et_4Me_4Ph_1P)Zn$ (blue square) to various acceptors in PhCN at 298 K. The dotted lines are calculated by the Marcus equation, with $\lambda = 0.50$, 1.10 eV (red), and 0.74–1.21 eV (blue), respectively. (Adapted from Ref. 55.)

between the porphyrin (donor) and acceptor molecules with increase in the driving force of photoinduced electron transfer, because the distances (R_{DA}) between donor and acceptor molecules are inversely proportional to the solvent reorganization energy (λ_s) in accordance with Eq. 5,

$$\lambda_s = \frac{e^2}{4\pi\varepsilon_0}\left(\frac{1}{2r_D}+\frac{1}{2r_A}-\frac{1}{R_{DA}}\right)\left(\frac{1}{\varepsilon_{op}}-\frac{1}{\varepsilon_s}\right), \tag{5}$$

where e is electric charge, ε_0 is the electric constant, r_D and r_A are the ionic radii of the donor and the acceptor, and ε_{op} and ε_s are the optical and static dielectric constants of the solvent, respectively.[38,62,63]

Figure 10 shows the driving force dependence of the λ values of the dimer and monomer porphyrins, which were determined from the k_{et} values using Eq. 3.[55] The λ values of all of the porphyrins increase linearly with increase in the driving force of photoinduced electron transfer. Because the λ values of $(DPB)Zn_2$ and $(DPOx)Zn_2$ are consistently smaller than those of $(Et_4Me_4Ph_1P)Zn$ by *ca.* 0.19 eV irrespective of the difference in the driving force of electron transfer (Figure 10), the difference in the total reorganization energy (λ) between the dimer and the monomer is attributed mainly to the smaller λ_s values of the porphyrin dimers as compared to the monomer.[55] The smaller λ value of the porphyrin dimer results in the acceleration of the forward photoinduced electron transfer but the deceleration of the back electron transfer.[55] The acceleration of the photoinduced electron

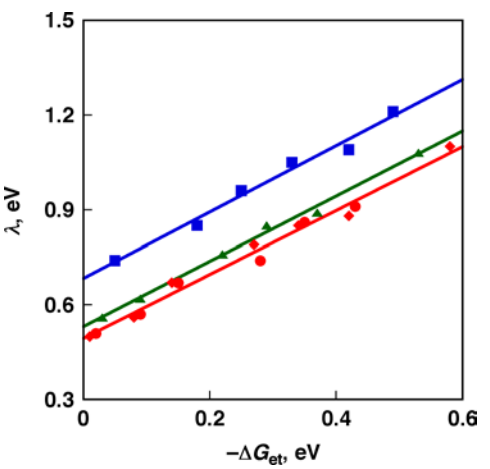

Figure 10. Driving force ($-\Delta G_{et}$) dependence of λ for electron transfer from $(DPB)Zn_2$ (red circle), $(DPOx)Zn_2$ (red diamond), $(DPO)Zn_2$ (green triangle), and $(Et_4Me_4Ph_1P)Zn$ (blue square) to various acceptors in PhCN at 298 K. (Adapted from Ref. 55.)

transfer and the deceleration of the back electron transfer of the porphyrin dimers are the key factors in attaining the high efficiency of the energy conversion in the photosynthetic reaction center, where the special pair (chlorophyll dimer) plays the essential role. The minimum λ value of $(DPOx)Zn_2$ (0.50 eV) is fairly close to the reported value of the electron transfer reaction in the π-complex between a cofacial free-base porphyrin dimer and a sandwiched acridinium ion (0.54 eV).[12c] This is the first example that shows a systematic distance dependence of the λ values depending on the driving force of photoinduced electron transfer and also a clear difference in the λ values between the dimeric and monomeric systems.

V. Charge Separation Using Chlorophyll Analogs

Chlorophyll that participates in photosynthesis is a chlorin pigment, which is a dihydro-compound structurally similar to porphyrins; it is produced through the same biosynthetic pathway as other porphyrin pigments, such as heme. The number of reduced double bonds in the pyrrole rings is zero in the case of porphyrins, one in the case of chlorins and two (diagonal to each other) in the case of bacteriochlorins. The one-electron oxidation potential decreases with increasing peripheral saturation.[64,65] Such a change in the oxidation potential results in a drastic difference in terms of the photodynamics of electron donor–acceptor-linked dyads in which zinc and free-base chlorins and porphyrins in Figure 11 act as electron donors and C_{60} acts as an electron acceptor, as described below.[65,66]

Laser photoexcitation of a deoxygenated PhCN solution containing the zinc chlorine–C_{60} dyad (ZnCh–C_{60}) affords a transient absorption spectrum with maxima

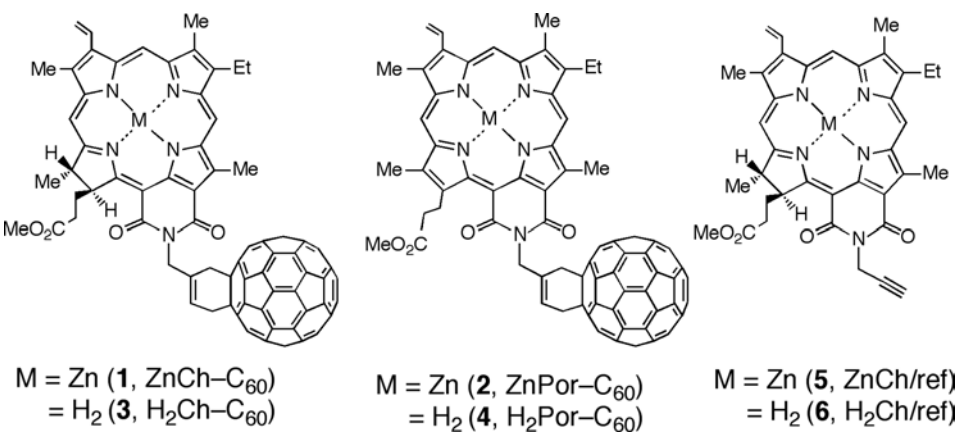

Figure 11. Zinc and free-base chlorin–C_{60}, zinc and free-base porphyrin–C_{60}, and the reference compounds without C_{60}.

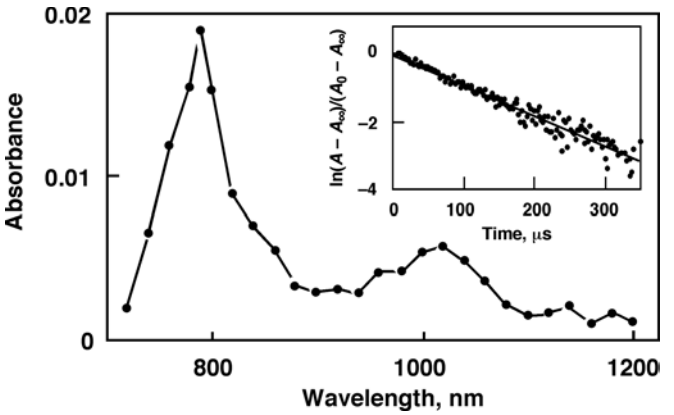

Figure 12. Transient absorption spectra of **1** in deaerated PhCN at 298 K at 0.1 μs after laser excitation at 355 nm. Inset: First-order decay plot of absorbance at 790 nm. (Adapted from Ref. 66.)

at 790 and 1020 nm, as shown in Figure 12.[66] The absorption band at 790 nm is assigned to the radical cation of the ZnCh moiety, and the absorption band at 1020 nm is a diagnostic marker of the monofunctionalized fullerene radical anion.[67]

The reference chlorin compound **5** shows a fluorescence band at 690 nm with a quantum yield (Φ) of 0.10, whereas the fluorescence emission is significantly quenched in **1** (Φ = 0.002 in PhCN) due to electron transfer from the singlet excited state of **1** to C_{60}.[66] The driving force of photoinduced electron transfer from the singlet excited state of **1** to C_{60} in PhCN is determined to be 0.47 eV from the one-electron oxidation potential of **1** and the excitation energy (S_1 = 1.80 eV) of the ZnCh moiety and the one-electron reduction potential of the C_{60} moiety in **1**.[66] The charge-separated (CS) state ($ZnCh^{\bullet+}$–$C_{60}^{\bullet-}$) is lower in energy (1.33 eV) than both the triplet excited state of C_{60} (1.45 eV)[68] and ZnCh (1.36–1.45 eV).[66] Thus, photoinduced electron transfer from the singlet excited state of ZnCh ($^1ZnCh^*$) to the C_{60} moiety of **1** occurs to produce the CS state, in competition with the intersystem crossing to $^3ZnCh^*$ and energy transfer to produce ZnCh–$^1C_{60}^*$ and ZnCh–$^3C_{60}^*$, as shown in Scheme 2a.[66] Electron transfer from $^3ZnCh^*$ to C_{60} also results in the formation of the CS state.[66]

The CS state detected in Figure 12 decays via back electron transfer (BET) to the ground state rather than to the triplet excited state.[66] The BET rate was determined from the disappearance of the absorption band at 790 nm due to the CS state and the decay of the absorption band obeys first-order kinetics (inset of Figure 12).[66] The k_{BET} value is determined to be 9.1×10^3 s^{-1}.[66]

In contrast to the case of ZnCh–C_{60} (**1**), no transient formation of $C_{60}^{\bullet-}$ at 1020 nm was detected for any other dyad in Figure 11 (**2**–**4**).[66] In each case, only the

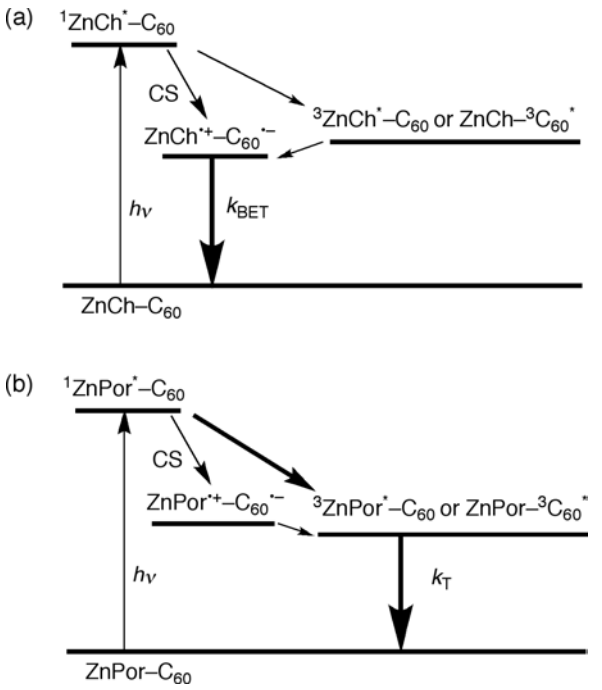

Scheme 2.

triplet–triplet absorption due to chlorin or porphyrin moiety was observed due to the higher energies of the CS state as compared to the triplet excited states (Scheme 2b).[66] This demonstrates the importance of the use of a chlorin chromophore with a zinc ion instead of a fully conjugated porphyrin system to obtain the long-lived CS state.

Photoexcitation of the free-base bacteriochlorin–C_{60} dyad with the same short methylene linkage leads to formation of the radical ion pair, which decays quickly to the triplet excited state of the bacteriochlorin moiety.[69] Figure 13 shows the driving force dependence of the intramolecular electron transfer rate constants (CS and BET) of zinc chlorin–C_{60} and zinc porphyrin–C_{60} dyads with different edge-to-edge distances (R_{ee}), which corresponds to the shortest distance between two molecules. In contrast to the case of **2** in Figure 11, the CS state energy of zinc porphyrin–C_{60} (**9**: 1.38 eV) in Figure 13 is lower than the energy of the triplet excited state of C_{60}.[70] The best fit of Eq. 1 provides and $\lambda = 0.51$ eV and $V = 7.8$ cm^{-1} for zinc chlorin–C_{60} (**8**: $R_{ee} = 5.9$ Å), and $\lambda = 0.66$ eV and $V = 3.9$ cm^{-1} for zinc porphyrin–C_{60} with a longer amide spacer (**9**: $R_{ee} = 11.9$ Å).[69] A directly linked ZnCh–C_{60} dyad which has an extremely short donor–acceptor distance (**7**: $R_{ee} = 2.6$ Å) affords the smallest reorganization energy ($\lambda = 0.42$ eV).[71] The smaller λ value with the shorter R_{ee} value may result from the smaller solvent reorganization energy of electron transfer, according to Eq. 5. On the other hand, the V value in Eq. 1 increases with decrease in the R_{ee}

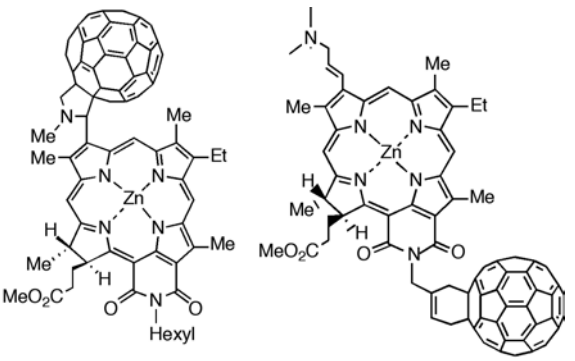

7: R_{ee} = 2.6 Å **8: R_{ee} = 5.9 Å**

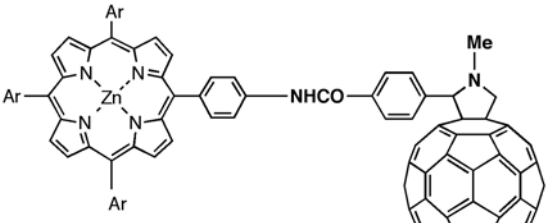

9: R_{ee} = 11.9 Å

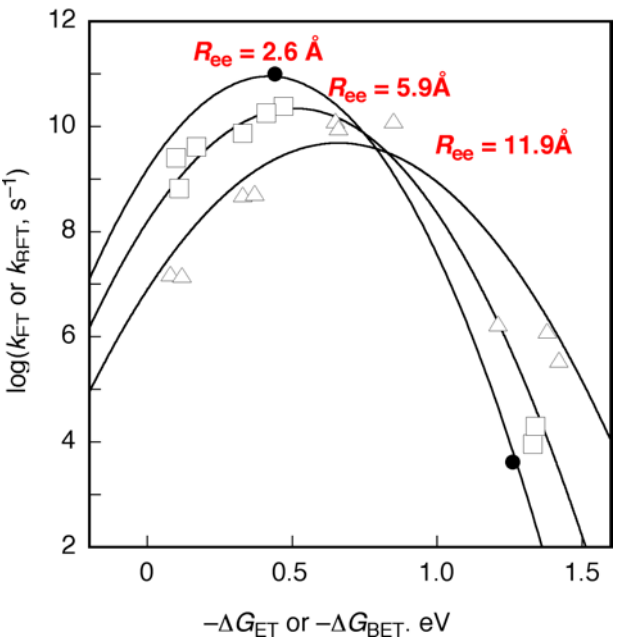

Figure 13. Driving force dependence of log k_{ET} and log k_{BET} for photoinduced electron transfer in zinc chlorine–, zinc porphyrin–fullerene dyads in PhCN linked with different spacers [edge-to-edge distances (R_{ee}) are 2.5, 5.9, and 11.9 Å]. (Adapted from Refs. 69–71.)

value due to the larger orbital overlap between the donor and acceptor moieties. The lifetime of the CS state of the ZnCh–C_{60} dyad (**7**) with the shortest donor–acceptor distance (R_{ee} = 2.6 Å) is determined to be 230 μs at 298 K, which is the longest CS lifetime in the series of dyads shown in Figure 13.[71] The temperature dependence of the decay rate constant (k_{BET}) was examined in PhCN solution observed by laser flash photolysis (25–65 °C) and also in frozen PhCN observed by the ESR signal decay (−150 to −100 °C).[71] The CS lifetime at −150 °C is determined to be as long as 120 s.[71]

A zinc imidazoporphyrin–C_{60} dyad [ZnImP–C_{60} (**10**)] with a short linkage (Figure 14a) also affords a long-lived CS state in PhCN with a lifetime of 330 μs at 278 K.[72] In nonpolar solvents, the CS state of donor–acceptor-linked systems becomes higher in energy than the triplet excited state of the donor or acceptor moiety when charge recombination results in formation of the triplet excited state rather than the ground state.[73] However, a zinc porphyrin–Au(III) porphyrin dyad with a short spacer [ZnPQ–$AuPQ^+$ (**11**) in Figure 14b] affords the long-lived CS state in a nonpolar solvent such as cyclohexane.[73] The introduction of quinoxaline into the porphyrin ring in **11** results in a lowering of the electron transfer state energy, which becomes lower than the energies of the triplet excited states of ZnPQ (1.32 eV) and $AuPQ^+$ (1.64 eV).[74] In this case, photoinduced electron transfer occurs from the singlet excited state of the ZnPQ ($^1ZnPQ^*$) to the metal center of the $AuPQ^+$ moiety to produce $ZnPQ^{\bullet+}$–$Au^{II}PQ$, which has the lifetime of 10 μs in cyclohexane.[74] The observed long lifetime of $ZnPQ^{\bullet+}$–$Au^{II}PQ$ results from a small reorganization energy for the metal-centered electron transfer of $AuPQ^+$ in nonpolar solvents due to the small change in solvation upon the electron transfer as compared with that in polar solvents.[74] The long-lived $ZnPQ^{\bullet+}$–$Au^{II}PQ$ was detected by EPR in toluene at 143 K, as shown in Figure 15. The broad signal with the hyperfine interaction with ^{197}Au (I = 3/2, A_1 = 180 G, A_2 = 14 G) at g_1 = 2.182, g_2 = 2.043, and g_3 = 1.979 clearly indicates that the site of electron transfer is the Au metal rather than the porphyrin ligand.[75–77]

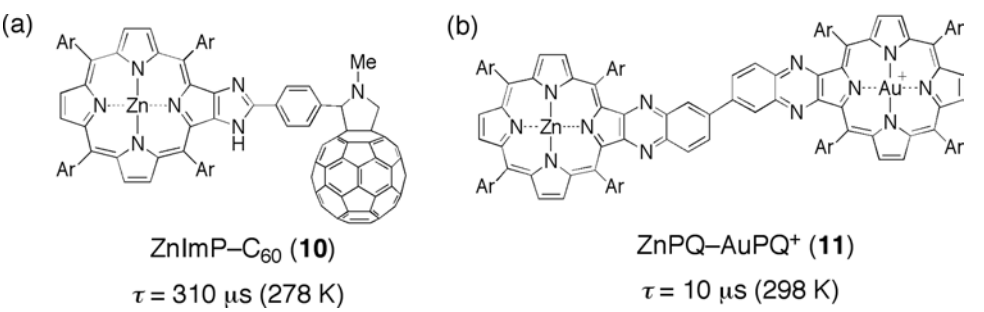

Figure 14. (a) A zinc imidazoporphyrin–C_{60} dyad (**10**: ZnImP–C_{60}); (b) a zinc porphyrin–Au(III) porphyrin dyad (**11**: ZnPQ–$AuPQ^+$). The CS lifetimes are given together.

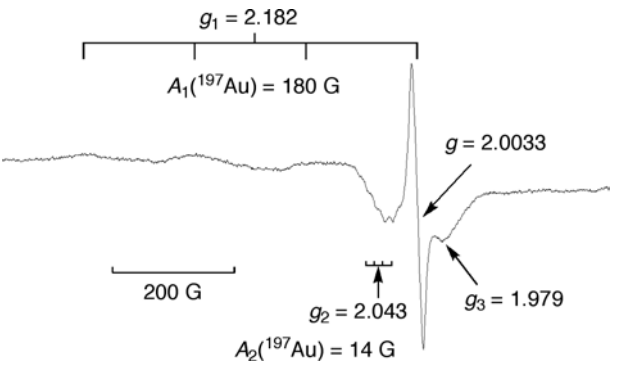

Figure 15. EPR spectrum observed under photoirradiation of a toluene solution of **11** at 143 K. (Adapted from Ref. 74.)

In a polar solvent such as PhCN, no CS state could be seen, but instead only the triplet–triplet absorption due to ^{3}ZnPQ*–AuPQ$^+$ was observed.[78] The absence of an observable CS state of **11** in the polar solvent PhCN may result from the much slower photoinduced electron transfer due to the large reorganization energy as compared with that in nonpolar solvents, allowing an efficient intersystem crossing process in **11** to produce the triplet excited state ^{3}ZnPQ*–AuPQ$^+$.[74,78]

A dodecafluorosubphthalocyanine [SubPc(F)$_{12}$] can also be used as an excellent electron acceptor unit, which is connected to the zinc porphyrin (ZnP) ring with three covalently linked triphenylamine entities at the *meso* position (Figure 16).[79]

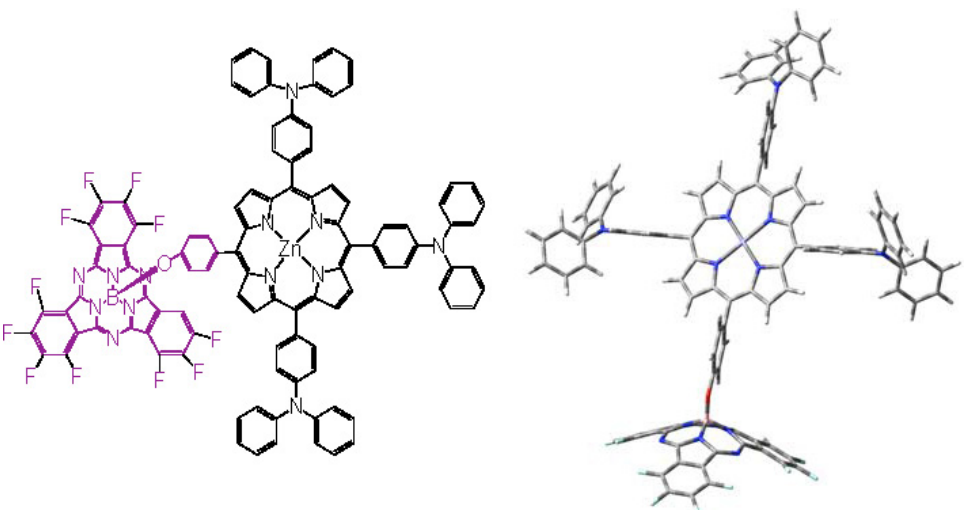

Figure 16. Molecular and optimized structure of ZnP(TPA)$_3$–SubPc(F)$_{12}$ (**12**). (Adapted from Ref. 79.)

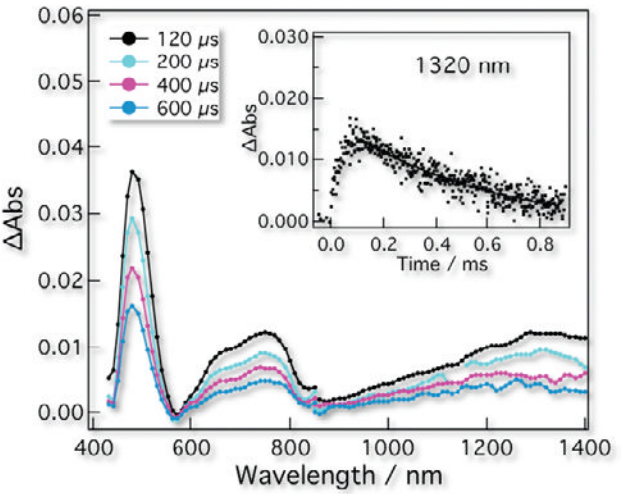

Figure 17. Nanosecond transient spectra obtained by 430 nm laser excitation of **12** in PhCN. (Adapted from Ref. 79.)

The conically shaped subphthalocyanines (SubPc) with their three *N*-fused units arranged around a central boron atom and π-electron aromatic core with their curved structures exhibit different photophysical and photochemical properties compared to their higher homologs, the phthalocyanines.[80–83] SubPcs act as electron acceptors for the photoactive assemblies.[84–86] The energy level of the CS state is below the triplet states of either of the donor and acceptor entities.[79] The CS state $[ZnP(TPA)_3^{\bullet+}–SubPc(F)_{12}^{\bullet-}]$ in PhCN is still alive at long time scales, reaching 2 milliseconds, as shown in Figure 17.[79] The absorption due to the $ZnP(TPA)_3$ radical cation in the near-IR region at 1320 nm in the figure serves as a diagnostic probe for identifying the CS state of **12**, allowing an accurate analysis of the intramolecular electron transfer dynamics without the interference of triplet absorption bands that have absorptions in the visible region.[79] The quantum yield of the CS state of **12** was determined to be 29%.[79] The time profile at 1320 nm shows a slow rise within 50 μs, followed by extremely slow decay.[79]

The rate of the slow rise was estimated at $5.3 \times 10^5\ s^{-1}$ and was referred to the rate of the CS process via $^3ZnP^*$.[79] However, the slow decay is due to the CR process of the radical ion pair with a triplet spin character, estimated at $1.7 \times 10^3\ s^{-1}$ ($\tau = 588\ \mu s$), which implies a significant increase in the triplet CS lifetime as compared to the singlet CS lifetime under the same conditions.[79]

Another example of formation of a long-lived CS state in a nonpolar solvent is tribasic corrole–C_{60} dyads (**13** and **14**), shown in Figure 18.[87] Corroles, which were first reported in 1965,[88] possess the skeleton of the corrin macrocycle (found in vitamin B_{12}) with only three *meso*-carbons between the four pyrrole rings.

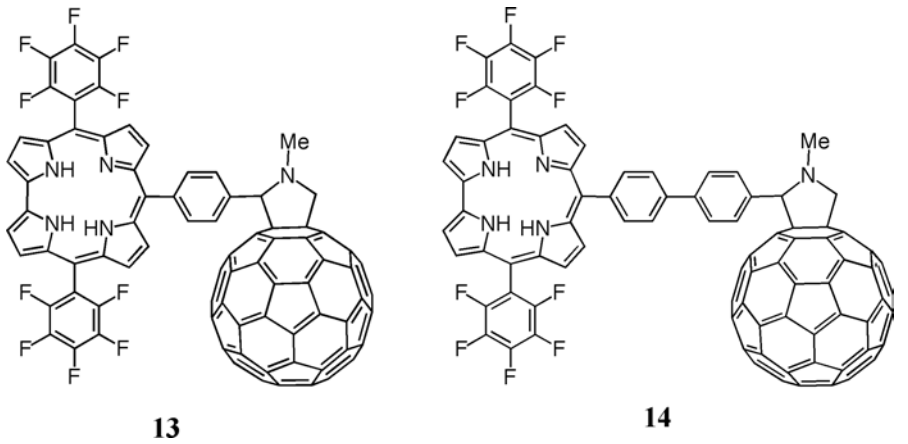

Figure 18. Molecular structures of corrole–C_{60} dyads (**13** and **14**).

Recent synthetic breakthroughs have made this macrocycle readily available.[89,90] When compared with porphyrins, these tribasic aromatic macrocycles exhibit excellent properties, including lower oxidation potentials, higher fluorescence quantum yields, larger Stokes shifts, and more intense absorption of red light.[91–94] The donor corrole entity, due to the facile oxidation compared to the traditionally used porphyrin analogs, yielded higher exothermicity for the photoinduced charge separation process. Consequently, efficient charge separation of corrole–C_{60} dyads (**13** and **14**) was observed from the time-resolved emission, and femto- and nanosecond laser flash photolysis measurements.[87] Because of the appropriate positioning of the energy levels of the CS state with respect to the triplet energy level and small reorganization energies of electron transfer in nonpolar solvents, the CS state with the lifetime of the order of a few microseconds was attained in nonpolar solvents.[87]

VI. Multistep Photoinduced Electron Transfer

Extensive efforts have been devoted to attaining a long distance charge separation via multistep photoinduced electron transfer, mimicking the natural photosynthetic reaction center.[95–100] A ferrocene unit was attached to ZnImP–C_{60} in Figure 14 to synthesize a triad (**15**: Fc–ZnImP–C_{60}).[101] Photoinduced electron transfer from ZnImP to C_{60} is followed by electron transfer to afford the final CS state (Fc^{+}–ZnImP–$C_{60}^{\bullet-}$), which has a much longer lifetime (630 μs) than the dyad ($ZnImP^{\bullet+}$–$C_{60}^{\bullet-}$: 230 μs) in PhCN at 298 K.[101] The energy diagram of photoinduced electron transfer of **15** is summarized in Scheme 3 with the lifetime of each transient species.[101] The CS lifetime (630 μs) of **15** is much longer than the

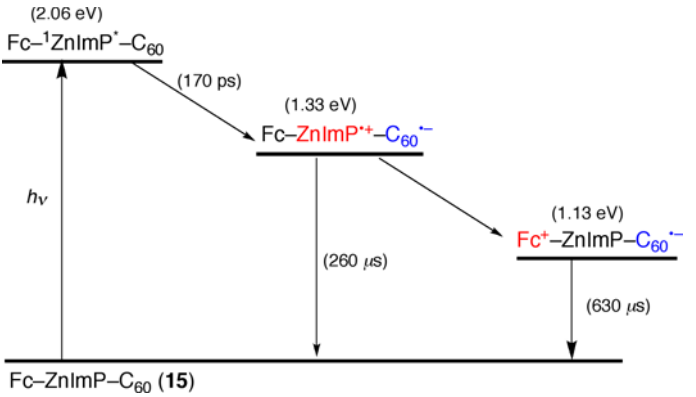

Scheme 3.

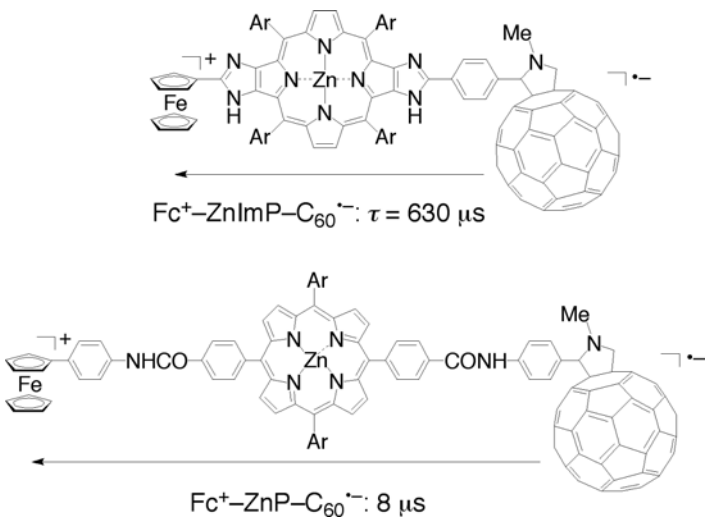

Figure 19. Comparison of the CS lifetime (τ) between Fc$^+$–ZnImP–$C_{60}^{•-}$ and Fc$^+$–ZnP–$C_{60}^{•-}$.

lifetime (8 μs) of a similar triad connected by a longer amide linkage, Fc–ZnP–C_{60} (**16**) in Figure 19.[101]

The longer CS lifetime of Fc$^+$–ZnImP–$C_{60}^{•-}$ is suggested to arise from partial cancelation of two effects: the rate reduction stemming from the smaller solvent reorganization energy with a shorter donor–acceptor distance (Eq. 5), and the rate enhancement due to increased coupling V which arises from the orbital delocalization.[101]

A ferrocene–zinc porphyrin–C_{60} triad (**16**) was further extended to a ferrocene–zinc porphyrin–free-base porphyrin–C_{60} tetrad [**17**: Fc–ZnP–H_2P–C_{60}; Figure 20a].[102]

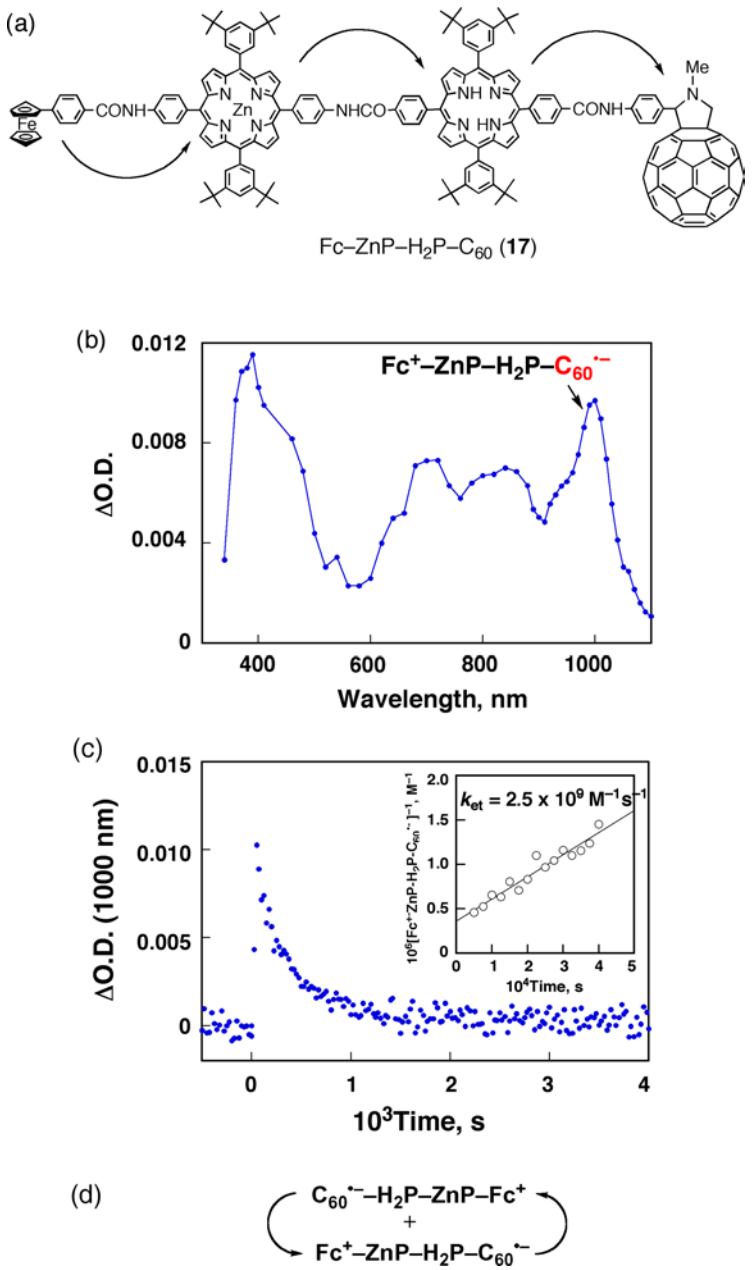

Figure 20. (a) The direction of photoinduced electron transfer in a Fc–ZnP–H_2P–C_{60} tetrad (**17**). (b) Differential absorption spectra obtained upon nanosecond flash photolysis (532 nm) of 7.2×10^{-6} M solutions of **17** in nitrogen-saturated PhCN with a time delay of 50 ns at 298 K. (c) The time profile of absorbance at 1000 nm obtained by nanosecond time-resolved absorption spectra of Fc–ZnP–H_2P–C_{60} (3.6×10^{-6} M) in argon-saturated DMF excited at 532 nm at 298 K. Inset: Second-order plot derived from the absorption change at 1000 nm. (d) Bimolecular back electron transfer between the CS state molecules. (Adapted from Ref. 102.)

Nanosecond transient absorption measurements of **17** reveal unambiguously the $C_{60}^{\bullet-}$ fingerprint (*ca.* 1000 nm), which matches quite reasonably that known for the π-radical anion of an *N*-methylfulleropyrrolidine (Figure 20b).[67,103] The transient absorption spectrum of **17** is virtually the same as that of Fc^{+}–ZnP–$C_{60}^{\bullet-}$ and Fc^{+}–H_2P–$C_{60}^{\bullet-}$.[70,104] The total quantum yields ($\Phi_{CS(total)}$) for the CS state of **17** were determined to be 0.20 (THF), 0.24 (PhCN), and 0.17 (DMF).[102] The relatively low quantum yields (0.17–0.24) result from the competition of charge shift from Fc–ZnP–$H_2P^{\bullet+}$–$C_{60}^{\bullet-}$ (1.63 eV) to Fc–$ZnP^{\bullet+}$–H_2P–$C_{60}^{\bullet-}$ (1.34 eV) versus the decay of Fc–ZnP–$H_2P^{\bullet+}$–$C_{60}^{\bullet-}$ to the triplet states of the free-base porphyrin (1.40 eV) and the C_{60} (1.50 eV).[102] In fact, the absorption due to $^3H_2P^*$ and $^3C_{60}^*$ (600–900 nm)[105] is observed together with that of Fc^{+}–ZnP–H_2P–$C_{60}^{\bullet-}$ in Figure 20b.[102]

The time profiles at 1000 nm due to the CS state of **17** obey second-order kinetics, rather than first-order kinetics, as shown in Figure 20c.[102] From the best fits, intermolecular ET dynamics were calculated that are nearly diffusion-controlled (PhCN: 5.4×10^9 M^{-1} s^{-1}; DMF: 2.5×10^9 M^{-1} s^{-1}).[102] The second-order rate law suggests that the intramolecular charge recombination in Fc^{+}–ZnP–H_2P–$C_{60}^{\bullet-}$ is too slow to compete with the diffusion-limited intermolecular charge recombination (Figure 20d). Thus, the rate of intramolecular charge recombination in Fc^{+}–ZnP–H_2P–$C_{60}^{\bullet-}$ was determined by electron paramagnetic resonance (EPR) measurements in a frozen matrix at variable temperatures using a low concentration in PhCN (1.0×10^{-5} M) under irradiation to stop the diffusion.[102] The EPR spectrum (Figure 21a) under irradiation at 203 K shows a characteristic broad signal attributable to $C_{60}^{\bullet-}$ (g = 2.0004).[67] As shown in Figure 21b, the EPR signal grows in immediately upon turning on the irradiation of **17** and upon turning off the irradiation source, the EPR signal decays, obeying first-order kinetics to afford a rate constant of 3.0 s^{-1} (Figure 21c) for the intramolecular CR process (k_{CR}). Only small temperature dependence of k_{CR} (2.6–3.0 s^{-1}) was observed upon varying the temperature between 163 and 203 K.[102] The lifetime of the CS state of **17** was determined to be 0.4 s, which is comparable to the lifetimes (~1 s) of the CS state in the bacterial photosynthetic reaction centers.[9–11,106]

The driving force dependence of the electron transfer rate constants (k_{ET}) of the dyad (**9**), triad (**16**), and tetrad (**17**) for CS and CR processes is shown in Figure 22, where log k_{ET} is plotted against the driving force ($-\Delta G_{ET}$).[102] The lines in the figure represent the best fit to Eq. 1 (**9**: λ = 0.66 eV, V = 3.9 cm^{-1}; **16**: λ = 1.09 eV, V = 0.019 cm^{-1}; **17**: λ = 1.32 eV, V = 0.00017 cm^{-1}).[102] The λ value increases, whereas the V value decreases with increasing edge-to-edge distance in the order of the dyad (R_{ee} = 11.9 Å), the triad (R_{ee} = 30.3 Å), and the tetrad (R_{ee} = 48.9 Å). In the case of the dyad, the CR rate in $ZnP^{\bullet+}$–$C_{60}^{\bullet-}$ in the Marcus inverted region is much slower than the CS rate constants from both the singlet and triplet excited states in the Marcus normal region (Figure 22). This enables a subsequent

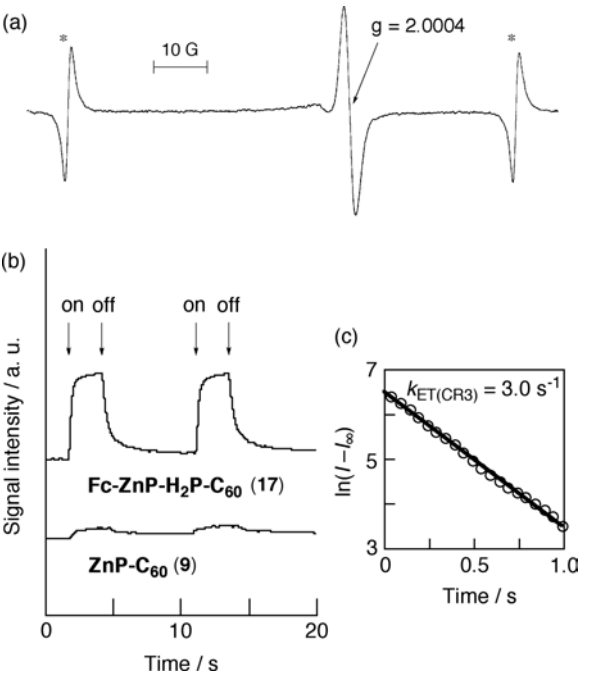

Figure 21. (a) ESR spectrum of **17** (1.0×10^{-5} M) in a frozen deaerated PhCN solution observed at 203 K under irradiation of UV-vis light from a high-pressure Hg lamp (* denotes a Mn marker). (b) Signal intensity response of **17** (1.0×10^{-5} M, top) and 9 (1.0×10^{-5} M, bottom) in a frozen deaerated PhCN solution at the maximum of the ESR signal intensity due to the $C_{60}^{\bullet-}$. (c) First-order plot for the decay of the ESR signal intensity (I) in **17** ($k_{ET(CR3)} = 3.0\ s^{-1}$). (Adapted from Ref. 102.)

electron transfer from Fc to $ZnP^{\bullet+}$ in the triad ($Fc–ZnP^{\bullet+}–C_{60}^{\bullet-}$) to produce the final CS state, $Fc^{+}–ZnP–C_{60}^{\bullet+}$, in competition with the back electron transfer in the initial CS states. In the case of the tetrad (**17**), the multistep electron transfer processes afford the final CS state, $Fc^{+}–ZnP–H_2P–C_{60}^{\bullet-}$, in which charges are separated at a long distance ($R_{ee} = 48.9$ Å).[102] The lifetime of the resulting CS state at such a long distance in a frozen PhCN becomes as long as 0.4 s (*vide supra*).[102] It should be noted that the CS lifetime is temperature-independent, since the CR process is at the Marcus top region (Figure 22).[102]

The maximum k_{ET} value (k_{ETmax}) of each Marcus plot in Figure 22 is correlated with the edge-to-edge distance (R_{ee}), separating the radical ions, according to Eq. 6,

$$\ln k_{ETmax} = \ln\left(\frac{2\pi^{3/2}V_0^2}{h(\lambda k_B)^{1/2}}\right) - \beta R_{ee}, \tag{6}$$

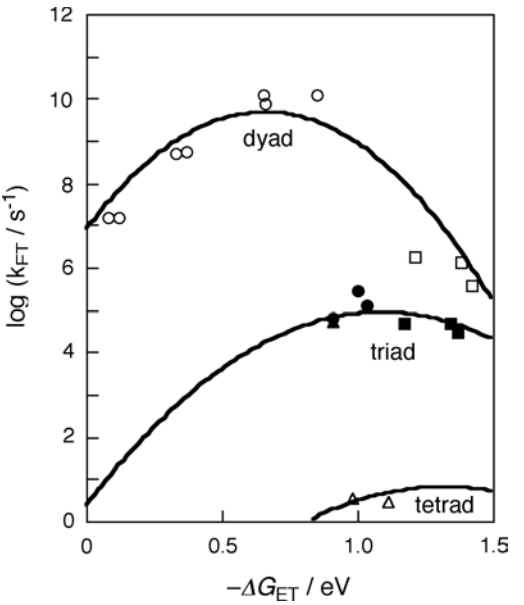

Figure 22. Driving force ($-\Delta G_{ET}$) dependence of intramolecular electron transfer rate constants (k_{ET}) in a dyad **9** (CS: white circles; CR: white squares), a triad **16** (black circles), and a tetrad **17** (white triangles). The data of other triads, Fc–H_2P–C_{60} (black triangles) and ZnP–H_2P–C_{60} (black squares), are also included. (Adapted from Ref. 102.)

where V_0 refers to the maximal electronic coupling element, while β is the decay coefficient factor (damping factor), which depends primarily on the nature of the bridging molecule.[102] From the linear plot of ln k_{ETmax} vs. R_{ee} in Figure 23, the β value is determined to be 0.60 Å^{-1}. This β value is located within the boundaries of nonadiabatic electron transfer reactions for saturated hydrocarbon bridges (0.8–1.0 Å^{-1}) and unsaturated phenylene bridges (0.4 Å^{-1}).[107]

The quantum yield for the final CS state was improved from 0.24 for Fc–ZnP–H_2P–C_{60} (**17**) in PhCN to 0.34 for Fc–ZnP–ZnP–C_{60} (**18**).[108] In addition, the CS lifetime was elongated to 1.3 s in DMF at 298 K.[107] This is by far the largest value ever reported for *intra*molecular charge recombination in synthetic donor–acceptor systems, including porphyrin–fullerene-linked systems. Substitution of the metal-free tetraphenylporphyrin chromophore (H_2P) by the corresponding zinc analog (ZnP) raises the excited state energy of the chromophore from 1.89 eV to 2.04 eV, and also lowers the one-electron oxidation potential of the electron donor by nearly 300 mV.[108] As a consequence of these two effects, the driving force of the charge separation is markedly increased, ensuring better efficiency.

The quantum yield for the CS state was further improved by employing a ferrocene-*meso*, *meso*-linked porphyrin trimer–fullerene pentad (**19**: Fc–$(ZnP)_3$–C_{60})

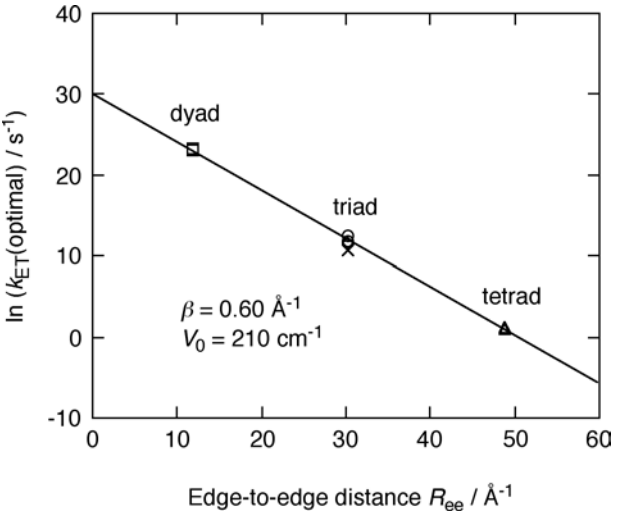

Figure 23. Edge-to-edge distance (R_{ee}) dependence of optimal electron transfer rate constants ($\ln[k_{ET}(\text{optimal})/s^{-1}]$) in **9** (square), **16** (circle), Fc–H_2P–C_{60} triad (diamond), ZnP–H_2P–C_{60} triad (cross), and **17** (triangle). The line represents the best fit to Eq. 1 ($\beta = 0.60$ Å^{-1}, $V_0 = 210$ cm^{-1}). (Adapted from Ref. 102.)

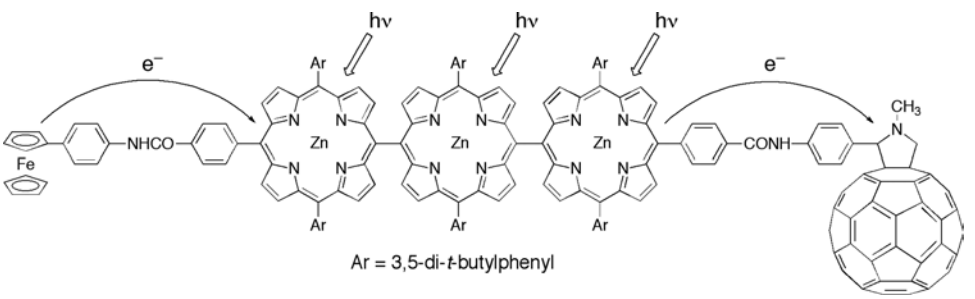

Figure 24. The direction of photoinduced electron transfer in a ferrocene-*meso,meso*-linked porphyrin trimer–fullerene pentad (**19**: Fc–$(ZnP)_3$–C_{60}). (Adapted from Ref. 109.)

in Figure 24.[109] Photoirradiation of **19** results in photoinduced electron transfer from both the singlet and triplet excited states of the porphyrin trimer [$^1(ZnP)_3^*$, $^3(ZnP)_3^*$] to the C_{60} moiety to produce the porphyrin trimer radical cation–C_{60} radical anion pair, Fc–$(ZnP)_3^{\bullet+}$–$C_{60}^{\bullet-}$.[109] The energy levels in PhCN are shown in Scheme 4.[109] Because a ferrocene unit is tethered at the end of $(ZnP)_3$–C_{60}, the pentad undergoes multistep photoinduced electron transfer, i.e. Fc–$^1(ZnP)_3^*$–C_{60} (1.95 eV) → Fc–$(ZnP)_3^{\bullet+}$–$C_{60}^{\bullet+}$ (1.36 eV) → Fc$^+$–$(ZnP)_3$–$C_{60}^{\bullet-}$ (1.03 eV) in PhCN (Scheme 4).[109]

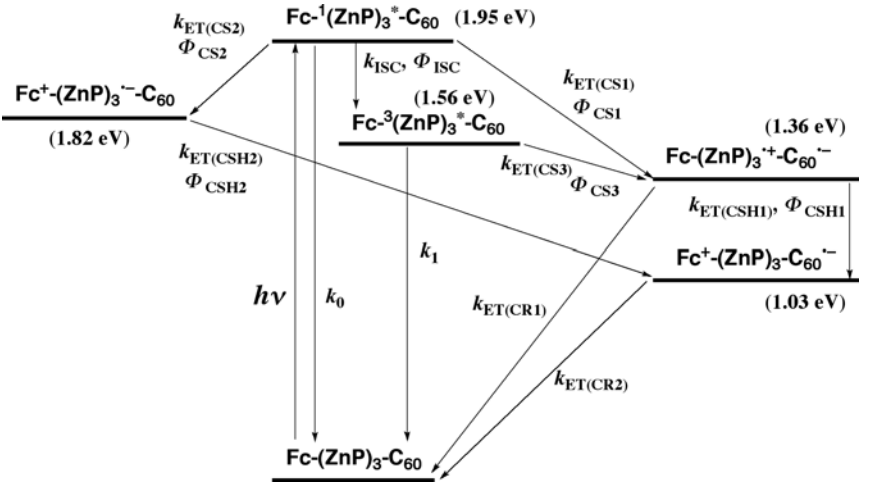

Scheme 4.

The time profiles at 1000 nm due to the final CS state of **19** also obey second-order kinetics in solution, because the bimolecular CR is predominant over the intramolecular CR.[109] When the diffusion was stopped in a frozen PhCN at 163 K, the ESR signal due to the CS state observed upon photoirradiation of **19** exhibited a slow and nearly seconds-lasting decay, which was best-fitted by first-order kinetics yielding a rate constant of 2.9 s^{-1} for the intramolecular CR process ($k_{ET(CR2)}$).[109] The CS lifetime of **19** was determined to be 0.53 s in frozen DMF at 163 K.[109] This CS lifetime is also comparable with the lifetime (~1 s) of the final CS state in the bacteria photosynthetic reaction centers.[106] The efficient formation of the final CS state with a high quantum yield (Φ = 0.83) has been achieved in the present pentad system.[109] Such excellent performance of **19** can be rationalized by the efficient charge separation because of the small reorganization energy of electron transfer and retarded charge recombination through the *meso*,*meso*-linked porphyrin trimer.[109]

Compared with the porphyrins described above, phthalocyanines (Pcs) emerge as attractive molecular building blocks for the artificial photosynthetic systems, in which they function as antennas with a wider absorbing range of the solar spectrum, where porphyrins fail to exhibit appreciable absorption.[110–112] Generally, Pcs undergo intermolecular π–π stacking interactions between the planar faces of the macrocycles, even at low concentration, giving rise to dimerization or aggregation which results in fluorescence quenching and low solubility. In contrast, axially substituted silicon Pcs have gained great attention because they do not aggregate due to their special structural features.[113–116] The integration of silicon Pc with two units of different electron acceptors, 1,4,5,8-naphthalenediimide

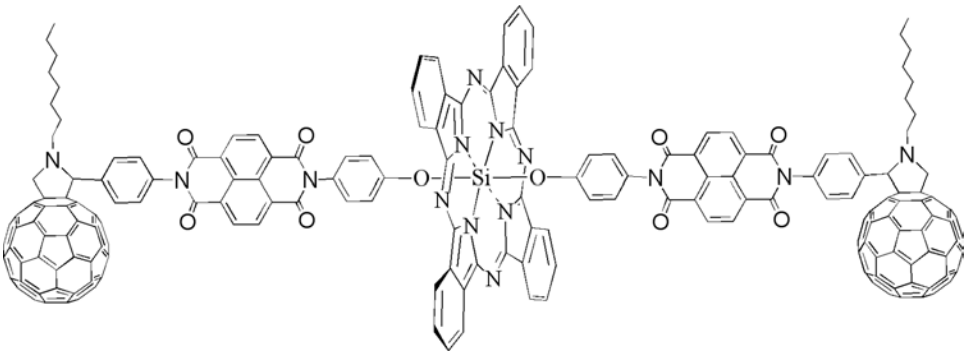

Figure 25. Silicon phthalocyanine linked with two units of different electron acceptors, 1,4,5,8-naphthalenediimide (NDI) and C_{60}, through the axial position (**20**: SiPc–$(NDI)_2$–$(C_{60})_2$). (Adapted from Ref. 117.)

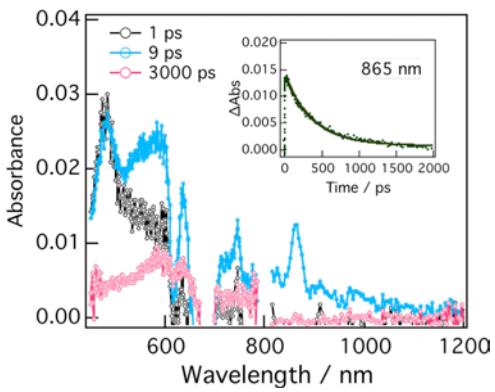

Figure 26. Femtosecond transient absorption spectra of **20** in deaerated PhCN after laser excitation at 380 nm. (Adapted from Ref. 117).

(NDI) and C_{60}, was made possible through the axial position to form the SiPc–$(NDI)_2$–$(C_{60})_2$ pentad (**20**) in Figure 25.[117] The pentad serves as light harvesting architecture with good spectral coverage in the visible and NIR regions. The planar NDI has the higher energy excited state than SiPc and C_{60}, as well as the lower one-electron reduction potential. Upon photoirradiation of a deaerated PhCN solution containing **20**, the characteristic absorption bands due to $SiPc^{\bullet+}$ (λ_{max} = 865 nm)[115] and $NDI^{\bullet-}$ (λ_{max} = 714 nm)[118] were observed as shown in Figure 26, where a weak absorption in the NIR region due to $C_{60}^{\bullet-}$ was also observed.[117] This indicates that an electron shifts from the $NDI^{\bullet-}$ to the adjoining C_{60} to generate $SiPc^{\bullet+}$–$(NDI)_2$–$(C_{60})_2^{\bullet-}$. The rate constants of CS and CR processes were determined be 3.0×10^{11} and 1.0×10^{9} s^{-1}, respectively.[117] The high k_{CS}/k_{CR} ratio

indicated the usefulness of **20** as a light-harvesting system. However, the decay of the CS state in deaerated PhCN affords the triplet excited state, SiPc–$(NDI)_2$–$^3(C_{60})_2^*$, which is converted to the lower triplet excited state, $^3SiPc^*$–$(NDI)_2$–$(C_{60})_2$, which decays to the ground state with a rate constant of 1.4×10^4 s^{-1}.[117]

VII. Supramolecular Porphyrin Complexes

In contrast to photosynthetic reaction center models in which each component is covalently bonded to the other (*vide supra*), each component of the photosynthetic reaction center is located at the required position by noncovalent bonding in the protein matrix to optimize the charge separation efficiency.[9–11] The use of noncovalent bonding situations such as metal–ligand coordination, electrostatic interaction, and hydrogen bonding provides simpler but more elegant ways to construct electron donor–acceptor ensembles mimicking the efficient biological electron transfer systems.[119–125] In particular, π–π interaction is one of the most important noncovalent binding methods because of its important role in biological systems such as π-stacking of double-strand DNA.[126–128] The acridinium ion is suitable as a component of an artificial photosynthetic reaction center because of the small reorganization energy (λ) of electron transfer,[129] which results in fast photoinduced electron transfer but extremely slow back electron transfer.[130,131]

A cofacial free-base bisporphyrin (H_4DPOx), which is regarded as a model compound of a bacteriochlorophyll dimer [$(BChl)_2$], forms a relatively strong π-complex with acridinium perchlorate ($AcH^+ClO_4^-$) in PhCN (**21** in Figure 27).[132]

The formation constant (K) of the H_4DPOx–AcH^+ complex is determined to be 97000 ± 1000 M^{-1} from spectral titration in PhCN, indicating relatively strong complex formation.[132] The π-complex formation is confirmed by ^{1}H NMR, in which signals due to both H_4DPOx and AcH^+ exhibit upfield shifts upon complexation.[132] The one-electron oxidation potential of H_4DPOx (E_{ox}) is shifted from 0.58 V in the absence of AcH^+ to 0.71 V by the insertion of AcH^+, because the bisporphyrin becomes more difficult to oxidize due to the repulsion of positive charges between the porphyrin radical cation and AcH^+.[132] The one-electron reduction potential of AcH^+ was also shifted from –0.46 V in the absence of the bisporphyrin to –0.57 V in the presence of the bisporphyrin due to complex formation.[132] As a result, the free energy change of electron transfer to form the ET state is changed from 1.04 eV to 1.28 eV in the π-complex (**21**).

Photoinduced electron transfer from the singlet excited state of H_4DPOx ($^1H_4DPOx^*$) to the AcH^+ moiety occurred efficiently in **21** to form the electron transfer state ($H_4DPOx^{\bullet+}$–$AcH^{\bullet}$), as indicated by the transient absorption spectra of a PhCN solution containing both H_4DPOx and AcH^+ observed upon laser excitation in Figure 28a.[132] The strong absorption in the range from 450 nm to 540 nm

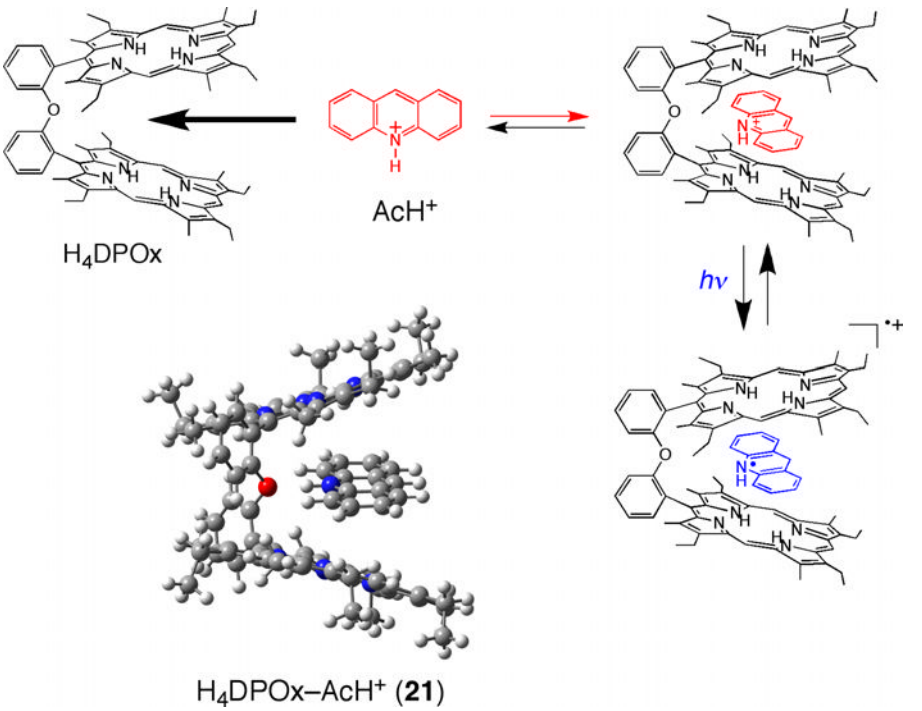

Figure 27. Formation of an electron transfer state of a π-complex of acridinium ion (AcH^+) inserted between porphyrin rings of a cofacial bisporphyrin (**21**: $H_4DPOx–AcH^+$). (Adapted from Ref. 132.)

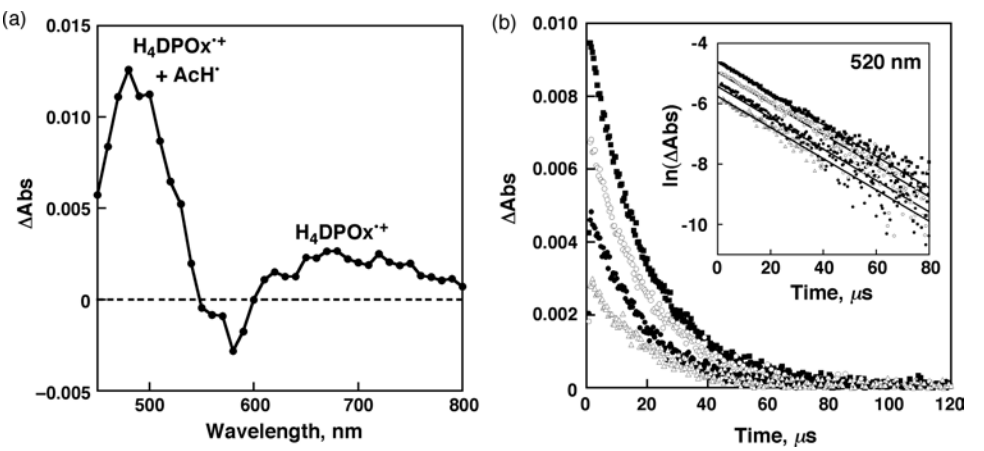

Figure 28. (a) Transient absorption spectrum of H_4DPOx (3.4×10^{-5} M) in the presence of AcH^+ (3.3×10^{-4} M) in deaerated PhCN at 273 K taken at 20 μs after laser excitation at 520 nm. (b) Time profiles of the absorption at 520 nm of $H_4DPOx^{\bullet+}$–$AcH^{\bullet}$ obtained with different laser intensities (1.5, 1.9, 2.1, and 3.8 mJ/pulse) in deaerated PhCN at 298 K. Inset: First-order plots. (Adapted from Ref. 132.)

is ascribed to $AcH^{\bullet}$,[129,130,133] and the transient absorption in the range from 620 nm to 800 nm is ascribed to $H_4DPOx^{\bullet+}$.[132] The decay time profiles of the absorption at 520 nm with the different laser intensities are shown in Figure 28b, where the first-order plots afford good linear correlations with the same slope, irrespective of the different laser intensities.[132] Such a first-order decay with the same slope strongly indicates that the back electron transfer from $AcH^{\bullet}$ to $H_4DPOx^{\bullet+}$ occurs in **21** and that no bimolecular decay is involved. The lifetime of the electron transfer state is determined to be 18 μs at 298 K ($k_{BET} = 5.5 \times 10^4$ s^{-1}).[132] The quantum yield of the electron transfer state is determined to be as high as 90%.[132] The electron transfer state lifetime exhibited large temperature dependence.[132] As a result, a remarkably long-lived electron transfer state has been attained at low temperature, and virtually no decay of the electron transfer state was observed at 77 K.[132]

The energy diagram of **21** is summarized in Scheme 5.[132] The rate constant (k_{ET}) of electron transfer from the singlet excited state of H_4DPOx ($^1H_4DPOx^*$) to AcH^+ in **21** was determined by time-resolved fluorescence measurements to be 2.9×10^8 s^{-1}.[132] The energy level of the electron transfer state of **21** (1.28 eV) is lower than that of the triplet states of H_4DPOx (1.59 eV) and AcH^+ (2.01 eV).[132,134] In addition to the π–π interaction described above, the axial coordination of pyridine compounds to the metal center of metalloporphyrins has been utilized to construct multiporphyrin assemblies as light-harvesting units by self-organization of Zn(II) porphyrins.[135–137] The axial coordination of pyridine was combined by complex formation of ammonium cation with crown ether to construct a biomimetic model of the bacterial "special pair", as shown in Figure 29.[138] A supramolecular complex (**22**) was formed between a cofacial zinc Pc dimer linked by complexation of four bis crown ether units with potassium ion, and a fullerene derivative functionalized with a pyridine coordinating entity and an alkyl ammonium cation entity for two-point binding.[138]

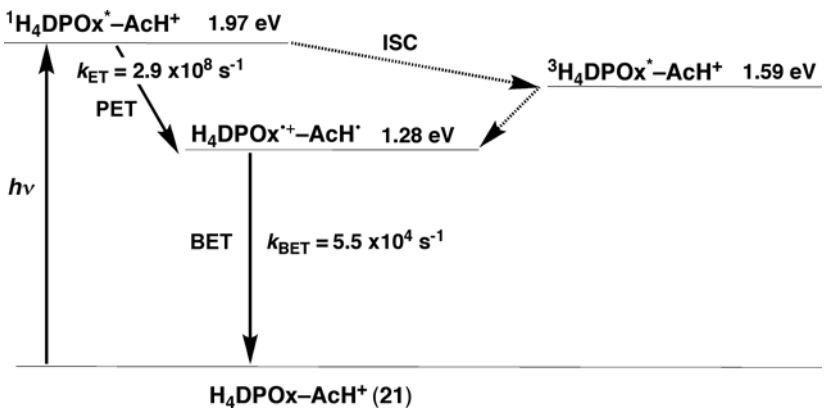

Scheme 5.

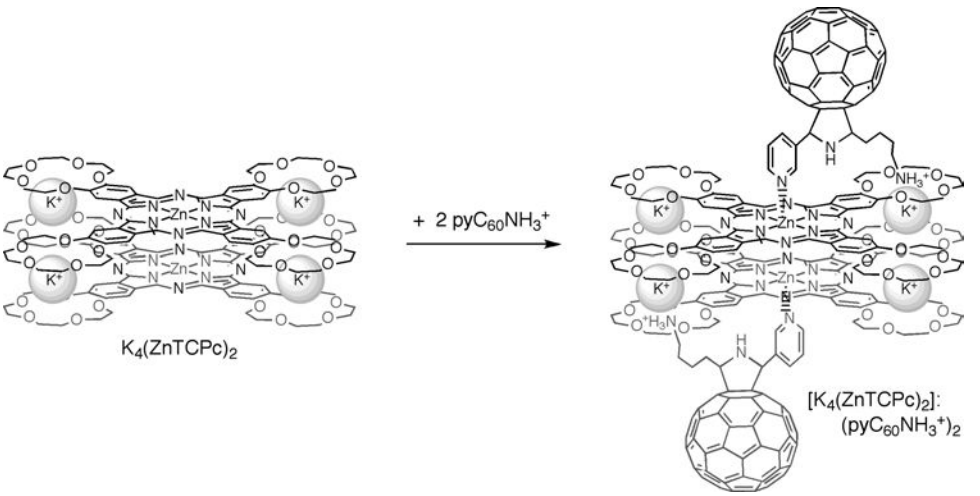

Figure 29. A supramolecular $K_4[ZnTCPc]_2$:$(pyC_{60}NH_3^+)_2$ conjugate (**22**). (Adapted from Ref. 138.)

Potassium-ion-induced dimerization of 4,5,4′,5′,4″,5″,4‴,5‴-tetrakis (1,4,7,10,13-pentaoxa-tridecamethylene)phthalocyanine zinc(II) (ZnTCPc) to afford the $K_4[ZnTCPc]_2$ dimer has been well established.[139–143] The K^+ ion is sandwiched between two 15-crown-5 entities from two different Pcs due to the size differences.[138] Then, the $K_4[ZnTCPc]_2$ dimer was allowed to interact with fullerene functionalized with a pyridine coordinating entity and an alkyl ammonium cation entity (Figure 29).[138] The calculated structure of **22** (Figure 30) revealed that the pyridine coordinates to the zinc center while the alkyl ammonium ion forms a complex with one of the crown ether entities without destroying the K^+-sandwich dimer via a "two-point" binding motif.[144–146] Utilization of such well-defined multiple modes of binding in a controlled fashion results in the formation of biomimetic supramolecular donor–acceptor conjugates.[138]

The photoexcitation of supramolecular $K_4[ZnTCPc]_2$–fullerene complex (**22**) affords a charge-separated state with a much longer lifetime (6.7 μs) as compared with the corresponding zinc porphyrin supramolecular complex (50 ns).[146] Such a drastically increased lifetime of the CS state in **22**, as compared to the corresponding porphyrin dimer complex, may result from a smaller reorganization energy of electron transfer for the more π-expanded Pc macrocycle relative to the porphyrin macrocycle.[138]

In order to further enhance the strength of axial coordination in Zn(II) macrocyclic compounds, the Lewis acidity of the Zn(II) center should be increased. The Lewis acidity of the Zn(II) center can be enhanced by macrocyclic ring distortion, which enforces lone pairs of nitrogen atoms in the pyrrole moieties to point out of

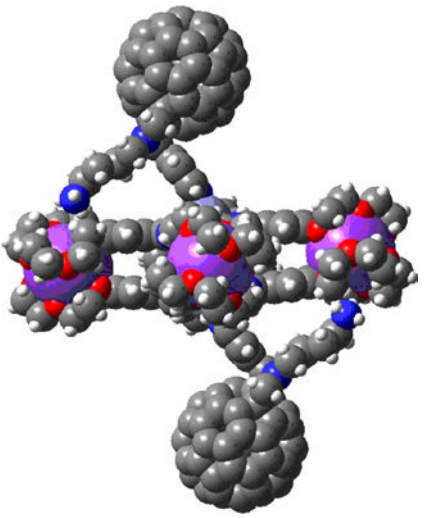

Figure 30. B3LYP/3-21G(*) optimized structure of the supramolecular $K_4[ZnTCPc]_2$:$(pyC_{60}NH_3^+)_2$ conjugate (**22**). The countercations and anions are omitted for clarity. (Adapted from Ref. 138.)

plane.[147] This misdirection of the lone pairs can weaken the interaction between the Zn(II) center and the nitrogen lone pairs to enhance the Lewis acidity of the Zn(II) center. Thus, the more the porphyrin ring is distorted as reflected on a larger ΔRMS value (see Figure 4), the stronger becomes the Lewis acidity of the Zn(II) to enhance the axial coordination bond strength with a base. The Zn(II) complexes of TPP^{2-} (tetraphenylporphyrin dianion) OPP^{2-} (octaphenylporphyrin dianion) and DPP^{2-} (dodecaphenylporphyrin dianion) showed different degrees of distortion of the porphyrin rings.[148–150] Among them, the DPP^{2-} ligand exhibited the largest nonplanarity as a saddle distortion and the largest displacement of the Zn(II) ion from the porphyrin mean plane.[147]

A saddle-distorted H_2DPP has also enabled facile protonation to give a stable diprotonated species, H_4DPP^{2+}, which can form intermolecular hydrogen bonds with electron donors.[151–154] The H_4DPP^{2+} can be combined with a nonplanar Zn(II) complex of saddle-distorted octaphenylphthalocyanine (H_2OPPc)[155,156] using pyridine-4-carboxylate (4-$PyCOO^-$) which can connect the Zn(OPPc) donor and the H_4DPP^{2+} acceptor by coordination bond and hydrogen bond.[157] The reaction of $[H_4DPP](4\text{-}PyCOO)_2$ with Zn(OPPc) in toluene gave a novel supramolecular assembly, $[(H_4DPP)\{Zn(OPPc)(\kappa^1\text{-}N\text{-}4\text{-}PyCOO)\}_2]$ (**23**).[157] The crystal structure is shown in Figure 31a.[156] The assembly contains one saddle-distorted H_4DPP^{2+} and two saddle-distorted Zn(OPPc) linked by two 4-$PyCOO^-$ anions (the components are shown in Figure 31b).[157] The bridging 4-$PyCOO^-$ coordinates to the Zn(II)

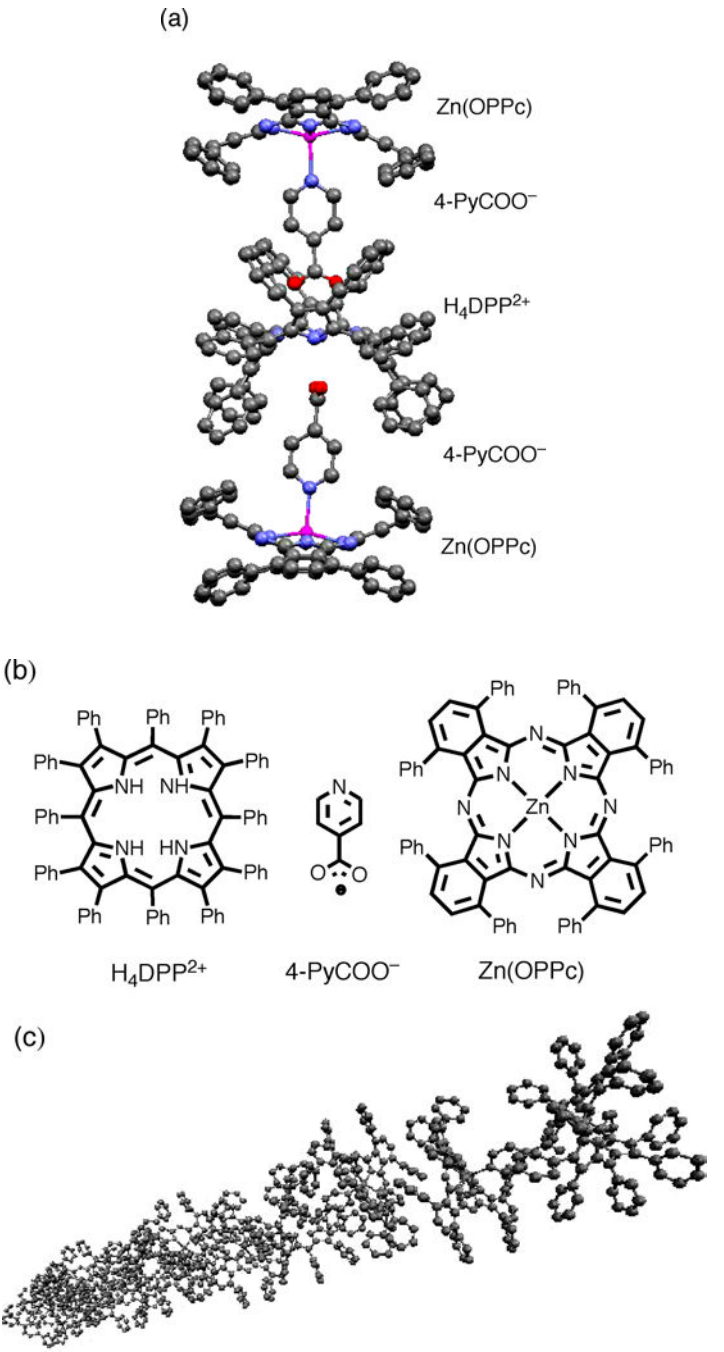

Figure 31. (a) Crystal structure of $[(H_4DPP)\{Zn(OPPc)(\kappa^1\text{-}N\text{-}4\text{-}PyCOO)\}_2]$ (**23**): purple — zinc; red — oxygen; blue — nitrogen; light gray — carbon. Hydrogen atoms and solvent molecules of crystallization are omitted for clarity. (b) Components of the supramolecular assembly. (c) One-dimensional nanowire structure in the crystal. (Adapted from Ref. 157.)

center of ZnOPPc through the axial coordination of pyridine nitrogen. It should be noted that there is two-point hydrogen bonding between H_4DPP^{2+} and 4-$PyCOO^-$ to connect the Zn(OPPc) units to the H_4DPP^{2+} moiety. The interatomic distances for those hydrogen bonds are in the range of 2.631(9)–2.725(7) Å, which suggests that hydrogen bonding is fairly strong.[157] The coordination of the pyridine linker is strong enough due to the remarkable saddle distortion of the $OPPc^{2-}$ ligand. The bond lengths of Zn1-N9 and Zn2-N18 are 2.117(3) and 2.140(3) Å, respectively, which are comparable with that found in [Zn(OPPc)(py)].[155,156] The crystal packing of **23** exhibits a one-dimensional nanowire structure (Figure 31c) by intermolecular π–π interactions of peripheral phenyl groups of the OPPc ligand.[157]

The supramolecular assembly in Figure 31 is stable enough in solution to maintain its structure, because ^{1}H diffusion-ordered spectroscopy (1H DOSY) in $CDCl_3$ allowed one to estimate its molecular volume (4849 $Å^3$), which was consistent with that (5096 $Å^3$) calculated on the basis of the crystal structure.[157] The stability of the supramolecular assembly in solution originates not only from the strong two-point hydrogen bonding between positively charged H_4DPP^{2+} and negatively charged 4-$PyCOO^-$ but also from the strengthened coordination of the nitrogen in 4-$PyCOO^-$ to the Zn(II) center with enhanced Lewis acidity within the saddle-distorted $OPPc^{2-}$ ligand.[157]

The energy diagram of the photoinduced electron transfer processes in **23** is shown in Scheme 6.[157] Femtosecond laser flash photolysis measurements revealed the photodynamics of **23** in PhCN.[157] Photoexcitation at 410 nm affords the singlet excited states of both H_4DPP^{2+} and Zn(OPPc) units ($^1[Por^{2+}]^*$ and $^1Pc^*$).[157] The singlet excited state of the porphyrin (Por) unit (1.66 eV) undergoes fast intra-supramolecular energy transfer with the rate constant of 4.2×10^{12} s^{-1}, which is comparable to that of

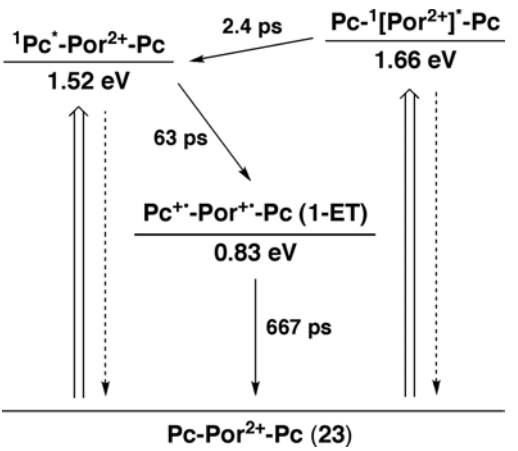

Scheme 6.

intramolecular energy transfer observed for a covalently linked ZnPor–ZnPc dyad.[158] This is followed by intra-supramolecular electron transfer from $^1Pc^*$ to Por^{2+} to give the electron transfer state at the energy level of 0.83 eV with the rate constant of 1.5×10^9 s^{-1}.[157] No energy transfer from the singlet excited state of $[H_4DPP](4\text{-}PyCOO)_2$ to Zn(OPPc) has occurred in **23**.[157] The electron transfer state has a lifetime of 667 ps, which is much longer than that observed in a covalently linked Zn (porphyrin)–Sn(phthalocyanine) dyad reported by Odobel and coworkers.[159]

The accessibility, stability, and reliability of multiporphyrin donor–acceptor systems can be further improved by using the stronger axial coordination in saddle-distorted Sn(IV) porphyrins with μ_3-O-centered and carboxylato-bridged trinulcear Ru^{III} clusters, as shown in Figure 32,[160] where the Sn(IV) ion, which is

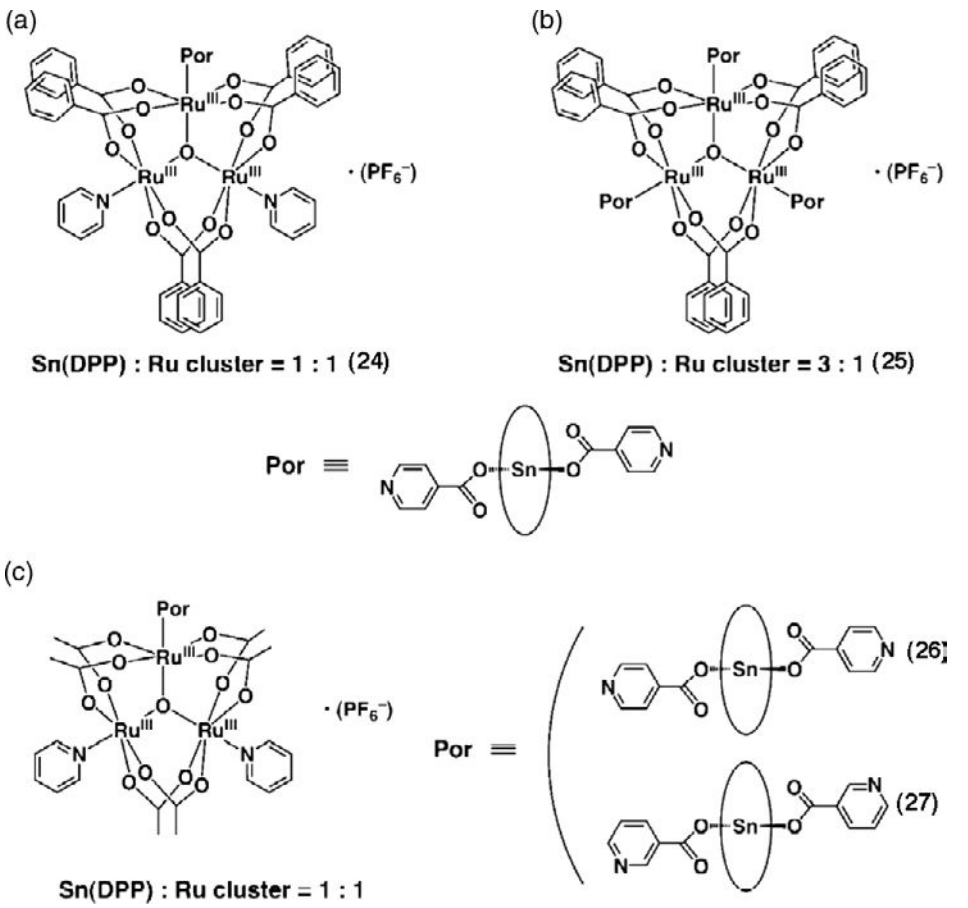

Figure 32. Schematic description of structures of conglomerates composed of Sn-DPP and Ru clusters: (a) a 1:1 complex (**24**), (b) a 3:1 complex (**25**), (c) 1:1 complexes (**26**, **27**). (Adapted from Ref. 160.)

a hard Lewis acid, binds with a hard base such as carboxylate oxygen to form a stable coordination bond with electron acceptors.[160] As electron acceptor, μ_3-oxo-centered and carboxylato-bridged trinuclear ruthenium clusters, $[Ru_3(\mu_3\text{-}O)(OC(O)R)_6L_3]^{n+}$, were employed due to their small structural change in the course of redox reactions for smaller reorganization energies.[161–164] The conglomerates are stable in solution, as demonstrated by ^{1}H NMR and ESI-MS spectroscopies.[160] This stability stems from the saddle distortion of the DPP^{2-} ligand to enhance the Lewis acidity of the Sn(IV) center, which strengthens the axial coordination of the linker.[160]

The conglomerates exhibited three reversible redox waves, as shown in Figure 33, where the Ru cluster moieties showed one reversible reduction wave due to $Ru^{III}{}_3/Ru^{II}Ru^{III}{}_2$ redox couples (0.03 V for **7**; 0.11 V for **25**) and one reversible oxidation wave ascribed to $Ru^{III}{}_3/Ru^{III}{}_2Ru^{IV}$ redox couples (1.06 V for **7**; 1.06 V for **25**).[160] The Sn(DPP) moieties exhibited reversible reduction waves (–0.91 V for **24**; –0.90 V for **25**) due to the Sn(DPP)/Sn($DPP^{\bullet-}$) redox couples and the oxidation waves ascribed to the Sn(DPP)/Sn($DPP^{\bullet+}$) redox couples (1.06 V for **24**; 1.06 V for **25**), which are overlapped with the oxidation waves of Ru cluster moieties in the case of **24** and **25**.[160]

The fast intramolecular photoinduced electron transfer from the Sn(DPP) unit to the trinuclear Ru^{III} cluster affording the electron transfer state [Sn($DPP^{\bullet+}$)–$Ru^{II}Ru^{III}{}_2$] was observed by femtosecond laser flash photolysis measurements.[160] The electron transfer state of the conglomerates showed lifetimes ranging from 98 ps to 405 ps, depending on the clusters and linkers employed.[160] The electron

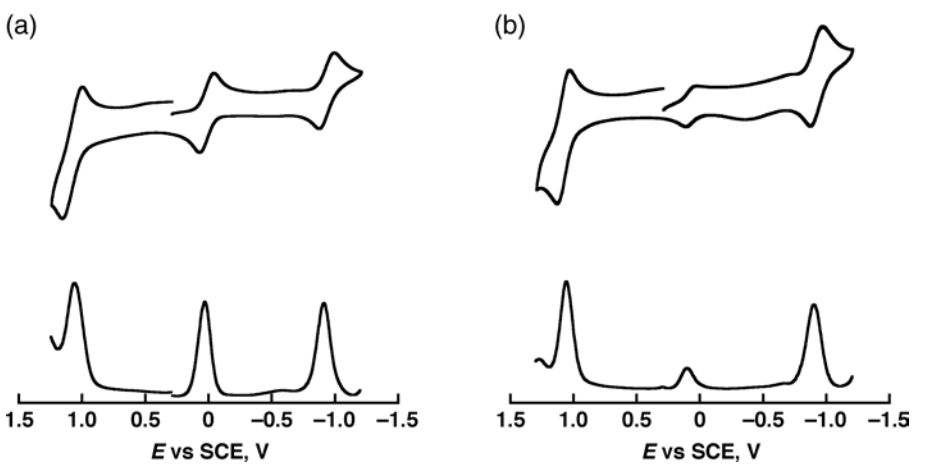

Figure 33. Cyclic voltammograms of conglomerates composed of Sn-DPP and Ru clusters: (a) a 1:1 complex (**24**) and (b) a 3:1 complex (**25**) in PhCN (0.1 M $TBAPF_6$ as an electrolyte). (Adapted from Ref. 160.)

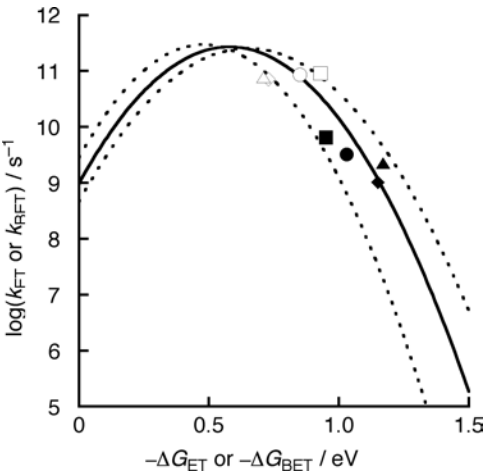

Figure 34. Driving force dependence of log k_{ET} (closed marks) or k_{BET} (open marks) for intramolecular electron transfer of conglomerates in PhCN at 298 K; **24** (circle), **25** (square), **26** (triangle), and **27** (rhombus). The fit of the curve based on the Marcus theory of electron transfer (Eq. 1) is shown by the solid line with $\lambda = 0.58$ eV and $V = 28.2$ cm^{-1} and the dotted lines with $\lambda = 0.50$ and 0.66 eV and $V = 28.2$ cm^{-1}, respectively. (Adapted from Ref. 160.)

transfer state decays via back electron transfer to recover the ground state, Sn(DPP)–Ru^{III}_3.[160] The lifetimes of the electron transfer states are determined from the back electron transfer rate constants to be 305 ps for **7**, 154 ps for **25**, 446 ps for **26**, and 98 ps for **27**, respectively.[160] The driving force dependence of log(k_{ET} or k_{BET}) for photoinduced electron transfer and back electron transfer is shown in Figure 34.[160] The fitting of the results to Eq. 1 afforded the reorganization energy of $\lambda = 0.58$ eV and $V = 28.2$ cm^{-1}, as shown (as the solid line) in Figure 34.[160] Both the rate constants of photoinduced electron transfer and back electron transfer in the conglomerates fall in the Marcus inverted region. This is a rare case in which both electron transfer and back electron transfer rates are located in the Marcus inverted region due to the small reorganization energy of electron transfer.[165] This reorganization energy of electron transfer is relatively small in comparison with other related dyads, giving rise to CS or electron transfer states.[4-6,14,15]

VIII. Porphyrin–Nanocarbon Composites

Formation of nanoscale donor–acceptor ensembles is also made possible by π–π interaction between multiporphyrin compounds such as the porphyrin–peptide hexadecamer [$P(H_2P)_{16}$][166,167] and single-walled carbon nanotubes (SWNTs), as shown in Figure 35.[168] The novel and unique electronic properties of SWNTs make them excellent candidates for next-generation nanoelectronic applications.[169–172]

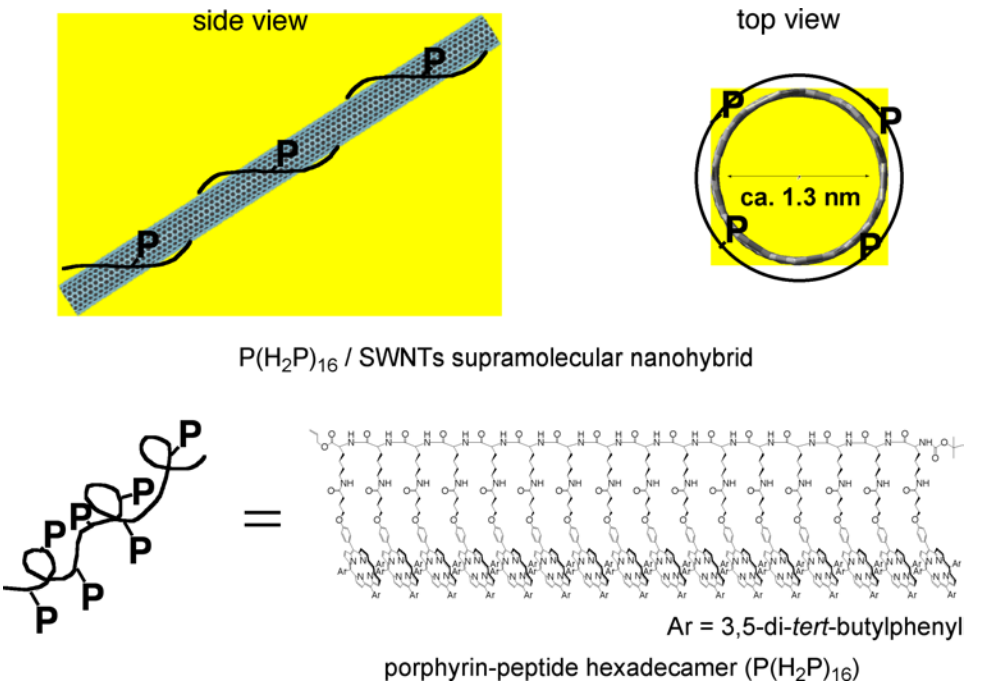

Figure 35. Formation of a supramolecular complex (**28**) between porphyrin–peptide hexadecamer [$P(H_2P)_{16}$] and single-walled carbon nanotube (SWNTs). (Adapted from Ref. 168.)

Supramolecular formation occurs through π–π interaction between porphyrins and nanotubes together with wrapping of the peptidic backbone in $P(H_2P)_{16}$.[168] This makes it possible to extract the large-diameter nanotubes (*ca.* 1.3 nm) as revealed by ultraviolet–visible–near-infrared and Raman spectroscopy as well as high-resolution transmission electron microscopy, as shown in Figure 36, where only an individual nanotube with a diameter below 2 nm and individual nanotubes with small-diameter bundles are observed.[168]

Laser photoexcitation of $P(H_2P)_{16}$/SWNTs nanohybrid (**28**) in DMF results in appearance of a transient absorption at 450 nm together with a broad absorption band in the 500–800 nm region, which exhibits a number of bleaching bands (Figure 37a).[168] Taking into account the fact that the bleaching bands agree with the absorption bands due to **28** (inset of Figure 37a) and no transient absorption was observed upon photoexcitation of $P(H_2P)_{16}$, the observed transient absorption spectrum was assigned to the CS state of **28**, which was produced by photoinduced electron transfer from the excited states of $P(H_2P)_{16}$ to SWNTs.[168] The decay of the CS state of **28** obeyed first-order kinetics with the same slope irrespective of any difference in the laser intensities, as shown in Figure 37b.[168] The same slope, irrespective of difference in the laser intensities in Figure 37b, strongly indicates

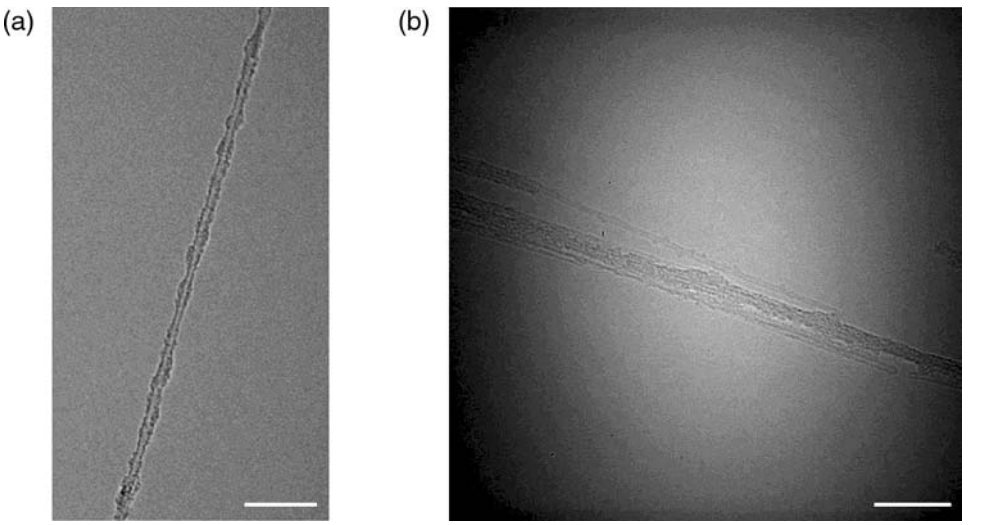

Figure 36. HRTEM images of **28** (scale bar = 20 nm): (a) an individual nanotube and (b) individual nanotubes with small-diameter bundles. (Adapted from Ref. 168.)

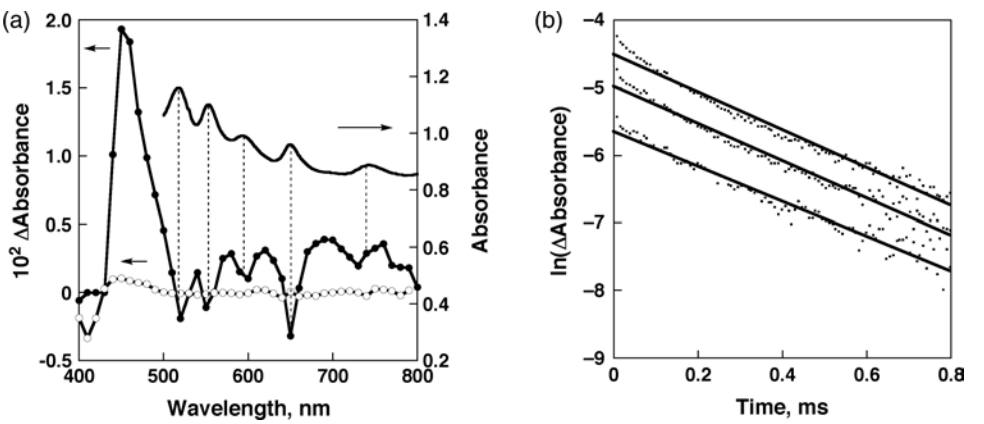

Figure 37. (a) Transient absorption spectra of **28** (solid line with black circles) and $P(H_2P)_{16}$ (solid line with white circles) in DMF at 298 K taken at 6 μs after laser excitation at 440 and 427 nm, respectively. Inset: UV–vis–NIR absorption spectra of **28**. (b) First-order plots at 480 nm with different laser powers (7, 3, and 1 mJ, respectively). (Adapted from Ref. 168.)

that the decay of the porphyrin radical cation results from the back electron transfer from the reduced SWNTs to the porphyrin radical cation in the supramolecular complex.[168] The CS lifetime is determined to be 370 μs, which is significantly shorter than the reported triplet lifetimes of porphyrin–peptide oligomers.[167] Formation of such nanohybrids affording the long-lived CS state of **28** opens up a new strategy for the extraction of large-diameter SWNTs without destruction of

the π-conjugated system within SWNTs and the development of efficient light energy conversion devices.

Although SWCNTs exhibit excellent chemical and physical properties,[173–177] the fine control of the size (i.e. length) of SWCNTs is a great challenge for solubilization and construction of nanoscale architectures and devices. The control of the diameter and size of carbon nanotubes has recently been made possible using cup-stacked carbon nanotubes (CSCNTs) that consist of truncated conical graphene layers with a hollow tubular morphology, composed of cup-shaped carbon units with diameters ranging from 50 to 150 nm and lengths of up to 200 μm.[178–180] In addition, the availability of reactive edges on the outer and inner surfaces of cup-shaped carbons to chemical functionalization or surface modification will open up new ways to utilize them in electronic, catalytic, and photovoltaic applications.[181] CSCNTs were efficiently destacked by the electron transfer reduction with sodium naphthalenide to produce individual cup-shaped carbons with controlled diameter and size, as shown in Figures 38a and b.[182] Addition of 1-iodododecane to reduced cup-shaped carbons leads to functionalized cup-shaped carbons (**29**), which are stable in air and highly dispersible in nonpolar solvents for long time periods (Figure 38c).[182] Photoinduced electron transfer reduction of CSCNTs with dimeric 1-benzyl-1,4-dhihydronicotinamide also results in the highly dispersible cup-shaped nanocarbons with size homogeneity.[183]

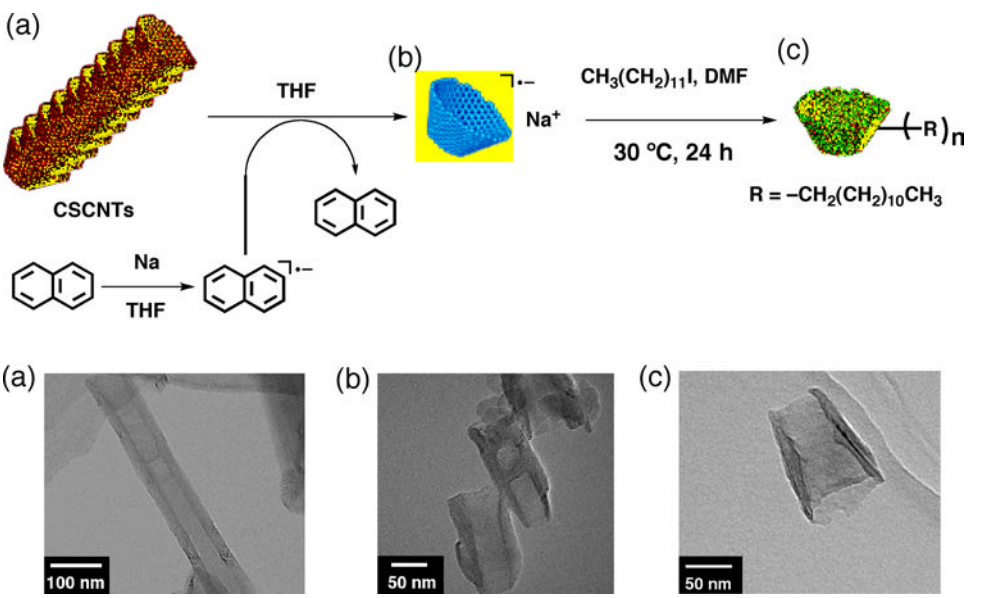

Figure 38. Electron transfer reduction of (a) cup-stacked carbon nanotubes (CSCNTs) to prepare (b) reduced CSCNTs and (c) docecylated CSCNTs (**29**) with controlled diameter and size, with their TEM images. (Adapted from Ref. 182.)

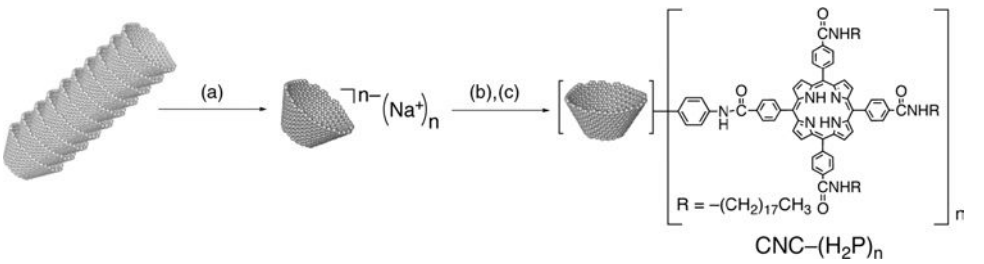

Figure 39. Synthesis of the porphyrin-functionalized cup-shaped nanocarbons (**30**: CNC–$(H_2P)_n$). Reagents and conditions: (a) naphthalene (Na), THF, r.t., 24 h; (b) 4-iodoaniline, DMF, 30 °C, 24 h; (c) porphyrin–COCl, pyridine, DMF, 120 °C, 72 h. (Adapted from Ref. 184.)

The cup-shaped nanocarbons generated by the electron transfer reduction of CSCNTs can be readily functionalized with porphyrins for use as light-capturing chromophores.[184] The general procedure for the synthesis of the porphyrin-functionalized cup-shaped nanocarbons [CNC–$(H_2P)_n$] (**30**) consists of two steps, as shown in Figure 39.[184] The first step involves cup-shaped nanocarbons functionalized with aniline as the precursor for functionalization with porphyrins. In the second step, the aniline-functionalized nanocarbons react with the porphyrin derivatives to construct the nanohybrids.[184] The resulting donor–acceptor nanohybrid (**30**) has been well characterized by thermogravimetric analysis (TGA), Raman and IR spectroscopy, transmission electron microscopy, elemental analysis, and ultraviolet–visible–near-infrared (UV–vis–NIR) spectroscopy.[184] The weight of porphyrins attached to the cup-shaped nanocarbons was determined to be 20% by the TGA and elemental analysis.[184] This corresponds to one functional group per 640 carbon atoms of the nanocup framework for **30** on average.[184] This result was supported by the elemental analysis that indicated a chemical formula of $C_{640}H_{55}(C_{108}H_{145}N_8O_4)$, from which the amount of porphyrins grafted to the cup-shaped carbons was determined to be 21.0%.[184] The structure of the cup-shaped nanocarbons of **30** was revealed by the TEM image in Figure 40, which shows the independently cup-shaped nanocarbon with a well-controlled diameter (*ca*. 50 nm) and size (*ca*. 100 nm).[184]

Laser photoexcitation of **30** in DMF results in appearance of the transient absorption, as shown in Figure 41a (solid line with open circles).[184] The triplet–triplet absorption of ref-H_2P (Figure 41b) exhibits quite different features as compared to **30** [see the near-infrared region (600–800 nm) as well as the peak top positions].[184] Thus, the observed transient absorption spectrum is assigned to the CS state of **30**, which is produced by photoinduced electron transfer from the singlet excited states of H_2P to cup-shaped nanocarbons in the nanohybrid. The formation of the CS state was also detected by electron spin resonance (ESR)

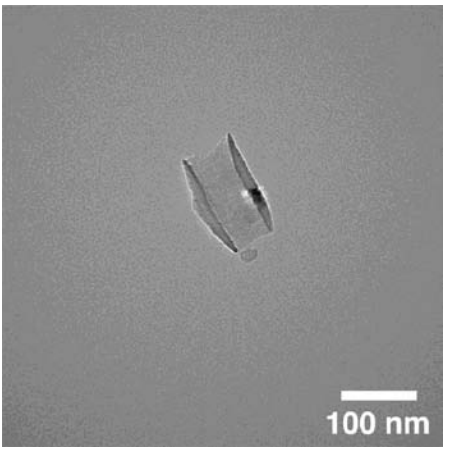

Figure 40. TEM image of porphyrin-functionalized cup-shaped nanocarbons (**30**); scale bar = 100 nm. (Adapted from Ref. 184.)

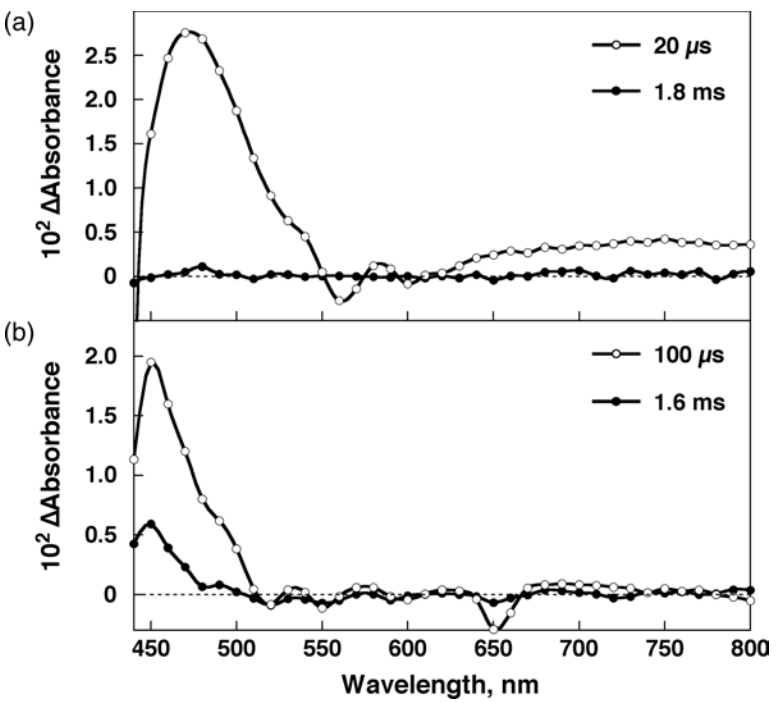

Figure 41. Transient absorption spectra of (a) CNC–$(H_2P)_n$ in deaerated DMF at 298 K taken at 20 μs (solid line with open circles) and 1.8 ms (solid line with black circles) after laser excitation at 426 nm and (b) ref-H_2P in deaerated DMF at 298 K taken at 100 μs (solid line with open circles) and 1.6 ms (solid line with black circles) after laser excitation at 426 nm. (Adapted from Ref. 184.)

measurements under photoirradiation of **30** with a high-pressure mercury lamp in frozen DMF at 153 K.[184]

The CS state detected in Figure 41a decayed obeying clean first-order kinetics.[184] Thus, the decay process is ascribed to intramolecular back electron transfer in the nanohybrid rather than intermolecular back electron transfer between $H_2P^{\bullet+}$ and $CNC^{\bullet-}$ produced by photoinduced electron transfer. The CS lifetime of **30** is determined from the first-order plots to be 0.64 ± 0.01 ms, which is the longest lifetime ever reported for electron-donor-attached nanocarbon materials. Such a long CS lifetime may result from the efficient electron migration in the cup-shaped nanocarbons following the charge separation.[184]

Nanocarbon structures can be obtained using only synthetic porphyrins which form aggregates in the form of fibers, nanorods, and nanotubes.[185–187] Robust porphyrin nanotubes can be prepared by ionic self-assembly of two oppositely charged porphyrins in aqueous solution.[187] The nanotubes are composed entirely of porphyrins and electrostatic, van der Waals, hydrogen bonding, axial coordination, and other weak intermolecular interactions, which typically contribute to the formation of porphyrin aggregates, and enhance the structural stability of these nanostructures.[187]

When $[H_4DPP_2]Cl_2$ is employed as a building block, this compound acts as a starting material to form a variety of novel porphyrin nanochannel (PNC) structures, in which various electron donors are incorporated.[188,189] In the presence of hydroquinone derivatives, the starting PNC (PNC-water) underwent guest exchange from the water molecules to a series of guest molecules in the course of recrystallization.[188] The crystal structure of the PNC including hydroquinone (**31**: PNC-H_2Q) was determined as shown in Figure 42.[188] The structure of the skeleton unit is the same as that of PNC-water and the water molecules are just replaced by hydroquinone.[188] The hydroquinone molecule was included due to intermolecular π–π interactions with H_4DPP^{2+}.[188] Hydrogen bonding was found for the hydroxyl groups of hydroquinone with the nitrogen atoms of the acetonitrile molecules in the skeleton units in the distance of 2.85 Å.[188] This hydrogen bonding fixes the configuration of the two hydrogens of the hydroxyl groups to be *trans* PNC compounds.[187] In the case of benzoquinone derivatives, which are two-electron oxidized species of corresponding hydroquinones, no inclusion was observed for those molecules under the same conditions.[188] These results indicate that electron-donating molecules are included selectively.[188] When tetrabromohydroquinone (H_2QBr_4) was employed as a guest molecule, however, it was not included in the PNC.[188] This indicates that steric factors are also important in the inclusion process of PNC-guest formation.[188]

The photodynamics of **31** is shown in Scheme 7.[188] The photoirradiation of **31** affords the singlet excited state of the porphyrin dication, $^1(H_4DPP^{2+})^*$, which

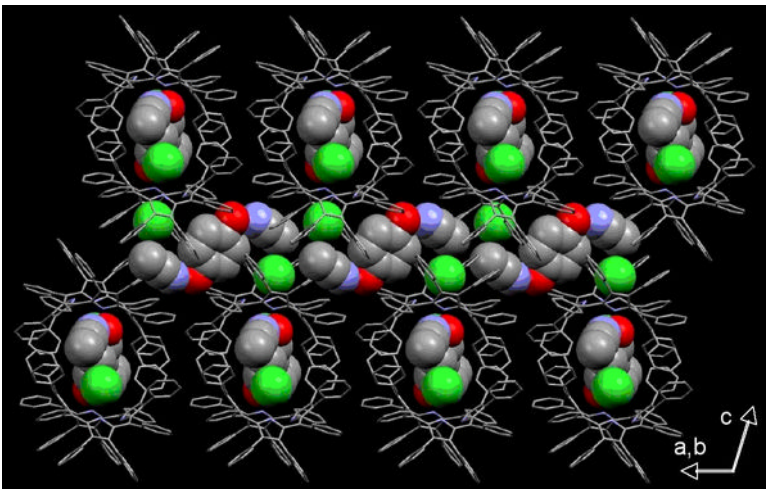

Figure 42. Crystal structure of PNC-H_2Q (**31**). The H_4DPP^{2+} unit is drawn with a wire frame. Carbon — gray; Oxygen — red; nitrogen — blue; chloride — light green. (Adapted from Ref. 188.)

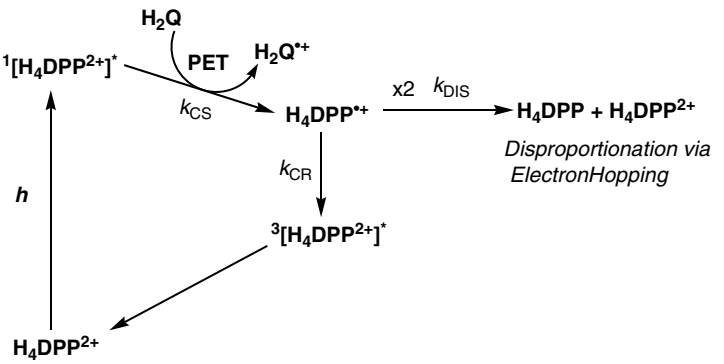

Scheme 7.

accepts one electron from the guest molecule, hydroquinone, to give the corresponding radical cation. The reduced radical cation of $H_4DPP^{\bullet+}$ undergoes fast disproportionation based on electron hopping in the solid state due to close contacts with other H_4DPP^{2+} via intermolecular π–π interactions to give the original H_4DPP^{2+} and the two-electron reduced species of H_4DPP (Scheme 7).[188] In addition, $H_4DPP^{\bullet+}$ undergoes back electron transfer (charge recombination) to form $^3(H_4DPP^{2+})^*$, the energy of which is lower than that of the electron transfer state. The photoinduced electron transfer process from guest donor molecules to $^1(H_4DPP^{2+})^*$ occurs much more efficiently than the intersystem crossing to give the

triplet state, $^3(H_4DPP^{2+})^*$, due to close and secure contact and inevitable intermolecular interactions with the guest molecules in the PNC.[188] Thus, the PNC provides an excellent opportunity to construct and develop porphyrin-based photofunctional materials.[188]

Supramolecular porphyrin nanochannels (PNCs), including tetrathiafulvalene (TTF) acting as a strong electron-donating guest in the inner space, were also prepared with the hydrochloride salt of dodecaphenylporphyrin ($[H_4DPP]Cl_2$) by self-assembly based on intermolecular π–π interactions, as shown in the crystal structure of the TTF-included PNC (**32**: PNC-TTF) in Figure 43.[189] Intermolecular π–π interaction was also recognized among peripheral phenyl groups of the porphyrin, mainly in the direction of the crystallographic *c* axis to form a column structure.[189] Photoinduced electron transfer from TTF to $^1(H_4DPP^{2+})^*$ occurred to afford the electron transfer state, $TTF^{\bullet+}$ and $H_4DPP^{\bullet+}$ in PNC.[189]

A single crystal ($0.87 \times 0.23 \times 0.10$ mm^3) of **32** exhibited photoconductivity upon photoirradiation at 633 nm with a He–Ne laser (5 mW) and the photocurrent was 0.7 nA at an electrical field strength of 3.5×10^4 V cm^{-1}.[189] The photocurrent showed direction dependence toward the crystallographic *c* axis.[189] This indicates that the main electron conduction path of the photocurrent is the π–π interactions among phenyl groups to facilitate electron hopping.[189]

In the case of a cyclic porphyrin dimer (Ni_2-CPD_{Py}) linked by butadiyne moieties bearing 4-pyridyl groups (Figure 44a),[190] Ni_2-CPD_{Py} acts as an electron donor to form a 1:1 inclusion π-complex with an electron acceptor C_{60} (**33**: $C_{60}\subset Ni_2$-CPD_{Py}).[191] The titration in solution indicated that Ni_2-CPD_{Py} included C_{60} to give a

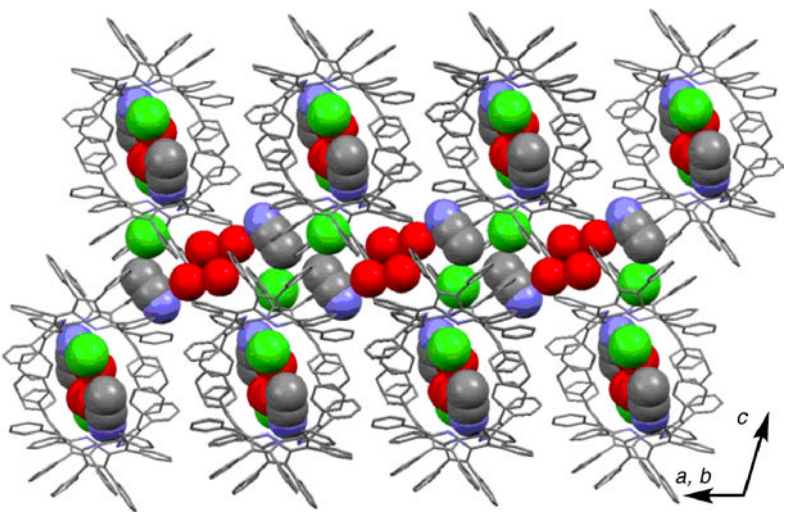

Figure 43. The crystal structure of PNC-TTF (**32**). (Adapted from Ref. 189.)

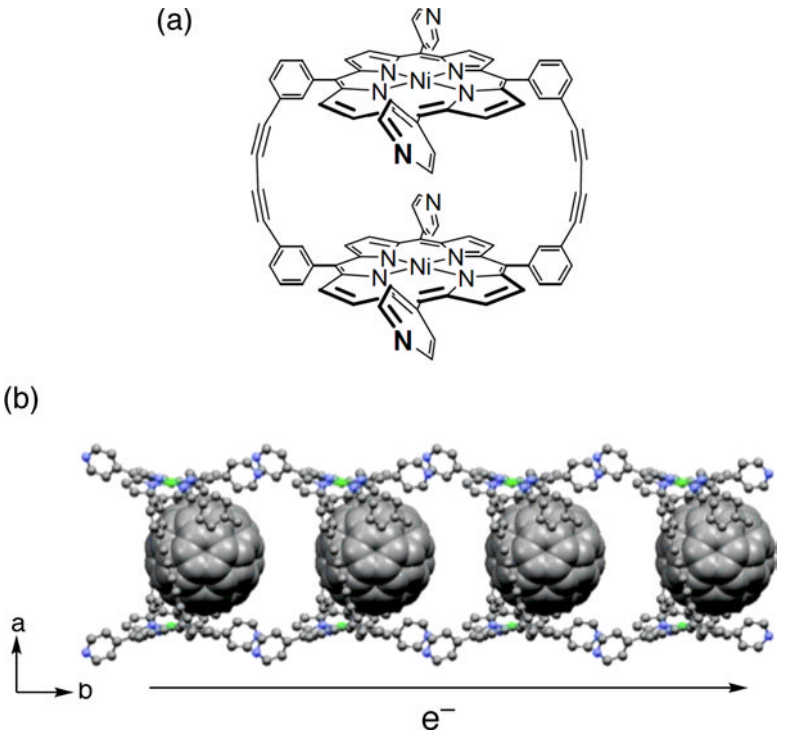

Figure 44. (a) Chemical structure of Ni_2-CPD_{Py}. (b) Crystal structures of tubular assemblies of C_{60}⊂Ni_2-CPD_{Py} (**33**). Hydrogen atoms are omitted for clarity. (Adapted from Ref. 191.)

1:1 inclusion complex (**33**) with an association constant (K) of 2.0×10^5 M^{-1}.[191] X-ray crystallography confirmed the 1:1 inclusion complex of C_{60} with Ni_2-CPD_{Py} (Figure 44b).[191] A nanosized tubular assembly is observed in the crystal packing of **33**. The tubular structure along the crystallographic b axis is formed by self-assembly through two kinds of cooperative noncovalent interactions between Ni_2-CPD_{Py} molecules.[191] One is a pair of complementary C–H···N hydrogen bonding interactions between the pyrrole β-CH and the nitrogen atoms of the pyridyl groups.[191] The other noncovalent interaction is a weak π–π interaction between the pyridyl groups.[191] In the crystal structure of **33**, a porphyrin nanotube is formed by the self-assembly of Ni_2-CPD_{Py}. Ni_2-CPD_{Py} molecules link together through non-classical C–H···N hydrogen bonds and π–π interactions of the pyridyl groups along the crystallographic b axis.[191] The included C_{60} molecules are linearly arranged in the nanotube to afford a supramolecular peapod. The charge carrier mobility of the single crystal of **33** was determined by flash photolysis time-resolved microwave conductivity (FP-TRMC) measurements. It has an anisotropic high electron mobility ($\Sigma\mu = 0.72$ cm^2 V^{-1} s^{-1}) along the linear array of C_{60}

(crystallographic *b* axis).[191] Such a high electron mobility in **33** suggests that supramolecular complexes of self-assembled porphyrin nanotubes and fullerenes provide promising materials for photovoltaic applications.

IX. Porphyrin Solar Cells

The important role of porphyrin derivatives combined with electron donors and acceptors in mimicking light harvesting and photoinduced electron transfer in the photosynthesis described above suggests that porphyrin molecules could serve as potential photosensitizers in dye-sensitized solar cells as well as electron donors in bulk heterojunction solar cell application.[192–198]

The PNC-TTF supramolecules in Figure 43 have been utilized to prepare porphyrin supramolecular solar cells.[188] Schematic description of the solar cell using an OTE/SnO_2/PNC-TTF anode is shown in Figure 45.[189] The PNC crystals-deposited films were prepared by the drop-cast method.[189] Photoelectrochemical measurements were carried out in a standard two-compartment cell consisting of a working electrode and a Pt wire gauze counterelectrode in the electrolyte (0.5 M LiI and 0.01 M I_2) in MeCN.[189] The incident photon-to-current efficiency (IPCE) values at various excitation wavelengths were determined from Eq. 7,[195]

$$\text{IPCE}\ (\%) = \frac{\frac{I_{SC}}{I_{inc}}}{\frac{1240}{\lambda}} \times 100, \tag{7}$$

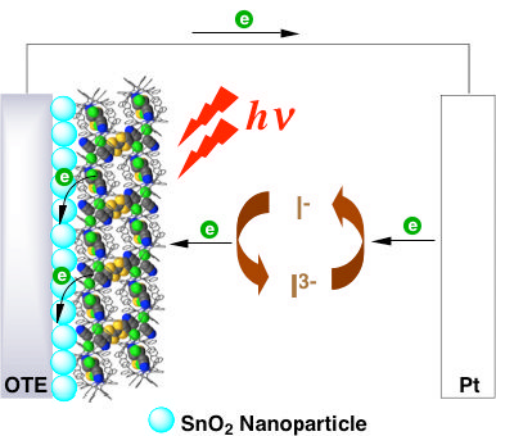

Figure 45. A schematic description of a photoelectrochemical cell using an OTE/SnO_2/PNC-TTF anode.

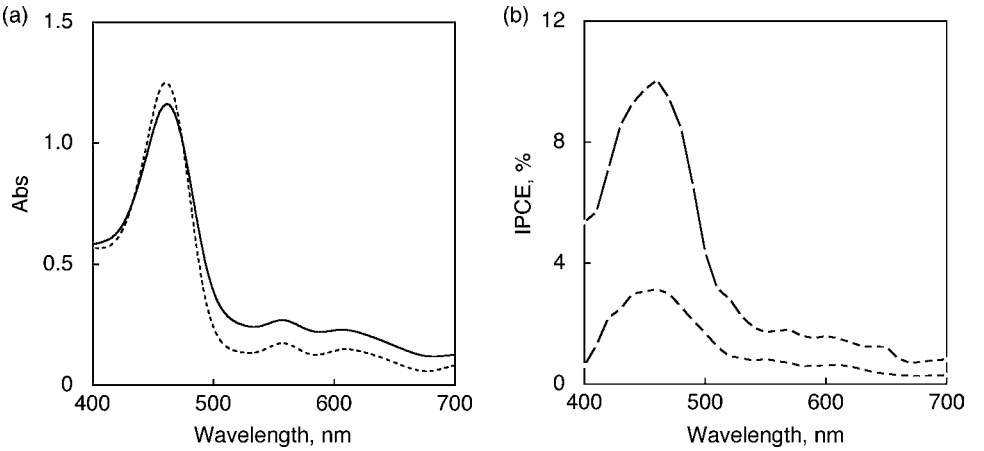

Figure 46. (a) Absorption spectra of OTE/SnO_2/PNC-TTF (solid line) and OTE/SnO_2/PNC-water (dotted line); (b) IPCE plots for OTE/SnO_2/PNC-TTF (circle) and OTE/SnO_2/PNC-water (square). (Adapted from Ref. 189.)

where I_{inc} is the incident light intensity (W cm^{-2}) and λ is the excitation wavelength (nm). The action spectra of both the OTE/SnO_2/PNC-TTF and the OTE/SnO_2/PNC-water electrodes are shown in Figure 46.[189] The close match in the absorption and action spectra indicates that the singlet excited state of $[H_4DPP]Cl_2$ is responsible for the photocurrent generation. Photoinduced electron transfer from TTF to $^1\{[H_4DPP]Cl_2\}^*$ followed by intermolecular electron hopping results in enhancement of photocurrent generation, because the maximum IPCE value (10.1%) for the OTE/SnO_2/PNC-TTF is more than three times higher than that for the OTE/SnO_2/PNC-water (3.1%).[189]

A combination of porphyrin dendrimers (chromophores and electron donor) and fullerenes (electron acceptor) is expected to result in enhanced light-harvesting efficiency of chromophores throughout the solar spectrum. Thus, a new type of solar cell has been constructed using molecular clusters of porphyrin dendrimer (donor) and fullerene (acceptor) dye units assembled on SnO_2 electrodes, which have high charge separation efficiency as well as efficient hole and electron transport.[199,200] The porphyrin dendrimers [D_nP_n; n = 4 (**34**), 8 (**35**), 16 (**36**)] are shown in Figure 47 together with the reference porphyrin compound (H_2P-ref).[199,200] Porphyrin dendrimers (D_nP_n) form supramolecular complexes with C_{60} in toluene and they are clustered in an acetonitrile/toluene mixed solvent system.[199,200] Then, the clusters are attached on nanostructured SnO_2 electrodes by an electrophoretic deposition method to afford the modified electrodes [denoted as OTE/SnO_2/$(D_nP_n+C_{60})_m$ (n = 4, 8, 16)].[199,200] The photoelectrochemical measurements were performed with a standard two-electrode system consisting of a

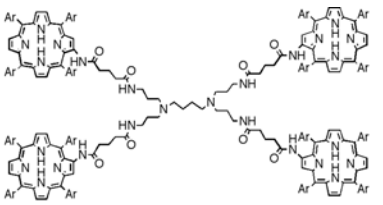

D_4P_4 (**34**)

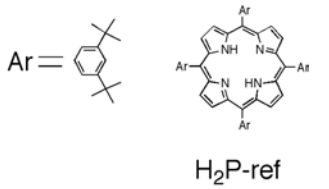

H_2P-ref

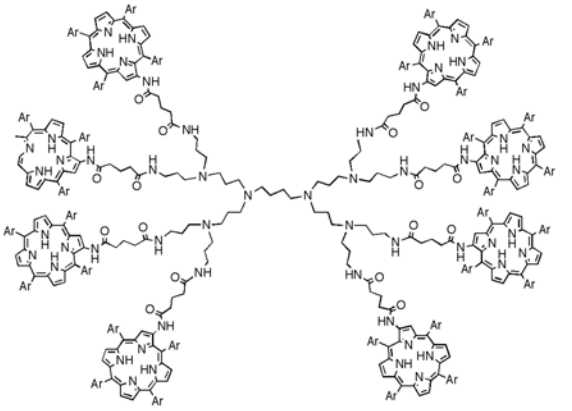

D_8P_8 (**35**)

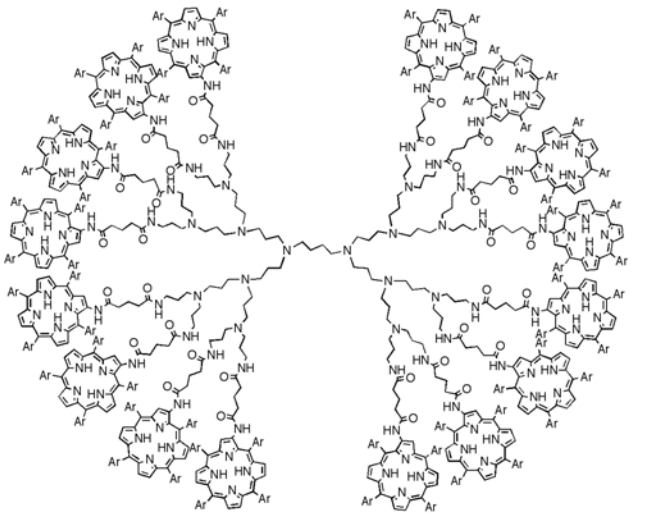

$D_{16}P_{16}$ (**36**)

Figure 47. Porphyrin dendrimers (**34**–**36**) and the reference compound employed for construction of organic solar cells composed of multiporphyrin/C_{60} supramolecular assemblies. (Adapted from Refs. 199 and 200.)

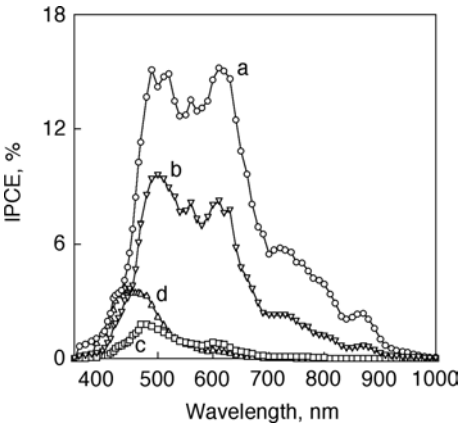

Figure 48. Photocurrent action spectra (IPCE vs. wavelength) of OTE/SnO_2/$(D_nP_n+C_{60})_m$ systems [(a) $n = 4$ (**34**); (b) $n = 8$ (**35**); (c) $n = 16$ (**36**)], (d) OTE/SnO_2/$(H_2P\text{-ref}+C_{60})_m$ and [D_4P_4] = 0.048 mM, [D_8P_8] = 0.024 mM, [$D_{16}P_{16}$] = 0.012 mM and [H_2P-ref] = 0.19 mM; [C_{60}] = 0.31 mM in MeCN/toluene = 3/1. (Adapted from Ref. 200.)

working electrode and a Pt wire gauze electrode in 0.5 M NaI and 0.01 M I_2 in air-saturated MeCN.[199,200] Figure 48 shows the wavelength dependence of the IPCE of the OTE/SnO_2/$(D_nP_n+C_{60})_m$ system and the reference system (OTE/SnO_2/$(H_2P\text{-ref}+C_{60})_m$) at a constant concentration ratio of porphyrin to C_{60}.[200] The OTE/SnO_2/$(D_4P_4+C_{60})_m$ system has the maximum IPCE value of 15% as well as the broad photoresponse, which extends well into the infrared (up to 1000 nm).[200]

Comparison of the photoelectrochemical properties between the OTE/SnO_2/$(D_4P_4+C_{60})_m$ system and the reference system indicates that the composite clusters of porphyrin dendrimers with C_{60} exhibit remarkable enhancement in photoelectrochemical performance due to the effective π–π interaction between porphyrins and fullerenes in the interpenetrating structure of the supramolecular clusters as compared with the reference system.[200] The broad long-wavelength absorption in the NIR region is diagnostic of the charge transfer absorption band due to the π-complex formed between the porphyrin and C_{60}, because similar charge transfer interactions leading to extended absorption have been observed for porphyrin–C_{60} dyads linked in close proximity.[201,202] The IPCE value decreases with increase in the number of dendrimer generation, and the OTE/SnO_2/$(D_{16}P_{16}+C_{60})_m$ system has even smaller IPCE values compared with the reference system [OTE/SnO_2/$(H_2P\text{-ref}+C_{60})_m$] (Figure 48).[200] In the case of $D_{16}P_{16}$ (**36**), the space between porphyrin rings may be too small for the interaction with C_{60}. This indicates that the distance between two porphyrin rings is also an essential factor in forming such a supramolecular complex.

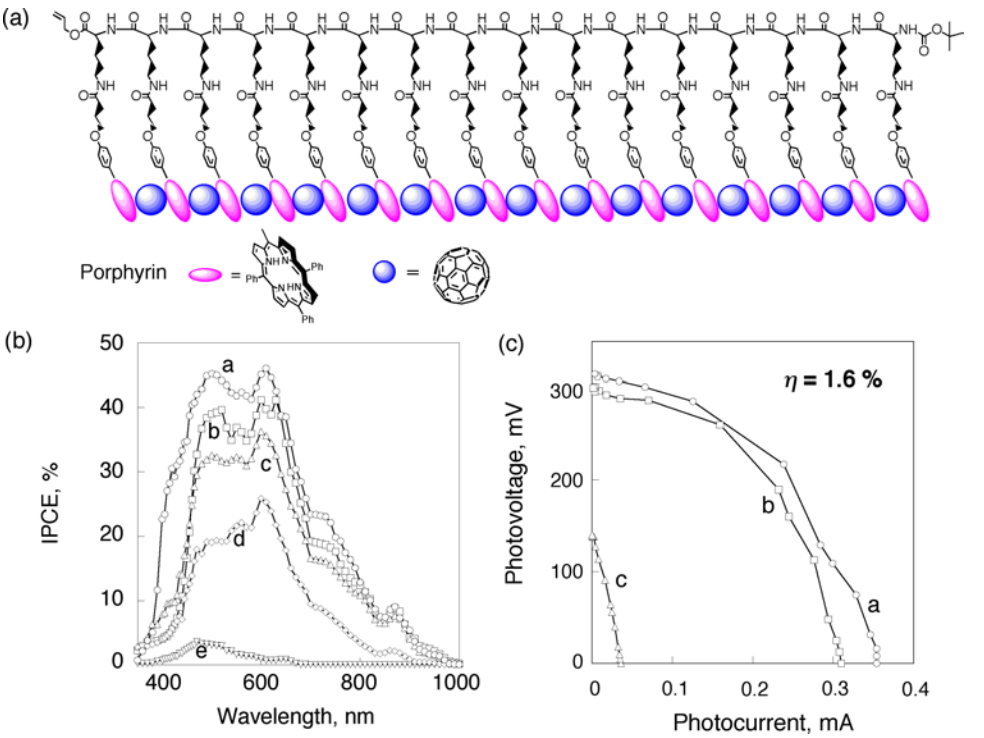

Figure 49. (a) Supramolecular complex between porphyrin–peptide hexadecamer $[P(H_2P)_{16}]$ (**41**) and C_{60}. (b) The photocurrent action spectra (IPCE vs. wavelength) of (a) (**41**+$C_{60})_m$, (b) (**40**+$C_{60})_m$, (c) (**39**+$C_{60})_m$, (d) (**38**+$C_{60})_m$, and (e) (**37**+$C_{60})_m$ modified OTE/SnO_2 electrodes under short circuit conditions. (c) Current–voltage characteristics of (a) OTE/SnO_2/(**41**+$C_{60})_m$, (b) OTE/SnO_2/(**40**+$C_{60})_m$, and (c) OTE/SnO_2/(**37**+$C_{60})_m$. (Adapted from Ref. 204.)

Porphyrin oligomers with a polypeptidic backbone, shown in Figure 49, are flexible enough to accommodate C_{60} between the porphyrin units.[203,204] The organization of $P(H_2P)_n$ and C_{60} composite clusters onto an optically transparent electrode (OTE) of a nanostructured SnO_2 electrode (denoted as OTE/SnO_2/$(P(H_2P)_n+C_{60})_m$ [n = 1 (**37**), 2 (**38**), 4 (**39**), 8 (**40**), 16 (**41**)]) was performed as the case of porphyrin dendrimers (*vide supra*). The IPCE value of OTE/SnO_2/$(P(H_2P)_n+C_{60})_m$ (n = 1, 2, 4, 8, 16) exhibits a remarkable rise with increase in the number of porphyrins in a polypeptide unit, as shown in Figure 49(b).[204] The OTE/SnO_2/$(P(H_2P)_{16}+C_{60})_m$ system has the maximum IPCE value of 48% at 600 nm as well as a broad photoresponse extending into the infrared region (up to 1000 nm).[204] This indicates that efficient photoinduced electron transfer occurs from the excited state of the porphyrin unit to C_{60} in the supramolecular complex with increase in the number of porphyrins in a polypeptide unit. Such an effective

light energy conversion is largely ascribed to the polypeptide structure which controls the three-dimensional organization between porphyrin and C_{60}.

The current–voltage (*I/V*) characteristics of OTE/SnO_2/(**41**+C_{60})$_m$, OTE/SnO_2/(**40**+C_{60})$_m$, and OTE/SnO_2/(**37**+C_{60})$_m$ electrodes are shown in Figure 49(c).[204] The (**41**+C_{60})$_m$ system has a fill factor (FF) of 0.47, an open circuit voltage (V_{oc}) of 320 mV, a short circuit current density (I_{sc}) of 0.36 mA cm^{-2}, and the overall power conversion efficiency (η) of 1.6% at input power of 3.4 mW cm^{-2}.[204] The *I/V* characteristics of the OTE/SnO_2/(**41**+C_{60})$_m$ system is remarkably enhanced (more than 40 times) as compared with the OTE/SnO_2/(**37**+C_{60})$_m$ electrode under the same experimental conditions.[204]

Supramolecular porphyrin solar cells have also been constructed using porphyrin-alkanethiolate monolayer protected-gold nanoclusters and C_{60} by clustering with gold nanoparticles and the electrophoretic deposition on SnO_2 electrodes to attain the power conversion efficiency of 1.5%.[205,206] Thus, supramolecular approaches between porphyrins and fullerenes provide a promising perspective for the development of efficient organic solar cells.

X. Concluding Remarks

As demonstrated in this chapter, porphyrins and phthalocyanines exhibit excellent photoinduced energy transfer and electron transfer properties with electron donors and acceptors, efficiently mimicking the functions in natural photosynthesis. The small reorganization energies of electron transfer of these functional π-compounds are essential for the design of artificial photosynthetic systems with fast charge separation but extremely slow charge recombination, which can be successfully applied to construct efficient light energy conversion systems such as photovoltaic devices. In particular, three-dimensional steric control in the supramolecular complexes of porphyrins and phthalocyanines with electron donors and acceptors contributes to efficient charge separation as well as hole and electron migration. Further improvement of energy transfer and electron transfer properties of photosynthetic reaction center models composed of porphyrins and phthalocyanines will certainly provide promising perspectives for the development of efficient light energy conversion systems.

XI. Acknowledgments

The author gratefully acknowledges the contributions of his collaborators and coworkers who are mentioned in the references. He also thanks the Ministry of Education, Culture, Sports, Science and Technology, Japan, and KOSEF/MEST through a WCU (R31-2008-000-10010-0) project for continuous support.

XII. References

1. Royer, D. L.; Berner, R. A.; Park, J. *Nature* **2007**, *446*, 530.
2. Lewis, N. S.; Nocera, D. G. *Proc. Natl. Acad. Sci. USA* **2006**, *103*, 15729.
3. Lewis, N. S. *ChemSusChem* **2009**, *2*, 383.
4. Fukuzumi, S. *Org. Biomol. Chem*. **2003**, *1*, 609.
5. Fukuzumi, S. *Bull. Chem. Soc. Jpn*. **2006**, *79*, 177.
6. Fukuzumi, S. *Phys. Chem. Chem. Phys*. **2008**, *10*, 2283-2297.
7. Hambourger, M.; Moore, G. F.; Kramer, D. M.; Gust, D.; Moore, A. L.; Moore, T. A. *Chem. Soc. Rev*. **2009**, *38*, 25.
8. Fukuzumi, S. *Eur. J. Inorg. Chem*. **2008**, 1351.
9. Deisenhofer, J.; Michel, H. *Angew. Chem. Int. Ed. Engl.* **1989**, *28*, 829.
10. Hoff, A. J.; Deisenhofer, J. *Phys. Rep*. **1997**, *287*, 1.
11. Nelson, N.; Yocum, C. F. *Annu. Rev. Plant Biol*. **2006**, *57*, 521.
12. Wasielewski, M. R. *Acc. Chem. Res*. **2009**, *42*, 1910.
13. Lewis, F. D.; Letsinger, R. L.; Wasielewski, M. R. *Acc. Chem. Res*. **2001**, *34*, 159.
14. Fukuzumi, S.; Guldi, D. M. In *Electron Transfer in Chemistry*; Balzani, V., Ed.; Wiley-VCH: Weinheim, **2001**; Vol. 2, pp. 270–337.
15. Guldi, D. M.; Illescas, B. M.; Atienza, C. M.; Wielopolski, M.; Martin, N. *Chem. Soc. Rev*. **2009**, *38*, 1587.
16. Martin, N.; Sanchez, L.; Herranz, M. A.; Illescas, B.; Guldi, D. M. *Acc. Chem. Res*. **2007**, *40*, 1015.
17. Fukuzumi, S.; Kojima, T. *J. Mater. Chem*. **2008**, *18*, 1427.
18. Fukuzumi, S.; Honda, T.; Ohkubo, K.; Kojima, T. *Dalton Trans*. **2009**, 3880.
19. Ohkubo, K.; Fukuzumi, S. *J. Porphyrins Phthalocyanines* **2008**, *12*, 993.
20. D'Souza, F.; Ito, O. *Coord. Chem. Rev*. **2005**, *249*, 1410.
21. Paddon-Row, M. N. In *Electron Transfer in Chemistry*; Balzani, V., Ed.; Wiley-VCH: Weinheim, **2001**; Vol. 3, pp. 179–271.
22. Flamigni, L.; Barigelletti, F.; Armaroli, N.; Collin, J.-P.; Dixon, I. M.; Sauvage, J.-P.; Williams, J. A. G. *Coord. Chem. Rev*. **1999**, *190–192*, 671.
23. Gust, D.; Moore, T. A.; Moore, A. L. In *Electron Transfer in Chemistry*; Balzani, V., Ed; Wiley-VCH: Weinheim, **2001**; Vol. 3, pp. 272–336.
24. Gust, D.; Moore, T. A. In *The Porphyrin Handbook*; Kadish, K. M.; Smith, K. M.; Guilard, R., Eds.; Academic Press: San Diego, CA, **2000**; Vol. 8, pp. 153–190.
25. Marcus, R. A. *Annu. Rev. Phys. Chem.* **1964**, *15*, 155.
26. Marcus, R. A. *Angew. Chem. Int. Ed. Engl*. **1993**, *32*, 1111.
27. Closs, G. L.; Miller, J. R. *Science* **1988**, *240*, 440.
28. Gould, I. R.; Farid, S. *Acc. Chem. Res*. **1996**, *29*, 522.
29. McLendon, G. *Acc. Chem. Res*. **1988**, *21*, 160.
30. Winkler, J. R.; Gray, H. B. *Chem. Rev*. **1992**, *92*, 369.
31. McLendon, G.; Hake, R. *Chem. Rev*. **1992**, *92*, 481.
32. Fukuzumi, S. In *The Porphyrin Handbook*; Kadish, K. M.; Smith, K.; Guilard, R., Eds.; Academic Press: San Diego, **2000**; Vol. 8, p. 115.
33. Shelnutt, J. A.; Medforth, C. J.; Berber, M. D.; Barkigia, K. M.; Smith, K. M. *J. Am. Chem. Soc.* **1991**, *113*, 4077.
34. Medforth, C. J.; Senge, M. O.; Smith, K. M.; Sparks, L. D.; Shelnutt, J. A. *J. Am. Chem. Soc*. **1992**, *114*, 9859.

35. Nakanishi, T.; Kojima, T.; Ohkubo, K.; Fukuzumi, S. *J. Am. Chem. Soc*. **2009**, *131*, 577.
36. Birnbaum, E. R.; Hodge, J. A.; Grinstaff, M. W.; Schaefer, W. P.; Henling, L.; Labinger, J. A.; Bercaw, J. E.; Gray, H. B. *Inorg. Chem*. **1995**, *34*, 3625.
37. Kavarnos, G. J. *Fundamentals of Photoinduced Electron Transfer*; Wiley–VCH: New York, **1993**.
38. Brunschwig, B. S.; Ehrenson, S.; Sutin, N. J. *J. Am. Chem. Soc*. **1984**, *106*, 6858.
39. Jentzen, W.; Turowska-Tyrk, I.; Scheidt, W. R.; Shelnutt, J. A. *Inorg. Chem*. **1996**, *35*, 3559.
40. Fukuzumi, S.; Nakanishi, I.; Tanaka, K.; Suenobu, T.; Tabard, A.; Guilard, R.; Van Caemelbecke, E.; Kadish, K. M. *J. Am. Chem. Soc*. **1999**, *121*, 785.
41. Ferreira, K. N.; Iverson, T. M.; Maghlaoui, K.; Barber, J.; Iwata, S. *Science* **2004**, *303*, 1831.
42. Pascal, A. A.; Liu, Z.; Broess, K.; van Oort, B.; van Amerongen, H.; Wang, C.; Horton, P.; Robert, B.; Chang, W.; Ruban, A. *Nature* **2005**, *436*, 134.
43. Amunts, A.; Drory, O.; Nelson, N. *Nature* **2007**, *447*, 58.
44. Ganesan, V.; Rosokha, S. V.; Kochi, J. K. *J. Am. Chem. Soc*. **2003**, *125*, 2559.
45. Lu, J.-M.; Rosokha, S. V.; Kochi, J. K. *J. Am. Chem. Soc*. **2003**, *125*, 12161.
46. Scheidt, W. R.; Cheng, B.; Haller, K. J.; Mislankar, A.; Rae, A. D.; Reddy, K. V.; Song, H.; Orosz, R. D.; Reed, C. A.; Cukiernik, F.; Marchon, J.-C. *J. Am. Chem. Soc*. **1993**, *115*, 1181.
47. Brancato-Buentello, K. E.; Kang, S.-J.; Scheidt, W. R. *J. Am. Chem. Soc*. **1997**, *119*, 2839.
48. Scheidt, W. R. *J. Biol. Inorg. Chem*. **2001**, *6*, 727.
49. Wasielewski, M. R.; Svec, W. A.; Cope, B. T. *J. Am. Chem. Soc*. **1978**, *100*, 1961.
50. Osuka, A.; Nakajima, S.; Maruyama, K.; Mataga, N.; Asahi, T.; Yamazaki, I.; Nishimura, Y.; Ohno, T.; Nozaki, K. *J. Am. Chem. Soc*. **1993**, *115*, 4577.
51. Pognon, G.; Boudon, C.; Schenk, K. J.; Bonin, M.; Bach, B.; Weiss, J. *J. Am. Chem. Soc*. **2006**, *128*, 3488.
52. Ozeki, H.; Nomoto, A.; Ogawa, K.; Kobuke, Y.; Murakami, M.; Hosoda, K.; Ohtani, M.; Nakashima, S.; Miyasaka, H.; Okada, T. *Chem. Eur. J*. **2004**, *10*, 6393.
53. D'Souza, F.; Chitta, R.; Gadde, S.; Rogers, L. M.; Karr, P. A.; Zandler, M. E.; Sandanayaka, A. S. D.; Araki, Y.; Ito, O. *Chem. Eur. J*. **2007**, *13*, 916.
54. Kuramochi, Y.; Satake, A.; Itou, M.; Ogawa, K.; Araki, Y.; Ito, O.; Kobuke, Y. *Chem. Eur. J*. **2008**, *14*, 2827.
55. Takai, A.: Gros, C. P.; Guilard, R.; Fukuzumi, S. *Chem. Eur. J*. **2009**, *15*, 3110.
56. Collman, J. P.; Hutchinson, J. E.; Lopez, M. A.; Tabard, A.; Guilard, R.; Seok, W. K.; Ibers, J. A.; L'Her, M. *J. Am. Chem. Soc*. **1992**, *114*, 9869.
57. Deng, Y.; Chang, C. J.; Nocera, D. G. *J. Am. Chem. Soc*. **2000**, *122*, 410.
58. Gros, C. P.; Brisach, F.; Meristoudi, A.; Espinosa, E.; Guilard, R.; Harvey, P. D. *Inorg. Chem*. **2007**, *46*, 125.
59. Tomo, T.; Okubo, T.; Akimoto, S.; Yokono, M.; Miyashita, H.; Tsuchiya, T.; Noguchi, T.; Mimuro, M. *Proc. Natl. Acad. Sci. USA* **2007**, *104*, 7283.
60. Vasudevan, J.; Stibrany, R. T.; Bumby, J.; Knapp, S.; Potenza, J. A.; Emge, T. J.; Schugar, H. J. *J. Am. Chem. Soc*. **1996**, *118*, 11676.
61. Fujitsuka, M.; Cho, D. W.; Tojo, S.; Yamashiro, S.; Shinmyozu, T.; Majima, T. *J. Phys. Chem. A* **2006**, *110*, 5735.
62. Shen, X.; Lind, J.; Merenyi, G. *J. Phys. Chem*. **1987**, *91*, 4403.
63. Shen, X.; Lind, J.; Eriksen, T. E.; Merenyi, G. *J. Chem. Soc. Perkin Trans. 2* **1989**, 555.
64. Ghosh, A. *J. Phys. Chem. B* **1997**, *101*, 3290.
65. Fukuzumi, S.; Ohkubo, K.; Chen, Y.; Pandey, R. K.; Zhan, R.; Shao, J.; Kadish, K. M. *J. Phys. Chem. A* **2002**, *106*, 5105.

66. Fukuzumi, S.; Ohkubo, K.; Imahori, H.; Shao, J.; Ou, Z.; Zheng, G.; Chen, Y.; Pandey, R. K.; Fujitsuka, M.; Ito O.; Kadish, K. M. *J. Am. Chem. Soc*. **2001**, *123*, 10676.
67. Fukuzumi, S.; Suenobu, T.; Hirasaka, T.; Sakurada, N.; Arakawa, R.; Fujitsuka, M.; Ito, O. *J. Phys. Chem. A* **1999**, *103*, 5935.
68. Anderson, J. L.; An, Y.-Z.; Rubin, Y.; Foote, C. S. *J. Am. Chem. Soc*. **1994**, *116*, 9763.
69. Ohkubo, K.; Imahori, H.; Shao, J.; Ou, Z.; Kadish, K. M.; Chen, Y.; Zheng, G.; Pandey, R. K.; Fujitsuka, M.; Ito, O.; Fukuzumi, S. *J. Phys. Chem. A* **2002**, *106*, 10991.
70. Imahori, H.; Tamaki, K.; Guldi, D. M.; Luo, C.; Fujitsuka, M.; Ito, O.; Sakata, Y.; Fukuzumi, S. *J. Am. Chem. Soc*. **2001**, *123*, 2607.
71. Ohkubo, K.; Kotani, H.; Shao, J.; Ou, Z.; Kadish, K. M.; Li, G.; Pandey, R. K.; Fujitsuka, M.; Ito, O.; Imahori, H.; Fukuzumi, S. *Angew. Chem. Int. Ed*. **2004**, *43*, 853.
72. Kashiwagi, Y.; Ohkubo, K.; McDonald, J. A.; Blake, I. M.; Crossley, M. J.; Araki, Y.; Ito, O.; Imahori, H.; Fukuzumi, S. *Org. Lett*. **2003**, *5*, 2719.
73. Imahori, H.; El-Khouly, M. E.; Fujitsuka, M.; Ito, O.; Sakata, Y.; Fukuzumi, S. *J. Phys. Chem. A* **2001**, *105*, 325.
74. Fukuzumi, S.; Ohkubo, K.; E, W.; Ou, Z.; Shao, J.; Kadish, K. M.; Hutchison, J. A.; Ghiggino, K. P.; Sintic, P. J.; Crossley, M. J. *J. Am. Chem. Soc*. **2003**, *125*, 14984.
75. Kadish, K. M.; Wenbo, E.; Ou, Z.; Shao, J.; Sintic, P. J.; Ohkubo, K.; Fukuzumi, S.; Crossley, M. J. *Chem. Commun*. **2002**, 356.
76. Kadish, K. M.; Wenbo, E.; Ou, Z.; Shao, J.; Sintic, P. J.; Ohkubo, K.; Fukuzumi, S.; Crossley, M. J. *Inorg. Chem*. **2004**, *43*, 2078.
77. Ohkubo, K.; Garcia, R.; Sintic, P. J.; Khoury, T.; Crossley, M. J.; Kadish, K. M.; Fukuzumi, S. *Chem. Eur. J*. **2009**, *15*, 10493.
78. Ohkubo, K.; Sintic, P. J.; Tkachenko, N. V.; Lemmetyinen, H.; Wenbo, E.; Ou, Z.; Shao, J.; Kadish, K. M.; Crossley, M. J.; Fukuzumi, S. *Chem. Phys*. **2006**, *326*, 3.
79. El-Khouly, M. E.; Ryu, J. B.; Kay, K.-Y.; Ito, O.; Fukuzumi, S. *J. Phys. Chem. C* **2009**, *113*, 15444.
80. de la Torre, G.; Torres, T.; Agulló-López, F. *Adv. Mater*. **1997**, *9*, 265.
81. Kobayashi, N.; Ishizaki, T.; Ishii, K.; Konami, H. *J. Am. Chem. Soc*. **1999**, *121*, 9096.
82. Kobayashi, N. *Bull. Chem. Soc. Jpn*. **2002**, *75*, 1.
83. Torres, T. *Angew. Chem. Int. Ed*. **2006**, *45*, 2834.
84. González-Rodríguez, D.; Torres, T.; Olmstead, M. M.; Rivera, J.; Herranz, M. Á.; Echegoyen, L.; Atienza Castellanos, C.; Guldi, D. M. *J. Am. Chem. Soc*. **2006**, *128*, 10680.
85. El-Khouly, M. E.; Shim, S. H.; Araki, Y.; Ito, O.; Kay, K.-Y. *J. Phys. Chem*. **2008**, *112*, 3910.
86. Medina, A.; Glassens, C. G.; Aminur Rahman, G. M.; Lamsabhi, A.; Mo, O.; Yanez, M.; Guldi, D. M.; Torres, T. *Chem. Commun*. **2008**, 1759.
87. Chitta, R.; Ohkubo, K.; Tasior, M.; Subbaiyan, N. K.; Zandler, M. E.; Gryko, D. T.; Fukuzumi, S.; D'Souza, F. *J. Am. Chem. Soc*. **2008**, *130*, 14263.
88. Johnson, A. W.; Kay, I. T. *J. Chem. Soc*. **1965**, 1620.
89. Vogel, E.; Will, S.; Shulze-Tilling, A.; Neumann, L.; Lex, J.; Bill, E.; Trautwein, A. X.; Wieghardt, K. *Angew. Chem. Int. Ed. Engl*. **1994**, *33*, 731.
90. Gryko, D. T. *Eur. J. Org. Chem*. **2002**, 1735.
91. Ding, T.; Alemán, E. A.; Mordarelli, D. A.; Ziegler, C. J. *J. Phys. Chem. A* **2005**, *109*, 7411–7417.
92. Bendix, J.; Dmochowski, I. J.; Gray, H. B.; Mahammed, A.; Simkhovic, L.; Gross, Z. *Angew. Chem. Int. Ed*. **2000**, *39*, 4048–4051.

93. Van der Boom, T.; Hayes, R. T.; Zhao, Y.; Bushard, P. J.; Weiss, E. A.; Wasielewski, M. R. *J. Am. Chem. Soc*. **2002**, *124*, 9582.
94. Tomizaki, K.; Loewe, R. S.; Kirmaier, C.; Scwartz, J. K.; Retsek, J. L.; Bocian, D. F.; Holten, D.; Lindsey, J. S. *J. Org. Chem*. **2002**, *67*, 6519–6534.
95. Wenger, O. S. *Coord. Chem. Rev*. **2009**, *253*, 1439.
96. Springer, J.; Kodis, G.; De La Garza, L.; Moore, A. L.; Moore, T. A.; Gust, D. *J. Phys. Chem. A* **2003**, *107*, 3567.
97. Baranoff, E.; Barigelletti, F.; Bonnet, S.; Collin, J.-P.; Flamigni, L.; Mobian, P.; Sauvage, J.-P. *Struct. Bond*. **2007**, *123*, 41.
98. Imahori, H.; Tamaki, K.; Araki, Y.; Sekiguchi, Y.; Ito, O.; Sakata, Y.; Fukuzumi, S. *J. Am. Chem. Soc*. **2002**, *124*, 5165.
99. Flamigni, L.; Dixon, I. M.; Collin, J.-P.; Sauvage, J.-P. *Chem. Commun*. **2000**, 2479.
100. Gabrielsson, A.; Hartl, F.; Zhang, H.; Lindsay Smith, J. R.; Towrie, M.; Vlcek, A., Jr.; Perutz, R. N. *J. Am. Chem. Soc*. **2006**, *128*, 4253.
101. Curiel, D.; Ohkubo, K.; Reimers, J. R.; Fukuzumi, S.; Crossley, M. J. *Phys. Chem. Chem. Phys*. **2007**, *9*, 5260.
102. Imahori, H.; Guldi, D. M.; Tamaki, K.; Yoshida, Y.; Luo, C.; Sakata, Y.; Fukuzumi, S. *J. Am. Chem. Soc*. **2001**, *123*, 6617.
103. Guldi, D. M.; Hungerbühler, H.; Asmus, K.-D. *J. Phys. Chem*. **1995**, *99*, 9380.
104. Fukuzumi, S.; Imahori, H.; Yamada, H.; El-Khouly, M. E.; Fujitsuka, M.; Ito, O.; Guldi, D. M. *J. Am. Chem. Soc.* **2001**, *123*, 2571.
105. Luo, C.; Guldi, D. M.; Imahori, H.; Tamaki, K.; Sakata, Y. *J. Am. Chem. Soc*. **2000**, *122*, 6535.
106. Blankenship, R. E.; Madigan, M. T.; Bauer, C. E., Eds. *Anoxygenic Photosynthetic Bacteria*; Kluwer Academic Publishing: Dordrecht, **1995**.
107. Helms, A.; Heiler, D.; McLendon, G. *J. Am. Chem. Soc*. **1992**, *114*, 6227.
108. Guldi, D. M.; Imahori, H.; Tamaki, K.; Kashiwagi, Y.; Yamada, H.; Sakata, Y.; Fukuzumi, S. *J. Phys. Chem. A* **2004**, *108*, 541.
109. Imahori, H.; Sekiguchi, Y.; Kashiwagi, Y.; Sato, T.; Araki, Y.; Ito, O.; Yamada, H.; Fukuzumi, S. *Chem. Eur. J*. **2004**, *10*, 3184.
110. Hanack, M.; Heckmann, H.; Polley, R. In *Methods in Organic Chemistry* (Houben-Weyl); Schaumann, E., Ed.; Thieme: Stuttgart, **1998**; Vol. E 9d, p. 717.
111. de la Torre, G.; Nicolau, M.; Torres, T. In *Phthalocyanines: Syntheses, Supramolecular Organization and Physical Properties (Supramolecular Photosensitive and Electroactive Materials)*; Nalwa, H. S., Ed.; Academic Press: New York, **2001**; pp. 1–111.
112. de la Torre, G.; Vázquez, P.; Agulló-López, F.; Torres, T. *Chem. Rev*. **2004**, *104*, 3723–3750.
113. Cheng, G.; Peng, X.; Hao, G.; Kennedy, V. O.; Ivano I. N.; Knappenberger, K.; Hill, T. J.; Rodgers, M. A. J.; Kenney M. E. *J. Phys. Chem. A* **2003**, *107*, 3503.
114. Ohkubo, K.; Fernández-Lázaro, F.; Fukuzumi, S.; Sastre-Santos, Á. *Org. Lett*. **2007**, *9*, 3441.
115. Martín-Gomis, L.; Ohkubo, K.; Fernández-Lázaro, F.; Fukuzumi, S.; Sastre-Santos, Á. *J. Phys. Chem. A* **2008**, *112*, 17694.
116. McKeown, N. B. *J. Mater. Chem*. **2000**, *10*, 1979–1995.
117. El-Khouly, M. E.; Kim, J. H.; Kay, K.-Y.; Choi, C. S.; Ito, O.; Fukuzumi, S. *Chem. Eur. J*. **2009**, *15*, 5301.
118. Okamoto, K.; Mori, Y.; Yamada, H.; Imahori, H.; Fukuzumi, S. *Chem. Eur. J*. **2004**, *10*, 474.
119. de Rege, P. J. F.; Williams, S. A.; Therien, M. J. *Science* **1995**, *269*, 1409.
120. Sessler, J. L.; Wang, B.; Harriman, A. *J. Am. Chem. Soc*. **1995**, *117*, 704.

121. Sessler, J. L.; Wang, B.; Springs, S. L.; Brown, C. T. In *Comprehensive Supramolecular Chemistry*; Atwood, J. L., Davies, J. E. D., Eds.; Pergamon, **1996**.
122. Chang, C. J.; Brown, J. D. K.; Chang, M. C. Y.; Baker, E. A.; Nocera, D. G. In *Electron Transfer in Chemistry*; Balzani, V., Ed.; Wiley-VCH: Weinheim, **2001**; Vol. 3, pp. 409–461.
123. D'Souza, F.; Ito, O. *Chem. Commun*. **2009**, 4913.
124. Blanco, M.-J.; Jiménez, M. C.; Chambron, J.-C.; Heitz, V.; Linke, M.; Sauvage, J.-P. *Chem. Soc. Rev*. **1999**, *28*, 293.
125. D'Souza, F.; Ito, O. *Coord. Chem. Rev*. **2005**, *249*, 1410.
126. Sun, D.; Tham, F. S.; Reed, C. A.; Chaker, L.; Boyd, P. D. W. *J. Am. Chem. Soc*. **2002**, *124*, 6604.
127. Mizutani, T.; Wada, K.; Kitagawa, S. *J. Am. Chem. Soc*. **2001**, *123*, 6459.
128. Wada, K.; Mizutani, T.; Matsuoka, H.; Kitagawa, S. *Chem. Eur. J.* **2003**, *9*, 2368.
129. Fukuzumi, S.; Ohkubo, K.; Suenobu, T.; Kato, K.; Fujitsuka, M.; Ito, O. *J. Am. Chem. Soc.* **2001**, *123*, 8459.
130. Fukuzumi, S.; Nishimine, M.; Ohkubo, K.; Tkachenko, N. V.; Lemmetyinen, H. *J. Phys. Chem. B* **2003**, *107*, 12511.
131. Fukuzumi, S.; Kotani, H.; Ohkubo, K.; Ogo, S.; Tkachenko, N. V.; Lemmetyinen, H. *J. Am. Chem. Soc.* **2004**, *126*, 1600.
132. Tanaka, M.; Ohkubo, K.; Gros, C. P.; Guilard, R.; Fukuzumi, S. *J. Am. Chem. Soc*. **2006**, *128*, 14625.
133. Ohkubo, K.; Suga, K.; Morikawa, K.; Fukuzumi, S. *J. Am. Chem. Soc*. **2003**, *125*, 12850.
134. Kikuchi, K.; Sato, C.; Watabe, M.; Ikeda, H.; Takasaki, Y.; Miyashi, T. *J. Am. Chem. Soc*. **1993**, *115*, 5180.
135. Kobuke, Y. *Struct. Bond*. **2006**, *121*, 49.
136. Bouamaied, I.; Coskun, T.; Stulz, E. *Struct. Bond*. **2006**, *121*, 1.
137. Anderson, S.; Anderson, H. L.; Sanders, J. K. M. *Acc. Chem. Res*. **1993**, *26*, 469.
138. D'Souza, F.; Maligaspe, E.; Ohkubo, K.; Zandler, M. E.; Subbaiyan, N. K.; Fukuzumi, S. *J. Am. Chem. Soc*. **2009**, *131*, 8787.
139. Kobayashi, N.; Lever, A. B. P. *J. Am. Chem. Soc*. **1987**, *109*, 7433.
140. Kobayashi, N.; Togashi, M.; Osa, T.; Ishii, K.; Yamauchi, S.; Hino, H. *J. Am. Chem. Soc.* **1996**, *118*, 1073.
141. Sielcken, O. E.; van Tilborg, M. V.; Roks, M. F. M.; Hendriks,R.; Drenth, W.; Nolte, J. M. *J. Am. Chem. Soc*. **1987**, *109*, 4261.
142. Thanabal, V.; Krishnan, V. *J. Am. Chem. Soc*. **1982**, *104*, 3643.
143. Chitta, R.; Rogers, L. M.; Wanklyn, A.; Karr, P. A.; Kahol, P. K.; Zandler, M. E.; D'Souza, F. *Inorg. Chem*. **2004**, *43*, 6969.
144. D'Souza, F.; Chitta, R.; Gadde, S.; Zandler, M. E.; Sandanayaka, A. S. D.; Araki, Y.; Ito, O. *Chem. Commun*. **2005**, 1279.
145. D'Souza, F.; Chitta, R.; Gadde, S.; Zandler, M. E.; McCarty, A. L.; Sandanayaka, A. S. D.; Araki, Y.; Ito, O. *Chem. Eur. J*. **2005**, *11*, 4416.
146. D'Souza, F.; Chitta, R.; Gadde, S.; Rogers, L. M.; Karr, P. A.; Zandler, M. E.; Sandanayaka, A. S.; Araki, Y.; Ito, O. *Chem. Eur. J*. **2007**, *13*, 916.
147. Kojima, T.; Nakanishi, T.; Honda, T.; Harada, R.; Shiro, M.; Fukuzumi, S. *Eur. J. Inorg. Chem*. **2009**, 727.
148. Chan, K. S.; Zhou, X.; Luo, B.-S.; Mak, T. C. W. *J. Chem. Soc. Chem. Commun*. **1994**, 271.
149. Medforth, C. J.; Senge, M. O.; Smith, K. M.; Sparks, L. D.; Shelnutt, J. A. *J. Am. Chem. Soc*. **1992**, *114*, 9859.

150. Liu, C.-J.; Yu, W.-Y.; Peng, S.-M.; Mak, T. C. W.; Che, C.-M. *J. Chem. Soc. Dalton Trans*. **1998**, *11*, 1805.
151. Harada, R.; T. Kojima, T. *Chem. Commun*. **2005**, 716.
152. Honda, T.; Kojima, T.; Fukuzumi, S. *Chem. Commun*. **2009**, 4994.
153. Yokoyama, A.; Kojima, T.; Ohkubo, K.; Fukuzumi, S. *Chem. Commun*. **2007**, 3999.
154. Kojima, T.; Nakanishi, T.; Honda, T.; Fukuzumi, S. *J. Porphyrins Phthalocyanines* **2009**, *13*, 14.
155. Kobayashi, N.; Fukuda, T.; Ueno, K.; Ogino, H. *J. Am. Chem. Soc*. **2001**, *123*, 10740.
156. Fukuda, T.; Homma, S.; Kobayashi, N. *Chem. Eur. J*. **2005**, *11*, 5205.
157. Kojima, T.; Honda, T.; Ohkubo, K.; Shiro, M.; Kusukawa, T.; Fukuda, T.; Kobayashi, N.; Fukuzumi, S. *Angew. Chem. Int. Ed*. **2008**, *47*, 6712.
158. Soares, A. R. M.; Martínez-Díaz, M. V.; Bruckner, A.: Pereira, A. M. V. M.; Tomé, J. P. C.; Alonso, C. M. A.; Faustino, M. A. F.; Neves, M. G. P. M. S.; Tomé, A. C.; Silva, A. M. S.; Cavaleiro, J. A. S.; Torres, T.; Guldi, D. M. *Org. Lett*. **2007**, *9*, 1557.
159. Fortage, J.; Göransson, E.; Blart, E.; Becker, H.-C.; Hammarström, L.; Odobel, F. *Chem. Commun*. **2007**, 4629.
160. Kojima, T.; Hanabusa, K.; Ohkubo, K.; Shiro, M.; Fukuzumi, S. *Chem. Eur. J*. **2010**, *16*, 3646.
161. Baumann, J. A.; Salmon, D. J.; Wilson, S. T.; Meyer, T. J.; Hatfield, W. E. *Inorg. Chem*. **1978**, *17*, 3342.
162. Abe, M.; Sasaki, Y.; Yamaguchi, T.; Ito, T. *Bull. Chem. Soc. Jpn*. **1992**, *65*, 1585.
163. Ito, T.; Hamaguchi, T.; Nagino, H.; Yamaguchi, T.; Kido, H.; Zavarine, I. S.; Richmond, T.; Washington, J.; Kubiak, C. P. *J. Am. Chem. Soc*. **1999**, *121*, 4625.
164. Abe, M.; Michi, T.; Sato, A.; Kondo, T.; Zhou, W.; Ye, S.; Uosaki, K.; Sasaki, Y. *Angew. Chem. Int. Ed*. **2003**, *42*, 2912.
165. Sessler, J. L.; Karnas, E.; Kim, S. K.; Ou, Z.; Zhang, M.; Kadish, K. M. Ohkubo, K.; Fukuzumi, S. *J. Am. Chem. Soc*. **2008**, *130*, 15256.
166. Solladié, N.; Hamel, A.; Gross, M. *Tetrahedron Lett*. **2000**, *41*, 6075.
167. Fujitsuka, M.; Hara, M.; Tojo, S.; Okada, A.; Troiani, V.; Solladié, N.; Majima, T. *J. Phys. Chem. B* **2005**, *109*, 33.
168. Saito, K.; Qiu, H.; Troiani, V.; Solladié, N.; Sakata, T.; Mori, H.; Ohama, M.; Fukuzumi, S. *J. Phys. Chem. C* **2007**, *111*, 1194.
169. Guldi, D. M.; Rahman, G. M. A.; Zerbetto, F.; Prato, M. *Acc. Chem. Res*. **2005**, *38*, 871.
170. Avouris, P. *Acc. Chem. Res*. **2002**, *35*, 1026.
171. Guldi, D. M. *J. Phys. Chem. B* **2005**, *109*, 11432.
172. Misewich, J. A.; Martel, R.; Avouris, Ph.; Tsang, J. C.; Heinze, S.; Tersoff, J. *Science* **2003**, *300*, 783.
173. O'Connell, M. J. *Carbon Nanotubes: Properties and Applications*; CRC Press: Boca Raton, FL, **2006**.
174. Meyyapan, M. *Carbon Nanotubes: Science and Applications*; CRC Press: Boca Raton, FL, **2005**.
175. Dresselhaus, M. S.; Dresselhaus, G.; Avouris, P. *Carbon Nanotubes: Synthesis, Structure, Properties, and Applications*; Springer-Verlag: Berlin, **2001**.
176. Hasobe, T.; Fukuzumi, S.; Kamat, P. V. *J. Am. Chem. Soc*. **2005**, *127*, 11884.
177. Ohtani, M.; Fukuzumi, S. *Chem. Commun*. **2009**, 4997.
178. Endo, M.; Kim, Y. A.; Hayashi, T.; Fukai, Y.; Oshida, K.; Terrones, M.; Yanagisawa, T.; Higaki, S.; Dresselhaus, M. S. *Appl. Phys. Lett*. **2002**, *80*, 1267.

179. Kim, Y. A.; Hayashi, T.; Fukai, Y.; Endo, M.; Yanagisawa, T.; Dresselhaus, M. S. *Chem. Phys. Lett*. **2002**, *355*, 279.
180. Endo, M.; Hayashi, T.; Kim, Y.-A.; Tantrakarn, K.; Yanagisawa, T.; Dresselhaus, M. S. *Carbon* **2004**, 42, 2329.
181. Hasobe, T.; Fukuzumi, S.; Kamat, P. V. *Angew. Chem. Int. Ed*. **2006**, *45*, 755.
182. Saito, K.; Ohtani, M.; Fukuzumi, S. *J. Am. Chem. Soc*. **2006**, *128*, 14216.
183. Saito, K.; Ohtani, M.; Fukuzumi, S. *Chem. Commun*. **2007**, 55.
184. Ohtani, M.; Saito, K.; Fukuzumi, S. *Chem. Eur. J*. **2009**, *15*, 9160.
185. Fuhrhop, J.-H.; Binding, U.; Siggel, U. *J. Am. Chem. Soc*. **1993**, *115*, 11036.
186. Schwab, A. D.; Smith, D. E.; Rich, C. S.; Young, E. R.; Smith, W. F.; de Paula, J. C. *J. Phys. Chem. B* **2003**, *107*, 11339.
187. Wang, Z.; Medforth, C. J.; Shelnutt, J. A. *J. Am. Chem. Soc*. **2004**, *126*, 15954.
188. Kojima, T.; Nakanishi, T.; Harada, R.; Yamauchi, S.; Ohkubo, K.; Fukuzumi, S. *Chem. Eur. J*. **2007**, *13*, 8714.
189. Nakanishi, T.; Kojima, T.: Ohkubo, K.; Hasobe, T.; Nakayama, K.; Fukuzumi, S. *Chem. Mater*. **2008**, *20*, 7492.
190. Nobukuni, H.; Shimazaki, Y.; Tani, F.; Naruta, Y. *Angew. Chem. Int. Ed*. **2007**, *46*, 8975.
191. Nobukui, H.; Tani, F.; Shimazaki, Y.; Naruta, Y.; Ohkubo, K.; Nakanishi, T.; Kojima, T.; Fukuzumi, S.; Seki, S. *J. Phys. Chem. C* **2009**, *113*, 19694.
192. Hasobe, T.; Fukuzumi, S.; Kamat, P. V. *Interface* **2006**, *15*, 47.
193. Imahori, H.; Umeyama, T. *J. Phys. Chem. C* **2009**, *113*, 9029.
194. Cheng, Y.-J.; Yang, S.-H.; Hsu, C.-S. *Chem. Rev*. **2009**, *109*, 5868.
195. Khazraji, A. C.; Hotchandani, S.; Das, S.; Kamat, P. V. *J. Phys. Chem. B* **1999**, *103*, 4693.
196. Hasobe, T.; Imahori, H.; Kamat, P. V.; Ahn, T. K.; Kim, D.; Hanada, T.; Hirakawa, T.; Fukuzumi, S. *J. Am. Chem. Soc*. **2005**, *127*, 1216.
197. Hasobe, T.; Fukuzumi, S.; Kamat, P. V. *Interface* **2006**, *15*, 47.
198. Imahori, H.; Fukuzumi, S. *Adv. Funct. Mater*. **2004**, *14*, 525.
199. Hasobe, T.; Kashiwagi, Y.; Absalom, M. A.; Hosomizu, K.; Crossley, M. J.; Imahori, H.; Kamat, P. V.; Fukuzumi, S. *Adv. Mater*. **2004**, *16*, 975.
200. Hasobe, T.; Kamat, P. V.; Absalom, M. A.; Kashiwagi, Y.; Sly, J.; Crossley, M. J.; Hosomizu, K.; Imahori, H.; Fukuzumi, S. *J. Phys. Chem. B* **2004**, *108*, 12865.
201. Tkachenko, N. V.; Lemmetyinen, H.; Sonoda, J.; Ohkubo, K.; Sato, T.; Imahori, H.; Fukuzumi, S. *J. Phys. Chem. A* **2003**, *107*, 8834.
202. Kesti, T. J.; Tkachenko, N. V.; Vehmanen, V.; Yamada, H.; Imahori, H.; Fukuzumi, S.; Lemmetyinen, H. *J. Am. Chem. Soc*. **2002**, *124*, 8067.
203. Hasobe, T.; Kamat, P. V.; Troiani, V.; Solladié, N.; Ahn, T. L.; Kim, S. K.; Kim, D.; Kongkanand, A.; Kuwabata, S.; Fukuzumi, S. *J. Phys. Chem. B* **2005**, *109*, 19.
204. Hasobe, T.; Saito, K.; Kamat, P. V.; Troiani, V.; Qiu, H.; Solladié, N.; Ahn, T. K.; Kim, K. S.; Kim, S. K.; Kim, D.; D'Souza, F.; Fukuzumi, S. *J. Mater. Chem*. **2007**, *17*, 4160.
205. Hasobe, T.; Imahori, H.; Kamat, P. V.; Fukuzumi, S. *J. Am. Chem. Soc*. **2003**, *125*, 14962.
206. Hasobe, T.; Imahori, H.; Kamat, P. V.; Ahn, T. K.; Kim, D.; Hanada, T.; Hirakawa, T.; Fukuzumi, S. *J. Am. Chem. Soc*. **2005**, *127*, 1216.

This page intentionally left blank

47 Anchoring of Porphyrins and Phthalocyanines on Conductors and Semiconductors for Use in Hybrid Electronics

Florence Duclairoir and Jean-Claude Marchon

Laboratoire de Chimie Inorganique et Biologique*,
Institut Nanosciences et Cryogénie, CEA-Grenoble,
17 rue des martyrs, 38054 Grenoble cedex 9, France

*Unité mixte de recherche du Commissariat à l'Energie Atomique
et de l'Université Joseph Fourier

List of Abbreviations

AFM	atomic force microscopy
BDMD	boron-doped microcrystalline diamond
BDND	boron-doped nanocrystalline diamond
BE	binding energy
CcO	cytochrome c oxidase
CMOS	complementary metal oxide semiconductor
CNT	carbon nanotube
Cyt c	cytochrome c
o-DCB	o-dichlorobenzene
DDQ	dichlorodicyanobenzoquinone
DMF	dimethylformamide
DIPEA	N,N-diisopropylethylamine
DRAM	dynamic random access memory
EDC	N-(3-dimethylaminopropyl)-N″-ethylcarbodiimide
EMOS	electrolyte molecule oxide silicon
EMS	electrolyte molecule silicon
FTIR	Fourier transform infrared
HOBt	1-hydroxybenzotriazole
IR	infrared
ITO	indium tin oxide
MBJC	molecular break junction
MC	macrocycle
MWCNT	multi-walled carbon nanotube
MOS	metal oxide silicon
Nc	naphthalocyanine
NMR	nuclear magnetic resonance
OEP	octaethylporphyrin
OLED	organic light-emitting diode
P	porphyrin
Pc	phthalocyanine
PDMS	polydimethylsiloxane
RAM	random access memory
SAM	self-assembled monolayer
SC	semiconductor
STM	scanning tunneling microscopy
SWCNT	single-walled carbon nanotube
TD	triple-decker
TEM	transmission electron microscopy

THF	tetrahydrofuran
TPP	tetraphenylporphyrin
Tyr	tyrosine
UV	ultraviolet
vis	visible
VdW	van der Waals
XPS	X-ray photoelectron spectroscopy

I. Introduction

For several decades chemists have invented methods for grafting porphyrins and phthalocyanines onto the surfaces of organic or inorganic solids using strong covalent bonds, with the view of designing novel materials such as supported homogeneous catalysts or chemically modified electrodes. In a related field, basic studies on the transfer of electrons between an electrical conductor and a surface-anchored molecule, and on the effect of light on this process, have induced the development of chemical methods for anchoring species such as metalloporphyrins on gold and other metal electrodes. Concurrent to these investigations, potential applications in the fields of photoinduced electron transfer, biomimetic models of the photosynthetic special pair, and photovoltaic cells have been proposed.

The need for ultimate miniaturization in microelectronics, combined with the emergence of molecular electronics, have led to the idea of coupling redox-active molecules, such as porphyrins and phthalocyanines, to the surface of silicon and to carbon nanotubes, with the view of designing novel devices with improved performance such as OLEDs, transistors, and memories. With the continuous increase in the density of silicon-based electronic devices (the Moore law), the process scaling in semiconductor technology will soon reach physical and technical limits preventing miniaturization below about 10 nm. Molecular electronics seeks to bring an answer to that problem by implementing new technologies in which one or a few molecules will function as switches, connections, and other logic or memory devices.[1]

With these considerations in mind, in this chapter we review the current methods used for anchoring porphyrins and phthalocyanines to the surface of conductors and semiconductors that are of current or potential use in microelectronics technology. This review successively addresses the functionalization of gold, silicon, carbon nanotubes, and oxide surfaces. For each material the basic chemical reactions of common use are first summarized. This overview of the field is followed by a collection of concise reports that are meant to illustrate the current state of the art. Even though the collection of examples is selective, the authors

have tried to be exhaustive in their coverage of the literature and in the list of references. Inclusion of experimental details in some examples has been made when these were deemed pertinent. A short final section summarizes a few innovative technologies and concepts in hybrid silicon/molecular electronics. The authors hope that this concise review may help the emergence of novel ideas and processes combining molecular chemistry and microelectronics.

II. Surface Functionalization of Gold

A. Overview

Sulfur has a strong affinity for gold. The spontaneous adsorption of sulfur-containing compounds on gold affords self-assembled monolayers (SAMs) that are well organized and homogeneous,[2] and it provides an efficient method for integrating molecules to electronic components. The modified Au surfaces are ideally suited to basic studies of molecular packing and orientation, surface-molecule coupling or charge-transfer.[3]

Bonding probably involves a (RS^-)–Au(I) species obtained by oxidative addition of the S–H bond to Au(0). One of the most commonly used techniques to generate this Au–S bond is to expose the gold surface to a thiol (B in Scheme 1).[2–4] Disulfide compounds (C and E in Scheme 1) are also used. The C type yields a SAM similar to that obtained with a thiol, but the E type yields a SAM with two Au–S bonds as anchors, which confers a more robust surface-bound system. During SAM formation thiol molecules can be oxidized to disulfides but also to other species. In order to avoid the formation of these parasitic derivatives other types of sulfur-containing species have been investigated, such as thioacetate and thiocyanates (A and D in Scheme 1). Metalloporphyrins and phthalocyanines have been immobilized on Au using thiol, disulfide or thioacetate derivatives. The thiocyanate route has been worked out to provide an alternative to harsh deprotection conditions that are not always compatible with molecular endurance.[5,6] To our knowledge this chemistry has not yet been tested on pyrrolic macrocycles.

To form a dense and well-ordered SAM experimental parameters such as reaction time, temperature, thiol concentration, and substrate roughness have to be taken into account. The grafting process can be divided into two steps: a fast initial adsorption (Scheme 2, left) and a subsequent slow reorganization (Scheme 2, right).[4,7] The initial step can be compared to a diffusion-controlled Langmuir adsorption. The thiol concentration has a strong impact, and a concentration in the mM range is commonly used in order for this step to be completed in minutes. The kinetics also depends on the reactivity of the thiol molecule, i.e. on the electron density on sulfur. The following step is a “packing step”: the molecules develop

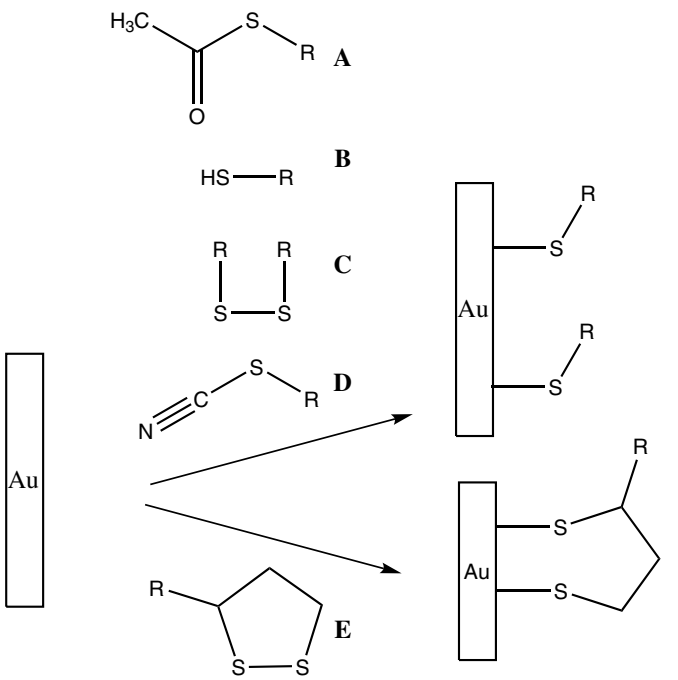

Scheme 1. Immobilization of sulfur compounds on the surface of gold.

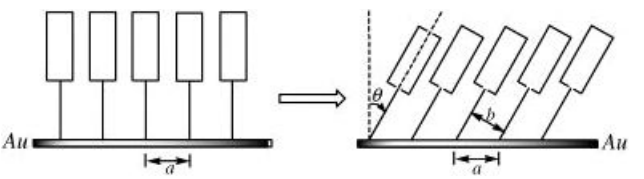

Scheme 2. Successive steps in the formation of a porphyrin SAM on gold. *a* is the S–S distance, *b* the chain-to-chain distance, and θ the tilt-angle. (Adapted from Ref. 7.)

inter-molecular interactions (VdW, π–π stacking, dipole–dipole, etc.) leading to a well-packed and ordered monolayer. This step can require hours to be completed.[8] A generally successful method is to dip a clean Au substrate in an ethanol solution of thiol at a mM concentration- for ~10–20 hours at room temperature.

Optimal surface coverage and ordering of the SAM result from maximized attractive lateral interactions between thiol molecules, and these interactions can be restricted by steric crowding leading to lower SAM quality. In order to obtain a good quality SAM with specifically chosen molecular units protruding from the surface, a sequential grafting can be performed, or the diluent technique can be used. For the first method a spacer thiol is immobilized and in a subsequent step

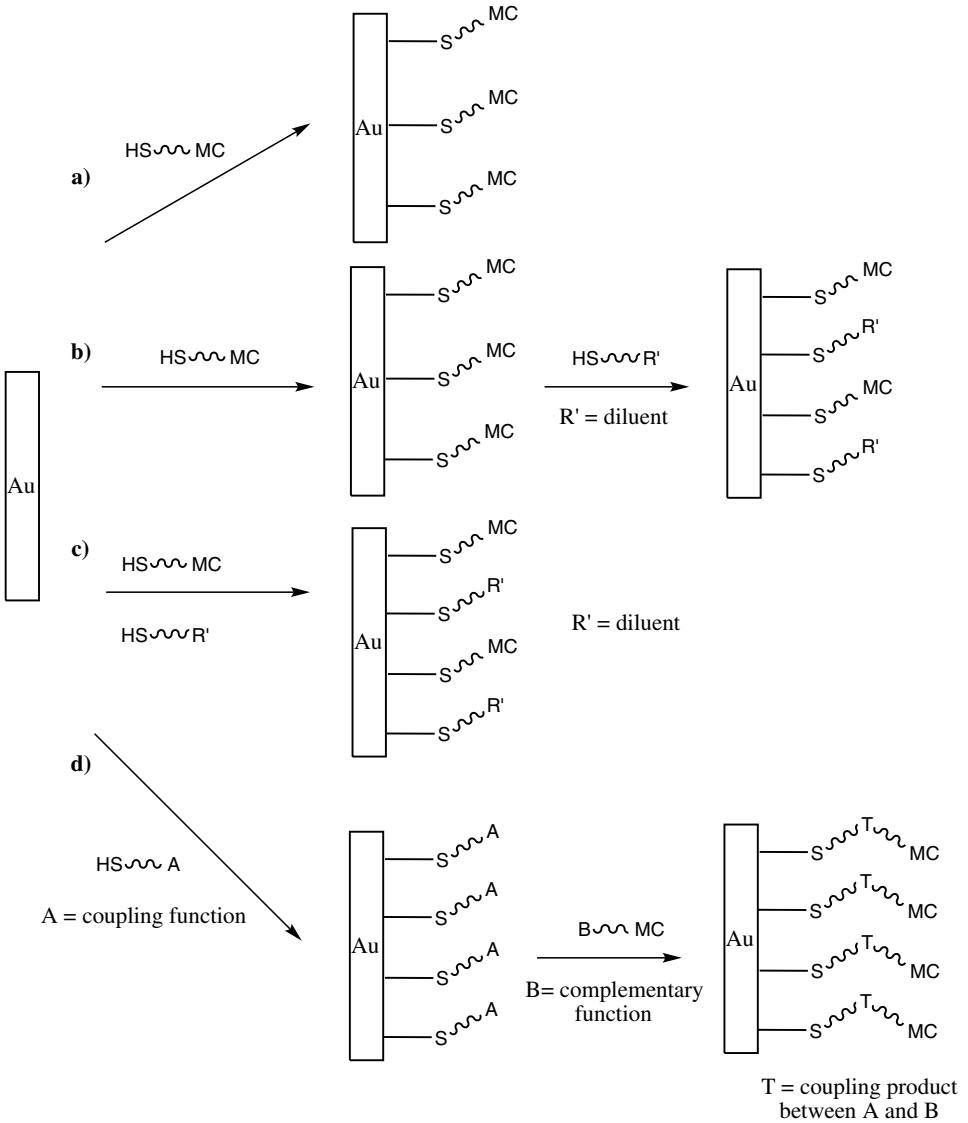

Scheme 3. Methods used for anchoring porphyrin and phthalocyanine macrocycles on gold. (a) Single-step adsorption; (b) diluent post-immobilization; (c) co-adsorption procedure; (d) sequential grafting (MC = macrocycle).

the molecule of interest is coupled to this spacer ad-layer (Scheme 3d). The molecules will therefore react within the limits of their coulombic repulsion and steric crowding. The diluent technique involves the co-adsorption of the molecule of interest along with an alkylthiol that should be co-immobilized on the surface (Scheme 3c).[9] This co-adsorption can sometimes lead to monolayers with

nonreproducible properties, resulting from segregation into islands of the different thiol compounds. To avoid such problems a post-adsorption of the diluent thiol is sometimes performed (Scheme 3b). In such cases the monolayer interstices are filled by the diluent forming a tighter monolayer that displays the expected properties.

Sequential grafting has been investigated for a variety of compounds. Spacer molecules bearing terminal amine or carboxylic acid functions have been immobilized on Au and further reacted with carboxylic acid or alcohol and amine derivatives to yield an ester or amide coupling link between the spacer and the compound of interest. In the case of pyrrolic macrocycles, such ester and amide coupling links are less common, and spacers bearing terminal end groups that are able to coordinate to the metal center have been used. In such cases the coupling link is a coordination bond (Scheme 4a). Another method involves the immobilization of a

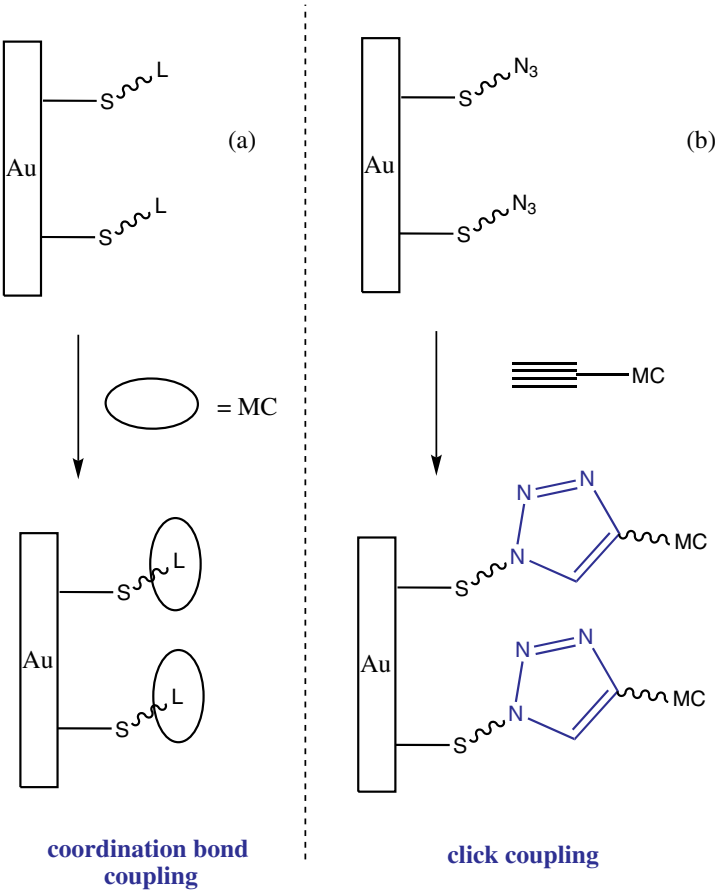

Scheme 4. Coupling methods used to sequentially immobilize tetrapyrrolic macrocycles on gold via (a) a coordination bond or (b) a cycloaddition.

spacer bearing a terminal azide function that is able to undergo click-coupling via 1,3-Huisgen cycloaddition with a macrocycle possessing a C–C triple bond. The coupling link obtained is a triazole (Scheme 4b).

B. Selected Examples

1. *Direct Immobilization of the Macrocycle*

a. *TPP derivatives*

Tetraphenylporphyrin (TPP) derivatives such as (**1**) and (**2**) have been immobilized on Au via the use of a thiol substituent (Figure 1).[10] These porphyrins are obtained from an aldehyde bearing a protected thiol function. Metalation is accomplished prior to the alkaline deprotection step, but in some cases metal insertion can be performed post-assembly.[11] The SAM is obtained by dipping the gold substrate in a chloroform solution of the thiol at a concentration around 1 μM.

This method has been used to study the charge-transfer between the TPP derivative and the Au surface through the SAM.[12] Modification of the surface has been evidenced by measuring the contact angle of water for a bare gold surface and a functionalized surface (Figure 2). The modified surface is more hydrophobic as the measured contact angle is larger.

Disulfide porphyrin derivatives have been prepared to allow their subsequent immobilization on Au.[13] Here the porphyrin SAM was prepared by dipping the

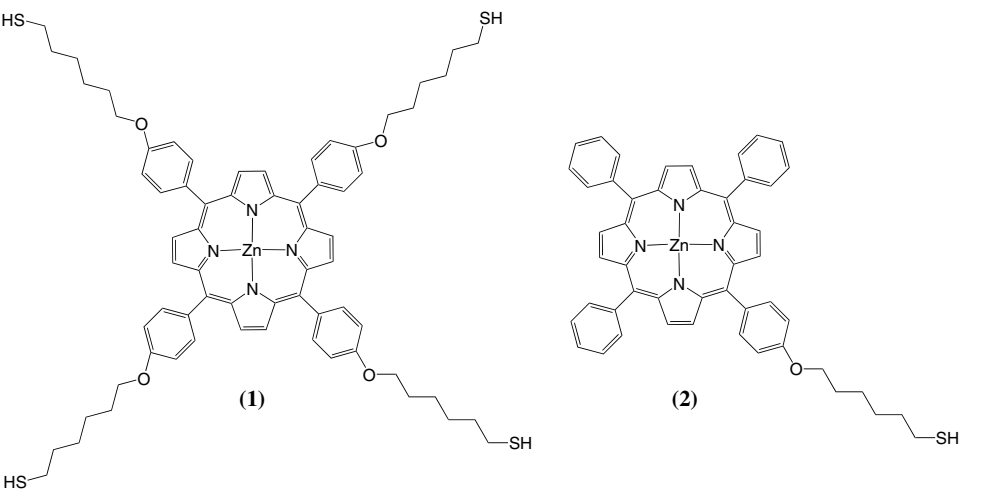

Figure 1. Structures of typical porphyrins bearing thiol anchoring units.

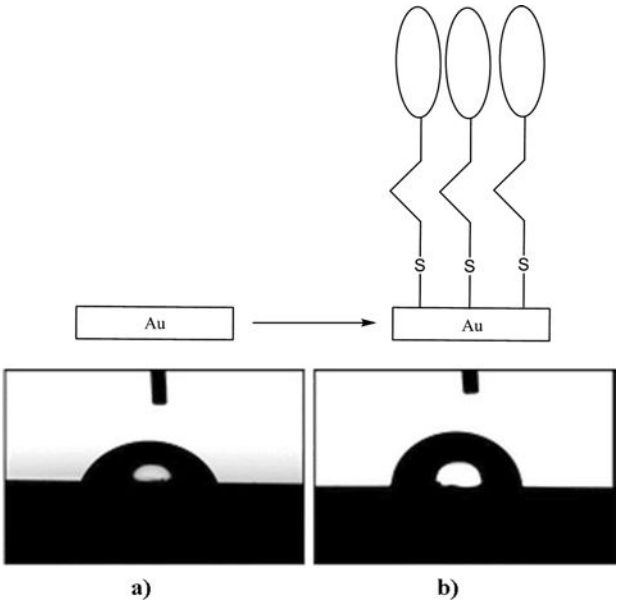

Figure 2. Top: schematic view of a porphyrin thiol SAM on gold. Bottom: Images of the contact angles of a H_2O drop on (a) a bare gold surface, and (b) on a TPP SAM. (Adapted from Ref. 12.)

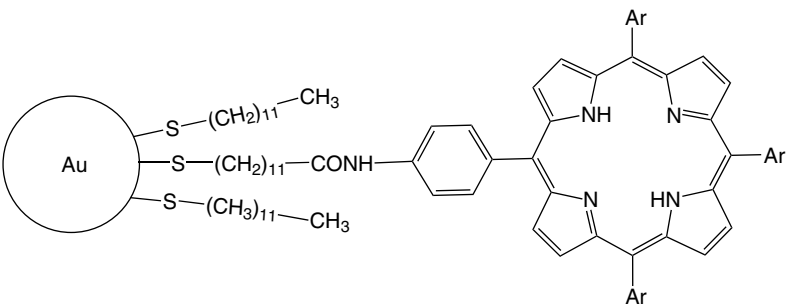

Figure 3. Schematic view of a SAM resulting from the diluent co-adsorption procedure on a gold nanocluster.

gold electrode in a porphyrin solution (50 mM in chloroform) for 12 hours at room temperature. The SAM was characterized electrochemically giving access to the surface coverage in redox compound. A coverage of 150 pmol.cm^{-2} was reached for a Mn porphyrin monolayer, and the surface concentration for porphyrin rings oriented perpendicular is estimated to be 330 pmol.cm^{-2}, and that of porphyrins oriented flat to be 70 pmol.cm^{-2}. Thus a tilted orientation of the porphyrins was proposed.

Several studies illustrate the diluent co-adsorption procedure for the formation of a packed monolayer (Figure 3).[14–17]

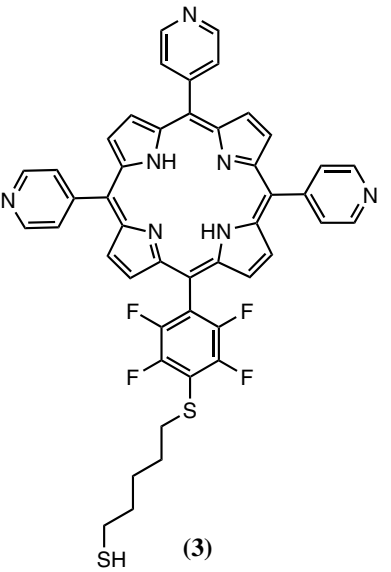

Figure 4. A tripyridylporphyrin with a terminal thiol.

Tripyridylporphyrins such as (**3**) (Figure 4) have been immobilized on Au via a phenylthiol anchoring group.[18] In this case the diluent SAM was prepared first, and the thiol macrocycle was then adsorbed in the remaining molecular interstices. The Au film was dipped in a 1 mM solution of diluent (*n*-dodecanethiol) dissolved in ethanol for 24 hours. After copious rinsing with ethanol, the functionalized surface was soaked for 5 days in a 0.5 mM solution of porphyrin thiol dissolved in dichloromethane. This step is longer in order to increase the chances of filling the holes with the porphyrin compound. STM analysis showed that this interchange of the immobilization steps leads to deposition of single porphyrins, or of assemblies of 3 to 5 porphyrins, at the edges of the diluent SAM defects. The resulting SAM is able in principle to coordinate and assemble additional porphyrin layers.

The thiol anchoring group is often protected in order to avoid side reactions or decomposition during macrocycle synthesis, and also to prevent possible coordination of the thiol to the metal center. Studies have been conducted on various protecting groups [S-cyano, S-(*N*-ethylcarbamoyl), S-acetyl, S-(9-anthrylmethyl), S-(2,4-dinitrophenyl), S-pivaloyl] and showed that most of them survive porphyrin formation and metalation with zinc.[19] However only three groups, i.e. S-cyano, S-(*N*-ethylcarbamoyl), and S-acetyl, can be cleaved *in situ* upon exposure to Au thus allowing binding to this surface.

Deuteroporphyrin complexes (Co, Fe) such as (**4**) (Figure 5) bearing a disulfide anchoring substituent linking two adjacent β positions have been immobilized

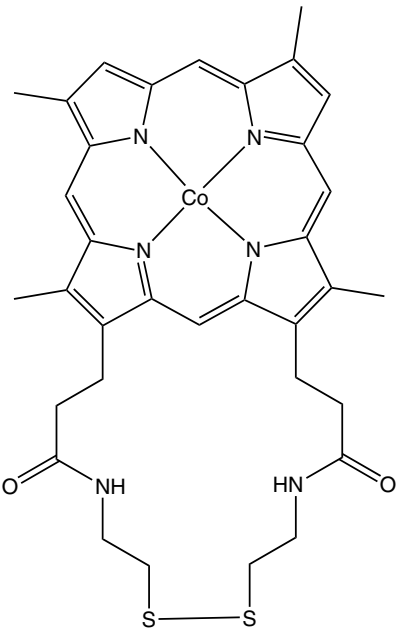

(4)

Figure 5. A deuteroporphyrin derivative with a disulfide anchoring unit.

on Au, leading to two S–Au bonds per porphyrin complex.[20] The SAM was formed by simply immersing the Au sample in a 2 mM solution of porphyrin derivative dissolved in ethanol for 24 hours at 4 °C. Ellipsometry and cyclic voltammetry studies confirmed the immobilization of the porphyrin on the surface and suggested that the SAM formed is robust. These SAMs have been used for catalytic electrochemical reduction of O_2 to H_2O_2 or H_2O.

b. *Modulation of the linker between the surface and the macrocycle*

Electrochemical studies of various porphyrin SAMs obtained with different spacer lengths suggested that the surface concentration of electroactive species is higher when a longer spacer is used.[13,14] This points to a higher stability of the SAM with long chains that develop more important lateral interactions than those with short chains. It was also observed that the electron-transfer rate decreases with increasing surface coverage and with increasing distance between the redox centre and the surface.

Bocian, Lindsey and coworkers have conducted an extensive study of the effects of linker length and nature (conjugated or not) using a large library of porphyrin compounds immobilized on Au (Figure 6).[21]

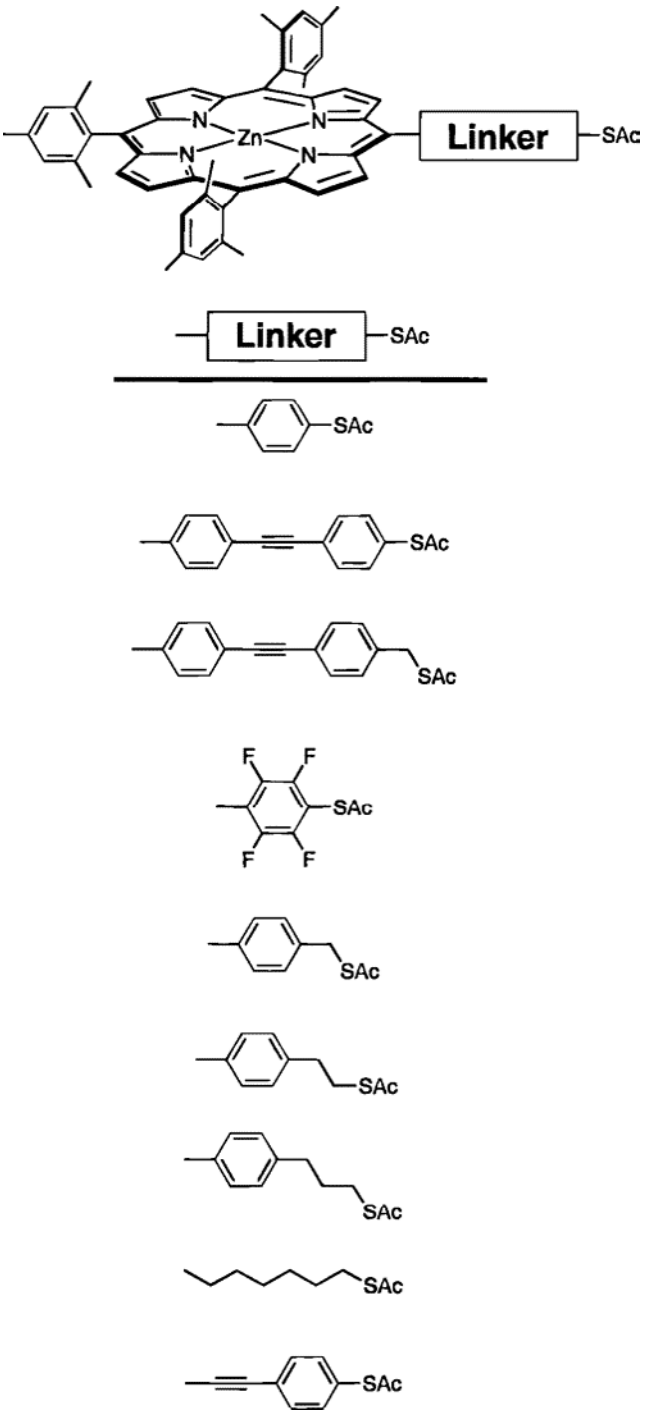

Figure 6. Various porphyrin-linker-thiol derivatives investigated for molecular-based information storage. (Adapted from Ref. 21.)

To perform these studies a specific 75-micron wide Au band substrate was prepared via e-beam evaporation on a glass slide covered with Cr. A 3 mm deep PDMS well was deposited on the Au band. Then the SAM was formed on the Au area at the bottom of the well by filling it with a 1 mM solution of porphyrin in absolute ethanol at room temperature for 30 minutes. Using this experimental setup the rate of electron-transfer (k°) for oxidation and the rate of charge dissipation $\tau_{1/2}$ (i.e. the charge retention half-time once the potential is switched off) were determined by electrochemical measurements.[22] Overall the k° values for most of these SAMs lie in the 10^4 to 10^5 s^{-1} range. Among the methylene containing linker SAMs, it was shown that the longer the alkyl chain, the slower will be the electron-transfer. Moreover the k° values are higher for fully conjugated than for aliphatic linkers. For the fully conjugated linkers, adding a phenyl ring between the macrocycle and the C–C triple bond decreases the value of k°. This is presumably due to a loss of conjugation between the macrocycle and the perpendicular phenyl substituent. The fastest electron transfer is obtained when the *meso* position is directly linked to the C–C triple bond of a conjugated linker. For a conjugated linker, an additional methylene group next to the sulfur anchor results in slower electron transfer, due to the breaking of the conjugation. The charge dissipation remains on average six times slower than the electron transfer. Opposite trends are observed for the rates of electron transfer and charge dissipation: if charge-transfer is fast, the charge retention time will be low, and *vice versa*. When a long aliphatic linker is used, the resulting SAMs exhibit the highest charge retention time. Both parameters decrease with increasing surface coverage. This was explained by hampered solvent/counterions diffusion and space-charge effects. For each linker used a different surface coverage was reached (surface crowding, tilt angle, molecular orientation) so this interdependence between surface coverage and k° or $\tau_{1/2}$ can screen the linker effect.

The influence of the electron abstraction site (metal center for Fe–P, or porphyrin ring for Zn–P) has been studied (Figure 7).[23] For ring-centered electron-transfer

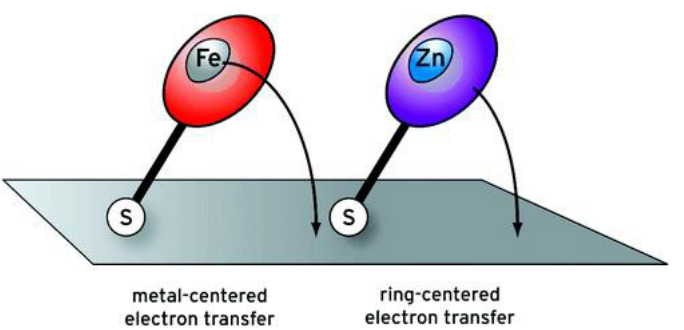

Figure 7. Schematic view of (*left*) metal-centered and (*right*) ring-centered electron transfer in porphyrin monolayers on gold. (Adapted from Ref. 23.)

the value of k^0 is 10 to 40 times higher than for the metal-centered case. This has been assigned to the delocalized nature of the molecular orbitals involved and to their proximity to the surface, compared to a d-orbital localized on the metal center.

c. *Multi-linkage between the surface and the macrocycle*

i. Two or four S containing *meso* substituents

Varying the number of anchoring groups has been investigated as a potential means of controlling the macrocycle orientation (parallel or perpendicular) relative to the Au surface, as well as the electron transfer rate (Figure 8).[24–29]

ii. Tripodal anchoring groups

A rigid aryl tripod based on a tris[4-(*S*-acetylthiomethyl)phenyl]-derivatized methane was constructed on a tetraarylporphyrin (Figure 9), in order to enforce perpendicular orientation of the macrocycle relative to the Au electrode.[30] Tests have been conducted on porphyrins, phthalocyanines, triple-decker (TD) and ferrocene-porphyrin systems. Electrochemical responses recorded for the tripod SAMs are more stable over time than when monopodal units are used. Therefore

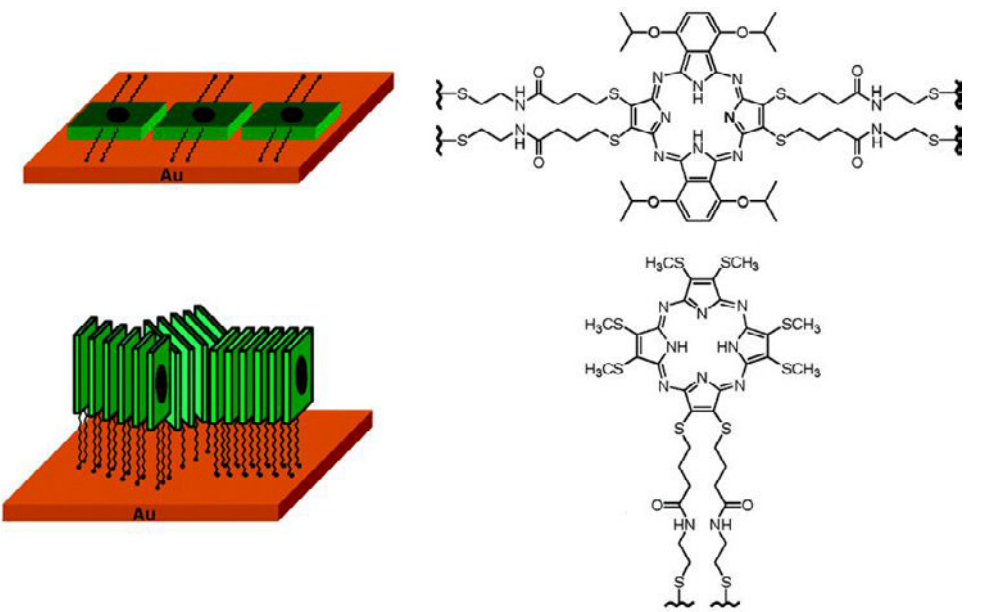

Figure 8. Schematic views of the expected SAM orientations of porphyrazines possessing two or four anchoring units. (Adapted from Ref. 25.)

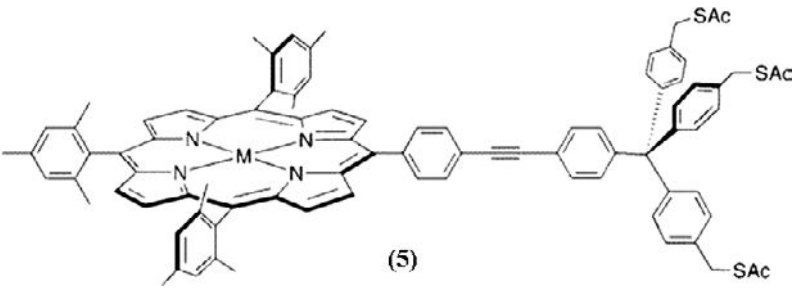

Figure 9. Substitution by a tripod is expected to allow anchoring of the porphyrin redox-active unit in upright position on gold. (Adapted from Ref. 31.)

these tripods lead to more robust SAMs with k° and $\tau_{1/2}$ parameters similar to those observed for monopodal SAMs.[31]

d. *Immobilization of complex porphyrin systems*

Porphyrin-ferrocene conjugates with a thioacetate anchoring unit on the macrocycle have been synthesized.[32] On the resulting SAM the ferrocene unit is positioned away from the gold surface, and the distance between the macrocycle and the ferrocene unit can be tuned by modifying the nature of the linker (Figure 10a). In related systems the ferrocene units are positioned on both sides of the macrocycle (Figure 10b). Electrochemical studies confirmed SAM formation on Au and they showed three oxidation waves: one for the ferrocene unit and two for the porphyrin core. These systems give access to larger numbers of redox states and various values of $k^\circ/\tau_{1/2}$ parameters that could be interesting for the design of molecular memory devices.

In similar systems such as (**6**) and (**7**) (Figure 11), a redox unit such as ferrocene[33] or a quinone[34] is placed between the porphyrin core and the surface, giving well-packed SAMs with high surface coverage which exhibit interesting photoinduced electron transfer properties.

In a search of good molecular candidates for multibit information storage, molecules with multiple redox states have been prepared, such as linear porphyrin dimers (**8**) (Figure 12), trimers[35,36] and triple-deckers.[37,38] SAM formation on Au was successful. For the porphyrin dimer SAMs the oxidation potentials are sufficiently resolved to identify individual states, whereas for trimers the waves overlap. Moreover the *meso–meso* linkage is not really stable upon oxidation of the porphyrin macrocycle. Other studies have been conducted with a linker added between the two porphyrins.[36]

Triple-decker (TD) systems such as (**9**) in which two Eu centers are sandwiched between three porphyrins and/or phthalocyanines (Figure 13) have

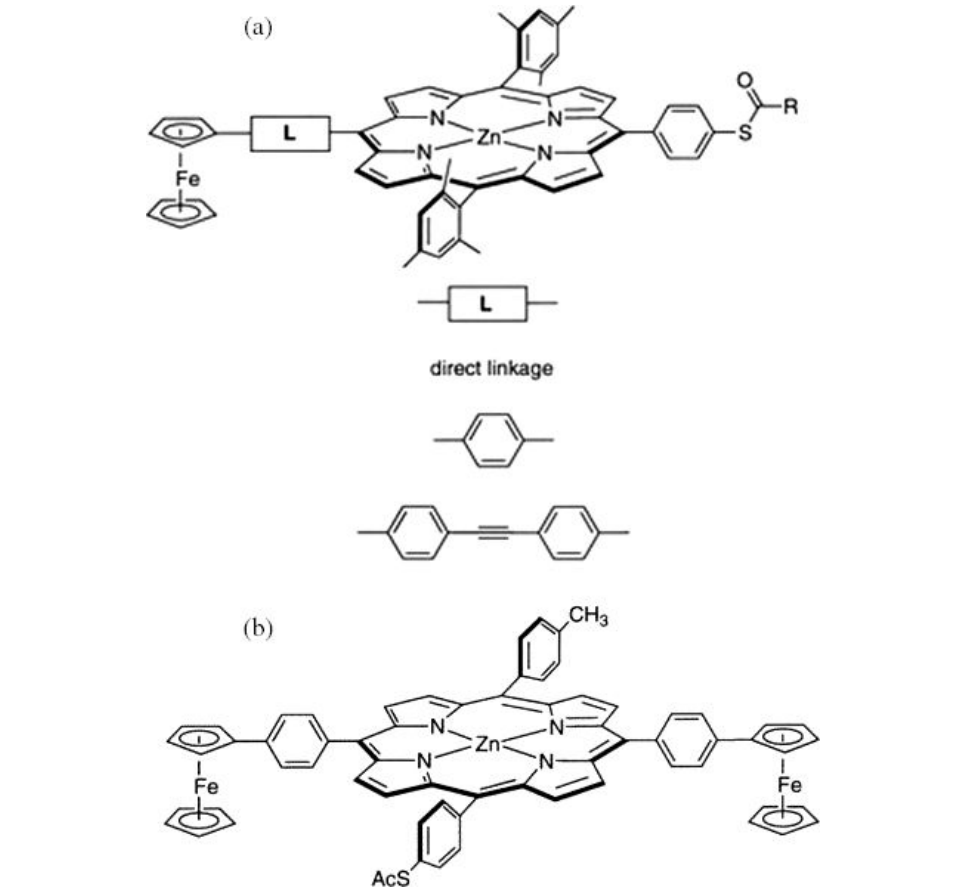

Figure 10. Structures of porphyrin-ferrocene conjugates synthesized for multibit information storage. (Adapted from Ref. 32.)

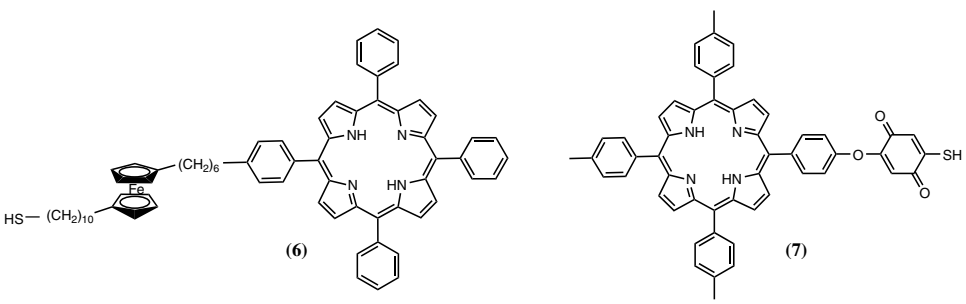

Figure 11. Porphyrin-ferrocene and -quinone conjugates used in photoinduced electron transfer studies.

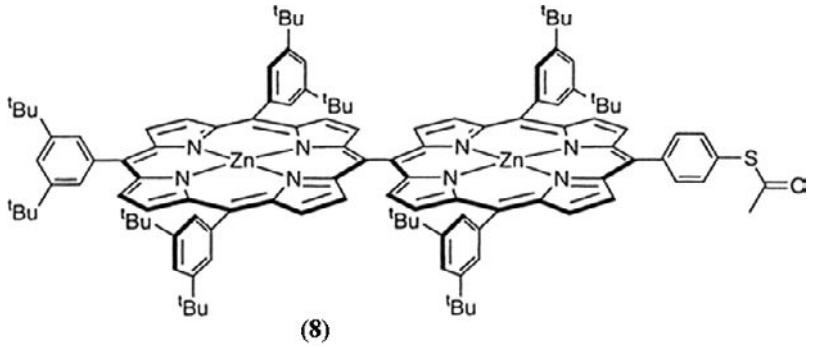

Figure 12. Structure of a linear porphyrin dimer synthesized for multibit information storage. (Adapted from Ref. 35.)

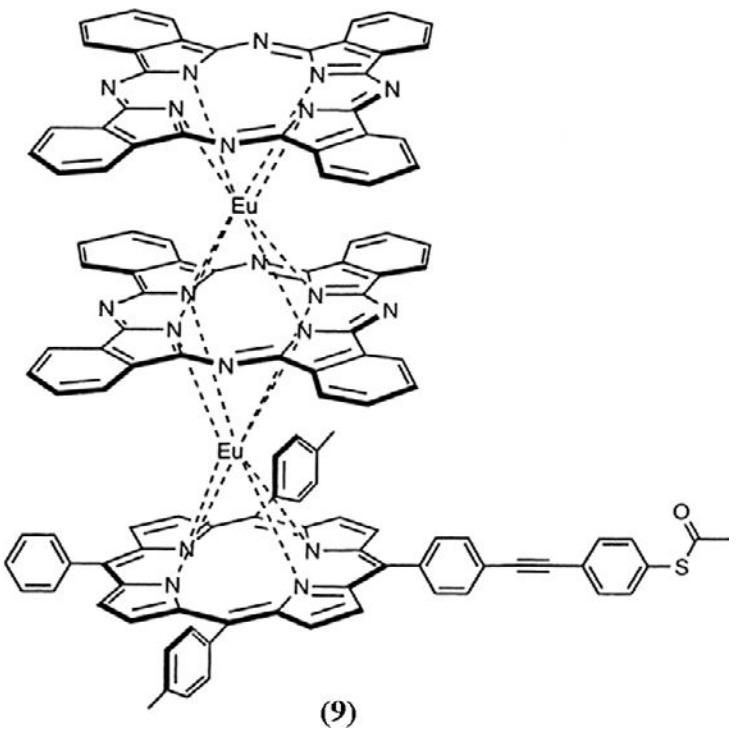

Figure 13. Structure of a typical triple-decker complex that has been immobilized on Au. (Adapted from Ref. 37.)

been synthesized.[37,38] A thioacetate anchoring unit is placed on the porphyrin of the TD.

A "pacman" structure (**10**) composed of two co-facial porphyrins linked by their available *meso* position with an aromatic bridge has been immobilized on Au

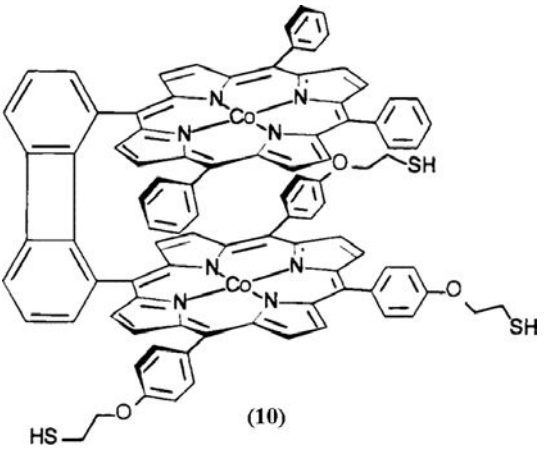

Figure 14. A thiolated bis(cobalt) cofacial diporphyrin used as a catalyst for the electrochemical reduction of dioxygen. It is a 4-electron reduction catalyst producing water when adsorbed on graphite. When chemisorbed on a gold electrode surface, the same catalyst exhibits the activity of only a two-electron catalyst, producing hydrogen peroxide. (Adapted from Ref. 39.)

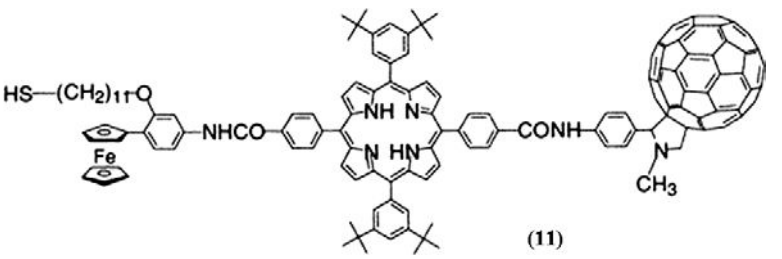

Figure 15. Structure of a ferrocene-porphyrin-fullerene triad used as a SAM on gold for light harvesting and photocurrent generation by gold electrodes. (Adapted from Ref. 40.)

(Figure 14).[39] On this structure only one of the two porphyrins bear three thiol anchoring functions in order to immobilize the structure parallel to the Au surface.

Ferrocene-porphyrin-fullerene conjugates with a thiol function such as (**11**) have been prepared (Figure 15) in a study dedicated to the understanding of photosynthetic energy and electron transfer on a gold surface.[40] Mixed SAMs of such system and boron-dipyrrin have been obtained by dipping the gold substrate in a 10 μM solution of both systems in various molar ratios and dissolved in CH_2Cl_2 for about 20 hours. Electrochemical and photochemical studies showed that a cascade of photoinduced energy transfer and multistep electron transfer takes place giving rise to photocurrent output with a high quantum yield (50 ± 8%).

2. *Sequential Immobilization of the Macrocycle*

Sequential grafting allows the benefit of a well-packed and ordered underlayer to be combined with the presence of sterically crowded species such as porphyrin macrocycles.

a. *Coordination bond coupling*

An appealing procedure is the immobilization of a bi-functional spacer possessing a terminal end group such as a pyridine or imidazole that can act as a ligand of the metalloporphyrin compound, or that can be transformed into a potential ligand (Figure 16).[41] Co-immobilization of a diluent thiol is required to accommodate the bulky macrocyclic species on the Au surface. Two distinct methods, labelled

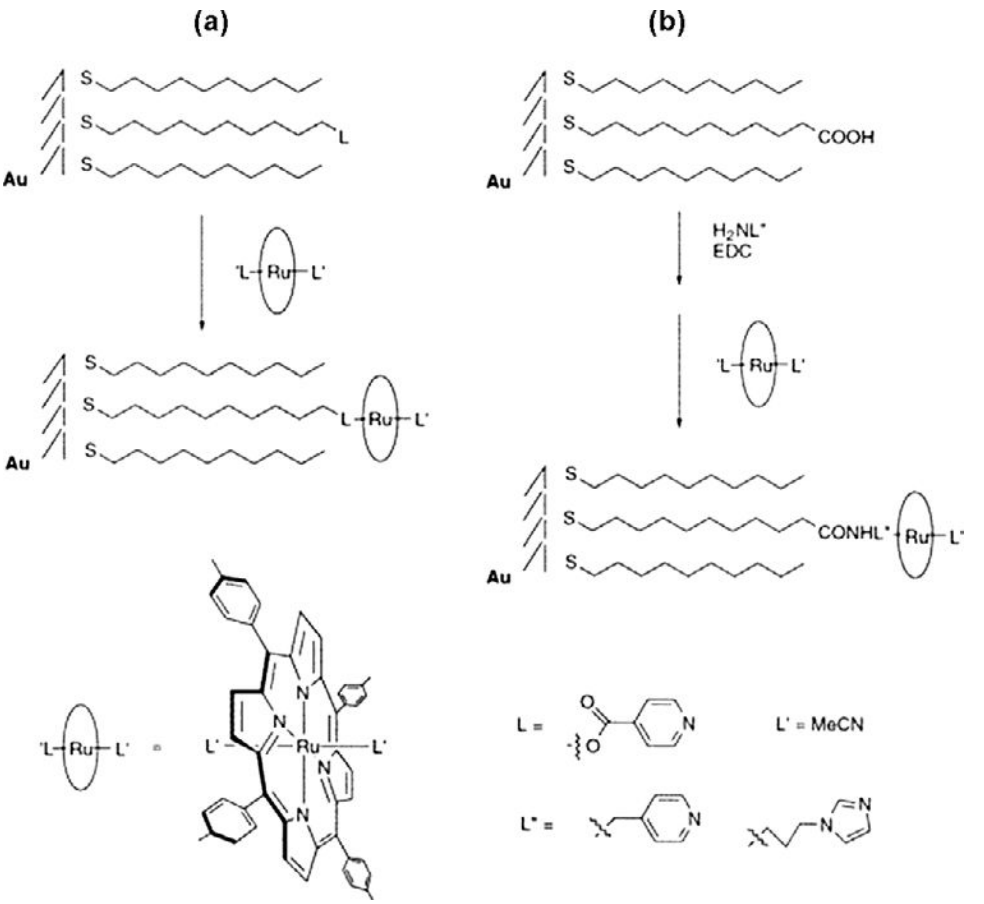

Figure 16. Modular formation on gold of monolayer assemblies containing axially ligated metalloporphyrins. (Adapted from Ref. 41.)

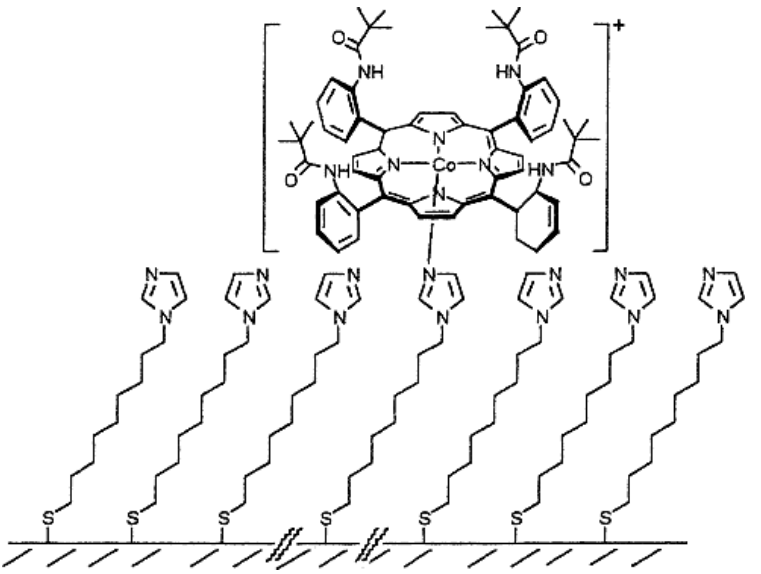

Figure 17. Self-assembled monolayers of 1-(10-mercaptodecyl)imidazole on gold electrodes used to bind cobalt "picket fence" porphyrin to the electrode surface. The binding involves coordination of the cobalt(III) center of the porphyrin to the pendant imidazole groups in the monolayer coating. (Adapted from Ref. 45.)

(a) and (b) in Figure 16, have been used to form a RuTPP SAM. To ease the chemical process the diluent is chosen so as to be slightly shorter than the bi-functional spacer to give access to the reactive function. The monolayers formed are quite stable. Both the Ru and macrocycle oxidation waves are visible in the cyclic voltammogram. Such procedures could be used for the growth of an array of different layers of metalloporphyrins.[42]

Various TPP and OEP derivatives have been similarly immobilized on Au using a pre-assembled pyridine SAM.[43,44]

The axial ligation immobilization technique has been used to form a SAM of a Co "picket fence" porphyrin (Figure 17).[45] The spacer used exhibits an imidazole end group that can coordinate to the metal center of the porphyrin. Cyclic voltammetry studies indicated good cycling stability.

Phosphorous TPP derivatives have been immobilized using a related method but the coordination to the thiol spacer via its terminal alcohol function was performed prior to SAM formation (Figure 18).[46]

b. *Click coupling*

The Huisgen 1,3-cycloaddition also known as the "click" reaction is a convenient and high-yielding process now used in numerous fields of chemistry and materials

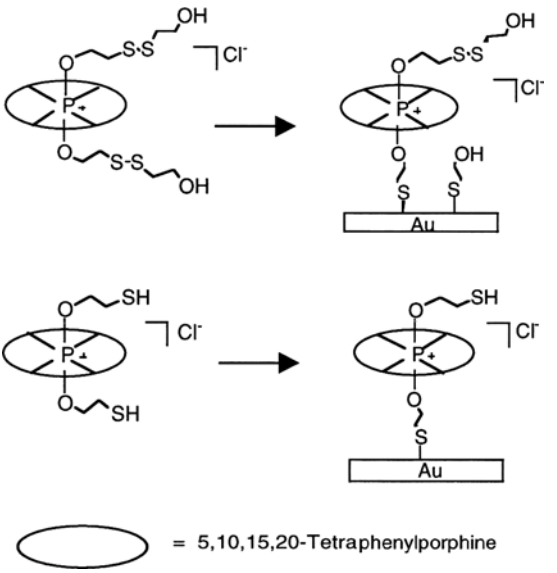

Figure 18. SAM formation on gold by a phosphorus TPP derivative via coordination of a thiol-containing axial ligand. (Adapted from Ref. 46.)

design.[47,48] It is also used to immobilize various species,[49–53] such as pyrrolic macrocycles on Au by sequential grafting. A Cu(I)-catalyzed click reaction was used to immobilize ferrocene and also porphyrins on Au (Figure 19).[9,54] In the first step a diluent and a bi-functional spacer — bearing a N_3 terminal end group — were co-adsorbed on the electrode surface. Each azide group then reacted with an acetylenic porphyrin derivative in the steric limit. Chidsey and coworkers investigated the impact of the resulting triazole linkage on the electron transfer between the surface and redox center. They showed that this linkage has the same electronic behaviour as an ester group. The electron transfer rate can be tuned by varying the nature and the length of the spacer. This prototypical N_3-functionalized surface seems to be a very interesting scaffold for the immobilization of porphyrins and other compounds on Au, and it has been adapted to other surfaces. Moreover, the electrochemically controlled reduction of the Cu(II) catalyst gives access to site selective functionalization.[55,56]

In a landmark study cytochrome *c* oxidase (C*c*O) models have been immobilized on Au using the same click procedure (Figure 20).[57,58] The C*c*O model reproduces the coordination environment and relative locations of Fe_{a3}, Cu_B, and Tyr_{244}. Various control experiments were performed by immobilizing models without the Cu centre or without the phenol which mimicks the Tyr group. By tuning the

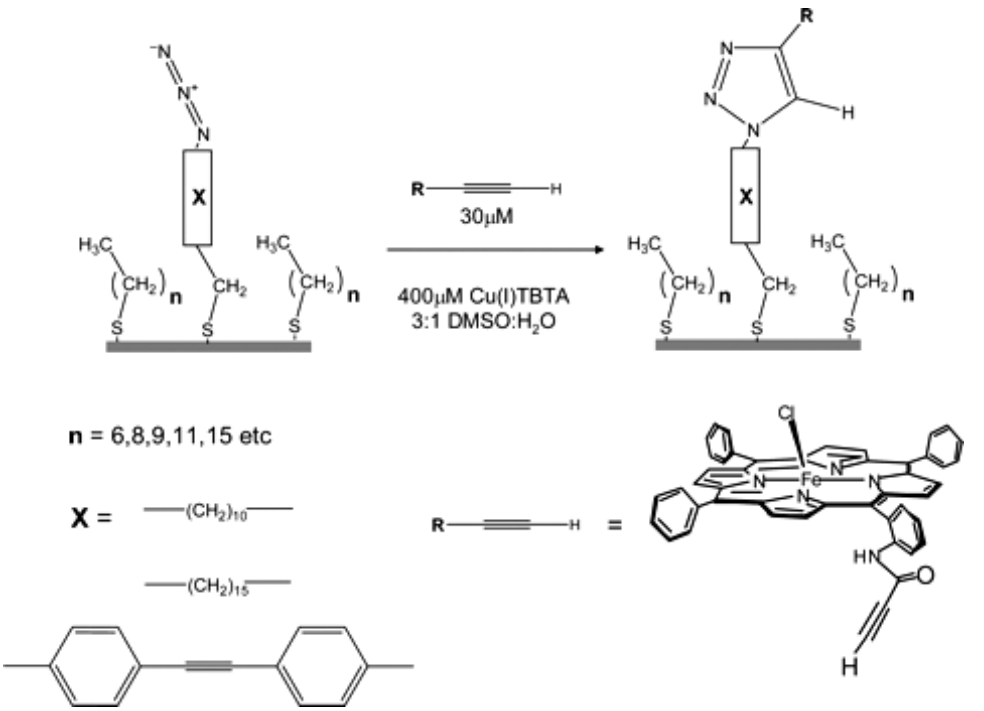

Figure 19. Scheme depicting the formation on gold electrodes of mixed monolayers coupled to redox species via Cu(I)-catalyzed azide-acetylene cycloaddition. The modular nature of the approach facilitates studies by allowing the diluent thiol, the nature of the tunneling bridge, X, and the redox species, R, to be independently varied. (Adapted from Ref. 56.)

spacer/diluent length and nature, the slow electron transfer occurring in the enzyme could be mimicked, and its significance in the efficiency of the four-electron reduction of O_2 catalyzed by C*c*O was delineated.

III. Surface Functionalization of Silicon

A. Overview

For molecular electronics the most appealing substrate is silicon as it has been used in the industry for years and because Si–O (~108 kcal.mol^{-1}) or Si–C (~76 kcal.mol^{-1}) bonds are stronger than the Au–S bond (~45 kcal.mol^{-1}).[59] The most commonly used techniques for silicon surface modification are the hydrosilylation reaction[60,61] and the grafting of aryldiazonium species[62] leading to Si–C surface bonds (Figure 21c–e). Another technique that has been used for porphyrin immobilization is the surface substitution reaction with hydroxyl anchoring units leading to Si–O surface bonds (Figure 21a).[59,63,64]

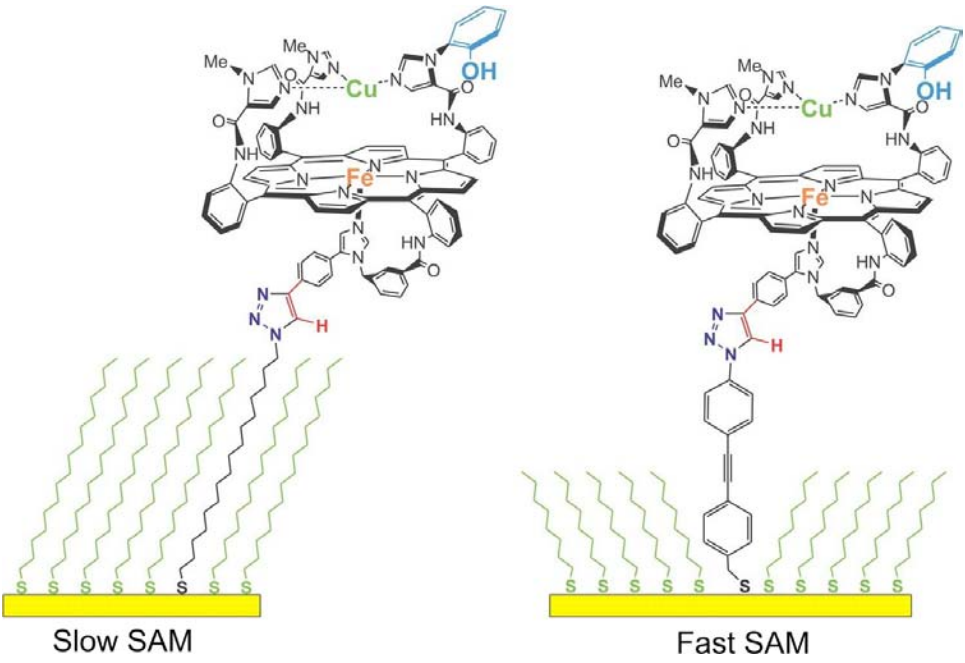

Figure 20. A functional model of cytochrome *c* oxidase active site covalently attached onto self-assembled monolayer-coated gold electrodes. When the electron transfer rate was made rate limiting via a slow SAM (left), both copper and phenol were required to enhance selective reduction of oxygen to water. (Adapted from Ref. 57.)

Alcohols can be immobilized on a Si substrate after an appropriate surface treatment[63,64]: hydrogenation by HF and/or halogenation by Cl_2 or PCl_5. The substitution reaction is often a "neat-grafting" procedure performed without any solvent or additional chemical. Thus liquid compounds are good candidates or else highly concentrated solutions (~ 0.1 M) are required. A reaction time of about 14 hours and a temperature of ~ 60–70 °C are necessary to obtain a good quality monolayer. This reaction has also been used to immobilize alcohols on porous Si.[65] This Si–O linkage can also be obtained by reaction of an aldehyde with the hydrogenated silicon surface,[66] which can be photoinitiated. To our knowledge this technique has been used to immobilize ferrocene[67] but not metalloporphyrins or phthalocyanines.

These procedures are useful but it seems that the Si–O bond is less stable than the Si–C bond when it comes to ageing and chemical resistance.[68] So in a number of studies the carbosilane linkage has been favoured. This linkage can be obtained by two methods: hydrosilylation or aryldiazonium addition. In the first method, the reagents are the hydrogenated Si surface and a compound bearing an unsaturation. The reaction is known to proceed through a radical mechanism (Figure 22).

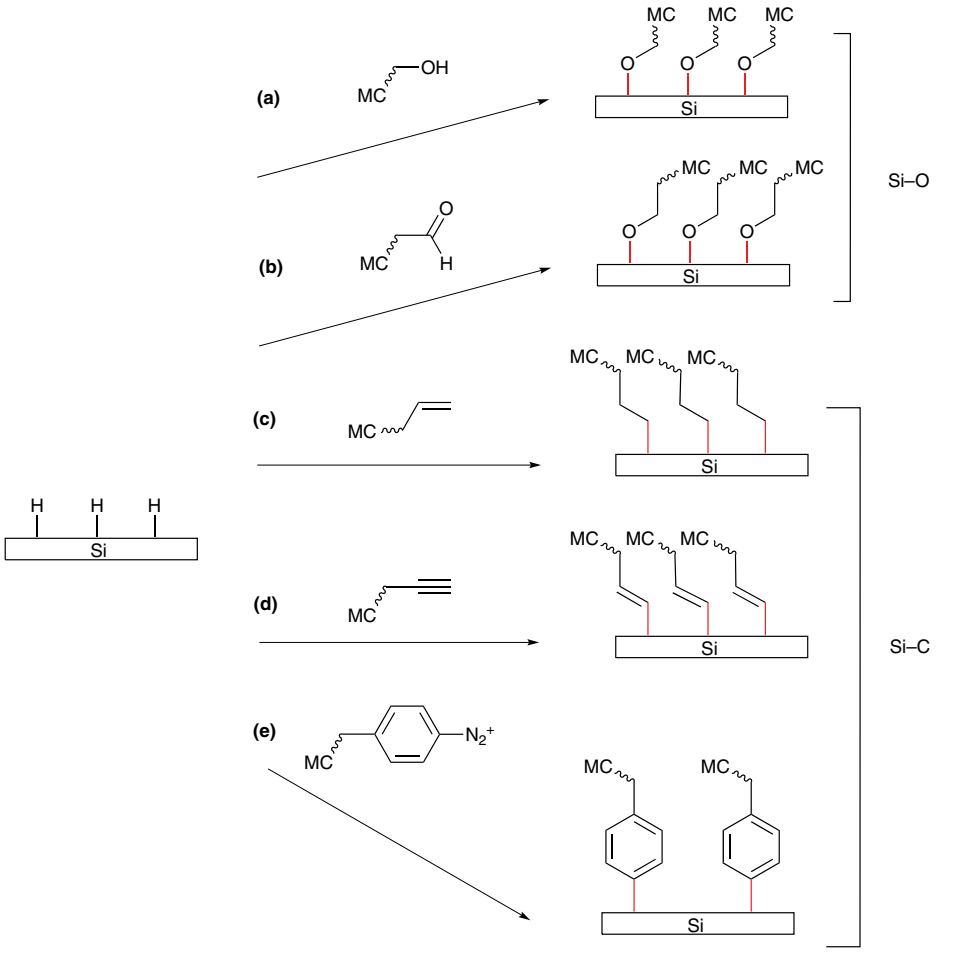

Figure 21. Methods used for anchoring porphyrin and phthalocyanine macrocycles on silicon by (a, b) Si–O or (c–e) Si–C bonds.

Si-centered radicals are formed upon cleavage of Si–H dangling bonds. A Si radical abstracts an H from the unsaturated molecule leading to a C• radical and a Si–C bond. In turn this C• abstracts an H from an adjacent surface Si–H group leaving another surface radical that will then propagate the reaction. The radical initiation can be obtained by electrochemical, chemical, thermal or by photochemical methods.

Figure 23 depicts the hydrosilylation of a C–C triple bond. In that case, different linkage types can be obtained: either the unsaturated site reacts with the adjacent Si–H site creating a cyclic linkage, or it does not react further and only abstracts an H from the adjacent Si–H site. This linkage diversity is hard to characterize.

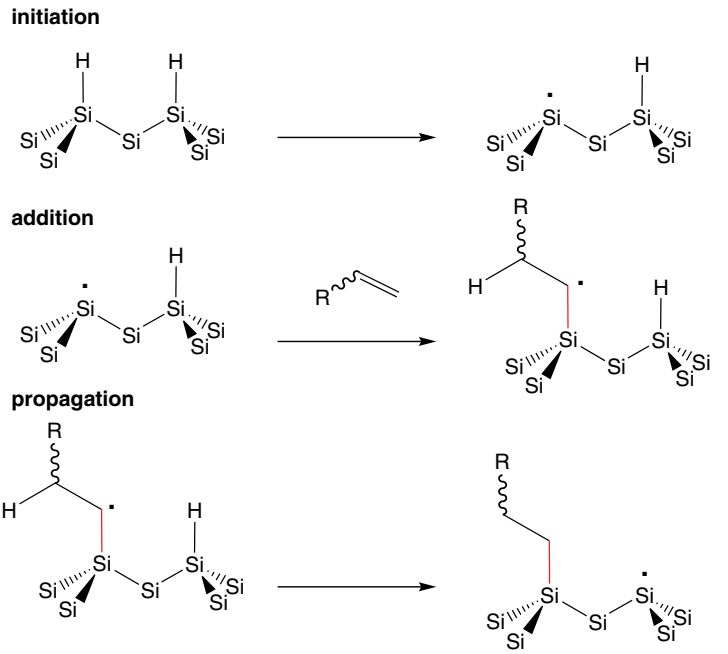

Figure 22. Radical mechanism of alkene hydrosilylation on the surface of hydrogenated silicon.

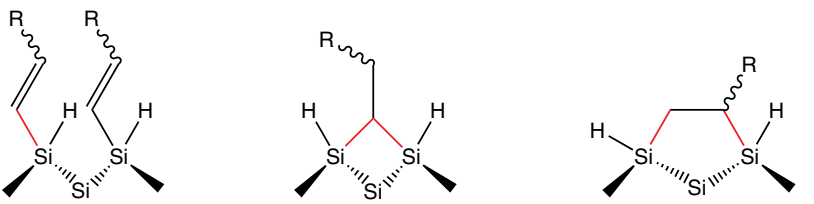

Figure 23. Various types of surface species obtained upon hydrosilylation of an alkyne by hydrogenated silicon.

The nature of the Si atomic plane has a strong impact on the type of Si–C bond, its tilt angles, and surface coverage. The Si–H site on Si(100) is a dihydride species with a Si–H bond angle of ~45° which is somewhat maintained in the resulting Si–C bond. The tilt angle also depends on the nature and volume of the immobilized molecule. In contrast, the Si–H site on Si(111) is a monohydride so the resulting alkyl chains are much less tilted, and higher surface coverage can be reached with this substrate.

Prior to surface grafting, the Si sample is dipped in an acidic fluoride solution in order to etch the SiO_2 layer and leave a Si–H reactive surface. For Si(100) HF

solutions (10%) are commonly used, whereas for Si(111) NH_4F solutions are necessary. Such hydrogenated surfaces can be easily re-oxidized if left in air; thus most reactions are performed under inert atmosphere in Schlenk-like apparatus or in a glove box. The experimental conditions of the hydrosilylation reaction depend on the starting material. If it is a liquid available in large quantities a "neat-grafting" procedure is performed: the substrate is covered with a small volume of compound and heated above 110 °C. For photochemical initiation a drop of compound is placed on the substrate. If the starting material is a solid, or if it is available in small quantities, it is dissolved in a high-boiling solvent like mesitylene or xylene. The substrate is dipped in the solution and the temperature is raised above 110 °C.

The second method leading to Si–C bonding is the aryldiazonium reaction with reductive Si–H surface.[62] This reaction involves an aryldiazonium salt that is reduced chemically or electrochemically to an aryl radical that subsequently abstracts an hydrogen atom from a Si–H site (Scheme 5). Once the aryl monolayer is formed it can be attacked by aryl radicals in solution yielding multi-layers. Tuning of the film thickness by controlling the applied current has been attempted.

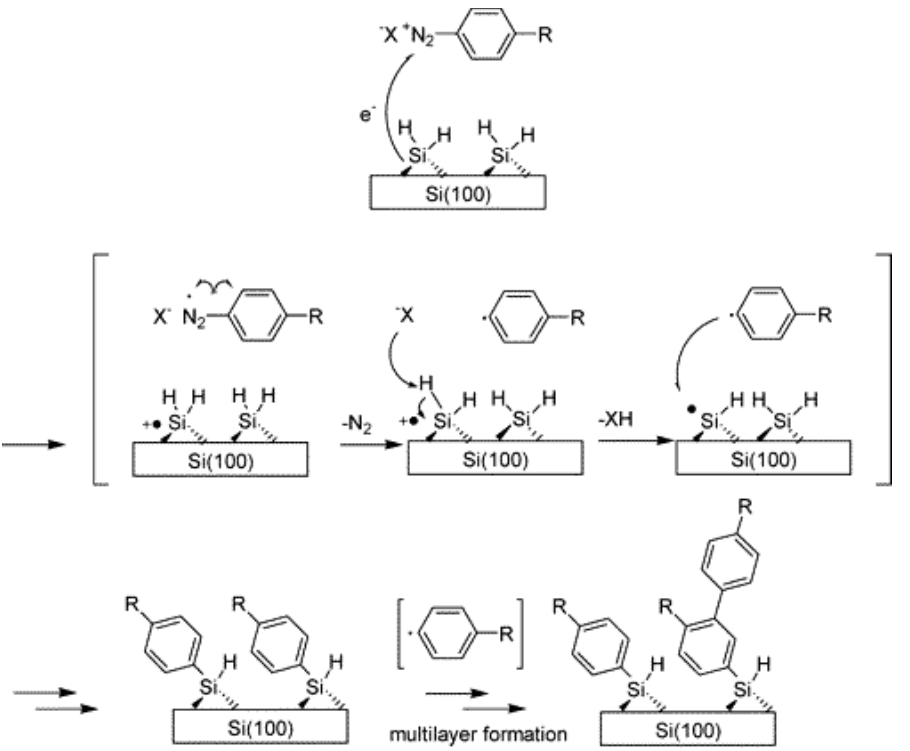

Scheme 5. Mechanism of the reaction of aryldiazonium salts with hydrogenated Si(100) surface. (Adapted from Ref. 69.)

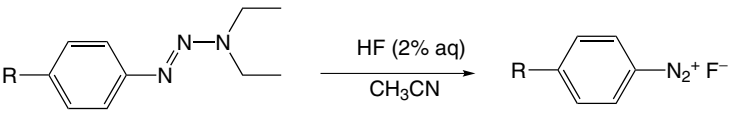

Scheme 6. *In situ* generation of aryldiazonium salt from an aryldiethyltriazene.

The hydrated Si surface is very reductive, and the diazonium function can also be spontaneously reduced by the Si surface, but in such cases only low thickness films are obtained.

Another route to obtain surface generation of aryl radicals has been explored. Replacement of sensitive aryldiazonium salts by stable aryldiethyltriazenes as starting compounds has been successfully investigated (Scheme 6).[69] This method is appealing because the charged species is generated *in situ*.

B. Selected Examples

1. *Si–O Bonding of the Macrocycle*

Zn and free base TPP derivatives have been immobilized on Si(100) and Si(111)[70] by reaction of a hydroxyl substituent with a pre-treated Si-I surface (Scheme 7). Preliminary iodination was performed by exposing a hydrogenated Si(111) sample in a Schlenk-tube to a CH_2Cl_2 solution of I_2 for 30 minutes at room temperature under N_2. This Si sample was then transferred to a stoppered tube containing a solution of 0.05–1 mM of porphyrin dissolved in THF for 2 hours at 373 K. XPS and AFM characterization confirmed that the grafting was successful. The XPS data showed that partial demetalation is observed.

Bocian, Lindsey and coworkers have studied porphyrins and triple-decker structures possessing hydroxyl anchoring units (Figure 24).[59,71] The usual room temperature attachment of hydroxyl species onto a Si–H surface apparently did not yield good quality SAMs. Increasing the temperature to 170 °C did not significantly enhance monolayer quality. So another strategy was followed with the periodical deposition of microdrops of porphyrin solution onto the heated Si–H surface over 3 hours. More ordered SAMs were obtained but their quality was not

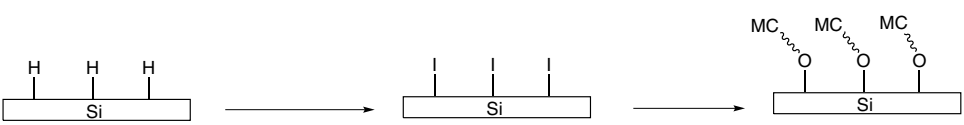

Scheme 7. Immobilization of hydroxyl containing porphyrins via iodination of the silicon surface.

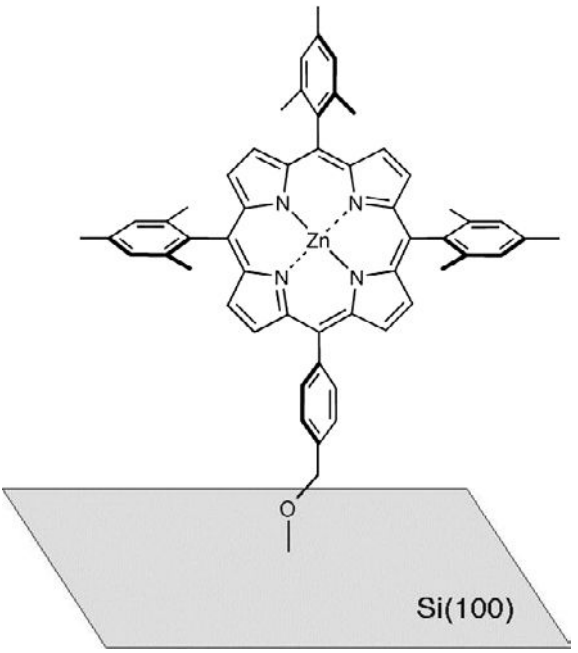

Figure 24. A typical porphyrin species tethered on silicon through a Si–O bond. (Adapted from Ref. 71.)

sufficient to record reproducible cyclic voltammetry data. Therefore the hydride surface was first iodized by dipping a Si–H sample in a saturated solution of I_2 in anhydrous $CHCl_3$. The macrocycle monolayer was obtained by placing on the Si–I surface microdrops (ca. 2 μL) of porphyrins in benzonitrile (10 mM) containing 1% pyridine. This base catalyzes the surface reaction and traps the HI formed during the reaction. One drop was deposited every 20 minutes over 3 hours while the substrate was heated to 165 °C. This drop deposition coupled to the heat control procedure yielded Si surfaces with the highest surface coverage. It was found that the modulation of the deposition time or the co-adsorption of a diluent can have an impact on the surface coverage. The success of the protocols was confirmed by electrochemical analyses. The surface coverage reached for the porphyrin macrocycles was in the 10^{-11} mol.cm^{-2} range. Good values of the k° and $\tau_{1/2}$ were obtained, similar to those obtained for modified Au surfaces, and they decrease with increasing surface coverage.[59]

Thiol- and selenol-containing porphyrins have been immobilized as monolayers on Si substrates via Si–S or Si–Se linkages.[72] The immobilization technique is adapted from the previously described baking procedure. The rate of electron transfer through the corresponding porphyrin monolayers does not depend on the nature of the group VI atom. The spacer nature and length have an impact on the

orientation and surface coverage, which in turn affect the monolayer electronic properties.

2. *Si–C Bonding of the Macrocycle*

a. *Hydrosilylation reaction*

Co and free base metalloporphyrins bearing four alkyne substituents have been immobilized on Si(100) and Si(111).[70] The immobilization was performed by dipping the Si substrates in a 4 mM solution of macrocycle dissolved in THF, for 24 hours at 373 K. A base was added to avoid demetalation. SAM formation was confirmed by XPS analysis. Tabulation of bonding energies (BE) for the porphyrin N1s and C1s revealed differences for free base porphyrins and metalloporphyrins. For free bases two values of ΔBE are found at 113 and 115 eV, consistent with two electronically inequivalent nitrogen atoms. Upon complexation, the Ns become equivalent and a single value is observed at 114 eV.

Two other hydrosilylation-related procedures (baking and sublimation) have been proposed for solid porphyrin compounds that are temperature resistant but unavailable in large quantities.[61,73] These techniques require high temperatures but only short reaction times (minutes). The porphyrin compound is placed on the substrate as a drop of solution, and it is baked at 400 °C, or it is sublimed onto a heated (400 °C) Si surface. In this case no solvent is required. Characterization of surfaces obtained after both types of treatment revealed the formation of porphyrin SAMs, and the electroactivity of the film was confirmed. This procedure is quite versatile as a variety of grafting substituents (ethynyl, vinyl, allyl, formyl, hydroxyl, acetylthio, acetylseleno, bromomethyl, bromo and iodo) have been tested, and good quality monolayers have been obtained. It seems that a polymerization is taking place on the surface and that covalent Si–C linkages are formed.

Two porphyrin derivatives bearing multiple allyl substituents (Figure 25) have been immobilized on Si via two anchoring units at two β-positions of the porphyrin core (**12**) or using a specific "tripodal" anchoring unit (**13**).[61,74] In both cases organosilane linkages are obtained. The tripod immobilization yielded monolayers displaying quite high retention time for the first porphyrinic oxidation state (ranging from 10 to 200 s depending on surface coverage). The baking procedure applied to the immobilization of these species can lead to high surface coverages (10^{-11} mol.cm^{-2} to 2×10^{-10} mol.cm^{-2}). It was suggested that the restricted motion of the linker arm between the surface and the macrocycle can explain this high coverage. The very robust and dense monolayers obtained with this compound prompted Bocian, Lindsey and coworkers to use it as a "starting block" for the

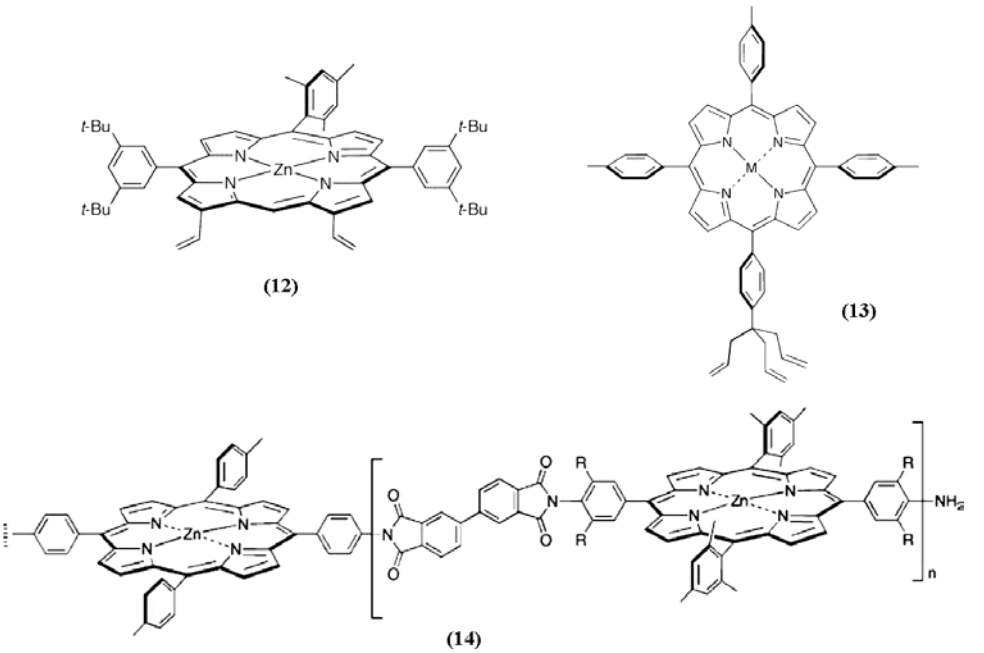

Figure 25. Porphyrins bearing two anchoring units in β-positions (**12**), an allylic tripod unit (**13**) and a "multad" immobilized on Si (**14**). (Adapted from Refs. 61, 74 and 75.)

sequential immobilization of porphyrinic "multads" (**13**).[75] These monolayers of porphyrin oligomers allowed higher storage capacities to be reached (Figure 25).

b. *Diazonium salt reaction*

Syntheses of porphyrins bearing an aryldiethyltriazene unit such as (**15**) have been performed and the resulting compounds were reacted with a Si surface (Figure 26a).[76] With these functional groups the difficult isolation of the diazonium salt is avoided. Immobilization was achieved by immersing the Si sample in a solution of porphyrins dissolved in a 1% HF/CH_3CN solution, which converted the aryldiethyltriazene to an aryldiazonium species that in turn reacted *in situ* with the Si–H surface. For compounds that are insoluble in this mixture, another method has been devised. The Si surface was passivated with HF and then immersed in a CH_3CN solution containing the porphyrin and a small amount of HBF_4 that generates the aryldiazonium salt. The concentration of the solution (0.1 to 0.5 mM) and the immersion time (10 to 120 minutes) can be tuned to obtain samples with various thicknesses. Smooth films of up to 80 nm can be conveniently obtained (Figure 26b).

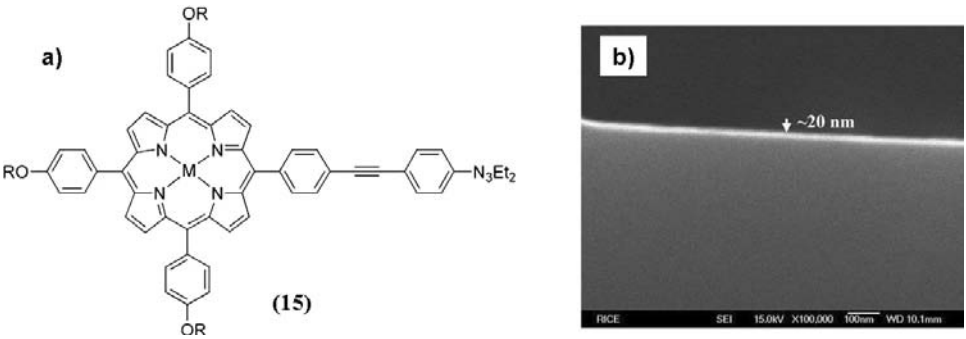

Figure 26. (a) Porphyrin bearing an aryldiethyltriazene substituent; (b) a SEM image of a film with an ellipsometric thickness of about 20 nm obtained with *in situ* aryldiazonium conversion conditions. (Adapted from Ref. 76.)

3. *Sequential Grafting*

Sequential grafting provides an efficient procedure for immobilization of sensitive compounds on silicon.[77] A robust bi-functional spacer is first immobilized using one of the techniques described earlier, and the coupling to the molecule of interest can then take place.

Cu, Co and Zn porphyrins have been immobilized on Si(100) and Si(111).[70] Two different types of grafting have been tested: one with a pre-treated Si–I surface and another with a pre-functionalized Si substrate bearing a chloromethyl end group (Scheme 8).

Click-chemistry based grafting has also been adapted to Si surface modification.[78–83] This technique has been used to immobilize ferrocene and porphyrins on Si(100).[84,85] Delapierre and coworkers immobilized porphyrins bearing a single C–C triple bond on a phenyl substituent onto a functionalized Si substrate with

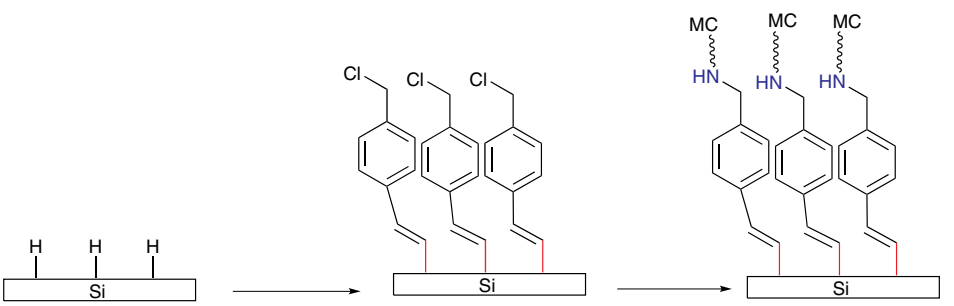

Scheme 8. Sequential immobilization of porphyrin macrocycles on Si using a chlorinated spacer.

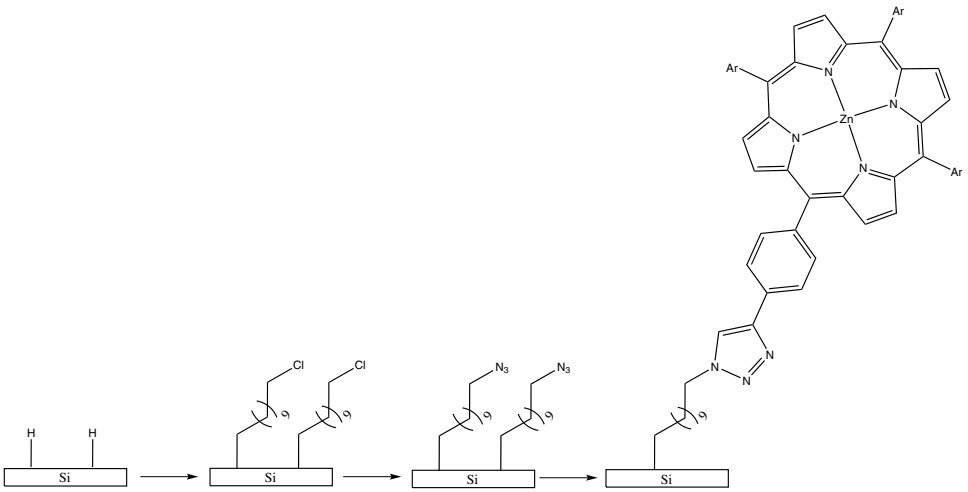

Scheme 9. Immobilization of a zinc tetraphenylporphyrin complex on Si by successive hydrosilylation, substitution, and click cycloaddition on a *meso* phenyl position.

azide functional groups protruding from the surface.[84] Immobilization takes place in three steps (Scheme 9). Chloro-undecene is first anchored on the surface by dipping the Si sample in a mesitylene solution (10% vol.) for 2 hours at reflux. The second step is the substitution of the Cl atom by the N_3 function by immersion of the previously modified Si sample in a saturated solution of NaN_3 in DMF at 80 °C for 18 hours under argon. The final step consists in dipping the sample for 24 hours at room temperature in a dichloromethane solution containing porphyrin (1 mM) and CuI (0.1 mM) and DIPEA (1 mM) to catalyze the cycloaddition reaction. Each functionalization step was monitored and confirmed by IR, ellipsometry and XPS. Electrochemical studies showed that tuning the linker length has an impact on the electron-transfer rate between Si and the porphyrin, which is slower with longer alkyl linkers.

This study has been extended to porphyrins bearing an azide substituent on a β-position and a Si modified sample with C–C triple bond protruding from the surface (Scheme 10).[85] In the first step, the alkyne-containing compound is immobilized on the Si–H substrate by dipping the hydrogenated sample in pure nonadiyne for 12 hours at 140 °C. The presence on the IR spectra of the signal of the alkyne unreacted unsaturation coupled with ellipsometric data show that only one end of the nonadiyne has reacted with the surface. Then the modified surface is coupled to the porphyrin by dipping the Si sample in a dry DMF solution of porphyrin also containing $CuSO_4$ and ascorbic acid to catalyze the cycloaddition reaction. AFM, ellipsometry, XPS and electrochemical studies showed that the monolayer formation via β-linking was successful. The surface coverage obtained

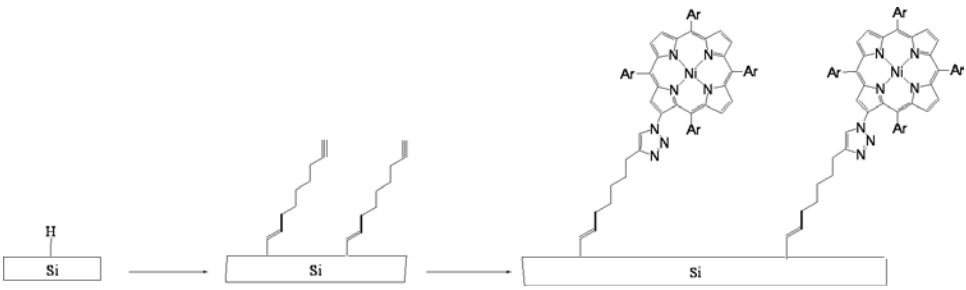

Scheme 10. Immobilization of a nickel tetraphenylporphyrin complex on Si by successive hydrosilylation, substitution and click cycloaddition on a β pyrrole position. (Adapted from Ref. 85.)

was 6×10^{-11} mol.cm^{-2}. No demetalation of the porphyrin was observed. It is noteworthy that the XPS signature of the triazole ring is very specific and can be used to confirm the surface cycloaddition reaction.

IV. Functionalization of Carbon Nanotubes and Surfaces

A. Overview

Carbon nanotubes (CNT) have been investigated as basic building blocks for electronic or photovoltaic devices. Their coupling to molecular species should allow the tuning of the properties of the resulting assembly and therefore lead to applications.[86] Porphyrins and phthalocyanines are among the molecules that have been immobilized on these substrates.[87] The anticipated applications lie mainly in the design of photoactive materials. The use of these hybrid systems in the electrocatalysis of reactions such as oxygen and hydrogen peroxide reduction, nitric oxide oxidation, oxidation of thiols and other pollutants has also been proposed.[88] A few molecular electronics applications have also been put forward.

Two different immobilization approaches, covalent[89,90] and noncovalent, have been suggested. Among the covalent procedures,[91] the most commonly used to modify CNTs with pyrrolic macrocycles are (Scheme 11): (1) amide or ester formation with the pending CO_2H functions, (2) reaction of aryldiazonium species with the CNT π-conjugated network,[92] and (3) 1,3-cycloaddition between an azomethine ylide and the CNT π-conjugated network (Prato reaction), yielding a pyrrolidine (Scheme 12).[89] In some cases, the macrocycle is immobilized in more than one step. The CNT surface is first decorated with a spacer using the aryldiazonium or the 1,3-cycloaddition reactions. In the following step the terminal end group of the spacer is reacted with the corresponding function on the macrocycle. Here again this coupling between the macrocycle and the spacer often uses an ester

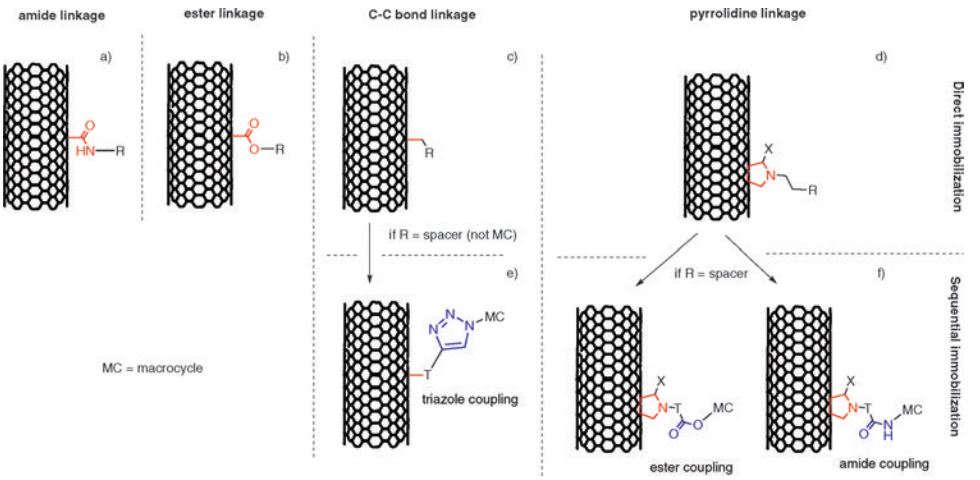

Scheme 11. Methods used for anchoring porphyrin and phthalocyanine macrocycles on carbon nanotubes by (a–d) direct and (e, f) sequential immobilization.

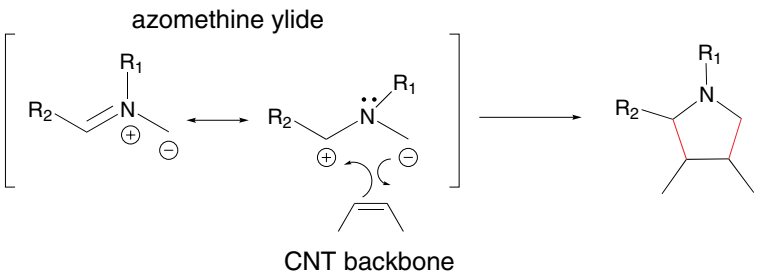

Scheme 12. Reaction of an azomethine ylide with the CNT backbone.

or amide coupling link. But this link can also be a triazole when the spacer bears a C–C triple bond end group and the macrocycle possesses an azide function.

CNTs are very sensitive to surface perturbation, and covalent grafting is not always the chosen technique as it can lead to an important change of the CNT properties. Alternatively a molecule — most often a functionalized pyrene — is chosen to interact with the CNT by π–π interactions. This noncovalent linkage is called the pyrene linkage. A second set of intermolecular interactions is used in order to immobilize the macrocycle on the decorated CNT (Figure 27). Pyrene and macrocycle units have been synthesized so as to possess two complementary functions that are able to "recognize" each other. The intermolecular interactions that could be used are numerous, and they include hydrogen bonding, coordination bonding, electrostatic interactions, etc. Sometimes the assembly is strengthened by using more than one type of interactions.

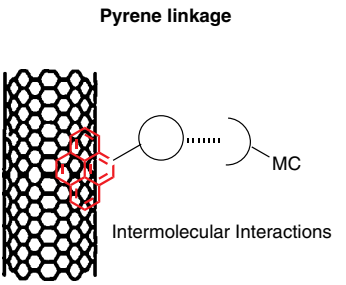

Figure 27. Noncovalent CNT surface modification involving pyrene interaction.

In the following section a few selected examples of phthalocyanines or porphyrins immobilized on CNT using one of these techniques are presented. Graphene and diamond substrates will also be briefly mentioned as the anchoring chemistry involved is very similar.

B. Selected Examples

1. *Covalent Linkage Between CNT and Macrocycle*

a. *Amide linkage with oxidized CNT*

Phthalocyanines have been coupled to CNTs to study the optical properties of the assembly.[93] After a purification step the single walled CNT (SWCNT) is oxidized in concentrated H_2SO_4/HNO_3 mixtures in order to produce carboxylic acid functions on the edges and on the defect sites of the CNT sidewalls. These functions were converted into acid chloride after reflux in $SOCl_2$. In parallel an aminophthalocyanine derivative was synthesized. This compound also bears hydrophobic groups to enhance the solubility of the final system. An amide formation reaction is then conducted between the Pc derivative and the acid chloride functionalized SWCNT in toluene in the presence of NEt_3. Due to poor solubility the system could not be characterized by NMR, however the UV-vis spectra of a dispersion of these species in $CHCl_3$ showed the broad absorption of the Pc core Q-bands. These bands are shifted towards the red indicating an electronic interaction with the SWCNT. Comparative IR analyses of KBr disks containing only CNT, Pc and the Pc-SWCNT system also confirmed the surface modification of the CNT. Electron-transfer processes within the system have been studied.

b. *Ester linkage with oxidized CNT*

Porphyrins have been covalently immobilized on CNT using an ester linkage.[94] Hydroxylated TPP derivatives were reacted with the pendant carboxylic functions of oxidized CNT. TPP derivatives possessing three hydrophobic C_{16} substituents and two linker lengths — between the OH group and the phenyl substituent — have been

tested. In this case, the ester formation was a solvent-free reaction: both CNT and porphyrin were put in contact in the solid state and stirred vigorously at 105 °C under N_2 for 24 hours. After a specific cleaning procedure, the systems were characterized by ^{1}H NMR and FTIR spectroscopies. The systems are soluble and the ^{1}H NMR spectra show the porphyrin signals with broader peaks that are consistent with the reduced mobility of immobilized species. In the IR spectra recorded in solution the signal of the C=O stretch of the ester linkage is clearly visible at 1734 cm^{-1} and 1730 cm^{-1}. TEM images showed CNT encapsulated by soft material that can be correlated to the porphyrin layer. The UV-vis and fluorescence data showed the predominant influence of the porphyrin properties, but the quantum yield analysis revealed the impact of the coupling between the molecules and the CNT, as the fluorescence quantum yield is reduced by 70% compared with the isolated porphyrin. This decrease can be explained by the intramolecular fluorescence quenching associated to the photoinduced electron transfer from the porphyrin to the nanotube. It was suggested that the linker length could have an impact on the molecular orientation at the nanotube surface leading to electron transfer modification. For a short linker no fluorescence quenching was observed. These results pave the way to the design of new nanometric photoactive material that could compete with dye-functionalized nanoparticles.

In a related procedure,[95] the acid chloride functions generated on CNTs were reacted with the hydroxylated porphyrin in toluene in presence of NEt_3 at 100 °C for 24 hours. FTIR analysis showed the presence of porphyrins on the nanotubes (Figure 28). The Soret band of the porphyrins around 450 nm was observed on the UV-vis spectra. For SWCNT even the Q bands were visible whereas for the multi-walled CNT (MWCNT) the absorption of the nanowire predominates and masks them. Upon excitation at 550 nm, the spectra recorded for a solution of porphyrin-nanowire system shows a ~95–100% quenching of the emission bands at 650 and 725 nm. This observation also suggests an intra-system electron-transfer process in this case.

c. *C–C Bond linkage between CNT and macrocycle*

i. Direct immobilization

The following example involves the immobilization of porphyrins on CNT using aryldiazonium chemistry and the formation of a C–C bond between the macrocycle and the nanowire.[96] For this surface modification procedure, prior oxidation of the CNT is not required. The purified SWNT are sonicated in o-dichlorobenzene (ODB) for 4 hours and an amino-TPP solution in acetonitrile is added. Then the reducing agent — isoamylnitrite — is added to the mixture that is stirred in the dark at 70 °C for 48 hours. Reduction of the *in situ* generated diazonium salt, followed by N_2 release, generates an aryl radical that reacts readily with the SWNT surface (Scheme 13) over a period of 48 hours. The final system was washed in DMF. The functionalization was confirmed by FTIR and UV-vis analysis.

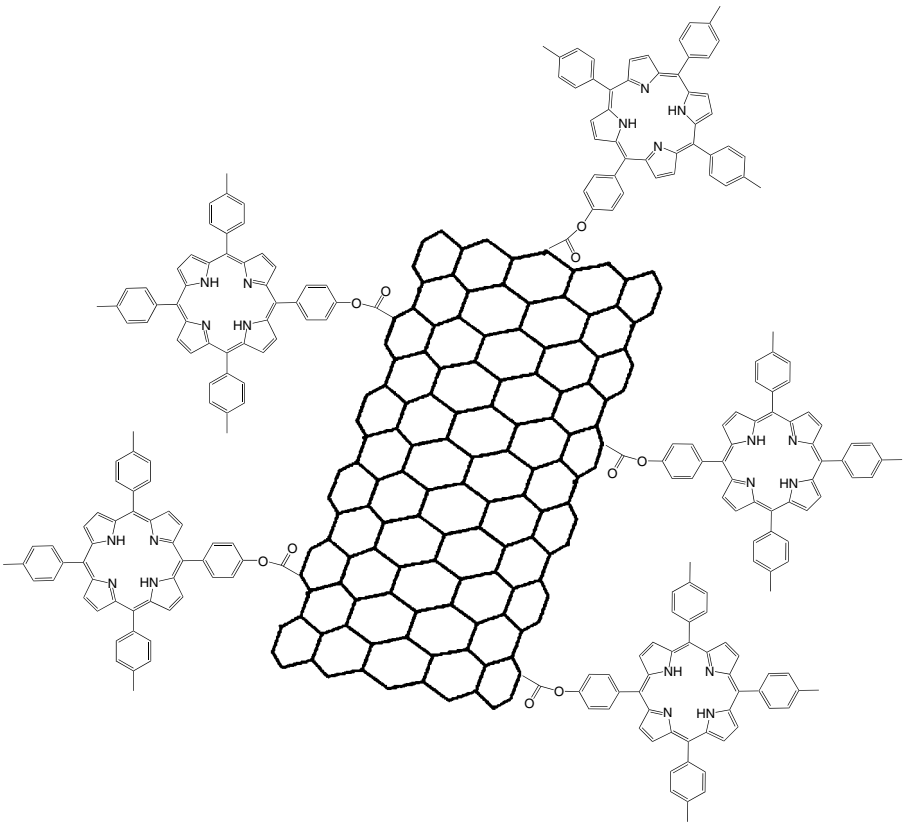

Figure 28. Porphyrins immobilized on SWNT by ester formation mediate photoinduced electron transfer. (Adapted from Ref. 95.)

Thermogravimetric analysis showed that the porphyrin surface coverage is higher than 28%. UV-visible and fluorescence analyses showed that there is an important charge transfer between the molecule and the nanotube by a rapid through-bond mechanism: the Soret band is shifted and fluorescence is quenched by 97%.

The effect of the chemical link between the nanotube and porphyrins has been investigated by comparing the optical properties of assemblies obtained by ester formation, amide formation and diazonium salt reaction (Figure 29).[97] Upon excitation of the porphyrin at the Soret wavelength, an important fluorescence quenching is observed: for the C–C linker and TPP-SWNT system a 97% quenching is recorded for the fluorescence emission at 651 nm and 717 nm. For the amide linker and TPP-SWNT system a 25% quenching is observed. For the even shorter ester axial linkage almost no fluorescence quenching occurs. The length of the linker has a similar impact on the system properties. It is interesting to note that this aryldiazonium reaction takes place between an aminoporphyrin derivative and a CNT, whereas a Si surface is inert under the same conditions.[76]

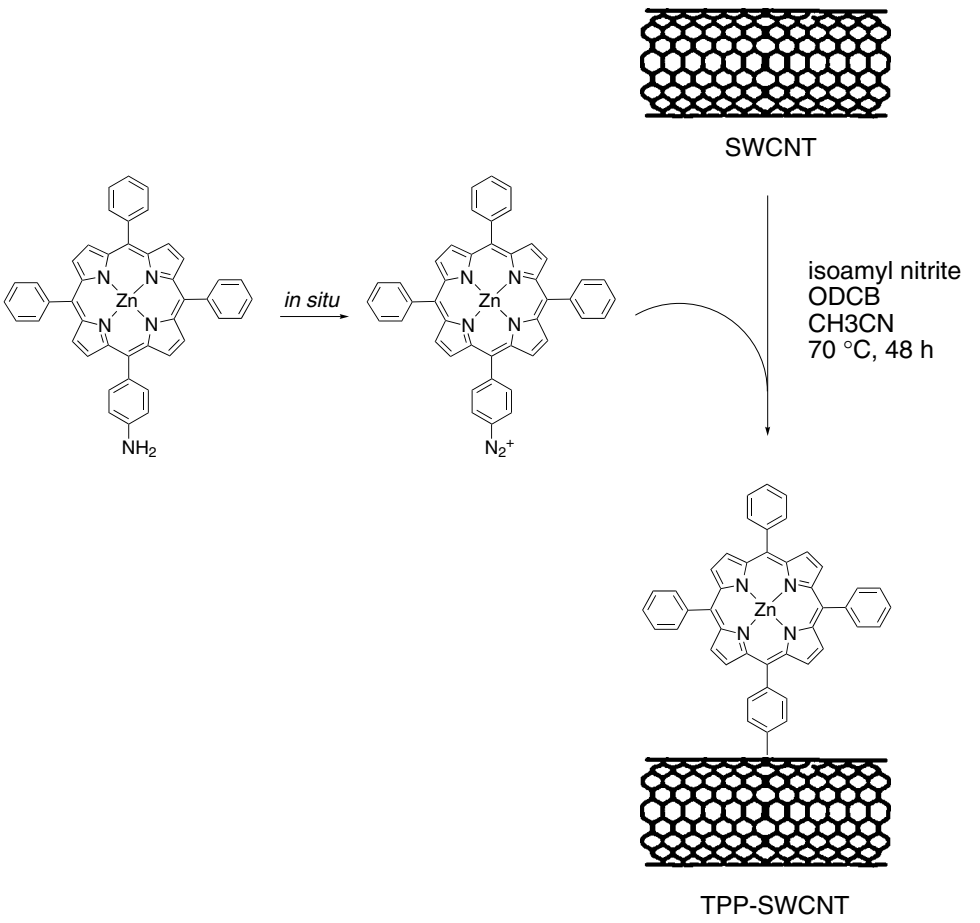

Scheme 13. Anchoring porphyrin on CNT by *in situ* formation of an aryldiazonium salt.

ii. Click coupling

Phthalocyanine compounds have been immobilized on SWCNT using a method based on the high yielding and mild click-chemistry cycloaddition described in the preceding sections.[98–101] In a typical study,[102] a C–C bond linkage is first formed between the CNT and the spacer, and in a subsequent step a triazole coupling link is produced between the spacer end group and a phthalocyanine. The chosen anchor molecule — 4-(trimethylsilyl)ethynylaniline — is converted into a diazonium salt and then linked to the SWCNTs. The alkyne substituent is then deprotected and reacted with an azide-functionalized phthalocyanine (Figure 30).

The click reaction was performed in NMP at 70 °C for 48 hours in presence of $CuSO_4$ and sodium ascorbate. A polar solvent such as NMP was used to enhance the rate and yield of the reaction and to allow the solubilization of the

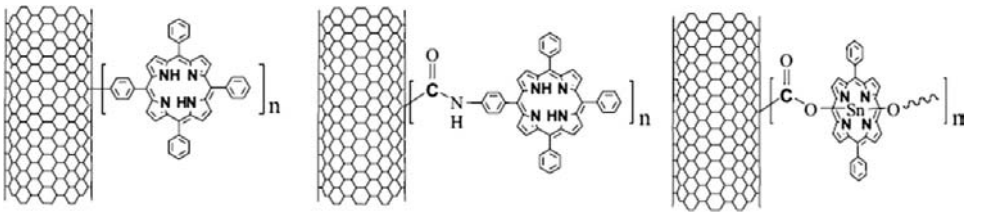

Figure 29. Porphyrin immobilization on SWNT via (left) a C–C bond linkage, (middle) an amide linkage and (right) an ester linkage. (Adapted from Ref. 97.)

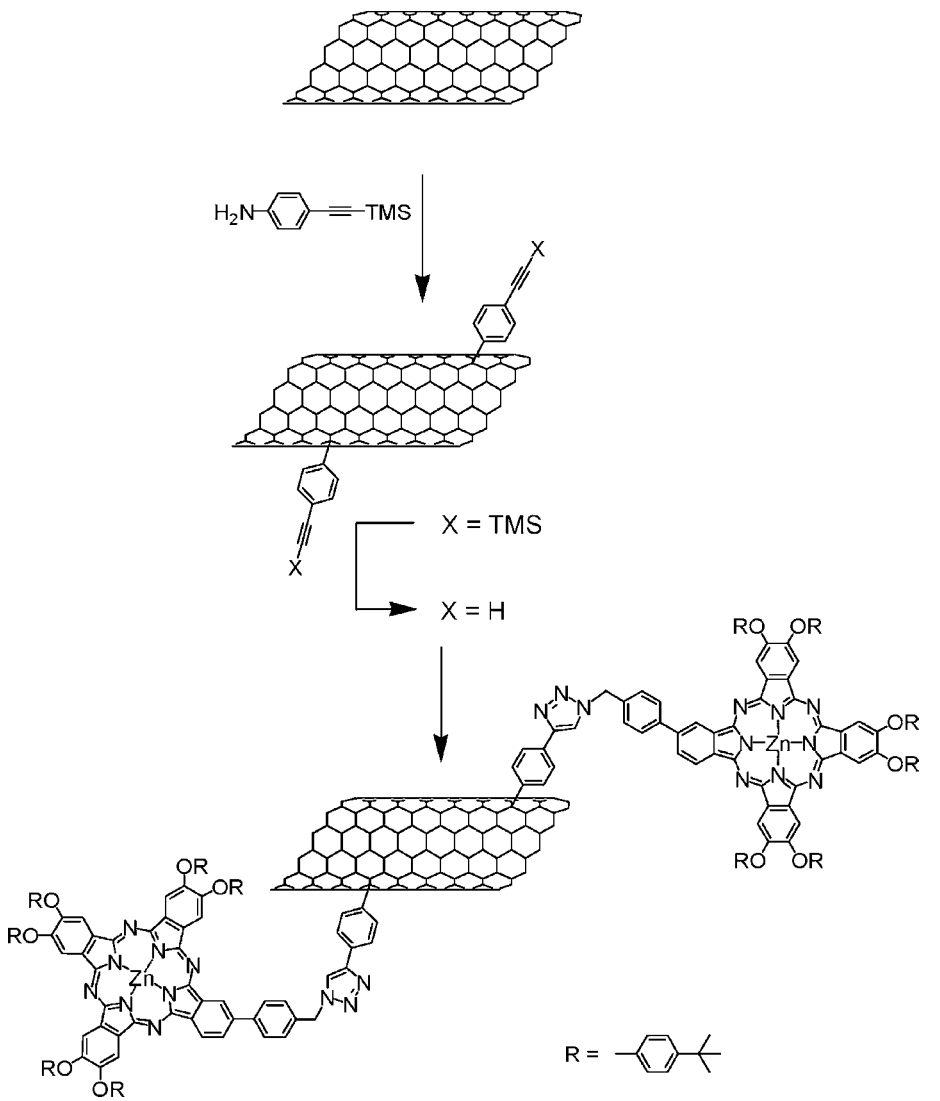

Figure 30. Phthalocyanine immobilization on SWNT via a click-chemistry based procedure. (Adapted from Ref. 102.)

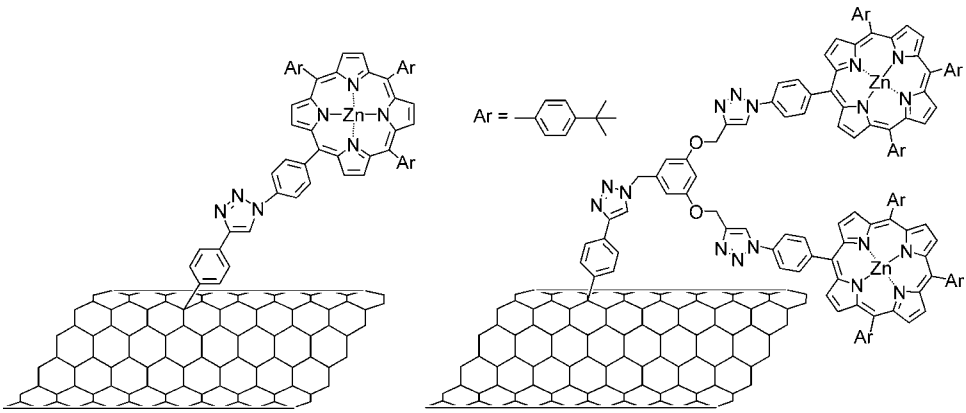

Figure 31. Porphyrin immobilization on SWNT via a click-chemistry based procedure. (Adapted from Ref. 107.)

phthalocyanines. It was shown that metallic nanotubes display higher surface coverage, which was explained by the higher reactivity of these substrates towards aryldiazonium derivatives. Phthalocyanine immobilization was confirmed by UV-vis and Raman spectroscopy, and by thermogravimetry. Photovoltaic properties have been investigated using a photoelectrochemical cell. The system was deposited on an ITO substrate. An electrolytic solution of 0.1 M Na_3PO_4 in presence of ascorbic acid (to avoid Pc photooxidation) was used along with a three electrode set-up consisting of the ITO modified electrode, a Pt wire and a Ag/AgCl electrode. The photocurrent yield reached values as high as 17%.

The 1,3-Huisgen cycloaddition has already been widely used to prepare dendrimeric materials.[103–105] Azido porphyrins[106] have been immobilized on CNT using anchoring dendrons designed to react by the Huisgen cycloaddition (Figure 31).[107,108] The advantage of using a dendron is to increase the amount of porphyrin material linked to the nanometric species while limiting the disruption of π-conjugation by a large number of surface covalent bonds.

d. *Pyrrolidine linkage between CNT and a spacer unit*

i. Amide coupling of the spacer to the macrocycle

The previously described procedures yielded poorly soluble or totally insoluble systems. Another procedure leading to enhanced solubilities has been investigated.[109] This procedure had been used previously on nonpyrrolic macrocycles.[110] It is based on the Prato reaction, i.e. the 1,3-dipolar cycloaddition that occurs between an azomethine ylide and the CNT yielding a pyrrolidine linkage (Scheme 14). Immobilization of a spacer compound by a pyrrolidine linkage is followed by amide coupling to a specifically synthesized Pc compound. In the

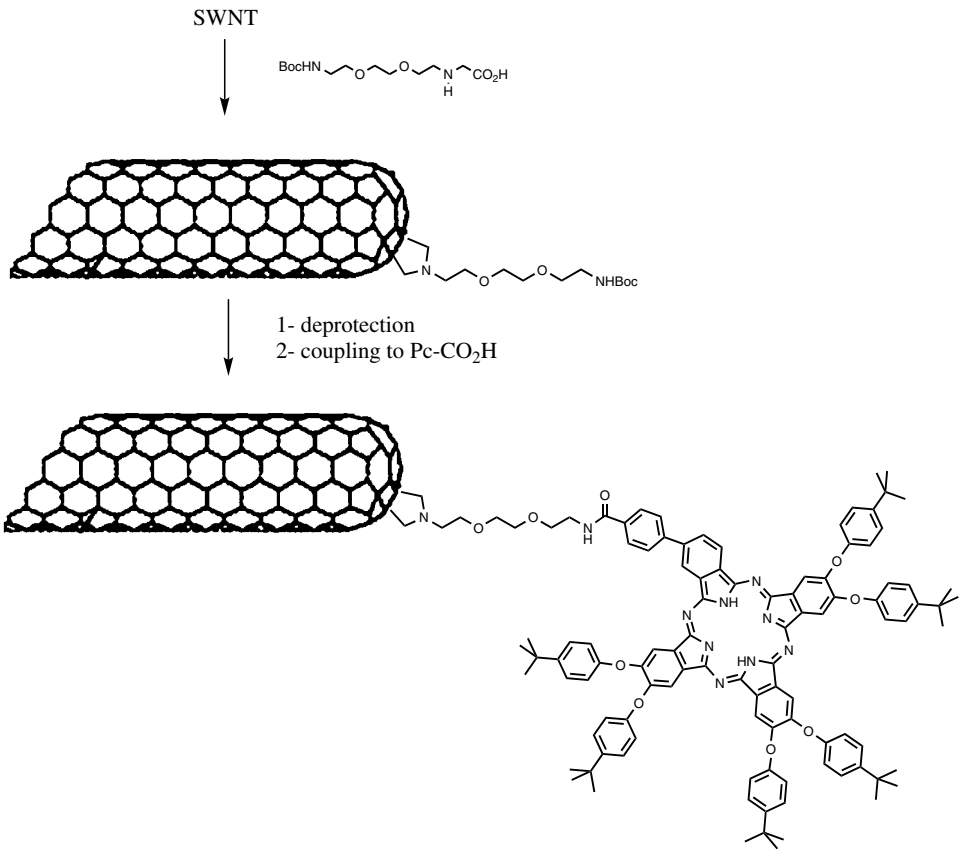

Scheme 14. Phthalocyanine immobilization on SWCNT by a Prato reaction and amide formation. (Adapted from Ref. 109.)

first step, the SWNT are placed in a mixture of a N-protected aminoacid and paraformaldehyde that react *in situ* to yield the reactive azomethine ylide. The N-protecting group was cleaved by bubbling HCl in DMF. The Pc bearing an acid carboxylic function was then reacted with the SWNT-$NH_3^+Cl^-$ nanotube modified system in the presence of *N*-(3-dimethylaminopropyl)-*N*′′-ethylcarbodiimide (EDC), 1-hydroxybenzotriazole (HOBt) in ethyldiisopropylamine. Thermogravimetric analysis revealed a 43% Pc surface coverage. The system solubility was sufficient to conduct photophysical studies. Absorption spectra were recorded in THF, and immobilization was further confirmed by a small emission band around 700 nm.

A similar grafting technique involving a pyrrolidine linkage between the CNT and a dendrimeric anchor compound was performed and the system was further reacted with a porphyrin derivative (Figure 32).[108] The first anchor was immobilized

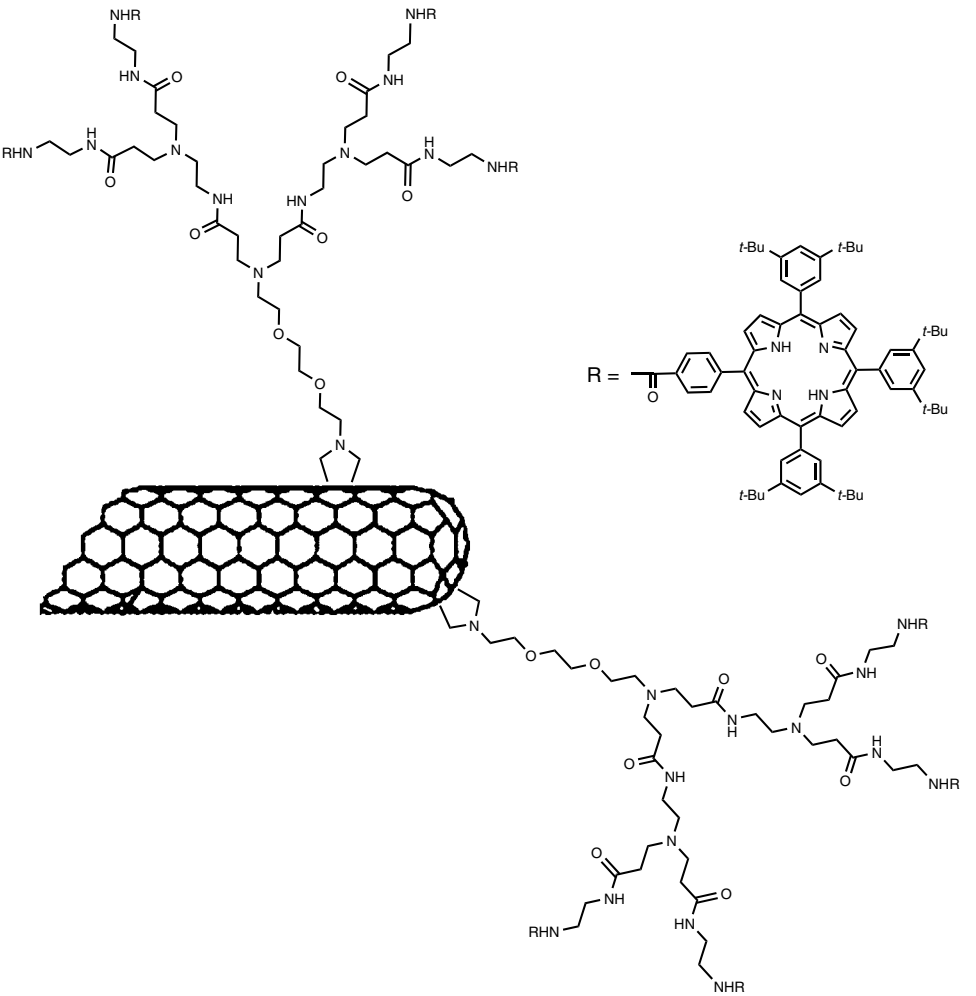

Figure 32. Porphyrin immobilization on SWNT via a dendronic approach. (Adapted from Ref. 108.)

using the procedure just described. Then the SWNT-$NH_3^+Cl^-$ was reacted with methyl acrylate in methanol for 3 days at 80 °C. After washing and filtration the ester functions were reacted with ethylenediamine providing a dendron with two terminal amines. To obtain the second generation dendron the previous one was further reacted with methyl acrylate followed by another ester formation reaction with ethylenediamine. Then the final four amines were coupled to TPP derivatives possessing carboxylic acid functions. The overall method allowed an increase of the surface coverage in the redox compound while limiting the π-conjugation system disruption. AFM imaging showed that the diameter of the SWCNT increases

upon porphyrin grafting. Thermogravimetric analysis indicated the presence of two porphyrins per dendrimer. The photoactivity of the hybrid systems has been studied.

ii. Ester coupling of the spacer to the macrocycle

The Prato reaction can also be used to immobilize phthalocyanines in one or two steps (Scheme 15).[111] For the first procedure a phthalocyanine aldehyde derivative is required, whereas for the sequential grafting the pyrrolidine linkage is first

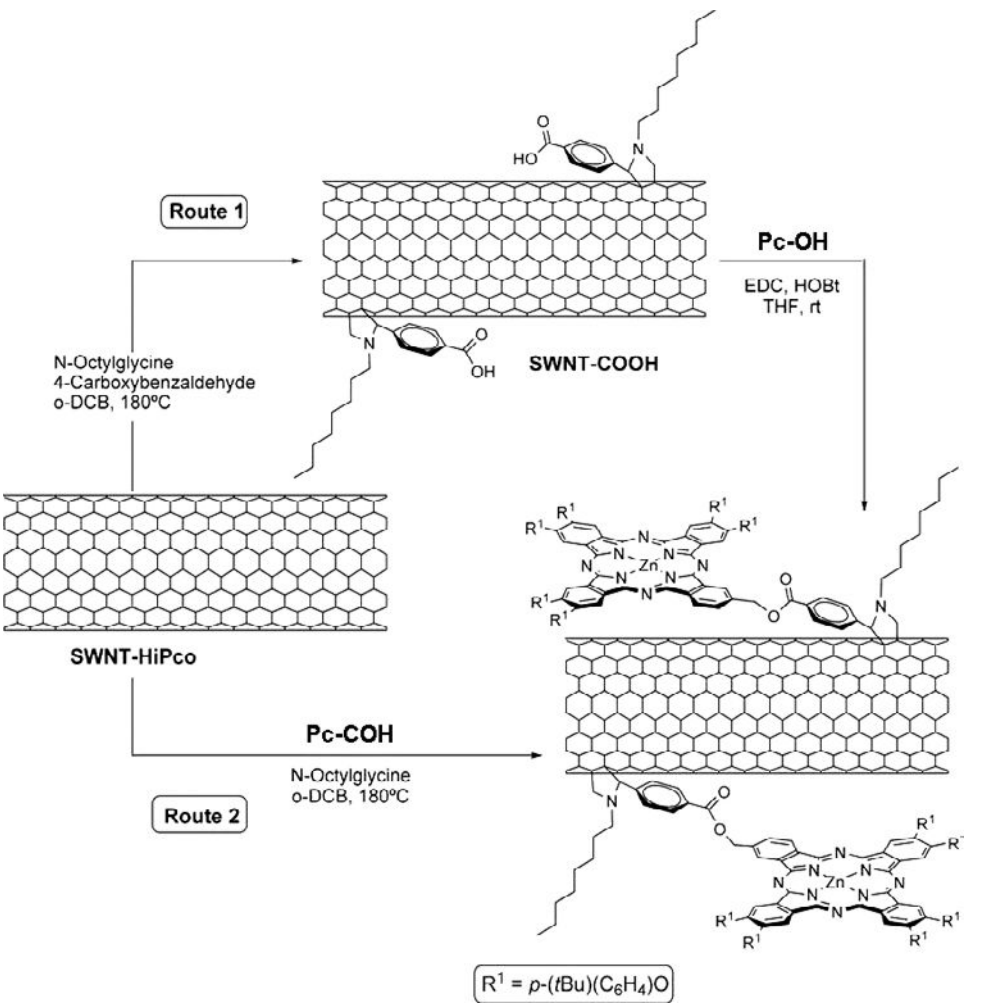

Scheme 15. Phthalocyanine immobilization on CNT by single-step and two-step grafting procedures. (Adapted from Ref. 111.)

obtained and the acid carboxylic end group of the spacer is then reacted with the hydroxyphthalocyanine. For the direct immobilization *N*-octylglycine and the Pc aldehyde derivative are mixed in o-DCB at 130 °C for 5 days yielding the Pc-functionalized SWNT. For the sequential grafting, the first step is the functionalization of the SWNT with a spacer bearing carboxylic acid functions. This reaction is performed in o-DCB with *N*-octylglycine and carboxybenzaldehyde at 180 °C for 5 days. The following step is the ester coupling between the Pc derivative and the CO_2H functions at room temperature for 4 days in THF using HOBt and EDC as coupling agents. Both procedures yielded Pc-CNT systems. With the sequential grafting higher Pc surface coverage is reached: 30% by weight compared to 20% by weight for the direct immobilization. In both methods *N*-octylglycine was used to facilitate the cycloaddition and impart higher solubilities.

2. *Noncovalent Linkage Between CNT and Macrocycle: π–π Interactions*

Studies have shown that tuning the length of the tether can influence the quenching behavior of the system. The nature of this tether is also important as the use of a C–C linker between an aromatic substituent and the nanotube leads to almost complete fluorescence quenching. In order to tune the system properties while keeping the nanotube as defect-free as possible, noncovalent functionalization procedures have been developed. The aromatic character of porphyrin and phthalocyanine derivatives has already been exploited to develop intermolecular interactions with CNT. Thus oligomers or polymers of porphyrins and sapphyrins have been immobilized irreversibly on the SWNT surface.[112–114]

An usual functionalization procedure involves the synthesis of a compound of interest bearing a pyrene "foot" that is able to interact via strong π–π interactions with the CNT backbone. In a few cases the pyrene compound bears a substituent that can act as a coordinating ligand,[115] or it bears a positive charge that interacts with negatively charged carboxylate function of the macrocyclic derivative.[116,117]

a. *Coordination bond coupling*

A pyrene bearing an imidazole moiety was immobilized on the SWNT surface (Figure 33). Then Zn–Pc and Zn–P were coordinated to the as-modified nanotubes. The presence of the macrocycle was confirmed by TEM imaging, UV-vis-NIR spectroscopy and electrochemical methods. Fluorescence quenching was also observed confirming the interaction between the macrocycle and the SWNT. Photoexcitation of the system resulted in the one-electron oxidation of the macrocycle (donor unit) and the simultaneous SWNT reduction (acceptor unit).

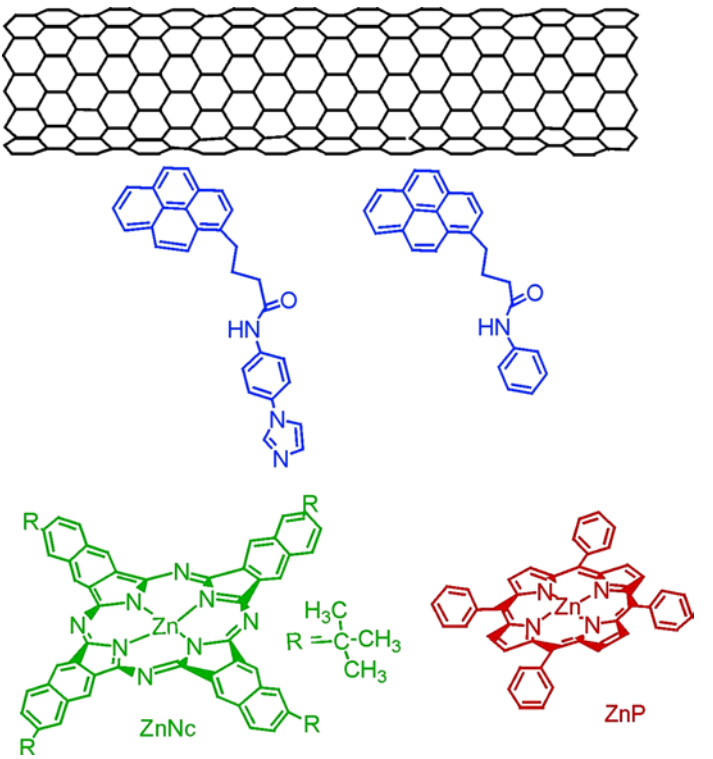

Figure 33. Representation of P and Nc immobilized on a CNT through coordination bond to a pyridino- or imidazolo-modified pyrene unit. (Adapted from Ref. 115.)

b. *Electrostatic coupling*

A positively charged pyrene has been designed so as to interact via electrostatic interactions with a negatively charged porphyrin (ZnP^{8-}).[116] To obtain the pyrene linkage 1-(trimethylammoniumacetyl)pyrene ($pyrene^{+}$) was dissolved in H_2O and water-soluble SWNT were added to the medium. The suspension was stirred overnight and then cleaned to afford the $pyrene^{+}$-SWNT system. The positively charged ammonium head group was used as an electrostatic anchor to bind the 8 anionic carboxylic groups of the zinc complex (ZnP^{8-}) (Figure 34). The modified SWNTs were dipped in dilute $Zn–P^{8-}$ solution and the success of the electrostatic immobilization was confirmed by TEM analysis and absorption spectroscopy.

c. *Crown ether-cation coupling*

Using the same pyrene foot as anchor for immobilization on the CNT, the electrostatic interactions can be replaced by crown ether-alkylammonium cation interactions to immobilize the porphyrin on the pyrene foot (Figure 35).[118] Mono- or

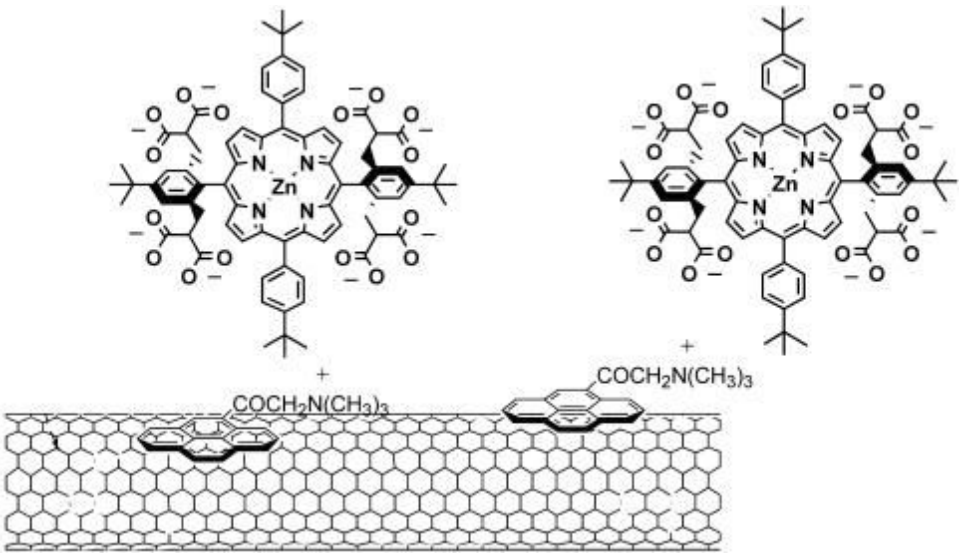

Figure 34. Porphyrin immobilization on a CNT through electrostatic coupling between positively charged pyrene units and negatively charged porphyrin substituents. (Adapted from Ref. 116.)

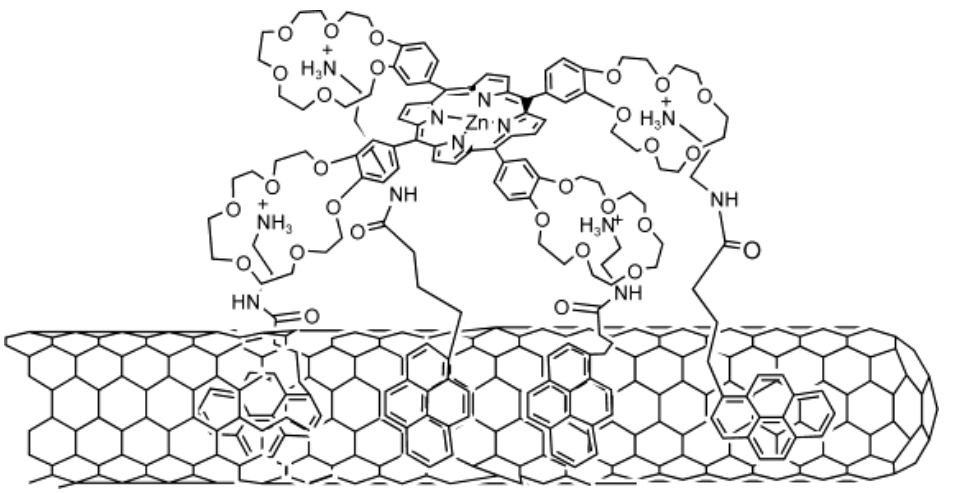

Figure 35. Porphyrin immobilization on a CNT through noncovalent interactions between ammonium cation modified pyrene unit and crown ether-substituted porphyrin derivative. (Adapted from Ref. 118.)

tetra- substituted porphyrins have been used and porphyrins with different arms between the aromatic ring and the crown ether have also been synthesized. The pyrene-SWNT system was formed upon stirring the CNT and pyrene in dry DMF at room temperature for 48 hours. The porphyrin interaction was characterized by

analyzing the photochemical properties of the systems, by TEM imaging and by electrochemistry. The porphyrins with four crown ether groups have been shown to interact more strongly with the SWNT.

3. *Graphene Functionalization via Amide Linkage*

Phthalocyanine and porphyrin deposition on graphite have been investigated for several decades[119]; however, it is only in the early 2000s that porphyrins have been covalently immobilized on graphene.[120,121] This material exists mainly as graphene oxide possessing various oxygen containing functional groups. These groups are reactive towards the amino groups of a porphyrin derivative. Thus, an amide linkage binds the porphyrin to the graphene layer (Figure 36). The success of this reaction has been confirmed by FTIR, UV-visible absorption and TEM analysis. Porphyrin grafting makes the system more soluble and processable and it affords a material with interesting optical properties.

As for the oxidized CNT, the carboxylic acid functions of graphene oxide can be converted to acid chloride by the use of $SOCl_2$ (Scheme 16).[122] These functions react in a second step with an aminoporphyrin also yielding a porphyrin linked to the graphene via an amide linkage.

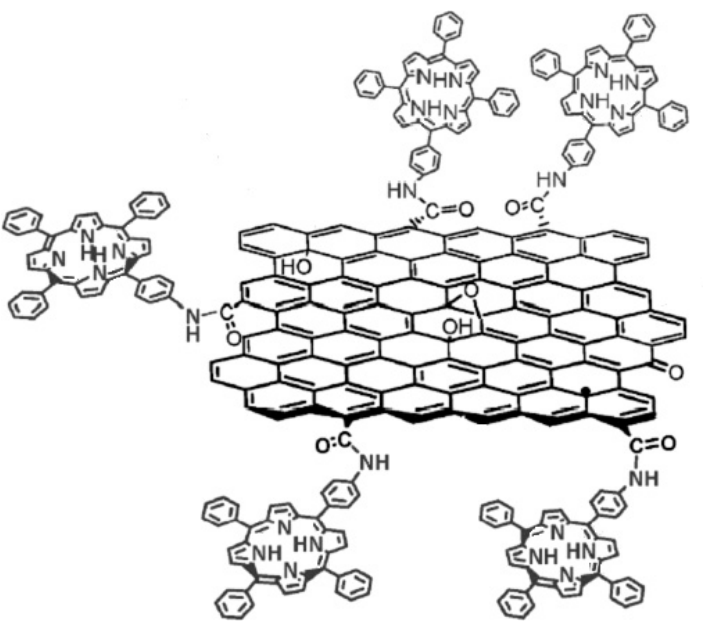

Figure 36. Porphyrins immobilization on graphene by ester formation with pendant acid carboxylic functions. (Adapted from Ref. 121.)

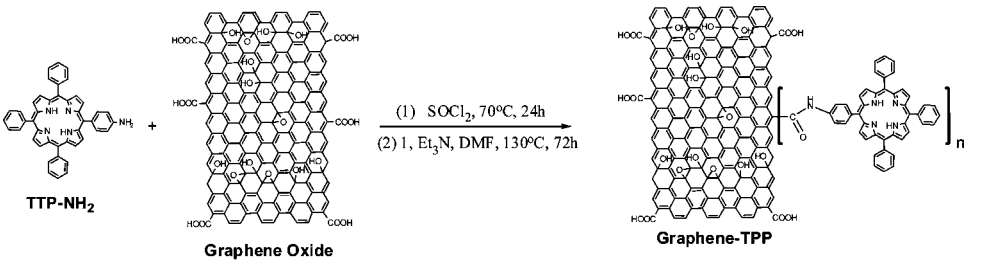

Scheme 16. Porphyrin immobilization on graphene by amide formation. (Adapted from Ref. 122.)

4. *Diamond Functionalization via C–C Linkage and Amide Coupling*

Investigations have been directed toward diamond surface modification. The reactions involved are comparable with those used to modify CNT.[123] Aryldiazonium grafting remains a convenient method to functionalize this material.[124] A cycloaddition between an allylic compound and the C backbone is also commonly used. Due to its compatibility with water diamond is a very attractive surface for functionalization with biomolecules.[125,126]

Cytochrome *c* has been covalently immobilized on a modified diamond electrode (Scheme 17) by amide coupling.[127] The electrode was boron-doped in order to decrease the material resistivity and to allow better electrical detection. The diamond was subjected to a hydrogen plasma for 45 minutes at 700 °C to produce a hydrogen-terminated surface that was then reacted with undecylenic acid methyl ester under photoirradiation. After a hydrolysis step, the amine function of cytochrome *c* was coupled to the immobilized carboxylic acid functions. Electrochemical analysis of the system showed the characteristic response of the cytochrome *c*, with a proportional trend between scan rate and current intensity confirming a surface-confined redox process. The surface coverage determined was ~1.2×10^{-11} mol.cm^{-2}. This study also showed that the electron-transfer between the redox species and the

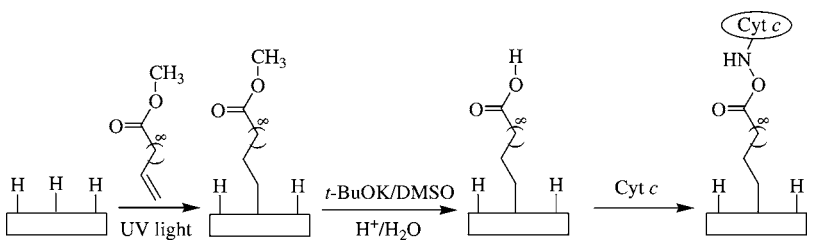

Scheme 17. Immobilization of cytochrome *c* on diamond following a sequential grafting procedure. (Adapted from Ref. 127.)

boron-doped nanocrystalline diamond (BDND) electrode is faster than with the boron-doped microcrystalline diamond (BDMD). The system also showed a good response toward the catalytic reduction of H_2O_2. This study showed that the coupling between a biological compound and a diamond electrode can lead to very sensitive electrochemical detection along with a stable response over time. Such hybrid systems could be of importance for the study of many proteins.

V. Functionalization of Oxide Surfaces

A. Overview

The most widely used technique to covalently immobilize compounds on oxide surfaces such as SiO_2, glass, TiO_2, or ITO is the silanization process, in which organosilanes possessing trialkoxysilane or trichlorosilane anchoring units are reacted with the oxide surface (Scheme 18a). The presence of water at the substrate interface seems to be mandatory for the reaction to proceed; it allows the initial hydrolysis of the reagent leaving silanol head groups which form hydrogen bonds to the protruding OH group of the substrate and with adjacent molecules. The subsequent step is a condensation releasing H_2O, forming a polymeric ad-layer of polysiloxane covalently immobilized on the surface. The coverage density and monolayer quality are improved if the solid substrate exhibits a large number of protruding silanol groups.[128] This is achieved by dipping the substrate in an acidic mixture (piranha) or by exposing the substrate to an oxygen plasma. These steps both clean the substrate and yield a hydrophilic surface that is prone to the deposition of water catalyst. The

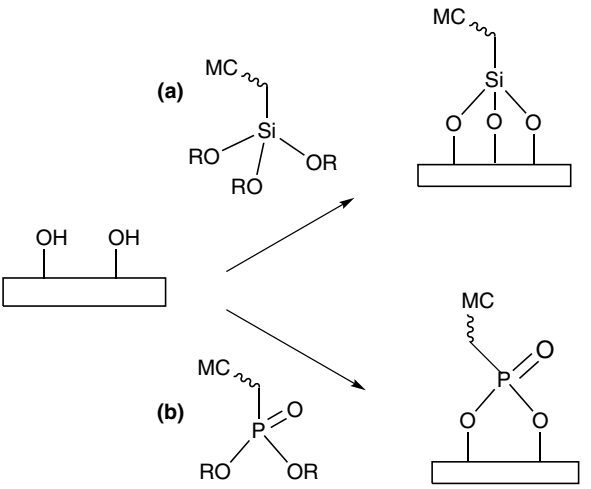

Scheme 18. Schematic representation of the linkage between a hydroxylated surface and (a) a triethoxylsilane or (b) a phosphonic acid.

monolayer quality depends on factors such as the nature of silane and solvent, temperature and reaction time.[128] Another popular technique uses phosphonic acid anchoring units that are reacted with surface hydroxyl groups (Scheme 18b).

B. Selected Examples

1. *Silanization*

a. *Direct immobilization*

Figure 37 shows a fluorescent free base porphyrin (**16**) that has been immobilized on a silica xerogel matrix.[129] Despite the chemical bonding between the molecule and the silica template no fluorescence quenching was observed.

b. *Sequential immobilization*

The click-chemistry based sequential grafting procedure has been used to derivatize silica.[130,131] Porphyrins bearing one or four C–C triple bonds were reacted with azide-functionalized SiO_2 nanoparticles for application in epoxidation catalysis (Scheme 19). The multiple anchors led to a low porphyrin coverage as the flat macrocycle lies parallel to the surface. This is an advantage as the distance between active centers remains sufficiently large to minimize interporphyrin electron-transfer and bleaching. However turnover numbers are low.

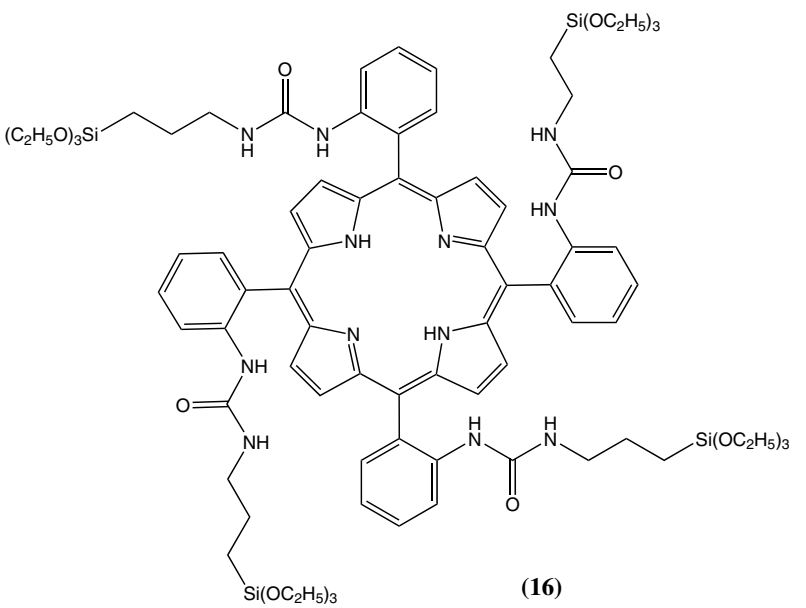

(16)

Figure 37. A porphyrin bearing four triethoxysilane anchoring units for parallel immobilization on the oxidized Si surface. (Adapted from Ref. 129.)

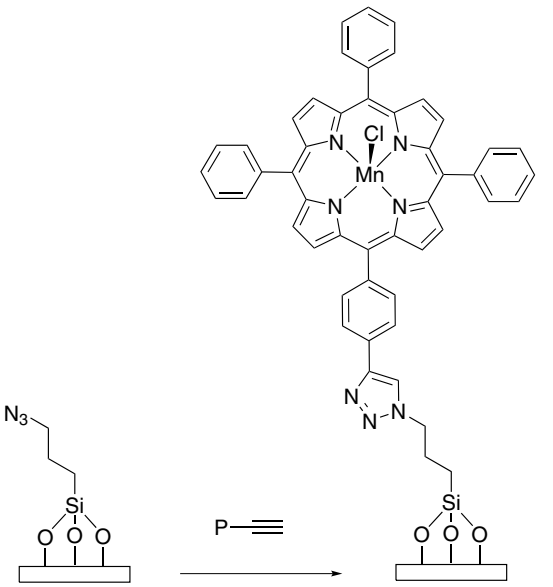

Scheme 19. Combination of alkoxysilane and click chemistries for the sequential immobilization of TPP derivatives on SiO_2 nanoparticules.

A porphyrin derivative has been immobilized on SiO_2 in two steps for acidic pH sensing applications (Scheme 20).[132] The compound used has one hydroxyl group for coupling to a spacer, and three 3-methoxy-3-(oxyethylene) *meso*-substituents to improve hydrophilicity. In the first step, a trichlorosilane coupling agent (CA) was grafted onto the surface by dipping the previously oxidised Si substrate in a 1:100 (v:v) solution of CA in hexane for 20 minutes at room temperature. Then the CA modified sample was immersed in a 5×10^{-3} mol.L^{-1} porphyrin solution in THF for 48 hours at 60 °C. This immobilization method was successful and yielded monolayers with 1.91×10^{13} molecules.cm^{-2} surface coverage. With this modified silica indicator pH can be monitored optically via changes of the Soret band of the porphyrin upon protonation.

The same protocol was used to immobilize a porphyrin bearing one hydroxyl unit for attachment to a modified silica sample and three aryl meso substituents possessing long alkyl chains.[133] This silica material-derivatized free base porphyrin monolayer has been tested as an optical gas sensor for NO_2 detection. Sensitivity to NO_2 is only observed with TPP derivatives, and not with OEP monolayers.

ITO electrodes have been modified with porphyrins using another sequential grafting procedure. A silanization reaction between the hydroxylated surface and a trimethoxysilane coupling agent is followed by amide formation between the terminal

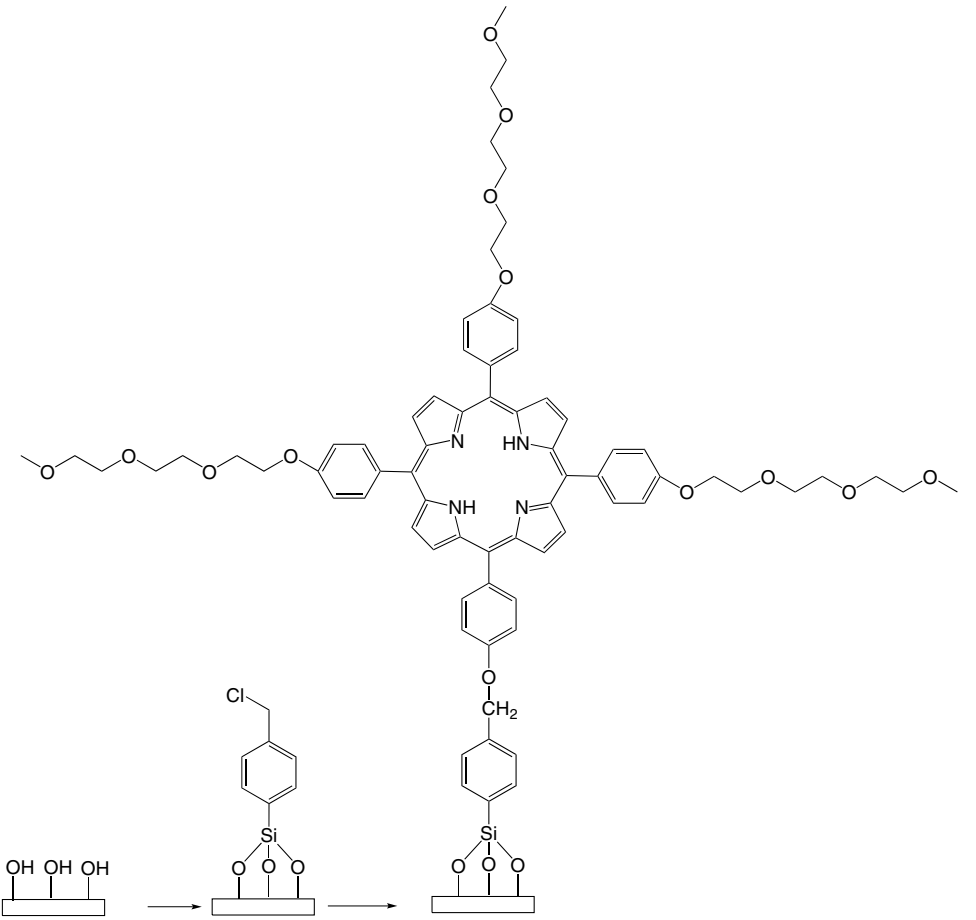

Scheme 20. Representation of the sequential process used to immobilize porphyrins on silica.

amine function of the CA and carboxylic acid porphyrins.[134] SAMs of porphyrins with or without tert-butyl groups (R = H or t-Bu in Figure 38) have been obtained. Photo- and electro-chemical analyses of the monolayers showed that interactions between porphyrins are more important for the nonsterically hindered species. The good quality of the porphyrin SAMs gives access to long-lived excited singlet state apparently similar to those of the antenna function of photosystem I in cyanobacteria, opening the field to the construction of artificial light harvesting systems.

2. *Phosphonate Linkage*

Bocian, Lindsey and coworkers have prepared porphyrin derivatives (**17**) and (**18**) possessing protected phosphonic acid anchoring units (Figure 39).[135,136]

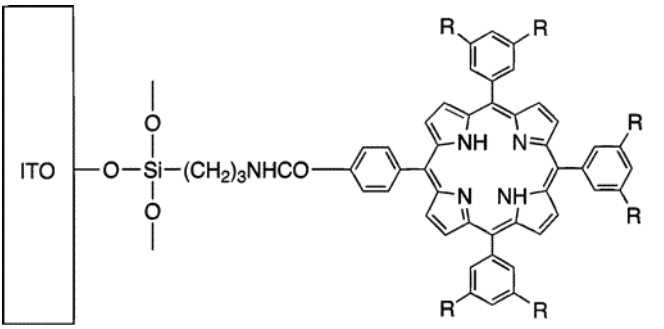

Figure 38. Self-assembled monolayers of porphyrins on ITO. (Adapted from Ref. 134.)

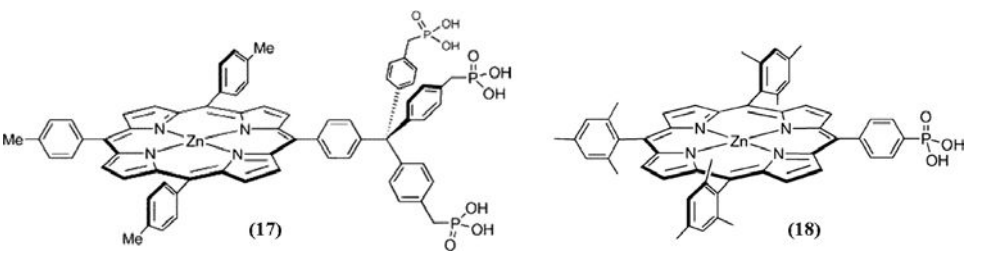

Figure 39. Porphyrin compounds bearing tripod- or mono-phosphonic acid anchoring units. (Adapted from Refs. 135 and 136.)

The di-*tert*butyloxyphosphoryl protected phosphonic acid is stable under the conditions of the coupling reaction, metallation, and DDQ oxidation; and the deprotection step does not lead to demetalation. The monolayer is formed by the baking method. Eight drops of a DMF porphyrin solution were deposited on the SiO_2 sample. Between each drop deposition, the sample is heated at 170 °C for 10 minutes. Electrochemical studies were conducted on these modified surfaces as the SiO_2 layer is thin and grown on a highly doped Si sample. The conducting samples thus obtained showed electrochemical characteristics consistent with the presence of robust monolayers.

Deutero-porphyrin derivatives bearing phosphonate residues such as (**19**) have been synthesized for immobilization on TiO_2 (Figure 40).[137] Co porphyrin monolayers seemed to be sensitive toward detection of organohalogen compounds.

Slipped co-facial Zn porphyrins have been immobilized on a titanium-modified ITO anode using a phosphonic acid anchoring unit (Scheme 21).[138] These compounds have been investigated as special-pair mimic porphyrin assemblies. In the first step, a porphyrin bearing a phosphonate anchor and two terminal olefin groups was grafted on ITO. Pair formation with another Zn porphyrin was achieved in a second step by Zn-imidazole coordination followed by ring-closure

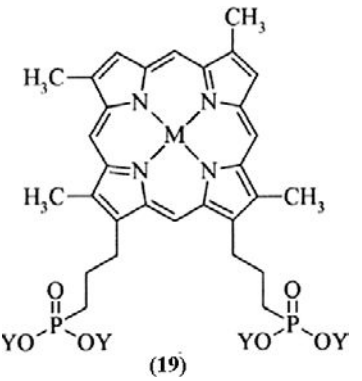

(19)

Figure 40. Deuteroporphyrin with phosphonate anchoring units for immobilization on TiO_2. (Adapted from Ref. 137.)

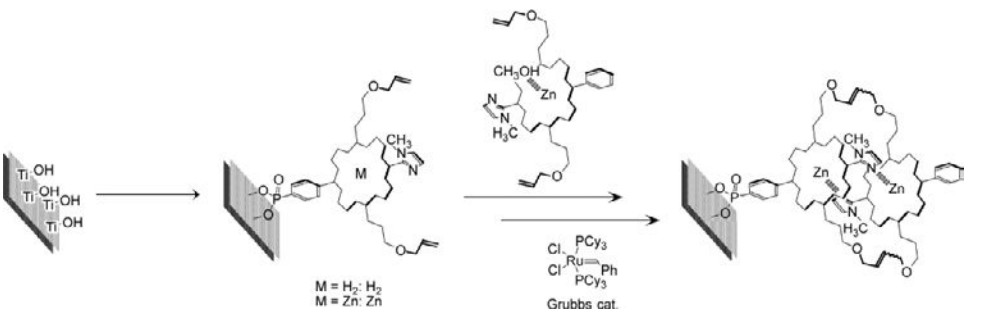

Scheme 21. Immobilization of a porphyrinic dimer on ITO with a phosphonic acid anchoring unit. (Adapted from Ref. 138.)

metathesis. These special-pair mimics exhibited efficient charge injection from the S_2 photoexcited state. High photocurrents were generated upon photoirradiation of the system in aqueous media containing hydroquinone.

Phosphonate coordination to Zr(IV) centers has been used to form multilayers of porphyrins on solid surfaces.[139–141] While this chemistry is useful for Langmuir-Blodgett film formation, it does not fit within the scope of a review devoted to surface functionalization.

VI. Innovative Technologies and Concepts in Hybrid Electronics

A. Overview

Porphyrins have been physically deposited on semiconductors for the design of hybrid devices based on their photoredox properties, such as light-sensitive Si- or

CNT-based transistors or optoelectronic memories.[142–145] Physical deposition methods are relatively simple to carry out, but they do not provide a controllable pathway for electrons at the interface between the bulk substrate and surface molecular materials. In contrast, chemical anchoring methods, such as those reviewed in the preceding paragraphs, afford strong coupling of the SAM molecular orbitals to the conduction and valence bands of the substrate, which in turn dictates the charge transport properties of the final device and warrants some reproducibility. Chemical approaches for hybrid silicon-molecular electronics have been reviewed.[146–150]

Porphyrin macrocycles and their metal complexes are regarded as key building blocks for this type of technology, as they remain robust under high-temperature processing steps and operating conditions. They also exhibit several redox states that are useful for multibit information storage, and they remain stable over a very large number of operational cycles.[71]

B. Selected Examples

1. *Molecular Capacitor Memory Cell*

Several libraries of specifically designed metalloporphyrins with various linker lengths and anchoring units have been constructed by Bocian, Lindsey and coworkers for the design of hybrid silicon memory devices. Electrochemical studies were first performed to determine values of the k° and $\tau_{1/2}$ parameters that can be linked to values of write/erase voltage and information retention time, respectively.[22,151] Information is stored as a charge in the redox monolayer. For capacitive electrochemical cell devices, a potential is applied between the reference/counter electrode and the porphyrin-decorated metal substrate (Figure 41). Once the voltage is high enough electrons flow from the molecule to the substrate and the molecule is oxidized. When the voltage is switched off, the molecule returns

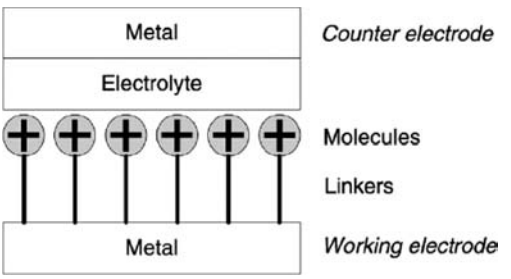

Figure 41. A typical example of molecular capacitor structure designed by Bocian, Misra and coworkers. (Adapted from Ref. 158.)

to its neutral state more or less rapidly. Initial studies were performed on capacitive cells based on metal electrodes.[152] In 2003, the substrate was switched to silicon in the design of so-called EMS (electrolyte molecule silicon) and EMOS (electrolyte molecule oxide silicon) structures.[153–155] The role of the tunnel oxide and of its thickness has been studied. The porphyrin monolayer showed good thermal stability (about 1 hour at 400 °C) and was stable upon continuous read-write cycling (10^{12} cycles).[71]

These results prompted the development of DRAM architectures (dynamic random access memory) using this hybrid technology by a startup company, ZettaCore, founded in 1999 for that purpose.[156] In brief, molecular capacitor cells offer several competitive advantages relative to the current DRAMs.[157] Self-assembly of the charge-carrying units in a single, uniform, dense monolayer, and higher charge density than in a conventional capacitor hold the key to increasing the density of DRAM in a cost-effective manner. Moreover, switching from a deep capacitor trench in conventional architectures to a flat electrochemical cell in the so-called ZettaRAM molecular capacitor is economically appealing. This will reduce the volume of the memory components on the chip, and also the lithography costs inherent to the engineering of capacitor trenches with a high aspect ratio (Figure 42). The ZettaRAM has the added benefit of being a low-power memory system.[158]

Following a similar strategy, De Salvo and coworkers have described novel types of capacitive cells in which metalloporphyrins are anchored to Si by

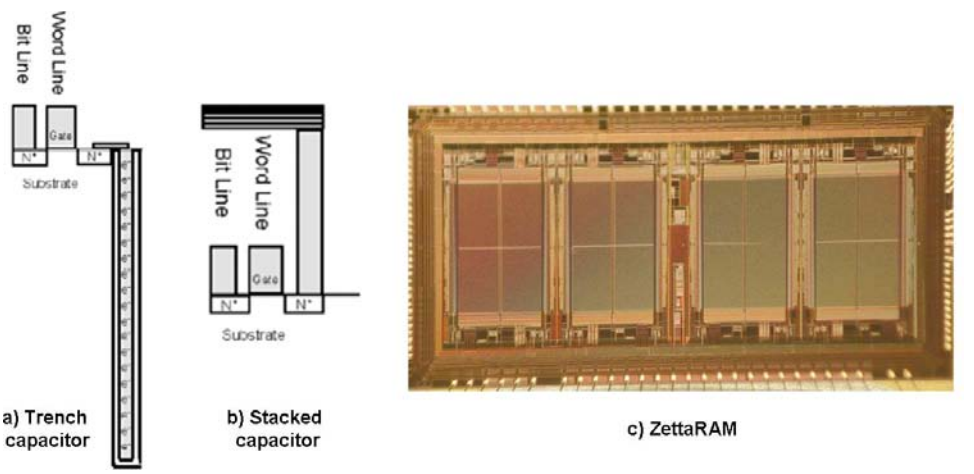

Figure 42. Examples of (a) trench and (b) stacked cell geometries for the DRAM capacitor, and (c) a photomicrograph of 1 MBit ZettaCore hybrid CMOS/molecular DRAM. (Adapted from Ref. 157.)

hydrosilylation, either in a single step or followed by a click cycloaddition.[159,160] Their potential in the design of advanced memory devices has been described,[161] and it has been highlighted in the International Technology Roadmap for Semiconductors (2009 edition).[162]

2. *Hybrid CMOS Transistor Memory*

Hybrid devices inspired from transistor and flash memory structures have been designed (Figure 43a).[163] The cell is made of a n-Si bulk with highly doped implanted p-Si source (S) and drain (D) regions. Between the S and D lies the channel above which a thin layer of SiO_2 tunnel oxide is deposited. The molecules are immobilized on the oxide layer via their phosphonate anchoring units, and this charging/discharging zone mimics the floating gate of flash memories. An electrolyte solution (or an ionic liquid) is then deposited and a metal top gate electrode is positioned in contact with the electrolyte.[164,165] All-solid pseudo-MOS hybrid silicon/molecular cells have been described (Figure 43b).[166,167]

3. *Hybrid Nanowire Transistor Memory*

An advanced memory structure obtained by immobilization of a Co porphyrin on an InO_2 nanowire linking two source and drain metallic dices (Figure 44a) has been described.[168] The procedure used to immobilize the porphyrin on the nanowire presumably generates a In–S bond. The I/V curve of the device was recorded upon

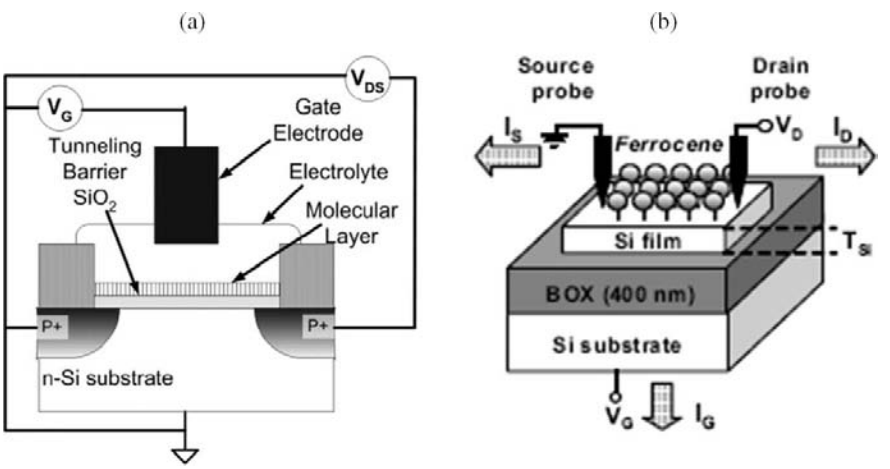

Figure 43. (a) Schematic view of a hybrid CMOS structure with a SiO_2 tunnel oxide layer. Adapted from Ref. 163. (b) An all solid pseudo-MOS device functionalized with ferrocene molecules. (Adapted from Ref. 167.)

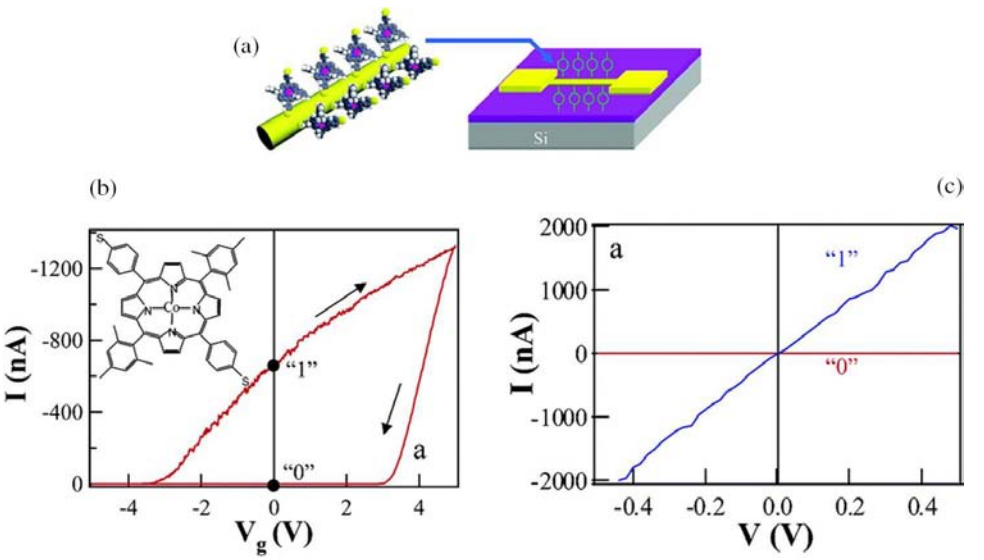

Figure 44. (a) Schematic view of a InO_2 nanowire transistor modified with a Co porphyrin SAM; (b) I/V_G characteristic recorded for this devices and (c) I/V_{DS} profile with $V_G = -0.1$ V after a write and a erase cycle leading to a "on-1" state and a "off-0" state. (Adapted from Ref. 168.)

sweeping the gate voltage (–5 V to 5 V) and recording the current in the nanowire with source-drain voltage set at 0.1 V. An important hysteresis was observed (Figure 44b). The memory states were probed by applying a positive (5 V) or a negative (–5 V) gate voltage to the Si (back gate), then the gate voltage was grounded and the memory state was identified by recording the conductance of the device through the nanowire (Figure 44c). In one case, the conductance of the nanowire varies linearly with V_{DS} and in the other case the conductance remains equal to 0. These two states correspond to an "on" and an "off" state. From the change of threshold voltage when the molecule are charged or discharged the number of electrons exchanged can be estimated (3 e^- per nm length of nanowire). The retention time was 41 seconds at room temperature, and could be increased up to hours by decreasing the temperature. The device also seemed stable upon write/erase cycling.

Similar measurements have been performed with a free base porphyrin rather than with a Co complex, and no hysteresis has been observed. This has been tentatively explained by the different natures of the oxidation sites — delocalized porphyrin orbitals in the second case vs. localized metal d orbitals in the first.

4. *Molecular Break-Junction Device*

Molecular break junctions are devices with a structure dedicated to mono-molecular electronics. A nanogap electrode is fabricated and presumably filled with a single

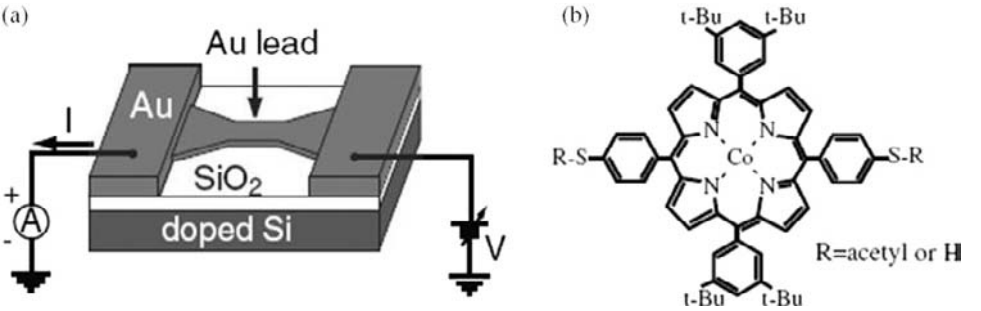

Figure 45. (a) Schematic view of the experimental setup used to study a molecular break junction on gold. The nanoscale break in the Au lead is not shown. (b) Chemical structure of molecule used to fill the nanogap. (Adapted from Ref. 169.)

molecule. A trans-A_2B_2 CoTPP derivative bearing two protected thiol anchoring units has been placed in a gold nanogap electrode (Figure 45).[169] Electron transport through the molecule has been studied.

VII. Conclusion

The wealth of chemical functionalization methods summarized in the preceding sections may lead one to consider that anchoring any porphyrin or phthalocyanine complex on any type of conductor or semiconductor is technically possible at this time. In this field again porphyrin compounds have the edge, due to their easy synthesis and derivatization. Sequential methods using the surface immobilization of a spacer and the subsequent coupling of an active molecule, such as those based on click chemistry, appear to be a major breakthrough for the anchoring of chemically or thermally sensitive molecules. A number of significant results have emerged which are of enormous interest in the design of molecular electronic devices. Due to their high stability in various redox states, porphyrin and phthalocyanine complexes faithfully play their role of charge storage sites which proves useful for information storage. Electron transport kinetics between the conductor (or semiconductor) substrate and the anchored molecule can be adjusted by changing the nature of the charge storage site (central metal or macrocyclic ring), and it can be finely tuned by modifying the nature (conjugated or not) and length of the linker. Such versatility may prove interesting for emerging technologies.

The development of hybrid silicon-molecular technologies thus seems foreseeable, but it may not be expected in the near future. A major hurdle lies in the inherent incompatibility of molecular chemistry with the techniques used for the elaboration of silicon chips. Clean room operations such as silicon etching and metal deposition require the exclusion of any possible source of contamination,

and molecular compounds and organic solvents clearly are potential contaminants. In this respect it is worth noting that in the few hybrid technologies developed so far (for the Zettaram memory cell), the anchoring of porphyrin and the steps involving molecular chemistry are conducted in the ultimate phase of the fabrication process. It will be interesting to watch the success met by this innovative product, and to see if its competitive advantages are recognized by the market.

In the meantime, molecular memory will still be viewed as a long term research goal. The knowledge base for molecular electronics obviously needs further fundamental work, which is currently under way in many laboratories all over the world.[162]

VIII. References

1. Carroll, R. L.; Gorman, C. B. *Angew. Chem. Int. Ed.* **2002**, *41*, 4378.
2. Ulman, A. *Chem. Rev*. **1996**, *96*, 1533.
3. Love, J. C.; Estroff, L. A.; Kriebel, J. K.; Nuzzo, R. G.; Whitesides, G. M. *Chem. Rev*. **2005**, *105*, 1103.
4. Bain, C. D.; Biebuyck, H. A.; Whitesides, G. M. *Langmuir* **1989**, *5*, 723.
5. Choi, Y.; Jeong, Y.; Chung, H.; Ito, E.; Hara, M.; Noh, J. *Langmuir* **2008**, *24*, 91.
6. Ciszek, J. W.; Tour, J. M. *Chem. Mater.* **2005**, *17*, 5684.
7. Zuo, G.; Liu, X.; Yang, J.; Li, X.; Lu, X. *J. Electroanal. Chem.* **2007**, *605*, 81.
8. Lu, X.; Zhang, L.; Li, M.; Wang, X.; Zhang, Y.; Liu, X.; Zuo, G. *ChemPhysChem* **2006**, *7*, 854.
9. Devaraj, N. K.; Decreau, R. A.; Ebina, W.; Collman, J. P.; Chidsey, C. E. D. *J. Phys. Chem. B* **2006**, *110,* 15955.
10. Shimazu, K.; Takechi, M.; Fujii, H.; Suzuki, M.; Saiki, H.; Yoshimura, T.; Uosaki, K. *Thin Solid Films* **1996**, *273*, 250.
11. Nishimura, N.; Ooi, M.; Shimazu, K.; Fujii, H.; Uosaki, K. *J. Electroanal. Chem.* **1999**, *473*, 75.
12. Lu, X. Q.; Li, M. R.; Yang, C. H.; Zhang, L. M.; Li, Y. F.; Jiang, L.; Li, H. X.; Jiang, L.; Liu, C. M.; Hu, W. P. *Langmuir* **2006**, *22*, 3035.
13. Yamada, T.; Hashimoto, T.; Kikushima, S.; Ohtsuka, T.; Nango, M. *Langmuir* **2001**, *17*, 4634.
14. Imahori, H.; Norieda, H.; Ozawa, S.; Ushida, K.; Yamada, H.; Azuma, T.; Tamaki, K.; Sakata, Y. *Langmuir* **1998**, *14*, 5335.
15. Imahori, H.; Norieda, H.; Nishimura, Y.; Yamazaki, I.; Higuchi, K.; Kato, N.; Motohiro, T.; Yamada, H.; Tamaki, K.; Arimura, M.; Sakata, Y. *J. Phys Chem. B* **2000**, *104*, 1253.
16. Imahori, H.; Arimura, M.; Hanada, T.; Nishimura, Y.; Yamazaki, I.; Sakata, Y.; Fukuzumi, S. *J. Am. Chem. Soc.* **2001**, *123*, 335
17. Imahori, H.; Kashiwagi, Y.; Endo, Y.; Hanada, T.; Nishimura, Y.; Yamazaki, I.; Araki, Y.; Ito, O.; Fukuzumi, S. *Langmuir* **2004**, *20*, 73.
18. Chan, Y.-H.; Schuckman, A. E.; Perez, L. M.; Vinodu, M.; Drain, C. M.; Batteas, J. D. *J. Phys. Chem. C* **2008**, *112*, 6110.
19. Gryko, D. T.; Clausen, C.; Lindsey, J. S. *J. Org. Chem.* **1999**, *64*, 8635.
20. Viana, A. S.; Leupold, S.; Montforts, F.-P.; Abrantes, L. M. *Electrochim. Acta* **2005**, *50*, 2807.
21. Gryko, D. T.; Clausen, C.; Roth, K. M.; Dontha, N.; Bocian, D. F.; Kuhr, W. G.; Lindsey, J. S. *J. Org. Chem.* **2000**, *65*, 7345.

22. Roth, K. M.; Gryko, D. T.; Clausen, C.; Li, J.; Lindsey, J. S.; Kuhr, W. G.; Bocian, D. F. *J. Phys. Chem. B* **2002**, *106*, 8639.
23. Jiao, J.; Schmidt, I.; Taniguchi, M.; Lindsey, J. S.; Bocian, D. F. *Langmuir* **2008**, *24*, 12047.
24. Zak, J.; Yuan, H.; Ho, M.; Woo, L. K.; Porter, M. D. *Langmuir* **1993**, *9*, 2772.
25. Vesper, B. J.; Salaita, K.; Zong, H.; Mirkin, C. A.; Barrett, A. G. M.; Hoffman, B. M. *J. Am. Chem. Soc.* **2004**, *126*, 16653.
26. Zong, H.; Sun, P.; Mirkin, C. A.; Barrett, A. G. M.; Hoffman, B. M. *J. Phys. Chem. B* **2009**, *113*, 14892.
27. Hutchison, J. E.; Postlethwaite, T. A.; Murray, R. W. *Langmuir* **1993**, *9*, 3277.
28. Postlethwaite, T. A.; Hutchison, J. E.; Hathcock, K. W.; Murray, R. W. *Langmuir* **1995**, *11*, 4109.
29. Éll, A. H.; Csjernyik, G.; Slagt, V. F.; Bäckvall, J.-E.; Berner, S.; Puglia, C.; Ledung, G.; Oscarsson, S. *Eur. J. Org. Chem.* **2006**, 1193.
30. Wei, L.; Padmaja, K.; Youngblood, W. J.; Lysenko, A. B.; Lindsey, J. S.; Bocian, D. F. *J. Org. Chem.* **2004**, *69*, 1461.
31. Wei, L.; Tiznado, H.; Liu, G.; Padmaja, K.; Lindsey, J. S.; Zaera, F.; Bocian, D. F. *J. Phys. Chem. B* **2005**, *109*, 23963.
32. Gryko, D. T.; Zhao, F.; Yasseri, A. A.; Roth, K. M.; Bocian, D. F.; Kuhr, W. G.; Lindsey, J. S. *J. Org. Chem.* **2000**, *65,* 7356.
33. Uosaki, K.; Kondo, T.; Zhang, X.-Q.; Yanagida, M. *J. Am. Chem. Soc.* **1997**, *119*, 8367.
34. Kondo, T.; Ito, T.; Nomura, S.-I.; Uosaki, K. *Thin Solid Films* **1996**, *284–285*, 652.
35. Clausen, C.; Gryko, D. T.; Yasseri, A. A.; Diers, J. R.; Bocian, D. F.; Kuhr, W. G.; Lindsey, J. S. *J. Org. Chem.* **2000**, *65*, 7371.
36. Clausen, C.; Gryko, D. T.; Dabke, R. B.; Dontha, N.; Bocian, D. F.; Kuhr, W. G.; Lindsey, J. S. *J. Org. Chem.* **2000**, *65*, 7363.
37. Li, J.; Gryko, D.; Dabke, R. B.; Diers, J. R.; Bocian, D. F.; Kuhr, W. G.; Lindsey, J. S. *J. Org. Chem.* **2000**, *65,* 7379.
38. Padmaja, K.; Youngblood, W. J.; Wei, L.; Bocian, D. F.; Lindsey, J. S. *Inorg. Chem.* **2006**, *45*, 5479.
39. Hutchison, J. E.; Postlethwaite, T. A.; Chen, C.-H.; Hathcock, K. W.; Ingram, R. S.; Ou, W.; Linton, R. W.; Murray, R. W.; Tyvoll, D. A.; Chng, L. L.; Collman, J. P. *Langmuir* **1997**, *13*, 2143.
40. Imahori, H.; Norieda, H.; Yamada, H.; Nishimura, Y.; Yamazaki, I.; Sakata, Y.; Fukuzumi, S. *J. Am. Chem. Soc.* **2001**, *123*, 100.
41. Eberspacher, T. A.; Collman, J. P.; Chidsey, C. E. D.; Donohue, D. L.; Van Ryswyk, H. *Langmuir* **2003**, *19*, 3814.
42. Offord, D. A.; Sachs, S. B.; Ennis, M. S.; Eberspacher, T. A.; Griffin, J. H.; Chidsey, C. E. D.; Collman, J. P. *J. Am. Chem. Soc.* **1998**, *120,* 4478.
43. Zhang, Z.; Hou, S.; Zhu, Z.; Liu, Z. *Langmuir* **2000**, *16*, 537.
44. Zhang, Z.; Imae, T.; Sato, H.; Watanabe, A.; Ozaki, Y. *Langmuir* **2001**, *17*, 4564.
45. Zou, S.; Clegg, R. S.; Anson, F. C. *Langmuir* **2002**, *18*, 3241.
46. Boeckl, M. S.; Bramblett, A. L.; Hauch, K. D.; Sasaki, T.; Ratner, B. D.; Rogers, J. W. *Langmuir* **2000**, *16*, 5644.
47. Nandivada, H.; Jiang, X.; Lahann, J. *Adv. Mater.* **2007**, *19*, 2197.
48. Nebhcni, L.; Barner-Kowollik, C. *Adv. Mater.* **2009**, *21*, 3442.
49. Chelmowski, R.; Kafer, D.; Köster, S. D.; Klasen, T.; Winkler, T.; Terfort, A.; Metzler-Nolte, N.; Wöll, C. *Langmuir* **2009**, *25*, 11480.

50. Mahouche, S.; Mekni, N.; Abbassi, L.; Lang, P.; Perruchot, C.; Jouini, M.; Mammeri, F.; Turmine, M.; Romdhane, H. B.; Chehimi, M. M. *Surf. Sci.* **2009**, *603*, 3205.
51. Ringot, C.; Sol, V.; Granet, R.; Krausz, P. *Mater. Lett.* **2009**, *63*, 1889.
52. Gole, A.; Murphy, C. J. *Langmuir* **2008**, *24*, 266.
53. Fleming, D. A.; Thode, C. J.; Williams, M. E. *Chem. Mater.* **2006**, *18*, 2327.
54. Collman, J. P.; Devaraj, N. K.; Eberspacher, T. P. A.; Chidsey, C. E. D. *Langmuir* **2006**, *22*, 2457.
55. Devaraj, N. K.; Dinolfo, P. H.; Chidsey, C. E. D.; Collman, J. P. *J. Am. Chem. Soc.* **2006**, *128*, 1794.
56. Devaraj, N. K.; Decreau, R. A.; Ebina, W.; Collman, J. P.; Chidsey, C. E. D. *J. Phys. Chem. B* **2006***, 110*, 15955.
57. Collman, J. P.; Devaraj, N. K.; Decréau, R. A.; Yang, Y.; Yan, Y.-L.; Ebina, W.; Eberspacher, T. A.; Chidsey, C. E. D. *Science* **2007***, 315*, 1565.
58. Decréau, R. A.; Collman, J. P.; Yang, Y.; Yan, Y.; Devaraj, N. K. *J. Org. Chem.* **2007**, *72*, 2794.
59. Roth, K. M.; Yasseri, A. A.; Liu, Z.; Dabke, R. B.; Malinovskii, V.; Schweikart, K.-H.; Yu, L.; Tiznado, H.; Zaera, F.; Lindsey, J. S.; Kuhr, W. G.; Bocian, D. F. *J. Am. Chem. Soc.* **2003**, *125*, 505.
60. Buriak, J. M. *Chem. Soc. Rev*. **2002**, *102*, 5, 1271.
61. Liu, Z.; Yasseri, A. A.; Loewe, R. S.; Lysenko, A. B.; Malinovskii, V. L.; Zhao, Q.; Surthi, S.; Li, Q.; Misra, V.; Lindsey, J. S.; Bocian, D. F. *J. Org. Chem.* **2004**, *69*, 5568.
62. Pinson, J.; Podvorica, F. *Chem. Soc. Rev.* **2005**, *34*, 429.
63. Zhu, X.-Y.; Boiadjiev, V.; Mulder, J. A.; Hsung, R. P.; Major, R. C. *Langmuir* **2000**, *16,* 6766.
64. Cleland, G.; Horrocks, B. R.; Houlton, A. *J. Chem. Soc. Faraday. T.* **1995**, *91*, 4001.
65. Kim, N. Y.; Laibinis, P. E. *J. Am. Chem. Soc.* **1997**, *119,* 2297.
66. Effenberger, F.; Götz, G.; Bidlingmaier, B.; Wezstein, M. *Angew. Chem. Int. Edit.* **1998**, *37*, 2462.
67. Aurora, A.; Bernardini, G.; Cattaruzza, F.; Flamini, A.; Pallavicini, P.; Zanoni, R.; Decker, F. *J. Electroanal. Chem.* **2005**, *579*, 133.
68. Sano, H.; Maeda, H; Ichii, T.; Murase, K.; Noda, K.; Matsushige, K.; Sugimura, H. *Langmuir* **2009**, *25,* 5516.
69. Chen, B.; Flatt, A. K.; Jian, H.; Hudson, J. L.; Tour, J. M. *Chem. Mater.* **2005**, *17,* 4832.
70. Zanoni, R.; Aurora, A.; Cattaruzza, F.; Decker, F.; Fastiggi, P.; Menichetti, V.; Tagliatesta, P.; Capodilupo, A.-L.; Lembo, A. *Mater. Sci. Eng. C* **2007**, *27*, 1351.
71. Liu, Z.; Yasseri, A. A.; Lindsey, J. S.; Bocian, D. F. *Science* **2003**, *302*, 1543.
72. Yasseri, A. A.; Syomin, D.; Loewe, R. S.; Lindsey, J. S.; Zaera, F.; Bocian, D. F. *J. Am. Chem. Soc.* **2004**, *126*, 15603.
73. Liu, Z.; Schmidt, I.; Thamyongkit, P.; Loewe, R. S.; Syomin, D.; Diers, J. R.; Zhao, Q.; Misra, V.; Lindsey, J. S.; Bocian, D. F. *Chem. Mater.* **2005**, *17,* 3728.
74. Padmaja, K.; Wei, L.; Lindsey, J. S.; Bocian, D. F. *J. Org. Chem.* **2005**, *70*, 7972.
75. Jiao, J.; Anariba, F.; Tiznado, H.; Schmidt, I.; Lindsey, J. S.; Zaera, F.; Bocian, D. F. *J. Am. Chem. Soc.* **2006**, *128*, 6965.
76. Lu, M.; Chen, B.; He, T.; Li, Y.; Tour, J. M. *Chem. Mater.* **2007**, *19,* 4447.
77. Chen, B.; Lu, M.; Flatt, A. K.; Maya, F.; Tour, J. M. *Chem. Mater.* **2008**, *20,* 61.
78. Ciampi, S.; Böcking, T.; Kilian, K. A.; James, M.; Harper, J. B.; Gooding, J. J. *Langmuir* **2007**, *23*, 9320.
79. Ciampi, S.; Le Saux, G.; Harper, J. B.; Gooding, J. J. *Electroanal.* **2008**, *20*, 1513.

80. Ciampi, S.; Bocking, T.; Kilian, K. A.; Harper, J. B.; Gooding, J. J. *Langmuir* **2008**, *24*, 5888.
81. Delapierre, G.; Duclairoir, F.; Marchon, J.-C. *French Patent* WO/2007/048924.
82. Rohde, R. D.; Agnew, H. D.; Yeo, W.-S.; Bailey, R. C.; Heath, J. R. *J. Am. Chem. Soc.* **2006**, *128*, 9518.
83. Haensch, C.; Ott, C.; Hoeppener, S.; Schubert, U. S. *Langmuir* **2008**, *24*, 10222.
84. Huang, K.; Duclairoir, F.; Pro, T.; Buckley, J.; Marchand, G.; Martinez, E.; Marchon, J.-C.; De Salvo, B.; Delapierre, G.; Vinet, F. *ChemPhysChem* **2009**, *10*, 963.
85. Liu, H.; Duclairoir, F.; Fleury, B.; Dubois, L.; Chenavier, Y.; Marchon, J.-C. *Dalton T.* **2009**, *19,* 3793.
86. Ciraci, S.; Dag, S.; Yildirim, T.; Gülseren, O.; Senger, R. T. *J. Phys.-Condens. Mat.* **2004**, *16*, R901.
87. De La Torre, G. *J. Porphyr. Phthalocya.* **2009**, *13*, 637–644.
88. Zagal, J. H.; Griveau, S.; Ozoemena, K. I.; Nyokong, T.; Bedioui, F. *J. Nanosci. Nanotechno.* **2009**, *9*, 2201.
89. Bahr, J. L.; Tour, J. M. *J. Mater. Chem.* **2002**, *12*, 1952.
90. Banerjee, S.; Hemraj-Benny, T.; Wong, S. S. *Adv. Mater.* **2005**, *17*, 17.
91. Hirsch, A. *Angew. Chem. Int. Edit.* **2002**, *41*, 1853.
92. Bahr, J. L.; Tour, J. M. *Chem. Mater.* **2001**, *13*, 3823.
93. De la Torre, G.; Blau, W.; Torres, T. *Nanotechnology* **2003**, *14*, 765.
94. Li, H.; Martin, R. B.; Harruff, B. A.; Carino, R. A.; Allard, L. F.; Sun, Y.-P. *Adv. Mater.* **2004**, *16*, 896.
95. Baskaran, D.; Mays, J. W.; Zhang, X. P.; Bratcher, M. S. *J. Am. Chem. Soc.* **2005**, *127*, 6916.
96. Guo, Z.; Du, F.; Ren, D.; Chen, Y.; Zheng, J.; Liu, Z.; Tian, J. *J. Mater. Chem.* **2006**, *16*, 3021.
97. Liu, Z.-B.; Tian, J.-G.; Guo, Z.; Ren, D.-M.; Du, F.; Zheng, J.-Y.; Chen, Y.-S. *Adv. Mater.* **2008**, *20*, 511.
98. Zhang, Y.; He, H.; Gao, C.; Wu, J. *Langmuir* **2009**, *25*, 5814.
99. Li, H.; Cheng, F.; Duft, A. M.; Adronov, A. *J. Am. Chem. Soc.* **2005**, *127*, 14518.
100. Liu, J.; Nie, Z.; Cao, Y.; Adronov, A.; Li, H. *J. Polym. Sci. A1* **2008**, *46*, 7187.
101. Landis, E.C.; Hamers, R. J. *Chem. Mater.* **2009**, *21*, 724.
102. Campidelli, S.; Ballesteros, B.; Filoramo, A.; Díaz, D. D.; De La Torre, G.; Torres, T.; Rahman, G. M. A.; Ehli, C.; Kiessling, D.; Werner, F.; Sgobba, V.; Guldi, D. M.; Cioffi, C.; Prato, M.; Bourgoin, J.-P. *J. Am. Chem. Soc.* **2008**, *130*, 11503.
103. Carlmark, A.; Hawker, C.; Hult, A.; Malkoch, M. *Chem. Soc. Rev.* **2009**, *38*, 352.
104. Binder, W. H.; Sachsenhofer, R. *Macromol. Rapid Comm.* **2008**, *29*, 952.
105. Malkoch, M.; Schleicher, K.; Drockenmuller, E.; Hawker, C. J.; Russell, T. P.; Wu, P.; Fokin, V. V. *Macromolecules* **2005**, *38*, 3663.
106. Séverac, M.; Pleux, L. L.; Scarpaci, A.; Blart, E.; Odobel, F. *Tetrahedron Lett.* **2007**, *48*, 6518.
107. Palacin, T.; Le Khanh, H.; Jousselme, B.; Jegou, P.; Filoramo, A.; Ehli, C.; Guldi, D. M.; Campidelli, S. *J. Am. Chem. Soc.* **2009**, *131*, 15394.
108. Campidelli, S.; Sooambar, C.; Diz, E. L.; Ehli, C.; Guldi, D. M.; Prato, M. *J. Am. Chem. Soc.* **2006**, *128*, 12544.
109. Ballesteros, B.; Campidelli, S.; de la Torre, G.; Ehli, C.; Guldi, D. M.; Prato, M.; Torres, T. *Chem. Commun*. **2007**, 2950.
110. Georgakilas, V.; Kordatos, K.; Prato, M.; Guldi, D. M.; Holzinger, M.; Hirsch, A. *J. Am. Chem. Soc.* **2002**, *124*, 760.
111. Ballesteros, B.; De La Torre, G.; Ehli, C.; Rahman, G. M. A.; Agulló-Rueda, F.; Guidi, D. M.; Torres, T. *J. Am. Chem. Soc.* **2007**, *129*, 5061.

112. Cheng, F.; Zhang, S.; Adronov, A.; Echegoyen, L.; Diederich, F. *Chem.-Eur. J.* **2006**, *12*, 6062.
113. Cheng, F.; Adronov, A. *Chem.-Eur. J.***2006**, *12*, 5053.
114. Boul, P.J.; Cho, D.-G.; Rahman, G. M. A.; Marquez, M.; Ou, Z.; Kadish, K. M.; Guldi, D. M.; Sessler, J. L. *J. Am. Chem. Soc.* **2007**, *129*, 5683.
115. Chitta, R.; Sandanayaka, A. S. D.; Schumacher, A. L.; D'Souza, L.; Araki, Y.; Ito, O.; D'Souza, F. *J. Phys. Chem. C* **2007**, *111*, 6947.
116. Guldi, D. M.; Rahman, G. M. A.; Jux, N.; Tagmatarchis, N.; Prato, M. *Angew. Chem. Int. Edit.* **2004**, *43*, 5526.
117. Ehli, C.; Rahman, G. M. A.; Jux, N.; Balbinot, D.; Guldi, D. M.; Paolucci, F.; Marcaccio, M.; Paolucci, D.; Melle-Franco, M.; Zerbetto, F.; Campidelli, S.; Prato, M. *J. Am. Chem. Soc.* **2006**, *128*, 11222.
118. D'Souza, F.; Chitta, R.; Sandanayaka, A. S. D.; Subbaiyan, N. K.; D'Souza, L.; Araki, Y.; Ito, O. *Chem.-Eur. J.* **2007**, *13*, 8277.
119. Liu, A.-Z.; Lei, S.-B. *Surf. Interface Anal.* **2007**, *39,* 33.
120. Boukhvalov, D. W.; Katsnelson, M. I. *J. Phys.-Condens. Mat.* **2009**, *21*, 344205.
121. Xu, Y.; Liu, Z.; Zhang, X.; Wang, Y.; Tian, J.; Huang, Y.; Ma, Y.; Zhang, X.; Chen, Y. *Adv. Mater*. **2009**, *21*, 1275.
122. Liu, Z.-B.; Xu, Y.-F.; Zhang, X.-Y.; Zhang, X.-L.; Chen, Y.-S.; Tian, J.-G. *J. Phys. Chem. B* **2009**, *113*, 9681.
123. Szunerits, S.; Boukherroub, R. *J. Solid State Electr.* **2008**, *12*, 1205.
124. Mangeney, C.; Qin, Z.; Dahoumane, S. A.; Adenier, A.; Herbst, F.; Boudou, J.-P.; Pinson, J.; Chehimi, M. M. *Diam. Relat. Mater.* **2008**, *17*, 1881.
125. Yang, N.; Uetsuka, H.; Nebel, C. E. *Adv. Funct. Mater.* **2009**, *19*, 887.
126. Wenmackers, S.; Vermeeren, V.; VandeVen, M.; Ameloot, M.; Bijnens, N.; Haenen, K.; Michiels, L.; Wagner, P. *Phys. Status Solidi A* **2009**, *206(3)*, 391.
127. Zhou, Y.; Zhi, J.; Zou, Y.; Zhang, W.; Lee, S.-T. *Anal. Chem.* **2008**, *80*, 4141.
128. Silberzan, P.; Leger, L.; Ausserre, D.; Benattar, J. J. *Langmuir* **1991**, *7,* 1647.
129. García-Sánchez, M.-A.; De la Luz, V.; Estrada-Rico, M. L.; Murillo-Martínez, M. M.; Coahuila-Hernández, M. I.; Sosa-Fonseca, R.; Tello-Solís, S. R.; Rojas, F.; Campero, A. *J. Non-Cryst. Solids* **2009**, *355*, 120.
130. Lummerstrofer, T.; Hoffmann, H. *J. Phys. Chem. B* **2004**, *108*, 3963.
131. McDonald, A. R.; Franssen, N.; van Klink, G. P. M.; van Koten, G. *J. Organomet. Chem.* **2009**, *694*, 2153.
132. Gulino, A.; Mineo, P.; Bazzano, S.; Vitalini, D.; Fragalà, I. *Chem. Mater.* **2005**, *17*, 4043.
133. Gulino, A.; Bazzano, S.; Mineo, P.; Scamporrino, E.; Vitalini, D.; Fragalà, I. *Chem. Mater.* **2005**, *17*, 521.
134. Imahori, H.; Hosomizu, K.; Mori, Y.; Sato, T.; Ahn, T. K.; Kim, S. K.; Kim, D.; Nishimura, Y.; Yamazaki, I.; Ishii, H.; Hotta, H.; Matano, Y. *J. Phys. Chem. B* **2004**, *108*, 5018.
135. Muthukumaran, K.; Loewe, R. S.; Ambroise, A.; Tamaru, S.-I.; Li, Q.; Mathur, G.; Bocian, D. F.; Misra, V.; Lindsey, J. S. *J. Org. Chem.* **2004**, *69*, 1444.
136. Loewe, R. S.; Ambroise, A.; Muthukumaran, K.; Padmaja, K.; Lysenko, A. B.; Mathur, G.; Li, Q.; Bocian, D. F.; Misra, V.; Lindsey, J. S. *J. Org. Chem.* **2004**, 69, 1453.
137. Wedel, M.; Walter, A.; Montforts, F.-P. *Eur. J. Org. Chem.* **2001**, 1681.
138. Morisue, M.; Haruta, N.; Kalita, D.; Kobuke, Y. *Chem. Eur. J.* **2006**, *12*, 8123.
139. Massari, A. M.; Gurney, R. W.; Wightman, M. D.; Huang, C.-H. K.; Nguyen, S. T.; Hupp, J. T. *Polyhedron* **2003**, *22*, 3065.
140. Nixon, C. M.; Le Claire, K.; Odobel, F.; Bujoli, B.; Talham, D. R. *Chem. Mater.* **1999**, *11,* 965.

141. Benítez, I. O.; Bujoli, B.; Camus, L. J.; Lee, C. M.; Odobel, F.; Talham, D. R. *J. Am. Chem. Soc.* **2002**, *124*, 4363.
142. Hecht, D. S.; Ramirez, R. J. A.; Briman, M.; Artukovic, E.; Chichak, K. S.; Stoddart, J. F.; Grüner, G. *Nano Lett.* **2006**, *6*, 2031.
143. Liu, C.-Y.; Bard, A. J. *Electrochem. Solid St.* **2001**, *4*, E39–E41.
144. Liu, C.-Y.; Pan, H.-I.; Fox, M. A.; Bard, A. J. *Science* **1993**, *261*, 897–899.
145. Winkelmann, C. B.; Ionica, I.; Chevalier, X.; Royal, G.; Bucher, C.; Bouchiat, V. *Nano Lett.* **2007**, *7*, 1454.
146. Li, Q. *Mod. Phys. Lett. B* **2008**, *22*, 1183.
147. Tour, J. M. *J. Org. Chem.* **2007**, *72*, 7477.
148. Ashkenasy, G.; Cahen, D.; Cohen, R.; Shanzer, A.; Vilan A. *Accounts Chem. Res.* **2002**, *35*, 121.
149. Wolkow, R. A. *Annu. Rev. Phys. Chem.* **1999**, *50*, 413.
150. Aswal, D. K.; Lenfant, S.; Guerin, D.; Yakhmi, J. V.; Vuillaume, D. *Anal. Chim. Acta* **2006**, *568*, 84.
151. Carcel, C.M.; Laha, J. K.; Loewe, R. S.; Thamyongkit, P.; Schweikart, K.-H.; Misra, V.; Bocian, D. F.; Lindsey, J. S. *J. Org. Chem.* **2004**, *69*, 6739.
152. Roth, K. M.; Gryko, D. T.; Clausen, C.; Li, J.; Lindsey, J. S.; Kuhr, W. G.; Bocian, D. F. *J. Phys. Chem. B* **2002**, *106*, 8639.
153. Li, Q.; Surthi, S.; Mathur, G.; Gowda, S.; Misra, V.; Sorenson, T. A.; Tenent, R. C.; Kuhr, W. G.; Tamaru, S.-I.; Lindsey, J. S.; Liu, Z.; Bocian, D. F. *Appl. Phys. Lett.* **2003**, *83*, 198.
154. Li, Q.; Surthi, S.; Mathur, G.; Gowda, S.; Zhao, Q.; Sorenson, T. A.; Tenent, R. C.; Muthukumaran, K.; Lindsey, J. S.; Misra, V. *App. Phys. Lett.* **2004**, *85*, 1829.
155. Mathur, G.; Gowda, S.; Li, Q.; Surthi, S.; Zhao, Q.; Misra, V. *IEEE T. Nanotechnol.* **2005**, *4*, 278.
156. Venkatesan, R. K.; Al-Zawawi, A. S.; Rotenberg, E. *Proceedings — International Symposium on High-Performance Computer Architecture* **2005**, 83.
157. Kuhr, W. G. *Electrochemical Society Interface* **2004**, *13*, 34.
158. Venkatesan, R. K.; Al-Zawawi, A. S.; Sivasubramanian, K.; Rotenberg, E. *IEEE T. Comput.* **2007**, *56*, 147.
159. Pro, T.; Buckley, J.; Huang, K.; Calborean, A.; Gely, M.; Delapierre, G.; Ghibaudo, G.; Duclairoir, F.; Marchon, J.-C.; Jalaguier, E.; Maldivi, P.; De Salvo, B.; Deleonibus, S. *IEEE T. Nanotechnol.* **2009**, *8*, 204.
160. Duclairoir, F.; Dubois, L.; Calborean, A.; Fateeva, A.; Fleury, B.; Kalaiselvan, A.; Marchon, J.-C.; Maldivi, P.; Billon, M.; Bidan, G.; de Salvo, B.; Delapierre, G.; Buckley, J.; Huang, K.; Barattin, R.; Pro, T. *Int. J. Nanotechnology* **2010**, *7*, 719.
161. De Salvo, B.; Molas, G.; Perniola, L.; Jahan, C.; Buckley, J.; Jalaguier, E.; Gely, M. *ECS Transactions* **2009**, *25*, 151.
162. *International Technology Roadmap For Semiconductors*, **2009**, *Emerging Research Devices* p. 8. http://www.itrs.net/links/2009itrs/2009chapters_2009tables/2009_erd.pdf
163. Gowda, S.; Mathur, G.; Li, Q.; Surthi, S.; Misra, V. *IEEE T. Nanotechnol.* **2006**, *5*, 258.
164. Jiao, J.; Nordlund, E.; Lindsey, J. S.; Bocian, D. F. *J. Phys. Chem. C* **2008**, *112*, 6173.
165. Anariba, F.; Tiznado, H.; Diers, J. R.; Schmidt, I.; Muresan, A. Z.; Lindsey, J. S.; Zaera, F.; Bocian, D. F. *J. Phys. Chem. C* **2008**, *112*, 9474.
166. He, T.; Corley, D. A.; Lu, M.; Di Spigna, N. H.; He, J.; Nackashi, D. P.; Franzon, P. D.; Tour, J. M. *J. Am. Chem. Soc.* **2009**, *131*, 10023.

167. Pro, T.; Buckley, J.; Barattin, R.; Calborean, A.; Aiello, V.; Nicotra, G.; Huang, K.; Gély, M.; Delapierre, G.; Jalaguier, E.; Duclairoir, F.; Chevalier, N.; Lombardo, S.; Maldivi, P.; Ghibaudo, G.; De Salvo, B.; Deleonibus, S. From atomistic to device level investigation of hybrid redox molecular/silicon field-effect memory devices, *IEEE T. Nanotechnol*., accepted for publication.
168. Li, C.; Ly, J.; Lei, B.; Fan, W.; Zhang, D.; Han, J.; Meyyappan, M.; Thompson, M.; Zhou, C. *J. Phys. Chem. B* **2004**, *108*, 9646.
169. Noguchi, Y.; Nagase, T.; Ueda, R.; Kamikado, T.; Kubota, T.; Mashiko, S. *Jpn. J. Appl. Phys.* **2007**, *1*, *46*, 2683.

This page intentionally left blank

48 Bioinspired Catalysts with B_{12} Enzyme Functions

Yoshio Hisaeda and Hisashi Shimakoshi

Department of Chemistry and Biochemistry,
Graduate School of Engineering, Kyushu University,
Fukuoka 819-0395, Japan

List of Abbreviations

AB	arsenobatetaine
As_2O_3	arsenic trioxide
BDHC	1,19-dimethyl-AD-didehydrocorrin
CFC-113	1,1,2-trichloro-1,2,2-trifluoroethane
CFC-113a	1,1,1-trichloro-2,2,2-trifluoroethane
CH_3-H_4folate	N^5-methyltetrahydrofolate
Cob(II)7C_1ester	heptamethyl cobyrinate
Cob(II)7C_3ester	heptapropyl cobyrinate
1,2-DCE	1,2-dichoroethene
DDAB	didodecyldimethylammonium bromide
DDD	1,1-dichloro-2,2-bis(4-chlorophenyl)ethane
DDE	1,1-dichloro-2,2-bis(4-chlorophenyl)ethylene
DDMS	1,1′-(2-chloroethylidene)-bis(4-chlorobenzene)
DDMU	1-chloro-2,2-bis(4-chlorophenyl)ethylene
DDNU	1,1′-(ethenylidene)-bis(4-chlorobenzene)
DDO	1,1′-(ethylidene)-bis(4-chlorobenzene)
DDT	1,1,1-trichloro-2,2-bis(4-chlorophenyl)ethane
DH	dimethylglyoximato
DMA	dimethylarsinic acid
DTT	dithiothreitol
ECA	ethyl chloroacetate
GSH	glutathione
HSA	human serum albumin
HCB	hexachlorobenzene
HCH	hexachlorocyclohexane
H_2salen	*N*,*N*′-ethylenebis(salicylideneamine)

MMA	monomethylarsonous acid
PCB	pentachlorobenzene
PCE	tetrachloroethene
PFOS	perfluorooctane sulfonate
SCE	saturated calomel electrode
SHE	standard hydrogen electrode
TMAO	trimethylarsine oxide
TCE	trichloroethene
TCPP	5,10,15,20-tetrakis(4-carboxyphenyl)porphyrin
$TsOCH_3$	methyl tosylate
TTDB	2,3-dichloro-1,1,4,4-tetrakis(4-chlorophenyl)but-2-ene

I. Introduction

A. Enzymic Reactions

Vitamin B_{12} is a term found in health and nourishment studies, and has the chemical name of cyanocobalamin. However, this name is typically used for a cobalamin derivative. Vitamin B_{12} derivative denotes the cobalamin family that will be discussed in this chapter. Vitamin B_{12} derivatives consist of a cobalt atom coordinated with the tetrapyrrole ring system (corrin ring) and also linked to a heterocyclic base, 5,6-dimethylbenzimidazole, as shown in Figure 1. The corrin ring is similar to that in porphyrins, which are found in heme, chlorophyll, or cytochromes, but also different from porphyrin in that it is highly reduced and is missing one carbon atom from the carbon macro-ring. The porphyrin is a dianionic ligand; on the other hand, the corrin ring is a monoanionic ligand. Therefore, the corrin ring can stabilize the low oxidation states of the central cobalt.

Two coenzymatically active forms of vitamin B_{12} exist, i.e. adenosylcobalamin and methylcobalamin, as shown in Figure 1. The B_{12}-dependent enzymes catalyze various molecular transformations, for example, the rearrangement reactions as typified by the conversion of methylmalonyl-CoA to succinyl-CoA, the methylation reaction as in the synthesis of methionine, and the dehalogenation reaction of perchloroethylene, all as shown in Figure 2. These B_{12}-dependent enzymic reactions have been reviewed in the literature.[1–5] These reactions are very interesting from the viewpoint of organic synthesis. In this chapter, the biomimetic and bioinspired catalytic reactions with vitamin B_{12} enzyme functions are summarized.

B. B_{12} Model Complexes

Various cobalt complexes have been synthesized as model complexes of vitamin B_{12}.[6] However, all of these complexes cannot be qualified as favorable

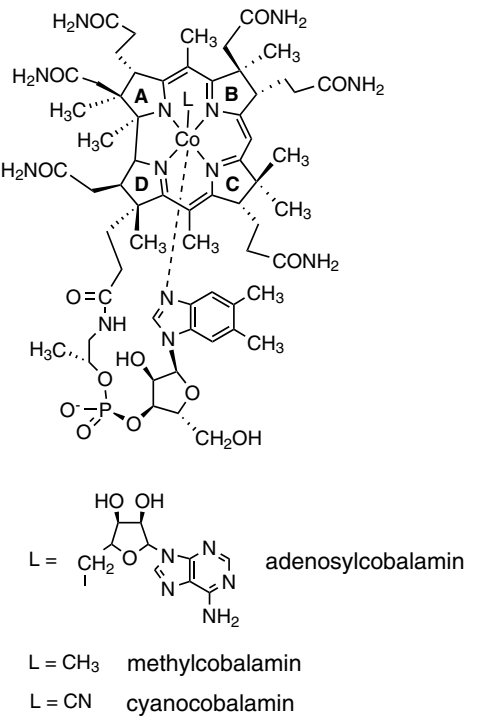

Figure 1. Structure of vitamin B_{12} derivatives.

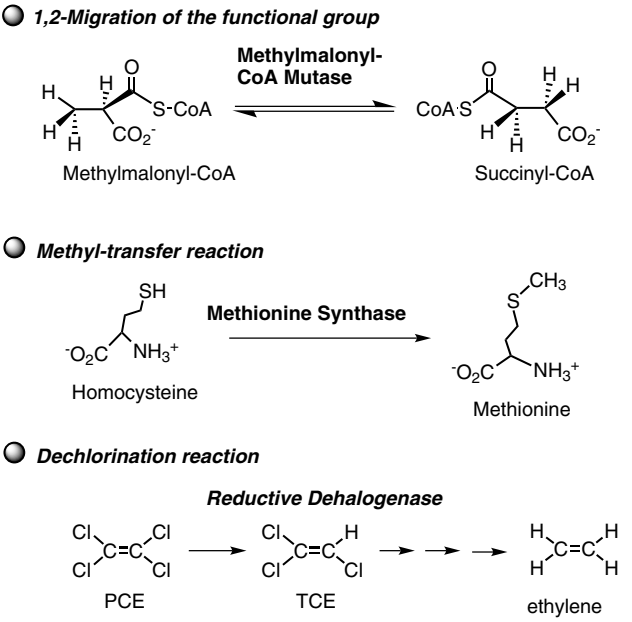

Figure 2. B_{12}-dependent enzymic reactions.

model complexes using the following criteria. (i) The redox behavior of the central cobalt, which is mainly controlled by the basicity of an equatorial ligand, must be similar to that for the naturally occurring B_{12}. (ii) The electronic properties must be equivalent to those of the natural B_{12}, which are provided by the corrin ring with eight double bonds and a direct bond between the rings A and D. (iii) The steric effects, which are caused by a methyl moiety and a hydrogen atom at the C(1) and C(19) positions in the corrin ring, respectively, may be important for the reactivity of the central cobalt.

The cobalt complexes have been extensively used not only as B_{12} models, but also as novel catalysts for organic syntheses by taking advantage of the high nucleophilicity of their univalent cobalt species. Typical model complexes are shown in Figure 3. However, most of these complexes cannot be used as functional simulations of B_{12}-dependent enzymes. For example, cobaloxime [bis(dimethylglyoximato)cobalt], [$Co(DH)_2$], which is readily prepared and frequently utilized, is capable of forming the cobalt–carbon bond with various ligands in the same manner as observed for the vitamin B_{12} derivative.[7] Nevertheless, this cobalt complex is not considered to be a good model since its redox behavior is different from that of B_{12}.[8] A cobalt complex of 1,19-dimethyl-AD-didehydrocorrin, [Co(BDHC)], has additional double bonds at the peripheral sites and an extra angular methyl group compared to the parent corrinoid.[9] This complex was found to be analogous to corrinoids on the basis of its electronic properties, but failed to simulate the reactions mediated by B_{12} because of the significant steric repulsion effect exerted by the angular methyl groups. As for the diimine-dioxime complex, [Co(DO)(DOH)pn], though this complex has a very simple structure compared to natural vitamin B_{12}, it shows redox behavior analogous to that of B_{12} with respect to the central cobalt.[10,11]

The naturally occurring apoproteins, which provide relevant reaction sites for B_{12}, are considered to perform additional important roles that lead to the desolvation and close association of reacting species. Based on this, the catalytic activity of B_{12} in hydrophobic microenvironments in order to simulate the catalytic functions of holoenzymes has shown some interesting characteristics. Under such circumstances, hydrophobic vitamin B_{12} derivatives (lipophilic derivatives), which have ester groups in place of the peripheral amide moieties of natural vitamin B_{12}, were reported.[12,13]

C. Construction of Artificial Enzymes

Naturally occurring holoenzymes are typical supramolecules composed of a specific apoprotein and an additional cofactor, such as a coenzyme or metal ions. Some artificial enzyme systems with organic/inorganic hybrid nanomaterials have

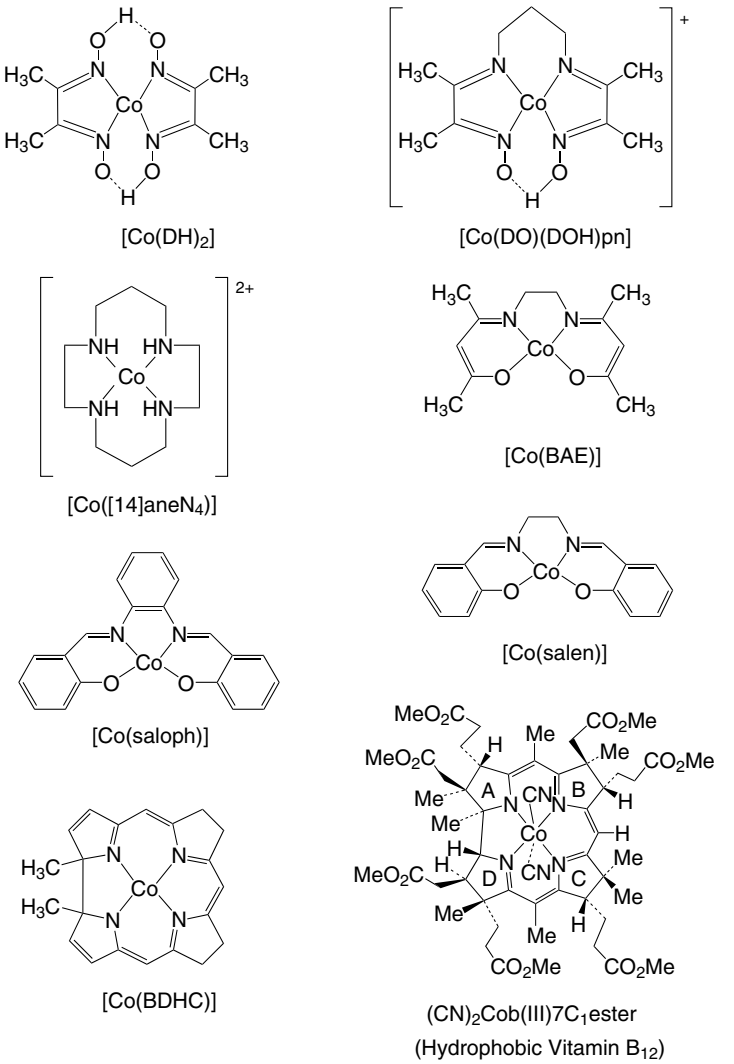

Figure 3. B_{12} derivative and model complexes.

been reported, as shown in Figure 4. One example is a vesicle-type artificial enzyme composed of peptide lipids and hydrophobic vitamin B_{12}.[14] The second example is a silica gel bearing vitamin B_{12} derivatives, formed by the sol-gel method.[15] The third is an organic/inorganic hybrid nanomaterial, i.e. human serum albumin (HSA) containing vitamin B_{12} derivatives.[16] The fourth example is a titanium dioxide–B_{12} hybrid system.[17] The electrochemical catalytic system and above

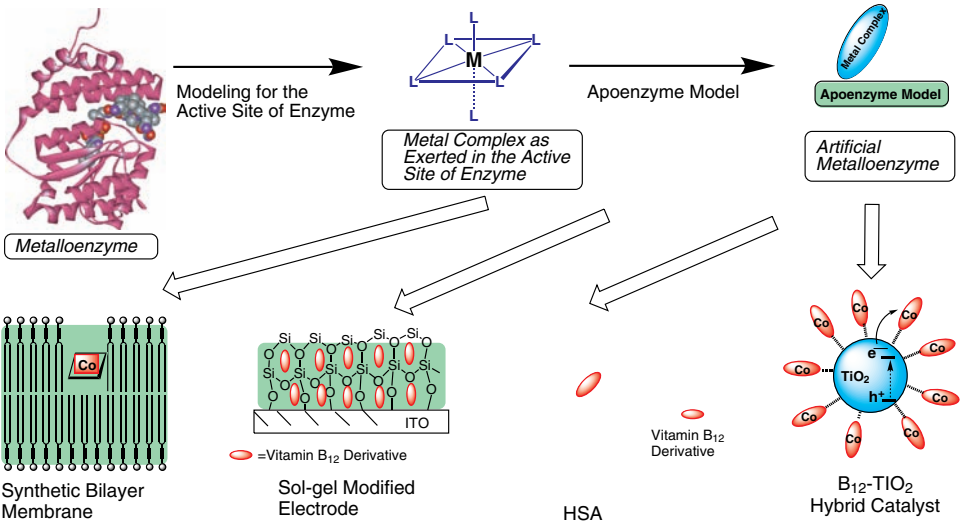

Figure 4. Artificial enzymes with organic/inorganic hybrid nanomaterials (adapted from Ref. 16).

artificial enzyme systems are very useful for various molecular transformations. The catalytic simulations of B_{12} enzymes with bioinspired systems are summarized in this chapter.

II. Bioinspired 1,2-Migration Reactions

The rearrangement reactions involve the intramolecular exchange of a functional group (X) and a hydrogen atom between neighboring carbon atoms [refer to Eq. 1].[18,19] These reactions have attracted much attention because of their novel nature from the viewpoints of organic and organometallic chemistry. Carbon-skeleton rearrangement reactions, mediated by methylmalonyl-CoA mutase, glutamate mutase, and α-methyleneglutarate mutase are shown in Eqs. 2–4.

(1)

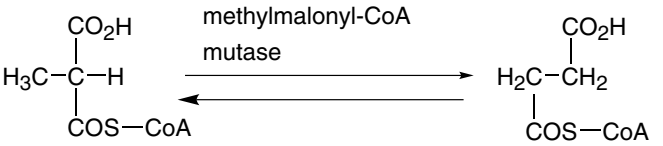

(2)

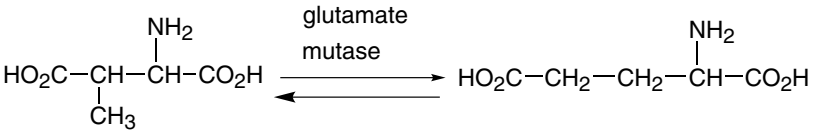

(3)

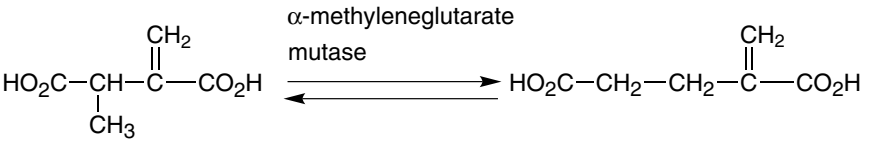

(4)

A. 1,2-Migration of Functional Groups on Cobalt Complexes

In B_{12} model reactions from the 1970s and 1980s, vitamin B_{12} derivatives or their model complexes are reduced to a super-nucleophilic Co(I) species, and alkylated complexes with the Co–C bond were obtained by reaction with the corresponding alkyl halide as the substrate. The products from the alkylated complex obtained by photolysis or thermolysis were then analyzed. Some typical and interesting reaction examples were shown as follows.

Dowd and Shapiro reported that the methylmalonate-bound cobalamin was prepared and the 1,2-migration product was obtained by the thermal cleavage of the Co–C bond at low yield as shown by Eq. 5.[20]

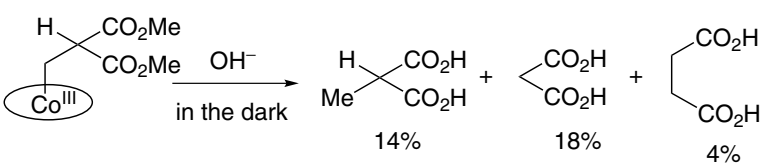

(5)

Scott and Kang reported that methylmalonyl monothiolate-bound cobalamin was prepared by the reaction between B_{12s} [Co(I) species of cobalamin] and the brominated substrate, and then the thioester-migrated product was obtained as the majority, as shown by Eq. 6.[21] This reaction is interesting from the viewpoint of

the migrating group, which is the thioester not the carboxylic ester. This tendency is similar to the enzymic reaction of methylmalonyl-CoA mutase.

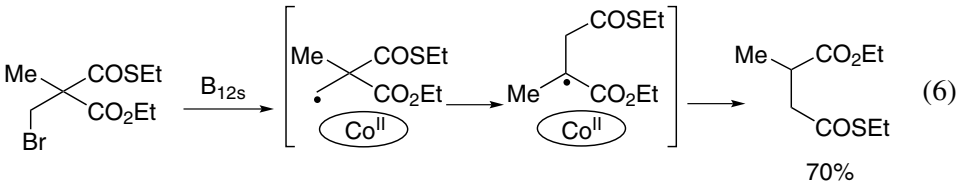

(6)

Schrauzer and coworkers also reported the reaction of the methylmalonyl monothiolate-bound cobalamin that was investigated under reduced reaction conditions, and proposed a rearrangement mechanism with an anionic intermediate as shown in Eq. 7.[22] The reaction mechanism was not different from that for the enzymic reaction, but this report showed that the 1,2-migration reaction proceeded effectively via an anionic intermediate.

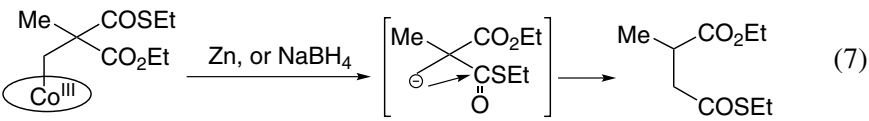

(7)

These reactions are interesting as pioneer model reactions for B_{12}-dependent enzymic reactions.

B. Electrochemical 1,2-Migration of Functional Groups

1. *Catalytic Simulation of Methylmalonyl-CoA Mutase*

The redox behavior of vitamin B_{12} derivatives was investigated in organic solvents, and a Co(I) species as a super-nucleophile is readily formed by electrochemical reduction.[23] On the basis of the redox behavior, the electrochemical catalytic cycles were established as shown in Figure 5. An alkylated complex, generated by the reaction of the Co(I) species and an alkyl halide, is generally decomposed by photolysis or electrolysis to afford reduction and/or rearrangement products.[24–26] One example using the hydrophobic vitamin B_{12}, [Cob(II)7C_1ester] ClO_4 (see Figure 6), is shown.

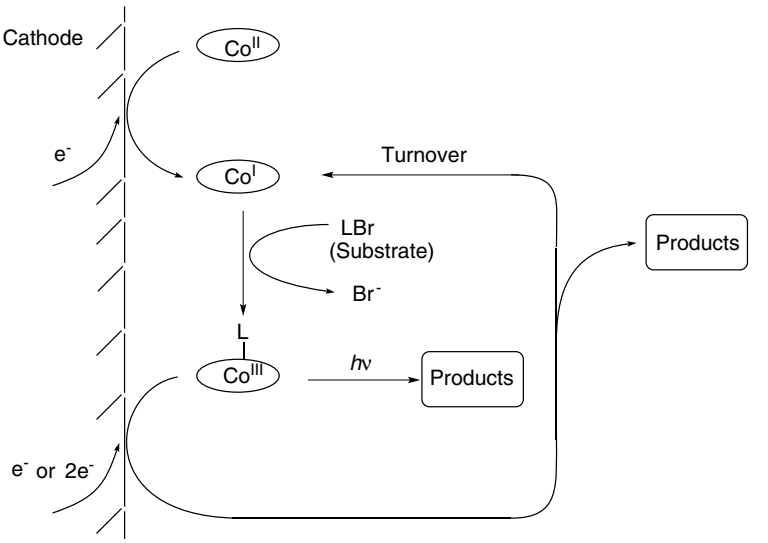

Figure 5. Electrochemical reactions mediated by B_{12} model complex.

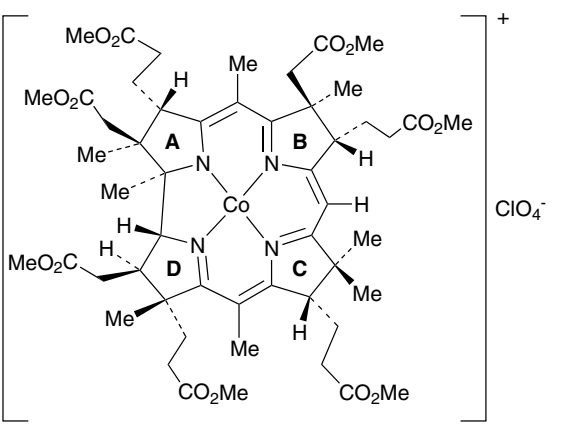

Figure 6. Structure of hydrophobic vitmain B_{12}, [Cob(II)7C_1ester]ClO_4.

2,2-Bis(ethoxycarbonyl)-1-bromopropane has been adopted as a model substrate for methylmalonyl-CoA mutase. The redox behavior of [Cob(II)7C_1ester]ClO_4 in DMF containing the substrate was examined by cyclic voltammetry. The redox potential for the Co(II)/Co(I) couple was observed to be −0.59 V vs. SCE in the presence of the substrate. An irreversible reduction peak was observed at *ca.* −1.3 V vs. SCE and assigned to the formation of the one-electron reduction intermediate of the alkylated complex, which was generated by the reaction between the Co(I) species

and the substrate. In addition, the second irreversible reduction peak was observed at *ca.* −1.8 V vs. SCE. This peak was assigned to the formation of the two-electron reduction intermediate of the alkylated complex. This redox behavior indicates that different intermediates will be formed at −1.0 V, −1.5 V, and −2.0 V vs. SCE.

Electrolysis of the substrate was carried out after the addition of a catalytic amount of [Cob(II)7C_1ester]ClO_4 in DMF under various conditions (refer to Eq. 8).[26] The catalysis was quite efficient at −2.0 V vs. SCE as reflected in the yields of the rearrangement product.

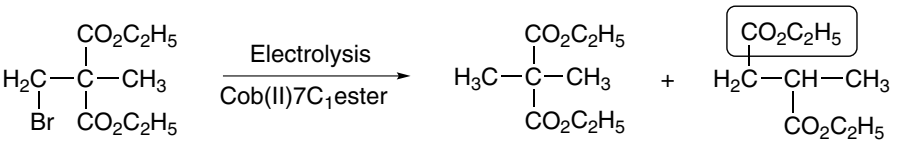

(8)

1) -1.0 V vs. SCE (hv)	10%	trace
2) -1.5 V vs. SCE	30%	trace
3) -1.5 V vs. SCE (AcOH)	17%	43%
4) -2.0 V vs. SCE	15%	80%

Reaction mechanisms involved in the controlled-potential electrolysis have been investigated by various spectroscopic methods.[25,26] The results are consistent with the overall feature of the electrolysis shown in Figure 7. At −1.0 V vs. SCE, the divalent cobalt complex is first converted into the corresponding univalent cobalt species by electrochemical reduction. The alkylated complex is subsequently formed by reaction of the super-nucleophilic Co(I) species with the alkyl halide. The complex is then decomposed by visible light to give the Co(II) species and the alkyl radical, and the latter abstracts a hydrogen atom to afford the simple reduction product. At −1.5 V vs. SCE, the alkylated complex is further reduced to form the one-electron reduction intermediate in the dark. The electronic structure of the intermediate seems to be represented by two canonical forms. A proton attack on the β-carbon of the substrate induces the carbon-skeleton rearrangement, followed by the cobalt–carbon bond cleavage. On the other hand, the one-electron reduction intermediate is spontaneously decomposed to the Co(I) chelate and the alkyl radical in the absence of an efficient proton source. The reduction product is mainly derived from the alkyl radical by rapid abstraction of a hydrogen atom. At −2.0 V vs. SCE, the alkylated complex is converted into the two-electron reduction intermediate in the dark. This intermediate is decomposed to the Co(I) chelate and an anionic species, and the rearrangement product is obtained from the latter. Since the identical radical species, which is produced by the reaction of the present substrate with tributyltin hydride or by photolysis of the

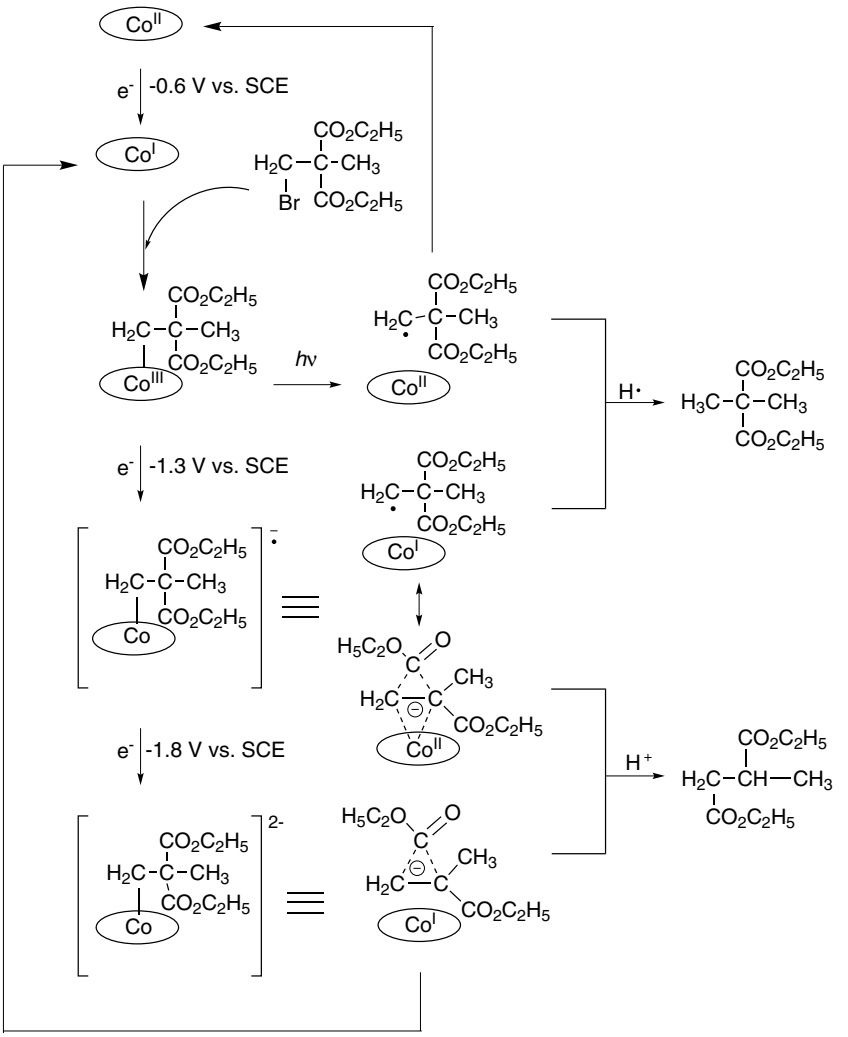

Figure 7. Overall electrochemical catalytic reactions mediated by hydrophobic vitamin B_{12} (adapted from Ref. 26).

present substrate bound to cobaloxime, does not undergo the rearrangement reaction,[27] both of the anionic reduction intermediates given in Figure 7 are the primary sources for the rearrangement product.

2. *Catalytic 1,2-Migration of Functional Groups*

In order to further characterize the catalytic proficiency of the hydrophobic vitamin B_{12} and to clarify the migratory aptitude of functional groups in the electrochemical rearrangement reaction, several kinds of substrates were also

used.[26] These substrates and the corresponding products are summarized in Eqs. 9 and 10. Substrates with two electron-withdrawing groups on the β-carbon atom tend to give the corresponding rearrangement products that are derived from the individual migration of the groups. Based on these results, the apparent migratory aptitude of electron-withdrawing groups decreases in the following sequence: COR > CO_2R > CN. Both steric bulkiness and the electronic character of the migrating groups are responsible for this tendency.

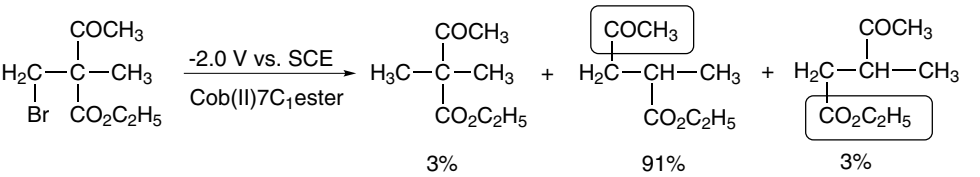

(9)

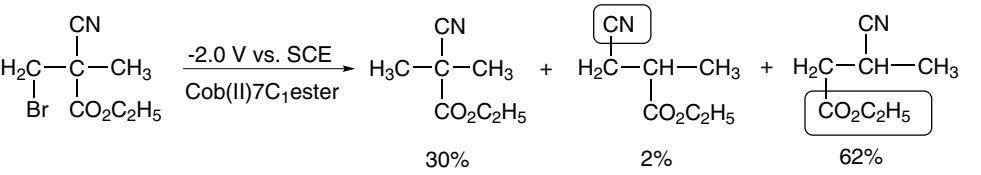

(10)

The steric effect in the carbon-skeleton rearrangement catalyzed by [Cob(II)7C_1ester]ClO_4 was investigated under the same conditions.[28] The controlled-potential electrolyses of alkyl halides having two carboxylic ester groups of different bulkiness on the same carbon atom were carried out in DMF (see Eq. 11). As for the correlation between the bulkiness of an ester group and migratory aptitude, a smaller ester group tends to migrate to the adjacent carbon atom more readily than a larger one. This steric effect is determined by the stereo-electronic effect.

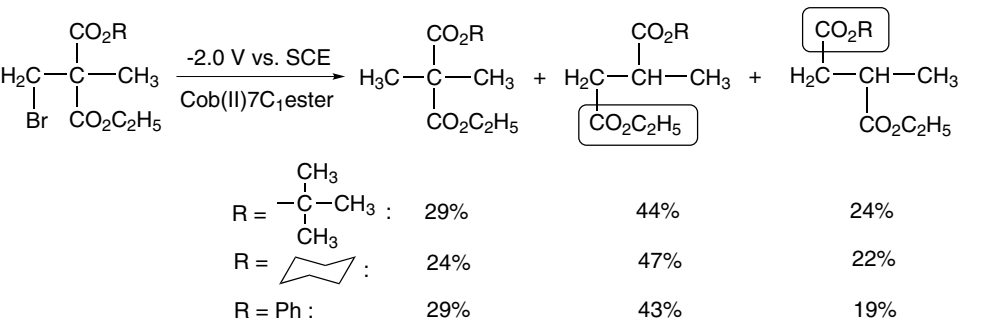

(11)

3. *Ring-Expansion Reactions*

Although naturally occurring B_{12}-dependent enzymes do not catalyze ring-expansion reactions, such reactions are mediated by vitamin B_{12} model complexes under electrochemical conditions. The ring-expansion of cyclic α-(bromomethyl)-β-keto esters by one carbon unit has been examined extensively by generating radical species with Bu_3SnH.[29–32] Torii and coworkers investigated the ring-expansion reactions of 2-alkyl-2-(bromomethyl)cycloalkanones, which have 5- and 6-membered rings, mediated by cobaloxime in methanol by constant-current electrolysis under irradiation with visible light.[33] Other ring-expansion reactions can be applied to vitamin B_{12} derivatives. [Cob(II)7C_1ester]ClO_4 was utilized to catalyze ring-expansion reactions under controlled-potential electrolysis conditions.

The electrolyses of alkyl halides with a cyclic ketone (5-, 6-, 7-, and 8-membered rings) and an ester group were carried out in DMF in the presence of [Cob(II)7C_1ester]ClO_4 at –2.0 V vs. SCE (see Eq. 12).[34] A simply reduced product, a ring-expanded product, and an ester-migrated product were reported. The major product was a ring-expansion product for all the substrates. The following facts became obvious based on these data: (i) The ring-expansion reactions are effectively catalyzed by the hydrophobic vitamin B_{12}. (ii) As for the reactivity of the substrates, an alicyclic ketone with a larger ring size (8-membered one) is less reactive than those with the smaller ring sizes (5-, 6-, and 7-membered). The formation of an alkylated complex with the substrate ($n = 4$) seems to be less favorable relative to that with other substrates due to steric reasons. (iii) As for the product selectivity, the major products are the ring-expanded ones for all substrates. Even when numbered substrates ($n = 2$ and 4) are used, ester-migrated products are obtained to some extent. Since the 6-membered ring is structurally stable, the 5-membered substrate ($n = 1$) readily afforded the ring-expansion product. On the other hand, the molar ratios of the nonexpanded products vs. the ring-expansion product are much higher for reactions with the 6-membered substrate ($n = 2$) than those for the other reactions.

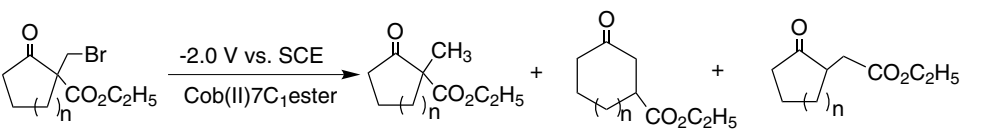

n = 1 (5-membered ring)	1.5%	43%	0%
n = 2 (6-membered ring)	14%	49%	12%
n = 3 (7-membered ring)	3%	44%	trace
n = 4 (8-membered ring)	2%	21%	4%

(12)

C. Artificial Enzymes Composed of Apoenzyme Model and B_{12} Model Complexes

Various cobalt complexes have been synthesized as model complexes of B_{12}.[35] The naturally occurring apoproteins, which provide relevant reaction sites for vitamin B_{12}, are considered to perform additional important roles that lead to the desolvation and close association of the reacting species.[36,37] Based on this concept, the activity of B_{12} in hydrophobic microenvironments has been studied in order to simulate the catalytic functions of holoenzymes.

One interesting example is a cyclophane-type B_{12} artificial enzyme that is constructed with a combination of an octopus cyclophane and a hydrophobic vitamin B_{12} (Figure 8).[27,38–41] The hydrophobic vitamin B_{12} is noncovalently incorporated into the octopus cyclophane in a 1:1 molar ratio by a hydrophobic interaction. The vesicle-type B_{12} artificial enzyme has also been reported as another example.[42–46] This artificial B_{12} enzyme is noncovalently constructed with a combination of a single-walled bilayer vesicle composed of $N^{+}C_5Ala2C_{16}$ and

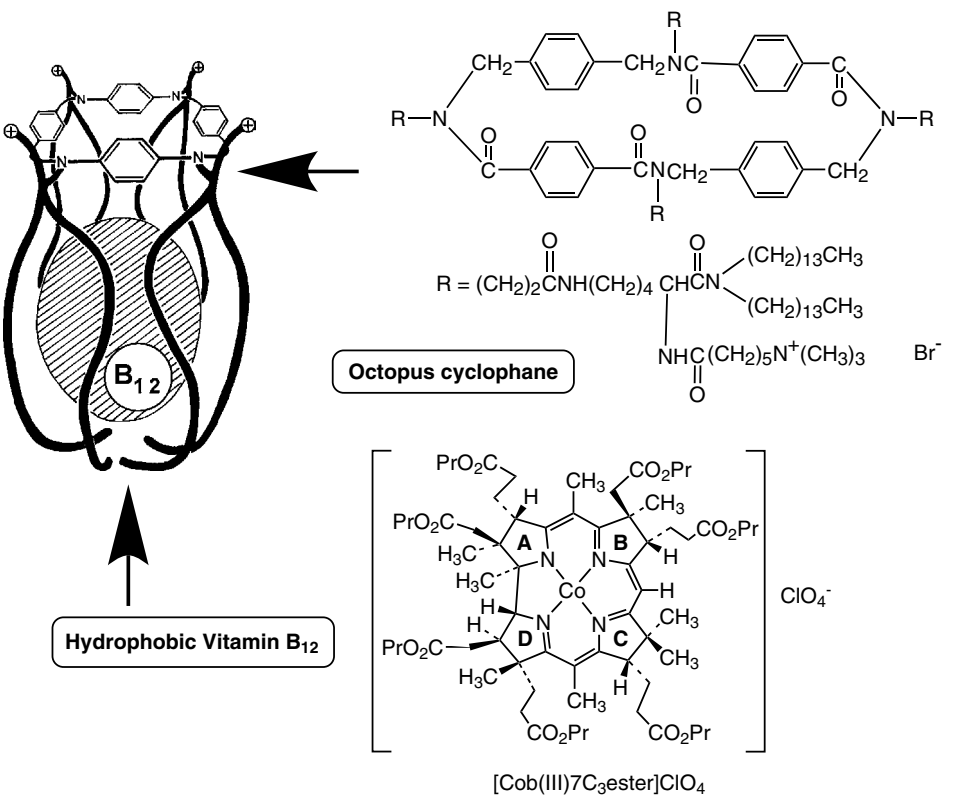

Figure 8. Cyclophane-type B_{12} artificial enzyme.

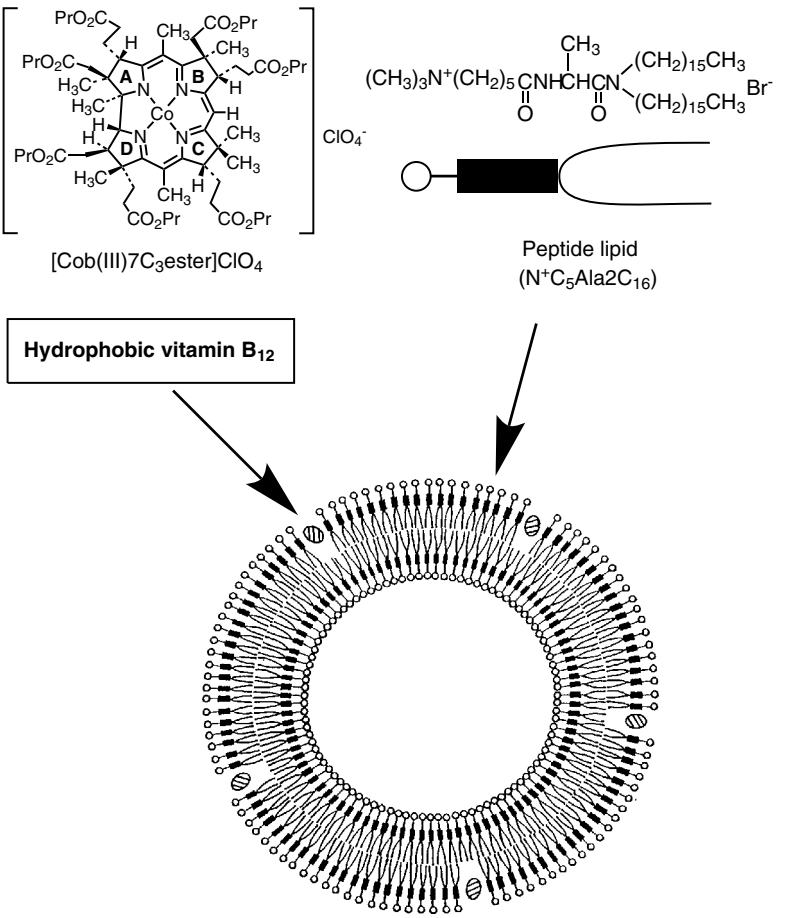

Figure 9. Vesicle-type B_{12} artificial enzyme.

the hydrophobic vitamin B_{12} (Figure 9). The morphological stability of the synthetic bilayer vesicle is not perturbed by the noncovalent incorporation of the hydrophobic vitamin B_{12}.[14,44] The model reactions of methylmalonyl-CoA mutase and glutamate mutase using artificial enzymes are outlined in the following section.

1. *Methylmalonyl-CoA Mutase-like Reactions*

Methylmalonyl-CoA mutase catalyzes the interconversion of methylmalonyl-CoA and succinyl-CoA. A characteristic aspect of the substrate, methylmalonyl-CoA, is that it has two electron-withdrawing groups on the same carbon atom. Successful model reactions have been reported in some papers.[27,44] The electrochemical

1,2-migration reactions proceed via anionic intermediates as described earlier. On the other hand, 1,2-migration reactions proceed via radical intermediates in artificial enzymes such as the cyclophane- and vesicle-type. Substrate species were bound to the hydrophobic vitamin B_{12} at one axial site of the nuclear cobalt, and the resulting alkylated complexes were noncovalently fixed in the bilayer membrane domain in aqueous media and then irradiated with visible light, resulting in the homolytic cleavage of the Co–C bond. Some typical experimental results are shown in Eqs. 13–16 and compared with the data obtained for the reactions in homogeneous solution. The apparent migratory aptitude of the electron-withdrawing groups was observed to increase as follows: CN ≈ $CO_2C_2H_5$ < $COCH_3$. The rearrangement reactions, which are slow in homogeneous solution, readily proceed in the vesicle by the cage effect of the apoenzyme model. Such microenvironmental effects provided by the bilayer membrane become more pronounced when the hydrophobic vitamin B_{12} is covalently bound to the lipid species.[47–51] A simpler artificial vitamin B_{12} holoenzyme has been constructed by combination of a bilayer membrane and a simple B_{12} model complex using the same procedure.[52,53]

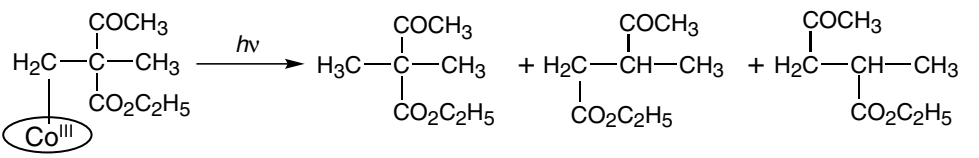

Methanol	70%	Trace	8%
Benzene	65%	Trace	10%
Vesicle	25%	Trace	63%
Cyclophane	23%	Trace	65%

(13)

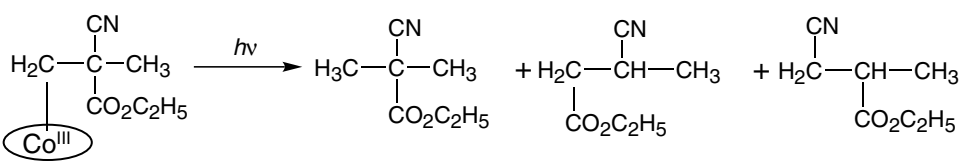

Methanol	87%	0%	0%
Benzene	78%	Trace	Trace
Vesicle	41%	23%	18%
Cyclophane	40%	21%	19%

(14)

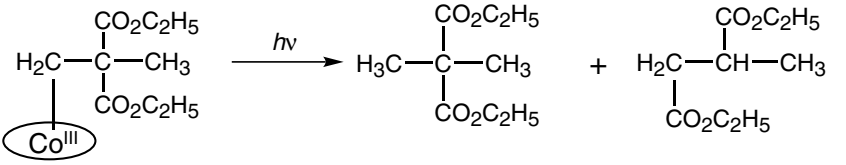

Methanol	88%	0%
Benzene	82%	1.3%
Vesicle	75%	9%
Cyclophane	75%	13%

(15)

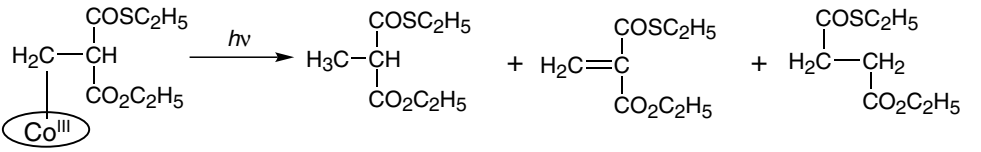

Methanol	83%	0%	0%
Benzene	80%	Trace	Trace
Vesicle	61%	4%	13%
Cyclophane	60%	4%	14%

(16)

The above reactions are stoichiometric rather than catalytic, even though the substrate species undergoes isomerization. In order to improve this situation, an effective process for activation of the substrates was coupled with the catalytic mediator composed of [Cob(II)7C_3ester]ClO_4 and the N^+C_5Ala2C_{16} vesicle.[44] An appropriate amount of [Cob(II)7C_3ester]ClO_4 and a large excess of vanadium trichloride were dissolved in an aqueous medium containing the N^+C_5Ala2C_{16} vesicle and an appropriate excess of the substrate. The solution was irradiated with visible light under aerobic conditions. The overall reaction cycle is shown in Figure 10. A substrate is activated by vanadium(III) ions and molecular oxygen,[54–57] and the resulting radical species undergoes coupling with [Cob(II)7C_3ester]$^+$ to afford the corresponding alkylated complex. The alkylated complex is subjected to homolytic cleavage to give the original substrate and the isomerized products, the former being subjected to catalysis. Similar reactions occur in the cyclophane-type artificial enzyme.[39,39]

The following aspects became apparent from these investigations. (i) A combination of vanadium trichloride and atmospheric oxygen abstracts a hydrogen atom from the terminal methyl group of a substrate species to

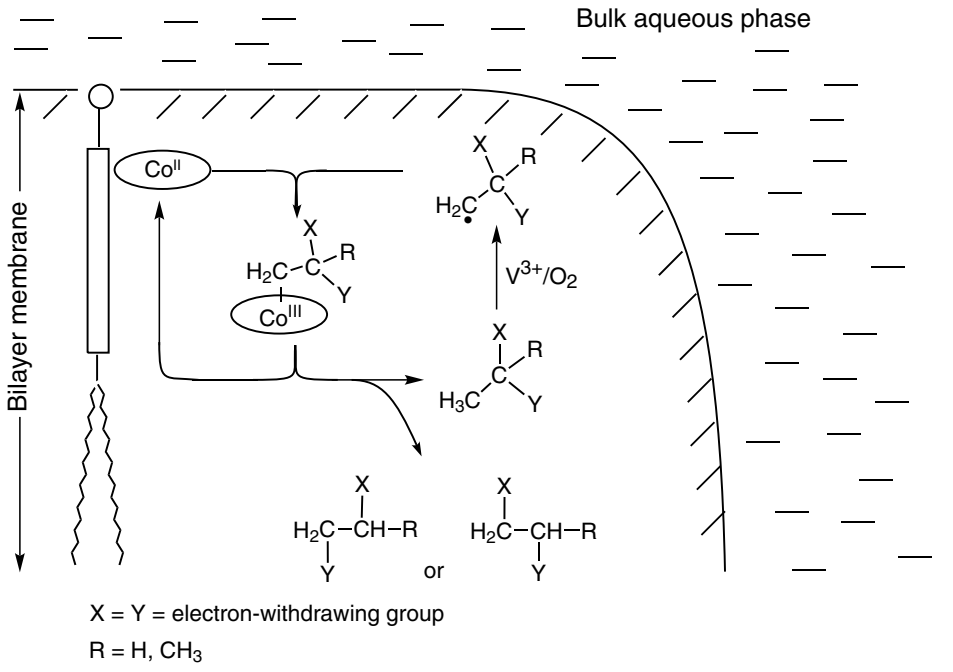

Figure 10. 1,2-Migration reactions activated by V^{3+}/O_2 in vesicle-type B_{12} artificial enzyme (adapted from Ref. 44).

form the corresponding radical species, which then undergoes a reaction with $[Cob(II)7C_3ester]^+$ to form the Co–C bond. (ii) Since both suppression of the molecular motion and desolvation effects operate on the chemical species incorporated into the bilayer vesicle, $[Cob(II)7C_3ester]^+$ and the substrate radical, which are produced by homolytic cleavage of the Co–C bond upon photolysis, must form a tight pair. Under such conditions, the nuclear cobalt promotes the 1,2-migration of the electron-withdrawing groups. This artificial holoenzyme is expected to be applied to other nonenzymatic reactions that undergo similar reaction mechanisms.[44]

2. *Glutamate Mutase-like Reactions*

Glutamate mutase mediates the interconversion of methylaspartic acid and glutamic acid. A model reaction with the apoenzyme functions has been reported.[43,45] Diethyl methylaspartate was bound to the hydrophobic vitamin B_{12}, and the resulting alkylated complex underwent homolytic cleavage of the Co–C bond upon

irradiation with visible light. It is apparent from Eq. 17 that the isomerization reaction takes place only in the apoenzyme models.

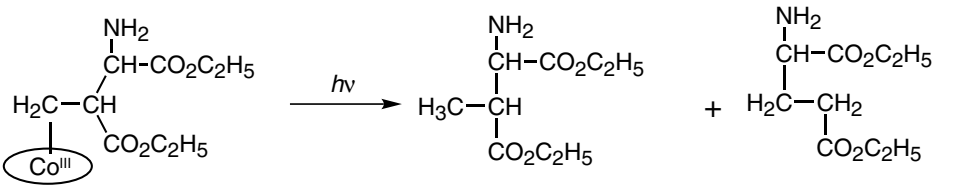

Methanol	83%	0%
Benzene	78%	Trace
Vesicle	66%	14%
Cyclophane	68%	15%

(17)

The overall reaction sequence mediated by the artificial glutamate mutase in the single-walled bilayer vesicle is illustrated in Figure 11; a substrate bound to a hydrophobic vitamin B_{12} undergoes the homolytic Co–C bond cleavage upon irradiation with visible light, the generated substrate radical is converted into the product radical, and the product radical abstracts a hydrogen atom from its vicinity to produce the final product.

Which functional group preferentially migrates to the neighboring carbon atom, the glycyl group or the carboxylic ester, in a reaction mediated by the artificial glutamate mutase? It became clear by utilizing a deuterated substrate that the glycyl group predominantly migrates in a similar manner as observed for the corresponding enzymic reaction, as shown in Eq. 18.[46] Dowd and coworkers observed that the β-methylaspartate-glutamate rearrangement readily took place via formation of a ketimine Schiff base derivative of diethyl β-methylaspartate, as mediated by vitamin B_{12}. Based on these results, they suggested the possible formation of

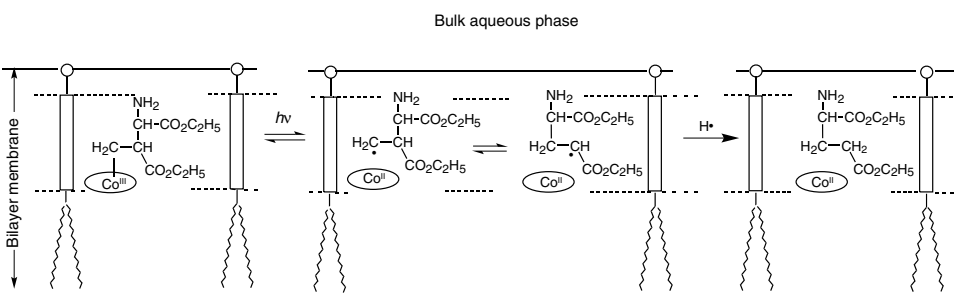

Figure 11. Overall reaction sequence in artificial glutamate mutase.

such a Schiff base intermediate in the corresponding enzymic reaction.[58,59] However, the glycyl group can migrate without the Schiff base formation in the apoenzyme model, though the yield is relatively low under the stated conditions.

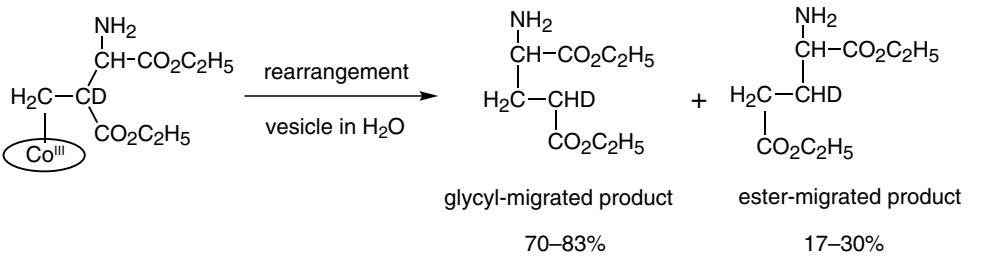

(18)

3. *Other Carbon-Skeleton Rearrangement Reactions*

Even though naturally occurring B_{12}-dependent enzymes do not catalyze ring-expansion reactions, such reactions are mediated by artificial enzymes under experimental conditions comparable to those applied in the abovementioned reactions. The reactions shown by Eqs. 19 and 20 were carried out in various media under anaerobic irradiation by visible light. The products, 2-methyl-1,3-cyclopentanedione (simple reduction product), 1,4-cyclohexanedione (ring-expansion product), 3-methyl-2-pyrrolidinone (simple reduction product) and 2-piperidinone (ring-expansion product), were obtained. These results indicated that the conversions of the 5-membered ring compounds into the corresponding 6-membered products take place much more favorably in the vesicle or the octopus cyclophane, relative to those in methanol and benzene.[38,60]

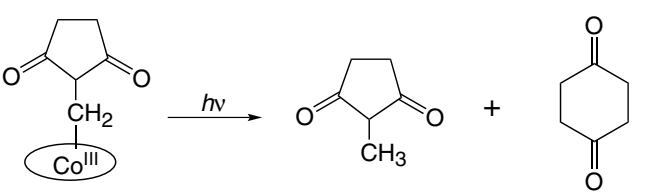

(19)

Methanol	69%	19%
Benzene	57%	28%
Vesicle	19%	67%
Cyclophane	15%	73%

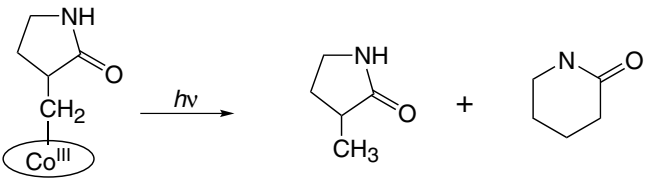

(20)

Methanol	83%	3%
Benzene	76%	9%
Vesicle	63%	24%
Cyclophane	61%	26%

III. Bioinspired Methyl Transfer Reactions

The methyl transfer reaction in methionine synthase catalyzed methylation at the sulfur of homocysteine using a methyl group from N^5-methyltetrahydrofolate (CH_3-H_4folate), which leads to tetrahydrofolate and methionine.[2] This reaction is also very interesting from the viewpoint of organic synthesis.

A. Methyl Transfer to Alkylthiols

The cobalamin-dependent methionine synthase that catalyzed the above methyl transfer reaction is one major role for the B_{12} coenzyme as shown in Figure 12. The cobalamin cofactor plays an integral role in methyl transfer, accepting methyl groups from CH_3-H_4folate and donating them to the homocysteine. During catalytic turnover, the cofactor cycles between the methylcobalamin and cob(I)alamin forms, alternately demethylated by homocysteine and remethylated by CH_3-H_4folate.[61]

It is difficult to achieve an efficient methyl transfer cycle under nonenzymatic conditions. Therefore, in model studies the methyl transfer cycle was often divided into two parts: the first half-reaction involving the methyl transfer from CH_3-H_4folate to cob(I)alamin, and the second half-reaction involving the methyl transfer from methylcob(III)alamin to homocysteine.[62] Zn^{2+} ions have been considered by many researchers to be the essential cofactor in this enzymic reaction.[63–65]

For the complete methyl transfer cycle, Keese, Darbre and coworkers in a pioneering study, reported that the methylated vitamin B_{12} derivatives involve the model methyl transfer reactions from methylamines to 1-hexanethiol in the presence of Zn and $ZnCl_2$ in refluxing ethanol.[66] They found that the methyl

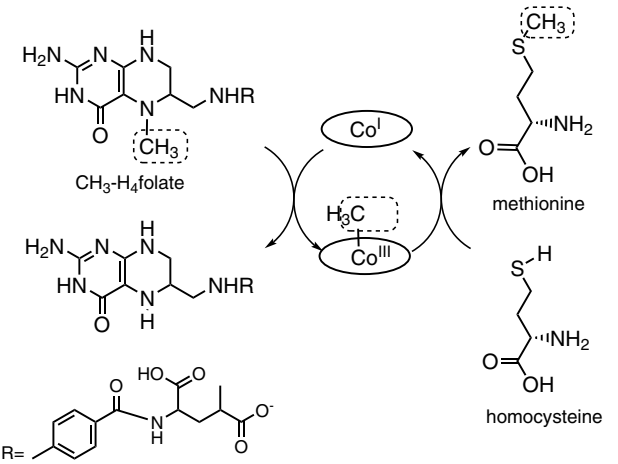

Figure 12. Catalytic cycle of methionine synthase.

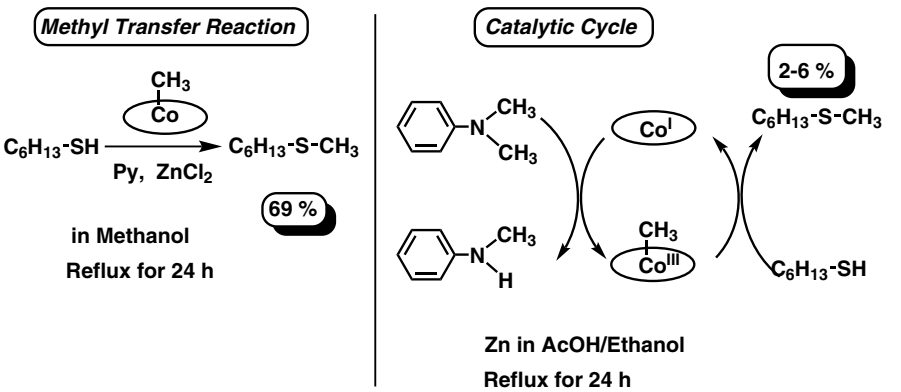

Figure 13. Model reaction of methionine synthase.

transfer reaction from methyl heptamethyl cobyrinate to 1-hexanethiol occurs in the presence of pyridine and $ZnCl_2$ in a 69% yield. They then used *N,N*-dimethylaniline as the methyl source, and constructed the catalytic cycle as shown in Figure 13. The methyl group first transfers to the Co(I) species from *N,N*-dimethylaniline to form methyl heptamethyl cobyrinate, and then it transfers to 1-hexanethiol. The authors carried out this reaction in the presence of Zn powder in acetic acid/ethanol under reflux conditions. The total yield of the hexyl methyl sulfide was about 6% based on the vitamin B_{12} derivative. The low yield may be attributed to the activity conflict between the methyl donor and methyl acceptor in the same environment, especially under neutral conditions.

A catalytic methyl transfer reaction from methyl tosylate ($TsOCH_3$) to 1-octanethiol mediated by heptamethyl cobyrinate perchlorate, [Cob(II)7C_1ester]ClO_4, was reported using an electrochemical method with a sacrificial Zn electrode as shown in Figure 14.[67] The catalytic methyl transfer reaction effectively proceeded under continuous controlled-potential electrolysis at −1.0 V vs. Ag/AgCl at 50 °C in the dark with a carbon-felt cathode and a sacrificial Zn-plate anode. Turnover behavior was observed for the first time under nonenzymatic conditions. During the electrolysis, Zn^{2+} ions from the sacrificial zinc plate anode played essential roles in the catalytic cycle. The mechanism for such methyl transfer reactions, as shown in Figure 15, was clarified by product analysis, electronic spectroscopy and ESR spin-trapping experiments, as well as cyclic voltammetry.[68] The formation

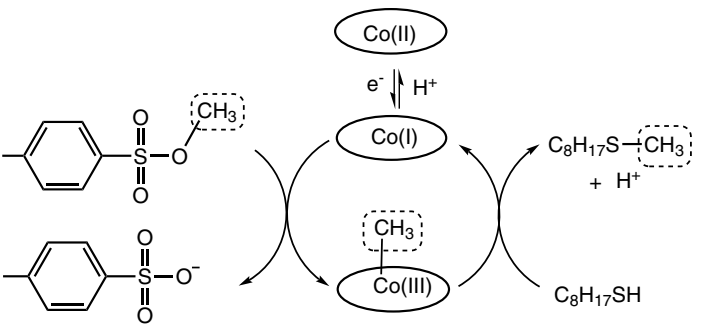

Figure 14. Methyl transfer cycle from methyl tosylate to 1-octanethiol catalyzed by B_{12} model complex (adapted from Ref. 67).

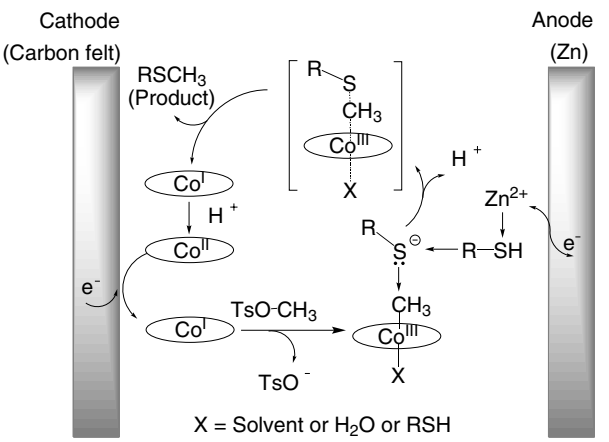

Figure 15. Mechanism of electrochemical methyl transfer reaction catalyzed by B_{12} model complex (adapted from Ref. 68).

and cleavage of the CH_3–Co bond is the indispensable intermediate during the catalytic methyl transfer reaction. Continuous electrolysis at −1.0 V vs. Ag/AgCl in the presence of $TsOCH_3$ insured a continuous Co(I) species, which facilitated the formation of the CH_3–Co intermediate by the reaction with methyl tosylate. Under thermodynamic conditions, with the help of Zn^{2+} and the interaction between the CH_3–Co bond and the activated 1-octanethiol, the CH_3–Co bond was cleaved, resulting in the methyl group transferred to the 1-octanethiol to form the methylated product. The Co(I) species formed may react with the proton from 1-octanethiol to form the Co(II) species. The catalyst will then be activated to the Co(I) species under electrochemical conditions.

B. Methyl Transfer to Inorganic Arsenics

Inorganic arsenic has caused serious chronic diseases through environmental pollution.[69] However, some methylated arsenic compounds, especially trimethylarsine oxide (TMAO) and arsenobatetaine (AB), have much lower toxicities than arsenic trioxide (As_2O_3). The acute toxicity of AB, as determined from animal experiments, is approximately one three-hundredth of that of arsenic trioxide.[70] Meanwhile, in marine ecosystems, inorganic arsenicals are biologically methylated through the food chain, which involves a methyltransferase and a reductase.[71–73] An interesting application of the methyl transfer reaction with vitamin B_{12} to the detoxification system for inorganic arsenic has been reported. A new synthetic pathway was designed for the transformation of arsenic trioxide into arsenobatetaine via trimethylarsine oxide, as shown in Figure 16.[74,75] It is a new and selective detoxification method for inorganic arsenic, which is the biomimetic methylation of arsenic trioxide (As_2O_3) to give trimethylarsine oxide (TMAO).

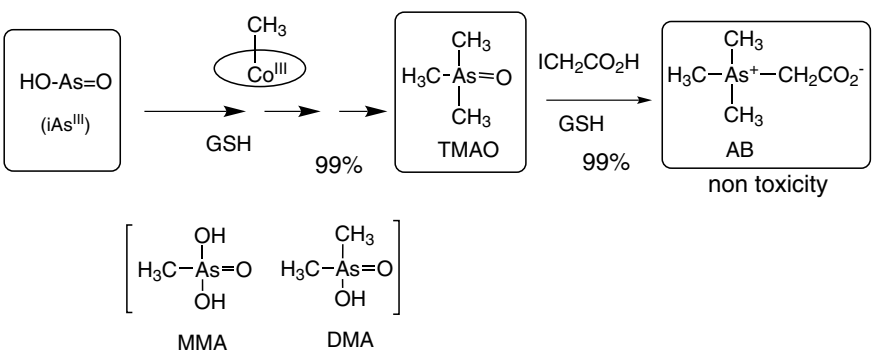

Figure 16. Methylation and detoxification of inorganic arsinic by methylated vitamin B_{12} derivative.

The methylation reaction of As_2O_3 was performed at 37 °C for 24 hours in an aqueous buffer solution using methyl heptamethyl cobyrinate as the methyl donor, in the presence of glutathione (GSH).[75] More than 98% of the arsenic trioxide (As_2O_3) was methylated to monomethylarsonous acid (MMA) 56%, dimethylarsinic acid (DMA) 41% and TMAO 1.4%. The generation of TMAO was not observed when methylcobalamin was used as the methyl donor under the same conditions.[76–78] Such activation may partly contribute to the interaction of GSH and the methylated hydrophobic vitamin B_{12}, which was observed by electronic spectroscopy. When such a methylation was performed at 100 °C in an aqueous buffer solution for 2 hours in the presence of glutathione with methyl cobyrinic acid as the methyl donor, the arsenic trioxide (As_2O_3) was almost quantitatively methylated to TMAO (99%).[74] This is the first report of the selective conversion of arsenic trioxide into TMAO using an artificial cofactor.

TMAO was quantitatively converted into AB in the presence of GSH and iodoacetic acid in an aqueous buffer solution at 37 °C.[74] The vitamin B_{12} derivatives and the GSH that are used in this detoxification method are safe and environmentally friendly materials. This method for the detoxification of inorganic arsenics could be used for the prevention of poisoning by inorganic arsenical compounds that are present in well water, which has been a widespread cause of chronic poisoning by arsenic.

IV. Bioinspired Dehalogenation Reactions

Vitamin B_{12}-dependent enzymes catalyze various molecular transformations that are of particular interest from the viewpoint of organometallic and catalytic chemistry. One of the most significant properties of the corrinoid compound (B_{12}) is the high nucleophilicity toward several organic halides to form an alkylated complex via dehalogenation. Much attention has been focused on such reductive dehalogenation reactions because of their potential application for the treatment of halogenated solvent wastes as well as for environmental remedial methods.[79] Within the past few decades, it has been demonstrated that certain bacteria can use tetrachloroethene as an electron acceptor by reducing it to *cis*-dichloroethene via trichloroethene and H_2 as an electron donor for energy conservation (dehalorespiration) (Figure 17).[80–83] Reductive dehalogenase isolated from the anaerobic bacteria contains the corrinoid compound as a cofactor.[84,85] Thus, the substantial ability of the corrinoid compound (B_{12}) to accomplish reductive dehalogenation prompted many researchers to investigate the catalysis of B_{12} for the degradation of various organic halides. Furthermore, efforts to clarify a mechanism for reductive dehalogenation of polychloroethylene in an enzymatic process have been reported using several model systems.[86–97] This

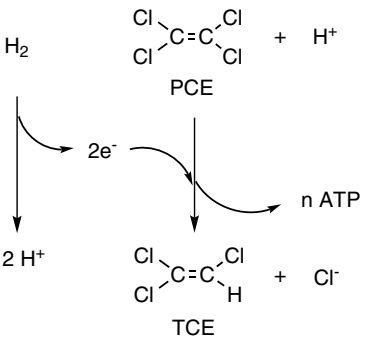

Figure 17. Scheme of dehalorespiration with H_2 as electron donor and tetrachloroethene as electron acceptor.

section highlights the catalytic dechlorination of chlorinated organic compounds by B_{12} and its models.

A. Reduction of Organic Halides by B_{12} Derivatives

In an early study, the reaction of the Co(I) state of B_{12} (vitamin B_{12s}) with various alkyl halides was investigated by kinetic experiments using sodium borohydride as the reducing reagent.[98,99] The nucleophilicity of vitamin B_{12s} was evaluated using Pearson's nucleophilic reactivity constants, n_{CH_3I} (Table 1).[100] Vitamin B_{12s} was recognized as a powerful nucleophile. Thus, the reductive dechlorinations of chlorinated organic molecules catalyzed by B_{12} derivatives were achieved using various chemical reductants. The catalytic and stoichometric reactions of two insecticides, mirex (1,1a,2,2,3,3a,4,5,5a,5b,6-dodecachlorooctahydro-1,3,4-metheno-1*H*-cyclobuta-[cd]pentalene) and kepone (1,1a,3,3a,5,5a,5b,6-decachlorooctahydro-1,3,4-methano-2*H*-cyclobuta[cd]pentalen-2-one) were conducted using vitamin B_{12s} in the presence of some reductants (either $NaBH_4$, 1-thioglycerol, 2,3-dimercaptopropanol, or

Table 1. Nucleophilic reactivity constants toward CH_3I.[a]

Nucleophile	n_{CH_3I}
CH_3OH	0.00
Cl^-	4.37
Br^-	5.79
I^-	7.42
Cobaloxime (aqua)	14.3
Vitamin B_{12s}	14.4

[a]Data taken from the Refs. 98 and 99.

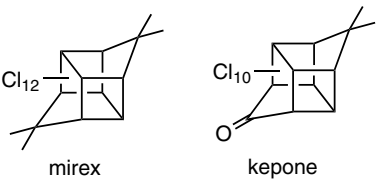

Figure 18. Structures of mirex and kepone.

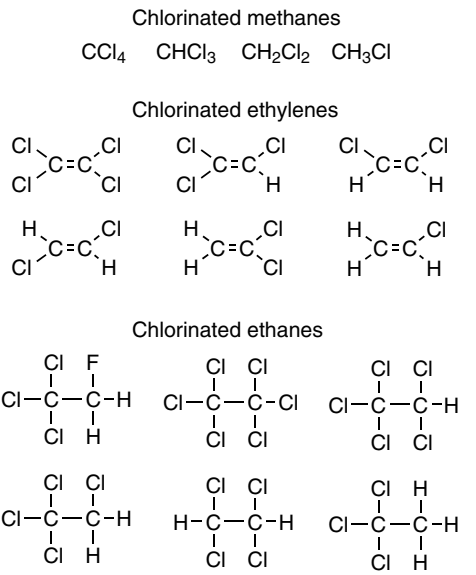

Figure 19. Structures of chlorinated methanes, ethylenes, and ethanes.

acetoin in alkali) (Figure 18).[101] A titanium(III) citrate was commonly used as the water-soluble reductant for the B_{12} activation. Chlorinated methanes, chlorinated ethylenes and ethanes, such as carbon tetrachloride, chloroform, dichloromethane, chloromethane, tetrachloroethylene, trichloroethylene, *cis*-dichloroethylene, *trans*-dichloroethylene, 1,1-dichloroethylene, vinyl chloride, trichlorofluoroethane, hexachloroethane, pentachloroethane, 1,1,1,2-tetrachloroethane, 1,1,2,2-tetrachloroethane, and 1,1,1-trichloroethane were dechlorinated to the corresponding alkanes and alkenes, catalyzed by cyanocobalamin (vitamin B_{12}) (Figure 19).[102–111] Toxaphene, a complex organochlorine pesticide mixture formed by the chlorination of camphene, was also dechlorinated by dicyanocobinamide and cyanocobalamin (Figure 20).[112] The most persistent metabolite in the environmental sample of toxaphene, 2-exo,3-endo,6-exo,8,8,10-hexachlorobornane, was also transformed. Reductive dechlorination of α-,β-,δ-,γ-hexachlorocyclohexane (HCH) isomers by

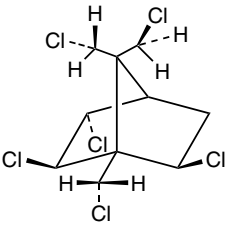

Figure 20. Structure of 2-*exo*, 3-*endo*, 6-*exo*, 8,9,10-hexachlorobornane.

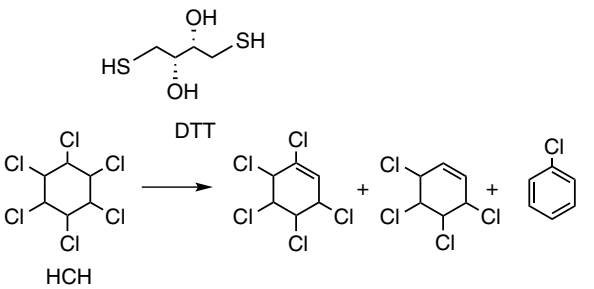

Figure 21. Dechlorination of hexachlorocyclohexane (HCH) by hydroxocobalamin/DTT system.

hydroxocobalamin was carried out in the presence of titanium(III) citrate (–0.48 V vs. SHE, pH above 7.3) and dithiothreitol (DTT) (–0.33 V vs. SHE, pH 7).[113,114] The reaction profiles for the dechlorination of HCH were dependent on the reductant. When DTT was used as the external electron source, α- and γ-HCH were transformed into pentachlorocyclohexane, tetrachlorocyclohexane, and chlorobenzene, whereas chlorobenzene was detected in all the HCH dechlorination systems together with small amounts of pentachlorocyclohexane and tetrachlorocyclohexane when titanium(III) citrate was used as the reductant (Figure 21).

The reductive dechlorination using the DTT/cyanocobalamin system was also applied to the degradation of carbon tetrachloride.[115] The Co(II) form of B_{12} (vitamin B_{12r}) was expected to be the predominant cobalt species that reacts with the organic halide, while cob(I)alamin (vitamin B_{12s}) did not participate in the reaction since DTT is a weak reductant. Therefore, the one-electron reduction of vitamin B_{12} followed by atom transfer to form the cobalt-trichloromethyl intermediate was proposed for the dechlorination mechanism (Figure 22).

As a thiol reductant, cysteine (–0.21 V vs. SHE, pH 7) was used for the carbon tetrachloride transformation mediated by cyanocobalamin.[116] The Co(II) form of B_{12} (vitamin B_{12r}) exhibited little reactivity toward carbon tetrachloride in the

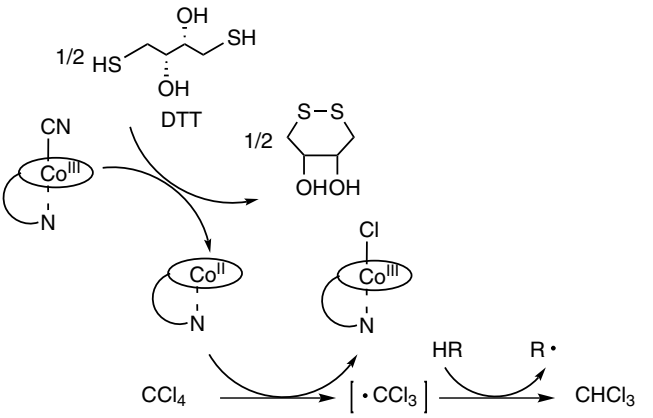

Figure 22. Proposed mechanism of CCl_4 reduction to $CHCl_3$ in the B_{12}-DTT system (adapted from Ref. 115).

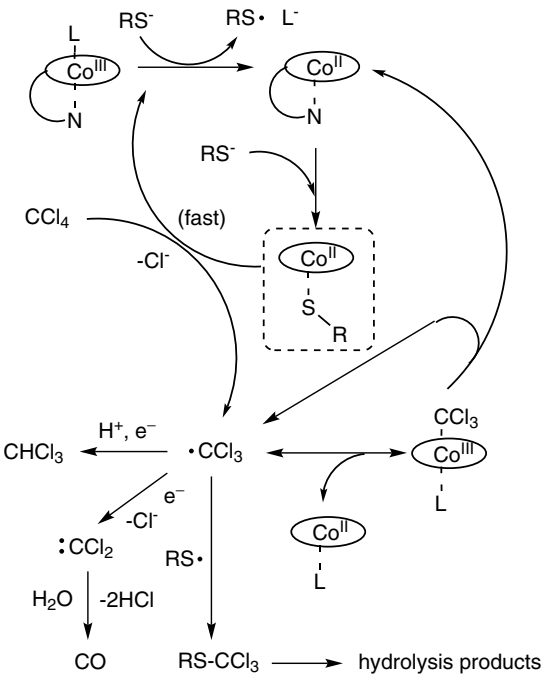

Figure 23. Hypothesized reaction scheme for CCl_4 transformation by B_{12} in cysteine solution (adapted from Ref. 116).

absence of cysteine, and the reactive B_{12} species was hypothesized to be the pentacoordinated Co(II)-cysteinate complex (Figure 23).

Dehalogenation of fluorinated organic compounds was also achieved by the B_{12} catalyst. Reductive defluorination of perfluorooctane sulfonate (PFOS)

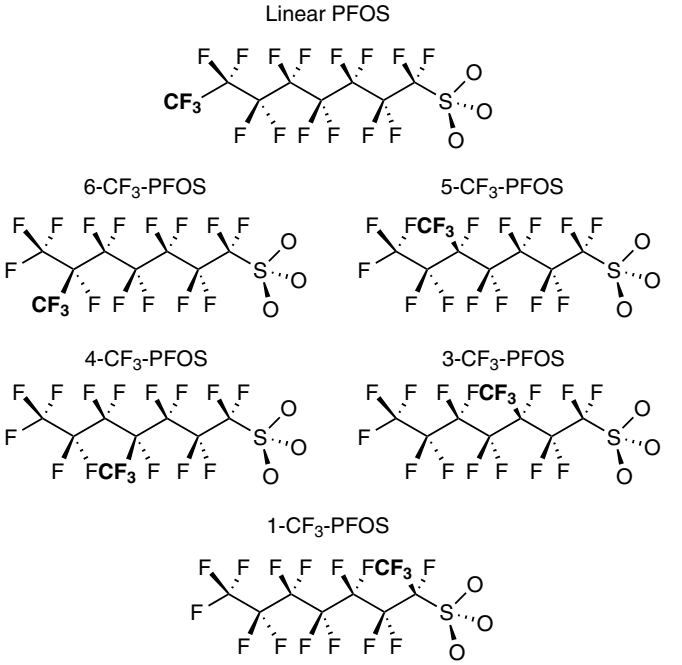

Figure 24. Structure of linear perfluorooctane sulfonate (PFOS) and branched isomers (6-CF_3-PFOS, 5-CF_3-PFOS, 4-CF_3-PFOS, 3-CF_3-PFOS, and 1-CF_3-PFOS).

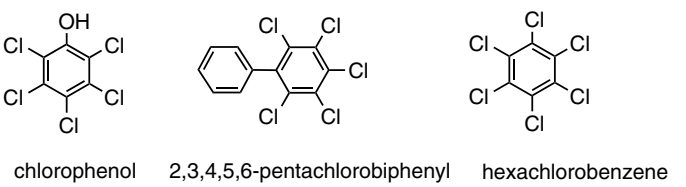

Figure 25. Structure of chlorophenol, 2,3,4,5,6-pentachlorobiphenyl, and hexachlorobenzene.

(Figure 24) was carried out using cyanocobalamin (vitamin B_{12}) as the catalyst and titanium(III) citrate as the bulk reductant in an anoxic aqueous solution at 70 °C and pH 9.[117] Partial defluorination of technical PFOS and PFOS branched isomers proceeded in seven days, with 18% and 71% fluoride releases, respectively.

Removal of the chlorine from the aromatic ring in chlorophenols,[118,119] 2,3,4,5,6-pentachlorobiphenyl[120,121] and hexachlorobenzene[121] were investigated by vitamin B_{12}/titanium(III) citrate or using the DTT system (Figure 25). Reductive dechlorination of such chlorinated benzenes by the B_{12} catalyst

proceed several days to weeks. For example, an approximately 10% chlorine removal for 2,3,4,5,6-pentachlorobiphenyl was observed for 36 days in aqueous condition at 20 °C.

Due to environmental concerns, zero valent metals were used as the reducing reagent for the B_{12} activation since a heterogeneous metal is easy to remove after the reaction.[122] Iron does not have enough reducing potential for Co(I) generation, while zinc efficiently reduced vitamin B_{12} to form the Co(I) species, as confirmed by UV-visible spectroscopy. The vitamin B_{12} and zinc combination system significantly enhances the reaction rates for both the PCE and TCE dechlorination compared with those for the metal only.

B. Electrocatalytic Reduction of Organic Halides by B_{12} Derivatives

Vitamin B_{12} derivatives are electrochemically active, and the Co(I) form of B_{12} is produced at the cathode in various media, such as DMF, DMSO, CH_3CN, alcohols, and aqueous solutions.[23,123] *In situ* generated Co(I) species in an electrolyte solution reacts with organic halides by dehalogenation. Ethylene dibromide, a suspected human carcinogen, was reduced to form an alkene at glassy carbon electrodes in a surfactant-stabilized emulsion using an electrocatalytic cycle involving vitamin B_{12} (Eqs. 21–25).[124,125] The catalysis of the Co(I) form of B_{12} saved an overpotential of 0.84 V compared to the direct reduction of ethylene dibromide. The intermediate (β-bromoalkyl)cobalamin (Eq. 21) was predicted but was kinetically invisible on the time scale under the investigated experimental conditions. Reductive dehalogenation of α-haloacetic acids to give acetic acid was achieved by vitamin B_{12s} during electrolysis at −0.9~−1.1 V vs. SCE in acetonitrile/water (1:1), pH 3 phosphate buffer.[126] Analysis by cyclic voltammetry showed the formation of a reduced organic product at the formal potential of Co(II)/Co(I). The organocobalt intermediate was also not observed in the reaction due to the carboxylic acid group that reductively destabilized the alkylated complex. In this way, the Co(I) species also formally acts as a powerful reductant toward these substrates.

$$Co(II) + e \longrightarrow Co(I) \tag{21}$$

$$Co(I) + CH_2BrCH_2Br \longrightarrow [BrCo(III)CH_2CH_2Br] \tag{22}$$

$$\longrightarrow Co(II) + \cdot CH_2CH_2Br + Br^- \tag{23}$$

$$Co(I) + \cdot CH_2CH_2Br \longrightarrow Co(II) + CH_2CH_2Br^- \tag{24}$$

$$CH_2CH_2Br^- \longrightarrow CH_2{=}CH_2 + Br^- \tag{25}$$

The electrolysis of 1,1,1-trichloro-2,2-bis(4-chlorophenyl)ethane (DDT) in the presence of corrinoid compound, heptamethyl cobyrinate perchlorate, was also reported.[127] Among the chlorinated organic compounds, DDT is characterized by a pronounced insecticidal property and has been used worldwide despite its known hazardous effects on human health and wildlife. DDT was catalytically dechlorinated by B_{12} to form 1,1-dichloro-2,2-bis(4-chlorophenyl)ethane (DDD), 1,1-dichloro-2,2-bis(4-chlorophenyl)ethylene (DDE), 1-chloro-2,2-bis(4-chlorophenyl)ethylene (DDMU), and (*E*/*Z*) 2,3-dichloro-1,1,4,4-tetrakis(4-chlorophenyl) but-2-ene (TTDB) in DMF containing tetra-*n*-butylammonium perchlorate (Figure 26). A photosensitive intermediate having a Co–C bond formed during the electrolysis was identified by electronic spectroscopy.

A voltammetric study of the electrocatalytic reduction of vicinal dibromoalkanes, (*trans*-1,2-dibromocyclohexane, 1,2-dibromobutane) in ionic liquid media of cyanocobalamin (vitamin B_{12}) was reported.[128] Cyanocobalamin was hard to dissolve in a dry ionic liquid, but was dissolved in an ionic liquid (butyl-3-methylimidazolium trifluoromethanesulfonate) containing water (5–20% v/v). In contrast, the corrinoid compound, heptamethyl cobyrinate perchlorate, was soluble in the dry ionic liquid. Interestingly, enhancement for reactivity of the Co(I) form of B_{12} toward DDT in the ionic liquid, 1-butyl-3-methylimidazolium

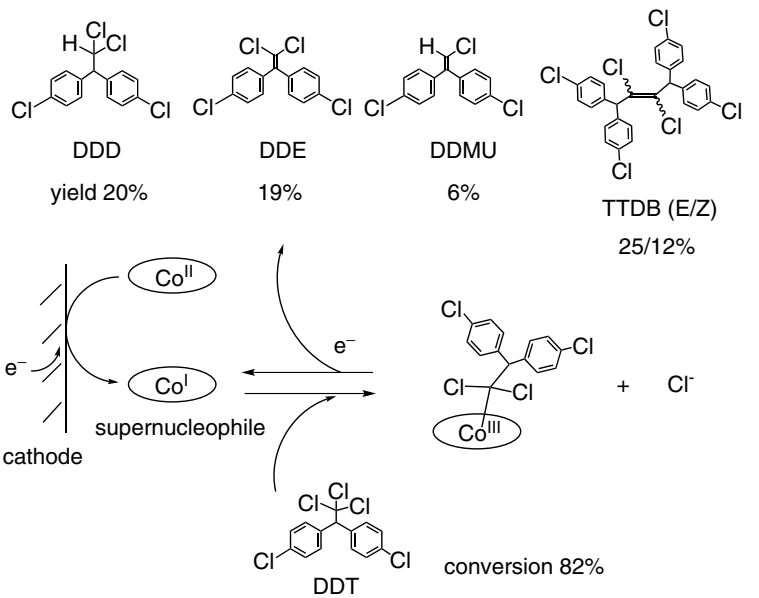

Figure 26. Dechlorination of DDT catalyzed by heptamethyl cobyrinate perchlorate under electrochemical conditions in DMF (adapted from Ref. 127).

tetrafluoroborate, was reported.[129] More highly dechlorinated products, 1,1′-(2-chloroethylidene)-bis(4-chlorobenzene) (DDMS), 1,1′-(ethenylidene)-bis(4-chlorobenzene) (DDNU), and 1,1′-(ethylidene)-bis(4-chlorobenzene) (DDO) were produced under electrolysis in an ionic liquid in the presence of the B_{12} catalyst compared to the result in DMF mentioned above (Eq. 26). The enhanced reactivity of the B_{12}-ionic liquid system over the B_{12}-DMF system for the electrolysis of DDT was explained by an application of the Hughes-Ingold predictions of solvent polarity effects on reaction rates.[130] Two neutral reactants, the Co(I) form of B_{12} and an organic halide, react to form charged products via a charge-separated activated complex in the polar ionic liquid, which decreases the $\Delta G^{\ddagger}$ value, resulting in an increase in the reaction rate. The solvent polarity parameter, the E_T^N value of the ionic liquid, is greater than that of DMF.[131]

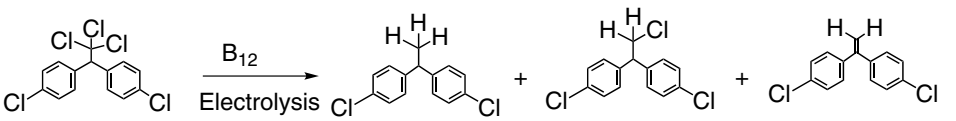

DDT → DDO 44% + DDMS 27% + DDNU trace (26)

The mechanism for the dechlorination of an organic chloride by B_{12} under electrochemical conditions was investigated by cyclic voltammetry.[132] Using chloroacetonitrile as an example, the crucial step in the catalytic process was elucidated as the proton transfer decomposition of the alkylcobalt(II) complex, which was formed by the reduction of the alkylcobalt(III) complex in DMF with the addition of an acid. Furthermore, it was pointed out that the reduction step of the alkylcobalt(III) complex was affected by the axial ligand, such as the chloride ion derived from the substrate (Figure 27). The stronger this ligand is, the more negative the potential required for this step which influences the catalytic process.

C. Photocatalytic Reduction of Organic Halides by B_{12} Derivatives

A photoredox compound was utilized for the activation of B_{12} to form a Co(I) species by irradiation with light. An inorganic complex, $[Ru(bpy)_3]Cl_2$ (where bpy is 2,2′-bipyridine) is widely used as a photosensitizer due to its ability to mediate electron transfer.[133–136] In the case of the B_{12} catalytic system, the

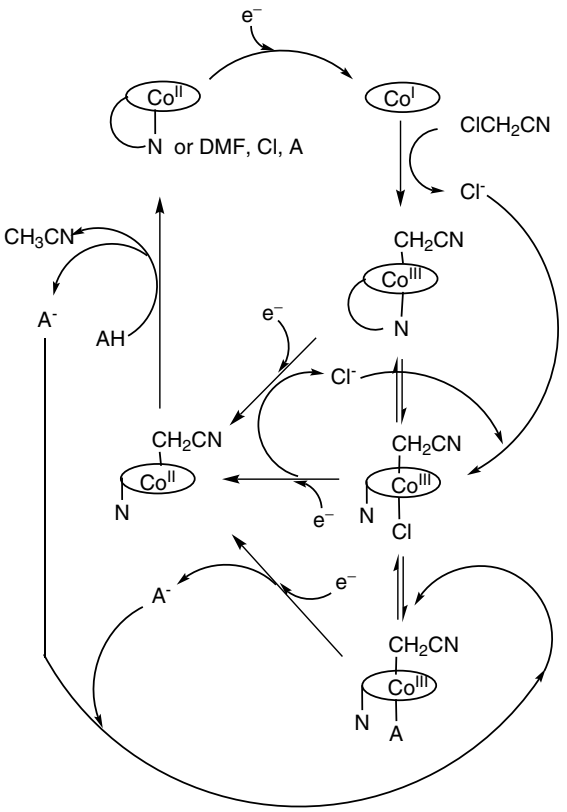

Figure 27. Proposed mechanism for dechlorination of organic chloride by B_{12} under electrochemical conditions (adapted from Ref. 132).

combined use of cyanocobalamin (vitamin B_{12}) and $[Ru(bpy)_3]Cl_2$ was first reported for the photochemical reduction of carbon dioxide and water by visible light irradiation.[137] Application of this combination for the dehalogenation of organic halides was also reported. The mono-dechlorination of DDT effectively proceeded using a heptamethyl cobyrinate perchlorate catalyst in the presence of $[Ru(bpy)_3]Cl_2$ by irradiation with visible light (Figure 28). The formation of the reactive Co(I) form of B_{12} was confirmed by the ESR spectral change in this system.[138,139]

Titanium oxide (TiO_2) was also utilized as the photosensitizer to mediate the electron transfer toward B_{12} (Figure 29). It is well known that TiO_2 generates an electron-hole pair under band gap excitation by UV light irradiation.[140–142] The conductive band electron for TiO_2 ($E_{red} = -0.5$ V vs. NHE in neutral aqueous solution) could reduce the B_{12} derivatives to form Co(I) species. A corrinoid compound having seven carboxylic acid groups, cobyrinic acid, was immobilized on TiO_2,

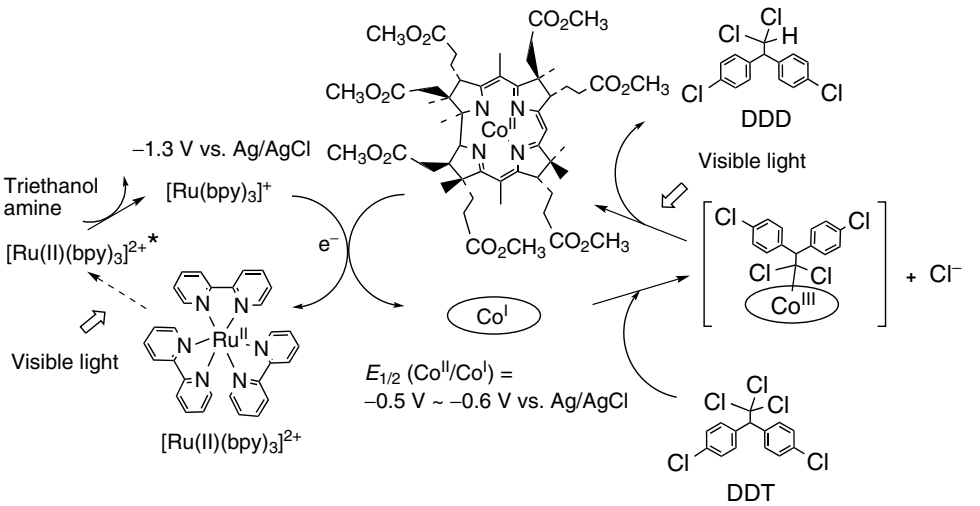

Figure 28. Strategy for photosensitized system for B_{12} catalysis (adapted from Ref. 138).

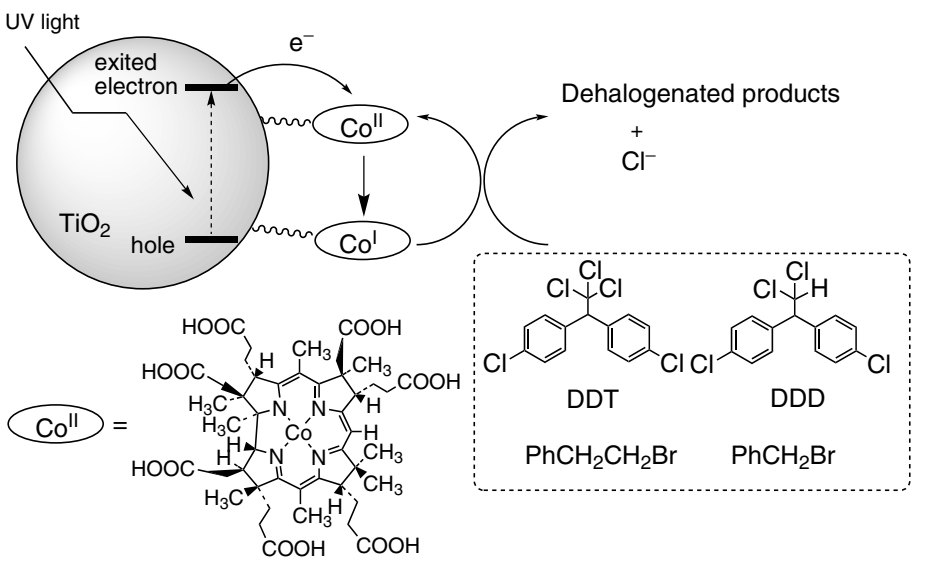

Figure 29. B_{12}-TiO_2 hybrid catalyst.

and the immobilized B_{12} was then reduced to the Co(I) state by irradiation with UV light (365 nm). The B_{12}–TiO_2 hybrid catalyst effectively dehalogenated various organic halides, such as DDT, DDD, and phenethyl bromide.[143] The powder type of B_{12}–TiO_2 hybrid catalyst can be immobilized on a glass plate. By irradiation

with UV light (365 nm), the immobilized catalyst (hybrid glass) shows efficient reactivity for the dechlorination of PCE to TCE and 1,2-DCE (*E*/*Z*) with product yields of 43% and 1/1%, respectively.[144]

D. Dechlorination of Organic Halides by Other Cobalt Complexes

Cobalt complexes, except for the corrinoid compound, have been synthesized and utilized for catalytic reactions. Tetradentate chelate compounds, such as porphyrin, phthalocyanine, cobaloxime, and H_2salen, where H_2salen is *N*,*N*′-ethylenebis(salicylideneamine), were extensively studied. The characteristics of each catalyst such as the stability, solubility, and redox potential of the cobalt center were dependent on each complex. The electrogenerated cobalt(I) salen was widely used for the dechlorination of various organic chlorides, such as ethyl chloroacetate (ECA),[145] 1,1,2-trichloro-1,2,2-trifluoroethane (CFC-113),[146] 1,1,1-trichloro-2,2,2-trifluoroethane (CFC-113a),[147] DDT,[148] hexachlorobenzene (HCB),[149] and pentachlorobenzene (PCB).[150] As for the photocatalytic system, cobalt(II) tetrasulfonatophthalocyanine[151] and cobalt(III) *meso*-tetra-(4-carboxyphenyl)porphyrin chloride[152] (Figure 30) were combined with TiO_2 for the reductive dechlorination of bromoform, carbon tetrachloride, and chloroform. The catalytic dechlorination

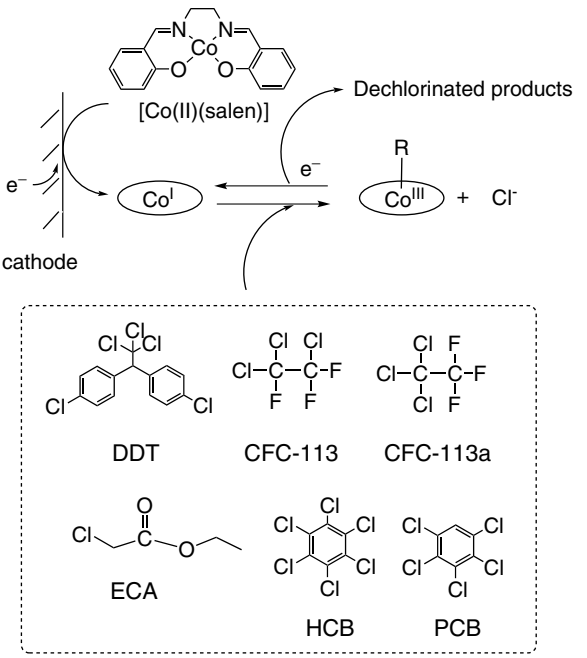

Figure 30. Electrolysis of various chlorinated organic compounds with [Co(II)(salen)].

of PCE and TCE by 5,10,15,20-tetrakis(4-carboxyphenyl)porphyrin cobalt [(TCPP)Co] with titanium(III) citrate as the bulk reductant was reported.[153] The bimolecular rate constants for the chlorinated ethylenes (PCE, TCE, *cis*-DCE, and *trans*-DCE) with the Co(I) form of (TCPP)Co and vitamin B_{12} were compared. The values of (TCPP)Co are 5.6 and 14 times for PCE and TCE, respectively, over B_{12}.

V. Bioinspired Immobilized Catalysts

A. B_{12} Modified Electrodes

Immobilized catalysts are generally considered to have many advantages: only a small amount is needed, they are usable in various media, and the products and catalyst can be easily separated. The catalyst can also be recovered and recycled, reducing waste significantly.[154] Various materials such as metals, polymers, clays, silica, and zeolite have been used as supports for the catalyst. Each support has different functions that are dependent on their properties. Among them, the electronic conductivity of the support is of importance and some materials were used as electrodes. Modified electrodes are a result of purposeful modification of a conductive substrate to produce an electrode suited for a particular function and they have properties which are different from those of the unmodified substrate. Therefore, modification of the electrode surface with a metal complex was developed as a good catalyst for electro-organic reactions.[155] This section highlights the studies of the B_{12} immobilized catalyst, and especially B_{12} modified electrodes for electro-organic reactions. The electro-catalytic utilities of the immobilized B_{12} result from the ready availability of the active Co(I) species by electron transfer from the electrode.

B. Noncovalently Bound B_{12} Modified Electrodes

The adsorption of a catalyst to an electrode surface has been known to modify the electrochemical behavior of the substrate. Zagal and coworkers have found that vitamin B_{12} (cyanocobalamine) strongly adsorbs on pyrolytic graphite.[156–158] The resulting vitamin B_{12} modified electrode catalyzed the oxidations of cysteine and glutathione and the reduction of cystine, while the bare electrodes are completely inert.

Vitamin B_{12} hexacarboxylate 8-aminocob(III)yrinic acid *c*-lactam [$B_{12}(COOH)_6$] was used to incorporate a catalytic activity into insoluble liquid crystal films of a cationic surfactant on carbon electrodes (Figure 31).[159] Didodecyldimethylammonium bromide (DDAB) films loaded with the vitamin B_{12} derivative catalyzed

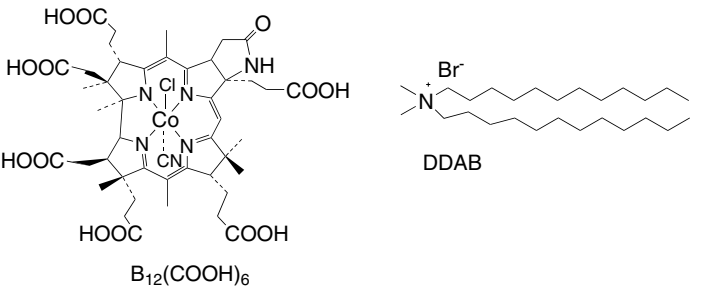

Figure 31. Structure of vitamin B_{12} hexacarboxylate ($B_{12}(COOH)_6$) and didodecyldimethylammonium bromide (DDAB).

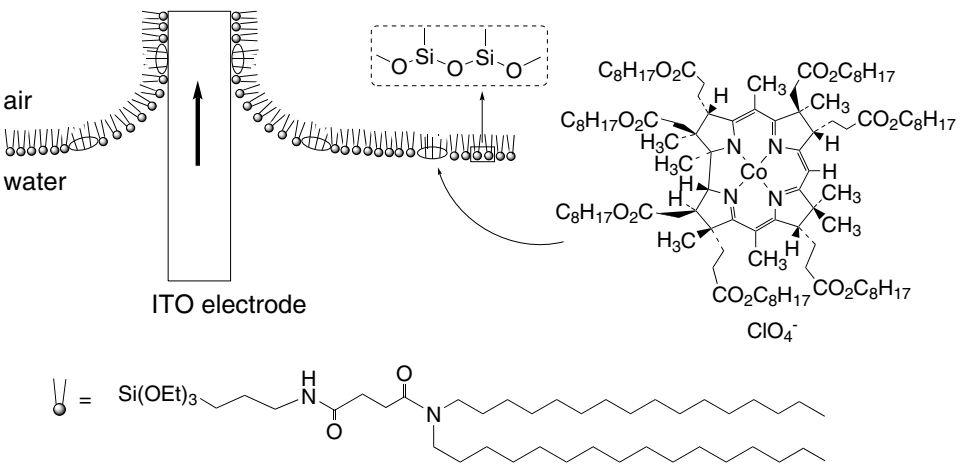

Figure 32. Illustration of B_{12}/LB film modified electrode.

the reductions of trichloroacetic acid and 1,2-dibromoethane at potentials of the Co(I) formation.

The corrinoid compound having seven long alkyl chains, heptaoctylcobyrinate perchlorate, was incorporated in a monolayer of an organosilane amphiphile, and the monolayer was transferred to an indium tin oxide (ITO) electrode as an X-type Langmuir-Blodgett (LB) film (Figure 32).[160] The redox behavior of the modified electrode was investigated by cyclic voltammetry, and the reversible Co(II)/Co(I) redox couple was observed at −0.65 V vs. Ag/AgCl in an aqueous solution. However the application of this modified electrode for electroorganic reactions was not reported.

A B_{12} modified electrode using sol-gel techniques was reported (Figure 33).[15] A hydrophobic heptapropyl cobyrinate perchlorate was readily trapped on an ITO

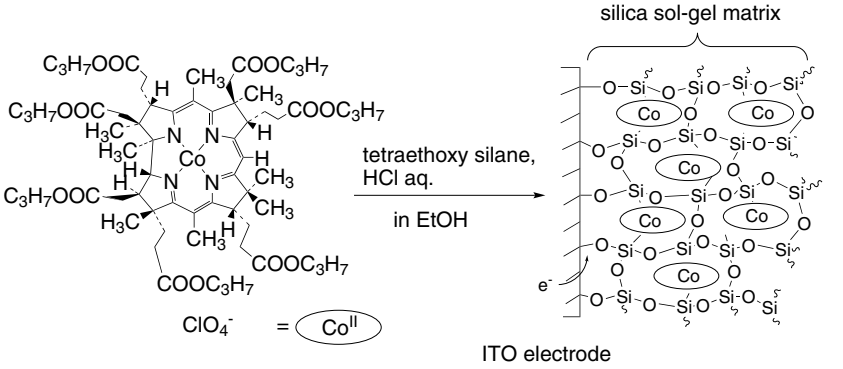

Figure 33. A sol-gel modified electrode containing the trapped B_{12} derivative (adapted from Ref. 15).

electrode by a sol-gel reaction. The complex was physically retained in a silica gel film formed on an ITO electrode. The electrolysis of benzyl bromide was performed at −1.20 V vs. Ag/AgCl by irradiation with visible light using the modified electrode to form bibenzyl and toluene.

C. Polymer-coated B_{12} Modified Electrodes

A surface modification of the carbon electrodes by polymers consisting of epoxy resins and a B_{12} derivative has been reported (Figure 34).[161] The polymeric monomer, Araldite CT-200 and the B_{12} derivative having a 3,5-diaminobenzoyl moiety at its peripheral site were co-polymerized onto an oxidized glassy carbon electrode surface at 373 K. The structure of the modified electrode was estimated to be a cross-linked polymer. Polymer-modified electrodes with large specific surfaces have been used in electroorganic synthesis. The synthesis of valeronitrile by the reductive cross-coupling of ethyl iodide and acrylonitrile effectively proceeded using the modified electrode (Eq. 27). This B_{12} modified carbon electrode was also used as an electrochemical sensor for alkylating agents, i.e. organic halides.[162] The oxidative addition

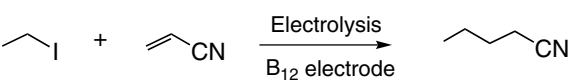

(27)

of an organic halide from dilute solutions to the immobilized Co(I) species of the B_{12} derivative yielded a surface-confined alkylated complex. The same modified electrode was applied to various electroorganic reactions as a functional simulation of the cobalamin-dependent enzymic reaction.[163] The

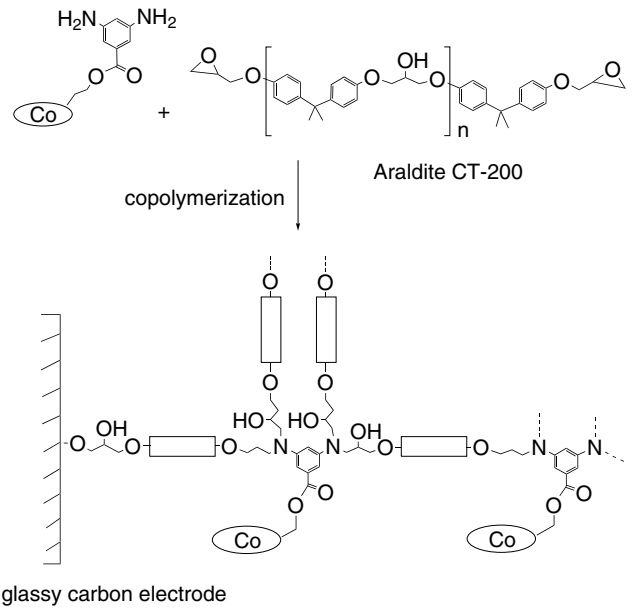

Figure 34. Polymerization by thermal curing of the B_{12} derivative and the diepoxide (Araldite) on basal plane pyrolytic graphite electrodes (adapted from Ref. 161).

carbon-skeleton rearrangement reactions of organic halides efficiently proceeded using the polymer-coated B_{12} modified electrode (Eqs. 28–30). The polymer matrix may provide an efficient microenvironmental effect on the rearrangement reaction catalyzed by B_{12}.

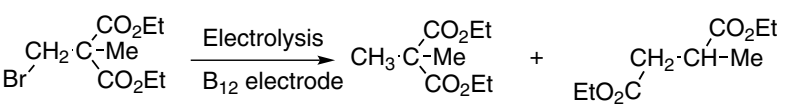

-2.0 V vs. SCE	2%	18–25%
-1.5 V vs. SCE	2%	2%

(28)

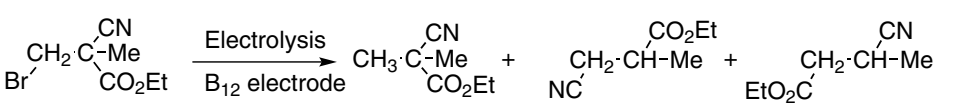

-2.0 V vs. SCE	3–5%	trace	10–20%
-1.5 V vs. SCE	3%	1%	2%

(29)

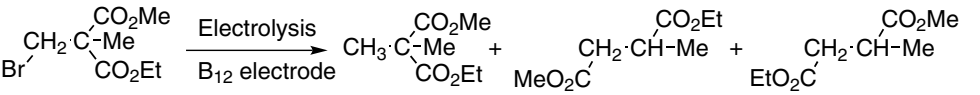

(30)

Another type of polymer-coated electrode was prepared.[164–167] Poly-*L*-lysine was covalently linked to carbon electrodes, and an amide linkage from polylysine to the B_{12} derivative was efficiently formed (Figure 35). The modified electrode showed a reversible electron transfer for the Co(II)/Co(I) couple. The electrocatalytic activities for various molecular transformations were conducted in microemulsions as the reaction medium (Eqs. 31 and 32).

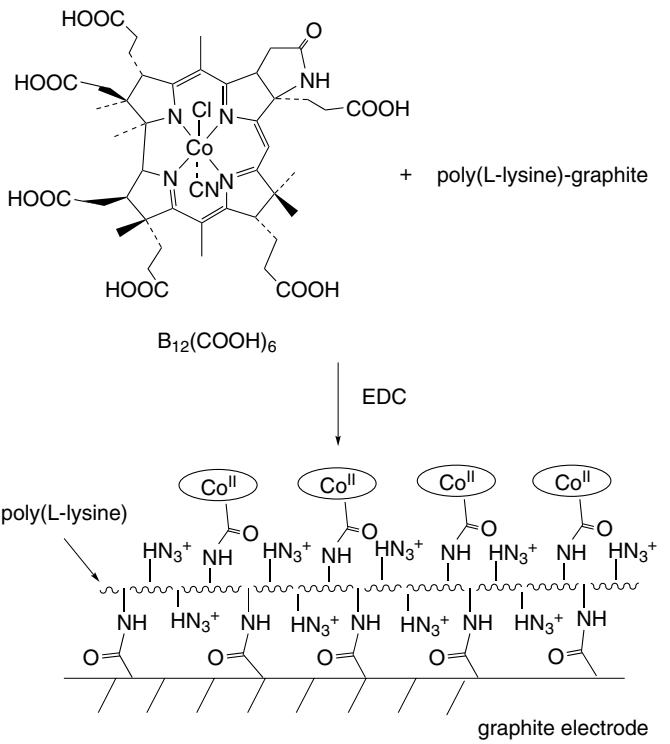

Figure 35. Illustration of preparation of vitamin B_{12} hexacarboxylate-poly(L-lysine) [$B_{12}(COOH)_6$-PLL] network on graphite electrode (adapted from Ref. 167).

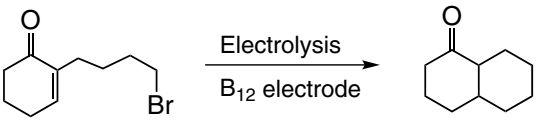

(31)

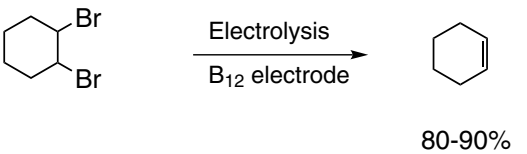

(32)

The electrochemical polymerization of a B_{12} derivative containing a pyrrole group in a peripheral alkyl chain on a platinum electrode surface has been reported (Figure 36).[168–170] The dissolved oxygen reduction reaction was chosen to obtain preliminary information about the catalytic activity of the B_{12}-containing polymer-modified electrodes. However, the application of this modified electrode for electroorganic reactions was not reported.

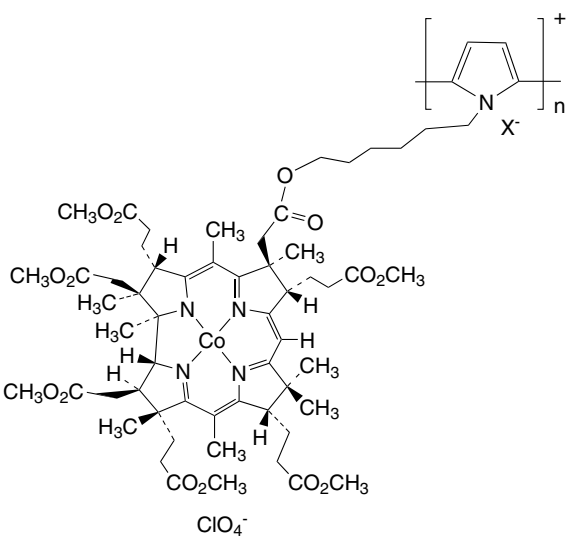

Figure 36. Polypyrrole branched B_{12}.

D. Covalently Bound B_{12} Modified Electrodes

The direct modification of the electrode surface with catalyst species provided some advantages compared to those of the previously described matrix-assisted modified electrodes. The predominant utility is facilitating the electron transfer from the electrode to the catalyst and easy access of the substrate to the bound catalyst. Synthesis of a B_{12} derivative having a trimethoxysilyl group at the peripheral position was reported (Figure 37).[171] This complex was easily immobilized onto an oxidized platinum electrode surface, and the immobilized complex exhibited a definitive Co(II)/Co(I) redox couple. The Co(I) species formed on the electrode surface reacts with phenethyl bromide to form styrene by irradiation with visible light and have a turnover number of over 6,000 for an hour.

A monolayer type B_{12} modified electrode was prepared using the self-assembly technique. A B_{12} disulfide derivative was spontaneously adsorbed onto the gold surface (Figure 38).[172] The modified electrode showed electrocatalytic activity for the reduction of dissolved oxygen. However, the application of this modified electrode for electroorganic reactions was not reported.

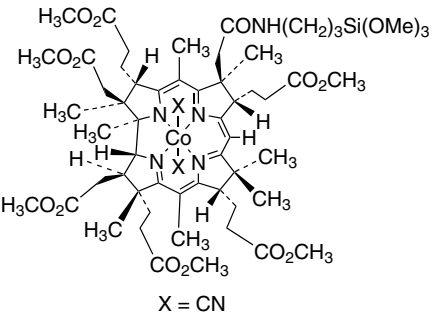

Figure 37. Structure of B_{12} derivative having a trimethoxysilyl group.

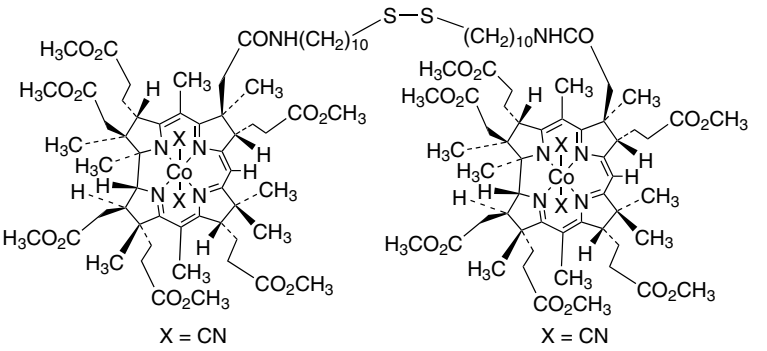

Figure 38. Structure of B_{12} disulfide derivative.

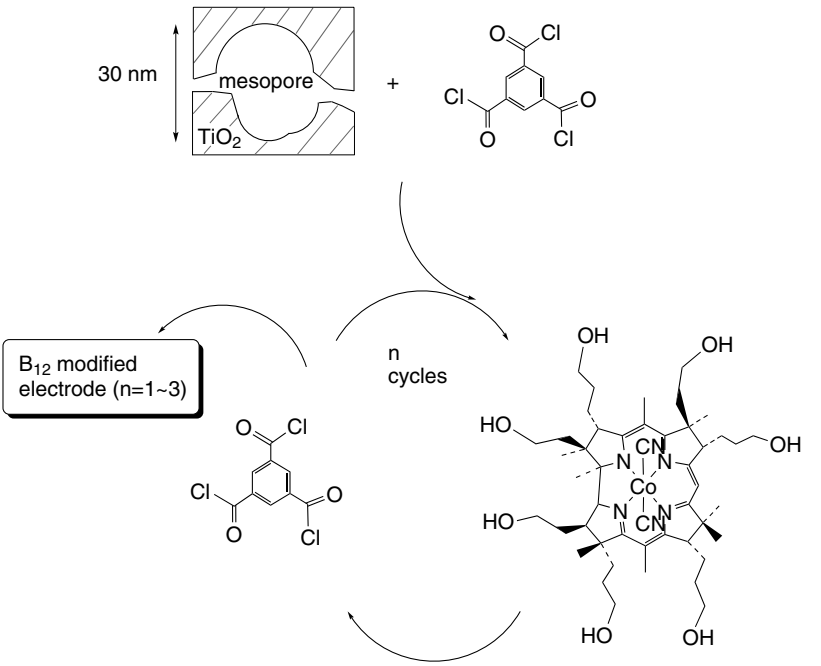

Figure 39. Preparation of B_{12}-modified electrode by cascade type surface modification of mesoporous TiO_2 electrodes (adapted from Ref. 174).

A mesoporous TiO_2 was also used as an electrode. A vitamin B_{12} hexacarboxylate, namely 8-aminocob(III)yrinic acid *c*-lactam ($B_{12}(COOH)_6$), was chemisorbed on a nanocrystalline TiO_2 electrode to form a B_{12} modified electrode.[173] The modified electrode was active for the debromination of dibromocyclohexane and the stereoselective cyclization of 2-(4-bromobutyl)-2-cyclohexen-1-one to 1-decalone in a microemulsion (Eqs. 31 and 32). Binding of the B_{12} catalyst to the TiO_2 electrode enhanced the electron-transfer rates and catalytic efficiency though about 70% of the B_{12} catalyst was desorbed from the TiO_2 electrodes during the reaction. A cross-linking of the B_{12} catalyst on the pore walls of a mesoporous TiO_2 electrode was achieved, based on a solid phase supported synthesis, to obtain a highly stable modified electrode (Figure 39).[174] The modified electrodes showed high electrocatalytic reactivity for the dehalogenation of vicinal dihalides (dibromoethane and *trans*-dibromocyclohexane).

E. B_{12} Immobilized Polymers

The use of a soluble polymer as catalyst support may be applicable as an advantageous alternative to conventional solid-phase supports. A soluble polymer

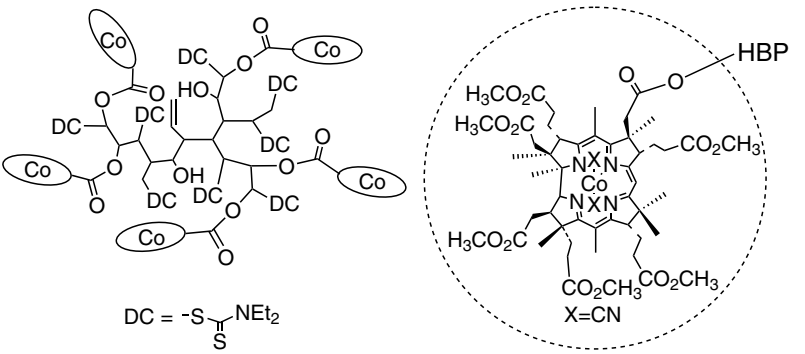

Figure 40. Structure of B_{12}-hyperbranched polymer (HBP).

support provides homogeneous reaction conditions that do not depress the access of the substrate. A hyperbranched polymer is one of the dendric polymers that are synthesized via a one-step polymerization reaction in an inexpensive and easy way, and it has various advantages when compared to dendrimers, which are synthesized via multiple-step polymerizations.[175] The B_{12}-hyperbranched polymers were synthesized and characterized by UV-visible and NMR spectroscopy as well as DLS (Figure 40).[176,177] The spherical shape of the hybrid polymer was observed by TEM. The hybrid polymer exhibits catalysis for the dehalogenation of phenethyl bromide to form ethylbenzene and 2,3-diphenylbutane by irradiation with UV light at room temperature.

VI. Other Bioinspired Reactions

A. Asymmetric Reactions

One of the fascinating functions of naturally occurring vitamin B_{12} is its potential as a chiral catalyst for asymmetric synthesis, since B_{12} creates a chiral reaction site provided by a corrin ring and peripheral substituents. B_{12} catalyzes asymmetric reduction of α,β-unsaturated carbonyl derivatives (esters and amides) in aqueous acetic acid in presence of zinc (Eq. 33).[178,179] Both cyanocobalamin and heptamethyl dicyanocobyrinate produce the (*S*)-isomer as product. Enantiometric excesses depended on the applied reaction conditions. The alkylated complex formed by *Re*-face attack of a Co(I) to substrate was considered as an intermediate, and subsequent reductive cleavage of cobalt–carbon bond afforded the (*S*)-configuration product in varying enantiometric excesses.[180] Schrauzer and coworkers investigated the asymmetric alkylation of cob(II)alamin with D/L-alanine in the presence of V^{3+} and oxygen radicals, and obtained the alanine-bound cobalamin with a 12% e.e. of the D-alanine-bound complex, as shown in Eq. 34.[54]

Ogoshi and coworkers studied the alkylation of cob(I)alamin with prochiral 1-acetyl-1-alkylcyclopropanes that induced an asymmetric center in the resulting alkyl ligands, as shown in Eq. 35, and found a 24% e.e. for X=Ac and Y=Et, and a 33% e.e. for X=Ac and Y=CH_2Ph.[181] Golding and coworkers carried out the alkylation of cob(I)alamin with *tert*-butyloxirane and methyloxirane as shown in Eq. 36, preferentially affording the (*R*)-alkyl-bound products in 62% and 50% e.e., respectively.[182,183] Bonhôte and Scheffold reported the asymmetric isomerization of 1,2-epoxycyclopentane to give (*R*)-2-cyclopenten-1-ol via the formation of the corresponding alkylated cobalamin, in 62% e.e.[184] Achiral epoxides and *N*-aziridines are isomerized to optically active allylic alcohols and *N*-acyl-allylamines by the hydroxocobalamin hydrochloride (vitamin B_{12a})/Zn/NH_4Cl system (Eqs. 37 and 38).[185,186] Using this system, an optically active cyclopenta[b] furan was obtained for prostaglandin synthesis.[187] Murakami and coworkers have investigated the enantioselective alkylation of hydrophobic vitamin B_{12} derivatives, which bear a chiral binaphthyl moiety, with various racemic 3-bromo-2-methylpropionic esters in methanol, and *S*-enantioselectivity with as high as 65% e.e. was observed regardless of the chiral nature of the binaphthyl moiety.[188,189] The higher *S*-enantiomer selectivity with hydrophobic vitamin B_{12} derivative has been reported as follows. The controlled-potential electrolysis of racemic ethyl 3-bromo-2-methoxy-2-phenylpropionate was carried out at −1.8 V vs. SCE in DMF, as mediated by hydrophobic vitamin B_{12} derivatives to afford ethyl 2-methoxy-2-phenylpropionate and ethyl 2-methoxy-3-phenylpropionate in the dark as shown in Eq. 39.[190] The best enantiomeric excess is 87% for the [Cob(II)7C_1ester]ClO_4.

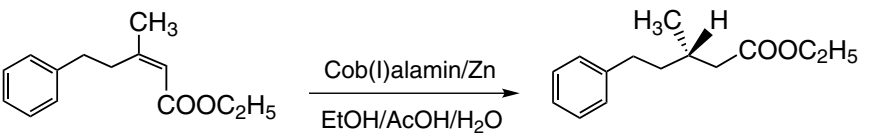

(33)

(*S*)-form (21% ee)

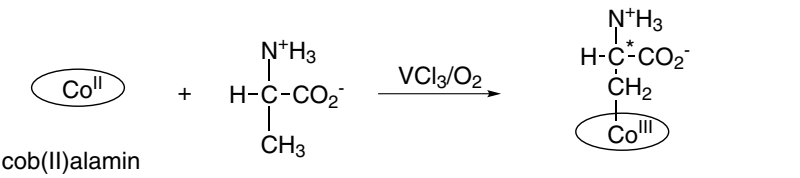

(34)

cob(II)alamin

DL-alanine

(D-alanine)-cobalamin
12% e.e.

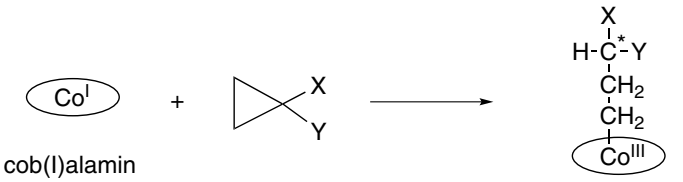

(35)

X = $COCH_3$, Y = C_2H_5 : 24% e.e.
X = $COCH_3$, Y = CH_2Ph : 33% e.e.

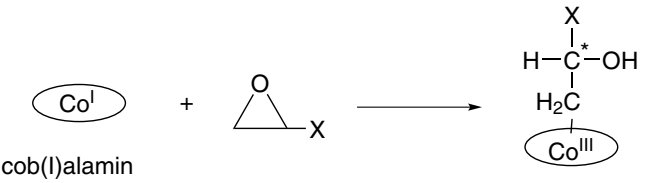

(36)

X =CH_3 : 50% e.e. (*R*-config)
X = $C(CH_3)_3$: 62% e.e. (*R*-config)

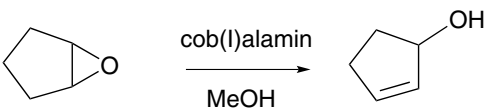

(37)

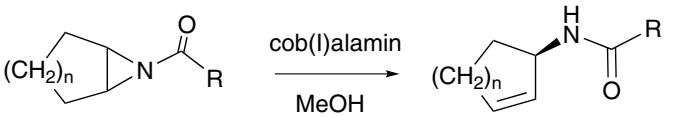

(38)

R = *t*-BuO, n = 1; R = *t*-BuO, n = 2
R = Ph, n = 1; R = Ph, n = 2
R = Et, n = 2

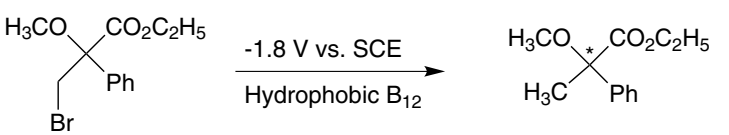

(39)

[Cob(II)7C_1ester]ClO_4 : 87% e.e. (*S*-config)
[Cob(II)7C_3ester]ClO_4 : 55% e.e. (*S*-config)

The enantioselective cyclopropanation of alkenes with ethyl diazoacetate was carried out in the presence of B_{12} (Eq. 40).[191] Among the cobalamin derivatives (cyanocobalamin, methylcobalamin, adenosylcobalamin, hydroxocobalamin hydrochloride), hydroxocobalamin hydrochloride (vitamin B_{12a}) exhibited the most effective catalysis for a variety of alkenes, which afforded the *cis*-dominant cyclopropanes in excellent yields and moderate enantioselectivities.

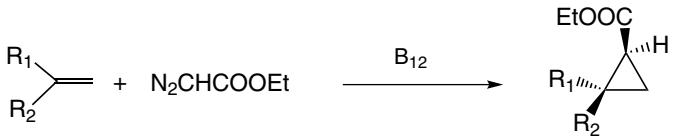

(40)

B. Other Reactions

Reductive removal of β-haloethyl protecting groups from acids was conducted using vitamin B_{12} and vitamin B_{12} model compounds.[192] The catalytically active Co(I) species formed by electrolysis or treatment with zinc reacts with β-chloroethyl or β-bromoethyl esters to form alkylated Co(III) intermediates and the subsequent cleavage of the cobalt–carbon bond to produce the corresponding acids and ethylene (Eq. 41). Such a reductive elimination was used for the synthesis of glycols (unsaturated sugars) (Eq. 42).[193] The tetra- or triacetyl-1-bromosugar was converted to the tri- or diacetyl sugars by the vitamin B_{12}/zinc system in neutral media, MeOH.

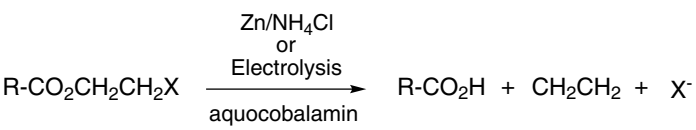

(41)

R = C_6H_5, *p*-CH_3-C_6H_5-NH- X = Cl, Br

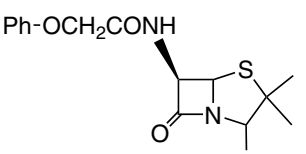

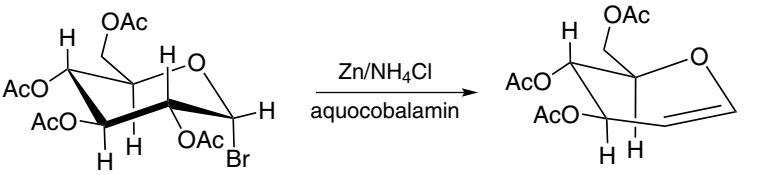

(42)

Reductive acylation of activated olefins with anhydrides was catalyzed by vitamin B_{12a}. 4-Oxo-aldehydes, ketones, esters, and nitriles were synthesized from the corresponding carboxylic anhydrides and activated olefins (Eq. 43).[194] The nucleophilic Co(I) form of B_{12} reacted with carboxylic anhydrides and other acyl derivatives to form Co(III) acyl compounds.[195] Photolysis or electrolysis of the cobalt–carbon bond provided the final product in the presence of an activated olefin.

$$(R^1CO)_2O + R^3HC{=}CR^2Z \xrightarrow[\text{vitamin } B_{12a}]{\text{Electrolysis, } h\nu} (R^1CO)R^3HC\text{-}CHR^2Z + R^1COO^- \quad (43)$$

R^1 = CH_3, *n*-C_7H_{15}, *n*-C_6H_{13}, C_6H_5
R^2 = H, CH_3
R^3 = H, CH_3

A unique reductive dimerization of arylalkenes catalyzed by the B_{12}/Zn or Ti(III) citrate system was reported in an environmentally benign solvent (ethanol/water).[196] Mono- and 1,1-disubstituted alkenes regioselectively provided the corresponding dimers along with some reduced product (Eq. 44), and dienes containing one aryl alkene afforded an intramolecular cyclized product (Eqs. 45 and 46). This reaction expands to the intramolecular cyclization reaction of N-substituted pyrroles and α-alkylstyrenes (Eqs. 47 and 48).[197]

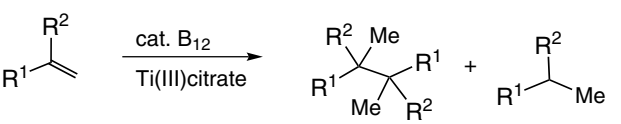

(44)

R^1 = Ph, 4-MeC_6H_4, 2,5-$(Me)_2C_6H_3$, 4-ClC_6H_4, 4-FC_6H_4
R^2 = H, Me, Ph

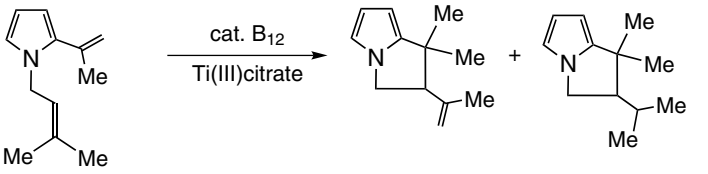

(45)

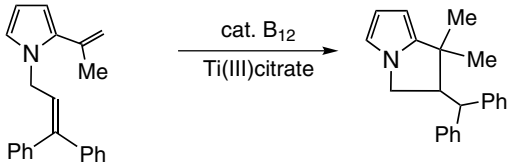

(46)

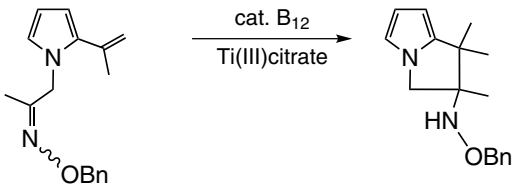

(47)

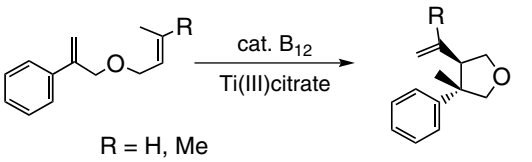

(48)

The photoreduction of CO_2 to CO catalyzed by a corrinoid compound, such as cyanocobalamin, hydroxocobalamin, and cobinamide, was carried out in acetonitrile/methanol solutions containing *p*-terphenyl and triethylamine as a photosensitizer and a sacrificial reductant, respectively.[198] The catalytic efficiency of the cobalt complexes for the photochemical production ($\lambda \geq 300$ nm) of CO and H_2 were compared for the corrinoid compounds and cobalt tetra-*m*-tolylporphyrin. The corrinoid compounds had higher product formation rates and yields than those of the porphyrin complex.

The photochemical catalytic reaction was also reported using the binuclear $Ru(bpy)_3$-B_{12} system. A radical-type cyclization of methyl 1-(3-bromopropyl)-4-oxocyclohexa-2,5-diene-1-carboxylate to the corresponding indene derivative was

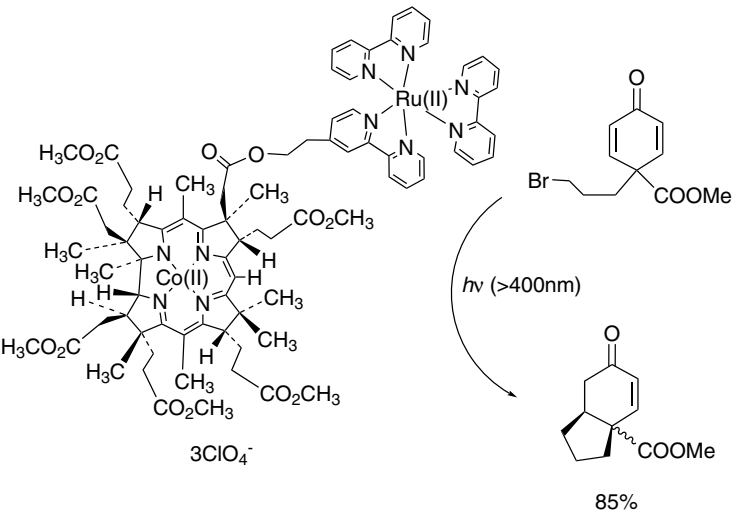

Figure 41. Photochemical catalytic reaction catalyzed by binuclear Ru(bpy)$_3$-B$_{12}$ system.

conducted using the photoredox-photocatalyst in the presence of triethanolamine (Figure 41).[199]

VII. Conclusions

The catalytic simulations, model reactions, and application reactions of B_{12} enzymes with bioinspired systems have been summarized in this chapter. Various cobalt complexes which act as B_{12} models exhibit a variety of wonderful reactivities. Hybrid catalysts composed of synthesized metal complexes and nano-space materials, which are similar to the active center of the B_{12} enzyme, enabled various molecular transformations, including environmental-friendly organic synthesis reactions and degradation reactions of organic halide pollutants by electroorganic or photochemical reactions. Combining the benefits of natural enzymes and engineering methods, this will allow the development of a new catalyst system that will exceed biological reactions. The development of bioinspired catalysts will play an important role in the next generation of science and technology.

VIII. References

1. Brown, K. L. *Chem. Rev.* **2005**, *105*, 2075–2149.
2. Kräutler, B.; Ostermann, S. Structure, reactions, and functions of B_{12} and B_{12}-proteins. In *The Porphyrin Handbook*; eds. Kadish, K. M.; Smith, K. M.; Guilard, R. Academic Press: San Diego, **2003**; Vol. 11, pp. 229–276.

3. Toraya, T. *Chem. Rev.* **2003**, *103*, 2095–2127.
4. Wohlfarth G.; Diekert, G. Reductive dehalogenase. In *Chemistry and Biochemistry of B_{12}*; ed. Banerjee, R. Wiley-Interscience: New York, **1999**; pp. 871–893.
5. Kräutler, B. *Vitamin B_{12} and B_{12}-Proteins*, eds. Kräutler, B.; Arigoni, D.; Golding, B. T. Wiley-VCH; Weinheim, **1998**.
6. Halpern, J. Chemistry and Significance of Vitamin B_{12} Model System. In *B_{12}*; ed. Dolphin, D. John Wiley: New York, **1982**; Vol. 1, pp. 501–542.
7. Schrauzer, G. N. *Acc. Chem. Res.* **1968**, *1*, 97–103.
8. Elliot, C. M.; Herschenhart, H.; Finke R. G.; Smith, B. L. *J. Am. Chem. Soc.* **1981**, *103*, 5558–5566.
9. Murakami, Y.; Aoyama Y.; Tokunaga, K. *J. Am. Chem. Soc.* **1980**, *102*, 6736–6744.
10. Costa, G. *Coord. Chem. Rev.* **1972**, *8*, 63–75.
11. Murakami, Y.; Hisaeda, Y.; Fan S.-D.; Matsuda, Y. *Bull. Chem. Soc. Jpn.* **1989**, *62*, 2219–2228.
12. Werthemann, L.; Keese R.; Eschenmoser, A. unpublished results; see Werthemann, L. Dissertation, ETH Zürich (Nr. 4097), Juris Druck and Verlag, Zürich, **1968**.
13. Murakami, Y.; Hisaeda Y.; Kajihara, A. *Bull. Chem. Soc. Jpn.* **1983**, *56*, 3642–3646.
14. Murakami, Y.; Hisaeda Y.; Ohno, T. *Bull. Chem. Soc. Jpn.* **1984**, *57,* 2091–2097.
15. Shimakoshi, H.; Nakazato, A.; Tokunaga, M.; Katagiri, K.; Ariga, K.; Kikuchi, J.; Hisaeda, Y. *Dalton Trans.* **2003**, 2308–2312.
16. Hisaeda, Y.; Masuko, T.; Hanashima, E.; Hayashi, T. *Sci. Tech. Adv. Mater.* **2006**, *7*, 655–661.
17. Shimakoshi, H.; Abiru, M.; Izumi, S.; Hisaeda, Y. *Chem. Commun.* **2009**, 6427–6429.
18. Golding, B. T.; Rao, D. N. R. Adenosylcobalamin-dependent enzymic reactions. In *Enzyme Mechanisms*; eds. Page, M. I.; Williams, A. The Royal Society of Chemistry: London, **1987**; pp. 404–428.
19. Pratt, J. M. Coordination chemistry of the B_{12} dependent isomerase reactions. In *B_{12}*; ed. Dolphin, D., John Wiley: New York, **1982**; Vol. 1, pp. 325–392.
20. Dowd, P.; Shapiro, M. *J. Am. Chem. Soc.* **1976**, *98*, 3724–3725.
21. Scott, A. I.; Kang, K. *J. Am. Chem. Soc.* **1977**, *99*, 1997–1999.
22. Grate, J. H.; Grate, J. W.; Schrauzer, G. N. *J. Am. Chem. Soc.* **1982**, *104*, 1588–1594.
23. Murakami, Y.; Hisaeda, Y.; Kajihara, A.; Ohno, T. *Bull. Chem. Soc. Jpn.* **1984**, *57*, 405–411.
24. Murakami, Y.; Hisaeda, Y.; Tashiro, T.; Matsuda, Y. *Chem. Lett.* **1985**, 1813–1816.
25. Murakami, Y.; Hisaeda, Y.; Tashiro, T.; Matsuda, Y. *Chem. Lett.* **1986**, 555–558.
26. Murakami, Y.; Hisaeda, Y.; Ozaki, T.; Tashiro, T.; Ohno, T.; Tani, Y.; Matsuda, Y. *Bull. Chem. Soc. Jpn.* **1987**, *60*, 311–324.
27. Murakami, Y.; Hisaeda, Y.; Kikuchi, J.; Ohno, T.; Suzuki, M.; Matsuda, Y.; Matsuura, T. *J. Chem. Soc., Perkin Trans. 2* **1988**, 1237–1246.
28. Murakami, Y.; Hisaeda, Y.; Ozaki, T. *J. Coord. Chem.* **1991**, *23*, 77–89.
29. Dowd P.; Choi, S.-C. *J. Am. Chem. Soc.* **1987**, *109*, 3493–3494.
30. Dowd P.; Choi, S.-C. *J. Am. Chem. Soc.* **1987**, *109*, 6548–6549.
31. Dowd P.; Choi, S.-C. *Tetrahedron* **1989**, *45*, 77–90.
32. Beckwith, A. L. J.; O'Shea, D. M.; Gerba, S.; Westwood, S. W. *J. Chem. Soc., Chem. Commun.* **1987**, 666–667.
33. Inokuchi, T.; Tsuji, M.; Kawafuchi, H.; Torii, S. *J. Org. Chem.* **1991**, *56*, 5945–5948.
34. Hisaeda, Y.; Takenaka, J.; Murakami, Y. *Electrochimica Acta* **1997**, *42*, 2165–2172.
35. Murakami, Y. Vitamin B_{12} models with macrocyclic ligands. In *Biomimetic Chemistry*; eds. Dolphin, D.; McKenna, C.; Murakami, Y.; Tabushi, I. American Chemical Society: Washington D. C., **1980**; pp. 179–199.

36. Pratt, J. M. *Chem. Soc. Rev.* **1985**, *14*, 161–170.
37. Finke, R. G.; Schiraldi, D. A.; Mayer, B. J. *Coord. Chem. Rev.* **1984**, *54*, 1–22.
38. Murakami, Y.; Hisaeda, Y.; Ohno, T. *J. Coord. Chem.* **1990**, *21*, 13–22.
39. Murakami, Y.; Hisaeda, Y.; Ohno, T. *Bioorg. Chem.* **1990**, *18*, 49–62.
40. Murakami, Y.; Hisaeda, Y.; Kikuchi, J.; Ohno, T.; Suzuki, M.; Matsuda, Y. *Chem. Lett.* **1986**, 727–730.
41. Murakami, Y.; Hisaeda, Y.; Kikuchi, J.; Ohno, T.; Suzuki, M.; Matsuda, Y. *Stud. Org. Chem.* **1987**, *31*, 433–438.
42. Murakami, Y.; Hisaeda, Y.; Ohno, T.; Matsuda, Y. *Chem. Lett.* **1986**, 731–734.
43. Murakami, Y.; Hisaeda, Y.; Ohno, T. *Chem. Lett*. **1987**, 1357–1360.
44. Murakami, Y.; Hisaeda, Y.; Ohno, T. *J. Chem. Soc. Perkin Trans.* **1991**, 405–416.
45. Murakami, Y.; Hisaeda, Y.; Ohno, T. *J. Chem. Soc. Chem. Commun.* **1988**, 856–858.
46. Murakami, Y.; Hisaeda, Y.; Song, X.-M.; Ohno, T. *J. Chem. Soc. Perkin Trans. 2*, **1992**, 1527–1528.
47. Murakami, Y.; Hisaeda, Y.; Ogawa, A.; Miyajima, T.; Hayashida, O.; Ohno, T. *Tetrahedron Lett.* **1993**, *34*, 863–866.
48. Murakami, Y.; Hisaeda, Y.; Ogawa, A.; Ohno, T. *Chem. Lett*. **1994**, 1657–1660.
49. Ohno, T.; Ogawa, A.; Hisaeda, Y.; Murakami, Y. *J. Chem. Soc. Perkin Trans. 2* **1994**, 2271–2273.
50. Ohno, T.; Ogawa, A.; Hisaeda, Y.; Murakami, Y. *Tetrahedron Lett.* **1994**, *35*, 9589–9592.
51. Murakami, Y.; Ogawa, A.; Hisaeda, Y.; Ohno, T. *J. Chem. Soc. Perkin Trans. 2* **1994**, 189–191.
52. Murakami, Y.; Hisaeda, Y.; Song, X.-M.; Fan, S.-D. *Chem. Lett.* **1989**, 877–880.
53. Murakami, Y.; Hisaeda, Y.; Song, X.-M.; Fan, S.-D.; Ohno, T. *Bull. Chem. Soc. Jpn.* **1991**, *64*, 2744–2750.
54. Maihub, A.; Grate, J.; Xu, H. B.; Schrauzer, G. N. *Z. Naturforsch.* **1983**, *38b*, 643–647.
55. Schrauzer, G. N.; Hashimoto, M. *J. Am. Chem. Soc.* **1979**, *101*, 4593–4601.
56. Schrauzer, G. N.; Hashimoto, M.; Maihub, A. *Z. Naturforsch., Teil B* **1980**, *35*, 588–593.
57. Maihub, A.; Xu, H. B.; Schrauzer, G. N. *Z. Naturforsch., Teil B* **1980**, *35*, 1435–1438.
58. Dowd, P.; Choi, S.-C.; Duah, F.; Kaufman, C. *Tetrahedron* **1988**, *44*, 2137–2148.
59. Choi, S.-C.; Dowd, P. *J. Am. Chem. Soc.* **1989**, *111*, 2313–2314.
60. Murakami, Y.; Hisaeda, Y.; Ohno T.; Matsuda, Y. *Chem. Lett.* **1988**, 445–451.
61. Banerjee, R. V.; Frasca, V.; Ballou, D. P.; Matthews, R. G. *Biochem.* **1990**, *29*, 11101–11109.
62. Matthews, R. G. *Acc. Chem. Res.* **2001**, *34*, 681–689.
63. Gonzales, J. C.; Peariso, K.; Penner-Hahn, J. E.; Matthews, R. G. *Biochemistry* **1996**, *35*, 12228–12234.
64. Peariso, K.; Goulding, C. W.; Huang, S.; Matthews, R. G.; Penner-Hahn, J. E. *J. Am. Chem. Soc.* **1998**, *120*, 8410–8416.
65. Zhou, Z. S.; Peariso, K.; Penner-Hahn, J. E.; Matthews, R. G. *Biochemistry* **1999**, *38*, 15915–15926.
66. Exl, C. W.; Darbre, T.; Keese, R. *Helv. Chim. Acta* **1999**, *82*, 1173–1184.
67. Pan, L.; Shimakoshi, H.; Hisaeda, Y. *Chem. Lett.* **2009**, 26–27.
68. Pan, L.; Shimakoshi, H.; Masuko, T.; Hisaeda, Y. *Dalton Trans.* **2009**, 9898–9905.
69. Yamauchi, H.; Aminaka, Y.; Yoshida, K.; Sun, G.; Pi, J.; Waalkes, M. P. T*oxicol. Appl. Pharmacol*. **2004**, *198*, 291–296.
70. Kaise, T.; Watanabe, S.; Ito, K. *Chemosphere* **1985**, *14*, 1327–1332.
71. Edmonds, J. S.; Francesconi, K. A. *Experientia* **1987**, *43*, 553–557.

72. Edmonds, J. S. *Bioorg. Med. Chem. Lett.* **2000**, *10*, 1105–1108.
73. Thomas, D. J.; Waters, S. B.; Styblo, M. *Toxicol. Appl. Pharmacol.* **2004**, *198*, 319–326.
74. Nakamura, K.; Hisaeda, Y.; Pan, L.; Yamauchi, H. *Chem. Commun.* **2008**, 5122–5124.
75. Nakamura, K.; Hisaeda, Y.; Pan, L.; Yamauchi, H. *J. Organometal. Chem.* **2009**, *694*, 916–921.
76. Pergantis, S. A.; Miguens-Rodriguez, M.; Vela, N. P.; Heitkemper, D. T. *J. Anal. At. Spectrom.* **2004**, *19*, 178–182.
77. Zakharyan R. A.; Aposhian, H. V. *Toxicol. Appl. Pharmacol.* **1999**, *154*, 287–291.
78. Schrauzer, G. N.; Seck, J. A.; Holland, R. J.; Beckham, T. M.; Rubin E. M.; Sibert, J. W. *Bioinorg. Chem.* **1972**, *2*, 93–124.
79. Alonso, F.; Beletskaya, I. P.; Yus, M. *Chem. Rev*. **2002**, *102*, 4009–4091.
80. Fetzner, S.; Lingens, F. *Microbiol. Rev*. **1994**, *58*, 641–685.
81. Wohlfarth, G.; Diekert, G. *Curr. Opin. Biotechnol*. **1997**, *8*, 290–295.
82. Holliger, C.; Wohlfarth, G.; Diekert, G. *FEMS Microbiol. Rev*. **1999**, *22*, 383–398.
83. Holliger, C.; Regeard, C.; Diekert, G. In *Dehalogenation*; eds. Häggblom, M. M.; Bossert, I. D. Kluwer Academic Publishers: Boston, USA, **2003**; pp. 115–157.
84. Neumann, A.; Wohlfarth, G.; Diekert, G. *J. Biol. Chem*. **1996**, *271*, 16515–16519.
85. Kräutler, B.; Fieber, W.; Ostermann, S.; Fasching, M.; Ongania, K.-H.; Gruber, K.; Kratky, C.; Mikl, C.; Siebert, A.; Diekert, G. *Helv. Chim. Acta* **2003**, *86*, 3698–3716.
86. Shey, J.; van der Donk, W. A. *J. Am. Chem. Soc*. **2000**, *122*, 12403–12404.
87. McCauley, K. M.; Wilson, S. R.; van der Donk, W. A. *Inorg. Chem*. **2002**, *41*, 5844–5848.
88. McCauley, K. M.; Wilson, S. R.; van der Donk, W. A. *J. Am. Chem. Soc*. **2003**, *125*, 4410–4411.
89. Pratt, D. A.; van der Donk, W. A. *J. Am. Chem. Soc*. **2005**, *127*, 384–396.
90. McCauley, K. M.; Pratt, D. A.; Wilson, S. R.; Shey, J.; Burkey, T. J.; van der Donk, W. A. *J. Am. Chem. Soc*. **2005**, *127*, 1126–1136.
91. Pratt, D. A.; van der Donk, W. A. *Chem. Commun*. **2006**, 558–560.
92. Rich A. E.; DeGreeff, A. D.; McNeill, K. *Chem. Commun*. **2002**, 234–235.
93. Follett, A. D.; McNeill, K. *J. Am. Chem. Soc*. **2005**, *127*, 844–845.
94. Follett, A. D.; McNeill, K. *Inorg. Chem*. **2006**, *45*, 2727–2732.
95. Fritsch, J. M.; Retka, N. D.; McNeill, K. *Inorg. Chem*. **2006**, *45*, 2288–2295.
96. Follett, A. D.; McNabb, K. A.; Peterson, A. A.; Scanlon, J. D.; Cramer, C. J.; McNeill, K. *Inorg. Chem*. **2007**, *46*, 1645–1654.
97. Kliegman, S.; McNeill, K. *Dalton Trans*. **2008**, 4191–4201.
98. Schrauzer, G. N.; Deutsch, E. Windgassen, R. J. *J. Am. Chem. Soc*. **1968**, *90*, 2441–2442.
99. Schrauzer, G. N.; Deutsch, E. *J. Am. Chem. Soc*. **1969**, *91*, 3341–3350.
100. Pearson, R. G.; Sobel, H.; Songstad, J. *J. Am. Chem. Soc*. **1968**, *90*, 319–326.
101. Schrauzer, G. N.; Nathankatz, R. *Bioinorg. Chem*. **1978**, *9*, 123–143.
102. Krone, U. E.; Thauer, R. K.; Hogenkamp, H. P. C. *Biochemistry* **1989**, *28*, 4908–4914.
103. Krone, U. E.; Thauer, R. K.; Hogenkamp, H. P. C. Steinbach, K. *Biochemistry* **1991**, *30*, 2713–2719.
104. Gantzer, C. J.; Wackett, L. P. *Environ. Sci. Technol*. **1991**, *25*, 715–722.
105. Schanke, C. A.; Wackett, L. P. *Environ. Sci. Technol*. **1992**, *26*, 830–833.
106. Chiu, P.-C.; Reinhard, M. *Environ. Sci. Technol*. **1995**, *29*, 595–603.
107. Burris, D. R.; Delcomyn, C. A.; Smith, M. H.; Roberts, A. L. *Environ. Sci. Technol*. **1996**, *30*, 3047–3052.
108. Glod, G.; Angst, W.; Holliger, C.; Schwarzenbach, R. P. *Environ. Sci. Technol*. **1997**, *31*, 253–260.

109. Glod, G.; Brodmann, U.; Angst, W.; Holliger, C.; Schwarzenbach, R. P. *Environ. Sci. Technol*. **1997**, *31*, 3154–3160.
110. Burris, D. R.; Delcomyn, C. A.; Deng, B.; Buck, L. E.; Hatfield, K. *Environ. Toxi. Chem*. **1998**, *17*, 1681–1688.
111. Semadeni, M.; Chiu, P.-C.; Reinhard, M. *Environ. Sci. Technol*. **1998**, *32*, 1207–1213.
112. Ruppe, S.; Neumann, A.; Diekert, G.; Vetter, W. *Environ. Sci. Technol*. **2004**, *38*, 3063–3067.
113. Marks, T. S.; Allpress, J. D.; Maule, A. *Appl. Environ. Microbiol*. **1989**, *55*, 1258–1261.
114. Rodríguez-Garrido, B.; Arbestain, M. C.; Monterroso, M. C.; Macías, F. *Environ. Sci. Technol*. **2004**, *38*, 5046–5052.
115. Assaf-Anid, N.; Hayes, K. F.; Vogel, T. M. *Environ. Sci. Technol*. **1994**, *28*, 246–252.
116. Chiu, P.-C.; Reinhard, M. *Environ. Sci. Technol*. **1996**, *30*, 1882–1889.
117. Ochoa-Herrera, V.; Sierra-Alvarez, R.; Somogyi, A.; Jacobsen, N. E.; Wysocki, V. H.; Field, J. A. *Environ. Sci. Technol*. **2008**, *42*, 3260–3264.
118. Smith, M. H.; Woods, S. L. *Appl. Environ. Micro*. **1994**, *60*, 4107–4110.
119. Smith, M. H.; Woods, S. L. *Appl. Environ. Micro*. **1994**, *60*, 4111–4115.
120. Woods, S. L.; Trobaugh, D. J. *Environ. Sci. Technol*. **1999**, *33*, 857–863.
121. Assaf-Anid, N.; Nies, L.; Vogel, T. M. *Appl. Environ. Micro*. **1992**, *58*, 1057–1060.
122. Kim, Y.-H.; Carraway, E. R. *Environ. Tech*. **2002**, *23*, 1135–1145.
123. Lexa, D.; Saveant, J. M. *Acc. Chem. Res*. **1983**, *16*, 235–243.
124. Rusling, J. F.; Connors, T. F.; Owlia, A. *Anal. Chem*. **1987**, *59*, 2123–2127.
125. Connors, T. F.; Arena, J. V.; Rusling, J. F. *J. Phys. Chem*. **1988**, *92*, 2810–2816.
126. Rusling, J. F.; Miaw, C. L.; Couture, E. C. *Inorg. Chem*. **1990**, *29*, 2025–2027.
127. Shimakoshi, H.; Tokunaga, M.; Hisaeda, Y. *Dalton Trans*. **2004**, 878–882.
128. Lagunas, M. C.; Silvester, D. S.; Aldous, L.; Compton, R. G. *Electroanalysis,* **2006**, *18*, 2263–2268.
129. Jabbar, Md. A.; Shimakoshi, H.; Hisaeda, Y. *Chem. Commun*. **2007**, 1653–1655.
130. Cooper, K. A.; Dhar, M. L.; Hughes, E. D.; Ingold, C. K.; MacNulty, B. J.; Woolf, L. I. *J. Chem. Soc*. **1948**, 2043–2049.
131. Muldoon, M. J.; Gordon, C. M.; Dunkin, I. R. *J. Chem. Soc., Perkin Trans*. **2001**, *2*, 433–435.
132. Argüello, J. E.; Costentin, C.; Griveau, S.; Savéant, J.-M. *J Am. Chem. Soc*. **2005**, *127*, 5049–5055.
133. Kalyanasundaram, K. *Coord. Chem. Rev*. **1982**, *46*, 159–244.
134. Juris, A.; Balzani, V.; Barigelletti, F.; Campagna, S.; Belser, P.; Zelewsky, A. V. *Coord. Chem. Rev*. **1988**, *84*, 85–277.
135. Sun, L.; Hammarström, L.; Akermark, B.; Styring, S. *Chem. Soc. Rev*. **2001**, *30*, 36–49.
136. Wang, M.; Na, Y.; Gorlov, M.; Sun, L. *Dalton Trans*. **2009**, 6458–6467.
137. Ziessel, R.; Hawecker, J.; Lehn, J.-M. *Helv. Chim. Acta* **1986**, *69*, 1065–1084.
138. Shimakoshi, H.; Tokunaga, M.; Baba, T.; Hisaeda, Y. *Chem. Commun*. **2004**, 1806–1807.
139. Shimakoshi, H.; Kudo, S.; Hisaeda, Y. *Chem. Lett*. **2005**, *34*, 1096–1097.
140. Fox, M. A.; Dulay, M. T. *Chem. Rev*. **1993**, *93*, 341–357.
141. Hoffmann, M. R.; Martin S. T.; Choi, W.; Bahnemann, D. W. *Chem. Rev*. **1995**, *65*, 69–96.
142. Fujishima, A.; Rao, T. N.; Tryk, D. A. *J. Photochem. Photobiol. C: Photochem. Rev*. **2000**, *1,* 1–21.
143. Shimakoshi, H.; Sakumori, E.; Kaneko, K.; Hisaeda, Y. *Chem. Lett*. **2009**, *38*, 468–469.
144. Shimakoshi, H.; Abiru, M.; Kuroiwa, K.; Kimizuka, N.; Watanabe, M.; Hisaeda, Y. *Bull. Chem. Soc. Jpn*. **2010**, *83*, 170–172.

145. Klein, L. J.; Alleman, K. S.; Peters, D. G.; Karty, J. A.; Reilly, J. P. *J. Electroanal. Chem*. **2000**, *481*, 24–33.
146. Persinger, J. D.; Hayes, J. L.; Klein, L. J.; Peters, D. G.; Karty, J. A.; Reilly, J. P. *J. Electroanal. Chem*. **2004**, *568*, 157–165.
147. Bishop, G. W.; Karty, J. A.; Peters, D. G. *J. Electrochem. Soc*. **2007**, *154*, F65–F69.
148. Gach, P. C.; Mubarak, M. S.; Karty, J. A.; Peters, D. G. *J. Electrochem. Soc*. **2007**, *154*, F1–F6.
149. Páramo-Garcío, U.; Ávila-Rodríguez, M.; García-Jiménez, M. G.; Gutieérrez-Granados, S.; Ibánez-Cornejo, J. G. *Electroanalysis* **2006**, *18*, 904–910.
150. Gach, P. C.; Karty, J. A.; Peters, D. G. *J. Electroanal. Chem*. **2008**, *612*, 22–28.
151. Kuhler, R. J.; Santo, G. A.; Caudlll, T. R.; Betterton, E. A.; Arnold, R. G.; *Environ. Sci. Technol*. **1993**, *27*, 2104–2111.
152. Obare, S. O.; Ito T.; Meyer, G. J. *Environ. Sci. Technol*. **2005**, *29*, 6266–6272.
153. Fritsch, J. M.; McNeill, K. *Inorg. Chem*. **2005**, *44*, 4852–4861.
154. Special issue of recoverable catalysts and reagents, *Chem. Rev*. **2002**, *102*, Issue 10.
155. Scheffold, R.; Rytz, G.; Walden, L. In *Modern Synthetic Methods*; ed. Sheffold R. Wiley: Frankfurt, **1983**; Vol. 3, pp. 355–440.
156. Zagal, J. H.; Páez, M.; Páez, C. *J. Electroanal. Chem*. **1987**, *237*, 145–148.
157. Zagal, J. H.; Aguirre, M. J.; Parodi, C. G. *J. Electroanal. Chem*. **1994**, *374*, 215–222.
158. Mimica, D.; Bedioui, F.; Zagal, J. H. *Electrochimica Acta* **2002**, *48*, 323–329.
159. Miaw, C. L.; Hu, N.; Bobbitt, J. M.; Ma, Z.; Ahmadi, M. F.; Rusling, J. F. *Langmuir* **1993**, *9*, 315–322.
160. Ariga, K., Tanaka, K.; Katagiri, K.; Kikuchi, J.; Shimakoshi, H.; Ohshima, E.; Hisaeda, Y. *Phys. Chem. Chem. Phys*. **2001**, *3*, 3442–3446.
161. Ruhe, A.; Walder, L.; Scheffold, R. *Helv. Chim. Acta* **1985**, *68*, 1301–1311.
162. Steiger, B.; Ruhe, A.; Walder, L. *Anal. Chem*. **1990**, *62*, 759–766.
163. Murakami, Y.; Hisaeda, Y.; Ozaki, T.; Matsuda, Y. *J. Chem. Soc., Chem. Commun*. **1989**, 1094–1096.
164. Zhou, D.-L.; Njue, C. K.; Rusling, J. F. *J. Am. Chem. Soc*. **1999**, *121*, 2909–2914.
165. Njue, C. K.; Rusling, J. F. *J. Am. Chem. Soc*. **2000**, *122*, 6459–6463.
166. Rusling, J. F. *Pure Appl. Chem*. **2001**, *73*, 1895–1905.
167. Campbell, C. J.; Njue, C. K.; Rusling, J. F. *Electrochem. Commun*. **2002**, *4*, 340–343.
168. Dabre, T.; Siljegovic, V.; Amolins, A.; Otten, T.; Keese, R.; Abrantes, L.; Correia, J. P. *Novel Trends in Electroorganic Synthesis* ed. Torii, S. Springer **1998**; pp. 395–399.
169. Fraga, R.; Keese, R. *Synlett* **2000**, *11*, 1694–1696.
170. Fraga, R.; Correia, J. P.; Keese, R.; Abrantes, L. M. *Electrochimica Acta* **2005**, *50*, 1653–1659.
171. Shimakoshi, H.; Tokunaga, M.; Kuroiwa, K.; Kimizuka, N.; Hisaeda, Y. *Chem. Commun*. **2004**, 50–51.
172. Viana, A. S.; Kalaji, M.; Abrantes, L. M. *Electrochimica Acta* **2002**, *47*, 1587–1594.
173. Mbindyo, J. K. N.; Rusling, J. F. *Langmuir* **1998**, *14*, 7027–7033.
174. Asaftei, S.; Walder, L. *Langmuir* **2006**, *22*, 5544–5547.
175. Voit, B. I.; Ledere, A. *Chem. Rev*. **2009**, *109*, 5924–5973.
176. Tahara, T.; Shimakoshi, H.; Tanaka, A.; Hisaeda, Y. *Tetrahedron Lett*. **2007**, *48*, 5065–5068.
177. Shimakoshi, H.; Nishi, M.; Tanaka, A.; Chikama, K.; Hisaeda, Y. *Chem. Lett*. **2009**, *39*, 22–23.
178. Fischli, A.; Süss, D. *Helv. Chim. Acta* **1979**, *62*, 48–58.
179. Fischli, A.; Süss, D. *Helv. Chim. Acta* **1979**, *62*, 2361–2373.
180. Fischli, A.; Daly, J. J. *Helv. Chim. Acta* **1980**, *63*, 1628–1643.

181. Ogoshi, H.; Kikuchi, Y.; Yamaguchi, T.; Toi, H.; Aoyama, Y. *Organometallics* **1987***, 6*, 2175–2178.
182. Anderson, R. J.; Dixon, R. M.; Golding, B. T. *J. Organomet. Chem.* **1992**, *437*, 227–237.
183. Davies, A. G.; Golding, B. T.; Hay-Motherwell, R. S.; Mwesigye-Kibende, S.; Rao, D. N.; Symons, M. C. R. *J. Chem. Soc., Chem. Commun.* **1988**, 378–380.
184. Bonhôte, P.; Scheffold, R. *Helv. Chim. Acta* **1991**, *74*, 1425–1444.
185. Su, H.; Walder, L.; Zhang, Z.-da.; Scheffold, R. *Helv. Chim. Acta* **1988**, *71*, 1073–1078.
186. Zhang, Z.-da.; Scheffold, R. *Helv. Chim. Acta* **1993**, *76*, 2602–2615.
187. Busato, S.; Tinembart, O.; Zhang, Z.-da, Scheffold, R. *Tetrahedron* **1990**, *46*, 3155–3166.
188. Murakami, Y.; Hisaeda, Y.; Kohno, H.; Ohno, T. *Chem. Lett.* **1992**, 909–912.
189. Murakami, Y.; Hisaeda, Y.; Kohno, H.; Ohno, T.; Nishioka, T. *Bull. Chem. Soc. Jpn.* **1992***, 65*, 3094–3102.
190. Ohno, T.; Nishioka, T.; Hisaeda, Y.; Murakami, Y. *J. Mol. Struct.* **1994**, *308*, 207–218.
191. Chen, Y.; Zhang, X. P. *J. Org. Chem*. **2004**, *69*, 2431–2435.
192. Scheffold, R.; Amble, E. *Angew. Chem. Int. Ed. Engl.* **1980**, *19*, 629–630.
193. Forbes, C. L.; Franck, R. W. *J. Org. Chem.* **1999**, *64*, 1424–1425.
194. Scheffold, R.; Orlinski, R. *J. Am. Chem. Soc*. **1983**, *105*, 7200–7202.
195. Walder, L.; Orlinski, R. *Organometallics* **1987**, *64*, 1424–1425.
196. Shey, J.; McGinley, C. M.; McCauley, K. M.; Dearth, A. S.; Young, B. T.; van der Donk, W. A. *J. Org. Chem*. **2002**, *67*, 837–846.
197. McGinley, C. M.; Relyea, H. A.; van der Donk, W. A. *Synlett* **2006**, 211–214.
198. Grodkowski, J.; Neta, P. *J. Phys. Chem. A* **2000**, *104*, 1848–1853.
199. Steiger, B.; Eichenberger, E.; Walder, L. *Chimia* **1991**, *45*, 32–37.

Index to Volume 10

B

D

E

F

G

H

N

O

P

Q

R

S

T

U

V

Z

Cumulative Index to Volumes 1–10*

*Volume numbers are given in Roman numerals followed by a colon and precede the relevant pages.

B

C

D

E

F

G

H

I

J

K

L

M

O

P

Q

R

S

T

U

X